Activity and stability of rat liver xanthine oxidase in the presence of pyridine

Kaveh Amini, Mohammad-Hossein Sorouraddin, and Mohammad-Reza Rashidi

Abstract: In the present study, rat liver xanthine oxidase activity and its thermostability in the presence of pyridine were investigated. The activity of the enzyme was determined by following the formation of uric acid spectrophotometrically. The thermal stability of the enzyme was studied in the presence of 0.0%–2.0% of pyridine in Sorenson's buffer. Thermal stability parameters (half-life, inactivation constant, and activation energies for enzyme inactivation), thermodynamic constants (ΔH^*, ΔS^*, and ΔG^*) and the kinetic parameters (K_m and V_{max}), were determined in pyridine-free and pyridine-containing buffer solution. A dramatic reduction was observed in xanthine oxidase activity in the presence of pyridine. However, the pyridine-treated enzyme showed a marked enhancement in thermal stability compared with the native enzyme. The ΔG values for the enzyme activity in the presence of pyridine were found to be about 1.5-fold larger than that calculated for the native enzyme, indicating that the enzyme becomes kinetically more stable in the presence of pyridine. The K_m value for xanthine oxidase in the presence of 0.5% pyridine increased by 4.8-fold compared with the enzyme in the pyridine-free buffer solution; however, there was 1.8-fold reduction in the V_{max} value in the hydro-organic solution compared with the enzyme activity in the buffer solution. As the stability of enzymes is one of the most difficult problems in protein chemistry, this thermostability property of xanthine oxidase could be of great value in developing novel strategies to improve and expand its application in various areas.

Key words: xanthine oxidase, pyridine, inactivation, thermostability, thermodynamic, kinetic constants.

Résumé : Dans ce travail, on a étudié l'activité et la thermostabilité de l'oxydase de la xanthine du foie de rat en présence de pyridine. On a déterminé l'activité de l'enzyme en suivant d'une façon spectrophotométrique la formation d'acide urique. On a étudié la stabilité thermique de l'enzyme en présence de 0,0 % à 2,0 % de pyridine dans un tampon de Sorenson. Les paramètres de stabilité thermique (demi-vie, constante d'inactivation et énergies d'activation de l'inactivation de l'enzyme), les constantes thermodynamiques (ΔH^*, ΔS^* et ΔG^*) et les paramètres cinétiques (K_m et V_{max}) ont été déterminés dans des solutions tamponnées sans pyridine ainsi que d'autres contenant de la pyridine. On a remarqué une diminution dramatique de l'activité de l'oxydase de la xanthine en présence de pyridine. Toutefois, l'enzyme traité par de la pyridine présence une augmentation marquée de sa stabilité thermique lorsqu'elle est comparée à l'enzyme non traité. On a trouvé que les valeurs du ΔG pour l'activité de l'enzyme en présence de pyridine est environ 1,5 fois plus élevée que celle calculée pour l'enzyme non traité; ceci indique que l'enzyme devient cinétiquement plus stable en présence de pyridine. Par comparaison avec l'enzyme dans une solution tamponnée sans pyridine, la valeur de K_m pour l'oxydase de la xanthine en présence de 0,5 % pyridine est 4,8 fois plus élevée; toutefois, on remarque la valeur de V_{max} pour l'activité de l'enzyme en solution hydro-organique est 1,8 fois plus faible que celle dans une solution tamponnée. Comme la stabilité des enzymes est un des problèmes les plus difficiles en chimie des protéines, cette propriété de thermostabilité de l'oxydase de la xanthine pourrait avoir une grande valeur dans le développement de nouvelles stratégies visant à améliorer et à étendre son application dans divers domaines.

Mots-clés : oxydase de la xanthine, pyridine, inactivation, thermostabilité, thermodynamique, constantes cinétiques.

Can. J. Chem. Downloaded from www.nrcresearchpress.com by 80.58.250.72 on 09/16/12
For personal use only.

Introduction

Although enzyme catalysis has been traditionally investigated in aqueous medium, the activity of enzymes in hydro-organic – nonaqueous media has undergone significant progress in recent years and enzymatic reactions in hydro-organic – nonaqueous systems have received a great deal of attention. The enzymatic reactions are usually reduced in the presence of organic solvents, but it is not always the case. Recent years have witnessed a growing interest in the application of hydro-organic – nonaqueous systems to increase enzyme activity.[1,2] These systems have also been used to enhance enzyme stability, particularly at higher temperatures.[3,4] As the stability of enzymes is one of the most

Received 16 June 2010. Accepted 21 September 2010. Published on the NRC Research Press Web site at canjchem.nrc.ca on 15 December 2010.

K. Amini[1] and M.-H. Sorouraddin. Department of Analytical Chemistry, Faculty of Chemistry, University of Tabriz, Tabriz, 51666-16471, Iran.
M.-R. Rashidi.[2] Drug Applied Research Center, Research and Development Complex, Tabriz University of Medical Sciences, Tabriz, 51664-14766, Iran.

[1]Present address: Department of Chemistry, York University, Toronto, ON M3J1P3, Canada.
[2]Corresponding author (e-mail: rashidi@tbzmed.ac.ir).

Can. J. Chem. Downloaded from www.nrcresearchpress.com by 80.58.250.72 on 09/16/12
For personal use only.

difficult problems in protein chemistry,[5] this application of hydro-organic – nonaqueous systems could be of great value.

Xanthine oxidase (EC 1.17.3.2) is a flavoprotein enzyme that plays an important role in the metabolism of endogenous purines, xenobiotics, and drugs. This enzyme serves as an important biological source of some reactive oxygen species that are involved in many pathological processes such as inflammation, atherosclerosis, cancer, and aging.[6,7] Xanthine oxidase has been used in biosensors for estimation of fish and meat freshness in the food industry,[8] evaluation of ischemic myocyte injury,[9] and measurement of theophylline.[10] In spite of these broad and important investigations on the activity of xanthine oxidase, there are only limited studies on the activity of this enzyme in nonaqueous media.[11–13] More recently, we investigated xanthine oxidase activity in various hydro-organic mixtures including pyridine.[14] According to this study, a dramatic reduction was observed in the xanthine oxidase activity in the presence of pyridine. Despite this significant inhibitory effect, the enzyme was quite stable in the presence of pyridine and >65% of the original activity remained after a 24 h incubation at 37 °C.[14] To evaluate this finding in more detail, the activity and thermal stability of rat liver xanthine oxidase in the presence of pyridine was investigated.

Experimental section

Chemicals

All experiments were performed with analytical reagent grade chemicals. Xanthine and uric acid were purchased from Sigma-Aldrich (Dorset, UK). All other chemicals were obtained from Merck (Darmstadt, Germany).

Apparatus and software

Spectrophotometric measurements were carried out using a Shimadzu 2550 UV–vis spectrophotometer that was controlled by a Shimadzu UV Probe personal software package including kinetics software. The instrument was connected to a Shimadzu cell temperature control unit. The cuvette used had a path length of 1.0 cm. The total volume used for the spectrophotometric measurements was constant at 1.0 mL. All data were saved in ASCII format.

Preparation of partially purified xanthine oxidase

Mature male Sprague–Dawley rats (150–250 g,; Tabriz University of Medical Sciences, Tabriz, Iran) were used in this study. They were fed with a standard laboratory diet and allowed food and water adlibitum. The temperature and humidity were kept at 18 ± 1 °C and 50%, respectively, and the lighting cycle was 7:00–19:00 h light and 19:00–7:00 h dark. Animals were handled with humane care in accordance with the National Institute of Health guidelines.

The animals were sacrificed between 9:00 and 10:00 by cervical dislocation. Livers were immediately excised, placed in an ice-cold isotonic potassium chloride solution (1.15% KCl *w*/*v*) containing 0.1 mmol/L EDTA. The livers were then homogenized on ice in a homogenizer fitted with a Teflon pestle. Partially purified enzyme was prepared from the liver homogenate by heat treatment and ammonium sulfate precipitation as described elsewhere.[15]

Enzyme activity assay

The activity of the enzyme solution was determined by following the formation of uric acid spectrophotometrically at 35 °C. After addition of 50 μL enzyme to a cuvette containing 0.95 mL of Sorenson's phosphate buffer (67 mmol/L, pH 7.0 containing 0.1 mmol/L EDTA) and 20 μmol/L of xanthine (prepared in the same phosphate buffer), the solution was immediately mixed and the formation of uric acid from xanthine oxidation was monitored at 295 nm up to 3 min. The initial rate was calculated from the linear part of the progress curve and one unit of xanthine oxidase was defined as the amount of the enzyme catalyzing the oxidation of 1.0 μmol/L xanthine to uric acid per minute at 35 °C.[16] The reaction was also carried out in the same manner in the presence of different concentrations of pyridine ranging from 0.5% to 2.0%. Experiments confirmed that the presence of either the substrate or pyridine did not affect the pH of the phosphate buffer significantly.

Thermal stability studies

The thermal stability of rat liver xanthine oxidase in the presence of pyridine was studied as follows: a volume of 1.33 mL of the enzyme solution (prepared in 67 mmol/L phosphate buffer, pH 7.0, containing 0.1 mmol/L EDTA) was mixed separately with 19 mL of Sorenson's buffer containing 0.0% (as a control), 0.5%, 1.0%, 1.5%, and 2.0% pyridine. The mixtures were then incubated in a water bath at 35, 45, 55 and 65 °C for 24 h and 750 μL of each solution was taken at different time intervals and the enzyme activity was measured as described above. The time-dependent loss in activity was used to calculate the half-life for each enzyme solution. According to the classical first-order kinetics of enzyme inactivation,[17] the first-order inactivation rate constants were determined as the slopes of the ln$V$ vs t plots, where V is the residual enzyme activity after incubation at a specific temperature for a specific period and t is the incubation time. Activation energies for the thermal inactivation were measured by plotting logarithms of the inactivation rate constants vs reciprocals of the absolute temperatures according to the Arrhenius equation.[18]

Kinetic data analysis

Thermal inactivation kinetics of rat liver xanthine oxidase was described using a first-order reaction model:

$$[1] \qquad -\mathrm{d}A/\mathrm{d}t = kA$$

where –dA/dt represents the loss of xanthine oxidase activity rate constant (min^{-1}), A is the xanthine oxidase activity after heating for time t, and k is the thermal inactivation rate constant of xanthine oxidase at the temperature studied.

The residual enzyme activity at treatment time t and at a constant temperature can be calculated by eq. [2] derived from eq. [1]:

$$[2] \qquad 1\mathrm{n}A/A_0 = kt$$

The inactivation rate constant (k) can be estimated by linear regression analysis of the natural logarithm of residual activity vs treatment time.

If the inactivation rate constants are obtained at different

Can. J. Chem. Downloaded from www.nrcresearchpress.com by 80.58.250.72 on 09/16/12
For personal use only.

temperatures, it would be possible to estimate the energy of activation for denaturation using the Arrhenius equation:

$$[3] \quad \ln k = \ln A - E_a/RT$$

where k is the rate constant at T, A is the Arrhenius constant, E_a the apparent activation energy, R and T are the universal gas constant (8.314 J/mol/K) and the absolute temperature, respectively.

The activation energy can be estimated by linear regression analysis of the natural logarithm of rate constant vs the reciprocal of the absolute temperature.

The thermodynamic parameters for thermostability were calculated by rearranging the Eyring's absolute rate equation derived from the transition-state theory[19] as described before:[20]

$$[4] \quad K_d = (k_B T/h)e^{(-\Delta H/RT)}e^{(\Delta S/R)}$$

where h = Planck's constant = 6.63×10^{-34} J s, k_B = Boltzmann's constant (R/N) = 1.38×10^{-23} J/K, and N = Avogadro's number = 6.02×10^{23} mol^{-1}.

$$[5] \quad \Delta H^* \text{ (enthalpy of activation)} = E_a - RT$$

$$[6] \quad \Delta H^* \text{ (free energy of activation)} = -RT \ln(k_d, h/k_B T)$$

where k_d is the first-order rate constant for thermal denaturation.

$$[7] \quad \Delta S^* \text{ (entropy of activation)} = (\Delta H^* - \Delta G^*)/T$$

Determination of Michaelis–Menten parameters

To obtain the Michaelis–Menten constant (K_m) and the maximum velocity of the reaction (V_{max}), the initial oxidation rate of different concentrations of xanthine in Sorenson's phosphate buffer (67 mmol/L, pH 7.0 containing 0.1 mmol/L EDTA) in the absence and presence of 0.5% and 2.0% pyridine at 55 °C following addition of the enzyme fraction was determined. The K_m and V_{max} values were obtained from the Lineweaver–Burk plots.

Results and discussion

Effect of pyridine on spectral changes of product formation

The activity of xanthine oxidase was assayed by measuring the production of uric acid at 295 nm in aqueous solution. No changes were observed in the spectrum of uric acid in the presence of pyridine. Therefore, it was possible to determine the activity of xanthine oxidase by following the formation of uric acid at 295 nm without any spectroscopic interference from pyridine.

Effect of pyridine on xanthine oxidase thermal stability

The thermal stability of both pyridine-free and pyridine-treated enzymes was studied by incubating the enzyme in Sorenson's phosphate buffer at different temperatures (35, 45, 55, and 65 °C) for 24 h and measuring the residual activities at desired time intervals. As expected, the activity of the enzyme either in the absence or presence of pyridine decreased with temperature and treatment time; however, pyridine-treated enzyme showed a marked enhancement in thermal stability compared with the native enzyme (Fig. 1).

As the concentration of pyridine increased from 0.5% to 2.0%, the thermal stability of the enzyme also increased. In the presence of 2.0% pyridine, there was >60% of the residual activity even 24 h after incubation of the enzyme at 35 °C, whereas the activity reached almost zero after 10 h in the absence of pyridine (Fig. 1). The half-life values for thermal inactivation of xanthine oxidase in the presence of 0.5%–2.0% pyridine at 35 °C were found to be 2.0- to 21.7-fold greater than that obtained in the absence of pyridine (Table 1). As temperature increased, the half-life was reduced for both pyridine-free and pyridine-treated enzymes. At all studied temperatures, the half-life values for xanthine oxidase in the presence of different concentrations of pyridine were much higher than those of the native enzyme, indicating that xanthine oxidase becomes more thermostable in the hydro-organic mixture.

The increase in the thermal stability of xanthine oxidase in the presence of pyridine was further supported by the inspection of the inactivation rate constants (k). The thermal inactivation of the enzyme appeared to follow first-order inactivation kinetics, giving correlation coefficient values in the range of 0.951 to 0.996. In Table 1, the inactivation rate constants together with the r values of the correlation have been summarized. The rate constants increased with higher heating temperatures. However, at all studied temperatures, the inactivation rate constants decreased in the presence of pyridine. A higher inactivation rate constant would imply a less stable enzyme. Therefore, an increase in the inactivation rate constant of xanthine oxidase in the presence of pyridine indicates that this organic solvent is capable of protecting the enzyme from thermal denaturation. This protective effect of pyridine was found to be concentration-dependent. It was also found that the protection of xanthine oxidase from thermal inactivation by pyridine decreased at higher temperatures. Therefore, the smallest k value (the highest protective effect) was obtained for the 2.0% pyridine-treated enzyme at 35 °C, which was ~22-fold smaller than that of the native enzyme.

The calculated inactivation rate constants were plotted against the pyridine concentration (Fig. 2). At any temperature examined, the k values decreased as the concentration of pyridine increased, which indicates that pyridine makes xanthine oxidase more heat stable than when no pyridine is present.

The dependence of the xanthine oxidase inactivation rate constants on temperature adequately fitted the Arrhenius equation. The E_a values for thermal inactivation of the enzyme were obtained from the Arrhenius plots of logarithms of the inactivation rate constants vs reciprocals of the absolute temperatures (Fig. 3).

The E_a value was determined to be 14.173 kJ/mol for the native enzyme. However, the E_a values increased with an increase in the pyridine concentration, giving the highest value of 64.663 kJ/mol in the presence of 2.0% pyridine (Table 1). The activation energy could be an index of the thermal stability of protein; lower activation energy for denaturation would imply a less stable enzyme.[21] Therefore, an increase in the E_a value in the presence of pyridine further suggests

Fig. 1. Thermal inactivation profiles of the rat liver xanthine oxidase in the absence and presence of different concentrations of pyridine.

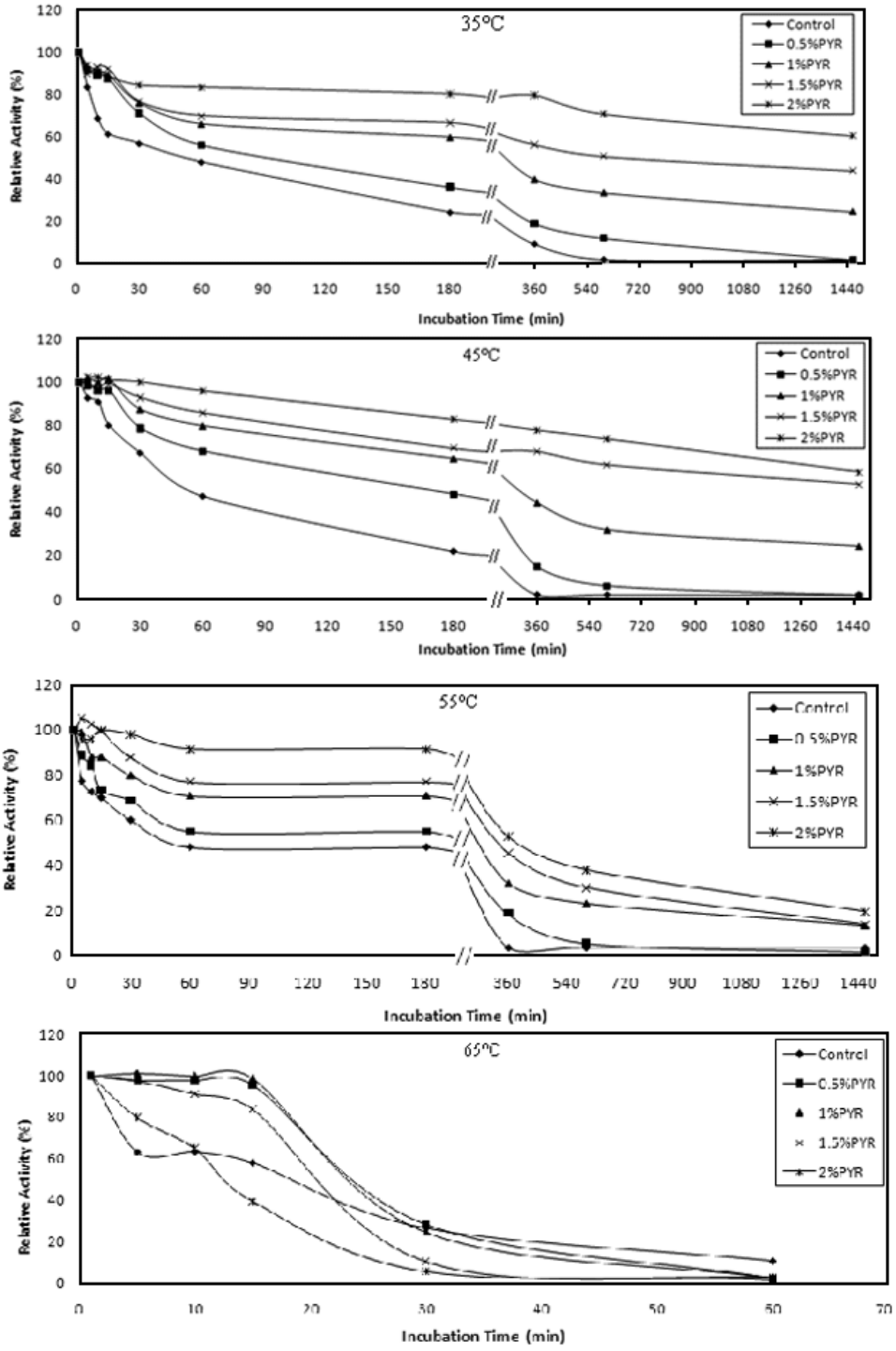

Can. J. Chem. Downloaded from www.nrcresearchpress.com by 80.58.250.72 on 09/16/12
For personal use only.

that pyridine is able to protect xanthine oxidase against thermal inactivation.

The thermodynamic activation parameters ΔG^*, ΔH^*, and ΔS^* were evaluated from the temperature dependence of the inactivation rate constant using Eyring equations and are summarized in Table 2. The enthalpy of denaturation (ΔH^*) of xanthine oxidase increased markedly in the presence of pyridine. This thermodynamic parameter represents the amount of heat required to denature the enzyme. A large and positive enthalpic value obtained for the denaturation process in the presence of pyridine indicates that xanthine oxidase in a medium containing pyridine is more thermostable than the enzyme in the buffer solution, since higher ΔH^* values suggest that more energy is required for enzyme denaturation to take place. There was also an increase in the entropy of denaturation (ΔS^*) when pyridine was present in the solution. The entropic parameter is the amount of energy per degree involved in the transition from a native to a denatured state. The value of ΔS^* also increased significantly in the presence of pyridine. As a positive value for

Can. J. Chem. Downloaded from www.nrcresearchpress.com by 80.58.250.72 on 09/16/12
For personal use only.

Table 1. Inactivation rate constants and half-life values for rat liver xanthine oxidase in the presence of 0.0%–2.0% pyridine at different temperatures.

Temperature (°C)		2% PYR	1.5% PYR	1% PYR	0.5% PYR	Control
35	$k\times10^2$ (min^{-1})	0.030	0.070	0.150	0.310	0.650
	r	0.953	0.978	0.956	0.985	0.994
	$t_{1/2}$ (min)	2310.0	990.0	462.0	223.6	106.6
45	$k\times10^2$ (min^{-1})	0.060	0.110	0.200	0.420	0.800
	r	0.951	0.979	0.988	0.995	0.991
	$t_{1/2}$ (min)	1155.0	630.0	346.5	165.0	86.6
55	$k\times10^2$ (min^{-1})	0.140	0.190	0.260	0.520	0.910
	r	0.988	0.996	0.976	0.994	0.995
	$t_{1/2}$ (min)	495.0	364.7	266.5	133.3	76.2
Activation energy (kJ/mol)		64.663	41.918	23.149	21.775	14.173

Note: PYR, pyridine. k, inactivation rate constant; r, correlation coefficient; $t_{1/2}$, half-life value for rat liver xanthine oxidase.

Fig. 2. Dependence of xanthine oxidase thermal inactivation rate constants (k) on pyridine concentration. Thermal inactivation of the enzyme was carried out according to the methods described in the Experimental section.

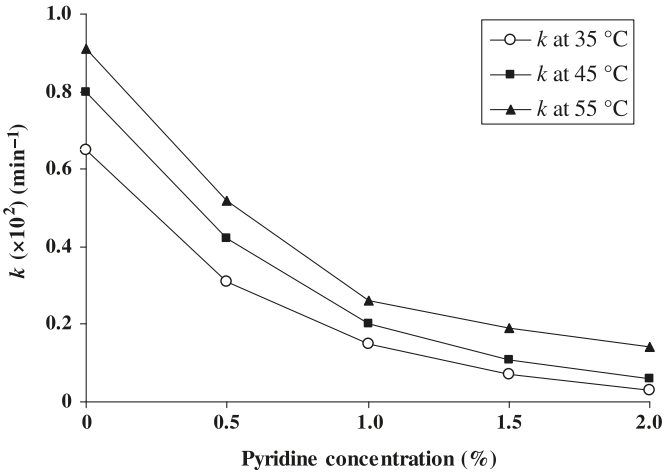

ΔS^* is indicative of the disorder of the system upon denaturation, based on entropic considerations, it seems that the thermal stability of xanthine oxidase decreases in the presence of pyridine. The free energy of denaturation (ΔG^*), which includes the contributions from both enthalpic and entropic terms, is a more accurate and reliable indicator of enzyme stability. The ΔG^* values for the enzyme activity in the presence of pyridine were found to be ~1.5-fold higher than that calculated for the native enzyme. ΔG^* can be regarded as a parameter for the kinetic stability of protein; a smaller ΔG^* change is associated with a more spontaneous process. Therefore, it appears that the energy barrier for denaturation of xanthine oxidase in a pyridine-containing buffer is high, and the enzyme becomes kinetically more stable in the presence of pyridine. The observed stabilization effect was enhanced when the concentration of pyridine increased from 0.5% to 2.0% (Table 2).

The thermal denaturation of enzymes usually results in the breakage of noncovalent linkages with an increase in the disorder or ΔS^*. Pyridine is an aromatic heterocyclic organic compound and is miscible with a broad range of polar and nonpolar solvents such as water and hexane. An increase in the enthalpic term of the xanthine oxidase denaturation in the pyridine-containing solution may indicate that pyridine stabilizes the modified form of the enzyme by adding noncovalent bonds, probably through both polar and hydrophobic interactions. A more positive ΔS^* value obtained for the denaturation of xanthine oxidase in pyridine-containing media shows that the water ordering in the enzyme hydration shell decreases in the new environment following the interaction of pyridine with water molecules, and this interaction is accompanied by an increase in the disorder or ΔS^*. It is also possible that in a dehydrated state, the conformational rigidity of the enzyme and its resistance to deleterious processes increase.[22] As, there was also an increase in the ΔG^* value, it seems that formation of new noncovalent bonds between the enzyme molecule and pyridine-containing solution plays an important role in the thermal stabilization of xanthine oxidase. The increase in both the enthalpies and entropies of xanthine oxidase thermal denaturation is an example of enthalpy–entropy compensation.

To further elucidate the behavior of xanthine oxidase in a pyridine-containing buffer solution, the Michaelis–Menten constants (K_m and V_{max}) for xanthine oxidase-catalyzed oxidation of xanthine were also determined in the absence and presence of pyridine at 55 °C. For xanthine oxidase in a buffer solution, the apparent K_m and V_{max} values were found to be 8.0 μmol/L and 0.10 μmol/L/min, respectively. However, the apparent K_m for xanthine oxidase in the presence of 0.5% pyridine was increased by 4.8-fold compared with the enzyme in the pyridine-free buffer solution. Therefore, it appears that the affinity of xanthine oxidase towards xanthine decreases when pyridine is present in the reaction medium. The V_{max} value of the enzyme in the hydro-organic solution also decreased 1.8-fold compared with the enzyme activity in the buffer solution. No significant difference was found in the kinetic parameters when the concentration of pyridine increased from 0.5% to 2.0% (Table 3). Therefore, both the affinity and the turnover number of xanthine oxidase are altered in the presence of pyridine.

However, in spite of a reduction in the efficiency of the reaction (expressed by V_{max}/K_m) in a pyridine-containing solution, the thermal stability of the enzyme increases in the presence of pyridine. The reduction in the catalytic efficiency of xanthine oxidase in a pyridine-containing buffer

Fig. 3. Kinetics of the thermal inactivation of rat liver xanthine oxidase. (*a*) Time-dependent loss in enzyme activity at 35 °C. (*b*) Arrhenius plots of xanthine oxidase inactivation.

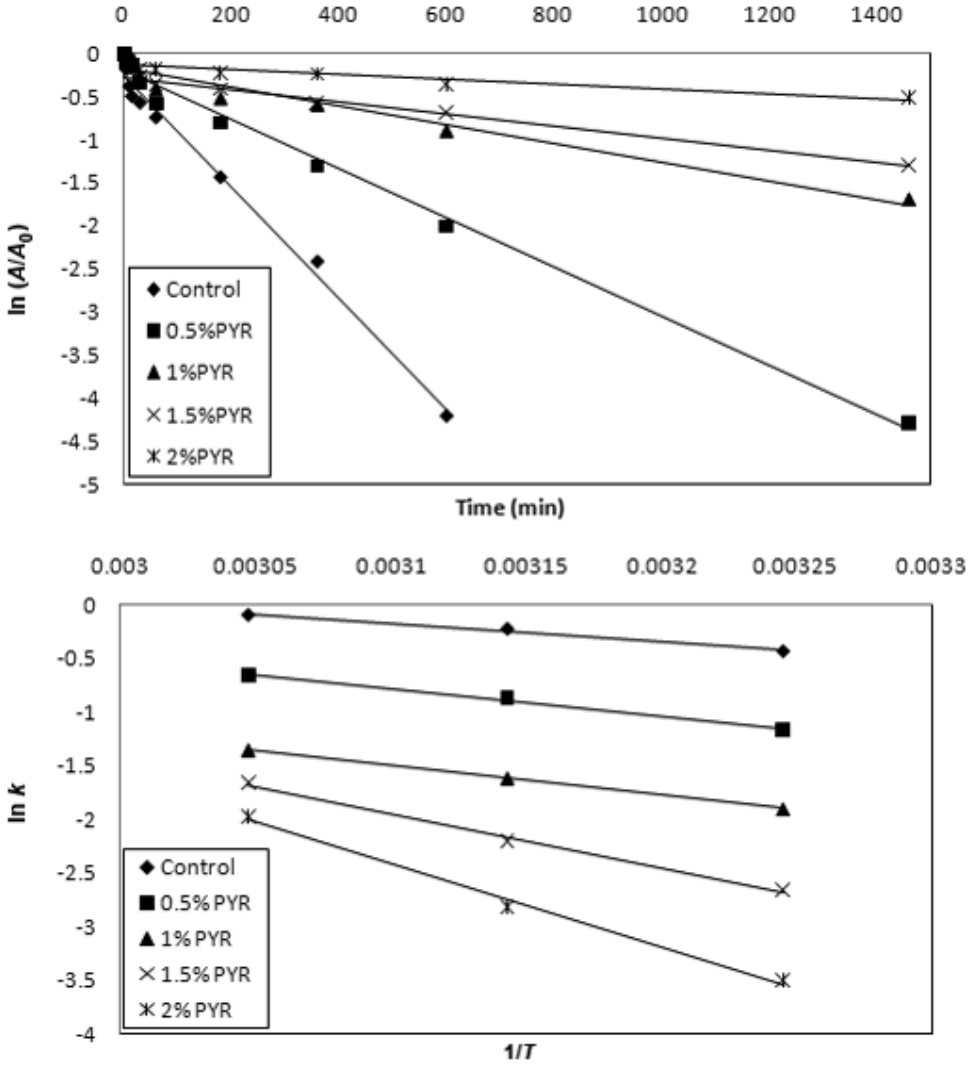

Table 2. Thermodynamic parameters for rat liver xanthine oxidase activity in the absence and presence of 0.5% and 2% pyridine at different temperatures.

Temperature (°C)	ΔG^* (kJ/mol)			ΔH^* (kJ/ mol)			ΔS^* (kJ/mol)		
	Control	0.5% PYR	2% PYR	Control	0.5% PYR	2% PYR	Control	0.5% PYR	2% PYR
35	12.902	14.799	20.781	11.611	19.213	62.101	0.004	0.014	0.134
45	12.772	14.476	19.624	11.527	19.129	62.017	0.004	0.014	0.134
55	12.822	14.348	17.928	11.444	19.046	61.934	0.004	0.014	0.134

Note: PYR, pyridine. ΔG^*, free energy of denaturation; ΔH^*, enthalpy of denaturation; and ΔS^*, entropy of denaturation.

Table 3. Michaelis–Menten constants for rat liver xanthine oxidase towards xanthine as the substrate in the absence and presence of 0.5% and 2% pyridine at 55 °C.

Constant	Control	0.5% PYR	2% PYR
K_m (μmol/L)	8.0	38.2	35.4
V_{max} ((μmol/L)/min)	0.100	0.180	0.170
V_{max}/K_m	0.012	0.004	0.005

Note: PYR, pyridine. K_m, Michaelis–Menten constant; V_{max}, maximum velocity of the enzymatic reaction.

could be attributed to the destruction of the enzyme hydration shell by the interaction of the organic solvent with water molecules.[23] It has been recognized that the replacement of water molecules from the enzyme leads to the unfolding of the enzyme molecule making the inner important residues of the enzyme molecule more exposed to the organic solvent. A higher exposure to the organic solvent could result in a faster denaturation rate.[24] It is also possible that the observed changes in the reaction kinetics arise from a direct interaction of pyridine as an inhibitor of the enzyme or even from a reduction in the number of the enzyme ac-

Can. J. Chem. Downloaded from www.nrcresearchpress.com by 80.58.250.72 on 09/16/12
For personal use only.

tive sites. Xanthine oxidase is a metalloenzyme composed of two identical subunits. Each subunit contains one atom of molybdenum, one molecule of enzyme-bound flavin adenine dinucleotide (FAD), and two iron–sulfur (2Fe–2S) centers, with the molybdenum center acting as the substrate-binding pocket.[25] There is some evidence indicating the sensitivity of the molybdenum center of xanthine oxidase for interacting with pyridine. According to Okamoto et al.,[26] the molybdenum center of xanthine oxidase is able to form a complex with 4-[5-pyridin-4-yl-1*H*-[1,2,4]triazol-3-yl]pyridine-2-carbonitrile (FYX-051, a potent inhibitor of xanthine oxidase). They showed that in the complex, a covalent linkage is formed between molybdenum and the pyridine ring of FYX-051. On the other hand, the presence of pyridine in an aqueous reaction medium provides a new environment in which the enzyme finds a new three-dimensional structure that is more resistant to deleterious processes.[22]

Conclusion

Xanthine oxidase activity was reduced in the presence of pyridine; however, in spite of this reduction, a remarkable increase was observed in the enzyme stability in the pyridine-containing reaction medium. As the stability of enzymes is one of the most difficult problems in protein chemistry,[15] this thermostability property of xanthine oxidase could be of great value in the development of novel strategies to improve and expand its application in various areas.

References

(1) Yoon, J. H.; Mckenzie, D. *Enzyme Microb. Technol.* **2005**, *36* (4), 439. doi:10.1016/j.enzmictec.2004.09.014.

(2) Tsai, S. -W.; Chen, C. -C.; Yang, H. -S.; Ng, I. -S.; Chen, T. -L. *Biochim. Biophys. Acta* **2006**, *1764*, 1424. doi:10.1016/j.bbapap.2006.07.001.

(3) Lima, V. M. G.; Krieger, N.; Mitchell, D. A.; Fontana, J. D. *Biochem. Eng. J.* **2004**, *18* (1), 65. doi:10.1016/S1369-703X(03)00165-7.

(4) Wu, J. C.; Lee, S. S.; Mahmood, M. M. B.; Chow, Y.; Talukder, M. M. R.; Choi, W. J. *J. Mol. Catal., B Enzym.* **2007**, *45* (3-4), 108. doi:10.1016/j.molcatb.2007.01.003.

(5) Szabó, A.; Bázár, G.; Andrássy-Baka, G.; Locsmándi, L.; Romvári, R. *Acta Aliment.* **2009**, *38* (1), 97. doi:10.1556/AAlim.2008.0023.

(6) Halliwell, B.; Cutteridge, M. C. *Free Radicals in Biology and Medicine,* 3rd ed.; New York: Oxford University Press, 1999; p 28.

(7) Ohta, Y.; Matsura, T.; Kitagawa, A.; Tokunaga, K.; Yamada, K. *Free Radic. Res.* **2007**, *41* (2), 135. doi:10.1080/10715760600953842.

(8) Nakatani, H. S.; dos Santos, L. V.; Pelegrine, C. P.; Gomes, S. T. M.; Matsushita, M.; de Souza, N. E.; Visentaine, J. V. *Am. J. Biochem. Biotechnol.* **2005**, *1* (2), 85. doi:10.3844/ajbbsp.2005.85.89.

(9) Mao, L.; Xu, F.; Xu, Q.; Jin, L. *Anal. Biochem.* **2001**, *292* (1), 94. doi:10.1006/abio.2001.5067.

(10) Stredansky, M.; Pizzariello, A.; Miertus, S.; Svorc, J. *Anal. Biochem.* **2000**, *285* (2), 225. doi:10.1006/abio.2000.4746.

(11) Fridovich, I. *J. Biol. Chem.* **1966**, *10*, 3624.

(12) Dastoli, F. R.; Price, S. *Arch. Biochem. Biophys.* **1967**, *118* (1), 163. doi:10.1016/0003-9861(67)90292-5.

(13) Dastoli, F. R.; Price, S. *Arch. Biochem. Biophys.* **1967**, *122* (2), 289. doi:10.1016/0003-9861(67)90197-X.

(14) Rashidi, M. R.; Soruraddin, M. H.; Taherzadeh, F.; Jouyban, A. *Biochemistry (Mosc.)* **2009**, *74* (1), 97. doi:10.1134/S0006297909010155.

(15) Johnson, C.; Stubley-Beedham, C.; Godfrey, J.; Stell, P. *Biochem. Pharmacol.* **1985**, *34* (24), 4251. doi:10.1016/0006-2952(85)90280-1.

(16) Duckworth, H. W.; Coleman, J. E. *J. Biol. Chem.* **1970**, *245*, 1613.

(17) Toscano, G.; Pirozzi, D.; Maremonti, M.; Gianfreda, L.; Greco, G., Jr. *Catal. Today* **1994**, *22* (3), 489. doi:10.1016/0920-5861(94)80119-3.

(18) Xu, S.; Labuza, T. P.; Diez-Gonzalez, F. *Appl. Environ. Microbiol.* **2006**, *72* (6), 4479. doi:10.1128/AEM.00096-06.

(19) Eyring, H.; Stearn, A. E. *Chem. Rev.* **1939**, *24* (2), 253. doi:10.1021/cr60078a005.

(20) Siddiqui, K. S.; Shamsi, A. M.; Anwar, M. A.; Rashid, M. H.; Rajoka, M. I. *Enzyme Microb. Technol.* **1999**, *24* (8–9), 599. doi:10.1016/S0141-0229(98)00170-7.

(21) Chaniotakis, N. A. *Anal. Bioanal. Chem.* **2004**, *378* (1), 89. doi:10.1007/s00216-003-2188-3.

(22) Volkin, D. B.; Staubli, A.; Langer, R.; Klibanov, A. M. *Biotechnol. Bioeng.* **1991**, *37* (9), 843. doi:10.1002/bit.260370908.

(23) Simon, L. M.; Kotormán, M.; Szabó, A.; Nemcsók, J.; Laczkó, I. *Process Biochem.* **2007**, *42* (5), 909. doi:10.1016/j.procbio.2007.01.014.

(24) d'Acunzo, F.; Barreca, A. M.; Galli, C. *J. Mol. Catal., B Enzym.* **2004**, *31* (1–3), 25. doi:10.1016/j.molcatb.2004.07.001.

(25) Rashidi, M. R.; Nazemiyeh, H. *Expert Opin. Drug Metab. Toxicol.* **2010**, *6* (2), 133. doi:10.1517/17425250903426164.

(26) Okamoto, K.; Matsumoto, K.; Hille, R.; Eger, B. T.; Pai, E. F.; Nishino, T. *Proc. Natl. Acad. Sci. U.S.A.* **2004**, *101* (21), 7931. doi:10.1073/pnas.0400973101.

Can. J. Chem. Downloaded from www.nrcresearchpress.com by 80.58.250.72 on 09/16/12
For personal use only.

Voltammetric detection of nitroaromatic compounds using carbon-nanomaterials-based electrodes

Hong-Xia Zhang and Jun-Hong Zhang

Can. J. Chem. Downloaded from www.nrcresearchpress.com by 80.58.250.72 on 09/16/12
For personal use only.

Abstract: The morphology of glassy carbon surfaces was investigated by the atomic force microscope (AFM) method. Multi-wall carbon nanotubes (MWCNTs) were purified and investigated with a scanning electron microscope (SEM) and a transmission electron microscope (TEM). An electrochemical technique based on the glassy carbon electrode (GCE) or MWCNT-modified GCEs was used for the detection of nitroaromatic compounds (NACs), namely 2,4,6-trinitrotoluene (TNT), 1,3,5-trinitrobenzene (TNB), 2,4-dinitrotoluene (2,4-DNT), and 1,3-dinitrobenzene (1,3-DNB). MWCNT-modified GCEs were more sensitive than GCEs to TNB, 2,4-DNT, and 1,3-DNB, with the detection limit down to ppb level, whereas the modified GCEs showed lower sensitivity to TNT. In varying degrees, the accumulation of nitro compounds can be promoted by MWCNT-modified GCEs in the detection process, a property which can be attributed to the large surface area and graphene-sheet structure of MWCNTs.

Key words: glassy carbon, carbon nanotubes, modified, electrochemical detection, nitro compounds, sensitivity.

Résumé : Faisant appel à la microscopie des forces atomiques (MFA), on a étudié la morphologie de la surface d'un carbone vitreux. On a purifié des nanotubes de carbone à surfaces multiples (NTCSM) et on en a étudié les propriétés par microscopie électronique à balayage (MEB) et par microscopie électronique de transmission (MET). On a utilisé une technique électrochimique basée sur une électrode de carbone vitreux (ECV) et des électrodes de carbone vitreux modifiées par des nanotubes de carbone à surfaces multiples pour la détection de composés nitroaromatiques (CNA), tels le 2,4,6-trinitrotoluène (TNT), le 1,3,5-trinitrobenzène (TNB), le 2,4-dinitrotoluène (2,4-DNT) et le 1,3-dinitrobenzène (1,3-DNB). Par comparaison avec les électrodes de carbone vitreux, on a observé une plus grande sensibilité des électrodes modifiées par des nanotubes de carbone à surfaces multiples pour le TNB, le 2,4-DNT et le 1,3-DNB alors que la limite de détection descend au niveau de la ppb; toutefois, pour le TNT, l'inverse est vrai. Dans le processus de détection, l'accumulation des composés nitrés peut être majorée à des degrés divers par les électrodes modifiées par des nanotubes de carbone à surfaces multiples et ceci peut être attribué à la grande superficie de sa surface et à la structure en feuille de graphène des nanotubes de carbone à surfaces multiples.

Mots-clés : carbone vitreux, nanotubes de carbone, modifié, détection électrochimique, composés nitro, sensibilité.

[Traduit par la Rédaction]

Introduction

Today, security and environmental protection are two important topics all over the world; for this reason, research in detecting ultra-trace amounts of explosive and toxic nitroaromatic compounds (NACs) has accelerated.[1–6] Many techniques are used in this research. Electrochemical detection has several advantages over other methods, in that the instrument is simple and suitable for constructing inexpensive and portable detectors. Moreover, electrochemical detection can utilize an excellent materials-based electrode or a chemically modified electrode (CME) for sensitive and selective analyses, and the electrode itself can act as a reactant to pump or withdraw electrons in the reaction (reduction–oxidation).[6–9] During detection, the target compounds such as NACs will selectively adsorb onto and enrich the chemically modified surface, making ultra-trace detection possible. Therefore, one way of improving the sensitivity of an electrochemical sensor is to use materials sensitive to the analytes; thus, the search for new materials sensitive to NACs becomes an important topic in security and environmental protection research.

Carbon materials with different morphology and structure are widely used as electrode materials. Among them, glassy carbon has a disordered structure, whereas the carbon nanotube (CNT) is built from sp^2 carbon units and has hexagonal honeycomb lattices. These structural distinctions result in their different properties, and the unique structural characteristic of CNT makes it of scientific interest. Recent studies have shown that CNTs can mediate electron transfer reactions when used as electrode materials, and CNTs have more useful properties than traditional carbon electrodes, including good conducting ability and high chemical stability.

Received 7 December 2009. Accepted 6 April 2010. Published on the NRC Research Press Web site at canjchem.nrc.ca on 16 December 2010.

H.X. Zhang[1] and J.H. Zhang. Department of Chemistry, Liaocheng University, Liaocheng 252059, P. R. China.

[1]Corresponding author (e-mail: hxzhang@iccas.ac.cn).

Can. J. Chem. Downloaded from www.nrcresearchpress.com by 80.58.250.72 on 09/16/12
For personal use only.

More importantly, CNTs are excellent candidates for sensors because of their interfacial adsorption properties and enhanced electrocatalytic activity.[10–14]

We have previously demonstrated that SiO_2 based materials can improve the detection sensitivity of NACs, and that mesoporous MCM-41 and SiO_2 nanospheres show differing sensitivities to NACs owing to their different morphology and structure.[5] In an ongoing effort to find materials sensitive to NACs, we investigated the electrochemical sensitivity of carbon-based materials of glassy carbon and MWCNT to NACs. MWCNT-modified GCEs showed higher sensitivity to three NACs, namely, TNB, 2,4-DNT, and 1,3-DNB, and lower sensitivity to TNT, than unmodified GCEs. And the detection limits by MWCNT-modified GCEs to TNB, 2,4-DNT, and 1,3-DNB was down to the ppb level.

Experimental

Materials

TNT (1g/L in acetonitrile), TNB, 2,4-DNT, and 1,3-DNB were obtained from Tokyo Kasei Kogyo Co. Ltd; GCE and MWCNTs were obtained from Chenhua (Shanghai, China) and Shenzhen Nanotech Port Co., Ltd. (Shenzhen, China), respectively; and *N*,*N*-dimethylformamide (DMF) and sodium chloride (NaCl) were obtained from Beijing Chemical Reagent Ltd., China. All the water used in this experiment was Milli-Q water. The solid NACs (TNB, 2,4-DNT, and 1,3-DNB) were dissolved in acetonitrile to form 1 g/L solutions.

Before the experiment, MWCNTs were first purified by refluxing in nitric acid for 5 h, followed by centrifugation, resuspension, filtration, and drying under vacuum at 100 °C.

Morphological characterization

The morphology of the GCE surface was imaged on a Nano IIIa atomic force microscope (AFM) (Digital Instruments) operating in a tapping mode using hard silicon tips with spring constants of ~40 N/m. Purified MWCNTs were characterized using a scanning electron microscope (SEM) (Hitachi S-4300F) and a transmission electron microscope (TEM) (Philips TECNAI-20). For SEM and TEM observations, the samples of purified MWCNTs were redispersed in DMF by ultrasonic treatment and dropped onto a silicon substrate and a carbon–copper grid, respectively.

Electrochemical detection

Electrochemical detection was performed with an EG&G Princeton Applied Research (PAR) advanced electrochemical system (PARSTAT 2263) controlled by a microcomputer with EG&G PARC M250 software as reported previously.[10] All experiments were performed at room temperature (about 25 °C). An electrochemical cell with the three-electrode configuration was employed in the experiment, including a glassy carbon disk 3 mm in diameter as working electrode, a saturated calomel electrode (SCE) as the reference electrode, and a platinum wire as the counter electrode. Before modification, the GCEs were well polished with 0.3 μm alumina slurry, ultrasonicated in Milli-Q water, and finally dried in an oven at about 45 °C.

To modify the GCEs, the purified MWCNTs were first dispersed in DMF at a concentration of about 10 mg/mL, and 5 μL of this suspension was dispersed directly onto the surface of the clean and dried electrode. After DMF evaporation, a thin film of MWCNT formed on the surface of GCE. The supporting electrolyte used in the experiments was 0.5 mol/L NaCl aqueous solution, which was thoroughly deoxygenated by bubbling high-purity nitrogen gas before the experiment, and maintaning a constant flow of high-purity nitrogen over the solution during the measurements. The potential was scanned linearly at 100 mV/S in the electrochemical detection.

Results and discussion

Materials morphology

AFM images show that the surface morphology of GCE is composed of disordered nanoparticles (see Fig. 1).[15,16] The SEM and TEM images of the purified MWCNTs are shown in Fig. 2. From the SEM image, it can be seen that the sample of MWCNTs is composed of nanotubes with uniform shape. The average diameter of a tube is about 70 nm and its length is several μm. It is evident that these nanotubes possess multiple walls, as indicated in the TEM image.

Electrochemical detection by GCEs

Electrochemical studies on NACs have shown repeatedly that the reduction of the nitro group in nitro compounds usually occurs in two steps including the formation of amine and hydroxylamine. Each nitro group undergoes sequential 6 e^- reduction to an amine group.[17–22] The voltammograms of NACs (TNT, TNB, 2,4-DNT, and 1,3-DNB) on cleaned GCEs are shown in Fig. 3. On GCEs, the intensity of the redox peak weakens with the decrease of NAC concentration in the electrolyte solution. The detection limit is defined as the lowest concentration with identifiable response compared with the blank solution;[23] the detection limit for TNT by GCEs is about 120 ppb. The first two redox potentials of three nitro groups of TNT on GCEs are at –0.54 and –0.70 V, respectively, while the third redox potential cannot be identified in a solution concentration of 300 ppb. The three nitro groups of TNB are reduced at about –0.48, –0.63, and –0.74 V on GCEs, and the corresponding detection limit is down to 60 ppb. With 2,4-DNT, the redox potential of the two nitro groups are at –0.66 and –0.81 V, and its detection limit is about 120 ppb. As for 1,3-DNB, the two nitro groups are reduced at –0.65 and –0.78 V, and the detection limit of 1,3-DNB by GCEs is about 30 ppb. The influence of scan rate on NAC reduction on GCEs was investigated by voltammetry from 10 to 500 mV/S; in all cases, the peak current of these four NACs was found to be linear with the scan rate, illustrating that the reduction signal originates from NACs adsorbed onto the glassy-carbon-terminated surface. Further experiment showed that the peak intensity of NACs on GCEs is independent of increased accumulation times.[6b]

Electrochemical detection by MWCNT-modified GCEs

MWCNT-modified GCEs were also used to detect TNT, TNB, 2,4-DNT, and 1,3-DNB. As shown in Fig. 4a, the redox potential of the three nitro groups of TNT are at –0.50, –0.62, and –0.77 V, respectively. The intensity of the redox peak weakens with the decrease of TNT concentration in the

Can. J. Chem. Downloaded from www.nrcresearchpress.com by 80.58.250.72 on 09/16/12
For personal use only.

Fig. 1. Images of the GCE surface; (a) AFM height (z = 10 nm) and (b) AFM phase (z = 20 nm); scanning region is 1 μmol/L × 1 μmol/L.

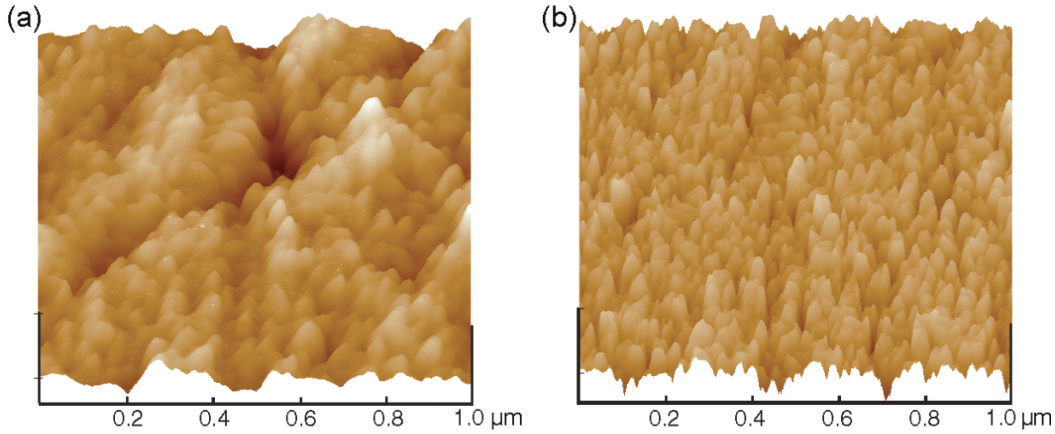

Fig. 2. SEM (a) and TEM (b) images of purified MWCNTs.

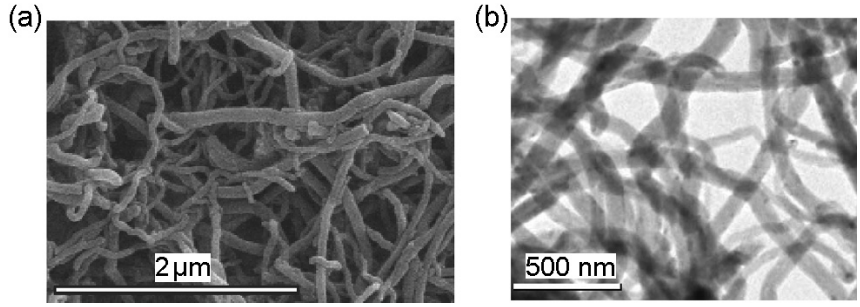

Fig. 3. Voltammograms of (a) TNT, (b) TNB, (c) 2,4-DNT, and (d) 1,3-DNB by unmodified GCEs in NaCl (0.5 mol/L) electrolyte.

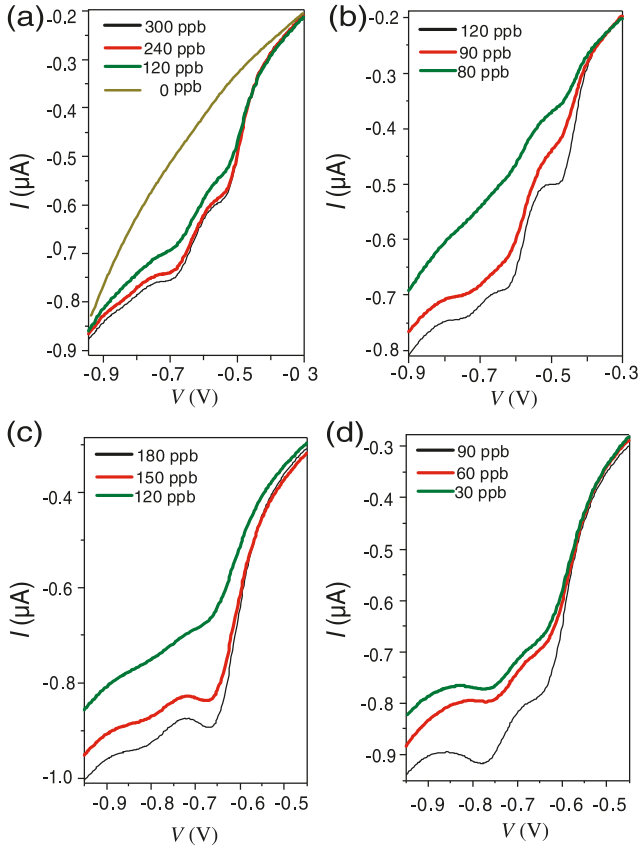

electrolyte solution, and the detection limit of TNT by MWCNT-modified GCEs is about 500 ppb without accumulation times.[6] Further experiments demonstrated that MWCNT-modified GCEs can greatly promote the accumulation of TNT as shown in Fig. 5a. With increasing accumulation times from 0 to 120 s, the intensity of the redox peak of TNT is distinctly enhanced, as has been reported in the literature.[6] The influence of scan rate on TNT reduction at MWCNT-modified GCEs was investigated by voltammetry from 10 to 500 mV/S. The relationship between peak current (I_p) and scan rate is linear (r^2 = 0.9952) with the equation of I_p = –0.30752(±0.00867)v – 8.81481(±2.28), which indicates that the reduction signal originates from TNT adsorbed onto the MWCNTs-terminated surface.

The voltammograms were then recorded in 0.5 mol/L NaCl solution containing different concentrations of TNB using MWCNT-modified GCEs, and the corresponding voltammograms are shown in Fig. 4b, indicating that MWCNT is very sensitive to TNB. TNB in a solution concentration of 36 ppb generates three well-defined redox signals at –0.49, –0.64, and –0.75 V, respectively. With decreasing TNB concentration, the peak intensity reduces. However, when TNB concentration was reduced to 6 ppb, the three redox peaks were still visible. This result indicates that MWCNTs is much more sensitive to TNB than is glassy carbon. Figure 5b shows the relationship between the accumulation times and the intensity of redox peak of TNB, showing that MWCNT-modified GCEs can also promote the accumulation of TNT, but that this promotion is weaker than with TNT. The relationship between the first peak current (I_p) of TNB and the scan rate is linear (I_p = –0.27833(±0.00401)v – 4.1853(±1.05387), r^2 = 0.9988).

Can. J. Chem. Downloaded from www.nrcresearchpress.com by 80.58.250.72 on 09/16/12
For personal use only.

Fig. 4. Voltammograms of TNT (a), TNB (b), 2,4-DNT (c), and 1,3-DNB (d) by MWCNT-modified GCEs in NaCl (0.5 mol/L) electrolyte.

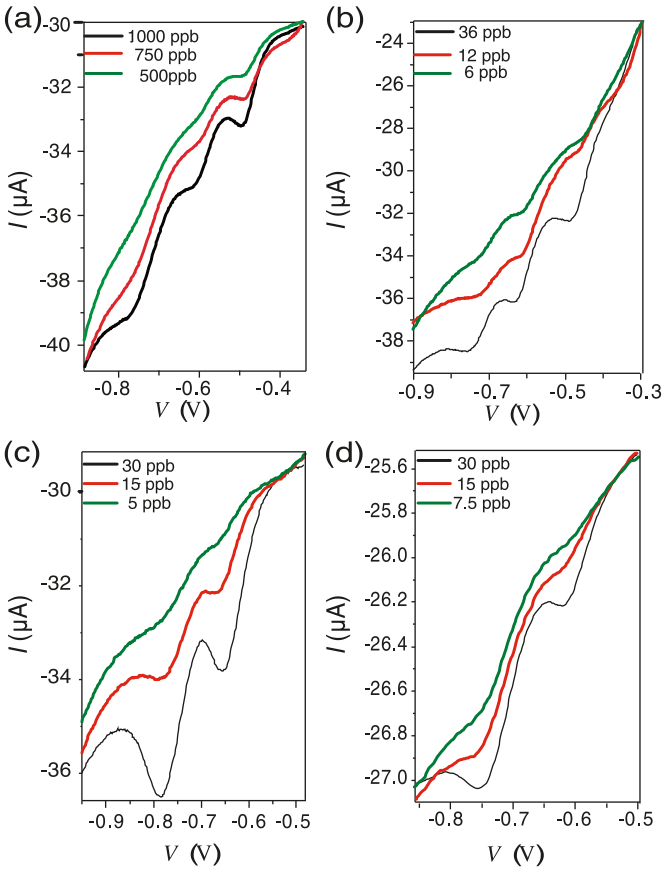

Experiments were also carried out to detect other NACs with MWCNT-modified electrodes in 0.5 mol/L NaCl solution. As shown in Fig. 4c, a 30 ppb 2,4-DNT solution generated two well-defined redox signals at –0.66 and –0.78 V, respectively, corresponding to the stepwise reduction of two nitro groups to the corresponding amine. There were still two weak peaks when 2,4-DNT concentration was reduced to 5 ppb. Experiment also showed that MWCNT-modified GCEs can greatly promote the accumulation of 2,4-DNT as shown in Fig. 5c. With increasing accumulation times from 0 to 120 s, the intensity of the redox peak of 2,4-DNT becomes clearly enhanced. The relationship between the first peak current and the scan rate is also linear.

Figure 4d shows the voltammograms of trace 1,3-DNB by MWCNT-modified GCEs. There are two strong redox signals at –0.62 and –0.75 V in 0.5 mol/L NaCl solution containing 30 ppb 1,3-DNB, corresponding to the stepwise reduction of two Ar–NO_2 groups to the corresponding Ar–NH_2 groups. And the detection limit of 1,3-DNB is down to 7.5 ppb. With increased accumulation times, the peak intensity of 1,3-DNB is also enhanced (see Fig. 5d). The peak current of 1,3-DNB is linear to the scan rate.

The redox potential and detection limit of four NACs on unmodified and MWCNT-modified GCEs are listed in Table 1. Without accumulation times, the detection limits for TNT, TNB, 2,4-DNT, and 1,3-DNB by MWCNT-modified GCEs are 500, 6, 5, and 7.5 ppb, respectively. By contrast,

Fig. 5. Voltammograms of NACs by MWCNT-modified GCEs in NaCl (0.5 mol/L) electrolyte at increasing accumulation times of 0, 60, and 120 s: (a) TNT at 1000 ppb concentration, (b) TNB at 71 ppb concentration, (c) 2,4-DNT at 30 ppb concentration, and (d) 1,3-DNB at 30 ppb concentration.

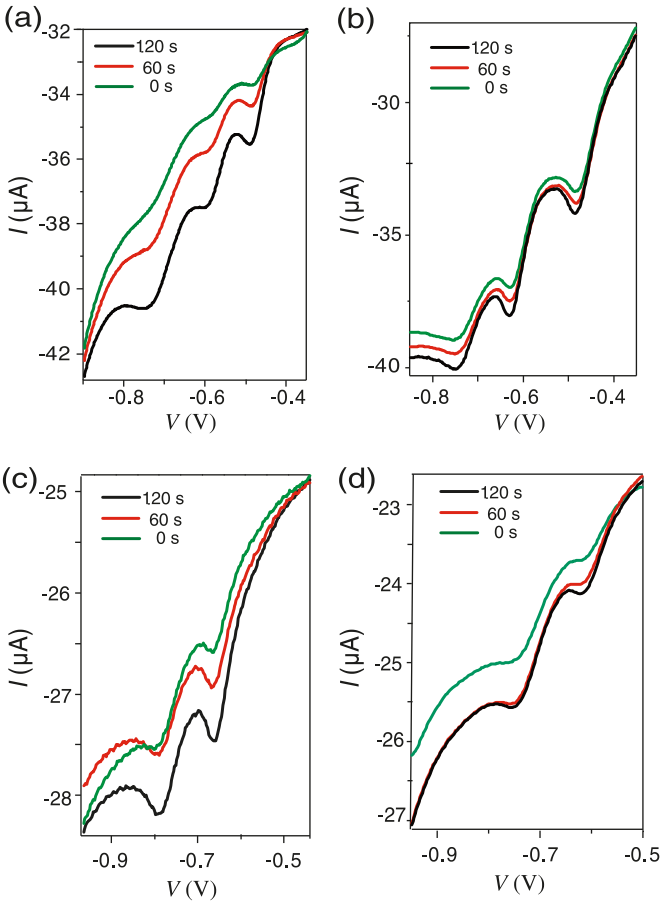

on unmodified GCEs, the detection limits for TNT, TNB, 2,4-DNT, and 1,3-DNB are 120, 80, 120, and 30 ppb, respectively. MWCNTs show higher sensitivity to TNB, 2,4-DNT, and 1,3-DNB than glassy carbon. Moreover, MWCNTs can greatly promote the accumulation of NACs onto electrodes in solution, which can further improve the detection sensitivity of NACs. This difference between glassy carbon and MWCNTs results from their distinct structure; the large surface area and graphene-sheet structure of MWCNTs contribute to this sensitivity.[6]

Conclusion

In the present study, the morphology of glassy carbon was studied by AFM. MWCNTs were purified and investigated by SEM and TEM. The electrochemical sensitivity of these two different carbon materials to NACs has been investigated by cathodic voltammetry. Compared with glassy carbon, MWCNT showed higher sensitivity to TNB, 2,4-DNT, and 1,3-DNB, and excellent accumulation of NACs, which may be attributed to the large surface area and graphene-sheet structure of MWCNTs. The results reported in this study indicate that the MWCNT-modified electrode is an excellent sensor candidate for high sensitivity and fast detection

Table 1. The redox potential and detection limit of four NACs on unmodified and MWCNT-modified GCEs.

	TNT	TNB	2,4-DNT	1,3-DNB
Unmodified GCEs				
Detection limit (ppb)	120	80	120	30
Redox potential (V)	–0.54, –0.70, –0.84	–0.48, –0.63, –0.74	–0.66, –0.81	–0.66, –0.78
MWCNT-modified GCEs				
Detection limit (ppb)	500	6	5	7.5
Redox potential (V)	–0.50, –0.62, –0.77	–0.49, –0.64, –0.75	–0.66, –0.78	–0.62, –0.75

of trace amounts of the nitro compounds TNB, 2,4-DNT, and 1,3-DNB. This will be important in both NAC sensor fabrication and carbon nanotube applications.

Acknowledgment

The authors thank the Shandong Tai-Shan Scholar Research Fund, and the Liaocheng University Foundation for Dr. Zhang.

References

(1) Gao, D.; Zhang, Z.; Wu, M.; Xie, C.; Guan, G.; Wang, D. *J. Am. Chem. Soc.* **2007**, *129* (25), 7859. doi:10.1021/ja070975k. PMID:17550249.

(2) Martin, A. N.; Farquar, G. R.; Gard, E. E.; Frank, M.; Fergenson, D. P. *Anal. Chem.* **2007**, *79* (5), 1918. doi:10.1021/ac061581z. PMID:17249636.

(3) Zhang, H.-X.; Chen, Q.; Wen, R.; Hu, J.-S.; Wan, L.-J. *Anal. Chem.* **2007**, *79* (5), 2179. doi:10.1021/ac0618268. PMID:17269652.

(4) Zhang, H.-X.; Cao, A.-M.; Hu, J.-S.; Wan, L.-J.; Lee, S. T. *Anal. Chem.* **2006**, *78* (6), 1967. doi:10.1021/ac051826s. PMID:16536434.

(5) Zhang, H.-X.; Hu, J.-S.; Yan, C.-J.; Jiang, L.; Wan, L.-J. *Phys. Chem. Chem. Phys.* **2006**, *8* (30), 3567. doi:10.1039/b604587c. PMID:16871348.

(6) (a) Krausa, M.; Schorb, K. *J. Electroanal. Chem.* **1999**, *461* (1-2), 10. doi:10.1016/S0022-0728(98)00162-4.; (b) Wang, J.; Hocevar, S. B.; Ogorevc, B. *Electrochem. Commun.* **2004**, *6* (2), 176. doi:10.1016/j.elecom.2003.11.010.

(7) Li, S.; Wang, X.; Beving, D.; Chen, Z.; Yan, Y. *J. Am. Chem. Soc.* **2004**, *126* (13), 4122. doi:10.1021/ja031985y. PMID:15053598.

(8) Weng, J.; Xue, J.; Wang, J.; Ye, J.-S.; Cui, H.; Sheu, F.-S.; Zhang, Q. *Adv. Funct. Mater.* **2005**, *15* (4), 639. doi:10.1002/adfm.200400049.

(9) Liu, G.; Lin, Y. *Anal. Chem.* **2005**, *77* (18), 5894. doi:10.1021/ac050791t. PMID:16159119.

(10) Wang, J.; Timchalk, C.; Lin, Y. *Environ. Sci. Technol.* **2008**, *42* (7), 2688. doi:10.1021/es702335y. PMID:18505017.

(11) Hu, P.; Huang, C. Z.; Li, Y. F.; Ling, J.; Liu, Y. L.; Fei, L. R.; Xie, J. P. *Anal. Chem.* **2008**, *80* (5), 1819. doi:10.1021/ac702187y. PMID:18232709.

(12) Kawano, T.; Chiamori, H. C.; Suter, M.; Zhou, Q.; Sosnowchik, B. D.; Lin, L. *Nano Lett.* **2007**, *7* (12), 3686. doi:10.1021/nl071964s. PMID:18001108.

(13) Robinson, J. A.; Snow, E. S.; Badescu, S. C.; Reinecke, T. L.; Perkins, F. K. *Nano Lett.* **2006**, *6* (8), 1747. doi:10.1021/nl0612289. PMID:16895367.

(14) Wang, F.; Gu, H.; Swager, T. M. *J. Am. Chem. Soc.* **2008**, *130* (16), 5392. doi:10.1021/ja710795k. PMID:18373343.

(15) McDermott, M. T.; McCreery, R. L. *Langmuir* **1994**, *10* (11), 4307. doi:10.1021/la00023a062.

(16) Shi, K.; Shiu, K.-K. *Anal. Chem.* **2002**, *74* (4), 879. doi:10.1021/ac010734+. PMID:11866068.

(17) Wang, J.; Bhada, R. K.; Lu, J.; MacDonald, D. *Anal. Chim. Acta* **1998**, *361* (1-2), 85. doi:10.1016/S0003-2670(97)00702-2.

(18) Bratin, K.; Kissinger, P. T. *Anal. Chim. Acta* **1981**, *130* (2), 295. doi:10.1016/S0003-2670(01)93007-7.

(19) Esteve-Núñez, A.; Caballero, A.; Ramos, J. L. *Microbiol. Mol. Biol. Rev.* **2001**, *65* (3), 335. doi:10.1128/MMBR.65.3.335-352.2001. PMID:11527999.

(20) Hawari, J.; Halasz, A.; Paquet, L.; Zhou, E.; Spencer, B.; Ampleman, G.; Thiboutot, S. *Appl. Environ. Microbiol.* **1998**, *64* (6), 2200. PMID:9603835.

(21) Williams, R. E.; Rathbone, D. A.; Scrutton, N. S.; Bruce, N. C. *Appl. Environ. Microbiol.* **2004**, *70* (6), 3566. doi:10.1128/AEM.70.6.3566-3574.2004. PMID:15184158.

(22) Hess, T. F.; Lewis, T. A.; Crawford, R. L.; Katamneni, S.; Wells, J. H.; Watts, R. J. *Water Res.* **1998**, *32* (5), 1481. doi:10.1016/S0043-1354(97)00364-3.

(23) Hrapovic, S.; Majid, E.; Liu, Y.; Male, K.; Luong, J. H. T. *Anal. Chem.* **2006**, *78* (15), 5504. doi:10.1021/ac060435q. PMID:16878889.

Can. J. Chem. Downloaded from www.nrcresearchpress.com by 80.58.250.72 on 09/16/12
For personal use only.

New active and recyclable catalytic systems based on $[Zn_4(H_2O)_2(PW_9O_{34})_2]^{10-}$ for alcohol oxidation with hydrogen peroxide in water

Yong Ding, Wei Zhao, Bao-chun Ma, and Wen-yuan Qiu

Abstract: A "sandwich" type tungstophosphate, $[Zn_4(H_2O)_2(PW_9O_{34})_2]^{10-}$, was used as the efficient and reusable catalyst for alcohol oxidation. The catalyst I of $K_{10}Zn_4(H_2O)_2(PW_9O_{34})_2{\cdot}20H_2O$ and the catalyst II of $[(C_{18}H_{37})_2(CH_3)_2N]_8K_2[Zn_4(H_2O)_2(PW_9O_{34})_2]$ were used to catalyze the oxidation of alcohols in water. High yields of the corresponding carbonyl compounds were obtained. The catalysts were recycled several times without loss in activity.

Key words: polyoxometalate, recyclable, catalyst, oxidation, alcohol.

Résumé : On a utilisé un tungstophosphate de type « sandwich », $[Zn_4(H_2O)_2(PW_9O_{34})_2]^{10-}$ comme catalyseur efficace et réutilisable pour l'oxydation d'alcools. On a utilisé les catalyseurs I, de formule $K_{10}Zn_4(H_2O)_2(PW_9O_{34})_2{\cdot}20H_2O$, et II, de formule $[(C_{18}H_{37})_2(CH_3)_2N]_8K_2$ $[Zn_4(H_2O)_2(PW_9O_{34})_2]$, pour catalyser l'oxydation d'alcools dans l'eau. On a obtenu des rendements élevés des dérivés carbonylés correspondants. Les catalyseurs ont été recyclés plusieurs fois sans perte d'activité.

Mots-clés : polyoxométalate, recyclable, catalyseur, oxydation, alcool.

[Traduit par la Rédaction]

Can. J. Chem. Downloaded from www.nrcresearchpress.com by 80.58.250.72 on 09/16/12
For personal use only.

Introduction

Carbonyl compounds are important precursors of various chemicals.[1–3] The selective oxidation of alcohols to the corresponding carbonyl compounds is an active field of research. Hydrogen peroxide used as the oxidant in liquid-phase oxidation has attracted much attention from researchers from the viewpoint of green chemistry. It overcomes the disadvantage of the toxic traditional inorganic oxidants,[4] and it is much cheaper and safer than other organic peroxides or peracids.[5] Polyoxometalates as effective catalysts for oxidation reactions have attracted wide attention in the past. Most examples of alcohol oxidation with hydrogen peroxide employed polyoxometalates as catalysts and have been reported, e.g., $[(n\text{-}C_8H_{17})_3NCH_3]_3\{PO_4[WO(O_2)_2]_4\}$,[6] $[\pi\text{-}C_5H_5N(CH_2)_{15}CH_3]_3\{PO_4[MoO(O_2)_2]_4\}$,[7] tetrakis(diperoxotungsto)phosphates,[8] lacunary polyoxotungstate of $[\gamma\text{-}SiW_{10}O_{36}(PhPO)_2]^{4-}$,[9] sodium tungstate + quaternaryammoniumhydrogen sulfate,[10] $[PW_{11}O_{39}]^{7-}$,[11] $[NaP_5W_{30}O_{110}]^{14-}$,[12] and so on. However, in these catalytic systems, the use of chlorocarbon poisonous solvents or the difficult recovery and reuse of those catalysts has restricted their wide applications in industrial and laboratorial synthesis.

From the viewpoint of green chemistry, water as an excellent solvent used in the catalytic oxidation of alcohols has received much attention recently. Although a number of methods have been developed,[13–19] the search for effective, new, environmentally benign, and reusable procedures for alcohol oxidation still remains an important challenge.

To the best of our knowledge, the "sandwich" type tungstophosphate, $[Zn_4(H_2O)_2(PW_9O_{34})_2]^{10-}$, has not been reported on the catalytic activity for the oxidation of alcohols in water. We report here two new catalytic systems for alcohol oxidation using it as a recyclable and active catalyst with hydrogen peroxide in water. (*i*) The potassium of the tungstophosphate ($K_{10}Zn_4(H_2O)_2(PW_9O_{34})_2{\cdot}20H_2O$) was used to oxidize several alcohols in water with hydrogen peroxide. The catalyst was reused for the next cycle from the organic product by separation of the aqueous phase. There was no discernable loss in activity and selectivity even after 10 cycles. (*ii*) High yields of ketones were obtained in the oxidation of secondary alcohols in water using $[(C_{18}H_{37})_2(CH_3)_2N]_8K_2[Zn_4(H_2O)_2(PW_9O_{34})_2]$. The catalyst was separated from the reaction mixture by adding diethyl ether to the system after the reaction. Comparing previous reports, there are some advantages in using our system: (*i*) water (a green solvent) was used as the solvent in the oxidation, (*ii*) the active catalysts could be easily reused, and (*iii*) some solid alcohols like DL-menthol and benzhydrol were

Received 6 April 2010. Accepted 24 September 2010. Published on the NRC Research Press Web site at canjchem.nrc.ca on 22 December 2010.

Y. Ding.[1] Lanzhou University, College of Chemistry and Chemical Engineering, Lanzhou University, Lanzhou 730000, China, Lanzhou 730000, China.
W. Zhao, B.-c. Ma, and W.-y. Qiu. State Key Laboratory of Applied Organic Chemistry, College of Chemistry and Chemical Engineering, Lanzhou University, Lanzhou 730000, China.

[1]Corresponding author (e-mail: dingyong1@lzu.edu.cn).

also successfully oxidized with excellent yields in our catalytic system.

Experimental

Reagents

All chemicals were analytical grade, commercially available, and used without further purification unless otherwise stated.

Preparation of catalysts

The potassium of the sandwich type tungstophosphate, $[Zn_4(H_2O)_2(PW_9O_{34})_2]^{10-}$ (catalyst I), was synthesized by the procedure reported in ref. 20. The catalyst II of $[(C_{18}H_{37})_2(CH_3)_2N]_8K_2[Zn_4(H_2O)_2(PW_9O_{34})_2]$ was obtained from $K_{10}Zn_4(H_2O)_2(PW_9O_{34})_2{\cdot}20H_2O$ by the following procedure: 0.9 g of $K_{10}Zn_4(H_2O)_2(PW_9O_{34})_2{\cdot}20H_2O$ was dissolved in 55 mL of water. To this solution, 0.9 g of dioctadecyl dimethyl ammonium chloride dissolved in 10 mL of *tert*-butyl alcohol was added slowly. The mixture was stirred vigorously for 4 h at 40 °C. A white solid was filtered off and then washed with an excess amount of water. The yield was 97%. Anal. calcd. for $[(C_{18}H_{37})_2(CH_3)_2N]_8K_2[Zn_4(H_2O)_2(PW_9O_{34})_2]$: C 39.51, H 6.97, N 1.21, P 0.67, W 35.84, Zn 2.82; found: C 40.68, H 6.98, N 1.13, P 0.60, W 35.23, Zn 2.74.

Characterization techniques

Infrared spectra were recorded on a Nicolet FTIR-360 FTIR spectrometer. The catalysts were measured using 2%–4% (*w*/*w*) KBr pellets prepared by manual grinding. ^{31}P MAS NMR spectra were recorded at 9.4 T on a Bruker Avance-400 wide bore spectrometer. GC analyses were performed on Shimadzu GC-9AM with a flame ionization detector equipped with a FFAP capillary. Mass spectra were recorded on a Finnigan Trace DSQ (Thermo Electron Corporation) at an ionization voltage of 70 eV and equipped with a DB-5 capillary column. Chemical elemental analysis of the catalysts was done on an ICP-atomic emission spectrometer (IRIS ER/S), and C, H, and N contents were measured on a German Elementar Vario EL spectrometer.

Catalytic reaction

The oxidation was carried out in two procedures. Procedure A: catalyst I of $K_{10}Zn_4(H_2O)_2(PW_9O_{34})_2{\cdot}20H_2O$ (9 μmol), water (3 mL), substrate (1 mmol), and H_2O_2 (5 mmol, 30% aq) were added to the reaction flask at 363 K. When the reaction was over, the organic products were separated from the aqueous phase by extraction. Then, readdition of alcohols (1 mmol) and H_2O_2 (30% aq) to the aqueous phase containing the catalyst were carried out for the next oxidation. Procedure B: catalyst II of $[(C_{18}H_{37})_2(CH_3)_2N]_8K_2[Zn_4(H_2O)_2(PW_9O_{34})_2]$ (18 μmol), substrate (4 mmol), and H_2O_2 (20 mmol, 30% aq) were added to the reaction flask. The reaction was carried out at 363 K. When the reaction was over, the catalyst precipitated with cooling and was collected completely from the solution by adding diethyl ether to the system. Assignments of products were made by comparison with authentic samples. Selected samples were also analyzed by GC–MS (Finnigan Trace DSQ), and some isolated products were characterized by NMR.

Results and discussion

Table 1 summarizes the catalytic oxidation of various alcohols with 30% H_2O_2 by catalyst I and II in procedures A and B, respectively. High yields of ketones were obtained in the oxidation of cyclohexanol and cyclopentanol in both procedures. For DL-menthol, a low yield of 8% was detected using procedure A after 10 h. However, a high yield of menthone (97%) was obtained using procedure B after 6 h. This difference should be attributed to whether the catalyst could be in good contact with the substrates during the oxidation. In procedure A, the poor water solubility of DL-menthol resulted in the substrate not being in good contact with the catalyst dissolving in water. But in procedure B, the cation of dioctadecyl dimethyl ammonium promoted the contact between the aqueous phase and the substrate. So, there were obvious differences between procedures A and B during the oxidation of these hydrophobic alcohols. This phenomenon was also presented in the oxidation of linear alcohols. For the oxidation of *sec*-butyl alcohol, 2-pentanol, and 2-octanol, the reaction time in procedure B was shorter than that in procedure A, but the activity of catalyst II in procedure B was much higher than that of catalyst I in procedure A. This was especially true for 2-octanol; the yield of 2-octanone in procedure A was only 39% in 10 h, but a high yield of 99% was obtained in procedure B after 6 h. Even so, procedure A based on catalyst I is actually an active catalytic system for most of the substrates listed in Table 1. Benzhydrol and 1-phenylethanol were oxidized to their corresponding ketones with high yields using procedure A, producing similar results with procedure B. For a more active substrate (1-phenylethanol), a two molar excess of H_2O_2 using catalyst I in water was sufficient (not listed here). Interestingly, catalyst I was also active for the primary alcohol of benzyl alcohol, and the products of benzaldehyde and benzoic acid were obtained, respectively, in high yields by controlling the amount of H_2O_2 in the system. Benzaldehyde is a very important chemical that has widespread applications in the fields of flavors, odorants, and pharmaceutical intermediates.[21] Therefore, we tried to get benzaldehyde from the oxidation of benzyl alcohol in our system. When the ratio of H_2O_2–substrate was 1:2, benzaldehyde as the sole product with a 94% yield was obtained using catalyst I in water. Increasing the amount of hydrogen peroxide to a molar excess five times greater than the substrate, the conversion of benzyl alcohol reached up to 100%, but benzoic acid as the main product was obtained with 93% selectivity. The results indicated that increasing the amount of hydrogen peroxide enhanced the activity of oxidation, but the excessive oxidant would also bring in deep oxidation.

$K_{10}Zn_4(H_2O)_2(PW_9O_{34})_2{\cdot}20H_2O$ is a "water-soluble" catalyst, and it effectively catalyzes the oxidation of alcohols in water. After reaction, the organic products were separated from the aqueous phase by extraction. The aqueous phase containing the catalyst could be kept to do the next oxidation. The catalytic results in the oxidation of cyclohexanol on catalyst I for different cycles are shown in Fig. 1. It can be seen that the activity of the reused catalyst did not

Can. J. Chem. Downloaded from www.nrcresearchpress.com by 80.58.250.72 on 09/16/12
For personal use only.

Can. J. Chem. Downloaded from www.nrcresearchpress.com by 80.58.250.72 on 09/16/12
For personal use only.

Table 1. Oxidation of various alcohols catalyzed by $[Zn_4(H_2O)_2(PW_9O_{34})_2]^{10-}$ with H_2O_2.

Entry	Substrate	Product	Procedure	Time (h)	Yield (mol%)	Selectivity (mol%)
1	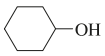		A	6	99	99
2	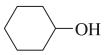		B	6	99	99
3	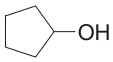		A	8	90	99
4	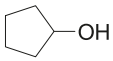		B	8	99	99
5			A	10	8	98
6			B	6	97	98
7			A	9	97	99
8			B	5	98	99
9	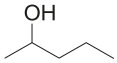	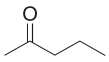	A	10	88	99
10	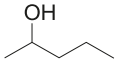	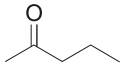	B	5	98	99
11	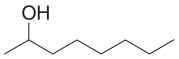	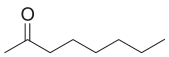	A	10	39	99
12	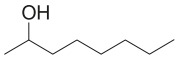	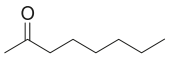	B	6	99	99
13			A	3	99	99
14			B	3	99	99
15	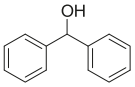	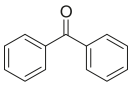	A	8	99	99
16	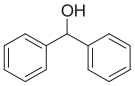	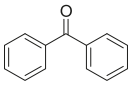	B	6	99	99
17	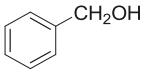	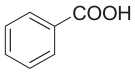	A	7	93	93
18[a]	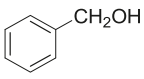	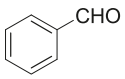	A	8	94	99

Note: Reaction conditions: Procedure A: 9 μmol catalyst I; 3 mL water; 1 mmol alcohol; 5 mmol (30 % aq) H_2O_2. Procedure B: 18 μmol catalyst II; 4 mmol alcohol; 20 mmol (30 % aq) H_2O_2; reaction temperature: 90 °C. The selectivity was based on ketone, aldehyde, or acid.
[a] 9 μmol catalyst I; 3 ml water; 2 mmol alcohol; 1 mmol (30 % aq) H_2O_2, the yield was based on H_2O_2; the selectivity was based on benzaldehyde.

change. Even after 10 consecutive cycles of the reaction, a 97% yield of the cyclohexanone with 99% selectivity was still kept in this catalytic system, indicating that this system is a robust and reusable oxidation system.

To evaluate the reusable property of catalyst II, the oxidation system in procedure B was investigated. The countercation of dioctadecyl dimethyl ammonium made the catalyst disperse in the mixture to form an emulsion with heating. After the reaction finished with the temperature dropping, the system changed to turbid. Then, some diethyl ether was added to the system to precipitate the catalyst completely. The catalyst was recovered by centrifugation and used for the next cycle. Table 2 shows the oxidation of 2-octanol using procedure B for different cycles. A yield of 98% was

Can. J. Chem. Downloaded from www.nrcresearchpress.com by 80.58.250.72 on 09/16/12
For personal use only.

Fig. 1. Oxidation of cyclohexanol by catalyst I in procedure A for different cycles. Reaction conditions were similar to that in Table 1.

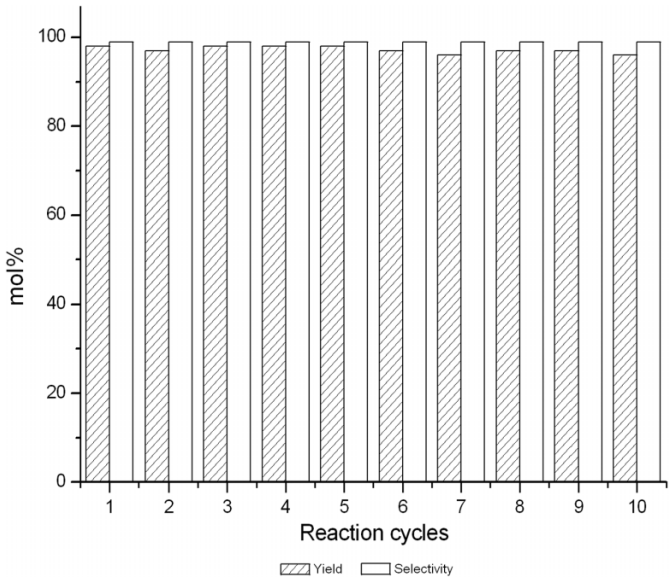

Table 2. Oxidation of 2-octanol by catalyst II for different cycles.

Catalyst	Yield (mol%)	Selectivity (mol%)
Fresh	98	99
Cycle 1	98	99
Cycle 2	97	99
Cycle 3	98	99

Note: Reaction conditions were the same as for procedure B.

Fig. 2. IR spectra of the two catalysts before and after oxidation reaction: (*a*) fresh catalyst I, (*b*) used catalyst I, (*c*) fresh catalyst II, and (*d*) used catalyst II.

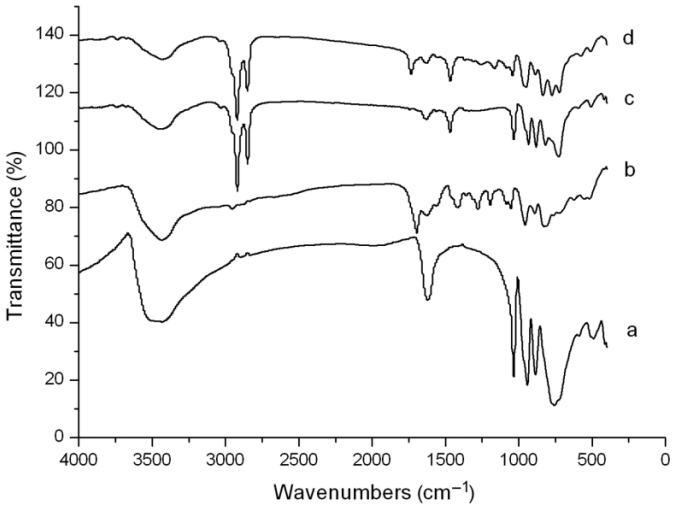

kept after three cycles, indicating that this catalytic system based on catalyst II is also a recyclable oxidation system.

The fresh catalysts and the used ones were characterized with FTIR spectra. As shown in Fig. 2, the IR spectrum of

Fig. 3. ^{31}P MAS NMR spectra of the two catalysts before and after an oxidation reaction: (*a*) fresh catalyst I, (*b*) used catalyst I, (*c*) fresh catalyst II, and (*d*) used catalyst II.

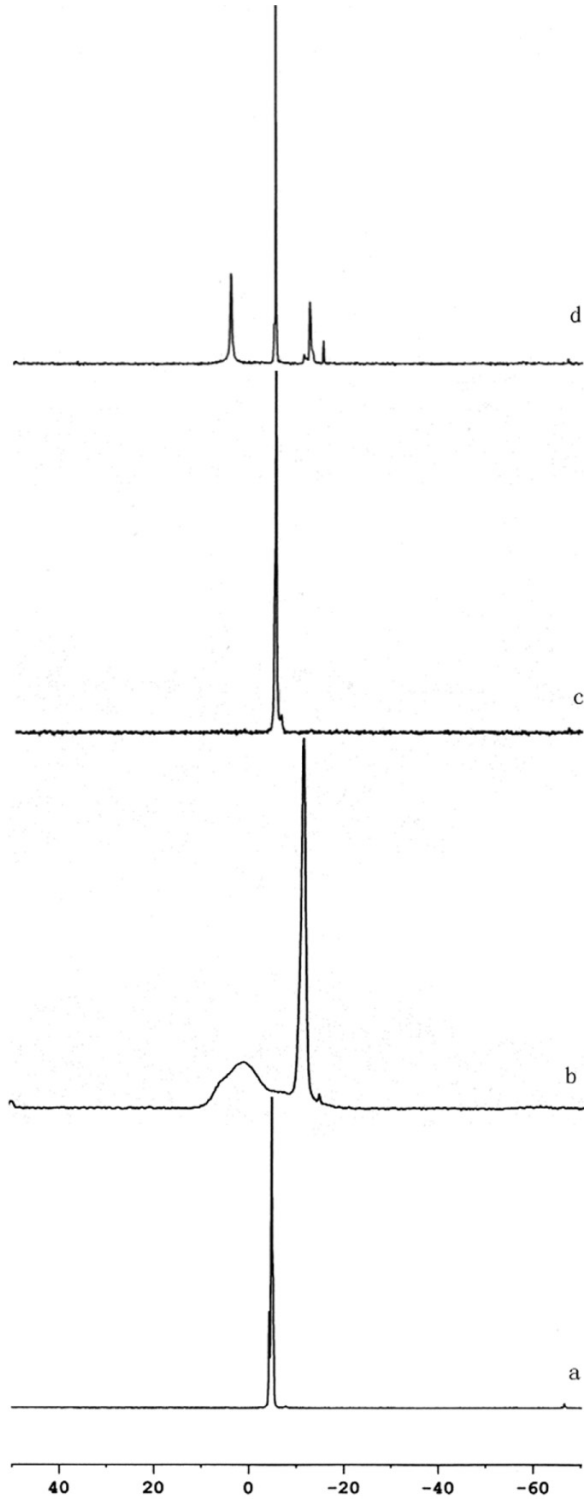

the fresh catalyst $K_{10}Zn_4(H_2O)_2(PW_9O_{34})_2{\cdot}20H_2O$ (Fig. 2*a*) exhibited characteristic peaks at 1034, 942, 886, and 756 cm^{-1} and were similar to the reference reports.[20] The single band at ~1034 cm^{-1}, near the P–O band position (1080 cm^{-1}) of $[PW_{12}O_{40}]^{3-}$, suggests that significant restoration of tetrahedral symmetry to the phosphate group has

Can. J. Chem. Downloaded from www.nrcresearchpress.com by 80.58.250.72 on 09/16/12
For personal use only.

occurred on metal substitution. There were obvious differences between the IR spectra of the fresh catalyst I and the used one. Several peaks were moved to new positions at 1054, 955, 889, 831, and 762 cm^{-1}, indicating that the structure of the catalyst has changed. It was not surprising that it could be ascribed to the recovery method of the catalyst. There have been several papers[16,22] that reported that the alteration of polyoxotungstate catalyst in the presence of H_2O_2 followed by the recovery of the initial structure after evaporation of solvents has always taken place, and the change of the structures cannot be ruled out. Considering the activity of the used catalyst, the fresh catalyst of $K_{10}Zn_4(H_2O)_2(PW_9O_{34})_2 \cdot 20H_2O$ seems to act as a precatalyst, which then maintains the catalytic activity during the later cycles. The IR spectra of the fresh catalyst II and the used one are also shown in Fig. 2; the peaks at 2919 and 2850 cm^{-1} were attributed to the C–H bonds of the quaternary ammonium cation of catalyst II. The peaks at 1033, 933, and 881 cm^{-1} were similar to that of catalyst I. Those revealed that catalyst II was synthesized containing a sandwich type tungstophosphate joined with the quaternary ammonium cation. The IR spectrum of the used catalyst II (Fig. 2*d*) was similar to the fresh one (Fig. 2*c*) except that some intensities of the peaks changed. There were no obvious changes between the fresh catalyst II and the used one.

This phenomenon was consistent with the ^{31}P MAS NMR characterization of the catalysts. As shown in Fig. 3, the strong peak at –4.7 ppm in Fig. 3*a* could be attributed to the sandwich type tungstophosphate structure of $[Zn_4(H_2O)_2(PW_9O_{34})_2]^{10-}$, which was very different from the structure of the keggin polytungstophosphate of $[PW_{12}O_{40}]^{3-}$ at about –15.8 ppm.[23,24] There were obvious changes shown in Fig. 3*b* of the used catalyst I; new peaks at 1.0 and –11.9 ppm appeared, which might be attributed to other keggin structures of polytungstophosphate. The structure of the catalyst has changed during the recovery course by evaporation of H_2O_2 aqueous solution. The ^{31}P MAS NMR of the fresh catalyst II kept the original structure of $[Zn_4(H_2O)_2(PW_9O_{34})_2]^{10-}$ (shown in Fig. 3*c*) at –5.0 ppm. After oxidation, the main species was also the sandwich type structure. Other peaks at 4.3, –12.4, and –15.3 ppm should be different kinds of polytungstophosphate species, which were obtained during the reaction with hydrogen peroxide. The original structure of $[Zn_4(H_2O)_2(PW_9O_{34})_2]^{10-}$ that could be kept in the used catalyst II might be attributed to the solvent precipitation recovery method of the catalyst. In addition, the countercation of the catalyst was also an important factor in this behavior. The countercation of catalyst II could prevent the change of the catalyst during the reaction, and the different amount of water in the reaction conditions might also play an important role.

Conclusions

In summary, we have demonstrated two new active and recyclable catalytic systems based on a sandwich type tungstophosphate, $[Zn_4(H_2O)_2(PW_9O_{34})_2]^{10-}$, for alcohol oxidation with hydrogen peroxide in water. Secondary alcohols were selectively oxidized to the corresponding ketones with high yields. Benzyl alcohol was converted to benzaldehyde at a high conversion rate and selectivity by controlling the amount of H_2O_2. The catalysts were recycled several times without an obvious loss in activity. These catalytic systems are environmentally friendly and practical systems for alcohol oxidation.

Acknowledgements

This work was financially supported by the National Natural Science Foundation of China (Grant No. 20803032). We gratefully thank Professor Wei Wang for the measurement of solid-state NMR.

References

(1) Fey, T.; Fischer, H.; Bachmann, S.; Albert, K.; Bolm, C. *J. Org. Chem.* **2001**, *66* (24), 8154. doi:10.1021/jo010535q.
(2) Sheldon, R. A.; Arends, I. W. C. E.; Dijksman, A. *Catal. Today* **2000**, *57* (1–2), 157. doi:10.1016/S0920-5861(99)00317-X.
(3) Singh, R. P.; Subbarao, H. N.; Dev, S. *Tetrahedron* **1979**, *35* (14), 1789. doi:10.1016/0040-4020(79)88010-2.
(4) Zhang, S. J.; Zhao, G. D.; Gao, S.; Xi, Z. W.; Xu, J. *J. Mol. Catal. Chem.* **2008**, *289* (1–2), 22. doi:10.1016/j.molcata.2008.04.004.
(5) Clark, J. H. *Green Chem.* **1999**, *1* (1), 1. doi:10.1039/a807961g.
(6) Venturello, C.; Gambaro, M. *J. Org. Chem.* **1991**, *56* (20), 5924. doi:10.1021/jo00020a040.
(7) Ishii, Y.; Yamawaki, K.; Yoshida, T.; Ura, T.; Ogawa, M. *J. Org. Chem.* **1987**, *52* (9), 1868. doi:10.1021/jo00385a042.
(8) Ishii, Y.; Tanaka, H.; Nishiyama, Y. *Chem. Lett.* **1994**, *23* (1), 1. doi:10.1246/cl.1994.1.
(9) Carraro, M.; Sandei, L.; Sartorel, A.; Scorrano, G.; Bonchio, M. *Org. Lett.* **2006**, *8* (17), 3671. doi:10.1021/ol061197o.
(10) Sato, K.; Hyodo, M.; Aoki, M.; Zheng, X. Q.; Noyori, R. *Tetrahedron* **2001**, *57* (13), 2469. doi:10.1016/S0040-4020(01)00068-0.
(11) Weng, Z. H.; Wang, J. Y.; Jian, X. G. *Catal. Commun.* **2008**, *9* (8), 1688. doi:10.1016/j.catcom.2007.11.017.
(12) Bamoharram, F. F.; Roshani, M.; Heravi, M. M.; Safaie, S. *Phosphorus Sulfur Silicon Relat. Elem.* **2006**, *181* (12), 2833. doi:10.1080/10426500600865004.
(13) ten Brink, G.-J.; Arends, I. W. C. E.; Shelden, R. A. *Science* **2000**, *287* (5458), 1636. doi:10.1126/science.287.5458.1636.
(14) ten Brink, G.-J.; Arends, I. W. C. E.; Shelden, R. A. *Adv. Synth. Catal.* **2002**, *344* (3–4), 355. doi:10.1002/1615-4169(200206)344:3/4<355::AID-ADSC355>3.0.CO;2-S.
(15) Sloboda-Rozner, D.; Alsters, P. L.; Neumann, R. *J. Am. Chem. Soc.* **2003**, *125* (18), 5280. doi:10.1021/ja0344821.
(16) Neumann, R.; Gara, M. *J. Am. Chem. Soc.* **1995**, *117* (18), 5066. doi:10.1021/ja00123a008.
(17) Ding, Y.; Zhao, W.; Zhang, Y. S.; Ma, B. C.; Qiu, W. Y. *React. Kinet. Mech. Catal.* [Online early access]. **2010**. doi:10.1007/s11144-010-0241-8.
(18) Ma, B.; Zhang, Y.; Ding, Y.; Zhao, W. *Catal. Commun.* **2010**, *11* (9), 853. doi:10.1016/j.catcom.2010.02.022.
(19) Zhao, W.; Zhang, Y. S.; Ma, B. C.; Ding, Y.; Qiu, W. Y. *Catal. Commun.* **2010**, *11* (6), 527. doi:10.1016/j.catcom.2009.12.010.
(20) Finke, R. G.; Droege, M. W.; Domaille, P. J. *Inorg. Chem.* **1987**, *26* (23), 3886. doi:10.1021/ic00270a014.
(21) *Ullmann's Encyclopedia of Industrial Chemistry,* 5th ed.; VCH Publishers: Weinheim, 1985; Vol. A3, p 469.
(22) Santos, I. C. M. S.; Simões, M. M. Q.; Pereira, M. M. M. S.;

Martins, R. R. L.; Neves, M. G. P. M. S.; Cavaleiro, J. A. S.; Cavaleiro, A. M. V. *J. Mol. Catal. Chem.* **2003**, *195* (1–2), 253. doi:10.1016/S1381-1169(02)00582-4.

(23) Ding, Y.; Zhao, W.; Hua, H.; Ma, B. *Green Chem.* **2008**, *10* (9), 910. doi:10.1039/b808404a.

(24) Zhao, W.; Ma, B. C.; Hua, H.; Zhang, Y. S.; Ding, Y. *Catal. Commun.* **2008**, *9* (14), 2455. doi:10.1016/j.catcom.2008.06.013.

Can. J. Chem. Downloaded from www.nrcresearchpress.com by 80.58.250.72 on 09/16/12
For personal use only.

Gas-phase reaction chemistry of 1,1-dimethyl-1-silacyclobutane as a precursor gas in the hot-wire chemical vapor deposition process—Formation of tetramethylsilane and trimethylsilane

L. Tong and Y.J. Shi

Can. J. Chem. Downloaded from www.nrcresearchpress.com by 80.58.250.72 on 09/16/12
For personal use only.

Abstract: The secondary gas-phase reaction products of 1,1-dimethyl-1-silacyclobutane (DMSCB) and its isotopomer, 1,1-di(perdeuteratedmethyl)-1-silacyclobutane (DMSCB-d_6), in a hot-wire chemical vapour deposition reactor were investigated using vacuum UV laser single photon ionization with time-of-flight mass spectrometry. Dimethylsilylene, one of the primary decomposition products, undergoes π-type addition across the double and triple C–C bond and an insertion reaction into the Si–H bond. A short-chain reaction mechanism, initiated by methyl radicals produced in the primary decomposition, is found to exist for both the source DMSCB molecule and its stable secondary products. The formation of tetramethylsilane and trimethylsilane via the reaction of 1,1-dimethylsilene with a methyl radical and an H_2 molecule, respectively, has been demonstrated. These are two new reaction channels involving 1,1-dimethylsilene in secondary gas-phase reactions.

Key words: 1,1-dimethyl-1-silacyclobutane, gas-phase reaction chemistry, hot-wire chemical vapour deposition, vacuum UV laser single photon ionization mass spectrometry, silene, silylene.

Résumé : Faisant appel à la spectrométrie de masse en temps de vol avec ionisation par un photon unique d'un laser UV à vide, on a étudié la nature des produits secondaires de la réaction du 1,1-diméthyl-1-silacyclobutane (DMSCB) et de son isotopomère, le 1,1-di(perdeutérométhyl)-1-silacyclobutane (DMSCB-d_6) dans un réacteur à dépôt de vapeur chimique sur un filament chauffé. Le diméthylsilylène, un des produits de décomposition primaire, subit une addition de type-π sur les doubles et triples liaisons C–C et une réaction d'insertion dans la liaison Si–H. On a trouvé qu'il existe un mécanisme réactionnel à courte chaîne, initié par les radicaux méthyles produits dans la décomposition primaire, tant pour la molécule source DMSCB que pour ses produits secondaires stables. On a démontré qu'il y a formation de tétraméthylsilane et de triméthylsilane par le biais de la réaction du 1,1-diméthylsilène avec respectivement un radical méthyle et une molécule de H_2. Ce sont deux voies réactionnelles nouvelles impliquant le 1,1-diméthylsilène dans des réactions secondaires en phase gazeuse.

Mots-clés : 1,1-diméthyl-1-silacyclobutane, chimie d'une réaction en phase gazeuse, dépôt de vapeur chimique sur un filament chauffé, spectrométrie de masse avec ionisation par un photon unique d'un laser UV à vide, silène, silylène.

Introduction

1,1-Dimethyl-1-silacyclobutane (DMSCB) has been used as a single-source precursor to deposit SiC thin films by low-pressure chemical vapour deposition (LP-CVD)[1] and hot-wire CVD (HW-CVD)[2]. In this molecule, both Si–H bonds in the parent silacyclobutane are substituted by Si–methyl connections. The milestone experiment done by Flowers and Gusel'nikov[3,4] in 1967 demonstrated that pyrolysis of DMSCB produced a clean unimolecular decomposition to ethene and dimethylsilene that can either be trapped or allowed to dimerize to 1,1,3,3-tetramethyl-1,3-disilacyclobutane (TMDSCB). The pyrolysis[5–11] and photolysis[12–14] of DMSCB have since been widely studied. However, the secondary gas-phase reactions, especially those in the HW-CVD process, are not yet well understood. Zaharias et al.[2] showed that Si and CH_3 radicals were produced in the primary gas-phase decomposition of DMSCB in HW-CVD. Our group has recently demonstrated that aside from the decomposition route to produce ethene and 1,1-dimethylsilene found in the pyrolysis of DMSCB, two other decomposition channels exist to form methyl radicals via the Si–CH_3 bond cleavage and the propene–dimethylsilylene species.[15] (Equations [1]–[3]: primary decomposition pathways of DMSCB on a heated W filament).

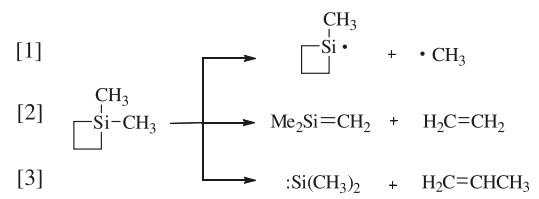

Received 20 June 2010. Accepted 4 October 2010. Published on the NRC Research Press Web site at canjchem.nrc.ca on 17 December 2010.

L. Tong and Y.J. Shi.[1] Department of Chemistry, University of Calgary, 2500 University Drive NW, Calgary, AB T2N 1N4, Canada.

[1]Corresponding author (e-mail: shiy@ucalgary.ca).

Can. J. Chem. Downloaded from www.nrcresearchpress.com by 80.58.250.72 on 09/16/12
For personal use only.

We have shown that both ethene and propene are formed through a stepwise diradical mechanism via the cleavage of a ring C–C and ring Si–C bond, respectively. The formation of ethene is favoured over that of propene. When DMSCB was contained in a HW-CVD reactor with a partial pressure of 0.48 torr (1 torr = 133.3224 Pa), the dominant product detected came from TMDSCB, which resulted from the dimerization of the 1,1-dimethylsilene formed from direct hot-filament decomposition. The other two products detected were 1,1,3-trimethyl-1,3-disilacyclobutane (TriMDSCB) and 1,3-dimethyl-1,3-disilacyclobutane (DMDSCB), which indicates that the isomerization between dimethylsilylene and methylsilene occurs in the process. However, the secondary gas-phase reactions involving the methyl radicals were missing. In addition, other reactions involving the reactive silene and silylene species than the cycloaddition of silene were not studied. In this work, we have extended our previous work on the gas-phase reaction chemistry of DMSCB in a HW-CVD process to study the secondary gas-phase reaction products involving all reactive species and aim to provide a complete picture of the reaction chemistry. The products from secondary gas-phase reactions when using DMSCB as a source gas in a HW-CVD reactor were probed by nonresonant single-photon ionization (SPI) with a 10.5 eV vacuum UV (VUV) wavelength of 118 nm coupled with time-of-flight mass spectrometry. This technique ionizes all chemical species with an ionization potential <10.5 eV and minimizes the dissociative fragmentation if the appearance potential is >10.5 eV.[16–18] This proves to be advantageous in diagnosing the reaction products in a complex system, such as those characteristic of combustion,[19] pyrolysis,[20,21] and CVD[22,23] processes. An isotopomer of DMSCB, 1,1-di(perdeuteromethyl)-1-silacyclobutane (DMSCB-d_6), was also synthesized in this work, and similar experiments with it replacing DMSCB help to understand the details of the gas-phase reaction chemistry.

Experimental details

The experimental setup used to record the VUV laser SPI TOF mass spectra of the secondary gas-phase reaction products from a HW-CVD reactor has been previously described in detail.[23,24] Briefly, the reactor is a cylindrical chamber housing a resistively heated tungsten filament (10 cm in length and 0.5 mm in diameter), a sample inlet tubing, and an IR-grade window for filament temperature measurement using a two-colour pyrometer (CHINO Works America Inc., Torrance, California). The reactor is incorporated through a 0.15 mm diameter pinhole to the ionization chamber housing a linear TOF mass spectrometer (R. M. Jordan Co., Inc., Grass Valley, California). The total pressure in the reactor was kept at 12 torr using a mass flow controller (type 1179 A; MKS Instruments, Andover, Maryland) and was monitored by a capacitance manometer (MKS Baratron, type 626 A). This gives a partial pressure of 0.48 torr when using a 4% DMSCB (or DMSCB-d_6) in He mixture. At this pressure, collision-free conditions were not maintained; this allowed for the detection of secondary gas-phase reaction products from the reactor. The 118 nm VUV laser radiation (10.5 eV) used to ionize the chemical species sampled from the reactor was produced in a nonresonant third-harmonic generation process of the 355 nm UV output from a Nd:YAG laser (LAB-170-10; Spectra-Physics, Santa Clara, California) in a gas cell containing 210 torr of a phase-matched 10:1 Ar–Xe gas mixture. Signals from the microchannel plate (MCP) detector in the TOF-MS were preamplified, averaged over 512 laser pulses, and saved into a computer for analysis. In this work, mass spectra for filament temperatures ranging from 900 to 2000 °C were recorded. For each temperature, a mass spectrum was collected every 5 min for 1 h.

DMSCB (≥97%; Sigma-Aldrich, St. Louis, Missouri) was used without further purification, and its purity was verified in situ by our TOF-MS. DMSCB-d_6 was synthesized by reacting 1,1-dichloro-1-silacyclobutane with CD_3MgI (99% atom% D; Sigma-Aldrich) based on an established method.[8] Its structure and purity (>98%) were checked by NMR and GC–MS. The isotope purity of DMSCB-d_6 (99% atom% D) was confirmed by our TOF-MS. The DMSCB or DMSCB-d_6 in He mixtures were prepared by entraining the room-temperature vapour of either compound in He (99.999%; Praxair) after degassing the liquid sample using several cycles of freeze–pump–thaw.

Results and discussion

Figures 1a and 1b show the room-temperature mass spectra of DMSCB and DMCB-d_6, respectively. The parent ion peak at m/z = 100 (base peak) and two fragment ion peaks of $[(CH_3)_2Si{=}CH_2]^{+\bullet}$ at m/z = 72 (78.2% ± 1.7%) and of $[(CH_3)Si(CH_2)_3]^{+\bullet}$ at m/z = 85 (3.8% ± 0.3%) were found to dominate the mass spectrum of DMSCB. The percentage for each fragment ion represents the relative ratio to the base peak. The assignment of the two fragment peaks were confirmed by the mass spectrum of DMSCB-d_6 in Fig. 1b. The isotope peaks of the parent ion and the fragment peak at m/z = 72 ascribed to ^{29}Si, ^{30}Si, and ^{13}C were also observed. It was noted that the isotope peaks of the one at m/z = 85 were not resolved. This is due to the slow dissociation of the parent ion[25] through the Si–CH_3 bond cleavage. From the inset of Fig. 1a, other weak fragment peaks were observed at m/z = 43 ($[CH_3Si]^{+\bullet}$, 0.091% ± 0.009%), 44 ($[(CH_3)HSi]^{+\bullet}$, 0.094% ± 0.006%), 58 ($[(CH_3)_2Si]^{+\bullet}$, 0.042% ± 0.003%), and 59 ($[C_2H_7Si]^{+\bullet}$, 0.20% ± 0.03%). Their corresponding peaks for DMCB-d_6 (inset of Fig. 1b) were observed at m/z = 46, 48, 64, and 65, respectively. The impurity (125 amu) in the synthesized DMSCB-d_6 sample was found to be <1%, which is consistent with the results of the NMR analysis. Figure 2a shows the mass spectra of the 4% DMSCB–He mixture at 12 torr recorded after the filament was turned on for 15 min at different filament temperatures ranging from 900 to 1500 °C. For comparison, the room-temperature mass spectrum is also shown. The intensities of the parent mass peak at m/z = 100 and its two dominant photofragmentation peaks at m/z = 72 and 85 decrease with increasing filament temperatures. This indicates that the DMSCB molecules decompose on the filament and are consumed in the secondary gas-phase reactions in the HW-CVD reactor. The analysis of the intensity ratios of the peaks at m/z = 72 and 85, respectively, to that of the parent molecules at different filament-on times and different filament temperatures found that the ratio of $I(m/z = 72)$:$I(m/z = 100)$

Can. J. Chem. Downloaded from www.nrcresearchpress.com by 80.58.250.72 on 09/16/12
For personal use only.

Fig. 1. Room-temperature mass spectra of (a) 1,1-dimethyl-1-silacyclobutane (DMSCB) and (b) 1,1-di(perdeuteromethyl)-1-silacyclobutane (DMSCB-d_6) recorded with 118 nm vacuum UV (VUV) laser ionization. The insets are expanded mass spectra in the mass region of 10–70 amu.

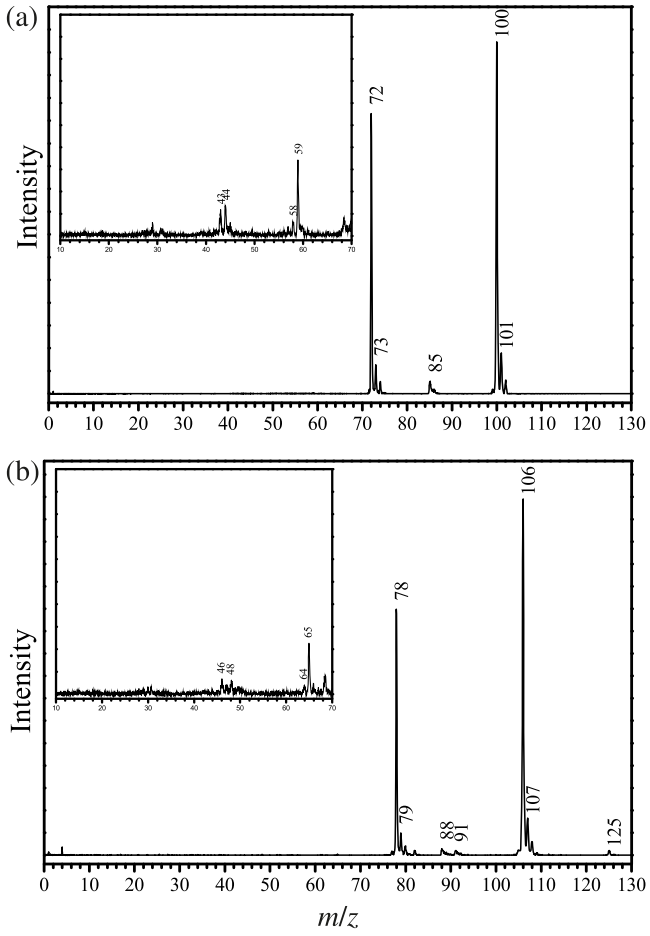

did not change with the filament-on time and filament temperatures, whereas the ratio of $I(m/z = 85)$:$I(m/z = 100)$ when the filament was on was above the room-temperature ratio of 0.038:1. This suggests that the peak intensity at $m/z = 72$ originates only from photofragmentation of the parent DMSCB ions, whereas sources other than the photofragmentation of the DMSCB ion are responsible for the peak intensity at $m/z = 85$. This will be discussed later. When the parent molecules decreased in intensity, new peaks at $m/z = 28$ (ethene), 42 (propene), 116 (DMDSCB), 130 (TriMDSCB), and 144 (TMDSCB) were observed, with the peak at $m/z = 144$ being the most dominant. The formation mechanisms for these dominant new mass peaks have been described in full detail in our previous study.[15] The enlarged mass spectra in three different mass regions are shown in Figs. 2b–2d. It is clear that other mass peaks at $m/z = 58$, 84, 86, 88, 98, 114, 128, 142, 156, 158, 170, 172, 174, 186, 188, 198, 202, 203, 217, 232, and 244 were also observed, although they were not as strong. This study focuses on understanding the formation of these new mass peaks, which originated from the stable products formed in the secondary gas-phase reactions in the HW-CVD reactor.

Reactions involving reactive intermediates silylenes

The decomposition of DMSCB on the hot W filament produced dimethylsilene and dimethylsilylene, as shown in eqs. [2] and [3]. Dimethylsilylene ($:Si(CH_3)_2$) is a very reactive species that once formed, can undergo a variety of reactions. They react with unsaturated alkenes and alkynes such as acetylene, ethene, propene, and propyne produced in the reactor, through π-type addition reactions.[26] Reactions shown in eqs. [4]–[7] produced 1,1-dimethylsilirene (84 amu), 1,1-dimethylsilirane (86 amu), 1,1,2-trimethylsilirene (98 amu), and 1,1,2-trimethylsilirane (100 amu). The first three peaks at m/z = 84, 86, and 98 are shown in Fig. 2b. The 1,1,2-trimethylsilirane (m/z =100) peak overlaps with the parent ion peak of DMSCB.

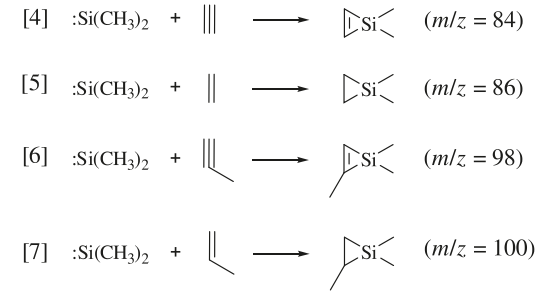

According to our previous study,[15] when using DMSCB-d_6, H–D scrambling for the peaks at m/z = 28 (ethene, C_2H_4) and m/z = 42 (propene, C_3H_6) was observed. Consequently, their complimentary peaks dimethylsilene (SiC_3H_8) and dimethylsilylene (SiC_2H_6) also show the H–D scrambling. The scrambling pattern is summarized in the following. (Equations [8] and [9]: the decomposition of DMSCB-d_6 on a heated W filament).

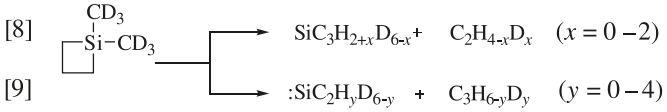

Therefore, the minimum mass shift for the peak at m/z = 84, representing the product from eq. [4], should be 2, and the maximum mass shift for the peak at m/z = 86 from eq. [5] should be 8. Figure 3 shows the mass spectra of the 4% DMSCB-d_6–He mixture recorded at a filament temperature of 1300 °C. It is clear from the expanded mass spectrum for the mass region of 70–170 amu (Fig. 3b) that a group of mass peaks between m/z = 86 and m/z = 98 was observed. As will be discussed later, the peaks from m/z = 95 to m/z = 98 originate from deuterated tetramethylsilane. Similarly, the minimum mass shift for the peak at m/z = 98 from eq. [6] should also be 2, which agrees well with the observation that the next group of peaks starts at m/z = 100. This suggests that π-addition reactions of dimethylsilylene occurred in our experiment. A second type of reaction involving dimethylsilylene is its insertion into the Si–H bond.[27] The DMSCB source molecule and the dominant secondary reaction product (TMDSCB) do not have Si–H bonds in their structures. However, the two other dominant products (DMDSCB (m/z = 116) and TriMDSCB (m/z = 130)) have Si–H bonds in their structures. The reactions of dimethylsilylene with DMDSCB and TriMDSCB (as demonstrated in

Fig. 2. (a) Mass spectra of a 4% 1,1-dimethyl-1-silacyclobutane (DMSCB) – He mixture at 12 torr (1 torr = 133.3224 Pa) at filament temperatures ranging from 900 to 1500 °C. The spectrum at 20 °C was recorded when the filament was off. The enlarged spectra of the mass regions of (b) 0–100 amu, (c) 100–200 amu, and (d) 200–300 amu.

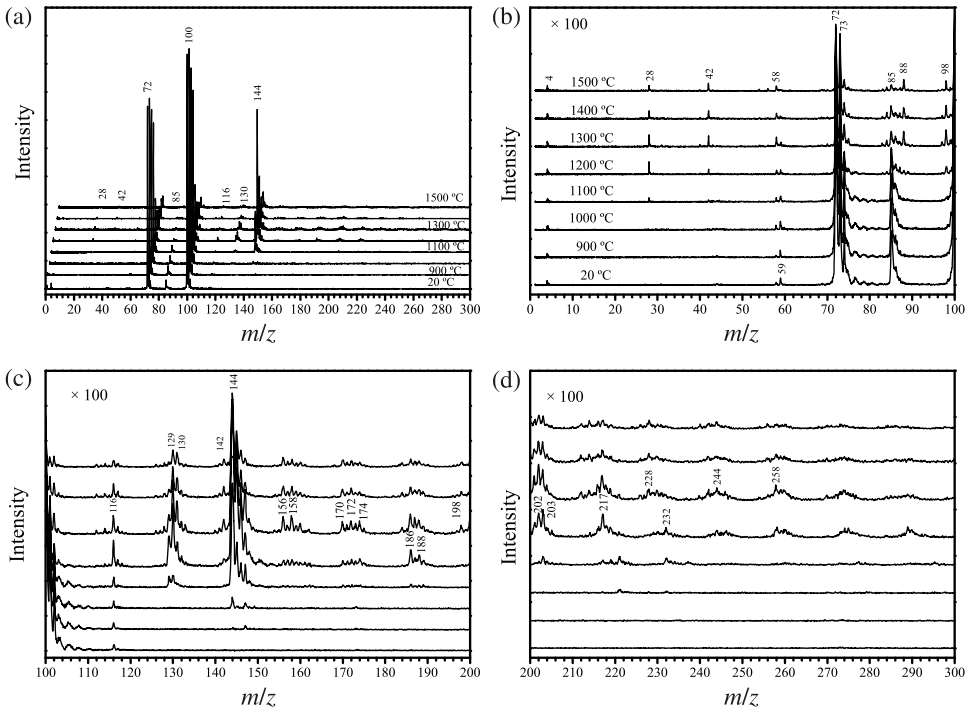

Can. J. Chem. Downloaded from www.nrcresearchpress.com by 80.58.250.72 on 09/16/12
For personal use only.

eqs. [10]–[12]) produced species with masses of 174, 188, and 232 amu. Figures 2c and 2d clearly show that the three peaks were observed in our experiments.

[10] 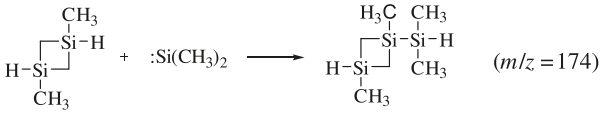

[11] 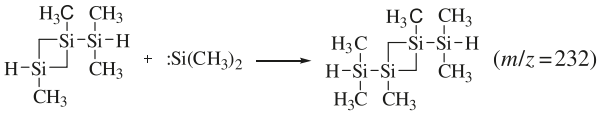

[12] 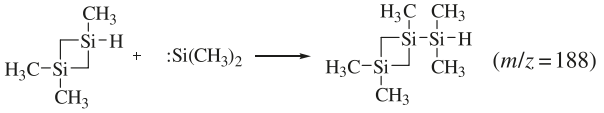

Our previous studies on tetramethylsilane,[24] hexamethylsilane,[28] and TMDSCB[29] demonstrated that a common and dominant photofragmentation pathway upon exposure to the 118 nm VUV radiation is the product of $[M-CH_3]^{+\bullet}$ radical ions. Similarly, the peaks at m/z = 116, 130, 174, 188, and 232 can lose one methyl group upon ionization by VUV radiation. This leads to the formation of various peaks with odd masses at m/z = 101, 115, 159, 173, and 217, all of which are shown in Figs. 2c and 2d. The peak at m/z = 101 overlaps with one of the isotope peaks of the parent molecule DMSCB. The contribution from ^{29}Si and ^{13}C at m/z = 101 amounts to 9.5% of the m/z = 100 peak intensity. However, the peak intensity ratio of m/z = 101 to m/z = 100 when the filament was on was found to be as high as 32.8%. The increase is likely due to the contribution from the photofragmentation of the peak at m/z = 116 (DMDSCB).

Formation of trimethylsilane (TriMS) and tetramethylsilane (TMS) — Reactions involving the reactive intermediate silene

In the experiments with DMSCB in the HW-CVD reactor, a new peak at m/z = 88 was observed starting from 1200 °C, as shown in Fig. 2b. This peak was assigned to TMS. TMS was also observed when using TMDSCB as a source gas,[29] where it was believed to be formed through the reaction between dimethylsilene and methyl radical followed by the addition of H_2 produced in the reactor.[30] In the room-temperature mass spectrum of TMS upon irradiation of the 118 nm VUV laser, the only characteristic photofragment peak was trimethylsilyl ion at m/z = 73 with an intensity four times that of the parent TMS ion.[24] In this work, the peak at m/z = 73 overlaps with one of the isotope peaks of the strong photofragment peak at m/z = 72 from the DMSCB parent ion. The contribution from the ^{29}Si and ^{13}C isotopes to the peak intensity at m/z = 73 amounts to 8.3% of the peak at m/z = 72 when the filament was off. However, the peak intensity ratio of m/z = 73 to m/z = 72 observed with DMSCB when the filament was on increased significantly with filament temperature when $T \geq 1200$ °C, as shown in Fig. 4. The photofragmentation of the formed TMS contributes partially to the peak intensity increase at m/z = 73.

The peak at m/z = 58 is a weak photofragment peak from the parent DMSCB ion; however, it was noted that the intensity of this peak increased with temperature and it sur-

Can. J. Chem. Downloaded from www.nrcresearchpress.com by 80.58.250.72 on 09/16/12
For personal use only.

Fig. 3. (a) Mass spectra of a 4% 1,1-dimethyl-1-silacyclobutane (DMSCB)-d_6 – He mixture at 12 torr (1 torr = 133.3224 Pa) at a filament temperature of 1300 °C. Inset: enlarged mass spectra in the mass regions of 25–70 amu. (b) Enlarged mass spectra in the mass region of 70–170 amu.

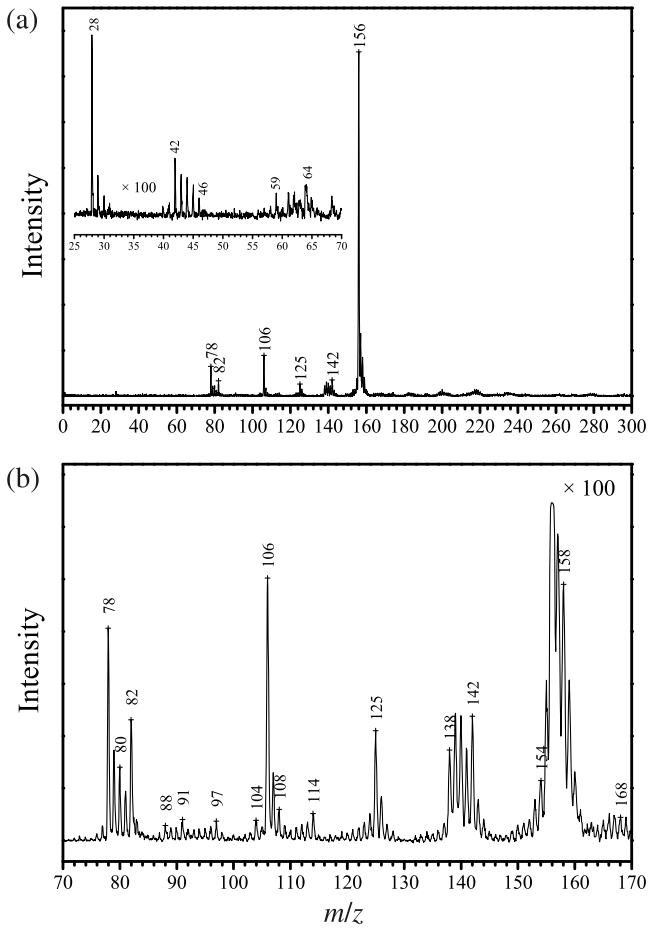

passed that of the peak at m/z = 59 (another photofragment peak from the DMSCB ion) at temperatures >1200 °C. As discussed in our previous study of TMDSCB,[29] 1,1-dimethylsilene can directly react with H_2 to form TriMS.[31] The room-temperature mass spectrum of TriMS when using 118 nm VUV laser ionization is dominated by two fragment peaks at m/z = 58 and 73 with an intensity ratio of 1:2.9. Therefore, the increase in the intensity of the peak at m/z = 58 is due to the formation of TriMS in the reactor and its photofragmentation upon VUV laser ionization. The photofragmentation of TriMS also contributes to the increase in the peak intensity at m/z = 73. Figure 5 shows the net intensity increase of the peak at m/z = 73 excluding the isotope contribution from the peak at m/z = 72 and the intensity contribution assumed from the photofragmentation of TriMS and TMS at 1400 and 1700 °C. It is clear that the intensity increase of the peak at m/z = 73 after the filament was turned on is mainly from the photofragmentation of TriMS and TMS. Similar behaviour was observed for other temperatures at 1300 and 1500–1600 °C. This strongly supports that both TriMS and TMS were produced in our HW-CVD reactor when using DMSCB as a source gas.

Moreover, if the aforementioned formation mechanisms

Fig. 4. The intensity ratio of the mass peak at m/z = 73 to that of the peak at m/z = 72 from a 4% 1,1-dimethyl-1-silacyclobutane (DMSCB) – He mixture at 12 torr (1 torr = 133.3224 Pa) vs filament-on time at different filament temperatures. The ratio at t = –5 min represents that at room temperature.

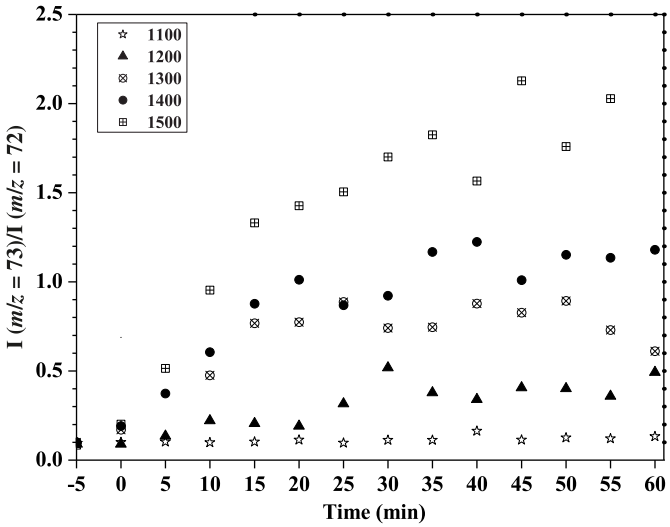

for the peaks at m/z = 58, 73, and 88 with DMSCB stand, a complex H–D scrambling for these peaks with DMSCB-d_6 is expected. As mentioned before, deuterated dimethylsilenes ($SiC_3H_{2+x}D_{6-x}$, x = 0–2) were produced from decomposition of DMSCB-d_6, with $SiC_3H_2D_6$ the most abundant of all[15]. H_2 will be the dominant species among H_2, HD, and D_2 formed via the elimination reaction from ethene, propene, and their isotopomers. Therefore, the deuterated TMS produced when using DMSCB-d_6 should have D atoms ranging from 7 to 10 and it is expected that TMS-d_9 (its formation shown in the following) should be the most abundant.

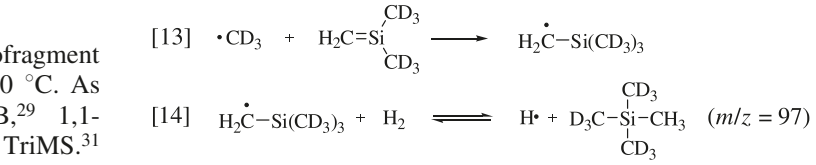

As shown in Fig. 3b, a group of peaks ranging from m/z = 95 to 98 were indeed observed, with the one at m/z = 97 being the most dominant of all. Upon irradiation by 118 nm VUV light, TMS-d_m (m = 7–10) fragments to produce deuterated trimethylsilyl ions (m/z = 77–82). These peaks are visible in Fig. 3b, of which the peak at m/z = 82 appeared to be the strongest. The peaks at m/z = 78–80 overlapped with the dominant photofragment ions (CH_2=$Si(CD_3)_2^{+\bullet}$) from the parent DMSCB-d_6 ion and their isotopes. TMS-d_9, the most abundant one, fragments to produce the peaks at m/z = 82 and 79 by losing one CH_3 and one CD_3 group, respectively. This explains the strong appearance of the peak at m/z = 82. The peak at m/z = 79 overlaps with one of the isotope peaks of the photofragment at m/z = 78 from the DMSCB-d_6 ion. However, after the filament was turned on, the peak intensity ratio of m/z = 79 to m/z = 78 increased with increasing filament temperature, as shown in Fig. 6. The ratio is much greater than the isotope contributions of 8.3%, and the photofragmentation from deuterated TMS ac-

Can. J. Chem. Downloaded from www.nrcresearchpress.com by 80.58.250.72 on 09/16/12
For personal use only.

Fig. 5. The intensity of the peak at m/z = 73 from a 4% 1,1-dimethyl-1-silacyclobutane (DMSCB) – He mixture at 12 torr (1 torr = 133.3224 Pa) vs filament-on time at a filament temperature of (a) 1400 °C and (b) 1700 °C. I73net (□) represents the net increase in the peak intensity at m/z = 73 observed from the experiment excluding the isotope contribution from the peak at m/z = 72 and (○) represents the contribution to the peak intensity from the photofragmentation of TriMS and TMS combined.

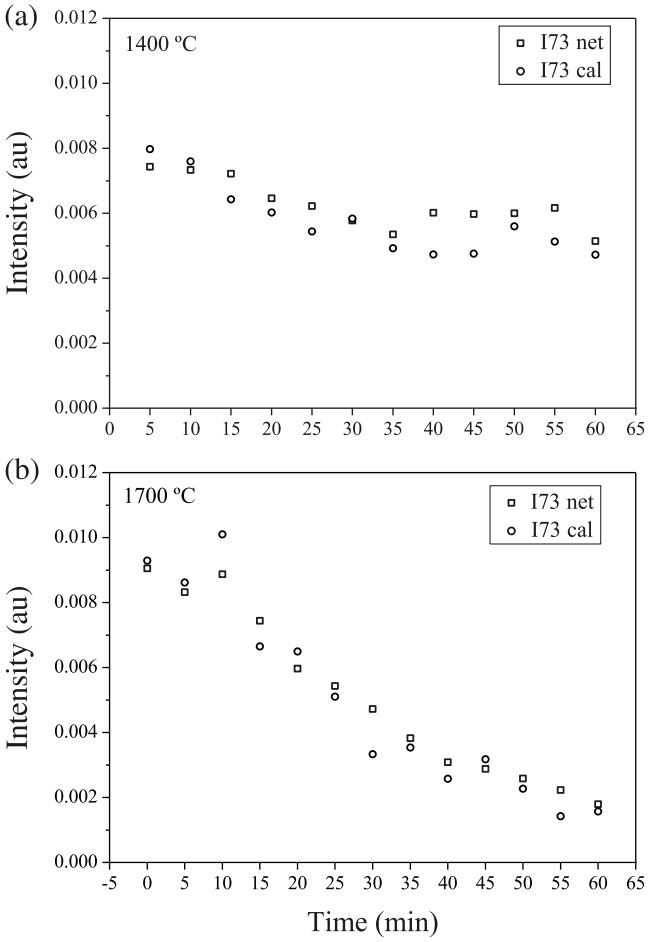

counts for a majority of the increase in the peak intensity at m/z = 79.

One of the characteristic products from secondary reactions when using TMS in the same reactor was found to be ethyltrimethylsilane (TriMES, m/z = 102),[24] which was formed by a biradical combination reaction between methyl and trimethylsilylmethyl originated from H-abstraction reactions. When using DMSCB, this peak overlaps with one of the isotope peaks from the parent DMSCB (m/z = 100). However, the intensity ratio of the peak at m/z = 102 to the peak at m/z = 100 was found to increase with filament-on time and filament temperature. The ratio when the filament was on ranged from 5.6%–64.1%, which is much greater than the expected isotope contribution of 3.7%. Therefore, TriMES contributed to the increased intensity of the peak at m/z = 102 when the filament was turned on. When using DMSCB-d_6, based on the scrambling pattern described before, it is expected that TriMES-d_6 to -d_{12} will be produced, with TriMES-d_{12} being the most abundant of all. In Fig. 3b,

Fig. 6. The intensity ratio of the mass peak at m/z = 79 to the peak at m/z = 78 from a 4% 1,1-dimethyl-1-silacyclobutane (DMSCB-d_6 – He mixture at 12 torr (1 torr = 133.3224 Pa) vs filament-on time at different filament temperatures. The ratio at t = –5 min represents that at room temperature.

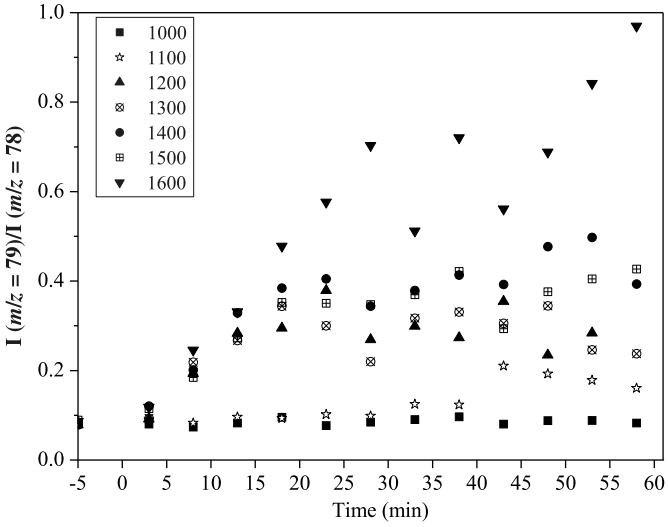

the peaks at m/z = 108–114 are shown. However, it should be noted that the H–D scrambling for the peak at m/z = 100 originating from eq. [7] could produce a mass shift between 2 and 10, contributing to the peaks up to m/z = 110. The peaks from m/z = 111 to 114 are believed to be from TriMES-d_9 to -d_{12}, and the peak at m/z = 114 is indeed the strongest.

Following the same argument for the formation of deuterated TriMS with DMSCB-d_6, the reaction between the dominant dimethylsilene-d_6 and H_2 is shown in eq. [15].

Overall, TriMS-d_n (n = 4–8) with masses ranging from 77 to 81 amu could be produced. These peaks overlap with the photofragmentation peak of TMS-d_m (m = 7–10), which is not conclusive. However, upon VUV photoionization, TriMS-d_n (n = 4–8) could lose H (D) or (deuterated) methyl radicals. The latter will produce peaks ranging from m/z = 59 to 65, all of which was observed in our experiments, as shown in the inset in Fig. 3a. This provides more strong evidence that TriMS was formed in the reactor from the reaction between dimethylsilene and H_2 when using DMSCB.

Hydrogen abstraction and biradical combination reactions

Our previous studies on TMS[24] and hexamethyldisilane[28] using the same process have shown that the H-abstraction reactions of either alkyl-substituted silanes or silyl-substituted alkanes by methyl radicals followed by biradical combination are the dominant pathways in the secondary gas-phase reactions. As shown in eq. [1], DMSCB also decomposes on the W filament to produce methyl and 1-methyl-1-

silacyclobutane-1-yl radicals. In the HW-CVD reactor, where the pressure of 4% DMSCB–He is 12 torr, the secondary gas-phase reactions of methyl radicals with the parent DMSCB molecule are likely to occur.

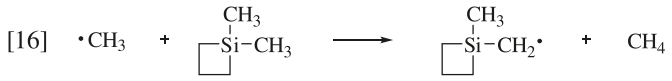

This can then be followed by the biradical combination reactions shown in the following:

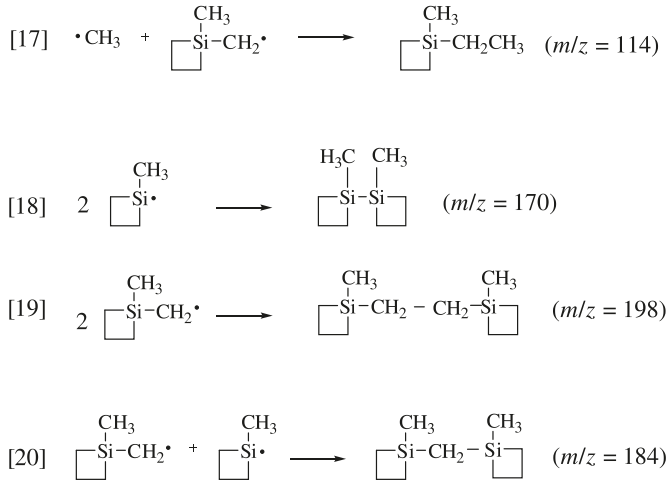

The products of the above four reactions, namely 1-methyl-1-ethyl-1-silacyclobutane at m/z = 114, 1,1′-dimethyl-1,1′-bisilacyclobutane at m/z = 170, 1,2-bis(1-methyl-1-silacyclobutane-1-yl)ethane at m/z = 198, and 1,2-bis(1-methyl-1-silacyclobutane)methane at m/z = 184 were observed experimentally. This suggests that a H-abstraction reaction of DMSCB by methyl radicals occurred in the HW-CVD reactor. These four observed products contain the structure unit of 1-methyl-1-silacyclobutane-1-yl and could produce the fragment ion at m/z = 85 upon exposure to the VUV radiation. This explains the increase in the intensity ratio of m/z = 85 to that of the parent ion in the HW-CVD reactor when the filament was turned on. The 1-methyl-1-ethyl-1-silacyclobutane at m/z = 114 continues to react with methyl radicals through reactions similar to eqs. [16] and [17] to produce a series of peaks with a mass difference of 14, representing a CH_2 group, at m/z = 128, 142, 156, and 170. All these peaks were experimentally observed, as shown in Fig. 2c.

As shown in Fig. 2a, the peak intensities from the dominant product from the secondary gas-phase reactions, TMDSCB, surpasses that of the DMSCB source molecules at filament temperatures >1200 °C. Therefore, the primary decomposition reactions and secondary reactions involving TMDSCB play an important role at higher temperatures. The detailed reaction chemistry when using TMDSCB as a source gas in the same HW-CVD reactor has been reported previously.[29] It was found that TMDSCB decomposed on the W filament to produce methyl and 1,1,3-trimethyl-1,3-disilacyclobutane-1-yl radicals. In the HW-CVD reactor, the H-abstraction reactions and biradical combination reactions similar to those represented by eqs. [16]–[20] form species that are responsible for the peaks at m/z = 158, 286, 258, and 272, of which the peak intensity at m/z = 158 is the strongest. The observation of the peak at m/z = 158 (1,3,3-trimethyl-1-ethyl-1,3-disilcyclobutane) in our experiment with DMSCB (Fig. 2c) confirmed that TMDSCB was indeed formed from the secondary reactions in the reactor. It is interesting to note that although TMDSCB was produced relatively strongly at a low temperature at 1100 °C, its characteristic secondary gas-phase reaction products, e.g., 1,3,3-trimethyl-1-ethyl-1,3-disilcyclobutane at m/z = 158, were only observed at temperatures >1200 °C. This is consistent with the fact that the lowest decomposition temperature for TMDSCB in a HW-CVD reactor was 1200 °C.[29] As shown in Fig. 2c, the peak at m/z = 129 was also observed. The intensity ratio of this peak to that of the TMDSCB parent ion at m/z = 144 was found to be ~4% at temperatures <1200 °C. This is close to the same ratio when the filament was off.[29] This suggests that the peak at m/z = 129 is from photofragmentation of the parent TMDSCB ion at these low temperatures. When the filament temperature is >1200 °C, this intensity ratio increases with filament temperatures and filament-on time, ranging from 4% to 11.3%. Since 1,3,3-trimethyl-1-ethyl-1,3-disilcyclobutane and other products formed contain the structure unit of 1,1,3-trimethyl-1,3-disilacyclobutane-1-yl with m/z = 129, they could produce the fragment ion at m/z = 129 upon exposure to VUV radiation. This likely explains the increase of the intensity ratio of m/z = 129 to that of the parent TMDSCB at m/z = 144 when the filament temperature was >1200 °C.

Conclusions

When DMSCB is contained in a HW-CVD reactor with a relatively high pressure of 0.48 torr, secondary reactions in the gas phase between the source molecule and primary reactive species (e.g., CH_3, dimethylsilylene, and 1,1-dimethylsilene) formed from its decomposition on the heated W filament produced a variety of stable molecules that were detected by the TOF MS coupled with a "soft" ionization source. The π-type addition across the double and triple C–C bonds and the insertion reaction into the Si–H bond are important for dimethylsilyene in the HW-CVD reactor. The methyl radical produced on the hot W filament initiates a short-chain reaction, where it is quickly terminated by recombination between the radical chain carriers. This mechanism was found to dominate the gas-phase reaction chemistry when methyl is the main primary reactive species produced by hot-wire decomposition of source gases such as TMS and TMDSCB in our previous studies. When using DMSCB as a source gas, the H-abstraction and biradical combination reactions involving the source gas itself as well as the secondary products (i.e., TMDSCB, TriMDSCB, DMDSCB, and TMS) all occurred at the same time, making the gas-phase reaction chemistry quite complicated. Our previous study demonstrated that cycloaddition of the primary reactive intermediate, 1,1-dimethylsilene, produces the dominant secondary product, TMDSCB. The dominance of 1,1-dimethylsilene in the gas-phase chemistry when using DMSCB originates from the lower activation energy for its formation from the hot filament . In this work, two other reaction channels have been demonstrated to exist for 1,1-dimethylsilene, i.e., it reacts with CH_3 and H_2, respectively,

Can. J. Chem. Downloaded from www.nrcresearchpress.com by 80.58.250.72 on 09/16/12
For personal use only.

to form TMS and TriMS. The formation of TMS and TriMS via 1,1-dimethylsilene has been confirmed by examining the H–D scrambling pattern when using DMSCB-d_6 and the peak intensity distribution of the trimethylsilyl ions. This work, combined with our previous study on the primary decomposition and the dominant secondary reaction pathway, i.e., the cycloaddition of silenes, provides a relatively complete picture of the gas-phase reaction chemistry when using DMSCB in a HW-CVD reactor and will help in a future kinetic study of the key reaction steps.

Acknowledgements

The financial support for this work by Natural Sciences and Engineering Research Council of Canada (NSERC), the University of Calgary, and the Canadian Foundation for Innovation (New Opportunities Fund) is gratefully acknowledged. The authors thank B. Eustergerling and R. Toukabri for their assistance in the experiments.

References

(1) Chiu, H.-T.; Lee, S.-F. *J. Chin. Chem. Soc.* **1992**, *39*, 293.
(2) Zaharias, G. A.; Duan, H. L.; Bent, S. F. *J. Vac. Sci. Technol. A* **2006**, *24* (3), 542. doi:10.1116/1.2194023.
(3) Flowers, M. C.; Gusel'nikov, L. E. *J. Chem. Soc. B* **1968**, 419. doi:10.1039/j29680000419.
(4) Gusel'nikov, L. E.; Flowers, M. C. *Chem. Commun.* **1967**, 864.
(5) Basu, S.; Davidson, I. M. T.; Laupert, R.; Potzinger, P. *Ber. Bunsenges. Phys. Chem.* **1979**, *83*, 1282.
(6) Gusel'nikov, L. E.; Nametkin, N. S. *J. Organomet. Chem.* **1979**, *169* (2), 155. doi:10.1016/S0022-328X(00)81154-7.
(7) Mahaffy, P. G.; Gutowsky, R.; Montgomery, L. K. *J. Am. Chem. Soc.* **1980**, *102* (8), 2854. doi:10.1021/ja00528a064.
(8) Gusel'nikov, L. E.; Volkova, V. V.; Avakyan, V. G.; Nametkin, N. S. *J. Organomet. Chem.* **1980**, *201* (1), 137. doi:10.1016/S0022-328X(00)92572-5.
(9) Nefedov, O. M.; Maltsev, A. K.; Khabashesku, V. N.; Korolev, V. A. *J. Organomet. Chem.* **1980**, *201* (1), 123. doi:10.1016/S0022-328X(00)92571-3.
(10) Koenig, T.; McKenna, W. *J. Am. Chem. Soc.* **1981**, *103* (5), 1212. doi:10.1021/ja00395a036.
(11) Dyke, J. M.; Josland, G. D.; Lewis, R. A.; Morris, A. *J. Phys. Chem.* **1982**, *86* (15), 2913. doi:10.1021/j100212a022.
(12) Tokach, S.; Boudjouk, P.; Koob, R. D. *J. Phys. Chem.* **1978**, *82* (11), 1203. doi:10.1021/j100500a001.
(13) Low, H. C.; John, P. *J. Organomet. Chem.* **1980**, *201* (2), 363. doi:10.1016/S0022-328X(00)87921-8.
(14) Brix, T.; Arthur, N. L.; Potzinger, P. *J. Phys. Chem.* **1989**, *93* (25), 8193. doi:10.1021/j100362a011.
(15) Tong, L.; Shi, Y. J. *J. Mass Spectrom.* **2010**, *45* (2), 215. doi:10.1002/jms.1712. PMID:20049692.
(16) Schühle, U.; Pallix, J. B.; Becker, C. H. *J. Am. Chem. Soc.* **1988**, *110* (7), 2323. doi:10.1021/ja00215a065.
(17) Butcher, D. J. *Microchem. J.* **1999**, *62* (3), 354. doi:10.1006/mchj.1999.1745.
(18) Shi, Y. J.; Lipson, R. H. *Can. J. Chem.* **2005**, *83* (11), 1891. doi:10.1139/v05-193.
(19) Li, J.; Bierbaum, V. M.; Leone, S. R. *Chem. Phys. Lett.* **1999**, *313* (1-2), 76. doi:10.1016/S0009-2614(99)01026-X.
(20) Chambreau, S. D.; Lemieux, J.; Wang, L.; Zhang, J. S. *J. Phys. Chem. A* **2005**, *109* (10), 2190. doi:10.1021/jp045010r. PMID:16838990.
(21) Shukla, B.; Susa, A.; Miyoshi, A.; Koshi, M. *J. Phys. Chem. A* **2007**, *111* (34), 8308. doi:10.1021/jp071813d. PMID:17685593.
(22) Duan, H. L.; Zaharias, G. A.; Bent, S. F. *Appl. Phys. Lett.* **2001**, *78* (12), 1784. doi:10.1063/1.1355994.
(23) Shi, Y. J.; Lo, B.; Tong, L.; Li, X. M.; Eustergerling, B. D.; Sorensen, T. S. *J. Mass Spectrom.* **2007**, *42* (5), 575. doi:10.1002/jms.1186. PMID:17285587.
(24) Li, X. M.; Eustergerling, B. D.; Shi, Y. J. *Int. J. Mass Spectrom.* **2007**, *263* (2-3), 233. doi:10.1016/j.ijms.2007.02.051.
(25) Dávalos, J. Z.; Baer, T. *J. Phys. Chem. A* **2006**, *110* (27), 8572. doi:10.1021/jp0566358. PMID:16821843.
(26) Al-Rubaiey, N.; Carpenter, I. W.; Walsh, R.; Becerra, R.; Gordon, M. S. *J. Phys. Chem. A* **1998**, *102* (44), 8564. doi:10.1021/jp981957f.
(27) Apeloig, Y. In *The Chemistry of Organic Silicon Compounds*, Vol. 1; Patai, S., Rappoport, Z., Eds. New York: Wiley, 1989; p 57.
(28) Shi, Y. J.; Li, X. M.; Tong, L.; Toukabri, R.; Eustergerling, B. *Phys. Chem. Chem. Phys.* **2008**, *10* (18), 2543. doi:10.1039/b718743b. PMID:18446255.
(29) Tong, L.; Shi, Y. J. *Thin Solid Films* **2009**, *517* (12), 3461. doi:10.1016/j.tsf.2009.01.058.
(30) Arthur, N. L.; Potzinger, P.; Reimann, B.; Steenbergen, H. P. *J. Chem. Soc., Faraday Trans.* **1990**, *86* (9), 1407. doi:10.1039/ft9908601407.
(31) Auner, N.; Davidson, I. M. T.; Ijadi-Maghsoodi, S.; Lawrence, F. T. *Organometallics* **1986**, *5* (3), 431. doi:10.1021/om00134a006.

Can. J. Chem. Downloaded from www.nrcresearchpress.com by 80.58.250.72 on 09/16/12
For personal use only.

Influence of molecular weight on the spectroscopic properties of a series of well-defined poly(3-hexylthiophene) polymers

Qiliang Peng, Ian W. Wyman, Dehui Han, and Guojun Liu

Can. J. Chem. Downloaded from www.nrcresearchpress.com by 80.58.250.72 on 09/16/12
For personal use only.

Abstract: A series of five poly(3-hexylthiophene) (P3HT) polymers were prepared, and their spectroscopic properties were studied. These polymers were well defined, with polydispersity indices no larger than 1.20 and regioregularities that were above 90% for each member of the series. The P3HT polymers were characterized using UV–vis and fluorescence spectroscopy, and their specific refractive index increments were measured in tetrahydrofuran. The influence of the molecular weight of these polymers on their maximum absorbance and emission wavelengths, molar extinction coefficients, and refractive index increments was studied.

Key words: conjugated polymers, poly(3-hexylthiophene), regioregularity, polythiophenes.

Résumé : On a préparé une série de cinq polymères du poly(3-hexylthiophène) (P3HT) et on a étudié leurs propriétés spectroscopiques. Ces polymères sont bien définis, avec des indices de polydispersité qui ne dépassent pas 1,20 et des régiosélectivités supérieures à 90 % pour chaque membre de la série. Cette série de polymères du P3HT a été caractérisée par les spectroscopies UV–visible et de fluorescence et on a aussi mesuré leurs incréments d'indice de réfraction spécifique dans le tétrahydrofurane. On a étudié l'influence du poids moléculaire de ces polymères sur leur absorbance maximale et sur les longueurs d'ondes d'émission, sur les coefficients d'extinction molaire et sur les incréments d'indice de réfraction spécifique.

Mots-clés : polymères conjugués, poly(3-hexylthiophène), régiorégularité, polythiophènes.

[Traduit par la Rédaction]

Introduction

Polythiophenes have attracted interest because of their optical properties and their applications in photovoltaic devices.[1–3] The molecular weights of these polymers can affect their physical, structural, and spectroscopic properties.[4–6] Therefore, by studying the relationship between the molecular weight of a polymer and its physical properties, one can reveal basic information about the conformation of that polymer. Kline et al.[7] reported that the charge transport mobility of transistors composed of poly(3-hexylthiophene) (P3HT) was enhanced as the molecular weight of P3HT increased. This was also observed by Zen et al.,[8] who proposed that this behaviour resulted from the increased planarity of higher molecular weight polymers. Brinkmann and Rannou[9] used high-resolution transmission electron microscopy techniques to study the morphology of P3HT. They found that a 10-fold increase in the molecular weight of the polymer, from 7.3×10^3 to 6.96×10^4 g mol^{-1}, led to enhanced interconnectivity, with ordered polymers acting as bridges between different crystalline lamellae.

Interpretations of the relationship between the molecular weight of a polymer and its spectral properties can be affected by several parameters. The polydispersity index (PDI) of a polymer is an important factor, with interpretations being more accurate when a polymer with a narrow molecular weight distribution is studied.[10] Also, a polymer should have a high regioregularity, since a uniform chain microstructure can promote ordered chain packing and charge transport in solid films.[11] In particular, it has been demonstrated that polythiophenes that are coupled together by head-to-tail linkages have improved optical properties owing to their increased coplanarity.[5,12,13] The P3HT polymers analyzed in this study had a combination of regioregular structures and relatively low PDI values (ranging between 1.10 and 1.20) and also had regioregularities above 90% throughout the series. Although previous spectroscopic studies of regioregular P3HT included individual samples with PDI values as low as 1.1,[7] the PDI values within a given series ranged up to at least 1.4.[8,9,14,15]

In this study, we explored the relationship between the spectroscopic properties of P3HT and its molecular weight, using regioregular samples that had low polydispersity indices. The spectroscopic properties that we studied include the molar extinction coefficient, the wavelengths of the absorption and emission maxima, and specific refractive index

Received 12 July 2010. Accepted 30 September 2010. Published on the NRC Research Press Web site at canjchem.nrc.ca on 18 December 2010.

Q. Peng, I.W. Wyman, D. Han, and G. Liu.[1] Department of Chemistry, Queen's University, 90 Bader Lane, Kingston, ON K7L 3N6, Canada.

[1]Corresponding author (e-mail: guojun.liu@chem.queensu.ca).

Table 1. Properties of the five P3HT samples.

Sample name	M_n[a] (g mol^{-1})	M_w[a] (g mol^{-1})	No. of repeat units[a]	PDI[a]	No. of repeat units[b]	RR[b,c] (%)
T1	4 200	5 000	25	1.20	27	94
T2	5 500	6 100	33	1.10	34	94
T3	7 500	8 900	45	1.19	46	92
T4	8 700	9 600	53	1.12	55	93
T5	10 500	11 900	63	1.13	67	94

Note: M_n, number-average molecular weight; M_w, weight-average molecular weight; PDI, polydispersity index; RR, regioregularity.

[a]Determined by SEC analysis using a light scattering detector.

[b]Determined from ^{1}H NMR integration.

[c]Values are percentages corresponding to the head-to-tail–head-to-tail arrangement.

Can. J. Chem. Downloaded from www.nrcresearchpress.com by 80.58.250.72 on 09/16/12
For personal use only.

increments. A relationship was determined between the refractive index increment and the molecular weight of P3HT, which may potentially serve as a method of molecular weight determination of this polymer.

Results and discussion

Molecular weights, polydispersity indices, and regioregularities of the polymers

The five samples were denoted as T1, T2, T3, T4, and T5, and their properties are summarized in Table 1. The molecular weight differed between samples by at least 1000 g mol^{-1}. The regioregularities of these samples were all above 90%, with the major configuration being head-to-tail–head-to-tail. According to the size-exclusion chromatography (SEC) plots (Fig. 1), the five samples had a molecular weight range between 4 200 and 11 000 g mol^{-1}, and their PDI values were no higher than 1.20. The numbers of repeat units determined by SEC with the light scattering detector were also in close agreement with those determined by ^{1}H NMR integration.

Refractive index increments

Refractive index increments (dn/dc) of the samples were determined. From the change in the differential refractive index (DRI) detector voltage (ΔV), the difference in the refractive index between a pure solvent and the polymer solution (Δn) for each concentration c can be calculated as follows:

$$[1] \qquad \Delta n = \alpha \Delta V$$

where α is the DRI calibration constant. The slope of the Δn versus c plot represents dn/dc. The dn/dc values of the five polymer samples are summarized in Table 2.

UV–vis spectroscopy

The maximum absorbance wavelengths (λ_{max}) of the solution and thin-film samples of these polymers, as well as their molar extinction coefficients (ε), are summarized in Table 3. The spectra of the five samples in chloroform solution and as spin-coated thin films are shown in Fig. 2. In Table 3, it can be seen that the λ_{max} values are larger for the thin-film samples than for the solution samples of P3HT.

The absorbance spectra of the thin-film P3HT samples displayed vibrational fine structures, such as shoulder peaks on each side of the maximum absorbance peak. These features were enhanced by the coplanarization of the polymer and the corresponding π-electron delocalization. For example, the λ_{max} of sample T3 was observed at 541 nm and shoulder peaks were observed at 525 and 597 nm, corresponding to energy level transitions of 2.27, 2.39, and 2.08 eV, respectively. Enhanced red shifts and increased fine structures of thin-film samples of P3HT relative to those of solution samples were also observed by Trznadel et al.[4] and Zen et al.[8]

Fig. 1. SEC plots of the five P3HT samples (T1, T2, T3, T4, and T5) recorded with THF as the eluent at a flow rate of 1 mL min^{-1}.

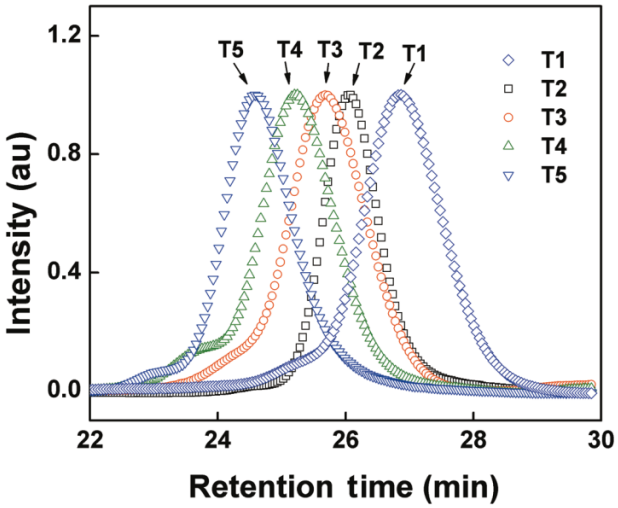

Table 2. Refractive index increment (dn/dc) values measured for a series of P3HT.

Sample name	dn/dc (mL g^{-1})[a]	M_n (g mol^{-1})
T1	0.244	4 200
T2	0.262	5 500
T3	0.277	7 500
T4	0.280	8 700
T5	0.283	10 500

[a]THF as solvent, t = 25.0 °C, flow rate = 0.33 mL min^{-1}, laser λ = 638 nm.

Fluorescence spectroscopy

The fluorescence spectroscopy measurement results of the

Table 3. UV–vis spectral properties of the P3HT samples.

Sample name	λ_{max} (nm) Chloroform solution	Thin film	ε (L mol^{-1} cm^{-1})[a]	M_n (g mol^{-1})
T1	439	478	4700	4 200
T2	448	537	7500	5 500
T3	450	541	7800	7 500
T4	451	549	7900	8 700
T5	451	550	8000	10 500

[a]Determined for the samples in chloroform solution.

Fig. 2. UV–vis absorbance spectra of P3HT samples in chloroform solutions (left) and as thin films (right).

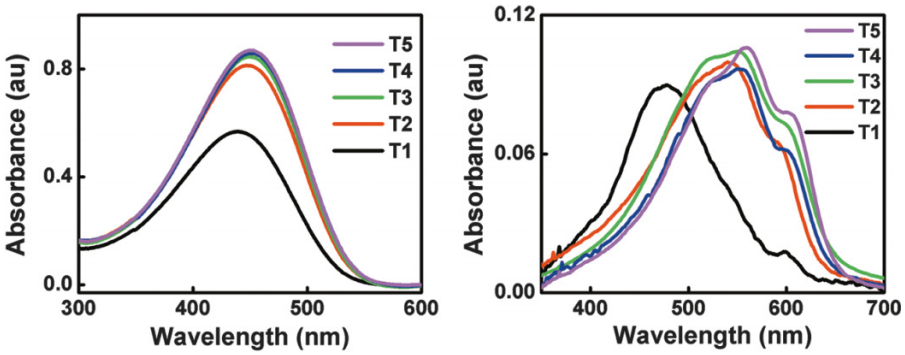

P3HT samples are shown in Table 4, while solution and thin-film fluorescence spectra are shown in Fig. 3. As shown in Table 4, the maximum emission wavelengths (λ_{em}) display red shifts as the molecular weight of the samples increases (as one progresses from T1 through to T5). This trend was observed for both the solution and the thin-film samples. Meanwhile, λ_{em} were longer for the polymers when they were analyzed as thin-film samples than when they were analyzed as solution samples. In a similar manner to the results of the UV–vis study, this may be due to enhanced π–π interactions within thin-film samples of the polymer compared with corresponding samples in solution. Owing to the self-quenching of the thin-film samples, the fluorescence spectra of the thin films were weaker in intensity than the corresponding solution spectra.

Table 4. Fluorescence properties of the P3HT samples.

Sample name	λ_{em} (nm) Chloroform solution	Thin film	M_n (g mol^{-1})
T1	570.5	643.5	4 200
T2	573.5	649.0	5 500
T3	575.0	653.0	7 500
T4	575.5	655.0	8 700
T5	575.5	656.0	10 500

Effect of the molecular weight of P3HT on its spectroscopic properties

Refractive index increments

The dn/dc measurements increased from 0.24 to 0.28 mL g^{-1} with increasing molecular weight. These results are consistent with the accepted trend of dn/dc values increasing with increasing molecular weight for smaller polymers, and then leveling off once the molecular weight of the polymer becomes larger (such as above 10^4 g mol^{-1}).[16] By combining the results for the five different polymer samples in THF, we determined the following relationship:

$$[2] \qquad dn/dc = 0.316 - 298/M_n$$

The dn/dc value of 0.307 mL g^{-1} in THF reported by Pearson et al.[15] for a sample of P3HT having a molecular weight of 2.23×10^5 g mol^{-1} agrees closely with this equation, indicating a potential method for the determination of the molecular weight of P3HT based on its dn/dc values. Other polymers, such as poly(ethylene oxide), poly(methyl methacrylate), and polystyrene, have dn/dc values that range between 0.11 and 0.20 mL g^{-1}.[17–19] The higher dn/dc value of P3HT can be attributed to the presence of the sulfur atoms of the thiophene units, which contribute to the larger refractive index.[20]

The relationship between the refractive index and the molecular weight of P3HT can be explained in terms of the variation of the polarizability of the polymer as its molecular weight increases.[21] As a chain of P3HT bearing delocalized electrons is extended, the polymer becomes more polarizable. As a result, for a conjugated polymer such as P3HT there is a pronounced relationship between the molecular weight and refractive index values.

Spectral properties

The maximum absorbance and emission wavelengths increased as the molecular weight of the P3HT samples increased. This trend was observed for both the solution

Can. J. Chem. Downloaded from www.nrcresearchpress.com by 80.58.250.72 on 09/16/12
For personal use only.

Fig. 3. Fluorescence spectra of P3HT samples in chloroform solution (left) and as thin films (right).

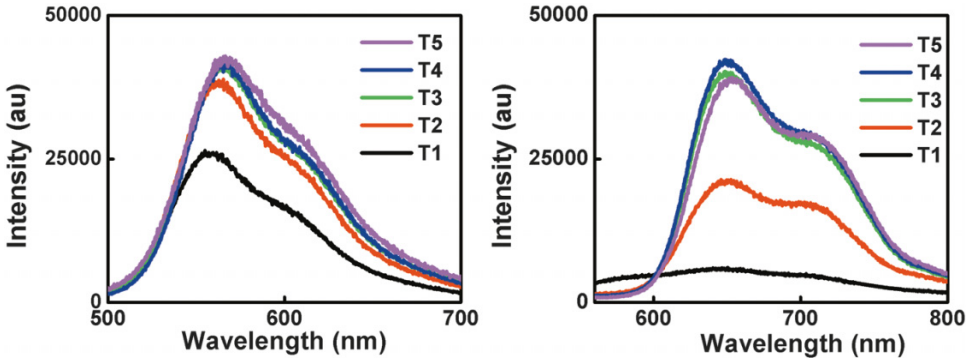

Fig. 4. Plots of the dependencies of λ_{max} (left) and λ_{em} (right) on the number of repeat units of P3HT, based on UV–vis and fluorescence data, respectively.

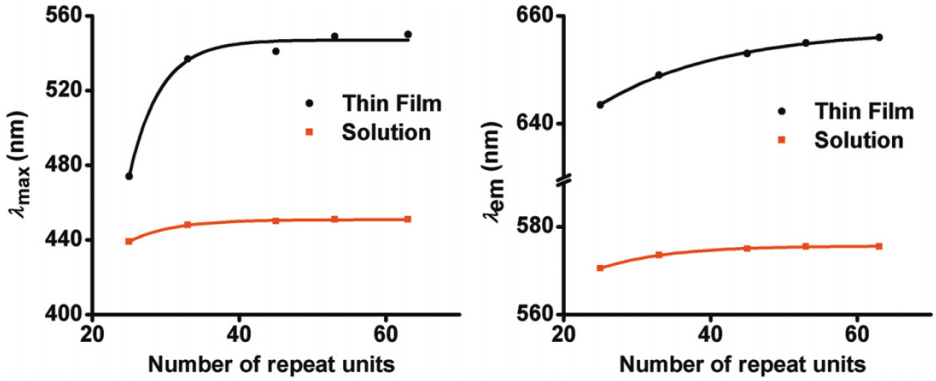

samples and the thin-film samples and was likely due to the decreases of the band gaps of the π–π* transitions as the lengths of the polymers increased and their conjugation was extended. The correlation between the absorbance and emission maxima of the P3HT samples and their number of repeat units is plotted in Fig. 4. The model used to fit this plot was that of Meier et al.,[22] and is described in the Supplementary data.

Extinction coefficient

In addition, a correlation exists between the molecular weight of the P3HT samples and their molar extinction coefficients (ε). For each P3HT sample, solutions were prepared in chloroform at varying concentrations. The values of ε were then plotted against the number of repeat units of the polymer samples, as shown in Fig. 5. The mathematical model[23] used to fit this plot is described in the Supplementary data. The ε values increased from 4700 to 8000 L mol^{-1} cm^{-1} as the molecular weight of the P3HT samples increased. As the conjugation length of a polymer is extended, its ε values also increase.[24,25] It is apparent from Fig. 5 that only slight increases of ε occurred once the molecular weight of the polymer exceeded 10^4 g mol^{-1}. This behaviour could explain the ε value of 8800 L mol^{-1} cm^{-1} reported previously for a P3HT polymer having a higher molecular weight of 4.8×10^4 g mol^{-1}.[26]

Izumi et al.[27] studied a series of well-defined beta-blocked oligothiophene derivatives and observed a continuous red shift of the absorbance maxima for polymers having up to 96 repeat units. They also observed dramatic increases of the molar extinction coefficient as the chain length increased, and large increases were observed even for samples with long chain lengths. In contrast, the molar extinction coefficients of P3HT observed by us increased only modestly as the length of the polymer exceeded 45 repeat units. Izumi et al. attributed their extended effective conjugation lengths to a lower degree of steric demand on their beta-blocked derivatives compared with that on derivatives bearing linear alkyl substituents, which may cause a greater extent of twisting of the backbone. This behaviour could also explain the saturation of the molar extinction coefficient increases that was observed in our samples beyond 45 repeat units (Fig. 5), as the bulk of the hexyl groups may have caused a greater degree of twisting of the polymer backbone, and thus a loss of conjugation, relative to the beta-blocked polythiophene derivatives studied by Izumi et al.[27]

Conclusions

From a series of five P3HT samples, a relationship between the molecular weight and the refractive index increment of this polymer was determined. Also, correlations between the molecular weight of P3HT and its spectral properties, such as its molar extinction coefficient and its maximum absorbance and emission wavelengths, were identified. The data presented in this study indicate that the refractive index increment (d*n*/d*c*), the maximum absorbance and emission wavelengths, and the extinction coefficients all increase with increasing molecular weight among our

Can. J. Chem. Downloaded from www.nrcresearchpress.com by 80.58.250.72 on 09/16/12
For personal use only.

Can. J. Chem. Downloaded from www.nrcresearchpress.com by 80.58.250.72 on 09/16/12
For personal use only.

Fig. 5. Plot of the relationship between the extinction coefficient of each P3HT sample in chloroform solution and its number of repeat units.

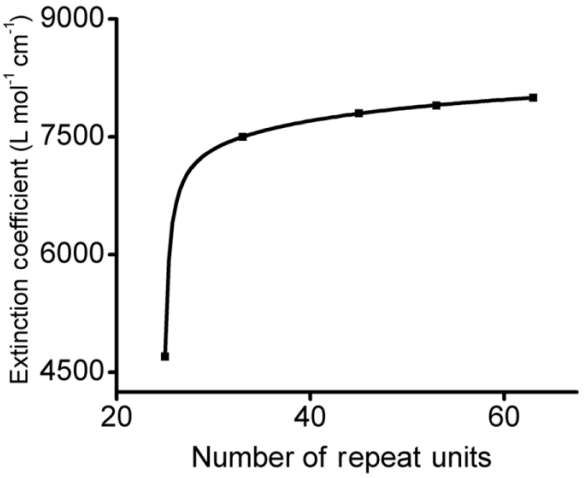

samples of relatively low molecular weight (>2.0 × 10^4 g mol^{-1}) P3HT polymers. This study's focus on lower molecular weight polymers was beneficial, as it could be seen that the spectral changes were smaller at higher molecular weights. These results may serve as benchmarks for subsequent studies of polythiophene-based materials for applications such as photovoltaic devices, and also for the comparison of the physical properties of polythiophene derivatives. With a solid understanding of the relationship between the structural and spectral properties of P3HT in hand, it may be possible to tailor the polymer for specific applications.

Experimental section

Materials

Spectroscopic grade chloroform was purchased from Sigma-Aldrich. Methanol (ACS grade) was purchased from Fisher Scientific. Tetrahydrofuran (ACS grade) was purchased from Fisher Scientific and dried by passing it through two alumina columns in a Grubb's system for solvent purification. Ni(dppp)Cl_2 and a 1.0 mol L^{-1} THF solution of *tert*-butyl magnesium chloride were purchased from Sigma-Aldrich.

Synthesis of P3HT

Vinyl-terminated poly(3-hexylthiophene) was prepared by utilizing a modified Grignard metathesis reaction procedure, as described by McCullough and co-workers.[28] Following the synthesis, the crude polymer was dissolved in THF and purified by three repeated precipitations from methanol. Samples T1, T2, and T3 were prepared by fractionation, while higher molecular weight samples T4 (53 repeat units) and T5 (63 repeat units) were prepared from separate batches. During the fractionation of the lower molecular weight batches, a sample of $P3HT_{41}$ (2.310 g) was dissolved in THF. This solution was then added to methanol to precipitate the polymer. The precipitate was subsequently filtered, washed with a water/methanol (1/9, *v*/*v*) solvent mixture, and dried. The polymer was extracted with acetone in a Soxhlet apparatus until the extracting acetone became colourless. The acetone was then removed by rotary evaporation to yield 0.050 g of sample T1, which had 25 repeat units. The remaining fractions were then consecutively Soxhlet extracted with hexane and then dichloromethane. The hexane and dichloromethane fractions yielded samples T2 (33 repeat units) and T3 (45 repeat units), respectively. The purpose of the terminal vinyl group was to allow the subsequent use of the P3HT polymers as macroinitiators for the preparation of diblock copolymers by anionic polymerization, as described by Dai et al.[29] The preparation and study of diblock copolymers containing a P3HT block will be described in a later publication. Given the large number of double bonds present in these conjugated polymers, we do not believe that the presence of the additional vinyl group will significantly affect the physical or spectroscopic properties of the polymers. Further details of the synthesis of the polymer samples, as well as their characterization by ^{1}H NMR and SEC, are described in the Supplementary data.

Refractive index measurements

The refractive index increment (d*n*/d*c*) of P3HT was measured in dilute THF solution in the off-line mode, using a Wyatt Optilab rEX differential refractive index (DRI) detector. The experiments were conducted at a constant temperature (25 °C) and a flow rate of 0.33 mL min^{-1} using a syringe pump (RAZEL, model R99) connected directly to the DRI detector.

The P3HT samples were dried in a vacuum overnight before they were used. For each sample, 15.0 mg of P3HT was fully dissolved in 6.0 mL of THF and centrifuged at 2000*g*. A stock solution of P3HT was then prepared with an original concentration of 2.50 mg mL^{-1}. This solution was diluted to prepare the other four solutions, with concentrations of 2.00, 1.50, 1.00, and 0.50 mg mL^{-1}. THF was first eluted through the detector cell to establish a baseline. Each solution was then passed through the DRI detector, beginning with the samples at the lowest concentrations. The data were collected and processed using the ASTRA version 5.3.4.10 software package provided by Wyatt Technology Corp.

Size-exclusion chromatography

SEC analyses were conducted using a set of three styragel columns (MZ Analysentechnik) with packing materials having pore diameters of 500, 10^4, and 10^5 Å. The columns showed a linear separation in the range of 5.0 × 10^2 to 1.0 × 10^6 g mol^{-1} and were placed in a column compartment with a thermostat set to 25 °C. A Wyatt Dawn Heleos-II multi-angle light scattering detector (Wyatt Technology Corp.) and a Wyatt Optilab refractive index detector were used to measure light scattering and refractive index values, respectively. The laser sources of these detectors were operated at 690 nm.

Each polymer solution was filtered through a 0.45 μm Teflon syringe filter before injection. The SEC analyses were performed on THF solutions of P3HT at 25 °C, with sample concentrations of 5 mg mL^{-1} and eluent flow rates of 1 mL min^{-1}. The data processing was performed using the ASTRA 5.3.4.10 software package provided by Wyatt Technology Corp. The number of repeat units of the P3HT polymers (Table 1) was calculated by dividing the molecular

weight of the P3HT polymers (as determined by SEC using the light scattering detector) by the molecular weight of the repeat unit, which was 166 g mol^{-1}.

UV–vis and fluorescence spectroscopy

All P3HT solutions studied by UV–vis analysis were prepared using spectroscopic grade chloroform. The concentrations of the solutions ranged between 2.0×10^{-3} and 1.8×10^{-2} mg mL^{-1}. UV–vis measurements were performed using a Cary 300 Bio spectrophotometer (Varian) with a spectral range between 200 and 800 nm. Ten millimetre Varian quartz cells were used for all measurements, and spectroscopic grade chloroform was used as the blank.

To prepare the P3HT films, a chloroform solution of P3HT was spin-coated onto a pre-cleaned glass microscope slide at a speed of 1000 rpm for 50 s and subsequently annealed at room temperature under high vacuum for 12 h. The dried samples were then placed in a plate holder as described by Li et al.[30] for UV–vis analysis. We estimate that the thickness of these films is approximately 1 μm. This estimation was based on the Beer–Lambert Law, using a literature value of 1.1 g mL^{-1} as the density of P3HT.[31,32] These films were also used for analysis by fluorescence spectroscopy.

Fluorescence measurements were performed using a Photon Technology International Alphascan spectrometer with a 150 W Xenon compact light source, and 10 mm Hellma quartz cells were used. The P3HT solutions were prepared at a concentration of 2.0×10^{-3} mg mL^{-1} in chloroform, and the absorbances of the solutions at their maximum absorbance wavelengths were kept at 0.100. The excitation wavelength was 430 nm, and the excitation and emission slit widths were set at 5 and 3 nm, respectively.

^{1}H NMR spectroscopy

^{1}H NMR spectra were recorded on a Bruker Avance 400 MHz NMR spectrometer, with deuterated chloroform as the solvent. The relaxation delay was 3 s.

The regioregularities of the P3HT samples were calculated based on the relative integrals from the ^{1}H NMR spectra that corresponded to the head-to-tail–head-to-tail conformation.[33,34]

The number of repeat units could be determined by comparing the integrals of the end groups with those of the repeat units. This value could be used as a comparison to access the accuracy of the number of repeat units calculated based on SEC data.

Supplementary data

Supplementary data, including ^{1}H NMR spectra, formulae used to fit the plots in Figs. 4 and 5, d*n*/d*c* plots of the polymers, and further details of their preparation, are available on the journal Web site (canjchem.nrc.ca).

Acknowledgements

NSERC of Canada is gratefully acknowledged for funding this research. Dr. Liu thanks the Canada Research Chair program for a senior Canada Research Chair position in materials science.

References

(1) Pokrop, R.; Verilhac, J.-M.; Gasior, A.; Wielgus, I.; Zagorska, M.; Travers, J.-P.; Pron, A. *J. Mater. Chem.* **2006**, *16* (30), 3099. doi:10.1039/b605504d.
(2) Sirringhaus, H.; Tessler, N.; Friend, R. H. *Science* **1998**, *280* (5370), 1741. doi:10.1126/science.280.5370.1741.
(3) Li, G.; Shrotriya, V.; Huang, J.; Yao, Y.; Moriarty, T.; Emery, K.; Yang, Y. *Nat. Mater.* **2005**, *4* (11), 864. doi:10.1038/nmat1500.
(4) Trznadel, M.; Pron, A.; Zagorska, M.; Chrzaszcz, R.; Pielichowski, J. *Macromolecules* **1998**, *31* (15), 5051. doi:10.1021/ma970627a.
(5) Zen, A.; Saphiannikova, M.; Neher, D.; Grenzer, J.; Grigorian, S.; Pietsch, U.; Asawapirom, U.; Janietz, S.; Scherf, U.; Lieberwirth, I.; Wegner, G. *Macromolecules* **2006**, *39* (6), 2162. doi:10.1021/ma0521349.
(6) Schilinsky, P.; Asawapirom, U.; Scherf, U.; Biele, M.; Brabec, C. J. *Chem. Mater.* **2005**, *17* (8), 2175. doi:10.1021/cm047811c.
(7) Kline, R. J.; McGehee, M. D.; Kadnikova, E. N.; Liu, J.; Frechet, J. M. J. *Adv. Mater.* **2003**, *15* (18), 1519. doi:10.1002/adma.200305275.
(8) Zen, A.; Pflaum, J.; Hirschmann, S.; Zhuang, W.; Jaiser, F.; Asawapirom, U.; Rabe, J. P.; Scherf, U.; Neher, D. *Adv. Funct. Mater.* **2004**, *14* (8), 757. doi:10.1002/adfm.200400017.
(9) Brinkmann, M.; Rannou, P. *Macromolecules* **2009**, *42* (4), 1125. doi:10.1021/ma8023415.
(10) Menon, A.; Dong, H.; Niazimbetova, Z. I.; Rothberg, L. J.; Galvin, M. E. *Chem. Mater.* **2002**, *14* (9), 3668. doi:10.1021/cm010936m.
(11) Sirringhaus, H.; Brown, P. J.; Friend, R. H.; Nielsen, M. M.; Bechgaard, K.; Langeveld-Voss, B. M. W.; Spiering, A. J. H.; Janssen, R. A. J.; Meijer, E. W.; Herwig, P.; de Leeuw, D. M. *Nature* **1999**, *401* (6754), 685. doi:10.1038/44359.
(12) Xu, B.; Holdcroft, S. *Macromolecules* **1993**, *26* (17), 4457. doi:10.1021/ma00069a009.
(13) Xu, B.; Lowe, J.; Holdcroft, S. *Thin Solid Films* **1994**, *243* (1–2), 638. doi:10.1016/0040-6090(93)04113-7.
(14) Verilhac, J.-M.; LeBlevennec, G.; Djurado, D.; Rieutord, F.; Chouiki, M.; Travers, J.-P.; Pron, A. *Synth. Met.* **2006**, *156* (11–13), 815. doi:10.1016/j.synthmet.2006.04.012.
(15) Heffner, G. W.; Pearson, D. S. *Macromolecules* **1991**, *24* (23), 6295. doi:10.1021/ma00023a035.
(16) Mori, S.; Barth, H. G. *Size Exclusion Chromatography*; Springer-Verlag: Berlin, 1999; Chapter 8.
(17) Fragouli, P. G.; Iatrou, H.; Hadjichristidis, N. *Polymer (Guildf.)* **2002**, *43* (25), 7141. doi:10.1016/S0032-3861(02)00455-X.
(18) Tumolo, T.; Angnes, L.; Baptista, M. S. *Anal. Biochem.* **2004**, *333* (2), 273. doi:10.1016/j.ab.2004.06.010.
(19) Sauzedde, F.; Hunkeler, D. J. *Int. J. Polym. Anal. Charact.* **2001**, *6* (3), 295. doi:10.1080/10236660108033949.
(20) You, N.-H.; Suzuki, Y.; Yorifuji, D.; Ando, S.; Ueda, M. *Macromolecules* **2008**, *41* (17), 6361. doi:10.1021/ma800982x.
(21) Binboga, N.; Kisakürek, D.; Baysal, B. M. *J. Polym. Sci.: Polym. Phys. Ed.* **1985**, *23* (5), 925. doi:10.1002/pol.1985.180230507.
(22) Meier, H.; Stalmach, U.; Kolshorn, H. *Acta Polym.* **1997**, *48* (9), 379. doi:10.1002/actp.1997.010480905.
(23) Graham, D. *J. Phys. Chem.* **1953**, *57* (7), 665. doi:10.1021/j150508a014.
(24) Choi, H.; Raabe, I.; Kim, D.; Teocoli, F.; Kim, C.; Song, K.;

Can. J. Chem. Downloaded from www.nrcresearchpress.com by 80.58.250.72 on 09/16/12
For personal use only.

Yum, J.-H.; Ko, J.; Nazeeruddin, M. K.; Gratzel, M. *Chem. Eur. J.* **2010**, *16* (4), 1193. doi:10.1002/chem.200902197.
(25) Kuang, D.; Klein, C.; Ito, S.; Moser, J.-E.; Humphry-Baker, R.; Zakeeruddin, S. M.; Gratzel, M. *Adv. Funct. Mater.* **2007**, *17* (1), 154. doi:10.1002/adfm.200600483.
(26) Linton, J. R.; Frank, C. W.; Rughooputh, S. D. D. V. *Synth. Met.* **1989**, *28* (1–2), 393. doi:10.1016/0379-6779(89)90551-1.
(27) Izumi, T.; Kobashi, S.; Takimiya, K.; Aso, Y.; Otsubo, T. *J. Am. Chem. Soc.* **2003**, *125* (18), 5286. doi:10.1021/ja034333i.
(28) Jeffries-El, M.; Sauve, G.; McCullough, R. D. *Macromolecules* **2005**, *38* (25), 10346. doi:10.1021/ma051096q.
(29) Dai, C.-A.; Yen, W.-C.; Lee, Y.-H.; Ho, C.-C.; Su, W.-F. *J. Am. Chem. Soc.* **2007**, *129* (36), 11036. doi:10.1021/ja0733991.
(30) Li, G.; Yao, Y.; Yang, H.; Shrotriya, V.; Yang, G.; Yang, Y. *Adv. Funct. Mater.* **2007**, *17* (10), 1636. doi:10.1002/adfm.200600624.
(31) Tashihiro, K.; Ono, K.; Minagawa, M.; Kobayashi, M.; Kawai, T.; Yoshino, K. J. *Polym. Sci. Part B: Polym. Phys.* **1991**, *29* (10), 1223. doi:10.1002/polb.1991.090291007.
(32) van Bavel, S.; Sourty, E.; de With, G.; Frolic, K.; Loos, J. *Macromolecules* **2009**, *42* (19), 7396. doi:10.1021/ma900817t.
(33) Sato, M.-A.; Morii, H. *Macromolecules* **1991**, *24* (5), 1196. doi:10.1021/ma00005a035.
(34) Mao, H.; Xu, B.; Holdcroft, S. *Macromolecules* **1993**, *26* (5), 1163. doi:10.1021/ma00057a041.

Can. J. Chem. Downloaded from www.nrcresearchpress.com by 80.58.250.72 on 09/16/12
For personal use only.

Computational study of proper and improper hydrogen bonding in methanol complexes

C. Dale Keefe and Zuzana Istvankova

Abstract: The bulk properties of alcohols, like those of aqueous solutions, are governed mostly by hydrogen bonding; however, in contrast with water molecules, the chemical structure of a simple alcohol such as methanol offers an opportunity to explore the effects of both proper and improper hydrogen bonding on a single hydrogen donor. The presence of the hydroxyl group generally gives rise to a strong proper hydrogen bond, while the methyl group of methanol is likely involved in the weaker improper hydrogen bond, among other weak non-covalent interactions. The effects of the two types of hydrogen bonds on the stability, geometric parameters, and properties of electron density of methanol complexes are examined while considering different geometrical arrangements of the methanol dimer and the binary complexes of methanol with water, acetonitrile, and chloromethane. Subsequently, potential conclusions about the nature of improper hydrogen bonding and the origin of the C–H bond contraction that results upon complex formation are discussed. Quantum theory of atoms in molecules and natural bond orbital methods were used in the analysis; all calculations were performed at the MP2(full)/6-311++G(d,p) level of theory.

Key words: infrared frequencies and intensities, red and blue shift, ab initio, atoms in molecules, methanol dimer, methanol complexes with water, acetonitrile, chloromethane, hydrogen bonding.

Résumé : Les propriétés globales des alcools, comme celles des solutions aqueuses, sont principalement déterminées par les liaisons hydrogènes ; toutefois, contrairement à ce qui est observé avec les molécules d'eau, la structure chimique d'un alcool simple, tel le méthanol, permet d'explorer les effets tant des liaisons hydrogènes propres et impropres d'un donneur d'hydrogène spécifique. La présence d'un groupe hydroxyle donne généralement lieu à une forte liaison hydrogène propre alors que le groupe méthyle du méthanol est vraisemblablement impliqué dans une liaison hydrogène impropre et plus faible parmi d'autres interactions faibles non covalentes. On a examiné les effets de ces deux types de liaisons hydrogènes sur la stabilité, les paramètres géométriques et sur les propriétés de la densité d'électron des complexes du méthanol tout en considérant divers arrangements géométriques du dimère du méthanol et de complexes binaires du méthanol avec l'eau, l'acétonitrile et le chlorométhane. On discute ensuite de conclusions potentielles concernant la nature de la liaison hydrogène impropre et de l'origine de la contraction de la liaison C–H qui résulte de la formation de complexes. Pour cette analyse, on a fait appel aux méthodes de la théorie quantique des atomes dans les molécules et de l'orbitale de liaison naturelle; tous les calculs ont été effectués au niveau MP2(complet)/6-311++G(d,p) de la théorie.

Mots-clés : fréquences et intensités infrarouges, déplacements vers le rouge et vers le bleu, ab initio, atomes dans les molécules, dimère du méthanol, complexes du méthanol avec l'eau, l'acétonitrile et le chlorométhane, liaison hydrogène.

[Traduit par la Rédaction]

Can. J. Chem. Downloaded from www.nrcresearchpress.com by 80.58.250.72 on 09/16/12
For personal use only.

Introduction

Among several different types of non-covalent interactions, the hydrogen bond (HB) plays an exceptionally important role in many fields of chemistry, biochemistry, and molecular biology.[1–4] The experimental and theoretical study of hydrogen bonding in methanol complexes has been an active topic of research for many years.[5–17] The idea of an unconventional improper HB has been brought forward by Hobza and Havlas.[18] Whereas the traditional HB is generally defined as an X–H···Y interaction, where X is an electronegative atom and Y is a region of excess electrons (lone electron pairs, π system), it has been found that a stabilizing intermolecular interaction also exists between carbon proton donors and regions rich in electron density.[19–21] Numerous experimental and theoretical studies have been performed on the C–H bond interactions involving both aromatic and nonaromatic molecules as electron density donors (HB acceptors),[21–28] as well as on other weak electron density acceptors (HB donors, such as Si–H and P–H bonds as well as N–H and F–H bonds).[29–32] A recent ab initio study from our laboratory investigated the interaction of X_3CH (X=H, F, Cl, or Br) with benzene and hexafluorobenzene.[33] Generally, the formation of a HB is associated with a vibrational spectral shift. A shift towards lower frequencies (red shift) is observed for proper HBs, together with an increase in vibrational intensity and, typically, bond elongation; on the other hand, a shift towards higher frequencies (blue shift) is usually observed for improper HBs, along with a decrease in

Received 9 August 2010. Accepted 20 October 2010. Published on the NRC Research Press Web site at canjchem.nrc.ca on 18 December 2010.

C.D. Keefe[1] and Z. Istvankova. Department of Chemistry, Cape Breton University, Sydney, NS B1P 6L2, Canada.

[1]Corresponding author (e-mail: Dale_Keefe@cbu.ca).

Can. J. Chem. Downloaded from www.nrcresearchpress.com by 80.58.250.72 on 09/16/12
For personal use only.

vibrational intensity and bond contraction.[34] The major source of the attraction in a proper HB is electrostatic interaction, explaining its strength and directionality.[19] Even though many similarities between proper and improper HBs have been reported in recent years,[18,31,32,35–37] the nature of unconventional hydrogen bonding and the origin of the bond contraction and concurrent blue shift of the stretching frequency are being actively studied by many groups, and several theories have emerged in recent years. Hobza and Havlas reported several similarities between the two HB types; however, they concluded that in contrast to the proper HB, the improper HB is formed by an indirect, two-step process where the charge transfer from the electron-rich region of the HB acceptor is directed mainly to the antibonding orbitals or the lone electron pairs in the remote parts of the HB donor.[19] A secondary effect is the structural reorganization of the proton donor, resulting in the strengthening and contraction of the X–H bond and the blue shift of the X–H stretching frequency.[19] Tsuzuki and Fujii[38] found that the nature of the CH···π interaction depends on the acidity of the interacting C–H bond. While the major source of attraction in CH···π bonding has been attributed to a dispersion interaction, similar to the interaction in a van der Waals cluster, the nature of some activated CH···π interactions of highly acidic C–H bonds may have some similarity with proper HBs. However, the electrostatic contribution in the activated CH···π interactions is substantially weaker than that in proper HBs, where the electrostatic contribution is the dominant attraction.[38]

On the other hand, Scheiner and Kar[35] concluded that there is no fundamental difference between the proper HB and the improper HB, and they attributed the changes in the X–H bond length to the net resultant of 2 sets of forces, the first (electrostatic interaction, polarization, charge transfer, and dispersion) tending towards elongation and the second (exchange forces associated with steric repulsion) tending towards contraction. Whereas in the proper HB the former set of forces dominates and results in the weakening of the X–H bond and the red shift of its stretching frequency, in the improper HB the short-range repulsive forces overcome the former set and the resulting stabilized complex exhibits the X–H bond strengthening and consequent blue shift of its stretching frequency. Likewise, other studies, for example those by Hermansson,[36] Alabugin et al.,[31] Qian and Krimm,[39] Li et al.,[32] and Joseph and Jemmis,[40] concluded that the red-shifted and blue-shifted HBs are governed by interactions of the same nature.

Although the same theory using perturbation model analysis, as suggested by Buckingham and colleagues,[37] could describe proper and improper HBs reasonably well, it still cannot unambiguously explain the origin of the C–H bond contraction and consequent blue shift of its stretching frequency. In many cases electrostatic models can give a good description of the nature of both red- and blue-shifting hydrogen bonding,[37] where the necessary condition for the meaningful use of these models is the negative sign of the proton donor dipole moment derivative with respect to the stretching coordinate,[36] which means that the dipole moment increases with the bond contraction; however, as Hobza and colleagues have indicated, the improper, blue-shifting HB has also been detected in complexes where the proton donor does not exhibit a negative gradient.[41]

Fig. 1. Schematic representation of the methanol complexes investigated. System **A**: a proper hydrogen bond (HB) in which the hydroxyl hydrogen of methanol is the HB donor. System **B**: an improper HB in which the methyl group of methanol is the HB donor. System **B′**: C···Y interaction in which the methyl group of methanol is the HB donor. System **C**: methanol is the HB acceptor. System **D**: two improper HB interactions, one involving the methyl hydrogen of methanol (HB donor) and the second involving the oxygen atom of methanol (HB acceptor) (could be thought of as a combination of **B** and **C**). System **E**: two HB interactions involving the hydroxyl group of methanol as HB donor and HB acceptor (could be thought of as a combination of **A** and **C**). The two equivalent hydrogens of the methyl group of methanol are labeled H_a, while the methyl hydrogen in the C–O–H plane is labeled H_b.

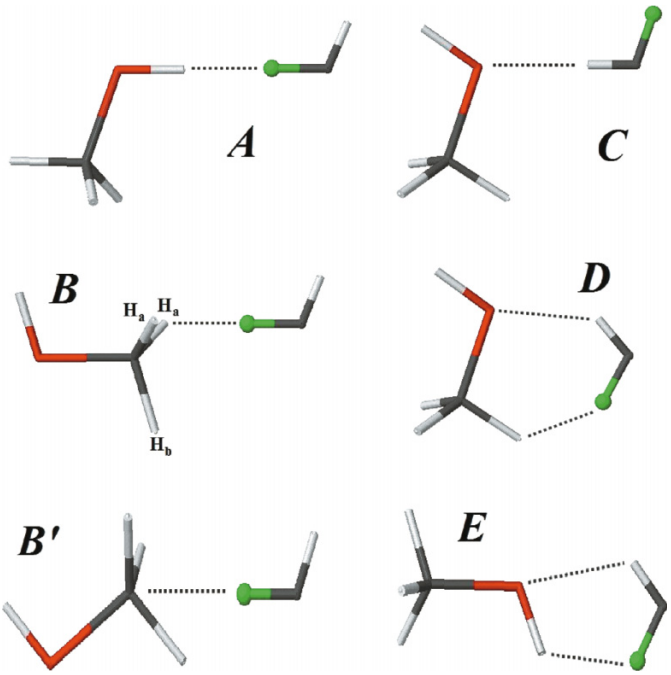

In this paper, we present the results of a computational study of methanol dimers and binary complexes of methanol with water, acetonitrile, and chloromethane. The optimized geometries, stabilization energies, harmonic frequencies, and vibrational intensities are reported. A net attraction is predicted for all of the optimized structures, and most of the complexes have no imaginary frequencies and are minima on the potential energy surface; small imaginary frequencies (less than $i40$ cm^{-1}) are observed for some systems and are noted where applicable. The purpose of this study is not only to analyze the changes that result upon complex formation in the bonds directly involved in the hydrogen bonding, but also to focus our attention on the changes in the remote parts of the molecules not directly involved in the intermolecular interactions to investigate whether the nature of proper and improper HBs is significantly different. The atoms in molecules (AIM) method provides useful insights into the description of chemical bonding[42–46] and it was used in the analysis of the electronic structure of the monomers and binary methanol systems. The topological features of the electron density can be described in terms of

Fig. 2. Topologies of the methanol complexes investigated; molecular graphs were constructed using AIM2000 software.[57] The larger circles represent the nuclei and the smaller red and yellow circles represent bond and ring critical points, respectively. The curves represent the bond paths linking the nuclei via bond critical points. [a]The structures are optimized to stable complexes, but calculated frequencies show one small imaginary frequency. [b]The structures are optimized to stable complexes, but calculated frequencies show two small imaginary frequencies. [c]The optimization of the methanol complex with chloromethane starting with the "**A**" structural arrangement of monomers always resulted in the optimized structure "**E**" when counterpoise (CP) correction was included. [d]The optimization of **D** and **E** arrangements of the CH_3OH/H_2O complex was not successful at the level of theory used. [e]For the CH_3OH/CH_3CN complex, only system **B′** (and not system **B**) was successfully optimized at the MP2 level with the CP correction included.

Can. J. Chem. Downloaded from www.nrcresearchpress.com by 80.58.250.72 on 09/16/12
For personal use only.

the critical points, the regions where the gradient vector of electron density is zero. The electron density, $\rho(r_c)$, and the Laplacian of the electron density, $\nabla^2\rho(r_c)$, evaluated at the intermolecular bond critical points and at the ring critical points as well as the integrated atomic properties were used in the description of proper and improper HBs. The natural bond orbitals (NBO) analysis, developed by Weinhold and co-workers, was performed to evaluate the orbital interactions within the pairs of interacting atoms.[47–49] NBO describes the chemical bonding in terms of hybridization or charge donation;[50,51] we have examined the occupancy and its changes upon HB formation at the lone pairs of the electronegative atom (O, N, and Cl) and at the antibonding orbitals of CO, CH, and OH, as well as the hybridization changes of the carbon atom and oxygen atom in the methanol molecule as an HB donor or HB acceptor.

The analysis of the above parameters is performed on the complexes with several different geometrical arrangements. Our goal is to complement earlier work on proper and improper HBs as well as to aid in describing the results of the experimental spectroscopic study of methanol complexes performed in our laboratory.[52]

Computational methods

The ab initio calculations were performed using Gaussian 03[53] on an AMD Opteron cluster. The geometries of all of the monomers and complexes were optimized at the second-order Møller–Plesset theory with the inner shells included (MP2(full)), with the 6-311++G(d,p) basis set; the energies, vibrational frequencies, and intensities were calculated at the same level of theory with the basis set superposition error approximated using the counterpoise correction method of Boys and Bernardi,[54] included in Gaussian 03. The stabilization energy of each dimer system was calculated as the difference between the calculated energy of the complex and the sum of the calculated energies of the isolated monomers, including the zero-point vibrational energy. Atomic charges were evaluated at the MP2(full)/6-311++G(d,p) level of theory using NBO (natural bond orbital),[55] a built-in subroutine of Gaussian 03, and using the AIM method.[44] Electron densities, bond critical point (BCP) properties, and atomic properties were analyzed using AIMAll software[56] and molecular graphs were constructed using AIM2000.[57]

Results and discussion

Five different arrangements (systems **A**, **B**, **C**, **D**, and **E**) of the binary complexes were considered. The structural arrangement of the monomers within each system is illustrated in Fig. 1. In systems **A** and **B**, methanol is a HB donor. In system **A**, a traditional HB exists between the hydroxyl hydrogen of methanol and the acceptor atom Y (Y= O, N, Cl), while in system **B** the unconventional HB interactions between the methyl group of methanol and Y are considered. Systems **B** and **B′** are very similar, though the AIM analysis shows 2 different electron density distributions (Fig. 2): in system **B** the BCP is found between a hydrogen atom and the acceptor Y, whereas in system **B′** the BCP is found between the carbon atom and the acceptor Y. Hence, system **B′** generally would not be considered as hydrogen bonded because the bond path does not connect the H atom to the Y acceptor atom through the BCP.[44] We first considered these systems as distinct; however, no significant difference with respect to the investigated parameters, other than the location of the BCP, was found between structures **B** and **B′**.

In system **C**, the oxygen atom in methanol acts as a HB acceptor (**C** and **C′** are used to distinguish between an improper HB and a proper HB, respectively). Systems **C** and **C′** were included in the study to examine the effects of the HB formation on the methanol molecule accepting the proton and to differentiate between changes due to HB donor and HB acceptor roles. The oxygen atom of methanol is the atom primarily involved in the HB interaction in these systems; however, the remote parts of the molecule, specifically the methyl group, show significant changes in the investigated parameters upon the non-covalent bond formation. System **D** has two improper HBs: one involves the methyl group of methanol and a Y atom, while the second involves the oxygen atom of methanol and a methyl group of the second unit of the complex. Finally, system **E** has the hydroxyl group involved in a proper HB and an improper HB (in the case of the methanol dimer the optimization of this arrangement resulted in a distinct interaction between two hydroxyl groups (we call it **E′**), and it will be treated separately). The optimizations of the **D** and **E** arrangements of the methanol–water complex were not successful at the level of theory used.

The stabilization energies and the corresponding distances between the monomers in the hydrogen-bonded complexes along with the values of the electron density and its Laplacian evaluated at the BCP found between the interacting atoms are summarized in Table 1, and the corresponding molecular graphs are illustrated in Fig. 2. It was found that with decreasing distance between the monomers within a hydrogen-bonded complex, the stabilization energy generally increases, and the values of the electron density, $\rho(r_c)$, and the Laplacian of electron density, $\nabla^2\rho(r_c)$, increase as well.[51,58,59]

Additionally, a good exponential relationship was observed between $\rho(r_c)$ or $\nabla^2\rho(r_c)$ and the intermolecular distance, as reported by others,[26,35,42,58,60–63] and an excellent linear relationship was found between $\rho(r_c)$ and $\nabla^2\rho(r_c)$, as

Can. J. Chem. Downloaded from www.nrcresearchpress.com by 80.58.250.72 on 09/16/12
For personal use only.

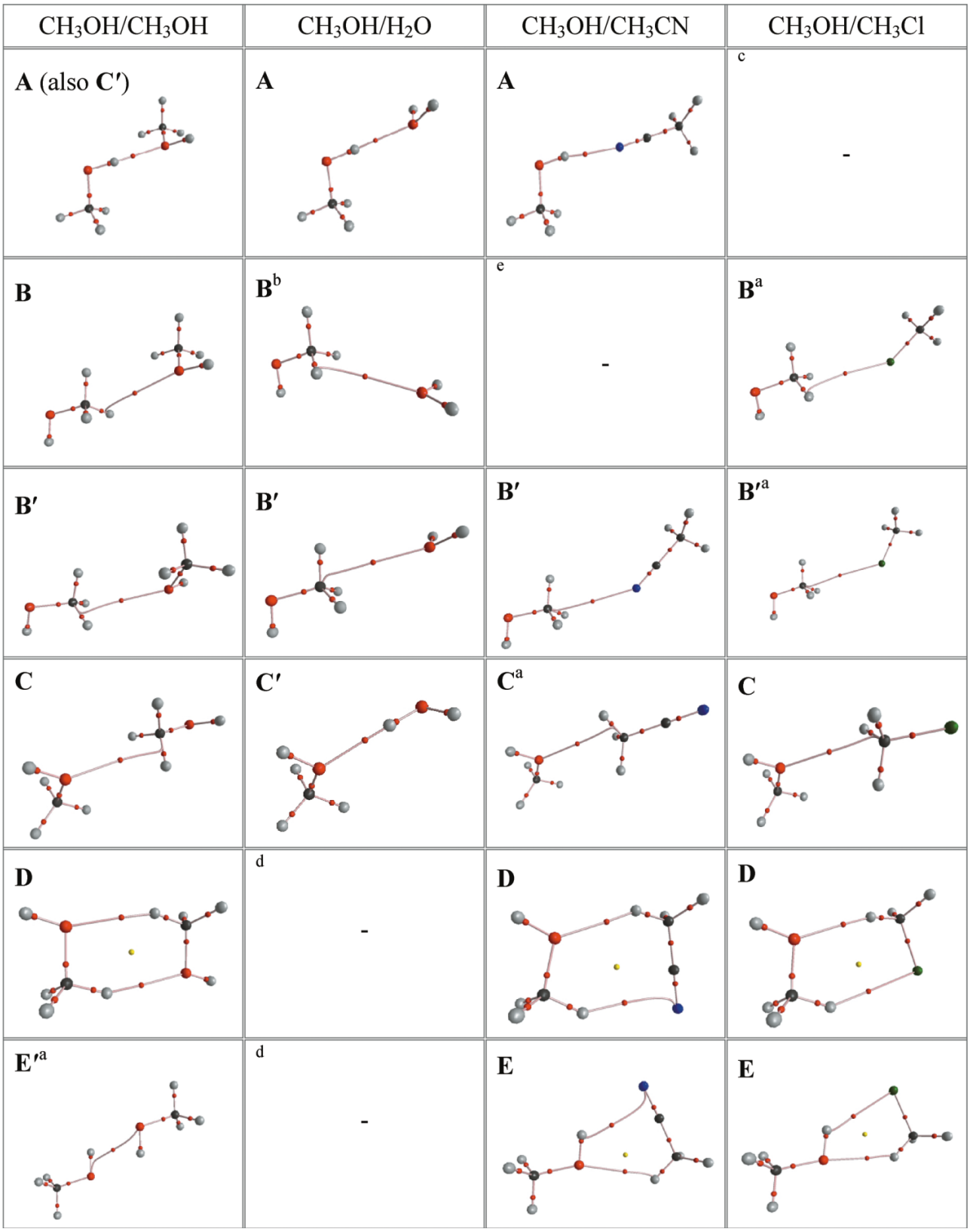

shown in Fig. 3. Reasonable logarithmic correlation was obtained between ΔE and the sum of the electron density evaluated at all critical points found between the monomers, or between ΔE and the sum of $\rho(r_c)$ evaluated at all BCPs between the monomers; the latter correlation was somewhat better, in agreement with the discussion by Rozas in the review of the nature of HBs.[21]

As expected,[41] the proper HB complexes (systems **A** and **C**′) are the most stable among all of the systems investigated, and the calculated stabilization energies (in the range

Can. J. Chem. Downloaded from www.nrcresearchpress.com by 80.58.250.72 on 09/16/12
For personal use only.

Table 1. Stabilization energies (ΔE), distances between monomers within the hydrogen-bonded complexes, and values of the electron density ($\rho(r_c)$) and the Laplacian of electron density ($\nabla^2\rho(r_c)$) evaluated at the intermolecular bond critical points (BCPs).

System	Complex	ΔE^a (kJ mol^{-1})	Distance (Å)	$\rho(r_c)$ (au)	$\nabla^2\rho(r_c)$ (au)
A	CH_3OH/CH_3OH	–16.4	1.99	0.021	0.083
	CH_3OH/H_2O	–12.9	2.05	0.019	0.072
	CH_3OH/CH_3CN	–15.2	2.15	0.016	0.060
B	CH_3OH/CH_3OH	–3.2	2.94	0.004	0.019
	CH_3OH/H_2O	–2.1	3.12	0.003	0.013
	CH_3OH/CH_3Cl	–1.5	3.47	0.002	0.009
B′	CH_3OH/CH_3OH	–3.1	2.97	0.004	0.019
	CH_3OH/H_2O	–2.1	3.14	0.004	0.017
	CH_3OH/CH_3CN	–3.9	3.16	0.004	0.016
	CH_3OH/CH_3Cl	–1.6	3.56	0.002	0.009
C	CH_3OH/CH_3OH	–3.1	2.97	0.004	0.019
	CH_3CN/CH_3OH	–7.2	2.97	0.005	0.022
	CH_3Cl/CH_3OH	–5.3	2.93	0.005	0.022
C′	CH_3OH/CH_3OH	–16.4	1.99	0.021	0.083
	H_2O/CH_3OH	–14.0	2.00	0.021	0.081
D[b]	CH_3OH/CH_3OH	–5.6	2.51, 2.51	0.008, 0.008	0.027, 0.027
	CH_3OH/CH_3CN	–11.2	2.91, 2.40	0.005, 0.010	0.014, 0.035
	CH_3OH/CH_3Cl	–6.9	3.20, 2.41	0.004, 0.010	0.011, 0.033
E[b]	CH_3OH/CH_3CN	–13.8	2.55, 2.66	0.008, 0.007	0.031, 0.023
	CH_3OH/CH_3Cl	–8.5	2.77, 2.48	0.007, 0.008	0.026, 0.030
E′[b]	CH_3OH/CH_3OH	–12.7	2.31, 2.33	0.013	0.059

[a]Energy of complex relative to total energy of the two free monomers; all energies include the zero-point vibrational energy.

[b]Two intermolecular BCPs are found in systems **D** and **E**; the values corresponding to the interaction involving the hydrogen of methanol are the first values shown for each set of parameters.

of –12 to –17 kJ mol^{-1}) are typical values for normal HBs.[21] The interaction energies for the improper HB complexes (systems **B** and **C**) are much smaller; however, stabilization energies in the range of –1 to –8 kJ mol^{-1} are still predicted upon complex formation. Furthermore, when two intermolecular improper HBs are present between the monomers, such as in systems **D**, the stabilization energies increase (approximately twice those of corresponding systems **B**), so cooperativity is predicted with two improper HBs within one system, where the directionality is known to make a smaller contribution to the strength of the interaction.[38,64] In contrast, changing the geometry of system **A** and introducing an additional CH···O interaction in addition to the proper OH···Y hydrogen bond (systems **E**) results in a slight lowering of the stabilization energy. The loss of directionality, which is known to be very important for proper HBs owing to a large contribution of the orientation-dependent electrostatic interaction, as well as an increased steric strain on the hydroxyl group contribute to the decrease in the stability of these complexes with respect to system **A**.

Vibrational frequencies and integrated intensities for the methanol monomer and the shifts in the vibrational frequencies for each of the complexes studied are summarized in Table 2. Corresponding changes in the bond lengths and changes in the electron density at BCPs are summarized in Table S2 of the Supplementary data. We shall emphasize the correlations between the frequency shifts of the stretching vibrations, the bond length changes, and the changes in the electron density evaluated at the intramolecular BCPs, which give a clear indication of either bond strengthening (bond length contraction, blue shift of the vibrational frequency, and decrease in the $\rho(r_c)$) or bond weakening (bond length elongation, red shift of the vibrational frequency, and increase in the $\rho(r_c)$) upon HB formation. To gain a better understanding of the nature of the interaction, all of the parts of the molecule directly or indirectly involved in the HB were examined; hence, we would like to draw attention to the remote parts of the methanol molecule in addition to the bonds directly involved in the HB.

The conceptual summary of the above relating to the frequency shifts of the methanol stretching vibrations is shown in Table 3. The significant red shift of the O–H stretching frequency (with the large increase in the vibrational intensity) and the blue shift of the C–O stretching frequency are observed only when methanol is donating a hydroxyl hydrogen in the proper HB (systems **A** and **E**), whereas the red shift of the C–O stretching frequency is expected for the improper HB involving the methyl hydrogen (systems **B** and **D**); however, the red shifts are smaller in magnitude, corresponding to weaker interactions. The considerable red shifts of the C–H stretching frequencies with the increase in the intensity of absorption are observed only for the proper HB complexes involving the hydroxyl hydrogen of methanol (systems **A**), in agreement with the study by Scheiner[65] investigating the spectroscopic patterns of CH···O hydrogen bonds in proteins. In all other cases, such as the improper HB involving hydrogen of a methyl group or the proper or improper HBs with methanol as an HB acceptor, blue shifts

Can. J. Chem. Downloaded from www.nrcresearchpress.com by 80.58.250.72 on 09/16/12
For personal use only.

Fig. 3. The relationship observed between $\rho(r_c)$ or $\nabla^2\rho(r_c)$ and the intermolecular distance, as well as the relationship between $\rho(r_c)$ and $\nabla^2\rho(r_c)$, calculated at the MP2(full) level using quantum theory of atoms in molecules for the binary methanol complexes with methanol, water, acetonitrile, and chloromethane.

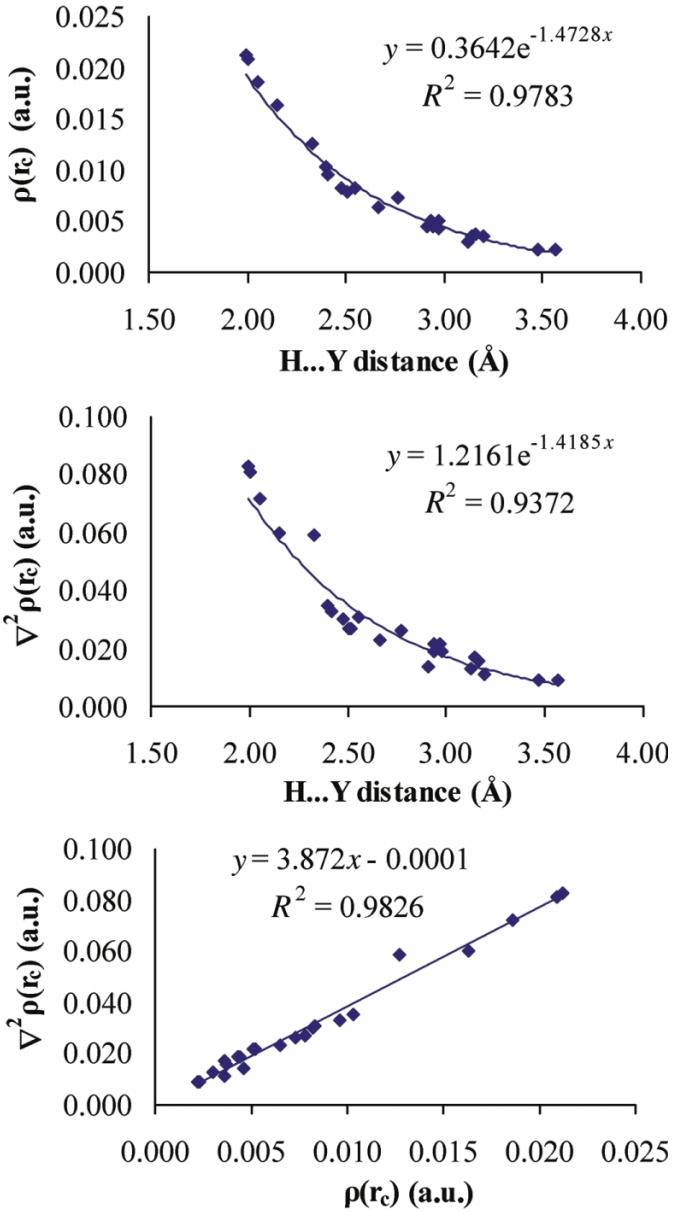

of the C–H stretching frequencies are predicted. The frequency shifts of the C–H stretching vibrations towards higher wavenumbers observed experimentally in the methanol solutions[52] might be an indication of hydrogen bonding involving the methyl group as HB donor, or they can also be understood as a result of methanol acting as an HB acceptor through the electronegative oxygen atom. The larger blue shifts in the C–H stretching frequencies result upon improper HB formation involving the methyl group of methanol as a proton donor or when methanol acts as an electron density donor in the proper HB, while the blue shifts of the C–H stretching frequencies are smaller when methanol acts as a proton acceptor in the improper HB (refer to Table 2). This might prove to be useful information when analyzing the experimental vibrational spectra of various methanol solutions; therefore, it is possible to conclude that the changes occurring at the remote parts of the molecule as a result of the intermolecular interactions should be considered an important factor in the description and characterization of the proper and improper hydrogen bonds.

AIM and NBO atomic charges are given in Table S3 of the Supplementary data. In the discussion below we refer to the AIM charges, since these were found to be more suitable[66] (carbon atom carries a positive charge when calculated with the AIM method and a negative charge when calculated using the NBO method); however, both methods give similar trends with respect to the charge distribution in methanol. The additional NBO data, including the changes in the atomic charges, in the natural bond orbital occupancy, and in the orbital energy, are listed in the Supplementary data (Tables S4, S5, and S6, respectively). The magnitude of the charge transfer from the HB acceptor to the HB donor and the most significant values of $E(2)$, the stabilization energy associated with delocalization for the intermolecular orbital interactions, are summarized in Table 4, while the changes in $E(2)$ corresponding to the intramolecular orbital interactions in the methanol molecule are shown in Table 5.

Joseph and Jemmis[40] have suggested that two complexes having the same density distribution, regardless of their nature, will give the same NBO data because the natural bond orbitals are generated from the final density of the complex; therefore, the NBO data alone cannot fully explain the origin of the C–H bond contraction in the improper HB. However, since the changes associated with the occupancy in σ*(C–H) are correlated with the inter- and intramolecular orbital interactions, the analysis of these could provide a considerable amount of information about the red- and blue-shifting nature of hydrogen bonds.[19,67] Intramolecular hyperconjugation plays a significant role in the electronic structure of methanol, contributing to the molecular stability of the methanol monomer, so it is reasonable to examine the changes in the intramolecular orbital interactions that occur upon the formation of a HB within the strongly or weakly bound complexes.

The charge transfer from HB acceptor towards HB donor is considerable (Table 4) for the proper HB methanol complexes (systems **A, C′**, and **E**). Although the percent s character of O in OH increases upon complex formation, the O–H bond is weakened and elongated owing to the dominant effect of the charge density being directed from the lone pair on the HB acceptor atom (Y) into the antibonding O–H orbital, σ*(O–H) (Table 4). The intramolecular orbital interaction LP(O) → σ*(C–H) in methanol increases in systems **A** (Table 5), in correlation with the C–H bond elongation and the red shift of the C–H stretching frequencies upon proper HB formation involving the hydroxyl hydrogen (refer to Table 2 and Table S2). In contrast with systems **A**, a decrease in the intramolecular orbital interaction LP(O) → σ*(C–H) is generally observed for systems **E**, possibly because of the presence of an O···HC interaction, and thus less charge is transferred to the antibonding CH orbital from LP(O) and could explain the C–H bond strengthening and contraction as the calculated $E(2)$ decreases.

The intermolecular charge transfer from HB acceptor towards HB donor is considerably smaller (Table 4) for the

Can. J. Chem. Downloaded from www.nrcresearchpress.com by 80.58.250.72 on 09/16/12
For personal use only.

Table 2. Shifts in the stretching frequencies (cm^{-1}) and the vibrational intensities (km mol^{-1}) upon hydrogen bond formation in the binary complexes of methanol with methanol, water, acetonitrile, and chloromethane calculated at the MP2(full) level with the 6-311++G(d,p) basis set.

		$\nu_{1,\ CH}$		$\nu_{2,\ CH}$		$\nu_{3,\ CH}$		$\nu_{4,\ CO}$		$\nu_{5,\ CO}$		$\nu_{6,\ OH}$	
System	Complex	$\Delta\tilde{\nu}$	A_j	$\Delta\tilde{\nu}$	A_j	$\Delta\tilde{\nu}$	A_j	$\Delta\tilde{\nu}$	A_j	$\Delta\tilde{\nu}$	A_j	$\Delta\tilde{\nu}$	A_j
	CH_3OH[a]	3058	58.58	3128	52.03	3194	23.61	1076	114.10	1097	7.51	3915	35.78
A	CH_3OH/CH_3OH	–12	70.23	–17	62.03	–16	37.06	22	97.58	28	6.54	–93	343.11
	CH_3OH/H_2O	–10	68.37	–15	61.87	–15	35.53	21	108.53	26	6.24	–71	306.02
	CH_3OH/CH_3CN	–13	67.95	–18	62.97	–18	41.35	21	105.34	25	1.79	–65	348.19
B	CH_3OH/CH_3OH	12	52.15	15	46.34	9	23.89	–7	137.62	–8	7.71	1	33.40
	CH_3OH/H_2O	13	52.38	18	45.92	0	27.61	–4	124.89	–4	2.51	1	32.56
	CH_3OH/CH_3Cl	3	65.54	5	44.47	2	21.64	–3	123.45	–3	9.11	1	35.69
B′	CH_3OH/CH_3OH	12	52.92	15	45.26	8	24.21	–6	137.51	–8	7.08	1	33.71
	CH_3OH/H_2O	11	56.99	13	48.92	13	22.28	–7	124.17	–8	8.87	2	32.05
	CH_3OH/CH_3CN	13	58.75	18	41.86	3	24.26	–8	136.56	–9	4.25	–1	33.94
	CH_3OH/CH_3Cl	4	63.71	5	44.61	3	21.83	–3	121.61	–4	9.26	1	35.97
C	CH_3OH/CH_3OH	2	57.79	4	46.39	0	24.48	–1	105.66	–1	3.43	–2	38.10
	CH_3CN/CH_3OH	6	57.38	9	42.97	–1	24.18	–2	119.65	–1	1.21	–4	40.67
	CH_3Cl/CH_3OH	4	58.97	7	44.36	–1	23.57	–1	116.75	–1	2.45	–3	39.27
C′	CH_3OH/CH_3OH	14	52.36	21	38.41	11	15.09	1	133.53	–4	5.89	1	44.66
	H_2O/CH_3OH	15	50.48	22	38.88	12	15.81	0	127.56	–3	6.13	–2	47.01
D	CH_3OH/CH_3OH[b]	0	66.26	1	51.59	13	2.05	–5	112.48	–1	3.94	–1	31.97
	CH_3OH/CH_3CN	8	57.87	12	43.23	14	8.10	–6	105.99	–2	3.36	–3	36.96
	CH_3OH/CH_3Cl	5	58.56	8	45.09	9	12.92	–3	96.09	–3	0.46	–2	36.81
E	CH_3OH/CH_3CN	3	65.04	4	47.26	–3	25.38	11	135.27	13	7.33	–30	74.61
	CH_3OH/CH_3Cl	1	66.27	3	48.64	–2	24.78	12	88.16	9	2.46	–23	70.95
E′	CH_3OH/CH_3OH[b]	2	64.40	3	49.00	–3	26.00	10	165.62	17	0.75	–37	83.54

[a]The vibrational wavenumbers are for the monomer molecule and not shifts.

[b]Average value for frequency shifts (negative indicates a red shift and positive a blue shift) and intensity of absorption of symmetric and asymmetric stretches with respect to individual methanol molecules in the dimer system are listed.

Published by NRC Research Press

Can. J. Chem. Downloaded from www.nrcresearchpress.com by 80.58.250.72 on 09/16/12
For personal use only.

Table 3. Summary of the changes in the vibrational frequencies of the OH, CH, and CO stretching vibrations of the methanol molecule involved in proper and improper hydrogen bonds (HBs) as either HB donor or HB acceptor.

	Proper HB	Improper HB
CH_3OH as HB donor		
OH	Large red shift	No change
CH	Red shift	Blue shift
CO	Blue shift	Red shift
CH_3OH as HB acceptor		
OH	No change	No change
CH	Blue shift	Small blue shift
CO	No change	No change

improper HB methanol complexes (systems **B, C**, and **D**). The electron density is directed away from H_a and slightly towards H_b, which could relate to the observation that the BCP is not found between H_b and Y (Y is the HB accepting atom) in systems **B** and **B′**, even though H_b carries the most positive charge (refer to Fig. 1). The insignificant charge transfer from the HB acceptor towards the HB donor might suggest that the changes in the atomic charges within the HB donor molecule are predominantly due to the intramolecular charge redistribution, and as suggested by Li,[67] the intramolecular hyperconjugation plays an important role along with the intermolecular hyperconjugation in the red- and blue-shifted HBs. A slightly weaker LP(Y) → σ*(C–O) intermolecular orbital interaction and a significant increase in the occupancy in σ*(C–O) are predicted, which correlates with the C–O bond weakening and elongation. A decrease in the LP(O) → σ*(C–H) intramolecular orbital interaction is observed for the improper HB complexes; therefore, a consequent decrease in occupancy in the σ*(C–H) orbital could explain the strengthening and contraction of the C–H bond. The occupancy in the σ(C–H) bonding molecular orbital decreases as well; however, it is of lower magnitude, so its effects would not prevail.

When methanol acts as a HB acceptor, the strengthening of the C–H bonds upon complex formation can be attributed to a decrease in the LP(O) → σ*(C–H) intramolecular orbital interaction and subsequent decrease in the NBO occupancy in σ*(C–H_a) and σ*(C–H_b), where the changes are larger for the proper HB, correlating with the larger frequency shifts. At the same time, the occupancy in one lone pair on the oxygen atom decreases, while for the second lone pair the occupancy increases by a small amount, and the increase in the NBO occupancy in σ*(C–O) corresponds to the C–O bond weakening, elongation, and subsequent red shift of its stretching frequency.

In systems **D**, the positive atomic charge on H_b, the hydrogen primarily involved in the HB interaction, increases considerably; this increase is comparable to the increase in the positive charge on the hydroxyl hydrogen involved in the proper HB (systems **A**). Even though the intermolecular orbital interaction LP(Y) → σ*(C–H) is more important in systems **D,** blue shifts of all of the C–H stretching frequencies are predicted; in contrast, the LP(Y) → σ*(C–H) interaction would have the opposite effect. The C–H bond contraction can be explained by the intramolecular charge transfer within the methanol molecule — specifically, by a decrease in the LP(O) → σ*(C–H) intramolecular orbital interaction — along with the considerable rehybridization of C in CH (percent s increase). However, there is also an important accepting role of the oxygen involved in the complex formation in systems **D**, and as described earlier, this additional interaction increases the complex stability; the charge transfer from the lone pair on the oxygen of methanol directed towards the HB donor would also cause C–H bond contraction.

Using the AIM analysis we also included evaluation of the 8 criteria for hydrogen bonding proposed by Popelier.[44] These criteria are as follows: (1) a BCP and two bond paths are found between the interacting atoms; (2) the meaningful range for the electron density, ρ(r), evaluated at the BCP is between 0.002 au and 0.04 au; (3) the range for $\nabla^2\rho(r)$ evaluated at the BCP is positive and between 0.02 and 0.15 au; (4) there is a penetration of the hydrogen atom and an acceptor atom (typically, the ρ value of the contour as an approximate boundary of the molecule in each monomer is taken to be 0.001 au); (5) the hydrogen atom loses electrons and (6) is destabilized; and (7) the dipolar polarization as well as (8) the atomic volume of the hydrogen atom decrease upon complex formation.

The results of the AIM analysis are given in Table 6. Since criteria 2 and 4–7 are satisfied for all of the complexes investigated, we will not discuss these in any more detail here, and only note that there seems to exist a correlation between the strength of the interaction and the magnitude of the change in the specific parameter, which might arise because not all of the proposed criteria are completely independent.[44]

Conventional hydrogen bonds (OH···Y interaction, Y=O, N, Cl (systems **A**, **C′** and **E**)) satisfy all 8 criteria, and as suggested by Popelier[44] and Koch and Popelier,[61] the verification of medium to strong hydrogen bonding is successful using the above analysis. Relatively large values of $\nabla^2\rho(r_c)$ correlate with the large decrease in the atomic volume of the hydroxyl hydrogen involved in the traditional OH···H hydrogen bond when the O–H–O angle is approximately 180° (systems **A** and **C′**), and these values decrease with a decreasing O–H–O angle (system **E**), as does the stabilization energy (Table 1). For the methanol dimer system **E′,** the intermolecular BCP is found between two oxygen atoms instead of between the hydrogen atom and oxygen atom; therefore, the basic topological character of traditional hydrogen bonding is not met. Considering that all of the other 7 criteria for hydrogen bonding are satisfied, this arrangement might be classified as a strained hydrogen-bonded complex. The calculated imaginary frequency might suggest that this arrangement is not the minimum at the potential energy surface; however, the size of the imaginary frequency is on the order of numerical accuracy and indicates a flat potential energy surface.[68]

The CH···O interaction within systems **E** and **D,** where the oxygen of methanol is the HB accepting atom, also satisfies all 8 criteria. In contrast, for the CH···Y interaction, where the methyl group of methanol is donating hydrogen (systems **B** and **D**), the calculated values of the Laplacian

Table 4. The magnitude of the charge transfer from the HB acceptor to the HB donor (positive values) calculated using the AIM method, and the most significant values of $E(2)$, the stabilization energy associated with delocalization for the intermolecular orbital interactions obtained from NBO analysis.

System	Complex	Intermolecular charge transfer from HB acceptor to HB donor (au)	Intermolecular orbital interaction from HB acceptor to HB donor	$E(2)$ (kcal mol^{-1})
A (**C′**)	CH_3OH/CH_3OH	0.013	LP(O) → σ*(O–H)	3.35
A	CH_3OH/H_2O	0.012	LP(O) → σ*(O–H)	4.87
A	CH_3OH/CH_3CN	0.015	LP(N) → σ*(O–H)	3.36
B (**C**)	CH_3OH/CH_3OH	–0.001	LP(O) → σ*(C–O)	0.25
B	CH_3OH/H_2O	–0.002	None above the threshold (0.05)	—
B	CH_3OH/CH_3Cl	0.003	LP(Cl) → σ*(C–O)	0.09
B′	CH_3OH/CH_3OH	–0.001	LP(O) → σ*(C–O)	0.21
B′	CH_3OH/H_2O	–0.001	LP(O) → σ*(C–O)	0.16
B′	CH_3OH/CH_3CN	0.002	LP(O) → σ*(C–O)	0.21
B′	CH_3OH/CH_3Cl	0.003	LP(O) → σ*(C–O)	0.14
C	CH_3CN/CH_3OH	0.000	LP(O) → σ*(C–C)	0.39
C	CH_3Cl/CH_3OH	–0.001	LP(O) → σ*(C–Cl)	0.38
C′	H_2O/CH_3OH	0.013	LP(O) → σ*(O–H)	3.24
D	CH_3OH/CH_3OH	0.000	LP(O) → σ*(C–H)	0.80
D	CH_3OH/CH_3CN	0.002	LP(O) → σ*(C–H)	1.38
D	CH_3OH/CH_3Cl	0.003	LP(O) → σ*(C–H)	1.48
E	CH_3OH/CH_3CN	0.008	LP(O) → σ*(C–N)	0.35
E	CH_3OH/CH_3Cl	0.009	LP(Cl) → σ*(O–H)	0.72
E′	CH_3OH/CH_3OH	0.000	LP(O) → σ*(O–H)	0.30

Can. J. Chem. Downloaded from www.nrcresearchpress.com by 80.58.250.72 on 09/16/12
For personal use only.

of electron density at the BCP are generally too low and outside of the suggested range; however, as pointed out by Popelier, the range of the values of electron density and its Laplacian at the intermolecular BCP serves more as a guide than as a rigid constraint.[44] For some cases though, the atomic volume of hydrogen increases upon complex formation; therefore, this criterion for hydrogen bonding would not be met in addition to the low value of $\nabla^2\rho(r_c)$.

The close similarity between systems **B** and **B′** (or systems **E** and **E′**) suggests that the presence of a BCP between the hydrogen and the Y atom is not as significant in the description of a HB as the value of the Laplacian at the particular critical point or the change in the atomic volume of an interacting atom, as has been proposed by Li and Yan.[69] Alternatively, electron density and its Laplacian evaluated at an intermolecular BCP might be used to quantify the strength of the HB interactions.[21] As Parthasarathi et al. discussed,[63] the smooth change in the nature of non-covalent interactions proceeds from the dispersive forces dominated by van der Waals interactions through classical to strong hydrogen bonding, which is mainly electrostatic in nature. This differs from the dramatic change in $\nabla^2\rho(r_c)$ from positive to negative values observed when going from a strong non-covalent hydrogen bond to a covalent bond.[63]

Conclusion

Several distinct geometrical arrangements of methanol dimers and binary systems of methanol with water, acetonitrile, and chloromethane were considered in this study, and the nature of proper and improper hydrogen bonds was investigated. The formation of a considerably stronger, proper HB interaction involving the hydroxyl hydrogen of methanol leads to weakening and elongation of the O–H bond, accompanied by a red shift of the O–H stretching frequency and an increase in the intensity of absorption. On the other hand, the improper HB involving the methyl group of methanol is a weak interaction and leads to strengthening and contraction of the C–H bond, accompanied by a blue shift of the C–H stretching frequencies and a decrease in the vibrational intensity.

The changes occurring at the remote parts of the HB donor molecule as a consequence of the intermolecular interaction should be considered an important factor in the description and characterization of proper and improper hydrogen bonds. The frequency shifts of the C–H stretching vibrations towards higher wavenumbers could be used as an indication of hydrogen bonding involving the methyl group as a HB donor, or these could also be understood as a result of methanol acting as a HB acceptor through the electronegative oxygen atom. The red shift of the C–H stretching frequency is predicted only upon proper HB formation involving the hydroxyl hydrogen of methanol. This might prove to be useful information when analyzing the experimental vibrational spectra of various methanol solutions.

Our study of binary methanol complexes suggests that along with a balance between opposing physical forces (electrostatic interaction, polarization, Pauli exclusion) that influence the lengthening or contraction of the bonds involved in the non-covalent interactions, the orbital overlap and electron charge transfer also play an important role and influence the resulting observable red or blue shift of the corresponding stretching frequencies. A close resemblance between the topological features of the electron density and its Laplacian for a proper HB and an improper HB suggests that the nature of these hydrogen bonds is similar, though there are some differences in the molecular orbital interactions and electronic charge transfer within the monomers or between the monomers of proper and improper HB complexes. The charge transfer from the HB acceptor to the HB

Can. J. Chem. Downloaded from www.nrcresearchpress.com by 80.58.250.72 on 09/16/12
For personal use only.

Table 5. NBO changes in the intramolecular orbital interactions between the lone pairs on oxygen and σ*(C–H) of methanol as a result of complex formation.

		Intramolecular orbital interaction $\Delta E(2)$ (kcal mol^{-1})				
System	Complex	LP1(O) → σ*(C–H_a)	LP2(O) → σ*(C–H_a)	LP1(O) → σ*(C–H_a)	LP2(O) → σ*(C–H_a)	LP1(O) → σ*(C–H_b)
	CH_3OH[a]	0.95	8.35	0.96	8.33	3.28
A	CH_3OH/CH_3OH[b]	0.19	0.20	0.05	0.70	0.15
	CH_3OH/H_2O	0.11	0.41	0.11	0.41	0.14
	CH_3OH/CH_3CN	0.12	0.47	0.11	0.50	0.11
B	CH_3OH/CH_3OH[b]	–0.01	–0.23	–0.04	–0.16	–0.07
	CH_3OH/H_2O	–0.04	–0.26	–0.05	–0.25	–0.10
	CH_3OH/CH_3Cl	–0.01	–0.10	–0.02	–0.11	–0.04
B′	CH_3OH/CH_3OH[b]	–0.04	–0.15	–0.01	–0.23	–0.06
	CH_3OH/H_2O	–0.03	–0.17	–0.02	–0.22	–0.07
	CH_3OH/CH_3CN	0.05	–0.49	–0.12	–0.03	–0.10
	CH_3OH/CH_3Cl	–0.01	–0.09	–0.01	–0.11	–0.03
C	CH_3OH/CH_3OH[c]	–0.07	–0.24	0.01	–0.04	–0.02
	CH_3CN/CH_3OH	–0.02	–0.29	–0.05	–0.20	–0.12
	CH_3Cl/CH_3OH	–0.06	–0.16	–0.02	–0.21	–0.06
C′	CH_3OH/CH_3OH[c]	–0.45	0.36	1.35	–2.83	–0.37
	H_2O/CH_3OH	1.30	–2.78	–0.46	0.29	–0.37
D	CH_3OH/CH_3OH[d]	–0.04	–0.36	–0.05	–0.34	–0.28
	CH_3OH/CH_3CN	–0.08	–0.53	–0.09	–0.51	–0.28
	CH_3OH/CH_3Cl	–0.06	–0.35	–0.07	–0.33	–0.16
E	CH_3OH/CH_3CN	0.05	–0.08	0.05	–0.08	–0.17
	CH_3OH/CH_3Cl	0.02	–0.07	0.01	–0.05	–0.06
E′	CH_3OH/CH_3OH[d]	0.21	–0.19	0.19	–0.36	–0.02

[a]Actual values for the monomer molecule.
[b]The changes calculated for the HB donor are shown.
[c]The changes calculated for the HB acceptor are shown.
[d]The values are averaged for the equivalent methanol units within a complex.

Published by NRC Research Press

Can. J. Chem. Downloaded from www.nrcresearchpress.com by 80.58.250.72 on 09/16/12
For personal use only.

Table 6. The AIM-based criteria for hydrogen bonding proposed by Popelier.[44]

System	Complex	Interaction	BCP	$\rho(r_c)$ (au)	$\nabla^2\rho(r_c)$ (au)	ρ_{donor} (au)	$\rho_{acceptor}$ (au)	ΔN (au)	ΔE (au)	ΔM (au)	ΔV (au)	H bonding?
A	CH_3OH/CH_3OH	OH···O	Yes	0.021	0.083	0.013	0.032	0.045	0.025	–0.040	–7.928	Yes
	CH_3OH/H_2O	OH···O	Yes	0.019	0.072	0.010	0.157	0.042	0.023	–0.037	–7.160	Yes
	CH_3OH/CH_3CN	OH···N	Yes	0.016	0.060	0.006	0.008	0.038	0.023	–0.031	–6.110	Yes
B	CH_3OH/CH_3OH	CH···O	Yes	0.004	0.019	0.003	0.002	0.008	0.002	–0.005	–0.019	No
	CH_3OH/H_2O	CH···O	Yes	0.003	0.013	0.002	0.180	0.010	0.003	–0.004	0.279	No
	CH_3OH/CH_3Cl	CH···Cl	Yes	0.002	0.009	0.001	0.001	0.002	0.001	–0.002	1.438	No
B′	CH_3OH/CH_3OH	C···O	No	0.004	0.019	0.002	0.002	0.009	0.002	–0.004	0.021	No
	CH_3OH/H_2O	C···O	No	0.004	0.017	0.002	0.416	0.004	0.001	–0.001	0.316	No
	CH_3OH/CH_3CN	C···N	No	0.004	0.016	0.002	0.006	0.008	0.003	–0.002	0.112	No
	CH_3OH/CH_3Cl	C···Cl	No	0.002	0.009	0.001	0.001	0.002	0.001	–0.001	1.201	No
C	CH_3CN/CH_3OH	C···O	No	0.005	0.022	0.003	0.002	0.009	0.003	–0.001	–0.592	No
	CH_3Cl/CH_3OH	C···O	No	0.005	0.022	0.003	0.004	0.008	0.002	–0.003	–0.515	No
C′	H_2O/CH_3OH	OH···O	Yes	0.021	0.081	0.052	0.074	0.042	0.023	–0.038	–7.560	Yes
D	CH_3OH/CH_3OH	CH···O	Yes	0.008	0.027	0.004	0.004	0.042	0.015	–0.025	–4.659	Yes
		CH···O	Yes	0.008	0.027	0.004	0.004	0.042	0.015	–0.025	–4.659	Yes
	CH_3OH/CH_3CN	CH···O	Yes	0.010	0.035	0.006	0.006	0.051	0.019	–0.023	–6.016	Yes
		CH···N	Yes	0.005	0.014	0.003	0.003	0.023	0.009	–0.012	–0.842	No
	CH_3OH/CH_3Cl	CH···O	Yes	0.010	0.033	0.005	0.004	0.051	0.019	–0.029	–5.845	Yes
		CH···Cl	Yes	0.004	0.011	0.001	0.002	0.014	0.006	–0.006	0.868	No
E	CH_3OH/CH_3CN	CH···O	Yes	0.006	0.023	0.004	0.003	0.038	0.015	–0.011	–3.277	Yes
		OH···N	Yes	0.008	0.031	0.004	0.005	0.018	0.013	–0.011	–1.754	Yes
	CH_3OH/CH_3Cl	CH···O	Yes	0.008	0.030	0.005	0.004	0.042	0.016	–0.019	–5.203	Yes
		OH···Cl	Yes	0.007	0.026	0.003	0.004	0.010	0.009	–0.005	–0.594	Yes
E′	CH_3OH/CH_3OH	HO···OH	No	0.013	0.059	0.053	0.089	0.025	0.015	–0.013	–2.720	No

Note: In the cases where the BCP exists between the HB acceptor atom (Y) and an HB donor atom other than hydrogen (O or C), the atomic properties values are calculated for the hydrogen atom closest to the HB acceptor rather than for the oxygen or carbon atom linked to the Y atom via the BCP. ΔN, ΔM, and ΔV are the change in charge, dipolar polarization, and volume upon complex formation.

Can. J. Chem. Downloaded from www.nrcresearchpress.com by 80.58.250.72 on 09/16/12
For personal use only.

donor is significant in a strong proper HB, which is mostly electrostatic in nature. The electrostatic forces and the intermolecular charge transfer are less dominating for an improper HB; instead, the intramolecular hyperconjugation plays a more significant role in the electronic structure of the improper HB methanol complexes.

Although the fundamental nature of proper and improper hydrogen bonding seems to be comparable, the origin of the C–H bond contraction in an improper HB can be explained by a different effect than the origin of the O–H bond elongation in a proper HB. Specifically, the elongation of the O–H bond is predominantly due to a strong electrostatic interaction between the OH group of the HB donor and an electron-rich region, accompanied by a considerable intermolecular charge transfer from the HB acceptor toward the antibonding σ*(O–H) orbital, upon which the weakening of the O–H bond is observed. On the other hand, the contraction of the C–H bond arises from a decrease in the intramolecular LP(O) → σ*(C–H) orbital interaction, causing strengthening of the C–H bond and a consequent blue shift of its stretching frequency. The weakening of the intramolecular LP(O) → σ*(C–H) orbital interaction in an improper HB complex can be explained as a result of a secondary structural reorganization of the proton donor due to the interactions between a HB acceptor and the remote parts of the HB donor, supporting the theory of Hobza.[19,41] Further work is ongoing to gain a better understanding of the above interactions and to extend existing theories, so that it will be possible to predict the spectroscopic shifts in the stretching frequencies based solely on the nature of the HB donor and HB acceptor and to use the experimental spectroscopic data to predict a possible type of non-covalent bonding interaction between the molecules.

Supplementary material

Supplementary data for this article, including the archives for all geometry optimizations of the structures discussed in this paper, are available on the journal Web site (canjchem.nrc.ca). Figures S1 and S2 show the relationships between the stabilization energy, the HB distance, and the sum of ρ(r) or the sum of $\nabla^2\rho(r)$ evaluated at the intermolecular BCPs and at all intermolecular critical points; the calculated data are listed in Tables S1 and S2. Figures S3–S6 show the envelope maps of the Laplacian of electron density. Changes in the stabilization energy in the formation of proper and improper hydrogen bonds with a methyl substitution in the HB donor and HB acceptor are illustrated in Fig. S7. Atomic charges calculated using AIM and NBO methods are compared in Table S3. Tables S4–S6 show the additional NBO results. Molecular graphs illustrating additional H_2O, MeCN, and MeCl complexes are shown in Fig. S8; corresponding data are summarized in Table S7.

Acknowledgements

C.D.K. thanks the Canada Research Chairs program, Canada Foundation for Innovation (CFI), Cape Breton University, Natural Sciences and Engineering Research Council Canada (NSERC), Nova Scotia Research and Innovation Trust, and Petroleum Research Fund for their financial support of this work. Z.I. thanks NSERC for an undergraduate summer research award. Computational facilities are provided in part by the Atlantic Computational Excellence Network (ACEnet, www.ace-net.ca), the regional high-performance computing consortium for universities in Atlantic Canada. ACEnet is funded by the CFI, the Atlantic Canada Opportunities Agency (ACOA), and the provinces of Newfoundland & Labrador, Nova Scotia, and New Brunswick.

References

(1) Jeffrey, G. A. *An Introduction to Hydrogen Bonding*; Oxford University Press: New York, 1997.
(2) Scheiner, S. *Hydrogen Bonding*; Oxford University Press: New York, 1997.
(3) Desiraju, G. R.; Steiner, T. *The Weak Hydrogen Bond in Structural Chemistry and Biology*; IUCr Monographs on Crystallography 9; Oxford University Press: Oxford, 1999.
(4) Grabowski, S. J., Ed. *Hydrogen Bonding – New Insights*; Challenges and Advances in Computational Chemistry and Physics, Vol. 3; Springer: Dordrecht, 2006.
(5) Bertie, J. E.; Zhang, S. L. *J. Mol. Struct.* **1997**, *413–414*, 333. doi:10.1016/S0022-2860(97)00152-X.
(6) Mó, O.; Yáñez, M.; Elguero, J. *J. Chem. Phys.* **1997**, *107* (9), 3592. doi:10.1063/1.474486.
(7) Martín, M. E.; Sánchez, M. L.; Olivares del Valle, F. J.; Aguilar, M. A. *J. Chem. Phys.* **2002**, *116* (4), 1613. doi:10.1063/1.1430253.
(8) Adya, A. K.; Bianchi, L.; Wormald, C. J. *J. Chem. Phys.* **2000**, *112* (9), 4231. doi:10.1063/1.480969.
(9) Deng, J. Q.; Lipson, R. H. *Can. J. Chem.* **2006**, *84* (6), 886. doi:10.1139/V06-085.
(10) Bahr, S.; Toubin, C.; Kempter, V. *J. Chem. Phys.* **2008**, *128* (13), 134712. doi:10.1063/1.2901970.
(11) Cao, D.-l.; Ren, F.-d.; Wang, J.-l.; Wang, W.-l. *J. Mol. Struct. THEOCHEM* **2007**, *805* (1–3), 53. doi:10.1016/j.theochem.2006.09.024.
(12) Boyd, S. L.; Boyd, R. J. *J. Chem. Theory Comput.* **2007**, *3* (1), 54. doi:10.1021/ct6002912.
(13) Liu, G.; He, T. *Struct. Chem.* **2007**, *18* (3), 387. doi:10.1007/s11224-007-9183-9.
(14) Suresh, S. J.; Prabhu, A. L.; Arora, A. *J. Chem. Phys.* **2007**, *126* (13), 134502. doi:10.1063/1.2647105.
(15) Wu, X.; Chen, Y.; Yamaguchi, T. *J. Mol. Spectrosc.* **2007**, *246* (2), 187. doi:10.1016/j.jms.2007.09.012.
(16) Oliveira, B. G.; Vasconcellos, M. L. A. A. *J. Mol. Struct. THEOCHEM* **2006**, *774* (1–3), 83. doi:10.1016/j.theochem.2006.06.018.
(17) Handgraaf, J.-W.; van Erp, T. S.; Meijer, E. J. *Chem. Phys. Lett.* **2003**, *367* (5–6), 617. doi:10.1016/S0009-2614(02)01779-7.
(18) Hobza, P.; Havlas, Z. *Chem. Rev.* **2000**, *100* (11), 4253. doi:10.1021/cr990050q.
(19) Hobza, P.; Havlas, Z. *Theor. Chem. Acc.* **2002**, *108*, 325.
(20) Fujii, A.; Patwari, G. N.; Ebata, T.; Mikami, B. *Int. J. Mass Spectrom.* **2002**, *220* (2), 289. doi:10.1016/S1387-3806(02)00774-1.
(21) Rozas, I. *Phys. Chem. Chem. Phys.* **2007**, *9* (22), 2782. doi:10.1039/b618225a.
(22) Desiraju, G. R. *Chem. Commun. (Camb.)* **2005**, (24): 2995. doi:10.1039/b504372g.
(23) Barnes, A. J. *J. Mol. Struct.* **2004**, *704* (1–3), 3. doi:10.1016/j.molstruc.2004.02.040.

Can. J. Chem. Downloaded from www.nrcresearchpress.com by 80.58.250.72 on 09/16/12
For personal use only.

(24) Scheiner, S.; Kar, T.; Pattanayak, J. *J. Am. Chem. Soc.* **2002**, *124* (44), 13257. doi:10.1021/ja027200q.
(25) van der Veken, B. J.; Herrebout, W. A.; Szostak, R.; Shchepkin, D. N.; Havlas, Z.; Hobza, P. *J. Am. Chem. Soc.* **2001**, *123* (49), 12290. doi:10.1021/ja010915t.
(26) Wojtulewski, S.; Grabowski, S. J. *Chem. Phys.* **2005**, *309* (2–3), 183. doi:10.1016/j.chemphys.2004.09.008.
(27) Tsuzuki, S.; Honda, K.; Uchimaru, T.; Mikami, M.; Tanabe, K. *J. Am. Chem. Soc.* **2000**, *122* (15), 3746. doi:10.1021/ja993972j.
(28) Tâme Parreira, R. L.; Galembeck, S. E.; Hobza, P. *ChemPhysChem* **2007**, *8* (1), 87. doi:10.1002/cphc.200600435.
(29) Chęcińska, L.; Grabowski, S. J. *Chem. Phys.* **2006**, *327* (2–3), 202. doi:10.1016/j.chemphys.2006.04.011.
(30) Yang, Y.; Zhang, W. *J. Mol. Struct. THEOCHEM* **2007**, *814* (1–3), 113. doi:10.1016/j.theochem.2007.03.005.
(31) Alabugin, I. V.; Manoharan, M.; Peabody, S.; Weinhold, R. *J. Am. Chem. Soc.* **2003**, *125* (19), 5973. doi:10.1021/ja034656e.
(32) Li, X.; Liu, L.; Schlegel, H. B. *J. Am. Chem. Soc.* **2002**, *124* (32), 9639. doi:10.1021/ja020213j.
(33) Keefe, C. D.; Isenor, M. *J. Phys. Chem. A* **2008**, *112* (14), 3127. doi:10.1021/jp076563f.
(34) Weizhou, W.; Pitoňák, M.; Hobza, P. *ChemPhysChem* **2007**, *8* (14), 2107. doi:10.1002/cphc.200700415.
(35) Scheiner, S.; Kar, T. *J. Phys. Chem.* **2002**, *106*, 1784.
(36) Hermansson, K. *J. Phys. Chem.* **2002**, *106*, 4695.
(37) Buckingham, A. D.; Del Bene, J. E.; McDowell, S. A. C. *Chem. Phys. Lett.* **2008**, *463* (1–3), 1. doi:10.1016/j.cplett.2008.06.060.
(38) Tsuzuki, S.; Fujii, A. *Phys. Chem. Chem. Phys.* **2008**, *10* (19), 2584. doi:10.1039/b718656h.
(39) Qian, W.; Krimm, S. *J. Phys. Chem. A* **2005**, *109* (25), 5608. doi:10.1021/jp040683v.
(40) Joseph, J.; Jemmis, E. D. *J. Am. Chem. Soc.* **2007**, *129* (15), 4620. doi:10.1021/ja067545z.
(41) Hobza, P.; Zahradnik, R.; Muller-Dethlefs, K. *Collect. Czech. Chem. Commun.* **2006**, *71* (4), 443. doi:10.1135/cccc20060443.
(42) Bader, R. F. W. *Atoms in Molecules: A Quantum Theory*; Oxford University Press: Oxford, 1990.
(43) Bader, R. F. W. *Chem. Rev.* **1991**, *91* (5), 893. doi:10.1021/cr00005a013.
(44) Popelier, P. L. A. *Atoms in Molecules: An Introduction*. Prentice Hall: London, 2000.
(45) Castillo, N.; Boyd, R. J. *J. Chem. Theory Comput.* **2006**, *2* (2), 271. doi:10.1021/ct050238j.
(46) Matta, C. F.; Castillo, N.; Boyd, R. J. *J. Phys. Chem. B* **2006**, *110* (1), 563. doi:10.1021/jp054986g.
(47) Foster, J. P.; Weinhold, F. *J. Am. Chem. Soc.* **1980**, *102* (24), 7211. doi:10.1021/ja00544a007.
(48) Carpenter, J. E.; Weinhold, F. *J. Am. Chem. Soc.* **1988**, *110* (2), 368. doi:10.1021/ja00210a008.
(49) Weinhold, F.; Landis, C. R. *Chem. Educ. Res. Pract. Eur.* **2001**, *2*, 91.
(50) Szatyłowicz, H.; Krygowski, T. M.; Hobza, P. *J. Phys. Chem. A* **2007**, *111* (1), 170. doi:10.1021/jp065336v.
(51) Szatyłowicz, H.; Krygowski, T. M.; Panek, J. J.; Jezierska, A. *J. Phys. Chem. A* **2008**, *112* (40), 9895. doi:10.1021/jp803592v.
(52) Keefe, C. D.; Gillis, E. A. L.; MacDonald, L. *J. Phys. Chem. A* **2009**, *113* (11), 2544. doi:10.1021/jp8092034.
(53) Frisch, M. J.; Trucks, G. W.; Schlegel, H. B.; Scuseria, G. E.; Robb, M. A.; Cheeseman, J. R.; Montgomery, J. A., Jr.; Vreven, T.; Kudin, K. N.; Burant, J. C.; Millam, J. M.; Iyengar, S. S.; Tomasi, J.; Barone, V.; Mennucci, B.; Cossi, M.; Scalmani, G.; Rega, N.; Petersson, G. A.; Nakatsuji, H.; Hada, M.; Ehara, M.; Toyota, K.; Fukuda, R.; Hasegawa, J.; Ishida, M.; Nakajima, T.; Honda, Y.; Kitao, O.; Nakai, H.; Klene, M.; Li, X.; Knox, J. E.; Hratchian, H. P.; Cross, J. B.; Bakken, V.; Adamo, C.; Jaramillo, J.; Gomperts, R.; Stratmann, R. E.; Yazyev, O.; Austin, A. J.; Cammi, R.; Pomelli, C.; Ochterski, J. W.; Ayala, P. Y.; Morokuma, K.; Voth, G. A.; Salvador, P.; Dannenberg, J. J.; Zakrzewski, V. G.; Dapprich, S.; Daniels, A. D.; Strain, M. C.; Farkas, O.; Malick, D. K.; Rabuck, A. D.; Raghavachari, K.; Foresman, J. B.; Ortiz, J. V.; Cui, Q.; Baboul, A. G.; Clifford, S.; Cioslowski, J.; Stefanov, B. B.; Liu, G.; Liashenko, A.; Piskorz, P.; Komaromi, I.; Martin, R. L.; Fox, D. J.; Keith, T.; Al-Laham, M. A.; Peng, C. Y.; Nanayakkara, A.; Challacombe, M.; Gill, P. M. W.; Johnson, B.; Chen, W.; Wong, M. W.; Gonzalez, C.; Pople, J. A. *Gaussian 03*, revision C.02; Gaussian, Inc.: Wallingford, 2004.
(54) Boys, S. F.; Bernardi, F. *Mol. Phys.* **1970**, *19* (4), 553. doi:10.1080/00268977000101561.
(55) Reed, A. E.; Curtiss, L. A.; Weinhold, F. *Chem. Rev.* **1988**, *88* (6), 899. doi:10.1021/cr00088a005.
(56) Keith, T. A. *AIMAll*, version 08.05.04, 2008. http://aim.tkgristmill.com.
(57) Biegler-König, F.; Schonbohm, J. *AIM2000*, version 2.0; Büro für Innovative Software, Fröbelstrasse 68, 33604 Bielefeld, Germany, 2002. http://www.aim2000.de.
(58) Popelier, P. L. A. *Coord. Chem. Rev.* **2000**, *197* (1), 169. doi:10.1016/S0010-8545(99)00189-7.
(59) Nakanishi, W.; Hayashi, S.; Narahara, K. *J. Phys. Chem. A* **2008**, *112* (51), 13593. doi:10.1021/jp8054763.
(60) Scheiner, S.; Grabowski, S. J.; Kar, T. *J. Phys. Chem. A* **2001**, *105* (46), 10607. doi:10.1021/jp0131267.
(61) Koch, U.; Popelier, P. L. A. *J. Phys. Chem.* **1995**, *99* (24), 9747. doi:10.1021/j100024a016.
(62) Cubero, E.; Orozco, M.; Luque, F. J. *Chem. Phys. Lett.* **1999**, *310* (5–6), 445. doi:10.1016/S0009-2614(99)00831-3.
(63) Parthasarathi, R.; Subramanian, V.; Sathyamurthy, N. *J. Phys. Chem. A* **2006**, *110* (10), 3349. doi:10.1021/jp060571z.
(64) Kar, T.; Scheiner, S. *J. Phys. Chem. A* **2004**, *108* (42), 9161. doi:10.1021/jp048546l.
(65) Scheiner, S. *J. Phys. Chem. B* **2009**, *113* (30), 10421. doi:10.1021/jp9035138.
(66) Wang, W.; Hobza, P. *J. Phys. Chem. A* **2008**, *112* (17), 4114. doi:10.1021/jp710992h.
(67) Li, A. Y. *J. Chem. Phys.* **2007**, *126* (15), 154102. doi:10.1063/1.2715561.
(68) We examined the potential energy surface around this motion and it is basically flat. We are confident that the imaginary frequency is due to round-off error in the calculations.
(69) Li, A. Y.; Yan, X. H. *Phys. Chem. Chem. Phys.* **2007**, *9* (47), 6263. doi:10.1039/b712001j.

Poly(*para*-phenylene ethynylene)s functionalized with Gd(III) chelates as potential MRI contrast agents

Katelyn M. Atkins, Francisco M. Martínez, Ali Nazemi, Timothy J. Scholl, and Elizabeth R. Gillies

Can. J. Chem. Downloaded from www.nrcresearchpress.com by 80.58.250.72 on 09/16/12
For personal use only.

Abstract: A poly(*para*-phenylene ethynylene) with water-solubilizing groups and Gd(III) chelates conjugated to the polymer backbone was designed and synthesized. Pre- and post-polymerization functionalization approaches were explored and the pre-polymerization approach for the introduction of the Gd(III) chelate was found to be more successful. The UV–vis absorption and fluorescence emission properties of the protected polymers were characterized and were found to be consistent with the results expected for this class of polymers. Removal of the protecting groups followed by chelation of Gd(III) led to a water-dispersible polymer. Relaxivity measurements were performed on this polymer with the aim of evaluating its potential as a new MRI contrast agent, and an r_1 of 1.37 L mmol^{-1} s^{-1} at 310 K and 20 MHz was determined. These results, along with dynamic light scattering analyses, suggested that the polymers formed micrometre-sized assemblies in aqueous solution. Although the relaxivity was relatively modest, these results provide important insights into the assembly properties of this new class of polymers and into the design criteria for future agents.

Key words: poly(*para*-phenylene ethynylene), magnetic resonance imaging, contrast agent.

Résumé : On a développé et synthétisé un poly(*para*-phénylèneéthylène) portant des groupes solubles dans l'eau et des chélates de Gd(III) conjugués au squelette du polymère. On a exploré des approches de fonctionnalisations avant et après les polymérisations et on a trouvé que l'approche prépolymérisation est meilleure pour l'introduction du chélate de Gd(III). On a caractérisé les propriétés d'absorption UV–visible et d'émission de fluorescence des polymères protégés et on a trouvé qu'ils sont en accord avec les résultats attendus pour cette classe de polymères. L'enlèvement des groupes protecteurs, suivi par la chélation du Gd(III) conduit à l'obtention d'un polymère qui peut être dispersé dans l'eau. On a effectué des mesures de relaxation sur ce polymère dans le but d'évaluer son potentiel comme un nouvel agent de contraste en imagerie de résonance magnétique (IRM) et on a déterminé que sa valeur de r_1 est égale à 1,37 L mmol^{-1} s^{-1}, à 310 K et à 20 MHz. Ces résultats, avec les analyses de dispersion dynamique de la lumière, suggèrent qu'en solution aqueuse les polymères forment des assemblées de la taille du micron. Même si la relaxation est relativement faible, ces résultats fournissent connaissances importantes dans les propriétés d'assemblage de cette nouvelle classe de polymère et dans les critères de conceptualisation des futurs agents.

Mots-clés : poly(*para*-phénylèneéthylène), imagerie de résonance magnétique (IRM), agent de contraste.

[Traduit par la Rédaction]

Introduction

Over the past few decades, magnetic resonance imaging (MRI) has emerged as a powerful noninvasive diagnostic tool in medicine.[1–3] It provides excellent spatial resolution and soft tissue contrast for conveying anatomical structure. In cases where the inherent soft tissue contrast is insufficient to distinguish diseased tissues from normal tissues, contrast agents are routinely used.[2,3] These agents are typically stable chelates of the lanthanide ion Gd(III). While these small-molecule agents have enabled significant advancements in MRI, they possess several limitations.

First, the relaxivities of the commercially available agents are only a few percent of the theoretically predicted values.[4] The low sensitivity of these agents imparts a requirement for gram-scale doses to obtain the required contrast. This raises concerns regarding the toxicity of these agents, particularly in patients with kidney disease.[5] Furthermore, there is increasing interest in the development of contrast agents tar-

Received 20 August 2010. Accepted 21 October 2010. Published on the NRC Research Press Web site at canjchem.nrc.ca on 21 December 2010.

K.M. Atkins, A. Nazemi, and E.R. Gillies.[1] Department of Chemistry, The University of Western Ontario, 1151 Richmond Street, London, ON N6A 5B7, Canada.
F.M. Martínez and T.J. Scholl. Department of Medical Biophysics, The Schulich School of Medicine and Dentistry, The University of Western Ontario, 1151 Richmond Street, London, ON N6A 5C1, Canada.

[1]Corresponding author (e-mail: egillie@uwo.ca).

Can. J. Chem. Downloaded from www.nrcresearchpress.com by 80.58.250.72 on 09/16/12
For personal use only.

geted to specific diseases via binding to receptors in the target tissues. Considering a stoichiometric 1:1 binding of the agent to the target, the target must be present at a concentration of approximately 125 μmol L^{-1}.[3] Unfortunately, many targets are not present at this relatively high concentration in vivo.

To address these limitations, significant efforts have been aimed at enhancing the relaxivities of Gd(III)-based contrast agents. It has been predicted by Solomon–Bloembergen–Morgan theory that increases in the rotational correlation times of the current agents can result in significantly increased relaxivities.[6,7] As macromolecules have slower tumbling rates in solution, much research has involved the conjugation of Gd(III) chelates such as diethylenetriaminepentaacetic acid (DTPA) and 1,4,7,10-tetraazacyclododecane-1,4,7,10-tetraacetic acid (DOTA) to macromolecules. Early efforts involving conventional linear macromolecules led to relatively disappointing results.[8–14] However, the conjugation of these chelates to macromolecules such as proteins[15,16] and dendrimers[17–25] provided much greater enhancements in relaxivity. These results highlight the importance of macromolecular structure and architecture, as flexible backbones allow the Gd(III) chelates to tumble in solution in a manner similar to the small molecules, while those structures possessing well-defined and rigidified conformations provide longer rotational correlation times and thus higher relaxivities.

With the importance of molecular rigidity in mind, our group was interested in investigating poly(*para*-phenylene ethynylene) (PPE) as a backbone for the conjugation of Gd(III) chelates. This polymer backbone, comprising alternating phenyl and alkyne moieties, exists in an elongated linear conformation, with backbone conjugation leading to high levels of fluorescence.[26–31] This fluorescence and its sensitivity to its environment have been exploited for the development and commercialization of sensors.[29–31] More recently, water-soluble analogues of these polymers have been developed and have been investigated as sensors for DNA,[32–34] proteins,[35] and bacteria.[36,37] However, to the best of our knowledge PPEs have never been investigated as MRI contrast agents. We proposed that the rigidified, elongated conformation of PPE would lead to significant enhancements in relaxivity of conjugated Gd(III) chelates. Furthermore, the fluorescence may enable the optical detection of these agents in cells and tissues, thus facilitating biological studies of the agents and potentially providing a dual modality imaging probe, perhaps even with sensor capabilities. Described here is the synthesis of a new PPE with conjugated Gd(III) chelates and the characterization of its optical properties and relaxivity.

Results and discussion

Polymer design

The structure of the target copolymer **1** is shown in Fig. 1. A modified DTPA[38] was selected as the Gd(III) chelate in this polymer, as the extra carboxylate incorporated in the aspartic acid linker allows 8 chelation sites of the ligand to be preserved for binding to the metal ion. Direct use of one of the carboxylates of DTPA for conjugation to the polymer backbone would lead to decreased complex stability, thus increasing the chances of transmetallation by Zn(II), a process that would potentially release toxic free Gd(III) in vivo.[39] In addition, although the conjugation of the modified DTPA chelate to the phenols of the polymer backbone would be expected to provide the highest relaxivity, this conjugation was not efficient in preliminary work. Therefore, an ethyl spacer was incorporated between the polymer backbone and the chelate to introduce a more nucleophilic amine group for the conjugation to the acid-functionalized DTPA.

Although the chelates were expected to impart some aqueous solubility to the PPEs, water-solubilizing oligo(ethylene glycol) moieties were also incorporated in the design. PPEs, like other conjugated polymers having a rigid and hydrophobic backbone, have inherently very poor water solubility that results in aggregation and subsequent fluorescence quenching.[40–42] Carboxylic acid terminated oligo(ethylene glycol) moieties were chosen because they have been previously demonstrated by Wosnick et al. to impart aqueous solubility to PPEs.[37] Indeed, preliminary work in our laboratory demonstrated that neutral tri(ethylene glycol) monomethyl ether derivatives were insufficient to impart aqueous solubility.

PPEs are typically prepared from diiodophenylene and dialkyne monomers via Sonogashira–Hagihara copolymerizations.[43,44] Based on this strategy, the proposed design incorporated the modified DTPA chelates into the diiodophenylene monomer **2** and the tetra(ethylene glycol) moieties into the dialkyne monomer **3** (Fig. 1). In addition, it was of interest to explore the postpolymerization functionalization of the PPE backbone as an alternative means of preparing the target polymers. This would potentially provide a versatile synthetic method that would allow easy incorporation of targeting ligands in future generations of the agent. Therefore, polymer **4** was also designed as a target, which would be prepared from monomers **3** and **5**.

Monomer syntheses

The synthesis of the dialkyne monomer **3** was performed following a protocol similar to that reported by Wosnick et al. for slightly different oligo(ethylene glycol) lengths (di(ethylene glycol) and penta(ethylene glycol)).[37] As shown in Scheme 1, 2,5-diiodo-1,4-hydroquinone (**6**)[30] was reacted with the tosylate **7**,[45] providing **8**. The alkyne moieties were then introduced by a Sonogashira reaction with trimethylsilylacetylene (TMSA) in the presence of catalytic copper(I) iodide and bis(triphenylphosphine)palladium(II) chloride. Finally, the trimethylsilyl protecting groups were removed by treatment of **9** with tetrabutylammonium fluoride (TBAF), providing **3**.

The synthesis of monomer **2** began with the reaction of the tosylate **10**[46] with 2,5-diiodo-1,4-hydroquinone to give the diazide **11** (Scheme 2). The azides were then reduced to amines under Staudinger conditions, providing **12**. Finally, the amines were conjugated to the previously reported DTPA derivative **13**[38] using dicyclohexylcarbodiimide (DCC) in the presence of 4-(dimethylamino)pyridine (DMAP) and 4-(dimethylamino)pyridinium *p*-toluenesulfonate (DPTS) to provide monomer **2**. For the preparation of monomer **5**, *tert*-butyl carbamate (Boc) protected 2-bromoethylamine (**14**)[47] was reacted with 2,5-diiodo-1,4-hydroquinone as shown in Scheme 3.

Can. J. Chem. Downloaded from www.nrcresearchpress.com by 80.58.250.72 on 09/16/12
For personal use only.

Fig. 1. Design of two alternative routes to a PPE with Gd(III) chelates and water-solubilizing side chains.

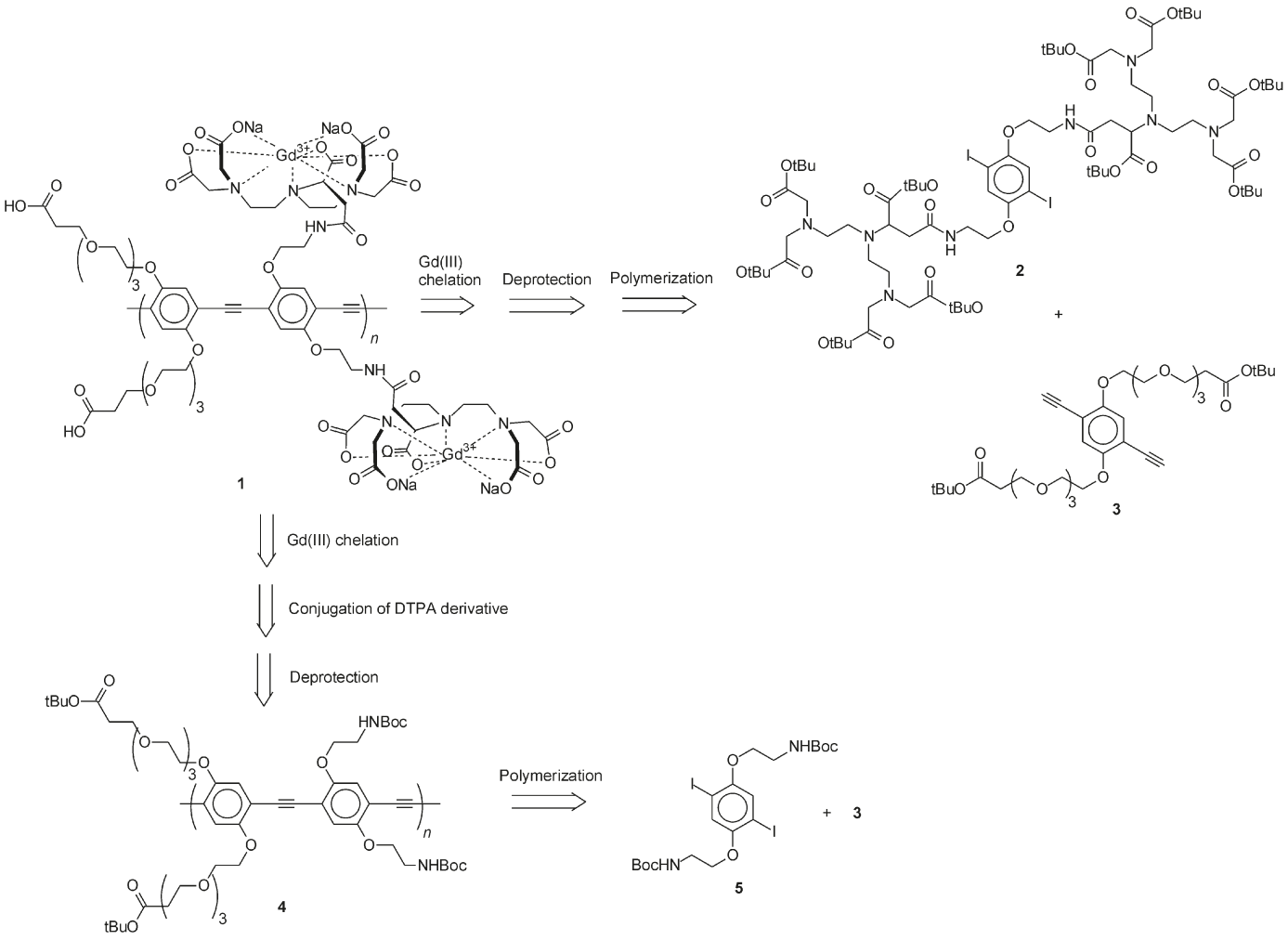

Scheme 1. Synthesis of monomer **3**.

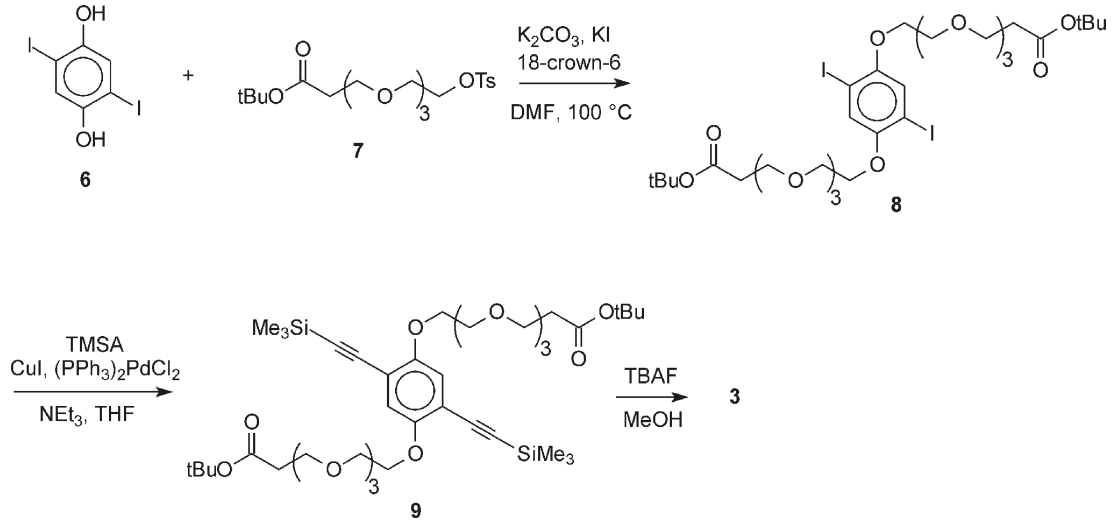

Polymer syntheses and characterization

Monomers **2** and **3** were copolymerized under Sonogashira–Hagihara conditions[43,44] to provide the protected polymer **15**, which was purified by dialysis in *N*,*N*-dimethylformamide (DMF) (Scheme 4). Using size exclusion chromatography (SEC) (Fig. 2), **15** was found to have a weight-average molecular weight (M_w) of 31 300 g mol^{-1} and a polydispersity index (PDI) of 2.6 as determined by a conventional calibration relative to polystyrene standards. Following determination of the refractive index increment (d*n*/d*c*) for

Scheme 2. Synthesis of monomer **2**.

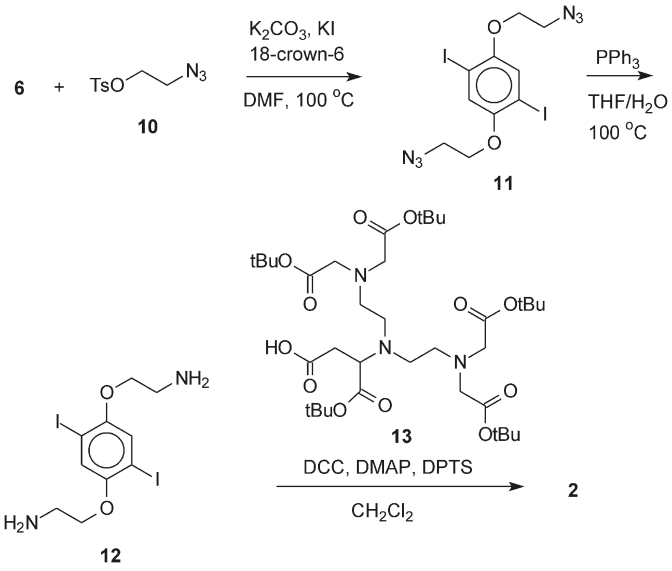

Scheme 3. Synthesis of monomer **5**.

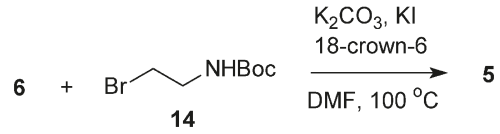

Fig. 2. Size exclusion chromatography traces for polymers **15** and **4**.

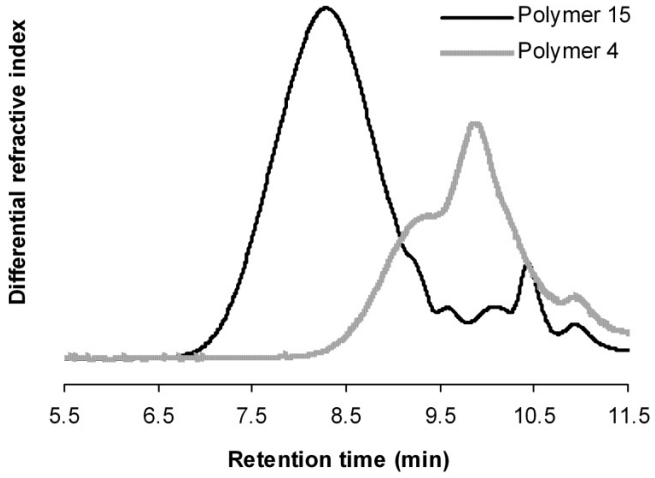

the polymer, its absolute molecular weight was also determined by multi-angle light scattering (MALS). This measurement provided an M_w of 40 500 g mol^{-1} and a PDI of 1.9. The values obtained by the conventional calibration and light scattering were therefore in relatively good agreement.

Monomers **3** and **5** were polymerized under the same conditions described above, leading to polymer **4**, which was also purified by dialysis in DMF. This polymer was found by SEC (Fig. 2) to have an M_w of 2640 g mol^{-1} and a PDI of 2.4. The lower M_w of this polymer in comparison with **15** can be attributed at least in part to the lower average monomer molecular weight but was also likely due to a lower degree of polymerization for unknown reasons.

As shown in Fig. 3, both polymers **15** and **4** exhibited red-shifted absorption maxima (λ_{max}) at 430 nm and 406 nm, respectively, relative to that of the dialkyne monomer **3** at 327 nm. This bathochromic shift can be attributed to the significantly increased conjugation of the polymers relative to the monomer and is typical of PPEs.[26,29] Concomitantly, the emission maxima also shifted to 465 nm and 460 nm for polymers **15** and **4**, respectively, relative to the monomer's emission λ_{max} of 372 nm (Fig. 4). These emission maxima are similar to those of other previously reported PPEs.[37,48]

Polymer deprotection and Gd(III) chelation

The *tert*-butyl ester groups on both the tetra(ethylene glycol) and DTPA derivatives of polymer **15** were easily removed by treatment of the polymer with 1:1 trifluoroacetic acid (TFA):CH_2Cl_2 to provide polymer **16** (Scheme 5). The resulting polymer was then dissolved in pure water and the pH was adjusted to 7.4 prior to the introduction of Gd(III) in the form of $GdCl_3 \cdot 6H_2O$, giving the target polymer **1**. Following purification by extensive dialysis, the Gd(III) content was measured by inductively coupled plasma mass spectrometry. Based on these measurements, Gd(III) was successfully introduced into each chelation site and no extra Gd(III) was detected.

Polymer **4** could also be fully deprotected by treatment with 1:1 TFA/CH_2Cl_2 to give **17** (Scheme 6). The next step towards the target was the introduction of the Gd(III) chelates by reaction of **17** with an *N*-hydroxysuccinimidyl ester derivative of **13** or the commercially available *p*-isothiocyanatobenzyl derivative of DTPA. Unfortunately, although **17** was soluble in organic solvents such as DMF and $CHCl_3$ when the amines were present as their TFA salts, all attempts to neutralize or basify the solution or to dissolve the polymer in aqueous buffer for the conjugation led to rapid polymer precipitation. The use of other polar solvents such as dimethylsulfoxide or methanol did not result in enhanced solubility, so this polymer could not be further functionalized.

Relaxivity measurements

The longitudinal relaxivity (r_1) of polymer **1** in 100 mmol L^{-1} pH 7.4 phosphate buffer was measured at 298 and 310 K between 0.01 and 35 MHz using a field cycling relaxometer. The results are shown in Fig. 5. When calculated on a per Gd(III) ion basis, the results corresponded to an r_1 of 1.37 ± 0.03 L mmol^{-1} s^{-1} at 310 K and 20 MHz. This result was unexpectedly low relative to the value of 4.1 L mmol^{-1} s^{-1} measured for Gd-DTPA under the same conditions.[15] In addition, although **1** appeared "soluble" upon first inspection, it was noted that after prolonged standing some material settled from solution, resulting in even lower relaxivities. This material could be redispersed by mixing, resulting in recovery of the relaxivity to the original value. This behaviour, along with a complete lack of polymer fluorescence, suggested that the polymer may have assembled into micrometre-sized particles in solution.

The suspension of polymer **1** was investigated by dynamic light scattering. As shown in Fig. 6, micrometre-sized particles were indeed detected. Optical microscopy was also

Can. J. Chem. Downloaded from www.nrcresearchpress.com by 80.58.250.72 on 09/16/12
For personal use only.

Scheme 4. Synthesis of polymer **15**.

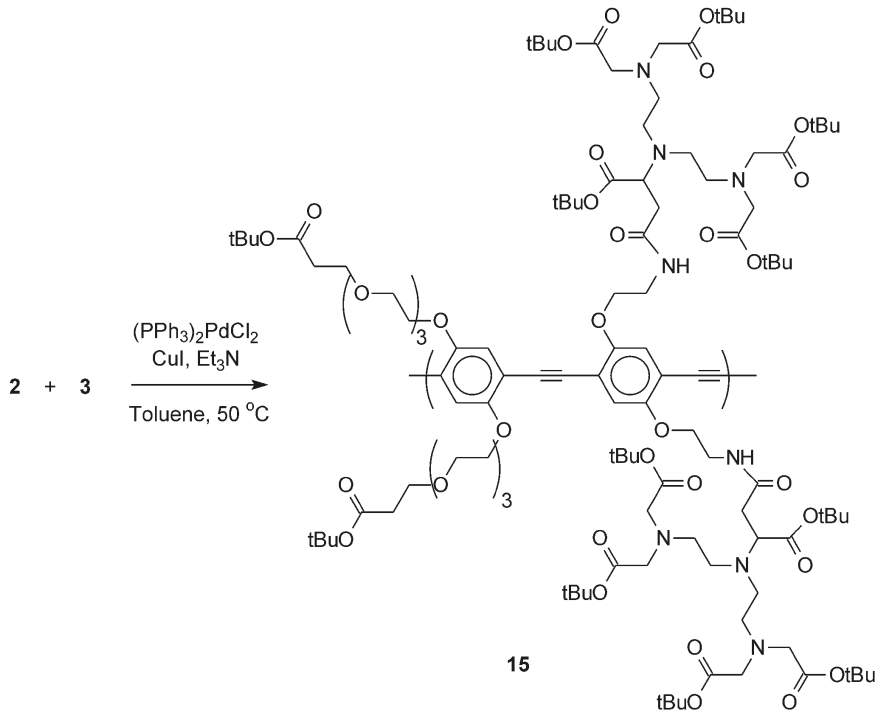

Fig. 3. UV–vis absorption spectra of polymers **15** and **4** and monomer **3** (in CH_3OH).

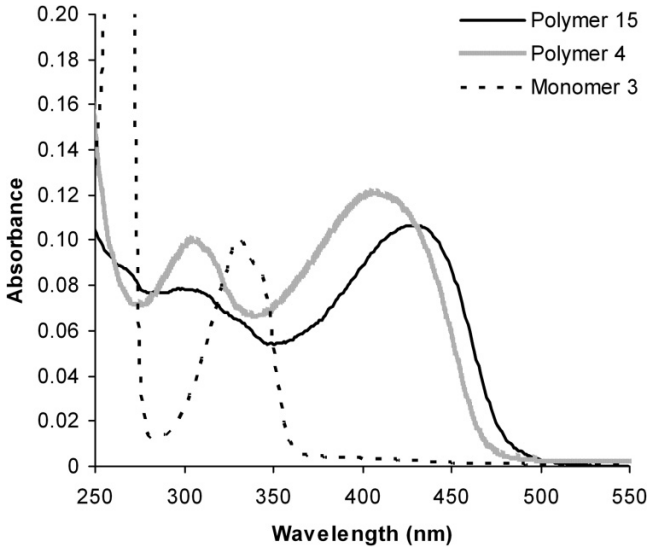

Fig. 4. Fluorescence emission spectra of polymers **15** and **4** and monomer **3** (in CH_3OH).

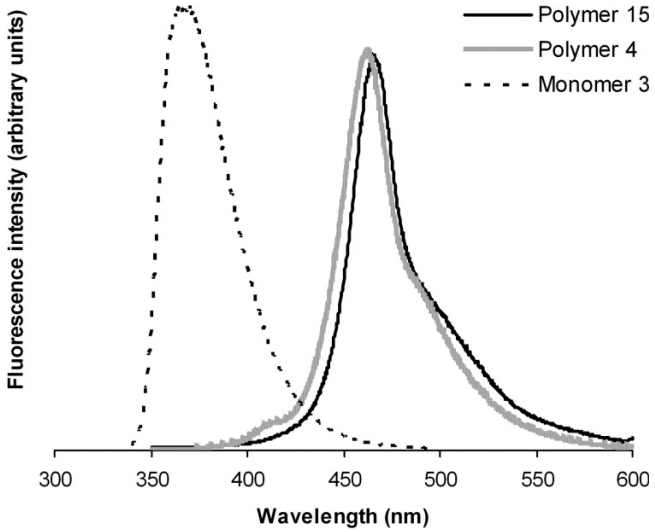

used to verify the size and revealed that the particles were solid and approximately spherical (Fig. 7). By extensive centrifugation it was possible to remove essentially all of the polymer from the suspension. Combined, these results suggest that the relaxivity exhibited by polymer **1** arose primarily through the interaction of water molecules with the Gd(III) ions at the surface of the particles, while the Gd(III) ions on the interior would have very poor access to water, a property that is known to substantially decrease the relaxivities of Gd(III) agents.[49–51] As the r_1 value was calculated based on the total concentration of Gd(III) ions in the sample, it is likely that the relaxivities of the complexes on or near the particle surface were much higher than 1.37 L mmol^{-1} s^{-1}, while those on the interior were much lower. For example, based on a mean particle size of 1.5 μm and assuming that water can freely penetrate the particle to a depth of 10 nm, the relaxivity on a per Gd(III) ion basis would be approximately 35 L mmol^{-1} s^{-1}, much higher than that for Gd-DTPA. However, this estimation is clearly very dependent on the value used for the depth of water penetration and the result ranges from 115 L mmol^{-1} s^{-1} for a penetration depth of 3 nm to 3.9 L mmol^{-1} s^{-1}, very close to the relaxivity of Gd-DTPA, if a penetration depth of 100 nm is assumed (see Supplementary data).

Overall, the significant aggregation of polymer **1** was surprising given the solubilizing carboxylic acid terminated

Can. J. Chem. Downloaded from www.nrcresearchpress.com by 80.58.250.72 on 09/16/12
For personal use only.

Scheme 5. Synthesis of the target polymer **1**.

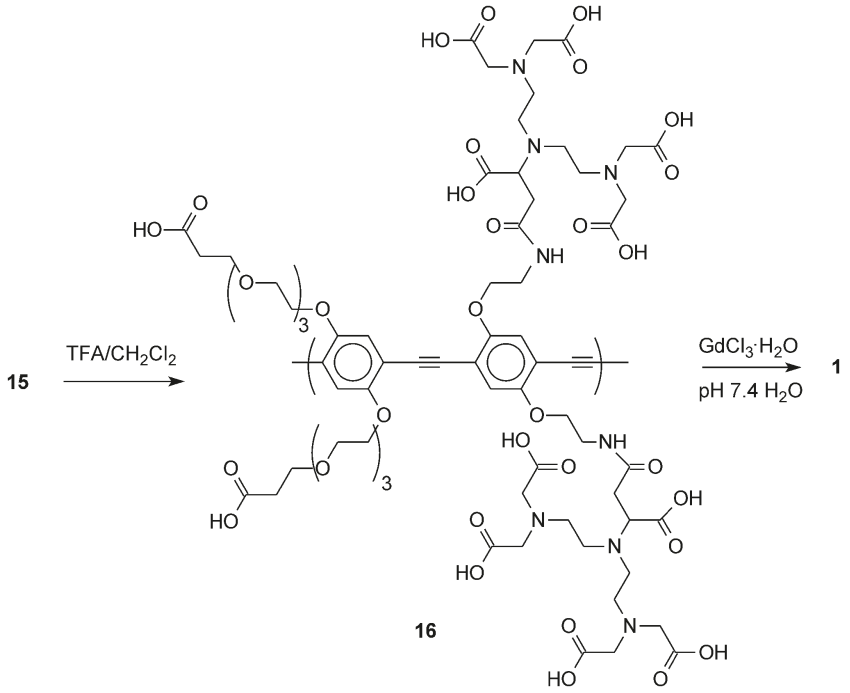

Scheme 6. Deprotection of polymer **4**.

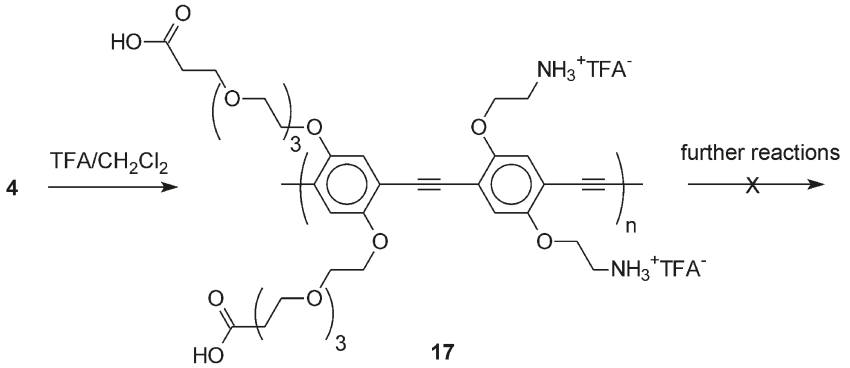

tetra(ethylene glycol) units, the inherently water-soluble Gd(III) complexes, and the previous reports of water-soluble PPEs bearing similar densities of charged moieties.[32,34,37] Considering the multiple competing effects that the incorporation of the polymeric complexes into the micrometre-sized aggregates would have on the relaxivity, it is not possible to confirm definitively that increased relaxivity would result from the rigidified polymer backbone. Thus, the unexpected assembly of polymer **1** introduces a new form of Gd(III) where each particle carries many Gd(III) ions along conjugated polymer backbones. However, to further investigate the effects of the PPE backbone on relaxivity and to exploit its fluorescence properties it will be necessary to design polymers that do not aggregate in water.

Conclusions

In summary, a PPE with conjugated water-solubilizing groups and DTPA derivatives was designed with the aim of obtaining Gd(III) complexes with high relaxivity due to the rigidity of the polymer backbone. Two synthetic routes to the target were explored, one involving the polymerization of a DTPA-functionalized monomer and the other involving a postpolymerization modification. While the postpolymerization modification was not successful owing to poor polymer solubility, the former route successfully led to a polymer having two Gd(III) complexes on alternating phenyl rings. Unexpectedly, this polymer assembled into microparticles in aqueous solution with a relaxivity of 1.37 L $mmol^{-1}$ s^{-1} on a per Gd(III) ion basis. This relaxivity is likely an average of Gd(III) complexes on the microparticle surface with high relaxivities and complexes on the particle interior with low relaxivities due to poor water accessibility.

Experimental

General procedures and materials

All chemicals were purchased from commercial suppliers and used without further purification unless otherwise noted. Anhydrous *N*,*N*-dimethylformamide (DMF), tetrahydrofuran

Can. J. Chem. Downloaded from www.nrcresearchpress.com by 80.58.250.72 on 09/16/12
For personal use only.

Can. J. Chem. Downloaded from www.nrcresearchpress.com by 80.58.250.72 on 09/16/12
For personal use only.

Fig. 5. Longitudinal relaxivity (r_1) of polymer **1** in pH 7.4 buffer as a function of field strength and temperature.

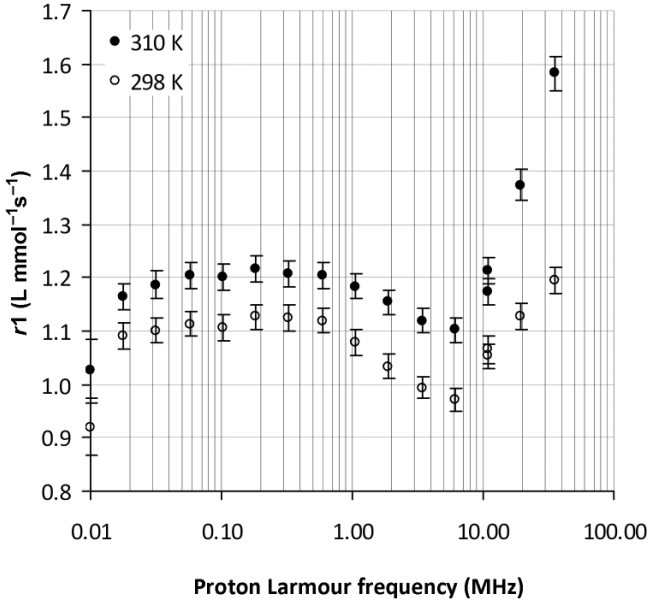

Fig. 6. Size distribution of aggregates formed by polymer **1** in pH 7.4 phosphate buffer, as measured by dynamic light scattering.

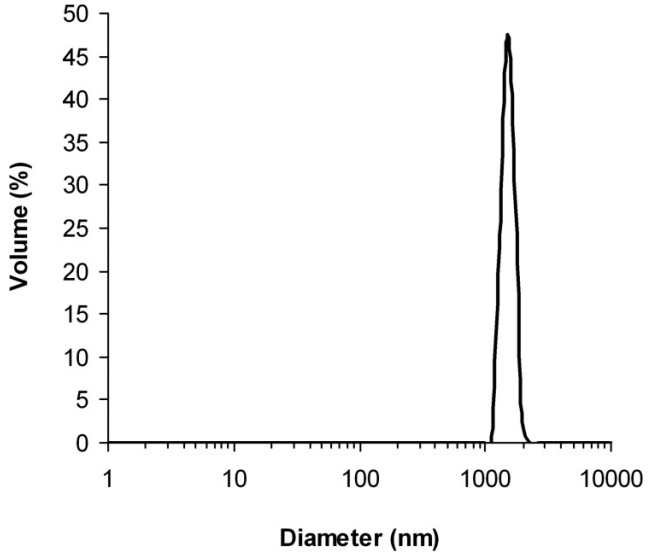

(THF), and toluene were obtained from a solvent purification system. CH_2Cl_2 and NEt_3 were distilled over CaH_2. Ultrapure water was obtained from a Barnstead EASYpure II system. Column chromatography was performed using silica gel (0.063–0.200 mm particle size, 70–230 mesh). ^{1}H NMR spectra were obtained at 400 MHz and ^{13}C NMR data were obtained at 100 MHz. Chemical shifts are reported in ppm and are calibrated against residual solvent signals of $CDCl_3$ (δ 7.26, 77.2) or D_2O (δ 4.75). High-resolution mass spectrometry (HRMS) was performed using a Micromass LCT (electrospray time-of-flight (ES+)) mass spectrometer or a Finnigan MAT 8200 mass spectrometer in time-of-flight ES+ mode. UV–vis absorption spectroscopy was performed on a Varian Cary 300 Bio UV–vis spectrophotometer. Emission spectra were obtaining using a Photon Technology International QM-4 SE spectrofluorometer. Size exclusion chromatography (SEC) was performed in THF using a Waters 515 HPLC pump, Wyatt Optilabrex RI and miniDAWN-TREOS detectors, and a ResiPore (300 mm × 7.5 mm) column from Polymer Laboratories. Column calibration was performed using polystyrene standards from Polymer Laboratories. Dynamic light scattering was performed on a Zetasizer Nano ZS instrument from Malvern Instruments. Optical microscopy was performed using an Olympus model IX71S8F-3 microscope equipped with a 20× (NA 0.50) objective. Dialyses were performed using Spectra/Por regenerated cellulose membranes with a molecular weight cutoff of 3500 Da. The inductively coupled plasma mass spectrometry (ICP-MS) analysis was performed at the Environmental Analytical Laboratories of the Saskatchewan Research Council. Relaxation rate measurements were performed on a Stelar Spinmaster FFC2000 1T C/DC relaxometer. The concentration of the polymer was 0.17 mg mL^{-1} in a 100 mmol L^{-1} pH 7.4 phosphate buffer solution.

Fig. 7. Optical microscopy image of assemblies formed by polymer **1**.

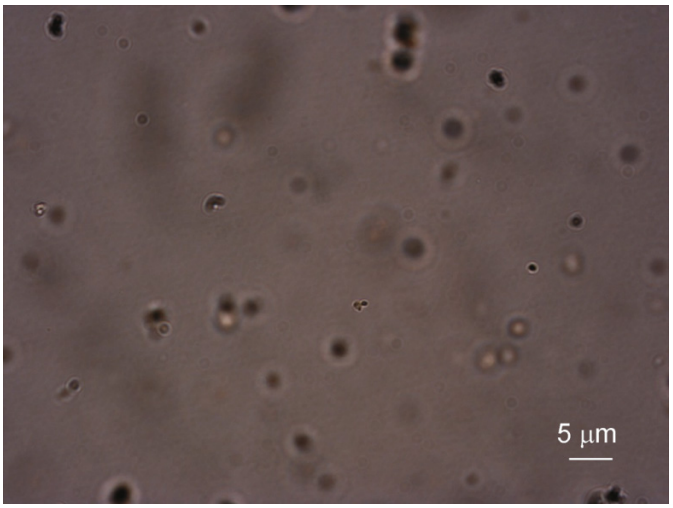

Synthesis of compound 8

To a flame-dried flask were added 2,5-diiodo-1,4-hydroquinone (0.64 g, 1.8 mmol, 1.0 equiv.), the tosylate **7** (1.9 g, 4.4 mmol, 2.5 equiv.), potassium iodide (0.15 g, 0.88 mmol, 0.50 equiv.), potassium carbonate (1.5 g, 11 mmol, 6.0 equiv.), and 18-crown-6 (0.92 g, 3.5 mmol, 2.0 equiv.). DMF (30 mL) was added and the resulting solution was heated to 100 °C for 48 h under an argon atmosphere. The solvent was removed in vacuo and the resulting residue was dissolved in a small amount of CH_2Cl_2, concentrated to dryness on a small amount of silica gel, and purified by column chromatography on silica gel (20:80 ethyl acetate – hexanes eluent) to yield compound **8** (0.71 g, 46%). IR (cm^{-1}, thin film from CH_2Cl_2): 3088, 2967, 2866, 1726. ^{1}H NMR (400 MHz, $CDCl_3$, δ): 1.44 (s, 18 H), 2.49 (t, J = 6.63 Hz, 4 H), 3.57–3.80 (m, 20 H), 3.83–3.91 (m, 4 H), 4.04–4.12 (m, 4 H), 7.23 (s, 2 H). ^{13}C NMR (100 MHz, $CDCl_3$, δ): 170.8, 153.1, 123.4, 86.4, 80.4, 71.1, 70.7, 70.5, 70.4, 70.2, 69.6, 66.9, 36.24, 28.1. HRMS calcd. for $[M]^+$ ($C_{32}H_{52}I_2O_{12}$): 882.1548; found: 882.1546.

Can. J. Chem. Downloaded from www.nrcresearchpress.com by 80.58.250.72 on 09/16/12
For personal use only.

Synthesis of compound 9

Compound **8** (0.69 g, 0.78 mmol, 1.0 equiv.) was added to a flame-dried flask and put under argon atmosphere. Dry THF (6 mL) was added, followed by trimethylsilylacetylene (0.76 g, 7.8 mmol, 10 equiv.) and triethylamine (5.4 mL, 39 mmol, 50 equiv.). Copper(I) iodide (4.5 mg, 23 μmol, 0.029 equiv.) and bis(triphenylphosphine)palladium(II) chloride (11 mg, 16 μmol, 0.020 equiv.) were added to the solution under a flow of argon. The mixture was stirred at room temperature for 48 h, and then the solvent was removed in vacuo. The resulting residue was purified by column chromatography (10:90 ethyl acetate – hexanes to 40:60 ethyl acetate – hexanes eluent gradient) to afford compound **9** (0.54 g, 96%). IR (cm^{-1}, thin film from CH_2Cl_2): 3010, 2954, 2867, 2151, 1729, 1495. ^1H NMR (400 MHz, $CDCl_3$, δ): 0.17 (s, 18 H), 1.37 (s, 18 H), 2.42 (t, J = 6.64 Hz, 4 H), 3.46–3.75 (m, 20 H), 3.80 (t, J = 4.88 Hz, 4 H), 4.05 (t, J = 4.88 Hz, 4 H), 6.85 (s, 2 H). ^{13}C NMR (100 MHz, $CDCl_3$, δ): 170.8, 153.8, 117.7, 114.1, 100.8, 100.3, 80.4, 71.1, 70.7, 70.5, 70.3, 69.6, 69.4, 66.8, 36.2, 28.0, –0.1. HRMS calcd. for $[M + Na]^+$ ($C_{42}H_{70}O_{12}NaSi_2$): 845.4304; found: 845.4329.

Synthesis of monomer 3

To a solution of compound **9** (0.51 g, 0.71 mmol, 1.0 equiv.) in methanol (4 mL) was added 1 mol L^{-1} tetrabutylammonium fluoride in THF (1.8 mL, 2.5 equiv.). The resulting solution was stirred for 12 h, and then the solvent was removed in vacuo and the resulting residue was purified by column chromatography (50:50 ethyl acetate – hexanes to 80:20 ethyl acetate – hexanes eluent gradient) to afford monomer **3** (0.36 g, 87%). UV–vis absorption (CH_3OH) λ_{max}: 327 nm. Emission λ_{max}: 372 nm. IR (cm^{-1}, thin film from CH_2Cl_2): 3242, 3010, 2972, 2866, 2092, 1727, 1495. ^1H NMR (400 MHz, $CDCl_3$, δ): 1.42 (s, 18 H), 2.48 (t, J = 6.64 Hz, 4 H), 3.34 (s, 2 H), 3.51–3.77 (m, 20 H), 3.84 (t, J = 5.08 Hz, 4 H), 4.12 (t, J = 4.88 Hz, 4 H), 6.97 (s, 2 H). ^{13}C NMR (100 MHz, $CDCl_3$, δ): 170.9, 154.0, 118.2, 113.5, 82.8, 80.4, 79.5, 71.0, 70.6, 70.5, 70.4, 69.6, 69.5, 66.8, 36.2, 28.1. HRMS calcd. for $[M]^+$ ($C_{36}H_{54}O_{12}$): 678.3615; found: 678.3605.

Synthesis of compound 11

To a flame-dried flask were added 2,5-diiodo-1,4-hydroquinone (3.3 g, 9.0 mmol, 1.0 equiv.), the tosylate **10** (5.1 g, 23 mmol, 2.5 equiv.), potassium iodide (0.60 g, 3.6 mmol, 0.40 equiv.), potassium carbonate (5.0 g, 36 mmol, 4.0 equiv.), and 18-crown-6 (2.4 g, 9.2 mmol, 1.0 equiv.). DMF (30 mL) was added and the resulting solution was heated at 100 °C for 48 h under an argon atmosphere. The solvent was removed in vacuo and the resulting residue was dissolved in a small amount of dichloromethane, concentrated to dryness on a small amount of silica gel, and purified by column chromatography (10:90 ethyl acetate – hexanes to 30:70 ethyl acetate – hexanes eluent gradient) to yield compound **11** (1.3 g, 32%). IR (cm^{-1}, KBr pellet): 3043, 2920, 2867, 2106, 1692. ^1H NMR (400 MHz, $CDCl_3$, δ): 3.65 (t, J = 5.08 Hz, 4 H), 4.11 (t, J = 5.08 Hz, 4 H), 7.23 (s, 2 H). ^{13}C NMR (100 MHz, $CDCl_3$, δ): 153.1, 123.7, 85.9, 67.8, 49.2. HRMS calcd. for $[M]^+$ ($C_{10}H_{12}I_2N_6O_2$): 499.8955; found: 499.8964.

Synthesis of compound 12

The diazide **11** (0.25 g, 0.58 mmol, 1.0 equiv.) and triphenylphosphine (0.76 g, 2.9 mmol, 5.0 equiv.) were dissolved in THF (10 mL). Water (5 mL) was added and the resulting mixture was heated at 60 °C for 2 h. The solvent was then removed in vacuo and the residue was purified by column chromatography (90:10 dichloromethane–methanol to 100% methanol eluent gradient) to yield compound **12** (0.19 g, 88%). IR (cm^{-1}, KBr pellet): 3360, 3038, 2925, 2869, 1693, 1526. ^1H NMR (400 MHz, $CDCl_3$, δ): 1.51 (br s, 4 H), 3.10 (t, J = 4.88 Hz, 4 H), 3.99 (t, J = 4.88 Hz, 4 H), 7.21 (s, 2 H). ^{13}C NMR (100 MHz, $CDCl_3$, δ): 152.8, 123.5, 86.3, 69.8, 45.3. HRMS calcd. for $[M]^+$ ($C_{10}H_{14}I_2N_2O_2$): 447.9145; found: 447.9158.

Synthesis of monomer 2

To a flame-dried flask were added the diamine **12** (0.038 g, 0.10 mmol, 1.0 equiv.), DTPA derivative **13** (0.18 g, 0.25 mmol, 2.5 equiv.), DMAP (0.012 g, 0.10 mmol, 1.0 equiv.), and DPTS (0.029 g, 0.10 mmol, 1.0 equiv.). The flask was placed under nitrogen and dry CH_2Cl_2 (5 mL) was added. Once the reagents had dissolved, DCC (0.12 g, 0.60 mmol, 6.0 equiv.) was added and the reaction mixture was stirred for 3 h at room temperature. The reaction mixture was then filtered through cotton to remove the dicyclohexylurea by-product and the solvent was removed in vacuo. The resulting material was purified by column chromatography (20:80 ethyl acetate – cyclohexane eluent) to afford compound **2** (0.074 g, 40%). IR (cm^{-1}, thin film from CH_2Cl_2): 3310, 3060, 2974, 2925, 1729, 1663, 1535, 1455. ^1H NMR (400 MHz, $CDCl_3$, δ): 1.36–1.56 (m, 90 H), 2.55 (br s, 2 H), 2.72 (br s, 2 H), 2.80 (br s, 16 H), 3.38–3.47 (m, 16 H), 3.61–3.81 (m, 4 H), 3.88 (br s, 2 H), 3.94–4.14 (m, 4 H), 7.23 (s, 2 H), 7.83 (br s, 2 H). ^{13}C NMR (100 MHz, $CDCl_3$, δ): 178.4, 171.2, 170.4, 152.8, 123.2, 86.3, 81.5, 81.0, 68.9, 60.9, 55.8, 53.1, 50.1, 41.9, 29.6, 28.21, 28.17. HRMS calcd. for $[M + H]^+$ ($C_{82}H_{141}I_2N_8O_{24}$): 1875.8148; found: 1875.8074.

Synthesis of monomer 5

To a flame-dried flask was added 2,5-diiodo-1,4-hydroquinone (0.56 g, 1.5 mmol, 1.0 equiv.), bromide **14** (0.86 g, 3.8 mmol, 2.5 equiv.), potassium iodide (0.13 g, 0.76 mmol, 0.50 equiv.), potassium carbonate (1.3 g, 9.2 mmol, 6.0 equiv.), and 18-crown-6 (0.81 g, 3.1 mmol, 2.0 equiv.). DMF (30 mL) was added and the resulting solution was heated at 100 °C for 24 h under an argon atmosphere. The solvent was removed in vacuo and the resulting residue was dissolved in a small amount of dichloromethane, concentrated to dryness on a small amount of silica gel, and purified by column chromatography on silica gel (10:90 ethyl acetate – hexanes eluent) to yield compound **5** (0.39 g, 40%). IR (cm^{-1}, thin film from CH_2Cl_2): 3356, 3052, 2974, 1688, 1532. ^1H NMR (400 MHz, $CDCl_3$, δ): 1.47 (s, 18 H), 3.56 (dt, J = 5.08, 5.07 Hz, 4 H), 4.01 (t, J = 5.07 Hz, 4 H), 5.08 (br s, 2 H), 7.19 (s, 2 H). ^{13}C NMR (100 MHz, $CDCl_3$, δ): 164.6, 152.77, 123.2, 86.5, 71.5, 69.9, 40.8, 28.42. HRMS calcd. for $[M]^+$ ($C_{20}H_{30}I_2N_2O_6$): 648.0193; found: 648.0176.

Can. J. Chem. Downloaded from www.nrcresearchpress.com by 80.58.250.72 on 09/16/12
For personal use only.

Synthesis of polymer 15

Monomer **2** (61 mg, 33 μmol, 1.0 equiv.) and monomer **3** (19 mg, 33 μmol, 1.0 equiv.) were added to a flame-dried two-neck round-bottom flask. The monomers were put under a nitrogen atmosphere and dry toluene (2 mL) was added, followed by dry NEt_3 (0.23 mL, 1.6 mmol). To this solution were added bis(triphenylphosphine)palladium(II) chloride (1.0 mg, 1.4 μmol, 0.040 equiv.) and copper(I) iodide (1.0 mg, 5.2 μmol, 0.16 equiv.). The reaction mixture was heated at 50 °C for 48 h. The solvent was removed in vacuo and the resulting residue was dissolved in DMF (2 mL). This solution was then dialyzed against DMF for 24 h to yield polymer **27** (71 mg, quantitative yield). UV–vis absorption (CH_3OH) λ_{max}: 430 nm. Emission λ_{max}: 465 nm. ^1H NMR (400 MHz, $CDCl_3$, δ): 1.23 (s, 18 H), 1.42 (s, 90 H), 2.29–2.46 (m, 10 H), 2.69–2.94 (m, 16 H), 3.06–4.15 (m, 52 H), 7.00 (br s, 2 H), 7.42 (br s, 2 H). SEC: M_w (conventional calibration) = 31 300 g mol^{-1}, PDI = 2.6; M_w (MALS; d*n*/d*c* = 0.138) = 40 500 g mol^{-1}, PDI = 1.9.

Synthesis of polymer 4

Monomer **3** (0.37 g, 0.63 mmol, 1.0 equiv.) and monomer **5** (0.41 g, 0.63 mmol, 1.0 equiv.) were added to a flame-dried two-neck round-bottom flask. The monomers were put under a nitrogen atmosphere and dry toluene (5 mL) was added, followed by dry NEt_3 (4.4 mL, 32 mmol). To this solution were added bis(triphenylphosphine)palladium(II) chloride (8.0 mg, 13 μmol, 0.020 equiv.) and copper(I) iodide (4.0 mg, 19 μmol, 0.030 equiv.). The reaction mixture was heated at 50 °C for 48 h. The solvent was then removed in vacuo and the resulting residue was dissolved in DMF (2 mL). This solution was then dialyzed against DMF for 24 h to yield polymer **4** (0.29 g, 47%). UV–vis absorption (CH_3OH) λ_{max}: 406 nm. Emission λ_{max}: 460 nm. ^1H NMR (400 MHz, $CDCl_3$, δ): 1.43 (br s, 36 H), 2.48 (t, *J* = 6.63 Hz, 4 H), 3.52–4.29 (m, 36 H), 7.06–7.09 (m, 4H). SEC: M_n = 1100 g mol^{-1}, PDI = 2.42.

Deprotection of polymer 15 and complexation of Gd(III)

In a flame-dried flask under a nitrogen atmosphere, polymer **15** (70 mg, 32 μmol, 1.0 equiv.) was dissolved in CH_2Cl_2 (1 mL) and trifluoroacetic acid (TFA) (1 mL) was added. The resulting solution was stirred for 2 h at room temperature and then the solvent was removed in vacuo and the resulting residue was dissolved in ultrapure water (2 mL). The solution was dialyzed against ultrapure water for 24 h. The resulting solution was then lyophilized to yield the deprotected polymer **16** (0.034 g, 71%). ^1H NMR (400 MHz, D_2O, δ; note that aromatic peaks were not observed, likely because of solubility limitations and aggregation): 2.30–2.42 (m, 8 H), 2.63–4.02 (m, 70 H). Polymer **16** (10 mg, 7.0 μmol, 1.0 equiv.) was then redissolved in ultrapure water (5 mL) and combined with a solution of gadolinium chloride hexahydrate (1.0 mg, 28 μmol, 4.0 equiv.) in 2 mL of ultrapure water and the pH was adjusted to 7.4 using 0.1 mol L^{-1} NaOH. The resulting solution was stirred for 12 h at room temperature and then the solvent was reduced in vacuo to a volume of 2 mL. This solution was then dialyzed against ultrapure water for 24 h. The solvent was removed using a lyophilizer to yield polymer **1** (12 mg, quantitative yield.). ^1H NMR could not be obtained because of the paramagnetic Gd. ICP-MS: mass of polymer analyzed: 0.2 mg; mass of Gd(III) expected: 35 μg; mass of Gd(III) found: 34.8 μg.

Deprotection of polymer 4

In a flame-dried flask under a nitrogen atmosphere, polymer **4** (0.28 g, 0.29 mmol, 1.0 equiv.) was dissolved in dichloromethane (1 mL) and TFA (1 mL) was added. The resulting solution was stirred for 2 h at room temperature and then the solvent was removed in vacuo and the resulting residue was dissolved in DMF (2 mL). The solution was then dialyzed against DMF for 24 h to yield the deprotected polymer **17** (0.118 g, 62%). ^1H NMR (400 MHz, D_2O, δ) 2.44 (br s, 4 H), 3.10–4.33 (m, 36 H), 7.01 (br s, 4 H).

Supplementary data

Supplementary data for this article are available on the journal Web site (canjchem.nrc.ca).

Acknowledgements

We thank the Natural Sciences and Engineering Research Council of Canada and the Ontario Institute for Cancer Research for funding. The Lagugné-Labarthet group is thanked for assistance with optical microscopy.

References

(1) Caravan, P.; Ellison, J. J.; McMurry, T. J.; Lauffer, R. B. *Chem. Rev.* **1999**, *99* (9), 2293. doi:10.1021/cr980440x.
(2) Hermann, P.; Kotek, J.; Kubicek, V.; Lukes, I. *Dalton Trans.* **2008**, *23* (23), 3027. doi:10.1039/b719704g.
(3) Caravan, P. *Chem. Soc. Rev.* **2006**, *35* (6), 512. doi:10.1039/b510982p.
(4) Raymond, K. N.; Pierre, V. C. *Bioconjug. Chem.* **2005**, *16* (1), 3. doi:10.1021/bc049817y.
(5) Hasebroock, K. M.; Serkova, N. J. *Expert Opin. Drug Metab. Toxicol.* **2009**, *5* (4), 403. doi:10.1517/17425250902873796.
(6) Strandberg, E.; Westlund, P. O. J. *Magn. Reson. Ser. A* **1996**, *122* (2), 179. doi:10.1006/jmra.1996.0193.
(7) Lauffer, R. B. *Chem. Rev.* **1987**, *87* (5), 901. doi:10.1021/cr00081a003.
(8) Gibby, W. A.; Bogdan, A.; Ovitt, T. W. *Invest. Radiol.* **1989**, *24* (4), 302. doi:10.1097/00004424-198904000-00009.
(9) Armitage, F. E.; Richardson, D. E.; Li, K. C. P. *Bioconjug. Chem.* **1990**, *1* (6), 365. doi:10.1021/bc00006a001.
(10) Rongved, P.; Fritzell, T. H.; Strande, P.; Klaveness, J. *Carbohydr. Res.* **1996**, *287* (1), 77. doi:10.1016/0008-6215(96)00062-6.
(11) Rebizak, R.; Schaefer, M.; Dellacherie, E. *Bioconjug. Chem.* **1997**, *8* (4), 605. doi:10.1021/bc970062n.
(12) Kellar, K. E.; Henrichs, P. M.; Hollister, R.; Koenig, S. H.; Eck, J.; Wei, D. *Magn. Reson. Med.* **1997**, *38* (5), 712. doi:10.1002/mrm.1910380506.
(13) Ladd, D. L.; Hollister, R.; Peng, X.; Wei, D.; Wu, G.; Delecki, D.; Snow, R. A.; Toner, J. L.; Kellar, K.; Eck, J.; Desai, V. C.; Raymond, G.; Kinter, L. B.; Desser, T. S.; Rubin, D. L. *Bioconjug. Chem.* **1999**, *10* (3), 361. doi:10.1021/bc980086+.
(14) Tóth, E.; Helm, L.; Kellar, K. E.; Merbach, A. E. *Chem. Eur. J.* **1999**, *5* (4), 1202. doi:10.1002/(SICI)1521-3765(19990401)5:4<1202::AID-CHEM1202>3.0.CO;2-Y.
(15) Lauffer, R. B.; Brady, T. J. *Magn. Reson. Imaging* **1985**, *3* (1), 11. doi:10.1016/0730-725X(85)90004-9.

Can. J. Chem. Downloaded from www.nrcresearchpress.com by 80.58.250.72 on 09/16/12
For personal use only.

(16) Lauffer, R. B.; Brady, T. J.; Brown, R. D., III; Baglin, C.; Koenig, S. H. *Magn. Reson. Med.* **1986**, *3* (4), 541. doi:10.1002/mrm.1910030407.
(17) Wiener, E. C.; Brechbiel, M. W.; Brothers, H.; Magin, R. L.; Gansow, O. A.; Tomalia, D. A.; Lauterbur, P. C. *Magn. Reson. Med.* **1994**, *31* (1), 1. doi:10.1002/mrm.1910310102.
(18) Wiener, E. C.; Auteri, F. P.; Chen, M. W.; Brechbiel, M. W.; Gansow, O. A.; Schneider, D. S.; Belford, R. L.; Clarkson, R. B.; Lauterbur, P. C. *J. Am. Chem. Soc.* **1996**, *118* (33), 7774. doi:10.1021/ja9536126.
(19) Kobayashi, H.; Sato, N.; Kawamoto, S.; Saga, T.; Hiraga, A.; Haque, T. L.; Ishimori, T.; Konishi, J.; Togashi, K.; Brechbiel, M. W. *Bioconjug. Chem.* **2001**, *12* (1), 100. doi:10.1021/bc000075s.
(20) Bryant, L. H., Jr.; Brechbiel, M.; Wu, C.; Bulte, J. W.; Herynek, V.; Frank, J. A. *J. Magn. Reson. Imaging* **1999**, *9* (2), 348. doi:10.1002/(SICI)1522-2586(199902)9:2<348::AID-JMRI30>3.0.CO;2-J.
(21) Rudovský, J.; Hermann, P.; Botta, M.; Aime, S.; Lukeš, I. *Chem. Commun. (Camb.)* **2005**, (18): 2390. doi:10.1039/b418712a.
(22) Langereis, S.; de Lussanet, Q. G.; van Genderen, M. H. P.; Backes, W. H.; Meijer, E. W. *Macromolecules* **2004**, *37* (9), 3084. doi:10.1021/ma035983+.
(23) Langereis, S.; de Lussanet, Q. G.; van Genderen, M. H. P.; Meijer, E. W.; Beets-Tan, R. G. H.; Griffioen, A. W.; van Engelshoven, J. M. A.; Backes, W. H. *NMR Biomed.* **2006**, *19* (1), 133. doi:10.1002/nbm.1015.
(24) Misselwitz, B.; Schmitt-Willich, H.; Ebert, W.; Frenzel, T.; Weinmann, H. J. *Magn. Reson. Mater. Phys. Biol. Med.* **2001**, *12* (2–3), 128. doi:10.1016/S1352-8661(01)00109-0.
(25) Schwickert, H. C.; Roberts, T. P. L.; Muhler, A.; Stiskal, M.; Demsar, F.; Brasch, R. C. *Eur. J. Radiol.* **1995**, *20* (2), 144. doi:10.1016/0720-048X(95)00645-7.
(26) Dellsperger, S.; Dotz, F.; Smith, P.; Weder, C. *Macromol. Chem. Phys.* **2000**, *201* (2), 192. doi:10.1002/(SICI)1521-3935(20000201)201:2<192::AID-MACP192>3.0.CO;2-E.
(27) Weder, C.; Sarwa, C.; Montali, A.; Bastiaansen, C.; Smith, P. *Science* **1998**, *279* (5352), 835. doi:10.1126/science.279.5352.835.
(28) Pschirer, N. G.; Miteva, T.; Evans, U.; Roberts, R. S.; Marshall, A. R.; Neher, D.; Myrick, M. L.; Bunz, U. H. F. *Chem. Mater.* **2001**, *13* (8), 2691. doi:10.1021/cm010226g.
(29) Swager, T. M.; Gil, C. J.; Wrighton, M. S. *J. Phys. Chem.* **1995**, *99* (14), 4886. doi:10.1021/j100014a003.
(30) Zhou, Q.; Swager, T. M. *J. Am. Chem. Soc.* **1995**, *117* (26), 7017. doi:10.1021/ja00131a031.
(31) Yang, J.-S.; Swager, T. M. *J. Am. Chem. Soc.* **1998**, *120* (46), 11864. doi:10.1021/ja982293q.
(32) Lee, K.; Povlich, L. K.; Kim, J. *Adv. Funct. Mater.* **2007**, *17* (14), 2580. doi:10.1002/adfm.200700218.
(33) Lee, K.; Rouillard, J. M.; Pham, T.; Gulari, E.; Kim, J. *Angew. Chem. Int. Ed. Engl.* **2007**, *46* (25), 4667. doi:10.1002/anie.200700419.
(34) Pun, C.-C.; Lee, K.; Kim, H.-J.; Kim, J. *Macromolecules* **2006**, *39* (22), 7461. doi:10.1021/ma061330s.
(35) Miranda, O. R.; You, C.-C.; Phillips, R.; Kim, I.-B.; Ghosh, P. S.; Bunz, U. H. F.; Rotello, V. M. *J. Am. Chem. Soc.* **2007**, *129* (32), 9856. doi:10.1021/ja0737927.
(36) Disney, M. D.; Zheng, J.; Swager, T. M.; Seeberger, P. H. *J. Am. Chem. Soc.* **2004**, *126* (41), 13343. doi:10.1021/ja047936i.
(37) Wosnick, J. H.; Mello, C. M.; Swager, T. M. *J. Am. Chem. Soc.* **2005**, *127* (10), 3400. doi:10.1021/ja043134b.
(38) Amedio, J. C., Jr.; Van Wagenen, G., Jr.; Zavlin, G.; Gyorkos, A.; Peterson, S. A. *Synth. Commun.* **2000**, *30* (20), 3755. doi:10.1080/00397910008087003.
(39) Laurent, S.; Parac-Vogt, T. N.; Kimpe, K.; Thirifays, C.; Binnemans, K.; Muller, R. N.; Vander Elst, L. *Eur. J. Inorg. Chem.* **2007**, *2007* (14), 2061. doi:10.1002/ejic.200601170.
(40) Lavigne, J. J.; Broughton, D. L.; Wilson, J. N.; Erdogan, B.; Bunz, U. H. F. *Macromolecules* **2003**, *36* (20), 7409. doi:10.1021/ma0348167.
(41) Tan, C.; Atas, E.; Muller, J. G.; Pinto, M. R.; Kleiman, V. D.; Schanze, K. S. *J. Am. Chem. Soc.* **2004**, *126* (42), 13685. doi:10.1021/ja046856b.
(42) Chen, L.; McBranch, D. W.; Wang, H.; Helgeson, R.; Wudl, F.; Whitten, D. G. *Proc. Natl. Acad. Sci. U.S.A.* **1999**, *96* (22), 12287. doi:10.1073/pnas.96.22.12287.
(43) Kim, J.; Swager, T. M. *Nature* **2001**, *411* (6841), 1030. doi:10.1038/35082528.
(44) Kim, I.-B.; Phillips, R.; Bunz, U. H. F. *Macromolecules* **2007**, *40* (15), 5290. doi:10.1021/ma070795v.
(45) Wilbur, D. S.; Pathare, P. M.; Hamlin, D. K.; Buhler, K. R.; Vessella, R. L. *Bioconjug. Chem.* **1998**, *9* (6), 813. doi:10.1021/bc980055e.
(46) Carboni, B.; Vaultier, M.; Carrie, R. *Tetrahedron* **1987**, *43* (8), 1799. doi:10.1016/S0040-4020(01)81491-5.
(47) Bonnard, V.; Azoulay, S.; Di Giorgio, A.; Patino, N. *Chem. Commun. (Camb.)* **2009**, (17): 2302. doi:10.1039/b815324h.
(48) Lee, K.; Cho, J. C.; Deheck, J.; Kim, J. *Chem. Commun. (Camb.)* **2006**, (18): 1983. doi:10.1039/b602267g.
(49) Tilcock, C.; Unger, E.; Cullis, P.; MacDougall, P. *Radiology* **1989**, *171* (1), 77.
(50) Tilcock, C.; MacDougall, P.; Unger, E.; Cardenas, D.; Fajardo, L. *Biochim. Biophys. Acta* **1990**, *1022* (2), 181. doi:10.1016/0005-2736(90)90112-2.
(51) Fossheim, S. L.; Fahlvik, A. K.; Klaveness, J.; Muller, R. N. *Magn. Reson. Imaging* **1999**, *17* (1), 83. doi:10.1016/S0730-725X(98)00141-6.

(–)-6α-Hydroxy polyanthellin A — A novel antifouling diterpenoid from the Indian soft coral *Cladiella krempfi* (Hickson)

V.P. Limna Mol, T.V. Raveendran, P.S. Parameswaran, R.J. Kunnath, and P.R. Rajamohanan

Can. J. Chem. Downloaded from www.nrcresearchpress.com by 80.58.250.72 on 09/16/12
For personal use only.

Abstract: Bioassay-guided purification of methanol extract of the soft coral *Cladiella krempfi* (Octocorallia: Alcynocea) yielded a novel eunicellin-type diterpenoid, (–)-6α-hydroxy polyanthellin A (**1**), active against the cyprids of the fouling barnacle, *Balanus amphitrite* (EC_{50} 9.02 μg/mL; LC_{50} 36 μg/mL; and therapeutic ratio = 4). The structure of compound **1** was determined from its spectral data, including IR, NMR (1D and 2D NMR), and mass spectra.

Key words: biofouling, antifouling, *Cladiella krempfi*, *Balanus amphitrite*, diterpenes.

Résumé : Une purification orientée par des bioessais du produit obtenu par extraction au méthanol du corail mou, *Cladiella krempfi* (Octacorallia : Alcynocea), a permis d'isoler un nouveau diterpénoïde de type eunicelline, la (–)-6α-hydroxypolyanthelline A (**1**), active contre les cyprides de la barnacle encrassante, *Balanus amphritrite* (CE_{50} 9,02 μg/mL; CL_{50} 36 μg/mL) et un rapport thérapeutique de 4). La structure du composé **1** a été déterminée à partir de données spectroscopiques, dont les spectres IR, RMN (1D et 2D) et de masse.

Mots-clés : encrassage biologique, antisalissure, *Cladiella krempfi*, *Balanus amphritrite*, diterpènes.

Introduction

The genus *Cladiella* belongs to the order Alcyonacea, class Anthozoa. These soft corals, which grow as thick carpetlike colonies, extending up to several square meters are widely distributed in the tropical and subtropical shallow-water habitats.[1] Several bioactive cembrane/eunicellane diterpenes, sesquiterpenes, sterols, and glycolipids have been reported from this genus by different groups.[2] These include Cladidiol and polyanthellin A, an acetylcholinesterase-inhibiting sesquiterpene and an antibacterial diterpene, respectively, from a *Cladiella* sp. found in the Andaman and Nicobar area; a new hemiketal steroid, cladiellin A, with antioxidant activity from China; cladiellaperoxide, a diterpenoid (toxic to brine shrimps) from *Cladiella sphaeroides*; and several pregnane glycosides from *Cladiella krempfi* (antitumour) collected from Miyazaki Prefecture, Japan.[2–6]

Despite their abundance in Indian waters, only limited studies on their chemical/biological properties are available in the literature.[7] Herein, we report the isolation and structure determination of a novel diterpenoid, (–)-6α-hydroxy polyanthellin A (**1**), active against the cyprids of the fouling barnacle, *Balanus amphitrite*, from *C. krempfi* from Lakshadweep Islands (India).

Experimental

General

NMR spectra were recorded in $CDCl_3$ solution on Bruker Avance 300 and 500 MHz NMR spectrometers, using a standard 5 mm probe while HR-MS analysis was performed on an Applied Biosystem instrument (QTOF type) and IR spectrum was recorded using Jasco FTIR 4100 IR spectrometer. For column chromatography, silica gel (60–120 mesh size) from s.d. Fine Chem Limited was used. All solvents were procured from s.d. Fine Chem Limited (AR Grade) and used as received.

Cladiella krempfi was collected from the shallow coastal waters of Kavaratti Island (Lakshadweep, lat. 10°34′0 N; long. 72°37′0 E). The thick carpetlike colonies were light brown in colour. The specimen (1 kg wet mass) was washed with fresh water and soaked in methanol before being transported to the laboratory. In the laboratory, the animals were cut into smaller pieces and repeatedly extracted with fresh MeOH. The combined MeOH supernatants were concentrated under reduced pressure using a rotavapor. The crude extract was then partitioned into petroleum ether, ethyl acetate, and aqueous fractions in the usual way. The active petroleum ether fraction (Fr 1, 2 g) was purified on Sephadex LH-20 (eluant: chloroform/methanol, 1:1) into four broad fractions (Fr 1–1 to Fr 1–4). Bioassay of the fractions indi-

Received 27 April 2010. Accepted 11 October 2010. Published on the NRC Research Press Web site at canjchem.nrc.ca on 23 December 2010.

V.P. Limna Mol, T.V. Raveendran,[1] P.S. Parameswaran, and R.J. Kunnath. National Institute of Oceanography (Regional Centre), Council of Scientific and Industrial Research, Dr. Salim Ali Road, Kochi, Kerala 682018, India.
P.R. Rajamohanan. National Chemical Laboratory, Council of Scientific and Industrial Research, Pune, India.

[1]Corresponding author (e-mail: tvravi@nio.org).

Table 1. MS fragmentation pattern of (–)-6α-hydroxy polyanthellin A.

Observed *m/z*	Calculated *m/z*	Molecular formula of the fragment ion	Stable fragment expelled from the parent ion
381.2630	381.2635	$C_{22}H_{37}O_5$	$[M + H]^+$
321.2371	321.2424	$C_{20}H_{33}O_3$	$[M – CH_3COOH + H]^+$
303.2319	321.2318	$C_{20}H_{31}O_2$	$[321 – H_2O]$
293.2527	293.2475	$C_{19}H_{33}O_2$	[321 – CO]
285.2221	285.2212	$C_{20}H_{29}O$	$[M – AcOH – 2H_2O + H]^+$
267.2091	267.2107	$C_{20}H_{27}$	$[285 – H_2O]$
225.1668	225.1637	$C_{17}H_{21}$	$[267 – C_3H_6]$
201.1611	201.1637	$C_{15}H_{21}$	

Table 2. Comparison of the ^1H and ^{13}C chemical shifts of (–)-6α-hydroxy polyanthellin A and polyanthellin A.

	(–)-6α-Hydroxy polyanthellin A		Polyanthellin A	
Carbon No.	δ_c	δ_h	δ_c	δ_h
1	41.9	2.20 (1H, dd, 7.2,10.5, $H_{ax/\beta}$)	41.6	2.30 (1H,m)
2	90.8	3.54 (1H, brs, Heq/β)	93.7	3.54 (1H, brs)
3	74.6	—	75.5	—
4	40.1	1.72 (1H, dd, 7, 1.5, eq/β), 1.85 (1H, m, ax/α)	36.2	1.41 (1H, m); 1.79 (1H, m)
5	29.2	2.05 (1H, m, eq/α); 1.55 (1H, m, ax/β)	18.1	1.49 (1H, m); 2.32 (1H, m)
6	80.3	4.55 (1H, brd, 6.3, eq/β)	39.6	1.42 (2H, m)
7	77.2	—	74.3	—
8	46.9	2.35 (1H, dd, 14.7, 11, eq/β); 1.76 (1H, dd, 14.7, 3.5, ax/α)	47.5	1.86 (1H, brd, 14.2); 2.19 (1H, dd, 4.9, 14.2)
9	75.5	4.05 (1H, ddd, 11, 7.2, 3.5, ax/β)	77.2	3.89 (1H, t, 5.3)
10	54.2	2.84 (1H, t, 7.2, eq/β)	51.0	3.21 (1H, t, 6)
11	82.9	—	83.1	—
12	30.6	2.38 (1H, m, eq/β);1.4 (1H, m, ax/α)	29.7	2.41 (1H, m); 1.25 (1H, m)
13	17.9	1.4 (1H, m, eq/α);1.22 (1H, m, ax/β)	17.5	1.14 (1H, m); 1.40 (1H, m)
14	42.5	1.25 (1H, m, ax/α)	42.3	1.15 (1H, m)
15	29.1	1.7 (1H, m)	29.6	1.67 (1H, m)
16	21.8	0.96 (3H, d, 6.9)	21.7	0.92 (3H, d, 6.9)
17	15.6	0.83 (3H, d, 6.9)	15.5	0.79 (3H, d, 6.9)
18	30.28	1.14 (3H, s, β-Me)	27.5	1.07 (3H, s)
19	23.16	1.23 (3H, s, β-Me)	35.6	1.33 (3H, s)
20	24.4	1.47 (3H, s, ax/β-Me)	24.0	1.48 (3H, s)
21	170.1s	—	170.3	—
22	22.6q	2.01 (3H, s)	22.5	1.99 (3H, s)

Can. J. Chem. Downloaded from www.nrcresearchpress.com by 80.58.250.72 on 09/16/12
For personal use only.

cated Fr 1–3 (100 mg) to be active, which was further purified on silica gel columns (gradient acetone/hexane), yielding the active compound as a single spot on TLC (R_f = 0.52). The structure of the purified compound (10 mg) was determined based on its IR, MS, and NMR spectral data.

The antibacterial screening of different fractions was carried out against seven strains of fouling bacteria (*Bacillus cereus*, *Bacillus pumilus*, *Bacillus megaterium*, *Pseudoalteromonas haloplanktis*, *Pseudomonas chlororaphis*, *Pseudomonas putida*, and *Pseudomonas aeruginosa*) using the disc diffusion method, with 100 μg of compound per disc.[8] The settlement inhibition activity was performed against *B. amphitrite* (= *Amphibalanus amphitrite*) cyprids at 50 μg/mL.[9,10] The effective and lethal concentrations (EC_{50} and LC_{50}) of the pure compound were determined using serial dilution method from 100 to 6.25 μg/mL.[8,11,12] The data were analyzed by one-way ANOVA, followed by Tukey's multiple comparison test at 95% confidence level.[13] One-way ANOVA was performed with SPSS, Version 10. EC_{50} and LC_{50} values were calculated using Probit analysis.[14,15] The experiment was repeated twice with different batches of larvae.

Results and discussion

Structure determination

IR absorptions of compound **1** (yield = 10 mg, $[\alpha]_D^{27} = -20^\circ$ (0.17%, $CHCl_3$) at 3450, 1730, and 1050 cm^{-1} indicated the presence of hydroxyl and ester groups in the molecule. Among these, the ester group could be an acetate, as confirmed by the characteristic NMR peaks at δ 2.01 (3H, s, CO–CH_3), 22.6 (CO–CH_3), and 170.1 (CO–CH_3) and the facile loss of 60 mass units in the mass spectrum (Table 1). ^{13}C NMR confirmed the presence of 22 carbons, distributed as four quarternary, seven CH, five CH_2, and six methyl carbons as confirmed by DEPT 135 and DEPT 90 spectra. Noteworthy was the presence of six oxygenated carbons (90.8d, 82.9s, 80.3d, 77.2s, 75.5d, and 74.6s) but relatively lower polarity of the compound (i.e., eluted with hexane/acetone,

Can. J. Chem. Downloaded from www.nrcresearchpress.com by 80.58.250.72 on 09/16/12
For personal use only.

Fig. 1. Schematic representation of the major HMBC correlations of (–)-6α-hydroxy polyanthellin A.

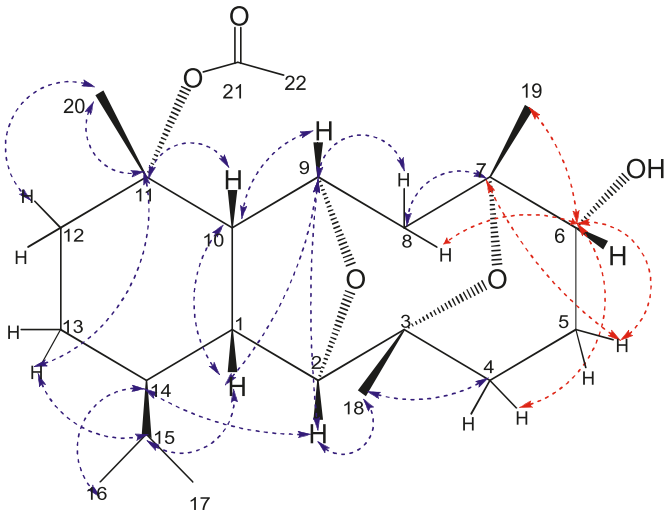

Fig. 2. Schematic representation of the strong and medium (dotted line) nOe correlations of (–)-6α-hydroxy polyanthellin A.

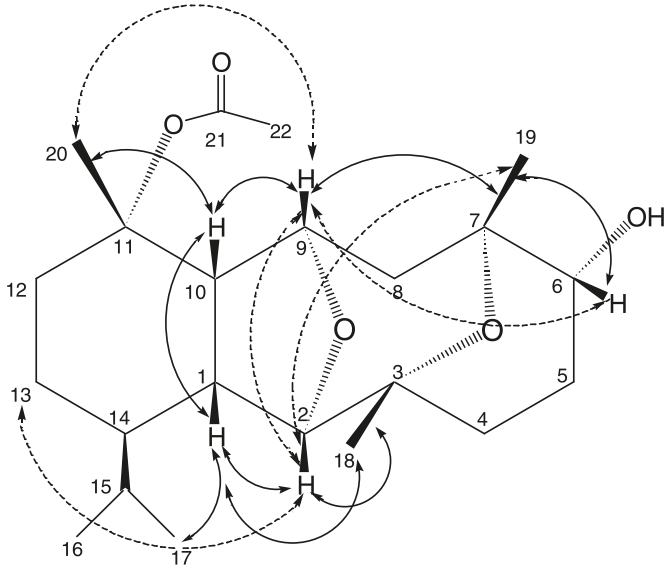

60:40, from SiO_2 column, R_f = 0.52 with hexane/acetone, 70:30, and its easy solubility in $CHCl_3$), indicating the possible presence of one or more cyclic ether/epoxides in the molecule. HR-MS revealed the accurate mass of its $[M + H]^+$ pseudomolecular ion to be 381.2630, corresponding to an elemental composition of $C_{22}H_{37}O_5$ (calcd.: 381.2635), thus indicating its diterpenoid nature. The above molecular formula indicated a degree of hydrogen deficiency of 5. One of these could be accounted for by the acetate group. NMR spectra ruled out the presence of any unsaturations, indicating that the molecule is tetracyclic.

Comparison of its NMR spectral data with those of different soft coral and gorgonian diterpenoids indicated its close structural similarity to polyanthellin A, a diterpenoid isolated from the gorgonian *Briareum polyanthes* (Table 2).[16] The major differences were the observed downfield shift of C-4 to C-6 signals from δ 36.2, 18.1, and 39.6 in polyanthellin A to δ 40.1 (CH_2), 29.2 (CH_2), and 80.3 (CH), respectively,

Fig. 3. (–)-6α-Hydroxy polyanthellin A.

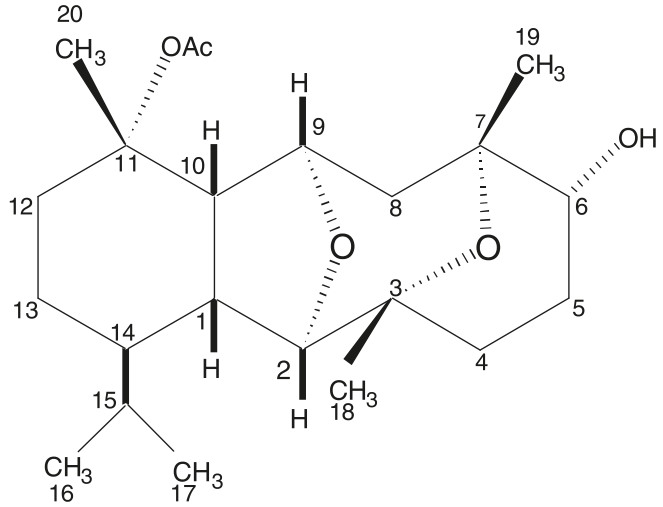

Fig. 4. Effect of (–)-6α-hydroxy polyanthellin A on the settlement and mortality of cyprids. (A) Batch 1 cyprids. (B) Batch 2 cyprids. % Settlement (▲); % mortality (●). Data plotted are means ± SD of six replicates.

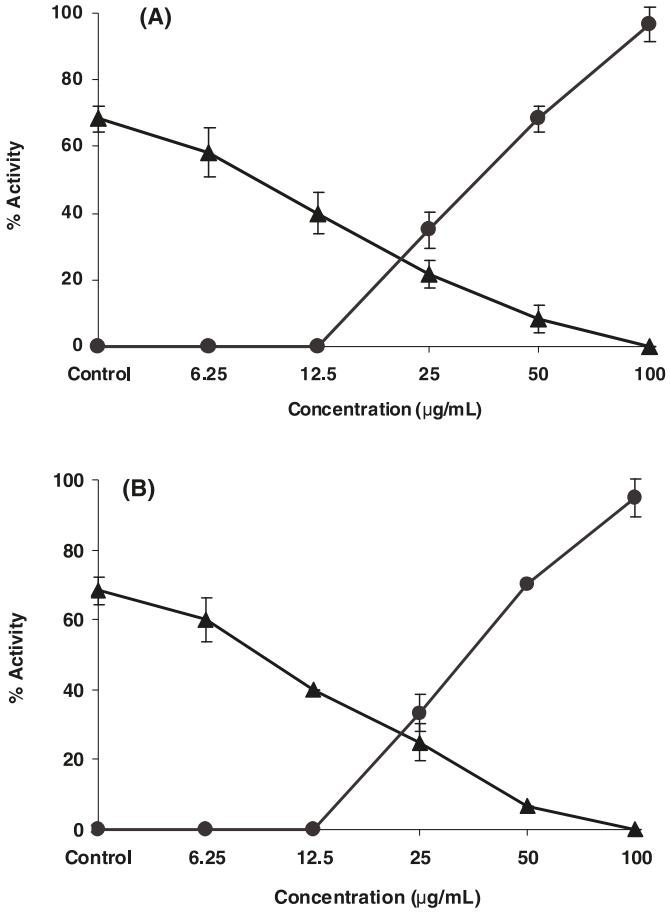

in compound **1**. Comparison of these values with those of related compounds briarellin M and O,[16] as well as examination of COSY, HSQC, and HMBC data indicated the presence of the additional hydroxyl group at C-6 (Table 2 and Fig. 1). The large downfield chemical shift of C-6 at

Can. J. Chem. Downloaded from www.nrcresearchpress.com by 80.58.250.72 on 09/16/12
For personal use only.

δ 80.26 indicated the presence of a hydroxyl group at this position. This was confirmed by the expected downfield shifts of C-4 and C-5 by 4 and 11 ppm, respectively.

The similarities in ^{1}H and ^{13}C chemical shifts, except for C-4, C-5, and C-6 of the isolated compound and polyanthellin A, indicated their relative stereochemistry also to be identical. The relatively small coupling constant observed for the 6-H (J = 6.3 Hz) indicated this proton to be equatorial. The observed strong nOe cross peaks H1 (δ 2.20)/H10 (δ 2.84) and H2 (δ 3.54), H10/H9 (δ 4.05) and 20 Me (δ 1.47), H9/19 Me (δ 1.23) and 19 Me/H6 (δ 4.55), as well as the medium size cross peaks between H2/H9, H2/H19, and H6/H9 (Fig. 2) further confirmed the sterochemistry. The observed optical rotation of compound **1** ($[\alpha]_D^{27} = -20^\circ$ (0.17%, $CHCl_3$)) is also comparable to that of polyanthellin A ($[\alpha]_D^{20} = -9.9^\circ$ (*c* 1.0, $CHCl_3$)) and other related eunicellin diterpenoids, indicating the absolute stereochemistry to be the same. From the above results, the structure of compound **1** could be established as (–)-6α-hydroxy polyanthalin A (Fig. 3).

Antifouling activity

The crude extract, partially purified fractions/compounds, were inactive against the seven strains of fouling bacteria. Duplicate experiments with varying dosages between 6.25 and 100 μg/mL confirmed the anti-settlement properties of compound **1** against *B. amphitrite* cyprids in a dose-dependent manner (Fig. 4; batch 1: $p = 0.05$; $F_{5,30} = 184.818$, EC_{50} 8.82 μg/mL, LC_{50} 35.72 μg/mL; batch 2: $p = 0.05$; $F_{5,30} = 322.760$, EC_{50} 9.23 μg/mL, LC_{50} 36.22 μg/mL; one-way ANOVA). The therapeutic ratio was calculated to be 4 from the above results.

Marine invertebrates, especially soft corals and gorgonians are a rich source for novel and bioactive secondary metabolites.[17,18] Since the first isolation of eunicellin, a diterpene from *Eunicella stricta* in 1968, over 50 eunicellin and related cladiellins have been isolated so far.[19,20] Many of these metabolites possess promising cytotoxic properties.[17,19] while a few are known to play a functional role as antifeedants, as indicated by mollusc and fish lethality studies.[21]

To the best of our knowledge, no studies have been reported so far on the antifouling properties of cladiellin diterpenes. Our studies indicate (–)-6α-hydroxy polyanthalin A (**1**) to be active against cyprids of *B. amphitrite*. With an LC_{50} of ~36 μg/mL and favourable EC_{50} value of ~9 μg/mL, its therapeutic ratio works out to be 4, which agrees well with the recommended value (i.e., >1) for environmentally compatible antifouling coatings.[22] Further studies on structure–activity relationships of this compound using different synthetic analogs/derivatives may lead to an environmentally benign antifouling agent of commercial potential.

Supplementary data

Supplementary data for this article are available on the journal Web site (canjchem.nrc.ca).

Acknowledgements

Our sincere thanks are due to the Centre for Marine Living Resources and Ecology (CMLRE), Ministry of Earth Sciences, New Delhi, for partial financial support; Director, National Institute of Oceanography (NIO), for the facilities provided; Department. of Science and Technology, Lakshadweep Islands, for the collection of samples; and Dr. Yehuda Benayahu for taxonomic identification. One of the authors (VPL) is thankful to the Council of Scientific and Industrial Research (CSIR), Government of India, for the grant of Senior Research Fellowship. This is NIO contribution No. 4869.

References

(1) Tentori, E.; Allemand, D. *Biol. Bull.* **2006**, *211* (2), 193. doi:10.2307/4134593.
(2) Huang, X. P.; Deng, Z. W.; Ofwegen, L. V.; Li, J.; Fu, H. Z.; Zhu, X. B.; Lin, W. H. *J. Asian Nat. Prod. Res.* **2006**, *8* (4), 287. doi:10.1080/10286020500034782.
(3) Yamada, K.; Ogata, N.; Ryu, K.; Miyamoto, T.; Komori, T.; Higuchi, R. *J. Nat. Prod.* **1997**, *60* (4), 393. doi:10.1021/np9605605.
(4) Lan, W.; Lin, C. W.; Su, J. Y.; Zeng, L. M. *Chem. J. Chin. Univ.* **2003**, *24*, 2019.
(5) Ata, A.; Ackerman, J.; Bayoud, A.; Radhika, P. *Helv. Chim. Acta* **2004**, *87* (3), 592. doi:10.1002/hlca.200490056.
(6) Zhang, G. W.; Ma, X. Q.; Kurihara, H.; Zhang, C. X.; Yao, X. S.; Su, J. Y.; Zeng, L. M. *Org. Lett.* **2005**, *7* (6), 991. doi:10.1021/ol0477475.
(7) Raveendran, T. V.; Limna Mol, V. P. *Curr. Sci.* **2009**, *97*, 508.
(8) Limna Mol, V. P.; Raveendran, T. V.; Parameswaran, P. S. *Int. Biodeter. Biodegr.* **2009**, *63* (1), 67. doi:10.1016/j.ibiod.2008.07.001.
(9) Clare, A. S.; Hoeg, J. T. *Biofouling* **2008**, *24* (1), 55. doi:10.1080/08927010701830194.
(10) Carlton, J. T.; Newman, W. A. *Biofouling* **2009**, *25* (1), 77. doi:10.1080/08927010802535247.
(11) Rittschof, D.; Clare, A. S.; Gerhart, D. J., Sr.; Mary, S. A.; Bonaventura, J. *Biofouling* **1992**, *6* (2), 115. doi:10.1080/08927019209386217.
(12) Maréchal, J. P.; Culioli, G.; Hellio, C.; Thomas-Guyon, H.; Callow, M. E.; Clare, A. S.; Ortalo-Magne, A. *J. Exp. Mar. Biol. Ecol.* **2004**, *313* (1), 47. doi:10.1016/j.jembe.2004.07.016.
(13) Conover, W. J.; Iman, L. *Am. Stat.* **1981**, *35* (3), 124. doi:10.2307/2683975.
(14) Finney, D. J. *Probit Analysis,* 3rd ed.; Cambridge University Press: Cambridge, 1971.
(15) Sakuma, M. *Appl. Entomol. Zool. (Jpn.)* **1998**, *33*, 339.
(16) Ospina, C. A.; Rodriguez, A. D.; Ortega-Barria, E.; Capson, T. L. *J. Nat. Prod.* **2003**, *66* (3), 357. doi:10.1021/np0204500.
(17) Coll, J. C. *Chem. Rev.* **1992**, *92* (4), 613. doi:10.1021/cr00012a006.
(18) Faulkner, D. J. *Nat. Prod. Rep.* **2002**, *19*, 1.
(19) Bernardelli, P.; Paquette, L. A. *Heterocycles* **1998**, *49* (1), 531. doi:10.3987/REV-98-SR2.
(20) MacMillan, D. W. C.; Overman, L. E.; Pennington, L. D. *J. Am. Chem. Soc.* **2001**, *123* (37), 9033. doi:10.1021/ja016351a.
(21) Harvell, C. D.; West, J. M.; Griggs, C. *Invertebr. Reprod. Dev.* **1996**, *30*, 239.
(22) Rittschof, D.; Lai, C.-H.; Kok, L.-M.; Teo, S. L.-M. *Biofouling* **2003**, *19*, 207. doi:10.1080/0892701021000083769.

Theoretical investigation of second-order nonlinear optical response — Hexamolybdate as a superior donor over metal carbonyl complexes in the D–π–A model

Ping Song, Chunguang Liu, Wei Guan, Likai Yan, Xiaolei Sun, Chan Yao, and Zhongmin Su

Can. J. Chem. Downloaded from www.nrcresearchpress.com by 80.58.250.72 on 09/16/12
For personal use only.

Abstract: Density functional theory (DFT) calculations were carried out to investigate the nonlinear optical (NLO) response for the donor-conjugated bridge-accepter (D–π–A) model of *p*-nitroaniline (PNA) – hexamolybdate derivatives and PNA–metal–carbonyl complexes. The bond length alternation (BLA) values decrease with lengthening of the π-conjugated bridge, especially for PNA–hexamolybdate derivatives, which dramatically enhances the NLO response. In addition, the introduction of Mo≡N in PNA–hexamolybdate derivatives is expected to provide a better electron transition channel, consequently generating lower BLA values and an outstanding NLO response compared with PNA–metal–carbonyl complexes. It is shown that the hexamolybdate acts as an electron donor when incorporating metal–carbonyl complexes into one molecule. All these behaviors reflect the superiority of hexamolybdate as a donor moiety in the D–π–A model for the design of potential NLO materials.

Key words: bond length alternation, PNA–hexamolybdate, metal–carbonyl complexes, NLO response, electron transition.

Résumé : On a effectué des calculs selon la théorie de la fonctionnelle de la densité (TFD) dans le but d'étudier la réponse optique non linéaire (ONL) du modèle D–π–A des dérivés hexamolybdate de *p*-nitroaniline (PNA) et des complexes PNA–métal–carbonyle. Les valeurs d'alternation de la longueur de liaison (ALL) diminuent avec un allongement du pont π-conjugué, particulièrement avec les dérivés hexamolybdatde de PNA qui augmentent d'une façon dramatique la réponse ONL. De plus, il est prévu que l'introduction de Mo≡N dans les dérivés hexamolybdatde de PNA conduira à une meilleure voie de transition pour les électrons et, en conséquence, qu'elle générera des valeurs plus basses pour l'ALL et une réponse ONL exceptionnelle par rapport à celle des complexes PNA–métal–carbonyle. On a démontré que l'hexamolybdate agit comme donneur d'électron lorsqu'il incorpore des complexes métal-carbonyle dans une molécule. Tous ces comportements reflètent la supériorité de l'hexamolybdate comme groupe donneur dans le modèle D–π–A de conception de matériaux potentiellement ONL.

Mots-clés : alternation de la longueur de liaison, hexamolybdate de *p*-nitroaniline, complexes métal–carbonyle, réponse optique non linéaire, transition électronique.

Introduction

The area of second-order nonlinear optical (NLO) properties continues to receive much attention in recent years. Organic compounds containing a donor and an acceptor connected by a conjugated bridge (D–π–A) have been confirmed to behave excellent NLO properties,[1–4] and the NLO response is related to the length of the organic bridge chain.[5–7] *p*-Nitroaniline (PNA) has been considered as a prototype of a conventional D–π–A model that exhibits a large NLO response, and a number of push–pull phenylene derivatives have been widely explored to investigate the charge transfer in the molecules.[8,9] Effective methods to enhance the second-order NLO response are applied by increasing the electronic asymmetry with more potent donating or accepting chromophores or increasing the length of the π-conjugated chain between the donor and the acceptor,[10–12] and the reduction of the bond length alternation (BLA) values for the π-conjugated bridge is another advisable approach.

As typical NLO materials, organic materials are of major interest because of their relatively low cost, high laser damage thresholds, low dielectric constants, and fast nonlinear optical response times. However, they have several disadvantages: low energy transitions in the UV–vis region result in a tradeoff between nonlinear efficiency and optical transparency with low thermal stability. Robust inorganic salts are available as large single crystals, and they possess a large transparency range and suffer very low optical losses, but the response times are slow. The organic–inorganic hybrid

Received 12 July 2010. Accepted 20 October 2010. Published on the NRC Research Press Web site at canjchem.nrc.ca on 23 December 2010.

P. Song, C. Liu, W. Guan, L. Yan, X. Sun, C. Yao, and Z. Su.[1] Institute of Functional Material Chemistry, Key Laboratory of Polyoxometalate Science of Ministry of Education, Faculty of Chemistry, Northeast Normal University, Changchun 130024, P. R. China.

[1]Corresponding author (e-mail: zmsu@nenu.edu.cn).

Can. J. Chem. Downloaded from www.nrcresearchpress.com by 80.58.250.72 on 09/16/12
For personal use only.

materials may combine the advantages of the two materials with little loss of optical transparency accompanying the large increase in β. The attachment of the chromophoric group to the main chain of the compound increases the stability of the orientation polarization.

The transition-metal complexes in organometallic and coordination chemistry offer large numbers of NLO structures closely related to their special metal *n*d configuration, oxidation states, etc.[13–17] The participation of the transition metals may induce low-energy metal-to-ligand charge transfer (MLCT), ligand-to-metal charge transfer (LMCT) or intraligand charge transfer (ILCT) excitation, consequently resulting in better NLO properties. Many metal complexes behave in an electronically amphoteric manner, i.e., as an ambivalent donor or acceptor, depending on the substituents on the conjugated side chain, and they can even replace the bridge moieties in the organic D–π–A structure and, consequently, with satisfactory NLO response. Among the transition-metal complexes, metalloporphyrins and metal Schiff base complexes with π-conjugated chains have been investigated to reveal dramatic NLO response.[18–20]

As large transition-metal oxides, polyoxometalates (POMs) are excellent electron acceptors and can form electron donor–acceptor compounds.[21,22] These compounds are favorable materials with high thermal stability and are expected to be better NLO materials than transition-metal complexes and pure organic compounds. Among many of the organic derivatives of POMs, organoimido derivatives have attracted more attention because of the fascinating synergistic effects resulting from the strong d–π interaction between the organic delocalized π electrons and the d electrons of the cluster.[23] The structure–property relationships with organoimido POM derivatives will be helpful in designing new promising NLO materials.[24–26] Although much research has been carried out on the NLO response for POMs, it is rare to compare POMs with organic or organometallic species for NLO properties, in particular the superiority of POMs. Previous work on the NLO properties for organoimido derivatives of hexamolybdate indicates that POMs act as an acceptor in the organoimido-substituted derivatives and they turn out to be donors with the increasing length of the organic conjugated chain.[27] Whether organometallic complexes act as donor or acceptor with the increasing length of a conjugated chain will be investigated, and a comparison of the donor ability of POMs with organometallic complexes will be performed.

Based on the typical D–π–A model PNA, three kinds of series are listed in Fig. 1: (*a*) PNA derivatives of a hexamolybdate compound (Mo_6NPhNO_2), (*b*) a PNA–molybdenum–pentacarbonyl complex (PNA–MoCO), and (*c*) a PNA–iron–tetracarbonyl complex (PNA–FeCO), as well as the derivatives with π-conjugated bridges for the three series. For series **a**, the hydrogen atom of the amido group in PNA has been replaced by hexamolybdate, consequently forming PNA derivatives of hexamolybdates. In general, metal–carbonyl fragments can be primarily regarded as electron-withdrawing groups with strong π acceptor abilities for CO ligands. However, the introduction of a strong acceptor (nitryl group) at the end of the conjugated side chain turns the metal–carbonyl into a donor moiety.

Fig. 1. The calculation models (n = 0–6).

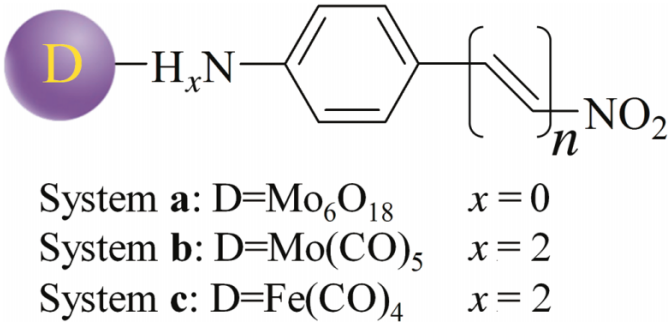

Computational details

Systems as large as the polyoxometalate compounds of heavy metal atoms entail a large computational cost, and it is additionally complicated owing to the requirement for properly treating the electron correlation and relativistic effects. Therefore, ab initio and semiempirical methods are unreliable for these large systems. A sensible alternative is the DFT method, which has been confirmed to be effective for the treatment of heavy metal compounds.[28,29] Therefore, DFT calculations were carried out using the ADF2006.01 programs.[30,31] The zero-order regular approximation (ZORA) was adopted in all the calculations to account for the scalar relativistic effects.[32,33] The local density approximation (LDA) characterized by the Vosko–Willk–Nusair (VWN)[34] parametrization was adopted for the correlation functional. In addition, the generalized-gradient approximation (GGA) was employed in the geometry optimization by using Beck[35] and Perdew[36] nonlocal corrections for the exchange and for the correlation functionals, respectively. Triple-ξ plus polarization Slater basis sets were taken to describe the electron of main group elements (O, C, N, and H) and the valence electrons of all transition-metal atoms (Mo and Fe), applied with the frozen-core approximation. The approximation of a frozen core for O, N, and C atoms was used up to the 1s shell and to the 3d and 2p shells, respectively, for Mo and Fe atoms. As an effective method in the evaluation of electronic spectra for a wide range of compounds, time-dependent density functional theory (TDDFT) was carried out to calculate the excitation properties of the species mentioned in the title. Moreover, a finite field (FF) approach at MP2 level was executed to calculate the second-order polarizability. The natural bond orbital (NBO) analysis was carried out using the Gaussian03 program[37] to investigate the bond character between two atoms, and the B3LYP method was used at the LANL2DZ level for all the transition-metal atoms and the 6–31G(d) level for main group elements.

Results and discussion

In our present study, as a prototype for the series of D–π–A models, the second-order NLO response for PNA was calculated to be 7.9×10^{-30} esu, which is in good agreement with reported values.[38,39] When PNA replaces its amido hydrogen atoms with the terminal oxygen atoms of hexamolybdate, Mo_6NPhNO_2 (**a1**) was formed with a second-order NLO response four times higher than that of PNA. PNA–MoCO (**b1**) and PNA-FeCO (**c1**) were preferred for showing

Can. J. Chem. Downloaded from www.nrcresearchpress.com by 80.58.250.72 on 09/16/12
For personal use only.

the effect on the second-order NLO response for transition-metal complexes. The series that could produce a larger enhancement in the NLO response was given more attention, and the conjugated repeating units $(C_2H_2)_n$ (n = 0–6) were introduced as π-conjugated bridges in series **a**, **b**, and **c** to observe the changes in the second-order NLO response.

The BLA values

BLA values are defined as the average change of length between adjacent single and double bonds.[40] As an important organic NLO chromophore, the ground-state structure for a donor–acceptor substituted polyene molecule can be viewed as a combination of two resonance forms, differing in the extent of charge separation.[41,42] When the donor and acceptor substituents connected by the conjugated bridge are stronger, the contribution of the charge-separated resonance form to the ground state increases and the BLA values decrease. BLA values have been confirmed to be a significant factor in NLO properties. Figure 2 shows that BLA values tend to decrease with the growing conjugated chains in series **a** and **b**. However, the BLA values for PNA–Mo_6 derivatives (series **a**) are much lower than those for PNA–MoCO derivatives (series **b**) with the same conjugated bridge. For example, the BLA value for **a2** with one conjugated unit is 0.067, nearly half of that for **b2** with a value of 0.110. However, when the number of conjugated bridge units increases to six, the BLA value for **a7** decreases to 0.020 and becomes less than the half of the **b7** value (0.057). Another type of PNA–FeCO derivative (series **c**) was chosen to further confirm the influence of conjugated length on BLA values. Figure 2 demonstrates that the BLA values for series **c** are in accord with those in series **b**, and the two curves coincide well with each other. In other words, the decreasing rate of the BLA values for series **a** is faster than that for series **b** and **c** with increasing conjugation length, indicating a better NLO response for POM-substituted compounds than for organometallic complexes.

The bonding characters between metal and nitrogen atoms

It is very interesting to note that the BLA values for series **a** are much smaller than those in series **b** and **c**, which belong to organometallic complexes, and hence the bond characters between the metal and the adjacent nitrogen atom should be investigated. The bond characters in previous works verified strong triple Mo≡N bonds existing in organoimido-substituted POMs.[43] NBO analysis has successfully described the bonding characters when nitryl is introduced at the end of the phenyl in organoimido-substituted POMs. In our present study, the Mo–N bond with short length (1.822 Å) in compound **a1** is still composed of one σ bond ($0.4682sd^{1.85}$Mo + $0.8836sp^{0.85}$N) and two π bonds (0.5969dMo + 0.8023pN and 0.4544dMo + 0.8908pN), which confirms the significant covalent character of Mo≡N interaction, and the strong synergistic effect stabilizes the POM derivatives. However, the Wiberg bond indices for the M–N bond in compounds **b1** and **c1** are 0.200 and 0.243, respectively, much lower than the index of 1 expected for a single bond, indicating no chemical bond exists between the metal and nitrogen atom in organometallic complexes, whereas the strong donor–acceptor interaction may be

Fig. 2. The change trends in BLA values for each series with increasing n.

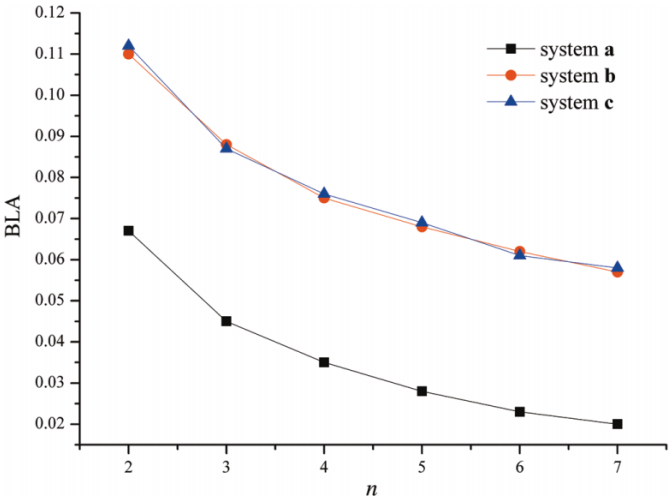

formed as treated by the second-perturbation energy $E(2)$ in eq. [1]:

$$[1] \qquad E(2) = E_{ij} = q_i F_{ij}^2 / \varepsilon_j \varepsilon_i$$

where F_{ij} is the off-diagonal element in the NBO Fock matrix, q_i is the donor occupancy, and ε_i and ε_j are diagonal elements (orbital energies). The values for $E(2)$ shown in Table 1 reveal that strong donor–acceptor interaction rather than covalent character exists from the lone electron pair of the nitrogen atom in the amido group to σ* of the M–C bond opposite to nitrogen, or to the lone pair of metal atoms. Therefore, the strong synergistic effect of Mo≡N in series **a** is expected to enhance the conjugation of the organic bridge and provide a better electron-transfer channel and, consequently, to improve the NLO response.

Static second-order polarizabilities

The total second-order polarizabilities β_0 for the studied series are defined using the following equation:

$$[2] \qquad \beta_0 = (\beta_x^2 + \beta_y^2 + \beta_z^2)^{1/2}$$

where β_x, β_y, and β_z are the components of the second-order polarizability tensor along the x, y, and z axes, respectively, and β_i is defined by eq. [3]:

$$[3] \qquad \beta_i = \beta_{iii} + \frac{1}{3}\sum_{j\neq 1}(\beta_{ijj} + \beta_{jij} + \beta_{jji})$$

From Table 2, the β_0 values for metal–carbonyl complexes **b1** and **c1** are 6.1 × 10^{-30} and 9.5 × 10^{-30} esu, respectively, and dramatically increases to 62.8 × 10^{-30} esu when the hexamolybdate moiety is substituted for the metal–carbonyl (nearly 8 times greater than that of PNA). Moreover, it is obvious from Fig. 3 that the β_0 values in the three series increase with the growing length of the conjugated bridges. However, the growth rate for β_0 in series **a** is dramatically faster, consequently resulting in larger second-order polarizabilities than in series **b** and **c** with the same conjugated bridge unit numbers.

The dipole moments for the three series illustrated in Ta-

Can. J. Chem. Downloaded from www.nrcresearchpress.com by 80.58.250.72 on 09/16/12
For personal use only.

Table 1. The second-perturbation energies $E(2)$ (kJ/mol) between the N atom in the amido and the metal in compounds **b1** and **c1**.

Compound	Bond length (Å)	Donor	Acceptor	Interaction	$E(2)$
b1	2.415	BD(1)N–H	BD*(1)Mo–C	σ→σ*	30.37
		LP(1)N	LP(5)Mo	n→n	33.89
		LP(1)N	BD*(1)Mo–C	n→σ*	285.97
c1	2.131	LP(1)N	LP*(5)Fe	n→n*	66.61
		LP(1)N	BD*(1)Fe–C	n→σ*	255.85

Table 2. The β_0 ($\times 10^{-30}$ esu) values and dipole moments μ (D) for each compound in each series.

Compound	β_0	μ
a1	62.8	2.83
a2	212.0	4.91
a3	514.1	6.47
a4	1114.7	8.00
a5	2108.5	9.30
a6	3660.5	10.28
a7	6229.5	11.19
b1	6.1	4.64
b2	18.2	5.14
b3	39.1	5.55
b4	72.2	7.08
b5	118.2	8.24
b6	180.9	8.80
b7	260.1	9.25
c1	9.5	4.30
c2	6.7	4.77
c3	11.1	5.32
c4	35.2	6.04
c5	93.7	6.90
c6	147.3	8.07
c7	227.5	8.54

Fig. 3. The change in trend of β_0 values for each series with different n.

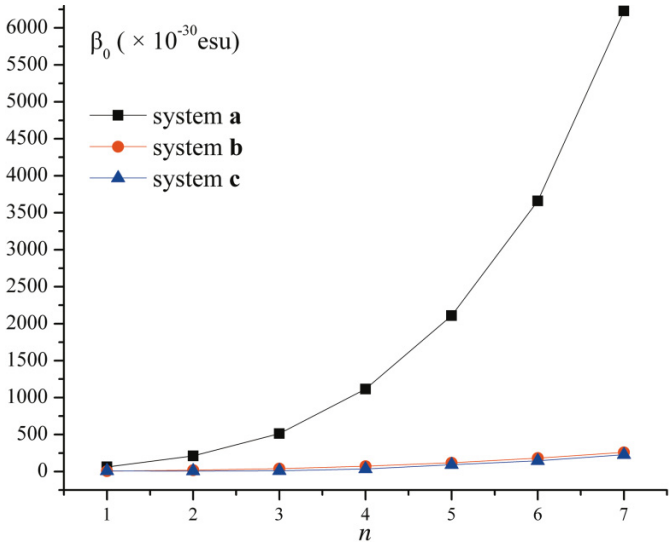

ble 2 are enhanced by increasing the length of the conjugated bridge, which lengthens the π conjugation of the molecule. Although the dipole moments for the first two compounds (n = 0 and 1) in series **a** are lower than the corresponding ones in series **b** and **c**, it starts to increase when n = 2. Therefore, the polarization for the ground-state molecule of the PNA–Mo_6 derivative (series **a**) tends to be higher than that of the organometallic complexes (series **b** and **c**), giving rise to larger NLO responses for series **a**, which is in agreement with the results calculated in Table 2.

The first main state with a large oscillator strength (f) value contributed to the electronic spectrum is shown in Table S1 (Supplementary data). As seen in Table S1, the transition energies E for the three series tended to decrease, and the f values increased as a result of the consecutive conjugated bridges, which is responsible for the increase in β_0 values (Fig. 3). For example, in series **a**, the value for E in compound **a1** is 2.74 eV and f increases to 0.739, resulting in a β_0 value of 62.8 $\times$ 10^{-30} esu, whereas E decreases to 1.58 eV and f increases to 1.950 in compound **a7** owing to the growing length of the conjugated bridge and generating a higher β_0 value of 6229.5 $\times$ 10^{-30} esu, nearly 30 times larger than compounds **b1** and **c1**. Similar trends were observed in series **b** and **c**. In comparison with the corresponding compounds with the same conjugated bridge in series **b** and **c**, the compounds in series **a** possess relatively smaller transition energies and greater oscillator strengths, which may induce a greater range of enhancement in β_0 values than in series **b** and **c**. The transition energies for compound **b7** and **c7** are 2.45 and 2.05 eV, respectively, indicating a blue-shift occurring in the organometallic complexes.

To further analyze the differences in the charge transfer between PNA–Mo_6 derivatives and PNA–MCO (M=Mo and Fe) complexes, the main contributions to the major transition were investigated and are found in Table S1 (Supplementary data). It was determined that the most important transitions for series **a** are generated by the promotion of the electron from HOMO to LUMO (HOMO and LUMO are represented by H and L, respectively, for simplicity), and the significant secondary transitions attribute the electron transition from H–5 to L. In comparison, the main transitions for series **b** and **c** are irregular, and the main donor moieties are located from H–4 to H with acceptor ones focusing on L and L+2. Therein, the first and seventh compounds in the three series have been chosen as representative, and the molecular orbitals contributing to the main transitions are shown in Fig. 4. It is obvious that the charge transfer in **a1** mainly originates from the π orbital of Mo≡N with a phenyl ring and partly from the p orbitals of oxygen atoms in the polyanion to the electron-withdrawing

Can. J. Chem. Downloaded from www.nrcresearchpress.com by 80.58.250.72 on 09/16/12
For personal use only.

Fig. 4. The main charge transfer contributing to the major transition states for typical compounds.

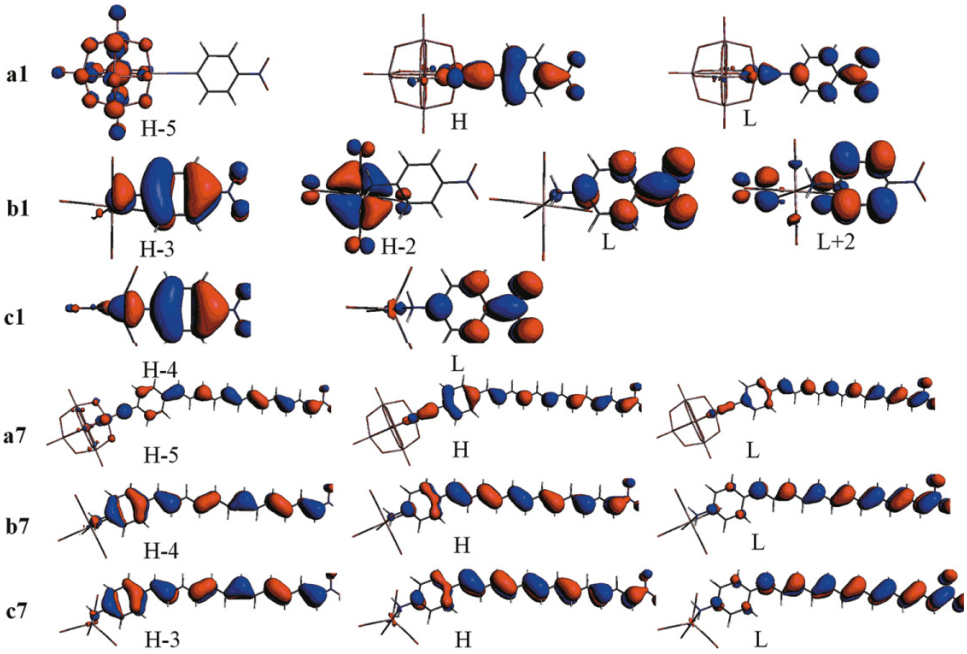

nitryl group. In contrast, **b1** and **c1** localize their donor moieties on the lone electron pair of the nitrogen atom in the amido group and the π orbital on the whole phenyl ring, and the acceptor ones concentrate on the nitryl group. In addition, Mo in **b1** also acts as a donor to offer d electrons to the π orbital of the phenyl ring and the electron transition can be assigned to MLCT. When the conjugated bridge linking donor and the acceptor moieties has been extended and the charge transfer has occurred in the conjugated bridge (ILCT) and tends to transfer to the part close to the nitryl acceptor. However, the electrons have been transferred throughout the conjugated chain according to the extended conjugated bridge and tend to transfer to the moiety with the nitryl acceptor. It is more interesting that the π orbital of Mo≡N in system **a** still contributes to the donor. Therefore, the electrons tend to transfer to the side with the acceptor moiety and the donor electrons not only concentrate on the left side, but begin to gradually extend over the conjugated bridge with the enhanced chain. In addition, it is proposed that the presence of Mo≡N in PNA–Mo_6 derivatives may take a role in transferring the electrons from the polyanion to the conjugated chain, consequently gaining more obvious electron transition to enhance the NLO response.

The electron transition for compound d

To shed further light on the superior donor properties of hexamolybdate over metal–carbonyl complexes in second-order NLO response in the D–π–A model, one new compound **d** combining a hexamolybdate framework and metal–carbonyl segment via a conjugated *p*-phenylenediamine bridge was investigated (Fig. 5). Compound **d** possesses a much large NLO response (362.2 × 10^{-30} esu), indicating the larger charge transfer from donor to acceptor. According to the TDDFT calculation, the main charge transfer with the largest oscillator strength originates from the polyanion framework to the conjugated bridge and the metal–carbonyl segment. Therefore, this revealed the superiority of hexamolybdate as a donor over the metal–carbonyl complexes and evoked its use for a promising NLO response.

Fig. 5. The main charge transfer contributing to the main transition states for compound **d**.

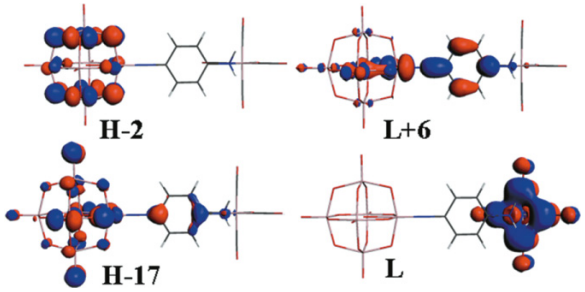

Conclusions

It is obvious that the NLO responses have been enhanced in each series with the growing length of the conjugated bridge and decreasing BLA values. However, the BLA values of PNA–Mo_6 derivatives are much lower than that of other organometallic complexes, resulting in a better NLO response. In addition, the link of hexamolybdate and PNA with Mo≡N is expected to supply a better electron-transfer channel and enhance the conjugation of the organic bridge and, consequently, generate outstanding NLO response over PNA–MCO complexes. In conclusion, POMs have exhibited a superiority in donor moiety as potential NLO materials.

Supplementary data

Supplementary data for this article are available on the journal Web site (canjchem.nrc.ca).

Can. J. Chem. Downloaded from www.nrcresearchpress.com by 80.58.250.72 on 09/16/12
For personal use only.

Acknowledgments

The authors gratefully acknowledge financial support from the National Natural Science Foundation of China (Project No. 20971020), the Program for Changjiang Scholars and Innovative Research Team in University (IRT0714), the Department of Science and Technology of Jilin Province (20082103), the Training Fund of Northeast Normal University's (NENU) Scientific Innovation Project (STC07017), and the Science Foundation for Young Teachers of Northeast Normal University (20090401). We also acknowledge Y.H.K. for computational support.

References

(1) Chemla, D.; Zyss, S. J. *Nonlinear Optical Properties of Organic Molecules and Crystals;* New York: Academic Press, 1987; Vol. 1.
(2) Locknar, S. A.; Peteanu, L. A.; Shuai, Z. G. *J. Phys. Chem. A* **1999**, *103* (14), 2197. doi:10.1021/jp9831381.
(3) Zyss, J.; Ledoux, I. *Chem. Rev.* **1994**, *94* (1), 77. doi:10.1021/cr00025a003.
(4) Meyers, F.; Marder, S. R.; Pierce, B. M.; Bredas, J. L. *J. Am. Chem. Soc.* **1994**, *116* (23), 10703. doi:10.1021/ja00102a040.
(5) Chandra Jha, P.; Krishnan, A.; Das, P. K.; Ramasesha, S. *J. Chem. Phys.* **2002**, *117* (6), 2873. doi:10.1063/1.1491878.
(6) Bulat, F. A.; Toro-Labbé, A.; Champagne, B.; Kirtman, B.; Yang, W. T. *J. Chem. Phys.* **2005**, *123* (1),o. 014319. doi:10.1063/1.1926275.
(7) Liu, C. G.; Qiu, Y. Q.; Sun, S. L.; Li, N.; Yang, G. C.; Su, Z. M. *Chem. Phys. Lett.* **2007**, *443* (1–3), 163. doi:10.1016/j.cplett.2007.06.060.
(8) Champagne, B.; Kirtman, B. *Handbook of Advanced Electronic and Photonic Materials;* H.S. Nalwa, Ed.; San Diego: Academic Press, 2001; Vol. 9, Chapter 2, p 63.
(9) Morley, J. O. *J. Phys. Chem.* **1994**, *98* (46), 11818. doi:10.1021/j100097a003.
(10) Carters, G.; Zyss, J. *J. Opt. Soc. Am. B* **1987**, *4*, 945.
(11) Williams, D. J. *Angew. Chem. Int. Ed. Engl.* **1984**, *23* (9), 690. doi:10.1002/anie.198406901.
(12) Williams, D. J., Ed. *Nonlinear Optical Properties of Organics and Polymeric Materials;* ACS Symposium Series 233; American Chemical Society: Washington, DC, 1984; p 103.
(13) Di Bella, S.; Fragalà, I.; Ledoux, I.; Marks, T. J. *J. Am. Chem. Soc.* **1995**, *117* (37), 9481. doi:10.1021/ja00142a014.
(14) Di Bella, S.; Fragalà, I.; Marks, T. J.; Ratner, M. A. *J. Am. Chem. Soc.* **1996**, *118* (50), 12747. doi:10.1021/ja960561j.
(15) Di Bella, S.; Fragalà, I.; Ledoux, I.; Diaz-Garcia, M. A.; Marks, T. J. *J. Am. Chem. Soc.* **1997**, *119* (40), 9550. doi:10.1021/ja971349y.
(16) Di Bella, S. *Chem. Soc. Rev.* **2001**, *30* (6), 355. doi:10.1039/b100820j.
(17) Dalton, G. T.; Cifuentes, M. P.; Watson, L. A.; Petrie, S.; Stranger, R.; Samoc, M.; Humphrey, M. G. *Inorg. Chem.* **2009**, *48* (14), 6534. doi:10.1021/ic900469y.
(18) de la Torre, G.; Vázquez, P.; Agulló-López, F.; Torres, T. *Chem. Rev.* **2004**, *104* (9), 3723. doi:10.1021/cr030206t.
(19) Di Bella, S.; Fragalà, I.; Ledoux, I.; Zyss, J. *Chem. Eur. J.* **2001**, *7* (17), 3738. doi:10.1002/1521-3765(20010903)7:17<3738::AID-CHEM3738>3.0.CO;2-I.
(20) Liu, C. G.; Qiu, Y. Q.; Sun, S. L.; Chen, H.; Li, N.; Su, Z. M. *Chem. Phys. Lett.* **2006**, *429* (4–6), 570. doi:10.1016/j.cplett.2006.07.097.
(21) Attanasio, D.; Bonamico, M.; Fares, V.; Imperatori, P.; Suber, L. *J. Chem. Soc., Dalton Trans.* **1990**, (11): 3221. doi:10.1039/dt9900003221.
(22) Williamson, M. M.; Bouchard, D. A.; Hill, C. L. *Inorg. Chem.* **1987**, *26* (9), 1436. doi:10.1021/ic00256a022.
(23) Katsoulis, D. E. *Chem. Rev.* **1998**, *98* (1), 359. doi:10.1021/cr960398a.
(24) Yan, L. K.; Jin, M. S.; Zhuang, J.; Liu, C. G.; Su, Z. M.; Sun, C. C. *J. Phys. Chem. A* **2008**, *112* (40), 9919. doi:10.1021/jp804342h.
(25) Yang, G. C.; Guan, W.; Yan, L. K.; Su, Z. M.; Xu, L.; Wang, E. B. *J. Phys. Chem. B* **2006**, *110* (46), 23092. doi:10.1021/jp062820p.
(26) Yan, L. K.; Yang, G. C.; Guan, W.; Su, Z. M.; Wang, R. S. *J. Phys. Chem. B* **2005**, *109* (47), 22332. doi:10.1021/jp0542120.
(27) Janjua, M. R. S. A.; Liu, C. G.; Guan, W.; Zhuang, J.; Muhammad, S.; Yan, L. K.; Su, Z. M. *J. Phys. Chem. A* **2009**, *113* (15), 3576. doi:10.1021/jp808707q.
(28) Ziegler, T. *Chem. Rev.* **1991**, *91* (5), 651. doi:10.1021/cr00005a001.
(29) Pierloot, K.; Ceulemans, A.; Merchán, M.; Serrano-Andrés, L. *J. Phys. Chem. A* **2000**, *104* (19), 4374. doi:10.1021/jp993384s.
(30) te Velde, G.; Bickelhaupt, F. M.; Baerends, E. J.; Fonseca Guerra, C.; van Gisbergen, S. J. A.; Snijders, J. G.; Ziegler, T. *J. Comput. Chem.* **2001**, *22* (9), 931. doi:10.1002/jcc.1056.
(31) ADF2006.01. *SCM;* Theoretical Chemistry, Vrije Universiteit, Amsterdam, The Netherlands. Available from http://www.scm.com.
(32) van Lenthe, E.; Baerends, E. J.; Snijders, J. G. *J. Chem. Phys.* **1993**, *99* (6), 4597. doi:10.1063/1.466059.
(33) van Lenthe, E.; Ehlers, A. E.; Baerends, E. J. *J. Chem. Phys.* **1999**, *110* (18), 8943. doi:10.1063/1.478813.
(34) Vosko, S. H.; Wilk, L.; Nusair, M. *Can. J. Phys.* **1980**, *58* (8), 1200. doi:10.1139/p80-159.
(35) Becke, A. D. *Phys. Rev. A* **1988**, *38* (6), 3098. doi:10.1103/PhysRevA.38.3098.
(36) Perdew, J. P. *Phys. Rev. B* **1986**, *33* (12), 8822. doi:10.1103/PhysRevB.33.8822.
(37) Frisch, M. J.; Trucks, G. W.; Schlegel, H. B.; Scuseria, G. E.; Robb, M. A.; Cheeseman, J. R.; Montgomery, J. A., Jr.; Vreven, T.; Kudin, K. N.; Burant, J. C.; Millam, J. M.; Iyengar, S. S.; Tomasi, J.; Barone, V.; Mennucci, B.; Cossi, M.; Scalmani, G.; Rega, N.; Petersson, G. A.; Nakatsuji, H.; Hada, M.; Ehara, M.; Toyota, K.; Fukuda, R.; Hasegawa, J.; Ishida, M.; Nakajima, T.; Honda, Y.; Kitao, O.; Nakai, H.; Klene, M.; Li, X.; Knox, J. E.; Hratchian, H. P.; Cross, J. B.; Bakken, V.; Adamo, C.; Jaramillo, J.; Gomperts, R.; Stratmann, R. E.; Yazyev, O.; Austin, A. J.; Cammi, R.; Pomelli, C.; Ochterski, J. W.; Ayala, P. Y.; Morokuma, K.; Voth, G. A.; Salvador, P.; Dannenberg, J. J.; Zakrzewski, V. G.; Dapprich, S.; Daniels, A. D.; Strain, M. C.; Farkas, O.; Malick, D. K.; Rabuck, A. D.; Raghavachari, K.; Foresman, J. B.; Ortiz, J. V.; Cui, Q.; Baboul, A. G.; Clifford, S.; Cioslowski, J.; Stefanov, B. B.; Liu, G.; Liashenko, A.; Piskorz, P.; Komaromi, I.; Martin, R. L.; Fox, D. J.; Keith, T.; Al-Laham, M. A.; Peng, C. Y.; Nanayakkara, A.; Challacombe, M.; Gill, P. M. W.; Johnson, B.; Chen, W.; Wong, M. W.; Gonzalez, C.; Pople, J. A. *Gaussian 03, Revision C.02;* Wallingford, CT: Gaussian Inc., 2004.
(38) Balakina, M. Y.; Nefediev, S. E. *Comput. Mater. Sci.* **2007**, *38* (3), 467. doi:10.1016/j.commatsci.2005.05.011.

(39) Sophy, K. B.; Shedge, S. V.; Pal, S. *J. Phys. Chem. A* **2008**, *112* (44), 11266. doi:10.1021/jp806204q.
(40) Meyers, F.; Marder, S. R.; Pierce, B. M.; Brédas, J. L. *J. Am. Chem. Soc.* **1994**, *116* (23), 10703. doi:10.1021/ja00102a040.
(41) Brooker, L. G. S.; Sprague, R. H. *J. Am. Chem. Soc.* **1941**, *63* (11), 3214. doi:10.1021/ja01856a088.
(42) Brooker, L. G. S.; Craig, A. C.; Heseltine, D. W.; Jenkins, P. W.; Lincoln, L. L. *J. Am. Chem. Soc.* **1965**, *87* (11), 2443. doi:10.1021/ja01089a025.
(43) Yan, L. K.; Su, Z. M.; Guan, W.; Zhang, M.; Chen, G. H.; Xu, L.; Wang, E. B. *J. Phys. Chem. B* **2004**, *108* (45), 17337. doi:10.1021/jp0478256.

Can. J. Chem. Downloaded from www.nrcresearchpress.com by 80.58.250.72 on 09/16/12
For personal use only.

Supported task-specific ionic liquid catalyst for highly efficient and recyclable aerobic oxidation of benzyl alcohols

Lin Liu, Juanjuan Ma, Zhen Sun, Jianping Zhang, Jingjing Huang, Shanzhong Li, and Zhiwei Tong

Can. J. Chem. Downloaded from www.nrcresearchpress.com by 80.58.250.72 on 09/16/12
For personal use only.

Abstract: A novel catalytic system was prepared by impregnating ionic liquid immobilized 2,2,6,6-tetramethylpiperidyl-1-oxyl (TEMPO) and copper salt onto various silica supports. This catalytic system was capable of rapidly converting different benzylic and allylic alcohols into the corresponding aldehydes under O_2 atmosphere with high conversion. Recycling results showed that the catalyst could be easily recovered and reused.

Key words: supported ionic liquid, selective alcohol oxidation, 2,2,6,6-tetramethylpiperidyl-1-oxyl (TEMPO).

Résumé : On a préparé un nouveau système catalytique en imprégnant du 2,2,6,6-tétraméthylpiperidine-1-oxyle (TEMPO) immobilisé sur un liquide ionique et un sel de cuivre sur divers supports à base de silice. Ce système catalytique, dans une atmosphère d'oxygène (O_2), est capable d'oxyder divers alcools benzyliques et allyliques en aldéhydes correspondants avec des taux élevés de conversion. Des résultats de recyclage ont montré que le catalyseur peut facilement être récupéré et réutilisé.

Mots-clés : liquide ionique sur un support, oxydation sélective d'alcool, 2,2,6,6-tétraméthylpiperidine-1-oxyle (TEMPO).

[Traduit par la Rédaction]

Introduction

In general, heterogeneous catalysis is preferred in industrial processes to homogeneous catalysis. The attractive features of heterogeneous catalysis include a large interfacial reaction area, ease of separation of products and catalysts, high system stability, and the potential to use very simple processing techniques such as fixed-bed reactor technology.[1] However, in some heterogeneous catalysis reactions, the diffusion rate of the reactants to the solid catalyst is often so low as to lead to a decrease of the reactivity of the catalytic system. Moreover, in comparison with homogeneous catalysis, lower selectivity is often obtained.

Ionic liquids are defined as salts with melting points below 100 °C. Favorable properties such as low vapor pressure, tunable hydrophilic or lipophilic properties, high thermal stability, low toxicity, and ease of handling make ionic liquids attractive alternatives to traditional organic solvents.[2] Unfortunately, high viscosity of ionic liquids may lead to mass or heat transfer limitations in the reaction system, implying that highly energy-consuming stirring is needed for industrial applications. Consequently, a new strategy integrating the advantages of ionic liquids and heterogeneous catalysis would be highly desirable.

In this context, the concept of confining ionic liquids on solid supports to obtain heterogenized homogeneous catalyst systems, described as supported ionic liquid catalysts, has recently attracted increasing attention. In a supported ionic liquid system, a thin film of ionic liquid is supported on the surface of a solid material (such as silica gel, diatomic earth, molecular sieves, or montmorillonite) via covalent anchoring or adsorption. Compared with the homogeneous catalyst system, the supported ionic liquid system provides 3 major advantages: (*i*) a small amount of ionic liquid; (*ii*) good activity, which is attributed to a higher concentration of the active species at the ionic liquid film; and (*iii*) convenient product separation and easy recovery of catalyst.[3,4] During the last decade, supported ionic liquid catalysts have been applied in hydroformylation,[5,6] hydrogenation,[7,8] Heck reaction,[9,10] hydroamination,[11] aldol reaction,[12] and epoxidation.[13]

The selective oxidation of alcohols to the corresponding aldehydes or ketones is the foundation of many important industrial and fine-chemical processes. Many highly efficient systems have been developed for catalytic aerobic alcohol oxidation using transition metals such as palladium,[14] ruthenium,[15] copper,[16,17] iron,[18] and vanadium.[19] Of particu-

Received 6 June 2010. Accepted 1 November 2010. Published on the NRC Research Press Web site at canjchem.nrc.ca on 23 December 2010.

L. Liu,[1] J. Ma, Z. Sun, J. Zhang, J. Huang, and S. Li. Department of Chemical Engineering, Huaihai Institute of Technology, Lianyungang 222005, China.
Z. Tong.[2] Department of Chemical Engineering, Huaihai Institute of Technology, Lianyungang 222005, China; SORST, Japan Science and Technology Agency (JST), Kawaguchi-shi, Saitama, Japan.

[1]Corresponding author (e-mail: spliulin@gmail.com).
[2]Corresponding author (e-mail: zhiweitong575@hotmail.com).

Scheme 1. Aerobic oxidation of alcohols catalyzed by TEMPO-IL/$CuCl_2$/SiO_2.

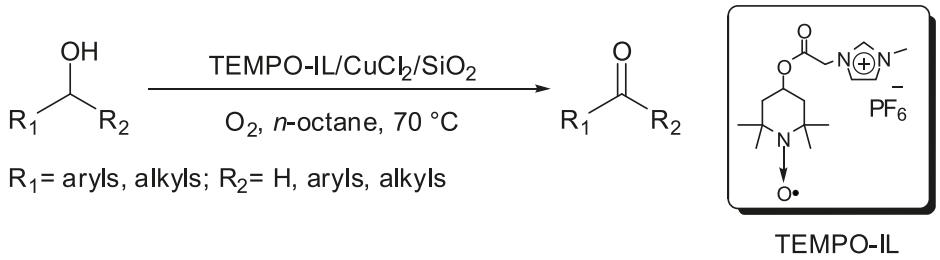

lar interest are the catalytic systems consisting of an inexpensive transition metal compound (e.g., copper) and 2,2,6,6-tetramethylpiperidyl-1-oxyl (TEMPO) for mild and selective aerobic alcohol oxidations. Recently, numerous immobilized TEMPO variants on both organic and inorganic supports have been developed.[20,21] For the aerobic alcohol oxidation promoted by these systems, the recycling of TEMPO could be achieved easily, but prolonged reaction times are usually needed for high conversion.[22]

Our recent work was focused on the oxidation of organic compounds with molecular oxygen as oxidant.[23,24] Earlier, we disclosed a catalytic system, TEMPO-IL/CuCl /MS3A (molecular sieve 3A), for the aerobic oxidation of a wide range of benzyl alcohols in the ionic liquid [bmim]PF_6, where MS3A serves as a heterogeneous Brønsted base to enhance the reaction rate remarkably.[25] In light of the newly developed supported ionic liquid catalyst systems, in this work we developed a novel catalytic aerobic oxidation system by impregnating the task-specific ionic liquid TEMPO-IL and copper salt onto various silica supports. The resulting system, TEMPO-IL/$CuCl_2$/SiO_2, catalyzed aerobic oxidation of most benzylic or allylic alcohols in *n*-octane to the corresponding aldehydes in less than 3 h with high conversion (Scheme 1). The catalyst system could easily be recycled and reused at least 3 times.

Results and discussion

The experimental results for *p*-nitrobenzyl alcohol oxidation using the supported task-specific ionic liquid catalyst system are listed in Table 1. Three kinds of copper salts — $Cu(OAc)_2$, $Cu(NO_3)_2$, and $CuCl_2$ — were used as co-catalyst in the TEMPO-IL/copper salt/SiO_2 catalyst system for the aerobic oxidation in *n*-octane (Table 1, entries 1–3). The catalyst system of TEMPO-IL/$CuCl_2$/SiO_2 was found to be most efficient, with more than 99% conversion in 1.5 h. The limitation of solvent for a supported ionic liquid catalyst system is that the solvent phase and the ionic liquid have to form a biphasic system without any ionic liquid leaching, otherwise the ionic liquid film would be washed out of the supporting material and the catalytic system would be deactivated.[4,26] The best catalytic activity was observed in *n*-octane (poor solvent for TEMPO-IL) (Table 1, entry 3); moderate catalytic activity was found in toluene, with 89% conversion in 12 h (Table 1, entry 4); and in the case of DMF and [bmim]PF_6 (good solvents for TEMPO-IL), poor catalytic activity was observed (Table 1, entries 5 and 6). In good solvents, TEMPO-IL and $CuCl_2$ are completely dissolved and the oxidation takes place mainly in solvent. In *n*-octane, on the other hand, the oxidation occurs mainly in the ionic liquid film, in which the relatively high concentration of catalyst may be beneficial to catalytic activity.

In previous studies, we found that when copper salt / TEMPO-IL catalyst systems were used for the aerobic oxidation of benzyl alcohols, CuCl exhibited better catalytic performance than $CuCl_2$.[23] Owing to the poor solubility of CuCl in water or methanol, it is hard to immobilize CuCl onto silica gel directly. However, we were surprised to find that the system of TEMPO-IL/$CuCl_2$/SiO_2 was even more effective for catalyzing the aerobic oxidation of benzyl alcohols than TEMPO-IL/CuCl. To verify the importance of immobilization in the catalysis, we carried out the oxidation of *p*-nitrobenzyl alcohol with TEMPO-IL/$CuCl_2$ as catalyst in the absence of the solid support. The results revealed that only a small amount of product could be achieved in the ionic liquid [bmim]PF_6 (Table 1, entry 7). In the case of *n*-octane as solvent (Table 1, entries 8 and 9), the substrate could be oxidized efficiently. However, the separation of the product from the reaction system and the recovery of the catalyst were tedious.

On the basis of the above results, we found that the immobilization of TEMPO-IL / copper salt resulted in higher activity as compared with their homogeneous counterparts. The question is, do other commonly used silicas have a similar effect on the aerobic oxidation of alcohol? We prepared the supported catalysts with three different silica supports: MCM-41, SBA-15, and silica gel (200–300 mesh). As shown in Table 2, the solid supports make hardly any difference in the oxidation of alcohol.

After determining the optimal reaction conditions for the supported task-specific ionic liquid catalysis, we examined the range of alcohols to which this catalytic aerobic oxidation could be applied. As shown in Table 3, benzylic alcohols were converted into their corresponding aldehydes in high conversions (Table 3, entries 1–5). The rates of these benzylic alcohol oxidations were not significantly affected by the electronic property of the substituents on the benzene ring. Similarly, allylic and heterocyclic primary alcohols could be smoothly oxidized to the corresponding aldehydes in high conversions using this catalyst system (Table 3, entries 6 and 7). The catalytic system shows high selectivity, only a trace amount of acid (less than 1%) was formed, and the double bond of allylic alcohol was unaffected. In spite of the good results with benzylic, allylic, and heterocyclic alcohols, the conversion obtained with aliphatic alcohol under the same conditions was quite low even after 12 h (Table 3, entry 8).

The recyclability of the catalyst system was then studied. At the end of each cycle the catalyst was separated by cen-

Can. J. Chem. Downloaded from www.nrcresearchpress.com by 80.58.250.72 on 09/16/12
For personal use only.

Can. J. Chem. Downloaded from www.nrcresearchpress.com by 80.58.250.72 on 09/16/12
For personal use only.

Table 1. Effects of catalysts and solvents on oxidation of *p*-nitrobenzyl alcohol.

Entry	Catalyst	Solvent	Time (h)	GC conversion (%)	Isolated yield (%)
1	TEMPO-IL/$Cu(OAc)_2/SiO_2$	*n*-Octane	1.5	78	70
2	TEMPO-IL/$Cu(NO_3)_2/SiO_2$	*n*-Octane	1.5	94	88
3	TEMPO-IL/$CuCl_2/SiO_2$	*n*-Octane	1.5, 5.5[a]	>99, >99[a]	90, 91[a]
4	TEMPO-IL/$CuCl_2/SiO_2$	Toluene	12	89	82
5	TEMPO-IL/$CuCl_2/SiO_2$	DMF	12	6	—
6	TEMPO-IL/$CuCl_2/SiO_2$	[bmim]PF_6	12	35	—
7	TEMPO-IL/$CuCl_2$	[bmim]PF_6	12	30	—
8	TEMPO-IL/$CuCl_2$	*n*-Octane	1.5	80	74
9	TEMPO/$CuCl_2$	*n*-Octane	1.5	82	74
10	TEMPO-IL/CuCl	[bmim]PF_6	12	85	76
11	SiO_2	*n*-Octane	12	Trace	—
12[b]	TEMPO-IL	[bmim]PF_6-H_2O	5 min	—	93

Note: Reaction conditions were as follows: *p*-nitrobenzyl alcohol (1 mmol), TEMPO-IL or TEMPO (0.05 mmol), copper salt (0.05 mmol), and solvent (10 mL) under O_2 at 70 °C.

[a]25 mg TEMPO-IL/$CuCl_2/SiO_2$ used.

[b]Ref. 27, sodium hypochlorite as oxidant.

Table 2. Effects of various silica supports on the oxidation of *p*-nitrobenzyl alcohol.

Entry	Support	Time (h)	Conversion (%)
1	SiO_2	0.5	76
2	MCM-41	0.5	79
3	SBA-15	0.5	80

Note: Reaction conditions were as follows: *p*-nitrobenzyl alcohol (1 mmol), catalyst (0.1 g), and *n*-octane (10 mL) under O_2 at 70 °C.

Table 3. Catalytic aerobic oxidation of various alcohols.

Entry	Substrate	Product	Time (h)	Conv./Select. (%)[a]	Yield (%)[b]
1	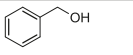		1.2	99/99	92
2	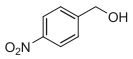	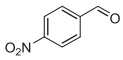	1.5	99/99	90
3	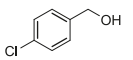	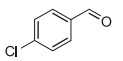	1.5	99/99	91
4	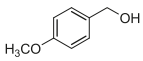	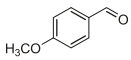	0.5	99/99	87
5	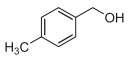	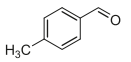	1.5	99/99	93
6	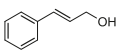	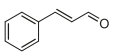	2.5	98/99	88
7	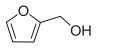		2	98/97	85
8	n-$C_{11}H_{23}$-CH_2OH	n-$C_{11}H_{23}$-CHO	12	39/99	—

Note: Reaction conditions were as follows: alcohol (1 mmol), TEMPO-IL/$CuCl_2/SiO_2$ (100 mg), and *n*-octane (10 mL) under O_2 at 70 °C.

[a]GC conversion and selectivity.

[b]Isolated yield.

trifugation and washed with *n*-octane. As shown in Fig. 1, the catalytic activity decreased gradually over 3 consecutive runs. However, the aerobic oxidation was still completed in 4 h at the 3rd cycle. In the supernatant, Cu was not detected by inductively coupled plasma analysis, whereas trace TEMPO-IL species were detected by HPLC analysis. The leaching of TEMPO-IL would be the main reason for the loss of activity, which may be due to the weak interaction between silica and TEMPO-IL.

Fig. 1. Recycling of the catalytic system for the oxidation of *p*-nitrobenzyl alcohol. Reaction conditions were as follows: *p*-nitrobenzyl alcohol (1 mmol), TEMPO-IL/$CuCl_2/SiO_2$ (0.1 g), and *n*-octane (10 mL) under O_2 at 70 °C; ■, run 1; □, run 2; ▲, run 3.

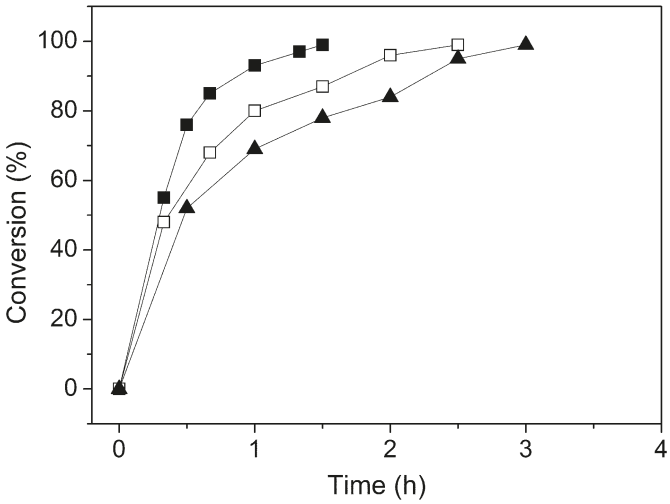

Conclusion

In summary, a highly efficient TEMPO-IL/$CuCl_2/SiO_2$ catalytic system based on the concept of supported ionic liquid catalysts has been developed and used for aerobic alcohol oxidation under an oxygen atmosphere. The amount of task-specific ionic liquid involved in the preparation of the catalyst was very low and the preparation procedure was simple. Moreover, the catalyst could be easily recovered by centrifugation and reused. From an economic point of view, our results indicate that supported task-specific ionic liquid

Can. J. Chem. Downloaded from www.nrcresearchpress.com by 80.58.250.72 on 09/16/12
For personal use only.

catalysis could be an interesting methodology. Further applications are currently under investigation in our laboratory.

Experimental

The ionic liquid [bmim]PF_6 was synthesized according to the literature.[27] Silica gel (200–300 mesh) was activated at 180 °C under vacuum overnight before use. All other chemicals were obtained from commercial sources with more than 99% purity and used without further purification. Gas chromatography (GC) analysis was performed on an Agilent GC-6820 equipped with a 30 m × 0.32 mm × 0.5 μm HP-Innowax capillary column and a flame ionization detector. The elemental analysis of copper was determined by inductively coupled plasma atomic emission spectroscopy (Thermo Scientific iCAP 6300). Products were all known compounds and were identified by comparing their physical and spectral data with those reported in the literature.

Catalyst preparation

TEMPO-IL was prepared according to the literature.[28] To a stirred solution of TEMPO-IL (1.0 g, 2.26 mmol) in 25 mL of methanol, $CuCl_2 \cdot 2H_2O$ (0.386 g, 2.26 mmol) was added. After that, silica gel (3.15 g) was added. The mixture was stirred for 5 h and then evaporated under reduced pressure for 3 h to give a powder of TEMPO-IL/$CuCl_2$/SiO_2. The obtained product was dried at 50 °C under vacuum overnight before use.

Typical experimental procedure for oxidation of alcohols

Alcohol (1 mmol) and TEMPO-IL/$CuCl_2$/SiO_2 (100 mg) were mixed with *n*-octane (10 mL) and stirred at 70 °C under O_2 (10 mL/min, 1 atm (1 atm = 101.325 kPa)) for the given time. After completion (monitored by TLC and GC), the mixture was centrifuged to separate the catalyst, which was washed several times with *n*-octane, dried, and recharged with fresh substrate and solvent for the next catalytic cycle. The combined solvent phase was concentrated under vacuum, and the crude product was purified by column chromatography (petroleum ether / ethyl acetate, 10/1) to provide the analytically pure aldehyde, which was characterized by ^{1}H NMR and IR analysis.

Acknowledgements

This work was supported by National Natural Science Foundation of China (grant No. 50873042) and the Scientific Research Program of the HuaiHai Institute of Technology (Z2009015, Z2009021).

References

(1) Mizuno, N.; Misono, M. *Chem. Rev.* **1998**, *98* (1), 199. doi:10.1021/cr960401q.
(2) Welton, T. *Coord. Chem. Rev.* **2004**, *248* (21–24), 2459. doi:10.1016/j.ccr.2004.04.015.
(3) Mehnert, C. P. *Chem. Eur. J.* **2005**, *11* (1), 50. doi:10.1002/chem.200400683.
(4) Gu, Y. L.; Li, G. X. *Adv. Synth. Catal.* **2009**, *351* (6), 817. doi:10.1002/adsc.200900043.
(5) Mehnert, C. P.; Cook, R. A.; Dispenziere, N. C.; Afeworki, M. *J. Am. Chem. Soc.* **2002**, *124* (44), 12932. doi:10.1021/ja0279242.
(6) Riisager, A.; Fehrmann, R.; Flicker, S.; van Hal, R.; Haumann, M.; Wasserscheid, P. *Angew. Chem. Int. Ed.* **2005**, *44* (5), 815. doi:10.1002/anie.200461534.
(7) Mehnert, C. P.; Mozeleski, E. J.; Cook, R. A. *Chem. Commun. (Camb.)* **2002**, (24): 3010. doi:10.1039/b210214e.
(8) Kume, Y.; Qiao, K.; Tomida, D.; Yokoyama, C. *Catal. Commun.* **2008**, *9* (3), 369. doi:10.1016/j.catcom.2007.07.012.
(9) Qiao, K.; Sugimura, R.; Bao, Q.; Tomida, D.; Yokoyama, C. *Catal. Commun.* **2008**, *9* (15), 2470. doi:10.1016/j.catcom.2008.06.016.
(10) Tao, R.; Miao, S.; Liu, Z.; Xie, Y.; Han, B.; An, G.; Ding, K. *Green Chem.* **2009**, *11* (1), 96. doi:10.1039/b811587g.
(11) Jimenez, O.; Müller, T. E.; Sievers, C.; Spirkl, A.; Lercher, J. A. *Chem. Commun. (Camb.)* **2006**, (28): 2974. doi:10.1039/b605567b.
(12) Likhar, P. R.; Roy, S.; Roy, M.; Subhas, M. S.; Kantam, M. L. *Catal. Commun.* **2009**, *10* (5), 728. doi:10.1016/j.catcom.2008.11.026.
(13) Lou, L. L.; Yu, K.; Ding, F.; Peng, X.; Dong, M.; Zhang, C.; Liu, S. *J. Catal.* **2007**, *249* (1), 102. doi:10.1016/j.jcat.2007.03.016.
(14) Buffin, B. P.; Clarkson, J. P.; Belitz, N. L.; Kundu, A. *J. Mol. Catal. Chem.* **2005**, *225* (1), 111. doi:10.1016/j.molcata.2004.08.035.
(15) Kato, C. N.; Shinohara, A.; Moriya, N.; Nomiya, K. *Catal. Commun.* **2006**, *7* (6), 413. doi:10.1016/j.catcom.2005.12.016.
(16) Figiel, P. J.; Sibaouih, A.; Ahmad, J. U.; Nieger, M.; Räisänen, M. T.; Leskela, M.; Repo, T. *Adv. Synth. Catal.* **2009**, *351* (16), 2625. doi:10.1002/adsc.200900478.
(17) Kumpulainen, E. T. T.; Koskinen, A. M. P. *Chem. Eur. J.* **2009**, *15* (41), 10901. doi:10.1002/chem.200901245.
(18) Huang, G.; Cai, C. C.; Luo, J.; Zhou, H.; Guo, Y. A.; Liu, S. Y. *Can. J. Chem.* **2008**, *86* (3), 199. doi:10.1139/V08-002.
(19) Jiang, N.; Ragauskas, A. J. *Tetrahedron Lett.* **2007**, *48* (2), 273. doi:10.1016/j.tetlet.2006.11.032.
(20) Gheorghe, A.; Matsuno, A.; Reiser, O. *Adv. Synth. Catal.* **2006**, *348* (9), 1016. doi:10.1002/adsc.200606043.
(21) Miao, C. X.; He, L. N.; Wang, J. Q.; Wang, J. L. *Adv. Synth. Catal.* **2009**, *351* (13), 2209. doi:10.1002/adsc.200900285.
(22) Dijksman, A.; Arends, I.; Sheldon, R. A. *Synlett* **2001**, 102.
(23) Liu, L.; Liuyan, J.; Yunyang, W. *Catal. Commun.* **2008**, *9* (6), 1379. doi:10.1016/j.catcom.2007.11.041.
(24) Liu, L.; Ji, L.-Y.; Wei, Y.-Y. *Monatsh. Chem.* **2008**, *139* (8), 901. doi:10.1007/s00706-008-0861-0.
(25) Lin, L.; Juanjuan, M.; Liuyan, J.; Yunyang, W. *J. Mol. Catal. Chem.* **2008**, *291* (1–2), 1. doi:10.1016/j.molcata.2008.06.001.
(26) *Ionic Liquids in Synthesis*; Wasserscheid, P., Welton, T., Eds.; 2nd ed.; Wiley-VCH: Weinheim, 2008.
(27) Dzyuba, S. V.; Bartsch, R. A. *Chem. Commun. (Camb.)* **2001**, (16): 1466. doi:10.1039/b104512c.
(28) Wu, X. E.; Ma, L.; Ding, M. X.; Gao, L. X. *Synlett* **2005**, 607.

Pseurotin A_1 and A_2, two new 1-oxa-7-azaspiro[4.4]non-2-ene-4,6-diones from the holothurian-derived fungus *Aspergillus fumigatus* WFZ-25

Fa-Zuo Wang, De-Hai Li, Tian-Jiao Zhu, Min Zhang, and Qian-Qun Gu

Can. J. Chem. Downloaded from www.nrcresearchpress.com by 80.58.250.72 on 09/16/12
For personal use only.

Abstract: Two new metabolites containing a 1-oxa-7-azaspiro[4.4]non-2-ene-4,6-dione core, pseurotin A_1 (**1**) and A_2 (**2**), as well as pseurotin A (**3**), were isolated from the holothurian-derived fungus *Aspergillus fumigatus* WFZ-25. These compounds were determined using extensive analysis of their spectroscopic data, including 1D and 2D NMR, HR-ESI-MS, and circular dichroism (CD) experiments.

Key words: pseurotin A, *Aspergillus fumigatus*, structure elucidation, cytotoxicity.

Résumé : On a isolé deux nouveaux métabolites à base de 1-oxa-7-azaspiro[4,4]non-2-ène-4,6-dione, les pseurotines A_1 (**1**) et A_2 (**2**), ainsi que la pseurotine A (**3**) à partir de l'*Aspergillus fumigatus* WFZ-25 dérivé de l'holothuriane. Les structures de ces composés ont été déterminées par une analyse extensive de leurs données spectroscopiques, dont des spectres de RMN 1D et 2D, de la spectrométrie de masse à haute résolution avec ionisation par électronébulisation (SM-HR-IEN) et des expériences de dichroïsme circulaire (DC).

Mots-clés : pseurotine A, *Aspergillus fumigatus*, élucidation de structure, cytotoxicité.

[Traduit par la Rédaction]

Introduction

In our ongoing efforts to discover antitumor metabolites from marine microorganisms, we found that ethyl acetate extracts of the marine-derived fungus *Aspergillus fumigatus* WFZ-25, isolated from the holothurian *Stichopus japonicus* collected from Lingshan Island, Qingdao, China, contained cytotoxic constituents. We have previously reported seven new prenylated indole diketopiperazine alkaloids and twelve known ones from this strain.[1] Further investigations of the active fractions led to the isolation of two new diastereomers of pseurotin A (**3**),[2] pseurotin A_1 (**1**) and A_2 (**2**) (Fig. 1).

Pseurotin A was previously isolated from the fungal strains *Pseudeurotium ovalis* Stolk and *A. fumigatus*,[3,4] and its absolute stereochemistry was determined by X-ray crystallographic analysis of its 12,13-dibromo derivatives.[3,5] Structurally, pseurotin A belongs to a family of natural products containing an unusual 1-oxa-7-azaspiro[4.4]non-2-ene-4,6-dione core and diverse biological activities. To the best of our knowledge, this family of natural products only possessed very few compounds, including pseurotins A-F1, F2 (8-*O*-demethylpseurotin A),[2,4,6,7] 14-norpseurotin A,[8] synerazol,[9] azaspirene,[10] FD-838,[11] and cephalimysins A–D.[12,13] In this paper, we report the isolation, structure elucidation, and cytotoxic activities of pseurotin A_1 (**1**) and A_2 (**2**).

Results and discussion

Compound **1** was isolated as a white amorphous powder. The molecular formula of $C_{22}H_{25}NO_8$ was established by HR-ESI-MS with a $[M + Na]^+$ peak at m/z = 454.1458 (calcd. for $C_{22}H_{25}NO_8Na^+$: 454.1478), indicating 11 degrees of unsaturation. The UV spectrum of **1** exhibiting absorption maxima at 251 (4.12) and 277 (3.97) nm was compatible with a phenyl ketone and one of the simple 3-(2*H*)-furanone systems.[14,15] The IR spectrum showed the presence of a lactame and an α,β-saturated ketone at 3204, 1726, 1706, and 1633 cm^{-1}.[2] In the ^1H NMR spectrum of **1**, four exchangeable protons appeared in the downfield region at δ 4.96 (d, J = 5.1 Hz, 11-OH), 5.75 (d, J = 5.5 Hz, 10-OH), 6.07 (d, J = 6.2 Hz, 9-OH), and 9.94 (s, 7-NH) owing to the presence of hydroxyl or amide protons. Five aromatic protons at δ 7.52 (2H, t, J = 7.7 Hz, H-20, 22), 7.63 (t, J = 7.3 Hz, H-21), and 8.10 (2H, d, J = 7.3 Hz, H-19, 23), as well as two olefinic methine protons at δ 5.39 (dd, J = 8.1, 11.0 Hz, H-

Received 31 July 2010. Accepted 25 October 2010. Published on the NRC Research Press Web site at canjchem.nrc.ca on 23 December 2010.

F.Z. Wang. Key Laboratory of Marine Bio-resources Sustainable Utilization, Research Center for Marine Microbes, Guangdong Key Laboratory of Marine Materia Medica, South China Sea Institute of Oceanology, Chinese Academy of Sciences, Guangzhou 510301, P. R. China.
D.H. Li, T.J. Zhu, M. Zhang, and Q.Q. Gu.[1] Key Laboratory of Marine Drugs, Chinese Ministry of Education, School of Medicine and Pharmacy, Ocean University of China, Qingdao 266003, P. R. China.

[1]Corresponding author (e-mail: guqianq@ouc.edu.cn).

Fig. 1. Structures of compounds **1**–**3**.

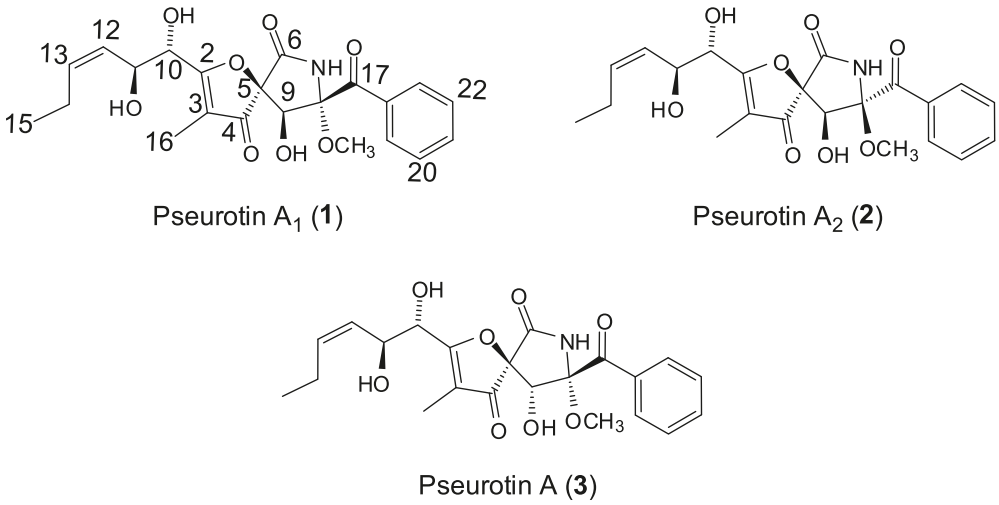

12) and 5.42 (dd, J = 7.0, 11.0 Hz, H-13) in the downfield region, revealed the presence of one monosubstituted phenyl group and a cis double bond. Furthermore, three oxygenated methine protons at δ 4.36 (t, J = 5.2 Hz, H-10), 4.45 (ddd, J = 5.5, 7.7, 10.6 Hz, H-11), and 4.62 (d, J = 6.2 Hz, H-9), three methyl protons at δ 0.86 (3H, dd, J = 7.3, 7.7 Hz, H-15), 1.66 (3H, s, H-16), and 3.12 (3H, s, 8-OMe) as well as one methylene proton at δ 1.95 (m, H-14a) and 2.01 (m, H-14b) were observed. The ^{13}C NMR and DEPT spectra of **1** revealed the presence of 21 carbons, including three methyls, one mehylene, seven sp^2 methines, two sp^3 quaternary carbons, three sp^2 quaternary carbons (one oxygenated), and three carbonyls. The HMQC spectrum revealed all of the one bond H–C connectivities (Table 1). The above data together with the ^{1}H–^{1}H COSY and HMBC correlation experiments (Fig. 2) further established the planar structure of **1**, which possessed a 1-oxa-7-azaspiro[4.4]non-2-ene-4,6-dione skeleton and was a diastereomer of pseurotin A (**3**).[2] Further comparison of the 1D NMR spectral data of **1** with those of **3** showed the main differences were that the chemical shifts at δ 200.0 (s, C-4), 97.1 (s, C-8), and 4.62 (d, J = 6.2 Hz, H-9) of **1** were strongly deshielded compared with **3**, whereas δ 88.2 (s, C-5), 194.8 (s, C-17), and 6.07 (d, J = 6.2 Hz, 9-OH) were shielded (Table 1). These data indicated that the configuration of C-9 of the two compounds could be different. Further confirmation were provided by NOESY correlations between H-9 and 8-OMe (δ 3.12, s), 9-OH, and 10-OH (δ 5.75, d, J = 5.5 Hz) (Fig. 3). The circular dichroism (CD) spectra of **1** and **3** gave similar Cotton effects (Fig. 4), which also suggested that the stereochemistry of C-9 in **1** should be changed but not that of C-5 and C-8. The above results were finally identified by comparison with CD data of FD-838 and cephalimysin B in the literature.[13] The structural differences between compounds **1** and **2** resembled those between FD-838 and cephalimysin B, which was compatible with the changes of their CD data. So the structure of **1** was assigned as (5*S*,8*S*,9*S*,10*S*,11*S*,12*Z*)-8-benzoyl-2-(10,11-dihydroxy-12-hexenyl)-9-hydroxy-8-methoxy-3-methyl-1-oxa-7-azaspiro[4.4]non-2-ene-4,6-dione and named pseurotin A_1 (Fig. 1).

Compound **2** was isolated as a white amorphous powder. The HR-ESI-MS, showing a $[M + Na]^+$ peak at m/z = 454.1465 (calcd. for $C_{22}H_{25}NO_8Na^+$: 454.1478), established the molecular formula as $C_{22}H_{25}NO_8$, equal to those of **1** and **3**. Detailed analysis of the UV, IR, and 1D NMR data of **1**–**3** indicated that **2** was a diastereomer of **1** and **3**, and the structure of **2** was closer to that of compound **1**. The chemical shifts of C-8 (δ 94.8, s) and H-9 (δ 4.18, d, J = 9.9 Hz) in **2** were strongly shielded compared with **1**, whereas 9-OH (δ 6.35, d, J = 9.9 Hz) was deshielded. We speculated that the configuration of C-8 was different from that of **1** (Table 1). This could be further determined by the NOESY correlation experiment and the CD spectrum of **2**. A NOESY correlation between 9-OH and 10-OH (δ 5.87, d, J = 5.5 Hz) was observed, but no correlation between H-9 and 8-OMe (δ 3.20, s) was noted. These results supported the above supposition (Fig. 3). Compared with the CD spectrum of compound **1**, the spectrum of **2** displayed a different Cotton effect with maxima at 251.6 (–2.7) and 227 (+9.4) nm (Fig. 4). This showed that the configuration of C-8 in **1** should be changed and that the one of C-5 (δ 87.1, s) was the same as the one in **2**. Similar to compound **1**, the configuration of **2** was finally assigned by comparison with the CD data of cephalimysin C and its enantiomer. The similar Cotton effects showed that the configurations of C-5, C-8, and C-9 in compound **2** were the same as the ones in the enantiomer of cephalimysin C.[13] Therefore, the structure of **2** was assigned as (5*S*,8*R*,9*S*,10*S*,11*S*,12*Z*)-8-benzoyl-2-(10,11-dihydroxy-12-hexenyl)-9-hydroxy-8-methoxy-3-methyl-1-oxa-7-azaspiro[4.4]non-2-ene-4,6-dione and named pseurotin A_2 (Fig. 1).

Compounds **1**–**3** were evaluated for their cytotoxicities against the P388, HL-60, A549, and BEL-7402 cell lines. The results showed that compound **2** displayed a slight cytotoxicity against the A549 and HL-60 cell lines and that compound **3** was slightly cytotoxic against the HL-60 cell lines, and the IC_{50} values for them were 48.0, 70.8, and 67.0 μmol/L, respectively. VP16 (etoposide) was used as a positive control.[1]

The pseurotins and their analogs have an interesting spirofuranone–lactam core and diverse biological activities. Structurally, the changes in configuration of C-5, C-8, and C-9 in the core could produce some stereoisomers. Recently,

Can. J. Chem. Downloaded from www.nrcresearchpress.com by 80.58.250.72 on 09/16/12
For personal use only.

Can. J. Chem. Downloaded from www.nrcresearchpress.com by 80.58.250.72 on 09/16/12
For personal use only.

Table 1. ^{1}H and ^{13}C NMR spectral data of compounds **1–3** in DMSO-d_6.

	1[a]		**2**		**3**	
Position	^{1}H (J in Hz)	^{13}C (mult.)	^{1}H (J in Hz)	^{13}C (mult.)	^{1}H (J in Hz)	^{13}C (mult.)
2		187.6 (s)		188.1 (s)		187.0 (s)
3		111.3 (s)		112.3 (s)		111.6 (s)
4		200.0 (s)		201.2 (s)		196.7 (s)
5		88.2 (s)		87.1 (s)		92.6 (s)
6		167.7 (s)		167.3 (s)		166.6 (s)
7-NH	9.94 (s)		9.99 (s)		9.96 (s)	
8		97.1 (s)		94.8 (s)		91.2 (s)
9	4.62 (d, J = 6.2)	75.7 (d)	4.18 (d, J = 9.9)	74.4 (d)	4.40 (d, J = 9.2)	75.0 (d)
10	4.36 (t, J = 5.2)	72.8 (d)	4.51 (t, J = 5.5)	71.9 (d)	4.35 (dd, J = 5.5, 5.9)	72.0 (d)
11	4.45 (ddd, J = 5.5, 7.7, 10.6)	68.3 (d)	4.57 (ddd, J = 5.5, 8.4, 11.0)	68.0 (d)	4.46 (ddd, J = 5.5, 8.2, 11.0)	68.2 (d)
12	5.39 (dd, J = 8.1, 11.0)	129.0 (d)	5.42 (dd, J = 8.5, 11.0)	128.7 (d)	5.39 (dd, J = 8.2, 11.0)	129.1 (d)
13	5.42 (dd, J = 7.0, 11.0)	133.8 (d)	5.47 (dd, J = 7.0, 11.0)	134.1 (d)	5.43 (dd, J = 6.8, 11.0)	133.9 (d)
14	1.95 (m)	20.7 (t)	2.08 (m)	20.8 (t)	1.98 (m)	20.7 (t)
	2.01 (m)		2.08 (m)		2.04 (m)	
15	0.86 (dd, J = 7.3, 7.7)	14.2 (q)	0.93 (dd, J = 7.3, 7.7)	14.2 (q)	0.88 (dd, J = 7.3,7.8)	14.2 (q)
16	1.66 (s)	5.7 (q)	1.66 (s)	5.7 (q)	1.64 (s)	5.7 (q)
17		194.8 (s)		195.9 (s)		196.4 (s)
18		134.7 (s)		133.7 (s)		133.5 (s)
19	8.10 (d, J = 7.3)	129.7 (d)	8.28 (d, J = 7.3)	130.3 (d)	8.26 (d, J = 6.9)	130.3 (d)
20	7.52 (t, J = 7.7)	128.4 (d)	7.55 (dd, J = 7.7, 8.0)	128.5 (d)	7.54 (dd, J = 7.4, 8.2)	128.4 (d)
21	7.63 (t, J = 7.3)	133.2 (d)	7.69 (t, J = 7.3)	134.0 (d)	7.68 (t, J = 7.4)	133.8 (d)
22	7.52 (t, J = 7.7)	128.4 (d)	7.55 (dd, J = 7.7, 8.0)	128.4 (d)	7.54 (dd, J = 7.4, 8.2)	128.4 (d)
23	8.10 (d, J = 7.3)	129.7 (d)	8.28 (d, J = 7.3)	130.3 (d)	8.26 (d, J = 6.9)	130.3 (d)
8-OMe	3.12 (s)	51.5 (q)	3.20 (s)	51.6 (q)	3.24 (s)	51.7 (q)
9-OH	6.07 (d, J = 6.2)		6.35 (d, J = 9.9)		6.26 (d, J = 9.2)	
10-OH	5.75 (d, J = 5.5)		5.87 (d, J = 5.5)		5.76 (d, J = 5.5)	
11-OH	4.96 (d, J = 5.1)		5.09 (d, J = 5.5)		4.90 (d, J = 5.6)	

[a]Assignment made on the basis of DEPT, ^{1}H –^{1}H COSY, HMQC, and HMBC data.

Fig. 2. ^{1}H–^{1}H COSY and key HMBC correlations of compound **1**.

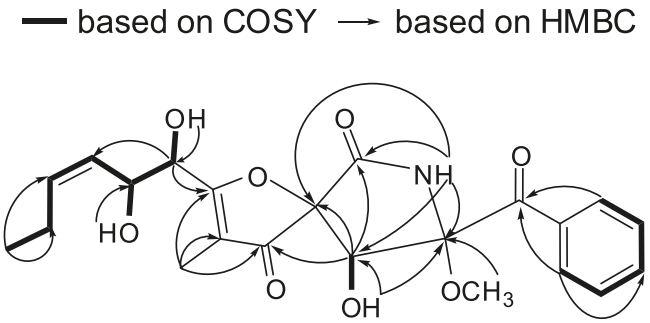

1

Fig. 3. Key NOESY correlations of compounds **1** and **2**.

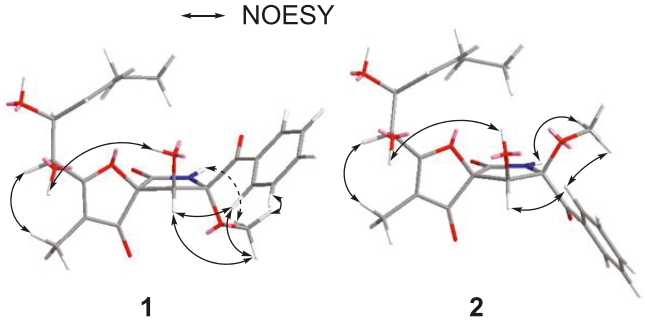

1 **2**

the absolute configurations of cephalimysins B–D and their synthetic stereoisomers were unambiguously established by studying CD Cotton effects.[13] Herein, we also successfully identified the absolute stereochemistry of **2** and **3** by comparison of their NMR data and CD spectra with those of pseurotin A (**3**). These results showed that the analysis of CD spectra was valuable for determining the absolute configuration of related compounds. However, the cytotoxicities of **1–3** against four tumor cell lines did not imply a structure–activity relationship.[13] Furthermore, the test of inhibitory activity of protein kinase for **1–3** is in progress.

Experimental

General

Column chromatography (CC): silica gel (SiO_2; Qingdao Haiyang Chemical Group Co., Ltd., China) and Sephadex LH-20 (Pharmacia). Optical rotations: JASCO P-1020 digital polarimeter. UV spectra: Beckman DU 640 spectrophotometer. IR spectra (KBr): Nicolet NEXUS 470 spectrophotometer. CD spectra: JASCO J-810 spectropolarimeter. NMR spectra (^{1}H NMR, ^{13}C NMR, DEPT, ^{1}H–^{1}H COSY, HMQC, HMBC, and NOESY): JEOL JNM-ECP 600 (600 MHz for ^{1}H NMR and 150 MHz for ^{13}C NMR) spectrometer; δ in ppm relative to Me_4Si as the internal standard, J in Hz. HR-ESI-MS: Q-TOF Ultima Global GAA076 LC mass

Fig. 4. Circular dichroism (CD) spectra for compounds **1**–**3**.

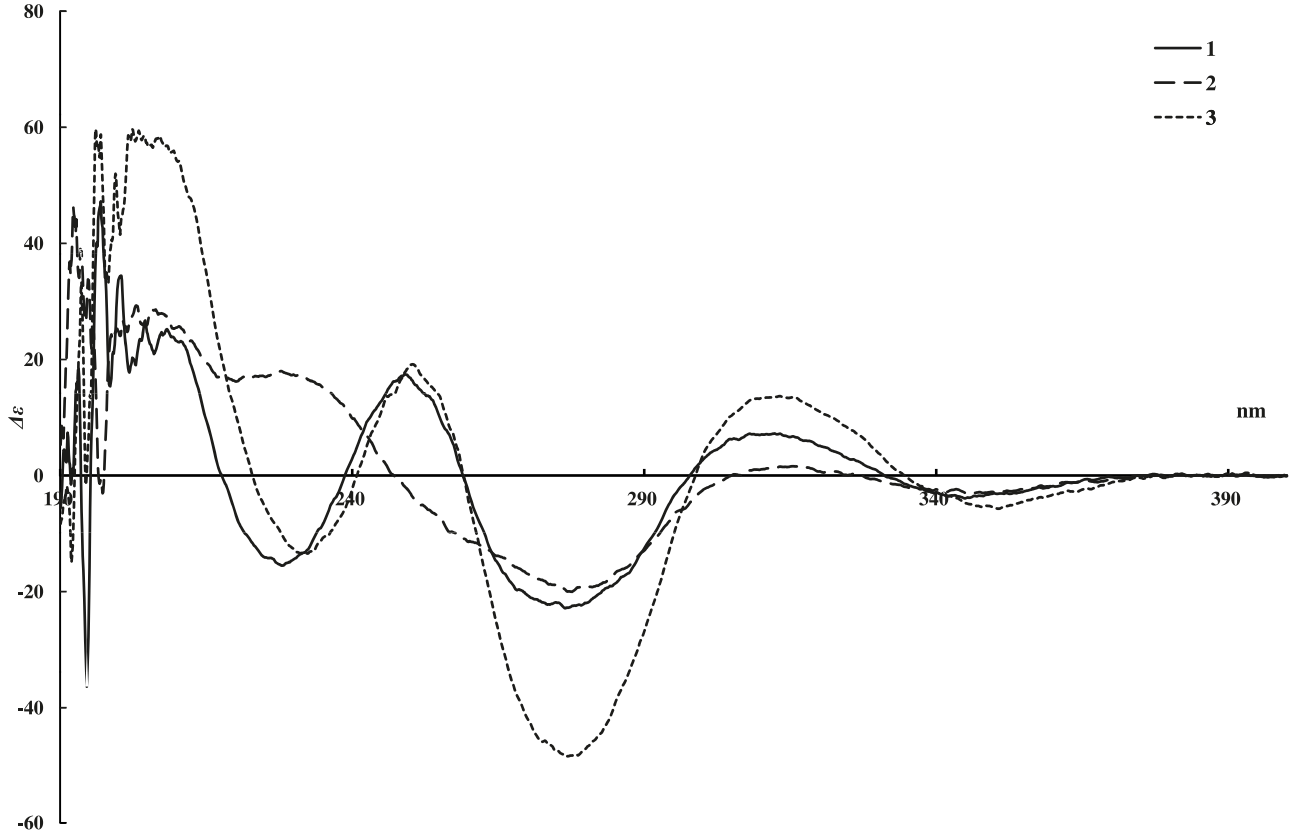

Can. J. Chem. Downloaded from www.nrcresearchpress.com by 80.58.250.72 on 09/16/12
For personal use only.

spectrometer; in *m/z* (rel %). Semipreparative HPLC: ODS column (Shin-pak ODS (H), 20 mm × 250 mm, 5 μm, 4 mL/min) and monitored by a UV detector.

Fungal material

The fungus *A. fumigatus* WFZ-25 was isolated from the holothurian *S. japonicus* collected in August 2005 from Lingshan Island, Qingdao, China. It was preserved in the Key Laboratory of Marine Drugs, Chinese Ministry of Education, Institute of Marine Drugs and Food, Ocean University of China. Working stock cultures were prepared on potato dextrose agar slants and stored at –20 °C.

Fermentation, extraction, and isolation

The fungus was inoculated in 500 mL Erlenmeyer flasks containing 150 mL liquid medium (20.0 g maltose, 20.0 g mannitol, 10.0 g glucose, 10.0 g monosodium glutamate, 0.5 g KH_2PO_4, 0.3 g $MgSO_4$, 3.0 g yeast extract paste, and 1.0 g maize paste dissolved in 1.0 L seawater, pH 6.5), followed by shaking incubation at 165 rpm for 9 days at 28 °C. The fermented whole broth (60 L) was filtered through cheesecloth to separate the supernatant and the mycelia. The former was concentrated under reduced pressure to about a quarter of the original volume and then extracted three times with ethyl acetate to give an ethyl acetate solution, while the latter was extracted three times with acetone–H_2O (80:20). The acetone solution was concentrated under reduced pressure to afford an aqueous solution. The aqueous solution was extracted three times with ethyl acetate to give another ethyl acetate solution. Both ethyl acetate solutions were combined and concentrated under reduced pressure to give a crude extract (100 g).

The crude extract was separated into 10 fractions (Fr.1–Fr.10) on a silica gel column using a stepwise gradient elution of petroleum ether (PE) – $CHCl_3$ – MeOH. Fraction Fr.6 (6.5 g) was subjected to repeated silica gel CC using a stepwise gradient elution of PE–$CHCl_3$–MeOH, followed by chromatographing on Sephadex LH-20, eluting with $CHCl_3$–MeOH (1:1), to yield subfraction Fr.6-2-1 (780.0 mg). Subfraction Fr.6-2-1 was subjected to Sephadex LH-20 eluting with $CHCl_3$–MeOH (1:1) and then purified by semipreparative HPLC using MeOH–H_2O (60:40) at a wavelength of 201 nm to yield compounds **3** (47.2 mg), **1** (34.0 mg), and **2** (8.6 mg).

Pseurotin A_1 (1)

White amorphous powder. $[\alpha]_D^{23}$ –4.2 (*c* 0.1, MeOH). UV (MeOH) λ_{max} (nm; log ε): 206 (4.15), 251 (4.12), 277 (3.97). CD (MeOH) λ_{max} (nm; $\Delta\varepsilon$): 208.3 (+13.1), 232.1 (–6.8), 249.3 (+9.1), 276.5 (–11.9), 308.1 (+3.8), 346.1 (–1.6). IR (KBr, cm^{-1}) ν_{max}: 3204, 1726, 1706, 1633, 1448, 1182, 1076, 1010, 785, 745, 539. ^1H (600 MHz) and ^{13}C (150 MHz) NMR data, see Table 1. HR-ESI-MS: 454.1458 $[M + Na]^+$ (calcd. for $C_{22}H_{25}NO_8Na^+$: 454.1478).

Pseurotin A_2 (2)

White amorphous powder. $[\alpha]_D^{23}$ –30.6 (*c* 0.1, MeOH). UV (MeOH) λ_{max} (nm; log ε): 205 (4.28), 252 (4.17), 278 (4.01). CD (MeOH) λ_{max} (nm; $\Delta\varepsilon$): 206.6 (+14.6), 227.8 (+9.4), 251.6 (–2.7), 278.1 (–10.3), 315.8 (+0.8), 344.9 (–1.6). IR (KBr, cm^{-1}) ν_{max}: 3204, 1741, 1739, 1693, 1448, 1215,

1176, 877, 751. ^{1}H (600 MHz) and ^{13}C (150 MHz) NMR data, see Table 1. HR-ESI-MS: 454.1465 $[M + Na]^+$ (calcd. for $C_{22}H_{25}NO_8Na^+$: 454.1478).

Pseurotin A (3)

White amorphous powder. $[\alpha]_D^{23}$ –2.5 (*c* 0.1, MeOH). UV (MeOH) λ_{max} (nm; log ε): 206 (3.98), 252 (3.93), 280 (3.77). CD (MeOH) λ_{max} (nm; $\Delta\varepsilon$): 206.8 (+30.5), 228.1 (–8.1), 250.4 (+10.0), 277.7 (–25.2), 308.1 (+3.8), 312.5 (+7.1), 350.4 (–3.0). IR (KBr, cm^{-1}) ν_{max}: 3211, 1725, 1705, 1632, 1440, 1079, 1041, 1017, 807, 666. ^{1}H (600 MHz) and ^{13}C (150 MHz) NMR data, see Table 1. ESI-MS: 432.2 $[M + H]^+$, 454.2 $[M + Na]^+$, 470.2 $[M + K]^+$.

Biological assays

Active fractions were assayed using the MTT (3-(4,5-dimethylthiazol-2-yl)-2,5-diphenyl tetrazolium bromide) method with the P388 cell line. Cytotoxic activities were evaluated by the MTT method[16] using the P388 and HL-60 cell lines and the SRB (sulforhodamine B) method[17] using the A549 and BEL-7402 cell lines.

In the MTT assay, the cell suspensions (200 μL) at a density of 5×10^4 cells mL^{-1} were plated in 96 well microtiter plates and incubated for 24 h at 37 °C in a humidified incubator at 5% CO_2. The test compound solution (2 μL in DMSO) at different concentrations was added to each well and further incubated for 72 h under the same conditions. Then, 20 μL of the MTT solution was added to each well and incubated for 4 h. The old medium (150 μL) containing MTT was then gently replaced by DMSO and pipetted to dissolve any formazan crystals formed. Absorbance was then determined on a Spectra Max Plus plate reader at 540 nm.

In the SRB assay, 200 μL of the cell suspensions were placed in 96 well plates at a density of 2×10^5 cells mL^{-1}. Then, 2 μL of the test compound solution (in MeOH) at different concentrations was added to each well and the culture was further incubated for 24 h at 37 °C in a humidified incubator at 5% CO_2. Following drug exposure, the cells were fixed with 12% trichloroacetic acid and the cell layer was stained with 0.4% SRB. The absorbance of the SRB solution was measured at 515 nm. Dose–response curves were generated and the IC_{50} values were defined as the concentration of compound required to inhibit cell proliferation by 50%.

Acknowledgments

This work was financially supported by the National Natural Science Foundation of China (No. 40906076) and the Shandong Provincial Natural Science Fund (No. ZR2009CZ016). The *A. fumigatus* was identified by Professor H. Kui at the Chinese Academy of Tropical Agricultural Sciences (CATAS) and South China University of Tropical Agriculture (SCUTA). The antitumor assay was performed at the Shanghai Institute of Materia Medica, Chinese Academy of Sciences.

References

(1) Wang, F. Z.; Fang, Y. C.; Zhu, T. J.; Zhang, M.; Lin, A. Q.; Gu, Q. Q.; Zhu, W. M. *Tetrahedron* **2008**, *64* (34), 7986. doi:10.1016/j.tet.2008.06.013.

(2) Bloch, P.; Tamm, C. *Helv. Chim. Acta* **1981**, *64* (1), 304. doi:10.1002/hlca.19810640131.

(3) Bloch, P.; Tamm, C.; Bollinger, P.; Petcher, T. J.; Weber, H. P. *Helv. Chim. Acta* **1976**, *59* (1), 133. doi:10.1002/hlca.19760590114.

(4) Wenke, J.; Anke, H.; Sterner, O. *Biosci. Biotechnol. Biochem.* **1993**, *57* (6), 961. doi:10.1271/bbb.57.961.

(5) Weber, H. P.; Petcher, T. J.; Bloch, P.; Tamm, C. *Helv. Chim. Acta* **1976**, *59* (1), 137. doi:10.1002/hlca.19760590115.

(6) Breitenstein, W.; Chexal, K. K.; Mohr, P.; Tamm, C. *Helv. Chim. Acta* **1981**, *64* (2), 379. doi:10.1002/hlca.19810640203.

(7) Wink, J.; Grabley, S.; Gareis, M.; Thiericke, R.; Kirsch, R. Eur. Pat. Appl. EP546474, 1993.

(8) Zhang, M.; Wang, W. L.; Fang, Y. C.; Zhu, T. J.; Gu, Q. Q.; Zhu, W. M. *J. Nat. Prod.* **2008**, *71* (6), 985. doi:10.1021/np700737g.

(9) Ando, O.; Satake, H.; Nakajima, M.; Sato, A.; Nakamura, T.; Kinoshita, T.; Furuya, K.; Haneishi, T. *J. Antibiot. (Tokyo)* **1991**, *44* (4), 382.

(10) Asami, Y.; Kakeya, H.; Onose, R.; Yoshida, A.; Matsuzaki, H.; Osada, H. *Org. Lett.* **2002**, *4* (17), 2845. doi:10.1021/ol020104+.

(11) Hayashi, Y.; Sankar, K.; Ishikawa, H.; Nozawa, Y.; Mizoue, K.; Kakeya, H. *Bioorg. Med. Chem. Lett.* **2009**, *19* (14), 3863. doi:10.1016/j.bmcl.2009.03.154.

(12) Yamada, T.; Imai, E.; Nakatuji, K.; Numata, A.; Tanaka, R. *Tetrahedron Lett.* **2007**, *48* (36), 6294. doi:10.1016/j.tetlet.2007.07.024.

(13) Yamada, T.; Kitada, H.; Kajimoto, T.; Numata, A.; Tanaka, R. *J. Org. Chem.* **2010**, *75* (12), 4146. doi:10.1021/jo100496f.

(14) Scott, A. J. *Interpretation of UV Spectra of Natural Products;* Pergamon Press: London, 1964.

(15) Rosenkranz, R. E.; Allner, K.; Good, R.; Philipsborn, W. v.; Eugster, C. H. *Helv. Chim. Acta* **1963**, *46* (4), 1259. doi:10.1002/hlca.19630460422.

(16) Mosmann, T. *J. Immunol. Methods* **1983**, *65* (1–2), 55. doi:10.1016/0022-1759(83)90303-4.

(17) Skehan, P.; Storeng, R.; Scudiero, D.; Monks, A.; McMahon, J.; Vistica, D.; Warren, J. T.; Bokesch, H.; Kenney, S.; Boyd, M. R. *J. Natl. Cancer Inst.* **1990**, *82* (13), 1107. doi:10.1093/jnci/82.13.1107.

Can. J. Chem. Downloaded from www.nrcresearchpress.com by 80.58.250.72 on 09/16/12
For personal use only.

Modifications of commercial pressurized solvent extraction (PSE) systems for the analysis of polychlorinated biphenyls in avian whole blood and serum

Stacey D. Haskins, Christina M. Harrison, David G. Kelly, and Ron D. Weir

Can. J. Chem. Downloaded from www.nrcresearchpress.com by 80.58.250.72 on 09/16/12
For personal use only.

Abstract: The present study considers simple and cost-effective modifications to commercial pressurised solvent extraction cells to extract polychlorinated biphenyls (PCBs) from avian blood and serum. Blood and serum samples of mass 0.2 g were examined. Such masses are consistent with those which may be obtained from many avian species without sacrificing individuals or compromising breeding and (or) migratory success. Extraction vessels are modified by the use of Teflon inserts, which are readily fabricated at low cost. These inserts reduce internal cell volume and surface area. Thus, background contamination is reduced whilst extraction and rinse solvent is used more effectively to afford a small extract volume. Packing of the cell void with sodium sulfate and florisil achieves in situ sample dehydration and lipid removal. When combined with extraction concentration and large volume injection gas chromatography – ion-trap mass spectrometry (LVI-GC–ITMS), the extraction method is capable of polychlorinated biphenyl analysis without post-extraction clean-up. Validation was accomplished using commercial chicken whole blood and serum, and PCB congeners 28, 77, 105, 126, 153, 167, 170, 180, 183, and 194. Surrogate corrected recoveries in the range of 75% to120% for whole blood and 80% to115% for serum were obtained. Detection limits were in the range of 0.01 to 0.22 ng g^{-1} for whole blood and 0.03 to 0.45 ng g^{-1} for serum. The relative standard deviations for all congeners investigated were better than 15%.

Key words: polychlorinated biphenyls, pressurized solvent extraction, avian blood, large-volume injection gas chromatography, ion-trap mass spectrometry, tandem mass spectrometry.

Résumé : Dans ce travail, on considère diverses modifications simples et rentables aux cellules d'extraction commerciales avec solvants sous pression pour extraire les biphényles polychlororés (BPC) à partir de sang et de sérum aviaire. On a examiné des échantillons de sérum et de sang de masse égale à 0,2 g. De telles masses sont en accord avec celles qui peuvent être obtenues à partir de plusieurs espèces aviaires sans devoir sacrifier les individus ou compromettre les aptitudes à la reproduction et (ou) à la migration. Les tubes d'extraction ont été modifiés par l'utilisation d'insert en Teflon qui peuvent facilement être fabriqués à de faibles coûts. Ces inserts réduisent le volume et la superficie de la cellule. La contamination de fond est ainsi réduite alors que le solvant d'extraction et de rinçage est utilisé d'une façon plus efficace de façon à avoir un faible volume d'extraction. Le remplissage du vide de la cellule avec du sulfate de sodium et du florisil permet de réaliser in situ la déshydratation de l'échantillon et l'enlèvement des lipides. Lorsqu'elle est combinée avec une concentration de l'extraction et un appareil de spectrométrie de masse avec piège d'ion et une injection d'un grand volume (« LVI-GC–ITMS »), la méthode d'extraction permet d'effectuer une analyse de biphényle polychloré sans purification post-extraction. On a réalisé la validation de la méthode en utilisant des échantillons commerciaux de sang complet et du sérum de poulet avec les congénères 28, 77, 105, 126, 167, 170, 183 et 194 des BPC. On a obtenu des récupérations corrigées pour les substitutions qui varient de 75 % à 120 % pour le sang complet et de 80 % à 115 % pour le sérum. Les limites de détection varient de 0,01 à 0,22 ng g^{-1} pour le sang complet et de 0,03 à 0,45 ng g^{-1} pour le sérum. Les déviations standards relatives pour tous les congénères étudiés sont meilleures que 15 %.

Mots-clés : biphényles polychlorés, extraction par solvant sous pression, sang aviaire, chromatographie gazeuse à grand volume d'injection, spectrométrie de masse à trappe ionique, spectrométrie de masse en tandem.

[Traduit par la Rédaction]

Received 5 August 2010. Accepted 31 October 2010. Published on the NRC Research Press Web site at canjchem.nrc.ca on 5 January 2011.

S.D. Haskins, C.M. Harrison, D.G. Kelly,[1] and R.D. Weir. Analytical Sciences Group, Department of Chemistry and Chemical Engineering, Royal Military College of Canada, 11 General Crerar Crescent, Box 17000 Station Forces, Kingston, ON K7K 7B4, Canada.

[1]Corresponding author (e-mail: David.Kelly@rmc.ca).

Can. J. Chem. Downloaded from www.nrcresearchpress.com by 80.58.250.72 on 09/16/12
For personal use only.

Introduction

Polychlorinated biphenyls (PBCs) represent 209 congener compounds, which were historically produced as complex mixtures under a number of trade names, such as Aroclors. The commercialization of these mixtures, as well as their release and transport in the environment, environmental persistence, and negative environmental impacts, has been extensively documented.[1–4] Legislation and regulation, intended to ban PCB production, limit use of existing PCBs stocks, and require environmental remediation, began in the 1970s in developed nations, such as Canada[5] and has continued into the 21st century.[6,7] However, PCBs were employed in a number of dissipative applications such as plasticizers, paints, wood-floor finishes, and pesticide extenders.[8] Moreover, several locations associated with industrial applications, such as those in the US states of New York (General Electric Company), Illinois (Outboard Marine Corporation), Massachusetts (Federal Pacific Electric Company), and Pennsylvania (Westinghouse Elevator Company),[9–14] are acutely contaminated. Environmental transport from dissipative sources and acutely contaminated sites has made PCBs global contaminants.[15] As the result of legislation and remedial action, driven by public concern, PCBs levels in sediment, birds, and fish have decreased in areas such as the Great Lakes.[16–19] However, PCB concentrations in Great Lakes fish remain in the part per billion range (10^{-9}); concentrations that are sufficient to impact higher species within foodwebs and to restrict human consumption.[20,21] The lipophilicity of PCBs and their resistance to degradation contribute to this bioaccumulation.[2] The effects of PCBs include interferences with thyroid activities and developmental abnormalities, with piscivorous avian species being particularly effected.[22–26] Population declines, and more recently population stress, have been noted. Numerous studies have sacrificed individual birds to assess PCB burdens.[27–30] However, facile methods of low-cost analysis using samples that do not require the sacrifice of individual birds and animals remain important in the assessment of PCB distribution and transport. In a recent study, we reported the analysis of PCBs in avian blood using uniquely designed and engineered pressurized extraction cells.[31] The present work investigates a simplified, and low cost, modification to commercial extraction vessels for the analysis of small volumes of both whole blood and serum.

Experimental

Reagents and materials

Unless otherwise stated, consumables were obtained from ThermoFisher Scientific. Solvent and acid grades were as follows: acetone (pesticide grade), dichloromethane (Optima), absolute ethanol (certified A.C.S.), concentrated sulfuric acid (trace metal grade), and phosphoric acid (reagent grade). Double deionized water (17.8 MΩ) was prepared using an E-pure water purification system, Barnstead International. Teflon was obtained from Warehouse Plastics Inc. (Toronto, Ontario). Florisil was obtained from Diagnostix (Mississauga, Ontario). Whole blood and serum were obtained separately as pooled 500 cm^3 samples from Animal Technologies Inc. (Tyler, Texas). Protocols used to prevent clotting, temperatures and periods of storage, and protein denaturation methods are described elsewhere for whole blood.[31] Similar protocols were employed in the use and storage of serum. Heparin was added to the blood prior to shipping to prevent clotting.

PCB congener standards were obtained as five mixtures containing all 209 PCB congeners (M-1668A-0.01X) from Chromatographic Specialties Inc. (Brockville, Ontario). Elution order was confirmed for all congeners and the capacity to report the full congener series was retained. A three-point calibration in the range 0.1 to 10.0 ng cm^{-3} was employed with the requirement for the R^2 obtained by linear regression to exceed 0.99. Ten environmentally relevant congeners, including ortho-substituted congeners, were considered in the present study. Four $^{13}C_{12}$-labeled PCB congeners 32, 101, 153, and 194 (Cambridge Isotopes Laboratories Inc.) were used as surrogates. The congeners studied and surrogates for correction of extraction efficiency are shown in Table 1. The PAH internal standards (naphthalene-d_8, phenanthrene-d_{10}, anthracene-d_{10}, and benzo(*a*)anthracene-d_{12}) were prepared at a concentration of 20 ng cm^{-3} (Supelco). All standards were prepared in dichloromethane.

Pressurized solvent extraction (PSE)

An Applied Separations (Allentown, Pennsylvania) *fast* pressurized solvent extraction (PSE) unit, capable of six simultaneous extractions, was used. Cells were 33 cm^3 (internal volume) and constructed of stainless steel (Applied Separations). Teflon inserts (length: 3.0 cm, radius: 1.0 cm, centre bore hole: 0.10 cm) were designed and crafted by the Analytical Sciences Group for the extraction vessels (Fig. 1). Three inserts were placed in each extraction vessel to reduce the volume to approximately 5 cm^3 (Fig. 2). All extractions (whole blood or serum) were performed using the following procedure: Extraction vessels were loaded (Fig. 2) sequentially with Teflon inserts,[2] filter paper, florisil, sodium sulfate, sample (0.2 g whole blood or serum), glass wool, and Teflon insert. The PCB congener and internal standards were spiked directly onto the blood prior to being covered with glass wool. Extraction conditions were as follows: solvent (1:3, acetone–DCM), static cycles (3 static cycles of 5 min duration), flushing time (1 min), temperature (100 °C), and pressure (10 MPa). Sample extracts were evaporated at room temperature (25 °C) under a flow of nitrogen gas to a final volume of 2 cm^3. Deuterated PAH internal standards were added to the extracts prior to GC–MS analysis.

Lipid determination

Lipid determination was performed colorimetrically using a sulfo-phospho-vanillin reaction.[32] Extractions were performed using 0.8 g samples in the absence of florisil reagent and sodium sulfate. Five replicates of whole blood and serum extracts were evaluated. A detailed description of the methods used to assess lipid in blood and blood products has been described elsewhere.[31]

Gas chromatography – mass spectrometry (GC–MS)

GC–MS analysis was performed using a PolarisQ ion-trap mass spectrometer (ThermoFisher) fitted with a programmed temperature vaporizing injector (PTVI) capable of large-volume injection. An extract volume of 0.150 cm^3 was used

Can. J. Chem. Downloaded from www.nrcresearchpress.com by 80.58.250.72 on 09/16/12
For personal use only.

Table 1. PCB congeners investigated, total number of chlorines, number of chlorines in ortho-substituted positions, masses evaluated for PCB quantification, and collision voltages.

Congener	No. of chlorine substituents	No. of *ortho*-chlorines	Retained[a] mass range	Quantitation[a] mass range	Collision voltage (V)
PCB 28	3	1	254–258	182–190	3
PCB 77	4	0	289–292	218–226	3
PCB 105	5	1	324–328	254–260	4
PCB 126	5	0	324–328	254–260	4
PCB 153	6	2	358–362	286–294	4
PCB 167	6	1	358–362	286–294	4
PCB 170	7	2	392–396	321–329	4
PCB 180	7	2	392–396	321–329	4
PCB 183	7	1	392–396	321–329	4
PCB 194	8	2	426–430	356–364	5

[a]The retained and quantitation mass ranges are denoted as (*m*/*z*).

Fig. 1. Teflon pressurized solvent extraction (PSE) vessel inserts.

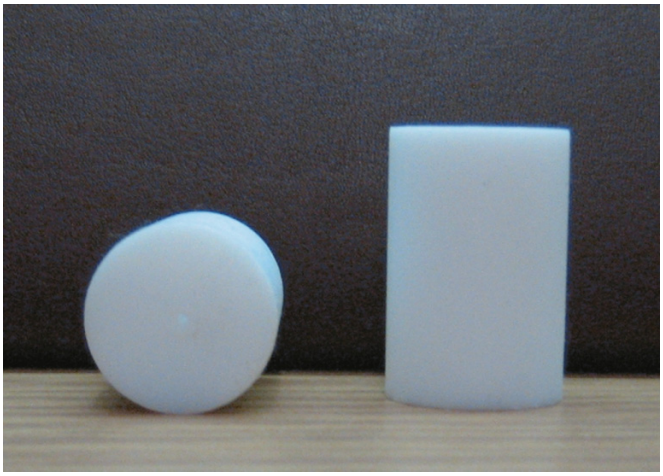

Fig. 2. Schematic of Teflon pressurized solvent extraction (PSE) vessel inserts and packing procedure.

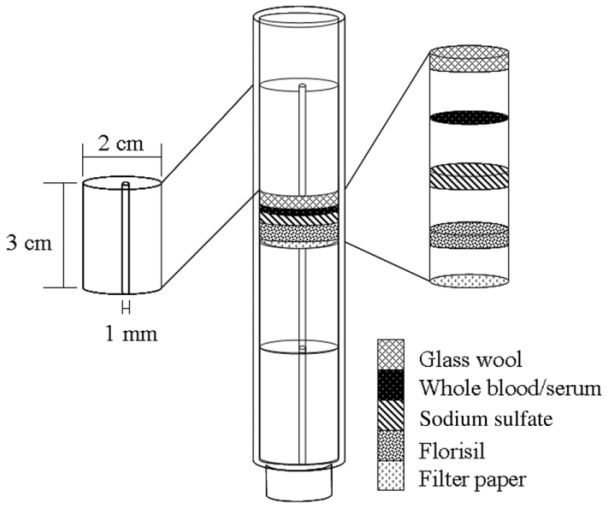

in split mode with an injection rate of 0.002 cm^3 s^{-1}. Separation was achieved in temperature-programmed mode using a Restek RTx-5MS fused-silica capillary column (60 m × 0.25 mm i.d., 0.25 μm phase thickness) and helium carrier gas. Full injection and separation parameters have been reported.[31] Mass spectral data were acquired in MS–MS mode using a damping/collision gas flow of 2.0 cm^3 min^{-1} and trap Q_v = 0.45. Mass ranges retained before and after collision, and well as collision voltages, are shown in Table 1. Data acquisition and analysis were performed using Xcaliber 1.4 software.

Fig. 3. Analyte percent recovery for 0.025 ng of PCB 167 and ^{13}C-labeled PCB 101 surrogate standard in 0.001, 0.002, 0.010, 0.050, and 0.150 cm^3 injection volumes. Recoveries are presented as the average of triplicate analysis; error bars denote the standard deviation of those triplicates.

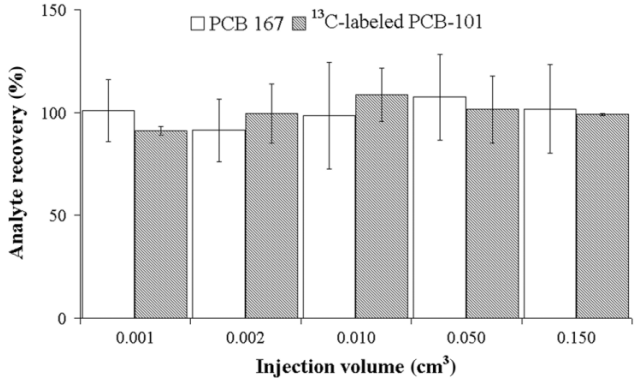

Results and discussion

Lipid determination

As there is a tendency in the field to report PCBs as lipid-based concentrations, the lipid content of both the serum and whole blood used in this study was determined so that the data presented here may be easily compared against other studies. Using colorimetry, mean lipid content was measured in six replicates of each blood type (serum and whole blood) and one control sample (NIST 1589a). The control sample result was within 20% of the certified value (0.60%),[33] whilst the results for blood and serum were 0.66% ± 0.01% and 0.69% ± 0.04%, respectively. As expected, lipid results from whole blood and serum in the present study are statistically equivalent to those found in a different batch of chicken blood used in a previous study using novel PSE vessels.[31] Data are in good agreement with the findings of a recent study conducted using NIST 1589a.[34] Moreover, the

Table 2. Replicate sample concentrations, accuracy, precision, and detection limits for the developed pressurized solvent extraction (PSE) method in serum samples (n = 5).

	Replicate sample analyte concentration (ng cm^{-3})[a]					Recovery	RSD	LOD[b]	MDL[c]
Compound	1	2	3	4	5	(%)	(%)	(ng cm^{-3})	(ng cm^{-3})
PCB 28	1.09	0.99	0.89	1.11	1.04	102	9	0.03	0.37
PCB 77	0.83	0.77	0.99	0.81	0.71	82	13	0.05	0.45
PCB 105	1.11	1.06	0.93	1.19	1.21	110	10	0.04	0.47
PCB 126	0.95	0.90	1.05	0.86	0.71	90	14	0.05	0.59
PCB 153	1.13	1.08	0.92	1.30	1.33	115	15	0.45	0.72
PCB 167	0.87	1.07	1.01	0.99	1.11	101	9	0.05	0.44
PCB 170	0.98	0.91	0.82	1.04	1.10	98	11	0.07	0.52
PCB 180	1.22	1.11	1.13	1.03	1.18	113	6	0.06	0.34
PCB 183	1.03	0.94	0.85	1.06	1.10	100	10	0.05	0.48
PCB 194	0.83	0.83	0.85	0.94	0.95	88	7	0.08	0.28

[a]Target concentration for all compounds in 1 ng cm^{-3}.
[b]Limit of detection based on a three S/N of a serum sample.
[c]Method detection limit based on replicate analysis as per ISO 17 025 requirements.

Table 3. Replicate sample concentrations, accuracy, precision, and detection limits for the developed pressurized solvent extraction (PSE) method in whole blood samples (n = 5).

	Replicate sample analyte concentration (ng cm^{-3})[a]					Recovery	RSD	LOD[b]	MDL[c]
Compound	1	2	3	4	5	(%)	(%)	(ng cm^{-3})	(ng cm^{-3})
PCB 28	10.22	8.96	9.54	10.08	8.68	95	7	0.15	2.66
PCB 77	8.65	7.61	7.71	8.08	7.68	80	5	0.22	0.95
PCB 105	9.19	9.94	10.09	9.99	10.18	99	4	0.01	1.64
PCB 126	7.39	7.92	7.95	7.61	7.56	77	3	0.02	0.82
PCB 153	11.41	14.46	11.59	10.70	10.53	117	14	0.16	2.86
PCB 167	9.90	10.72	10.15	10.87	10.53	104	4	0.05	1.50
PCB 170	10.90	11.82	11.16	12.20	10.50	113	6	0.07	2.47
PCB 180	9.38	11.88	10.96	11.01	11.36	109	9	0.05	3.44
PCB 183	8.61	9.78	9.59	8.89	9.46	93	6	0.05	1.68
PCB 194	8.27	9.68	10.60	10.21	9.5	97	9	0.03	3.28

[a]Target concentration for all compounds in 10 ng cm^{-3}.
[b]Limit of detection based on a three S/N of a serum sample.
[c]Method detection limit based on replicate analysis as per ISO 17 025 requirements.

Can. J. Chem. Downloaded from www.nrcresearchpress.com by 80.58.250.72 on 09/16/12
For personal use only.

results compare well with other independent studies conducted using avian blood,[35,36] and the precision reported on the results is well within published values from more extensive studies.[37,38] However, from the literature, it is apparent that lipid determinations are highly dependent on the methodology used. Thus, the method used to determine lipid content of blood and serum in this study could be reliably compared against other internal studies of the same nature; however, given the variability in the results from lipid analyses as a function of the analytical procedure employed, it is likely more prudent to report PCB concentrations as whole blood or serum values, rather than lipid-based values, for interlaboratory comparisons.

Large-volume injection gas chromatography – ion-trap mass spectrometry (LVI-GC–ITMS)

Large-volume injection utilizes the separation of solvent and analyte at low temperatures using large split ratios. It is inevitable that a portion of the analyte will be lost during this process, and retention efficiencies will drop as analyte volatility approaches solvent volatility. Reproducible rather than complete transfer to the GC column is required. In the present work, equal analyte masses were injected using 0.001, 0.002, 0.010, 0.050, and 0.150 cm^3 injections. Mean injection efficiencies for PCB 167 and surrogate standard ^{13}C-labeled PCB 101, normalized to 0.001 cm^3, are presented in Fig. 3. It is evident that 0.150 cm^3 injections represent an efficient and precise method of sample introduction. Average injection efficiencies were >90% for all congeners studied, and relative standard deviation values ranged from 15% to 26%.

Blood and serum extraction

Extraction efficiency was determined by the analysis of control samples (m = 0.2 g; n = 5), which were prepared using chicken whole blood or serum. Samples were spiked directly with 10 PCB congeners in dichloromethane to afford a blood concentration of 10 or 1 ng g^{-1}, for whole blood and serum, respectively. Whole blood was spiked at a higher concentration, as elevated detection limits were expected due to the increased sophistication of the sample matrix. Extractions were performed using three static cycles, as other studies have demonstrated that PCB recovery is increased with additional extraction cycles.[34,39,40] Such work additionally

Can. J. Chem. Downloaded from www.nrcresearchpress.com by 80.58.250.72 on 09/16/12
For personal use only.

demonstrates that little advantage accrues by the use of more than three cycles. Extracts were introduced directly to the GC–MS without additional clean up. The avoidance of post-extraction clean up increases throughput, reduces potential contamination and cross-contamination, and reduces analytical costs. However, the removal of sufficient matrix materials is also essential to facilitate large-volume injection, to avoid column and inlet contamination, and to prevent degradation of mass spectrometer performance. Tables 2 and 3 summarize relevant analyte data related to the proposed PCB extraction method for whole blood and serum samples, respectively. Recoveries were within 75% to 120% of expected values with corresponding RSD values of 15% or better. Surrogate and internal standard recoveries were all >90% when compared against calibration standard response. These data suggest that sufficient in-cell lipid removal has occurred to facilitate PCB analysis. The results conform well to those achieved using PSE to examine low-level PCBs in fatty foodstuffs[41] and to those reported from other solid phase extraction (SPE) studies as well as methods that use significantly greater sample volumes.[34,41–45] While SPE systems can detect PCBs in serum samples of comparable size, the method cannot be extended to whole blood; a challenge which does not extend to PSE systems.

Analytical performance is often assessed on the basis of a statistically based detection limit. Several methods may be employed to determine this limit.[46–49] As with our previous work,[31] the present study reports detection limits as both three times the signal-to-noise ratio of unspiked whole blood and serum samples and two times the standard deviation of replicate analyses multiplied by the Student's t value based on the appropriate number of samples used. The former calculation is used to place the data in the context of that reported by other workers.[41,43,44] The latter method was performed in accordance with ISO/IEC 17025, the standard that defines the competency of testing and calibration laboratories.[50] The increasing legal importance of environmental data in terms of legislation and litigation makes the use of the latter increasingly important. The detection limits based on a signal-to-noise ratio of 3:1 are between 0.01 and 0.22 ng cm^{-3} per congener for whole blood and between 0.03 and 0.45 ng cm^{-3} per congener for serum (see Tables 2 and 3). The detection limits based on replicate analysis, which are consistent with the ISO/IEC 17025 standard, are between 0.82 and 3.44 ng cm^{-3} per congener for whole blood and between 0.28 and 0.72 ng cm^{-3} per congener for serum (see Tables 2 and 3). Detection limits based on the signal-to-noise ratio, for both whole blood and serum, are in the same range as those reported for SPE serum extractions;[42,51] as SPE cannot be used for whole blood analysis, serum comparisons have been made. It is evident that replicate-based detection limits are generally higher for serum and whole blood than those obtained by signal-to-noise determinations. Inevitably, these detection limits will compare less favourably with those of other studies. Limits of detection calculated from replicate analyses in this study are at best comparable with some of the LODs reported elsewhere,[42,51] and in other instances, those limits are almost one order of magnitude higher. However, it must be noted that these differences represent a fundamentally different approach to the determination of detection limits, and that these less favourable data represent limits that could have a more widely accepted legal standing. In general, the proposed PSE method appears to produce broadly comparable results to more commonly used techniques. The replicate-based detection limits for whole blood were generally found to be higher in this study than in the study using novel pressurized solvent extraction vessels.[31] The detection limits for PCBs 77 and 126 were found to be approximately equivalent between studies; however, for the five other PCBs shared between studies, the detection limits in this study ranged from 4 (PCB 105) to 55 (PCB 194) times higher. However, the detection limits remain in the low part-per-billion range (10^{-9}) for 0.2 g samples. Similar detection limits using traditional methods often require sample masses 5 times greater than those used here to obtain comparable detection limits. Although the detection limits using the current system are somewhat higher than those using the more intricate extraction vessels, the limits obtained in the present work are consistent with the requirements of environmental analysis. Moreover, depending on the study and the level of sensitivity required, the use of Teflon inserts presents an attractive alternative as the cost associated with their fabrication is approximately 5% of the cost associated with manufacturing the more specialized extraction vessels; the approximate costs of coiled vessels and inserts being $500 and $25, respectively. Furthermore, coiled vessels require a level of engineering support that is not available to all laboratories.

Conclusions

The low blood volumes that can be taken from small avian species without sacrifice create specialized challenges for PCB extraction and quantification. A new extraction vessel was designed in 2010,[31] which offers detection limits at or under 1.5 ng g^{-1} per congener for the analysis of whole blood; however, the equipment is quite costly for the end-user. This study reports on the accuracy, precision, and detection limits for the extraction of 10 environmentally relevant PCB congeners from 0.2 g samples of avian whole blood and serum, using conventional PSE cells that have had their internal volume decreased by the use of Teflon inserts. These inserts can be fabricated for a mere fraction of the cost of the specialized vessels, yet they still allow the addition of lipid and moisture-removing packing materials in situ. Whilst the detection limits are somewhat higher in the present study, they still remain in the low ng g^{-1} range, making the technique competitive with more commonly used methods of PCB extraction. The detection limits for each of the congeners examined ranged from 0.01 to 0.22 ng g^{-1} in whole blood and from 0.03 to 0.45 ng g^{-1} in serum, with RSDs better than 15% in all instances. Given the findings of this study, the PSE method reported here should be considered suitable as a rapid and low-cost alternative for the analysis of environmentally relevant PCB congeners in both whole blood and serum samples.

Acknowledgements

The staff of the Analytical Sciences Group at the Royal Military College of Canada is gratefully acknowledged for their assistance in the completion of this research.

Can. J. Chem. Downloaded from www.nrcresearchpress.com by 80.58.250.72 on 09/16/12
For personal use only.

References

(1) Waid, J. S., Ed. *PCBs and the Environment;* CRC Press: Boca Raton, FL, 1986.

(2) Erickson, M. D. *The Analytical Chemistry of PCBs,* 2nd ed.; CRC Press: Boca Raton, FL, 1997.

(3) Tanabe, S. *Environ. Pollut.* **1988**, *50* (1–2), 5. doi:10.1016/0269-7491(88)90183-2.

(4) Risebrough, R. W.; Rieche, P.; Peakall, D. B.; Herman, S. G.; Kirven, M. N. *Nature* **1968**, *220* (5172), 1098. doi:10.1038/2201098a0.

(5) *Environmental Contaminants Act;* Environment Canada and Health and Welfare Canada: Ottawa, ON, 1977.

(6) *Controlling PCBs Management of PCBs in Canada;* Environment Canada: Toronto, ON, 1981.

(7) Environment Canada. *Canada Gazette* **2009**, *143* (39), 2915.

(8) Durfee, R. L.; Contos, G.; Whitmore, F. C.; Barden, J. D.; Hackman, E. E., III; Westin, R. A. *PCBs in the United States — Industrial Use and Environmental Distributions,* EPA 560/6–76–005, NTIS No. PB252 012, Prepared for the Office of Toxic Substances, United States Environmental Protection Agency (USEPA): Washington, DC, 1976.

(9) Gustafson, C. G. *Environ. Sci. Technol.* **1970**, *4* (10), 814. doi:10.1021/es60045a008.

(10) *General Electric Co – Hudson Falls;* ID No. NYD002080075; United States Environmental Protection Agency (USEPA): New York.

(11) *Outboard Marine Corp.;* ID No. ILD000802827; United States Environmental Protection Agency (USEPA): Chicago, IL.

(12) de Percin, P. R. *J. Hazard. Mater.* **1995**, *40* (2), 203. doi:10.1016/0304-3894(94)00085-U.

(13) *New Bedford Harbor;* ID No. MAD980731335; United States Environmental Protection Agency (USEPA): Boston, MA.

(14) *Westinghouse Elevator Company Plant;* ID No. PAD043882281; United States Environmental Protection Agency (USEPA): Philadelphia, PA.

(15) Beyer, A.; Biziuk, M. *Rev. Environ. Contam. Toxicol.* **2009**, *201*, 137. doi:10.1007/978-1-4419-0032-6_5.

(16) Baumann, P. C.; Whittle, D. M. *Aquat. Toxicol.* **1988**, *11* (3–4), 241. doi:10.1016/0166-445X(88)90077-X.

(17) Jeremiason, J. D.; Hornbuckle, K. C.; Eisenreich, S. J. *Environ. Sci. Technol.* **1994**, *28* (5), 903. doi:10.1021/es00054a023.

(18) Mackay, D. *J. Great Lakes Res.* **1989**, *15* (2), 283. doi:10.1016/S0380-1330(89)71482-9.

(19) Swackhamer, D. L. *J. Environ. Monit.* **2005**, *7* (6), 540. doi:10.1039/b506709j.

(20) *Update: National Listing of Fish and Wildlife Advisories;* EPA 823-F-03-003; Office of Water, United States Environmental Protection Agency (USEPA): Washington, DC, 2003.

(21) *2005–2006 Guide to Eating Ontario Sport Fish;* Ontario Ministry of the Environment: Toronto, ON, 2005.

(22) Verreault, J.; Skaare, J. U.; Jenssen, B. M.; Gabrielsen, G. W. *Environ. Health Perspect.* **2004**, *112* (5), 532. doi:10.1289/ehp.6756.

(23) Gould, J. C.; Cooper, K. R.; Scanes, C. G. *Ecotoxicol. Environ. Saf.* **1999**, *43* (2), 195. doi:10.1006/eesa.1999.1776.

(24) Webb, C. M.; McNabb, F. M. A. *Gen. Comp. Endocrinol.* **2008**, *155* (3), 650. doi:10.1016/j.ygcen.2007.09.010.

(25) Marsili, L.; Fossi, M. C.; Casini, S.; Focardi, S. *Chemosphere* **1996**, *33* (4), 699. doi:10.1016/0045-6535(96)00222-6.

(26) Jenssen, B. M.; Nilssen, V. H.; Murvoll, K. M.; Skaare, J. U. *Chemosphere* **2001**, *44* (3), 483. doi:10.1016/S0045-6535(00)00284-8.

(27) Braune, B. M.; Simon, M. *Environ. Sci. Technol.* **2003**, *37* (14), 3071. doi:10.1021/es021082p.

(28) Kunisue, T.; Minh, T. B.; Fukuda, K.; Watanabe, M.; Tanabe, S.; Titenko, A. M. *Environ. Sci. Technol.* **2002**, *36* (7), 1396. doi:10.1021/es011051e.

(29) Champoux, L.; Rodrigue, J.; Desgranges, J.-L.; Trudeau, S.; Hontela, A.; Boily, M.; Spear, P. *Environ. Monit. Assess.* **2002**, *79* (2), 193. doi:10.1023/A:1020289425542.

(30) Papp, Z.; Bortolotti, G. R.; Sebastian, M.; Smits, J. E. G. *Arch. Environ. Contam. Toxicol.* **2007**, *52* (2), 257. doi:10.1007/s00244-006-0037-z.

(31) Haskins, S. D.; Kelly, D. G.; Weir, R. D. *Anal. Chim. Acta* **2010**, *677* (1), 19. doi:10.1016/j.aca.2009.12.036.

(32) Frings, C. S.; Fendley, T. W.; Dunn, R. T.; Queen, C. A. *Clin. Chem.* **1972**, *18*, 673.

(33) *Standard Reference Material 1589a;* National Institute of Standards and Technology (NIST) Certificate of Analysis: Gaithersburg, MD, 2007.

(34) Keller, J. M.; Swarthout, R. F.; Carlson, B. K. R.; Yordy, J.; Guichard, A.; Schantz, M. M.; Kucklick, J. R. *Anal. Bioanal. Chem.* **2009**, *393* (2), 747. doi:10.1007/s00216-008-2453-6.

(35) Pascalon-Pekelniczky, A. *Vet. Res.* **1998**, *29*, 197.

(36) Rivetz, B.; Bogin, E.; Weisman, Y.; Avidar, J.; Hadani, A. *Avian Pathol.* **1977**, *6* (4), 343. doi:10.1080/03079457708418244.

(37) Lizenko, M. V.; Regerand, T. I.; Bakhirev, A. M.; Lizenko, E. I. *J. Evol. Biochem. Physiol.* **2008**, *44* (5), 581. doi:10.1134/S0022093008050071.

(38) Bernert, J. T.; Turner, W. E.; Patterson, D. G., Jr.; Needham, L. L. *Chemosphere* **2007**, *68* (5), 824. doi:10.1016/j.chemosphere.2007.02.043.

(39) Popp, P.; Keil, P.; Möder, M.; Paschke, A.; Thuss, U. *J. Chromatogr. A* **1997**, *774* (1–2), 203. doi:10.1016/S0021-9673(97)00337-3.

(40) Björklund, E.; von Holst, C.; Anklam, E. *Trends Analyt. Chem.* **2002**, *21* (1), 40. doi:10.1016/S0165-9936(01)00120-0.

(41) Ramos, J. J.; Gonzalez, M. J.; Ramos, L. *J. Sep. Sci.* **2004**, *27* (7–8), 595. doi:10.1002/jssc.200301648.

(42) Gómara, B.; Ramos, L.; Gonzalez, M. J. *J. Chromatogr. B Analyt. Technol. Biomed. Life Sci.* **2002**, *766* (2), 279. doi:10.1016/S0378-4347(01)00508-4.

(43) Ramos, J. J.; Gomara, B.; Fernandez, M. A.; Gonzalez, M. J. *J. Chromatogr. A* **2007**, *1152* (1–2), 124. doi:10.1016/j.chroma.2006.12.050.

(44) Ramos, J. J.; Dietz, C.; Gonzalez, M. J.; Ramos, L. *J. Chromatogr. A* **2007**, *1152* (1–2), 254. doi:10.1016/j.chroma.2006.11.097.

(45) García, I.; Ignacio, M.; Mouteira, A.; Cobas, J.; Carro, N. *Anal. Bioanal. Chem.* **2008**, *390* (2), 729. doi:10.1007/s00216-007-1680-6.

(46) Hubaux, A.; Vos, G. *Anal. Chem.* **1970**, *42* (8), 849. doi:10.1021/ac60290a013.

(47) Currie, L. *Anal. Chem.* **1968**, *40* (3), 586. doi:10.1021/ac60259a007.

(48) ACS Committee on Environmental Improvement. *Anal. Chem.* **1980**, *52* (14), 2242. doi:10.1021/ac50064a004.

(49) Keith, L. H.; Crummett, W.; Deegan, J., Jr.; Libby, R. A.; Taylor, J. K.; Wentler, G. *Anal. Chem.* **1983**, *55* (14), 2210. doi:10.1021/ac00264a003.

(50) *General Requirements for the Competence of Testing and Calibration Laboratories;* ISO/IEC 17025; 2005.

(51) Pauwels, A.; Wells, D. A.; Covaci, A.; Schepens, P. J. C. *J. Chromatogr. B Analyt. Technol. Biomed. Life Sci.* **1999**, *723* (1–2), 117. doi:10.1016/S0378-4347(98)00493-9.

Efficient process for the conversion of xylose to furfural with acidic ionic liquid

Furong Tao, Huanling Song, and Lingjun Chou

Abstract: An efficient and simple process for the dehydration of xylose into furfural was studied, which was catalyzed by 1-(4-sulfonic acid)butyl-3-methylimidazolium hydrogen sulfate (IL-1) under mild conditions. A xylose conversion of 95.3% with a furfural yield of 91.45% was achieved in a 25 min reaction time at 150 °C; the xylose conversion and furfural yield greatly depended on the operation conditions, such as reaction time and temperature. IL-1 could be recycled and exhibited constant activity for five successive trials. This system was an important improvement, relative to the reactions using mineral acids at high temperatures, for further development on a pilot scale.

Key words: xylose, dehydrate, furfural, ionic liquids.

Résumé : On a étudié une méthode simple et efficace de déshydratation du xylose en furfural qui est catalysée par le sulfate acide de l'acide 1-(4-sulfonique)butyl-3-méthylimidazolium (IL-1) dans des conditions douces. Avec un temps de réaction de 25 min à une température de 150 °C, on a obtenu un degré de conversion de 95,3 % du xylose en furfural et un rendement en furfural de 91,45 %; la conversion du xylose et le rendement en furfural dépendent fortement des conditions de la réaction, particulièrement du temps de réaction et de la température. Le IL-1 peut être recyclé et il présente encore une activité constante après cinq essais successifs. Dans l'optique d'un développement d'un système à l'échelle pilote, ce système correspond à une amélioration importante par rapport aux réactions faisant appel à des acides minéraux et à des températures plus élevées.

Mots-clés : xylose, déshydratation, furfural, liquides ioniques.

[Traduit par la Rédaction]

Can. J. Chem. Downloaded from www.nrcresearchpress.com by 80.58.250.72 on 09/16/12
For personal use only.

Introduction

Diminishing fossil fuel reserves and growing concerns about global warming indicate that sustainable sources of energy are needed in the near future.[1–5] The development of the chemistry of furanic compounds from carbohydrates for the preparation of nonpetroleum polymeric materials was recently updated.[6–13] Within this framework, furfural is one of the key compounds that is produced on an industrial scale, and improving the chemical technology for its production still remains of great interest.

At present, furfural is usually obtained through dehydration of pentoses, particularly xylose or hemicelluloses, at high temperature (200–250 °C) or in the presence of mineral acids as catalysts.[14] Under these conditions, the selectivity of furfural does not exceed 70%. Sako et al.[15] reported that in the case of continuous extraction with supercritical CO_2, the yield of furfural reached 80% in the hydrolysis of xylose. Moreau et al.[16] demonstrated that the selectivity of furfural was up to 90% over microporous solid acid catalysts at 170 °C from xylose. Recently, Zhang and Zhao[17] studied microwave-assisted conversion of lignocellulosic biomass into furans in ionic liquids; the yield of furfural was about 30%, and it was difficult to separate furfural from the reaction system.

In this work, we developed a simple and efficient catalytic process for the conversion of xylose into furfural, using water as a pertinent solvent, methylisobutylketone (MIBK) as a phase modifier,[18] and the acidic ionic liquid, 1-(4-sulfonic acid)butyl-3-methylimidazolium hydrogen sulfate (IL-1), was used as catalyst. With the given catalytic process and with xylose as the starting material, a furfural yield of 91.4% could be achieved at 150 °C for a reaction time of 25 min. The IL-1 could be recycled, and the catalyst exhibited constant activity over five cycles of evaluation.

Experimental

Materials

D-(+)-Xylose (98%), 1-methyl imidazole (CP, >99%), and 1,4-butanesultone (>99%) were purchased from Alfa Aesar and used without further purification. 4-Methyl-2-pentanone (AR, >90%), furfural (CP, >90%), and acetonitrile (HPLC) were purchased from Tianjin Chemical Reagent Company

Received 28 May 2010. Accepted 25 August 2010. Published on the NRC Research Press Web site at canjchem.nrc.ca on 23 December 2010.

F. Tao. State Key Laboratory for Oxo Synthesis and Selective Oxidation, Lanzhou Institute of Chemical Physics, Chinese Academy of Sciences, Lanzhou 730000, P. R. China; Graduate School of Chinese Academy of Sciences, Beijing 100049, P. R. China.
H. Song and L. Chou.[1] State Key Laboratory for Oxo Synthesis and Selective Oxidation, Lanzhou Institute of Chemical Physics, Chinese Academy of Sciences, Lanzhou 730000, P. R. China.

[1]Corresponding author (e-mail: ljchou@licp.cas.cn).

Can. J. Chem. Downloaded from www.nrcresearchpress.com by 80.58.250.72 on 09/16/12
For personal use only.

(Tianjin, China). All other reagents and solvents were reagent grade and were used as received.

Preparation of IL-1

1-Methyl imidazole (16.4 g) and 1,4-butanesultone (27.28 g) were mixed in a flask (250 mL), stirred for 17 h at 42–45 °C, and a white solid was received. Then the white solid was ground, washed repeatedly with a small portion of ether, filtrated, and vacuumized for 4 h. Equimolar white solid was added to H_2SO_4 (98%), and the mixture was stirred at 80 °C for 6 h. The obtained viscous liquid was washed with ether three times and dried in vacuum to form the ionic liquid IL-1 (1-(4-sulfonic acid)butyl-3-methylimidazolium hydrogen sulfate). ^{1}H NMR (400 MHz, D_2O) δ: 1.53 (m, 2H), 1.80 (m, 2H), 2.72 (t, 2H), 3.67 (s, 3H), 4.02 (t, 2H), 7.24 (d, 2H), 8.47 (s, 1H). ESI-MS *m*/*z*: (+)218.6, (–)96.3.

General procedure for the conversion of xylose to furfural

Experiments were carried out in a stainless steel autoclave with a glass liner tube (100 mL); the reactor was loaded with 1.0 g of xylose, 0.5 g of catalyst, 1.5 mL of H_2O, and 8 mL of MIBK. The reaction mixture was heated by an electrical heating jacket to 150 °C for 25 min, and then the reactor was removed and quickly quenched in a cool water bath. After filtration, extraction, and separation, the organic and aqueous phases were collected to characterize the products. For the recycling of IL-1, furfural was extracted from the water phase five times with 8 mL of ethyl acetate. After extraction, the aqueous phase was heated at 60 °C for 24 h in a vacuum oven to remove water and residual ethyl acetate. The IL-1 was then used directly for the next run by adding xylose and solvents. All results were replicated at least three times.

Analyses

The xylose concentration in the products was analyzed by the dinitrosalicylic acid (DNS) method.[19] Analysis of furfural was performed by HPLC on an Waters Alliance 2695 series equipped with a Waters 2996 PDA detector and an intersil ODS-EP C18 reversed-phase column (250 mm × 4.6 mm, 5 μm). During this process, the column temperature remained constant at 30 °C, and the mobile phase applied was water–acetonitrile (15:85, *v*/*v*) at a flow rate of 0.5 mL/min with UV detection at 280 nm.

Results and discussion

Xylose conversion with various catalysts

To obtain efficient acidic catalysts for the hydrolysis of xylose, the catalytic activities of different catalysts were tested. As shown in Fig. 1, the present method was effective for various acidic catalysts, which included mineral acids (HCl, H_2SO_4), Lewis acids ($AlCl_3$, $SnCl_2$), heteropolyacid ($H_3PW_{12}O_{40}$), and acidic ionic liquids (IL-1, $C_4mimH_2PO_4$). It can be seen that $H_3PW_{12}O_{40}$ exhibited weaker catalytic activity than others under the same experimental conditions, whereas HCl and $C_4mimH_2PO_4$ had obvious activity. On the other hand, IL-1, $SnCl_2$, and H_2SO_4 showed very high catalytic activity for the conversion of xylose to furfural. Under the reaction conditions, IL-1 gave a 95.3% of xylose conversion and 91.4% of furfural yield at 150 °C for 25 min. Since the results were most favorable for IL-1, this catalyst was chosen to be studied in detail.

Also, compared with the results that other authors have achieved with ionic liquids for xylose conversion to furfural, our work showed that the efficiency and simplicity of xylose dehydration mainly depended on the reaction media and catalyst employed. It has been reported that there was an obvious relationship between activity and catalyst acidity in the reaction, and that high catalyst acidity leads to high reaction activity.[9] So we considered that the higher acidity of IL-1 over that of other catalysts, such as $AlCl_3$ and

Fig. 1. Conversion of xylose to furfural in the presence of different catalysts (xylose = 1.0 g, catalyst = 0.5 g, H_2O = 1.5 mL, methylisobutylketone (MIBK) = 8 mL, *T* = 150 °C, *t* = 25 min, *P* = 1 atm; 1 atm = 101.325 kPa).

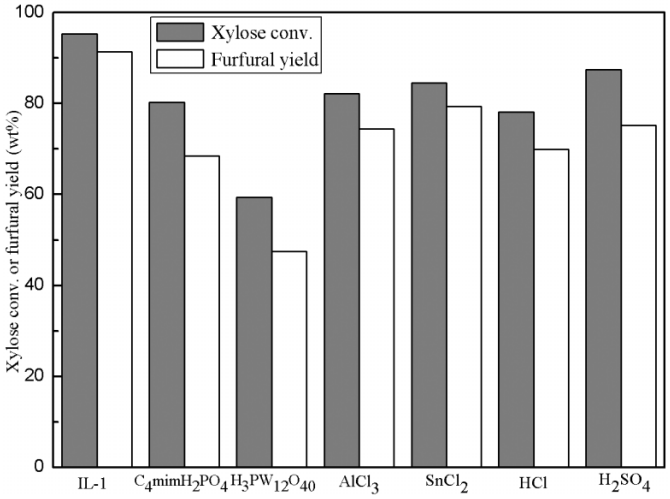

Fig. 2. Effect of catalyst dosage on xylose conversion and furfural yield (xylose = 1.0 g, H_2O = 1.5 mL, methylisobutylketone (MIBK) = 8 mL, *T* = 150 °C, *t* = 25 min, *P* = 1 atm; 1 atm = 101.325 kPa).

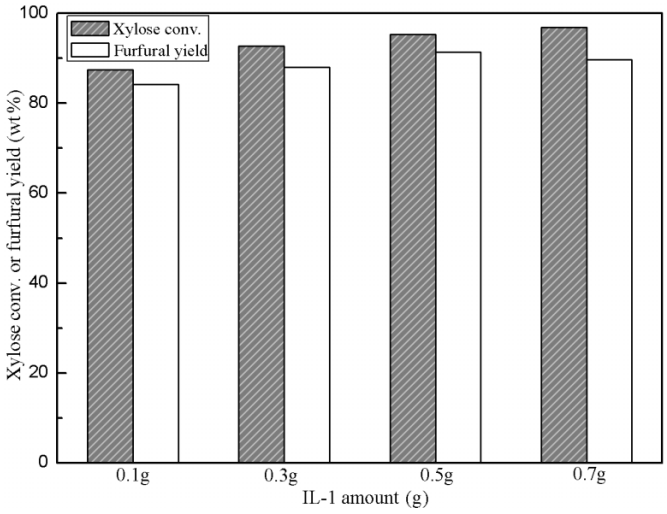

Can. J. Chem. Downloaded from www.nrcresearchpress.com by 80.58.250.72 on 09/16/12
For personal use only.

Table 1. Effect of reaction conditions on the conversion of xylose to furfural (xylose = 1.0 g, H_2O = 1.5 mL, methylisobutylketone (MIBK) = 8 mL, P = 1 atm; 1 atm = 101.325 kPa).

Reaction temperature (°C)	Reaction time (min)	Xylose conversion (wt%)	Furfural yield (wt%)	Furfural selectivity (wt%)
60	20	20.5	13.9	67.8
	40	45.5	31.0	68.1
	60	59.7	43.8	73.4
80	15	27.3	18.4	67.4
	35	52.9	37.5	70.9
	55	67.4	52.7	78.2
100	10	54.1	40.9	75.6
	25	60.7	49.0	81.7
	40	71.3	62.1	87.1
120	5	82.3	74.4	90.4
	15	85.7	79.2	92.4
	25	89.0	83.5	93.8
	35	92.1	87.6	95.1
150	5	88.6	80.3	90.6
	15	92.7	85.1	91.8
	25	95.3	91.4	95.9
	35	97.5	88.7	91.0

$H_3PW_{12}O_{40}$, should probably be responsible for its higher catalytic activity in this work.

Effect of catalyst dosage on xylose conversion and furfural yield

Figure 2 shows the effect of the catalyst dosage on xylose conversion and furfural yield. The amount of IL-1 used was 0.1, 0.3, 0.5, and 0.7 g. In the absence of catalyst, at a 150 °C reaction temperature, no xylose conversion was observed for a reaction time of 25 min (not shown in Fig. 2). In the presence of IL-1, the formation of furfural occurred. When the catalyst dosage increased from 0.3 to 0.5 g, the furfural yield increased from 88% to 92%. However, when the amount of IL-1 was increased from 0.5 to 0.7 g, there was little change in xylose conversion and furfural yield. As the xylose conversion and furfural yield had no further change with further IL-1 dosage over 0.5 g, this implied that there were sufficient catalytic sites available for the substrate xylose (1.0 g) in the system at this experimental condition.

Effect of reaction temperature and time

The effects of reaction temperature and time on xylose conversion are shown in Table 1. It can be seen that the reaction temperature and time had a large effect on both the xylose conversion and furfural yield. When the reaction temperature was 60 °C, with a 40 min reaction time, the xylose conversion was 45.5% and a furfural yield of 31% was obtained. The furfural yield increased from 31% to 83.5% when conditions changed from 60 to 120 °C in a 25 min reaction time. A furfural yield of 91.45% could be obtained for 25 min at a reaction temperature of 150 °C.

As listed in Table 1, by prolonging the reaction time, the reaction proceeded more thoroughly, and the color of the organic phase changed from almost colorless to a deep yellow. The selectivity of furfural was up to 96% when the reaction was performed at 150 °C for 25 min, which was a little higher than the results for 35 min at the same temperature. Indeed, it was reported that further degradation of furfural led to fragmentation reactions of furfural to compounds identified as pyruvaldehyde, formaldehyde, glyceraldehyde, or glycolaldehyde.[14] Other side reactions, such as condensation or resinification of furfural, were easier to perform than fragmentation reactions. We considered that maybe it was these side reactions that led to the decrease of furfural selectivity. Nevertheless, it should be mentioned in the case of xylose dehydration that the formation of heavy compounds is less probable compared with what occurs in fructose hydrolysis to 5-hydroxymethylfurfural (5-HMF), which can react through its hydroxymethyl function, thus yielding higher molecular weight compounds.

Effect of initial xylose concentration

From a practical point of view, if higher concentrations of xylose could be used as feedstock, the technique could be economical. In the acid catalytic dehydration of xylose, the initial xylose concentration has a large effect on furfural yield and selectivity. Different initial concentrations of xylose were studied, which were 0.3, 0.7, 1.0, 1.5, and 2.0 g. It can be seen from Fig. 3 that the rate of xylose conversion had little effect with different initial concentrations of xylose, but the furfural yield reduced gradually with increasing initial xylose concentration. As shown in Fig. 3, the highest furfural yield was 91.4% with 1.0 g of initial xylose loadings, but the yield was reduced to 78% when the amount of xylose was 2.0 g. The loss in furfural yield was thought to be due to the higher xylose concentration, which would increase the probability that reactive compounds such as xylose and furfural would collide with each other or cross polymerize.[20]

Influence of water content on the conversion of xylose

Since IL-1 is a hydrophilic ionic liquid, the influence of water content on xylose dehydration was studied, which is shown in Fig. 4. Previous works already indicated that water had a negative effect on the dehydration of fructose to 5-HMF;[8,21–22] this point was also suitable for the hydrolysis of xylose. As shown in Fig. 4, when the water content in the system was <1.5 g, it had little effect on the xylose conversion and furfural yield. However, as the amount of water increased from 1.5 to 3.5 g, the conversion of xylose and furfural yield decreased significantly, only 86% and 79%, respectively. Zhao et al.[23] also reported on adding water or organic solvents such as glycerol into ionic liquids and proposed that lowering the dielectric constant of the reaction media would result in the loss of catalytic activity.

Recycling of IL-1

In the principles of green engineering,[24] the recycling of a catalyst is essential, so this walso also examined in our work. Experiments were conducted at 150 °C for a reaction time of 25 min. As the catalyst IL-1 was only in an aqueous phase after the reaction, the product furfural was separated from the water phase after reaction by extracting five times with 8 mL ethyl acetate, which is similar to the procedure in the literature.[25] IL-1 and xylose were found to be insoluble in ethyl acetate and furfural was the sole product in the

Can. J. Chem. Downloaded from www.nrcresearchpress.com by 80.58.250.72 on 09/16/12
For personal use only.

Fig. 3. Effect of xylose initial loading on the reaction (IL-1 = 0.5 g, H_2O = 1.5 mL, methylisobutylketone (MIBK) = 8 mL, T = 150 °C, t = 25 min, P = 1 atm; 1 atm = 101.325 kPa).

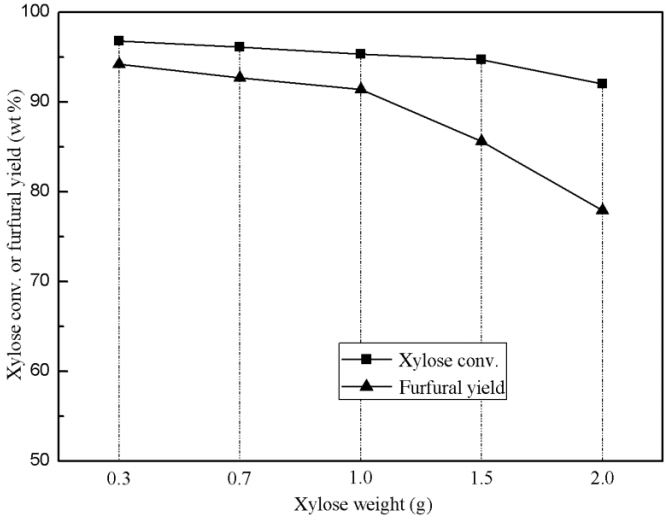

Fig. 4. Influence of water content on xylose conversion (xylose = 1.0 g, methylisobutylketone (MIBK) = 8 mL, T = 150 °C, t = 25 min, P = 1 atm; 1 atm = 101.325 kPa).

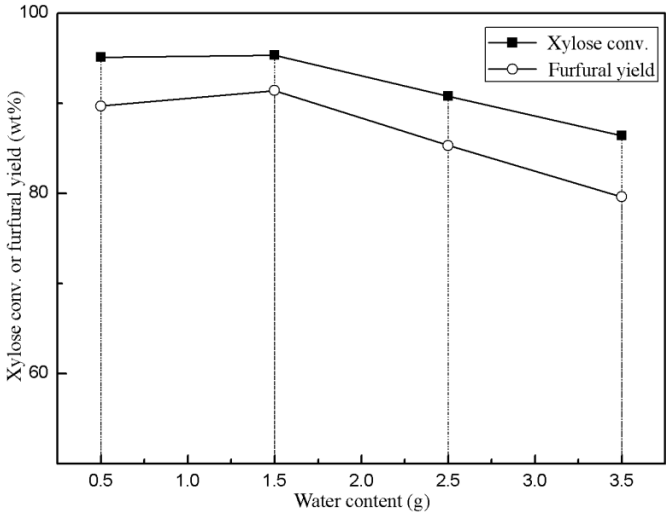

ethyl acetate phase, similar to that noted by Hu et al.[21] After extraction, the aqueous phase was heated at 60 °C for 24 h in a vacuum oven to remove the water and residual ethyl acetate. Such an operation is rather important as three water molecules are produced during the course of the reaction. It was then used directly for the next run by adding an equal amount of xylose and solvents. It can be seen in Fig. 5 that in the recycled reaction, IL-1 gave almost a comparable amount of furfural, which indicated that the catalyst IL-1 retained a very high activity for the conversion of xylose into furfural. The yield of furfural and xylose conversion were not obviously decreased over five runs with the recycled catalyst.

Conclusions

Preparation of furfural through the dehydration reaction of xylose is one of the most important approaches to utilize

Fig. 5. Recycling of IL-1 (xylose = 1.0 g, IL-1 = 0.5 g, H_2O = 1.5 g, methylisobutylketone (MIBK) = 8 mL, T = 150 °C, t = 25 min, P = 1 atm; 1 atm = 101.325 kPa).

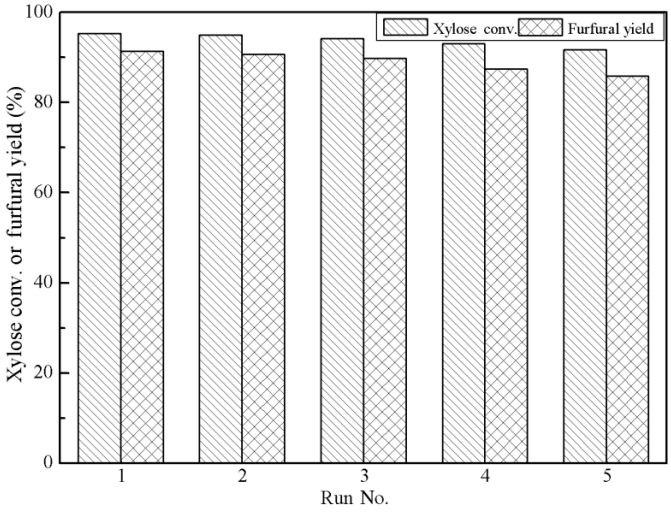

biomass as a promising substitute for petroleum-based chemicals. It was demonstrated herein that this reaction could be smoothly carried out by using the acidic ionic liquid IL-1 as catalyst in a biphase separation system. The process we developed was shown to be efficient, and a xylose conversion of 95.3% with a 91.45% furfural yield was obtained when the reaction was carried out at 150 °C for a reaction time of 25 min. As the reaction time increased to 35 min at 150 °C, the selectivity of furfural decreased from 95.9% to 91%. Initial loadings of up to 2.0 g of xylose in the system led to an obvious decrease in furfural yield, which was about 14%, but the conversion of xylose seldom decreased (~2%). A water content <1.5 g had little effect on the xylose conversion and furfural yield, but a significant decrease was detected both in the xylose conversion and furfural yield when water content was >1.5 g. The catalyst IL-1 could be recycled almost without loss of activity for five times after the product furfural was separated with ethyl acetate. The results strongly suggested that the ionic liquid IL-1 could play an important role in exploring new, efficient, and easy-to-use processes for the preparation of furfural from xylose. Although the process developed efficiently for the conversion of xylose to furfural, further work is required to improve the furfural yield under milder conditions.

Acknowledgement

We gratefully acknowledge the financial support of the State Key Laboratory for Oxo Synthesis and Selective Oxidation of China.

References

(1) Kunkes, E. L.; Simonetti, D. A.; West, R. M.; Serrano-Ruiz, J. C.; Gärtner, C. A.; Dumesic, J. A. *Science* **2008**, *322* (5900), 417. doi:10.1126/science.1159210.
(2) Dodds, D. R.; Gross, R. A. *Science* **2007**, *318* (5854), 1250. doi:10.1126/science.1146356.
(3) Huber, G. W.; Corma, A. *Angew. Chem. Int. Ed.* **2007**, *46* (38), 7184. doi:10.1002/anie.200604504.
(4) Chheda, J. N.; Huber, G. W.; Dumesic, J. A. *Angew. Chem. Int. Ed.* **2007**, *46* (38), 7164. doi:10.1002/anie.200604274.

(5) Huber, G. W.; Iborra, S.; Corma, A. *Chem. Rev.* **2006**, *106* (9), 4044. doi:10.1021/cr068360d.
(6) Román-Leshkov, Y.; Barrett, C. J.; Liu, Z. Y.; Dumesic, J. A. *Nature* **2007**, *447* (7147), 982. doi:10.1038/nature05923.
(7) Ilgen, F.; Ott, D.; Kralisch, D.; Reil, C.; Palmberger, A.; König, B. *Green Chem.* **2009**, *11* (12), 1948. doi:10.1039/b917548m.
(8) Qi, X. H.; Watanabe, M.; Aida, T. M.; Smith, R. L., Jr. *Green Chem.* **2008**, *10* (7), 799. doi:10.1039/b801641k.
(9) Bao, Q. X.; Qiao, K.; Tomida, D.; Yokoyama, C. *Catal. Commun.* **2008**, *9* (6), 1383. doi:10.1016/j.catcom.2007.12.002.
(10) Lansalot-Matras, C.; Moreau, C. *Catal. Commun.* **2003**, *4* (10), 517. doi:10.1016/S1566-7367(03)00133-X.
(11) Qi, X.; Watanabe, M.; Aida, T. M.; Smith, R. L., Jr. *Catal. Commun.* **2009**, *10* (13), 1771. doi:10.1016/j.catcom.2009.05.029.
(12) Yan, H.; Yang, Y.; Tong, D.; Xiang, X.; Hu, C. *Catal. Commun.* **2009**, *10* (11), 1558. doi:10.1016/j.catcom.2009.04.020.
(13) Moreau, C.; Finiels, A.; Vanoye, L. *J. Mol. Catal. Chem.* **2006**, *253* (1–2), 165. doi:10.1016/j.molcata.2006.03.046.
(14) Antal, M. J., Jr.; Leesomboon, T.; Mok, W. S.; Richards, G. N. *Carbohydr. Res.* **1991**, *217* (1), 71. doi:10.1016/0008-6215(91)84118-X.
(15) Sako, T.; Taguchi, T.; Sugeta, T.; Nakazawa, N.; Okubo, T.; Hiaki, T.; Sato, M. *J. Chem. Eng. of Jpn* **1992**, *25* (4), 372. doi:10.1252/jcej.25.372.
(16) Moreau, C.; Durand, R.; Peyron, D.; Duhamet, J.; Rivalier, P. *Ind. Crops Prod.* **1998**, *7* (2–3), 95. doi:10.1016/S0926-6690(97)00037-X.
(17) Zhang, Z.; Zhao, Z. K. *Bioresour. Technol.* **2010**, *101* (3), 1111. doi:10.1016/j.biortech.2009.09.010.
(18) Román-Leshkov, Y.; Chheda, J. N.; Dumesic, J. A. *Science* **2006**, *312* (5782), 1933. doi:10.1126/science.1126337.
(19) Wang, W. L.; Huang, X. S. *Food Sci. (Beijing, China)* **2006**, *4*, 196.
(20) Kuster, B. F. M. *Starch* **1990**, *42* (8), 314. doi:10.1002/star.19900420808.
(21) Hu, S. Q.; Zhang, Z. F.; Zhou, Y. X.; Han, B. X.; Fan, H. L.; Li, W. J.; Song, J. L.; Xie, Y. *Green Chem.* **2008**, *10* (12), 1280. doi:10.1039/b810392e.
(22) Qi, X. H.; Watanabe, M.; Aida, T. M.; Smith, R. L., Jr. *Green Chem.* **2009**, *11* (9), 1327. doi:10.1039/b905975j.
(23) Zhao, H. B.; Holladay, J. E.; Brown, H.; Zhang, Z. C. *Science* **2007**, *316* (5831), 1597. doi:10.1126/science.1141199.
(24) Tang, S. Y.; Bourne, R. A.; Smith, R. L.; Poliakoff, M. *Green Chem.* **2008**, *10* (3), 268. doi:10.1039/b719469m.
(25) Yong, G.; Zhang, Y. G.; Ying, J. Y. *Angew. Chem. Int. Ed.* **2008**, *47* (48), 9345. doi:10.1002/anie.200803207.

Can. J. Chem. Downloaded from www.nrcresearchpress.com by 80.58.250.72 on 09/16/12
For personal use only.

Synthesis of a new chiral auxiliary — Non-cross-linked polystyrene-supported oxazolidine-2-selone

Xiping He, Jia Li, Cuifen Lu, Zuxin Chen, and Guichun Yang

Abstract: A new chiral auxiliary, non-cross-linked polystyrene-supported oxazolidine-2-selone was synthesized using *N*-Boc-L-tyrosine ethyl ester as starting material. The structure of the target product was detected by IR, NMR, elemental analysis, and the spectrum result was consistent with the molecular structure.

Key words: non-cross-linked polystyrene, support, oxazoline-2-selone, chiral auxiliary.

Résumé : Faisant appel à l'ester éthylique de la *N*-Boc-L-tyrosine comme produit de départ, on a réalisé la synthèse d'un nouvel auxiliaire chiral, l'oxazolidine-2-sélone supportée par du polystyrène non réticulé. La structure du produit de synthèse a été confirmée par spectroscopies IR et RMN et par analyse élémentaire et les résultats spectraux sont en accord avec la structure moléculaire.

Mots-clés : polystyrène non réticulé, support, oxazoline-2-sélénone, auxiliaire chiral.

[Traduit par la Rédaction]

Can. J. Chem. Downloaded from www.nrcresearchpress.com by 80.58.250.72 on 09/16/12
For personal use only.

Introduction

Carbon–carbon bond-forming reactions involving asymmetric aldol reactions have emerged as powerful tools in organic synthesis. Chiral oxazolidine-2-selone was found to be an excellent auxiliary in asymmetric aldol reactions.[1–4] However, in most cases, the separation and purification of the chiral auxiliaries were troublesome. To recycle and reuse expensive chiral auxiliaries is a challenge in organic synthesis.

Insoluble polymer supports, such as Merrifield resin and Wang resin provided a simple procedure "filtration" for rapidly achieving the isolation of desired compounds or recovering expensive reagents or catalysts attached onto solid support for recycling.[5,6] But several shortcomings were shown because of nonlinear kinetic behavior, unequal distribution or access to the chemical reaction, and synthetic difficulties in transferring standard organic reactions to the solid phase. Soluble polymer supports have been studied as a way to overcome the problems of insoluble supports. Soluble polymer supports allow expeditious transfer of solution-based synthetic protocols, circumventing the extensive optimization process often required in heterogeneous reactions.[7,8] After the addition of an appropriate poor solvent, the polymer support can be precipitated and filtered, allowing its expeditious recovery.

Non-cross-linked polystyrene (NCPS) and functionalized NCPS show a more restrictive solubility profile because of their high stereoregular configuration of phenyl rings along the polymer main chain and the resulting tendency toward crystallization.[9,10] We theorized that this solubility versus recovery relationship of crystalline polymer — a well-known phenomenon in polymer chemistry — could lead to a better recovery yield of the polymer support when precipitated with a poor solvent.

Our group has undertaken a research program to develop novel chiral auxiliaries using NCPS as support.[11,12] In this article, we report the synthesis of a new NCPS-supported oxazolidine-2-selone chiral auxiliary from *N*-Boc-L-tyrosine ethyl ester (Scheme 1). Reagents and conditions: (a) K_2CO_3 (2.0 equiv), BnBr (1.2 equiv), DMF (dimethylformamide), 40 °C, 24 h; (b) $LiAlH_4$ (1.2 equiv), THF, 0 °C ~ RT (RT, room temperature), 18 h; (c) acetyl chloride (1.1 equiv), EtOAc–MeOH (1:2, *v*/*v*), 0 °C ~ RT, 24 h ; (d) DMF–DMA (dimethyl acetal) (1.1 equiv), TsOH (catalytic amount), N_2, toluene, reflux, 48 h; (e) 20% $Pd(OH)_2$ (catalytic amount), THF–MeOH (1:1, *v*/*v*), RT, 6 h; (f) K_2CO_3 (3.5 equiv), functionalized NCPS (**1**, 1.05 equiv), 40 °C, 24 h; and (g) Methyl lithium (1.2 equiv), hexamethyl disilylamine (1.15 equiv), Se (1.0 equiv), –78 °C ~ RT, 2 h.

Results and discussion

As shown in Scheme 1, NCPS-supported oxazolidine-2-selone was synthesized using *N*-Boc-L-tyrosine ethyl ester as the starting material. A benzylation reaction is used as the most common way to protect the hydroxy, therefore, *N*-Boc-L-tyrosine ethyl ester was first treated with BnBr to

Received 24 July 2010. Accepted 17 October 2010. Published on the NRC Research Press Web site at canjchem.nrc.ca on 5 January 2011.

X. He, J. Li, C. Lu,[1] Z. Chen, and G. Yang. Ministry-of-Education Key Laboratory for the Synthesis and Application of Organic Functional Molecules, Faculty of Chemistry and Chemical Engineering, Hubei University, Wuhan 430062, P.R. China.

[1]Corresponding author (e-mail: lucuifen0511@yahoo.com.cn).

Scheme 1. Synthesis of non-cross-linked polystyrene (NCPS)-supported oxazolidine-2-selenone **8**.

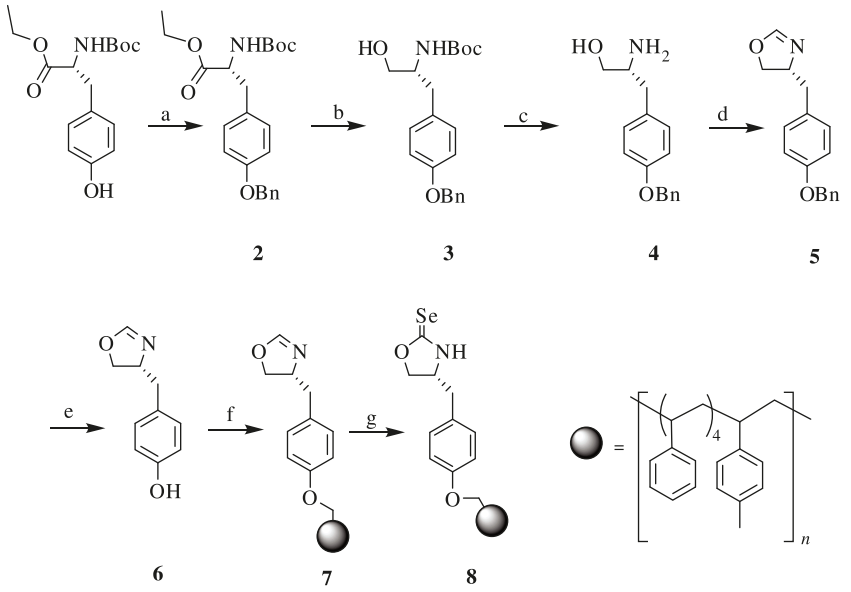

afford the benzylated product **2** in 80% yield. Then compound **2** was reduced by $LiAlH_4$ to obtain the alcohol **3** in 84% yield. Removal of the Boc group from **3** using acetyl chloride under MeOH–EtOAc obtained the amino alcohol **4** in 87% yield. Treating **4** with DMF–DMA produced the oxazoline **5** through a ring-closing reaction.[7] Removal of the benzyl group of **5** was carried out by 20% $Pd(OH)_2$ under H_2 to provide the chiral oxazoline **6** in 84% yield. Then **6** was linked to **1** to afford NCPS-supported oxazoline **7**. Compound **1** (Fig. 1) was prepared according to ref. 9, by copolymerizing 4-vinylbenzyl chloride and styrene in a ratio of 1:4. Finally, **7** was treated with selenium in the presence of lithium amide to obtain NCPS-supported oxazolidine-2-selone **8** in 75% yield. The structure of the chiral auxiliary **8** was detected by IR, NMR, elemental analysis, and the spectrum result was consistent with the molecular structure. This chiral auxiliary is soluble in typical organic solvents, such as $CHCl_3$, CH_2Cl_2, EtOAc, THF, DMF, and benzene, and insoluble in MeOH, EtOH, and H_2O, and this solubility versus recovery relationship of the crystalline polymer could lead to better recovery yield of the chiral auxiliary.

Conclusions

In conclusion, we have developed a new NCPS-supported oxazolidine-2-selone chiral auxiliary. This chiral auxiliary has potential value in asymmetric reactions such as high stereoselectivity and better recovery yield. Further application of this NCPS-supported oxazolidine-2-selone chiral auxiliary in aldol reactions is currently underway in our laboratory.

Experimental

General

All solvents were obtained from commercial sources and dried or purified by standard procedures before use. Melting points were measured on a WRS-1A digital melting point apparatus and uncorrected; optical rotations were measured

Fig. 1. Functionalized non-cross-linked polystyrene (NCPS).

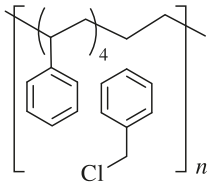

using a sodium D line on a WZZ-2B automatic polarimeter; IR spectra were recorded on a IR-spectrum one (PerkinElmer) spectrometer. NMR spectra were recorded on a Varian Unity INOVA 600 spectrometer in $CDCl_3$ using TMS as the internal standard; elemental analyses were done on a VarioEL III (Elementar, Germany) analyzer.

Synthesis of *N*-Boc-*O*-benzyl-L-tyrosine ethyl ester (2)

To a solution of *N*-Boc-L-tyrosine ethyl ester (8.64 g, 27.95 mmol) in dry DMF (50 mL) were added benzyl bromide (3.98 mL, 33.54 mmol), anhyd K_2CO_3 (7.71 g, 55.90 mmol), and 18-crown-6 (catalytic amount). Then the resulting mixture was stirred at 40 °C for 24 h. After evaporation of the solvent, the residue was dissolved in ethyl acetate (100 mL) and washed with brine (3 × 10 mL). The organic phase was dried over $MgSO_4$, filtered, and concentrated to afford a pale yellow solid. Recrystallization from EtOAc and petroleum ether (PE; 1:5, *v*/*v*) gave **2** (8.9 g, 80%); mp 63.2–63.7 °C. $[\alpha_D^{25}]$ = +16.2 (*c* 0.05, THF). IR (NaCl, cm^{-1}): 3371, 1716, 1611, 1584, 1511. ^1H NMR ($CDCl_3$, 600 MHz) δ: 7.43–7.27 (m, 5H), 7.05 (d, J = 7.8 Hz, 2H), 6.90 (d, J = 8.4 Hz, 2H), 5.04 (s, 2H), 4.96 (t, J = 7.8 Hz, 1H), 4.51 (s, 1H), 4.15 (dd, J_1 = 7.2 Hz, J_2 = 13.8 Hz, 2H), 3.03 (dd, J_1 = 6.0 Hz, J_2 = 11.4 Hz, 2H), 1.43 (s, 9H), 1.23 (t, J = 6.9 Hz, 3H). ^{13}C NMR ($CDCl_3$, 150 MHz) δ: 172.1, 158.3, 155.6, 137.7, 131.0, 128.8, 128.6, 128.2, 127.7, 115.2, 80.5, 70.6, 61.3, 54.5, 37.4, 28.3, 14.3.

Can. J. Chem. Downloaded from www.nrcresearchpress.com by 80.58.250.72 on 09/16/12
For personal use only.

Can. J. Chem. Downloaded from www.nrcresearchpress.com by 80.58.250.72 on 09/16/12
For personal use only.

Synthesis of *N*-Boc-*O*-benzyl-L-tyrosinol (3)

To a solution of compound **2** (8.65 g, 21.65 mmol) in anhyd THF (50 mL), $LiAlH_4$ (0.96 g, 25.98 mmol) in THF (20 mL) was added dropwise at 0 °C. The mixture was allowed to stir at RT for 18 h before acidification to pH 6∼7 with 1 N HCl, and the insoluble solid was filtered. After evaporation of the solvent, the residue was dissolved in ethyl acetate (100 mL), washed with brine (3 × 10 mL). The organic phase was dried over $MgSO_4$, filtered, and concentrated to afford a white solid. Recrystallization from EtOAc and PE (1:3, *v*/*v*) gave **3** (6.2 g, 84%); mp 105.0–105.6 °C. $[\alpha_D^{25}]$ = –17.5 (*c* 0.02, THF). IR (NaCl, cm^{-1}): 3360, 2923, 1816, 1611, 1524, 694. ^1H NMR ($CDCl_3$, 600 MHz) δ: 7.43–7.26 (m, 5H), 7.12 (d, *J* = 8.4 Hz, 2H), 6.91 (d, *J* = 8.4 Hz, 2H), 6.05 (s, 2H), 5.03 (s, 2H), 3.81 (m, 1H), 3.63 (m, 1H), 3.58 (m, 1H), 2.77 (d, *J* = 7.2 Hz, 2H), 1.42 (s, 9H). ^{13}C NMR ($CDCl_3$, 150 MHz) δ: 158.6, 156.5, 137.3, 130.1, 129.4, 128.5, 127.8, 115.6, 80.3, 70.5, 64.7, 60.3, 54.1, 37.5, 29.3.

Synthesis of *O*-benzyl-L-tyrosinol (4)

To a solution of compound **3** (5.6 g, 15.68 mmol) in mixed solvents of EtOAc (30 mL) and MeOH (60 mL) was added acetyl chloride (3.91 mL, 31.36 mmol) at 0 °C. After 30 min, the reaction mixture was stirred at RT for 24 h. NaOH (1.5 N) was added to counteract produced acids, then most of the solvent was removed under reduced pressure. The residue was dissolved in CH_2Cl_2 (100 mL) and washed with brine (3 × 10 mL). The organic phase was dried over $MgSO_4$, filtered, and concentrated to afford a yellow solid. The crude product was further purified by column chromatography (MeOH–CH_2Cl_2, 1:20, *v*/*v*) to give **4** (3.5 g, 87%); mp 174.4–174.8 °C. $[\alpha_D^{25}]$ = –12.0 (*c* 0.04, CH_3OH). IR (NaCl, cm^{-1}): 3704, 3360, 3032, 1609, 1580, 748. ^1H NMR ($CDCl_3$, 600 MHz) δ: 7.45–7.35 (m, 5H), 7.19 (d, *J* = 8.4 Hz, 2H), 7.01 (d, *J* = 9.0 Hz, 2H), 5.13 (s, 2H), 3.74–3.55 (m, 2H), 3.47 (m, 1H), 2.89 (d, *J* = 6.6 Hz, 1H), 2.77 (t, *J* = 6.9 Hz, 1H), 1.85 (s, 3H). ^{13}C NMR ($CDCl_3$, 150 MHz) δ: 157.3, 137.5, 131.1, 130.6(2C), 129.7, 128.3, 127.8, 115.6, 70.1, 66.2, 54.7, 40.1.

Synthesis of (4*S*)-4-(4′-benzyloxy)benzyl-4,5-dihydrooxazoline (5)

DMF–DMA (1.16 mL, 8.79 mmol) and TsOH (0.06 g) under N_2 were added to a solution of **4** (2.06 g, 8.0 mmol) in toluene (85 mL). The solution was refluxed for 48 h in a flask equipped with a Soxhlet extraction device containing 20 g of 4 Å molecular sieves under N_2. The reaction mixture was washed with 10% $NaHCO_3$ (30 mL) and brine (30 mL) and dried over Na_2SO_4. The residue was purified by flash column chromatography (EtOAc–PE–Et_3N, 1:4:1, *v*/*v*) to give **5** (1.71 g, 80%) as a white solid; mp 117.9–118.3 °C. IR (NaCl, cm^{-1}): 3035, 1630, 1513, 1114. ^1H NMR ($CDCl_3$, 600 MHz) δ: 8.10 (s, 1H), 7.30–7.42 (5H, m), 7.09 (d, *J* = 9.0 Hz, 2H), 6.91 (d, *J* = 9.0 Hz, 2H), 5.01 (s, 2H), 4.18 (t, *J* = 3.0 Hz, 1H), 3.70 (d, *J* = 7.2 Hz, 1H), 3.58 (dd, J_1 = 3.6 Hz, J_2 = 10.2 Hz, 1H), 2.82 (m, 2H). ^{13}C NMR ($CDCl_3$, 150 MHz) δ: 161.8, 157.9, 137.2, 130.6, 130.4, 129.7, 128.8, 127.7, 115.3, 70.2, 63.8, 52.2, 36.2.

Synthesis of (4*S*)-4-(4′-*p*-hydroxy)benzyl-4,5-dihydrooxazoline (6)

Compound **5** (1.34 g, 5.0 mmol) was dissolved in THF (25 mL) and MeOH (25 mL), and 20% $Pd(OH)_2$ (0.27 g) was added, and the mixture was then stirred under H_2 at room temperature for 6 h. After filtration through Celite, washing with methanol and THF, and evaporation of the solvents, the residue was purified by flash column chromatography (EtOAc–PE–Et_3N, 1:2:1, *v*/*v*) to give **6** (0.74 g, 84%) as a white solid; mp 60.5–60.8 °C. $[\alpha_D^{20}]$ = –68.6 (*c* 0.04, MeOH). IR (NaCl, cm^{-1}): 3197, 1628, 1515, 1380, 1244. ^1H NMR ($CDCl_3$, 600 MHz) δ: 8.10 (s, 1H), 7.12 (d, *J* = 9.0 Hz, 2H), 6.89 (d, *J* = 9.0 Hz, 2H), 5.40 (s, 1H), 4.24 (t, *J* = 4.2 Hz, 1H), 3.84 (d, *J* = 8.4 Hz, 1H), 3.52 (dd, J_1 = 4.8 Hz, J_2 = 12.4 Hz, 1H), 2.64 (m, 2H). ^{13}C NMR ($CDCl_3$, 150 MHz) δ: 160.4, 157.9, 130.6, 130.4, 115.3, 76.2, 70.2, 39.8.

Synthesis of NCPS-supported (4*S*)-4-substituted 4,5-dihydrooxazoline (7)

To a solution of compound **6** (0.66 g, 3.71 mmol) in DMF (30 mL) were added the functionalized NCPS **1** (2.20 g), anhyd K_2CO_3 (1.80 g, 13.0 mmol), and 18-crown-6 (catalytic amount). The resulting mixture was stirred at 40 °C for 24 h. Then most of the solvent was removed under reduced pressure. The viscous solution was dropped into cold EtOH (100 mL), and the precipitated solid was filtered and dried to afford polymer **7** (2.43 g, 85%). IR (NaCl, cm^{-1}): 3302, 1629, 1237, 699. ^{13}C NMR ($CDCl_3$, 150 MHz) δ: 158.0, 155.0, 145.5, 130.4, 130.1, 128.2, 127.8, 125.9, 115.1, 70.8, 70.2, 66.9, 52.0, 41.0, 40.5. Elementary analysis for polymer **7**: C, 86.31%; H, 7.21%; N, 1.89%.

Synthesis of NCPS-supported (4*S*)-4-benzyloxyl oxazolidine-2-selenone (8)

Methyllithium (2.26 mL, 3.17 mmol) and hexamethyl disilylamine (0.63 mL, 3.04 mmol) were added to dry THF (15 mL) under N_2 at 0 °C. The solution was stirred for 10 min and then cooled to –78 °C. Compound **7** (1.50 g, 2.64 mmol) in dry THF (30 mL) was added dropwise to the solution and the mixture was stirred for 30 min at –78 °C. Se (0.24 g, 2.68 mmol) was added in batches, stirred for an additional 2 h at RT, and then the pH was adjusted to 4–5 by aq saturated citric acid. After filtrating through Celite, the filtrate was concentrated under reduced pressure. The viscous solution was dropped into cold EtOH (50 mL), and the precipitated solid was filtered and dried to afford polymer **8** (1.30 g, 75%). IR (NaCl, cm^{-1}): 3340, 1510, 1261, 698. ^{13}C NMR ($CDCl_3$, 150 MHz) δ: 188.2, 158.1, 137.6, 136.4, 136.3, 130.1, 127.7, 127.1, 126.5, 126.3, 115.7, 114.2, 75.5, 68.8, 56.9, 52.2, 39.2. ^{77}Se NMR ($CDCl_3$, 150 MHz) δ: –319.80 (relative to (*R*)-4-benzyloxazolidine-2-selenone at –328.70). Elementary analysis for polymer **8**: C, 77.71%; H, 6.58%; N, 1.69%.

Acknowledgments

We gratefully acknowledge the National Natural Sciences Foundation of China (grant Nos. 20772026 and 20372019).

References

(1) Li, Z. Zh.; Wu, R. L.; Michalczyk, R.; Dunlap, R. B.; Odom, J. D.; Silks, L. A. III. *J. Am. Chem. Soc.* **2000**, *122*, 386.

(2) Silks, L. A., III; Kimball, D.; Hatch, D.; Ollivault-Shiflett, M.; Michalczyk, R.; Moody, E. *Synth. Commun.* **2009**, *39* (4) 641. doi:10.1080/00397910802419706.

(3) Silks, L. A. P.; Wu, R.; Dunlap, R. B.; Odom, J. *Phosphorus Sulfur Silicon Relat. Elem.* **1998**, *136* (1), 209. doi:10.1080/10426509808545945.

(4) Wu, R. L.; Odom, J. D.; Dunlap, R. B.; Dunlap, R. B. *Tetrahedron Asymmetry* **1999**, *10* (8), 1465. doi:10.1016/S0957-4166(99)00140-8.

(5) Kotake, T.; Rajesh, S.; Hayashi, Y.; Mukai, Y.; Ueda, M.; Kimura, T.; Kiso, Y. *Tetrahedron Lett.* **2004**, *45* (18), 3651. doi:10.1016/j.tetlet.2004.03.043.

(6) Yamashita, M.; Lee, S. H.; Koch, G.; Zimmermann, J.; Clapham, B.; Janda, K. D. *Tetrahedron Lett.* **2005**, *46* (33), 5495. doi:10.1016/j.tetlet.2005.06.061.

(7) For an excellent review see: Chung, C. W. Y.; Toy, P. H. *Tetrahedron: Asymmetry* **2004**, *15* (3), 387. doi:10.1016/j.tetasy.2003.12.015.

(8) (a) Desimoni, G.; Faita, G.; Galbiati, A.; Pasini, D.; Quadrelli, P.; Rancati, F. *Tetrahedron Asymmetry* **2002**, *13* (4), 333. doi:10.1016/S0957-4166(02)00117-9.; (b) Giffels, G.; Beliczey, J.; Felder, M.; Kragl, U. *Tetrahedron: Asymmetry.* **1998**, *9* (4), 691. doi:10.1016/S0957-4166(98)00011-1.; (c) Enholm, E. J.; Gallagher, M. E.; Moran, K. M.; Lombardi, J. S.; Schulte, J. P., II. *Org. Lett.* **1999**, *1* (5), 689. doi:10.1021/ol990613k.

(9) Narita, M.; Itsuno, S.; Hirata, M.; Kusano, K. *Bull. Chem. Soc. Jpn.* **1978**, *51* (5), 1477. doi:10.1246/bcsj.51.1477.

(10) (a) Malanga, M. *Adv. Mater.* **2000**, *12* (23), 1869. doi:10.1002/1521-4095(200012)12:23<1869::AID-ADMA1869>3.0.CO;2-#.; (b) Su, Z.; Hsu, S. L.; Li, X. *Macromolecules* **1994**, *27* (1), 287. doi:10.1021/ma00079a042.; (c) Dong, J. Y.; Manias, E.; Chung, T. C. *Macromolecules* **2002**, *35* (9), 3439. doi:10.1021/ma012215e.

(11) (a) Lu, C. F.; Li, D. L.; Wang, Q. Y.; Yang, G. C.; Chen, Z. X. *Eur. J. Org. Chem.* **2009**, *2009* (7), 1078. doi:10.1002/ejoc.200800758.; (b) Wan, Y. D.; Lu, C. F.; Nie, G. C.; Chen, Z. X. *J. Chem. Res.* **2007**, *2007*, 84. doi:10.3184/030823407X198212.

(12) (a) Chen, J. N.; Nie, J. Q.; Huang, Y. L.; Chen, Z. X.; Yang, G. C. *J. Chem. Res.* **2006**, *2006*, 696. doi:10.3184/030823406779173370.; (b) Li, J.; Lu, C. F.; Chen, Z. X.; Yang, G. C.; Yang, G. C. *J. Chem. Res.* **2010**, *2010*, 86. doi:10.3184/030823410X12653142350782.

Can. J. Chem. Downloaded from www.nrcresearchpress.com by 80.58.250.72 on 09/16/12
For personal use only.

Electronic structure of *S*-nitrosothiols from sulfur K-edge X-ray absorption spectroscopy

Vlad Martin-Diaconescu, Inna Perepichka, D. Scott Bohle, and Pierre Kennepohl

Abstract: Sulfur K-edge X-ray absorption spectroscopy (S K-edge XAS) was applied to investigate the electronic structure of primary and tertiary *S*-nitrosothiols. Our experimental data, supported by density functional calculations, indicate that changes at C_α affect the *S*-nitroso group through both inductive and direct orbital effects. Furthermore, our data are consistent with a weakening of the S–N bond in tertiary *S*-nitrosothiols as compared to their primary *S*-nitroso analogues. These results support existing computational models and suggest that the reactivity of *S*-nitrosothiols is not dominated by the electronics of the S–N bond.

Key words: *S*-nitrosothiols, X-ray absorption spectroscopy (XAS), *S*-nitroso-*N*-acetylpenicillamine (SNAP), nitrosoglutathione.

Résumé : On a fait appel à la spectroscopie d'absorption des rayons-X près du seuil K du soufre (SAX près du seuil K du soufre) pour étudier la structure électronique de *S*-nitrothiols primaires et tertiaires. Les données expérimentales et les calculs de la fonctionnelle de la densité indiquent que les changements au niveau du C_α affectent le groupe *S*-nitroso par des effets inductifs ainsi que par des effets directs d'orbitales. De plus, les données sont en accord avec un affaiblissement de la liaison S–N dans les *S*-nitrosothiols primaires par rapport à leurs analogues *S*-nitroso primaires. Ces résultats supportent les modèles existants dérivés de calculs théoriques et ils suggèrent que la réactivité des *S*-nitrosothiols n'est pas dominée par les effets électroniques de la liaison S–N.

Mots-clés : *S*-nitrosothiols, spectroscopie d'absorption des rayons X (SAX), *S*-nitroso-*N*-acétylpénicillamine (SNAP), nitrosoglutathion.

[Traduit par la Rédaction]

Introduction

S-Nitrosothiols are important nitric oxide (NO) derivatives with potential therapeutic applications.[1] Nitric oxide has been implicated in various physiological processes, including neurotransmission,[2] induction of smooth muscle relaxation,[3,4] inhibition of platelet aggregation,[5] and modulation of enzyme activity via S-nitrosation.[6] Nitric oxide release from *S*-nitrosothiols is facilitated by heat, light, and catalyzed by metal ions such as Cu^+.[7] However, the factors that control the reactivity of *S*-nitrosothiols have yet to be completely elucidated.

It is generally accepted that primary *S*-nitrosothiols are less stable than their tertiary counterparts. For example, the primary nitrosothiol *S*-nitroso-*N*-acetylcysteine (SNAC) has a very short lifetime,[8,9] whereas tertiary *S*-nitrosothiols such as *S*-nitroso-*N*-acetylpenicillamine (SNAP) and trityl thionitrite (Ph_3CSNO) are inert and isolable.[10] One exception is *S*-nitrosoglutathione (GSNO), which can be readily obtained even though it is a primary *S*-nitrosothiol.[11] The general stability of tertiary versus primary *S*-nitrosothiols has been attributed to steric constraints, which hinder the formation of disulfides, the primary product of *S*-nitrosothiol decomposition.[9] In the case of GSNO, its resistance to Cu^+-mediated decomposition has been attributed to chelation of the metal ions, which might explain the resistance of GSNO to Cu^+ decomposition as compared to SNAP.[12]

To address the reactivity of *S*-nitrosothiols, several theoretical models for S–NO bonding have been proposed. Density functional methods have been used to suggest that the S–N bond is most appropriately described as a single bond;[13] such single bond character seems to be supported by the long S–N bond observed in trityl thionitrite.[14] However, the identification of cis–trans isomers with a measurable rotational barrier about the S–N bond (by ^{15}N NMR) suggests the presence of significant S=N double bond character.[14,15] More recently, valence-bond calculations have supported this idea, implying that significant S=N character is required.[16]

We have used sulfur K-edge X-ray absorption spectroscopy[17,18] (XAS) as a means of probing details of the electronic structure of a series of *S*-nitrosothiols (see Fig. 1); an earlier study provided a preliminary assignment and analysis

Received 2 November 2009. Accepted 24 February 2010. Published on the NRC Research Press Web site at canjchem.nrc.ca on 18 November 2010.

This article is part of a Special Issue dedicated to Professor J. C. Scaiano.

V. Martin-Diaconescu and P. Kennepohl.[1] Department of Chemistry, The University of British Columbia, Vancouver, BC V6T 1Z1.
I. Perepichka and D.S. Bohle. Department of Chemistry, McGill University, Montreal, QC H3A 2K6.

[1]Corresponding author (e-mail: pierre@chem.ubc.ca).

Can. J. Chem. Downloaded from www.nrcresearchpress.com by University of Electronic and Science Techonology of China on 09/18/12
For personal use only.

Can. J. Chem. Downloaded from www.nrcresearchpress.com by University of Electronic and Science Techonology of China on 09/18/12
For personal use only.

Fig. 1. *S*-Nitrosothiols model compounds investigated using sulfur K-edge XAS: *S*-nitrosoglutathione (GSNO), trityl thionitrite (Ph_3CSNO), and *S*-nitroso-*N*-acetylpenicillamine (SNAP).

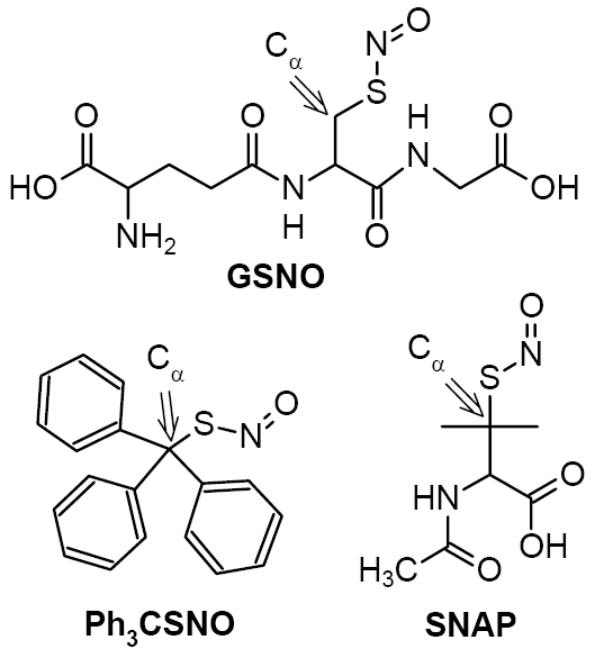

of the electronic structure of GSNO and SNAP XAS.[19] However, we have undertaken a more detailed analysis to more directly evaluate the electronic effects of C_α substitution. We have therefore used a combination of S K-edge XAS and DFT methods to explore the bonding in GSNO, SNAP, and Ph_3CSNO and provide experimental insights into the nature of bonding in these nitrosylated thiols.

Results and discussion

Normalized and energy-calibrated sulfur K-edge XAS spectra of selected *S*-nitrosothiols are shown in Fig. 2. The spectrum of the primary *S*-nitrosothiol (GSNO, Fig. 2A) exhibits three intense low energy features at 2471.4 eV, 2473.4 eV, and 2475.0 eV; these have been previously attributed to the $SN_{\pi^*} \leftarrow S_{1s}$, $SN_{\sigma^*} \leftarrow S_{1s}$, and $SC_{\sigma^*} \leftarrow S_{1s}$, respectively.[19] SNAP, a tertiary alkyl *S*-nitrosothiol, exhibits a similar spectroscopic profile; however, the features are shifted to lower energy (see Fig. 2B): the $SN_{\pi^*} \leftarrow S_{1s}$ shifts only slightly to 2471.2 eV ($\Delta E \approx -0.2$ eV), but the $SN_{\sigma^*} \leftarrow S_{1s}$ (2472.8 eV) and $SC_{\sigma^*} \leftarrow S_{1s}$ (2474.5 eV) transitions are shifted by –0.6 eV and –0.5 eV, respectively. The overall shift to lower energy in tertiary alkyls has been previously attributed to increased electron donation from the alkyl substituents on the proximal carbon (C_α), which would decrease the effective nuclear charge (Z_{eff}) of the sulfur atom and thus increase the energy of the S_{1s} orbital.[19] However, the observed shift in the $SN_{\pi^*} \leftarrow S_{1s}$ transition is quite different from that observed for the $SN_{\sigma^*} \leftarrow S_{1s}$ and $SC_{\sigma^*} \leftarrow S_{1s}$ transitions, which suggests that other factors likely contribute.

The S K-edge XAS spectrum of Ph_3CSNO (Fig. 2C) exhibits even greater spectroscopic differences, with only two major features visible in the spectrum. The feature due to the $SN_{\pi^*} \leftarrow S_{1s}$ transition at 2471.1 eV is well-resolved

Fig. 2. Sulfur K-edge XAS spectra with features assigned according to acceptor orbitals of sulfur 1s bound transitions for (A) *S*-nitrosoglutathione (dashed), (B) *S*-nitroso-*N*-acetylpenicillamine (solid), (C) trityl thionitrite (dotted), and (D) second derivative of XAS spectra.

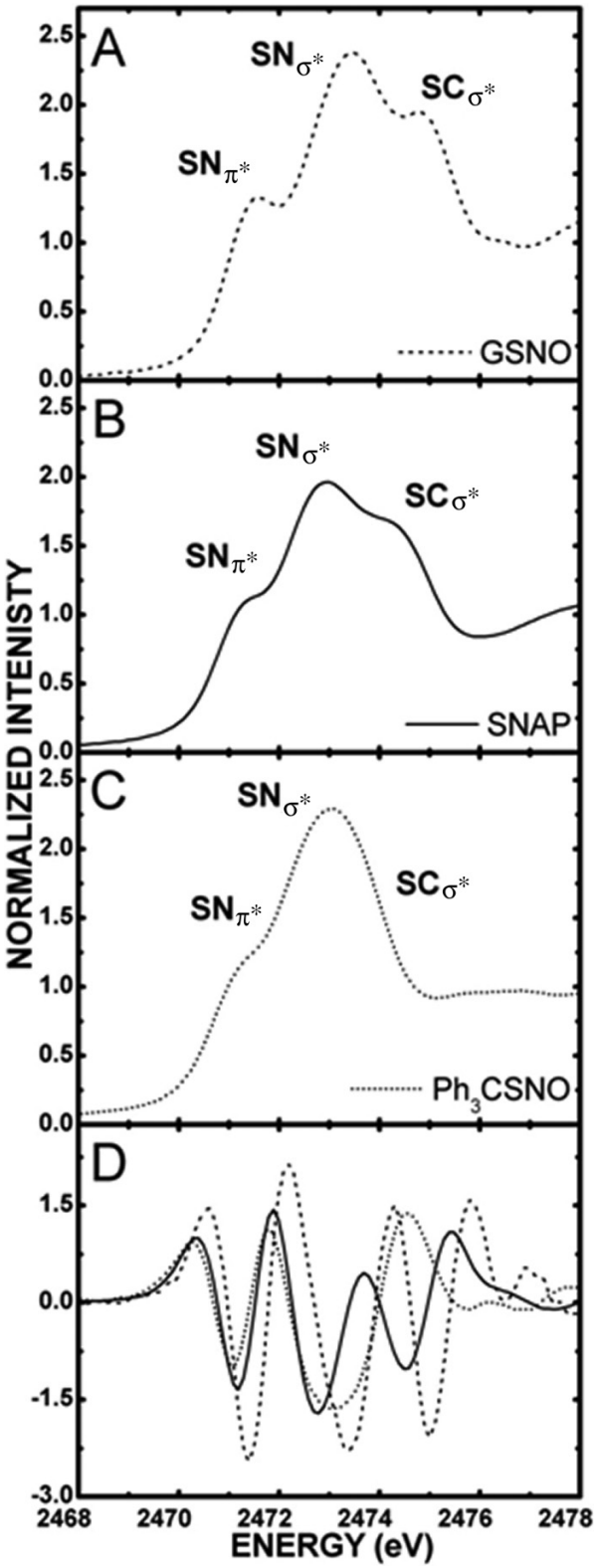

Can. J. Chem. Downloaded from www.nrcresearchpress.com by University of Electronic and Science Techonology of China on 09/18/12
For personal use only.

from a single broad feature at 2473.1 eV. The presence of this broad feature suggests strong overlap between the $SN_{\sigma^*} \leftarrow S_{1s}$ and $SC_{\sigma^*} \leftarrow S_{1s}$ transitions, yielding a single feature at 2473.1 eV. Given that the energy of this broad feature is in good agreement with the $SN_{\sigma^*} \leftarrow S_{1s}$ transition in GSNO and SNAP, it is most reasonable to anticipate that the $SC_{\sigma^*} \leftarrow S_{1s}$ transition has shifted to lower energy due to aryl substitution, with much smaller changes in the energetics of the $SN_{\sigma^*} \leftarrow S_{1s}$ transition. This interpretation is in good agreement with DFT calculations (vide infra). Unsurprisingly, changes in the substitution at C_α produces large energy shifts in the $SC_{\sigma^*} \leftarrow S_{1s}$, with more subtle effects occurring in the S–NO bonding manifold (as represented by the $SN_{\pi^*} \leftarrow S_{1s}$ and $SN_{\sigma^*} \leftarrow S_{1s}$ transitions).

To further explore possible contributions to the observed effect, time-dependent density functional theory (TD-DFT) calculations were carried out on a series of primary, secondary, and tertiary model systems. Qualitatively, our TD-DFT results match the spectroscopic assignments (see Fig. 3); our results are also consistent with previous calculations on these and related systems.[15,16,19] As observed experimentally, primary *S*-nitrosothiols exhibit three major features in their simulated S K-edge XAS spectra in the following energy order: $SN_{\pi^*} \leftarrow S_{1s} < SN_{\sigma^*} \leftarrow S_{1s} < SC_{\sigma^*} \leftarrow S_{1s}$. The observed splittings between the different features corresponds quite well with experiment (see Supplementary data S1 for details). The intensity of the lowest lying SN_{π^*} feature directly reflects the degree of π character in the S–N bond. The strong intensity of the SN_{π^*} feature clearly indicates the importance of π contributions, in agreement with recent theoretical work.[16] A more quantitative determination of π-contributions and its modulation with solvation and other effects is currently ongoing.

Our computational results also indicate a splitting of the $SC_{\sigma^*} \leftarrow S_{1s}$ contributions into two transitions, due to mixing with CH_{σ^*} at C_α (e.g., see Fig. 3). Not surprisingly, this mixing decreases as a function of substitution, with tertiary systems exhibiting only a single feature in this energy range (vide infra, see Fig. 4). In addition to this loss of mixing, the energy of $SC_{\sigma^*} \leftarrow S_{1s}$ decreases markedly with substitution, in agreement with our S K-edge XAS data. The shift in $SC_{\sigma^*} \leftarrow S_{1s}$ transition energy brings this feature closer to the $SN_{\sigma^*} \leftarrow S_{1s}$ peak, consistent with the behavior seen in Ph_3CSNO.

Calculated $SN_{\pi^*} \leftarrow S_{1s}$ and $SN_{\sigma^*} \leftarrow S_{1s}$ excitation energies also decrease with increasing substitution but the changes are more subtle. In each of these transitions, the largest effect occurs between the methyl and ethyl nitrosothiols (–0.3 eV and –0.4 eV), with only small changes occurring upon further substitution (–0.03 eV and –0.1 eV). As has been noted previously,[19] the $SN_{\pi^*} \leftarrow S_{1s}$ transition should not be directly affected by changes in SC bonding, since its π interaction is perpendicular to the σ framework. We further note that our DFT results also indicate that the SN_{π^*} orbital is not significantly affected by changes at C_α. Therefore, shifts in the energy of the $SN_{\pi^*} \leftarrow S_{1s}$ can be used as an indicator of the Z_{eff} of the sulfur atom. From this, we find that $Z_{eff}^{S(GSNO)} > Z_{eff}^{S(SNAP)} > Z_{eff}^{S(Ph_3CSNO)}$. However, this effect does not account for the larger shifts observed in the energies of the $SN_{\sigma^*} \leftarrow S_{1s}$ and $SC_{\sigma^*} \leftarrow S_{1s}$ transitions. These additional shifts to lower energy are observed both experimentally and computationally and appear as the result of a lowering of the energy of the SN_{σ^*} and SC_{σ^*} acceptor orbitals, respectively. This implies that changes at C_α decrease the magnitude of the σ interactions and result in weakening both the SC and SN σ bonds. This is in agreement with previously reported SC bond dissociation energies for alkylthiols, which decrease in energy with increased alkyl substitution at the C_α,[20] as well as calculated bond dissociation energies, which predict that S–N bonds in tertiary *S*-nitrosothiols should be slightly weaker than S–N bonds in the primary ones.[21]

Fig. 3. TD-DFT generated electron density contour plots (isovalue = 0.05 e Å^{-3}) of acceptor orbitals corresponding to the lowest empty valence molecular orbital of the primary *S*-nitrosothiol, ethyl-*S*-nitrosothiol.

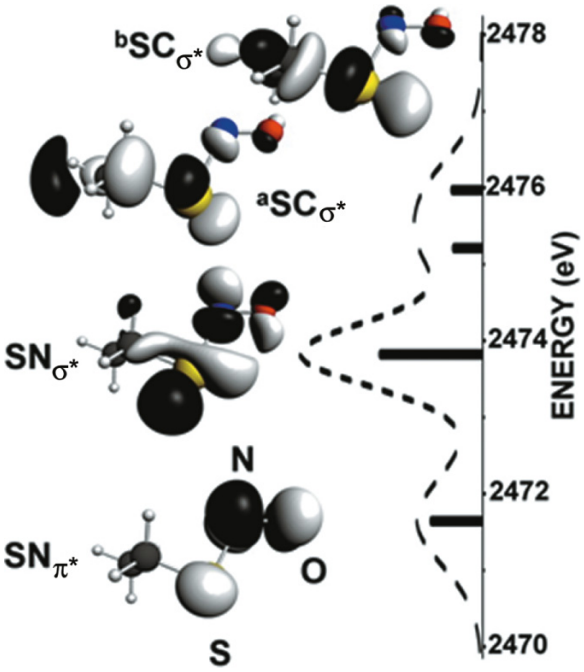

As previously noted, primary *S*-nitrosothiols are generally less stable than tertiary *S*-nitrosothiols, with GSNO being a notable exception.[8–11] Such behavior has been attributed to steric effects,[9] given that electronic differences have generally been assumed to be relatively small. This assumption has previously been explored theoretically, but direct experimental validation was lacking until now. Our current work demonstrates that electronic differences do exist between primary and tertiary *S*-nitrosothiols, indicating relatively large differences in the S–C bond and somewhat more modest differences in the S–N bond. Our data strongly suggest that the S–N bond in tertiary nitrosothiols is weaker than S–N bond in primary nitrosothiols, as indicated by a decrease in the energy of the $SN_{\pi^*}/SN_{\sigma^*} \leftarrow S_{1s}$ transitions in Ph_3CSNO and SNAP vs. GSNO. This would imply that the reactivity of *S*-nitrosothiols should be greater in the tertiary cases, in apparent contradiction with observed thermal and Cu^+-catalyzed disulfide bond formation as a function of C_α substitution (see Fig. 4).

The relative differences in S–N bonding between these species are inconsistent with direct electronic control of either the thermal or Cu^+-catalyzed reactivity of *S*-nitroso-

Can. J. Chem. Downloaded from www.nrcresearchpress.com by University of Electronic and Science Techonology of China on 09/18/12
For personal use only.

Fig. 4. TD-DFT simulated sulfur K-edge XAS spectra for the primary (1′) *S*-nitrosothiols with a methyl and ethyl molecular backbone; the secondary (2′) *S*-nitrosothiol with an isopropyl molecular backbone; and the tertiary (3′) *S*-nitrosothiol with a *tert*-butyl molecular backbone. Excitation energies were shifted by +77.3 eV from calculated values.

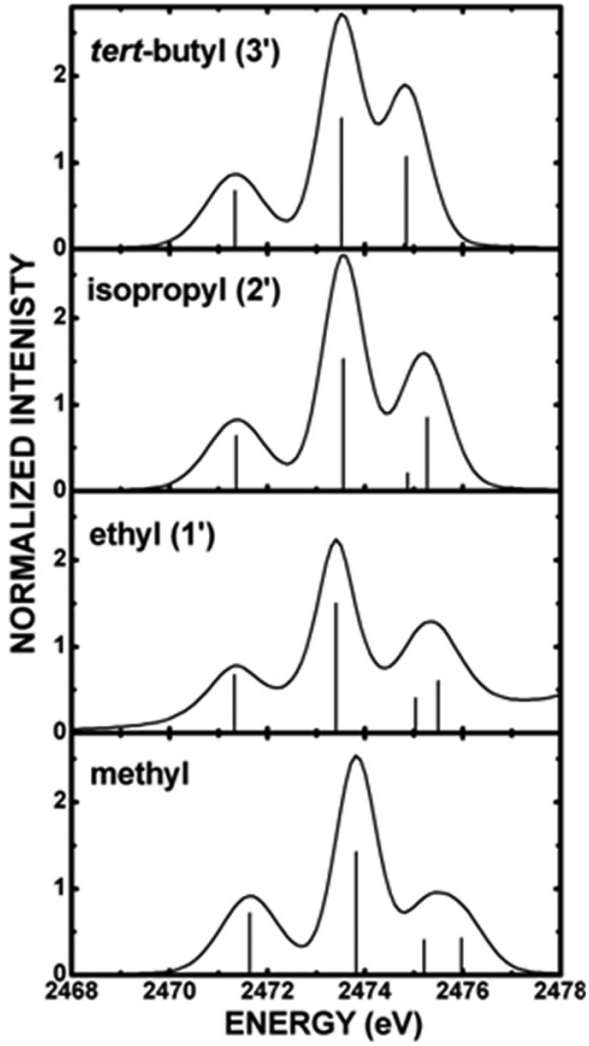

thiols, leaving either indirect (e.g., solvation) and (or) steric factors as primary considerations. We have begun to explore these alternative factors to provide an effective predictive model for the reactivity of *S*-nitrosothiols.

Experimental

Materials

The RSNO compounds used in this study, *S*-nitrosoglutathione,[11] *S*-nitroso-*N*-acetylpenicillamine,[10,14] and tritylthionitrite were prepared and purified by literature methods.[14]

XAS data collection

Sulfur K-edge XAS data were acquired at the new beamline 4–3 of the Stanford Synchrotron Radiation Lightsource (SSRL), using a low *Z* setup allowing low-temperature data acquistions.[22] Samples were mixed with 50% (*v*/*v*) boron nitride to minimize self-absorption, and mounted as a thin layer of finely ground powder on sulfur-free Kapton tape. Data were acquired using a Lytle detector at ambient temperature and pressure (~1 atm, 298 K) (1 atm = 101.325 kPa). Spectral energy calibration was carried out using hydrated sodium thiosulfate with the first pre-edge feature being calibrated at 2472.02 eV.[23] Spectra were normalized according to previously published procedures using BlueprintXAS.[24]

DFT calculations

DFT calculations were carried out using the Amsterdam Density Functional Package Software 2007.01.[25–27] Full geometry optimizations were carried out for the model compounds: methyl-*S*-nitrosothiol (CH_3SNO), ethyl-*S*-nitrosothiol (CH_3CH_2SNO), isopropyl-*S*-nitrosothiol ($(CH_3)_2CHSNO$), and *tert*-butyl-*S*-nitrosothiol ($(CH_3)_3CSNO$); followed by single-point calculations and TD-DFT using a TZ2P basis set, BP86 (Becke-Perdew 86) functional, and no molecular symmetry. XAS spectra for sulfur 1s excitations were calculated using no core for any of the atoms and the ModifyExcitation key (see Supplementary data, S2–S5). The resulting excitations were shifted by +77.3 eV to account for computational discrepancies in the calculated core excited-state energies.

Supplementary data

Supplementary data for this article are available on the journal Web site (canjchem.nrc.ca).

Acknowledgements

This project was funded through the Natural Sciences and Engineering Research Council (NSERC) of Canada Discovery Grants to PK and DSB and by the Canada Research Chair for DSB. Special thanks to Dr. Matthew Latimer at the Stanford Synchrotron Radiation Lightsource for his technical and scientific assistance during data collection. Portions of this research were carried out at the Standard Synchrotron Radiation Lightsource (SSRL), a national user facility operated by Stanford University on behalf of the US Department of Energy-Office of Basic Energy Sciences (DOE-BES). The SSRL Structural Molecular Biology Program is supported by the DOE, Office of Biological and Environmental Research, and the National Institutes of Health (NIH), National Center for Research Resources, Biomedical Technology Program.

References

(1) Al-Sa'doni, H.; Ferro, A. *Clin. Sci. (Lond.)* **2000**, *98* (5), 507. doi:10.1042/CS19990267. PMID:10781381.
(2) Garthwaite, J. *Trends Neurosci.* **1991**, *14* (2), 60. doi:10.1016/0166-2236(91)90022-M. PMID:1708538.
(3) Ignarro, L. J.; Kadowitz, P. J. *Annu. Rev. Pharmacol. Toxicol.* **1985**, *25* (1), 171. doi:10.1146/annurev.pa.25.040185.001131. PMID:2988418.
(4) Ignarro, L. J. *Pharmacol. Toxicol.* **1990**, *67* (1), 1. doi:10.1111/j.1600-0773.1990.tb00772.x. PMID:1975691.
(5) Radomski, M. W.; Palmer, R. M. J.; Moncada, S. *Br. J. Pharmacol.* **1987**, *92* (3), 639. PMID:3322462.
(6) Konorev, E. A.; Kalyanaraman, B.; Hogg, N. *Free Radic.*

Biol. Med. **2000**, *28* (11), 1671. doi:10.1016/S0891-5849(00)00281-1. PMID:10938464.
(7) Williams, D. L. H. *Org. Biomol. Chem.* **2003**, *1* (3), 441. doi:10.1039/b209748f. PMID:12926240.
(8) Askew, S. C.; Barnett, D. J.; McAninly, J.; Williams, D. L. H., J. Chem. Soc. Perkin Trans. 2 **1995**, *4*, 741.
(9) Bainbrigge, N.; Butler, A. R.; Gorbitz, C. H., J. Chem. Soc. Perkin Trans. 2 **1997**, *2*, 351.
(10) Field, L.; Dilts, R. V.; Ravichandran, R.; Lenhert, P. G.; Carnahan, G. E. *J. Chem. Soc. Chem. Commun.* **1978**, (6): 249. doi:10.1039/c39780000249.
(11) Hart, T. W. *Tetrahedron Lett.* **1985**, *26* (16), 2013. doi:10.1016/S0040-4039(00)98368-0.
(12) Al-Sa'doni, H. H.; Khan, I. Y.; Poston, L.; Fisher, I.; Ferro, A. *Nitric Oxide-Biol. Chem.* **2000**, *4* (6), 550.
(13) Baciu, C.; Gauld, J. W. *J. Phys. Chem. A* **2003**, *107* (46), 9946. doi:10.1021/jp035205j.
(14) Arulsamy, N.; Bohle, D. S.; Butt, J. A.; Irvine, G. J.; Jordan, P. A.; Sagan, E. *J. Am. Chem. Soc.* **1999**, *121* (30), 7115. doi:10.1021/ja9901314.
(15) Bartberger, M. D.; Houk, K. N.; Powell, S. C.; Mannion, J. D.; Lo, K. Y.; Stamler, J. S.; Toone, E. J. *J. Am. Chem. Soc.* **2000**, *122* (24), 5889. doi:10.1021/ja994476y.
(16) Timerghazin, Q. K.; Peslherbe, G. H.; English, A. M. *Org. Lett.* **2007**, *9* (16), 3049. doi:10.1021/ol0711016. PMID:17616141.
(17) Glaser, T.; Hedman, B.; Hodgson, K. O.; Solomon, E. I. *Acc. Chem. Res.* **2000**, *33* (12), 859. doi:10.1021/ar990125c. PMID:11123885.
(18) Solomon, E. I.; Hedman, B.; Hodgson, K. O.; Dey, A.; Szilagyi, R. K. *Coord. Chem. Rev.* **2005**, *249* (1–2), 97. doi:10.1016/j.ccr.2004.03.020.
(19) Szilagyi, R. K.; Schwab, D. E. *Biochem. Biophys. Res. Commun.* **2005**, *330* (1), 60. doi:10.1016/j.bbrc.2005.02.127. PMID:15781232.
(20) Fine, D. H.; Westmore, J. B. *Can. J. Chem.* **1970**, *48* (3), 395. doi:10.1139/v70-064.
(21) Bartberger, M. D.; Mannion, J. D.; Powell, S. C.; Stamler, J. S.; Houk, K. N.; Toone, E. J. *J. Am. Chem. Soc.* **2001**, *123* (36), 8868. doi:10.1021/ja0109390. PMID:11535101.
(22) Kennepohl, P.; Wasinger, E. C.; DeBeer George, S. *J. Synchrotron Radiat.* **2009**, *16* (4), 484. doi:10.1107/S0909049509021384. PMID:19535861.
(23) Hedman, B.; Frank, P.; Gheller, S. F.; Roe, A. L.; Newton, W. E.; Hodgson, K. O. *J. Am. Chem. Soc.* **1988**, *110* (12), 3798. doi:10.1021/ja00220a013.
(24) Delgado-Jaime, M. U.; Conrad, J. C.; Fogg, D. E.; Kennepohl, P. *Inorg. Chim. Acta* **2006**, *359* (9), 3042. doi:10.1016/j.ica.2005.12.058.
(25) Velde, G. T.; Bickelhaupt, F. M.; Baerends, E. J.; Guerra, C. F.; Van Gisbergen, S. J. A.; Snijders, J. G.; Ziegler, T. *J. Comput. Chem.* **2001**, *22* (9), 931. doi:10.1002/jcc.1056.
(26) Guerra, C. F.; Snijders, J. G.; te Velde, G.; Baerends, E. J. *Theor. Chem. Acc.* **1998**, *99* (6), 391. doi:10.1007/s002140050021.
(27) ADF2007.01 [computer program]. SCM, Theoretical Chemistry, Vrije Universiteit: Amsterdam, The Netherlands. http://www.scm.com.

Can. J. Chem. Downloaded from www.nrcresearchpress.com by University of Electronic and Science Techonology of China on 09/18/12
For personal use only.

Luminescence studies of copper(I)-containing [2]pseudorotaxanes

Breeze N. Briggs, Fabien Durola, David R. McMillin, and Jean-Pierre Sauvage

Abstract: This report describes photoluminescence studies of copper-containing [2]pseudorotaxanes that mimic elements of functioning molecular machines. Excitation with visible light induces a formal oxidation of the metal center and simulates an actuation process. In all four [2]pseudorotaxanes studied, the ring ligand is the same, but the thread ligand is variable, namely 2,9-di(anisol-4-yl)-1,10-phenanthroline (dap), 6,6′-di(anisol-4-yl)-2,2′-bipyridine (o-dabipy), 5,5′-di(anisol-4-yl)-2,2′-bipyridine (m-dabipy), or 8,8′-di(anisol-4-yl)-3,3′-bi-isoquinoline (dabiiq). The absorbance bandshapes suggest that aryl substituents extending from the core ligands engage in stacking interactions and induce a partially flattened structure in the ground state. More severe flattening occurs in the excited state and precludes the observation of emission if inter-ligand steric forces do not limit the distortion. Thus, the [2]pseudorotaxanes containing dap or o-dabipy as the thread ligand exhibit uncorrected emission maxima at around 720 nm in room-temperature dichloromethane, while the less constrained analogues, containing dabiiq or m-dabipy, are not emissive in fluid solution and barely exhibit a signal in rigid media. In dichloromethane, the luminescence quantum yields of the dap- and o-dabipy-containing systems are 6×10^{-4} and 4×10^{-4}, and the excited-state lifetimes are 98 ns and 90 ns, respectively.

Key words: copper(I), luminescence, rotaxane, charge transfer.

Résumé : On a effectué des études de photoluminescence de [2]pseudorotaxanes contenant d cuivre et qui imitent les éléments de machines moléculaires opérationnelles. L'excitation à l'aide de lumière visible induit une oxydation formelle du centre métallique et simule un processus d'activation. Dans les quatre [2]pseudorotaxanes étudiés, le noyau du ligand est le même, mais le ligand commun est variable, soit la 2,9-di(anisol-4-yl)-1,10-phénanthroline (dap), la 6,6′-di(anisol-4-yl)-2,2′-bipyridine (o-dabipy), la 5,5′-di(anisol-4-yl)-2,2′-bipyridine (m-dabipy) et la 8,8′-di(anisol-4-yl)-3,3′-biisoquinoléine (dabiiq). Les formes des bandes d'absorption suggèrent que les substituants aryles qui s'orientent vers l'extérieur des ligands de coeur donnent lieu à des interactions d'empilement et qu'ils induisent une structure partiellement aplatie dans l'état fondamental. Un aplatissement plus important se produit dans l'état excité et il empêche l'observation de l'émission si les forces stériques inter-ligand ne limitent pas la distorsion. Ainsi, les [2]pseudorotaxanes qui contiennent du « dap » ou du « o-dibipy » comme ligand commun donnent lieu à des maxima d'émission non corrigée autour de 720 nm, à la température ambiante, dans le dichlorométhane, alors que les analogues avec moins de contraintes, contenant du « dabiiq » ou du « m-dapiry » ne donnent pas lieu à de l'émission en solution fluide et ils présentent à peine un signal en milieu solide. Dans la dichlorométhane, les rendements quantiques de luminescence des systèmes contenant du « dab » ou du « o-dabipy » sont de 6×10^{-4} et 4×10^{-4} et les temps de vie des états excités sont respectivement de 98 et 90 ns.

Mots-clés : cuivre(I), luminescence, rotaxane, transfert de charge.

[Traduit par la Rédaction]

Introduction

Copper(I) is a useful templating agent for the synthesis of molecules exhibiting interesting topologies.[1] An example is a two-component molecular assembly known as a [2]rotaxane, which threads together like an axle through a wheel. Elaborate versions can function as molecular machines, i.e., molecular device prototypes that execute mechanical motion in response to an external input.[2–4] For example, a copper-containing [2]rotaxane with 1,10-phenanthroline and 2,2′:6′,6″-terpyridine stations in the ring ligand is capable of displaying rotary motion, as recently demonstrated by Raehm et al.[5] Electrochemical actuation is possible because the copper(I) and copper(II) oxidation states characteristically prefer different coordination numbers. Thus, the thermodynamically favored copper(I) form is four-coordinate and

Received 6 April 2010. Accepted 17 June 2010. Published on the NRC Research Press Web site at canjchem.nrc.ca on 25 November 2010.

This article is part of a Special Issue dedicated to Professor J. C. Scaiano.

B.N. Briggs and D.R. McMillin.[2] Department of Chemistry, Purdue University, 560 Oval Drive, West Lafayette, IN 47907-2084, USA.
F. Durola.[1] Centre de Recherche Paul Pascal, UPR 8641 du CNRS, 115 avenue Schweitzer, 33600 Pessac, France.
J. Sauvage. Laboratoire de Chimie Organo-Minérale, Institut de Chimie, LC3 UMR 7177 du CNRS, Université de Strasbourg, 4 rue Blaise Pascal, 67070 Strasbourg CEDEX, France.

[1]Corresponding author (e-mail: durola@crpp-bordeaux.cnrs.fr).
[2]Corresponding author (e-mail: mcmillin@purdue.edu).

Can. J. Chem. Downloaded from www.nrcresearchpress.com by University of Electronic and Science Techonology of China on 09/18/12
For personal use only.

Can. J. Chem. Downloaded from www.nrcresearchpress.com by University of Electronic and Science Techonology of China on 09/18/12
For personal use only.

entails complexation to the phenanthroline embedded in the ring component. Upon oxidation of the copper center, the metal prefers to be five-coordinate, hence the ring ligand pirouettes about the thread and coordinates to the metal via the terpyridine moiety.[5] Regeneration of the phenanthroline-bound form occurs with reduction back to copper(I).

Photoluminescence studies are potentially relevant to the dynamics of the system because population of the emitting metal-to-ligand charge-transfer (MLCT) excited state entails formal oxidation of the metal center.[6–9] In general, two important structural changes occur in a $Cu(NN)_2^+$ system after absorption to the Franck–Condon state. (Herein, NN designates a diimine ligand such as 1,10-phenanthroline or 2,2′-bipyridine). First, the excited state undergoes a flattening distortion,[7–11] which is complete in less than a picosecond.[12,13] Subsequently, at least in donor media, expansion of the coordination number and solvent-induced exciplex quenching occurs on a nanosecond time scale.[12,13] There are, however, few reports about luminescence studies involving copper(I)-containing [2]rotaxanes and related systems.[14] Most of the work focuses on systems designed to produce charge separation. Armaroli et al.[15] have, for example, studied a copper(I)-containing [2]rotaxane that incorporated a bis(1,10-phenanthroline) ligand environment for the metal center as well as bulky C_{60} groups as termini at both ends of the thread ligand. They find that photoexcitation induces net electron transfer from the copper center to a C_{60} and virtually complete quenching of the CT emission from the copper center as well as the fluorescence from the C_{60} unit.[15] Using a related structure, which included a zinc porphyrin as well, Li et al. have detected MLCT luminescence from the bis(1,10-phenanthroline)copper center, but the lifetime is very short due to oxidative quenching by C_{60} acceptors.[16]

For convenience, the emission studies described below utilize [2]pseudorotaxanes, which lack the bulky "stopper" groups that prevent unthreading in a true [2]rotaxane. Figure 1 shows the structure of the m-30 ring ligand, which all systems have in common. The thread component is any one of four different ligands also depicted in Fig. 1, namely 2,9-di(anisol-4-yl)-1,10-phenanthroline (dap), 6,6′-di(anisol-4-yl)-2,2′-bipyridine (o-dabipy), 5,5′-di(anisol-4-yl)-2,2′-bipyridine (m-dabipy), or 8,8′-di(anisol-4-yl)-3,3′-bi-isoquinoline (dabiiq).

Experimental

Synthesis

Previously published procedures yielded the coordinating macrocycle m-30[17] and the ligands dap,[18] o-dabipy,[19] and dabiiq.[20]

5,5′-Dianisyl-2,2′-bipyridine (m-dabipy)

The 5,5′-dibromo-2,2′-bipyridine precursor[21] (150 mg, 0.32 mmol), 4-methoxyphenyl boronic acid (106 mg, 0.704 mmol), and Na_2CO_3 (675 mg, 6.4 mmol) were placed in a two-necked round-bottom flask under argon. Then, toluene (30 mL), deionized water (10 mL), and ethanol (5 mL) were added. The solution was degassed and stirred under argon, then $Pd(PPh_3)_4$ (37 mg, 0.032 mmol) was added. The mixture was then degassed again and stirred at 90 °C for 16 h. Solvents were evaporated and a poorly soluble product was obtained. The crude product was thoroughly washed with water to remove sodium carbonate. The product was then washed five times with CH_2Cl_2 to remove starting material and soluble byproducts. The title product was thus obtained pure as a white solid (54 mg, 46% yield).

^{1}H NMR (DMSO-d_6, 300 MHz): δ (ppm) = 9.00 (d, 2H, J = 2.3 Hz), 8.45 (d, 2H, J = 8.3 Hz), 7.93 (dd, 2H, J = 8.3, 2.3 Hz), 7.79 (d, 4H, J = 8.8 Hz), 7.10 (d, 4H, J = 8.8 Hz), 3.84 (s, 6H).

Fig. 1. Copper-containing [2]pseudorotaxanes studied along with m-30 the ring ligand for each.

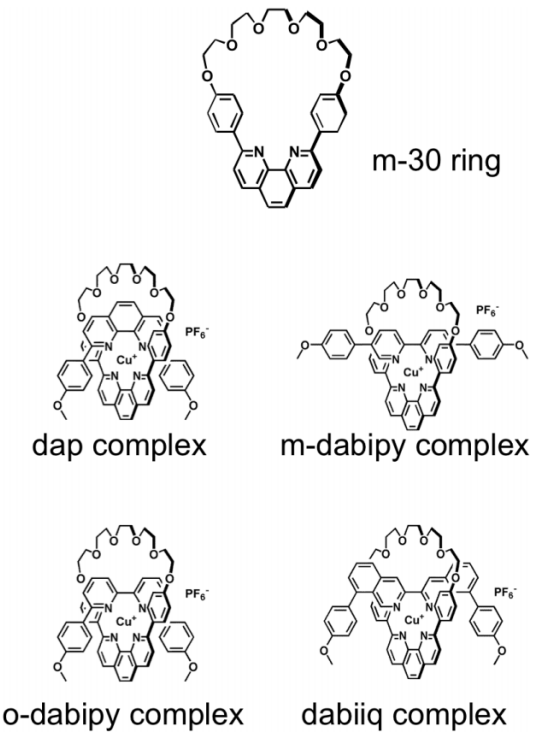

Threaded complexes: Cu(m-30)(NN)$^+$ PF_6^-

In a typical procedure, $Cu(CH_3CN)_4PF_6$ (1 equiv.) in degassed CH_3CN (0.5 mL per mg of complex) was added to a stirred degassed solution of macrocycle m-30 (1 equiv.) in CH_2Cl_2 (0.3 mL per mg of m-30). A deep orange color appeared instantly. A short while later, a solution in CH_2Cl_2 (0.3 mL per mg ligand) of 1 equiv. of the diimine ligand (NN, respectively, dap, o-dabipy, m-dabipy, or dabiiq) was added at room temperature, and the solution immediately turned dark red. After the solution was stirred for 2 h under argon at room temperature, the solvents were removed under vacuum. The dark red solid thus obtained was dissolved again in a minimum of degassed CH_3CN. As a precaution, the solution was filtered, after which evaporation of the filtrate yielded the copper complex quasi-quantitatively.

Cu(m-30)(dap)$^+$ PF_6^-

^{1}H NMR (CD_3CN, 300 MHz): δ (ppm) = 8.65 (d, 2H, J = 8.4 Hz), 8.55 (d, 2H, J = 8.4 Hz), 8.25 (s, 2H), 8.09 (s, 2H), 7.92 (d, 2H, J = 8.4 Hz), 7.88 (d, 2H, J = 8.4 Hz), 7.55 (d, 4H, J = 8.7 Hz), 7.34 (d, 4H, J = 8.7 Hz), 6.09 (d, 4H, J = 8.8 Hz), 6.01 (d, 4H, J = 8.8 Hz), 3.82 (s, 4H), 3.73–3.70 (m, 4H), 3.60–3.57 (m, 4H), 3.55–3.51 (m, 4H), 3.46 (s,

Can. J. Chem. Downloaded from www.nrcresearchpress.com by University of Electronic and Science Techonology of China on 09/18/12
For personal use only.

6H), 3.44–3.41 (m, 4H). ES-MS *m/z* = 1021.3218 (calcd. 1021.3238 for $C_{60}H_{54}CuN_4O_8^+$).

***Cu(m-30)(o-dabipy)*$^+$ *PF*$_6^-$**

^{1}H NMR (CD_3CN, 300 MHz): δ (ppm) = 8.50 (d, 2H, *J* = 8.4 Hz), 8.27 (d, 2H, *J* = 8.0 Hz), 8.10 (t, 2H, *J* = 8.0 Hz), 8.02 (s, 2H), 7.90 (d, 2H, *J* = 8.4 Hz), 7.56 (d, 2H, *J* = 8.0 Hz), 7.54 (d, 4H, *J* = 8.8 Hz), 7.39 (d, 4H, *J* = 8.8 Hz), 6.44 (d, 4H, *J* = 8.8 Hz), 6.00 (d, 4H, *J* = 8.8 Hz), 4.02–3.99 (m, 4H), 3.76 (s, 4H), 3.74 (br, 8H), 3.73–3.70 (m, 4H), 3.36 (s, 6H). ES-MS *m/z* = 997.3212 (calcd. 997.3238 for $C_{58}H_{54}CuN_4O_8^+$).

***Cu(m-30)(m-dabipy)*$^+$ *PF*$_6^-$**

^{1}H NMR (CD_3CN, 300 MHz): δ (ppm) = 8.74 (d, 2H, *J* = 8.4 Hz), 8.29–8.16 (m, 10H), 7.55 (d, 8H, *J* = 8.6 Hz), 7.06 (d, 4H, *J* = 8.6 Hz), 6.27 (d, 4H, *J* = 8.6 Hz), 3.85 (s, 6H), 3.82–3.79 (m, 4H), 3.78 (s, 4H), 3.77–3.74 (m, 4H), 3.69–3.66 (m, 4H), 3.65–3.62 (m, 4H). ES-MS *m/z* = 997.3207 (calcd. 997.3238 for $C_{58}H_{54}CuN_4O_8^+$).

***Cu(m-30)(dabiiq)*$^+$ *PF*$_6^-$**

^{1}H NMR (CD_3CN, 300 MHz): δ (ppm) = 9.04 (s, 2H), 8.69 (d, 2H, *J* = 8.4 Hz), 8.63 (s, 2H), 8.18 (d, 2H, *J* = 8.3 Hz), 8.14 (s, 2H), 8.10 (d, 2H, *J* = 8.4 Hz), 7.93 (dd, 2H, *J* = 8.2, 7.2 Hz), 7.60 (d, 2H, *J* = 7.1 Hz), 7.49 (d, 4H, *J* = 8.8 Hz), 7.26 (d, 4H, *J* = 8.8 Hz), 6.92 (d, 4H, *J* = 8.8 Hz), 6.15 (d, 4H, *J* = 8.8 Hz), 3.87 (s, 4H), 3.77 (s, 6H), 3.76–3.73 (m, 4H), 3.65–3.62 (m, 4H), 3.58–3.55 (m, 4H), 3.48–3.44 (m, 4H). ES-MS *m/z* = 1097.3534 (calcd. 1097.3551 for $C_{66}H_{58}CuN_4O_8^+$).

Methods

In the emission studies involving solid-state or frozen-glass samples, a 620 nm long-pass filter was in place to reject scattered light. The excitation beam also passed through a notch filter centered at 450 nm. For excitation and emission, the slit settings were 10 nm and 20 nm, respectively. The glassing solvent was a 4:1 mixture of ethanol:methanol, and the sample holder was a 3 mm i.d. quartz tube immersed in a finger dewar filled with liquid nitrogen. The same assembly without cryogen also allowed for measurements from solid-state samples. For frozen glass and solid-state emission measurements, the blank was either an empty capillary tube or one loaded with a non-emissive, solid-state copper(I) compound. The procedure for deoxygenation of dichloromethane entailed a sequence of freeze–pump–thaw cycles. For lifetime measurements, a combination of 620 and 700 nm long pass filters prevented scattered light from impinging on the detector. The setup also included a 450 nm notch filter in the laser beam. The laser dye was Coumarin 440 in ethanol at a concentration of 6.1×10^{-3} mol/L. The method of Parker and Rees yielded estimates of emission quantum yields.[22] Residual solvent protons (^{1}H NMR: CD_3CN: 1.96 ppm, DMSO-d_6: 2.50 ppm) served for referencing NMR signals.

Instrumentation

The spectrophotometer for the absorbance measurements was a Varian Cary 300 Bio unit. A Varian Cary Eclipse unit yielded photoluminescence data. A description of the apparatus used for the lifetime measurements is in the literature.[23] The NMR spectrometer was a Bruker AVANCE 300 (300 MHz). The mass spectrometer was a Bruker MicroTOF (ES-MS).

Fig. 2. Absorbance spectra of dap, o-dabipy, dabiiq, and m-dabipy complexes in dichloromethane at room temperature.

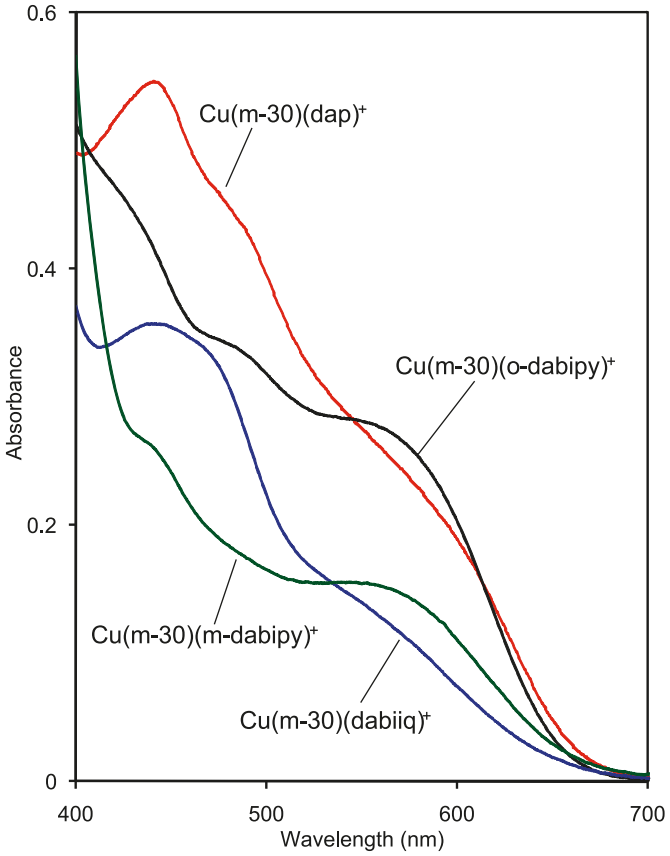

Results

The solvent employed for most of the solution work was dichloromethane (DCM) wherein the four copper complexes exhibit the visible absorption spectra depicted in Fig. 2. In each case, a strong, variably structured absorption occurs in the vicinity of 450 nm along side a broad shoulder that appears at ~580 nm. The shoulder is especially prominent in the spectra of the o-dabipy and m-dabipy complexes. Despite similar absorption throughout the series, only the dap and o-dabipy complexes exhibit a detectable emission signal in room-temperature solution. The emission is broadband in both cases and maximizes between 710 nm and 720 nm (Table 1); see Fig. 3 for data pertaining to the o-dabipy complex. In deoxygenated DCM at room temperature, the luminescence quantum yields are 6×10^{-4} and 4×10^{-4} for the dap and o-dabipy complexes, respectively. The corresponding emission lifetimes are 98 ns and 90 ns. In an alcohol glass at 77 K, the same two complexes exhibit an emission maximum at about 740 nm, and the lifetime of the emission signal extends considerably to 990 ns for the dap complex and 870 ns for the o-dabipy analogue. In the frozen glass, the dabiiq and m-dabipy complexes also emit, though very weakly, and exhibit lifetimes of 185 ns and 155 ns, re-

Can. J. Chem. Downloaded from www.nrcresearchpress.com by University of Electronic and Science Techonology of China on 09/18/12
For personal use only.

Table 1. Emission data for Cu(m-30)(NN)$^+$ systems.

	λ^a nm (τ, ns)		
Complex	298 K in DCM[b]	77 K in EtOH/MeOH	298 K in solid state
Cu(m-30)(dap)$^+$	718 (98)	745 (990)	720 (270)
Cu(m-30)(o-dabipy)$^+$	715 (90)	740 (870)	730 (150)
Cu(m-30)(m-dabipy)$^+$	—[c]	760 (155)	770 (—[c])
Cu(m-30)(dabiiq)$^+$	—[c]	760 (185)	770 (—[c])

[a]From uncorrected spectra.
[b]Quantum yields: dap complex 6.4 × 10^{-4}; o-dabipy complex 4.0 × 10^{-4}.
[c]Not resolved.

Fig. 3. Uncorrected emission spectra of the hexafluorophosphate salt of Cu(m-30)(o-dabipy)$^+$ measured in room-temperature dichloromethane (thin), the solid state (thick × 1/2), as well as a 77 K alcohol glass (-Δ- × 1/6), and from the corresponding salt of Cu(m-30)(m-dabipy)$^+$ in an alcohol glass at 77 K (-□-). Emission intensities are arbitrary.

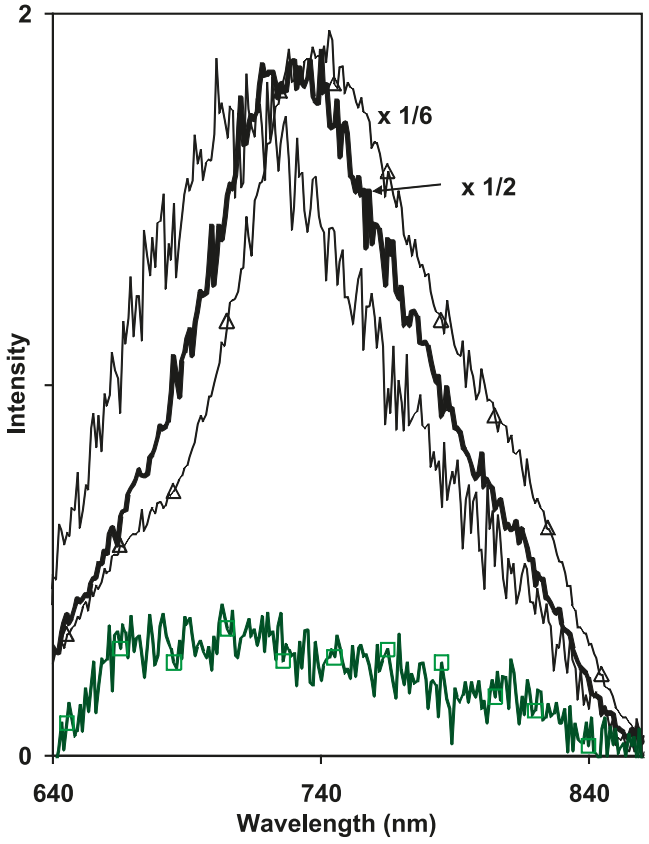

Fig. 4. Uncorrected emission spectra measured from solid samples of [Cu(m-30)(dap)]PF_6, [Cu(m-30)(o-dabipy)]PF_6, [Cu(m-30)(m-dabipy)]PF_6, and [Cu(m-30)(dabiiq)]PF_6 at room temperature.

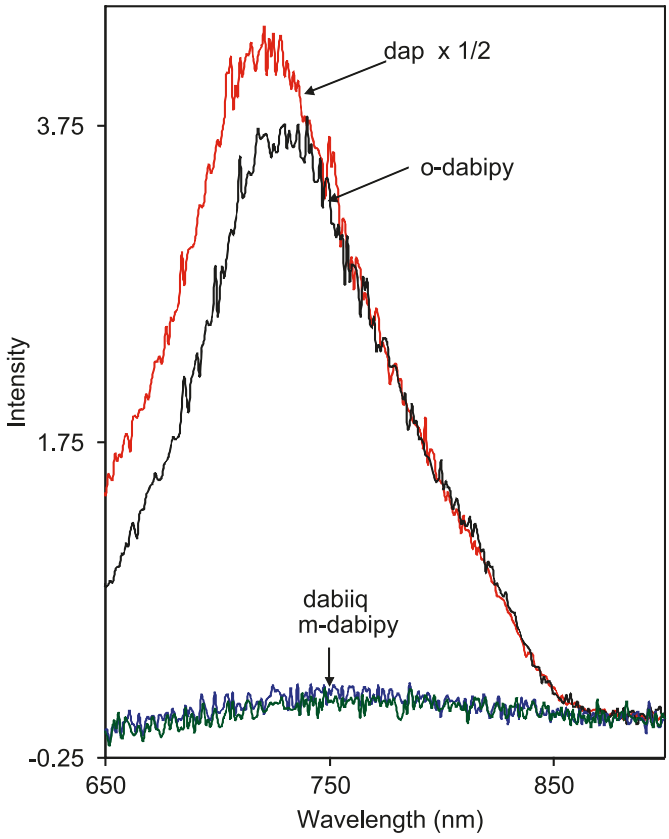

spectively. See Fig. 3 for the 77 K spectrum of the [2]pseudorotaxane with m-dabipy as the thread ligand. The emissions from the dap and o-dabipy complexes are both much more intense and durable enough to persist in the weakly basic solvent acetonitrile at room temperature, although the lifetimes contract to 50 ns and 30 ns, respectively.

The emission results are qualitatively similar in the solid state; see Fig. 4. In the case of the dap complex, the solid-state emission spectrum virtually coincides with that obtained in room-temperature, fluid solution, but the lifetime extends to 270 ns. On the other hand, the emission maximum for the o-dabipy complex shifts to slightly longer wavelength (730 nm), and that may account for the smaller increase in the emission lifetime (to 150 ns). Figure 4 shows that the dabiiq and m-dabipy complexes both exhibit weak emissions, centered at ~770 nm in the solid state. Unfortunately, neither signal is strong enough to permit a lifetime measurement.

Discussion

CT absorption and emission

Previous work has shown that the MLCT excitation that dominates the visible spectrum of a Cu(NN)$_2^+$ complex originates in the dπ orbitals of the metal that have nonzero overlap with empty π*(NN) acceptor orbitals of the ligand.[24,25] The presence of ligands with chemically distinct π systems in the thread and ring components may introduce

Can. J. Chem. Downloaded from www.nrcresearchpress.com by University of Electronic and Science Techonology of China on 09/18/12
For personal use only.

Fig. 5. Schematic view of bonding overlap formed by the half-occupied dσ orbital of a copper(II) center and the donor orbitals of two α,α-diimine ligands in the limit of a planar coordination geometry.

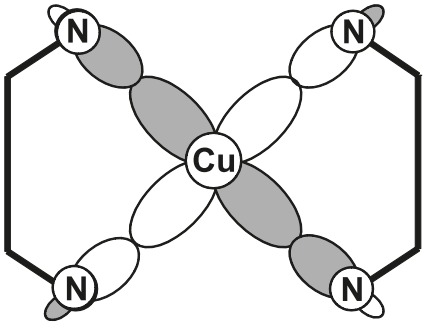

a broadening of the visible spectrum. Moreover, the shoulders that appear at λ ~575 nm in Fig. 2 are *characteristic* of $Cu(NN)_2^+$ systems in which at least one of the ligands has an aryl substituent positioned ortho to one or both of the imine nitrogens.[26,27] The shoulders result from two distinct *ground-state* distortions that destroy idealized D_{2d} symmetry and split the dπ orbital energies.[28–30] One is a "rocking" distortion that imparts a pyramidal coordination geometry, probably promoted by the formation of a stacking interaction involving an aryl substituent on one ligand and the aromatic core of the opposite ligand.[29] The second distortion entails a tetragonal flattening of the N_4 donor set about the copper center.[30] For the latter distortion, the driving force is presumably the mesomeric interaction(s) that results (result) when the aryl substituent(s) adopts (adopt) smaller dihedral angle(s) relative to the mean plane of the NN ligand.[30] Significant flattening is possible with a very modest driving force because the major opposing force derives from interligand steric interactions when the central ion is a d^{10} closed-shell metal center. The same interactions account for notable differences in the formation constants of $Cu(NN)^+$ and $Cu(NN)_2^+$ systems with aryl- as opposed to alkyl-substituted NN ligands.[31]

Further structural changes occur in the MLCT excited state due to the d-shell vacancy created, another consequence of which is the shift in the X-ray absorption edge of the copper center.[12] Nominally containing copper(II), the thermally equilibrated excited state becomes even more flattened, as a consequence of a second-order Jahn–Teller effect.[11] In more descriptive terms, additional flattening occurs because it leads to improved overlap amongst sigma-donor orbitals of the ligand and the half-occupied d orbital of copper in the CT excited state (Fig. 5). Indeed, the same kind of flattening is evident in the structures of oxidized $Cu(NN)_2^{2+}$ analogues.[32,33] When the flattening is severe, as in the case of $Cu(phen)_2^+$, the excited-state potential energy surface may impinge on the ground-state surface. The emission yield then becomes vanishingly small due to efficient non-radiative decay, even in frozen solution.[34,35] Indeed, for a $Cu(NN)_2^+$ system to exhibit emission in solution, sterically active groups must be present adjacent to the donor nitrogens to limit the extent of flattening.[7,9,36]

Within the [2]pseudorotaxane series studied herein, the m-30 ring ligand is a key structural element that clearly has a salutary effect on the emission lifetime of the o-dabipy complex (90 ns in DCM). Normally, $Cu(NN)_2^+$ complexes based on 2,2′-bipyridine ligands have relatively short-lived excited states, e.g., 34 ns for Cu(6,6′-diphenyl-4,4′-dimethyl-2,2-bipyridine)$_2^+$.[33] For comparison, the corresponding excited-state lifetime is 310 ns for Cu(2,9-diphenyl-4,7-dimethyl-1,10-phenanthroline)$_2^+$.[37] Ligand-dependent distortions may account for the difference in lifetimes of the two controls, especially torsional relaxation about the 2,2′ bond of the bipyridine ligand. In each case, bond length changes also occur in the excited state due to population of a π* orbital of the ligand. Bond length changes are apt to be greater in a bipyridine complex because the π* orbital delocalizes over fewer atoms than is the case with a phenanthroline moiety. One possibility is that the structural changes are less important in the o-dabipy-containing [2]pseudorotaxane because the CT excitation actually localizes on the m-30 ring ligand. In line with this possibility, the emission occurs at about the same energy whether the thread ligand is dap or o-dabipy. The m-30 ring ligand is no panacea, however, because the bis-thread complex $Cu(dap)_2^+$ exhibits a *longer* excited-state lifetime (260 ns[26]) than the dap-containing [2]pseudorotaxane. Vibrationally assisted radiationless decay may be less efficient for $Cu(dap)_2^+$ if the absence of a ring ligand permits better nesting of the ground- and excited-state potential energy surfaces.

Moreover, the m-30 ligand is not sufficiently structure-preserving to permit a photoluminescence signal if fluid solution from the [2]pseudorotaxane containing either m-dabipy or dabiiq as the thread ligand. In both cases, the anisole substituents of the thread ligand are evidently far enough removed from the opposite m-30 ligand that appreciable flattening occurs in the excited state and quenches the emission. Even in the solid state, where packing forces can come into play and help preserve structure,[11] the emissions from the m-dabipy and dabiiq complexes are very weak and maximize at relatively long wavelengths.

In summary, absorbance bandshapes reveal that all of the [2]pseudorotaxanes studied adopt low symmetry, partially flattened structures due to intra- and inter-ligand interactions involving bulky anisole substituents. Sterically active ligand substituents must be present to inhibit a flattening distortion in the excited state that quenches the photoluminescence. However, the steric interactions may produce inter-ligand "friction" that affects the mechanical response time. In fact, the [2]pseudorotaxanes that contain either the relatively open dabiiq or m-dabipy ligand (and exhibit faster mechanical motion[38]) are non-luminescent in room-temperature dichloromethane solution, whereas the dap and o-dabipy analogues exhibit emissions that maximize at ~720 nm and decay with time constants of 98 ns and 90 ns, respectively. The lifetime for the Cu(m-30)(o-dabipy)$^+$ system is more than twice what one would expect for a simple bis-bipyridine analogue. At 77 K in a frozen glass, the decay times for the emissions from Cu(m-30)(dap)$^+$ and Cu(m-30)(o-dabipy)$^+$ extend to almost a microsecond, whereas in room-temperature acetonitrile solution, the same complexes undergo solvent-induced exciplex quenching on a time scale of just under a microsecond, according to lifetime data.

Acknowledgements

The authors acknowledge support from the National Sci-

ence Foundation grant No. CHE-08011776 to D. R. M. and the Région Alsace for fellowships to F. D.

References

(1) Dietrich-Buchecker, C. O.; Sauvage, J. P. *Chem. Rev.* **1987**, *87* (4), 795. doi:10.1021/cr00080a007.

(2) Balzani, V.; Credi, A.; Venturi, M. *Molecular Devices and Machines: a Journey into the Nano World;* Wiley-VCH: Weinheim, 2003.

(3) Balzani, V.; Credi, A.; Raymo, F. M.; Stoddart, J. F. *Angew. Chem. Int. Ed.* **2000**, *39*, 3349. doi:10.1002/1521-3773(20001002)39.

(4) Kay, E. R.; Leigh, D. A.; Zerbetto, F. *Angew. Chem. Int. Ed.* **2007**, *46* (1-2), 72. doi:10.1002/anie.200504313.

(5) Raehm, L.; Kern, J. M.; Sauvage, J. P. *Chem. Eur. J.* **1999**, *5* (11), 3310. doi:10.1002/(SICI)1521-3765(19991105)5:11<3310::AID-CHEM3310>3.0.CO;2-R .

(6) Blaskie, M. W.; McMillin, D. R. *Inorg. Chem.* **1980**, *19* (11), 3519. doi:10.1021/ic50213a062.

(7) McMillin, D. R.; McNett, K. M. *Chem. Rev.* **1998**, *98* (3), 1201. doi:10.1021/cr9601167. PMID:11848930.

(8) Sakaki, S.; Mizutani, H.; Kase, Y. *Inorg. Chem.* **1992**, *31* (22), 4575. doi:10.1021/ic00048a026.

(9) Lavie-Cambot, A.; Cantuel, M.; Leydet, Y.; Jonusauskas, G.; Bassani, D. M.; McClenaghan, N. D. *Coord. Chem. Rev.* **2008**, *252* (23–24), 2572. doi:10.1016/j.ccr.2008.03.013.

(10) Eggleston, M. K.; Fanwick, P. E.; Pallenberg, A. J.; McMillin, D. R. *Inorg. Chem.* **1997**, *36* (18), 4007. doi:10.1021/ic970135e.

(11) Cunningham, C. T.; Moore, J. J.; Cunningham, K. L. H.; Fanwick, P. E.; McMillin, D. R. *Inorg. Chem.* **2000**, *39* (16), 3638. doi:10.1021/ic000082s. PMID:11196827.

(12) Shaw, G. B.; Grant, C. D.; Shirota, H.; Castner, E. W.; Meyer, G. J.; Chen, L. X. *J. Am. Chem. Soc.* **2007**, *129* (7), 2147. doi:10.1021/ja067271f. PMID:17256860.

(13) Iwamura, M.; Takeuchi, S.; Tahara, T. *J. Am. Chem. Soc.* **2007**, *129* (16), 5248. doi:10.1021/ja069300s. PMID:17397161.

(14) Flamigni, L.; Heitz, V.; Sauvage, J. P. *Struct. Bonding. (Berlin, Ger.)* **2006**, *121*, 217. doi:10.1007/430_018.

(15) Armaroli, N.; Diederich, F.; Dietrich-Buchecker, C. O.; Flamigni, L.; Marconi, G.; Nierengarten, J. F.; Sauvage, J. P. *Chem. Eur. J.* **1998**, *4* (3), 406. doi:10.1002/(SICI)1521-3765(19980310)4:3<406::AID-CHEM406>3.0.CO;2-#.

(16) Li, K.; Bracher, P. J.; Guldi, D. M.; Herranz, M. A.; Echegoyen, L.; Schuster, D. I. *J. Am. Chem. Soc.* **2004**, *126* (30), 9156. doi:10.1021/ja047548g. PMID:15281785.

(17) Dietrich-Buchecker, C. O.; Sauvage, J. P.; Kintzinger, J. P. *Tetrahedron Lett.* **1983**, *24* (46), 5095. doi:10.1016/S0040-4039(00)94050-4.

(18) Dietrich-Buchecker, C. O.; Sauvage, J. P. *Tetrahedron* **1990**, *46* (24), 503. doi:10.1016/S0040-4020(01)85433-8.

(19) Collin, J. P.; Jouvenot, D.; Koizumi, M.; Sauvage, J. P. *Inorg. Chem.* **2005**, *44* (13), 4693. doi:10.1021/ic050246a. PMID:15962977.

(20) Durola, F.; Hanss, D.; Roesel, P.; Sauvage, J. P.; Wenger, O. S. *Eur. J. Org. Chem.* **2007**, *125*. doi:10.1002/ejoc.200600796.

(21) Bruce, J. I.; Chambron, J. C.; Kolle, P.; Sauvage, J. P. *J. Chem. Soc., Perkin Trans. 1* **2002**, *1226*. doi:10.1039/b202407c.

(22) Parker, C. A.; Rees, W. T. *Analyst (Lond.)* **1960**, *85* (1013), 587. doi:10.1039/an9608500587.

(23) Cunningham, K. L.; Hecker, C. R.; McMillin, D. R. *Inorg. Chim. Acta* **1996**, *242* (1-2), 143. doi:10.1016/0020-1693(95)04859-6.

(24) Day, P.; Sanders, N. *J. Chem. Soc. A* **1967**, 1536. doi:10.1039/j19670001536.

(25) Phifer, C. C.; McMillin, D. R. *Inorg. Chem.* **1986**, *25* (9), 1329. doi:10.1021/ic00229a008.

(26) Gushurst, A. K. I.; McMillin, D. R.; Dietrich-Buchecker, C. O.; Sauvage, J. P. *Inorg. Chem.* **1989**, *28* (22), 4070. doi:10.1021/ic00321a008.

(27) Felder, D.; Nierengarten, J. F.; Barigelletti, F.; Ventura, B.; Armaroli, N. *J. Am. Chem. Soc.* **2001**, *123* (26), 6291. doi:10.1021/ja0043439. PMID:11427053.

(28) Everly, R. M.; McMillin, D. R. *J. Phys. Chem.* **1991**, *95* (23), 9071. doi:10.1021/j100176a011.

(29) Cesario, M.; Dietrich-Buchecker, C. O.; Guilhem, J.; Pascard, C.; Sauvage, J. P. *J. Chem. Soc. Chem. Commun.* **1985**, (5): 244. doi:10.1039/c39850000244.

(30) Klemens, F. K.; Palmer, C. E. A.; Rolland, S. M.; Fanwick, P. E.; McMillin, D. R.; Sauvage, J. P. *N. J. Chem.* **1990**, *14*, 129.

(31) Meyer, M.; Albrecht-Gary, A. M.; Dietrich-Buchecker, C. O.; Sauvage, J. P. *Inorg. Chem.* **1999**, *38* (10), 2279. doi:10.1021/ic981259+.

(32) Miller, M. T.; Gantzel, P. K.; Karpishin, T. B. *Inorg. Chem.* **1998**, *37* (9), 2285. doi:10.1021/ic971164s. PMID:11670386.

(33) Williams, R. M.; De Cola, L.; Hartl, F.; Lagref, J. J.; Planeix, J. M.; De Cian, A.; Hosseini, M. W. *Coord. Chem. Rev.* **2002**, *230* (1-2), 253. doi:10.1016/S0010-8545(02)00046-2.

(34) Everly, R. M.; Ziessel, R.; Suffert, J.; McMillin, D. R. *Inorg. Chem.* **1991**, *30* (3), 559. doi:10.1021/ic00003a041.

(35) Shinozaki, K.; Kaizu, Y. *Bull. Chem. Soc. Jpn.* **1994**, *67* (9), 2435. doi:10.1246/bcsj.67.2435.

(36) Eggleston, M. K.; McMillin, D. R.; Koenig, K. S.; Pallenberg, A. J. *Inorg. Chem.* **1997**, *36* (2), 172. doi:10.1021/ic960698a.

(37) Cunningham, C. T. Synthetic and Geometric Perturbations of the Excited States of Metal-Polypyridine Systems, Ph. D. Thesis, Purdue University: West Lafayette, 1998.

(38) Durola, F.; Sauvage, J. P. *Angew. Chem. Int. Ed.* **2007**, *46* (19), 3537. doi:10.1002/anie.200604815.

Can. J. Chem. Downloaded from www.nrcresearchpress.com by University of Electronic and Science Techonology of China on 09/18/12
For personal use only.

Reverse Stern–Volmer behavior for luminescence quenching in carbon nanoparticles

Li Cao, Parambath Anilkumar, Xin Wang, Jia-Hui Liu, Sushant Sahu, Mohammed J. Meziani, Ethan Myers, and Ya-Ping Sun

Abstract: Photoluminescence properties of carbon nanoparticles from different treatments in various suspensions were evaluated, and the results were in general agreement with those available in the literature. An interesting observation was that the quenching of luminescence emissions in the aqueous suspended carbon nanoparticles by aliphatic amines deviated from the classical Stern–Volmer behavior in a somewhat unusual fashion, exhibiting reversed quenching (increasing luminescence intensities) at very low quencher concentrations. The implication of the observation to the mechanistic framework that may account for photoluminescence emissions in both functionalized and naked carbon nanoparticles is proposed and discussed.

Key words: carbon nanoparticles, luminescence, quenching, surface passivation, Stern–Volmer.

Résumé : On a évalué les propriétés de photoluminescence de nanoparticules de carbone obtenues par divers traitements dans des suspensions variées et les résultats obtenus sont généralement en accord avec eux qu'on retrouve dans la littérature. On a toutefois fait l'observation intéressante que la décroissance des émissions de luminescence des nanoparticules de carbone en suspension aqueuse, sous l'influence d'amines aliphatiques, dévie du comportement classique de Stern–Volmer d'une façon assez inhabituelle alors qu'elle présente une décroissance inversée (augmentation des intensités de luminescence) à des concentrations très faibles de désactivateur. On propose et on discute des implications de ces observations aux concepts mécanistiques qui pourraient expliquer les émissions de photoluminescence des nanoparticules nues ou fonctionnalisées.

Mots-clés : nanoparticules de carbone, luminescence, désactivation, passivation superficielle, Stern–Volmer.

[Traduit par la Rédaction]

Introduction

Quantum-sized semiconductor nanoparticles or quantum dots (QDs) have attracted much attention for their excellent optical properties and many related potential applications.[1–6] Among well-established QDs are those based on cadmium selenide nanoparticles and associated core–shell nanostructures.[7,8] However, since cadmium is a heavy metal known for its significant toxic effects and environmental hazards,[9–12] there has been extensive effort on the search for alternative QD-like photoluminescent materials. For example, nanosized silicon as an indirect bandgap semiconductor has been modified and (or) processed specifically for much improved fluorescence quantum efficiencies.[13–15]

Carbon is hardly considered as a member of the "semiconductor family", but it was found and demonstrated unambiguously by Sun and co-workers[16,17] that nanoscale carbon particles could be made brightly fluorescent with both one- and two-photon excitations. There have since been a large number of studies on fluorescent carbon nanoparticles from many different sources and processing or functionalization schemes and conditions.[18–24] While the bright fluorescence (with yields up to 50% and, performance-wise, competitive with that of the well-established semiconductor QDs)[18] has generally been associated with surface-functionalized carbon nanoparticles, there have been a number of reports on the detection of luminescence emissions in "naked" carbon nanoparticles.[21,25–30] For example, photoluminescence was found in acid-treated candle soot in aqueous suspension,[25,26] and subsequently many other suspended soot-like carbon materials (such as natural gas soot[27] or carbonized sugars[21]). Among other naked carbon nanoparticles found to be photoluminescent were those from electrochemical decomposition and (or) oxidation of carbon-based or carbon-rich nanomaterials suspended in water or other solvents.[28–30] These carbon nanoparticles were generally small (less than 10 nm), and their luminescence quantum yields were generally low (mostly less than 1%).

In the work reported here, we examined carbon nanoparticles from different treatments for evaluation and confirmation of their photoluminescence properties in suspensions

Received 30 April 2010. Accepted 17 June 2010. Published on the NRC Research Press Web site at canjchem.nrc.ca on 11 December 2010.

This article is part of a Special Issue dedicated to Professor J. C. Scaiano.

L. Cao, P. Anilkumar, X. Wang, J. Liu, S. Sahu, M.J. Meziani, E. Myers, and Y.-P. Sun.[1] Department of Chemistry and Laboratory for Emerging Materials and Technology, Clemson University, Clemson, SC 29634-0973, USA.

[1]Corresponding author (e-mail: syaping@clemson.edu).

Can. J. Chem. Downloaded from www.nrcresearchpress.com by University of Electronic and Science Techonology of China on 09/18/12
For personal use only.

Can. J. Chem. Downloaded from www.nrcresearchpress.com by University of Electronic and Science Techonology of China on 09/18/12
For personal use only.

under various experimental conditions. An interesting observation was that the quenching of luminescence emissions in the aqueous suspended carbon nanoparticles by aliphatic amines deviated from the classical Stern–Volmer behavior in a somewhat unusual fashion, exhibiting reversed quenching (increasing luminescence intensities) at very low quencher concentrations. The implication of the results to the mechanistic framework that may account for photoluminescence emissions in both functionalized and naked carbon nanoparticles is proposed and discussed.

Results and discussion

The aqueous suspension of the as-purified carbon nanoparticles (produced in the arc discharge of pure graphite rods) was centrifuged at 3 500*g* to yield a colored supernatant. Upon dialysis against pure water, the apparently homogeneous particle suspension was still colored (denoted as fraction S, Fig. 1), with the observed absorption spectrum of a featureless curve (Fig. 1). The excitation at various visible wavelengths resulted in significant luminescence emissions (Fig. 1), in general agreement with what has been reported in the literature for suspended carbon nanoparticles from different sources and preparations.[21,25–30] The observed emission quantum yields (for example, 0.24% at 440 nm excitation) were at the lower end of the values already in the literature.

The carbon nanoparticles in the homogeneous suspension were, size-wise, broadly distributed according to atomic force microscopy imaging (Fig. 2). The results from transmission electron microscopy (TEM) analysis of the same sample were generally consistent with such an assessment, though the relatively low contrast between the smaller carbon nanoparticles and the carbon coating on the TEM grid hindered a more quantitative determination of size distributions.

The carbon nanoparticles could also be suspended in polar organic solvents, in which the luminescence emission properties were somewhat different. The luminescence spectra remained very broad, with some variations in the spectral peak and band width (Fig. 3), and the observed emission quantum yields were clearly solvent dependent, obviously more luminescent in the solvent dimethyl sulfoxide (DMSO) (Table 1).

The presence of solvent was apparently necessary for the observation of luminescence emissions from carbon nanoparticles. No luminescence could be detected for the same particles under solvent-free conditions (for example, deposited on solid substrate). This has generally been the case for other naked carbon nanoparticles from different sources and preparations. Thus, it seems logical to assume that the solvent molecules may passivate the particle surface, similar to but understandably less effective than the surface passivation agents in the much more fluorescent functionalized carbon nanoparticles (dubbed "carbon dots").[16–18,21] In this regard, the higher luminescence quantum yields of the carbon nanoparticles suspended in DMSO (Table 1) might simply be due to relatively more effective particle surface passivation by DMSO molecules (conceptually similar to weak surface noncovalent "functionalization" of the carbon nanoparticles). Therefore, the photoluminescence in all

Fig. 1. Absorption and emission (—, 400 nm excitation; – –, 440 nm excitation) spectra of the aqueous suspended carbon nanoparticles (photo inset: fraction S).

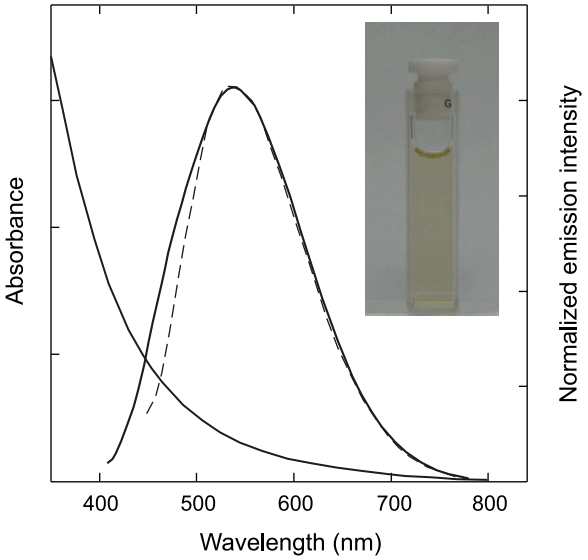

Fig. 2. A typical atomic force microscopy image of the carbon nanoparticles (fraction S).

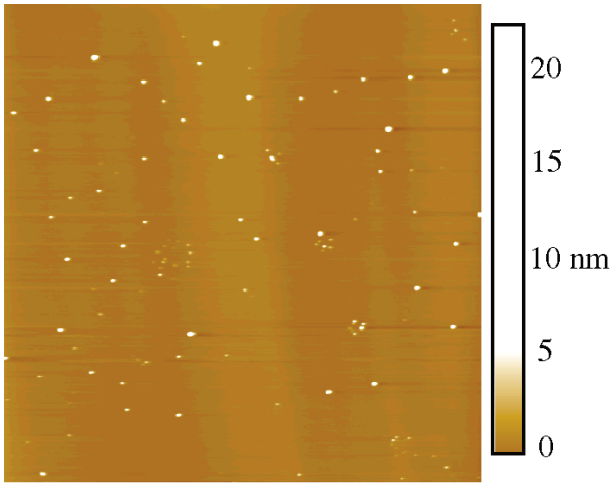

small carbon nanoparticles (naked or functionalized carbon dots) could have the same origin: the emissive energy trapping sites on the passivated surface of carbon nanoparticles.[16]

The effect of surface passivation on luminescence properties of the carbon nanoparticles was also reflected in the unusual quenching results with aliphatic amines as quenchers. Specifically for diethylamine (DEA) in aqueous suspension of the carbon nanoparticles, as a representative example, the observed luminescence intensities increased with an increasing amount of quencher molecules at low DEA concentrations, namely the reversed Stern–Volmer quenching behavior (Fig. 4). Beyond the low concentration region (~4 mmol/L for DEA in aqueous solution), the normal quenching took over, though the Stern–Volmer plot was curved downward at higher DEA concentrations (Fig. 4). The absorption and luminescence emission spectra of the carbon nanoparticles remained largely unchanged with DEA

Can. J. Chem. Downloaded from www.nrcresearchpress.com by University of Electronic and Science Techonology of China on 09/18/12
For personal use only.

Fig. 3. Luminescence spectra (400 nm excitation, normalized in the inset) of the carbon nanoparticles (fraction S) in DMSO (—), DMF (· · ·), water (– – –), ethanol (– · · –), and methanol (— —).

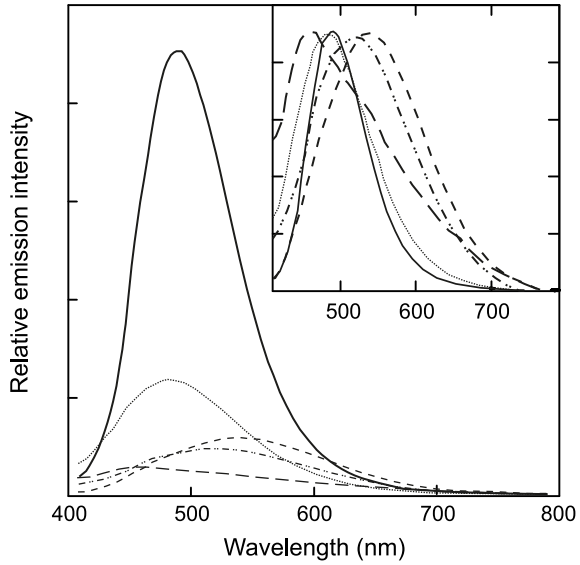

Table 1. Luminescence quantum yields of the carbon nanoparticles in different solvents.

Solvent	Φ_F for excitation at 440 nm (400 nm) (%)
DMSO	0.84 (0.73)
DMF	0.29 (0.25)
Water	0.24 (0.16)
Ethanol	0.2 (0.14)
Methanol	0.14 (0.09)

Fig. 4. Stern–Volmer plots for the quenching of luminescence intensities (○, 400 nm excitation; △, 440 nm excitation) of the carbon nanoparticles (fraction S) by diethylamine (DEA) in aqueous solution.

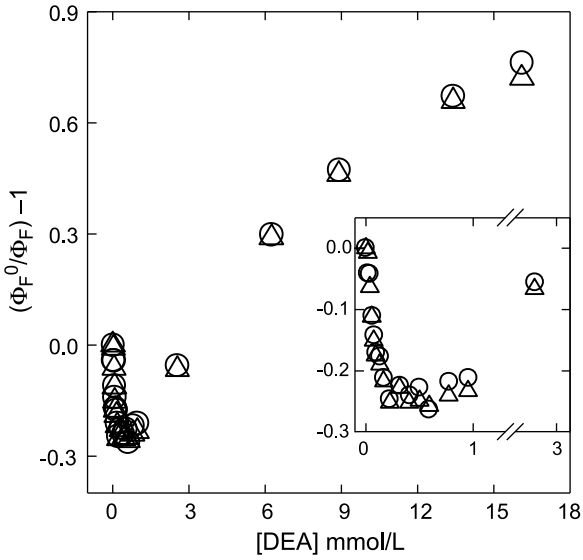

concentration in both the reversed and normal Stern–Volmer quenching regions.

The reversed Stern–Volmer quenching behavior at low quencher concentrations might be explained by the same mechanistic framework as that for the functionalized carbon nanoparticles, namely that the DEA molecules in initially low population could be "adsorbed" onto the carbon nanoparticles to improve the surface passivation, phenomenologically similar to weak noncovalent functionalization, to result in higher luminescence intensities. The effect of improved passivation might be overtaken by the normal Stern–Volmer quenching at higher quencher concentrations. Interestingly, similarly different quenching behaviors in low and high DEA concentration regions were observed for the carbon nanoparticles in methanol (Fig. 5), but not in DMSO (Fig. 5). The latter was a solvent in which the carbon nanoparticles were found to be significantly more luminescent (Table 1). The absence of the reversed quenching behavior in DMSO was consistent with the argument that the

Fig. 5. Stern–Volmer plots for the quenching of luminescence intensities (○, 400 nm excitation; △, 440 nm excitation) of the carbon nanoparticles (fraction S) by diethylamine (DEA) in methanol (top) and DMSO (bottom).

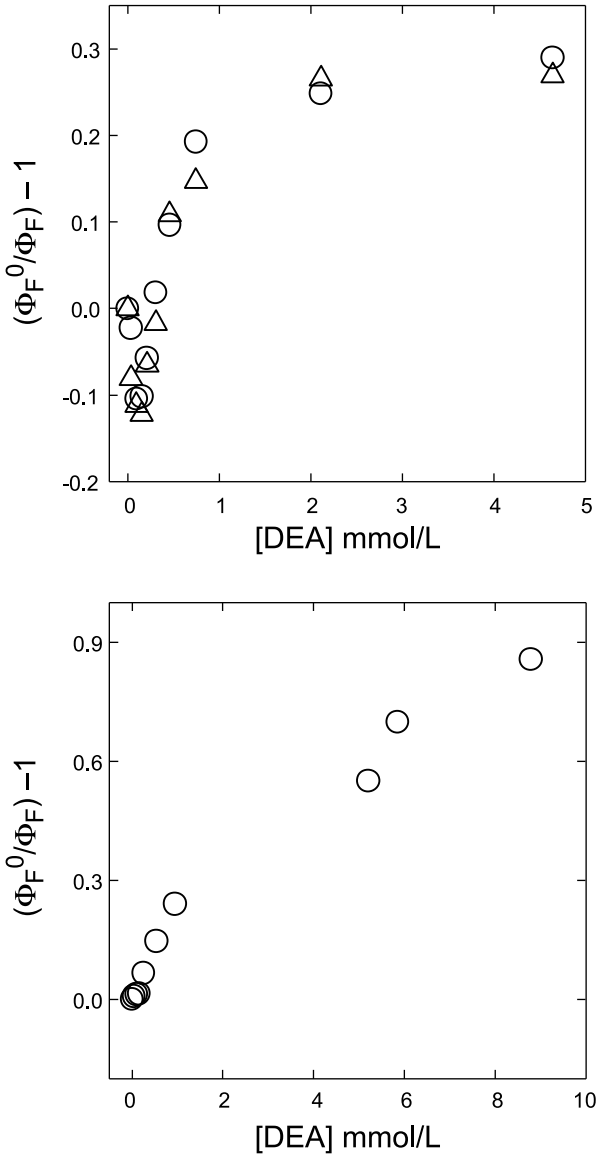

Can. J. Chem. Downloaded from www.nrcresearchpress.com by University of Electronic and Science Techonology of China on 09/18/12
For personal use only.

Fig. 6. Stern–Volmer plots for the quenching of luminescence intensities (400 nm excitation) of the carbon nanoparticles (fraction S) by ethylamine (top) and PEG_{550N} (bottom) in aqueous solution.

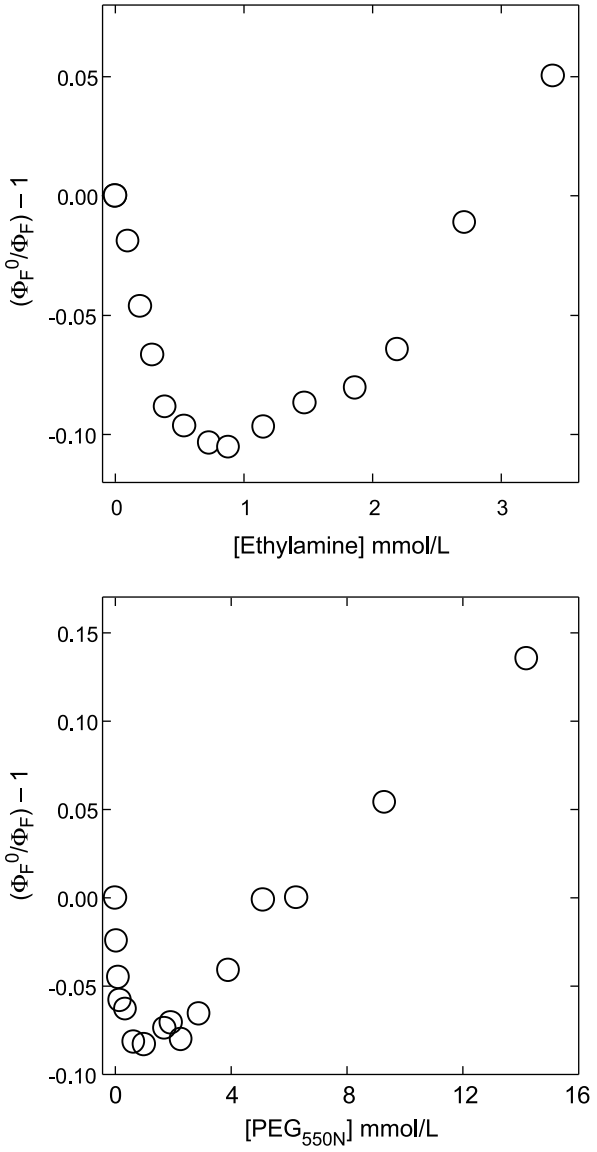

Table 2. Luminescence quantum yields of different fractions in water.

Fraction	Φ_F for excitation at 440 nm (400 nm) (%)
Fraction S	0.24 (0.16)
Fraction R_1	0.14 (0.11)
Fraction R_2	0.15 (0.11)
Fraction R_3	0.16 (0.13)
Fraction R_4	0.14 (0.11)

observed higher luminescence quantum yields in DMSO could be attributed to the more effective surface passivation by the solvent molecules, with which the similar passivation effect by the low-concentration DEA molecules was apparently not competitive.

Other water-soluble amines such as ethylamine and methoxy polyethylene glycol amine ($CH_3O(CH_2CH_2O)_{11}CH_2CH_2NH_2$, PEG_{550N}) exhibited similar reversed quenching behavior at

Fig. 7. Normalized luminescence spectra (400 nm excitation) of the carbon nanoparticles in water: fraction S (—), fraction R_1 (· · ·), fraction R_2 (– – –), fraction R_3 (– · · –), and fraction R_4 (— —).

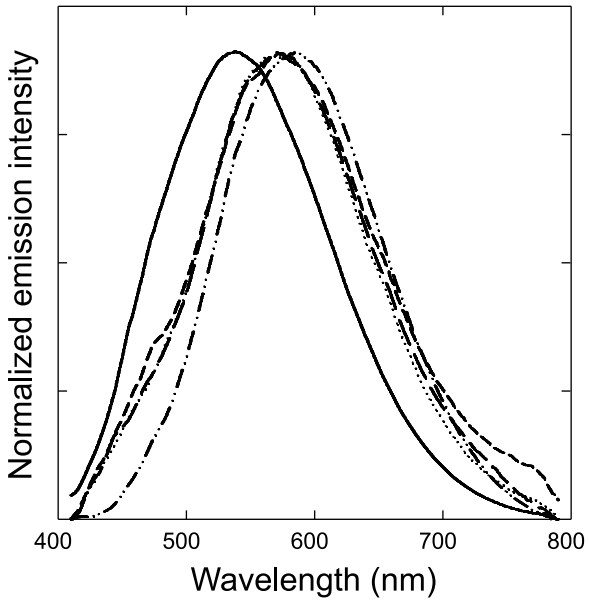

lower quencher concentrations (Fig. 6). The subsequent turnover in Stern–Volmer plots could again be attributed to the competition between the initial enhancement in luminescence intensities due to the improving particle surface passivation and the normal luminescence quenching. The latter was likely due to photoinduced electron transfer processes.[31]

The dispersion of purified carbon nanoparticles in aqueous solution was dependent on the solution pH, being more stable under neutral than acidic conditions. Therefore, the centrifugation at 3 500*g* to obtain the supernatant for the experiments described above was performed with the as-purified (nitric acid-treated, thus acidic) sample, followed by dialysis of the supernatant to result in an even more stable aqueous suspension at neutral pH (fraction S, as compared below with the other fractions). The residue from the same centrifugation was also dialyzed against deionized water to neutral pH (as fraction R), and the fraction was subdivided into various fractions (fraction R_1, R_2, R_3, and R_4, Table 2) via sequential centrifugation at different *g* values, as described in more details in the Experimental section. The fractions thus obtained were characterized and evaluated for their luminescence properties, in reference to those of the sample (fraction S) described above.

The atomic force microscopy results for these fractions suggested no major differences from fraction S (Fig. 2), except for the observation of some larger particles in low population (insignificant statistically). The absorption and luminescence properties of these fractions were also found to be mostly similar among fractions R (Fig. 7), though the luminescence spectra were somewhat shifted from that of fraction S (Figs. 1 and 7), and the observed luminescence quantum yields were also lower (Table 2). Nevertheless, for such inhomogeneous samples of suspended carbon nanoparticles, the changes in spectroscopic results across all samples could hardly be considered as dramatic, or they are actually qualitatively similar.

Can. J. Chem. Downloaded from www.nrcresearchpress.com by University of Electronic and Science Techonology of China on 09/18/12
For personal use only.

The results from this study, in general agreement with those reported in the literature, confirmed that neat carbon nanoparticles in aqueous and other solvent suspensions were photoluminescent, though with much lower emission quantum yields than those found in functionalized carbon nanoparticles or carbon dots. The fractionation aimed at size selection in terms of different centrifugation fields was apparently not so effective, probably because the gravimetric properties of the suspended carbon nanoparticles were affected by not just the particle sizes, but also surface characteristics such as the presence and population of oxidized groups (carboxylic acids, especially). Nevertheless, the general insensitivity of the observed spectroscopic properties to the fractionation seemed to suggest that the photoluminescent emissions were qualitatively similar across all of the suspended carbon nanoparticles. Mechanistically, the luminescence in these nanoparticles likely has the same origin as that in the functionalized carbon nanoparticles, both due to passivated surface energy trapping sites. A major difference is that the suspended carbon nanoparticles are passivated by solvent molecules (so the naked particles are not so naked after all), whereas the nanoparticles in brightly emissive carbon dots are passivated by surface functionalization. The significance for the observation of reversed Stern–Volmer quenching behavior in this study is that it helps to illustrate the importance of surface passivation to the luminescence emissions in carbon nanoparticles.

Experimental section

Materials

Fine-extruded graphite rods (carbon content > 99.9%) were purchased from Graphitestore.com, Inc. Dialysis membrane tubing was supplied by Spectrum Laboratories. Water was deionized and purified by being passed through a Labconco WaterPros water purification system.

Measurements

A Baxter Megafuge (model 2630) and Beckman-Coulter ultracentrifuge (Optima L90K with a type 90 Ti fixed-angle rotor) were used for centrifugation at various *g* values. Atomic force microscopy analyses were conducted in the acoustic AC mode on a Molecular Imaging PicoPlus system equipped with a multipurpose scanner for a maximum imaging area of 10 μm × 10 μm and a NanoWorld Pointprobe NCH sensor (125 μm in length). Transmission electron microscopy (TEM) studies were performed on Hitachi 9500 TEM and Hitachi HD-2000 S-TEM systems. Optical absorption spectra were recorded on a Shimadzu UV-2501PC spectrophotometer. Luminescence emission spectra were measured on a Jobin-Yvon fluorescence spectrometer equipped with a 450 W xenon source, Gemini-180 excitation monochromator and Tirax-550 emission monochromator, and a single-photon counting detector (Hamamatsu R928P PMT at 950 V). Quinine sulfate and 9,10-bis(phenylethynyl)-anthracene were used as the fluorescence standard.

Carbon nanoparticles

The carbon soot containing nanoparticles was produced in the arc discharge of graphite rods.[32] The discharge chamber was in a floating helium atmosphere (1 atm; 1 atm = 101.325 kPa) while the rods were burned with a direct current of 70 A (28 V). The as-produced carbon soot was dispersed in dimethylformamide (DMF) with ultrasonication (Crest Ultrasonics, Model 950DA, 50–60 Hz) for 24 h. The dispersion was then evaporated to remove DMF for the recovery of carbon particles.

The particle sample (3 g) in aqueous nitric acid solution (2.6 mol/L, 240 mL) was refluxed for 12 h. The resulting acidic suspension at room temperature was centrifuged at 3 500*g* for 5 min to collect the supernatant. It was then neutralized with sodium carbonate, followed by dialysis (membrane molecular weight cutoff ~500) against fresh deionized water for 3 days. The resulting stable dispersion of carbon nanoparticles, denoted as fraction S, was used in most of the measurements, including those that required a transfer from aqueous to another solvent.

The residue from the centrifugation above, denoted as fraction R, was added to water for the same dialysis to result in an aqueous suspension at neutral pH. Upon settling after 12 h, the sediment was harvested as fraction R_1, and the supernatant was centrifuged at 55 000*g* for 1 h to obtain the residue as fraction R_2. The new supernatant was again centrifuged in a higher field of 393 000*g* for 1 h to yield the residue as fraction R_3 and the final supernatant as fraction R_4.

Concentrations of the carbon nanoparticles in suspensions were generally low, less than 10 mg/L. At such low concentrations, the particle concentration effect on spectroscopic results was negligible.

Acknowledgements

This work was made possible by a grant from the National Science Foundation (NSF). L.C. was supported by a Susan G. Komen for the Cure Postdoctoral Fellowship. J.-H.L. was a visiting student from Peking University (the group of Prof. Haifang Wang and Prof. Yuanfang Liu) in Beijing, China. E.M. was a research participant supported by the Palmetto Academy, an education-training program managed by the South Carolina Space Grant Consortium.

References

(1) Alivisatos, P. *Nat. Biotechnol.* **2004**, *22* (1), 47. doi:10.1038/nbt927. PMID:14704706.
(2) Michalet, X.; Pinaud, F. F.; Bentolila, L. A.; Tsay, J. M.; Doose, S.; Li, J. J.; Sundaresan, G.; Wu, A. M.; Gambhir, S. S.; Weiss, S. *Science* **2005**, *307* (5709), 538. doi:10.1126/science.1104274. PMID:15681376.
(3) Medintz, I. L.; Uyeda, H. T.; Goldman, E. R.; Mattoussi, H. *Nat. Mater.* **2005**, *4* (6), 435. doi:10.1038/nmat1390. PMID:15928695.
(4) Tan, Z. N.; Zhang, F.; Zhu, T.; Xu, J.; Wang, A. Y.; Dixon, J. D.; Li, L. S.; Zhang, Q.; Mohney, S. E.; Ruzyllo, J. *Nano Lett.* **2007**, *7* (12), 3803. doi:10.1021/nl072370s. PMID:17975946.
(5) Resch-Genger, U.; Grabolle, M.; Cavaliere-Jaricot, S.; Nitschke, R.; Nann, T. *Nat. Methods* **2008**, *5* (9), 763. doi:10.1038/nmeth.1248. PMID:18756197.
(6) Kamat, P. V. *J. Phys. Chem. C* **2008**, *112* (48), 18737. doi:10.1021/jp806791s.
(7) Alivisatos, A. P. *Science* **1996**, *271* (5251), 933. doi:10.1126/science.271.5251.933.

Can. J. Chem. Downloaded from www.nrcresearchpress.com by University of Electronic and Science Techonology of China on 09/18/12
For personal use only.

(8) (a) Hines, M. A.; Guyot-Sionnest, P. *J. Phys. Chem.* **1996**, *100* (2), 468. doi:10.1021/jp9530562.; (b) Peng, X. G.; Schlamp, M. C.; Kadavanich, A. V.; Alivisatos, A. P. *J. Am. Chem. Soc.* **1997**, *119* (30), 7019. doi:10.1021/ja970754m.

(9) Lovrić, J.; Cho, S. J.; Winnik, F. M.; Maysinger, D. *Chem. Biol.* **2005**, *12* (11), 1227. doi:10.1016/j.chembiol.2005.09.008. PMID:16298302.

(10) Hardman, R. A. *Environ. Health Perspect.* **2006**, *114* (2), 165. doi:10.1289/ehp.8284. PMID:16451849.

(11) Lin, P.; Chen, J.-W.; Chang, L. W.; Wu, J.-P.; Redding, L.; Chang, H.; Yeh, T.-K.; Yang, C. S.; Tsai, M.-H.; Wang, H.-J.; Kuo, Y.-C.; Yang, R. S. H. *Environ. Sci. Technol.* **2008**, *42* (16), 6264. doi:10.1021/es800254a. PMID:18767697.

(12) Geys, J.; Nemmar, A.; Verbeken, E.; Smolders, E.; Ratoi, M.; Hoylaerts, M. F.; Nemery, B.; Hoet, P. H. M. *Environ. Health Perspect.* **2008**, *116* (12), 1607. doi:10.1289/ehp.11566. PMID:19079709.

(13) Wilson, W. L.; Szajowski, P. F.; Brus, L. E. *Science* **1993**, *262* (5137), 1242. doi:10.1126/science.262.5137.1242. PMID:17772645.

(14) Portolés, M. J. L.; Nieto, F. R.; Soria, D. B.; Amalvy, J. I.; Peruzzo, P. J.; Mártire, D. O.; Kotler, M.; Holub, O.; Gonzalez, M. C. *J. Phys. Chem. C* **2009**, *113* (31), 13694. doi:10.1021/jp903727n.

(15) Fojtik, A.; Henglein, A. *J. Phys. Chem. B* **2006**, *110* (5), 1994. doi:10.1021/jp058176g. PMID:16471774.

(16) Sun, Y.-P.; Zhou, B.; Lin, Y.; Wang, W. J.; Fernando, K. A. S.; Pathak, P.; Meziani, M. J.; Harruff, B. A.; Wang, X.; Wang, H.; Luo, P. G.; Yang, H.; Kose, M. E.; Chen, B.; Veca, L. M.; Xie, S. Y. *J. Am. Chem. Soc.* **2006**, *128* (24), 7756. doi:10.1021/ja062677d. PMID:16771487.

(17) Cao, L.; Wang, X.; Meziani, M. J.; Lu, F. S.; Wang, H. F.; Luo, P. G.; Lin, Y.; Harruff, B. A.; Veca, L. M.; Murray, D.; Xie, S.-Y.; Sun, Y.-P. *J. Am. Chem. Soc.* **2007**, *129* (37), 11318. doi:10.1021/ja073527l. PMID:17722926.

(18) Sun, Y.-P.; Wang, X.; Lu, F.; Cao, L.; Meziani, M. J.; Luo, P. G.; Gu, L.; Veca, L. M. *J. Phys. Chem. C* **2008**, *112* (47), 18295. doi:10.1021/jp8076485.

(19) Bourlinos, A. B.; Stassinopoulos, A.; Anglos, D.; Zboril, R.; Karakassides, M.; Giannelis, E. P. *Small* **2008**, *4* (4), 455. doi:10.1002/smll.200700578. PMID:18350555.

(20) Liu, R.; Wu, D.; Liu, S.; Koynov, K.; Knoll, W.; Li, Q. *Angew. Chem. Int. Ed.* **2009**, *48* (25), 4598. doi:10.1002/anie.200900652.

(21) Peng, H.; Travas-Sejdic, J. *Chem. Mater.* **2009**, *21* (23), 5563. doi:10.1021/cm901593y.

(22) Zhu, H.; Wang, X.; Li, Y.; Wang, Z.; Yang, F.; Yang, X. *Chem. Commun. (Camb.)* **2009**, *5118*. doi:10.1039/b907612c.

(23) Mochalin, V. N.; Gogotsi, Y. *J. Am. Chem. Soc.* **2009**, *131* (13), 4594. doi:10.1021/ja9004514. PMID:19290627.

(24) Hu, S.-L.; Niu, K.-Y.; Sun, J.; Yang, J.; Zhao, N.-Q.; Du, X. W. *J. Mater. Chem.* **2009**, *19* (4), 484. doi:10.1039/b812943f.

(25) Liu, H. P.; Ye, T.; Mao, C. D. *Angew. Chem. Int. Ed.* **2007**, *46* (34), 6473. doi:10.1002/anie.200701271.

(26) Ray, S. C.; Saha, A.; Jana, N. R.; Sarkar, R. *J. Phys. Chem. C* **2009**, *113* (43), 18546. doi:10.1021/jp905912n.

(27) Tian, L.; Ghosh, D.; Chen, W.; Pradhan, S.; Chang, X.; Chen, S. *Chem. Mater.* **2009**, *21* (13), 2803. doi:10.1021/cm900709w.

(28) Zhou, J. G.; Booker, C.; Li, R. Y.; Zhou, X. T.; Sham, T. K.; Sun, X. L.; Ding, Z. F. *J. Am. Chem. Soc.* **2007**, *129* (4), 744. doi:10.1021/ja0669070. PMID:17243794.

(29) Zhao, Q.-L.; Zhang, Z.-L.; Huang, B.-H.; Peng, J.; Zhang, M.; Pang, D.-W. *Chem. Commun. (Camb.)* **2008**, *5116*. doi:10.1039/b812420e.

(30) Zheng, L.; Chi, Y.; Dong, Y.; Lin, J.; Wang, B. *J. Am. Chem. Soc.* **2009**, *131* (13), 4564. doi:10.1021/ja809073f. PMID:19296587.

(31) Wang, X.; Cao, L.; Lu, F.; Meziani, M. J.; Li, H.; Qi, G.; Zhou, B.; Harruff, B. A.; Kermarrec, F.; Sun, Y.-P. *Chem. Commun. (Camb.)* **2009**, *3774*. doi:10.1039/b906252a.

(32) Murooka, Y.; Maede, Y.; Ozaki, M.; Hibino, M. *Chem. Phys. Lett.* **2001**, *341* (5–6), 455. doi:10.1016/S0009-2614(01)00493-6.

A photoswitchable bichromophoric oxazine with fast switching speeds and excellent fatigue resistance

Erhan Deniz, Stefania Impellizzeri, Salvatore Sortino, and Françisco M. Raymo

Abstract: In search of strategies to regulate the photochemical and photophysical properties of photochromic oxazines, we designed a multichromophoric compound incorporating 3*H*-indole, benzooxazine, and 2-(4-dimethylaminophenyl)ethynyl fragments. We synthesized this molecule in two steps in an overall yield of 51%, starting from commercial precursors. The ultraviolet irradiation of this photochrome opens a [1,3]oxazine ring in less than 6 ns to generate a zwitterionic isomer with a quantum yield of 0.10. In particular, the photoinduced ring opening generates a 4-nitrophenolate anion and a 3*H*-indolium cation. Additionally, this process brings the 2-(4-dimethylaminophenyl)ethynyl appendage into conjugation with the 3*H*-indolium cation. As a result, two distinct bands for the anionic and cationic fragments of the photogenerated zwitterion appear in the visible region of the absorption spectrum. The photogenerated isomer has a lifetime of 2 μs and switches back to the original form with first-order kinetics. Furthermore, this bichromophoric photochrome tolerates hundreds of switching cycles with no sign of degradation and can be operated within rigid polymer matrices. Thus, this particular structural design can lead to the development of a new family of bichromophoric photochromes and photoresponsive materials with microsecond switching times and excellent fatigue resistances.

Key words: heterocycles, molecular switches, oxazines, photochromism, photoisomerization.

Résumé : Dans le cadre d'une recherche sur des stratégies qui pourraient permettre de régulariser les propriétés photochimiques et photophysiques d'oxazines photochromiques, on a développé un composé multichromophorique comportant des fragments 3*H*-indole, benzooxazine et 2-(4-diméthylaminophényl)éthynyle. Cette molécule a été synthétisée en deux étapes, avec un rendement de 51 %, à partir de précurseurs commerciaux. L'irradiation ultraviolette de ce photochrome provoque l'ouverture d'un noyau [1,3]diazine en moins de 6 ns pour conduire à la formation d'un isomère zwitterionique avec un rendement quantique de 0,10. En particulier, l'ouverture de cycle photoinduite génère un anion 4-nitrophénolate et un cation 3*H*-indolium. De plus, ce processus conduit le groupe 2-(4-diméthylaminophényl)éthynyle à se placer en conjugaison avec le cation 3*H*-indolium. Il en résulte que la région visible du spectre d'absorption comporte deux bandes distinctes, l'une pour le fragment anionique et l'autre pour le fragment cationique du zwitterion photogénéré. Le temps de vie de l'isomère photogénéré est de 2 μs et il retourne à la forme originale avec une cinétique du premier ordre. De plus, ce photochrome bichromophorique tolère des centaines de cycles sans signe apparent de dégradation et il peut être utilisé dans des matrices de polymères rigides. Cette structure particulière pourrait donc conduire au développement d'une nouvelle famille de photochromes bichromophoriques et de matériaux photosensibles ayant des temps de commutation de l'ordre de la microseconde et une excellente capacité à résister à la fatigue.

Mots-clés : hétérocycles, commutateurs moléculaires, oxazines, photochromie, photoisomérisation.

[Traduit par la Rédaction]

Introduction

The term photochromism refers to the photoinduced and reversible change in color of a collection of molecules.[1–5] The process can be a consequence of photoinduced ring opening–closing steps, cis–trans isomerizations, intramolecular proton transfers, intermolecular electron transfers, cycloadditions, or the reorganization of ligands around a metal center. All these transformations alter the electronic structure of the photoresponsive compound and result in significant changes in the absorption spectrum. In addition, these structural alterations at the molecular level can translate into noticeable changes in refractive index. As a result, photochromic transformations can be exploited to modulate the absorption coefficient and refractive index of a substrate under the influence of optical stimulations. Indeed, a diver-

Received 19 February 2010. Accepted 1 May 2010. Published on the NRC Research Press Web site at canjchem.nrc.ca on 17 December 2010.

This article is part of a Special Issue dedicated to Professor J. C. Scaiano.

E. Deniz, S. Impellizzeri, and F.M. Raymo.[1] University of Miami Department of Chemistry, 1301 Memorial Drive, Coral Gables, FL 33146-0431, USA.
S. Sortino. Dipartimento di Scienze Chimiche, Università di Catania, viale Andrea Doria 8, Catania, I-95125, Italy.

[1]Corresponding author (e-mail: fraymo@miami.edu).

Can. J. Chem. Downloaded from www.nrcresearchpress.com by University of Electronic and Science Techonology of China on 09/18/12
For personal use only.

Can. J. Chem. Downloaded from www.nrcresearchpress.com by University of Electronic and Science Techonology of China on 09/18/12
For personal use only.

sity of photoresponsive materials and devices have already been designed around the absorptive and dispersive effects associated with photochromic compounds.[6–8] In fact, promising examples of all-optical logic gates,[9–13] optical limiters,[14–18] photoresponsive filters,[19] and photoswitchable probes[20–26] have all been implemented on the basis of the photochromism associated with certain organic compounds.

Nitrospiropyrans switch from a colorless to a colored state under ultraviolet irradiation and revert thermally to the original form.[27–31] Because of their photochemical behavior and their synthetic accessibility, they have become one of the most popular classes of photochromic compounds. However, their switching speeds are relatively slow and a full switching cycle can only be completed on a timescale of minutes. Furthermore, the involvement of the triplet state in the photoisomerization mechanism tends to encourage degradation and these compounds can only tolerate a few tens of switching cycles. In search of strategies to improve their switching speeds and fatigue resistances, we developed a new family of photochromic compounds based on the photoinduced opening and thermal closing of [1,3]oxazine rings.[32] Our molecules switch from a colorless to a colored state in less than 6 ns upon ultraviolet excitation and revert to the original form on a nanosecond timescale. In addition, they survive thousands of switching cycles unaffected, even in the presence of molecular oxygen, and can be operated in solution as well as within rigid polymer matrices. The integration of these compounds into photonic materials and devices, however, requires a basic understanding of the stereoelectronic factors regulating their spectroscopic signature and photochromism. In particular, we need to learn how their molecular skeleton should be modified to tune the color of the photogenerated state, the timescales of the isomerization processes, and the quantum efficiency of their coloration without compromising their excellent fatigue resistance.

Laser excitation of **1a** (Fig. 1) at 355 nm opens its [1,3]oxazine ring in less than 6 ns to generate the zwitterionic isomer **1b** with a quantum yield of 0.10 in acetonitrile at 20 °C.[32a,32b] The original state **1a** does not absorb in the visible region, while the 4-nitrophenolate chromophore of the photogenerated species **1b** absorbs at 440 nm. Therefore, the photoinduced transformation of **1a** into **1b** is accompanied by the appearance of a transient band in the visible region of the absorption spectrum. This band decays monoexponentially on a nanosecond timescale with the thermal reisomerization of **1b** back to **1a**.

The introduction of a 2-(4-dimethylaminophenyl)ethynyl group in place of the phenyl ring of **1a** generates a bichromophoric switch in the shape of **2a**.[32g] Specifically, the photoinduced opening of the [1,3]oxazine ring of this compound brings the 2-(4-dimethylaminophenyl)ethynyl appendage into conjugation with the 3*H*-indolium cation. The resulting chromophore absorbs at 540 nm and, hence, the formation of **2b** is accompanied by the appearance of a transient band centered at this wavelength together with one at 440 nm for the 4-nitrophenolate anion. Both bands decay monoexponentially on a microsecond timescale and with identical kinetics, as **2b** reisomerizes thermally to **2a**. Thus, structural modifications of the group (R^2 in Fig. 1) attached to the chiral center at the junction of the two heterocyclic fragments

Fig. 1. Photoinduced transformation of the [1,3]oxazines **1a**–**4a** into the zwitterions **1b**–**4b**.

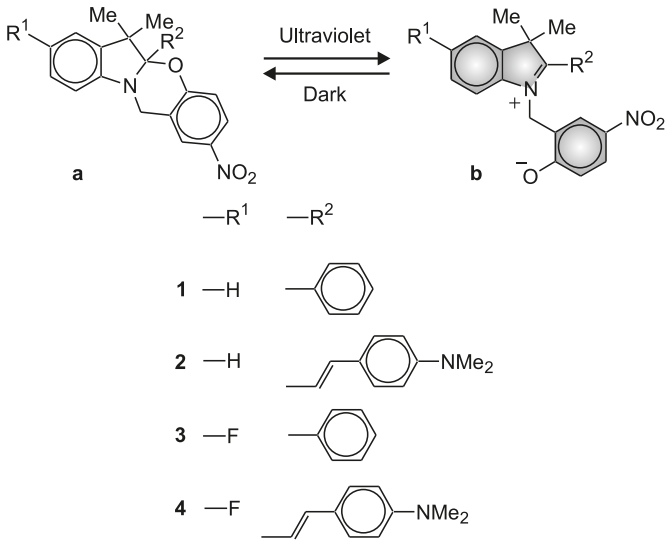

of our oxazines can be exploited to regulate the absorption properties of their photogenerated states in the visible region and impose bichromophoric character on them. However, the transition from **1a** to **2a** has a depressive effect on the photoisomerization efficiency and the quantum yield decreases from 0.10 to 0.07.

The introduction of a fluorine substituent in the para position (R^1 in Fig. 1) relative to the nitrogen atom of the 3*H*-indole fragment of **1a** facilitates the photoinduced opening of the [1,3]oxazine ring. Specifically, the quantum yield increases from 0.10 to 0.29 with the transition from **1a** to **3a**.[32g] On the basis of these considerations, we envisaged the possibility of introducing a fluorine substituent also on the 3*H*-indole fragment of the bichromophoric switch **2a** to improve the quantum yield for its photoisomerization. In particular, we designed compound **4a** and here we report its synthesis, spectroscopic characterization, and photochemical properties in solution and within a rigid polymer matrix.

Results and discussion

Synthesis

We synthesized **4a** in two steps (Fig. 2), starting from commercial precursors, with an overall yield of 51%. Specifically, the condensation of 2,3,3′-trimethyl-5-fluoro-3*H*-indole with *N,N*-dimethyl-4-aminobenzaldehyde under acidic conditions gave the extended 3*H*-indole **5**, which was reacted with 2-chloromethyl-4-nitrophenol to afford the target oxazine **4a**. Similarly, the reaction of **5** with methyl iodide produced the iodide salt of the model 3*H*-indolium cation **6**.

Steady-state absorption spectroscopy

The spectrum of **4a** reveals a band centered at 306 nm (*a* and *d* in Fig. 3) for the overlapping absorptions of the 2-(4-dimethylaminophenyl)ethynyl and 4-nitrophenoxy chromophores. Upon addition of acid, the [1,3]oxazine ring of **4a** opens to generate the cationic species **4c** (Fig. 4). This transformation extends the conjugation of the 2-(4-dimethylaminophenyl)ethynyl appendage and shifts its absorption to

Can. J. Chem. Downloaded from www.nrcresearchpress.com by University of Electronic and Science Techonology of China on 09/18/12
For personal use only.

Fig. 2. Synthesis of the [1,3]oxazine **4a** and model compound **6**.

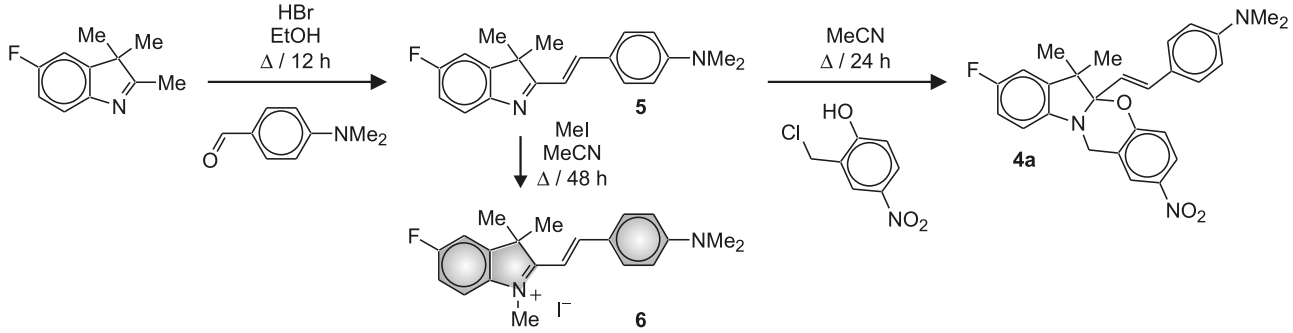

Fig. 3. Steady-state absorption spectra of solutions (0.1 mmol/L, MeCN, 20 °C) of **4a** before (*a* and *d*) and after the addition of either CF_3CO_2H (1 equiv., *b*) or Bu_4NOH (5 equiv., *e*), **6** (*c*), and 4-nitrophenol after the addition of Bu_4NOH (4 equiv., *f*).

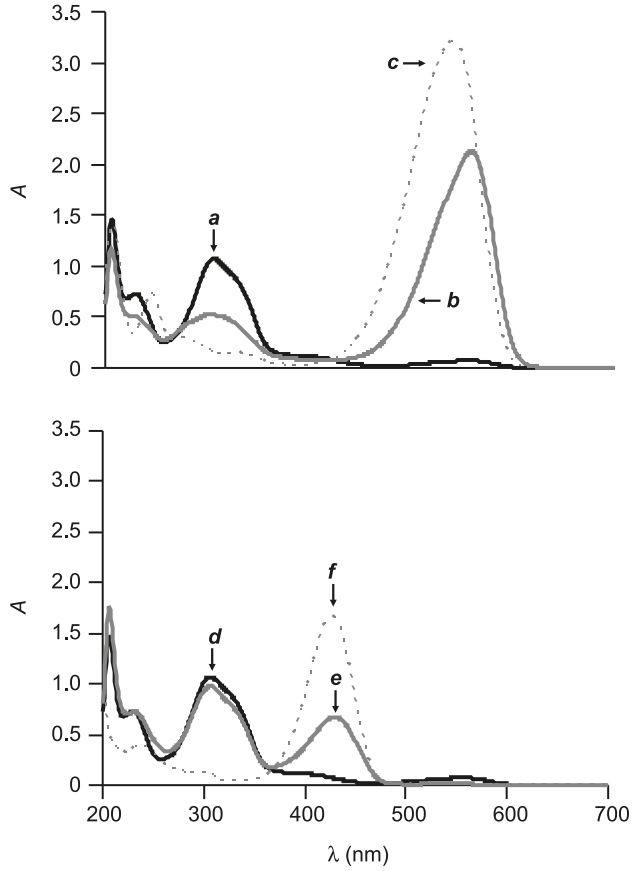

559 nm (*b* in Fig. 3). Indeed, this band resembles that of the model 3*H*-indolium cation **6** (*c* in Fig. 3).

The addition of base also opens the [1,3]oxazine ring of **4a** to generate the anionic species **4d**. This process causes the appearance of a band at 427 nm (*e* in Fig. 3), corresponding to the 4-nitrophenolate chromophore of **4d**. In fact, this absorption is reminiscent of that associated with the tetrabutylammonium salt of 4-nitrophenolate (*f* in Fig. 3).

Transient absorption spectroscopy

In acetonitrile at 20 °C, the laser excitation of **4a** at 355 nm is accompanied by the appearance within 6 ns of two transient bands at 420 and 540 nm (*a* in Fig. 5) in the absorption spectrum. They resemble those observed in the steady-state spectra of **4d** and **4c**, respectively (*e* and *b* in Fig. 3) and correspond to ground-state absorptions of the 4-nitrophenolate anion and 3*H*-indolium cation, respectively, of **4b**. Thus, the [1,3]oxazine ring of **4a** opens upon excitation to generate the bichromophoric isomer **4b**, in analogy to the behavior of **2a** and **2b**. However, the transition from **2a** to **4a** results in an increase in quantum yield from 0.07 to 0.10.[33] Indeed, plots (*b* and *c* in Fig. 5) of the absorbance change measured at 540 nm upon laser excitation against the pulse energy show a noticeable increase in slope on going from **2a** to **4a**, consistent with an enhancement in quantum efficiency. Thus, the presence of a fluorine substituent on the 3*H*-indolium fragment of **4a** facilitates the photochromic transformation. Presumably, this effect is a consequence of the reduced electron density on the nitrogen atom of the 3*H*-indole fragment of **4a**, relative to that of **2a**, with the suppression of competitive photoinduced electron transfer to the adjacent nitro group. Indeed, the cyclic voltammograms of the model compounds **7** and **8** (Fig. 6) demonstrate that the oxidation potential of the 3*H*-indole fragment shifts by 70 mV in the positive direction with the introduction of an electron-withdrawing fluorine substituent.[34]

The photogenerated isomer **4b** reverts spontaneously to **4a** on a microsecond timescale. As a result, the two bands of **4b** decay with identical first-order kinetics. Curve fitting of both temporal profiles (*d* and *e* in Fig. 5) reveals the lifetime of **4b** to be 2 μs in acetonitrile at 20 °C. This value is identical to that of **2b**, demonstrating that the fluorine substituent has no influence on the reisomerization kinetics. Thus, a full switching cycle can be completed in a few microseconds with both photochromic systems. In addition, they tolerate hundreds of switching cycles with no sign of degradation. Specifically, the steady-state absorption spectra recorded before and after 300 excitation cycles are virtually identical, indicating the lack of any significant degradation under these experimental conditions.

The bichromophoric photochrome **4a** can be incorporated within a rigid poly(methyl methacrylate) (PMMA) matrix on the basis of a spin-coating procedure. The laser excitation of the resulting film at 355 nm is also accompanied by the appearance within 6 ns of two transient bands (*a* in Fig. 7). Once again, these bands resemble those observed in the steady-state spectra of **4d** and **4c** in solution and correspond to ground-state absorptions of the 4-nitrophenolate anion and

Can. J. Chem. Downloaded from www.nrcresearchpress.com by University of Electronic and Science Techonology of China on 09/18/12
For personal use only.

Fig. 4. Transformation of the [1,3]oxazine **4a** into the cation **4c** or anion **4d** under the influence of acid or base, respectively.

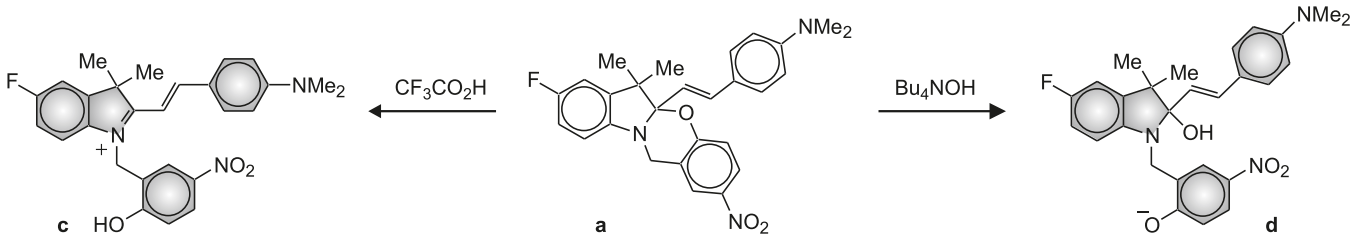

3*H*-indolium cation of **4b**. As observed in solution, the photogenerated isomer **4b** reverts spontaneously back to **4a** also within the PMMA matrix. Concomitantly, both absorption bands decay with the reisomerization process, though with biexponential kinetics in this instance. Curve fitting of the corresponding temporal profiles (*b* in Fig. 7) indicates lifetimes of 4 and 130 μs. The biexponential decay is consistent with that observed for **2b** in PMMA and suggests the coexistence of two main environments for the photochromic dopants within the polymer matrix.

Conclusions

Bichromophoric photochromes can be synthesized in two steps, starting from commercial precursors, by fusing 3*H*-indole and benzooxazine fragments and appending a 2-(4-dimethylaminophenyl)ethynyl group to the chiral center at the junction of the two heterocycles. The ultraviolet excitation of these compounds opens their [1,3]oxazine ring in less than 6 ns to produce a zwitterionic isomer, incorporating a 4-nitrophenolate anion and a 3*H*-indolium cation. These two chromophoric fragments absorb at 440 and 540 nm, respectively, and, therefore, the photoinduced transformation is accompanied by the appearance of two bands in the visible region of the absorption spectrum. The introduction of a fluorine substituent in the para position, relative to the nitrogen atom, of the 3*H*-indole heterocycle increases the photoisomerization quantum yield. Indeed, the electron-withdrawing character of the substituent reduces the electron density on the nitrogen atom of the 3*H*-indole heterocycle and facilitates the photoinduced ring-opening process. Instead, this particular substituent has essentially no influence on the lifetime of the photogenerated isomer, which reverts to the original form with first-order kinetics on a microsecond timescale. In fact, these bichromophoric photochromes can be switched back and forth between their two states in a few microseconds and tolerate hundreds of switching cycles with no sign of degradation. In addition, they can be operated within rigid PMMA matrices, though with slower reisomerization kinetics than in acetonitrile solution. Thus, our structural design for the realization of bichromophoric photochromes can lead to the development of novel photoresponsive materials with fast switching speeds and excellent fatigue resistances.

Experimental procedures

Materials and methods

Chemicals were purchased from commercial sources and used as received with the exception of MeCN, which was distilled over CaH_2. Compounds **7** and **8** were prepared according to literature procedures.[32a,32g] All reactions were monitored by thin-layer chromatography, using aluminum sheets coated with silica (60, F_{254}). Fast atom bombardment mass spectra (FABMS) were recorded with a VG Mass Lab Trio-2 spectrometer in a 3-nitrobenzyl alcohol matrix. Nuclear magnetic resonance (NMR) spectra were recorded with Bruker Avance 400 or 500 spectrometers. Steady-state absorption spectra were recorded with a Varian Cary 100 Bio spectrometer, using quartz cells with a path length of 0.5 cm. Time-resolved absorption spectra were recorded with a Luzchem Research mLFP–111 spectrometer, after excitation with a Continuum Surelite II–10 Nd–YAG laser (pulse width = 6 ns (FWHM), wavelength = 355 nm). The photochromic films were prepared by spin-coating a CH_2Cl_2 solution of **4a** (1.0 mg/mL) and PMMA (52 mg/mL) on a glass plate at 420 rpm for 9 s. The thickness (6 μm) of the resulting films was measured with a Tencor Instruments 10-00090 surface profilometer. Cyclic voltammograms were recorded with a CH Instruments 660 workstation in degassed MeCN solutions of Bu_4NPF_6 (0.1 mol/L) under an atmosphere of Ar, using a glassy-carbon working electrode, a platinum counter electrode, and a Ag/AgCl reference electrode.

Synthesis of 5

A solution of 2,3,3′-trimethyl-5-fluoro-3*H*-indole (1.09 g, 6.15 mmol), *N,N*-dimethyl-4-aminobenzaldehyde (0.92 g, 6.15 mmol), and HBr (0.5 mL, 33% in AcOH) in EtOH (10 mL) was heated under reflux for 12 h. After cooling to ambient temperature, the solvent was distilled off under reduced pressure. The residue was dissolved in CH_2Cl_2 (30 mL) and washed with a saturated aqueous solution of $NaHCO_3$ (2 × 20 mL). The organic phase was dried over Na_2SO_4 and the solvent was distilled off under reduced pressure to give **5** (1.6 g, 85%) as an orange solid. ^{1}H NMR ($CDCl_3$) δ : 1.44 (6H, s), 2.98 (6H, s), 6.69 (2H, d, J = 8 Hz), 6.85 (1H, d, J = 16 Hz), 7.00 (2H, t, J = 7 Hz), 7.49–7.51 (3H, m), 7.66 (1H, d, J = 16 Hz). ^{13}C NMR ($CDCl_3$) δ: 24.4, 40.6, 53.4, 109.3, 112.5, 115.0, 121.0, 124.3, 129.4, 139.0, 148.9, 150.7, 151.6, 160.3, 162.7, 184.3. FABMS *m/z*: 310 $[M + H]^+$.

Synthesis of 4a

A solution of **5** (278 mg, 0.9 mmol) and 2-chloromethyl-4-nitrophenol (169 mg, 0.9 mmol) in MeCN (20 mL) was heated under reflux for 24 h. After cooling to ambient temperature, the solvent was distilled off under reduced pressure and the residue was dissolved in CH_2Cl_2 (3 mL). The addition of Et_2O (20 mL) caused the precipitation of a purple solid. The solid was dissolved in CH_2Cl_2 (30 mL) and washed with H_2O (20 mL). The organic phase was dried over Na_2SO_4 and the solvent was distilled off under reduced

Can. J. Chem. Downloaded from www.nrcresearchpress.com by University of Electronic and Science Techonology of China on 09/18/12
For personal use only.

Fig. 5. Transient absorption spectrum (0.04 mmol/L, MeCN, 20 °C) of **4a** (*a*) recorded 0.1 μs after laser excitation (355 nm, 6 ns, 12 mJ). Absorbance change (0.04 mmol/L, MeCN, 20 °C) at 540 nm recorded 0.1 μs after laser excitation (355 nm, 6 ns) of **2a** (*b*) and **4a** (*c*) against the pulse energy. Temporal evolution of the absorbance (0.04 mmol/L, MeCN, 20 °C) at 440 (*d*) and 540 nm (*e*) after excitation (355 nm, 6 ns, 12 mJ) of **4a** and the corresponding monoexponential fittings.

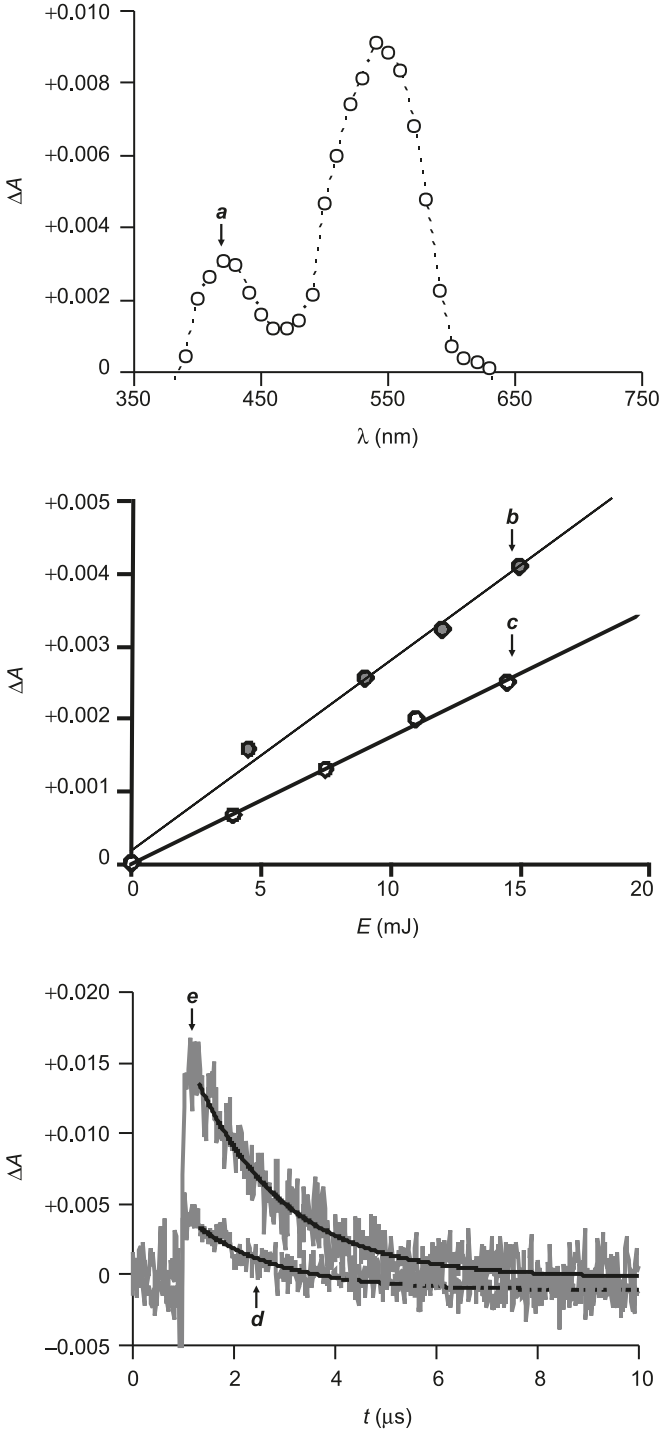

pressure to give **4a** (248 mg, 60%) as a purple solid. ^{1}H NMR (DMSO) δ: 1.34 (6H, s), 2.93 (6H, s), 4.85 (2H, s), 6.42 (1H, d, J = 16 Hz), 6.67 (2H, d, J = 9 Hz), 6.88–6.95 (4H, m), 7.20 (1H, d, J = 8 Hz), 7.44 (2H, d, J = 8 Hz), 7.95 (1H, d, J = 9 Hz), 8.10 (1H, s). ^{13}C NMR (DMSO) δ: 23.9, 24.8, 26.2, 45.0, 45.4, 50.8, 111.1, 111.3, 111.9, 112.8, 114.7, 118.3, 121.6, 123.8, 125.4, 130.2, 139.6, 141.9, 142.6, 152.2, 155.0, 157.9, 160.2, 190.7. FABMS *m/z*: 461 [M + H]$^+$

Fig. 6. Model compounds **7** and **8**.

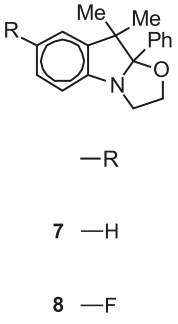

Fig. 7. Transient absorption spectrum (2% *w*/*w*, PMMA, 20 °C) of **4a** (*a*) recorded 0.1 μs after laser excitation (355 nm, 6 ns, 12 mJ). Temporal evolution of the absorbance at 640 nm (*b*) after excitation and the corresponding biexponential fitting.

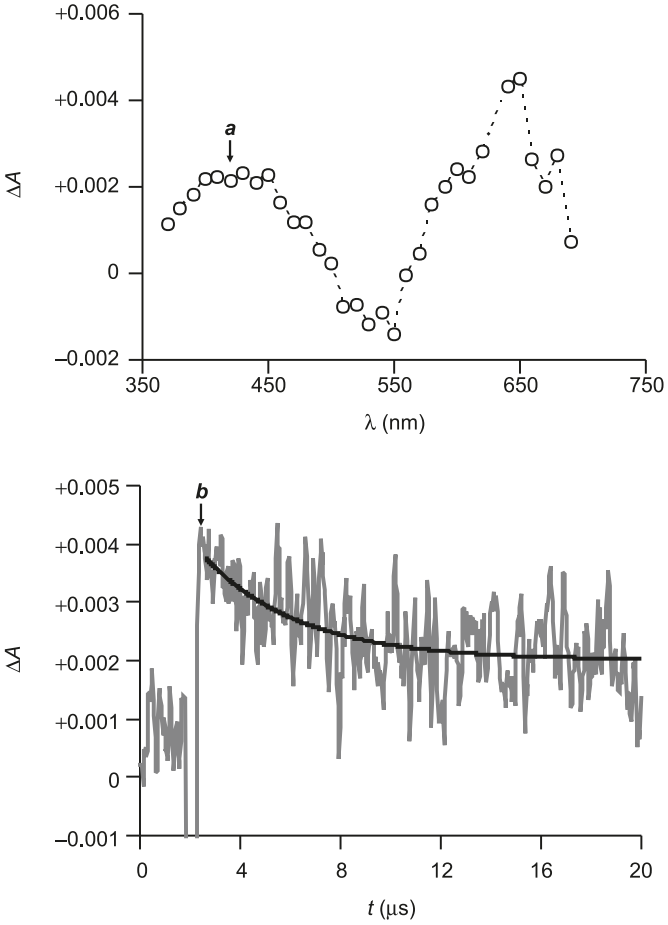

Synthesis of 6

A solution of **5** (120 mg, 0.39 mmol) and MeI (113 mg, 0.8 mmol) in MeCN (10 mL) was heated under reflux for 48 h. After cooling to ambient temperature, the solvent was

Can. J. Chem. Downloaded from www.nrcresearchpress.com by University of Electronic and Science Techonology of China on 09/18/12
For personal use only.

distilled off under reduced pressure and the residue was dissolved in CH_2Cl_2 (3 mL). The addition of Et_2O (20 mL) caused the precipitation of a purple solid, which was filtered off to give **6** (141 mg, 80%). ^{1}H NMR ($CDCl_3$) δ: 1.79 (6H, s), 3.19 (6H, s), 4.18 (3H, s), 6.79 (2H, d, J = 8 Hz), 7.18 (2H, d, J = 8 Hz), 7.26 (1H, d, J = 20 Hz), 7.44-–7.47 (1H, m), 8.04–8.08 (3H, m). ^{13}C NMR ($CDCl_3$) δ: 28.0, 36.2, 40.9, 51.4, 105.5, 110.8, 113.1, 114.9, 116.5, 122.9, 135.8, 138.3, 144.4, 155.1, 155.8, 163.9, 179.4. FABMS: m/z = 323 $[M - I]^+$.

Acknowledgments

We thank the NSF (CAREER Award CHE-0237578 and CHE-0749840) and MIUR (PRIN 2008) for financial support.

References

(1) *Photochromism*; Dorion, G. H., Wiebe, A. F., Eds.; Focal Press: New York, 1970.
(2) *Photochromism*; Brown, G. H., Ed.; Wiley: New York, 1971.
(3) *Organic Photochromes*; El'tsov, A. V., Ed.; Consultants Bureau: New York, 1990.
(4) *Photochromism: Molecules and Systems*; Bouas-Laurent, H., Dürr, H., Eds.; Elsevier: Amsterdam, 1990.
(5) *Organic Photochromic and Thermochromic Compounds*; Crano, J. C., Guglielmetti, R., Eds.; Plenum Press: New York, 1999.
(6) *Applied Photochromic Polymer Systems*; McArdle, C. B., Ed.; Blackie: Glasgow, 1992.
(7) (a) *Photo-Reactive Materials for Ultrahigh Density Optical Memory*; Irie, M., Ed.; Elsevier: Amsterdam, 1994; (b) Irie, M. *Chem. Rev.* **2000**, *100* (5), 1683. doi:10.1021/cr9800681. PMID:11777415.
(8) (a) Raymo, F. M.; Tomasulo, M. *Chem. Eur. J.* **2006**, *12*, 3186; doi:10.1002/chem.200501178.(b) Raymo, F. M. *Angew. Chem. Int. Ed.* **2006**, *45*, 5249. doi:10.1002/anie.200602516.
(9) (a) de Silva, A. P.; McClean, G. D.; McClenaghan, N. D.; Moody, T. S.; Weir, S. M. *Nachr. Chem.* **2001**, *49*, 602; doi:10.1002/nadc.20010490506.(b) Brown, G. J.; de Silva, A. P.; Pagliari, S. *Chem. Commun. (Camb.)* **2002**, 2461; doi:10.1039/b207795g.(c) de Silva, A. P.; McClenaghan, N. D. *Chem. Eur. J.* **2004**, doi:10.1002/chem.200305054.*10*, 574; (d) de Silva, A. P.; Uchiyama, S. *Nat. Nanotechnol.* **2007**, *2* (7), 399. doi:10.1038/nnano.2007.188. PMID:18654323.
(10) Ward, M. D. *J. Chem. Educ.* **2001**, *78*, 321. doi:10.1021/ed078p321.
(11) Raymo, F. M. *Adv. Mater.* **2002**, *14*, 401. doi:10.1002/1521-4095(20020318).
(12) Steinitz, D.; Remacle, F.; Levine, R. D. *ChemPhysChem* **2002**, *3* (1), 43. doi:10.1002/1439-7641(20020118). PMID:12465475.
(13) (a) Balzani, V.; Credi, A.; Venturi, M. *ChemPhysChem* **2003**, *4* (1), 49. PMID:12596465.; (b) Credi, A. *Angew. Chem. Int. Ed.* **2007**, *46*, 5472.
(14) Tutt, L. W.; Boggess, T. F. *Prog. Quantum Electron.* **1993**, *17*, 299. doi:10.1016/0079-6727(93)90004-S.
(15) Perry, J. W. Organic and Metal-Containing Reverse Saturable Absorbers for Optical Limiting. In *Nonlinear Optics of Organic Molecules and Polymers*; Nalwa, H. S., Miyata, S., Eds.; CRC Press: Boca Raton, 1997; pp 813–840.
(16) Van Stryland, E. W.; Hagan, D. J.; Xia, T.; Said, A. A. Applications of Nonlinear Optics to Passive Optical Limiting. In *Nonlinear Optics of Organic Molecules and Polymers*; Nalwa, H. S., Miyata, S., Eds.; CRC Press: Boca Raton, 1997; pp 841–860.
(17) Sun, Y.-P.; Riggs, J. E. *Int. Rev. Phys. Chem.* **1999**, *18*, 43. doi:10.1080/014423599230008.
(18) Ganeev, R. A. *J. Opt. A: Pure Appl. Opt.* **2005**, *7*, 717. doi:10.1088/1464-4258/7/12/004.
(19) Crano, J. C.; Kwak, W. S.; Welch C. N. Spirooxazines and Their Use in Photochromic Lenses. In *Applied Photochromic Polymer Systems*; McArdle, C. B., Ed.; Blackie: Glasgow, 1992; pp 31–79.
(20) (a) Hell, S. W. Increasing the Resolution of Far-Field Fluorescence Light Microscopy by Point-Spread-Function Engineering. In *Topics in Fluorescence Spectroscopy*; Lakowicz, J. R., Ed.; Plenum Press: New York, 1997; pp 361–426; (b) Hell, S. W. *Nat. Biotechnol.* **2003**, *21* (11), 1347. doi:10.1038/nbt895. PMID:14595362.; (c) Hell, S. W.; Dyba, M.; Jakobs, S. *Curr. Opin. Neurobiol.* **2004**, *14* (5), 599. doi:10.1016/j.conb.2004.08.015. PMID:15464894.; (d) Hell, S. W. *Phys. Lett. A* **2004**, *326*, 140; doi:10.1016/j.physleta.2004.03.082.(e) Hell, S. W.; Willig, K. I.; Dyba, M.; Jakobs, S.; Kastrup, L.; Westphal, V. Nanoscale Resolution with Focused Light: STED and Other RESOLFT Microscopy Concepts. In *Handbook of Biological Confocal Microscopy*; Pawley, J. B., Ed.; Springer: New York, 2006; pp 571–579; (f) Hell, S. W.; Kastrup, L. *Nachr. Chem.* **2007**, *55*, 47; doi:10.1002/nadc.200744314.(g) Hell, S. W. *Science* **2007**, *316* (5828), 1153. doi:10.1126/science.1137395. PMID:17525330.; (h) Schönle, A.; Hell, S. W. Nanoscale resolution in far-field fluorescence microscopy. In *Science of Microscopy*; Hawkes, P. W., Spence, J. C. H., Eds.; Springer: New York, 2007;Vol. 2, pp 790–834; (i) Hell, S. W. *Nat. Methods* **2009**, *6* (1), 24. doi:10.1038/nmeth.1291. PMID:19116611.
(21) Bates, M.; Huang, B.; Zhuang, X. *Curr. Opin. Chem. Biol.* **2008**, *12* (5), 505. doi:10.1016/j.cbpa.2008.08.008. PMID:18809508.
(22) Fernández-Suárez, M.; Ting, A. Y. *Nat. Rev. Mol. Cell Biol.* **2008**, *9* (12), 929. doi:10.1038/nrm2531. PMID:19002208.
(23) Gustafsson, M. G. L. *Nat. Methods* **2008**, *5* (5), 385. doi:10.1038/ nmeth0508-385. PMID:18446157.
(24) Heilemann, M.; Dedecker, P.; Hofkens, J.; Sauer, M. *Laser Photon. Rev.* **2009**, *3*, 180. doi:10.1002/lpor.200810043.
(25) Lippincott-Schwartz, J.; Manley, S. *Nat. Methods* **2009**, *6* (1), 21. doi:10.1038/nmeth.f.233. PMID:19116610.
(26) (a) Hess, S. T. *Nat. Methods* **2009**, *6* (2), 124. doi:10.1038/nmeth0209-124. PMID:19180093.; (b) Gould, T. J.; Verkhusha, V. V.; Hess, S. T. *Nat. Protoc.* **2009**, *4* (3), 291. doi:10.1038/nprot.2008.246. PMID:19214181.
(27) (a) Bertelson, R. C. Photochromic Processes Involving Heterolytic Cleavage. In *Photochromism*; Brown, G.H., Ed.; Wiley: New York, 1971; pp 45–431; (b) Bertelson, R. C. Spiropyrans. In *Organic Photochromic and Thermochromic Compounds*; Crano, J. C., Guglielmetti, R., Eds.; Plenum Press: New York, 1999; Vol. 1, pp 11–83.
(28) Kholmanskii, A. S.; Dyumanev, K. M. *Russ. Chem. Rev.* **1987**, *56*, 136. doi:10.1070/RC1987v056n02ABEH003262.
(29) (a) Guglielmetti, R. 4n + 2 Systems: Spiropyrans. In *Photochromism: Molecules and Systems*; Bouas-Laurent, H., Dürr, H., Eds.; Elsevier: Amsterdam, 1990; pp 314–466; (b) Guglielmetti, R. Spiropyrans and Related Compounds. In *Photochromism: Molecules and Systems*; Bouas-Laurent, H., Dürr, H., Eds.; Elsevier: Amsterdam, 1990; pp 855–878.

(30) Tamai, N.; Miyasaka, H. *Chem. Rev.* **2000**, *100*, 1875.
(31) Minkin, V. I. *Chem. Rev.* **2004**, *104* (5), 2751. doi:10.1021/cr020088u. PMID:15137806.
(32) (a) Tomasulo, M.; Sortino, S.; White, A. J. P.; Raymo, F. M. *J. Org. Chem.* **2005**, *70* (20), 8180. doi:10.1021/jo051417w. PMID:16277345.; (b) Tomasulo, M.; Sortino, S.; Raymo, F. M. *Org. Lett.* **2005**, *7* (6), 1109. doi:10.1021/o1050045a. PMID:15760151.; (c) Tomasulo, M.; Sortino, S.; Raymo, F. M. *Asian Chem. Lett.* **2007**, *11*, 219; (d) Tomasulo, M.; Sortino, S.; Raymo, F. M. *Adv. Mater.* **2008**, *20*, 832; doi:10.1022/adma.200602843.(e) Tomasulo, M.; Sortino, S.; Raymo, F. M. *J. Org. Chem.* **2008**, *73* (1), 118. doi:10.1021/jo7017119. PMID:18052385.; (f) Tomasulo, M.; Sortino, S.; Raymo, F. M. *J. Photochem. Photobiol. A* **2008**, *200*, 44; doi:10.1016/j.photochem.2008.03.016.(g) Deniz, E.; Tomasulo, M.; Sortino, S.; Raymo, F. M. *J. Phys. Chem. C* **2009**, *113*, 8491; doi:10.1021/jp901494c.(h) Åxman Petersen, M.; Deniz, E.; Brøndsted Nielsen, M.; Sortino, S.; Raymo, F. M. *Eur. J. Org. Chem.* **2009**, 4333; doi:10.1002/ejoc.200900604.(i) Tomasulo, M.; Deniz, E.; Benelli, T.; Sortino, S.; Raymo, F. M. *Adv. Funct. Mater.* **2009**, *19*, 3956; doi:10.1002/adfm.200901364.(j) Tomasulo, M.; Deniz, E.; Sortino, S.; Raymo, F. M. *Photochem. Photobiol. Sci.* **2010**, *9* (2), 136. doi:10.1039/b9pp00114j. PMID:20126786.
(33) The quantum yield of **4a** was determined using **2a** as standard, according to a literature procedure (ref. 32g).
(34) The oxidation potentials of **7** and **8** are +1.16 and +1.23 V vs. Ag/AgCl, respectively.

Can. J. Chem. Downloaded from www.nrcresearchpress.com by University of Electronic and Science Techonology of China on 09/18/12
For personal use only.

Chemoselective photochemical surface reaction — Ketene versus carbene reactivity from the photolysis of saturated monolayers of pyridyl diazoesters on single-crystal Pt

Jason L. Pitters, Dana K. Adkinson, Keith Griffiths, Peter R. Norton, and Mark S. Workentin

Abstract: Irradiation of saturated monolayers of 3- and 4-substituted pyridyl diazoacetates on single-crystal Pt surfaces leads to either the corresponding reactive carbene or stable ketene intermediate with the chemoselectivity determined by the position of the photoreactive substituent on the pyridyl ring, which ultimately directs the available interactions with neighboring substrates.

Key words: ketene, carbene, diazoester, saturated monolayer, photochemistry, Pt surfaces.

Résumé : L'irradiation de monocouches saturées de diazoacétates de pyridyles substitués dans les positions 3 et 4 sur des surfaces de monocristaux de platine conduit à la formation soit du carbène réactif correspondant ou de l'intermédiaire cétène stable dans lesquels la chimiosélectivité est déterminée par la position du substituant photoréactif sur le noyau pyridyle qui en fin de compte dirige les interactions disponibles avec les substrats avoisinants.

Mots-clés : cétène, carbène, diazoester, monocouche saturée, photochimie, surfaces de platine.

[Traduit par la Rédaction]

Introduction

The ability to precisely control the reactivity of organic molecules as saturated monolayers on metal surfaces is a significant challenge. Results of such studies remain of interest because of the continued need for efficient methods for the selective chemical modification of the surface for a host of applications.[1] Most studies with these goals concentrate on monolayers based on long alkyl chains with surface active groups bound to Au or Si, while studies of smaller, less flexible organic molecular architectures are relatively unexplored.[2,3] Monolayers of smaller and more rigid molecules should allow for more careful control and understanding of the orientation of the organic substrate and allow for selectivity in the interfacial reactivity as a function of the position of the reactive moiety on the rigid structure of the moiety forming the monolayer.

Here, we report a remarkable and unprecedented chemoselectivity in a monolayer surface photoreaction, namely the photoreaction of pyridyl diazoacetates (3- and 4-PDE) on single-crystal platinum surfaces. The chemoselectivity results from the relative position of the reactive group on the rigid molecular architecture of the base pyridyl rings. Diazoesters are known to react thermally and photochemically with loss of nitrogen to form the corresponding carbene intermediate.[4] Unlike diazoketones or diazoaldehydes, they do not generally undergo efficient Wolff-type rearrangements to generate a ketene because of the poor migratory aptitude of the –OR group; instead, they generally react through a carbene.[4] For example, aryl diazoester derivatives show only traces (<1%) of Wolff rearrangement.[4c] Pyridyl diazoesters are not well studied, and only in the case of 3-PDE was the formation of a ketene observed, but this was at 10 K in an Ar matrix.[5] In solution, we found 98% of the products from irradiation of 3- or 4-PDE are from trapping of the carbene intermediate.[6] However, in this report, we show that we can select the reactivity between the carbene and ketene by simply altering the position of the diazoester function on the pyridyl ring that is bound to the metal surface (Scheme 1). Such control sheds important insights into the reactivity in this type of monolayer environment and suggests that this experimental approach also provides a method for characterizing reactive intermediates.

Received 1 June 2010. Accepted 22 July 2010. Published on the NRC Research Press Web site at canjchem.nrc.ca on 7 January 2011.

This article is part of a Special Issue dedicated to Professor J. C. Scaiano.

J.L. Pitters. National Institute for Nanotechnology (NINT), National Research Council (NRC) of Canada, 11421 Saskatchewan Drive, Edmonton, AB T6G 2M9, Canada.
D.K. Adkinson, K. Griffiths, P.R. Norton, and M.S. Workentin.[1] Department of Chemistry, The University of Western Ontario, London, ON N6A 5B7, Canada.

[1]Corresponding author (e-mail: mworkent@uwo.ca).

Can. J. Chem. Downloaded from www.nrcresearchpress.com by University of Electronic and Science Techonology of China on 09/18/12
For personal use only.

Can. J. Chem. Downloaded from www.nrcresearchpress.com by University of Electronic and Science Techonology of China on 09/18/12
For personal use only.

Scheme 1. Chemoselectivity in the surface photochemistry of 3- and 4-PDE on Pt.

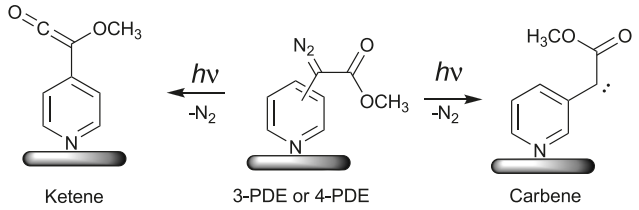

Experimental

All ultra-high vacuum (UHV) experiments were performed in a stainless steel chamber pumped with a 330 L s^{-1} turbo molecular pump and a titanium sublimation pump. With these pumps, background pressures in the low 10^{-10} torr range (1 torr = 133.322 Pa) could be achieved. The chamber was interfaced to a Mattson Cygnus 100 Fourier transform infrared spectrometer for FTIR–RAIR (reflection absorption infrared) spectroscopy. The external optical system for the RAIRS consisted of a flat plane mirror that redirected the collimated IR light from the spectrometer to a parabolic mirror that focused the light on the sample surface in the chamber at a grazing angle. The reflected light from the sample then left the chamber to be re-collimated by another parabolic mirror and then focused on the detector with a final parabolic mirror. The UHV chamber was fitted with KCl windows, and a liquid-nitrogen-cooled narrow-band mercury cadmium telluride detector with a spectral range of 800–4000 cm^{-1} was used for the experiments. The optical system was purged with dried air and scrubbed of CO_2 with a Balston FTIR gas-purge generator system. A PIKE Technologies wire grid polarizer was also used to filter out the s-polarized light. Also interfaced to the UHV chamber was an Ar^+ ion gun, a quadrupole mass spectrometer for temperature-programmed desorption (TPD), and low energy electron diffraction (LEED) optics that could be substituted for an Auger system with a cylindrical mirror analyzer. Through a separately pumped gas manifold, Ar for sputtering, O_2 for cleaning, and CO could be introduced to the chamber with the use of leak valves. Two separate leak valves were also available for the introduction of samples to the surface for analysis. Dosing of samples was directed through steel tubes to the surface to ensure surface coverage without chamber contamination.

The Pt crystal, either Pt(110) or Pt(111), was attached to the sample mount (two nickel-coated copper posts) by spot-welding four 0.010 inch (1 inch = 2.54 cm) diameter Pt wire to the back of the crystal. A K-type thermocouple was spot-welded to the edge of the crystal for temperature monitoring. The crystal was initially annealed for 3 days at 1073 K with periodic Ar^+ sputtering to remove impurities from the bulk of the Pt. This was followed by a final annealing at 1273 K for 3 h. The crystals were also cleaned prior to each experiment. The cleaning procedure consisted of Ar^+ sputtering (3 KeV, 6 $\mu A\,cm^{-2}$ at an Ar pressure of 1×10^{-5} torr) at 298–1073 K, followed by annealing in 1×10^{-6} O_2 at 1273 K for up to 30 min. A final annealing at 1373 K for up to 20 min was also performed. The cleanliness of the crystal was checked with LEED and Auger electron spectroscopy (AES). The crystal was determined to be clean and ordered when impurities of carbon, sulfur, and oxygen were not observed with AES and a sharp LEED pattern was observed.[7]

The surface photochemical experiments were performed using a 200 W mercury–xenon arc lamp supplied by Oriel. The lamp was filtered with a series of mirrors and cut-off filters to transmit light from 300 to 400 nm. The light entered the UHV chamber through a quartz window and was focused on the sample through a series of external fused-silica optical lenses.

Methyl diazo(3-pyridyl)acetate (3-PDE)

A procedure adapted from Tomioka et al.[5] was used for the synthesis of 3-PDE. The compound 3-acetyl pyridine (30 g, 0.25 mol) was heated to reflux in morpholine (37.5 g, 0.43 mol) with sulfur (13 g, 0.41 mol) for 6 h in a modified Willgerodt reaction.[8] The mixture was poured onto ice and allowed to stand overnight. The resulting crystals were then filtered and recrystallized from a 50% benzene/petroleum ether mixture to give a pure thioacetomorpholide (63%). The thioacetomorpholide (8 g, 0.036 mol) was heated to reflux in 80 mL of a 50% ethanol/water mixture with excess KOH for 12 h. The water and ethanol were removed and the mixture was taken up in methanol (MeOH), which was acidified with dry HCl. This mixture was then heated to reflux for 24 h. The MeOH was removed and the salt was taken up in water and made basic with solid $NaHCO_3$. The resulting pyridyl ester was then extracted with ether and dried with magnesium sulfate and the ether was removed under vacuum to give a pale yellow liquid. This liquid was distilled at 100 °C at 0.1 mm Hg (1 mm Hg = 133.322 Pa) to give a colorless liquid of methyl (3-pyridyl)acetate (59%). The methyl (3-pyridyl)acetate (2 g, 0.013 mol) was stirred for 3 days at room temperature in 50 mL acetonitrile with tosyl azide (0.026 mol) and 4 g of KF/Al_2O_3 solid support.[9,10] The solid support was then filtered off and the acetonitrile was removed, leaving an orange solid. The solid was chromatographed on silica 60 (80 g silica per 1 g diazoester) with ethyl acetate. The removal of the ethyl acetate left an orange crystal that was shown to be pure methyl diazo(3-pyridyl)acetate (87%). Mp 58–60 °C. UV–vis (MeCN) λ_{max}, nm (ε, L mol^{-1} cm^{-1}): 272 (11800), 248 (12400), 207 (11770). IR (CCl_4) ν (cm^{-1}): 3035, 30003, 2955, 2845, 2091 (C=N=N), 1713 (C=O), 1587, 1565, 1481, 1437, 1421, 1360, 1348, 1261, 1195, 1063, 1032, 1020, 911. ^1H NMR (200 MHz, $CDCl_3$) δ (ppm): 3.89 (s, 3H), 7.31 (m, 1H), 7.88 (m, 1H), 8.43 (dd, 1H), 8.69 (m, 1H). ^{13}C NMR (50 MHz, $CDCl_3$) δ (ppm): 52, 63, 122, 123, 131, 145, 147, 165. MS *m/z* (% relative intensity): 177 (25), 149 (11), 106 (100), 78 (56), 63 (25). Exact mass MS calcd.: 177.0538, found: 177.0541.

Methyl diazo(4-pyridyl)acetate (4-PDE)

The synthesis of methyl diazo(4-pyridyl)acetate was accomplished using the method described above for the synthesis of methyl diazo(3-pyridyl)acetate, except that 4-acetyl pyridine was used as the starting material. Methyl diazo(4-pyridyl)acetate was isolated as a yellow powder. Mp 84–85 °C. UV–vis (MeCN) λ_{max}, nm (ε, L mol^{-1} cm^{-1}): 280 (14100), 250 (14300), 215 (13000). IR (CCl_4) ν (cm^{-1}): 3062, 3030, 2956, 2846, 2097 (C=N=N), 1719 (C=O),

Can. J. Chem. Downloaded from www.nrcresearchpress.com by University of Electronic and Science Techonology of China on 09/18/12
For personal use only.

1593, 1545, 1494, 1438, 1419, 1358, 1258, 1224, 1194, 1158, 1048, 990. ^{1}H NMR (200 MHz, $CDCl_3$) δ (ppm): 3.88 (s, 3H), 7.40 (dd, 4.7, 1.7 Hz, 2H), 8.52 (dd, 4.7, 1.7 Hz, 2H). ^{13}C NMR (50 MHz, $CDCl_3$) δ (ppm): 52, 64, 117, 136, 150, 164. MS *m*/*z* (% relative intensity): 177 (31), 149 (10), 106 (100), 78 (54), 63 (21). Exact mass MS calcd.: 177.0538, found: 177.0541.

Results and discussion

Saturated monolayers of analytically pure 3- and 4-PDE on Pt were formed through a sublimation process in a UHV chamber. In this method, the diazoester is introduced from the gas phase where it condenses onto a cooled and cleaned single-crystal Pt(110) or Pt(111) surface at 223 K using a technique we have previously described.[3,6] The multilayers resulting from the sublimation process are thermally desorbed by slowly warming the Pt crystal; the maximum rate of desorption for 3- and 4-PDE was found to be ~266–269 K using TPD and mass spectroscopic (MS) detection of the desorbed molecules. At temperatures above that of the maximum rate of desorption, only molecules chemisorbed on the metal are present. For subsequent experiments, dosing to form the monolayer was accomplished by holding the temperature of the cleaned Pt above the temperature for multilayer desorption, typically 293 K, but below that for any further reaction.

Reflection absorption infrared (RAIR) spectroscopy was used to characterize the resulting saturated monolayers formed using one of the two approaches presented above. The RAIR spectra of the saturated layer of 4-PDE and 3-PDE on Pt(110) are shown in Figs. 1 and 2, respectively. These are presented along with solution-phase transmission IR spectra for comparison. Key IR bands in the monolayer spectra include the C=N=N asymmetric and symmetric stretches at 2098 and 1337 cm^{-1} and 2093 and 1362 cm^{-1}, for 4-PDE and 3-PDE, respectively. The corresponding C=O stretches are at 1712 and 1710 cm^{-1}, respectively. Additional modes due to the C=C and C=N of the pyridyl ring in the range of 1570 and 1440 cm^{-1} are also evident. While there are slight intensity differences in the C=O and C=N=N bands between the solution and monolayer spectra due to the difference in the two experiments (transmission vs. RAIR) there is no significant shift in the position of the IR bands of either the diazo C=N=N or the ester C=O bands; the asymmetric and symmetric C=N=N and C=O bands in the solution-phase transmission spectra occur at 2091, 1361, and 1713 cm^{-1} and 2097, 1358, and 1719 cm^{-1} for 3- and 4-PDE, respectively. Because of this similarity, we conclude that these functional groups do not interact significantly with the metal surface in the monolayer. In the region between 1600 and 1400 cm^{-1}, there are differences on the order of 40–60 cm^{-1} when one compares the corresponding bands in the monolayer spectrum to those in the solution phase. The modes in this region are largely associated with the pyridyl ring. Together, the results indicate that the monolayer is bound through the pyridyl nitrogen, and that the rings have a mostly perpendicular orientation because of the strong $C{\equiv}N_2$ and C=O bands.[11] Similar spectra were recorded for 3- and 4-PDE on Pt(111) and these are provided in the Supplementary data.

Fig. 1. IR spectra of 4-PDE. (*a*) Solution transmission IR spectrum of 4-PDE in CCl_4 at 298 K, 4 cm^{-1}, scaled to fit. (*b*) RAIR spectrum of 4-PDE monolayer on Pt(110) at 298 K, 8 cm^{-1}. (*c*) RAIR spectrum of 4-PDE monolayer after photolysis, 8 cm^{-1}. Inset at top shows an expansion of the region between 2200 and 2000 cm^{-1} illustrating loss of C=N=N asymmetric stretch at 2098 cm^{-1} and growth of C=C=O stretch at 2124 cm^{-1}.

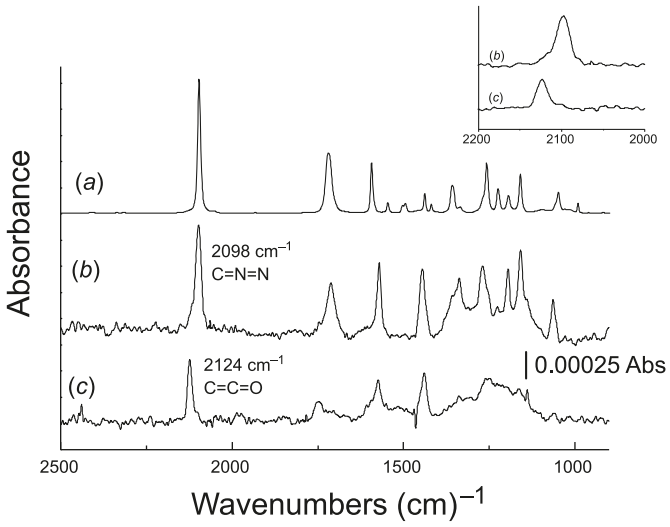

Fig. 2. IR spectra of 3-PDE. (*a*) Solution transmission IR spectrum of 3-PDE in CCl_4 at 298 K, 4 cm^{-1}, scaled to fit. (*b*) RAIR spectrum of 3-PDE monolayer on Pt(110) at 298 K, 4 cm^{-1}. (*c*) RAIR spectrum of 3-PDE monolayer after photolysis, 4 cm^{-1}.

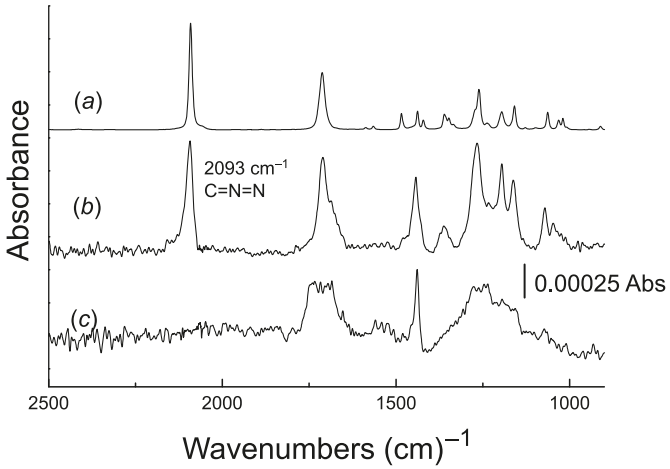

The monolayer was shown to be saturated by co-dosing carbon monoxide onto the monolayer formed as described above. Any available Pt sites would be indicated by the appearance of the Pt–CO stretch;[12] however, no Pt sites were observed. The thermal stability of the saturated monolayer was investigated by TPD experiments and by monitoring changes in the IR spectra as the temperature of the crystal was increased. The TPD spectra monitored several masses that corresponded to the major fragment ions for compounds (*m*/*z* = 106 and 78). The TPD spectra also monitored mass 28 to detect the release of nitrogen gas that evolves during the thermal decomposition of the diazoesters. For 3-PDE, the only detected signal was that of *m*/*z* = 28 and no other changes were detected for the fragments from the 3-PDE pa-

Can. J. Chem. Downloaded from www.nrcresearchpress.com by University of Electronic and Science Techonology of China on 09/18/12
For personal use only.

rent molecule. The detection of mass 28 indicated that there was a thermal decomposition of the diazo group during the heating of the monolayer. The onset of the detection occurred at 375 K and reached a maximum at 455 K. This decomposition temperature agrees well with that measured for similar diazoesters such as ethyl diazophenylacetate, where a half-life of 95 min at 373 K has been determined.[13] The fact that no fragments from the parent molecule were detected (m/z = 106 and 78) indicated that the diazo group decomposes on the surface before any desorption of the pyridyl groups occurs. Similar results were obtained for 4-PDE where the onset of the release of nitrogen was observed in the TPD at 390 K with a maximum at 465 K. The similarities between the thermal stability of the diazoesters as saturated monolayers and that measured for similar molecules when not bound to a surface suggest that the Pt surface does not alter the thermal stability of the diazo group, further indicating that this functionality is not interacting with the surface (vide supra). Saturated monolayers are stable indefinitely at temperatures below the temperature of onset of loss of nitrogen. Photoreactions described below were thus performed at 293 K, above the maximum rate of desorption of the multilayer and well below the thermal decomposition temperature.

RAIR spectra measured after irradiation of the saturated monolayers with light of wavelength 300–400 nm are shown in Figs. 1*c* and 2*c*, respectively. Particularly diagnostic during the photolysis in both is the loss of the asymmetric and symmetric C=N=N absorptions and the concomitant change in the C=O region. The loss of nitrogen occurs only during photolysis and this can be monitored by mass spectroscopy. In the case of 4-PDE, there is a concomitant growth of an absorption at 2124 cm^{-1} that can be assigned to the ketene C=C=O stretch.[5,14] The ketene formed remains stable indefinitely. The ketene is the result of the Wolff rearrangement and its observation is surprising because it has only been observed in an Ar matrix at 10 K. Under other conditions at higher temperatures, the ketenes are reactive. On the other hand, for 3-PDE, the ketene stretch does not form and the major change accompanying loss of the diazo stretches is a broadening and shifting of the C=O regions at 1730 cm^{-1} and 1100–1350 cm^{-1}.

The IR spectral changes observed on irradiation of 3-PDE are similar to those measured on irradiation of multilayers of these substrates. In multilayer (and in solid-state irradiations of 3- and 4-PDE),[6] it is easy to establish that the products observed are due to carbene reactions, either coupling to form the alkene or reaction with another 3- or 4-PDE to form an azine. In the multilayer and solid-state reactions, the azine and alkene products can be identified by MS (multilayer) and NMR and IR analytical spectroscopic techniques (solid state). Formation of the carbene and the resulting azine and alkene products on the saturated monolayer are less easy to characterize. The RAIR spectrum obtained (Fig. 2*c*) has less identifiable features. The only characteristic peak is a shifting and broadening of the absorption in the C=O region at 1730 cm^{-1}. A similar RAIR spectrum, with a broadened peak in the C=O region is obtained when the 3-PDE-saturated monolayer is heated above 373 K, the temperature where *thermal* loss of nitrogen occurs. For both the thermal and photochemical experiments, we obtained evi-

Scheme 2. Proposed surface reaction of surface-generated carbene.

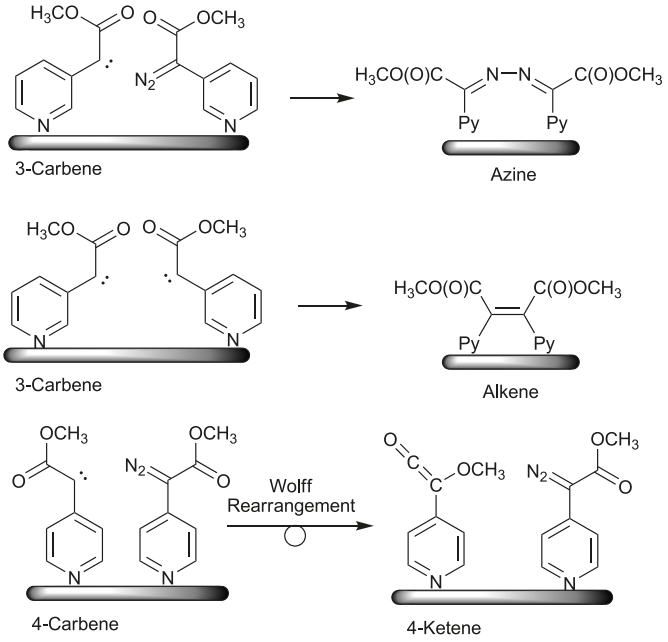

dence for the formation of the azine and alkene products from carbene reaction by MS identification of their parent ions (and known major fragments) upon TPD of the photolyzed monolayers. The identification of the alkene and azine molecules was established by monitoring fragments unique to each of the alkene and azine, respectively. The fragmentation pattern for the alkene include major m/z at 298, 270, 267, and 239, while the azines had major m/z at 267 and 207. The parent ion for the azine at 326 amu could not be observed in the electron ionization mode. The fragmentation patterns of the alkenes and azines were determined from the solid-state photolysis experiments.[6] Because m/z 298 and 239 were unique for the alkene and 207 was unique for the azines, these masses were monitored during the TPD for identification of the molecules. Of course, other products from the carbene reacting through other pathways cannot be ruled out.

We attempted to trap the carbene intermediate on the surface by photolyzing the 3-PDE monolayer surface in the presence of an overlayer of known carbene traps, such as methanol, methyl amine (X–H insertion), and benzene (C=C insertion). In each case, the resulting RAIR spectrum looked identical to that shown in Fig. 2*c* (see Supplementary data) and suggests that even in the presence of the overlayer of reactant, the carbene reacts similar to when generated in the absence of the trap. The reasons for this may include that the intramonolayer reactions are faster than the reaction of the generated carbene with the trapping reagent or that the reaction with the trap is hindered because the experiment has to be done at temperatures where the reactant is in the solid state (frozen). Details are provided in the Supplementary data.

Taken together, the experimental evidence suggests that irradiation of the 3-PDE-saturated monolayer results in formation of the carbene that is efficiently scavenged by neighboring 3-PDE or analogous carbene to form alkene and azine structures on the surface (Scheme 2); these structures lead to a broadening of the C=O ester region.

Can. J. Chem. Downloaded from www.nrcresearchpress.com by University of Electronic and Science Techonology of China on 09/18/12
For personal use only.

The inescapable conclusion is that the difference in reactivity of 3- and 4-PDE as saturated monolayers of Pt is related to the position of the photoreactive substituent on the pyridyl ring. For 3-PDE, the initially formed carbene is presumably formed in an orientation more closely positioned with respect to its neighbors allowing bimolecular reactions to occur. By contrast, the 4-PDE carbene is held at an orientation where the inefficient Wolff rearrangement, with the migration of the $–OCH_3$ to form ketene, can compete because of the inability of intramonolayer carbene bimolecular reactivity. Besides the remarkable chemoselectivity observed in this study, the observation of the ketene for 4-PDE suggests that for pyridyl substrates, the surface can act to isolate molecules and allow for the characterization of reactive intermediates usually only seen in Ar matrixes. We are currently trying to exploit this possibility in addition to investigating the reactivity of the ketene and carbene monolayers.

Supplementary data

Supplementary data for this article (additional spectra for 3-PDE and 4-PDE on Pt(111), TPD data, tables of IR stretching frequencies with assignments, and details of carbene trapping experiments) are available on the journal Web site (canjchem.nrc.ca).

Acknowledgements

The Natural Sciences and Engineering Research Council of Canada (NSERC), the Government of Ontario (Premier's Research Excellence Award), Ontario Research Development Fund, and the Canadian Foundation for Innovation (CFI) are thanked for financial support.

References

(1) (a) Chechik, V.; Crooks, R. M.; Stirling, C. J. M. *Adv. Mater.* **2000**, *12* (16), 1161. doi:10.1002/1521-4095(200008)12:16<1161::AID-ADMA1161>3.0.CO;2-C.; (b) Mrksich, M. *Chem. Soc. Rev.* **2000**, *29* (4), 267. doi:10.1039/a705397e.; (c) Willner, I.; Willner, B. *Pure Appl. Chem.* **2001**, *73* (3), 535. doi:10.1351/pac200173030535.; (d) Sullivan, T. P.; Huck, W. T. S. *Eur. J. Org. Chem.* **2003**, *2003* (1), 17. doi:10.1002/1099-0690(200301)2003:1<17::AID-EJOC17>3.0.CO;2-H.; (e) Daniel, M. C.; Astruc, D. *Chem. Rev.* **2004**, *104* (1), 293. doi:10.1021/cr030698+. PMID:14719978.; (f) Ulman, A. *Chem. Rev.* **1996**, *96* (4), 1533. doi:10.1021/cr9502357. PMID:11848802.; (g) Hamers, R. J. *Annu. Rev. Anal. Chem.* **2008**, *1* (1), 707. doi:10.1146/annurev.anchem.1.031207.112916.; (h) Haensch, C.; Hoeppener, S.; Schubert, U. S. *Chem. Soc. Rev.* **2010**, *39* (6), 2323. doi:10.1039/b920491a. PMID:20424728.

(2) (a) Zhou, X. L.; Zhu, X.-Y.; White, J. M. *Surf. Sci. Rep.* **1991**, *13* (3–6), 73 [and references cited therein]. doi:10.1016/0167-5729(91)90009-M.; (b) Zhu, X.-Y. *Surf. Sci.* **1997**, *390* (1–3), 224. doi:10.1016/S0039-6028(97)00556-6.

(3) Pitters, J. L.; Griffiths, K.; Kovar, M.; Norton, P. R.; Workentin, M. S. *Angew. Chem. Int. Ed.* **2000**, *39* (12), 2144. doi:10.1002/1521-3773(20000616)39:12<2144::AID-ANIE2144>3.0.CO;2-V.

(4) (a) Kirmse, W. *Eur. J. Chem.* **2002**, 2193; (b) Regitz, M.; Maas, G. *Diazo Compounds. Properties and Synthesis;* Academic Press, Inc.: Toronto, 1986.; (c) Tomioka, H.; Okuno, H.; Izawa, Y. *J. Chem. Soc., Perkin Trans. 2* **1980**, (11): 1636. doi:10.1039/p29800001636.

(5) Tomioka, H.; Ichikawa, N.; Komatsu, K. *J. Am. Chem. Soc.* **1993**, *115* (19), 8621. doi:10.1021/ja00072a015.

(6) Pitters, J. L. Ph. D. Thesis, The University of Western Ontario, 2001.

(7) Kasza, R. V.; Shapter, J. G.; Griffiths, K.; Norton, P. R.; Sloan, J. J. *Surf. Sci.* **1994**, *321* (3), L239. doi:10.1016/0039-6028(94)90181-3.

(8) Schwenk, E.; Papa, D. *J. Org. Chem.* **1946**, *11* (6), 798. doi:10.1021/jo01176a023.

(9) Regitz, M.; Hocker, J.; Liedhegener, A. *Org. Synth.* **1973**, *5*, 179.

(10) Yamawaki, J.; Ando, T. *Chem. Lett.* **1979**, *8* (7), 755. doi:10.1246/cl.1979.755.

(11) (a) Francis, S. A.; Ellison, A. H. *J. Opt. Soc. Am.* **1959**, *49* (2), 131. doi:10.1364/JOSA.49.000131.; (b) Haq, S.; King, D. A. *J. Phys. Chem.* **1996**, *100* (42), 16957. doi:10.1021/jp960814v.

(12) (a) Froitzheim, H.; Hopster, H.; Ibach, H.; Lehwald, S. *Appl. Phys. (Berl.)* **1977**, *13*, 147; (b) Robbins, J. L.; Marucchi-Soos, E. *J. Phys. Chem.* **1987**, *91* (8), 2026. doi:10.1021/j100292a007.

(13) Regitz, M.; Bartz, W. *Chem. Ber.* **1970**, *103* (5), 1477. doi:10.1002/cber.19701030519.

(14) (a) Kuhn, A.; Plug, C.; Wentrup, C. *J. Am. Chem. Soc.* **2000**, *122* (9), 1945. doi:10.1021/ja993859t.; (b) Acton, A. W.; Allen, A. D.; Antunes, L. M.; Fedorov, A. V.; Najafian, K.; Tidwell, T. T.; Wagner, B. D. *J. Am. Chem. Soc.* **2002**, *124* (46), 13790. doi:10.1021/ja027347h. PMID:12431108.

Aggregation of zinc tetraphenylporphyrin characterized by ensemble and single-molecule fluorescence spectroscopy

Jaclyn A. O'Brien, Yin Lu, Emma N. Hooley, Kenneth P. Ghiggino, Ronald P. Steer, and Matthew F. Paige

Abstract: The aggregation of metalloporphyrins is believed to play a crucial role in the excited-state annihilation process known as triplet–triplet annihilation, which in turn has significant potential applications in photon upconversion schemes. In this work, the propensity of the water-soluble metalloporphyrin zinc (II) *meso*-tetra(4-sulfonatophenyl)porphine to undergo aggregation when adsorbed to glass cover slips was investigated by single-molecule fluorescence microscopy. In proof-of-principle experiments, it was demonstrated (1) that individual molecules of the metalloporphyrin can be directly visualized in spite of their very weak fluorescence emission, and (2) that at low concentrations (10^{-8} mol/L), the molecule has a strong tendency to form multimolecular aggregates. A subset of the multimolecular aggregates shows a significant blue-shift in fluorescence emission, though at present the precise nature of the molecular aggregates remains unclear.

Key words: aggregation, spectroscopy, metalloporphyrin, single-molecule fluorescence, microscopy, photobleaching.

Résumé : On croit que l'agrégation des métalloporphyrines joue un rôle crucial dans le processus d'annihilation de l'état excité, connu comme annihilation triplet-triplet, qui a des applications potentielles dans les schémas de conversion ascendante du proton. Dans ce travail, faisant appel à la microscopie de fluorescence de molécules uniques, on a étudié la propensité d'une métalloporphyrine soluble dans l'eau, le sel de zinc (II) de la *méso*-tétra(4-sulfonatophényl)porphine, à subir une agrégation lorsqu'elle est adsorbée sur des lamelles de verre. Dans des expériences de principe de la preuve, il a été démontré (1) que des molécules individuelles de la métalloporphyrine peuvent être visualisées directement malgré leur très faible émission de fluorescence et (2) que, à très faible concentration (10^{-8} mol/L), la molécule possède une forte tendance à former des agrégats multimoléculaires. Un sous-ensemble d'agrégats multimoléculaires présente un déplacement important vers le bleu dans l'émission de fluorescence, même si pour le moment, la nature précise de l'agrégat moléculaire n'est pas claire.

Mots-clés : agrégation, spectroscopie, métalloporphyrine, fluorescence de molécule unique, fluorescence, microscopie, photoblanchiment.

[Traduit par la Rédaction]

Introduction

Intermolecular aggregation, both in solution and in solid media, plays an important role in a wide range of photochemical and photophysical phenomena. Of particular recent interest has been the influence of intermolecular aggregation on excited-state annihilation processes,[1–4] in part because of the potential application of these processes in non-coherent photon upconversion, the conversion of low-energy photons into high-energy photons. Photon upconversion has been proposed as an approach to enhance the energy conversion efficiency of dye-sensitized solar cells, and as such is an area of intense research interest and societal importance. At present, a number of groups are actively investigating the importance of intermolecular aggregation on the excited-state annihilation process known as triplet–triplet annihilation (TTA; schematically written as $2T_1 \rightarrow S_n\ (n \geq 1) + S_0$) because TTA holds significant practical promise for implementation in solar photon upconversion schemes, particularly in the photon-rich red and near-infrared regions of the solar spectrum.

Metalloporphyrins are arguably the most thoroughly investigated class of molecules for TTA upconversion schemes, in part because homomolecular TTA in porphyrins can populate higher excited states (S_n, $n = 1$) and potentially gather a larger fraction of the absorbed photon energy than systems in which $n \leq 1$ are the product states. Recently, Baluschev investigated TTA in a mixed Pt (or Pd) metalloporphyrin sensitizer and blue-emitter system in solution and

Received 29 April 2010. Accepted 30 June 2010. Published on the NRC Research Press Web site at canjchem.nrc.ca on 5 January 2011.

This article is part of a Special Issue dedicated to Professor J. C. Scaiano.

J.A. O'Brien, Y. Lu, R.P. Steer, and M.F. Paige.[1] Department of Chemistry, University of Saskatchewan, 110 Science Place, Saskatoon, SK S7N 5C9, Canada.
E.N. Hooley and K.P. Ghiggino. School of Chemistry, Bio21 Institute, University of Melbourne, Melbourne, Victoria, 3010, Australia.

[1]Corresponding author (e-mail: matthew.paige@usask.ca).

Can. J. Chem. Downloaded from www.nrcresearchpress.com by University of Electronic and Science Techonology of China on 09/18/12
For personal use only.

Can. J. Chem. Downloaded from www.nrcresearchpress.com by University of Electronic and Science Techonology of China on 09/18/12
For personal use only.

solid state, and proposed several schemes that give rise to photon upconversion.[1,2] The first involves homomolecular TTA between metalloporphyrins to yield an S_2 state, followed by intermolecular energy transfer (resonant) to the blue emitter compound, and the second requires heteromolecular energy transfer between the photoexcited sensitizer and blue emitter, leading to a triplet-state blue emitter, followed by homomolecular TTA in the blue emitter to yield a final blue emitter S_1 state. However, recent publications by Steer and co-workers[4–6] have called into question these mechanisms and suggested that aggregation of the porphyrin sensitizer (and (or) the acceptor, for the mixed sensitizer and emitter system) must be taking place for TTA to occur at the observed efficiencies. Experimental evidence for porphyrin aggregation under a variety of conditions has been reported previously by other researchers.[7–10] Furthermore, Steer and co-workers have reported aggregation of closed-shell zinc *meso*-tetraphenylporphine (ZnTPP) in thin poly(methyl methacrylate) (PMMA) films that exhibit TTA.[5] Evidence for aggregation included Soret absorption band widths that increased as a function of ZnTPP loading with no corresponding emission band broadening, and the ratio of emission to absorption band intensities (proportional to quantum yield at low dye loading levels) decreasing with the extent of dye loading, indicating self-quenching of the ZnTPP. Furthermore, fluorescence lifetime measurements of ZnTPP in PMMA give bi-exponential decays, with decreasing lifetime as a function of dye loading levels, which again is entirely consistent with intermolecular aggregation effects.

To gain further direct evidence for porphyrin aggregation in solid systems, we have applied a combination of ensemble and single-molecule fluorescence spectroscopy methods to samples of zinc (II) *meso*-tetra(4-sulfonatophenyl)porphine (ZnTPPS; structure shown in Fig. 1), a water-soluble variant of the model metalloporphyrin ZnTPP, immobilized on glass cover slips. Single-molecule fluorescence spectroscopy is an experimental approach in which the fluorescence emission of individual molecules is observed, typically through the use of ultrasensitive, laser-based fluorescence microscopy on highly diluted (10^{-8}–10^{-9} mol/L) samples.[11,12] Detecting the extremely low levels of fluorescence emission from an individual fluorophore is possible only through careful selection of fluorophores and detection systems; one seeks to minimize unwanted background fluorescence through the use of ultraclean samples while maximizing fluorescence signals through the use of high numerical aperture oil-immersion objective lenses, low noise, high-gain photodetectors, and fluorophores with sufficiently good spectroscopic properties.

Maximizing fluorescence signals is the primary challenge that one is faced with when applying single-molecule fluorescence approaches to detection of ZnTPP, its derivatives, and its aggregates. Typical fluorophores used in single-molecule measurements have high absorption cross-sections, high fluorescence quantum yields (and correspondingly long excited state lifetimes), an absence of triplet bottlenecks, and low photobleaching quantum yields. Although a wide range of fluorophores have been used (laser dyes and related fluorescent labels, autofluorescent proteins, and others[13]), metalloporphyrins, and ZnTPP in particular, would appear, at least upon initial inspection, to be challenging fluorophores for these measurements. ZnTPP has an S_1 fluorescence quantum yield of ~0.04[5,14] and a high intersystem crossing yield (ideal for a high triplet yield in TTA applications, but undesirable for single-molecule fluorescence, as these are "dark" states) and is known to undergo photodegradation in the presence of oxygen.[15] The molar extinction coefficient in the Q-band is typically modest (ε_{max} ~3000 cm^{-1} $(mol/L)^{-1}$ in water; see Fig. 2), though reasonably efficient Q-band excitation is possible through the use of a CW solid-state diode laser.

Fig. 1. Chemical structure of zinc (II) *meso*-tetra(4-sulfonatophenyl)phenylporphine.

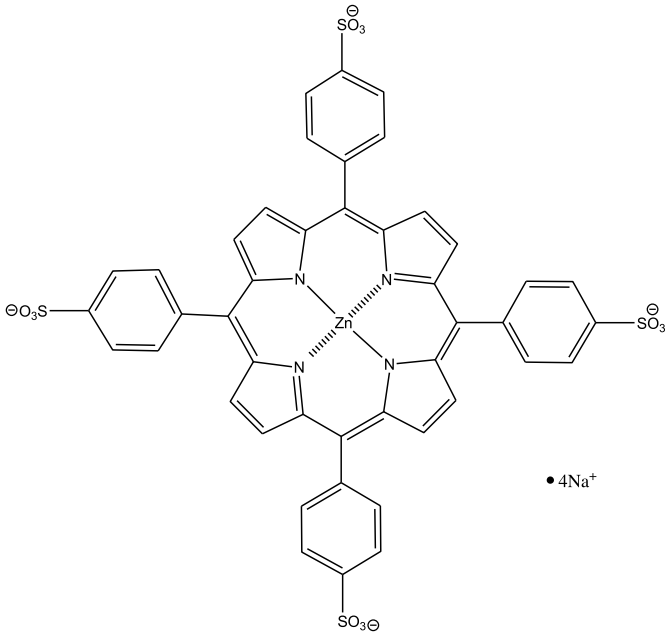

Although the task of measuring individual ZnTPPS molecules and aggregates of the metalloporphyrin appears daunting in the face of this evidence, a series of recent publications by Kim[16–21] in which the single-molecule emission of covalently linked porphyrin arrays was reported suggest that these measurements might indeed be feasible. Of particular interest is a report by Kim in which the emission from linked zinc metalloporphyrin arrays (containing $n = 1$ up to $n = 96$ porphyrin monomer units) was observed.[16] In these systems, fluorescence time trajectories displayed steps corresponding to the photobleaching of individual zinc porphyrin units, up to $n = 8$ monomer units. After this limit had been reached, more complex photobleaching behavior was observed, which was explained by means of an excitonic coupling model. The observation of discrete steps in these array systems (albeit with a signal-to-noise ratio that was not ideal) provides reasonable hope that individual ZnTPPS molecules, as well as aggregates that contain a small number of molecules, can be detected and characterized through single-molecule fluorescence techniques.

On the basis of these results, we have carried out a combination of single-molecule and ensemble fluorescence measurements in an attempt to characterize the aggregation state of ZnTPPS at low concentrations (10^{-8} mol/L) on glass cover slips. Our selection of the water-soluble ZnTPPS over ZnTPP was made because of experimental limitations (many of the common organic solvents used to dissolve ZnTPP are

Can. J. Chem. Downloaded from www.nrcresearchpress.com by University of Electronic and Science Techonology of China on 09/18/12
For personal use only.

Fig. 2. (*a*) Expanded-scale absorption spectrum of ZnTPPS in water (1×10^{-5} mol/L) displaying both B- and Q-bands. (*b*) Absorption spectrum of ZnTPPS in water displaying the Q-band region of the spectrum. (*c*) Emission spectrum of ZnTPPS in water (5×10^{-4} mol/L). Fluorescence excitation was performed at 532 nm to provide a close spectral match to the excitation laser used in subsequent microscopy and spectromicroscopy measurements. Q-band emission has not been corrected for re-absorption events.

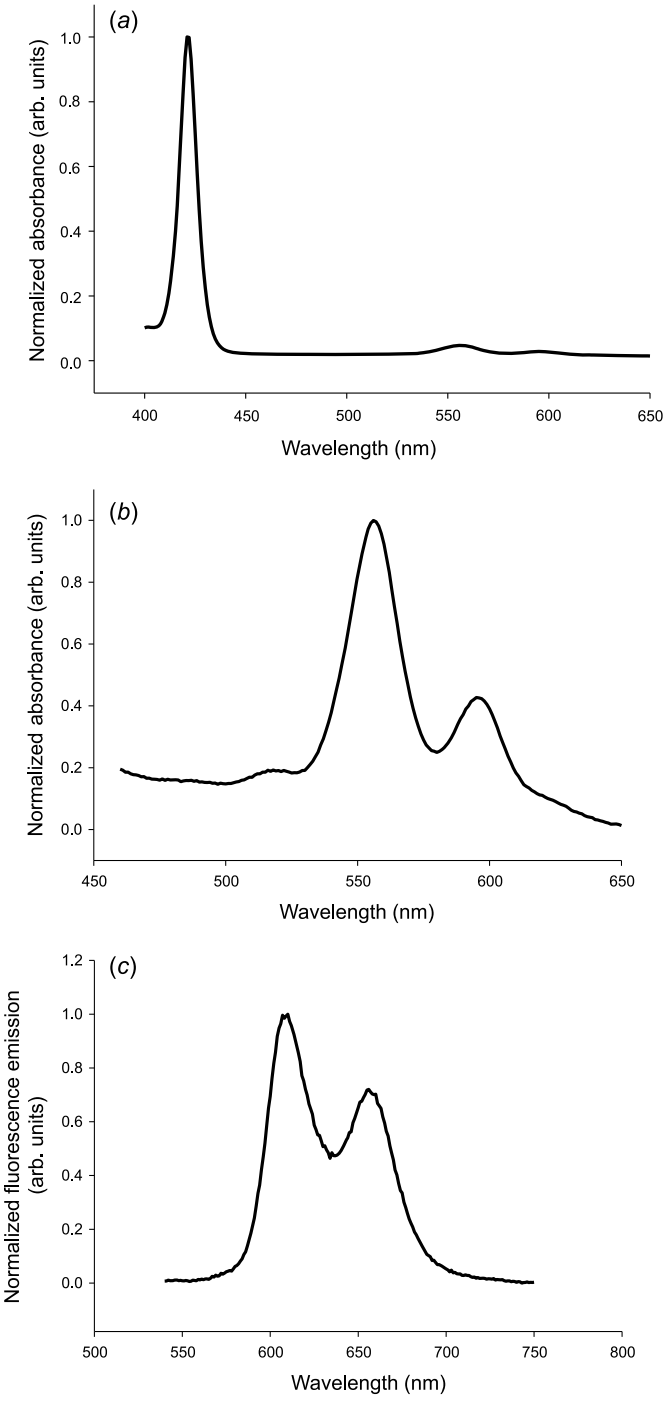

heavily contaminated with fluorescent impurities, making single-molecule measurements of such weakly fluorescent molecules extremely difficult), as well as because ZnTPPS has previously been reported to undergo a considerable amount of aggregation in aqueous solution (for a review of this and other relevant aggregation behavior see the review by Harvey[7]), thereby providing a simple method to ensure at least some degree of metalloporphyrin aggregation. Single-molecule epifluorescence microscopy has revealed the presence of both individual ZnTPPS molecules and multimolecular aggregates at the concentration regime investigated, providing direct supporting evidence of porphyrin aggregation at even these low concentrations. Further spectroscopic characterization of the aggregates (emission spectra) was carried out through spectromicroscopic characterization.

Materials and methods

Sample preparation

Samples were prepared by dissolving ZnTPPS (Frontier Scientific) in water (Millipore, resistivity 18 MΩ·cm) to a final concentration of ~10^{-8} mol/L. Glass cover slips (borosilicate float glass, VWR Scientific) were cleaned by repeated passes through the flame of a propane torch before sample deposition. Solutions were spin-cast onto the clean glass cover slips and imaged directly in the single-molecule microscope. Control samples of the cover slips alone and cover slips that had been treated with solvent alone showed no significant impurities when imaged in the fluorescence microscope.

Fluorescence microscopy

Single-molecule fluorescence imaging experiments were carried out on a wide-field epifluorescence microscope. A CW solid-state diode laser (532 nm, vertical polarization, Dragon Lasers) was focused onto the back focal plane of a 60×, 1.4NA oil-immersion microscope objective (PlanApo, Nikon) and fluorescence emission was passed through 2 long-pass filters (540LP, Omega Optical) before being focused onto an electron multiplying CCD camera (Cascade 512F, Photometrics).

For spectromicroscopy measurements, the microscope layout was altered. The excitation laser was focused via the oil-immersion objective into a small (estimated ~2 μm) spot; fluorescence emission was passed through the same long-pass filters as described above and then focused into an imaging spectrograph (MS125 Spectrograph, Newport (Oriel) Instruments). The spectrograph output was imaged onto an electron multiplying CCD camera (iXon, Andor Technology) and converted into a 2D spectrum of the region of interest. The wavelength of the instrument was calibrated with an Hg pen lamp. Since the quantum yield of the CCD camera does not change substantially over the spectral region of interest, there was no need to correct spectral data for the wavelength-dependent response of the photodetector. For spectromicroscopy measurements, a frame exposure time of 100 ms was used, and CCD pixels were binned to ensure maximum possible signal-to-noise ratio in the collected emission spectra.

Results and discussion

Absorption and emission spectra of ZnTPPS in ultrapure water were collected and are shown in Fig. 2. The absorption spectrum of ZnTPPS consisted of 2 well-defined bands

Can. J. Chem. Downloaded from www.nrcresearchpress.com by University of Electronic and Science Techonology of China on 09/18/12
For personal use only.

(B-band and Q-band), the first centered at 421 nm and the second (2 peaks) at 557 nm and 596 nm, which is consistent with other metalloporphyrin absorption spectra found in the literature. Extinction coefficients of 3165 cm^{-1} $(mol/L)^{-1}$ and 1457 cm^{-1} $(mol/L)^{-1}$ were measured at 596 nm (the 0–0 transition from S_0 to S_1) and 532 nm (laser excitation wavelength used for fluorescence microscopy measurements), respectively. Again, the magnitude of the ε_{max} is quite modest, suggesting that the single-molecule fluorescence measurements will be challenging. For comparison purposes, consider the approximate difference in fluorescence signal that might be anticipated between ZnTPPS and an excellent laser dye such as R6G: R6G, a good dye for single-molecule measurements, has a molar absorptivity of ~63 000 cm^{-1} $(mol/L)^{-1}$ at 514 nm (limiting extinction coefficients for organic molecules with oscillator strengths $f = 1$ are approximately 10^5 cm^{-1} $(mol/L)^{-1}$), an excitation wavelength that is readily accessible with an argon-ion laser, and a fluorescence quantum yield in ethanol of 0.95.[14] Accounting for the differences in molar absorptivity and fluorescence quantum yield, one estimates that the approximate fluorescence intensity difference between R6G and ZnTPPS should be ~3 orders of magnitude. While R6G is readily detected in single-molecule fluorescence measurements, compensating for the anticipated 3 orders of magnitude loss in signal represents a considerable technical challenge. Details explaining how this challenge was met are described later in this manuscript. The fluorescence emission spectrum of ZnTPPS upon excitation at 532 nm consisted of 2 well-defined peaks at 610 nm and 656 nm, which is again consistent with reports found in the literature.

Heavily diluted samples of ZnTPPS (10^{-8}–10^{-9} mol/L) were deposited on clean glass cover slips and imaged in the single-molecule microscope. Extensive control testing was performed to ensure that any emission observed in these samples was from ZnTPPS alone, and not from any fluorescent contaminants that might be found in solvents or on cover slips or transferred from glassware or other sources. Control samples of the cleaned cover slips alone and cleaned cover slips that had been dosed with aliquots of fresh Millipore water (the solvent used for ZnTPPS) were tested rigorously for contamination. It is common in many single-molecule measurements to spin-cast a thin polymer layer onto the dye-covered cover slips to minimize exposure of fluorophores to oxygen and thereby decrease photobleaching. However, for these measurements, a polymer layer was not used because control experiments revealed extensive contamination of the polymer at the single-molecule level. It is worth noting that trace-level contamination of organic solvents and polymers places considerable limits on the range of samples and systems that can be investigated by single-molecule fluorescence. In many cases, the source of these contaminants is not clear (though for organic solvents, likely contributors are the products of photochemical-based radical reactions as well as trace levels of antioxidants added to minimize potential formation of peroxides), and this is an area of technical development that needs considerable attention to forward the field of research.

Samples prepared as described above yielded discrete, luminescent spots (~300 nm, as dictated by the diffraction limit of ~$\lambda_{exc}/2$) on a dark background when imaged in the single-molecule microscope. Time trajectories (Fig. 3), that is, plots showing fluorescence emission as a function of time, were collected for the luminescent spots and analyzed. In general, the luminescent spots demonstrated two different types of photobleaching behavior: one group photobleached in a single step and the other group photobleached in a more complex manner, either through multiple steps or through a gradual (approximately exponential) decrease in signal. There was typically a ~3:1 ratio of single-step photobleaching entities to more complex photobleaching entities observed per image. Single-step photobleaching in conjunction with low fluorophore concentration and diffraction-limited spots is a strong signature of individual molecules; therefore, we consider the spots that photobleached in a single step to be due to individual ZnTPPS molecules. Molecules that photobleached in a single step generally remained non-emissive for the remainder of the experiment and rarely exhibited repeated on–off "blinking", which has been reported in some other single-molecule systems.[11,13]

Fig. 3. Single-molecule fluorescence time trajectory for an individual molecule of ZnTPPS dispersed on clean glass cover slip substrates. The fluorescence intensity is plotted as CCD counts per 100 ms integration bin (arbitrary units) after subtraction of the mean background signal. The excitation intensity was 1.0 kW/cm^2, as determined by measuring laser power at the focal plane divided by the illumination area.

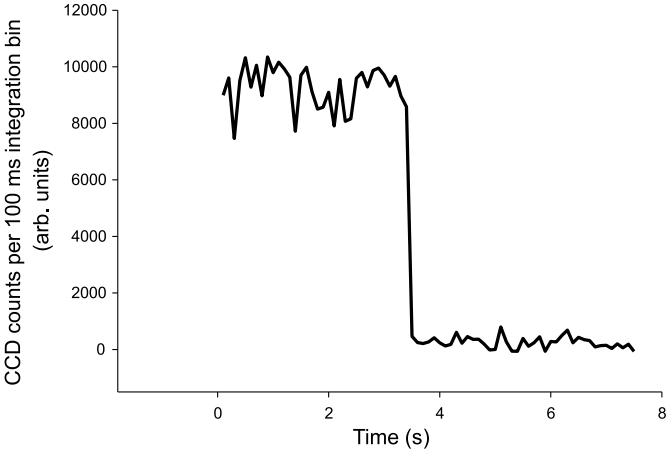

Before examining the fluorescent properties of individual ZnTPPS molecules in greater detail, it is worth considering more carefully some of the technical aspects of the microscopy experiments that made visualization of such a weakly fluorescent fluorophore possible. First, we have made use of the largest possible illumination intensity that could be used without immediately photobleaching the sample (typical fluorophores emit ~10^6 photons prior to photobleaching, with higher incident photon flux resulting in larger fluorescence signals but more rapid photobleaching). The illumination intensity was optimized such that the majority of molecules measured emitted for at least several CCD frame periods (100 ms integration period per frame) prior to photobleaching. Next, contamination issues aside, foregoing the use of a protective polymer layer reduces background scattering and hence results in improved signal-to-background ratios, though again, with commensurate increases in photobleaching rates. An additional key factor in these experiments, and

Can. J. Chem. Downloaded from www.nrcresearchpress.com by University of Electronic and Science Techonology of China on 09/18/12
For personal use only.

one that is often overlooked in single-molecule imaging, are recent improvements in the performance characteristics of fluorescence emission filters. Recent innovations in dielectric emission filter technology (see, for example, the 3RD Millennium line of filters from Omega Filters) have enabled the production of filters with much sharper cutoff frequencies, improved transmission properties, and greater attenuation than filters of previous generations. The primary role of the emission filter in single-molecule imaging is to remove scattered laser excitation light from the measurement, and steeper cutoff frequencies allow the selection of filters whose spectral cutoffs are extremely close (in some cases several nanometres) to the excitation wavelength. This in turn allows a greater fraction of the total fluorescence emission to be passed to the detector, resulting in substantially greater signals. Improved transmission properties of emission filters also give greater signal intensities in single-molecule imaging experiments, and these factors in combination contribute significantly to the successful visualization of such weak fluorophores.

By measuring large numbers of individual ZnTPPS molecules (entities that photobleached in a single step), histograms of useful spectroscopic parameters can be constructed. Figures 4*a* and 4*b* show histograms of single-molecule photobleaching times and single-molecule fluorescent intensities, respectively. The photobleaching time data are well represented by a single-exponential decay curve ($N = A_0\exp(-t/\tau_{on})$, where N is the number of molecules, A_0 is a fitting constant, and τ_{on} is a photobleaching time constant equal to 0.7 s), suggesting the existence of a single population of emitters adsorbed on the glass surface. For comparison purposes, previous measurements of R6G imaged under comparable illumination intensities but in the presence of a protective polymer coating gave a $\tau_{on} = 2.0$ s, indicating that ZnTPPS is less photostable than good organic dye molecules.[22] As stated previously, the participation of metalloporphyrin in oxygen-based photochemical reactions is well documented, consistent with its low photostability in single-molecule measurements.

In terms of fluorescence intensities (Fig. 4*b*), experimental results are again consistent with the existence of a single population of emitters on the glass substrates. Mean signal intensities were equal to ~4500 counts per 100 ms integration bin. It is notable that these intensities are comparable with those we have reported previously for a rhodamine-like calcium ion sensor (Calcium Green-1),[23] albeit with a significantly higher photobleaching rate and a significantly greater illumination intensity. While it is difficult to compare measurements quantitatively between different microscope setups and illumination conditions, we also note that our signal-to-noise ratios appear to be significantly better than those reported by Kim[16] in his initial investigations of metalloporphyrin-based arrays, though this is based only on inspection of a few published fluorescence time trajectories.

A similar analysis was undertaken for the second type of photobleaching behavior, in which more complex fluorescence trajectories were observed. Unlike for the single-molecule data, a wide variety of photobleaching behaviors were observed for this set of entities, 2 examples of which are shown in Figs. 5*a* and 5*b*. In the case of the trajectory shown in Fig. 5*a*, 3 clear-cut photobleaching events occur

Fig. 4. (*a*) Histogram of photobleaching times for individual ZnTPPS molecules collected from time trajectories. Excitation intensity was 1.0 kW/cm^2. Data have been fit with a single-exponential function ($N = A_0\exp(-t/\tau_{on})$), where τ_{on} is the photobleaching time constant. The photobleaching time constant was calculated to be $\tau_{on} = 0.7$ s. (*b*) Histogram of individual ZnTPPS molecule fluorescence intensities (measured in CCD counts / 10 (arbitrary units)).

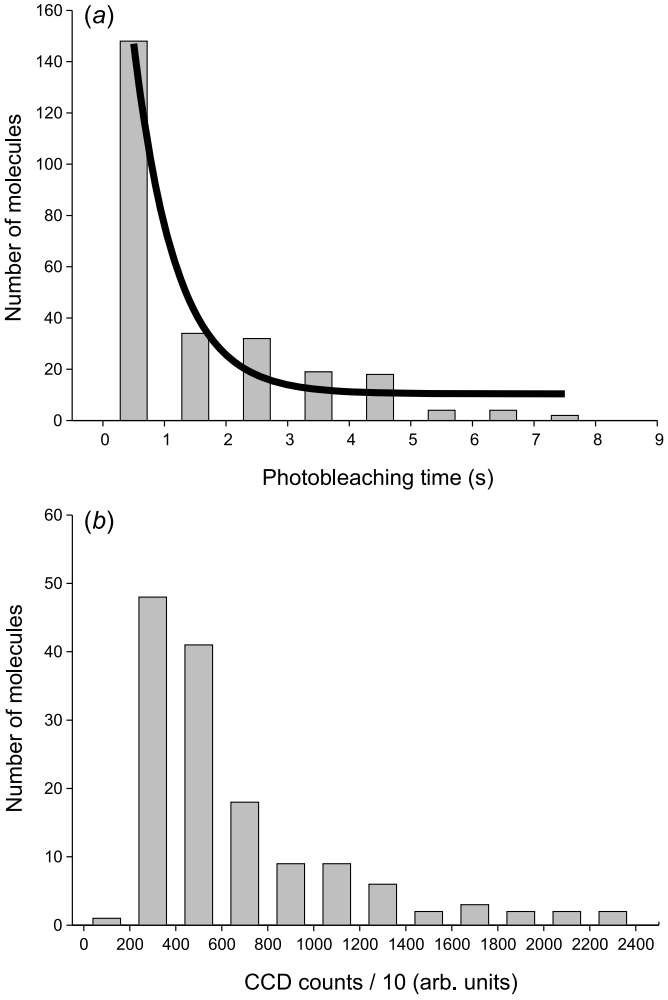

sequentially, suggesting that the spot is due to an aggregate containing at least 3 independently radiating ZnTPPS molecules. Similar multiple-step photobleaching events have been reported in a number of single-molecule studies of multifluorophoric systems (see refs. 24 and 25, for example), including the low-monomer-number porphyrin arrays of Kim.[16] Finally, in still other systems, there have been demonstrations of more complex excitonic coupling between subunits, often resulting in collective photobleaching of the entire aggregate via the formation of exciton trap states.[24–26] However, this behavior is typically observed in highly organized antenna array-like systems rather than the nonspecific molecular aggregates that are likely formed here. The time trajectory shown Fig. 5*b* exhibits more complex behavior (in some instances, fluorescence intensity increases with time), though there are fluctuations in these trajectories that suggest the photobleaching of discrete molecular subunits. We note that substantially larger and brighter aggregates

Can. J. Chem. Downloaded from www.nrcresearchpress.com by University of Electronic and Science Techonology of China on 09/18/12
For personal use only.

Fig. 5. (*a*) Fluorescence trajectory for multimolecular aggregate of ZnTPPS exhibiting three well-defined photobleaching events. (*b*) Fluorescence trajectory for multimolecular aggregate of ZnTPPS exhibiting complex photobleaching behavior. The dotted lines (red in the Web version) highlight one of the single-step transitions observed in this time trajectory. The excitation intensity in both cases was 1.0 kW/cm^2.

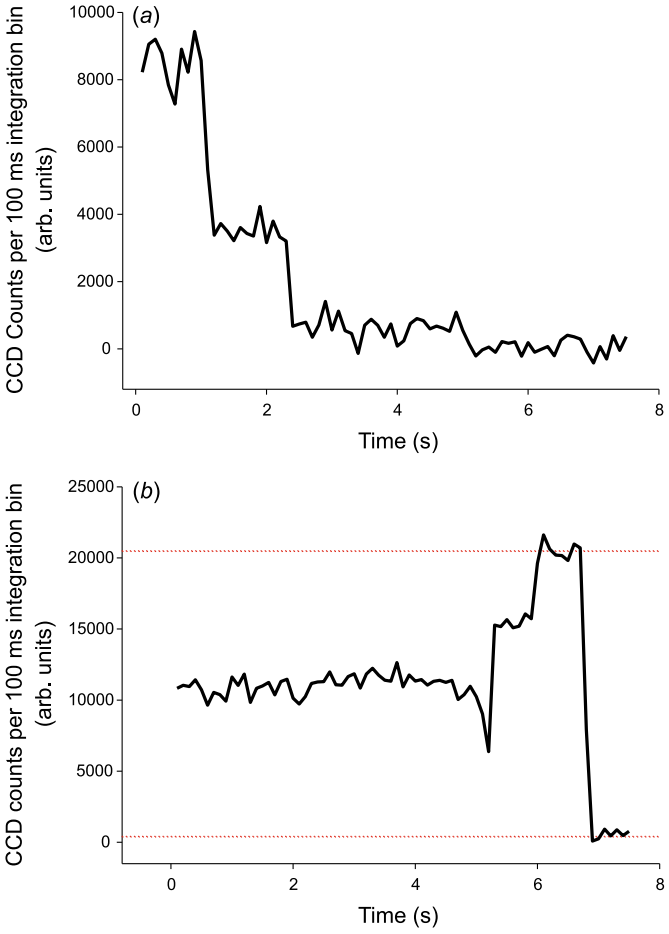

Fig. 6. (*a*) Histogram showing fluorescence intensity of multimolecular ZnTPPS aggregates (measured in CCD counts / 100 (arbitrary units)). (*b*) Histogram showing fluorescence intensity of individual decay steps in multimolecular ZnTPPS aggregates (measured in CCD counts / 100 (arbitrary units)). The excitation intensity was 1.0 kW/cm^2.

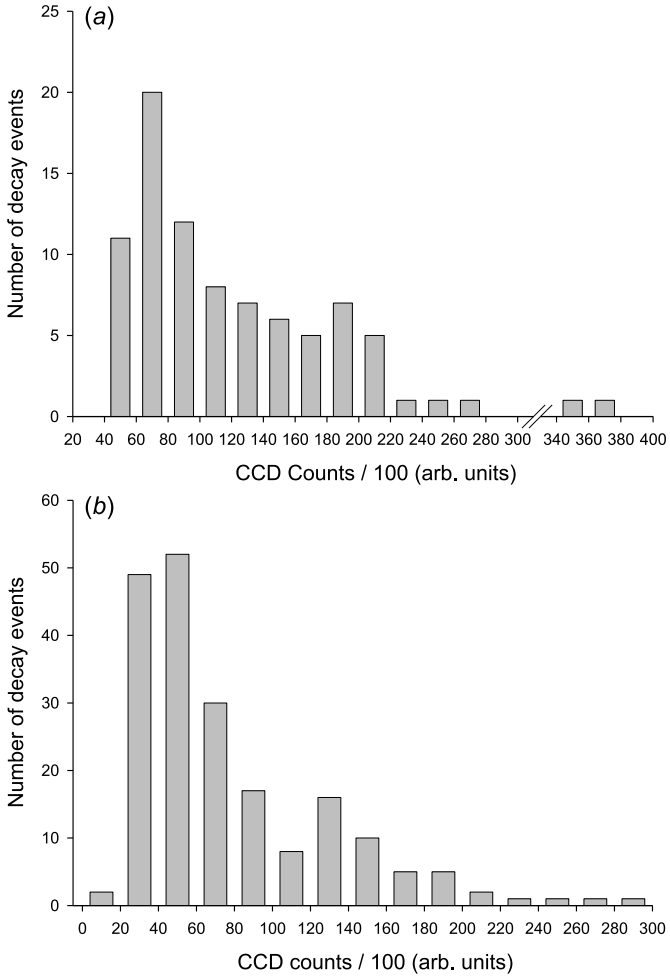

can be formed in this system through controlling the concentration of the dye solution.

A substantial fraction of the aggregates that were measured exhibited one or more quantized, step-like decay stages and were amenable to further analysis. The total fluorescence intensities of the aggregates as well as the intensities for individual photobleaching steps were determined and are shown as histograms in Figs. 6*a* and 6*b*. While the total intensity of an aggregate was greater than the intensity of an individual molecule, the intensity histogram for the individual photobleaching steps in the aggregate was comparable with the intensity histogram for the single-molecule measurements (Fig. 4*b*). There are several key points that can be extracted from these measurements. The first is that, given the correlation between the fluorescence intensity histograms, the individual photobleaching steps in the aggregates are likely caused by the photobleaching of individual molecules in the aggregate. In addition, given that independent photobleaching steps are detectable and there was no observable tendency for the aggregates to undergo collective photobleaching, it seems reasonable to assume that exciton coupling is of negligible importance in these aggregates, suggesting perhaps that they are not due to stacked arrays. Finally, since the aggregates themselves have a greater intensity than the individual constituent molecules, there appears to be minimal quenching upon aggregation, though of course this might simply be a selection bias of the experiment; if the emission is sufficiently quenched, then the aggregates will not be observable under these conditions.

To directly examine the effect of aggregation on the emission spectrum of the ZnTPPS aggregates, spectromicroscopic characterization was performed using a modified version of the fluorescence microscope setup. In these measurements, the excitation beam was focused into a small (~2 μm) spot and the fluorescence emission dispersed via a spectrograph onto an electron multiplying CCD detector. Although the spectromicroscopy setup was not sufficiently optimized for single-molecule fluorescence detection, the system was capable of measuring emission spectra from the more strongly fluorescent ZnTPPS aggregates when sufficiently high illumination intensities were used. A typical

Can. J. Chem. Downloaded from www.nrcresearchpress.com by University of Electronic and Science Techonology of China on 09/18/12
For personal use only.

Fig. 7. Fluorescence emission spectrum of ZnTPPS aggregates taken from sample prepared at 1×10^{-8} mol/L concentration via spectromicroscopy (blue; excitation intensity = 17.0 kW/cm^2). For comparison purposes, the ensemble emission spectrum taken in water using a spectrofluorimeter is also shown (red). The sharp peak located at 629 nm in the blue spectrum is caused by Raman scattering from the glass cover slip.

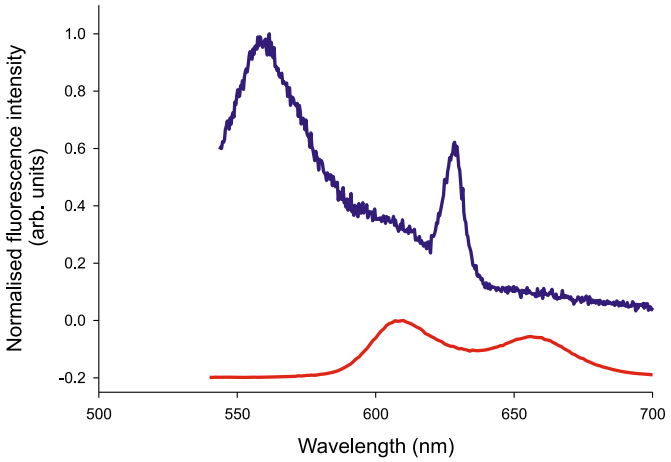

emission spectrum from an aggregate is shown in Fig. 7; the bulk emission spectrum of ZnTPPS in water collected on a spectrofluorimeter is also shown (in red) for comparison purposes. The emission spectrum for the aggregates consisted of 2 strong bands, the first a broad band with a maximum at 562 nm and the second a sharp band with a maximum at 629 nm. Control experiments with a clean cover glass that had been dosed with water yielded a similar sharp peak at 629 nm, suggesting that this peak is caused by Raman scattering (observable because of the high excitation intensity, 17 kW/cm^2, used in these experiments) rather than fluorescence emission from the metalloporphyrin. The 562 nm band had a broad shoulder centered at ~600 nm, though the component peaks were strongly overlapped and resolving individual peak maxima was difficult. The peak separation is consistent with that measured for the two Q-bands in the absorption spectrum, and it is likely that these are the corresponding Q-band emission peaks. It is worth noting, however, that the emission spectrum collected from the spectromicroscopy measurements is significantly blue-shifted with respect to the ensemble counterpart measured in water (610 nm and 656 nm, respectively).

While spectral data for this system are currently limited and should be considered preliminary, we note that reports of J- and H-aggregate formation as well as nonspecific aggregates in metalloporphyrin systems are plentiful in the literature.[7–10,27] In comparison with the literature results, the precise nature of the aggregates formed in these experiments is currently unclear. For example, porphyrin dimers and trimers are known to exhibit significant blue-shifts of Soret absorption bands upon face-to-face π aggregation with an accompanying quenching in fluorescence.[7] While we are unable to carry out absorption measurements on the individual aggregates, the emission spectra show a significant blue-shift with respect to the ensemble measurements, and the samples are easily detected in the system, suggesting that quenching is minimal. However, as stated previously, these measurements may well be preferentially selecting for the most strongly fluorescent aggregates and few conclusions as to the precise nature of the aggregates can be made at this time. Further spectral analysis of the aggregates, in conjunction with ultrasensitive fluorescence lifetime imaging measurements, will provide greater insight into the precise nature of the aggregation state of the metalloporphyrin. It should also be noted that attempting to extrapolate these results to ZnTPP in polymer (the systems that were used to demonstrate TTA) must be done with considerable caution, because the sulfate functional groups that render ZnTPPS soluble in aqueous solution are likely to promote aggregation of the chromophore. Furthermore, direct adsorption of ZnTPPS to the hydrophilic glass surfaces may also give rise to aggregation. Therefore, these experiments should be considered only as proof-of-principle demonstrations of the single-molecule methodology for porphyrin analysis. Nonetheless, this approach has been successful in this regard and holds considerable promise for providing insight into porphyrin aggregation and the influence of aggregation on fluorescence upconversion processes.

Summary

Individual molecules and multimolecular aggregates of zinc (II) *meso*-tetra(4-sulfonatophenyl)phenylporphine deposited onto glass cover slips have been examined by single-molecule fluorescence microscopy and spectromicroscopy. Although the procedure is experimentally challenging, individual molecules of ZnTPPS can be visualized through careful optimization of single-molecule imaging parameters including sample preparation, illumination intensity, and selection of emission filters. Multimolecular aggregates of ZnTPPS photobleach in a complex manner, though in many cases their fluorescence time trajectories contain discrete photobleaching steps that correspond to the photobleaching of individual molecules. The more strongly fluorescent aggregates could be examined by spectromicroscopy, and the emission spectrum of these aggregates exhibited a significant blue-shift in comparison with the emission spectrum collected from standard fluorimeter-based ensemble measurements. These measurements show that metalloporphyrin aggregation occurs and is detectable even at 10^{-8} mol/L concentration, suggesting that the single-molecule fluorescence approach is a viable one for investigating the importance of metalloporphyrin aggregation in fluorescence upconversion schemes.

Acknowledgements

The authors are pleased to acknowledge the Natural Sciences and Engineering Research Council of Canada (NSERC), the Canada Foundation for Innovation (CFI), the Province of Saskatchewan, the Australian Research Council, and the University of Saskatchewan for providing financial support for this research. Acknowledgment is made to the Donors of the American Chemical Society Petroleum Research Fund for support of this research. We also thank Professors Trevor Smith (University of Melbourne) and Toby Bell (Monash University) for their assistance and for insightful comments during this project.

Can. J. Chem. Downloaded from www.nrcresearchpress.com by University of Electronic and Science Techonology of China on 09/18/12
For personal use only.

References

(1) Baluschev, S.; Miteva, T.; Yakutkin, V.; Nelles, G.; Yasuda, A.; Wegner, G. *Phys. Rev. Lett.* **2006**, *97* (14), 143903. doi:10.1103/PhysRevLett.97.143903.

(2) Baluschev, S.; Yakutkin, V.; Wegner, G.; Minch, B.; Miteva, T.; Nelles, G.; Yasuda, A. *J. Appl. Phys.* **2007**, *101* (2), 023101. doi:10.1063/1.2409618.

(3) Singh-Rachford, T. N.; Haefele, A.; Ziessel, R.; Castellano, F. N. *J. Am. Chem. Soc.* **2008**, *130* (48), 16164. doi:10.1021/ja807056a.

(4) Sugunan, S. K.; Tripathy, U.; Brunet, S. M. K.; Paige, M. F.; Steer, R. P. *J. Phys. Chem. A* **2009**, *113* (30), 8548. doi:10.1021/jp9034776.

(5) O'Brien, J. A.; Rallabandi, S.; Tripathy, U.; Paige, M. F.; Steer, R. P. *Chem. Phys. Lett.* **2009**, *475* (4–6), 220. doi:10.1016/j.cplett.2009.05.039.

(6) Steer, R. P. *J. Appl. Phys.* **2007**, *102* (7), 076102. doi:10.1063/1.2787156.

(7) Harvey, P. D. Recent Advances in Free and Metalated Multi-Porphyrin Assemblies and Arrays. A Photophysical Perspective. In *The Porphyrin Handbook*; Kadish, K. M., Smith, K. M., and Guilard, R., Eds.; Academic Press: San Diego, 2003; Vol. 18.

(8) Khairutdinov, R. F.; Serpone, N. *J. Phys. Chem.* **1995**, *99* (31), 11952. doi:10.1021/j100031a024.

(9) Maiti, N. C.; Mazumdar, S.; Periasamy, N. *J. Porphyr. Phthalocyanines* **1998**, *2* (4–5), 369. doi:10.1002/(SICI)1099-1409(199807/10)2:4/5<369::AID-JPP92>3.0.CO;2-3.

(10) Maiti, N. C.; Mazumdar, S.; Periasamy, N. *J. Phys. Chem. B* **1998**, *102* (9), 1528. doi:10.1021/jp9723372.

(11) Moerner, W. E. *J. Phys. Chem. B* **2002**, *106* (5), 910. doi:10.1021/jp012992g.

(12) Moerner, W. E.; Orrit, M. *Science* **1999**, *283* (5408), 1670. doi:10.1126/science.283.5408.1670.

(13) Moerner, W. E.; Fromm, D. P. *Rev. Sci. Instrum.* **2003**, *74* (8), 3597. doi:10.1063/1.1589587.

(14) Dixon, J. M.; Taniguchi, M.; Lindsey, J. S. *Photochem. Photobiol.* **2005**, *81* (1), 212. doi:10.1562/2004-11-06-TSN-361.1.

(15) Kowalska, D.; Steer, R. P. *J. Photochem. Photobiol. Chem.* **2008**, *195* (2–3), 223. doi:10.1016/j.jphotochem.2007.10.011.

(16) Park, M.; Cho, S.; Yoon, Z. S.; Aratani, N.; Osuka, A.; Kim, D. *J. Am. Chem. Soc.* **2005**, *127* (43), 15201. doi:10.1021/ja0544861.

(17) Yang, J.; Cho, S.; Yoo, H.; Park, J.; Li, W. S.; Aida, T.; Kim, D. *J. Phys. Chem. A* **2008**, *112* (30), 6869. doi:10.1021/jp800337y.

(18) Yang, J.; Kim, D. *J. Mater. Chem.* **2009**, *19* (8), 1057. doi:10.1039/b815813d.

(19) Yang, J.; Park, M.; Yoon, Z. S.; Hori, T.; Peng, X. B.; Aratani, N.; Dedecker, P.; Hotta, J. I.; Uji-I, H.; Sliwa, M.; Hofkens, J.; Osuka, A.; Kim, D. *J. Am. Chem. Soc.* **2008**, *130* (6), 1879. doi:10.1021/ja075701b.

(20) Yang, J. S.; Yoo, H.; Aratani, N.; Osuka, A.; Kim, D. *Angew. Chem. Int. Ed.* **2009**, *48* (24), 4323. doi:10.1002/anie.200901375.

(21) Yoo, H.; Yang, J.; Nakamura, Y.; Aratani, N.; Osuka, A.; Kim, D. *J. Am. Chem. Soc.* **2009**, *131* (4), 1488. doi:10.1021/ja807105n.

(22) Bagh, S.; Paige, M. F. *Can. J. Chem. 83* (5), 435. doi:10.1139/v05-053.

(23) Lu, Y.; Paige, M. F. *J. Fluoresc.* **2007**, *17* (6), 739. doi:10.1007/s10895-007-0185-1.

(24) Vanden Bout, D. A.; Yip, W. T.; Hu, D. H.; Fu, D. K.; Swager, T. M.; Barbara, P. F. *Science* **1997**, *277* (5329), 1074. doi:10.1126/science.277.5329.1074.

(25) Yip, W. T.; Hu, D. H.; Yu, J.; Vanden Bout, D. A.; Barbara, P. F. *J. Phys. Chem. A* **1998**, *102* (39), 7564. doi:10.1021/jp981808x.

(26) Lounis, B.; Deich, J.; Rosell, F. I.; Boxer, S. G.; Moerner, W. E. *J. Phys. Chem. B* **2001**, *105* (21), 5048. doi:10.1021/jp010116x.

(27) Maiti, N. C.; Ravikanth, M.; Mazumdar, S.; Periasamy, N. *J. Phys. Chem.* **1995**, *99* (47), 17192. doi:10.1021/j100047a024.

Photogeneration and reactivity of acyl nitroso compounds

Anthony S. Evans, Andrew D. Cohen, Zachary A. Gurard-Levin, Naod Kebede, Tevye C. Celius, Alexander P. Miceli, and John P. Toscano

Abstract: Acyl nitroso compounds have been generated by photolysis of several different classes of precursors including 9,10-dimethylanthracene adducts, nitrodiazo compounds, and 1,2,4-oxadiazole-4-oxides. Consideration of the nitronate-like resonance structure of nitrodiazo compounds led to an examination of the photochemistry of nitronates with α-leaving groups. Photolysis of such nitronates has been shown to generate an acyl nitroso species along with a carbene intermediate. Nanosecond time-resolved infrared (TRIR) spectroscopy has been used to detect photogenerated acyl nitroso compounds directly and to examine their reaction kinetics with amines and thiols. The mechanism of acyl nitroso aminolysis by primary amines involves general base catalysis, while the mechanism of aminolysis by secondary amines is strictly bimolecular. Thiols do not seem to be reactive with acyl nitroso compounds on the microsecond time scale, but thiolates are quite reactive. The reaction between benzoyl nitroside and an organic-soluble thiolate, tetrabutylammonium dodecanethiolate, proceeds via a proposed tetrahedral intermediate, which is observable by TRIR spectroscopy.

Key words: acyl nitroso, nitrodiazo, nitronate photochemistry, 1,2,4-oxadiazole-4-oxides, time-resolved IR spectroscopy.

Résumé : On a généré des composés acylnitroso par photolyse des plusieurs classes différentes de précurseurs, y compris des adduits du 9,10-diméthylanthracène, des composés nitrodiazo et des 4-oxydes de 1,2,4-oxadiazoles. Une considération de la structure des composés nitrodiazo qui est similaire à la structure de résonance des nitronates a conduit à un examen de la photochimie des nitronates possédant un groupe partant en position α. On a montré que la photolyse de tels nitronates conduit à la formation d'espèces acylnitroso aux côtés d'un intermédiaire carbène. On a fait appel à la spectroscopie infrarouge résolue en fonction du temps (IR-RT) pour détecter directement les composés acylnitroso photogénérés et pour déterminer la cinétique de leurs réactions avec des amines et des thiols. Le mécanisme de l'aminolyse d'un acylnitroso par les amines primaires implique une catalyse basique générale alors que le mécanisme de l'aminolyse d'un acylnitroso par les amines secondaires est strictement bimoléculaire. Les thiols ne semblent pas être réactifs vis-à-vis des composés acylnitroso à l'échelle de temps de la microseconde, mais les thiolates sont très réactifs. La réaction entre le nitroside de benzoyle et le thiolate organique soluble, décanethiolate de tétrabutylammonium, se fait par le biais d'une intermédiaire tétraédrique que l'on peut observer par spectroscopie IR-RT.

Mots-clés : acylnitroso, nitrodiazo, photochimie du nitronate, 4-oxydes de 1,2,4-oxadiazoles, spectroscopie infrarouge résolue en fonction du temps (IR-RT).

[Traduit par la Rédaction]

Introduction

Acyl nitroso (*C*-nitrosocarbonyl) compounds (**1**) are transient electrophiles that were originally proposed as intermediates in the pyrolysis of alkyl nitrites in the presence of aldehydes[1] as well as in the oxidation of hydroxamic acids.[2–4] Seminal work strongly suggesting the intermediacy of acyl nitroso compounds in the oxidation of hydroxamic acids was reported in a series of papers by Kirby[5] and Kirby and Sweeney.[6,7] Building on previous studies of the dienophilic character of nitrosyl cyanide, it was reasoned that the electron-withdrawing character of the carbonyl functionality ought to render acyl nitroso species reactive in [4 + 2] cycloadditions as well. Indeed, the mild periodate oxidation of aceto- and benzohydroxamic acid in the presence of a variety of conjugated dienes such as 9,10-dimethylanthracene (DMA) yields the Diels–Alder product **2** in high yield (Scheme 1). Further studies with these Diels–Alder adducts revealed that they can undergo a retro-Diels–Alder reaction at elevated temperatures and that the generated acyl nitroso intermediate could be trapped by a different diene.[7]

Received 1 June 2010. Accepted 17 June 2010. Published on the NRC Research Press Web site at canjchem.nrc.ca on 5 January 2011.

This article is part of a Special Issue dedicated to Professor J. C. Scaiano in appreciation of his contributions to photochemistry and organic reaction mechanisms.

A.S. Evans, A.D. Cohen, Z.A. Gurard-Levin, N. Kebede,[1] T.C. Celius,[2] A.P. Miceli, and J.P. Toscano.[3] Department of Chemistry, Johns Hopkins University, Baltimore, MD 21218, USA.

[1]Present address: Department of Chemistry, Edinboro University of Pennsylvania, Edinboro, PA 16444, USA.
[2]Present address: Department of Chemistry and Biochemistry, Ohio Northern University, Ada, OH 45810, USA.
[3]Corresponding author (e-mail: jtoscano@jhu.edu).

Can. J. Chem. Downloaded from www.nrcresearchpress.com by University of Electronic and Science Techonology of China on 09/18/12
For personal use only.

Can. J. Chem. Downloaded from www.nrcresearchpress.com by University of Electronic and Science Techonology of China on 09/18/12
For personal use only.

Scheme 1. The oxidative generation of acyl nitroso compounds (**1**) and subsequent reaction with DMA to form Diels–Alder adducts (**2**).

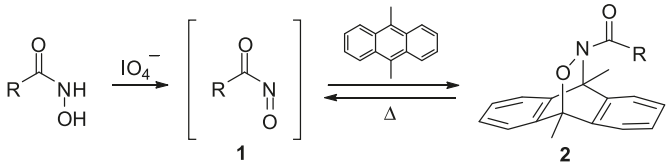

Scheme 2. The reaction of acyl nitroso compounds (**1**) with nucleophiles to generate HNO.

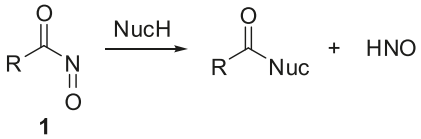

Scheme 3. The generation of acyl nitroso compounds (**1**) from nitrodiazo precursors (**3**).

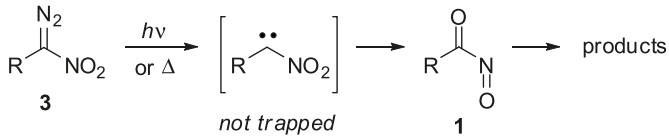

Reactions of acyl nitroso species with nucleophiles had been suggested by initial observations but were more carefully examined by Corrie et al.[8] Periodate oxidation of benzohydroxamic acid in aqueous media yields predominantly benzoic acid, while tetraalkyl-ammonium periodate oxidation in dichloromethane yields *O*-benzoylbenzohydroxamic acid. Atkinson et al.[9] studied the reaction of acyl nitroso compounds with amines to give amides in reasonable yields. Clearly, **1** is able to acylate nucleophiles such as water, hydroxamic acids, and amines, presumably with concomitant generation of nitroxyl (HNO) (Scheme 2). The detection of nitrous oxide (N_2O), the product of HNO dimerization and subsequent dehydration, in the reaction of **1** with amines is consistent with HNO formation.[9]

Acyl nitroso species have also been proposed as intermediates in the decomposition of nitrodiazo compounds (**3**). Although nitrocarbene intermediates can be trapped following rhodium-catalyzed decomposition,[10–14] thermolysis or photolysis leads only to acyl nitroso-derived products (Scheme 3).[15,16] Calculations predict that singlet nitrocarbene has little to no barrier to rearrangement to nitrosoformaldehyde.[17]

Quadrelli et al. have developed 1,2,4-oxadiazole-4-oxide derivatives (**4**) as efficient photochemical[18] and thermal[19] precursors to acyl nitroso compounds (Scheme 4), and Quadrelli and Caramella[20] have made use of these precursors in a wide variety of synthetic applications. We have recently utilized 3,5-diphenyl-1,2,4-oxadiazole-4-oxide (**4**, R = Ph) in the first direct observation of an acyl nitroso species in solution by nanosecond time-resolved infrared (TRIR) spectroscopy.[21] In this study, the strongest diagnostic signal for benzoyl nitroside (**1**, R = Ph) appeared at 1735 cm^{-1}; it was produced faster than the time resolution of our spectrometer ($k_{obs} > 2.0 \times 10^7$ s^{-1}) and was stable for at least 1 ms in the absence of nucleophiles.

Scheme 4. The generation of acyl nitroso compounds (**1**) from 1,2,4-oxadiazole-4-oxide derivatives (**4**).

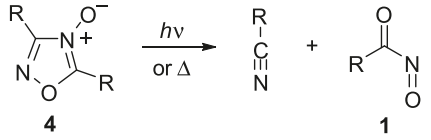

Fig. 1. TRIR difference spectra averaged over the time frames indicated following laser photolysis (266 nm, 5 ns, 3 mJ) of a 5 mmol L^{-1} solution of **2** (R = Ph) in dichloromethane.

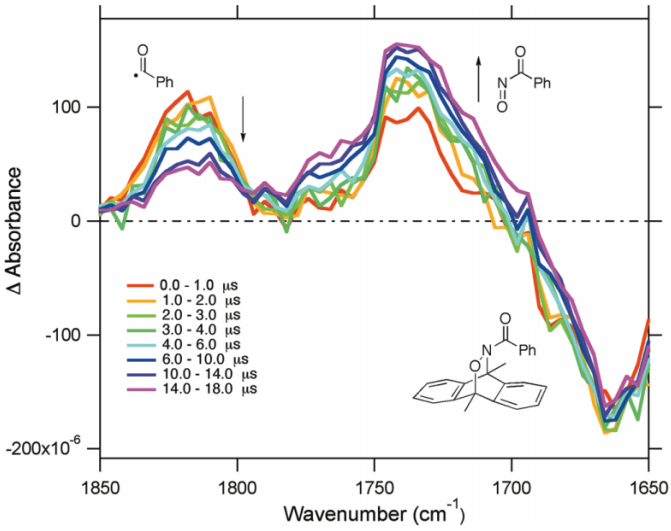

In this manuscript, we are pleased to extend our original TRIR studies of acyl nitroso compounds generated from **4** and also to report on the photochemistry of DMA adducts (**2**), nitrodiazo compounds (**3**), and related nitronate derivatives.

Results and discussion

Photogeneration of acyl nitroso compounds from DMA adducts

Following our initial TRIR studies of benzoyl nitroside generated from a 1,2,4-oxadiazole-4-oxide,[21] we have performed analogous studies on its DMA adduct (**2**, R = Ph). Laser photolysis (266 nm, 5 ns, 3 mJ) of a 5 mmol L^{-1} solution of **2** (R = Ph) in dichloromethane produces the TRIR difference spectrum shown in Fig. 1. Interestingly, in addition to the diagnostic acyl nitroso band at 1735 cm^{-1}, another prominent band is observed at 1820 cm^{-1}. The 1820 cm^{-1} band is formed faster than the time resolution of our spectrometer ($k_{obs} > 2.0 \times 10^7$ s^{-1}) and decays on the microsecond time scale with concomitant additional growth of the 1735 cm^{-1} acyl nitroso band.

IR absorbances above 1800 cm^{-1} are relatively rare for organic species and are typically observed only for highly strained carbonyls, carbonyls substituted with strongly electron-withdrawing groups, and acyl radicals. Acyl radicals have been extensively studied in hydrocarbon solvent by TRIR spectroscopy.[22,23] Benzoyl radical is reported to absorb at 1828 cm^{-1}, consistent with our 1820 cm^{-1} signal in dichloromethane. We envision two potential pathways consistent with the TRIR data of Fig. 1: (*i*) simple secondary photoly-

Can. J. Chem. Downloaded from www.nrcresearchpress.com by University of Electronic and Science Techonology of China on 09/18/12
For personal use only.

Scheme 5. Two potential photochemical pathways for the DMA adduct (**2**, R = Ph).

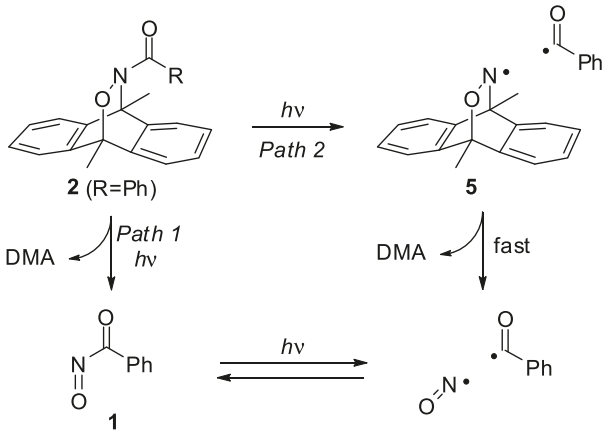

sis of benzoyl nitroside within the 266 nm laser pulse to form nitric oxide (NO) and benzoyl radical, which subsequently recombine (Scheme 5, path 1), or (*ii*) Norrish type I cleavage of precursor **2** to form benzoyl radical and NO/DMA adduct (**5**), which rapidly dissociates to NO and DMA, followed by NO–benzoyl radical recombination (Scheme 5, path 2). Similar photochemistry has very recently been proposed for other acyl nitroso Diels–Alder cycloadducts.[24]

Analogous TRIR experiments on the acetyl nitroside/DMA adduct (**2**, R = Me) reveal only the characteristic acyl nitroso band, in this case observed at 1780 cm^{-1} (consistent with B3LYP/6-31G* calculations), with no evidence for the acetyl radical (Supplementary data). Since acetyl nitroside is not expected to absorb at 266 nm, whereas benzoyl nitroside should, these experiments suggest that the secondary photolysis pathway (Scheme 5, path 1) is operative.

Photogeneration of acyl nitroso compounds from nitrodiazo compounds

We have also examined the photogeneration of acyl nitroso compounds from nitrodiazo precursors by TRIR spectroscopy. Ethyl nitrodiazoacetate (**3**, R = CO_2Et) and nitrodiazomethyl *tert*-butyl ketone (**3**, R = C(O)-*t*-Bu) both provide the characteristic acyl nitroso TRIR signal at 1788 and 1756 cm^{-1}, respectively, consistent with B3LYP/6-31G* calculations (Supplementary data). Each of these bands was produced faster than the time resolution of our spectrometer ($k_{obs} > 2.0 \times 10^7$ s^{-1}) and was stable for at least 1 ms in dichloromethane. In the spectral region between 2200 and 2000 cm^{-1}, we also observe diazo depletion bands with no TRIR evidence for the formation of ketene,[25,26] which could potentially be formed via Wolff rearrangement from either of these precursors (Supplementary data). Consistent with the lack of Wolff rearrangement, nearly quantitative yields of N_2O (formed via acyl nitroso-produced HNO) are observed following the photolysis of ethyl nitrodiazoacetate in 75:25 acetonitrile/water (Scheme 6).

Given the above results and previous observations that photogenerated nitrocarbenes are not trappable,[15,16] we have begun to explore an alternative photochemical pathway to acyl nitroso compounds from nitrodiazo precursors that arose from consideration of their nitronate-like resonance structure (**3-N**). Alkyl nitronates (**6**) have been shown to undergo a photoinduced rearrangment to hydroxamic acids (Scheme 7*a*).[27–31] An analogous reaction from a nitrodiazo compound leads to the *N*-oxirane intermediate **7**, which could undergo further rearrangement, via two potential pathways, to the acyl nitroso product (Scheme 7*b*).

Photogeneration of acyl nitroso compounds from nitronates with α-leaving groups

To test the reaction scheme shown in Scheme 7*b* we have examined the photochemistry of nitronates with α-leaving groups. Our initial studies have focused on phenylcyanonitromethane nitronate (**8**); results similar to those reported below have also been observed in preliminary experiments with the 4-chloro and 4-methoxy analogues.

Nitronate **8** is stable in sodium hydroxide or methanol solutions. As shown in Scheme 8, photolysis (Rayonet, 254 nm) of **8** in methanol cleanly provides two products, methyl benzoate (**10**) and methoxyphenylacetonitrile (**12**). HPLC and GC–MS analysis reveal a 29% ± 5% yield of **10** and a 63% ± 7% yield of **12** (values are means ± SD). The production of methyl benzoate was confirmed by comparison with an authentic sample; the GC–MS data for nitrile **12** match well with its reported mass spectrum.[32] N_2O quantification following photolysis of nitronate **8** in methanol indicates that HNO is formed in a 26% ± 5% yield, consistent with the yield of methyl benzoate.

To explain the formation of nitrile **12**, we propose that *N*-oxirane intermediate **9** partitions between the anticipated loss of cyanide ion and the loss of nitrite ion to form phenylcyano carbene (**11**), which is trapped by methanol to form nitrile **12**, as has been previously observed.[33,34] Although we have not yet conducted experiments that indicate whether carbene **11** is formed thermally or photochemically (analogous to epoxide photochemistry[34–36]) from *N*-oxirane **9**, this hypothesis is consistent with earlier studies of nitronate photochemistry where carbene intermediates were proposed.[30]

Further experimental evidence for the formation of carbene **11** is provided by additional trapping experiments. GC–MS analysis following photolysis of nitronate **8** in acetonitrile containing either cyclohexene or 2,3-dimethyl-2-butene reveals carbene–alkene adducts (both C–H and C=C insertion products).[36] Moreover, the addition of increasing concentrations of alkene to a methanol-containing acetonitrile solution of nitronate **8** results in a decrease of the carbene–methanol adduct **12** accompanied by a concomitant increase in carbene–alkene derived products. Finally, photolysis of nitronate **8** in THF results in products (**14** and **15**, Scheme 8) consistent with the rearrangement of carbene-derived ylide **13**. Analogous THF–ylide rearrangement products have been observed in the study of 2-naphthyl(carbomethoxy)carbene.[37]

Reactivity of acyl nitroso compounds with amines

We have examined the reactivity of three acyl nitroso compounds (**1**, R = Ph, Me, and 4-Cl-Ph) with a variety of amines in dichloromethane. Acyl nitroso compounds (**1**, R = Ph and 4-Cl-Ph) were generated from 1,2,4-oxadiazole-4-oxides (**4**), and acyl nitroso **1** (R = Me) was generated from

Can. J. Chem. Downloaded from www.nrcresearchpress.com by University of Electronic and Science Techonology of China on 09/18/12
For personal use only.

Scheme 6. The photodecomposition of ethyl nitrodiazoacetate in 75:25 acetonitrile/water.

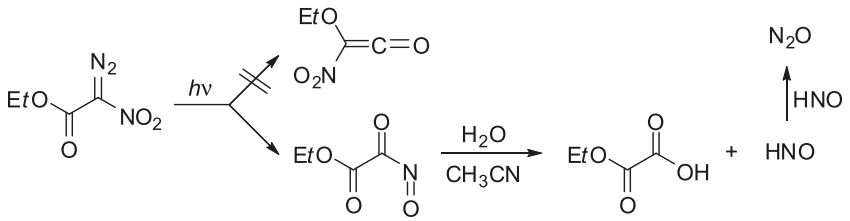

Scheme 7. (*a*) The photochemistry of alkyl nitronates. (*b*) The analogous photochemistry of nitrodiazo precursors to produce acyl nitroso compounds.

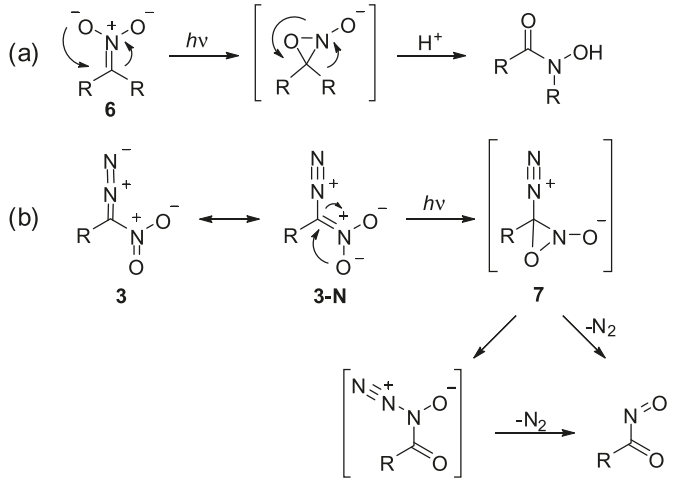

its DMA adduct (**2**). The decay kinetics of the characteristic acyl nitroso TRIR signals were monitored as a function of varying concentrations of added amine to derive reaction rate constants.

For the secondary amines, diethylamine (DEA) and piperidine (PIP), plots of observed decay rates (k_{obs}) versus amine concentration are linear and fit well to the pseudo-first-order rate equation $k_{obs} = k_o + k_{amine}$[amine] (Fig. 2 and Supplementary data). Derived second-order rate constants are shown in Table 1. (Note that the reaction of benzoyl nitroside (**1**, R = Ph) with DEA has been refined slightly from that originally reported ($k_{DEA} = 1.3 \times 10^5 \pm 0.5 \times 10^5$ L mol^{-1} s^{-1}).[21]) The twofold faster rate constant for the reaction of **1** (R = Ph) with PIP versus DEA is consistent with the decreased steric bulk of the ring-constrained PIP.

For the primary amines, *n*-butylamine (NBA) and benzylamine (BA), in contrast to the above secondary amines, plots of k_{obs} versus amine concentration are not linear, but rather fit to the rate equation $k_{obs} = k_o + k_{amine}$[amine]^2 (Fig. 3 and Supplementary data), indicating that the reaction of acyl nitroso species with primary amines is a third-order reaction, requiring two molecules of the primary amine. Relative rate constants derived for NBA and BA (Table 1) are again consistent with expected reactivity. No reactivity was observed with *tert*-butylamine (TBA), even at concentrations approaching 2 mol L^{-1}, owing to the steric bulk of this poorly nucleophilic amine.

The dependence of the reaction order of the aminolysis of acyl nitroso species on amine structure (i.e., primary vs. secondary) is consistent with previous reports of the aminolysis of esters by primary and secondary amines in organic solvent.[38–40] Our results indicate that the mechanism of acyl nitroso aminolysis by primary amines involves general base catalysis, while the mechanism of aminolysis by secondary amines is strictly bimolecular.

For a given amine, the rate of aminolysis is also dependent on the structure of the acyl nitroso compound. Consistent with expected electronic effects, **1** (R = 4-Cl-Ph) reacts 2 to 3 times more rapidly than **1** (R = Ph) with DEA and NBA, respectively. Also, aliphatic acyl nitroso (**1**, R = Me) reacts 2.5 to 10 times more rapidly than aromatic acyl nitroso (**1**, R = Ph) with NBA and PIP, respectively.

Reactivity of acyl nitroso compounds with thiols

We have also examined the kinetics and mechanism of the reaction of **1** (R = Ph) with thiols. Initial experiments surprisingly revealed no observed increase in the acyl nitroso decay rate upon the addition of up to 100 mmol L^{-1} *N*-acetylcysteine methyl ester (NAC). However, in the presence of 3.4 mmol L^{-1} NAC and 48 mmol L^{-1} DEA, the decay of **1** was observable and faster than that in the presence of 48 mmol L^{-1} DEA alone. We postulate that although the thiol itself is not reactive (on the microsecond time scale), the in situ generated diethylammonium thiolate is. We examined thiolate reactivity directly using organic-soluble tetrabutylammonium dodecanethiolate (TBA-D). The dependence of the acyl nitroso decay rate fit well to the pseudo-first-order rate equation $k_{obs} = k_o + k_{TBA\text{-}D}$[TBA-D] and a value of $k_{TBA\text{-}D} = 4.2\ (\pm 0.6) \times 10^7$ L mol^{-1} s^{-1} was determined (Supplementary data).

For all amines examined, acyl nitroso decay is accompanied by concomitant growth of the corresponding amide product ($\sim$1660 cm^{-1}). In the case of the reaction of TBA-D with **1** (R = Ph), however, the acyl nitroso (1735 cm^{-1}) decays over the microsecond time scale to a strongly absorbing intermediate that is observed at 1615 cm^{-1} (Fig. 4). This intermediate subsequently decays on the millisecond time scale to the product thiobenzoate (**17**), observed at 1706 cm^{-1}, consistent with the reported carbonyl stretching frequency of ethylthiobenzoate.[41] We have tentatively assigned this 1615 cm^{-1} band to tetrahedral intermediate **16** (Scheme 9), which is calculated (Supplementary data) to have a very intense N=O stretch at 1597 cm^{-1}, reasonably consistent with the observed TRIR band.

The rate of decay of the intermediate 1615 cm^{-1} band and the rate of growth of the 1706 cm^{-1} product band are both independent of the concentration of TBA-D, consistent with a unimolecular reaction of **16**. A similar tetrahedral intermediate has been proposed in the alkaline hydrolysis of thiobenzoates.[42]

Can. J. Chem. Downloaded from www.nrcresearchpress.com by University of Electronic and Science Techonology of China on 09/18/12
For personal use only.

Scheme 8. The photochemistry of phenylcyanonitromethane nitronate (**8**).

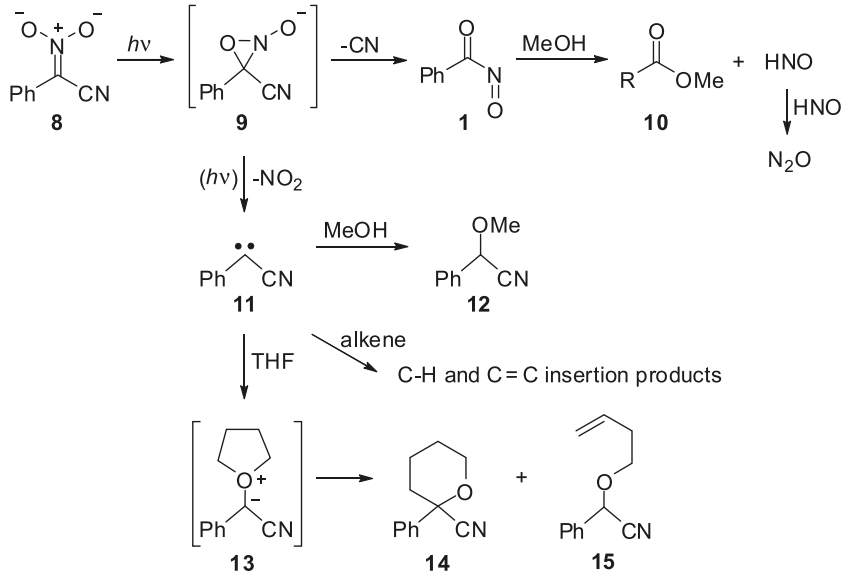

Table 1. Rate constants for the reaction of acyl nitroso compounds with amines.

	$k \times 10^{-5}$ (L mol^{-1} s^{-1})		$k \times 10^{-4}$ (L^{-1} mol^{-2} s^{-1})		
Acyl nitroso **1**, R =	DEA	PIP	NBA	BA	TBA
Ph	1.2±0.1	2.0±0.1	2.8±0.1	0.36±0.9	No rxn
Me	ND	22±1	7.1±0.1	ND	No rxn
4-Cl-Ph	2.3±0.1	ND	10.1±0.1	ND	No rxn

Note: DEA, diethylamine; PIP, piperidine; NBA, *n*-butylamine; BA, benzylamine; TBA, *tert*-butylamine; ND, not determined; no rxn, no reaction observed on the microsecond time scale.

Fig. 2. Plots of observed rate of decay of **1** (R = Ph) in dichloromethane monitored at 1735 cm^{-1} as a function of diethylamine (squares) or piperidine (circles) concentration. The dotted lines are the least-squares fit to a linear function.

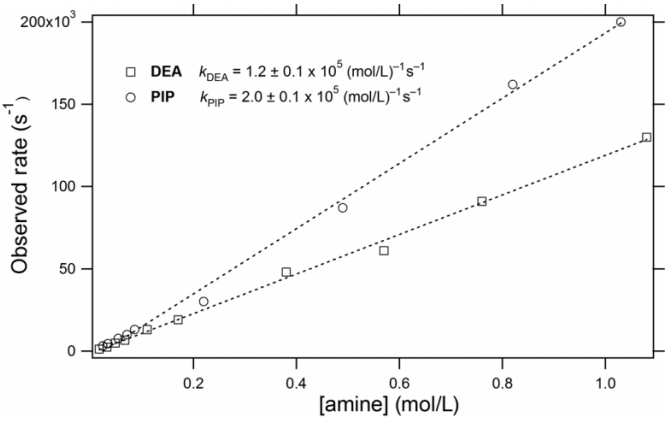

Fig. 3. Plots of observed rate of decay of **1** (R = Ph) in dichloromethane monitored at 1735 cm^{-1} as a function of benzylamine (squares) or *n*-butylamine (circles) concentration. The dotted lines are the least-squares fit to a polynomial function.

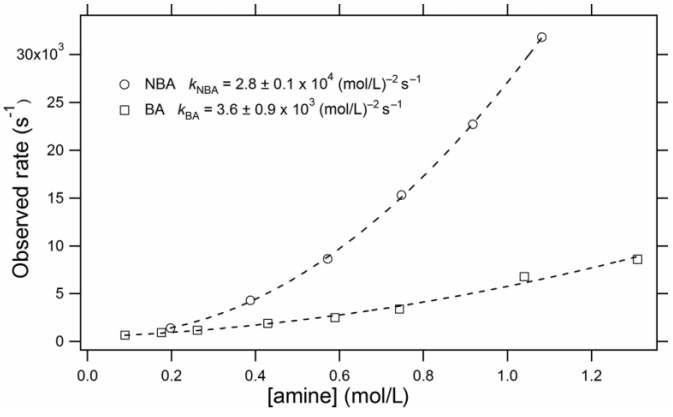

Conclusions

Acyl nitroso compounds have been generated by photolysis of several different classes of precursors including DMA adducts (**2**), nitrodiazo compounds (**3**), and 1,2,4-oxadiazole-4-oxides (**4**). Consideration of the nitronate-like resonance structure of nitrodiazo compounds led to an examination of the photochemistry of nitronates with α-leaving groups (e.g., **8**). Photolysis of nitronate **8** has been shown to generate an acyl nitroso species along with a carbene intermediate.

Nanosecond TRIR spectroscopy has been used to detect photogenerated acyl nitroso compounds directly and to examine their reaction kinetics with amines and thiols. The mechanism of acyl nitroso aminolysis by primary amines involves general base catalysis, while the mechanism of aminolysis by secondary amines is strictly bimolecular. Thiols do not seem to be reactive with acyl nitroso compounds on the microsecond time scale, but thiolates are quite reactive. The reaction between benzoyl nitroside (**1**, R = Ph) and the organic-soluble thiolate TBA-D proceeds via a proposed tet-

Can. J. Chem. Downloaded from www.nrcresearchpress.com by University of Electronic and Science Techonology of China on 09/18/12
For personal use only.

Fig. 4. (*a*) TRIR difference spectra averaged over the time frames indicated and (*b* and *c*) kinetic traces observed following laser photolysis (355 nm, 5 ns, 4 mJ) of a 1 mmol L^{-1} solution of **4** (R = Ph) containing 10 mmol L^{-1} TBA-D in dichloromethane.

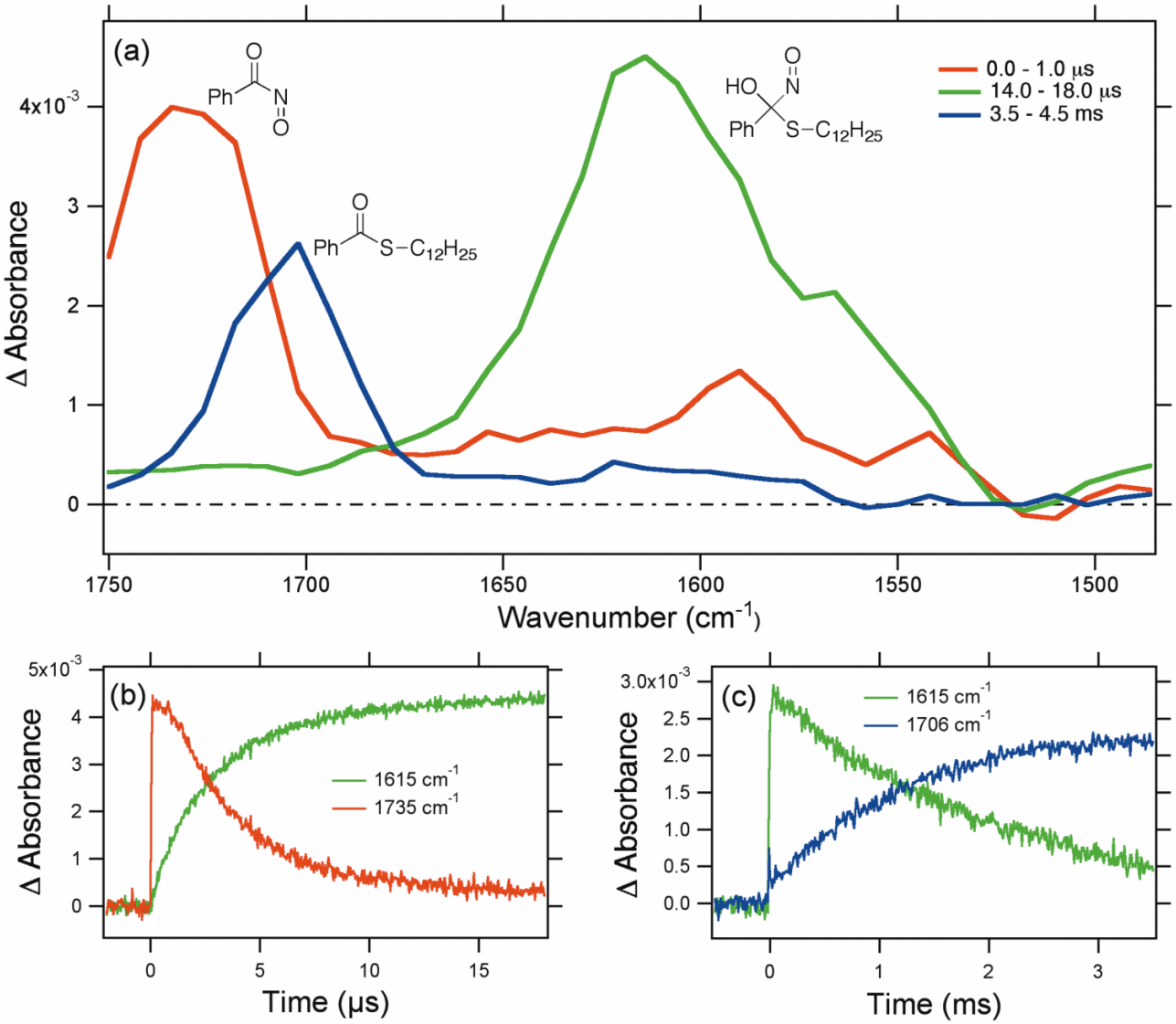

Scheme 9. The postulated mechanism for the thiolysis of benzoyl nitroside illustrating the intermediacy of **16**.

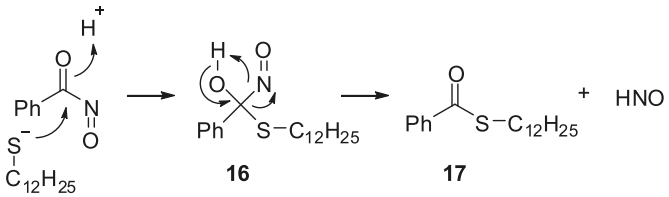

rahedral intermediate, which is observable by TRIR spectroscopy.

Experimental section

General methods

Unless otherwise noted, materials were obtained from the Sigma-Aldrich Chemical Company, Fisher Scientific, or Cambridge Isotope Laboratories. All solvents were purified with a PureSolv MD 5 solvent purification system. All amines were redistilled prior to use and stored over potassium hydroxide.

^{1}H NMR spectra were recorded on a Bruker Avance 400 MHz FT NMR operating at 400 MHz; ^{13}C NMR spectra were recorded on a Bruker Avance 300 MHz FT NMR operating at 75 MHz. All ^{1}H resonances are reported in parts per million, and are referenced to solvent (^{1}H NMR (chloroform-*d*) δ: 7.26, (methanol-d_4) δ: 3.3). Melting points were recorded on a Mel-Temp apparatus and are uncorrected. High resolution mass spectra were obtained on a VG70SE double focusing magnetic sector mass spectrometer operating in fast atom bombardment ionization mode. Reported masses were referenced to a doubly potassiated PEGMME mass calibrant. Ultraviolet–visible (UV–vis) absorption spectra were obtained using a Hewlett Packard 8453 diode array spectrometer. Infrared (IR) absorption spectra were obtained using a Bruker IFS 55 Fourier transform infrared spectrometer. All density functional theory (DFT) calculations were performed using Spartan '04 (Wavefunction, Inc.) for Macintosh or

Can. J. Chem. Downloaded from www.nrcresearchpress.com by University of Electronic and Science Techonology of China on 09/18/12
For personal use only.

Spartan '08 (Wavefunction, Inc.) for Windows using the B3LYP/6-31G* method and basis set.

Time-resolved IR methods

TRIR experiments were conducted following the method of Iwata and Hamaguchi[43] as described previously.[25] Briefly, the broadband output of a $MoSi_2$ IR source (JASCO) is crossed with excitation pulses from a Continuum Minilite II Nd:YAG laser (266 nm or 355 nm) operating at 15 Hz. Changes in IR intensity are monitored using an AC-coupled mercury/cadmium/tellurium (MCT) photovoltaic IR detector (Kolmar Technologies, KMPV11-J1/AC), amplified, digitized with a Tektronix TDS520A oscilloscope, and collected on a Macintosh with IGOR for data processing. The experiment is conducted in dispersive mode with a JASCO TRIR 1000 spectrometer.

N_2O quantification via GC headspace analysis

GC headspace analysis was performed on a Varian CP-3800 instrument equipped with a Restek ShinCarbon ST 80/100 molecular sieve-packed column and an electron capture detector.

Photolysis of Angeli's salt (a classic HNO donor under physiologically relevant conditions[44]) has been shown to produce HNO/NO^-, which subsequently yields N_2O.[45] To quantify the amount of N_2O produced following photolysis of Angeli's salt, a 1 mmol L^{-1} solution in 0.01 mol L^{-1} NaOH was prepared and 1 mL of this solution was placed in series of 1 cm quartz cuvettes. The cuvettes were sealed with rubber septa and sparged with argon for 20 min. Samples were then photolyzed (Rayonet, 254 nm) until completion as indicated by the disappearance of the characteristic Angeli's salt UV absorbance at 254 nm. Samples were allowed to equilibrate at 37 °C for 1 h and then 100 μL of headspace was analyzed for N_2O. N_2O yields are taken as an average of five injections. The theoretical yield of Angeli's salt-derived N_2O was calculated for the NaOH solution using Henry's law and was found to be quantitative versus authentic samples. N_2O yields were determined analogously for ethyl nitrodiazoacetate (**3**, R = CO_2Et) in 75:25 acetonitrile/water and phenylcyano-nitromethane nitronate (**8**) in methanol and compared with that found for Angeli's salt (assumed to be 100%) in 75:25 acetonitrile/water and methanol, respectively.

GC–MS methods

GC–MS analysis was performed on a Shimadzu GC17A/QP5050A instrument equipped with electron ionization. Nitronate samples were prepared in methanol, THF, or acetonitrile, sparged with argon, photolyzed (Rayonet, 254 nm), concentrated under vacuum, reconstituted in 1 mL of methanol, and then analyzed by GC–MS. Carbene trapping by alkenes (cyclohexene and 2,3-dimethyl-2-butene) was analyzed analogously in acetonitrile solutions. Competitive carbene trapping by methanol versus alkene (cyclohexene or 2,3-dimethyl-2-butene) was also performed in acetonitrile with 10 mmol L^{-1} methanol and 0–50 mmol L^{-1} alkene. Yields are reported as an average of four individual experiments.

HPLC methods

HPLC data were collected on a Waters Delta 600 system equipped with a Model 6000A pump and a Model 2487 dual wavelength UV detector monitoring at 230 nm equipped with a Waters C-18 symmetry column. All HPLC eluents contained 0.1% trifluoroacetic acid. Nitronate samples were prepared in methanol, sparged with argon, and then photolyzed (Rayonet, 254 nm). HPLC analysis was then performed with a flow rate of 1 mL min^{-1} with 35:65 acetonitrile/water. Yields are reported as an average of four individual experiments.

General procedure for the synthesis of DMA cycloadducts (2)

The synthesis of DMA cycloadducts (**2**) was carried out in accordance with a literature procedure, using tetrabutylammonium periodate instead of tetraethyl-ammonium periodate.[7] Benzoyl nitroside/DMA cycloadduct (**2**, R = Ph): mp 126–128 °C (lit. value[7] mp 127–128 °C). Acetyl nitroside/DMA cycloadduct (**2**, R = Me): mp 133–136 °C (lit. value[7] mp 133–136 °C).

General procedure for the synthesis of nitrodiazocarbonyl compounds (3)

Ethylnitrodiazoacetate and nitrodiazomethyl *tert*-butyl ketone were synthesized by the method reported by Charette et al.[46] Ethylnitrodiazoacetate (**3**, R = CO_2Et): IR (film, cm^{-1}) ν_{max}: 2148, 1750, 1693. ^1H NMR ($CDCl_3$) δ: 4.42 (2H, q), 1.38 (3H, t). Nitrodiazomethyl *tert*-butyl ketone (**3**, R = C(O)-*t*-Bu): IR (film, cm^{-1}) ν_{max}: 2142, 2180, 1690, 1650. ^1H NMR ($CDCl_3$) δ: 1.35 (s, 9 H).

General procedure for the synthesis of 1,2,4-oxadiazole-4-oxides (4)

The synthesis of 1,2,4-oxadiazole-4-oxides was performed using a slight modification of a literature procedure.[47] The synthesis of 3,5-diphenyl-1,2,4-oxadiazole-4-oxide is shown below as a general procedure.

3,5-Diphenyl-1,2,4-oxadiazole-4-oxide (4, R = Ph)

Benzohydroximoyl chloride was prepared from benzaldehyde oxime in accordance with literature procedures and used directly for the next step.[48] Dehydrohalogenation was performed in ethanol using triethanolamine to yield benzonitrile oxide. The nitrile oxide dimerization was accomplished in situ with triethanolamine, yielding a mixture of three dimeric species. The desired dimer was initially purified by silica gel column chromatography (10%–30% ethyl acetate / hexanes). The column-purified product was further purified by recrystallization from methanol/water, yielding white needles; mp 132–133 °C (lit. value[49] mp 134 °C).

3,5-Bis(4-chlorophenyl)-1,2,4-oxadiazole-4-oxide (4, R = 4-Cl-Ph)

Prepared from 4-chlorobenzaldehyde oxime using the general procedure; mp 189–190 °C (lit. value[49] mp 189–190 °C).

General procedure for the synthesis of arylcyanonitromethane potassium nitronates

Arylcyanonitromethane potassium nitronate derivatives

Can. J. Chem. Downloaded from www.nrcresearchpress.com by University of Electronic and Science Techonology of China on 09/18/12
For personal use only.

were prepared via modification of a literature procedure.[50] Synthesis of phenylcyanonitromethane potassium nitronate is shown below as a general procedure.

Phenylcyanonitromethane potassium nitronate (8)

Benzyl cyanide (2.93 g, 0.025 mol) was added to a solution of potassium *tert*-butoxide (9.25 g, 0.0825 mol) in 90 mL of THF at –50 °C in a dry ice / acetone bath. Isoamyl nitrate (7.3 g, 0.55 mol) was added dropwise, maintaining the temperature at –45 to –50 °C. The cooling bath was removed and the reaction mixture allowed to warm to room temperature. The precipitate that formed was filtered and washed with THF and then ether. The residue was recrystallized from ethanol/hexanes (2.25 g, 45%). IR (mineral oil, cm^{-1}) ν_{max}: 2201, 1495, 1455, 1417, 1366, 1339, 1310, 1284, 1264, 1190, 1167, 1034, 1005, 989, 762. ^1H NMR (methanol-d_4) δ: 7.15 (1H, t), 7.32 (2H, d), 7.90 (2H, d). ^{13}C NMR (D_2O) δ: 129.40, 128.52, 127.68, 125.87, 117.88, 102.10. HR-FAB-MS *m/z*: 238.9629 $[M + 2K]^+$. Calcd. for $C_8H_5K_2N_2O_2$: 238.9625.

4-Chloro-phenylcyanonitromethane potassium nitronate

Prepared from 4-chlorobenzyl cyanide using the general procedure. IR (mineral oil, cm^{-1}) ν_{max}: 2200, 1497, 1397, 1303, 1279, 1248, 1115, 1098, 996, 824. ^1H NMR (methanol-d_4) δ: 7.32 (2H, d), 7.90 (2H, d). ^{13}C NMR (D_2O) δ: 132.14, 128.31, 128.05, 126.89, 117.48, 101.49. HR-FAB-MS *m/z*: 272.9232 $[M + 2K, {}^{35}Cl]^+$, 274.9210 $[M + 2K, {}^{37}Cl]^+$. Calcd. for $C_8H_4ClK_2N_2O_2$: 272.9235.

4-Methoxy-phenylcyanonitromethane potassium nitronate

Prepared from 4-methoxybenzyl cyanide using the general procedure. IR (mineral oil, cm^{-1}) ν_{max}: 2205, 1600, 1514, 1412, 1351, 1310, 1290, 1241, 1189, 1151, 1028, 991, 828. ^1H NMR (methanol-d_4) δ: 3.79 (3H, s), 6.90 (2H, d), 7.80 (2H, d). ^{13}C NMR (D_2O) δ: 158.07, 127.60, 122.14, 117.60, 113.87, 101.80, 55.28. HR-FAB-MS *m/z*: 268.9726 $[M + 2K]^+$. Calcd. for $C_9H_7K_2N_2O_3$: 268.9731.

Synthesis of tetrabutylammonium dodecanethiolate (TBA-D)

The synthesis was carried out in accordance with the published procedure.[51,52]

Supplementary data

Supplementary data (additional TRIR data, kinetic analyses, and computational results) for this article are available on the journal Web site (canjchem.nrc.ca).

Acknowledgment

J.P.T. thanks the U.S. National Science Foundation (CHE-0911305) for generous support of this research.

References

(1) Beckwith, A. L. J.; Evans, G. W. *J. Chem. Soc.* **1962**, 130. doi:10.1039/jr9620000130.
(2) Sklarz, B.; Al-Sayyab, A. F. *J. Chem. Soc.* **1964**, 1318. doi:10.1039/jr9640001318.
(3) Moffatt, J. G.; Lerch, U. *J. Org. Chem.* **1971**, *36* (22), 3391. doi:10.1021/jo00821a027.
(4) Rowe, J. E.; Ward, A. D. *Aust. J. Chem.* **1968**, *21* (11), 2761.
(5) Kirby, G. W. *Chem. Soc. Rev.* **1977**, *6* (1), 1. doi:10.1039/cs9770600001.
(6) Kirby, G. W.; Sweeny, J. G. *J. Chem. Soc., Chem. Commun.* **1973**, 704. doi:10.1039/c39730000704.
(7) Kirby, G. W.; Sweeny, J. G. *J. Chem. Soc., Perkin Trans. 1* **1981**, 3250. doi:10.1039/p19810003250.
(8) Corrie, J. E. T.; Kirby, G. W.; Mackinnon, J. W. M. *J. Chem. Soc., Perkin Trans. 1* **1985**, 883. doi:10.1039/p19850000883.
(9) Atkinson, R. N.; Storey, B. M.; King, S. B. *Tetrahedron Lett.* **1996**, *37* (52), 9287. doi:10.1016/S0040-4039(97)82943-7.
(10) O'Bannon, P. E.; Dailey, W. P. *J. Org. Chem.* **1989**, *54* (13), 3096. doi:10.1021/jo00274a027.
(11) O'Bannon, P. E.; Dailey, W. P. *Tetrahedron Lett.* **1989**, *30* (32), 4197. doi:10.1016/S0040-4039(01)80688-2.
(12) O'Bannon, P. E.; Dailey, W. P. *Tetrahedron* **1990**, *46* (21), 7341. doi:10.1016/S0040-4020(01)89052-9.
(13) O'Bannon, P. E.; Dailey, W. P. *J. Org. Chem.* **1991**, *56* (6), 2258. doi:10.1021/jo00006a058.
(14) Charette, A. B.; Wurz, R. P.; Ollevier, T. *Helv. Chim. Acta* **2002**, *85* (12), 4468. doi:10.1002/hlca.200290023.
(15) Schöllkopf, U.; Markusch, P. *Justus Liebigs Ann. Chem.* **1971**, *753*, 143. doi:10.1002/jlac.19717530113.
(16) O'Bannon, P. E.; Dailey, W. P. *Tetrahedron Lett.* **1988**, *29* (45), 5719. doi:10.1016/S0040-4039(00)82171-1.
(17) O'Bannon, P. E.; Dailey, W. P. *Tetrahedron Lett.* **1988**, *29* (9), 987. doi:10.1016/0040-4039(88)85315-2.
(18) Quadrelli, P.; Mella, M.; Caramella, P. *Tetrahedron Lett.* **1999**, *40* (4), 797. doi:10.1016/S0040-4039(98)02416-2.
(19) Quadrelli, P.; Campari, G.; Mella, M.; Caramella, P. *Tetrahedron Lett.* **2000**, *41* (12), 2019. doi:10.1016/S0040-4039(00)00093-9.
(20) Quadrelli, P.; Caramella, P. *Curr. Org. Chem.* **2007**, *11* (11), 959. doi:10.2174/138527207781058745.
(21) Cohen, A. D.; Zeng, B.-B.; King, S. B.; Toscano, J. P. *J. Am. Chem. Soc.* **2003**, *125* (6), 1444. doi:10.1021/ja028978e. PMID:12568581.
(22) Neville, A. G.; Brown, C. E.; Rayner, D. M.; Lusztyk, J.; Ingold, K. U. *J. Am. Chem. Soc.* **1991**, *113* (5), 1869. doi:10.1021/ja00005a082.
(23) Brown, C. E.; Neville, A. G.; Rayner, D. M.; Ingold, K. U.; Lusztyk, J. *Aust. J. Chem.* **1995**, *48* (2), 363.
(24) Matsuo, K.; Nakagawa, H.; Adachi, Y.; Kameda, E.; Tsumoto, H.; Suzuki, T.; Miyata, N. *Chem. Commun. (Camb.)* **2010**, *46* (21), 3788. doi:10.1039/c001502d. PMID:20393655.
(25) Wang, Y.; Yuzawa, T.; Hamaguchi, H.; Toscano, J. P. *J. Am. Chem. Soc.* **1999**, *121* (12), 2875. doi:10.1021/ja983278o.
(26) Wang, Y.; Toscano, J. P. *J. Am. Chem. Soc.* **2000**, *122* (18), 4512. doi:10.1021/ja9937775.
(27) Imam, S. H.; Marples, B. A. *Tetrahedron Lett.* **1977**, *18* (30), 2613. doi:10.1016/S0040-4039(01)83834-X.
(28) Yamada, K.; Kanekiyo, T.; Tanaka, S.; Naruchi, K.; Yamamoto, M. *J. Am. Chem. Soc.* **1981**, *103* (23), 7003. doi:10.1021/ja00413a056.
(29) Yamada, K.; Tanaka, S.; Naruchi, K.; Yamamoto, M. *J. Org. Chem.* **1982**, *47* (27), 5283. doi:10.1021/jo00148a011.

(30) Edge, G. J.; Imam, S. H.; Marples, B. A. *J. Chem. Soc., Perkin Trans. 1* **1984**, 2319. doi:10.1039/p19840002319.
(31) Lipczynska-Kochany, E. *Chem. Rev.* **1991**, *91* (4), 477. doi:10.1021/cr00004a002.
(32) Kumamoto, K.; Nakano, K.; Ichikawa, Y.; Kotsuki, H. *Synlett* **2006**, 1968.
(33) Meek, J. S.; Fowler, J. S. *J. Am. Chem. Soc.* **1967**, *89* (8), 1967. doi:10.1021/ja00984a046.
(34) Boyer, J. H.; Selvarajan, R. *J. Am. Chem. Soc.* **1969**, *91* (22), 6122. doi:10.1021/ja01050a033.
(35) Petrellis, P. C.; Griffin, G. W. *Chem. Commun.* **1967**, 691. doi:10.1039/C19670000691.
(36) Petrellis, P. C.; Dietrich, H.; Meyer, E.; Griffin, G. W. *J. Am. Chem. Soc.* **1967**, *89* (8), 1967. doi:10.1021/ja00984a047.
(37) Wang, J.-L.; Yuzawa, T.; Nigam, M.; Likhotvorik, I.; Platz, M. S. *J. Phys. Chem.* **2001**, *105* (15), 3752.
(38) Shawali, A. S. A. S.; Biechler, S. S.; Biechler, S. S. *J. Am. Chem. Soc.* **1967**, *89* (12), 3020. doi:10.1021/ja00988a039.
(39) Menger, F. M.; Smith, J. H. *J. Am. Chem. Soc.* **1969**, *91* (19), 5346. doi:10.1021/ja01047a025.
(40) Anderson, D. J.; Gilchrist, T. L.; Horwell, D. C.; Rees, C. W. *Chem. Commun.* **1969**, 146. doi:10.1039/C29690000146.
(41) Baker, A. W.; Harris, G. H. *J. Am. Chem. Soc.* **1960**, *82* (8), 1923. doi:10.1021/ja01493a022.
(42) Boopsingh, B.; Satchell, D. P. N. *J. Chem. Soc., Perkin Trans. 2* **1972**, 1702. doi:10.1039/P29720001702.
(43) Iwata, K.; Hamaguchi, H. *Appl. Spectrosc.* **1990**, *44* (9), 1431. doi:10.1366/0003702904417742.
(44) Miranda, K. M.; Nagasawa, H. T.; Toscano, J. P. *Curr. Top. Med. Chem.* **2005**, *5* (7), 649. doi:10.2174/1568026054679290.
(45) Shafirovich, V.; Lymar, S. V. *Proc. Natl. Acad. Sci. U.S.A.* **2002**, *99* (11), 7340. doi:10.1073/pnas.112202099. PMID: 12032284.
(46) Charette, A. B.; Wurz, R. P.; Ollevier, T. *J. Org. Chem.* **2000**, *65* (26), 9252. doi:10.1021/jo001235w. PMID: 11149883.
(47) Sumengen, D. *Chim. Acta Turc.* **1985**, *13* (3), 393.
(48) Liu, K.-C.; Shelton, B. R.; Howe, R. K. *J. Org. Chem.* **1980**, *45* (19), 3916. doi:10.1021/jo01307a039.
(49) Quadrelli, P.; Invernizzi, A. G.; Falzoni, M.; Caramella, P. *Tetrahedron* **1997**, *53* (5), 1787. doi:10.1016/S0040-4020(96)01088-5.
(50) Feuer, H.; Savides, C. *J. Am. Chem. Soc.* **1959**, *81* (21), 5826. doi:10.1021/ja01530a069.
(51) Rybakova, I. A.; Shekhtman, R. I.; Prilezhaeva, E. N., *Izv. Akad. Nauk SSSR, Ser. Khim.* **1991**, 2146.
(52) Koval', I. V. *Russ. J. Org. Chem.* **2005**, *41* (5), 631. doi:10.1007/s11178-005-0220-0.

Can. J. Chem. Downloaded from www.nrcresearchpress.com by University of Electronic and Science Techonology of China on 09/18/12
For personal use only.

Supramolecular encapsulation of benzimidazole-derived drugs by cucurbit[7]uril

Apurba L. Koner, Indrajit Ghosh, Na'il Saleh, and Werner M. Nau

Abstract: UV–vis and NMR spectroscopic techniques were employed to demonstrate the ability of the synthetic macrocyclic host cucurbit[7]uril (CB7) to solubilize and stabilize widely used fungicides and anthelmintic drugs of the benzimidazole family in water, namely, albendazole (ABZ), carbendazim (CBZ), thiabendazole (TBZ), fuberidazole (FBZ), and the parent benzimidazole (BZ). CB7 binds the protonated forms of these guests very strongly (e.g., $K = 2.6 \times 10^7$ L/mol for ABZ) but their neutral forms significantly more weakly (e.g., $K = 6.5 \times 10^4$ L/mol for ABZ), which reflects a complexation-induced increase of their pK_a values by 2.6 units for ABZ, 2.5 units for CBZ, 4.0 units for TBZ, 3.8 units for FBZ, and 3.5 units for BZ. The absolute drug solubilities increased upon complexation from 0.003 to 0.300 mmol/L for ABZ, from 0.160 to 1.12 mmol/L for CBZ, from 0.110 to 1.11 mmol/L for TBZ, and from 0.25 to 0.75 mmol/L for FBZ (for BZ, the solubility enhancement was found to be insignificant). Complexation by CB7 further improves the photostability of the drugs and alters their photophysical properties.

Key words: supramolecular chemistry, cucurbit[*n*]urils, benzimidazole drugs, pK_a shifts, solubility enhancement, photostability, drug delivery.

Résumé : On a fait appel aux techniques spectroscopiques d'UV–vis et de RMN pour évaluer l'habilité de l'hôte macrocyclique de synthèse, cucurbit[7]urile (CB7) à solubilizer et à stabiliser dans l'eau des fongicides et des médicaments antihelmintiques largement utilisés, de la famille du benzimidazole, en particulier l'albenzole (ABZ), la carbendazime (CBZ), le thiabendazole (TBZ), le fubéridazole (FBZ) et le produit fondamental, le benzimidazole (BZ). Le CB7 se lie fortement à la forme protonée de ces hôtes (par exemple, $K = 2{,}6 \times 10^7$ L/mol pour l'ABZ), mais les formes neutres sont beaucoup plus faibles (par exemple, $K = 6{,}5 \times 10^4$ L/mol pour l'ABZ) ce qui est un reflet de l'augmentation induite par la complexation des valeurs de leurs pK_a qui est de 2,6 unités pour l'ABZ, de 2,5 unités pour le CBZ, de 4,0 unités pour le TBZ, de 3,8 unités pour le FBZ et de 3,5 unités pour le BZ. Les solubilités absolues des médicaments augmentent par complexation de 0,003 à 0,300 mmol/L pour l'ABZ, de 0,160 à 1,12 mmol/L pour le CBZ, de 0,110 à 1,11 mmol/L pour le TBZ et de 0,25 à 0,75 mmol/L pour la FBC ; pour le BC, on a trouvé que l'augmentation de solubilité est insignifiante. La complexation des médicaments avec le CB7 augmente de plus la photostabilité des médicaments et elle altère leurs propriétés photophysiques.

Mots-clés : chimie supramoléculaire, cucurbit[*n*]uriles, médicaments à base de benzimidazole, pK_a, administration des médicaments.

[Traduit par la Rédaction]

Introduction

When guest molecules are noncovalently encapsulated inside water-soluble macrocyclic container compounds such as cyclodextrins, calixarenes, or cucurbiturils, a modification of their chemical and physicochemical properties always occurs owing to the altered microenvironment as well as the confinement and isolation of the guest.[1–10] Frequently, the complexation of the guest has beneficial effects on its aqueous solubility, because the encapsulation reduces the tendency of the guest to undergo aggregation or unspecific adsorption.[11–15] Further, the complexation may enhance the thermal, as well as photochemical, stability of a guest by isolating it from the aqueous bulk and thereby preventing bimolecular reactions — in the simplest case, oxidation by molecular oxygen.[16,17] Such solubility and stability enhancements are particularly desirable for (hydrophobic) drug molecules. Accordingly, macrocyclic encapsulation of drugs has emerged as a viable complementary technique to other established formulation strategies, such as organic solvents as solubilizers[18] or the use of liposomes or micellar systems.[19–21] An important aspect for the use of macrocycles in drug delivery is the reversibility of the host–guest complexation process, which allows full or partial retention of the

Received 30 April 2010. Accepted 11 June 2010. Published on the NRC Research Press Web site at canjchem.nrc.ca on 15 January 2011.

This article is part of a Special Issue dedicated to Professor J. C. Scaiano.

A.L. Koner, I. Ghosh, and W.M. Nau.[2] School of Engineering and Science, Jacobs University Bremen, Campus Ring 1, D-28759 Bremen, Germany.
N. Saleh.[1] Department of Chemistry, College of Science, UAE University, P.O. Box 17551, Al-Ain, UAE.

[1]Corresponding author (e-mail: n.saleh@uaeu.ac.ae).
[2]Corresponding author (e-mail: w.nau@jacobs-university.de).

Can. J. Chem. Downloaded from www.nrcresearchpress.com by University of Electronic and Science Techonology of China on 09/18/12
For personal use only.

Can. J. Chem. Downloaded from www.nrcresearchpress.com by University of Electronic and Science Techonology of China on 09/18/12
For personal use only.

Scheme 1. Chemical structures of the examined benzimidazoles and cucurbit[7]uril.

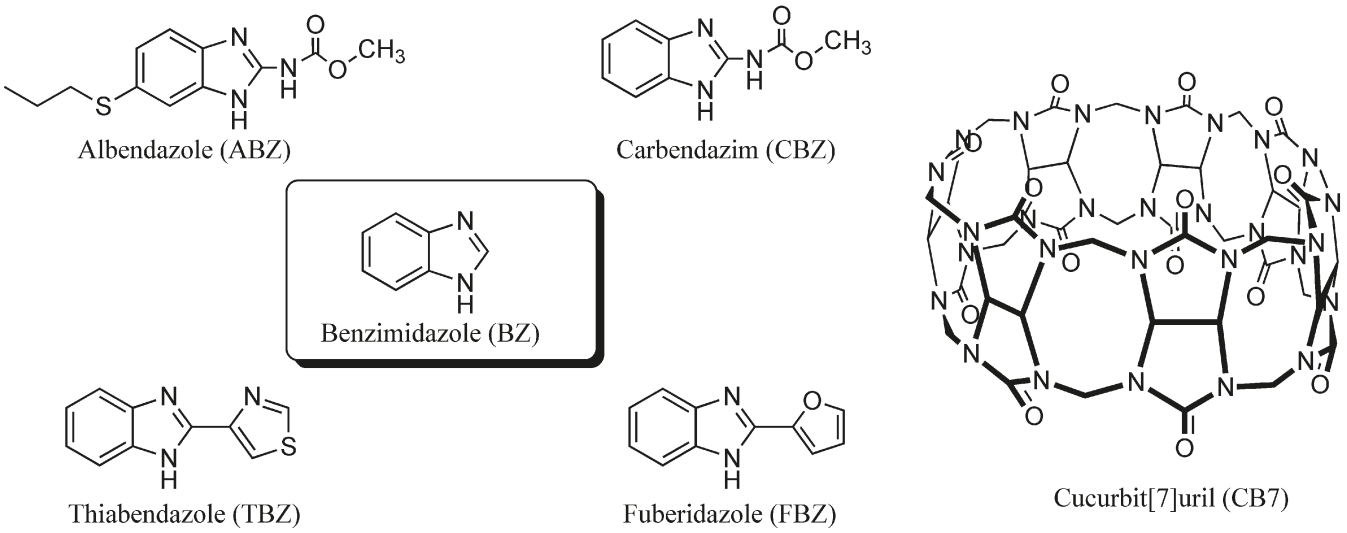

biological or medicinal activity of the encapsulated drugs.[22–30]

Amongst the macrocyclic container compounds used in drug formulations, cyclodextrins have received the most attention owing to their availability from natural sources and their biocompatibility.[28–30] However, cyclodextrins frequently suffer from low binding constants, with typical values on the order of 10^3 L/mol,[1,31,32] which limits their application owing to the subtle concentration dependence of supramolecular complexation equilibria. Cucurbiturils, which have just recently been demonstrated to show a low, if not negligible, cellular and acute toxicity,[33] are another interesting class of macrocycles with potential for drug delivery and stabilization.[23–26] They stand out, in particular, with respect to their high binding constants with hydrophobic as well as cationic guest molecules.[3,9,34–41] Moreover, they have been shown to effectively shift the pK_a values of encapsulated guests,[5–7,12,41–47] which also differentiates them from cyclodextrins.[42] We have recently exploited these pK_a shifts for the development of fluorescent reporter pairs employed for assaying and sensing[7,42,48–51] and for supramolecular catalysis of hydrolytic reactions,[52] and have communicated the use for the activation and stabilization of prodrugs.[43]

In chemical and structural detail, cucurbit[*n*]urils (CB*n*) are cyclic oligomers composed of a varying number of, but more than four, glycoluril units bridged by methylene groups. They form a rigid barrel-like molecular container structure that can take up suitably sized guests through its two carbonyl-laced portals.[3,53] CB6 was first made in 1905[54] but was characterized only in 1981.[55] In the context of drug delivery, the subsequently prepared[56–58] larger homologue CB7 (see Scheme 1) has become especially important owing to its high water solubility[59] and intermediate cavity volume.[3,33] The latter allows the strong binding of mono-, di-, and trinuclear aromatic residues,[6,41,42,60,61] which are omnipresent in numerous drugs. More specifically, recent studies have revealed a high affinity of the benzimidazole residue with CB7,[6,23,43,62] which we have used as an incentive to study herein the binding of different benzimidazole-derived drugs, namely albendazole (ABZ), carbendazim (CBZ), thiabendazole (TBZ), and fuberidazole (FBC) (see Scheme 1), as well as the parent compound (benzimidazole, BZ) with CB7. We also studied the effects of CB7 on their photophysical properties, photochemical stabilities, and aqueous solubilities.

Results

Optical spectroscopy and determination of pK_a values of the uncomplexed guests

In water at pH 7.2, ABZ, CBZ, TBZ, FBZ, and BZ show far-UV absorptions (<320 nm) and fluorescence in the region of 290–360 nm (Table S1 in the Supplementary data). The absorption spectra undergo slight but characteristic shifts at lower pH values (Fig. S4 in the Supplementary data), which are attributable to a protonation of the benzimidazole residue. The pK_a values of the uncomplexed guests were accordingly determined by UV titrations (Table 1) and were found to be in good agreement with those previously reported for ABZ,[65] CBZ,[66] TBZ,[67] FBZ,[68] and BZ.[69]

Determination of binding constants

The addition of CB7 to the guests led to characteristic changes of their absorption spectra (see Fig. S2 in the Supplementary data), which were assigned, based on literature precedent for related compounds[6,43,70] and complementary NMR investigations (see the following), to the immersion of the benzimidazole residue inside the macrocyclic cavity. The effects of added CB7 on the fluorescence properties of the guests (fluorescence spectra, intensities, and lifetimes) were also determined, but were less systematic (see the Supplementary data). The host–guest binding constants were subsequently determined by means of UV titrations (see Fig. 1, Table 1). These titrations were performed either below the pK_a value of the uncomplexed guests or above the pK_a' values of the complexed guests (the latter were determined in a separate set of experiments, see the following) to ensure that the protonation state of the guest did not significantly change upon complexation. Note that CB7 acts as a cation receptor and accordingly displays consistently higher (at least two orders of magnitude larger) binding con-

Can. J. Chem. Downloaded from www.nrcresearchpress.com by University of Electronic and Science Techonology of China on 09/18/12
For personal use only.

Table 1. pK_a values of benzimidazole derivatives in their uncomplexed (pK_a) and CB7-complexed states (pK_a') in water, and binding constants of their neutral (K_{BZ}) and protonated (K_{BZH^+}) forms with CB7.

Guest	pK_a	pK_a'[a]	ΔpK_a	K_{BZ} (10^3 L/mol)[b]	K_{BZH^+} (10^6 L/mol)[c]
ABZ	3.5	6.1	2.6	65	26
CBZ	4.5	7.0	2.5	24	7.6
TBZ	4.6	8.6	4.0	0.150±0.025	1.5
FBZ	4.8	8.6	3.8	0.05±0.01	0.32
BZ	5.5	9.0	3.5	1.5	4.7

[a]Obtained from fitting of the pH titrations in the presence of host according to a four-state model, cf. refs. 63 and 64; estimated error is ±0.3 units.
[b]Determined at pH 10.5 except for ABZ (pH 8.4); 10% error unless stated differently; error refers to the standard deviation of the nonlinear fitting according to a 1:1 complexation model.
[c]Estimated from the thermodynamic cycle in Scheme 2 and the relation $K_{BZH^+} = K_{BZ} \times K_a / K_a'$.

Fig. 1. Host–guest titrations of the unprotonated benzimidazole guests with CB7 for (*a*) ABZ at pH 8.4 and (*b*) CBZ at pH 10.5. The titration curves for the other guests as well as the actual variations in the UV–vis spectra with the addition of CB7 are shown in the Supplementary data (Figs. S1 and S2).

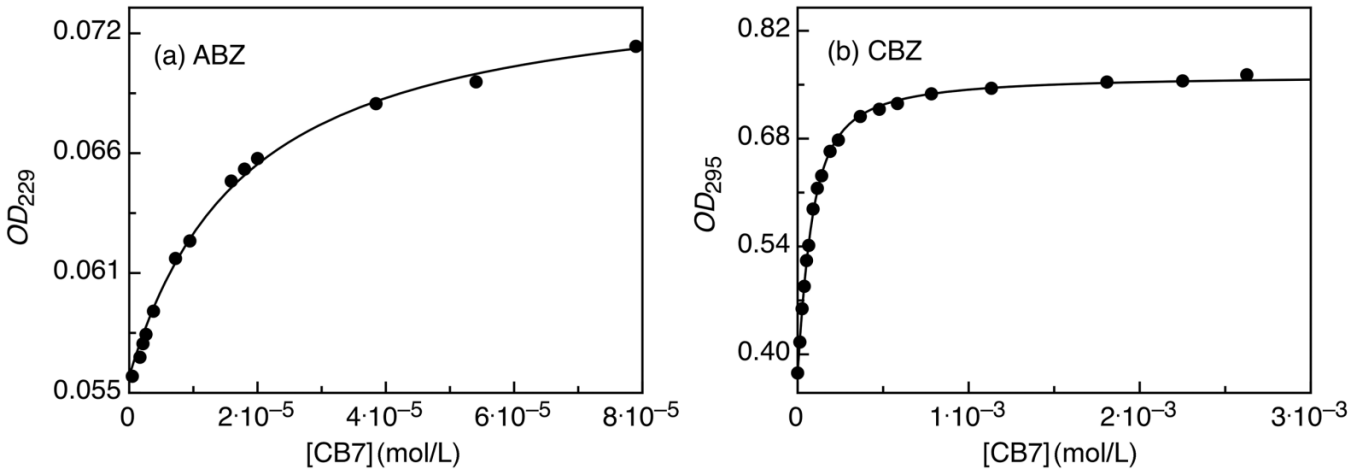

stants with the protonated guests (K_{BZH^+} vs K_{BZ} values in Table 1). For example, the binding constant of CB7 with the protonated form of ABZ is estimated to be 2.6×10^7 L/mol, with the neutral form only 6.5×10^4 L/mol. It should be noted that the host–guest titrations could be fitted in all cases according to a 1:1 binding model. This was also consistent with the isosbestic points observed in the UV titrations with CB7.

^{1}H NMR spectroscopy and determination of binding mode

NMR measurements were performed to gain structural insights into the host–drug complexes. As an example, the ^{1}H NMR spectrum of FBZ in D_2O at pH 2 (pD 2.4) in the absence and in the presence of 2.5 mmol/L CB7 is shown in Fig. 2 (see Table S2 in the Supplementary data for the complexation-induced chemical shifts of all guests). As can be seen, the imidazolium protons are upfield shifted in the presence of CB7 by up to 1 ppm, while the furanyl protons are hardly affected or even slightly downfield shifted (Fig. 2). In analogy to the NMR spectral shifts for other guest molecules complexed to cucurbit[7]uril,[43] these characteristic shifts are interpreted as a preferential encapsulation of the benzimidazole residue inside the CB7 macrocycle, while the furanyl ring is positioned near the rim

Fig. 2. ^{1}H NMR spectra of 0.25 mmol/L FBZ (*a*) without CB7 and (*b*) with 2.5 mmol/L CB7 in D_2O at pD 2.4.

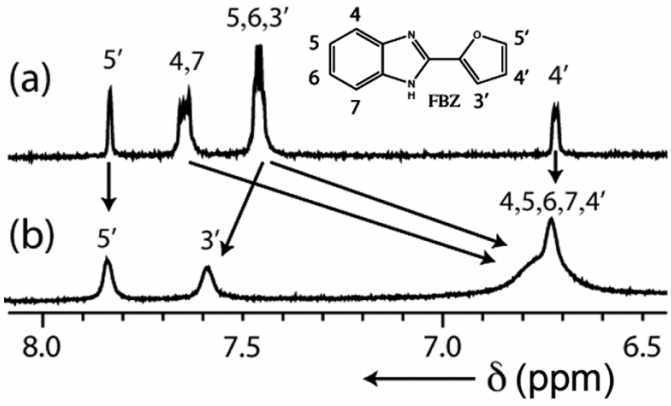

region or slightly outside. The NMR spectral data for the remaining benzimidazole derivatives were consistent with this proposed binding mode; for ABZ, the hydrophobic propylthio moiety also shows upfield shifts (see the Supplementary data, Fig. S3), which suggests that this hydrophobic group also shuttles, at least occasionally, inside CB7, such that on average a partial or temporary inclusion applies.

As a negative control experiment, and to expose the bene-

Can. J. Chem. Downloaded from www.nrcresearchpress.com by University of Electronic and Science Techonology of China on 09/18/12
For personal use only.

fitsof CB7 as the macrocycle of choice, we conducted the NMR measurements with CB6 as an alternative host, which, however, is too small to encapsulate the benzimidazole ring. This smaller macrocycle does indeed show (according to the complexation-induced shifts) no inclusion of the benzimidazole group,[71] but encapsulates other groups of the drugs, e.g., the carbamate methyl groups in ABZ and CBZ (upfield shift of 1 ppm, Table S2 in the Supplementary data). The ^{1}H NMR spectra of TBZ and FBZ in the absence and presence of CB6 were identical, suggesting the absence of sizable binding.

pK_a values of the complexed guests and complexation-induced pK_a shifts

The protonated forms of the guests experience an additional stabilization due to ion–dipole interactions with the carbonyl portals of CB7. Accordingly, the propensity of the guests to become protonated is increased when they are complexed by CB7, an intuitive conjecture, which manifests itself experimentally in a pK_a shift upon addition of macrocycle, i.e., larger pK_a values in the complexed compared with the uncomplexed form. Others[5,45–47,72–74] and we[6,7,12,41–44,64] have previously observed such pK_a shifts accompanying host–guest complexation, and we have developed fitting algorithms for pH titrations in the presence of host based on a four-state model involving (*i*) the uncomplexed unprotonated guest, (*ii*) the uncomplexed protonated guest, (*iii*) the unprotonated host–guest complex, and (*iv*) the protonated host–guest complex, which are all connected through a thermodynamic cycle as illustrated in Scheme 2.[6,63,64,75]

The fitting allowed us to extract the pK_a' of the complexes (Fig. 3, Table 1) and to extrapolate the second binding constant when at least one of the binding constants and the pK_a value of the uncomplexed guest were known from independent measurements. In the case of the benzimidazole guests investigated herein, the binding constants of the unprotonated guests could be more accurately determined than those of the protonated guests; the latter were in several cases too high to allow precise determinations by UV titrations, and they were consequently estimated from the fitted pK_a values through the condition imposed by the thermodynamic cycle ($K_{BZH^+} = K_{BZ} \times K_a / K_a'$).[76] Note that the observed pK_a shifts range from 2.5 to 4.0 units, with the largest value observed for TBZ.

Solubility enhancement

The effect that the addition of CB7 has on the solubility of the guests was determined by UV spectrophotometry (see Fig. 4 and the Materials and methods) at the physiological pH (7.2). In the presence of 2 mmol/L CB7, the solubility of ABZ increased by a factor of 100, that of CBZ increased by a factor of 7, that of TBZ increased by a factor of 10 and that of FBZ increased by a factor of 3 (Fig. 4, Table S3 in the Supplementary data). In terms of absolute solubilities (these were determined from the optical density (OD) values), they increased upon complexation from 0.003 to 0.300 mmol/L for ABZ, from 0.160 to 1.12 mmol/L for CBZ, from 0.110 to 1.11 mmol/L for TBZ, and from 0.25 to 0.75 mmol/L for FBZ (for BZ, the solubility enhancement was found to be insignificant). Note that there appears to be a rough inverse correlation between the intrinsic water solubility of the drug (in the absence of CB7) and its binding constant with CB7 (in its unprotonated form, Table 1). This is expected, since both properties are governed by the hydrophobicity of the drug and guest.[63] The use of macrocycles for drug solubilization is consequently particularly promising for the least soluble drugs.

Scheme 2. Four-state complexation model of the neutral and protonated benzimidazoles with CB7.

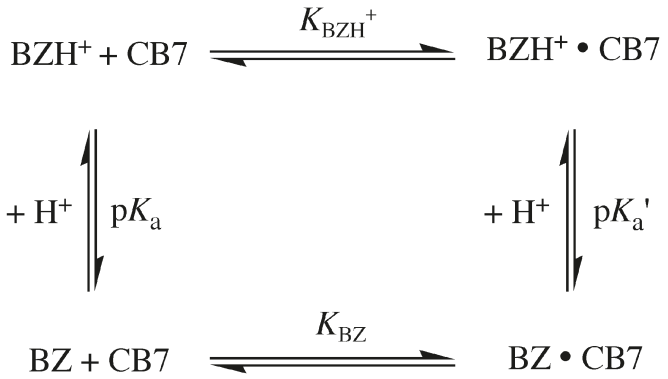

Photostabilization

Encapsulation in CB7 also enhanced the photostability of FBZ and TBZ. Under intense UV irradiation at pH 2.4, FBZ decomposed 7 times more slowly and TBZ 3 times more slowly in their complexes with CB7 than in their free forms (Fig. 5). For ABZ, CBZ, and BZ, no significant photostabilizing effects caused by CB7 were observed.

Discussion

The benzimidazole-derived drugs investigated herein are being used extensively worldwide as fungicides and anthelmintic drugs.[23,77–85] TBZ is used against fungally caused diseases and for the preservation of citrus fruits and bananas. Even more, marketed as Mintezol, Tresaderm, or Arbotect, it is used to treat dogs and cats infected with hookworms and other helminthes.[77–80] ABZ, marketed as Albenza, Eskazole, or Zentel, is used against pork and dog tapeworm infestations.[23,82–85] Surprisingly, ABZ also exhibits antitumor activity and is toxic for a number of cancer cell lines including colorectal and ovarian cancers and leukaemia. CBZ and FBZ are used only as fungicides;[81–83] CBZ, in particular, is broadly used to protect cereals, fruits, rice, and tomatoes.[78–80] One common feature is their low aqueous solubility, which is particularly undesirable for their use as anthelmintic drugs.

As a potential additive to increase the solubility of benzimidazole-derived drugs, we have investigated herein CB7. CB7 was known from previous studies to bind strongly to the benzimidazole residues,[6,23,43,86] and we have combined this knowledge with our interest to investigate complexation-induced pK_a shifts of guest molecules.[5–7,12,41–47,64] Specifically, we have already communicated that the pK_a values of benzimidazole derivatives would dramatically increase upon complexation by CB7.[43] We presumed that this could interconvert an uncharged (at

Can. J. Chem. Downloaded from www.nrcresearchpress.com by University of Electronic and Science Techonology of China on 09/18/12
For personal use only.

Fig. 3. pH titrations of the BZ drugs, monitored by UV in the absence (filled circles) and presence of CB7 (2.5 mmol/L, empty circles). The changes in the UV–vis spectra are shown in the Supplementary data (Figs. S4 and S5).

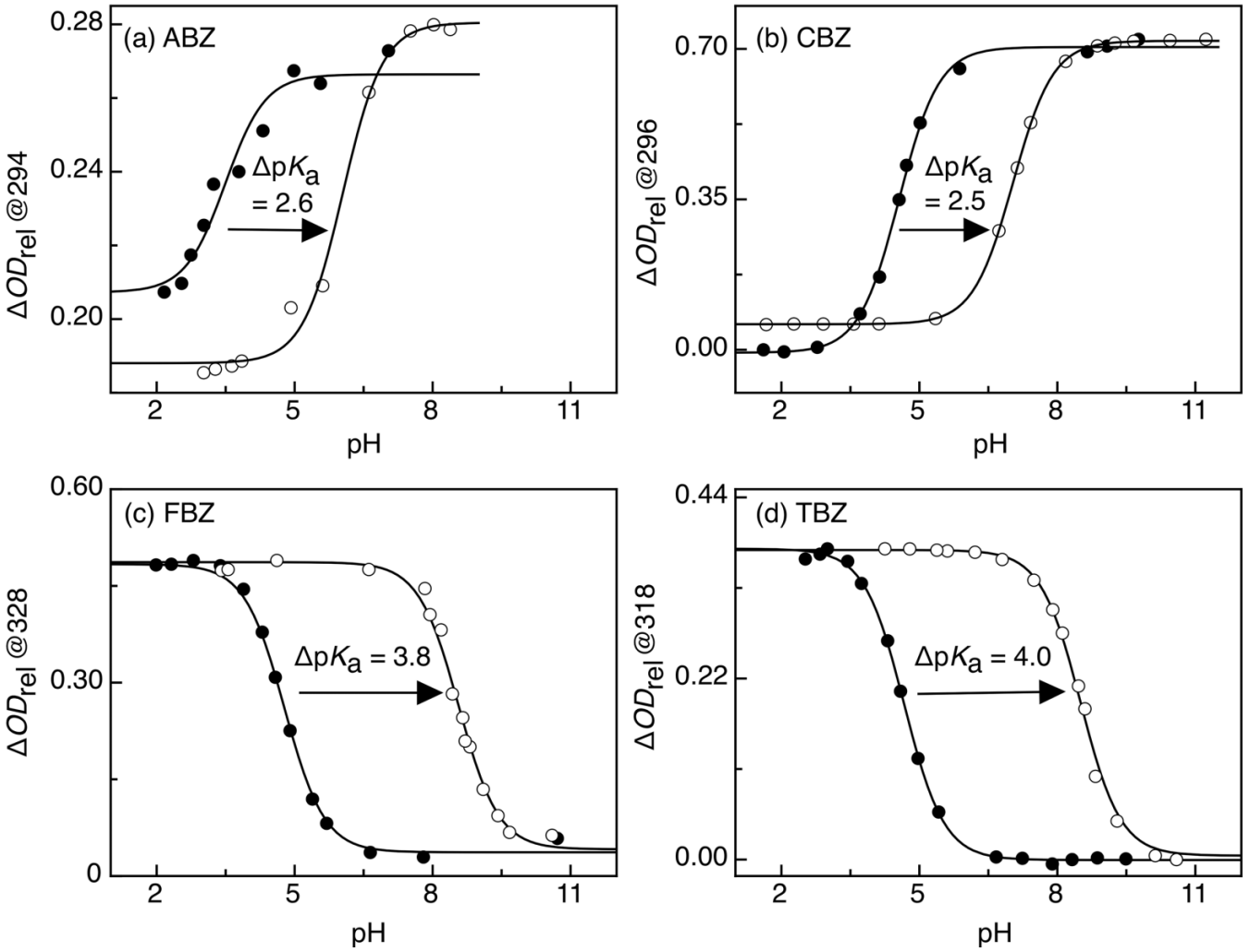

pH 7.2), intrinsically insoluble guest into an encapsulated charged guest with an intuitively expected higher solubility.

Supramolecular pK_a shifts, in particular those effected by macrocyclic complexation of guests, have recently attracted significant attention, for example, with the perspective of catalysis.[52,72] The largest presently known pK_a shifts reach values of 4.5 units, coming close to the values known for some enzymes.[44,73,64] pK_a shifts are caused either by a (relative) destabilization of charged species in hydrophobic environments or by a selective stabilization of a charged guest in macrocycles with cation or anion receptor properties. Cucurbiturils are cation receptors and as such stabilize cationic species, thereby facilitating the protonation of basic functionalities and increasing the pK_a values, for example, of ammonium ions. In detail, the carbonyl portals of CB7, the homologue used in the present study, stabilize cations by ion–dipole interactions. These electrostatic interactions add to the hydrophobic interactions that bind the guest even in its neutral form, which results in overall higher binding constants for the protonated forms. In fact, according to Scheme 2, the binding constants of the protonated forms can be readily predicted from a thermodynamic cycle.[63]

All investigated benzimidazoles indeed undergo large pK_a shifts upon complexation by CB7, ranging from 2.5 to 4.0 units. Even though the substituent-dependent variations of the absolute values of the pK_a shifts are not well understood at present, the large values reveal that, at a given pH value, the CB7 complexation increases the concentration ratio in favor of the protonated form of the benzimidazoles by 300 fold to 10 000 fold, owing to the logarithmic nature of the pK_a scale. Effectively, in the pH region in between the rise parts of the two titration curves (Fig. 3), i.e., also in the physiological pH region, the encapsulation of the drugs into CB7 converts a poorly soluble hydrophobic compound into a positively charged and presumably more soluble inclusion complex. This manifests itself in an apparently increased (from μmol/L to low mmol/L) solubility of the drugs, which reaches a factor of 100 in the most impressive case of the most hydrophobic (and least water soluble) drug, ABZ. Zhao et al.[23] have previously reported a larger solubility enhancement factor of 600–700 for ABZ, which could be related to the use of a higher CB7 concentration and (or) the use of deuterated water as an alternative solvent. Because the solubilization strongly depends on the degree of drug encapsulation, the solubility enhancement factor depends not

Can. J. Chem. Downloaded from www.nrcresearchpress.com by University of Electronic and Science Techonology of China on 09/18/12
For personal use only.

Fig. 4. Absorption spectra measured at the physiological pH (7.2) for the free BZ drugs in the absence (dashed lines) and presence of CB7 (2.0 mmol/L, solid lines). The solubility enhancement factors are indicated along the arrows. Note that the UV absorption spectrum of ABZ in the presence of CB7 was obtained for a 30 times diluted solution to obtain an OD value inside the instrumental range.

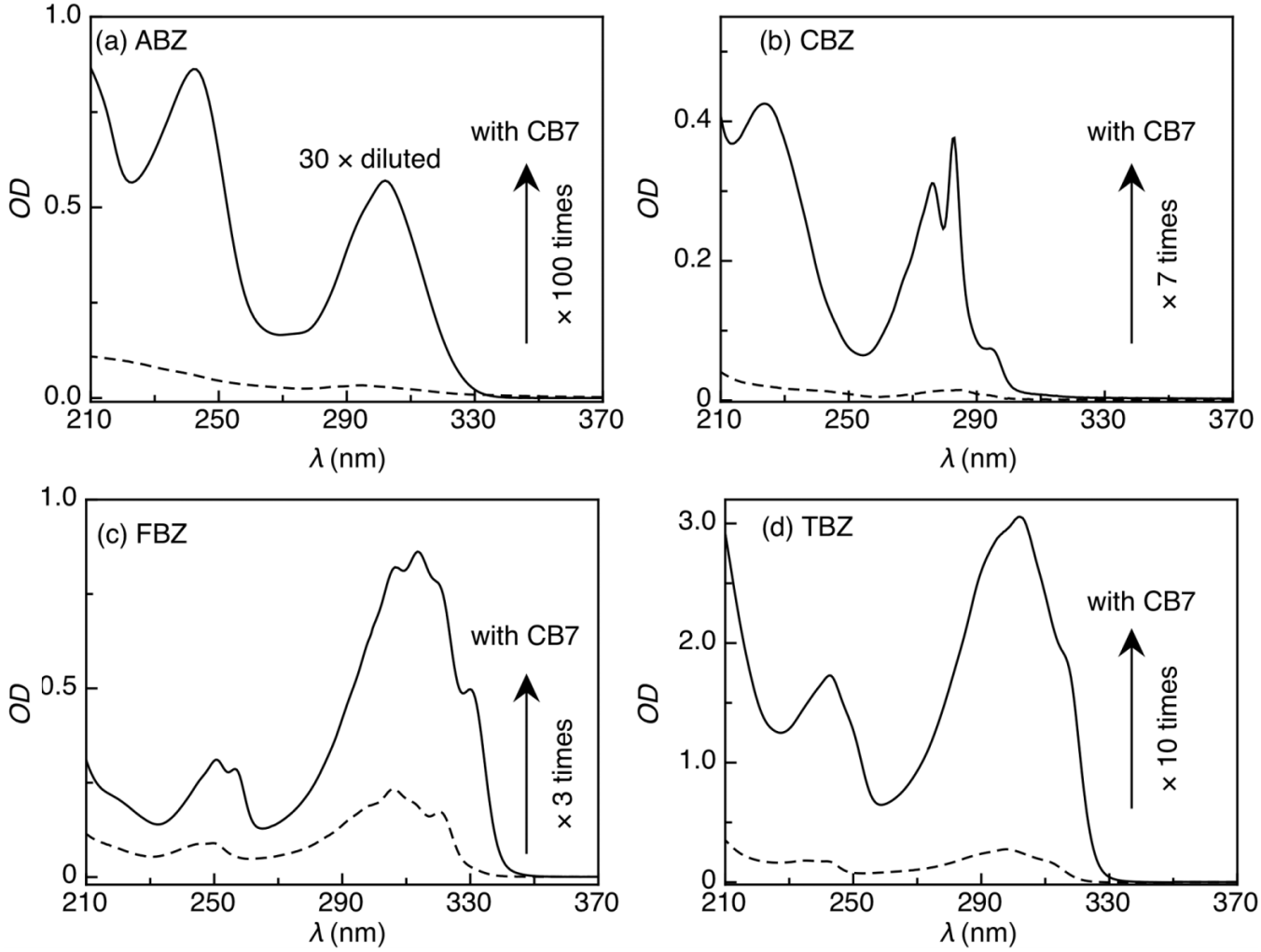

Fig. 5. Photodecomposition in the absence (dashed lines) and presence of CB7 (2.0 mmol/L, solid lines) of (*a*) FBZ and (*b*) TBZ, followed through the decrease of the UV absorption band with increasing time of photoirradiation by UV lamps (350 nm) in a photoreactor (60 min for TBZ and 17 min for FBZ). In the inset, the characteristic photodecomposition decay function, $f = \log[(10^{A_0} - 1)/(10^{A} - 1)]$, is plotted versus time and from the slope the relative photodecomposition quantum yields were determined.

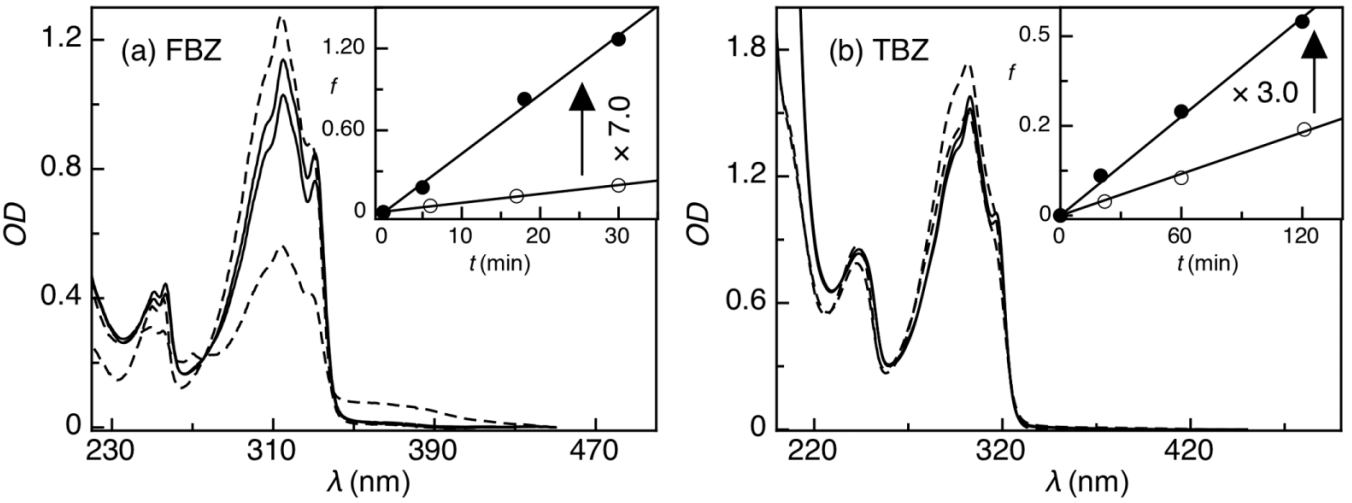

Can. J. Chem. Downloaded from www.nrcresearchpress.com by University of Electronic and Science Techonology of China on 09/18/12
For personal use only.

only on the binding constants but also on the concentration of CB7 used.

Any prospective applications of cucurbiturils in drug delivery must compete with those involving cyclodextrins as drug carriers. Both are expected to be useful additives to prevent aggregation by macrocyclic encapsulation. It turns out that CB7 enhances the solubility of the investigated drugs more efficiently, reflected in the use of lower additive concentrations as well as higher solubilities. For example, 2 mmol/L CB7 enhances the solubility of CBZ more (factor of 7) than even a five times higher concentration of β-cyclodextrin (factor of 1.6). For TBZ, the difference is similar (factor of 10 vs 1.9), while for FBZ the result is somewhat smaller, but still significant (factor of 3 vs 1.7). The lower efficiency of β-cyclodextrin encapsulation can be accounted for on one hand by its lower binding constants (<100 L/mol)[87] and on the other hand by its inability to induce protonation, and thereby increased solubility, of the drugs. In fact, cyclodextrins are known to affect pK_a shifts in the "wrong" direction[41] because they tend to preferentially complex the neutral forms of drugs.[63] The pK_a shifts effected by cucurbituril encapsulation therefore constitute a novel stand-alone feature of these drug carriers.

Conclusions

The macrocycle cucurbit[7]uril binds strongly to all investigated fungicides and anthelmintic drugs and increases their pK_a values, which results in host-induced protonation. The strong binding and protonation of the guests lead jointly to increased solubility, an effect that could be potentially exploited for drug delivery. Research along this line is assisted by the very low toxicity of cucurbiturils.[33]

Materials and methods

All guest molecules were purchased from Sigma-Aldrich and used as received. CB7 was synthesized according to our previously reported method.[56] Deionized and doubly distilled water was used. The pH of the solutions was adjusted (±0.2) using a pH meter (WTW 330i equipped with a combined Sen Tix Mic pH glass electrode) by adding the required amount of NaOH or HCl.

All UV–vis and fluorescence spectral measurements were performed using a Varian Cary 4000 UV–vis spectrophotometer and a Varian Cary Eclipse fluorometer (5 nm slit width for both excitation and emission monochromators). The fluorescence lifetimes of the drugs were measured by using time-correlated single photon counting (FLS920, Edinburgh Instruments Ltd., Livingston, UK). Excitation was made by using a PicoQuant pulsed LED (PLS-280, λ_{ex} = 280 nm, full width at half-maximum = 450 ps). ^{1}H NMR spectra were recorded with a JEOL ECX 400 MHz NMR spectrometer in D_2O (99.9% from Sigma-Aldrich). The photostabilization of the drugs was monitored through the change in the absorbance of the free and complexed drugs at pH 2.0 upon irradiation in a Luzchem LZC-4V photoreactor equipped with 14 Hitachi FL8BL-B UVA lamps (λ_{ex} = 350 nm).

In the solubility measurements, aqueous saturated solutions of the drugs were prepared by preadjusting the solution to pH 7.2. The solutions were then initially vortexed for about 10 min and then sonicated for 30 min. Then the solutions were filtered and absorption spectra were measured at pH 7.2. The same procedure was followed in the presence of 2.0 mmol/L CB7 at the same pH. The concentration of the drugs in water and inside the CB7 cavity was calculated from the obtained molar extinction coefficients measured independently in our laboratory.

Supplementary data

Supplementary data for this article are available on the journal Web site (canjchem.nrc.ca).

Acknowledgements

Financial support from the Deutsche Forschungsgemeinschaft (DFG, NA 686/3-1 and NA 686/4-1), the Deutscher Akademischer Austausch Dienst (DAAD) exchange program (grant No. A/06/11962), the Fonds der Chemischen Industrie, and both host universities is gratefully acknowledged.

References

(1) Rekharsky, M. V.; Inoue, Y. *Chem. Rev.* **1998**, *98* (5), 1875. doi:10.1021/cr970015o. PMID:11848952.
(2) Kim, J. S.; Quang, D. T. *Chem. Rev.* **2007**, *107* (9), 3780. doi:10.1021/cr068046j. PMID:17711335.
(3) Lagona, J.; Mukhopadhyay, P.; Chakrabarti, S.; Isaacs, L. *Angew. Chem. Int. Ed.* **2005**, *44* (31), 4844. doi:10.1002/anie.200460675.
(4) Lee, J. W.; Samal, S.; Selvapalam, N.; Kim, H. J.; Kim, K. *Acc. Chem. Res.* **2003**, *36* (8), 621. doi:10.1021/ar020254k. PMID:12924959.
(5) Wu, J.; Isaacs, L. *Chem. Eur. J.* **2009**, *15* (43), 11675. doi:10.1002/chem.200901522.
(6) Shaikh, M.; Dutta Choudhury, S.; Mohanty, J.; Bhasikuttan, A. C.; Nau, W. M.; Pal, H. *Chem. Eur. J.* **2009**, *15* (45), 12362. doi:10.1002/chem.200900390.
(7) Koner, A. L.; Nau, W. M. *Supramol. Chem.* **2007**, *19* (1), 55. doi:10.1080/10610270600910749.
(8) Liu, Y.; Han, B. H.; Chen, Y. T. *J. Phys. Chem. B* **2002**, *106* (18), 4678. doi:10.1021/jp015603r.
(9) Rankin, M. A.; Wagner, B. D. *Supramol. Chem.* **2004**, *16* (7), 513. doi:10.1080/10610270412331283583.
(10) Wagner, B. D.; Fitzpatrick, S. J.; Gill, M. A.; MacRae, A. I.; Stojanovic, N. *Can. J. Chem.* **2001**, *79* (7), 1101. doi:10.1139/cjc-79-7-1101.
(11) Mohanty, J.; Pal, H.; Ray, A. K.; Kumar, S.; Nau, W. M. *ChemPhysChem* **2007**, *8* (1), 54. doi:10.1002/cphc.200600625. PMID:17171726.
(12) Nau, W. M.; Mohanty, J. *Int. J. Photoenergy* **2005**, *7* (3), 133. doi:10.1155/S1110662X05000206.
(13) Mohanty, J.; Nau, W. M. *Angew. Chem. Int. Ed.* **2005**, *44* (24), 3750. doi:10.1002/anie.200500502.
(14) Arunkumar, E.; Forbes, C. C.; Smith, B. D. *Eur. J. Org. Chem.* **2005**, *2005* (19), 4051. doi:10.1002/ejoc.200500372.
(15) Politzer, I. R.; Crago, K. T.; Hampton, T.; Joseph, J.; Boyer, J. H.; Shah, M. *Chem. Phys. Lett.* **1989**, *159* (2–3), 258. doi:10.1016/0009-2614(89)87420-2.
(16) González-Béjar, M.; Montes-Navajas, P.; García, H.; Scaiano, J. C. *Langmuir* **2009**, *25* (18), 10490. doi:10.1021/la9011923. PMID:19735127.
(17) Mohanty, J.; Nau, W. M. *Photochem. Photobiol. Sci.* **2004**, *3* (11–12), 1026. doi:10.1039/b412936a. PMID:15570390.

Can. J. Chem. Downloaded from www.nrcresearchpress.com by University of Electronic and Science Techonology of China on 09/18/12
For personal use only.

(18) Avdeef, A.; Kansy, M.; Bendels, S.; Tsinman, K. *Eur. J. Pharm. Sci.* **2008**, *33* (1), 29. PMID:17983735.
(19) Schroeder, A.; Kost, J.; Barenholz, Y. *Chem. Phys. Lipids* **2009**, *162* (1–2), 1. doi:10.1016/j.chemphyslip.2009.08.003. PMID:19703435.
(20) Malam, Y.; Loizidou, M.; Seifalian, A. M. *Trends Pharmacol. Sci.* **2009**, *30* (11), 592. doi:10.1016/j.tips.2009.08.004. PMID:19837467.
(21) Fanciullino, R.; Ciccolini, J. *Curr. Med. Chem.* **2009**, *16* (33), 4361. doi:10.2174/092986709789712916. PMID: 19835568.
(22) Montes-Navajas, P.; González-Béjar, M.; Scaiano, J. C.; García, H. *Photochem. Photobiol. Sci.* **2009**, *8* (12), 1743. doi:10.1039/b9pp00041k. PMID:20024172.
(23) Zhao, Y. J.; Buck, D. P.; Morris, D. L.; Pourgholami, M. H.; Day, A. I.; Collins, J. G. *Org. Biomol. Chem.* **2008**, *6* (24), 4509. doi:10.1039/b813759e. PMID:19039358.
(24) Wheate, N. J. *J. Inorg. Biochem.* **2008**, *102* (12), 2060. doi:10.1016/j.jinorgbio.2008.06.005. PMID:18653238.
(25) Wheate, N. J.; Buck, D. P.; Day, A. I.; Collins, J. G. *Dalton Trans.* **2006**, 451. doi:10.1039/b513197a. PMID:16395444.
(26) Jin Jeon, Y.; Kim, S.-Y.; Ho Ko, Y.; Sakamoto, S.; Yamaguchi, K.; Kim, K. *Org. Biomol. Chem.* **2005**, *3* (11), 2122. doi:10.1039/b504487a. PMID:15917899.
(27) Da Silva, E.; Lazar, A. N.; Coleman, A. W. *J. Drug Delivery Sci. Technol.* **2004**, *14*, 3.
(28) Challa, R.; Ahuja, A.; Ali, J.; Khar, R. K. *AAPS PharmSciTech* **2005**, *6* (2), E329. doi:10.1208/pt060243. PMID: 16353992.
(29) Hirayama, F.; Uekama, K. *Adv. Drug Deliv. Rev.* **1999**, *36* (1), 125. doi:10.1016/S0169-409X(98)00058-1. PMID:10837712.
(30) Uekama, K.; Hirayama, F.; Irie, T. *Chem. Rev.* **1998**, *98* (5), 2045. doi:10.1021/cr970025p. PMID:11848959.
(31) Houk, K. N.; Leach, A. G.; Kim, S. P.; Zhang, X. Y. *Angew. Chem. Int. Ed.* **2003**, *42* (40), 4872. doi:10.1002/anie.200200565.
(32) Connors, K. A. *Chem. Rev.* **1997**, *97* (5), 1325. doi:10.1021/cr960371r. PMID:11851454.
(33) Uzunova, V. D.; Cullinane, C.; Brix, K.; Nau, W. M.; Day, A. I. *Org. Biomol. Chem.* **2010**, *8* (9), 2037. doi:10.1039/b925555a. PMID:20401379.
(34) Wang, R. B.; Wyman, I. W.; Wang, S. H.; Macartney, D. H. *J. Incl. Phenom. Macrocycl. Chem.* **2009**, *64* (3–4), 233. doi:10.1007/s10847-009-9556-3.
(35) Miskolczy, Z.; Biczók, L.; Megyesi, M.; Jablonkai, I. *J. Phys. Chem. B* **2009**, *113* (6), 1645. doi:10.1021/jp8098329. PMID:19159198.
(36) Wyman, I. W.; Macartney, D. H. *Org. Biomol. Chem.* **2008**, *6* (10), 1796. doi:10.1039/b801650j. PMID:18452015.
(37) Rekharsky, M. V.; Mori, T.; Yang, C.; Ko, Y. H.; Selvapalam, N.; Kim, H.; Sobransingh, D.; Kaifer, A. E.; Liu, S. M.; Isaacs, L.; Chen, W.; Moghaddam, S.; Gilson, M. K.; Kim, K. M.; Inoue, Y. *Proc. Natl. Acad. Sci. U.S.A.* **2007**, *104* (52), 20737. doi:10.1073/pnas.0706407105. PMID:18093926.
(38) Kemp, S.; Wheate, N. J.; Stootman, F. H.; Aldrich-Wright, J. R. *Supramol. Chem.* **2007**, *19* (7), 475. doi:10.1080/10610270601124019.
(39) Moon, K.; Kaifer, A. E. *Org. Lett.* **2004**, *6* (2), 185. doi:10.1021/ol035967x. PMID:14723524.
(40) Ong, W.; Gómez-Kaifer, M.; Kaifer, A. E. *Org. Lett.* **2002**, *4* (10), 1791. doi:10.1021/ol025869w. PMID:12000300.
(41) Mohanty, J.; Bhasikuttan, A. C.; Nau, W. M.; Pal, H. *J. Phys. Chem. B* **2006**, *110* (10), 5132. doi:10.1021/jp056411p. PMID:16526757.
(42) Shaikh, M.; Mohanty, J.; Singh, P. K.; Nau, W. M.; Pal, H. *Photochem. Photobiol. Sci.* **2008**, *7* (4), 408. doi:10.1039/b715815g. PMID:18385882.
(43) Saleh, N.; Koner, A. L.; Nau, W. M. *Angew. Chem. Int. Ed.* **2008**, *47* (29), 5398. doi:10.1002/anie.200801054.
(44) Praetorius, A.; Bailey, D. M.; Schwarzlose, T.; Nau, W. M. *Org. Lett.* **2008**, *10* (18), 4089. doi:10.1021/ol8016275. PMID:18722450.
(45) Wyman, I. W.; Macartney, D. H. *J. Org. Chem.* **2009**, *74* (21), 8031. doi:10.1021/jo901861e. PMID:19799399.
(46) Wyman, I. W.; Macartney, D. H. *Org. Biomol. Chem.* **2010**, *8* (1), 253. doi:10.1039/b917610a. PMID:20024156.
(47) Wyman, I. W.; Macartney, D. H. *Org. Biomol. Chem.* **2010**, *8* (1), 247. doi:10.1039/b915694a. PMID:20024155.
(48) Hennig, A.; Bakirci, H.; Nau, W. M. *Nat. Methods* **2007**, *4* (8), 629. doi:10.1038/nmeth1064. PMID:17603491.
(49) Bailey, D. M.; Hennig, A.; Uzunova, V. D.; Nau, W. M. *Chem. Eur. J.* **2008**, *14* (20), 6069. doi:10.1002/chem.200800463.
(50) Nau, W. M.; Ghale, G.; Hennig, A.; Bakirci, H.; Bailey, D. M. *J. Am. Chem. Soc.* **2009**, *131* (32), 11558. doi:10.1021/ja904165c. PMID:19627092.
(51) Bhasikuttan, A. C.; Mohanty, J.; Nau, W. M.; Pal, H. *Angew. Chem. Int. Ed.* **2007**, *46* (22), 4120. doi:10.1002/anie.200604757.
(52) Klöck, C.; Dsouza, R. N.; Nau, W. M. *Org. Lett.* **2009**, *11* (12), 2595. doi:10.1021/ol900920p. PMID:19462966.
(53) Jeon, Y. M.; Kim, H.; Whang, D.; Kim, K. *J. Am. Chem. Soc.* **1996**, *118* (40), 9790. doi:10.1021/ja962071x.
(54) Behrend, R.; Meyer, E.; Rusche, F. *Liebigs Ann. Chem.* **1905**, *339* (1), 1. doi:10.1002/jlac.19053390102.
(55) Freeman, W. A.; Mock, W. L.; Shih, N. Y. *J. Am. Chem. Soc.* **1981**, *103* (24), 7367. doi:10.1021/ja00414a070.
(56) Marquez, C.; Huang, F.; Nau, W. M. *IEEE Trans. Nanobioscience* **2004**, *3* (1), 39. doi:10.1109/TNB.2004.824269. PMID:15382642.
(57) Day, A. I.; Blanch, R. J.; Arnold, A. P.; Lorenzo, S.; Lewis, G. R.; Dance, I. *Angew. Chem. Int. Ed.* **2002**, *41* (2), 275. doi:10.1002/1521-3773(20020118)41:2<275::AID-ANIE275>3.0.CO;2-M.
(58) Kim, J.; Jung, I. S.; Kim, S. Y.; Lee, E.; Kang, J. K.; Sakamoto, S.; Yamaguchi, K.; Kim, K. *J. Am. Chem. Soc.* **2000**, *122* (3), 540. doi:10.1021/ja993376p.
(59) Marquez, C.; Nau, W. M. *Angew. Chem. Int. Ed.* **2001**, *40* (23), 4387. doi:10.1002/1521-3773(20011203)40:23<4387::AID-ANIE4387>3.0.CO;2-H.
(60) Liu, S. M.; Ruspic, C.; Mukhopadhyay, P.; Chakrabarti, S.; Zavalij, P. Y.; Isaacs, L. *J. Am. Chem. Soc.* **2005**, *127* (45), 15959. doi:10.1021/ja055013x. PMID:16277540.
(61) Wang, R. B.; Yuan, L.; Macartney, D. H. *Chem. Commun. (Camb.)* **2005**, 5867. doi:10.1039/b513246k. PMID:16317457.
(62) Wang, R. B.; Macgillivray, B. C.; Macartney, D. H. *Dalton Trans.* **2009**, 3584. doi:10.1039/b904028e. PMID:19381421.
(63) Zhang, X. Y.; Gramlich, G.; Wang, X. J.; Nau, W. M. *J. Am. Chem. Soc.* **2002**, *124* (2), 254. doi:10.1021/ja011866n. PMID:11782177.
(64) Bakirci, H.; Koner, A. L.; Schwarzlose, T.; Nau, W. M. *Chem. Eur. J.* **2006**, *12* (18), 4799. doi:10.1002/chem.200501479.
(65) Takacsnovak, K.; Jozan, M.; Szasz, G. *Int. J. Pharm.* **1995**, *113* (1), 47. doi:10.1016/0378-5173(94)00176-6.
(66) Aharonson, N.; Kafkafi, U. *J. Agric. Food Chem.* **1975**, *23* (3), 434. doi:10.1021/jf60199a069. PMID:239036.

Can. J. Chem. Downloaded from www.nrcresearchpress.com by University of Electronic and Science Techonology of China on 09/18/12
For personal use only.

(67) Tway, P. C.; Love, L. J. C. *J. Phys. Chem.* **1982**, *86* (26), 5227. doi:10.1021/j100223a032.
(68) Melo, M. J.; Macanita, A. L.; Melo, E.; Wamhoff, H.; Pina, F. *J. Photochem. Photobiol. Chem.* **1994**, *83* (3), 237. doi:10.1016/1010-6030(94)03831-7.
(69) Peral, F.; Gallego, E. *Spectrochim. Acta, Part A* **2000**, *56* (11), 2149. doi:10.1016/S1386-1425(00)00270-5.
(70) Pischel, U.; Uzunova, V. D.; Remón, P.; Nau, W. M. *Chem. Commun. (Camb.)* **2010**, *46* (15), 2635. doi:10.1039/b927595a. PMID:20461873.
(71) Saleh, N.; Al-Rawashdeh, N. A. F. *J. Fluoresc.* **2006**, *16* (4), 487. doi:10.1007/s10895-006-0106-8. PMID:16807778.
(72) Pluth, M. D.; Bergman, R. G.; Raymond, K. N. *Science* **2007**, *316* (5821), 85. doi:10.1126/science.1138748. PMID:17412953.
(73) Pluth, M. D.; Bergman, R. G.; Raymond, K. N. *J. Am. Chem. Soc.* **2007**, *129* (37), 11459. doi:10.1021/ja072654e. PMID:17713905.
(74) Pluth, M. D.; Bergman, R. G.; Raymond, K. N. *J. Am. Chem. Soc.* **2008**, *130* (34), 11423. doi:10.1021/ja802839v. PMID:18680290.
(75) Marquez, C.; Nau, W. M. *Angew. Chem. Int. Ed.* **2001**, *40* (17), 3155. doi:10.1002/1521-3773(20010903)40:17<3155::AID-ANIE3155>3.0.CO;2-7.
(76) Another complication in the determination of the binding constants of the protonated guests was the low pH (approximately 2), which was required to ensure that the guests were quantitatively protonated. At such low pH, protonation of CB7 or competitive binding of hydronium ions might interfere. A UV absorption titration for ABZ at pH 2.4 indeed provided a slightly lower binding constant of the protonated form (5.9×10^6 L/mol) than the one projected from the thermodynamic cycle (2.6×10^7 L/mol, Table 1).
(77) Gallidis, E.; Papadopoulos, E.; Ptochos, S.; Arsenos, G. *Vet. Parasitol.* **2009**, *164* (1), 53. doi:10.1016/j.vetpar.2009.04.011. PMID:19409707.
(78) Williamson, S. M.; Guzman, M.; Marin, D. H.; Anas, O.; Jin, X.; Sutton, T. B. *Biol. Control* **2008**, *46* (3), 279. doi:10.1016/j.biocontrol.2008.05.016.
(79) Schirra, M.; D'Aquino, S.; Palma, A.; Angioni, A.; Cabras, P. *J. Agric. Food Chem.* **2008**, *56* (22), 10793. doi:10.1021/jf802295m. PMID:18973341.
(80) Gould, M.; Nelson, L.; Waterer, D.; Hynes, R. *Biocontrol Sci. Technol.* **2008**, *18* (10), 1005. doi:10.1080/09583150802478189.
(81) Yenjerla, M.; Cox, C.; Wilson, L.; Jordan, M. A. *J. Pharmacol. Exp. Ther.* **2009**, *328* (2), 390. doi:10.1124/jpet.108.143537. PMID:19001156.
(82) Lahlali, R.; Massart, S.; De Clercq, D.; Serrhini, M. N.; Creemers, P.; Jijakli, M. H. *Eur. J. Plant Pathol.* **2009**, *123* (1), 37. doi:10.1007/s10658-008-9337-7.
(83) Omar, I.; O'Neill, T. M.; Rossall, S. *Plant Pathol.* **2006**, *55* (1), 92. doi:10.1111/j.1365-3059.2005.01315.x.
(84) Horton, J. *Parasitology* **2000**, *121* (S1), S113. doi:10.1017/S0031182000007290. PMID:11386684.
(85) Pourgholami, M. H.; Szwajcer, M.; Chin, M.; Liauw, W.; Seef, J.; Galettis, P.; Morris, D. L.; Links, M. *Cancer Chemother. Pharmacol.* **2010**, *65* (3), 597. doi:10.1007/s00280-009-1157-8. PMID:19904538.
(86) Ge, J. Y.; Xue, S. F.; Zhu, Q. J.; Tao, Z.; Zhang, J. X. *J. Incl. Phenom. Macrocycl. Chem.* **2007**, *58* (1–2), 63. doi:10.1007/s10847-006-9120-3.
(87) Lezcano, M.; Al-Soufi, W.; Novo, M.; Rodríguez-Núñez, E.; Tato, J. V. *J. Agric. Food Chem.* **2002**, *50* (1), 108. doi:10.1021/jf010927y. PMID:11754552.

Strain-promoted 1,3-dipolar cycloadditions of diazo compounds with cyclooctynes

Joseph Moran, Craig S. McKay, and John Paul Pezacki

Abstract: Strain-promoted cycloadditions of diazo compounds with dibenzocyclooctyne proceed with second-order rate constants of >10 L mol^{-1} s^{-1} at 25 °C. These reactions display rate constants that are comparable or greater than those of the analogous reactions of nitrones or azides with cyclooctynes.

Key words: metal-free click chemistry, diazo compounds, 1,3-dipolar cycloaddition, dibenzocyclooctyne, rate constants.

Résumé : Les cycloadditions catalysées par une tension de composés diazo avec le dibenzocyclooctyne se produisent avec des constantes de vitesse du deuxième ordre supérieures à 10 L mol^{-1} s^{-1}, à 25 °C. Les constantes de vitesse de ces réactions sont comparables ou supérieures à celles de réactions analogues de nitrones ou d'azotures sur les cyclooctynes.

Mots-clés : chimie par cliquage sans métal, composés diazo, cycloaddition 1,3-dipolaire, dibenzocyclooctyne, constantes de vitesse.

[Traduit par la Rédaction]

Introduction

"Click chemistry" was first coined by Kolb et al. in 2001,[1] and has come to describe chemical reactions that are rapid, selective, thermodynamically favourable, and devoid of side products.[1] In less than a decade, this philosophy has been embraced in numerous areas of the chemical sciences, including small-molecule library synthesis,[2] the construction of supramolecular materials,[3] and biomolecule conjugation.[4] Although the vast majority of these examples have relied on the copper-catalyzed [3+2] azide–alkyne cycloaddition (CuAAC) to provide a reliable reaction, biological applications have demanded the development of "click" reactions that do not require the presence of toxic copper species. Biocompatible variants that are kinetically driven by strain-release of cyclooctynes activated by gem difluoro[5a–5c] or dibenzo[5d] groups have subsequently been shown to be as effective for azide–alkyne cycloadditions without the requirement of copper catalysis. Other bio-orthogonal reactions involving 1,3-dipoles, such as nitrile oxides[6] or photochemically generated nitrile imines,[7] have also been reported and have reaction kinetics that are comparable or superior to azide–alkyne cycloadditions and are also highly chemoselective in the context of biological systems.

Our laboratory has recently demonstrated that strain-promoted cycloadditions of nitrones with cyclooctynes are up to 25 times faster than comparable reactions of azides.[8] Nitrone cycloadditions have also been successfully applied to protein functionalization.[9] Increased reaction rates are valuable as a means for reducing the required concentration of labeling reagents in bioorthogonal reactions. Inspired by the pioneering work done by Huisgen et al.[10] on 1,3-dipolar cycloadditions of diazoalkanes with acyclic alkynes,[10–12] we set out to investigate whether a strain-promoted variant could serve as a rapid alternative to reactions of nitrones or azides with cyclooctynes (Fig. 1).[13] Herein, we report that diazoalkanes are rapid dipoles for 1,3-dipolar cycloadditions with cyclooctynes.

Fig. 1. Overview of strain-promoted 1,3-dipolar cycloadditions of azides, nitrones, and diazo compounds with cyclooctynes.

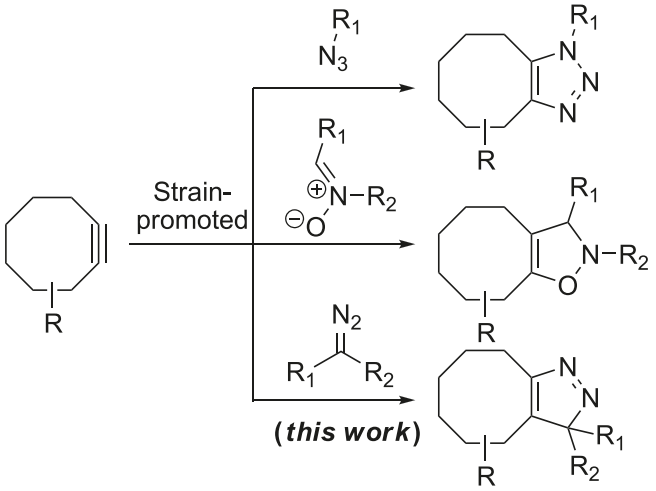

Received 28 April 2010. Accepted 30 June 2010. Published on the NRC Research Press Web site at canjchem.nrc.ca on 8 January 2011.

This article is part of a Special Issue dedicated to Professor J. C. Scaiano on the occasion of his 65th birthday.

J. Moran. Steacie Institute for Molecular Sciences, National Research Council of Canada, 100 Sussex Drive, Ottawa, ON K1A 0R6, Canada.

C.S. McKay and J.P. Pezacki.[1] Steacie Institute for Molecular Sciences, National Research Council of Canada, 100 Sussex Drive, Ottawa, ON K1A 0R6, Canada; Department of Chemistry, University of Ottawa, 10 Marie Curie, Ottawa, ON K1N 6N5, Canada.

[1]Corresponding author (e-mail: John.Pezacki@nrc-cnrc.gc.ca).

Can. J. Chem. Downloaded from www.nrcresearchpress.com by University of Electronic and Science Techonology of China on 09/18/12
For personal use only.

Can. J. Chem. Downloaded from www.nrcresearchpress.com by University of Electronic and Science Techonology of China on 09/18/12
For personal use only.

Table 1. Second-order rate constants, k_2 (L mol^{-1} s^{-1}), for the reactions of diazo compounds **1a**–**1d** with **2**.

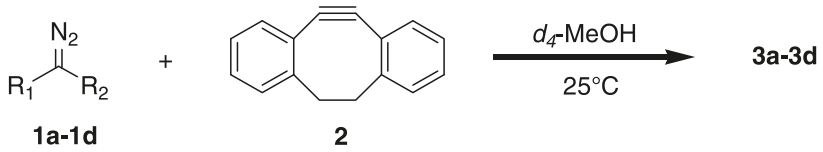

1a-1d **2**

Entry	Diazo compound	Product	Time (min)	Yield %[a]	k_2 (L mol^{-1} s^{-1})[b]
1	**1a** 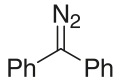	**3a** 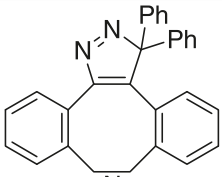	98	>99	0.070 ± 0.003
2	**1b** 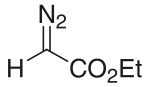	**3b**[c] 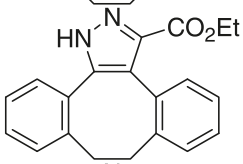	1062	97	0.0053 ± 0.0002
3	**1c** 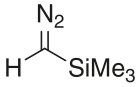	**3c**[c] 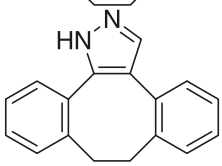	<1 min	34	>10[d]
4	**1d** 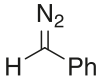	**3d**[c] 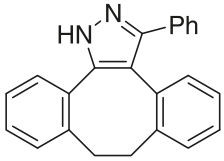	<1 min	93	>10[d]

Note: Conditions: diazo compound (50 mmol/L); **2** (50 mmol/L), 25 ºC, d_4-MeOH.
[a] Isolated yield.
[b] Kinetic evaluation of diazo compounds: the appropriate substrate and **2** were predissolved in d_4-MeOH and mixed at an equimolar concentration of ~25 mmol/L.
[c] Representative tautomer isolated after column chromatography.
[d] Reactions were too fast to be measured by ^{1}H NMR even at 2.5 mmol/L of substrate.

Results and discussion

There are number of ways in which diazoalkanes can be conveniently synthesized.[14] Here, standard literature procedures were used to prepare diazoalkanes just prior to use.[15] The diazoalkane scope was evaluated with respect to its electronics and conformational rigidity (Table 1). The reaction of diphenyldiazomethane **1a** with dibenzocyclooctyne **2** in d_4-methanol yielded the substituted pyrazole **3a** in >95% yield within 96 min, corresponding to a second-order rate constant, k_2 = 0.07 L mol^{-1} s^{-1}. Substitution with stronger electron-withdrawing groups, such as ethyl 2-diazoacetate **1b**, reduced the reaction rate by 13-fold, k_2 = 0.0053 L mol^{-1} s^{-1} (Table 1, entry 2), reaching >95% conversion within 18 h.

Diazoalkanes bearing electron-donating groups or groups less capable of resonance stabilization displayed dramatic rate enhancements. Trimethylsilyl diazomethane (**1c**) reacted rapidly with **2** and reached maximum conversion within 1 min, and phenyl diazomethane reached >95% conversion within 1 min. We were unable to determine rate constants for diazoalkanes **1c** and **1d** by ^{1}H NMR, since reactions were complete upon acquisition of the first data point. The modest yield of **3c** most likely resulted from competitive reaction pathways, including carbene reaction pathways of **1c**. The cycloadducts arising from reactions of diazoalkanes **1b** and **1d** underwent rapid tautomerization to the aromatic pyrazoles **3b** and **3d**, respectively. The primary cycloadduct from the reaction of **1b** with **2** underwent loss of the trimethylsilyl group under the aqueous reaction conditions yielding **3c**.

In general, **2** reacts with resonance-stabilized diazoalkanes at rates comparable to acyclic nitrones bearing phenyl substituents at the α-position (Table 2, entries 1 and 2) or benzyl azide (k_2 = 0.062 L mol^{-1} s^{-1}).[8] However, more weakly stabilized diazoalkanes, **1c** and **1d**, displayed faster intrinsic kinetics for cycloaddition with **2** than either strained endocyclic nitrones (Table 2, entry 3)[8] or nitrones equipped with ester or amide[9] groups at the α-position (Table 2, entries 4 and 5).

Lastly, a screen of various deuterated solvents was used to evaluate the generality of the reaction as well as to determine if there was a solvent effect on the rate of cycloaddition. Fortunately, the reaction of **1a** with **2** proceeded to >95% yield in less than 4 h for all solvents employed (Table 3). In contrast to the solvent effect observed with nitrones, where protic solvents were slowest,[8] d_4-methanol

Table 2. Rate constants for the reactions of nitrones with **2**.

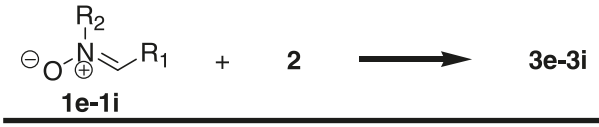

1e-1i

Entry	Nitrone		Product	k_2 (L mol^{-1} s^{-1})
1[a]	R_1= Ph	R_2= Bn	**3d**	0.09
2[a]	R_1= Ph	R_2= Me	**3e**	0.13
3[a]	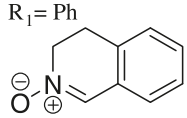		**3f**	1.5
4[b]	R_1= CO_2Et	R_2= Me	**3g**	3.9
5[b]	R_1= C(O)NHBn	R_2= Me	**3h**	2.2

Note: Rate constants were determined by ^{1}H NMR in analogy with experiments involving diazoalkanes.

[a] See ref. 8.

[b] Unfunctionalized dibenzocyclooctynol was used in place of **2**; see ref. 9.

Table 3. Solvent screen for the reaction of **1a** with **2**.

1a

Entry	Solvent	Reaction time for 95% conversion to **3a** (min)
1	C_6D_6	245 + 15
2	*CD_3OD*	98 ± 5
3	*d_6*-DMSO	108 + 5
4	CD_3CN	139 + 5

Note: Conditions: **2** was added to **1a** (both pre-dissolved, 100 mmol/L, 1:1) in an NMR tube and monitored by ^{1}H NMR at 25 °C.

was found to be the optimal solvent, reaching 95% yield within 98 min.

Diazoalkanes can be protonated to form alkanediazonium ions in aqueous solution in biological systems that can alkylate nucleic acids as well as protein side chains, causing cellular stress and carcinogenesis.[16] Although the biomolecular rate constants for strain-promoted cycloaddition are slower than those of proton transfer ($k_{H^+} \approx 10^2$–10^6 L mol^{-1} s^{-1})[16] under neutral conditions, at physiological pH where hydronium ion concentration is low (10^{-7} mol/L), cycloaddition rates may be competitive or even dominate over diazonium ion chemistry. Interestingly, cyclooctynes might also serve as in vivo quenchers of diazoalkanes that might be formed through nitrosative stress.

Diazoalkanes can give rise to carbene intermediates either through photolytic or thermolytic processes.[17] Carbenes can then undergo O–H or C–H insertion reactions, cyclopropanation reactions, as well as intramolecular rearrangements such as 1,2-hydrogen shifts.[17] Pioneering work by Scaiano's group and others have established rate constants for many of these processes.[17–19] Although these rates can be high, any carbene intermediates formed in biological media would be expected to react preferentially with water to form the corresponding alcohol or undergo intramolecular rearrangements. However, the rate constants reported here suggest that even unstabilized diazoalkanes should react rapidly and spontaneously with cyclooctyne **2** before significant thermolysis or photolysis can occur under ambient conditions.

Conclusion

Strain-promoted cycloadditions of diazoalkanes with cyclooctynes represent an alternative rapid conjugation technique for material sciences and a valid method for constructing functionalized pyrazoles. Rate enhancements of >10 L mol^{-1} s^{-1} were observed for diazoalkanes containing electron-donating groups adjacent to the diazo moiety. These rates are comparable with those of analogous reactions involving endocyclic nitrones or nitrones bearing ester or amide moieties at the α-position. Optimization of the stability and reactivity of the diazoalkane group may lead to diazoalkanes as reactive and useful alternatives to nitrone and azide dipoles for use in strain-promoted cycloadditions with cyclooctynes.

Supplementary data

Supplementary data for this article are available on the journal Web site (canjchem.nrc.ca).

Acknowledgements

We thank Professor J. C. Scaiano for his pioneering work in areas of photochemistry and physical organic chemistry, which has inspired and enabled new research in diverse fields.

References

(1) Kolb, H. C.; Finn, M. G.; Sharpless, K. B. *Angew. Chem. Int. Ed.* **2001**, *40* (11), 2004. doi:10.1002/1521-3773(20010601)40:11<2004::AID-ANIE2004>3.0.CO;2-5.

(2) Kolb, H. C.; Sharpless, K. B. *Drug Discov. Today* **2003**, *8* (24), 1128. doi:10.1016/S1359-6446(03)02933-7. PMID: 14678739.

(3) Lutz, J. F. *Angew. Chem. Int. Ed.* **2007**, *46* (7), 1018. doi:10.1002/anie.200604050.

(4) Wu, P.; Fokin, V. V. *Aldrichim Acta* **2007**, *40*, 7.

(5) (a) Agard, N. J.; Prescher, J. A.; Bertozzi, C. R. *J. Am. Chem. Soc.* **2004**, *126* (46), 15046. doi:10.1021/ja044996f. PMID:15547999.; (b) Oh, E. C.; Khan, N.; Novelli, E.; Khanna, H.; Strettoi, E.; Swaroop, A. *Proc. Natl. Acad. Sci. U.S.A.* **2007**, *104* (5), 1679. doi:10.1073/pnas.0605934104. PMID:17242361.; (c) Codelli, J. A.; Baskin, J. M.; Agard, N. J.; Bertozzi, C. R. *J. Am. Chem. Soc.* **2008**, *130* (34), 11486. doi:10.1021/ja803086r. PMID:18680289.; (d) Ning, X.; Guo, J.; Wolfert, M. A.; Boons, G.-J. *Angew. Chem. Int. Ed.* **2008**, *47* (12), 2253. doi:10.1002/anie.200705456.

(6) (a) Singh, I.; Vyle, J. S.; Heaney, F. *Chem. Commun. (Camb.)* **2009**, (22): 3276. doi:10.1039/b904185k. PMID: 19587938.; (b) Himo, F.; Lovell, T.; Hilgraf, R.; Rostovtsev, V. V.; Noodleman, L.; Sharpless, K. B.; Fokin, V. V. *J. Am. Chem. Soc.* **2005**, *127* (1), 210. doi:10.1021/ja0471525. PMID:15631470.

(7) (a) Song, W.; Wang, Y.; Qu, J.; Madden, M. M.; Lin, Q. *Angew. Chem. Int. Ed.* **2008**, *47* (15), 2832. doi:10.1002/anie.200705805.; (b) Song, W.; Wang, Y.; Qu, J.; Lin, Q. *J. Am. Chem. Soc.* **2008**, *130* (30), 9654. doi:10.1021/ja803598e. PMID:18593155.; (c) Wang, Y.; Hu, W. J.; Song, W.; Lim,

Can. J. Chem. Downloaded from www.nrcresearchpress.com by University of Electronic and Science Techonology of China on 09/18/12
For personal use only.

Can. J. Chem. Downloaded from www.nrcresearchpress.com by University of Electronic and Science Techonology of China on 09/18/12
For personal use only.

R. K.; Lin, Q. *Org. Lett.* **2008**, *10* (17), 3725. doi:10.1021/ol801350r. PMID:18671406.

(8) McKay, C. S.; Moran, J.; Pezacki, J. P. *Chem. Commun. (Camb.)* **2010**, *46* (6), 931. doi:10.1039/b921630h. PMID: 20107654.

(9) Ning, X.; Temming, R. P.; Dommerholt, J.; Guo, J.; Ania, D. B.; Debets, M. F.; Wolfert, M. A.; Boons, G.-J.; van Delft, F. L. *Angew. Chem. Int. Ed.* **2010**, *49* (17)(Guo), 3065. doi:10.1002/anie.201000408.

(10) Huisgen, R.; Stangl, H.; Sturm, H. J.; Wagenhofer, H. *Angew. Chem.* **1961**, *73* (5), 170. doi:10.1002/ange.19610730508.

(11) For reviews, see: (a) Korobitsyna, I. K.; Bulusheva, V. V.; Rodina, L. L. *Chem. Heterocycl. Compd.* **1978**, *14* (5), 471. doi:10.1007/BF00673325.; (b) Padwa, A. *1,3-Dipolar Cycloaddition Chemistry;* John Wiley & Sons: New York, 1984; Vol. I.

(12) For recent papers concerning 1,3-dipolar cycloadditions of diazo compounds with alkynes, see: (a) Vuluga, D.; Legros, J.; Crousse, B.; Bonnet-Delpon, D. *Green Chem.* **2009**, *11* (2), 156. doi:10.1039/b812242c.; (b) Qi, X.; Ready, J. M. *Angew. Chem. Int. Ed.* **2007**, *119*, 3306.; (c) Jiang, N.; Li, C.-J. *Chem. Commun. (Camb.)* **2004**, (4): 394. doi:10.1039/b311763d. PMID:14765225.; (d) Aggarwal, V. K.; de Vicente, J.; Bonnert, R. V. *J. Org. Chem.* **2003**, *68* (13), 5381. doi:10.1021/jo0268409. PMID:12816503.

(13) For an isolated example of the reactivity of a diazo compound with a cyclooctyne, see: Wittig, G.; Hutchison, J. J. *Liebigs Ann. Chem.* **1970**, *741* (1), 79. doi:10.1002/jlac.19707410109.

(14) Zollinger, H. In *Diazo Chemistry;* VCH: New York, 1995; Vol. 1–2.

(15) Kumar, S.; Murray, R. W. *J. Am. Chem. Soc.* **1984**, *106* (4), 1040. doi:10.1021/ja00316a037.

(16) (a) Laali, K.; Olah, G. A. *Res. Chem. Intermed.* **1985**, *6* (3), 237. doi:10.1007/BF03055537.; (b) Kirmse, W. *Angew. Chem. Int. Ed. Engl.* **1976**, *15* (5), 251. doi:10.1002/anie.197602511.; (c) Collins, C. J. *Acc. Chem. Res.* **1971**, *4* (9), 315. doi:10.1021/ar50045a004.; (d) More O'Ferrall, R. A. *Adv. Phys. Org. Chem.* **1967**, *5*, 331. doi:10.1016/S0065-3160(08)60313-5.; (e) Rieche, A.; Schmitz, E. *Angew. Chem.* **1955**, *67* (9-10), 273. doi:10.1002/ange.19550670909.; (f) Pezacki, J. P.; Wagner, B. D.; Lew, C. S. Q.; Warkentin, J.; Lusztyk, J. *J. Am. Chem. Soc.* **1997**, *119* (7), 1789. doi:10.1021/ja962550w.; (g) Whittaker, D. In *The Chemistry of Diazonium and Diazo Compounds;* Patai, S., Ed.; Wiley-Interscience: Chichester, 1978; pp 617–639; (h) Leung, K. H.; Archer, M. C. *Chem. Biol. Interact.* **1984**, *48* (2), 169. doi:10.1016/0009-2797(84)90118-2. PMID: 6697420.; (i) Lawson, T.; Nagel, D. *Carcinogenesis* **1988**, *9* (6), 1007. doi:10.1093/carcin/9.6.1007. PMID:3370746.; (j) Liberato, D. J.; Saavedra, J. E.; Farnsworth, D. W.; Lijinsky, W. *Chem. Res. Toxicol.* **1989**, *2* (5), 307. doi:10.1021/tx00011a007. PMID:2519822.

(17) (a) Brinker, U. In *Advances in Carbene Chemistry;* Elsevier: New York, 1998; Vol. 1–2; (b) Moss, R. A.; Platz, M. S.; Jones, M. In *Reactive Intermediate Chemistry;* John Wiley and Sons: New York, 2004.

(18) Some representative papers: (a) Pezacki, J. P.; Pole, D. L.; Warkentin, J.; Chen, T. Q.; Ford, F.; Toscano, J. P.; Fell, J.; Platz, M. S. *J. Am. Chem. Soc.* **1997**, *119* (13), 3191. doi:10.1021/ja961933r.; (b) Pezacki, J. P.; Wood, P. D.; Gadosy, T. A.; Lusztyk, J.; Warkentin, J. *J. Am. Chem. Soc.* **1998**, *120* (34), 8681. doi:10.1021/ja973469b.; (c) Pezacki, J. P. *Can. J. Chem.* **1999**, *77* (7), 1230. doi:10.1139/cjc-77-7-1230.; (d) Pezacki, J. P.; Couture, P.; Dunn, J. A.; Warkentin, J.; Wood, P. D.; Lusztyk, J.; Ford, F.; Platz, M. S. *J. Org. Chem.* **1999**, *64* (12), 4456. doi:10.1021/jo990171q.; (e) Tae, E. L.; Zhu, Z. D.; Platz, M. S.; Pezacki, J. P.; Warkentin, J. *J. Phys. Chem.* **1999**, *103*, 5336.

(19) Some representative papers: (a) Barcus, R. L.; Hadel, L. M.; Johnston, L. J.; Platz, M. S.; Savino, T. G.; Scaiano, J. C. *J. Am. Chem. Soc.* **1986**, *108* (14), 3928. doi:10.1021/ja00274a013.; (b) Barra, M.; Fisher, T. A.; Cernigliaro, G. J.; Sinta, R.; Scaiano, J. C. *J. Am. Chem. Soc.* **1992**, *114* (7), 2630. doi:10.1021/ja00033a041.; (c) Belt, S. T.; Bohne, C.; Charette, G.; Sugamori, S. E.; Scaiano, J. C. *J. Am. Chem. Soc.* **1993**, *115* (6), 2200. doi:10.1021/ja00059a014.; (d) Griller, D.; Liu, M. T. H.; Scaiano, J. C. *J. Am. Chem. Soc.* **1982**, *104* (20), 5549. doi:10.1021/ja00384a074.; (e) Werstiuk, N. H.; Casal, H. L.; Scaiano, J. C. *Can. J. Chem.* **1984**, *62* (11), 2391. doi:10.1139/v84-410.

A porphyrin-stabilized iridium oxide water oxidation catalyst

Benjamin D. Sherman, Smitha Pillai, Gerdenis Kodis, Jesse Bergkamp, Thomas E. Mallouk, Devens Gust, Thomas A. Moore, and Ana L. Moore

Abstract: Colloidal solutions of iridium oxide hydrate ($IrO_2 \cdot nH_2O$) were formed using porphyrin stabilizers bearing malonate-like functional groups at each of the four meso positions of the porphyrin ring. Cyclic voltammetry and monitoring of solution oxygen concentrations under constant applied potential demonstrated the electrochemical catalytic activity of the porphyrin–$IrO_2 \cdot nH_2O$ complexes for the oxidation of water to oxygen. Quenching of the porphyrin fluorescence in the complex implies strong interaction between the porphyrin and the $IrO_2 \cdot nH_2O$. These results mark a step toward developing a porphyrin-based photoanode for use in a photoelectrochemical water-splitting cell.

Key words: water oxidation, electrochemical catalysis, iridium oxide, porphyrin.

Résumé : Il se forme des solutions colloïdales d'hydrate d'oxyde d'iridium ($IrO_2 \cdot nH_2O$) lorsqu'on utilise comme stabilisants des porphyrines portant sur chacune des quatre positions méta du noyau porphyrine des groupes fonctionnels apparentés au malonate. La voltampérométrie cyclique et le monitorage des concentrations d'oxygène dans la solution, sous potentiel appliqué constant, démontrent l'activité catalytique électrochimique des complexes porphyrine–$IrO_2 \cdot nH_2O$ pour l'oxydation de l'eau en oxygène. Le piégeage de la fluorescence de la porphyrine dans le complexe implique une forte interaction entre la porphyrine et le $IrO_2 \cdot nH_2O$. Ces résultats marque une étape en avant dans le développement d'une photoanode à base de porphyrine pour l'utilisation d'une cellule photoélectrochimique pour la division de l'eau.

Mots-clés : oxydation de l'eau, catalyse électrochimique, oxyde d'iridium, porphyrine.

[Traduit par la Rédaction]

Introduction

Work carried out by Harriman et al. over 20 years ago demonstrated that hydrated iridium oxide ($IrO_2 \cdot nH_2O$) is an active, stable, and efficient catalyst for water oxidation.[1–3] Colloidal $IrO_2 \cdot nH_2O$ in solution with either $Ru(II)(bpy)_3$ (bpy = 2,2′-bipyridine) or porphyrin dye could carry out the photochemical generation of O_2 from water.[2,3] These studies, however, required the presence of a strong oxidant ($S_2O_8^{2-}$) to generate the photo-oxidized dye that would then oxidize the catalyst. Subsequent electrochemical studies by other groups investigated techniques for immobilizing $IrO_2 \cdot nH_2O$ on the surface of transparent glass electrodes.[4–6] Yagi et al. showed that adsorbed layers formed on the surface of indium-doped tin oxide and fluorine-doped tin oxide electrodes when the electrodes were allowed to soak in a solution containing citrate-stabilized colloidal $IrO_2 \cdot nH_2O$.[5,6] Electrochemical studies of prepared electrodes showed the onset of catalytic current near 1.0 V versus saturated calomel electrode (SCE) at pH 5.3 (no $IrO_2 \cdot nH_2O$ in solution). Murray et al. have studied $IrO_2 \cdot nH_2O$ particles formed at high pH, without the use of stabilizing groups, both on a surface and in solution.[7,8] Their work has shown the need for only 0.15 V of overpotential for the onset of water oxidation and 100% current efficiency for the generation of O_2 from water at an overpotential of 0.29 V.[7,8] Although the catalytic activity of $IrO_2 \cdot nH_2O$ has been well established, only recently has a system capable of driving the catalyst photoelectrochemically been demonstrated.[9]

We have reported the development of a water-splitting photoelectrochemical cell employing a $Ru(II)(bpy)_3$–$IrO_2 \cdot nH_2O$ based photoanode.[9] In that work, the dye–$IrO_2 \cdot nH_2O$ complex was formed using a heteroleptic $Ru(II)(bpy)_3$ complex containing phosphonate groups on one of the bipyridyl ligands and a malonate group on another. Previous work had demonstrated the preference of carboxylate groups over phosphonate groups for binding to the surface of $IrO_2 \cdot nH_2O$.[10] This chemistry allowed for the formation of small $IrO_2 \cdot nH_2O$ particles (1–5 nm) capped with $Ru(II)(bpy)_3$ dye molecules containing exposed phosphonate groups.[9,10] The dye–$IrO_2 \cdot nH_2O$ constructs could then be attached to metal oxide semiconductors, such as titanium dioxide (TiO_2), via the phosphonate group.

In this system, the photoanode consisted of the dye–$IrO_2 \cdot nH_2O$ complex adsorbed to a TiO_2 layer on top of a

Received 2 June 2010. Accepted 23 July 2010. Published on the NRC Research Press Web site at canjchem.nrc.ca on 11 January 2011.

This article is part of a Special Issue dedicated to Professor J. C. Scaiano.

B.D. Sherman, S. Pillai, G. Kodis, J. Bergkamp, D. Gust, T.A. Moore, and A.L. Moore.[1] Center for Bioenergy and Photosynthesis and Department of Chemistry and Biochemistry, Arizona State University, Tempe, AZ 85287-1604, USA.
T.E. Mallouk. Department of Chemistry, The Pennsylvania State University, University Park, PA 16802, USA.

[1]Corresponding author (e-mail: AMoore@asu.edu).

Can. J. Chem. Downloaded from www.nrcresearchpress.com by University of Electronic and Science Techonology of China on 09/18/12
For personal use only.

Can. J. Chem. Downloaded from www.nrcresearchpress.com by University of Electronic and Science Techonology of China on 09/18/12
For personal use only.

fluorine-doped tin oxide electrode. When this photoanode was combined with a platinum cathode in a photoelectrochemical cell, the cell produced a photocurrent of 12.7 μA cm^{-2} upon illumination with 450 nm light at an intensity of 7.8 mW cm^{-2}, giving an internal quantum yield of 0.9%.[9] Three principal factors limited the performance of this system: slow electron transfer from the $IrO_2 \cdot nH_2O$ catalyst to the oxidized dye, bleaching of the dye likely resulting from nucleophilic attack on the oxidized dye, and the need for applied bias to achieve overall water splitting. Transient spectroscopic studies showed electron transfer from the $IrO_2 \cdot nH_2O$ to the photo-oxidized dye (2.8 ms) to be an order of magnitude slower than the back electron transfer from TiO_2 to the oxidized dye (0.37 ms).[9] An additional issue with Ru(II)$(bpy)_3$ complexes as photosensitizers is that they absorb strongly in the blue region of the spectrum but cannot efficiently utilize light in the red region of the spectrum.

The work outlined herein seeks to improve the stability, electron transfer rate, and spectral properties of the dye–$IrO_2 \cdot nH_2O$ complex by incorporating a porphyrin rather than the Ru(II)$(bpy)_3$ dye. We report the synthesis of a porphyrin–$IrO_2 \cdot nH_2O$ complex that shows an electrochemical catalytic response similar to that of other $IrO_2 \cdot nH_2O$ complexes.[5] Finally, fluorescence lifetime measurements indicate quenching of the porphyrin fluorescence in the porphyrin–$IrO_2 \cdot nH_2O$ complex.

Experimental

Materials

Sephadex with a 5 000 molecular weight cutoff, Na_2HPO_4, NaH_2PO_4, tetrabutylammonium hexafluorophosphate, and benzonitrile were obtained from Sigma-Aldrich. Benzonitrile was distilled prior to use. K_2IrCl_6 was used as received from Alfa Aesar. KNO_3 was obtained from Fluka. Tetrahydrofuran for synthesis was distilled from sodium/benzophenone. Dimethylformamide was dried over activated 4 Å molecular sieves. Dichloromethane used for chromatography was distilled from calcium hydride.

Porphyrin synthesis

General methods

5,10,15,20-Tetrakis(4-bromomethylphenyl)porphyrin was synthesized by a published method.[11] The malonate substitution and cleavage of the esters were performed by literature procedures used for related compounds.[12–14] Palladium insertion was achieved by adapting Durantini's procedure.[13]

Porphyrin 1

Sodium hydride (387 mg, 16 mmol) was suspended in 10 mL of dry THF under nitrogen atmosphere. Diethyl malonate (0.61 mL, 4 mmol) in 20 mL THF was added dropwise under ice cooling. After being stirred for 1 h at room temperature, a solution of 5,10,15,20-tetrakis(4-bromomethylphenyl)porphyrin (200 mg, 0.20 mmol) in 20 mL of dry THF was added dropwise to the mixture and stirred for 1 h. The reaction mixture was then poured into an ice-cold saturated NH_4Cl solution. The aqueous layer was extracted with CH_2Cl_2. The organic solution was washed thoroughly with water and dried over Na_2SO_4. The crude material was purified by column chromatography on silica gel (solvent CH_2Cl_2:EtOAc, 20:1). Yield: 120 mg (45%). UV–vis (CH_2Cl_2, nm) λ_{max}: 419, 516, 551, 591, 647. ^{1}H NMR (400 MHz, $CDCl_3$, RT) δ: –2.82 (s, 2H, NH), 1.34 (t, 24H, J = 7.2 Hz, ethyl CH_3), 3.56 (d, 8H, J = 7.7 Hz, CH_2), 3.96 (t, 4H, J = 7.7 Hz, CH), 4.3 (m, 16H, J = 7.2 Hz, ethyl CH_2), 7.58 (d, 8H, J = 8.0 Hz, phenyl CH_2), 8.10 (d, 8H, J = 8.0 Hz, phenyl CH_2), 8.77 (s, 8H pyrrolic H). MALDI-TOF–MS m/z calcd. for $C_{76}H_{78}N_4O_{16}$: 1302.54; found: 1302.67.

Porphyrin 1a

A 50 mg (0.038 mmol) portion of **1** and finely ground sodium hydroxide (292 mg, 7.5 mmol) were suspended in 40 mL of ethanol. The mixture was refluxed for 15 h and a precipitate was formed. The mixture was cooled to room temperature and filtered. The residue was washed with a little ice-cold ethanol and dried in high vacuum. Yield: 43 mg (89.5%). UV–vis (H_2O, nm) λ_{max}: 415, 519, 557, 582, 635. ^{1}H NMR (400 MHz, D_2O, RT) δ: 3.3 (d, 8H, J = 7.9 Hz, CH_2), 3.59 (t, 4H, J = 7.9 Hz, CH), 7.58 (d, 8H, J = 7.8 Hz, phenyl CH_2), 7.9 (d, 8H, J = 7.8 Hz, phenyl CH_2), 8.47 (s, 4H, pyrrolic H), 8.98 (s, 4H, pyrrolic H). MALDI-TOF–MS m/z calcd. for $C_{76}H_{78}N_4O_{16}$: 1079.02; found: 1079.41.

Porphyrin 2

To a solution of **1** (24 mg, 0.018 mmol) in 10 mL DMF was added palladium(II) chloride (32.6 mg, 0.18 mmol). The mixture was stirred for 1 h at 55 °C under nitrogen. The solvent was removed under reduced pressure and the compound was purified by column chromatography on silica gel (solvent CH_2Cl_2:EtOAc, 20:1). Yield: 21 mg (81%). UV–vis (CH_2Cl_2, nm) λ_{max}: 416, 523. ^{1}H NMR (400 MHz, $CDCl_3$, RT) δ: 1.35 (t, 24H, J = 7.2 Hz, ethyl CH_3), 3.56 (d, 8H, J = 7.7 Hz, CH_2), 3.96 (t, 4H, J = 7.7 Hz, CH), 4.3 (m, 16H, J = 7.2 Hz, ethyl CH_2), 7.58 (d, 8H, J = 8.0 Hz, phenyl CH_2), 8.06 (d, 8H, J = 8.0 Hz, phenyl CH_2), 8.75 (s, 8H, pyrrolic H). MALDI-TOF–MS m/z calcd. for $C_{76}H_{78}N_4O_{16}$: 1302.54; found: 1302.67.

Porphyrin 2a

Porphyrin **2** (20 mg, 0.014 mmol) and finely ground sodium hydroxide (107 mg, 2.7 mmol) were suspended in 20 mL of ethanol. The mixture was refluxed for 15 h and a precipitate was formed. The mixture was cooled to room temperature and filtered. The residue was washed with a little ice-cold ethanol and dried in high vacuum. Yield: 17 mg (88%). UV–vis (H_2O, nm) λ_{max}: 413, 522. ^{1}H NMR (400 MHz, D_2O, RT) δ: 3.28 (d, 8H, J = 7.9 Hz, CH_2), 3.59 (t, 4H, J = 7.9 Hz, CH), 7.58 (d, 8H, J = 7.8 Hz, phenyl CH_2), 7.96 (s, 8H, phenyl CH_2), 8.47 (s, 8H, pyrrolic H).

Preparation of the porphyrin–$IrO_2 \cdot nH_2O$ complex

The complex was formed in a solution containing 50 μmol L^{-1} of the porphyrin sodium salt, either **1a** or **2a**, and 1 mmol L^{-1} of K_2IrCl_6. The solution was adjusted to pH 8 with 0.25 mol L^{-1} NaOH and heated to 35 °C, and the reaction was allowed to proceed (~2–3 days) until the starting red-brown solution became pale yellow. The pH of the solution was monitored throughout the reaction period and NaOH was added as necessary to maintain mildly basic pH.

Can. J. Chem. Downloaded from www.nrcresearchpress.com by University of Electronic and Science Techonology of China on 09/18/12
For personal use only.

The resulting colloids were either used as such or purified by size exclusion chromatography using a Sephadex gel filtration medium. The malonate–$IrO_2{\cdot}nH_2O$ was prepared as previously described.[10]

Electrochemical measurements

All electrochemical measurements were done using a CH Instruments 760D potentiostat along with software provided by the manufacturer. A glassy carbon or platinum working electrode was used as indicated along with a Ag^+/Ag quasi reference or Ag/AgCl (in saturated KCl) reference and a Pt wire mesh counter electrode. Ferrocene was used to calibrate the potential of the Ag^+/Ag quasi reference with Cp_2Fe^+/Cp_2Fe taken as 0.45 V versus SCE. Cyclic voltammetric measurements of **1** and **2** were done in benzonitrile with 0.1 mol L^{-1} tetrabutylammonium hexafluorophosphate. Porphyrin–$IrO_2{\cdot}nH_2O$ measurements were done in 0.1 mol L^{-1} KNO_3 aqueous solution at the scan rates and potentials indicated. Some measurements were taken in 0.1 mol L^{-1} phosphate buffer with pH near 7 as indicated.

Clark electrode measurements

A Yellow Springs Instrument Co. 5300 Biological Oxygen Monitor was used to measure the percent O_2 in solution, with air-saturated solution set as 100% O_2. Solutions were purged of O_2 by bubbling Ar until the O_2 level reached 30%–50%. Argon was then flowed into the headspace of the cell to keep atmospheric O_2 from entering. After reading a stable percent O_2 level for 2–5 min, the amperometry experiment was initiated. A line was fitted to the stable percent O_2 reading for the 60 s before applying potential in the experiment and was subtracted from the trace to give $\Delta\%O_2$ (change in percent O_2 during the experiment) as shown in Fig. 1.

Time-resolved fluorescence measurements

Fluorescence decay measurements were performed by the time-correlated single-photon-counting method. The excitation source for the system was a mode-locked Ti:Sapphire laser (Spectra Physics, Millennia-pumped Tsunami) with a 130 fs pulse duration operating at 80 MHz. The laser output was sent through a frequency doubler and pulse selector (Spectra Physics Model 3980) to obtain 370–450 nm pulses at 4 MHz. Fluorescence emission was detected at the magic angle using a double grating monochromator (Jobin Yvon Gemini-180) and a microchannel plate photomultiplier tube (Hamamatsu R3809U-50). The instrument response function was 35–55 ps. The spectrometer was controlled by software based on the LabView programming language and data acquisition was done using a single photon counting card (Becker-Hickl, SPC-830).

Data analysis was carried out using locally written software (ASUFIT) developed in a MATLAB environment (Mathworks Inc.). Random errors associated with the reported lifetimes obtained from fluorescence were typically ≤ 5%.

Results and discussion

This work centers on the use of tetrakis(methylphenylmalonate)porphyrins as stabilizers for the formation of $IrO_2{\cdot}nH_2O$ colloidal solutions. It builds on the previous finding that bidentate carboxylic acid groups act as effective stabilizers for the formation of small $IrO_2{\cdot}nH_2O$ colloidal particles.[10] The porphyrins used in this study contain methylphenylmalonate groups at each of the para positions of the four meso phenyl groups; it is expected that the colloidal particles formed with these stabilizers will be similar in structure to those reported by Hoertz et al.[10]

Fig. 1. Oxygen concentration relative to air-saturated water measured with a Clark electrode. Green line: porphyrin **2a**–$IrO_2{\cdot}nH_2O$, glassy carbon working electrode poised at 1.4 V vs. Ag/AgCl. Blue line: porphyrin **2a**–$IrO_2{\cdot}nH_2O$, glassy carbon working electrode poised at 0.6 V vs. Ag/AgCl. Black line: buffer only, glassy carbon working electrode poised at 0.6 V vs. Ag/AgCl. Red line: buffer only, glassy carbon working electrode poised at 1.4 V vs. Ag/AgCl. All measurements taken in H_2O at pH 6.95 with 0.1 mol L^{-1} KNO_3 and 0.1 mol L^{-1} phosphate buffer. Potential applied starting at t = 60 s.

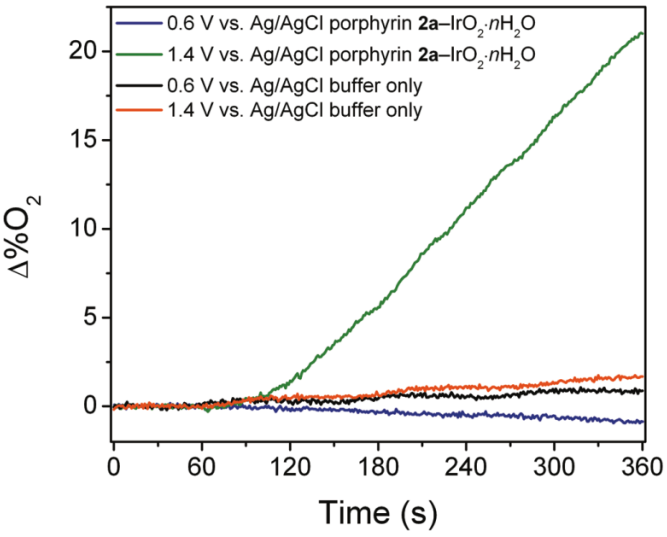

Colloidal $IrO_2{\cdot}nH_2O$ particles were successfully formed using porphyrin **1a** and its Pd analogue, **2a**, shown in Fig. 2 along with their protected ester forms (**1** and **2**). Synthesis of the $IrO_2{\cdot}nH_2O$ colloids entailed heating a solution containing K_2IrCl_6 and the porphyrin at 35 °C for ~2–3 days. The initial pH of the solution was adjusted to near pH 8 with NaOH and monitored and adjusted throughout the synthesis to maintain moderately basic conditions. The resulting colloidal solution was pale yellow. In some cases, the resulting preparation was purified over a size-exclusion column to remove salts and unused starting material. Solutions prepared in this way were stored under mildly basic conditions and remained stable on the benchtop for several months.

Cyclic voltammetry experiments were carried out to elucidate the electrochemical characteristics of the colloids. A typical voltammogram reveals the onset of strong anodic current near 1.1 V versus Ag/AgCl, indicative of water oxidation. Poising of the working electrode at sufficiently positive potentials causes the generation of bubbles at the electrode surface in solutions containing the porphyrin–$IrO_2{\cdot}nH_2O$. Figure 3 shows an overlay of several voltammograms performed in the presence of $IrO_2{\cdot}nH_2O$ catalysts. The various $IrO_2{\cdot}nH_2O$ complexes give comparable voltammograms, with strong anodic signals indicative of water ox-

Can. J. Chem. Downloaded from www.nrcresearchpress.com by University of Electronic and Science Techonology of China on 09/18/12
For personal use only.

Fig. 2. Structures of porphyrin **1**, the octasodium salt of **1** (**1a**), porphyrin **2**, and the octasodium salt of **2** (**2a**).

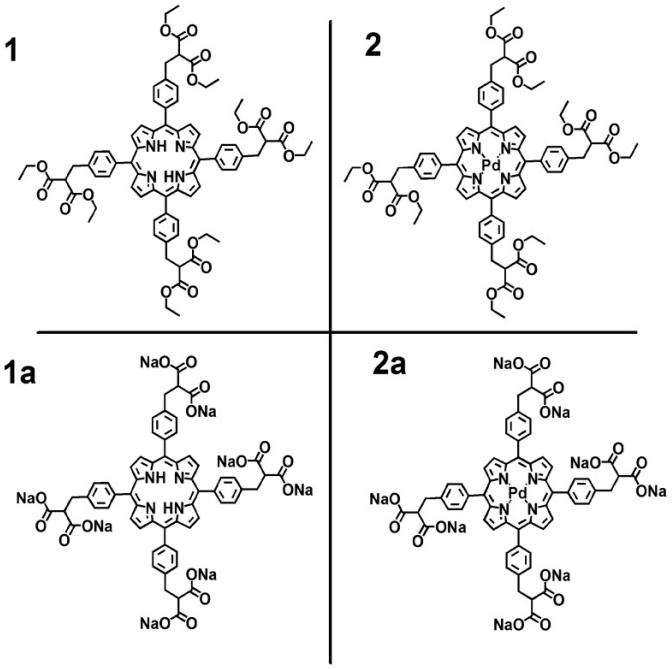

Fig. 3. Comparison of cyclic voltammograms taken in solutions containing porphyrin **1a**–$IrO_2{\cdot}nH_2O$ (red), porphyrin **2a**–$IrO_2{\cdot}nH_2O$ (orange), malonate–$IrO_2{\cdot}nH_2O$ (blue), or only supporting electrolyte (black). All scans were taken with a glassy carbon working electrode, at a scan rate of 100 mV s^{-1}, with voltages referenced to a Ag/AgCl electrode. The solutions contained $IrO_2{\cdot}nH_2O$ colloidal catalyst at different concentrations and the currents observed should not be taken as a quantitative comparison of catalytic activity.

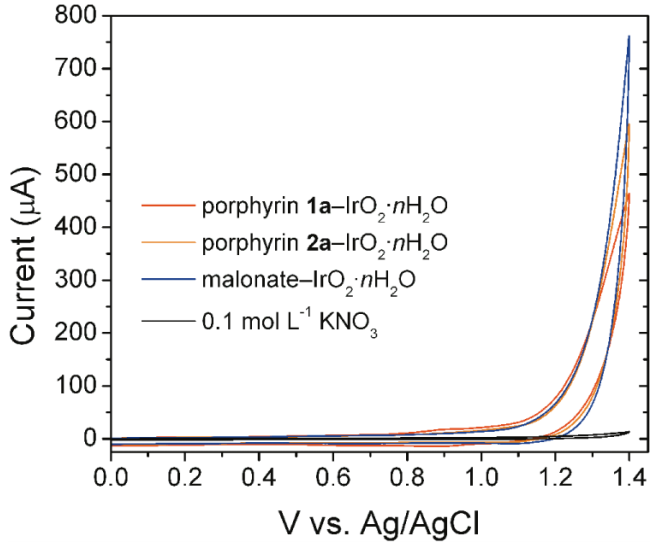

idation. Comparison with the scan in the absence of any $IrO_2{\cdot}nH_2O$ clearly shows the signal originates from the presence of the catalyst. It should be emphasized that Fig. 3 is not intended as a quantitative comparison between the various $IrO_2{\cdot}nH_2O$ complexes, as the concentration and likely the size of the colloid was different in each case, but rather as a means of demonstrating that the behavior of the

Fig. 4. Porphyrin fluorescence lifetime measurements. Red line: porphyrin **1a** in solution with malonate-stabilized $IrO_2{\cdot}nH_2O$, lifetime 8.79 ns. Blue line: porphyrin **1a**–$IrO_2{\cdot}nH_2O$ colloidal particles, major component lifetime 46.7 ps (see text).

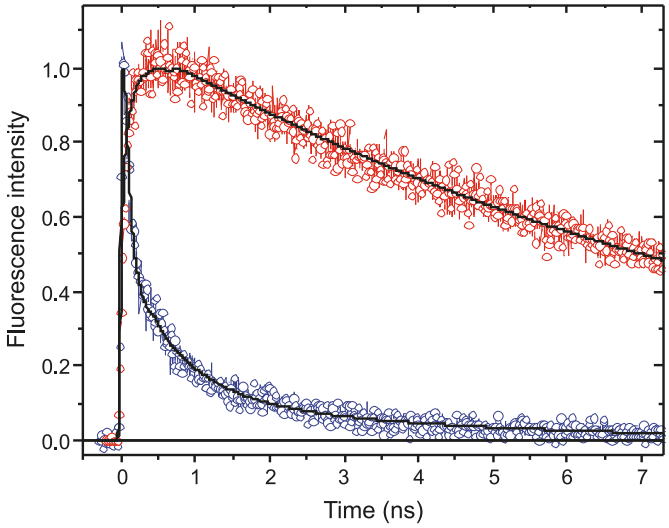

porphyrin–$IrO_2{\cdot}nH_2O$ complexes is similar to that of the carboxylic acid (malonate or citrate) stabilized $IrO_2{\cdot}nH_2O$ complexes described in the literature.[5,6]

To demonstrate that the observed catalytic signal corresponds to the oxidation of water to O_2, a Clark electrode was employed to monitor the O_2 concentration in the solution during electrochemical measurements. After purging the cell of O_2 by bubbling with argon, the cell was sealed and the O_2 concentration was monitored while poising the glassy carbon working electrode at various potentials versus Ag/AgCl (Fig. 1). With porphyrin **2a**–$IrO_2{\cdot}nH_2O$ in solution, the O_2 concentration does not increase with time at 0.6 V versus Ag/AgCl but does increase at 1.4 V. When the same working electrode is used in a solution containing only supporting electrolyte and no catalyst, no increase in O_2 occurs at either 0.6 or 1.4 V versus Ag/AgCl. Thus, oxygen is produced only in the presence of the catalyst at a suitable potential.

As one means of assessing the interaction of the porphyrin dye with the $IrO_2{\cdot}nH_2O$, the porphyrin fluorescence lifetimes in the porphyrin–$IrO_2{\cdot}nH_2O$ complex and with the porphyrin dissolved in a solution containing malonate–$IrO_2{\cdot}nH_2O$ were determined. As shown in Fig. 4, the fluorescence lifetime of the free porphyrin **1a** in the presence of malonate–$IrO_2{\cdot}nH_2O$ was 8.79 ns. This lifetime is typical for a free base porphyrin of this general type. The fluorescence lifetime of the same porphyrin complexed with $IrO_2{\cdot}nH_2O$ was quenched, with the major component having a lifetime of 46.7 ps (70.4%), and minor components with lifetimes of 316.9 ps (18.6%), 1.81 ns (9.1%), and 7.09 ns (1.9%). These results suggest that different populations of porphyrin molecules in the material experience different interactions with the $IrO_2{\cdot}nH_2O$. The dominant short fluorescence lifetime component implies a significant interaction between the porphyrin and the $IrO_2{\cdot}nH_2O$ particle. Quenching by energy transfer, electron transfer, enhanced intersystem crossing, or some combination of these is possible; the exact mechanism has not been assigned. Fortunately, the porphyrin excited state is not quenched to the point that the

Can. J. Chem. Downloaded from www.nrcresearchpress.com by University of Electronic and Science Techonology of China on 09/18/12
For personal use only.

Fig. 5. Cyclic voltammograms of (*a*) porphyrin **1** and (*b*) porphyrin **2**. Voltammograms were taken with a platinum working electrode in benzonitrile with 0.1 mol L^{-1} tetrabutylammonium hexafluorophosphate, at a scan rate of 100 mV s^{-1}.

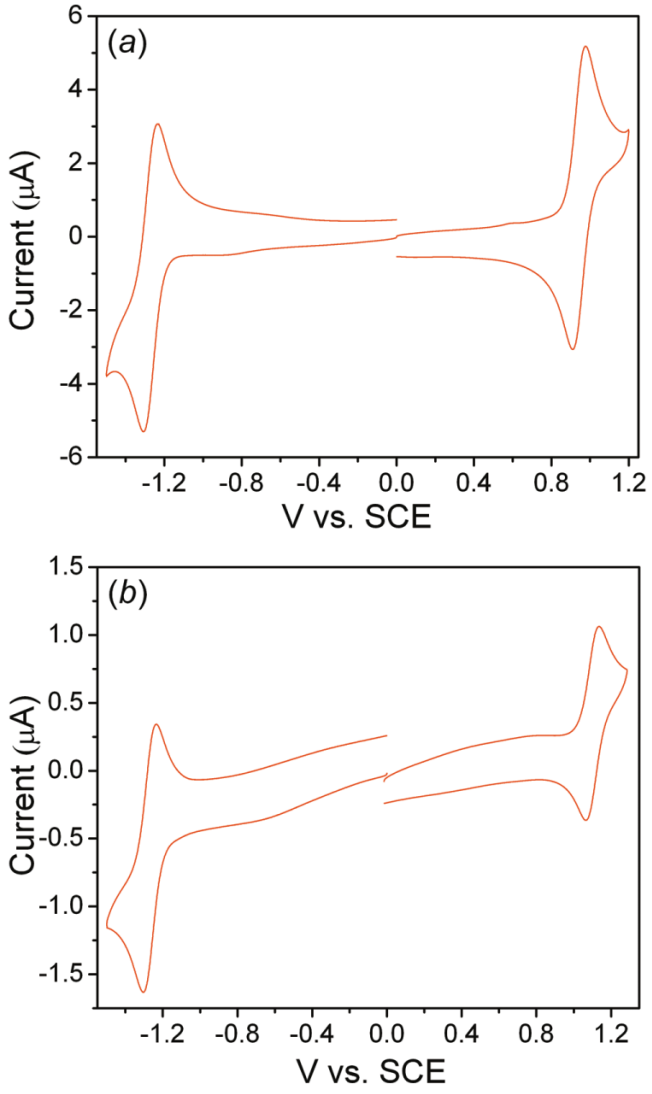

Table 1. Electrochemical potentials for **1** and **2**.

	1st oxidation		1st reduction	
Porphyrin	V vs. SCE	ΔE_p (mV)	V vs. SCE	ΔE_p (mV)
1	0.94	67	–1.28	75
2	1.10	72	–1.28	71

Note: ΔE_p, difference between anodic and cathodic peak potentials of the corresponding process from the cyclic voltammogram. Scan rate, 100 mV s^{-1}.

quantum yield of electron injection into a nanostructured Ti or Sn oxide would be expected to be limited.

In these photoanodes, the driving force for electron transfer from the $IrO_2 \cdot nH_2O$ catalyst to the sensitizer is provided by the electrochemical potential for the reduction of the porphyrin radical cation. Figure 5 shows cyclic voltammograms of free base porphyrin **1** and its Pd analog **2**. As seen in Table 1, the addition of Pd increases the potential by ~160 mV. Having these two sensitizers available will facilitate mechanistic studies designed to determine the yield-limiting steps in the photooxidation of water.

Conclusion

We report the use of a high-potential, porphyrin-based stabilizer in the formation of $IrO_2 \cdot nH_2O$ colloidal particles and have demonstrated catalytic electrochemical water oxidation by this complex. The porphyrin was designed to incorporate dicarboxylic acid groups at each of the four meso positions, as such groups are known to interact favorably with the $IrO_2 \cdot nH_2O$ surface.[10] This work is a step towards the synthesis of a high-potential porphyrin carrying the appropriate moieties, namely *para*-malonate and phosphonate groups on the porphyrin ring, to allow formation of the catalytic complex and then its subsequent adsorption to a transparent conductive electrode. This construct will be the photoanode of a porphyrin-based analogue of the $Ru(II)(bpy)_3$-based water-splitting photoelectrochemical cells that have previously been reported by us[9] as well as by others.[15]

Acknowledgments

This work is supported as part of the Center for Bio-Inspired Solar Fuel Production, an Energy Frontier Research Center funded by the US Department of Energy, Office of Science, Office of Basic Energy Sciences under Award Number DE-SC0001016, and by the Office of Basic Energy Sciences, Division of Chemical Sciences, Geosciences, and Energy Biosciences, Department of Energy under contract DE-FG02-07ER15911. B.D.S. thanks Science Foundation Arizona for their support in this work through a graduate research fellowship.

References

(1) Harriman, A.; Thomas, J. M. *New J. Chem.* **1987**, *11* (11–12), 757.
(2) Harriman, A.; Pickering, I. J.; Thomas, J. M.; Christensen, P. A. *J. Chem. Soc., Faraday Trans.* **1988**, *84* (8), 2795. doi:10.1039/f19888402795.
(3) Nahor, G. A.; Neta, P.; Hambright, P.; Thompson, A. N.; Harriman, A. *J. Phys. Chem.* **1989**, *93* (16), 6181. doi:10.1021/j100353a044.
(4) Petit, M. A.; Plichon, V. *J. Electroanal. Chem.* **1998**, *444* (2), 247. doi:10.1016/S0022-0728(97)00570-6.
(5) Yagi, M.; Tomita, E.; Sakita, S.; Kuwabara, T.; Nagai, K. *J. Phys. Chem. B* **2005**, *109* (46), 21489. doi:10.1021/jp0550208.
(6) Kuwabara, T.; Tomita, E.; Sakita, S.; Hasegawa, D.; Sone, K.; Yagi, M. *J. Phys. Chem. C* **2008**, *112* (10), 3774. doi:10.1021/jp7098416.
(7) Nakagawa, T.; Beasley, C. A.; Murray, R. W. *J. Phys. Chem. C* **2009**, *113* (30), 12958. doi:10.1021/jp9060076.
(8) Nakagawa, T.; Bjorge, N. S.; Murray, R. W. *J. Am. Chem. Soc.* **2009**, *131* (43), 15578. doi:10.1021/ja9063298.
(9) Youngblood, W. J.; Lee, S. A.; Kobayashi, Y.; Hernandez-Pagan, E. A.; Hoertz, P. G.; Moore, T.; Moore, A. L.; Gust, D.; Mallouk, T. E. *J. Am. Chem. Soc.* **2009**, *131* (3), 926. doi:10.1021/ja809108y.
(10) Hoertz, P. G.; Kim, Y.; Youngblood, W. J.; Mallouk, T. E. *J. Phys. Chem. B* **2007**, *111* (24), 6845. doi:10.1021/jp070735r.

(11) Wen, L. Q.; Li, M.; Schlenoff, J. B. *J. Am. Chem. Soc.* **1997**, *119* (33), 7726. doi:10.1021/ja970612s.
(12) Yokomatsu, T.; Minowa, T.; Murano, T.; Shibuya, S. *Tetrahedron* **1998**, *54* (32), 9341. doi:10.1016/S0040-4020(98)00586-9.
(13) Scalise, I.; Durantini, E. N. *J. Photochem. Photobiol., A* **2004**, *162* (1), 105. doi:10.1016/S1010-6030(03)00317-4.
(14) Guldi, D. M.; Zilbermann, I.; Anderson, G.; Li, A.; Balbinot, D.; Jux, N.; Hatzimarinaki, M.; Hirsch, A.; Prato, M. *Chem. Commun. (Camb.)* **2004**, (6): 726. doi:10.1039/b400027g.
(15) Brimblecombe, R.; Koo, A.; Dismukes, G. C.; Swiegers, G. F.; Spiccia, L. *J. Am. Chem. Soc.* **2010**, *132* (9), 2892. doi:10.1021/ja910055a.

Can. J. Chem. Downloaded from www.nrcresearchpress.com by University of Electronic and Science Techonology of China on 09/18/12
For personal use only.

Dye-sensitized solar cells made of titania nanoparticles structured into a mesoporous material

Carmela Aprile, Laura Teruel, Mercedes Alvaro, and Hermenegildo García

Abstract: Using cetyltrimethylammonium bromide as the structure-directing agent, titania nanoparticles (3–5 nm) were organized into a mesoporous material (8.6 nm average pore size and 99 m^2/g). The textural and spatial structuring of the mesoporous material were studied by isothermal gas adsorption, X-ray diffraction, and transmission electron microscopy. Dye-sensitized solar cells using mesoporous material exhibit a one order of magnitude increase in the overall efficiency with respect to analogous cells prepared using the same nanoparticles without periodic mesoporous material. This photovoltaic enhancement is due to increased adsorption of the dye (ruthenium polypyridyl N719) to the mesoporous material arising from the larger area of this mesoporous solid with respect to the same unstructured nanoparticles.

Key words: dye-sensitized solar cells, semiconductors, Pluronic as structure-directing agent, spatial ordering of titania nanoparticles, N719 dye.

Résumé : Utilisant le bromure de cétyltriméthylammonium comme agent dirigeant la structure, il a été possible d'organiser des nanoparticules (3–5 nm) de dioxyde de titane en un matériau mésoporeux (taille moyenne des pores de 8,6 nm et 99 m^2/g). On a étudié la structure texturale et spatiale du matériau mésoporeux par adsorption gazeuse isotherme, diffraction des rayons-X et microscopie électronique à transmission. L'efficacité globale de cellules solaires sensibilisées par un colorant et comportant de ce matériel mésoporeux donnent lieu à une augmentation d'un ordre de grandeur par rapport à des cellules analogues préparées utilisant les mêmes nanoparticules sans matériau mésoporeux périodique. Cette hausse photovoltaïque est due à une augmentation de l'adsorption du colorant (polypyridyl ruthénium N719) du matériau mésoporeux provenant de la plus grande surface du ce solide mésoporeux par rapport aux mêmes nanoparticules non structurées.

Mots-clés : cellules solaires sensibilisées par un colorant, Pluronic comme agent directeur de la structure, ordonnance spatiale de nanoparticules de dioxyde de titane, colorant N719.

[Traduit par la Rédaction]

Introduction

The dye-sensitized solar cell (DSSC) based on titanium dioxide is a topic of much current interest.[1,2] In this type of photovoltaic device, light in the visible region is absorbed by the dye, which upon excitation injects one electron into the semiconductor conduction band, leading to charge separation. The electron in the semiconductor conduction band goes through the external circuit to the metal cathode (typically a platinized electrode) and is transported by the electrolyte redox couple (typically I^-/I_3^-) to the positive hole of the dye. In this type of DSSC, the use of a layer of nanoparticulated titania (about 10 nm size) to construct the solar cell was a breakthrough in this area in the 1990s.[2] Because of the pivotal role played by titania, there is continued interest in producing new forms of this material that eventually can lead to improved photovoltaic activity.[2]

The preparation by Mobil researchers of mesoporous silicas, such as MCM-41 (Mobil Corporate Material Number 41), with remarkable spatial periodicity and strict uniformity of pore size in the nanometre scale was a significant contribution to material science.[3] Mesoporous silicas rank at the top of the list of large surface area solids, possessing high pore volumes and being able to adsorb large quantities of guests compared with amorphous or microporous silicas.[4] Since the initial reports describing the preparation of mesoporous silicas, there has been an interest in expanding these results to other metal oxides besides silica.[5] Preparation of periodic mesoporous oxides is a topic that has been extensively reviewed.[6–10] Given its photovoltaic and photocatalytic activity, titanium dioxide is one metal oxide that will benefit from being prepared with a large surface area and pore volume.[11–15] Thus, starting from compounds containing a single titanium atom, such as $Ti(OiPr)_4$, the synthesis of periodic mesoporous titania has been attempted using commercial amphiphilic polymer Pluronic 123 as the structure-directing agent to produce the spatial ordering in the nanometre length scale.[12–15]

Received 17 March 2010. Accepted 9 July 2010. Published on the NRC Research Press Web site at canjchem.nrc.ca on 20 January 2011.

This article is part of a Special Issue dedicated to Professor J. C. Scaiano.

C. Aprile, L. Teruel, M. Alvaro, and H. García.[1] Instituto de Tecnología Química CSIC-UPV, Universidad Politécnica de Valencia, 46022 Valencia, Spain.

[1]Corresponding author (e-mail: hgarcia@qim.upv.es).

Can. J. Chem. Downloaded from www.nrcresearchpress.com by University of Electronic and Science Techonology of China on 09/18/12
For personal use only.

Can. J. Chem. Downloaded from www.nrcresearchpress.com by University of Electronic and Science Techonology of China on 09/18/12
For personal use only.

One of the general problems encountered in mesoporous materials obtained from molecular precursors is the lack of structural stability upon removal of the structure-directing agent, leading to collapse of the material.[6,16] This instability is generally attributed to the thin walls constituted by a few metal–oxygen bonds. Moreover, in the particular case of titanium dioxide, most of the attempts to prepare periodic mesoporous materials from molecular compounds having a single Ti atom have led to the formation of nanoparticulated materials with a variable degree of ordering and porosity. One way in which this instability has been circumvented is by pyrolizing the organic template inside the mesopores instead of removing it.[17] The hard carbonaceous residue inside the channels produces remarkable stability, thereby preventing the collapse of the structure.[17] However, a disadvantage of this strategy for increasing the structural stability is that the pore volume is notably reduced and incorporation of dye molecules inside the mesopores is impeded by the remaining carbon.

Recently, we and others have reported the preparation of periodic mesoporous titania using small nanoparticles rather than molecular precursors as building blocks and have observed remarkable photocatalytic properties.[11,18] The advantage of using nanoparticles as building blocks to construct the material instead of condensing molecules of a single titanium atom is the robustness of the structure. It has been shown for related mesoporous metal oxides constituted by the corresponding nanoparticles that the mesoporosity can resist steaming for long periods.[19] Similar steaming treatment with much shorter time and milder conditions will produce the complete collapse of mesoporous solids synthesized from molecular precursors. In addition, the empty pore volume allows adsorption of a large dye loading that is crucial to reach high efficiencies of the photovoltaic cell.

In this context, we report the spatial structuring of small titania nanoparticles (3–5 nm) (pre-TiO_2) in the micrometric length using cetyltrimethylammonium bromide (CTABr) as the structure-directing agent, forming a mesoporous material with some spatial structuring (mp-TiO_2), as determined by isothermal gas adsorption and transmission electron microscopy (TEM) images. The use of mp-TiO_2 leads to a one order of magnitude increase in the current density of DSSCs as compared with identical cells prepared with the unstructured precursor TiO_2 nanoparticles (pre-TiO_2). There are some precedents in the literature showing that spatial structuring of the photoactive titania layer or the use of structured mesoporous titania is beneficial for the efficiency of the resulting solar cells.[17,20–26] The main contribution of our work is to show that the origin of this remarkable enhancement is the larger amount of adsorbed sensitizing dye as compared with pre-TiO_2. This higher dye adsorption of mp-TiO_2 as compared with pre-TiO_2 arises from the increase in surface area upon nanoparticle structuring in the micrometric scale forming a mesoporous material.

Experimental methods

Synthesis of mp-TiO_2

In a typical procedure, CTABr was added to a solution of NH_4OH and deionized water, and the solution was stirred for 30 min in a closed polyethylene bottle to form a homogeneous solution. Nanoparticles of TiO_2 suspended in ethanol (20 mL) and the appropriate amount of tetraethyl orthosilicate (TEOS) dissolved in ethanol (5 mL) were mixed and added slowly to the CTABr solution at 50 °C for 2 h. TiO_2 nanoparticles (pre-TiO_2) were prepared by the hydrolysis of titanium isopropoxide in aqueous solution as previously reported.[18] The resulting sample consists of TiO_2 nanoparticles with a size distribution between 3 and 5 nm as determined by TEM, as has been previously reported.[18] The molar ratio of the materials was 1.00:0.12:8.0:114 $X : CTABr : NH_3$ (20%) : H_2O, where X corresponds to the sum of the Ti and Si atoms. The Ti:Si atomic ratio was 99:1. The mixture was stirred at 50 °C for 1 h. Then the resulting gel was heated at 100 °C in static conditions for 4 days. The solid obtained was washed thoroughly with water and ethanol and dried at 100 °C for 3 h. The structure-directing agent was removed by calcination using the following temperature program: room temperature, temperature increasing by 3 °C/min, 500 °C for 5 h. Initially the sample was purged with nitrogen (1 mL/min), and after the first 5 h the nitrogen flow was gradually replaced with air to complete surfactant combustion. An analogous preparation procedure in the complete absence of TEOS results in a material with significantly less spatial ordering and mesoporosity, as evidenced by isothermal gas adsorption and TEM.[18]

Fig. 1. Isothermal N_2 adsorption profile measured for mp-TiO_2. The inset shows the estimated pore-size distribution.

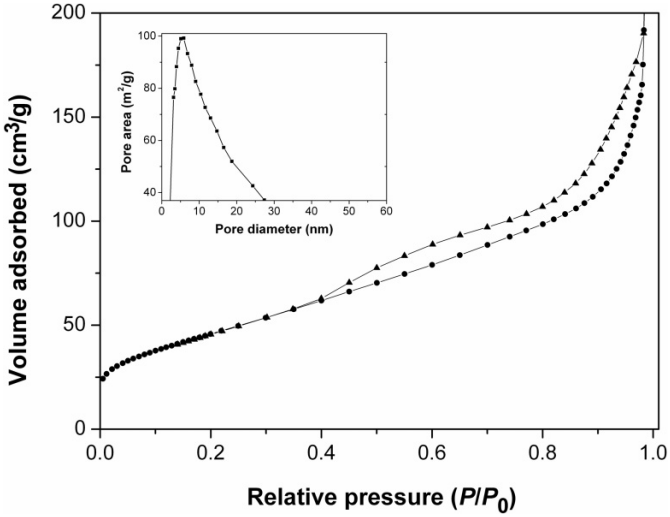

Photovoltaic measurements

DSSCs were prepared according to the literature.[27,28] Thus, pre-TiO_2 or mp-TiO_2 semiconductors (100 mg) were dispersed in an ethylcellulose (6%) – α-terpineol paste. The paste was spread onto freshly cleaned transparent conductive glass (FTO) and the layer was sintered at 450 °C. After cooling to 50 °C, the films were immersed in a 0.3 mmol/L solution of commercial polypyridyl ruthenium complex N719 dye (Solaronix) in a 1:1 CH_3CN–*tert*-butanol mixture for 2 days. The TiO_2 electrodes were assembled with platinized counter electrodes using a separator of adhesive polymer film (Surlyn M). To obtain the I–V curves of cells containing pre-TiO_2 and mp-TiO_2, a thin layer of these ma-

Can. J. Chem. Downloaded from www.nrcresearchpress.com by University of Electronic and Science Techonology of China on 09/18/12
For personal use only.

Fig. 2. Raman spectra (left) and X-ray diffraction pattern (right) of mp-TiO_2 (*a*) and pre-TiO_2 (*b*). The spectra and diffraction patterns coincide with those of the anatase phase.

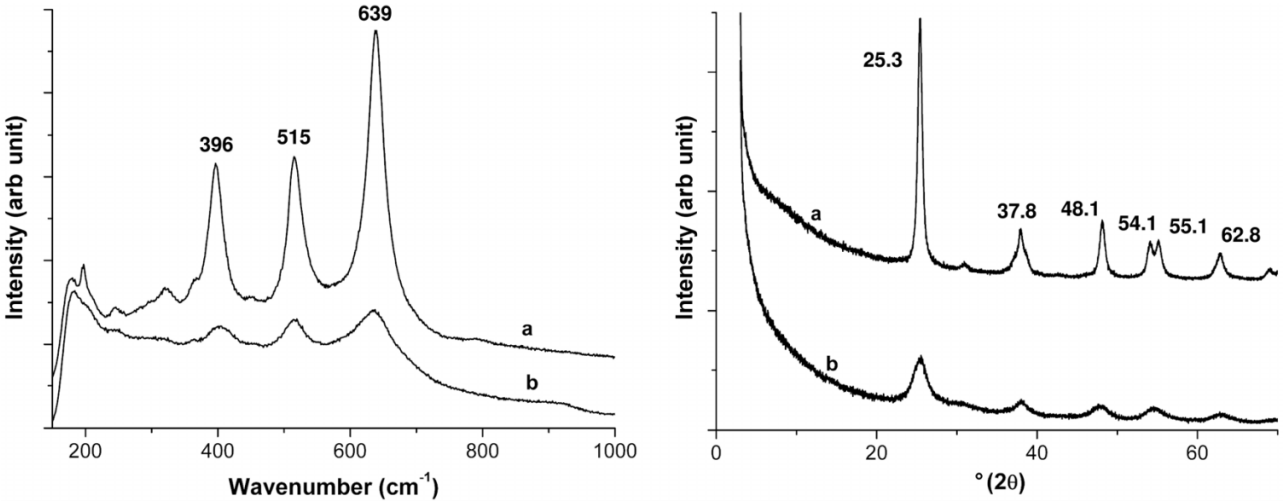

Fig. 3. TEM images of pre-TiO_2 nanoparticles (*a*, dark field) and views parallel (*b*) and perpendicular (*c*) to mp-TiO_2 channels.

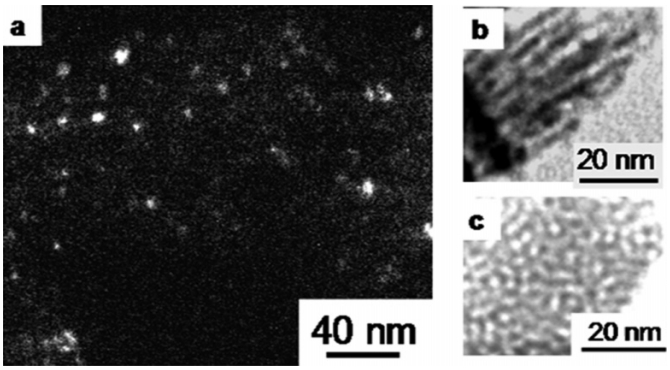

terials was prepared by spreading the semiconductor paste onto a transparent conductive FTO electrode, using the razor blade method. The resulting layer was sintered in an oven at 450 °C for 30 min. The photovoltaic cell was constructed by using the titania layer on FTO as anode and a platinized electrode as cathode and using a solution of 0.5 mol/L lithium iodide, 0.5 mol/L iodine, and 0.4 mol/L *tert*-butylpyridine in acetonitrile as electrolyte. The electrodes (0.6 cm × 0.6 cm) were connected to a potentiostat (Amel) and illuminated with a solar simulator (Oriel) with an AM 1.5G filter. The nominal power for the measurements was 1000 W/m^2.

Results and discussion

The preparation of mp-TiO_2 was undertaken using pre-TiO_2 nanoparticles (3–5 nm size) as building blocks and CTABr as the structure-directing agent in the presence of minimum amounts of TEOS as chemical binder. Under these synthesis conditions, the spatial structuring originated by the CTABr liquid crystal serves to template the mesopores of the solid, whose nanoparticles are bound by strong Si–O bonds from TEOS hydrolysis and co-condensation.[18] Isothermal nitrogen adsorption shows that mp-TiO_2 has mesoporosity with a broad pore size (distribution between 6 and 20 nm) having a maximum at 8.6 nm, and a BET surface area determined according to the Brunauer–Emmett–Teller algorithm[29] of 99 m^2/g was estimated (see inset of Fig. 1). This surface-area value compares favorably with the surface area of pre-TiO_2 (35 m^2/g) and that of conventional P25 TiO_2, which is typically around 45 m^2/g.

The solid was annealed from room temperature to 500 °C at a rate of 3 °C/min. The pre-TiO_2 used as building blocks was also submitted to the same treatment as mp-TiO_2 but in the absence of CTABr. Importantly, the anatase phase of pre-TiO_2 and mp-TiO_2 was established by Raman spectroscopy and X-ray diffraction (Fig. 2). The spectra and diffractograms of both pre-TiO_2 and mp-TiO_2 coincide with those expected for the anatase phase, which are different from those for the amorphous and rutile phases.[18] It is known that the photovoltaic activity of TiO_2 in the anatase phase is higher than that in the rutile phase.[18]

Transmission electron microscopy clearly demonstrates the presence of mesopores and the occurrence of some spatial ordering of mp-TiO_2. Figure 3 presents the TEM dark-field image showing that TiO_2 nanoparticles (small white spots) are well dispersed all over the material with some variation in size, whereas the bright field reveals the mesoporous structure of the material. Thus, the characterization based on isothermal gas adsorption, X-ray diffraction, and TEM images shows that the material consists of small TiO_2, the anatase nanoparticles, with some spatial structuring introduced by the surfactant as template.

Two sets of DSSCs were prepared by the same procedure using pre-TiO_2 or mp-TiO_2 as semiconductor, polypyridyl ruthenium complex N719 as dye, and a solution of 0.5 mol/L lithium iodide, 0.05 mol/L iodine, and 0.4 mol/L *tert*-butylpyridine in acetonitrile as electrolyte. For comparison, an analogous set of DSSCs was also prepared using standard P25 TiO_2 with an average particle size of 30 nm.

The performance of the DSSCs prepared with pre-TiO_2 and mp-TiO_2 was measured for a set of 3 independent cells. A summary of the data obtained is shown in Table 1. Figure 4 shows selected I–V plots from which the data of Table 1 have been obtained. As can be seen there, the voltage at open circuit (V_{OC}) was somewhat higher for mp-TiO_2, but the most remarkable difference is the higher current density

Can. J. Chem. Downloaded from www.nrcresearchpress.com by University of Electronic and Science Techonology of China on 09/18/12
For personal use only.

Table 1. Efficiency of DSSCs based on pre-TiO_2, mp-TiO_2, and P25.

	V_{oc} (V)	J_{sc} (mA/cm^2)	Fill factor	Efficiency (%)	Dye content (mol dye / mg $TiO_2 \times 10^8$)
Pre-TiO_2 (8 μm)	0.57	0.66	0.48	0.18	0.18
Mp-TiO_2 (8 μm)	0.66	4.87	0.52	1.67	3
P25 (18 μm)	0.66	5.53	0.52	1.89	2.4
Mp-TiO_2 (18 μm)	0.69	8.93	0.45	2.77	2.7

Fig. 4. I–V curves of pre-TiO_2 (8 μm) (*a*), mp-TiO_2 (8 μm) (*b*), P25 (18 μm) (*c*), and mp-TiO_2 (18 μm) (*d*).

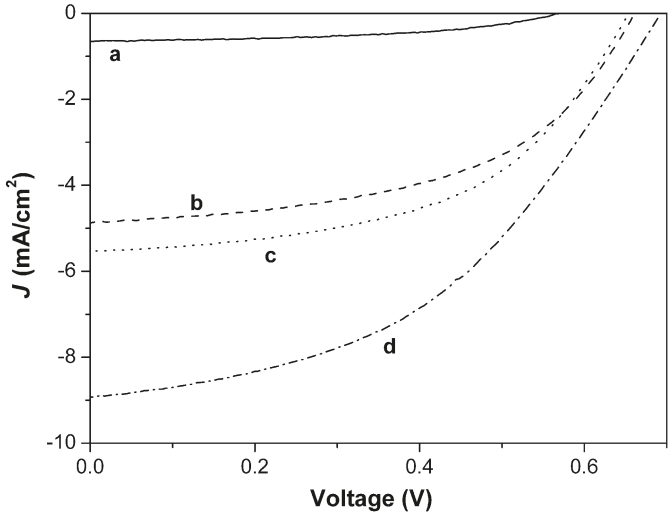

Fig. 5. Photocurrent spectra of solar cells based on pre-TiO_2 (*a*), mp-TiO_2 (*b*), and P25 (*c*).

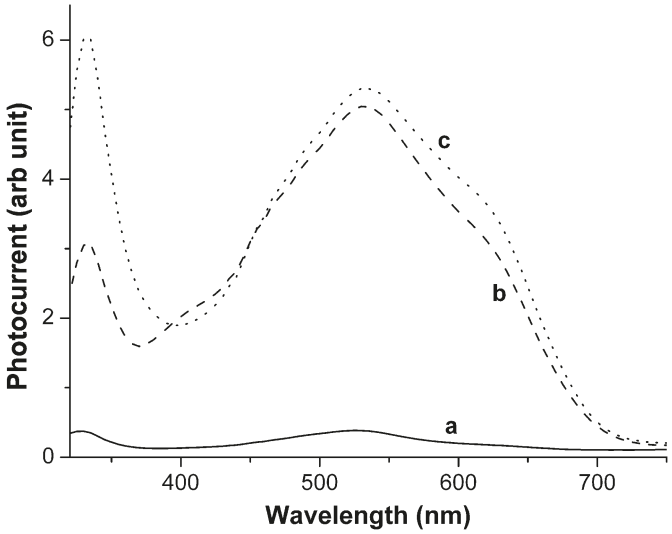

(J_{SC}) for mp-TiO_2 compared with pre-TiO_2. As a result of the higher J_{SC}, the efficiency of DSSCs prepared with mp-TiO_2 is significantly higher than that of DSSCs prepared with pre-TiO_2. As can also be seen in Table 1, the efficiency of the DSSC prepared with mp-TiO_2 is better than that obtained using the P25 TiO_2 standard when films of the same thickness are compared (Table 1). Concerning the efficiency data of Table 1, they are somewhat lower than the typical values previously reported in the literature for DSSCs, which are around 6%.[11,14] However, we notice that the absolute efficiency value strongly depends on the DSSC surface area and preparation conditions.[30] In our case, the DSSC cells were 0.6 cm × 0.6 cm, which is larger than the area of reported cells with higher efficiency.

Table 2. Mass of TiO_2 and dye content of the films in the photovoltaic cells depending on the material.

Material	Thickness (μm)	Mass content of the film (mg/cm^2)	Dye content (mol N719 / cm$^2 \times 10^9$)
Pre-TiO_2	8	0.53	1
Mp-TiO_2	8	0.78	24
P25	18	1.28	30
Mp-TiO_2	18	1.96	54

The data presented in Table 1 were obtained for cells immediately after addition of the electrolyte. No variation in the efficiency parameters was observed for measurements carried out 2 h after preparation. However, probably owing to solvent evaporation, no photovoltaic response was observed when the cells were measured days after preparation.

When comparing DSSCs of mp-TiO_2 and P25 of the same thickness, mp-TiO_2 is more active (Table 1). Comparison of DSSCs of the same thickness should minimize differences arising from light scattering. To confirm the higher efficiency of mp-TiO_2 DSSCs with respect to pre-TiO_2 DSSCs constituted by the same nanoparticles and correlate it with the spatial structuring of the material, we measured the photocurrent spectra of 3 solar cells based on pre-TiO_2, mp-TiO_2, and P25 (Fig. 5). As can be concluded from the plots presented in Fig. 5, and in agreement with the operation of DSSCs, the photocurrent spectra match the absorption spectrum of the dye (N719), indicating that this is the species harvesting light and injecting electrons to the semiconductor conduction band.

Based on this photocurrent spectrum, it becomes apparent that the loading of dye onto the semiconductor surface should be one of the most important parameters controlling the relative efficiency. For this reason, the mass of titania and the amount of N719 dye adsorbed in each cell were determined. Visually, the color intensity of the mp-TiO_2 layers was higher than that of pre-TiO_2 layers. Adsorbed N719 dye was quantified by colorimetry; the dye was desorbed by immersing the layer in diluted aqueous base and the optical density of a given volume of the resulting solution was measured at 530 nm. The dye content is given in Table 2. These data show that the amount of N719 adsorbed on mp-TiO_2 for the same thickness is 24 times higher than that adsorbed on pre-TiO_2. We also noticed that the mass of semiconductor for the same thickness is about 1.5 times higher for mp-TiO_2 than for pre-TiO_2. Both factors, but particularly the much higher dye content, favor the photovoltaic response

Can. J. Chem. Downloaded from www.nrcresearchpress.com by University of Electronic and Science Techonology of China on 09/18/12
For personal use only.

of mp-TiO_2 with respect to that of pre-TiO_2. A similar trend was found when comparing P25 and mp-TiO_2, i.e., higher dye adsorption (1.8 times) and higher mass (1.5 times) for mp-TiO_2 than for P25.

The ability of mp-TiO_2 to adsorb higher amounts of N719 is a reflection of its larger surface area (99 m^2/g) as result of the spatial structuring with respect to pre-TiO_2 (35 m^2/g). The high adsorption capacity of periodic mesoporous metal oxides compared with amorphous materials is well documented.[3] It has to be noted that the higher dye adsorption capacity of mp-TiO_2 is inherent to its mesoporous ordering and its total surface area. In other words, at the same thickness the amount of dye adsorbed by mp-TiO_2 has to be higher than that adsorbed by P25.

It is also noteworthy that structuring increases the mass density of mp-TiO_2 films compared with pre-TiO_2 and even P25 TiO_2 films. This higher density must be related to the morphology of the particles and the way in which these particles are packed. Apparently better loose-particle packing is achieved using small (pre-TiO_2) or medium-sized (P25) nanoparticles rather than mp-TiO_2.

In summary, by structuring titania nanoparticles in a mesoporous solid, the resulting material possesses higher pore volume and greater surface area than the nanoparticulated unstructured precursor. This high surface area plays a positive role, adsorbing significantly larger amounts of the photosensitizing dye. The result of this high adsorption capacity is an enhancement of the current density of DSSCs of about one order of magnitude. This result illustrates the advantages of high surface area titania for enhancing the efficiency of DSSCs.

Acknowledgements

Financial support by the Spanish DGI (CTQ2009-11586) is gratefully acknowledged. C. A. thanks the Spanish Ministry of Education for a Juan de la Cierva research associate contract.

References

(1) Gratzel, M. *J. Photochem. Photobiol. Chem.* **2003**, *4* (2), 145. doi:10.1016/S1389-5567(03)00026-1.
(2) Gratzel, M. *Cur. Opin. Coll. Interf. Sci.* **1999**, *4* (4), 314. doi:10.1016/S1359-0294(99)90013-4.
(3) Kresge, C. T.; Leonowicz, M. E.; Roth, W. J.; Vartuli, J. C.; Beck, J. S. *Nature* **1992**, *359* (6397), 710. doi:10.1038/359710a0.
(4) Corma, A. *Chem. Rev.* **1997**, *97* (6), 2373. doi:10.1021/cr960406n.
(5) Soler-Illia, G. J. D.; Sanchez, C.; Lebeau, B.; Patarin, J. *Chem. Rev.* **2002**, *102* (11), 4093. doi:10.1021/cr0200062.
(6) Ryoo, R.; Jun, S. *J. Phys. Chem. B* **1997**, *101* (3), 317. doi:10.1021/jp962500d.
(7) Yang, Q. H.; Li, Y.; Zhang, L.; Yang, J.; Liu, J.; Li, C. *J. Phys. Chem. B* **2004**, *108* (23), 7934. doi:10.1021/jp040124o.
(8) Kondo, J. N.; Domen, K. *Chem. Mater.* **2008**, *20* (3), 835. doi:10.1021/cm702176m.
(9) Llusar, M.; Sanchez, C. *Chem. Mater.* **2008**, *20* (3), 782. doi:10.1021/cm702141e.
(10) Tiemann, M. *Chem. Mater.* **2008**, *20* (3), 961. doi:10.1021/cm702050s.
(11) Kartini, I.; Menzies, D.; Blake, D.; da Costa, J. C. D.; Meredith, P.; Riches, J. D.; Lu, G. Q. *J. Mater. Chem.* **2004**, *14* (19), 2917. doi:10.1039/b406286h.
(12) Choi, S. Y.; Lee, B.; Carew, D. B.; Mamak, M.; Peiris, F. C.; Speakman, S.; Chopra, N.; Ozin, G. A. *Adv. Funct. Mater.* **2006**, *16* (13), 1731. doi:10.1002/adfm.200500507.
(13) Malfatti, L.; Falcaro, P.; Amenitsch, H.; Caramori, S.; Argazzi, R.; Bignozzi, C. A.; Enzo, S.; Maggini, M.; Innocenzi, P. *Microp. Mesop. Mater.* **2006**, *88* (1–3), 304. doi:10.1016/j.micromeso.2005.09.027.
(14) Ngamsinlapasathian, S.; Pavasupree, S.; Suzuki, Y.; Yoshikawa, S. *Sol. Energy Mater. Sol. Cells* **2006**, *90* (18–19), 3187. doi:10.1016/j.solmat.2006.06.021.
(15) Zukalová, M.; Zukal, A.; Kavan, L.; Nazeeruddin, M. K.; Liska, P.; Gratzel, M. *Nano Lett.* **2005**, *5* (9), 1789. doi:10.1021/nl0514011.
(16) Wang, H.; Liu, Y.; Pinnavaia, T. J. *J. Phys. Chem. B* **2006**, *110* (10), 4524. doi:10.1021/jp056688p.
(17) Lee, J.; Orilall, M. C.; Warren, S. C.; Kamperman, M.; DiSalvo, F. J.; Wiesner, U. *Nat. Mater.* **2008**, *7* (3), 222. doi:10.1038/nmat2111.
(18) Alvaro, M.; Aprile, C.; Benitez, M.; Carbonell, E.; Garcia, H. *J. Phys. Chem. B* **2006**, *110* (13), 6661. doi:10.1021/jp0573240.
(19) Alvaro, M.; Aprile, C.; Garcia, H.; Gomez-Garcia, C. J. *Adv. Funct. Mater.* **2006**, *16* (12), 1543. doi:10.1002/adfm.200500766.
(20) Aprile, C.; Corma, A.; Garcia, H. *Phys. Chem. Chem. Phys.* **2008**, *10* (6), 769. doi:10.1039/b712168g.
(21) Kim, Y. J.; Lee, Y. H.; Lee, M. H.; Kim, H. J.; Pan, J. H.; Lim, G. I.; Choi, Y. S.; Kim, K.; Park, N. G.; Lee, C.; Lee, W. I. *Langmuir* **2008**, *24* (22), 13225. doi:10.1021/la802340g.
(22) Liu, Z. F.; Li, Y. J.; Zhao, Z. G.; Cui, Y.; Hara, K.; Miyauchi, M. J. *Mater. Chem.* **2010**, *20*, 492.
(23) Nedelcu, M.; Lee, J.; Crossland, E. J. W.; Warren, S. C.; Orilall, M. C.; Guldin, S.; Huttner, S.; Ducati, C.; Eder, D.; Wiesner, U.; Steiner, U.; Snaith, H. J. *Soft Matter* **2009**, *5* (1), 134. doi:10.1039/b815166k.
(24) Yoon, J. H.; Jang, S. R.; Vittal, R.; Lee, J.; Kim, K. J. *J. Photochem. Photobiol. Chem.* **2006**, *180* (1–2), 184. doi:10.1016/j.jphotochem.2005.10.013.
(25) Yue, W. B.; Randorn, C.; Attidekou, P. S.; Su, Z. X.; Irvine, J. T. S.; Zhou, W. Z. *Adv. Funct. Mater.* **2009**, *19* (17), 2826. doi:10.1002/adfm.200900658.
(26) Yue, W. B.; Xu, X. X.; Irvine, J. T. S.; Attidekou, P. S.; Liu, C.; He, H. Y.; Zhao, D. Y.; Zhou, W. Z. *Chem. Mater.* **2009**, *21* (12), 2540. doi:10.1021/cm900197p.
(27) Nazeeruddin, M. K.; Bessho, T.; Cevey, L.; Ito, S.; Klein, C.; De Angelis, F.; Fantacci, S.; Comte, P.; Liska, P.; Imai, H.; Graetzel, M. *J. Photochem. Photobiol. Chem.* **2007**, *185* (2-3), 331. doi:10.1016/j.jphotochem.2006.06.028.
(28) Nazeeruddin, M. K.; Splivallo, R.; Liska, P.; Comte, P.; Grätzel, M. *Chem. Commun.* **2003**, (12), 1456. doi:10.1039/b302566g.
(29) Brunauer, S.; Emmett, P. H.; Teller, E. *J. Am. Chem. Soc.* **1938**, *60* (2), 309. doi:10.1021/ja01269a023.
(30) Lee, W. J.; Ramasamy, E.; Lee, D. Y. *Sol. Energy Mater. Sol. Cells* **2009**, *93* (8), 1448. doi:10.1016/j.solmat.2009.03.002.

Fluorescence studies of a series of monodisperse telechelic α,ω-dipyrenyl poly(*N*-isopropylacrylamide)s in ethanol and in water

Jamie Yip, Jean Duhamel, Xing Ping Qiu, and Françoise M. Winnik

Abstract: Steady-state and time-resolved fluorescence measurements were performed on solutions in ethanol and in water (23 °C) of a series of poly(*N*-isopropylacrylamide)s labeled with a pyrenyl group at each chain end (Py_2-PNIPAM) and ranging in molecular weight (M_n) from 5 900 to 44 500 g·mol^{-1}. Water and ethanol are of similar solvent quality towards the PNIPAM chain. The pyrene labels, in contrast, are soluble in ethanol but not in water. The efficiency of excimer formation for Py_2-PNIPAM samples in ethanol decreased with increasing chain length, a trend typical of pyrene end-labeled polymers in good solvents. The ratio I_E/I_M, where I_E is the Py excimer emission intensity and I_M is the Py monomer emission intensity, scaled as $M_n^{-1.4}$, where M_n is the number-average molecular weight of the sample. The kinetics of excimer formation were more complex for aqueous Py_2-PNIPAM solutions, as a consequence of pyrene–pyrene association prior to excitation. The excimer time-dependent profiles exhibited significantly faster rise times, compared with the situation in ethanol, and they could not be fitted with the traditional Birks scheme. The results are discussed in the context of the solution properties of telechelic amphiphilic PNIPAMs and are compared with data gathered previously in studies of dipyrenyl end-labeled poly(ethylene oxides), the only other polymers soluble in water and organic solvents subjected to similar studies in the past.

Key words: telechelic amphiphilic poly(*N*-isopropylacrylamide), pyrene excimer, time-resolved fluorescence spectroscopy, polymer cyclization dynamics.

Résumé : On a mesuré la fluorescence à l'état stationnaire et résolue en fonction du temps, de solutions dans l'éthanol ou dans l'eau, à 23 °C, d'une série de poly(*N*-isopropylacrylamides) marqués par un groupe pyrényle aux deux extrémités des chaînes (Py_2-PNIPAM) et dont les poids moléculaires (M_n) varient de 5 900 à 44 500 g·mol^{-1}. Les qualités de l'eau et de l'éthanol vis-à-vis des chaînes de PNIPAM sont semblables. Toutefois, le pyrène utilisé comme marqueur est soluble dans l'éthanol, mais pas dans l'eau. L'efficacité de la formation de l'excimère pour les échantillons de Py_2-PNIPAM dans l'éthanol diminue avec une augmentation de la longueur de la chaîne, une tendance typique dans les bons solvants pour les polymères marqués aux extrémités avec des pyrènes. Le rapport I_E/I_M dans lequel I_E est l'intensité de l'émission de l'excimère Py et I_M est l'intensité de l'émission du monomère Py, a une pente de $M_n^{-1.4}$, M_n étant la valeur moyenne du poids moléculaire de l'échantillon. En raison de l'association pyrène–pyrène avant l'excitation, la cinétique de la formation de l'excimère est plus complexe pour les solutions aqueuses de Py_2-PNIPAM. Par rapport à ce qui est observé dans l'éthanol, les profils de l'excimère en fonction du temps présentent des temps de croissance qui sont beaucoup plus rapides et ils n'ont pas pu être ajustés au schéma traditionnel de Birks. On discute des résultats dans le contexte des propriétés en solution des PNIPAM amphiphiles téléchéliques et on les compare aux données accumulées antérieurement dans les études de poly(oxydes d'éthylène) marqués aux extrémités par des groupes dipyrényles, les seuls autres polymères solubles dans l'eau et les solvants organiques à avoir été soumis à des études semblables dans le passé.

Mots-clés : poly(*N*-isopropylacrylamide) amphiphile et téléchélique, excimère pyrène, spectroscopie de fluorescence résolue en fonction du temps, dynamique de la cyclisation d'un polymère.

[Traduit par la Rédaction]

Introduction

Some 35 years ago, studies of the end-to-end cyclization of polymer chains were of considerable interest, since they shed light onto fundamental aspects of processes such as the synthesis of cyclic polymers, the cyclization of DNA, and the dynamics of chains in solution. An important breakthrough was achieved in the early 1980s when theoretical

Received 31 May 2010. Accepted 9 July 2010. Published on the NRC Research Press Web site at canjchem.nrc.ca on 22 January 2011.

This article is part of a Special Issue dedicated to Professor J. C. Scaiano.

J. Yip and J. Duhamel. Institute for Polymer Research, Department of Chemistry, University of Waterloo, Waterloo, ON N2L 3G1, Canada.
X.P. Qiu and F.M. Winnik.[1] Faculty of Pharmacy and Department of Chemistry, Université de Montréal, CP 6128 Succursale Centre Ville, Montréal, QC H3C 3J7, Canada.

[1]Corresponding author (e-mail: Francoise.winnik@umontreal.ca).

Can. J. Chem. Downloaded from www.nrcresearchpress.com by University of Electronic and Science Techonology of China on 09/18/12
For personal use only.

Can. J. Chem. Downloaded from www.nrcresearchpress.com by University of Electronic and Science Techonology of China on 09/18/12
For personal use only.

predictions[1,2] and experimental observations[3,4] indicated that the end-to-end cyclization process can be probed by two pyrenyl moieties covalently attached to the ends of a monodisperse polymer and is described under these conditions by a single rate constant (k_{cy}). The experiment is straightforward: one pyrene chromophore is excited and its emission is monitored as it encounters a ground-state pyrene to form an excimer.[5] The extreme sensitivity of fluorescence allows one to conduct such experiments with solutions with concentrations usually low enough to ensure that no intermolecular interactions take place, so that the fluorescence signal being detected reports solely on processes that occur intramolecularly.[6–18] The rate constant of excimer formation is a measure of k_{cy}, which in turn provides information about the long-range polymer chain dynamics and as such is a measure of the flexibility of a given chain.

The most complete set of information about the rate constant k_{cy} has been obtained for a series of pyrene-labeled monodisperse polystyrenes, which were synthesized by anionic polymerization.[6] Other backbones that have been investigated include polytetrahydrofuran,[7] polydimethylsiloxane,[8–10] poly(ε-caprolactone),[11] polycarbonates,[12,13] and poly(ethylene oxide) (PEO).[14–18] The latter studies stand out, as PEO is the only polymer in the list that is soluble in organic solvents and also in water. Since the pyrene label is soluble in organic solvents, its presence at the ends of the chain does not significantly affect the properties of the polymer in organic solvents and, consequently, Py_2-PEO displays the typical kinetics expected for excimer formation via the diffusive encounters of two pyrenyl (Py) moieties in organic solvents.[14–18] Pyrene groups, however, are poorly soluble in water and their incorporation on PEO chain ends has profound effects on the properties of the polymer and on the kinetics of end-to-end cyclization. The photophysical properties of pyrene are also affected by its confinement in an aqueous environment.[16,18–22] For instance, a substantial fraction of the excimer is formed instantaneously through direct excitation of ground-state pyrene aggregates, which are stabilized by the water-soluble PEO backbone. Nonetheless, given that end-to-end cyclization is described by a single rate constant, it has been possible to derive kinetic models that follow relatively well the process of excimer formation in aqueous solutions of Py_2-PEO and also account for the presence of pyrene ground-state dimers.[16,18–23]

Our research interests have focused on poly(*N*-isopropylacrylamide) (PNIPAM), which, like PEO, is a nonionic polymer soluble in organic solvents and in water at room temperature. The two polymers share a number of properties and have often been compared with regard to their interactions with surfactants[24,25] and with proteins.[26] But in some important thermal and conformational properties, they differ markedly from each other. For instance, the lower critical solution temperatures (LCSTs) of aqueous PEO solutions show a strong molecular-weight dependence, while the LCST of PNIPAM is almost independent of the molecular weight, exhibiting very flat cloud point lines. Also, from molecular dynamics simulations, PEO chains are inferred to adopt a loose helical form (11/2 helix), and the size of each turn is such that it can accommodate one water molecule linked to the chain via hydrogen bonds. In contrast, PNIPAM chains in water are partially collapsed by the association of hydrophobic isopropyl groups. One may expect, therefore, differences in the end-to-end cyclization dynamics of PNIPAM and PEO in water and in organic solvents. The objective of the work reported here was to investigate the fluorescence properties of α,ω-dipyrenyl-PNIPAM in ethanol and in water to assess the cyclization dynamics of PNIPAM in the two solvents and to compare them with those of PEO in the same solvents, using data previously reported for Py_2-PEO.

Recent advances in controlled radical polymerization have led to the development of synthetic protocols for the preparation of monodisperse polymers bearing reactive groups at their ends,[27] creating entries into families of polymers soluble in water and (or) organic solvents carrying a fluorescent tag at one or both chain ends. Several examples can be found in the literature where PNIPAM prepared by living radical polymerization has been labeled with a pyrenyl group at one[28–31] or both chain ends.[32] Using a procedure similar to previously reported syntheses, we prepared Py_2-PNIPAMs ranging in number-average molecular weight (M_n) from 6 000 to 45 000 g·mol^{-1} and evaluated the steady-state and time-resolved fluorescence properties of the polymers in ethanol and in water. This study of the kinetics of excimer formation of monodisperse dipyrenyl end-labeled PNIPAM is the first new example, in addition to studies of Py_2-PEO, that provides the opportunity to compare the photophysics of identical pyrene-tethered chains in water and an organic solvent. Conversely, it allows one to gain further insight into the properties of amphiphilic telechelic PEOs and PNIPAMs, which have been compared and contrasted on the basis of scattering and rheology measurements that probe different length scales than the pyrene excimer.

Experimental

Materials

All chemicals were purchased from Sigma-Aldrich Chemicals Co. unless otherwise specified. *N*-Isopropylacrylamide (NIPAM, 99%) was obtained from Acros Organics and recrystallized from an acetone–hexanes (4:6, *v*/*v*) mixture. Acryloyl chloride (97%), sodium bicarbonate ($NaHCO_3$, 99.5%), anhydrous sodium sulfate (Na_2SO_4, 99.0%), and triethylamine (99.5%) were used as received. Dimethyl sulfoxide (DMSO, 99.9%) was used without purification. 1,4-Dioxane and tetrahydrofuran (THF) were purified by a solvent purification system with two packed columns of activated alumina provided by Innovative Technology Inc. 4-(1-Pyrenyl)butyl iodide was synthesized as described earlier.[28] All other solvents were of reagent grade and used as received. Water was deionized using a Millipore MilliQ system. Ethanol (Fisher Scientific, HPLC grade) was used as received.

Preparation of α,ω-dipyrenyl poly(*N*-isopropylacrylamide)

The polymer was prepared by a two-step end group transformation procedure, starting from a precursor telechelic polymer, α,ω-diisobutylsulfanylthiocarbonylsulfanyl poly(*N*-isopropylacrylamide) (iBS_2-PNIPAM),[27] prepared according to a previously reported procedure (Fig. 1).[32] In the first

Can. J. Chem. Downloaded from www.nrcresearchpress.com by University of Electronic and Science Techonology of China on 09/18/12
For personal use only.

Fig. 1. Synthetic scheme of telechelic α,ω-dipyrenyl poly(*N*-isopropylacrylamide).

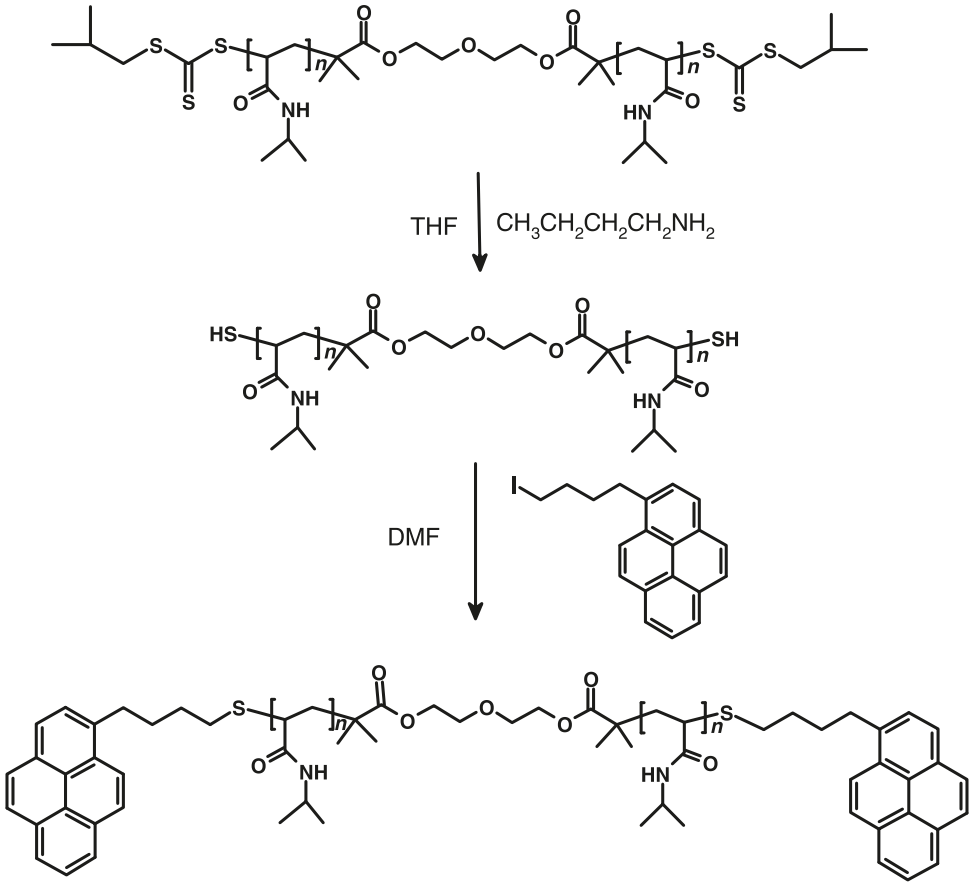

step, the precursor polymer, iBS_2-PNIPAM, was aminolyzed by *n*-butylamine (10-fold molar excess with respect to the thiocarbonylthio moiety) in THF to generate α,ω-dimercapto PNIPAM (HS_2-PNIPAM). In the second step, HS_2-PNIPAM was reacted with 4-(1-pyrenyl)butyl iodide (1.5-fold molar excess with respect to the mercapto (SH) groups) in dimethylformamide (DMF) to yield the targeted polymer. This nucleophilic substitution reaction was catalyzed with potassium carbonate (K_2CO_3), and a small amount of the reducing agent triphenylphosphine was added to prevent the formation of disulfide linkages between polymer chain ends. The polymer in DMF was first recovered by precipitation in diethyl ether. It was purified by two consecutive precipitations from THF to diethyl ether.

Determination of pyrene end functionality

The pyrene end functionality was evaluated by UV–visible absorption spectroscopy. First, the isobutylsulfanylthiocarbonylsulfanyl (iBS) moiety content of the corresponding precursor polymer (iBS_2-PNIPAM) was determined for solutions of the polymer in chloroform, using the absorbance at 310 nm. A solution of diethylene glycol di(2-(1-isobutyl)-sulfanylthiocarbonylsulfanyl-2-methyl propionate) in chloroform was used as the standard (ε_{310} = 28 600 $L \cdot mol^{-1} \cdot cm^{-1}$). Second, the pyrene content of Py_2-PNIPAM was determined for solutions of the polymer in methanol, using the absorbance of the pyrenyl chromophore at 342 nm, where iBS moieties do not absorb. The molar extinction coefficient of the pyrenyl group in methanol was approximated by using that of 4-(1-pyrenyl)butanol (PyButOH) in methanol (ε_{342} = 43 450 $L \cdot mol^{-1} \cdot cm^{-1}$). The molar extinction coefficient of PyButOH was determined by preparing solutions with known concentrations of PyButOH in methanol and plotting their absorbance obtained with a 1 cm path length UV cell as a function of PyButOH concentration. A straight line was obtained whose slope yielded the molar extinction coefficient of PyButOH in methanol according to the Beer–Lambert law. A comparison of the iBS concentration (end functionality assumed to be 100%) and the measured pyrene concentration gave the pyrene functionality values listed in Table 1.

Sample preparation for fluorescence measurements

Since the pyrenyl pendants of the Py_2-PNIPAM samples form pyrene aggregates or dimers in aqueous solution, absorption measurements conducted in water must be carefully interpreted if they are to be used to determine polymer concentration. Indeed, it has been shown in one example that the molar absorption coefficient of a pyrenyl moiety is about 1.7 times larger when the pyrenyl unit exists as an isolated monomer than when it is part of a ground-state pyrene aggregate.[33] Taking this into consideration, the Py_2-PNIPAM concentrations in water were determined as follows. First, the polymer was dissolved in ethanol, where no pyrene

Can. J. Chem. Downloaded from www.nrcresearchpress.com by University of Electronic and Science Techonology of China on 09/18/12
For personal use only.

Table 1. Number-average molecular weights (M_n) and polydispersity indices (PDI) of the Py_2-PNIPAM samples.

Sample	M_n (kg·mol^{-1})	PDI	Py functionality (%)
Py_2-PNIPAM-6K	5.9	1.05	85.4
Py_2-PNIPAM-8K	7.6	1.08	82.6
Py_2-PNIPAM-14K	13.7	1.10	87.4
Py_2-PNIPAM-25K	25.4	1.07	75.5
Py_2-PNIPAM-45K	44.5	1.10	74.8

aggregates are generated. The concentration of pyrenyl pendants was determined from the molar absorption coefficient of 4-(1-pyrene)butanol in ethanol (ε_{342} = 42 600 L·mol^{-1}·cm^{-1}) determined in the laboratory. The Py_2-PNIPAM solution was diluted to the desired concentration of pyrenyl groups in ethanol. Then, the ethanol was evaporated off and the same volume of water was added to the dried film of Py_2-PNIPAM. This solution was placed in the fridge for 30 min. This counterintuitive procedure is often employed to enhance the dissolution in water of polymers, such as PNIPAM, that exhibit a lower critical solution temperature (LCST). For PNIPAM, the LCST is ~32 °C. The polymer loses its solubility in water above this temperature. Finally, the solution was stirred vigorously and allowed to warm to room temperature (23 ± 1 °C). Following this protocol, the pyrene concentration of the Py_2-PNIPAM solutions in water was the same as the one determined for the Py_2-PNIPAM solutions in ethanol. A pyrene concentration of 2.4×10^{-6} mol·L^{-1} was used for the fluorescence measurements done in ethanol. All Py_2-PNIPAM solutions in ethanol were degassed by bubbling a gentle flow of nitrogen through the solution for 30 min before steady-state or time-resolved fluorescence measurements were conducted. Aerated aqueous solutions of Py_2-PNIPAM were used for fluorescence measurements.

Size exclusion chromatography

The size exclusion chromatography system consisted of an Agilent 1100 isocratic pump, a set of TSK-gel α-M (particle size, 13 μm; exclusion limit, 1×10^7 Da for polystyrene in DMF) and TSK-gel α-3000 (particle size, 7 μm; exclusion limit, 1×10^5 Da for polystyrene in DMF) columns (Tosoh Biosep), a Dawn EOS multiangle laser light scattering detector (λ = 690 nm; Wyatt Technology Co.), and an Optilab DSP interferometric refractometer (λ = 690 nm; Wyatt Technology Co.) and the conditions were as follows: injection volume, 100 μL; flow rate, 0.5 mL·min^{-1}; eluent, DMF; and temperature, 40 °C. The refractive index increment (dn/dc) value of PNIPAM was determined to be 0.0738 mL·g^{-1} at 690 nm in DMF at 40 °C using an Optilab DSP interferometric refractometer (Wyatt Technology Co.).

Steady-state fluorescence

The fluorescence spectra of the Py_2-PNIPAM samples in ethanol and water were acquired on a Photon Technology International (PTI) LS-100 steady-state fluorometer. The fluorometer was equipped with an Ushio UXL-75Xe xenon arc lamp and a PTI 814 photomultiplier detection system. Py_2-PNIPAM solutions in ethanol and water were, respectively, degassed and nondegassed. The solutions were excited at 344 nm. The monomer fluorescence intensity (I_M) was obtained by taking the integral under the fluorescence spectrum from 372 to 378 nm. The fluorescence intensity of the excimer (I_E) was determined by first normalizing the fluorescence spectrum of 4-(1-pyrene)butanol at a concentration of 2.5×10^{-6} mol·L^{-1} in ethanol and 0.6×10^{-6} mol·L^{-1} in water to the peak at 375 nm of the fluorescence spectrum of the Py_2-PNIPAM solutions. At such low concentration, 4-(1-pyrene)butanol emits as the pyrene monomer. Second, the normalized spectrum of 4-(1-pyrene)butanol was subtracted from that of the Py_2-PNIPAM solution. Third, the fluorescence intensity of the subtracted spectrum was integrated from 500 to 530 nm to yield I_E.

Time-resolved fluorescence

The fluorescence decays of the pyrene monomer and excimer of the Py_2-PNIPAM solutions were acquired on an IBH time-resolved fluorometer equipped with a nano-LED light source. The Py_2-PNIPAM solutions were prepared with a pyrene concentration of 1.2×10^{-6} mol·L^{-1}. The solutions were excited at 344 nm and the fluorescence decays were monitored at 375 and 510 nm for the pyrene monomer and excimer, respectively, using a cutoff filter at 370 and 495 nm, respectively. A Ludox solution was used at the excitation wavelength to determine the instrument response function, which was convoluted with the desired theoretical function for the decay analysis.

Analysis of the fluorescence decays

All monomer and excimer fluorescence decays were first fitted with a sum of exponentials according to eq. [1].

$$[1] \qquad f(t) = \sum_{i=1}^{N} a_{X_i} \times \exp\left(-t/\tau_{X_i}\right)$$

where X = M (monomer) or E (excimer).

Themonomer and excimer fluorescence decays acquired for the Py_2-PNIPAM solutions in ethanol were also fitted with eqs. [2] and [3], which are based on the Birks scheme given in Scheme 1.[5] In Scheme 1, the parameters k_{cy}, k_{-cy}, τ_M, and τ_E represent the rate constant of excimer formation, the rate constant of excimer dissociation, the monomer lifetime, and the excimer lifetime, respectively.

$$[2] \qquad [Py^*] = \frac{[Py^*_{diff}]_0}{\sqrt{(X-Y)^2 + 4k_{cy}k_{-cy}}}\left((X-\tau_2^{-1}) \times \exp(-t/\tau_1) - (X-\tau_1^{-1}) \times \exp(-t/\tau_2)\right) + [Py^*_{free}]_0 \exp(-t/\tau_M)$$

Can. J. Chem. Downloaded from www.nrcresearchpress.com by University of Electronic and Science Techonology of China on 09/18/12
For personal use only.

$$[3] \qquad [E^*] = \frac{k_{cy}[Py^*_{diff}]_0}{\sqrt{(X-Y)^2 + 4k_{cy}k_{-cy}}}\left(-\exp(-t/\tau_1) + \exp(-t/\tau_2)\right) + [Py^*_S]_0 \exp(-t/\tau_S)$$

Scheme 1. Birks' scheme for the formation of an excimer with a pyrene end-labeled monodisperse polymer.[5,18]

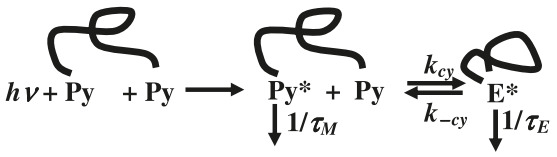

The parameters $X = k_{cy} + \tau_M^{-1}$ and $Y = k_{-cy} + \tau_E^{-1}$ are used in the expressions of the decay times τ_1 and τ_2, which are given in eqs. [4] and [5]. The initial concentrations of pyrenes that form an excimer by diffusion or do not form an excimer because they are attached to monolabeled chains are represented by $[Py^*_{diff}]_0$ and $[Py^*_{free}]_0$, respectively, in eqs. [2] and [3]. Occasionally, a short-lived pyrene species with a decay time of 2–4 ns and denoted as Py^*_S is encountered when excimer formation occurs in restricted geometries, such as when the pyrene pendants are confined to a polymer.[18] The origin of this spike is discussed further in the Results and discussion section. The monomer lifetime, τ_M, in ethanol was estimated to equal 220 ns by analyzing the monoexponential fluorescence decay of 4-(1-pyrene)butanol in ethanol.

$$[4] \qquad \tau_1^{-1} = \frac{X + Y + \sqrt{(X-Y)^2 + 4k_{cy}k_{-cy}}}{2}$$

$$[5] \qquad \tau_2^{-1} = \frac{X + Y - \sqrt{(X-Y)^2 + 4k_{cy}k_{-cy}}}{2}$$

The monomer and excimer fluorescence decays were fitted globally to ensure that the decay times τ_1 and τ_2 remained the same in the analysis of the monomer and excimer decays. The decay time τ_S was fixed to 2 ns in the analysis.

Results and discussion

Preparation and characterization of the polymers

The synthesis of α,ω-dipyrenyl poly(*N*-isopropylacrylamide)s (Py_2-PNIPAMs) is depicted in Fig. 1. First, PNIPAMs of narrow size distribution bearing a trithiocarbonate group at each chain end were prepared by reversible addition-fragmentation chain transfer polymerization of NIPAM using a difunctional trithiocarbonate compound, i.e., diethylene glycol di(2-(1-isobutyl)sulfanylthiocarbonylsulfanyl-2-methyl propionate), as the chain transfer agent.[27] The isobutyltrithiocarbonate groups were aminolyzed, yielding thiol end groups, which were subjected to nucleophilic substitution using 4-(1-pyrenyl)butyl iodide in the presence of sodium carbonate. Evidence for the successful end labeling was obtained by monitoring the UV absorption of the pyrenylbutyl pendants at 342 nm. The number-average molecular weight (M_n) and polydispersity index (PDI) of the polymers, shown in Table 1, were determined by size exclusion chromatography analysis in DMF, a good solvent for PNIPAM and its hydrophobically modified analogues.[32] The extent of pyrene incorporation onto the polymer chain ends (end functionality of the polymers, Table 1) was determined from the absorbance of the pyrenyl groups for solutions of the polymers in methanol.

Overview of the solution properties of the polymers in ethanol and in water

The two solvents selected for the study have similar viscosities at 25 °C (ethanol: η = 1.07 mPa·s; water: η = 0.89 mPa·s). The intrinsic viscosity of a commercial PNIPAM sample at 25 °C was determined to be 48.5 ± 0.5 and 46.6 ± 0.6 mL·g^{-1} in ethanol and water, respectively, indicating that the dimensions (radius of gyration or end-to-end distance) of the PNIPAM polymer coil should be similar in water and ethanol. All Py_2-PNIPAM samples were soluble in ethanol, but only the Py_2-PNIPAM samples with M_n values of 14 000 g·mol^{-1} or higher were soluble in water at 23 °C, which is the temperature of the fluorescence measurements reported here. Samples with lower molecular weight (5 900 and 7 600 g·mol^{-1}), which were reluctant to dissolve in water, were used only for the studies of Py_2-PNIPAM in ethanol. Fluorescence spectra, normalized at the 0-0 transition, of Py_2-PNIPAM samples in ethanol and in water are shown in Figs. 2A and 2B, respectively. The spectra present a strong contribution from the pyrene monomer emission, with bands at 376–396 nm, as well as a weak pyrene excimer emission, with its characteristic broad emission centered at 470 nm. The excimer emission intensity decreases with increasing chain length. The contribution of the excimer emission was weaker for polymers dissolved in ethanol, indicating that in water hydrophobic interactions between the pyrene end groups tend to overcome the natural tendency of the polymer to stretch owing to excluded volume effects, bringing the pyrene pendants into close contact under the form of pyrene aggregates where an excimer is generated efficiently.[16,18–21]

Solutions of Py_2-PNIPAM samples in ethanol

The experiments reported below aimed at characterizing intramolecular excimer formation. If an excimer is generated intramolecularly, its emission intensity, relative to the pyrene monomer intensity, should be independent of polymer concentration. We established that the ratio of pyrene excimer to monomer emission intensities, I_E/I_M, was constant (= 3.1×10^{-3}) for Py_2-PNIPAM-45K solutions in ethanol ranging in concentration from 23 to 530 mg·L^{-1}, equivalent to a pyrene concentration of 0.32 to 25 μmol·L^{-1}. The fluorescence spectra of all Py_2-PNIPAM samples in ethanol were acquired at a pyrene concentration of 2.5×10^{-6} mol·L^{-1}, a value for which excimer formation occurs exclusively be-

Can. J. Chem. Downloaded from www.nrcresearchpress.com by University of Electronic and Science Techonology of China on 09/18/12
For personal use only.

Fig. 2. Fluorescence spectra of pyrene end-labeled PNIPAM normalized at the 0-0 transition, λ_{ex} = 344 nm. (A) [Py] = 2.5 × 10^{-6} mol·L^{-1} in ethanol; top to bottom: Py_2-PNIPAM-6K, Py_2-PNIPAM-8K, Py_2-PNIPAM-14K, Py_2-PNIPAM-25K, Py_2-PNIPAM-45. (B) [Py] = 1.25 × 10^{-6} mol·L^{-1} in water; top to bottom: Py_2-PNIPAM-14K, Py_2-PNIPAM-25K, Py_2-PNIPAM-45K.

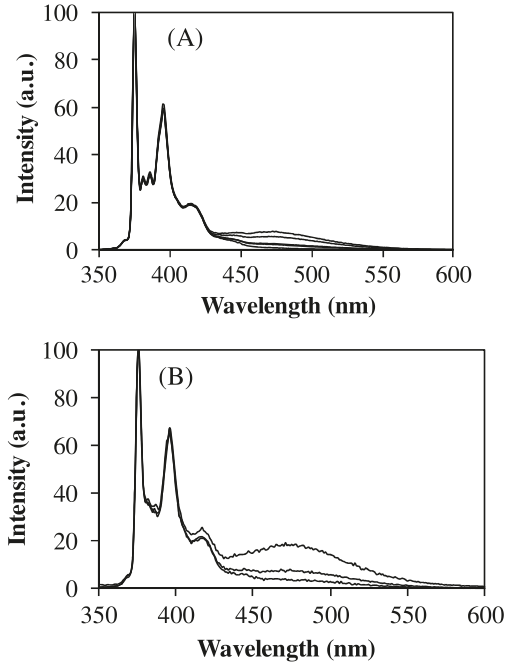

tween pyrenes linked to the same chain. The effect of chain length on the I_E/I_M ratio is seen in Fig. 3, where the I_E/I_M ratios are reported as a function of M_n. The slope of the log–log plot shown in Fig. 3 equals 1.4 ± 0.2 for solutions in ethanol (symbol: ◇).

The scaling relationship $I_E/I_M \propto M_n^{-1.4}$ found in ethanol for the Py_2-PNIPAM samples is in agreement with values expected from theoretical work conducted by Cuniberti and Perico,[34,35] who proposed eq. [6] to estimate the I_E/I_M ratio for pyrene-labeled polymers at temperatures <30 °C, where the rate constant for excimer dissociation can be neglected with respect to τ_E^{-1}.

$$[6] \qquad \frac{I_E}{I_M} = \kappa \frac{\phi_E^\circ}{\phi_M^\circ} \tau_M k_1 [Py]_{loc}$$

In eq. [6], κ is a constant that depends on the geometry and sensitivity of the spectrofluorometer used; k_1 is the bimolecular encounter rate constant, which for free pyrenes would equal 2 × RT/(3 × η) with R, T, and η being, respectively, the ideal gas constant, the absolute temperature in Kelvin, and the solvent viscosity; ϕ_M° and ϕ_E° are the fluorescence quantum yields of, respectively, the pyrene monomer and excimer; τ_M is the natural lifetime of the pyrene monomer; and $[Py]_{loc}$ represents the effective concentration of the unexcited chromophores in the neighborhood of the excited species. The end-to-end cyclization rate constant, k_{cy}, is taken as the product k_1 × $[Py]_{loc}$. Since the parameters ϕ_M°, ϕ_E°, κ, and τ_M are constants that do not depend on chain length, eq. [6] implies that the I_E/I_M ratio depends only on k_{cy}, which has been shown theoretically[35,36] and experimentally[6,8,12,14] to scale with the number-average degree of polymerization, N, as $N^{-\gamma}$, where γ has been found to take values between 0.9 and 1.9 depending on the polymer backbone and solvent. Based on the above, the I_E/I_M ratio found to scale as $M_n^{-1.4}$ (Fig. 4) for the Py_2-PNIPAM samples in ethanol conforms to what is theoretically[35,36] and experimentally[6,8,12,14] expected for the intramolecular excimer formation of a pyrene end-labeled monodisperse polymer in an organic solvent.

Fig. 3. Plot of $\ln(I_E/I_M)$ vs $\ln(M_n)$ for pyrene end-labeled PNIPAM in water (□, [Py] = 1.25 × 10^{-6} mol·L^{-1}) and ethanol (◇, [Py] = 2.5 × 10^{-6} mol·L^{-1}). Ethanol: slope = 1.4 ± 0.2; water: slope = 1.5 ± 0.1.

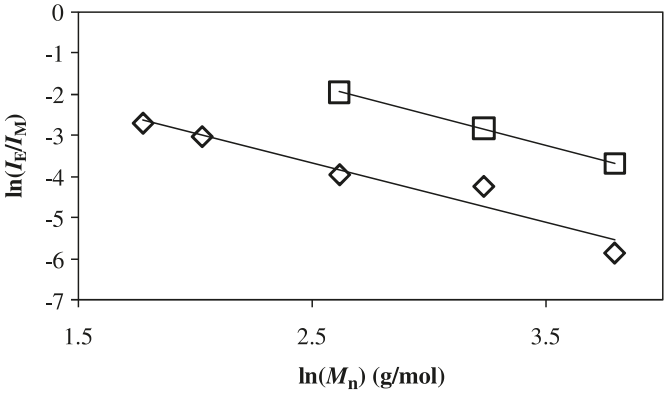

Next, fluorescence decays for the pyrene monomer and excimer emissions were acquired for the Py_2-PNIPAM samples in ethanol to gain information about the dynamics of excimer formation. All time-resolved fluorescence experiments were carried out with solutions where the pyrene concentration was 2.5 × 10^{-6} mol·L^{-1}. The decays recorded for the monomer and excimer emissions are shown in Figs. 4A and 4B, respectively. The pyrene monomer decay rate increases with decreasing polymer chain length, reflecting the increasingly more facile excimer formation. In fact, measurable excimer formation takes place only in ethanolic solutions of Py_2-PNIPAM samples of M_n = 14 000 g·mol^{-1} or less (see Fig. 2A), so that the excimer fluorescence decays of Py_2-PNIPAM-26K and Py_2-PNIPAM-45K in ethanol could not be acquired. The excimer fluorescence decays of the shorter chains exhibited a well-defined rise time (Fig. 4B), confirming that excimer formation occurs by diffusive encounters of the chain ends. As the polymer chain length increases, the excimer decays more slowly in the same manner as the pyrene monomer, which is a consequence of the coupling that exists between the concomitant disappearance of the pyrene monomer and formation of the pyrene excimer.[5] A spike was found early in the excimer decay of Py_2-PNIPAM-14K. The origin of this spike is debatable. Such a spike is usually observed for pyrene end-labeled polymers of high molecular weight or in viscous solvents when excimer formation by diffusion is not favored.[18,36] It can also be the result of some residual light scattering making its way through the detector and the monochromator despite the use of a 495 nm cutoff filter, or possibly it could originate from an impurity that emits weakly and is observed only when little excimer is formed.

The monomer and excimer fluorescence decays were first

Can. J. Chem. Downloaded from www.nrcresearchpress.com by University of Electronic and Science Techonology of China on 09/18/12
For personal use only.

Fig. 4. Fluorescence decays of pyrene end-labeled PNIPAM, λ_{ex} = 344 nm. (A) Ethanol, [Py] = 2.5 × 10^{-6} mol·L^{-1}, λ_{em} = 375 nm; top to bottom: Py_2-PNIPAM-45K, Py_2-PNIPAM-25K, Py_2-PNIPAM-14K, Py_2-PNIPAM-8K, Py_2-PNIPAM-6K. (B) Ethanol, [Py] = 2.5 × 10^{-6} mol·L^{-1}, λ_{em} = 510 nm; top to bottom: Py_2-PNIPAM-14K, Py_2-PNIPAM-8K, Py_2-PNIPAM-6K. (C) Water, [Py] = 1.2 × 10^{-6} mol·L^{-1}, λ_{em} = 375 nm; top to bottom: Py_2-PNIPAM-45K, Py_2-PNIPAM-25K, Py_2-PNIPAM-14K. (D) Water, [Py] = 1.2 × 10^{-6} mol·L^{-1}, λ_{em} = 510 nm; top to bottom: Py_2-PNIPAM-45K, Py_2-PNIPAM-25K, Py_2-PNIPAM-14K.

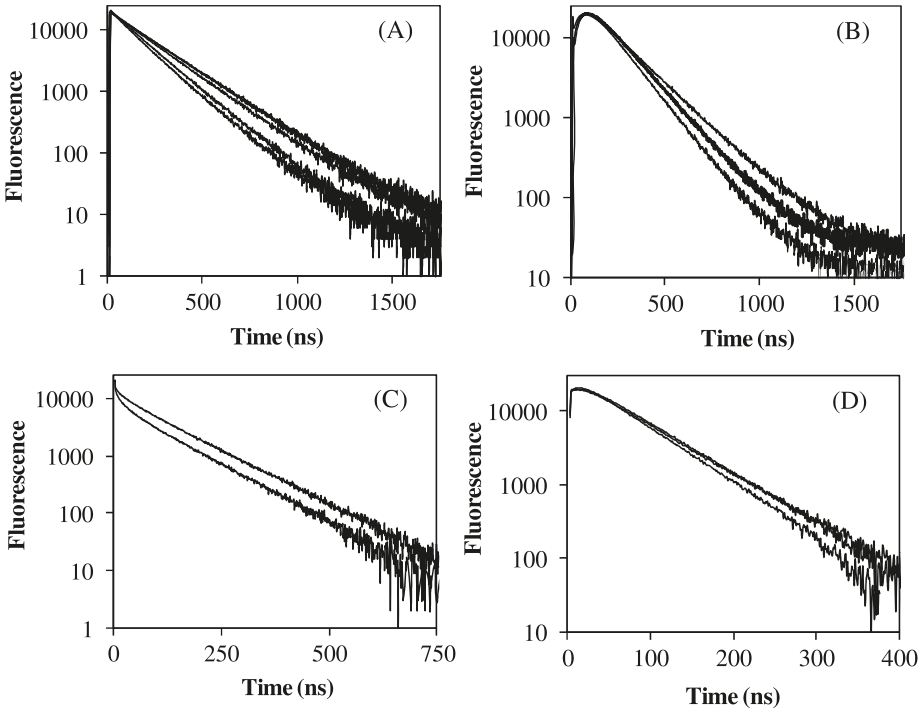

fitted with a sum of exponentials (i.e., eq. [1]), yielding the pre-exponential factors and decay times listed in Tables 2 and 3. As the chain length of the Py_2-PNIPAM sample increases, the number-average lifetime ($<\tau>$) increases, eventually reaching a value close to 220 ns, which is the lifetime of 4-(1-pyrene)butanol in ethanol. The increase in $<\tau>$ reflects the decrease in efficiency for excimer formation as the pyrene end groups are separated by increasing chain length. For Py_2-PNIPAM-45K, the pyrenes are kept so far apart that they emit only as independent monomers and do not form excimers. The excimer decays have a short component whose origin could be light scattering, a trace of impurity, or ground-state dimers.[18,37] The ratio a_{E2}/a_{E3} is negative and equals –0.90 for Py_2-PNIPAM-6K and Py_2-PNIPAM-8K. This value is close to –1.0, which indicates that excimer formation is diffusion controlled, as expected from the prominent rise time observed in the excimer decays shown in Fig. 4B. As the chain length increases and excimer formation is less efficient, the a_{E2}/a_{E3} ratio becomes more positive and equals –0.72 for Py_2-PNIPAM-14K.

A global analysis of the monomer and excimer fluorescence decays of the Py_2-PNIPAM solutions in ethanol was performed according to Birks' scheme with eqs. [2] and [3]. The fits were excellent, with χ^2 values smaller than 1.30 and residuals and the autocorrelation function of the residuals being randomly distributed around zero. The parameters k_{cy}, k_{-cy}, τ_E, and f_{free} ($f_{free} = [Py^*_{free}]_0/([Py^*_{free}]_0 + [Py^*_{diff}]_0)$) retrieved from the analysis are listed in Table 4. The rate constant for excimer formation decreases with increasing chain length as $k_{cy} \propto M_n^{-\gamma}$ with $\gamma = 0.91 \pm 0.03$. The γ value is smaller than the values of 1.62 found for Py_2-polystyrene in cyclohexane at 34.5 °C,[6] 1.52 found for Py_2-polytetrahydrofuran,[8] and 1.9 and 1.7 found for Py_2-polycarbonate in acetonitrile and acetone, respectively,[12] but it is similar to the values of 1.1, 0.90, and 0.91 found for Py_2-poly(ethylene oxide) in diethyleneglycol diethyl ether at 50 °C, toluene at 45 °C, and tetrahydrofuran at 20 °C, respectively.[14] Although τ_E and k_{-cy} increase somewhat with increasing chain length (mostly for Py_2-PNIPAM-14K), this increase is believed to be an artifact because τ_E and k_{-cy} describe intrinsic properties of the pyrene excimer, which should not depend on polymer chain length as long as the chain is long enough, as should be the case with the Py_2-PNIPAM samples. This artifact is due to limitations in the Birks scheme analysis of fluorescence decays acquired with long pyrene end-labeled polymer constructs that do not generate much excimer. Indeed, as can be seen in Fig. 2, excimer formation is strongly reduced for the Py_2-PNIPAM samples having a M_n greater than 14 000 g·mol^{-1}. This increase of τ_E and k_{-cy} with increasing polymer chain length has been observed in at least one other instance.[37] If τ_E and k_{-cy} are averaged, one finds that the excimer lifetime equals 66 ± 7 ns, which is reasonable for a pyrene excimer in organic solvent.[5] The excimer dissociation rate constant is small and equals 6 ± 3 × 10^6 s^{-1}. These results are typical for excimer formation of a pyrene end-labeled monodisperse polymer in organic solvents.[5]

Solutions of Py_2-PNIPAM samples in water at 23 °C

In Fig. 5, the I_E/I_M ratio is plotted as a function of the molar pyrene concentration for solutions in water of Py_2-PNIPAM ($M_n \geq$ 14 000 g·mol^{-1}). The ratio I_E/I_M increases

Can. J. Chem. Downloaded from www.nrcresearchpress.com by University of Electronic and Science Techonology of China on 09/18/12
For personal use only.

Table 2. Pre-exponential factors and decay times obtained by fitting the monomer and excimer fluorescence decays of the Py_2-PNIPAM samples in ethanol with a sum of exponentials (eq. [1] with $N = 2$ and 3 for the monomer and excimer, respectively).

Sample	τ_{M1} (ns)	a_{M1}	τ_{M2} (ns)	a_{M2}	χ^2	$\langle\tau\rangle$ (ns)	τ_{E1} (ns)	a_{E1}	τ_{E2} (ns)	a_{E2}	τ_{E3} (ns)	a_{E3}	χ^2	a_{E2}/a_{E3}
Py_2-PNIPAM-6K	109	0.42	174	0.58	1.01	147	1.2	0.83	47	–1.59	142	1.76	1.05	–0.91
Py_2-PNIPAM-8K	91	0.15	172	0.85	1.08	160	1.9	0.78	49	–2.06	159	2.29	1.10	–0.90
Py_2-PNIPAM-14K	112	0.10	204	0.90	1.05	194	1.5	0.77	43	–0.59	190	0.82	1.05	–0.72
Py_2-PNIPAM-25K	71	0.07	214	0.93	1.07	203								
Py_2-PNIPAM-45K	95	0.04	218	0.96	1.20	213								

Table 3. Pre-exponential factors and decay times obtained by fitting the monomer and excimer fluorescence decays of the Py_2-PNIPAM samples in water with a sum of exponentials (eq. [1] with $N = 3$).

Sample	τ_{M1} (ns)	a_{M1}	τ_{M2} (ns)	a_{M2}	τ_{M3} (ns)	a_{M3}	χ^2	$\langle\tau\rangle$ (ns)	τ_{E1} (ns)	a_{E1}	τ_{E2} (ns)	a_{E2}	τ_{E3} (ns)	a_{E3}	χ^2	a_{E-}/a_{E+}
Py_2-PNIPAM-14K	4.5	0.30	28	0.26	109	0.43	1.10	56	11	–0.74	58	1.66	106	0.08	1.01	–0.42
Py_2-PNIPAM-25K	6.8	0.20	44	0.20	118	0.61	1.05	82	18	–0.66	56	1.40	96	0.25	1.18	–0.40
Py_2-PNIPAM-45K	4.9	0.13	38	0.18	118	0.68	1.09	101	16	–0.76	60	1.57	99	0.19	1.12	–0.43

Table 4. Excimer formation rate constants (k_{cy}), excimer dissociation rate constants (k_{-cy}), excimer lifetimes (τ_E), and molar fractions of pyrene monomers that do not form excimer (f_{free}).

Sample	k_{cy} (10^7 s^{-1})	k_{-cy} (10^7 s^{-1})	τ_E (ns)	f_{free}
Py_2-PNIPAM-6K	0.34	0.36	60	0.10
Py_2-PNIPAM-8K	0.26	0.43	64	0.10
Py_2-PNIPAM-14K	0.15	0.94	74	0.24

Fig. 5. Plot of I_E/I_M vs [Py] for Py_2-PNIPAM-45K (◇), Py_2-PNIPAM-25K (□), and Py_2-PNIPAM-14K (△) in water and Py_2-PNIPAM-45K (○) in ethanol.

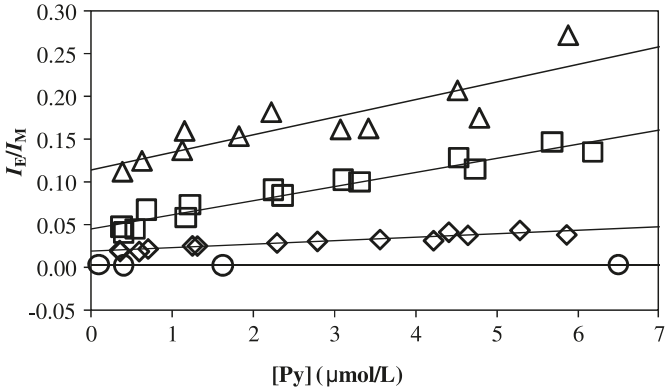

linearly with increasing polymer concentration, an indication that intermolecular excimer formation is taking place in this concentration range ($1 < [Py] < 7 \times 10^{-6}$ mol·L^{-1}).[9] For solutions of identical Py concentration, the I_E/I_M ratio decreases with increasing chain length, as was the case for Py_2-PNIPAM in ethanol. The I_E/I_M ratio of the Py_2-PNIPAM solutions having a pyrene concentration of 1.25 μmol·L^{-1} was plotted as a function of M_n in Fig. 3 (symbol: □). For this pyrene concentration, the I_E/I_M ratio was found to scale as $M_n^{-\gamma}$, where $\gamma = 1.5 \pm 0.1$, an exponent similar to the one of 1.4 ± 0.2 found in ethanol and within the range of exponents obtained for other Py_2-polymers in organic solvents.[6,8,12,14] Since the viscosities of water and ethanol are rather close to each other, viscosity is not expected to significantly affect the value of k_1 in eq. [6]. Furthermore, the similarity of the intrinsic viscosity values of unmodified PNIPAM in water and in ethanol suggests that the dimensions of the polymer coil are the same in water and ethanol. Therefore, the enhancement of excimer formation observed in Figs. 2 and 3 for Py_2-PNIPAM in water is an indication that hydrophobic associations between pyrene pendants occur, inducing a decrease of the average size of the polymer coil and an increase in $[Py]_{loc}$ in eq. [6].

Fluorescence decays of Py_2-PNIPAM solutions in water were acquired only for the longer chains. The excimer decays were not biexponential (see Table 3), which rules out the possibility of using the typical Birks scheme to fit the fluorescence decays.[5] This departure from the traditional Birks scheme is attributed to the presence of ground-state pyrene aggregates, which form excimers instantaneously upon direct excitation, as previously observed in studies of aqueous solutions of Py_2-PEO.[18–22] The presence of ground-state pyrene aggregates is supported by the values taken by

Can. J. Chem. Downloaded from www.nrcresearchpress.com by University of Electronic and Science Techonology of China on 09/18/12
For personal use only.

the ratio of the sum of the negative pre-exponential factors divided by the sum of the positive pre-exponential factors, a_{E-}/a_{E+}. For Py_2-PNIPAM-14K, the only polymer amenable to studies in both ethanol and water, the a_{E-}/a_{E+} ratio is more positive in water (–0.42) than in ethanol (–0.72). For aqueous solutions, the a_{E-}/a_{E+} ratio did not change much with M_n, having values of –0.40 and –0.43 for Py_2-PNIPAM-25K and Py_2-PNIPAM-45K, respectively. The presence of the ground-state pyrene aggregates complicates the quantitative analysis of the fluorescence decays. A detailed analysis of the decays is beyond the scope of this report.

Conclusions

Five pyrene end-labeled PNIPAM samples of narrow molecular weight distribution (ranging in size from $M_n \sim 6000$ to 45 000 g·mol^{-1}) (Fig. 1 and Table 1) were prepared and their solutions in ethanol and in water were studied by fluorescence spectroscopy. All polymers were soluble in ethanol, but only samples of $M_n \geq 14\,000$ g·mol^{-1} were water soluble. In the case of the polymers of M_n = 14 000, 25 000, and 45 000 g·mol^{-1}, the excimer emission was enhanced for polymers in water compared with solutions in ethanol, an effect attributed to the presence of pyrene aggregates via intra- and interchain association. This association process is triggered by the hydrophobicity of the pyrene end groups and bears similarity to the process of flower micelle formation in aqueous solutions of di-(*n*-octadecyl)-PNIPAM.[38] It is also akin to the micellization induced by Py in aqueous solutions of semitelechelic Py-PNIPAM reported previously.[39] Time-resolved fluorescence measurements, which revealed a diminished rise time in the excimer profiles of the Py_2-PNIPAM samples in water (Fig. 4), confirmed the presence of pyrene ground-state aggregates. The ratio I_E/I_M, taken as a measure of the rate of excimer formation, was found to scale as $M_n^{-\gamma}$, where $\gamma = 1.4 \pm 0.2$ and 1.5 ± 0.1 in ethanol and water, respectively. These exponents are within the range of exponents typically obtained with pyrene end-labeled monodisperse polymers.[6,8,12,14] All parameters retrieved from the analysis of the fluorescence decays of polymers in ethanol were reasonable, and the rate of excimer formation, k_{cy}, was found to scale as $M_n^{-0.9}$, an exponent that is smaller than the one obtained by analysis of steady-state data (I_E/I_M ratio). The discrepancy may be a consequence of the smaller set of data points available for k_{cy}. Since it was possible to determine k_{cy} accurately for only three polymers (Py_2-PNIPAM-6K, Py_2-PNIPAM-8K, and Py_2-PNIPAM-14K; see Table 4), whereas all five Py_2-PNIPAM samples yielded accurate I_E/I_M ratios (Fig. 3). The photophysical properties of Py_2-PNIPAM in ethanol are similar to those of Py_2-PEO of similar size in organic solvents, forming excimers according to Birks' scheme. As observed for solutions of Py_2-PEO in water, excimer formation kinetics are complex for aqueous solutions of Py_2-PNIPAM owing to the presence of aggregates of ground-state pyrenes, and they need to be subjected to a detailed data treatment to compare the properties of the two families of polymers in water. Work towards this goal is ongoing, as it is expected to unveil how differences in the hydration of the PEO and PNIPAM main chains[40] can impact the association of their amphiphilic derivatives in water monitored on the time and distance scales of pyrene excimer formation.

Acknowledgements

This study was supported by funding from the Natural Sciences and Engineering Research Council of Canada (NSERC). J. Y. and J. D. are thankful to Manoj Mathew for his help in confirming the reproducibility of the measurements done in water.

References

(1) Wilemski, G.; Fixman, M. *J. Chem. Phys.* **1974**, *60* (3), 866. doi:10.1063/1.1681162.
(2) Wilemski, G.; Fixman, M. *J. Chem. Phys.* **1974**, *60* (3), 878. doi:10.1063/1.1681163.
(3) Cuniberti, C.; Perico, A. *Eur. Polym. J.* **1977**, *13* (5), 369. doi:10.1016/0014-3057(77)90097-0.
(4) Winnik, M. A.; Redpath, T.; Richards, D. H. *Macromolecules* **1980**, *13* (2), 328. doi:10.1021/ma60074a023.
(5) Birks, J. B. *Photophysics of Aromatic Molecules*; Wiley: New York, 1970.
(6) Winnik, M. A. *Acc. Chem. Res.* **1985**, *18* (3), 73. doi:10.1021/ar00111a002.
(7) Slomkowski, S.; Winnik, M. A. *Macromolecules* **1986**, *19* (2), 500. doi:10.1021/ma00156a053.
(8) Svirskaya, P.; Danhelka, J.; Redpath, A. E. C.; Winnik, M. A. *Polymer (Guildf.)* **1983**, *24* (3), 319. doi:10.1016/0032-3861(83)90270-7.
(9) Kim, S. D.; Torkelson, J. M. *Macromolecules* **2002**, *35* (15), 5943. doi:10.1021/ma0200322.
(10) Gardinier, W. E.; Bright, F. V. *J. Phys. Chem. B* **2005**, *109* (31), 14824. doi:10.1021/jp0440939.
(11) Piçarra, S.; Gomes, P. T.; Martinho, J. M. G. *Macromolecules* **2000**, *33* (10), 3947. doi:10.1021/ma992106o.
(12) Boileau, S.; Méchin, F.; Martinho, J. M. G.; Winnik, M. A. *Macromolecules* **1989**, *22* (1), 215. doi:10.1021/ma00191a041.
(13) Duhamel, J.; Khaykin, Y.; Hu, Y. Z.; Winnik, M. A.; Boileau, S.; Mechin, F. *Eur. Polym. J.* **1994**, *30* (1), 129. doi:10.1016/0014-3057(94)90242-9.
(14) Ghiggino, K. P.; Snare, M. J.; Thistlethwaite, P. J. *Eur. Polym. J.* **1985**, *21* (3), 265. doi:10.1016/0014-3057(85)90230-7.
(15) Lee, S.; Winnik, M. A. *Macromolecules* **1997**, *30* (9), 2633. doi:10.1021/ma961351u.
(16) Lee, S.; Duhamel, J. *Macromolecules* **1998**, *31* (26), 9193. doi:10.1021/ma981160m.
(17) Farinha, J. P. S.; Piçarra, S.; Miesel, K.; Martinho, J. M. G. *J. Phys. Chem. B* **2001**, *105* (43), 10536. doi:10.1021/jp011467e.
(18) Costa, T.; Seixas de Melo, J.; Burrows, H. D. *J. Phys. Chem. B* **2009**, *113* (3), 618. doi:10.1021/jp806555x.
(19) Cheung, S.-T.; Winnik, M. A.; Redpath, A. E. C. *Makromol. Chem.* **1982**, *183* (7), 1815. doi:10.1002/macp.1982.021830720.
(20) Char, K.; Frank, C. W.; Gast, A. P. *Macromolecules* **1989**, *22* (7), 3177. doi:10.1021/ma00197a047.
(21) Duhamel, J.; Yekta, A.; Hu, Y.; Winnik, M. A. *Macromolecules* **1992**, *25* (25), 7024. doi:10.1021/ma00051a046.
(22) Winnik, F. M. *Chem. Rev.* **1993**, *93* (2), 587. doi:10.1021/cr00018a001.
(23) Farinha, J. P. S.; Martinho, J. M. G.; Xu, H.; Winnik, M. A.;

Quirk, R. P. *J. Polym. Sci., Part B: Polym. Phys.* **1994**, *32* (9), 1635. doi:10.1002/polb.1994.090320906.
(24) Walter, R.; Rička, J.; Quellet, Ch.; Nyffenegger, R.; Binkert, T. *Macromolecules* **1996**, *29* (11), 4019. doi:10.1021/ma951529x.
(25) Gan, D.; Lyon, A. L. *Macromolecules* **2002**, *35* (26), 9634. doi:10.1021/ma021186k.
(26) Tasaki, K. *J. Am. Chem. Soc.* **1996**, *118* (35), 8459. doi:10.1021/ja951005c.
(27) Qiu, X.-P.; Winnik, F. M. *Macromolecules* **2007**, *40* (4), 872. doi:10.1021/ma062225l.
(28) Duan, Q.; Miura, Y.; Narumi, A.; Shen, X.; Sato, S.-I.; Satoh, T.; Kakuchi, T. *J. Polym. Sci. Part Polym. Chem.* **2006**, *44* (3), 1117. doi:10.1002/pola.21208.
(29) Scales, C. W.; Convertine, A. J.; McCormick, C. L. *Biomacromolecules* **2006**, *7* (5), 1389. doi:10.1021/bm060192b.
(30) Rao, J.; Xu, J.; Luo, S.; Liu, S. *Langmuir* **2007**, *23* (23), 11857. doi:10.1021/la7020148.
(31) Rao, J.; Zhang, J.; Xu, J.; Liu, S. *J. Colloid Interface Sci.* **2008**, *328* (1), 196. doi:10.1016/j.jcis.2008.09.001.
(32) Segui, F.; Qiu, X.-P.; Winnik, F. M. *J. Polym. Sci., Part A: Polym. Chem.* **2008**, *46* (1), 314. doi:10.1002/pola.22382.
(33) Siu, H.; Duhamel, J. *J. Phys. Chem. B* **2008**, *112* (48), 15301. doi:10.1021/jp801105q.
(34) Cuniberti, C.; Perico, A. *Eur. Polym. J.* **1980**, *16* (9), 887. doi:10.1016/0014-3057(80)90121-4.
(35) Cuniberti, C.; Perico, A. *Prog. Polym. Sci.* **1984**, *10* (4), 271. doi:10.1016/0079-6700(84)90007-8.
(36) Siu, H.; Duhamel, J.; Sasaki, D. Y.; Pincus, J. L. *Langmuir* **2010**, *26* (13), 10985. doi:10.1021/la9045429.
(37) Ingratta, M.; Hollinger, J.; Duhamel, J. *J. Am. Chem. Soc.* **2008**, *130* (29), 9420. doi:10.1021/ja800897m.
(38) Koga, T.; Tanaka, F.; Motokawa, R.; Koizumi, S.; Winnik, F. M. *Macromolecules* **2008**, *41* (23), 9413. doi:10.1021/ma800957z.
(39) Winnik, F. M.; Adronov, A.; Kitano, H. *Can. J. Chem.* **1995**, *73* (11), 2030. doi:10.1139/v95-251.
(40) Okada, Y.; Tanaka, F. *Macromolecules* **2005**, *38* (10), 4465. doi:10.1021/ma0502497.

Can. J. Chem. Downloaded from www.nrcresearchpress.com by University of Electronic and Science Techonology of China on 09/18/12
For personal use only.

Insights into the effect of ketylimine, aldimine, and vinylene group attachment and regiosubstitution on the fluorescence deactivation of fluorene

Stéphane Dufresne, Thomas Skalski, and W.G. Skene

Abstract: The spectroscopic and electrochemical properties of a 9-substituted fluorene ketylimine (**3**) were investigated and compared with those of its vinylene analogue (**4**) to determine the origins of the quenched fluorescence of these compounds. The predominate mode of singlet excited state deactivation of the heteroatomic fluorene was found to be internal conversion involving bond rotation. Meanwhile, its carbon counterpart was found to undergo deactivation preferentially by intersystem crossing to form its triplet, which was confirmed by laser flash photolysis. Both **3** and **4** quenched the fluorescence of fluorene with diffusion-controlled rate constants, implying that the singlet excited states of **3** and **4** are also quenched by intramolecular photoinduced electron transfer (PET). This deactivation mode was found to be exergonically favorable (–90 kJ/mol for **3** and –81 kJ/mol for **4**) according to the Rehm–Weller equation. The position of the heteroatomic bond on the fluorene moiety was further found to influence the singlet excited state deactivation pathway. The 2-substituted regioisomer decayed predominately by intramolecular PET and its fluorescence can be restored by acid protonation. Conversely, the PET mechanism is a minor deactivation mode for the 9-substituted fluorene derivative and its fluorescence can be enhanced by suppressing bond rotational modes, possible at low temperature and potentially in thin films.

Key words: fluorenyl ketylimines, intramolecular photoinduced electron transfer, Stern–Volmer quenching, azomethines.

Résumé : Afin de déterminer les origines de la fluorescence dégénérée de ces composés, on a étudié les propriétés spectroscopiques et électrochimiques des cétylimines de fluorènes portant un substituant en position 9 (**3**) et on les a comparées à celles de son analogue vinylène (**4**). On a trouvé que le mode dominant de la désactivation de l'état singulet excité du fluorène hétéroatomique se produit par une conversion interne impliquant une rotation de liaison. On a trouvé par ailleurs que sa contrepartie carbonée subit une désactivation préférentielle par un croisement intersystème conduisant à la formation de son triplet, ce qui est confirmé par la photolyse laser éclair. Les composés **3** et **4** désactivent tous la fluorescence du fluorène avec des constantes de vitesse contrôlées par la diffusion impliquant que l'état singulet excité des composés **3** et **4** est aussi désactivé par un transfert d'électron photoinduit (TEP) intramoléculaire. On a trouvé que, suivant l'équation de Rehm–Weller, ce mode de désactivation est favorable d'un point de vue exorgonique (–90 kJ/mol pour **3** et –81 kJ/mol pour **4**). On a trouvé aussi que la position de la liaison hétéroatomique dans la portion fluorène influence aussi la voie de désactivation de l'état singulet excité. On a aussi observé que le régioisomère portant un substituant en position 2 se désactive d'une façon prédominante par un TEP intramoléculaire et que sa fluorescence peut être restaurée par protonation acide. Inversement, le mécanisme de TEP n'est qu'un mode mineur de désactivation pour les dérivés du fluorènes portant un substituant en position 9 pour lesquels la fluorescence peut être augmentée par une suppression des modes de rotation des liaisons possibles à basse température et possiblement dans des films minces.

Mots-clés : cétylimines de fluorényles, transfert d'électron photoindut (TEP) intramoléculaire, désactivation de Stern–Volmer, azométhines.

[Traduit par la Rédaction]

Introduction

Conjugated materials have received much attention as a result of their photophysical and electrochemical properties, which make them suitable for organic electronics such as field-effect transistors, light-emitting diodes, and photovoltaics, to name but a few.[1–4] In particular, fluorene-based materials have been extensively studied because of their

Received 30 March 2010. Accepted 8 June 2010. Published on the NRC Research Press Web site at canjchem.nrc.ca on 13 January 2011.

This article is part of a Special Issue dedicated to Professor J. C. Scaiano.

S. Dufresne, T. Skalski,[1] and W.G. Skene.[2] Centre for Self-Assembled Chemical Structures, Département de Chimie, Université de Montréal, CP 6128, Centre-ville, Montreal, QC H3C 3J7, Canada.

[1]Present address: Université d'Artois, Unité de Catalyse et de Chimie du Solide, UMR CNRS n° 8181, Faculté Jean Perrin, rue Jean Souvraz, S.P. 18, 62307, Lens CEDEX, France.
[2]Corresponding author (e-mail: w.skene@umontreal.ca).

Can. J. Chem. Downloaded from www.nrcresearchpress.com by University of Electronic and Science Techonology of China on 09/18/12
For personal use only.

Can. J. Chem. Downloaded from www.nrcresearchpress.com by University of Electronic and Science Techonology of China on 09/18/12
For personal use only.

inherent high fluorescence, which makes them ideal for use in emitting devices.[5] Fluorene and its derivatives can additionally withstand the harsh oxidative and reductive environment of a device, further making them ideal materials for use in emitting devices.[6–8] Despite these advantages, the fluorescence quantum yield and color emitted by fluorene are highly sensitive to its environment and its substitution. This is evidenced by keto defects in the 9-position of fluorene, resulting in both decreased emission and undesired green emission.[6,9,10]

Although the fluorenone defect (**1**) (Chart 1) in polyfluorenes is undesired because it reduces device efficiency and results in color contamination, the ketone group is nonetheless interesting because it affords the means to introduce functionality into the conjugated fluorene polymer and to subsequently modulate the polymer's properties.[7,11–13] Simple condensation of amines with fluorene's ketone leads to ketylimines. The properties of the polyfluorenes such as solubility, electronic effects, color, and emission yields, to name but a few, can potentially be tailored by judicious choice of the amine used in preparing the ketylimine.

Despite the potential ease of preparing fluorene ketylimines such as **3** by simple condensation methods, few examples of these compounds are known.[14–16] Interestingly, no modern reports have described the successful synthesis of **3** or its derivatives, while only classic literature reports the preparation of some derivatives using harsh and extremely stringent reaction conditions.[17,18] The limited number of reports detailing the preparation of **3** and its derivatives, together with the absence of reported characterization, prompted us to prepare **3** to investigate the influence of the heteroatomic bond on the photophysical properties of fluorene. We were further incited to investigate the photophysical properties of both **3** and **4** by the lack of previous photophysical studies and by a desire to understand the origins of their unknown quenched fluorescence. The knowledge gained from investigating these model compounds is of importance not only for understanding the influence of the homo- and heteroatomic bonds on the photophysical properties, but also for designing and preparing future generations of fluorenyl compounds with tailored properties for specific applications. We additionally examined **3** because it is complementary to our previous aldimine studies of fluorene derivatives such as **5** and **6** and would provide vital structure–property information as well as information about the regiosubstitution effect on the photophysical properties.[19–24] The preparation and photophysical studies of **3** are therefore reported herein to understand the effect of the N=C group and its placement on the fluorenyl excited state properties.

Experimental procedures

General procedures

All reagents, including **1**, **2**, and **4**, were commercially available from Sigma-Aldrich and were used as received unless otherwise stated. Anhydrous and deaerated solvents were obtained with a Glass Contour solvent purification system. ^{1}H NMR and ^{13}C NMR spectra were recorded on a Bruker 400 MHz spectrometer with the appropriate deuterated solvents.

Chart 1.

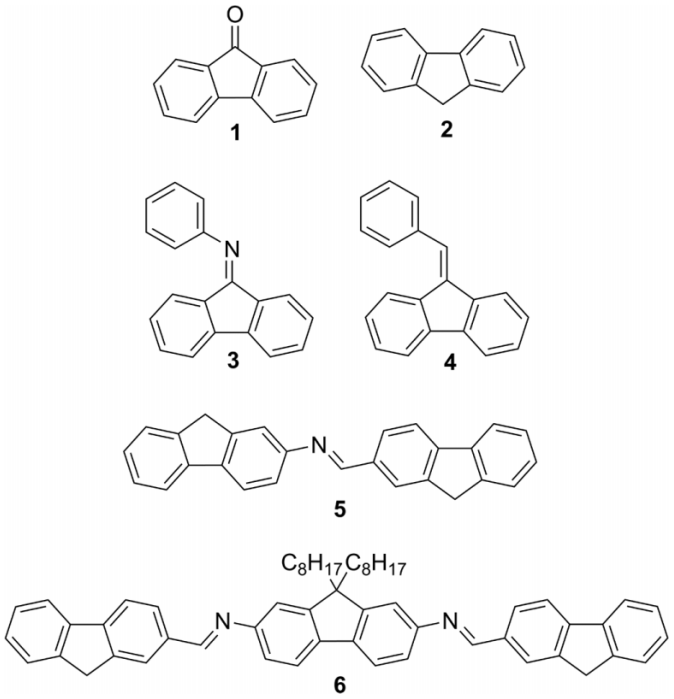

Spectroscopic measurements

The absorption measurements were done on a Cary 500 spectrometer, while the fluorescence studies were performed on an Edinburgh Instruments FLS-920 fluorimeter after deaerating the samples thoroughly with nitrogen for 20 min. Fluorescence absolute quantum yields were measured at 10^{-5} mol/L by exciting the compounds of study at the corresponding maximum absorption in spectroscopic grade dichloromethane at room temperature in an integrating sphere.[25] The ΔE values were calculated from the intercept of normalized absorption and fluorescence spectra of the corresponding compounds. The spectroscopic band gaps (E_g) were calculated from the tangent from the absorption onset.

Electrochemical measurements

Cyclic voltammetric measurements were performed on a Bioanalytical Systems EC epsilon potentiostat. Compounds were dissolved in anhydrous and deaerated dichloromethane at 10^{-4} mol/L with NBu_4PF_6 at sufficient concentration to achieve highly conductive solutions. A platinum electrode was used as the auxiliary and the working electrode, while a saturated Ag/AgCl electrode was used as the reference electrode. Ferrocene was added at the end of the analyses to serve as an internal reference. The electrochemical band gaps (E_g) were calculated from the measured oxidation and reduction potentials according to $E_{pa} + E_{pc} + 0.4$.

Laser flash photolysis

Laser flash photolysis experiments were done on a Luzchem mini-LFP system exciting at 355 nm with the third harmonic of a Nd-YAG laser. The solutions were prepared with matched absorbances between 0.3 and 0.5 at the excitation wavelength and deaerated for 20 min with nitrogen.

Highest occupied molecular orbital (HOMO) and lowest

Can. J. Chem. Downloaded from www.nrcresearchpress.com by University of Electronic and Science Techonology of China on 09/18/12
For personal use only.

unoccupied molecular orbital (LUMO) energy levels were calculated semiempirically using density functional theory (DFT) calculation methods available in Spartan 06 (Wavefunction, Inc.) with the 6-31g* basis set. The bond angles, distances, torsions, and other parameters were experimentally derived from the X-ray data from the corresponding structures.

N-*(9H-Fluoren-9-ylidene)benzenamine (3)*

Aniline (153 mg, 1.64 mmol) was dissolved with DABCO (500 mg, 4.45 mmol) in anhydrous toluene at 0 °C. This was followed by the slow addition of 1.0 mol/L $TiCl_4$ solution in toluene (2.77 mL, 2.77 mmol). Compound **1** (100 mg, 0.55 mmol) was added and then refluxed for 3–4 h. The solvent was removed and the product was isolated as a yellow solid after purification by recrystallization in 50:50 dichloromethane/hexanes or by flash chromatography on alumina with neat hexanes with 1% triethylamine increased to hexanes/ethyl acetate (95:5) (57 mg, 41%); mp 92–94 °C. ^{1}H NMR (acetone-d_6) δ: 7.85 (d, 1H, J = 7.6 Hz), 7.77 (m, 2H), 7.52 (m, 1H), 7.43 (m, 4H), 7.21 (m, 1H), 6.98 (m, 2H), 6.55 (d, 1H, J = 8.0 Hz). ^{13}C NMR (acetone-d_6) δ: 164.0, 153.9, 145.6, 143.6, 139.4, 139.3, 133.9, 132.7, 131.2, 130.7, 130.3, 130.0, 129.5, 128.5, 127.1, 125.7, 124.8, 122.4, 121.8, 119.7.

Crystal structure determination

Diffraction data for **3** were collected on a Bruker FR591 diffractometer using graphite-monochromatized Cu Kα radiation (1.54178 Å). The structures were solved by direct methods (SHELXS97, University of Göttingen). All nonhydrogen atoms were refined based on Fobs2 (SHELXS97, University of Göttingen), while hydrogen atoms were refined on calculated positions with fixed isotropic U, using riding model techniques.

Synthesis

Given the limited experimental protocols for the preparation of **3** and the lack of its detailed characterization, we set out to prepare this compound. We first attempted to prepare **3** via our previously successful methods for aldimines by simple condensation of **2** with aniline in absolute ethanol and in neat aniline.[26–28] Although some desired product was detected by both TLC and crude NMR, purification by standard methods yielded insufficient material for characterization and photophysical studies. The low yield is most likely a result of reduced reactivity because of steric hindrance of the ketone, while the product formed was most likely extremely hydrolytically sensitive and subsequently decomposed with standard chromatographic preparative methods.[14,17,29,30] The latter is supported by the absence of isolated products after silica gel chromatography. Stringent reaction protocols using $TiCl_4$ and an excess of DABCO were used for activating the hindered ketone and preventing imine hydrolysis, respectively. Product isolation was possible by column chromatography over activated basic alumina. Alternatively, the desired product could also be obtained by recrystallization of the crude reaction mixture from a 50:50 dichloromethane/hexanes mixture. We also attempted to prepare an aliphatic derivative of **3** using butylamine to understand the photodeactivation modes of the N=C bond with a limited degree of conjugation on the fluorophores. However, the desired product could not be obtained despite the various reaction conditions employed. Its instability is most likely a result of its extreme sensitivity to hydrolysis and it spontaneously decomposes under ambient conditions. Nonetheless, the unprecedented and complete characterization by standard methods confirmed the formation of **3** in high purity and sufficient amounts for spectroscopic measurements, albeit in low yield.

X-ray crystallographic data

Unlike aldimines, ketylimines lack the characteristic imine peak, allowing for unequivocal product identification by ^{1}H NMR. The lack of characteristic proton resonance at 8.5 ppm makes product identification challenging. Undeniable evidence for correct product formation is, however, possible by X-ray diffraction. In addition to this, the relation of the phenyl unit to the fluorene moiety can be determined from the X-ray diffraction data, allowing for comparison of the structures with analogous aldimines such as **6**.

Compound **3** was crystallized by slow evaporation from a saturated solution of acetone to give small yellow plates. The resolved structure (Fig. 1, left panel) confirms that **3** was formed and crystallizes in an orthorhombic unit as per Table 1. Three different molecules of **3** were found within the crystal lattice for a total of 24 molecules per lattice. Despite the large number of different molecules per lattice, only small variances were found between them. As seen in the right panel of Fig. 1, depicting the crystal structure shown along the *b*-axis, the phenyl moiety is not coplanar with the fluorene moiety. In fact, the planes described by the two aromatic moieties are twisted by 70°, 80°, and 85° for each of the three distinct molecules isolated per lattice. The twisting between the two planes is required to minimize the steric hindrance between the ortho protons of the phenyl and fluorene units. This is evident from the calculated HOMO and LUMO energy levels seen in Fig. 2 using the X-ray crystallographic data for the optimized geometry. It should be noted that the observed twisting between the two planes is greater than that for its aldimine regioisomer (**6**), whose two terminal fluorenes are twisted by 26° and 65° relative to the central fluorene.[24] Although the mean plane angles differ for **3** and its regioisomer (**6**), the corresponding bond distances and angles for the two analogues are identical within experimental error. The large twisting angle between the aromatic units nonetheless implies not only that the 9-position of the fluorene is sterically hindered, but that **3** has a limited degree of conjugation extending only through the fluorene=N portion. The latter is supported spectroscopically (vide infra). The severe steric hindrance and the large twisting of the fluorenyl and phenyl mean plane angles observed from the crystallographic data for **3** prevent any higher ordered structure arising from intermolecular interactions. In fact, the three-dimensional crystal network of **3** is governed by only weak face-to-π interactions. This is in contrast to **6**, which has a high degree of 3D ordering owing to many intermolecular π-stacking and C–H–π interactions.

Can. J. Chem. Downloaded from www.nrcresearchpress.com by University of Electronic and Science Techonology of China on 09/18/12
For personal use only.

Fig. 1. ORTEP X-ray structure of **3** with the ellipsoids shown at 50% probability along the *a*-axis (left) and *b*-axis (right).

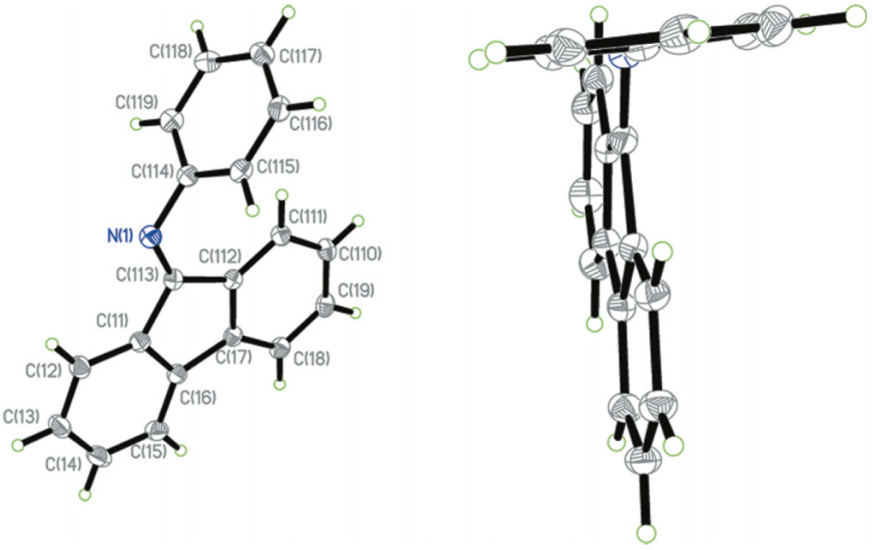

Table 1. Details of crystal structure determination for **3**.

	Compound **3**
Formula	$C_{19}H_{13}N$
M_w (g/mol); $F(000)$	255.30; 3216
Crystal color and form	Yellow plate
Crystal size (mm)	0.15 × 0.13 × 0.05
T (K); $D_{calcd.}$ (g/cm^3)	150(2); 1.247
Crystal system	Orthorhombic
Space group	*Pbca*
Unit cell	
a (Å)	9.6721(2)
b (Å)	16.4370(3)
c (Å)	51.3027(10)
α (°)	90.000
β (°)	90.000
γ (°)	90.000
V (Å^3); Z	8156.1(3); 24
θ range (°); completeness	1.76–72.26; 0.996
Reflections: collected/independent; R_{int}	8022/7112; 0.041
μ (mm^{-1})	0.556
Abs. corr.	Semiempirical
$R_1(F)$; $wR(F^2)$ [$I > 2\sigma(I)$]	0.0571; 0.1549
$R_1(F)$; $wR(F^2)$ (all data)	0.0629; 0.1580
GoF (F^2)	1.297
Max. residual e density (e Å^{-3})	–0.426

Spectroscopy

Given the limited reports examining the fluorescence of **3** and its analogous vinylene derivative (**4**),[31–33] we examined the photophysical properties of these two compounds. Such studies are required to understand the effect and the placement of the heteroconjugated bond on the fluorescence and the origin of the weak fluorescence of these compounds. This is possible by comparing the spectroscopic properties of **3**–**5**. As seen in Table 2, the three compounds exhibit approximately the same absorption maxima and differ only in their long wavelength absorption. The same trend of spectral shifts as a function of structures is also observed for their fluorescence spectra. It can be concluded from the absorption and fluorescence spectra of **3** and **4** that the heteroconjugated fluorene is more conjugated than its all-carbon counterpart. This is further supported by the shorter N=C bond distance (1.279 Å) compared with the corresponding C=C bond distance (1.340 Å) for **4**, derived from the X-ray crystallographic data. The shorter bond distance implies a greater sp^2 character to the bond and hence a higher degree of conjugation, which is further corroborated by the band gaps (E_g).

Both **3** and **4** possess substantially lower fluorescence quantum yields than **1** in dichloromethane, as seen in Table 2. More specifically, **4** does not fluoresce, while **3** only weakly fluoresces at room temperature. To better understand the origins of the differences between the two analogues and their quenched fluorescence relative to **1**, the fluorescence at 77 K was measured. All modes of rotational deactivation are suppressed at this temperature and an observed fluorescence increase would denote internal conversion deactivation by bond rotation. The fluorescence yield of **3** increased to 0.6 at 77 K, while no change was observed for **4** at this low temperature. Although an accurate ratio between the emission at 77 K and that at room temperature cannot be determined owing to the weak room temperature fluorescence, it can nonetheless be confirmed that the major mode of singlet excited state deactivation of **3** is by nonradiative means involving bond rotation, most likely the N–phenyl bond. Meanwhile, the singlet excited state deactivation of **4** occurs by other means. It can be concluded from the temperature fluorescence measurements that deactivation of excited fluorene is highly influenced by its substituents. This is evident from the temperature-dependent fluorescence of the regioisomers **3** and **4**, where two different deactivation modes occur despite the vinylene and imine bonds being isoelectronic. The different effect of the homoaryl and heteroconjugated bonds on the fluorene properties is further evidenced from the calculated HOMO and LUMO levels for **3** and **4**. As seen in Fig. 2, the HOMO is localized exclusively over the phenyl–N moiety and the LUMO is distributed across the fluorenyl moiety for **3**. This is in contrast to **4**, whose HOMO is distributed across the fluorenyl moiety while the

Can. J. Chem. Downloaded from www.nrcresearchpress.com by University of Electronic and Science Techonology of China on 09/18/12
For personal use only.

Fig. 2. HOMO (left) and LUMO (right) energy levels of **3** calculated using the DFT 6-31g* basis set using the X-ray crystallographic data for the optimized geometry.

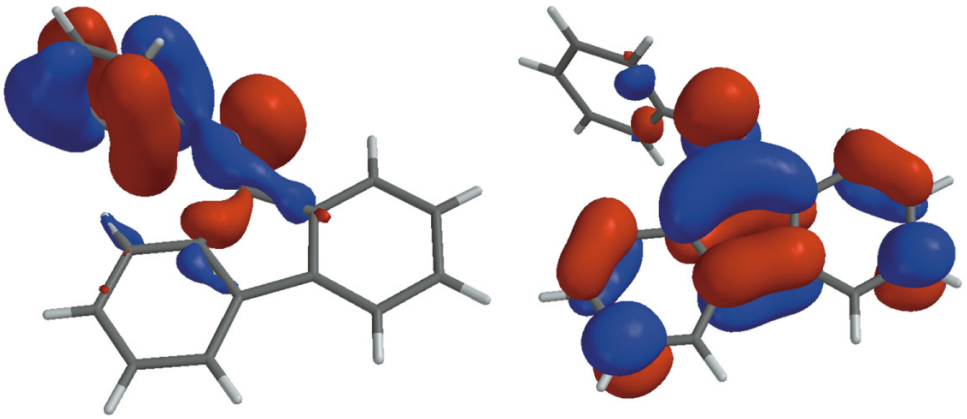

Table 2. Various spectroscopic data.

Compound	Absorbance (nm)[b,c]	Fluorescence (nm)[b]	ΔE (eV)	E_g spec (eV)	Fluorescence quantum yield[a] CH_2Cl_2	CH_2Cl_2 + TFA	77 K / RT[d]
1	258 (377)	505	2.9	3.6	0.02	0	7
2	261	302	4.4	3.9	0.50	0.45	4
3	258, 298 (388)	478	2.8	2.6	0.04	0.03	15
4	259 (328)	402	3.4	3.1	0	0	0
5[e]	361	445	2.9	2.9	0.40	—	—

[a]Absolute fluorescence quantum yield measured using an integrating sphere.

[b]Measured in CH_2Cl_2.

[c]Values in parentheses denote the most bathochromically shifted absorption maximum.

[d]Fluorescence quantum yield ratio measured at 77 K in a 4:1 methanol/ethanol matrix and at room temperature (RT) in methanol. The change in refractive index is minimal for the two temperatures, and therefore no temperature-dependent fluorescence correction is required.

[e]Ref. 21.

Fig. 3. HOMO (left) and LUMO (right) energy levels of **4** calculated using the DFT 6-31g* basis set using the X-ray crystallographic data for the optimized geometry.

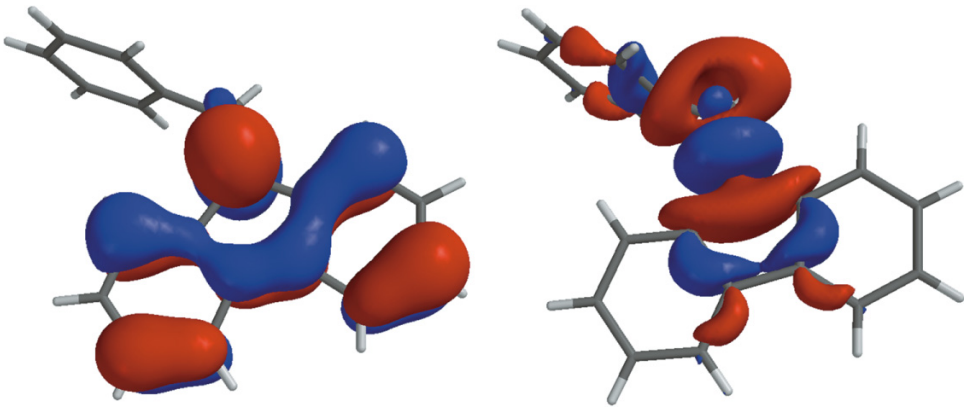

LUMO covers the cyclopentyl, imino, and phenyl moieties (Fig. 3).

The nonexistent room temperature fluorescence and the absence of increased fluorescence at a reduced temperature of **4** would suggest the presence of deactivation modes other than internal conversion. A possible deactivation mode would be intersystem crossing to form the triplet state. Both **3** and **4** were therefore further investigated by laser flash photolysis to spectroscopically confirm the formation of a triplet state. As seen in Fig. 4, a strong transient signal is apparent at 450 nm for the excitation of **4** at 355 nm by laser flash photolysis. The quenching of this transient with 1,3-cyclohexadiene and the unimolecular decay confirm the triplet nature of the transient. The similar transient intensities observed for optically matched samples of xanthone and **4** suggest that the triplet quantum yield of **4** is similar to that of xanthone ($\Phi_{TT} = 1$).[34–37] Conversely, no transient signal was detected for **3**, implying the absence of triplet

Can. J. Chem. Downloaded from www.nrcresearchpress.com by University of Electronic and Science Techonology of China on 09/18/12
For personal use only.

Fig. 4. Transient absorption spectra of xanthone (black) and **4** (red) measured at 0.12 μs after the 355 nm laser pulse in deaerated dichloromethane. Inset: monoexponential decay of transient **4** monitored at 450 nm.

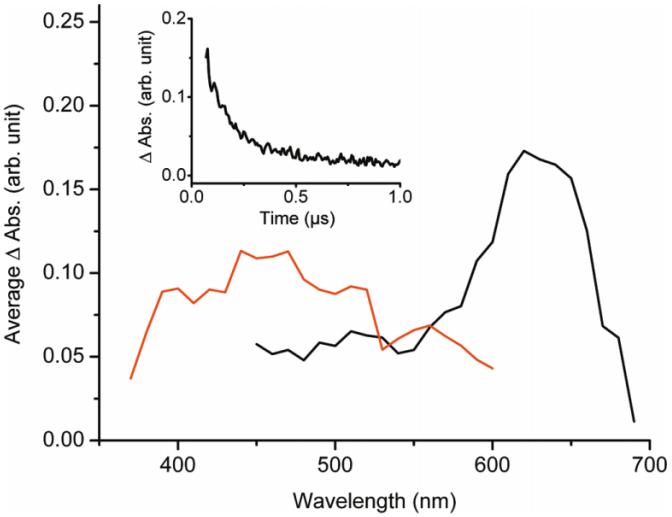

Fig. 5. Stern–Volmer fluorescence quenching of **2** with 0 (black), 20 (red), 40 (green), 60 (blue), and 80 (orange) mmol of **3** in dichloromethane. Inset: change in fluorescence of **2** with the addition of **3**, monitored at 318 nm.

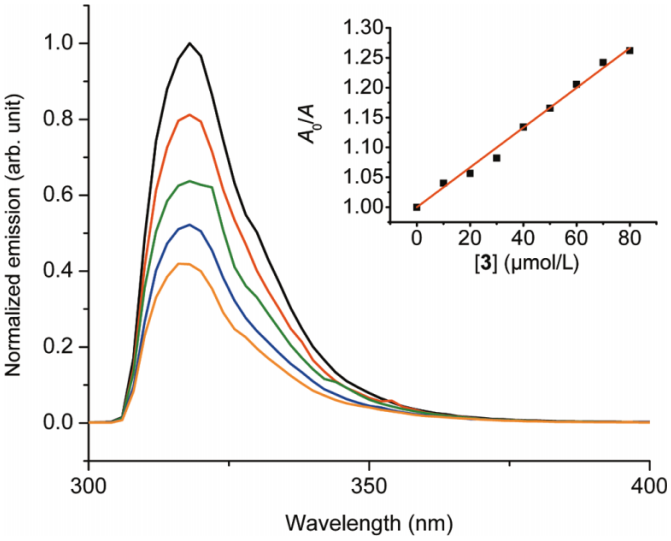

formation and hence no deactivation by intersystem crossing for the heteroatomic compound. The time-resolved and steady-state spectroscopic methods confirm that **3** preferentially deactivates by internal conversion, while the singlet excited state of **4** is predominately deactivated by intersystem crossing.

Although the temperature-dependent fluorescence confirms that the singlet excited state of **3** deactivates by internal conversion, the quantum yield of this process cannot be accurately measured. This is a result of the large error associated with comparing the intense fluorescence signal at 77 K with the extremely weak room temperature signal. Therefore, internal deactivation modes other than rotational internal conversion energy dissipation, such as photoinduced electron transfer (PET), cannot be dismissed. Stern–Volmer quenching studies of **3** and **4** were subsequently undertaken to determine whether other modes of singlet excited state deactivation occurred.[38] Owing to the quenched fluorescence of **3** and **4**, quantitative and accurate quenching studies were not possible using these two compounds as fluorophores. The quenching measurements were therefore done with fluorophore **2** because of its inherent high fluorescence yield. As seen in Fig. 5, **3** quenches the fluorescence of **2** with a bimolecular quenching rate constant (k_q) of 3.3×10^{11} L mol^{-1} s^{-1}, from the measured fluorescence lifetime of **2** (τ_o = 10 ns). Similarly, **4** also quenches **2** with $k_q = 4.0 \times 10^{11}$ L mol^{-1} s^{-1}. Higher quenching ratios of ϕ_o/ϕ would be beneficial to derive accurate k_q values. However, these were not possible because of spectroscopic screening effects of the quenchers at higher concentrations leading to deviations from linearity of the Stern–Volmer plots. The rate constants measured are slighter greater than the diffusion-controlled limit in dichloromethane ($k_q = 2 \times 10^{10}$ L mol^{-1} s^{-1}).[38] This is a result of overlapping absorbances between the fluorophore and the quencher at the excitation wavelength making it difficult to make accurate quenching measurements. Nonetheless, the calculated diffusion-controlled k_q confirm that the fluorene singlet excited state is efficiently deactivated by both **3** and **4**. The results are consistent with previous quenching studies of **1** with aliphatic imines that were deactivated by PET. The similarity of the quenching rate constants of **3** and **4** with their fluorophore-free quenching counterparts, concomitant with the favorable energetics (vide infra), implies that the singlet excited state deactivation occurs by intramolecular PET.[19–21]

The diffusion-controlled k_q quenching of **2** by both **3** and **4** implies deactivation by PET. The energetics of PET were empirically calculated according to the Rehm–Weller equation to corroborate the fluorescence quenching data: $\Delta G^\circ_{eT} = E_{pa}$ (fluorophore) – E_{pc} (quencher) – $\Delta E_{0,0}$ – λ.[39] The equation takes into account the fluorophore's oxidation potential (E_{pa}), the quencher's reduction potential by accepting the transferred electron from the fluorophore (E_{pc}), and the solvent reorganization energy (λ). The energy gap ($\Delta E_{0,0}$) between the ground and excited singlet states of **2** must also be taken into account, since PET involves electron transfer from the excited state. The required value is calculated from the intercept of the normalized plot of the absorption and fluorescence spectra of the fluorophores (see the Supplementary data). The E_{pa} and E_{pc} values (Table 3) were measured by cyclic voltammetry and correspond to the oxidation and reduction potentials of **2** and quenchers (**3** and **4**), respectively. The combined spectroscopic and electrochemical data (Tables 2 and 3) were used to calculate the energetics of PET. The exergonic values of –90 and –84 kJ/mol calculated for the quenching of **1** by **3** and **4**, respectively, support the Stern–Volmer quenching data and imply that deactivation of the singlet excited states of **3** and **4** also occurs by intramolecular PET. This deactivation mode is consistent with the 2-fluorenyl aldimine regioisomers that also deactivate by intramolecular PET.[19–21] Interestingly, the PET deactivation mode of 2-substituted regioisomers can be suppressed by protonating the azomethine, resulting in fluorescence yields near unity.[19–21] However, the fluorescence yield of **3** does not increase upon protonation (Table 2). This is most likely a result of the steric hindrance at the

Can. J. Chem. Downloaded from www.nrcresearchpress.com by University of Electronic and Science Techonology of China on 09/18/12
For personal use only.

Table 3. Electochemical data recorded in anhydrous and deaerated dichloromethane with a saturated Ag/Ag^+ reference electrode.

Compound	E_{pa} (eV)	E_{pc} (eV)	E_g (eV)
1	0.86	–1.03	2.3
2	0.91	–1.31	2.6
3	1.50	–1.40	3.3
4	1.73	–1.85	4.0

fluorenyl 9-position and as such, the imine cannot be efficiently protonated. Nonetheless, the spectroscopic and electrochemical data support the conclusion that the singlet excited states of **3** and **4** deactivate by intramolecular PET. While this degenerate manifold is also efficiently deactivated by rotational internal conversion in the case of **3**, **4** is efficiently deactivated predominately by intersystem crossing to form its triplet. The net outcome of these different deactivation processes is suppressed fluorescence for both **3** and **4**.

Conclusion

The origin of the previously unknown fluorescence suppression for 9-substituted fluorenes has been determined. Deactivation of the fluorophore excited state occurs by combined efficient rotational internal conversion and intramolecular photoinduced electron transfer for the heteroatomic ketylimine **3**. Although the singlet excited state of its carbon analogue (**4**) also deactivates by PET, the major mode of deactivation is by intersystem crossing resulting in efficient triplet formation. While the triplet manifold was spectroscopically confirmed by laser flash photolysis, evidence for the intramolecular PET mechanism was supported by examining the fluorescence rate constants for quenching of fluorene by both the ketylimine and vinylene fluorene derivatives. The PET mechanism was further supported by calculating the energetics according to the Rehm–Weller equation. Not only was the PET mechanism found to be exergonically favorable with these two quenchers, but deactivation of the singlet excited state occurred with diffusion-controlled rate constants. Unlike its 2-substituted fluorenyl regioisomers, the fluorescence of **3** cannot be restored by suppressing the PET mechanism by protonation. Nonetheless, the fluorescence quenching of **3** occurs predominately by rotational internal conversion, while that of its 2-substituted regioisomer occurs predominately by PET. The fluorescence of **3** can therefore be dramatically increased by reducing bond rotation deactivation modes, which is possible at low temperature or potentially in the solid state (e.g., by spin coating as thin films). The fluorescence enhancement possible with 9-heteroatomic fluorenyl imines makes these compounds beneficial and better suited for emitting devices than both their vinylene and 2-substituted regioisomer analogues, which waste their desired singlet excited state energy by uncontrollable means. Although the N=C bond is understood to be isoelectronic to the C=C bond, it was found that deactivation of the singlet excited state occurs by different modes depending on the type of unsaturated bond. The location of the N=C moiety on the fluorene was also found to play an important role in determining the fluorescence quenching mechanism. The future generation of materials for a given emitting or sensing application can therefore be prepared with the knowledge gained from the discovered fluorescence quenching mechanism.

Supplementary data

Supplementary data for this article are available on the journal Web site (canjchem.nrc.ca). CCDC 781760 contains the crystallographic data for this manuscript. These data can be obtained, free of charge, via www.ccdc.cam.ac.uk/conts/retrieving.html (or from the Cambridge Crystallographic Data Centre, 12 Union Road, Cambridge CB2 1EZ, UK; fax +44 1223 336033; or deposit@ccdc.cam.ac.uk).

Acknowledgements

The Natural Sciences and Engineering Research Council of Canada (NSERC) is thanked for a Discovery Grant, Strategic Research Grant, and Research Tools and Instruments grant allowing this work to be performed, and the Canada Foundation for Innovation (CFI) is thanked for additional equipment funding. W. G. S. also thanks the Royal Society of Chemistry for a JWT Jones Travelling Fellowship, thus allowing this manuscript to be completed. S. D. and T. S. thank NSERC and Le conseil général du Nord Pas de Calais and Le conseil municipal de Vaulx Vraucourt for graduate scholarships, respectively. T. S. also thanks the Direction des Relations Internationales of the Université de Montréal.

References

(1) Brédas, J.-L.; Norton, J. E.; Cornil, J.; Coropceanu, V. *Acc. Chem. Res.* **2009**, *42* (11), 1691. doi:10.1021/ar900099h. PMID:19653630.

(2) Bredas, J.-L.; Durrant, J. R. *Acc. Chem. Res.* **2009**, *42* (11), 1689. doi:10.1021/ar900238j. PMID:19916562.

(3) Kamtekar, K. T.; Monkman, A. P.; Bryce, M. R. *Adv. Mater.* **2010**, *22* (5), 572. doi:10.1002/adma.200902148. PMID: 20217752.

(4) Lee, K.; Nair, P. R.; Scott, A.; Alam, M. A.; Janes, D. B. *J. Appl. Phys.* **2009**, *105* (10), 102046. doi:10.1063/1.3116630.

(5) Grimsdale, A. C.; Chan, K. L.; Martin, R. E.; Jokisz, P. G.; Holmes, A. B. *Chem. Rev.* **2009**, *109* (3), 897. doi:10.1021/cr000013v. PMID:19228015.

(6) Chan, K. L.; Sims, M.; Pascu, S. I.; Ariu, M.; Holmes, A. B.; Bradley, D. D. C. *Adv. Funct. Mater.* **2009**, *19* (13), 2147. doi:10.1002/adfm.200990055.

(7) Jo, J.; Vak, D.; Noh, Y.-Y.; Kim, S.-S.; Lim, B.; Kim, D.-Y. *J. Mater. Chem.* **2008**, *18* (6), 654. doi:10.1039/b714138f.

(8) Rathnayake, H. P.; Cirpan, A.; Delen, Z.; Lahti, P. M.; Karasz, F. E. *Adv. Funct. Mater.* **2007**, *17* (1), 115. doi:10.1002/adfm.200600089.

(9) Montilla, F.; Mallavia, R. *Adv. Funct. Mater.* **2007**, *17* (1), 71. doi:10.1002/adfm.200600141.

(10) Romaner, L.; Pogantsch, A.; Scandiucci de Freitas, P.; Scherf, U.; Gaal, M.; Zojer, E.; List, E. J. W. *Adv. Funct. Mater.* **2003**, *13* (8), 597. doi:10.1002/adfm.200304360.

(11) Pijper, T. C.; Pijper, D.; Pollard, M. M.; Dumur, F.; Davey, S. G.; Meetsma, A.; Feringa, B. L. *J. Org. Chem.* **2010**, *75* (3), 825. doi:10.1021/jo902348u. PMID:20055375.

(12) Kappaun, S.; Scheiber, H.; Trattnig, R.; Zojer, E.; List, E. J. W.; Slugovc, C. *Chem. Commun. (Camb.)* **2008**, 5170. doi:10.1039/b808407f. PMID:18956058.

Can. J. Chem. Downloaded from www.nrcresearchpress.com by University of Electronic and Science Techonology of China on 09/18/12
For personal use only.

(13) Becker, K.; Lupton, J. M.; Feldmann, J.; Nehls, B. S.; Galbrecht, F.; Gao, D. Q.; Scherf, U. *Adv. Funct. Mater.* **2006**, *16* (3), 364. doi:10.1002/adfm.200500550.
(14) Suzuki, K.; Matsu-Ura, N.; Horii, H.; Sugita, Y.; Sanda, F.; Endo, T. *J. Appl. Polym. Sci.* **2002**, *83* (8), 1744. doi:10.1002/app.10101.
(15) Meng, Q.; Thibblin, A. *J. Am. Chem. Soc.* **1997**, *119* (6), 1224. doi:10.1021/ja9624681.
(16) Dai, W.; Srinivasan, R.; Katzenellenbogen, J. A. *J. Org. Chem.* **1989**, *54* (9), 2204. doi:10.1021/jo00270a034.
(17) O'Donnell, M. J.; Polt, R. L. *J. Org. Chem.* **1982**, *47* (13), 2663. doi:10.1021/jo00134a030.
(18) Pickard, P. L.; Tolbert, T. L. *Org. Synth.* **1964**, *5*, 51.
(19) Dufresne, S.; Pérez Guarìn, S. A.; Bolduc, A.; Bourque, A. N.; Skene, W. G. *Photochem. Photobiol. Sci.* **2009**, *8* (6), 796. doi:10.1039/b819735k. PMID:19492107.
(20) Dufresne, S.; Callaghan, L.; Skene, W. G. *J. Phys. Chem. B* **2009**, *113* (47), 15541. doi:10.1021/jp907391y.
(21) Bourque, A. N.; Dufresne, S.; Skene, W. G. *J. Phys. Chem. C* **2009**, *113* (45), 19677. doi:10.1021/jp907263p.
(22) Tsang, D.; Bourgeaux, M.; Skene, W. G. *J. Photochem. Photobiol. A* **2007**, *192* (2–3), 122. doi:10.1016/j.jphotochem.2007.05.013.
(23) Pérez Guarìn, S. A.; Skene, W. G. *Mater. Lett.* **2007**, *61* (29), 5102. doi:10.1016/j.matlet.2007.04.015.
(24) Guarìn, S. A. P.; Dufresne, S.; Tsang, D.; Sylla, A.; Skene, W. G. *J. Mater. Chem.* **2007**, *17*, (27), 2801. doi:10.1039/b618098a.
(25) Bolduc, A.; Dufresne, S.; Hanan, G. S.; Skene, W. G. *Can. J. Chem.* **2010**, *88* (3), 236. doi:10.1139/V09-166.
(26) Dufresne, S.; Skene, W. G. *J. Org. Chem.* **2008**, *73* (10), 3859. doi:10.1021/jo8002503. PMID:18410143.
(27) Guarìn, S. A.; Bourgeaux, M.; Dufresne, S.; Skene, W. G. *J. Org. Chem.* **2007**, *72* (7), 2631. doi:10.1021/jo070100o. PMID:17343421.
(28) Bourgeaux, M.; Skene, W. G. *J. Org. Chem.* **2007**, *72* (23), 8882. doi:10.1021/jo701515j. PMID:17956121.
(29) Saroja, G.; Pingzhu, Z.; Ernsting, N. P.; Liebscher, J. *J. Org. Chem.* **2004**, *69* (3), 987. doi:10.1021/jo035204n. PMID:14750836.
(30) Meng, Q.; Thibblin, A. *J. Am. Chem. Soc.* **1997**, *119* (6), 1224. doi:10.1021/ja9624681.
(31) Liao, W.-Y.; Wang, S.-S.; Yao, H.-H.; Chen, C.-W.; Tasi, H.-P.; Chu, W.-P.; Chen, J.-H.; Lee, S.-B. *IEEE Trans.* Magn. **2005**, *41*, 1019. doi:10.1109/TMAG.2004.842039.
(32) He, F.; Xia, H.; Tang, S.; Duan, Y.; Zeng, M.; Liu, L.; Li, M.; Zhang, H.; Yang, B.; Ma, Y.; Liu, S.; Shen, J. *J. Mater. Chem.* **2004**, *14* (18), 2735. doi:10.1039/b407262f.
(33) Liu, L.; Qiao, L.-X.; Liu, S.-Z.; Cui, D.-M.; Zhang, C.-M.; Zhou, Z.-J.; Du, Z.-L.; Wong, W.-Y. *J. Polym. Chem. A* **2008**, *46* (10), 3193. doi:10.1002/pola.22654.
(34) Carmichael, I.; Helman, W. P.; Hug, G. L. *J. Phys. Chem. Ref. Data* **1987**, *16* (2), 239. doi:10.1063/1.555782.
(35) Carmichael, I.; Hug, G. L. *J. Phys. Chem. Ref. Data* **1986**, *15* (1), 1. doi:10.1063/1.555770.
(36) Scaiano, J. C. *CRC Handbook of Organic Photochemistry;* CRC Press: Boca Raton, FL, 1989.
(37) Signals of identically matched intensity are not expected owing to the different triplet–triplet molar absorptivity coefficients of **4** and xanthone.
(38) Turro, N. J.; Ramamurthy, V.; Scaiano, J. C. *Principles of Molecular Photochemistry: An Introduction;* University Science Books: Sausalito, CA, 2009.
(39) Gilbert, A.; Baggott, J. *Essentials of Molecular Photochemistry;* CRC Press: Boca Raton, FL, 1991.

Distribution and reactivity of gallates toward galvinoxyl radicals in SDS micellar solutions — Effect of the alkyl chain length

Raquel Bridi, Carolina Aliaga, Alexis Aspée, Elsa Abuin, and Eduardo Lissi

Can. J. Chem. Downloaded from www.nrcresearchpress.com by University of Electronic and Science Techonology of China on 09/18/12
For personal use only.

Abstract: In this work, we have evaluated the reactivity of methyl gallate, propyl gallate, and *n*-octyl gallate toward galvinoxyl radicals in homogeneous solution (ethanol) and sodium dodecyl sulfate micelles. In ethanol, the rate of galvinoxyl consumption was independent of the gallate's alkyl chain length. On the other hand, reaction rates in micelles were dependent on the length of the gallate alkyl chain. Measurements of the rate of the reaction at different pH show that, even at pH 7.0, the reaction mainly involves the monodeprotonated anionic form of the gallates. Plots of reaction rates as a function of the surfactant concentration allowed us to evaluate the distribution of the gallates (K_{GH}) and an apparent rate constant defined by the product between the intramicellar rate constant of the anion (k_{G^-}) and its partition constant (K_{G^-}). The values of the increment of the apparent rate constant per methylene group in the alkyl chain strongly suggest that intramicellar rate constant values are independent of the alkyl chain length. This points to a similar intramicellar localization of the phenolate moiety in the three gallates considered.

Key words: galvinoxyl radical, gallates, rate-constant values, sodium dodecyl sulfate (SDS) micelles.

Résumé : Dans ce travail, on a évalué la réactivité du gallate de méthyle, du gallate de propyle et du gallate d'octyle vis-à-vis les radicaux galvinoxyles, en solution homogène dans l'éthanol et dans des micelles de dodécylsulfate de sodium. Dans l'éthanol, la vitesse de disparition du galvinoxyle est indépendante de la longueur de la chaîne alkyle des gallates. Par ailleurs, les vitesses de réaction dans les micelles dépendent de la longueur de la chaîne alkyle des gallates. Des mesures de vitesse de réaction à divers pH montrent que même à un pH de 7,0, la réaction implique principalement la forme anionique monodéprotonée des gallates. Des courbes des vitesses de réaction en fonction de la concentration d'agent de surface a permis d'évaluer la distribution des gallates (K_{GH}) et une constante de vitesse apparente définie par le produit entre la constante de vitesse intramicellaire de l'anion (k_{G^-}) et sa constante de partition (K_{G^-}). Les valeurs des incréments de la constante de vitesse apparente par groupe méthylène de la chaîne alkyle suggèrent fortement que les valeurs la constante de vitesse intramicellaire sont indépendantes de la longueur de la chaîne alkyle. On a considéré ces points pour une localisation intramicellaire semblable de la portion phénolate dans les trois gallates considérés.

Mots-clés : radical galvinoxyle, gallates, valeurs des constantes de vitesse, micelles de dodécylsulfate de sodium (DSS).

[Traduit par la Rédaction]

Introduction

Oxidative stress imposed by reactive oxygen species may play a crucial role in the pathophysiology associated with neoplasia, atherosclerosis, and neurodegenerative diseases. The oxidative damage can be controlled by compounds that remove active free radicals. These compounds can be endogenous or exogenous and most of them have phenolic groups as active moieties. They show a wide range of activities in vitro and are thought to exert protective effects against major diseases such as cancer and cardiovascular diseases.[1–3] The efficiency of a compound to remove reactive radicals will depend on the reactivity of its phenolic groups and the relative localization of the radical and the free-radical scavenger.[4] The synthetic *n*-alkyl esters of gallic acid, in particular propyl and octyl gallates, are widely employed as antioxidants in food and pharmaceutical industries. Besides the antioxidant activity, other biological roles have been described for this group of molecules, such as anticancer, antibacterial, and antifungal roles.[5]

Several studies have shown a good correlation between the inhibition of lipid oxidation of a given compound and its reactivity toward stable radicals.[6,7] However, in dispersed (microheterogeneous) systems like emulsions, antioxidant activity is related to several parameters determined by the interface. In particular, depending on the emulsifier used, an

Received 16 March 2010. Accepted 11 June 2010. Published on the NRC Research Press Web site at canjchem.nrc.ca on 20 January 2011.

This article is part of a Special Issue dedicated to Professor J. C. Scaiano.

R. Bridi.[1] Universidade Federal de Rio Grande do Sul, Av. Ipiranga 2752 Porto Alegre, Rio Grande do Sul 90610-000, Brazil.
C. Aliaga, A. Aspée, E. Abuin, and E. Lissi. Facultad de Química y Biología, Universidad de Santiago de Chile, Av. L. B. O'Higgins 3363, Casilla 40, Correo 33, Santiago, Region Metropolitana, Chile.

[1]Corresponding author (e-mail: raquel.bridi@ufrgs.br).

Can. J. Chem. Downloaded from www.nrcresearchpress.com by University of Electronic and Science Techonology of China on 09/18/12
For personal use only.

accumulation of antioxidants at the interface can be achieved. Although lipidic domains are the main sites of lipid peroxidation, association of antioxidants at the interface does not necessarily result in an improvement of their antioxidant activity. This efficiency can be determined by interactions between antioxidants and emulsifiers at the interface, which may be hydrophobic or due to hydrogen bonding.[6,7] The hydrophobicity of the substrate will strongly influence its distribution between the microphase and the external medium and can also determine the intraparticle substrate distribution, affecting its reactivity toward the hydrophobic radical.[6,8] In this work, we have evaluated the reactivity of methyl gallate (MG), propyl gallate (PG), and *n*-octyl gallate (OG) toward galvinoxyl radicals in homogeneous solution and sodium dodecyl sulfate (SDS) micelles. Galvinoxyl, a stable phenoxyl radical, has a strong absorption peak at 428 nm in ethanol. In the presence of phenolic compounds, it is reduced by electron and (or) hydrogen-atom transfer. This last process has been related to the O–H bond dissociation energy of the donor group.[6,9]

Results and discussion

Figure 1A presents the depletion of galvinoxyl radicals (3 μmol/L) in ethanol solution in the presence of 100 μmol/L methyl, propyl, or octyl gallate. This figure shows that the course of the reaction, and in particular the initial rate of the process, is barely modified by the length of the alkyl chain. This result suggests an identical reactivity of the phenol moiety in ethanol for methyl, propyl, or octyl gallate.[10]

On the other hand, different rates are observed for the different gallates in SDS solutions. Figure 1B represents, as an example, the depletion of galvinoxyl radicals (3 μmol/L) in SDS (0.1 mol/L) in the presence of 100 μmol/L MG, PG, or OG. In particular, the data obtained in these systems show that the rate of the process increases when the length of the gallate alkyl chain increases.

For a given gallate, at fixed gallate and galvinoxyl concentrations, the rate of the process depends on the surfactant concentration. Initial rates measured in these conditions are shown in Fig. 2. The data of this figure show that (*i*) over the whole surfactant concentration range, the initial rate of galvinoxyl consumption follows the order OG > PG > MG (observed differences are larger at low surfactant concentrations); and (*ii*) the rate of the process decreases when the surfactant concentration increases.

These results can be due to the following: (*i*) distribution of galvinoxyl between the external solvent and the micellar ensemble; (*ii*) distribution of the gallates between the external solvent and the micelles; and (or) (*iii*) dependence of the intramicellar rate constant on the length of the gallate alkyl chain.

To assess the localization and environment of galvinoxyl radicals, electron paramagnetic resonance (EPR) spectra were recorded in buffer and SDS solutions (0.025 and 0.1 mol/L). The spectra are shown in Fig. 3.

Galvinoxyl EPR spectra in buffer showed a broad singlet characteristic of solid microaggregates.[11] On the other hand, well-resolved spectra were observed in micellar solutions, with a hyperfine structure that is very little dependent on the surfactant concentration. This would indicate that, in the tested SDS range, all the radicals are incorporated to the micelles and that their surroundings are similar, independent of the surfactant concentration.[6]

Fig. 1. Depletion of galvinoxyl radicals (3 μmol/L) by 100 μmol/L methyl gallate (○), propyl gallate (△), and octyl gallate (□) in ethanol (A) and in 0.1 mol/L SDS in phosphate buffer, pH 7.0 (B).

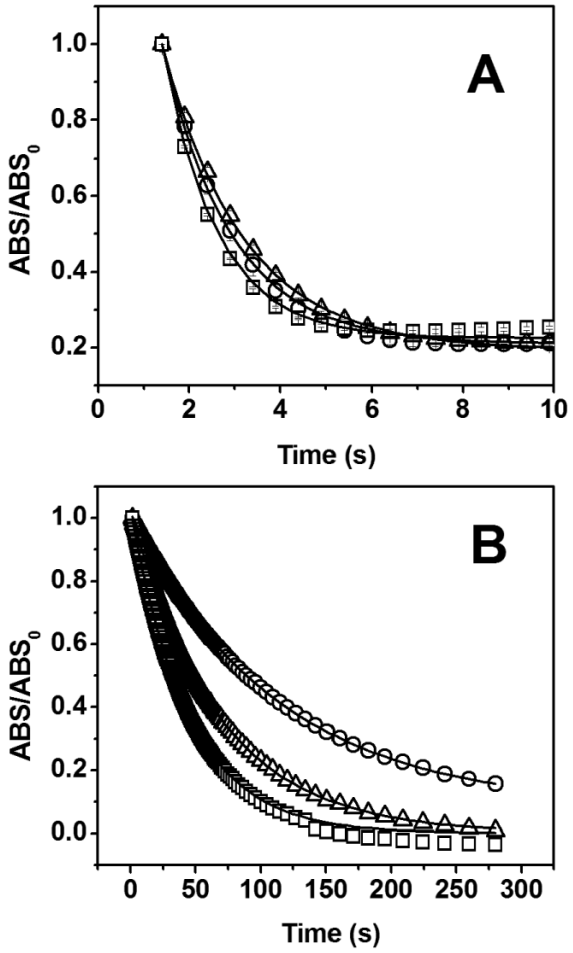

Fig. 2. Initial rate of galvinoxyl consumption elicited by the addition of 100 μmol/L methyl gallate (○), propyl gallate (△), and octyl gallate (□) as a function of SDS concentration.

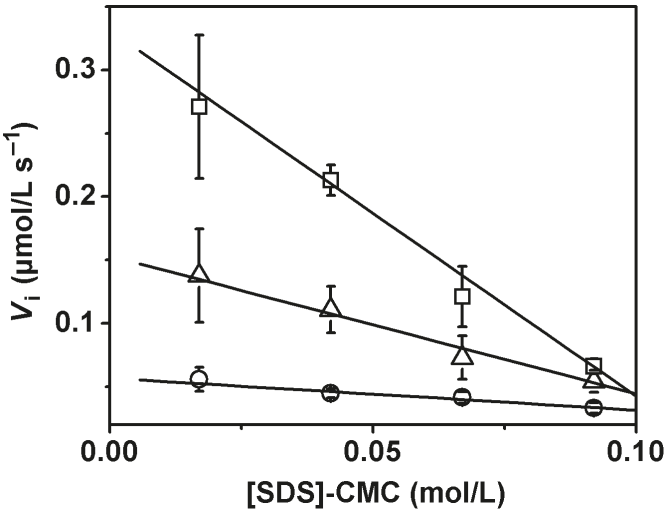

Can. J. Chem. Downloaded from www.nrcresearchpress.com by University of Electronic and Science Techonology of China on 09/18/12
For personal use only.

Fig. 3. Electron paramagnetic resonance spectra of 20 μmol/L gavinoxyl in phosphate buffer at pH 7 (A), 0.025 mol/L SDS (B), and 0.1 mol/L SDS (C).

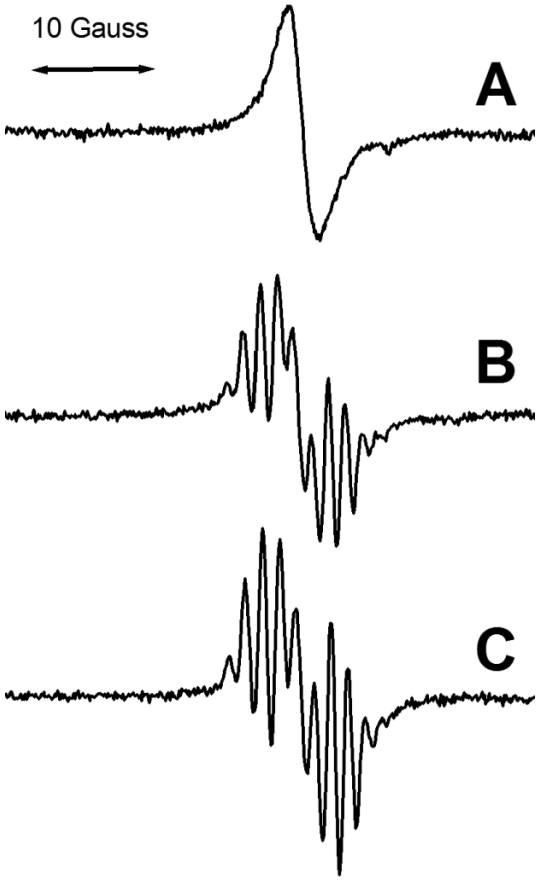

Campos et al.[10] have developed a data treatment to evaluate the antioxidant partition constant and the intramicellar second-order rate constant for the reaction of gallates and 2,2-diphenyl-1-picrylhydrazyl (DPPH). The procedure assumes that the reaction takes place from the gallate in its phenolic form (non-ionized). Nevertheless, under our experimental conditions (phosphate buffer, pH 7 in bulk solution) gallates are partially deprotonated (pK_a = 8.03). The reactivity of gallates and their ionized forms toward galvinoxyl radicals can be different, as can their contribution to the overall reaction rate due to differences in their partition constants.

The galvinoxyl consumption rate in micelles was strongly dependent on the pH of the phosphate media. The data given in Fig. 4 show that, for MG, the reaction rate increases ~20 times when the pH changes from 5 to 9. These results clearly indicate a much faster reaction of the ionized gallate (G^-) than the protonated form (GH).

Measurements in SDS micelles at pH 7.0 showed a decrease in rate when SDS concentration increases (Fig. 5). The following mechanism can explain the reaction rate observed in the presence of micelles:

[1] $\mathrm{GH} = \mathrm{G}^- + \mathrm{H}^+$

[2] $\mathrm{GH} + \mathrm{SDS} = \mathrm{GH}_{\mathrm{mic}}$

Fig. 4. Observed first-order rate constant of galvinoxyl consumption by 100 μmol/L methyl gallate in 0.1 mol/L SDS at different pH values.

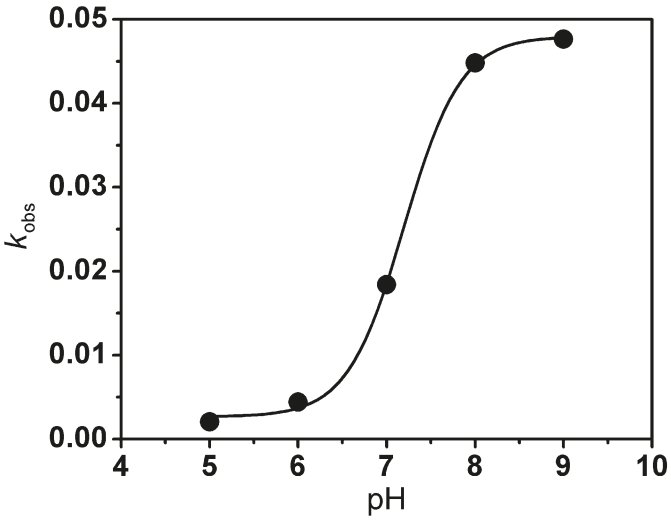

[3] $\mathrm{G}^- + \mathrm{SDS} = \mathrm{G}^-_{\mathrm{mic}}$

[4] $\mathrm{Galv}^{\bullet}_{\mathrm{mic}} + \mathrm{GH}_{\mathrm{mic}} \rightarrow \mathrm{Products}$

[5] $\mathrm{Galv}^{\bullet}_{\mathrm{mic}} + \mathrm{G}^-_{\mathrm{mic}} \rightarrow \mathrm{Products}$

where GH and G^- represent the non-ionized and ionized forms of gallates, respectively; Galv• is the galvinoxyl radical and the subscript mic indicates the micellar pseudophase.

The galvinoxyl depletion rate (v), due to eqs. [4] and [5], can be written as

[6] $$v/\mathrm{Galv}^{\bullet} = (k_{\mathrm{GH}}\mathrm{GH}_{\mathrm{mic}} + k_{\mathrm{G}^-}\mathrm{G}^-_{\mathrm{mic}})/f$$

where f is the fraction of volume of micelles, defined as $f = V^{\circ}[\mathrm{SDS}]/1000$, and V° is the surfactant molar volume.

The previous reaction can be expressed in terms of the concentration in aqueous phase if partition constants of the gallate (K_{GH}) and the ionized form (K_{G^-}) are incorporated in eq. [6].

[7] $$v/\mathrm{Galv}^{\bullet} = \frac{1000}{V^{\circ}}(k_{\mathrm{GH}}K_{\mathrm{GH}}\mathrm{GH} + k_{\mathrm{G}^-}K_{\mathrm{G}^-}\mathrm{G}^-)$$

From the data given in Fig. 4, it can be concluded that the contribution of the $k_{\mathrm{GH}}K_{\mathrm{GH}}$ factor is much smaller than that of the ionized gallate ($k_{\mathrm{G}^-}K_{\mathrm{G}^-}$). The overall rate can then be written as

[8] $$\mathrm{Galv}^{\bullet}[\mathrm{G}]/v = a + b[\mathrm{SDS}]$$

where [G] represents the analytical gallate concentration, $[\mathrm{G}] = \mathrm{GH} + \mathrm{G}^- + \mathrm{GH}_{\mathrm{mic}} + \mathrm{G}^-_{\mathrm{mic}}$, and

[9] $$a = \left(1 + \frac{K_a}{[\mathrm{H}^+]}\right) \Big/ \frac{1000}{V^{\circ}} K_{\mathrm{G}^-} \frac{K_a}{[\mathrm{H}^+]} k_{\mathrm{G}^-}$$

Can. J. Chem. Downloaded from www.nrcresearchpress.com by University of Electronic and Science Techonology of China on 09/18/12
For personal use only.

Fig. 5. (A) Depletion of galvinoxyl radicals by 100 μmol/L propyl gallate at different concentrations of SDS: 0.1 mol/L (○), 0.075 mol/L (△), and 0.025 mol/L (□). (B) Initial rate of galvinoxyl consumption elicited by the addition of octyl gallate in 0.1 mol/L (□) and 0.05 mol/L (○) SDS. Bar lines represent the standard deviation of three independent measurements.

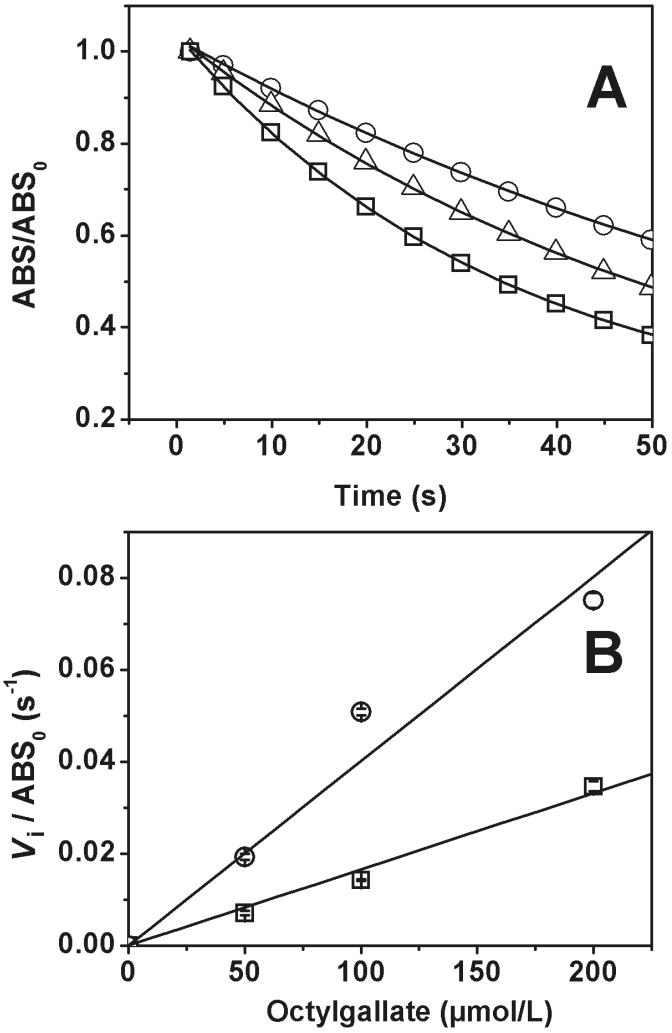

$$[10] \qquad b = \left(K_{GH} + K_G \frac{K_a}{[H^+]}\right) \Big/ \frac{1000}{V^o} K_{G^-} \frac{K_a}{[H^+]} k_{G^-}$$

If the dissociation constant of the gallates (K_a) and the charge of the micelles are considered, it can be concluded that in our experimental conditions the concentration of the ionized gallate in the aqueous solution and in the micelle is much lower than the analytical gallate concentration. This consideration allows simplification of the values of a and b in this expression to

$$[11] \qquad a = V^o[H^+]/1000K_{G^-}K_a k_{G^-}$$

$$[12] \qquad b = K_{GH}V^o[H^+]/1000K_{G^-}K_a k_{G^-}$$

A plot of the left-hand side of eq. [8] against the free surfactant concentration (Fig. 6) allows the evaluation of K_{GH} (from the slope and intercept). It is interesting to note that

Fig. 6. Inverse initial rate of galvinoxyl consumption elicited by the addition of 100 μmol/L methyl gallate (○), propyl gallate (△), and octyl gallate (□) as a function of SDS concentration. Bar lines represent the standard deviation of three independent measurements. The critical micelle concentration was taken as 8 mmol/L.

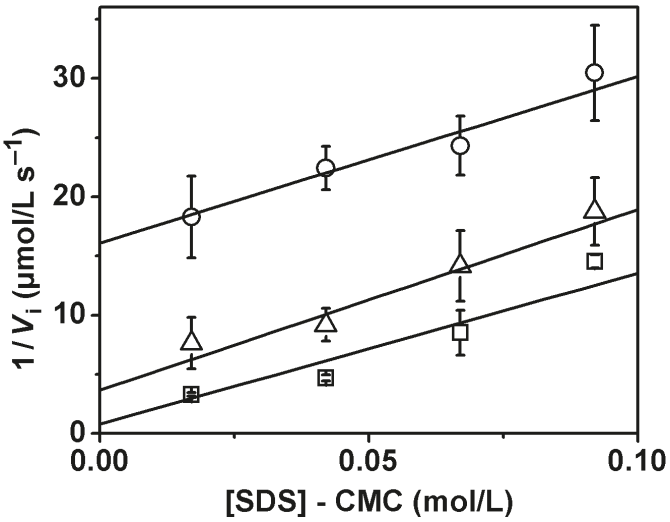

in spite of the fact that the reactive species is the deprotonated gallate, the rate of the process is determined by the partition of GH. This apparent anomaly is due to the fact that the partition of GH regulates the amount of free G^- and that this determines the amount of the reactive species associated to the micelles.

If V° is taken as –250 mL/mol, the intercept of the plot allows determination of the product between the intramicellar rate constant of the ionized gallate and its partition constant ($K_{G^-}k_{G^-}$). These values are shown in Table 1, where the results obtained in homogeneous (ethanol) solution are also included.

The data treatment employed to obtain $k_{G^-}K_{G^-}$ values implies that K_{G^-} is independent of SDS concentration, in spite of the change in surface potential that could be elicited by the concomitant increase in free sodium concentration. To test the pertinence of this assumption, we measured the rate of galvinoxyl consumption by MG, employing a fixed SDS concentration (50 mmol/L) in the absence and presence of 30 mmol/L NaCl. No significant differences were observed (data not shown), indicating that under the present experimental conditions, we can assume that the factor $k_{G^-}K_{G^-}$ can be considered to be nearly independent of the free sodium concentration.

The data collected in Table 1 show that, as expected, the gallate association constant to SDS micelles increases with the length of the alkyl chain. A plot of $\ln(K_{GH})$ against the number of methylene groups in the gallate alkyl chain renders a contribution to the free energy of transfer ($\Delta\Delta G^o$) of nearly 1 kJ per methylene group. This value can be subject to a large error given the uncertainty in the OG distribution constant, but is similar to those reported in other systems comprising ionic micelles.[12,13] Furthermore, it is considerably larger than that obtained for the same gallates in Triton X-100 micelles.[9] This difference can be related to a more hydrophobic environment sensed by the gallates' alkyl chains in SDS than in Triton X-100 micelles.

Can. J. Chem. Downloaded from www.nrcresearchpress.com by University of Electronic and Science Techonology of China on 09/18/12
For personal use only.

Table 1. Experimentally determined K_{GH} and $K_{G^-}k_{G^-}$ values in SDS micellar solutions.

	K_{GH} (L mol^{-1})[a]	$K_{G^-}k_{G^-}$ (L^2 mol^{-2} s^{-1})[b]	k_{EtOH} (L mol^{-1} s^{-1})
Methyl gallate	8.7	550	4900
Propyl gallate	41.7	2400	4600
Octyl gallate	157	11000	6500

[a]Values calculated in terms of molar surfactant concentrations.
[b]Values assuming V°= 250 mL/mol.

The factor $K_{G^-}k_{G^-}$ shows the same trend as the partition coefficient of the protonated gallate (K_{GH}) with the length of the gallate alkyl chain (Table 1). In agreement with this, a plot of $\log(K_{G^-}k_{G^-})$ versus the number of methylene groups renders a slope of 0.18, a value that is very close to that obtained for the change of K_{GH} with the number of methylene groups. If it is assumed that the length of the alkyl chain influences K_{G^-} and K_{GH} in similar ways, the similar slopes imply that k_{G^-} is nearly independent of the number of methylene groups. These results would suggest a similar intramicellar location of the reactive moiety.[7] Therefore, the differences observed (Fig. 1B) would be mainly a consequence of the different partition constants for the three deprotonated gallate alkyl esters.

A similar conclusion has been obtained regarding the reaction of gallates with DPPH in neutral Triton X-100 micelles.[10] The slower rates observed in SDS micelles compared with the rates observed in ethanol (Fig. 1) can be mostly ascribed to the small G^- fraction associated to the anionic micelles. This fraction can lead to an electron-transfer process at the micellar surface between the phenolate group of the gallate and the micelle-associated galvinoxyl radicals.

Conclusions

Different rates observed for the reaction of gallates with different alkyl chain lengths with galvinoxyl radicals in SDS micelle solutions are mainly due to partitioning of the anionic gallates. In fact, the results indicate similar intramicellar rate constants for the three compounds considered, indicating that the intramicellar localization of the reactive group is independent of the length of the alkyl chain.

Experimental

Materials

Thestable free-radical galvinoxyl (2,6-di-*tert*-butyl-α-(3,5-di-*tert*-butyl-4-*oxo*-2,5-cyclohexadiene-1-ylidene), anionic SDS (sodium dodecyl sulfate, 99%), and the gallates methyl gallate (98%), propyl gallate, and *n*-octyl gallate (98%) were obtained from Sigma-Aldrich. Stock solutions of the gallates and galvinoxyl were prepared daily in analytical grade ethanol (Merck). The reactions carried out in micelles contained 1% ethanol. Micellar solutions of SDS were prepared in 10 mmol/L sodium phosphate buffer, pH 7.0.

Instruments

UV–visible spectra were recorded using a UV–vis spectrophotometer (Hewlett Packard 8453; Palo Alto, California, USA). A stopped-flow apparatus from Applied Photophysics was used for kinetic measurements. The rate of the reaction was followed by registering the absorbance of galvinoxyl at 428 nm. EPR spectra were obtained on a Bruker EMX 1572 spectrometer that operates in the X-band (9.2–9.9 GHz), equipped with a thermal cavity at 25 °C.

Acknowledgements

Raquel Bridi gratefully acknowledges the Universidade Federal do Rio Grande do Sul for supporting a postdoctoral stay at the Universidad de Santiago de Chile. Financial support from FONDECYT 1085177 is also acknowledged.

References

(1) Halliwell, B.; Gutteridge, J. *Free Radicals in Biology and Medicine;* Oxford University Press Inc.: New York, 2007; Chapter 9.
(2) Rice-Evans, C. A.; Miller, N. J.; Bolwell, P. G.; Bramley, P. M.; Pridham, J. B. *Free Radic. Res.* **1995**, *22* (4), 375. doi:10.3109/10715769509145649. PMID:7633567.
(3) Boudet, A.-M. *Phytochemistry* **2007**, *68* (22–24), 2722.
(4) Barclay, L. R.; Vinqvist, M. R. *Free Radic. Biol. Med.* **1994**, *16* (6), 779. doi:10.1016/0891-5849(94)90193-7. PMID: 8070681.
(5) Kratz, J. M.; Andrighetti-Fröhner, C. R.; Leal, P. C.; Nunes, R. J.; Yunes, R. A.; Trybala, E.; Bergström, T.; Barardi, C. R. M.; Simões, C. M. O. *Biol. Pharm. Bull.* **2008**, *31* (5), 903. doi:10.1248/bpb.31.903. PMID:18451516.
(6) Heins, A.; McPhail, D. B.; Sokolowski, T.; Stöckmann, H.; Schwarz, K. *Lipids* **2007**, *42* (6), 573. doi:10.1007/s11745-007-3052-6. PMID:17473943.
(7) Stöckmann, H.; Schwarz, K.; Huynh-Ba, T. *J. Am. Oil Chem. Soc.* **2000**, *77* (5), 535. doi:10.1007/s11746-000-0085-6.
(8) Abuin, E.; Lissi, E.; Ortiz, P.; Henriquez, C. *Bol. Soc. Chil. Quim.* **2002**, *47*, 145.
(9) Shi, H.; Niki, E. *Lipids* **1998**, *33* (4), 365. doi:10.1007/s11745-998-0216-8. PMID:9590623.
(10) Campos, A. M.; Ponce, E.; Lissi, E. A. *J. Phys. Org. Chem.* **2009**, *22* (12), 1208. doi:10.1002/poc.1580.
(11) Stasko, A.; Brezová, V.; Biskupic, S.; Misík, V. *Free Radic. Res.* **2007**, *41* (4), 379. PMID:17454120.
(12) Sepulveda, L.; Lissi, E.; Quina, F. *Adv. Colloid Interface Sci.* **1986**, *25* (1), 1. doi:10.1016/0001-8686(86)80001-X. PMID:3333129.
(13) Ulloa, Y.; Rubio, M. A.; Lissi, E. A.; Aspée, A. *Bol. Soc. Chil. Quim.* **1994**, *39*, 129.

Photochemistry of matrix-isolated 5-cyano-2*H*-pyran-2-one (δ-cyano-α-pyrone) and cyanocyclobuta-1,3-diene

Jessica L. Menke and Robert J. McMahon

Abstract: Matrix-isolation photochemistry (λ > 299 nm; Ar, 10 K) of 5-cyano-2*H*-pyran-2-one (**5**, δ-cyano-α-pyrone) shows complete conversion to a mixture of several ring-opened ketene isomers (**6**) and a ring-closed Dewar lactone (**7**), as detected by infrared spectroscopy. Subsequent irradiation (λ > 200 nm) causes decarboxylation of the Dewar lactone (**7**) to produce cyanocyclobuta-1,3-diene (**8**). Continued irradiation (λ > 200 nm) results in the photodecomposition of cyanocyclobuta-1,3-diene (**8**) to cyanoacetylene and acetylene. 4-Cyanopyridine (**10**) was explored as an alternative photochemical precursor to cyanocyclobuta-1,3-diene (**8**). It was found, however, that **10** does not exhibit observable photochemistry under our irradiation conditions.

Key words: astrochemistry, cyclobutadiene, matrix-isolation spectroscopy, physical-organic chemistry, reactive intermediates.

Résumé : La photochimie (λ > 299 nm; Ar, 10 K) de la 5-cyano-2*H*-pyran-2-one (**5**, δ-cyano-α-pyrone) isolée dans une matrice donne lieu à une conversion complète qui, d'après les détections faites par spectroscopie infrarouge, comporte un mélange de plusieurs isomères céténiques en chaîne ouverte, **6**, et un sous forme cyclique, la lactone de Dewar **7**. Une irradiation subséquente (λ > 220 nm) provoque une décarboxylation de la lactone de Dewar, **7**, et la formation du cyanocyclobuta-1,3-diène (**8**). Une continuation de l'irradiation (λ > 220 nm) conduit à une photodécomposition du cyanocyclobuta-1,3-diène (**8**) et à l'obtention du cyanoacétylène et de l'acétylène. On a aussi examiné la possibilité d'utiliser la 4-cyanopyridine (**10**) comme précurseur photochimique pour le cyanocyclobuta-1,3-diène (**8**). On a trouvé toutefois que le produit **10** ne donne lieu à aucune photochimie observable dans les conditions d'irradiation utilisées ici.

Mots-clés : astrochimie, cyclobutadiène, spectroscopie en isolement dans une matrice, chimie organique physique, intermédiaires réactifs.

[Traduit par la Rédaction]

Introduction

Interest in the photochemistry of 2*H*-pyran-2-one (**1**, α-pyrone) derives from its utility in generating cyclobuta-1,3-diene (**4**),[1–16] a reactive molecule of considerable theoretical interest in organic chemistry.[11,17,18] In the current study, we explored the photochemistry of 5-cyano-2*H*-pyran-2-one (**5**, δ-cyano-α-pyrone) in an effort to generate cyanocyclobuta-1,3-diene (**8**) (Scheme 1).

Our interest in producing cyanocyclobutadiene (**8**) stems from the general relevance of cyanoacetylene and other unsaturated organic nitriles to the chemistry of the interstellar medium[19–23] and the atmosphere of Titan, Saturn's largest moon.[24–27] Cyanocyclobutadienes are predicted intermediates in the thermal[28,29] and photochemical[30,31] trimerization of cyanoacetylene and acetylene to give cyanobenzenes, and recent computational work reveals that cyano substituents confer a thermodynamic stabilization to the cyclobutadiene ring.[32,33] We now describe the photochemical transformations involving cyanopyrone **5**, cyanoketene isomers **6**, Dewar lactone **7**, and cyanocyclobuta-1,3-diene (**8**). We also describe efforts to utilize 4-cyanopyridine (**10**) as an alternative photochemical precursor to cyanocyclobuta-1,3-diene (**8**).

Background

Irradiation of α-pyrone (**1**) initiates both a ring-opening reaction to produce ketene **2** and a ring-closing reaction to produce bicyclic lactone **3**, which we refer to as a Dewar lactone. Under photochemical reaction conditions, ketene **2** exists as multiple conformational and geometric isomers. Close examination of the ketene-stretching region of the IR spectrum gives insight into how many isomers are present and how they interconvert with further irradiation.[14,16] In the unsubstituted α-pyrone (**1**) system, a [1,5] sigmatropic hydrogen shift in ketene **2** is a degenerate process. In certain substituted systems, however, the [1,5]-hydrogen shift pro-

Received 29 April 2010. Accepted 17 June 2010. Published on the NRC Research Press Web site at canjchem.nrc.ca on 21 January 2011.

This article is part of a Special Issue dedicated to Professor J. C. Scaiano.

J.L. Menke and R.J. McMahon.[1] Department of Chemistry, University of Wisconsin, 1101 University Avenue, Madison, WI 53706-1322, USA.

[1]Corresponding author (e-mail: mcmahon@chem.wisc.edu).

Can. J. Chem. Downloaded from www.nrcresearchpress.com by University of Electronic and Science Techonology of China on 09/18/12
For personal use only.

Can. J. Chem. Downloaded from www.nrcresearchpress.com by University of Electronic and Science Techonology of China on 09/18/12
For personal use only.

Scheme 1.

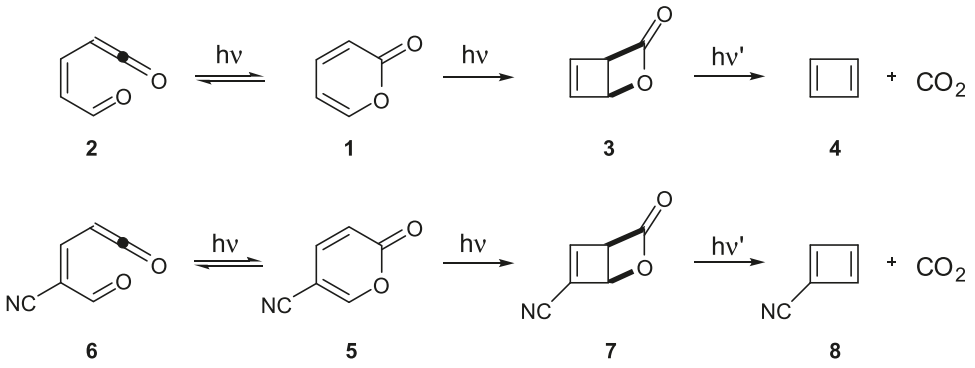

duces a different ketene isomer.[16] Ring-closing of this ketene can produce a different isomer of α-pyrone.

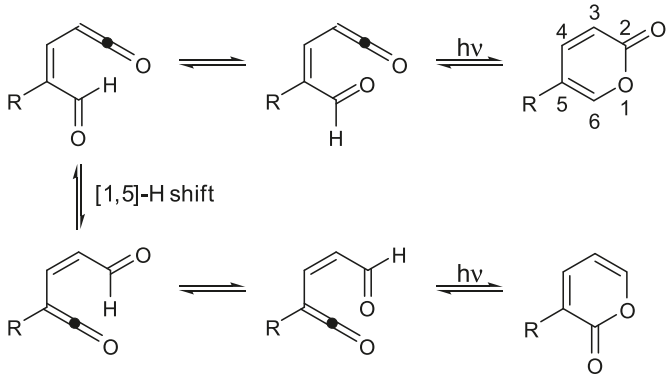

The Dewar lactone **3**, as well as several substituted derivatives, photodecompose to produce cyclobuta-1,3-diene (**4**) and CO_2.[2,3,5,6,9,10,12–16,34–40] When cyclobutadiene and CO_2 are cage-confined in a matrix, they form a complex in which CO_2 lies parallel to the plane of the cyclobutadiene ring.[13,41,42]

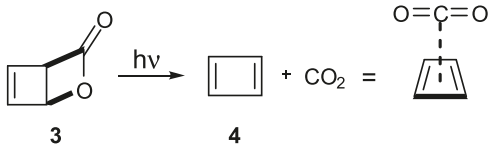

Pyridine (**9**) also serves as a photochemical precursor to cyclobutadiene.[3,43] A benefit of pyridine precursors is the lack of ring-opening products. However, two Dewar isomers are possible (type I and type II).[3,43–45] Kudoh et al. showed that pyridine (**9**) selectively forms the type I Dewar isomer under UV irradiation.[43] Careful selection of substituted pyridines may lead to the corresponding substituted cyclobutadienes.

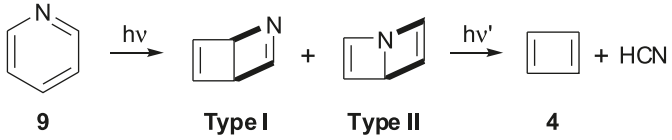

Results and discussion

Photochemistry of 5-cyano-2*H*-pyran-2-one (5): IR spectroscopy

5-Cyano-2*H*-pyran-2-one (**5**) was sublimed at 70 °C and co-deposited with argon to afford a clean matrix-isolated sample. The IR spectrum obtained after deposition can be found as Supplementary data (Fig. S1). UV irradiation (λ > 299 nm, 2 h) provides complete conversion of **5** to a mixture of the Dewar lactone **7** and several ketenes **6** (Scheme 2) (Fig. 1). The production of a Dewar lactone has been seen previously for the parent system[2,5,7–10,12,14] and several substituted α-pyrones.[13,15,16] The identity of **7** is confirmed by comparison of the experimental and computed (B3LYP/6-31G*) IR spectra (Fig. 1). The shift of the carbonyl stretching vibration of **7** to higher frequency, relative to cyanopyrone **5**, is common for carbonyl groups in small ring systems and is a characteristic signature for the formation of Dewar lactones from α-pyrones. The complete disappearance of cyanopyrone **5** rules out the possibility of a photostationary state, as seen for 5-carbomethoxy-2*H*-pyran-2-one.[15] A raw spectrum showing the complete conversion of **5** to **6** and **7** can be found in the Supplementary data, Fig. S2.

The presence of the ring-opened ketene isomers **6** is revealed by the asymmetric –C=C=O stretching vibration centered at 2135 cm^{-1} (Fig. 2). Figure 2*a*, which is taken from the same experiment shown in Fig. 1, exhibits 4 absorptions, at 2146, 2140, 2134, and 2127 cm^{-1}, with an additional very weak band at 2118 cm^{-1}. For the unsubstituted system, several different ketene isomers (**2**) are also observed, and these isomers interconvert with further irradiation.[14] The absorption pattern for the cyanoketene isomers **6** (Fig. 2) is very similar to the spectrum obtained by Breda et al. after irradiation of α-pyrone at λ > 285 nm for 1 min. The peaks for the cyanoketene isomers **6** are shifted to higher frequency by approximately 10 cm^{-1}, relative to the unsubstituted system.[14]

An additional experiment was performed using a Xe lamp (lower intensity than the Hg lamp) to follow the isomerization of the ketene isomers. Figure 2*b* shows the evolution of the –C=C=O stretching region as a function of irradiation time (λ > 299 nm). The absorptions at 2140, 2134, and 2127 cm^{-1} appear to grow at a fairly consistent rate. The absorptions at 2146 and 2118 cm^{-1}, however, initially grow at a faster rate and then begin to disappear after 2 to 6 h of irradiation, indicating a secondary photochemical process.

Can. J. Chem. Downloaded from www.nrcresearchpress.com by University of Electronic and Science Techonology of China on 09/18/12
For personal use only.

Scheme 2.

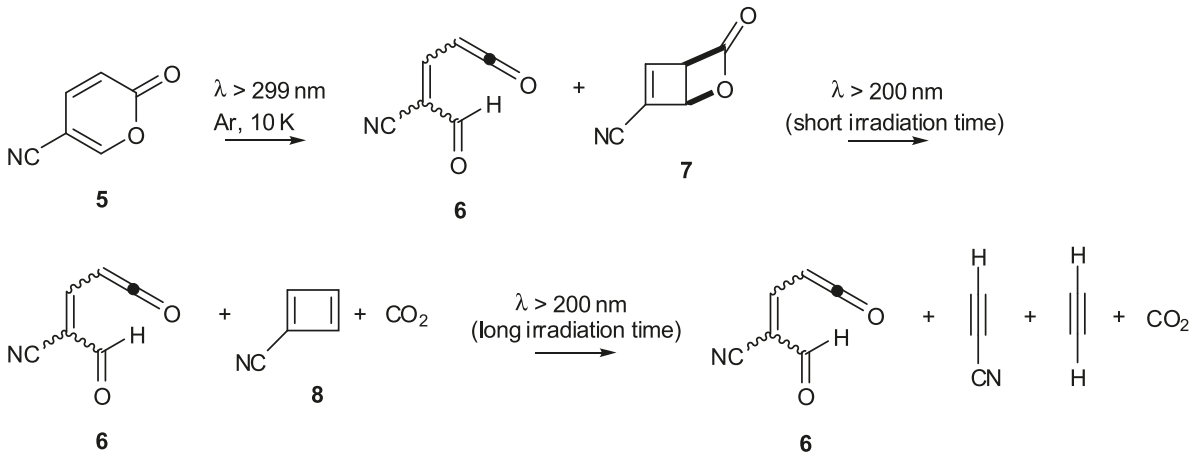

Fig. 1. Top: Unscaled computed (B3LYP/6-31G*) IR spectrum of Dewar lactone **7**. Middle: IR subtraction spectrum obtained after irradiation (λ > 299 nm; 2 h) of 5-cyano-2*H*-pyran-2-one (**5**) showing the appearance (positive peaks) of ketenes **6** and Dewar lactone **7** with the simultaneous disappearance (negative peaks) of **5** (Ar, 10 K). Bottom: Unscaled computed IR spectrum of **5**.

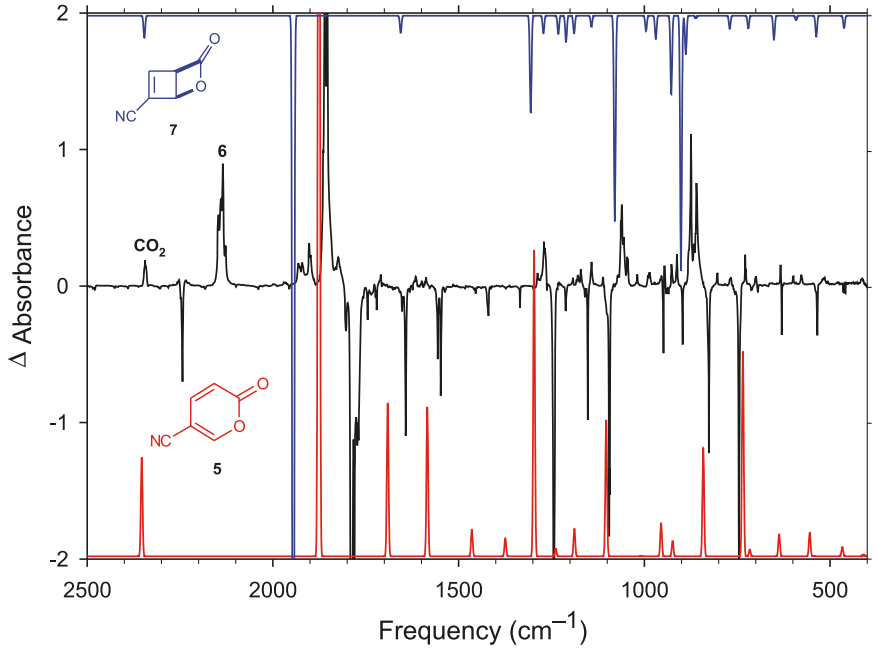

To better understand the structure, energetics, and spectroscopy of the possible cyanoketene isomers **6a**–**6g**, we performed a computational survey using DFT methods (B3LYP/6-31G*) (Fig. 3). The cyanoketene structures **6a**–**6g** lie within 8 kcal mol^{-1} of each other. Although not all of the transition states connecting the cyanoketene isomers were computed, the lowest (**6a** to **6b**) and highest (**6b** to **6f**) barriers reported for the unsubstituted isomers were computed. In terms of energetics, all structures appear to be viable intermediates under the photochemical reaction conditions. Despite the fact that the computed IR spectrum for each cyanoketene isomer **6a**–**6g** is available to us, we are unable to provide a detailed assignment for the isomers present in the experimental spectrum. Apart from the strong absorptions of the –C=C=O stretching vibrations, the remainder of the IR absorptions of **6a**–**6g** are relatively weak and are further obscured by the presence of the strongly absorbing Dewar lactone **7** in the matrix.

Photochemical conversion of Dewar lactone 7 to cyanocyclobuta-1,3-diene (8)

After the complete conversion of 5-cyano-2*H*-pyran-2-one (**5**) to ketenes (**6**) and Dewar lactone **7** (λ > 299 nm), the matrix was irradiated at shorter wavelengths (λ > 200 nm). After 30 min of irradiation, the major photoproducts were CO_2 (3702, 3596, 2345, 661 cm^{-1}),[46] acetylene (3284, 3268, 3257, 3247, 744, 736 cm^{-1}),[47] and cyanoacetylene (3315, 2269, 2076, 667 cm^{-1}),[48] as shown in Fig. 4*a*. In addition, several weak absorptions can be attributed to cyanocyclobuta-1,3-diene (**8**) (2184, 1211, 602, 518 cm^{-1}). These bands correspond rather well with the most intense absorptions in the computed IR spectrum of **8** (Fig. 4*a*, top). Apart from the nitrile stretch (2184 cm^{-1}), these bands are also similar to

Can. J. Chem. Downloaded from www.nrcresearchpress.com by University of Electronic and Science Techonology of China on 09/18/12
For personal use only.

Fig. 2. The asymmetric –C=C=O stretching region of the IR spectrum of ketenes (**6**). (*a*) Spectrum obtained after irradiation of 5-cyano-2*H*-pyran-2-one (**5**) with a Hg lamp (λ > 299 nm; Ar, 10 K) for 2 h. (*b*) Spectra obtained after irradiation of **5** with a Xe lamp (λ > 299 nm; Ar, 10 K) for 1, 10, 35, 60, 90 min; 2, 6, 8, 12, and 29 h. Absorptions at 2140, 2134, and 2127 cm^{-1} grow at a fairly consistent rate throughout the course of the irradiation.

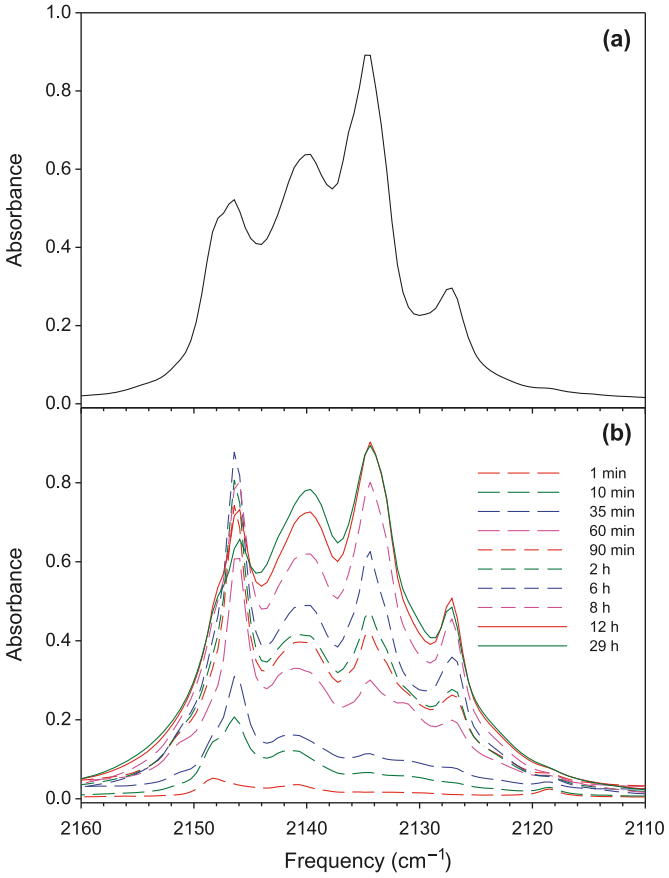

Fig. 3. Computed relative energies (kcal mol^{-1}, B3LYP/6-31G*, ZPVE included) of cyanoketene isomers (**6a**–**6g**), along with transition-state energies for the thermal conversion of **6a** to **6b** and **6b** to **6f**.

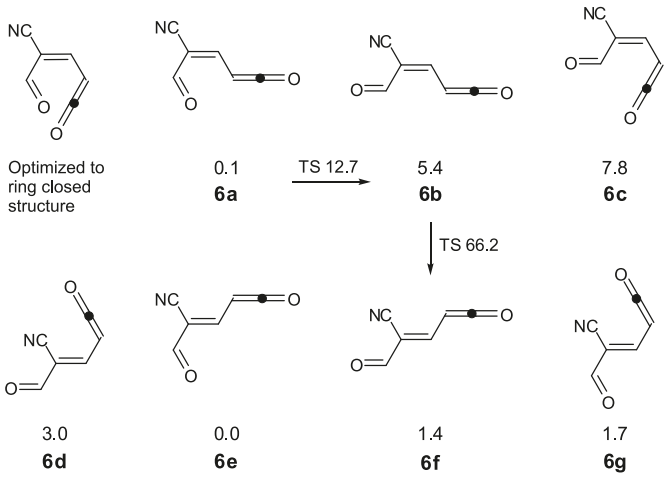

those of the unsubstituted cyclobutadiene (**4**) (1245, 655, 575 cm^{-1}).[2,6,8,12] Further support for the cyanocyclobuta-1,3-diene (**8**) assignment comes from consideration of the subsequent photochemistry. Continued irradiation (λ > 200 nm; 60 min) reveals an increase in the IR absorptions of both acetylene and cyanoacetylene with concomitant disappearance of the IR absorptions attributed to **8**.

When cyclobutadiene derivatives are photochemically produced from the corresponding Dewar lactones under matrix isolation conditions, the cyclobutadiene and CO_2 are formed in a single matrix cavity and thus exist as a complex.[9,14,41,49] To probe the possible involvement of a complex in the current system, we carried out a computational investigation of the complex between cyanocyclobuta-1,3-diene (**8**) and CO_2. A complex was indeed obtained as an energy minimum on the potential energy surface (B3LYP/6-31G*). The computed IR spectrum of the complex, however, did not display any significant differences when compared with the spectrum of **8** itself (see Supplementary data). There is a very slight decrease (0.7 kcal mol^{-1}) in the relative energy of the **8**–CO_2 complex as compared with the fully separated **8** and CO_2. Although it is likely that the complex is present in the matrix, this conclusion cannot be experimentally confirmed or denied on the basis of the data available to us.

During the short-wavelength irradiation (λ > 200 nm), additional minor changes are observed in the IR spectrum (Fig. 4). The simultaneous growth and loss of peaks in the –C=C=O stretching region (ca. 2135 cm^{-1}) indicate further photoequilibration of the ketene isomers **6**. New peaks at 2234 and 503 cm^{-1} remain unassigned at this time.

Photochemistry of 5-cyano-2*H*-pyran-2-one (5): UV–vis spectroscopy

The electronic absorption spectrum of 5-cyano-2*H*-pyran-2-one (**5**; Ar, 10 K) exhibits absorption maxima at 233 and 291 nm (Fig. 5). Photoexcitation into the longer wavelength absorption feature, using λ > 299 nm, bleaches the absorptions of **5**. The residual absorption maximum shifts to 250 nm, which presumably arises from the mixture of isomeric ketenes **6**, since the chromophore for the nonconjugated Dewar lactone **7** is expected to lie deeper in the UV. Irradiation at shorter wavelengths (λ > 200 nm) bleaches the absorption at 250 nm. The resulting spectrum reveals only the tailing absorptions of species absorbing in the deep UV. IR spectra, taken under analogous conditions, show the appearance of acetylene and cyanoacetylene, neither of which absorbs strongly at λ > 200 nm.[50] During the λ > 200 nm irradiation, we were unable to identify an absorption feature — first growing, then disappearing — that could be correlated with cyanocyclobuta-1,3-diene (**8**).

Cyanopyridines as photochemical precursors for cyanocyclobuta-1,3-dienes

In light of the earlier reports that pyridine serves as a photochemical precursor for the production of Dewar pyridine[3,43–45] and cyclobutadiene,[3,43,45] we identified 4-cyanopyridine (**10**) as a potential precursor for cyanocyclobuta-1,3-diene (**8**). Each of the cyanopyridine isomers is commercially available, but the 4-substituted isomer became

Can. J. Chem. Downloaded from www.nrcresearchpress.com by University of Electronic and Science Techonology of China on 09/18/12
For personal use only.

Fig. 4. (*a*) Top: Unscaled computed (B3LYP/6-31G*) IR spectrum of cyanocyclobuta-1,3-diene (**8**). Middle: IR subtraction spectrum obtained after irradiation (λ > 200 nm; 30 min) of a matrix containing ketenes **6** and Dewar lactone **7** showing the appearance of CO_2, acetylene (HCCH), cyanoacetylene (HCCCN), and cyanocyclobuta-1,3-diene (*, **8**) (Ar, 10 K). Isomerization of ketenes **6** and the presence of an unknown species (X) are also observed. Bottom: Unscaled computed spectrum of Dewar lactone **7**. (*b*) Middle: IR subtraction spectrum obtained after irradiation (λ > 200 nm; 60 min) showing the increase in acetylene (HCCH) and cyanoacetylene (HCCCN) and loss of cyanocyclobuta-1,3-diene (*, **8**) (Ar, 10 K). Bottom: Unscaled computed spectra of **8** (blue) and **7** (red). The 1800–1400 cm^{-1} spectral region is omitted for clarity. The full spectrum is available in the Supplementary data, Fig. S3.

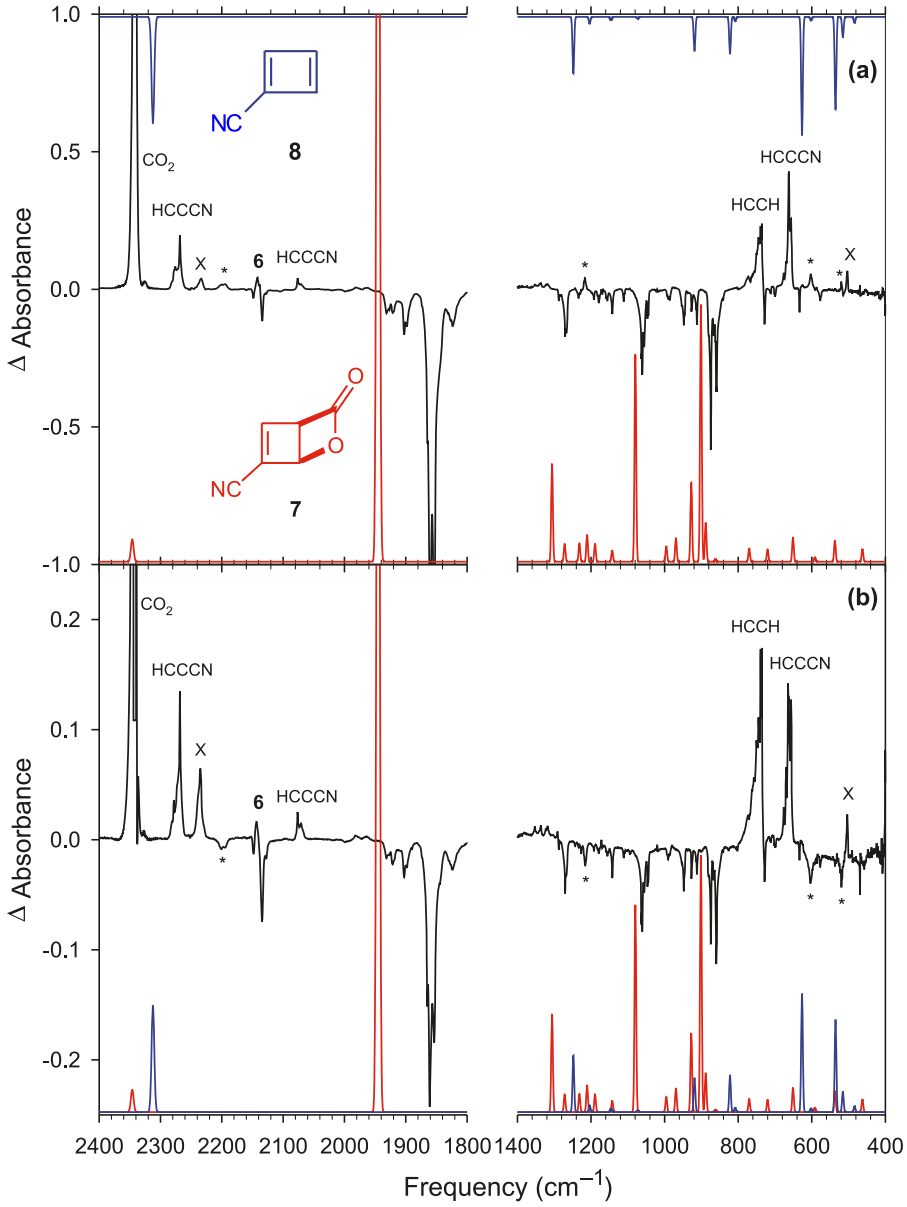

the focus of our study because it would produce the fewest Dewar isomers (Fig. 6).

4-Cyanopyridine (**10**) was sublimed at 25 °C and co-deposited with argon to afford a clean matrix-isolated sample. The IR spectrum obtained after deposition can be found as Supplementary data (Fig. S4). The sample was irradiated at several wavelengths, including λ > 200 nm, for 10 h with no photochemical changes apparent by IR spectroscopy (Fig. S5). Thus, under our experimental conditions, 4-cyanopyridine is not a viable precursor for the production of cyanocyclobuta-1,3-diene (**8**). The cyano substituent apparently perturbs the excited state of the pyridine moiety such that photocyclization to the Dewar isomer does not occur. In this regard, it is worth commenting that the electronic absorption spectrum of 4-cyanopyridine (**10**) differs notably from that of pyridine (**9**),[51] and that 4-cyanopyridine is phosphorescent, while pyridine is not.[52]

Several dicyanopyridines are also commercially available and may be considered potential precursors to the dicyanocyclobuta-1,3-dienes. These systems were computationally surveyed (Fig. 7). 3,4-Dicyanopyridine (**13**) represents an attractive target because the Dewar isomer (2-aza-5,6-dicyanobicyclo[2.2.0]hexa-2,5-diene, **14**) is the lowest in energy of all the dicyano Dewar isomers, and because both type I

Can. J. Chem. Downloaded from www.nrcresearchpress.com by University of Electronic and Science Techonology of China on 09/18/12
For personal use only.

Fig. 5. UV–vis spectra obtained after 3 min deposition of 5-cyano-2*H*-pyran-2-one (**5**) at 50 °C (black) (Ar, 25 K), followed by irradiation at λ > 299 nm (Ar, 10 K) for 5 and 10 min, then irradiation at λ > 200 nm for 5 and 10 min. (Because UV–vis absorptions are much more intense than IR absorptions, the matrix used for UV–vis spectroscopy is much thinner than that used for IR spectroscopy, resulting in much shorter irradiation times.)

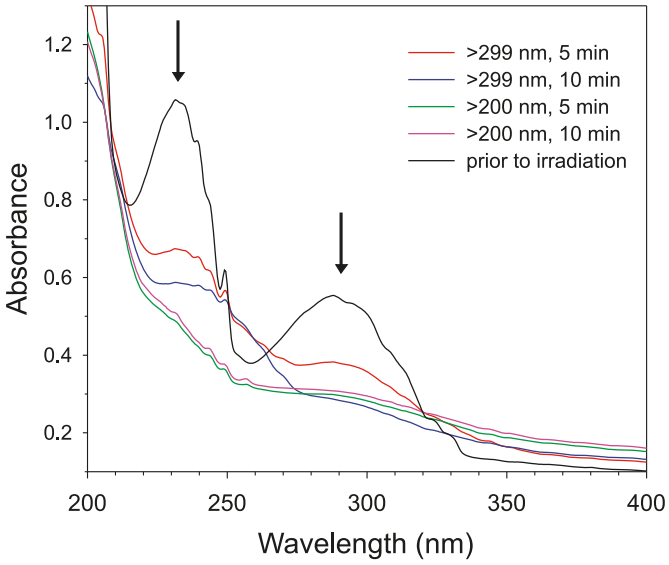

Fig. 6. Computed relative energies (kcal mol^{-1}, B3LYP/6-31G*, ZPVE included) for the cyanopyridine isomers and the corresponding Dewar isomers of type I and type II.

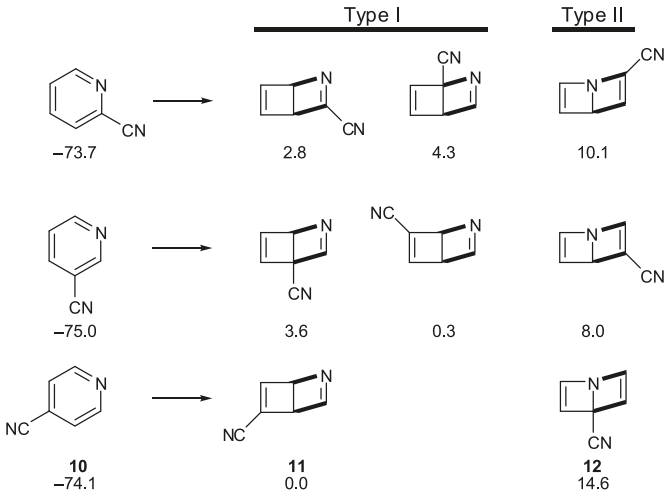

Dewar isomers (**14** and **15**) have the requisite connectivity to eliminate HCN to give a dicyanocyclobuta-1,3-diene. Future work will be directed toward the generation of dicyanocyclobuta-1,3-dienes from dicyanopyridines or other suitable precursors.

Summary

Matrix isolation photochemistry (λ > 299 nm) of 5-cyano-2*H*-pyran-2-one (**5**) shows complete conversion to a mixture containing several ring-opened ketene isomers (**6**) and a bicyclic Dewar lactone (**7**), as detected by infrared spectroscopy. Subsequent irradiation (λ > 200 nm) effects

Fig. 7. Computed relative energies (kcal mol^{-1}, B3LYP/6-31G*, ZPVE included) for the dicyanopyridine isomers and the corresponding Dewar isomers of type I and type II.

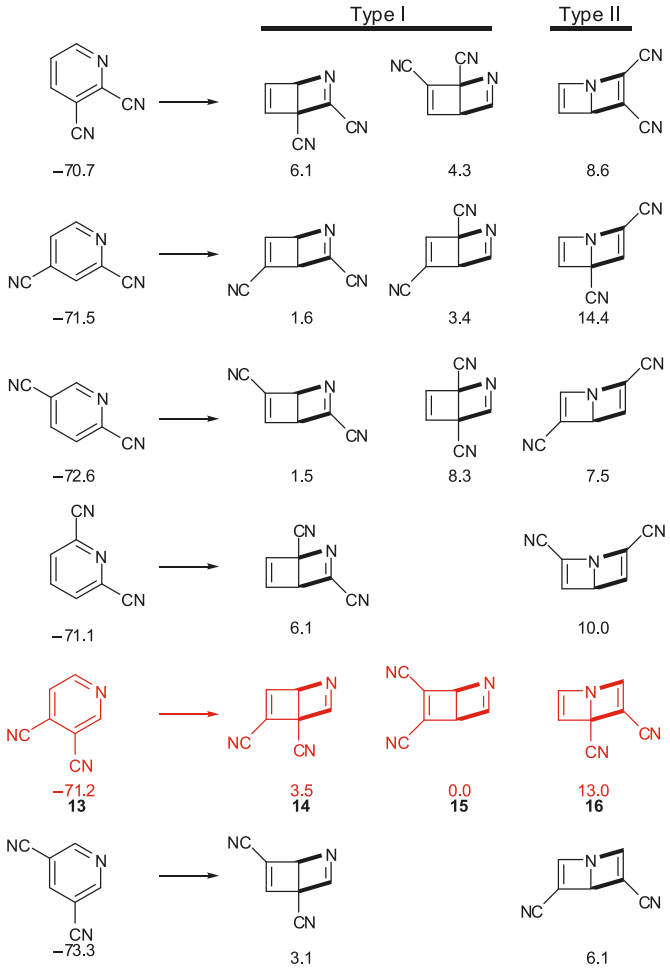

decarboxylation of the Dewar lactone (**7**) to afford cyanocyclobuta-1,3-diene (**8**). Continued irradiation causes photodecomposition of cyanocyclobuta-1,3-diene (**8**) to cyanoacetylene and acetylene. UV–vis spectra were also obtained, although they do not show features that can be assigned to **8**. Although pyridine (**9**) has been previously shown to serve as a photochemical precursor to cyclobuta-1,3-diene (**4**), 4-cyanopyridine (**10**) is not a viable precursor to cyanocyclobuta-1,3-diene (**8**) under our experimental conditions.

Methods

Computational methods

Density functional theory computations were performed using Gaussian03[53] and the Becke 3-parameter gradient-corrected exchange functional[54] with the correlation functional of Lee et al.[55] (B3LYP). The 6-31G* basis set[56] was employed for geometry optimizations, relative energies, and harmonic vibrational frequency computations. All energies have been corrected for zero-point vibrational energies (ZPVE). Vibrational frequencies were used to determine the nature of the stationary points as an energy minimum (no imaginary modes), transition state (one imaginary mode), or higher order saddle point (more than one imaginary mode).

Can. J. Chem. Downloaded from www.nrcresearchpress.com by University of Electronic and Science Techonology of China on 09/18/12
For personal use only.

Estimated transition states for the thermal conversion of **6a** to **6b** and **6b** to **6f** were optimized under the constraint of a fixed dihedral angle of 90°.[14]

Experimental methods

Infrared spectra were obtained with a Thermo Nicolet Nexus 870-FT-IR instrument (MCT-B detector). UV–vis spectra were obtained on a Varian Cary 5000 UV–vis–NIR spectrophotometer. NMR spectra were obtained on a Varian MercuryPlus 300 spectrometer.

Matrix-isolation spectroscopy

The apparatus and experimental technique for low-temperature matrix-isolation spectroscopy have been described previously[57,58] and minor modifications are described here. The compressor for the closed-cycle refrigeration system was manufactured by ASC-Cryogenics (model 125). The window temperature was measured and controlled by a temperature controller from Lake Shore Cryotronics (model 331).

Sample deposition

Solid 5-cyano-2*H*-pyran-2-one (**5**) (0.010 g) was placed in a short glass tube and attached to the spectroscopic vacuum shroud. The deposition tube was evacuated, and the sample was kept under high vacuum for 1 h before the matrix-isolation apparatus was cooled to 25 K. The sample was heated with an oil bath to 70 °C for 45 min for an IR spectroscopy experiment (CsI inner window and KBr outer windows) and 3 min for a UV–vis experiment (sapphire inner window and quartz outer windows). The sample was deposited along with an inert gas (Ar or N_2) at a rate of approximately 1.5 Torr min^{-1} (1 Torr = 133.322 Pa). Two torr of Ar were deposited both before and after the sample deposition. The matrix window was then cooled to 10 K.

Solid 4-cyanopyridine (**10**) (Sigma-Aldrich, used without further purification) was deposited using a deposition tube with a stopcock, owing to the volatility of the sample. The sample (0.015 g) was held under high vacuum for 1 h (sample kept at 77 K) before subliming onto the matrix window at room temperature (2×10^{-7} Torr) along with Ar at a rate of approximately 1.5 Torr min^{-1}. Two torr of Ar were deposited both before and after the sample deposition.

Sample irradiation

Irradiations were performed using a Hg arc lamp (Photon Technology International 100 W Hg lamp and model LPS-220B power supply, voltage set to 26 V). A Xe arc lamp (ILC Technology LX300UV 300 W Xe lamp and EM500xl power supply) was used for one of the UV–vis experiments. Cutoff filters were used to provide proper wavelengths for irradiation.

Synthesis of 5-cyano-2*H*-pyran-2-one (5)

*Conversion of 2*H*-pyran-2-one-5-carboxylic acid (13) to 2*H*-pyran-2-one-5-carbonyl chloride (14)*

The procedure given by Csihony et al.[59] was followed, with a few modifications. 2*H*-Pyran-2-one-5-carboxylic acid (2.0 g, 14.3 mmol) and $SOCl_2$ (6 mL, 30.8 mmol) (both used as received from Sigma-Aldrich) were placed in a 3-neck, 50 mL round-bottom flask equipped with a reflux condenser, N_2 inlet, and magnetic stir bar. The reaction mixture was heated to 100 °C for 8 h. A hot 1:10 mixture of CH_2Cl_2–hexanes was added to the reaction mixture to dissolve the solid that formed during reflux. Additional hexane was added until a white precipitate formed. This mixture was then cooled to finish crystallization. 2*H*-Pyran-2-one-5-carbonyl chloride (**14**) was isolated as a light green solid by filtration (1.5 g, 67% yield). ^{1}H NMR (300 MHz, $CDCl_3$) δ: 6.39 (d, J = 10.5 Hz, 1H), 7.77 (d, J = 10.5 Hz, 1H), 8.58 (s, 1H). ^{13}C NMR (300 MHz, $CDCl_3$) δ: 162.9, 162.7, 158.2, 140.2, 116.6, 115.4.

*Conversion of 2*H*-pyran-2-one-5-carbonyl chloride (14) to 5-cyano-2*H*-pyran-2-one (5)*[60]

2*H*-Pyran-2-one-5-carbonyl chloride (**14**) (1.5 g, 9.5 mmol) and sulfamide (0.8 g, 8.3 mmol) were added to a 25 mL round-bottom flask equipped with an N_2 inlet. The solid mixture was heated to 120 °C for 1 h. The solids melted and bubbled as HCl was evolved, producing a dark red oil. When cooled, the reaction mixture solidified. The mixture was transferred to a separatory flask using 75 mL of 10% (*w*/*v*) $NaHCO_3$ solution. The product was extracted with 2 × 50 mL CH_2Cl_2. The organic layer was then washed with 2 × 25 mL sat. aq. NaCl. The organic layer was then dried using $MgSO_4$, and the product was isolated in vacuo to afford 5-cyano-2*H*-pyran-2-one (**5**) (0.23 g, 20% yield). Further purification was not undertaken because the NMR spectrum of the crude product was clean. ^{1}H NMR (300 MHz, $CDCl_3$) δ: 8.0 (1:1:1 t, J = 1.3 Hz, 1H), 7.4 (dd, J = 2.9, 9.4 Hz, 1H), 6.4 (d, J = 9.4 Hz, 1H). ^{13}C NMR (300 MHz, $CDCl_3$) δ: 160.0, 157.3, 140.6, 117.3, 113.5, 95.3.

Supplementary data

Supplementary data for this article are available on the journal Web site (canjchem.nrc.ca).

Acknowledgements

We gratefully acknowledge financial support from the U. S. National Science Foundation (NSF-0715305). We also acknowledge NSF support for departmental computing facilities (NSF-0091916) and NMR instrumentation (NSF-0342998).

References

(1) Corey, E. J.; Streith, J. *J. Am. Chem. Soc.* **1964**, *86* (5), 950. doi:10.1021/ja01059a059.
(2) Lin, C. Y.; Krantz, A. *J. Chem. Soc. Chem. Commun.* **1972**, (19): 1111. doi:10.1039/c39720001111.
(3) Chapman, O. L.; McIntosh, C. L.; Pacansky, J. *J. Am. Chem. Soc.* **1973**, *95* (1), 244. doi:10.1021/ja00782a047.
(4) McIntosh, C. L.; Chapman, O. L. *J. Am. Chem. Soc.* **1973**, *95* (1), 247. doi:10.1021/ja00782a048.
(5) Pong, R. G. S.; Shirk, J. S. *J. Am. Chem. Soc.* **1973**, *95* (1), 248. doi:10.1021/ja00782a049.
(6) Chapman, O. L.; McIntosh, C. L.; Pacansky, J. *J. Am. Chem. Soc.* **1973**, *95* (2), 614. doi:10.1021/ja00783a066.
(7) Chapman, O. L.; De La Cruz, D.; Roth, R.; Pacansky, J. *J. Am. Chem. Soc.* **1973**, *95* (4), 1337. doi:10.1021/ja00785a056.

Can. J. Chem. Downloaded from www.nrcresearchpress.com by University of Electronic and Science Techonology of China on 09/18/12
For personal use only.

(8) Krantz, A.; Lin, C. Y.; Newton, M. D. *J. Am. Chem. Soc.* **1973**, *95* (8), 2744. doi:10.1021/ja00789a088.
(9) Pong, R. G. S.; Huang, B. S.; Laureni, J.; Krantz, A. *J. Am. Chem. Soc.* **1977**, *99* (12), 4153. doi:10.1021/ja00454a043.
(10) Huang, B. S.; Pong, R. G. S.; Laureni, J.; Krantz, A. *J. Am. Chem. Soc.* **1977**, *99* (12), 4154. doi:10.1021/ja00454a044.
(11) Bally, T.; Masamune, S. *Tetrahedron* **1980**, *36* (3), 343. doi:10.1016/0040-4020(80)87003-7.
(12) Arnold, B. R.; Michl, J. *J. Phys. Chem.* **1993**, *97* (50), 13348. doi:10.1021/j100152a046.
(13) Breda, S.; Lapinski, L.; Reva, I.; Fausto, R. *J. Photochem. Photobiol., A* **2004**, *162* (1), 139. doi:10.1016/S1010-6030(03)00339-3.
(14) Breda, S.; Reva, I.; Lapinski, L.; Fausto, R. *Phys. Chem. Chem. Phys.* **2004**, *6* (5), 929. doi:10.1039/b309660b.
(15) Reva, I. D.; Nowak, M. J.; Lapinski, L.; Fausto, R. *Chem. Phys. Lett.* **2006**, *429* (4–6), 382. doi:10.1016/j.cplett.2006.08.061.
(16) Reva, I.; Nowak, M. J.; Lapinski, L.; Fausto, R. *Chem. Phys. Lett.* **2008**, *452* (1–3), 20. doi:10.1016/j.cplett.2007.12.027.
(17) Maier, G. *Angew. Chem. Int. Ed. Engl.* **1988**, *27* (3), 309. doi:10.1002/anie.198803093.
(18) Bally, T. *Angew. Chem. Int. Ed.* **2006**, *45* (40), 6616. doi:10.1002/anie.200602279.
(19) Winnewisser, G.; Herbst, E. *Rep. Prog. Phys.* **1993**, *56* (10), 1209. doi:10.1088/0034-4885/56/10/001.
(20) Herbst, E. *Annu. Rev. Phys. Chem.* **1995**, *46* (1), 27. doi:10.1146/annurev.pc.46.100195.000331.
(21) Thaddeus, P.; McCarthy, M. C.; Travers, M. J.; Gottlieb, C. A.; Chen, W. *Faraday Discuss.* **1998**, *109*, 121. doi:10.1039/a800286j.
(22) Ehrenfreund, P.; Charnley, S. B. *Annu. Rev. Astron. Astrophys.* **2000**, *38* (1), 427. doi:10.1146/annurev.astro.38.1.427.
(23) Herbst, E. *Chem. Soc. Rev.* **2001**, *30* (3), 168. doi:10.1039/a909040a.
(24) Kunde, V. G.; Aikin, A. C.; Hanel, R. A.; Jennings, D. E.; Maguire, W. C.; Samuelson, R. E. *Nature* **1981**, *292* (5825), 686. doi:10.1038/292686a0.
(25) Owen, T. *Nature* **2005**, *438* (7069), 756. doi:10.1038/438756a. PMID:16363022.
(26) McCord, T. B.; Hansen, G. B.; Buratti, B. J.; Clark, R. N.; Cruikshank, D. P.; D'Aversa, E.; Griffith, C. A.; Baines, E. K. H.; Brown, R. H.; Dalle Ore, C. M.; Filacchione, G.; Formisano, V.; Hibbitts, C. A.; Jaumann, R.; Lunine, J. I.; Nelson, R. M.; Sotin, C. *Planet. Space Sci.* **2006**, *54* (15), 1524. doi:10.1016/j.pss.2006.06.007.
(27) Suits, A. G. *J. Phys. Chem. A* **2009**, *113* (42), 11097. doi:10.1021/jp908522j. PMID:19827848.
(28) Hopf, H.; Witulski, B. *Pure Appl. Chem.* **1993**, *65* (1), 47. doi:10.1351/pac199365010047.
(29) Hopf, H.; Mlynek, C.; McMahon, R. J.; Menke, J. L.; Lesarri, A.; Rosemeyer, M.; Grabow, J.-U. *Chem. Eur. J.* **2010**, *16* (47), 14115. doi:10.1002/chem.201001648.
(30) Ferris, J. P.; Guillemin, J. C. *J. Org. Chem.* **1990**, *55* (21), 5601. doi:10.1021/jo00308a017. PMID:11543604.
(31) Guillemin, J. C.; Ferris, J. P. Photochemistry of Unsaturated Nitriles on Titan. In *Proceedings of the Symposium on Titan*, Toulouse, France, Sept 9–12, 1991; ESA SP-338, 1991; pp 177–181.
(32) Eckert-Maksić, M.; Lischka, H.; Maksić, Z. B.; Vazdar, M. *J. Phys. Chem. A* **2009**, *113* (29), 8351. doi:10.1021/jp9015273. PMID:19569708.
(33) Menke, J. L.; Patterson, E. V.; McMahon, R. J. *J. Phys. Chem. A* **2010**, *114* (22), 6431. doi:10.1021/jp101963p. PMID:20465222.
(34) Pirkle, W. H.; McKendry, L. H. *J. Am. Chem. Soc.* **1969**, *91* (5), 1179. doi:10.1021/ja01033a025.
(35) Hedaya, E.; Miller, R. D.; McNeil, D. W.; D'Angelo, P. F.; Schissel, P. *J. Am. Chem. Soc.* **1969**, *91* (7), 1875. doi:10.1021/ja01035a063.
(36) Rieke, R. D.; Copenhafer, R. A. *Tetrahedron Lett.* **1971**, *12* (13), 879. doi:10.1016/S0040-4039(01)96579-7.
(37) Krantz, A. *J. Am. Chem. Soc.* **1974**, *96* (15), 4992. doi:10.1021/ja00822a049.
(38) Cram, D. J.; Tanner, M. E.; Thomas, R. *Angew. Chem. Int. Ed. Engl.* **1991**, *30* (8), 1024. doi:10.1002/anie.199110241.
(39) Kuş, N.; Breda, S.; Reva, I.; Tasal, E.; Ogretir, C.; Fausto, R. *Photochem. Photobiol.* **2007**, *83* (5), 1237. doi:10.1111/j.1751-1097.2007.00152.x. PMID:17880520.
(40) Kuş, N.; Breda, S.; Fausto, R. *J. Mol. Struct.* **2009**, *924–926*, 81. doi:10.1016/j.molstruc.2008.10.013.
(41) Maier, G.; Hartan, H.-G.; Sayrac, T. *Angew. Chem. Int. Ed. Engl.* **1976**, *15* (4), 226. doi:10.1002/anie.197602262.
(42) Redingon, R. L. *J. Chem. Phys.* **1998**, *109* (24), 10781. doi:10.1063/1.477776.
(43) Kudoh, S.; Takayanagi, M.; Nakata, M. *J. Photochem. Photobiol., A.* **1999**, *123* (1-3), 25. doi:10.1016/S1010-6030(99)00035-0.
(44) Wilzbach, K. E.; Rausch, D. J. *J. Am. Chem. Soc.* **1970**, *92* (7), 2178. doi:10.1021/ja00710a088.
(45) Johnstone, D. E.; Sodeau, J. R. *J. Phys. Chem.* **1991**, *95* (1), 165. doi:10.1021/j100154a033.
(46) Irvine, M. J.; Mathieson, J. G.; Pullin, A. D. *Aust. J. Chem.* **1982**, *35*, 1971.
(47) Becker, R. S.; Hong, J. H. *J. Phys. Chem.* **1983**, *87* (1), 163. doi:10.1021/j100224a035.
(48) Guennoun, Z.; Couturier-Tamburelli, I.; Piétri, N.; Aycard, J. P. *Chem. Phys. Lett.* **2003**, *368* (5–6), 574. doi:10.1016/S0009-2614(02)01898-5.
(49) Neumann, F.; Jug, K. *J. Org. Chem.* **1994**, *59* (21), 6437. doi:10.1021/jo00100a055.
(50) Seki, K.; He, M.; Liu, R.; Okabe, H. *J. Phys. Chem.* **1996**, *100* (13), 5349. doi:10.1021/jp952787z.
(51) Olsher, U.; Lubart, R.; Brith, M. *Chem. Phys.* **1976**, *17* (2), 237. doi:10.1016/0301-0104(76)80104-8.
(52) Akiyama, S.; Yamauchi, S.; Hirota, N.; Nagaoka, S.-i. *J. Phys. Chem.* **1993**, *97* (1), 40. doi:10.1021/j100103a010.
(53) Frisch, M. J.; Trucks, G. W.; Schlegel, H. B.; Scuseria, G. E.; Robb, M. A.; Cheeseman, J. R.; Montgomery, J. A.; Vreven, T.; Kudin, K. N.; Burant, J. C.; Millam, J. M.; Iyengar, S. S.; Tomasi, J.; Barone, V.; Mennucci, B.; Cossi, M.; Scalmani, G.; Rega, N.; Petersson, G. A.; Nakatsuji, H.; Hada, M.; Ehara, M.; Toyota, K.; Fukuda, R.; Hasegawa, J.; Ishida, M.; Nakajima, T.; Honda, Y.; Kitao, O.; Nakai, H.; Klene, M.; Li, X.; Knox, J. E.; Hratchian, H. P.; Cross, J. B.; Bakken, V.; Adamo, C.; Jaramillo, J.; Gomperts, R.; Stratmann, R. E.; Yazyev, O.; Austin, A. J.; Cammi, R.; Pomelli, C.; Ochterski, J. W.; Ayala, P. Y.; Morokuma, K.; Voth, G. A.; Salvador, P.; Dannenberg, J. J.; Zakrzewski, V. G.; Dapprich, S.; Daniels, A. D.; Strain, M. C.; Farkas, O.; Malick, D. K.; Rabuck, A. D.; Raghavachari, K.; Foresman, J. B.; Ortiz, J. V.; Cui, Q.; Baboul, A. G.; Clifford, S.; Cioslowski, J.; Stefanov, B. B.; Liu, G.; Liashenko, A.; Piskorz, P.; Komaromi, I.; Martin, R. L.; Fox, D. J.; Keith, T.; Al-Laham,

M. A.; Peng, C. Y.; Nanayakkara, A.; Challacombe, M.; Gill, P. M. W.; Johnson, B.; Chen, W.; Wong, M. W.; Gonzalez, C.; Pople, J. A. *Gaussian 03*, Revision B.05; Gaussian, Inc.: Wallingford, CT, 2004.

(54) Becke, A. D. *Phys. Rev. A* **1988**, *38* (6), 3098. doi:10.1103/PhysRevA.38.3098. PMID:9900728.

(55) Lee, C.; Yang, W.; Parr, R. G. *Phys. Rev. B* **1988**, *37* (2), 785. doi:10.1103/PhysRevB.37.785.

(56) Hehre, W. J.; Radom, L.; Schleyer, P. V.; Pople, J. A. *Ab Initio Molecular Orbital Theory*; Wiley: New York, 1986.

(57) McMahon, R. J.; Chapman, O. L.; Hayes, R. A.; Hess, T. C.; Krimmer, H.-P. *J. Am. Chem. Soc.* **1985**, *107* (25), 7597. doi:10.1021/ja00311a063.

(58) Seburg, R. A.; McMahon, R. J. *J. Am. Chem. Soc.* **1992**, *114* (18), 7183. doi:10.1021/ja00044a034.

(59) Csihony, S.; Mika, L. T.; Vlad, G.; Barta, K.; Mehnert, C. P.; Horvath, I. T. *Collect. Czech. Chem. Commun.* **2007**, *72* (8), 1094. doi:10.1135/cccc20071094.

(60) Ashworth, I. W.; Bowden, M. C.; Dembofsky, B.; Levin, D.; Moss, W.; Robinson, E.; Szczur, N.; Virica, J. *Org. Process Res. Dev.* **2003**, *7* (1), 74. doi:10.1021/op025571l.

Can. J. Chem. Downloaded from www.nrcresearchpress.com by University of Electronic and Science Techonology of China on 09/18/12
For personal use only.

Determination of oxygen permeabilities in thin polymer films using quenching of upconverted fluorescence in porphyrins

Sunish K. Sugunan, Matthew F. Paige, and Ronald P. Steer

Abstract: Proof-of-principle is demonstrated for a method of measuring the oxygen diffusion properties of thin polymer films based on quenching of the delayed upconverted S_2 fluorescence of Zn(II) *meso*-tetraphenylporphine (ZnTPP). Empirical oxygen diffusion coefficients and permeability coefficients for poly(vinyl alcohol) (PVA) have been computed using Stern–Volmer kinetics in the steady-state regime and a nonlinear gas solubility model in the time domain. Simplified dual-mode theory has been used to calculate crude theoretical oxygen permeability coefficients to compare with the experimental values. It is confirmed that oxygen permeability in the PVA matrix is controlled largely by the characteristics of the polymer matrix, particularly its water content and distribution.

Key words: oxygen diffusion, triplet–triplet annihilation, upconverted fluorescence, Stern–Volmer kinetics, nonlinear gas solubility model, dual-mode theory.

Résumé : On présente une démonstration du principe de preuve pour une méthode de mesure des propriétés de diffusion de l'oxygène à partir de films minces de polymère ; elle est basée sur le piégeage de la fluorescence S_2 retardée et non convertie du sel de zinc(II) de la *méso*-tétraphénylporphyne (ZnTPP). On a calculé les coefficients empiriques de diffusion de l'oxygène et les coefficients de perméabilité de l'alcool polyvinylique en faisant appel à la cinétique de Stern–Volmer dans le régime d'état stationnaire et un modèle de solubilité gazeuse non linéaire dans le domaine du temps. On a fait appel à la théorie simplifiée du double mode pour calculer les coefficients bruts de perméabilité théorique de l'oxygène afin de les comparer aux valeurs expérimentales. Il est confirmé que la perméabilité de l'oxygène dans la matrice d'alcool polyvinylique est contrôlée principalement par les caractéristiques de la matrice de polymère, en particulier par son contenu en au et sa distribution.

Mots-clés : diffusion de l'oxygène, annihilation triplet–triplet, fluorescence non convertie, cinétique de Stern–Volmer, modèle de solubilité gazeuse non linéaire, théorie du double mode.

[Traduit par la Rédaction]

Introduction

The transport properties of gas molecules through polymer media has been an area of long-standing interest from both fundamental and applied perspectives.[1–3] In addition to the fundamental interest in the oxidative degradation of polymers,[2,3] research in this field is motivated by the many potential applications of polymers as protective barriers (for food, chemicals, etc.), as gas separation membranes, as an ingredient in pressure-sensitive paints, and, most recently, as host materials for organic or organometallic dyes in dye-sensitized solar cells.[2–9] Measuring the rate of molecular oxygen transport through polymer materials is therefore important and devising simple, accurate, and rapid methods to make such measurements continues to be an active area of research.

Over the years, many techniques have been developed to measure the diffusion rate of molecular oxygen in polymer thin films. In the time-lag method, a defined concentration of oxygen is applied to one side of a polymer membrane positioned at the center of an evacuated chamber and the buildup of a partial pressure of oxygen on the other side of the membrane is monitored as a function of time. This method suffers from technical difficulties such as the requirements for relatively large, free-standing, defect-free thick films, large chamber volumes, and long observation times for polymers having very low values of oxygen permeability.[8,10] The most widely used alternatives involve methods of optically sensing the oxygen concentration.[1–20] For most of these methods, an optically excited organic dye molecule or inorganic complex in its singlet or triplet state dissolved or embedded in a polymer thin film is quenched by molecular oxygen introduced into the film, thereby forming the ground state of the dye (plus singlet molecular oxygen in many cases). The rate of oxygen diffusion is monitored by observing either the luminescence quenching of the dye molecule or the rate of singlet oxygen production.

Received 2 May 2010. Accepted 17 June 2010. Published on the NRC Research Press Web site at canjchem.nrc.ca on 21 January 2011.

This article is part of a Special Issue dedicated to Professor J. C. Scaiano.

S.K. Sugunan, M.F. Paige, and R.P. Steer.[1] Department of Chemistry, University of Saskatchewan, Saskatoon, SK S7N 5C9, Canada.

[1]Corresponding author (e-mail: ron.steer@usask.ca).

Can. J. Chem. Downloaded from www.nrcresearchpress.com by University of Electronic and Science Techonology of China on 09/18/12
For personal use only.

Can. J. Chem. Downloaded from www.nrcresearchpress.com by University of Electronic and Science Techonology of China on 09/18/12
For personal use only.

The rate of oxygen diffusion across the polymer matrix is then analyzed using either Fick's diffusion kinetics as a function of the time taken to reach a steady state of oxygen concentration in the film or Stern–Volmer and diffusion-controlled reaction kinetics once a steady state of oxygen concentration in the film is reached.[10] These methods are particularly attractive because of their high sensitivity, low consumption of oxygen, simple experimental setup, and shorter experimental time.[9] Typical dye molecules employed in optical oxygen sensing include porphyrins, transition-metal complexes, naphthalene, perylene, and triphenylene.[6,8–20] Even though other techniques such as mass spectrometry and fluorescence microscopy[5,9] can also monitor oxygen transport in polymers, the use of a simple steady-state or time-resolved spectrofluorimeter or phosphorimeter remains the simplest and the most popular method.

The method of finding the oxygen permeability of polymer films through steady-state Stern–Volmer kinetics was initiated by Jones[21] and was extended by Yekta et al.[10] and Douglas and co-workers.[14–17] In these cases, a sensor film composed of a phosphorescent dye molecule embedded in a polymer film was employed to provide the optical signal. Later, Rharbi et al.[7] used a method in which a polymer film was used as the separating membrane in the time-lag method described earlier, but the buildup of a partial pressure of oxygen in the receiving chamber was monitored by luminescence quenching of a separate sensor film containing a phosphorescent dye. Oxygen permeation through bilayer polymer films was investigated by Poulsen and Ogilby.[3] Here, the polymer film of interest was coated on a sensor layer composed of a porphyrin dissolved in a second polymer. The rate of oxygen permeation through the polymer film was measured by detecting the near infrared phosphorescence of singlet oxygen.

The oxygen permeability coefficients of different polymers have been summarized in a recent article by Hess et al.[8] The effects of water content on the permeability of poly(vinyl alcohol) (PVA), a test material used in our experiments, have recently been investigated by Lien et al.[22]

In this article, we aim to show proof-of-principle that oxygen permeability and diffusion kinetics in polymer films can be measured by observing the quenching of delayed (upconverted) fluorescence in a suitable dye. In this demonstration, we have chosen to examine oxygen transport through thin layers of PVA coated on a thicker layer of Zn(II) *meso*-tetraphenylporphine (ZnTPP) dissolved in poly(ethyl methacrylate) (PEMA). We have previously shown that upconverted S_2 (Soret band) fluorescence can be generated relatively efficiently both in solution and in the solid phase by triplet–triplet annihilation (TTA) in ZnTPP upon excitation in its Q band with a continuous wave (CW) laser at 532 nm.[23,24] When molecular oxygen quenches the triplet state of ZnTPP, the S_2 fluorescence of ZnTPP is also quenched. The mechanisms of TTA and the oxygen quenching of the triplets are outlined below.

$$[i] \quad S_0(\mathrm{ZnTPP}) + h\nu_{(532\,\mathrm{nm})} \rightarrow S_1(\mathrm{ZnTPP})$$

$$[ii] \quad S_1(\mathrm{ZnTPP}) \rightarrow T_1(\mathrm{ZnTPP})\ (\eta_{\mathrm{ISC}} \approx 1.0)$$

$$[iii] \quad 2T_1(\mathrm{ZnTPP}) \rightarrow S_2(\mathrm{ZnTPP}) + S_0(\mathrm{ZnTPP})$$

$$[iv] \quad S_2(\mathrm{ZnTPP}) \rightarrow S_0(\mathrm{ZnTPP}) + h\nu_{(\mathrm{upconverted})}$$

$$[v] \quad T_1(\mathrm{ZnTPP}) + O_2(^3\Sigma_g^-) \rightarrow {}^{1,3,5}(\mathrm{ZnTPP}\cdots O_2) \rightarrow S_0(\mathrm{ZnTPP}) + O_2(^1\Sigma_g^+) \text{ or } O_2(^1\Delta g) \text{ or } O_2(^3\Sigma_g^-)$$

Note that the TTA, step (*iii*), can occur by molecular diffusion in fluid media but relies on triplet exciton migration in porphyrin aggregates in thin films and other nonfluid media.

By measuring the rate of S_2 fluorescence intensity quenching of ZnTPP upon interaction of the annihilating triplets with different partial pressures of oxygen, one can, in principle, calculate the rate of oxygen diffusion in the PVA layer. Employing the quenching of TTA-generated upconverted fluorescence from ZnTPP for measuring the diffusion of oxygen in polymers offers two significant advantages over other optical techniques. (*i*) The S_2–S_0 fluorescence from ZnTPP occurs in the violet region of the spectrum; it is strongly allowed (oscillator strength, $f \sim 1$) and is therefore very easy to detect, even though the efficiency of the TTA process can be low.[23–25] (*ii*) The experimental setup required is very simple, involving only a steady-state spectrofluorimeter equipped with a vacuum sample chamber and a low-power CW visible laser as the excitation source.

Assumptions, theory, and data analysis

We have selected PEMA as the host polymer in the sensor layer to dissolve ZnTPP because PEMA has a very large oxygen permeability compared with PVA under the same conditions.[8,22] We chose PVA as the test polymer in this demonstration primarily because the fluorescent reporter in the sensor layer, ZnTPP, is relatively insoluble in it. Previous experience with trying to coat layers of organic solvent-soluble polymers on top of the sensor layer resulted in the dissolution and migration of the ZnTPP into the top test layer. We assume that the interface between the polymer sensor and test layers will not serve as a significant barrier to oxygen diffusion. On this basis, we then reasonably assume that the concentration of oxygen will be uniform in the sensor PEMA film on the time scale of the experiment and that diffusion of oxygen within the sensor layer will not interfere with measurements of the diffusion properties of oxygen in the PVA test film. We also assume that the oxygen diffusion process can be described by standard models and that the oxygen quenching of the triplet states that participate in the excited-state annihilation that produces the observed fluorescence is a pseudo-first-order kinetic process. We do nothing to control or measure the water content of the PVA film or to determine the degree of crystallinity of the polymer itself. We therefore do not anticipate being able to exactly reproduce any of the previous values of the oxygen diffusion and permeability coefficients that have been correlated with PVA's water content.[22]

The fundamental theories regarding the transport properties of gases in polymers have been summarized in an excellent monograph by Crank and Park.[26] The rate of luminescence decay at any time t from a sensor film when one

Can. J. Chem. Downloaded from www.nrcresearchpress.com by University of Electronic and Science Techonology of China on 09/18/12
For personal use only.

side of a defect-free thin film of a polymer having thickness l is exposed to a partial pressure of oxygen is given by[27]

$$[1] \qquad I(t) = \int_0^1 I(X, t)\, \mathrm{d}X$$

where $I(X, t)$ is the luminescence intensity as a function of the position within the film, X, and the time of observation is t. X is the normalized depth of oxygen penetration in the film, which varies from 0 to 1 and is given by $X = x/l$, where x is the perpendicular depth within the film. Here, we assume a uniform distribution of ZnTPP in the PEMA film, a uniform layer of PVA on top of it, uniform laser illumination throughout the film, and a uniform rate of oxygen diffusion in the test film and through the interface between the films based on the assumption that the oxygen diffusion in the PVA layer is not affected by that in the PEMA layer. We use the nonlinear gas solubility model[27] to assess the oxygen concentration at any point in the film:

$$[2] \qquad \frac{I(X, t)}{I_0} = [\gamma a C^2 + (\gamma + a + b)C + 1]^{-1}$$

where C is the concentration of oxygen, γ, a, and b are fitting parameters, and I_0 is the unquenched luminescence intensity of the sensor film in the absence of oxygen.

Assuming that the polymer film is uniformly planar throughout the test area, the concentration of oxygen in the polymer film for all time scales is given by

$$[3] \qquad C = C_0 + (C_1 - C_0) \times \left\{ 1 - \frac{4}{\pi} \sum_{i=0}^{\infty} \left[\frac{(-1)^i}{(2i+1)} \right] \exp\left[\frac{-(2i+1)^2 \pi^2 D t}{4l^2} \right] \cos\left[\frac{(2i+1)\pi X}{2} \right] \right\}$$

where C_0 is the initial concentration of oxygen in the film, C_1 is the oxygen concentration at the film surface during the diffusion process, and D is the diffusion coefficient of oxygen in the film. Since our sample film is allowed to outgas under vacuum prior to the introduction of oxygen, we approximate that $C_0 = 0$. Because of the oscillatory behaviour of this equation and the large computational time required, we used an alternative form of it for shorter time scales assuming that $C_0 = 0$:

$$[4] \qquad C = C_1 \left[\sum_{i=0}^{\infty} (-1)^i \mathrm{erfc} \frac{(2i+1)l + lX}{\sqrt{4Dt}} + \sum_{i=0}^{\infty} (-1)^i \mathrm{erfc} \frac{(2i+1)l - lX}{\sqrt{4Dt}} \right]$$

where erfc is the complimentary error function.

Substituting eq. [4] into eq. [2] and subsequently eq. [2] into eq. [1] gives the rate of fractional luminescence intensity quenching ($I(t)/I_0$) as a function of time t.

Once the steady-state concentration of oxygen is reached in the film, the system should follow Stern–Volmer kinetics:

$$[5] \qquad \frac{I_0}{I_q} = 1 + k_q \tau_0 [O_2]$$

where I_q is the luminescence intensity under steady-state conditions where the oxygen concentration is $[O_2]$, k_q is the bimolecular quenching rate constant, and τ_0 is the lifetime (of the lowest triplet state of ZnTPP in our case) of the excited dye molecule.

Smoluchowski's diffusional encounter theory can be applied to relate the bimolecular quenching constant to the diffusion coefficient, k_{diff}, that specifies the limiting rate at which the oxygen molecule can form an encounter complex with the excited dye molecule:[8,10]

$$[6] \qquad k_q = \alpha k_{diff} = \alpha 4\pi\sigma N_A D$$

Here, the proportionality constant, α, is the luminescence quenching probability in an encounter complex of the dye with oxygen, σ is the diameter of the encounter complex (which should be the sum of the van der Waals' radii of the dye molecule and oxygen; a value of 10 Å is used), N_A is Avogadro's number, and D is the diffusion coefficient. Even though α may increase with multiple encounters between the dye molecule and oxygen trapped in the polymer, we take a value of 1/9 for α on the basis that both ZnTPP and molecular oxygen are in the triplet state prior to forming a diffusional encounter complex and the formation of the product singlet states is limited by a spin statistical factor of 1/9. Likewise, formation of the fluorescing S_2 excited state of ZnTPP is limited by a spin statistical factor of 1/9 when produced from the TTA encounter complex.[25]

Finally, Henry's law can be applied to relate the equilibrium oxygen concentration to the solubility coefficient of oxygen in the film (S) and the partial pressure of oxygen (P_{O_2}) in the low to moderate pressure range:[8,10]

$$[7] \qquad [O_2]_{eq} = S P_{O_2}$$

Combining eqs. [5], [6], and [7] gives the desired equation relating the steady-state luminescence intensity to the permeability (P) of oxygen, which is a product of the diffusion coefficient (D) and the solubility coefficient (S), i.e., $P = DS$:

$$[8] \qquad \frac{I_0}{I_q} = 1 + (P)(4\pi\alpha\sigma N_A \tau_0)(P_{O_2})$$

Both time-based and steady-state data were analyzed in Origin 7.5 (OriginLab). Simpson's rule for integration was used to numerically integrate the fitting function in eq. [2].

Experimental

Zn(II) *meso*-tetraphenylporphine (low chlorin; ZnTPP), poly(ethyl methacrylate) (PEMA; average molecular weight

Can. J. Chem. Downloaded from www.nrcresearchpress.com by University of Electronic and Science Techonology of China on 09/18/12
For personal use only.

(MW) ~ 515 000 by gel permeation chromatography (GPC)), and toluene (high-performance liquid chromatography (HPLC) grade, ≥99.9%) were obtained from Sigma-Aldrich and were used as received. Poly(vinyl alcohol) (PVA; 99.7 mol% hydrolyzed, MW ~ 78 000) was purchased from Polysciences and was used as received. Millipore water was used to prepare the PVA solution. The sensor films were prepared by spin casting (800 rpm) aliquots of solution containing 4.0 mmol·L^{-1} ZnTPP and 2.0% (*w*/*v*) PEMA in toluene onto thoroughly precleaned 1.2 mm thick glass slides (VWR). About 50 μL of the solution was used for a layer. For each test sample, 40 aliquots were spin cast sequentially. The thickness of the ultimate sensor layer was considerably less than the sum of the individual PEMA and ZnTPP layers deposited and the absorbance of the sensor film did not scale with the number of layers deposited, suggesting that dissolution and loss of ZnTPP occurred during the spin casting of each layer. Thin layers of the test film were made by spin casting (1000 rpm) about 100 μL per layer of the PVA solution in water onto the sensor film. The spectra and state of aggregation of the ZnTPP in such sensor films have been previously reported.[24]

The thickness of the PVA films was measured by using an LSE Stokes ellipsometer (7109-C-351A) using the thickness and psiC/DeltaC calculation mode. The oxygen diffusion measurements were performed on a Photon Technology International QuantaMaster spectrofluorometer custom fitted with a low-power, frequency-doubled 532 nm CW Nd:YAG laser (WSTech, TECGL-30) as the sample excitation source. A calibrated graded neutral density filter (Edmund Optics) was used to attenuate the power of the laser beam when necessary and a mechanical beam shutter (Copal shutter, Edmund Optics) was used to chop the laser beam at every 30 s to minimize photochemical damage to the sample from prolonged exposure to the laser radiation. A notch filter was placed between the sample and the emission monochromator to remove scattered excitation radiation. The laser "on" power density delivered to the sample at 532 nm was typically 0.38 W·cm^{-2}.

The sample slides were fitted as windows on the front side of an evacuated triangular brass cell with the sample thin film on the inner, evacuated side. The brass cell was evacuated by connecting it to a grease-free glass vacuum line. The sample was allowed to outgas under vacuum for at least 1 h prior to any experiment. The sample was excited at less than a critical angle of incidence of ~30° and the emission was collected in a front-face geometry. The sample was continuously irradiated with the laser prior to any experiment until stable fluorescence intensity at the S_2 peak maximum of ZnTPP (~435 nm) as a function of time was achieved. The porphyrin emission intensity decreased slightly during this preirradiation procedure and we assume that this was due to photo-oxidation of the dye by residual oxygen in the sensor films and possibly due to slight additional outgassing of water vapour from the PVA film upon gentle laser-induced warming of the sample in the excitation volume. The vacuum- and gas-handling system included a gas mixing chamber that was connected to N_2 and O_2 gas cylinders. Different proportions of dry N_2 and O_2 gases were mixed in this chamber by gentle heating and were then exposed to the outgassed sample at time $t = 0$. In all cases, the total pressure of N_2 and O_2 was constant and kept at slightly less than 1.0 atm (1 atm = 101.325 kPa). After completing a measurement, continuous pumping of gases from the sample chamber usually returned the upconverted fluorescence intensity to within a few percent of the intensity observed at $t = 0$.

Results and discussion

Figure 1 demonstrates proof-of-principle that variations in the intensity of delayed (upconverted) fluorescence caused by oxygen quenching of the triplet states of an appropriately chosen fluorescent dye can be used to measure the diffusion kinetics of oxygen in a polymer film. Figure 1*a* shows the time-of-exposure dependent S_2 fluorescence quenching of ZnTPP resulting from when a thin film of PVA spin cast from a 0.5% (*w*/*w*) solution is brought into contact with an oxygen partial pressure of 13.4 kPa in dry nitrogen at approximately room temperature. The dye luminescence is quenched and attains a constant value after about 500 s of exposure to oxygen. The best fit of eq. [1] to these data yielded a diffusion coefficient of $D = 4.5 \times 10^{-9}$ cm^2·s^{-1}. The time-of-exposure dependent quenching of a thin layer of PVA made from a solution having a concentration of 2% (*w*/*w*) PVA in water is shown in Fig. 1*b*. Here, the partial pressure of oxygen is 27 kPa and the luminescence profile reaches a steady state in slightly longer than 4500 s, but the relative steady-state (equilibrium) intensity is substantially higher than in the previous example. The best fit to these data resulted in a significantly smaller value of the diffusion coefficient, $D = 2.0 \times 10^{-10}$ cm^2·s^{-1}. Note that although the fits between the diffusion theory expression and the data are not perfect, two diffusional processes were not needed to obtain the observed agreement, thus substantiating the assumption that the oxygen concentration in the sensor layer is approximately constant on the time scale of the experiment. Note also that these two films were of similar thickness: 6.9×10^{-6} cm for the film cast from the 0.5% solution and 7.1×10^{-6} cm for the film cast from the 2% solution. Both the content and the distribution of the water in these two films, however, are expected to be rather different (vide infra).

A difference in the magnitude of the oxygen permeability values for samples prepared from 0.5% and 2.0% solutions was also found in the Stern–Volmer kinetic analysis of the samples under steady-state conditions. Here, the equilibrium intensity of the dye's upconverted S_2 fluorescence was measured for the same film exposed to different partial pressures of oxygen in dry nitrogen at a total pressure of a little less than 1 atm. The data are amenable to a straightforward Stern–Volmer analysis as shown in Fig. 2*a* for the sample prepared from 0.5% PVA in water. The slope of the curve is 1.3×10^{-3} Pa^{-1}, which, when substituted into eq. [8], gives a permeability coefficient of 2.2×10^{-16} cm^3(gas at STP)·cm·cm^{-2}·s^{-1}·Pa^{-1}. A Stern–Volmer kinetic plot for oxygen diffusion in a thin test layer of PVA made from a 2.0% solution in water, shown in Fig. 2*b*, resulted in a slope of 9.9×10^{-6} Pa^{-1} and a permeability coefficient of 1.7×10^{-18} cm^3(gas at STP)·cm·cm^{-2}·s^{-1}·Pa^{-1}, which is a factor of 130 lower than that found in the 0.5% sample. Note that the same value of the unquenched lifetime of triplet ZnTPP, τ_0 =

Can. J. Chem. Downloaded from www.nrcresearchpress.com by University of Electronic and Science Techonology of China on 09/18/12
For personal use only.

Fig. 1. Luminescence quenching profiles of (*a*) one thin layer of 0.5% (*w*/*w*) PVA exposed to a partial pressure of 100 torr (1 torr = 133.3224 Pa) of oxygen and (*b*) one thin layer of 2.0% (*w*/*w*) PVA exposed to a partial pressure of 200 torr of oxygen. The empty circles represent the data points and the solid curves represent the best fit for the data as determined by the reduced χ^2 values.

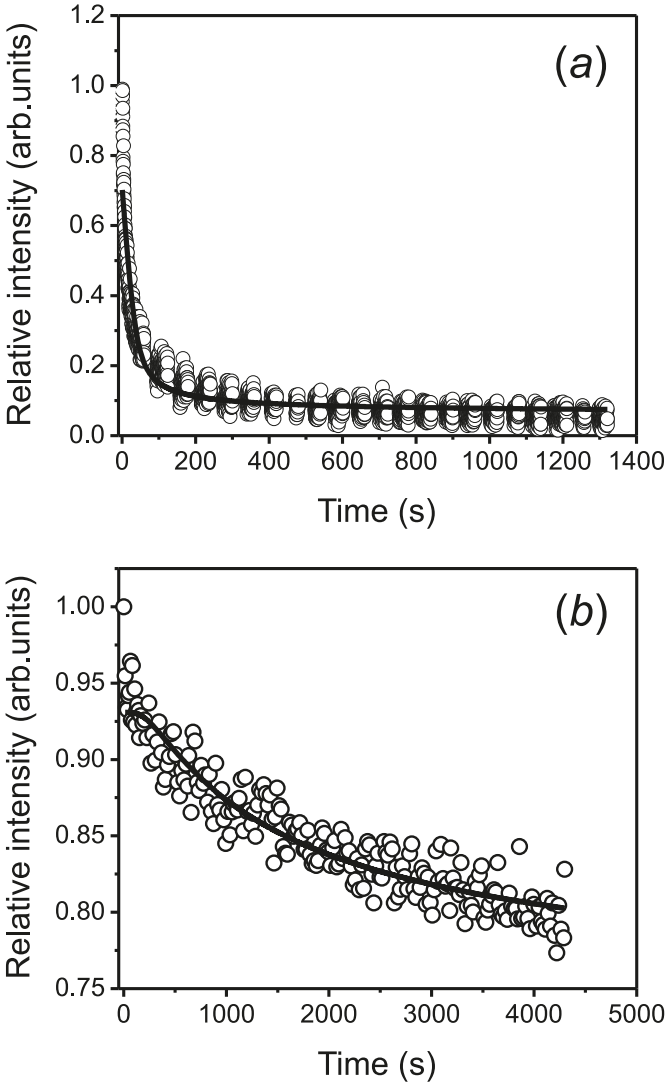

Fig. 2. Stern–Volmer kinetic analysis of (*a*) one layer of 0.5% (*w*/*w*) PVA and (*b*) one layer of 2.0% (*w*/*w*) PVA. The empty circles represent the data points and the solid curves represent the best least-squares fit to the data.

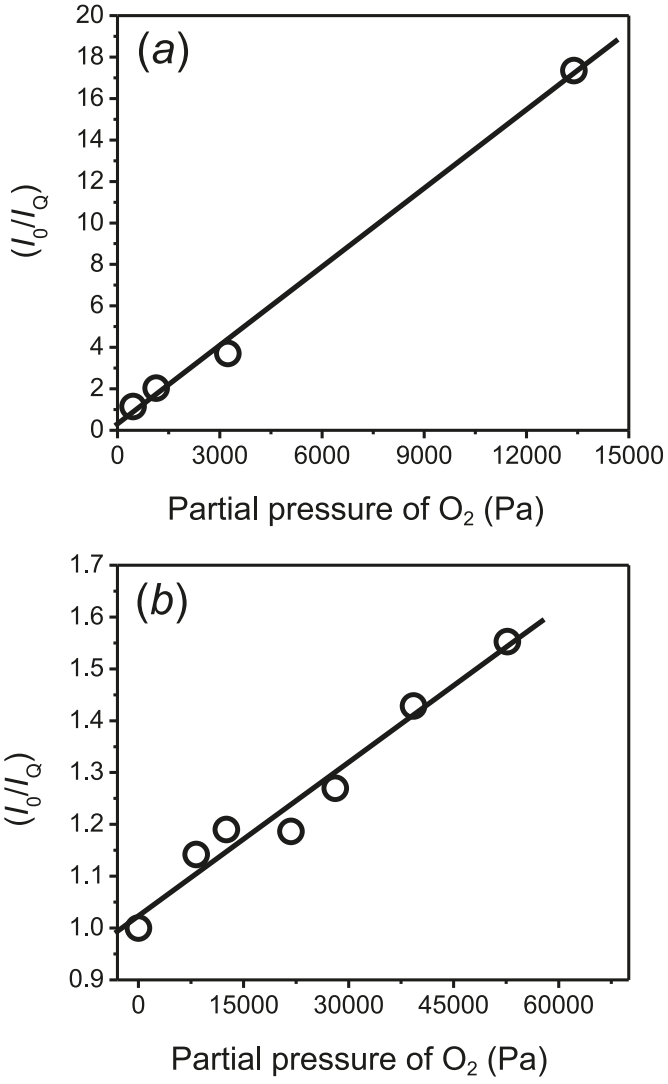

6.86×10^{-3} s, previously measured[28] for ZnTPP in PMMA, has been used in both of these calculations. The actual triplet lifetime was not measured in these proof-of-principle experiments, and any difference would constitute a source of systematic error in the determination of the values of *P* reported here.

We have also determined whether the thickness of the polymer membrane would affect the measured oxygen permeability of PVA. The temporal luminescence quenching profiles for two different thicknesses of PVA are shown in Fig. 3 and the corresponding diffusion coefficients calculated as above are shown in Table 1. Note that the value of the apparent oxygen diffusion coefficient decreases with increasing thickness of the PVA test film. Because both *D* and *P* should be independent of film thickness if the films themselves are of the same composition and morphology, this observation implies that at least one uncontrolled variable (in our case the water content and distribution and perhaps the degree of polymer crystallinity) is responsible for the differences.

These measured values of *D* and *P* can be compared only crudely with literature values because of the largely unknown water contents and distributions of both the samples under evaluation here and those for which data are reported in the literature. Values of *D* for absolutely dry PVA have been obtained[29,31] by molecular dynamics simulations for samples at 375 K ($D = 5.0 \times 10^{-7}$ cm^2·s^{-1}) and 500 K ($D = 1.6 \times 10^{-6}$ cm^2·s^{-1}). However, these values apply to conditions in which PVA will be in its glassy state with a large free volume, where a much faster rate of oxygen diffusion is expected compared with those measured here. The permeability values measured here may be compared with a reported[30] permeability value for oxygen diffusion in PVA (of unknown water content) of 9.16×10^{-16} cm^3(gas at STP)·cm·cm^{-2}·s^{-1}·Pa^{-1}, in order-of-magnitude agreement.

The glass transition temperature of PVA is near 358 K,

Can. J. Chem. Downloaded from www.nrcresearchpress.com by University of Electronic and Science Techonology of China on 09/18/12
For personal use only.

Fig. 3. Luminescence quenching profiles of (*a*) three layers of 0.5% (*w*/*w*) PVA exposed to a partial pressure of 100 torr of oxygen and (B) five layers of 0.5% (*w*/*w*) PVA exposed to a partial pressure of 100 torr of oxygen. The empty circles represent the data points and the solid curves represent the best fit for the data as determined by the reduced χ^2 values.

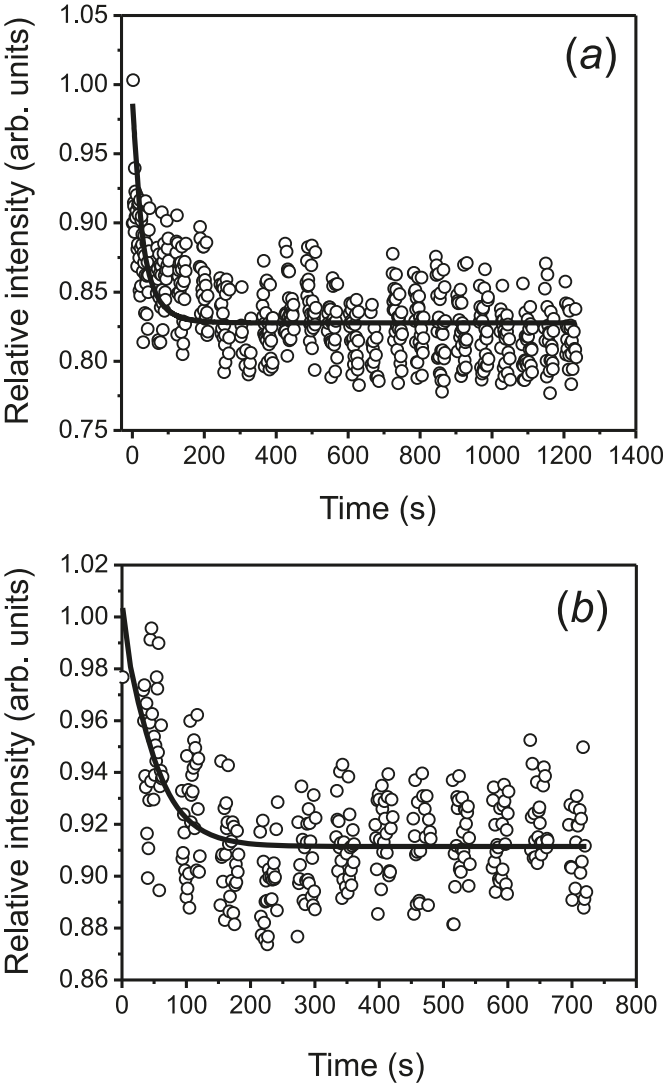

well above the near-room temperatures used in our experiments. When a polymer is in a semicrystalline state well below its glass transition temperature, nanocrystalline clusters dispersed in a continuous network of a low fraction of amorphous polymer are formed.[32–35] The crystalline part in the polymer matrix is generally impermeable to gas penetration, whereas gas diffusion is relatively facile in the amorphous phase. Moreover, PVA films prepared from aqueous media can contain variable amounts of water and this water can be distributed in a continuum of strongly to weakly bound environments.[22] Gas diffusion in the amorphous regions follows the free-volume model,[33] and whereas the diffusive motion of gas molecules is generally faster than the mobility of the polymer segments, the polymer does respond to provide space to accommodate the diffusing gas.[36] It is not unreasonable to assume that the free volume in the polymer thin film and hence the water content and distribution in our films will depend on the initial concentration of the polymer in solution and the exact conditions used to cast the film. All other factors remaining the same, the number density of the polymer molecules should be expected to increase with increasing concentration of the polymer in the spin-cast solution. The relation between the initial polymer concentration in aqueous solution and the resulting free volume and distribution of water in the thin film should explain why the measured diffusion coefficient and permeability are substantially reduced when the polymer concentration in the spin-cast solution is increased. We proceed with a largely empirical analysis based on this hypothesis.

Consider two different samples of the same polymer film that are formed from two different concentrations of the polymer in solution. The resulting films have different water contents and hence different oxygen solubilities, S_1 and S_2. Let the measured oxygen diffusion coefficients in the two films be D_1 and D_2, respectively, and let the measured permeability coefficients be P_1 and P_2, respectively. Since $P = DS$, the ratios of the values of P and D will give an estimate of the differences in oxygen solubilities in the two films. Using the data for D and P presented above, for the two starting PVA concentrations employed we find that $S_1 = 5.7S_2$, i.e., using this analysis, oxygen would be about 6 times more soluble in the PVA film made from the lower concentration solution. Since the two films are of approximately the same thickness, the pores of the film made from the lower concentration solution must be significantly larger and contain more bulk-like water than those in the film formed from the higher concentration solution. Since oxygen solubility increases with the bulk-like water content of PVA,[22] this interpretation is consistent with the above starting hypothesis.

The solubility of oxygen in the PVA thin film can be computed by correlating the equilibrium concentration of the oxygen dissolved in the polymer film (C) with the partial pressure, P_{O_2}, of the gas at the polymer surface using the dual-mode theory:[30,37]

$$[9] \qquad C = K_H P_{O_2} + C_\infty \frac{bP_{O_2}}{1 + bP_{O_2}}$$

Here, K_H is the Henry's law constant (Pa^{-1}), which characterizes the first term in eq. [9] as a Henry's isotherm; C_∞ is the steady-state concentration of oxygen in the polymer film; and b is the ratio of the rates of the adsorption and desorption processes, which, when included in the second term of eq. [9], yields a Langmuir-type isotherm. While using this model, it must be assumed that the absorption and desorption processes do not alter the PVA matrix, that the matrix is homogeneous, and that only one oxygen molecule occupies a given site in the polymer matrix at a time.

In addition, because oxygen is a small, rapidly diffusing molecule and the pressures of oxygen applied in the experiments are less than 1.0 atm, ideal gas behaviour for the dissolution of oxygen in the polymer can be assumed. If one can neglect the Langmuir-type isotherm part in eq. [9], as is the usual case,[30] then the solubility of oxygen in the PVA polymer matrix is governed by Henry's law for the gas pressures applied here. Therefore, the solubility coefficient can be computed by using the simple equation

Can. J. Chem. Downloaded from www.nrcresearchpress.com by University of Electronic and Science Techonology of China on 09/18/12
For personal use only.

Table 1. Experimental diffusion coefficients and calculated[29,30] (see text) permeability coefficients for oxygen in PVA membranes having different thicknesses.

Thickness of thin layers made from 0.5% solution of PVA, l (cm)	Experimental diffusion coefficient, D ($cm^2 \cdot s^{-1}$)	Calculated permeability coefficient, P (cm^3(gas at STP)$\cdot cm \cdot cm^{-2} \cdot s^{-1} \cdot Pa^{-1}$)
6.9×10^{-6}	4.6×10^{-9}	$2.0 \times 10^{-14} < \mu < 2.5 \times 10^{-14}$
5.5×10^{-5}	2.4×10^{-11}	$1.1 \times 10^{-16} < \mu < 1.3 \times 10^{-16}$
8.6×10^{-5}	7.8×10^{-11}	$3.4 \times 10^{-16} < \mu < 4.2 \times 10^{-16}$

Table 2. Experimental and calculated[29,30] (see text) diffusion coefficients and permeability coefficients of oxygen in thin films of PVA cast from two different concentrations of PVA in water.

Concentration of PVA (%, *w/w*) in aqueous solution	Experimental permeability coefficient, P (cm^3(gas at STP)$\cdot cm \cdot cm^{-2} \cdot s^{-1} \cdot Pa^{-1}$	Experimental diffusion coefficient, D ($cm^2 \cdot s^{-1}$)	Calculated solubility coefficient, S (cm^3(gas at STP)$\cdot cm^{-3} \cdot Pa^{-1}$	Calculated permeability coefficient, P (cm^3(gas at STP)$\cdot cm \cdot cm^{-2} \cdot s^{-1} \cdot Pa^{-1}$)
0.5	2.2×10^{-16}	4.5×10^{-9}	$4.4 \times 10^{-6} < \mu < 5.4 \times 10^{-6}$	$2.0 \times 10^{-14} < \mu < 2.5 \times 10^{-14}$
2.0	1.7×10^{-18}	2.0×10^{-10}	$4.4 \times 10^{-6} < \mu < 5.4 \times 10^{-6}$	$8.9 \times 10^{-16} < \mu < 1.1 \times 10^{-15}$

$$[10] \qquad S = K_H(T/T_0)P_0$$

where T = 298 K is the experimental temperature, P_0 = 1.0 atm, and T_0 = 273 K.

The Henry's constant, K_H, for dry PVA has been computed using Monte Carlo simulations by Cozmuta et al.[30] Owing to the complex dynamics of oxygen in the voids and channels of the polymer and owing to the possible structural modifications of the polymer matrix during the adsorption process, K_H was calculated as a 95% confidence interval rather than as an average value and was reported as ($0.4 < \mu < 0.5$) $cm^3 \cdot cm^{-3} \cdot atm^{-1}$. We have used the lower and upper limits of this range of K_H values to compute a theoretical solubility coefficient of oxygen in dry PVA, also expressed as a 95% confidence interval (Table 2). We then used this calculated solubility coefficient range together with the values of the experimentally observed diffusion coefficients to calculate a range of values of the permeability coefficient. These values are compared with the experimentally determined values of the permeability coefficients. The experimental permeability coefficients and experimental diffusion coefficients measured for PVA containing residual amounts of water are compared with the calculated solubility coefficient and the calculated permeability coefficients for dry PVA in Tables 1 and 2. The calculated permeability coefficients are two to three orders of magnitude larger than the experimentally observed ones (Table 2).

Although some of this discrepancy could be due to experimental uncertainties in the measured values of D and S, a more likely source is the presence of water in the polymer. It should be noted that severe discrepancies exist in the literature regarding the magnitudes of the oxygen permeation coefficients of a wide range of polymers.[8] For PVA, however, Lien et al.[22] have shown that the oxygen permeability is a strong function only of the water content of the films and increases rapidly by over a factor of 100 as the water content increases by a few weight percent.

Conclusions

We have demonstrated proof-of-principle that quenching of delayed fluorescence in a visible light absorbing system that exhibits photon upconversion can be used to measure the diffusion properties of oxygen in thin polymer films. Although we have used upconverted fluorescence from the S_2 state of ZnTPP as the reporting luminescence in this demonstration, other molecular systems exhibiting photon upconversion by TTA or by triplet–singlet annihilation could also be employed and might be useful in overcoming some of the limitations encountered in our study. Here, we have been limited by the choice of polymer matrices for the porphyrin-containing sensor; the capping test film must be chosen so that spin casting it onto the sensor film does not dissolve the porphyrin so that it becomes embedded in the test film. Although reliable diffusion and permeability coefficients cannot be claimed to have been measured with the system reported here, the data obtained were readily interpretable using standard gas transport and luminescence quenching methodology. Time-of-exposure luminescence decay data were amenable to analysis using standard diffusion models; luminescence quenching at equilibrium oxygen concentrations produced excellent linear Stern–Volmer plots. Order-of-magnitude agreement with literature data was obtained.

The discrepancies between the values of the diffusion and permeability coefficients for oxygen in PVA obtained by spin casting from aqueous solutions of different PVA concentrations have been rationalized by considering how the differences in film structure and water content affect the solubility of oxygen in the films. Water content and distribution in the PVA films were not controlled or measured. Future work, based on the useful report of Lien et al.[22] that identifies the role of water in the gas transport properties of PVA, should be expected to resolve the serious discrepancies that currently exist in the literature. Better results using the system described here might be obtained by using a sensor-containing polymer that has a glass transition temperature below room temperature. Such an arrangement would permit the test polymer layer to be deposited in intimate contact with the sensor layer and then, as needed for PVA, pre-equilibrated with water vapour at various partial pressures. Nevertheless, the existing information is extremely useful in assessing the viability of proposed photon upcon-

version schemes for improving the efficiencies of dye-sensitized solar cells,[23,24] in which oxygen quenching of triplet states must be avoided.

Acknowledgements

The Natural Sciences and Engineering Research Council of Canada, the Canada Foundation for Innovation, and the University of Saskatchewan are gratefully acknowledged for financial support of this research program. We are also grateful to the donors of the American Chemical Society Petroleum Research Fund for support of this research. The authors thank Dr. Jedrzej Szmytkowski for writing the fitting program in Origin. We are also grateful to one of the referees of the original manuscript, who suggested the use of sensor-containing polymers with glass transition temperatures lower than room temperature.

References

(1) Cisse, A. L.; Grossman, E.; Sibener, S. J. *J. Phys. Chem.* **2008**, *112* (24), 7166. doi:10.1021/jp801393b.

(2) Poulsen, L.; Zebger, I.; Tofte, P.; Klinger, M.; Hassager, O.; Ogilby, P. R. *J. Phys. Chem.* **2003**, *107* (50), 13885. doi:10.1021/jp0362739.

(3) Poulsen, L.; Ogilby, P. R. *J. Phys. Chem. A* **2000**, *104* (12), 2573. doi:10.1021/jp993449r.

(4) Bowyer, W. J.; Xu, W.; Demas, J. N. *Anal. Chem.* **2004**, *76* (15), 4374. doi:10.1021/ac0497961. PMID:15283575.

(5) Kneas, K. A.; Demas, J. N.; DeGraff, B. A.; Periasamy, A. *Microsc. Microanal.* **2000**, *6* (6), 551. doi:10.1007/S100050010052. PMID:11116304.

(6) Obata, M.; Matsuura, N.; Mitsuo, K.; Nagai, H.; Asai, K.; Harada, M.; Hirohara, S.; Tanihara, M.; Yano, S. *J. Polym. Sci. Part A: Polym. Chem.* **2010**, *48* (3), 663. doi:10.1002/pola.23818.

(7) Rharbi, Y.; Yekta, A.; Winnik, M. A. *Anal. Chem.* **1999**, *71* (22), 5045. doi:10.1021/ac990193c.

(8) Hess, S.; Becker, A.; Baluschev, S.; Yakutkin, V.; Wegner, G. *Macromol. Chem. Phys.* **2007**, *208* (19–20), 2173. doi:10.1002/macp.200700196.

(9) López-Gejo, J.; Haigh, D.; Orellana, G. *Langmuir* **2010**, *26* (3), 2144. doi:10.1021/la902546k.

(10) Yekta, A.; Masoumi, Z.; Winnik, M. A. *Can. J. Chem.* **1995**, *73* (11), 2021, and refs. cited therein. doi:10.1139/v95-250.

(11) Tian, Y.; Shumway, B. R.; Meldrum, D. R. *Chem. Mater.* **2010**, *22* (6), 2069. doi:10.1021/cm903361y. PMID:20352057.

(12) Mills, A.; Lepre, A. *Anal. Chem.* **1997**, *69* (22), 4653. doi:10.1021/ac970430g.

(13) Xu, W.; McDonough, R. C., III; Langsdorf, B.; Demas, J. N.; DeGraff, B. A. *Anal. Chem.* **1994**, *66* (23), 4133. doi:10.1021/ac00095a004. PMID:7847622.

(14) Evans, R. C.; Douglas, P. *Anal. Chem.* **2006**, *78* (16), 5645. doi:10.1021/ac060288w. PMID:16906707.

(15) Eaton, K.; Douglas, B.; Douglas, P. *Sens. Actuators B* **2004**, *97* (1), 2. doi:10.1016/S0925-4005(03)00269-7.

(16) Douglas, P.; Eaton, K. *Sens. Actuators B* **2002**, *82* (2–3), 200. doi:10.1016/S0925-4005(01)01006-1.

(17) Douglas, P.; Eaton, K. *Sens. Actuators B* **2002**, *82* (1), 48. doi:10.1016/S0925-4005(01)00988-1.

(18) Hartmann, P.; Leiner, J. P.; Lippitsch, M. E. *Anal. Chem.* **1995**, *67* (1), 88. doi:10.1021/ac00097a015.

(19) Õige, K.; Avarmaa, T.; Suisalu, A.; Jaaniso, R. *Sens. Actuators B* **2005**, *106* (1), 424. doi:10.1016/j.snb.2004.09.001.

(20) Badocco, D.; Pastore, P. *Anal. Chem.* **2008**, *80* (6), 2091. doi:10.1021/ac702202t. PMID:18275221.

(21) Jones, P. F. *J. Polym. Sci. Part B: Polym. Lett.* **1968**, *6* (7), 487. doi:10.1002/pol.1968.110060706.

(22) Lien, L.; Fellows, C. M.; Copeland, L.; Hawkett, B. S.; Gilbert, R. G. *Aust. J. Chem.* **2002**, *55* (8), 507. doi:10.1071/CH02007.

(23) Sugunan, S. K.; Tripathy, U.; Brunet, S. M. K.; Paige, M. F.; Steer, R. P. *J. Phys. Chem. A* **2009**, *113* (30), 8548. doi:10.1021/jp9034776. PMID:19719312.

(24) O'Brien, J. A.; Rallabandi, S.; Tripathy, U.; Paige, M. F.; Steer, R. P. *Chem. Phys. Lett.* **2009**, *475* (4–6), 220. doi:10.1016/j.cplett.2009.05.039.

(25) Turro, N. J.; Ramamurthy, V.; Scaiano, J. C. *Principles of Molecular Photochemistry: An Introduction;* University Science Books: Sausalito, California, 2009. Note: Recently, Schmidt's group has established for tetrakisquinoxalinoporphyrin palladium(II) and rubrene that the TTA efficiency does not follow the usually accepted 1/9 spin-statistical limitation, and obtained a TTA upconversion efficiency as high as 33% (see Cheng, Y. Y.; Khoury, T.; Clady, R. G. C. R.; Tayebjee, M. J. Y.; Ekins-Daukes, N. J.; Crossley, M. J.; Schmidt, T. W. *Phys. Chem. Chem. Phys*. **2010,** *12* (1), 66. doi: 10.1039/b913243k). However, for ZnTPP, we have no comparable data and we therefore assume that the TTA efficiency in ZnTPP is subject to the usual spin-statistical limitation so that $\alpha = 1/9$.

(26) Crank, J.; Park, G. S. *Diffusion in Polymers;* Academic Press: New York, 1968.

(27) Kneas, K. A.; Demas, J. N.; Nguyen, B.; Lockhart, A.; Xu, W.; DeGraff, B. A. *Anal. Chem.* **2002**, *74* (5), 1111, and refs. cited therein. doi:10.1021/ac010867v. PMID:11924972.

(28) Furuto, T.; Lee, S.-K.; Amao, Y.; Asai, K.; Okura, I. *J. Photochem. Photobiol. A* **2000**, *132* (1–2), 81. doi:10.1016/S1010-6030(00)00203-3.

(29) Karlsson, G. E.; Gedde, U. W.; Hedenqvist, M. S. *Polymer (Guildf.)* **2004**, *45* (11), 3893. doi:10.1016/j.polymer.2003.12.082.

(30) Cozmuta, I.; Blanco, M.; Goddard, W. A., III. *J. Phys. Chem. B* **2007**, *111* (12), 3151. doi:10.1021/jp062942h. PMID:17388466.

(31) Karlsson, G. E.; Johansson, T. S.; Gedde, U. W.; Hedenqvist, M. S., J. Macromol. Sci. Part B: Phys. **2002**, *41* (2), 185. doi:10.1081/MB-120003080.

(32) Hiltner, A.; Liu, R. Y. F.; Hu, Y. S.; Baer, E. *J. Polym. Sci. Part B: Polym. Phys.* **2005**, *43* (9), 1047. doi:10.1002/polb.20349.

(33) Horas, J. A.; Rizzotto, M. G. *J. Polym. Sci. Part B: Polym. Phys.* **1996**, *34* (9), 1541. doi:10.1002/(SICI)1099-0488(19960715)34:9<1541::AID-POLB2>3.0.CO;2-O.

(34) Biscoglio, M. *J. Phys. Chem. B* **1999**, *103* (43), 9070. doi:10.1021/jp9840228.

(35) Van der Bruggen, B.; Jansen, J. C.; Figoli, A.; Geens, J.; Van Baelen, D.; Drioli, E.; Vandecasteele, C. *J. Phys. Chem. B* **2004**, *108* (35), 13273. doi:10.1021/jp048249g.

(36) Budd, P. M.; McKeown, N. B.; Fritsch, D. *J. Mater. Chem.* **2005**, *15* (20), 1977. doi:10.1039/b417402j.

(37) Mueller-Plathe, F. *Macromolecules* **1991**, *24* (24), 6475. doi:10.1021/ma00024a017.

Can. J. Chem. Downloaded from www.nrcresearchpress.com by University of Electronic and Science Techonology of China on 09/18/12
For personal use only.

Dynamics of capsuleplex formed between octaacid and organic guest molecules — Photophysical techniques reveal the opening and closing of capsuleplex

Nithyanandhan Jayaraj, Steffen Jockusch, Lakshmi S. Kaanumalle, N.J. Turro, and V. Ramamurthy

Abstract: This manuscript is concerned with the opening and closing of a capsuleplex made up of organic guest molecules and two cavitand molecules known as octaacid (OA). The capsuleplex is loosely held together in water through weak interactions. We have investigated the opening–closing of the OA capsuleplex by monitoring the quenching of excited singlet and (or) triplet states of nine different guest molecules encapsulated within a capsule by molecular oxygen that is dissolved in water surrounding the capsule. The rate constants for oxygen quenching of the excited guest molecules were estimated by monitoring the intensity of fluorescence/phosphorescence or lifetimes of excited states of guest molecules in the presence of different concentrations of oxygen in water. Guest molecules were chosen such that one could probe the opening–closing process during a time range of 0.05 to 922 μs. We believe that the oxygen quenching constant reflects the accessibility of oxygen to the guest enclosed within the OA capsuleplex, and this in turn depends on the capsule opening–closing rate constant. Based on the quenching studies, we conclude that guests whose lifetimes are shorter than 5 μs are inaccessible to oxygen. Results presented in this report suggest that the extent and time scale for opening depends on the guest.

Key words: capsuleplex, octaacid, energy transfer, quenching by oxygen, capsule opening and closing.

Résumé : Dans ce travail on a étudié l'ouverture et la fermeture d'un capsuleplexe qui est formé de molécules organiques hôtes et de deux molécules de cavitands et qui est connu comme l'octa-acide (OA). Le capsuleplexe faiblement retenu ensemble dans l'eau par le biais de faibles interactions. On a étudié le cycle d'ouverture–fermeture du capsuleplexe OA en suivant la désactivation des états singulet excité et triplet des neuf molécules invitées différentes encapsulées par une capsule d'oxygène moléculaire qui est dissous dans l'eau entourant la capsule. On a évalué les constantes de vitesse de désactivation des molécules invitées excitées par l'oxygène en suivant l'intensité de fluorescence/phosphorescence ou les temps de vie des états excités des molécules invitées en présence de concentrations variables d'oxygène dans l'eau. Les molécules invitées ont été choisies d'une façon telle qu'on puisse étudier d'ouverture–fermeture durant un intervalle de temps allant de 0,05 à 922 μs. On croit que la constante de désactivation par l'oxygène est un reflet de l'accessibilité de l'oxygène à la molécule invitée incluse dans le capsuleplexe d'OA qui dépendrait à son tour sur la constante de vitesse d'ouverture–fermeture de la capsule. Sur la base des études de désactivation, on conclut que les invités dont les temps de vie sont inférieurs à 5 μs ne sont pas accessibles à l'oxygène. Les résultats rapportés ici suggèrent que le degré et l'échelle de temps pour l'ouverture dépendent de l'invité.

Mots-clés : capsuleplexe, octa-acide, transfert d'énergie, désactivation par l'oxygène, ouverture et fermeture de la capsule.

[Traduit par la Rédaction]

Introduction

This manuscript is concerned with the dynamics of a capsuleplex made up of an organic guest and two host molecules. The host octaacid (OA, **1**, Scheme 1), having a cuplike shape, belongs to a class of hosts known as cavitands.[1] The capsuleplex we are concerned with in this report is made up of two OA cavitand molecules and guest molecules that are loosely held by weak interactions in water. Examples of 1:2 and 2:2 (guest:host ratio) capsuleplexes of octaacid are known, and this article deals with both types of capsuleplexes.[2]

We have recently established that an organic guest molecule, confined within a capsule made up of two molecules of OA, undergoes motion corresponding to rotations along its

Received 26 April 2010. Accepted 17 June 2010. Published on the NRC Research Press Web site at canjchem.nrc.ca on 21 January 2011.

This article is part of a Special Issue dedicated to Professor J. C. Scaiano.

N. Jayaraj, L.S. Kaanumalle, and V. Ramamurthy.[1] Department of Chemistry, University of Miami, Coral Gables, FL 33124, USA.
S. Jockusch and N.J. Turro. Department of Chemistry, Columbia University, New York, NY 10027, USA.

[1]Corresponding author (e-mail: murthy1@miami.edu).

Can. J. Chem. Downloaded from www.nrcresearchpress.com by University of Electronic and Science Techonology of China on 09/18/12
For personal use only.

Can. J. Chem. Downloaded from www.nrcresearchpress.com by University of Electronic and Science Techonology of China on 09/18/12
For personal use only.

Scheme 1. (i) Structure and dimensions of the octaacid (OA) and its complexes; (a–h) represent the various protons in OA. The dimensions indicated for OA refer to atom-to-atom in (ii) and include van der Walls radius in (iii). Cartoon representations of the 1:2 and 2:2 octaacid complexes are shown in (iv).

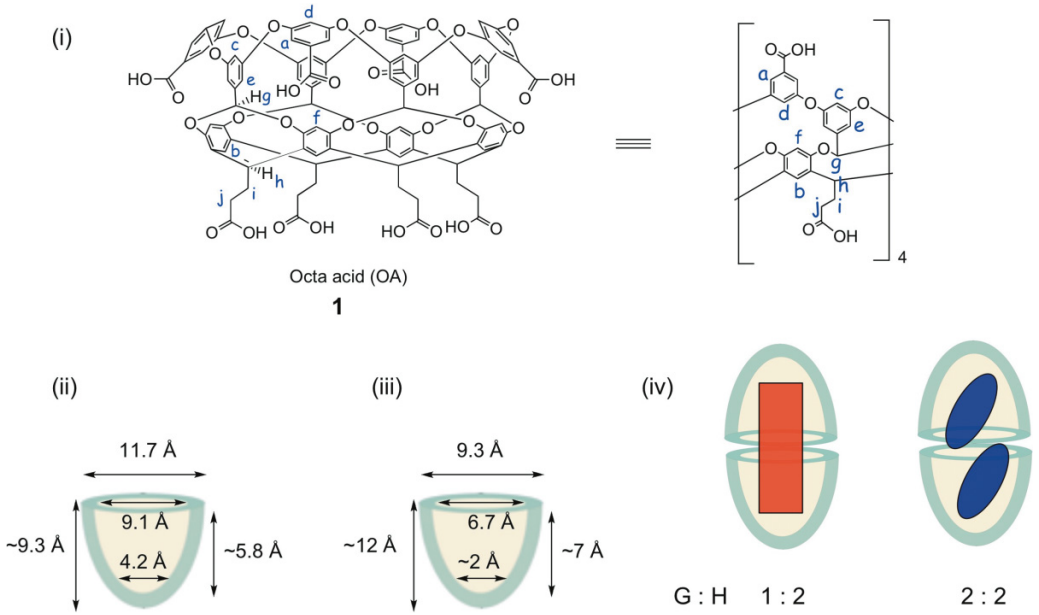

Scheme 2. Three types of motions exerted by guests within octaacid (OA) capsuleplexes are illustrated in (a–c). The equilibrium between capsuleplex opening and closing is illustrated in (d).

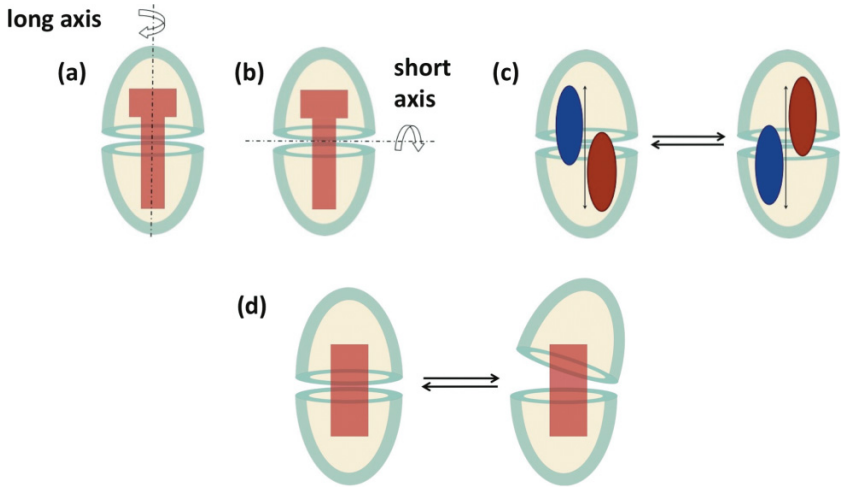

short and long axes.[3] Examination of a number of guest molecules by ^{1}H NMR and EPR experiments suggested that the extent of rotation depends on the structure of the guest molecule. In addition, when two guest molecules form a capsuleplex with OA, they can undergo sliding motion. These three types of motion that we have established as occurring within the OA capsuleplex are illustrated in a cartoon fashion in Schemes 2a–2c. In this manuscript, we are concerned with yet another motion, namely partial opening and closing of the capsuleplex (Scheme 2d). We define opening to mean that the two cavitand molecules that make up the capsule come apart enough for a quencher such as oxygen to access the guest present inside. Since the capsuleplex is made up of two weakly interacting host molecules, a legitimate question comes to mind: "Does the capsuleplex remain closed all the time or does it open and close periodically? If the latter, what is the time scale in which such a process takes place?"

In this study, we have probed the opening–closing of a capsuleplex by monitoring the quenching of excited singlet and (or) triplet states of guest molecules (Scheme 3) present inside a capsule by molecular oxygen that is present outside the capsule. The rate of quenching was estimated by monitoring the intensity of fluorescence/phosphorescence or lifetimes of excited states of guest molecules in the presence of different concentrations of oxygen in water. Guest molecules were chosen such that one could probe the opening–closing process during a wide time range. Structures and molecular dimensions of guests employed whose excited-state lifetimes cover 0.05 to 922 μs are listed in Scheme 3. Based on the results presented in the following, we conclude that guests whose lifetimes are shorter than 5 μs are not accessible to

Can. J. Chem. Downloaded from www.nrcresearchpress.com by University of Electronic and Science Techonology of China on 09/18/12
For personal use only.

Scheme 3. Structures and dimensions of the guests used in this study. The dimensions indicated for various guests refer to atom-to-atom and do not include the van der Waals radius.

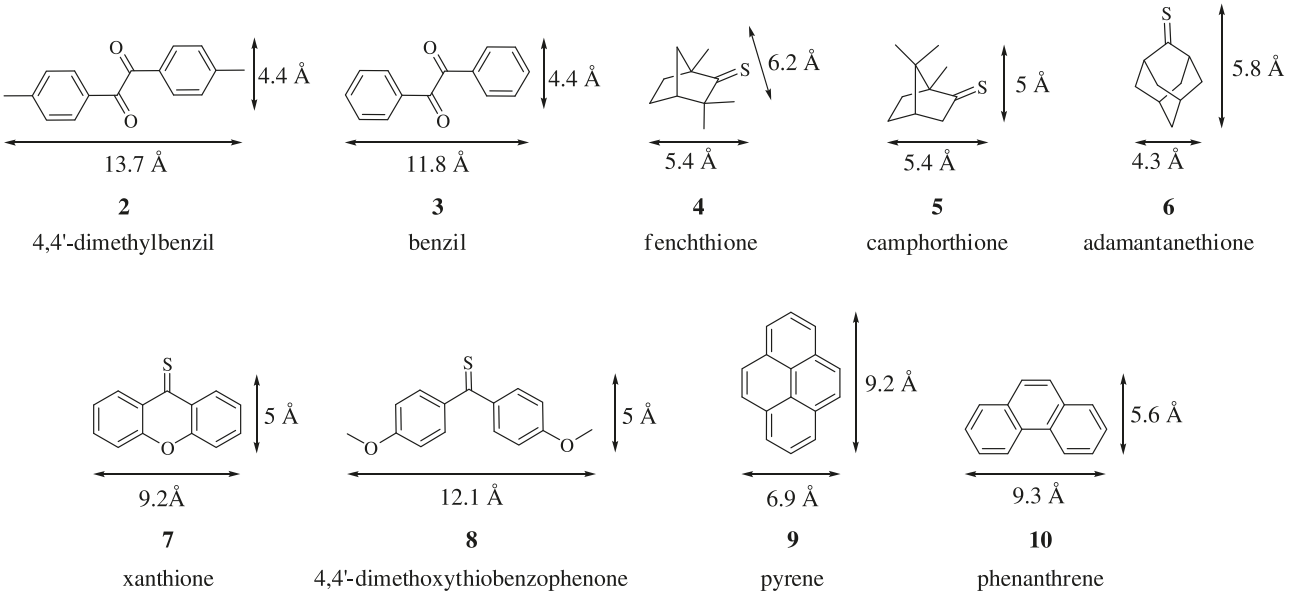

oxygen. However, guests with lifetimes longer than 15 μs are accessible to oxygen. Based on the measured quenching rate constants, we conclude that the extent and time scale for opening depends on the guest.

Results and discussion

Capsuleplexes composed of guests **2**–**10** and OA were prepared in water at pH ~9.0 (borate buffer).[4,5] Details are provided in the Experimental section of the Supplementary data. ^{1}H NMR spectral data confirmed the inclusion of guests within the OA capsule and provided information about the stoichiometry of the complex. NOESY experiments helped us infer the orientation of guest molecule(s) within the OA capsule. The ^{1}H NMR experimental details for one guest molecule, 4,4′-dimethoxythiobenzophenone (**8**), as a representative of guests **2**–**10**, are described in the following. A similar approach yielded information about the inclusion of other guest molecules and are listed in Scheme 3. The ^{1}H NMR spectra of free OA in water, **8** in $CDCl_3$, and **8**@OA_2 capsuleplex (represented as guest@host; stoichiometry indicated as a subscript) in water are provided in Fig. 1. In this case, the signals owing to OCH_3 in compound **8** appear at δ 3.9 ppm in $CDCl_3$, whereas within OA in D_2O, it is upfield shifted to δ –0.81 ppm. Such an upfield shift owing to diamagnetic shielding by the aromatic ring that forms the OA capsule has been established earlier.[6,7] Similar upfield shifts for various protons in compounds **2**–**7**, **9**, and **10** confirmed the inclusion of these probe molecules within the OA capsule (the spectra are provided as Supplementary data). As seen in Fig. 1, in addition to the shift in the ^{1}H signals of the guest, the signals owing to the OA molecule were also affected. Interpretation of these changes has been discussed in prior publications and will not be repeated here. ^{1}H NMR titration experiments established the stoichiometry of the **8**@OA_2 complex to be 1:2. Titration spectra in the case of OA with **8** are provided in Fig. 2. As can be seen in the spectra, upon addition of the guest up to 0.5 equiv, there are changes in the host region. Addition of more than 0.5 equiv of the guest did not result in any further changes in the spectra, suggesting that **8** forms a 1:2 complex with OA. Also, addition of more than 0.5 equiv of **8** to the OA solution resulted in turbidity, suggesting that **8** is insoluble in water in the absence of OA. The appearance of sharp signals owing to guest **8** and the absence of a shift in the guest peaks with varying ratios of host-to-guest suggested that in the NMR time scale, **8** remains within the OA capsule. Capsule formation was further confirmed by measuring the diffusion constant of the capsuleplex by ^{1}H NMR DOSY experiments. For example, free OA has a diffusion constant of 1.88×10^{-6} cm^2 s^{-1}, whereas the **8**@OA_2 complex has a diffusion constant of 1.38×10^{-6} cm^2 s^{-1}. Similar diffusion constants were observed for complexes of **2**–**7**, **9**, and **10** (see Supplementary data). Guest-to-host ratios for all capsuleplexes discussed in this study are included in Table 1.

The experiments we performed to gain information concerning the capsule opening–closing process rely on the quenching of excited states (S_1 or T_1) of guest molecules by molecular oxygen.[8] Guest molecules **2**–**8**, having very high rate constants of intersystem crossing (ISC) from S_1 to T_1, show phosphorescence at room temperature in solution (see Table 1 for the quenching of the excited state).[8,9] On the other hand, probes **9** and **10**, having low rate constants of ISC from S_1 to T_1, fluoresce at room temperature. In the first set of compounds (**2**–**8**), the T_1 state (phosphorescence), and in the latter two molecules (**9** and **10**), the S_1 state (fluorescence), are quenched by molecular oxygen via energy transfer in organic solvents with rate constants $>5 \times 10^8$ (mol/L)$^{-1}$ s^{-1} (Table 1).[10,11] Since pyrene (**9**) did not phosphoresce at room temperature, quenching in the case of the pyrene triplet was monitored by its T–T absorption. As indicated in Table 1, the pyrene triplet was quenched by oxygen in a cyclohexane solution with a rate constant of 1.6×10^9 (mol/L)$^{-1}$ s^{-1}.[10] Since the excited states of all the guest

Can. J. Chem. Downloaded from www.nrcresearchpress.com by University of Electronic and Science Techonology of China on 09/18/12
For personal use only.

Fig. 1. ^{1}H NMR spectra of (i) 4,4′-dimethoxythiobenzophenone (**8**) in $CDCl_3$, (ii) capsuleplex, octaacid (OA) :**8** (2:1), [OA] = 1 mmol/L in 10 mmol/L tetraborate D_2O buffer, and (iii) OA (1 mmol/L in 10 mmol/L tetraborate D_2O buffer). Signals marked with * represent the residual proton resonances from the corresponding solvents.

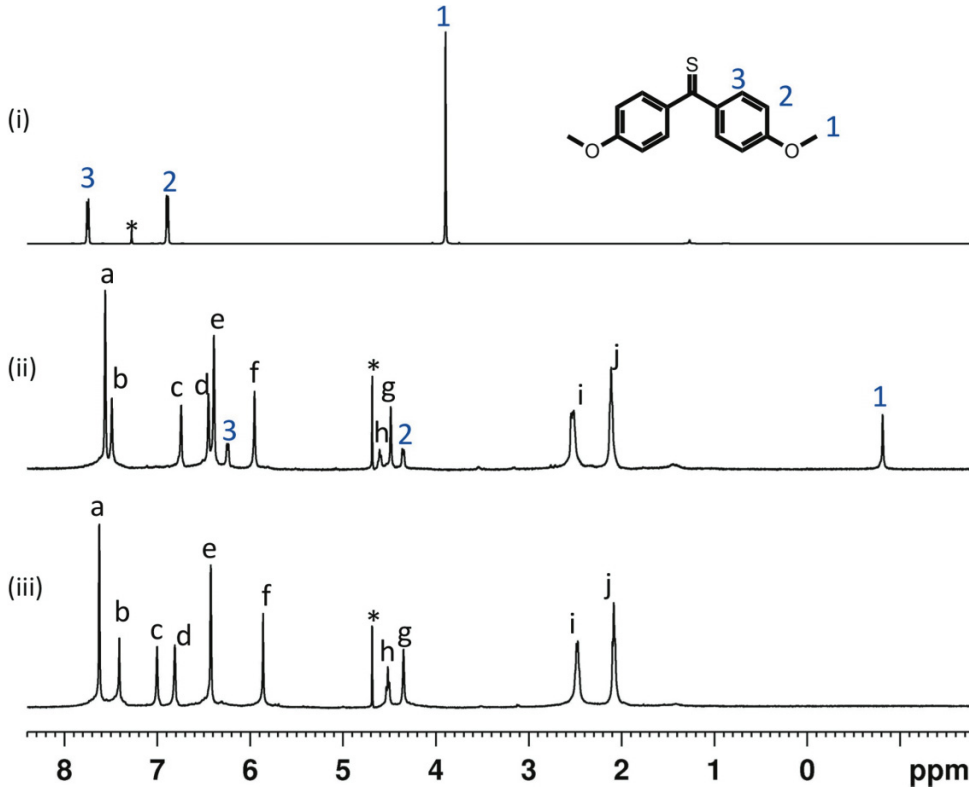

molecules we chose were quenched with very high rate constants in solution,[12] we believed that oxygen should be able to quench the excited states of guest molecules **2**–**10** entrapped within the OA, provided that the excited guest molecules were accessible to oxygen during their lifetime. Alternatively, the quenching could occur through the wall of the capsuleplex. We believed that information on the rate constants of oxygen quenching of the excited states of various guests would be able to distinguish between the two mechanistic possibilities. If the quenching occurs through donor–acceptor contact, the accessibility of oxygen to the excited guest molecule would depend on the opening–closing of the capsuleplex. The cavitand that forms the capsule has two ports, one small and one large. Oxygen with a molecular width of ~3 Å (including the van der Waals' radius) will not be able to access the entrapped guest through the smaller port of the OA capsuleplex, which has a diameter of ~2 Å (including the van der Waals' radius, see Scheme 1). Therefore, we believe that oxygen and the entrapped guest could meet only through the larger port that is present at the middle of the capsuleplex. The larger port would become available only if the capsuleplex opens at least partially. We need to address several questions before drawing conclusions regarding the opening–closing process of the capsuleplex from the oxygen quenching data: (*i*) Is the probe molecule entrapped within a capsule accessible to oxygen? (*ii*) Is the quenching static or dynamic? (*iii*) What are the rates of quenching of the capsule-trapped guests? (*iv*) What is the rate-determining step in the quenching process?

In this section, we present experimental data for benzil (**3**) as a representative of guests **2**–**6**. Experimental data for guests **2** and **4**–**6** are provided in the Supplementary data. Room-temperature emission spectra of **3**@OA_2 in water (borate buffer) consisting of fluorescence, delayed fluorescence (480–520 nm), and phosphorescence (530–650 nm) are shown in Fig. 3a. As illustrated in the figure, the phosphorescence intensity is significantly reduced in the presence of oxygen compared with that in nitrogen-saturated buffer solution. The displayed spectra clearly show that emission intensities are dependent on the concentration of oxygen in water. The phosphorescence (530–650 nm) was significantly quenched by oxygen, whereas the fluorescence (direct and delayed fluorescence at 480–520 nm) shows only minor oxygen quenching. Consistent with the steady-state emission data, the excited triplet state decay profiles displayed in Fig. 3b also exhibit oxygen-concentration dependence.

Rate constants for quenching of the benzil triplet by oxygen were determined by monitoring the decay profiles of benzil triplet states at varying concentrations of oxygen. Triplet-state decay profiles were monitored by two independent methods, phosphorescence (Fig. 3b) and triplet–triplet absorption measurements. The rate constants for quenching were obtained from the slope of the plots of the pseudo-first-order decay rate constants of benzil triplet states vs the oxygen concentration (Fig. 4). Quenching rate constants obtained by the two methods (included in the figure) are identical within experimental error.[13,14] These data suggest that oxygen is able to quench the benzil triplet in spite of it being enclosed within the OA capsule. However, the rate constant for quenching of benzil in a capsuleplex is

Can. J. Chem. Downloaded from www.nrcresearchpress.com by University of Electronic and Science Techonology of China on 09/18/12
For personal use only.

Fig. 2. ^{1}H NMR titration studies of the octaacid (OA) with **8** (500 MHz, D_2O). [OA] = 1 mmol/L in 10 mmol/L tetraborate D_2O buffer. Signals marked with * represent the residual proton resonances from the solvent.

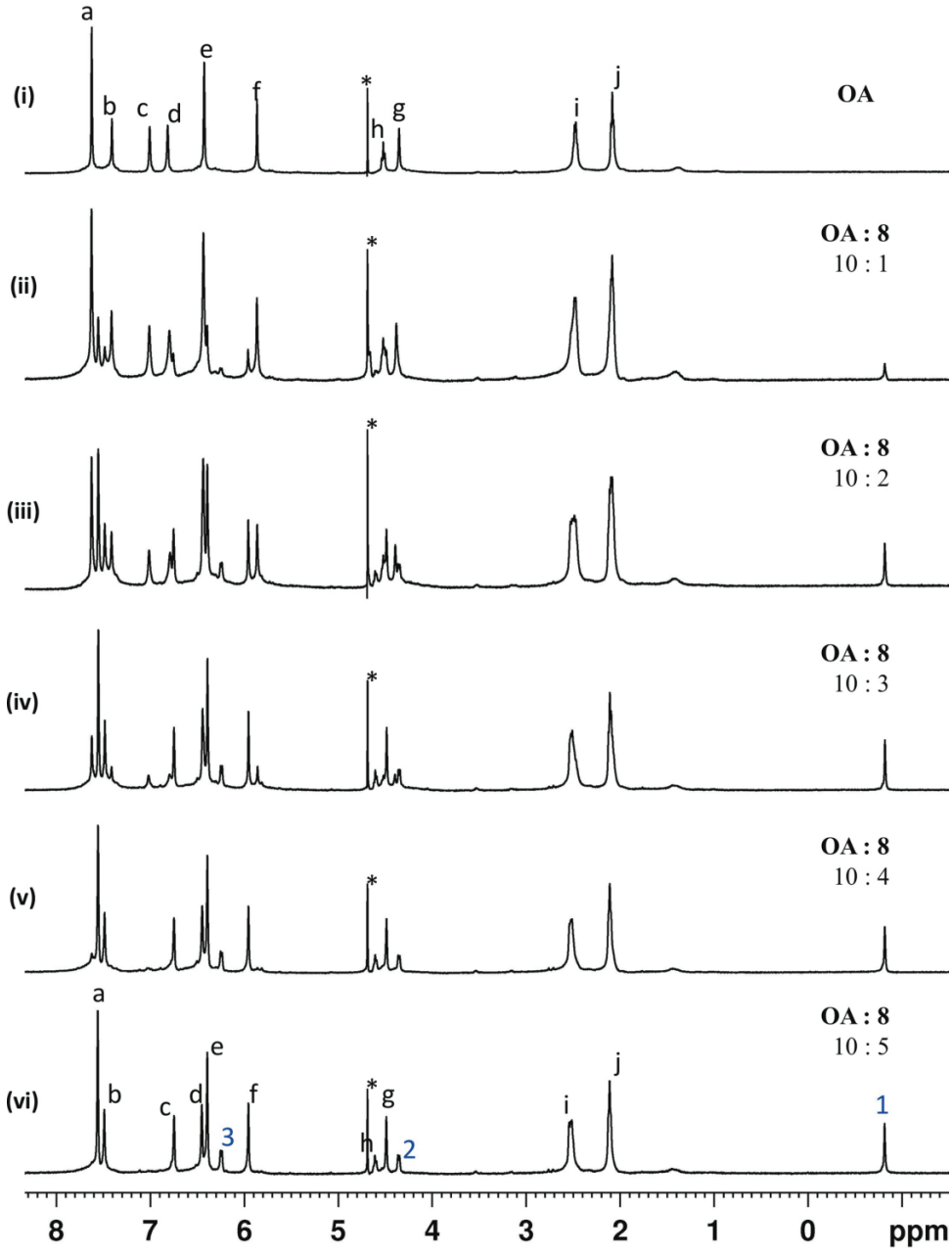

significantly lower (1.2×10^7 $(mol/L)^{-1}$ s^{-1} vs 6.0×10^8 $(mol/L)^{-1}$ s^{-1}) than in an organic solvent (Table 1). Rate constants for oxygen quenching of the triplets of guest molecules **2**–**6** and **9** captured with the OA capsule are provided in Table 1. As noted, the numbers are more than an order of magnitude lower in the capsule than in an organic solvent.

To interpret the data, we need to ascertain whether the quenching is static or dynamic. The data provided in Fig. 3 suggest that the quenching is a dynamic process. Had it been a fully static process, no variation in lifetime would have occurred. Further support comes from the Stern–Volmer plots with points taken from both steady-state emission and lifetime data (Fig. 3c). The linear lines with almost identical slopes are consistent with a dynamic process. This conclusion is also consistent with the difference in rise time of singlet oxygen phosphorescence and decay time of benzil phosphorescence (Fig. 5c).

To probe the mechanism of the quenching process, phosphorescence emission from singlet oxygen was monitored upon quenching the **3**@OA_2 triplet by ground-state oxygen. As illustrated in Fig. 5a, quenching of benzil triplet resulted in phosphorescence from singlet oxygen, suggesting that quenching is the result of energy transfer. Furthermore, the difference in emission intensities (Fig. 5a) and lifetimes (Figs. 5b and 5c; 5 and 41 μs in H_2O and D_2O buffer, respectively)[15] of singlet oxygen observed between H_2O and D_2O solutions suggested that singlet oxygen, generated by the above energy-transfer process, spends most of its life-

Can. J. Chem. Downloaded from www.nrcresearchpress.com by University of Electronic and Science Techonology of China on 09/18/12
For personal use only.

Table 1. Excited-state lifetime and oxygen-quenching data for capsuleplexes made up of octaacid (OA) and organic guests **2–10** listed in Scheme 3.

Compound	H:G	Excited state		O_2 quenching in OA (%)	k_q (O_2) ((mol/L)$^{-1}$ s^{-1}) in OA[a]	k_q (O_2) ((mol/L)$^{-1}$ s^{-1}) in solution
		Type	Lifetime in OA (μs)[a]			
Pyrene (**9**)	2:1	T_1	922[b]	38[c]	5×10^{5}[a]	1.6×10^{9}[d]
4,4′-Dimethylbenzil (**2**)	2:1	T_1	596[e]	85[f]	8.7×10^{7}[a] 7.9×10^{7}[b]	8.2×10^{8}[b,g]
Fenchthione (**4**)	2:2	T_1	187[e]	55[f]	1.6×10^{6}[b]	$>10^{9}$
Benzil (**3**)	2:1	T_1	151[e]	63[f]	1.3×10^{7}[a] 1.2×10^{7}[e]	6.0×10^{8}[b,g]
Camphorthione (**5**)	2:2	T_1	65[e]	59[f]	2.4×10^{7}[e]	$>10^{9}$
Adamantanethione (**6**)	2:2	T_1	17[e]	48[f]	2.8×10^{7}[e]	$>10^{9}$
Xanthione (**7**)	2:1	T_1	4.8[e]	3[f]	—	$>10^{9}$
4,4′-Dimethoxy thiobenzophenone (**8**)	2:1	T_1	0.62[e]	0[f]	—	$>10^{9}$
Pyrene (**9**)	2:1	S_1	0.34[h]	0[f]	—	2.5×10^{10}[d]
Phenanthrene (**10**)	2:1	S_1	0.05[h]	0[f]	—	2.3×10^{10}[d]

Note: H, host; G, guest; and k_q, quenching rate constant.

[a]Error limit ~10%.

[b]Determined by triplet–triplet absorption.

[c]Determined by comparing the triplet absorption decay traces in both nitrogen- and oxygen-saturated solutions of guest@OA capsuleplexes.

[d]In cyclohexane solution.

[e]Determined by phosphorescence.

[f]Determined by comparing the relative luminescence intensities (at λ_{max}) of the spectra recorded in both nitrogen- and oxygen-saturated solutions of guest@OA capsuleplexes.

[g]In acetonitrile solution.

[h]Determined by fluorescence.

time in water. Since our earlier studies have shown that the capsuleplex is nonpolar and has no water molecules inside the capsule,[16] we believe that singlet oxygen following energy transfer, if it occurs within the capsule, escapes to water. Alternatively, the energy transfer might be occurring when the capsule is partially open so that water molecules surround the donor and acceptor pair. We favor the latter model.

Triplets of xanthione (**7**) and 4,4′-dimethoxythiobenzophenone (**8**) included within OA capsule were not quenched by oxygen, although they were quenched at diffusion-limited rates in organic solvents.[17–19] Phosphorescence spectra and triplet decay profiles in the presence of oxygen and nitrogen, shown in Fig. 6 for xanthione, are distinctly different from those shown in Fig. 3 for benzil. In Fig. 6, the phosphorescence intensities and triplet decays are almost identical for nitrogen- and oxygen-saturated solutions. This behavior also extended to S_1 of pyrene (**9**) and phenanthrene (**10**). As illustrated in Fig. 7a, the fluorescence spectra of pyrene@OA_2 in nitrogen-saturated and oxygen-saturated buffer solutions are identical. The S_1 lifetime of pyrene was nearly identical under nitrogen- and oxygen-saturated conditions (Fig. 7b). This is distinctly different from that in cyclohexane solution where pyrene S_1 is quenched by oxygen at a diffusion-limited rate. Thus, while the S_1 states of pyrene and phenanthrene are quenched at diffusion-controlled rates in cyclohexane,[10,11] they are unquenched when they are included within the OA.

Examination of Table 1 reveals that there are two sets of molecules, one (triplet **2–6** and triplet **9**) includes the molecules that are quenched by oxygen when enclosed within the OA capsule, and the other (**7–10**) represents the molecules that are not quenched by oxygen when enclosed within the OA capsule. Since the second set of molecules involves both triplet (**7** and **8**) and excited singlet (**9** and **10**) states, we believe that the absence of quenching in the second set does not depend on the spin state. Closer examination of Table 1 suggests that the lifetime of the excited state is likely to play a role in the quenching process. Although in solution they are quenched at diffusion-controlled rate constants, guest molecules whose lifetimes are shorter than 5 μs are not quenched by oxygen when they are enclosed in the OA capsule. Also, it is important to note that the five guest molecules whose lifetimes span between 17 and 922 μs are quenched with rate constants varying between 5×10^5 (mol/L)$^{-1}$ s^{-1} and 8×10^7 (mol/L)$^{-1}$ s^{-1}. We need to address three important questions: (*i*) What exactly do the quenching rate constants imply? (*ii*) Why are some encapsulated guests quenched but not the others? (*iii*) Why do the quenching rate constants vary between the guests?

In Scheme 4, the sequence of steps involved in the energy-transfer process are summarized with rate constants listed above each step. The first step is the diffusion of the excited capsuleplex and oxygen to form a collision complex with a rate constant of k_d. The second step represents the access of oxygen to the excited guest present within the capsule. This step requires partial opening of the capsuleplex and the rate constant is represented as k_o. The third step is the true energy-transfer process between ground-state oxygen and the excited guest that are close to each other. This step is represented by the rate constant k'_{ET}. To differentiate between the energy transfer occurring across the wall of the capsuleplex and the one involving the collisional complex between ground-state oxygen and the excited guest (present within the host OA), the former process is represented by a rate constant of k_{ET}.

The sequence of steps involved in the quenching of guest@OA_2 by oxygen is shown in Scheme 4. We visualize

Can. J. Chem. Downloaded from www.nrcresearchpress.com by University of Electronic and Science Techonology of China on 09/18/12
For personal use only.

Fig. 3. (a) Steady-state emission spectra of **3**@OA_2 in solutions saturated with various oxygen–nitrogen mixtures. OA, octaacid. (b) Phosphorescence decay profile of **3**@OA_2 observed at 560 nm after excitation (308 nm, 15 ns pulse width). (c) Stern–Volmer plots with various concentrations of oxygen using steady-state phosphorescence intensity (I_o/I) and triplet lifetimes (τ_o/τ).

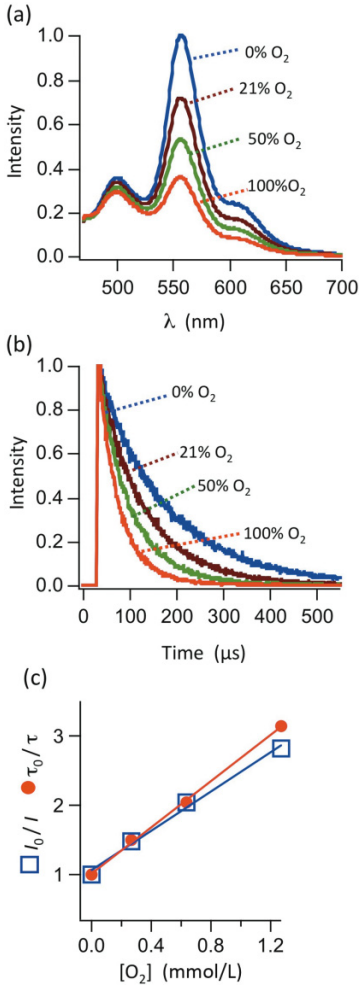

Fig. 4. Determination of the quenching rate constant (k_q) of benzil (**3**) triplets by oxygen. (a) Pseudo-first-order decay constant of the triplet–triplet absorption of **3** observed at 460 nm after excitation with laser pulses (355 nm, 5 ns pulse width) of **3**@OA_2 solutions at different oxygen concentrations. OA, octaacid. (b) Phosphorescence decay constant of **3** observed at 560 nm after excitation with laser pulses (308 nm, 15 ns pulse width) of **3**@OA_2 solutions at different oxygen concentrations. The black lines show the linear fits.

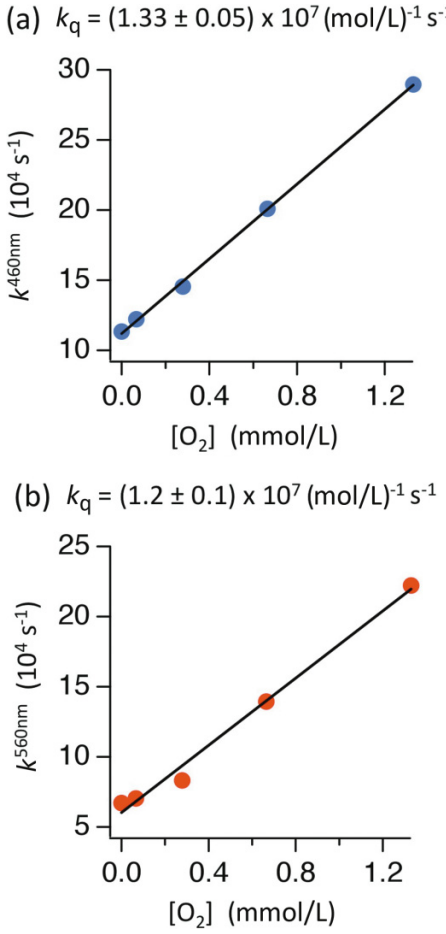

three possible mechanisms for the energy-transfer process: (*i*) Energy transfer occurs between the excited guest entrapped within the OA capsule and oxygen in water through the walls of the capsule. This type of energy transfer has been demonstrated to occur between benzil entrapped within a covalently linked capsule (carceplex) and oxygen.[20–24] The upper limit of the rate constant for this process was estimated to be 10^4 $(mol/L)^{-1}$ s^{-1}. Since the measured rate constants in the current study are orders of magnitudes higher, we believe that the energy transfer does not occur through the walls of the capsule. (*ii*) Energy transfer occurs between the donor guest and acceptor oxygen (both being present within the capsule). Under such conditions, static quenching is expected. Such a possibility has been ruled out by the results suggesting that the quenching is a dynamic rather than a static process (see Figs. 3 and 5 and related discussion). (*iii*) The third possibility, which we favor, is the one where quenching is controlled by the capsule opening–closing process. In this case, the quenching would be expected to be dynamic. In solution, the rate constant for energy transfer between benzil and oxygen was measured to be 6×10^8 $(mol/L)^{-1}$ s^{-1}, which is higher than the number measured in the presence of the OA.[13,14] Since the rate constants we have measured for benzil@OA_2 and five other guest@OA_2 capsuleplexes (Table 1) are lower than those in solution (in the absence of the OA), we believe that the measured rate constants do not represent the energy-transfer process, but they represent the accessibility of oxygen to the entrapped guest, which in turn depends on the capsule opening–closing process.

To fully understand the meaning of the quenching constant, we need to know exactly what the measured k_q represents. The steps involved in the quenching are the formation of the encounter complex between molecular oxygen and the excited guest – OA capsuleplex (k_d), the decomplexation of the encounter complex between oxygen and capsuleplex without energy transfer (k_{-d}), and the capsule opening that facilitates the interaction between oxygen and the excited encapsulated guest (k_o). Upon close interaction between ground-state oxygen and the excited guest, we assume that

Can. J. Chem. Downloaded from www.nrcresearchpress.com by University of Electronic and Science Techonology of China on 09/18/12
For personal use only.

Fig. 5. Quenching of benzil (**3**) phosphorescence and generation of singlet oxygen. (a) Steady-state phosphorescence of singlet oxygen from excitation (310 nm) of air-saturated buffer solutions (D_2O or H_2O) of **3**@OA_2. OA, octaacid. (b) (H_2O) and (c) (D_2O): Phosphorescence decay trace of **3** (blue trace observed at 560 nm) and $^1O_2$ (red trace observed at 1270 nm) after excitation with a laser pulse (308 nm, 15 ns pulse width). The **3**@OA_2 solutions in buffer were saturated with N_2/O_2 gas mixture (1:1). The black lines show the kinetic fits of benzil phosphorescence decay and growth + decay of $^1O_2$ phosphorescence. Bz in the figure represents benzil.

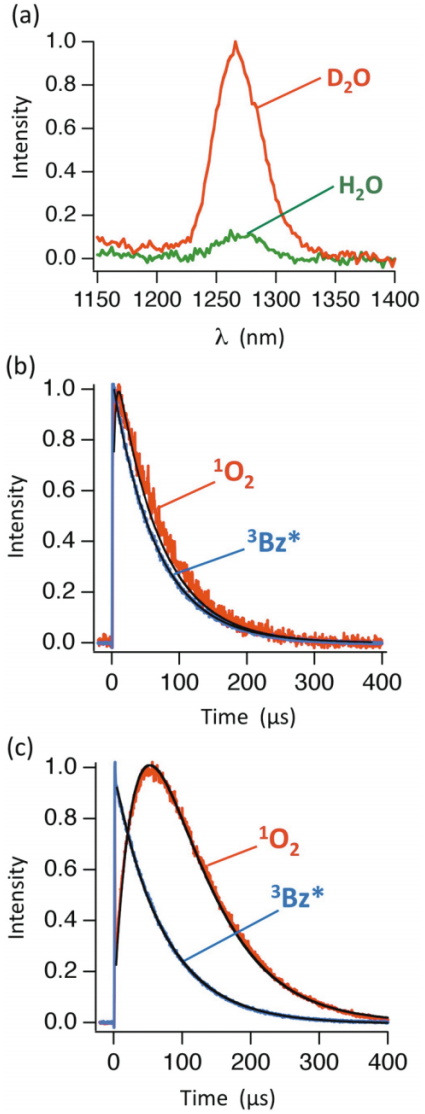

the energy transfer occurs instantaneously, and the slow step is the accessibility of oxygen to the trapped excited guest molecule. Under these conditions, the measured k_q would be given by eq. [1]. If we assume that $k_{-d} > k_o$, then k_q and k_o would be given by eqs. [2] and [3], respectively. Since no specific interactions are expected between oxygen and the capsuleplex, we believe that k_{-d} would be determined by the lifetime of the encounter complex (capsuleplex and oxygen) in water and k_d would be the diffusion rate constant in water, which is 7.4×10^9 $(mol/L)^{-1}$ s^{-1}.[25] Based on literature reports, we assume that the lifetime of the encounter complex between oxygen and the capsuleplex in water

Fig. 6. (a) Steady-state phosphorescence spectra of **7**@OA_2 in oxygen and nitrogen, excitation wavelength (400 nm). OA, octaacid. (b) Phosphorescence decay profile of **7**@OA_2 observed at 670 nm after excitation (355 nm, 5 ns pulse width) of **7**@OA_2 solutions in oxygen and nitrogen.

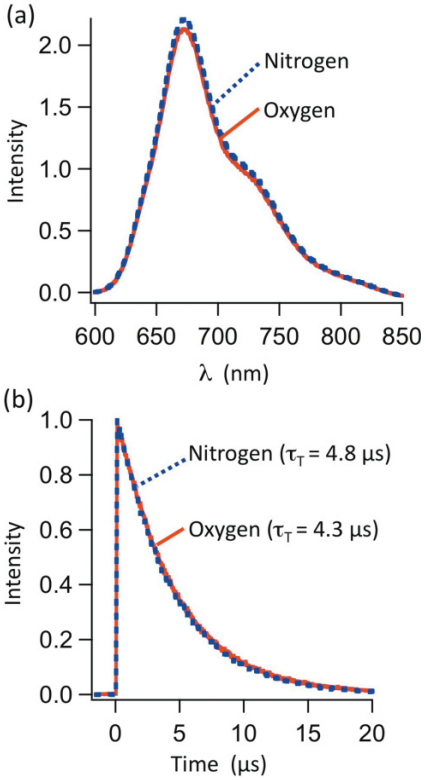

would be between 0.1 and 0.5 ns.[26,27] Thus, the value for k_{-d} would be between 2×10^9 and 1×10^{10} s^{-1}. Under such conditions, k_o would be between 0.3 and 1.3 $\times$ k_q. On the basis of these assumptions, we believe that the measured quenching constants listed in Table 1 indirectly reflect the rate constants for capsule opening and that the values vary over at least two orders of magnitude between the pyrene triplet and the 4,4′-dimethylbenzil triplet.

$$[1] \qquad k_q = \frac{k_d k_o}{k_{-d} + k_o}$$

$$[2] \qquad k_q = \frac{k_d k_o}{k_{-d}}$$

$$[3] \qquad k_o = \frac{k_{-d} k_q}{k_d}$$

Finally, we address the question of why the excited states of xanthione (T_1, 4.7 μs), 4,4′-dimethoxythiobenzophenone (T_1, 0.6 μs), pyrene (S_1, 0.3 μs), and phenanthrene (S_1, 0.05 μs) included within OA capsule are not quenched by oxygen (Table 1). To understand this process, one needs to recognize that guests with excited-state lifetimes longer than 17 μs are quenched by oxygen to varying percentages (see Table 1). For example, the phosphorescence of adamantanethione (**6**) with a lifetime of 17 μs is quenched to 48% by oxygen (based on relative phosphorescence intensities of

Can. J. Chem. Downloaded from www.nrcresearchpress.com by University of Electronic and Science Techonology of China on 09/18/12
For personal use only.

Scheme 4. Schematic representation of energy transfer between the encapsulated guest and oxygen. The rate constants indicated in the scheme are defined in the text.

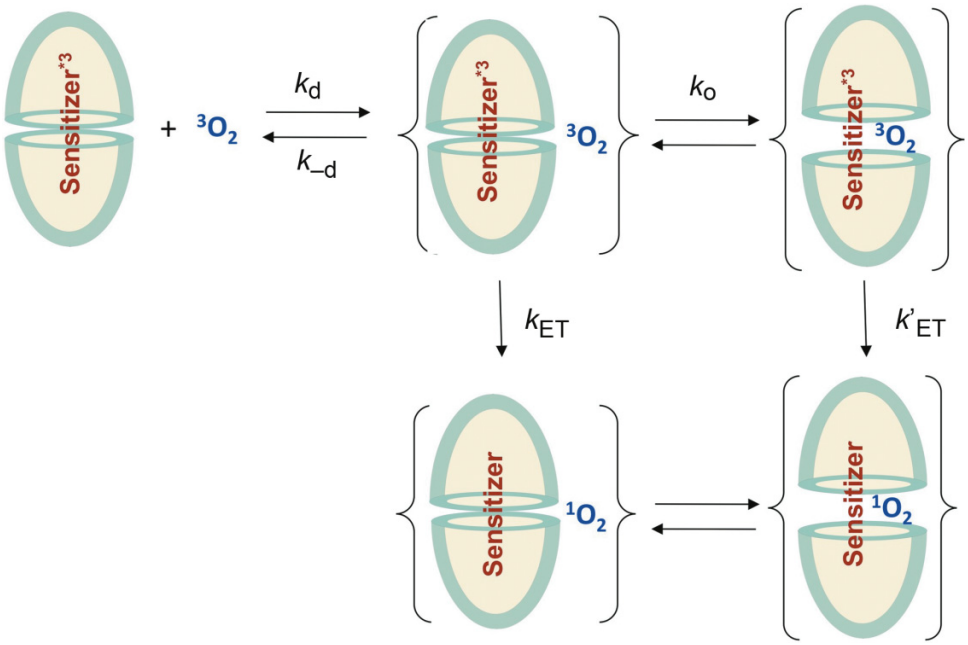

Fig. 7. (a) Steady-state fluorescence spectra of **9**@OA_2 in oxygen and nitrogen. OA, octaacid. (b) Fluorescence decay profile of **9**@OA_2 observed at 380 nm after excitation (330 nm) of **9**@OA_2 solutions in oxygen and nitrogen.

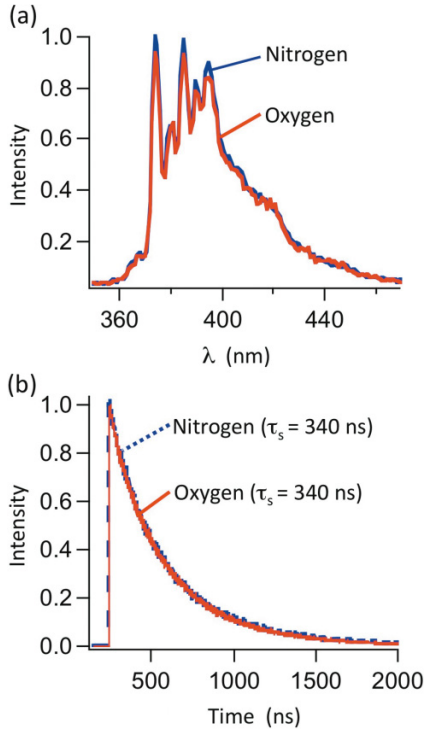

oxygen- and nitrogen-saturated solutions). On the other hand, 4,4′-dimethylbenzil with a lifetime of 596 μs is quenched to 85% of its initial phosphorescence intensity. Increased quenching cannot be solely due to the longer lifetime of the 4,4′-dimethylbenzil triplet. For example, the pyrene triplet with a much longer lifetime (922 μs) is quenched only to 38% as monitored by its T–T absorption. The most noteworthy feature is that molecules whose excited-state lifetimes are shorter than 5 μs remain unquenched by oxygen. We believe that 5 μs may be the cutoff point in terms of the accessibility of oxygen to the excited guest molecule. This suggests that the trapped guest excited state must live for longer than 5 μs for oxygen to access it. One could interpret this to mean that the capsule takes longer than 5 μs to open (at least in the case of xanthione).

As indicated by the quenching percentage (Table 1), the time it takes for the capsule to open may vary with the guest. The excited-state lifetime alone does not determine the quenching percentage. As seen in Table 1, there is no direct correlation between the lifetime and quenching percentage (compare the triplets of **2**, **6**, and **9**). The observed k_q range from 5×10^5 to 9×10^7 $(mol/L)^{-1}$ s^{-1}, depending on the guest molecule (Table 1). This variation in k_q values indicates that the structure of the guest plays an important role in the stability of the host–guest complex and the kinetics of the accessibility of oxygen to the entrapped guest. For example, for benzil, a k_q of 1.3×10^7 $(mol/L)^{-1}$ s^{-1} was observed, whereas for longer dimethylbenzil (11.8 vs 13.7 Å; see Scheme 3), a k_q approximately six times larger (8×10^7 $(mol/L)^{-1}$ s^{-1}) was observed (see Scheme 5 for cartoon representations of the capsuleplexes). This suggests that for the capsule to open just enough for oxygen to reach the excited guest, it takes about six times longer for benzil than for dimethylbenzil. Clearly, the length of the molecule that determines the compactness of the capsuleplex is important in the opening–closing process.

The most interesting observation was noticed with pyrene. In this case, a much smaller rate constant of 5×10^5 $(mol/L)^{-1}$ s^{-1} was observed. This small k_q could be explained by the different nature of the pyrene triplet state (π–π*) compared with the benzil derivatives with an n–π* nature. Triplet states of n–π* are localized at the C=O

Scheme 5. Structures of the guest@host complexes based on ^{1}H NMR data.

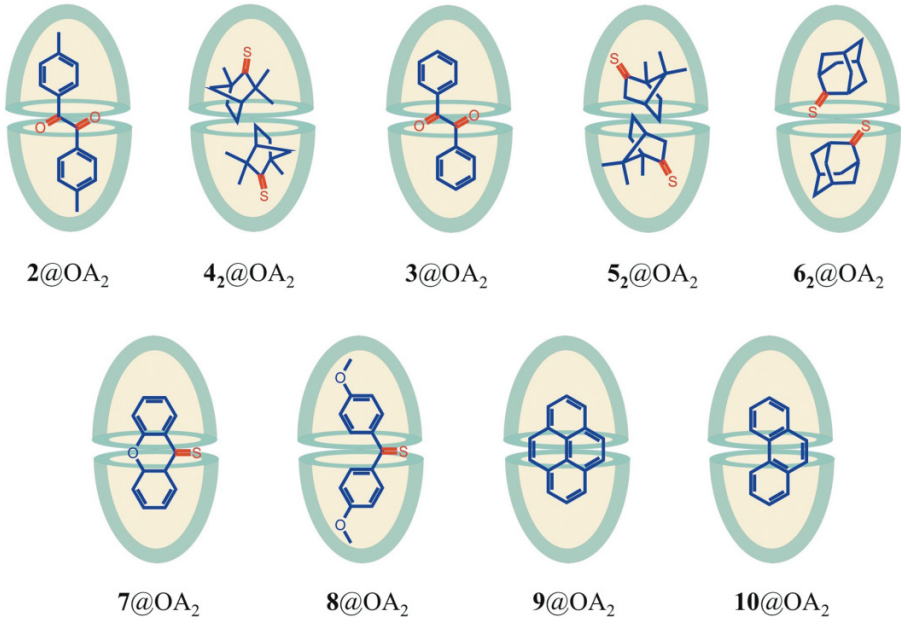

chromophore, which is located at the capsule entrance for benzil derivatives, and therefore, probably more accessible to oxygen. Pyrene triplet states (π–π^*) are delocalized over the entire molecule, which probably makes them less accessible to oxygen quenching at the capsule entrance. Thus, the measured quenching constant reflects the accessibility of oxygen to the excited guest for energy transfer to take place. Therefore, the extent of the required opening for each guest could vary, and this in turn may depend on the structure of the guest. We caution that the measured k_qs listed in Table 1 do not represent the same extent of opening in all cases. However, the lower than diffusion-limited value and higher than the energy-transfer rate constant (k_{ET}, Scheme 4) reported for a carcerand suggest that the measured k_qs provide information concerning the opening of the capsuleplex. From the quenching studies, we conclude that the capsuleplex is dynamic and it periodically opens and closes in the μs time scale.

The difference in rate constants between the three thiones **4**, **5**, and **6** is also interesting. In spite of having similar triplet-state lifetimes in solution, the triplet-state lifetimes and quenching constants in OA capsuleplexes differ by an order of magnitude between fenchthione and adamantanethione. Examination of the orientation of the thiones within the capsule accounts for the difference.[9] Orientations based on ^{1}H NMR data of the three thiones within the capsule are shown in Scheme 5. NMR experiments showed that the thiocarbonyl chromophore of fenchthione is deeply buried at the bottom of the OA cap, which shields the excited state from oxygen quenching and, consequently, a lower k_q is observed (1.6×10^6 (mol/L)$^{-1}$ s^{-1}). Clearly in this case, a small opening as in the case of benzil would not suffice for oxygen to reach the excited chromophore. On the other hand, in the case of adamantanethione, where the thione chromophore is in the middle of the capsule, it could be accessed (similar to benzil) with a slight opening of the capsule. The observed quenching constant for adamantanethione is comparable to that of benzil, although they have distinctly different lifetimes (17 vs 151 μs). From these studies, it is clear that capsuleplexes of organic guests and OA are dynamic, and one of the motions they exhibit is the opening and closing of the capsule (Scheme 2d). The time scale for this process depends on the structure and hydrophobicity of the guest. The extent to which the capsuleplex has to open for quenching to occur may vary with the orientation of the guest within the capsule.

Conclusion

In this study, we show that excited states of guests enclosed as capsuleplexes could be quenched by oxygen via an energy-transfer process. The rate constant measured for the quenching reflects the accessibility of oxygen to the guest enclosed within the OA capsuleplex, and this in turn depends on the capsule opening–closing. The rate constant of this process most likely depends on the structure of the guest.

Supplementary data

Supplementary data for this article are available on the journal Web site (canjchem.nrc.ca).

Acknowledgements

V.R. and N.J.T. are grateful to the National Science Foundation (NSF), USA, for generous financial support (CHE-0848017 and CHE-0717518, respectively). The authors thank Professor C. Bohne for insightful discussions.

References

(1) Gibb, C. L. D.; Gibb, B. C. *J. Am. Chem. Soc.* **2004**, *126* (37), 11408. doi:10.1021/ja0475611. PMID:15366865.
(2) Jayaraj, N.; Zhao, Y.; Parthasarathy, A.; Porel, M.; Liu, R. S. H.; Ramamurthy, V. *Langmuir* **2009**, *25* (18), 10575. doi:10.1021/la901367k. PMID:19496576.
(3) Kulasekharan, R.; Jayaraj, N.; Porel, M.; Choudhury, R.;

Can. J. Chem. Downloaded from www.nrcresearchpress.com by University of Electronic and Science Techonology of China on 09/18/12
For personal use only.

Sundaresan, A. K.; Parthasarathy, A.; Ottaviani, M. F.; Jockusch, S.; Turro, N. J.; Ramamurthy, V. *Langmuir* **2010**, *26* (10), 6943. doi:10.1021/la904196g. PMID:20055365.
(4) Parthasarathy, A.; Kaanumalle, L. S.; Ramamurthy, V. *Org. Lett.* **2007**, *9* (24), 5059. doi:10.1021/ol702322u. PMID: 17956116.
(5) Sundaresan, A. K.; Ramamurthy, V. *Org. Lett.* **2007**, *9* (18), 3575. doi:10.1021/ol0713990. PMID:17665921.
(6) Kaanumalle, L. S.; Gibb, C. L. D.; Gibb, B. C.; Ramamurthy, V. *J. Am. Chem. Soc.* **2005**, *127* (11), 3674. doi:10.1021/ja0425381. PMID:15771483.
(7) Natarajan, A.; Kaanumalle, L. S.; Jockusch, S.; Gibb, C. L. D.; Gibb, B. C.; Turro, N. J.; Ramamurthy, V. *J. Am. Chem. Soc.* **2007**, *129* (14), 4132. doi:10.1021/ja070086x. PMID: 17362015.
(8) Turro, N. J.; Ramamurthy, V.; Scaiano, J. C. *Modern Molecular Photochemistry of Organic Molecules;* University Science Books: Sausalito, CA, 2010.
(9) Jayaraj, N.; Maddipatla, M. V. S. N.; Prabhakar, R.; Jockusch, S.; Turro, N. J.; Ramamurthy, V. *J. Phys. Chem. B* **2010**, *114* (45), 14320. doi:10.1021/jp911698s. PMID: 20356085.
(10) Patterson, L. K.; Porter, G.; Topp, M. R. *Chem. Phys. Lett.* **1970**, *7* (6), 612. doi:10.1016/0009-2614(70)87019-1.
(11) Saltiel, J.; Atwater, B. W. *Adv. Photochem.* **1988**, *14*, 1. doi:10.1002/9780470133446.ch1.
(12) Montalti, M.; Credi, A.; Prodi, L.; Teresa Gandolfi, M. *Handbook of Photochemistry;* 3rd ed.; Taylor & Francis: Boca Raton, 2006.
(13) Fang, T.-S.; Brown, R. E.; Kwan, L. C.; Singer, L. A. *J. Phys. Chem.* **1978**, *82* (23), 2489. doi:10.1021/j100512a008.
(14) Parker, C. A.; Joyce, T. A. *Chem. Commun.* **1968**, 1421.
(15) Hurst, J. R.; Schuster, G. B. *J. Am. Chem. Soc.* **1983**, *105* (18), 5756. doi:10.1021/ja00356a009.
(16) Porel, M.; Jayaraj, N.; Kaanumalle, L. S.; Maddipatla, M. V. S. N.; Parthasarathy, A.; Ramamurthy, V. *Langmuir* **2009**, *25*, 3473. doi:10.1021/la804194w. PMID:19708142.
(17) Ramesh, V.; Ramnath, N.; Ramamurthy, V. *J. Photochem.* **1982**, *18* (3), 293. doi:10.1016/0047-2670(82)85014-4.
(18) Rajee, R.; Ramamurthy, V. *J. Photochem.* **1979**, *11* (2), 135. doi:10.1016/0047-2670(79)80046-5.
(19) Rajee, R.; Ramamurthy, V. *Tetrahedron Lett.* **1978**, *19* (51), 5127. doi:10.1016/S0040-4039(01)85829-9.
(20) Parola, J. A.; Pina, F.; Ferreira, E.; Maestri, M.; Balzani, V. *J. Am. Chem. Soc.* **1996**, *118* (46), 11610. doi:10.1021/ja962450q.
(21) Pina, F.; Parola, A. J.; Ferreira, E.; Maestri, M.; Armaroli, N.; Ballardini, R.; Balzani, V. *J. Phys. Chem.* **1995**, *99* (34), 12701. doi:10.1021/j100034a003.
(22) Farrán, A.; Deshayes, K. D. *J. Phys. Chem.* **1996**, *100* (9), 3305. doi:10.1021/jp9531467.
(23) Place, I.; Farran, A.; Deshayes, K.; Piotrowiak, P. *J. Am. Chem. Soc.* **1998**, *120* (48), 12626. doi:10.1021/ja982538z.
(24) Romanova, Z. S.; Deshayes, K.; Piotrowiak, P. *J. Am. Chem. Soc.* **2001**, *123* (44), 11029. doi:10.1021/ja011325y. PMID: 11686708.
(25) Turro, N. J.; Ramamurthy, V.; Scaiano, J. C. *Modern Molecular Photochemistry of Organic Molecules;* University Science Books: Sausalito, CA, 2010; pp 469–478.
(26) Noyes, R. M. *J. Am. Chem. Soc.* **1955**, *77* (8), 2042. doi:10.1021/ja01613a003.
(27) Czapski, G.; Ogdan, J.; Ottolenghi, M. *Chem. Phys. Lett.* **1969**, *3* (6), 383. doi:10.1016/0009-2614(69)80143-0.

Can. J. Chem. Downloaded from www.nrcresearchpress.com by University of Electronic and Science Techonology of China on 09/18/12
For personal use only.

Synthesis and spectroelectrochemical investigation of two tetraarylporphyrins

Robin A. Krüger, Andrea S. Terpstra, and Todd C. Sutherland

Abstract: A free-base tetraarylporphyrin was synthesized by the [2+2] macrocyclization of a dipyrromethane derivative with 3,4,5-tris(dodecyloxy)benzaldehyde in 61% yield. The free-base porphyrin was metallated with zinc acetate in 94% conversion. The free-base and metallated porphyrins show typical intense Soret bands at 426 and 425 nm, respectively, along with the expected number and intensity of Q-bands. Both porphyrins are also fluorescent and display small Stokes shifts between 13 and 18 nm. Cyclic voltammetry established that each porphyrin underwent two reversible one-electron oxidations at 492 and 725 mV (vs Fc/Fc^+ (ferrocene reference)) for the free-base porphyrin and at 329 and 589 mV (vs Fc/Fc^+) for the Zn-metalloporphyrin. Electron-transfer rates were also determined to fall between 1.2×10^{-3} and 2.4×10^{-3} cm s^{-1}. In addition, spectroelectrochemistry and density functional theory calculations of the oxidized products were carried out to confirm the macrocyclic ring oxidations.

Key words: porphyrinoids, electrochemistry, redox chemistry, photochemistry, density functional calculations.

Résumé : On a réalisé la synthèse d'une tétraaraylporphyrine sous la forme de base libre avec un rendement de 61 % par macrocyclisation [2+2] d'un dérivé de dipyrrométhane avec du 3,4,5-tris(docécyloxo)benzaldéhyde. On a effectué la métallation de la porphyrine à l'état de base libre, avec un rendement de 94 %, par traitement avec de l'acétate de zinc. La base libre et la porphyrine métallée présentent respectivement les bandes typiques intenses de Soret à 426 et à 425 nm ainsi que le nombre et l'intensité attendu des bandes Q. Les deux porphyrines sont aussi fluorescentes et elles présentent de faibles déplacements de Stokes, entre 13 et 18 nm. La voltampérométrie cyclique a permis d'établir que chaque porphyrine subit deux oxydations réversibles à un électron, à 492 et 725 mV (vs Fc/Fc^+) pour la base libre et à 329 et 589 mV (vs Fc/Fc^+) pour la Zn-métalloporphyrine. On a aussi déterminé que les vitesses de transfert d'électron se situent entre $1,2 \times 10^{-3}$ et $2,4 \times 10^{-3}$ cm s^{-1}. De plus, de la spectroélectrochimie et des calculs d'après la théorie de la fonctionnelle de la densité effectués sur les produits oxydés pour confirmer les oxydations des noyaux macrocycliques.

Mots-clés : porphyrinoïdes, électrochimie, chimie d'oxydoréduction, photochimie, calculs de la fonctionnelle de la densité.

[Traduit par la Rédaction]

Introduction

Porphyrinoids are commonly found compounds in both the animal and plant kingdoms, as they play important roles in the key steps of photosynthesis that ultimately convert sunlight into chemical energy.[1,2] Iron porphyrins play critical roles in oxygen transport,[3,4] peroxide reduction,[5–7] drug metabolism (cytochrome P450),[8,9] and the mitochondrial electron-transport chain.[10,11] Because of their prevalence in nature, exploration of their potential applications in organic materials is warranted. Photoinitiated charge-transfer reactions are key steps in solar energy conversion,[2,12,13] device applications,[14] and catalysis.[15,16] Progress in these applications necessitates a critical understanding of the thermodynamic factors that direct the charge-transfer reactions. Excited-state reactants are versatile intermediates because they are both better electron donors and better electron acceptors than their ground-state counterparts.[17–19] The reducing and oxidizing strength of these excited-state reagents is crucial to understanding the driving forces that are operating in the eventual applications. Generally, porphyrin ring systems can be easily oxidized to radical cations and sometimes dications.[20–24] Importantly, these cations are stable at room temperature and can be used as reactive intermediates that could be used in organic materials applications.

This contribution explores the electronic properties of two porphyrins and compares them with two well-characterized porphyrins, namely free-base tetraphenylporphyrin (TPP) and Zn-TPP. In addition, full electrochemical and density functional theory (DFT) studies were carried out to assess the charge-transport properties of the oxidized porphyrin ring systems. The goal of this work is to install electron-rich substituents to the meso positions of porphyrins to make stabilized cations for use as light-harvesting chromophores in solar cell applications. Important parameters for a candidate material are high molar absorptivity and excited-

Received 26 February 2010. Accepted 20 May 2010. Published on the NRC Research Press Web site at canjchem.nrc.ca on 25 January 2011.

This article is part of a Special Issue dedicated to Professor J. C. Scaiano.

R.A. Krüger, A.S. Terpstra, and T.C. Sutherland.[1] Department of Chemistry, University of Calgary, 2500 University Drive NW, Calgary, AB T2N 1N4, Canada.

[1]Corresponding author (e-mail: todd.sutherland@ucalgary.ca).

Can. J. Chem. Downloaded from www.nrcresearchpress.com by University of Electronic and Science Techonology of China on 09/18/12
For personal use only.

Can. J. Chem. Downloaded from www.nrcresearchpress.com by University of Electronic and Science Techonology of China on 09/18/12
For personal use only.

state redox potential that are compatible with a typical *n*-type material, such as phenyl-C_{61}-butyric acid methyl ester (PCBM), and ground-state stability of the radical cation. Furthermore, these compounds were synthesized to explore whether supramolecular structures, such as liquid crystals, could form using meso-aryl substituted porphyrins. A common motif, the trisalkoxyphenyl group, has been employed in a variety of functional materials[25–29] to impart supramolecular long-range ordering that may enhance charge transport in solar applications.

Experimental

Zinc-porphyrin (4)

Free-base porphyrin (30 mg, 10.6 μmol), $NaHCO_3$ (100 mg, 450 μmol) and zinc acetate dihydrate (100 mg, 450 mmol) were stirred at ambient temperature in $CHCl_3$ for 4 h in the dark. The red solution was then poured on diluted aqueous $NaHCO_3$ solution (50 mL). After phase separation, the aqueous layer was extracted with CH_2Cl_2 (1 × 20 mL) and the combined organic layers were dried with $MgSO_4$ and evaporated. The crude red oil was purified by column chromatography using CH_2Cl_2 as the eluent on alumina (N, III) and collection of the first red fraction. The yield was 29 mg (10 μmol, 94%). ^{1}H NMR (CD_2Cl_2, 400 MHz) δ: 9.10 (s, 8 H, aryl-H), 7.45 (s, 8 H, pyr-H), 4.29 (t, J = 6.6 Hz, 8 H, OCH_2), 4.11 (t, J = 6.5 Hz, 16 H, OCH_2), 2.01–1.94 (m, 8 H, CH_2), 1.93–1.86 (m, 16 H, CH_2), 1.72–1.65 (m, 8 H, CH_2), 1.56–1.25 (m, 208 H, CH_2), 0.93 (t, J = 7.0 Hz, 12 H, CH_3), 0.87 (t, J = 7.0 Hz, 24 H, CH_3). UV–vis (CH_2Cl_2) λ_{abs} (nm) [ε (L mol^{-1} cm^{-1})] = 425 [130 000], 550 [6600], 589 [1300]. λ_{em} (nm) (relative intensity) (λ_{ex} = 425 nm) = 607 (0.96), 649 (1). HR–MS (MALDI-TOF) calcd. for $C_{188}H_{316}N_4O_{12}Zn$: 2886.353; found: 2886.365.

Results and discussion

The synthesis of metal-free porphyrin **3** and Zn-porphyrin **4** is shown in Scheme 1. The synthesis of **1** was carried out using literature methods.[30,31] Condensation of freshly distilled excess pyrrole and TFA with **1** resulted in the formation of the dipyrromethane **2** in 57% yield. Note that **2** was moderately stable at room temperature under N_2 atmosphere and was immediately used in the ring-closing condensation with **1** to produce the free-base porphyrin **3** in 61% yield.[32] Porphyrin **3** was easily metallated with Zn-acetate at room temperature in the dark to give Zn-porphyrin **4** in 94% yield. The electronic absorption and emission properties of porphyrins **3** and **4** are summarized in Table 1, and the spectra are included in the Supplementary data. Both **3** and **4** exhibit strong near-UV absorptions (Soret) attributed to the $S_0 \rightarrow S_2$ transition and sets of weaker visible transitions (Q-bands) attributed to the $S_0 \rightarrow S_1$ transitions, typical of porphyrins.[33] The absorption and emission properties of **3** and **4** are consistent with other reports, which have been extensively reviewed.[34]

The Soret peak, B(0,0), for **3** is positioned at 426 nm with a full width at half maximum (FWHM) of 20 nm, which is similar to the Soret band of **4** at 425 nm with a narrower FWHM of 14 nm (see Supplementary data). The Soret bands of **3** and **4** are slightly red-shifted compared with Soret bands of free-base tetraphenylporphyrin (H_2-TPP) and Zn-tetraphenylporphyrin (Zn-TPP) because of the electron-donating tris(alkoxy) meso-substituents.

Scheme 1. Synthesis of Zn-porphyrin.

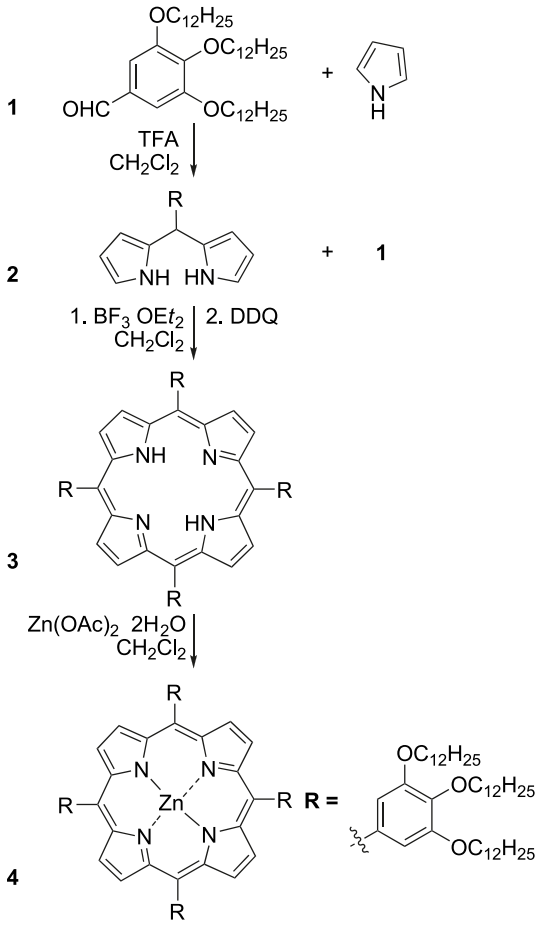

The emission spectra of **3** and **4** are similar to the emission spectra of H_2-TPP and Zn-TPP, respectively. Note the excitation wavelength used in each compound was the peak of the Soret band. Free-base porphyrin **3** has two emission peaks at 661 nm and 722 nm with peak height ratios of 1 to 0.44. The Q(0,0) peak position of **3** is red-shifted by 11 nm compared with H_2-TPP, whereas the vibronic sideband of **3** is red-shifted by only 5 nm, accompanied by a ~50% decrease in peak intensity compared with H_2-TPP. The emission spectrum of Zn-porphyrin **4** also exhibits two red-shifted peaks compared with Zn-TPP at 607 nm and 649 nm. The emission peaks are typical for porphyrinoid compounds and are consistent with emission from singlet excited states. Triplet emissions typically show at 800 nm and greater wavelengths.

Charge-transfer dynamics were assessed by cyclic voltammetry (CV) for the oxidation reaction. Figure 1*a* shows the cyclic voltammagrams of **3** at various scan rates. Each voltammagram shows two quasi-reversible oxidation waves, which are assigned to two, one-electron oxidation steps, consistent with other reports of related porphyrins.[35–40] The half-wave potentials ($E^{ox}_{1/2}$) were calculated from the average of the anodic and cathodic peaks of each step, which results

Can. J. Chem. Downloaded from www.nrcresearchpress.com by University of Electronic and Science Techonology of China on 09/18/12
For personal use only.

Table 1. Absorption and luminescence peaks of **3** and **4** in CH_2Cl_2 at room temperature.

		Absorption peaks[a]			Luminescence peaks[b]			
	B(0,0)	$Q_y(1,0)$	$Q_y(0,0)$	$Q_x(1,0)$	$Q_x(0,0)$	Q(0,0)	Q(0,1)	Stokes shift (nm)
H_2-TPP[c]	419(413)	514(19.4)	547(8.2)	592(6.6)	646(4.6)	650(1)	717(0.84)	4
3	426(151)	518(7.1)	555(3.4)	592(2.2)	648(1.7)	661(1)	722(0.44)	13
Zn-TPP[c]	422(574)			548(29.9)	588(5.1)	595(1)	645(2.1)	7
4	425(130)			550(6.6)	589(1.3)	607(1)	649(1.1)	18

Note: H_2-TPP, free-base tetraphenylporphyrin; Zn-TPP, zinc-tetraphenylporphyrin.

[a]All absorption peaks are shown in nanometres followed by molar absorptivities in parentheses with units of 10^3 L mol^{-1} cm^{-1}.

[b]All luminescence peaks are shown in nanometres followed by ratio of intensities. Compounds were excited at B bands.

[c]These data were taken from PhotoChemCAD.

in $E^{ox}_{1/2}(1)$ of 492 mV and $E^{ox}_{1/2}(2)$ of 725 mV vs Fc/Fc^+ (ferrocene reference). The difference between the two oxidation half-wave potentials is 233 mV, which is similar to H_2-TPP.

The CV at slow scan rate (20 mV s^{-1}) provides a good indication of reversibility with peak separations of 78 mV between anodic and cathodic redox couples, where peak separations of 57 mV are considered ideal reversible Nernstian behaviour. The capacitive current, which is quantified as the difference between anodic and cathodic currents in a region that does not contain Faradic responses, is unexpectedly large. There are reports of alkyl-derivatized porphyrins that form liquid crystals[41–44] or films on electrodes[45–48] and this is possible with compound **3**; however, porphyrin **3** is very soluble in CH_2Cl_2, which should minimize film formation. In addition, the linear plot in Fig. 1*b* indicates the redox reaction is diffusion controlled. Peak current is related to scan rate according to eq. [1][49]

$$[1] \qquad i_p = (2.69 \times 10^5) n^{3/2} A D_O^{1/2} C_O^* \upsilon^{1/2}$$

where i_p is the peak current in amperes, n is the number of electrons involved in the redox reaction, A is the area of the electrode surface in cm^2, D_O is the diffusion constant of the oxidized species in cm^2 s^{-1}, C_O is the concentration of redox species in mol cm^{-3}, and υ is the scan rate in V s^{-1}. From eq. [1], plots in Fig. 1*b* can be used to determine the diffusion coefficient, assuming the diffusion coefficients of the oxidized and reduced porphyrins are equal ($D_O \approx D_R$). The diffusion coefficients for $\mathbf{3}^+$ and $\mathbf{3}^{2+}$ were found to be 3.3×10^{-7} cm^2 s^{-1} and 5.6×10^{-7} cm^2 s^{-1}, respectively. Using the Stokes–Einstein equation and assuming spherical compounds, these diffusion coefficients correspond to radii of 16 nm and 9 nm for $\mathbf{3}^+$ and $\mathbf{3}^{2+}$, respectively. Clearly, these hydration radii are much larger than the molecular dimensions and could indicate aggregates are forming in solution under CV conditions that are not present at the concentrations used for optical studies. The proposal of aggregate formation is also consistent with the large non-Faradic currents and broad peaks due to different sizes of aggregates. The estimate of the diffusion coefficient enables the use of Nicholson's approach[50] to calculating the electron-transfer rate constant from the difference in peak potentials at each scan rate. The standard rate constants (k_0) for the first and second one-electron oxidations, shown in eq. [2], are 2.4×10^{-3} cm s^{-1} and 1.4×10^{-3} cm s^{-1}, respectively, for **3**. The electron-transfer rate constants for **3** are typical for numerous porphyrin systems.[51]

Fig. 1. (*a*) Cyclic voltammagram of **3** (4.5×10^{-4} mol L^{-1}) in CH_2Cl_2 containing 0.1 mol L^{-1} tetrabutylammonium hexafluorophosphate ($TBAPF_6$) at various scan rates using a glassy carbon electrode, a Ag|AgCl|KCl3M reference electrode, and a Pt wire counter electrode at 25 °C. (*b*) Peak heights of the two oxidation and reduction peaks as a function of the square root of the scan rate for porphyrin **3**.

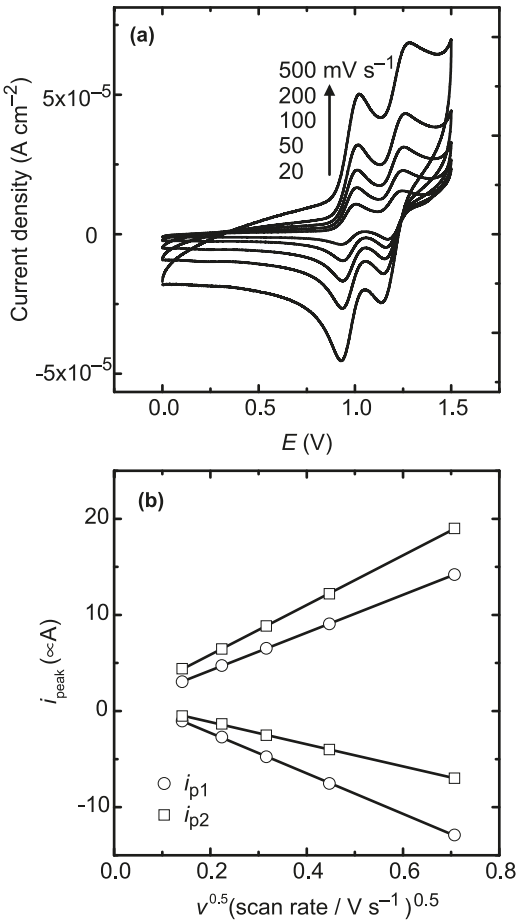

$$[2] \qquad \mathbf{3} \underset{k_0^1}{\overset{-e^-}{\rightarrow}} \mathbf{3}^+ \underset{k_0^2}{\overset{-e^-}{\rightarrow}} \mathbf{3}^{2+}$$

The CVs at increasing scan rates of Zn-porphyrin **4** are included in the Supplementary data because they are similar to those of the free-base porphyrin **3**, exhibiting two quasi-reversible, one-electron oxidation steps. The two redox waves are typical for several Zn-porphyrinoid compounds[52]

Can. J. Chem. Downloaded from www.nrcresearchpress.com by University of Electronic and Science Techonology of China on 09/18/12
For personal use only.

Table 2. Summary of electrochemical parameters.

Compound	$E^{ox}_{1/2}(1)$ (mV)	$E^{ox}_{1/2}(2)$ (mV)	ΔE (mV)	$D_O(1)$ (10^{-6} cm^2 s^{-1})	$D_O(2)$ (10^{-6} cm^2 s^{-1})	$k_0(1)$ (10^{-3} cm s^{-1})	$k_0(2)$ (10^{-3} cm s^{-1})	$r_H(1)$ (nm)	$r_H(2)$ (nm)
3	492	725	233	0.33	0.56	2.4	1.4	16	9
4	329	589	260	1.4	2.8	1.2	1.9	4	2

Note: All potentials are referenced to Fc/Fc$^+$. Diffusion coefficients of oxidized and reduced species were assumed to be the same. Rate constants were calculated using Nicholson's method. Hydration radii were calculated using solvent viscosity of CH_2Cl_2 at 0.413 mPa s.

and the peaks are also easier to oxidize than **3**. The two half-wave potentials of **4**, $E^{ox}_{1/2}(1)$ and $E^{ox}_{1/2}(2)$, were 329 mV and 589 mV vs Fc/Fc$^+$, respectively. The difference between the two oxidation half-wave potentials is 260 mV, which is similar to the difference in the case of Zn-TPP. The peak separation at the slowest scan rate (10 mV s^{-1}) is 88 mV and 81 mV for the first and second oxidation peaks, respectively, consistent with quasi-reversible redox reactions.

The capacitive currents in Zn-porphyrin **4** are much less than in the CVs for free-base porphyrin **3**, even though the concentration of **4** in the electrochemical cell was higher than that of **3**. In comparing the CVs of **3** and **4**, it is clear that the CV of **3** displays unique diffusion effects. Employing eq. [1], the diffusion coefficients were calculated to be 1.4×10^{-6} cm^2 s^{-1} and 2.8×10^{-6} cm^2 s^{-1} for $\mathbf{4}^+$ and $\mathbf{4}^{2+}$, respectively, resulting in hydration radii of 4 nm and 2 nm for $\mathbf{4}^+$ and $\mathbf{4}^{2+}$, respectively. Although the diffusion coefficients are much higher in the Zn-porphyrin case, the standard electron-transfer rates constants for the first and second oxidation reactions are 1.2×10^{-3} cm s^{-1} and 1.9×10^{-3} cm s^{-1}, respectively, which are similar to those of compound **3**. A summary of all electrochemical results is included in Table 2.

The electrochemical oxidation potentials in conjunction with the highest-energy fluorescent band, corresponding to the lowest-lying singlet state, allow for the estimation of the excited-state oxidation potential, first described by Rehm and Weller[53,54] in eq. [3].

$$[3] \qquad E^{*ox}_{1/2} = E^{ox}_{1/2} - E_{00} + \omega_r$$

where $E^{*ox}_{1/2}$ is the excited-state oxidation potential, $E^{ox}_{1/2}$ is the ground-state redox potential, E_{00} is the energy gap between the zeroth vibrational levels of the ground and excited states, and ω_r is the electrostatic work term. For this work, it is assumed that the electrostatic work term has been adequately accounted for within the measurement of the ground-state redox potentials. The excited-state oxidation potentials for **3** and **4** are –1.39 V and –1.71 V vs Fc/Fc$^+$, respectively. For comparison, H_2-TPP is estimated to have a singlet excited-state redox potential of –1.32 V vs Fc/Fc$^+$.[55] The second oxidation potential was not calculated because the fluorescence spectrum of the radical cation is unknown.

The absorption spectrum of **3** oxidized to $\mathbf{3}^+$ is shown in Fig. 2*a*. Figure 2*a* shows three main features consistent with the ring oxidation.[56–60] The first is the decrease in the Soret band intensity. Concomitantly, there are two new features increasing in intensity at 470 nm and 696 nm. The isosbestic points at 400 nm and 453 nm suggest the UV–vis spectra represent two species that are in equilibrium, which is consistent with the reversible nature of the CV results for **3**. Figure 2*b* shows the absorbance difference spectra of the data shown in Fig. 2*a*. The resulting plot shows more of the smaller transitions and clearly indicates isosbestic points as the data cross the $y = 0$ line. The growth of the largest peak at 470 nm is similar to other spectroelectrochemical results of other porphyrins and is tentatively assigned to the Soret band of the radical cation, $\mathbf{3}^+$.

Fig. 2. Spectroelectrochemistry of **3**. (*a*) UV–vis spectra of compound **3** at an applied potential of +1.0 V. Each spectrum is recorded at 2 min intervals and arrows indicate the direction of peak change. (*b*) The absorbance difference spectra of the data shown in Fig. 2*a*. Positive peaks indicate peak growth compared with neutral porphyrin.

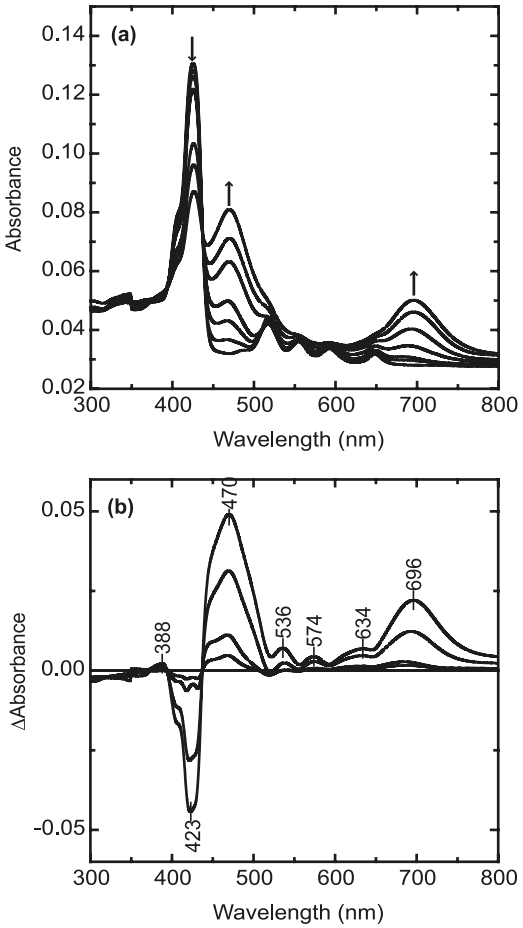

The smaller features that are visible in the difference spectra (Fig. 2*b*) at 536, 574, and 634 nm are assigned to the Q-bands of the oxidized porphyrin. After exhaustive oxidation of **3** to $\mathbf{3}^+$, the potential was stepped to 1.2 V, where the conversion of $\mathbf{3}^+$ to $\mathbf{3}^{2+}$ is expected to occur. The absorption spectrum of $\mathbf{3}^{2+}$ is not shown; however, no significant changes were observed with the exception of a slight increase in the peak at 696 nm. The lack of visible changes is due to two factors. First, the electronic transitions of $\mathbf{3}^{2+}$

Can. J. Chem. Downloaded from www.nrcresearchpress.com by University of Electronic and Science Techonology of China on 09/18/12
For personal use only.

could be weak, and second, the cell design uses a longer path length (1 mm) such that the resultant spectrum is a linear combination of all three species diffusing into the light path. In addition, the oxidized form may be more reactive and decompose. Although CV evidence supports a stable redox couple, the spectroelectrochemical cell design does not permit exclusion of O_2 from the cell.

Spectroelectrochemical experiments were carried out with **4** to investigate the electronic structure of the oxidized form of **4**, which is included in the Supplementary data. The oxidation of **4** to $\mathbf{4}^+$ shows a decrease in the Soret band with an applied potential of 0.8 V (first oxidation potential $\mathbf{4/4}^+$). Upon oxidation, a new Soret band is seen evolving at 442 nm, which is blue-shifted from the $\mathbf{3}^+$ radical cation species. New Q-bands of the radical cation ($\mathbf{4}^+$) appear at 523, 577, 643, and 680 nm. In addition, a new broad transition occurs at 897 nm. Spectroelectrochemical experiments were also carried out at applied potentials equal to the second oxidation. However, at the $E^{ox}_{1/2}(2)$, the spectral features were nearly the same as the spectrum of $\mathbf{4}^+$. After spectral subtraction of the oxidized spectrum ($\mathbf{4}^+$), a broad peak at ~900 nm was observed, but considering the long path length (1 mm), it is clear that the dication ($\mathbf{4}^{2+}$) spectrum consists of neutral **4**, radical cation $\mathbf{4}^+$, and the dication $\mathbf{4}^{2+}$, which precludes accurate spectral deconvolution.

Structures **3**, **4**, $\mathbf{3}^+$, $\mathbf{4}^+$, $\mathbf{3}^{2+}$, and $\mathbf{4}^{2+}$ were energy optimized using DFT methods with the B3LYP basis set and 6-31+G functional using the Gaussian03 software package.[61] The summaries of the frontier orbital energy levels are shown in Fig. 3. Based on the gas-phase calculations, the HOMO energy levels of the free-base porphyrin **3** and the Zn-metalloporphyrin **4** are very similar in energy. This HOMO energy level trend was not observed in the experimentally determined oxidation potential. Experimental results show the Zn-porphyrin is easier to oxidize, suggesting it has a higher-lying HOMO. This inconsistency could arise from solvent effects that are not accounted for in the calculations. The two highest occupied FMOs of **3** and **4** are nearly degenerate and both have nearly degenerate LUMOs, consistent with the four-orbit model.[33] The HOMO–LUMO energy gap is similar for **3** and **4**, which is consistent with the observed electronic absorption spectroscopy. Both radical cations, $\mathbf{3}^+$ and $\mathbf{4}^+$, show red-shifted adsorptions compared with their neutral parent compounds. The SOMO of $\mathbf{4}^+$ is nearly triply degenerate, whereas the SOMO of $\mathbf{3}^+$ does not follow the same pattern. The FMOs of $\mathbf{3}^+$ and $\mathbf{4}^+$ are shown in Fig. 4. The triply degenerate occupied orbitals of $\mathbf{4}^+$ are confined to the electron-rich trisalkoxy phenyl rings, in contrast to $\mathbf{3}^+$, where the SOMO orbital is delocalized over the macrocyclic ring and the four trisalkoxy phenyl rings. The dication species $\mathbf{3}^{2+}$ and $\mathbf{4}^{2+}$ show the lowest HOMO–LUMO energy difference of 0.8 eV, corresponding to 1550 nm, which was not observed in the absorption spectra. In addition, the HOMOs of both dications are triply degenerate and the LUMOs are non-degenerate.

FMOs for all compounds are included in the Supplementary data. Starting with the neutral porphyrins **3** and **4**, the doubly degenerate HOMOs and LUMOs show electron density confined to the porphyrin macrocyclic ring. In addition, the energy-minimized structures have the meso-substituted phenyl rings perpendicular to the macrocyclic ring, implying

Fig. 3. DFT-calculated (B3LYP/6-31+G) energy levels of the frontier orbitals of the neutral, radical cation, and dication of compounds **3** and **4**. The HOMO–LUMO energy differences are shown over the arrows.

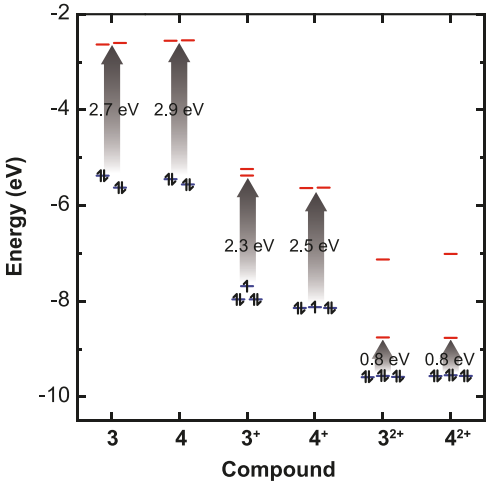

Fig. 4. FMOs of the radical cations $\mathbf{3}^+$ and $\mathbf{4}^+$ using DFT with the B3LYP basis set and 6-31G+ functional.

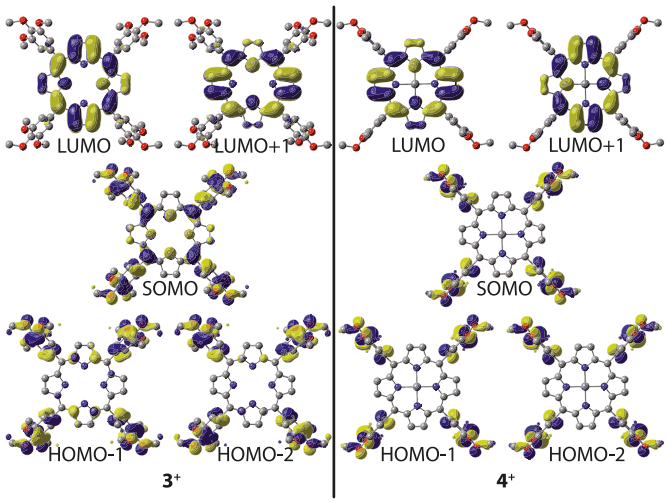

little electronic perturbations can occur from a meso-phenyl substitution pattern. The monocations $\mathbf{3}^+$ and $\mathbf{4}^+$ have different minimized structures. The free base $\mathbf{3}^+$ has a SOMO that is delocalized over the macrocyclic ring and the four phenyl meso-substituents and a twist in the meso-phenyl groups, such that contributions from the phenyl rings can participate in delocalization. In contrast, the Zn-porphyrin cation, $\mathbf{4}^+$, maintains the same geometry as neutral **4** and the SOMO is limited to the four meso-substituted phenyl rings. Both LUMO and LUMO+1 of both monocations ($\mathbf{3}^+$ and $\mathbf{4}^+$) are centered on the macrocyclic ring system. The removal of an additional electron to the dications results in HOMOs that reside on the four phenyl substituents. In addition, both dications $\mathbf{3}^{2+}$ and $\mathbf{4}^{2+}$ show a twist in the meso-phenyl substituents allowing for stabilization of the dicationic macrocycle. The LUMOs of the dications show coefficients on both the phenyl substituents and the macrocycle. The calculations indicate extensive electronic tuning is possible by modifying the β-pyrrole positions, and limited HOMO energy level tun-

Can. J. Chem. Downloaded from www.nrcresearchpress.com by University of Electronic and Science Techonology of China on 09/18/12
For personal use only.

ing is possible using phenyl-substituted meso positions. However, the mono- and dications can be strongly stabilized by electron-rich meso-derivatives.

Conclusions

The optical measurements of the tetraarylporphyrins display typical behaviour with intense Soret and Q-band absorptions and fluorescence spectra with small Stokes shifts. Electrochemical oxidations of both the free-base porphyrin **3** and Zn-metalloporphyrin **4** show two reversible one-electron redox waves by cyclic voltammetry methods. Further analysis of the cyclic voltammetry data revealed an unusually large diffusion coefficient for **3**, suggesting aggregate formation. Considering the size and number of alkoxy groups, aggregation is feasible, as others have used such motifs to build long-range order in liquid crystals. The electron-transfer rate constants were 1.2×10^{-3} cm s^{-1} and 2.4×10^{-3} cm s^{-1} for compounds **3** and **4**, respectively, which falls within the range of other porphyrins. Spectroelectrochemical experiments suggest that the electron removed to form the radical cations ($\mathbf{3}^{+}$ and $\mathbf{4}^{+}$) is part of the porphyrin macrocycle. In addition, the spectroelectrochemical results are supported by the DFT-calculated energy-optimized structures of **3** and **4** in their neutral and radical cation states. The reversibility and stability of the oxidized forms of both **3** and **4** support the use of these compounds in organic devices as light harvesters or supramolecular charge-transfer assemblies. Of particular utility could be the excited-state energy of the oxidized porphyrin ring systems to generate charge-separated components used in solar energy conversion. The electrochemically determined HOMO energy levels of **3** and **4** are –5.3 eV and –5.1 eV (assuming the HOMO energy level of Fc/Fc^{+} is –4.8 eV), respectively, which is comparable to the ubiquitous poly-3-hexylthiophene (P3HT) at –5.0 eV and LUMO energy of –3.3 eV. The Rehm and Weller equation gives an estimate of LUMO energy levels of **3** and **4** at –3.4 eV and –3.1 eV, respectively, which is similar to P3HT. The similar energy levels of **3** and **4** with P3HT indicate porphyrins with their superior molar absorptivities could be used as alternative light-harvesting compounds (*p*-type material) in organic photovoltaic cells. In addition, the LUMO level of PCBM, at –3.7 eV, is lower than the excited-state energy of either **3** or **4**, allowing for a thermodynamic driving force for charge separation. Unfortunately, the tetraaryl substituents did not impart supramolecular properties, which would lead to organized structures that could carry charge more efficiently over long distances. Nevertheless, the electron-rich, trisalkoxy meso-substituted porphyrins are remarkably air and electrochemically stable, which is a design necessity for devices.

Supplementary data

Supplementary data for this article are available on the journal Web site (canjchem.nrc.ca).

Acknowledgements

The authors are grateful to the Natural Sciences and Engineering Research Council of Canada (NSERC), Alberta Government, Canadian Foundation for Innovation (CFI), and the Institute for Sustainable Energy, Environment and Economy, for funding.

References

(1) Wasielewski, M. R. *Chem. Rev.* **1992**, *92* (3), 435. doi:10.1021/cr00011a005.
(2) Gust, D.; Moore, T. A.; Moore, A. L. *Acc. Chem. Res.* **2001**, *34* (1), 40. doi:10.1021/ar9801301. PMID:11170355.
(3) Henderson, B. W.; Dougherty, T. J. *Photochem. Photobiol.* **1992**, *55* (1), 145. doi:10.1111/j.1751-1097.1992.tb04222.x. PMID:1603846.
(4) Meunier, B. *Chem. Rev.* **1992**, *92* (6), 1411. doi:10.1021/cr00014a008.
(5) Traylor, T. G.; Tsuchiya, S.; Byun, Y. S.; Kim, C. *J. Am. Chem. Soc.* **1993**, *115* (7), 2775. doi:10.1021/ja00060a027.
(6) Anson, F. C.; Shi, C. N.; Steiger, B. *Acc. Chem. Res.* **1997**, *30* (11), 437. doi:10.1021/ar960264j.
(7) Batinić-Haberle, I.; Spasojević, I.; Hambright, P.; Benov, L.; Crumbliss, A. L.; Fridovich, I. *Inorg. Chem.* **1999**, *38* (18), 4011. doi:10.1021/ic990118k.
(8) Wrighton, S. A.; Stevens, J. C. *Crit. Rev. Toxicol.* **1992**, *22* (1), 1. doi:10.3109/10408449209145319. PMID:1616599.
(9) Guengerich, F. P. *Annu. Rev. Pharmacol. Toxicol.* **1999**, *39* (1), 1. doi:10.1146/annurev.pharmtox.39.1.1. PMID:10331074.
(10) Sottocasa, G. L.; Kuylenstierna, B.; Ernster, L.; Bergstrand, A. *J. Cell Biol.* **1967**, *32* (2), 415. doi:10.1083/jcb.32.2.415. PMID:10976232.
(11) Ferrer-Sueta, G.; Hannibal, L.; Batinić-Haberle, I.; Radi, R. *Free Radic. Biol. Med.* **2006**, *41* (3), 503. doi:10.1016/j.freeradbiomed.2006.04.028.
(12) Wöhrle, D.; Meissner, D. *Adv. Mater.* **1991**, *3*, 129. doi:10.1002/adma.19910030303.
(13) Imahori, H.; Fukuzumi, S. *Adv. Funct. Mater.* **2004**, *14* (6), 525. doi:10.1002/adfm.200305172.
(14) Lane, P. A.; Palilis, L. C.; O'Brien, D. F.; Giebeler, C.; Cadby, A. J.; Lidzey, D. G.; Campbell, A. J.; Blau, W.; Bradley, D. D. C. *Phys. Rev. B Condens. Matter* **2001**, 63.
(15) Grinstaff, M. W.; Hill, M. G.; Labinger, J. A.; Gray, H. B. *Science* **1994**, *264* (5163), 1311. doi:10.1126/science.8191283. PMID:8191283.
(16) Bhyrappa, P.; Young, J. K.; Moore, J. S.; Suslick, K. S. *J. Am. Chem. Soc.* **1996**, *118* (24), 5708. doi:10.1021/ja953474k.
(17) Bock, C. R.; Connor, J. A.; Gutierrez, A. R.; Meyer, T. J.; Whitten, D. G.; Sullivan, B. P.; Nagle, J. K. *J. Am. Chem. Soc.* **1979**, *101* (17), 4815. doi:10.1021/ja00511a007.
(18) Balzani, V.; Juris, A.; Venturi, M.; Campagna, S.; Serroni, S. *Chem. Rev.* **1996**, *96* (2), 759. doi:10.1021/cr941154y. PMID:11848772.
(19) Guldi, D. M.; Prato, M. *Acc. Chem. Res.* **2000**, *33* (10), 695. doi:10.1021/ar990144m. PMID:11041834.
(20) Dolphin, D.; Felton, R. H. *Acc. Chem. Res.* **1974**, *7* (1), 26. doi:10.1021/ar50073a005.
(21) Roberts, J. E.; Hoffman, B. M.; Rutter, R.; Hager, L. P. *J. Biol. Chem.* **1981**, *256* (5), 2118. PMID:6257699.
(22) Erman, J. E.; Vitello, L. B.; Mauro, J. M.; Kraut, J. *Biochemistry* **1989**, *28* (20), 7992. doi:10.1021/bi00446a004. PMID:2557891.
(23) Ravikanth, M.; Chandrashekar, T. K. Nonplanar Porphyrins and Their Biological Relevance: Ground and Excited-State Dynamics. In *Coordination Chemistry;* 1995; Vol. 82, pp 105–188.

Can. J. Chem. Downloaded from www.nrcresearchpress.com by University of Electronic and Science Techonology of China on 09/18/12
For personal use only.

(24) Kadish, K. M.; Lin, M.; van Caemelbecke, E.; De Stefano, G.; Medforth, C. J.; Nurco, D. J.; Nelson, N. Y.; Krattinger, B.; Muzzi, C. M.; Jaquinod, L.; Xu, Y.; Shyr, D. C.; Smith, K. M.; Shelnutt, J. A. *Inorg. Chem.* **2002**, *41* (25), 6673. doi:10.1021/ic0200702. PMID:12470062.

(25) Meier, H.; Müller, K. *Angew. Chem. Int. Ed. Engl.* **1995**, *34* (1314), 1437. doi:10.1002/anie.199514371.

(26) Pieterse, K.; Lauritsen, A.; Schenning, A. P. H. J.; Vekemans, J. A. J. M.; Meijer, E. W. *Chem. Eur. J.* **2003**, *9* (22), 5597. doi:10.1002/chem.200305073.

(27) Tanabe, K.; Yasuda, T.; Yoshio, M.; Kato, T. *Org. Lett.* **2007**, *9* (21), 4271. doi:10.1021/ol701741e. PMID:17887690.

(28) Terazzi, E.; Torelli, S.; Bernardinelli, G.; Rivera, J.-P.; Bénech, J.-M.; Bourgogne, C.; Donnio, B.; Guillon, D.; Imbert, D.; Bünzli, J. C.; Pinto, A.; Jeannerat, D.; Piguet, C. *J. Am. Chem. Soc.* **2005**, *127* (3), 888. doi:10.1021/ja0446101. PMID:15656627.

(29) van Gorp, J. J.; Vekemans, J. A. J. M.; Meijer, E. W. *J. Am. Chem. Soc.* **2002**, *124* (49), 14759. doi:10.1021/ja020984n. PMID:12465989.

(30) Wang, D. H.; Shen, Z.; Guo, M.; Cheng, S. Z. D.; Harris, F. W. *Macromolecules* **2007**, *40* (4), 889. doi:10.1021/ma061763v.

(31) Cheng, F.; Adronov, A. *Chem. Eur. J.* **2006**, *12* (19), 5053. doi:10.1002/chem.200600302.

(32) Nowak-Król, A.; Gryko, D.; Gryko, D. T. *Chem. Asian J.* **2010**, *5* (4), 904. doi:10.1002/asia.200900693. PMID: 20235275.

(33) Gouterman, M. *J. Mol. Spectrosc.* **1961**, *6*, 138. doi:10.1016/0022-2852(61)90236-3.

(34) Gouterman, M. In *The Porphyrins;* Dolphin, D., Ed.; Academic Press: New York, 1978; Vol. 3, pp 1–165.

(35) Giraudeau, A.; Callot, H. J.; Gross, M. *Inorg. Chem.* **1979**, *18* (1), 201. doi:10.1021/ic50191a042.

(36) Renner, M. W.; Barkigia, K. M.; Zhang, Y.; Medforth, C. J.; Smith, K. M.; Fajer, J. *J. Am. Chem. Soc.* **1994**, *116* (19), 8582. doi:10.1021/ja00098a019.

(37) Ghosh, A. *J. Am. Chem. Soc.* **1995**, *117* (16), 4691. doi:10.1021/ja00121a025.

(38) Woller, E. K.; DiMagno, S. G. *J. Org. Chem.* **1997**, *62* (6), 1588. doi:10.1021/jo962159t.

(39) Guilard, R.; Kadish, K. M. *Chem. Rev.* **1988**, *88* (7), 1121. doi:10.1021/cr00089a007.

(40) Kadish, K. M.; Vancaemelbecke, E.; Boulas, P.; Dsouza, F.; Vogel, E.; Kisters, M.; Medforth, C. J.; Smith, K. M. *Inorg. Chem.* **1993**, *32* (20), 4177. doi:10.1021/ic00072a005.

(41) Gregg, B. A.; Fox, M. A.; Bard, A. J. *J. Am. Chem. Soc.* **1989**, *111* (8), 3024. doi:10.1021/ja00190a041.

(42) Gregg, B. A.; Fox, M. A.; Bard, A. J. *J. Phys. Chem.* **1990**, *94* (4), 1586. doi:10.1021/j100367a068.

(43) Schouten, P. G.; Warman, J. M.; de Haas, M. P.; Fox, M. A.; Pan, H.-L. *Nature* **1991**, *353* (6346), 736. doi:10.1038/353736a0.

(44) van der Boom, T.; Hayes, R. T.; Zhao, Y. Y.; Bushard, P. J.; Weiss, E. A.; Wasielewski, M. R. *J. Am. Chem. Soc.* **2002**, *124* (32), 9582. doi:10.1021/ja026286k. PMID:12167053.

(45) Fleming, B. D.; Bond, A. M. *Electrochim. Acta* **2009**, *54* (10), 2713. doi:10.1016/j.electacta.2008.11.042.

(46) Kampas, F. J.; Yamashita, K.; Fajer, J. *Nature* **1980**, *284* (5751), 40. doi:10.1038/284040a0.

(47) Bedioui, F.; Devynck, J.; Bied-Charreton, C. *Acc. Chem. Res.* **1995**, *28* (1), 30. doi:10.1021/ar00049a005.

(48) Malinski, T.; Ciszewski, A.; Bennett, J.; Fish, J. R.; Czuchajowski, L. *J. Electrochem. Soc.* **1991**, *138* (7), 2008. doi:10.1149/1.2085915.

(49) Bard, A. J.; Faulkner, L. R. *Electrochemical Methods: Fundamentals and Applications,* 2nd ed.; Wiley: New York, 2001; p xxi, 833 p.

(50) Nicholson, R. S. *Anal. Chem.* **1965**, *37* (11), 1351. doi:10.1021/ac60230a016.

(51) Kadish, K. M.; Davis, D. G. *Ann. N. Y. Acad. Sci.* **1973**, *206* (1 The Chemical), 495. doi:10.1111/j.1749-6632.1973.tb43232.x. PMID:4518403.

(52) Kuo, M. C.; Li, L. A.; Yen, W. N.; Lo, S. S.; Lee, C. W.; Yeh, C. Y. *Dalton Trans.* **2007**, (14): 1433. doi:10.1039/b617170b. PMID:17387405.

(53) Rehm, D.; Weller, A. *Ber. Bunsen-Ges.* **1969**, *73*, 834.

(54) Rehm, D.; Weller, A. *Isr. J. Chem.* **1970**, *8*, 259.

(55) Pandian, R. P.; Chandrashekar, T. K.; Saini, G. S. S.; Verma, A. L. *J. Chem. Soc., Faraday Trans.* **1993**, *89* (4), 677. doi:10.1039/ft9938900677.

(56) El-Kasmi, A.; Lexa, D.; Maillard, P.; Momenteau, M.; Saveant, J. M. *J. Am. Chem. Soc.* **1991**, *113* (5), 1586. doi:10.1021/ja00005a022.

(57) Langhus, D. L.; Wilson, G. S. *Anal. Chem.* **1979**, *51* (8), 1139. doi:10.1021/ac50044a012.

(58) Kadish, K. M.; Mu, X. *Pure Appl. Chem.* **1990**, *62* (6), 1051. doi:10.1351/pac199062061051.

(59) Lin, C.-; Fang, M.-Y.; Cheng, S.-H. *J. Electroanal. Chem.* **2002**, *531* (2), 155. doi:10.1016/S0022-0728(02)01056-2.

(60) Sooambar, C.; Troiani, V.; Bruno, C.; Marcaccio, M.; Paolucci, F.; Listorti, A.; Belbakra, A.; Armaroli, N.; Magistrato, A.; De Zorzi, R.; Geremia, S.; Bonifazi, D. *Org. Biomol. Chem.* **2009**, *7* (11), 2402. doi:10.1039/b820210a. PMID:19462051.

(61) Frisch, M. J.; Trucks, G. W.; Schlegel, H. B.; Scuseria, G. E.; Robb, M. A.; Cheeseman, J. R.; Montgomery, J. A., Jr.; Vreven, T.; Kudin, K. N.; Burant, J. C.; Millam, J. M.; Iyengar, S. S.; Tomasi, J.; Barone, V.; Mennucci, B.; Cossi, M.; Scalmani, G.; Rega, N.; Petersson, G. A.; Nakatsuji, H.; Hada, M.; Ehara, M.; Toyota, K.; Fukuda, R.; Hasegawa, J.; Ishida, M.; Nakajima, T.; Honda, Y.; Kitao, O.; Nakai, H.; Klene, M.; Li, X.; Knox, J. E.; Hratchian, H. P.; Cross, J. B.; Bakken, V.; Adamo, C.; Jaramillo, J.; Gomperts, R.; Stratmann, R. E.; Yazyev, O.; Austin, A. J.; Cammi, R.; Pomelli, C.; Ochterski, J. W.; Ayala, P. Y.; Morokuma, K.; Voth, G. A.; Salvador, P.; Dannenberg, J. J.; Zakrzewski, V. G.; Dapprich, S.; Daniels, A. D.; Strain, M. C.; Farkas, O.; Malick, D. K.; Rabuck, A. D.; Raghavachari, K.; Foresman, J. B.; Ortiz, J. V.; Cui, Q.; Baboul, A. G.; Clifford, S.; Cioslowski, J.; Stefanov, B. B.; Liu, G.; Liashenko, A.; Piskorz, P.; Komaromi, I.; Martin, R. L.; Fox, D. J.; Keith, T.; Al-Laham, M. A.; Peng, C. Y.; Nanayakkara, A.; Challacombe, M.; Gill, P. M. W.; Johnson, B.; Chen, W.; Wong, M. W.; Gonzalez, C.; Pople, J. A. *Gaussian 03,* Revision E.01; Gaussian, Inc.: Wallingford, CT, 2004.

Competing photodehydration and excited-state intramolecular proton transfer (ESIPT) in adamantyl derivatives of 2-phenylphenols

Nikola Basarić, Nikola Cindro, Yunyan Hou, Ivana Žabčić, Kata Mlinarić-Majerski, and Peter Wan

Abstract: 2-Phenylphenol derivatives strategically substituted with a hydroxyadamantyl substituent were synthesized and their photochemical reactivity was investigated. Derivatives **9** and **10** undergo competitive excited-state intramolecular proton transfer (ESIPT) from the phenol to the carbon atom of the adjacent phenyl ring and formal ESPT from the phenol to the hydroxyl group coupled with dehydration. These two processes (both via S_1) give rise to two classes of quinone methides (QMs) that revert to starting material or react with nucleophiles, respectively. ESIPT to carbon atoms was studied by performing photolyses in the presence of D_2O, whereupon deuterium incorporation to the adjacent phenyl ring was observed (Φ = 0.1–0.2). The competing formal ESPT and dehydration takes place with quantum yields that are an order of magnitude lower and was studied by isolation of photomethanolysis products. Derivative **8** did not undergo ESIPT to carbon atom. Owing to the presence of an intramolecular H bond, an efficient ESIPT from the phenol to the hydroxyl group coupled with dehydration gives a QM that efficiently undergoes electrocyclization (overall Φ = 0.33), to give chroman **16**. In addition, spiro[adamantane-2,9′-(4′-hydroxy)fluorene] (**12**) undergoes ESIPT, unlike the previously reported unreactive parent 2-hydroxyfluorene. The reactive singlet excited states of the prepared biphenyl and fluorene molecules were characterized by fluorescence spectroscopy, whereas laser flash photolysis (LFP) was performed to characterize the longer lived QM intermediates.

Key words: adamantanes, ESIPT, proton transfer, photochemistry, quinone methides, photosolvolysis.

Résumé : On a réalisé la synthèse de dérivés du 2-phényléthanol substitués d'une façon stratégique par un substituant hydroxyadamantyle et on a étudié leur réactivité photochimique. Les dérivés **9** et **10** subissent des transferts de proton intramoléculaire dans l'état excité (TPIEE) du phénol vers l'atome de carbone du noyau phényle adjacent et un TPIEE formel du phénol vers le groupe hydroxyle couplé avec une déshydratation. Ces deux processus, qui se font tous les deux par le biais d'une réaction S_1, conduisent à la formation de deux classes de quinométhanes (QM) qui respectivement se reconvertissent en produit de départ ou qui réagissent avec des nucléophiles. On a étudié les TPIEE vers les atomes de carbone en effectuant des photolyse en présence de D_2O qui ont permis d'observer l'incorporation de deutérium dans le noyau phényle adjacent (Φ = 0,1–0,2). La réaction formelle de TPIEE et de déshydratation qui est en compétition se produit avec des rendements quantiques qui sont un ordre de grandeur plus faibles et qui ont été étudiés en isolant les produits de photométhanolyse. Le dérivé **8** ne donne pas lieu à un TPIEE vers l'atome de carbone. En raison de la présence d'une liaison hydrogène intramoléculaire, un TPIEE du phénol vers le groupe hydroxyle, couplé avec une déshydration, conduit à un QM qui subit une électrocyclisation (rendement quantique global de 0,33) et donne le chromane **16**. De plus, contrairement à ce qui a été rapporté antérieurement pour le 2-hydroxyfluorène qui n'est pas réactif, le spiro[adamantane-2,9′-(4′-hydroxy)fluorène (**12**) subit un TPIEE. On a caractérisé les états excités singulets réactifs des molécules portant des biphényles ou un fluorène en faisant appel à la spectroscopie de fluorescence alors qu'on a fait appel à la photolyse laser éclair (PLE) pour caractériser les intermédiaires QM de durée de vie plus longue.

Mots-clés : adamantanes, transfert de proton intramoléculaire dans l'état excité (TPIEE), transfert de proton, photochimie, quinométhane, photosolvolyse.

[Traduit par la Rédaction]

Received 8 March 2010. Accepted 7 May 2010. Published on the NRC Research Press Web site at canjchem.nrc.ca on 26 January 2011.

This article is part of a Special Issue dedicated to Professor J. C. Scaiano.

N. Basarić,[1] N. Cindro, I. Žabčić, and K. Mlinarić-Majerski. Department of Organic Chemistry and Biochemistry, Ruđer Bošković Institute, Bijenička cesta 54, 10 000 Zagreb, Croatia.
Y. Hou and P. Wan.[2] Department of Chemistry, Box 3065, University of Victoria, Victoria, BC V8W 3V6, Canada.

[1]Corresponding author (e-mail: nbasaric@irb.hr).
[2]Corresponding author (e-mail: pwan@uvic.ca).

Can. J. Chem. Downloaded from www.nrcresearchpress.com by University of Electronic and Science Techonology of China on 09/18/12
For personal use only.

Can. J. Chem. Downloaded from www.nrcresearchpress.com by University of Electronic and Science Techonology of China on 09/18/12
For personal use only.

Introduction

Excited-state intramolecular proton transfer (ESIPT) is a fundamental chemical process that has been intensively investigated[1] since it was discovered by Weller.[2] It occurs when electronic excitation of a molecule enhances the acidity and (or) basicity of sites that are in close proximity, allowing a fast proton transfer (PT) to take place on the excited-state surface. The ESIPT gives rise to high-energy tautomers, which usually revert very rapidly to the starting molecules. However, the presence of the photo-tautomers can be detected by fluorescence or transient absorption spectroscopy. Additionally, in some cases, the photo-tautomers can be transformed to stable photochemical products.

As part of on-going research into excited-state acid–base reactions involving phenols,[3] many were found to give rise to quinone methides (QM). For example, on excitation of *o*-hydroxybenzyl alcohol (**1**), ESIPT from the phenol OH to the hydroxyl group, coupled with a dehydration, gives rise to QM **2** (eq. [1]).[4] Similarly, QM **2** can be photogenerated from hydroxybenzylacetate[5] or ammoniummethylphenol derivatives.[6] Since QM **2** is not a photo-tautomer of the starting molecule (as would be the case if generated via a pure ESIPT reaction), the addition of H_2O is required to convert it back to phenol **1**. Hence, QMs photogenerated by dehydration (or similar photochemical reaction) usually have long lifetimes that can be readily detected by laser flash photolysis, and sometimes by conventional UV–vis spectrometry. For example, QMs **3**[4] and **4**[7] (in 1:1 CH_3CN:H_2O) have lifetimes of 5–10 s, and 0.5 s, respectively.

[1] 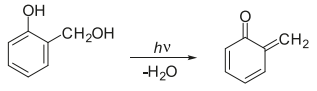

1 2

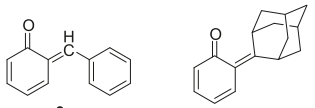

3 4

Since QMs are important intermediates in chemistry and biology, research on their photochemical formation and reactivity has intensified in the last few decades.[8] QMs are known to react with DNA and nucleobases.[9] They also have a pivotal role in the antibiotic action of antracyclines.[10] Rokita at al. have shown that electron-withdrawing groups make QMs more electrophilic and shorter lived, whereas electron-donating groups stabilize the structure.[11] Wan and co-workers have found that formal ESIPT reactions can give biphenyl[12] or terphenyl QM derivatives.[13] In these reactions, a basic site of the formal ESIPT is the oxygen of a benzyl alcohol moiety,[14,15] or a carbon atom of an adjacent phenyl,[16] naphthyl,[17] or the anthryl ring.[18] For example, irradiation of 2-phenylphenol (**5**) in the presence of D_2O gives deuterated QMs **6** and **7** (eq. [2]), which revert rapidly to the starting molecule **5**. However, the deuterium remains incorporated in **5** at the ortho (**5D2**) and the para positions (**5D4**) of the adjacent phenyl ring.

[2] 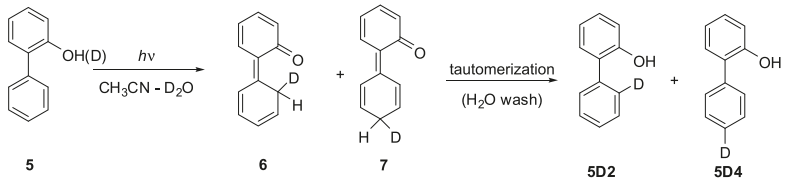

5 6 7 5D2 5D4

Recently, Behin Aein and Wan[12c] reported the competition between ESIPT to carbon atoms of an adjacent phenyl ring and formal excited-state proton transfer to oxygen of a benzyl alcohol moiety (coupled with dehydration) using the compound 4-(2-hydroxy-2-ethyl)-2′-hydroxybiphenyl, with both processes giving rise to QMs. The study was performed by carying out photolyses in CH_3CN–D_2O and CH_3OH–D_2O.[12c] To further investigate to what extent can ESIPT to carbon atoms compete with the formal excited-state proton transfer to heteroatom substituents (e.g., benzyl alcohol moiety) that would normally lead to photosolvolysis, we report herein on the photochemical reactivity of a series of *o*-phenylphenols **8**–**10** wherein both processes are possible. In addition, these phenylphenols were strategically substituted with a hydroxyadamantyl moiety, since we have found that this increases quantum yields of QM formation in photodehydration reactions.[7] Furthemore, we report on the photochemical reactivity of ammonium salt **11** that was expected to be less prone to the ESIPT because of the presence of a good nucleofugal ammonium group, which would encourage photosolvolysis. In addition, we probed for ESIPT in the adamantyl fluorene derivative **12** and compared its photochemistry with the parent fluorene compound **13** that does not undergo ESIPT.[16] The mechanisms of photochemical reactions were investigated by preparative irradiations, fluorescence measurements, and laser flash photolysis.

Can. J. Chem. Downloaded from www.nrcresearchpress.com by University of Electronic and Science Techonology of China on 09/18/12
For personal use only.

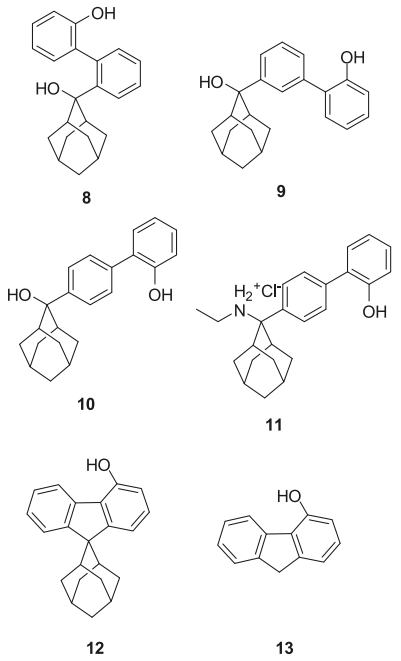

Results and discussion

Materials

Methoxybiphenyl derivatives **14a**–**14c** were prepared by Suzuki reactions from dibromobenzenes and *o*-methoxyphenylboronic acid. The biphenyls were transformed to the Grignard reagents that were reacted with 2-adamantanone to furnish adamantyl biphenyls **8a**–**10a** (eq. [3]). The methoxy ethers **8a**–**10a** were then treated with Lewis acid BBr_3 to give phenols **9** and **10** (eq. [4]) and fluorene **12**. The ortho derivative **10** was obtained by a modification of the published procedure[19] by a cleavage of the ether by sodium ethylthiolate (Scheme 1). The ammonium derivative **11** was synthesized from alcohol **10** according to a modification of the published procedure.[20] Alcohol **10** was first transformed to azide **15** and then reduced by Raney Ni to the corresponding amine that was transformed to *N*-ethyl hydrochloride **11** by purging the diethyl ether solution with dry HCl (eq. [5]). In the later reaction, the alkylation of the amine moiety probably took place by a nucleophilic attack of the amine to the carbon atom of the protonated ethyl ether.

Scheme 1.

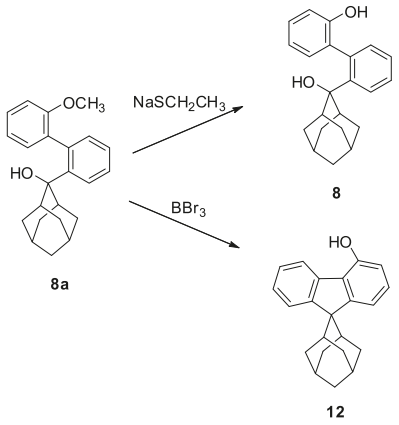

[3]

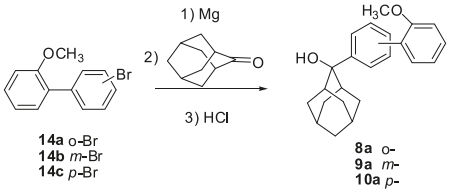

[4]

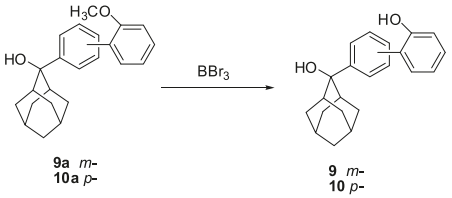

[5]

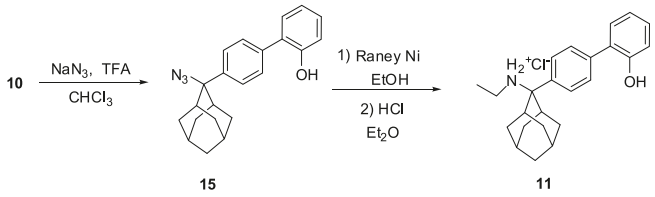

Preparative irradiations

According to previous reports on the photochemistry of benzhydrols,[4,5,7,15] and the corresponding similar biphenyl derivatives,[12,16] it is anticipated that electronic excitation of **8**–**10** in the presence of a protic solvent should give rise to a formal long range proton transfer from the phenol moiety to the alcohol that would couple with a dehydration. It should deliver QMs that can react with nucleophiles (e.g., CH_3OH) and give the substitution (or photosolvolysis) products. To probe for this photochemical process, **8**–**10** were photolyzed in CH_3OH–H_2O (4:1). The CH_3OH–H_2O mixture was chosen because it is known that proton transfer takes place more readily to the clusters of H_2O than CH_3OH.[21] Furthermore, photolyses of similar derivatives in neat CH_3OH sometimes led to the formation of by-products owing to competing pathways involving homolytic cleavage reactions.[7,15]

Can. J. Chem. Downloaded from www.nrcresearchpress.com by University of Electronic and Science Techonology of China on 09/18/12
For personal use only.

In aqueous solvent mixtures, the homolytic pathways can generally be reduced.

Photochemical reaction of **9** and **10** gave rise to methanolysis products **9b** and **10b** (eq. [6]), respectively, whereas **8** furnished chroman **16** (eq. [7]). The photolyses (254 nm, 16 lamps, 15 min) were clean, and the products from **8**, **9**, and **10** were isolated in 64%, 19%, and 19% yield, respectively. The unreacted starting materials could be completely recovered by chromatography. On irradiation of the ammonium derivative **11** under the same conditions, complete conversion was achieved. It delivered alcohol **10** (15%) and the methanolysis product **10b** (85%). Quantum yields of the photomethanolyses were determined by use of photomethanolysis of **1** as an actinometer (Φ = 0.23).[4] This actinometer was chosen because it undergoes the same type of reaction under the same conditions as investigated photolyses of **8**–**11**. In addition, it is very simple to analyze the composition of the irradiated solutions by HPLC. The results are compiled in Table 1.

[6] 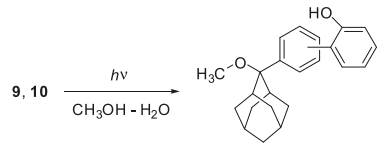

[7] 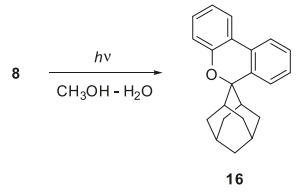

To probe for the ESIPT to the carbon atom of the adjacent ring in **8**–**12**, irradiations were performed in CH_3CN–D_2O. The concentration of D_2O was 0.1% or 25%. After irradiations and washing with H_2O, the samples were analyzed by NMR and MS to determine the position and the extent of deuteration, respectively. Photolysis of **8** (5 min) gave solely **16** without incorporated deuterium (according to NMR). The MS analysis of the photolyzed sample, however, detected traces of **8** and **8D** (1% of D on photolysis in 0.1% D_2O, and 5% of D on photolysis in 25% D_2O, eq. [8]). Photolysis of **9** (15 min, 0.1% D_2O) gave rise to **9D2** and **9D5** (eq. [9]) in a ratio ~1:1 (according to NMR). The MS analysis showed presence of 30% of monodeuterated compound and 70% of dideuterated compound. Similarly, irradiation of **10** (15 min) gave rise to **10D** and **10D2** (eq. [10]), and the MS analysis showed presence of 22% **10D** and 77% of **10D2**. Interestingly, photolysis of fluorene **12** (1 h, 0.1% D_2O) also furnished the deuterated compound **12D** (eq. [11]), unlike **13** that under the same conditions was not deuterated.

Table 1. Quantum yields of photochemical reactions of biphenyls **8**–**11** and fluorene **12**.

Compound	Φ_D[a]	Φ_{MeOH}[b]
8	—	0.33±0.03[c]
9	0.20±0.02 (0.16±0.02)	0.024±0.004
10	0.15±0.02 (0.09±0.02)	0.020±0.004
11	0.12±0.02	~0.1
12	$(2–3)\times10^{-3}$	—

[a]Quantum yield of deuterium incorporation into the adjacent phenyl ring on photolysis in CH_3CN–D_2O (0.1%); the values in parenthesis correspond to experiments carried out in CH_3CN–D_2O (25%).
[b]Quantum yields of photosolvolysis carried out in CH_3OH–H_2O (25%).
[c]Quantum yield for the photochemical formation of **16**.

[8] 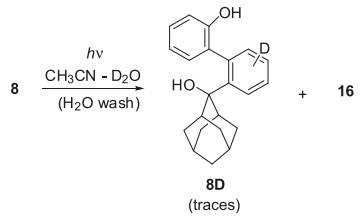

[9] 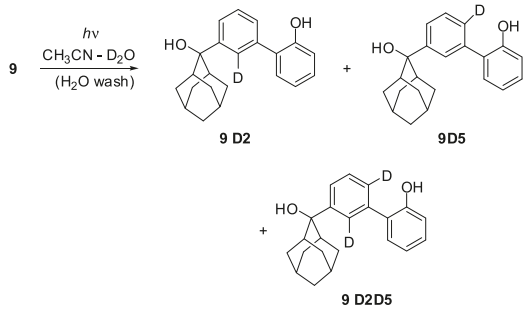

[10] 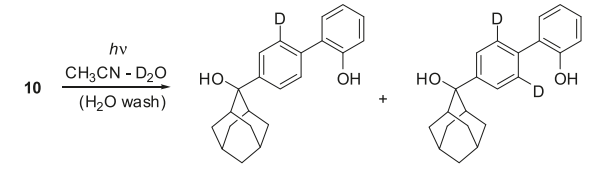

[11] 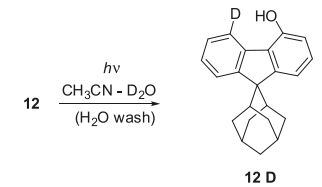

Quantum yields of deuterium exchange on photolysis of **9**–**12** were determined by the use of two actinometers, methanolysis of **1** (Φ = 0.23)[4] and deuterium exchange on photolysis of 2-phenylphenol (**5**, Φ = 0.041).[16] The extent of deuteration was determined by NMR and MS. Both actinometers gave quantum yields for deuteration that differed only within the experimental error of the method, so their mean value was reported (Table 1). It is interesting to note

Can. J. Chem. Downloaded from www.nrcresearchpress.com by University of Electronic and Science Techonology of China on 09/18/12
For personal use only.

Table 2. Fluorescence properties of **8**–**10** and **12**.

Compound	Φ_f (CH_3CN)[a]	Φ_f (CH_3CN–H_2O 1:4)[a]	τ_f (CH_3CN) (ns)[b]	τ_f (CH_3CN–H_2O 1:4) (ns)[b]
8	0.005±0.001	0.01±0.001	~0.3 (~4.6)[c]	n.d.
9	0.44±0.06	0.37±0.03	2.02±0.02	3.9±0.1 (phenol)
			5.0±0.3 (5%)	6.3±0.1 (phenolate)
10	0.50±0.04	0.28±0.02	1.74±0.03	3.5±0.1 (phenol)
			5.4±0.5 (5%)	6.6±0.1 (phenolate)
12	0.77±0.03	0.68±0.05	3.1	n.d.

Note: n.d.: Not determined.

[a]Quantum yield of fluorescence determined by use of fluorene in CH_3OH as a reference (Φ = 0.68).[24]

[b]Singlet excited-state lifetimes determined by single photon timing method.

[c]Decay time probably corresponds to **16** that was formed during measurement.

Fig. 1. Normalized fluorescence spectra of **10** (black) and **12** (red) in CH_3CN (full line) and CH_3CN–H_2O 1:4 (dashed line).

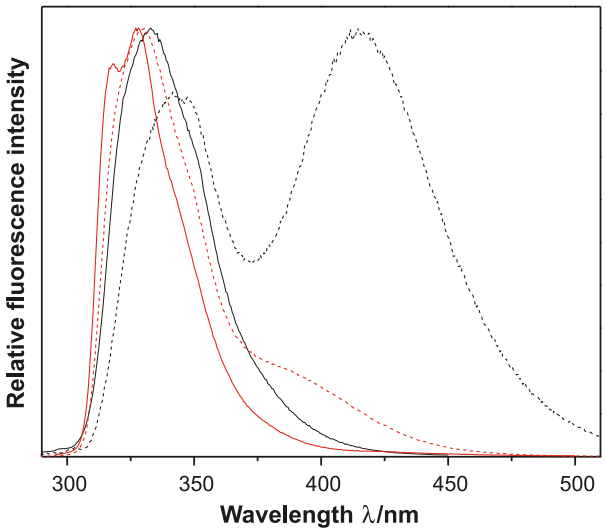

that quantum yields of deuteration were higher in solutions with lower concentration of D_2O, suggesting that increase of H_2O (D_2O) content results in lower quantum yields of ESIPT to carbon. Furthermore, introduction of the hydroxyadamantyl moiety into the parent 2-hydroxybiphenyl structure **5** increased the quantum yield of deuterium exchange by up to 2–5 times. The measured quantum yields for **9** and **10** show that deuteration is a process that takes place by an order of magnitude more efficiently than photomethanolysis. On the contrary, deuterium exchange in **8** did not compete with the efficient formation of chroman **16**.

To additionally probe for the competition between the photomethanolysis and the deuterium exchange, **9** and **10** were irradiated in CH_3OD. The NMR spectrum after photolysis of **10** showed a presence of 10% of **10b** and indicated that **10** and (or) **10b** were 35% deuterated.[22] A similar result was also obtained on photolysis of **9**, indicating the competition of deuteration and formation of **9b**. These results obtained on photolysis in CH_3OD would seem to suggest a smaller difference between the quantum yield of the deuterium incorporation and the photomethanolysis in **9** and **10** than it is presented in Table 1. However, the results are not directly comparable, since experiments were not carried out under the same conditions.

Fluorescence

ESIPT and proton-transfer reactions of phenol derivatives are generally singlet excited-state processes.[1,4,12] Hence, we examined fluorescence of **8**–**10** and **12** to gain more insight into properties of the corresponding singlet excited states. Proton-donor ability of the solvent should influence both the ESIPT and the proton transfer reactions.[23] Therefore, the fluorescence spectra were recorded in CH_3CN and CH_3CN–H_2O (1:4). Quantum yields of fluorescence were determined by using fluorene in methanol as a reference (Φ_f = 0.68).[24] Singlet excited-state lifetimes were obtained by use of the single photon timing method. The results are compiled in Table 2 and in the Supplementary data.

Generally, in CH_3CN solutions, phenols **9** and **10** and fluorene **12** are strongly fluorescent with the maxima of the emission at ~330 nm (Fig. 1). On the contrary, phenol **8** is very weakly fluorescent and shows emission with the maximum at ~320 nm. In CH_3CN–H_2O (1:4) solutions of **8**–**10** and **12**, a dual fluorescence was observed, with the additional band at longer wavelengths (400–450 nm) clearly assignable to the formation of phenolates in the excited state. Accordingly, quantum yields of fluorescence in the aqueous solutions (CH_3CN–H_2O 1:4) are lower (except for **8** where it is double).

To get better insight into the effect of added protic solvent, fluorescence titrations of CH_3CN solutions with H_2O were performed. Addition of H_2O to the solutions of **9** and **10** initially induced fluorescence quenching, which on further additions (>10 mol/L) increased the fluorescence. For **8** and **12**, the initial addition of H_2O already increased the fluorescence (see Supplementary data). However, except for **8**, in CH_3CN–H_2O (1:4) solution, fluorescence is quenched compared with the neat CH_3CN. The unusual influence of added H_2O to fluorescence of **9**–**12** may be ascribed to high lipophylicity and unusual solvation of these derivatives, in accordance with previous report.[7] Addition of H_2O to the solution of **8** probably disrupts the intramolecular H bond between the phenol and the alcohol moiety in the ortho position. In turn, that probably results in a decrease of the efficiency of the ESIPT from the phenol to the alcohol, which is the major anticipated deactivation pathway of the singlet excited state of **8** in CH_3CN (causing low Φ_f and short τ). Similarly, an increase of Φ_f in aqueous media for **9** and **10** may be associated with a decrease of the Φ for the ESIPT pathway to the carbon at the ortho position, and hence, deuteration of the adjacent phenyl ring.

Singlet excited-state lifetimes for **8**–**10** and **12** in CH_3CN

Can. J. Chem. Downloaded from www.nrcresearchpress.com by University of Electronic and Science Techonology of China on 09/18/12
For personal use only.

are in line with the quantum yields of fluorescence in that solvent (Table 2). For **8**–**10**, decays of the fluorescence could not be fitted to single exponential functions. In the case of **8**, the longer decay component probably corresponds to the lifetime of **16** that was formed during measurement. Two decay times for **9** and **10** may be ascribed to the presence of two excited states, ^1L_a and ^1L_b, or conformers with different excited-state lifetimes. Formation of aggregates was disregarded by recording a fluorescence decay of a diluted solution of **10** that was also fitted by a biexponential function. However, the unambiguous assignation of the decay component contributing with ~5% was not made. In aqueous solutions, **9** and **10** clearly showed presence of two decay components that were assigned to phenols, more contributing at shorter wavelengths, and phenolates, the rising components contributing mainly at longer wavelengths.

The formation of phenolates from **8**–**10** in CH_3CN–H_2O (1:4) and the observation of dual fluorescence are clearly due to enhanced acidity of the phenol moiety in the singlet excited state. It is well-known that phenols in the excited state become more acidic; for example, the pK_a value for the deprotonation of 2-phenylphenol (**5**) in the singlet state was reported (pK_a^* = 1.15).[25] However, for the ESIPT, a presence of the basic site is also required that is capable of accepting the proton from the phenol. Hence, we performed fluorescence titrations of **9**, **10**, and **12** with acid to estimate the basicity of the corresponding singlet excited states. The CH_3CN–H_2O (1:4) solutions were titrated with aqueous $HClO_4$ resulting in the fluorescence quenching of both the phenol and the phenolate emission. Furthermore, inspection of the normalized fluorescence spectra indicated that phenol fluorescence was more quenched than for the phenolate. That finding suggests that the protonation site in the excited state is indeed not phenolate, but rather a more basic site, a carbon atom or the alcohol moiety. Stern–Volmer analyses of the quenching (see Supplementary data) revealed the diffusion-limited quenching constants (k_q ~ 1.3–1.5 × 10^{10} (mol/L)$^{-1}$ s^{-1}). The basicity was determined by use of the global factor analysis fitting program Specfit.[26] For **9** and **10**, the following pK_a values for the dissociation of the conjugated acids were estimated: 2.0 ± 0.1 and 2.1 ± 0.1, respectively.

Laser flash photolysis (LFP)

LFP was performed for biphenyls **8**–**11** to characterize detectable QMs or other potentially relevant intermediates in their photochemistry. LFP of **8** in CH_3CN and CH_3CN–H_2O, however, only gave rise to negative transient absorptions at the wavelengths <550 nm owing to fluorescence and reversible bleaching of the chromophore. On the other hand, LFP of N_2-purged CH_3CN solutions of **9** and **10** produced a very strong positive transient absorption with a maximum at 390 nm and shoulder stretching over the whole visible region. The signal decayed with a rate constant k = 2.4 × 10^5 s^{-1} and k = 1.3 × 10^6 s^{-1} for **9** and **10**, respectively. Since the transient could be quenched by O_2, in analogy to similar transients seen with other hydroxybiphenyl derivatives,[16] it was assigned to the triplet states of **9** and **10**.

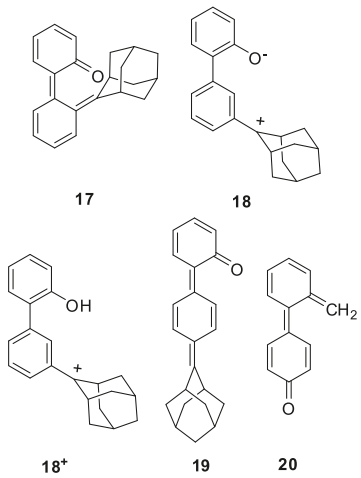

It is anticipated that photolysis of **9** in a protic solvent should give rise to zwitterionic QM **18**. Therefore, LFP was carried out in CH_3CN–H_2O and TFE (see Supplementary data). LFP in O_2-purged CH_3CN–H_2O gave rise to a fast-decaying transient (~30 ns) absorbing with a maximum at 400 nm and stretching to longer wavelengths (>500 nm) that partly overlapped with the signal of the triplet decaying with a similar rate constant. The fast-decaying transient might be ascribed to QM. However, it is more likely to be due to a radical cation. Transient spectra of radical cations with maxima at 350 nm and 550–650 nm decaying with similar lifetimes have been reported.[27] In TFE, which is a less nucleophilic solvent, radical cations, cations,[28] and zwitterionic QMs should be longer lived, and hence, more easily detectable. In an O_2-purged TFE solution of **9**, fast-decaying transient absorption (30–40 ns) was observed at 300–450 nm. Based on reported longer lifetimes of radical cations in TFE,[27] we tentatively assign it to the zwitterionic QM **18** or cation **18**$^+$. However, the transient overlapped with the signal of the triplet, which in addition to its short lifetime precluded further study.

In O_2-purged CH_3CN–H_2O (1:1) solutions of **10** and **11**, besides the signal of the quenched triplet (in O_2-purged solution, the triplet decays with the constant k = 3–5 × 10^7 s^{-1}), transients absorbing at 430 nm and longer wavelengths (550–800 nm) were observed (Fig. 2). These transients were not quenchable by O_2 or N_2O. Hence, they probably do not correspond to radicals, triplets, or solvated electrons. In addition, the intensity of the transient absorption depends linearly on the laser power, ruling out two-photon processes. However, the decay of the signal could not be fitted to a single exponential function. Two or three exponents were required, suggesting a presence of several species. The decay from **10** in O_2-purged solution (CH_3CN–H_2O 1:1) at 600 nm revealed a presence of the species with τ ~ 400 ns, 1 μs, and 30–60 μs, whereas transients from **11** were more persistent, with the main decay component at 600 nm corresponding to a lifetime of 6–8 μs. These transient absorptions in principle may be assigned as being due to radical cations and (or) QM **19**.

The positively charged molecule **11** is anticipated to be less prone to photoionization than noncharged alcohol **10**. On the contrary, the signal of the transient absorption was

Can. J. Chem. Downloaded from www.nrcresearchpress.com by University of Electronic and Science Techonology of China on 09/18/12
For personal use only.

Fig. 2. Transient absorption spectra of **10** and **11** recorded in O_2-purged CH_3CN–H_2O (1:1) 0.5 μs after the laser pulse. Insets: decays at 600 nm.

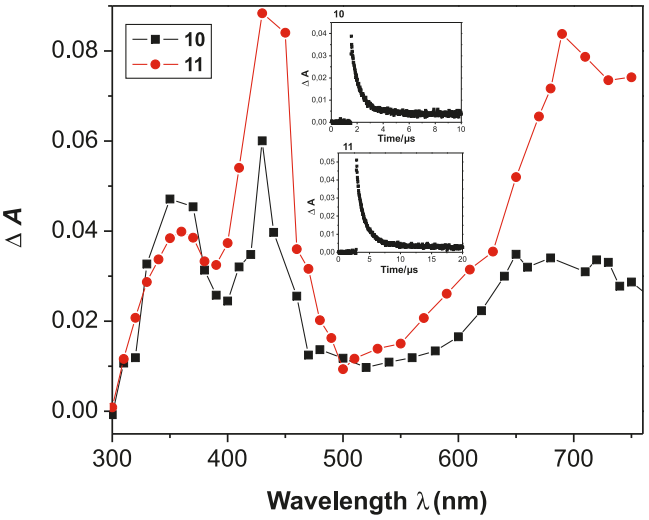

stronger for the ammonium derivative **11** than for alcohol **10**, suggesting that it is not due to the radical cation but rather the QM. The relatively high wavelength region of the transient absorption (550–800 nm), on the other hand, does not suggest that it would correspond to QM **19**. However, a similar transient absorption spectrum with a maximum at a similar wavelength region was reported for QM **20** (τ = 400 ns).[12b]

To be able to assign the transients (Fig. 2) to QM **19** or the radical cation, a quenching was performed with ethanolamine, an ubiquitous quencher of QMs. The transient from **10** decaying with $k = 1 \times 10^6$ s^{-1} was quenched with a rate constant $k_q = 7.7 \times 10^6$ $(mol/L)^{-1}$ s^{-1}. The value of the quenching constant is higher than the reported for the similar biphenyl QM derivative **20** ($k_q = 9 \times 10^4$ $(mol/L)^{-1}$ s^{-1}).[12b] However, it is smaller than those reported for the quenching of radical cations with primary amines (~2×10^9 $(mol/L)^{-1}$ s^{-1}).[27] To get further evidence for the assignation of the transients, LFP of the methoxy derivative **10a** was also performed. Namely, the photolysis of **10a** can give rise to radical cations but cannot give QMs. LFP of **10a** gave rise to transient absorption that in O_2-purged CH_3CN–H_2O showed maxima at 340 and 600 nm, decaying with a rate constant $k = 5 \times 10^4 - 8 \times 10^4$ s^{-1}. This transient was assigned to the radical cation of **10a**. Accordingly, we tentatively assign transients with similar decay times to those seen on the LFP of **10** and **11** to radical cations, whereas faster decaying transients (lifetime 1–6 μs) can be tentatively assigned to QM **19**. However, we were unable to record the representative transient spectrum corresponding only to QM **19** because of the overlapping with the signal of the radical cations.

Reaction mechanisms

From these product studies, fluorescence measurements, and LFP, a reaction mechanism can be proposed. In biphenyl **8**, because of the presence of an intramolecular H bond between the phenol OH and the alcohol at the ortho position, the major anticipated deactivation channel from the singlet excited state is ESIPT coupled with the dehydration. It takes place along the H-bond trajectory and gives rise to QM **17** that very rapidly and efficiently undergoes 6π electrocyclization giving chroman **16** (Scheme 2). The overall quantum yield for the formation of **16** in CH_3OH–H_2O (4:1) is 0.33. Since the electrocyclization reaction takes place very fast, QM **17** has a short lifetime (sub-nanoseconds), so we were unable to detect it by LFP. Because of efficient ESIPT and the formation of QM **17**, the quantum yield of fluorescence of **8** is low and the singlet-state lifetime is short. Addition of a protic solvent disrupts the intramolecular H bond, resulting in a decrease of the quantum yield of ESIPT from the phenol to the alcohol. In addition, in a highly protic medium, the singlet excited state of **8** deprotonates giving phenolates that may, or may not, undergo dehydration giving QM **17**. In any case, the ESIPT process from the phenol to the carbon atom of the adjacent phenyl ring giving **8QM** almost does not take place. That is, in the singlet excited state of **8**, protonation of the carbon atom of the adjacent phenyl ring cannot compete with the protonation of the hydroxyl group and dehydration.

Scheme 2.

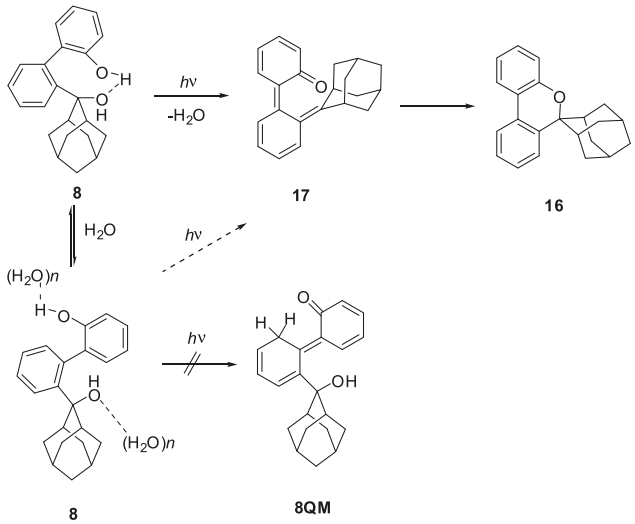

In biphenyl **9**, the hydroxyl group is further away from the phenol moiety. Hence, the intramolecular H bond does not exist, which is in line with the higher quantum yield of fluorescence and the longer singlet excited-state lifetime (compared with **8**). In the aprotic solvent, the phenolic OH probably forms a H–π interaction with the adjacent phenyl ring, as has been demonstrated for the parent system **5**.[12] The electronic excitation of the molecule results in the increased polarization of the resulting singlet state and the increased acidity of the phenolic OH ($pK_a^* = 1.15$).[25] These, coupled with the H–π interaction, probably form a trajectory for the ESIPT from the phenol to the C atom of the adjacent phenyl ring. The ESIPT gives rise to QMs **9QM5** and **9QM2** (Scheme 3), as indicated from the deuterium-exchange experiments. The QMs are formed in a 1:1 ratio, suggesting that there is no prevalence between the conformers of **9** in the ground state, or that free rotation between the phenyl rings in the singlet excited state is much faster than deactivation pathways.

Addition of a protic solvent probably partly disrupts the H–π interaction, leading to a decrease of the ESIPT to

Can. J. Chem. Downloaded from www.nrcresearchpress.com by University of Electronic and Science Techonology of China on 09/18/12
For personal use only.

Scheme 3.

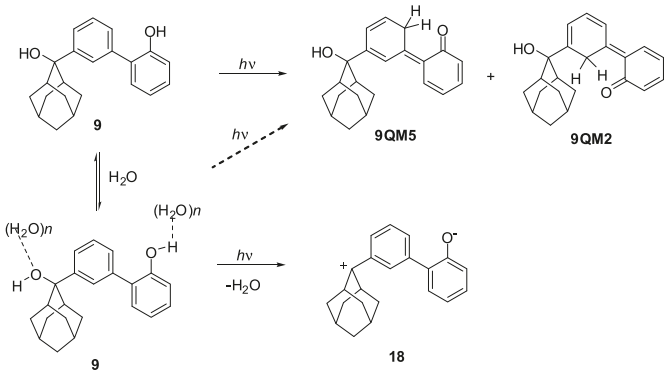

carbon atoms. Hence, in protic media **9QM5** and **9QM2** are formed with lower quantum yields, which is demonstrated by the lowering of the quantum yields for deuterium exchange on the increase of D_2O content. In highly protic media, phenol in the singlet excited state of **9** deprotonates giving phenolate, as evidenced from the fluorescence spectra. Furthermore, the fluorescence titration with acid indicated that the most basic site in the singlet excited state is not the phenolate. The finding is in accord with two mechanisms: (*i*) the ESIPT to the carbon atom and (*ii*) the formal ESPT from the phenol OH to the carbon atom or the hydroxyl group, via participation of H_2O molecules, which mediate this formal long-range proton transfer (Scheme 3). Consequently, in protic media, formal ESPT probably gives rise to both protonation of carbon giving **9QM5** and **9QM2** and dehydration delivering zwitterion QM **18**. Measured quantum yields for deuterium exchange and methanolysis demonstrate that ESIPT to carbon is by an order of magnitude more efficient than formal ESPT to the alcohol coupled with dehydration. QMs **9QM5** and **9QM2** are probably very short-lived. Their anticipated lifetimes are in the subnanosecond region. Hence, it was not possible to detect these on our nanosecond LFP. On the contrary, in TFE, we saw the transient absorption, which may be due to zwitterion QM **18** (lifetime ~30 ns).

Similar to **9**, in the singlet excited state of biphenyls **10** and **11** in aprotic solvent, the ESIPT from the phenol to the carbon atom of the adjacent phenyl ring represents an important deactivation pathway. It gives rise to **10QM2** (Scheme 4) and deuterium incorporation on irradiation in the presence of D_2O. Addition of a protic solvent opens new pathways. ESPT in the singlet excited state of **10** gives rise to phenolates, as seen by fluorescence. Phenolate may deliver **10QM2** or may dehydrate giving QM **19**. In protic media, formation of **10QM2** is minimally 5 times more efficient than formation of **19**. In **11**, on the contrary, ESIPT to carbon and formation of **10QM2** proceeds with similar efficiency to the formation of QM **19** because of the presence of a good nucleofugal ammonium group. Photochemistry of **10** and **11** gives rise to two classes of QMs. **10QM2** is probably too short-lived to be detected by nanosecond LFP. On the other hand, the transient absorption spectra of **19** overlap with the radical cationic intermediates observed for the LFP of **10** and **11**, which made its detection difficult. It is interesting to note that incorporation of the hydroxyadamantyl moiety increased quantum yields for the ESIPT to the carbon atom of the adjacent phenyl ring 3–5 times, as compared with the parent biphenyl **5**. This finding may be ascribed to an inductive effect of the adamantyl (alkyl) group that stabilizes the QM structure (e.g., *tert*-butyl $\sigma_m = -0.10$ and $\sigma_p = -0.10$).[24]

Scheme 4.

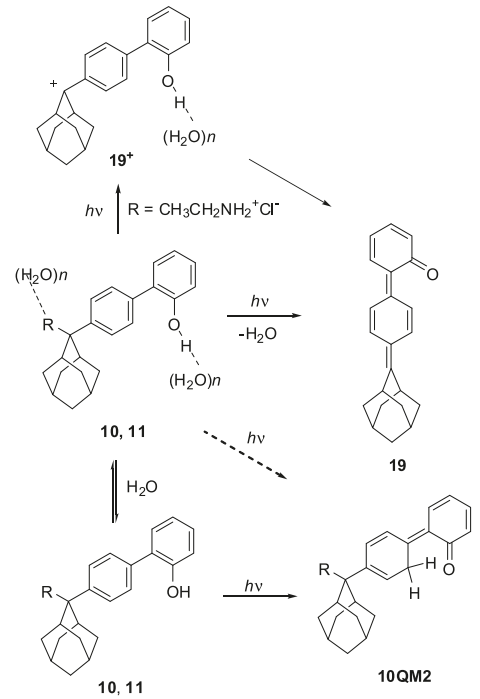

Wan and co-workers[12,16] reported that fluorene **13** does not undergo ESIPT because of the rigid planar structure wherein there is no interaction between the phenol OH and the π-electrons of the accepting ring. On the contrary, on irradiation of adamantylfluorene **12**, incorporation of the deuterium to the carbon atom indicated that ESIPT takes place, giving rise to **12QM** (eq. [12]), albeit with a low quantum yield of 2×10^{-3} to 3×10^{-3}. The reactivity of **12** can probably be ascribed to a slight change in the geometry upon introduction of the bulky adamantyl substituent. According to the B3LYP/6–31G calculation,[29] the most stable geometry of **13** is planar and the dihedral angle between the phenyl rings is 0°. On the contrary, in the most stable geometry of **12**, the biphenyl rings are not perfectly planar; the dihedral angle is 6.3°. In addition, owing to the angle between the phenyl rings, the phenolic OH comes slightly closer to the C atom with which it should form a new σ bond. The OH–C distance in **13** is 2.586 Å, whereas in **12** it is 2.523 Å. Furthermore, in the biphenyl systems **9** and **10**, it was shown that adamantyl increases the reactivity in the ESIPT reactions, presumably because of the inductive effect of the adamantyl (alkyl) group, which stabilizes the QM structure.

[12] 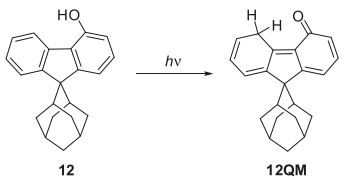

Can. J. Chem. Downloaded from www.nrcresearchpress.com by University of Electronic and Science Techonology of China on 09/18/12
For personal use only.

Conclusion

Adamantyl derivatives of 2-phenylphenol **8**–**11** were synthesized and their photochemical reactivity was investigated. Except for the ortho derivative **8**, excitation to the S_1 state leads to competitive ESIPT from the phenol to the carbon atom of the adjacent ring, and formal ESPT from the phenol to the alcohol, coupled with the dehydration. Both processes give rise to QMs that tautomerize to the starting molecules or react with nucleophiles (**18** and **19**). ESIPT to carbon takes place by an order of magnitude more efficiently than photodehydration. In the ortho derivative **8**, efficient ESIPT from the phenol to the alcohol, coupled with dehydration, gives QM **17** and, further, chroman **16**. ESIPT to the carbon atom of the adjacent phenyl ring in **8** cannot compete with the former efficient process. Introduction of the adamantyl moiety to the biphenyl increased reactivity of the molecule in the ESIPT reaction to the carbon atom. Furthermore, distortion of the planarity in the fluorene molecule by the introduction of the adamantyl opened a possibility for ESIPT reaction in the system, which is otherwise nonreactive. The results presented herein show the importance of the ESIPT to carbon atom in the photochemistry of a variety of biphenyl systems.

Experimental

General

^{1}H and ^{13}C NMR spectra were recorded on a Bruker AV-300, 500, or 600 MHz instrument. The NMR spectra were taken in $CDCl_3$ or DMSO-d_6 at room temperature (RT) using TMS as a reference and chemical shifts are reported in ppm. Melting points were determined using an original Köfler mikroheiztisch aparatus (Reichter, Wien) and are uncorrected. UV–vis spectra were recorded on a Varian Cary 100 Bio spectrophotometer at RT. IR spectra were recorded on a FTIR ABB Bomem MB 102 spectrophotometer in KBr. MS were recorded on an Agilent 6410 triple quadrupole mass spectrometer using the electrospray ionization technique. The spectra were obtained in positive and negative modes in the presence of formic acid. HR-MS were obtained on an Applied Biosystems 4800 Plus MALDI TOF/TOF instrument (AB, Foster City, California). For the sample analysis, a Shimadzu HPLC equipped with a diode-array detector and a Phenomenex Luna 3u C18(2) column was used. The mobile phase was CH_3OH–H_2O (20%). For the chromatographic separations silicagel (Merck 0.05–0.2 mm) was used. Analytical thin layer chromatography was performed on Polygram SILG/UV_{254} (Machery–Nagel) plates. Irradiation experiments were performed in a Rayonet reactor equipped with 16 lamps with the output at 254 nm. During irradiations, the irradiated solutions were continuously purged with Ar and cooled by a tap-water finger condenser. Solvents for irradiation were of HPLC purity. Chemicals (dibromobenzenes, bromoanisoles, 2-adamantanone, and a solution of BBr_3) were purchased from the usual commercial sources and were used as received. Solvents for chromatographic separations were purified by distillation.

General procedure for Grignard reaction

The reaction was carried out in a two-neck round-bottom flask (100 mL) under a N_2 inert atmosphere equipped with a condenser and a dropping funnel. Magnesium (10 mmol), which was freshly activated prior to reaction, was placed in the flask and suspended in THF (10 mL). A THF solution (20 mL) of bromobiphenyl (10 mmol) was placed in the dropping funnel. A few drops of the solution were added to the suspension in the flask, and the reaction was initiated by adding a crystal of iodine and heating. The remaining solution in the funnel was added over 30 min at RT. After the addition was completed, the reaction mixture was refluxed until all the magnesium reacted (1–1.5 h). The solution of the Grignard reagent was cooled to RT and a THF solution (20 mL) of 2-adamantanone (10 mmol) was added dropwise over an 1 h period. After the addition was completed, the reaction mixture was refluxed for 4 h and stirred at RT overnight. The next day, a saturated solution of ammonium chloride (100 mL) was added to the reaction mixture, the layers were separated, and the aqueous layer was additionally acidified with 1 mol/L HCl until all solid dissolved. The acidified aqueous layer was extracted with diethyl ether (3×30 mL) and the organic extracts were combined and then dried over anhyd $MgSO_4$. After filtration and removal of the solvent, the crude product obtained was additionally purified by chromatography on silica gel using CH_2Cl_2 or CH_2Cl_2–EtOAc as an eluent.

2-(2-Hydroxyadamantan-2-yl)-2′-methoxybiphenyl (8a)

Grignard reagent was prepared from 2-bromo-2′-methoxybiphenyl (**14a**)[30] (1.80 g, 6.84 mmol) and magnesium (0.17 g, 6.84 mmol) and reacted with 2-adamantanone (1.03 g, 6.85 mmol) to afford 2.33 g of the crude product **8a** that was purified on a column of silica gel to give the product (1.74 g, 76%) in the form of colourless crystals; mp 114–115 °C. IR (KBr) ν_{max} (cm^{-1}): 3415 (OH), 2900 (CH), 2849 (CH). ^{1}H NMR ($CDCl_3$, 600 MHz) δ (ppm): 7.68 (d, 1H, J = 8.1 Hz, H-Ar), 7.38 (dt, 1H, J = 1.6 Hz, J = 8.1 Hz, H-Ar), 7.34 (dt, 1H, J = 1.7 Hz, J = 8.1 Hz, H-Ar), 7.27 (dt, 1H, J = 1.1 Hz, J = 7.4 Hz, H-Ar), 7.18 (dd, 1H, J = 1.6 Hz, J = 7.4 Hz, H-Ar), 7.00–7.04 (m, 2H, H-Ar), 6.93 (d, 1H, J = 8.3 Hz, H-Ar), 3.86 (br s, 1H, OH), 3.74 (s, 3H, OCH_3) 2.59 (br s, 1H, H-Ad), 2.34 (dt, 1H, J = 2.2 Hz, J = 12.4 Hz, H-Ad), 2.11 (dt, 1H, J = 2.2 Hz, J = 12.4 Hz, H-Ad), 1.80–1.90 (m, 2H, H-Ad), 1.60–1.72 (m, 5H, H-Ad), 1.54 (dt, 1H, J = 2.2 Hz, J = 12.4 Hz, H-Ad), 1.40 (dt, 1H, J = 2.2 Hz, J = 12.4 Hz, H-Ad), 1.32 (dq, 1H, J = 3.2 Hz, J = 12.4 Hz, H-Ad), 1.23 (dq, 1H, J = 3.2 Hz, J = 12.4 Hz, H-Ad). ^{13}C NMR ($CDCl_3$, 150 MHz) δ (ppm): 154.68 (s), 142.69 (s), 136.48 (s), 134.30 (s), 133.08 (d), 129.81 (d), 128.54 (d), 127.76 (d), 127.12 (d), 126.61 (d), 121.32 (d), 111.04 (d), 76.56 (s), 55.68 (q), 37.52 (t), 35.14 (d), 34.87 (t), 34.75 (d), 34.02 (t), 33.07 (t), 32.68 (t), 27.29 (d), 26.53 (d). HR-MS calcd. for $C_{23}H_{26}O_2$–OH: 317.1900; found: 317.1907.

3-(2-Hydroxyadamantan-2-yl)-2′-methoxybiphenyl (9a)

Grignard reagent was prepared from 3-bromo-2′-methoxybiphenyl (**14b**)[31] (1.88 g, 7.14 mmol) and magnesium (0.18 g, 7.19 mmol) and reacted with 2-adamantanone (0.98 g, 6.49 mmol) to afford 2.27 g of the crude product **9a** that was purified on a column of silica gel to give the product (0.94 g, 39%) in the form of colourless oil. IR

Can. J. Chem. Downloaded from www.nrcresearchpress.com by University of Electronic and Science Techonology of China on 09/18/12
For personal use only.

(KBr) ν_{max} (cm^{-1}): 3473 (OH), 2906 (CH), 2853 (CH). ^1H NMR ($CDCl_3$, 300 MHz) δ (ppm): 7.71 (s, 1H, H-Ar), 7.49 (tt, 1H, *J* = 1.7 Hz, *J* = 7.3 Hz, H-Ar), 7.38–7.44 (m, 2H, H-Ar), 7.28–7.34 (m, 2H, H-Ar), 7.02 (dt, 1H, *J* = 0.7 Hz, *J* = 7.4 Hz, H-Ar), 6.98 (d, 1H, *J* = 8.5 Hz, H-Ar), 3.80 (s, 3H, OCH_3), 2.59 (br s, 2H, H-Ad), 2.44 (br s, 1H, H-Ad), 2.40 (br s, 1H, H-Ad), 1.65–2.10 (m, 11H, H-Ad). ^{13}C NMR ($CDCl_3$, 75 MHz) δ (ppm): 156.29 (s), 144.73 (s), 138.59 (s), 130.74 (d), 130.66 (s), 128.50 (d), 128.25 (d, 2C), 126.83 (d), 123.89 (d), 120.73 (d), 111.12 (d), 75.59 (s), 55.40 (q), 37.62 (t), 35.60 (d, 2C), 34.74 (t, 2C), 32.89 (t, 2C), 27.37 (d), 26.86 (d). HR-MS calcd. for $C_{23}H_{26}O_2$–OH: 317.1900; found: 317.1902.

4-(2-Hydroxyadamantan-2-yl)-2′-methoxybiphenyl (10a)

Grignard reagent was prepared from 4-bromo-2′-methoxybiphenyl (**14c**)[32] (1.70 g, 6.46 mmol) and magnesium (0.16 g, 6.58 mmol) and reacted with 2-adamantanone (0.99 g, 6.55 mmol) to afford 2.29 g of the crude product **10a** that was purified on a column of silica gel to give the product (1.17 g, 54%) in the form of colourless crystals; mp 132–133 °C. IR (KBr) ν_{max} (cm^{-1}): 3477 (OH), 2190 (CH), 2856 (CH). ^1H NMR ($CDCl_3$, 300 MHz) δ (ppm): 7.56 (br s, 4H, H-Ar), 7.29–7.34 (m, 2H, H-Ar), 7.02 (dt, 1H, *J* = 0.8 Hz, *J* = 7.6 Hz, H-Ar), 6.98 (d, 1H, *J* = 8.4 Hz, H-Ar), 3.81 (s, 3H, OCH_3), 2.59 (br s, 2H, H-Ad), 2.45 (br s, 1H, H-Ad), 2.40 (br s, 1H, H-Ad), 1.91 (br s, 1H, OH), 1.69–1.80 (m, 10H, H-Ar). ^{13}C NMR ($CDCl_3$, 75 MHz) δ (ppm): 156.35 (s), 143.75 (s), 137.28 (s), 130.72 (d), 130.00 (s), 129.67 (d, 2C), 128.48 (d), 124.97 (d, 2C), 111.06 (d), 75.46 (s), 55.38 (q), 37.61 (t), 35.58 (d, 2C), 34.80 (t, 2C), 32.88 (t, 2C), 27.35 (d), 26.87 (d). HR-MS calcd. for $C_{23}H_{26}O_2$–OH: 317.1900; found: 317.1909.

2-(2-Hydroxyadamantan-2-yl)-2′-hydroxybiphenyl (10)

The reaction was carried out under a N_2 atmosphere in a round-bottom flask (100 mL) equipped with a condenser and a dropping funnel, and the outlet of the N_2 from the condenser was purged through a solution of sodium ethoxyde in ethanol. Sodium hydride (0.46 g, 20 mmol) was placed in the flask and then suspended in 5 mL of dry DMF. The suspension was cooled using an ice bath, and a solution of ethyl mercaptane (1.4 mL, 20 mmol) in DMF (5 mL) was added dropwise. When the addition was completed, the reaction mixture was stirred for 10 min and the ice bath was removed. Methoxybiphenyl derivative **8a** (1.7 g, 5.08 mmol) was dissolved in DMF (10 mL) and added to the reaction mixture. After addition, the mixture was refluxed over 4 h, cooled, and poured into 100 mL of H_2O. The aqueous mixture was washed with hexane (2 × 50 mL) and acidified by a saturated solution of ammonium chloride. Extraction with ethyl acetate was carried out (3 × 100 mL), the extracts were dried over anhyd $MgSO_4$, the solid was removed by filtration, and then the solvent was removed on the rotary evaporator. The reaction furnished 1.61 g of the crude product, which was purified by crystallization from carbon tetrachloride to afford 1 g (62%) of the pure product **8** in the form of colourless crystals; mp 194–196 °C (lit.[33] mp 213–214 °C).

General procedure for the removal of the methyl ether groups from phenols with BBr_3

The reaction was carried out under a N_2 atmosphere in a three-neck round-bottom flask (250 mL) equipped with a septum and a syringe. Methoxybiphenyl derivative **8a**–**10a** (10 mmol) was placed in the flask, then dissolved in dry CH_2Cl_2 (100 mL), and the solution was cooled to 0 °C using an ice bath. To the cold solution, by use of a syringe, a solution of BBr_3 in CH_2Cl_2 (1 mol/L, 10 mL) was added dropwise over a 1 h period. After the addition was completed, the stirring was continued for 1 h at 0 °C and then at RT overnight. The next day, to the reaction mixture 100 mL of cold water was added, the layers were separated, and the aqueous layer extracted with CH_2Cl_2 (3 × 50 mL). The combined organic extracts were dried over anhyd $MgSO_4$, the solid was removed by filtration, and then the solvent was removed on a rotary evaporator. The obtained crude product was purified on a column filled with silica gel using CH_2Cl_2 or CH_2Cl_2–EtOAc (4:1) as the eluent.

Spiro[adamantane-2,9′-(4′-hydroxy)fluorene] (12)

From 2-(2-hydroxyadamantan-2-yl)-2′-methoxybiphenyl (**8a**, 0.94 g, 2.81 mmol) and a solution of BBr_3 (14.1 mL), the reaction gave 0.92 g (99%) of the crude fluorene product **12** that was additionally purified for the purpose of analysis on a column of silica gel using CH_2Cl_2 as the eluent. Colourless crystals, mp 158–160 °C. IR (KBr) ν_{max} (cm^{-1}): 3519 (OH-phenol), 3365 (CH), 2900 (CH), 2854 (CH). ^1H NMR ($CDCl_3$, 600 MHz) δ (ppm): 8.31 (dd, 1H, *J* = 1.0 Hz, *J* = 7.7 Hz, H-Ar), 8.11 (d, 1H, *J* = 8.1 Hz, H-Ar), 7.71 (d, 1H, *J* = 7.9 Hz, H-Ar), 7.37 (dt, 1H, *J* = 0.8 Hz, *J* = 7.6 Hz, H-Ar), 7.26 (dt, 1H, *J* = 1.5 Hz, *J* = 7.5 Hz, H-Ar), 7.12 (t, 1H, *J* = 7.9 Hz, H-Ar), 6.72 (d, 1H, *J* = 7.9 Hz), 5.08 (s, 1H, OH-phenol), 2.85–3.00 (m, 4H, H-Ad), 2.18 (br s, 2H, H-Ad), 1.98 (br s, 2H, H-Ad), 1.70–1.80 (m, 4H, H-Ad), 1.55–1.60 (m, 2H, H-Ad). ^{13}C NMR ($CDCl_3$, 75 MHz) δ (ppm): 153.50 (s), 151.32 (s), 150.29 (s), 139.83 (s), 128.61 (d), 127.52 (s), 126.80 (d), 125.93 (d), 124.82 (d), 123.91 (d), 122.03 (d), 113.94 (d), 58.47 (s), 41.59 (t), 34.83 (d, 2C), 34.22 (t, 2C), 34.12 (t, 2C), 27.28 (d), 27.24 (d). MS (ESI) *m/z*: 301 ($M - H^+$). HR-MS calcd. for $C_{22}H_{22}O$: 302.1676; found: 302.1674.

3-(2-Hydroxyadamantan-2-yl)-2′-hydroxybiphenyl (9)

From 3-(2-hydroxyadamantan-2-yl)-2′-methoxybiphenyl (**9a**, 0.76 g, 2.27 mmol) and a solution of BBr_3 (11.3 mL), the reaction gave 0.50 g (69%) of product **9** in the form of colourless crystals; mp 179–181 °C. IR (KBr) ν_{max} (cm^{-1}): 3452 (OH-phenol), 3190 (OH-alcohol), 2900 (CH), 2852 (CH). ^1H NMR (DMSO-d_6, 300 MHz) δ (ppm): 9.45 (s, 1H, OH-phenol), 7.62 (br s, 1H, H-Ar), 7.32–7.44 (m, 3H, H-Ar), 7.23 (dd, 1H, *J* = 1.6 Hz, *J* = 7.5 Hz, H-Ar), 7.14 (dt, 1H, *J* = 1.6 Hz, *J* = 8.0 Hz, H-Ar), 6.92 (dd, 1H, *J* = 0.8 Hz, *J* = 8.0 Hz, H-Ar), 6.87 (dt, 1H, *J* = 1.0 Hz, *J* = 7.4 Hz, H-Ar), 4.60 (br s, 1H, OH), 2.50 (br s, 2H, H-Ad), 2.41 (br s, 1H, H-Ad), 2.38 (br s, 1H, H-Ad), 1.55–1.85 (m, 10H, H-Ad). ^{13}C NMR (DMSO-d_6, 75 MHz) δ (ppm): 154.28 (s), 145.69 (s), 138.19 (s), 130.32 (d), 128.30 (d), 128.24 (s), 127.67 (d), 127.11 (d), 126.53 (d), 123.87 (d), 119.42 (d), 116.04 (d), 73.59 (s), 37.50 (t), 34.88 (d, 2C),

Can. J. Chem. Downloaded from www.nrcresearchpress.com by University of Electronic and Science Techonology of China on 09/18/12
For personal use only.

34.30 (t, 2C), 32.62 (t, 2C), 27.00 (d), 26.62 (d). HR-MS calcd. for $C_{22}H_{24}O_2$–H: 319.1703; found 319.1703.

4-(2-Hydroxyadamantan-2-yl)-2′-hydroxybiphenyl (10)

From 4-(2-hydroxyadamantan-2-yl)-2′-methoxybiphenyl (**10a**, 1.84 g, 5.5 mmol) and a solution of BBr_3 (20 mL), the reaction gave 1.25 g (69%) of product **10** that was additionally purified on a column of silica gel using CH_2Cl_2–EtOAc (4:1) to afford 700 mg (40%) of the pure product in the form of colourless crystals; mp 215–217 °C. IR (KBr) ν_{max} (cm^{-1}): 3517 (OH-alcohol), 3220 (OH-phenol), 2932 (CH), 2903 (CH), 2857 (CH). ^{1}H NMR (DMSO-d_6, 300 MHz) δ (ppm): 9.48 (s, 1H, OH-phenol), 7.52 (d, 2H, J = 8.6 Hz), 7.48 (d, 2H, J = 8.6 Hz), 7.25 (dd, 1H J = 1.5 Hz, J = 7.4 Hz), 7.13 (dt, 1H J = 1.5 Hz, J = 8.1 Hz), 6.93 (dd, 1H, J = 1.0 Hz, J = 8.1 Hz), 6.86 (dt, 1H J = 1.0 Hz, J = 7.4 Hz), 4.57 (s, 1H, OH), 2.50 (br s, 1H, H-Ad, covered by DMSO), 2.42 (br s, 1H, H-Ad), 2.38 (br s, 1H, H-Ad), 1.82 (br s, 1H, H-Ad), 1.55–1.75 (m, 10 H, H-Ad). ^{13}C NMR (DMSO-d_6, 75 MHz) δ (ppm): 154.36 (s), 144.37 (s), 136.54 (s), 130.20 (d), 128.78 (d, 2C), 128.27 (d), 127.54 (s), 125.16 (d, 2C), 119.40 (d), 116.00 (d), 73.41 (s), 37.47 (t), 34.77 (d, 2C), 34.38 (t, 2C), 32.59 (t, 2C), 27.00 (d), 26.61 (d). HR-MS calcd. for $C_{22}H_{24}O_2$–H: 319.1703; found: 319.1703.

4-(2-Azidoadamantan-2-yl)-2′-hydroxybiphenyl (15)

A two-neck flask (50 mL) was charged with sodium azide (127 mg, 1.96 mmol) and $CHCl_3$ (4 mL). The obtained suspension was cooled by a salt–ice bath and TFA (365 μL, 4.9 mmol) was slowly added using a syringe. After 10 min of stirring, a suspension of alcohol **10** (314 mg, 0.98 mmol) in $CHCl_3$ (3 mL) was added. The reaction mixture was stirred at –5 °C for 4 h and then at RT overnight. To the reaction mixture, aqueous ammonia (10 mL, 15%) was added and the layers were separated. The aqueous layer was extracted with $CHCl_3$ (2 × 25 mL) and with EtOAc (2 × 25 mL). The combined extracts were dried over anhyd MgSO4, the solution was filtered, and the solvent was removed on a rotary evaporator to afford pure azide (340 mg) quantitatively. Colourless crystals, mp 121–122 °C. IR (KBr) ν_{max} (cm^{-1}): 3516 (OH-phenol), 2942 (CH), 2901 (CH), 2856 (CH), 2103 (N_3). ^{1}H NMR ($CDCl_3$, 300 MHz) δ (ppm): 7.57 (d, 2H, J = 7.5 Hz, H-Ar), 7.54 (d, 2H, J = 7.5 Hz, H-Ar), 7.22–7.30 (m, 2H, H-Ar), 6.96–7.03 (m, 2H, H-Ar), 5.30 (br s, 1H, OH), 2.67 (br s, 2H, H-Ad), 2.36 (br s, 1H, H-Ad), 2.31 (br s, 1H, H-Ad), 1.97 (br s, 1H, H-Ad), 1.73–1.86 (m, 9H, H-Ad). ^{13}C NMR ($CDCl_3$, 75 MHz) δ (ppm): 152.36 (s), 139.84 (s), 136.35 (s), 130.18 (d), 129.31 (d, 2C), 129.11 (d), 127.37 (s), 126.24 (d, 2C), 120.81 (d), 115.84 (d), 69.89 (s), 37.44 (t), 33.79 (t, 2C), 33.15 (t, 2C), 32.83 (d, 2C), 27.12 (d), 26.52 (d). HR-MS calcd. for $C_{22}H_{23}N_3O$–H: 344.1768; found: 344.1784.

4-[2-(N-ethylaminoadamantan-2-yl)]-2′-hydroxybiphenyl hydrochloride (11)

A two-neck flask (250 mL) equipped with a condenser was charged with an absolute ethanol solution (50 mL) of azide **15** (200 mg, 0.58 mmol). To the solution was added a suspension of freshly activated Raney Ni (~10 g). The suspension was heated at ~70 °C overnight. The next day, the reaction mixture was filtered to remove the Raney Ni, and the ethanol solution was evaporated to afford 200 mg of the crude amine. The amine was dissolved in dry ethyl ether (100 mL) and purged with HCl over a 30 min period whereupon colourless precipitate formed. The precipitate was filtered through a sinter funnel, washed with ether and CH_2Cl_2, and dried in vacuum to afford the pure product (60 mg, 27%). Colourless crystals, mp 242–245 °C. IR (KBr) ν_{max} (cm^{-1}): 3400–2800 (broad, NH, OH), 2920 (CH), 2860 (CH). ^{1}H NMR (DMSO-d_6, 300 MHz) δ (ppm): 9.69 (s, 1H, OH), 8.43 (br s, 2H, NH_2), 7.69 (d, 2H, J = 7.6 Hz, H-Ar), 7.65 (d, 2H, J = 7.6 Hz, H-Ar), 7.31 (dd, 1H, J = 7.3 Hz, J = 1.3 Hz, H-Ar), 7.18 (dt, 1H, J = 8.0 Hz, J = 1.5 Hz, H-Ar), 6.99 (d, 1H, J = 8.0 Hz, H-Ar), 6.89 (dd, 1H, J = 7.3 Hz, J = 8.0 Hz), 3.35 (q, 2H, J = 7.4 Hz, NCH_2), 2.90 (br s, 2H, H-Ad), 2.61 (br s, 1H, H-Ad), 2.47 (br s, 1H, H-Ad), 2.42 (br s, 1H, H-Ad), 1.94 (br s, 1H, H-Ad), 1.62–1.86 (m, 8H, H-Ad), 1.05 (t, 3H, J = 7.4 Hz, CH_3). ^{13}C NMR (DMSO-d_6, 75 MHz) δ (ppm): 154.51 (s), 138.80 (s), 133.77 (s), 130.23 (d), 129.13 (d, 2C), 128.82 (d), 127.73 (d, 2C), 126.43 (s), 119.45 (d), 116.24 (d), 67.11 (s), 37.33 (t), 36.52 (t), 33.55 (t, 2C), 30.64 (t, 2C), 30.60 (d, 2C), 26.45 (d), 25.58 (d), 11.55 (q). HR-MS calcd. for $C_{24}H_{30}ClNO$–HCl: 346.2176; found: 346.2183.

Photolysis experiments: general procedure

A CH_3OH or CH_3OH–H_2O (25%) solution (100 mL, c = 3.1 × 10^{-3} mol/L) of hydroxybiphenyl derivative **8**–**11** (100 mg, 0.31 mmol) was placed in a quartz vessel and irradiated in a Rayonet reactor using 16 lamps at 254 nm. Prior to (15 min) and during the irradiation, the solution was continuously purged with a stream of Ar and cooled by a cold-finger condenser. After irradiation, the solvent was removed on a rotary evaporator and the residue was chromatographed on a thin layer of silica gel using CH_2Cl_2 or CH_2Cl_2–EtOAc (30%) as the eluent.

Spiro[adamantane-2,6′-benzo[c]chromene] (16)

Yield: 60 mg (64%), mp 123–124 °C (lit.[33] mp 123–124 °C).

3-(2-Methoxyadamantan-2-yl)-2′-hydroxybiphenyl (9b)

Colourless crystals (20 mg (19%)), mp 179–181 °C. IR (KBr) ν_{max} (cm^{-1}): 3270 (OH-phenol), 2916, 2855 (CH). ^{1}H NMR ($CDCl_3$, 300 MHz) δ (ppm): 7.54 (br s, 1H, H-Ar), 7.43–7.50 (m, 2H, H-Ar), 7.37 (dt, 1H, J = 1.8 Hz, J = 6.8 Hz, H-Ar), 7.20–7.28 (m, 2H, H-Ar), 6.99 (dt, 1H, J = 1.0 Hz, J = 6.3 Hz, H-Ar), 6.96 (d, 1H, J = 7.0 Hz, H-Ar), 5.20 (br s, 1H, OH), 2.83 (s, 3H, OCH_3), 2.63 (br s, 2H, H-Ad), 2.32 (br s, 1H, H-Ad), 2.28 (br s, 1H, H-Ad), 1.88 (br s, 1H, H-Ad), 1.60–1.80 (m, 9H, H-Ad). ^{13}C NMR ($CDCl_3$, 75 MHz) δ (ppm): 152.35 (s), 142.37 (s), 136.49 (s), 130.20 (d), 129.01 (d), 128.85 (d), 128.27 (s), 128.22 (d), 127.51 (d), 126.79 (d), 120.73 (d), 115.70 (d), 79.78 (s), 48.10 (q), 37.54 (t), 34.45 (t, 2C), 32.70 (d, t, 4C), 27.62 (d), 26.72 (d). HR-MS calcd. for $C_{23}H_{26}O_2$–H: 333.1860; found: 333.1875.

4-(2-Methoxyadamantan-2-yl)-2′-hydroxybiphenyl (10b)

Colourless crystals (20 mg (19%)), mp 157–158 °C. IR

Can. J. Chem. Downloaded from www.nrcresearchpress.com by University of Electronic and Science Techonology of China on 09/18/12
For personal use only.

(KBr) ν_{max} (cm^{-1}): 3234 (OH-phenol), 2933 (CH), 2901 (CH), 2856 (CH). ^1H NMR ($CDCl_3$, 300 MHz) δ (ppm): 7.55 (d, 2H, J = 8.4 Hz, H-Ar), 7.44 (d, 2H, J = 8.4 Hz, H-Ar), 7.18–7.26 (m, 2H, H-Ar), 6.92–6.98 (m, 2H, H-Ar), 5.33 (br s, 1H, OH), 2.82 (s, 3H, OCH_3), 2.63 (br s, 2H, H-Ad), 2.33 (br s, 1H, H-Ad), 2.29 (br s, 1H, H-Ad), 1.88 (br s, 1H, H-Ad), 1.60–1.85 (m, 9H, H-Ad). ^{13}C NMR ($CDCl_3$, 75 MHz) δ (ppm): 152.40 (s), 140.81 (s), 135.67 (s), 130.14 (d), 128.96 (d), 128.48 (d, 2C), 128.15 (d, 2C), 127.64 (s), 120.72 (d), 115.75 (d), 79.68 (s), 48.08 (q), 37.56 (t), 34.40 (t, 2C), 32.76 (d, 2C), 32.71 (t, 2C), 27.61 (d), 26.73 (d). HR-MS calcd. for $C_{23}H_{26}O_2$–H: 333.1860; found: 333.1875.

Quantum yields

Four quartz cuvettes, containing solutions of **8**–**11** (5 mg, 0.015 mmol or 0.013 mmol for **11**) in CH_3OH–H_2O (4:1, 25 mL, $c = 6 \times 10^{-4}$ mol/L), and a quartz cuvette with a solution of **1** (5 mg, 0.029 mmol) in CH_3OH–H_2O (1:1, 25 mL $c = 1 \times 10^{-3}$ mol/L) were purged with N_2 for 20 min, sealed, and irradiated at the same time in a Rayonet reactor equipped with 6 lamps with the output at 254 nm for 1, 2, 3, and 6 min. The composition of the irradiated solutions was analyzed by HPLC. Quantum yields for the methanolysis were calculated using the quantum yield for the methanolysis of **1** as the actinometer (Φ = 0.23).[4]

Alternatively, a quartz cuvette containing a solution of **8**–**11** (10 mg, 0.03 mmol) in CH_3CN–D_2O (100 mL, 0.1% or 25% D_2O) was purged with Ar for 30 min and irradiated in a Rayonet reactor equipped with 16 lamps for 3 min. After the irradiation, H_2O was added (100 mL) to the photolyzed solution and extractions with CH_2Cl_2 were carried out (3 × 50 mL). The extracts were dried over anhyd $MgSO_4$, the solution was filtered, and the solvent was removed on a rotary evaporator. The deuterium content was determined by NMR and MS. A solution of **1** in CH_3OH–H_2O (1:1, Φ = 0.23) was irradiated for 3 min and worked up in the same way under the same conditions. The conversion to the photomethanolysis product was obtained from the NMR spectrum. A solution of **5** (10 mg, 0.058 mmol) in 100 mL CH_3CN–D_2O (Φ = 0.041) also was irradiated under the same conditions.[16] After the workup, the content of deuterium was determined by NMR and MS. Using both actinometers, the quantum yields for deuterium incorporation in **8**–**11** were calculated and the mean value was reported.

Steady-state and time-resolved fluorescence measurements

The steady-state measurements were performed on a Photon Technology International (PTI) Quanta-Master QM-2 luminescence spectrometer. The samples were dissolved in CH_3CN or CH_3CN–H_2O (1:4), and the concentrations were adjusted to have optical densities at the excitation wavelength (270 nm) <0.1. Solutions were purged with nitrogen for 15 min prior to analysis. The measurements were performed at 20 °C. Fluorescence quantum yields were determined by comparison of the integral of emission bands with the one of fluorene in methanol (Φ = 0.68).[24] Typically, three absorption traces were recorded (and averaged) and three fluorescence emission traces were collected with excitation at three different wavelengths. Three quantum yields were calculated and the mean value was reported.

Fluorescence titrations were performed by adding aliquots (60 μL) of aqueous $HClO_4$ (pH 2.09) to 2 mL of the CH_3CN–H_2O (1:4) solution. The pH of aqueous $HClO_4$ was measured by a pH meter. The titration was performed at RT in air-saturated solutions.

Fluorescence-decay histograms were obtained on an Edinburgh instrument OB920, equipped with a hydrogen flash lamp, using a time-correlated single photon counting technique in 1023 channels. Histograms of the instrument response functions (using a LUDOX scatterer) and sample decays were recorded until they typically reached 3×10^3 counts in the peak channel (except for **8** where only 500 counts were collected). The half-width of the instrument response function was typically ~1.5 ns. The time increment per channel was 0.049 or 0.02 ns. Obtained histograms were fitted as sums of exponential using Gaussian-weighted nonlinear least-squares fitting based on Marquardt–Levenberg minimization implemented in the software package of the instrument. The fitting parameters (decay times and preexponential factors) were determined by minimizing the reduced χ^2. An additional graphical method was used to judge the quality of the fit that included plots of surface "carpets" of the weighted residuals vs channel number.

Laser flash photolysis (LFP)

All LFP studies were conducted at the University of Victoria LFP facility employing a YAG laser, with a pulse width of 10 ns and an excitation wavelength of 266 nm. Static cells (0.7 cm) were used, and solutions were purged with nitrogen or oxygen for 20 min prior to measurements. Optical densities at 266 nm were ~0.4–0.6.

Supplementary data

Supplementary data for this article are available on the journal Web site (canjchem.nrc.ca).

Acknowledgements

We thank the National Foundation for Science, Higher Education, and Technological Development (NZZ grant No. 02.05/25) and the Ministry of Science, Education, and Sports of the Republic of Croatia (grant No. 098-0982933-2911), the Natural Sciences and Engineering Research Council of Canada (NSERC), and the University of Victoria, Victoria, British Columbia, for financing.

References

(1) (a) Ireland, J. F.; Wyatt, P. A. H. *Adv. Phys. Org. Chem.* **1976**, *12*, 131. doi:10.1016/S0065-3160(08)60331-7.; (b) Klöpffer, W. *Adv. Photochem.* **1977**, *10*, 311. doi:10.1002/9780470133408.ch5.; (c) Arnaut, L. G.; Formosinho, S. J. *J. Photochem. Photobiol. Chem.* **1993**, *75* (1), 1. doi:10.1016/1010-6030(93)80157-5.; (d) Formosinho, S. J.; Arnaut, L. G. *J. Photochem. Photobiol. Chem.* **1993**, *75* (1), 21. doi:10.1016/1010-6030(93)80158-6.; (e) Ormson, S. M.; Brown, R. G. *Prog. React. Kinet.* **1994**, *19*, 45; (f) Le Gourrierec, D.; Ormson, S. M.; Brown, R. G. *Prog. React. Kinet.* **1994**, *19*, 211; (g) Hynes, J. T.; Klinman, J. P.; Limbach, H.-H.; Schowen, R.L., Eds.; *Hydrogen-transfer Reactions;* Wiley-VCH: Weinheim, 2007.

(2) Weller, K. *Naturwissenschaften* **1955**, *42* (7), 175. doi:10.1007/BF00595299.

(3) (a) Wan, P.; Shukla, D. *Chem. Rev.* **1993**, *93* (1), 571.

Can. J. Chem. Downloaded from www.nrcresearchpress.com by University of Electronic and Science Techonology of China on 09/18/12
For personal use only.

doi:10.1021/cr00017a024.; (b) Wan, P.; Barker, B.; Diao, L.; Fischer, M.; Shi, Y.; Yang, C. *Can. J. Chem.* **1996**, *74* (4), 465. doi:10.1139/v96-051.; (c) Wan, P.; Brousmiche, D. W.; Chen, C. Z.; Cole, J.; Lukeman, M.; Xu, M. *Pure Appl. Chem.* **2001**, *73* (3), 529. doi:10.1351/pac200173030529.; (d) Lukeman, M.; Wan, P. In *Handbook of Organic Photochemistry and Photobiology,* 2nd ed.; Horspool, W.; Lenci, F., Eds.; CRC Press: Boca Raton, 2004; Chap. 39, pp 1–19.

(4) (a) Wan, P.; Chak, B. *J. Chem. Soc., Perkin Trans. 2* **1986**, (11): 1751. doi:10.1039/p29860001751.; (b) Diao, L.; Yang, C.; Wan, P. *J. Am. Chem. Soc.* **1995**, *117* (19), 5369. doi:10.1021/ja00124a024.

(5) (a) Chiang, Y.; Kresge, A. J.; Zhu, Y. *J. Am. Chem. Soc.* **2000**, *122* (40), 9854. doi:10.1021/ja001557h.; (b) Chiang, Y.; Kresge, A. J.; Zhu, Y. *J. Am. Chem. Soc.* **2001**, *123* (33), 8089. doi:10.1021/ja010826g. PMID:11506565.; (c) Chiang, Y.; Kresge, A. J.; Zhu, Y. *J. Am. Chem. Soc.* **2002**, *124* (4), 717. doi:10.1021/ja0120375. PMID:11804503.; (d) Chiang, Y.; Kresge, A. J.; Zhu, Y. *J. Am. Chem. Soc.* **2002**, *124* (22), 6349. doi:10.1021/ja020020w. PMID:12033864.

(6) Modica, E.; Zanaletti, R.; Freccero, M.; Mella, M. *J. Org. Chem.* **2001**, *66* (1), 41. doi:10.1021/jo0006627. PMID:11429928.

(7) Basarić, N.; Žabčić, I.; Mlinarić-Majerski, K.; Wan, P. *J. Org. Chem.* **2010**, *75* (1), 102. doi:10.1021/jo902004n. PMID:19957924.

(8) Rokita, S. E., Ed.; *Quinone Methides;* Wiley: Hoboken, 2009.

(9) (a) Zeng, Q.; Rokita, S. E. *J. Org. Chem.* **1996**, *61* (26), 9080. doi:10.1021/jo961864z.; (b) Rokita, S. E.; Yang, J.; Pande, P.; Greenberg, W. A. *J. Org. Chem.* **1997**, *62* (9), 3010. doi:10.1021/jo9700336. PMID:11671669.; (c) Veldhuyzen, W. F.; Pande, P.; Rokita, S. E. *J. Am. Chem. Soc.* **2003**, *125* (46), 14005. doi:10.1021/ja036943o. PMID:14611237.; (d) Zhou, Q.; Rokita, S. E. *Proc. Natl. Acad. Sci. U.S.A.* **2003**, *100* (26), 15452. doi:10.1073/pnas.2533112100. PMID:14673113.; (e) Wang, P.; Liu, R.; Wu, X.; Ma, H.; Cao, X.; Zhou, P.; Zhang, J.; Weng, X.; Zhang, X. L.; Qi, J.; Zhou, X.; Weng, L. *J. Am. Chem. Soc.* **2003**, *125* (5), 1116. doi:10.1021/ja029040o. PMID:12553783.; (f) Richter, S. N.; Maggi, S.; Mels, S. C.; Palumbo, M.; Freccero, M. *J. Am. Chem. Soc.* **2004**, *126* (43), 13973. doi:10.1021/ja047655a. PMID:15506758.

(10) (a) Egholm, M.; Koch, T. H. *J. Am. Chem. Soc.* **1989**, *111* (21), 8291. doi:10.1021/ja00203a047.; (b) Gaudiano, G.; Frigerio, M.; Bravo, P.; Koch, T. H. *J. Am. Chem. Soc.* **1990**, *112* (18), 6704. doi:10.1021/ja00174a038.; (c) Angle, S. R.; Yang, W. *J. Org. Chem.* **1992**, *57* (4), 1092. doi:10.1021/jo00030a012.; (d) Angle, S. R.; Rainier, J. D.; Woytowicz, C. *J. Org. Chem.* **1997**, *62* (17), 5884. doi:10.1021/jo970539o.

(11) Weinert, E. E.; Dondi, R.; Colloredo-Melz, S.; Frankenfield, K. N.; Mitchell, C. H.; Freccero, M.; Rokita, S. E. *J. Am. Chem. Soc.* **2006**, *128* (36), 11940. doi:10.1021/ja062948k. PMID:16953635.

(12) (a) Lukeman, M.; Wan, P. *Chem. Commun. (Camb.)* **2001**, (11): 1004. doi:10.1039/b100817j.; (b) Xu, M.; Lukeman, M.; Wan, P. *Photochem. Photobiol.* **2006**, *82* (1), 50. doi:10.1562/2005-02-17-RA-444. PMID:15934790.; (c) Behin Aein, N.; Wan, P. *J. Photochem. Photobiol. Chem.* **2009**, *208* (1), 42. doi:10.1016/j.jphotochem.2009.08.004.

(13) (a) Xu, M.; Chen, C. Z.; Wan, P. *J. Photochem. Photobiol. Chem.* **2008**, *198* (1), 26. doi:10.1016/j.jphotochem.2008.02.012.; Nayak, M. K.; Wan, P. *Photochem. Photobiol. Sci.* **2008**, *7* (12), 1544. doi:10.1039/b810111f. PMID:19037508.

(14) Brousmiche, D. W.; Xu, M.; Lukeman, M.; Wan, P. *J. Am. Chem. Soc.* **2003**, *125* (42), 12961. doi:10.1021/ja036808b. PMID:14558845.

(15) Diao, L.; Wan, P. *Can. J. Chem.* **2008**, *86* (2), 105. doi:10.1139/V07-125.

(16) Lukeman, M.; Wan, P. *J. Am. Chem. Soc.* **2002**, *124* (32), 9458. doi:10.1021/ja0267831. PMID:12167041.

(17) Lukeman, M.; Wan, P. *J. Am. Chem. Soc.* **2003**, *125* (5), 1164. doi:10.1021/ja029376y. PMID:12553807.

(18) (a) Flegel, M.; Lukeman, M.; Huck, L.; Wan, P. *J. Am. Chem. Soc.* **2004**, *126* (25), 7890. doi:10.1021/ja039078g. PMID:15212537.; (b) Basarić, N.; Wan, P. *J. Org. Chem.* **2006**, *71* (7), 2677. doi:10.1021/jo0524728. PMID:16555820.

(19) Mirrington, R. N.; Feutrill, G. I. *Org. Synth.* **1973**, *53*, 90.

(20) Kalir, A.; Balderman, D. *Org. Synth.* **1981**, *7*, 443.

(21) (a) Lee, J.; Robinson, G. W.; Webb, S. P.; Philips, L. A.; Clark, J. H. *J. Am. Chem. Soc.* **1986**, *108* (21), 6538. doi:10.1021/ja00281a016.; (b) Robinson, G. W. *J. Phys. Chem.* **1991**, *95* (25), 10386. doi:10.1021/j100178a027.; (c) Tolbert, L. M.; Haubrich, J. E. *J. Am. Chem. Soc.* **1994**, *116* (23), 10593. doi:10.1021/ja00102a028.

(22) The signals of the adjacent phenyl ring H atoms where deuteration takes place in **10** and **10a** are overlapping; 500 MHz NMR cannot resolve these signals.

(23) (a) Fischer, M.; Wan, P. *J. Am. Chem. Soc.* **1998**, *120* (11), 2680. doi:10.1021/ja974144y.; (b) Solntsev, K. M.; Huppert, D.; Agmon, N.; Tolbert, L. M. *J. Phys. Chem. A* **2000**, *104* (19), 4658. doi:10.1021/jp994454y.; (c) Tolbert, L. M.; Solntsev, K. M. *Acc. Chem. Res.* **2002**, *35* (1), 19. doi:10.1021/ar990109f. PMID:11790085.; (d) Agmon, N. *J. Phys. Chem. A* **2005**, *109* (1), 13. doi:10.1021/jp047465m. PMID:16839085.

(24) Montalti, M.; Credi, A.; Prodi, L.; Gandolfi, M. T. *Handbook of Photochemistry;* CRC Taylor and Francis: Boca Raton, 2006.

(25) Townsend, R.; Schulman, S. G. *Chim. Oggi* **1992**, *10*, 49.

(26) (a) Gampp, H.; Maeder, M.; Meyer, C. J.; Zuberbühler, A. D. *Talanta* **1985**, *32* (2), 95. doi:10.1016/0039-9140(85)80035-7. PMID:18963802.; (b) Grampp, H.; Maeder, M.; Meyer, C. J.; Zuberbühler, A. D. *Talanta* **1985**, *32*, 257; (c) Gampp, H.; Maeder, M.; Meyer, C. J.; Zuberbühler, A. D. *Talanta* **1985**, *32* (12), 1133. doi:10.1016/0039-9140(85)80238-1. PMID:18963968.

(27) (a) Johnston, L. J.; Schepp, N. P. *J. Am. Chem. Soc.* **1993**, *115* (15), 6564. doi:10.1021/ja00068a013.; (b) Johnston, L. J.; Schepp, N. P. *Pure Appl. Chem.* **1995**, *67* (1), 71. doi:10.1351/pac199567010071.

(28) (a) McClelland, R. A.; Chan, C.; Cozens, F.; Modro, A.; Steenken, S. *Angew. Chem. Int. Ed. Engl.* **1991**, *30* (10), 1337. doi:10.1002/anie.199113371.; (b) Cozens, F. L.; Kanagasabapathy, V. M.; McClelland, R. A.; Steenken, S. *Can. J. Chem.* **1999**, *77* (12), 2069. doi:10.1139/cjc-77-12-2069.

(29) Calculated for the gas phase by B3LYP-6–31g calculation: Frisch, M. J.; Trucks, G. W.; Schlegel, H. B.; Scuseria, G. E.; Robb, M. A.; Cheeseman, J. R.; Zakrzewski, V. G.; Montgomery, J. A., Jr.; Stratmann, R. E.; Burant, J. C.; Dapprich, S.; Millam, J. M.; Daniels, A. D.; Kudin, K. N.; Strain, M. C.; Farkas, O.; Tomasi, J.; Barone, V.; Cossi, M.; Cammi, R.; Mennucci, B.; Pomelli, C.; Adamo, C.; Clifford, S.; Ochterski, J.; Petersson, G. A.; Ayala, P. Y.; Cui, Q.;

Morokuma, K.; Salvador, P.; Dannenberg, J. J.; Malick, D. K.; Rabuck, A. D.; Raghavachari, K.; Foresman, J. B.; Cioslowski, J.; Ortiz, J. V.; Baboul, A. G.; Stefanov, B. B.; Liu, G.; Liashenko, A.; Piskorz, P.; Komaromi, I.; Gomperts, R.; Martin, R. L.; Fox, D. J.; Keith, T.; Al-Laham, M. A.; Peng, C. Y.; Nanayakkara, A.; Challacombe, M.; Gill, P. M. W.; Johnson, B.; Chen, W.; Wong, M. W.; Andres, J. L.; Gonzalez, C.; Head-Gordon, M.; Replogle, E. S.; Pople, J. A. *Gaussian 98;* Gaussian, Inc.: Pittsburgh, PA; 2001.

(30) (a) Leroux, F. R.; Bonnafoux, L.; Heiss, C.; Colobert, F.; Lanfranchi, D. A. *Adv. Synth. Catal.* **2007**, *349* (17-18), 2705. doi:10.1002/adsc.200700211.; (b) Han, P.; Zhang, H.; Qiu, X.; Ji, X.; Gao, L. *J. Mol. Catal. Chem.* **2008**, *295* (1–2), 57. doi:10.1016/j.molcata.2008.08.016.; (c) Dong, C.-G.; Liu, T.-P.; Hu, Q.-S. *Synlett* **2009**, *7*, 1081.

(31) Tasaka, A; Kaku, T.; Kusaka, M. 1-Substituted Phenyl-1-(1*H*-imidazol-4-yl) Alcohols, Process for Producing the Same and Use Thereof. Int. Patent WO 2001/030764, May 3, 2001 [in Japanese].

(32) (a) Arai, N.; Narasaka, K. *Bull. Chem. Soc. Jpn.* **1995**, *68* (6), 1707. doi:10.1246/bcsj.68.1707.; (b) Ishikawa, S.; Manabe, K. *Chem. Lett.* **2007**, *36* (11), 1302. doi:10.1246/cl.2007.1302.

(33) Wang, B.; Li, M.; Xu, S.; Song, H.; Wang, B. *J. Org. Chem.* **2006**, *71* (21), 8291. doi:10.1021/jo061415r. PMID: 17025329.

Can. J. Chem. Downloaded from www.nrcresearchpress.com by University of Electronic and Science Techonology of China on 09/18/12
For personal use only.

A computational study of the fluctional behaviour of group 14 substituted *ortho*-semiquinone radicals

K.U. Ingold and Gino A. DiLabio

Abstract: The dynamics of the 1,4-migration of some *O*-substituted 3,5-di-*tert*-butyl-*ortho*-semiquinone radicals have been calculated by density-functional theory (DFT). There is very good agreement in the rate constant and Arrhenius parameters between these calculations and experimental values for migration of H, D, and the Me_3Si group. For the Me_3Sn group, the calculations indicate an incredibly fast migration ($k^{293K} = 2.0 \times 10^{12}$ s^{-1}), a result that is consistent with experimental data ($k^{293K} > 10^9$ s^{-1}). Other *O*-substituents examined by DFT and compared with experimental data were H_3C and Me_2ClSn.

Key words: semiquinone radicals, group migration, group-coupled electron transfer, kinetics, density functional theory.

Résumé : Faisant appel à la théorie de la fonctionnelle de la densité (TFD), on a calculé la dynamique de la migration-1,4 de quelques radicaux 3,5-di-*tert*-butyl-*ortho*-semiquinones *O*-substituées. Il existe un très bon accord entre les constantes de vitesse et les paramètres d'Arrhenius calculées et les valeurs expérimentales pour la migration de H, D et du groupe Me_3Si. Pour le groupe Me_3Sn, les calculs prédisent une vitesse de migration incroyablement rapide ($k^{293K} = 2{,}0 \times 10^{12}$ s^{-1}), une valeur qui est en accord avec les données expérimentales ($k^{293K} > 10^9$ s^{-1}). Les autres *O*-substituants examinés par la TFD et comparés avec des données expérimentales sont le H_3C et Me_2ClSn.

Mots-clés : radicaux semiquinones, migration de groupe, transfert d'électron couplé à un groupe, cinétique, théorie de la fonctionnelle de la densité.

[Traduit par la Rédaction]

An anomaly in the electron paramagnetic resonance (EPR) spectra of tri-organo group 14 peroxyl radicals, $R_3XOO^{\bullet}$, recently drew our attention.[1] Briefly, the *g*-values for this family of radicals are rather similar (increasing from 2.015 for X = C, through 2.024 for X = Sn, to 2.034 for X = Pb), which implies that they all have rather similar structures. However, their ^{17}O hyperfine splittings (hfs) appeared inconsistent with similar structures. For X = C, Si, and Ge, the two oxygen atoms are magnetically inequivalent, with the outer ^{17}O hfs being larger than the inner ^{17}O hfs (outer/inner ^{17}O hfs ratios 1.33 (C), 1.74 (Si), 1.67 (Ge)), which implies an $R_3X–O–O^{\bullet}$ structure for these peroxyls. However, for X = Sn the two oxygen atoms had been reported[2] to be magnetically equivalent.[3] This led to the suggestion that trialkyltin peroxyl radicals have "a penta-coordinate, trigonal bipyramidal structure … in which the vacant Sn 5d orbitals are used to form a dative bond with the lone pair of electrons on the terminal oxygen" of the peroxy function, structure ***A***.[2] Since this appeared unlikely in view of the similarities in the *g*-values of the group 14 peroxyls, we hypothesized that $R_3SnOO^{\bullet}$ radicals had a similar structure, with the magnetically equivalent oxygen atoms arising from a fast (on the EPR time scale, i.e., > ~10^7 s^{-1}) 1,2-shift of the R_3Sn group, reaction 1. Density-functional theory (DFT) calculations supported this hypothesis, giving inequivalent oxygen atoms (outer/inner ^{17}O hfs ratio = 1.47 (Sn)), with $k_1 = 5 \times 10^8$ s^{-1} at the experimental temperature of ~200 K.[1]

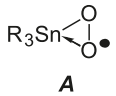

A

[1]

Since the computed rate constant for reaction 1 could not be checked against experimental data, we searched for analogous reactions for which such data were available and settled on the 1,4-shift of some trisubstituted group 14 moieties between the two oxygen atoms in 3,6-di-*tert*-butyl-*ortho*-semiquinone radicals, reaction 2.[4]

Received 2 May 2010. Accepted 11 June 2010. Published on the NRC Research Press Web site at canjchem.nrc.ca on 27 January 2011.

This article is part of a Special Issue dedicated to Professor J. C. Scaiano.

K.U. Ingold. National Research Council, 100 Sussex Drive, Ottawa, ON K1A 0R6, Canada.
G.A. DiLabio.[1] National Institute for Nanotechnology, National Research Council, 11421 Saskatchewan Drive, Edmonton, AB T6G 2M9, Canada.

[1]Corresponding author (e-mail: Gino.DiLabio@nrc.ca).

Can. J. Chem. Downloaded from www.nrcresearchpress.com by University of Electronic and Science Techonology of China on 09/18/12
For personal use only.

Can. J. Chem. Downloaded from www.nrcresearchpress.com by University of Electronic and Science Techonology of China on 09/18/12
For personal use only.

[2] 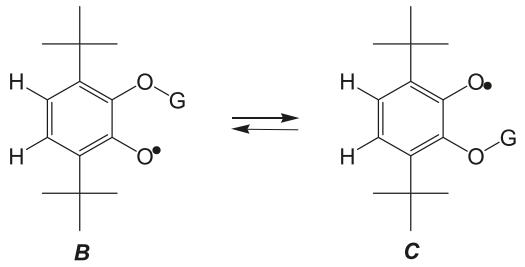

B ***C***

In these radicals, the two *tert*-butyl substituents serve three practical functions: (1) they simplify the EPR spectra to splittings only by the two aromatic hydrogen atoms (and **G**), (2) they ensure that the group, **G**, points towards the O• moiety (rather than away), and (3) they increase the persistence of the radicals, making the signals more intense and easier to measure than would be the case for the unsubstituted radicals. These two substituents probably cause some acceleration in the rates of reaction 2 relative to those of similar reactions in *ortho*-semiquinones that lack these bulky groups.

For **G** = Me_3Sn, reaction 2 has been reported to be so rapid that its rate constant could not be measured by EPR line-broadening effects even at 183 K, the lowest temperature employed[5] (a lower limit of 10^9 s^{-1} for this rate constant was later estimated at 293 K[6]). The possibility that the absence of line broadening effects with **G** = Me_3Sn was due to the formation of a symmetric bridged structure, ***D***, was considered improbable for two very good reasons[6]: (1) ***D*** would have considerable spin density on the tin and cause very significant hfs by the ^{117}Sn and ^{119}Sn isotopes, but these hfs were small (12.8 and 13.3 G, respectively)[6]; and (2) for **G** = Me_3Sn, the two ring protons give a 3.6 G triplet, indicating that they are magnetically equivalent. The 3.6 G hfs for this triplet was essentially identical to the hfs of the two ring protons in radicals with **G** = Me_2SnCl[5] and **G** = Me_3Si[6] at temperatures where these groups were migrating rapidly (on the EPR time scale) between the two oxygen atoms, namely 3.6 G[5] (3.7 G)[7] and ~3.9 G[6], respectively. For these last two **G**, the two aromatic hydrogen atoms become magnetically inequivalent at low temperatures, transforming into doublets of doublets: 5.2 and 2.6 G[5] (5.0 and 2.5 G)[7] for **G** = Me_2SnCl, and 8.4 and 0.62 G[6] for **G** = Me_3Si. For the tin-centered **G**, the earlier observations and conclusions have been confirmed by Davies and Hawari,[7] who greatly expanded the number of such tin-containing semiquinone radicals and who also examined the migration dynamics for **G** = Me_2PbCl.[8,9]

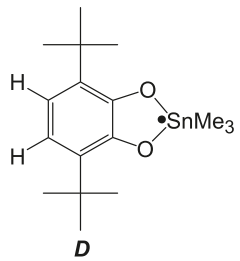

D

Values of k_2 and the Arrhenius parameters for reaction 2 have been estimated from EPR line-broadening effects and reported for **G** = Me_2SnCl[5,7] and Me_3Si[6] (see Table 1). The 1,4-shift for **G** = H_3C was too slow to measure.[6] It was concluded that the coordinative unsaturation of tin and silicon facilitates their coordination with a lone pair on the phenoxyl oxygen atom,[10,11] which lowers the barrier for group transfer.[6] It was suggested that Me_2SnCl migrates more slowly than Me_3Sn because the outer electrons of the chlorine interact with the tin d orbitals, reducing the coordinative unsaturation of the tin atom.[6] It is the dynamics of reaction 2 with **G** = Me_2SnCl and **G** = Me_3Si that we hoped to match by DFT computations to further support our hypothesis[1] that an $R_3SnOO^•$ radical has 2 magnetically equivalent oxygen atoms[2] because of a rapid 1,2-shift of the R_3Sn group.

Since line-broadening effects have also been employed to determine the values of k_2 and the Arrhenius parameters for **G** = H[12] and **G** = D[12] (see Table 1), our calculations were extended to cover these two *ortho*-semiquinones.[18–21] Before we describe our computational results, it is important to recognize that there are "oddities" in the reported Arrhenius parameters listed in Table 1 that probably arise from the quite limited temperature range available in EPR line-broadening kinetic measurements. That is, chemical thermodynamics[22] teaches us to "expect" an Arrhenius pre-exponential factor (A) for reaction 2 with **G** = H and **G** = D of ~$10^{13–14}$ s^{-1}. The same value, or possibly a slightly lower value (~$10^{12.5–13.5}$ s^{-1}), should be expected for **G** = Me_2SnCl and **G** = Me_3Si, implying that the experimental values for the former group[5–7] may have been slightly overestimated. The experimental pre-exponential factors for **G** = H and **G** = D are more than one log unit lower than "expected". This suggests that quantum mechanical tunneling may be significant for both H and D transfers at the temperatures investigated, an idea that is supported by the slightly higher value of $\log A_2$ for **G** = D than for **G** = H (see Table 1).

It is also important to keep in mind that theory is not yet capable of predicting Arrhenius parameters with high fidelity to experimental values. Although significant improvements in theoretical methods continue unabated, the exponential sensitivity of kinetic parameters to computed energies makes this a particularly challenging task for computational chemistry. For anything but the smallest systems, a better than order-of-magnitude accuracy from theory cannot (yet) be expected.

We begin with the intramolecular H and D transfer processes. (Analogous intramolecular transfers in diamagnetic systems have been studied by microwave and infrared spectroscopy.[23]) Our calculated values for $\log(A/s^{-1})$ for ***B*→*C*** with **G** = H and **G** = D are about 12.6 and are therefore in reasonable accordance with our "thermochemical expectations", being roughly one log unit larger than the reported values. Computed rate constants, with tunneling corrections obtained using an Eckart approach,[24] are in excellent agreement with experimental values. The computed kinetic isotope effect (k_H/k_D) of 10 with tunneling (4.3 without tunneling) is in very good agreement with the experimental value of 10.7.

In addition to quantum mechanical tunneling, the mechanism for the hydrogen and deuterium exchange must also involve intramolecular proton-coupled electron transfer (PCET).[25] Figure 1*a* shows a side view of ***B*** (**G** = H) showing relevant orbitals. The minimum energy structure of ***B*** has an intramolecular hydrogen bond between the OH group

Can. J. Chem. Downloaded from www.nrcresearchpress.com by University of Electronic and Science Techonology of China on 09/18/12
For personal use only.

Table 1. Experimental and calculated[13–17] rate constants for reaction 2 at 293 K and Arrhenius parameters (E_a in kcal/mol).

	Experimental			Calculated		
G	k_2 (s^{-1})	log(A/s^{-1})	E_a	k_2 (s^{-1})	log(A/s^{-1})	E_a
H[a,b]	3.2×10^9	11.5	2.9	2.0×10^{9}[c]	12.7	2.0[d]
D[a,e]	0.3×10^9	11.8	4.5	0.2×10^{9}[f]	12.6	2.5[g]
H_3C[h,i]	$<10^4$			1.0×10^{-16}	13.1	39.6
Me_3Si[h,j]	2.5×10^6	13.2	9.3	5.9×10^5	12.4	9.0
Me_2SnCl[h,k]	2.5×10^6	14.4	10.7	6.9×10^7	12.8	5.3
Me_2SnCl[l]	2.2×10^6	14.1	10.4	6.9×10^7	12.8	5.3
Me_3Sn[h,m]	$>10^9$			2.0×10^{12}	12.8	0.7

[a]Experimental data in heptane, ref. 17.
[b]273–393 K.
[c]Without tunneling: 2.3×10^8 s^{-1}.
[d]Without tunneling: 5.8 kcal/mol.
[e]293–393 K.
[f]Without tunneling: 5.3×10^7 s^{-1}.
[g]Without tunneling: 6.6 kcal/mol.
[h]Experimental data in toluene, ref. 6.
[i]263–473 K.
[j]273–333 K.
[k]163–223 K.
[l]Experimental data in xylene, ref. 7. 208–404 K. This reference also includes the following kinetic data: **G**; $k_2/10^6$ s^{-1}; log(A/s^{-1}); E_a (kcal/mol): Bu_2SnCl, 0.47, 13.6, 10.6; Ph_2SnCl, 0.49, 14.4, 11.7; $(MeCO_2)_3Sn$, 25, 14.1, 8.9; Me_2PbCl, 4.6, 11.7, 6.7.
[m]183–403 K.

Fig. 1. (*a*) Simplified illustration of the orbitals of the minimum energy structure of ***B*** (di-*tert*-butyl groups omitted). The lone-pair orbitals are shaded gray and singly occupied orbitals are white. The intramolecular hydrogen bond is indicated by the red dashed line, which also indicates the path transited by the proton during the exchange reaction. (*b*) Top-down and (*c*) tilted views of the hydrogen exchange transition state (TS) of an unsubstituted semiquinone with its singly occupied molecular orbital (SOMO). The SOMO is π-type and delocalized across the O···H···O centres as well as through the ring. The colours of the orbital represent its relative phases. (*d*) Side view of a ball-and-stick model of the hydrogen exchange TS of semiquinone. The black arrow indicates the direction of transfer of a proton, the path for which lies in the plane of the ring. The blue arrow shows one possible route of the transferring electron, along a path that is parallel to the path of the proton but out of the plane of the ring. The green, curved arrow shows a second route for the electron, along a path through the ring orbitals and also out of the plane of the ring.

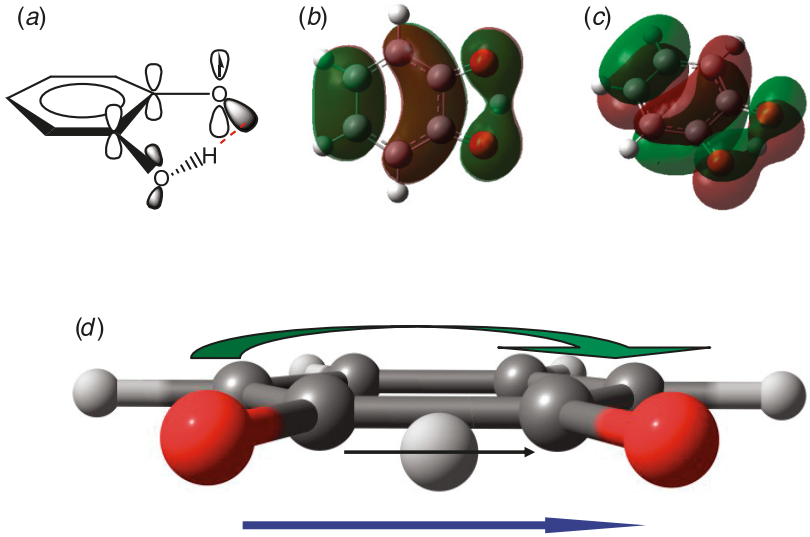

and the lone pair of electrons on the (formal) O• centre. This hydrogen bond lies in the plane of the ring. Hydrogen exchange cannot occur easily via a hydrogen atom transfer (i.e., a proton with its electron) because the lone pair on the "receiving" oxygen atom cannot accept an extra electron. Instead, exchange occurs through a transition state involving a proton transfer from the OH group to the O• across the hydrogen bond. Concurrent with proton transfer, an electron

Can. J. Chem. Downloaded from www.nrcresearchpress.com by University of Electronic and Science Techonology of China on 09/18/12
For personal use only.

Fig. 2. Transition state structures for reaction 2 with (*a*) **G** = CH_3, R(H_3C–O) = 2.09 Å, (*b*) **G** = Me_3Si, R(Me_3Si–O) = 1.98 Å, and (*c*) **G** = Me_2SnCl, R(Me_2ClSn–O) = 2.24 Å.

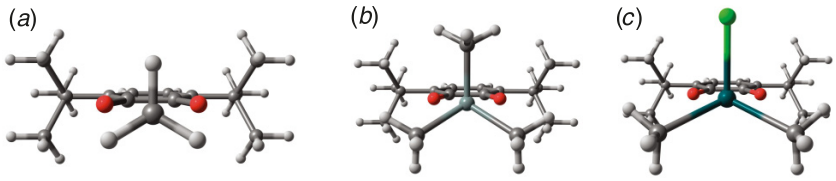

Fig. 3. (*a*) The minimum energy and (*b*) transition state (R(Me_3Sn–O) = 2.27 Å) structures for ***B*** with **G** = Me_3Sn.

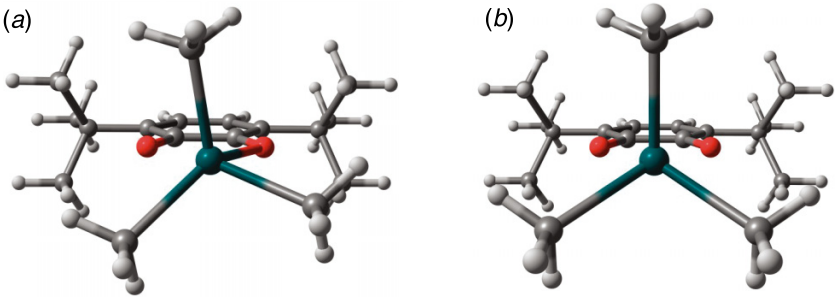

is transferred via the π-type bond involving the O···H···O atoms, which is perpendicular to the ring. This is clearly seen in the singly occupied molecular orbital (SOMO) of the hydrogen exchange transition state (TS) illustrated in Figs. 1*b* and 1*c*. The conjugative delocalization of the O orbitals into the ring provides a second "route" for the electron to take in the PCET process and this is also demonstrated by the SOMO shown in Figs. 1*b* and 1*c*. The path taken by the proton and possible paths used for transferring the accompanying electron are illustrated in Fig. 1*d*. Theory has previously implicated multiple paths for transferring the electron in PCET processes that involve the following bimolecular identity reactions: oxime + iminoxyl,[26] toluene + benzyl, and phenol + phenoxyl.[27]

In principle, processes similar to PCET as described for **G** = H and D in reaction 2 should also occur for other **G**, provided that the central atom in **G** is able to undergo facile valence shell expansion. If this is the case, we may generalize the PCET mechanism to "GCET", or group-coupled electron transfer. It is clear that for **G** = CH_3, GCET is not able to occur. This is simply because pentavalent carbon is energetically highly disfavoured (i.e., there is no energetically low-lying empty orbital on CH_3). The calculations indicate that the O–CH_3 bond would need to lengthen by 0.65 Å to reach the TS structure. Therefore, the barrier to group transfer is very high and results in a very low rate constant. A picture of the TS associated with reaction 2 for **G** = CH_3 is shown in Fig. 2*a*.

Additional calculations indicate that the barrier associated with hydrogen atom transfer from **G** = CH_3 to the (formal) O• is much more likely than group transfer. The activation barrier for this endothermic process is predicted by theory to be about 25.5 kcal/mol.

The calculated kinetic parameters with **G** = Me_3Si are in very gratifying agreement with experimental values. To reach the TS (see Fig. 2*b*), the O–$SiMe_3$ bond must lengthen by approximately 0.25 Å. This results in a much lower barrier height and larger rate constant for transfer with **G** = Me_3Si than for transfer with **G** = CH_3. A detailed examination of the reaction coordinate reveals that the TS can be reached by rotation of the $SiMe_3$ group about the Si–O bond. The resultant steric repulsion between the methyl groups on **G** and the neighbouring *tert*-butyl substituent is then sufficiently high that the Me_3Si–O bond is lengthened to the TS value.

For **G** = Me_2SnCl, the predictions made by theory are in somewhat poorer agreement with experimental data. However, the calculated log(A/s^{-1}) is in line with thermochemical expectations, vide supra. Calculations predict a rather small activation energy of 5.3 kcal/mol, which contributes to the large rate constant. The minimum energy structure of ***B*** with **G** = Me_2SnCl has the chlorine atom pointed toward the adjacent *tert*-butyl group. To reach the TS (Fig. 2*c*), the Me_2(Cl)Sn group must rotate by about 90° while the Me_2(Cl)Sn–O bond must lengthen by about 0.09 Å.

The case of **G** = Me_3Sn is particularly interesting. The calculations indicate that ***B*** (**G** = Me_3Sn) has an asymmetric energy minimum wherein there is no Me–Sn bond exactly perpendicular to the plane of the aromatic ring (Fig. 3*a*). This minimum energy structure produces all positive vibration frequencies, verifying that it is indeed a minimum on the potential energy surface. Similarly, the TS structure, shown in Fig. 3*b*, was verified as such with the calculations giving one imaginary frequency associated with group transfer (reaction 2). The magnitude of the imaginary frequency is only 37.8 cm^{-1}, indicating that reaching the TS requires very little energy. In fact, the Me_3Sn–O bond length in the minimum energy structure only needs to be lengthened by about 0.03 Å to reach its TS length. Vibrational analyses and potential energy surface scans show that the TS can be reached from the minimum energy structure by a slight rotation of the Me_3Sn group about the Sn–O bond, as is evident upon examination of Fig. 3. Inclusion of thermal corrections (293 K) to the electronic energies results in a predicted E_a of 0.70 kcal/mol. This calculated E_a value is too small to be reliable but it does imply that transfer of the **G** = Me_3Sn group is extremely facile, in accordance with the experimental observations.[28,29] Moreover, theory indicates that the

Can. J. Chem. Downloaded from www.nrcresearchpress.com by University of Electronic and Science Techonology of China on 09/18/12
For personal use only.

minimum energy structure should be represented by ***B*** and not by ***D***, which is also in accordance with the conclusions reached by Prokof'ev et al.[6] on the basis of EPR spectral evidence, vide supra.

The present calculations are in sufficiently good agreement with experimental data that it is fairly safe to conclude that we have been employing appropriate methodology to study these kinds of dynamic processes and they therefore provide additional support for our earlier conclusion[1] that the R_3Sn group in $R_3SnOO^{\bullet}$ radicals undergoes such a fast 1,2-shift that the two oxygen atoms are magnetically equivalent on the EPR time scale.

Acknowledgements

We thank Prof. A. G. Davies for sharing his extensive knowledge and for his continued advice and encouragement and Dr. Bun Chan (University of Sydney) for helpful discussions. We also thank P. Boulanger (University of Alberta) for computational resources.

References

(1) Ingold, K. U.; DiLabio, G. A. *Can. J. Chem.* **2010**, *88* (11), 1053. doi:10.1139/V10-071.

(2) Howard, J. A.; Tait, J. C. *J. Am. Chem. Soc.* **1977**, *99* (25), 8349. doi:10.1021/ja00467a053.

(3) Experimental ^{17}O hfs have not been reported for $R_3PbOO^{\bullet}$. Calculated values are given in ref. 1.

(4) For reviews of these and analogous reactions, see: (a) Bubnov, N. N.; Solodovnikov, S. P.; Prokof'ev, A. I.; Kabachnik, M. I. *Russ. Chem. Rev.* **1978**, *47* (6), 549. doi:10.1070/RC1978v047n06ABEH002238.; (b) Prokof'ev, A. I.; Prokof'eva, T. I.; Belostotskaya, I. S.; Burnov, N. N.; Solodnikov, S. P.; Ershov, V. V.; Kabachnik, M. I. *Tetrahedron* **1979**, *35* (20), 2471. doi:10.1016/S0040-4020(01)93765-2. For a review of solvent viscosity effects on the rates of these fast unimolecular reactions, see: (c) Rakhimov, R. R.; Prokof'ev, A. I.; Lebedev, Ya. S. *Russ. Chem. Rev.* **1993**, *62* (6), 509. doi:10.1070/RC1993v062n06ABEH000030.

(5) Kukes, S. G.; Prokof'ev, A. I.; Bubnov, N. N.; Solodovnikov, S. P.; Korniets, E. D.; Kravtsov, D. N.; Kabachnik, M. I. *Dokl. Chem.* **1976**, *229*, 519.

(6) Prokof'ev, A. I.; Prokof'eva, T. I.; Bubnov, N. N.; Solodovnikov, S. P.; Belostotskaya, I. S.; Ershov, V. V.; Kabachnik, M. I. *Dokl. Chem.* **1978**, *239*, 165.

(7) Davies, A. G.; Hawari, J. A.-A. *J. Organomet. Chem.* **1983**, *251*, 53. doi:10.1016/0022-328X(83)80243-5.

(8) Similar results and conclusions have been reported for adducts of tri-substituted group 14 radicals with other 1,2-dicarbonyl compounds.[9]

(9) See for example: (a) Alberti, A.; Hudson, A. *Chem. Phys. Lett.* **1977**, *48* (2), 331. doi:10.1016/0009-2614(77)80326-6.; (b) Alberti, A.; Hudson, A. *J. Chem. Soc., Perkin Trans. 2* **1978**, (10): 1098. doi:10.1039/p29780001098.; (c) Razuvaev, G. A.; Tsarjapkin, V. A.; Gorbunova, L. V.; Cherkasov, V. K.; Abakumov, G. A.; Klimov, E. S. *J. Organomet. Chem.* **1979**, *174* (1), 47. doi:10.1016/S0022-328X(00)96161-8.; (d) Davies, A. G.; Hawari, J. A.-A. *J. Organomet. Chem.* **1980**, *201* (1), 221. doi:10.1016/S0022-328X(00)92578-6.; (e) Barker, P. J.; Davies, A. G.; Hawari, J. A.-A.; Tse, M.-W. *J. Chem. Soc. Perkin Trans. 2*, **1980**, 1488. doi:10.1039/P29800001488.; (f) Davies, A. G.; Hawari, J. A.-A.; Gaffney, C.; Harrison, P. G. *J. Chem. Soc. Perkin Trans. 2*, **1982**, 631. doi:10.1039/P2980000625.

(10) In this connection, it has recently been demonstrated that oxygen-centered radical attack on alkyl and aryl borane substrates does not occur by a traditional S_H2 process.[11] Instead, it involves a nucleophilic attack of an oxygen lone pair on the empty boron p orbital. The unpaired electron on the oxygen is not directly involved, but the boron–ligand bond aligned with the SOMO cleaves and the ligand leaves promptly. The mechanism was described as a nucleophilic homolytic substitution at boron.

(11) Carra, C.; Scaiano, J. C. *Eur. J. Org. Chem.* **2008**, *2008* (26), 4454. doi:10.1002/ejoc.200800187.

(12) Prokof'ev, A. I.; Bubnov, N. N.; Solodnikov, S. P.; Kabachnik, M. I. *Tetrahedron Lett.* **1973**, *14* (27), 2479. doi:10.1016/S0040-4039(01)96183-0.

(13) Calculations were performed using B3[14]LYP[15]/6-311+G(d,p) as implemented in ref. 16. For radicals containing Sn, we used the averaged relativistic effective potentials of LaJohn et al.[17] with the accompanying basis set, which was used uncontracted.

(14) Becke, A. D. *J. Chem. Phys.* **1993**, *98*, 5648. doi:10.1063/1.464913.

(15) Lee, C.; Yang, W.; Parr, R. G. *Phys. Rev. B* **1988**, *37*, 785. doi:10.1103/PhysRevB.37.785.

(16) Frisch, M. J.; Trucks, G. W.; Schlegel, H. B.; Scuseria, G. E.; Robb, M. A.; Cheeseman, J. R.; Montgomery, J. A., Jr.; Vreven, T.; Kudin, K. N.; Burant, J. C.; Millam, J. M.; Iyengar, S. S.; Tomasi, J.; Barone, V.; Mennucci, B.; Cossi, M.; Scalmani, G.; Rega, N.; Petersson, G. A.; Nakatsuji, H.; Hada, M.; Ehara, M.; Toyota, K.; Fukuda, R.; Hasegawa, J.; Ishida, M.; Nakajima, T.; Honda, Y.; Kitao, O.; Nakai, H.; Klene, M.; Li, X.; Knox, J. E.; Hratchian, H. P.; Cross, J. B.; Adamo, C.; Jaramillo, J.; Gomperts, R.; Stratmann, R. E.; Yazyev, O.; Austin, A. J.; Cammi, R.; Pomelli, C.; Ochterski, J. W.; Ayala, P. Y.; Morokuma, K.; Voth, G. A.; Salvador, P.; Dannenberg, J. J.; Zakrzewski, V. G.; Dapprich, S.; Daniels, A. D.; Strain, M. C.; Farkas, O.; Malick, D. K.; Rabuck, A. D.; Raghavachari, K.; Foresman, J. B.; Ortiz, J. V.; Cui, Q.; Baboul, A. G.; Clifford, S.; Cioslowski, J.; Stefanov, B. B.; Liu, G.; Liashenko, A.; Piskorz, P.; Komaromi, I.; Martin, R. L.; Fox, D. J.; Keith, T.; Al-Laham, M. A.; Peng, C. Y.; Nanayakkara, A.; Challacombe, M.; Gill, P. M. W.; Johnson, B.; Chen, W.; Wong, M. W.; Gonzalez, C.; Pople, J. A. *Gaussian 03*, revision D.01; Gaussian, Inc.: Pittsburgh, PA, 2004.

(17) LaJohn, L. A.; Christiansen, P. A.; Ross, R. B.; Atashroo, T.; Ermler, W. C. *J. Chem. Phys.* **1987**, *87* (5), 2812. doi:10.1063/1.453069.

(18) It has been reported that "solvents capable of forming hydrogen bonds" retard the rate of reaction 2 for **G** = H.[4a] This is to be expected because phenols containing intramolecular H bonds are capable of forming bifurcated intra/intermolecular H bonds,[19] which reduces the rates of H-atom abstraction[20] just as intermolecular H bonding reduces the rates of abstraction from simple phenols.[21] Fortunately, the experiments in question[4a] were done in heptane, which is neither an H-bond donor nor acceptor, so the kinetic measurements should be directly comparable with the computed dynamics.

(19) Litwinienko, G.; DiLabio, G. A.; Mulder, P.; Korth, H.-G.; Ingold, K. U. *J. Chem. Phys. A* **2009**, *113* (22), 6275. doi:10.1021/jp900876q.

(20) de Heer, M. I.; Mulder, P.; Korth, H.-G.; Ingold, K. U.;

Lusztyk, J. *J. Am. Chem. Soc.* **2000**, *122* (10), 2355. doi:10.1021/ja9937674.
(21) Snelgrove, D. W.; Lusztyk, J.; Banks, J. T.; Mulder, P.; Ingold, K. U. *J. Am. Chem. Soc.* **2001**, *123* (3), 469. doi:10.1021/ja002301e.
(22) Benson, S. W. *Thermochemical Kinetics*; Wiley: New York, 1976; 2nd ed.
(23) For a summary, see: Wilson, E. B.; Smith, Z. *Acc. Chem. Res.* **1987**, *20* (7), 257. doi:10.1021/ar00139a004.
(24) Eckart, C. *Phys. Rev.* **1930**, *35*, 1303. doi:10.1103/PhysRev.35.1303.
(25) Mayer, J. M.; Hrovat, D. A.; Thomas, J. L.; Borden, W. T. *J. Am. Chem. Soc.* **2002**, *124* (37), 11142. doi:10.1021/ja012732c. PMID:12224962.
(26) DiLabio, G. A.; Ingold, K. U. *J. Am. Chem. Soc.* **2005**, *127* (18), 6693. doi:10.1021/ja0500409. PMID:15869291.
(27) DiLabio, G. A.; Johnson, E. R. *J. Am. Chem. Soc.* **2007**, *129* (19), 6199. doi:10.1021/ja068090g. PMID:17444643.
(28) This particular reaction could be referred to as a stannylium[29] coupled electron transfer.
(29) Lambert, J. B. "Stable stannylium cations in condensed phases". In *Tin Chemistry, Fundamentals, Frontiers, and Applications*; Davies, A. G., Gielen, M., Pannell, K. H., Kiekink, E. R. T., Eds.; Wiley: Chichester, UK, 2009; pp 152–159.

Can. J. Chem. Downloaded from www.nrcresearchpress.com by University of Electronic and Science Techonology of China on 09/18/12
For personal use only.

Kinetic and mechanistic studies of the reactions of diarylgermylenes and tetraaryldigermenes with carbon tetrachloride

Lawrence A. Huck and William J. Leigh

Can. J. Chem. Downloaded from www.nrcresearchpress.com by University of Electronic and Science Techonology of China on 09/18/12
For personal use only.

Abstract: The mechanisms of the reactions of diphenylgermylene ($GePh_2$) with CCl_4 in hydrocarbon solvents and in THF solution have been studied, employing 3,4-dimethyl-1,1-diphenylgermacyclopent-3-ene (**6a**) and 1,1-diphenylgermacyclobutane (**17**) as photochemical precursors to $GePh_2$. In hydrocarbon solvents, the reaction produces Ph_2GeCl_2 (**10**) and $Ph_2Ge(Cl)CCl_3$ (**12**) in a ratio of **10**:**12** $\approx$ 7, along with a variety of other radical-derived products and small amounts of $Ph_2GeH(D)Cl$ (**11**), which is formed partly by reaction of $GePh_2$ with adventitious HCl. The reaction is much cleaner in THF, where **12** is formed as the major product (**10**:**12** $\approx$ 0.8); a similar product distribution is obtained in hexanes containing 0.05 mol/L THF, while **12** is the exclusive product in hexanes containing 3 mmol/L NEt_3. Rate constants for the reactions of CCl_4 with $GePh_2$ and five ring-substituted derivatives were determined by laser flash photolysis, as well as Arrhenius parameters for reaction of the parent ($GePh_2$), in the two solvents. The reactions of $GePh_2$ with CCl_4 and $CHCl_3$ have also been studied in 3-methylpentane solution at 78–90 K. Different reaction mechanisms are clearly operative in hydrocarbon and complexing solvents, but both involve modest charge donation from germanium to the substrate in the transition state for the rate-determining step. For the reaction in hydrocarbon solvents, the data are consistent with inner-sphere electron transfer following or in concert with weak Lewis acid–base complexation. A similar mechanism is proposed for the reaction in THF solution, in competition with a second involving nucleophilic attack of the germylene–THF complex at a chlorine atom of the substrate. Rate constants were also determined for reaction of CCl_4 with the corresponding tetraaryldigermenes at low halocarbon concentrations in hexanes, along with Arrhenius parameters for the parent (Ge_2Ph_4). These reactions also proceed via initial Cl-atom abstraction, based on the identity of the products formed in the reaction of CCl_4 with tetramesityldigermene.

Key words: germylene, halocarbon, free radical, kinetics, abstraction, electron transfer.

Résumé : On a étudié les mécanismes des réactions du diphénylgermylène ($GePh_2$) avec le CCl_4, dans des solvants hydrocarbonés, en utilisant les 3,4-diméthyl-1,1-diphénylgermacyclopent-3-ène (**6a**) et 1,1-diphénylgermacyclobutane (**17**) comme précurseurs photochimiques du $GePh_2$. Dans les solvants hydrocarbonés, la réaction conduit à la formation de Ph_2GeCl_2 (**10**) et de $Ph_2Ge(Cl)CCl_3$ (**12**) dans un rapport **10**:**12** approximativement égal à 7, aux côtés d'une variété d'autres produits dérivés de radicaux et de faibles quantités de $Ph_2GeH(D)Cl$ (**11**) dont la formation résulte en partie d'une réaction adventice avec du HCl. La réaction dans le THF est beaucoup plus propre et elle la formation du produit **12** est majoritaire (**10**:**12** = 0,8); on obtient une distribution de produit semblable dans les hexanes contenant 0,05 mol/L de THF alors que le produit **12** est le produit exclusif dans les hexanes content 3 mmol/L de NEt_3. Les constantes de vitesse des réactions du CCl_4 avec le $GePh_2$ et les dérivés de cycles à cinq chaînons substitués ont été déterminées par photolyse éclair au laser et on a aussi déterminé les paramètres d'Arrhenius de la réaction du germylène parent, $GePh_2$, dans les deux solvants. On a aussi étudié les réactions du $GePh_2$ avec le CCl_4 et le $CHCl_3$, en solution dans le 3-méthylpentane et à des températures allant de 78 à 90 K. Il est clair que divers mécanismes de réaction interviennent dans l'hydrocarbure et les solvants complexants, mais les deux comportent une étape cinétiquement déterminante de l'état de un état de transition qui implique un modeste transfert de charge du germanium vers le substrat. Les paramètres d'Arrhenius pour la réaction du germylène libre dans les hexanes indiquent que l'état de transition est bien structuré mais faiblement lié; les données sont en accord avec un transfert d'électron dans la sphère interne à la suite de, ou de concert avec, une faible complexation acide–base de Lewis. On propose un mécanisme similaire pour la réaction en solution dans le THF; il serait en compétition avec un autre impliquant une attaque nucléophile du complexe germylène–THF au niveau de l'atome de chlore du substrat. On a aussi déterminé les constantes de vitesse pour la réaction du CCl_4 avec les tétraaryldigermènes correspondants à des faibles concentrations d'halocarbones dans les hexanes et on a aussi déterminé les paramètres d'Arrhenius pour le (Ge_2Ph_4) parent. Sur la base de l'identité des produits qui se forment dans la réaction du CCl_4 avec le tétramésityldigermène, ces réactions se produisent aussi par le biais d'un enlèvement initial d'un atome de chlore.

Received 17 May 2010. Accepted 28 July 2010. Published on the NRC Research Press Web site at canjchem.nrc.ca on 31 January 2011.

This article is part of a Special Issue dedicated to Professor J. C. Scaiano.

L.A. Huck and W.J. Leigh.[1] Department of Chemistry and Chemical Biology, McMaster University, 1280 Main Street West, Hamilton ON L8S 4M1, Canada.

[1]Corresponding author (e-mail: leigh@mcmaster.ca).

Mots-clés : germylène, halocarbone, radical libre, cinétique, enlèvement, transfert d'électron.

[Traduit par la Rédaction]

Can. J. Chem. Downloaded from www.nrcresearchpress.com by University of Electronic and Science Techonology of China on 09/18/12
For personal use only.

Introduction

There has been great interest over the past few decades in the chemistry of silylenes and germylenes, the silicon and germanium analogues of singlet carbenes, respectively. Much of this has been directed toward the synthesis and study of the structures and reactivities of isolable derivatives,[1–7] which owe their stabilities to electronic stabilization and (or) steric protection of the divalent group 14 atom by substituents. The dimerization process that these effects inhibit occurs at rates within a factor of about 10 of the diffusional limit in solution in the cases of simpler "tetrylenes" such as the dimethyl-, diphenyl-, and dimesityl-substituted derivatives.[8–12] These simpler derivatives and the parent dihydrides (SiH_2 and GeH_2) thus require fast time-resolved spectroscopic methods to be studied directly,[13] but they can be expected to provide a more precise definition of the range of chemical behavior inherent to silicon and germanium in their divalent states. They are also key intermediates in many thermal and photochemical reactions of organosilicon[14,15] and –germanium[16,17] compounds and are important ligands in a number of metal-catalyzed processes.[18]

Tetrylenes bearing hydrido or simple alkyl or aryl substituents are voracious electrophiles, reacting exceedingly rapidly with even weak nucleophiles such as alcohols and alkenes.[9,11,13,19–23] The large majority of the reactions these species undergo, particularly those with heteroatom (i.e., O–, N–, S–, etc.) containing substrates, are thought to begin with the formation of a Lewis acid–base complex between the tetrylene and the substrate.[4] Indeed, transient silylene-[9,19,22–25] and germylene-[20,21,25–27] donor complexes have been detected directly in a large number of instances, both in low-temperature matrix experiments and in solution at ambient temperatures by laser flash photolysis methods. Complexation with a nonreactive Lewis base such as THF reduces the reactivity of the tetrylene toward both dimerization and reactions with other substrates that require access to the vacant p orbital on the (ground-state singlet) tetrylene to proceed.[19,28–31] Complexation can also be expected to increase the nucleophilic character of the tetrylene, and hence promote reactions with electrophilic substrates that might be relatively unreactive toward the free species.[30,32–36]

The reactions of silylenes[3–5] and germylenes[4,16] with halocarbons are particularly fascinating, as they proceed in one of two directions depending on the halocarbon: C–X insertion and X-atom abstraction. Singlet carbenes behave similarly.[37,38] Halogen atom abstraction is the main process that occurs with benzyl halides and carbon tetrachloride, whereas C–X insertion predominates with allyl, vinyl, and (in the case of silylenes) aliphatic halides. Again, the reactions are generally thought to proceed via an initially formed tetrylene–halocarbon Lewis acid–base complex, which can then react by concerted insertion into the C–X bond or by homolytic C–X cleavage to form the corresponding singlet radical pair via an electron transfer process (eq. [1]).[3,39] The caged radical pair either couples to generate the formal R′–X insertion product or undergoes cage escape; the resulting halosilyl or halogermyl free radical then abstracts a halogen atom from a second molecule of the halocarbon to form the corresponding dihalosilane or –germane. Interestingly, the reaction of $GeMe_2$ with CCl_4 also proceeds in THF solution, with a rate constant only slightly smaller than that for reaction with the free germylene in hydrocarbon solvents.[30] While product studies were not carried out, it is relevant to note that the reaction of $GeMe_2$ with CCl_4 is known to afford the C–Cl insertion product essentially exclusively in the presence of catalytic amounts of triphenylphosphine.[40] This suggests that the presence of a "spectator" donor opens up yet another mechanistic pathway for reaction of the germylene with this halocarbon.

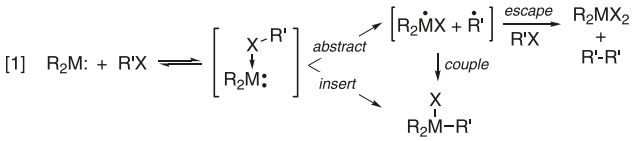

The reactions of halocarbons with disilenes[41,42] and digermenes,[43–45] the M=M doubly bonded dimers of silylenes and germylenes, respectively, also appear to proceed via initial halogen atom abstraction in most known cases. Kira et al.[42] carried out a detailed experimental study of the reactions of a series of three kinetically stable tetrasilyldisilenes (**1**) with CCl_4, $CHCl_3$, and various other chloro- and bromocarbons in hexane solution (eq. [2]), and found the product distributions and rate constants to vary systematically as a function of both the halocarbon and steric bulk in the disilene. Through a combination of kinetic, electron paramagnetic resonance (EPR), and electrochemical studies on these systems, they concluded that the reaction proceeds by simple chlorine atom abstraction to generate the corresponding halodisilanyl and R′ radicals (eq. [3]), which they proposed is promoted by a significant degree of 1,2-biradical character of the Si=Si bond. Mochida et al.[43] reported the major product of the reaction of (transient) tetramethyldigermene (Ge_2Me_4) with CCl_4 to be the corresponding 1,2-dichlorodigermane (**4**), whereas Baines and co-workers[45] isolated the formal Cl–R′ addition product (**5**) from the reaction of the sterically stabilized digermene Ge_2Mes_4 with $CHCl_3$ (eq. [3]). A similar difference in product distribution was also observed by Kira et al.[42] for the reactions of tetrasilyldisilenes **1a** and **1b** with these two halocarbons, CCl_4 being the more reactive of the two by roughly three orders of magnitude. The reactions of several simple disilenes and digermenes with CCl_4 have been studied computationally by Su,[46] the results of which indicate that Cl abstraction is indeed the lowest energy reaction pathway in these systems.

Can. J. Chem. Downloaded from www.nrcresearchpress.com by University of Electronic and Science Techonology of China on 09/18/12
For personal use only.

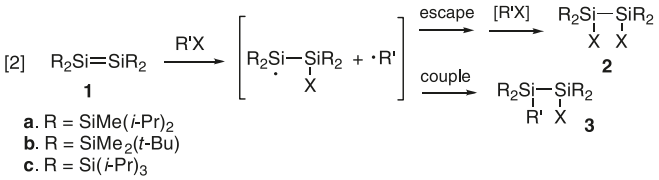

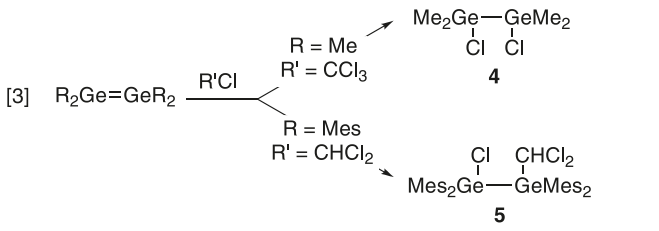

Kinetic studies of the reactions of CCl_4 with Ge_2Me_4,[11,43] Ge_2Et_4,[43] $(GeMePh)_2$,[47] and Ge_2Ph_4[20] in hydrocarbon solvents reveal a ca. 20-fold span in the rate constants, which decrease in the order $k_{Ge_2Et_4} \approx 2k_{Ge_2Me_4} \approx 6k_{GeMePh_2} \approx 20k_{Ge_2Ph_4}$. The trend may be indicative of a modest degree of charge transfer from the Ge=Ge bond to the halocarbon in the transition state for Cl abstraction, as Kira et al.[42] concluded from a kinetic study of the reactions of a series of substituted benzyl chlorides with disilene **1c**.

In the present paper, we report the results of product, kinetic, and low-temperature spectroscopic studies of the reactions of $GePh_2$ and its (digermene) dimer (Ge_2Ph_4) with CCl_4 in hexanes and THF solution, which was carried out with the goal of elucidating the detailed mechanisms of these reactions in both noncomplexing and (for $GePh_2$) complexing solvents. Arrhenius parameters have been determined, and the role of electronic factors in the transition states for the rate-determining steps of these reactions have been assessed through an examination of the effect of polar ring substituents on the absolute rate constants. As in earlier kinetic studies,[27,30,48] we employed the substituted 1,1-diaryl-3,4-dimethylgermacyclopent-3-enes **6a–6f** as photochemical precursors to the corresponding diarylgermylenes (**8a–8f**) and tetraaryldigermenes (**9a–9f**; eq. [4]), each pair of which can be studied in the same experiment. It is not practical to carry out product studies of the digermene reactions using these precursors because formation of the digermene requires dimerization of the significantly more reactive germylene, so tetramesityldigermene (**9g**) has been employed as a model compound. The latter was generated by low-temperature photolysis of hexamesitylcyclotrigermane (**7g**).[49,50]

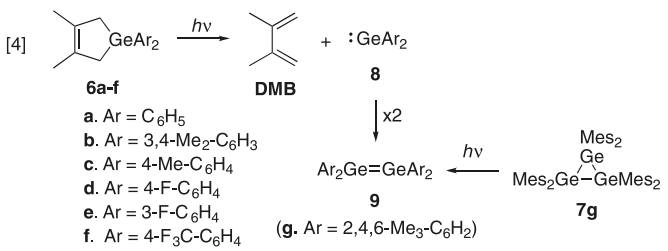

Results

Product studies

Steady-state photolyses of deoxygenated solutions of **6a** (0.02 mol/L) in C_6D_{12} containing varying initial concentrations of CCl_4 (0.02–0.5 mol/L) and hexamethyldisilane (ca. 0.002 mol/L; internal standard) were monitored over the 0%–10% conversion range (in **6a**) by ^1H NMR spectroscopy and GC–MS, which allowed the identification of chlorogermanes **10–12** (eq. [5]), DMB, chlorocyclohexane-d_{11}, chloroform, and trace amounts of hexachloroethane (C_2Cl_6). The yields of DMB and **10–12** were determined relative to consumed **6a** from the slopes of concentration vs time plots, constructed for the five compounds from the NMR integrals. Significant amounts of unidentified products giving rise to resonances in the allylic (δ 3.4–3.7) and aliphatic (δ 1.5–2.2) regions of the NMR spectrum were also detected; their yields relative to the other products increased with increasing photolysis times, consistent with them being derived from (secondary) radical reactions involving (mainly) DMB, whose concentration vs time plots displayed significant downward curvature. Broad baseline absorptions in the aromatic region of the NMR spectra were also observed and became more pronounced with increased photolysis times, consistent with the formation of oligomeric material containing phenyl groups. The yields of these unidentified materials increased with increasing initial CCl_4 concentration, as did the severity of the curvature in the concentration vs time plots for DMB. This suggests that they arise to a large extent from secondary radical reactions resulting from photolysis of CCl_4,[51–53] which absorbs weakly at 254 nm (ε_{254nm} = 0.44 $(mol/L)^{-1}$ cm^{-1} compared with ε_{254nm} = 340 $(mol/L)^{-1}$ cm^{-1} for **6a**). Indeed, H(D)Cl was also detected qualitatively in the photolyzed mixtures in the head space above the solutions. Table 1 lists the yields of **10–12** and DMB (the latter calculated from the initial slopes of the curved plots) that were obtained in the experiments using initial CCl_4 concentrations in the 0.02–0.1 mol/L range (see Supplementary data).

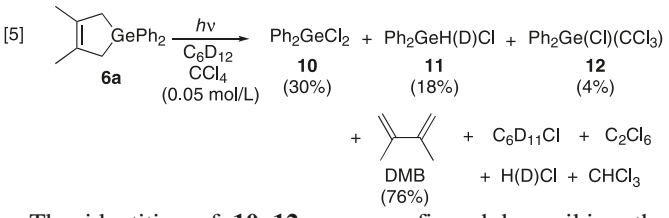

The identities of **10–12** were confirmed by spiking the photolyzed mixtures with independently prepared authentic samples. Compound **12** was prepared by reaction of 2 equiv of PhMgBr with **13**[55] (eq. [6]), and was obtained as a viscous, moisture-sensitive liquid. Unintentional hydrolysis of the compound afforded germanol **14** (eq. [7]), whose structure was determined by single crystal X-ray crystallography (see Supplementary data). The crystallographic data are of fairly low quality, but nevertheless clearly establish the connectivity and identity of the compound.

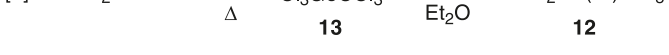

Can. J. Chem. Downloaded from www.nrcresearchpress.com by University of Electronic and Science Techonology of China on 09/18/12
For personal use only.

Table 1. Product yields (%) from 254 nm photolysis of 3,4-dimethyl-1,1-diphenylgermacyclopent-3-ene (**6a**; 0.02 mol/L) with CCl_4 in deoxygenated C_6D_{12} or THF-d_8 solution under various conditions.

		Product yields (%)				
Solvent	$[CCl_4]$ (mol/L)	Ph_2GeCl_2 (**10**)	$Ph_2GeH(D)Cl$ (**11**)	$Ph_2Ge(Cl)CCl_3$ (**12**)	DMB	%D (**11**)
C_6D_{12}	0.02	20±4	22±3	3.3±0.7	96±6	67
C_6D_{12}	0.05	30±5	18±3	4.1±0.7	76±6	56
C_6D_{12}	0.10	33±4	27±4	3.9±0.5	78±8	44
THF-d_8	0.05	33±4	20±5	49±6	87±7	25

[7] $Ph_2Ge(Cl)CCl_3$ (**12**) $\xrightarrow[-HCl]{H_2O}$ $Ph_2Ge(OH)CCl_3$ (**14**)

Chlorodiphenylgermane (**11**) was readily recognizable in the NMR spectra of the photolysis mixtures owing to its characteristic Ge–H resonance at δ 6.76, which was present even after ca. 1% conversion of **6a**; its intensity relative to those of the (ortho) aromatic protons indicated the compound was ca. 50% deuterated. The concentration vs time plots for this product exhibited good linearity throughout the (ca. 10%) conversion range in most experiments, but exhibited mild upward curvature in those carried out at higher (>0.1 mol/L) CCl_4 concentrations. The yield of the compound relative to the other products also increased with increasing CCl_4 concentration >0.05 mol/L. One possible route for the formation of the compound is by reaction of $GePh_2$ with H(D)Cl,[56] produced by H(D) abstraction by chlorine atoms formed by competing photolysis of CCl_4. Indeed, photolysis of a solution of **6a** (0.04 mol/L) in C_6D_{12} saturated with HCl(g) resulted in the clean formation of **11** and DMB in high yields (eq. [8]). This mechanism is consistent with the significantly higher yields of the product that were obtained in runs carried out with the higher CCl_4 concentrations, where >0.5% of the incident light is absorbed by the halocarbon. HCl might also be formed by hydrolysis of **10** or **12** by water introduced inadvertently throughout the course of the photolysis; this seems a less likely possibility, but it cannot be ruled out.

[8] 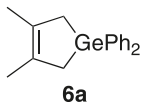 (**6a**) $\xrightarrow[C_6D_{12}, HCl\ (sat)]{h\nu}$ Ph_2GeHCl (**11**) (83 ± 3%) + DMB (80 ± 2%)

Photolysis of **6a** (0.02 mol/L) in THF-d_8 containing CCl_4 (0.05 mol/L) afforded the same products as were obtained in C_6D_{12}, but the material balance was considerably higher and the formal C–Cl insertion product (**12**) was formed as the major product (eq. [9]) (see Supplementary data). The broad baseline absorptions in the aromatic region of the NMR spectrum were much less pronounced, the unidentified resonances in the δ 1.5–2.2 and δ 3.4–3.7 regions of the spectrum were absent, and the concentration vs time plot for DMB exhibited only slight nonlinearity over the 0%–10% conversion range in **6a**, indicating a significantly smaller contribution to the overall product distribution from radical-derived side reactions. The yield of **11** (relative to **11**-*d*) was also higher than in the C_6D_{12} photolyses, which we interpret as being due mainly to increased amounts of HCl being formed during the experiment. This could be due in part to hydrolysis of the other chlorogermane products by adventitious water in the solvent, the presence of which could be detected by NMR. The water peak broadened throughout the course of the experiment, an effect consistent with the formation of HCl in the product mixture,[57] and the concentration vs time plot for **11** exhibited upward curvature. These observations are all consistent with the main source of **11** (in this experiment) being via reaction of $GePh_2$ with HCl.

[9] (**6a**) $\xrightarrow[CCl_4\ (0.05\ mol/L)]{h\nu,\ THF\text{-}d_8}$ Ph_2GeCl_2 (**10**) (26%) + Ph_2GeHCl (**11**) (22%) + $Ph_2Ge(Cl)(CCl_3)$ (**12**) (35%) + DMB (80%)

A similar product distribution was obtained upon photolysis of a cyclohexane solution of **6a** (0.02 mol/L) containing CCl_4 (0.05 mol/L) and THF (0.06 mol/L), which afforded **10** and **12** in an approximate 1:1 ratio, according to GC–MS analysis of the mixture. Another experiment employing the same concentrations of **6a** and CCl_4 in cyclohexane containing triethylamine (NEt_3, 0.003 mol/L) afforded **12** as the major germanium-containing product, and only trace amounts of **10** and **11** could be detected by GC–MS.

The course of the reaction of CCl_4 with tetramesityldigermene (**9g**) was also studied, following the reported procedure for the synthesis of the digermene by low-temperature photolysis of hexamesitylcyclotrigermane (**7g**; 1.3 mmol/L) in deoxygenated toluene containing triethylsilane.[45,58] Addition of a cold solution of CCl_4 in toluene to a preprepared solution of **9g** at –40 °C ($[CCl_4] \approx 0.35$ mol/L) caused the characteristic yellow colour of the digermene to decolourize within a few seconds. The solvent was evaporated and the ^1H NMR spectrum of the residue showed evidence for the formation of several products (see Supplementary data), amongst which 1,2-dichlorotetramesityldigermane (**15**; eq. [10]) was identified by spiking the mixture with an independently prepared sample.[59] The yield of **15** was estimated to be ~20% from the contribution of the area of its aromatic proton resonance to the total area of the aromatic proton region of the spectrum (δ 6.50–8.85), excluding the contributions from residual **7g** and $Mes_2Ge(H)SiMe_3$.[60] Attempts to identify the other products by GC–MS allowed only C_2Cl_6 (in trace amounts) to be unambiguously identified in the mixture.

Can. J. Chem. Downloaded from www.nrcresearchpress.com by University of Electronic and Science Techonology of China on 09/18/12
For personal use only.

[10] $Mes_2Ge{=}GeMes_2$ (**9g**) $\xrightarrow[\text{-40 °C}]{CCl_4,\ \text{toluene}}$ $Mes_2Ge(Cl)-Ge(Cl)Mes_2$ (**15**, ca. 20%) + C_2Cl_6 + other products

Only trace amounts of **15** could be detected in the product mixture obtained in a similar experiment employing $CHCl_3$ as substrate. In this case, addition of a cold solution of $CHCl_3$ to a toluene solution containing **9g** at –40 °C ($[CHCl_3] \approx 0.8$ mol/L) resulted in no change in the yellow colour of the solution, even after standing at –40 °C for 30 min. Raising the temperature to ca. –20 °C caused the yellow colour to disappear within ~5 min. The ^{1}H NMR spectrum of the evaporated mixture was similar to that described previously by Baines and co-workers,[45] and verified the formation of compound **16** (eq. [11]) as the major product of the reaction of the digermene with $CHCl_3$.

[11] $Mes_2Ge{=}GeMes_2$ (**9g**) $\xrightarrow[\text{-20 °C}]{CHCl_3,\ \text{toluene}}$ $Mes_2Ge(Cl)-Ge(CHCl_2)Mes_2$ (**16**, ca. 25%) + other products

Laser flash photolysis studies

Laser flash photolysis experiments were carried out using flowed, deoxygenated solutions of **6a**-**6f** (ca. 0.003 mol/L) in anhydrous hexanes and the pulses from a KrF excimer laser (~25 ns, ~100 mJ, 248 nm) for excitation. The behaviour observed for the six compounds in the absence of added CCl_4 has been described previously.[10,27,30,48] Briefly, the photolysis pulse results in the prompt formation of the characteristic absorptions owing to the corresponding transient diarylgermylenes (**8a**–**8f**; λ_{max} = 300 nm and 480–500 nm), which decay with second-order kinetics with the concomitant growth of absorptions centered at ca. 440 nm owing to the corresponding digermenes (**9a**–**9f**). In each case, addition of CCl_4 causes the decay of the germylene absorptions (monitored at 500 nm) to accelerate and produces concomitant reductions in the maximum signal intensities and apparent lifetimes of the digermene absorptions, as we reported previously for **6a**.[20] The digermenes could be detected and their decay kinetics characterized in the presence of lower concentrations of CCl_4, over a range that varied depending on the reactivity of its germylene precursor toward the substrate. The germylenes remained detectable at much higher (0.1–1.0 mol/L) CCl_4 concentrations, where their decays proceeded completely to baseline and followed clean first-order kinetics. Rate constants for reaction of CCl_4 with each of the germylenes (**8a**–**8f**) and the corresponding digermenes (**9a**–**9f**) were obtained from the slopes of plots of the first-order decay rate coefficients (k_{decay}) vs [CCl_4] according to eq. [12], where k_0 is the hypothetical pseudo-first-order rate coefficient for decay of the monitored species in the absence of substrate and k_{CCl_4} is the second-order rate constant for reaction with the substrate, respectively. These plots exhibited good to excellent linearity in each case (see Supplementary data). For example, Fig. 1 shows selections of representative transient absorbance vs time profiles obtained for digermene **9c** and germylene **8c** in the presence of varying amounts of CCl_4, along with the corresponding plots of k_{decay} vs [CCl_4] as insets. The absolute rate constants obtained in the experiments with the six compounds are listed in Table 2; the values obtained for **8a** and **9a** are in excellent agreement with the previously reported values.[20]

$$[12] \qquad k_{decay} = k_0 + k_{CCl_4}[CCl_4]$$

Co-absorption of the excitation light by the substrate (ε_{248nm} = 1.23 mol/L^{-1} cm^{-1} for CCl_4, compared with ε_{248nm} = 290 mol/L^{-1} cm^{-1} for **6a**) was impossible to avoid in these experiments, and so a control experiment was carried out to assess the possible contributions to the germylene and digermene decay kinetics owing to the formation of HCl, trichloromethyl, and solvent-derived radicals[61,62] within the reaction volume owing to competing CCl_4 photolysis. We chose germacyclopentene **6d** for the experiment because the corresponding germylene and digermene exhibit reactivity toward CCl_4 that is roughly in the middle of the ranges exhibited by the six germylenes and corresponding digermenes that were studied in this work. Decay rate coefficients were determined for **8d** and **9d** at several CCl_4 concentrations between 0.03 and 0.5 mol/L as a function of excitation laser intensity, on which the concentrations of these CCl_4-derived species should depend. The decay rate coefficients for both species were found to be approximately constant over a two- to four-fold range in laser intensity at each CCl_4 concentration that was examined, indicating that co-absorption of the excitation light by the substrate has minimal effects on the measured rate constants for reaction of CCl_4 with **8a**–**8f** and **9a**–**9f** owing to the presence of HCl, CCl_3, and solvent-derived radicals produced in the laser pulse. The presence of CCl_4 did cause modest reductions in the intensities of the transient signals, but no more than would be expected because of simple screening of the excitation light by the substrate. It can thus be further concluded that CCl_4 does not quench the excited (singlet) states of **6a**–**6f** within the concentration ranges that were studied.

A transient absorption spectrum recorded with a solution of **6a** in hexanes containing 0.5 mol/L CCl_4, conditions under which the lifetime of $GePh_2$ is reduced to $\tau \approx$ 165 ns and digermene formation is completely suppressed, showed no difference in the relative intensities of the $GePh_2$ absorption maxima (500 and ca. 300 nm) compared to those in the absence of added substrate, and no new absorptions (transient or stable) that could be ascribed to intermediates or products of reaction of $GePh_2$ with the halocarbon.

We also attempted to measure a rate constant for the reaction of CCl_4 with tetramesityldigermene (**9g**) in hexanes, employing **7g** (1.3×10^{-5} mol/L) as precursor. Laser photolysis of **7g** produces the strong absorptions owing to **9g** (λ_{max} = 405 nm) both within the laser pulse and (in the absence of added substrates) over a 20–30 μs time period after the pulse owing to dimerization of $GeMes_2$ (**8g**), the photolysis co-product;[63] the latter was not monitored in these experiments. Addition of small amounts of CCl_4 to the solution caused the signal owing to **9g** to decay, exhibiting lifetimes that decreased from ca. 1.4 to 0.8 ms over the 1.3–5 mmol/L concentration range in added halocarbon. A plot of k_{decay} vs [CCl_4] afforded k_{CCl_4} = (2.0 ± 0.1) × 10^5 (mol/L)$^{-1}$ s^{-1} (see Supplementary data), which should be considered an upper limit of the true value; the lifetimes showed a modest dependence on laser intensity, suggesting

Can. J. Chem. Downloaded from www.nrcresearchpress.com by University of Electronic and Science Techonology of China on 09/18/12
For personal use only.

Fig. 1. Transient absorbance vs time profiles for (*a*) tetraaryldigermene **9c** and (*b*) diarylgermylene **8c**, from laser flash photolysis of **6c** in deoxygenated hexanes containing (*a*) 0–0.04 mol/L CCl_4 and (*b*) 0.24 mol/L (—) and 0.56 mol/L (○) at 25 °C. The insets show the plots of k_{decay} vs [CCl_4] obtained from the two sets of data.

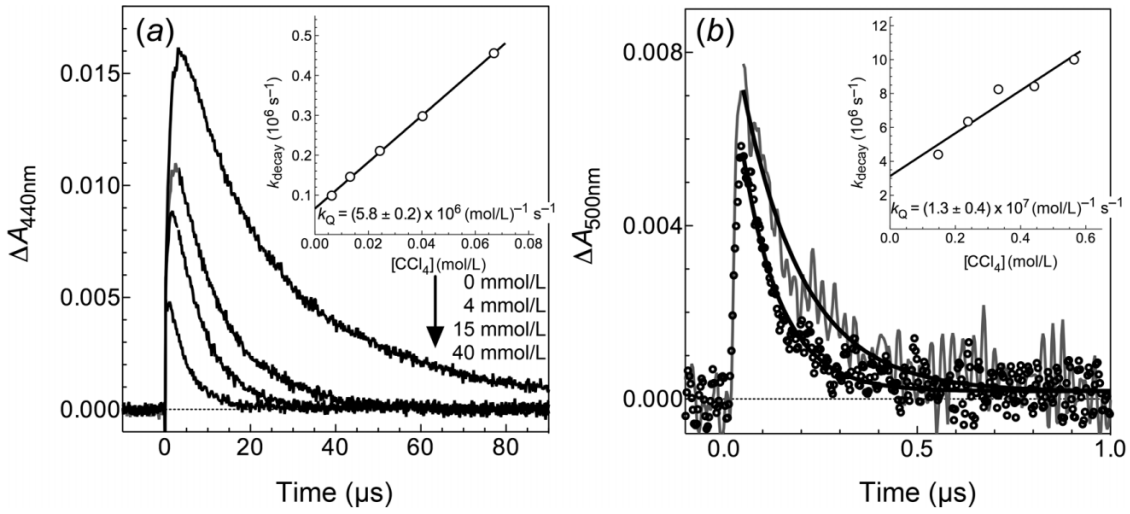

Table 2. Second-order rate constants for the reactions of CCl_4 with germylenes **8a**–**8f** and digermenes **9a**–**9g** in deoxygenated hexanes solution and with the corresponding germylene–THF complexes in THF at 25 °C.

	Second-order rate constant		
8 or **9**	k_{CCl4}[8] (10^6 (mol/L)$^{-1}$ s^{-1})	k_{CCl4}[9] (10^6 (mol/L)$^{-1}$ s^{-1})	k_{CCl4}^{8-THF} (10^6 (mol/L)$^{-1}$ s^{-1})
a (H)	12±1	3.9±0.5	4.3±0.3
b (3,4-Me_2)	12±2	8.9±1.0	6.4±0.6
c (4-Me)	13±4	5.8±0.2	2.3±0.2
d (4-F)	6.9±1.6	2.5±0.1	0.86±0.07
e (3-F)	8.0±0.8	1.3±0.1	0.56±0.08
f (4-CF_3)	2.6±1.2	0.91±0.08	1.3±0.2
g (2,4,6-Me_3)	—	≤0.20	—

Note: Errors are reported as twice the standard error from linear least-squares analysis according to eq. [10].

they may be affected by competing photolysis of the substrate, as discussed above.

Laser photolysis experiments with **6a**–**6f** in deoxygenated THF solution afforded the strong, long-lived transient absorptions owing to the corresponding germylene–THF complexes, as reported previously for **6a**, **6c**, **6d**, and **6f**.[30] The spectra and lifetimes measured for the THF complexes with **8b** and **8e** (see Supplementary data) were quite similar to those of the other four; the complexes exhibited absorption maxima in the 340–350 nm range and decayed over several tens of microseconds, coincident with the growth of weak absorptions (centered at 440 nm) owing to the corresponding digermenes.[30] Addition of 0.01–0.4 mol/L CCl_4 to the solutions caused the absorptions owing to the complexes to decay with clean pseudo-first-order kinetics and quenched the formation of the corresponding digermenes; again, plots of k_{decay} vs [CCl_4] according to eq. [10] were linear in each case (see Supplementary data), and afforded the absolute rate constants listed in Table 2. Figure 2*a* shows a series of representative transient decay profiles for the **8a**–THF complex at various substrate concentrations, whereas Fig. 2*b* shows the plot of k_{decay} vs [CCl_4]. Chloroform was also found to shorten the lifetime of the **8a**–THF complex, and a plot of k_{decay} vs [$CHCl_3$] was linear with slope k_{CHCl_3} = (2.4 ± 0.5) × 10^4 (mol/L)$^{-1}$ s^{-1} (see Supplementary data).

Rate constants were determined at four additional temperatures over the 10–60 °C range, for the reactions of CCl_4 with **8a** and **9a** in hexanes and with the **8a**–THF complex in THF (see Supplementary data). The resulting Arrhenius plots afford activation parameters of E_a = –0.7 ± 0.7 kcal/mol (1 cal = 4.184 J) and log(A/(mol/L)$^{-1}$ s^{-1}) = 6.5 ± 0.5 for the reaction of free **8a** in hexanes, E_a = +4.3 ± 0.8 kcal/mol and log(A/(mol/L)$^{-1}$ s^{-1}) = 9.6 ± 0.6 for that of **9a** in hexanes, and E_a = +5.9 ± 0.4 kcal/mol and log(A/(mol/L)$^{-1}$ s^{-1}) = 10.9 ± 0.3 for the reaction of the **8a**–THF complex in THF. Figure 3*a* shows the plots for **8a** (in hexanes) and **8a**–THF (in THF) and that for **9a** in hexanes is shown in Fig. 3*b*.

Low-temperature spectroscopic studies

A study of the reactions of $GePh_2$ (**8a**) with CCl_4 and $CHCl_3$ in 3-methylpentane (3-MP) solution at 78–95 K was also carried out. These experiments employed 1,1-diphenylgermacyclobutane (**17**) as the photochemical precursor to $GePh_2$, which is produced in ca. 20% chemical yield along with cyclopropane, 1,1-diphenylgermene (**18**; 60%), and ethylene from photolysis of this compound in hexanes at 25 °C (eq. [13]).[64] We anticipated that $GePh_2$ should be detectable from **17** under these conditions since its co-product (cyclopropane) is inert; we have previously shown that the photolysis of **6a** in low-temperature glasses does not afford

Can. J. Chem. Downloaded from www.nrcresearchpress.com by University of Electronic and Science Techonology of China on 09/18/12
For personal use only.

Fig. 2. (*a*) Transient decay profiles of the **8a**–THF complex in THF containing various concentrations of CCl_4, recorded at 350 nm. The black lines are the fit of the decays to first-order kinetics. (*b*) Plot of k_{decay} vs [CCl_4] from the experiment of (*a*).

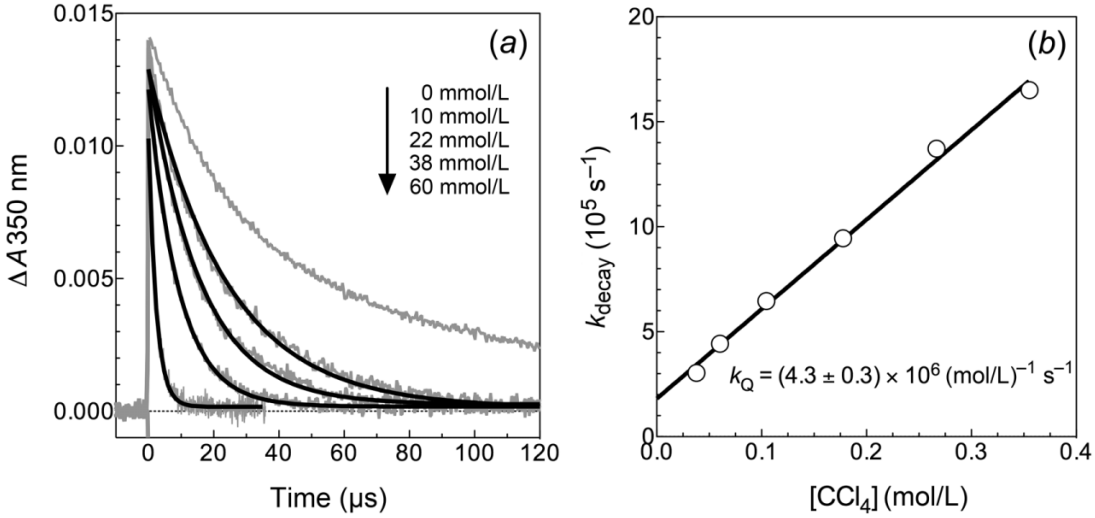

Fig. 3. Arrhenius plots for the reactions of CCl_4 with (*a*) $GePh_2$ (**8a**) in deoxygenated hexanes (○) and the **8a**–THF complex in THF (□), and (*b*) Ge_2Ph_4 (**9a**) in hexanes (○), determined by laser photolysis of **6a** over the range of 10–60 °C.

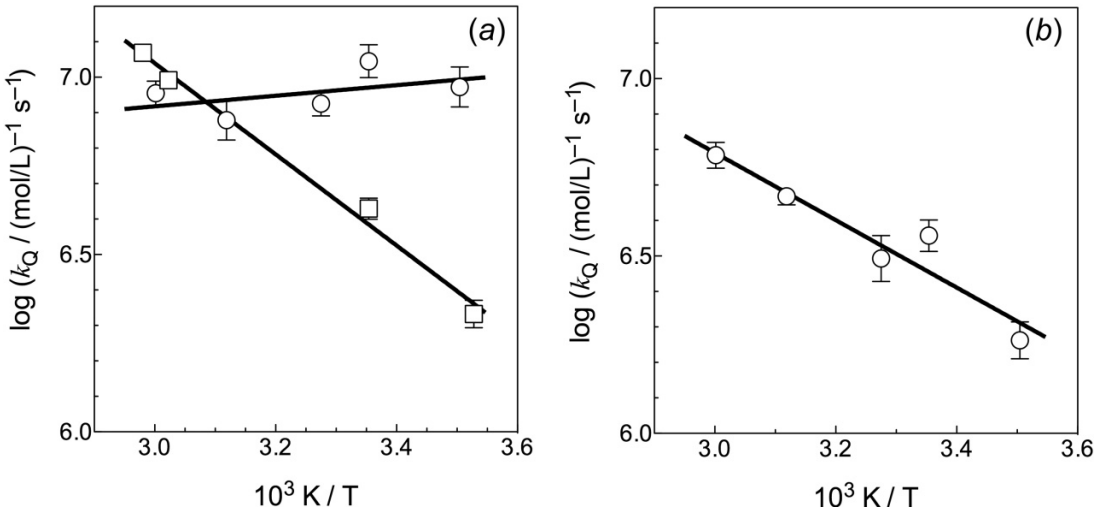

$GePh_2$ in detectable amounts owing (presumably) to rapid reaction with DMB in the solvent cage.[65]

[13] Ph_2Ge□ (**17**) $\xrightarrow{h\nu}$ $GePh_2$ + △ (**8a**, ~ 20%) + $Ph_2Ge{=}CH_2$ + $H_2C{=}CH_2$ (**18**, ~ 60%)

As expected, photolysis of a solution of **17** in 3-MP (glass transition temperature ≈ 77 K[66]) at 78 K afforded two distinct transient products that were detectable by low-temperature UV–vis spectroscopy, one exhibiting λ_{max} = 460 nm and a second exhibiting a shoulder absorption centred at 326 nm, on the edge of an intense band centred below 300 nm (see Fig. 4*a*). The absorption at 326 nm is assigned to germene **18**,[64,67] whereas the 460 nm absorption band is assigned to $GePh_2$. The latter spectrum agrees well with those obtained in low-temperature experiments using other precursors, such as the known disilylgermane **19**[26,68] and disilyldigermane **20**.[69] The solution was then warmed in 1 K increments and a spectrum was recorded at each temperature. At ca. 82 K the 460 nm absorption band began to decrease in intensity slightly and shift to longer wavelengths, ending up finally at λ_{max} = 474 nm; the spectrum recorded at 87 K is shown as the broken line in Fig. 4*a*. The spectrum also shows a slight red-shift of the band below 300 nm, which is also due (at least partly) to $GePh_2$. The red-shift of the spectrum upon warming the solution between 78 and 82 K is consistent with geometrical relaxation of the solute, formed in a nonequilibrium geometry during the photochemical reaction that produces it.[70,71] Warming the solution further caused an accelerated reduction in the intensity of the (474 nm) band and a slight blue-shift (to λ_{max} = 470 nm), until it had all but disappeared entirely by the time the temperature reached 91 K, and the remaining spectrum consisted mainly of that owing to **18**. The latter disappeared upon further warming of the solution, presumably because of dimerization.[67,72]

Can. J. Chem. Downloaded from www.nrcresearchpress.com by University of Electronic and Science Techonology of China on 09/18/12
For personal use only.

Fig. 4. (*a*) UV–vis spectra from photolysis of a deoxygenated 3-methylpentane solution containing **17** at 78 K (solid line); the same solution after warming to ca. 87 K is shown as the broken line. (*b*) As in (*a*) except the solution contained 0.15 mol/L CCl_4. (*c*) As in (*a*) except the solution contained 0.15 mol/L $CDCl_3$.

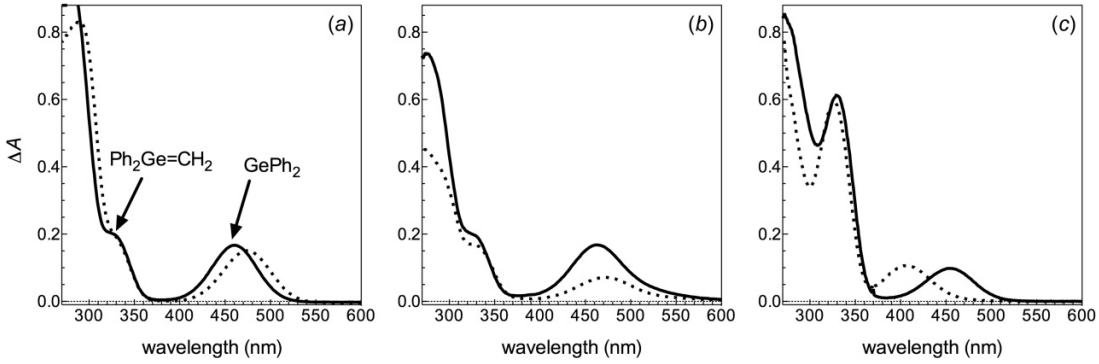

The procedure was repeated with a solution of **17** in 3-MP containing 0.15 mol/L CCl_4, the results of which are shown in Fig. 4*b*. In this case, warming the solution from 78 to 87 K resulted in a similar red-shift of the 460 nm band to what was observed in the absence of the halocarbon, but it was accompanied by a much more rapid decrease in intensity. This is consistent with reaction of $GePh_2$ with the halocarbon substrate; the spectrum showed no evidence for a detectable product of the reaction.

Finally, the procedure was repeated again with a solution of **17** in 3-MP containing 0.15 mol/L $CDCl_3$. This experiment afforded considerably different results than were observed in the others (see Fig. 4*c*); the 326 nm band at the end of the photolysis period was considerably more intense relative to the long wavelength band, and the latter was centered at slightly shorter wavelengths (λ_{max} = 453 nm). More importantly, warming the solution resulted in a blue-shift of the long wavelength band to 405 nm and a concomitant reduction in the intensity of the absorption below 300 nm; the intensity of the 326 nm band remained unaffected. Warming the solution past 88 K led to a gradual decrease in the intensity of the 405 nm absorption band until it eventually disappeared. This is again consistent with a halocarbon-induced reaction of $GePh_2$, but to yield a new transient product. Similar results were obtained (for the 450–460 nm band owing to $GePh_2$) using **20** as the $GePh_2$ precursor.

Taken together, the results of these experiments indicate that $GePh_2$ reacts with both CCl_4 and $CDCl_3$ at 82–90 K, but only with $CDCl_3$ does a transient product build up in high enough concentrations to be detected. We tentatively assign the species formed in the reaction with $CDCl_3$ under these conditions to the $GePh_2$–$CDCl_3$ Lewis acid–base complex.

Discussion

Reaction of CCl_4 with diarylgermylenes

The product studies are complicated somewhat by side reactions owing to the accompanying formation of H(D)Cl and the high reactivity of the diene co-product (DMB) toward radical reactions, but they nevertheless show conclusively that the reaction of $GePh_2$ with CCl_4 in hydrocarbon solvents proceeds mainly by initial Cl-atom abstraction, producing the corresponding germanium dichloride (**10**) as the major product along with minor amounts of the formal C–Cl insertion product, **12**. The behaviour is thus closely analogous to that exhibited by $GeMe_2$, which was studied by several groups using both thermal and photochemical methods and a variety of different precursors,[40,73–75] most of them considerably less prone to the radical side reactions that complicate the product mixtures in the present study. The formation of **11** is particularly difficult to account for completely, as it is clear that it is formed via a number of mechanisms. Roughly 50% of the compound is formed as the deuterated isotopomer, which must be derived ultimately from radical reactions involving the relatively strong C–D bonds associated with the solvent. Of the various radical species that we can anticipate being formed under the conditions of our experiments, only chlorine atoms possess sufficient potency to abstract deuterium from C_6D_{12}.[76] Some of the **11**-*d* that is formed could then arise from reaction of $GePh_2$ with DCl. The most obvious route to chlorine atoms is via photolysis of CCl_4,[61,77] yet the conditions of our steady-state experiments were such that only ca. 0.7% of the excitation light could be absorbed by the substrate at an initial concentration of 0.1 mol/L. The quantum yield for $GePh_2$ formation from **6a** is 0.55,[10] so it seems unlikely that all of the **11**-*d* is formed in this way unless the quantum yield for CCl_4 photolysis is significantly greater than the value of ~0.2 reported for the process in the gas phase.[52] It is similarly difficult to account completely for the formation of protiated **11**; its formation from the Ph_2GeCl radical via radical disproportionation processes and (perhaps) via H abstraction from an allylic hydrogen in the precursor, which is thermodynamically plausible based on predicted bond dissociation energies,[76,78] is a possibility at low conversions. We thus conclude that the cage-escape:recombination ratio of the (singlet)[73] [Ph_2GeCl + CCl_3] radical pair formed in the primary reaction of $GePh_2$ with CCl_4 in hydrocarbon solvents is on the order of about 10:1, assuming that roughly half of the **11** that is formed is derived from Ph_2GeCl radical reactions.

The present results also demonstrate that the presence of nonreactive Lewis bases such as THF or NEt_3, either as the solvent or in low concentration in hexanes, shifts the product

Can. J. Chem. Downloaded from www.nrcresearchpress.com by University of Electronic and Science Techonology of China on 09/18/12
For personal use only.

distribution in favor of the formal C–Cl insertion product, **12**. This too is consistent with early studies of $GeMe_2$; Egorov et al.[40] obtained high yields of the formal C–Cl insertion product from the reaction of $GeMe_2$ with CCl_4 in the presence of triphenylphosphine. It thus seems likely that the detailed mechanisms of the reactions of this halocarbon with $GePh_2$ and $GeMe_2$ are quite similar. Our reported rate constants for the reaction of $GeMe_2$ with CCl_4 in hexanes ($k = (9 \pm 1) \times 10^7$ $(mol/L)^{-1}$ s^{-1})[11,79] and THF ($k = (3.3 \pm 0.3) \times 10^7$ $(mol/L)^{-1}$ s^{-1})[30] are both 7–8 times larger than the corresponding values reported here for $GePh_2$, differences that are typical of those observed for the reactions of most (common) substrates with these two transient germylenes in solution.[11,20,21,30]

The various kinetic and spectroscopic data reported in the present work provide a potentially much more detailed picture of the mechanism of the reaction than has been possible in previous studies with $GeMe_2$. A Hammett plot of the rate constants for the reactions of the substituted derivatives in hexanes (Fig. 5*a*) shows a modest correlation, affording a reaction constant of $\rho = -0.4 \pm 0.1$. This indicates there is significant charge donation from germanium to the substrate in the rate-determining step for the reaction. The Arrhenius parameters for the reaction of the parent diarylgermylene (**8a**) in hexanes ($E_a = -0.7 \pm 0.7$ kcal/mol; $\log(A/(mol/L)^{-1}\ s^{-1}) = 6.5 \pm 0.5$; $\Delta S^{\ddagger} = -31 \pm 3$ cal K^{-1} mol^{-1} at 35 °C) indicate the reaction to be entirely entropically controlled, with no enthalpic barrier. Interestingly, these features are broadly similar to those exhibited by the reaction of (singlet) chlorophenylcarbene with CCl_4, which was studied in detail by Platz and co-workers[38] in the early 1990s.

The negative Hammett ρ value and the observed temperature dependence are consistent with a mechanism involving the initial reversible formation of a weakly bound germylene–halocarbon Lewis acid–base complex, which undergoes rate-controlling dissociative inner-sphere electron transfer (“iset”) from germanium to the halocarbon moiety to afford the [Ph_2GeCl + CCl_3] radical pair (eq. [14]). It should be noted that our data do not demand a discrete reactive complex as a steady-state intermediate in the reaction; it is merely suggested by our detection of the corresponding $GePh_2$–$CDCl_3$ complex in the low-temperature UV–vis experiments (vide infra). The data for CCl_4 are equally compatible with a single step concerted mechanism.[80] The reaction must involve a surface crossing with the (excited) open-shell singlet state of the germylene as it proceeds, as Platz and co-workers[38] indicated in their study of the reaction of PhCCl with CCl_4; this, presumably, is where the free energy barrier to the process is located.

[14] 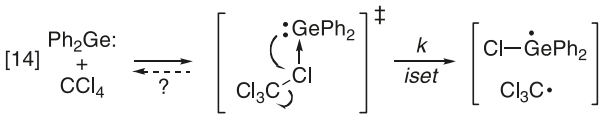

Ando et al.[26] reported the spectroscopic detection of the complexes of various germylenes (including $GePh_2$) with chlorohexane and chlorobenzene in hydrocarbon glasses at 77 K, prompting the later proposal by Neumann[16] for their involvement in the reactions of $GeMe_2$ with halocarbons; computational evidence for the intermediacy of analogous complexes in the reactions of some stable silylenes with CCl_4 has been reported by Su and co-workers.[81–83] If a reactive complex is involved as a discrete intermediate in the reaction of $GePh_2$ with CCl_4, we are unable to detect it even at 80–90 K, so the free energy barrier for its further transformation must be relatively small. The low-temperature experiments with $CDCl_3$ as substrate are consistent with the formation of a complex in this case, judging from the similarity of the spectrum to those of the complexes of $GePh_2$ with the chlorocarbons reported by Ando et al.[26] The rate constant for reaction of $GePh_2$ with $CHCl_3$ in hexanes at 25 °C is at least 50 times smaller than that with CCl_4,[20] consistent with a significantly higher barrier for the second step of the reaction with $CHCl_3$, whose C–Cl bond is ca. 5 kcal/mol stronger than that in CCl_4[76] and which is less easily reduced.[84] As a result, the $GePh_2$–$CHCl_3$ complex is detectable at low temperatures, whereas the putative $GePh_2$–CCl_4 complex (assuming it exists at all) is not. We were also unable to detect the product radical (Ph_2GeCl) in our laser photolysis experiments, which is an interesting point of difference between $GePh_2$ and its silicon homolog, $SiPh_2$. In the latter case, the primary reaction with CCl_4 produces a second intermediate that was assigned to the $SiPh_2Cl$ radical on the basis of its UV spectrum and the fact that its lifetime decreases with increasing CCl_4 concentration.[22] The reason for the difference is likely due to the fact that the primary Cl-abstraction step is roughly two orders of magnitude faster for the silylene than the germylene, but there is a much smaller difference in the rate constants for Cl abstraction by the Ph_2GeCl and Ph_2SiCl radicals.[85–87]

The reaction in THF, where the germylene exists essentially exclusively as the Lewis acid–base complex with the solvent, proceeds with a rate constant that is only ca. 3 times smaller than that of the free germylene in hexanes and produces a substantially higher yield of the formal C–Cl insertion product, **12**. While it is clear that some portion of the reaction continues to follow the free radical pathway, it appears to be a relatively minor component. We thus conclude that a different mechanism operates (either in whole or in part) in the presence of the nonreactive complexing agent compared with that in pure hexanes. The product distribution is quite similar in hexanes containing 0.05 mol/L THF and the reaction is similarly well-behaved, so it is clear that bulk solvent properties have nothing to do with the effect of the O donor on the product distribution. More dramatically, C–Cl insertion is essentially the exclusive reaction pathway (**10**:**12** $\approx$ 1:60) in hexanes containing 3 mmol/L NEt_3, which binds much more strongly to $GePh_2$ than does THF;[20,21] the presence of the amine would have the added benefit of soaking up any H(D)Cl that is formed, thus eliminating the formation of **11**. This all suggests that in the presence of O or N donors, the formation of the C–Cl insertion product proceeds via nucleophilic attack of the substrate by germanium in the germylene–donor complex. The Hammett plot of the rate constants for reaction of the substituted derivatives in THF solution (Fig. 5*b*) exhibits a significantly greater degree of scatter compared with that observed in hexanes, but is nevertheless broadly consistent with the germylene–O-donor complex playing the role of nucleophile in the reaction. The temperature dependence for the reaction of the parent (**8a**) leads to activation parameters of

Can. J. Chem. Downloaded from www.nrcresearchpress.com by University of Electronic and Science Techonology of China on 09/18/12
For personal use only.

Fig. 5. Hammett plots of the rate constants for the reaction of CCl_4 with (*a*) free **8a**–**8f** in hexanes and (*b*) **8a**–**8f**–THF complexes in THF, at 25 °C.

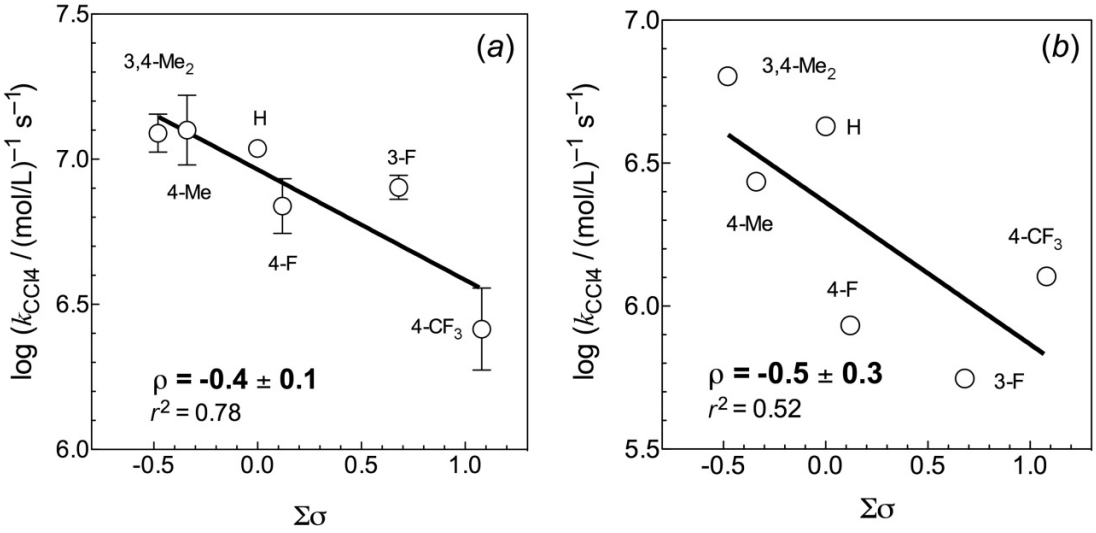

E_a = +5.9 ± 0.4 kcal/mol and log(A/(mol/L)$^{-1}$s $^{-1}$) = 10.9 ± 0.3, the latter corresponding to an overall entropy of activation of $\Delta S^{\ddagger}$ = –11.6 ± 1.3 cal K^{-1} mol^{-1} at 35 °C.

The results suggest that the **8a**–THF complex reacts with CCl_4 via two competing mechanisms, as depicted in eq. [15]. We propose that the formation of **10** (along with perhaps a small fraction of the total amount of **12** that is produced) is due to Cl-atom abstraction as it is in hexanes, the only difference being that the coordinated THF moiety is liberated (presumably) at some stage during the formation of the resulting radical pair. We suggest that the formation of **12** arises mainly via nucleophilic attack of the germanium lone pair in the complex at a chlorine atom in the substrate, to yield a contact ion pair that rapidly annihilates to form the product. The process requires prior coordination with the Lewis base, both to impart nucleophilic character at germanium and stabilize the formation of the ion pair. This pathway would be expected to be enhanced relative to the other in the presence of a stronger Lewis base, as indeed we observe. The latter mechanism, as opposed to one involving nucleophilic attack at carbon in the substrate, is consistent with the roughly 200-fold lower reactivity of the $GePh_2$–THF complex with $CHCl_3$ ($k_{CHCl_3} \approx 2.4 \times 10^4$ (mol/L)$^{-1}$ s^{-1}) compared with CCl_4 under similar conditions. An electron-transfer mechanism might also be consistent with the observed results, provided the transfer of chlorine in the contact radical ion pair occurs largely as an atom transfer rather than ion transfer.

[15]

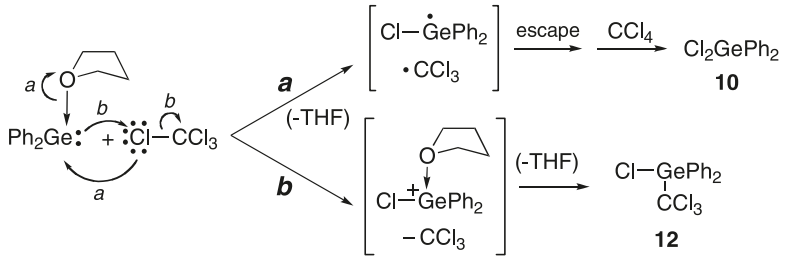

Reaction of CCl_4 with tetraaryldigermenes

The reaction of CCl_4 with tetramesityldigermene (**9g**) affords the corresponding 1,2-dichlorodigermane (**15**) as a major product, allowing the conclusion that Cl-atom abstraction to yield the 2-chlorodigermyl radical (**21**; eq. [16]) is a dominant mode of reaction of the Ge–Ge bond in this compound with CCl_4. The reaction produces a number of unidentified additional products, some of them presumably derived from side reactions resulting from the accompanying formation of the CCl_3 radical. This supports our inference that the primary reaction of the other tetraaryldigermenes (**9a**–**9f**) with CCl_4 is Cl-atom abstraction, as Mochida et al.[43] found to be the case for Ge_2Me_4. It is interesting to note that the reactions of **9g** with CCl_4 and $CHCl_3$[45] (which affords the 1,2-dichloride in only trace amounts; vide supra) exhibit similar differences in product distribution as Kira et al.[42] reported for the reactions of these two halocarbons with the less sterically hindered (**1a** and **1b**) of the three tetrasilyldisilene derivatives they studied. The more sterically hindered derivative (**1c**) afforded the corresponding 1,2-dichlorides in both cases; it did as well with CH_2Cl_2 as substrate, whereas **1a** afforded only the formal cage recombination product.

Can. J. Chem. Downloaded from www.nrcresearchpress.com by University of Electronic and Science Techonology of China on 09/18/12
For personal use only.

They interpreted these differences in terms of steric effects on the cage-escape–recombination ratio of the initially formed radical pairs, but the possibility that the formal recombination product (when it is observed) might be formed at least in part via an entirely different mechanism cannot be discounted. In any event, it is certainly clear that with all the disilenes they studied, the reaction with CCl_4 proceeds to a very large extent via initial Cl-atom abstraction. This is also true for Ge_2Me_4,[43] and probably as well for **9g** and the other less-hindered systems that we have characterized kinetically in the present work. It is also clear from the results of Kira et al.[42] that $CHCl_3$ *can* react the same way, and does so exclusively when the Si=Si bond is severely sterically hindered. It is also clear from their results that $CHCl_3$ is a characteristically much less reactive substrate than CCl_4 toward Si=Si bonds. This is true as well for the Ge=Ge bonds in Ge_2Me_4,[43] Ge_2Mes_4 (vide supra), and Ge_2Ph_4.[20] The difference in absolute rate constant is on the order of 1000 or more for both disilene **1c**[42] and Ge_2Me_4.[43] Kira et al.[42] reported activation parameters of $\Delta H^{\ddagger}$ = +7.0 ± 0.1 kcal/mol and $\Delta S^{\ddagger}$ = –43.9 ± 0.1 cal K^{-1} mol^{-1} for Cl abstraction from $CHCl_3$ by **1c**, but unfortunately did not study the temperature dependence of the corresponding reaction with CCl_4.

[16] $Mes_2Ge{=}GeMes_2$ (**9g**) $\xrightarrow{CCl_4}$ $[Mes_2Ge(Cl)-\dot{G}eMes_2 \cdot CCl_3]$ (**21**)

The Arrhenius plot of the absolute rate constants for reaction of **9a** with CCl_4 in hexanes (Fig. 3*b*) affords activation parameters of E_a = +4.3 ± 0.8 kcal/mol and $\log(A/(\text{mol/L})^{-1}\ s^{-1})$ = 9.6 ± 0.6, corresponding to an enthalpy and entropy of activation of $\Delta H^{\ddagger}$ = +3.7 ± 0.8 kcal/mol and $\Delta S^{\ddagger}$ = –16.7 ± 1.3 cal K^{-1} mol^{-1} at 35 °C, respectively, which we tentatively ascribe to those characterizing the Cl-abstraction process from this substrate by the Ge=Ge bond in Ge_2Ph_4. Su[46] reported a calculated value of $\Delta E^{\ddagger}$ = +0.6 kcal/mol at the B3LYP/6–311G(d,p) level of theory for the Cl-abstraction reaction of Ge_2Me_4 with CCl_4, which is the only direct comparison possible with the results of earlier studies on related systems.

The Hammett plot of the rate constants for the reactions of **9a** and the five substituted derivatives (Fig. 6) reveals an excellent correlation with substituent constants and affords a reaction constant of ρ = –0.31 ± 0.03. The value is indicative of significant charge donation from the Ge=Ge bond in **9** to the substrate in the transition state for the Cl-atom abstraction and is again broadly consistent with the results of Kira et al.[42] for disilene **1c**. They observed a good two-parameter correlation between the rates of reaction of disilene **1c** with a series of substituted benzyl chlorides and polar (Hammett σ_p) and spin delocalization (σ_{JJ}) substituent constants; the polar reaction constant was ρ = +0.9, which reflects the effects of substituent polarity from the opposite frame of reference to that probed in the present study.

Conclusions

The reaction of $GePh_2$ with CCl_4 in hydrocarbon solvents proceeds exclusively via Cl-atom abstraction, as is known also to be the case for $GeMe_2$ based on the results of early studies of the simpler germylene derivative using both thermal and photochemical methods for its generation. The present study affords considerably greater information in regards to the detailed mechanism of the process. The temperature dependence of the rate constant indicates the reaction is entropically controlled and possesses little or no enthalpic barrier, consistent with a two-step mechanism involving a reversibly formed intermediate whose collapse to the primary products is rate-controlling. It is well-established that $GePh_2$ (and other transient germylenes) form detectable Lewis acid–base complexes with other, less reactive halocarbons, and the present work extends the list of such substrates to include chloroform. We thus envisage the reaction with CCl_4 to begin with such an interaction, which allows the Cl-atom transfer to occur via a dissociative inner-sphere electron transfer process; if a discrete Lewis acid–base complex is involved, it is a steady-state intermediate that is undetectable even at very low temperatures. Reactivity is enhanced modestly by electron-donor substituents on the germylene, which supports the proposed mechanism. So too does the sizeable reduction in rate constants exhibited by the reactions of $GePh_2$ with $CHCl_3$ and other less easily reduced halocarbons.

A second mechanism comes into play in the presence of "spectator" donors such as THF (either as solvent or a catalyst) and NEt_3, which lead to increased yields of the formal C–Cl insertion product at the expense of radical-derived products, to an extent that depends on donor basicity. The reaction of $GePh_2$ with CCl_4 in THF solution exhibits activation parameters of E_a = +5.9 ± 0.4 kcal/mol and $\Delta S^{\ddagger}$ = –11.6 ± 1.3 cal K^{-1} mol^{-1} at 35 °C, the interpretation of which is complicated by the fact that competing reaction channels are operative and product studies have not been carried out over the full temperature range probed in the kinetic experiments. The rate constants for reaction of the substituted derivatives in this solvent correlate poorly with Hammett substituent constants, but show a trend toward higher reactivity with the more electron-rich derivatives in the series; this too may be a reflection of the competing reaction

Fig. 6. Hammett plot of the rate constants for the reactions of tetraaryldigermenes **9a**–**9f** with CCl_4 in hexanes at 25 °C.

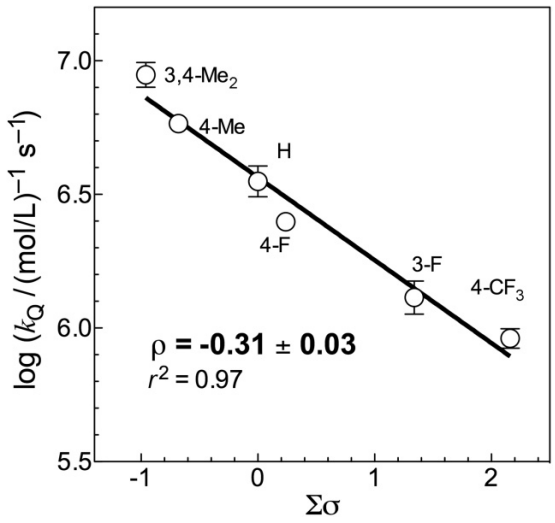

Can. J. Chem. Downloaded from www.nrcresearchpress.com by University of Electronic and Science Techonology of China on 09/18/12
For personal use only.

channels that may operate. Neverthless, a mechanism involving nucleophilic attack at the chlorine of the substrate by the germylene lone pair in the germylene–donor complex, to yield a contact ion pair that rapidly annihilates to form the observed product, is consistent with the data and explains the higher yield of formal C–Cl insertion product that is obtained.

The reaction of CCl_4 with the corresponding tetraaryldigermenes also proceeds via Cl-atom abstraction in hexanes solution, affording the corresponding 1,2-dichlorodigermane as the main product. Activation parameters of E_a = +4.3 ± 0.8 kcal/mol and $\Delta S^{\ddagger}$ = –16.7 ± 1.3 cal K^{-1} mol^{-1} have been determined for the reaction of Ge_2Ph_4, which are consistent with theoretical estimates for Ge_2Me_4 and the results of earlier studies of the corresponding reactions with sterically stabilized tetrasilyldisilenes. The process involves significant charge donation from the Ge=Ge bond to the substrate in the transition state for the rate-determining step, as revealed by an excellent correlation of the rate constants for reaction of the substituted tetraaryldigermenes with Hammett substituent constants.

Carbon tetrachloride represents an extreme in the reactions of transient germylenes, silylenes, and their corresponding dimers with halocarbon substrates, reacting exclusively by Cl-atom abstraction. This behaviour is shared by benzyl chloride, which possesses a C–Cl bond of similar strength to that in CCl_4. Interestingly, allyl chloride undergoes exclusive C–Cl insertion with $GeMe_2$ in spite of a similar C–Cl bond strength to those in CCl_4 and benzyl chloride.[16] This and other reactions of transient silylenes and germylenes are the subject of continued study in our laboratory.

Experimental

^1H and ^{13}C NMR spectra were recorded on Bruker AV200 or AV600 spectrometers in $CDCl_3$, CD_3CN, C_6D_6, C_6D_{12}, or THF-d_8 (Cambridge Isotope Laboratories). High-resolution mass spectra were recorded on a Micromass TofSpec 2E mass spectrometer using electron impact or chemical ionization (NH_3 reagent gas). MALDI mass spectra were recorded on a WatersMicromass MALDI MicroMX mass spectrometer operating in reflectron mode (matrix: α-cyano-4-hydroxycinnamic acid). GC–MS analysis of product mixtures was performed using a Varian Saturn 2200 GC–MS–MS system equipped with a VF-5ms capillary column (30 m × 0.25 mm; 0.25 μm; Varian, Inc.) using electron impact or chemical ionization (MeOH reagent gas); an asterisk by an *m/z* value indicates it is the most intense peak of a Ge isotopomeric cluster. X-ray crystallographic analysis was performed in the McMaster Analytical X-Ray (MAX) Diffraction Facility on a single crystal (grown from slow evaporation of hexanes), mounted and cooled to –100 °C on a SMART APEX II diffractometer with a 3 kW sealed tube Mo generator.

All synthetic preparations were carried out in flame-dried glassware under an atmosphere of dry nitrogen. The germacyclopentenes **6a**–**6f**,[10,27,30,48] hexamesitylcyclotrigermane (**7g**),[88] 1,2-dichloro-1,1,2,2-tetramesityldigermane (**15**),[59] 1,1-diphenyl-1-germacyclobutane (**17**),[67] and diphenylgermanium dichloride (**10**)[89] were prepared as previously described.

Trichloro(trichloromethyl)germane (Cl_3GeCCl_3) was prepared following the method of Nefedov and co-workers.[55] $GeCl_2$–dioxane (10.3 g, 44 mmol) was dissolved in CCl_4 (150 mL) and refluxed for 4 h under nitrogen. The reaction mixture was stirred under vacuum (~0.1 mm Hg; 1 mm Hg = 133.322 4 Pa) at ambient temperature until the solvent had been removed, yielding the crude product as a pale yellow solid. While still under vacuum, the flask was gently warmed with a water bath (ca. 40–50 °C) and the product, a white solid (8.68 g, 29 mmol, 66%), sublimed onto a cold-finger cooled to –(30–40)°C using dry ice – isopropanol. The melting point was measured in a sealed tube (mp 104–106 °C; lit.[55] mp 106–107 °C). MS (*m/z* (I)): 297.7* (3) $[M^+]$, 260.8* (80) $[M - Cl]^+$, 178.8* (28) $[M - CCl_3]^+$, 159.9* (18), 116.9 (100).

Chloro(trichloromethyl)diphenylgermane (**17**): A two-neck 250 mL round bottom flask, fitted with a dropping funnel and a condenser, was charged with Cl_3GeCCl_3 (0.80 g, 2.7 mmol) and anhyd ether (20 mL). The dropping funnel was charged with freshly prepared PhMgBr (10.8 mmol, 4 equiv) in ether (50 mL). The Grignard reagent was added dropwise over 40 min, causing the formation of white insoluble salts. After the addition was complete, the mixture was allowed to stir for 2 h at room temperature. The solvent was removed under vacuum and the residue was washed with pentane (5 × 20 mL). The combined washes were filtered and the solvent removed under vacuum to yield a yellow oil (0.66 g). The product was isolated from the crude reaction mixture by Kugelrohr distillation as a colourless oil (0.10 g, 0.3 mmol, 11%), distilling at 110–120 °C (P = 0.05 mm Hg). IR (cm^{-1}, intensity): 3075 (m), 3055 (m), 1960 (w), 1885 (w), 1816 (w), 1585 (w), 1485 (s), 1434 (s), 1092 (s), 998 (s). ^1H NMR (C_6D_{12}): 7.34–7.42 (m, 6H), 7.79–7.87 (m, 4H). ^1H NMR (CD_3CN): 7.55–7.59 (m, 4H, *ortho*), 7.61–7.67 (m, 2H, *para*), 7.87–7.91 (m, 4H, *meta*). ^{13}C NMR (CD_3CN): 92.05 (CCl_3), 130.19 (*ortho*), 130.69 (*ipso*), 133.09 (*para*), 135.38 (*meta*). Note: the ^{13}C shift of CCl_3 is consistent with literature data for this group on Ge.[40,90,91] GC–MS (Saturn, CI) *m/z*: 344.7* (20) $(M - Cl)^+$, 299.2* (44), 201.3 (100), 161.1 (30), 159.2 (50). GC–MS (Saturn, EI) *m/z*: 263.2* (100)$(M - CCl_3)^+$. MS (Micromass, CI) (*m/z*, intensity): 306.9* (7), 280.0* (4), 263.0* (18), 151.0* (8), 108.9* (9), 94.1 (24), 93.1 (28), 78.0 (100). HRMS calcd for $C_{12}H_{10}{}^{74}GeCl$ $(M - CCl_3)^+$: 262.9683; found: 262.9621.

Attempts to crystallize the compound were unsuccessful; however, slow evaporation of a hexane solution in contact with atmospheric moisture led to the formation of colourless crystals of trichloromethyldiphenylgermanol (**14**) (mp 65.6–67.7 °C). IR (cm^{-1}, intensity): 3375 (br, m), 1961 (w), 1882 (w), 1810 (w), 1481 (m), 1431 (s), 999 (s). ^1H NMR (CD_3CN): 7.50–7.54 (m, 4H, *ortho*), 7.56–7.60 (m, 2H, *para*), 7.82–7.87 (m, 4H, *meta*).

Chlorodiphenylgermane (**11**) was prepared following the method of Kunai and co-workers.[92] The product was isolated from the crude reaction mixture as a colourless oil by Kugelrohr distillation (T = 100 °C, P = 0.2 mm Hg). IR (cm^{-1}): 3071 (m), 3052 (m), 3008 (br, w), 2076 (br, s), 1484 (m), 1433 (s), 1334 (w), 1305 (w), 1095 (s), 1027 (w), 998 (w), 855 (br, w). ^1H NMR δ: 6.56 (s, H), 7.46–7.54 (m, 6H, *ortho/para*), 7.63–7.73 (m, 4H, *meta*). ^{13}C NMR δ:

Can. J. Chem. Downloaded from www.nrcresearchpress.com by University of Electronic and Science Techonology of China on 09/18/12
For personal use only.

128.9 (*meta*), 130.8 (*para*), 133.8 (*ortho*), 135.3 (*ipso*). MS *m/z* (I): 263.0* (15), 227.0* (13), 185.9* (100), 151.0* (48), 108.9* (49), 79.1* (60). HRMS $C_{12}H_{10}{}^{74}GeCl$ (M – H) calcd: 262.9683; found: 262.9675.

Steady-state photolysis experiments were carried out using a Rayonet photochemical reactor (Southern New England Ultraviolet Co.) equipped with a merry-go-round and 2 × RPR2537 (254 nm) lamps. For those monitored by NMR spectrosccopy, aliquots (ca. 0.7 mL) of solutions in C_6D_{12} or THF-d_8 containing Si_2Me_6 (ca. 2 mmol/L) as an internal integration standard were placed in quartz NMR tubes, sealed with a septum, and deoxygenated with a fine stream of dry argon for ca. 10 min prior to the experiment. Reaction products were identified by spiking the mixture with authentic samples as well as by GC–MS analysis at the end of the experiment.

For those monitored by GC–MS only, solutions of the compounds and CCl_4 were prepared in dry cyclohexane or THF (5 mL) containing dodecane (1 mmol/L) as the internal integration standard. If applicable, THF or NEt_3 (Sigma-Aldrich, refluxed over and distilled from KOH) was added as well. The solution was transferred to a quartz NMR tube, sealed with a rubber septum, and deoxygenated with a stream of dry argon for 5 min. Aliquots were removed at regular intervals and analyzed by GC–MS, repurging the sample with argon after each aliquot was taken.

Nanosecond laser flash photolysis experiments were carried out using the pulses from a Lambda-Physik Compex 120 excimer laser, filled with F_2–Kr–Ne (248 nm; ca. 25 ns; 100 ± 5 mJ) and a Luzchem Research mLFP-111 laser flash photolysis system, modified as described previously.[10] Solutions were prepared in a calibrated 100 mL reservoir fitted with a glass frit to allow bubbling of argon through the solution for at least 30 min prior to and then throughout the duration of each experiment. Concentrations were such that the absorbance at the excitation wavelength was between ca. 0.7 and 0.9. The solutions were pumped from the reservoir through Teflon tubing connected to a 7 mm × 7 mm Suprasil flow cell using a Masterflex 77390 peristaltic pump. The glassware, sample cell, and transfer lines were dried in a vacuum oven (65–85 °C) before use. In experiments carried out at 25 °C, solution temperatures were measured with a Teflon-coated copper–constantan thermocouple inserted into the thermostatted sample compartment in close proximity to the sample cell; those in which the solution temperature was varied were carried out using a flow cell that allowed insertion of the thermocouple directly into the sample solution. Reagents were added directly to the reservoir by microliter syringe as aliquots of standard solutions. Transient absorbance–time profiles at each concentration of scavenger are the signal-averaged result of 7–40 laser shots. Decay rate constants were calculated by nonlinear least-squares analysis of the transient absorbance–time profiles using the Prism 5.0 software package (GraphPad Software, Inc.) and the appropriate user-defined fitting equations, after importing the raw data from the Luzchem mLFP software and applying the necessary corrections to remove the minor contributions from the corresponding digermenes at low substrate concentrations.[20,27] Rate constants were calculated by linear least-squares analysis of decay rate – concentration data (generally 4–7 points) that spanned as large a range in transient decay rate as possible. Errors are quoted as twice the standard error obtained from the least-squares analyses. Rate constants determined at temperatures other than 25 °C were corrected for thermal solvent expansion.[93]

Low-temperature UV–vis spectrophotometry employed a 2 cm × 1 cm × 1 cm cuvette constructed from quartz tubing (Vitrocom, Inc.) and an Oxford Optistat liquid nitrogen cryostat equipped with an Oxford ITC601 temperature controller. Solutions of **6a** (ca. 0.001 mol/L; $A_{254\ nm} \sim 0.8$) in 3-methylpentane (Sigma-Aldrich spectrophotometric grade) were deoxygenated with argon, sealed in the cuvette with a rubber septum, and placed in the cryostat, which was then cooled to 78 K. The entire assembly was placed in a Rayonet photochemical reactor equipped with twelve RPR-2537 lamps to irradiate the sample, with UV–vis spectra being obtained before and during the photolysis procedure at selected time intervals. The cryostat was then warmed in 1 K increments and a spectrum recorded after ca. 5 min equilibration at the new temperature. The spectra shown in Fig. 4 are difference spectra, obtained by subtracting the UV spectrum obtained prior to photolysis from those obtained after irradiation and subsequent warming.

Supplementary data

Supplementary data (concentration vs time plots and representative NMR spectra from steady-state photolysis experiments and kinetic data determined in laser flash photolysis experiments) for this article are available on the journal Web site (canjchem.nrc.ca). CCDC 788625 contains the X-ray data (for **14**) in CIF format for this manuscript. These data can be obtained, free of charge, via http://www.ccdc.cam.ac.uk/conts/retrieving.html (or from the Cambridge Crystallographic Data Centre, 12 Union Road, Cambridge CB2 1EZ, UK; fax +44 1223 336033; or deposit@ccdc.cam.ac.uk).

Acknowledgments

We thank the Natural Sciences and Engineering Research Council of Canada (NSERC) for financial support and for a graduate scholarship to L.A.H. We also thank Teck-Cominco Metals Ltd. for a generous gift of germanium tetrachloride, Mr. S. Chitnis for the synthesis of **6b** and Drs. J. Britten and H. Jenkins for their assistance with X-ray crystallography. Finally, we thank Tito for his enthusiastic advice, guidance, and support over the past 30 (or so) years.

References

(1) Tokitoh, N.; Okazaki, R. *Coord. Chem. Rev.* **2000**, *210* (1), 251. doi:10.1016/S0010-8545(00)00313-1.
(2) Weidenbruch, M. *J. Organomet. Chem.* **2002**, *646* (1–2), 39. doi:10.1016/S0022-328X(01)01262-1.
(3) Hill, N. J.; West, R. *J. Organomet. Chem.* **2004**, *689* (24), 4165. doi:10.1016/j.jorganchem.2004.09.012.
(4) Tokitoh, N.; Ando, W. In *Reactive Intermediate Chemistry*; Moss, R. A.; Platz, M. S.; Jones, M., Jr., Eds.; John Wiley and Sons: New York, 2004; pp 651–715.
(5) Kira, M.; Iwamoto, T.; Ishida, S. *Bull. Chem. Soc. Jpn.* **2007**, *80* (2), 258. doi:10.1246/bcsj.80.258.

Can. J. Chem. Downloaded from www.nrcresearchpress.com by University of Electronic and Science Techonology of China on 09/18/12
For personal use only.

(6) Nagendran, S.; Roesky, H. W. *Organometallics* **2008**, *27* (4), 457. doi:10.1021/om7007869.
(7) Mizuhata, Y.; Sasamori, T.; Tokitoh, N. *Chem. Rev.* **2009**, *109* (8), 3479. doi:10.1021/cr900093s.
(8) Conlin, R. T.; Netto-Ferreira, J. C.; Zhang, S.; Scaiano, J. C. *Organometallics* **1990**, *9* (4), 1332. doi:10.1021/om00118a074.
(9) Yamaji, M.; Hamanishi, K.; Takahashi, T.; Shizuka, H. *J. Photochem. Photobiol. Chem.* **1994**, *81* (1), 1. doi:10.1016/1010-6030(93)03775-C.
(10) Leigh, W. J.; Harrington, C. R.; Vargas-Baca, I. *J. Am. Chem. Soc.* **2004**, *126* (49), 16105. doi:10.1021/ja046308y.
(11) Leigh, W. J.; Lollmahomed, F.; Harrington, C. R. *Organometallics* **2006**, *25* (8), 2055. doi:10.1021/om0600083.
(12) Moiseev, A. G.; Leigh, W. J. *Organometallics* **2007**, *26* (25), 6268. doi:10.1021/om7006584.
(13) Becerra, R.; Walsh, R. *Phys. Chem. Chem. Phys.* **2007**, *9* (22), 2817. doi:10.1039/b617844h.
(14) Steinmetz, M. G. *Chem. Rev.* **1995**, *95* (5), 1527. doi:10.1021/cr00037a017.
(15) Gaspar, P. P.; West, R. In *The Chemistry of Organic Silicon Compounds;* Rappoport, Z.; Apeloig, Y., Eds.; John Wiley and Sons: New York, 1998; Vol. 2, pp 2463–2568.
(16) Neumann, W. P. *Chem. Rev.* **1991**, *91* (3), 311. doi:10.1021/cr00003a002.
(17) Boganov, S. E.; Egorov, M. P.; Faustov, V. I.; Nefedov, O. M. In *The Chemistry of Organic Germanium, Tin, and Lead Compounds;* Rappoport, Z., Ed.; John Wiley and Sons: New York, 2002; Vol. 2, pp 749–839.
(18) Waterman, R.; Hayes, P. G.; Tilley, T. D. *Acc. Chem. Res.* **2007**, *40* (8), 712. doi:10.1021/ar700028b.
(19) Levin, G.; Das, P. K.; Bilgrien, C.; Lee, C. L. *Organometallics* **1989**, *8* (5), 1206. doi:10.1021/om00107a013.
(20) Leigh, W. J.; Harrington, C. R. *J. Am. Chem. Soc.* **2005**, *127* (14), 5084. doi:10.1021/ja043072p.
(21) Leigh, W. J.; Lollmahomed, F.; Harrington, C. R.; McDonald, J. M. *Organometallics* **2006**, *25* (22), 5424. doi:10.1021/om060595s .
(22) Moiseev, A. G.; Leigh, W. J. *Organometallics* **2007**, *26* (25), 6277. doi:10.1021/om700659d.
(23) Leigh, W. J.; Kostina, S. S.; Bhattacharya, A.; Moiseev, A. G. *Organometallics* **2010**, *29* (3), 662. doi:10.1021/om9009747.
(24) Gillette, G. R.; Noren, G. H.; West, R. *Organometallics* **1989**, *8* (2), 487. doi:10.1021/om00104a033.
(25) Boganov, S. E.; Faustov, V. I.; Egorov, M. P.; Nefedov, O. M. *Russ. Chem. Bull.* **2004**, *53* (5), 960. doi:10.1023/B:RUCB.0000041298.37114.c6.
(26) Ando, W.; Itoh, H.; Tsumuraya, T. *Organometallics* **1989**, *8* (12), 2759. doi:10.1021/om00114a004.
(27) Huck, L. A.; Leigh, W. J. *Organometallics* **2007**, *26* (6), 1339. doi:10.1021/om0609362.
(28) Riviere, P.; Satge, J.; Castel, A. *C. R. Acad. Sci. Paris* **1975**, *281*, 835.
(29) Wienken, S.; Neumann, W. P. *Chem. Ber.* **1993**, *126* (3), 769. doi:10.1002/cber.19931260330.
(30) Lollmahomed, F.; Huck, L. A.; Harrington, C. R.; Chitnis, S. S.; Leigh, W. J. *Organometallics* **2009**, *28* (5), 1484. doi:10.1021/om8010323.
(31) Steele, K. P.; Weber, W. P. *J. Am. Chem. Soc.* **1980**, *102* (19), 6095. doi:10.1021/ja00539a020.
(32) Schoeller, W. W.; Schneider, R. *Chem. Ber.* **1997**, *130* (7), 1013. doi:10.1002/cber.19971300731.
(33) Belzner, J.; Ihmels, H. *Adv. Organomet. Chem.* **1998**, *43*, 1. doi:10.1016/S0065-3055(08)60668-1.
(34) Bharatam, P. V.; Moudgil, R.; Kaur, D. *Organometallics* **2002**, *21* (18), 3683. doi:10.1021/om011096o.
(35) Oláh, J.; De Proft, F.; Veszprémi, T.; Geerlings, P. *J. Phys. Chem. A* **2005**, *109* (8), 1608. doi:10.1021/jp0468556.
(36) Sanji, T.; Mitsugi, H.; Tanaka, M.; Fujiyama, H.; Sakurai, H. *Organometallics* **2006**, *25* (26), 6159. doi:10.1021/om060671r.
(37) Roth, H. D. *Acc. Chem. Res.* **1977**, *10* (3), 85. doi:10.1021/ar50111a003.
(38) Jones, M. B.; Maloney, V. M.; Platz, M. S. *J. Am. Chem. Soc.* **1992**, *114* (6), 2163. doi:10.1021/ja00032a034.
(39) Egorov, M. P.; Gal'minas, A. M.; Basova, A. A.; Nefedov, O. M. *Dokl. Akad. Nauk SSSR (Engl. transl.)* **1993**, *329*, 102.
(40) Egorov, M. P.; Dvornikov, A. S.; Ezhova, M. B.; Kuz'min, V. A.; Kolesnikov, S. P.; Nefedov, O. M. *Organomet. Chem. USSR* **1991**, *4*, 582.
(41) Fanta, A. D.; Belzner, J.; Powell, D. R.; West, R. *Organometallics* **1993**, *12* (6), 2177. doi:10.1021/om00030a029.
(42) Kira, M.; Ishima, T.; Iwamoto, T.; Ichinohe, M. *J. Am. Chem. Soc.* **2001**, *123* (8), 1676. doi:10.1021/ja002798s.
(43) Mochida, K.; Kayamori, T.; Wakasa, M.; Hayashi, H.; Egorov, M. P. *Organometallics* **2000**, *19* (17), 3379. doi:10.1021/om000471u.
(44) Leshina, T. V.; Volkova, O. S.; Taraban, M. B. *Russ. Chem. Bull.* **2001**, *50* (11), 1916. doi:10.1023/A:1015051923766.
(45) Samuel, M. S.; Jennings, M. C.; Baines, K. M. *Organometallics* **2001**, *20* (3), 590. doi:10.1021/om0008530.
(46) Su, M. D. *J. Phys. Chem. A* **2004**, *108* (5), 823. doi:10.1021/jp031021t.
(47) Leigh, W. J.; Dumbrava, I. G.; Lollmahomed, F. *Can. J. Chem.* **2006**, *84* (7), 934. doi:10.1139/V06-107.
(48) Huck, L. A.; Leigh, W. J. *Organometallics* **2009**, *28* (23), 6777. doi:10.1021/om900791e.
(49) Tsumuraya, T.; Batcheller, S. A.; Masamune, S. *Angew. Chem. Int. Ed. Engl.* **1991**, *30* (8), 902. doi:10.1002/anie.199109021.
(50) Dixon, C. E.; Liu, H. W.; Vander Kant, C. M.; Baines, K. M. *Organometallics* **1996**, *15* (26), 5701. doi:10.1021/om9606911.
(51) Yu, W. H. S.; Wijnen, M. H. J. *J. Chem. Phys.* **1970**, *52* (8), 4166. doi:10.1063/1.1673626.
(52) Davis, D. D.; Schmidt, J. F.; Neeley, C. M.; Hanrahan, R. J. *J. Phys. Chem.* **1975**, *79* (1), 11. doi:10.1021/j100568a003.
(53) Rebbert, R. E.; Ausloos, P. J. *J. Photochem.* **1976/77**, *6* (4), 265. doi:10.1016/0047-2670(76)85084-8.
(55) Kolesnikov, S. P.; Perl'mutter, B. L.; Nefedov, O. M. *Dokl. Akad. Nauk SSSR* **1971**, *196*, 85.
(56) Satgé, J.; Massol, M.; Rivière, P. *J. Organomet. Chem.* **1973**, *56*, 1. doi:10.1016/S0022-328X(00)89951-9.
(57) Murakhtina, T.; Heuft, J.; Meijer, E. J.; Sebastiani, D. *ChemPhysChem* **2006**, *7* (12), 2578. doi:10.1002/cphc.200600385.
(58) Hurni, K. L.; Rupar, P. A.; Payne, N. C.; Baines, K. M. *Organometallics* **2007**, *26* (23), 5569. doi:10.1021/om7005358.
(59) Cooke, J. A.; Dixon, C. E.; Netherton, M. R.; Kollegger, G. M.; Baines, K. M. *Synth. React. Inorg. Met.-Org. Chem.* **1996**, *26* (7), 1205. doi:10.1080/00945719608004362.
(60) Baines, K. M.; Cooke, J. A.; Vittal, J. J. *Chem. Commun.* **1992**, 1484.
(61) Chateauneuf, J. E. *J. Am. Chem. Soc.* **1990**, *112* (1), 442. doi:10.1021/ja00157a066.
(62) Hawari, J. A.; Davis, S.; Engel, P. S.; Gilbert, B. C.; Griller,

Can. J. Chem. Downloaded from www.nrcresearchpress.com by University of Electronic and Science Techonology of China on 09/18/12
For personal use only.

D. *J. Am. Chem. Soc.* **1985**, *107* (16), 4721. doi:10.1021/ja00302a020.
(63) Toltl, N. P.; Leigh, W. J.; Kollegger, G. M.; Stibbs, W. G.; Baines, K. M. *Organometallics* **1996**, *15* (17), 3732. doi:10.1021/om960334q.
(64) Leigh, W. J.; Potter, G. D.; Huck, L. A.; Bhattacharya, A. *Organometallics* **2008**, *27* (22), 5948. doi:10.1021/om800574s.
(65) Leigh, W. J.; Huck, L. A.; Held, E.; Harrington, C. R. *Silicon Chem.* **2005**, *3* (3–4), 139. doi:10.1007/s11201-006-9017-4.
(66) Ling, A. C.; Willard, J. E. *J. Phys. Chem.* **1968**, *72* (6), 1918. doi:10.1021/j100852a010.
(67) Toltl, N. P.; Leigh, W. J. *J. Am. Chem. Soc.* **1998**, *120* (6), 1172. doi:10.1021/ja973756f.
(68) Ando, W.; Tsumuraya, T.; Sekiguchi, A. *Chem. Lett.* **1987**, *16* (2), 317. doi:10.1246/cl.1987.317.
(69) Laser flash photolysis of **20** in hexanes solution affords long-lived absorptions centred at 300 and 450 nm, assignable to the diphenyl(trimethylsilyl)germyl radical, but no evidence for the formation of $GePh_2$. See Supplementary data.
(70) Nazran, A. S.; Gabe, E. J.; LePage, Y.; Northcott, D. J.; Park, J. M.; Griller, D. *J. Am. Chem. Soc.* **1983**, *105* (9), 2912. doi:10.1021/ja00347a073.
(71) Tukada, H.; Sugawara, T.; Murata, S.; Iwamura, H. *Tetrahedron Lett.* **1986**, *27* (28), 235. doi:10.1016/S0040-4039(00)83985-4.
(72) Toltl, N. P.; Stradiotto, M. J.; Morkin, T. L.; Leigh, W. J. *Organometallics* **1999**, *18* (26), 5643. doi:10.1021/om990447k.
(73) Koecher, J.; Lehnig, M.; Neumann, W. P. *Organometallics* **1988**, *7* (5), 1201. doi:10.1021/om00095a029.
(74) Shusterman, A. J.; Landrum, B. E.; Miller, R. L. *Organometallics* **1989**, *8* (8), 1851. doi:10.1021/om00110a004.
(75) Mochida, K.; Yoneda, I.; Wakasa, M. *J. Organomet. Chem.* **1990**, *399* (1-2), 53. doi:10.1016/0022-328X(90)80083-C.
(76) Luo, Y.-R.; Kerr, J. A. In *CRC Handbook of Chemistry and Physics* [Online], 87 ed.; Lide, D. R., Ed.; CRC Press/Taylor and Francis: Boca Raton, FL, 2007; pp 9.54–9.82. http://www.hbcnetbase.com (accessed 28 April 2010).
(77) Hanf, A.; Läuter, A.; Volpp, H.-R. *Chem. Phys. Lett.* **2003**, *368* (3-4), 445. doi:10.1016/S0009-2614(02)01896-1.
(78) Clark, K. B.; Griller, D. *Organometallics* **1991**, *10* (3), 746. doi:10.1021/om00049a039.
(79) Lollmahomed, F.; Leigh, W. J. *Organometallics* **2009**, *28* (11), 3239. doi:10.1021/om9000814.
(80) Houk, K. N.; Rondan, N. G.; Mareda, J. *Tetrahedron* **1985**, *41* (8), 1555. doi:10.1016/S0040-4020(01)96395-1.
(81) Su, M. D. *J. Am. Chem. Soc.* **2003**, *125* (7), 1714. doi:10.1021/ja0210751.
(82) Li, R. E.; Sheu, J. H.; Su, M. D. *Inorg. Chem.* **2007**, *46* (22), 9245. doi:10.1021/ic7012446.
(83) Chen, C.-H.; Su, M. D. *Chem. Eur. J.* **2007**, *13* (24), 6932. doi:10.1002/chem.200601736.
(84) Totten, L. A.; Roberts, A. L. *Crit. Rev. Environ. Sci. Technol.* **2001**, *31* (2), 175. doi:10.1080/20016491089208.
(85) Ito, O.; Hoteiya, K.; Watanabe, A.; Matsuda, M. *Bull. Chem. Soc. Jpn.* **1991**, *64* (3), 962. doi:10.1246/bcsj.64.962.
(86) Leigh, W. J.; Toltl, N. P.; Apodaca, P.; Castruita, M.; Pannell, K. H. *Organometallics* **2000**, *19* (16), 3232. doi:10.1021/om000174p.
(87) Lalevée, J.; Blanchard, N.; Graff, B.; Allonas, X.; Fouassier, J. P. *J. Organomet. Chem.* **2008**, *693* (24), 3643. doi:10.1016/j.jorganchem.2008.08.039.
(88) Ando, W.; Tsumuraya, T. *J. Chem. Soc. Chem. Commun.* **1987**, (20): 1514. doi:10.1039/c39870001514.
(89) Sharutin, V. V.; Sharutina, O. K.; Pavlov, K. V.; Shcherbinin, V. V. *Russ. J. Gen. Chem.* **1994**, *64*, 949.
(90) Komoriya, H.; Kako, M.; Nakadaira, Y.; Mochida, K. *Organometallics* **1996**, *15* (8), 2014. doi:10.1021/om9509150.
(91) Nemes, G.; Escudié, J.; Silaghi-Dumitrescu, I.; Ranaivonjatovo, H.; Silaghi-Dumitrescu, L.; Gornitzka, H. *Organometallics* **2007**, *26* (21), 5136. doi:10.1021/om061188j.
(92) Ohshita, J.; Toyoshima, Y.; Iwata, A.; Tang, H.; Kunai, A. *Chem. Lett.* **2001**, *30* (9), 886. doi:10.1246/cl.2001.886.
(93) Lide, D. R., Ed. *CRC Handbook of Chemistry and Physics* [Online], 87 ed.; CRC Press/Taylor and Francis: Boca Raton, FL, 2007; pp 15–25. http://www.hbcnetbase.com (accessed 28 April 2010).

REVIEW / SYNTHÈSE

Photoinduced charge separation in microporous and mesoporous materials

Ranjit T. Koodali

Abstract: A review of photoinduced charge separation of organic molecules in microporous and mesoporous materials is presented. In particular, the photoionization of *N*-alkylphenothiazine (PC_n), *N*,*N*,*N*′,*N*′-tetramethylbenzidine (TMB), and porphyrin in microporous materials, such as zeolites, aluminophosphates (AlPOs), silicoaluminophosphates (SAPOs), and mesoporous materials, such as MCM-41, MCM-48, and SBA-15, is discussed.

Key words: photoinduced charge separation, photoionization, microporous, mesoporous materials.

Résumé : On présente une revue de la séparation de charge photoinduite des molécules organiques dans des matériaux microporeux et mésoporeux. On discute particulièrement des cas des *N*-alkylphénothiazines (PC_n), de la *N*,*N*,*N*′,*N*′-tétraméthylbenzidine (TMB) et de la porphyrine dans des matériaux microporeux tels les zéolites, les aluminophosphates (AlPO) et les silicoaluminophosphates (SAPO) ainsi que les matériaux mésoporeux tels le MCM-41, le MCM-48 et le SBA-15.

Mots-clés : séparation de charge photoinduite, photoionisation, matériaux microporeux et mésoporeux.

[Traduit par la Rédaction]

Introduction

Solar energy conversion and storage has gained renewed interest in the past few years.[1–11] The scientific community is engaged in the pursuit of exploring the possibility of using sunlight as the source to produce clean, renewable, and environment friendly based energy alternative to the widely used fossil fuels. Research in this area can be broadly classified into solar electricity (production of electricity through the use of inorganic and organic solar cells), solar fuels (photoelectrochemical cells), and solar thermal systems (typically through the use of solar concentrators). Nature provides scientists with inspiration and hope to find possibilities to solve this global challenge. In natural photosynthesis, solar energy is converted into chemical energy in the form of biomass. The overall efficiency is very low, i.e., <8% of the incident insolation is stored as chemical fuel. In spite of the relative low efficiency, this process is responsible for sustaining living organisms on earth. The natural photosynthetic process involves four essential steps. The first step is light absorption and propagation through an organized biomolecular membrane. This step is accomplished by nature through a light-harvesting complex that consists of several pigments (primarily chlorophylls, carotenes, and xanthophylls) and redox proteins that are arranged in a well-defined spatial geometry and work in tandem. The next step involves vectorial or unidirectional photoinduced electron transfer through a co-operative interaction between the various components of the membrane. This is followed by electron transport through a chain of reactions in which, ultimately, the electron is used to reduce NADP to NADPH. All of these three steps occur in the thylakoid membrane. The final step involves the fixation of carbon dioxide to generate energy in the form of carbohydrates and the simultaneous oxidation of water to oxygen.[12]

The intricate and highly organized structure found in nature has inspired chemists to explore the possibility of designing artificial photosynthetic systems. Intense research in this area is pursued with the purpose of harvesting sunlight and its conversion to electricity or fuels. From a chemist's perspective, the photoinduced electron transfer is a key step and, thus, the study of photoinduced electron-transfer reactions is important in the design of artificial photoredox systems.[13] Artificial photoredox systems may provide ways by which sunlight reaching the earth's surface can be exploited to generate useful energy or chemicals. Nature provides chemists with a toolbox for designing artificial photoredox systems, and it may soon be possible for us to mimic all, if not most, of the essential intricacies of the natural photosynthetic system with new and revolutionary discoveries being made in unraveling the photosynthesis mechanism at the atomic level. Indeed, artificial nanoscale assemblies consisting of organic–inorganic hybrid materials synthesized in the laboratory are capable of mimicking the photosynthesis reaction. One must, however, realize that success is limited to

Received 1 June 2010. Accepted 14 July 2010. Published on the NRC Research Press Web site at canjchem.nrc.ca on 2 February 2011.

This article is part of a Special Issue dedicated to Professor J. C. Scaiano.

R.T. Koodali. Department of Chemistry, University of South Dakota, Vermillion, SD 57069, USA (e-mail: Ranjit.Koodali@usd.edu).

Can. J. Chem. Downloaded from www.nrcresearchpress.com by University of Electronic and Science Techonology of China on 09/18/12
For personal use only.

Can. J. Chem. Downloaded from www.nrcresearchpress.com by University of Electronic and Science Techonology of China on 09/18/12
For personal use only.

the laboratory scale and, currently, the technology is not mature enough for large-scale deployment. The challenges are poor efficiency, long-term instability, and high cost.

The drawback of most photochemical processes is the thermodynamically favorable rapid back-electron transfer (BET) reaction that results in the loss of any converted energy in the form of heat. Thus, an objective is to design systems in which long-lived charge separation can be achieved; furthermore, it is desirable if this can be achieved at room temperature. An important requirement is to achieve net charge separation, since efficient photoionization followed by rapid BET is not a practical way of storing energy.

Photoinduced charge separation in organized molecular assemblies

The photoinduced charge separation can be represented by the following equations:

$$[1] \quad D \rightarrow D^*$$

$$[2] \quad D^* + A \rightarrow D^+ + A^-$$

$$[3] \quad D^+ + A^- \rightarrow D + A$$

where D and A represent donor and acceptor molecules. Light excitation in step [1] creates the excited species, D*. The second step is the photoionization step in which an electron transfer occurs. The excitation of the donor molecule makes it a better reducing agent and thus it can easily donate an electron to A. If the redox properties of D^+ and A^- are tailored appropriately then they may be used to drive reactions such as the photosplitting of water or the fixing of carbon dioxide to generate fuels. The reaction in step [3]) is the recombination or the BET reaction that occurs readily in homogeneous solutions and thereby wastes the energy created by excitation. An important goal is to minimize rxn. [3] so that the free energy converted from light may be stored and subsequently used for driving a chemical reaction.

As discussed, minimizing the BET reaction in photoredox systems is critical. Owing to the importance of this problem, many attempts have been made to design systems that can minimize BET.[14,15] In this respect, microheterogeneous systems provide appropriate spatial organization of both donor and acceptor molecules to retard BET and increase the lifetime of the photogenerated species.[16–19] The term microheterogeneous system encompasses several classes of systems ranging from surfactants, lipid vesicles, liposomes, micelles, and microemulsions to organic and inorganic materials. Extensive studies using molecular assemblies were carried out in the 1980s and 1990s, and several excellent papers and reviews were published and are not the focus of this review.[20–31] An important aspect of the microheterogeneous systems is the fact that they exhibit efficient light-induced electron transfer compared with homogeneous solvents. Also, efficiency losses owing to self-quenching reactions are minimized in microheterogeneous systems and thus a relatively high concentration of dye molecules may be used. Also, the observed photophysical behavior and the reaction kinetics in microheterogeneous systems are quite different when compared with homogeneous systems.

The photoinduced charge separation of organic molecules in lipids, micelles, vesicles, and polymers has been described in many reports.[26–31] The main drawback of these systems is that the lifetime of the photoproduced species is only a few milliseconds (ms), and, typically, these are stable only at relatively low temperatures, i.e., 77 K. In micelles and vesicles, the photoinduced charge separation efficiency is affected by many factors such as the nature of the head group of the surfactant, charge and alkyl length of the surfactant, location of the electron donors and acceptors relative to the surfactant–water interface, surface charge distribution of the surfactants, and the ionic strength of the interface. The net quantum efficiency of organic molecules in micelles and vesicles is typically higher than that in homogeneous solutions, but the photoinduced radicals are not typically stable at room temperature as stated previously.[30,31] The quantum efficiencies are usually higher in vesicles when compared with micelles. The yields showed a dependence upon the surface charge of the aggregate, increasing in the order anionic (micelles) < cationic (micelles) < anionic (vesicles) < neutral (vesicles) < cationic (vesicles).[29] Furthermore, in several instances, the quantum efficiencies in micelles and vesicles are limited by the solubility of the photoactive molecules. Polymer systems with chemical or physical incorporation of electron donors and acceptors show promise, but they still have significant degrees of molecular motion that decrease the stability of the photoproduced radicals.[32,33] The synthesis of acceptors and donors connected by covalent bonds or more complex combinations, such as donor–spacer–acceptor, have also generated new systems for efficient photoinduced charge separation.[34] But covalently linked architecture alone has not provided long-lived photoinduced charge separation at room temperature. A big drawback of the these systems is the fact that the photoinduced charge separation is short lived at room temperature, and, more importantly, photolysis of such systems was found to cause degradation of the systems and thus they were not very robust. It became clear that heterogeneous solid supports provide a novel way to arrange the photoactive molecules and they also have the potential of other functional requirements of an artificial photoredox system such as membranelike properties.[14,15]

Photoinduced charge separation in layered materials

Initial studies of the photoinduced charge separation of organic molecules in oxide materials were carried out on clay, alumina, and silica. The clays were a logical choice of support to be investigated as solid supports, since they were used extensively in the petroleum industry until the use of zeolites.[30,35] Clays may be broadly classified into expandable (in water) and nonexpandable materials or alternatively called as the 2:1 or 1:1 clay. The expandable clays, such as montmorillonite and hectorite, have interlayer space that can be varied depending on the nature of the material intercalated. The photoinduced charge separation of polycyclic aromatic hydrocarbons,which include anthracene, naphthalene, pyrene (Py), and tris(2,2′-bipyridine)ruthenium(II) ($Ru(bpy)_3^{2+}$), were the subject of numerous investigations in the laboratory of Thomas and co-workers.[36–44] The fluorescent probe $Ru(bpy)_3^{2+}$ was used to investigate the nature of the surfaces of both naturally occurring clays like hectorite and

Can. J. Chem. Downloaded from www.nrcresearchpress.com by University of Electronic and Science Techonology of China on 09/18/12
For personal use only.

montmorillonite and synthetic clay such as laponite. The lifetime and quantum yield are dependent on the location of the adsorbed ions or molecules, for example, $Ru(bpy)_3^{2+}$ is adsorbed in the interlayer spacings in hectorite and montmorillonite, whereas it is adsorbed on the surface in laponite. The lifetime of the photogenerated species, namely $Ru(bpy)_3^{3+}$, is ~0.5 ms.[36] The photophysical properties of pyrene in alumina, silica, and laponite were studied by Thomas and co-workers[35–37] They reported that pyrene cation radicals are produced by irradiation with UV light and that the mechanism of photoionization on the solid can take place via a monophotonic or biphotonic process. The lifetime of the photoproduced pyrene cation radical was found to be ~10 ms. Aromatic amines such as benzidene (BD) and *N*,*N*,*N*′,*N*′-tetramethylbenzidine (TMB) have also been investigated.[45] UV irradiation ($\lambda < 400$ nm) leads to photoionization given by the following equation:

$$[4] \quad TMB \rightarrow TMB^{+} + e_{aq}^{-}$$

The hydrated electron reacts in the presence of oxygen to give the superoxide radical ($O_2^{-\bullet}$). The lifetime of the photoproduced TMB^+ is ~1 ms. Since studies with clays did not necessarily increase the lifetime of the photogenerated species, other layered materials such as zirconium phosphate were explored as hosts.

Inorganic layered phosphates such as α-zirconium phosphate (α-ZrP) have been used for constructing supramolecular assemblies.[46] The phosphate group carries an ionizable hydroxyl group that can be easily deprotonated, and hence cations can be incorporated by ion exchange. The photoinduced electron transfer of $Ru(bpy)_3^{2+}$, *N*-alkylphenothiazines (PC_n), and TMB have been examined in these layered materials.[47–49] The quantum efficiency of the PC_n cation radical increases from methyl to hexyl, and as the chain length increases further, the photo-oxidation yield decreases.[48] The stability of the photoproduced PC_n^+ cation was found to decrease from methyl to hexadecyl, and this was attributed to the increased inductive effect of PC_n^+ with an increase in the alkyl chain length. Also, it has been reported that with anincrease in chain length, the PC_ns tend to form clusters that may self-quench by a mechanism involving intermolecular transfer to a surface trap.[50] Thus, there is an optimum chain length in the quantum efficiency. In a separate study, Krishna and Kevan have reported the photooxidation of TMB in α-ZrP.[49] The half-life of TMB^+ was determined to be 10 h at room temperature, whereas the half-life of PC_n^+ was found to range from several days to several weeks depending on the chain length as discussed previously.

Photoinduced charge separation in silica gels

A dramatic increase in the lifetime (up to a few hours) of the photogenerated species was observed when the reactions were carried out in silica gels. The research group of Avnir has done pioneering study involving molecular excited states in sol–gel matrices.[51,52] Some interesting features of pyrene-doped SiO_2 gels are that the photoionization process is biphotonic, the lifetime of the solvated electron is fairly long, and phosphorescence is observed at room temperature. This has an important consequence in that the sol–gel matrix allows for photophysical studies to be usually conducted at room temperatures. Exceedingly long-lived photoinduced charge separation was reported in an artificial photosynthetic system that consisted of dimethylviologen (MV^{2+}) as the electron acceptor and Py as the electron donor immobilized in a porous sol–gel silica glass.[53–55] Photoinduced electron transfer from PC_ns, TMB, porphyrin, and $Ru(bpy)_3^{2+}$ in amorphous silica gels have also been reported.[22,23,56,57] The guest molecules were introduced into the host system either by their addition to the synthesis solution during the room-temperature synthesis process or were incorporated by a post-impregnation method after the silica gels were separately synthesized. The photoionization of PC_n and TMB were studied by ESR and diffuse reflectance spectroscopy. The quantum efficiency was found to depend on the pore size of the silica used. In a small-pore silica gel (average pore sizes of 1.7 and 2.5 nm), *N*-methylphenothiazine cation radical ($PC_1^{+\bullet}$) and TMB cation radical ($TMB^{+\bullet}$) have a larger quantum efficiency when compared with a large-pore-sized silica gel (6.0 and 14 nm).[22,56] The relatively low quantum efficiency in the larger pores was partly attributed to the formation of TMB_2^{2+}. Although the quantum efficiency was found to depend on the pore sizes, the stability of the photoproduced TMB^+ was found to be similar in all the silica materials examined in this study. The half-life of TMB^+ ions was found to be ~2 h. It was suggested that the mobility of the photoproduced cations controls the yield and photostability. Interestingly, no effect on the quantum efficiency and stability of the PC_n cation radicals were observed when the alkyl chain lengths were varied from 1 to 16 carbons. The results obtained for the photoionization of PC_n and TMB show the same dependency on pore size, suggesting that the photo-oxidation mechanisms for these two photochromic molecules are the same. These studies indicate that the silica gel framework acts as an electron acceptor and the surface silanol groups of silica gels are probably the principal sites responsible for the adsorption of PC_n and TMB. Surface hydroxyl groups may serve as electron acceptors in large-pore-sized silica with production of a hydrogen atom. However, in small-pore-sized materials no ESR signal owing to trapped hydrogen atoms were detected, although the yield of the photoproduced cations was found to be higher in them. Thus, the results do not clearly clarify the role of the silanol groups as electron acceptors. In a follow-up study, Xiang and Kevan[57] studied the effects of chloromethanes on the photoionization of *N*-methylphenothiazine in silica gels of 14 nm pore size at room temperature. The net quantum efficiency of $PC_1^{+\bullet}$ was compared with the samples that did not have the chloromethanes. It was found that addition of CCl_4 and $CHCl_3$ increased the photoionization yield of $PC_1^{+\bullet}$, and this was attributed to the higher electron affinities (2.12 and 1.75 eV).[58] In comparison, addition of CH_2Cl_2 and CH_3Cl did not enhance the quantum efficiency, presumably because of their lower electron affinities. MV^{2+} is an efficient electron acceptor and has been investigated extensively in photoredox systems. The quantum efficiency and stability of the photoproduced MV^+ radical was found to also depend on the pore size; however, the yield of MV^+ radical was higher in the large-pore silica (14 nm) compared with the small-pore silica (1.7 nm).[59] This trend was attributed to the fact that the counter chloride

Can. J. Chem. Downloaded from www.nrcresearchpress.com by University of Electronic and Science Techonology of China on 09/18/12
For personal use only.

anion in the dimethylviologen dichloride was the electron donor. The separation distance between the MV^+ and the chloride trapping site is larger in the large-pore silica, and hence the BET is minimized in the 14 nm average pore size silica. Increasing the chain length of the viologen from one to seven did not significantly affect the quantum efficiency or stability when the pore size was kept the same. Interestingly, the method of incorporation was found to affect the quantum efficiency; the quantum efficiencies were found to be greater when the impregnation method was used compared with a direct incorporation of MV^{2+}.

The photo-oxidation of $Ru(bpy)_3^{2+}$ in silica gels was reported by Matsuura and Kevan.[23] The stabilization of $Ru(bpy)_3^{3+}$, particularly at room temperature, is usually a challenge, since the BET reaction is fairly rapid and usually exothermic. $Ru(bpy)_3^{3+}$ was stabilized in silica gel after photolysis in the presence of electron acceptors such as persulfonate ion or tetrachloro-1,4-benzoquinone (*p*-chloranil). The yield of $Ru(bpy)_3^{3+}$ was found to be similar for silica gels with average pore sizes of 2.5 and 14 nm at 77 K for the same loading of $Ru(bpy)_3^{2+}$ using $S_2O_8^{2-}$ as the electron acceptor. The yield of $Ru(bpy)_3^{3+}$ was calculated to be 50% and 1% in the presence of persulfonate and *p*-chloranil, respectively. The efficient quenching of the $Ru(bpy)_3^{2+*}$ by $S_2O_8^{2-}$ has been attributed to the strong affinity of $S_2O_8^{2-}$ and the strong attractive force between the positively charged $Ru(bpy)_3^{2+}$ and the negatively charged $S_2O_8^{2-}$ ions. The yield of $Ru(bpy)_3^{3+}$ is an order of magnitude lower at room temperature compared with the yield at 77 K, and this limits their applicability.

Metalloporphyrins are involved in several important electron transfer reactions in biological reactions and photosynthetic systems.[60–64] Metalloporphyrins can be easily photoionized. The photoionization can take place through the oxidation of the ligand or the central metal ion leading to the formation of metalloporphyrin π-cation radicals or an increase in the oxidation state of the metal ion.[65] In a study, the photoionization of several metalloporphyrins (H_2TPP, CuTPP, NiTPP, and ZnTPP) adsorbed in 4 nm silica gel irradiated with visible light was examined at room temperature and 77 K.[66] The photoionization efficiency was found to decrease in the order ZnTPP > H_2TPP > NiTPP >> CuTPP. The half-life of $Zn(II)TPP^{+\bullet}$ was determined to be 16 days at room temperature, a remarkable improvement compared with other systems investigated earlier. The main drawback of these studies is the fact that the average pore sizes of the silica materials were reported with no specific information regarding the pore-size distribution, and thus it is fairly difficult to correlate the effect of pore sizes on the quantum efficiencies, if any. In addition, silica gels have no long-range order and a have wide pore-size distribution compared with zeolites and may not serve as a useful biomimetic artificial photoredox system.

Photoinduced charge separation in microporous materials

Extensive research has been done on zeolites as hosts for photoinduced charge separation.[67–70] Over the last decade, considerable progress has been made in using zeolites to extend the lifetime of the photoproduced species from hours to several days, if not weeks. Zeolites are crystalline aluminosilicates with a three-dimensional structure made up of corner-sharing SiO_4 and AlO_4 tetrahedra with cations occupying extra framework positions to balance the charge of the negative framework. Zeolites have been popular choices as host materials because their periodic and regular framework not only replicates the spatial organization observed in nature, but the inherent electrostatic environment provides an opportunity to retard BET.[71–73] The negatively charged aluminosilicate framework provides a polar environment that can be further modified by varying the number and type of charge-compensating cations. The arrangement of channels and pores in these crystalline materials allows for the placement of molecules in well-defined and unique spatial arrangements. Thus, the architecture of zeolites allows for novel arrangements of molecules in space with considerable long-range order. The difference between molecules encapsulated in zeolites and species encapsulated in matrices such as micelles and vesicles is that the zeolite framework can act as an active host and influence the structure and reactivity of the encapsulated molecules. Kochi and co-workers studied the photoinduced charge transfer between neutral aromatic donors and cationic bipyridinium viologen acceptors in zeolite L, Y, mordenite, and mazzite cavities.[69,73–75] They found that the lifetime of the charge-separated state in the zeolite was in the order of milliseconds compared with that in homogeneous solution (picoseconds). Zeolites have also been employed as a medium for artificial supramolecular assembly of various donor–acceptor pairs in an effort to understand the factors that govern the charge-separation states. In particular, studies have been carried out to achieve long-lived charge separation across zeolite–solution interfaces.[13,16,17] Zeolites Y and L internally exchanged with electron acceptor MV^{2+} and externally with bulky electron donors $Ru(bpy)_3^{2+}$ or $Zn(II)Por^{4+}$ (Por = tetrakis(*N*-methyl-4-pyridyl)porphyrin); these were prepared and the photoinduced charge separation was studied.[76] The small quantum yield (0.0003%) suggests that the BET process is very fast and efficient. A dramatic improvement in the yield and efficiency of charge separation across the zeolite–solution interface was achieved by filling the empty cages of zeolite Y with an appropriate photosensitized donor $Ru(bpy)_3^{2+}$ and a charge-relaying compound *N*,*N*′-tetramethylene-2,2′-bipyridinium. The electron acceptor chosen was propylviologen sulfonate (PVS). On irradiation, the system approached a steady state as the radical yield reached ~60% of the total sensitizer concentration.[13] A further increase in the yield of charge separation across the zeolite–solution interface was obtained by simultaneously introducing an electron relay compound and electron donor in adjacent cages of a zeolite. This led to an approximately fourfold increase in the yield of charge separation.[17]

In a series of papers published from the Kevan group, the photoionization of PC_n, MV^{2+}, and TMB were examined in aluminosilicate zeolites.[77,78–80] Na forms of Zeolite A, X, and Y were ion-exchanged by Li^+, K^+, or Cs^+ and prepared first. Then, alkylmethylviologen (MV^{2+}_n) was ion-exchanged and the sample evacuated to 10^{-5} torr (1 torr = 133.3224 Pa) at 90 °C. Upon irradiation at 77 K, peaks corresponding to the methylviologen cation radical were observed. The yield was found to be in the order zeolites Y > zeolites X >> zeolite A. Experiments were also carried out using the dibromide

Can. J. Chem. Downloaded from www.nrcresearchpress.com by University of Electronic and Science Techonology of China on 09/18/12
For personal use only.

salt of diheptylviologen, but the yield of the diheptylviologen cation radical was higher when compared with the yield of the dimethylviologen dichloride cation radical. This result suggests that the aluminosilicate framework of zeolites is the electron source because bromide is a weaker reducing anion than chloride, and one would have expected an opposite trend if the halide ions were the electron source. Furthermore, it is highly unlikely that the halide ions are ion-exchanged into the extra-framework positions because zeolites are known to selectively exchange cationic species only. In this study, the presence of Li^+, K^+, or Cs^+ instead of Na^+ did not have any observable effect on the yield of the MV^+ cation radical. This result was surprising, since it has been reported that the donor strength of the zeolites framework can be modulated by the extra-framework ions.[81–83] Alvaro et al.[84] reported that the yield of $MV^{+\bullet}$ was found to depend on the nature of the alkali metal ion-exchanged into zeolite Y. Yoon and co-workers[85] reported the formation of $MV^{+\bullet}$ in MV^{2+}–arene donor charge-transfer (CT) complexes in K^+-, Rb^+-, and Cs^+-containing zeolite X. However, in the absence of any arene, $MV^{+\bullet}$ was not detected. In subsequent studies, Ranjit and Kevan[78,79] reported that the quantum efficiency of $MV^{+\bullet}$ increased in the order Li–X < Na–X < K–X < Rb–X < Cs–X. The donor strength of the zeolite framework also increases in the same order, suggesting that the aluminosilicate framework is the electron donor. This was further confirmed by a linear correlation between the quantum efficiency and the Sanderson's partial charge of the framework oxygen. The half-lives for $MV^{+\bullet}$ were determined to be 63, 24, 20, 12, and 10 days for Cs–X, Rb–X, K–X, Na–X and Li–X zeolites, respectively, and consistent with the trend observed for the quantum efficiency. The quantum efficiency of $MV^{+\bullet}$ in Na–A zeolite was found to be two times lower than Na–X, and this was attributed to the fact that the pore opening in zeolite A is much smaller and that MV^{2+} is only adsorbed on the external surface. The photoionization of TMB was studied in chromium ion-exchanged zeolite X at room temperature.[80] The quantum efficiency of $TMB^{+\bullet}$ was found to be higher in Cr(V)–X zeolite compared with Cr(III)–X zeolite. The quantum efficiency of $TMB^{+\bullet}$ was determined to be highest in the sample containing the least amount of Cr, i.e., Si/Cr = 222. Increasing the Cr amount leads to the formation of greater amounts of non-paramagnetic $(TMB)_2^{2+}$ and evidence for this was supported by UV–vis diffuse reflectance spectroscopy (DRS) studies because ESR can only detect paramagnetic species such as $TMB^{+\bullet}$. Zeolites indeed have proven to be a versatile media for the study of photoinduced charge separation.

Other microporous materials such as ETS-10, clinoptilolite, and mordenite have also been examined for the photoinduced charge separation of methylphenothiazine (PC_1).[86–88] A series of metal-ion-exchanged microporous titanosilicates were prepared and *N*-methylphenothiazine (PC_1) was incorporated in them. UV irradiation at room temperature led to the formation of $PC_1^{+\bullet}$. The quantum efficiency of $PC_1^{+\bullet}$ was found to decrease in the order H–ETS-10 > Na,K–ETS-10 > Na–ETS-10 > Ni–ETS-10 > Li–ETS-10 > Cu–ETS-10 > Co–ETS-10. Also, the photoionization yield was found to decrease with an increase in chain length.[86] When clinoptilolite was used as the host, the quantum efficiency of $PC_1^{+\bullet}$ was found to decrease in the order H–clinoptilolite > Ni–clinoptilolite > K–clinoptilolite > Na–clinoptilolite > Co–clinoptilolite > Na,K–clinoptilolite > Cu–clinoptilolite.[87] Taken together, these results suggest that the photochemistry of PC_1 is sensitive to the pore opening and the nature of the metal ion. It has been suggested that the protons and the alkali metal ions act as electron acceptors in these two systems, which is consistent with previously reported systems; however, no studies confirming this postulate have been carried out.

H–, Na–, and Na,K–mordenites were examined as molecular hosts for the photoionization of *N*,*N*,*N*′,*N*′-tetramethyl-*p*-phenylenediamine (TMPD).[88] The quantum efficiency was found to decrease in the order Na–mordenite/TMPD > Na,K–mordenite/TMPD > Na–mordenite/TMB > Na,K–mordenite/TMB > H–mordenite/TMPD > H–mordenite/TMB. The higher quantum efficiency found for TMPD was due to the lower gas-phase ionization potential (4.9 eV) compared with 6.1 eV for TMB. However, the photostabilities of $TMPD^{+\bullet}$ and $TMB^{+\bullet}$ are only a few hours. Ion exchange of Na^+ by Ni^{2+} and Cu^{2+} further increases the quantum efficiency twofold.

Aluminophosphates (AlPO-*n*) belong to a class of microporous molecular sieves comparable to zeolites.[89] The structure of AlPO covers a wide range of structure types; some are analogous to zeolites such as chabazite (AlPO-34), but there are a number of AlPOs that are unique and have no zeolite analogue such as AlPO-5 and AlPO-11. In recent years, microporous AlPO and silicoaluminophosphate (SAPO) materials have been examined as hosts.[90,91] Furthermore, they seem more amenable to framework substitution of Al(III) and (or) P(V) by a variety of transition metal ions.[92–94] The AlPO-5 (SAPO-5) is composed of 4-ring, 6-ring, and 12-ring channels; AlPO-8 (SAPO-8) consists of 4-ring, 6-ring, and 14-ring channels, whereas AlPO-11 (SAPO-11) consists of 4-ring, 6-ring, and 10-ring channels. This leads to channels with pore openings of 7.3, 8.7, and 6.3 Å, respectively. The molecular dimensions of organic molecules PC_1 and Py are 6.5 Å × 10 Å and 6.9 Å × 10 Å, respectively.

One of the first reports of the photoionization of methylphenothiazine in a transition metal containing SAPO was reported by Kurshev et al.[95] They studied the photoionization of methylphenothiazine at room temperature in SAPO-5, SAPO-11 (channel-type microporous materials), SAPO-34, and VPI-5 (cage-type microporous materials structurally similar to AlPO-8). The quantum efficiency was found to decrease in the order Ni–VPI-5 > Ni–SAPO-5 >> Ni–SAPO-11 ~ Ni–SAPO-34. The yield and stability of the photoproduced cation radicals was found to negligible in H-SAPO-5 and H-AlPO-5. Thermogravimetric analysis (TGA) of the methylphenothiazine (PC_1) containing microporous materials showed that PC_1 completely penetrated inside the channels of Ni–VPI-5 and Ni–SAPO-5, only partly penetrated into Ni–SAPO-11 channels, and did not penetrate into the channels and cages of Ni–SAPO-34. This study clearly indicates that the pore diameter is a critical parameter affecting the quantum efficiency. In a subsequent study, the photoionization of PC_1 was examined in V- and Ti-containing AlPO-5 and AlPO-11 microporous materials.[91] The quantum efficiency of $PC_1^{+\bullet}$ was found to increase in the order AlPO-11< AlPO-5 < TAPO-11 < TAPO-5 <

Can. J. Chem. Downloaded from www.nrcresearchpress.com by University of Electronic and Science Techonology of China on 09/18/12
For personal use only.

VAPO-11 < VAPO-5. ESR studies clearly indicate the formation of V^{4+} on irradiation, suggesting that the V^{5+} ions act as electron-trapping sites. Efforts to detect Ti^{3+} were unsuccessful because the signal owing to Ti^{3+} overlaped with the signal formed owing to $PC_1^{+\bullet}$. The quantum efficiency was found to depend on the amount of V^{5+} and Ti^{4+} incorporated into the microporous material, and the optimum amount was found to vary depending on the nature of the host employed. In a closely related study, metal-containing silicoaluminophosphate M–SAPO-*n* (M = Cr, Fe, or Mn, and *n* = 5, 8, or 11) were examined as hosts for the photoionization of PC_1.[96] Cr–SAPO-8 exhibited the highest quantum efficiency among the transition-metal ions examined in this study. ESR studies indicated that the transition-metal ions acted as electron acceptors. These new microporous materials with "*built-in*" transition-metal ions as electron acceptors offer the potential for creating photoactive systems with long-lived charge separation. The photoionization efficiency was found to depend on the nature of the metal ion, the concentration of the metal ion, and also on the pore size of the microporous SAPO material used, with Cr–SAPO-8 exhibiting the highest quantum efficiency. The half-life of $PC_1^{+\bullet}$ in Cr–SAPO-5 (Si/Cr = 105) was estimated to be 100 days. The high quantum efficiency and excellent photostability in this material was attributed to the high electron affinity of Cr^{5+}. The photooxidation of TMB was examined in Cr-containing SAPO materials.[90] The quantum efficiency was found to decrease in the order CrH–SAPO-11 > CrH–SAPO-5 > CrH–SAPO-8. The pore size increased in the order SAPO-8 > SAPO-5 > SAPO-11. The decrease in the quantum efficiency in the larger pores was attributed to the greater mobility of $TMB^{+\bullet}$. The stability of the photoproduced $TMB^{+\bullet}$ was found to be significantly lower compared with $PC_1^{+\bullet}$. The half-life of $TMB^{+\bullet}$ in SAPO-5 was found to be <1 h. Nevertheless, these materials were able to stabilize the photoproduced cation radicals at room temperature. In another study, the photoionization of Py was examined in Cr–SAPO-5, Cr–SAPO-11, and Cr–SAPO-34 materials.[97] ESR studies indicated that Cr(V) acted as an electron acceptor. The quantum efficiency and stability of photoproduced $Py^{+\bullet}$ was found to depend on the pore size of the microporous material, the concentration, and the oxidation state of the chromium ions. The quantum efficiency was found to decrease in the order Cr–SAPO-5 > Cr–SAPO-11 > Cr–SAPO-34. The half-life ($t_{1/2}$) of $Py^{+\bullet}$ was estimated to be 45 days. The drawback of these host systems is that the pore size is too small for the incorporation of bulky molecules such as porphyrins and *N*-alkylphenothiazines (alkyl = hexyl, heptyl, octyl, decyl, etc.) and *N*-alkylpyrenes (alkyl = butyl, pentyl, hexyl, etc.).

Photoinduced charge separation in mesoporous materials

In heterogeneous reactions using microporous materials, diffusion of the reactant molecules and accessibility of the active sites to them are important factors. Bulky molecules with molecular dimensions >10 Å cannot be incorporated in the pores of microporous materials such as zeolites, AlPO, and SAPO.[98] Hence, it is important to study the feasibility of new materials with larger pore dimensions as hosts. Such materials can immobilize bulky photoactive molecules within their pores and stabilize them. *N*-Alkylphenothiazines PC_1, PC_3, PC_6, PC_{10}, and PC_{16} were incorporated into transition-metal-ion-containing mesoporous silicoaluminophosphates (Me–UHM-3, where Me = Cu, Cr, Ni, or Mn) and their photooxidation examined after UV excitation.[99] The pore diameter of these materials was determined to be 1.7 nm by using the Barrett–Joyner–Helena (BJH) equation and applying it to the desorption branch of the nitrogen isotherm. The effect of the ratio of Si/Al, the nature of the transition metal, and the concentration of the metal on the quantum efficiency was examined in this study. The highest quantum efficiency was obtained for mesoporous Cu–UHM-3 with PC_{10} as the electron donor. The TGA results indicate that PC_1, PC_3, PC_6, and PC_{10} mostly penetrate into the mesoporous host because their molecular dimensions are less than the pore diameter of the host employed. However, when the alkyl chain length increases to 16, the TGA results indicate that PC_{16} has very little penetration into the mesoporous material of Me–UHM-3. To examine the role of pore size in the photoionization of PC_n, mesoporous UHM-3 with three different pore sizes, 1.9, 2.9, and 3.8 nm, were prepared. The photoionization of PC_n (*n* = 1, 6, 10, or 18) was examined in these materials. The quantum efficiencies and stabilities of $PC_n^{+\bullet}$ generally increase with increases in pore size except for $PC_6^{+\bullet}$, which decreased with an increase in the pore size. This is attributed to the greater mobility, which leads to smaller quantum efficiencies and faster decay.

MCM-41 is mesoporous silica containing a regular array of uniform linear one-dimensional pores with a high surface area in the range of 700–1000 m^2/g and a pore-size distribution nearly as sharp as that of zeolites.[100,101] In addition, the pore diameter can be varied from 15 Å to as high as 100 Å. The tetrahedral Si(IV) ions in the MCM-41 framework can be replaced by other metal ions such as Al(III), Ti(IV), Mn(II), etc., further extending the range of materials that can be synthesized and examined as hosts.[102–104] Photoinduced electron transfer of bulky molecules such as 2,4,6-triphenylpyrylium cations,[105] tritylium cations[106], and porphyrins in MCM-41 mesoporous materials have been reported.[107,108] Porphyrin π-cation radicals ($H_2TPP^{+\bullet}$) were generated by visible light irradiation. The quantum efficiency was found to increase with an increase in pore size. Incorporation of Ti into the MCM-41 material was found to further increase the quantum efficiency of $H_2TPP^{+\bullet}$; however, substitution of Al into siliceous MCM-41 was detrimental to the quantum efficiency because protonation of H_2TPP to H_4TPP^{2+} was found to occur. The $H_2TPP^{+\bullet}$ radical decays only by 5% after 2 days at room temperature. Since the Ti-MCM-41 materials were promising hosts for enhanced quantum efficiency and stability, a further detailed study was carried out.[109] A series of TiMCM-41 materials with variable amounts of Ti in the MCM-41 framework was synthesized and used for the photoionization of PC_n. The quantum efficiency was found to increase in the order Si–MCM-41 < Al–MCM-41 < Ti–MCM-41. The photo-oxidation yields were found to decrease as the alkyl chain lengths increased from PC_1 to PC_{16}. An impregnated Ti-MCM-41 sample was also prepared for comparison, and the quantum efficiency was found to be lower compared with the sample Ti–MCM-41 in which Ti was incorporated into the framework (Si/Ti ratios of 200, 140, and 80). The stability of the

Can. J. Chem. Downloaded from www.nrcresearchpress.com by University of Electronic and Science Techonology of China on 09/18/12
For personal use only.

photoproduced $PC_n^{+\bullet}$ was found to increase from PC_1 to PC_{16} owing to the inductive effect. In a related study, transition-metal-ion-exchanged Me–AlMCM-41 was examined as a host for the photoionization of PC_n.[110] Among the transition-metal ions studied, Ni–AlMCM-41 exhibited the highest quantum efficiency compared with Fe– and Cu–AlMCM-41. The photoionization yield was found to decrease with an increase in the alkyl chain length as reported previously. To test the generality of the photoinduced charge separation, *N*-alkylpyrenes (Py_n) were photoionized in SiMCM-41 and transition-metal-ion-containing Me–MCM-41 (Me = Co^{2+}, Cu^{2+}, Ni^{2+}, V^{5+}, or Ti^{4+}).[111] The quantum efficiency was found to increase in the order Ti–MCM-41 > Ni–MCM-41 > V–MCM-41 > Si–MCM-41 > Co–MCM-41 > Cu–MCM-41. The quantum efficiency was found to decrease with an increase in the alkyl chain length. This was partly attributed to the formation of molecular aggregates because Py_ns with longer alkyl chain lengths are more prone to this phenomenon. Another reason for the decrease was due to the exclusion of Py_n with an increase in the alkyl chain length, a result confirmed by TGA experiments.

Mesoporous MCM-41 molecular sieves were found to be promising hosts for long-lived photoinduced charge separation between carotenoid radical cations and the MCM-41 framework.[112] Incorporation of metal ions such as Ni(II), Ti(IV), Cu(II), and Fe(III) into siliceous MCM-41 was found to enhance the efficiency of carotenoid oxidation.[113–115]

Among the M41S class of materials, extensive studies have been carried out using the hexagonal form, MCM-41. Less studied is the cubic form, MCM-48. One of the reasons for this is due to the fact that the synthesis of the cubic form is inherently challenging. Thus, the photoionization of PC_n and H_2TPP was examined in this material.[91,108] The photooxidation efficiency of $PC_n^{+\bullet}$ increased in the order Si–MCM-48 < Al–MCM-48 < V–MCM-48. The net quantum efficiency was found to increase monotonically with an increase in the V content in MCM-48. The quantum efficiency was found to decrease with increasing alkyl chain length, whereas the photostability was found to increase with an increase in the alkyl chain length, which is consistent with previous reports involving MCM-41.

SBA-15 belongs to the mesoporous family of materials and, unlike MCM-41, has relatively thicker pores (60 Å) and hence is thermally more stable.[116,117] It has a hexagonal structure with highly uniform tubular channels that can be varied from 50 to 300 Å. Hence, it is an interesting material for encapsulating guest molecules. V–SBA-15 was prepared by incipient wetness impregnation and used as a host for the photoionization of PC_n (n = 1, 6, 10, or 16).[118] The photoionization results indicate that $PC_n^{+\bullet}$s are more stable in V–SBA-15 compared with the siliceous form and that the quantum efficiency was found to increase with an increase in V loading. In contrast to previous studies, both the quantum efficiency and photostability were found to increase with an increase in the alkyl chain length. The half-life of $PC_n^{+\bullet}$ is, however, only a few days and lower compared with several microporous materials examined previously, indicating a high mobility in these large-pore-sized (53 Å) materials. In a follow-up study, the photoionization of PC_ns (n = 1, 6, 10, or 16) were examined in Ti–SBA-15 materials at room temperature.[119] The overall quantum efficiency and stability of $PC_n^{+\bullet}$ was found to increase with an increase in Ti content and with an increase in alkyl chain length for PC_n.

Conclusion and future outlook

This review clearly illustrates that heterogeneous solid supports are versatile materials for the encapsulation of photochromic molecules. Of the various microporous and mesoporous structures that have been synthesized and characterized, only a handful of framework types have been investigated in detail for applications related to photoinduced charge separation. There are a large number of structure types that have been unexplored and possibly untapped, and concerted research is required to bridge our gap using these materials. Although it is clear that periodic materials provide a novel way to arrange molecules in three-dimensional space and the potential to mimic the natural photosynthetic system, there are several challenges and issues that need to be addressed before they can be deployed in large-scale applications and become practical. These are outlined below:

1. The efficiency of the photoinduced charge separation process needs to be improved and BET further minimized to increase the lifetime of the photogenerated species.
2. Several of the artificial photoredox systems reported in the literature require the use of high-energy UV light or visible light. Chromophores should be designed such that they can absorb the broad spectrum of the solar radiation, including UV, visible, and the near-IR wavelengths, and transfer the energy efficiently to the active redox centers.
3. Currently, the host molecules are randomly or statistically encapsulated in the channels, cages, or pores of the host material. In principle, one should be able to achieve spatial control of the placement of these molecules a priori in predetermined and specific positions.

Acknowledgement

Thanks are due to the State of South Dakota supported 2010 Center for the Research and Development of Light-Activated Materials and the National Science Foundation (NSF-EPS-0903804).

References

(1) Kalyanasundaram, K.; Grätzel, M. *Curr. Opin. Biotechnol.* **2010**, *21* (3), 298. doi:10.1016/j.copbio.2010.03.021.
(2) Smith, A. M.; Nie, S. *Acc. Chem. Res.* **2010**, *43* (2), 190. doi:10.1021/ar9001069.
(3) Spitler, M. T.; Parkinson, B. A. *Acc. Chem. Res.* **2009**, *42* (12), 2017. doi:10.1021/ar900232m.
(4) Dau, H.; Zaharieva, I. *Acc. Chem. Res.* **2009**, *42* (12), 1861. doi:10.1021/ar900225y.
(5) Gust, D.; Moore, T. A.; Moore, A. L. *Acc. Chem. Res.* **2009**, *42* (12), 1890. doi:10.1021/ar900209b.
(6) Grätzel, M. *Inorg. Chem.* **2005**, *44* (20), 6841. doi:10.1021/ic0508371.
(7) Cox, A. *Photochemistry* **2002**, *33*, 405. doi:10.1039/9781847554826-00405.
(8) Grätzel, M.; Moser, J.-E. In *Electron Transfer in Chemistry;*

Can. J. Chem. Downloaded from www.nrcresearchpress.com by University of Electronic and Science Techonology of China on 09/18/12
For personal use only.

Balzani, V., Ed.; Wiley-VCH, 2001: Weinheim, Germany; pp 589–644.
(9) Barachevsky, V. A. *High Energy Chem.* **2003**, *37* (1), 6. doi:10.1023/A:1021905408521.
(10) Alexander, N. *Photosynth. Res.* **2001**, *70*, 129. doi:10.1023/A:1017909325669 .
(11) Gust, D.; Moore, T. A.; Moore, A. L. *Acc. Chem. Res.* **2001**, *34* (1), 40. doi:10.1021/ar9801301.
(12) Kalyanasundaram, K. *Photochemistry in Microheterogeneous Systems;* Academic: New York, 1987.
(13) Dutta, P. K.; Ledney, M. In *Molecular Level Artificial Photosynthetic Materials;* Meyer, G. J., Ed.; John Wiley: New York, 1997; pp 209–271.
(14) Grätzel, M. *Energy Resources Through Photochemistry and Catalysis;* Academic: New York, 1983.
(15) Ramamurthy, V. *Photochemistry in Organized and Constrained Media;* VCH: New York, 1991.
(16) Borja, M.; Dutta, P. K. *Nature* **1993**, *362* (6415), 43. doi:10.1038/362043a0.
(17) Sykora, M.; Kincaid, J. R. *Nature* **1997**, *387* (6629), 162. doi:10.1038/387162a0.
(18) Gessner, F.; Scaiano, J. C. *J. Photochem. Photobiol. Chem.* **1992**, *67* (1), 91. doi:10.1016/1010-6030(92)85171-P.
(19) Krueger, J. S.; Mayer, J. E.; Mallouk, T. E. *J. Am. Chem. Soc.* **1988**, *110* (24), 8232. doi:10.1021/ja00232a044.
(20) Infelta, P. P.; Grätzel, M.; Fendler, J. H. *J. Am. Chem. Soc.* **1980**, *102* (5), 1479. doi:10.1021/ja00525a001.
(21) Kang, Y. S.; Kevan, L. *J. Phys. Chem.* **1994**, *98* (16), 4389. doi:10.1021/j100067a029.
(22) Bosong, X.; Kevan, L. *Colloids Surf. A Physicochem. Eng. Asp.* **1993**, *72*, 11. doi:10.1016/0927-7757(93)80446-L.
(23) Matsuura, K.; Kevan, L. *J. Phys. Chem.* **1996**, *100* (25), 10652. doi:10.1021/jp953078o.
(24) Kevan, L. *Radiat. Phys. Chem.* **1992**, *39*, 333.
(25) Kevan, L. *Radiat. Phys. Chem.* **1990**, *37*, 629.
(26) Narayana, P. A.; Li, A. S. W.; Kevan, L. *J. Am. Chem. Soc.* **1982**, *104* (24), 6502. doi:10.1021/ja00388a004.
(27) McManus, H. J. D.; Kang, Y. S.; Kevan, L. *J. Phys. Chem.* **1993**, *97* (1), 255. doi:10.1021/j100103a044.
(28) McManus, H. J. D.; Kang, Y. S.; Kevan, L. *J. Phys. Chem.* **1992**, *96* (5), 2274. doi:10.1021/j100184a046.
(29) Baglioni, P.; Rivara-Minten, E.; Stenland, C.; Kevan, L. *J. Phys. Chem.* **1991**, *95* (24), 10169. doi:10.1021/j100177a098.
(30) Arce, R.; Kevan, L. *J. Chem. Soc., Faraday Trans. I* **1985**, *81* (7), 1669. doi:10.1039/f19858101669.
(31) Narayana, P. A.; Li, A. S. W.; Kevan, L. *J. Am. Chem. Soc.* **1981**, *103* (12), 3603. doi:10.1021/ja00402a073.
(32) Fossum, R. D.; Fox, M. A. *J. Phys. Chem. B* **1997**, *101* (33), 6384. doi:10.1021/jp9704123.
(33) Dupray, L. M.; Meyer, T. J. *Inorg. Chem.* **1996**, *35* (21), 6299. doi:10.1021/ic9516222.
(34) Gust, D.; Moore, T. A.; Moore, A. L. *Acc. Chem. Res.* **1993**, *26* (4), 198. doi:10.1021/ar00028a010.
(35) Laszlo, P. *Science* **1987**, *235* (4795), 1473. doi:10.1126/science.235.4795.1473.
(36) Nakamura, T.; Thomas, J. K. *Langmuir* **1985**, *1* (5), 568. doi:10.1021/la00065a010.
(37) Thomas, J. K. *Acc. Chem. Res.* **1988**, *21* (7), 275. doi:10.1021/ar00151a004.
(38) Liu, X.; Iu, K. K.; Thomas, J. K. *J. Phys. Chem.* **1989**, *93* (10), 4120. doi:10.1021/j100347a049.
(39) Kuykendall, V. G.; Thomas, J. K. *J. Phys. Chem.* **1990**, *94* (10), 4224. doi:10.1021/j100373a064.
(40) Iu, K. K.; Thomas, J. K. *J. Phys. Chem.* **1991**, *95* (2), 506. doi:10.1021/j100155a002.
(41) Pankasem, S.; Thomas, J. K. *J. Phys. Chem.* **1991**, *95* (18), 6990. doi:10.1021/j100171a049.
(42) Pankasem, S.; Thomas, J. K. *J. Phys. Chem.* **1991**, *95* (19), 7385. doi:10.1021/j100172a051.
(43) Pankasem, S.; Thomas, J. K. *J. Photochem. Photobiol. Chem.* **1991**, *62* (1), 53. doi:10.1016/1010-6030(91)85104-O.
(44) Liu, X.; Thomas, J. K. *Langmuir* **1991**, *7* (11), 2808. doi:10.1021/la00059a065.
(45) Kovar, L.; DellaGuardia, R.; Thomas, J. K. *J. Phys. Chem.* **1984**, *88* (16), 3595. doi:10.1021/j150660a043.
(46) Ungashe, S. B.; Wilson, W. L.; Katz, H. E.; Scheller, G. R.; Putvinski, T. M. *J. Am. Chem. Soc.* **1992**, *114* (22), 8717. doi:10.1021/ja00048a065.
(47) Yeates, R. C.; Kuznicki, S. T.; Lloyd, L. B.; Eyring, E. M. *J. Inorg. Nucl. Chem.* **1981**, *43* (10), 2355. doi:10.1016/0022-1902(81)80264-3.
(48) Krishna, R. M.; Kurshev, V.; Kevan, L. *Phys. Chem. Chem. Phys.* **1999**, *1* (11), 2833. doi:10.1039/a901801h.
(49) Krishna, R. M.; Kevan, L. *Microporous Mesoporous Mater.* **1999**, *32* (1-2), 169. doi:10.1016/S1387-1811(99)00102-X.
(50) Pelizzetti, E.; Mentasti, E. *Inorg. Chem.* **1979**, *18* (3), 583. doi:10.1021/ic50193a012.
(51) Kaufman, V. R.; Levy, D.; Avnir, D. *J. Non-Cryst. Solids* **1986**, *82* (1-3), 103. doi:10.1016/0022-3093(86)90117-1.
(52) Kaufman, V. R.; Avnir, D. *Langmuir* **1986**, *2* (6), 717. doi:10.1021/la00072a008.
(53) Slama-Schwok, A.; Ottolenghi, M.; Avnir, D. *Nature* **1992**, *355* (6357), 240. doi:10.1038/355240a0.
(54) Slama-Schwok, A.; Avnir, D.; Ottolenghi, M. *J. Am. Chem. Soc.* **1991**, *113* (10), 3984. doi:10.1021/ja00010a047.
(55) Slama-Schwok, A.; Avnir, D.; Ottolenghi, M. *J. Phys. Chem.* **1989**, *93* (22), 7544. doi:10.1021/j100359a004.
(56) Xiang, B.; Kevan, L. *Langmuir* **1994**, *10* (8), 2688. doi:10.1021/la00020a030.
(57) Xiang, B.; Kevan, L. *Langmuir* **1995**, *11* (3), 860. doi:10.1021/la00003a030.
(58) Saperstein, D.; Levine, E. *J. Phys. Chem.* **1975**, *62* (9), 3560. doi:10.1063/1.430948.
(59) Xiang, B.; Kevan, L. *J. Phys. Chem.* **1994**, *98* (19), 5120. doi:10.1021/j100070a029.
(60) Dolphin, D.; Felton, R. H. *Acc. Chem. Res.* **1974**, *7* (1), 26. doi:10.1021/ar50073a005.
(61) Hewson, W. D.; Hager, L. P. In *The Porphyrins;* Dolphin, D. Ed.; Academic Press: New York, 1979; Vol. 4, Chapter 4.
(62) Fajer, J.; Davis, H. S. In *The Porphyrins;* Dolphin, D. Ed.; Academic Press: New York, 1979; Vol. 7, Chapter 6.
(63) Whitten, D. G. *Acc. Chem. Res.* **1980**, *13* (3), 83. doi:10.1021/ar50147a004.
(64) Davis, M. S.; Forman, A.; Fajer, J. *Proc. Natl. Acad. Sci. U.S.A.* **1979**, *76* (9), 4170. doi:10.1073/pnas.76.9.4170.
(65) Wolberg, A.; Manassen, J. *Inorg. Chem.* **1970**, *9* (10), 2365. doi:10.1021/ic50092a035.
(66) Sung-Suh, H. M.; Kevan, L. *J. Chem. Soc., Faraday Trans.* **1998**, *94* (10), 1417. doi:10.1039/a800067k.
(67) Dutta, P. K.; Incavo, J. A. *J. Phys. Chem.* **1987**, *91* (17), 4443. doi:10.1021/j100301a005.
(68) Li, Z.; Mallouk, T. E. *J. Phys. Chem.* **1987**, *91* (3), 643. doi:10.1021/j100287a029.

Can. J. Chem. Downloaded from www.nrcresearchpress.com by University of Electronic and Science Techonology of China on 09/18/12
For personal use only.

(69) Yoon, K. B.; Kochi, J. K. *J. Phys. Chem.* **1991**, *95* (9), 3780. doi:10.1021/j100162a063.
(70) Ramamurthy, V.; Schanze, K., Eds. *Solid State and Surface Photochemistry;* Marcel-Dekker: New York, 2000.
(71) Ramamurthy, V.; Eaton, D. F.; Caspar, J. V. *Acc. Chem. Res.* **1992**, *25* (7), 299. doi:10.1021/ar00019a005.
(72) Van Bekkum, H.; Flanigen, E. M.; Jansen, J. C., Eds. *Introduction to Zeolite Science and Practice;* Elsevier: Amsterdam, 1991.
(73) Yoon, K. B.; Hubig, S. M.; Kochi, J. K. *J. Phys. Chem.* **1994**, *98* (14), 3865. doi:10.1021/j100065a050.
(74) Yoon, K. B.; Kochi, J. K. *J. Am. Chem. Soc.* **1989**, *111* (3), 1128. doi:10.1021/ja00185a053.
(75) Sankararaman, S.; Yoon, K. B.; Yabe, T.; Kochi, J. K. *J. Am. Chem. Soc.* **1991**, *113* (4), 1419. doi:10.1021/ja00004a057.
(76) Persaud, L.; Bard, A. J.; Campion, A.; Fox, M. A.; Mallouk, T. E.; Webber, S. E.; White, J. M. *J. Am. Chem. Soc.* **1987**, *109* (24), 7309. doi:10.1021/ja00258a011.
(77) McManus, H. J. J.; Finel, C.; Kevan, L. *Radiat. Phys. Chem.* **1995**, *45* (5), 761. doi:10.1016/0969-806X(94)00095-2.
(78) Ranjit, K. T.; Kevan, L. *J. Phys. Chem. B* **2002**, *106* (5), 1104. doi:10.1021/jp013194t.
(79) Ranjit, K. T.; Kevan, L. *Stud. Surf. Sci. Catal.* **2002**, *142*, 763. doi:10.1016/S0167-2991(02)80099-4.
(80) Ranjit, K. T.; Kevan, L. *J. Phys. Chem. B* **2002**, *106* (36), 9306. doi:10.1021/jp021276r.
(81) Uytterhoeven, L.; Dompas, D.; Mortier, W. J. *J. Chem. Soc., Faraday Trans.* **1992**, *88* (18), 2753. doi:10.1039/ft9928802753.
(82) Barr, T. L. *Zeolites* **1990**, *10* (8), 760. doi:10.1016/0144-2449(90)90058-Y.
(83) Mirodatos, C.; Pichat, P.; Barthomeuf, D. *J. Phys. Chem.* **1976**, *80* (12), 1335. doi:10.1021/j100553a016.
(84) Alvaro, M.; Garcia, H.; Garcia, S.; Marquez, F.; Scaiano, J. C. *J. Phys. Chem. B* **1997**, *101* (16), 3043. doi:10.1021/jp9628850.
(85) Park, Y. S.; Um, S. Y.; Yoon, K. B. *J. Am. Chem. Soc.* **1999**, *121* (13), 3193. doi:10.1021/ja980912p.
(86) Krishna, R. M.; Prakash, A. M.; Kurshev, V.; Kevan, L. *Phys. Chem. Chem. Phys.* **1999**, *1* (17), 4119. doi:10.1039/a903461g.
(87) Krishna, R. M.; Chang, Z.; Choo, H.; Ranjit, K. T.; Kevan, L. *Phys. Chem. Chem. Phys.* **2000**, *2* (14), 3335. doi:10.1039/b002878i.
(88) Bae, J. Y.; Ranjit, K. T.; Choo, H.; Kevan, L. *Phys. Chem. Chem. Phys.* **2001**, *3* (24), 5602. doi:10.1039/b104678k.
(89) Hartmann, M.; Kevan, L. *Chem. Rev.* **1999**, *99* (3), 635. doi:10.1021/cr9600971.
(90) Ranjit, K. T.; Kevan, L. *Phys. Chem. Chem. Phys.* **2001**, *3* (14), 2921. doi:10.1039/b102626g.
(91) Chang, Z.; Koodali, R.; Krishna, R. M.; Kevan, L. *J. Phys. Chem. B* **2000**, *104* (23), 5579. doi:10.1021/jp000505b.
(92) Prakash, A. M.; Hartmann, M.; Zhu, Z.; Kevan, L. *J. Phys. Chem. B* **2000**, *104* (7), 1610. doi:10.1021/jp993818j.
(93) Prakash, A. M.; Kevan, L. *J. Phys. Chem. B* **1999**, *103* (12), 2214. doi:10.1021/jp9836630.
(94) Zhu, Z.; Kevan, L. *Phys. Chem. Chem. Phys.* **1999**, *1* (1), 199. doi:10.1039/a807149g.
(95) Kurshev, V.; Prakash, A. M.; Krishna, R. M.; Kevan, L. *Microporous Mesoporous Mater.* **2000**, *34* (1), 9. doi:10.1016/S1387-1811(99)00150-X.
(96) Ranjit, K. T.; Chang, Z.; Krishna, R. M.; Prakash, A. M.; Kevan, L. *J. Phys. Chem. B* **2000**, *104* (33), 7981. doi:10.1021/jp001485g.
(97) Ranjit, K. T.; Kevan, L. *J. Phys. Chem. B* **2003**, *107* (11), 2610. doi:10.1021/jp022284a.
(98) Ranjit, K. T.; Kevan, L. *J. Phys. Chem. B* **2001**, *105* (1), 118. doi:10.1021/jp001918f.
(99) Bae, J. Y.; Ranjit, K. T.; Luan, Z.; Krishna, R. M.; Kevan, L. *J. Phys. Chem. B* **2000**, *104* (41), 9661. doi:10.1021/jp001500h.
(100) Beck, J. S.; Vartuli, J. C.; Roth, W. J.; Leonowicz, M. E.; Kresge, C. T.; Schmitt, K. D.; Chu, C. T. W.; Olson, D. H.; Sheppard, E. W. *J. Am. Chem. Soc.* **1992**, *114* (27), 10834. doi:10.1021/ja00053a020.
(101) Chen, C.-Y.; Li, H.-X.; Davis, M. E. *Microporous Mater.* **1993**, *2* (1), 17. doi:10.1016/0927-6513(93)80058-3.
(102) Luan, Z.; Cheng, C.-F.; Zhou, W.; Klinowski, J. *J. Phys. Chem.* **1995**, *99* (3), 1018. doi:10.1021/j100003a026.
(103) Alba, M.; Luan, Z.; Klinowski, J. *J. Phys. Chem.* **1996**, *100* (6), 2178. doi:10.1021/jp9515895.
(104) Zhang, J.; Goldfarb, D. *J. Am. Chem. Soc.* **2000**, *122* (29), 7034. doi:10.1021/ja994165n.
(105) Corma, A.; Fornes, V.; Garcia, H.; Miranda, M. A.; Sabater, A. *J. Am. Chem. Soc.* **1994**, *116* (21), 9767. doi:10.1021/ja00100a059.
(106) Cano, M. L.; Cozens, F. L.; Garcia, H.; Marti, V.; Scaiano, J. C. *J. Phys. Chem.* **1996**, *100* (46), 18152. doi:10.1021/jp960730m.
(107) Sung-Suh, H. M.; Luan, Z.; Kevan, L. *J. Phys. Chem. B* **1997**, *101* (49), 10455. doi:10.1021/jp972772w.
(108) Chang, Z.; Kevan, L. *Langmuir* **2002**, *18* (3), 911. doi:10.1021/la011414o.
(109) Krishna, R. M.; Prakash, A. M.; Kevan, L. *J. Phys. Chem. B* **2000**, *104* (8), 1796. doi:10.1021/jp993450q.
(110) Sinlapadech, S.; Krishna, R. M.; Luan, Z.; Kevan, L. *J. Phys. Chem. B* **2001**, *105* (19), 4350. doi:10.1021/jp0044882.
(111) Krishna, R. M.; Kevan, L. *Phys. Chem. Chem. Phys.* **2001**, *3* (23), 5348. doi:10.1039/b107371k.
(112) (a) Konovalova, T. A.; Gao, Y.; Schad, R.; Kispert, L. D.; Saylor, C. A.; Brunel, L.-C. *J. Phys. Chem. B* **2001**, *105* (31), 7459. doi:10.1021/jp0108519.
(113) Konovalova, T. A.; Gao, Y.; Kispert, L. D.; van Tol, J.; Brunel, L.-C. *J. Phys. Chem. B* **2003**, *107* (4), 1006. doi:10.1021/jp021565f.
(114) Gao, Y.; Konovalova, T. A.; Lawrence, J. N.; Smitha, M. A.; Nunley, J.; Schad, R.; Kispert, L. D. *J. Phys. Chem. B* **2003**, *107* (11), 2459. doi:10.1021/jp027164h.
(115) Gao, Y.; Konovalova, T. A.; Xu, T.; Kispert, L. D. *J. Phys. Chem. B* **2002**, *106* (42), 10808. doi:10.1021/jp025978s.
(116) Zhao, D.; Huo, Q.; Feng, J.; Chmelka, B. F.; Stucky, G. D. *J. Am. Chem. Soc.* **1998**, *120* (24), 6024. doi:10.1021/ja974025i.
(117) Luan, Z.; Hartmann, M.; Zhao, D.; Zhou, W.; Kevan, L. *Chem. Mater.* **1999**, *11* (6), 1621. doi:10.1021/cm9900756.
(118) Luan, Z.; Bae, J. Y.; Kevan, L. *Chem. Mater.* **2000**, *12* (10), 3202. doi:10.1021/cm000318q.
(119) Luan, Z.; Bae, J. Y.; Kevan, L. *Microporous Mesoporous Mater.* **2001**, *48* (1-3), 189. doi:10.1016/S1387-1811(01)00364-X.

Intramolecular H-atom transfer reactions in rigid peptides — Correlated solvent and structural effects

Anna Lewandowska, Gordon L. Hug, Gerald Hörner, Dariusz Pogocki, Franciszek Kazmierczak, and Bronislaw Marciniak

Can. J. Chem. Downloaded from www.nrcresearchpress.com by Xi'an Jiaotong University on 09/19/12
For personal use only.

Abstract: The rates and the mechanism of intramolecular hydrogen-atom transfer across the rigid diketopiperazine spacer in two epimeric benzophenone–tyrosine dyads were studied by nanosecond laser flash photolysis in 12 non-protic and protic solvents. Effects of the stereochemistry on the ground-state structures and conformational equilibria and dynamics have been addressed by means of NMR-based population analysis and long-term molecular-dynamics simulations. The excited triplet state of the benzophenone is found to be quenched intramolecularly by the remote phenol moiety with rates that are highly dependent on the solvent and on the relative benzophenone–phenol orientation. In agreement with previous studies, the kinetic diversity, with rates ranging from $<10^5$ s^{-1} to 2×10^7 s^{-1}, can be attributed to retarding effects of the bulk viscosity and to effects of specific solvation, which can be both rate retarding and rate accelerating. As an extension of the previous knowledge, however, the phenomenology of the kinetic solvent effects, that is, the nature of the predominating solvent parameter and its absolute impact on the reactivity, is found to be highly correlated with structural effects.

Key words: kinetic solvent effect, stereoselectivity, biradicals, tyrosyl radical, molecular dynamics.

Résumé : Utilisant la photolyse laser éclair, au niveau de la nanoseconde, on a étudié les vitesses et le mécanisme de réaction du transfert d'atome d'hydrogène intramoléculaire à travers l'espaceur dicétopipérazine rigide dans deux dyades de benzophénone–tyrosine dans douze solvants protiques et aprotiques. Faisant appel à l'analyse de populations à l'aide de la RMN et de simulations de dynamique moléculaire à long terme, on a étudié les effets de la stéréochimie sur les structures de l'état fondamental et sur la dynamique et les équilibres conformationnels. On a trouvé que l'état triplet excité de la benzophénone est piégé d'une façon intramoléculaire par la portion phénolique éloignée avec des vitesses qui dépendent beaucoup du solvant et des orientations relatives de la benzophénone et du phénol. En accord avec les études antérieures, la diversité cinétique des vitesses qui varient de moins de 10^5 s^{-1} à 2×10^7 s^{-1} peut être attribuée aux effets de viscosité globale qui les diminuent et aux effets de solvatation spécifique qui peuvent soit les accélérer ou les retarder. Toutefois, comme extension aux connaissances acquises antérieurement, on a trouvé que la phénoménologie des effets cinétiques du solvant, c'est-à-dire la nature du paramètre prédominant du solvant et son impact absolu sur la réactivité, est intimement reliée aux effets structuraux.

Mots-clés : effet cinétique du solvant, stéréosélectivité, biradicaux, radical tyrosyle, dynamique moléculaire.

[Traduit par la Rédaction]

Introduction

Photoinduced hydrogen-abstraction reactions by triplet-excited carbonyl compounds have been a central topic of photochemical research for many years.[1] Starting off with the seminal study by Das and Scaiano in 1981,[2] the reactions of phenols with triplet-excited carbonyl compounds have stimulated recurrent interest.[3–26] Hydrogen-atom transfer (HAT) from the phenol to the excited carbonyl provides, quite invariantly with respect to the nature of the carbonyl compound, an efficient source of metastable radicals, namely the carbonyl-derived ketyl radical and the phenoxyl

Received 29 April 2010. Accepted 30 June 2010. Published on the NRC Research Press Web site at canjchem.nrc.ca on 15 February 2011.

This article is part of a Special Issue dedicated to Professor J. C. Scaiano.

A. Lewandowska, F. Kazmierczak, and B. Marciniak.[2] Faculty of Chemistry, Adam Mickiewicz University, 60-780 Poznan, Poland.
G.L. Hug. Faculty of Chemistry, Adam Mickiewicz University, 60-780 Poznan, Poland; Radiation Laboratory, University of Notre Dame, Notre Dame, IN 46556, USA.
G. Hörner.[1] Faculty of Chemistry, Adam Mickiewicz University, 60-780 Poznan, Poland; Institut für Chemie, Technische Universität Berlin, 10623 Berlin, Germany.
D. Pogocki. Faculty of Biology and Agriculture, University of Rzeszow, 35-601 Rzeszow, Poland; Centre of Radiation Research and Technology, Institute of Nuclear Chemistry and Technology, 03-195 Warsaw, Poland.

[1]Corresponding author (e-mail: hoerner@amu.edu.pl).
[2]Corresponding author (e-mail: marcinia@amu.edu.pl).

Can. J. Chem. Downloaded from www.nrcresearchpress.com by Xi'an Jiaotong University on 09/19/12
For personal use only.

radical. Ample use of these clean radical-affording pathways has allowed the selective formation and the characterization of biologically relevant phenoxyl radicals that are derived, for instance, from the phenolic amino acid tyrosine (Tyr)[7] and from the phenolic neurotransmitter adrenaline.[6] Selective generation of fluorinated tyrosyl radicals within biological matrices has allowed their use as a mechanistic probe and as an external trigger of proton-coupled electron transfer reactions in native proteins.[27]

This biochemical application was based on an intramolecular variation of the carbonyl–phenol theme within covalently bound dyads. Mechanistic studies of the intramolecular HAT pathways corroborated the view that such dyads share the reaction pathways with their bimolecular congeners and, thus, produce the corresponding biradicals with high selectivity and efficiency as long as the structural constraints of the dyad allow close contacts between the reacting moieties. The intramolecular HAT quenching of, for instance, the benzophenone triplet state (^{3}bp) by an H-atom donor, RH, implies that >C=O···HR distances below 3.1 Å are successful.[28] Studies of the intramolecular HAT of several benzophenone-based dyads have provided evidence that the chemical nature of the linker between the chromophores (that is, the flexibility and the directionality of the linker) is one major source of kinetic diversity. Remarkable variations in the reaction rates of isomeric benzophenone–phenol dyads (regiomers and stereomers) have been attributed to modulations of the distance distributions and relative orientations of the reacting moieties.[10,12,19]

In extension of previous work on the solvent effects of the intramolecular HAT by Scaiano, Miranda, Leigh, and others,[2,12,16,19,23] our recent systematic studies of the HAT reactions of peptide-linked benzophenone–tyrosine dyads (bp∪Tyr) have shown that this interpretation of structurally imposed kinetic effects is incomplete. Instead, specific solvent–solute interactions have been identified as the second important control of the intramolecular HAT dynamics.[29,30] Our results imply that the kinetic effects that are imposed by the solvent and those that are due to the dyad structure are correlated with each other and that they must not be treated separately. In non-protic solvents the intramolecular reactivity was generally found to be linearly correlated with the solvents' hydrogen-acceptor strength, which parallels the phenomenology of the solvent dependence of bimolecular HAT reactions of phenols.[31–36] In particular, the HAT reaction in two epimeric bp∪Tyr dyads exhibited significantly solvent-dependent stereoselectivity, which could be attributed to specific solvent–solute interactions.[29]

In the latter work the chromophores were connected by open-chain peptide structures (see Scheme 1; A denotes ^{3}bp as the hydrogen acceptor; HD denotes hydrogen donor PhOH), wherein the high intrinsic flexibility of the linker blurs the stereoselectivity. Therefore, limiting the flexibility of the peptide linker should allow deeper insights into the relations between the kinetic phenomenology and the molecular structure. The diketopiperazine (DKP) ring system provides such a peptide environment with reduced flexibility. First, the DKP ring imposes a distinct orientation between the reacting chromophores for epimeric dyads (see Scheme 1; from left to right, the structures denote the (L-L) and (L-D) epimers). In addition, the presence of the DKP ring exerts unique control over the conformations of the respective side chains of the attached amino acids. Previous studies of the conformations of substituted diketopiperazines revealed structural preferences that significantly differed from those of their open-chain analogues.[37,38] Such structural preferences are expected to be reflected in the nonbonding distances of the side chains and the inter-side-chain reactivity.

Preliminary work on the HAT between tyrosine and 4-benzoyl-phenylalanine (bpa) side chains of the epimeric diketopiperazines **1** and **2** (see Scheme 2*a*) actually showed significantly enhanced stereoselectivity.[39]

Herein, we present the results of extended laser-flash photolysis studies of **1** and **2** that address the medium dependence of the excited-state dynamics in more detail. These studies are supplemented by the results of molecular-dynamics simulations and NMR investigations of the ground-state structures and conformations that establish a quantitative picture of the conformer distributions of the dyads and define the molecular prerequisites of the individual quenching geometries. As will be shown, the presence of the rigid DKP linker imposes very different structural constraints on the intramolecular mobility of epimers **1** and **2**. These structural differences translate into individual phenomenology of the solvent effects for both of the dyads.

Experimental section

Synthesis and characterization

Chemicals and solvents (Sigma-Aldrich and BACHEM) for synthesis were of the highest available analytical grade and were used without further purification. Products were identified by means of NMR techniques and combustion analysis. Routine ^{1}H NMR and ^{13}C NMR spectra were recorded at 200/400 MHz and 50.3 MHz, respectively, in perdeuterated dimethyl sulfoxide (DMSO-d_6) and in deuterated trifluoroacetic acid (TFA-*d*), with the resonances being reported in parts per million downfield from tetramethylsilane. Assignments of ^{1}H and ^{13}C resonances were based on two-dimensional homo- and heteronuclear NMR techniques. An unambiguous assignment of the strongly overlapping β-proton resonances of the bpa and the Tyr residues in **1** and **2**, as required for the analysis of the ground-state rotamer distribution, was accomplished by two-dimensional nuclear Overhauser enhancement spectra (see Figs. S1 and S2 in the Supplementary data). The assignment of the $H^{\beta R}$ and $H^{\beta S}$ in the Tyr side chain of **1** and **2** as the high-field and the low-field doublet-of-doublet parts of the AB sub-spectrum, respectively, followed established conventions.[40] The same assignment was assumed to hold for the bpa side chain. The synthesis of the cyclic dipeptides (diketopiperazines, DKPs) **1** and **2** followed the method invented by Nitecki et al.[41] The fully protected open-chain precursors *N*-boc-(L/D)-bpa-(L)-Tyr-OMe were obtained by standard peptide-coupling methods as recently described in detail.[29] The cyclic peptides were obtained from the precursors after acidic deprotection of the N-terminus in formic acid followed by thermally

Scheme 1. Schematic of the structural constraints of the intramolecular H-atom transfer between a hydrogen donor (HD) and an acceptor (A) within linear and cyclic dipeptide scaffolds (asterisks denote chiral carbon centers; curved arrows (blue in the Web version) denote additional degrees of rotational freedom in the open-chain arrangements).

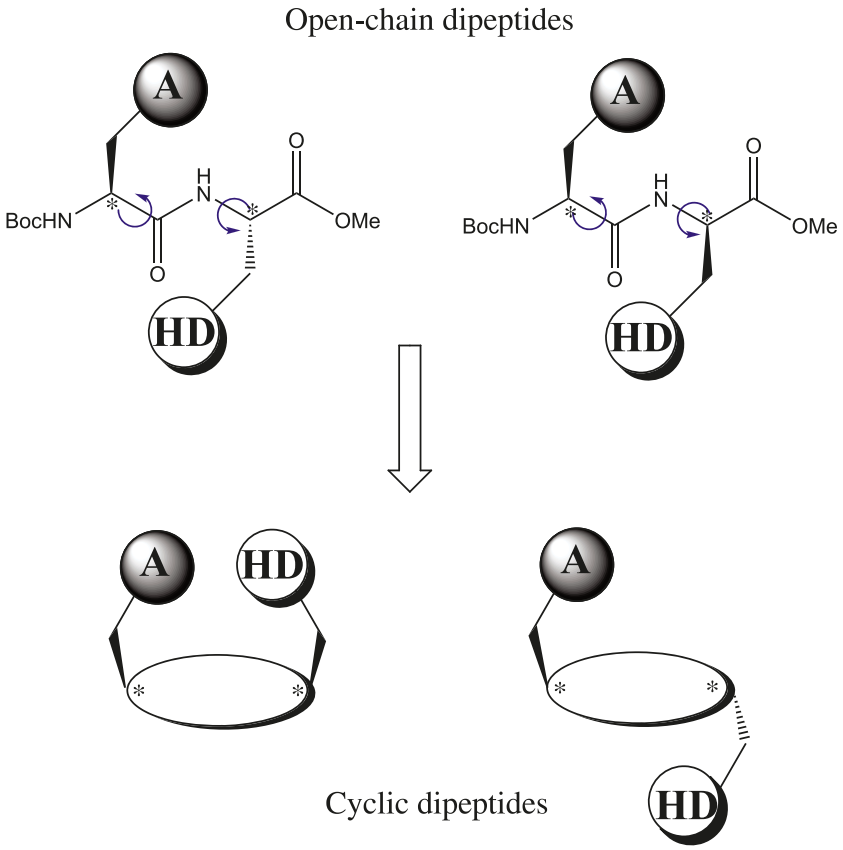

Scheme 2. (*a*) Structures of the diketopiperazines **1** and **2** and notation of atom positions; (*b*) notation of the side-chain rotamers for the L-configured side chains in **1** and **2** (R denotes the respective aromatic moiety); the D-configured bpa residue in dyad **1** is accounted for by an interchange of the >NH and >CO groups.

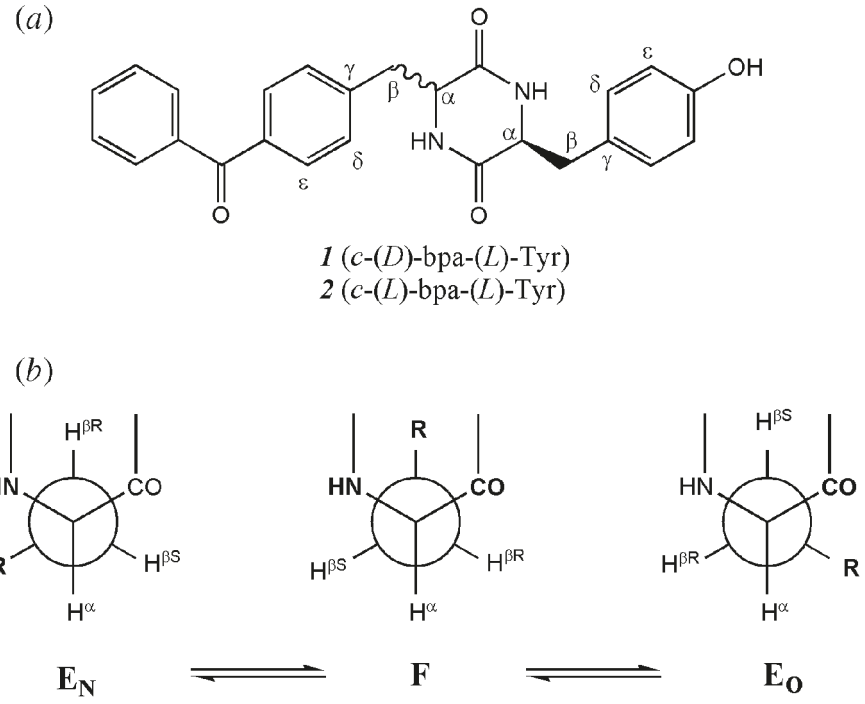

Can. J. Chem. Downloaded from www.nrcresearchpress.com by Xi'an Jiaotong University on 09/19/12
For personal use only.

Can. J. Chem. Downloaded from www.nrcresearchpress.com by Xi'an Jiaotong University on 09/19/12
For personal use only.

induced cyclization (full synthetic procedures and details of characterization are given in the Supplementary data).

Molecular modeling details

The conformational space of the DKPs **1** and **2** was sampled by means of Langevin dynamics (LD)[42–48] done in conjunction with the CHARMM27[49] all-atom empirical potential. Since there is no representation of the diphenylketone functionality in the original CHARMM force field, the parameters for the atoms of its aromatic rings were taken from the atoms of the phenylalanine residue. Similarly, the carbonyl oxygen and carbon atoms of the ketone functionality were calculated with parameters provided for these atoms in the peptide bond. To achieve consistency of charge distribution in the molecules, the atomic charges were recalculated using the partial equalization of orbital electronegativity method of Gasteiger and Marsili.[50] In the LD no explicit solvent molecules were used, but the usual LD frictional drag of the solvent was factored in using a collision frequency for all heavy atoms equal to approx. 20 ps^{-1}, which reflects the viscosity of acetonitrile, fitting molecular dynamics and experimental data.[44,51] The free LD simulations were done with the 2 fs time step and 100 ns propagation time, preceded by 12 ps of heating from 0 K to 300 K and 18 ps of equilibration. For the force field calculations we used version 7.1 of the HyperChem PC molecular modeling package,[52] which integrates the Langevin equation of motion using the method of Allen and Tildesley.[53]

The rate constants of the close-contact formation between the reacting moieties, here k_{OO}, have been evaluated from the simulations by means of number correlation functions, following the routines that have been described in detail previously.[54] If the reactive and non-reactive conformations are considered as being in equilibrium but the overall H-abstraction reaction is very fast compared with the relaxation of equilibrium between the conformations, then the observed rate constant k_H should be comparable to a theoretical rate constant, k_{OO}, computed from the simulation via eqs. [1–3].[54] The numerator, $\langle N_{OO}\rangle$, in eq. [1] is the fraction of the time that the distance between the carbonyl and hydroxyl oxygens was less than 4 Å during an 80 ns LD trajectory. The denominator, τ_{rxn}, in eq. [1] is the relaxation time for the equilibrium between the reactive and non-reactive conformations. It is related to a correlation function by the fluctuation-dissipation theorem.[55] The normalized number correlation function $C_N(t)$ was used for this calculation (see eq. [2]).

$$[1] \qquad k_{OO} = \frac{\langle N_{OO}\rangle}{\tau_{rxn}}$$

$$[2] \qquad \tau_{rxn} = \int_0^{+\infty} C_N(t)\,dt$$

which has the form

$$[3] \qquad C_N(t) = \frac{\langle \delta N_{OO}(t)\delta N_{OO}(0)\rangle}{\langle \delta N_{OO}{}^2\rangle}$$

Here $\delta N_{OO}(t) = N_{OO}(t) - \langle N_{OO}\rangle$ and $N_{OO}(t) = 1$ for $d_{OO} \leq 4.0$ Å and $N_{OO}(t) = 0$ for $d_{OO} \geq 4.0$ Å. Note that $\langle \delta N_{OO}{}^2\rangle = \langle N_{OO}\rangle - \langle N_{OO}\rangle^2$. The statistical error of the evaluation has been taken into account following the approach of Zwanzig and Ailawadi.[55,56]

Nanosecond flash photolysis

The setup for the nanosecond laser flash photolysis (LFP) experiments and the data acquisition system have been previously described in detail.[57,58] LFP experiments employed a pulsed N_2 laser (337 nm, 5 mJ, ≈8 ns) and a Nd:YAG laser (266 nm and 355 nm, 5 mJ, 7–9 ns) for excitation. Transient decays were recorded at individual wavelengths by the step-scan method with a step distance of 10 nm in the range of 320 to 700 nm as the mean of 10 pulses. Samples for LFP were deoxygenated with high-purity argon for 15 min prior to the measurements. Experiments were performed in rectangular quartz cells (1 cm × 1 cm). All experiments were performed with freshly prepared solutions at room temperature (295 ± 1 K). In the case of 266 nm photolysis, excitation of both chromophores (bp and Tyr) cannot be avoided. However, analysis of the molar absorption coefficients measured for bp and Tyr[59] shows that excitation of the tyrosine moiety was less than 10%. We used 266 nm excitation (which allowed us to use lower dyad concentrations) to avoid bimolecular hydrogen abstraction by the triplet state from the ground state of the dyad (self-quenching). Solvents for time-resolved spectroscopy were of the highest available analytical grade and were used without further purification.

Results

NMR study of ground-state conformations

A previous density functional theory (DFT) study of the DKPs **1** and **2** revealed the structural details of the respective quenching geometries and a qualitative interrelation between the inter-side-chain reactivity and structural preferences, which are reflected in the non-bonding distances of the side chains.[39] The cited work has shown that a variety of structures that differ in their relative side-chain orientations should be energetically accessible in solution. Therefore it was of interest to obtain quantitative information about the populations of the side-chain rotamers in the dyads' ground state. Herein we present the results of an NMR-based analysis of the absolute populations of the side-chain rotamers of the DKPs **1** and **2**. An important result is that the NMR-derived populations are distinctly different between the epimeric dyads **1** and **2**.

The populations of the rotamers $p(\boldsymbol{i})$ were extracted from the vicinal coupling constants of the diastereotopic β-protons and the α-protons of both of the amino-acid side chains, $^3J(H^{\alpha}–H^{\beta R})$ and $^3J(H^{\alpha}–H^{\beta S})$ (here bpa and Tyr; see Scheme 2*a* for the notation of the proton positions),[60] as recently used in the analysis of open-chain dyads.[29,30] The acronyms $\mathbf{E_N}$, $\mathbf{E_O}$, and **F** denote side-chain rotamers wherein the aromatic substituent R is extended to the adjacent nitrogen atom, extended to the adjacent carbonyl oxygen atom, and folded back across the DKP ring, respectively. This rotamer notation is based on the orientation of the side-chain substituent R (see Scheme 2*b*) rather than on the dihedral angles, to simplify the comparison between the epimeric compounds **1** and **2**. The computed rotamer populations for DMSO-d_6 and TFA-*d* are summarized in Table 1. The limited

Table 1. Summary of the side-chain rotamer populations $p(i)$ of the diketopiperazines **1** and **2** computed from experimental coupling constants (DMSO-d_6; 200 MHz).

	bpa residue			Tyr residue		
	$p(\mathbf{E_N})$	$p(\mathbf{E_O})$	$p(\mathbf{F})$	$p(\mathbf{E_N})$	$p(\mathbf{E_O})$	$p(\mathbf{F})$
1	0.22 (0.40)	0.10 (0.17)	0.68 (0.43)	0.18 (0.21)	0.07 (0.21)	0.75 (0.58)
2	0.42 (0.55)	0.20 (0.16)	0.38 (0.29)	0.26 (0.33)	0.20 (0.16)	0.54 (0.51)

Note: Estimated uncertainty $\Delta p(i) = \pm 0.02$ and ± 0.04 for $p(\mathbf{E_N})$ ($p(\mathbf{E_O})$) and $p(\mathbf{F})$, respectively. Data in parentheses denote the populations in TFA-*d*.

Fig. 1. DFT minimized structures of highly populated solution-phase conformations of **1** (**F–F**) and **2** (**F–E$_N$**). (Note that the **1** shown here is the stereoisomer used in the LFP experiments, but the **1** shown in Scheme 2 is the stereoisomer used in the NMR and LD simulations. These two species, both labeled **1**, are identical molecules, being the mirror image of each other, and a limited set of duplicate LFP experiments verified their identical chemical behavior.)

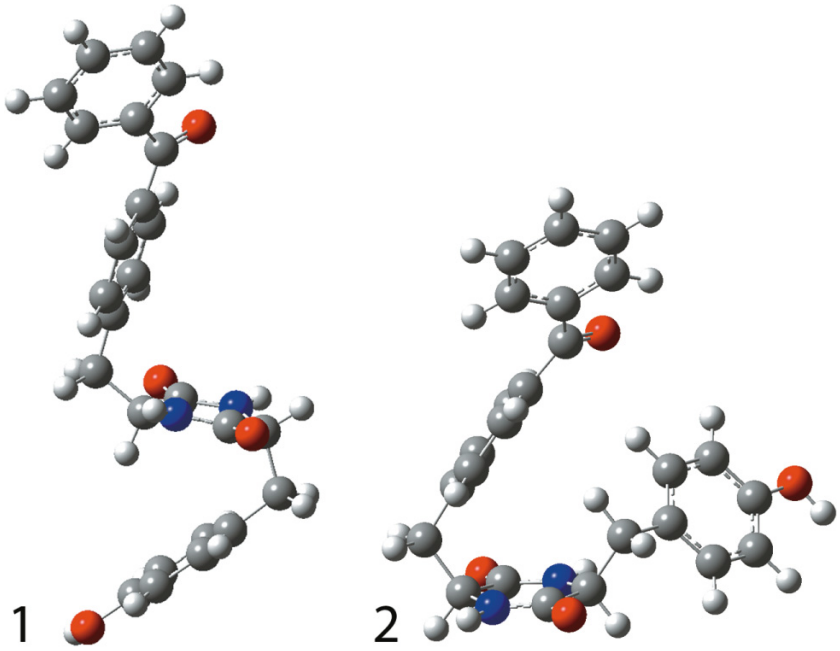

Can. J. Chem. Downloaded from www.nrcresearchpress.com by Xi'an Jiaotong University on 09/19/12
For personal use only.

solubility of the DKPs under study interfered with a detailed investigation of the solvent dependence of the rotamer populations. It is noted that the population preferences of **1** and **2** are somewhat blurred in solutions of the very strong H-bond donor TFA.

The NMR-derived populations for DMSO solutions of **1** and **2** reveal side-chain conformational preferences that differ significantly from those of open-chain congeners. The aromatic side chains in linear peptides preferably populate the rotamer $\mathbf{E_N}$ in polar solvents such as DMSO, with $p(\mathbf{E_N}) \geq 0.7$.[61–64] In contrast, $\mathbf{E_N}$ appears to be much less favorable in the cyclic peptide **1**, where both aromatic residues preferably populate the back-folded **F** conformation instead. This behavior is quite common for the DKPs that carry aromatic amino acids and has been associated with dipole-induced dipole interactions between the DKP amides and the aromatic ring.[65,66] Based on the assumption that the conformer populations of the two side chains of **1** are statistically independent, a favored population of the **F–F** conformation can be expected with $p(\mathbf{F–F}) = 0.68 \times 0.75 = 0.51$. Thus, in full agreement with the outcomes of the previous DFT studies in an acetonitrile (ACN) continuum, a "double-sandwich" like structure of **1** also prevails in DMSO solution, which implies long inter-side-chain distances (see Fig. 1).

For **2**, wherein both aromatic residues share the same half-room above the DKP ring, the side-chain preferences are less expressed. When compared with dyad **1**, significantly smaller populations of the **F** conformation are obtained for **2**. In particular, the **F–F** conformation of **2** would contribute only with $p(\mathbf{F–F}) = 0.38 \times 0.54 = 0.20$, if statistically independent conformer populations can be reasonably assumed. In fact, the molecular-dynamics simulations show that this latter assumption is not valid for **2** and that even smaller populations prevail (vide infra). This finding of diminished populations of **F–F** is important for the interpretation of the excited-state dynamics of **2**, because photoinduced HAT within **2** is limited to the **F–F** conformation of the side chains wherein both aromatic moieties are back-folded across the DKP ring at the same time. It appears that repulsive interactions between the bulky aromatic groups favor the population of sterically less crowded conformations in the latter structure. In particular, a simultaneous population of the **F** rotamer by both side chains appears less probable.

Can. J. Chem. Downloaded from www.nrcresearchpress.com by Xi'an Jiaotong University on 09/19/12
For personal use only.

Fig. 2. Extracts of long-term molecular-dynamics simulations for **2** (Langevin dynamics; implicit-solvent model for ACN): (*a*) time variation of the inter-side-chain distance *d*(O–O) between the tyrosine (Tyr) hydroxylic oxygen atom and the 4-benzoyl-phenylalanine (bpa) carbonyl oxygen atom; (*b*) time variation of the bpa side-chain dihedral angle; (*c*) time variation of the Tyr side-chain dihedral angle.

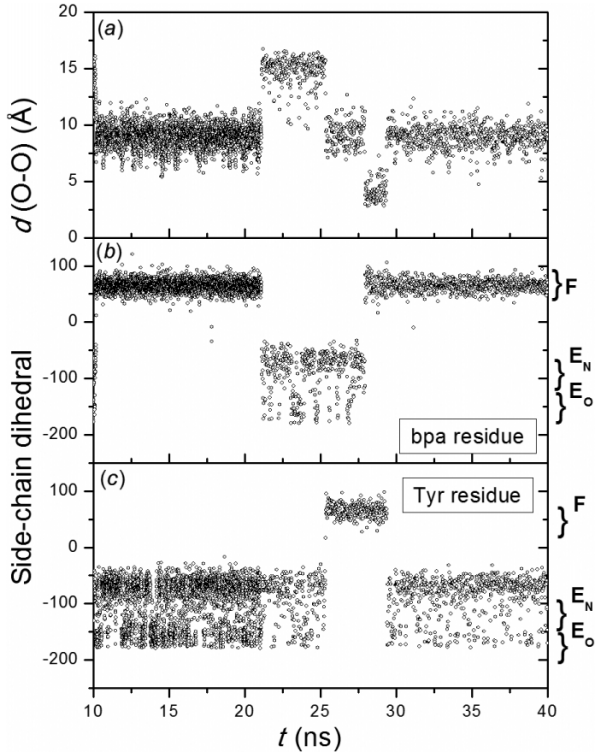

Conformational dynamics

The interconversion between different molecular conformations has been studied by means of long-term molecular-dynamics simulations (100 ns duration; implicit-solvent model for ACN). Figure 2 summarizes the time variation of 3 molecular parameters (both side-chain dihedral angles and the characteristic inter-side-chain distance) within a 30 ns simulation window for dyad **2**. In Fig. 2*a* the sum of the resident times at each distance (*d*(O–O)) should be viewed in regard to the total period of the simulation (100 ns); i.e., when the sums of these resident times are divided by the total time of the simulation, they basically reflect the relative existence of the dyad at each O–O distance (probability distribution). (Respective plots for **1** are given in the Supplementary data.)

In agreement with the NMR results, mainly 3 rotamers ($\mathbf{E_N}$, $\mathbf{E_O}$, and **F**) of each side chain are populated during the simulation of both compounds. Of particular interest was the probability of the **F–F** conformation of **2**, which allows for close contacts of <4.0 Å (Fig. 2) between the reacting moieties and closely resembles the quenching geometry of this dyad. As stated above, the simulations strongly disfavor this conformation: the calculated probability of the population of the **F–F** conformation is only 1.4%. In conclusion, the **F–F** conformation, although shown to be a rare conformation during the simulations for **2**, irrespective of the chosen starting geometry, is sufficient to explain the reactivity toward intramolecular HAT in the range of 10^7 s^{-1} (see further discussion).

As shown by DFT studies, close contacts of <3.2 Å within dyad **1** require the population of conformations that do not refer to side-chain rotamers. The formation of such structures does not appear at all during the 100 ns simulation (see Fig. S3 in the Supplementary data).

Laser flash photolysis: spectral and kinetic analyses

The excited-state dynamics of the dyads **1** and **2** were studied by means of nanosecond laser photolysis in 12 different solvents and solvent mixtures. Transient products were identified, and the efficiency of their formation was quantified by means of transient-absorption spectroscopy and spectral resolutions.

In all cases the triplet state was identified as the predominate intermediate in the early spectra by its characteristic absorption maxima at 325 nm (not shown) and 520 nm in addition to a long-wavelength absorption above 600 nm. The triplet state spectra of both dyads were indistinguishable and showed little variation with the change in solvent.

For bp∪Tyr dyads that are related to **1–2**, intramolecular HAT was found to be the predominate quenching pathway. The quantum yields for the formation of the respective biradicals were reported to be unity.[61] Thus, any significant spectral evolution with a spectral shift from 525 to 540 nm and accompanied by a growth at 405 nm would be indicative of the formation of ketyl and tyrosyl radicals, respectively. We found that the two dyads showed distinctly different spectral evolution during and after the decay of the triplet state.

This effect of the structure is illustrated by the transient spectra observed for solutions of **1** and **2** in ACN (Fig. 3). While the spectrum obtained for **1** in pure ACN after 200 ns largely resembles the original triplet spectrum, with its distinctive 520 nm absorption, the spectrum obtained for **2** carries significant contributions from a tyrosyl radical and a ketyl radical after only 100 ns. Note in particular the spectral shift of dyad **2** from the initial maximum of 520 nm to 540 nm, indicating the transition from its triplet to its ketyl radical. As shown in Fig. 3*b*, a change in the solvent did not significantly affect the transient absorption spectra of dyad **2**, an observation that holds for all of the studied solvents. Accordingly, deconvolution of the transient absorption spectra for compound **2** in an ACN–H_2O (2:1 *v*/*v*) mixture gave the same results as previously reported for pure ACN.[39] The quenching is found to proceed intramolecularly with high efficiency. This finding is in accordance with the lack of a concentration dependence of the triplet decay rate constants (see below). However, the intermediate (biradical) decays on the same time scale as it is formed. This behavior interferes with biradical accumulation and is contrary to the general observation that biradicals decay on a much longer time scale than do their parent triplets.[12,16,19,61]

In contrast to the largely solvent-independent behavior of **2**, the evolution of the transient spectra of dyad **1** is strongly dependent on the nature of the solvent. In particular, the spectrum obtained after 200 ns in the ACN–H_2O (2:1 *v*/*v*) mixture differs dramatically from the one in pure ACN and is fully consistent with efficient formation of ketyl and tyrosyl radicals. To clarify the nature of this solvent effect, the

Fig. 3. Transient absorption spectra obtained during laser flash photolysis at 355 nm of deoxygenated solutions (9×10^{-4} mol L^{-1}) of (*a*) compound **1** with a time delay of 200 ns and (*b*) compound **2** with a time delay of 100 ns; measurements in ACN (filled symbols) and in ACN–H_2O (2:1 *v*/*v*) (open symbols).

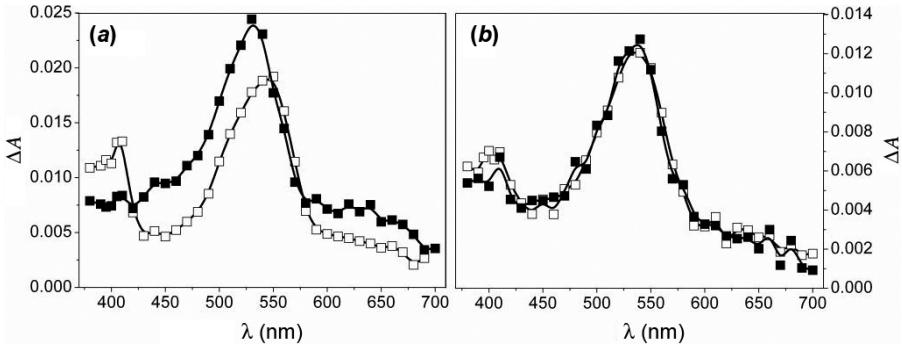

Fig. 4. (*a*) Resolutions of transient absorption spectra taken 1400 ns after 355 nm laser pulsing (5 mJ) of a solution of **1** in ACN. (*b*) Concentration profiles for the transients obtained from the deconvolution of transient absorption spectra of **1** in ACN. (*c*) Resolutions of transient absorption spectra taken 130 ns after 355 nm laser pulsing (5 mJ) of a solution of **1** in ACN–H_2O (1:1 *v*/*v*). (*d*) Concentration profiles for the transients obtained from the deconvolution of transient absorption spectra of **1** in ACN–H_2O (1:1 *v*/*v*). □, triplet state ^{3}bp; ○, ketyl radical bpH$^\bullet$; Δ, tyrosyl radical Tyr(O$^\bullet$); ◇, bp radical anion bp$^{\bullet-}$; *, experimental data. Solid curves are the resulting fits from the regression analysis.

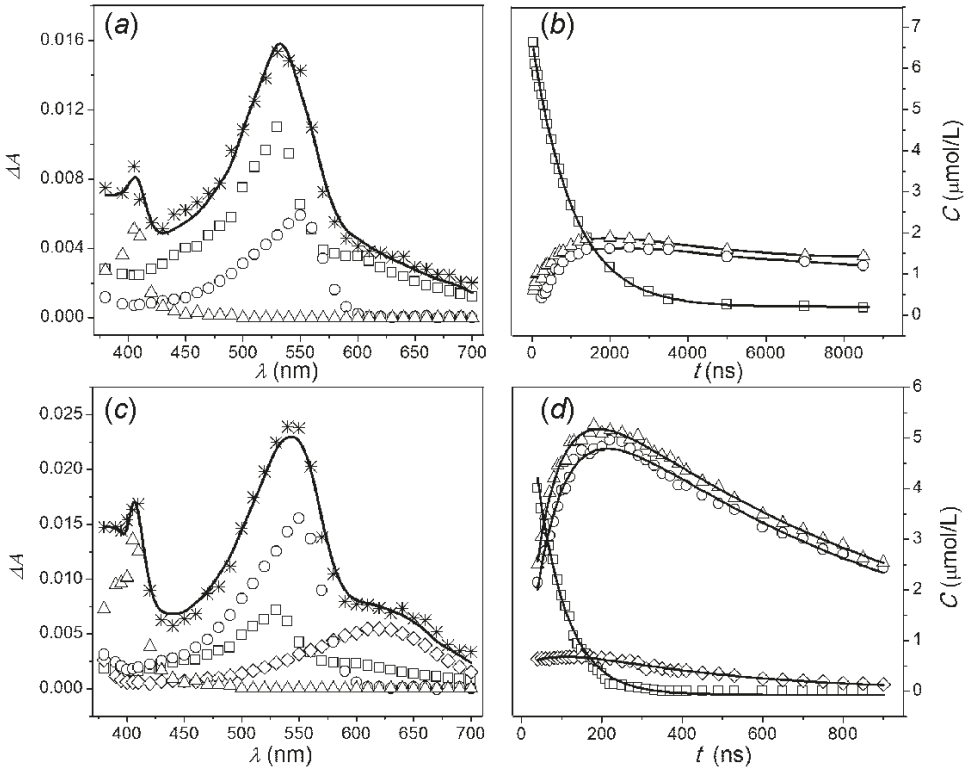

transient spectra obtained for compound **1** in ACN and ACN–H_2O (1:1 *v*/*v*) were deconvoluted into their spectral components, from which concentration–time profiles were constructed. Exemplary resolutions are given in Figs. 4*a* and 4*c* and the resulting profiles are displayed in Figs. 4*b* and 4*d*. These profiles reveal the distinct difference in the triplet quenching of dyad **1** in the two solvents. That is, the reaction is found to be intermolecular in ACN, whereas it is predominantly intramolecular in the ACN–H_2O (1:1 *v*/*v*) mixture. To simulate quantitatively the experimental data obtained in ACN for dyad **1**, only 3 components were needed: the triplet state ^{3}bp, ketyl radicals (bpH$^\bullet$), and tyrosyl radicals (Tyr(O$^\bullet$)) (see Fig. 4*a*). The concentrations of bpH$^\bullet$ and Tyr(O$^\bullet$) were found to be equal within the error estimation. The triplet decay obtained from the concentration profile is 1 μs, which is well in agreement with the triplet lifetime obtained from the kinetic traces at 630 nm. From the decomposition of the transient absorption spectra and the resulting concentration profile, the quantum yield for the formation of both radicals was calculated to be equal to 25% in ACN. Based on the long lifetimes of the radicals, which are decaying for tens of microseconds, we can conclude that they are formed mainly in self-quenching reactions (see Scheme 3).

Can. J. Chem. Downloaded from www.nrcresearchpress.com by Xi'an Jiaotong University on 09/19/12
For personal use only.

Can. J. Chem. Downloaded from www.nrcresearchpress.com by Xi'an Jiaotong University on 09/19/12
For personal use only.

Scheme 3. Deactivation paths (red, bimolecular; blue, unimolecular) of the triplet-excited state of the dyads **1** and **2**.

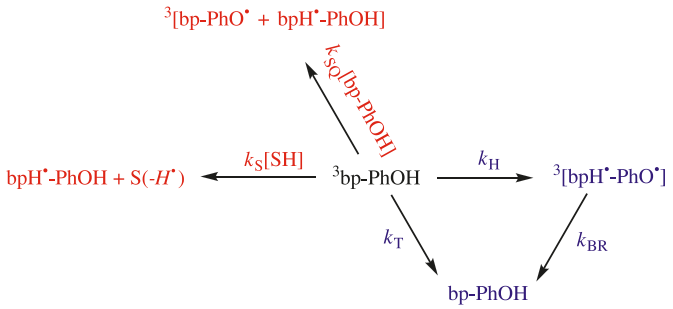

A totally different situation was observed for dyad **1** in ACN–H_2O (1:1 *v*/*v*). First, the triplet lifetime was reduced by a factor of 10. Second, to reproduce the experimental data, 4 components had to be used, namely ^{3}bp, ketyl radicals (bpH$^\bullet$), bp radical anions (bp$^{\bullet-}$), and tyrosyl radicals (Tyr(O$^\bullet$)). The rates of formation of the radical species bpH$^\bullet$, bp$^{\bullet-}$, and Tyr(O$^\bullet$) were, within experimental error, identical to the triplet-decay rate of dyad **1**. The total amount of bpH$^\bullet$ and bp$^{\bullet-}$ together was equal to the Tyr(O$^\bullet$) concentration, within experimental error. Formation and decay of both the ketyl radical and the tyrosyl radical appear to follow the same decay law. This is in accordance with an intramolecular reaction mechanism. The initial triplet concentration, after extrapolation to the end of the pulse, was 7.1 μmol L^{-1}. The maximum concentration of the tyrosyl radical was determined to be 6.9 μmol L^{-1}. This value was obtained from fitting the Tyr(O$^\bullet$) concentration profile to a function that takes into account the growth and the decay of the species. From this value and the above triplet concentration (actinometer), the quantum yield of the tyrosyl radical is seen to be close to unity. The same procedure was applied to the bp radical anion, and its quantum yield of formation was estimated to be 0.18. The results proved that not only can dyad **1** (which has the benzophenone and phenol moieties on opposite sides of the DKP ring) undergo intramolecular HAT, but this reaction can occur with quantum yields close to unity. Analogous behavior has been observed in other solvents such as ACN–H_2O mixtures, 2,2,2-trifluoroethanol (TFE), and 1,1,1,2,2,2-hexafluoropropanol (HFIP), except that the bp radical anion was detected only in ACN–H_2O mixtures.

The steering effects of the solvents on the efficiency of the intramolecular triplet quenching of dyads **1** and **2** manifest themselves also in the triplet lifetimes, which exhibit a remarkably distinct influence of the solvents. Some exemplary kinetic profiles, recorded at 630 nm, that illustrate the distinct solvent dependencies of the triplet decays of **1** and **2** are given in Fig. 5. For dyad **2**, where the benzophenone and tyrosine moieties occupy the same side of the DKP ring, the kinetic profiles coincide with each other, irrespective of the solvent. This indicates little impact of the solvent on the triplet lifetimes. Contrasting behavior was seen in dyad **1**, where the triplet lifetimes were very sensitive to the solvents and varied between approx. 50 ns in HFIP and >1000 ns in ACN or EtOAc. In general, the triplet lifetimes of **1** are reduced dramatically on going from non-protic to protic solvents. Thus, in contrast to the previous study of a pair of open-chain epimeric dyads, the triplet lifetimes of the two cyclic structures studied here exhibit completely distinct solvent dependencies.

To study the solvent effects on the intramolecular HAT pathway, the corresponding rate constants, k_H, have been isolated from the observed gross triplet-decay rate constants, k_{obs}. The latter have been extracted from the decay profiles at 630 nm (mono-exponential fits), the decay profiles at 520 nm (bi-exponential fits), and, in some cases, the triplet component of the concentration profiles (as in Figs. 4*b* and 4*d*; mono-exponential fits). Agreement between these methods was within 5%. The absolute value of the triplet-decay rate constant, k_{obs}, is the sum of the rate constants of the individual decay processes (Scheme 3). The evaluation procedures take into account (*i*) the solvent dependence of the intrinsic triplet lifetime of the bp chromophore by referencing it to the behavior of unsubstituted bp in the respective solvent and (*ii*) the effects of self-quenching (see Supplementary data). Due to the low laser power, effects of triplet–triplet annihilation were negligible.

A detailed kinetics data evaluation and a description of the way that we dealt with competition between intra- and intermolecular quenching paths can be found in the Supplementary data.

While the triplet decay of dyad **2** exhibited no significant concentration dependence, LFP results for dyad **1** in non-protic solvents, such as ACN or dichloromethane, show that the values for k_{obs} were concentration dependent. This behavior is due to contributions to bimolecular quenching from self-quenching, which leads to the ketyl radical and the tyrosyl radical with the rate constant k_{SQ}. The latter species decayed by bimolecular processes within tens of microseconds and therefore gave a virtually constant offset in the transient spectra on the time scale of the experiment. The self-quenching process was efficient in non-protic solvents where the reactivity toward intramolecular HAT was small. Notably, the k_H calculated from experiments at different concentrations, 2×10^{-5} mol L^{-1} (λ_{exc} = 266 nm) or 9×10^{-4} mol L^{-1} (λ_{exc} = 337 nm), were in a good agreement (Table 2).

The rate constants for the intramolecular HAT, k_H, calculated for dyad **1** range from $<1 \times 10^5$ s^{-1} in EtOAc to 2×10^7 s^{-1} in HFIP (see Table 2). The rate constants for the intramolecular HAT for dyad **2** varied only from 2.2×10^7 s^{-1} in ACN to 8.2×10^6 s^{-1} in TFE. The uncertainty in the rate constant values derived in this manner increases significantly with H-abstraction contributions from the solvent.

The results presented in Table 2 show a striking contrast between the two diastereomers with regard to the dependence of their k_H on solvent. The results show that a change in the configuration of just one chiral center produced completely distinct changes in the reactivity of the intramolecular HAT with a change in the solvent. The reaction rates for dyad **1** were found to be strongly solvent dependent, while the solvent was found to be of minor importance for the reaction rates of dyad **2**.

This contrasting solvent behavior toward the intramolecular HAT observed in **1** and **2** is unusual for a pair of diastereomers. In this regard they are found to be a unique pair of diastereomers with a unique solvent dependence of the

Fig. 5. Normalized decay profiles observed at 630 nm and mono-exponential fits to the decays for solutions of dyads **1** (*a*) and **2** (*b*). a, ethyl acetate; b, ACN; c, ACN–H_2O (2:1 *v*/*v*); d, trifluoroethanol.

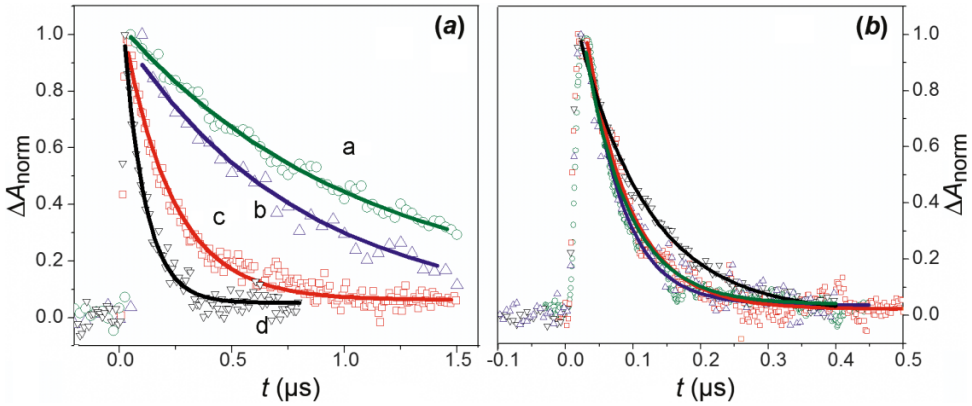

Table 2. Summary of solvent parameters and the kinetic data of dyads **1** and **2**.

		Solvent parameters			Rate constants		
	Solvent	$\Sigma\alpha_2^{Ha}$	$\Sigma\beta_2^{Ha}$	η^b	k_H (**1**)^c	k_H (**2**)^c	S^d
1	Chloroform	0.15	0.02	0.537	(2.2)	(11.5)	5.2
2	Dichloromethane	0.1	0.05	0.437	1.9 (2.0)	(14.5)	7.2
3	1,2-Dichloroethane	0.1	0.11	0.77	(1.7)	(13.6)	10.7
4	Acetonitrile	0.07	0.32	0.37	*0.3 (0.3)*	20.7 (20.0)	73.7
5	Benzonitrile	0	0.33	1.2	*0.3*	9.5	31.6
6	Ethyl acetate	0.0	0.45	0.423	*0.1*	14.4	131
7	Trifluoroethanol	0.57	0.25	1.8^e	8.5	8.2	0.97
8	Methanol	0.43	0.47	0.544	*2.3 (2.8)*	*9.2*	3.9
9	Hexafluoro-2-propanol	0.77	0.10	1.02	21.1	15.7	0.74
10a	Acetonitrile/H_2O (9:1 *v*/*v*)	0.55^f	≈0.34^g	—	3.0	—	—
10b	Acetonitrile/H_2O (4:1 *v*/*v*)	0.61^f	≈0.34^g	—	5.5	—	—
10c	Acetonitrile/H_2O (2:1 *v*/*v*)	0.62^f	≈0.34^g	—	8.4	13.9	1.7

[a]Taken from ref. 67.

[b]At 25 °C (ref. 68).

[c]Results from 355 nm and 337 nm LFP (10^6 s^{-1}); experimental error ±5%, 0.7 mmol/L ≤ [**1**], [**2**] ≤ 2.6 mmol/L. Data in italics: experimental error ±20%. Data in parentheses from 266 nm LFP, 20 μmol/L ≤ [**1**], [**2**] ≤ 40 μmol/L.

[d]$S = k_H$ (**2**) / k_H (**1**).

[e]Taken from ref. 69.

[f]Interpolated from data in ref. 70.

[g]Linear interpolation from data in pure solvents, weighted by molar fractions.

stereoselectivity. Both epimers showed reactivity with respect to intramolecular HAT, but with a remarkable chiral discrimination in their rate constants, and this chiral discrimination strongly depends on the solvents. We and others previously reported stereoselection in HAT rates of diastereomeric ketone–phenol dyads in the range of 2–10 when expressed as the ratio of the rate constants of the intramolecular HAT between remote phenol and ketone moieties of these compounds.[16,19,29] The stereoselectivity ($S = k_H$ (**2**) / k_H (**1**)) found in this work varied from 131 to 0.74 (Table 2). In particular, the epimers revealed marked stereoselectivity in some of the non-protic solvents such as EtOAc and benzonitrile, much higher than has ever been reported previously. Quite unexpectedly, the stereoselectivity was significantly reduced in protic solvents. At extremes, compound **1**, which has the reactive moieties on opposite sides of the DKP ring, became more reactive than **2** in hexafluoro-2-propanol as a medium.

Discussion

In this study the excited-state dynamics of **1** and **2** have been taken as probes of structural effects on the efficiencies and rates of intramolecular hydrogen-atom transfer reactions. We find that the distinct steric constraints of the dyads, as outlined above, are reflected in distinct dynamics of the dyads' triplet states. The dyads particularly differ in their dependencies on the medium, as discussed below.

The intramolecular HAT in dyad **1** was found to be strongly solvent dependent, with the rate constants, k_H, ranging from $<1 \times 10^5$ s^{-1} to 2×10^7 s^{-1}. We recently observed a similar range of rate constants for the intramolecular HAT in one open-chain bp∪Tyr dyad,[30] whereas the HAT reactions in the open-chain congeners of **1** and **2** in a given solvent are generally faster by one to two orders of magnitude.[29] Such solvent-driven modulations of bimolecular HAT reaction rates of phenols have been generally attributed to effects of specific solvation of the phenol, which

Can. J. Chem. Downloaded from www.nrcresearchpress.com by Xi'an Jiaotong University on 09/19/12
For personal use only.

Can. J. Chem. Downloaded from www.nrcresearchpress.com by Xi'an Jiaotong University on 09/19/12
For personal use only.

Fig. 6. (*a*) Plot of H-atom transfer rate constants, $\log k_H$, against Abraham's effective H-bond acceptor ability (refs. 71, 73), $\Sigma\beta_2^H$, for protic solvents (open symbols) and non-protic solvents (filled symbols); (*b*) plot of H-atom transfer rate constants, $\log k_H$, against Abraham's effective H-bond donor ability (refs. 71, 73), $\Sigma\alpha_2^H$, for solvents with $\Sigma\beta_2^H \geq 0.25$ (filled symbols) and solvents with $\Sigma\beta_2^H \leq 0.11$ (open symbols); red symbols represent data for the **1**-(D,L) epimer and blue symbols represent data for the **2**-(L,L) epimer. (*c*) Semilogarithmic plot of stereoselectivity of H-atom transfer in dyads **1** and **2** as a function of the solvents' H-bond acceptor ability; open symbols represent protic solvents. (*d*) Semilogarithmic plot of stereoselectivity of H-atom transfer in dyads **1** and **2** as a function of the solvents' H-bond donor ability; open symbols represent solvents with $\Sigma\beta_2^H \leq 0.11$. Solvent codes as in Table 2.

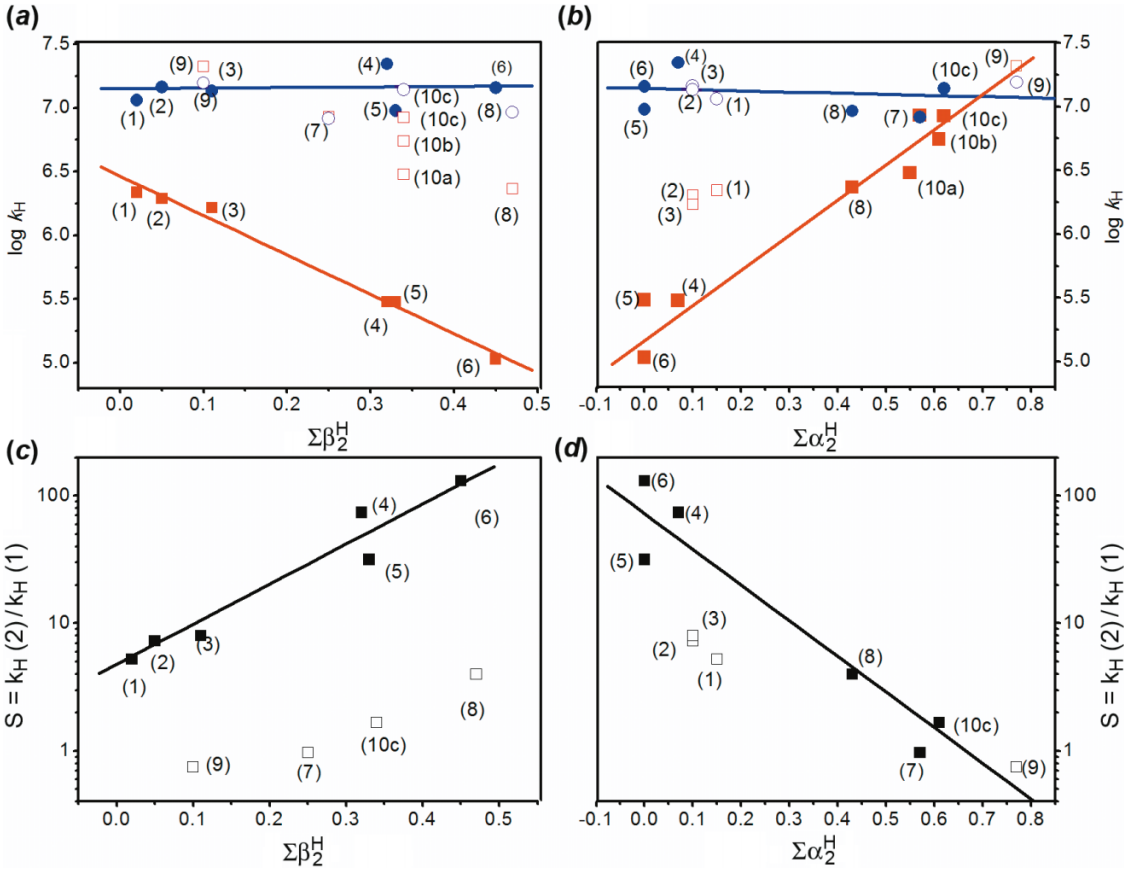

were coined as kinetic solvent effects. In particular, the previous work on the bimolecular HAT of phenols has shown that rate constants are correlated with the solvents' hydrogen-bond acceptor ability.[31–36,71,72] That is, the logarithmic rate constants depended linearly on a single solvent parameter, namely Abraham's H-bond acceptor ability,[71,73] irrespective of the molecularity of the reaction.[29] Notably, the solvent dependence cannot be fully explained by solute–solvent interactions of the tyrosine moiety. As shown here, the single-parameter dependence of the intramolecular HAT reaction that sufficed to explain the reactivity of the open-chain congeners of **1** and **2**[29] is not sufficient to explain the difference in reaction rate constants of the cyclic dyad **1**. Our results show that, in contrast to the phenomenology of the kinetic solvent effect, which necessarily connects specific solvation with reaction hindrance, specific solvation can also promote the HAT reactions of phenols.

In the following discussion the focus will first be on the data for dyad **1** displayed in Figs. 6*a* and 6*b* (red symbols).

A plot of the kinetic data for dyad **1** from Table 2 against the effective H-bond acceptor ability of the solvents (Fig. 6*a*) exhibits two different regions that reflect the character of the solvents. HAT rates in non-protic solvents with weak effective H-bond donor abilities, $\Sigma\alpha_2^H$ (red filled symbols in Fig. 6*a*), have a linear dependence on $\Sigma\beta_2^H$, with a slope $b = -3.1$ ($r^2 = 0.995$) and an intercept of 6.5. Thus, this dyad is another example where the slopes of the logarithmic intramolecular HAT rate constants versus $\Sigma\beta_2^H$ plots are characteristic for each dyad but not characteristic for each donor.[29,30]

The second region in Fig. 6*a* is that formed by the protic solvents with significant H-bond donor abilities. The protic solvents seem to allow much higher rate constants than their non-protic counterparts having similar H-bond acceptor abilities (nearly matching $\Sigma\beta_2^H$). For example, ethyl acetate and MeOH have almost the same H-bond acceptor ability, but k_H values for **1** differ by a factor of 10. Another example is the contrasting behavior of pure ACN and the ACN–H_2O (2:1 *v*/*v*) mixture, in which k_H values for **1** differ by a factor of 25. The large increase in the intramolecular HAT rate constant in protic solvents might be due to a switch in the mechanism.

The decrease of the HAT rates with the H-bond acceptor ability of the non-protic solvents suggests that negligible intramolecular reactivity is expected for dyad **1** in solvents with $\Sigma\beta_2^H > 0.3$. However, the data in Table 2 show that

Can. J. Chem. Downloaded from www.nrcresearchpress.com by Xi'an Jiaotong University on 09/19/12
For personal use only.

protic solvents with high $\Sigma\beta_2^H$ values show significant reactivity for dyad **1**. In Fig. 6*b*, data from Table 2 are plotted against $\Sigma\alpha_2^H$; with the exception of the chlorohydrocarbons, there is a linear correlation for dyad **1** with a positive slope of 2.3 ($r^2 = 0.977$) and an intercept of 5.2. That is, the reactivity increases with the strength of the solvent–solute interaction.

In summary, opposite effects were exerted by non-protic and protic solvents on intramolecular HAT in dyad **1**. The relevant solvent parameters favoring efficient intramolecular HAT for dyad **1** are the solvents' small $\Sigma\beta_2^H$ values and high $\Sigma\alpha_2^H$ values. This was realized by HFIP, for example. The opposite behavior was seen in the poor reactivity in EtOAc, which can be explained on the basis of its high $\Sigma\beta_2^H$ (0.45) and low $\Sigma\alpha_2^H$ (0.00).

In conclusion, the solvent dependence of the cyclic dyad **1** sharply diverges from the behavior of its open-chain congener[29] but largely coincides with the phenomenology observed recently for a more rigid open-chain dyad.[30] Obviously, the observed phenomenology of the kinetic solvent effects reflects structural parameters of the dyads. This is most evident from the behavior of the cyclic dyad **2**, which lacks any significant dependence on the H-bonding properties of the solvent.

The plot of the logarithmic rate constants versus $\Sigma\beta_2^H$ for dyad **2** exibits no significant variance with the solvents' H-bond accepting or H-bond donating properties (blue symbols in Figs. 6*a* and 6*b*). Actually, the slopes are close to zero in both cases, which means that the rate constants for HAT for dyad **2** are independent of these parameters. Accordingly, the stereoselectivity of the HAT in **1** and **2**, expressed as the ratio of the rate constants and shown in Figs. 6*c* and 6*d*, directly reflects the solvent dependence of the HAT of **1**. The sharp decrease of the HAT reaction rates for dyad **1** in non-protic solvents with hydrogen-bond acceptor tendencies and, on the other hand, the sharp increase of the reaction rates in protic solvents with hydrogen-bond donor tendencies are the dominant sources of the solvent dependence of the stereoselectivity (Figs. 6*c* and 6*d*). Our findings are in contrast with other results where the stereoselectivity of the HAT process was solely dependent on the $\Sigma\beta_2^H$, irrespective of the protic or non-protic character of the solvents.

In conclusion, we have studied the behavior of the two cyclic-bridged dyads **1** and **2** in 12 different solvents and mixtures. It was shown that the properties of a solvent, i.e., its ability to act as a hydrogen bond donor or acceptor, play an important role in determining the HAT rate constants in only one of the two epimers in this study.

The contrasting solvent dependencies of the HAT rate constants for dyad **1** in protic and non-protic solvents can be interpreted as being due to fundamentally different HAT mechanisms in the respective solvents. In favor of this interpretation are the significant enhancement of the reaction rates in protic solvents and the presence of the bp radical anion in an ACN–H_2O (1:1 *v*/*v*) mixture. In addition, it is important to note that the intercepts of the single-solvent parameter regressions in Figs. 6*a* and 6*b* (red lines) differ by almost 2 orders of magnitude. These values represent the isolated and solvent-independent HAT rate constants and, thus, they should not vary if there is only a single common mechanism of HAT in protic and non-protic solvents.[30]

Moreover, NMR, molecular-dynamics simulations, and DFT results[39] have shown that conformations with extremely long distances (12.8 Å) between the reactive moieties are the most favorable ones in solution (Fig. 1; Table 1). The HAT rates in non-protic solvents are limited by the accessibility of free (i.e., not H-bonded) tyrosine. In contrast, the kinetic data obtained in protic media show a correlation between HAT rates and the H-bond donor ability of the solvent. Thus, at least for intramolecular HAT reactions, the solvation of the abstracting species should be considered, a priori, as important as the solvation of the H-donating species. However, the action of the protic solvent in this case and its impact on the mechanism of the HAT step remain under discussion and are the subject of further work.

Several pieces of evidence favor electron transfer involving pathways that are driven by specific H-bonding interactions of the electron acceptor with the protic solvent. An electron-transfer pathway in protic solvents has been observed recently for a sterically restricted bp∪TyrOH dyad. In this structure, the directionality of the benzamide linker of the dyad effectively excludes close intramolecular contacts. Studies of the solvent effects on the nanosecond-transient dynamics and on the chemically induced dynamic nuclear polarization following LFP have shown that in protic solvents the H abstraction reaction is initiated by electron transfer (G. Hörner and colleagues, unpublished data). Similar conclusions have been drawn from studies of the bimolecular electron transfer between anisole and ^{3}bp, where dramatic activating effects of strongly H-bonding solvents on the one-electron oxidation of anisole by ^{3}bp show that this phenomenon is not limited to phenols and might be of general significance.[74]

In contrast to the above discussion, neither of the rate-determining effects of solvation seems to be important for the HAT in dyad **2**, as there was little variation in the k_H rate constant among solvents. The ratio of the highest k_H obtained in ACN and the smallest k_H obtained in TFE is just 2.4 for the triplet state of dyad **2**. The absence of a marked solvent dependence, which was observed for all other dyads, therefore deserves further consideration. In particular, it raises the question, what are the factors determining the rate constants if there is no impact of specific solvation?

The observation that the triplet state of dyad **2** was quenched slightly more slowly in solvents with higher viscosity, which led to smaller values of k_H (TFE and benzonitrile, see Table 2), points to the importance of the intramolecular dynamics. Similar observations were made for its open-chain analogue.[29] The observation of a greatly diminished triplet reactivity of **2** in highly viscous *tert*-butanol further corroborates viscosity as another source of kinetic diversity. That is, the dynamics of the molecular motions bringing dyad **2** to its reactive state appear to be rate determining in all solvents, which implies that the intrinsic HAT reaction rate of the dyad, irrespective of its state of solvation, markedly exceeds the rates of the intramolecular motions.

To check whether molecular dynamics are the rate-determining steps of the intramolecular HAT of dyad **2**, we have estimated the rate constant for the formation of close-contact conformations, k_{OO}, based on the LD trajectories de-

Can. J. Chem. Downloaded from www.nrcresearchpress.com by Xi'an Jiaotong University on 09/19/12
For personal use only.

scribed above. In the calculation of the relaxation time (τ_{rxn} from the integration in eq. [2]), we have neglected the negative values of $C_N(t)$, which occur for $t > 1.4$ ns, since they were becoming artificially large with increasing delay times. Neglecting these negative values of $C_N(t)$ means that our computed value of 0.4 ns for the relaxation time is an upper limit. The average fraction of conformations, $\langle N_{OO} \rangle$, with the O–O distance less than 4 Å was determined to be equal to 0.01. Using this value and the τ_{rxn} from eq. [2], the estimated value of k_{OO} was calculated to be $2.5 \pm 0.1 \times 10^7$ s^{-1} (from eq. [1]). The resulting good agreement between the rate constant of formation of close-contact conformations and the experimental value of the intramolecular HAT rate constant in ACN (see Table 2) indicates that intramolecular dynamics is the rate-determining step of the intramolecular HAT.

As discussed previously,[39] DFT calculations suggested the presence of a number of different conformers of **2** with nearly degenerate energies. In particular, calculations on dyad **2** in an ACN continuum highlighted the competition between a conformer with a short O–O distance (favorable for the quenching geometry) with other, more extended conformers of similar energy (but having unfavorable geometries for HAT). This situation has been put to the test in the current work using NMR studies and molecular-dynamics simulations. Taking into account the error in DFT calculations, we can state that the NMR data and the theoretical calculations are in quite good agreement. The NMR data and the simulations both show that conformers that allow for close contacts between the reacting centers have to overcome significant steric constraints.

While the energetic differences between all of the side-chain rotamers appear to be rather small according to the NMR data (<1.0 kcal mol^{-1}), other intrinsically non-reactive structures of dyad **2** with only one aromatic side chain folded over the DKP ring are certainly favored, as evident from NMR data and the simulations (Fig. 2). Thus, significant intramolecular rearrangements must precede the reaction and can even be rate determining as soon as the intrinsic HAT rate exceeds the rate of formation of the quenching geometry. This condition actually seems to hold for dyad **2**. As stressed before (see Fig. 2), the long-term dynamics simulations indicated that the formation of close-contact structures occurs for dyad **2**. In particular, the rate of this formation in an ACN continuum with $k_{OO} = 2.5 \pm 0.1 \times 10^7$ s^{-1} (computed from eqs. [1–3]) shows very good agreement with the observed rate constants of the HAT in this solvent (see Table 2).

Conclusions

In this work we addressed the solvent effects on unimolecular HAT reactions in two epimeric benzophenone–tyrosine dyads. In agreement with previous work,[29] effects of specific solvation as well as effects of the bulk viscosity have been identified as important controls of the intramolecular reactivity. Most interestingly, the limited intramolecular mobility imposed by the rigid peptide environment of the diketopiperazine spacer translates into a strongly contrasting phenomenology of the solvent effects between the two epimers. For the anti-configured epimer **1**, where both amino acid side chains occupy different half rooms of the diketopiperazine spacer, two solvent parameters influence the H abstraction rates, namely the effective H-bond acceptor ability, $\Sigma\beta_2^H$, and the effective H-bond donor ability, $\Sigma\alpha_2^H$, as defined by Abraham.[67] In sharp contrast, the syn-configured dyad **2** represents the first example for HAT reactions from a sterically unhindered phenol without any sizable dependence on specific solvation effects. The reciprocal dependence of the HAT rates of **2** on the bulk viscosity points to the intramolecular dynamics as the rate-determining step.

In conclusion, the presented experimental and theoretical work fully confirmed our hypothesis that the solvent-effect phenomenology of intramolecular HAT reactions of phenols is dependent on and correlated with the donor-acceptor geometry. Intramolecular HAT reactions from phenols yield kinetic solvent effects that are significantly correlated with structural features; that is, individual kinetic solvent effects are expected to prevail for every single system. This mechanistic feature will be put to the test in further work.

Supplementary data

Supplementary data for this article are available on the journal Web site (canjchem.nrc.ca).

Acknowledgements

Financial support from the Ministry of Science and Higher Education (Poland) (grant No. N204 143138) and from the Foundation for Polish Science is gratefully acknowledged. This work was supported by COST Chemistry CM0603. This is document No. NDRL 4851 from the Notre Dame Radiation Laboratory, which is supported by the Office of Basic Energy Sciences at the United States Department of Energy. The computation was supported by the Interdisciplinary Centre for Mathematical and Computational Modeling of Warsaw University (G28-21). A. L. is a scholar of Adam Mickiewicz University Foundation at 2010. A. L. thanks the Director of the Radiation Laboratory for a stipend that supported part of this work.

References

(1) Turro, N. J.; Ramamurth, V.; Scaiano, J. C. *Modern Molecular Photochemistry of Organic Molecules*; University Science Books: Sausalito, CA, 2010.
(2) Das, P. K.; Encinas, M. V.; Scaiano, J. C. *J. Am. Chem. Soc.* **1981**, *103* (14), 4154. doi:10.1021/ja00404a029.
(3) Biczók, L.; Berces, T.; Linschitz, H. *J. Am. Chem. Soc.* **1997**, *119* (45), 11071. doi:10.1021/ja972071c.
(4) Boate, D. R.; Johnston, L.; Scaiano, J. C. *Can. J. Chem.* **1989**, *67* (5), 927. doi:10.1139/v89-142.
(5) Canonica, S.; Hellrung, B.; Wirz, J. *J. Phys. Chem. A* **2000**, *104* (6), 1226. doi:10.1021/jp9930550.
(6) Cosa, G.; Scaiano, J. C. *Org. Biomol. Chem.* **2008**, *6* (24), 4609. doi:10.1039/b810765c. PMID:19039370.
(7) Galian, R. E.; Pastor-Perez, L.; Miranda, M. A.; Perez-Prieto, J. *Chem. Eur. J.* **2005**, *11* (11), 3443. doi:10.1002/chem.200401118.
(8) Galian, R. E.; Litwinienko, G.; Pérez-Prieto, J.; Ingold, K. U. *J. Am. Chem. Soc.* **2007**, *129* (30), 9280. doi:10.1021/ja071716y. PMID:17625849.
(9) Koner, A. L.; Pischel, U.; Nau, W. M. *Org. Lett.* **2007**, *9* (15), 2899. doi:10.1021/ol071165g. PMID:17580891.

Can. J. Chem. Downloaded from www.nrcresearchpress.com by Xi'an Jiaotong University on 09/19/12
For personal use only.

(10) Lathioor, E. C.; Leigh, W. J. *Can. J. Chem.* **2001**, *79* (12), 1851. doi:10.1139/cjc-79-12-1851.
(11) Lathioor, E. C.; Leigh, W. J. *Photochem. Photobiol.* **2006**, *82* (1), 291. doi:10.1562/2005-06-20-RA-581. PMID: 16042506.
(12) Lathioor, E. C.; Leigh, W. J.; St. Pierre, M. J. *J. Am. Chem. Soc.* **1999**, *121* (51), 11984. doi:10.1021/ja991207z.
(13) Leigh, W. J.; Lathioor, E. C.; St. Pierre, M. J. *J. Am. Chem. Soc.* **1996**, *118* (49), 12339. doi:10.1021/ja961973v.
(14) Wakasa, M.; Hayashi, H. *J. Phys. Chem.* **1995**, *99* (47), 17074. doi:10.1021/j100047a004.
(15) Yamaji, M.; Aoyama, Y.; Furukawa, T.; Itoh, T.; Tobita, S. *Chem. Phys. Lett.* **2006**, *420* (1–3), 187. doi:10.1016/j.cplett. 2005.12.072.
(16) Miranda, M. A.; Lahoz, A.; Martınez-Manez, R.; Bosca, F.; Castell, J. V.; Perez-Prieto, J. *J. Am. Chem. Soc.* **1999**, *121* (49), 11569. doi:10.1021/ja990823s.
(17) Pérez-Prieto, J.; Boscá, F.; Galian, R. E.; Lahoz, A.; Domingo, L. R.; Miranda, M. A. *J. Org. Chem.* **2003**, *68* (13), 5104. doi:10.1021/jo034225e. PMID:12816463.
(18) Pérez-Prieto, J.; Galian, R. E.; Morant-Miñana, M. C.; Miranda, M. A. *Chem. Commun. (Camb.)* **2005**, (25): 3180. doi:10.1039/b500697j. PMID:15968364.
(19) Pérez-Prieto, J.; Lahoz, A.; Boscá, F.; Martinez-Mañez, R.; Miranda, M. A. *J. Org. Chem.* **2004**, *69* (2), 374. doi:10. 1021/jo0356199. PMID:14725449.
(20) Pérez-Prieto, J.; Stiriba, S. E.; Boscá, F.; Lahoz, A.; Domingo, L. R.; Mourabit, F.; Monti, S.; Miranda, M. A. *J. Org. Chem.* **2004**, *69* (25), 8618. doi:10.1021/jo048973v. PMID: 15575737.
(21) Pischel, U.; Nau, W. M. *Photochem. Photobiol. Sci.* **2002**, *1* (2), 141. doi:10.1039/b110108k. PMID:12659131.
(22) Pischel, U.; Patra, D.; Koner, A. L.; Nau, W. M. *Photochem. Photobiol.* **2006**, *82* (1), 310. doi:10.1562/2005-02-07-RA-434. PMID:15882091.
(23) Scaiano, J. C.; McGimpsey, W. G.; Leigh, W. J.; Jakobs, S. *J. Org. Chem.* **1987**, *52* (20), 4540. doi:10.1021/ jo00229a021.
(24) Seyedsayamdost, M. R.; Reece, S. Y.; Nocera, D. G.; Stubbe, J. *J. Am. Chem. Soc.* **2006**, *128* (5), 1569. doi:10. 1021/ja055926r. PMID:16448128.
(25) Sul'timova, N. B.; Levin, P. P.; Chaikovskayab, O. N. *Russ. Chem. Bull., Int. Ed.* **2005**, *56*, 1397.
(26) Yamaji, M.; Oshima, J.; Hidaka, M. *Chem. Phys. Lett.* **2009**, *475* (4–6), 235. doi:10.1016/j.cplett.2009.05.063.
(27) Stubbe, J.; van der Donk, W. A. *Chem. Rev.* **1998**, *98* (2), 705. doi:10.1021/cr9400875.
(28) Wagner, P. J.; Pabon, R.; Park, B. S.; Zand, A. R.; Ward, D. L. *J. Am. Chem. Soc.* **1994**, *116* (2), 589. doi:10.1021/ ja00081a020.
(29) Hörner, G.; Hug, G. L.; Lewandowska, A.; Kazmierczak, F.; Marciniak, B. *Chem. Eur. J.* **2009**, *15* (13), 3061. doi:10. 1002/chem.200802674.
(30) Hörner, G.; Lewandowska, A.; Hug, G. L.; Marciniak, B. *J. Phys. Chem. C* **2009**, *113* (27), 11695. doi:10.1021/ jp901740z.
(31) Avila, D. V.; Ingold, K. U.; Lusztyk, J.; Green, W. H.; Procopio, D. R. *J. Am. Chem. Soc.* **1995**, *117* (10), 2929. doi:10. 1021/ja00115a029.
(32) Banks, J. T.; Ingold, K. U.; Lusztyk, J. *J. Am. Chem. Soc.* **1996**, *118* (28), 6790. doi:10.1021/ja961032i.
(33) Litwinienko, G.; Ingold, K. U. *J. Org. Chem.* **2003**, *68* (9), 3433. doi:10.1021/jo026917t. PMID:12713343.
(34) Litwinienko, G.; Ingold, K. U. *J. Org. Chem.* **2004**, *69* (18), 5888. doi:10.1021/jo049254j. PMID:15373474.
(35) Litwinienko, G.; Ingold, K. U. *J. Org. Chem.* **2005**, *70* (22), 8982. doi:10.1021/jo051474p. PMID:16238337.
(36) Litwinienko, G.; Ingold, K. U. *Acc. Chem. Res.* **2007**, *40* (3), 222. doi:10.1021/ar0682029. PMID:17370994.
(37) Hug, G. L.; Bobrowski, K.; Pogocki, D.; Hörner, G.; Marciniak, B. *ChemPhysChem* **2007**, *8* (15), 2202. doi:10.1002/ cphc.200700369. PMID:17910022.
(38) Kopple, K. D.; Ohnishi, M. J. *J. Am. Chem. Soc.* **1969**, *91* (4), 962. doi:10.1021/ja01032a029. PMID:5778278.
(39) Lewandowska, A.; Hug, G. L.; Hörner, G.; Carmichael, I.; Kazmierczak, F.; Marciniak, B. *Chem. Phys. Lett.* **2009**, *473* (4–6), 348. doi:10.1016/j.cplett.2009.03.085.
(40) Kirby, G. W.; Michael, J. *J. Chem. Soc. Chem. Commun.* **1971**, *187*, 415.
(41) Nitecki, D. E.; Halpern, B.; Westley, J. W. *J. Org. Chem.* **1968**, *33* (2), 864. doi:10.1021/jo01266a091.
(42) Leach, A. R. *Molecular Modelling: Principles and Applications*; Longman: Harlow, England, 1996.
(43) Frenkel, D.; Smit, B. *Understanding Molecular Simulation. From Algorithms to Applications*; Academic Press: San Diego, 1996.
(44) Widmalm, G.; Pastor, R. W. *J. Chem. Soc., Faraday Trans.* **1992**, *88* (13), 1747. doi:10.1039/ft9928801747.
(45) Levy, R. M.; Karplus, M.; McCammon, J. A.. *Chem. Phys. Lett.* **1979**, *65* (1), 4. doi:10.1016/0009-2614(79)80114-1.
(46) He, S.; Scheraga, H. A. *J. Chem. Phys.* **1998**, *108* (1), 287. doi:10.1063/1.475379.
(47) Field, M. J. *A Practical Introduction to the Simulation of Molecular Systems*; Cambridge University Press: Cambridge, 1999.
(48) Hinchliffe, A. *Chemical Modeling. From Atoms to Liquids*; John Wiley & Sons: Chichester, UK, 1999.
(49) MacKarell, A. D., Jr.; Bashford, D.; Bellott, M.; Dunbrack, R. L., Jr.; Evanseck, J. D.; Field, M. J.; Fischer, S.; Gao, J.; Guo, H.; Ha, S.; Joseph-McCarthy, D.; Kuchnir, L.; Kuczera, K.; Lau, F. T. K.; Mattos, C.; Michnick, S.; Ngo, T.; Nguyen, D. T.; Prodhom, B.; Reiher, W. E., III; Roux, B.; Schlenkrich, M.; Smith, J. C.; Stote, R.; Straub, J.; Watanabe, M.; Wiórkiewicz-Kuczera, J.; Yin, D.; Karplus, M. *J. Phys. Chem. B* **1998**, *102* (18), 3586. doi:10.1021/jp973084f.
(50) Gasteiger, J.; Marsili, M. *Tetrahedron* **1980**, *36* (22), 3219. doi:10.1016/0040-4020(80)80168-2.
(51) Venable, R. M.; Zhang, Y.; Hardy, B. J.; Pastor, R. W. *Science* **1993**, *262* (5131), 223. doi:10.1126/science. 8211140. PMID:8211140.
(52) Hypercube. *HyperChem® Computational Chemistry*; Hypercube, Inc.: Gainesville, FL, 2002.
(53) Allen, M. P.; Tildesley, D. J. *Computer Simulation of Liquids*; Oxford University Press: New York, 1987.
(54) Pogocki, D.; Schöneich, C. *Chem. Res. Toxicol.* **2002**, *15* (3), 408. doi:10.1021/tx0101550. PMID:11896689.
(55) Chandler, D. *Introduction to Modern Statistical Mechanics*; Oxford University Press: Oxford, 1987.
(56) Zwanzig, R.; Ailawadi, N. K. *Phys. Rev.* **1969**, *182* (1), 280. doi:10.1103/PhysRev.182.280.
(57) Pedzinski, T.; Markiewicz, A.; Marciniak, B. *Res. Chem. Intermed.* **2009**, *35* (4), 497. doi:10.1007/s11164-009-0046-4.
(58) Thomas, M. D.; Hug, G. L. *Comput. Chem.* **1988**, *22* (6), 491. doi:10.1016/S0097-8485(98)00022-9.
(59) Ludwig, M.; Asher, S. A. *J. Am. Chem. Soc.* **1988**, *110* (4), 1005. doi:10.1021/ja00212a004.
(60) Laws, W. R.; Ross, J. B. A.; Wyssbrod, H. R.; Beechem, J.

M.; Brand, L.; Sutherland, J. C. *Biochemistry* **1986**, *25* (3), 599. doi:10.1021/bi00351a013.
(61) Hörner, G.; Hug, G. L.; Pogocki, D.; Filipiak, P.; Bauer, W.; Grohmann, A.; Lämmermann, A.; Pedzinski, T.; Marciniak, B. *Chem. Eur. J.* **2008**, *14* (26), 7913. doi:10.1002/chem.200800315.
(62) Kobayashi, J.; Higashijima, T.; Miyazawa, T. *Int. J. Pept. Protein Res.* **1984**, *24* (1), 40. doi:10.1111/j.1399-3011.1984.tb00925.x.
(63) Kobayashi, J.; Higashijima, T.; Sekido, S.; Miyazawa, T. *Int. J. Pept. Protein Res.* **1981**, *17* (4), 486. doi:10.1111/j.1399-3011.1981.tb02018.x.
(64) Kobayashi, J.; Nagai, U. *Biopolymers* **1978**, *17* (9), 2265. doi:10.1002/bip.1978.360170918.
(65) Donzel, B.; Gauduchon, P.; Wahl, Ph. *J. Am. Chem. Soc.* **1974**, *96* (3), 801. doi:10.1021/ja00810a027.
(66) Chandrasekaran, R.; Lakshminarayanan, A. V.; Mohanakrishnan, P.; Ramachandran, G. N. *Biopolymers* **1973**, *12* (6), 1421. doi:10.1002/bip.1973.360120615.
(67) Abraham, M. H. *Chem. Soc. Rev.* **1993**, *22* (2), 73. doi:10.1039/cs9932200073.
(68) *CRC Handbook of Chemistry and Physics*, 76th ed.; D. R. Lide (Ed.); CRC Press: Boca Raton, 1995.
(69) Sierra, P. S.; Tejuca, C. C.; Garcia-Blanca, F. *Helv. Chim. Acta* **2005**, *88*, 312.
(70) Marcus, Y.; Migron, Y. *J. Phys. Chem.* **1991**, *95*, 400.
(71) Snelgrove, D. W.; Lusztyk, J.; Banks, J. T.; Mulder, P.; Ingold, K. U. *J. Am. Chem. Soc.* **2001**, *123* (3), 469. doi:10.1021/ja002301e.
(72) Valgimigli, L.; Banks, J. T.; Ingold, K. U.; Lusztyk, J. *J. Am. Chem. Soc.* **1995**, *117* (40), 9966. doi:10.1021/ja00145a005.
(73) Abraham, M. H.; Grellier, P. L.; Prior, D. V.; Morris, J. J.; Taylor, P. J. *J. Chem. Soc., Dalton Trans.* **1990**, *20*, 521.
(74) Lewandowska, A.; Hug, G. L.; Hörner, G.; Pedzinski, T.; Filipiak, P.; Marciniak, B. *ChemPhysChem* **2010**, *11* (10), 2108. doi:10.1002/cphc.201000196. PMID:20540143.

Can. J. Chem. Downloaded from www.nrcresearchpress.com by Xi'an Jiaotong University on 09/19/12
For personal use only.

Zirconium oxide nanoparticles coated on sepiolite by sol–gel process — Their application as a solvent-free catalyst for condensation reactions

Sadok Letaief, Yun Liu, and Christian Detellier

Abstract: An inorganic nanocomposite made of zirconia nanoparticles coated on the external surfaces of the fibrous clay mineral sepiolite was prepared by using the sol–gel process under soft conditions using zirconium(IV) propoxide in 1-propanol as the precursor. The resulting materials were characterized by X-ray diffraction (XRD), thermal gravimetric analyses (TGA) and differential thermal analyses (DTA), microporosimetry, ^{29}Si magic-angle spinning (MAS) nuclear magnetic resonance (NMR), and high-resolution transmission electron microscopy (HR-TEM). The organic material from the precursor was fully removed after calcination at 450 °C, concurrently with the crystallization of the cubic phase of zirconium oxide. The coordinated water molecules of sepiolite were fully removed and its symmetrical layered structure was folded after calcination at 650 °C, as observed by XRD and ^{29}Si cross-polarization (CP)/MAS NMR. The arrangement of the nanoparticles of zirconium oxide on the sepiolite external surfaces maintains a fibrous morphology for the nanocomposite. This material was applied as a catalyst for the Knoevenagel condensation reaction of benzaldehyde and malononitrile under solvent-free conditions. Strongly improved yields of reaction, attributed to larger catalytically active surfaces, were obtained compared with either the sepiolite clay mineral or the zirconium oxide tested individually.

Key words: nanocomposites, zirconia, clay minerals, sepiolite, Knoevenagel reaction, condensation reaction, sol–gel process, nanohybrid materials, heterogeneous catalysis, solvent-free reaction.

Résumé : Faisant appel à un processus sol–gel dans des conditions douces et utilisant du propylate de zirconium(IV) dans le 1-propanol comme précurseur, on a préparé un nanocomposite inorganique fait de nanoparticules de zircone recouvrant les surfaces externes de sépiolite, un mineral d'argileux fibreux. Les matériaux résultant ont été caractérisés par diffraction des rayons-X (DRX), par analyse thermogravimétrique (ATG) et analyse thermique différentielle (ATD), par microporosimétrie, par RMN du ^{29}Si avec rotation à l'angle magique avec polarisation croisée (RMN ^{29}Si RAM/PC) et par microscopie électronique de transmission à haute résolution (ME–THR). Les résidus du produit organique précurseur ont été éliminés complètement, après calcination à 450 °C, et cette opération s'est produite simultanément avec la cristallisation de la phase cubique de l'oxyde de zirconium. Après calcination à 650 °C, tel qu'observé par DRX et RMN ^{29}Si RAM/PC, les molécules d'eau de coordination de la sépiolite étaient enlevées complètement et la structure en couche symétrique était repliée. L'arrangement des nanoparticules d'oxyde de zirconium sur les surfaces externes de la sépiolite permet au nanocomposite de maintenir sa morphologie fibreuse. On a appliqué ce matériel comme catalyseur pour une réaction de condensation de Knoevenagel du benzaldéhyde et du malonitrile, dans des conditions sans solvant. Par comparaison avec la sépiolite ou l'oxyde de zirconium utilisés individuellement, le nanocomposite conduit à des rendements beaucoup plus élevés pour la réaction et ce résultat est attribué à une plus grande quantité de surfaces catalytiquement actives.

Mots-clés : nanocomposites, zircone, mineraux argileux, sépiolite, réaction de Knoevenagel, réaction de condensation, processus sol–gel, matériaux nanohybrides, catalyse hétérogène, réaction sans solvant.

[Traduit par la Rédaction]

Introduction

Sepiolite, a nonswelling clay mineral, is a hydrated magnesio-silicate[1] with a theoretical half cell unit formula of $Si_{12}O_{30}Mg_8(OH)_4(OH_2)_4{\cdot}8H_2O$.[2] Unlike most other clay minerals (montmorillonite, vermiculite, kaolinite, etc.), it is characterized by a fibrous structure consisting of continuous talc-like two-dimensional octahedral layers of magnesium sandwiched between two tetrahedral layers of silicon. Different units are linked to each other through an inverted Si–O–Si bond happening every six silicon atoms.[3] This arrangement of discontinuous sheets creates an extended porous

Received 17 May 2010. Accepted 6 August 2010. Published on the NRC Research Press Web site at canjchem.nrc.ca on 15 February 2011.

In honour of the outstanding career contributions of Professor J.C. (Tito) Scaiano to the chemical sciences. This article is part of a Special Issue dedicated to Professor J. C. Scaiano.

S. Letaief, Y. Liu, and C. Detellier.[1] Centre for Catalysis Research and Innovation and Department of Chemistry, University of Ottawa, 10 Marie Curie, Ottawa, ON K1N 6N5, Canada.

[1]Corresponding author (e-mail: dete@uottawa.ca).

Can. J. Chem. Downloaded from www.nrcresearchpress.com by University of Electronic and Science Techonology of China on 09/18/12
For personal use only.

Can. J. Chem. Downloaded from www.nrcresearchpress.com by University of Electronic and Science Techonology of China on 09/18/12
For personal use only.

structure of tunnels and channels of molecular dimensions at the interior and at the exterior, respectively, of the fibres. The cross section of each tunnel is approximately 10.6 Å × 3.7 Å in diameter and runs parallel to the fibre axis.[4] This particularity of the structure, shared only with palygorskite, a clay mineral of similar structure but with different tunnel dimension, gives sepiolite interesting physicochemical properties such as microporosity and absorption. Despite its fascinating chemical and structural properties, its applications in the industrial domain are still quite limited compared with montmorillonite or kaolinite for example.

A small number of studies have reported on the preparation of metal nanoparticles supported on the external surfaces of sepiolite: by precipitation and reduction,[5,6] ion exchange,[7,8] impregnation,[9] grafting through vinylsilanes,[10,11] and sol–gel methods.[12,13] All these nanohybrid materials resulting from deposition of a variety of metallic species from, for example, titanium, osmium, iron, nickel, cupper, palladium, silver, platinum, gold, or cobalt have been used as heterogeneous catalysts or as support for potential use of their optical and magnetic properties.[5,7,12,14–21] To the best of our knowledge, the decoration of sepiolite fibres with zirconium oxide has not yet been reported.

Zirconium dioxide (ZrO_2) is one of the most studied ceramic materials owing to its chemical, mechanical, and optical properties. It is stable under three different structures: monoclinic, tetragonal, and cubic.[22] The monoclinic phase is stable from room temperature (RT) to 1175 °C. The tetragonal phase is stable from 1175 to 2370 °C and, finally, the cubic phase is stable from 2370 to 2680 °C. The stability of the phases may vary depending on the support surfaces.[22] Zirconium oxide was exploited for various applications such as catalysis,[23,24] electrochemistry,[25,26] and in membrane preparations.[27]

The Knoevenagel condensation is an important reaction in organic chemistry for the synthesis of intermediate compounds. It is one of the most useful and widely employed methods for carbon–carbon bond formation.[28] Generally, this reaction is performed in an organic solvent in the presence of a base such as an amine. In the search for more environmentally friendly reaction media, heterogeneous catalysts such as orthophosphates,[29] Ni impregnated on SiO_2 or TiO_2 supports,[30] K_2CO_3,[31] zeolites,[32] alkali-exchanged sepiolites,[33] silica gel,[34] ammonium acetate – basic alumina,[35] nanocrystalline ZnO,[36] ionic liquid[37,38], or mesoporous $Ce_xZr_{1-x}O_2$ solid solutions[39] have been reported for Knoevenagel condensations between aldehydes and malononitrile. Zirconia supported on MgO[40] or impregnated with sulfate ions[41] was used as catalyst for this reaction under solvent-free conditions.

In this study, the remarkable structural features of sepiolite were used to prepare an efficient catalyst for the Knoevenagel condensation of benzaldehyde derivatives with malononitrile under solvent-free conditions. The external surface of sepiolite was decorated by nanoparticles of zirconium oxide. These modifications, which take place at the nanometer scale under soft conditions, produce a functional nanocomposite material combining the textural properties of the pristine clay mineral and the catalytic activity of zirconium oxide. The material was characterized by a series of techniques. It was applied to the solvent-free reaction of condensation of benzaldehyde and malononitrile.

Scheme 1. A schematic illustration of the deposition of zirconium oxide nanoparticles on the external surfaces of sepiolite.

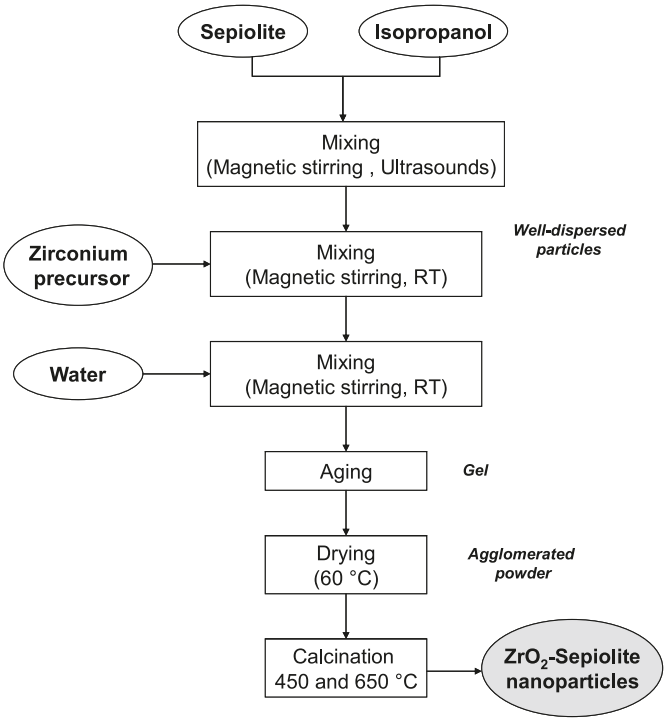

Experimental

Reagents

Sepiolite (SepSp-1) was obtained from the Source Clays Repository, Purdue University, West Lafayette, Indiana. Purified sepiolite was obtained by standard sedimentation techniques and the <2 μm fraction was used in the experiments. More details about the sepiolite purification procedures are described in the literature.[42]

Zirconium(IV) propoxide solution (70 wt% in 1-propanol) was purchased from Sigma-Aldrich and always kept in an anhydrous environment. Benzaldehyde, *para*-nitrobenzaldehyde, and *para*-hydroxylbenzaldehyde were purchased from Sigma-Aldrich and were used as received.

Preparation of ZrO_2–sepiolite nanoparticles (Scheme 1)

A procedure similar to previously reported ones for the preparation of silica–smectite,[43] titania–sepiolite,[12] or TiO_2/SiO_2 – clay porous materials[13] was used for the preparation of the nanocomposite sepiolite–zirconia nanoparticles using the sol–gel technique without addition of cationic surfactant, in contrast to the previously reported procedures.[12,13,43] Two grams of sieved sepiolite (<100 μm) were dispersed in 40 mL of 2-propanol. The suspension was stirred for 30 min, sonicated for another 6 min (3 × 2 min), and maintained again under magnetic stirring in a closed vial for 3 days to obtain a homogeneous dispersion. A selected amount of zirconium propoxide was slowly added to the suspension. Two sets of the experiment were carried out: (*i*) the amount of zirconium propoxide added was equal to the

Can. J. Chem. Downloaded from www.nrcresearchpress.com by University of Electronic and Science Techonology of China on 09/18/12
For personal use only.

amount of clay mineral and (*ii*) the amount of zirconium propoxide was twice the amount of clay mineral. The mixture was stirred again at room temperature for 20 min, and then the amount of water necessary for a complete hydrolysis of the propoxide was added dropwise under magnetic stirring. After the addition of water, the dispersion became very viscous because of the sol–gel transition. The resulting gel was then dried at 60 °C, grounded, and heated at two different temperatures (450 and 650 °C).

Catalytic activity

The catalytic properties of the zirconium oxide nanoparticles supported on the external surfaces of sepiolite were tested for the Knoevenagel condensation reaction between aromatic aldehyde derivatives (benzaldehyde, *para*-nitrobenzaldehyde, and *para*-hydroxylbenzaldehyde) and malononitrile. A mixture of 0.5 g of benzaldehyde (47 mmol), 0.34 g of malononitrile (51 mmol), and 40 mg of the sepiolite–zirconium oxide nanoparticle material was refluxed, vigorously stirred, and heated for 2 h at 100 °C. The resulting product was extracted by diethyl ether, purified using column chromatography on silica gel with diethyl ether – *n*-hexane, and analyzed by ^{1}H and ^{13}C NMR.

Characterization

X-ray diffraction (XRD) patterns were obtained with a Philips PW 3710 instrument equipped with a Ni filter and Cu Kα radiation (λ = 0.154 18 nm) operating at 45 kV and 40 mA. Differential thermal analyses (DTA) and thermal gravimetric analyses (TGA) were recorded on a SDT 2960 simultaneous DSC-TGA instrument under N_2 flow (100 mL/min) with a heating rate of 10 °C/min.

Transmission electron microscopy (TEM) and high-resolution (HR)-TEM images were obtained on a JEOL JEM-2100F electron microscope. Samples were suspended in ethanol for ~10 min under ultrasonic treatment before depositing them on carbon-film-coated copper grids. TEM photos of different areas of analysis at various magnifications were analysed.

Brunauer–Emmett–Teller (BET) surface area and micropore measurements of the samples were processed on a Micromeritics ASAP-2010 instrument. The samples were predegassed at room temperature under vacuum to eliminate adsorbed moisture and zeolitic water within the micropores. The degas process was terminated when the vacuum pressure decreased to 3 μmHg (1 mmHg = 133.3224 Pa). The molecular cross section of nitrogen used in the data analysis was 0.1620 nm^2. The typical range of thickness chosen for *t*-plot measurements was 3.5–5 Å.

^{29}Si cross-polarization / magic-angle spinning (CP/MAS) spectra were collected on a Bruker AVANCE 500 NMR spectrometer operating at 99.35 MHz. The ^{29}Si chemical shifts were referenced to TMS at 0 ppm using the high-frequency signal of tetrakis(trimethylsilyl) silane at 29.9 ppm as a secondary standard.

Results and discussion

TGA

Figure 1 gives a differential thermal gravimetry (DTG) comparison between pure sepiolite (Fig. 1a) and the hybrid material prepared by hydrolysis and condensation of zirconium propoxide at the external surface of sepiolite, dried at 60 °C (Fig. 1b). In the case of sepiolite, the first weight loss occurring at 77 °C corresponds to the zeolitic water elimination as well as surface water elimination. The second loss at 276 °C corresponds to the elimination of the first coordinated water molecule. The third loss at 524 °C corresponds to the elimination of the second coordinated water molecule. Finally, the fourth loss at 828 °C is due to the dehydroxylation of the internal Mg–OH bonds.[2,44] The DTG results of the hybrid materials show additional weight losses at 161 and 364 °C owing to the decomposition of the organic moieties. After production of the ZrO_2 nanoparticles, the loss of the second water molecule and the dehydroxylation of sepiolite take place in the same temperature range as in the case of the original sepiolite. This is an indication that the structure of sepiolite is not altered during the deposition of the zirconium oxide, as observed also on the XRD pattern (see Fig. 2d). It is clear from Fig. 1b that after heating the hybrid material at temperatures >400 °C, the organic material was fully removed, resulting in the formation of zirconium oxide. Two temperatures of calcinations were chosen, 450 and 650 °C. The DTG results are given in Figs. 1c and 1d, respectively. Two major weight losses, corresponding to the

Fig. 1. Differential thermal gravimetry (DTG) traces of (a) sepiolite, (b) the hybrid material prepared by hydrolysis and condensation of zirconium propoxide at the external surface of sepiolite and dried at 60 °C , (c) sample (b) calcined at 450 °C, and (d) sample (b) calcined at 650 °C.

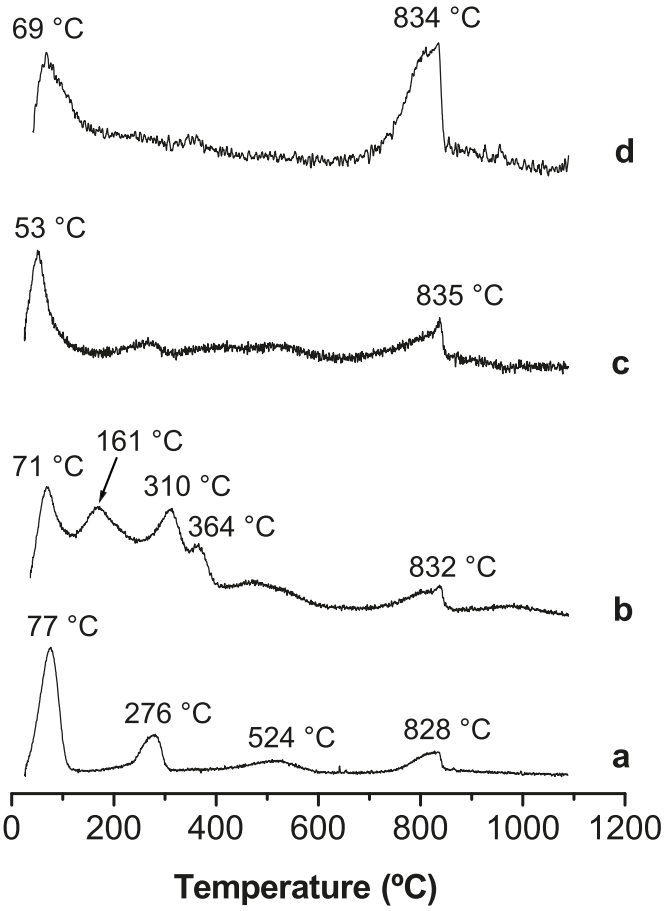

Can. J. Chem. Downloaded from www.nrcresearchpress.com by University of Electronic and Science Techonology of China on 09/18/12
For personal use only.

Fig. 2. Powder X-ray diffraction (XRD) diffractograms of (a) pure sepiolite, (b) zirconium oxide prepared by hydrolysis and condensation of zirconium propoxide without sepiolite, (c) the hybrid material prepared by hydrolysis and condensation of zirconium propoxide at the external surface of sepiolite and dried at 60 °C , (d) sample (*b*) calcined at 450 °C, and (e) sample (b) calcined at 650 °C.

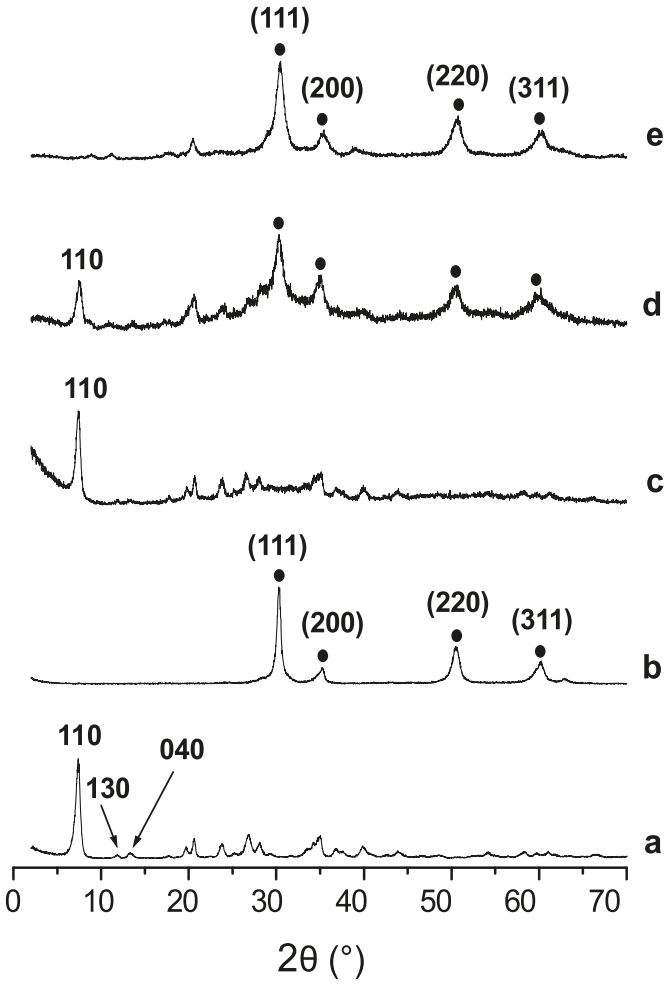

removal of water adsorbed at the external surface and to the dehydroxylation of sepiolite at high temperature, could be observed. TGA–DTG results indicate that the organic moieties on the nanohybrid materials can be removed by calcination above 450 °C. At these temperatures, ZrO_2 nanoparticles are formed. The coordinated water molecules are fully removed by calcination at 650 °C.

XRD

Figure 2 shows the XRD spectra of the starting sepiolite (Fig. 2a), the hybrid material prepared by hydrolysis and condensation of zirconium isopropoxide at the external surface of sepiolite and dried at 60 °C (Fig. 2c), and the hybrid material obtained after heating at 450 °C (Fig. 2d) and 650 °C (Fig. 2e). The diffractogram of the hybrid material recuperated after drying at 60 °C exhibits the typical reflections of sepiolite. It shows only wide bands around 2θ = 25°–35°, owing to the presence of amorphous solid, as expected. After calcination at 450 °C, new reflections appear

Fig. 3. Transmission electron microscopy (TEM) images of untreated sepiolite at two different scales.

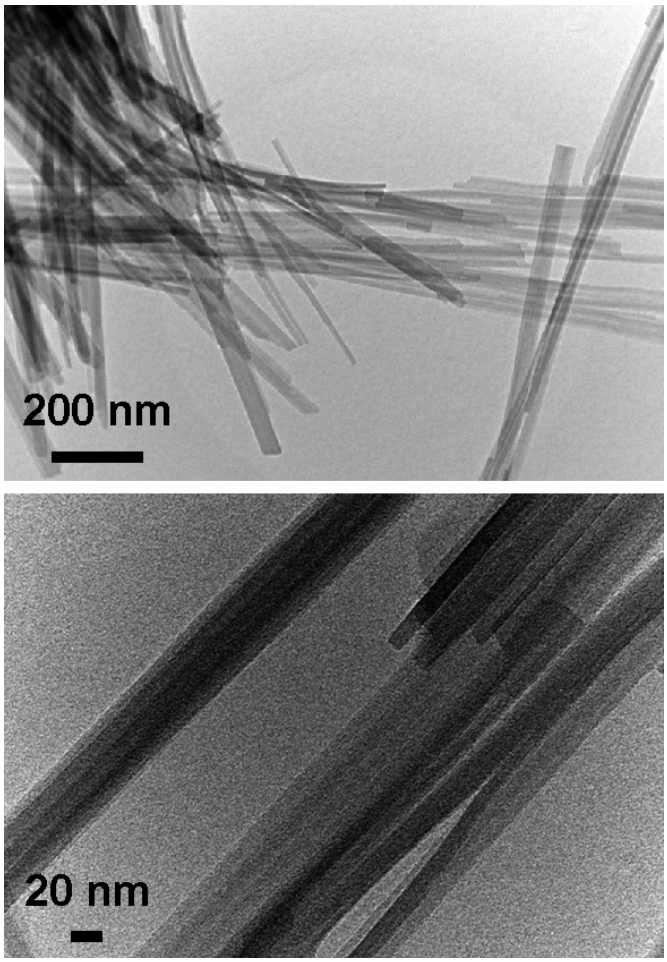

in the XRD pattern at 2θ = 30.3°, 35.3°, 50.5°, and 60.2°. These reflections are characteristic of the zirconium oxide in tetragonal or cubic phase. They are more pronounced in the case of the nanohybrid material obtained after heating at 650 °C. Their positions are identical to the zirconium dioxide prepared by hydrolysis and condensation of zirconium propoxide without sepiolite (Fig. 2b). The values of the relative intensities of the reflections present in the X-ray diffractogram of the zirconium dioxide particles prepared in this work were compared with the relative intensities of reflections observed for zirconium dioxide in cubic and tetragonal phases.[45,46] The reflections observed at 30.3°, 35.3°, 50.50°, and 60.2° correspond to the (111), (200), (220), and (311) planes, respectively, of the cubic phase.

The disappearance of the 001 reflection of sepiolite (2θ = 7.8°) after heating the nanohybrid material at 650 °C indicates that the structure of sepiolite is folded.[47,48] As it will be discussed in the next section, even when sepiolite is folded, the arrangement of the nanoparticles of zirconium oxide maintains the fibre morphology.

HR-TEM

TEM analysis performed on the pristine sepiolite clay mineral (untreated sepiolite) show needle structures characterized by a variety of lengths between 100 and 600 nm

Can. J. Chem. Downloaded from www.nrcresearchpress.com by University of Electronic and Science Techonology of China on 09/18/12
For personal use only.

Fig. 4. Transmission electron microscopy (TEM) images of the hybrid material prepared by hydrolysis and condensation of zirconium propoxide at the external surface of sepiolite and then dried at 60 °C.

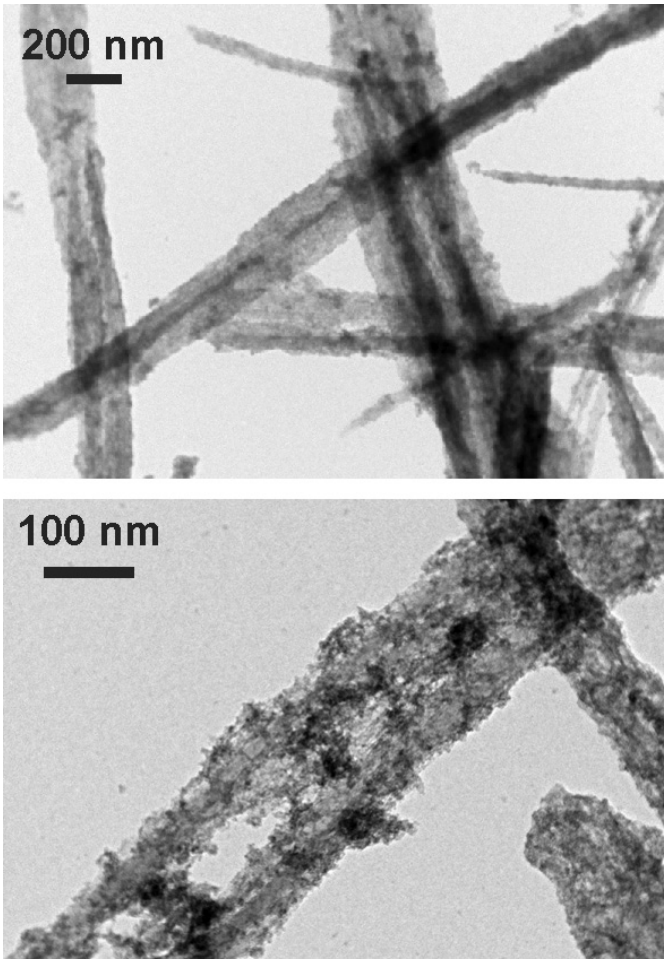

(Fig. 3, top image). These needles are randomly distributed and formed by the superposition of a number of fibres. HR-TEM measurement on the untreated sepiolite shows smooth, thin fibres having a thickness close to 15 nm. These can be aggregated in needles of typically 50–100 nm in thickness (Fig. 3, bottom image). After deposition of the Zr propoxide on the sepiolite external surfaces, the TEM of the samples still show long needles randomly distributed (Fig. 4). The surfaces of the fibres have become rough compared with those of pure sepiolite. This is due to the sticking of zirconium propoxide on the external surfaces of sepiolite. In contrast with the case of sepiolite where it was possible to observe individual fibres, in the case of the nanohybrid material, an agglomeration of the fibres takes place during the deposition of zirconium oxide. This agglomeration results in needles with enlarged cross sections compared with those of sepiolite. Figures 5 and 6 show examples of ZrO_2 nanoparticles prepared at the external surfaces of sepiolite and calcined at 450 and 650 °C, respectively. ZrO_2 nanoparticles are easily distinguished because of the high contrast of zirconium. They are homogeneously distributed on the external surfaces of sepiolite. Even after calcination at 650 °C, the structure of the nanocomposite maintains a fibrous morphology. XRD results indicated that the structure of sepiolite is folded at this temperature.

Fig. 5. Transmission electron microscopy (TEM) image of the hybrid material after calcination at 450 °C.

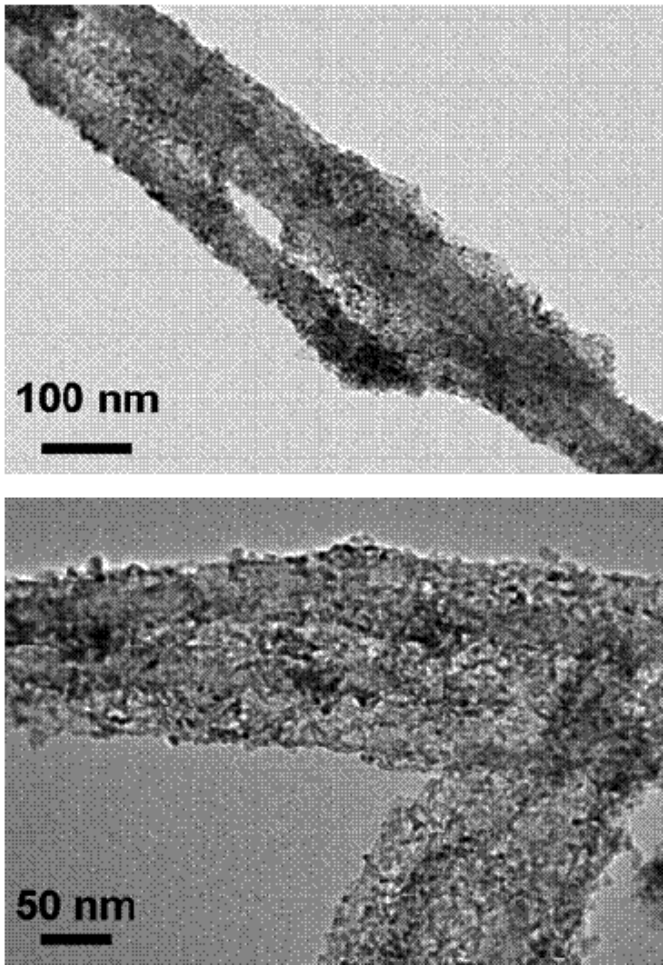

^{29}Si NMR CP/MAS

^{29}Si NMR spectra of pure sepiolite and of the hybrid material prepared by hydrolysis and condensation of zirconium propoxide at the external surface of sepiolite showed the expected three Q^3 peaks within the sepiolite structure at approx. –92.0, approx. –95, and approx. –97 (Figs. 7a and 7b).[44,49] The Q^2 peak owing to the surface silanol groups was observed at –85 ppm.[4] This peak had diminished significantly in intensity after reaction with zirconium propoxide, an indication that the latter has reacted with the silanol groups. Heating the material at 450 and 650 °C results in the observation of more than three signals, indicating the loss of symmetry of the silicium atoms owing to a structural change of sepiolite.[4] At 450 °C, a fraction of the coordinated water molecules has been lost, the structure is partially folded, and the ^{29}Si NMR spectrum is the superposition of partially and fully dehydrated sepiolite. At 650 °C, sepiolite is fully dehydrated and completely folded,[4,47,48] resulting in the loss of the tunnel structure and in the loss of symmetry of the silicon atoms, with all six having become chemically distinct. At this temperature, the Mg(II) dehydroxylation has not yet been reached.

Can. J. Chem. Downloaded from www.nrcresearchpress.com by University of Electronic and Science Techonology of China on 09/18/12
For personal use only.

Fig. 6. Transmission electron microscopy (TEM) image of the hybrid material after calcination at 650 °C.

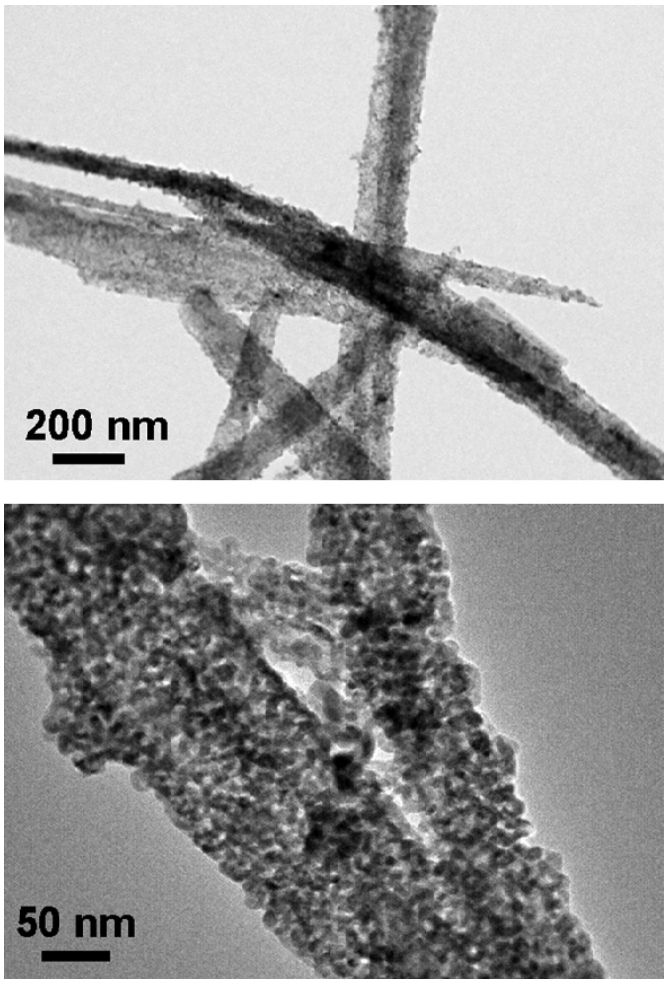

Fig. 7. Solid-state ^{29}Si NMR cross-polarization / magic-angle spinning (CP/MAS) of (a) pure sepiolite, (b) the hybrid material prepared by hydrolysis and condensation of zirconium propoxide at the external surface of sepiolite and dried at 60 °C, (c) sample (b) calcined at 450 °C, and (d) sample (b) calcined at 650 °C.

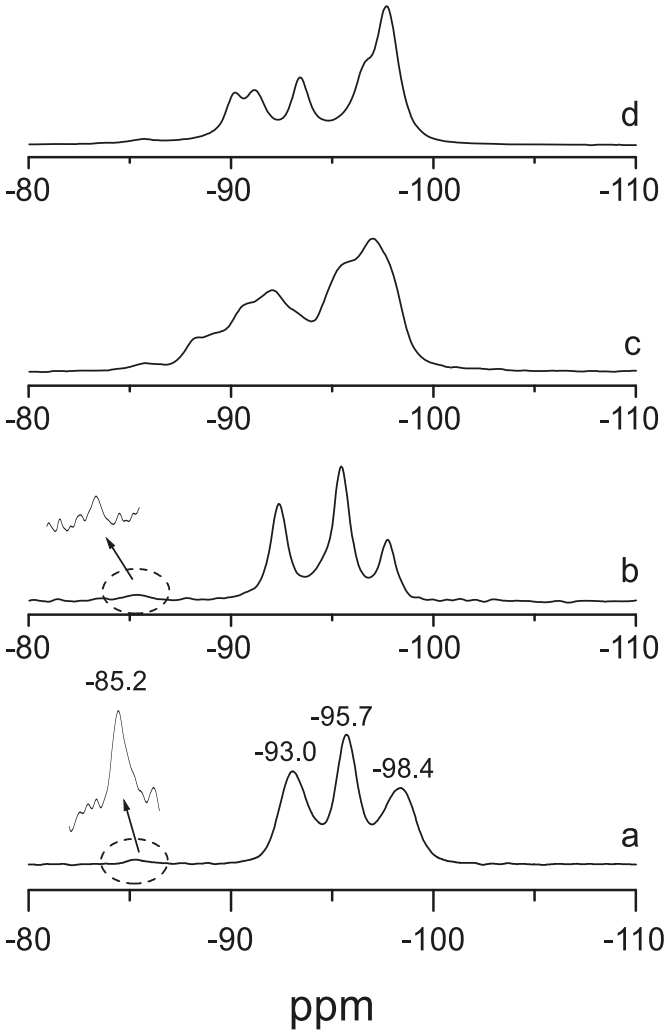

Porosimetry

Table 1 gives the surface area values calculated by the BET equation[50] from N_2 adsorption isotherms of pure sepiolite, pure zirconium oxide, and the resulting nanocomposites after calcinations at 450 and 650 °C. The sol–gel deposition of zirconium propoxide on sepiolite results in a decrease of the surface area from 298 m^2/g for pure sepiolite to 181 and 246 m^2/g for Sep–Zr 1/1 and Sep–Zr 1/2, respectively, where 1/1 and 1/2 represent the mass ratio of sepiolite to ZrO_2. The fibrous structure of sepiolite contains a series of channels and tunnels leading to a large surface area. The deposition of zirconium propoxide blocks some tunnels and also results in agglomeration of individual fibres of sepiolite. This textural change results in a decrease of the surface area after deposition of the zirconium propoxide. After calcination of the samples at 450 °C, the surface area of the nanocomposites is larger compared with the pristine sepiolite. At this temperature, pure sepiolite is partially folded and the nanocomposites are covered by zirconium oxide. After heating the nanocomposites at 650 °C, the surface areas of the resulting nanocomposites were decreased by more than 50% compared with those at RT because of the complete folding of the structure of the sepiolite and agglomeration of the fibres. Nanocomposites heated at 450 °C were used for catalytic tests because they have the highest surface area values.

Table 1. Values of the Brunauer–Emmett–Teller (BET) surface area for sepiolite (**Sep**), zirconium oxide (**ZrO_2**), and the nanohybrid materials made of ZrO_2 deposited on sepiolite with mass ratios of 1/1 (**Sep–Zr 1/1**) and 1/2 (**Sep–Zr 1/2**). The measurements were recorded on the samples unheated and preheated at 450 and 650 °C.

	RT (m^2/g)	450 °C (m^2/g)	650 °C (m^2/g)
Sep	298	114	99
Sep–Zr 1/1	181	156	82
Sep–Zr 1/2	246	140	103
ZrO_2	—	36	24

Catalytic activity

Catalytic activity studies were carried out under solvent-free conditions using untreated sepiolite, zirconium oxide, and zirconium oxide deposited on the external surfaces of

Table 2. Conversion and selectivity (%) of the Knoevenagel condensation reaction of benzaldehyde derivatives with malonitrile.

Derivative	Sep		Sep–Zr 1/1		Sep–Zr 1/2		ZrO_2	
	Yield	Sel.	Yield	Sel.	Yield	Sel.	Yield	Sel.
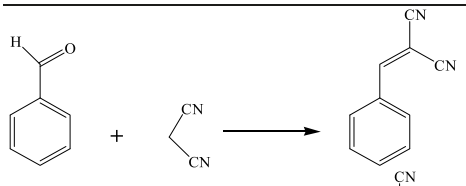	37	*100*	94	*100*	83	*100*	44	*100*
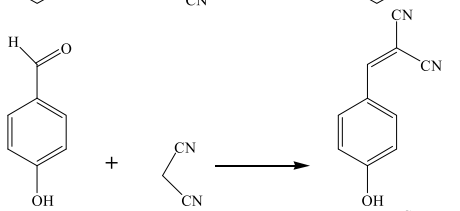	30	*100*	89	*100*	80	*100*	45	*100*
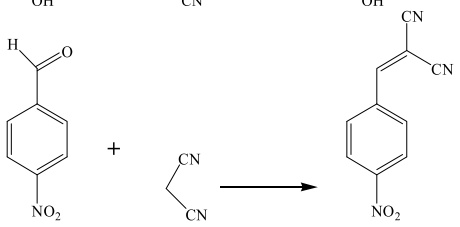	49	*100*	83	*100*	88	*100*	38	*100*

Note: Sep, sepiolite. Values in italic typeface indicate selectivity.

sepiolite. The results of the Knoevenagel condensation of benzaldehyde derivatives are given in Table 2. The nature of the catalyst was found to influence the catalytic efficiency. When the reaction was carried out using untreated sepiolite as the support, the conversion was modest (<50%). These yields were improved but still limited when the reaction was carried out using zirconium oxide (Table 2). However, the nanohybrid catalysts calcined at 450 °C gave much higher conversion rates. For example, the yield obtained for the catalyst Sep–Zr 1/1 is 94% for the condensation of benzaldehyde and 88% for the catalyst Sep–Zr 1/2 in the case of the condensation of *para*-nitrobenzaldehyde.

A higher amount of ZrO_2 deposited on sepiolite does not significantly increase the yield of the reaction. On the contrary, it is lower in some cases. This result can be interpreted by the porosity of these materials. The BET surface area of Sep–Zr 1/2 (140 m^2/g) is lower than the area of sample Sep–Zr 1/1 (156 m^2/g), resulting in less accessibility of the substrate to the active catalytic sites.

Conclusion

The remarkable structural features of the clay mineral sepiolite were used to prepare an efficient catalyst for the Knoevenagel condensation of benzaldehyde derivatives under solvent-free conditions. An inorganic nanocomposite was prepared by the deposition of zirconium oxide nanoparticles on the external surfaces of sepiolite. The nanoparticles were prepared by a sol–gel technique, from solutions of zirconium(IV) propoxide in 1-propanol as precursor. After calcination at 650 °C, the organic material from the precursor was lost, the coordinated water of sepiolite was fully removed, and the layered structure of sepiolite was folded. However, the arrangement of the nanoparticles of zirconium oxide on the external surfaces maintains a fibrous morphology for the nanocomposite. These modifications, which take place at the nanometer scale under soft conditions, produce a functional nanocomposite material combining the textural properties of the pristine clay mineral and the catalytic activity of zirconium oxide.

The material was applied to the solvent-free reaction of the condensation of benzaldehyde and malononitrile. The condensation reaction, which necessitates mild basic conditions, is here governed by the porosity of the supporting sepiolite (increasing the density of supported nanoparticles) and the basicity and catalytic effect of the ZrO_2 nanoparticles. Strongly improved yields of reaction, attributed to larger catalytically active surfaces, were obtained in the case of the inorganic nanocomposite material, compared with either the sepiolite mineral or the zirconium oxide tested individually.

Acknowledgements

This work was financially supported by a Discovery Grant of the Natural Sciences and Engineering Research Council of Canada (NSERC). The Canada Foundation for Innovation and the Ontario Research Fund are gratefully acknowledged for infrastructure grants to the Centre for Catalysis Research and Innovation, University of Ottawa, Ottawa, Ontario.

References

(1) Brown, G.; Brindley, G. W., Eds. *Crystal Structures of Clay Minerals and Their X-ray Identification;* Mineralogical Society: London, 1980.

(2) Kuang, W.; Facey, G. A.; Detellier, C.; Casal, B.; Serratosa, J. M.; Ruiz-Hitzky, E. *Chem. Mater.* **2003**, *15* (26), 4956. doi:10.1021/cm034867i.

(3) Jones, B. F.; Galan, E. Sepiolite and Palygorskite. In *Hydrous Phyllosilicates. Reviews in Mineralogy;* Bailey, S. W., Ed., 1988; Vol. 19, pp 631–674.

Can. J. Chem. Downloaded from www.nrcresearchpress.com by University of Electronic and Science Techonology of China on 09/18/12
For personal use only.

Can. J. Chem. Downloaded from www.nrcresearchpress.com by University of Electronic and Science Techonology of China on 09/18/12
For personal use only.

(4) Eir, M. R. W.; Kuang, W.; Facey, G. A.; Detellier, C. *Clays Clay Miner.* **2002**, *50* (2), 240. doi:10.1346/000986002760832838.
(5) Zhu, L.; Letaief, S.; Liu, Y.; Gervais, F.; Detellier, C. *Appl. Clay Sci.* **2009**, *43* (3–4), 439. doi:10.1016/j.clay.2008.10.004.
(6) Tao, R.; Miao, S.; Liu, Z.; Xie, Y.; Han, B.; An, G.; Ding, K. *Green Chem.* **2009**, *11* (1), 96. doi:10.1039/b811587g.
(7) Shimizu, K.; Maruyama, R.; Komai, S.; Kodama, T.; Kitayama, Y. *J. Catal.* **2004**, *227* (1), 202. doi:10.1016/j.jcat.2004.07.012.
(8) Kou, M. R. S.; Mendioroz, S.; Fierro, J. L. G.; Rodriguez-Ramos, I.; Palacios, J. M.; Guerrero-Ruiz, A.; De Andres, A. M. *Clays Clay Miner.* **1992**, *40* (2), 167. doi:10.1346/CCMN.1992.0400205.
(9) Güngör, N.; Isci, S.; Günister, E.; Teterycz, W.; Klimkiewicz, H. *Appl. Clay Sci.* **2006**, *32* (3–4), 291. doi:10.1016/j.clay.2006.03.005.
(10) Barrios-Neira, J.; Rodrique, L.; Ruiz-Hitzky, E. *J. Microsc. (Paris)* **1975**, *20*, 295.
(11) Casal, B.; Ruiz-Hitzky, E.; Bergaya, F.; Challal, D.; Fripiat, J.; Van Damme, H. *J. Mol. Catal.* **1985**, *33* (1), 83. doi:10.1016/0304-5102(85)85021-5.
(12) Aranda, P.; Kun, R.; Martin-Luengo, M. A.; Letaief, S.; Dekany, I.; Ruiz-Hitzky, E. *Chem. Mater.* **2008**, *20* (1), 84. doi:10.1021/cm702251f.
(13) Manova, E.; Aranda, P.; Martín-Luengo, M. A.; Letaïef, S.; Ruiz-Hitzky, S. *Microporous Mesoporous Mater.* **2010**, *131* (1–3), 252. doi:10.1016/j.micromeso.2009.12.031.
(14) Letaïef, S.; Grant, S.; Detellier, C. *Appl. Clay Sci.* **2011**. In press.
(15) Pecharromán, C.; Esteban-Cubillo, A.; Fernández, H.; Esteban-Tejeda, L.; Pina-Zapardiel, R.; Moya, J. S.; Solis, J.; Afonso, C. N. *Plasmonics* **2009**, *4* (4), 261. doi:10.1007/s11468-009-9101-7.
(16) Blanco, J.; Petre, A. L.; Yates, M.; Martin, M. P.; Martin, J. A.; Martin-Luengo, M. A. *Appl. Catal., B* **2007**, *73* (1–2), 128. doi:10.1016/j.apcatb.2006.06.017.
(17) Güngür, N.; Isci, S.; Günister, E.; Mista, W.; Teterycz, H.; Klimkiewicz, R. *Appl. Clay Sci.* **2006**, *32* (3–4), 291. doi:10.1016/j.clay.2006.03.005.
(18) Pecharromán, C.; Esteban-Cubillo, A.; Montero, I.; Moya, J. S.; Aguilar, E.; Santaren, J.; Alvarez, A. *J. Am. Ceram. Soc.* **2006**, *89* (10), 3043. doi:10.1111/j.1551-2916.2006.01190.x.
(19) Luo, L.; Li, S. *J. Nat. Gas Chem.* **2004**, *13*, 45.
(20) Salvador, R.; Casal, B.; Yates, M.; Martin-Luengo, M. A.; Ruiz-Hitzky, E. *Appl. Clay Sci.* **2002**, *22* (3), 103. doi:10.1016/S0169-1317(02)00132-1.
(21) Kou, M. R. S.; Mendioroz, S.; Fierro, J. L. G.; Rodriguez-Ramos, I.; Palacios, J. M.; Guerrero-Ruiz, A.; De Andres, A. M. *Clays Clay Miner.* **1992**, *40* (2), 167. doi:10.1346/CCMN.1992.0400205.
(22) (a) Garvie, R.; Nicholson, P. S. *J. Am. Ceram. Soc.* **1972**, *55* (6), 303. doi:10.1111/j.1151-2916.1972.tb11290.x.; (b) Shukla, S.; Seal, S. *J. Phys. Chem. B* **2004**, *108* (11), 3395. doi:10.1021/jp037532x.
(23) Liu, J.; Zhao, Z.; Liang, P.; Xu, C.; Duan, A.; Jiang, G.; Lin, W.; Wachs, I. E. *Catal. Lett.* **2008**, *120* (1–2), 148. doi:10.1007/s10562-007-9267-6.
(24) Ilyas, M.; Sadiq, M. *Catal. Lett.* **2009**, *128* (3–4), 337. doi:10.1007/s10562-008-9750-8.
(25) Sivaprakash, S.; Majumder, S. B.; Katiyar, R. S. *J. Electrochem. Soc.* **2009**, *156* (4), A328. doi:10.1149/1.3078401.
(26) Saccà, A.; Gatto, I.; Carbone, A.; Pedicini, R.; Passalacqua, E. *J. Power Sources* **2006**, *163* (1), 47. doi:10.1016/j.jpowsour.2005.12.062.
(27) Fernández, E.; Benito, J. M.; Pazos, C.; Coca, J. *J. Membr. Sci.* **2005**, *246* (1), 1. doi:10.1016/j.memsci.2004.04.007.
(28) Jones, G., Ed. *Organic Reactions;* John Wiley and Sons: New York, 1967; Vol. 15, p 204.
(29) Priya, K.; Buvaneswari, G. *Mater. Res. Bull.* **2009**, *44* (6), 1209. doi:10.1016/j.materresbull.2009.01.014.
(30) Rajasekhar Pullabhotla, V. S. R.; Rahman, A.; Jonnalagadda, S. B. *Catal. Commun.* **2009**, *10* (4), 365. doi:10.1016/j.catcom.2008.09.021.
(31) Ren, Y. M.; Cai, C. *Synth. Commun.* **2007**, *37* (13), 2209. doi:10.1080/00397910701397375.
(32) (a) Reddy, T. I.; Varma, R. S. *Tetrahedron Lett.* **1997**, *38* (10), 1721. doi:10.1016/S0040-4039(97)00180-9.; (b) Corma, A.; Iborra, S. Zeolites & Related Materials in Knoevenagel Condensations and Michael Additions. In *Fine Chemicals Through Heterogeneous Reactions;* Sheldon, R. A., van Bekkum, H., Eds.; Wiley-VCH: Weinheim, 2001; Chapter 7.1, pp 309–326; (c) Román-Leshkov, Y.; Moliner, M.; Davis, M. E. *Chem. Mater.* **2010**, *22* (8), 2646. doi:10.1021/cm100108e.
(33) (a) Corma, A.; Martin-Aranda, R. M. *J. Catal.* **1991**, *130* (1), 130. doi:10.1016/0021-9517(91)90097-N.; (b) Corma, A.; Garcia, H.; Leyva, A.; Primo, A. *Appl. Catal. Gen.* **2004**, *257* (1), 77. doi:10.1016/S0926-860X(03)00635-5.
(34) de la Cruz, P.; Diez-Barra, E.; Loupy, A.; Langa, F. *Tetrahedron Lett.* **1996**, *37* (7), 1113. doi:10.1016/0040-4039(95)02318-6.
(35) Balalaie, S.; Nemati, N. *Synth. Commun.* **2000**, *30* (5), 869. doi:10.1080/00397910008087099.
(36) Hosseini-Sarvari, M.; Sharghi, H.; Etemad, S. *Helv. Chim. Acta* **2008**, *91* (4), 715. doi:10.1002/hlca.200890072.
(37) Yue, C.; Mao, A.; Wei, Y.; Lü, M. *Catal. Commun.* **2008**, *9* (7), 1571. doi:10.1016/j.catcom.2008.01.002.
(38) Ranu, B. C.; Jana, R. *Eur. J. Org. Chem.* **2006**, *2006* (16), 3767. doi:10.1002/ejoc.200600335.
(39) Postole, G.; Chowdhury, B.; Karmakar, B.; Pinki, K.; Banerji, J.; Auroux, A. *J. Catal.* **2010**, *269* (1), 110. doi:10.1016/j.jcat.2009.10.022.
(40) Gawande, M. B.; Jayaram, R. V. *Catal. Commun.* **2006**, *7* (12), 931. doi:10.1016/j.catcom.2006.03.008.
(41) Reddy, B. M.; Patil, M. K.; Rao, K. N.; Reddy, G. K. *J. Mol. Catal. Chem.* **2006**, *258* (1–2), 302. doi:10.1016/j.molcata.2006.05.065.
(42) Weir, M. R.; Rutinduka, E.; Detellier, C.; Feng, C. Y.; Wang, Q.; Matsuura, T.; Le Van Mao, R. *J. Membr. Sci.* **2001**, *182* (1–2), 41. doi:10.1016/S0376-7388(00)00547-0.
(43) Letaïef, S.; Martín-Luengo, M. A.; Aranda, P.; Ruiz-Hitzky, E. *Adv. Funct. Mater.* **2006**, *16* (3), 401. doi:10.1002/adfm.200500190.
(44) Hubbard, B.; Kuang, W.; Moser, A.; Facey, G. A.; Detellier, C. *Clays Clay Miner.* **2003**, *51* (3), 318. doi:10.1346/CCMN.2003.0510308.
(45) Vahldiek, F. W.; Robinson, L. B.; Lynch, C. T. *Science* **1963**, *142* (3595), 1059. doi:10.1126/science.142.3595.1059.
(46) Goedicke, K.; Liebig, J. S.; Zywitzki, O.; Sahm, H. *Thin Solid Films* **2000**, *377–378* (1–2), 37. doi:10.1016/S0040-6090(00)01381-X.
(47) Nagata, H.; Shimoda, S.; Sudo, T. *Clays Clay Miner.* **1974**, *22* (3), 285. doi:10.1346/CCMN.1974.0220310.
(48) (a) Rautureau, M.; Mifsud, A. *Clay Miner.* **1977**, *12* (4), 309. doi:10.1180/claymin.1977.012.4.04.; (b) Serna, C.; Ahlrichs,

J. L.; Serratosa, J. M. *Clays Clay Miner.* **1975**, *23* (6), 452. doi:10.1346/CCMN.1975.0230607.
(49) (a) Facey, G. A.; Kuang, W.; Detellier, C. *J. Phys. Chem. B* **2005**, *109* (47), 22359. doi:10.1021/jp053832y.; (b) Kuang, W.; Facey, G. A.; Detellier, C. *J. Mater. Chem.* **2006**, *16* (2), 179. doi:10.1039/b512575h.
(50) Brunauer, S.; Emmett, P. H.; Teller, E. *J. Am. Chem. Soc.* **1938**, *60* (2), 309. doi:10.1021/ja01269a023.

Can. J. Chem. Downloaded from www.nrcresearchpress.com by University of Electronic and Science Techonology of China on 09/18/12
For personal use only.

Photoautoionization structure in the halogen systems Br_2, I_2, BrCl, ICl, and IBr

Andrew J. Yencha and Devinder Kaur

Abstract: The photoabsorption ion-yield spectra of the titled molecules have been recorded in the threshold ionization region between the two spin-orbit components of the ground states of the molecular ions. All ion-yield spectra display rather simple autoionization structure superimposed on a smoothly rising continuum in the ionization energy region. The structure was analyzed in terms of autoionizing Rydberg states and their vibrational profiles simulated using Rydberg–Klein–Rees (RKR) derived potential energy curves and calculated Franck–Condon factors using Gaussian line-shape functions. All of the structure observed is attributed to spin-orbit autoionization. There seems to be a propensity for autoionization of sσ Rydberg states in all of the interhalogen molecules studied.

Key words: autoionization, Rydberg states, halogens, interhalogens, photoionization yields.

Résumé : On a enregistré les spectres de rendement ionique de photoabsorption des molécules mentionnées dans le titre en opérant dans la région de seuil entre les deux composantes spin-orbites des états fondamentaux des ions moléculaires. Tous les spectres de rendement ionique présentent une structure d'autoionisation relativement simple superposée sur un continuum croissant régulièrement dans la région d'énergie d'ionisation. On a analysé la structure en termes d'états de Rydberg autoionisants, on a simulé leurs profils vibrationnels en utilisant des courbes d'énergie potentielle dérivées du modèle de Rydberg–Klein–Rees (RKR) et on a calculé les facteurs de Franck–Condon en faisant appel à des fonctions gaussiennes de la forme des courbes. Toute la structure observée est attribuée à une autoionisation spin-orbite. Il semble qu'il existe une propensité à l'autoionisation des états sσ des états de Ryderg dans toutes les molécules interhalogènes qui ont été étudiées.

Mots-clés : autoionisation, états de Rydberg, halogènes, interhalogènes, rendements de photoionisation.

[Traduit par la Rédaction]

Introduction

The photochemical utility of diatomic halogen and interhalogen molecules in flash photolysis studies for the photodissociative production of excited- and ground-state halogen atoms has been known for a long time.[1–5] More recently, diatomic halogen and interhalogen molecules have received considerable attention owing to their interesting spectroscopic properties and because of the reactivity of their excited states, particularly with rare gas atoms related to excimer laser-light generation.[6] Theoretical studies have revealed how complicated the excited-state potentials are even in the simplest of these systems,[7–9] while experimental studies are beginning to unravel the potential-energy picture in the more complicated systems, as well as confirming theoretical predictions in simpler systems.[10] An important characteristic of these molecules is their ability to support numerous, stable, energetically low-lying valence ion-pair states because of the relatively low ionization potentials and high electron affinities of the atomic constituents. These states are known to possess potential minima at relatively long bond lengths, have large dissociation energies, exhibit small vibrational frequencies, and have a tendency to group in clusters. We are now beginning to understand that these ion-pair states can interact with Rydberg states lying in the vacuum-ultraviolet (VUV) spectral region affecting their absorption, fluorescence, and ionization spectroscopic properties. The situation is further complicated by the fact that the Rydberg states in these molecules are extensively predissociated by repulsive states associated with ground- and excited-state atoms. In addition, in all of the diatomic halogen and interhalogen molecules, except Cl_2, the thermodynamic dissociation limit for producing the lowest energy set of ion pairs occurs just below the onset of molecular ionization. Hence, Rydberg states lying in the energy region just above the ionization limit may interact with two types of continua, that is the ionization continuum and the ion-pair continuum. Thus, structures in the molecular photoionization yield spectra owing to autoionization in these molecules may possess a resemblance to the structure in the photodissociative excitation functions for ion-pair formation. Although the photoionization yield spectra have been obtained for 7 of the 10

Received 28 April 2010. Accepted 10 August 2010. Published on the NRC Research Press Web site at canjchem.nrc.ca on 9 February 2011.

This article is part of a Special Issue dedicated to Professor J. C. Scaiano.

A.J. Yencha[1] and D. Kaur.[2] Department of Chemistry, State University of New York at Albany, Albany, NY 12222, USA.

[1]Corresponding author (e-mail: yencha@albany.edu).
[2]Present address: Rockwood Specialties (Singapore) Pte. Ltd., 14 Tuas Avenue 20, Singapore 638826.

Can. J. Chem. Downloaded from www.nrcresearchpress.com by University of Electronic and Science Techonology of China on 09/18/12
For personal use only.

Can. J. Chem. Downloaded from www.nrcresearchpress.com by University of Electronic and Science Techonology of China on 09/18/12
For personal use only.

diatomic halogen and interhalogen molecules,[11–19] only two, F_2[18] and Cl_2,[19] have been analyzed with respect to their autoionizing structure just above their lowest ionization limits. We have recorded both the photoionization yield spectra and the ion-pair photodissociative excitation function spectra in the vicinity of the ionization limits of the molecules Br_2, I_2, BrCl, ICl, and IBr and have analyzed these in terms of their formation mechanisms. We have found a strong correlation between these two types of spectra. We report here on the autoionizing structure in the photoionization yield spectra of these molecules. We have previously published our analyses of the ion-pair formation excitation function spectra for the same molecules.[20–22]

Experimental

The photoabsorption ion-yield spectra reported here were obtained using synchrotron radiation at the National Synchrotron Light Source (NSLS) facility of the Brookhaven National Laboratory, Upton, New York, on beam line U-11. The molecular beam apparatus used has been described in detail previously[23,24] and the method for recording photoexcitation spectra reported,[20–22,25–27] so only a brief experimental description will be given here.

A supersonic beam made up of a mixture of ~1%–2% of the halogen being studied in helium was produced using a 200 μm diameter glass nozzle, heated to ~100 °C with backing pressures in the range of 100–200 Torr (1 Torr = 133.3224 Pa), and a skimmer of 1 mm diameter located 5–10 mm downstream of the nozzle. The position of the nozzle relative to the skimmer was adjusted to give the maximum Ar^+ signal through the quadrupole mass spectrometer at an energy just above the ionization potential of Ar. The backing pressure of the sample plus helium, as measured on a Baratron capacitance manometer, was adjusted to give the maximum molecular ion signal at an energy just above the ionization limit of the molecule. Under typical conditions, the pressure in the nozzle chamber was of the order of 1×10^{-5} Torr, while the pressure in the interaction chamber was ~6×10^{-7} Torr. Based on an analysis of the hot-band structure in the ion-pair excitation functions for Br_2,[20] we estimated a vibrational temperature of our sample of ~250 K. This temperature was used throughout our analysis procedure for the simulated spectral results presented here (see the following). We have no information as to the rotational temperatures of our samples, but we assume them to be quite low (e.g., <20 K). The molecular beam intersected the focused (1 mm^2) tunable synchrotron radiation beam of 0.09 nm bandpass (FWHM) (equivalent to an energy resolution of ~48 cm^{-1} at 130 nm). Prior to entering the interaction chamber the synchrotron radiation was passed through a 2 mm thick LiF filter to eliminate second and higher order radiation. The resolution and calibration of the synchrotron light was accomplished by setting the monochromator wavelength scale to zero wavelength at the maximum intensity for zero-order radiation (totally reflective grating, i.e., acting as a mirror) and then by measuring the ionization threshold for argon in first order. In this way we found the wavelength scale to be accurate to within ±0.02 nm. The intensity of the synchrotron light intersecting the molecular beam was monitored using a sodium salicylate quantum converter plus photomultiplier. This signal allowed for correcting the quadrupole mass spectrometer signal for the decay with time of the synchrotron radiation as well as the wavelength-dependent transmission function of the monochromator. Ions formed in the interaction volume were extracted with a static field of ~50 V cm^{-1} and focused onto the entrance aperture of a quadrupole mass spectrometer where they were mass analyzed. Photoionization yield spectra were obtained by standard pulse counting procedures, a CAMAC interface, and a PDP 11/23 minicomputer.

The samples studied were obtained from the following sources: Br_2 (J. T. Baker Co., 99.8% purity), I_2 (Eastman Kodak Co., 99.9% purity), ICl (Eastman Kodak Co., 98% purity), and IBr (Aldrich Chemicals, 98% purity). BrCl was prepared from a stoichiometric mixture of Br_2 and Cl_2 (Matheson Gas Products, 99.9% purity). The mixture was refluxed about six or seven times by repeated heating and cooling (condensing) before being stored in a glass bulb. All samples were degassed at liquid nitrogen temperature prior to being used. Except for ICl and IBr, the samples were premixed (1%–2%) in helium and stored in separate 4 L stainless steel cylinders at a total pressure of ~7 atm (1 atm = 101.325 kPa). For ICl and IBr, 1%–2% mixtures in helium were prepared by passing helium gas over neat ICl or IBr, maintained at a constant temperature in a thermostated box, prior to entering the nozzle tube of the apparatus.

Analysis procedure

Analyses of the autoionizing structure found in the photoabsorption ion-yield spectra were accomplished by means of simulation calculations of the Franck–Condon factors for transitions from the ground states of the molecules to various accessible Rydberg states.[27] The energy levels (E_n) for the states in a particular Rydberg series can be calculated using the Rydberg formula:[28]

$$E_n = \mathrm{IP} - R/(n - \delta)^2$$

where IP is the ionization potential, R is the Rydberg constant = 109 737 cm^{-1}, n is the principal quantum number, and δ is the quantum defect. The δ (or screening constant) depends on the azimuthal (or orbital) quantum number l, and as l increases, δ rapidly approaches zero. As n increases, the energy increases and eventually approaches the convergence limit (or ionization potential).

Individual Rydberg systems were obtained employing Gaussian line-shape functions for each vibrational band, in which the identical width of all bands in a system was an adjustable parameter. The total simulated spectrum was derived from the sum of the individual Rydberg systems with appropriate (adjustable) weighting factors to give the best overall fit to the experimental spectrum. Contribution from hot bands were incorporated into the simulation calculations assuming a vibrational Boltzmann temperature of 250 K.[20–22,27] This procedure assumes that the coupling between the rovibrational levels of a Rydberg state with the ionization continuum is the same for all levels and, furthermore, that the coupling between different Rydberg states with the ionization continuum is also the same.

Can. J. Chem. Downloaded from www.nrcresearchpress.com by University of Electronic and Science Techonology of China on 09/18/12
For personal use only.

Results and discussion

The approach to analyzing and simulating the photoabsorption molecular ion-yield spectra in the threshold ionization region recognizes the so-called "heavy-atom effect" in the ionization properties of interhalogen molecules. That is, in mixed diatomic halogen molecules the lowest ionization potential is always associated with the heavier of two constituent atoms, whereas the second ionization potential is always associated with the lighter of the two constituent atoms. In his 1934 paper, Mulliken[29] presented formulations for the lowest energy electron configurations for the homonuclear and heteronuclear diatomic halogens. In the case of a diatomic homonuclear halogen (X_2), the initial approximation using molecular orbitals is

$$X_2 : \ldots (\sigma + \sigma, \sigma_g)^2(\pi + \pi, \pi_u)^4(\pi - \pi, \pi^*_g)^4, \quad {}^1\Sigma^+_g$$

where g and u indicate the even or odd symmetry property about the center-of-mass of the molecule. Since the atomic orbitals are identical in this case, the best approximation for the electron configuration is given using the atomic orbitals for the π electrons:

$$X_2 : \ldots (\sigma + \sigma, \sigma_g)^2(n\mathrm{p}\pi_u)^4(n\mathrm{p}\pi^*_g)^4, \quad {}^1\Sigma^+_g$$

where n is the principal quantum number of the outermost filled atomic orbital from which the molecular orbital was formed and ${}^1\Sigma^+_g$ is its term symbol using Hund's case (a) notation. The generalized valence electron configuration using pure atomic orbitals for the formation of the molecular orbitals for a mixed diatomic halogen molecule, XY, where X is the heavier atom, was given by Mulliken[29] as

$$XY : \ldots (\sigma_y + \sigma_x, \sigma)^2(n_y\mathrm{p}\pi)^4(n_x\mathrm{p}\pi^*)^4, \quad X\ {}^1\Sigma^+$$

where the g/u symmetry property no longer applies. It follows that the electron configurations of the three lowest energy ionized states of XY would be

$$X^+Y : \ldots (\sigma_y + \sigma_x, \sigma)^2(n_y\mathrm{p}\pi)^4(n_x\mathrm{p}\pi^*)^3, \quad X\ {}^2\Pi_{3/2,1/2}$$

$$XY^+ : \ldots (\sigma_y + \sigma_x, \sigma)^2(n_y\mathrm{p}\pi)^3(n_x\mathrm{p}\pi^*)^4, \quad A\ {}^2\Pi_{3/2,1/2}$$

$$(XY)^+ : \ldots (\sigma_y + \sigma_x, \sigma)^1(n_y\mathrm{p}\pi)^4(n_x\mathrm{p}\pi^*)^4, \quad B\ {}^1\Sigma^+$$

where the charge is localized on the atoms X^+ and Y^+, respectively, on the ground state (X) and first-excited state (A) of the molecular ions, and where the charge is symmetrically situated between the two atoms ($X^{\pm}Y$) in the second-excited state (B). In the homonuclear diatomic halogens, the term symbols of the ground and the first two excited states of the molecular ions are, respectively, X ${}^2\Pi_{3/2,1/2,g}$, A ${}^2\Pi_{3/2,1/2,u}$, and B ${}^1\Sigma^+_g$, using Hund's case (a) notation. In the discussion to follow the molecules with the same heavy atom are grouped together.

Formation of the molecular ions Br_2^+ and $BrCl^+$

The upper trace of Fig. 1 shows the experimental photoabsorption ion-yield spectrum of the parent molecular ion Br_2^+ in the threshold ionization region. It consists of a series of autoionization band structures superimposed on a steeply rising ionization function towards shorter wavelengths. We

Fig. 1. A comparison of the experimental photoabsorption ion-yield curve for Br_2^+ formation and calculated autoionization function for Br_2. The calculated spectrum was obtained from the sum of the three simulated autoionizing Rydberg state profiles shown in the figure. The upper number in the assignment refer to the principal quantum numbers (n) and the lower numbers refer to the excited-state vibrational quantum numbers (v').

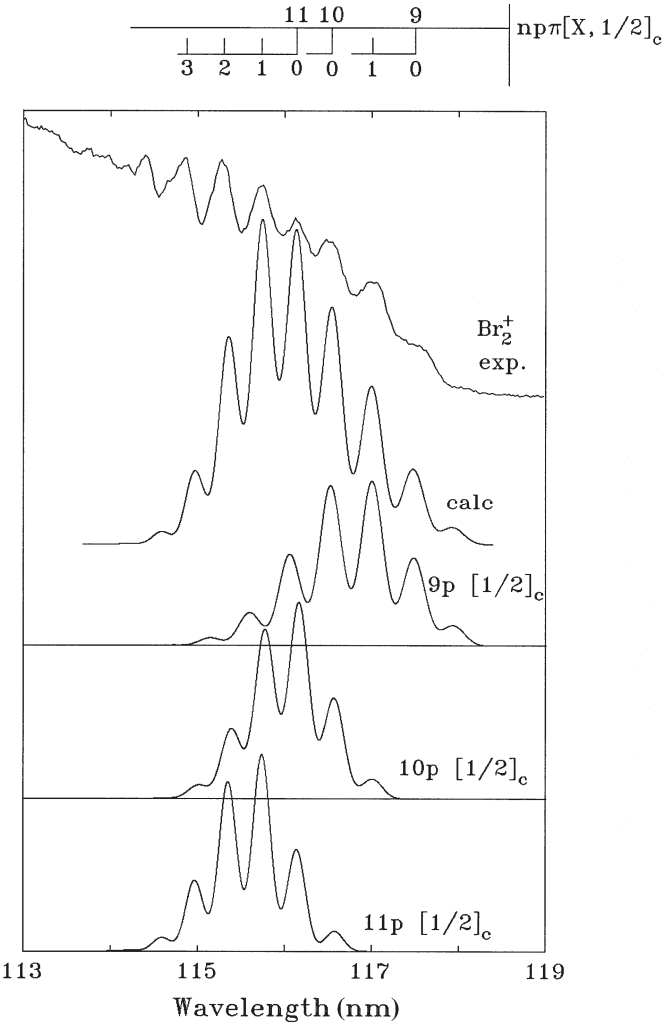

assigned and simulated this structure to be due to the Rydberg series [X 1/2]$_c n$pπ, for n = 9–11, where [X 1/2]$_c$ represents the core ion convergence limit Br_2^+ [X ${}^2\Pi_{1/2g}$] at 114.1 nm (87 645,[20,30] 87 647,[31] and 87 648[32] cm^{-1}). This series represents a continuation of a Rydberg state, [X 1/2]$_c$8pπ, found to be important in ion-pair formation in Br_2 at slightly longer wavelengths (118.73 nm, 84 225 cm^{-1}).[20] Also shown in Fig. 1 are the individual simulated Rydberg states with their calculated vibrational profiles and the summed calculated autoionization spectrum. The three Rydberg states were simulated using a quantum defect of 2.335 for the npπ Rydberg series derived from an analysis of the [X 1/2]$_c$8pπ Rydberg state using the (0,0) band position of 84 225 cm^{-1},[20] the convergence limit of the [X ${}^2\Pi_{1/2g}$] state of 87 645 cm^{-1},[20,30] an equilibrium internuclear distance of 2.188 Å, and vibrational constants of 353, 300, and 350 cm^{-1} for the 9pπ, 10pπ, and 11pπ states, respectively.[27] The calculated peak energy positions of the (0,0) bands for

Can. J. Chem. Downloaded from www.nrcresearchpress.com by University of Electronic and Science Techonology of China on 09/18/12
For personal use only.

the 9pπ, 10pπ, and 11pπ states were 85 174, 85 777, and 86 183 cm^{-1}, respectively, corresponding to the wavelengths 117.4, 116.6, and 116.0 nm, respectively. As can be seen in Fig. 1, there is a good correspondence between the observed and calculated autoionization structure in the ion-yield spectrum. No attempt was made to simulate the underlying ionization continuum in the calculated spectrum.

The experimental photoabsorption ion-yield spectrum of the parent molecular ion $BrCl^+$ in the threshold ionization region is shown as the upper trace in Fig. 2. The autoionization peak structure superimposed on a smoothly rising ionization function appears to be less extensive than for Br_2^+. In fact, the autoionization structure can be attributed mainly to a single Rydberg state, $[X\ 1/2]_c11s\sigma$, of BrCl, although a shoulder peak appears to shorter wavelengths on each of the major peaks. We have calculated the peak position of the (0,0) vibrational band of the 11sσ Rydberg state to be at 111.9 nm (89 332 cm^{-1}) using a quantum defect of 3.07[27] and the convergence limit for $BrCl^+$ [$X\ ^2\Pi_{1/2}$] formation of 11.29 eV[22] (109.8 nm, 91 060 cm^{-1}). This can be compared to the observed peak position of 111.8 nm. The vibrational profile for the 11sσ Rydberg state was calculated using an equilibrium internuclear distance of 2.045 Å[33] and a vibrational constant of 463 cm^{-1} and is shown as the lower trace in Fig. 2. No attempt was made to simulate an underlying ionization continuum or the shoulder peaks in the calculated spectrum. We note that the highest energy Rydberg state assigned in the ion-pair excitation functions of BrCl was the 10sσ state converging onto the X ($^2\Pi_{1/2}$) ion state of BrCl.[22] Hence, the autoionizing Rydberg state, $[X\ 1/2]_c11s\sigma$, of BrCl, represents a continuation of the Rydberg series $[X\ 1/2]_cns\sigma$ for n = 8–10, found to be important in ion-pair formation below the onset of ionization in BrCl at 112.5 nm (11.02 eV, 88 882 cm^{-1}).[22] We further note that the structure owing to ion-pair formation essentially ends upon the opening of the channels to the more dominant processes of photoionization and autoionization.

Formation of the molecular ions I_2^+, ICl^+, and IBr^+

The experimental photoabsorption ion-yield spectrum of the parent molecular ion I_2^+ in the threshold ionization region is shown as the top trace in Fig. 3. It is more complicated than the two previous ion-yield spectra for Br_2^+ and $BrCl^+$. The ion-yield spectrum for I_2^+ shows two very broad peak structures between 133 and 128 nm immediately following the onset of ionization at 133.2 nm (75 069[34–36] and 75 098[37] cm^{-1}) followed by more or less typical autoionizing structure superimposed on a steeply rising ionization function and terminating in the vicinity of the I_2^+ [$X\ ^2\Pi_{1/2g}$] ionization limit at 124.6 nm (80 266 cm^{-1}[34–36] and 80 228 cm^{-1}[37]). We interpret the two broad autoionizing features as owing to the overlapping of two Rydberg series: $[X\ 1/2]_cnp\pi$, for n = 9 and 10 and $[X\ 1/2]_cnf$, for n = 5 and 6, as identified in Fig. 3.

It is worthwhile discussing how we came to the conclusion that the 5f and 6f Rydberg states play a role in the autoionization structure in the ion-yield spectrum of I_2^+, in spite of the fact that the 4f Rydberg state was not identified as being present in the ion-pair excitation function.[21] Originally, the observed vibrational structure in the ion-pair excitation functions of I_2 was assigned[21] to three Rydberg states,

Fig. 2. A comparison of the experimental photoabsorption ion-yield curve for $BrCl^+$ formation and calculated autoionization function for BrCl. Each of the peaks is assigned to a simulated vibrational band v' (lower number) in the $[X\ 1/2]_c11s\sigma$ autoionizing Rydberg state as indicated in the figure.

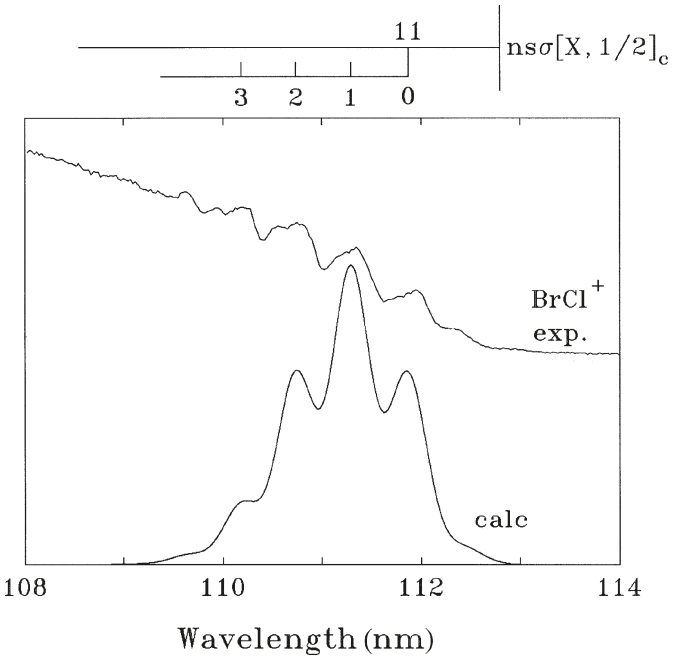

$[X\ 3/2]_c9p\pi$, $[X\ 3/2]_c10p\pi$, and $[X\ 3/2]_c11p\pi$, whose origins were predicted at 72 463, 73 099, and 73638 cm^{-1} based on the high-resolution VUV absorption spectrum analysis of I_2.[38] Subsequently, a reanalysis of the absorption spectrum of I_2 using ionization energies determined from zero electron kinetic energy (ZEKE) – pulsed-field ionization (PFI) photoelectron spectra of I_2[39] indicate that the above Rydberg states should be reassigned to three $[X\ 1/2]_c4f$ Rydberg states whose origins are at 72 647, 73 138, and 73 658 cm^{-1}.[40] The approximate wavelength positions of the cluster of $[X\ 1/2]_cnf$ Rydberg states were calculated to be at 136.8, 132.1, and 129.7 nm for 4f, 5f, and 6f, respectively, using a quantum defect of 0.066.[41] The first wavelength position is very close to that derived from the mean energy of the three $[X\ 1/2]_c4f$ Rydberg states given directly above (73 148 cm^{-1}, 136.7 nm), and the second two wavelength values fall well within the two broad autoionizing features in the ion-yield spectrum, as shown in Fig. 3. Additional evidence for the involvement of f-state Rydbergs in autoionization comes from the high-resolution study of the photoionization of HI in the threshold ionization region.[42] The HI molecule is expected to behave very similarly in the threshold ionization region as the I_2 molecule. This is because in the threshold ionization region in both molecules the electronic structure is dominantly due to the nonbonding electrons localized on the iodine atom. The Rydberg series $[X\ 1/2]_cnf(\sigma,\pi)$ for n = 5–8 were clearly identified as the autoionization structure between the two lowest ionization potentials in HI.[42] The lack of perceptible vibrational structure in the two broad bands in the autoionization spectrum of I_2 suggests that a cluster of Rydberg states, e.g., $[X\ 1/2]_cnf(\sigma)$, $-nf(\pi)$, and $-nf(\delta)$, are present whose energy positions are very close and make for a continuum-like band

Can. J. Chem. Downloaded from www.nrcresearchpress.com by University of Electronic and Science Techonology of China on 09/18/12
For personal use only.

Fig. 3. A comparison of the experimental photoabsorption ion-yield curve for I_2^+ formation and calculated autoionization function for I_2. The calculated spectrum was obtained from the sum of the simulated ion-yield curves owing to transitions to the four autoionizing Rydberg states shown. The upper numbers in the assignment refer to the principal quantum numbers (n) and the lower numbers refer to the excited-state vibrational quantum numbers (v').

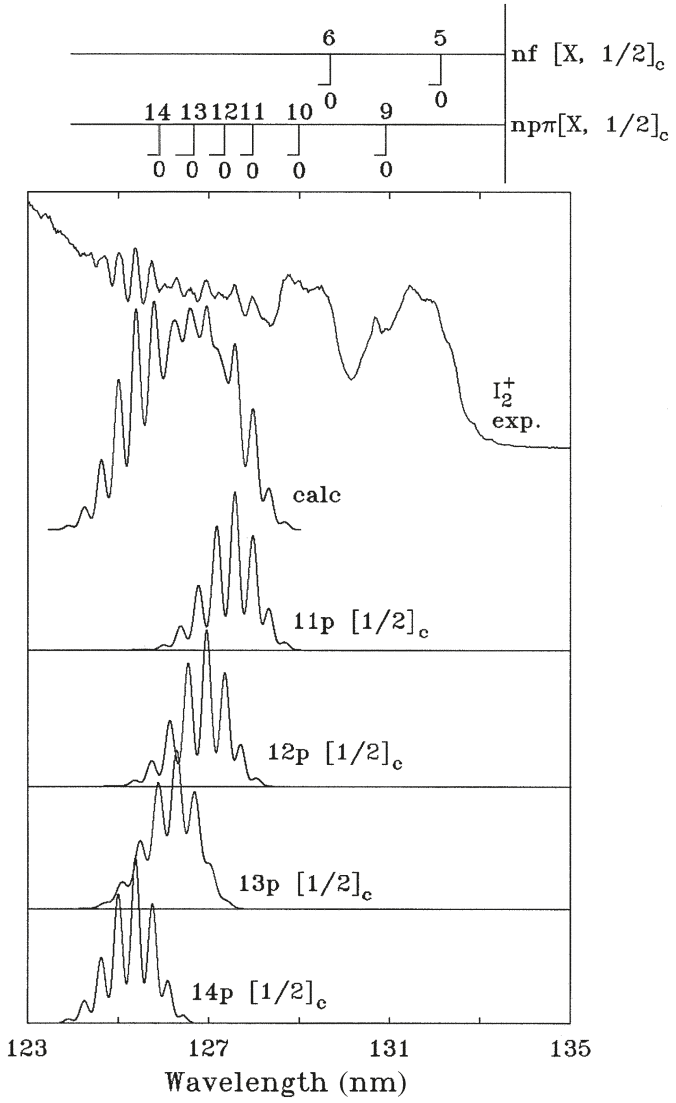

(see, for example, the photoionization spectrum of HI[42] and the VUV absorption spectrum of I_2.[38])

The extensive breadth of the two broad bands in Fig. 3 (between 133 and 128 nm) suggests that the widths of the observed features are primarily due to the separation of the origins of the unresolved component nf states. That is, the separation of the origins of the 4f states is ~1000 cm^{-1} (see above), so assuming that the quantum defect does not change with n, the equivalent separations of the 5f and 6f states should be ~600 and 350 cm^{-1}, respectively. This appears to be consistent with the observed spectrum.

An additional factor contributing to the broadness of the first two autoionization bands is the presence of the $[X\ 1/2]_c np\pi$ Rydberg states, for n = 9 and 10. The wavelength positions of the (0,0) bands for these two states have been calculated to be at 130.9 nm for 9pπ and 129.0 nm for 10pπ using the convergence limit for the I_2^+ $[X\ ^2\Pi_{1/2g}]$ state of 9.95 eV[34–37] and a quantum defect of 3.58[41] for the npπ series. However, a slight decrease of 0.01 eV in the convergence limit gave rise to a much better fit between the experimental and calculated values. The calculated wavelength positions of the (0,0) bands for the Rydberg series $[X\ 1/2]_c np\pi$, for n = 11, 12, 13, and 14 are 127.9, 127.2, 126.6, and 126.3 nm, respectively. All of the Rydberg states (11p, 12p, 13p and 14p) were simulated with respect to their vibrational profiles using an equilibrium internuclear distance of 2.578 Å and vibrational constants of 245, 250, 240, and 250 cm^{-1}, respectively, and are individually displayed in Fig. 3. In addition, the sum of these vibrational profiles is shown as the calculated spectrum. You will note that the calculated and experimental spectra agree quite nicely in peak positions and overall profiles. No attempt was made to simulate the two broad autoionization peaks nor the underlying ionization continuum in the calculated spectrum.

Owing to the similarity between the photoabsorption ion-yield spectra for ICl and IBr, these molecules will be treated together. As can be seen in the upper traces of Figs. 4 and 5, the experimental photoabsorption ion-yield spectra for the formation of the parent molecular ions ICl^+ and IBr^+, respectively, in the threshold ionization region are quite similar. The spectra consists of a fairly extensive number of autoionization peaks superimposed on a smoothly rising ionization function from the onset of ionization at 123.0 nm (10.076 eV)[43] in the case of ICl and at 126.6 nm (9.796 eV)[44] in the case of IBr. The appearance of these spectra are quite similar to the ion-yield spectrum for $BrCl^+$ (see Fig. 2). In fact, in all three interhalogen molecules, all of the autoionizing structure between the spin-orbit component states is assigned to sσ Rydberg states as given in Table 1.

We have calculated the peak positions of the (0,0) vibrational bands of the $[X\ 1/2]_c ns\sigma$ Rydberg series for n = 9–12 for ICl using a quantum defect of 4.01[27] and the convergence limit for ICl^+ $[X\ ^2\Pi_{1/2}]$ formation of 10.67 eV[22] (116.2 nm, 86 059 cm^{-1}) as shown at the top of Fig. 4. The vibrational profiles for these Rydberg states were simulated using an equilibrium internuclear distance of 2.225 Å[27] and vibrational constants of 415, 415, 440, and 447 cm^{-1} for n = 9, 10, 11, and 12, respectively, and are shown individually in the lower portion of Fig. 4. The calculated spectrum shown in Fig. 4 is the sum of these individual vibrational autoionization profiles. The calculated peak energy positions of the (0,0) bands for the 9sσ, 10sσ, 11sσ, and 12 sσ Rydberg states were 81 699, 83 056, 83 822, and 84 388 cm^{-1}, respectively, corresponding to the wavelengths 122.4, 120.4, 119.3, and 118.5 nm, respectively. As can be seen in Fig. 4, there is a good correspondence between the observed and calculated autoionization structure in the ion-yield spectrum. No attempt was made to simulate the underlying ionization continuum in the calculated spectrum.

Continuing our analysis procedure in IBr, we calculated the peak positions of the (0,0) vibrational bands of the $[X\ 1/2]_c ns\sigma$ Rydberg series for n = 9–14 for IBr using a quantum defect of 3.99[27] and the convergence limit for IBr^+ $[X\ ^2\Pi_{1/2}]$ formation of 10.39 eV[45,46] (119.3 nm, 83 801 cm^{-1}) as shown at the top of Fig. 5. The vibrational

Can. J. Chem. Downloaded from www.nrcresearchpress.com by University of Electronic and Science Techonology of China on 09/18/12
For personal use only.

Fig. 4. A comparison of the experimental photoabsorption ion-yield curve for ICl^+ formation and calculated autoionization function for ICl. The calculated spectrum was obtained from the sum of the simulated ion-yield curves owing to transitions to the four autoionizing Rydberg states shown. The upper numbers in the assignment refer to the principal quantum numbers (n) and the lower numbers refer to the excited-state vibrational quantum numbers (v').

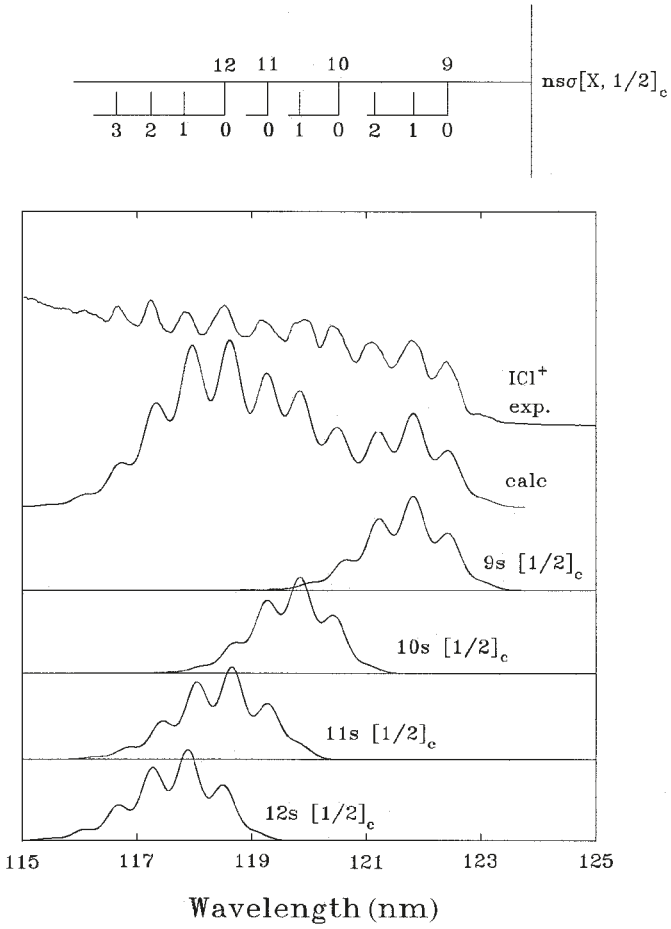

profiles for these Rydberg states were simulated using an equilibrium internuclear distance of 2.383 Å[27] and vibrational constants of 280, 230, 276, 290, 290, and 290 cm^{-1} for n = 9, 10, 11, 12, 13, and 14, respectively, and are shown individually in the lower portion of Fig. 5. The calculated spectrum shown in Fig. 5 is the sum of these individual vibrational autoionization profiles. The calculated peak energy positions of the (0,0) bands for the 9sσ, 10sσ, 11sσ, 12sσ, 13sσ, and 14sσ Rydberg states were 79 491, 80 841, 81 566, 82 102, 82 440, and 82713 cm^{-1}, respectively, corresponding to the wavelengths 125.8, 123.7, 122.6, 121.8, 121.3, and 120.9 nm, respectively. As can be seen in Fig. 5, there is a good correspondence between the observed and calculated autoionization structure in the ion-yield spectrum. No attempt was made to simulate the underlying ionization continuum in the calculated spectrum.

Conclusions

Because all the autoionization structure in the photoabsorption ion-yield spectra presented here and listed in Table 1 for the treated halogen and interhalogen molecules

Fig. 5. A comparison of the experimental photoabsorption ion-yield curve for IBr^+ formation and calculated autoionization function for IBr. The calculated spectrum was obtained from the sum of the simulated ion-yield curves owing to transitions to the six autoionizing Rydberg states shown. The upper numbers in the assignment refer to the principal quantum numbers (n) and the lower numbers refer to the excited-state vibrational quantum numbers (v').

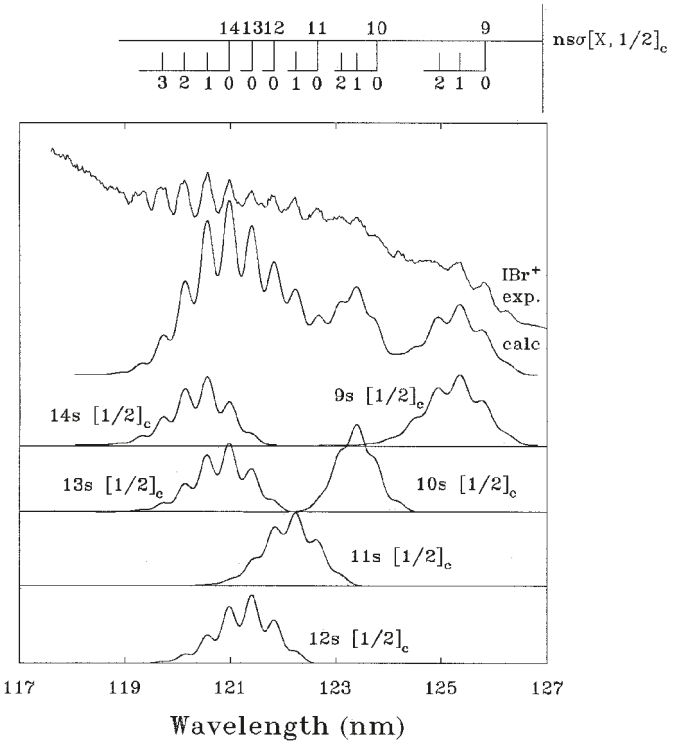

Table 1. Summary of the dominant autoionizing Rydberg state features assigned in the photoabsorption ion-yield spectra of some halogen and interhalogen molecules as identified in Figs. 1–5.

Molecule	Rydberg state assignment
Br_2	$[X\ 1/2g]_c np\pi_u$ for n = 9, 10, 11
I_2	$[X\ 1/2g]_c nf$ for n = 5, 6
	$[X\ 1/2g]_c np\pi_u$ for n = 9, 10, 11, 12, 13, 14
BrCl	$[X\ 1/2]_c ns\sigma$ for n = 11
ICl	$[X\ 1/2]_c ns\sigma$ for n = 9, 10, 11, 12
IBr	$[X\ 1/2]_c ns\sigma$ for n = 9, 10, 11, 12, 13, 14

reside between the ionization energies of the respective spin-orbit components of the ground-state ion, it is expected that spin-orbit autoionization[47] is the mechanism for the production of this structure. This type of autoionization is common for heavy-atom molecules.[47] The autoionization structures observed in the photoabsorption ion-yield spectra in the threshold ionization region of the halogen and interhalogen molecules studied here are all rather simple, in most cases only involving a single Rydberg series, the exception being the case of the iodine molecule. However, we point out that in this rather low-resolution study it is possible to not detect the presence of all contributing Rydberg systems. There appears to be a propensity for autoionizing sσ Rydberg states in the interhalogen molecules that represent a continuation of the same series found to be important

Can. J. Chem. Downloaded from www.nrcresearchpress.com by University of Electronic and Science Techonology of China on 09/18/12
For personal use only.

in ion-pair formation in the energy region below the onset of ionization.[22]

Acknowledgements

The authors thank the National Synchrotron Light Source facility of the Brookhaven National Laboratory, Upton, New York, for providing beam time and facilities for carrying out this study. The authors are also grateful to Dr. J. Robb Grover for providing instruction in the operation of his beam line equipment and for providing us with laboratory facilities for the preparation of our sample gas mixtures.

References

(1) Christie, M. I.; Roy, R. S.; Thrush, B. A. *Trans. Faraday Soc.* **1959**, *55*, 1139. doi:10.1039/tf9595501139.
(2) Christie, M. I.; Roy, R. S.; Thrush, B. A. *Trans. Faraday Soc.* **1959**, *55*, 1149. doi:10.1039/tf9595501149.
(3) Donovan, R. J.; Husain, D. *Nature* **1965**, *206* (4980), 171. doi:10.1038/206171a0.
(4) Donovan, R. J.; Husain, D. *Trans. Faraday Soc.* **1966**, *62*, 2643. doi:10.1039/tf9666202643.
(5) Donovan, R. J.; Husain, D. *Trans. Faraday Soc.* **1968**, *64*, 2325. doi:10.1039/tf9686402325.
(6) Krauss, M.; Mies, F. H. In *Excimer Lasers, Topics in Applied Physics,* 2nd ed.; Rhodes, Ch. K., Ed.; Springer-Verlag: Berlin, 1984; Vol. 30, p 5.
(7) Peyerimhoff, S. D.; Buenker, R. J. *Chem. Phys.* **1981**, *57* (3), 279. doi:10.1016/0301-0104(81)80208-X.
(8) Cartwright, D. C.; Hay, P. J. *Chem. Phys.* **1987**, *114* (3), 305. doi:10.1016/0301-0104(87)85044-9.
(9) Balasubramanian, K. *Chem. Phys.* **1988**, *119* (1), 41. doi:10.1016/0301-0104(88)80004-1.
(10) See, for example, as representative literature, the following: (a) Wang, S.; Lawley, K. P.; Ridley, T.; Donovan, R. J. *J. Chem. Soc. Faraday Discuss.* **2000**, *115*, 345; (b) Kvaran, A.; Yencha, A. J.; Lawley, K. P.; Donovan, R. J. *Mol. Phys.* **1992**, *75* (1), 197. doi:10.1080/00268979200100151.; (c) Ishiwata, T.; Si, J.; Obi, K. *J. Chem. Phys.* **1992**, *96* (8), 5678. doi:10.1063/1.462667.; (d) Ishiwata, T.; Kasai, Y.; Obi, K. *J. Chem. Phys.* **1991**, *95* (1), 60. doi:10.1063/1.461463.; (e) Ishiwata, T.; Ishiguro, A.; Obi, K. *J. Mol. Spectrosc.* **1991**, *147* (2), 300. doi:10.1016/0022-2852(91)90057-H.; (f) Lawley, K. P.; Kerr, E. A.; Donovan, R. J.; Hopkirk, A.; Shaw, D.; Yencha, A. J. *J. Phys. Chem.* **1990**, *94* (16), 6201. doi:10.1021/j100379a012.; (g) Wörmer, J.; Moller, T.; Zimmerer, G.; Le Calvé, J.; Castex, M. C. *Chem. Phys. Lett.* **1990**, *170* (5–6), 419. doi:10.1016/S0009-2614(90)87077-5.; (h) Bowman, R. M.; Dantus, M.; Zewail, A. H. *Chem. Phys. Lett.* **1989**, *161* (4–5), 297. doi:10.1016/0009-2614(89)85088-2.; (i) Koenders, B. G.; Koeckhoven, S. M.; Kuik, G. J.; Drabe, K. E.; de Lange, C. A. *J. Chem. Phys.* **1989**, *91* (10), 6042. doi:10.1063/1.457422.; (j) Yencha, A. J.; Donovan, R. J.; Hopkirk, A.; Shaw, D. *J. Phys. Chem.* **1988**, *92* (19), 5523. doi:10.1021/j100330a038.
(11) Morrison, J. D.; Hurzeler, H.; Inghram, M. G.; Stanton, H. E. *J. Chem. Phys.* **1960**, *33* (3), 821. doi:10.1063/1.1731268.
(12) Dibeler, V. H.; Walker, J. A.; McCulloh, K. E. *J. Chem. Phys.* **1969**, *50* (10), 4592. doi:10.1063/1.1670937.
(13) Dibeler, V. H.; Walker, J. A.; McCulloh, K. E. *J. Chem. Phys.* **1969**, *51* (10), 4230. doi:10.1063/1.1671784.
(14) Myer, J. A.; Samson, J. A. R. *J. Chem. Phys.* **1970**, *52* (2), 716. doi:10.1063/1.1673044.
(15) Dibeler, V. H.; Walker, J. A.; McCulloh, K. E. *J. Chem. Phys.* **1970**, *53* (12), 4414. doi:10.1063/1.1673966.
(16) Dibeler, V. H.; Walker, J. A.; McCulloh, K. E. *J. Chem. Phys.* **1970**, *53* (12), 4715. doi:10.1063/1.1674004.
(17) Dibeler, V. H.; Walker, J. A.; McCulloh, K. E.; Rosenstock, H. M. *Int. J. Mass Spectrom. Ion Phys.* **1971**, *7* (3), 209. doi:10.1016/0020-7381(71)80017-7.
(18) Berkowitz, J.; Chupka, W. A.; Guyon, P. M.; Holloway, J. H.; Spohr, R. *J. Chem. Phys.* **1971**, *54* (12), 5165. doi:10.1063/1.1674811.
(19) Berkowitz, J.; Mayhew, C. A.; Ruscic, B. *Chem. Phys.* **1988**, *123* (2), 317. doi:10.1016/0301-0104(88)87278-1.
(20) Yencha, A. J.; Kela, D. K.; Donovan, R. J.; Hopkirk, A.; Kvaran, A. *Chem. Phys. Lett.* **1990**, *165* (4), 283. doi:10.1016/0009-2614(90)87189-X.
(21) Kvaran, A.; Yencha, A. J.; Kela, D. K.; Donovan, R. J.; Hopkirk, A. *Chem. Phys. Lett.* **1991**, *179* (3), 263. doi:10.1016/0009-2614(91)87035-A.
(22) Kaur, D.; Yencha, A. J.; Donovan, R. J.; Kvaran, A.; Hopkirk, A. *Org. Mass Spectrom.* **1993**, *28* (4), 327. doi:10.1002/oms.1210280411.
(23) White, M. G.; Grover, J. R. *J. Chem. Phys.* **1983**, *79* (9), 4124. doi:10.1063/1.446361.
(24) Grover, J. R.; Walters, E. A.; Newman, J. K.; White, M. G. *J. Am. Chem. Soc.* **1985**, *107* (25), 7329. doi:10.1021/ja00311a020.
(25) Yencha, A. J.; Kaur, D.; Donovan, R. J.; Kvaran, A.; Hopkirk, A.; Lefebvre-Brion, H.; Keller, F. *J. Chem. Phys.* **1993**, *99* (7), 4986. doi:10.1063/1.466000.
(26) Yencha, A. J.; Hopkirk, A.; Grover, J. R.; Cheng, B.-M.; Lefebvre-Brion, H.; Keller, F. *J. Chem. Phys.* **1995**, *103* (8), 2882. doi:10.1063/1.470501.
(27) Kaur-Kela, D. Ph.D. Thesis, State University of New York at Albany, 1991.
(28) Stebbings, R. F.; Dunning, F. B. *Rydberg States of Atoms and Molecules;* Cambridge University Press: Cambridge, UK, 1982; p 117.
(29) Mulliken, R. S. *Phys. Rev.* **1934**, *46* (7), 549. doi:10.1103/PhysRev.46.549.
(30) Donovan, R. J.; Flexen, A. C.; Lawley, K. P.; Ridley, T. *Chem. Phys.* **1998**, *226* (1–2), 217. doi:10.1016/S0301-0104(97)00324-8.
(31) Cockett, M. C. R.; Beattie, D. A.; Macleod, N. A.; Lawley, K. P.; Ridley, T.; Donovan, R. J. *Phys. Chem. Chem. Phys.* **2002**, *4* (8), 1419. doi:10.1039/b109560a.
(32) Yencha, A. J.; Hopkirk, A.; Hiraya, A.; Donovan, R. J.; Goode, J. G.; Maier, R. R. J.; King, G. C.; Kvaran, A. *J. Phys. Chem.* **1995**, *99* (19), 7231. doi:10.1021/j100019a004.
(33) Dunlavey, S. J.; Dyke, J. M.; Morris, A. *J. Electron Spectrosc. Relat. Phenom.* **1977**, *12* (3), 259. doi:10.1016/0368-2048(77)85077-9.
(34) Cockett, M. C. R.; Goode, J. G.; Lawley, K. P.; Donovan, R. J. *J. Chem. Phys.* **1995**, *102* (13), 5226. doi:10.1063/1.469248.
(35) Cockett, M. C. R. *J. Phys. Chem.* **1995**, *99* (44), 16228. doi:10.1021/j100044a005.
(36) Cockett, M. C. R.; Donovan, R. J.; Lawley, K. P. *J. Chem. Phys.* **1996**, *105* (9), 3347. doi:10.1063/1.472535.
(37) Yencha, A. J.; Cockett, M. C. R.; Goode, J. G.; Donovan, R. J.; Hopkirk, A.; King, G. C. *Chem. Phys. Lett.* **1994**, *229* (4–5), 347. doi:10.1016/0009-2614(94)01060-9.
(38) Venkateswarlu, P. *Can. J. Phys.* **1970**, *48*, 1055. doi:10.1139/p70-136.
(39) Ridley, T.; Beattie, D. A.; Cockett, M. C. R.; Lawley, K. P.;

Donovan, R. J. *Phys. Chem. Chem. Phys.* **2002**, *4* (8), 1398. doi:10.1039/b109555m.
(40) Lawley, K. P.; Flexen, A. C.; Maier, R. R. J.; Manck, A.; Ridley, T.; Donovan, R. J. *Phys. Chem. Chem. Phys.* **2002**, *4* (8), 1412. doi:10.1039/b109558g.
(41) Kiess, C. C.; Corliss, C. H. *J. Res. Natl. Bur. Stand. A* **1959**, *63A*, 1.
(42) Hart, D. J.; Hepburn, J. W. *Chem. Phys.* **1989**, *129* (1), 51. doi:10.1016/0301-0104(89)80018-7.
(43) Yencha, A. J.; Lopes, M. C. A.; King, G. C. *Chem. Phys. Lett.* **2000**, *325* (5–6), 559. doi:10.1016/S0009-2614(00)00719-3.
(44) Yencha, A. J.; Malins, A. E. R.; King, G. C. *Chem. Phys. Lett.* **2003**, *370* (5–6), 756. doi:10.1016/S0009-2614(03)00166-0.
(45) Mason, S. M.; Tuckett, R. P. *Chem. Phys.* **1989**, *109* (2–3), 383. doi:10.1016/0301-0104(86)87067-7.
(46) Higginson, B. R.; Lloyd, D. R.; Roberts, P. J. *Chem. Phys. Lett.* **1973**, *19* (4), 480. doi:10.1016/0009-2614(73)85130-9.
(47) Lefebvre-Brion, H.; Field, R. W. *Perturbations in the Spectra of Diatomic Molecules;* Academic Press Inc.: Orlando, FL, 1986; pp 331–412.

Can. J. Chem. Downloaded from www.nrcresearchpress.com by University of Electronic and Science Techonology of China on 09/18/12
For personal use only.

Photochromic benzo[*g*]quinoxalines

Muriel Rakotomalala, Michael Katz, Emilie Voisin, Tamara C. S. Pace, Cornelia Bohne, and Vance E. Williams

Abstract: The photochromism of two 2,3-diarylbenzo[*g*]quinoxaline derivatives was explored. Irradiating 2,3-diphenylbenzo[*g*]quinoxaline with 350 nm light led to the formation of its photodimer, which could be reverted to its monomers either thermally or photochemically.The resulting photodimer absorbs at a longer wavelength than analogous dianthracene derivatives. 2,3-Dipyridylbenzo[*g*]quinoxaline was also observed to undergo photodimerization. The ability of these readily prepared benzoquinoxaline derivatives to undergo [4 + 4]-photocycloaddition reactions makes them attractive alternatives to anthracene derivatives.

Key words: cycloaddition, photochromism, benzoquinoxaline.

Résumé : On a étudié la photochromie de deux dérivés de 2,3-diarylbenzo[*g*]quinoxaline. L'irradiation de la 2,3-diphénylbenzo[*g*]quinoxaline avec de la lumière à 350 nm conduit à la formation de son photodimère qui peut revenir à sa forme monomère d'une façon soit thermique ou photochimique. Le photodimère qui en résulte absorbe à une longueur d'onde plus grande que celle des dérivés dianthracènes analogues. On a observé que la 2,3-dipyridylbenzo[*g*]quinoxaline subit aussi une photodimérisation. L'habilité de ces dérivés de la benzoquinoxaline facilement accessibles à subir des réactions de [4 + 4]-photocycloaddition en font des alternatives attrayantes aux dérivés de l'anthracène.

Mots-clés : cycloaddition, photochromie, benzoquinoxaline.

[Traduit par la Rédaction]

Introduction

Since the discovery of anthracene photochromism in the 19th century,[1] extensive studies have been carried out on the photodimerization of this and related molecules.[2,3] Although these reversible reactions have been exploited in a variety of contexts,[4–10] their practical utility is limited by the pronounced tendency of anthracene derivatives to photo-oxidize[3,11–13] and the short wavelengths (<300 nm) needed to photolyze the dimers back into their monomers.[3] Functional groups at the 2 and 3 positions of anthracene can shift the absorption of both the monomer and dimer to longer wavelengths, but such derivatives are often difficult to synthesize.[14–18] In contrast, 2,3-disubstituted benzo[*g*]quinoxalines can be prepared in a single step from commercially available starting materials[19] and, given their structural similarities to anthracene, are also expected to undergo [4 + 4]-photocycloaddition reactions. Although numerous benzo[*g*]-quinoxaline derivatives have been prepared,[20,21] their photochemistry has not been studied; indeed, the photochromism of nitrogen-containing analogues of anthracene remains largely unexplored.[22–29]

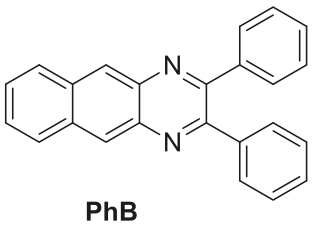

PhB

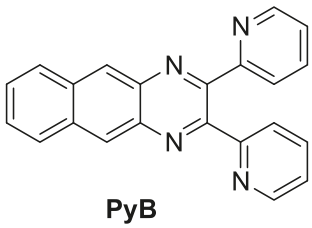

PyB

These considerations prompted us to investigate the photochemistry of two 2,3-diarylbenzo[*g*]quinoxaline derivatives, **PhB** and **PyB**. The presence of either phenyl or pyridyl groups at the 2 and 3 positions of these derivatives was anticipated to confer several advantages on these chromophores; not only are these groups expected to shift the absorbance to longer wavelengths, but they may also improve the solubility by inhibiting aggregation between the benzo[*g*]quinoxaline cores. The pyridyl derivative **PyB** was of further interest for its potential ability to complex to metals, which suggests a means to modulate the photoreactivity through chemical stimuli.

Received 1 June 2010. Accepted 22 July 2010. Published on the NRC Research Press Web site at canjchem.nrc.ca on 14 February 2011.

M. Rakotomalala, M. Katz, E. Voisin, and V.E. Williams.[1] Department of Chemistry, Simon Fraser University, 8888 University Dr., Burnaby, BC V5A 1S6, Canada.
T.C.S. Pace and C. Bohne. Chemistry Department, University of Victoria, P.O. Box 3065, Victoria, BC V8W 3V6, Canada.

[1]Corresponding author (e-mail: vancew@sfu.ca).

Can. J. Chem. Downloaded from www.nrcresearchpress.com by University of Electronic and Science Techonology of China on 09/18/12
For personal use only.

Can. J. Chem. Downloaded from www.nrcresearchpress.com by University of Electronic and Science Techonology of China on 09/18/12
For personal use only.

Scheme 1.

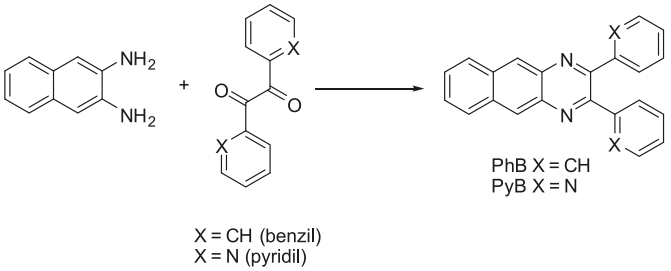

Results and discussion

PhB and **PyB** were prepared from the condensation of 2,3-diaminonaphthalene with benzil[19] and pyridil,[30] respectively (Scheme 1). Pyridil was obtained in two steps via a benzoin condensation of picolinaldeyde followed by oxidation using a slightly modified literature procedure.[31]

The UV–vis absorption spectrum of **PhB** in acetonitrile reveals a strong absorbance centred at 270 nm and a less intense set of bands at longer wavelengths (λ_{max} = 380 nm). Irradiation of a degassed 4.4 mmol/L acetonitrile solution of **PhB** with lamps centered at 350 nm for 150 min led to the formation of a single photoproduct in a 20% yield. The yield of this reaction increased to 72% when a filter solution of KNO_3 was employed to block wavelengths below 340 nm,[32] which suggests that the product may be undergoing photoreversion to **PhB** upon exposure to shorter wavelengths. This conjecture was supported by the observation that the photoproduct has an absorption maximum at 328 nm, where there is considerable output from the lamps employed (vide infra). This photoproduct is thermally stable at room temperature and was readily separated from the starting material.

The MALDI-TOF spectrum of this photoproduct exhibits an intense peak at *m*/*z* 333 and a weaker peak at 665, which correspond to the M + 1 peaks of **PhB** and its photodimer, respectively. The low intensity of the dimer peak is in keeping with the behaviour of anthracene photodimers, which typically dissociate during mass spectrometry experiments.[2] The ^{1}H NMR spectrum of the product was consistent with that of the head-to-tail (ht) photodimer, ***ht*-di-PhB**. The most significant feature of this spectrum is a singlet at 5.06 ppm, which is within the range expected for protons attached to the sp^3-hybridized bridgehead carbons of dianthracene-like photodimers. The observation of only a single photoproduct from this reaction is likely due to the steric bulk of the phenyl groups, which may inhibit formation of the head-to-head (hh) stereoisomer, ***hh*-di-PhB**. It is also possible that this second isomer was formed in trace quantities that could not be detected, or that it exhibits appreciably lower thermal stability than the ht dimer and therefore decomposes.

The identification of the photoproduct as ***ht*-di-PhB** was confirmed by X-ray crystallography (Fig. 1) of single crystals obtained by slow evaporation of a 1:1 acetonitrile/chloroform solution. Under these conditions, the dimer crystallizes in the monoclinic space group *P*21*n*. The bond lengths between the sp^3-hybridized bridgehead carbons are 1.61(6) Å, which are longer than a typical carbon–carbon single bond, but similar to the lengths of the corresponding bonds in dianthracene (1.624 Å) and related systems.[2]

Fig. 1. Structure of the head-to-tail photodimer of 2,3-diphenylbenzo[*g*]quinoxaline (***ht*-di-PhB**) determined by X-ray crystallography.

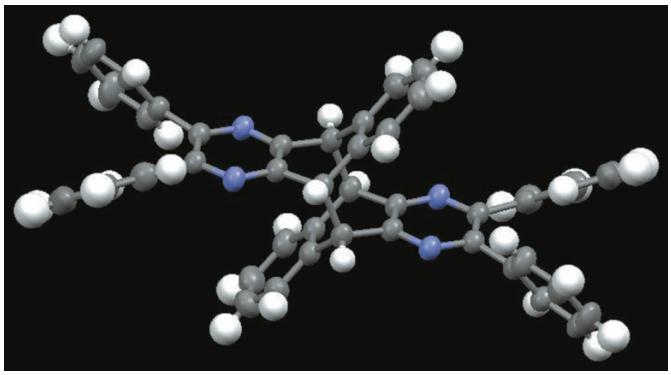

The relatively long bridgehead bonds observed in the crystal structure suggested that, like anthracene derivatives, these dimers might thermally revert to monomers at elevated temperatures. The thermal stability of ***ht*-di-PhB** was studied by monitoring the UV–vis spectrum of a 1 mmol/L solution heated in DMSO at a variety of temperatures. No decomposition was observed for a sample heated at 120 °C for 5 h, indicating that the dimer is thermally stable at moderate temperatures. In contrast, heating this compound to 150 °C led to a continuous decrease in absorption bands and an accompanying increase in peaks associated with the monomer **PhB**. At this temperature, reversion of the dimer to **PhB** was complete after 2.5 h.

To examine whether ***ht*-di-PhB** also undergoes photoreversion, a 0.1 mmol/L acetonitrile solution of the dimer was irradiated with 328 nm light and the progress of the reaction was monitored by UV–vis spectroscopy (Fig. 2). During irradiation, the absorbance at 328 nm steadily decreased while a new peak at 380 nm grew in, indicating that the product dissociates to the corresponding monomer. The ^{1}H NMR spectrum confirmed that **PhB** was being formed during the course of these experiments. Dissociation reached completion after 240 min of irradiation. The spectral changes with time show that two isobestic points may be located at 321 and 342 nm. However, close inspection of these wavelength regions (Fig. 2, inset) reveals a very small systematic drift as time progresses, which suggests that only two major species are present in solution, but a minor species, probably present at very low concentrations, is also possibly formed. It is unclear at this time what the nature of this additional photoproduct is, although it may arise from the cyclization of the peripheral phenyl groups to form a triphenylene-like product.[33]

In an effort to better understand the mechanism of photodimerization, the excited state lifetimes of **PhB** were determined by single-photon counting for the singlet excited state and by laser flash photolysis for the triplet state. The singlet state lifetimes were found to be 1.9 ns ± 0.1 ns in acetonitrile and <0.5 ns in cyclohexane.[34] The triplet lifetimes are long (≥10 μs) in acetonitrile and cyclohexane. In comparison, the singlet excited state of anthracene has a lifetime of 5.3 ns in nonpolar solvents.[35] We observed no appreciable difference in the efficiency for photodimerization when this reaction was carried out in aerated solutions, which excludes reactivity from the triplet excited state. In addition, unlike

Can. J. Chem. Downloaded from www.nrcresearchpress.com by University of Electronic and Science Techonology of China on 09/18/12
For personal use only.

Fig. 2. UV–vis absorption spectra of the photodissociation of a 0.1 mmol/L solution of the head-to-tail photodimer of 2,3-diphenylbenzo[*g*]quinoxaline (***ht*-di-PhB**) in CH_3CN using a 328 nm light. Inset: expansion of the 315–355 nm region.

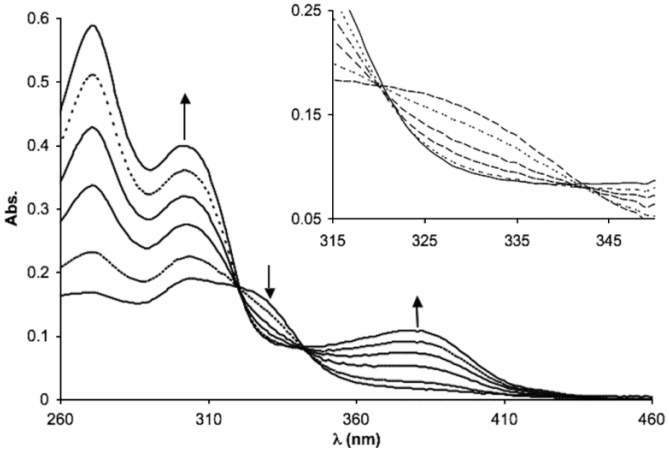

many anthracene derivatives, **PhB** does not appear to be prone to photoreactions with oxygen, as no additional products such as endoperoxides were observed when the reaction was performed in air. These results suggest that photodimerization occurs from the singlet excited state. The absence of endoperoxide formation makes it possible to perform the reaction in aerated solutions, which represents a distinct advantage of this system for practical applications.

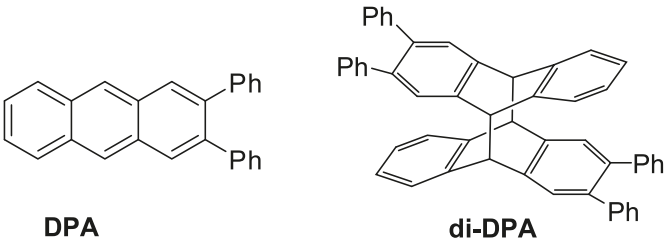

The photochromic properties of **PhB** compare favourably to those of 2,3-diphenylanthracene, **DPA**.[35] **DPA** also undergoes [4 + 4]-cycloaddition to form a single photodimer, which also appeared to be the ht stereoisomer. The UV–vis absorption spectra of **DPA** and **PhB** are similar, although the absorption of the latter is redshifted by ~20 nm relative to that of the former. A dramatic difference is also observed between the absorption spectra of the corresponding photodimers (Fig. 3). Whereas ***ht*-di-PhB** exhibits a large peak at 328 nm, the photodimer of **DPA** (**di-DPA**) has no appreciable absorption above 320 nm, and the parent compound, dianthracene (**di-A**) does not absorb above 300 nm. As a consequence, switching between **PhB** and its dimer can be induced with longer wavelengths than is achievable with most anthracene derivatives. It is also worth noting that although both **PhB** and **DPA** can be prepared from benzil, **PhB** is prepared in a single step in a high yield, whereas **DPA** is prepared in three steps in considerably lower overall yields.[15,36]

The photochemistry of the dipyridyl derivative **PyB** is similar to that of **PhB**. A 1.33 mmol/L acetonitrile solution of **PyB** was irradiated with lamps centered at 350 nm for

Fig. 3. Absorption spectra of dianthracene (**di-A**), the photodimer of 2,3-diphenylanthracene (**di-DPA**), and the head-to-tail photodimer of 2,3-diphenylbenzo[*g*]quinoxaline (***ht*-di-PhB**) in acetonitrile.

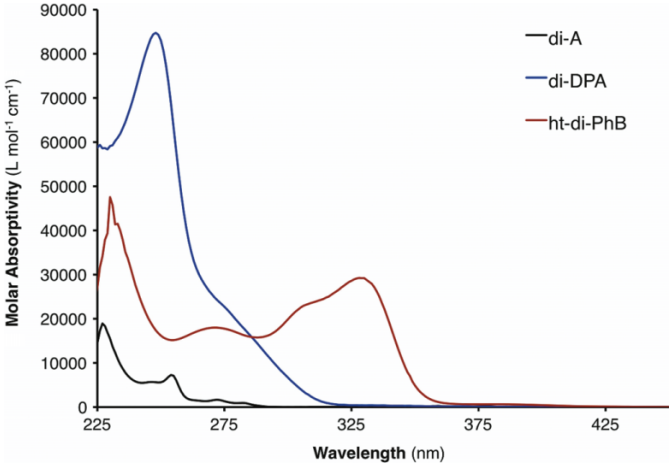

150 min. The ^{1}H NMR spectrum of the residue obtained by evaporation of the reaction solvent showed a new set of peaks in the aromatic region accompanied by a singlet at 5.2 ppm associated with the formation of the bridgehead across the central ring of two benzo[*g*]quinoxaline moieties. The MALDI-TOF mass spectrum of this mixture showed a peak at *m*/*z* 669, corresponding to M(**di-PyB**) + 1, and a more intense peak for M(**PyB**) + 1. These results are therefore consistent with the identification of the photoproduct as **di-PyB**. The photoadduct formed could be separated from **PyB** by slow evaporation of CH_3CN, which led to selective precipitation of the photodimer. A priori, we expect the ht dimer, ***ht*-di-PyB**, to preferentially form as the major product. This prediction is borne out by the observation of an NOE between protons **a** and **b** (Fig. 4) in the NOESY spectrum of this photoproduct in $CDCl_3$. This NOE would not be expected for the hh dimer.

In addition to its photochromic properties, **PyB** is also capable of binding a variety of metal cations.[37–40] It would therefore be of interest whether the presence of species capable of binding to this compound would also alter its reactivity. However, initial attempts to modulate the tendency of this compound to undergo [4 + 4]-photocycloaddition reactions by the addition of transition metals such as zinc have been unsuccessful. Controlling the photoreactivity of this compound by protonation of the pyridyl groups also proved impractical, as **PyB** becomes insoluble at low pH. Further investigations into the reactivity of this compound in the presence of transition metals and other species are underway.

Conclusion

In conclusion, we have demonstrated that both **PhB** and **PyB** photochemically dimerize in solution. It was also shown that the dimer ***ht*-di-PhB** can be dissociated back to **PhB** using either heat or light. **PhB** offers several advantages over anthracene derivatives to which it is structurally related. This compound is straightforward to prepare, is not prone to photooxidation, and can be switched between its dimer and monomer forms using relatively long wavelengths

Can. J. Chem. Downloaded from www.nrcresearchpress.com by University of Electronic and Science Techonology of China on 09/18/12
For personal use only.

Fig. 4. Proposed structure of the photoproduct formed upon irradiation of 2,3-dipyridylbenzo[*g*]quinoxaline (**PyB**).

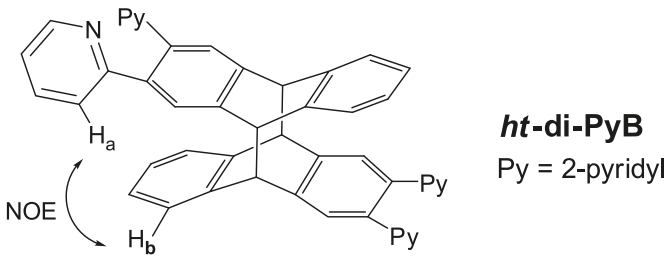

of light. As such, benzoquinoxalines represent a promising new class of photochromic compounds that overcome many of the shortcomings of anthracene derivatives, and we are currently investigating the photochemistry of other members of this family of molecules.

Experimental

Materials

All chemicals were used as provided from the supplier. Acetonitrile, 2,3-diaminonaphthalene, and benzil were purchased from Caledon Laboratories Ltd., Sigma-Aldrich Chemical Co., and Matheson Colleman & Bell, respectively. Potassium nitrate, acetic acid, and toluene were purchased from Anachemia.

Instruments

^{1}H NMR and ^{13}C NMR spectroscopic characterization were carried out using a Bruker AMX-400 400 MHz spectrometer; IR spectra were obtained using a Thermo Nicolet Nexus 670 FT-IR ESP spectrometer, performed in KBr. Low-resolution EI mass spectrometry (70 eV) was carried out using a Hewlett Packard 5985 mass spectrometer. MALDI-TOF mass spectra were carried out using a Perspective Voyager-DE STR from PE Applied Biosystems with a nitrogen laser (337 nm) and using 2,5-dihydroxybenzoic acid as the matrix. Microanalysis (C, H, and N) were performed at Simon Fraser University, Burnaby, British Columbia, by M. Yang and S. Wong. Melting points were determined using a Fisher melting point apparatus and are uncorrected. UV–vis absorption spectra were obtained on a Cary 300 biospectrophotometer.

Fluorescence spectra were measured with a PTI QM-2 spectrometer, and the singlet excited state lifetimes were measured with an OB920 single-photon counter from Edinburgh. The excitation wavelength was 380 nm and emission spectra were collected between 395 and 700 nm (slit bandwidth of 3 nm), while decays were collected at 460 nm in cyclohexane or 490 nm in acetonitrile (slit bandwidth of 16 nm). For a description of the laser flash photolysis system, see ref. 33. Samples were excited with a Nd:YAG laser at 266 nm, and the kinetics were monitored at 400–410 and 460 nm. For all photophysical experiments, samples were deoxygenated by bubbling nitrogen for 20 min.

X-ray crystallography

Crystal data for ht-di-DPBQ

$C_{48}H_{32}N_4$, MW = 664.79, monoclinic, space group = *P* 1 21/*n*1, a = 8.6132(9) Å, b = 18.4915(17) Å, c = 10.9618(16) Å, β = 96.550(6), V = 1734.5(4) Å^3, T = 293 K, Z = 2, ρ_{calcd} = 1.273 g/cm^{-3}, μ (Cu Kα) = 0.580, 3014 unique reflections, 2639 observed ($I_o > 2.5\sigma(I_o)$). The final RF = 0.0436 and RWF = 0.0645 (observed data).

Synthesis

Synthesis of 2,3-dibenzylbenzo[g]quinoxaline (PhB)

A solution of 2,3-diaminonaphtalene (1.0 mmol) and benzil (1.1 mmol) in acetic acid (10 mL) was refluxed overnight. Reaction progress was monitored by TLC (eluent: toluene). Once all 2,3-diaminonaphtalene was consumed, the hot reaction mixture was poured over crushed ice. The resulting off-brown suspension was then neutralized with satd. $NaHCO_3$. The aqueous solution was extracted with dichloromethane (3 × 80 mL). The organic washes were combined and dried over $MgSO_4$, filtered, and dried in vacuo yielding an off-yellow powder (88%). The product was purified by flash column chromatography (eluent: dichloromethane) to yield a yellow crystalline powder (75%). Uncorrected mp 184–185 °C (lit. value[19] mp 187–189 °C). UV–vis λ_{max} (nm) (ε ((mol/L)/cm): 271 (61 292), 302 (3683), 381 (12 341) 88. IR (KBr, cm^{-1}) ν: 3053, 2919, 2849, 1436, 1346, 1249. ^{1}H NMR (400 MHz, $CDCl_3$) δ_H: 8.75 (s, 2H), 8.13 (q, 2H), 7.57 (m, 6H), 7.37 (m, 6H). ^{13}C NMR (100 MHz, $CDCl_3$) δ_C: 154.1, 139.1, 137.9, 134.0, 129.8, 128.9, 128.5, 128.2, 127.5, 126.7. MS *m/e* (CI): 333.3 (M + 1). Anal. calcd for $C_{24}H_{16}H_2$ (%): C 86.72, H 4.85, N 8.43; found: C 86.56, H 5.00, N 8.21.

Synthesis of 1,2-di(pyridin-2-yl)ethane-1,2-dione (pyridil)

Picolinaldehyde (3.22 g, 30.0 mmol) and potassium cyanide (1.92 g, 30.0 mmol) were dissolved in ethanol (5 mL) and water (20 mL) and heated to reflux. After 4 h, TLC analysis (hexane / ethyl acetate, 1:1) showed that all picolinaldehyde was consumed; the hot reaction mixture was poured over crushed ice. The resulting brown suspension was filtered with a Buchner funnel and washed with cold ethanol to yield 2-hydroxy-1,2-di(pyridine-2-yl)ethanone (95%), which was used without further purification. ^{1}H NMR (500 MHz, $CDCl_3$, ppm) δ_H: 8.47 (d, J = 5.0 Hz, 2.0H), 7.93–7.88 (m, 2H), 7.84 (dt, J_1 = 8.2, J_2 = 1.8 Hz, 2H), 7.19 (ddd, J_1 = 7.3, J_2 = 5.0, J_3 = 1.2 Hz, 2H).

2-Hydroxy-1-(pyridine-2-yl)ethanone (1.611 g, 7.5 mmol) was dissolved in pyridine (25 mL). To this solution was added a solution of $CuSO_4$ (1.870 g, 7.5 mmol) in H_2O (10 mL). Once addition was complete, the reaction mixture was stirred at reflux for 1 h. The hot reaction was poured over crushed ice and filtered to yield 0.857 g of pure pyridil (54%) as a yellow crystalline solid; mp 155–157 °C (lit. value[31] mp 156–157 °C). MS *m/z* (CI): 213 (M + 1). ^{1}H NMR (500 MHz, $CDCl_3$, ppm) δ_H: 8.60 (d, J = 4.7 Hz, 2.0H), 8.23 (d, J = 7.8 Hz, 2H), 7.94 (dt, J = 7.7, 1.8 Hz, 2H), 7.50 (ddd, J_1 = 7.6, J_2 = 4.8, J_3 = 1.2 Hz, 2H).

Synthesis of PyB

This compound was synthesized according to literature procedure.[30] The product was recrystallized from hot ethanol yielding **PyB** (73%) as shiny yellow crystals; mp 183–185 °C (lit. value[30] mp 184–185 °C). MS *m/z* (CI) 335

Can. J. Chem. Downloaded from www.nrcresearchpress.com by University of Electronic and Science Techonology of China on 09/18/12
For personal use only.

(M + 1). ^{1}H NMR (400 MHz, $CDCl_3$, ppm) δ_H: 8.80 (s, 2H), 8.36 (d, J = 4.8 Hz, 2H), 8.15 (m, 2H), 8.09 (d, J = 7.8 Hz, 2H), 7.87 (dt, J_1 = 1.7, J_2 = 7.7 Hz, 2H), 7.61 (m, 2H), 7.26 (m, 4H).

Photochemical experiments

All photodimerization experiments were carried out in glass tubes in a Rayonet photoreactor fitted with seven RPR3500A lamps.

For the experiments in which a filter solution was employed, 3.32 mg **PhB** was dissolved in 0.75 mL of CH_3CN. The solution was transferred to an NMR tube and immersed into a test tube filled with a 2.0 mol/L solution of KNO_3 in water. The sample was irradiated in a Rayonet for 150 min. The solvent was then removed in vacuo and redissolved in a minimum volume of $CDCl_3$. The ^{1}H NMR sprectrum showed a 4:1 ratio of dimer to monomer.

Synthesis of ht-di-PhB

PhB (3.3 mg) was dissolved in spectral grade benzene (1.5 mL) and deoxygenated. The sample was then irradiated in a Rayonet fitted with seven 350 nm lamps for 2 h. After irradiation, a white powder was precipitated on the side of the glass. The solution was decanted and the white product on the side of the glass vessel was collected. MALDI-TOF *m/z*: 665 (M + 1). UV–vis λ_{max} (nm) (ε (mol/L)/cm): 230 (47 543), 270 (17 967), 308 (23 337), 328 (29 242). IR (KBr, cm^{-1}) ν: 3057, 2959, 2919, 2849, 1389, 1144. ^{1}H NMR (400 MHz, $CDCl_3$, ppm) δ_H: 7.23 (m, 16H), 7.14 (m, 8H), 7.03 (m, 4H), 5.05 (s, 4H). ^{13}C NMR (100 MHz, $CDCl_3$, ppm) δ_C: 156.3, 148.7, 140.4, 138.8, 129.4, 128.1, 128.0, 126.9, 52.7. (Note: due to the limited solubility of this compound, we were unable to observe the signals for quaternary carbons.) Anal. calcd for $C_{48}H_{32}N_4$ (%): C 86.72, H 4.85, N 8.43; found: C 86.61, H 4.98, N 8.15.

Thermal dissociation of ht-di-PhB

***ht*-di-PhB** (6.6 mg) was dissolved in 100 mL DMSO in a 100 mL volumetric flask. The solution (20 mL, 1.00×10^{-5} mol/L) was transferred into four 25 mL glass vials. The open vials were then heated in oil baths at 60, 80, 100, and 150 °C.

Photodissociation of ht-di-PhB

***ht*-di-PhB** (6.6 mg) was used to prepare a 10 mL solution of 1×10^{-4} mol/L in acetonitrile using several dilutions. The solution was transferred to a 1 cm quartz cuvette and irradiated at 328 nm in the fluorimeter. Dissociation progress was followed by UV–vis spectroscopy.

Synthesis of ht-di-PyB

***ht*-di-PyB** was prepared using the method described above for ***ht*-di-PhB** to afford a white solid that precipitated from the reaction solution. MALDI-TOF *m/z*: 669 (M + 1). ^{1}H NMR (500 MHz, $CDCl_3$, ppm) δ_H: 8.43 (d, J = 4.8 Hz, 2H), 7.69–7.63 (m, 2H), 7.45–7.37 (m, 2H), 7.25 (dd, J_1 = 5.4, J_2 = 3.3 Hz, 2H), 7.21–7.14 (m, 1H), 7.00 (dd, J_1 = 5.4, J_2 = 3.2 Hz, 2H), 5.16 (s, 2 H). ^{13}C NMR (125 MHz, $CDCl_3$, ppm) δ_C: 157.3, 156.9, 149.1, 147.9, 140.0, 136.2, 128.0, 127.3, 124.3, 122.6, 109.7, 52.7.

Supplementary data

Supplementary data (UV–vis absorption spectra of **PhB** with ***ht*-di-PhB** and spectra showing the progress of the thermal dissociation experiment) for this article are available on the journal Web site (canjchem.nrc.ca). CCDC 653177 contains the X-ray data in CIF format for this manuscript. These data can be obtained, free of charge, via http://www.ccdc.cam.ac.uk/conts/retrieving.html (or from the Cambridge Crystallographic Data Centre, 12 Union Road, Cambridge CB2 1EZ, UK; fax +44 1223 336033; or deposit@ccdc.cam.ac.uk).

Acknowledgement

The authors gratefully acknowledge the Natural Sciences and Engineering Research Council of Canada (NSERC), the University of Victoria, Victoria, British Columbia, and Simon Fraser University, Burnaby, British Columbia, for funding; T.C.S.P. thanks NSERC for a Canada Graduate Scholarships – Doctoral (CGS-D) scholarship; and M.-K. Yang and F. Haftbaradaran are acknowledged for carrying out the microanalysis.

References

(1) Fritzsche, J. *Bull. Acad. Imp. Sci. St. Petersbourg* **1867**, *11*, 385.
(2) Bouas-Laurent, H.; Castellan, A.; Desvergne, J.-P.; Lapouyade, R. *Chem. Soc. Rev.* **2000**, *29* (1), 43. doi:10.1039/a801821i.
(3) Bouas-Laurent, H.; Castellan, A.; Desvergne, J.-P.; Lapouyade, R. *Chem. Soc. Rev.* **2001**, *30* (4), 248. doi:10.1039/b006013p.
(4) Nakatsuji, S.; Ojima, T.; Akutsu, H.; Yamada, J. *J. Org. Chem.* **2002**, *67* (3), 916. doi:10.1021/jo010943u.
(5) Ojima, T.; Akutsu, H.; Yamada, J.; Nakatsuji, S. *Polyhedron* **2001**, *20* (11–14), 1335. doi:10.1016/S0277-5387(01)00615-5.
(6) Jones, J. R.; Liotta, C. L.; Collard, D. M.; Schiraldi, D. A. *Macromolecules* **2000**, *33* (5), 1640. doi:10.1021/ma990041j.
(7) Schäfer, C.; Eckel, R.; Ros, R.; Mattay, J.; Anselmetti, D. *J. Am. Chem. Soc.* **2007**, *129* (6), 1488. doi:10.1021/ja067734h.
(8) McSkimming, G.; Tucker, J. H. R.; Bouas-Laurent, H.; Desvergne, J. P.; Coles, S. J.; Hursthouse, M. B.; Light, M. E. *Chem. Eur. J.* **2002**, *8* (15), 3331. doi:10.1002/1521-3765(20020802)8:15<3331::AID-CHEM3331>3.0.CO;2-C.
(9) De Schryver, F. C.; Anand, L.; Smets, G.; Switten, J. *J. Polym. Sci., Polym. Lett. Ed.* **1971**, *9* (10), 777.
(10) Matsui, J.; Ochi, Y.; Tamaki, K. *Chem. Lett.* **2006**, *35* (1), 80. doi:10.1246/cl.2006.80.
(11) Yang, C.; Jacob, J.; Mullen, K. *Macromolecules* **2006**, *39* (17), 5696. doi:10.1021/ma060722w.
(12) Bratschkov, C.; Karpuzova, P.; Müllen, K.; Klapper, M.; Schopov, I. *Polym. Bull.* **2001**, *46* (5), 345. doi:10.1007/s002890170041.
(13) Wasserman, H. H.; Scheffer, J. R.; Cooper, L. J. *J. Am. Chem. Soc.* **1972**, *94* (14), 4991. doi:10.1021/ja00769a034.
(14) Bailey, D.; Williams, V. E. *Tetrahedron Lett.* **2004**, *45* (12), 2511. doi:10.1016/j.tetlet.2004.02.010.
(15) Bailey, D.; Murphy, J. N.; Williams, V. E. *Can. J. Chem.* **2006**, *84* (4), 659. doi:10.1139/V06-054.
(16) Bowles, D. W.; Anthony, J. E. *Org. Lett.* **2000**, *2* (1), 85. doi:10.1021/ol991254w.
(17) Lagodzinski, K. *Liebigs Ann. Chem.* **1905**, *342* (1/3), 90.
(18) Bailey, D.; Williams, V. E. *Chem. Commun. (Camb.)* **2005**, 2569. doi:10.1039/b502183a.

(19) Goldstein, H.; Streuli, M. *Helv. Chim. Acta* **1937**, *20* (1), 650. doi:10.1002/hlca.19370200197.
(20) Carlson, D. L.; Huchital, D. H.; Mantilla, E. J.; Sheardy, R. D.; Murphy, W. R. *J. Am. Chem. Soc.* **1993**, *115* (14), 6424. doi:10.1021/ja00067a073.
(21) Gazit, A.; App, H.; McMahon, G.; Chen, J.; Levitzki, A.; Bohmer, F. D. *J. Med. Chem.* **1996**, *39* (11), 2170. doi:10.1021/jm950727b.
(22) Ihmels, H.; Mohrschladt, C. J.; Schmitt, A.; Bressanini, M.; Leusser, D.; Stalke, D. *Eur. J. Org. Chem.* **2002**, No. 15, 2624. doi:10.1002/1099-0690(200208)2002:15<2624::AID-EJOC2624>3.0.CO;2-Q.
(23) Bradsher, C. K.; Beavers, I. E.; Jones, J. H. *J. Org. Chem.* **1957**, *22* (12), 1740. doi:10.1021/jo01363a640.
(24) Jouvenot, D.; Glazer, E. C.; Tor, Y. *Org. Lett.* **2006**, *8* (10), 1987. doi:10.1021/ol060253i.
(25) Warrener, R. N.; Golic, M.; Butler, D. N. *Tetrahedron Lett.* **1998**, *39* (26), 4717. doi:10.1016/S0040-4039(98)00865-X.
(26) Kuckling, D.; Ivanova, I. G.; Adler, H.-J. P.; Wolff, T. *Polymer (Guildf.)* **2002**, *43* (6), 1813. doi:10.1016/S0032-3861(01)00766-2.
(27) Lehnberger, C.; Wolff, T. *J. Colloid Interface Sci.* **1999**, *213* (1), 187. doi:10.1006/jcis.1999.6126.
(28) Lehnberger, C.; Scheller, D.; Wolff, T. *Heterocycles* **1997**, *45* (10), 2033. doi:10.3987/COM-97-7891.
(29) Nees, D.; Cichos, U.; Wolff, T. *Ber. Bunsenges. Phys. Chem* **1996**, *100* (8), 1372.
(30) Yeomans, B. D.; Kelso, L. S.; Tregloan, P. A.; Keene, F. R. *Eur. J. Inorg. Chem.* **2001**, No. 1, 239. doi:10.1002/1099-0682(20011)2001:1<239::AID-EJIC239>3.0.CO;2-2.
(31) Schaefer, J. P.; Bertram, J. L. *J. Am. Chem. Soc.* **1967**, *89* (16), 4121. doi:10.1021/ja00992a029.
(32) Parker, C. A. *Photoluminescence in Solution;* Elsevier: New York, 1968.
(33) Sato, T.; Shimada, S.; Hata, K. *Bull. Chem. Soc. Jpn.* **1971**, *44* (9), 2484. doi:10.1246/bcsj.44.2484.
(34) Liao, Y.; Bohne, C. *J. Phys. Chem.* **1996**, *100* (2), 734. doi:10.1021/jp951697r.
(35) Murov, S. L.; Carmichael, I.; Hug, G. L. *Handbook of Photochemistry,* 2nd, revised and expanded, ed.; Marcel Dekker, Inc.: New York, 1993; p 420.
(36) Bailey, D.; Williams, V. E. *J. Org. Chem.* **2006**, *71* (15), 5778. doi:10.1021/jo060838q.
(37) Holliday, B. J.; Mirkin, C. A. *Angew. Chem. Int. Ed.* **2001**, *40* (11), 2022. doi:10.1002/1521-3773(20010601)40:11<2022::AID-ANIE2022>3.0.CO;2-D.
(38) Wang, J. H.; Fang, Y.-Q.; Bourget-Merle, L.; Polson, M. I. J.; Hanan, G. S.; Juris, A.; Loiseau, F.; Campagna, S. *Chem. Eur. J.* **2006**, *12* (33), 8539. doi:10.1002/chem.200600245.
(39) Polson, M. I. J.; Howell, S. L.; Flood, A. H.; Burrell, A. K.; Blackman, A. G.; Gordon, K. C. *Polyhedron* **2004**, *23* (8), 1427. doi:10.1016/j.poly.2004.02.012.
(40) For an example of transition metals modulating the photodimerization of acridiziniums, see Bendig, J.; Geppert, B.; Kerysig, D. *J. Prakt. Chem.* **1978**, *320* (5), 739. doi:10.1002/prac.19783200506.

Can. J. Chem. Downloaded from www.nrcresearchpress.com by University of Electronic and Science Techonology of China on 09/18/12
For personal use only.

Fluorescence from the A $^2\Sigma^+$ state suggests a non-Franck–Condon $N_2O^{+\bullet}$ vibrational state population after keV collisional activation with helium

Yawei Lin and Paul M. Mayer

Abstract: A commercial analytical mass spectrometer coupled with a spectrograph and charge-coupled device (CCD) detector was used to obtain the collision-induced emission (CIE) spectra (190–1020 nm) from ion–molecule collisions between $N_2O^{+\bullet}$ and He at laboratory frame collision energies of 4–8 keV. The observed emissions were from the A $^2\Sigma^+ \rightarrow$ X $^2\Pi^+$ system of $N_2O^{+\bullet}$, excited fragments of the parent molecule, and the target gas. The relative emission intensities of the $N_2O^{+\bullet}$ ions and their fragments were independent of the ion translational energy within the 4–8 keV range, confirming the curve-crossing mechanism for translational-to-internal energy transfer in this system. Band emission intensities of 1_0^1 and 3_1^1 relative to the 1_0^0 band within the $N_2O^{+\bullet}$ (A $\rightarrow$ X) system have been measured and compared with reference data. The results indicated that the collisionally excited ion has a decidedly non-Franck–Condon vibrational state distribution.

Key words: Frank–Condon principle, curve-crossing mechanism, collisional activation, mass spectrometry, predissociation.

Résumé : On a utilisé un spectromètre de masse analytique commercial couplé à un spectrographe et à un dispositif détecteur de charge couplée pour obtenir des spectres d'émission induite par une collision (EIC) (190–1020 nm) à partir de collisions ion–molécule entre du $N_2O^{+\bullet}$ et du He à des énergies de collision de 4 à 8 keV disponible au laboratoire. Les émissions observées à partir du système A $^2\Sigma^+ \rightarrow$ X $^2\Pi^+$ du $N_2O^{+\bullet}$, les fragments excités de la molécule de base et du gaz cible. Les intensités relatives de l'émission des ions $N_2O^{+\cdot}$ et de leurs fragments sont indépendantes de l'énergie translationnelle dans la fourchette de 4 à 8 keV, ce qui confirme le mécanisme de croisement de coure pour le transfert d'énergie translationnelle à interne dans ce système. On a mesuré les intensités des bandes d'émission 1_0^1 et 3_1^1 par rapport à la bande 1_0^0 dans le système $N_2O^{+\bullet}$ (A $\rightarrow$ X) et on les a comparées avec des données de référence. Les résultats indiquent que l'ion excité par collision n'est définitivement pas une distribution d'état vibrationnel de Franck-Condon.

Mots-clés : principe de Franck–Condon, mécanisme de croisement de courbe, activation par collision, spectrométrie de masse, prédissociation.

Introduction

The triatomic ion $N_2O^{+\bullet}$ is isoelectronic with NCO, $CO_2^{+\bullet}$, and BO_2. It is the intermediate in an important ion–molecule reaction in the upper atmosphere (eq. [1]).[1]

$$[1] \quad O + (^4S_u) + N_2(X^1\Sigma_g^+) \rightarrow N_2O^{+\bullet}(A^2\Sigma^+) \rightarrow NO^+(X^1\Sigma^+) + N(^4S)$$

The dominant emission band systems of $N_2O^{+\bullet}$, extending from 335 to 405 nm, are the A $^2\Sigma^+ \rightarrow$ X $^2\Pi^+$ transitions from three dominant levels 1^0, 1^1, and 3^1 of the A state. Here the capital number represents the normal vibrational mode involved (1 being the symmetric stretch, 2 being the degenerate bend, and 3 the asymmetric stretch) and the superscript and subscript represent the vibrational quanta in the upper and lower states, respectively).[2] Higher excited states of $N_2O^{+\bullet}$, such as the B and C states, are predissociative and not observed in emission spectra.[3] Also, the state crossings between the potential surfaces of the predissociative states and that of the A $^2\Sigma^+$ state occurs near the bottom of the potential surface of the A state, restricting the number of vibrational levels in which the A state is formed.[4–6]

Emission cross sections and vibrational level ratios of $N_2O^{+\bullet}$ have been measured by a variety of techniques including photoionization, Penning ionization, electron impact, and charge exchange.[7–10] It is well-known that when an ion is formed by vertical excitation, the vibrational branching ratio is equal to the ratio of the corresponding Franck–Condon factors. Tokue et al.[11] determined the vibrational distributions of the 1^1 and 3^1 levels relative to the 1^0 level of the A state, using Penning ionization. The branching ratio for the 1^1 level strongly depended on the excitation energy, showing non-Franck–Condon behaviour, resulting from autoioni-

Received 12 March 2010. Accepted 9 July 2010. Published on the NRC Research Press Web site at canjchem.nrc.ca on 9 February 2011.

This article is part of a Special Issue dedicated to Professor J. C. Scaiano.

Y. Lin and P.M. Mayer.[1] Department of Chemistry, University of Ottawa, 10 Marie-Curie, Ottawa, ON K1N 6N5, Canada.

[1]Corresponding author (e-mail: pmmayer@uottawa.ca).

Can. J. Chem. Downloaded from www.nrcresearchpress.com by University of Electronic and Science Techonology of China on 09/18/12
For personal use only.

Can. J. Chem. Downloaded from www.nrcresearchpress.com by University of Electronic and Science Techonology of China on 09/18/12
For personal use only.

zation and shape resonant ionization, indicating that a vertical transition is not always available.

In this study, we have focused on keV (laboratory frame) ion–molecule collisional activation. In mass spectrometry, collisional activation is an essential method for fragmenting ions to gain further structure determination.[12–16] When a projectile ion with keV translational energy collides with a relatively stationary target gas moiety, a portion of the ion's translational energy is converted to internal energy, sufficient for the ion to undergo dissociation reactions. Of the potential mechanisms for this energy transfer, the most widely applicable one is the curve-crossing mechanism.[17–19] The qualitative and quantitative description of curve-crossing adiabatic energy transfer to produce electronic excitation has been described by Massey et al.[20] and Nikitin.[21] As shown in Fig. 1,[17] during the collision process, when the projectile ion approaches the target, the energy of the collision complex increases along the adiabatic curve of the ground state, until the ground-state potential surface crosses with that of an excited state through point C. The strength of the nonadiabatic coupling of the two curves can be represented as the Massey parameter, ξ, in the Massey equation $\xi = a\Delta E/h\upsilon$ (ΔE is the smallest energy gap between two adiabatic states, a is the width of the nonadiabatic interaction region, and υ is the classical nuclear velocity). The curve-crossing then brings about a radiationless transition between the ground and electronic excited states of the collision complex. During separation of the collision complex, the projectile ion may return to its original energy surface or remain in an excited electronic state. In the latter case, the electronic excitation can be removed by emission of a photon or converted to ro-vibrational excitation of the ground state by intramolecular vibrational relaxation (IVR). As the relative velocity of the interacting pair increases the time of interaction decreases, decreasing the Massey parameter, thereby increasing the probability that the system crosses into an excited state. Thus, this direct T→E (translational to electronic) energy transfer is operable at keV collision energies.

Recent work by our group showed that for keV $N_2^{+\bullet}$–He and $CO_2^{+\bullet}$–He collisions, the relative emission intensity between the fragments and the projectile ions are independent of ion translational energy in the 3–8 keV range, results consistent with the formation of a discrete distribution of excited states by the curve-crossing mechanism.[22–24] The purpose of this paper is to extend our collision-induced emission (CIE) study to the $N_2O^{+\bullet}$–He system, and by comparing our results with those obtained from other activation methods, to get a clearer picture of the mechanism of high-energy ion–molecule collisions.

Experimental procedures

All experiments were performed on a modified VG ZAB mass spectrometer[14] with an added third field-free region (3FFR) as previously described.[25,26]

$N_2O^{+\bullet}$ ions were generated from N_2O by 80–90 eV electron ionization in the ion source of the instrument. The ions were transmitted to the 3FFR where they collided with the target gas in the collision cell at a collision gas pressure that reduces the pre-cell ion flux by 10% (i.e., essentially single collision conditions).[14] With 80–90 eV electrons, ionization of $N_2O^{+\bullet}$ could result in $N_2O^{+\bullet}$ A $^2\Sigma^+$ being formed in the ion source.[27] However, the radiative lifetime of the A state is shorter than 400 ns.[28–30] When compared with the time required for the ions to reach the collision chamber, which ranges from 17 to 34 μs depending on the accelerating voltage, virtually all ions that are formed initially in the A $^2\Sigma^+$ would have returned to the ground state by the time they collide with the target gas.

Fig. 1. A simplified diagram illustrating curve-crossings during ion–target collisions. The behaviour of the excited states is drawn as a single entity.

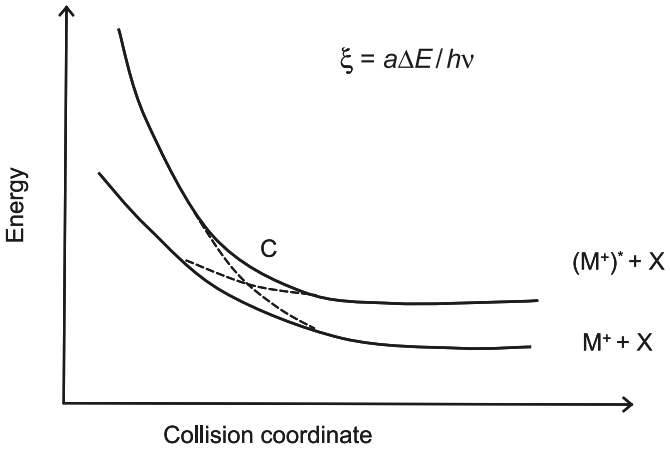

A spectrograph (Acton SpectraPro 275, 27.5 focal length, 1200 g mm^{-1} holographic grating) and a thermoelectrically cooled charge-coupled device (CCD) detector (Andor DV401-UV, front-illuminated with UV coating) were installed above the collision cell for the detection of photon emissions resulting from ion–target collisions.[22] Emissions from the excited-state species were directly observed with the CCD detector cooled to a temperature of –35 °C. The time window of observation ranges from 30 to 60 ns for 8 to 4 keV $N_2O^{+\bullet}$. The entrance slit of the spectrograph was set to 3.0 mm, providing a spectral resolution of 8.5 nm (measured at full width at half-height for atomic lines). Optical emissions were recorded from 190 to 1020 nm using the Andor MCD 2.63.1.8 program and were recorded in 14 separate segments, each being 50–70 nm wide. Two accumulations of 30 min were collected at 8 keV ion translational energy for each segment at full vertical binning reading mode. For other ion translational energies, the total acquisition time for each of the separate segments ranged from 1 to 4 h. Each segment was background-subtracted, and background spectra were collected prior to signal acquisition with exactly the same conditions except without an ion beam. Spectral spikes resulting from cosmic rays were removed digitally by the program. Horizontal binning was performed manually in the ASCII file by combining data of every 20 pixel columns, and the overlapping portion of the spectrum at the two ends of each window was averaged.

A higher resolution spectrum (330–400 nm) was obtained by reducing the entrance slit width to 1.0 mm, resulting in a spectral resolution of 3.0 nm, and the data acquisition time of each segment was increased to 4 h.

Can. J. Chem. Downloaded from www.nrcresearchpress.com by University of Electronic and Science Techonology of China on 09/18/12
For personal use only.

Fig. 2. Collision-induced emission spectra (190–1020 nm) of $N_2O^{+\bullet}$–He collisions at 8 keV. Collision gas pressure corresponded to 90% ion beam transmission. The arrows with different shapes represent photoemission from O^+, N^+, He, N, and O.

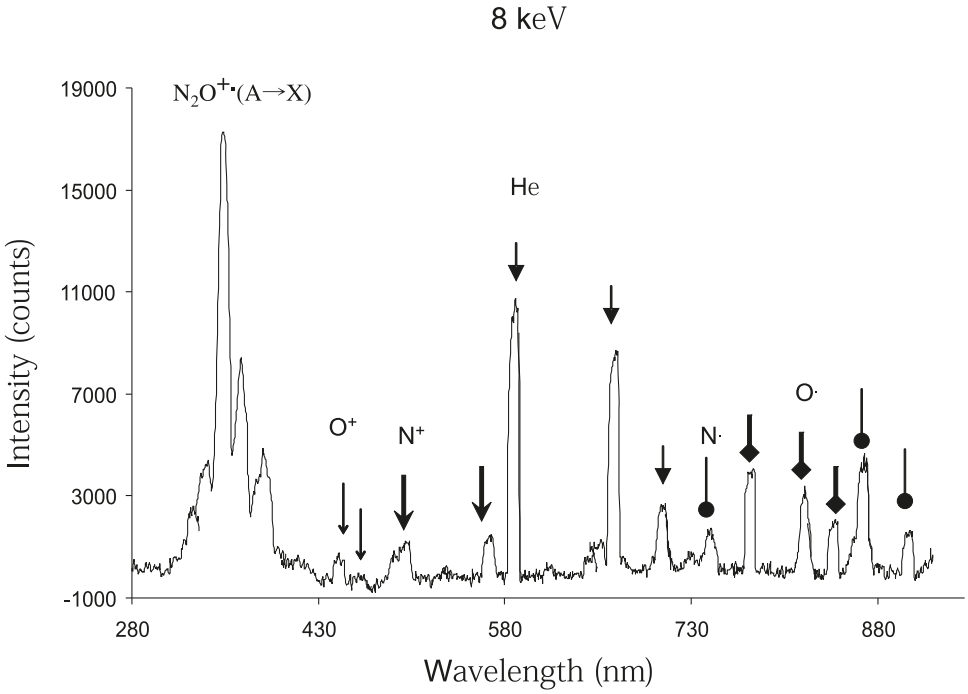

Results and discussion

Emission spectrum from $N_2O^{+\bullet}$–He collisions

The emission spectrum obtained from $N_2O^{+\bullet}$–He collisions at 8 keV ion translational energy is shown in Fig. 2 and is compared with those obtained at 6 and 4 keV in Fig. 3. A summary of the peak and transition assignments is presented in Table 1. Emission signals observed in the lower wavelength region (330–400 nm) correspond to the $N_2O^{+\bullet}$ ($A\ ^2\Sigma^+ \rightarrow X\ ^2\Pi^+$) system. Three dominant vibrational bands, 1^1, 3^1, and 1^0 were observed. Other peaks observed in the spectrum arise from the emissions of the target gas He and electronically excited fragments N^+, N, O^+, and O.

In our earlier study of the $CO_2^{+\bullet}$–He system,[24] two obvious band emissions resulting from electronic transitions of the $B\ ^2\Sigma_u^+$ and $A\ ^2\Pi_u$ states to the ground $X\ ^2\Pi_g$ state of $CO_2^{+\bullet}$ were observed. The vibrational progression in $CO_2^{+\bullet}$ $A\ ^2\Pi_u \rightarrow X\ ^2\Pi_g$ transition showed emission from high vibrational levels (7, 0, 0) in the $A\ ^2\Pi_u$ state. In the present $N_2O^{+\bullet}$He system, only the expected $A\ ^2\Sigma^+ \rightarrow X\ ^2\Pi^+$ transition was observed, and in addition, emissions arise only from low (indeed $v = 1$) vibrational levels of the A state. Also, the $CO_2^{+\bullet}$–He CIE spectra only showed two atomic emissions from the oxygen radicals O(^{5}P) and O(^{3}P), meanwhile in the $N_2O^{+\bullet}$–He CIE spectra, nine more atomic emissions from fragments N^+, N, O^+, and O were observed. The intensity ratio between the molecular emission and atomic emission from O(^{5}P) and O(^{3}P) were calculated: $I_{N_2O^+}/I_{O(^5P)}$ and $I_{CO_2^+}/I_{O(^5P)}$ are 19 and 31, respectively; $I_{N_2O^+}/I_{O(^3P)}$ and $I_{CO_2^+}/I_{O(^3P)}$ are 11 and 22, respectively, indicating the greater tendency to form excited fragments in the collisional activation of $N_2O^{+\bullet}$, in agreement with the dissociative nature of the $N_2O^{+\bullet}$ higher excited states.[3,33] According to ab initio calculations of the potential surfaces by Komiha,[33,34] shown in Fig. 4, two repulsive potential curves of $1^4\Pi$ and $1^4\Sigma^-$ state curve-cross with the A and X state surfaces, leading to different state-specified fragments. Also, there are avoided crossings between the $1^4\Sigma^-$ and $2^4\Sigma^-$ states. We have identified a number of higher energy fragments in our CIE spectra indicative of the dissociation of the higher electronic states of $N_2O^{+\bullet}$ (Table 1). This example shows that one benefit of the CIE experiment is that it not only offers rich information on the excited states of the projectile ion generated in a collision, but also on the excited states of CID products.

Relative intensities as a function of ion translational energy

The emission spectra over the wavelength range of 280–950 nm from 8 to 4 keV ion translational energy are presented in Fig. 3. The intensities of the emissions from the target gas cannot be directly compared with those from the projectile ions or the fragments, since the spatial distribution of collisions across the collision cell is unknown. The relative emission intensities of $N_2O^{+\bullet}$, N^+, O^+, and O at various collision energies are presented in Fig. 5. The intensities have been corrected for their differences in radiative lifetime, as only a portion of the emission from each excited-state species is detected. The correction was performed based on our previous conclusion that the majority of collision events take place under the window.[22] In Fig. 5, all the points falls on the $y = x$ line indicating that the relative emission intensities do not change with ion translational energy, supporting the curve-crossing mechanism for collisional excitation, which will produce the same distribution of excited states in the projectile ion, only the probability with which they are formed changes with translational energy according to the Massey equation.

Can. J. Chem. Downloaded from www.nrcresearchpress.com by University of Electronic and Science Techonology of China on 09/18/12
For personal use only.

Fig. 3. Collision-induced emission spectra (190–1020 nm) of $N_2O^{+\bullet}$–He collisions at 8, 6, and 4 keV. Collision gas pressure corresponded to 90% ion beam transmission.

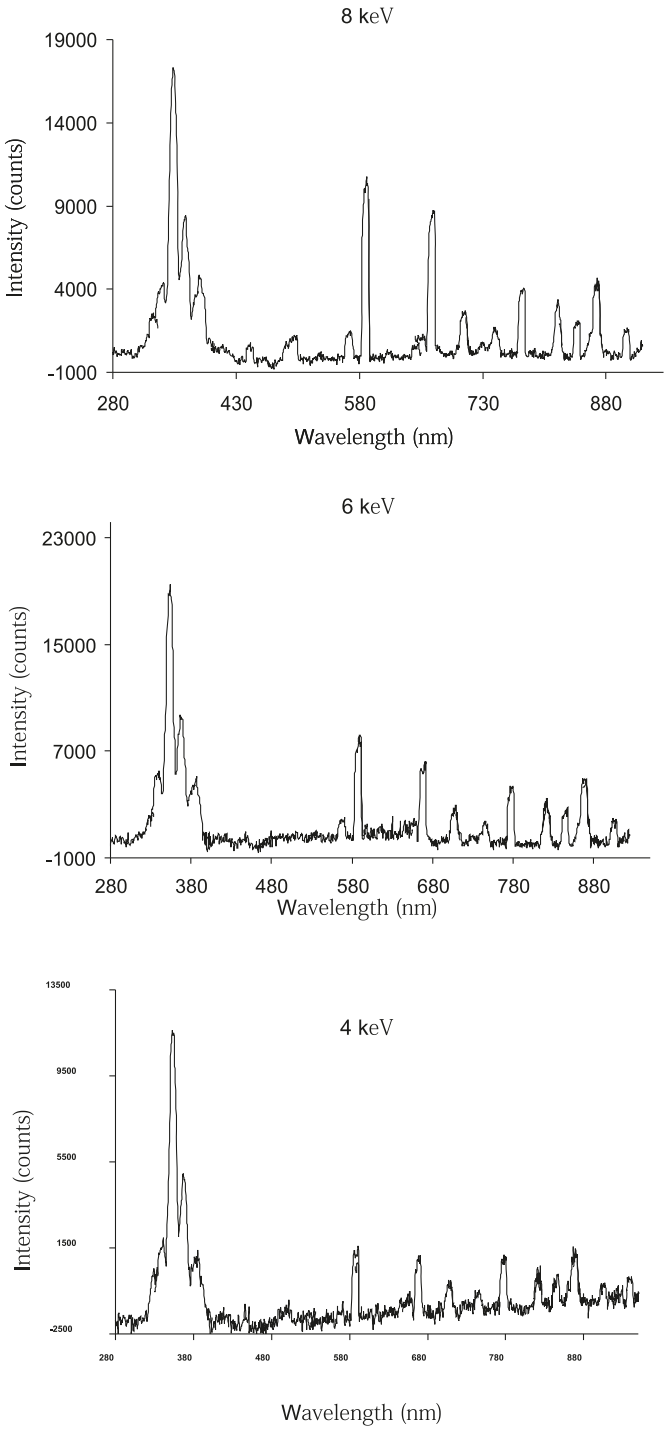

Table 1. Observed emissions in Fig. 2 and their corresponding radiative lifetimes.

Transition			τ (ns)	λ (nm)	Ref.
$N_2O^{+\bullet}$	A $^2\Sigma^+ \rightarrow$ X $^2\Pi^+$	1_0^1	180	338	29
		3_1^1	199	344	
		1_0^0	243	355	
		1_1^0	243	368	
		1_2^0	243	383	
		$1_1^0 3_1^1$	195		
360					
O^+	(3p) $^6P \rightarrow$ (3s) $^6S^0$		11	446	36, 37
	(3p) $^4D^0 \rightarrow$ (3s) 4P		39	468	
O	(3d) $^5P \rightarrow$ (3s) $^5S^0$		27	779	36, 37
	(3p) $^4P^0 \rightarrow$ (3s) ^4P		34	822	
	(3p) $^3P \rightarrow$ (3s) $^3S^0$		31	847	
N^+	(3d) $^3F^0 \rightarrow$ (3p) ^3D		8	503	36, 37
	(3p) $^3S \rightarrow$ (3s) $^3P^0$		13	503	
	(3p) $^3D \rightarrow$ (3s) $^3P^0$		18	570	
	(3p) $^3P \rightarrow$ (4l) $^3P^0$		33	659	
N	(3p) $^4S^0 \rightarrow$ (3s) ^4P		31	748	36, 37
	(3p) $^4D^0 \rightarrow$ (3s) ^4P		44	872	
	(3d) $^2P \rightarrow$ (3p) $^2S^0$		52	906	
	(3p) $^2F^0 \rightarrow$ (3s) ^2D		39	906	
He	(3p) $^3P^0 \rightarrow$ (2s) ^3S		18	389	36, 37
	(3d) $^3D \rightarrow$ (2p) $^3P^0$		14	590	
	(3d) $^1D \rightarrow$ (2p) $^1P^0$		16	671	

Relative band strength for in the A $^2\Sigma^+$ state $N_2O^{+\bullet}$

Figure 6 shows a higher resolution CIE spectrum of the $N_2O^{+\bullet}$ A $^2\Sigma^+ \rightarrow$ X $^2\Pi^+$ system in the 330–400 nm region produced by 8 keV collisions. The three bands 1_0^0, 1_0^1, and 3_1^1 are located at 354 338, and 347 nm, respectively, together with related transitions 1_1^0 and 1_2^0 and the combination band $1_1^0\ 3_1^1$. Each $N_2O^{+\bullet}$ A $^2\Sigma^+ \rightarrow$ X $^2\Pi^+$ vibrational band consists of a pair of sub-bands with nearly equal intensity owiwng to the spin-orbit splitting of the X $^2\Pi^+$ state. The band-emission intensities have been lifetime-corrected for later calculation of the relative intensities.[30]

The relative emission cross section is known to be related to the vibrational branching ratios and emission intensities as described in equations below

$$[2] \quad \frac{\sigma_{em}(\upsilon_i', \upsilon_k'')}{\sigma_{em}(\upsilon_j', \upsilon_l'')} \doteq \frac{I_{em}(\upsilon_i', \upsilon_k'')/\varepsilon(\upsilon_i', \upsilon_k'')}{I_{em}(\upsilon_j', \upsilon_l'')/\varepsilon(\upsilon_j', \upsilon_l'')}$$

$$[3] \quad \frac{\sigma_{em}(\upsilon_i', \upsilon_k'')}{\sigma_{em}(\upsilon_j', \upsilon_l'')} \doteq \frac{\nu(\upsilon_i', \upsilon_k'')^3 q(\upsilon_i', \upsilon_k'')\sigma(\upsilon_i')f(\upsilon_i')}{\nu(\upsilon_j', \upsilon_l'')^3 q(\upsilon_j', \upsilon_l'')\sigma(\upsilon_j')f(\upsilon_j')}$$

where $I_{em}(\upsilon', \upsilon'')$, $q(\upsilon', \upsilon'')$, $\varepsilon(\upsilon', \upsilon'')$, and $\sigma_{em}(\upsilon', \upsilon'')$ are the emission intensity, the Franck–Condon factor, the transition frequency, and the cross section, respectively, for the υ'–υ'' band. The $f(\upsilon')$ and $\sigma(\upsilon')$ represent the fluorescence vs the predissociation branching ratio and excitation cross sections, respectively, for the υ' level of the A state. By transforming the equations and obtaining the $f(\upsilon')$ and $q(\upsilon', \upsilon'')$ values based on the photoelectron–photoion coincidence measurement,[27] the branching ratios can be determined from the relative intensities of the vibrational bands.[11,13] The band strength of the 1_0^1 and 3_1^1 bands relative to that of the 1_0^0 band are listed in Table 2, along with values from photoionization and Penning ionization. In photoionization, $I(1_0^1)/I(1_0^0)$ and $I(3_1^1)/I(1_0^0)$ maintain constant values of 0.27 and 0.05, respectively, when the photon energy is >45 eV. Since the energy range above 45 eV is free of autoionization and shape resonance, these values are regarded as the branching factors in the Franck–Condon limit. Penning ioni-

Can. J. Chem. Downloaded from www.nrcresearchpress.com by University of Electronic and Science Techonology of China on 09/18/12
For personal use only.

Fig. 4. Ab initio potential curves for a collinear $N_2O^{+\bullet}$ geometry calculated by Komiha (ref. 34). From Richard-Viard et al. 1990, reproduced with permission of J. Chem. Phys., Vol. 93, p. 8881, © 1990 American Institute of Physics.

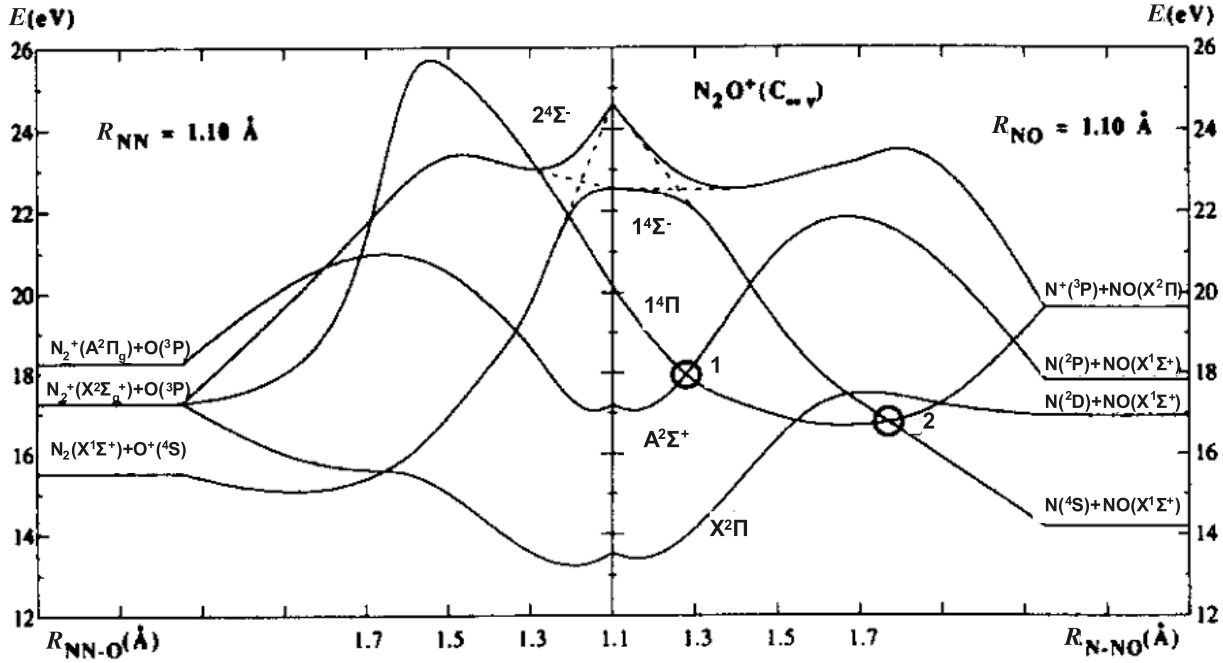

Fig. 5. The plot of the lifetime-corrected relative emission intensities of $N_2O^{+\bullet}$, N^+, N, and O at various ion translational energies vs those at 8 keV. All ion translational energies were obtained by varying the source accelerating voltages. Spectra are normalized to the ion flux at 8 keV. Collision gas pressure corresponded to 90% ion beam transmission.

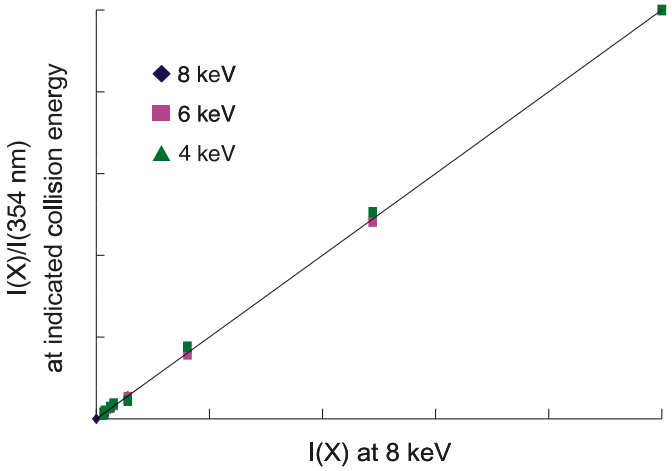

Fig. 6. Collision-induced emission spectrum (330–400 nm) of 8 keV $N_2O^{+\bullet}$–He collisions obtained with an entrance slit width of 1.0 mm (total data acquisition time per section was 8 h).

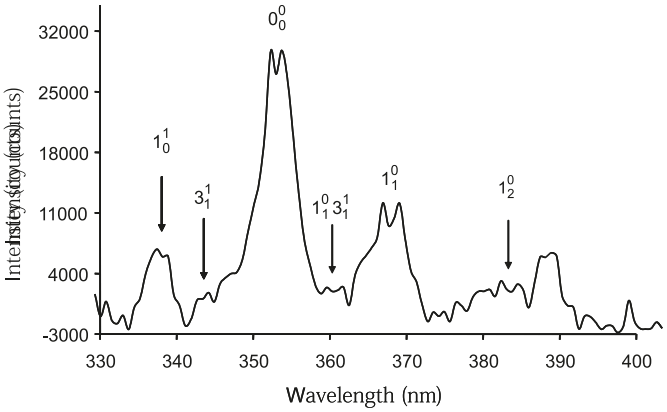

zation obtained by Ne(^{3}P: 16.6 eV) and He(2^3S: 19.9 eV) is similar to photoionization, showed non-Franck–Condon behaviour when the excitation energy was <45 eV. Since autoionization is from the Rydberg state of the neutral molecule and shape resonant ionization is due to the interaction of the photoelectron or metastable atom and the target neutral molecule,[35–31] neither of them have relevance to the $N_2O^{+\bullet}$–He system in this study. In the present CIE experiments, the$I(1_0^1)/I(1_0^0)$ and $I(3_1^1)/I(1_0^0)$ ratios in the $N_2O^{+\bullet}$ A state show obvious deviation from Franck–Condon behaviour, unlike our previous observations with $CO_2^{+\bullet}$–He.[23] This is a clear example of collisional excitation producing a decidedly non-Franck–Condon distribution of vibrational levels. This must be due to the fact that many predissociative states (such as the $1^4\Pi$ and $1^4\Sigma^-$ states, Fig. 4) cross with, and populate the vibrational levels of, the A state of $N_2O^{+\bullet}$.

Conclusion

Using a modified VG-ZAB mass spectrometer, the emission from electronic excited projectile $N_2O^{+\bullet}$ ions and their collision-induced dissociation products were observed, giving a relatively full picture of the activation process. Collision-induced emission spectroscopy produced from high keV $N_2O^{+\bullet}$–He collisions showed that the relative populations of electronically excited $N_2O^{+\bullet}$, N, O, O^+, and N^+ states remains constant as the collision energy is increased from 4 to 8 keV, a result consistent with the curve-crossing mechanism of collisional activation. The relative vibrational

Can. J. Chem. Downloaded from www.nrcresearchpress.com by University of Electronic and Science Techonology of China on 09/18/12
For personal use only.

Table 2. Band-emission intensities of 101 and 311 relative to the 100 band of $N_2O^{+\bullet}$ (A→X).

Method	Ionizing energy (eV)	$I(1^1_0)/I(1^0_0)^a$	$I(3^1_1)/I(1^0_0)^a$	Ref.
CIE		0.227 (2)	0.124 (3)	This work
PI	17.1–26.8	0.162(17)	0.057(6)	38
	17	0.237(6)	0.047(2)	32
	20	0.113(4)	0.038(3)	
	45–53	0.272(6)	0.049(3)	
He(2^3S)-FA	Thermal	0.137(12)	0.062(3)	9
Ne(^{3}P)-FA	Thermal	0.208(43)	0.019–0.061(9)	10
He(2^3S)-FA	0.15	0.105(7)	0.045(3)	11

Note: PI, photoionization; FA, Penning ionization; and CIE, collision-induced emission.

[a]Numbers in parentheses represent uncertainties attached to the last digit.

branching ratios of $N_2O^{+\bullet}$ after collisional activation were compared with those obtained by different activation processes. Results indicate that owing to the complex curve-crossing between predissociation states and the A and X states of $N_2O^{+\bullet}$, the vibrational population in the A state appears more evenly distributed than that resulting from Franck–Condon photoexcitation. This was also different than that seen in the case of $CO_2^{+\bullet}$–He collisions and is the result of the many predissociative higher energy states populating the vibrational levels of $N_2O^{+\bullet}$ A $^2\Sigma^+$.

Acknowledgments

P.M.M. thanks the Natural Sciences and Engineering Research Council of Canada (NSERC) for continuing financial support.

References

(1) Danilov, A. D. *Chemistry of the Iionosphere;* Plenum: New York, 1970.
(2) Callomon, J. H.; Creutzberg, F. *Philos. Trans. R. Soc. Lond.* **1974**, *277* (1266), 157. doi:10.1098/rsta.1974.0048.
(3) Brehm, B.; Frey, R.; Küstler, A.; Eland, J. H. D. *Int. J. Mass Spectrom. Ion Phys.* **1974**, *13* (3), 251. doi:10.1016/0020-7381(74)80029-X.
(4) Fellows, C. E.; Vervloet, M. *Chem. Phys.* **2001**, *264* (2), 203. doi:10.1016/S0301-0104(00)00401-8.
(5) Hopper, D. G. *J. Am. Chem. Soc.* **1978**, *100* (4), 1019. doi:10.1021/ja00472a001.
(6) Richard-Viard, M.; Delboulbé, A.; Vervloet, M. *Chem. Phys.* **1996**, *209* (2-3), 159. doi:10.1016/0301-0104(96)00164-4.
(7) Berkowitz, J.; Eland, J. H. D. *J. Chem. Phys.* **1977**, *67* (6), 2740. doi:10.1063/1.435188.
(8) Ferrett, T. A.; Parr, A. C.; Southworth, S. H.; Hardis, J. E.; Dehmer, J. L. *J. Chem. Phys.* **1989**, *90* (3), 1551. doi:10.1063/1.456098.
(9) Tsuji, M.; Tsuji, K.; Nishimura, Y. *Int. J. Mass Spectrom. Ion Phys.* **1979**, *30* (2), 175. doi:10.1016/0020-7381(79)80094-7.
(10) Tsuji, M.; Maier, J. P. *Chem. Phys.* **1988**, *126* (2–3), 435. doi:10.1016/0301-0104(88)85051-1.
(11) Tokue, I.; Kudo, T.; Ito, Y. *Chem. Phys. Lett.* **1992**, *199* (5), 435. doi:10.1016/0009-2614(92)87023-I.
(12) Holmes, J. L.; Mayer, P. M.; Aubry, C. *Assigning Structures to Ions in the Mass Spectrometry;* CRC: New York, 2007.
(13) Cooks, R. G. *Collision Spectroscopy*; Plenum: New York, 1978.
(14) Holmes, J. L. *Org. Mass Spectrom.* **1985**, *20* (3), 169. doi:10.1002/oms.1210200302.
(15) Levsen, K.; Schwarz, H. *Mass Spectrom. Rev.* **1983**, *2* (1), 77. doi:10.1002/mas.1280020104.
(16) Todd, P. J.; Mclafferty, F. W. *Tandem Mass Spectrometry;* Wiley: New York, 1983.
(17) Mayer, P. M.; Poon, C. *Mass Spectrom. Rev.* **2009**, *28* (4), 608. doi:10.1002/mas.20225.
(18) Durup, J. *Recent Developments in Mass Spectrometry;* University Park: Baltimore, 1970.
(19) McLuckey, S. A. *J. Am. Soc. Mass Spectrom.* **1992**, *3* (6), 599. doi:10.1016/1044-0305(92)85001-Z.
(20) Massey, H. S. W.; Burhop, E. H. S.; Gilbody, H. B. *Electronic and Ionic Impact Phenomena;* Clarendon: Oxford, 1974.
(21) Nikitin, E. E. *Theory of Elementary Atomic and Molecular Processes in Gases;* Clarendon: Oxford, 1974.
(22) Poon, C.; Mayer, P. M. *J. Phys. Chem. A* **2007**, *111* (5), 777. doi:10.1021/jp066755v.
(23) Poon, C.; Mayer, P. M. *J. Am. Soc. Mass Spectrom.* **2008**, *19* (10), 1551. doi:10.1016/j.jasms.2008.06.004.
(24) Poon, C.; Lin, Y.; Mayer, P. M. *J. Phys. Chem. A* **2008**, *112* (34), 7761. doi:10.1021/jp8017524.
(25) Burgers, P. C.; Holmes, J. L.; Szulejko, J. E.; Mommers, A. A.; Terlouw, J. K. *Org. Mass Spectrom.* **1983**, *18* (6), 254. doi:10.1002/oms.1210180607.
(26) Holmes, J. L.; Mayer, P. M.; Mommers, A. A. *Int. J. Mass Spectrom. Ion Process.* **1994**, *135* (2-3), 213. doi:10.1016/0168-1176(94)04000-1.
(27) Hiroshi, K.; Shimada, H.; Kobayashi, M.; Tokue, I.; Ito, Y. *Chem. Phys. Lett.* **1991**, *109*, 179.
(28) van Sprang, H. A.; Möhlmann, G. R.; De Heer, F. J. *Chem. Phys.* **1978**, *33* (1), 65. doi:10.1016/0301-0104(78)87071-2.
(29) Ibuki, T.; Sugita, N. *J. Chem. Phys.* **1984**, *80* (10), 4625. doi:10.1063/1.446547.
(30) Maier, J. P.; Thommen, F. *Chem. Phys.* **1980**, *51* (3), 319. doi:10.1016/0301-0104(80)80106-6.
(31) Tsuji, M.; Obase, H.; Endoh, M.; Yamaguchi, S.; Yamaguchi, K.; Kobarai, K.; Nishimura, Y. *J. Chem. Phys.* **1988**, *89* (11), 6753. doi:10.1063/1.455349.
(32) Bashkin, S.; Stoner, J. O. *Atomic Energy Levels & Grotrian Diagrams 1;* North-Holland: New York, 1975.
(33) Richard-Viard, M.; Atabek, O.; Dutuit, O.; Guyon, P. M. *J. Chem. Phys.* **1990**, *93* (12), 8881. doi:10.1063/1.459227.
(34) Komiha, N. *Thèsè de Troisième cycle;* Paris: Université Pierre et Marie Curie, 1981.
(35) Braunstein, M.; Mckoy, V. *J. Chem. Phys.* **1989**, *90* (3), 1535. doi:10.1063/1.456096.

(36) Niehaus, A. *Adv. Chem. Phys.* **1981**, *45*, 399. doi:10.1002/9780470142646.ch5.
(37) Wiese, W. L.; Smith, M. W.; Glenno, B. M. *Atomic Transition Probabilities;* National Bureau of Standards: Washington, DC, 1966.

Can. J. Chem. Downloaded from www.nrcresearchpress.com by University of Electronic and Science Techonology of China on 09/18/12
For personal use only.

Photophysical aspects of 6-methylcoumarin–cucurbit[8]uril host–guest complexes

Barry C. Pemberton, Elango Kumarasamy, Steffen Jockusch, D.K. Srivastava, and J. Sivaguru

Can. J. Chem. Downloaded from www.nrcresearchpress.com by Xi'an Jiaotong University on 09/19/12
For personal use only.

Abstract: Photophysical measurements of 6-methylcoumarin (**1**) encapsulated within cucurbit[8]uril (CB[8]) indicate a pronounced red shift in the fluorescence maximum with an increase in the emission quantum yield and fluorescence lifetime. In addition, at 77 K, there is observable phosphorescence upon encapsulation within CB[8]. The photophysical measurements add credibility to our previously proposed dynamic nature of the CB–coumarin complex in solution. The dynamic nature of the CB[8]–coumarin host–guest complex in water is critical to a CB acting as a supramolecular catalytic nanoreaction vessel to facilitate the photodimerization of coumarins leading to syn dimers.

Key words: cucurbiturils, supramolecular catalysis, host–guest photochemistry, coumarin photophysics, coumarin–CB[8] host–guest complex, lifetime of coumarin–CB[8].

Résumé : Des mesures photophysiques sur la 6-méthylcoumarine (**1**) encapsulée dans du cucurbit[8]urile (CB[8]) mettent en évidence un déplacement prononcé vers le rouge dans le maximum de fluorescence avec une augmentation dans le rendement quantique d'émission et le temps de vie de fluorescence. De plus, à 77 K, l'encapsulation dans du CB[8] provoque une phosphorescence qui peut être détectée. Les mesures photophysiques ajoutent de la crédibilité à la proposition que nous avons faite antérieurement relative à la nature dynamique du complexe CB–coumarine en solution. La nature dynamique du complexe hôte–invité CB[8]–coumarine dans l'eau est critique pour le CB qui agit comme récipient pour la nanoréacton catalytique supramoléculaire afin de faciliter la photodimérisation des coumarines conduisant aux dimères syn.

Mots-clés : cucurbituriles, catalyseur sapramoléculaire, photochimie hôte–invité, coumarine, photophysique, complexe hôte–invité coumarine–CB[8], temps de vie du complexe coumarine–CB[8].

[Traduit par la Rédaction]

Introduction

Coumarin has historically been the subject of intense photochemical and spectroscopic interest mainly as a consequence of its importance in biological systems and its use in various materials of commercial interest.[1–7] Based on this precedence, we chose to investigate the photophysics of coumarin upon complexation within cucurbit[8]uril (CB[8])[8–16] in aqueous solution to understand the environmental perturbations on the excited state of coumarins.[6,7]

In the last few years, we have been exploring the role of CB[8] in altering the photoreactivity of coumarin derivatives.[17–20] We chose 6-methylcoumarin (**1**) to understand the role of CBs in the alteration of the photochemistry of encapsulated coumarin guests. Photodimerization of **1** in water and in other isotropic media was postulated to occur from the triplet state.[21,22] Our investigations[17–19] revealed that CB[8] and **1** form a dynamic complex in water with a host–guest ratio of 1:1.6 and with a binding constant of 1.33×10^4 $(mol/L)^{-1}$ (K_1) and 2.00×10^6 $(mol/L)^{-1}$ (K_2).[23,24] Photodimerization proceeded very efficiently in the presence of CB[8]. There was no noticeable difference in the reaction efficiency under N_2-, air-, and O_2-saturated conditions. Additionally, we successfully employed a catalytic amount (10 mol%) of CB[8] leading to selective formation of syn dimers during photodimerization (Scheme 1). We proposed a catalytic cycle involving CB[8] where the high photodimerization rate within the cavity compared with the photodimerization in water outside the CB[8] cavity (background reaction) determines the efficiency of the catalytic cycle and the selectivity in the photodimerization process (syn–anti ratio). The extent of the background reaction compared with the reaction within the cavity was understood based on the photoproduct distribution. In the present case involving **1**, the anti dimer is formed only outside the cavity, whereas the syn isomers are formed within the cavity. Thus, the ratio of the syn–anti isomer not only reflects the selectivity within the confined environment of CB[8] but also the efficiency of the catalytic cycle. By employing CBs in catalytic amounts, we were able to overcome one of the limitations of employing CB[8] as a nanoreaction vessel for chemical transformations,

Received 2 May 2010. Accepted 9 July 2010. Published on the NRC Research Press Web site at canjchem.nrc.ca on 15 February 2011.

This article is part of a Special Issue dedicated to Professor J. C. Scaiano.

B.C. Pemberton, E. Kumarasamy, D.K. Srivastava, and J. Sivaguru.[1] Department of Chemistry and Biochemistry, North Dakota State University, Fargo, ND 58103, USA.
S. Jockusch. Department of Chemistry, Columbia University, New York, NY 10027, USA.

[1]Corresponding author (e-mail: sivaguru.jayaraman@ndsu.edu).

Scheme 1. Photodimerization of 6-methylcoumarin (**1**).

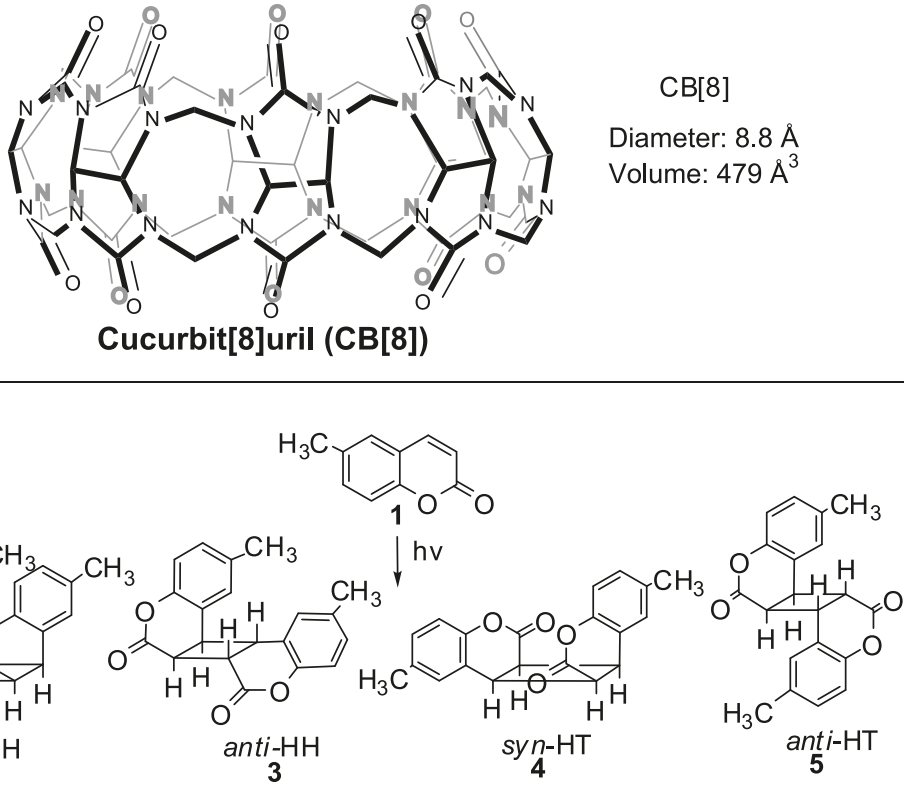

Can. J. Chem. Downloaded from www.nrcresearchpress.com by Xi'an Jiaotong University on 09/19/12
For personal use only.

namely, limited solubility of CB[8] at higher concentrations in water (maximum solubility is ~0.2 mmol/L).[8–16] To rationalize the photochemical transformation under catalytic conditions, it is important to identify the reactive spin state in the catalytic cycle. Considering that the photodimerization of **1** in alcohol leads to the anti head-to-head (*anti*-HH; **3**) exclusively,[21] the photoproduct selectivity upon inclusion of **1** within CBs cannot be attributed to a change in polarity alone (as the polarity of the cucurbituril cavity was previously reported to be similar to that of *n*-octanol[25]). As all four dimers (**2**–**5**) could fit within CB[8],[18,19] characterizing the nature of the excited state (singlet and (or) triplet excited state, excited species lifetime inside the cavity) is critical to understanding the supramolecular aspects leading to catalysis.[17] In this report, we present the photophysical investigations for the comprehension of the role of CB[8] in altering the photochemistry of encapsulated **1**.

Results and discussion

To understand the photophysical aspects of **1** within CB[8], steady-state luminescence spectroscopy and fluorescence lifetime measurements at room temperature were performed in water in the presence and in the absence of CB[8]. In the absence of CB[8], a structureless emission centered around 411 nm with a lifetime shorter than 0.1 ns (Fig. 1) was observed (Table 1). The emission intensity increased upon increasing the mole equivalents of CB[8] from 5 to 190 mol% of CB[8]. The emission intensity remained constant when the mole equivalents of CB[8] were increased beyond 100 mol% to 190 mol%. In addition, there was a noticeable red shift in the emission maximum (Fig. 1). For example, the emission maxima shifted from 430 nm for 5 mol% to 443 nm for 100 mol%. Fluorescence lifetime measurements in the presence of CB[8] showed a bi- or triexponential decay with distinct lifetime components. The uncomplexed **1** in water decays in <0.1 ns and CB[8]–**1** host–guest (H–G) complexes decay at ~3.7 and ~0.7 ns. We tentatively assign the long-lived component (~3.7 ns) as the decay from a 1:1 H–G complex and the short-lived component (~0.7 ns) as the 1:2 H–G complex. As the fluorescence of the 1:2 H–G complex competes with photodimerization and nonradiative decay, a shorter lifetime when compared with a 1:1 H–G complex is expected for the 1:2 H–G complex. Because of instrumental limitations owing to the relatively long instrument response function compared with the fast decaying lifetime components, we fitted the fluorescence decays in the presence of CB[8] to only two components, which are listed in Table 1. In the biexponential fit, the long-lived component corresponds to a 1:1 H–G complex, whereas the short-lived component corresponds to both the free **1** and the 1:2 H–G complex. As we have a dynamic H–G complex, the relative contribution of the decay components depend on the mol% of CB[8]. Based on the biexponential fit (Table 1), we believe that the decay components of all three species, namely, uncomplexed **1**, the 1:1 H–G complex, and the 1:2 H–G complex, are present at a lower mol% of CB[8] (i.e., from 5 to 40 mol%). At a higher mol% of CB[8] (i.e., ≥100 mol%), the decay components from 1:1 H–G complex predominate with minor contributions from 1:2 H–G complex. Fluorescence quantum yield measurements (quinine sulfate in 0.5 mol/L H_2SO_4 as the standard) showed an increase in the quantum yield (Φ_{em}) from 0.008 in the absence of CB[8] to 0.04 in the presence

Fig. 1. (A) Steady-state emission of 6-methylcoumarin (**1**; 1×10^{-5} mol/L) at 298 K (λ_{ex} = 320 nm). (B) Fluorescence decay of **1** at 298 K (λ_{ex} = 340 nm; λ_{em} = 411 nm for decay in water and λ_{em} = 443 nm for 100 mol% of cucurbit[8]uril (CB[8])); IRF = instrument response function. (C) Phosphorescence of **1** at 77 K in water recorded from a 30 to 60 ms time window with various mol% of CB[8] (relative to the concentration of **1**); λ_{ex} = 345 nm.

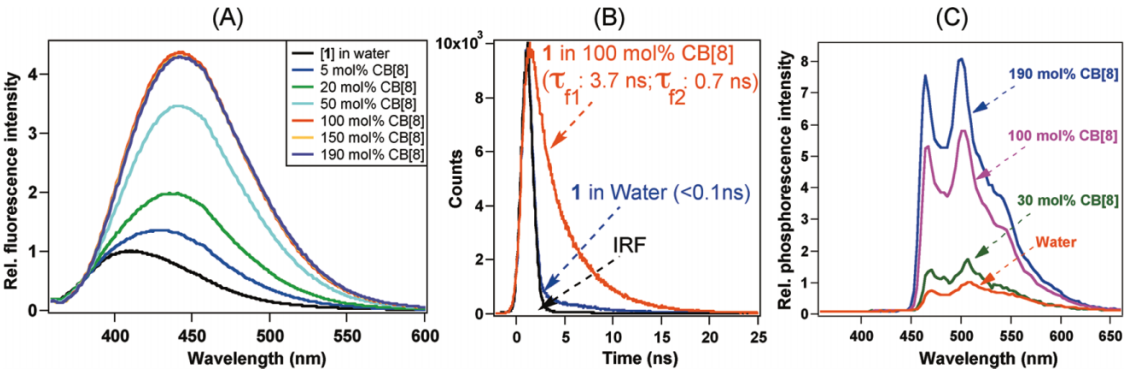

Table 1. Photophysical and photochemical properties of the photodimerization of the 6-methylcoumarin–cucurbit[8]uril host–guest complex in water at room temperature.

Entry	CB[8] (mol%)	Emission parameters			Photodimerization (syn dimers)	
		λ_{max}[a]	Φ_{em}[b]	τ (ns)[c]	Φ_{dim}[d]	r_{dim} ((mol/L) min^{-1})[e]
1	0	411	0.008	<0.1	0.006	4.28×10^{-7}
2	5	430	0.010	0.1 (41%); 3.7 (59%)	—	5.13×10^{-7}
3	10	432	0.013	0.2 (35%); 3.8 (65%)	0.007	5.20×10^{-7}
4	20	436	0.018	0.2 (24%); 3.7 (75%)	—	6.95×10^{-7}
5	30	441	0.020	1.1 (33%); 3.7 (67%)	0.008	1.06×10^{-6}
6	40	442	0.027	0.5 (15%); 3.7 (84%)	—	1.24×10^{-6}
7	50	443	0.030	0.7 (15%); 3.7 (85%)	0. 016	1.61×10^{-6}
8	70	443	0.037	0.8 (14%); 3.7 (86%)	—	2.22×10^{-6}
9	100	443	0.038	0.7 (14%); 3.7 (86%)	0. 021	3.03×10^{-6}
10	130	443	0.040	0.7 (14%); 4.0 (86%)	0. 020	—
11	150	443	0.040	0.8 (15%); 3.7 (85%)	—	3.62×10^{-6}
12	160	443	0.041	—	0. 021	3.85×10^{-6}
13	170	443	0.039	0.7 (15%); 3.7 (85%)	—	3.64×10^{-6}
14	190	443	0.039	0.8 (15%); 3.7 (85%)	0. 020	3.18×10^{-6}

Note: CB[8], cucurbit[8]uril.

[a]Steady-state emission of **1** was recorded with λ_{ex} = 320 or 340 nm.

[b]Optical density (absorbance) of **1** is ~0.11 at λ_{ex} = 345 nm for determining the quantum yield. Quinine sulfate in 0.5 mol/L H_2SO_4 (Φ_{fl} = 0.55) was used as the standard. Reported Φ_{em} are an average of a minimum of three runs with an error <5%.

[c]λ_{ex} = 340 nm. Fluorescence decay was monitored at 411 nm (entry 1) and at 443 nm (entries 2–14). The percent intensity contributions are in brackets.

[d]Photodimerization quantum yields were measured using ferrioxalate actinometry. Irradiations were performed with a 450 W medium pressure Hg lamp using a 313 nm band pass filter. Reported values are an average of a minimum of 10 runs with an error <10%. The number of moles of the photodimer **2** formed was computed from the decrease in the absorbance of **1**, as there was a clear isosbestic point indicating a one-to-one conversion from **1** to **2**.

[e]Photodimerization rate (r_{dim}) was monitored by UV–vis spectroscopy. Reported r_{dim} are an average of a minimum of three runs with an error <10%. [**1**] = 0.05 mmol/L was irradiated with a 450 W medium pressure Hg lamp under an aerated condition.

of CB[8] in water (Table 1). The maximum Φ_{em} was observed for 100 mol% CB[8] (Fig. 1) with a Φ_{em} value of 0.04 and stayed constant upon increasing the CB[8] concentration beyond 100 mol%. (Note: Φ_{em} levels off beyond 100 mol% of CB[8] as shown in in Fig. 2A.) Additionally, in spite of forming a poor glass at 77 K, we were able to observe phosphorescence (Fig. 1C) in water with various mol% of CB[8], showing the formation of 6-methylcoumarin excited triplet (^{3}**1***).

The photodimerization of coumarins was originally postulated to depend on the multiplicity of the excited state, with the singlet excited state favoring the syn dimers and the triplet excited state favoring the anti dimer.[1–5] Recently,[21,22] the multiplicity dependent pathway was questioned for the photodimerization of **1** and a reactive triplet excited state (^{3}**1***) was postulated in isotropic media irrespective of the type of solvent. It was reasoned that the high intersystem crossing rate (isc), especially in polar solvents (water, trifluoroethanol, etc.), probably caused by appropriate shifting of spectroscopically not accessible energy levels led to the reactivity from the triplet excited state (^{3}**1***).[21,22] The excited triplet chromophore reacts with a ground state monomer to

Can. J. Chem. Downloaded from www.nrcresearchpress.com by Xi'an Jiaotong University on 09/19/12
For personal use only.

Can. J. Chem. Downloaded from www.nrcresearchpress.com by Xi'an Jiaotong University on 09/19/12
For personal use only.

Fig. 2. (A) Change in fluorescence quantum yield, (B) photodimerization rate increase, and (C) photodimerization quantum yield (r_{uncat} = r_{dim} at 0 mol% of cucurbit[8]uril (CB[8])) upon varying the mol% of CB[8].

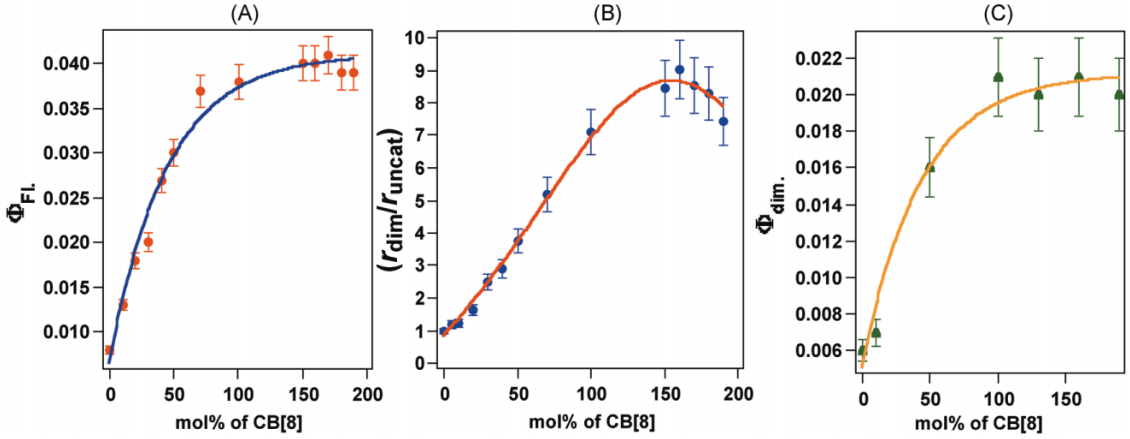

Scheme 2. Photodimerization of 6-methylcoumarin (**1**) within cucurbit[8]uril (CB[8]) in water.

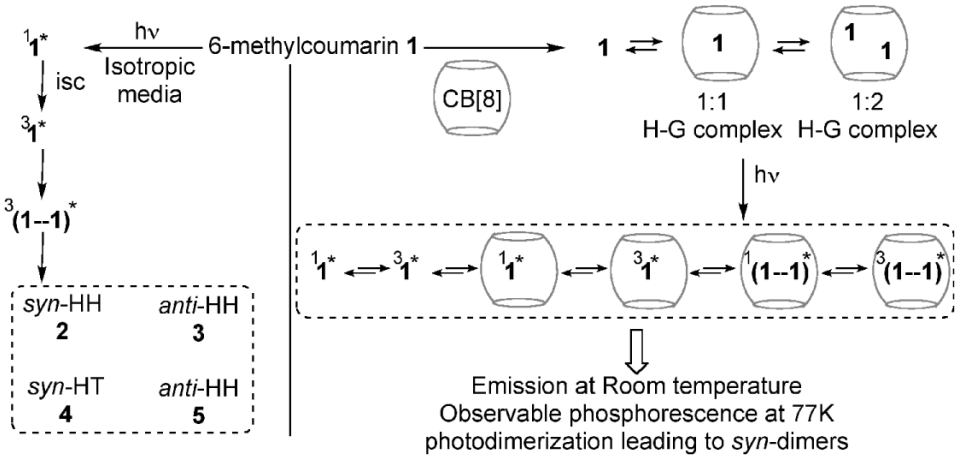

form an excited complex, ^{3}(**1**–**1**)*. The stability of the complexes, namely, $^3(\mathbf{1}\text{–}\mathbf{1})_{\text{anti-HH}}$*, $^3(\mathbf{1}\text{–}\mathbf{1})_{\text{anti-HT}}$*, $^3(\mathbf{1}\text{–}\mathbf{1})_{\text{syn-HH}}$*, and $^3(\mathbf{1}\text{–}\mathbf{1})_{\text{syn-HT}}$*, and their corresponding reactive rates were theorized to determine the product distribution (Scheme 2).[21,22] Based on absorbance and emission measurements, the excited singlet and triplet states of **1** were assigned a ππ* configuration, with the singlet excited state at ~78 kcal/mol and the triplet excited state at ~61 kcal/mol.[21,22,26–30] The photophysics for **1** has been reported for various solvents. Low-temperature photophysical measurements (at 77 K) showed fluorescence emission maxima centered around 406 nm with a quantum yield (Φ_f) of 0.015 in ethanol.[26] The fluorescence lifetime of the emission centered around 405 nm was found to be ≤0.3 ns at 295 K in 1,4-dioxane.[27] Additionally, the phosphorescence spectra at 77 K[30] showed a (0,0) transition at 465 nm with a quantum yield (Φ_p) of 0.066 in ethanol[26] and a triplet quantum yield of 0.04 in benzene at 298 K.[27] Further, extensive photophysical investigations revealed that the greatest majority of the quanta are lost within the singlet manifold for **1**.[21,22,28] The very weak fluorescence from **1** at low concentrations in solvents of low and medium polarity and the low Φ_f in highly polar solvents were cited as the reasons for the exclusion of any significant contribution of a singlet state (or singlet state excited complex) during the photodimerization.

Upon complexation of **1** with CB[8], the room-temperature fluorescence intensity increases with a noticeable red shift. This cannot be attributed to polarity alone, as **1** is weakly fluorescent in a nonpolar solvent (the solvent polarity is less than that for methanol). We believe that the confinement of **1** within the hydrophobic CB[8] cavity is crucial and is likely responsible for the enhanced emission and longer lifetime. Similarly, the confinement of **1** within CB[8] is likely responsible for the observed phosphorescence at 77 K. The phosphorescence intensity cannot be quantified to a mol% of CB[8] under our experimental conditions, as water does not form a transparent glass at 77 K. Nevertheless, a clear increase in the phosphorescence intensity (Fig. 1C) was observed upon complexation with CB[8].

The quantum yield of photodimerization (Φ_{dim}) was calculated by ferrioxalate actinometry (Fig. 2C and Table 1). The Φ_{dim} was found to increase with an increase in the mole equivalents (mol%) of CB[8]. Upon increasing the mole equivalents of CB[8] beyond 100 mol%, there was no noticeable change in Φ_{dim}, indicating that the amount of photodimer formed per unit of time to the number of photons absorbed after 100 mol% of CB[8] occurs at the same

Can. J. Chem. Downloaded from www.nrcresearchpress.com by Xi'an Jiaotong University on 09/19/12
For personal use only.

efficiency. (Note: Φ_{dim} levels off beyond 100 mol% of CB[8] as shown in Fig. 2C.) On the other hand, the rate of photodimerzation (r_{dim}) depends on the relative population of 1:2 H–G complex, 1:1 H–G complex, and uncomplexed **1**, which in turn are dependent on the amount of CB[8] present. We previously postulated a dynamic H–G complex of **1** with CB[8] (a mixture of 1:1 H–G complex, 1:2 H–G complex, and uncomplexed **1**) in solution to rationalize the catalytic nature of photodimerization. (Note: r_{dim} increases until 160 mol% of CB[8] and then decreases as displayed in Fig. 2B.) As the maximum r_{dim} was observed at 160 mol% of CB[8], this corresponds to a concentration at which the dynamic equilibrium favors the highest concentration of the 1:2 H–G complex, resulting in increased reaction efficiency. Increasing the mol% of CB[8] beyond this optimum concentration decreases the rate, as the dynamic equilibrium possibly shifts away from the 1:2 H–G complex, thereby lowering the reaction efficiency (Fig. 2B). Qualitatively, this aspect can be understood based on thermodynamic features leading to complexation. In the case of a 1:2 H–G complex, both host–guest interaction (H–G) and guest–guest (G–G) interaction play a dominant role. In the case of a 1:1 complex, the major interaction is the interaction between the host and the guest (H–G). So, to shift the equilibrium away from a 1:2 complex, the H–G interaction would have to override both the [(H–G) + (G–G)] interactions. Based on our data, it is clear that this happens at a CB[8] concentration >160 mol%. If the above aspect holds true, changing the coumarin concentration must shift the concentration of CB[8] that corresponds to the maximum photodimerization rate. We observed that the concentration of CB[8] corresponding to the maximum reaction rate changes with a change in the coumarin concentration (~160 and ~170 mol% of CB[8] for 0.05 and 0.04 mmol/L of **1**, respectively).[17,20]

The photophysical aspects can also be understood based on this dynamic behavior of the CB[8]–**1** H–G complex. Photoexcitation of the dynamic H–G complex and uncomplexed coumarin leads to their corresponding excited states (singlet and triplet excited states) in solution. The reactivity of the dynamic H–G complex depends on the lifetime of the excited species in solution. Thus, the cavity not only templates the coumarin leading to selective formation of syn photodimers but enhances the reactivity by altering the photophysics of the excited coumarin, which is reflected in the enhanced photodimerization rate.

One aspect that is yet to be ascertained is the nature of the reactive species involved in the photodimerization process. As the photodimerization of **1** in water and in other isotropic media was postulated to occur from the triplet state,[21,22] we carried out the reaction under N_2-, air-, or O_2-saturated conditions in the presence of CB[8].[20] There was no noticeable difference in the reaction efficiency in N_2-, air-, or O_2-saturated conditions. Recently,[31] triplet-energy transfer from CB-encapsulated methylene blue to molecular oxygen to yield singlet oxygen was observed to occur at a lower rate, when compared with the rate of singlet oxygen generation in the absence of CBs. This suggests that excited state quenching of CB-encapsulated guests is indeed feasible but at a lower rate. Thus, two distinct possibilities arise in our case for CB[8]–**1** H–G complex, namely, (*i*) the triplet state of encapsulated coumarins within CBs is shielded from external quencher(s),[25,32,33] namely, oxygen for a longer time compared with free coumarin **1** outside the cavity leading to photoreactivity from the triplet state; and (*ii*) the singlet spin state is involved in the photodimerization pathway within the CB[8]. As we have observed both fluorescence and phosphorescence, we cannot ascertain if the photodimerization occurs from the singlet or the triplet manifold and if the photodimerization likely involves a singlet ^{1}(**1**–**1**)* excited complex or a triplet ^{3}(**1**–**1**)* excited complex within CB[8]. Further studies are needed to understand this aspect.

Conclusion

Photophysical investigation of **1** within CB[8] adds credibility to our proposed dynamic behavior of the CB[8]–**1** H–G complex in water. We observe an increase in the emission quantum yield and an increase in fluorescence lifetime upon encapsulation within CB[8]. The maximum emission intensity is observed for the 1:1 complex, and the emission intensity decreases for the 1:2 complex. There is also observable phosphorescence at 77 K in the presence of CB[8].

Experimental

General methods

1 was purchased from Alfa Aesar and was used as received without further purification. CB[8] was synthesized using previously reported procedures.[34–38] Diethyl ether was used for the extraction process as received without further purification. Nanopure water (≥17.8 MΩ/cm, Barnstead Ultrapure) was used as the solvent for carrying out photoreactions and photophysical measurements. Stock solutions of CB[8] (0.1 mmol/L) and **1** (1 mmol/L) were prepared and diluted appropriately for the different experiments.

Photophysical methods[25,31–33]

Spectrophotometric solvents were used wherever necessary unless or otherwise mentioned. UV quality fluorimeter cells (with a range up to 190 nm) were purchased from Luzchem. Absorbance measurements were performed using a Shimadzu UV-2501PC UV–vis spectrophotometer. For actinometry studies, a 310 nm ± 5 nm band pass filter purchased from Aashi Spectra, Japan, was used.

Emission spectra were recorded on a Horiba Jobin Yvon Fluorolog 3 spectrometer (FL3-22) equipped with double-grating monochromators, a dual lamp housing containing a 450 W CW xenon lamp and a UV xenon flash lamp (FL-1040), Fluorohub/MCA/MCS electronics, and a R928 PMT detector. Emission and excitation spectra were corrected in all cases for source intensity (lamp and grating) and emission spectral response (detector and grating) by standard instrument correction provided in the instrument software. Fluorescence lifetime measurements were performed using a 340 nm nanoLED as the light source with a pulse repetition rate of 1 MHz. The instrument response function was collected using a scatter solution (Sigma-Aldrich, Ludox TM-40 colloidal silica). The goodness-of-fit was assessed by minimizing the reduced χ^2 function and further judged by the symmetrical distribution of the residuals. For Φ_{em}, optically dilute solutions (absorbance value $\sim$ 0.11) were

Can. J. Chem. Downloaded from www.nrcresearchpress.com by Xi'an Jiaotong University on 09/19/12
For personal use only.

used with quinine sulfate (recrystalized from water 3×)[39] in 0.5 mol/L H_2SO_4 (Φ_{fl} = 0.55) as the standard. Steady-state emission spectra were processed by FluorEssence software. Lifetime measurements were done using DAS6 v6.4 software.

Determining the quantum yield of emission[20]

Appropriate amounts of stock solutions[20] were mixed to get various ratios of the CB[8]–**1**. The emission was monitored by exciting at 345 nm with a slit width of 0.5 nm and monitoring from 360 to 660 nm with a slit width of 1.4 nm and an integration time of 0.1 s. Quinine sulfate in 0.5 mol/L H_2SO_4 (Φ_{fl} = 0.55) was used as the reference (Φ_{em}). Optically dilute solutions (absorbance value ~ 0.11 at excitation wavelength) were employed, and the emission was integrated using the FluorEssence software package. Using the following equation, the quantum yields for the solutions was calculated.[39]

$$\Phi_s = \Phi_r(I_s/I_r)(A_r/A_s)(\eta_s^2/\eta_r^2)$$

where Φ_s is the fluorescence quantum yield of the sample (i.e., **1**–CB[8] mixture), Φ_r is the fluorescence quantum yield for the reference solution (i.e., 0.5 mol/L H_2SO_4 quinine sulfate), I_s is the fluorescence intensity of the sample (**1**–CB[8] mixture), I_r is the fluorescence intensity of the reference solution (0.5 mol/L H_2SO_4 quinine sulfate), A_s is the absorbance value of the sample (**1**–CB[8] mixture), A_r is the absorbance value of the reference solution (0.5 mol/L H_2SO_4 quinine sulfate), η_s is the refractive index of the solvent (water) for the sample, and η_r is the refractive index of the solvent (water) for the reference (0.5 mol/L H_2SO_4 quinine sulfate).

Actinometry to determine photodimerization quantum yields[20]

The moles of product formed for the reaction of interest were done by irradiating the sample alongside the ferrioxalate actinometer solution (prepared by Hammond variation of the Hatchard and Parker procedure).[40] The moles of product formed were determined by the disappearance of the starting moles using UV–vis spectroscopy. As the reaction showed a clear isosbestic point indicating a one-to-one conversion of the reactant to photoproduct, the number of moles of product formed was computed from the decrease in absorbance (reacted starting material). The number of moles of product per unit time is related to the number of photons absorbed. The slope yields the quantum yield of the photoreaction (Φ_{dim}).[20]

Monitoring reaction rates by absorbance measurements[20]

Appropriate amounts of stock solutions were mixed to get various ratios of CB[8]–**1** with a total concentration of **1** being 5.00×10^{-5} mol/L and varying the CB[8] concentration between 0 and 2.50×10^{-6} mol/L.[20] The solution was irradiated (295 nm cutoff) under different reaction conditions (N_2, O_2, and air) with varying mole percents of CB[8] as listed in Table S4 in the Supplementary data, and the reaction progress was monitored at specified time intervals (1, 2, 3, 4, 5, 6, 7, 8, 9, 10, 15, 20, 25, 30, 35, 45, and 60 min). A clear isosbestic point under the conditions investigated indicated that the reaction was stoichiometric with a one-to-one conversion from **1** to the photodimer. This was also confirmed by NMR analysis,[20] which did not show any side products. Control studies were carried out simultaneously in the presence (various mol%) and in the absence of CB[8].[20]

Kinetics of photodimerization

The photodimerization with 0.05 mmol/L (or 0.04 mmol/L) of **1** (>295 nm irradiation) was followed by absorbance measurements at various mol% of CB[8], and the $r_{dim}$was computed. The percentage rate increase of uncatalyzed reaction (r_{uncat}) in the absence of CB[8] was taken as the reference for the computation of the the percent rate increase. The maximum rate increase (a 9× increase in reaction rate) was observed at ~160 mol% of CB[8] upon employing 0.05 mmol/L **1**. Similarly, the maximum rate increase (a 7.5× increase in reaction rate) was observed at ~70 mol% of CB[8] upon employing 0.04 mmol/L **1**.[20]

Fluorescence lifetime measurements[20]

The emission was monitored by exciting the samples using a 340 nm nanoLED light source and monitoring the emission at 411 nm (for **1** in water) and at 443 nm (for **1** with various mol% of CB[8]). The following parameter was maintained during acquisition: emission slit width = 5.0 nm. Fitting analysis was done by fitting to tri- or bi-exponential decay kinetics of the sample components taking the instrument response function (IRF) into consideration.

Phosphorescence measurements at 77 K[20]

The phosphorescence spectra were recorded at 77 K by exciting the samples at 345 nm using a pulsed Xenon lamp and monitoring the emission from 360 to 660 nm. The following parameters were maintained during acquisition: excitation slit width = 8 nm, emission slit width = 8 nm; flash per count = 10; and wavelength increments = 3 nm. For a sample window of 30 ms, time per flash of 100 ms with a delay time of 30 ms was employed. For a sample window of 10 ms, time per flash of 61 ms with a delay time of 10 ms was employed.

Photoirradiation of 1 in water at various mol% of CB[8]

Photoirradiation of **1** (0.05 mmol/L) with various mol% of CB[8] in water was carried out with a 450 W medium pressure mercury lamp. In a typical experiment, an appropriate amount of **1** stock solution[20] was pipetted to a 100 mL volumetric flask and made up to the mark with nanopure water. In a separate 100 mL volumetric flask an appropriate mol% of CB[8] stock solution was added and made to the mark with nanopure water. The two solutions were added to a 250 mL Erlenmeyer flask and mixed for 10 min. This solution was deaerated with N_2 or O_2 for 15 min and the Erlenmeyer flask was sealed. For aerated conditions, the flask was kept open without prior N_2 or O_2 bubbling. The aqueous solution was irradiated for 60 min (Pyrex cutoff) at room temperature. After photoirradiation, ammonium chloride (50 mg) was added to the solution followed by the addition of 50 mL of diethyl ether. The reaction mixture was stirred for 1 h at room temperature. The organic layer was separated and the aqueous layer was extracted with diethyl ether (2 × 25 mL). The combined ether extract was dried over anhydrous sodium sulfate and concentrated under reduced

pressure. The concentrated reaction mixture was analyzed by NMR spectroscopy without additional purification. Control studies were carried out under identical concentrations of **1** (0.05 mmol/L) without the addition of CB[8] to ascertain the role of CB[8] in the photodimerization processes.

Supplementary data

Supplementary data for this article are available on the journal Web site (canjchem.nrc.ca).

Acknowledgments

This work was carried out with generous financial support from the National Science Foundation (NSF). J.S. is grateful for the financial support of NSF through CAREER: CHE-0748525. The authors are grateful for the financial support of NSF through Grant EPS-0814442 for an ND-EPSCoR SEED II grant and a doctoral dissertation fellowship for B.P.

References

(1) Hammond, G. S.; Stout, C. A.; Lamola, A. A. *J. Am. Chem. Soc.* **1964**, *86* (15), 3103. doi:10.1021/ja01069a026.
(2) Hoffman, R.; Wells, P.; Morrison, H. *J. Org. Chem.* **1971**, *36* (1), 102. doi:10.1021/jo00800a022.
(3) Muthuramu, K.; Murthy, V. R. *J. Org. Chem.* **1982**, *47* (20), 3976. doi:10.1021/jo00141a035.
(4) Ramasubbu, N.; Row, T. N. G.; Venkatesan, K.; Ramamurthy, V.; Rao, C. N. R. *J. Chem. Soc., Chem. Commun.* **1982**, 178. doi:10.1039/C39820000178.
(5) Moorthy, J. N.; Venkatesan, K.; Weiss, R. G. *J. Org. Chem.* **1992**, *57* (12), 3292. doi:10.1021/jo00038a012.
(6) Turro, N. J. *Proc. Natl. Acad. Sci. U.S.A.* **2005**, *102* (31), 10766. doi:10.1073/pnas.0501376102.
(7) Ramamurthy, V., Ed. *Photoprocesses of Organic Molecules Included in Zeolites;* Wiley-VCH: New York, 1991.
(8) Behrend, R.; Meyer, E.; Rusche, F. *Liebigs Ann. Chem.* **1905**, *339* (1), 1. doi:10.1002/jlac.19053390102.
(9) Mock, W. L. *Top. Curr. Chem.* **1995**, *175*, 1. doi:10.1007/3-540-58800-0_16.
(10) Lee, J. W.; Samal, S.; Selvapalam, N.; Kim, H.-J.; Kim, K. *Acc. Chem. Res.* **2003**, *36* (8), 621. doi:10.1021/ar020254k.
(11) Day, A.; Arnold, A. P.; Blanch, R. J.; Snushall, B. *J. Org. Chem.* **2001**, *66* (24), 8094. doi:10.1021/jo015897c.
(12) Lagona, J.; Mukhopadhyay, P.; Chakrabarti, S.; Isaacs, L. *Angew. Chem. Int. Ed.* **2005**, *44* (31), 4844. doi:10.1002/anie.200460675.
(13) Maddipatla, M. V. S. N.; Kaanumalle, L. S.; Natarajan, A.; Pattabiraman, M.; Ramamurthy, V. *Langmuir* **2007**, *23* (14), 7545. doi:10.1021/la700803k.
(14) Wang, R.; Yuan, L.; Macartney, D. H. *J. Org. Chem.* **2006**, *71* (3), 1237. doi:10.1021/jo052136r.
(15) Wu, X.-L.; Luo, L.; Lei, L.; Liao, G.-H.; Wu, L.-Z.; Tung, C.-H. *J. Org. Chem.* **2008**, *73* (2), 491. doi:10.1021/jo701998e.
(16) Yang, C.; Mori, T.; Origane, Y.; Ko, Y. H.; Selvapalam, N.; Kim, K.; Inoue, Y. *J. Am. Chem. Soc.* **2008**, *130* (27), 8574. doi:10.1021/ja8032923.
(17) Pemberton, B. C.; Barooah, N.; Srivatsava, D. K.; Sivaguru, J. *Chem. Commun. (Camb.)* **2010**, *46* (2), 225. doi:10.1039/b920605a.
(18) Barooah, N.; Pemberton, B.; Sivaguru, J. *Org. Lett.* **2008**, *10* (15), 3339. doi:10.1021/ol801256r.
(19) Barooah, N.; Pemberton, B.; Johnson, A. C.; Sivaguru, J. *Photochem. Photobiol. Sci.* **2008**, *7* (12), 1473. doi:10.1039/b814230k.
(20) Refer to the Supplementary data.
(21) Wolff, T.; Göerner, H. *Phys. Chem. Chem. Phys.* **2004**, *6* (2), 368. doi:10.1039/b312335a.
(22) Yu, X.; Scheller, D.; Rademacher, O.; Wolff, T. *J. Org. Chem.* **2003**, *68* (19), 7386. doi:10.1021/jo034627m.
(23) Wang, Z. X.; Srivastava, D. K. *Anal. Biochem.* **1994**, *216* (1), 15. doi:10.1006/abio.1994.1002.
(24) Gharibi, H.; Safarpour, M. A.; Rafati, A. A. *J. Colloid Interface Sci.* **1999**, *219* (2), 217. doi:10.1006/jcis.1998.6041.
(25) Mohanty, J.; Nau, W. M. *Angew. Chem. Int. Ed.* **2005**, *44* (24), 3750. doi:10.1002/anie.200500502.
(26) Mantulin, W. W.; Song, P.-S. *J. Am. Chem. Soc.* **1973**, *95* (16), 5122. doi:10.1021/ja00797a004.
(27) Becker, R. S.; Chakravorti, S.; Gartner, C. A.; de Graca Miguel, M. *J. Chem. Soc., Faraday Trans.* **1993**, *89* (7), 1007. doi:10.1039/ft9938901007.
(28) de Melo, S. S. J.; Becker, R. S.; Maqanita, A. L. *J. Phys. Chem.* **1994**, *98* (24), 6054. doi:10.1021/j100075a002.
(29) Fedorin, G. F.; Georgievskii, V. P. *J. Appl. Spectrosc.* **1974**, *20* (1), 122. doi:10.1007/BF00617307.
(30) Allen, S. K.; Todd, A.; Allen, J. M. *Biochem. Biophys. Res. Commun.* **1997**, *235* (3), 615. doi:10.1006/bbrc.1997.6848.
(31) González-Béjar, M.; Montes-Navajas, P.; García, H.; Scaiano, J. C. *Langmuir* **2009**, *25* (18), 10490. doi:10.1021/la9011923.
(32) Buschmann, H.-J.; Wolff, T. *J. Photochem. Photobiol. Chem.* **1999**, *121* (2), 99. doi:10.1016/S1010-6030(98)00459-6.
(33) Wagner, B. D. *Curr. Anal. Chem.* **2007**, *3* (3), 183. doi:10.2174/157341107781023839.
(34) Day, A.; Arnold, A. P.; Blanch, R. J.; Snushall, B. *J. Org. Chem.* **2001**, *66* (24), 8094. doi:10.1021/jo015897c.
(35) Day, A. I.; Arnold, A. P.; Blanch, R. J. *Molecules* **2003**, *8* (1), 74. doi:10.3390/80100074.
(36) Lagona, J.; Mukhopadhyay, P.; Chakrabarti, S.; Isaacs, L. *Angew. Chem. Int. Ed.* **2005**, *44* (31), 4844. doi:10.1002/anie.200460675.
(37) Lagona, J.; Fettinger, J. C.; Isaacs, L. *J. Org. Chem.* **2005**, *70* (25), 10381. doi:10.1021/jo051655r.
(38) Ong, W.; Gómez-Kaifer, M.; Kaifer, A. E. *Org. Lett.* **2002**, *4* (10), 1791. doi:10.1021/ol025869w.
(39) Morris, J. V.; Mahaney, M. A.; Huber, J. R. *J. Phys. Chem.* **1976**, *80* (9), 969. doi:10.1021/j100550a010.
(40) Murov, S. L. *Handbook of Photochemistry;* Marcel Dekker: New York, 1973.

Can. J. Chem. Downloaded from www.nrcresearchpress.com by Xi'an Jiaotong University on 09/19/12
For personal use only.

Synthesis and characterization of a naphthalimide–dye end-labeled copolymer by reversible addition–fragmentation chain transfer (RAFT) polymerization

Binxin Li, Daniel Majonis, Peng Liu, and Mitchell A. Winnik

Abstract: We describe the synthesis of an end-functionalized copolymer of *N*-(2-hydroxypropyl)methacrylamide (HPMA) and *N*-hydroxysuccinimide methacrylate (NMS) by reversible addition–fragmentation chain transfer (RAFT) polymerization. To control the polymer composition, the faster reacting monomer (NMS) was added slowly to the reaction mixture beginning 30 min after initating the polymerization (ca. 16% HPMA conversion). One RAFT agent, based on azocyanopentanoic acid, introduced a –COOH group to the chain at one end. Use of a different RAFT agent containing a 4-amino-1,8-naphthalimide dye introduced a UV–vis absorbing and fluorescent group at this chain end. The polymers obtained had molecular weights of 30 000 and 20 000, respectively, and contained about 30 mol% NMS active ester groups.

Key words: RAFT, semi-batch polymerization, dye-labeled polymer, HPMA, *N*-hydroxysuccinimide methacrylate.

Résumé : On décrit la synthèse d'un copolymère fonctionnalisé aux extrémités du *N*-(2-hydroxypropyl)méthacrylamide (HPMA) et de méthacrylate de *N*-hydroxysuccinimide (NMS) par polymérisation impliquant une addition et une fragmentation radicalaire avec transfert de chaîne (AFRT). Dans le but de contrôler la composition du polymère, le monomère qui réagit le plus rapidement (NMS) est additionné lentement au mélange réactionnel 30 min après que la polymérisation a été initiée (conversion approximative de 16 % du HPMA). Un agent AFRT à base d'acide azocyanopentanoïque permet d'introduire un groupe –COOH à une extrémité de la chaîne. L'utilisation d'un agent AFRT différent, contenant un colorant 4-amino-1,8-naphtalimide, introduit un groupe fluorescent et absorbant dans l'UV–vis à l'extrémité de la chaîne. Les polymères obtenus possèdent respectivement des poids moléculaires de 30 000 et 20 000 et ils contiennent approximativement 30 mol% de groupes esters du NMS.

Mots-clés : polymérisation impliquant une addition et une fragmentation radicalaire avec transfert de chaîne (AFRT), polymérisation semi-discontinue, polymère marqué avec un colorant, *N*-(2-hydroxypropyl)méthacrylamide (HPMA), méthacrylate de *N*-hydroxysuccinimide (NMS).

[Traduit par la Rédaction]

Introduction

Poly-*N*-(2-hydroxypropyl)methacrylate (PHPMA) is a nontoxic, nonimmunogenic, and biocompatible polymer that offers great promise as the host carrier of polymer–drug conjugates. These conjugates (polymer therapeutics) offer some important advantages over conventional chemotherapeutic agents, such as increased solubility, longer circulation times, and lower nonspecific cytotoxicity.[1,2] Early examples of polymer–drug conjugates based on PHPMA involved polymers synthesized by traditional free radical polymerization.[3,4] This led to polymers with rather broad molecular weight distributions. More recently, there has been a strong interest in the synthesis of PHPMA and its copolymers by controlled radical polymerization as a means of obtaining material with a narrower molecular weight distribution. This is important in therapeutic applications because molecular weight can influence the phamacokinetics, toxicity, and inhibitory potency of the conjugate.[5,6]

Several groups have reported an indirect synthesis of PHPMA by atom transfer radical polymerization (ATRP). In this approach, one begins with the polymerization of *N*-methacryloxysuccinimide (NMS) followed by treatment of the PNMS obtained with excess 1-amino-2-propanol.[7] This approach takes advantage of the fact that the succinimide ester group of NMS can react with amines to form amides. For therapeutic applications, complete removal of the Cu ion catalyst can be problematic. This is one reason that a greater effort has been devoted to the development of the synthesis of PHPMA and its copolymers by reversible addition–

Received 26 April 2010. Accepted 29 July 2010. Published on the NRC Research Press Web site at canjchem.nrc.ca on 22 February 2011.

This article is part of a Special Issue dedicated to Professor J. C. Scaiano.

B. Li, D. Majonis, P. Liu, and M.A. Winnik.[1] Department of Chemistry, University of Toronto, 80 St. George Street, Toronto, ON M5S 3H6, Canada.

[1]Corresponding author (e-mail: mwinnik@chem.utoronto.ca).

Can. J. Chem. Downloaded from www.nrcresearchpress.com by University of Electronic and Science Techonology of China on 09/18/12
For personal use only.

Can. J. Chem. Downloaded from www.nrcresearchpress.com by University of Electronic and Science Techonology of China on 09/18/12
For personal use only.

fragmentation chain transfer (RAFT) polymerization. McCormick and co-workers[8] prepared hydrophilic–cationic block copolymers of HPMA and *N*-[3-(dimethylamino)propyl]methacrylamide (DMAPMA) by RAFT polymerization in water. These polymers lack pendant functionality for attachment of drugs or dyes. To address this issue, they developed a synthesis of copolymers of HPMA with *N*-(3-aminopropyl)methacrylamide) (APMA). Here, APMA provided amine functional groups for bioconjugation. They described modification of these copolymers with folic acid[9] or with *N*-succinimidyl 3-(2-pyridyldithio)-propionate to attach 5′-thiolated RNAs through a thiol–disulfide exchange reaction.[10] Hong and Pan[11] reported the synthesis of P(HPMA-*b*-NIPAM) (NIPAM = *N*-isopropylacrylamide) block copolymers by RAFT polymerization. These polymers were obtained with molecular weights in the range of 7 800–26 300 g/mol with narrow polydispersites (PDI = 1.15–1.29). Zentel and co-workers[12] synthesized functional amphiphilic poly(*N*-(2-hydroxypropyl) methacrylamide)-*b*-lauryl methacrylate) by RAFT polymerization. They investigated the influence of nanoaggregates formed by this block polymer on cell viability and on the motility of adherent cells.

A more general strategy for the preparation of functional HPMA copolymers involves the synthesis of an activated polymer with pendant active ester groups along the backbone. A random copolymer of HPMA and NMS would be an effective scaffold for the attachment of amine derivatives of dyes or drugs. The challenge in this synthesis is that the reactivity ratios (r_{HPMA} = 0.12 and r_{NMS} = 3.46)[13] favor rapid consumption of the NMS comonomer. Kane and co-workers[13,14] addressed this problem by using a "semi-batch" approach to the synthesis,[15] by adding the more reactive monomer slowly as the RAFT polymerization proceeded. They monitored the kinetics of the reaction and the composition of the polymer as the reaction proceeded, obtaining polymer that contained ~20 mol% NMS groups throughout the reaction. These polymers could be functionalized with a peptide known to disrupt anthratoxin assembly. The reaction in DMSO involved substitution of the active ester with an amino group from the peptide.

We are interested in this approach to the synthesis of functional HPMA copolymers, but with a higher NMS content. Here, we report a modified synthesis that follows the Kane and co-workers[13] strategy, but introduces functional and dye-containing chain-transfer agents (CTAs). As is well-established for RAFT polymerization, these transfer agents allow one to introduce functional groups or dyes at the initiating end of the polymer chains.[16–18] We are particularly interested in dyes based on the naphthalimide ring structure. The 1,8-naphthalimide chromophore and its derivatives have been studied for many years.[19–22] Many of these derivatives are easily synthesized from the corresponding naphthalic anhydrides. They have relatively high fluorescent quantum yields, high photostability, and tunable spectroscopic properties. Many 1,8-naphthalimide derivatives have been incorporated covalently or non-covalently into various polymeric materials to study the properties and behavior of the polymers. Our group has examined a family of 1,8-naphthalimide derivatives as donor–acceptor pairs to monitor polymer morphology or the diffusion of polymers by Förster resonance energy transfer (FRET) measurements.[23] Polymers containing the 1,8-naphthalimide group have also been studied for other applications such as sensors, probes, OLEDs, and solar cells, as well as photochemotherapy.[24]

Here, we describe the synthesis of a copolymer of HPMA and NMS with a naphthalimide-labeled end through RAFT polymerization. This dye-containing polymeric precursor can be further modified and potentially used in bioconjugation, drug delivery, and gene delivery applications.

Experimental

General characterization

^{1}H NMR (400 MHz) spectra were recorded on a Varian Mercury 400 spectrometer. $CDCl_3$ and d_6-DMSO were purchased from Cambridge Isotope Laboratories, Inc. 3-(Trimethylsilyl)propionic acid-d_4 sodium salt (TSP) was purchased from Sigma-Aldrich. For gel permeation chromatography (GPC) measurements, the eluant was 1-methyl-2-pyrrolidinone (NMP) containing 0.2 wt% LiCl, and the column was calibrated with poly(methyl methacrylate) (PMMA) standards. The analysis was carried out at 80 °C at a flow rate of 0.6 mL/min using a Viscotek VE1121 GPC solvent pump, with a Viscotek VE 3580 refractive index detector and a Viscotek VE3210 UV–vis absorbance detector. UV–vis measurements were carried out with a PerkinElmer Lambda 6 spectrometer.

Materials

4-Bromo-1,8-naphthalimide anhydride (BNA) (95%, Sigma-Aldrich), isobutylamine (99%, Sigma-Aldrich), ethylenediamine (99%, Sigma-Aldrich), oxalyl chloride (98%, Sigma-Aldrich), 2,2′-azobis(2-methylpropionitrile) (AIBN) (98%, Sigma-Aldrich), 1,3,5-trioxane (≥99%, Sigma-Aldrich), *tert*-butyl alcohol (*t*-BuOH) (≥99.5%, Sigma-Aldrich), *N*,*N*-dimethylformamide (DMF) (99.8%, Sigma-Aldrich), 1-methyl-2-pyrrolidinone (NMP) (≥99%, Sigma-Aldrich), and other chemicals were used as received. *N*-(2-Hydroxypropyl)methacrylamide (HPMA) was prepared according the literature procedure reported by Ulbrich et al.[25] *N*-Methacryloxysuccinimide (NMS) was synthesized according to the literature procedure reported by Shunmugam and Tew.[26] 4-Cyanopentanoic acid dithiobenzoate (CIDB) was synthesized as described previously.[27]

Synthesis of 9-isobutyl-4-ethylenediamino-1,8-naphthalimide

9-Isobutyl-4-ethylenediamino-1,8-naphthalimide was synthesized in two steps. 4-Bromo-1,8-naphthalic anhydride (1.4 g, 5.1 mmol) and isobutylamine (2.0 mL, 21 mmol) were added to 1,4-dioxane (40 mL) at room temperature. The solution was stirred for 4.5 h at 100 °C. The solvent was removed by rotary evaporation. The yellow solid was purified by silica column chromatography using heptanes–acetone (12:1, v:v) as the eluent. Finally, the yellow solid product (9-isobutyl-4-bromo-1,8-naphthalimide) was dried under vacuum at 50 °C overnight. Yield: 1.14 g (72%); mp 130.0–131.5 °C. ^{1}H NMR ($CDCl_3$, ppm) δ: 0.98 (d, 6H), 2.24 (m, 1H), 4.04 (d, 2H), 7.85 (dd, 1H), 8.04 (d, 1H), 8.42 (d, 1H), 8.58 (d, 1H), 8.66 (d, 1H). Elemental anal. calcd: C 57.85, H 4.25, N 4.22; found: C 57.98, H 4.32, N 4.50.

Can. J. Chem. Downloaded from www.nrcresearchpress.com by University of Electronic and Science Techonology of China on 09/18/12
For personal use only.

Table 1. Characteristics of the naphthalimide–dye end-labeled poly(HPMA-co-NMS).

NPMA mol%[a]	NMS mol%[a]	DP_{HPMA}[a]	DP_{NMS}[a]	M_n (NMR)[a]	M_n (NMR)[b]	M_n (UV)[c]
69	31	54	24	16 000	18 000	18 000

Note: HPMA, *N*-(2-hydroxypropyl)methacrylamide; NMS, *N*-methacryloxysuccinimide; DP_{HPMA}, mean number of HPMA units per polymer; and DP_{NMS}, mean number of NMS units per polymer.

[a]Calculated with eqs. [1] and [2].

[b]From the determination of the moles of the dye end group using TPS as an internal standard, calculated as M_n = [mass of poly(HPMA-co-NMS)]/[moles of naphthalimide–dye].

[c]From the absorbance at 430 nm using a value of $\varepsilon = 1.3 \times 10^4$ $(mol/L)^{-1}$ cm^{-1}.

9-Isobutyl-4-bromo-1,8-naphthalimide (3.020 g, 9.123 mmol) was added to ethylenediamine (50 mL, 0.75 mol). The solution was stirred at 50 °C for 2.5 h. The reaction mixture was treated with toluene (200 mL), and then the volatile liquids were removed by rotary evaporation. The crude product was dissolved in 1 mol/L aq HCl (70 mL). The product was precipitated by adding 1 mol/L aq NaOH until the solution became weakly basic (pH ~8). The mixture was then filtered. The yellow solid product (9-isobutyl-4-ethylenediamino-1,8-naphthalimide) was dried under vacuum at 50 °C overnight. Yield: 2.66 g (94%); mp 162–164 °C. ^{1}H NMR ($CDCl_3$, ppm) δ: 0.98 (d, 6H), 1.24 (broad, 2H), 2.25 (m, 1H), 3.18 (t, 2H), 3.42 (m, 2H), 4.03 (d, 2H), 6.14 (broad, 1H), 6.72 (d, 1H), 7.62 (t, 1H), 8.16 (d, 1H), 8.45 (d, 1H), 8.58 (d, 1H). Elemental anal. calcd.: C 69.43, H 6.80, N 13.49; found: C 68.52, H 6.66, N 13.66.

Synthesis of bis(benzenethiocarbonyl) disulfide

Magnesium turnings (3.00 g, 0.125 mol) were placed into a round-bottom flask with a catalytic amount of iodine. Bromobenzene (18.84 g, 0.1200 mol) was mixed with dry THF (90 mL). Then a 10 mL mixture of bromobenzene and THF was added to the flask and heated slightly. The remaining mixture was added slowly, while the temperature of reaction remained below 40 °C. The reaction was then stirred at room temperature for 1 h, after which the flask was cooled to 0 °C. Carbon disulfide (9.15 g, 0.120 mol) was added to the Grignard mixture at 0 °C. When the reaction finished after 2 h, deionized water (350 mL) was added, and the salts were removed by filtration. Concentrated HCl (~10 mL) was added to the filtrate and the mixture was extracted with diethyl ether. After evaporating the solvent with a rotary evaporator, absolute ethanol (100 mL) was added into the dithiobenzoic acid along with DMSO (18.75 g, 0.24 mol) and a catalytic amount of iodine. The reaction proceeded at room temperature for 2 h, and then the mixture was filtered. The purple solid (bis(thiocarbonyl) disulfide) was dried under vacuum at room temperature overnight. Yield: 11.04 g (60%); mp 96–98 °C. ^{1}H NMR ($CDCl_3$, ppm) δ: 7.45 (t, 4H), 7.61 (t, 2H), 8.07 (t, 4H).

Synthesis of the naphthalimide–dye-labeled CTA (NapDB)

Oxalyl chloride (5.3 mL, 62 mmol) was added to a stirred suspension of 4,4′-azobis(4-cyanovaleric acid) (1.708 g, 6.775 mmol) in anhyd CH_2Cl_2 with a catalytic amount of *N*,*N*-dimethylformamide at room temperature. After 3 h, the reaction mixture turned clear and was evaporated with a rotary evaporator to leave a yellow solid of 4,4′-(diazene-1,2-diyl)bis(4-cyanopentanoyl chloride). Yield: 1.820 g (95.6%). ^{1}H NMR ($CDCl_3$, ppm) δ: 1.72 (d, 6H), 2.62 (m, 4H), 3.14 (m, 4H).

9-Isobutyl-4-ethylenediamino-1,8-naphthalimide (1.557 g, 4.788 mmol) was dissolved in 100 mL anhyd CH_2Cl_2. The solution was cooled to 0 °C. A solution of 4,4′-(diazene-1,2-diyl)bis(4-cyanopentanoyl chloride) (0.632 g, 2.19 mmol) and *N*,*N*-diisopropylethylamine (2.29 mL, 13.1 mmol) in 20 mL anhyd CH_2Cl_2 was added dropwise to the dye solution via an addition funnel under N_2 protection. The reaction was stirred for 12 h at room temperature and then concentrated with a rotary evaporator. The mixture was washed with saturated sodium bicarbonate solution, 1% aq HCl, and finally 2 mol/L aq NaCl. The organic layer was dried over magnesium sulfate, filtered, and concentrated. The naphthalimide–dye-labeled CTA precursor was precipitated in diethyl ether and lyophilized overnight. Yield: 1.36 g (79%). ^{1}H NMR ($CDCl_3$, ppm) δ: 0.98 (d, 12H, CH_3), 1.69 (d, 6H, CH_3), 2.22–2.52 (m, 8H, CH_2CH_2), 3.44 (m, 4H, CH_2), 3.68 (t, 4H, CH_2), 4.01 (d, 4H, CH_2), 6.57 (d, 2H), 7.60 (t, 2H), 8.12 (d, 2H), 8.35 (d, 2H), 8.51 (d, 2H).

A solution of bis(thiocarbonyl) disulfide (0.156 g, 0.510 mmol) and the naphthalimide–dye-labeled CTA precursor (0.213 g, 0.246 mmol) in ethyl acetate was degassed with nitrogen and heated at 80 °C for 20 h. The solvent was removed with a rotary evaporator, and the residue was purified by silica column chromatography using ethyl acetate – hexane as the eluent. Yield: 0.049 g (34%); mp 90–93 °C. ^{1}H NMR ($CDCl_3$, ppm) δ: 0.99 (d, 6H, CH_3), 1.93 (s, 3H, CH_3), 2.44–2.71 (m, 4H, CH_2CH_2), 3.54 (t, 2H, CH_2), 3.77 (t, 2H, CH_2), 4.04 (d, 2H, CH_2), 6.17 (broad, 1H, NH), 6.60 (d, 1H, naphthalic-H), 6.91 (broad, 1H, NH), 7.66 (t, 1H), 7.35 (m, 2H, m-ArH), 7.38 (t, 1H, p-ArH), 7.84 (dd, 2H, o-ArH), 8.24 (d, 1H), 8.45 (d, 1H), 8.57 (d, 1H). Elemental anal. calcd.: C 65.01, H 5.63, N 9.78; found: C 64.83, H 5.77, N 9.23.

The homopolymerization of HPMA

The polymerizations were carried out under an Argon (Ar) atmosphere using the Shlenck technique. A typical polymerization procedure is described in the following. A stock solution was prepared comprised of AIBN (140.08 mg, 0.851 mmol), CIDB (41.08 mg, 0.155 mmol), and 1,3,5-trioxane (internal standard, 449 mg, 4.98 mmol) in degassed DMF (5 mL). HPMA (0.458 g, 3.55 mmol) was evacuated and back-filled with Ar three times. The degassed *t*-BuOH (3.2 mL) was injected into a round-bottom flask containing HPMA to form a 1 mol/L solution, and a solution of AIBN, CIDB, and 1,3,5-trioxane in DMF (200 μL) was transferred

Can. J. Chem. Downloaded from www.nrcresearchpress.com by University of Electronic and Science Techonology of China on 09/18/12
For personal use only.

into the same flask. The reaction was carried out at 80 °C immediately and finally quenched in an acetone – dry ice bath. Aliquots (0.1 mL) were taken out for NMR analysis throughout the reaction. The final polymer was precipitated using a mixture of anhydrous diethyl ether and anhydrous acetone (1:1 v/v), recovered by centrifugation, and then lyophilized overnight for further analysis by NMR and GPC.

The copolymerization of HPMA and NMS

The copolymerization reactions were carried out under an Argon (Ar) atmosphere on a Shlenck line. A typical copolymerization procedure (Table 1) is described in the following. A stock solution was prepared consisting of AIBN (6.6 mg, 0.040 mmol), NCTA (45.7 mg, 0.0799 mmol), and 1,3,5-trioxane (internal standard, 77.6 mg. 0.861 mmol) in degassed DMF (1 mL). The monomers were evacuated and backfilled with Ar three times. The solvents were degassed by bubbling with Ar gas. *t*-BuOH (1.9 mL) was added to a round-bottom flask containing HPMA (0.275 g, 2.13 mmol) to form a 1 mol/L solution, and then the solution of AIBN, NCTA, and 1,3,5-trioxane in DMF (200 μL) was transferred into the flask. The mixture was heated at 80 °C for 30 min, and then a solution of NMS in DMF (0.5 mol/L) was added continuously into the reaction mixture at 0.43 mL/h through an airtight syringe by a syringe pump (KD Scientific, model 780100). After the addition of the NMS solution, the reaction was kept at 80 °C for an additional 30 min and was then quenched in an acetone – dry ice bath. Aliquots (0.1 mL) were taken out for NMR analysis throughout the reaction. The final polymer was precipitated using a mixture of anhydrous diethyl ether and anhydrous acetone (1:1 v/v), recovered by centrifugation, and then lyophilized overnight. A sample for end-group analysis was subjected to a second precipitation from DMF into ether–acetone. The polymer product (26 mg) was stored at 4 °C.

Molecular weight determination

A sample of the dye-labeled polymer was examined by UV–vis spectroscopy. A sample of the dye-labeled poly(HPMA-co-NMS) (1.134 mg) was dissolved in 1.0 mL DMF to form a 1.13 g/L solution. The calibration curve of the UV absorbance of the naphthalimide–dye was built using 9-isobutyl-4-ethylenediamino-1,8-naphthalimide (BEAN) as a model compound. A series of solutions of BEAN in DMF was prepared with accurately known concentrations. The absorbance of these solutions at 440 nm was measured by UV–vis spectrometry. For the ^{1}H NMR experiments, dye-labeled copolymers were dissolved into DMSO-d_6 to form solutions at 10 mg/mL. In the GPC experiments, dye-labeled polymers were dissolved in NMP containing 0.2 wt% LiCl to form 1 mg/mL solutions.

Results and discussion

In a RAFT polymerization employing a thiocarbonylthio compound ZC(=S)SR as a chain transfer agent, the R group will become attached to the initiating end of the chain. The –SC(=S)Z at the other end can act as a protected thiol for further transformation of the polymer. In the initial polymerization reactions described below, CIDB (see below, Scheme 1) was used as the chain-transfer agent (CTA). It

Scheme 1. Reversible addition–fragmentation chain transfer (RAFT) copolymerization of *N*-(2-hydroxypropyl)methacrylamide (HPMA) and *N*-methacryloxysuccinimide (NMS).

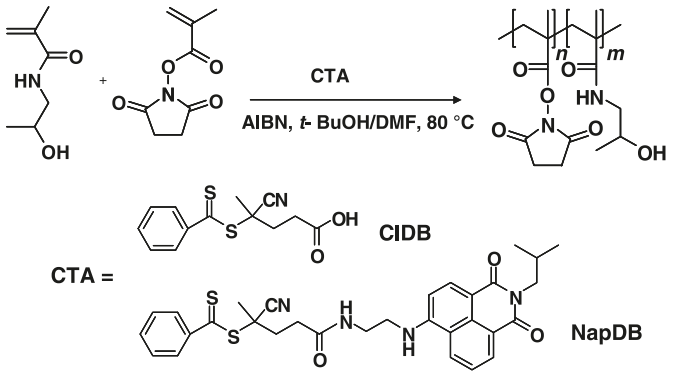

was synthesized as described in ref. 27. This CTA introduces a carboxylic acid into the R-group. If the R-group bears important functionality (such as a fluorescent dye) for applications in aqueous media, it is important that the attachment of the dye not involve ester groups which can slowly hydrolyze in water. In the design of the naphthalimide chain transfer agent used in these experiments, it is incorporated as an amide. The synthesis of this CTA is shown in Scheme 2. It was synthesized from bis(benzenethiocarbonyl) disulfide and the dye-containing azo-initiator in a single step. The yield was only 34% after column chromatography, but ^{1}H NMR and elemental analysis indicated that the product was pure. It showed only one spot by TLC.

We initially examined the kinetics of the polymerization of HPMA at 80 °C in the presence of CIDB as the chain-transfer agent and AIBN as the initiator. The ratio of [HPMA]–[CIDB]–[AIBN] was 320:2:1. As shown in the Supplementary data, $\ln([M]_0/[M]_t)$ increased linearly with reaction time over the first 4 h of the polymerization. Later, the rate of the polymerization became slower. The molecular weight increased monotonically but not quite linearly throughout the polymerization (see Fig. S2 in the Supplementary data), and maintained a narrow polydispersity. At 70% conversion, the sample was characterized by GPC (PMMA standards), yielding M_n = 32 000 with PDI = 1.3. These results establish that CIDB is an effective CTA for this RAFT polymerization. These results also provide information about the monomer conversion kinetics that we used to design the addition rate of NMS for the copolymerization of HPMA and NMS.

Semi-batch copolymerization of HPMA and NMS with CIDB as the CTA

Initial studies of the copolymerization of HPMA and NMS were carried out using CIDB as the RAFT agent. This reaction is shown in Scheme 1. In this copolymerization, all of the reactants except NMS (that is, AIBN, the CTA, 1,3,5-trioxane as an internal standard, and HPMA monomer, in a mixture of DMF and *tert*-butyl alcohol as the solvent) were introduced into a flask on a Schlenk line equipped with a septum and thoroughly outgassed as described in the Experimental section. The reaction was initiated by heating the solution to 80 °C and, after 30 min, a solution of NMS

Can. J. Chem. Downloaded from www.nrcresearchpress.com by University of Electronic and Science Techonology of China on 09/18/12
For personal use only.

Scheme 2. The synthesis of the naphthalimide–dye-labeled chain-transfer agent (CTA).

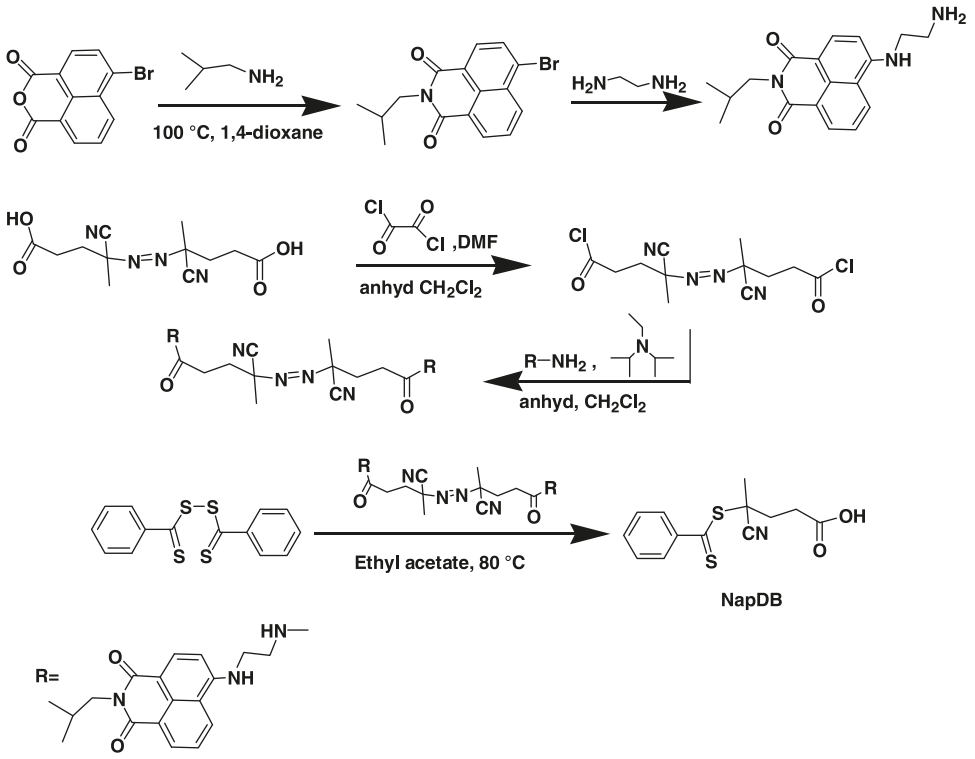

Fig. 1. ^{1}H NMR spectra for the conversion of *N*-(2-hydroxypropyl)methacrylamide (HPMA) and *N*-methacryloxysuccinimide (NMS) in reversible addition–fragmentation chain transfer (RAFT) copolymerization. The numbers in different colour zones indicate the average value of the vinyl protons of each corresponding monomer compared with the peak of the internal standard.

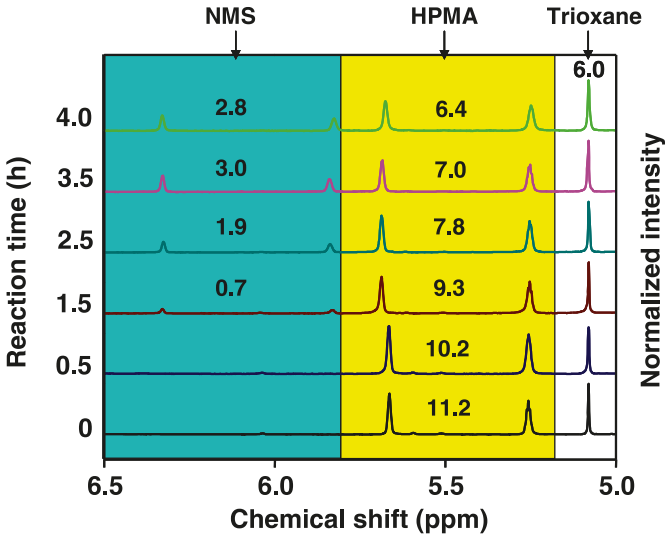

(0.5 mol/L) in DMF was added continuously into the reaction mixture at 0.43 mL/h via a syringe pump.

The conversion of HPMA and NMS was determined by ^{1}H NMR (in $CDCl_3$) (Fig. 1). The peaks at 5.2 and 5.7 ppm are ascribed to the vinyl protons of HPMA, and the peaks at 5.8 and 6.3 ppm are ascribed to the vinyl protons of NMS. The peak of 1,3,5-trioxane at 5.1 ppm was used as an internal standard to determine the amounts of HPMA and NMS remaining in the reaction mixture. In Fig. 1, the integral of this peak is arbitrarily assigned an integration value of 6.0. The numbers in the yellow zone of the spectra represent the average of the integrals of the two vinyl protons of HPMA, whereas the numbers in the blue zones of the spectra are the corresponding values of the two vinyl protons of NMS. These integral values indicate the amount of HPMA and NMS remaining at each point in the reaction. Over the first 30 min of the reaction, only HPMA was present. Then the addition of NMS began. Over the next 3.5 h, one can see a decrease in the concentration of HPMA in the reaction, accompanied by a slow steady build-up of NMS monomer in the reaction mixture. Even though NMS is more reactive in this copolymerization than HPMA, the consumption rate of NMS in the reaction was slower than its feed rate.

In Fig. 2A, we plot these data in terms of the time evolution of the amount of the monomers present in the system. The amount of HPMA in the reaction decreased essentially linearly with reaction time, and the amount of free NMS in the reaction mixture increased over time. After 4 h, 42% of the HPMA in the reaction and 24% of the NMS added were consumed. The composition of the poly(HPMA-co-NMS) obtained at different intervals of time was determined by ^{1}H NMR (in d_6-DMSO). Figure 2B shows that the percentage of HPMA in poly(HPMA-co-NMS) decreased slightly from 80% to 69% as the incorporation of NMS increased from 20% to 31%. The relatively high percentage of HPMA in the copolymer at 1.5 h is a consequence of the poly(HPMA) segment formed during the initial 30 min of the polymerization.

GPC measurements showed that the molecular weight of the copolymer increased over the first 3.5 h of the reaction. Individual traces were symmetrical (shown in Fig. S3B in

Can. J. Chem. Downloaded from www.nrcresearchpress.com by University of Electronic and Science Techonology of China on 09/18/12
For personal use only.

Fig. 2. (A) Amounts of monomer remaining at different reaction times in the semi-batch reversible addition–fragmentation chain transfer (RAFT) copolymerization of *N*-(2-hydroxypropyl)methacrylamide (HPMA) and *N*-methacryloxysuccinimide (NMS) with 4-cyanopentanoic acid dithiobenzoate (CIDB) as the chain-trnasfer agent (CTA). (B) The composition of the copolymer at these reaction times determined by ^{1}H NMR.

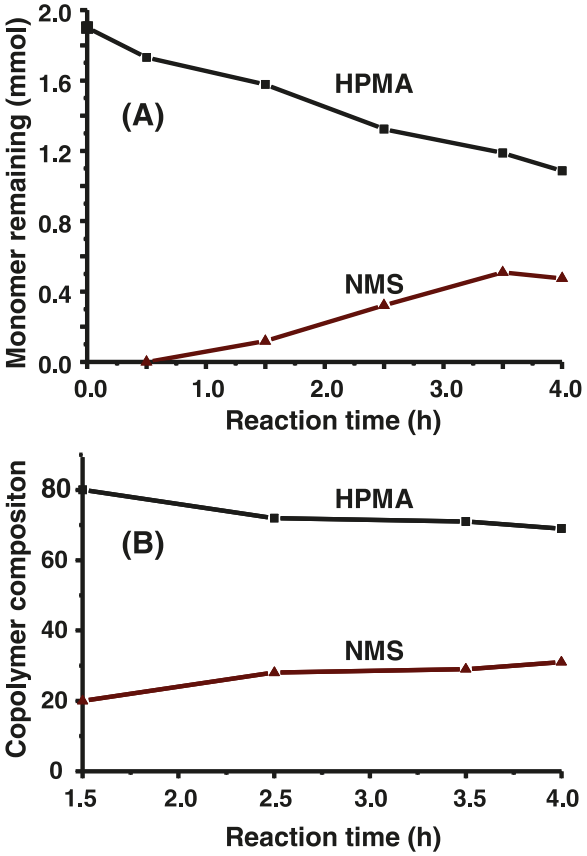

the Supplementary data), and the polydispersities were relatively narrow (PDI = 1.3–1.4). Based upon PMMA standards, M_n values increased from 10 000 g/mol after 1.5 h to 18 000 g/mol after 3.5 h, with little additional change found after 4 h, when the reaction was terminated. The poly(HPMA-co-NMS) obtained had M_n= 18 000 g/mol and PDI = 1.4. Analysis of the polymer by ^{1}H NMR revealed that the incorporation of NMS in the copolymer increased gradually as the copolymerization proceeded. We infer that the semi-batch method of synthesis enabled the formation of a polymer with a quasi-random distribution of NMS units, except for the segment of poly(HPMA) formed at the beginning of the polymerization.

Synthesis and characterization of the naphthalimide–dye end-labeled copolymer

To obtain a corresponding copolymer of HPMA and NMS with a strongly fluorescent dye at one end, the polymerization reaction was repeated using NapDB as the RAFT agent. This reaction is shown in Scheme 1. The copolymerization was carried out in the semi-batch mode at 80 °C over 4 h, with the addition of NMS (0.43 mL/h) initiated at the 30 min point of the reaction. The ratio of monomers

Fig. 3. Gel permeation chromatography (GPC) traces (UV and refractive index (RI) detectors) of the naphthalimide–dye end-labeled poly(HPMA-co-NMS) synthesized using a mol ratio ([HPMA + NMS]/[CTA]/[AIBN] = 320:2:1). The UV signal was monitored at 430 nm. HPMA, *N*-(2-hydroxypropyl)methacrylamide; NMS, *N*-methacryloxysuccinimide; CTA, chain-transfer agent; and AIBN, 2,2′-azobis(2-methylpropionitrile).

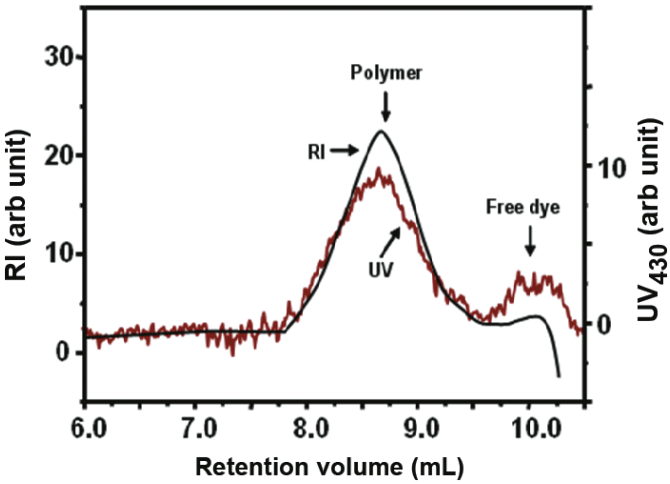

(HPMA + NMS) to NapDB to AIBN was maintained at 320:2:1. The ratio of HPMA to NMS remained 3:1. The conversion of HPMA and NMS was determined by ^{1}H NMR, using 1,3,5-trioxane as an internal standard. From GPC measurements on the dye-labeled poly(HPMA-co-NMS), using the refractive index (RI) detector in conjunction with PMMA standards, we obtained a nominal molecular weight of M_n = 21 000, M_w = 31 000, PDI = 1.5 (Fig. 3).

This sample also shows two peaks in the UV trace (λ = 430 nm) at retention times of 14.5 and 16.7 min. The former corresponds to the polymer and demonstrates that the dye is part of the polymer structure. The peak at longer retention time is due to residual CTA in the sample. The amount present is too small to give an appreciable signal in the RI detector.

The ^{1}H NMR spectrum of the purified naphthalimide–dye end-labeled poly(HPMA-co-NMS) in d_6-DMSO is presented in Fig. 4 along with the corresponding peak assignments. The characteristic resonances for the poly(HPMA-co-NMS) backbone appear at 0.4–1.4 ppm, along with the methacrylamide methyl protons and the methyl protons (k) of the HPMA unit. The peaks at 2.8 and 3.0 ppm are ascribed to the protons of the succinimide (o) and to the protons of the amide methylene (i), respectively. The signal of the alcohol methine (j) appears at 3.7 ppm. The signals of hydroxyl proton and amine proton appear at 4.7 and 7.3 ppm, respectively. The signals of the naphthalimide are also very clear and easily identified, such as the proton a at 8.6 ppm, the proton e at 8.5 ppm, and the proton c at 8.3 ppm. The peak at 3.3 ppm is due to traces of water present in the deuterated DMSO used as the NMR solvent.

For quantitative interpretation of the ^{1}H NMR signals, a spectrum was acquired with 1280 scans and a relaxation delay time of 25 s. The mean number of HPMA units per polymer (DP_{HPMA}) and of NMS units per polymer (DP_{NMS}) were

Can. J. Chem. Downloaded from www.nrcresearchpress.com by University of Electronic and Science Techonology of China on 09/18/12
For personal use only.

Fig. 4. [1]H NMR spectrum of the naphthalimide–dye end-labeled poly(HPMA-co-NMS) in DMSO-d_6. The inset is an enlargement of the region from 6.8 to 8.7 ppm.

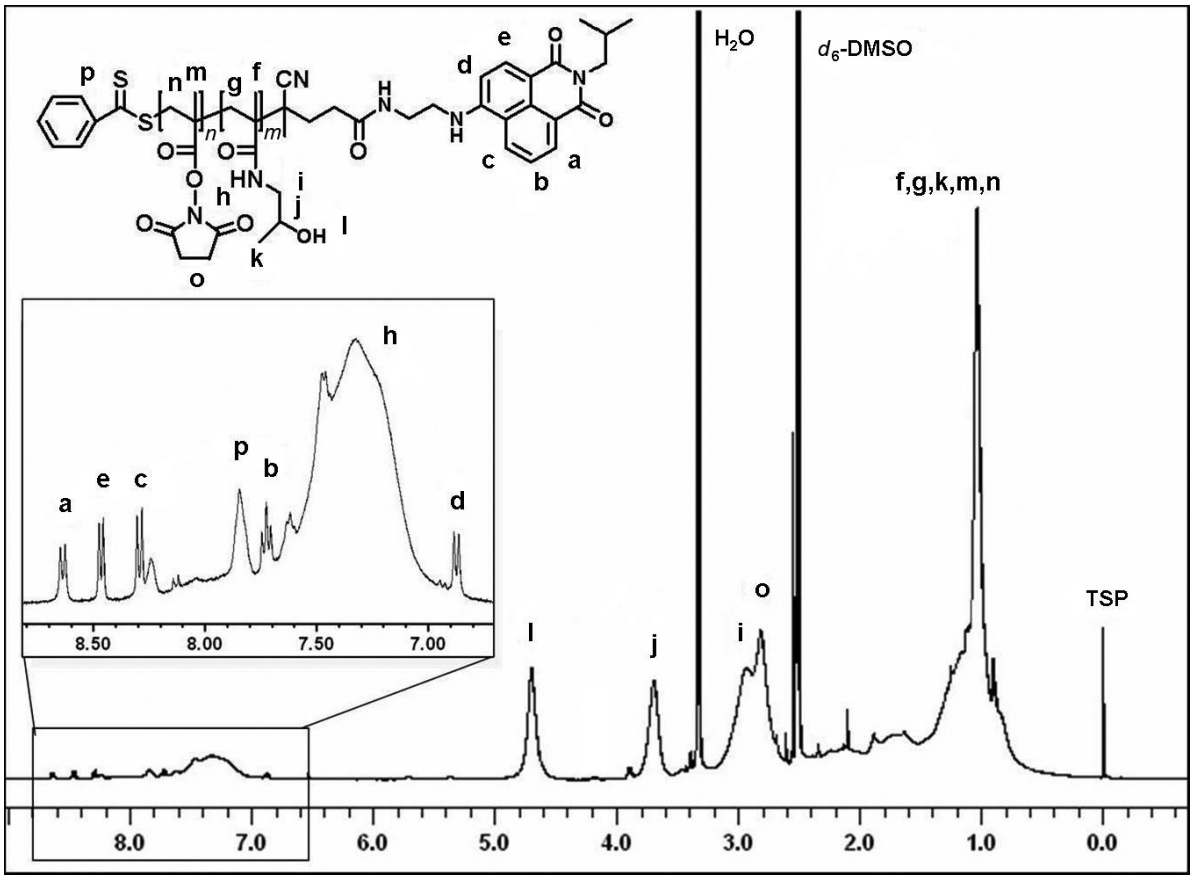

Fig. 5. UV–vis absorption spectrum of the naphthalimide–dye end-labeled poly(HPMA-co-NMS) (1.13 g/L) in *N*,*N*-dimethylformamide (DMF), with an absorbance at λ_{max} (440 nm) of 0.094.

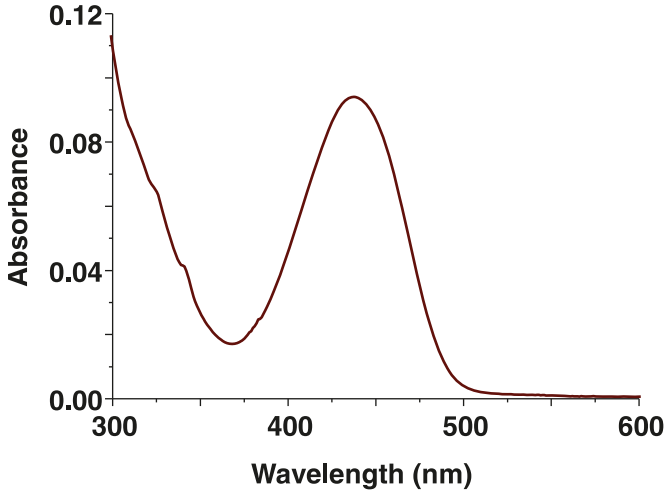

evaluated from the ratios of the peak integrals, using the signal a at 8.65 ppm as a measure of the naphthalimide end group. The signal j at 3.7 ppm represents one proton per HPMA unit. The signals i + o at 2.8–3.1 ppm represent contributions from the NMS group (4H) and 2H from the HPMA group. The desired information was calculated using eqs. [1] and [2].

$$[1] \quad DP_{HPMA} = \frac{I_j n_a}{I_a n_j}$$

$$[2] \quad DP_{NMS} = \frac{(I_{i+o} - I_j n_i / n_j) n_a}{I_a n_i}$$

Here I_a is the integral of peak a. I_i, I_j, and I_o are the integrals of peaks i, j, and o, respectively. n_a is the number of peak a protons. n_i, n_j, and n_o are the numbers of peak i, j, and o protons), respectively. The absolute number – average molecular weight of poly(HPMA-co-NMS) was calculated from the degrees of polymerization of monomers (HPMA and NMS), as well as the mass of the naphthalimide chain end assuming one dye molecule per chain.

As a check on this value of M_n, we used TSP as an external standard for the quantitative determination of M_n by NMR. In this procedure, a sample of the dye-labeled poly(HPMA-co-NMS) (6.17 mg) was dissolved in d_6-DMSO (0.6913 g), and a known amount (19.8 mg) of a solution of TSP in d_6-DMSO (1.0 mg/g) was added. The [1]H NMR spectrum was measured as described previously. The TSP signal can be seen as the peak at 0.0 ppm in Fig. 4. The integral of this signal was compared with the signal of the naphthalimide–dye at 8.65 ppm to obtain the mol ratio of the naphthalimide dye to TSP. The results obtained from [1]H NMR (d_6-DMSO) are summarized in Table 1. The M_n values determined with both methods are in good agreement. The mol ratio of

Can. J. Chem. Downloaded from www.nrcresearchpress.com by University of Electronic and Science Techonology of China on 09/18/12
For personal use only.

HPMA–NMS determined by NMR (69:31) is somewhat enhanced in its NMS content compared with the 3:1 mol ratio of monomers in the feed (25 mol%) NMS.

Figure 5 presents a UV–vis spectrum of the polymer in DMF solution. The solution shows λ_{max} at 440 nm. To estimate M_n based upon this absorption, we determined a value of the molar extinction coefficient of the chromophore in DMF ($\varepsilon = 1.3 \times 10^4$ (mol/L)$^{-1}$ cm^{-1}) using 9-isobutyl-4-ethylenediamino-1,8-naphthalimide as a model compound. In this way we calculated $M_n^{UV} = 18\,000$. These M_n values are compared in Table 1 and are seen to be in good agreement with each other. The value of M_n obtained from analysis of the GPC trace with a calibration curve based on PMMA standards was 21 000. The difference between this value and those obtained by NMR and UV–vis is an indication of the different hydrodynamic volumes of poly(HPMA-co-NMS) and PMMA in NMP at 80 °C.

Summary

Copolymers poly(HPMA-co-NMS) with molecular weight of ca. 20 000 and 30 000 were synthesized by RAFT polymerization, using two different RAFT agents. In one example, we used the carboxylic acid functionalized CIDB, whereas in the second example, we used NapDB containing a naphthalimide–dye derivative with an absorption λ_{max} at 430 nm. Both polymers contained ~30 mol% NMS groups. This pair of monomers is characterized by a serious reactivity ratio mismatch ($r_{HPMA} = 0.12$ and $r_{NMS} = 3.46$).[13] To overcome this problem, we followed the example of Kane and co-workers[13,14] and fed the more reactive monomer (NMS) into the reaction slowly as the polymerization proceeded. We began the addition of NMS as a solution in DMF 30 min after initiation of the polymerization of HPMA (~15% conversion). The reaction was not run under monomer-starved conditions. By NMR, we could show that the amount of free NMS monomer in the reaction built up slowly over the 3.5 h that it was fed into the reaction. An aliquot of the polymer taken after 1 h of reaction time contained 20 mol% NMS and, after 4 h, the polymer contained 30 mol% NMS. Values of M_n determined by end-group analysis by ^{1}H NMR and by UV–vis spectroscopy were in good agreement with each other.

Supplementary data

Supplementary data for this article are available on the journal Web site (canjchem.nrc.ca).

Acknowledgment

The authors thank the Natural Sciences and Engineering Research Council of Canada (NSERC) for their support of this research.

References

(1) Langer, R. *Nature* **1998**, *392* (Suppl.), 5.
(2) Duncan, R. *Nat. Rev. Drug Discov.* **2003**, *2* (5), 347. doi:10.1038/nrd1088.
(3) Kissel, M.; Peschke, P.; Šubr, V.; Ulbrich, K.; Strunz, A. M.; K hnlein,R.; Debus, J.; Friedrich, E. *Eur. J. Nucl. Med. Mol. Imaging* **2002**, *29* (8), 1055. doi:10.1007/s00259-002-0835-0.
(4) Satchi-Fainaro, R.; Puder, M.; Davies, J. W.; Tran, H. T.; Sampson, D. A.; Greene, A. K.; Corfas, G.; Folkman, J. *Nat. Med.* **2004**, *10* (3), 255. doi:10.1038/nm1002.
(5) Seymour, L. W.; Duncan, R.; Strohalm, J.; Kopeček, J. *J. Biomed. Mater. Res.* **1987**, *21* (11), 1341. doi:10.1002/jbm.820211106.
(6) Seymour, L. W.; Ulbrich, K.; Strohalm, J.; Kopecek, J.; Duncan, R. *Biochem. Pharmacol.* **1990**, *39* (6), 1125. doi:10.1016/0006-2952(90)90293-T.
(7) Godwin, A.; Hartenstein, M.; Muller, A. H. E.; Brocchini, S. *Angew. Chem. Int. Ed.* **2001**, *40* (3), 594. doi:10.1002/1521-3773(20010202)40:3<594::AID-ANIE594>3.0.CO;2-P.
(8) Scales, C. W.; Huang, F.; Li, N.; Vasilieva, Y. A.; Ray, J.; Convertine, A. J.; McCormick, C. L. *Macromolecules* **2006**, *39* (20), 6871. doi:10.1021/ma061453c.
(9) York, A. W.; Zhang, Y.; Holley, A. C.; Guo, Y.; Huang, F.; McCormick, C. L. *Biomacromolecules* **2009**, *10* (4), 936. doi:10.1021/bm8014768.
(10) York, A. W.; Huang, F.; McCormick, C. L. *Biomacromolecules* **2010**, *11* (2), 505. doi:10.1021/bm901249n.
(11) Hong, C. Y.; Pan, C. Y. *Macromolecules* **2006**, *39* (10), 3517. doi:10.1021/ma052593+.
(12) Barz, M.; Tarantola, M.; Fischer, K.; Schmidt, M.; Luxenhofer, R.; Janshoff, A.; Theato, P.; Zentel, R. *Biomacromolecules* **2008**, *9* (11), 3114. doi:10.1021/bm800684b.
(13) Yanjarappa, M. J.; Gujraty, K. V.; Joshi, A.; Saraph, A.; Kane, R. S. *Biomacromolecules* **2006**, *7* (5), 1665. doi:10.1021/bm060098v.
(14) Gujraty, K. V.; Yanjarappa, M. J.; Saraph, A.; Joshi, A.; Mogridge, J.; Kane, R. S. *J. Polym. Sci. Part Polym. Chem.* **2008**, *46* (21), 7249. doi:10.1002/pola.23031.
(15) Kreft, T.; Reed, W. F. *Macromolecules* **2009**, *42* (15), 5558. doi:10.1021/ma900745n.
(16) Moad, G.; Rizzardo, E.; Thang, S. H. *Aust. J. Chem.* **2006**, *59* (10), 669. doi:10.1071/CH06250.
(17) Moad, G.; Rizzardo, E.; Thang, S. H. Mater. Matters *2010*, **5**, 2 [Online]. Available from http://www.sigmaaldrich.com/etc/medialib/docs/Aldrich/Brochure/1/al_material_matters_v5n1.Par.0001.File.tmp/al_material_matters_v5n1.pdf
(18) Bathfield, M.; D'Agosto, F.; Spitz, R.; Charreyre, M. T.; Delair, T. *J. Am. Chem. Soc.* **2006**, *128* (8), 2546. doi:10.1021/ja057481c.
(19) Liu, J.; Cao, J.; Shao, S.; Xie, Z.; Cheng, Y.; Geng, Y.; Wang, L.; Jing, X.; Wang, F. *J. Mater. Chem.* **2008**, *18* (14), 1659. doi:10.1039/b716234k.
(20) Yuan, D.; Brown, R. G.; Hepworth, J. D.; Alexiou, M. S.; Tyman, J. H. P. *J. Heterocycl. Chem.* **2008**, *45* (2), 397. doi:10.1002/jhet.5570450216.
(21) Coronado, J. L. G.; MartÚn, E.; Montero, L. A.; Fierro, J. L. G.; GarcÚa de la Vega, J. M. *J. Phys. Chem. A* **2007**, *111* (39), 9724. doi:10.1021/jp075336a.
(22) Grabchev, I.; Sali, S.; Betcheva, R.; Gregoriou, V. *Eur. Polym. J.* **2007**, *43* (10), 4297. doi:10.1016/j.eurpolymj.2007.07.036.
(23) Felorzabihi, N.; Froimowicz, P.; Haley, J.; Bardajee, G. R.; Li, B.; Bovero, E.; van Veggel, F. C. J. M.; Winnik, M. A. *J. Phys. Chem. B* **2009**, *113* (8), 2262. doi:10.1021/jp807637s.
(24) Mei, C.; Tu, G.; Zhou, Q.; Cheng, Y.; Xie, Z.; Ma, D.; Geng, Y.; Wang, L. *Polymer (Guildf.)* **2006**, *47* (14), 4976. doi:10.1016/j.polymer.2006.03.085.
(25) Ulbrich, K.; Subr, V.; Strohalm, J.; Plocova, D.; Jelinkova, M.; Rihova, B. *J. Control. Release* **2000**, *64* (1-3), 63. doi:10.1016/S0168-3659(99)00141-8.

(26) Shunmugam, R.; Tew, G. N. *J. Polym. Sci. Part Polym. Chem.* **2005**, *43* (23), 5831. doi:10.1002/pola.21102.
(27) Sprong, E.; De Wet-Roos, D.; Tonge, M. P.; Sanderson, R. D. *J. Polym. Sci. Part Polym. Chem.* **2003**, *41* (2), 223. doi:10.1002/pola.10503.

Can. J. Chem. Downloaded from www.nrcresearchpress.com by University of Electronic and Science Techonology of China on 09/18/12
For personal use only.

Effect of positively charged backbone groups on radical cation migration and reaction in duplex DNA

Sriram Kanvah and Gary B. Schuster

Abstract: A series of DNA oligomers were prepared that contain guanidinium linkages (positively charged) positioned selectively in place of and among the normal negatively charged phosphodiester backbone groups of duplex DNA. One-electron oxidation of these DNA oligomers by UV irradiation of a covalently linked anthraquinone group generates a radical cation (electron "hole") that migrates by hopping through the DNA and is trapped at reactive sites, GG steps, to form mutated bases that are detected by strand cleavage after subsequent piperidine treatment of the irradiated DNA. Analysis of the strand cleavage pattern reveals that guanidinium substitution in these oligomers does not measurably affect the charge migration rate but it does inhibit reaction at nearby guanines.

Key words: DNA oxidation, anthraquinone photosensitizer, charge transport, guanidinium backbone.

Résumé : On a préparé une série d'oligomères de l'ADN qui contiennent des liaisons guanidinium (chargées positivement) positionnées d'une façon sélective à la place de et parmi les groupes normalement chargés d'une façon négative des groupes phosphodiesters du duplex de l'ADN. L'oxydation à un électron de ces oligomères d'ADN par une irradiation UV d'un groupe anthraquinone lié d'une façon covalente provoque la formation d'un cation radical (« trou » d'électron) qui se déplace par sauts à travers l'ADN, qui est piégé à ses sites réactifs, étapes GG, avec formation de bases ayant subi une mutation qui sont détectées par une coupure des brins après un traitement subséquent avec de la pipéridine des ADN irradiés. L'analyse des patrons de clivage des brins révèle que la substitution par des groupes guanidinium dans ces oligomères n'a pas d'effet mesurable sur la vitesse de migration de la charge, mais qu'elle inhibe la réaction au niveau des guanines adjacentes.

Mots-clés : oxydation de l'ADN, anthraquinone comme photosensibilisateur, transport de charge, squelette de guanidinium.

[Traduit par la Rédaction]

Introduction

Extensive research on long-distance radical cation ("hole") transport in duplex DNA has focused on understanding its implications to the oxidative damage caused by chemical and ionizing radiation that often leads to mutagenic lesions.[1] These experiments have generated a vigorous debate on the mechanism of charge transport in DNA.[2–9] Our work in this field has focused on charge transport and on the reactions of the nucleobase radical cations.[2,10–13] In this examination, we use UV irradiation of an anthraquinone group (AQ) covalently linked to duplex DNA to initiate one-electron oxidation, which occurs when an electron is transferred from a neighboring nucleobase to the excited AQ with the concomitant formation of the AQ radical anion and a base radical cation.[14] The radical anion is subsequently consumed by reaction with O_2 (forming superoxide) and the radical cation migrates through the DNA bases via a hopping mechanism[5,15] until it is trapped by an irreversible reaction, usually with water or oxygen, that results in a damaged (mutated) nucleobase. The damaged base is typically detected by strand cleavage following chemical or enzymatic treatment of the oxidized DNA. For a long time it was thought that reaction of the radical cation occurred primarily at the sites of lowest oxidation potential,[16] for instance the 5′ G of a GG doublet or at a GGG triplet. However, recent reports of reaction at thymine in oligonucleotides that do not contain guanines reveal instead that reaction generally occurs at the nucleobase radical cation having the highest reactivity.[17–20]

The effect of nucleobase sequence on charge hopping emerges from consideration of the entire sequence of nucleobases in the oligonucleotide. That is, in one instance a particular base sequence can facilitate charge hopping and in another that sequence can be a barrier to hopping.[21] The transport of a radical cation over such a barrier is a result

Received 28 April 2010. Accepted 9 June 2010. Published on the NRC Research Press Web site at canjchem.nrc.ca on 18 February 2011.

This article is part of a Special Issue dedicated to Professor J. C. Scaiano.

S. Kanvah[1,2] and G.B. Schuster. School of Chemistry and Biochemistry, Georgia Institute of Technology, Atlanta, GA 30332, USA.

[1]Corresponding author (e-mail: kanvah@gmail.com).
[2]Present address: Department of Chemistry, Indian Institute of Technology, Gandhinagar, VGEC Complex, Chandkheda, Visat-Gandhinagar Highway, Ahmedabad 382 424, India.

Can. J. Chem. Downloaded from www.nrcresearchpress.com by University of Electronic and Science Techonology of China on 09/18/12
For personal use only.

Can. J. Chem. Downloaded from www.nrcresearchpress.com by University of Electronic and Science Techonology of China on 09/18/12
For personal use only.

Fig. 1. Structures of DNA oligomers used in this work. The asterisk indicates the position of the ^{32}P radiolabel.

DNA																		
1	5'-AQ	AT	AA	GG_1	AA	GG_2	AA	GG_3	AA	GG_4	AA	GG_5	AA	GG_6	AA	TA	TA*	-3'
2	3'	TA	TT	CC	TT	CC	TT	CC	TT	CC	TT	CC	TT	CC	TT	AT	AT	-5'
3	3'	TA	TT	CC	TgT	CC	TT	CC	TT	CC	TT	CC	TT	CC	TT	AT	AT	-5'
4	3'	TA	TT	CC	TgT	CC	TT	CC	TgT	CC	TT	CC	TgT	CC	TT	AT	AT	-5'
5	5'-AQ	AT	AA	GG_1	AA	GG_2	AA	GG_3	TT	GG_4	AA	GG_5	AA	GG_6	AA	TA	TA*	-3'
6	3'	TA	TT	CC	TT	CC	TT	CC	AA	CC	TT	CC	TT	CC	TT	AT	AT	-5'
7	5'-AQ	AT	AA	GG_1	AA	GG_2	AA	GG_3	TgT	GG_4	AA	GG_5	AA	GG_6	AA	TA	TA*	-3'
8	3'-	TA	TT	CC	TT	CC	TgT	CC	TT	CC	TT	CC	TT	CC	TT	AT	AT	-5'

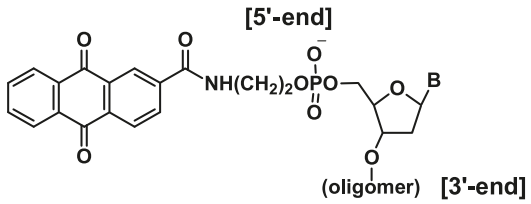

AQ-Linked DNA

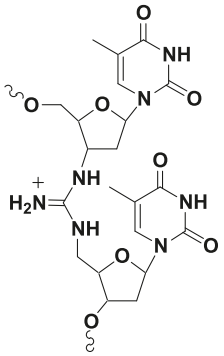

TgT

of the instantaneous fluctuations in the orientation of the nucleobases[10,22] and, most importantly, in the water (solvent) and counterion environment.[10,23] In this regard, it is important to understand the effect of perturbations to the normal stacking of bases in DNA charge transport[24] and to the solvent and counterion environment that occur with changes to the sugar-phosphate backbone.[10,25,26] In particular, we assessed the effect of positively charged groups substituted for the normally neutral nucleobases and the effect of replacing the negatively charged phosphate groups of the backbone with uncharged methylphosphonate groups. For example, in one case we inserted a cationic pyridinium nucleoside mimic for a base[27] and in another we substituted formally positively charged Hg(II) metal centers[28] for protons in thymine–thymine mispairs. These experiments revealed a robust radical cation migration process. On the other hand, replacement of backbone phosphate groups with methylphosphonates causes profound changes to the solvent and counterion environment and this results in significant changes to the reaction of the radical cation at nearby guanines in the oligonucleotide.[10,29] In this work, we extend the examination of backbone perturbation to the reversal of the charge in segments of a DNA oligonucleotide from negative to positive by examining mixed backbone sequences consisting of positively charged guanidinium linkages positioned selectively among the normal negatively charged phosphodiesters of duplex DNA.

Experimental section

N′-Acetyl-*N*-(3′-deoxythymidine-3′-yl)-*N*″-(5′-deoxythymidine-5′-yl) guanidine (TgT) was prepared as described elsewhere.[30] Sodium azide, instead of lithium azide, was used in the synthetic scheme described. The TgT-containing oligomers (Fig. 1) were prepared by standard procedures. The amidite building block of TgT was obtained using a standard phosphoramidite reaction strategy. A 15 min coupling time was used for the TgT phosphoramidite in an Expedite 8909 DNA synthesizer. Similarly, the anthraquinone phosphoramidite was attached to the 5′ end of the oligomer using a 15 min coupling time. The DNA oligomers were deprotected at 60 °C by reaction with 30% ammonium hydroxide solution overnight. The protected guanidine, on treatment with ammonium hydroxide, is deprotected to yield the positively charged guanidinium linkage.[31] All oligonucleotides were purified using a Hitachi HPLC system containing a reverse-phase Dynamax C-18 column in an acetonitrile and triethylammonium acetate buffer solvent system and characterized by mass spectrometry. Electrospray ionization spectra of the modified DNA are given in the Supplementary data (Figs. S3 to S10).

Melting temperatures were determined on a Cary 1E UV–vis spectrophotometer on 2.0 μmol/L samples at 260 nm. Circular dichroism spectra were determined using a JASCO spectropolarimeter. 3′-End labeled DNA oligomers were obtained by incubation of the single-stranded DNA with [α-^{32}P]ATP and terminal deoxynucleotidyl transferase at 37 °C for 45 min. Samples were purified on a 20% denaturing polyacrylamide gel; elution and precipitation with ethanol yielded the radiolabeled DNA.

Samples for irradiation were prepared by hybridization of a mixture of radiolabeled DNA and unlabeled DNA (5 μmol/L). The samples were heated to 90 °C for 10 min and allowed to cool slowly to room temperature. Samples were irradiated at approx. 30 °C in microcentrifuge tubes in a Rayonet photoreactor (Southern New England Ultraviolet Co., Barnsford, Connecticut) containing eight 350 nm

Can. J. Chem. Downloaded from www.nrcresearchpress.com by University of Electronic and Science Techonology of China on 09/18/12
For personal use only.

lamps, each having an intensity of 8 W. Irradiation times were adjusted by iteration to ensure single-hit conditions. After irradiation, the samples were precipitated once with ethanol, dried, and treated with piperidine at 90 °C for 30 min. After evaporation of the piperidine, the samples were dissolved in denaturing loading dye and analyzed on a 20% 19:1 acrylamide:bisacrylamide gel. The gels were dried and the cleavage sites were visualized by autoradiography. Quantification of cleavage bands was performed on a Fuji phosphorimager.

Results and discussion

Figure 1 shows the series of oligomers that were prepared to assess the effect of converting regions of the normal phosphate-linked negatively charged backbone of DNA to guanidinium-linked regions bearing positive charges. Each duplex contains a 5′-linked AQ group as photosensitizer, a 3′ ^{32}P radiolabel, and 6 GG steps that serve as traps for the radical cation, where reaction with H_2O or O_2 leads to base damage and subsequent strand cleavage after piperidine treatment. DNA(**1/2**) is a normal DNA duplex oligomer that serves as a control for analysis of DNA(**1/3**) and DNA(**1/4**), which have 1 and 3 guanidinium-containing TgT groups, respectively. DNA(**5/6**), which serves as a control for experiments with DNA(**7/8**), is similar to DNA(**1/2**) except that the nucleobase pairs separating GG_3 and GG_4 have been changed. In DNA(**1/2**), GG_3 and GG_4 are separated by an AA step, while in DNA(**5/6**) there is a TT step between GG_3 and GG_4. In DNA(**7/8**), GG_3 is surrounded by TgT groups — one is adjacent to the GG and the other is in the complementary strand.

The substitution of guanidinium groups for phosphate groups reduces the overall negative charge of the DNA duplexes by 2, 4, or 6 depending on the number of modifications. It is expected that the positively charged guanidinium groups will reduce the electrostatic repulsion of the phosphate groups of normal double-stranded DNA. However, the melting temperatures (T_m) of the TgT-containing duplexes are not greatly different from that of the normal DNA duplexes. For example, the T_m of DNA(**1/4**), which contains 3 TgT groups, is 47 °C in pH 7.0 sodium phosphate buffer solution, and DNA(**1/2**) melts at 50 °C. Likewise, the other guanidinium-containing duplexes melt at temperatures similar to their all-phosphate-containing control compounds. The first derivative melting curve profiles of these DNA duplexes are given in the Supplementary data. Circular dichroism spectra (Fig. S2 of the Supplementary data) of the guanidinium-containing duplexes are essentially indistinguishable from those of their control compounds, which indicates that the global B-DNA structure is not measurably affected by the guanidinium substitutions.

Irradiation of these AQ-containing DNA duplexes at 350 nm results in the one-electron oxidation of a nucleobase to form a radical cation. The radical cation then migrates through the DNA, encountering either normal phosphate groups or regions containing positively charged guanidinium groups in the backbone. The guanidinium modifications may affect either (or both) the rate constant for charge hopping from base to base (k_{hop}) or the rate constant for trapping (k_{trap}) of the radical cation by reaction with H_2O or O_2.

Fig. 2. Autoradiogram comparing the photocleavage of DNA duplexes (**1/2**), (**1/3**), and (**1/4**) having zero, one, and three guanidine modifications, respectively. The guanidine modifications are on the pyrimidine-dominated complementary strand. D, 5, 10, and 15 refer to irradiation times in minutes (D is "dark"; i.e., no irradiation) and GG_n refers to the GG step position (1–6) in the labeled DNA strand (see Fig. 1).

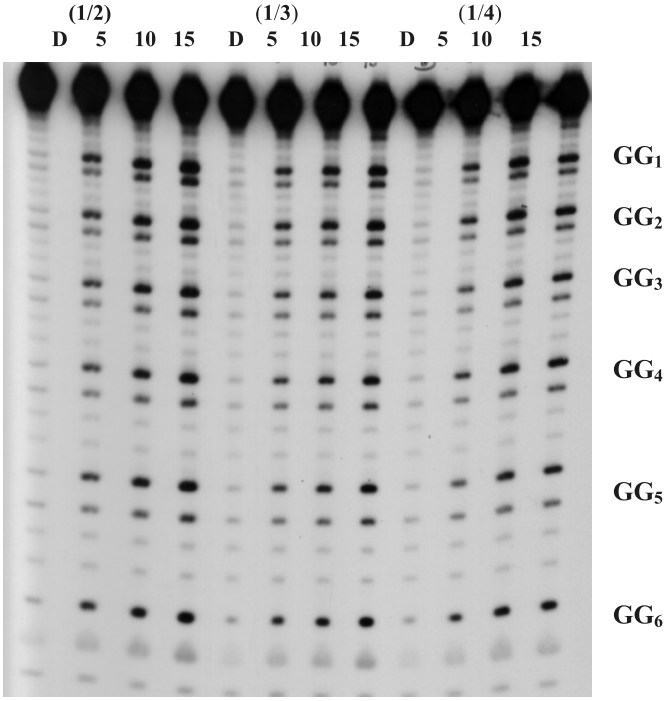

Changes to these rate constants would be reflected in the relative amounts of strand cleavage detected at GG steps in subsequent analyses. For example, if the TgT group presents an insurmountable barrier to radical cation migration, then no strand cleavage would be detected at GG steps 2–6 in DNA(**1/3**).

As shown in Fig. 2, irradiation of duplex DNA(**1/2**) leads, as expected, to similar amounts of strand cleavage at each of the 6 GG steps because the rate of hopping in this sequence is much greater than the rate of trapping.[22] Irradiation of DNA duplexes (**1/3**) and (**1/4**), which contain 1 and 3 guanidine substitutions, respectively, gives a similar result — essentially equal strand cleavage efficiency at each of the 6 GG steps. This is a surprising result that may have occurred because the path of radical cation migration is primarily through purines, which have lower oxidation potentials than pyrimidines, and the guanidinium modification is between two pyrimidines located on the complementary strand. We examined the reactions of DNA(**6/7**) and DNA(**7/8**) to address this possibility.

As indicated above, DNA(**6/7**) and DNA(**7/8**) differ from the first set of oligomers by changes in the nucleobase sequence. In these sequences a TT step separates the first three GG steps from the rest. Unlike a single T,[23] a TT step[31] between GG_3 and GG_4 of DNA(**5/6**) presents a significant barrier to radical cation migration, as is clearly seen in the relative amount of strand cleavage at each of the GG steps. Irradiation of DNA(**5/6**) at 350 nm causes essentially equivalent strand cleavage at GG_1, GG_2, and GG_3, and reduced

Can. J. Chem. Downloaded from www.nrcresearchpress.com by University of Electronic and Science Techonology of China on 09/18/12
For personal use only.

Fig. 3. Autoradiograms comparing photocleavage of DNA duplexes (**7/8**), (**6/7**), and (**5/6**). Arrow indicates position of backbone modification. D, 5, and 10 refer to irradiation times in minutes (D is "dark"; i.e., no irradiation) and GG_n refers to the GG step position (1–6) in the labeled DNA strand (see Fig. 1).

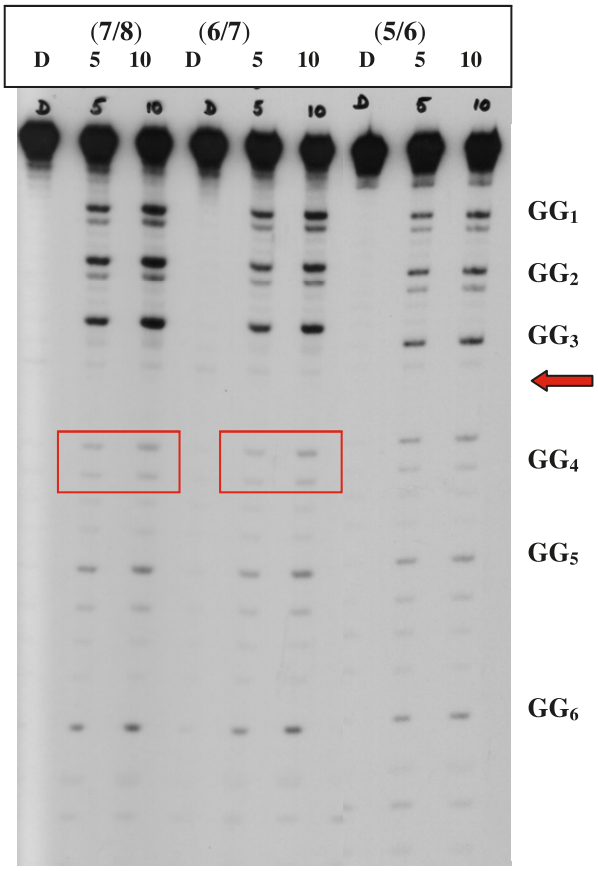

amounts of reaction at GG_4, GG_5, and GG_6 (see Fig. 3). The GG steps following the TT barrier react with similar efficiency, which can be attributed to the presence of charge transfer-facilitating purine bridges. In DNA(**6/7**), the guanidinium-containing TgT group is between GG_3 and GG_4 and the expected radical cation migration path through purines is further inhibited. In this case, substitution of the positively charged guanidinium group does reduce the amount of strand cleavage observed at GG_4, GG_5, and GG_6, as shown in Fig. 3 and in the histogram from quantitative phosphorimagery shown in Fig. 4. Similar results are obtained from the irradiation of DNA(**7/8**). The positive charge in DNA(**6/7**) leads to about 50% inhibition of reaction at GG_4, while the additional positive charge in DNA(**7/8**) has no additional influence. The positively charged backbone modification has a local effect on radical cation trapping, while there is no effect on radical cation hopping, as seen in reactions of GG_5 and GG_6 (Fig. 4).

Conclusions

We replaced portions of the phosphodiester backbone of DNA with segments containing positively charged guanidinium groups. The guanidinium groups connect thymines in a TT bridge that separates GG steps. The results of the one-electron oxidation experiments show that the presence of

Fig. 4. Histogram showing the relative amount of strand cleavage at respective GG steps for DNA duplexes (**6/7**), (**7/8**), and (**5/6**) after 10 min of irradiation at 350 nm and standard work-up with piperidine. The error bars are calculated from independent repetitions.

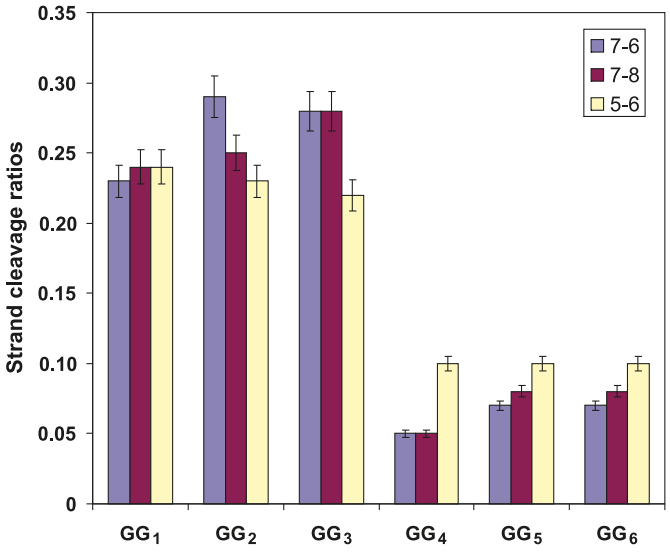

positively charged backbone groups does not affect the hopping rate constants for radical cations in these duplexes. This substitution does have a local effect when the positively charged backbone is introduced into the "purine pathway". This result is understood to be a consequence of radical cation ("hole") density that is localized largely on the relatively low oxidation potential nucleobase sites guanine and adenine. Apparently, although the phosphate backbone may also be involved in charge delocalization, its role is not significant enough to measurably affect the hopping of radical cations in DNA. The rate of the trapping reaction appears to be somewhat reduced at guanines adjacent to a guanidinium group.

Supplementary data

Supplementary data are available with the article through the journal Web site (www.nrcresearchpress.com/cjc).

Acknowledgements

We thank the Vasser Woolley Foundation for research support and Drs. Joshy Joseph, Wen Chen, and Elizabeth Kuruvilla of the Georgia Institute of Technology School of Chemistry and Biochemistry for helpful discussion.

References

(1) (a) Schuster, G. B., Ed. *Top. Curr. Chem.* **2004**, *236*; (b) Schuster, G. B., Ed. *Top. Curr. Chem.* **2004**, *237*.
(2) Kanvah, S.; Joseph, J.; Schuster, G. B.; Barnett, R. N.; Cleveland, C. L.; Landman, U. *Acc. Chem. Res.* **2010**, *43* (2), 280. doi:10.1021/ar900175a.
(3) Genereux, J. C.; Barton, J. K. *Chem. Rev.* **2010**, *110* (3), 1642. doi:10.1021/cr900228f.
(4) Lewis, F. D.; Zhu, H.; Daublain, P.; Sigmund, K.; Fiebig, T.; Raytchev, M.; Wang, Q.; Shafirovich, V. *Photochem. Photobiol. Sci.* **2008**, *7* (5), 534. doi:10.1039/b719715b.

Can. J. Chem. Downloaded from www.nrcresearchpress.com by University of Electronic and Science Techonology of China on 09/18/12
For personal use only.

(5) Giese, B.; Amaudrut, J.; Kohler, A. K.; Spormann, M.; Wessely, S. *Nature* **2001**, *412* (6844), 318. doi:10.1038/35085542.
(6) Lewis, F. D.; Liu, X.; Liu, J.; Miller, S. E.; Hayes, R. T.; Wasielewski, M. R. *Nature* **2000**, *406* (6791), 51. doi:10.1038/35017524.
(7) Berlin, Y. A.; Kurnikov, I. V.; Beratan, D.; Ratner, M. A.; Burin, A. L. *Top. Curr. Chem.* **2004**, *237*, 1.
(8) Saito, I.; Takayama, M.; Sugiyama, H.; Nakatani, K.; Tsuchida, A.; Yamamoto, M. *J. Am. Chem. Soc.* **1995**, *117* (23), 6406. doi:10.1021/ja00128a050.
(9) Misiaszek, R.; Crean, C.; Joffe, A.; Geacintov, N. E.; Shafirovich, V. *J. Biol. Chem.* **2004**, *279* (31), 32106. doi:10.1074/jbc.M313904200.
(10) Barnett, R. N.; Cleveland, C. L.; Joy, A.; Landman, U.; Schuster, G. B. *Science* **2001**, *294* (5542), 567. doi:10.1126/science.1062864.
(11) Cleveland, C. L.; Barnett, R. N.; Bongiorno, A.; Joseph, J.; Liu, C.; Schuster, G. B.; Landman, U. *J. Am. Chem. Soc.* **2007**, *129* (27), 8408. doi:10.1021/ja071893z.
(12) Liu, C. S.; Hernandez, R.; Schuster, G. B. *J. Am. Chem. Soc.* **2004**, *126* (9), 2877. doi:10.1021/ja0378254.
(13) Schuster, G. B. *Acc. Chem. Res.* **2000**, *33* (4), 253. doi:10.1021/ar980059z.
(14) Henderson, P. T.; Jones, D.; Hampikian, G.; Kan, Y. Z.; Schuster, G. B. *Proc. Natl. Acad. Sci. U.S.A.* **1999**, *96* (15), 8353. doi:10.1073/pnas.96.15.8353.
(15) Conwell, E. M. *Proc. Natl. Acad. Sci. U.S.A.* **2005**, *102* (25), 8795. doi:10.1073/pnas.0501406102.
(16) Steenken, S.; Jovanovic, S. V. *J. Am. Chem. Soc.* **1997**, *119* (3), 617. doi:10.1021/ja962255b.
(17) Kanvah, S.; Schuster, G. B. *Org. Biomol. Chem.* **2010**, *8* (6), 1340. doi:10.1039/b922881k.
(18) Ghosh, A.; Joy, A.; Schuster, G. B.; Douki, T.; Cadet, J. *Org. Biomol. Chem.* **2008**, *6* (5), 916. doi:10.1039/b717437c.
(19) Joy, A.; Ghosh, A. K.; Schuster, G. B. *J. Am. Chem. Soc.* **2006**, *128* (16), 5346. doi:10.1021/ja058758b.
(20) Joseph, J.; Schuster, G. B. *J. Am. Chem. Soc.* **2009**, *131* (39), 13904. doi:10.1021/ja9055917.
(21) Joseph, J.; Schuster, G. B. *J. Am. Chem. Soc.* **2006**, *128* (18), 6070. doi:10.1021/ja060655l.
(22) Liu, C. S.; Schuster, G. B. *J. Am. Chem. Soc.* **2003**, *125* (20), 6098. doi:10.1021/ja029333h.
(23) Barnett, R. N.; Cleveland, C. L.; Landman, U.; Boone, E.; Kanvah, S.; Schuster, G. B. *J. Phys. Chem. A* **2003**, *107* (18), 3525. doi:10.1021/jp022211r.
(24) Kratochvílová, I.; Todorciuc, T.; Král, K.; Němec, H.; Bunček, M.; Šebera, J.; Záliš, S.; Vokáčová, Z.; Sychrovský, V.; Bednárová, L.; Mojzeš, P.; Schneider, B. *J. Phys. Chem. B* **2010**, *114* (15), 5196. doi:10.1021/jp100264v.
(25) Ikeura-Sekiguchi, H.; Sekiguchi, T. *Phys. Rev. Lett.* **2007**, *99* (22), 228102. doi:10.1103/PhysRevLett.99.228102.
(26) Liu, T.; Barton, J. K. *J. Am. Chem. Soc.* **2005**, *127* (29), 10160. doi:10.1021/ja053025c.
(27) Onyemauwa, F. O.; Schuster, G. B. *Org. Lett.* **2006**, *8* (23), 5255. doi:10.1021/ol062075z.
(28) Joseph, J.; Schuster, G. B. *Org. Lett.* **2007**, *9* (10), 1843. doi:10.1021/ol070135a.
(29) Barnett, R. N.; Bongiorno, A.; Cleveland, C. L.; Joy, A.; Landman, U.; Schuster, G. B. *J. Am. Chem. Soc.* **2006**, *128* (33), 10795. doi:10.1021/ja061795y.
(30) Barawkar, D. A.; Bruice, T. C. *Proc. Natl. Acad. Sci. U.S.A.* **1998**, *95* (19), 11047. doi:10.1073/pnas.95.19.11047.
(31) Liu, C. S.; Schuster, G. B. *J. Am. Chem. Soc.* **2003**, *125* (20), 6098. doi:10.1021/ja029333h.

Comparison of photoenolization and alcohol release from alkyl-substituted benzoyl benzoic esters

Sivaramakrishnan Muthukrishnan, Tamara C.S. Pace, Qian Li, Brian Seok, Gerdien de Jong, Cornelia Bohne, and Anna D. Gudmundsdottir

Abstract: Photolysis of **1B** in argon-saturated solutions yields **4B** and releases methanol. Laser flash photolysis of **1B** shows formation of biradical **2B**, which has a lifetime of ~50 ns and a λ_{max} at 330 nm. Biradical **2B** undergoes an intersystem crossing to form photoenols **E-3B** and **Z-3B** with a λ_{max} at 390 nm. Laser flash photolysis shows that the lifetimes of **E-3B** and **Z-3B** are affected by the solvent. Density functional theory calculations demonstrate that the transition-state barrier for a 1,5-H atom shift from **Z-3B** to regenerate **1B** is affected by the *ortho*-alkyl substituents, whereas the stereoelectronics of the alkyl substituent affect the transition-state barrier of **E-3B** as it undergoes electrocyclic ring closure to form **4B**. The photoreactivity of **1B** was compared with its analogous methyl and isopropyl derivatives **1A** and **1C**, respectively, to better estimate the effect of the alkyl substituent on reactivity.

Key words: photoremovable protecting groups, photoenols, laser flash photolysis, 1,5 H-atom shift, electrocyclic ring closure, intramolecular lactonization.

Résumé : La photolyse de **1B** dans des solutions saturées en argon conduit à la formation de **4B** et à la libération de méthanol. La photolyse éclair au laser de **1B** conduit à la formation du biradical **2B** dont le temps de vie est d'environ 50 ns et un λ_{max} à 330 nm. Le biradical **2B** subit une transformation intersystème avec formation des photoénols **E-3B** et **Z-3B** avec un λ_{max} à 390 nm. La photolyse éclair au laser montre que les temps de vie des isomères **E-3B** et **Z-3B** sont affectés par le solvant. Des calculs selon la théorie de la fonctionnelle de la densité démontre que la barrière de l'état de transition pour un déplacement 1,5 d'atome d'hydrogène à partir de **Z-3B** et conduisant à la régénération du produit **1B** est affectée par les substituants *ortho*-alkyles alors que les effets stéréoélectroniques du substituant alkyle affectent la barrière de l'état de transition de l'isomère **E-3B** lorsqu'il subit une fermeture électrocyclique de cycle conduisant à la formation de **4B**. Dans le but de pouvoir mieux évaluer l'effet d'un substituant alkyle sur la réactivité, on a comparé la photoréactivité de **1B** à celles de ses analogues, les dérivés méthyle (**1A**) et isopropyle (**1C**).

Mots-clés : groupes protecteurs photolabiles, photoénols, photolyse éclair au laser, déplacement 1,5 d'un atome d'hydrogène, fermeture électrocyclique de cycle, lactonisation intramoléculaire.

[Traduit par la Rédaction]

Introduction

In the past few decades, various systems have been designed for use as photoremovable protecting groups, phototriggers, and photocaging groups.[1–7] Photoremovable protecting groups have potential use in a wide variety of applications, such as drug and gene delivery, release of fragrances in household products, and as an aid in multistep synthesis. Furthermore, photoremovable protecting groups have been used to release bioactive compounds in living tissue and thus make it possible to study physiological events such as enzyme activity, muscle contraction by ATP hydrolysis, and ion channel permeability. Because they have potential use in such a wide variety of applications, photoremovable protecting groups with diverse physical properties are desirable. Furthermore, detailed knowledge of the photorelease mechanism makes it easier to determine the best-suited photoremovable protecting groups for each application.

We have shown that ester **1C** releases its alcohol moiety upon irradiation, and that the release is independent of the reaction medium.[8,9] The release from **1C** is initiated by intramolecular H-atom abstraction by the triplet ketone in **1** to form 1,4-triplet biradical **2C**, which intersystem crosses to E and Z-photoenols **3C**. **Z-3C** is short-lived because it

Received 5 June 2010. Accepted 18 August 2010. Published on the NRC Research Press Web site at canjchem.nrc.ca on 25 February 2011.

This article is part of a Special Issue dedicated to Professor J. C. Scaiano.

S. Muthukrishnan, Q. Li, B. Seok, G. de Jong, and A.D. Gudmundsdottir.[1] Department of Chemistry, University of Cincinnati, Cincinnati, Ohio 45221, USA.
T.C.S. Pace and C. Bohne. Department of Chemistry, University of Victoria, Victoria, BC V8W 3V6, Canada.

[1]Corresponding author (e-mail: annag@uc.edu).

Can. J. Chem. Downloaded from www.nrcresearchpress.com by University of Electronic and Science Techonology of China on 09/18/12
For personal use only.

Can. J. Chem. Downloaded from www.nrcresearchpress.com by University of Electronic and Science Techonology of China on 09/18/12
For personal use only.

Scheme 1. Proposed reaction mechanism for photorelease from **1**.

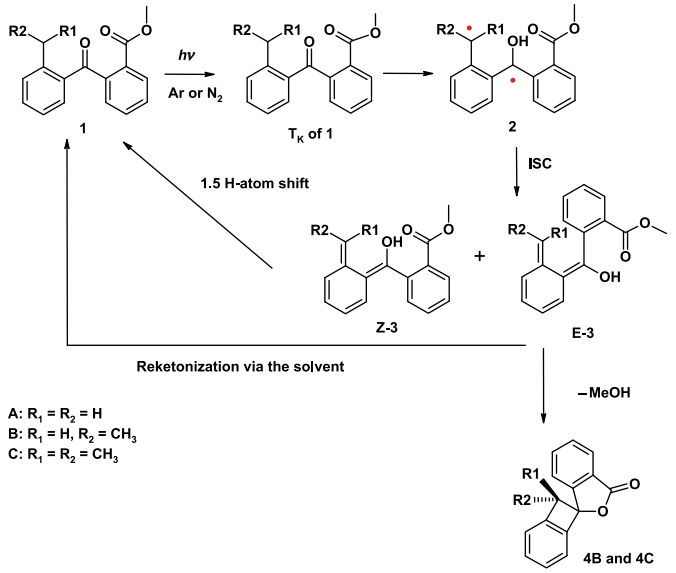

decays by a 1,5-H shift to regenerate **1C**. The longer lived **E-3C** undergoes electrocyclic ring closure and intramolecular lactonization to release the alcohol moiety. In comparison, **1A**, which has an *ortho*-methyl group, fails to release its alcohol moiety upon irradiation (Scheme 1), even though transient spectroscopy shows that the major reactivity of **1A** involves intramolecular H-atom abstraction to form **Z-3A** and **E-3A**.[10] It was concluded that the short lifetime of **E-3A** prevented it from undergoing intramolecular lactonization and releasing its alcohol.

In this paper, we compare the photoreactivities of methyl, ethyl, and isopropyl benzoyl benzoic esters **1A**, **1B**, and **1C**, respectively, in argon- or nitrogen-saturated solutions by performing product studies, transient absorption spectroscopy, and theoretical calculations. The lifetimes of **Z-3** and **E-3** are affected by intramolecular hydrogen bonding, the steric demand, and the stereoelectronic properties of the *ortho*-alkyl groups. The yields of photorelease from **1A**, **1B**, and **1C** depend on the yields of **E-3A**, **3B**, and **3C** and, more importantly, on their lifetimes.

Experiments

Laser flash photolysis

Laser flash apparatus

Laser flash photolysis studies were performed using Excimer[11] or YAG lasers.[12,13] Rate constants were determined by fitting an average of three to eight kinetic traces. Transient absorption spectra were obtained by plotting average absorbance values collected from decays at 10 or 20 nm intervals between 300 and 600 nm.

Sample preparation for laser flash photolysis

Stock solutions of **1A**, **1B**, and **1C** in methanol and acetonitrile were prepared with spectroscopic grade solvents, such that the solutions had absorptions between 0.6 and 0.8 at 266 nm. Stock solutions of **1A**, **1B**, and **1C** in spectroscopic grade benzene and acetonitrile were prepared so that the solutions had absorptions between 0.8 and 0.6 at 308 nm. Typically, about 2 mL of the solutions was placed in 7 mm × 7 mm Suprasil quartz cells capped with prewashed septa. These solutions were purged with nitrogen or argon for 10 min. The lifetimes of **E-3C** were measured as described earlier.[13]

Preparation of 1B

To a stirred solution of phthalic anhydride (2.29 g, 15 mmol) in a 1:1 anhydrous diethyl ether – toluene mixture was added 2-ethylphenyl magnesium bromide, prepared from 2-bromoethylbenzene (3.0 g, 16 mmol) and magnesium turnings (500 mg, 17.8 mmol) in anhydrous diethyl ether.[14] The resulting mixture was refluxed for 12 h and poured onto ice – hydrochloric acid, and the resulting mixture was extracted with diethyl ether (3 × 30 mL). The mixture was washed with a 10% $NaHCO_3$ solution, and the aqueous phase was acidified with 10% aq HCl and extracted with diethyl ether (3 × 30 mL). The organic layer was dried over anhydrous magnesium sulfate and evaporated under vacuum to yield 2-(2′-ethylbenzoyl)benzoic acid (2.2 g, 8.5 mmol, 56%). Without further purification, the material was dissolved in methanol, concd H_2SO_4 (5 mL) was added, and the mixture was refluxed overnight (16 h). The resulting mixture was cooled to room temperature, neutralized with aq $NaHCO_3$, and extracted with diethyl ether (3 × 40 mL). The organic layer was dried over anhydrous magnesium sulfate and evaporated under vacuum to yield a yellow residue. The residue was purified by silica gel column chromatography to yield methyl 2-(2′-ethylbenzoyl)benzoic acid ester **1B** as a pale yellow oil (2.2 g, 8.2 mmol, 51% yield).

1B: IR (neat, cm^{-1}): 2954, 1725, 1670, 1287, 929, 768. ^1H NMR (400 MHz, $CDCl_3$, ppm) δ: 7.92 (m, 1H), 7.38–7.62 (m, 5H), 7.13–7.24 (m, 2H), 3.64 (s, 3H), 3.05 (q, J = 8 Hz, 2H) 1.34 (t, J = 8 Hz, 3H). ^{13}C NMR (100 MHz, $CDCl_3$, ppm) δ: 198.4, 167.3, 145.8, 142.2, 136.4, 131.9, 131.7, 131.4, 130.4, 130.2, 130.1, 129.7, 128.8, 126.8, 52.6, 27.0, 15.7. HRMS (ESI-MS) *m/z* calcd for $C_{17}H_{16}O_3Na$ $[M + Na]^+$: 291.0997; found: 291.0983.

Photolysis of 1B in argon-saturated 2-propanol

Ester **1B** (71 mg, 0.27 mmol) was placed in a Pyrex tube and dissolved in 2-propanol (7 mL), and the resulting solution was purged with argon at room temperature for 15 min and sealed with a rubber septum. The solution was irradiated using a 450 W medium pressure mercury arc lamp immersed in a Pyrex well for 28 h at room temperature. The reaction was monitored through thin layer chromatography (10% ethyl acetate in hexane). After the majority of the starting material disappeared, the solvent was removed under vacuum, and the yellow residue was purified with a silica gel column using a 7:93 ethyl acetate – hexane mixture to yield **4B** as a yellow liquid (35 mg, 15 mmol, 56% yield) and recovered starting material (25 mg, 0.09 mmol, 35% recovery).

4B: IR (neat, cm^{-1}): 2924, 1771, 1465, 934. ^1H NMR (400 MHz, $CDCl_3$, ppm) δ: 7.03–7.17 (m, 2H), 7.31–7.64 (m, 5H), 7.98–8.00 (m, 1H), 4.31 (q, J = 8 Hz, 1H), 1.28 (d, J = 8 Hz, 3H). ^{13}C NMR (100 MHz, $CDCl_3$, ppm) δ: 169.8, 146.9, 141.9, 133.5, 131.1, 129.4, 128.7, 126.7, 125.6, 123.4, 123.4, 122.4, 90.3, 50.9, 14.7. HRMS (ESI-

Can. J. Chem. Downloaded from www.nrcresearchpress.com by University of Electronic and Science Techonology of China on 09/18/12
For personal use only.

Scheme 2. Photolysis of **1A**, **1B**, and **1C** in argon-saturated benzene.

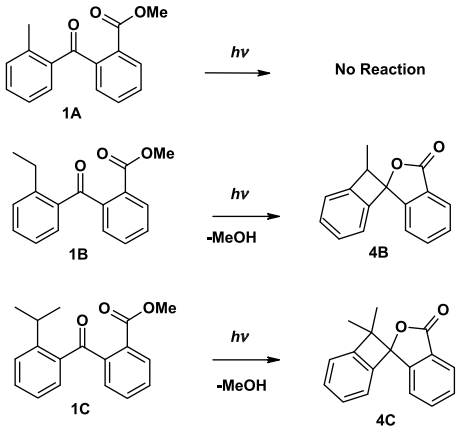

MS) *m/z* calcd for $C_{17}H_{16}O_2$ [M + 1]: 237.0916; found: 237.0904.

Quantum yields

Quantum yields for the photolysis of **1B** were determined both for depletion of the starting material and for formation of product **4B**. 2-Propanol was dried over molecular sieves and distilled prior to use. The mole to area ratio response of the GC traces was calibrated for compounds **1B** and **4B** and valerophenone in 2-propanol, which was the actinometer.[15] Irradiation of 0.1 mol/L argon- and nitrogen-saturated 2-propanol solutions of **1B** on a merry-go-round apparatus using a 450 W medium pressure mercury arc lamp and potassium chromate filter to isolate the 313 nm line was performed to about 10% conversion. At least three replicates of each sample were irradiated and analyzed with a GC equipped with an FID detector. The results from all three replicates were averaged.

Theoretical calculations

Density functional theory (DFT) calculations were performed using Gaussian03 at the B3LYP level of theory and with the 6–31+G(d) basis set.[16,17] All transition states were confirmed to have one imaginary vibrational frequency by the analytical determination of the second derivative of the energy with respect to the internal coordinates. Intrinsic reaction coordinate[18] calculations were used to verify that the transition states corresponded to the correct reactant and products.[19,20] Vertical UV absorption spectra were calculated using time-dependent density functional theory (TD-DFT).[21–25] The effect of solvation was calculated using the self-consistent reaction field (SCRF) method with the integral equation formalism polarization continuum model (IEFPCM) with methanol and acetonitrile as the solvents.[26–30]

Results and discussion

Product studies

Photolysis of **1B** in an argon-saturated solution results in lactone **4B**, which is similar to the photoreactivity of **1C** (Scheme 2). Irradiation of **1B** in solvents such as benzene, toluene, chloroform, and 2-propanol yields **4B** in comparable yields, indicating that the photorelease is not strongly affected by the solvent (Fig. 1). In contrast, we have reported that photolysis of **1A** yields no products in solvents such as benzene and chloroform, which do not have easily abstractable H atoms. However, in solvents with abstractable H atoms, **1A** yields **5** (Scheme 3), presumably from intermolecular H-atom abstraction from the solvent.[10]

Fig. 1. Photolysis of **1B** in $CHCl_3$, C_6H_6, 2-propanol, and toluene.

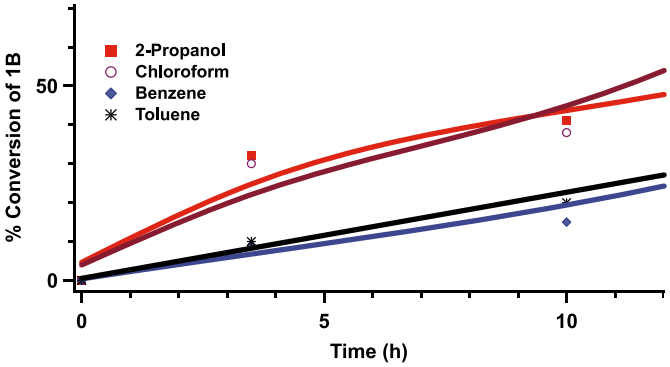

Scheme 3. Photolysis of **1A** in argon-saturated methanol.

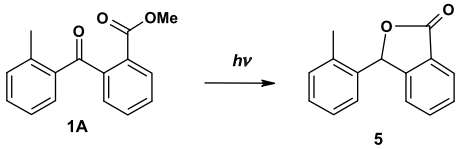

Table 1. Quantum yields for depletion of **1** and formation of **4.**

Quantum yield for depletion of **1**		Quantum yield for formation of **4**	
1A[a]	0.030±0.003	**4A**	0
1B	0.09±0.01	**4B**	0.07±0.01
1C[b]	0.17±0.01	**4C**	0.14±0.01

[a]See ref. 10.
[b]See ref. 8.

Quantum yields

The quantum yields for the depletion of **1B** and the formation of **4B** in 2-propanol are listed in Table 1. The quantum yields for **1C**, which have been published previously, are slightly higher than those for **1B** and are listed in Table 1 for comparison.

Calculations

To better understand why **1A**, **1B**, and **1C** react differently, we calculated the stationary points on their energy surfaces. We optimized the gas-phase structures of **1A**, **1B**, and **1C** and their respective first triplet excited states of the ketone. The C=O bond in the T_K of **1** is elongated to 1.311 Å compared with 1.225 Å in the S_0. The progression of the C–O bond stretch fits well with the T_K of **1** having an (n,π*) configuration.[31–34] The calculated energies of the T_Ks of **1A**, **1B**, and **1C** are ~8 kcal/mol (1 cal = 4.184 J) lower than the measured value for the analogous benzophenone. However, we have previously shown that DFT calculations

Can. J. Chem. Downloaded from www.nrcresearchpress.com by University of Electronic and Science Techonology of China on 09/18/12
For personal use only.

Table 2. Intramolecular hydrogen bonds in **Z-3** and **E-3**.

	Bond vibrational frequency	Bond length
Compound	O–H (cm^{-1})	C=O H–O– (Å)
Z-3A	3479	1.783
Z-3B	3480	1.782
Z-3C	3459	1.740
E-3A	3506	1.800
E-3B	3504	1.7821
E-3C	3490	1.756

underestimate the energy of triplet ketones with an (n,π*) configuration.[35]

We optimized the structures of biradicals **2A**, **2B**, and **2C** and found that their lowest energy conformers have intramolecular hydrogen bonding between the O–H group and the C=O ester group. The hydrogen-bonded conformers are ~5–8 kcal/mol lower in energy than those that do not have intramolecular hydrogen bonding. The calculated O–H and C=O stretches in the hydrogen-bonded conformer of **2A** are located at 2996 and 1662 cm^{-1}, respectively, but the corresponding stretches are at 3742 and 1768 cm^{-1} in a conformer of **2A** that does not undergo intramolecular hydrogen bonding. Thus, the calculated IR spectra confirm the intramolecular hydrogen bonding in the lowest energy conformers of **2A**, **2B**, and **2C**.

The structures of **Z-3** and **E-3** with intramolecular hydrogen bonding were also optimized. Enols **Z-3** and **E-3** are between 35 and 40 kcal/mol higher in energy than corresponding ketones **1A**, **1B**, and **1C**. Furthermore, **Z-3** is between 1 and 3 kcal/mol more stable than the corresponding **E-3** molecule. The intramolecular hydrogen bond in **Z-3C** is shorter and has a lower vibrational frequency than that in **Z-3A** and **Z-3B** and is therefore stronger (Table 2). Similarly, the intramolecular hydrogen bond in **E-3C** is found to be stronger than that for **E-3A** and **E-3B**.

We calculated the transition state for the T_K of **1** for the H-atom abstraction to form biradical **2**. The transition-state barrier for γ H-atom abstraction of the T_K of **1A** is ~8 kcal/mol, whereas the transition-state barriers for the T_Ks of **1B** and **1C** are less by 3 and 4 kcal/mol, respectively. The stationary points on the energy surfaces of **1A**–**1C** are plotted in Figs. 2–4. These plots highlight that the intramolecular H-atom abstraction from the T_K of **1A**, **1B**, and **1C** to form biradicals **2A**, **2B**, and **2C** can be easily achieved at ambient temperature. Even though biradical **2A** is a primary radical, it is only ~3 kcal/mol less stable than **2B** and **2C**, presumably because the radical center on the *ortho*-methylene is stabilized owing to conjugation with the aromatic rings. The driving force for the reactivity of **E-3** and **Z-3** must be the re-aromatization of the benzene ring.

We calculated the transition states for **Z-3** to reform **1** via 1,5 H-atom shifts (Table 3 and Fig. 5). The transition-state barrier for **Z-3A** to reform **1A** is 7.2 kcal/mol and 6.6 kcal/mol for **Z-3B** to form **1B**. Presumably, the electron-donating effect of the ethyl groups stabilizes the transition state more than the methyl group stabilizes it. In comparison, the steric demand of the isopropyl group, which cannot rotate away as

Scheme 4. Calculated transition state barriers for **E-3**, **6**, and **7**.

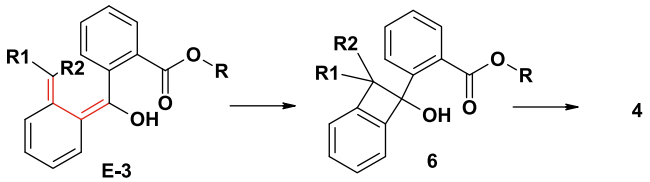

	Torsion Angle	Transition state for electrocyclic ring closure (kcal/mol)	Transition state for lactonization (kcal/mol)
E-3A	28	18.6	37.4
E-3B	33	16.1	36.8
E-3C	44	15.9	42.4

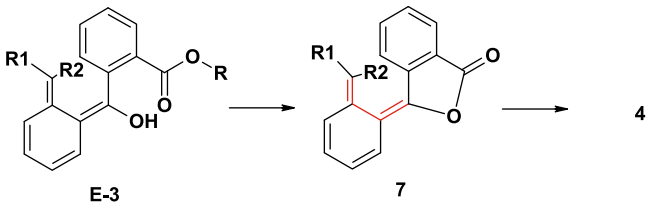

	Transition state for lactonization (kcal/mol)	Torsion Angle	Transition state for electrocyclic ring closure (kcal/mol)
E-3A	43.5	33	18.6
E-3B	43.2	35	17.6
E-3C	43.0	44	17.8

the ethyl group can, causes the transition-state barrier for the 1,5 H-atom shift in **Z-3C** to increase to 7.9 kcal/mol.

The calculated transition states for electrocyclic ring closure of **E-3** show that alkyl substituents stabilize this transition state (Scheme 4). Thus, the transition-state barrier for **E-3A** is the highest, and the barriers for **E-3B** and **E-3C** are lower. The steric effect of the dimethyl substituents in **E-3C** twists its butadienyl moiety. The torsion angle between the butadienyl moiety in **E-3C** is 44°, but only 33° and 28° in **E-3B** and **E-3A**, respectively. In the electrocyclic ring closures, twisting of the butadienyl moiety to a distorted structure moves the reactant along the potential energy surface towards the transition state's twisted geometry. So the steric effect of the dimethyl substituent in **E-3C** lowers the transition-state barrier for forming **6C** by twisting the butadienyl moiety.

Furthermore, we calculated the transition-state barrier for **6** to undergo lactonization and found that the barrier for lactonization is ~40 kcal/mol, which is considerably higher than the transition-state barrier for **E-3** to undergo electrocyclic ring closure. However, it is complicated to compare these transition-state barriers because solvation is expected to affect the lactonization significantly more than the electrocyclic ring closure. The calculated transition-state barriers make it possible to evaluate the effect of the alkyl substituents on these two processes rather than to obtain their absolute values. The steric demand of the dimethyl group in **6C** makes the lactonization slightly less feasible than for **6A** and **6B**.

We calculated the transition states for lactonization of **E-3A**, **3B**, and **3C** to form **7**. The transition-state barrier is

Can. J. Chem. Downloaded from www.nrcresearchpress.com by University of Electronic and Science Techonology of China on 09/18/12
For personal use only.

Fig. 2. Calculated stationary points on the energy surface for **1A**. The energies are in kcal/mol (1 cal = 4.184 J) and are obtained from the singlet- (black) and triplet-optimized structures with zero point energy corrections included. Numbers in parentheses are energies calculated with a polarization continuum model (PCM) model for methanol.

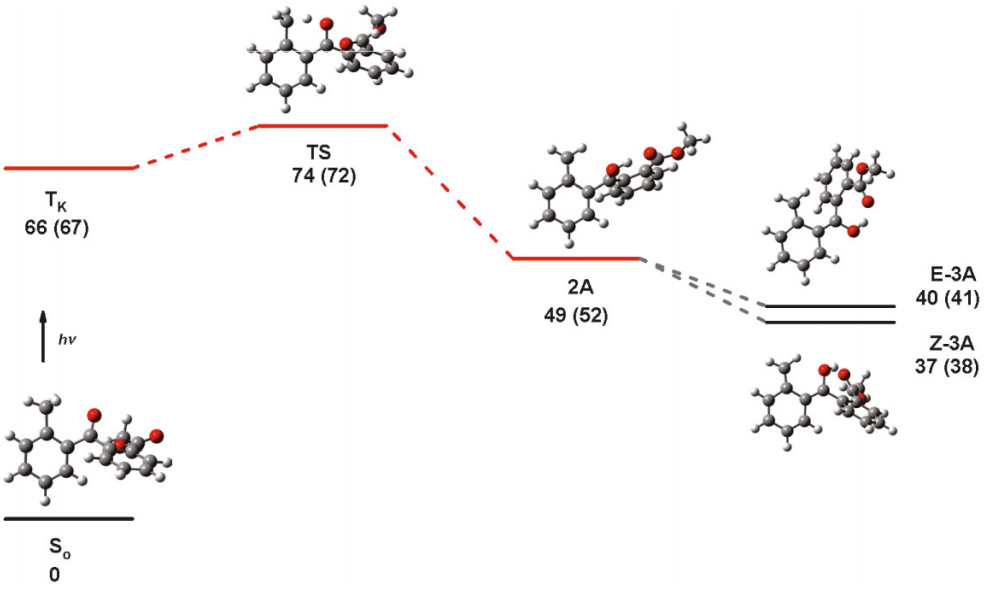

Fig. 3. Calculated stationary points of the energy surface for **1B**. The energies are in kcal/mol (1 cal = 4.184 J) and are obtained from the singlet- (black) and triplet-optimized structures with zero point energy corrections included. Numbers in parentheses are energies calculated with a polarization continuum model (PCM) model for methanol.

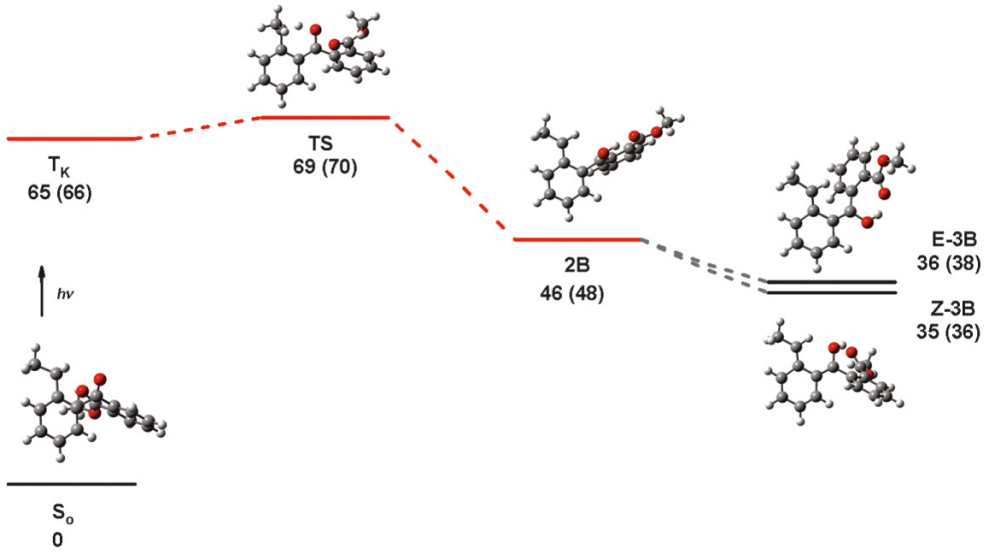

~43 kcal/mol for **E-3**. The calculations demonstrate that the *ortho*-alkyl substituent has minimal effect on the lactonization of **E-3**. In comparison, the calculated transition-state barrier for **7** to form **4** shows that ring closure of **7A** is the least favored as expected, since its butadienyl moiety is less twisted than for **7B** and **7C**.

Thus, the calculations show that the electrocyclic ring closure of **E-3** and **6** are affected by the alkyl substituents, whereas lactonization of **E-3** is not. However, the transition-state barrier for lactonization of **6C** is increased by the steric demand of the dimethyl group.

Laser flash photolysis of **1B** in nitrogen-saturated methanol produced a transient spectrum with a λ_{max} at ~330 nm with a lifetime of ~53 ns (Fig. 6) We assign this absorption to triplet biradical **2B** on the basis of its similarity to the transient spectra of the analogous 1,4-biradical **2A**.[9,10] The TD-DFT calculations support this assignment because the major calculated electronic transition for **2B** is located at 336 nm (f = 0.0871) in the gas phase and at 334 nm (f = 0.1104) in methanol. In oxygen-saturated solutions, the absorption owing to **2B** was quenched. As the absorption band for **2B** decayed, a new transient with a λ_{max} at 390 nm (Fig. 6) formed at the same rate. We assign this absorption to **Z-3B** and **E-3B**, based on comparison with the transient spectra of **3A** and **3C**.[8,10] The TD-DFT calculations also support this assignment as they revealed that the major absorption bands of **Z-3B** and **E-3B** are located at 426 nm (f = 0.1975) and 437 nm (f = 0.0699) in methanol, respec-

Can. J. Chem. Downloaded from www.nrcresearchpress.com by University of Electronic and Science Techonology of China on 09/18/12
For personal use only.

Fig. 4. Calculated stationary points on the energy surface for **1C**. The energies are in kcal/mol (1 cal = 4.184 J) and are obtained from the singlet- (black) and triplet-optimized structures with zero point energy corrections included. Numbers in parentheses are energies calculated with a polarization continuum model (PCM) model for methanol.

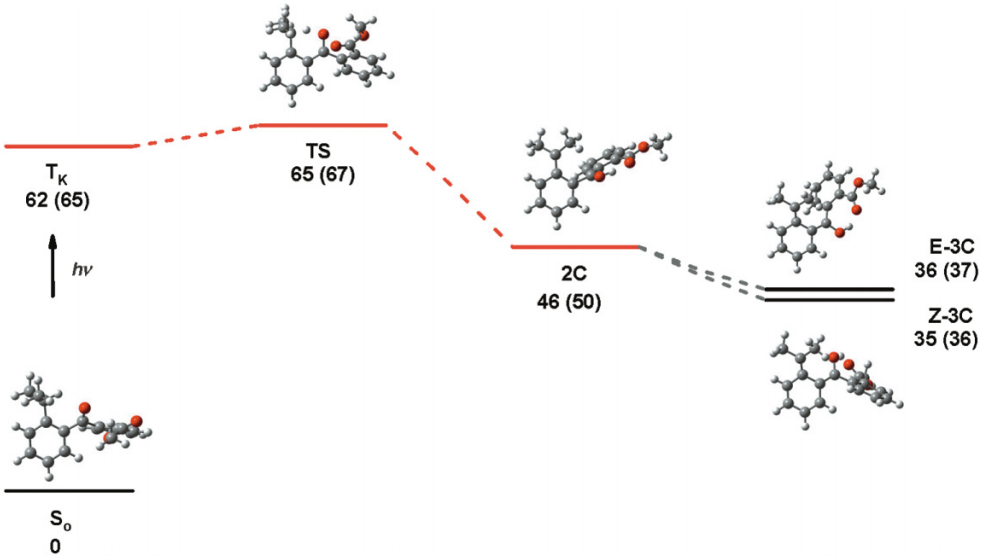

Table 3. Calculated transition-state (TS) barriers for the 1,5 H-atom shift in **Z-3**.

Compound	TS barrier (kcal/mol)
Z-3A	7.2
Z-3B	6.6
Z-3C	7.9

Note: 1 cal = 4.184 J.

Fig. 5. Transition state for 1,5 H-atom shift in **Z-3A**, **Z-3B**, and **Z-3C**.

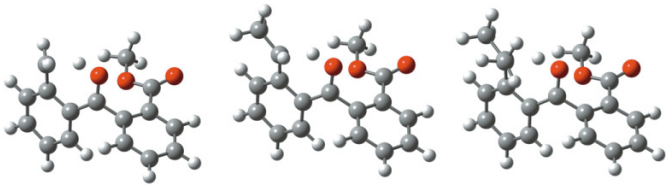

Fig. 6. Laser flash photolysis of **1B** in N_2-saturated methanol over (A) a time window of 1 μs and (B) a time window of 200 μs.

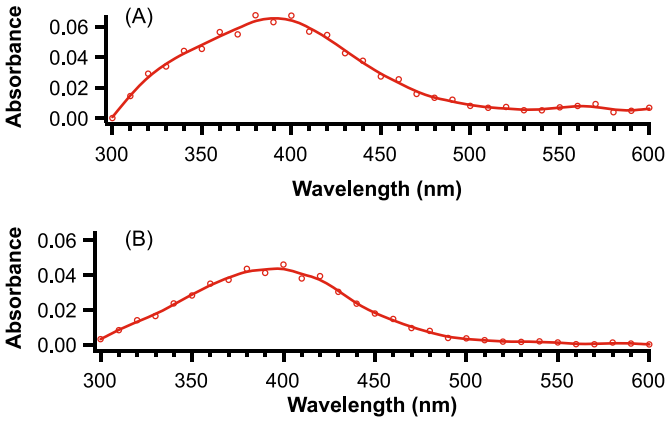

tively. The lifetimes of **Z-3B** and **E-3B** in methanol are 15 μs and >3 ms, respectively. The lifetimes for each component can be obtained by fitting the decay with a monoexponential function because the decay of **Z-E3** is complete before **E-3B** has decayed significantly (Fig. 7). In acetonitrile, the lifetime of **Z-3B** is reduced to 2.5 μs, and the lifetime of **E-3B** is >19 ms. This is in agreement with previous reports that show that the Z-photoenols from *o*-methyl benzophenone and *o*-methyl acetophenones are longer lived in solvents that can form hydrogen bonds with the photoenols.[36,37]

We have reported the laser flash photolysis of **1A** and **1C** previously;[8] however, in this paper we compare the lifetimes and yields of biradicals **2A**, **2B**, and **2C** and photoenols **3A**, **3B**, and **3C** (see Table 4). The lifetimes of biradicals **2A**, **2B**, and **2C** are similar within experimental error, which fits well with the calculations that predict that these biradicals have similar stabilities.

The ratios of **Z-3** and **E-3** in benzene (Fig. 7), which cannot form hydrogen bonds with the photoenols, are shown in Fig. 7. The ratios of Z-enol to E-enol were measured from the absorbance at 390 nm by measuring the combined absorptions of **Z-3** and **E-3** on shorter timescales and the absorption of **E-3** on longer timescales. The Z:E ratio was highest for **3A** at 1:1.2 and somewhat lower for **3C** (3.2:1) and **3B** (3.5:1). Thus, by assuming that **E-3** and **Z-3** have similar absorption coefficients, the quantum yields for enol formation from **1A** is only half that observed for **1B** and **1C** (Fig. 7). The lower yield of photoenols from **1A** is a reflection that the intramolecular H-atom abstraction is less favorable in the T_K of **1A** than in that of **1B** and **1C**. However, the **Z**:**E** ratio is the lowest for **3A**, presumably because intramolecular rotation in **2A** is less hindered than in **2B** and **2C**. We have previously shown that restricted intramolecular rotation in analogous biradicals results in less E-photoenol formation.[38]

The lifetime of **Z-3C** is the longest in all solvents (Table 4), whereas that of **Z-3B** is only somewhat shorter lived and that of **Z-3A** is considerably shorter. The lifetime

Can. J. Chem. Downloaded from www.nrcresearchpress.com by University of Electronic and Science Techonology of China on 09/18/12
For personal use only.

Fig. 7. Decay of **E-3** and **Z-3** at 390 nm in N_2-saturated benzene. The kinetic traces are obtained under identical conditions, thus showing relative yields for forming **Z-3** and **E-3**.

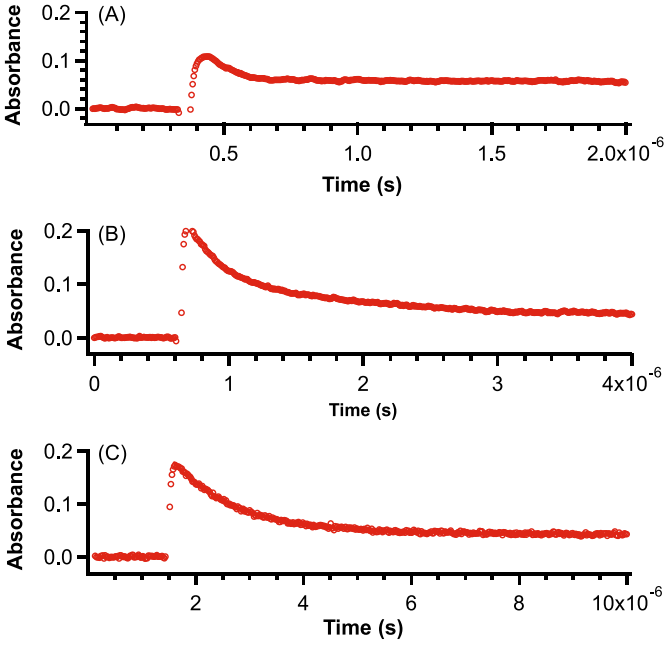

Table 4. Measured lifetimes of **2**, **E-3** and **Z-3** in N_2-saturated solutions.

	Lifetime		
Compound	Benzene	MeCN	MeOH
2A	77 ns	57 ns	54 ns
Z-3A	0.09 μs	1.2 μs	6.5 μs
E-3A	1<τ>8 ms	10 ms	162 μs
2B	50 ns	58 ns	33 ns
Z-3B	~0.7 μs	2.5 μs	15 μs
E-3B	1<τ>8 ms	19 ms	>3 ms
2C	70 ns	83 ns	60 ns
Z-3C	1.2 μs	8 μs	17 μs
E-3C	>500 ms	>0.1 s	>0.1 s

of **Z-3A** in methanol is comparable to the analogous Z-enol from 2,4-methyl benzophenone,[37] whereas the lifetime of **Z-3A** in benzene is considerably longer. Wagner and co-workers[37] showed that the 1,5 H-atom shifts are retarded by intermolecular hydrogen bonding. Thus, we theorize that intramolecular hydrogen bonding also renders **Z-3** more stable towards a 1,5 H-atom shift. The steric factors of the alkyl substituent in **Z-3B** and **Z-3C** also retard the 1,5-hydrogen shift, and thus they are longer lived than **Z-3A**.

The lifetime of **E-3A** was shorter than for **E-3B** in acetonitrile and methanol, whereas the lifetimes in benzene are comparable. **E-3C** is longer lived than both **E-3A** and **E-3B**. Unlike the Z-photoenols, the E-photoenol reketonization is solvent-assisted. Furthermore, in competition with reketonization, **E-3B** and **E-3C** must undergo electrocyclic ring closure and intramolecular lactonization to form **4B** and **4C**, respectively. **E-3A** reketonizes faster than it undergoes electrocyclic ring closure or lactonization. Thus, we theorize that in nonpolar solvents, **E-3B** and **E-3C** decay by electrocyclic ring closure followed by lactonization. Our hypothesis is based on the observation that **E-3A** does not produce **4A** in nonpolar solvent, whereas **E-3A** has lifetimes that are similar as observed for **E-3B** and that the transition-state barrier for **E-3A** to undergo electrocyclic ring closure is larger than that for **E-3B** and **E-3C**. In comparison, the calculated transition-state barrier for lactonization of **E-3** is not affected significantly by the alkyl substituents.

Conclusion

The product studies show that **1B** and **1C** release their alcohol moiety upon irradiation via photoenolization and form **4B** and **4C**, whereas **1A** also undergoes photoenolization, but both **Z-3A** and **E-3A** decay back to the starting material. Laser flash photolysis shows that **1A**, **1B**, and **1C** all undergo H-atom abstraction to form **2**, which intersystem crosses to form **E-3** and **Z-3**. The yields of the photoenols are similar for **1B** and **1C** and slightly less for **1A** in benzene. The calculations further support this because stationary points on the energy surface of these esters are very similar. The lifetime of **E-3A** is significantly shorter in methanol than that of both **E-3B** and **E3C**. Thus, **E-3A** does not react to release its alcohol moiety but rather regenerates **1A**. In comparison, the lifetime of **E-3A** is considerably longer in benzene and acetonitrile, however, because the electrocyclic ring closure for **E-3A** is less favorable than for **E-3B**, it reketonizes faster than it undergoes electrocyclic ring closure. Thus, in designing photoprotecting groups based on intramolecular photoenolization, it is important to consider the effect of the alkyl substituent on electrocyclic ring closure and lactonization.

Acknowledgement

This work was supported by the Petroleum Research Fund administrated by the American Chemical Society and the Ohio Supercomputer Center. Partial funding of this project was provided by the National Science Foundation (NSF). M.S. acknowledges the Harry Mark Research Fellowship. C.B. and T.C.S.P. thank the Natural Sciences and Engineering Research Council of Canada (NSERC) for funding at the University of Victoria, Victoria, British Columbia, and T.C.S.P. thanks NSERC for a Canada Graduate Scholarships – Doctoral (CGS-D) scholarship. A.D.G. is grateful for having had the opportunity to spend a sabbatical in the laboratory of Professor Scaiano.

References

(1) Sankaranarayanan, J.; Muthukrishnan, S.; Gudmundsdottir, A. D. *Adv. Phys. Org. Chem.* **2009**, *43*, 39. doi:10.1016/S0065-3160(08)00002-6.
(2) Herrmann, A. *Angew. Chem. Int. Ed.* **2007**, *46* (31), 5836. doi:10.1002/anie.200700264.
(3) Ellis-Davies, G. C. R. *Nat. Methods* **2007**, *4* (8), 619. doi:10.1038/nmeth1072.
(4) Mayer, G.; Heckel, A. *Angew. Chem. Int. Ed.* **2006**, *45* (30), 4900. doi:10.1002/anie.200600387.
(5) Bochet, C. G. *Pure Appl. Chem.* **2006**, *78* (2), 241. doi:10.1351/pac200678020241.
(6) *Dynamic Studies In Biology*; Goeldner, M.; Givens, R., Eds. Wiley-VCH: Weinheim, 2005.

Can. J. Chem. Downloaded from www.nrcresearchpress.com by University of Electronic and Science Techonology of China on 09/18/12
For personal use only.

(7) Pelliccioli, A. P.; Wirz, J. *Photochem. Photobiol. Sci.* **2002**, *1* (7), 441. doi:10.1039/b200777k.
(8) Pika, J.; Konosonoks, A.; Robinson, R. M.; Singh, P. N. D.; Gudmundsdottir, A. D. *J. Org. Chem.* **2003**, *68* (5), 1964. doi:10.1021/jo0261193.
(9) Pika, J.; Konosonoks, A.; Singh, P.; Gudmundsdottir, A. D. *Spectrum (Bowling Green, OH)* [Online] **2003**, *16* (4), 12. http://www.bgsu.edu/departments/photochem/assets/pdf/spectrum/winter2003spectrum.pdf.
(10) Konosonoks, A.; Wright, P. J.; Tsao, M.-L.; Pika, J.; Novak, K.; Mandel, S. M.; Krause Bauer, J. A.; Bohne, C.; Gudmundsdottir, A. D. *J. Org. Chem.* **2005**, *70* (7), 2763. doi:10.1021/jo048055x.
(11) Muthukrishnan, S.; Sankaranarayanan, J.; Klima, R. F.; Pace, T. C. S.; Bohne, C.; Gudmundsdottir, A. D. *Org. Lett.* **2009**, *11* (11), 2345. doi:10.1021/ol900754a.
(12) Liao, Y.; Bohne, C. *J. Phys. Chem.* **1996**, *100* (2), 734. doi:10.1021/jp951697r.
(13) Mitchell, R. H.; Bohne, C.; Wang, Y.; Bandyopadhyay, S.; Wozniak, C. B. *J. Org. Chem.* **2006**, *71* (1), 327. doi:10.1021/jo052153g.
(14) Wijtmans, M.; Rosenthal, S. J.; Zwanenburg, B.; Porter, N. A. *J. Am. Chem. Soc.* **2006**, *128* (35), 11720. doi:10.1021/ja063562c.
(15) Wagner, P. J. *J. Am. Chem. Soc.* **1967**, *89* (23), 5898. doi:10.1021/ja00999a028.
(16) Frisch, M. J.; Trucks, G. W.; Schlegel, H. B.; Scuseria, G. E.; Robb, M. A.; Cheeseman, J. R.; Montgomery, J. A., Jr.; Vreven, T.; Kudin, K. N.; Burant, J. C.; Millam, J. M.; Iyengar, S. S.; Tomasi, J.; Barone, V.; Mennucci, B.; Cossi, M.; Scalmani, G.; Rega, N.; Petersson, G. A.; Nakatsuji, H.; Hada, M.; Ehara, M.; Toyota, K.; Fukuda, R.; Hasegawa, J.; Ishida, M.; Nakajima, T.; Honda, Y.; Kitao, O.; Nakai, H.; Klene, M.; Li, X.; Knox, J. E.; Hratchian, H. P.; Cross, J. B.; Adamo, C.; Jaramillo, J.; Gomperts, R.; Stratmann, R. E.; Yazyev, O.; Austin, A. J.; Cammi, R.; Pomelli, C.; Ochterski, J. W.; Ayala, P. Y.; Morokuma, K.; Voth, G. A.; Salvador, P.; Dannenberg, J. J.; Zakrzewski, V. G.; Dapprich, S.; Daniels, A. D.; Strain, M. C.; Farkas, O.; Malick, D. K.; Rabuck, A. D.; Raghavachari, K.; Foresman, J. B.; Ortiz, J. V.; Cui, Q.; Baboul, A. G.; Clifford, S.; Cioslowski, J.; Stefanov, B. B.; Liu, G.; Liashenko, A.; Piskorz, P.; Komaromi, I.; Martin, R. L.; Fox, D. J.; Keith, T.; Al-Laham, M. A.; Peng, C. Y.; Nanayakkara, A.; Challacombe, M.; Gill, P. M. W.; Johnson, B.; Chen, W.; Wong, M. W.; Gonzalez, C.; Pople, J. A. Gaussian 03, Revision A.1. Pittsburgh, PA: Gaussian, Inc., 2003.
(17) Becke, A. D. *J. Chem. Phys.* **1993**, *98* (7), 5648. doi:10.1063/1.464913.
(18) Wilson, R. M.; Hannemann, K.; Heineman, W. R.; Kirchhoff, J. R. *J. Am. Chem. Soc.* **1987**, *109* (15), 4743. doi:10.1021/ja00249a060.
(19) Gonzalez, C.; Schlegel, H. B. *J. Chem. Phys.* **1989**, *90* (4), 2154. doi:10.1063/1.456010.
(20) Gonzalez, C.; Schlegel, H. B. *J. Phys. Chem.* **1990**, *94* (14), 5523. doi:10.1021/j100377a021.
(21) Parr, R. G.; Weitao, Y. *Density Functional Theory in Atoms and Molecules;* Oxford University Press: Oxford, UK, 1989.
(22) *Denisty Functional Methods in Chemistry*; Labanowksi, J. K.; Andzelm, J. W., Eds. Springer-Verlag: New York, 1991.
(23) Stratmann, R. E.; Scuseria, G. E.; Frisch, M. J. *J. Chem. Phys.* **1998**, *109* (19), 8218. doi:10.1063/1.477483.
(24) Bauernschmitt, R.; Ahlrichs, R. *Chem. Phys. Lett.* **1996**, *256* (4-5), 454. doi:10.1016/0009-2614(96)00440-X.
(25) Foresman, J. B.; Head-Gordon, M.; Pople, J. A.; Frisch, M. J. *J. Phys. Chem.* **1992**, *96* (1), 135. doi:10.1021/j100180a030.
(26) Tomasi, J.; Persico, M. *Chem. Rev.* **1994**, *94*, 2027. doi:10.1021/cr00031a013.
(27) Cramer, C. J.; Truhlar, D. G. *Chem. Rev.* **1999**, *99*, 2161. doi:10.1021/cr960149m.
(28) Tomasi, J.; Mennucci, B.; Cammi, R. *Chem. Rev.* **2005**, *105* (8), 2999. doi:10.1021/cr9904009.
(29) Mennucci, B.; Cances, E.; Tomasi, J. *J. Phys. Chem. B* **1997**, *101* (49), 10506. doi:10.1021/jp971959k.
(30) Cancès, E.; Mennucci, B. *J. Chem. Phys.* **2001**, *114* (10), 4744. doi:10.1063/1.1349091.
(31) Srivastava, S.; Yourd, E.; Toscano, J. P. *J. Am. Chem. Soc.* **1998**, *120* (24), 6173. doi:10.1021/ja981093b.
(32) He, H.-Y.; Fang, W.-H.; Phillips, D. L. *J. Phys. Chem. A* **2004**, *108* (25), 5386. doi:10.1021/jp037735l.
(33) Fang, W.-H.; Phillips, D. L. *J. Theor. Comput. Chem.* **2003**, *2* (1), 23. doi:10.1142/S0219633603000355.
(34) Fang, W.-H.; Phillips, D. L. *ChemPhysChem* **2002**, *3* (10), 889. doi:10.1002/1439-7641(20021018)3:10<889::AID-CPHC889>3.0.CO;2-U.
(35) Muthukrishnan, S.; Mandel, S. M.; Hackett, J. C.; Singh, P. N. D.; Hadad, C. M.; Krause, J. A.; Gudmundsdottir, A. D. *J. Org. Chem.* **2007**, *72* (8), 2757. doi:10.1021/jo062160k.
(36) Scaiano, J. C.; Wintgens, V.; Netto-Ferreira, J. C. *Tetrahedron Lett.* **1992**, *33* (40), 5905. doi:10.1016/S0040-4039(00)61085-7.
(37) Haag, R.; Wirz, J.; Wagner, P. J. *Helv. Chim. Acta* **1977**, *60* (8), 2595. doi:10.1002/hlca.19770600813.
(38) Muthukrishnan, S.; Sankaranarayanan, J.; Pace, T. C. S.; Konosonoks, A.; De Michiei, M. E.; Meese, M. J.; Bohne, C.; Gudmundsdottir, A. D. *J. Org. Chem.* **2010**, *75* (5), 1393. doi:10.1021/jo9021088.

Investigation of ligand effects on exciton recombination in PbS nanoparticles

Jennifer M. Zemke, Thomas E. Novet, and David R. Tyler

Abstract: Multiple exciton generation (MEG) and exciton recombination were studied by femtosecond transient absorption spectroscopy in PbS nanoparticles (NPs) capped with oleic acid (PbS–OLA) and 2,3-dimercaptopropane sulfonate (PbS–DMPS) ligands. Analysis of the transient absorption data showed that the PbS–DMPS nanoparticles exhibit increased rates of multi- and single-exciton recombination compared with the PbS–OLA nanoparticles; however, the MEG yield for both sets of particles was the same within experimental error. The origin of the differences in the exciton recombination decay rates is unknown, but it is speculated that it may be due to the ionic functionality of DMPS or to the different ligating atoms of the OLA and DMPS ligands. The PbS–DMPS nanoparticles were highly sensitive to the presence of oxygen, which caused a dramatic increase in nonradiative decay pathways, which can be mistaken for multiexciton absorbance and decay. Removal of oxygen eliminated the nonradiative decay pathways. Overall, this study showed that the dynamics of MEG can be modified by changing the NP ligand shell, a result that may be useful in the development of NP-based thin-film solar devices.

Key words: multiple exciton generation, surface modification of nanoparticles, exciton recombination, nanoparticle ligand exchange.

Résumé : On a étudié le génération d'excition multiple (GEM) et la recombinaison d'exciton par spectroscopie d'absorption des espèces transitoires au niveau de la femtoseconde, dans des nanoparticules de PbS coiffées de ligands d'acide oléique (PbS–OLA) et de sulfonate de 2,3-dimercaptopropane (PbS–DMPS). L'analyse des données d'absorption des espèces transitoires montre que, par comparaison avec les nanoparticules de PbS–OLA, les nanoparticules de PbS–DMPS présentent des vitesses accrues de recombinaison d'excitons simples et multiples; toutefois, les rendements pour la GEM sont les mêmes, aux erreurs expérimentales près, dans les deux cas. L'origine des différences dans les vitesses de décroissance de recombinaison de l'exciton est inconnue, mais il est possible de spéculer qu'elle pourrait être due à la fonctionnalité ionique du DMPS ou aux atomes de ligature différents des ligands OLA et DMPS. Les nanoparticules de PbS–DMPS sont très sensibles à la présence d'oxygène qui provoque une augmentation dramatique dans les voies non radiatives de décroissance, que l'on peut attribuer à tort à de l'absorbance multiexciton et à de la décroissance. L'enlèvement de l'oxygène permet d'éliminer ces voies de décroissance non radiatives. Dans l'ensemble, cette étude montre que la dynamique de la GEM peut être modifiée par un changement de la couche de ligand de nanoparticules, un résultat qui peut être utile dans le développement de dispositifs solaires en film mince à base de nanoparticules.

Mots-clés : génération d'excition multiple, modification de la surface de nanoparticules, recombinaison d'exction, échange de ligand d'une nanoparticule.

[Traduit par la Rédaction]

Introduction

Semiconductor nanoparticles (NPs) are favorable candidates for integration into cost-effective solar devices. This is primarily due to their broad optical tunability and ease of processing. In particular, lead chalcogenide (PbS, PbSe, or PbTe) NPs provide tunability through the near-infrared (NIR) portion of the electromagnetic spectrum while exhibiting quantum-confined properties, two desirable qualities for matching the solar spectrum in photovoltaic devices.[1–5]

Because of quantum confinement, an NP has a discrete energy spectrum. In semiconductor NPs, this spectrum is split by a forbidden energy gap much like in bulk semiconductors. However, owing to the discretized energy states, NPs exhibit very different properties from the bulk.[6] Most importantly, bulk semiconductors waste excess solar energy as heat. In semiconductor NPs, however, a process called multiple exciton generation (MEG) can lead to more efficient solar energy transduction. In the MEG process, multiple excitons are created per photon absorbed, provided energy and momentum requirements are met. For semiconductor NPs, the incident photon energy required to create

Received 28 May 2010. Accepted 28 November 2010. Published on the NRC Research Press Web site at canjchem.nrc.ca on 24 February 2011.

This article is part of a Special Issue dedicated to Professor J. C. Scaiano.

J.M. Zemke and D.R. Tyler.[1] Department of Chemistry, University of Oregon, 1253 University of Oregon, Eugene, OR 97403, USA.
T.E. Novet. Voxtel-Inc, University of Oregon, 1253 University of Oregon, Eugene, OR 97403, USA.

[1]Corresponding author (e-mail: dtyler@uoregon.edu).

Can. J. Chem. Downloaded from www.nrcresearchpress.com by University of Electronic and Science Techonology of China on 09/18/12
For personal use only.

Can. J. Chem. Downloaded from www.nrcresearchpress.com by University of Electronic and Science Techonology of China on 09/18/12
For personal use only.

multiple excitons is $2E_g$ or greater (where E_g is the NP bandgap energy).[7–11] In contrast, much greater excitation energies are needed for bulk semiconductor MEG.[12] In principle, if MEG occurs and charge separation and (or) transport is faster than or competitive with recombination, MEG can appreciably enhance the photocurrent of solar devices.

To attain efficient marketable NP-based devices, the lifetimes of single and multiple excitons, and what governs these lifetimes, must be understood. For this reason, substantial effort has gone into quantifying MEG decay times in various NP systems. It is well-documented that multiple excitons recombine through an Auger-type process much more quickly (tens to hundreds of picoseconds) than the long-lived (nanosecond to microsecond) radiative recombination of single excitons and that this process is dependent on the size, shape, and composition of the NPs studied.[7–11,13–18]

Because of the large surface-to-volume ratio inherent to NPs, it is hypothesized that the NP surface plays a significant role in the electron dynamics of the system.[19,20] Thus, a key component in designing NP-based solar cells is understanding the role of the stabilizing ligand shell. Provided that electron dynamics are not influenced by a large density of surface trap states,[21] it is hypothesized that by controlling the type of ligand on the NPs the MEG efficiency, multiexciton lifetime, and charge transport through a device can be optimized. Additionally, it was shown for PbSe that preparation techniques and post-treatment of NP films with various ligands and solvents yield very different recombination dynamics and MEG efficiencies.[22] The authors of this study suggested that the differences they observed are most likely attributable to the chemical species present on the NP surface or to the changes observed in average interparticle distance.[22] These results prompted our curiosity regarding using the structure of the ligand shell to control MEG, and we began a study to investigate ligand effects on MEG. In this paper we report the results of our first study. Specifically, oleic acid-capped PbS NPs (PbS–OLA) and 2,3-dimercaptopropanesulfonate capped PbS NPs (PbS–DMPS) were investigated with femtosecond transient absorption spectroscopy to determine if there is a ligand effect on MEG and exciton recombination dynamics.

Before presenting the results of our study, a few more introductory notes are necessary. Recently, there has been some controversy over MEG in NP systems. In particular, it has been argued that MEG is less efficient than what was previously reported[11,23–25] (Note, however, that the controversy is not about the existence of MEG). For example, a re-examination of CdSe and CdTe NPs led to the conclusion that MEG efficiency is negligible in these systems, contrary to prior results and contrary to the general idea that MEG is enhanced in quantum-confined systems.[23] In our view, much of the controversy stems from the fact that numerous experimental variables can affect the apparent MEG dynamics. For example, differences in apparent MEG efficiencies have been reported in different preparative batches of supposedly identical nanoparticles.[26,27] Because of this, controversy has developed over the existence of photocharging of the NPs leading to a misinterpretation of true MEG yields; however, stirring of the solutions to sample a fresh volume of NPs with each laser pulse greatly reduces the probability of photoionization and allows for the observation of true MEG yields.[26] Additionally, the extent of ligand coverage and oxidation of a NP surface may lead to increased carrier trapping, thus requiring additional considerations in analyzing the carrier dynamics.[27] All of these points serve to emphasize that to efficiently exploit MEG in working devices it is essential to understand the properties of the NPs, including elucidating the direct effect of the ligand shell.

Experimental section

Synthesis of PbS NPs

All reagents and solvents were obtained from Sigma-Aldrich except D_2O, which was purchased from Cambridge Isotope Laboratories. Lead sulfide NPs were synthesized by preparing a lead precursor solution according to the method of Hines and Scholes.[1] To synthesize the parent OLA-capped particles, a solution consisting of 4 mL octadecene and 4 mL OLA was prepared and 0.3 g PbO was added to the mixture. The solution was heated under vacuum to 100 °C for 30 min to dissolve the PbO and to drive off H_2O. The solution was subsequently heated to the appropriate injection temperature (100–150 °C) for the desired particle size and held at that temperature for at least 30 min.

While the lead solution was heating, a sulfur precursor solution of 0.167 mL hexamethyldisilathiane and 4 mL octadecene was degassed under nitrogen. When the lead solution reached the desired injection temperature, the sulfur precursor was quickly injected into the flask and allowed to cool to room temperature. Removal of excess ligand and octadecene was completed by repeated precipitation in acetone, centrifugation of the particles, and dispersion in small amounts of toluene.[1] NIR characterization of the particles was accomplished using a PerkinElmer Lambda 19 UV–vis–NIR spectrophotometer. Particle size and monodispersity were measured using a FEI Titan 80-300 TEM in STEM mode (PbS–OLA NP $d = 5.0 \pm 0.7$ nm).

Ligand exchange on the PbS–OLA particles was accomplished according to literature precedent.[28] D_2O was chosen as the solvent over H_2O because of its suppressed NIR absorption. Equal volumes of PbS–OLA solutions (25 mg/mL) and the 2,3-dimercaptopropanesulfonate sodium salt dissolved in D_2O (78 mmol/L) were stirred until phase transfer of the particles was complete (~1 h). The ionically functionalized NPs were centrifuged to break emulsions formed during stirring and phase transfer. The PbS–DMPS particles were then precipitated from D_2O using acetonitrile, centrifuged, and resuspended in D_2O. The particles were characterized by NIR absorbance spectroscopy and TEM imaging (PbS-DMPS NP $d = 5.2 \pm 0.9$ nm).

Transient absorption measurements

Femtosecond laser system

The optical setup used for obtaining the pump–probe transient absorption data included a passively mode-locked Ti:Sapphire oscillator (SpectraPhysics Tsunami, 750 mW) pumped by a solid-state Nd:YAG laser (SpectraPhysics Millenia Pro., 5 W). This source yielded 100 fs pulses centered at 800 nm. The pulses were seeded into a regenerative am-

Can. J. Chem. Downloaded from www.nrcresearchpress.com by University of Electronic and Science Techonology of China on 09/18/12
For personal use only.

Fig. 1. Optical layout of the femtosecond laser system.

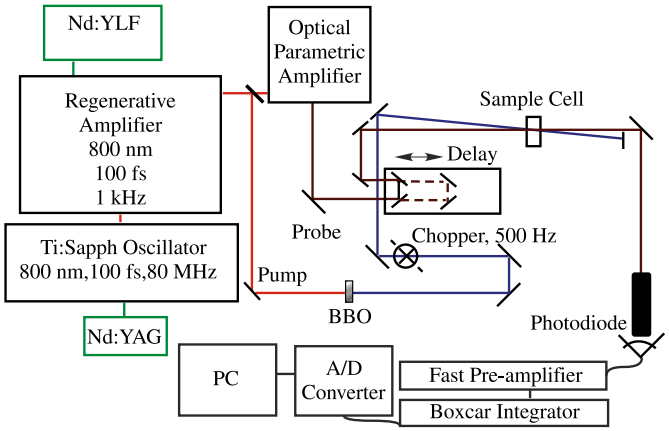

plifier (SpectraPhycics Spitfire Pro) pumped by a q-switched intracavity-doubled Nd:YLF laser (SpectraPhysics Empower, 15 W).

Optical layout

The beam from the amplifier (3.1 W, 1 kHz) was split into pump and probe components as shown in Fig. 1. The pump component was frequency doubled to 400 nm for MEG experiments (for non-MEG experiments it remained at 800 nm) and was chopped at 500 Hz, half the rate of the probe, with an optical chopper. The probe component was tuned in an optical parametric amplifier (OPA) to match the NIR first exciton absorbance of the nanoparticle samples. The probe pulses were delayed with respect to the pump by a micron resolution delay stage. The probe signal was detected on a fast biased InGaAs photodiode (Thorlabs DET 410), whereas the pump signal was indexed by a biased silicon photodiode (Thorlabs DET 210). The signal intensities were amplified and sampled using a fast preamplifier (SRS-SR445A) and boxcar integrator (SRS-SR250). The output from the boxcar integrator was connected to an analog-to-digital converter and then input into a PC. Transient absorption data was calculated using the probe pulse intensity with and without pump pulse excitation. IgorPro software was used for data analysis.

Sample preparation and handling

Solvents were degassed with nitrogen prior to use. Samples were prepared by dispersing NPs in an appropriate solvent at a desired concentration. Sample solutions were placed in cuvettes equipped with stir bars and PTFE stoppers. To ensure removal of oxygen, PbS–DMPS solutions were degassed a second time before transferring to a cuvette in the latter studies. The headspaces of all cuvettes were filled with nitrogen, and the cuvettes were taped and sealed for the duration of the femtosecond experiments.

As a special note, transients taken for stirred and static solutions of both PbS–OLA and PbS–DMPS sometimes showed an appreciable difference in the ratio of early to late population components. Also, as previously mentioned, there have been recent reports outlining the observation of ligand-dependent photocharging of NP solutions.[26] For these reasons, all of the samples used for MEG determination in this study were stirred.

Results and discussion

Choice of ligands

Because we are trying to elucidate the direct effect of the ligand on MEG, we determined that solution-phase samples were of interest primarily owing to the fact that, in solution, the effective concentration of NPs is less than in a film, which decreases the likelihood that interparticle distance is affecting MEG. During our initial investigations of NP ligand–shell substitution reactions, we found that substitution of PbS–OLA NPs by neutral organic thiol ligands led to precipitation of the NPs or to opaque solutions in a wide variety of solvents, rendering the NPs unsuitable for our transient absorption measurements. It was necessary, therefore, to find a ligand, other than one of the neutral thiols, which would allow the NPs to remain suspended in a transparent solution. A literature search revealed that substitution of OLA-capped nanoparticles by DMPS yielded stable NPs in solution, particularly under anaerobic conditions.[28] This same study suggested that, once the DMPS is coordinated to the NP, the ionic ligands repel one another, thereby maintaining a minimum interparticle distance that reduced the probability of precipitation brought on by agglomeration. Most importantly, this study determined that thin-film devices made with the PbS–DMPS NPs showed enhanced photoresponse in the NIR compared with PbS–OLA films, where no photocurrent was detected under the same conditions. This enhanced photoactivity was primarily attributed to the reduced interparticle spacing in the PbS–DMPS films over PbS–OLA films. Transient absorption studies of the PbS–OLA and PbS–DMPS NPs could reveal additional information regarding the differences in photoresponse of the films, such as enhancements of MEG quantum yields or longer exciton lifetimes. The synthetic ease of the DMPS-for-OLA substitution reaction, combined with the encouraging thin-film photocurrent results, was a strong incentive to carry out this study using the DMPS and OLA NP systems.

Transient absorption of OLA-capped NPs

Two fractions of OLA-capped NPs (from the same synthetic batch) with a first exciton absorbance at 1340 nm were excited with 800 and 400 nm laser pulses in toluene solution. In all transient absorption measurements, the probe wavelength was tuned to the maximum of the exciton absorbance in the NIR spectrum. The particles were excited under low-fluence excitation to prevent nonlinearities and to ensure that the average number of photons absorbed per NP (N_{abs}) was kept to a minimum. The value for N_{abs} is given by eq. [1].[11]

$$[1] \qquad N_{abs} = J(0)\frac{1 - e^{-\alpha L}}{cL}$$

where L is the path length of the cuvette, $J(0)$ is the photon fluence at the front face of the cuvette, c is the sample concentration, and αL = OD ln,[10] as calculated from the optical density (OD) of the NP absorbance spectrum.

Raw transient absorption traces at varied pump fluences obtained for 800 nm excitation (Fig. 2*a*) were fit using a global least-squares fitting routine. The subsequent analysis was performed according to the procedure outlined by Ellingson et al.[8] Within this analysis, the time constants for

Can. J. Chem. Downloaded from www.nrcresearchpress.com by University of Electronic and Science Techonology of China on 09/18/12
For personal use only.

Fig. 2. Transient decay curves for PbS – oleic acid (OLA) nanoparticles (NPs) excited at (*a*) 800 nm (1.55 eV, 1.68E_g, where E_g is the NP bandgap energy) and (*b*) 400 nm (3.11 eV, 3.35E_g), with various pump intensities.

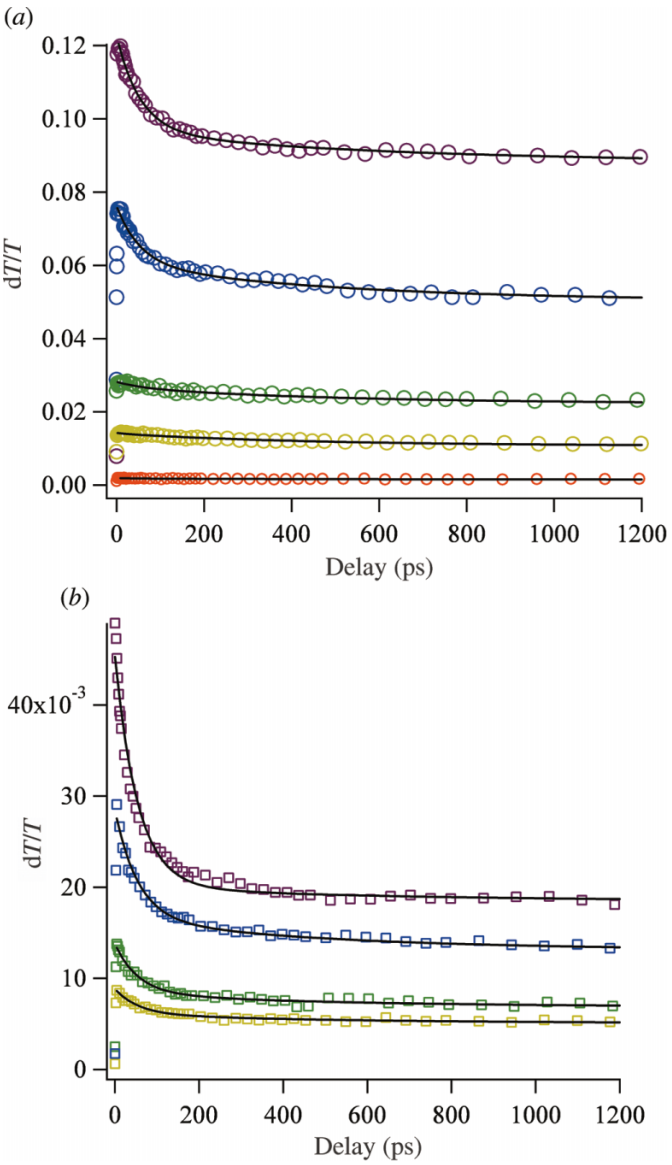

single exciton (τ_X) and biexciton (τ_{MX}) recombination were global parameters and were varied for at least four kinetic traces until the best fit results were obtained. The resulting time constants revealed a single exciton lifetime of 80 ns and a faster biexciton time constant of 436 ps. The amplitudes for these variable fluence traces at 800 nm excitation (<2E_g) are the Poisson amplitudes, which are influenced by N_{abs}. Upon extracting the amplitudes and exciton lifetimes in the case where MEG does not occur ($h\nu < 2E_g$), raw transients for MEG excitation can be analyzed. Figure 2*b* shows the variable fluence traces for the excitation of PbS–OLA at 400 nm (3.35E_g). In this case, the curves were fit by constraining τ_X and τ_{MX} to the extracted values obtained above; however, the amplitudes of these curves are no longer strictly Poissonian and now contain components of MEG. Extraction of the MEG quantum yield will be detailed later.

Fig. 3. Example NIR absorbance spectra showing the first exciton absorption ($1S_h$–$1S_e$) for parent PbS – oleic acid (OLA) (blue line) nanoparticles (NPs) vs ligand-exchanged PbS – 2,3-dimercaptopropanesulfonate (DMPS) particles (red line).

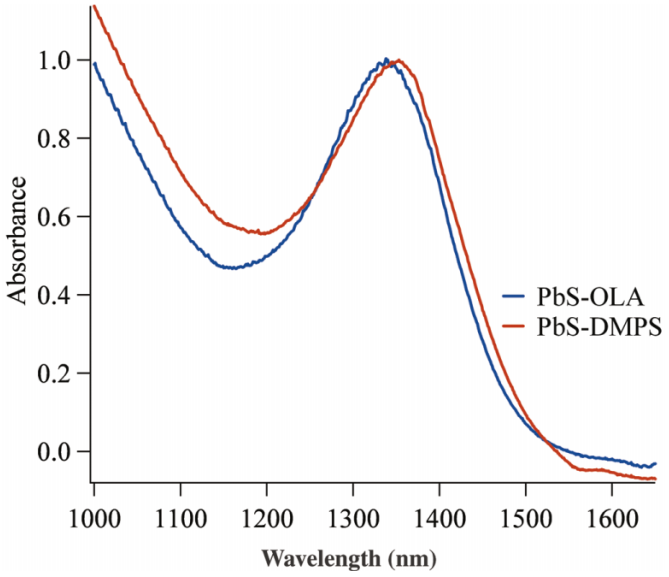

Ligand exchange and transient absorption of PbS–DMPS NPs

Ligand-exchange reactions were carried out on PbS–OLA NPs with DMPS (PbS–MPS). The PbS–DMPS NPs were characterized by TEM imaging and NIR absorption spectroscopy to confirm their size and exciton absorbance (see Experimental section). The red shift in the NIR spectrum for the PbS–DMPS NPs compared with PbS–OLA NPs (Fig. 3) is accounted for by the change in dielectric constant of the solvent[28] and not by a change in particle size, as confirmed by TEM imaging.

Ultrafast decay curves for a single batch of PbS–DMPS particles were obtained for 800 and 400 nm excitation (1.69 and 3.38 times the bandgap energy, respectively) at various pump fluences. The raw traces for both excitation wavelengths are shown in Fig. 4. It is interesting to note that the transient dynamics recorded for PbS–DMPS at 400 nm excitation (Fig. 4*b*) are very different from the OLA-capped particles under MEG conditions. At first glance, it appears that the PbS–DMPS nanoparticles excited under MEG conditions have a greatly enhanced MEG signature compared to the PbS–OLA NPs (the ratio of populations at early and late times; 2.5 and 3.4, respectively). However, experiments showed that the enhanced MEG in the PbS–DMPS NPs is likely attributable to NP decomposition leading to enhanced trapping. After 1–3 days in the sealed cuvettes, the particles precipitated out of solution. The precipitation time was loosely correlated to the care taken to remove oxygen in the samples. To investigate this phenomenon further, a second ligand exchange was performed from the same PbS–OLA parent batch but with care taken to remove O_2 from the PbS–DMPS product before sealing it in the sample cuvettes. Additionally, the PbS–DMPS and PbS–OLA NPs were monitored by NIR absorbance spectroscopy throughout the MEG laser experiments to ensure that the laser experiments were not carried out on decomposed NPs.

Can. J. Chem. Downloaded from www.nrcresearchpress.com by University of Electronic and Science Techonology of China on 09/18/12
For personal use only.

Fig. 4. Variable fluence transient curves and curve fits for PbS – 2,3-dimercaptopropanesulfonate (DMPS) under (*a*) 800 nm and (*b*) 400 nm excitation.

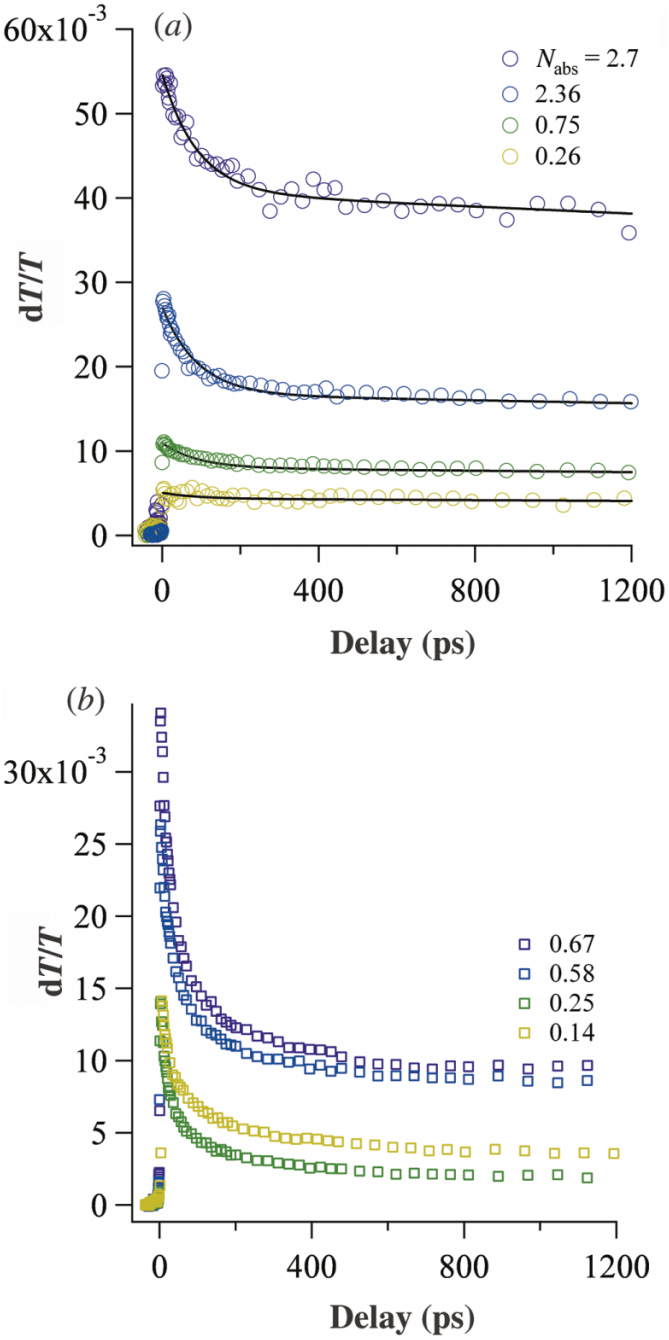

In the case of PbS–OLA NPs, shown in Fig. 5*a*, there is no change in the $1S_h$–$1S_e$ (first exciton) absorbance over the course of the femtosecond experiments. (It should be noted that there is a blue shift of the exciton absorbance in these NPs compared with freshly prepared NPs. This change is most likely due to some oxidation of the NP core[29] causing a change in size of the nanoparticles. Nevertheless, there is no evidence of the particles changing during the course of the MEG data collection.) In contrast to the PbS–OLA solution, the PbS–DMPS NPs do change during the MEG ex-

Fig. 5. Time-lapse absorbance spectra of (*a*) parent PbS – oleic acid (OLA) nanoparticles (NPs) and (*b*) ligand-exchanged PbS – 2,3-dimercaptopropanesulfonate (DMPS) particles throughout the transient absorption experiments.

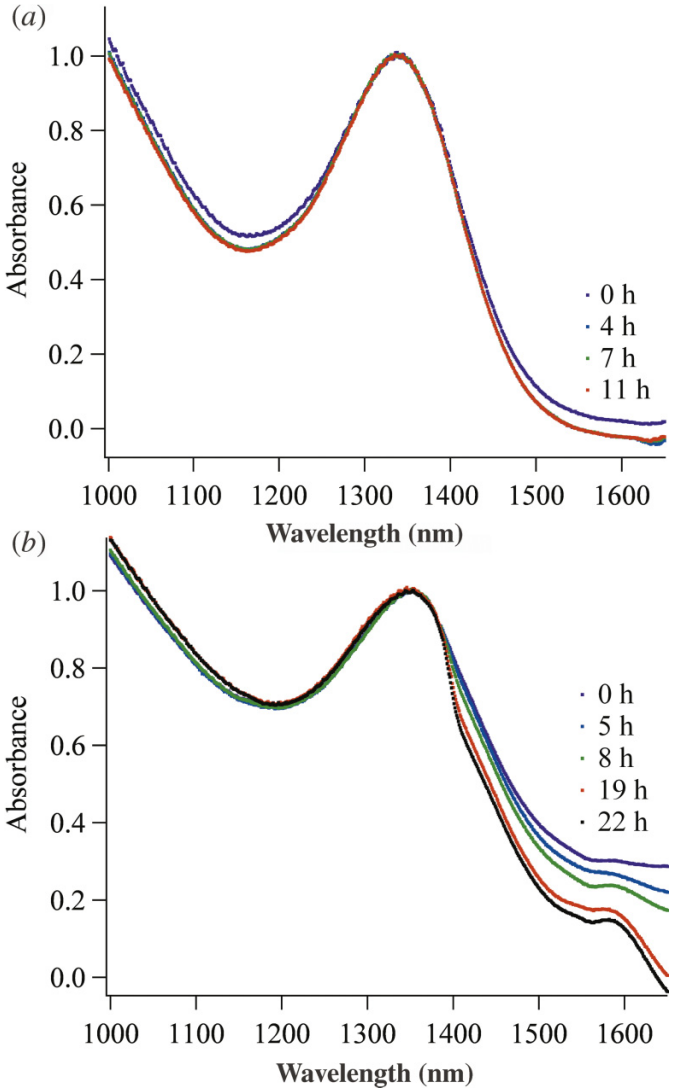

periment (Fig. 5*b*): the first exciton absorbance peak narrows and appears almost multimodal within 1 day.

To eliminate the effects of NP decomposition during the MEG experiments, only transient spectra taken within the first 8 h following sample preparation were used in the data analyses. Additionally, the samples were degassed a second time prior to sealing the cuvettes. Results of the MEG experiments on PbS–DMPS NPs prepared under these anaerobic conditions are shown in Fig. 6. Note there is no apparent decomposition in the spectra of the PbS–DMPS NPs.

The global fitting procedure described previously was used to fit the raw transient data for PbS–DMPS. Time constants extracted from the non-MEG curve fits are listed in Table 1 and compared with those obtained for PbS–OLA. Also shown in Table 1 are the MEG quantum yields (QYs) for the PbS–DMPS and PbS–OLA particles. In determining QY, the ratio of short and long time signal (A/B) is plotted as a function of N_{abs} (Fig. 7). Fits for the curves for 800 nm excitation assume Poisson statistics for the absorption of

Can. J. Chem. Downloaded from www.nrcresearchpress.com by University of Electronic and Science Techonology of China on 09/18/12
For personal use only.

Fig. 6. Decay curves for PbS – oleic acid (OLA) and batch 2 of the PbS – 2,3-dimercaptopropanesulfonate (DMPS) particles excited under multiple exciton generation (MEG) conditions.

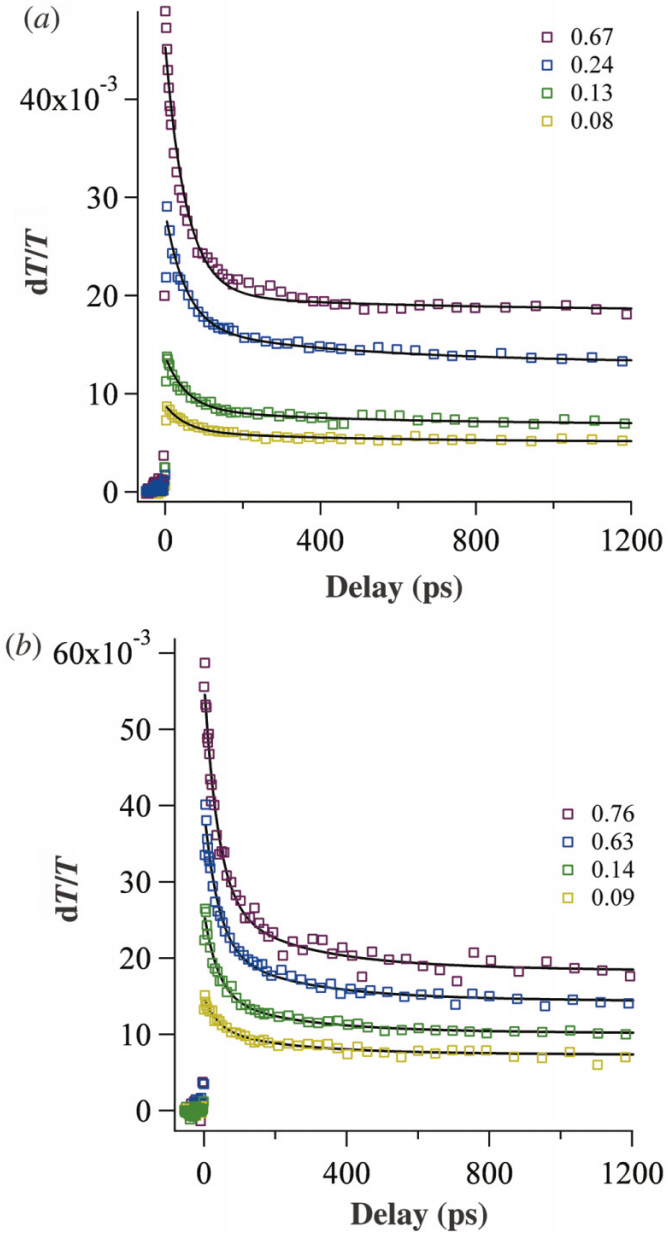

Table 1. Characteristic lifetimes of multiple (τ_{MX}) and single (τ_X) exciton recombination and extracted multiple exciton generation (MEG) quantum yields (QYs) for PbS – oleic acid (OLA) and PbS – 2,3-dimercaptopropanesulfonate (DMPS).

Sample	τ_{MX} (ps)	τ_X (ns)	MEG QY
PbS–OLA	436±45	80	1.4±0.1
PbS–DMPS	223±65	36	1.5±0.1

photons by the NPs. The curves for 400 nm excitation are non-Poissonian, but are fit by allowing for the adjustment of the QY, which accounts for the enhanced amplitudes owing to MEG. By extrapolating these fits back to vanishing photon fluence and dividing out the contribution of the

Fig. 7. Ratios of early to late time signals vs the average number of photons absorbed per nanoparticle at the front face of the sample cuvette (N_{abs}) for (*a*) PbS – oleic acid (OLA) and (*b*) PbS – 2,3-dimercaptopropanesulfonate (DMPS) particles.

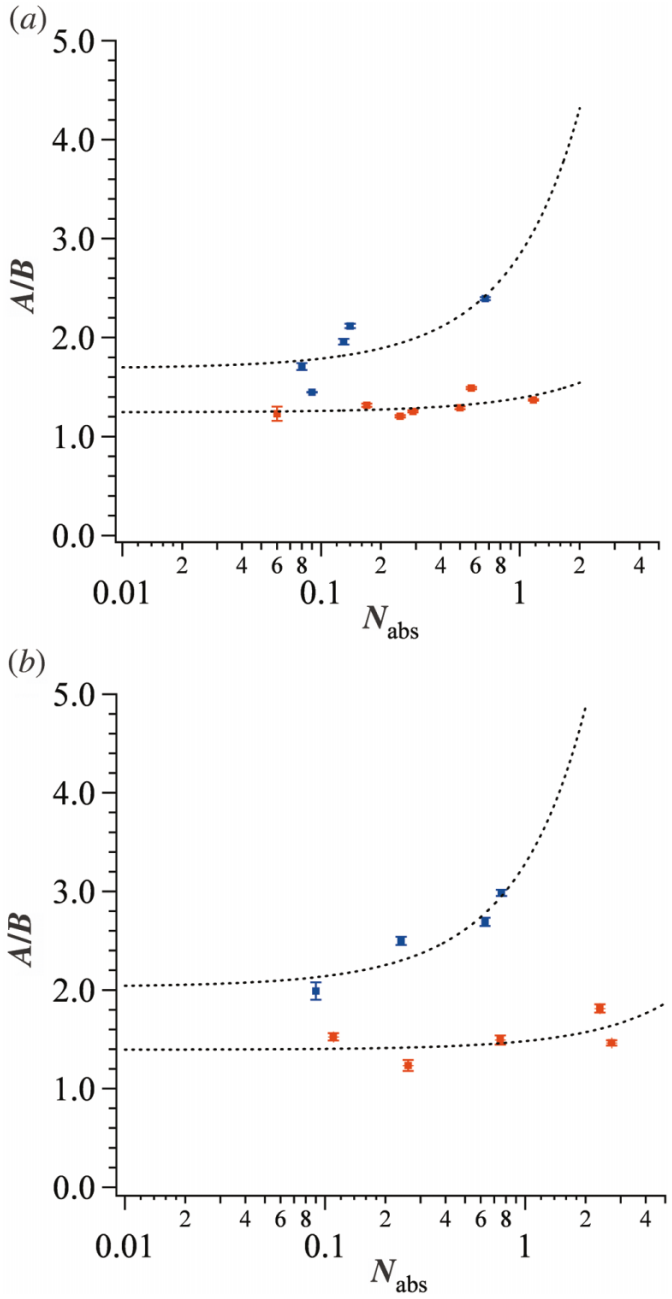

800 nm excitation curves, the MEG QY for each particle set was determined. Note in Table 1 that even the more rigorously deoxygenated PbS–DMPS NPs experience faster decay dynamics than their PbS–OLA parent batch; however, the MEG QY for each particle set is the same within experimental error. The time constants for multi- and single-exciton decay for the PbS–DMPS particles are less than half that of the PbS–OLA particles, indicating that the ligand has an effect on MEG and exciton recombination.[30]

The origin of the ligand effect on decay dynamics is unknown. One suggestion is that the faster decay rates for exciton recombination in the DMPS system are due to the

Can. J. Chem. Downloaded from www.nrcresearchpress.com by University of Electronic and Science Techonology of China on 09/18/12
For personal use only.

negative charge on the ligand. It is suggested that the electron is electrostatically repelled by the anionic ligand shell. This would prevent delocalization of the electrons over the surface of the NP, spatially confining them to the core, which causes them to recombine with holes more quickly. A related hypothesis is that the ligand effect can be attributed to the different ligating atoms in the two ligands. The DMPS ligand binds through sulfur instead of oxygen. Because oxygen is more electronegative than sulfur, it is more likely to accept electron density and, therefore, more likely to delocalize the electronic wave function over the surface of the NP, which would lead to slower electron–hole recombination rates. A final suggestion is that the differences in the decay dynamics may be due to a solvent effect. Previous studies suggested that the solvent can affect electron dynamics in NPs that have significant trap state densities,[31] but does not play as significant a role in passivated NPs.[32] The NPs used in this investigation are passivated by the ligands, leading to the conclusion that solvent effects may not be of great consequence. Investigations are underway in our laboratory to further probe these ligand effects and to provide insight into their origin.

Key insights and conclusions

PbS NPs with OLA and DMPS ligands were investigated to determine how the NP ligand shell affects MEG and exciton recombination dynamics. Experiments showed striking differences between the PbS–DMPS samples prepared in the presence of oxygen and those prepared anaerobically. With oxygen present in the samples, the kinetic decay curves exhibited large false MEG-type signatures and enhanced recombination rates owing to the photooxidation and degradation of the NPs and the ensuing increase in the number of nonradiative decay pathways. Rigorous removal of oxygen from the samples produced kinetic decay curves with time constants for PbS–DMPS NPs that were significantly shorter than those of the PbS–OLA NPs. The origin of the differences in the exciton recombination decay rates is unknown, but it is speculated that it may be due to the ionic functionality of the DMPS ligand or to the different ligating atoms of the OLA and DMPS ligands. This study shows that MEG dynamics can be tuned by changing the NP ligand shell, which may have implications for the development of NP-based efficient thin-film solar devices.

Acknowledgments

Funding for this paper was provided by the National Science Foundation (NSF) IGERT Fellowship Program under Grant Number DGE-0549503 and by NSF Grant CHE-080939. Additional funding for research materials was provided by Voxtel-Inc, University of Oregon. The authors would like to thank I. Moody for help with the ligand substitution reactions.

References

(1) Hines, M. A.; Scholes, G. D. *Adv. Mater.* **2003**, *15* (21), 1844. doi:10.1002/adma.200305395.

(2) Murray, C. B.; Sun, S. H.; Gaschler, W.; Doyle, H.; Betley, T. A.; Kagan, C. R. *IBM J. Res. Dev. (Srinagar)* **2001**, *45* (1), 47. doi:10.1147/rd.451.0047.

(3) Wehrenberg, B. L.; Wang, C.; Guyot-Sionnest, P. *J. Phys. Chem. B* **2002**, *106* (41), 10634. doi:10.1021/jp021187e.

(4) Murphy, J. E.; Beard, M. C.; Norman, A. G.; Ahrenkiel, S. P.; Johnson, J. C.; Yu, P. R.; Mićić, O. I.; Ellingson, R. J.; Nozik, A. J. *J. Am. Chem. Soc.* **2006**, *128* (10), 3241. doi:10.1021/ja0574973. PMID:16522105.

(5) Maria, A.; Cyr, P. W.; Klem, E. J. D.; Levina, L.; Sargent, E. H. *Appl. Phys. Lett.* **2005**, *87* (21), 213112. doi:10.1063/1.2135868.

(6) Norris, D. J. Electronic Structure in Semiconductor Nanocrystals. In *Semiconductor and Metal Nanocrystals, Synthesis and Electronic and Optical Properties;* Klimov, V. I. Ed.; Marcel Dekker: New York, 2004; p 65.

(7) Shabaev, A.; Efros, A. L.; Nozik, A. J. *Nano Lett.* **2006**, *6* (12), 2856. doi:10.1021/nl062059v. PMID:17163719.

(8) Ellingson, R. J.; Beard, M. C.; Johnson, J. C.; Yu, P.; Micic, O. I.; Nozik, A. J.; Shabaev, A.; Efros, A. L. *Nano Lett.* **2005**, *5* (5), 865. doi:10.1021/nl0502672. PMID:15884885.

(9) Schaller, R. D.; Sykora, M.; Pietryga, J. M.; Klimov, V. I. *Nano Lett.* **2006**, *6* (3), 424. doi:10.1021/nl052276g. PMID:16522035.

(10) Nozik, A. J. *Inorg. Chem.* **2005**, *44* (20), 6893. doi:10.1021/ic0508425. PMID:16180844.

(11) Trinh, M. T.; Houtepen, A. J.; Schins, J. M.; Hanrath, T.; Piris, J.; Knulst, W.; Goossens, A. P.; Siebbeles, L. D. A. *Nano Lett.* **2008**, *8* (6), 1713. doi:10.1021/nl0807225. PMID:18489170.

(12) Kolodinski, S.; Werner, J. H.; Wittchen, T.; Queisser, H. J. *Appl. Phys. Lett.* **1993**, *63* (17), 2405. doi:10.1063/1.110489.

(13) El-Sayed, M. A. *Acc. Chem. Res.* **2004**, *37* (5), 326. doi:10.1021/ar020204f. PMID:15147173.

(14) Ellingson, R. J.; Blackburn, J. L.; Yu, P.; Rumbles, G.; Micic, O. I.; Nozik, A. J. *J. Phys. Chem. B* **2002**, *106* (32), 7758. doi:10.1021/jp025666p.

(15) Klimov, V. I. *J. Phys. Chem. B* **2006**, *110* (34), 16827. doi:10.1021/jp0615959. PMID:16927970.

(16) Yu, P.; Nedeljkovic, J. M.; Ahrenkiel, P. A.; Ellingson, R. J.; Nozik, A. J. *Nano Lett.* **2004**, *4* (6), 1089. doi:10.1021/nl049524d.

(17) Schaller, R. D.; Pietryga, J. M.; Klimov, V. I. *Nano Lett.* **2007**, *7* (11), 3469. doi:10.1021/nl072046x. PMID:17967043.

(18) Gachet, D.; Avidan, A.; Pinkas, I.; Oron, D. *Nano Lett.* **2010**, *10* (1), 164. doi:10.1021/nl903172f. PMID:19911830.

(19) Zhang, J. Z. *Acc. Chem. Res.* **1997**, *30* (10), 423. doi:10.1021/ar960178j.

(20) Guyot-Sionnest, P.; Wehrenberg, B.; Yu, D. *J. Chem. Phys.* **2005**, *123* (7), 074709. doi:10.1063/1.2004818. PMID:16229612.

(21) Patel, A. A.; Wu, F.; Zhang, J. Z.; Torres-Martinez, C. L.; Mehra, R. K.; Yang, Y.; Risbud, S. H. *J. Phys. Chem. B* **2000**, *104* (49), 11598. doi:10.1021/jp000639p.

(22) Beard, M. C.; Midgett, A. G.; Law, M.; Semonin, O. E.; Ellingson, R. J.; Nozik, A. J. *Nano Lett.* **2009**, *9* (2), 836. doi:10.1021/nl803600v. PMID:19170560.

(23) Nair, G.; Bawendi, M. G. *Phys. Rev. B* **2007**, *76* (8), 081304. doi:10.1103/PhysRevB.76.081304.

(24) Nair, G.; Geyer, S. M.; Chang, L. Y.; Bawendi, M. G. *Phys. Rev. B* **2008**, *78* (12), 125325. doi:10.1103/PhysRevB.78.125325.

(25) Ben-Lulu, M.; Mocatta, D.; Bonn, M.; Banin, U.; Ruhman, S. *Nano Lett.* **2008**, *8* (4), 1207. doi:10.1021/nl080199u. PMID:18341299.

(26) McGuire, J. A.; Joo, J.; Pietryga, J. M.; Schaller, R. D.;

Klimov, V. I. *Acc. Chem. Res.* **2008**, *41* (12), 1810. doi:10.1021/ar800112v. PMID:19006342.
(27) Sykora, M.; Koposov, A. Y.; McGuire, J. A.; Schulze, R. K.; Tretiak, O.; Pietryga, J. M.; Klimov, V. I. *ACS Nano* **2010**, *4* (4), 2021. doi:10.1021/nn100131w. PMID:20369900.
(28) Moody, I. S.; Stonas, A. R.; Lonergan, M. C. *J. Phys. Chem. C* **2008**, *112* (49), 19383. doi:10.1021/jp807360q.
(29) Stouwdam, J. W.; Shan, J.; van Veggel, F. C. J. M.; Pattantyus-Abraham, A. G.; Young, J. F.; Raudsepp, M. *J. Phys. Chem. C* **2007**, *111* (3), 1086. doi:10.1021/jp0648083.
(30) Whereas the PbS–OLA particles did not exhibit signs of photooxidation during the laser studies, it is possible they might have undergone oxidation prior to the laser studies and prior to ligand exchange. It is also possible that having pre-oxidized particles during the ligand exchange facilitates the oxidation of the ligand or prevents satisfactory passivation of the NPs, leading to the precipitation of the NPs. During the course of our investigation, it was reported by Klimov and co-workers[27] that oxidation of the NP core has a slight effect on MEG dynamics. In the same manner, if oligosulfide formation of the DMPS ligand occurs because of oxidation then a coordination site (or dangling bond) can open up on the surface of the particle. Both the oxidation of the NP core and the presence of dangling bonds can contribute to electron-trapping states on the NP surface. Correcting for a trapping factor in such a case provides a better assessment of true MEG yields.

(31) Sengupta, A.; Jiang, B.; Mandal, K. C.; Zhang, J. Z. *J. Phys. Chem. B* **1999**, *103* (16), 3129. doi:10.1021/jp9842345.
(32) Roberti, T. W.; Cherepy, N. J.; Zhang, J. Z. *J. Chem. Phys.* **1998**, *108* (5), 2143. doi:10.1063/1.475593.

Can. J. Chem. Downloaded from www.nrcresearchpress.com by University of Electronic and Science Techonology of China on 09/18/12
For personal use only.

The reactivity of diarylmethyl carbocations within non-protic zeolites

Geniece L. Hallett-Tapley, Norman P. Schepp, and Frances L. Cozens

Can. J. Chem. Downloaded from www.nrcresearchpress.com by University of Electronic and Science Techonology of China on 09/18/12
For personal use only.

Abstract: The generation of diarylmethyl carbocations within non-protic zeolites (LiY, NaY, KY, RbY, CsY, and NaX) was carried out via laser excitation (266 nm or 266 nm / 308 nm) of diarylacetic acids. Rapid loss of CO_2, followed by photochemical oxidation of the diarylmethyl radicals resulted in the formation of the diarylmethyl carbocations. The reactivity of the diarylmethyl carbocations was found to be highly dependent on the alkali metal counterion and the Si/Al ratio of the zeolite framework. Furthermore, the effect of various para-electron donating substituents (4-H, 3-CH_3, 4-CH_3, 4,4′-CH_3, and 4-OCH_3) on the diarylmethyl carbocation reactivity was investigated. Comparison of the Hammett plots constructed for the reactivity of the diarylmethyl carbocations in zeolites with those in solution (CH_3CN–H_2O (1:2) and TFE) showed decreased sensitivity of the electrophilic species towards para-electron donating substituents in the heterogeneous media. The leveling effect observed in the zeolite Hammett plots has been attributed to the presence of an isokinetic relationship, specifically, a low isokinetic temperature for the reaction of diarylmethyl carbocations with the aluminosilicate zeolite framework.

Key words: zeolites, cation-exchanged Y, reactivity, carbocation, linear free energy relationships, Hammett plots, isokinetic temperatures.

Résumé : On a procédé à la génération de carbocations diarylméthyles dans des zéolites non protiques (LiY, NaY, KY, RbY, CsY et NaX) en effectuant une excitation laser (266 nm ou 266 nm / 308 nm) d'acides diarylacétiques. La perte rapide de CO_2, suivie par l'oxydation photochimique des radicaux diarylméthyles conduit à la formation des carbocations diarylméthyles. On a trouvé que la réactivité des carbocations diarylméthyles dépend beaucoup du contre-ion du métal alcalin et du rapport Si/Al du squelette du zéolite. De plus, on a étudié l'effet de divers substituants para électrodonneurs (4-H, 3-CH_3, 4-CH_3, 4,4′-CH_3 et 4-O-CH_3) sur la réactivité du carbocation diarylméthyle. Une comparaison des courbes de Hammett obtenues à partir de la réactivité des carbocations diarylméthyles dans des zéolites avec celles obtenues en solution (CH_3CN–H_2O (1 : 2), TFE) permet d'observer une diminution de la sensibilité des espèces électrophiles vis-à-vis des substituants para électrodonneurs en milieu hétérogène. L'effet de nivellement observé dans les courbes de Hammett pour le zéolite est attribué à la présence d'une relation isocinétique, spécifiquement une température isocinétique basse pour la réaction des carbocations diarylméthyles avec le squelette aluminosilicate du zéolite.

Mots-clés : zéolites, Y à cation échangé, réactivité, carbocation, relations linéaires d'énergie libre, courbes de Hammett, températures isocinétiques.

[Traduit par la Rédaction]

Introduction

Zeolites are crystalline aluminosilicate materials comprised of a network of $[SiO_4]^{4-}$ and $[AlO_4]^{5-}$ tetrahedra arranged in a fashion that gives rise to a highly organized network of microscopic voids in the form of channels or cavities.[1–6] Because of the tetravalent character, each aluminum atom in the zeolite framework possesses a negative charge that is often counterbalanced by small monovalent[1,3,5–7] or divalent cations,[5,8–10] such as the alkali metal cations (M^+ = Li^+, Na^+, K^+, Rb^+, or Cs^+), creating a non-protic polar environment that contains both Lewis acid[1,5,7,8,11–13] and base sites.[3,8,11,14,15] The polarity of the intrazeolite environment and the ability of the framework to restrict diffusional motion are fundamental characteristics that have been exploited in the development of zeolites as a host environment for the study of short-lived reactive intermediates.

The use of zeolites to study carbocation intermediates has been well-known over the past several decades, with most cases focusing on the study of these electrophilic species in Brönsted acid zeolites (M^+ = H^+).[16–21] More recently, xanthylium,[22] cumyl,[11,23] and fluorenyl[24,25] carbocations have been generated and their reactivities studied when contained within the framework cavities of non-protic cation-exchanged

Received 1 June 2010. Accepted 23 July 2010. Published on the NRC Research Press Web site at canjchem.nrc.ca on 25 February 2011.

This paper is dedicated to Professor Tito Scaiano in recognition of his tremendous contributions to the world of chemistry and also for being a great ambassador for the chemical community and a very good friend to many. This article is part of a Special Issue dedicated to Professor J. C. Scaiano.

G.L. Hallett-Tapley, N.P. Schepp, and F.L. Cozens.[1] Department of Chemistry, Dalhousie University, Halifax, NS B3H 4J3, Canada.

[1]Corresponding author (e-mail: fcozens@dal.ca).

Can. J. Chem. Downloaded from www.nrcresearchpress.com by University of Electronic and Science Techonology of China on 09/18/12
For personal use only.

Scheme 1.

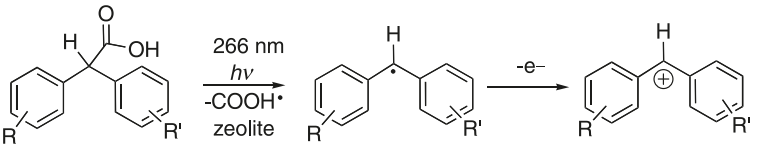

R = R' = H	D(COOH)	D•	D+
R = 4-CH_3;R' = H	4-(CH_3)D(COOH)	4-(CH_3)D•	4-(CH_3)D+
R = R' = 4-CH_3	4,4'-$(CH_3)_2$D(COOH)	4,4'-$(CH_3)_2$D•	4,4'-$(CH_3)_2$D+
R = 3-CH_3;R' = H	3-(CH_3)D(COOH)	3-(CH_3)D•	3-(CH_3)D+
R = 4-OCH_3;R' = H	4-(OCH_3)D(COOH)	4-(OCH_3)D•	4-(OCH_3)D+

zeolites. Studying the reactivity of short-lived carbocations within the cavities of non-protic zeolites presents an opportunity to investigate how variables such as zeolite basicity/nucleophilicity affect the reactivity and decay of these species.[11] Furthermore, non-protic zeolites have been shown to exhibit enhanced Lewis base properties that are highly dependent on the framework charge-balancing cations, as well as the Si/Al ratio of the solid support.[1,3,7,8] The active Lewis base sites, which have been implicated in the decay of reactive carbocations, are attributed to the nucleophilic framework oxygens of the [Al–O–Si]$^-$ bridge.[3,11,14,26,27] Smaller alkali metal counterions (e.g., Li^+ or Na^+) strongly interact with the active Lewis base sites, reducing the nucleophilicity of the zeolite framework and resulting in increased lifetimes of zeolite-encapsulated carbocations, whereas the larger counterions (e.g., Rb^+ or Cs^+) provide for a more nucleophilic environment and enhanced reactivity.

In the present work, the reactivity of a series of diarylmethyl carbocations are studied as a function of aryl substituent and zeolite composition. The diarylmethyl carbocations were generated by laser flash photolysis of the corresponding diarylacetic acids[28,29] within the cavities of cation-exchanged zeolites (Scheme 1). The absorption properties and reactivity of the carbocations investigated in this work have been thoroughly studied in homogenous solution.[29–36]

Of particular interest is the influence of the intrazeolite environment on the substituent effects for the carbocation decay within the zeolite environment. Previous work in our group has suggested that the decay of carbocations generated within the confines of non-protic zeolites is less sensitive towards substituents effects as compared with those same carbocations when generated in polar–protic solvents.[24,37] Using a more complete series of diarylacetic acids for the generation of aryl-substituted diarylmethyl carbocations allowed for a larger range of carbocation reactivity to be studied within the zeolite framework. This larger data set, along with temperature studies, has assisted in the development of a possible rationale for the zeolite leveling effect on carbocation reactivity.

Results

Diarylmethyl carbocations in alkali-metal-cation-exchanged zeolites

Laser irradiation with 266 nm excitation of di-*p*-tolylacetic acid (4,4′-$(CH_3)_2$D(COOH)) incorporated in zeolite NaY under evacuated conditions resulted in the formation of two well-defined transient absorption bands located at 340 and 470 nm (Fig. 1*a*). These absorption bands closely resemble those for the di-*p*-tolylmethyl radical (4,4′-$(CH_3)_2D^•$) at 340 nm and the di-*p*-tolylmethyl cation (4,4′-$(CH_3)_2D^+$) at 470 nm previously identified upon laser excitation of di-*p*-tolylmethylchloride in acetonitrile[30] and di-*p*-tolylmethane in MY zeolites.[38] Further support for the identification of the 340 nm band to a carbon-centred radical is the complete quenching of the band when molecular oxygen is added to the dry zeolite – organic composite prior to laser irradiation. The transient absorption band at 470 nm, which is identified as 4,4′-$(CH_3)_2D^+$, displays characteristics typical for a reactive carbocation generated within a dry cation-exchanged zeolite cavity. The transient decay is not influenced by the addition of molecular oxygen to the zeolite sample, but the rate constant for the decay significantly accelerates upon the introduction of nucleophiles such as co-absorbed water.

The decay of 4,4′-$(CH_3)_2D^+$ in dry NaY at room temperature is shown in Fig. 2. As is typical for reactions in zeolites, the decay did not fit to a single first-order expression, reflecting the heterogeneous environments within the zeolites cavities in which the carbocations react. In the present case, the decay did fit well to a double first-order (or bi-exponential) rate expression consisting of a fast component that decayed with a rate constant of 4.8×10^4 s^{-1} and a slow component with a rate constant of 5.3×10^3 s^{-1}. The fact that the decay fit well to a bi-exponential expression suggests that the cations exist in two distinct environments within the zeolites and indicates that the simple bi-exponential model is adequate in describing the rate constants for the decay of the carbocations studied in the present work.

Similar results to those described previously were observed upon 266 nm laser excitation of 4,4′-$(CH_3)_2$(COOH) incorporated within dry evacuated LiY, KY, RbY, and CsY. In each case, the transient absorption spectra contained two strong absorption bands, one centred at 340 nm owing to 4,4′-$(CH_3)_2D^•$ and the second centred at 470 nm owing to 4,4′-$(CH_3)_2D^+$. Rate constants for the decay of the 4,4′-$(CH_3)_2D^+$ within the cation-exchanged zeolites were determined by fitting the decays to a bi-exponential rate expression, and these rate constants are summarized in Table 1. The reactivity of 4,4′-$(CH_3)_2D^+$ increased as the size of the zeolite counterion increased from Li^+ to Cs^+, which is consistent with the greater nucleophilic environment provided by CsY as compared with LiY. In addition to the larger rate constants upon going from LiY to CsY, the relative amount of carbocation compared with radical decreased. Thus, in LiY, both the carbocation and radical absorptions were similar in amplitude, but, in CsY, the radical signal dominated.

Can. J. Chem. Downloaded from www.nrcresearchpress.com by University of Electronic and Science Techonology of China on 09/18/12
For personal use only.

Fig. 1. Transient diffuse reflectance spectra generated following 266 nm laser flash photolysis of (*a*) di-*p*-tolylacetic acid, (*b*) *p*-anisylphenylacetic acid, and (*c*) *p*-tolylphenylacetic acid in dry NaY under evacuated conditions (1×10^{-3} Torr (1 Torr = 133.322 Pa)). Transient diffuse reflectance spectra generated following two-laser two-colour laser flash photolysis (at 266 nm (●) and at 308 nm (○)) of (*d*) *p*-tolylphenylacetic acid in evacuated KY and (*e*) diphenylacetic acid and (*f*) *m*-tolylphenylacetic acid in evacuated NaY. Insets show the decay of the respective carbocations at their absorption maximum.

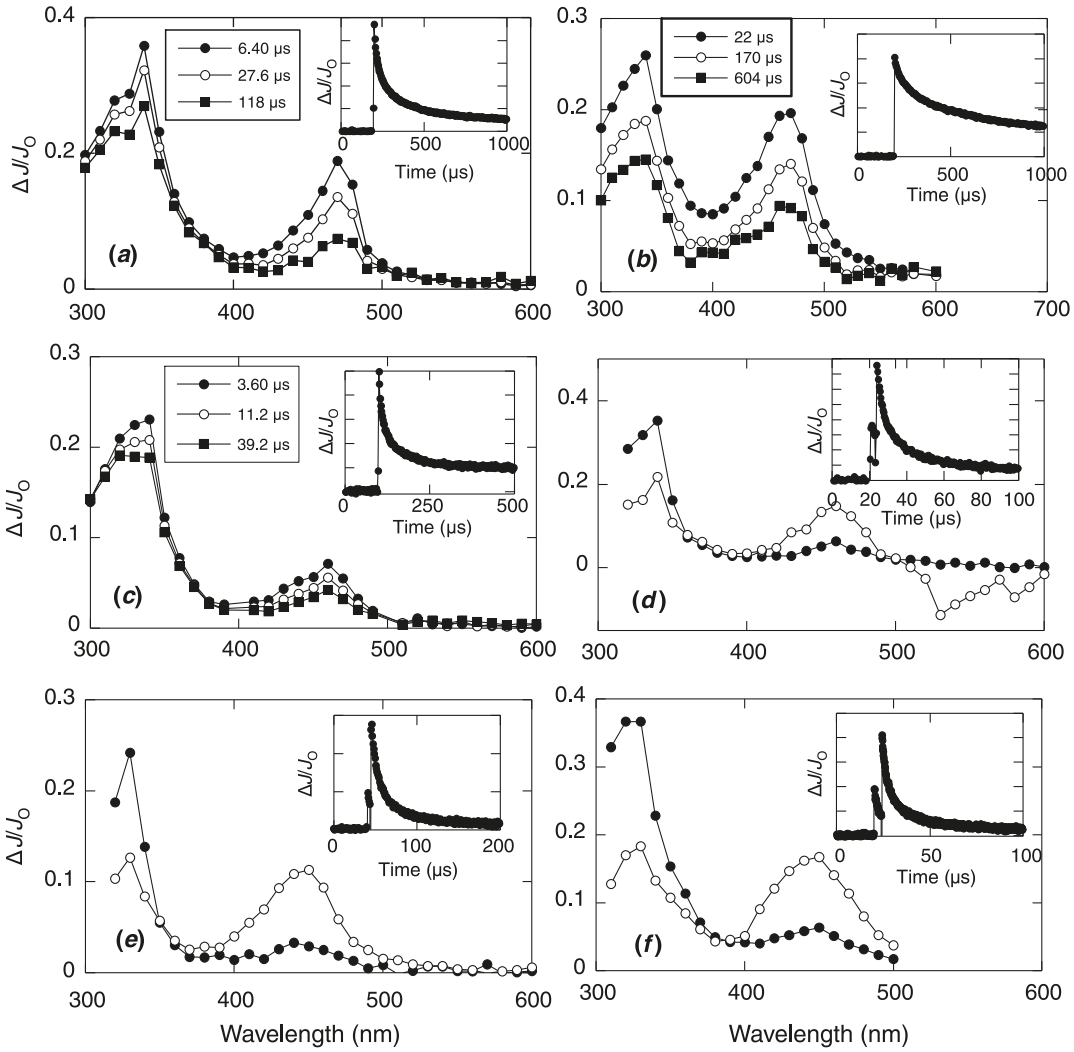

Laser irradiation of *p*-anisylphenylacetic acid (4-(OCH_3)D(COOH)) in dry, evacuated NaY produced the transient absorption spectra shown in Fig. 1*b*. The spectra shows the presence of two strong absorption bands, one centred at 340 nm owing to the *p*-anisylphenylmethyl radical[30,38] (4-(OCH_3)D•) and the second centred at 460 nm owing to the *p*-anisylphenylmethyl cation[30,38] (4-(OCH_3)D^+). The band at 340 nm was rapidly quenched upon the addition of oxygen to the zeolite sample, in agreement with the identification of the transient to a radical species. In addition, the reactivity of the band at 460 nm was significantly enhanced upon co-absorption of water, consistent with the identification of the band as the carbocation. Under dry evacuated conditions at room temperature, the decay of 4-(OCH_3)D^+ fit well to a bi-exponential rate expression, giving fast and slow decay rate constants of 2.5×10^4 and 2.6×10^3 s^{-1}, respectively.

The *p*-anisylphenylmethyl cation was also readily generated in the other cation-exchanged zeolites (LiY, KY, RbY, and CsY) upon 266 nm laser excitation of 4-(OCH_3)D(COOH) under dry evacuated conditions. As was the case for the di-*p*-tolylmethyl cation, the rate constant for the decay of the *p*-anisylphenylmethyl cation increased going from LiY to CsY, as expected for a carbocation incorporated within the cavities of the cation-exchanged Y zeolites. Furthermore, the relative yield of the carbocation formation compared with radical formation decreased moving from LiY to CsY. Rate constants for the decay of 4-(OCH_3)D^+ in the cation-exchanged zeolites are given in Table 1.

Laser irradiation of *p*-tolylphenylacetic acid (4-(CH_3)D(COOH) incorporated within dry, evacuated NaY produced the transient absorption spectra shown in Fig. 1*c*. Similar to the other substrates, the transient spectrum shows the presence of two absorption bands. The transient absorption band centred at 340 nm is assigned to the *p*-tolylphenylmethyl radical (4-(CH_3)D•) on the basis of the band's close similarity to that of the known absorption spectrum for the radical, and in a similar manner the longer wavelength band

Can. J. Chem. Downloaded from www.nrcresearchpress.com by University of Electronic and Science Techonology of China on 09/18/12
For personal use only.

Fig. 2. Time-resolved change in absorption at 470 nm after 266 nm laser irradiation of di-*p*-tolylacetic acid in dry evacuated NaY. The experimental data and line-of-best fit obtained using a bi-exponential equation are shown in the upper segment of the graph and the lower segment shows the residuals.

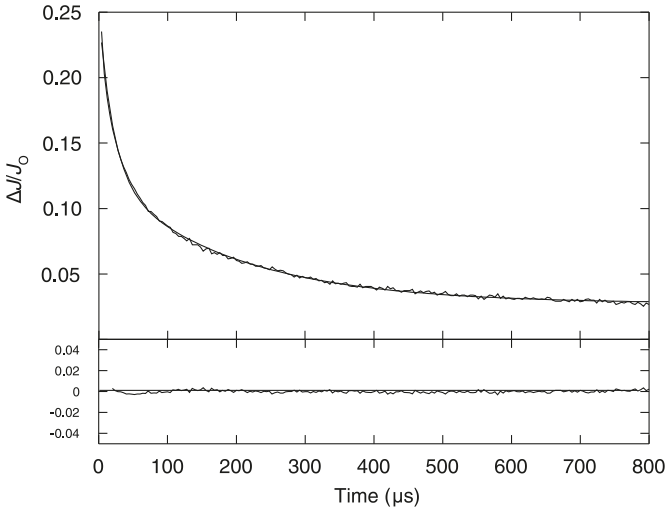

centred at 460 nm is assigned to the monosubstituted *p*-tolylphenylmethyl cation (4-$(CH_3)D^+$).[30] The intensity of the carbocation band at 460 nm is considerably weaker than that for the radical at 340 nm. As well, the carbocation decayed with fast and slow components, 1.2×10^5 and 1.5×10^4 s^{-1}, respectively (Table 1), which are considerably greater than those observed for the more stabilized di-*p*-tolylmethyl and *p*-anisylphenylmethyl carbocations.

Laser irradiation of 4-$(CH_3)D(COOH)$ incorporated within dry evacuated LiY produced very similar results to those in NaY, and the rate constants for decay in LiY are listed in Table 1. However, in dry evacuated KY, RbY, and CsY, only the radical at 340 nm was observed, with little evidence for carbocation formation at 460 nm. To enhance the yield of carbocation formation within these more nucleophilic and less ionizing cation-exchanged zeolites, two-laser two-colour experiments were conducted. In these experiments, the incorporated acid was subjected to 266 nm laser excitation in the usual way. However, within a short time period, typically ~6 μs, after the initial 266 nm laser pulse a second laser pulse at 308 nm was directed onto the sample to selectively excite the diarylmethyl radical and cause a rapid photoionization to yield the corresponding carbocation (eq. [1]).

[1]

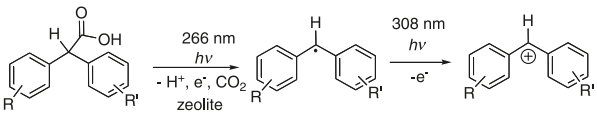

As shown in Fig. 1*d*, a 308 nm laser pulse delivered to the sample just after 266 nm irradiation of 4-$(CH_3)D(COOH)$ in KY caused bleaching of the *p*-tolylphenylmethyl radical signal at 340 nm and increased absorption at 460 nm owing to the formation of the *p*-tolylphenylmethyl carbocation by photoionization of the radical. Strong fluorescence from the excited diarylmethyl radical is also observed between 500 and 600 nm.[28,29,39,40] This fluorescence signal was short-lived and did not influence the kinetics of the carbocation decay taken at ~450 nm. In this manner the yield of 4-$(CH_3)D^+$ in all the cation-exchanged zeolites was sufficiently large for the carbocation decay within the MY zeolites to be accurately determined. Slow and fast components of the rate constants for the decay of the 4-$(CH_3)D^+$ in the cation-exchanged zeolites are given in Table 1.

Laser irradiation (266 nm) of diphenylacetic acid (D(COOH)) incorporated within dry evacuated NaY produced the transient absorption spectrum shown in Fig. 1*e* (●), which features a strong band owing to the diphenylmethyl radical ($D^\bullet$) at 330 nm and a much weaker band at 450 nm owing to the diphenylmethyl cation (D^+). Subsequent 308 nm laser irradiation strongly enhanced the cation signal (Fig. 1*e*, ○) so that reliable kinetic data could be obtained. Again, the decay of the cation fit well to a bi-exponential expression giving rate constants for fast and slow components of 3.1×10^5 and 5.1×10^4 s^{-1}, respectively. Two-colour two-laser experiments were also employed for generation of D^+ in the LiY, KY, RbY, and CsY zeolites. In each case, 308 nm laser excitation of the diphenylmethyl radical $D^\bullet$ generated by the initial 266 nm laser pulse led to the formation of the diphenylmethyl cation D^+ in sufficient yields so that rate constants could be readily obtained (Table 1).

Similar results were found upon irradiation of *m*-tolylphenylacetic acid (3-$(CH_3)D(COOH)$). Two-colour two-laser experiments were carried out in all five of the cation-exchanged zeolites to produce a high enough yield of the *m*-tolylphenylmethyl cation (3-$(CH_3)D^+$) for accurate kinetic analysis. The spectra generated upon two-colour two-laser excitation of 3-$(CH_3)D(COOH)$ in dry NaY are shown in Fig. 1*f*, where 3-$(CH_3)D^+$ at 450 nm can be readily seen. 3-$(CH_3)D^+$ decayed quickly in NaY with fast and slow components of 4.0×10^5 and 6.0×10^3 s^{-1}, respectively. Rate constants for the decay of 3-$(CH_3)D^+$ in the MY zeolites are also given in Table 1.

The five diarylacetic acids were also irradiated in NaX. In each case, the transient spectra included a band near 340 nm that is consistent with the formation of the diarylmethyl radicals. A band corresponding to a diarylmethyl cation was also observed upon irradiation of di-*p*-tolylacetic acid, *p*-anisylphenylacetic acid, and *p*-tolylphenylacetic acid in NaX, either by simple 266 nm or two-colour two-laser excitation, but no carbocation absorption was detected from diphenylacetic acid and *m*-tolylphenylacetic acid. The decays of the detectable carbocations fit well to a bi-exponential rate law, giving the rate constants included in Table 1. As expected, owing to the higher nucleophilicity of NaX, the rate constants for the decays of the carbocations in NaX are all considerably larger than those obtained in NaY.

Temperature study

Rate constants for the decay of the five substituted diarylmethyl carbocations were investigated as a function of temperature in the five cation-exchanged MY zeolites and in NaX. For each carbocation the decay rate constant was measured at a minimum of six different temperatures. In each case, the decays were fit to a bi-exponential rate expression, with attention being focused on the effect of temperature on the fast component. Representative data for the diarylmethyl carbocation in NaY are given in Table 2. As

Can. J. Chem. Downloaded from www.nrcresearchpress.com by University of Electronic and Science Techonology of China on 09/18/12
For personal use only.

Table 1. Rate constants for the fast and slow components of the decay of diarylmethyl carbocations (C^+) in cation-exchanged zeolites at 22 ± 1 °C.

		Rate constant					
C^+	λ_{max} (nm)	LiY (10^5 s^{-1})	NaY (10^5 s^{-1})	KY (10^5 s^{-1})	RbY (10^5 s^{-1})	CsY (10^5 s^{-1})	NaX (10^5 s^{-1})
D^+	450	3.2 (44%)	3.1 (44%)	13.4 (32%)	18 (42%)	19 (71%)	[a]
		0.57 (56%)	0.51 (56%)	2.7 (68%)	3.6 (59%)	4.8 (29%)	
3-$(CH_3)D^+$	460	3.9 (66%)	4.0 (62%)	10.2 (52%)	11 (53%)	12 (52%)	[a]
		0.58 (34%)	0.06 (38%)	1.65 (48%)	2.3 (47%)	4.6 (48%)	
4-$(CH_3)D^+$	460	2.5 (39%)	1.2 (34%)	5.1 (64%)	12 (47%)	14 (58%)	15 (44%)
		0.33 (61%)	0.15 (66%)	0.89 (36%)	2.2 (14%)	1.6 (42%)	1.4 (56%)
4,4′-$(CH_3)_2D^+$	470	0.53 (38%)	0.48 (56%)	3.4 (57%)	5.4 (59%)	9.6 (54%)	7.2 (58%)
		0.044 (62%)	0.053 (44%)	0.54 (43%)	0.91 (41%)	2.2 (46%)	1.2 (42%)
4-$(OCH_3)D^+$	460	0.06 (28%)	0.25 (36%)	2.4 (44%)	3.7 (53%)	4.4 (54%)	4.2 (74%)
		0.014 (72%)	0.026 (64%)	0.39 (56%)	0.87 (47%)	1.2 (46%)	0.24 (26%)

Note: Standard deviation ≤20%. Numbers in brackets represent the percentage of the bi-exponential fit corresponding to each component. Rate constants were determined by fit of the kinetic traces to a bi-exponential first-order equation.

[a]No time-resolved decay was detected in the kinetic profile.

Table 2. Fast components of the bi-exponential decay for the diarylmethyl carbocations (C^+) in NaY at 299, 281, and 239 K.

	Fast component		
C^+	k_1 ($\times 10^4$ s^{-1}) at 299 K	k_1 ($\times 10^4$ s^{-1}) at 281 K	k_1 ($\times 10^4$ s^{-1}) at 239 K
D^+	13.2±0.6	7.6±0.2	0.89±0.02
3-$(CH_3)D^+$	10.5±0.3	8.6±0.3	0.94±0.02
4-$(CH_3)D^+$	10.0±0.2	6.3±0.1	0.31[a]
4,4′-$(CH_3)_2D^+$	3.2±0.1	0.77±0.01	0.017[a]
4-$(OCH_3)D^+$	2.7±0.1	0.20±0.01	0.0052[a]

[a]Values extracted from exponential decay method (ESM).

well, lifetime distribution plots over several timescales were constructed at the various temperatures, and the rate constants for the fast component were calculated using the exponential series method (ESM).[41] This process was carried out for each of the kinetic profiles to ensure consistency in data analysis and also to confirm that the data extracted from the bi-exponential fits were comparable to the numbers collected from the ESM plots. In most cases the rate constants for the fast component calculated using the two methods were closely similar. However, at low temperatures, the ESM gave more reproducible results than the bi-exponential fit, and in these cases the rate constants determined using ESM were used.

Determination of activation parameters for the decay of diarylmethyl cations in zeolites

The activation parameters for the intrazeolite behaviour of the diarylmethyl carbocations were determined using the Eyring equation (eq. [2]).

$$[2] \qquad \ln\left(\frac{k_{decay}}{T}\right) = \ln\left(\frac{k_B}{h}\right) + \frac{\Delta S^{\neq}}{R} + \frac{\Delta H^{\neq}}{RT}$$

where k_{decay} is the decay rate constant, T is the temperature, k_B is the Boltzmann constant, h is Planck's constant, $\Delta S^{\neq}$ is the entropy of the reaction, $\Delta H^{\neq}$ is the enthalpy of the reaction, and R is the gas constant. An Eyring plot of $\ln(k_{decay}/T)$ vs $1/T$ results in a straight line, where $\Delta H^{\neq}$ and $\Delta S^{\neq}$ can be obtained from the slope and intersect of the graph, respectively. Representative Eyring plots constructed from the rate constants for the decay of the diarylmethyl carbocations in KY are given in Fig. 3. The activation parameters for the diarylmethyl carbocations studied in this work in the NaY, KY, RbY, and CsY zeolites and NaX are summarized in Table 3.

Substituent effects

Whereas the intrazeolite environment has been shown to be an important factor in determining the reactivity of encapsulated diarylmethyl carbocations, substituent effects on the diarylmethyl carbocations must also be considered to fully explain the reactivity of these species within the zeolite cavities. Hammett plots were constructed to evaluate the substituent effects experienced by the diarylmethyl carbocation in NaY, KY, RbY, CsY, and NaX at four different temperatures. Representative plots are shown in Fig. 4 for data obtained at 299 K. Data for the effect of substituents on the decay of the same carbocations in CF_3CH_2OH (TFE)[36] and CH_3CN–H_2O (1:2)[33] are also included in Fig. 4.

The slopes of these plots (ρ^+) represent the sensitivity of the reaction to substituents, and values of ρ^+ obtained for reaction of the diarylmethyl cations in the five zeolites at four different temperatures are summarized in Table 4.

Discussion

In the present work, diarylmethyl carbocations were generated by laser flash photolysis of the corresponding diarylacetic

Can. J. Chem. Downloaded from www.nrcresearchpress.com by University of Electronic and Science Techonology of China on 09/18/12
For personal use only.

Table 3. Activation parameters ($\Delta H^{\neq}$ (kJ/mol), $\Delta S^{\neq}$ (J K^{-1} mol^{-1}), and $\Delta G^{\neq}$ (kJ/mol)) for the decay of the diarylmethyl carbocations (C^+) in evacuated zeolites.

		C^+				
Zeolite	Activation parameter	D^+	3-$(CH_3)D^+$	4-$(CH_3)D^+$	4,4′-$(CH_3)_2D^+$	4-$(OCH_3)D^+$
NaY	$\Delta H^{\neq}$	26±2	24±2	34±3	51±4	60±6
	$\Delta S^{\neq}$	–58±3	–66±4	–37±3	14±1	35±7
	$\Delta G^{\neq}$	42±3	44±3	45±4	48±4	50±6
KY	$\Delta H^{\neq}$	11±2	13±3	19±2	21±2	26±5
	$\Delta S^{\neq}$	–92±5	–87±8	–69±3	–72±3	–66±7
	$\Delta G^{\neq}$	38±2	39±4	40±2	42±2	46±5
RbY	$\Delta H^{\neq}$	5±2	7±1	9±2	14±3	17±3
	$\Delta S^{\neq}$	–108±8	–106±7	–98±9	–88±8	–86±3
	$\Delta G^{\neq}$	37±3	38±2	39±3	40±4	43±3
CsY	$\Delta H^{\neq}$	6±2	13±1	8±1	12±2	17±1
	$\Delta S^{\neq}$	–101±6	–82±8	–98±4	–89±7	–81±6
	$\Delta G^{\neq}$	36±3	38±3	37±2	39±3	41±2
NaX	$\Delta H^{\neq}$			8±2	16±2	20±1
	$\Delta S^{\neq}$			–97±10	–71±3	–62±1
	$\Delta G^{\neq}$			37±4	36±2	39±1

Note: The free energies ($\Delta G^{\neq}$) were calculated at 298 K.

Fig. 3. Eyring plots for the decay of the diphenylmethyl (●), *m*-tolylphenylmethyl (○), *p*-tolylphenylmethyl (■), di-*p*-tolylmethyl (□), and *p*-anisylphenylmethyl (▲) carbocations in KY.

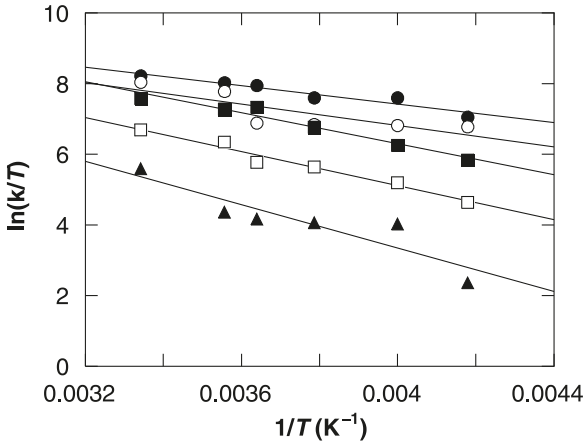

Fig. 4. Hammett plots illustrating the effect of para-aryl substituents on the decay of di-*p*-arylmethyl carbocations in CH_3CN–H_2O (1:2, ●; $\rho^+ = 3.1$), CF_3CH_2OH (TFE) (○; $\rho^+ = 4.2$), NaY (■; $\rho^+ = 1.43$), KY (□; $\rho^+ = 1.41$), RbY (▲; $\rho^+ = 1.10$), and CsY (△; $\rho^+ = 0.90$).

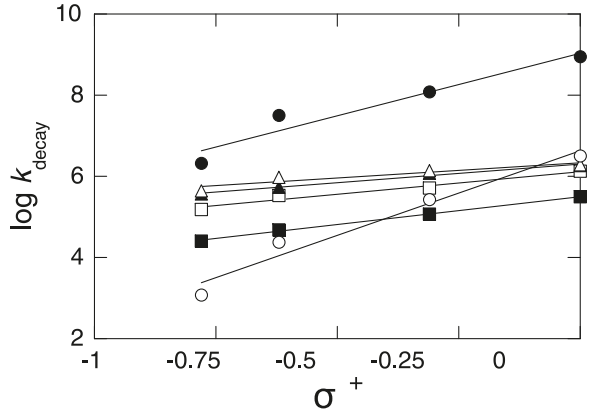

acids. The proposed mechanism for carbocation formation is shown in Scheme 2. Upon incorporation of the carboxylic acid into the zeolite framework, the acid undergoes an equilibrium deprotonation reaction to form the corresponding carboxylate ion. This is consistent with other deprotonation reactions for similar carboxylic acids in cation-exchanged zeolites.[22] Laser flash photolysis using 266 nm excitation of the carboxylate ion then results in the photochemical generation of the acyloxy radical, which undergoes a rapid loss of CO_2 (>10^8 s^{-1}) to form the diarylmethyl radical.[42–44] A subsequent photoionization of the carbon-centred radical either with the same laser pulse (266 nm) or with a second-colour second-laser pulse (308 nm) efficiently oxidizes the diarylmethyl radical to the corresponding diarylmethyl carbocation. The presence of the fluorescence on short timescales from excited diarylmethyl radicals between 530 and 580 nm in the transient spectra also supports the proposed radical photoionization mechanism.

Sufficient amounts of the more stabilized carbocations, such as 4,4′-$(CH_3)_2D^+$ and 4-$(OCH_3)D^+$, were generated for kinetic analysis using a single 266 nm laser pulse. Presumably, the yield of ionization from the small quantity of excited radicals generated by sequential absorption of 266 nm light from a single laser pulse was high enough for the production of adequate amounts of the carbocations. On the other hand, for the less stabilized carbocations, especially those in the less ionizing zeolites like KY, RbY, and CsY, the yield of ionization from the excited radical generated in a single 266 nm laser pulse was too low for adequate formation of the carbocations. In those cases, the second, 308 nm laser pulse was able to generate a far greater quantity of excited radical so that even inefficient ionization from the excited state still led to the formation of suitable amounts of carbocation for kinetic analysis.

Can. J. Chem. Downloaded from www.nrcresearchpress.com by University of Electronic and Science Techonology of China on 09/18/12
For personal use only.

Scheme 2.

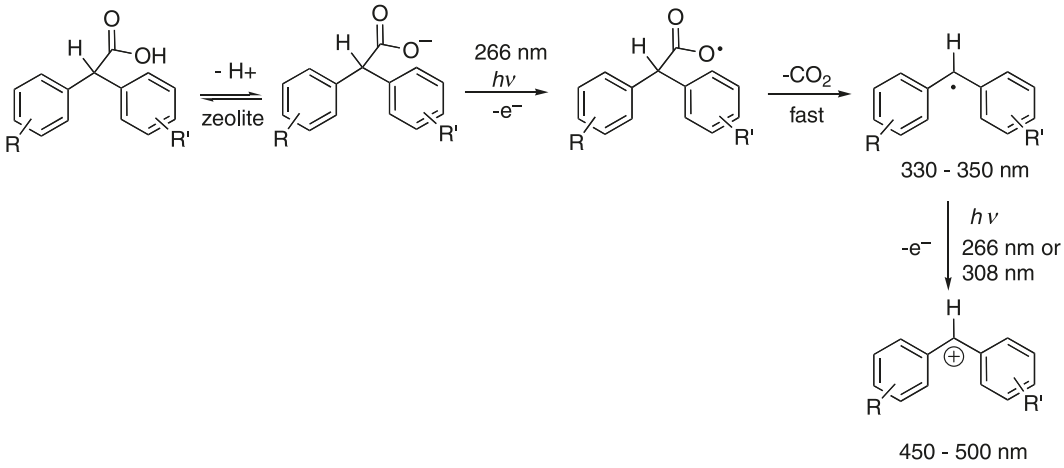

Table 4. Hammett slope (ρ^+) values obtained from the plots for the rate constants for the decay of the diarylmethyl carbocations in the cation-exchanged zeolites and different solutions at four temperatures.

	ρ^+			
Medium	299 K	274 K	264 K	239 K
Zeolite				
NaY	1.4	2.1	2.4	3.4
KY	1.4	1.7	1.8	2.2
RbY	1.0	1.2	1.3	1.7
CsY	0.7	0.8	0.9	1.2
NaX	0.47	0.9	1.2	1.6
Solution				
TFE	4.2[a,b]			
CH_3CN–H_2O (1:2)	3.1[a,c]			

Note: Standard deviation ≤20%.

[a]Room temperature (295 K).

[b]Data taken from ref. 36.

[c]Data taken from ref. 33.

The effect of zeolite nucleophilicity on the decay of diarylmethyl carbocations

The results presented in Table 1 clearly show that the reactivity of diarylmethyl carbocations is strongly influenced by the nucleophilicity of the intrazeolite environment. Notably, a systematic increase in reactivity of the diarylmethyl carbocations is observed upon varying the alkali-metal counterion from Li^+ to Cs^+. The Lewis basicity, or electron-donating ability, of the zeolite framework is highly influenced by the alkali-metal counterion, in particular the ionic interactions that occur between the counterion and the framework oxygens of the $[Si–O–Al]^-$ backbone. Small hard cations, such as Na^+, have stronger interactions with the active sites in the zeolite backbone than larger soft counterions, such as Cs^+. The weaker attractive force experienced between the softer counterions and the $[Si–O–Al]^-$ sites often translates into a more basic zeolite framework and stronger nucleophilic interactions between the framework oxygens and encapsulated electrophilic guests. The enhanced reactivity of the diarylmethyl carbocations can be readily illustrated by the ~20-fold increase in the rate constant for the decay of the di-*p*-tolylmethyl carbocation in CsY as compared with in NaY. A similar trend was observed for the *p*-anisylphenylmethyl, *p*-tolylphenylmethyl, diphenylmethyl, and *m*-tolylphenylmethyl carbocations, where 18-, 12-, 6- and 3-fold increases in reactivity were noted going from NaY to CsY. The decays of the photogenerated diarylmethyl carbocations in LiY were found to be slightly faster than expected. This increase in reactivity in LiY can be attributed to increased amounts of intrazeolite water present within the highly hydroscopic LiY, which increases the reactivity of the diarylmethyl carbocations generated within this intrazeolite environment.

The Si/Al ratio also influences the reactivity of zeolite-encapsulated diarylmethyl carbocations. For example, the rate constant for the decay of the di-*p*-tolylmethyl carbocation increases by a factor of 20 on going from NaY to NaX. NaX has an increased number of $[Si–O–Al]^-$ bridges, which provides a greater number of active nucleophilic sites (as compared with NaY) and a more nucleophilic zeolite environment. The increased reactivity of the diarylmethyl carbocations in NaX is consistent with the mechanism for carbocation decay that involves nucleophilic attack of the zeolite backbone onto the electrophilic cationic centre[14,45–47] and is in agreement for the decay of other reactive carbocation within cation-exchanged zeolites.[11,24,25]

Temperature effects

The data in Table 3 show an increase in the enthalpy of activation with more electron-rich *p*-aryl substituents. For example, for the more reactive diphenylmethyl carbocation in NaY, $\Delta H^{\neq}$ is 26 kJ/mol. However, substitution of the aryl ring with an electron-donating *p*-OCH_3 group more than doubles the $\Delta H^{\neq}$ for the reaction between the carbocations to 60 kJ/mol. The entropy of activation also increases with increasing electron-donating ability of the *p*-aryl substituents in NaY. This effect is again large, with the entropy of activation increasing by almost 100 J K^{-1} mol^{-1} upon going from the unsubstituted diphenylmethyl carbocation to the 4-OCH_3 derivative, and also changing from a negative to a positive value. Similar results are observed in the other MY zeolites. In all cases, $\Delta H^{\neq}$ more than doubles upon going from D^+ to (4-OCH_3)D^+. In addition, the values for $\Delta S^{\neq}$ decrease, although the decrease is smaller in KY,

Can. J. Chem. Downloaded from www.nrcresearchpress.com by University of Electronic and Science Techonology of China on 09/18/12
For personal use only.

Fig. 5. Enthalpy–entropy compensation plots for the decay of di-*p*-arylmethyl carbocations in (*a*) KY and (*b*) CsY at temperatures ≤299 K.

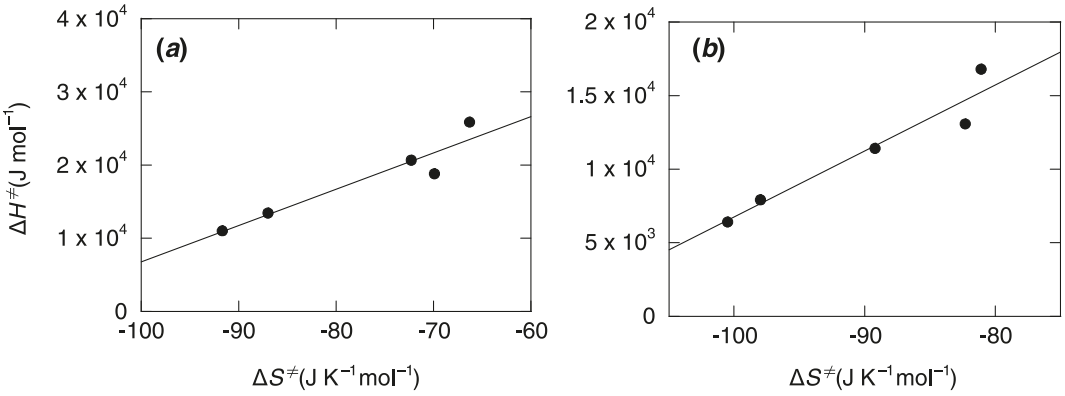

RbY, and CsY compared with NaY, and in some cases within the sum of the standard errors in $\Delta S^{\neq}$. Thus, the data show electron-donating substituents cause an increase in both the enthalpy and entropy of activation. The increase in $\Delta H^{\neq}$ serves to slow the reaction, whereas an increase in $\Delta S^{\neq}$ causes a faster reaction. Therefore, the observation that the reaction slows in the presence of electron-donating groups indicates that the effect of the substituents on the overall reactivity of diarylmethyl carbocations is driven by changes to the activation enthalpy and not the entropy of activation.

Substituent effects and isokinetic temperatures

From the ρ^+ values listed in Table 4 for the decay of diarylmethyl carbocations in TFE, CH_3CN–H_2O (1:2) and MY zeolites at 299 K, it is evident that the decay of the carbocations is substantially more sensitive to the effects of *p*-aryl substituents when formed in TFE and CH_3CN–H_2O solvents than when encapsulated within MY zeolites. For example, the ρ^+ value obtained in TFE (ρ^+ = 4.2) is more than two times the corresponding value in NaY (ρ^+ = 1.43). Even when compared with the more nucleophilic CH_3CN–H_2O (1:2) solvent mixture (ρ^+ = 3.1), the ρ^+ values in alkali-metal cation-exchanged X and Y zeolites, ranging from a low of ρ^+ = 0.7 to high of ρ^+ = 1.4 (at 299 K), are still significantly smaller. These results indicate that the intrazeolite environment tends to cause a "leveling effect" on the sensitivity of diarylmethyl carbocations towards the *p*-aryl substituent when formed within the confines of a solid support.

One possible explanation for the leveling effect is that the confines of the zeolite cavities force the aromatic rings to rotate relative to the empty p orbital of the carbocation centre, thus reducing the influence of the substituents on the aromatic ring. However, the data in Table 4 clearly show a sizeable increase in ρ^+ with decreasing temperature, indicating that the diarylmethyl carbocations in the MY zeolites are sensitive towards the electronic effects of the *p*-aryl substituents at low temperatures. This sensitivity to substituents at low temperatures argues against reduced coplanarity of the rings with the empty p orbital as being the main source of the leveling effect, although it still may play a secondary role.

On the other hand, the observed sensitivity of ρ^+ to temperature and the shallow Hammett plots that give small ρ^+ values are results that have, for other reactions, been attributed to low isokinetic temperatures (IKT).[48–53] Thus, an alternative explanation for the leveling effect observed in the reaction of substituted diarylmethyl cations in the zeolites is the presence of an unusually low IKT.[54,55]

To explore the possibility that the reactions of the diarylmethyl cations feature a low IKT, several methods were employed to determine the presence of an isokinetic relationship and the value of an IKT. One of the simplest methods is based on a linear relationship between $\Delta H^{\neq}$ and $\Delta S^{\neq}$ where the slope (β) is the corresponding IKT (eq. [3]).[49,54–59]

$$[3] \qquad \Delta H^{\neq} = \beta \Delta S^{\neq}$$

Figure 5 presents the enthalpy–entropy compensation plots constructed for the decay of diarylmethyl carbocations in KY and CsY. From these graphs, it is evident that the enthalpies and entropies of activation are complementary. Furthermore, analysis of the slopes of the linear fits produced values considered to be an approximation of the IKT for the reaction of the diarylmethyl carbocations with the $[Si–O–Al]^-$ framework. Table 5 presents the estimated IKTs in NaY, KY, RbY, CsY, and NaX as calculated from the linear fit. All of the values extracted from the enthalpy–entropy plots give low IKTs, ranging from lows of 333 to 360 K for reaction in NaX and NaY, respectively, to a high of 513 K for reaction in CsY.

The presence of an isokinetic relationship is also typically visible in Eyring plots, where the presence of a common point of intersection can be estimated to be the IKT for the organic reaction of interest.[60] Figures 6*a* and 6*b* depict the Eyring plots for the intrazeolite decay of the diarylmethyl carbocations in NaY and CsY. A distinct point of intersection can be seen in each plot. The Eyring plots constructed for the decay of the diarylmethyl carbocations in KY, RbY, and NaX also present a point of intersection, supporting the presence of an isokinetic relationship for the decay of diarylmethyl carbocations in non-protic zeolites. *F* value statistical calculations were also undertaken to validate the IKT (or point of intersection) observed in each Eyring plot.[60] Like the approximate IKTs obtained from the compensation plots, the values calculated from the Eyring plot / F-statistic method were also low. The average IKTs calculated using these methods are presented in Table 5. The IKTs for the decay of diarylmethyl carbocations in alkali-

Can. J. Chem. Downloaded from www.nrcresearchpress.com by University of Electronic and Science Techonology of China on 09/18/12
For personal use only.

Table 5. Isokinetic temperatures (IKT) for the decay of diarylmethyl cations in alkali metal cation-exchanged X and Y zeolites.

	IKT		
Zeolite	$\Delta H^{\neq}$ vs $\Delta S^{\neq}$ (K)	Eyring/F statistic (K)	Avg. (K)[a]
NaY	360	366	363±4
KY	497	505	501±4
RbY	482	518	500±18
CsY	511	520	515±5
NaX	333	345	339±6

Note: Standard deviation ≤20%.

[a]Errors were calculated using the standard deviation of the two values collected.

Fig. 6. Extended Eyring plots for the decay of the diphenylmethyl (—), *m*-tolylphenylmethyl (– –), *p*-tolylphenylmethyl (— —), di-*p*-tolylmethyl (- — -), and *p*-anisylphenylmethyl (- -) cations in (*a*) NaY and (*b*) CsY at temperatures ≤299 K. Extended Hammett plots for the decay of di-*p*-arylmethyl carbocations in (*c*) NaY and (*d*) CsY at 299 K (●), 274 K (○), 264 K (■), and 239 K (□).

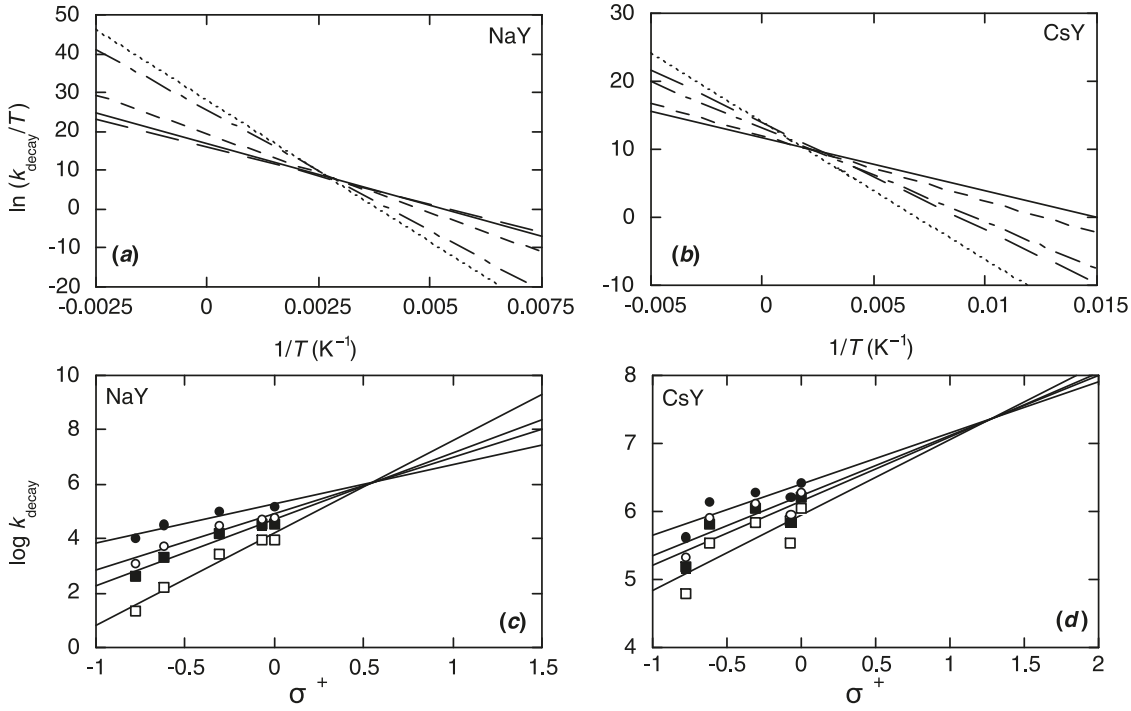

metal cation-exchanged Y zeolites were estimated to be between 345 and 518 K.

A reaction series that exhibits a common point of intersection in the Eyring plots will commonly present a common point of intersection in the Hammett plot as well.[48,49] The Hammett plots constructed for the decay of the diarylmethyl carbocations in NaY and CsY are presented in Figs. 6*c* and 6*d*. The point of intersection occurs at σ^+ = 0.58 for NaY and σ^+ = 1.23 in CsY. A carbocation possessing a substituent parameter equivalent to the point of intersection will have identical reactivity at all temperatures, commonly referred to as the isokinetic substituent. The low-temperature Hammett plots presented in Fig. 6 can also be used to illustrate the increased sensitivity of the diarylmethyl carbocations towards *p*-aryl substituents with decreasing temperature, as is reflected by the ρ^+ values presented in Table 5.

From the data presented in Table 5, it is evident that the IKTs for the decay of diarylmethyl carbocations in alkali-metal cation-exchanged Y and NaX zeolites are much lower than 1000 K and fall well within a normal experimental range. Several accounts on the reactivity of diarylmethyl carbocations towards π nucleophiles[48,61,62] can be likened to the nucleophilic attack of the diarylmethyl carbocations by the active Lewis base sites in the zeolite framework. The IKT for the reaction of diarylmethyl carbocations with various alkenes is close to 700 K higher than the IKT for the reaction of the analogous electrophilic species in non-protic X and Y zeolites.

Based on the previous publications in solution and the current results obtained in non-protic zeolites, it seems reasonable to suggest that the observed leveling effect of the *p*-aryl substituent effects in zeolite-encapsulated diarylmethyl carbocations can be explained by the lower IKT for the reaction of diarylmethyl carbocations with the [Si–O–Al]$^-$ backbone. Though no experimental or theoretical technique

Can. J. Chem. Downloaded from www.nrcresearchpress.com by University of Electronic and Science Techonology of China on 09/18/12
For personal use only.

Scheme 3.

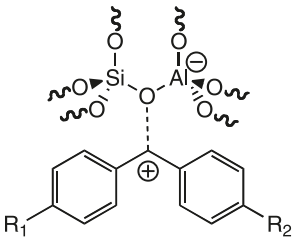

can predetermine the IKT for a given organic reaction, molecular complexation during the solvation process has been considered a determining factor for reactions with low IKTs [54]. Zeolites are commonly referred to as solid-state ionizing, solvents,[63] where co-encapsulated guest molecules undergo interactions with the aluminosilicate framework similar to solvation interactions in solution, as illustrated in Scheme 3. Thus, we propose that the solvation of the diarylmethyl carbocations in non-protic zeolites involves the formation of a framework-bound alkoxy adduct (Scheme 3).

Comparing the results obtained for the decay of the carbocations in NaY and NaX supports the solvation of the zeolite-encapsulated diarylmethyl carbocations as the potential source of the low IKTs. From the data presented in Table 5, it can be seen that the IKT for the decay of the diarylmethyl carbocations in NaX is an estimated 20 K lower than in NaY. The formation of a solvated cation would be more likely to occur within the confines of the more basic/nucleophilic environment of zeolite X based on the larger number of active base sites within this zeolite lattice.

Experimental

Materials

Diphenylacetic acid was commercially available (Sigma-Aldrich) and was used as received. The synthesis of di-*p*-tolylacetic acid,[64] *p*-tolylphenylacetic acid,[65] *p*-anisylphenylacetic,[65] and *m*-tolylphenylacetic acid[66,67] have been reported previously.

Zeolites

NaY (Si:Al = 2.4) and NaX (Si:Al = 1.3) were purchased from Sigma-Aldrich. All zeolites were activated in an oven at 450 °C for at least 12 h prior to use to ensure the removal of intrazeolite water. Alkali-metal cation-exchanged zeolites were prepared through aqueous ion exchange with the corresponding chloride salts (LiCl, KCl, RbCl, and CsCl) in the usual way.[11] The number of cations per unit cell of zeolite Y are 16 site I cations, 32 site II cations, and 8 site III cations. Only site II and site III cations are accessible to guest molecules.[7] The degree of cation exchange in Y zeolites is typically 47% for LiY, 97% for KY, 44% for RbY, and 47% for CsY. For larger cations, such as Rb^+ and Cs^+, only the Na^+ cations that occupy type II and type III sites can be readily exchanged.[68] Hydrated Li^+ does not readily exchange the type I cations, which results in a lower percent exchange. All solvents used during zeolite preparation were spectroscopic grade (99.98%, Omnisolv, BDH) and were used as received.

Sample preparation

The method of guest molecule incorporation into the zeolite was adapted from a procedure previously described.[69]

Laser flash photolysis

The computer-controlled ns laser flash photolysis system was employed in this study and has been previously described.[11] For one-laser irradiation experiments, the excitation source was the fourth harmonic (266 nm, ≤25 mJ, <8 ns/pulse) of a Nd:YAG laser. For the two-laser techniques, the first excitation source was the Nd:YAG 266 nm laser and the second was an excimer laser (308 nm, <70 mJ, 10 ns/pulse). Diffuse reflectance experiments involve measuring the fraction of reflected light absorbed by the transient, denoted as the reflectance change, $\Delta J/J_0$, where J_0 is the reflectance intensity before laser excitation and ΔJ is the change in reflectance intensity after excitation owing to absorption by photogenerated transients. Transient signals were directed into a monochromatic-photomulitipler tube system and subsequently captured using a digital oscilloscope and transferred to a computer controlled by software based on the Labview programming language. Samples contained in 3 mm × 7 mm quartz sample cells were used under reduced pressure or under oxygen-saturated conditions. Samples irradiated under an oxygen atmosphere were purged using high-purity molecular oxygen for a minimum of 20 min prior to laser flash photolysis.

Data analysis

Data analysis was based on the fraction of reflected light absorbed by the transient species, $\Delta J/J_0$. Owing to the large number of microenvironments found in the zeolite matrix, time-resolved kinetic spectra commonly contain multiple components. As such, the time-resolved decays of the transients investigated in this report fit well to bi-exponential first-order rate equations, rather than simple first-order expressions, unless otherwise reported.

The low-temperature time-resolved data was collected using a Thermo NESLAB CC-100 cooler, a NESLAB U-Tainer B thermostat, and a NESLAB Exatrol temperature control. To accurately determine the temperature conditions experienced by the solid-state samples, a sample probe was constructed that replicated the intrazeolite conditions. The temperature standard consisted of 300 mg of hydrated NaY zeolite placed into a 3 mm × 7 mm quartz sample cell. A digital thermometer was then securely placed into the heterogeneous material. The probe was placed into the cooled sample holder and allowed to equilibrate for 10–15 min, during which time the temperature reading on the thermometer stabilized. Following determination of the equilibrium experimental temperature, the sample to be studied was placed into the sample holder and allowed to equilibrate for the same amount of time as the temperature probe.

The rate constants for the decay of several of the more stable diarylmethyl carbocations were incomplete on the longest timescales of our ns laser flash photolysis apparatus, therefore, the corresponding rate constants were calculated from lifetime distribution plots. Rate constant distributions were calculated from transient decays using ESM.[41] The fitting function employed contained 200 exponential terms, which were fixed logarithmically spaced rate constants ranging

Can. J. Chem. Downloaded from www.nrcresearchpress.com by University of Electronic and Science Techonology of China on 09/18/12
For personal use only.

from 1 to 1 $\times$ 10^7 s^{-1} with variable pre-exponentials. Typically, three sets of rate constant distributions were revealed by ESM analysis of the transient decays. Each set of rate constant distributions was fit using nonlinear least-squares fitting to a Gaussian equation; the parameters from these fits were used to calculate the normalized area under each set of distributions. The rate constants were extracted from the lifetime data using a Gaussian fit.

Kinetic data used for the low-temperature Hammett plots were calculated using the Eyring activation parameters.

Supplementary data

Supplementary data (time-resolved spectral and kinetic data and low-temperature plots (enthalpy–entropy compensation, Eyring, and Hammett) are available with this article through the journal Web site (www.nrcresearchpress.com/cjc).

Acknowledgements

We gratefully acknowledge the Natural Sciences and Engineering Research Council of Canada (NSERC) and Dalhousie University, Halifax, Nova Scotia, for financial support of this research.

References

(1) Ramamurthy, V. J. *Photochem. Photobiol. C. Phytochem. Rev.* **2000**, *1* (2), 145. doi:10.1016/S1389-5567(00)00010-1.
(2) Ramamurthy, V. *Photoprocesses of Organic Molecules Included in Zeolites.* In *Photoprocesses of Organic Molecules Included in Zeolites;* Ramamurthy, V., Ed.; VCH Publishers: New York, 1991; pp 429–493.
(3) Hashimoto, S. J. *Photochem. Photobiol. C. Phytochem. Rev.* **2003**, *4* (1), 19. doi:10.1016/S1389-5567(03)00003-0.
(4) Scaiano, J. C.; Garcia, H. *Acc. Chem. Res.* **1999**, *32* (9), 783. doi:10.1021/ar9702536.
(5) García, H.; Roth, H. D. *Chem. Rev.* **2002**, *102* (11), 3947. doi:10.1021/cr980026x.
(6) Yoon, K. B. *Chem. Rev.* **1993**, *93* (1), 321. doi:10.1021/cr00017a015.
(7) Ramamurthy, V.; Turro, N. J. *J. Inclusion Phenom. Mol. Recognit. Chem.* **1995**, *21*, 239.
(8) Auerbach, S. M.; Karrado, K. A.; Dutta, P. K. *Handbook of Zeolite Science and Technology;* Marcel Dekker Inc.: New York, 2003.
(9) Rabo, J. A. *Zeolite Chemistry and Catalysis;* American Chemical Society Monograph: Washington, DC, 1976.
(10) Lakshminarasimhan, P.; Thomas, K. J.; Brancaleon, L.; Wood, P. D.; Johnston, L. J.; Ramamurthy, V. *J. Phys. Chem. B* **1999**, *103* (43), 9247. doi:10.1021/jp990913j.
(11) O'Neill, M. A.; Cozens, F. L.; Schepp, N. P. *J. Am. Chem. Soc.* **2000**, *122* (25), 6017. doi:10.1021/ja993619d.
(12) Corma, A. *Chem. Rev.* **1995**, *95* (3), 559. doi:10.1021/cr00035a006.
(13) Jacobs, P. A.; Beyer, H. K. *J. Phys. Chem.* **1979**, *83* (9), 1174. doi:10.1021/j100472a013.
(14) Haw, J. F.; Richardson, B. R.; Oshiro, I. S.; Lazo, N. D.; Speed, J. A. *J. Am. Chem. Soc.* **1989**, *111* (6), 2052. doi:10.1021/ja00188a016.
(15) Barthomeuf, D. *J. Phys. Chem.* **1984**, *88* (1), 42. doi:10.1021/j150645a010.
(16) Cozens, F. L.; Bogdanova, R.; Regimbald, M.; Garcia, H.; Marti, V.; Scaiano, J. C. *J. Phys. Chem. B* **1997**, *101* (35), 6921. doi:10.1021/jp9708963.
(17) Cozens, F. L.; Garcia, H.; Scaiano, J. C. *J. Am. Chem. Soc.* **1993**, *115* (24), 11134. doi:10.1021/ja00077a010.
(18) Cano, M. L.; Cozens, F. L.; Fornes, V.; Garcia, H.; Scaiano, J. C. *J. Phys. Chem.* **1996**, *100* (46), 18145. doi:10.1021/jp960729n.
(19) Cano, M. L.; Cozens, F. L.; Garcia, H.; Marti, V.; Scaiano, J. C. *J. Phys. Chem.* **1996**, *100* (46), 18152. doi:10.1021/jp960730m.
(20) Cano, M. L.; Corma, A.; Fornes, V.; Garcia, H. *J. Phys. Chem.* **1995**, *99* (12), 4241. doi:10.1021/j100012a053.
(21) Cozens, F. L.; Garcia, H.; Scaiano, J. C. *Langmuir* **1994**, *10* (7), 2246. doi:10.1021/la00019a036.
(22) Cozens, F. L.; Cano, M. L.; Garcia, H.; Schepp, N. P. *J. Am. Chem. Soc.* **1998**, *120* (23), 5667. doi:10.1021/ja971524a.
(23) Cozens, F. L.; O'Neil, M. A.; Schepp, N. P. *J. Am. Chem. Soc.* **1997**, *119* (32), 7583. doi:10.1021/ja970690f.
(24) O'Neill, M. A.; Cozens, F. L. *Can. J. Chem.* **2003**, *81* (6), 647. doi:10.1139/v03-071.
(25) O'Neill, M. A.; Cozens, F. L.; Schepp, N. P. *Tetrahedron* **2000**, *56* (36), 6969. doi:10.1016/S0040-4020(00)00518-4.
(26) Davis, M. E. *Acc. Chem. Res.* **1993**, *26* (3), 111. doi:10.1021/ar00027a006.
(27) Forester, T. R.; Howe, R. F. *J. Am. Chem. Soc.* **1987**, *109* (17), 5076. doi:10.1021/ja00251a004.
(28) Faria, J. L.; Steenken, S. *J. Am. Chem. Soc.* **1990**, *112* (3), 1277. doi:10.1021/ja00159a076.
(29) Faria, J. L.; Steenken, S. *J. Phys. Chem.* **1993**, *97* (9), 1924. doi:10.1021/j100111a034.
(30) Bartl, J.; Steenken, S.; Mayr, H.; McClelland, R. A. *J. Am. Chem. Soc.* **1990**, *112* (19), 6918. doi:10.1021/ja00175a028.
(31) Faria, J. L.; McClelland, R. A.; Steenken, S. *Chem. Eur. J.* **1998**, *4* (7), 1275. doi:10.1002/(SICI)1521-3765(19980710)4:7<1275::AID-CHEM1275>3.0.CO;2-X.
(32) Kirmse, W.; Krzossa, B.; Steenken, S. *J. Am. Chem. Soc.* **1996**, *118* (32), 7473. doi:10.1021/ja960268j.
(33) McClelland, R. A.; Kanagasabapathy, V. M.; Banait, N.; Steenken, S. *J. Am. Chem. Soc.* **1989**, *111* (11), 3966. doi:10.1021/ja00193a031.
(34) McClelland, R. A.; Kanagasabapathy, V. M.; Banait, N.; Steenken, S. *J. Am. Chem. Soc.* **1991**, *113* (3), 1009. doi:10.1021/ja00003a040.
(35) McClelland, R. A.; Kanagasabapathy, V. M.; Banait, N.; Steenken, S. *J. Am. Chem. Soc.* **1992**, *114* (5), 1816. doi:10.1021/ja00031a041.
(36) McClelland, R. A.; Kanagasabapathy, V. M.; Steenken, S. *J. Am. Chem. Soc.* **1988**, *110* (20), 6913. doi:10.1021/ja00228a066.
(37) O'Neill, M. A. Nanosecond Time-Resolved Diffuse Reflectance Studies of Reactive Carbocations and Charge Migration in Non-Acidic Zeolites. Ph.D. Thesis, Dalhousie University, 2001.
(38) Shea, S.; Schepp, N. P.; Keirstead, A. E.; Cozens, F. L. *Can. J. Chem.* **2005**, *83* (9), 1637. doi:10.1139/v05-208.
(39) Arnold, B. A.; Scaiano, J. C.; McGimpsey, W. G. *J. Am. Chem. Soc.* **1992**, *114* (25), 9978. doi:10.1021/ja00051a033.
(40) Weir, D.; Scaiano, J. C. *Chem. Phys. Lett.* **1986**, *128* (2), 156. doi:10.1016/0009-2614(86)80316-5.
(41) Siemiarczuk, A.; Wagner, B. D.; Ware, W. R. *J. Phys. Chem.* **1990**, *94* (4), 1661. doi:10.1021/j100367a080.
(42) Baciocchi, E.; Bietti, M. *J. Chem. Soc., Perkin Trans. 2* **2002**, *2* (4), 720. doi:10.1039/b200388k.

(43) Bockman, T. M.; Hubig, S. M.; Kochi, J. K. *J. Am. Chem. Soc.* **1996**, *118* (18), 4502. doi:10.1021/ja960112j.
(44) Bockman, T. M.; Hubig, S. M.; Kochi, J. K. *J. Org. Chem.* **1997**, *62* (7), 2210. doi:10.1021/jo9617833.
(45) Haw, J. F.; Nicholas, J. F.; Xu, T.; Beck, L. W.; Ferguson, D. B. *Acc. Chem. Res.* **1996**, *29* (6), 259. doi:10.1021/ar950105k.
(46) Xu, T.; Haw, J. F. *J. Am. Chem. Soc.* **1994**, *116* (22), 10188. doi:10.1021/ja00101a044.
(47) Xu, T.; Haw, J. F. *J. Am. Chem. Soc.* **1994**, *116* (17), 7753. doi:10.1021/ja00096a036.
(48) Mayr, H.; Schneider, R.; Grabis, U. *J. Am. Chem. Soc.* **1990**, *112* (11), 4460. doi:10.1021/ja00167a051.
(49) Pushparaj, F. J.; Kannan, S.; Vikram, L.; Kumar, L. S.; Rangappa, K. S. *J. Phys. Org. Chem.* **2005**, *18* (10), 1042. doi:10.1002/poc.968.
(50) Hamed, E. A. *Indian J. Chem.* **1997**, *36*, 102.
(51) Reddy, S. R.; Manikyamba, P. *J. Chem. Sci.* **2006**, *118* (3), 257. doi:10.1007/BF02708285.
(52) Srivastava, S. P.; Gupta, V. K.; Jain, M. C.; Ansari, M. N.; Kaushik, R. D. *Thermochim. Acta* **1983**, *68* (1), 27. doi:10.1016/0040-6031(83)80376-1.
(53) Schmid, R.; Soukup, R. W.; Sapunov, V. N.; Linert, W. *Z. Phys. Chem. Neue Folge* **1981**, *126*, 25.
(54) Leffler, J. E.; Grunwald, E. *Rates and Equilibria of Organic Reactions: As Treated by Statistical, Thermodynamical and Extrathermodynamical Methods;* John Wiley and Sons, Inc.: New York, 1963.
(55) Leffler, J. E. *J. Chem. Phys.* **1955**, *23* (11), 2199. doi:10.1063/1.1740710.
(56) Anslyn, E. V.; Doughtery, D. A. *Modern Physical Organic Chemistry;* University Science Books: New York, 2006.
(57) Corma, A.; Llopis, F.; Monton, J. B.; Weller, S. *J. Catal.* **1993**, *142* (1), 97. doi:10.1006/jcat.1993.1192.
(58) Corma, A.; Llopis, F.; Monton, J. B.; Weller, S. *J. Catal.* **1994**, *148* (1), 415. doi:10.1006/jcat.1994.1227.
(59) Palmero, A.; Suarez, M. P.; Aldao, C. M. *J. Catal.* **1994**, *148* (1), 413. doi:10.1006/jcat.1994.1226.
(60) Linert, W. *Chem. Soc. Rev.* **1994**, *23* (6), 429. doi:10.1039/cs9942300429.
(61) Mayr, H.; Schneider, R.; Schade, C.; Bartl, J.; Bederke, R. *J. Am. Chem. Soc.* **1990**, *112* (11), 4446. doi:10.1021/ja00167a049.
(62) Patz, M.; Mayr, H.; Bartl, J.; Steenken, S. *Angew. Chem. Int. Ed. Engl.* **1995**, *34* (4), 490. doi:10.1002/anie.199504901.
(63) Dutta, P. K.; Turbeville, W. *J. Phys. Chem.* **1991**, *95* (10), 4087. doi:10.1021/j100163a036.
(64) Clarke, L. F.; Hegarty, A. F.; O'Neill, P. *J. Org. Chem.* **1992**, *57* (1), 362. doi:10.1021/jo00027a062.
(65) McKenzie, A.; Widdows, S. T. *J. Chem. Soc. Trans.* **1915**, *107*, 702. doi:10.1039/ct9150700702.
(66) Shukla, D.; Wan, P. *J. Photochem. Photobiol. Chem.* **1998**, *113* (1), 53. doi:10.1016/S1010-6030(97)00298-0.
(67) Gualtieri, F.; Mordini, A.; Pecchi, S.; Scapecchi, S. *Synlett* **1996**, *1996* (5), 447. doi:10.1055/s-1996-5444.
(68) Van Bekkum, H.; Flanigen, E. M.; Janson, J. C. *Introduction to Zeolite Science and Practice;* Elsevier Science Ltd.: Amsterdam, 1991.
(69) Stamires, D.; Turkevich, J. *J. Am. Chem. Soc.* **1964**, *86* (5), 749. doi:10.1021/ja01059a001.

Can. J. Chem. Downloaded from www.nrcresearchpress.com by University of Electronic and Science Techonology of China on 09/18/12
For personal use only.

Fluorescence enhancement of amine-capped CdSe/ZnS quantum dots by thiol addition

Jordi Aguilera-Sigalat, Simon Rocton, Raquel E. Galian, and Julia Pérez-Prieto

Abstract: The present communication reports that while addition of alkyl thiols drastically reduces the fluorescence of CdSe core quantum dots, it actually enhances the emission properties of already highly fluorescent amine-capped CdSe/ZnS core-shell quantum dots.

Key words: CdSe/ZnS, core shell, fluorescence, ligand exchange, quantum dot.

Résumé : On montre dans ce travail que, alors que l'addition d'alkylthiols diminue d'une façon drastique la fluorescence des points quantiques d'un coeur CdSe, cette addition augmente en fait les propriétés d'émission de fluorescence déjà très élevées des points quantiques de la couche d'un coeur CdSe/ZnS chapeauté par une amine.

Mots-clés : CdSe/ZnS, couche d'un cœur, fluorescence, échange de ligand, point quantique.

[Traduit par la Rédaction]

Introduction

Quantum dots (QDs) have unique optical properties[1] that make them of interest for biological, medical, and engineering applications. They are highly fluorescent systems compared with organic dyes, though different factors, such as growth conditions, post-illumination treatment, the nature of the capping ligand, and storage conditions, seem to affect their fluorescence quantum yield (Φ_F). Some of these factors may induce the appearance of defects on the QD surface, producing an additional nonradiative pathway due to trapping of the electron or the hole generated after the absorption of light. To reduce the number of defects and, consequently, increase the Φ_F, good QD surface passivation is needed. This can be accomplished by adding an inorganic shell or using long-chain organic surfactants.[1]

With regard to using an inorganic shell as coating, a higher band gap material (ZnS, ZnSe, CdS) has been used to prepare core-shell QDs that have, in general, a much higher Φ_F.[2,3]

With respect to ligands, trioctylphosphine (TOP) and trioctylphosphine oxide (TOPO) are the most common ligands used in the synthesis of QDs.[1,2,4] However, the exchange of the phosphine ligands by fatty amines leads to an enhancement of the Φ_F of the resulting nanoparticle.[5] Functional thiol ligands have also been used as capping material to make QDs water-soluble and to add functionality to the nanoparticle.[6] Thiol ligands can replace TOPO and amine ligands and bind more strongly to the QD surface,[7,8] but such exchange decreases the Φ_F of CdSe core QDs.[5,8,9] This behavior has been attributed to the hole-trapping capacity of thiol molecules.[10]

Curiously, in the case of CdSe/ZnS core-shell QDs, where the shell should avoid the QD emission quenching by electron donors,[11] ligand exchange of TOPO by hydrophilic thiols to achieve water-soluble QDs also leads to a decrease in Φ_F. This has been explained by formation of thiolates in water, and such thiolates somehow add new hole trap states.[7,12]

To gain insight into the effect of thiols (rather than thiolates) on the fluorescence of organic-soluble core-shell QDs, we studied the QD emission in the presence of two model alkyl thiols: 11-mercapto-1-undecanol (MU) and a thiol functionalized with a benzophenone chromophore (KP-SH) (Scheme 1). For comparison purposes, studies using CdSe core QDs were also performed. We analyzed the influence of the native ligand (TOPO or TOP for CdSe and a long-chain amine for CdSe/ZnS) used as capping material, the QD size, and the thiol concentration on the variation of the QD fluorescence. Our results demonstrated that the CdSe and CdSe/ZnS QDs presented a different response to the addition of the assayed thiols.

Results and discussion

CdSe core QDs (QD-C) capped with TOPO and TOP ligands were synthesized according to the methodology reported by Peng and Peng.[4a] The size of the nanoparticles

Received 31 March 2010. Accepted 3 October 2010. Published on the NRC Research Press Web site at canjchem.nrc.ca on 25 February 2011.

This article is part of a Special Issue dedicated to Professor J. C. Scaiano on the occasion of his 65th birthday.

J. Aguilera-Sigalat, S. Rocton, and J. Pérez-Prieto.[2] Instituto de Ciencia Molecular (ICMol), Universidad de Valencia, Catedrático José Beltrán 2, 46980 Paterna, Valencia, Spain.
R.E. Galian.[1] Departamento de Química Analítica, ICMol, Dr. Moliner 50, 46100 Burjassot, Spain.

[1]Corresponding author (e-mail: raquel.galian@uv.es).
[2]Corresponding author (e-mail: Julia.perez@uv.es).

Can. J. Chem. Downloaded from www.nrcresearchpress.com by University of Electronic and Science Techonology of China on 09/18/12
For personal use only.

Can. J. Chem. Downloaded from www.nrcresearchpress.com by University of Electronic and Science Techonology of China on 09/18/12
For personal use only.

Scheme 1. Exchange of TOPO or TOP (core QDs) and amine (core-shell QDs) by thiol compounds.

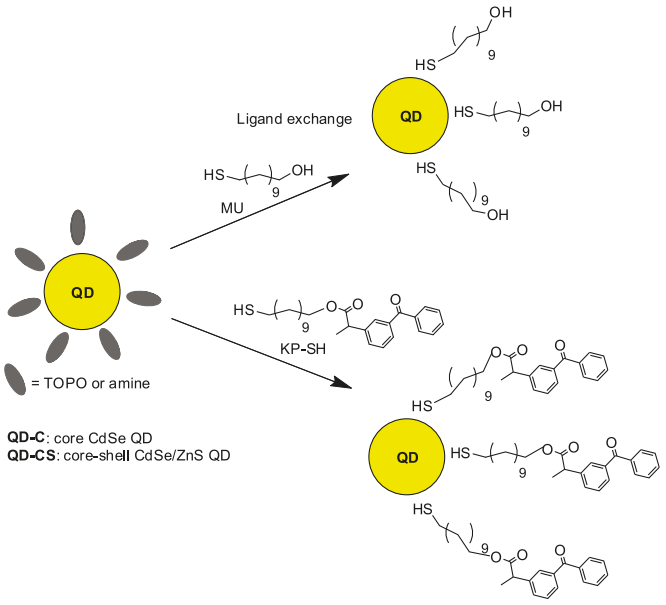

was estimated using the maximum of the first exciton peak in the UV–vis spectrum[13]; thus, the maximum at 513 nm for QD-C1 was indicative of a diameter of 2.5 nm. High-resolution transmission electron microscopy images confirmed the size of the nanoparticle as well as the crystalline properties and monodispersity of QD-C1 (size 2.6 ± 0.4 nm). In addition, different commercial CdSe/ZnS core-shell QDs (QD-CS), capped with a long-chain primary amine, were used. All QDs were soluble in organic solvents such as toluene and chloroform.

The effect of different thiol (MU, KP-SH[14]) concentrations on the optical properties of the QDs was studied using steady-state absorption and fluorescence spectroscopy. The addition of thiol did not cause a significant change in either the maximum of the first exciton peak or the emission maximum of core and core-shell QDs (Table S1 in the Supplementary data). However, important fluorescence quenching was detected upon addition of MU (5 mmol/L) to a toluene solution of QD-C1 (2.9 µmol/L) with a thiol/QD concentration ratio of 1724 (Fig. 1, Table 1). Similarly, fluorescence quenching was detected after addition of KP-SH to QD-C1 ([thiol]/[QD] = 6200).

By contrast, when the MU/QD concentration ratio was as low as 540, the initial fluorescence quenching was followed by fluorescence enhancement (reaching a plateau after 90 min) and the appearance of a broad photoluminescence at a longer wavelength than the band edge luminescence (maximum approx. 700 nm, see Fig. 2). The latter luminescence could be ascribed to new surface states with emission properties.[15] Likewise, after addition of KP-SH in a KP-SH/QD molar ratio of 620, an initial fluorescence quenching was followed by a fluorescence enhancement (Fig. S2 in the Supplementary data; Table 1). Also, an emission at longer wavelengths than the band edge was observed.

Similar results were obtained for another batch of homemade CdSe core QDs, QD-C2 (λ_{max} exciton peak at 523 nm, 2.6 nm). Moreover, the sensitivity of QD-C2 fluorescence to thiol addition was higher after 6 months of aging. This result shows the increase of QD surface defects with time.

Fig. 1. Fluorescence spectra of a deaerated toluene solution of QD-C1 (2.9 µmol/L) in the absence (●) and in the presence of MU (5 mmol/L) 0 min (▼), 30 min (■), and 80 min (○) after the addition of the MU; [MU]/[QD-C1] = 1724.

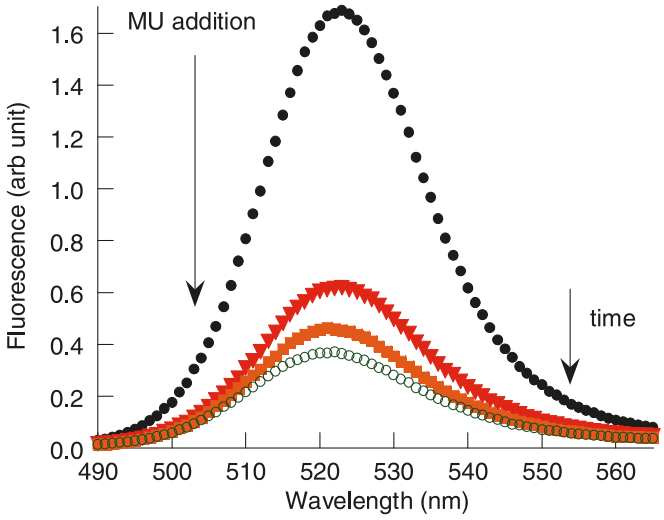

Table 1. Variation of the QD fluorescence quantum yield after the addition of MU and KP-SH, and kinetic rate constant of the ligand exchange (k_{LE}).

QD/thiol system	[Thiol]/[QD] molar ratio	$(I_{inf}–I_0)/I_0$[a]	k_{LE} (s^{-1} L mol^{-1})
QD-C1/MU	540	0.80	—
	1 724	–0.67	7.0±0.4
QD-C1/KP-SH	620	0.18	22.2±0.6
	6 200	–0.65	—
QD-CS1/MU	2 940	0.59	5.8±0.3
QD-CS1/KP-SH	3 600	1.34	11.5±0.4
QD-CS2/MU	12 500	0.93	13±1
QD-CS2/KP-SH	4 500	0.72	22±2

[a] I_0 and I_{inf}: fluorescence emission area of the QD in the absence of the thiol and 2 h after addition of the thiol, respectively.

To check whether this behavior also applied to core-shell QDs, we extended our studies to commercial core-shell QDs (QD-CS).[16] The addition of the functional thiol KP-SH to QD-CS1 (λ_{max} exciton peak at 504 nm) induced fluorescence enhancement at different concentrations; thus, an important emission increase (+1.34) with no change in the maximum was registered 2 h after the addition of KP-SH with a ligand/QD molar ratio of 3600 (Fig. 3). The same trend was detected for QD-CS2 (λ_{max} exciton peak at 565 nm) fluorescence, but it was less sensitive than that of QD-CS1 (Fig. S3 in the Supplementary data). The addition of MU to a QD-CS1 toluene solution (MU/QD concentration ratio of 2940) also produced an important fluorescence enhancement (+0.59) in a time-dependent process (Fig. S4). The fluorescence enhancement was observed even when using an [MU]/[QD] ratio in the 2 940 – 12 500 range (see Fig. S5 for a 12 500 molar ratio). This fluorescence enhancement

Can. J. Chem. Downloaded from www.nrcresearchpress.com by University of Electronic and Science Techonology of China on 09/18/12
For personal use only.

Fig. 2. Fluorescence spectra of a deaerated toluene solution of QD-C1 (2.9 μmol/L) before (○), immediately after (●), and 90 min after (■) the addition of MU (1.57 mmol/L); [MU]/[QD-C1]= 540.

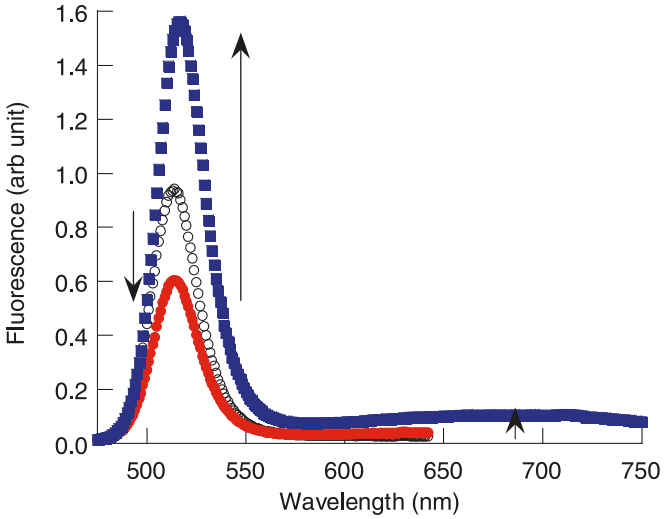

Fig. 3. Fluorescence spectra of a deaerated toluene solution of QD-CS1 in the absence (■, [QD] = 0.5 μmol/L) and in the presence of KP-SH ([KP-SH]/[QD] = 3600), the latter being registered 0 (○), 10 (▲), 30 (×), 60 (●), and 150 (□) min after the addition of the thiol.

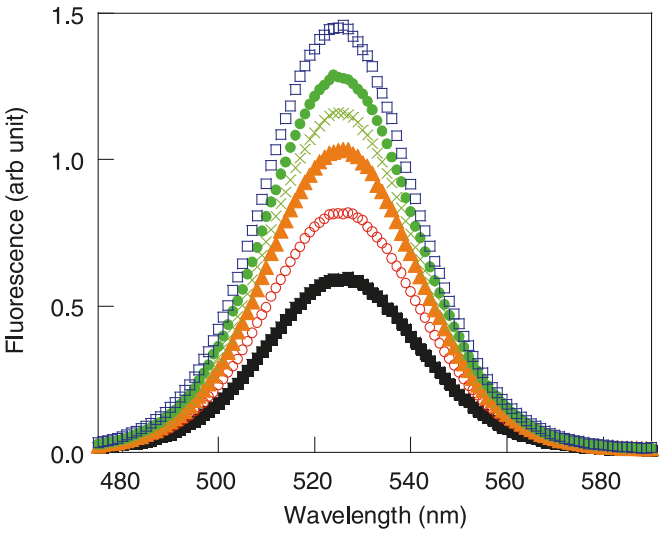

of the core-shell QDs upon thiol addition contrasts with the effect reported for the thiolates.[17,18]

Control experiments were performed to rule out the possibility that the different nature of the native ligand (TOPO in core QDs and a long-chain amine in core-shell QDs) was the origin of the different response to thiol addition of the core and core-shell QDs. So, the effect of the addition of octadecylamine (ODA), followed by MU 150 min later, on the QD-C1 fluorescence was monitored (Fig. 4). The addition of ODA to QD-C1 led to a considerable enhancement of the QD emission (+3.28) in a time-dependent process (Figs. 4 and S7). This increase was in agreement with the higher fluorescence quantum yield of amine-coated QDs compared with TOPO- or TOP-coated QDs.[4b] The exchange kinetics has been interpreted as being due to a combination

Fig. 4. Time dependence of the fluorescence intensity of QD-C1 (2.9 μmol/L) upon addition of ODA (6.5 mmol/L) followed by addition of MU (5.2 mmol/L) 150 min later; [amine]/[QD] = 2200 and [thiol]/[QD] = 1800.

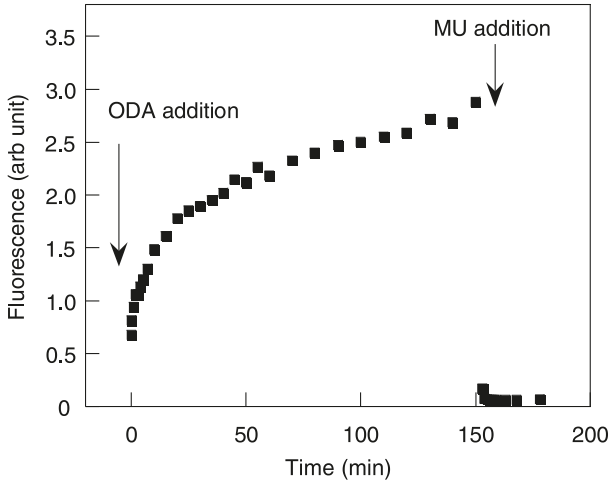

of ligand binding to vacant surface sites on CdSe QDs (fast coordination) and the ligand exchange itself (a slower process). After an equilibrium was reached, addition of MU caused a drastic decrease in the fluorescence emission of the system because the amine was replaced by the thiol ligand (Figs. 4 and S8). Therefore, the presence of amine as a native capping ligand (QD-CS) instead of TOPO (QD-C) is not responsible for the different behavior produced by thiol addition to these QDs.

The time-dependent fluorescence quenching observed for CdSe has been previously used as a tool to measure the exchange kinetics of native ligands for thiols on the CdSe surface.[8] Therefore, the changes in QD emission intensities were recorded as a time function, from which the kinetic rate constants (k_{LE}, Table 1) for the ligand exchange (TOPO, CdSe; amine, CdSe/ZnS) were calculated (see details in Figs. S9–S14 in the Supplementary data). The values for the addition of KP-SH were two times higher than those for the addition of MU, which is indicative of a higher replacement of a bulkier ligand.

To gain insight into the nature of the thiol binding to the QD, we prepared two samples (A and B) containing QD-CS3 (λ_{max} exciton peak at 520 nm, 48.1 × 10^{-9} mol) and KP-SH (2.4 × 10^{-4} mol) in deaerated chloroform (50 mL). They were maintained at room temperature for 2 h (sample A) and 48 h (sample B). After almost total solvent evaporation (2 mL) and the addition of methanol (30 mL), the samples were centrifugated at 8000 rpm (20 800*g*) for 20 min at 20 °C and the supernatants were decanted. The nanoparticles were dissolved in chloroform (2 mL) and the purification process was repeated twice, finally leading to CS3@KP_{2h} and CS3@KP_{48h} nanoparticles.

Both QD-CS3/KP-SH solutions exhibited a higher fluorescence than QD-CS3, and their emission maxima shifted slightly (1 nm) towards the red compared with that of QD-CS3 (Fig. 5). Remarkably, the emission of the cleansed QDs, CS3@KP_{2h} and CS3@KP_{48h}, was lower than that of QD-CS3 (Fig. 5), and the maxima were located at 542 nm (4 nm red-shifted compared with QD-CS3).[19] Therefore,

Can. J. Chem. Downloaded from www.nrcresearchpress.com by University of Electronic and Science Techonology of China on 09/18/12
For personal use only.

Fig. 5. Comparative fluorescence spectra of deaerated toluene solutions of QD-CS3 (■), QD-CS3/KP-SH (5×10^3 molar ratio) 2 h and 48 h after addition of the thiol (●), and cleansed CS3@KP_{2h} (▲) and CS3@KP_{48h} (□).

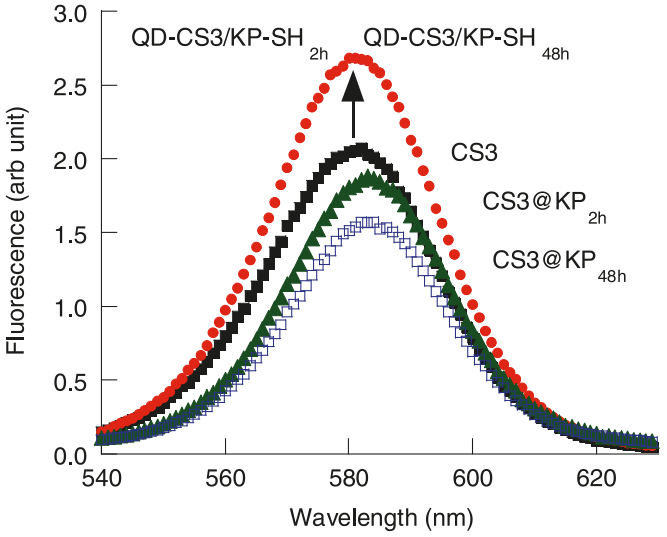

washing of the thiol-capped QDs resulted in a loss of the unbound (encapsulated) thiol and produced QDs with an emission lower than that of the initial core-shell QDs. The red-shifted emission exhibited by CS3@KP_{2h} and CS3@KP_{48h} indicated some thiol binding to the QD surface with time.

These results demonstrated that the replacement of amines by thiols on the core-shell QD surface resulted in better protection of the QD emission. The thiols encapsulated within the QD ligands were responsible for the fluorescence enhancement. In addition, the higher emission of CS3@KP_{48h} QDs than of CS3@KP_{2h} QDs suggested that thiolate binding to the QD surface appeared to be, at the least, nondetrimental for the QD emission.

Theoretical calculations have shown that thiol binding to ZnS surfaces is endothermic, while thiolate binding is a spontaneous process that can cause an alteration of the ZnS surface.[20] Consequently, we suggest that the replacement of amine ligands by thiols in the CdSe/ZnS QDs could benefit from the basicity of the amine ligands, allowing slow deprotonation of the thiol ligands to take place close to the nanoparticle surface and eventually resulting in thiolate binding to the shell with minimum surface alteration.

In summary, our results demonstrate that while addition of thiols drastically reduces the fluorescence of CdSe core QDs, it actually enhances the emission properties of already highly fluorescent amine-capped CdSe/ZnS core-shell QDs.

Supplementary data

Supplementary data (Table S1, Figs. S1–S15) are available with the article through the journal Web site (www.nrcresearchpress.com/cjc).

Acknowledgements

The authors thank Ministerio de Ciencia y Tecnología (Project CTQ2008-06777-CO2-01 contract granted to J.A.-S., and RyC contract granted to R.E.G), Generalitat Valenciana (Project ACOMP/2009/334), and Universidad de Valencia (Project UV-AE-09-5805) for their support.

References

(1) Alivisatos, A. P. *J. Phys. Chem.* **1996**, *100* (31), 13226. doi:10.1021/jp9535506.
(2) Carrillo-Carrión, C.; Cárdenas, S.; Simonet, B. M.; Valcárcel, M. *Chem. Commun. (Camb.)* **2009**, (35): 5214. doi:10.1039/b904381k.
(3) (a) Liu, Y.; Kim, M.; Wang, M.; Wang, Y. A.; Peng, X. *Langmuir* **2006**, *22* (14), 6341. doi:10.1021/la052747e.; (b) Hines, M. A.; Guyot-Sionnest, P. *J. Phys. Chem.* **1996**, *100* (2), 468. doi:10.1021/jp9530562.
(4) (a) Peng, Z. A.; Peng, X. *J. Am. Chem. Soc.* **2001**, *123* (1), 183. doi:10.1021/ja003633m.; (b) Talapin, D. V.; Rogach, A. L.; Kornowski, A.; Haase, M.; Weller, H. *Nano Lett.* **2001**, *1* (4), 207. doi:10.1021/nl0155126.
(5) Bullen, C.; Mulvaney, P. *Langmuir* **2006**, *22* (7), 3007. doi:10.1021/la051898e.
(6) Galian, R. E.; de la Guardia, M. *Trends Analyt. Chem.* **2009**, *28* (3), 279. doi:10.1016/j.trac.2008.12.001.
(7) Breus, V.; Heyes, C. D.; Nienhaus, G. U. *J. Phys. Chem. C* **2007**, *111* (50), 18589. doi:10.1021/jp075848p.
(8) Koole, R.; Schapotschnikow, P.; de Mello Donega, C.; Vlugt, T. J. H.; Meijerink, A. *ACS Nano* **2008**, *2* (8), 1703. doi:10.1021/nn8003247.
(9) Munro, A. M.; Plante, H. J.-L.; Ng, M. S.; Ginger, D. S. *J. Phys. Chem. C* **2007**, *111* (17), 6220. doi:10.1021/jp068733e.
(10) (a) For the photocatalytic role of CdSe QDs in the formation of disulfides, see: Aldana, J.; Wang, A. Y.; Peng, X. *J. Am. Chem. Soc.* **2001**, *123* (36), 8844. doi:10.1021/ja016424q.; (b) however, disulfide bond cleavage on the surface of CdSe QDs has also been reported: Billone, P. S.; Maretti, L.; Maurel, V.; Scaiano, J. C. *J. Am. Chem. Soc.* **2007**, *129* (46), 14150. doi:10.1021/ja076118y.
(11) Dabbousi, B. O.; Rodriguez-Viejo, J.; Mikulec, F. V.; Heine, J. R.; Mattoussi, H.; Ober, R.; Jensen, K. F.; Bawendi, M. G. *J. Phys. Chem. B* **1997**, *101* (46), 9463. doi:10.1021/jp971091y.
(12) (a) Jeong, S.; Achermann, M.; Nanda, J.; Ivanov, S.; Klimov, V. I.; Hollingsworth, J. A. *J. Am. Chem. Soc.* **2005**, *127* (29), 10126. doi:10.1021/ja042591p.; (b) Hohng, S.; Ha, T. *J. Am. Chem. Soc.* **2004**, *126* (5), 1324. doi:10.1021/ja039686w.
(13) Yu, W. W.; Qu, L.; Guo, W.; Peng, X. *Chem. Mater.* **2003**, *15* (14), 2854. doi:10.1021/cm034081k.
(14) MU was transformed into KP-SH following the Yamamoto procedure: Ishihara, K.; Nakayama, M.; Ohara, S.; Yamamoto, H. *Synlett* **2001**, *2001* (7), 1117. doi:10.1055/s-2001-15156.
(15) Kalyuzhny, G.; Murray, R. W. *J. Phys. Chem. B* **2005**, *109* (15), 7012. doi:10.1021/jp045352x.
(16) Commercial core-shell quantum dots were purchased from Evidenttech. They possess a fluorescence quantum yield higher than 50%.
(17) Algar, W. R.; Krull, U. J. *ChemPhysChem* **2007**, *8* (4), 561. doi:10.1002/cphc.200600686.
(18) In fact, addition of MU as thiolate to QS-CS3 nanoparticles led to a decrease in their fluorescence (see Fig. S6 in the Supplementary data).
(19) Full width at half maximum: 40 nm (QD-CS3), 39 nm (KP-

SH/QD-CS3), and 38 nm (CS3@KP). In addition, Fig. S15 in the Supplementary data shows the ^{1}H-NMR spectrum of KP-SH/QD-CS3, CS3@KP_{48h}, and the collected supernatants after washing of the QDs.

(20) Pong, B.-K.; Trout, B. L.; Lee, J.-Y. *Langmuir* **2008**, *24* (10), 5270. doi:10.1021/la703431j.

Can. J. Chem. Downloaded from www.nrcresearchpress.com by University of Electronic and Science Techonology of China on 09/18/12
For personal use only.

p-Hydroxyphenacyl photoremovable protecting groups — Robust photochemistry despite substituent diversity

Richard S. Givens, Kenneth Stensrud, Peter G. Conrad II, Abraham L. Yousef, Chamani Perera, Sanjeewa N. Senadheera, Dominik Heger, and Jakob Wirz

Can. J. Chem. Downloaded from www.nrcresearchpress.com by Xi'an Jiaotong University on 09/19/12
For personal use only.

Abstract: A broadly based investigation of the effects of a diverse array of substituents on the photochemical rearrangement of *p*-hydroxyphenacyl esters has demonstrated that common substituents such as F, MeO, CN, CO_2R, $CONH_2$, and CH_3 have little effect on the rate and quantum efficiencies for the photo-Favorskii rearrangement and the release of the acid leaving group or on the lifetimes of the reactive triplet state. A decrease in the quantum yields across all substituents was observed for the release and rearrangement when the photolyses were carried out in buffered aqueous media at pHs that exceeded the ground-state pK_a of the chromophore where the conjugate base is the predominant form. Otherwise, substituents have only a very modest effect on the photoreaction of these robust chromophores.

Key words: substituent, pH, pK_a, solvent effects, photorelease.

Résumé : Une étude détaillée des effets de divers arrangements de substituants sur le réarrangement photochimique des esters de *p*-hydroxyphénacyle a démontré que les substituants communs, tel F, MeO, CN, CO_2R ou CH_3, n'ont que peu d'effet sur la vitesse et les efficacités quantiques du réarrangement de photo-Favorskii et sur la libération du groupe acide partant ou sur les temps de vies de l'état triplet réactif. On a observé que tous ces substituants provoquent des diminutions des rendements quantiques pour la libération et le réarrangement quand les réactions de photolyse sont effectuées dans un milieu aqueux tamponné à un pH supérieur à celui du pK_a de l'état fondamental du chromophore pour lequel la base conjuguée est la forme prédominante. Autrement, les substituants n'ont qu'un effet modeste sur la photoréaction de ces robustes chromophores.

Mots-clés : substituant, pH, pK_a, effets de solvant, libération photochimique.

[Traduit par la Rédaction]

Introduction

Among the known photoremovable protecting groups, *p*-hydroxyphenacyl (pHP, **1**, eq. [1]) has consistently provided very fast (within a few nanoseconds after excitation or even less) and efficient, high conversion release of substrates. Moreover, the photoproducts are transparent at irradiation wavelengths ≥280 nm, permitting essentially complete conversion. Since developing the pHP as a "caging group" a decade ago,[1] pHP derivatives have found several applications in neurobiology,[2] enzyme catalysis,[3] and chemistry[4–6] that have demonstrated the advantages of its rapid, efficient release properties. An intriguing aspect of pHP photochemistry is the rearrangement of the chromophore that accompanies the release of the substrate. Anderson and Reese,[7] who discovered the photorearrangement by photolysis of *p*-hydroxyphenacyl chloride, isolated ethyl *p*-hydroxyphenylacetate (HPAA), which they described as a "photo-Favorskii" rearrangement product and depicted the skeletal rearrangement as passing through a putative spirocyclohexa-2,5-dienylcyclopropyl-4,8-dione intermediate (**I_2**) (eq. [1]).

Received 1 June 2010. Accepted 22 August 2010. Published on the NRC Research Press Web site at canjchem.nrc.ca on 2 March 2011.

Dedicated to Professor J. C. Scaiano, University of Ottawa, on the occasion of his 65th birthday. This article is part of a Special Issue dedicated to Professor J. C. Scaiano.

R.S. Givens,[1] K. Stensrud, P.G. Conrad II, A.L. Yousef, C. Perera, and S.N. Senadheera. Department of Chemistry, University of Kansas Lawrence, Lawrence, KS 66045, USA.
D. Heger. Research Centre for Toxic Compounds in the Environment (RECETOX) and Department of Chemistry, Faculty of Science, Masaryk University, Kamenice3, 625 00 Brno, Czech Republic.
J. Wirz. Department of Chemistry, University of Basel, Klingelbergstrasse 80, CH-4056 Basel, Switzerland.

[1]Corresponding author (e-mail: givensr@ku.edu).

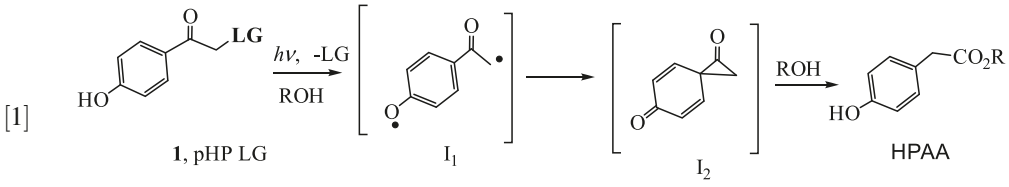

[1]

LG = leaving groups: including phosphates, carboxylates, thiols, imidazoles, phenols, and chloride.

Can. J. Chem. Downloaded from www.nrcresearchpress.com by Xi'an Jiaotong University on 09/19/12
For personal use only.

Our subsequent studies using a variety of leaving groups have affirmed that the major rearrangement pathway proceeds to the *p*-hydroxyphenylacetic acid as long as the reactions are carried out in aqueous or hydroxylic solvents.[8] Recent studies have been directed toward fine-tuning the requirements for the release and for the rearrangement of the pHP group, particularly, the effects of varying the leaving group (**LG**), the substituents on pHP, and the solvent.[8]

Details regarding the timing and multiplicity requirements of the bond-making and bond-breaking events in the photo-Favorskii rearrangement have been addressed in several mechanistic and theoretical investigations.[9–11] The release rates, as well as the product distribution, are sensitive to the presence of H_2O and other hydroxylic solvent combinations.[8–10] An adiabatic triplet sequence has been proposed[10,12] that involves both the deprotonation of the phenolic OH group and the heterolytic release of the leaving group[13] prior to formation of cyclopropanone $\mathbf{I_2}$ (eq. [1]). At least one additional intermediate, an oxyallyl–phenoxy triplet biradical ($\mathbf{I_1}$), has been proposed and evidence for $\mathbf{I_1}$ was recently reported.[9] Still, the molecular events including the multiplicities of the intermediates and the pathways that form $\mathbf{I_1}$ and $\mathbf{I_2}$ and their conversions to products are not fully established.

We report here the results of our investigations of the substituent effect on the photochemistry, multiplicity, quantum yield, reaction rate, and the effects of pK_a and pH. In addition, we have evaluated the substituent effect on the rearrangement including intermediates $\mathbf{I_1}$ and $\mathbf{I_2}$ suggested for the photo-Favorskii rearrangement. A series of substituted pHP esters (Fig. 1) were examined under a variety of conditions that included changes in solvent, pH, and ionic strength of the media. The mechanistic implications of these results provide a clearer understanding of this most interesting photorearrangement reaction.

Results and discussion

The array of substituted pHP derivatives was chosen to include both electron donor and acceptor functional groups (Fig. 1). Several of these compounds were also selected for future synthetic alterations or attachment sites for modifications desired for various applications of pHP photochemistry. There were a few instances where the γ-aminobutyric acid (GABA) leaving group was not easily installed, so the alternative acetate or diethyl phosphate leaving groups were inserted. These leaving groups are also well-documented in the literature of pHP photorelease chemistry and therefore can be related to the more numerous GABA representatives through comparisons of the known photochemistry of the parent, unsubstituted pHP acetate (**24**),[9,11] or diethyl phosphate (**27**).[1,2,10,11]

Synthesis of substituted pHP derivatives

Schemes 1A and 1B describe the synthetic protocols employed for the substituted pHP esters in Fig. 1. The GABA leaving group was chosen to assure good aqueous solubility. GABA is particularly advantageous in this respect, and in our laboratories it has served as the standard leaving group for several previous studies of pHP release rates and efficiencies. In general, the synthetic strategies for substituted pHP chromophores vary according to the availability of the substituted phenol, *p*-hydroxybenzoic acid, or *p*-hydroxyacetophenone precursor. The *p*-hydroxyacetophenones, when available, are converted directly to the pHP GABA and other leaving-group analogs by any one of a number of convenient transformations that activate the α-methyl group, e.g., bromination to the α-bromomethyl ketone followed by S_N2 displacement with N-BOC protected GABA and then deprotection with TFA, e.g., **13**–**23** (Scheme 1B).

The syntheses of the GABA derivatives of pHP (**1**), 3-methoxy-pHP (**2**), and 3,5-dimethoxy-pHP (**3**) followed the published protocols developed earlier for glutamates.[2a,2b] The 3-carboxymethyl-pHP (**10**) and 3-carbamoyl-pHP (**11**) derivatives were derived by the same sequence from the commercially available methyl 5-acetylsalicylate. The 2- and 3-cyano and all of the fluoro ketones (**13d**–**23d**), were synthesized from the corresponding phenols by a sequence of bromination of the phenol (**13b**–**23b**), then benzyl protection (**13c**–**23c**), followed by acylation through Stille coupling with Pd(0) and 1-ethoxyvinyl stannane to furnish, in excellent yield, the substituted *p*-benzyloxyacetophenone. Debenzylation gave acetophenones **13d**–**23d**, which were then converted to the GABA esters **13**–**23**.

The synthesis of new acetate derivatives **25** and **26** stemmed from a protocol uniform to the GABA esters, but commencing with the *p*-hydroxyacetophenones available from the Stille coupling route mentioned above and using sodium acetate in lieu of GABA according to the method of Phillips.[10]

The synthesis of the new diethyl phosphates **30**–**32** constituted an altogether separate series of steps. For the electron-donating methoxy scaffolds **30a** and **31a**, Friedel–Crafts acylation of corresponding pivalate-protected phenols with chloroacetyl chloride, followed by chloro displacement with sodium bromide engendered α-bromo derivatives **30d**–**31d**. Facile diethyl phosphate substitution of the bromoketones

Fig. 1. Substituted *p*-hydroxyphenacyl (pHP) esters.

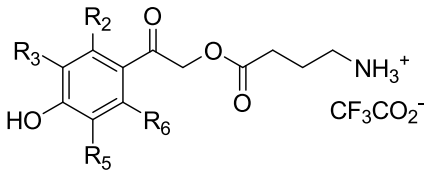

GABAs

1. R_2, R_3, R_5, R_6 = H
2. R_3 = OCH_3; R_2, R_5, R_6 = H
3. R_3, R_5 = OCH_3; R_2, R_6 = H
4. R_3 = OH; R_2, R_5, R_6 = H
5. R_2 = OH; R_3, R_5, R_6 = H
6. R_3 = CH_3; R_2, R_5, R_6 = H
7. R_2 = CH_3; R_3, R_5, R_6 = H
8. R_3, R_5 = CH_3; R_2, R_5 = H
9. R_3= CO_2H; R_2, R_5, R_6 = H
10. R_3 = CO_2CH_3; R_2, R_5, R_6 = H
11. R_3 = $CONH_2$; R_2, R_5, R_6 = H
12. R_3 = NO_2; R_2, R_5, R_6 = H
13. R_3 = CN; R_2, R_5, R_6 = H
14. R_3 = CF_3; R_2, R_5, R_6 = H
15. R_3 = OCF_3; R_2, R_5, R_6 = H
16. R_3 = F; R_2, R_5, R_6 = H
17. R_3 = H; R_2 = F; R_5, R_6 = H
18. R_2, R_3 = F; R_5, R_6 = H
19. R_3, R_5 = F; R_2, R_6 = H
20. R_2, R_5 = F; R_3, R_6 = H
21. R_3, R_5 = H; R_2, R_6 = F
22. R_2, R_3, R_6 = F; R_5 = H
23. R_2, R_3, R_5, R_6 = F

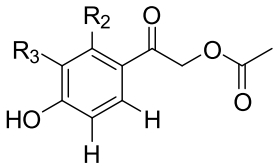

Acetates

24. R_2, R_3, R_5, R_6 = H
25. R_3 = CN, R_2 = H
26. R_2 = H, R_3 = CN

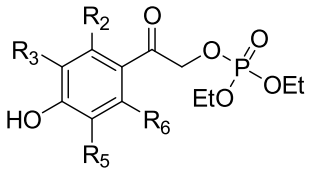

Diethyl phosphates

27. R_2, R_3, R_5, R_6 = H
28. R_2 = OCH_3; R_3, R_5, R_6 = H
29. R_2, R_5 = OCH_3; R_3, R_6 = H
30. R_3, R_5, R_6 = H; R_2 = OCH_3
31. R_3, R_5 = H; R_2, R_6 = OCH_3
32. R_3 = $COCH_3$; R_2, R_5, R_6 = H

was then mediated by Ag(I) followed by pivalate deprotection using ammonium acetate in aqueous methanol to furnish **30** and **31**.

An initial Fries rearrangement of acetyl-protected *p*-hydroxybenzoic acid **32b** provided the *o*-acetylated analog **32c**, whose carboxylic acid moiety was transformed into the α-diazo ketone through the acid chloride. After deacetylation with ammonium acetate in aqueous methanol, reaction with diethyl phosphoric acid gave **32**.

UV–vis spectral properties of substituted pHPs

The UV–vis spectral properties of **1–32** in H_2O and in aqueous buffer at pH 9 and the groundstate pK_as of the corresponding *p*-hydroxyacetophenones are given in Table 1. The pK_as range from 3.9 to >8.0, indicating that at physiological pH the chromophore will be a mixture of the conjugate base (phenoxide) and the neutral, un-ionized phenol. In most cases, the un-ionized form is prevalent at pH 5.0–7, whereas at pH 9, in all cases, the conjugate base prevails. It was anticipated that the photochemistry of the two forms might differ. In fact, the photochemistry will be shown to be sensitive to the solution pH as well as to the pK_a of the chromophore.

The UV–vis spectra of unsubstituted *p*-hydroxyacetophenone (pHA, **1d**) measured at neutral pH (phosphate buffer, pH 7) and in basic media (pH 8) typify the significant shifts in the absorption maxima upon ionization of these chromophores (Fig. 2).[4a] The spectrum of pHA displays a prominent π–π* absorption band with a maximum at 275 nm. In some solvents, a weak shoulder on the red edge of the π–π* band of the *p*-hydroxyketone (not shown) has been attributed to the carbonyl n–π* transition.[10c] The absorption band centered at 330 nm is assigned to the conjugate base π–π* transition. Based on the significant contributions of both chromophores in aqueous solutions between pH 5 and 8, it was necessary to study the photochemistry and physical properties of substituted pHP derivatives under buffered conditions to assure a constant ratio of the two forms of the

Can. J. Chem. Downloaded from www.nrcresearchpress.com by Xi'an Jiaotong University on 09/19/12
For personal use only.

Scheme 1. (A) Synthetic strategy for γ-aminobutyric acid (GABA) derivatives **4**–**23.** Conditions: (i) Br_2, TFA, room temperature (rt) 90%–100%. (ii) BnBr, K_2CO_3, CH_3CN, rt, 85%–95%. (iii) $Pd(PPh_3)_4$, 1-ethoxyvinyltributyltin, $PhCH_3$, 100 °C, 70%–92%. (iv) (a) (R′ = Bn), phenyltrimethylammonium tribromide (PTAB), CH_3OH–CH_2Cl_2 (1:1) rt, 90%–98%; (b) (R′ = H), $CuBr_2$, $CHCl_3$–EtOAc (1:1), reflux, 70%–80%. (v) (a) (R′ = Bn), N-*t*-Boc GABA, K_2CO_3, CH_3CN, rt, 40%–95%; (b) (R′ = H), N-*t*-Boc GABA, 1,8-diazabicyclo[5.4.0]undec-7-ene (DBU), benzene–DMF (20:1), 7 °C to rt, 55%–60%. (vi) TFA, 24 h, rt, 50%–85%. (vii) Pd–H_2, EtOAc, rt, 95%–100%. (viii) TFA–CH_2Cl_2 (1:1), rt, 70%–100%. (B) Synthetic strategies for diethyl phosphate derivatives **30**–**32**. Conditions (top reaction): (i) $(CH_3)_3COCl$, Et_3N, 0 °C to rt, 100%. (ii) $ClCH_2COCl$, $AlCl_3$, 0 °C, 20%–50%. (iii) NaBr, acetone, reflux, 90%–98%. (iv for **30**) HO–P(O)$(OEt)_2$, Ag_2O, CH_3CN, 60 °C, 76%. (v for **31**) K^+ OP(O)$(OEt)_2$, dibenzo[18]crown-6, CH_3CN, reflux, for 20%. (vi) NH_4OAc, H_2O–MeOH, 1:4, 50 °C, 24 h, 90%–95%. Conditions (bottom reaction): (i) $AlCl_3$, $PhNO_2$, 150 °C, 98%. (ii) AcCl, TEA, CH_2Cl_2, rt, 70%. (iii) (a) $SOCl_2$; (b) CH_2N_2, Et_2O; (c) MeOH(aq), NH_4OAc, 50 °C, 21% overall. (iv) Diethyl phosphoric acid, benzene, 60 °C, 79%

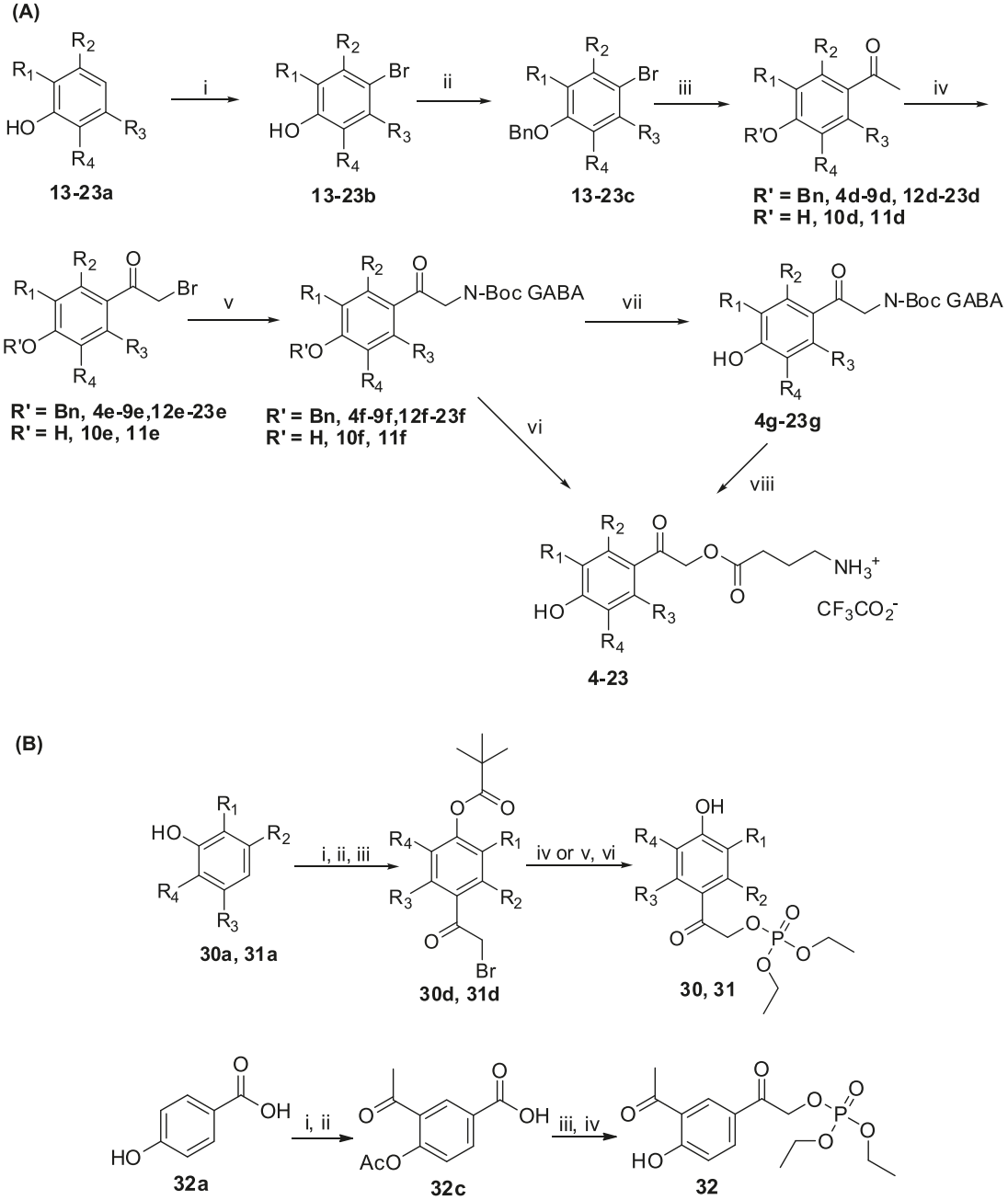

chromophore. Studies were also conducted in unbuffered aqueous media for comparison.

Product studies

Two major photolysis products were obtained from each substituted pHP derivative: the leaving group, i.e., GABA, diethyl phosphate, or acetate, and the substituted *p*-hydroxyphenylacetic acid (pHPAA), which is the rearrangement product from the photo-Favorskii reaction (eq. [1]). A minor product, the substituted *p*-hydroxybenzyl alcohol, is formed

Can. J. Chem. Downloaded from www.nrcresearchpress.com by Xi'an Jiaotong University on 09/19/12
For personal use only.

Can. J. Chem. Downloaded from www.nrcresearchpress.com by Xi'an Jiaotong University on 09/19/12
For personal use only.

Table 1. The pK_a and UV absorption maxima in H_2O and at pH 9 for substituted *p*-hydroxyphenacyl (pHP) γ-aminobutyric acid (GABA) derivatives arranged in order of ascending pK_a.

Derivatives	pK_a[a]	λ_{max} (nm) (log ε)[b]	λ_{max} (nm) (log ε) at pH 9[c]
23 (2,3,5,6-tetraF)	3.9	316 (3.95)	316 (4.10)
22 (2,3,5-triF)	4.5	324 (4.05)	323 (4.01)
12 (3-NO_2)	5.2	397 (3.20),[d] 334 (4.14)	399 (3.22), 335 (4.20)
13 (3-CN)	5.2	322 (3.46)[e]	321 (3.44)
19 (3,5-F)	5.3	331 (4.14)	330 (4.14)
14 (3-CF_3)	5.5	325 (4.22)[f]	328 (4.24)
20 (2,5-diF)	5.7	278 (3.26), 326 (3.92)	326 (4.12)
18 (2,3-diF)	5.9	272 (4.09), 328 (3.04)	323 (4.07)
11 (3-CO_2NH_2)	6.2	324 (4.15)	NA
15 (3-OCF_3)	6.5	273 (3.79), 328 (4.31)	329 (4.18)
16 (3-F)	6.7	274 (4.00), 335 (2.97)	351 (3.67), 328 (3.96)
21 (2,6-F)	6.8	274 (4.00)	313 (4.06)
17 (2-F)	7.2	271 (3.97)	328 (3.90), 319 (3.91)
10 (3-CO_2CH_3)	7.7	272 (4.09), 330 (3.94)	NA
3, **29** (3,5-OCH_3)	7.8	279, 300 (3.97), 355 (3.55)	357 (4.28)
5 (2-OH)	7.8	276 (3.85)	
2, **28** (3-OCH_3)	7.9	276 (3.93), 341 (3.58)	342 (4.27)
4 (3-OH)	7.9	309 (3.97), 279 (3.86)	
1, **24**, **27** (parent)	8.0	279 (4.09), 325 (3.40)	324 (4.33)
7 (2-CH_3)	8.0	287 (4.06)	343 (3.86), 328 (4.10)
6 (3-CH_3)	8.1	284 (3.84)	356 (3.75), 334 (3.97)
8 (3,5-CH_3)	8.2	304 (3.79), 287 (3.96)	362 (3.91), 348 (4.05)
26 (2-CN)	NA	275 (3.45), 305 (3.39)	
30 (2-OCH_3)	NA	278 (3.98), 307 (3.93)	
31 (2,6-OCH_3)	NA	283 (3.70)	
32 (3-$COCH_3$)	NA	274 (3.39), 319 (3.06)	
9 (3-CO_2H)	NA	280 (3.90), 310 (3.58)	

Note: NA, not available.

[a]The pK_a values of the corresponding *p*-hydroxyacetophenones were determined by spectrophotometric titration. Ionic strength was low (I < 0.05 mol/L) and not held constant. The ionization quotients pK_{ac} of the *p*-hydroxyacetophenone analogues of **1**–**3** and **9**–**11**, measured at constant ionic strength (I = 0.1 mol/L), were ~0.05 units lower.

[b]Water.

[c]*N*-(2-Hydroxyethyl)piperazine-*N*′-ethanesulfonic acid (HEPES, 0.01 mol/L).

[d]The absorption maxima (λ_{max} (nm) (log ε) for **12** was also measured at pH 5 in 0.01 mol/L ammonium acetate: 256 (3.92).

[e]The absorption maxima (λ_{max}(nm) (log ε) for **13** was also measured at pH 5 in 0.01 mol/L ammonium acetate: 270 (sh).

[f]The absorption maxima (λ_{max}(nm) (log ε) for **14** was also measured at pH 5 in 0.01 mol/L ammonium acetate: 274 (4.14).

in <5% yield and is derived by decarbonylation of the putative spirodienedione intermediate $\mathbf{I_2}$, followed by hydration of the resulting *p*-quinone methide.[9] All of the products were characterized by HRMS and by comparison of their ^{1}H and ^{13}C NMR spectral properties either with authentic samples or related products from our previous pHP studies.

Photolyses carried out in aprotic organic solvents generally produced reduction products such as the substituted pHA and other radical-derived products. These studies were not pursued further, and the products were not observed in the aqueous solution photolyzates.

Quantitative determination of the products was obtained by ^{1}H NMR or by LC–MS/MS. The ^{1}H NMR spectra of pHP caged GABAs in D_2O were cleanly transformed into spectra of the two major photoproducts accompanied by complete disappearance of pHP GABA. Product studies were routinely carried out to quantitative conversion.

Triplet-state pK_a, quantum yield, and Stern–Volmer studies

The pK_a of the excited triplet state of **1d** is strongly reduced by about 4.3 pK_a units relative to pHA's ground-state pK_a of 7.9.[8] Since proton transfer plays a significant role in the mechanism of the release of the leaving group,[4,8–13] changes in the pK_a of the chromophore will provide additional insight into the mechanistic features of the reaction. Currently, there remains a controversy over the timing and importance of the proton transfer to the solvent. One suggested pathway depicts proton transfer from the chromophore in concert with leaving group departure (vide infra).[10] For this scenario, the enhanced acidity of the pHP triplet would enhance the reactivity of the chromophore toward release and rearrangement. The second scenario suggests that the phenol group is merely a spectator and does not play a pivotal role in the release or rearrangement.[10,14] Therefore,

Can. J. Chem. Downloaded from www.nrcresearchpress.com by Xi'an Jiaotong University on 09/19/12
For personal use only.

Fig. 2. UV spectral data for *p*-hydroxyacetophenone (**1d**). The absorption spectra are of a 0.13 mmol/L solution of **1d** in NaH_2PO_4 buffer (3% CH_3CN) at pH 7 and 8 showing the shift in absorption from the phenol to its conjugate base. (From Givens and Yousef 2005, in *Dynamic Studies in Biology: Phototriggers, Photoswitches, and Caged Biomolecules*, Chap. 1.3.2.2, p. 60, reproduced with permission, ©Wiley-VCH Verlag CmbH & Co. KGaA.)

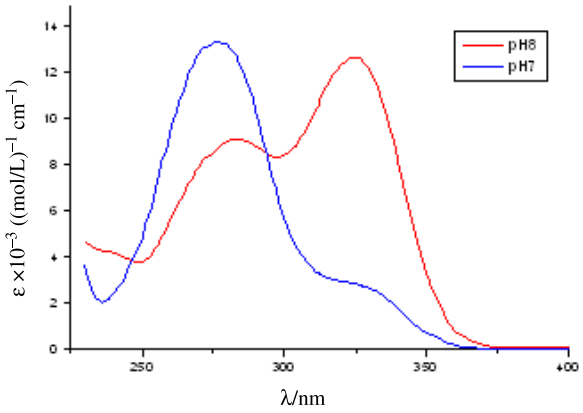

a study of the effect of pK_a on the reaction efficiency and rate of release should be valuable.

The quantum yields for the disappearance of pHP esters and for the appearance of the two major products were determined by LC–MS/MS and ^{1}H NMR at low conversion (<5%) in unbuffered H_2O (Table 2) and in buffered solutions (Table 3) at acidic, neutral, and basic pH.

The quantum yields were first determined in unbuffered H_2O (Table 2). However, these must be considered less accurate because the pH changes during photolysis. The mildly acidic phenolic *p*-hydroxyphenacyl chromophore (pK_a ~ 4–8) is converted into a series of three new acids, a bifunctional *p*-hydroxyphenylacetic acid along with the leaving group, which, in several cases, is the strongest acid present, e.g., a phosphoric or sulfonic acid. The contributions of the three newly created acids decrease the pH. Since the photolysis solution for a particular chromophore is a delicate balance of the phenolic pHP ester and its conjugate base and since their ratio is dependent on the chromophore's pK_a, the changing pH of the media will affect that ratio and, therefore, the quantum yield. Furthermore, as reported earlier and amplified in this paper, the quantum yields are dramatically different for the un-ionized chromophore and its conjugate base. Taken together, the quantum yields in unbuffered media are a complex function of the pK_a, a changing pH, and the relative quantum yields. Nevertheless, the quantum yields reported in Table 2 may be considered as representative because they were derived by extrapolation to initial efficiencies at low conversions (<2%). However, they are not corrected for the relative concentrations of the un-ionized and conjugate base present.

Table 3 reveals that in buffered media the efficiencies for release decrease as the pH of the media increases for essentially every pHP ester. The decrease in efficiency is most pronounced as the increasing pH approaches the pK_a of the pHP ester, reaching its lowest when the chromophore is completely converted to its conjugate base, which is graphically depicted in Fig. 3. This normally resulted in a reduction of 60%–80% in the quantum yield.

Table 2. The effect of pK_a on the quantum yields for substituted *p*-hydroxyphenacyl (pHP) γ-aminobutyric acid (GABA) in unbuffered H_2O. Entries are arranged according to decreasing disappearance quantum yields.

		Quantum yield in H_2O		
Substituted pHP GABA	pK_a	Φ_{dis}[a]	Φ_{app}[b]	Φ_{app}[c]
13 (3-CN)[d]	5.2	0.42	0.35	0.39
17 (2-F)	7.2	0.28	0.27	0.26
18 (2,3-diF)	5.9	0.24	0.24	0.22
20 (2,5-diF)	5.7	0.22	0.21	0.20
1 (parent)	8.0	0.20	0.19	0.16
14 (3-CF_3)	5.5	0.17	0.16	0.14
21 (2,6-F)	6.8	0.16	0.16	0.15
16 (3-F)	6.7	0.16	0.15	0.15
8 (3,5-CH_3)	8.2	0.15	0.14	0.13
6 (3-CH_3)	8.1	0.15	0.14	0.13
23 (tetraF)	3.9	0.11	0.10	0.10
19 (3,5-F)	5.3	0.11	0.11	0.10
7 (2-CH_3)	8.0	0.11	0.10	0.10
15 (3-OCF_3)	6.5	0.09	0.09	0.07
22 (2,3,5-triF)	4.5	0.08	0.07	0.06
2 (3-OCH_3)	7.9	0.07	0.06	NA
3 (3,5-OCH_3)	7.8	0.03	0.03	NA

Note: NA, not available.All runs were low conversions to products (<2%). Standard deviations are <±0.02. 3-NO_2 (**12**), 3-OH (**4**), and 2-OH (**5**) did not react under these conditions and are omitted. Unbuffered 18 MΩ Ultrapure H_2O was used.

[a]Quantum yield for the disappearance of pHP GABA.
[b]Quantum yield for the appearance of GABA.
[c]Quantum yield for the appearance of rearranged acid.
[d]CH_3CN–H_2O (1:1).

The lower quantum yield may be attributable to several factors including a decrease in intersystem crossing (isc) efficiency (Φ_{ST}) or in the rate constant of release relative to that of competing nonproductive pathways. One of these may simply be deprotonation to the triplet conjugate base (**1**$^-$).[3] Results in Table 4 suggest, however, that the rates for intersystem crossing are essentially insensitive to substitution for the un-ionized esters. Less is known for the rates of isc for the conjugate bases.

Two substituents of interest are cyano and methoxy. The ortho (or 2) substituted derivatives were not amenable to our synthetic strategies and difficulty was encountered in the attempts to synthesize the GABA derivatives, especially in the Boc deprotection step. However, acetate and phosphate analogs were synthetically accessible and, therefore, their photochemistries were examined. Disappearance quantum yields were measured for 2- and 3-cyano pHP OAc and for the four variations of the methoxy pHP diethyl phosphates. These are given in Table 5 along with the parent pHP OAc and diethyl phosphates reported earlier for comparison.[1,9–11]

Clearly, the cyano-substituted acetates are less efficient than the parent, which was surprising, since the GABA analog of the 3-CN pHP GABA gave an enhanced efficiency for photodeprotection. It should be noted that poorer aqueous solubility of acetate and other carboxylic esters requires cosolvents such as acetonitrile or DMSO. There is mounting evidence that the concentration of the organic cosolvent re-

Table 3. Substituent effects on the quantum yields for γ-aminobutyric acid (GABA) release at 300 nm in buffered CH_3CN–H_2O. Entries are arranged according to decreasing disappearance quantum yields at pH 7.3.

		Quantum yield								
		pH 5.0[a,b]			pH 7.3[a,c]			pH 8.2[a,c]		
pHP GABA	pK_a	Φ_{dis}[d]	Φ_{app}[e]	Φ_{app}[f]	Φ_{dis}[d]	Φ_{app}[e]	Φ_{app}[f]	Φ_{dis}[d]	Φ_{app}[e]	Φ_{app}[f]
13 (3-CN)	5.2	0.21	0.13	0.19	0.33[g]	0.28[g]	0.28[g]	0.19[h]		
1 (Parent)	8.0	0.21	0.20	0.18	0.21	0.20	0.20	0.09	0.09	0.06
17 (2-F)	7.2	0.24	0.23	0.23	0.21	0.20	0.19	0.06	0.06	0.03
8 (3,5-CH_3)	8.2				0.17	0.17	0.15	0.11	0.11	0.09
6 (3-CH_3)	8.1				0.15	0.16	0.13	0.08	0.08	0.06
14 (3-CF_3)	5.5	0.24	0.23		0.12	0.11	0.10	0.08	0.08	
16 (3-F)	6.7	0.15	0.14	0.14	0.12	0.12	0.11	0.02	0.02	<0.01
18 (2,3-diF)	5.9	0.16	0.16	0.15	0.11	0.11	0.09	0.05	0.05	0.04
23 (tetraF)	3.9	0.08	0.07		0.10	0.10	0.08	0.09	0.09	
7 (2-CH_3)	8.0				0.10	0.09	0.08	0.07	0.07	0.06
21 (2,6-F)	6.8				0.10	0.09	0.08	0.04	0.04	0.02
20 (2,5-diF)	5.7	0.07	0.07		0.10	0.09	0.09	0.02	0.02	<0.01
22 (2,3,5-F)	4.5	0.07	0.06		0.06	0.06	0.04	0.02	0.02	<0.01
15 (3-OCF_3)	6.5	0.07	0.05		0.06	0.06	0.05	0.02	0.02	0.01
19 (3,5-F)	5.3	0.08	0.07	0.07	0.05	0.05	0.04	0.02	0.02	<0.01

[a]Standard deviations were <±0.02.
[b]Ammonium acetate (0.01 mol/L).
[c]*N*-(2-Hydroxyethyl)piperazine-*N*′-ethanesulfonic acid (HEPES, 0.01 mol/L) and $LiClO_4$ (0.1 mol/L), pH 7.3.
[d]Quantum yield for the disappearance of *p*-hydroxyphenacyl (pHP) GABA.
[e]Quantum yield for the appearance of GABA.
[f]Quantum yield for the appearance of rearranged acid.
[g]Ammonium acetate (0.01 mol/L, pH 7).
[h]Ammonium acetate (0.01 mol/L, pH 9).

Can. J. Chem. Downloaded from www.nrcresearchpress.com by Xi'an Jiaotong University on 09/19/12
For personal use only.

duces quantum yields and rates of release.[9,11–13] This is not consistently the case, but may be a factor in the cyano acetate series.

Methoxy substitution, on the other hand, has little effect for the 3-MeO pHP phosphates but does enhance the reactivity of the 2-MeO pHP phosphates (**30** and **31**). These are among the most efficient photodeprotection efficiencies we have encountered in the phosphate series.[1,3c,4a,8,9,12] It was discovered, however, that these latter two derivatives were less soluble and less stable to aqueous hydrolysis.

Picosecond pump–probe spectroscopy on a cross section of the substituted pHP that included both electron-donating and -withdrawing derivatives and fluorinated examples showed little variation in the rate constants of triplet rise (k_1) and decay (k_2) (Table 4).

Scheme 2 summarizes a series of the parallel pathways available to the photoactivated pHP derivatives and their conjugate bases. The products are the same for both pathways, but the details concerning the excited states and the partitioning among their available decay and reaction pathways are different. We have a much less-detailed understanding of the mechanism for the reaction of the conjugate bases than the un-ionized pHP system. However, we have monitored the change in quantum yields at different pH and at a longer excitation wavelength (RPR 350 nm lamps). The values are uniformly much lower than those obtained for the un-ionized pHP analog using RPR 300 nm lamps. The conjugate bases display a weak fluorescence ($\Phi < 1 \times 10^{-4}$). Otherwise, the two forms show comparable rates of triplet formation and decay upon excitation at 350 nm. Thus, the low product quantum yields for the conjugate bases are most likely due to variations in the partitioning among the competing exit channels from the triplet excited states of the two chromophores.

Parallel studies on Stern–Volmer quenching of the ester disappearance and product appearance by sorbate for a few of the esters further indicated no significant differences in triplet lifetimes. This also suggests that there is little difference in the partitioning among the triplet decay pathways, but does not exclude the possibility of recombination of initially formed ion-triplet biradical pairs (See the Experimental section and Table 6 for details).

Heterolytic release of the leaving group generates an intermediate biradical–ion pair ([$\mathbf{I}_1{}^3$·**LG**]) raising the possibility of cage return, which might contribute to the differences in the photorelease quantum yields. Evidence for cage return was obtained by increasing the ionic strength of the aqueous solutions with $LiClO_4$, $NaClO_4$, $MgCl_2$, etc. With several derivatives, the quantum yields increased significantly, some by a factor of two or more, whereas others remained unchanged and, in a few cases, even decreased. The increased ionic strength had no effect on the LFP triplet decay rates.

Finally, the triplet energies of the pHP and its conjugate base may be a source of the differences in reactivity. The 71.6 kcal/mol (1 cal = 4.184 J) triplet energy of pHP is diminished to 61.2 kcal/mol for the conjugate base.[8] This ~10 kcal/mol decrease in energy may favor the barrierless or low-barrier processes over the more energy demanding

Fig. 3. Graphic representation of the effect of pK_a on the quantum yield of substituted *p*-hydroxyphenacyl (pHP) γ-aminobutyric acid (GABA) as a function of pH. Numerical identifications of the esters are placed adjacent to the pH 7.3 values. (A) Disappearance quantum yield of substituted pHP GABA as a function of its pK_a at pH 7.3 (●) and 8.2 (○). (B) Appearance quantum yields of GABA as a function of the pHP ester pK_a at pH 7.3 (●) and 8.2 (○). Data are from Table 3. The 3-CN derivative **13** is omitted because of a solvent change.

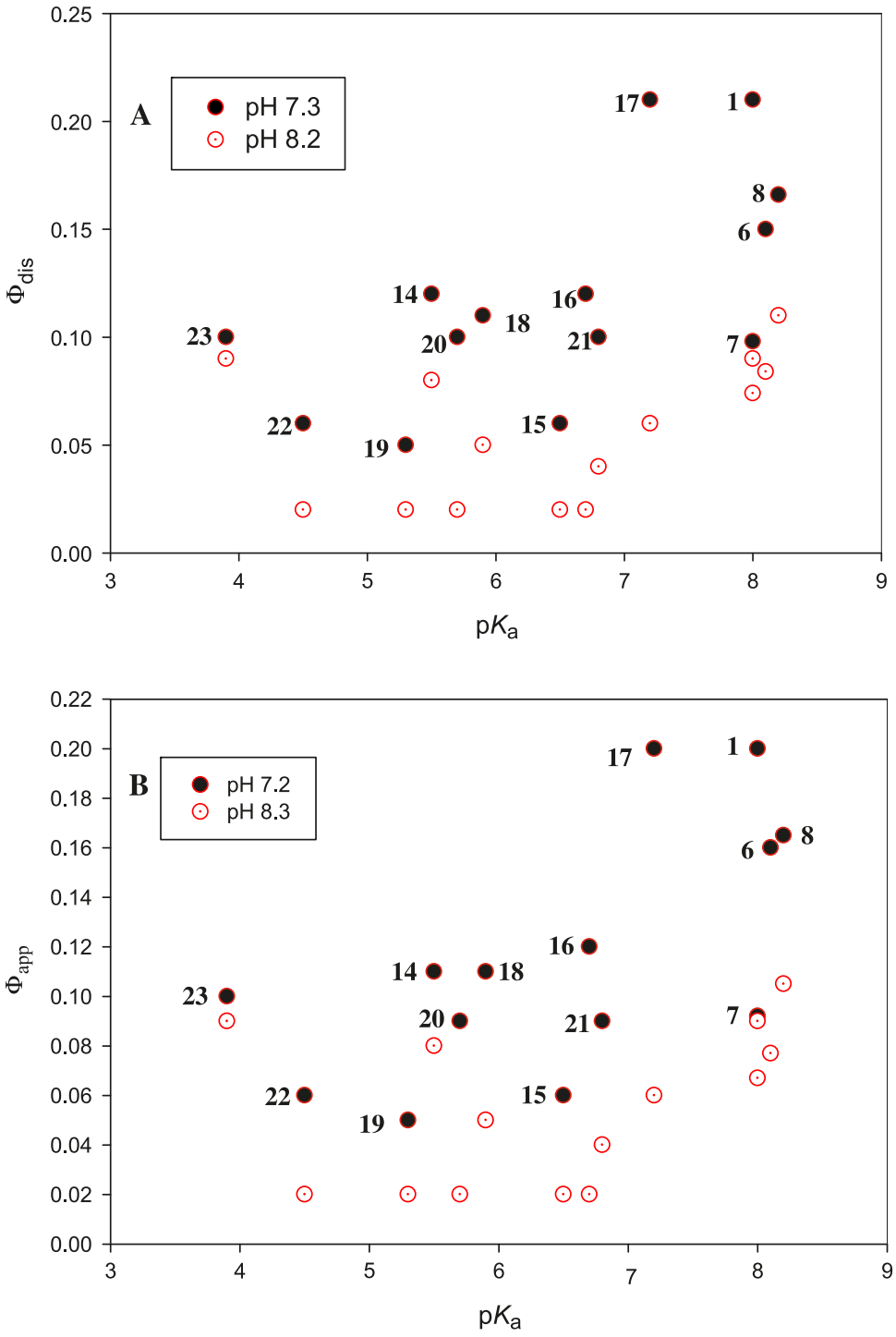

heterolytic release pathway of the photo-Favorskii rearrangement.

Pathways that may account for nonproductive decay of the triplet would include deprotonation to the conjugate base with subsequent rapid decay to its ground state[15] or proton tautomerization to **33**, the proton tautomer of pHP originally suggested by Wan and co-workers[11] (which was later shown to be a triplet[8]) that, following isc to the ground state, would rapidly tautomerize back to the pHP ester. Interestingly, there is a prominent, long-lived 340 nm transient that also is observed in the LFP spectra of most pHP derivatives. This band is appropriately positioned for assignment

Can. J. Chem. Downloaded from www.nrcresearchpress.com by Xi'an Jiaotong University on 09/19/12
For personal use only.

Can. J. Chem. Downloaded from www.nrcresearchpress.com by Xi'an Jiaotong University on 09/19/12
For personal use only.

Table 4. Laser flash photolysis studies on selected derivatives in unbuffered H_2O.

	Rate constant	
pHP GABA	k_1 (10^{11} s^{-1})[a,b]	k_2 (10^9 s^{-1})[b]
1 (Parent)	4.4	3.0[c]
2 (3-OCH_3)	2.2	1.3
3 (3,5-OCH_3)	2.7	2.8[d]
10 (3-CO_2CH_3)	3.2	1.3
11 (3-$CONH_2$)	ND	2.2
9 (3-CO_2H)	2.1	1.0
20 (2,5-diF)	3.0	2.6
22 (2,3,5-triF)	3.9	0.90
23 (tetraF)	3.6	3.4[d]

Note: pHP, *p*-hydroxyphenacyl; GABA, γ-aminobutyric acid.

[a]Singlet $\lambda_{max} \sim 315$ nm.

[b]k_1 is the rate constant for triplet rise and k_2 is the rate constant for triplet decay.

[c]Near the tail end of the triplet decay, new absorption bands appeared at 320, 420, and 440 nm, which have been assigned to the oxyallyl–phenoxy biradical $\mathbf{I_1}$ and decayed with a rate constant of $k_{birad} \approx 1.30 \times 10^9$ s^{-1}.[9,15]

[d]Acetonitrile (5%) was added to the aqueous solvent to dissolve these esters.

Table 5. Quantum yields for cyano-pHP acetates and methoxy-pHP phosphates at λ = 300 nm.

Compound	Φ_{dis}[a]
pHP acetates[b]	
24 (Unsubstituted)	0.30
25 (3-CN)	0.17
26 (2-CN)	0.08
pHP diethyl phosphates[c]	
27 (Unsubstituted)	0.40
28 (3-OCH_3)	0.39
29 (3,5-OCH_3)	0.44[d]
30 (2-OCH_3)	0.59
31 (2,6-OCH_3)	0.69
32 (3-$COCH_3$)	0.03

Note: pHP, *p*-hydroxyphenacyl.

[a]Error limits for disappearance quantum yields (±0.03%).

[b]Analysis carried out in 20% aq CH_3CN or DMSO.

[c]Analysis carried out in 50% aq CH_3CN.

[d]$\Phi_{dis} = 0.13$ at λ = 350 nm.

either to the ground-state conjugate base of the pHP group or to **33**.[11,14] As in the case of the conjugate base of pHP derivatives, the tautomer **33** is an unlikely candidate for room-temperature heterolysis.[9]

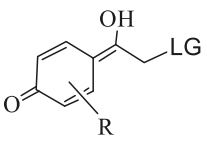

33

For the heterolytic pathway that proceeds on to the rearranged product, three scenarios have also been suggested.

Scheme 2. Parallel pathways for the photochemical and photophysical processes of *p*-hydroxyphenacyl (pHP) or its conjugate base.

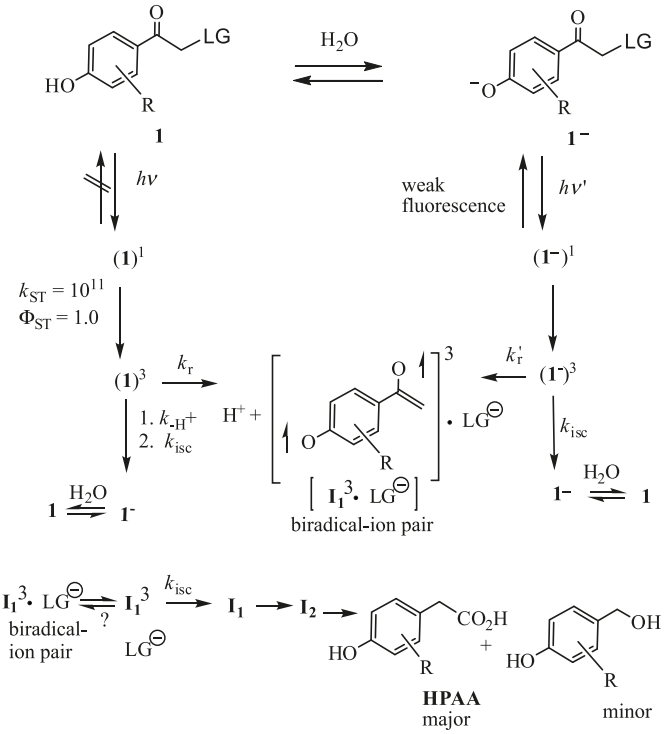

Proton loss[14] or heterolysis could be the initial step or the two could occur in concert. Two such stepwise scenarios can be envisaged, differing by only the order of departure of two entities. Evidence that militates against proton loss preceding the departure of the leaving group comes from the poor efficiencies of the conjugate bases and from our earlier analysis of solvent kinetic isotope effects (SKIE). A "proton inventory" of the SKIE revealed that either two or three protons are "in flight" in the release process.[9,16] The partition functions are consistent with the phenolic proton and two solvent water protons associated with two carbonyls during the extrusion of $\mathbf{I_1}$.

The other stepwise construct would involve the departure of the leaving group before loss of the proton, thereby generating a triplet α-keto carbenium ion. This pathway is also unlikely based on the known photochemistry of released derivatives such as *p*-methoxyphenacyl analogs, which, even in hydroxylic solvents, do not efficiently follow a rearrangement pathway for the chromophore.[1b,17] This is in keeping with the requirement that the *para* hydroxyl function and a leaving group positioned α to the carbonyl be present on the phenacyl chromophore to ensure efficient photo-Favorskii rearrangement.

Taken together, these results are viewed as favoring the concomitant loss of the phenolic proton and the leaving group. Thus, the evidence is most consistent with the interpretation that a concerted proton and leaving group departure occurs with the resulting extrusion of a neutral triplet biradical $\mathbf{I_1}$. This process is not only a minimum energy pathway for heterolysis, but also conserves spin.[18] The oxyallyl–phenoxy triplet biradical $\mathbf{I_1}$ then relaxes to a singlet and closes to the spirobicyclohexadienedione $\mathbf{I_2}$. The fate of $\mathbf{I_2}$ as a groundstate intermediate mimics a typical Favorskii

Can. J. Chem. Downloaded from www.nrcresearchpress.com by Xi'an Jiaotong University on 09/19/12
For personal use only.

Table 6. Stern–Volmer studies of *p*-hydroxyphenacyl (pHP) γ-aminobutyric acid (GABA) derivatives in unbuffered H_2O and in aqueous media at pH 7.3 buffer.

	Studies with water[a,b]		Studies with buffer at pH 7.3[b,c]	
Compound	K_{SV} ((mol/L)$^{-1}$)[d]	τ^3 (10^{-9}s)[e]	K_{SV} ((mol/L)$^{-1}$)[d]	τ^3 (10^{-9}s)[e]
13	299	40.5		
14	20.2	2.75	30.3	4.12
15	33.1	4.47	29.4	4.03
16	24.2	3.23	26.0	3.66
17	13.0	1.99	19.2	2.52
18	44.7	6.02	39.0	5.33
19	29.1	4.04	32.6	4.31
20	15.2	2.12	51.1	6.93
21	25.5	3.31	8.02	1.13
22	34.2	4.67	36.8	4.82
23	30.0	4.16	14.1	1.90

[a]Unbuffered 18 MΩ Ultrapure H_2O.
[b]Std. dev. <10%.
[c]*N*-(2-Hydroxyethyl)piperazine-*N*′-ethanesulfonic acid (HEPES, 0.01 mol/L) and $LiClO_4$ (0.1 mol/L).
[d]Sorbic acid quencher, Stern–Volmer constant.
[e]Triplet lifetime.

rearrangement[19] by ring-opening hydrolysis via nucleophilic attack of solvent (water) to produce rearranged *p*-hydroxyphenylacetic acid. Decarbonylation, a minor pathway open to $\mathbf{I_2}$, yields *p*-quinone methide that hydrolyzes to *p*-hydroxybenzyl alcohol, the minor product.

The effect of structure on the photolytic reactivity of substituted pHP GABAs

There appears to be no correlation between the ground-state pK_as of the chromophores and their photochemical behavior in terms of their quantum yields or rate constants for release. The pK_a dictates the ratio of the un-ionized and conjugate base, and this ratio in turn affects the photochemical reactivity. Therefore, the photochemical and photophysical properties do not change with the introduction of most substituents. The most notable exceptions are the effect of 3-nitro and the 2- and 3-hydroxyl groups, which completely quench reactivity. Similarly unreactive were the 3-acetyl and any appended auxochromes that could quench such as naphthyl (not shown).

Conclusions

A unique rearrangement, the photo-Favorskii reaction, of pHP esters combines the accelerated release of substrate ligands with a hypsochromic shift of the pHP chromophore. The rearrangement occurs on the triplet manifold by a spin-conserved extrusion of the chromophore as a triplet biradical $\mathbf{I_1}$ followed by relaxation of the biradical and closure to yield $\mathbf{I_2}$, the "Favorskii" intermediate, merging the photochemical pathway with a ground-state Favorskii reaction.[19] With few exceptions, substituents on the chromophore do not influence the mechanics of the rearrangement sequence and cause only small variations in the quantum yields and reaction-rate constants. The release of substrate is consistently more efficient for the un-ionized chromophores. Substituents do influence the chromophore pK_a; electron-donating and -withdrawing groups both lower the pK_a and, therefore, favor the conjugate base at neutral pH. This causes lower quantum yields, since the conjugate base is much less efficient at releasing the leaving group.

4-Hydroxybenzyl alcohol, a ubiquitous minor product, serves as additional supporting evidence for the intermediacy of $\mathbf{I_2}$ through its formation by decarbonylation and hydrolysis.[9]

Finally, these results provide evidence that further modification of the chromophore is possible without decreasing its photoreactivity, enhancing the pHP physical and photochemical versatility. Carboxyl, carbonyl, ether, and amide functional groups can be introduced to enhance the solubility, binding, and other physical properties without fear of losing reactivity.

Current studies on this intriguing chromophore and on the mechanism of the unusual photochemical rearrangement are in progress.

Experimental

Methods

Melting points were conducted with open-ended capillary tubes using a noncalibrated Thomas–Hoover melting-point apparatus. Lyophilization was performed using a Labconco FreezeZone device set at –52 °C and 0.04 mbar (1 bar = 100 kPa). Solution pH values were determined using a Fisher Scientific pH 510 meter calibrated with certified Fisher buffer solutions of pH 4, 7, and 10. Products of all reactions were assessed for purity using the following instrumental techniques: For ^{1}H, ^{13}C, and ^{19}F NMR, Bruker DRX 400 and DRX 500 MHz spectrometers were utilized with trifluoroacetic acid as an internal standard (δ = –76.55 ppm). GC–MS analysis was done on an Agilent 6890N Network GC system equipped with a Quattro Micromass triple quadrupole electron impact mass spectrometer. Exact masses were performed on a Quattro Micromass triple quadrupole electrospray ionization mass spectrometer. UV–vis data were obtained on a Carey Bio100 instrument using 1.5 mL quartz cuvettes. Fluorescence data were acquired on a Carey Eclipse fluorescence spectrophotometer using a 10 mm

Can. J. Chem. Downloaded from www.nrcresearchpress.com by Xi'an Jiaotong University on 09/19/12
For personal use only.

quartz cell. IR data were obtained using a Shimadzu FT-IR 8400 S instrument with pressed potassium bromide (KBr) pellets or a prefabricated sodium chloride (NaCl) chloroform cell for solid-phase analysis and NaCl prefabricated plates for oil analysis. Ground-state pK_as were determined through sample titration with increasing amounts of 0.0461 mol/L NaOH (standardized with potassium hydrogen phthalate), correlating pH vs [OH^-] and ascertaining the half equivalence point as the pK_a. Product separation was achieved by flash chromatography using EM Science silica gel and gradient hexanes – ethyl acetate as eluting solvents. All reactions were run under ambient conditions unless otherwise stated. ^{1}H NMR spectroscopy was utilized to monitor the progress of the photolysis of all new pHP cages. In general, a 1–10 mmol/L sample of pHP-caged GABA was prepared in 2 mL D_2O and ~2 mL was placed in an NMR tube. This was positioned in a photoreactor equipped with two 15 W, 3000 Å Rayonet lamps and a merry-go-round. Irradiation for 30 min generally led to 100% conversion as judged by the absence of the ester proton signals. Photoproduct identification was achieved through the spiking the samples of the irradiated mixture with authentic samples of the resolved GABA. Quantitative photolysis conditions for determination of quantum yields and Stern–Volmer quenching constants (K_{SV}) were as follows: The lamp light output (in mEinsteins/min) was established using the potassium ferrioxalate method.[7] Milligram quantities of caged compounds and caffeine or acetamidophenol were weighed out on a Fisher brand microbalance and dissolved in 4 mL of 18 MΩ ultrapure water salt solutions of various concentrations, buffers with or without adjusted ionic strengths, or purified organic solvents were then added to a quartz tube and vortexed, resulting in a homogenous solution of the caged compound and internal standard. Concentrations of the caged compounds ranged from 1 to 9 mmol/L. These tubes were then placed in a carousel within a Rayonet photochemical reactor equipped with two 3000 Å, 15 W Rayonet photochemical reactor RPR3000 mercury lamps as light sources. One hundred microlitre samples were removed at 30 s intervals up to 5 min using a 250 μL Hamilton microsyringe and diluted to 1 mL with water using 1 mL volumetric flasks.

Quantum efficiency determinations

Quantitative analysis was achieved by HPLC–UV or HPLC–MS/MS. The LC–MS/MS instrument was a Waters 2695 Liquid Chromatographer equipped with a Quattro Micromass triple quadrupole electrospray ionization mass spectrometer, outfitted with an autosampler. UV–vis detection consisted of a Waters 2497 type with a dual wavelength detector set at 220 and 240 nm. The reservoirs used were as follows: (*i*) 99% water, 1% methanol, 10 mmol/L ammonium formate, and 0.06% formic acid; and (*ii*) 99% methanol, 1% water, 10 mmol/L ammonium formate, and 0.06% formic acid. The column was a reverse-phase (C18), 4 μm mesh Altech Altima, 50 mm in length. Injections of 100 μL were made with an automated sampler for each run for a total of three injections per vial. A mobile phase gradient was utilized to optimize compound separation. The flow rate was set at 300 μL/min. Data analysis was performed by Mass Lynx Ultima software and Microsoft Excel. Smoothing functions were used for peak analysis of the chromatographic peaks. Calibration curves to obtain *R* values from linear least-squares regression were determined at concentrations of the reactants and products in photolyses by systematic increases of pHP-caged GABA, free GABA, and *p*-hydroxyphenylacetic acid concentrations to determine correlations with internal standards caffeine or 4-acetamidophenol. The quantum efficiencies were then calculated from the ratio of the reactant or product concentrations to the photons absorbed using the actinometer values obtains as indicated above.

Lifetime and rate measurements

The Stern–Volmer quenching technique[20] effectively distinguished the triplet lifetimes of pHP derivatives, using potassium sorbate as the quencher. Concentrations of pHP GABA solutions ranged from 0.001 to 0.01 mol/L; these were diluted with sorbate solutions of increasing concentration (0–0.1 mol/L) and subsequently photolyzed under previously indicated conditions to ascertain the change in quantum efficiencies of GABA release. Φ_0/Φ vs [*Q*], and K_{SV} were determined. To establish the triplet lifetime (τ^3), the rate of quenching (k_q) was assumed to be commensurate with the rate of bimolecular diffusion in water ($k_{diff} \sim 7.2 \times 10^9$ s^{-1}). The results are shown in Table 6.

Femtosecond pump–probe spectroscopy

Femtosecond transient absorption was measured with the pump – supercontinuum probe technique using a Ti/Sa laser system (Clark MXR CPA-2001; 775 nm, pulse energy 0.9 mJ, full width at half maximum 150 fs, and operating frequency 426 Hz). Part of the beam was fed into a Clark MXR NOPA. The output at 532 nm was frequency-doubled by a β-barium borate (BBO) crystal to 266 nm and upon compression, elicited pump pulses with an energy of 1 μJ and <150 fs pulse width. A probe beam continuum was generated by focusing the 775 nm beam in front of a CaF_2 plate with a 2 mm path length that produced a supercontinuum probe beam spanning a wavelength range of 270–690 nm. The pump and probe beams were focused to a 0.2 mm spot on the sample that was flowing in an optical cell with a thickness of 0.4 mm. The probe beam and a reference signal (passing the solution beside the pump beam) were spectrally dispersed and registered with two photodiode arrays (512 pixels). Transient absorption spectra were calculated from the ratio of the two beams. The pump–probe cross-correlation was <100 fs over the entire spectrum. Measurements on short time scales (up to 50 ps) were corrected for chirp using a program (SPAN) kindly provided by Professor N. Ernsting, Institut für Chemie, Humboldt Universität zu Berlin, Germany. To improve the signal-to-noise ratio, the data were averaged over multiple pump–probe scans (3–6 scans with 400 shots per temporal point).

Materials

Unless indicated, starting materials were obtained from Sigma-Aldrich or Matrix Scientific. Before usage, solvents were purified via simple distillation employing phosphorus pentoxide, calcium hydride, or calcium chloride and stored in containers with microwave-activated 4 Å molecular sieves. Ultrapure (18 MΩ) water was used in all instances.

Can. J. Chem. Downloaded from www.nrcresearchpress.com by Xi'an Jiaotong University on 09/19/12
For personal use only.

Synthesis

pHP GABAs

4-(2-(4-Hydroxyphenyl)-2-oxoethoxy)-4-oxobutan-1-aminium-2,2,2-trifluoroacetate (1)

The steps to synthesize **1** were described in the protocol by Givens et. al.[5]

4-(2-(4-Hydroxy-3-methoxyphenyl)-2-oxoethoxy)-4-oxobutan-1-amonium-2,2,2-trifluoroacetate (2)

The synthesis of **2** was accomplished by using the procedures of Givens et al.[5] and Conrad et al.[2] as reported for **1**. Under an inert atmosphere of argon, a flame-dried 100 mL round-bottom flask was charged with *N*-Boc-γ-aminobutyric acid (248 mg, 1.22 mmol), 2-bromo-1-(4-hydroxy-3-methoxyphenyl)ethanone (300 mg, 1.22 mmol), and acetonitrile (50 mL). Potassium carbonate (188 mg, 1.36 mmol) was added and the mixture was stirred at room temperature (rt) for 24 h. The solvent was removed under reduced pressure and the remaining residue was dissolved in ethyl acetate and washed with water (3 × 10 mL). The organic extract was dried with $MgSO_4$ and concentrated to afford a pink solid. The crude product was flash chromatographed on silica gel with 2:1, 1:1, and then 2:3 hexane – ethyl acetate. Collection of the appropriate fractions and removal of the solvent under reduced pressure provided 2-(4-hydroxy-3-methoxyphenyl)-2-oxoethyl-4-[(*tert*-butoxycarbonyl)amino]-butanoate as a light pink solid. Yield: 333 mg, 74%; mp 88–89 °C. The *t*-Boc group was removed by treating the 2-(4-hydroxy-3-methoxyphenyl)-2-oxoethyl-4-[(*tert*-butoxycarbonyl)amino]butanoate (281 mg, 0.76 mmol) with cold trifluoroacetic acid (TFA, 10 mL). The solution was stirred at 0 °C for 1 h. The excess TFA was removed under reduced pressure and the remaining residue was dissolved in water, and washed with ethyl acetate. The aqueous layer was collected and the water removed by lyophilization to give 4-(2-(4-hydroxy-3-methoxyphenyl)-2-oxoethoxy)-4-oxobutan-1-amonium-2,2,2-trifluoroacetate as a tan solid (**2**, 545 mg, 100% yield, mp 128–130 °C). IR (KBr, cm^{-1}): 3339, 3181, 3150, 2935, 2756, 2088, 1757, 1675, 1593, 1516, 1460, 1424, 1383, 1368, 1281, 1178, 1132, 1020. ^1H NMR (400 MHz, D_2O) δ: 1.94 (p, *J* = 7.3 Hz, 2H), 2.60 (t, *J* = 7.1 Hz, 2H), 3.00 (t, *J* = 7.7 Hz, 2H), 3.79 (s, 3H), 5.37 (s, 2H), 6.85 (d, *J* = 8.3 Hz, 1H), 7.36 (s, 1H), 7.43 (d, *J* = 8.4 Hz, 1H).

4-(2-(4-Hydroxy-3,5-dimethoxyphenyl)-2-oxoethoxy)-4-oxobutan-1-amonium-2,2,2-trifluoroacetate (3)

The synthesis of **3** was accomplished by using the procedure of Conrad et. al.[2] A solution of 2-bromo-1-(4-hydroxy-3-methoxyphenyl)ethanone[2] (600 mg, 2.18 mmol/L) was treated with 4-(*tert*-butoxycarbonylamino)butanoic acid (N-*t*-Boc-GABA; 443 mg, 2.18 mmol/L) in 10 mL of benzene at 7 °C to which was added 366 mg (2.41 mmol/L) of 1,8-diazabicyclo[5.4.0]undec-7-ene (DBU) in 10 mL of benzene. The mixture was allowed to reach rt and stirred overnight. The solvent was removed in vacuo and the crude product purified by silica gel chromatography (522 mg, 60% yield). The *t*-Boc protecting group was then removed by treatment with TFA (10 mL) at 0 °C for 4 h. The TFA was removed by rotary evaporation and the crude product was treated with H_2O–EA. The aqueous layer was collected and the water removed by lyophilization to give 4-(2-(4-hydroxy-3,5-dimethoxyphenyl)-2-oxoethoxy)-4-oxobutan-1-amonium-2,2,2-trifluoroacetate as a colorless oil (**3**, 100%). IR (film, cm^{-1}): 3388, 3179, 2943, 2847, 1737, 1693, 615, 1536, 1466, 1431, 1379, 1326, 1300, 1169, 1047. ^1H NMR (400 MHz, D_2O) δ: 1.94 (m, 2H), 2.58 (t, *J* = 7.1 Hz, 2H), 3.00 (t, *J* = 7.7 Hz, 2H), 3.63 (s, 6H), 5.18 (s, 2H), 6.75 (s, 2H). FAB MS (free amine) *m*/*z*: 342 (M +1). HRMS calcd for $C_{15}H_{20}NO_8$ (M + H): 342.1189; found: 342.1193.

Representative description, with 16

1-(Benzyloxy)-4-bromo-2-fluorobenzene (16b)

The general method of Frechét and co-workers[21] was followed. A solution of 4-bromo-2-fluorophenol (**16a**, 3.83 g, 20.0 mmol), benzyl bromide (2.38 mL, 20.0 mmol), and potassium carbonate (6.91 g, 50.0 mmol) in CH_3CN (30 mL) was stirred at rt for 15 h. The solution was diluted with 50 mL CH_2Cl_2, washed with water (3 × 30 mL), dried (magnesium sulfate), and concentrated to give 5.24 g (93%) of 1-(benzyloxy)-4-bromo-2-fluorobenzene (**16b**) as a white precipitate; mp 65–67 °C. IR ($CHCl_3$, cm^{-1}): 3020, 2987, 2684, 2304, 1498, 1421, 1265, 1217, 1051, 896, 738, 695. ^1H NMR (400 MHz, $CDCl_3$) δ (ppm): 7.41 (m, 5H), 7.27 (dd, *J* = 6.4, *J* = 2.2 Hz, 1H), 7.26 (dt, *J* = 4.3, *J* = 2.0 Hz, 1H), 6.89 (t, *J* = 8.8 Hz, 1H), 5.13 (s, 2H). ^{13}C NMR (125 MHz, $CDCl_3$) δ (ppm): 154.23, 151.73, 146.06, 136.02, 128.88, 127.73, 120.14, 117.23, 115.86, 113.02, 71.90. ^{19}F NMR (376 MHz, $CDCl_3$ + 1 drop of CF_3CO_2H) δ (ppm): –130.78. HRMS (M+) calcd for $C_{13}H_{10}FBrO$: 279.9899; found: 279.9905.

1-(Benzyloxy)-3-fluorophenyl)ethanone (16c)

The general method of Kosugi et al.[22] was used. The experimental procedure is described with that for **23** (vide infra).[28] White precipitate; yield: 89%, mp 79–81 °C. IR ($CHCl_3$, cm^{-1}): 3053, 2987, 1679, 1610, 1514, 1498, 1421, 1265, 1217, 1052, 896, 738, 696. ^1H NMR (400 MHz, $CDCl_3$) δ (ppm): 7.74 (dd, *J* = 11.3, *J* = 2.4 Hz, 1H), 7.69 (dd, *J* = 9.0, *J* = 1.6 Hz, 1H) 7.44, (m, 5H), 7.04 (t, *J* = 8.4 Hz, 1H), 5.23 (s, 2H), 2.55, (s, 3H). ^{13}C NMR (125 MHz, $CDCl_3$) δ (ppm): 196.05, 153.66, 151.16, 135.82, 130.92, 128.95, 127.57, 125.76, 116.36, 114.22, 71.25, 26.52. ^{19}F NMR (376 MHz, $CDCl_3$ + 1 drop of CF_3CO_2H) δ (ppm): –133.02. HRMS (M + H) calcd for $C_{15}H_{13}FO_2$: 245.0978; found: 245.0951.

1-(4-(Benzyloxy)-3-fluorophenyl)-2-bromoethanone (16d)

The method was adapted from Ohriand co-workers.[23] A 50 mL round-bottom flask was charged with **16c** (700 mg, 2.86 mmol) and phenyltrimethylammonium tribromide (PTAB) (1.07 g, 2.86 mmol). The mixture was subsequently dissolved by the addition of 40 mL of CH_2Cl_2–CH_3OH (1:1). The resultant solution was stirred at rt for 6 h, at which time full conversion was indicated by GC–MS. The solution was transferred to a separatory funnel, diluted with 50 mL of CH_2Cl_2, and washed profusely with water (3 × 50 mL). Excess solvent was removed under reduced pressure, affording an orange precipitate, 900 mg (2.58 mmol), ~95%.[24] IR ($CHCl_3$, cm^{-1}): 3055, 2988, 1679, 1615, 1511,

Can. J. Chem. Downloaded from www.nrcresearchpress.com by Xi'an Jiaotong University on 09/19/12
For personal use only.

1498, 1417, 1267, 1219, 1050, 891, 748, 696. ^{1}H NMR (400 MHz, $CDCl_3$) δ (ppm): 7.77 (dd, J = 10.0, J = 2.4 Hz, 1H), 7.72 (dd, J = 7.0, J = 2.8 Hz, 1H), 7.42 (m, 5H), 7.07 (t, J = 8.4 Hz, 1H), 5.24 (s, 2H), 4.37 (s, 2H). ^{19}F NMR (376 MHz, $CDCl_3$ + 1 drop of CF_3CO_2H) δ (ppm): –133.12.

*2-(4-(Benzyloxy)-3-fluorophenyl)-2-oxoethyl-4-(*tert-*butoxycarbonylamino)butanoate (16e)*

The general method of Fujita and Hiyama[25] was utilized. A solution of 1-(4-(benzyloxy)-3-fluorophenyl)-2-bromoethanone (**16d**, 900 mg, 2.78 mmol), potassium carbonate (1.15 mg, 8.35 mmol), and 4-(*tert*-butoxycarbonylamino) butanoic acid (N-Boc–GABA, 678 mg, 3.33 mmol) in 50 mL of CH_3CN was stirred for 24 h at rt. The solution was washed with EtOAc, water, the aqueous phase discarded, and the resulting phase evaporated under reduced pressure. Flash column chromatography (hexanes–EtOAc, 5:1) afforded **16e** as a white precipitate. Yield: 1.10 g (89%); mp 97–99 °C. IR (KBr, cm^{-1}): 3300, 3100–2800, 1742, 1701, 1600, 1517, 1437, 1400 1309, 1200, 1165, 953, 750, 700, 668. ^{1}H NMR (400 MHz, CD_3CN) δ (ppm): 7.80 (dd, J = 7.0, J = 2.4 Hz, 1H), 7.78 (dd, J = 7.0, J = 2.0 Hz, 1H), 7.47 (dd, J = 4.4, J = 1.8 Hz, 1H), 7.42 (m, 5H), 5.31 (s, 2H), 5.25 (s, 2H), 2.97 (t, J = 6.8 Hz, 2H), 2.45 (t, J = 7.6 Hz, 2H), 1.76 (m, 2H), 1.40 (s, 9H). ^{13}C NMR (125 MHz, d_6-DMSO) δ (ppm): 190.67, 172.51, 155.60, 152.30, 150.80, 135.82, 128.39, 128.14, 127.68, 126.93, 125.60, 115.28, 114.82, 77.45, 70.36, 66.12, 39.64, 30.63, 28.22, 24.96. ^{19}F NMR (376 MHz, CD_3CN + 1 drop of CF_3CO_2H) δ (ppm): –133.44. HRMS (M + Na) calcd for $C_{24}H_{28}FNO_6Na$: 468.1798; found: 468.1796.

4-(2-(3-Fluoro-4-hydroxyphenyl)-2-oxoethoxy)-4-oxobutan-1-aminium-2,2,2-trifluoroacetate (16)

The general method of Marsh and Goodman[26] was followed. To a flame-dried 50 mL round-bottom flask containing 2-(4-(benzyloxy)-3-fluorophenyl)-2-oxoethyl-4-(*tert*-butoxy-carbonylamino)-butanoate (**16e,** 850 mg, 1.91 mmol) was added 20 mL of freshly distilled TFA. Stirring continued for 24 h at rt under ambient conditions. The solution was evaporated under reduced pressure and washed with EtOAc–water. The water layer was then extracted, frozen, and then lyophilized, affording **16** as an adhesive precipitate. Yield: 550 mg (78%). IR (KBr, cm^{-1}): 3434, 3269, 3100–2800, 1741, 1693, 1610, 1553, 1420, 1201, 1050, 823, 759, 719. ^{1}H NMR (400 MHz, D_2O) δ (ppm): 7.70 (d, J = 9.0 Hz, 2H), 7.12 (t, J = 9.9 Hz, 1H), 5.50 (s, 2H), 3.09 (t, J = 7.6 Hz, 2H), 2.66 (t, J = 7.0 Hz, 2H), 2.05 (m, 2H). ^{13}C NMR (125 MHz, MeOD) δ (ppm): 190.05, 172.06, 161.60, 152.27, 151.07, 150.33, 126.03, 125.33, 117.30, 115.33, 65.95, 38.54, 30.02, 22.48. ^{19}F NMR (376 MHz, D_2O) δ (ppm): –133.58. HRMS (M+) calcd for $C_{12}H_{15}FNO_4$: 256.0985; found: 256.0977.

The synthetic protocol for generating compounds **14** and **15**[27] and **17**–**23**[28] has been previously published. The synthesis of **13** was analogous to that for **16** and, therefore, only the spectroscopic data for this is described.

1-Benzyloxy-4-bromo-2-cyanobenzene (13b)

White solid. Yield: 87%; mp 80–81 °C. IR (KBr, cm^{-1}): 3068, 3035, 2229, 1591, 1487, 1454, 1287, 1132, 1132, 1018, 813, 742, 696. ^{1}H NMR (400 MHz, CD_3CN) δ (ppm): 5.22 (s, 2H), 7.14 (d, 1H), 7.45 (m, 5H), 7.73 (dd, 1H), 7.81 (d, 1H). ^{13}C NMR (100 MHz, CD_3CN) δ (ppm): 71.9, 104.5, 112.5, 115.9, 116.2, 128.7, 129.4, 129.7, 136.7, 136.8, 138.4, 160.6. HRMS (M+) calcd for $C_{14}H_{10}BrNO$: 286.9946; found: 286.9937.

1-(4-Benzyloxy-3-cyanophenyl)ethanone (13c)

White solid. Yield: 90%; mp 120–123 °C. IR (KBr, cm^{-1}): 3068, 3033, 2229, 1681, 1602, 1500, 1419, 1355, 1275, 1137, 977, 817, 750, 630. ^{1}H NMR (400 MHz, CD_3CN) δ (ppm): 2.53 (s, 3H), 5.31 (s, 2H), 7.26 (d, 1H), 7.44 (m, 5H), 8.17 (dd, 1H), 8.26 (d, 1H). ^{13}C NMR (100 MHz, CD_3CN) δ (ppm): 25.45, 70.79. 101.53, 112.63, 115.27, 127.50, 128.19, 128.40, 130.15, 134.20, 134.50, 1335.27, 163.02, 194.85. HRMS (M + H) calcd for $C_{16}H_{13}NO_2$: 252.1024; found: 252.1022.

1-(4-Benzyloxy)-3-cyanophenyl)-2-bromoethanone (13d)

White solid. Yield: 91%; mp 94–96 °C. IR ($CDCl_3$, cm^{-1}): 688, 833, 1037, 1247, 1280, 1600, 1735, 2115, 2258, 3091. ^{1}H NMR (400 MHz CD_3CN) δ (ppm): 4.63 (s, 2H), 5.35 (s, 2H) 7.16 (d, 1H), 7.46 (m, 5H), 8.25 (dd, 1H), 8.32 (d, 1H). ^{13}C NMR (100 MHz, CD_3CN) δ (ppm): 32.30, 71.30, 102.26, 113.31, 115.34, 117.36, 127.28, 127.88, 128.60, 128.78, 135.10, 135.46, 135.48, 163.87, 188.96. HRMS (M+) calcd for $C_{16}H_{13}BrNO_2$: 330.0130; found: 330.0140.

*2-(4-(Benzyloxy)-3-cyanophenyl-2-oxoethyl-4-(*tert-*butoxycarbonylamino)butanoate (13e)*

White solid. Yield: 81%; mp 119–120 °C. IR ($CHCl_3$, cm^{-1}): 3456, 2252, 1743, 1706, 1600, 1502, 1271, 1166. ^{1}H NMR (400 MHz, CD_3CN) δ (ppm): 1.39 (s, 6H), 1.78 (t, 2H), 2.20 (m, 2H), 3.10 (t, 2H), 5.31 (s, 4H), 7.29 (d, 1H), 7.40 (m, 5H), 8.17 (dd, 1H), 8.25 (d, 1H). ^{13}C NMR (100 MHz, CD_3CN) δ (ppm): 24.47, 25.46, 27.27, 30.34, 39.01, 65.62, 70.79, 70.93, 77.73, 101.89, 112.64, 112.97, 115.01, 117.00, 127.02, 127.53, 128.24, 133.88, 134.15, 135.13, 155.58, 163.57, 172.21, 189.92. HRMS (M + H) calcd for $C_{25}H_{29}N_2O_6$: 452.2026; found: 453.2021.

4-(2-(3-Cyano-4-hydroxyphenyl)-2-oxoethoxy)-4-oxobutan-1-aminium-2,2,2-trifluoroacetate (13)

Waxy solid. Yield: 50%. IR (KBr, cm^{-1}): 3388, 2358, 2343, 2237, 1677 (broad), 1610, 1438, 1205, 1137, 842, 802, 723. ^{1}H NMR (400 MHz, D_2O) δ (ppm): 1.94 (t, 2H), 2.59 (m, 2H), 3.08 (t, 2H), 5.39 (s, 2H), 7.05 (d, 1H), 8.01 (dd, 1H), 8.18 (d, 1H). ^{13}C NMR (100 MHz, D_2O) δ (ppm): 21.96, 29.43, 38.54, 66.59, 99.25, 112.76, 115.10, 117.42, 119.74, 134.87, 162.83, 172.45, 192.32. HRMS (M+) calcd for $C_{13}H_{15}N_2O_4$: 263.1032; found: 263.1023.

The synthetic course towards **4**–**9** and **12** followed the same protocol as for **13**–**23**, but commenced with the commercially available corresponding *p*-hydroxyacetophenones. Hence, only spectroscopic data for these are indicated.

1-(3,4-Bis(benzyloxy)phenyl)ethanone (4d)

White solid. Yield: 98%. *This compound is known.* ^{1}H NMR (400 MHz, $CDCl_3$) δ (ppm): 7.63 (dd, J = 8.8, J = 2.3 Hz, 1H), 7.40 (m, 11H), 6.94 (dd, J = 9.2, J = 2.0 Hz, 1H), 5.25 (s, 2H), 5.22 (s, 2H), 2.52 (s, 3H).

Can. J. Chem. Downloaded from www.nrcresearchpress.com by Xi'an Jiaotong University on 09/19/12
For personal use only.

1-(3,4-Bis(benzyloxy)phenyl)-2-bromoethanone (4e)

Oil. Yield: 96%[7]. ^{1}H NMR (400 MHz, $CDCl_3$) δ (ppm): 7.68 (s, 1H), 7.41 (m, 11H), 6.96 (d, 1H), 5.24 (s, 2H), 5.22 (s, 2H), 4.46 (s, 2H).

2-(3,4-Bis(benzyloxy)phenyl)-2-oxoethyl-4-(*tert*-butoxycarbonylamino)butanoate (4f)

White precipitate. Yield: 90%; mp 112–114 °C. IR (KBr, cm^{-1}): 3310, 3100–2800, 1743, 1700, 1658, 1601, 1436, 1400, 1200, 1165, 955, 745, 742, 700, 697, 665, 651. ^{1}H NMR (400 MHz, d_6-DMSO) δ (ppm): 7.62 (dd, J = 7.2, J = 2.4 Hz, 1H), 7.56 (d, J = 1.8 Hz, 1H), 7.38 (m, 10H), 7.19 (d, J = 8.1 Hz, 1H), 6.92 (t, J = 7.2 Hz, 1H), 5.40 (s, 2H), 5.27 (s, 2H), 5.21 (s, 2H), 2.97 (t, J = 6.8 Hz, 2H), 2.40 (t, J = 7.7 Hz, 2H), 1.70 (m, 2H), 1.38 (s, 9H). ^{13}C NMR (125 MHz, d_6-DMSO) δ (ppm): 197.09, 171.80, 155.60, 152.85, 147.98, 136.85, 128.41, 127.94, 127.58, 126.84, 122.64, 113.04, 112.51, 77.47, 70.00, 66.07, 39.61, 30.67, 28.22, 24.54. HRMS (M + H) calcd for $C_{31}H_{36}NO_7$: 534.2492; found: 534.2484.

2-(2,4-Dihydroxyphenyl)-2-oxoethyl-4-(*tert*-butoxycarbonylamino)butanoate (4g)

An adapted method of Theodorakis and co-workers[29] was utilized. To a stoppered round-bottom flask containing a solution of **4f** (1.20 g, 2.24 mmol) and 120 mg of 10% *w*/*w* Pd/C in 25 mL of EtOAc was added H_2 via a needle from a reinforced balloon. The reaction was deemed complete after 4 h by the absence of the reagent band on TLC (hexanes–EtOAc, 1:1). Excess solvent was removed in vacuo to afford an adhesive precipitate. Yield: 98%. ^{1}H NMR (400 MHz, d_6-DMSO) δ (ppm): 7.32 (d, J = 7.2 Hz, 2H), 6.93 (s, 1H), 6.89 (t, J = 6.9 Hz, 1H), 5.39 (s, 2H), 2.98 (t, J = 6.8 Hz, 2H), 2.38 (t, J = 7.9 Hz, 2H), 1.68 (m, 2H), 1.40 (s, 9H). ^{13}C NMR (125 MHz, d_6-DMSO) δ (ppm): 197.34, 171.97, 155.66, 155.52, 136.92, 123.01, 113.09, 112.39, 77.55, 70.13, 39.56, 30.65, 28.19, 24.53.

4-(2-(3,4-Dihydroxyphenyl)-2-oxoethoxy)-4-oxobutan-1-aminium-2,2,2-trifluoroacetate (4)

White precipitate. Yield: 92%; mp 56–58 °C. IR (KBr, cm^{-1}): 3432, 3274, 3100–2800, 1739, 1691, 1602, 1520, 1421, 1377, 1309, 1298, 1201, 1178, 1128, 1055, 1027, 1008, 823, 762, 717, 613. ^{1}H NMR (400 MHz, D_2O) δ (ppm): 7.35 (s, 1H), 7.33 (s, 1H), 6.91 (d, J = 7.1 Hz, 1H), 5.36 (s, 2H), 3.07 (t, J = 6.8 Hz, 2H), 2.65 (t, J = 7.8 Hz, 2H), 2.00 (m, 2H). ^{13}C NMR (125 MHz, D_2O) δ (ppm): 194.29, 174.13, 163.06, 150.88, 144.11, 125.88, 122.69, 119.74, 117.42, 115.10, 66.56, 38.30, 30.23, 21.95. HRMS (M+) calcd for $C_{12}H_{16}NO_5$: 254.1028; found: 254.1032.

1-(2,4-Bis(benzyloxy)phenyl)ethanone (5d)

White precipitate. Yield: 97%. *This compound is known.* ^{1}H NMR (400 MHz, $CDCl_3$) δ (ppm): 7.86 (t, J = 7.6, 1H), 7.39 (m, 11H), 6.64 (dd, J = 8.7, J = 2.3 Hz, 1H), 5.12 (s, 2H), 5.10 (s, 2H), 2.57 (s, 3H).

1-(2,4-Bis(benzyloxy)phenyl)-2-bromoethanone (5e)

Waxy precipitate. Yield: 94%.[7] ^{1}H NMR (400 MHz, $CDCl_3$) δ (ppm): 7.78 (s, 1H), 7.35 (m, 10H), 6.60 (d, 2H), 5.12 (s, 2H), 5.09 (s, 2H), 4.51 (s, 2H).

2-(2,4-Bis(benzyloxy)phenyl)-2-oxoethyl-4-(*tert*-butoxycarbonylamino)butanoate (5f)

Adhesive precipitate. Yield: 48%. IR (KBr, cm^{-1}): 3310, 3100–2800, 1743, 1700, 1658, 1601, 1436, 1400, 1200, 1165, 955, 745, 742, 700, 697, 665, 651. ^{1}H NMR (400 MHz, d_6-DMSO) δ (ppm): 7.93 (t, J = 8.8 Hz, 1H), 7.43 (m, 10H), 7.14 (dd, J = 8.7, J = 2.2 Hz, 1H), 6.88 (t, J = 5.7 Hz, 1H), 6.62 (d, J = 4.7 Hz, 1H), 5.37 (s, 2H), 5.29 (s, 1H), 5.21 (s, 1H), 5.10 (s, 2H), 2.94 (t, J = 6.6 Hz, 2H), 2.37 (t, J = 7.5 Hz, 2H), 1.76 (m, 2H), 1.37 (s, 9H). ^{13}C NMR (125 MHz, d_6-DMSO) δ (ppm): 190.50, 172.15, 164.65, 159.78, 155.58, 135.99, 132.04, 128.35, 127.51, 118.10, 107.59, 103.90, 100.33, 77.43, 70.72, 69.19, 39.95, 30.68, 28.22, 24.88. HRMS (M + H) calcd for $C_{31}H_{36}NO_7$: 534.2492; found: 534.2504.

2-(2,4-Dihydroxyphenyl)-2-oxoethyl-4-(*tert*-butoxycarbonylamino)butanoate (5g)

Adhesive precipitate. Yield: 97%. ^{1}H NMR (400 MHz, d_6-DMSO) δ (ppm): 11.43, (s, 1H), 11.34 (s, 1H), 7.88 (s, 1H), 7.70 (d, 1H), 6.87 (t, 1H), 6.38 (d, 1H), 5.28 (s, 1H), 2.96 (t, 2H), 2.40 (t, 2H), 1.67 (m, 2H), 1.38 (s, 9H).

4-(2-(2,4-Dihydroxyphenyl)-2-oxoethoxy)-4-oxobutan-1-aminium-2,2,2-trifluoroacetate (5)

White precipitate. Yield: 85%; mp 136–138 °C. IR (KBr, cm^{-1}): 3432, 3274, 3100–2800, 1739, 1691, 1602, 1520, 1421, 1377, 1309, 1298, 1201, 1178, 1128, 1055, 1027, 1008, 823, 762, 717, 613. ^{1}H NMR (400 MHz, D_2O) δ (ppm): 7.97 (d, J = 6.8 Hz, 1H), 7.72 (d, J = 8.8 Hz, 1H), 6.53 (d, J = 7.6v, 1H), 5.48 (s, 1H), 5.43 (s, 1H), 3.14 (t, J = 7.6 Hz, 2H), 2.72 (t, J = 7.0 Hz, 2H), 2.08 (m, 2H). ^{13}C NMR (125 MHz, D_2O) δ (ppm): 193.77, 174.15, 162.75, 151.02, 144.22, 125.92, 122.70, 119.65, 117.37, 115.58, 66.60, 38.51, 30.28, 22.00. HRMS (M+) calcd for $C_{12}H_{16}NO_5$: 254.1028; found: 254.1038.

1-(4-(Benzyloxy)-3-methyl-phenyl)ethanone (6d)

White precipitate. Yield: 95%. *This compound is known.* ^{1}H NMR (400 MHz, $CDCl_3$) δ (ppm): 7.82 (s 1H), 7.80 (s, 1H), 7.40 (m, 5H), 6.90 (d, J = 8.8 Hz, 1H), 5.17 (s, 2H), 2.56 (s, 3H), 2.33 (s, 3H).

1-(4-(Benzyloxy)-3-methylphenyl)-2-bromoethanone (6e)

Oil. Yield: 97%.[7] ^{1}H NMR (400 MHz, $CDCl_3$) δ (ppm): 7.82 (d, 2H), 7.40 (m, 5H), 6.88 (d, J = 8.8 Hz, 1H), 5.19 (s, 2H), 4.33 (s, 2H), 2.33 (s, 3H).

2-(4-(Benzyloxy)-3-methylphenyl)-2-oxoethyl-4-(*tert*-butoxycarbonylamino)butanoate (6f)

White precipitate. Yield: 94%; mp 105–106 °C. IR (KBr, cm^{-1}): 3307, 3100–2800, 1742, 1701, 1659, 1606, 1437, 1407, 1209, 1167, 955, 743, 700, 667. ^{1}H NMR (400 MHz, d_6-DMSO) δ (ppm): 7.82 (d, J = 9.1 Hz, 2H), 7.40 (m, 5H), 7.14 (d, J = 8.1 Hz, 1H), 6.87 (t, J = 7.4 Hz, 1H), 5.39 (s, 2H), 5.25 (s, 2H), 2.96 (t, J = 6.8 Hz, 2H), 2.42 (t, J = 7.6 Hz, 2H), 2.24 (s, 3H), 1.70 (m, 2H), 1.38 (s, 9H). ^{13}C NMR (125 MHz, d_6-DMSO) δ (ppm): 191.14, 172.20, 161.40, 155.60, 136.67, 131.00, 130.10, 129.26, 128.50, 127.34, 126.45, 125.07, 111.62, 77.45, 69.55, 66.03, 39.33, 30.68, 28.18, 24.98, 16.04. HRMS (M + Na) calcd for $C_{25}H_{31}NO_6Na$: 464.2049; found: 464.2017.

Can. J. Chem. Downloaded from www.nrcresearchpress.com by Xi'an Jiaotong University on 09/19/12
For personal use only.

2-(4-Hydroxy-3-methylphenyl)-2-oxoethyl-4-(tert-butoxycarbonylamino)butanoate (6g)

Adhesive precipitate. Yield: 98%. ^{1}H NMR (400 MHz, d_6-DMSO) δ (ppm): 10.76 (s, 1H), 7.86 (d, J = 9.2 Hz, 2H), 7.66 (d, J = 8.0 Hz, 1H), 6.89 (t, 1H), 5.38 (s, 2H) 2.96 (t, J = 6.9 Hz, 2H), 2.42 (t, J = 7.8 Hz, 2H), 2.24 (s, 3H), 1.70 (m, 2H), 1.38 (s, 9H).

4-(2-(4-Hydroxy-3-methylphenyl)-2-oxoethoxy)-4-oxobutan-1-aminium-2,2,2-trifluoroacetate (6)

White precipitate. Yield: 89%; mp 118–120 °C. IR (KBr, cm^{-1}): 3432, 3274, 3100–2800, 1739, 1691, 1602, 1520, 1421, 1377, 1309, 1298, 1201, 1178, 1128, 1055, 1027, 1008, 823, 762, 717, 613. ^{1}H NMR (400 MHz, d_6-DMSO) δ (ppm): 7.86 (s, 3H), 7.72 (d, J = 6.2 Hz, 1H), 7.67 (dd, J = 9.0, J = 1.8 Hz, 1H), 5.39 (s, 1H), 2.88 (t, J = 7.0 Hz, 2H), 2.56 (t, J = 7.6 Hz, 2H), 2.16 (s, 3H), 1.87 (m, 2H). ^{13}C NMR (125 MHz, d_6-DMSO) δ (ppm): 190.67, 171.72, 160.98, 158.27, 130.76, 127.76, 125.10, 120.30, 117.94, 114.76, 66.11, 38.09, 30.15, 22.10, 15.80. HRMS (M+) calcd for $C_{13}H_{18}NO_4$: 252.1230; found: 252.1212.

1-(4-(Benzyloxy)2-methylphenyl)ethanone (7d)

White precipitate. Yield: 93%. *This compound is known.* GC–MS (EI): One peak; retention time, 8.24 min (initial temp 50 °C, ramp 25 °C/min until 300 °C). MS *m*/*z*: 240.0.

1-(4-(Benzyloxy)-2-methylphenyl)-2-bromoethanone (7e)

White precipitate. Yield: 92%. *This compound is known.* GC–MS (EI): One peak; retention time, 9.77 min (initial temp 50 °C, ramp 25 °C/min until 300 °C). MS *m*/*z*: 317.9, 319.9.

2-(4-(Benzyloxy)-2-methylphenyl)-2-oxoethyl-4-(tert-butoxycarbonylamino)butanoate (7f)

Adhesive precipitate.Yield: 91%. IR (KBr, cm^{-1}): 3307, 3100–2800, 1742, 1701, 1659, 1606, 1437, 1407, 1209, 1167, 955, 743, 700, 667. ^{1}H NMR (400 MHz, d_6-DMSO) δ (ppm): 7.86 (d, J = 9.1 Hz, 1H), 7.47–7.40 (m, 5H), 6.97 (t, J = 6.5 Hz, 2H), 6.87 (t, J = 7.4 Hz, 1H), 5.28 (s, 2H), 5.19 (s, 2H), 2.97 (t, J = 6.7 Hz, 2H), 2.42 (m, 5H), 1.68 (m, 2H), 1.37 (s, 9H). ^{13}C NMR (125 MHz, d_6-DMSO) δ (ppm): 193.63, 172.21, 161.05, 155.60, 141.48, 136.40, 132.04, 128.47, 127.42, 125.06, 118.30, 111.85, 107.74, 77.45, 69.30, 67.05, 38.83, 30.68, 28.22, 24.54, 21.11. HRMS (M + Na) calcd for $C_{25}H_{31}NO_6Na$: 464.2049; found: 464.2040.

2-(4-Hydroxy-2-methylphenyl)-2-oxoethyl-4-(tert-butoxycarbonylamino)butanoate (7g)

Adhesive precipitate. Yield: 98%. IR (KBr, cm^{-1}): 3460, 3300, 3100–2800, 1740, 1699, 1662, 1606, 1437, 1407, 1209, 1167, 955, 743, 700, 667. ^{1}H NMR (400 MHz, d_6-DMSO) δ (ppm): 10.30 (d, 1H), 7.78 (d, J = 9.1 Hz, 1H), 6.89 (t, J = 7.5 Hz, 1H), 6.71 (t, J = 6.3 Hz, 1H), 5.26 (s, 2H), 2.98 (t, J = 6.7 Hz, 2H), 2.41 (m, 5H), 1.69 (m, 2H), 1.39 (s, 9H). ^{13}C NMR (125 MHz, d_6-DMSO) δ (ppm): 192.91, 172.21, 160.96, 155.60, 141.83, 131.87, 125.29, 118.74, 112.51, 77.45, 66.86, 38.97, 30.46, 28.22, 24.95, 21.68. HRMS (M + Na) calcd for $C_{18}H_{25}NO_6Na$: 374.1580; found: 374.1577.

4-(2-(4-Hydroxy-2-methylphenyl)-2-oxoethoxy)-4-oxobutan-1-aminium-2,2,2-trifluoroacetate (7)

White precipitate. Yield: 95%; mp 110–112 °C. IR (KBr, cm^{-1}): 3460, 3300, 3100–2800, 1740, 1699, 1662, 1606, 1437, 1407, 1209, 1167, 955, 743, 700, 667. ^{1}H NMR (400 MHz, d_6-DMSO) δ (ppm): 7.86 (s, 3H), 7.80 (d, J = 9.0 Hz, 1H), 6.74 (t, J = 6.2 Hz, 1H), 5.28 (s, 2H), 2.96 (t, J = 6.7 Hz, 2H), 2.54 (t, J = 7.6 Hz, 2H), 2.40 (s, 3H), 1.87 (m, 2H). ^{13}C NMR (125 MHz, d_6-DMSO) δ (ppm): 192.71, 171.72, 161.19, 158.64, 141.88, 131.90, 124.55, 118.81, 117.56, 112.58, 67.02, 37.84, 30.14, 22.54, 20.34. HRMS (M+) calcd for $C_{13}H_{18}NO_4$: 252.1236; found: 252.1227.

1-(4-(Benzyloxy)-3,5-dimethylphenyl)ethanone (8d)

Oil. Yield: 95%. *This compound is known.* GC–MS (EI): One peak; retention time, 8.38 min (initial temp 50 °C, ramp 25 °C/min until 300 °C). MS *m*/*z*: 254.0.

1-(4-(Benzyloxy)-3,5-dimethylphenyl)-2-bromoethanone (8e)

White precipitate. Yield: 95%. *This compound is known.* GC–MS (EI): One peak; retention time, 9.87 min (initial temp 50 °C, ramp 25 °C/min until 300 °C). MS *m*/*z*: 331.9, 333.9.

2-(4-(Benzyloxy)-3,5-dimethylphenyl)-2-oxoethyl-4-(tert-butoxycarbonylamino)butanoate (8f)

Adhesive precipitate. Yield: 96%. IR (KBr cm^{-1}): 3307, 3100–2800, 1742, 1701, 1659, 1606, 1437, 1407, 1209, 1167, 955, 743, 700, 667. ^{1}H NMR (400 MHz, d_6-DMSO) δ (ppm): 7.70 (d, J = 8.6 Hz, 1H), 7.50–7.40 (m, 5H), 6.89 (t, J = 7.2 Hz, 1H), 5.42 (s, 2H), 4.88 (s, 2H), 2.97 (t, J = 6.9 Hz, 2H), 2.43 (t, J = 7.8 Hz, 2H), 2.29 (s, 6H), 1.68 (m, 2H), 1.36 (s, 9H). ^{13}C NMR (125 MHz, d_6-DMSO) δ (ppm): 191.84, 172.19, 160.04, 155.60, 137.06, 131.49, 129.59, 128.68, 128.36, 128.13, 127.85, 77.45, 73.52, 66.20, 38.97, 30.50, 28.18, 24.97, 16.20. HRMS (M + Na) calcd for $C_{26}H_{33}NO_6Na$: 478.2206; found: 478.2191; (M + H) calcd for $C_{26}H_{34}NO_6$: 456.2386; found: 456.2388.

2-(4-Hydroxy-3,5-dimethylphenyl)-2-oxoethyl-4-(tert-butoxycarbonylamino)butanoate (8g)

Adhesive precipitate. Yield: 99%. IR (KBr, cm^{-1}): 3548, 3301, 3100–2800, 1739, 1702, 1661, 1606, 1437, 1407, 1209, 1167, 955, 743, 700, 667. ^{1}H NMR (400 MHz, d_6-DMSO) δ (ppm): 9.40 (s, 1H), 7.59 (d, J = 8.6 Hz, 2H), 6.89 (t, J = 7.2 Hz, 1H), 5.36 (s, 2H), 2.98 (t, J = 7.0 Hz, 2H), 2.55 (t, J = 7.5 Hz, 2H), 2.20 (s, 6H), 1.92 (m, 2H). ^{13}C NMR (125 MHz, d_6-DMSO) δ (ppm): 190.91, 172.20, 159.67, 155.59, 128.60, 125.25, 123.74, 77.44, 65.91, 38.96, 30.90, 28.18, 24.98, 16.52. HRMS (M + Na) calcd for $C_{19}H_{27}NO_6Na$: 388.1736; found: 388.1735.

4-(2-(4-Hydroxy-3,5-dimethylphenyl)-2-oxoethoxy)-4-oxobutan-1-aminium-2,2,2-trifluoroacetate (8)

White precipitate. Yield: 92%; mp 125–127 °C. IR (KBr, cm^{-1}): 3550, 3301, 3100–2800, 1739, 1702, 1661, 1606, 1437, 1407, 1209, 1167, 955, 743, 700, 667. ^{1}H NMR (400 MHz, d_6-DMSO) δ (ppm): 9.36 (s, 1H), 7.86 (s, 3H), 7.62 (d, J = 8.6 Hz, 2H), 5.36 (s, 2H), 2.98 (t, J = 7.0 Hz, 2H), 2.43 (m, 5H), 2.22 (s, 6H), 1.69 (m, 2H), 1.37

Can. J. Chem. Downloaded from www.nrcresearchpress.com by Xi'an Jiaotong University on 09/19/12
For personal use only.

(s, 9H). ^{13}C NMR (125 MHz, d_6-DMSO) δ (ppm): 189.74, 170.61, 157.71, 156.71, 127.72, 124.97, 123.15, 116.95, 65.02, 37.10, 28.88, 21.48, 15.55. HRMS (M+) calcd for $C_{14}H_{20}NO_4$: 266.1392; found: 266.1389.

Benzyl 5-acetyl-2-(benzyloxy)benzoate (9d)

White precipitate. Yield: 93%; mp 98–100 °C. IR (KBr, cm^{-1}): 3325, 3100–2800, 1726, 1697, 1676, 1598, 1500, 1452, 1370, 1269, 1230, 1176, 1060, 1030, 1008, 821, 757, 721, 698. ^{1}H NMR (400 MHz, $CDCl_3$) δ (ppm): 8.46 (d, J = 2.1 Hz, 1H), 8.08 (dd, J = 9.0, J = 2.4 Hz, 1H), 7.44–7.33 (m, 10H), 7.09 (d, J = 8.8 Hz, 2H), 5.38 (s, 2H), 5.25 (s, 2H), 2.58 (s, 3H). ^{13}C NMR (125 MHz, $CDCl_3$) δ (ppm): 195.42, 165.04, 160.91, 135.11, 134.24, 133.04, 130.28, 129.16, 128.22, 127.81, 119.35, 117.36, 112.49, 70.08, 68.86, 25.74. HRMS (M + Na) calcd for $C_{23}H_{20}O_4Na$: 383.1259; found: 383.1262.

Benzyl 2-(benzyloxy)-5-(2-bromoacetyl)benzoate (9e)

Oil. Yield: 95%. IR (KBr, cm^{-1}): 3325, 3100–2800, 1726, 1697, 1676, 1598, 1500, 1452, 1370, 1269, 1230, 1176, 1060, 1030, 1008, 821, 757, 721, 698. ^{1}H NMR (400 MHz, $CDCl_3$) δ (ppm): 8.50 (d, J = 2.2 Hz, 1H), 8.10 (dd, J = 9.0, J = 2.4 Hz, 1H), 7.44–7.33 (m, 10H), 7.10 (d, J = 8.9 Hz, 2H), 5.38 (s, 2H), 5.25 (s, 2H), 4.41 (s, 2H). ^{13}C NMR (125 MHz, $CDCl_3$) δ (ppm): 189.39, 165.32, 162.18, 135.68, 135.48, 134.52, 133.49, 128.74, 128.26, 127.11, 126.47, 120.87, 113.44, 70.86, 67.21, 30.48. HRMS (M + Na) calcd for $C_{23}H_{19}BrO_4Na$: 461.0365; found: 461.0372.

Benzyl-2-(benzyloxy)-5-(2-(4-(*tert*-butoxycarbonylamino)butanoyloxy)acetyl)benzoate (9f)

White precipitate. Yield: 75%; mp 75–77 °C. IR (KBr, cm^{-1}): 3271, 3100–2800, 1733, 1701, 1697, 1600, 1577, 1500, 1454, 1415, 1365, 1269, 1251, 1215, 1166, 1056, 1028, 1008, 919, 875, 821, 758, 700. ^{1}H NMR (400 MHz, d_6-DMSO) δ (ppm): 8.26 (d, J = 2.4 Hz, 1H), 8.12 (dd, J = 9.0, J = 2.3 Hz, 1H), 7.44–7.33 (m, 11H), 6.89 (t, J = 5.5 Hz, 2H), 5.45 (s, 2H), 5.33 (s, 2H), 2.97 (t, J = 7.2 Hz, 2H), 2.42 (t, J = 7.0 Hz, 2H), 1.68 (m, 2H), 1.38 (s, 9H). ^{13}C NMR (125 MHz, $CDCl_3$) δ (ppm): 190.85, 172.13, 165.28, 161.01, 155.90, 135.82, 133.51, 130.81, 128.42, 128.04, 127.89, 127.33, 126.27, 113.95, 77.78, 70.10, 64.96, 59.73, 39.30, 30.64, 28.22, 25.24. HRMS (M + Na) calcd for $C_{32}H_{35}NO_8Na$: 584.2260; found: 584.2239.

5-(2-(4-(*tert*-Butoxycarbonylamino)butanoyloxy)acetyl)-2-hydroxybenzoic acid (9g)

Adhesive precipitate. Yield: 96%. ^{1}H NMR (400 MHz, d_6-DMSO) δ (ppm): 8.37 (d, J = 2.4 Hz, 1H), 8.08 (dd, J = 9.2, J = 2.3 Hz, 1H), 7.10 (d, J = 8.9 Hz, 2H) 6.90 (t, J = 5.5 Hz, 2H), 5.43 (s, 2H), 2.98 (t, J = 7.2 Hz, 2H), 2.44 (t, J = 7.0 Hz, 2H), 1.68 (m, 2H), 1.36 (s, 9H).

4-(2-(3-Carboxy-4-hydroxyphenyl)-2-oxoethoxy)-4-oxobutan-1-aminium-2,2,2-trifluoroacetate (9)

Adhesive precipitate. Yield: 94%. IR (KBr, cm^{-1}): 3440, 3274, 3100–2800, 1733, 1741, 1692, 1649, 1631, 1596, 1500, 1450, 1416, 1299, 1201, 1184, 1124, 1053, 1006, 823, 800, 760, 707, 680. ^{1}H NMR (400 MHz, D_2O) δ (ppm): 8.36 (s, 1H), 8.00 (d, J = 8.9 Hz, 1H), 7.08 (d, J = 8.1 Hz), 5.46 (s, 2H), 3.12 (t, J = 7.2 Hz, 2H), 2.68 (t, J = 7.0 Hz, 2H), 2.06 (m, 2H). ^{13}C NMR (125 MHz, D_2O) δ (ppm): 193.77, 174.11, 171.62, 165.14, 163.06, 134.87, 131.89, 119.72, 117.89, 115.09, 113.41, 66.60, 38.55, 30.45, 21.97. HRMS (M+) calcd for $C_{13}H_{16}NO_6$: 282.0978; found: 282.0967.

1-(4-(Benzyloxy)-3-nitrophenyl)ethanone (12d)

White precipitate. Yield; 96%. *This compound is known.* ^{1}H NMR (400 MHz, $CDCl_3$) δ (ppm): 8.45 (dd, J = 9.2, J = 2.4 Hz, 1H), 8.14 (dd, J = 9.2, J = 1.8 Hz, 1H), 7.42 (m, 6H), 5.34 (s, 2H), 2.60 (s, 2H).

1-(4-(Benzyloxy)-3-nitrophenyl)-2-bromoethanone (12e)

Oil. Yield: 97%.[7] ^{1}H NMR (400 MHz, $CDCl_3$) δ (ppm): 8.34 (s, 1H), 8.00 (d, 1H), 7.28 (m, 6H), 5.20 (s, 2H), 4.23 (s, 2H).

2-(4-(Benzyloxy)-3-nitrophenyl)-2-oxoethyl-4-(*tert*-butoxycarbonylamino)butanoate (12f)

White precipitate. Yield: 67%; mp 144–146 °C. IR (KBr, cm^{-1}): 3310, 3100–2800, 1740, 1700, 1655, 1603, 1433, 1400, 1204, 1170, 955, 745, 697, 665. ^{1}H NMR (400 MHz, CD_3CN) δ (ppm): 8.37 (dd, J = 7.2, J = 2.6 Hz, 1H), 8.12 (d, J = 1.5 Hz, 1H), 7.43 (m, 6H), 6.85 (t, J = 7.2 Hz, 1H), 5.34 (s, 2H), 3.09 (t, J = 6.8 Hz, 2H), 2.46 (t, J = 7.6 Hz, 2H), 1.77 (m, 2H), 1.40 (s, 9H). ^{13}C NMR (125 MHz, CD_3CN) δ (ppm): 195.22, 173.42, 160.65, 158.77, 139.23, 136.54, 135.40, 133.98, 131.78, 128.36, 125.89, 119.24, 116.82, 66.72, 38.44, 30.51, 29.11, 21.88. HRMS (M + Na) calcd for $C_{24}H_{28}N_2O_8Na$: 495.1743; found: 495.1755

4-(2-(4-Hydroxy-3-nitrophenyl)-2-oxoethoxy)-4-oxobutan-1-aminium-2,2,2-trifluoroacetate (12)

White precipitate. Yield: 78%; mp 76–78 °C. IR (KBr, cm^{-1}): 3441, 3265, 3100–2800, 1740, 1690, 1605, 1520, 1430, 1377, 1309, 1252, 1225, 1199, 1166, 1055, 820, 760. ^{1}H NMR (400 MHz, D_2O) δ (ppm): 8.72 (d, J = 2.2 Hz, 1H), 8.20 (d, J = 9.2 Hz, 1H), 7.32 (d, J = 8.8 Hz, 1H), 5.56 (s, 2H), 3.14 (t, J = 7.8 Hz, 2H), 2.72 (t, J = 9.2 Hz, 2H), 2.08 (m, 2H). ^{13}C NMR (125 MHz, D_2O) δ (ppm): 193.16, 174.10, 163.13, 157.81, 135.75, 134.33, 126.61, 120.50, 117.44, 115.12, 66.69, 38.54, 30.23, 21.96. HRMS (M+) calcd for $C_{12}H_{15}N_2O_6$: 283.0925; found: 283.0914.

The procedures for constructing **10** and **11** were the same as those described by Conrad et. al.;[2a,2c] therefore, only spectral data for these are indicated.

5-Bromoacetyl-2-hydroxybenzoic acid methyl ester (10b)

White solid. Yield: 73%; mp 91–92 °C. IR ($CHCl_3$, cm^{-1}): 3030, 3010, 2957, 1675, 1589, 1491, 1444, 1355, 1309, 1089, 965. ^{1}H NMR (400 MHz, $CDCl_3$) δ (ppm): 4.01 (s, 3 H), 4.41 (s, 2 H), 7.05 (d, J = 8.8 Hz, 1H), 8.09 (dd, J = 8.8 Hz, 2.2, 1H), 8.50 (d, J = 2.2 Hz, 1H). ^{13}C NMR (74.5 MHz, $CDCl_3$) δ (ppm): 30.4, 52.8, 112.3, 118.4, 125.6, 132.2, 133.1, 136.0, 165.8, 169.9, 189.3. HRMS (M + H) calcd for $C_{10}H_{10}BrO_4$: 272.9762; found: 272.9759.

Can. J. Chem. Downloaded from www.nrcresearchpress.com by Xi'an Jiaotong University on 09/19/12
For personal use only.

5-[4-*tert*-Butoxycarbonylaminobutyryloxy)acetyl]-2-hydroxybenzoic acid methyl ester (10c)

White solid. Yield: 46%; mp 113–114 °C. IR ($CHCl_3$, cm^{-1}): 3447, 3023, 2981, 2953, 1745, 1695, 1681, 1588, 1504, 1444, 1368, 1163, 1089, 962. ^1H (400 MHz, $CDCl_3$) δ (ppm): 1.44 (s, 9 H), 1.91 (q, J = 7.0 Hz, 2 H), 2.54 (t, J = 7.3 Hz, 2 H), 3.23 (q, J = 6.4 Hz, 2 H), 4.00 (s, 3 H), 5.32 (s, 2 H), 7.07 (d, J = 8.8 Hz, 1 H), 8.04 (dd, J = 8.8 Hz, 2.2, 1 H), 8.44 (d, J = 2.2 Hz, 1 H). ^{13}C NMR (74.5 MHz, $CDCl_3$) δ (ppm), 25.5, 28.6, 31.3, 53.0, 65.8, 112.5, 118.7, 126.0, 131.0, 135.1, 166.0, 170.0, 172.9, 190.2. HRMS (M + H) calcd for $C_{19}H_{26}NO_8$: 396.1650; found: 396.1648.

4-(2-(4-Hydroxy-3-(methoxycarbonyl)phenyl)-2-oxoethoxy)-4-oxobutan-1-aminium-2,2,2-trifluoroacetate (10)

Clear oil. Yield: 100%. IR (CH_2Cl_2, cm^{-1}) 3695, 3440, 3040, 2967, 1739, 1648, 1601, 1526, 1492, 1454, 1359, 1228, 1203, 773, 671. ^1H NMR (400 MHz, D_2O) δ (ppm): 2.04 (q, J = 7.0 Hz, 2H), 2.70 (t, J = 7.1 Hz, 2H), 3.10 (t, J = 7.3 Hz, 2H), 3.96 (s, 3H), 5.47 (s, 2H), 7.03 (d, J = 8.73 Hz, 1H), 8.02 (dd, J = 8.8 Hz, 2.2, 1H), 8.36 (d, J = 8.8 Hz, 2.2, 1H). ^{13}C NMR (74.5 MHz, D_2O) δ (ppm): 22.1, 30.4, 38.7, 53.0, 66.5, 112.7, 117.8, 125.1, 131.3, 134.9, 164.3, 169.4, 174.0, 193.2. HRMS (M+) calcd for $C_{14}H_{18}NO_6$: 296.1134; found: 296.1132.

5-Bromoacetyl-2-hydroxybenzamide (11b)

White solid. Yield: 29%; mp 185 °C (dec.). IR (film, cm^{-1}): 3417, 3364, 3305, 3280, 1671, 1650, 1625, 1587, 1487, 1427, 1363, 1286, 1228, 837, 592. ^1H NMR (400 MHz, $CDCl_3$) δ (ppm): 4.72 (s, 2 H), 7.03 (d, J = 8.2 Hz, 1H), 7.45 (bs, 1H), 8.12 (dd, J = 8.8 Hz, 2.20, 1H), 8.38 (bs, 1H), 8.56, (d, J = 2.0 Hz, 1H). ^{13}C NMR (74.5 MHz, $CDCl_3$) δ (ppm): 32.7, 114.6, 119.2, 126.2, 130.5, 135.8, 167.9, 173.4, 190.2. HRMS (M + H) calcd for $C_9H_9BrNO_3$ (M + H): 257.9766; found: 257.9783.

4-*tert*-Butoxycarbonylaminobutyric acid 2-(3-carbamoyl-4-hydroxyphenyl)-2-oxoethyl ester (11c)

White solid. Yield: 59%; mp 138–139 °C. IR ($CHCl_3$, cm^{-1}): 3535, 3462, 3414, 3028, 2975, 2931, 1750, 1699, 1663, 1611, 1508, 1417, 1368, 1166. ^1H NMR (400 MHz, acetone-d_6) δ (ppm): 1.4 (s, 9H), 1.85 (q, J = 7.2 Hz, 2H), 2.50 (t, J = 7.4 Hz, 2H), 3.17 (q, J = 6.6 Hz, 2H), 5.42 (s, 2H), 6.05 (bs, 1H), 7.02 (d, J = 8.7 Hz, 1H), 7.55 (bs, 1H), 8.07 (dd, J = 8.7, 1.7 Hz, 1H), 8.37 (bs, 1H), 8.51 (d, J = 1.8 Hz, 1H). ^{13}C NMR (75.4 MHz, acetone-d_6) δ (ppm): 26.3, 28.7, 31.7, 40.4, 66.7, 78.6, 114.5, 119.2, 126.2, 129.4, 134.6, 156.8, 167.7, 173.2, 173.4, 191.2. HRMS (M + H) calcd for $C_{18}H_{25}N_2O_7$: 381.1662; found: 381.1645.

4-(2-(3-Carbamoyl-4-hydroxyphenyl)-2-oxoethoxy)-4-oxobutan-1-aminium-2,2,2-trifluoroacetate (11)

Clear oil. Yield: 100%. IR ($CHCl_3$, cm^{-1}): 3415, 3219, 1728, 1692, 1665, 1629, 1497, 1432, 1377, 1238, 1200, 1144. ^1H NMR (400 MHz, D_2O) δ (ppm): 1.92 (q, J = 7.16 Hz, 2H), 2.61 (t, J = 7.4 Hz, 2H), 3.00 (q, J = 6.6 Hz, 2H), 5.40 (s, 2H), 6.94 (d, J = 8.7 Hz, 1H), 7.90 (dd, J = 8.72, 1.72 Hz, 1 H), 8.32 (d, J = 1.88 Hz, 1 H). ^{13}C NMR (75.4 MHz, D_2O) δ (ppm): 22.4, 30.6, 38.9, 66.9, 115.6, 118.2, 125.2, 130.4, 134.1, 163.2, 171.1, 174.4, 193.7. HRMS (M + H) calcd for $C_{13}H_{17}N_2O_5$: 281.1137; found: 281.1114.

The same protocol used for **13**–**23** was utilized for the synthesis of **24** and **25** up to the formation of benzyl-protected α-bromoacetophenones **13**–**23a**.

2-(4-Hydroxyphenyl)-2-oxoethyl acetate (24)

The sequence towards the synthesis of **24** conformed to that of Wan and co-workers.[30]

2-(Acetyloxy)-1-[3-cyano-4-(phenylmethoxy)phenyl]ethanone (26f)

A solution of NaOAc (175 mg, 2.13 mmol) and **25e** (470 mg, 1.42 mmol) in acetone was stirred overnight. The resulting solution was evaporated to dryness, 15 mL of water was added, and the mixture was extracted with ethyl acetate (3× 15 mL). The ethyl acetate layer was dried with anhyd $MgSO_4$. The solvent was removed and the resulting solid was further purified by column chromatography (hexanes – ethyl acetate, 1:1) to give 2-(acetyloxy)-1-[3-cyano-4-(phenylmethoxy)phenyl]ethanone (**25f**) as a white solid (250 mg, 57%); mp 122–124 °C. IR (KBr, cm^{-1}): 2225, 1735, 1701, 1595, 1321, 1222, 1078, 989, 761. ^1H NMR (400 MHz, CD_3Cl) δ (ppm): 2.20 (s, 3H), 5.17 (s, 2H), 5.27 (s, 2H), 7.21 (m, 1H), 7.37 (m, 6H), 7.87 (d, 1H). ^{13}C NMR (100 MHz, CD_3CN) δ (ppm): 19.3, 65.8, 70.3, 112.2, 118.0, 118.2, 122.2, 127.4, 127.6, 128.1, 128.3, 128.4, 128.4, 131.5, 135.5, 161.7, 169.9, 190.0. HRMS (M + Na) calcd for $C_{18}H_{15}NO_4Na$: 332.0899; found: 332.0901.

2-(3-Cyano-4-hydroxyphenyl)-2-oxoethyl acetate (26)

An adapted method from the synthesis of **4g** was employed. White solid. Yield: 80%; mp 158–160 °C. IR (KBr cm^{-1}): 3203, 2227, 1741, 1672, 1604, 1560, 1321, 1220, 1122, 1074, 896, 837, 740. ^1H NMR (400 MHz $(CD_3)_2CO$) δ (ppm): 2.13 (s, 3H), 5.37 (s, 2H), 7.23 (m, 1H), 7.25 (s, 1H), 8.10 (d, 1H). ^{13}C NMR (100 MHz, $(CD_3)_2CO$): 19.5, 65.9, 113.0, 117.2, 118.1, 122.5, 128.0, 132.1, 161.5, 169.6, 189.6. HRMS (M + Na) calcd for $C_{11}H_9NO_4Na$: 242.0429; found: 242.0417.

2-(Acetyloxy)-1-[2-cyano-4-(phenylmethoxy)phenyl]ethanone (25f)

The same procedure used for **26f** was followed. White solid. Yield: 90%; mp 92–94 °C. IR (KBr, cm^{-1}): 2231, 1741, 1691, 1604, 1377, 1284, 1224, 1085, 823, 738. ^1H NMR (400 MHz, $CDCl_3$) δ (ppm): 2.22 (s, 3H), 5.24 (s, 2H), 5.30 (s, 2H), 7.08 (d, 2H), 8.05 (m, 5H), 8.16 (d, 2H). ^{13}C NMR (100 MHz, $CDCl_3$) δ (ppm): 20.6, 65.6, 71.2, 113.2, 115.1, 127.0, 127.4, 128.7, 128.9, 134.1, 134.2, 134.6, 163.8, 170.4, 189.3. HRMS (M + Na) calcd for $C_{17}H_{16}NO_4Na$: 332.0899; found: 332.0916.

2-(2-Cyano-4-hydroxyphenyl)-2-oxoethyl acetate (25)

White solid. Yield: 90%; mp 185–186 °C. IR (KBr, cm^{-1}): 3150, 2237, 1739, 1666, 1585, 1508, 1421, 1379, 1240, 1124, 1083, 941, 835. ^1H NMR (400 MHz $(CD_3)_2CO$) δ (ppm): 2.14 (s, 3H), 5.42 (s, 2H), 7.19 (d, 1H) 8.12 (dd, 1H), 8.29 (d, 1H). ^{13}C NMR (100 MHz, $(CD_3)_2CO$): 19.5, 65.8, 100.0, 115.3, 116.8, 129.9, 133.8,

Can. J. Chem. Downloaded from www.nrcresearchpress.com by Xi'an Jiaotong University on 09/19/12
For personal use only.

134.0, 163.1, 169.6, 189.7. HRMS (M + H) calcd for $C_{11}H_8NO_4$: 218.0453: found: 218.

pHP Diethyl phosphates

Diethyl (2-(4-hydroxyphenyl)-2-oxoethyl) phosphate (27)

The synthesis of **27** was achieved using the protocol of Givens and Park.[1]

Diethyl (2-(4-hydroxy-3-methoxyphenyl)-2-oxoethyl) phosphate (28)

The synthesis of **28** was achieved using the same protocol used for **27**.[1]

Diethyl (2-(4-hydroxy-3,5-dimethoxyphenyl)-2-oxoethyl) phosphate (29)

The procedure for synthesizing **29** has been previously published.[25]

3-Methoxyphenyl pivalate (30b)

The general method of Gorobets et al.[31] was followed with modifications. To a cooled (0 °C), stirred solution of 3-methoxyphenol (**30a**, 2.0 g, 16.1 mmol) in dry CH_2Cl_2 (10 mL), freshly distilled triethyl amine (3.350 mL, 24.2 mmol) and catalytic amount of 4-dimethylaminopyridine (20 mg, 0.16 mmol) were added under Ar. After 10 min, pivaloyl chloride (2.98 mL, 24.2 mmol) was added dropwise to the reaction mixture. The reaction mixture was allowed to stir for 30 min at 0 °C, brought to rt, and then stirred overnight. At that point, water (10 mL) and ethyl acetate (30 mL) were added to the reaction mixture and the organic phase was washed sequentially with 10% HCl (3 × 25 mL), water (2 × 25 mL), saturated $NaHCO_3$ solution (3 × 25 mL) and brine (2 × 25 mL. The organic phase was separated, dried over anhyd $MgSO_4$, filtered, and the supernatant concentrated under reduced pressure to produce 3-methoxyphenyl pivalate (**30b**) as thick yellow oil (3.335 g, 100%). IR (Teflon film, cm^{-1}) 2972–2837, 1753, 1606, 1593, 1490, 1140, 1115, 1043, 766. ^1H NMR (500 MHz, CD_3COCD_3) δ (ppm): 7.31–7.28 (1H, t, J = 8.1 Hz), 6.82–6.82 (1H, d, J = 2.3 Hz), 6.81–6.80 (1H, d, J = 2.4 Hz), 6.69–6.66 (1H, m), 3.79 (3H, s), 1.33 (9H, s). ^{13}C NMR (125 MHz, CD_3COCD_3) δ (ppm): 177.8, 161.6, 153.4, 130.6, 114.7, 112.1, 108.7, 55.8, 39.6, 27.4. HRMS (M + H) calcd for $C_{12}H_{17}O_3$: 209.1178; found: 209.1182. The ^1H NMR data were similar to the literature values.[32]

4-(2-Chloroacetyl)-3-methoxyphenyl pivalate (30c)

The general method of Gonzalez-Gomez et al.[33] was followed with modifications. To a cooled (0 °C) stirred solution of $AlCl_3$ (4.73 g, 35.4 mmol) in chloroacetyl chloride (10 mL) under Ar was added 3-methoxyphenyl pivalate (**30b**, 3.355 g, 16.1 mmol). The reaction mixture was allowed to stir for 3 h at 0 °C under Ar. Then, water (20 mL) was added cautiously to quench the reaction and the resulting solution was extracted to EtOAc (4 × 25 mL). The organic phase was washed sequentially with saturated $NaHCO_3$ solution (3 × 25 mL) and brine (2 × 25 mL). The organic phase was separated, dried over anhyd $MgSO_4$, filtered, and the supernatant concentrated under reduced pressure to afford the crude product that was chromatographed on silica gel (EtOAc–hexanes–CH_2Cl_2, 1:2:2) to give 4-(2-chloroacetyl)-3-methoxyphenyl pivalate (**30c**) as green-white crystalline solid (2.32 g, 50%), mp 58–61 °C. IR (KBr, cm^{-1}): 2980–2854, 1757, 1686, 1606, 1420, 1271, 1186, 1117, 897, 791. ^1H NMR (500 MHz, CD_3COCD_3) δ (ppm): 7.85–7.84 (1H, d, J = 8.6 Hz), 7.01–7.00 (1H, d, J = 2.0 Hz), 6.86–6.83 (1H, d, J = 8.6 Hz), 4.90 (2H, s), 4.01 (3H, s), 1.34 (9H, s). ^{13}C NMR (125 MHz, CD_3COCD_3) δ (ppm): 190.4, 176.7, 161.3, 157.6, 132.6, 123.4, 115.4, 107.2, 56.8, 51.8, 39.8, 27.3. HRMS (M + H) calcd for $C_{14}H_{18}O_4Cl$: 285.0894; found: 285.0912.

4-(2-Diethoxyphosphoryloxyacetyl)-3-methoxyphenyl pivalate (30e)

The general methods of Finkelstein[34] and Yoh et al.[35] were utilized with modifications. A 50 mL round-bottom flask was charged with 4-(2-chloroacetyl)-3-methoxyphenyl pivalate (**30c**, 500 mg, 1.8 mmol) and NaBr (1.08 g, 10.5 mmol). Acetone (20 mL) was added and the resulting mixture was refluxed at 60 °C for 24 h. The reaction mixture was then concentrated and the resulting residue was suspended in ethyl acetate (20 mL) and washed sequentially with brine (2 × 20 mL) and water (20 mL). The ethyl acetate layer was separated, dried over anhyd $MgSO_4$, filtered, and the supernatant concentrated under reduced pressure to afford 4-(2-bromoacetyl)-3-methoxyphenyl pivalate (**30d**) as a white solid (95% conversion to the α-bromo ketone analog according to ^1H NMR). This compound was used directly in the next step without purification. To a stirred solution of 4-(2-bromoacetyl)-3-methoxyphenyl pivalate (**30d**, 548 mg, 1.66 mmol) in CH_3CN (10 mL), diethyl phosphoric acid (641 mg, 4.16 mmol) and Ag_2O (772 mg, 3.33 mmol) were added. The resulting mixture was stirred at 60 °C and the progress of the reaction was monitored by TLC. After 16 h, the black-colored suspension was filtered through a plug of Celite, the filtrate concentrated, and EtOAc (20 mL) was added. The organic layer was washed sequentially with saturated $NaHCO_3$ (40 mL) and water (20 mL) and dried over anhyd $MgSO_4$. The solvent was evaporated to afford the crude product as a yellow-brown liquid that was chromatographed on silica gel using a gradient solvent system (EtOAc–hexanes (1:2), EtOAc–hexanes (1:1), EtOAc–hexanes (2:1), EtOAc–hexanes (3:1), EtOAc–MeOH (19:1)) to produce the 4-(2-(diethoxyphosphoryloxy)acetyl)-2-methoxyphenyl pivalate (**30e**) as a yellow-brown solid (468 mg, 76%), mp 80–84 °C. IR (KBr, cm^{-1}): 2982–2852 (br), 1747, 1686, 1605, 1261, 1124, 1028, 854, 798. ^1H NMR (500 MHz, CD_3COCD_3) δ (ppm): 7.93–7.91 (1H, d, J = 8.6 Hz), 7.01 (1H, d, J = 2.0 Hz), 6.86–6.84 (1H, d, J = 8.5 Hz), 5.18–5.16 (2H, d, J = 10.8 Hz), 4.18–4.12 (4H, m), 4.00 (3H, s), 1.34 (9H, s), 1.32–1.29 (6H, m). ^{13}C NMR (125 MHz, $CDCl_3$) δ (ppm): 193.0, 192.9, 176.7, 161.7, 157.7, 132.4, 122.8, 115.4, 107.1, 73.0, 64.4, 64.3, 56.8, 39.8, 27.3, 16.5. ^{31}P NMR (162 MHz, CD_3COCD_3) δ (ppm): –0.24. HRMS (M + H) calcd for $C_{19}H_{26}O_8PNa$: 425.1341; found: 425.1323.

Diethyl (2-(4-hydroxy-2-methoxyphenyl)-2-oxoethyl) phosphate (30)

NH_4OAc (1.435 g, 18.61 mmol) was added to a stirred solution of 4-(2-(diethoxyphosphoryloxy)acetyl)-2-methoxyphenyl pivalate (**30e**, 468 mg, 1.16 mmol) in aq MeOH

Can. J. Chem. Downloaded from www.nrcresearchpress.com by Xi'an Jiaotong University on 09/19/12
For personal use only.

(H_2O–MeOH, 1:4, 20 mL). The resulting mixture was warmed at 50 °C and the progress of the reaction was monitored by TLC. After 36 h, the reaction mixture was concentrated and the residue was extracted with EtOAc (5 × 10 mL). Combined organic layers were dried over anhyd $MgSO_4$ and the solvent was evaporated to afford diethyl 2-(4-hydroxy-3-methoxyphenyl)-2-oxoethyl phosphate (**30**) as a dark yellow solid that was further purified on silica gel using a gradient solvent system (EtOAc–hexanes (3:1), EtOAc–MeOH (19:1)) to isolate the pure compound as a white crystalline solid (340 mg, 92%), mp 95–98 °C. IR (KBr, cm^{-1}): 3134, 1672, 1602, 1473, 1383, 1337, 1231, 1032, 984, 849. ^{1}H NMR (400 MHz, CD_3COCD_3) δ (ppm): 9.40 (1H, s) 7.83–7.81 (2H, d, J = 8.8 Hz), 6.56 (2H, m), 5.12–5.09 (2H, d, J = 11.2 Hz), 4.20–4.13 (4H, m), 3.94 (3H, s), 1.33–1.29 (6H, m). ^{13}C NMR (125 MHz, CD_3COCD_3) δ (ppm): 191.5, 164.97, 162.9, 133.4, 117.3, 109.4, 99.7, 73.1, 73.0, 64.4, 56.1, 16.5. ^{31}P NMR (162 MHz, CD_3COCD_3) δ (ppm): –0.37. HRMS (M – H) calcd for $C_{13}H_{18}O_7P$: 317.0790; found: 317.0795.

The same protocol was used for the synthesis of **31b** and **31d** except for the final step for **31** and only spectral data are conveyed for these derivatives.

3,5-Dimethoxyphenyl pivalate (31b)

Oil. Yield: 100%. IR (Teflon film, cm^{-1}): 2968–2839, 1751, 1618, 1475, 1130, 1063, 895, 835, 681. ^{1}H NMR (500 MHz, CD_3COCD_3) δ (ppm): 6.38–6.37 (1H, t, J = 2.3 Hz), 6.29 (1H, s), 6.28 (1H, s), 3.77 (6H, s), 1.32 (9H, s). ^{13}C NMR (125 MHz, CD_3COCD_3) δ (ppm): 176.9, 162.2, 154.0, 101.8, 98.4, 55.9, 39.6, 27.4. HRMS (M + Na) calcd for $C_{13}H_{18}O_4Na$: 261.1103; found: 261.1100.

4-(2-Bromoacetyl)-3,5-dimethoxyphenyl pivalate (31d)

White solid. Yield: 20%; mp 125–128 °C. IR (KBr, cm^{-1}): 3018–2841, 1749, 1732, 1597, 1464, 1412, 1221, 1128, 997, 892. ^{1}H NMR (500 MHz, CD_3COCD_3) δ (ppm): 6.53 (2H, s), 4.59 (2H, s), 3.81 (6H, s), 1.33 (9H, s). ^{13}C NMR (125 MHz, CD_3COCD_3) δ (ppm): 193.9, 176.8, 158.9, 155.6, 114.9, 99.7, 56.8, 51.0, 39.7, 27.4. HRMS (M + Na) calcd for $C_{15}H_{19}O_5BrNa$: 381.0314; found: 381.0312.

Diethyl (2-(4-hydroxy-2,6-dimethoxyphenyl)-2-oxoethyl) phosphate (31)

The general methods of Knopik et al.[36] and Das et al.[37] were followed with some modifications. The potassium salt of diethyl phosphoric acid (535 mg, 2.78 mmol) and dibenzo-[18]-crown-6 (50 mg, 0.14 mmol) were added to a stirred solution of 4-(2-bromoacetyl)-3,5-dimethoxyphenyl pivalate (**31d**, 500 mg, 1.40 mmol) in CH_3CN (10 mL). The resulting mixture was stirred at 80 °C and the progress of the reaction was monitored by TLC. After 16 h, the reaction mixture was concentrated and EtOAc (20 mL) was added. The organic layer was washed sequentially with saturated $NaHCO_3$ (40 mL) and water (20 mL) and dried over anhyd $MgSO_4$. The solvent was evaporated to afford the crude product as a yellow-white solid that was chromatographed on silica gel using a gradient solvent system (EtOAc–hexanes (1:2), EtOAc–hexanes (1:1), EtOAc–hexanes (2:1), EtOAc–hexanes (3:1), EtOAc–MeOH (19:1)) to isolate the crude diethyl 2-(4-hydroxy-2,6-dimethoxyphenyl)-2-oxoethyl phosphate as a dark yellow thick oil. Several attempts were made to purify the product on silica gel, but they were unsuccessful. Therefore, the crude product was used in the deprotection step without further purification. NH_4OAc (456 mg, 5.92 mmol) was added to a stirred solution of the crude phosphate from the previous step (160 mg) in aq MeOH (H_2O–MeOH, 1:4, 10 mL). The resulting mixture was warmed at 50 °C and the progress of the reaction monitored by TLC. After 36 h, the reaction mixture was concentrated and the residue was extracted with EtOAc (5 × 10 mL). The combined organic layers were dried over anhyd $MgSO_4$, and the solvent was evaporated to afford diethyl 2-(4-hydroxy-2,6-dimethoxyphenyl)-2-oxoethyl phosphate (**31**) as a yellow-brown thick oil that was further purified by preparative TLC (hexanes–isopropanol–chloroform, 1:1:11) to produce the pure product as a thick yellow oil (10 mg, overall 2%). UV–vis [H_2O–CH_3CN (1:1)] λ_{max} (ε $(mol/L)^{-1}$ cm^{-1}): 283 (5013). IR (Teflon film, cm^{-1}): 2959–2852, 1738, 1593, 1462, 1342, 1261, 1211, 1153, 1028, 800. ^{1}H NMR (400 MHz, CD_3COCD_3) δ (ppm): 9.04 (1H, s), 6.18 (1H, s), 4.81–4.79 (2H, d, J = 9.3 Hz), 4.13–4.05 (2H, m), 3.75 (3H, s), 1.30–1.27 (6H, m). ^{13}C NMR (125 MHz, CD_3COCD_3) δ ppm 196, 162.4, 160.2, 108.8, 92.9, 72.2, 64.4, 56.2, 16.5. ^{31}P NMR (162 MHz, CD_3COCD_3) δ (ppm): –0.75. MS (ESI (–)) m/z calcd for $(C_{14}H_{21}O_8P–H)^-$: 347.0896; found: 347.0887.

3-Acetyl-4-hydroxybenzoic acid (32b)

The general method of Nagano and Matsumura[38] was followed with modifications. Aluminum chloride (2.96 g, 22.2 mmol) was added into a flame-dried three-neck round-bottom flask containing a solution of 4-hydroxybenzoic acid (**32a**; 1.0 g, 5.55 mmol) in nitrobenzene (10 mL) under Ar. The reaction mixture was kept stirring vigorously at 150 °C for 14 h in the three-neck flask fitted with a $CaCl_2$ tube. On cooling, some crushed ice and 10% HCl (50 mL) were added to the flask, and the separated nitrobenzene was removed by distillation. The aqueous phase was extracted with EtOAc (3 × 25 mL) and washed with saturated $NaHCO_3$ solution (3 × 25 mL). The alkaline aqueous phase was acidified with 10% HCl and extracted again with EtOAc (3 × 25 mL). The combined later organic layers were dried over anhyd $MgSO_4$, filtered, and the supernatant concentrated under reduced pressure to afford 3-acetyl-4-hydroxybenzoic acid (**32b**) as a pink colored solid (980 mg, 98%), mp 227–230 °C. IR (KBr, cm^{-1}): 3433, 1684, 1643, 1610, 1578, 1420, 1325, 1296, 1215, 1122, 943, 825, 771. ^{1}H NMR (400 MHz, CD_3COCD_3) δ (ppm): 12.71 (1H, s), 8.56 (1H, s), 8.17–8.15 (1H, d, J = 8.0 Hz), 7.05–7.03 (1H, d, J = 8.0 Hz), 2.77 (3H, s). ^{13}C NMR (125 MHz, CD_3COCD_3) δ (ppm): 166.7, 166.6, 138.1, 134.6, 122.4, 120.2, 119.1, 119.0, 27.0. HRMS (M – H) calcd for $C_9H_7O_4$: 179.0344; found: 179.0323

4-Acetoxy-3-acetylbenzoic acid (32c)

Triethyl amine (1.465 mL, 10.55 mmol) followed by acetyl chloride dropwise (564 μL, 7.91 mmol) was added to a stirred solution of **32b** (950 mg, 5.27 mmol) in dry CH_2Cl_2 (15 mL) under Ar. The reaction mixture was allowed to stir for 45 min at rt. At that point, ethyl acetate (40 mL) was added to the reaction mixture, and the organic phase was

Can. J. Chem. Downloaded from www.nrcresearchpress.com by Xi'an Jiaotong University on 09/19/12
For personal use only.

washed with 10% HCl (3 × 25 mL) followed by saturated $NaHCO_3$ solution (3 × 25 mL). The aqueous fractions from the $NaHCO_3$ extraction were combined, acidified with 10% HCl, and extracted into EtOAc (3 × 25 mL). The EtOAc fractions were combined, dried over anhyd $MgSO_4$, filtered, and the supernatant concentrated under reduced pressure to afford the 4-acetoxy-3-acetylbenzoic acid (**32c**) as a pink solid (820 mg, 70%), mp 125–145 °C (dec.). IR (KBr, cm^{-1}) 3078–2552 (br), 1767, 1689, 1647, 1429, 1296, 1192, 918, 735; ^1H NMR (400 MHz, CD_3COCD_3) δ (ppm): 10.44 (1H, s), 8.48 (1H, d, *J* = 1.8 Hz), 8.23–8.21 (1H, d, *J* = 8.4 Hz), 7.35–7.33 (1H, d, *J* = 8.4 Hz), 2.60 (3H, s), 2.33 (3H, s). ^{13}C NMR (125 MHz, CD_3COCD_3) δ (ppm): 197.3, 169.4, 166.4, 153.5, 138.1, 135.1, 132.3, 129.3, 125.4, 119.1, 27.0, 21.2. HRMS (M – H) calcd for $C_{11}H_9O_5$: 221.0450; found: 221.0440.

1-(3-Acetyl-4-hydroxyphenyl)-2-diazoethanone (32d)

A flame-dried 50 mL round-bottom flask was charged with **32c** (830 mg, 3.74 mmol) and freshly distilled $SOCl_2$ (20 mL) was added under Ar. The resulting mixture was refluxed at 80 °C for 8 h and concentrated under reduced pressure to afford 4-acetoxy-3-acetylbenzoyl chloride as colorless oil. This acid chloride was used in next step without further purification. To a solution of KOH (3.0 g, 53.5 mmol) in 2-methoxyethanol (17 mL) and water (5 mL), diazold (5.0 g, 23.3 mmol) in diethyl ether (75 mL) was added carefully. The resulting mixture was gently heated to reflux temperatures (40–45 °C). The ether layer was distilled into the collection flask in an ice bath at 0 °C. The ether distillate was sequentially dried over KOH pellets for 1 h at 0 °C and with Na pieces for 1 h at 0 °C. Then a solution of acid chloride (899 mg, 3.74 mmol) in dry ether (10 mL) was added dropwise to the distillate (diazomethane) with vigorous stirring at –5 °C. The reaction mixture was allowed to come to 0 °C and stirred overnight. The solvent was evaporated, and the yellowish orange thick oil was used in the deptrotection step without purification. To a stirred solution of crude 2-acetyl-4-(2-diazoacetyl)phenyl acetate (340 mg, 1.38 mmol) in aq MeOH (H_2O–MeOH, 1:4, 20 mL), NH_4OAc (852 mg, 11.05 mmol) was added. The resulting mixture was warmed at 50 °C and the progress of the reaction was monitored by TLC. After 8 h, the reaction mixture was concentrated and the residue was extracted with acetone (5 × 10 mL). The combined organic layers were dried over anhyd $MgSO_4$ and the solvent was evaporated to afford 1-(3-acetyl-4-hydroxyphenyl)-2-diazoethanone (**32d**) as a yellowish brown oil that was further purified on silica gel (hexanes–EtOAc, 1:1) to generate the pure compound as a yellow oil (254 mg, 21% overall yield). IR (Teflon film, cm^{-1}): 3364, 2112, 1761, 1690, 1614, 1418, 1362, 1196, 1150, 1011, 914, 847, 733. ^1H NMR (400 MHz, CD_3COCD_3) δ (ppm): 12.68 (1H, s), 8.40 (1H, d, *J* = 2.2 Hz), 8.04–8.01 (1H, d, *J* = 8.8 Hz), 7.03–7.01 (1H, d, *J* = 8.8 Hz), 6.69 (1H, s), 2.76 (3H, s). ^{13}C NMR (125 MHz, CD_3COCD_3) δ (ppm): 197.5, 185.0, 169.5, 153.2, 135.3, 132.2, 129.6, 125.4, 54.9, 21.2. HRMS (M – H) calcd for $C_{10}H_7N_2O_3$: 203.0457; found: 203.0452.

2-(3-Acetyl-4-hydroxyphenyl)-2-oxoethyl diethyl phosphate (32)

To a stirred solution of **32d** (240 mg, 1.18 mmol) in benzene (10 mL), diethyl phosphoric acid (362 mg, 2.35 mmol) in benzene (5 mL) was added dropwise. The resulting mixture was stirred at 60 °C and the progress of the reaction was monitored by the TLC. After 24 h, EtOAc (20 mL) was added to the reaction mixture. The organic layer was washed sequentially with saturated $NaHCO_3$ (40 mL) and water (20 mL) and then dried over anhyd $MgSO_4$. The solvent was evaporated to afford the crude product as a brownish yellow oil that was chromatographed on silica gel (with a gradient solvent system: EtOAc–hexanes (1:2), EtOAc–hexanes (1:1), EtOAc–hexanes (2:1), EtOAc–hexanes (3:1)) to produce 2-(3-acetyl-4-hydroxyphenyl)-2-oxoethyl diethyl phosphate (**32**) as a thick brown oil (306 mg, 79% yield). IR (Teflon film, cm^{-1}): 3443, 2985–2872, 1703, 1643, 1597, 1369, 1265, 1209, 1153, 1030, 820. ^1H NMR (400 MHz, CD_3COCD_3) δ (ppm): 12.81 (1H, s), 8.59–8.58 (1H, d, *J* = 2.2 Hz), 8.17–8.14 (1H, d, *J* = 8.8 Hz), 7.08–7.06 (1H, d, *J* = 8.8 Hz), 5.42–5.39 (2H, d, *J* = 10.6 Hz), 4.18–4.13 (4H, m), 2.79 (3H, s), 1.33–1.30 (6H, m). ^{13}C NMR (125 MHz, CD_3COCD_3) δ (ppm): 191.6, 167.2, 136.5, 133.3, 126.8, 120.2, 119.4, 119.3, 69.5, 64.6, 27.2, 16.5, 16.4. ^{31}P NMR (162 MHz, CD_3COCD_3) δ (ppm): –0.14. HRMS (M – H) calcd for $C_{14}H_{18}O_7P$: 329.0790; found: 329.0772.

Acknowledgements

This work was supported by National Institutes of Health (NIH) grants GM069663 (R.S.G.) and R01 GM72910 (R.S.G.), grants MSM0021622413 and CZ.1.05/2.1.00/01.0001 (European Union, CETOCOEN) administered by the Ministry of Education, Youth and Sports of the Czech Republic (D.H.), and the Swiss National Science Foundation (J.W.).

References

(1) (a) Givens, R. S.; Park, C.-H. *Tetrahedron Lett.* **1996**, *37* (35), 6259. doi:10.1016/0040-4039(96)01390-1.; (b) Park, C.-H.; Givens, R. S. *J. Am. Chem. Soc.* **1997**, *119* (10), 2453. doi:10.1021/ja9635589.

(2) (a) Conrad, P. G., II; Givens, R. S.; Weber, J. F. W.; Kandler, K. *Org. Lett.* **2000**, *2* (11), 1545. doi:10.1021/ol005856n.; (b) Sul, J.-Y.; Orosz, G.; Givens, R. S.; Haydon, P. G. *Neuron Glia Biol.* **2004**, *1* (01), 3. doi:10.1017/S1740925X04000031.; (c) Conrad, P. G., II; Givens, R. S.; Weber, J. F. W.; Kandler, K. *Org. Lett.* **2000**, *2* (11), 1545. doi:10.1021/ol005856n.; (d) Givens, R. S.; Weber, J. F. W.; Jung, A. H.; Park, C.-H. *Methods Enzymol.* **1998**, *291*, 1. doi:10.1016/S0076-6879(98)91004-7.

(3) (a) Zou, K.; Cheley, S.; Givens, R. S.; Bayley, H. *J. Am. Chem. Soc.* **2002**, *124* (28), 8220. doi:10.1021/ja020405e.; (b) Zou, K.; Miller, T. W.; Givens, R. S.; Bayley, H. *Angew. Chem. Int. Ed.* **2001**, *40* (16), 3049. doi:10.1002/1521-3773(20010817)40:16<3049::AID-ANIE3049>3.0.CO;2-N.; (c) Geibel, S.; Barth, A.; Amslinger, S.; Jung, A. H.; Burzik, C.; Clarke, R. J.; Givens, R.; Fendler, K. *Biophys. J.* **2000**, *79* (3), 1346. doi:10.1016/S0006-3495(00)76387-9.; (d) Arabaci, G.; Guo, X.-C.; Beebe, K. D.; Coggeshall, K. M.; Pei, D. *J. Am. Chem. Soc.* **1999**, *121* (21), 5085. doi:10.1021/ja9906756.; (e) Du, X.; Frei, H.; Kim, S.-H. J. *Biol. Chem.* **2000**, *275* (12), 8492. doi:10.1074/jbc.275.12.8492.

Can. J. Chem. Downloaded from www.nrcresearchpress.com by Xi'an Jiaotong University on 09/19/12
For personal use only.

(4) (a) Givens, R. S.; Goeldner, M., Eds. Dynamic Studies in Biology: Phototriggers, Photoswitches, and Caged Biomolecules, Wiley-VCH Verlag GmbH & Co. KGaA: Weinheim, Germany, 2005; (b) Givens, R. S.; Weber, J. F. W.; Jung, A. H.; Park, C.-H. *Methods Enzymol.* **1998**, *291*, 1. doi:10.1016/S0076-6879(98)91004-7.

(5) Givens, R. S.; Jung, A.; Park, C.-H.; Weber, J.; Bartlett, W. *J. Am. Chem. Soc.* **1997**, *119* (35), 8369. doi:10.1021/ja971331n.

(6) Specht, A.; Loudwig, S.; Peng, L.; Goeldner, M. *Tetrahedron Lett.* **2002**, *43* (49), 8947. doi:10.1016/S0040-4039(02)02194-9.

(7) Anderson, J. C.; Reese, C. B. *Tetrahedron Lett.* **1962**, *3* (1), 1. doi:10.1016/S0040-4039(00)62031-2.

(8) (a) Conrad, P. G., II; Givens, R. S.; Hellrung, B.; Rajesh, C. S.; Ramseier, M.; Wirz, J. *J. Am. Chem. Soc.* **2000**, *122* (38), 9346. doi:10.1021/ja001134f.; (b) Sebej, P.; Lim, B. H.; Park, B. S.; Givens, R. S.; Klan, P. *Org. Lett.* **2011**, *13*, ASC Articles ASAP [Online].

(9) Givens, R. S.; Heger, D.; Hellrung, B.; Kamdzhilov, Y.; Mac, M.; Conrad, P. G.; Cope, E.; Lee, J. I.; Mata-Segreda, J. F.; Schowen, R. L.; Wirz, J. *J. Am. Chem. Soc.* **2008**, *130* (11), 3307. doi:10.1021/ja7109579.

(10) (a) Ma, C.; Zuo, P.; Kwok, W. M.; Chan, W. S.; Kan, J. T. Z.; Toy, P. H.; Phillips, D. L. J. *J. Org. Chem.* **2004**, *69*, 664; (b) Ma, C.; Chan, W. S.; Kwok, W. M.; Zuo, P.; Phillips, D. L. *J. Phys. Chem. B* **2004**, *108* (26), 9264. doi:10.1021/jp0376020.; (c) Ma, C.; Kwok, W. M.; Chan, W. S.; Zuo, P.; Kan, J. T. W.; Toy, P. H.; Phillips, D. L. *J. Am. Chem. Soc.* **2005**, *127* (5), 1463. doi:10.1021/ja0458524.; (d) Ma, C.; Kwok, W. M.; Chan, W. S.; Du, Y.; Kan, J. T. W.; Phillips, D. L. J. *Am. Chem. Soc.* **2006**, *128* (8), 2558. doi:10.1021/ja0532032.; (e) Chan, W. S.; Ma, C.; Kwok, W. M.; Phillips, D. L. *J. Phys. Chem. A* **2005**, *109* (15), 3454. doi:10.1021/jp044546+.; (f) Zuo, P.; Ma, C.; Kwok, W. M.; Chan, W. S.; Phillips, D. L. *J. Org. Chem.* **2005**, *70* (22), 8661. doi:10.1021/jo050761q.; (g) Chen, X. B.; Ma, C.; Kwok, W. M.; Guan, X.; Du, Y.; Phillips, D. L. *J. Phys. Chem. A* **2006**, *110* (45), 12406. doi:10.1021/jp064490e.

(11) Zhang, K.; Corrie, J. E. T.; Munasinghe, V. R. N.; Wan, P. *J. Am. Chem. Soc.* **1999**, *121* (24), 5625. doi:10.1021/ja984187u.

(12) Givens, R. S.; Conrad, P. G., II; Yousef, A. L.; Lee, J.-I. In *Photoremovable protecting groups;* CRC Handbook of Organic Photochemistry and Photobiology; 2nd ed.; CRC Press, Boca Raton, FL, 2004; pp 69/1–69/46.

(13) See Chapter 2.2, pp 110–115 of ref. 4a.

(14) Cao, Q.; Guan, X.; George, M. W.; Phillips, D. L.; Ma, C.; Kwok, W. M.; Li, M.; Du, Y.; Sun, X.-Z.; Xue, J. *Faraday Discuss.* **2010**, *145*, 171 and references therein. doi:10.1039/b908188g.

(15) (a) Stensrud, K. F.; Heger, D.; Šebej, P.; Wirz, J.; Givens, R. S. J. *Photochem. Photobiol.* **2008**, *7* (5), 614. doi:10.1039/b719367j.; (b) Stensrud, K. F.; Noh, J.; Kandler, K.; Wirz, J.; Heger, D.; Givens, R. S. *J. Org. Chem.* **2009**, *74* (15), 5219. doi:10.1021/jo900139h.

(16) (a) Alvarez, F. J.; Schowen, R. L. In *Isotopes in Organic Chemistry;* Buncel, E.; Lee, C. C., Eds., Elsevier Science Ltd: Amsterdam, 1987; Vol. 7, pp 1–59; (b) Kresge, A. J.; More O'Ferrall, R. A.; Powell, M. F. In *Isotopes in Organic Chemistry;* Buncel, E.; Lee, C. C., Eds., Elsevier Science Ltd: Amsterdam, 1987; Vol. 7, pp 177–273; (c) Hegazi, M.; Mata-Segreda, J. F.; Schowen, R. L. *J. Org. Chem.* **1980**, *45* (2), 307. doi:10.1021/jo01290a021.; (d) Quinn, D. M. In *Isotope Effects in Chemistry and Biology;* Kohen, A.; Limbach, H.-H., Eds.; Taylor and Francis, Oxford, UK, 2006; pp 995–1018.

(17) (a) Sheehan, J. C.; Umezawa, K. *J. Org. Chem.* **1973**, *38* (21), 3771. doi:10.1021/jo00961a027.; (b) Cameron, J. F.; Willson, C. G.; Frechet, J. M. J. *J. Am. Chem. Soc.* **1996**, *118* (51), 12925. doi:10.1021/ja954339a.; (c) Banerjee, A.; Falvey, D. E. *J. Org. Chem.* **1997**, *62* (18), 6245. doi:10.1021/jo970495j.; (d) Literák, J.; Dostalova, A.; Klan, P. *J. Org. Chem.* **2006**, *71* (2), 713. doi:10.1021/jo0521551.

(18) (a) Klan, P.; Wirz, J. *Photochemistry of Organic Compounds;* J. Wiley & Sons, Chichester, UK, 2009; (b) Turro, N. J.; Ramamurthy, V.; Scaiano, J. C. *Modern Molecular Photochemistry of Organic Molecules;* University Science Books, Sausalito, CA, 2010.

(19) Bordwell, F. G.; Scamehorn, G. R.; Springer, W. R. *J. Am. Chem. Soc.* **1969**, *91* (8), 2087. doi:10.1021/ja01036a037.

(20) Desilets, D. J.; Kissinger, P. T.; Lytle, F. E. *Anal. Chem.* **1987**, *59* (8), 1244. doi:10.1021/ac00135a040.

(21) Hawker, C. J.; Lee, R.; Frechet, J. M. *J. Am. Chem. Soc.* **1991**, *113* (12), 4583. doi:10.1021/ja00012a030.

(22) Kosugi, M.; Sumiya, T.; Obara, Y.; Suzuki, M.; Sano, H.; Migita, T. *Bull. Chem. Soc. Jpn.* **1987**, *60* (2), 767. doi:10.1246/bcsj.60.767.

(23) Vasquez-Martinez, Y.; Ohri, R. V.; Kenyon, V.; Holman, T. R.; Sepulveda-Boza, S. *Bioorg. Med. Chem.* **2007**, *15* (23), 7408. doi:10.1016/j.bmc.2007.07.036.

(24) Further purification was unnecessary to achieve the target and, therefore, was not pursued. The yield was approximated using ^{1}H NMR with DMF as an internal standard.

(25) Fujita, M.; Hiyama, T. *J. Org. Chem.* **1988**, *53* (23), 5405. doi:10.1021/jo00258a003.

(26) Marsh, J. P.; Goodman, L. *J. Org. Chem.* **1965**, *30* (7), 2491. doi:10.1021/jo01018a528.

(27) Stensrud, K.; Noh, J.; Kandler, K.; Wirz, J.; Heger, D.; Givens, R. S. *J. Org. Chem.* **2009**, *74* (15), 5219. doi:10.1021/jo900139h.

(28) Stensrud, K. F.; Heger, D.; Sebej, P.; Wirz, J.; Givens, R. S. *Photochem. Photobiol. Sci.* **2008**, *7* (5), 614. doi:10.1039/b719367j.

(29) Guizzunti, G.; Brady, T. P.; Malhotra, V.; Theodorakis, E. A. *J. Am. Chem. Soc.* **2006**, *128* (13), 4190. doi:10.1021/ja058259a.

(30) Zhang, K.; Corrie, J. E. T.; Munasinghe, V. R. N.; Wan, P. *J. Am. Chem. Soc.* **1999**, *121* (24), 5625. doi:10.1021/ja984187u.

(31) Gorobets, E.; Sun, G.; Wheatley, B. M. M.; Parvez, M.; Keay, B. A. *Tetrahedron Lett.* **2004**, *45* (18), 3597. doi:10.1016/j.tetlet.2004.03.073.

(32) Miyashita, M.; Shiina, I.; Miyoshi, S.; Mukaiyama, T. *Bull. Chem. Soc. Jpn.* **1993**, *66* (5), 1516. doi:10.1246/bcsj.66.1516.

(33) González-Gomez, J.; Santana, L.; Uriarte, E. *Synthesis 2002* (01), 43. doi:10.1055/s-2002-19292.

(34) Finkelstein, H. *Ber. Dtsch. Chem. Ges* **1910**, *43* (2), 1528. doi:10.1002/cber.19100430257.

(35) Yoh, S. D.; Park, K. H.; Kim, S. H.; Cheong, D. Y. *Tetrahedron* **1989**, *45* (11), 3321. doi:10.1016/S0040-4020(01)81011-5.

(36) Knopik, P.; Bruzik, K. S.; Stec, W. J. *Org. Prep. Proced. Int.* **1991**, *23* (2), 214. doi:10.1080/00304949109458318.

(37) Ramesh, C.; Mahender, G.; Ravindranath, N.; Das, B. *Tetrahedron* **2003**, *59* (7), 1049. doi:10.1016/S0040-4020(02)01635-6.

(38) Nagano, T.; Matsumura, K. *J. Am. Chem. Soc.* **1953**, *75* (24), 6237. doi:10.1021/ja01120a038.

Can. J. Chem. Downloaded from www.nrcresearchpress.com by University of Electronic and Science Techonology of China on 09/18/12
For personal use only.

Deposition of anionic conjugated poly(phenylenevinylene) onto silica nanoparticles via electrostatic interactions — Assembly and single-particle spectroscopy

An T. Ngo, Kai L. Lau, Jeffrey S. Quesnel, Robert Aboukhalil, and Gonzalo Cosa

Abstract: Fluorescent nanoparticles were prepared via adsorption of the conjugated polyelectrolyte poly[5-methoxy-2-(3-sulfopropoxy)-1,4-phenylenevinylene] (MPS-PPV) onto 50 and 100 nm aminosilane functionalized silica beads. The particles were investigated via ensemble and single-molecule or -particle spectroscopy techniques to quantify the effect of the silica bead core on the exciton migration efficiency within the polymer. Ensemble emission spectra and ensemble fluorescence quenching studies with methyl viologen are consistent with good exciton migration along the polymer in the polymer-coated bead. The silica nanobead scaffolding preserves the sensitivity of the free polymer and provides a controllable architecture that minimizes nonspecific interactions. Single-particle spectroscopy studies were conducted on particles immobilized onto the positively charged surface of glass cover slips. Particle immobilization enabled us to monitor the effect of oxygen scavenger solutions on individual particles by changing the surrounding solution. The intensity–time trajectories of individual beads provide a mechanism of signal transduction with potential applications in multiplexing studies. Hundreds of individual beads can be imaged in a rapid parallel fashion.

Key words: fluorescent sensor, water-soluble light-emitting polymer, energy migration, single-molecule spectroscopy, organic–inorganic nanoparticle.

Résumé : On a préparé des nanoparticules fluorescentes par adsorption du polyélectrolyte conjugué poly[5-méthoxy-2-(3-sulfopropoxy)-1,4-phénylènevinylène] (MPS-PPV) sur des billes de silice de 50 et de 100 nm fonctionnalisées avec de l'aminosilane. Afin de quantifier l'effet du coeur de la bille de silice sur l'efficacité de la migration de l'exciton dans le polymère, on a étudié les particules par des techniques de spectroscopie sur l'ensemble et sur les molécules et particules individuelles. Le spectre d'émission de l'ensemble et les études de désactivation de fluorescence par le viologène de méthyle sur l'ensemble sont en accord avec une bonne migration de l'exciton le long du polymère dans la bille couverte de polymère. L'échafaudage de la nanobille de silice permet de préserver la sensibilité du polymère libre et fournit une architecture contrôlable qui minimise les interactions non spécifiques. Des études de spectroscopie sur des particules individuelles ont été effectuées sur des particules immobilisées sur la surface chargée d'une façon positive de lamelles de verre. L'immobilisation des particules nous a permis de suivre l'effet des solutions pièges d'oxygène sur des particules individuelles par un changement de la solution environnante. Les trajectoires d'intensité et temps des billes individuelles fournit un mécanisme de transduction de signal avec des applications potentielles dans des études de multiplexage. Il est possible de faire l'image de centaines de billes individuelles d'une façon parallèle rapide.

Mots-clés : senseur fluorescent, polymère émettant de la lumière soluble dans l'eau, migration d'énergie, spectroscopie de molécule individuelle, nanoparticule organique–inorganique.

[Traduit par la Rédaction]

Introduction

Conjugated polyelectrolytes have attracted interest over the past 10 years as highly sensitive fluorescent molecules for the detection of biological and chemical analytes.[1–5] Their sensitivity stems from the delocalization of the excited state across multiple chromophore segments along the polymer backbone. Rapid exciton migration to molecular quenchers (analytes of interest) located along a polymer backbone accounts for amplified fluorescence quenching[1,2] or superquenching,[5] which gives these polymers a unique sensitivity.

A number of studies have shown that rapid exciton migration is normally encountered in polymer chains that are

Received 25 May 2010. Accepted 5 August 2010. Published on the NRC Research Press Web site at canjchem.nrc.ca on 1 March 2011.

This article is part of a Special Issue dedicated to Professor J. C. Scaiano.

A.T. Ngo, K.L. Lau, J.S. Quesnel, R. Aboukhalil, and G. Cosa.[1] Department of Chemistry, McGill University, 801 Sherbrooke Street West, Montreal, QC H3A 2K6, Canada; Centre for Self-Assembled Chemical Structures (CSACS/CRMAA), McGill University, Otto Maass Bldg, 801 Sherbrooke Street West, Montreal, QC H3A 2K6, Canada.

[1]Corresponding author (e-mail: gonzalo.cosa@mcgill.ca).

Can. J. Chem. Downloaded from www.nrcresearchpress.com by University of Electronic and Science Techonology of China on 09/18/12
For personal use only.

highly folded and (or) aggregated, where through-space energy transfer is a viable transport mechanism, but it is not common in extended polymer chains, where through-bond energy transfer is the dominant exciton transport mechanism.[6–8] Conditions that favour the aggregation of the polymer are therefore more conducive to rapid exciton transport and highly sensitive quenching.

The deposition of conjugated polyelectrolytes onto silica beads[9–12] or other substrates[13,14] via electrostatic interaction[15] has been proposed by a number of researchers as a means of providing a well-controlled environment with increased polymer backbone interaction that would allow for faster exciton transport and thus greater sensitivity in the conjugated polymer. Whitten and co-workers have explored the use of μm-sized beads coated with a cationic poly(phenylene ethynylene) (PPE) conjugated polyelectrolyte, which is in turn coated by a lipid bilayer, to report upon the degradation of the lipid bilayer by surfactants[9] or phospholipase enzymes.[11] Schanze and co-workers[16] have exploited the singlet-oxygen-producing ability of such supported conjugated polyelectrolytes as a potential biocide. Finally, Swager and co-workers,[10,17] working on sub-μm beads and employing a layer by layer deposition strategy, have reported on the preparation of 200 nm beads with alternating quaternary ammonium polycations and negatively charged PPE. They observed that the sensitivity of the 200 nm silica-bead-supported PPE increased upon the deposition of multiple PPE layers.[10]

Here we report on the functionalization of silica nanobeads (50 and 100 nm in diameter) with aminosilane groups and their subsequent coating with the anionic conjugated polyelectrolyte poly(phenylene vinylene) poly[5-methoxy-2-(3-sulfopropoxy)-1,4-phenylenevinylene] (MPS-PPV). We also describe the characterization of these particles via both ensemble and single-particle spectroscopy. Ensemble emission spectra and ensemble fluorescence quenching studies with methyl viologen are consistent with good exciton migration along the polymer in the polymer-coated bead. Single-particle studies on the nanobeads provide insight into the polymer photophysics and illustrate the use of conjugated polyelectrolytes in novel fluorescent assays, where the intensity–time trajectories of individual nanobeads provide a mechanism of signal transduction with potential applications in multiplexing studies. Hundreds of individual beads can be imaged in a rapid parallel fashion.

Results and discussion

Preparation of MPS-PPV-coated SiO_2 beads

To enable the adsorption of anionic MPS-PPV via electrostatic interactions, we first functionalized the silica beads with aminosilane groups to render them cationic. Anionic silica nanoparticles 50 and 100 nm in diameter were functionalized with 3-aminopropyltrimethoxysilane following the procedure described by Haller and co-workers.[18] 3-Aminopropyltrimethoxysilane (97%) was added to a suspension of silica nanoparticles in water. The concentration of nanobeads (stated as mol of bead/L unless otherwise specified) was 9.10×10^{-8} mol/L for 100 nm beads (5.65 wt% silica, d = 1.027 g/mL) and 3.7×10^{-6} mol/L for 50 nm beads (20–21 wt% silica). After several seconds of vortexing, 38% (12 N) HCl was added to quench the reaction. This was followed by thorough washing of the beads with distilled deionized water in various precipitation–resuspension steps. The functionalization process was verified by measuring the bead ζ potential (Figs. 1A and 1B). Prior to functionalization, and owing to the deprotonated silanol groups on the bead surface, the beads exhibited negative ζ potentials of –56 ± 13 mV (50 nm beads) and –38 ± 2 mV (100 nm beads). Functionalization introduced amine groups at an optimal ratio of three hydroxyl groups to one amine (Scheme 1). This reversed the sign of the surface potential at neutral pH, producing ζ potential values of +43 ± 9 mV (50 nm beads) and +37 ± 11 mV (100 nm beads). Functionalization did not affect the mean hydrodynamic diameter of the 50 or 100 nm beads, but produced a slight broadening in the size distribution of the 100 nm beads. The functionalized beads were used within 3 months following the aminosilanization, although the colloidal suspensions may be stable for years.[18]

Scheme 1. Amine functionalization of silica beads (drawing not to scale).[18]

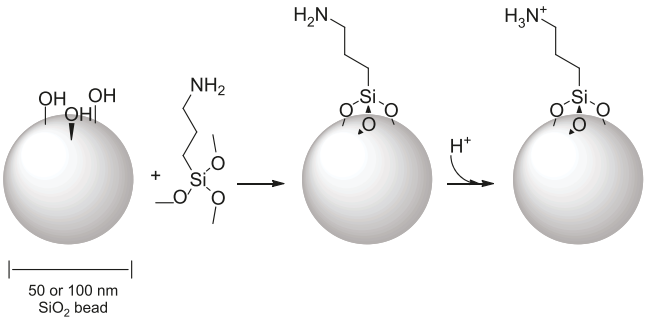

The beads were next coated with the conjugated polyelectrolyte MPS-PPV by adding aliquots of bead solution slowly, with mixing,[9] to ca. stoichiometric amounts of MPS-PPV in 1 mmol/L sodium acetate buffer, pH 5.80. A number of steps consisting of bead addition to MPS-PPV solutions, mechanical agitation, centrifugation, supernatant removal, and resuspension (first in a fresh MPS-PPV solution, and after 3 cycles, in a 1 mmol/L *N*-(2-hydroxyethyl)-piperazine-*N*′-ethanesulfonic acid (HEPES, pH 7.3) buffer for the next 4 cycles) followed. Use of insufficient polymer during the initial step of the coating procedure was visually indicated by a colourless rather than an orange supernatant (which is otherwise seen and indicates a large amount of un-adsorbed polymer). The order of addition (beads to polymer) was important to prevent aggregation between partially coated beads.

The coating process was verified by ζ potential and dynamic light scattering (Fig. 1). Following coating with MPS-PPV, the 50 and 100 nm beads exhibited ζ potentials of –34 ± 19 and –37 ± 22 mV, respectively. We measured a mean hydrodynamic diameter of 140 nm ± 14 nm for the MPS-PPV-coated 100 nm silica beads ($S100^{-}NH_3^{+}PPV^{-}$) (see Fig. 1B), which was within the standard deviation of the starting amino-functionalized bead ($S100^{-}NH_3^{+}$) diameter, 122 nm ± 25 nm. We may conclude that the coated beads formed no dimers or larger aggregates. In contrast the

Can. J. Chem. Downloaded from www.nrcresearchpress.com by University of Electronic and Science Techonology of China on 09/18/12
For personal use only.

Fig. 1. Zeta (ζ) potential (A) and mean hydrodynamic diameter (B) upon functionalization and coating of silica nanobeads with the anionic conjugated polyelectrolyte poly[5-methoxy-2-(3-sulfopropoxy)-1,4-phenylenevinylene] (MPS-PPV). Two different bead diameters (50 and 100 nm) were studied. S50, S100, anionic silica nanobeads; $S50^{-}NH_3^{+}$, $S100^{-}NH_3^{+}$, amine-functionalized silica nanobeads; and $S50^{-}NH_3^{+}PPV^{-}$, $S100^{-}NH_3^{+}PPV^{-}$, MPS-PPV coated onto amine-functionalized silica nanobeads.

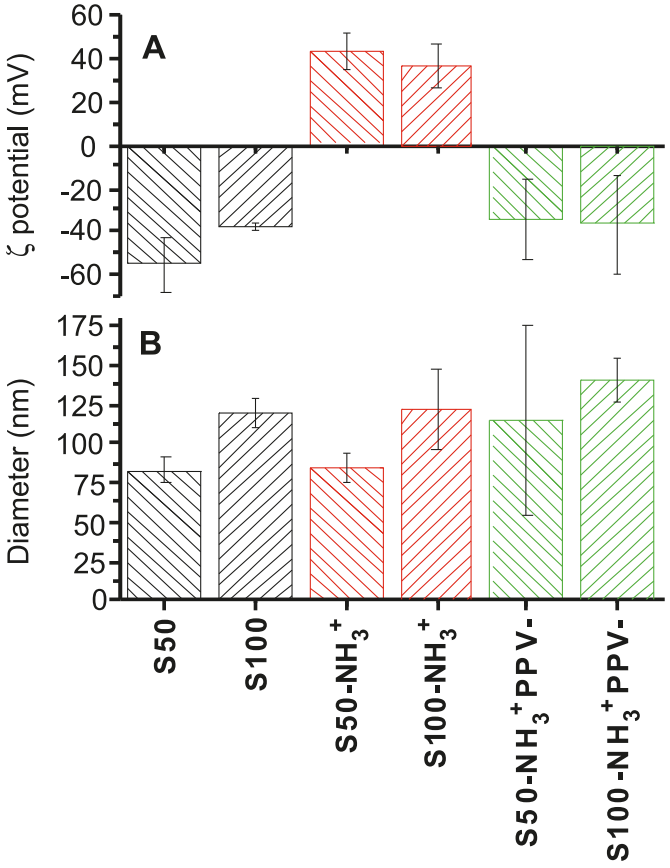

50 nm silica beads had an average diameter of 83 nm ± 8 nm when bare ($S50^{-}NH_3^{+}$) and 115 nm ± 60 nm when coated ($S50^{-}NH_3^{+}PPV^{-}$) (Fig. 1B). This increase in size would indicate that particle dimerization occurred during polymer coating.

The amount of MPS-PPV coating was next quantified by UV–vis absorbance of the supernatants. A final value of 69% coverage was calculated assuming one MPS-PPV monomer per 0.36 nm^2 of bead surface.[19] Table 1 shows representative absorbance values for the supernatants in the bead-coating procedure. We may note that the first three supernatants contained polymer that did not adsorb onto the beads when the beads were exposed to free polymer solutions on three consecutive resuspension–precipitation cycles. Also, the fraction of polymer remaining in solution increased substantially in consecutive cycles, consistent with significant coating occurring in the first adsorption cycle. The last five supernatants listed in Table 1 correspond to washing cycles. These supernatants contain excess polymer that was washed off the beads after coating in the first three cycles. Here the amount of polymer washed from the beads decreases with washing cycles.

Absorption and fluorescence

Following the preparation of MPS-PPV-coated nanobeads, we characterized them via ensemble spectroscopy. We acquired UV–vis absorption spectra after subtracting the contribution owing to scattering from the beads. Given that these beads are 6- to 100-fold smaller than those silica beads previously reported by other groups,[9–12] their light scattering is less pronounced at wavelengths where MPS-PPV absorbs. No major spectral differences were observed upon comparing the absorption or emission spectra of the MPS-PPV coated beads to those of the free polymer in solution (Fig. 2). The relative emission quantum yields (Φ_f) were also determined upon 450 nm excitation; MPS-PPV adsorption to silica beads reduced its emission quantum yield by 30%–50% (Table 2).

Fluorescence quenching studies

We next conducted ensemble quenching studies on MPS-PPV-coated beads and on free MPS-PPV employing methyl viologen (MV^{2+}) as a quencher.[3,14,20,21] The results are summarized in Table 3 and illustrated in Fig. 3. Whereas MPS-PPV coated onto 100 nm beads had essentially the same Stern–Volmer fluorescence quenching constant as the free polymer, MPS-PPV coated onto 50 nm beads exhibited a threefold increase in the Stern–Volmer constant (K_{sv}) compared with free polymer, this change may be accounted for by electronic and surface effects different in each of the two beads. Electronic and surface effects upon adsorption onto beads have been shown to magnify the K_{sv} of other fluorescent polymers (with respect to nitroaromatic quenchers) by up to 200-fold.[10,17]

The upward curvature observed in the Stern–Volmer plots (Fig. 3D) likely indicates that more than one quenching mechanism is operational, such as a combination of both static and dynamic quenching.[22] For free MPS-PPV, it has been shown that deviation from linearity with increasing quencher concentration arises from MV^{2+}-mediated aggregation of the polyanionic polymer.[23] Aggregation in turn increases the probability of exciton migration to the quencher site and leads to enhanced sensitivity to the quencher.[24]

Counter ion induced aggregation should play a less significant role when MPS-PPV is coated onto aminosilanized silica beads. Whereas deviations from linearity are not significant in 100 nm beads, they are, however, observed in quenching plots of MPS-PPV coated onto 50 nm beads. This observation, together with some extent of blue shift in the emission spectra with increasing MV^{2+} (see the following) would point to either the presence of short MPS-PPV oligomers in solution or to the presence of labile, nonaggregated, fragments on the surface.

We note that following increasing additions of quencher, the free MPS-PPV exhibited a gradual blue shift (Fig. 3) from 567 to 553 (3.52×10^{-7} mol/L) to 543 nm (5.57×10^{-7} mol/L MV^{2+}) and then finally to 519 nm (9.49×10^{-7} mol/L). Such a marked shift is not observed with MPS-PPV adsorbed onto silica beads. MPS-PPV coated onto 50 nm beads exhibits a small blue shift, from 570 (no MV^{2+}) to 561 nm (2.34×10^{-7} mol/L MV^{2+}); the blue shift for MPS-PPV coated onto 100 nm beads is negligible, from 567 (no MV^{2+}) to 563 nm (5.55×10^{-7} mol/L MV^{2+}).

Can. J. Chem. Downloaded from www.nrcresearchpress.com by University of Electronic and Science Techonology of China on 09/18/12
For personal use only.

Table 1. Percent coverage of 100 nm beads determined from absorbance of supernatants during the coating process.

		Adsorbed PPV		Desorbed PPV	
Supernatant	Concn (mol/L)	mol/L	%	mol/L	%
1	6.9×10^{-5}	6.5×10^{-5}	57.2		
2	1.2×10^{-4}	1.5×10^{-5}	13.0		
3	1.3×10^{-4}	7.6×10^{-6}	6.7		
4	4.7×10^{-6}			4.6×10^{-6}	4.1
5	1.9×10^{-6}			1.9×10^{-6}	1.7
6	1.0×10^{-6}			1.0×10^{-6}	0.9
7	1.0×10^{-6}			1.0×10^{-6}	0.9
8	7.5×10^{-7}			7.5×10^{-7}	0.7

Note: MPS-PPV, poly[5-methoxy-2-(3-sulfopropoxy)-1,4-phenylenevinylene]. The volume of each supernatant was 900 μL; 100 nm beads = 1.3 nmol/L; [MPS-PPV] = 1.34×10^{-4} mol/L for cycles 1–3. A molar extinction coefficient value of 3460 $(mol/L)^{-1}$ cm^{-1}, calculated in terms of monomer repeat units, was utilized for MPS-PPV. Stoichiometry: 1 MPS-PPV monomer repeat unit per 0.36 nm^2 of bead surface.[19]

Fig. 2. Poly[5-methoxy-2-(3-sulfopropoxy)-1,4-phenylenevinylene (MPS-PPV) absorption (A) and emission (B) spectra when adsorbed to 50 and 100 nm beads and when free in solution. Fluorescence was measured upon 450 nm excitation of optically matched MPS-PPV solutions; fluorescence spectra are normalized with respect to free polymer. All spectra were taken at pH 7.3 in 1 mmol/L *N*-(2-hydroxyethyl)piperazine-*N*′-ethanesulfonic acid (HEPES). 2.0×10^{-5} mol/L MPS-PPV (□), $S100^-NH_3^+PPV^-$, [beads] = 5×10^{-10} mol/L (○), and $S50^-NH_3^+PPV^-$, [beads] = 4.6×10^{-9} mol/L (△).

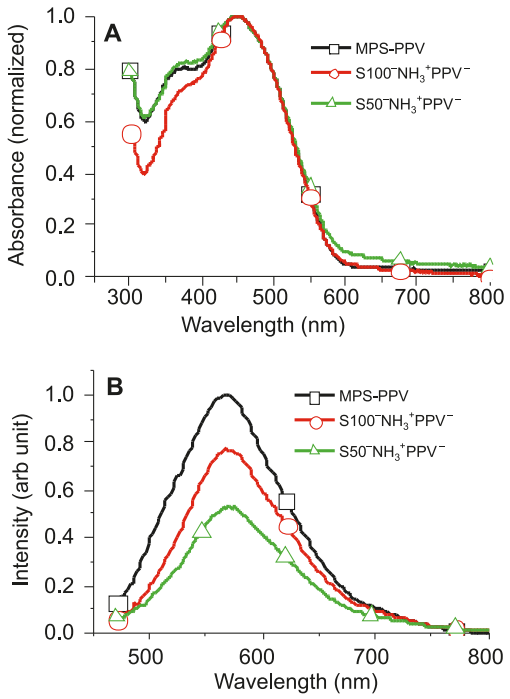

Likely, the blue shift observed in free polymer with increasing quencher concentration arises from the presence of short MPS-PPV oligomers in solution or the presence of labile, nonaggregated, fragments on the surface, which are not quenched under the sub-μmol/L quencher concentrations employed herein.

Table 2. Effect of bead support (100 and 50 nm) on the relative fluorescence quantum yield of poly[5-methoxy-2-(3-sulfopropoxy)-1,4-phenylenevinylene] (MPS-PPV) at 450 nm in 1 mmol/L *N*-(2-hydroxyethyl)piperazine-*N*′-ethanesulfonic acid (HEPES) (pH 7.3).

Sample	Φ_f (relative)
MPS-PPV	1.0
$S100^-NH_3^+PPV^-$	0.7
$S50^-NH_3^+PPV^-$	0.5

Table 3. Stern–Volmer constants (K_{sv}) for free poly[5-methoxy-2-(3-sulfopropoxy)-1,4-phenylenevinylene] (MPS-PPV) compared with MPS-PPV coated onto beads of 50 and 100 nm diameters.

Sample	K_{sv}
MPS-PPV	$2.61(\pm0.05)\times10^6$
$S50^-NH_3^+PPV^-$	$8.3(\pm0.3)\times10^6$
$S100^-NH_3^+PPV^-$	$2.2(\pm0.04)\times10^6$

Note: All Stern–Volmer constants were measured in 1 mmol/L *N*-(2-hydroxyethyl)piperazine-*N*′-ethanesulfonic acid (HEPES, pH 7.3). The error from the linear fit is indicated in parentheses.

Fluorescence enhancement upon nonspecific interactions with proteins

As part of the characterization of the MPS-PPV-coated silica beads we next studied the effects of nonspecific interactions with proteins on the polymer photophysics. Hydrophobic and electrostatic interactions with proteins can affect the fluorescence and quenching of conjugated polyelectrolytes free in solution.[25,26] An intensity enhancement and a blue shift in intensity, as well as a reduced Stern–Volmer fluorescence quenching constant all constitute signature features of the nonspecific interaction of conjugated polyelectrolyte

Can. J. Chem. Downloaded from www.nrcresearchpress.com by University of Electronic and Science Techonology of China on 09/18/12
For personal use only.

Fig. 3. Quenching of poly[5-methoxy-2-(3-sulfopropoxy)-1,4-phenylenevinylene] (MPS-PPV) by methyl viologen (MV^{2+}). (A), (B), and (C) show the fluorescence spectra under increasing [MV^{2+}] for (A) MPS-PPV 2.0×10^{-5} mol/L, (B) $S50^{-}NH_3^{+}PPV^{-}$ (the solution was 4.6×10^{-9} mol/L in beads and 2.0×10^{-5} mol/L in MPS-PPV), and (C) $S100^{-}NH_3^{+}PPV^{-}$ (the solution was 5×10^{-10} mol/L in beads and 2.0×10^{-5} mol/L in MPS-PPV). (D) The Stern–Volmer quenching plots and the linear fit to the first few experimental points for the various particles under study. Excitation was performed at 440 nm.

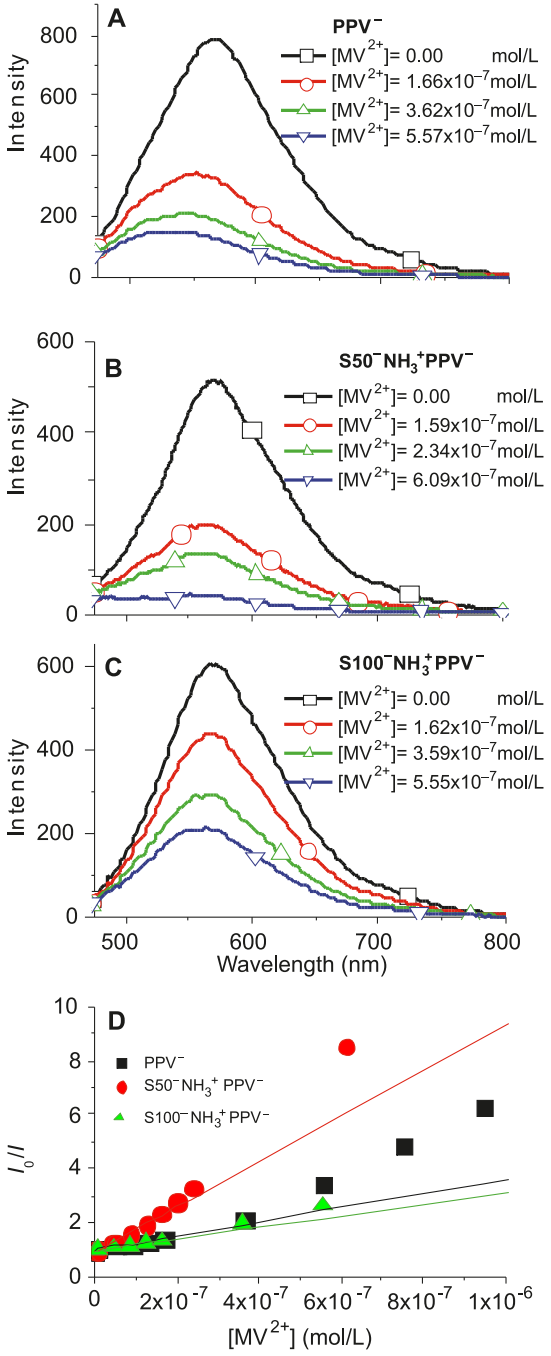

MPS-PPV with hydrophobic media.[27,28] The potential for these interactions must be taken into account when designing detection platforms utilizing conjugated polyelectrolytes.[29] By controlling the aggregation state of the polyelectrolyte, a silica bead support has the potential to minimize such effects.

Fig. 4. Bovine serum albumin (BSA, 69 kDa) added to 3.0×10^{-5} mol/L poly[5-methoxy-2-(3-sulfopropoxy)-1,4-phenylenevinylene] (MPS-PPV) and $S100^{-}NH_3^{+}PPV^{-}$. (A) Intensity enhancement, from integrated areas of background-subtracted peaks, for MPS-PPV (black) and for $S100^{-}NH_3^{+}PPV^{-}$ (red). (B) Normalized emission spectra at 450 nm excitation. MPS-PPV free (■), MPS-PPV plus 5 mg/mL BSA (□), $S100^{-}NH_3^{+}PPV^{-}$ (●), $S100^{-}NH_3^{+}PPV^{-}$ plus 5 mg/mL BSA (○). All solutions were in 1 mmol/L *N*-(2-hydroxyethyl)piperazine-*N*′-ethanesulfonic acid (HEPES, pH 7.3).

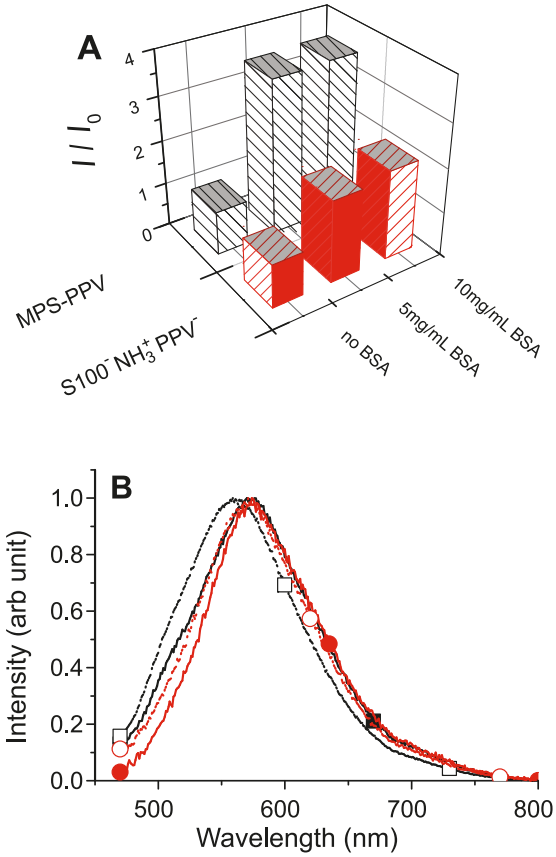

We exposed $S100^{-}NH_3^{+}PPV^{-}$ beads and free MPS-PPV to bovine serum albumin (BSA), a 69 kDa protein that has known surfactant properties. The fluorescence of the free MPS-PPV was enhanced 3.5-fold and blueshifted by 12 nm (576–564 nm), whereas the fluorescence of $S100^{-}NH_3^{+}PPV^{-}$ beads underwent only a twofold enhancement and no blue shift (Fig. 4). The bead-support configuration thus minimizes the fluorescence effects of nonspecific interactions on conjugated polyelectrolytes. It is also foreseeable to decorate the beads with suitable receptors for the specific (and sensitive) detection of analytes of interest.

Single-particle studies

We next used single-particle total internal reflection fluorescence microscopy (TIRF) to examine the initial intensity distribution and the evolution of intensity over time for $S50^{-}NH_3^{+}PPV^{-}$ and $S100^{-}NH_3^{+}PPV^{-}$ beads. Our imaging experiments were conducted both in air-saturated buffered solution and in a buffered solution containing an oxygen

Can. J. Chem. Downloaded from www.nrcresearchpress.com by University of Electronic and Science Techonology of China on 09/18/12
For personal use only.

Fig. 5. Poly[5-methoxy-2-(3-sulfopropoxy)-1,4-phenylenevinylene] (MPS-PPV) coated 100 nm beads ($S100^{-}NH_3^{+}PPV^{-}$) in 1 mmol/L *N*-(2-hydroxyethyl)piperazine-*N*′-ethanesulfonic acid (HEPES, pH 7.3), imaged in the absence (A) and presence (C) of glucose oxidase oxygen scavenger. Initial intensity histograms ((B) and (D)) are also shown for both conditions. Samples were illuminated via 488 nm excitation at 6.0 mW laser power, 500 ms exposure time, and a flow rate of 1 μL/min.

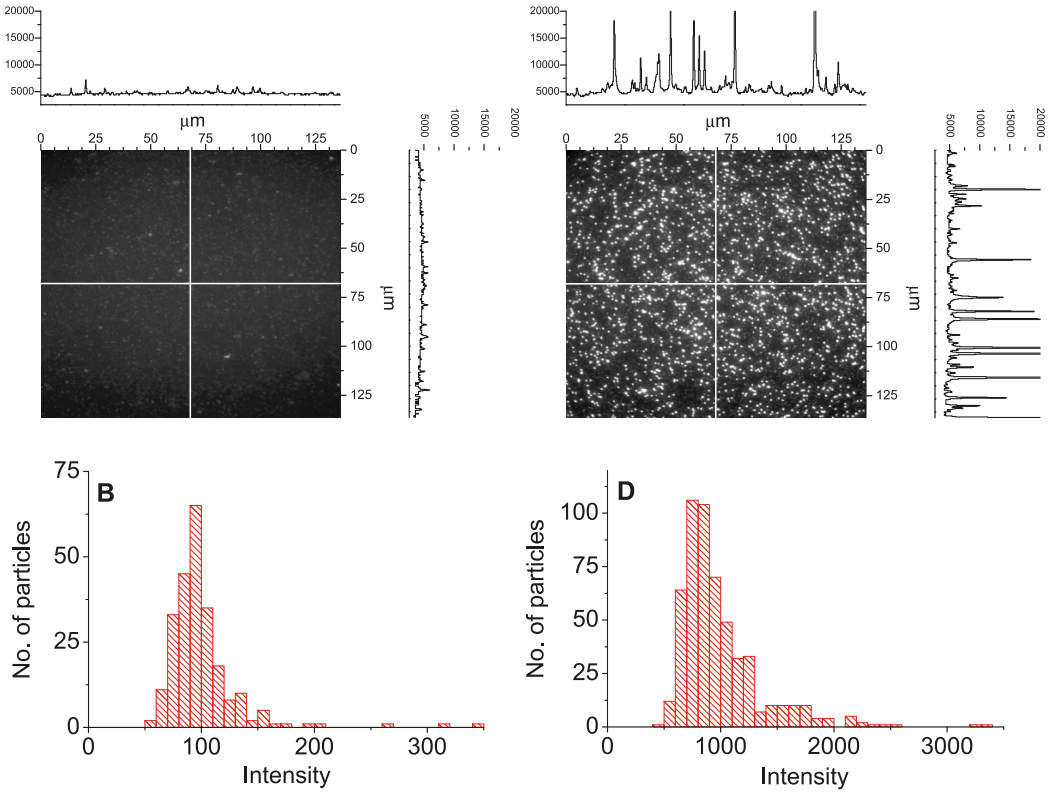

Fig. 6. Effect of oxygen scavenger on the photobleaching of poly[5-methoxy-2-(3-sulfopropoxy)-1,4-phenylenevinylene] (MPS-PPV) coated 50 nm beads ($S50^{-}NH_3^{+}PPV^{-}$). Samples were imaged at 500 ms integration time, at 6.0 mW ± 0.2mW laser power, in 1 mmol/L *N*-(2-hydroxyethyl)piperazine-*N*′-ethanesulfonic acid (HEPES, pH 7.3), and at a flow rate of 1 μL/min, in the presence and absence of glucose oxidase oxygen scavenger. (A)–(B) $S50^{-}NH_3^{+}PPV^{-}$ beads imaged in buffer, no oxygen scavenger (EMCCD gain = 3200). (C)–(D) $S50^{-}NH_3^{+}PPV^{-}$ beads imaged in oxygen scavenger (EMCCD gain = 1700). Examples of stepwise photobleaching behaviour are shown in (A) buffer and (C) oxygen scavenger. Examples of exponential decay are shown in (B) buffer and in (D) oxygen scavenger.

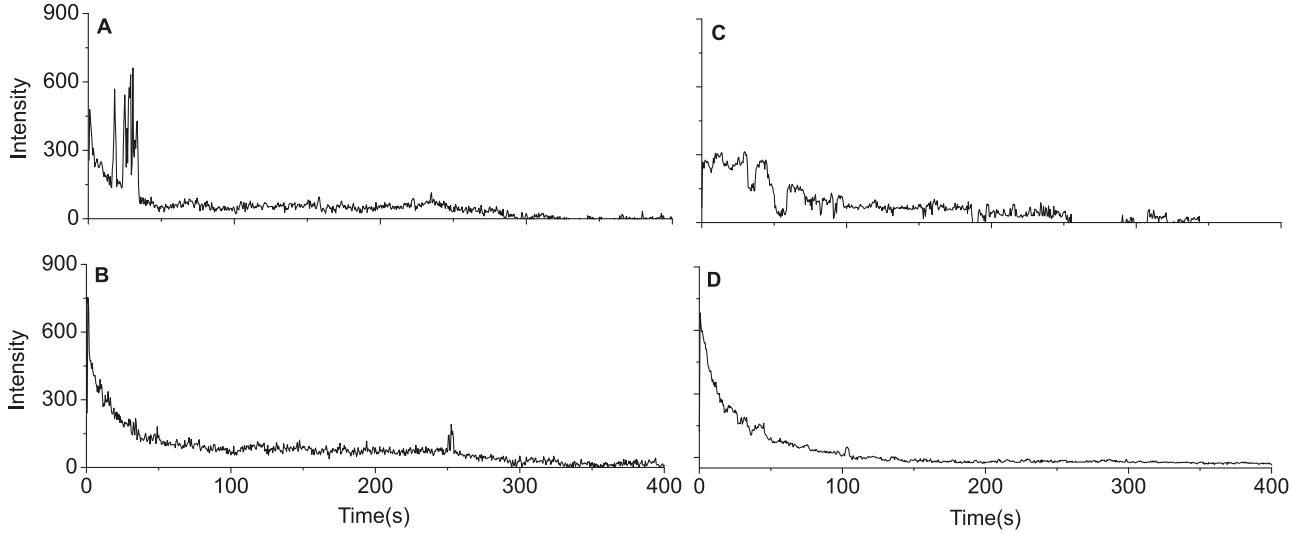

scavenger mixture consisting of α-D-glucose, glucose oxidase, catalase, and β-mercaptoethanol.[30]

We observed that when immersed in the oxygen scavenger solution the emission intensity and the photostability of the MPS-PPV-coated beads increased dramatically when compared with air-saturated solutions. We noted a ca. fourfold

Can. J. Chem. Downloaded from www.nrcresearchpress.com by University of Electronic and Science Techonology of China on 09/18/12
For personal use only.

increase in the survival time and an eightfold intensity increase over the air-saturated solution (Figs. 5 and 6). When the particles were monitored in a solution of glucose oxidase and catalase, with no glucose oxidase substrate α-D-glucose, no difference was observed vs air-saturated solutions (not shown). The glucose oxidase – catalase effect on the emissive properties of the particles thus arises from the oxygen-scavenging activity of the mixture rather than nonspecific protein-conjugated polyelectrolyte interactions. Ensemble experiments conducted with BSA (vide supra) further show that nonspecific interactions with proteins have only a minor effect on the photophysical properties of MPS-PPV-coated silica nanoparticles.

Oxygen in the solution is known to quench the emission of PPV-based conjugated polymers, where both reversible and irreversible quenching pathways may take place. For poly[2-methoxy-5-(2'ethyl-hexyloxy)1,4-phenylene-vinylene] (MEH-PPV) it has been shown that singlet-oxygen mediated photo-oxidation leads to the formation of carbonyl groups at the vinyl bond that turn the polymer irreversibly nonemissive.[31,32] Likely, a similar quenching phenomenon is observed with the closely related polymer MPS-PPV utilized in our studies. The glucose oxidase – catalase system,[30] widely used in single-molecule spectroscopy,[33] decreases the amount of oxygen in the solution, preventing oxidative damage to the fluorophore and lengthening its lifetime. The addition of β-mercaptoethanol further reduces the possibility of singlet-oxygen sensitization by the conjugated-polymer triplet states, since β-mercaptoethanol is a well-known triplet quencher.[34] The combined effect of the triplet quenching by β-mercaptoethanol and the oxygen depletion by glucose oxidase – catalase ultimately leads to a ca. 40-fold increase in the number of photons recorded per particle prior to their irreversible photobleaching. Preliminary experiments further show that β-mercaptoethanol on its own can also affect the fluorescence quantum yield. We are currently investigating the source of this effect.

Single-particle spectroscopy allows for the detection of multiple populations within a given sample.[35] Intensity–time trajectories report upon the extent of interchromophore communication in conjugated polymers[7,36], where on–off single-step transitions, characteristic of single chromophores, will indicate good electronic contact and (or) efficient exciton transport,[8,36,37] and intensity–time trajectories showing an exponential drop in emission over time will reflect on poor exciton transport and the presence of a large number of unrelated chromophores.[7]

Upon analyzing more than 500 intensity–time trajectories recorded for either $S50^{-}NH_3^{+}PPV^{-}$ or $S100^{-}NH_3^{+}PPV^{-}$, we observed that most beads exhibited a gradual photobleaching with time both in an oxygen scavenger solution[30] containing glucose oxidase and in an air-saturated solution (buffer only, no glucose oxidase). Given the time resolution of our experiments, where frames were acquired every 500 ms, the occasional stepwise photobleaching behaviour that we noticed, particularly in air-saturated solutions (see Figs. 6A and 6C) may be ascribed to rapid photobleaching of a number of chromophores in the particle within a given 500 ms frame. Indeed, in oxygen-scavenger-containing solutions we observed virtually no steps in the intensity photobleaching.

We note that there is no evidence that the particles behave as a single quantum state (i.e., particles undergoing one-step photobleaching much like single chromophores do) neither for 50 nor 100 nm MPS-PPV-coated beads. Such behaviour is, however, observed in single MPS-PPV polymer particles in solution or in MEH-PPV particles spin cast in a polymer matrix. The amount of polymer material required to coat the silica beads is likely too large for the exciton to explore the whole bead surface during the excited-state lifetime.

Conclusion

In conclusion, the anionic light-emitting poly(phenylene vinylene) MPS-PPV was adsorbed onto silica nanobeads of 50 and 100 nm diameter towards the creation of a novel material for fluorescence detection and imaging. The increased K_{SV} and decreased quantum yield in PPV-coated beads indicate that the bead support promotes interchain contact, as has been observed for poly(phenylene-ethynylene). The PPV-coated beads were further resistant to fluorescence modifications induced by nonspecific binding to serum proteins. Particle immobilization enabled us to monitor the effect of oxygen scavenger solutions on individual particles by changing the surrounding solution. Hundreds of individual beads can be imaged in a rapid parallel fashion. Glucose oxidase – catalase oxygen scavenger caused an eightfold increase in fluorescence intensity and a fourfold increase in the emissive time prior to photobleaching, which is consistent with reducing the possibility of permanent oxidative damage to the fluorophore. The intensity–time trajectories of individual beads provide a mechanism of signal transduction with potential applications in multiplexing studies. Our results provide new insights into the development of fluorescent sensors based on immobilized silica nanoparticles coated with water-soluble poly(phenylene vinylene) derivatives.

Experimental

Materials

Silica beads 100 nm (±30 nm) in diameter and 5.65 wt% in water were purchased from Polysciences Inc. (Warrington, Pennsylvania). Silica beads 40–50 nm in diameter and 20–21 wt% in water were generously provided free of charge from Nissan Chemical Industries Ltd. (Houston, Texas). Methyl viologen (MV^{2+}), 3-aminopropyltrimethoxysilane (97%), β-mercaptoethanol (14.3 mol/L), D-(+)-glucose (minimum 99.5%), and a 0.25 wt% solution of MPS-PPV in distilled deionized water were purchased from Sigma-Aldrich (Oakville, Ontario). Acetone, HPLC grade, 99.5% was obtained from ACP Chemicals Inc. (Montreal, Quebec). Vectabond was acquired from Vector Laboratories (Burlingame, California). Catalase (beef liver) and glucose oxidase were obtained from Roche Diagnostics (Indianapolis, Indiana). HEPES buffer (1 mol/L, pH 7.3, for molecular biology), acetic acid (99.7%), and sodium acetate (99.3%) were purchased from Fisher Scientific Canada (Ottawa, Ontario).

Functionalization of silica beads

Amino-silanized 100 nm silica beads ($S100^{-}NH_3^{+}$)

To 100 μL of 100 nm (±30 nm) silica beads, 5.65 wt% in water (9.1×10^{-8} mol/L beads), was added 0.16 mL of

Can. J. Chem. Downloaded from www.nrcresearchpress.com by University of Electronic and Science Techonology of China on 09/18/12
For personal use only.

3-aminopropyltrimethoxysilane (97%). The sample was vortexed for several seconds and incubated at room temperature for 5 min. 0.5 mL of 38% HCl was then added to protonate the amine groups. The sample was again vortexed thoroughly and centrifuged at 16 060*g* (13 000 rpm on a Fisher Accuspin microcentrifuge) for 5 min. 0.5 mL of the supernatant was replaced with 1 mL of MilliQ water. The beads were resuspended by brief sonication and then centrifuged. One millilitre of the supernatant was replaced with 1 mL of water; this wash step was repeated two additional times or until the pH of the supernatant was between 5 and 7. The samples were stored at 4 °C for up to 6 months. Yield: ~1 mL of 7.2×10^{-9} mol/L amino-silanized beads of 100 nm diameter ($S100^{-}NH_3^{+}$) in water.

Amino-silanized 50 nm silica beads ($S50^{-}NH_3^{+}$)

To 100 μL of 50 nm (±10 nm) silica beads, 20–21 wt% in water (3.65×10^{-6} mol/L beads), was added 0.05 mL of 3-aminopropyltrimethoxysilane (97%). The procedure for functionalizing 50 nm beads was otherwise identical to the procedure for the functionalization of 100 nm beads.

Amino-silanized PPV-coated 100 nm silica beads ($S100^{-}NH_3^{+}PPV^{-}$)

Aliquots of beads in water were added slowly, dropwise with agitation, to a solution of 1.4×10^{-4} mol/L MPS-PPV for a final bead concentration of 1.3×10^{-9} mol/L. The sample was vortexed for 1 h, incubated at room temperature for 1 h, and centrifuged at 16 060*g*. The supernatant was replaced with 1.4×10^{-4} mol/L MPS-PPV; the beads were resuspended by brief sonication and vortex, vortexed for 1 h and incubated at room temperature for 30 min, then centrifuged at 16 060*g*. The supernatant was replaced with 1.4×10^{-4} mol/L MPS-PPV; after resuspension the beads were vortexed for 10 min and incubated at room temperature for 15 min. The sample was then centrifuged, and the supernatant replaced with 1 mmol/L HEPES (pH 7.3) buffer. After resuspension in HEPES buffer, the beads were vortexed for 10 min and incubated at room temperature for 15 min. The sample was then centrifuged and the supernatant replaced with fresh buffer solution. This washing step was repeated four times.

Amino-silanized PPV-coated 50 nm silica beads ($S50^{-}NH_3^{+}PPV^{-}$)

The procedure was identical to that employed with 100 nm beads other than a final bead concentration of 1.3×10^{-8} mol/L was achieved when aliquots of beads were added to MPS-PPV solutions.

Dynamic light scattering

Aliquots of sample were added to buffer that had been filtered through 0.45 μm hydrophilic syringe filters. The intensity – intensity time correlation of scattered 532 nm laser light was measured at 25 °C, perpendicular to the incident beam, using a Brookhaven BI-9000 AT digital correlator and BI-200SM goniometer system. The optical density filter and detector slit were adjusted to yield a scattered intensity of 10–100 kcps. The normalized intensity – intensity time correlation function was transformed to the normalized electric field time correlation function via the Siegert relation and evaluated via the CONTIN regularization algorithm.

Zeta potential studies

Bead samples were diluted to a final concentration of 2.6×10^{-10} mol/L in 1 mmol/L HEPES buffer (pH 7.3) ($S100^{-}NH_3^{+}PPV^{-}$ and $S50^{-}NH_3^{+}PPV^{-}$) or 1 mmol/L sodium acetate buffer (pH 5.8) ($S100^{-}NH_3^{+}$ and $S50^{-}NH_3^{+}$). Several trials consisting of 10 cycles (i.e., 10 individual measurements) were taken for each sample on a ZetaPlus ζ potential analyzer (Brookhaven Instruments Corp.) at room temperature.

Absorption and fluorescence

Absorption and emission spectra were recorded on Cary 5000 UV–VIS–NIR and Cary Eclipse fluorescence spectrophotometers, respectively. The amount of MPS-PPV coating the beads was estimated by subtracting the bare-bead scattering from the absorbance spectrum of coated beads. A solution of MPS-PPV in 1 mmol/L HEPES (pH 7.3) buffer was prepared to match the amount of MPS-PPV coating the beads, within 5% and at an absorbance between 0.05 and 0.1. The fluorescence emission of both samples was recorded at 450 nm excitation with 10 nm excitation and emission slits and a scan range of 470–800 nm.

For quenching of MPS-PPV-coated silica beads with MV^{2+}, aliquots of MV^{2+} in 1 mmol/L HEPES (pH 7.3) buffer were added to the samples of free MPS-PPV or MPS-PPV-coated beads, and fluorescence spectra were recorded after mixing well. The final concentrations of MV^{2+} ranged from 1×10^{-10} to 1×10^{-5} mol/L.

TIRF microscopy imaging

Cover slips were cleaned with piranha solution (30% $H_2O_2 - H_2SO_4$, 1:3 (cc)) and rinsed with autoclaved deionized water until the pH of the rinse water was 6–7. Residual water was removed by three repeated washes with acetone. Vectabond, (0.5 mL) collected under argon gas, was added to the cover slips immersed in 25 mL of acetone. The cover slips were then incubated for 5 min. The reaction was quenched by replacing the acetone with water and rinsing twice. Cover slips were rinsed with HydroClone HyPure molecular biology grade water and dried via blown argon prior to fitting with flow chambers. Flow chambers were prepared with a predrilled polycarbonate film (Grace Biolabs) assembled on top of the cover slips, yielding a final volume of 10 μL. Silicone ports were glued on top of the chamber with double-sided tape.

Up to 40 μL of a 10 pmol/L bead solution was first flowed into the chambers; subsequently 20 μL of buffer were flowed at 5 μL/min to remove any beads not bound to the surface. Images were recorded during the flowing of buffer at a rate of 1 μL/min. Following imaging in buffer conditions, 20 μL of glucose oxidase oxygen scavenger solution were flowed over the sample. Images were then recorded while flowing oxygen scavenger at a rate of 1 μL/min. The oxygen scavenger solution consisted of β-mercaptoethanol (1% *v*/*v*), β-D-(+)-glucose (3% *w*/*v*), glucose oxidase (0.1 mg/mL), and catalase (0.02 mg/mL), where the glucose oxidase was added just prior to use. All experiments were conducted at room temperature (22–25 °C).

Can. J. Chem. Downloaded from www.nrcresearchpress.com by University of Electronic and Science Techonology of China on 09/18/12
For personal use only.

The experimental setup consisted of an Olympus IX 71 microscope adapted with a commercial turnkey TIRF module IX2-RFAEVA-2 by Olympus. The excitation involved objective-based TIRF. The samples were illuminated at the critical angle[38] using the 488 nm output of a cw Ar+ laser from SpectraPhysics at 6.0 mW ± 0.2 mW (measured at the nosepiece). The laser beam was introduced via a single mode fiber optic and directed by a dichroic beamsplitter (z488rdc; Chroma, Rockingham, Vermont) to the sample via a high numerical aperture (N.A. = 1.45) oil immersion objective (Olympus PLAN APO 60X). Fluorescence emission was collected through the same objective and then transmitted through an emission filter HQ530 LP (640DCXR Chroma) into a Cascade 512B EMCCD camera (Roper Scientific, Inc.) operated with Image Pro software. Images were recorded at exposure times of 500 ms for over 350 s. Individual beads in a series of images acquired over time were identified using software developed in our laboratory and based on MATLAB and IDL routines by T. Ha.[39]

Acknowledgements

G.C. is grateful to the Natural Sciences and Engineering Research Council of Canada (NSERC), the Canada Foundation for Innovation (CFI) New Opportunities Fund, and the Centre for Self-Assembled Chemical Structures (CSACS/CRMAA) for financial assistance. A.T.N. is thankful to the Canadian Institutes of Health Research (CIHR) for a Chemical Biology Scholarship. K.L.L. is thankful to the Faculty of Science, McGill University, Montreal, Quebec, for an undergraduate research scholarship. R.A. thanks NSERC for an Undergraduate Student Research Award (USRA).

References

(1) Swager, T. M. *Acc. Chem. Res.* **1998**, *31* (5), 201. doi:10.1021/ar9600502.
(2) Thomas, S. W.; Joly, G. D.; Swager, T. M. *Chem. Rev.* **2007**, *107* (4), 1339. doi:10.1021/cr0501339.
(3) Chen, L.; McBranch, D. W.; Wang, H.-L.; Helgeson, R.; Wudl, F.; Whitten, D. G. *Proc. Natl. Acad. Sci. U.S.A.* **1999**, *96* (22), 12287. doi:10.1073/pnas.96.22.12287.
(4) Wang, D.; Gong, X.; Heeger, P. S.; Rininsland, F.; Bazan, G. C.; Heeger, A. J. *Proc. Natl. Acad. Sci. U.S.A.* **2002**, *99* (1), 49. doi:10.1073/pnas.012581399.
(5) Achyuthan, K. E.; Bergstedt, T. S.; Chen, L.; Jones, R. M.; Kumaraswamy, S.; Kushon, S. A.; Ley, K. D.; Lu, L.; McBranch, D.; Mukundan, H.; Rininsland, F.; Shi, X.; Xia, W.; Whitten, D. G. *J. Mater. Chem.* **2005**, *15* (27-28), 2648. doi:10.1039/b501314c.
(6) Tan, C.; Atas, E.; Muller, J. G.; Pinto, M. R.; Kleiman, V. D.; Schanze, K. S. *J. Am. Chem. Soc.* **2004**, *126* (42), 13685. doi:10.1021/ja046856b.
(7) Huser, T.; Yan, M.; Rothberg, L. J. *Proc. Natl. Acad. Sci. U.S.A.* **2000**, *97* (21), 11187. doi:10.1073/pnas.97.21.11187.
(8) Yu, J.; Hu, D. H.; Barbara, P. F. *Science* **2000**, *289* (5483), 1327. doi:10.1126/science.289.5483.1327.
(9) Zeineldin, R.; Piyasena, M. E.; Bergstedt, T. S.; Sklar, L. A.; Whitten, D.; Lopez, G. P. *Cytometry A* **2006**, *69A* (5), 335. doi:10.1002/cyto.a.20250.
(10) Wosnick, J. H.; Liao, J. H.; Swager, T. M. *Macromolecules* **2005**, *38* (22), 9287. doi:10.1021/ma051182q.
(11) Chemburu, S.; Ji, E.; Casana, Y.; Wu, Y.; Buranda, T.; Schanze, K. S.; Lopez, G. P.; Whitten, D. G. *J. Phys. Chem. B* **2008**, *112* (46), 14492. doi:10.1021/jp803358j.
(12) Zeineldin, R.; Piyasena, M. E.; Sklar, L. A.; Whitten, D.; Lopez, G. P. *Langmuir* **2008**, *24* (8), 4125. doi:10.1021/la703575r.
(13) Ho, P. K. H.; Kim, J.-S.; Burroughes, J. H.; Becker, H.; Li, S. F. Y.; Brown, T. M.; Cacialli, F.; Friend, R. H. *Nature* **2000**, *404* (6777), 481. doi:10.1038/35006610.
(14) Chen, L.; McBranch, D.; Wang, R.; Whitten, D. *Chem. Phys. Lett.* **2000**, *330* (1-2), 27. doi:10.1016/S0009-2614(00)00970-2.
(15) Decher, G. *Science* **1997**, *277* (5330), 1232. doi:10.1126/science.277.5330.1232.
(16) Chemburu, S.; Corbitt, T. S.; Ista, L. K.; Ji, E.; Fulghum, J.; Lopez, G. P.; Ogawa, K.; Schanze, K. S.; Whitten, D. G. *Langmuir* **2008**, *24* (19), 11053. doi:10.1021/la8016547.
(17) Liao, J. H.; Swager, T. M. *Langmuir* **2007**, *23* (1), 112. doi:10.1021/la0616911.
(18) Peters, K. R.; Rutter, G.; Gschwender, H. H.; Haller, W. *J. Cell Biol.* **1978**, *78* (2), 309. doi:10.1083/jcb.78.2.309.
(19) To calculate the number of monomers for monolayer coverage of one bead, it was assumed that an MPS-PPV monomer lying flat on the bead surface occupies an area of ca. 36 $Å^2$. Considering that the surface area of a 100 nm bead is 3.14×10^4 nm^2 and the surface area of a 50 nm bead is 7.85×10^3 nm^2, a total of 8.7×10^4 monomers per 100 nm bead and 2.2×10^4 monomers per 50 nm bead are required for monolayer coverage.
(20) Chen, L.; Xu, S.; McBranch, D.; Whitten, D. *J. Am. Chem. Soc.* **2000**, *122* (38), 9302. doi:10.1021/ja001248r.
(21) Dalvi-Malhotra, J.; Chen, L. *J. Phys. Chem. B* **2005**, *109* (9), 3873. doi:10.1021/jp0455071.
(22) Lakowicz, J. R. *Principles of Fluorescence Spectroscopy;* 3rd ed.; Springer: New York, 2006.
(23) Wang, D.; Wang, J.; Moses, D.; Bazan, G. C.; Heeger, A. J. *Langmuir* **2001**, *17* (4), 1262. doi:10.1021/la001271q.
(24) Schanze, K. S.; Zhao, X. *In* Handbook of Conducting Polymers; Skotheim, T. A., Reynolds, J., Eds.; CRC Press, 2007; Vol. 1.
(25) Kaur, P.; Wu, M.; Anzaldi, L.; Waldeck, D. H.; Xue, C.; Liu, H. *Langmuir* **2007**, *23* (26), 13203. doi:10.1021/la7023007.
(26) Liu, M.; Kaur, P.; Waldeck, D. H.; Xue, C.; Liu, H. *Langmuir* **2005**, *21* (5), 1687. doi:10.1021/la047434i.
(27) Ngo, A. T.; Karam, P.; Fuller, E.; Burger, M.; Cosa, G. *J. Am. Chem. Soc.* **2008**, *130* (2), 457. doi:10.1021/ja076217b.
(28) Ngo, A. T.; Cosa, G. *Langmuir* **2010**, *26* (9), 6746. doi:10.1021/la904100q.
(29) Kim, I.-B.; Dunkhorst, A.; Bunz, U. H. F. *Langmuir* **2005**, *21* (17), 7985. doi:10.1021/la051152g.
(30) Kinosita, K.; Itoh, H.; Ishiwata, S.; Hirano, K.; Nishizaka, T.; Hayakawa, T. *J. Cell Biol.* **1991**, *115* (1), 67. doi:10.1083/jcb.115.1.67.
(31) Yan, M.; Rothberg, L. J.; Papadimitrakopoulos, F.; Galvin, M. E.; Miller, T. M. *Phys. Rev. Lett.* **1994**, *73* (5), 744. doi:10.1103/PhysRevLett.73.744.
(32) Bradley, D. D. C. *J. Phys. D Appl. Phys.* **1987**, *20* (11), 1389. doi:10.1088/0022-3727/20/11/007.
(33) Aitken, C. E.; Marshall, R. A.; Puglisi, J. D. *Biophys. J.* **2008**, *94* (5), 1826. doi:10.1529/biophysj.107.117689.
(34) Rasnik, I.; McKinney, S. A.; Ha, T. *Nat. Methods* **2006**, *3* (11), 891. doi:10.1038/nmeth934.
(35) Weiss, S. *Science* **1999**, *283* (5408), 1676. doi:10.1126/science.283.5408.1676.

(36) Van den Bout, D. A.; Yip, W.-T.; Hu, D.; Fu, D.-K.; Swager, T. M.; Barbara, P. F. *Science* **1997**, *277* (5329), 1074. doi:10.1126/science.277.5329.1074.
(37) Hu, D.; Yu, J.; Wong, K.; Bagchi, B.; Rossky, P. J.; Barbara, P. F. *Nature* **2000**, *405* (6790), 1030. doi:10.1038/35016520.
(38) Axelrod, D. *Traffic* **2001**, *2* (11), 764. doi:10.1034/j.1600-0854.2001.21104.x.
(39) Roy, R.; Hohng, S.; Ha, T. *Nat. Methods* **2008**, *5* (6), 507. doi:10.1038/nmeth.1208.

Can. J. Chem. Downloaded from www.nrcresearchpress.com by University of Electronic and Science Techonology of China on 09/18/12
For personal use only.

Temperature effects on xanthone–β-cyclodextrin binding dynamics

Tamara C. S. Pace and Cornelia Bohne

Can. J. Chem. Downloaded from www.nrcresearchpress.com by University of Electronic and Science Techonology of China on 09/18/12
For personal use only.

Abstract: The complexation dynamics of the triplet excited state of xanthone with β-cyclodextrin were studied at various temperatures between 10 and 50 °C. Association and dissociation rate constants were determined using the laser flash photolysis quenching methodology with Cu^{2+} as a quencher. The rate constants for the association and dissociation of triplet xanthone with β-cyclodextrin increased with temperature, while the equilibrium constant for the triplet excited state remained relatively constant. Equilibrium constants for the ground-state complexation of xanthone with β-cyclodextrin were determined from fluorescence studies at various temperatures. The ground-state binding efficiency decreased with temperature and was markedly greater than that of the triplet excited state at all temperatures. The enthalpy and entropy for the β-cyclodextrin complex formation of the ground and triplet excited states fall on the enthalpy–entropy compensation relationship previously established for cyclodextrin complexes. The activation enthalpies for the association and dissociation rate constants for triplet xanthone are similar. The activation entropy is favorable for the association process, whereas a negative activation entropy was measured for the dissociation process, suggesting that solvation plays a key role in the complex formation between xanthone and β-cyclodextrin.

Key words: xanthone, β-cyclodextrin, binding dynamics, temperature, excited states.

Résumé : Opérant à diverses températures en 10 et 50 °C, on a étudié la dynamique de la complexation de l'état excité triplet de la xanthone avec la β-cyclodextrine. Les constantes de vitesse d'association et de dissociation du triplet de la xanthone avec la β-cyclodextrine augmente avec la température alors que la constante d'équilibre pour l'état excité triplet demeure relativement constante. Les constantes d'équilibre pour la complexation de l'état fondamental de la xanthone avec la β-cyclodextrine ont été déterminées à partir d'études de fluorescence à diverses températures. L'efficacité de fixation de l'état fondamental diminue avec la température et sa valeur est beaucoup plus grande que celle de l'état excité triplet, à toutes les températures. L'enthalpie et l'entropie de formation du complexe avec la β-cyclodextrine des états fondamental et excité triplet se retrouvent tous sur la relation de compensation enthalpie-entropie établie antérieurement pour les complexes de la cyclodextrine. Les enthalpies d'activation pour les constantes de vitesse d'association et de dissociation pour l'état triplet de la xanthone sont semblables. L'entropie d'activation est favorable pour le processus d'association alors qu'on a mesuré une entropie d'activation négative pour le processus de dissociation, ce qui suggérerait que la solvatation joue un rôle clé dans la formation de complexe entre la xanthone et la β-cyclodextrine.

Mots-clés : xanthone, β-cyclodextrine, dynamique de fixation, température, états excités.

[Traduit par la Rédaction]

Introduction

Cyclodextrins (CDs) are cyclic oligosaccharides with relatively rigid hydrophobic internal cavities in which a number of organic and inorganic guest molecules can be incorporated. The size of the CD cavity is determined by the number of glucose units in the molecule (6, 7, or 8 for α, β, and γ-CD).[1,2] There is much thermodynamic information available for the complexation of guests to CDs. The efficiency of complex formation is largely determined by the hydrophobicity of the guest, as well as size complementarity between the guest and the CD cavity.[3,4] There is much less known about the binding dynamics of guests with CDs,[5–7] because in general the binding dynamics are fast. Early temperature jump[8] and stopped-flow experiments[9,10] showed that the association and dissociation rate constants for a series of azo dyes varied by three orders of magnitude, whereas changes in the equilibrium constants were much smaller. These results showed that the changes in the kinetics do not necessarily parallel changes in the thermodynamics of the guest complexation to CDs. Very little temperature-dependent kinetic data has been determined because fast kinetic techniques are required. In the case of a complex between the trinitrophenylated Meisenheimer complex of adenosine and γ-CD, the kinetics could be studied by NMR because of the unusually high equilibrium constant for this complex.[11] However, for the lower equilibrium constants usually seen for CD complexes with 1:1 stoichiometry, techniques with time resolution in the ns to μs time domain are required.

Received 6 June 2010. Accepted 29 July 2010. Published on the NRC Research Press Web site at canjchem.nrc.ca on 1 March 2011.

This article is part of a Special Issue dedicated to Professor J. C. Scaiano.

T.C.S. Pace and C. Bohne.[1] Department of Chemistry, University of Victoria, PO Box 3065, Victoria, BC V8W 3V6, Canada.

[1]Corresponding author (e-mail: cornelia.bohne@gmail.com).

Can. J. Chem. Downloaded from www.nrcresearchpress.com by University of Electronic and Science Techonology of China on 09/18/12
For personal use only.

Chart 1. Structure of xanthone.

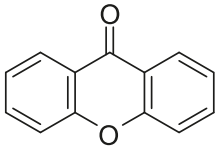

Dynamics studies using triplet excited states are suitable for this time domain.[6,7]

The size of the guest molecule contributes greatly to the binding efficiency of the guest–CD complex. In the case of xanthone (Chart 1) the highest equilibrium constant was for binding to β-CD, whereas binding to α-CD and γ-CD was less efficient because the cavities are, respectively, too small and too large.[12] Theoretical studies, combined with induced circular dichroism measurements, showed that xanthone binds to the rim of the CD cavity and is not deeply included in the cavity.[13]

In our previous work on the binding of xanthone to β-CD, we studied the binding dynamics at 20 °C directly[12,14,15] or using Cu^{2+} as a quencher.[16] These studies found quite different equilibrium constants for the ground state and triplet excited state of xanthone,[14] attributed to the higher basicity and greater dipole moment of the xanthone triplet excited state compared with the ground state.[16]

In this current work, we examined the effect of temperature on the triplet-excited-state binding dynamics of xanthone with β-CD, as well as the temperature effects on the equilibrium constants for the ground and excited states.

Results

Ground-state complexation

Equilibrium constants (K_{eq}) for ground-state guest molecules with a host can be determined when a spectroscopic observable of the guest changes upon complexation to the host. Addition of β-CD resulted in a decrease in xanthone fluorescence intensity and a small blue shift in the fluorescence emission maximum. The xanthone fluorescence intensity was also seen to decrease with increasing temperature.

The equilibrium constants (K_{eq}) for the binding of ground-state xanthone to β-CD were obtained at various temperatures from analysis of the change in xanthone fluorescence intensity (ΔI) with increasing β-CD concentrations ($[CD]_T$; eq. [1] and Fig. 1),

$$[1] \qquad \Delta I = \frac{[G]_T \Delta\phi K_{eq}[CD]_T}{1 + K_{eq}[CD]_T}$$

where $\Delta\phi$ is related to the difference in quantum yields for the free and bound guests and $[G]_T$ is the total guest concentration. This equation is valid for formation of a 1:1 host–guest complex when the concentration of CD exceeeds the guest concentration.[17] The nonlinear equation is preferable for the determination of K_{eq} values because it gives proper weight to the experimental data; however, a double reciprocal plot (eq. [2]) can be used to check the assumption of a 1:1 complex stoichiometry, because a linear relationship is expected if the correct stoichiometry is assumed. Linear double reciprocal plots were obtained at all temperatures studied (Fig. S1 in the Supplementary data).

Fig. 1. Changes in xanthone (25 μmol/L) fluorescence intensity with β-cyclodextrin (β-CD) concentration at (a) 10 °C (○), (b) 20 °C (□), (c) 30 °C (●), (d) 40 °C (■), and (e) 50 °C (◆). The solid lines correspond to the fit of the experimental data to eq. [1].

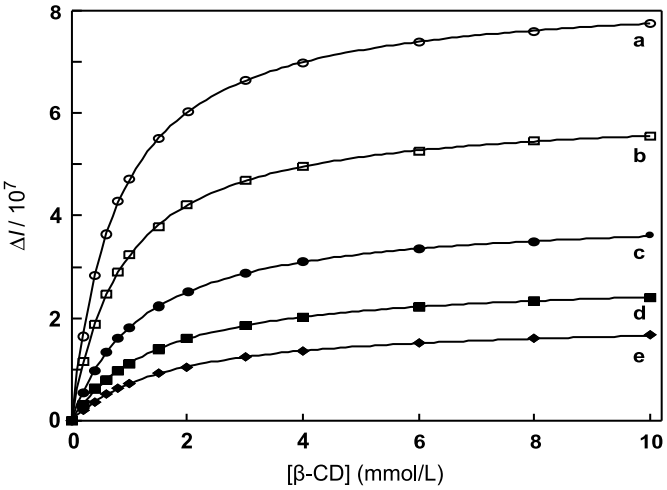

$$[2] \qquad \frac{1}{\Delta I} = \frac{1}{[G]_T \Delta\phi} + \frac{1}{[G]_T \Delta\phi K_{eq}[CD]_T}$$

The K_{eq} values determined for the xanthone–β-CD complex at various temperatures (Table 1) decreased with increasing temperature. The 20 °C data is in agreement with the previously determined value of 1100 ± 200 $(mol/L)^{-1}$.[14]

The change in K_{eq} with temperature was analyzed using the van't Hoff equation (eq. [3]). The enthalpy (ΔH^0) and entropy changes (ΔS^0) for the 1:1 complex formation between xanthone and β-CD were calculated from the van't Hoff plot (Fig. 2). Values of –14 ± 2 kJ mol^{-1} and +11 ± 4 J mol^{-1} K^{-1} were recovered for ΔH^0 and ΔS^0, respectively.

$$[3] \qquad \ln K_{eq} = -\frac{\Delta H^0}{RT} + \frac{\Delta S^0}{R}$$

Triplet-excited-state complexation

The binding dynamics of triplet xanthone to CDs[12,14,16] can be studied using the direct or the quenching methods.[6,18] The direct method takes advantage of the large shift in the triplet–triplet absorption spectra for xanthone in environments of different polarity.[19,20] When kinetic decays are monitored at wavelengths away from the isosbestic point, the decay is a sum of two exponentials, with a fast component attributed to relocation of xanthone from β-CD into the bulk solution. As the temperature was increased, the observed rate constant for the fast component increased. Unfortunately, the signal-to-noise ratio also increased at the higher temperatures, and the error in the direct kinetic measurements was too high for recovery of association and dissociation rate constants.

In the case of the quenching methodology, the triplet-excited-state kinetics of xanthone were measured at 600 nm. This monitoring wavelength corresponds to the isosbestic point for the triplet–triplet absorption spectra for xanthone in water and xanthone bound to β-CD.[12] The decays followed a mono-exponential function and the triplet

Can. J. Chem. Downloaded from www.nrcresearchpress.com by University of Electronic and Science Techonology of China on 09/18/12
For personal use only.

Table 1. Ground-state equilibrium constants (K_{eq}) for the binding of xanthone (25 μmol/L) to β-cyclodextrin (β-CD).

T (°C)	K_{eq} / (mol/L)$^{-1}$[a]
10	1200±100
20	1090±50
30	860±40
40	690±40
50	610±40

[a]Experiments were conducted twice and errors correspond to average deviations.

Fig. 2. van't Hoff plot for xanthone–β-cyclodextrin (β-CD) complexation.

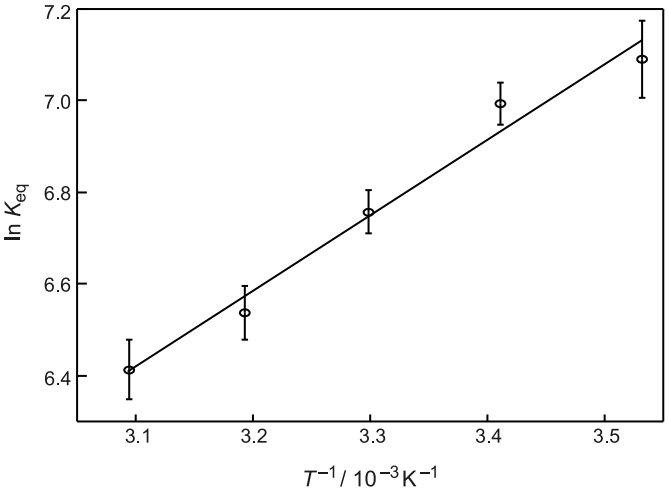

lifetimes for xanthone in water were in excess of 10 μs at all temperatures studied. The triplet lifetimes were somewhat longer in the presence of β-CD, and the lifetimes in the absence and presence of β-CD were shortened somewhat as the temperature was increased.

Quenchers for triplet excited states, such as Cu^{2+} or NO_2^-,[12,21] which reside primarily in the aqueous phase, can be employed to determine the values for the association (k_+^*) and dissociation (k_-^*) rate constants for triplet xanthone with β-CD. This quenching methodology has been previously used in the determination of the complexation dynamics of guest molecules with CDs.[6,22] For example, the binding dynamics of triplet chromone with β-CD was studied using Cu^{2+} or NO_2^- as quenchers, whereas the binding dynamics of triplet flavone could only be studied using Cu^{2+}.[16] In the present study Cu^{2+} was used as the quencher because preliminary experiments showed that with NO_2^- the qualitative trends with changes in temperature were the same as those observed with Cu^{2+}, but the rate constants recovered had larger errors.

The values for the quenching rate constant in water (k_q) were determined from quenching plots for xanthone in water in the absence of cyclodextrin. The observed triplet decay rate constant (k_{obs}) was obtained at several quencher concentrations, and the data were fit to eq. [4], where k_0 is the decay rate constant for xanthone in water in the absence of quencher. The plots for the quenching of triplet xanthone by Cu^{2+} in water were linear at all temperatures (Fig. 3).

Fig. 3. Quenching plots for the triplet-excited-state quenching of xanthone by Cu^{2+} in water (open symbols) and in the presence of 6 mmol/L β-cyclodextrin (β-CD; filled symbols) at 10 °C (◆), 30 °C (●), and 50 °C (■). The solid lines for the quenching plots in water correspond to the fit to eq. [4]. The solid lines for the quenching plots in the presence of β-CD correspond to the fit to eq. [5] when the decay rate constant for xanthone in water in the absence of cyclodextrin (k_0) and the quenching rate constant in water (k_q) are fixed to the values obtained in water, the decay rate constant for xanthone in the presence of β-CD without quencher (k_0^H) is fixed to the value for the decay in β-CD in the absence of quencher, and the quenching rate constant for the host (k_q^H) is fixed to 1 × 10^6 (mol/L)$^{-1}$ s^{-1}.

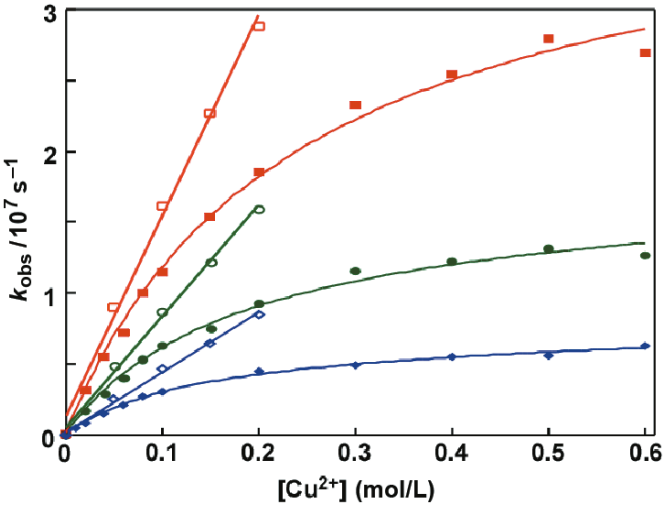

The quenching efficiencies in water increased with temperature and were two orders of magnitude smaller (Table 2) than the diffusion-controlled rate constant for a bimolecular reaction, e.g., 6.5 × 10^9 (mol/L)$^{-1}$ s^{-1} at 20 °C.[23]

$$[4] \qquad k_{obs} = k_0 + k_q[Cu^{2+}]$$

In the presence of β-CD, the plots for quenching triplet excited xanthone by Cu^{2+} were curved (Fig. 3). The curvature is due to less-efficient quenching of the triplet excited states bound to the CD cavity. Generally, quenchers that reside primarily in the aqueous phase are employed so that the quenching efficiency of excited-state guests in water is higher than that for guests bound to the host, k_q^H. At higher quencher concentrations, the rate-limiting step for quenching becomes the exit of the guest from the host or its intrinsic decay within the host, resulting in downward curvature in the quenching plots. Qualitatively, the larger the difference between the linear quenching plots obtained in aqueous solution and the curved quenching plots obtained in the presence of the host, the slower the binding dynamics in the host–guest system. If the concentration of free guest is small in comparison with the amount of bound guest, then the kinetics are pseudo-first-order and follow a mono-exponential decay, and k_{obs} is given by eq. [5],[22,24]

$$[5] \qquad k_{obs} = k_0^H + k_-^* + k_q^H[Cu^{2+}] - \frac{k_-^* k_+^* [CD]}{k_0 + k_q[Cu^{2+}] + k_+^*[CD]}$$

where k_0^H is the decay rate constant for xanthone in the pre-

Can. J. Chem. Downloaded from www.nrcresearchpress.com by University of Electronic and Science Techonology of China on 09/18/12
For personal use only.

Table 2. Quenching rate constants for xanthone in water (k_q) and bound to β-cyclodextrin (β-CD; k_q^H), association and dissociation rate constants (k_+^* and k_-^*), and equilibrium constants for triplet xanthone with β-CD (K_T; 6 mmol/L).

T (°C)[a]	k_q / 10^7 (mol/L)$^{-1}$ s^{-1}	k_q^H / 10^6 (mol/L)$^{-1}$ s^{-1}	k_+^* / 10^9 (mol/L)$^{-1}$ s^{-1}	k_-^* / 10^6 s^{-1}	K_T / (mol/L)$^{-1}$[b]
10 (1)	4.2±0.1	0–2	0.9±0.1	6.8±0.8	140±30
20 (1)	6.0±0.2	0–5	1.5±0.4	10±3	150±60
30 (1)	7.8±0.3	0–2	2.3±0.2	17±1	140±20
40 (2)	11.5±0.3	0–5	3.7±0.3	25±1	150±10
50 (1)	14.0±0.6	0–5	5.2±0.4	37±3	140±20

Note: The errors in k_q correspond to the statistical errors for the fit of the data to eq. [4], the ranges for k_q^H are the values for which the fit of the data to eq. [5] was acceptable and the errors in k_+^*, and k_-^* correspond to the average deviation for the maximum and minimum values recovered when k_q^H was fixed in the quoted range.

[a]Bracketed numbers correspond to the number of times experiments were performed.

[b]K_T values were calculated from k_+^*/k_-^*.

sence of β-CD, but without quencher. The k_0 and k_q values were fixed to those determined from quenching studies in the absence of cyclodextrin. A concentration of 6 mmol/L β-CD was used for these quenching studies. At too low a concentration of β-CD, the assumption that the concentration of free guest is less than that of the bound guest is no longer valid. Employing the highest host concentration may also not be ideal, because the curvature of the plot is defined by fewer points when host concentration is increased.[18]

When the quenching plots were fit to eq. [5] adequate fits were observed for a wide range of values for k_q^H, k_+^*, and k_-^*. The possible values for k_q^H range from complete protection from the quencher ($k_q^H = 0$) to no protection from the quencher ($k_q^H = k_q$). Fits were performed by fixing k_q^H to zero, then with incrementally larger values, until the fit was no longer adequate. The association and dissociation rate constants in Table 2 correspond to the average of the minimum and maximum values recovered for the range of k_q^H values that resulted in adequate fits (see Fig. S2 in the Supplementary data for adequate and inadequate fits over a range of k_q^H values at 10 °C). The equilibrium constant for triplet xanthone and β-CD (K_T) was calculated from the association and dissociation rate constants. The K_T values did not change significantly with temperature and were much smaller than the equilibrium constants for ground-state xanthone (see above). The values for k_+^*, k_-^*, and K_T at 20 °C were the same within experimental error as those determined previously in quenching experiments with Cu^{2+}.[16]

The changes in the association and dissociation rate constants were analyzed using the Eyring equation (eq. [6]) to obtain activation parameters,

$$[6] \qquad \ln\frac{k}{T} = -\frac{\Delta H^{\neq}}{RT} + \frac{\Delta S^{\neq}}{R} + \ln\frac{k_B}{h}$$

where $\Delta H^{\neq}$ is the activation enthalpy, $\Delta S^{\neq}$ is the activation entropy, k_B is the Boltzmann constant, h is Planck's constant, T is the temperature, and R is the gas constant.

$\Delta H^{\neq}$ and $\Delta S^{\neq}$ for the dissociation process recovered from the Eyring plot (Fig. 4) were +31 ± 1 kJ mol^{-1} and –7.1 ± 0.1 J mol^{-1} K^{-1}, respectively, whereas values of +30 ± 1 kJ mol^{-1} and +36 ± 1 J mol^{-1} K^{-1} were recovered for the association process.

Fig. 4. Eyring plots for the association (○) and dissociation (□) rate constants for triplet xanthone binding to β-cyclodextrin (β-CD).

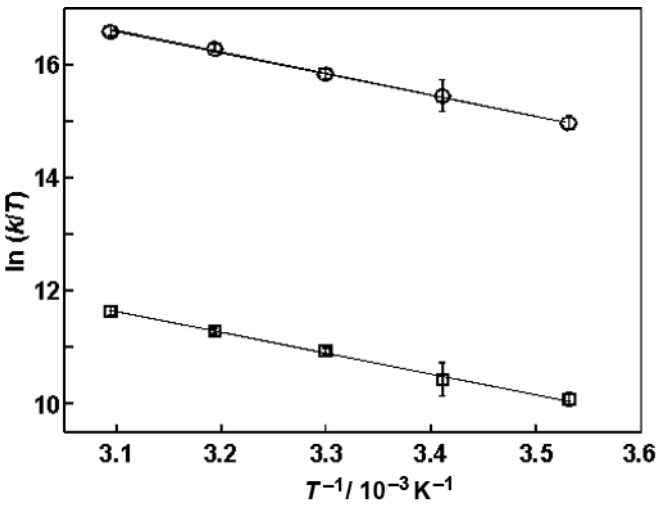

Discussion

Theoretical studies combined with spectroscopic validation using induced circular dichroism measurements showed that xanthone binds to the rim of β-CD with one of the rings included within the cavity.[6,13] Formation of the complex is enthalpically (ΔH^0 = –14 ± 2 kJ mol^{-1}) and entropically driven (ΔS^0 = +11 ± 4 J mol^{-1} K^{-1}). The gain in enthalpy is related to the hydrophobic interactions between the aromatic ring of xanthone included in the cavity and the CD. The structure of the complex was calculated to have the xanthone tilted towards one side of the CD cavity to gain further stabilization by the interaction of xanthone with the rim containing the secondary hydroxyl groups.[13] However, no specific hydrogen bonds were identified in these calculations. In addition, the structure of β-CD is significantly different from that determined in its crystal structure, suggesting that the CD is flexible enough to adapt to the guest so that the interactions between the guest and the CD are enhanced.[13] From the entropic point of view, the inclusion of xanthone within the CD cavity and the distortion of the CD to maximize interactions lead to a lowering of the degrees of freedom and a decrease of entropy. However, water molecules released from inside the CD cavity and from solvating the parts of the guest included in the com-

Can. J. Chem. Downloaded from www.nrcresearchpress.com by University of Electronic and Science Techonology of China on 09/18/12
For personal use only.

plex increase the entropy of the system.[4] Therefore, the positive ΔS^0 value observed for the formation of the xanthone β-CD complex is dominated by the release of water.

An analysis of over 1000 values for the equilibrium constants between guests and CDs showed that an enthalpy–entropy compensation occurs for the binding of guests with CDs.[4] For each increment in enthalpic gain for complex formation, some of this gain is lost in the form of a less favorable entropy. In the case of β-CD, 20% of the enthalpic gain is translated into a free-energy gain (eq. [7] derived from 488 equilibrium constant values). When ΔH^0 is equal to zero, the formation of host–guest complexes with β-CD are favored entropically by 11 kJ mol^{-1} (298.15 K) owing to the liberation of water molecules.[4] The $T\Delta S^0$ value calculated for the complexation of xanthone with β-CD from the experimentally determined ΔH^0 value is –0.2 ± 0.1 kJ mol^{-1}, which is comparable to the experimental $T\Delta S^0$ value of 3 ± 1 kJ mol^{-1}, considering the scatter of the enthalpy–entropy compensation plot (r = 0.89) used to derive eq. [7].[4] This comparison shows that the complexation of xanthone follows the same pattern as observed for other guests.

$$[7] \qquad T\Delta S^0 = 0.8\Delta H^0 + 11 \ \ (\text{kJ mol}^{-1})$$

The complexation dynamics of the triplet state of xanthone, determined in laser flash photolysis experiments, are faster than for the ground state, measured in laser temperature jump experiments.[14] The faster dynamics are due to the increase in the dissociation rate constant for the triplet state when compared with the dissociation rate constant for the ground state. This faster dissociation was attributed[14] to the higher dipole moment of triplet ketones with π,π* configuration[25] and (or) the high basicity of the excited state of triplet xanthone.[26] The equilibrium constants for the triplet excited state, calculated from the k_+^* and k_-^* values, were constant with the increase in temperature and were always smaller than the equilibrium constants for the ground state. The smaller equilibrium constant for the excited state is due to the faster dissociation process, whereas the lack of dependence of the triplet-state equilibrium constant on temperature indicates that the enthalpy change is negligible. Therefore, the β-CD complex formation for the triplet state of xanthone is exclusively driven by entropy owing to the release of solvation water molecules. The enthalpic component for complex formation was mainly attributed to the hydrophobic interaction of the portions of the guest that were desolvated with the walls of the CD with some contribution from possible hydrogen bonds between the guest and the hydroxyl groups of the CD.[4] The increase of ΔH^0 to ca. 0 for the triplet state compared with the ΔH^0 value of –14 kJ mol^{-1} for the ground state suggests that either a smaller area of the guest interacts with the CD, leading to the location of triplet xanthone further away from the CD cavity, or weaker hydrogen bonds are formed at the rim of the CD. In contrast, the $T\Delta S^0$ value for the triplet state (12.8 ± 0.3 kJ mol^{-1}, calculated from the activation parameters determined from the Eyring plots) is higher than the value for the ground state. This difference is either related to the formation of a more flexible triplet xanthone–CD complex or owing to the release of a larger number of water molecules for complex formation with the triplet state compared with the complex for ground state xanthone. The ΔH^0 and $T\Delta S^0$ values for triplet xanthone fall onto the enthalpy–entropy compensation relationship defined by eq. [7]. This result shows that the binding of the electronically excited state follows the same trends as for ground states. Finally, for an equilibrium constant, which is primarily determined by a gain in entropy, one would expect an increase in K_T at higher temperatures. However, such a trend was not observed owing to the narrow temperature range that could be employed in the current study.

In the case of the excited state, the enthalpy and entropy of activation for the association and dissociation processes were determined from the Eyring plots. The same enthalpies of activation for the association and dissociation processes are probably coincidental, since no apparent reason exists from the structural point of view why the $\Delta H^{\neq}$ values should be the same. The entropy of activation for the dissociation process is negative, showing that solvation by water of the separated CD and triplet xanthone molecules is the major contributor to this parameter. The positive $\Delta S^{\neq}$ for the association process is also consistent with the release of water molecules from the host and guest being the driving force for the complex formation. Indeed the large value for $\Delta S^{\neq}$ suggests that desolvation of the guest and host is the rate-limiting process for the formation of the complex.

Conclusions

The temperature-dependence studies showed that the binding of the ground state of xanthone with β-CD was enthalpically and entropically driven, whereas in the case of the triplet excited state only entropy played a role in the formation of the complex. The sign for $\Delta S^{\neq}$ for the association and dissociation rate constants of triplet xanthone further suggested that changes in solvation between the separated host and guest are a major determinant for complex formation with CDs. The ΔH^0 and ΔS^0 values for both the ground and triplet states of xanthone follow the enthalpy–entropy compensation dependence determined for other guest molecules with β-CD. This result showed that the binding of the electronically excited state follows the same trends as for ground states, and changes observed between the binding of ground and excited states of guests is dictated by changes in shape or electronic properties between the two states.

Experimental

Equipment

Fluorescence spectra were collected using a PTI QM-2 fluorimeter. Experiments were carried out on aerated solutions in 10 mm × 10 mm quartz cells, and the temperature was kept constant using a Haake water bath. Solutions were kept at the correct temperature in the water bath prior to measurement and were equilibrated at least 10 min in the sample holder before spectra were collected. The excitation wavelength was 345 nm, and emission was collected between 355 and 575 nm. Fluorescence spectra were corrected for the baseline emission of water, so that Raman emission from the solvent was subtracted from the spectra. Fluorescence intensities were determined by integration of the spec-

Can. J. Chem. Downloaded from www.nrcresearchpress.com by University of Electronic and Science Techonology of China on 09/18/12
For personal use only.

tra between 365 and 450 nm. The slits for the excitation and emission monochromators were set with a bandpass of 3 nm.

The laser flash photolysis system used to measure triplet decay kinetics has been described previously.[27] Samples were excited at 355 nm using a Spectra Physics Quanta Ray Lab 130–4 Nd:YAG laser. The sample holder was modified to incorporate a Unisoku USP-203 cryostat, which can be used to achieve temperatures from –150 to 100 °C. Each sample was allowed to equilibrate at least 10 min in the cryostat before measurements were made.

The cryostat was mounted on a home-built stage that can be moved in three dimensions to allow alignment with both the laser beam and the Xe-lamp monitoring beam, which are orthogonal to each other. The cryostat was fitted with four windows; the two windows in the laser path have AR coating for the laser wavelengths. A pinhole was fitted to the window on which the Xe lamp was incident to ensure that the size of the monitoring beam was smaller than the size of the incident laser beam.

All solutions for laser flash photolysis were placed in 10 mm × 10 mm quartz cells and deaerated with N_2O for at least 20 min prior to use. Ketones such as xanthone are easily photoionized in aqueous solutions, and N_2O acts as an efficient solvated electron trap.[28]

Materials

β-Cyclodextrin (Cargill) and $CuSO_4 \cdot 5H_2O$ (Sigma-Aldrich) were used as received. Xanthone (Sigma-Aldrich) was recrystallized from 95% ethanol prior to use. Deionized water (Sybron-Barnstead) was employed for all samples.

Solution preparation

Solutions for triplet-excited-state quenching experiments with Cu^{2+}

A solution of xanthone in water (25 μmol/L) was prepared by injection from a methanol stock solution (1 mmol/L). Xanthone (25 μmol/L) in β-CD (6 mmol/L) was prepared by dissolving β-CD in the aqueous xanthone solution. The solution was then heated to 60 °C for 30 min. The high Cu^{2+} concentrations used in the quenching experiments necessitated that each quencher concentration be prepared as a separate solution. The highest Cu^{2+} concentration solution (0.6 mol/L) was prepared by dissolving copper(II) sulfate in the xanthone–β-CD solution. Solutions with lower Cu^{2+} concentrations were prepared by dilution with the xanthone–β-CD solution. The solutions were left to shake for 12 h.

Solutions for fluorescence binding isotherms

A solution of xanthone in water (25 μmol/L) was prepared by injection from a methanol stock solution (1 mmol/L). The highest concentration xanthone–β-CD solutions (10 mmol/L) was prepared by dissolving β-CD in the aqueous xanthone solution. Solutions with lower β-CD concentrations were prepared by dilution with the aqueous xanthone solution. The solutions were left to shake for 12 h.

Supplementary data

Supplementary data (double reciprocal plots for ground-state xanthone binding to β-CD and fits with different parameters for the triplet xanthone quenching plots) for this article are available on the journal Web site (canjchem.nrc.ca).

Acknowledgement

The authors thank the Natural Sciences and Engineering Research Council of Canada (NSERC) for funding.

References

(1) Szejtli, J. *Chem. Rev.* **1998**, *98* (5), 1743. doi:10.1021/cr970022c.
(2) Szejtli, J.; Osa, T. In *Comprehensive Supramolecular Chemistry;* Atwood, J. L., Davies, J. E., MacNicol, D. D., Vögtle, F., Lehn, J.-M., Eds.; Elsevier Science Ltd.: New York, 1996; Vol. 3.
(3) Connors, K. A. *Chem. Rev.* **1997**, *97* (5), 1325. doi:10.1021/cr960371r.
(4) Rekharsky, M. V.; Inoue, Y. *Chem. Rev.* **1998**, *98* (5), 1875. doi:10.1021/cr970015o.
(5) Bohne, C. *Spectrum* **2000**, *13*, 14.
(6) Bohne, C. *Langmuir* **2006**, *22* (22), 9100. doi:10.1021/la061227w.
(7) Pace, T. C. S.; Bohne, C. *Adv. Phys. Org. Chem.* **2007**, *42*, 167. doi:10.1016/S0065-3160(07)42004-4.
(8) Cramer, F.; Saenger, W.; Spatz, H. C. *J. Am. Chem. Soc.* **1967**, *89* (1), 14. doi:10.1021/ja00977a003.
(9) Seiyama, A.; Yoshida, N.; Fujimoto, M. *Chem. Lett.* **1985**, (7): 1013. doi:10.1246/cl.1985.1013.
(10) Yoshida, N.; Seiyama, A.; Fujimoto, M. *J. Phys. Chem.* **1990**, *94* (10), 4246. doi:10.1021/j100373a068.
(11) Green, T. K.; Denoroy, L.; Parrot, S. *J. Org. Chem.* **2010**, *75* (12), 4048. doi:10.1021/jo1003357.
(12) Barra, M.; Bohne, C.; Scaiano, J. C. *J. Am. Chem. Soc.* **1990**, *112* (22), 8075. doi:10.1021/ja00178a034.
(13) Murphy, R. S.; Barros, T. C.; Barnes, J.; Mayer, B.; Marconi, G.; Bohne, C. *J. Phys. Chem. A* **1999**, *103* (1), 137. doi:10.1021/jp9821681.
(14) Liao, Y.; Frank, J.; Holzwarth, J. F.; Bohne, C. *J. Chem. Soc. Chem. Commun.* **1995**, (2): 199. doi:10.1039/c39950000199.
(15) Okano, L. T.; Barros, T. C.; Chou, D. T. H.; Bennet, A. J.; Bohne, C. *J. Phys. Chem. B* **2001**, *105* (11), 2122. doi:10.1021/jp002622c.
(16) Christoff, M.; Okano, L. T.; Bohne, C. *J. Photochem. Photobiol. Chem.* **2000**, *134* (3), 169. doi:10.1016/S1010-6030(00)00262-8.
(17) Connors, K. A. *Binding Constants — The Measurement of Molecular Complex Stability;* John Wiley & Sons: New York, 1987.
(18) Kleinman, M. H.; Bohne, C. In *Molecular and Supramolecular Photochemistry;* Ramamurthy, V., Schanze, K. S., Eds.; Marcel Dekker Inc.: New York, 1997; Vol. 1, pp 391–466.
(19) Evans, C. H.; Prud'homme, N.; King, M.; Scaiano, J. C. *J. Photochem. Photobiol. Chem.* **1999**, *121* (2), 105. doi:10.1016/S1010-6030(98)00455-9.
(20) Scaiano, J. C. *J. Am. Chem. Soc.* **1980**, *102* (26), 7747. doi:10.1021/ja00546a018.
(21) Treinin, A.; Hayon, E. *J. Am. Chem. Soc.* **1976**, *98* (13), 3884. doi:10.1021/ja00429a025.
(22) Turro, N. J.; Okubo, T.; Chung, C. J. *J. Am. Chem. Soc.* **1982**, *104* (7), 1789. doi:10.1021/ja00371a001.
(23) Murov, S. L.; Carmichael, I.; Hug, G. L. *Handbook of*

Photochemistry; 2nd revised and expanded ed.; Marcel Dekker, Inc.: New York, 1993.
(24) Almgren, M.; Grieser, F.; Thomas, J. K. *J. Am. Chem. Soc.* **1979**, *101* (2), 279. doi:10.1021/ja00496a001.
(25) Fessenden, R. W.; Carton, P. M.; Shimamori, H.; Scaiano, J. C. *J. Phys. Chem.* **1982**, *86* (19), 3803. doi:10.1021/j100216a020.
(26) Ireland, J. F.; Wyatt, P. A. H. *J. Chem. Soc., Faraday Trans. I* **1972**, *68*, 1053. doi:10.1039/f19726801053.
(27) Liao, Y.; Bohne, C. *J. Phys. Chem.* **1996**, *100* (2), 734. doi:10.1021/jp951697r.
(28) Janata, E.; Schuler, R. H. *J. Phys. Chem.* **1982**, *86* (11), 2078. doi:10.1021/j100208a035.

Can. J. Chem. Downloaded from www.nrcresearchpress.com by University of Electronic and Science Techonology of China on 09/18/12
For personal use only.

Locked nucleic acid hairpin detection of UV-induced DNA damage

Amira El-Yazbi and Glen R. Loppnow

Can. J. Chem. Downloaded from www.nrcresearchpress.com by University of Electronic and Science Techonology of China on 09/18/12
For personal use only.

Abstract: The exposure of DNA to radiation and chemical insults leads to damage and disease. Thus, detection and understanding of DNA damage is important for elucidating molecular mechanisms of disease. However, current methods of DNA damage detection are either time-consuming, destroy the sample, or are too specific to be used for generic detection of damage. In this paper, we examine the sensitivity of different locked nucleic acid (LNA) hairpin probes for detecting UV-induced oligonucleotide damage to LNA composition, target concentration, and ionic strength. We also compare the selectivity of the LNA hairpin probe with a DNA molecular beacon (MB) hairpin probe for detecting DNA damage. Our results show that the selectivity of the LNA hairpin probe to UV-induced nucleic acid damage increases with increasing ionic strength of the buffer and decreases with increasing target concentration and with increasing LNA ratio.

Key words: locked nucleic acids, fluorescence, nucleic acids, DNA damage, molecular beacons, sensors.

Résumé : L'exposition de l'ADN à des radiations et à des insultes chimiques provoque des dommages et des maladies. La détection et la compréhension des dommages à l'ADN sont donc des opérations importantes pour l'élucidation des mécanismes moléculaires des maladies. Toutefois, les méthodes actuelles courantes de détection des dommages à l'ADN demandent beaucoup de temps, détruisent l'échantillon ou sont trop spécifiques pour être utilisées par la détection générique des dommages. Dans ce travail, on examine la sensibilité des différentes sondes en épingle à cheveux d'acide nucléique bloqué (ANB) pour la détection de dommages dans l'oligonucléotide induits par l'UV à la composition de l'ANB, à la concentration de la cible et de la concentration ionique. On compare aussi la sélectivité de la sonde en épingle à cheveux d'ANB à une sonde en épingle à cheveux d'un faisceau moléculaire (FM) d'ADN pour la détection des dommages à l'ADN. Les résultats obtenus montrent que la sélectivité de la sonde en épingle à cheveux d'ANB aux dommages à l'acide nucléique induits par l'UV augmente avec une augmentation de la force ionique du tampon et qu'elle diminue avec une augmentation de la concentration de la cible et avec une augmentation du rapport d'ANB.

Mots-clés : acides nucléiques bloqués, fluorescence, acides nucléiques, dommages à l'ADN, faisceaux moléculaires, senseurs.

[Traduit par la Rédaction]

Introduction

Absorption of light by DNA produces molecular-scale lesions in the DNA and RNA, which can subsequently lead to cancer and other diseases.[1–4] Absorption of UVB (290–320 nm) and UVC (200–290 nm) light leads to the formation of thymidine cyclobutyl photodimers (CPD) as the primary photoproduct.[5] Other photoproducts with UV irradiation are pyrimidine pyrimidinone [6–4]-photoproducts, dewar pyrimidinones, and uracil and thymine photohydrates. All these photoproducts are localized on the pyrimidine nucleobases near the C5=C6 double bond, opposite to the site of base pairing. Other damage agents, such as oxidative conditions and ionizing radiation, lead to other DNA lesions, such as single- and double-strand breaks, 8-oxoguanosine and other oxidation products, and cross-links.

A number of techniques have been used to detect nucleic acid damage previously, either in vivo or in vitro. Most of these techniques isolate the DNA, melt it to obtain single-stranded DNA fragments, separate the fragments, and detect the lesions.[6–9] Such techniques include gel electrophoresis,[6] capillary electrophoresis,[7] electrochemistry,[7] HPLC,[8] and mass spectrometry.[9] While useful, these techniques are destructive and time-consuming. In addition, the electrophoretical and chromatographical techniques require prefiltering, which may itself introduce lesions.

Other spectroscopic-based techniques have recently been used to characterize nucleic acid damage. Differences in the fluorescence lifetime of a dye intercalated in undamaged and damaged DNA have been used to detect DNA damage.[10] Fluorescently labeled antibodies provide an exquisitely selective probe of particular damage photoproducts, such as thymine CPDs.[11] Most recently, molecular beacons (MBs) have been used as a broad-spectrum sensor of DNA and RNA damage[12] (A. Mah, S. Yarasi, and G. R. Loppnow,

Received 28 April 2010. Accepted 26 September 2010. Published on the NRC Research Press Web site at canjchem.nrc.ca on 3 March 2011.

This article is part of a Special Issue dedicated to Professor J. C. Scaiano.

A. El-Yazbi and G.R. Loppnow.[1] Department of Chemistry, University of Alberta, Edmonton, AB T6G 2G2, Canada.

[1]Corresponding author (e-mail: glen.loppnow@ualberta.ca).

Can. J. Chem. Downloaded from www.nrcresearchpress.com by University of Electronic and Science Techonology of China on 09/18/12
For personal use only.

manuscript in preparation). MBs are DNA hairpins labeled with a quencher on one end and a fluorophore on the other. In the hairpin form, the quencher and fluorophore are in close proximity and the fluorescence is quenched. However, binding of target DNA or RNA, which is complementary to the loop of the MB, separates the fluorophore and quencher, and the fluorescence is detectable. The inherent sensitivity of fluorescence makes the MBs sensitive probes of nucleic acid damage.

We have previously shown[12] (A. Mah, S. Yarasi, and G. R. Loppnow, manuscript in preparation) that the binding of the molecular beacon is sufficiently destabilized upon the occurrence of a single UV-induced, ionizing radiation-induced, or oxidation-induced damage site such that the hairpin configuration has a much lower melting temperature (i.e., free energy) than the hybridized probe. This condition results in lower fluorescence from the damaged target-loop hybrid and, consequently, a maximum discrimination of damaged vs undamaged oligonucleotide.

Fluorescently labeled locked nucleic acid (LNA) hairpins have the potential to detect UV-induced DNA damage. LNAs are nucleic acids containing ribonucleosides in which a methylene group connects the $C_{4'}$ and $O_{2'}$ atoms of the ribose sugar, locking it into the 3′ endo (North) conformation.[13] Such DNA probes appear to be more selective towards base pair mismatches[13] and have been used to enhance the specificity of probes for fluorescence in situ hybridization (FISH) assays, DNA microarrays, and real-time polymerase chain reaction (RT-PCR).[14–17] In this paper, we show that fluorescently labeled LNA hairpins can indeed detect UV-induced DNA damage, albeit with lower selectivity for damaged DNA than conventional MBs. The results show that the sensitivity of LNA MBs depends on ionic strength, target concentration, and the LNA composition of the hairpin. These results are discussed in the context of the conformation dynamics of LNA hairpins.

Experimental

Materials

The single-strand dT_{17} and dT_{24} oligonucleotide targets and the MBs were obtained from Integrated DNA Technologies Inc. (Coralville, Iowa) and are listed in Table 1. The target oligonucleotides were purified by standard desalting, whereas the MBs were purified by HPLC. The magnesium chloride ($MgCl_2$) and sodium chloride (NaCl) were both obtained from EMD Chemicals Inc. (Gibbstown, New Jersey). Tris and ethylenediaminetetraacetic acid (EDTA) were obtained from ICN Biomedicals, (Aurora, Ohio) and BDH Inc. (Toronto, Ontario), respectively. All chemicals were used as received. Nanopure water from a Barnsted Nanopure (Boston, Massachusetts) system was used for all solutions. The oligonucleotide samples and MBs were each dissolved in 1 mmol/L EDTA in nanopure water and kept frozen at –20 °C until needed.

UV irradiation

Nitrogen-purged solutions of 4 μmol/L dT_{24} in one of two buffers, either 10 mmol/L Tris, 1 mmol/L EDTA, and 3 mmol/L $MgCl_2$ adjusted to pH 7.5 or 20 mmol/L Tris, 1 mmol/L EDTA, 5 mmol/L $MgCl_2$, and 50 mmol/L NaCl adjusted to pH 7.5, were irradiated in sealed, UV-transparent 1 cm path length cuvettes. The cuvettes were placed in a water bath also contained in a UV-transparent water dish. The temperature, which was monitored by means of a Cole-Parmer DiGi-SENSE thermocouple (Niles, Illinois), was kept constant throughout the irradiation by the water bath. Oligonucleotide samples were irradiated in a Luzchem (Ottawa, Ontario) DEV photoreactor chamber with UVC light from lamps emitting principally at 254 nm. The samples were constantly stirred during irradiation, and the photoreactor was purged with nitrogen throughout the irradiation to flush out oxygen and any ozone subsequently generated from the UVC lamps. Control samples were handled identically, but were not exposed to UV radiation. The UVC lamps were turned on ~20 min before the start of irradiation to stabilize the lamp output.

Absorption and fluorescence measurements

Absorption spectra were recorded at intervals throughout the irradiation period on a Hewlett-Packard (Sunnyvale, California) 8452A diode array spectrophotometer by placing the irradiated cuvettes containing the target oligonucleotide solutions directly into the spectrophotometer. For the room-temperature fluorescence measurements, a 20 μL aliquot of each irradiated solution was taken at various time intervals and was later mixed with appropriate amounts of the probe and buffer solution to give final concentrations of 200 nmol/L oligonucleotide and 200 nmol/L probe for the MB–target (1:1) experiments and final concentrations of 1 μmol/L oligonucleotide target and 200 nmol/L probe for the MB–target (1:5) experiments. These solutions were then incubated in the dark at room temperature for about 24 h. Room-temperature fluorescence spectra of 200 μL aliquots of the incubated hybridization mixtures were measured using a Photon Technologies International (Birmingham, New Jersey) fluorescence system. The spectra were recorded between 500 and 700 nm with excitation at 495 nm. A 10 mm path length Suprasil quartz fluorescence cuvette was used for these measurements. The melting curves were baseline-corrected[19] to obtain accurate melting temperatures.

Results and discussion

The design and optimization of MBs to probe nucleic acid damage have been described previously in detail.[12] We use the same principles here for designing and optimizing the LNA MBs to ensure that these probes can selectively discriminate single damage sites in oligonucleotides. A representative melting curve of one of the MBs, both alone and in the presence of undamaged target, is shown in Fig. 1. In the absence of target DNA or RNA, the MB stem is closed and exhibits minimal fluorescence. In the presence of undamaged oligonucleotide, the MB opens and forms a stable target-loop hybrid with maximum fluorescence. Subsequently, the binding should be sufficiently destabilized upon the occurrence of a single damage site such that the hairpin configuration has a much lower melting temperature (i.e., free energy) than the hybridized probe. This condition results in lower fluorescence from the damaged target-loop hybrid and, consequently, a maximum discrimination of damaged vs undamaged oligonucleotide.

Can. J. Chem. Downloaded from www.nrcresearchpress.com by University of Electronic and Science Techonology of China on 09/18/12
For personal use only.

Table 1. Sequences of oligonucleotide.

Name[a]	Nucleotide sequence[b]	Melting temperature (°C)			
		MB stem	MB–dT_{24} hybrid	MB–dT_{17} hybrid	MB–rU_{17} hybrid
MB_{33}-4	5′-(6-FAM)-*CCCAAAAAAAAAAAAAAAAAA*(+A)A(+A)AAA(+A)AA(+A)*TTTGGG*-(3-DAB)-3′	40.6	38.3	—	—
MB_{33}-0	5′-(6-FAM)-*CCCAAAAAAAAAAAAAAAAAAAAAAAAATTTGGG*-(3-DAB)-3′	40.2	35.7	—	—
MB_{26}-4	5′-(6-FAM)-*CACAAA* AAA A(+A)A (+A)AA A(+A)A A(+A)*TTTGTG*-(3-BHQ_1)-3′	51.0	—	37.6	32.5
MB_{26}-5	5′-(6-FAM)-*CACAAAA*(+A)AA(+A)AA(+A)AA(+A)*TTTGTG*-(3-BHQ_1)-3′	51.6	—	42.0	32.9
MB_{26}-6	5′-(6-FAM)-*TCCAAAA*(+A)A(+A)A(+A)A(+A)A(+A) AA*TTTGGA*-(3-BHQ_1)-3′	54.4	—	43.1	40.1

[a]The subscript represents the total number of bases comprising the oligonucleotide sample and the number at the end represents the number of locked nucleic acids (LNAs) in the structure.
[b]"+" denotes the locked nucleotide, 6-FAM is 6-carboxyfluorescein, 3-DAB is 4-(4′-dimethylaminophenylazo)-benzoic acid) and 3-BHQ_1 is the black hole quencher-1.[20] The bases in italic typeface represent the stem of the molecular beacon (MB).

Fig. 1. Melting curve of 200 nmol/L molecular beacon $(MB)_{26}$-5 alone (○) and in the presence of 200 nmol/L target poly-dT_{17} (●) in 20 mmol/L Tris buffer containing 1 mmol/L EDTA, 5 mmol/L $MgCl_2$, and 50 mmol/L NaCl. Both curves were generated at a rate of 1.0 °C/min. This is a representative melting curve of the MBs alone and with targets, which all showed similar shapes.

The melting curves (Fig. 1) show that the MB stem melts at a slightly higher temperature than that of the target-loop hybrid, which is an important criterion for the optimal performance of the MB in the detection of damage.[12] To ensure this criterion is met, we performed thermal denaturation profiles of MBs in equilibrium with their targets and obtained the melting curves for the MBs alone and with the targets. The results are shown in Table 1. In all cases, the difference in melting temperature (T_m) between the hairpin and hybrid forms of the LNA MBs is similar to the difference in the T_m between the same forms of the non-LNA MB. This result suggests that both sensors may have similar selectivity to oligonucleotide damage.[12]

Target dT_{17} and rU_{17} were chosen for this study because of their well-known photochemistry. CPDs are the primary form of UV-induced damage in dT_{17}, in addition to the formation of small amounts of the pyrimidine–pyrimidinone [6–4] photoproduct.[5,20] In rU_{17} approximately equal amounts of the CPD and photohydrates are formed.[5,20] The quantum yields (Φ) for such processes are Φ = 0.044 for CPD formation in poly-dT and Φ = 0.012 and Φ = 0.015 for photohydrate and CPD formation, respectively, in poly-rU.[20] Therefore, comparing the MB hybridization with UV-damaged rU_{17} and dT_{17} will allow for a determination of the relative destabilizing effect of CPD and photohydrates on duplex formation. In addition, poly-dT and poly-rU targets exclude complications owing to other processes, such as spontaneous depurination because of thermal effects, UV-induced depurination of guanosine residues, and UV-induced oxidative damage for guanine bases.

The fluorescence of the LNA MBs with targets dT_{17} and rU_{17}, which have been irradiated with UVC, are shown in Fig. 2 as a function of irradiation time. As damage accumulates on the target oligonucleotide strand, the MB–target hybrid becomes less stable than the hairpin form at the

Can. J. Chem. Downloaded from www.nrcresearchpress.com by University of Electronic and Science Techonology of China on 09/18/12
For personal use only.

Fig. 2. Fluorescence intensity at 520 nm as a function of irradiation time for the targets. Only the 200 nmol/L (A) dT_{17} and (B) rU_{17} targets were irradiated (●) and the damage was detected by molecular beacon $(MB)_{26}$-5. Aliquots of the irradiated target were mixed with 200 nmol/L MB in buffer containing 200 mmol/L Tris, 5 mmol/L $MgCl_2$, 50 mmol/L NaCl, and 1 mmol/L EDTA at pH 7.5, and the fluorescence of this mixture was then measured. The control (○) is the unirradiated target sequences hybridized with the MB_{26}-5 in the same buffer. The black solid line through the irradiated sample points is a single exponential fit (eq. [1]) to the fluorescence intensity of the irradiated sample with (A) $I_0 = 0.3$, $A = 3.8$, and $\tau = 1.98$ min and (B) $I_0 = 0.2$, $A = 6.7$, and $\tau = 0.79$ min. The straight line through the control sample points is a linear fit drawn by eye.

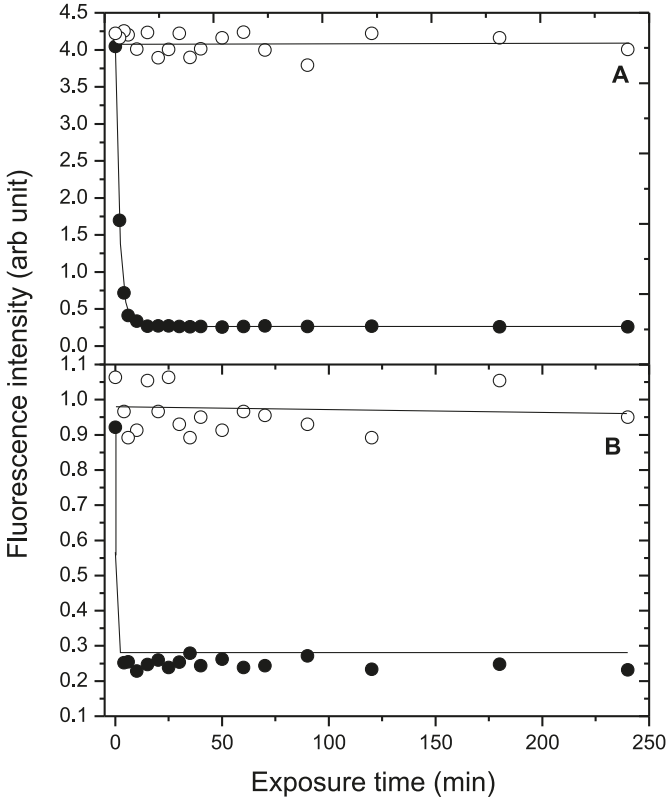

Fig. 3. Fluorescence intensity at 520 nm as a function of irradiation time for dT_{24} (●). Only the 1 μmol/L dT_{24} target was irradiated and the damage was detected by molecular beacon $(MB)_{33}$-4. Aliquots of the irradiated target were mixed with 200 nmol/L MB in buffer containing (A) 10 mmol/L Tris, 3 mmol/L $MgCl_2$, and 1 mmol/L EDTA at pH 7.5 and (B) 20 mmol/L Tris, 50 mmol/L NaCl, 5 mmol/L $MgCl_2$, and 1 mmol/L EDTA at pH 7.5. The fluorescence of this mixture was then measured. The control (○) is the unirradiated dT_{24} target sequence hybridized with MB_{33}-4 in the same buffer. The black solid line through the irradiated sample points is a single exponential fit (eq. [1]) to the fluorescence intensity of the irradiated sample with (A) $I_0 = 0.4$, $A = 1.3$, and $\tau = 8.4$ min and (B) $I_0 = 0.5$, $A = 3.5$, and $\tau = 5.6$ min. The straight line through the control sample points is a linear fit drawn by eye.

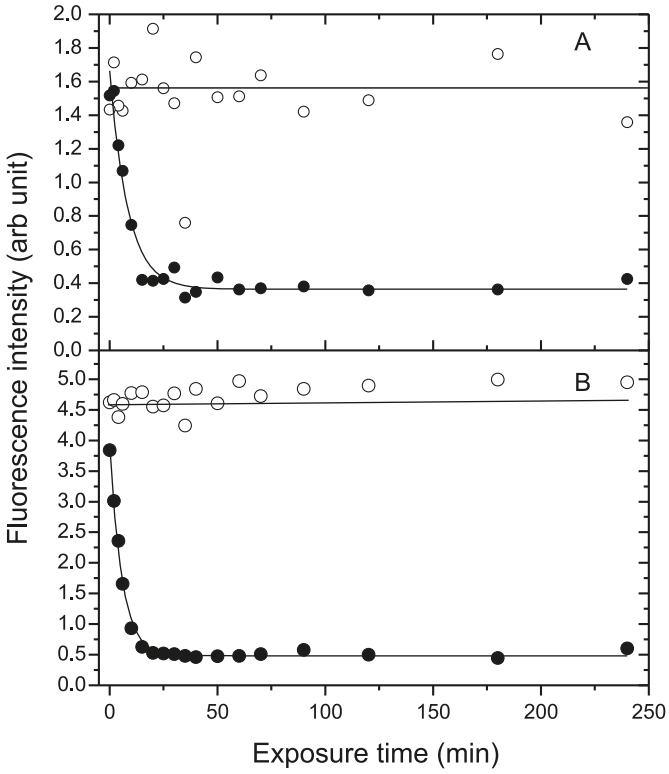

temperature used in the assay, effectively decreasing the fluorescence intensity. In Figs. 2–5, such a decrease with fluorescence is observed as the irradiation time increases. This result demonstrates that LNA MBs can detect DNA and RNA damage.

The damage curves shown in Figs. 2–5 have been fit with a single exponential function:

$$[1] \qquad I = I_0 + Ae^{-t/\tau}$$

where I is the fluorescence intensity at time t, I_0 is the fluorescence intensity at time 0, A is the amplitude, and $e^{-t/\tau}$ is the exponential decay. This fit allows us to determine the rate of decrease of fluorescence intensity with irradiation time. This decay in the fluorescence intensity represents the instability of the damaged target–MB hybrid. Therefore, the faster the rate of the fluorescence intensity decrease, the more selective the MB is at detecting UV-induced oligonucleotide damage under identical irradiation conditions for the same target. Because all of the target solutions were irradiated under the same conditions, with the same rate of oligonucleotide damage accumulation, the comparison of the rates of fluorescence intensity decrease provides a direct comparison of the selectivity of the different probes with oligonucleotide damage. We studied the effect of ionic strength, target–MB concentration ratios, and the LNA–DNA composition of the MB to determine the optimal conditions for the LNA MB to detect UV-induced damage with high selectivity.

Ionic strength of the medium

As shown previously,[12] MBs detect DNA damage at $[Mg^{2+}]$ of 1 mmol/L or higher. Tan and co-workers[13] showed that higher ionic strength buffers than that used for MBs may improve the LNA MB detection of single base pair mismatches. Figure 3 shows the fluorescence intensity decrease for the LNA MB as a function of target UVC irradiation time at two different conditions, one of low ionic

Can. J. Chem. Downloaded from www.nrcresearchpress.com by University of Electronic and Science Techonology of China on 09/18/12
For personal use only.

Fig. 4. Fluorescence intensity at 520 nm as a function of irradiation time for dT_{17} (●). Only (A) 1 μmol/L dT_{17} target and (B) 200 nmol/L dT_{17} target were irradiated and the damage was detected by molecular beacon $(MB)_{26}$-4. Aliquots of the irradiated target were mixed with 200 nmol/L MB in buffer containing 20 mmol/L Tris, 5 mmol/L $MgCl_2$, 50 mmol/L NaCl, and 1 mmol/L EDTA at pH 7.5, and the fluorescence of this mixture was then measured. The control (○) is the unirradiated dT_{17} target sequence hybridized with MB_{26}-4 in the same buffer. The black solid line through the irradiated sample points is a single exponential fit (eq. [1]) to the fluorescence intensity of the irradiated sample with (A) $I_0 = 0.2$, $A = 5.4$, and $\tau = 5.79$ min and (B) $I_0 = 0.2$, $A = 2.9$, and $\tau = 1.67$ min. The straight line through the control sample points is a linear fit drawn by eye.

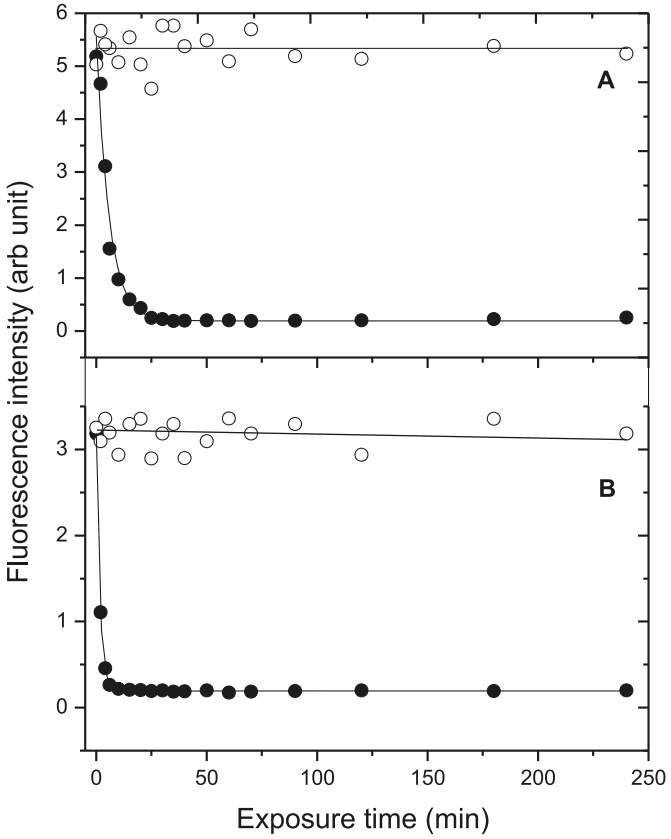

Fig. 5. Fluorescence intensity at 520 nm as a function of irradiation time for dT_{17}. Only the 200 nmol/L dT_{17} target was irradiated (●) and the damage was detected by (A) molecular beacon $(MB)_{26}$-4, (B) MB_{26}-5, and (C) MB_{26}-6. Aliquots of the irradiated target were mixed with 200 nmol/L MB in buffer containing 200 mmol/L Tris, 5 mmol/L $MgCl_2$, 50 mmol/L NaCl, and 1 mmol/L EDTA at pH 7.5, and the fluorescence of this mixture was measured. The control (○) is the unirradiated dT_{17} target sequence hybridized with the MBs in the same buffer. The black solid line through the irradiated sample points is a single exponential fit (eq. [1]) to the fluorescence intensity of the irradiated sample with (A) $I_0 = 0.2$, $A = 2.9$, and $\tau = 1.67$ min, (B) $I_0 = 0.3$, $A = 3.8$, and $\tau = 1.98$ min, and (C) $I_0 = 0.1$, $A = 3.3$, and $\tau = 2.13$ min. The straight line through the control sample points is a linear fit drawn by eye.

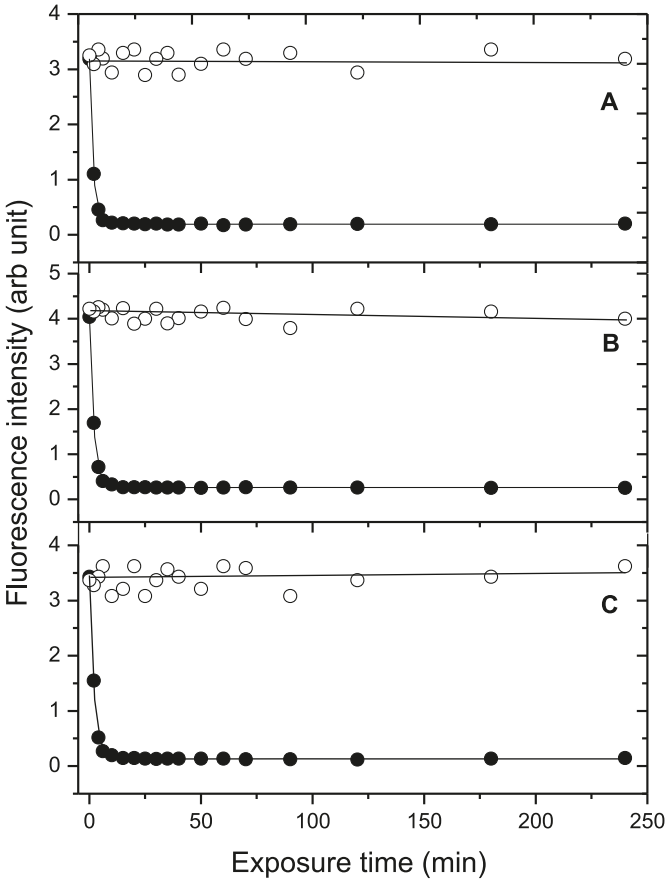

strength, having 1 mmol/L [Mg^{2+}], and the other is of higher ionic strength, incorporating both Na^+ and Mg^{2+} counterions. Table 2 presents the damage time constants for the decrease in fluorescence intensity when fit to eq. [1]. Results show that higher ionic strength increases the selectivity of the LNA MB probe to DNA damage (i.e., shows a more rapid decrease in MB fluorescence with irradiation time). With the conditions used here, a 1.5 times higher selectivity to damage is observed than with the lower ionic strength conditions. This result indicates the importance of ionic strength in determining the stability, structure, and binding behavior of MB probes.

The oligonucleotide target concentration

To study the effect of the target concentration in the presence of the high ionic strength medium on the selectivity of the LNA MBs to detect UV damage, we performed two experiments, one in which the MB_{26}-4 was incubated with UV-damaged dT_{17} target present in a 1:1 concentration ratio and one in which the concentration ratio is 1:5 for the MB–target. The results are shown in Table 2 and Fig. 4. These results show that high relative target concentration and high ionic strength yield longer damage constants than lower relative target concentrations. This result may suggest the formation of triplexes of two targets and one MB instead of the formation of a duplex hybrid between the target and the MB. Damage to one target of the triplex and subsequent dehybridization would still yield a stable MB–target duplex with high fluorescence. Not until both targets are damaged would the MB form a closed hairpin and exhibit fluorescence quenching. This scheme would yield longer damage constants than a system of only duplexes.

Can. J. Chem. Downloaded from www.nrcresearchpress.com by University of Electronic and Science Techonology of China on 09/18/12
For personal use only.

Table 2. Time constants of the first-order exponential decay of different samples.

Sample[a]	Ratio of MB:T	Ionic strength[b]	Regression coefficient	Time constant (min)
MB_{33}-4 + dT_{24}	1:5	Low	0.959	8.42
MB_{33}-4 + dT_{24}	1:5	High	0.993	5.61
MB_{33}-0 + dT_{24}	1:1	Low	0.996	1.34
MB_{26}-4 + dT_{17}	1:5	High	0.977	5.79
MB_{26}-4 + dT_{17}	1:1	High	1.000	1.67
MB_{26}-5 + dT_{17}	1:1	High	0.999	1.98
MB_{26}-6 + dT_{17}	1:1	High	0.997	2.13
MB_{26}-4 + rU_{17}	1:1	High	0.983	3×10^{-3}
MB_{26}-5 + rU_{17}	1:1	High	0.993	0.79
MB_{26}-6 + rU_{17}	1:1	High	0.997	1.54

[a]The subscript represents the total number of bases comprising the molecular beacon and the number at the end represents the number of locked nucleic acids (LNAs) in the structure.

[b]Low ionic strength, 10 mmol/L Tris + 3 mmol/L $MgCl_2$ + 1 mmol/L EDTA; and high ionic strength, 20 mmol/L Tris + 50 mmol/L NaCl + 5 mmol/L $MgCl_2$ + 1 mmol/L EDTA.

LNA–DNA ratio in the MB design

Previous studies[14] showed that the incorporation of LNA bases in the MB stem sequence significantly increases the stability of the hairpin structure. This increased stability greatly increases the energy barrier of opening the LNA–MB stem and, consequently, slows down its hybridization kinetics. In this work, we used MBs with LNA bases only in the loops, in different ratios, and with stems composed only of DNA bases. This design allows the study of the effect of LNA bases on the selectivity of the MB to detect UV damage in oligonucleotides and avoid the long hybridization kinetics of LNA bases in the MB stem.[13] Table 1 shows the four MBs used in this experiment, MB_{33}-0 (complement to dT_{24}), MB_{26}-4 (complement to dT_{17}), MB_{26}-5 (complement to dT_{17}), and MB_{26}-6 (complement to dT_{17}), with incorporation ratios of LNA bases in the MB loop of 0%, 24% (4/17), 29% (5/17), and 36% (6/17), respectively. The results after irradiating the target dT_{17} with UVC light and separately hybridizing aliquots of the damaged target with these four MBs are shown in Fig. 5 and Table 2. It is clear that the damage constants increase with increasing proportion of LNA bases in the loop, reflecting a decrease in selectivity of the LNA MB to detect UV damage with an increasing LNA ratio. Similar trends were obtained upon irradiating the rU_{17} target (Table 2). However, the damage constants of the single exponential decay fit (eq. [1]) are much lower for the rU_{17} target than for the dT_{17} one (Fig. 2). This result agrees with a previously published study,[12] which showed that the MB detection of UV-induced damage to poly-rU is much more selective than that to poly-dT, owing to a lower overall stability of damaged RNA–DNA hybrids compared with damaged DNA–DNA hybrids.

These results conclusively show that incorporation of LNA bases in the MB loop do not improve the sensitivity of the MBs to UVC-induced oligonucleotide damage. This is surprising in light of previous reports of LNA's greater sensitivity to single base pair mismatches.[13–16] Indeed, LNAs have been shown to be more sensitive than ssDNA probes in detecting single base pair mismatches.[13–16] However, these previous studies utilized LNA MBs that contained a greater proportion of locked nucleotides, up to a fully modified LNA MB loop.[14] The results presented here suggest that the difference in recognition sites for single base pair mismatches compared with UV-damage products (CPD and photohydrates) in the oligonucleotide target strand is significant enough to preclude the use of LNA MBs for selective detection of DNA damage.

A possible molecular explanation for this difference between damage and mismatch detection by the LNA MBs may lie in differences in the recognition site for single base mismatch (at the site of hydrogen bonding) compared with the recognition site of UV-damage products (at the C_5=C_6 bond, on the opposite side of the molecule from the base-pairing site). Although damage is known to disrupt the local DNA structure, such a perturbation may not be as large as the proximal change in hydrogen bonding that occurs upon single base-pair mismatch. Thus, damage may not destabilize the LNA MB as much as single base-pair mismatches. Future experiments should provide a more well-defined model for the detection of damage by the LNA MB and an explanation for the lower sensitivity of such detection by LNA MBs compared with MBs.

Conclusion

The results presented in this paper demonstrate the factors affecting the specificity of LNA MBs to detect UV-induced nucleic acid damage. High ionic strength and low target concentration improves the performance of these MBs in detecting UV-induced damage in dT and rU polynucleotides, as demonstrated by the shorter damage constants. Increasing the LNA ratio in the MB design leads to longer damage constants, reflecting a decrease in the selectivity of these MBs to detect damage. In conclusion, the results presented here show that, although LNA hairpin probes have greater selectivity to single base-pair mismatches than regular MB probes, they have lower specificity for detecting nucleic acid damage.

Acknowledgements

The authors acknowledge financial support for the work described in this paper from the Natural Sciences and Engineering Research Council of Canada (NSERC) Discovery

Grants-in-Aid of Research Programme, the Alberta Heritage Foundation for Medical Research (AHFMR), and the Alberta Cancer Foundation.

References

(1) Marrot, L.; Meunier, J. R. *J. Am. Acad. Dermatol.* **2008**, *58* (5), S139. doi:10.1016/j.jaad.2007.12.007.
(2) Lindahl, T. *Nature* **1993**, *362* (6422), 709. doi:10.1038/362709a0.
(3) Marnett, L. J.; Burcham, P. C. *Chem. Res. Toxicol.* **1993**, *6* (6), 771. doi:10.1021/tx00036a005.
(4) Ames, B. N.; Gold, L. S.; Willett, W. C. *Proc. Natl. Acad. Sci. U.S.A.* **1995**, *92* (12), 5258. doi:10.1073/pnas.92.12.5258.
(5) Mitchell, D. L. In *CRC Handbook of Organic Photochemistry and Photobiology;* Horspool, W. M.; Song, P.-S., Eds.; CRC Press: New York, 1995; pp 1326–1331.
(6) Weinfeld, M.; Soderlind, K.-J. M. *Biochemistry* **1991**, *30* (4), 1091. doi:10.1021/bi00218a031.
(7) Haab, B. B.; Mathies, R. A. *Anal. Chem.* **1995**, *67* (18), 3253. doi:10.1021/ac00114a023.
(8) Kaur, H.; Halliwell, B. *Biochem. J.* **1996**, *318*, 21.
(9) Dizdaroglu, M. *Methods Enzymol.* **1994**, *34*, 3. doi:10.1016/0076-6879(94)34072-2.
(10) Trevithick-Sutton, C. C.; Mikelsons, L.; Filippenko, V.; Scaiano, J. C. *Photochem. Photobiol.* **2007**, *83* (3), 556. doi:10.1562/2006-07-21-RA-976.
(11) Xing, J. Z.; Lee, J.; Leadon, S. A.; Weinfeld, M.; Le, X. C. *Methods* **2000**, *22* (2), 157. doi:10.1006/meth.2000.1056.
(12) Yarasi, S.; McConachie, C.; Loppnow, G. R. *Photochem. Photobiol.* **2005**, *81* (2), 467. doi:10.1562/2004-09-02-RA-301.1.
(13) Wang, L.; Yang, C. J.; Medley, C. D.; Benner, S. A.; Tan, W. *J. Am. Chem. Soc.* **2005**, *127* (45), 15664. doi:10.1021/ja052498g.
(14) Yang, C. J.; Wang, L.; Wu, Y.; Kim, Y.; Medley, C. D.; Lin, H.; Tan, W. *Nucleic Acids Res.* **2007**, *35* (12), 4030. doi:10.1093/nar/gkm358.
(15) Wu, Y.; Yang, C. J.; Moroz, L. L.; Tan, W. *Anal. Chem.* **2008**, *80* (8), 3025. doi:10.1021/ac702637w.
(16) Martinez, K.; Estevez, M.-C.; Wu, Y.; Phillips, J. A.; Medley, C. D.; Tan, W. *Anal. Chem.* **2009**, *81* (9), 3448. doi:10.1021/ac8027239.
(17) Morandi, L.; Ferrari, D.; Lombardo, C.; Pession, A.; Tallini, G. *J. Virol. Methods* **2007**, *140* (1-2), 148. doi:10.1016/j.jviromet.2006.11.014.
(18) See http://www.idtdna.com/catalog/Modifications/Modifications.aspx?ProductID=2059.
(19) Marky, L. A.; Breslauer, K. J. *Biopolymers* **1987**, *26* (9), 1601. doi:10.1002/bip.360260911.
(20) Ruzsicska, B. P.; Lemaire, D. G. E. In *CRC Handbook of Organic Photochemistry and Photobiology;* Horspool, W. M.; Song, P.-S., Eds.; CRC Press: New York, 1995; pp 1289–1317.

Can. J. Chem. Downloaded from www.nrcresearchpress.com by University of Electronic and Science Techonology of China on 09/18/12
For personal use only.

Density functional theory computational study on Diels–Alder reactions of cyclopentadiene with selected vinylsilanes and methylenecyclopropane

Nick Henry Werstiuk and Wojciech Sokol

Abstract: Aimed at predicting relative reactivities, density functional theory (DFT) calculations were carried out on a series of Diels–Alder reactions involving silylvinyl derivatives reacting with cyclopentadiene as part of a synthetic research project. Using three reactions for which experimental rate data are available to calibrate our calculations, we computationally pinpointed the best synthetic route to bicyclo[2.2.1]hept-5-ene-2,2-diylbis(trimethylsilane) (**1**). The synthesis begins with the Diels–Alder reaction of cyclopentadiene (**2**) with commercially available (1-bromovinyl)trimethylsilane (**6**).

Key words: DFT calculations, Diels–Alder reactions, bicyclic trimethylsilanes, activation parameters.

Résumé : Dans le cadre d'un projet de recherches en synthèse et dans le but de prédire les réactivités relatives, on a effectué des calculs de théorie de la fonctionnelle de la densité (TFD) sur une série de réactions de Diels–Alder impliquant des dérivés silylvinyles réagissant avec du cyclopentadiene. Utilisant trois réactions pour lesquelles des données expérimentales sur les vitesses sont disponibles pour calibrer nos calculs, on a précisé par calcul la meilleure voie de synthèse pour obtenir le bicyclo[2.2.1]hept-5-ène-2,2-diylbis(triméthylsilane) (**1**). La synthèse implique une réaction de Diels–Alder du cyclopentadiène (**2**) avec du (1-bromovinyl)triméthylsilane (**6**) disponible commercialement.

Mots-clés : calculs d'après la théorie de la fonctionnelle de la densité (TFD), réactions de Diels–Alder, triméthylsilanes, paramètres d'activation.

[Traduit par la Rédaction]

Introduction

Our interest in crystallizing the 6,6-trimethylsilyl- and 6,6-spirocyclopropyl-2-norbornyl cations — **6,6-diTMS-2-nbc** and **6,6-spirocyclo-2-nbc** — for low-temperature high-resolution X-ray determination of their electron densities as part of a quantum theory of atoms in molecules (QTAIM) study[1,2] led us to develop a new synthesis of bicyclo[2.2.1]-hept-5-ene-2,2-diylbis(trimethylsilane) (**1**); we reasoned that 2-bromo-bicyclo[2.2.1]heptane-6,6-diylbis(trimethylsilane) prepared from **1** would serve as a suitable precursor of **6,6-diTMS-2-nbc** at low temperature. To that end we undertook a density functional theory (DFT) study to assist us in pinpointing a new synthesis of **1** by utilizing a Diels–Alder (D–A) reaction for the first step (Scheme 1). The previously described route involved a two-stage process — the second step required 35 days to complete — from dicyclopentadiene (**2**) and 1,1-bis(trichlorosilyl)ethane (**3**).[3,4] In addition to the fact that the second step of the previous synthesis (**4** to **1**) required 35 days with frequent additions of MeMgI, **3** is not commercially available and its synthesis is not straightforward.[5,6] We considered three alternative D–A reactions summarized in Scheme 1: the reaction of ethene-1,1-diylbis(trimethylsilane) (**5**), commercially available (1-bromovinyl)trimethylsilane (**6**), and trichloro[1-(trimethylsilyl)vinyl]silane (**8**) with cyclopentadiene (**2**). To establish the best route, we carried out DFT calculations on the D–A reaction of **2** with **5**, **6**, and **8** to compute activation energies for the forward and reverse processes and, where possible, to determine the diastereoselectivities. We also studied the dimerization of **2** to **10N** and **10X**, its reaction with methylenecyclopropane (**11**) and with **3** to calibrate our calculations because activation energies for these reactions are available in the literature.[7–9] In this paper we report our computational results that pointed to the sequence of reactions **2** + **6** → **7X** + **7N** → **1** as the route of choice to **1**.

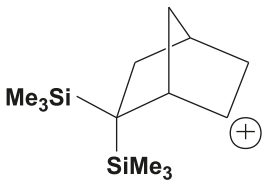

6,6-diTMS-2-nbc

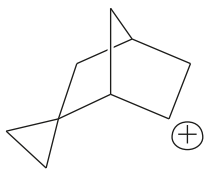

6,6-spirocyclo-2-nbc

Received 16 June 2010. Accepted 3 September 2010. Published on the NRC Research Press Web site at canjchem.nrc.ca on 3 March 2011.

This article is part of a Special Issue dedicated to Professor J. C. Scaiano.

N.H. Werstiuk[1] and W. Sokol. Department of Chemistry, McMaster University, Hamilton, ON L8S 4M1, Canada.

[1]Corresponding author (e-mail: werstiuk@mcmaster.ca).

Can. J. Chem. Downloaded from www.nrcresearchpress.com by University of Electronic and Science Techonology of China on 09/18/12
For personal use only.

Can. J. Chem. Downloaded from www.nrcresearchpress.com by University of Electronic and Science Techonology of China on 09/18/12
For personal use only.

Scheme 1. Synthetic routes to bicyclo[2.2.1]hept-5-ene-2,2-diylbis(trimethylsilane) (**1**).

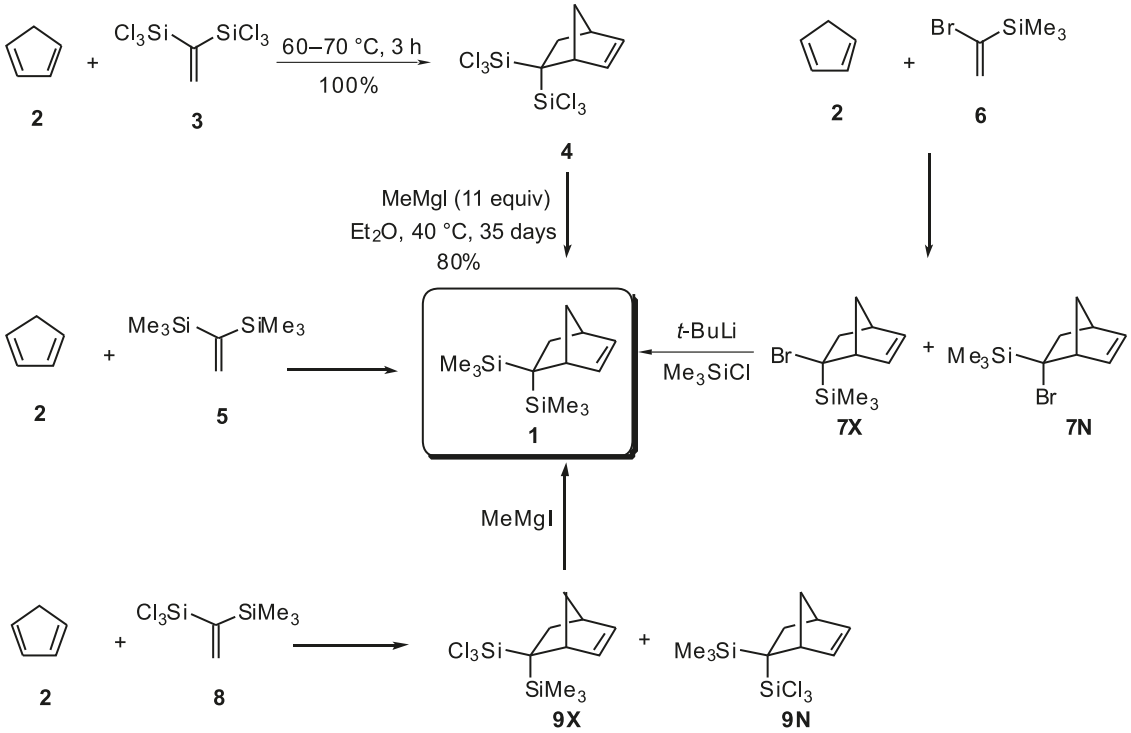

Computational methods

DFT calculations were performed with GAUSSIAN 03 (G03).[10] Geometries of all structures including transition states (TSs) were optimized at the MPW1PW91/6–31+G(d) level of theory as implemented in G03. The Cartesian coordinates and total energies of all structures are collected in the Supplementary data. We chose to use the MPW1PW91 functional because it was developed by Adamao and Berone[11] to better account for van der Waals forces. Frequency analyses, carried out at the same level of theory on the reactants, TSs, and products at 298.15 K for all species, confirmed that the transition states, as required, possessed one imaginary frequency. Calculations at the MPW1PW91/6–31+G(d) and B3PW91/6–31+G(d) levels on the dimerization of **2** yielded the results we reported previously.[12] Whereas calculations (the results are collected in the Supplementary data) at the B3PW91/6–31+G(d) level on the reactions of **2** with **3**, **5**, **6**, and **8** yielded results similar to those obtained at MPW1PW91/6–31+G(d), only the MPW1PW91/6–31+G(d) results are discussed in this paper. Frequency analyses were also carried out 463.15 K for selected molecules (the D–A synthesis of spiro[bicyclo[2.2.1]heptane-2,1′-cyclopropane]-5-ene is usually carried out at this temperature),[7a,7b] but the data are not reported. Energies of TSs were also corrected with basis set superposition error (BSSE)[13] calculations as implemented in G03. Thermochemical data for the forward and retro D–A reactions are collected in Table 1 and Table 2, respectively.

Results and discussion

To verify the accuracy of our calculations for the reaction of **2** with **5**, **6**, and **8**, we calibrated our approach by studying three reactions for which the experimental energies of activation are available, including the dimerization of **2**. As was found previously,[12,14] **10N-TS** exhibits C_2 symmetry. TSs **10N-TS** and **10X-TS** for formation of **10N** and **10X** are displayed in Fig. 1 along with the lengths (Å) of the incipient C–C bonds. It is seen that **10N-TS** exhibits a significantly larger asynchronicity (0.87 Å) than **10X-TS** (0.06). The key point is that our computed $\Delta H^{\ddagger}$ is in excellent agreement with the experimental value. The experimental Arrhenius activation energy (E_a) for the dimerization of **2** is 16.7 ± 0.6 kcal/mol (1 cal = 4.184 J).[9] Consequently, $\Delta H^{\ddagger}$ ($\Delta H^{\ddagger} = E_a - RT$, where R is the gas constant and T is the temperature) is estimated to be 16.1 kcal/mol at 298 K; our computed $\Delta H^{\ddagger}$ for endo dimerization is 17.0 kcal/mol ($\Delta G^{\ddagger}$ = 31.0 kcal/mol). That we found $\Delta H^{\ddagger}$ to be 20.3 kcal/mol ($\Delta G^{\ddagger}$ = 34.2 kcal/mol) for formation of **10X** — 3.3 kcal/mol higher than the endo reaction — is in keeping with the fact that **10N** is the kinetic product in the dimerization of **2**; experimentally, endo/exo > 49 ($\Delta\Delta G^{\ddagger}$ > 3.3 kcal/mol). We also found that $\Delta\Delta H$ for **10X** and **10N** is –1.1 kcal/mol at 298 K, in keeping with the fact that **10X** is the thermodynamic product in the dimerization of **2**. These results validate our computational studies.

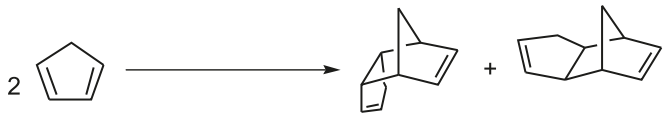

We also were interested in synthesis of spiro[bicyclo[2.2.1]heptane-2,1′-cyclopropane]-5-ene **12** and its conversion to the *exo*-2-bromo compound that would serve as a precursor to **6,6-spirocyclo-2-nbc** for our experimental electron density studies at low temperature. **12** is prepared in respectable yield from methylenecyclopropane and cyclo-

Can. J. Chem. Downloaded from www.nrcresearchpress.com by University of Electronic and Science Techonology of China on 09/18/12
For personal use only.

Table 1. MPW1PW91/6–31+G(d) activation parameters (kcal/mol; 1 cal = 4.184 J) for transition states at 298 K.

	Activation parameter (kcal/mol)				
TS for product (forward)	$\Delta E_{elec}^{\ddagger}$	$\Delta E_{elec}^{\ddagger}$+BSSE	$\Delta E_0^{\ddagger a}$	$\Delta H^{\ddagger b,c}$	$\Delta G^{\ddagger d}$
1	24.02	25.47	26.10	25.26	40.12
4	12.15	14.49	14.08	13.46	28.09
7X	16.74	22.90	18.27	17.66	31.05
7N	16.68	22.87	18.39	17.79	31.84
9X	19.24	21.13	21.09	20.48	34.82
9N	17.72	19.65	19.93	19.06	34.54
10X	19.29	20.39	21.14	20.35	34.16
10N	15.93	17.05	17.77	17.02	31.05
12	19.41	20.37	21.21	20.38	34.00

Note: BSSE, basis set superposition error; E_{elec}, uncorrected total energy; ZPE, zero point energy; E_{vib}, vibrational contribution to E; E_{rot}, rotational contribution to E; E_{trans}, translational contribution to E; R, gas constant; T, temperature; G, entropy of the reaction; and TS, transition state.

[a] $E_0 = E_{elec}$ + ZPE.
[b] $E = E_0 + E_{vib} + E_{rot} + E_{trans}$.
[c] $H = E + RT$.
[d] $G = H$ + TS.

Table 2. MPW1PW91/6–31+G(d) activation parameters (kcal/mol; 1 cal = 4.184 J) for retro Diels–Alder reactions at 298 K.

	Activation parameter (kcal/mol)				
From product	$\Delta E_{elec}^{\ddagger}$	$\Delta E_{elec}^{\ddagger}$+BSSE	$\Delta E_0^{\ddagger a}$	$\Delta H^{\ddagger b,c}$	$\Delta G^{\ddagger d}$
1	38.00	39.43	34.86	35.54	33.75
4	33.22	35.50	30.49	31.09	29.21
7X	45.76	51.93	42.53	43.06	42.05
7N	45.13	51.33	42.04	42.61	41.15
9X	35.54	37.41	32.46	33.75	29.79
9N	36.49	38.41	33.66	34.20	32.74
10X	44.57	45.66	41.01	41.60	40.27
10N	40.09	41.19	36.54	37.20	36.04
12	57.05	58.00	53.39	54.06	52.57

Note: BSSE, basis set superposition error; E_{elec}, uncorrected total energy; ZPE, zero point energy; E_{vib}, vibrational contribution to E; E_{rot}, rotational contribution to E; E_{trans}, translational contribution to E; R, gas constant; T, temperature; G, entropy of the reaction; and TS, transition state.

[a] $E_0 = E_{elec}$ + ZPE.
[b] $E = E_0 + E_{vib} + E_{rot} + E_{trans}$.
[c] $H = E + RT$
[d] $G = H$ + TS.

Scheme 2. Synthesis of spiro[bicyclo[2.2.1]heptane-2,1′-cyclopropane]-5-ene.

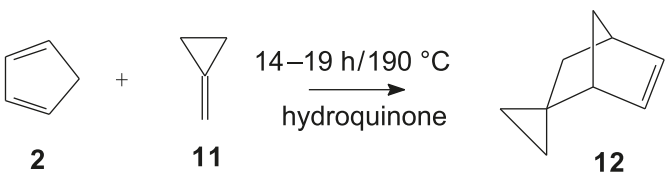

pentadiene[7a,7b] in the presence of hydroquinone (Scheme 2). Transition state **12-TS** for the reaction is displayed as Fig. 2 along with the incipient bond lengths. The asynchronicity is 0.10 Å — in this case the C1–C6 bond is shorter that the C4–C5 bond.

At 298 K the calculated $\Delta G^{\ddagger}$ was 34.0 kcal/mol, only 3.0 kcal/mol higher than $\Delta G^{\ddagger}$ for the endo dimerization of **2**. At 463 K, the temperature at which this reaction is typically carried out, $\Delta G^{\ddagger}$ was 41.5 kcal/mol, 3.3 kcal/mol higher than for the formation of **10N** at 463 K. The retro reaction of **12** has a much higher $\Delta G^{\ddagger}$ (52.6 kcal/mol) than the forward process, in keeping with the fact the **12** is the thermodynamic product.

We also studied the D–A reaction for the formation of **4** to calibrate our calculations. Kirmse and Söllenböhmer[3,4] showed that **4** is obtained quantitatively from **2** and **3** under relatively mild conditions at 333–343 K in 3 h, implying that the barrier for the reaction is lower than the barrier for dimerization of **2**. This reaction has a much lower computed

Can. J. Chem. Downloaded from www.nrcresearchpress.com by University of Electronic and Science Techonology of China on 09/18/12
For personal use only.

Fig. 1. Transition states (TS) (*a*) **10N-TS** and (*b*) **10X-TS** and incipient C–C bond lengths (Å) at MPW1PW91/6–31+G(d).

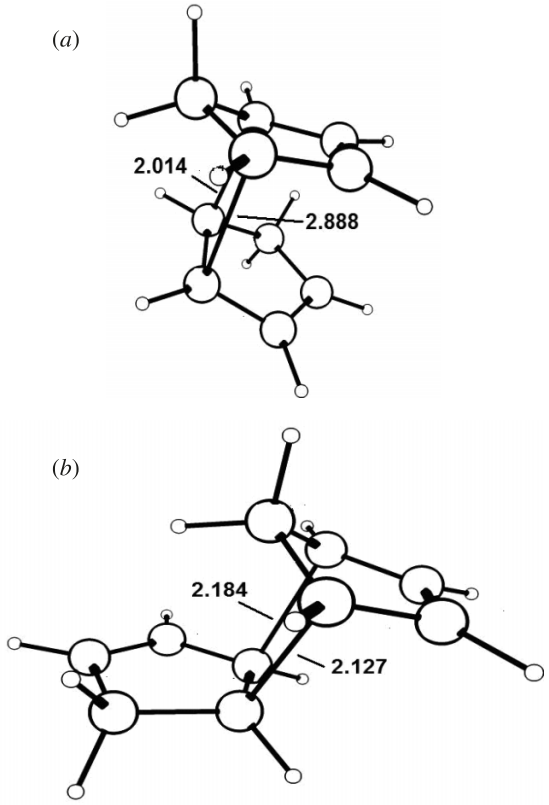

Fig. 2. Transition state (TS) **12-TS** and incipient C–C bond lengths (Å) at MPW1PW91/6–31+G(d).

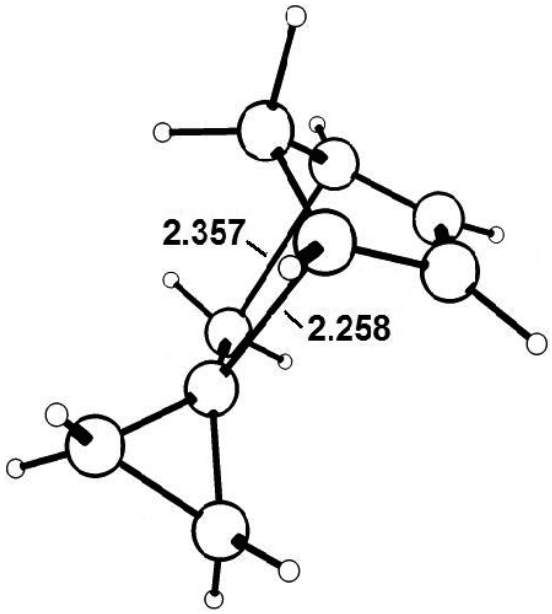

$\Delta H^{\ddagger}$ than endo dimerization of **2** (13.5 vs 17.0 kcal/mol) at 298 K. This is also seen in the relative free energies of activation (28.1 vs 31.0 kcal/mol). Of the six D–A reactions we studied, the formation of **4** has the lowest barrier, nicely in keeping with the experimental results. Transition state **4-TS** for the reaction of **2** + **3** is displayed as Fig. 3*a* along with

Fig. 3. Transition states (TS) (*a*) **4-TS** and (*b*) **1-TS** and incipient C–C bond lengths (Å) at MPW1PW91/6–31+G(d).

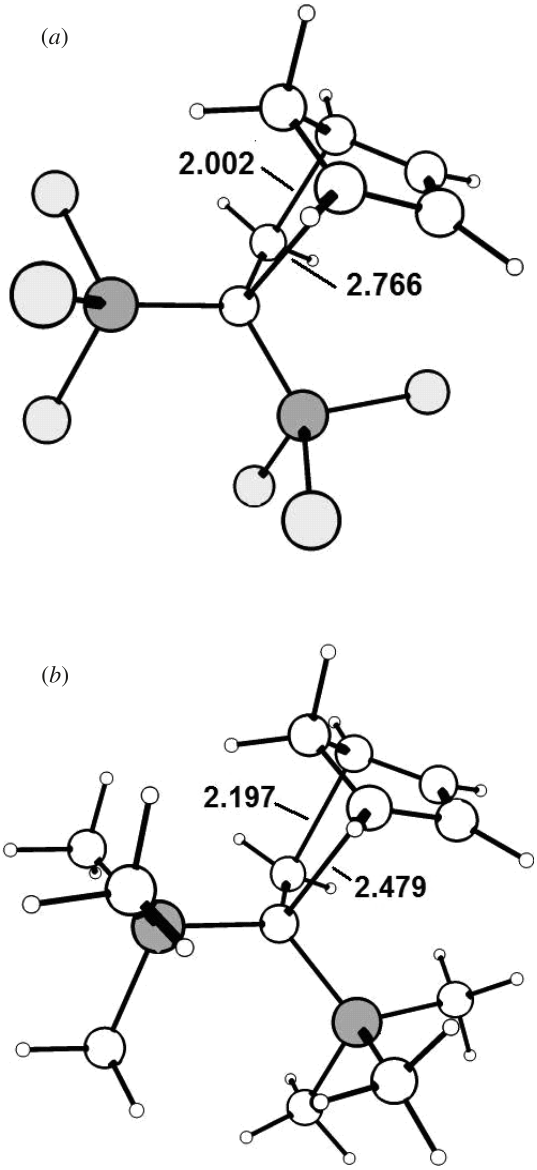

the incipient C–C bonds. In this case, the asynchronicity is large (0.76Å) with the incipient C1–C6 bond being much longer than the C4–C5 bond.

Given that our computational results on the formation of **10N**, **12**, and **4** correlated well with experimental studies documented in the literature, we expect the computed thermochemical parameters for the other D–A reactions included in this study to be of comparable accuracy and thereby assist us in selecting the best route to **1**; we proceeded to study alternative D–A reactions to **1** computationally. It should be pointed out that the BSSE corrections for the dimerization of **2** and its reactions with **11** and **3** did not significantly alter the differences in activation energies based on the uncorrected total energies ($\Delta\Delta E_{elec}^{\ddagger}$s) even though the BSSE-corrected $\Delta E_{elec}^{\ddagger}$ values (column 3 of Tables 1 and 2) were 2–3 kcal/mol higher than the uncorrected values. We expect that the same situation holds for the reactions of **2** with **5**, **6**, and **8**.

Can. J. Chem. Downloaded from www.nrcresearchpress.com by University of Electronic and Science Techonology of China on 09/18/12
For personal use only.

Fig. 4. Transition states (TS) (*a*) **9X-TS** and (*b*) **9N-TS** and incipient C–C bond lengths (Å) at MPW1PW91/6–31+G(d).

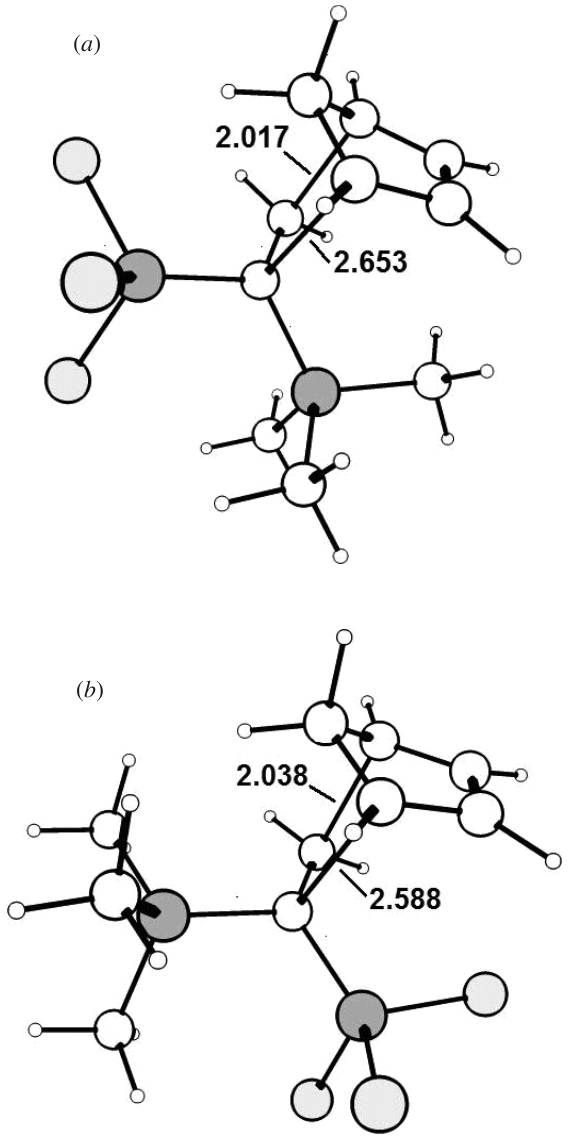

Fig. 5. Transition states (TS) (*a*) **7X-TS** and (*b*) **7N-TS** and incipient C–C bond lengths (Å) at MPW1PW91/6–31+G(d).

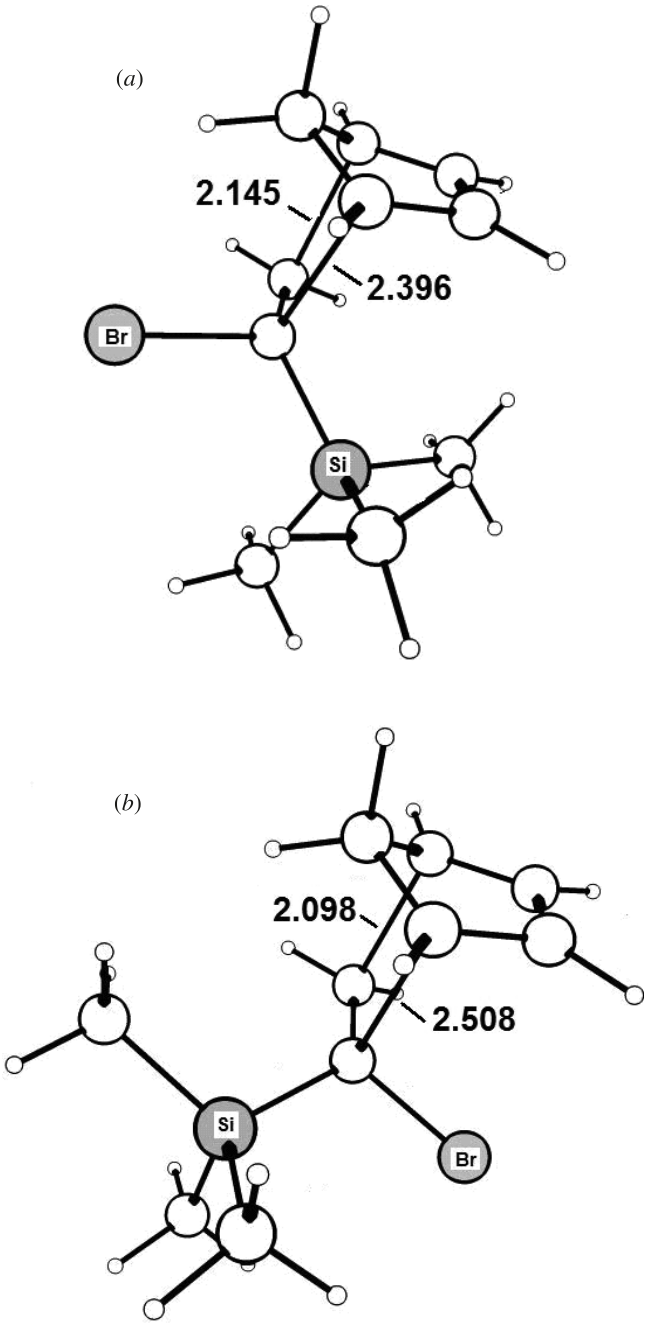

An alternative route directly to **1** involves the reaction of **2** with **5**. In this case, the asynchronicity (0.28 Å) is considerably smaller than in the case of the formation of **4**, with the C1–C6 incipient bond being longer than the C4–C5 bond even though the two trimethylsilyl groups are the largest pair of substiutents investigated at C6. At 298 K, $\Delta G^{\ddagger}$ is 40.1 kcal/mol, 12.0 and 9.1 kcal/mol higher than the $\Delta G^{\ddagger}$s for the formation of **4** and **10N**, respectively. Moreover, $\Delta G^{\ddagger}$ for the reverse reaction is 33.7 kcal/mol, 6.4 kcal/mol lower than $\Delta G^{\ddagger}$ for the forward reaction. At 463 K, the forward and reverse $\Delta G^{\ddagger}$s are 48.4 and 32.7 kcal/mol, respectively. This means that only trace amounts of **1** will be present when the reaction is attempted. Clearly, the **2** + **5** route to **1** is not a viable one.

The second alternate route we studied involved the reaction of **2** with **8**. The exo and endo TSs **9X-TS** and **9N-TS** are displayed in Fig. 4 along with the incipient C4–C5 and C1–C6 bond lengths. In this case diastereomeric products are possible. The asynchronicity indexes are relatively high; 0.64 for the **9X-TS** and 0.55 for **9N-TS**. That the $\Delta G^{\ddagger}$s for formation of *exo*-trichloro[2-(trimethylsilyl)bicyclo[2.2.1]-hept-5-en-2-yl]silane (**9X**) and *endo*-trichloro[2-(trimethylsilyl)bicyclo[2.2.1]hept-5-en-2-yl]silane (**9N**) at 298 K are 34.8 kcal/mol 34.5 kcal/mol, respectively, indicates that a small kinetic diastereoselectivity is expected. The barriers for the retro reactions of **9X** and **9N** were 29.8 and 32.7 kcal/mol, respectively. That the retro barriers are lower than the barriers for the forward reactions established that the reaction of **2** with **8** is also not a viable route to **1** via **9X** and **9N**. At 463 K the $\Delta G^{\ddagger}$s for the forward reactions for formation of *exo*- and *endo*-trichloro[2-(trimethylsilyl)bicyclo[2.2.1]hept-5-en-2-yl]silane are 42.7 and 43.1 kcal/mol,

Can. J. Chem. Downloaded from www.nrcresearchpress.com by University of Electronic and Science Techonology of China on 09/18/12
For personal use only.

respectively, 15.5 and 11.2 kcal/mol higher than the $\Delta G^{\ddagger}$s for the retro reactions. Clearly, the sequence **2** + **8** → **9X** + **9N** → **1** is not a viable route to **1**.

The third alternate route we explored computationally involved the reaction of (1-bromovinyl)trimethylsilane (**6**) with **2** to yield **7X** and **7N**, which would yield **1** via standard lithiation and silylation steps. Transition states **7X-TS** and **7N-TS** for the reaction of **2** + **6** are displayed in Figs. 5*a* and 5*b* along with the lengths of the incipient C–C bonds. The TSs exhibit asynchronicities of 0.25 and 0.41 Å, respectively. The computed $\Delta G^{\ddagger}$s for the formation of **7X** and **7N** are 31.0 and 31.8 kcal/mol at 298 K (importantly, the ΔGs are fairly large and negative (–10.1 for **7X** and –9.9 for **7N**)) with the retro barriers being 42.0 and 41.1 kcal/mol, respectively. Even at 463 K, the barriers for retro reactions remained higher (40.5 and 41.1 kcal/mol) than the forward reactions (28.4 and 38.2 kcal/mol) and, consequently, **7X** and **7N** will be the thermodynamic products in both cases. Based on the fact that (*i*) **6** is commercially available, (*ii*) the D–A reaction with **2** to yield **7X** and **7N** is expected to proceed readily based on the computed barriers, and (*iii*) **7X** and **7N** are the thermodynamic products, it is clear the pathway that includes the preparation of **7X** and **7N** is the sequence of choice for the synthesis of **1**.

Conclusion

This study demonstrated the advantage of using DFT calculations in a synthetic research project. We successfully used DFT calculations at the MPW1PW91/6–31+G(d) level to define the route of choice for the synthesis of bicyclo[2.2.1]hept-5-ene-2,2-diylbis(trimethylsilane) (**1**) beginning with a Diels–Alder reaction.

Supplementary data

Supplementary data are available with this article through the journal Web site (www.nrcresearchpress.com/cjc).

Acknowledgement

Financial support by the Natural Sciences and Engineering Research Council of Canada (NSERC) is gratefully acknowledged. Computing resources of the McMaster node of SHARCnet (Shared Hierarchical Academic Research Computing Network (of Ontario)) were used in this study.

References

(1) Bader, R. F. W. *Atoms in Molecules — A Quantum Theory;* Oxford University Press: Oxford, UK, 1990.

(2) Werstiuk, N. H.; Muchall, H. M. In *Proceedings of the Gordon Research Conference on Electron Distribution and Chemical Bonding:* Mount Holyoke College: South Hadley, MA, 2004.

(3) Kirmse, W.; Söllenböhmer, F. *J. Chem. Soc. Chem. Commun.* **1989** (12), 774. doi:10.1039/c39890000774.

(4) Kirmse, W.; Söllenböhmer, F. *J. Am. Chem. Soc.* **1989**, *111* (11), 4127. doi:10.1021/ja00193a070.

(5) Petrov, A. D.; Mironov, V. F.; Glukhovtsev, V. G. *Izv. Akad. Nauk SSSR, Ser. Khim.* **1956**, 461.

(6) Ruedinger, C.; Beruda, H.; Schmidbaur, H. *Z. Naturforsch. B: Chem. Sci.* **1994**, *49*, 1348.

(7) (a) Köster, R.; Arora, S.; Binger, P. *Synthesis* **1971**, *1971* (06), 322. doi:10.1055/s-1971-21733.; (b) Peiris, S.; Raguskas, A. J.; Sothers, J. B. *Can. J. Chem.* **1987**, *65*, 789.

(8) Harkness, J. B.; Kistiakowsky, G. B.; Mears, W. H. *J. Chem. Phys.* **1937**, *5* (9), 682. doi:10.1063/1.1750100.

(9) Benford, G. A.; Wassermann, A. *J. Chem. Soc.* **1939**, 362. doi:10.1039/jr9390000362.

(10) Frisch, M. J.; Trucks, G. W.; Schlegel, H. B.; Scuseria, G. E.; Robb, M. A.; Cheeseman, J. R.; Montgomery, J. A., Jr.; Vreven, T.; Kudin, K. N.; Burant, J. C.; Millam, J. M.; Iyengar, S. S.; Tomasi, J.; Barone, V.; Mennucci, B.; Cossi, M.; Scalmani, G.; Rega, N.; Petersson, G. A.; Nakatsuji, H.; Hada, M.; Ehara, M.; Toyota, K.; Fukuda, R.; Hasegawa, J.; Ishida, M.; Nakajima, T.; Honda, Y.; Kitao, O.; Nakai, H.; Klene, M.; Li, X.; Knox, J. E.; Hratchian, H. P.; Cross, J. B.; Bakken, V.; Adamo, C.; Jaramillo, J.; Gomperts, R.; Stratmann, R. E.; Yazyev, O.; Austin, A. J.; Cammi, R.; Pomelli, C.; Ochterski, J. W.; Ayala, P. Y.; Morokuma, K.; Voth, G. A.; Salvador, P.; Dannenberg, J. J.; Zakrzewski, V. G.; Dapprich, S.; Daniels, A. D.; Strain, M. C.; Farkas, O.; Malick, D. K.; Rabuck, A. D.; Raghavachari, K.; Foresman, J. B.; Ortiz, J. V.; Cui, Q.; Baboul, A. G.; Clifford, S.; Cioslowski, J.; Stefanov, B. B.; Liu, G.; Liashenko, A.; Piskorz, P.; Komaromi, I.; Martin, R. L.; Fox, D. J.; Keith, T.; Al-Laham, M. A.; Peng, C. Y.; Nanayakkara, A.; Challacombe, M.; Gill, P. M. W.; Johnson, B.; Chen, W.; Wong, M. W.; Gonzalez, C.; Pople, J. A. *Gaussian 03, Revisions B.02 and C.02;* Gaussian Inc.: Wallingford, CT, 2004.

(11) Adamo, C.; Barone, V. *J. Chem. Phys.* **1998**, *108* (2), 664. doi:10.1063/1.475428.

(12) Werstiuk, N. H.; Sokol, W. *Can. J. Chem.* **2008**, *86* (7), 737. doi:10.1139/V08-070.

(13) Simon, S.; Duran, M.; Dannenberg, J. J. *J. Chem. Phys.* **1996**, *105* (24), 11024. doi:10.1063/1.472902.

(14) Carmella, P.; Quadrelli, P.; Toma, L. *J. Am. Chem. Soc.* **2002**, *124*, 1130. doi:10.1021/ja016622h.

Luminescence and decay properties of the $^1D_2$ level of Pr^{3+}-doped YPO_4

J. Collins, M. Bettinelli, and B. Di Bartolo

Abstract: This investigation reports on the spectroscopic properties of trivalent Pr in YPO_4. In particular, we show how the luminescence from the $^1D_2$ level depends on the polarization of the emission and on the temperature of the sample. We also report on the decay kinetics of the $^1D_2$ level, which show the lifetime decreasing as temperature is increased. Our observed lifetime of 440 μs is at low temperature and is significantly longer than that reported by other workers. We explain the temperature dependence of the $^1D_2$ emission by considering the population redistribution in the $^1D_2$ level, without invoking the existence of multiphonon relaxation. Finally, we estimate the radiative decay rates of individual crystal field levels within the $^1D_2$ manifold.

Key words: luminescence, praseodymium, yttrium phosphate, $^1D_2$, radiative decay, lifetime, temperature dependence.

Résumé : On rapporte les propriétés spectroscopiques du Pr trivalent dans du YPO_4. En particulier, on a cherché à établir quelle est la dépendance de la luminescence du niveau $^1D_2$ sur la polarisation de l'émission et sur la température de l'échantillon. On a aussi déterminé la cinétique de décroissance du niveau $^1D_2$; elle montre que le temps de vie diminue avec une augmentation de la température. Le temps de vie observé dans cette étude à basse température, 440 μs, est beaucoup plus long que celui rapporté par d'autres auteurs. On explique cette dépendance de l'émission $^1D_2$ sur la température par une considération de la redistribution de la population dans le niveau $^1D_2$ sans invoquer l'existence d'une relaxation multiphoton. Enfin, on a évalué les vitesses de décroissance radiative des niveaux individuels du champ cristallin dans la voie $^1D_2$.

Mots-clés : luminescence, praséodyme, phosphate d'yttrium, $^1D_2$, décroissance radiative, temps de vie, dépendance sur la température.

[Traduit par la Rédaction]

Introduction

Pr^{3+}-doped insulators have been investigated for potential use in a variety of applications such as scintillators and phosphors. An energy level diagram of trivalent Pr in solids is shown in Fig. 1. The levels of primary interest for luminescence applications are the $^3P_0$ and $^1D_2$ levels. The $^1D_2$ level has been of recent interest for possible phosphor applications because of its strong emission in the red and because it is efficiently fed from the upper levels.[1,2] Pr-doped YPO_4 also shows efficient feeding of the $^1D_2$ level, and so it represents a system of potential interest.

Previous work on Pr-doped YPO_4 shows that the maximum phonon energies are greater than 1000 cm^{-1}, and that the multiphonon decay is very strong.[3,4] These factors often lead to weak luminescence from the $^3P_0$ level, and correspondingly low quantum efficiencies. The strong multiphonon relaxation from the $^3P_0$ level, however, results in favorable conditions for luminescence from the $^1D_2$ level. The reason for this is that when the system is pumped into the more strongly absorbing ^3P_J (J = 0, 1, 2) levels, efficient multiphonon relaxation leads to the vast majority of the ions ending up in the metastable $^1D_2$. The question that remains open at this point is whether the $^1D_2$ emission is an efficient one or whether nonradiative decay processes, such as multiphonon decay, compete effectively with radiative decay. This is the central question addressed in this paper.

The decay of the $^1D_2$ has been shown to involve several processes. In addition to radiative decay and multiphonon relaxation, the $^1D_2$ decays via a cross-relaxation process that tends to quench the emission at high concentrations. These processes are shown in Fig. 1. This cross-relaxation is observed in many samples, especially a high Pr doping.[5,6] In some systems, Pr^{3+} has also exhibited upconversion, but this has not been observed in the YPO_4 system.[7,8] In this work we study the decay from the $^1D_2$ level in Pr-doped YPO_4 and attempt to understand which processes are responsible for the decay.

Several workers have studied this system, and have come to varying conclusions regarding the decay of the $^1D_2$ level.

Received 9 May 2010. Accepted 3 September 2010. Published on the NRC Research Press Web site at canjchem.nrc.ca on 3 March 2011.

This article is part of a Special Issue dedicated to Professor J. C. Scaiano.

J. Collins.[1] Department of Physics and Astronomy, Wheaton College, Norton MA 02766, USA.
M. Bettinelli. Dipartmento di Biotechnologie, Universitá Delgi Studi di Verona, Verona, Italy.
B. DiBartolo. Department of Physics, Boston College, Chestnut Hill, MA 02467, USA.

[1]Corresponding author (e-mail: jcollins@wheatonma.edu).

Can. J. Chem. Downloaded from www.nrcresearchpress.com by University of Electronic and Science Techonology of China on 09/18/12
For personal use only.

Can. J. Chem. Downloaded from www.nrcresearchpress.com by University of Electronic and Science Techonology of China on 09/18/12
For personal use only.

Fig. 1. Energy level diagram of the Pr^{3+} in YPO_4. Decay processes shown are (1) radiative decay, (2) multiphonon decay, and (3) nonradiative cross-relaxation.

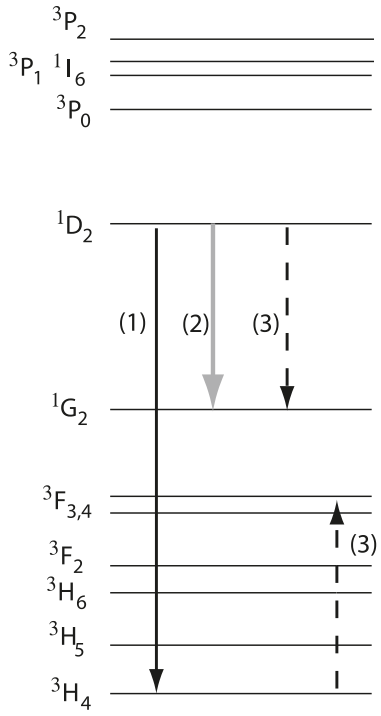

The literature contains conflicting values for the $^1D_2$ lifetime. Also, whereas some workers conclude that multiphonon relaxation is a prominent decay process, others conclude that there is no multiphonon decay and that cross-relaxation is the dominant nonradiative decay mechanism. We will discuss these results in more detail later. In this paper we present evidence showing that in low-doped systems the decay is overwhelmingly radiative. We demonstrate this by examining both the luminescence spectra and the response of the system to pulsed excitation in the temperature range from 30 to 300 K. The temperature dependence of the radiative lifetime closely follows the results as predicted from the luminescence data at all temperatures, so that there is no reason to invoke the presence of any nonradiative decay processes.

Experimental method

Single crystals of YPO_4 doped with 0.1 mol% Pr^{3+} (substituting for Y^{3+}) were grown by spontaneous nucleation from a $PbO–P_2O_5$ flux (1:1 molar ratio).[9] The reagents employed for the growths were $NH_4H_2PO_4$ (reagent grade), PbO (reagent grade), Y_2O_3 (99.99%), and Pr_6O_{11} (99.999%). The batch was put in a covered Pt crucible with a tightly fitting lid and heated up to 1300 °C inside a horizontal furnace. After a soaking time of about 15 h, the temperature was lowered to 800 °C with a rate of ≈1.8 °C/h; the crucible was then drawn out from the furnace and quickly inverted to separate the flux from the crystals grown at the bottom of the crucible. The flux was dissolved using hot diluted nitric acid. Single crystals of good optical quality were obtained in the form of platelets having sizes up to $10 \times 4 \times 0.5$ mm^3 elongated in the direction of the *c* axis of the xenotime crystal structure.

YPO_4 crystallizes in the tetragonal $I4_1/amd$ space group (No. 141) with $Z = 4$, $a = b = 6.8817(5)$, $c = 6.0177(6)$ Å, and $\alpha = \beta = \gamma = 90°$.[10] The xenotime structure is characterized by chains of alternating edge-sharing VO_4 (tetrahedral) and YO_8 (dodecahedral) units, which develop along the crystallographic *c* axis. The Pr^{3+} doping ions replace Y^{3+} in their eightfold coordinated sites having D_{2d} point symmetry.

Absorption measurements on the sample were taken at room temperature with a PerkinElmer model 750 UV–vis–NIR absorption spectrophotometer. For all luminescence measurements, the sample was excited with a Molectron model DL-II dye laser pumped by a Molectron model UV-400 nitrogen laser. The laser produces pulses having ~1 mJ of energy and a width of 8 ns. The luminescence from the sample is dispersed by a 1 m McPherson monochromator and detected with a Hamamatsu photomultiplier tube type R1387, which was cooled by a Products for Research TE-cooled housing. A filter was placed at the entrance slit of the monochromator to eliminate scattered light from the laser, and a polarizer was also placed at the entrance slit when required. For luminescence spectra, the signal from the photomultiplier was sent to an EG&GPARC model 4121B boxcar averager. So as to maximize the signal, we used the input having 1 MΩ of impedance; no attempt was made to do time-resolved studies. The signal was averaged over 30 pulses and stored on the computer using LabVIEW. For lifetime studies, the signal from the phototube was sent directly into an oscilloscope (Tektronix model TDS3052B) and averaged over 512 pulses. The sample was cooled using a Janis model RD closed-cycle He refrigerator connected to an Oerlikon Leybold Vacuum Coolpack 2200 compressor unit. The temperature was varied from 28 to 300 K using a Lake Shore model 805 temperature controller.

Experimental results

Absorption measurements at room temperature were taken between 800 and 300 nm and display the narrow peaks associated with the Pr ion, as well as a broad-band absorption beginning near 500 nm and continually increasing in strength. This band did not seem to affect the emission from the $^1D_2$ level of the Pr ion, which is the main focus of this paper, and so will not be discussed further.

Emission spectra were taken from 470 to 800 nm and show emission lines originating from both the $^1D_2$ and the $^3P_0$ levels. The red emission near 600 nm, corresponding to the $^1D_2 \rightarrow {}^3H_4$ transition, is the most prominent set of lines at all temperatures. Figure 2 shows the crystal field levels of the excited $^1D_2$ manifold and of the ground $^3H_4$ manifold. Emission from the $^3P_0$ level is very weak in YPO_4.

Emission spectra owing to the $^1D_2 \rightarrow {}^3H_4$ transitions in the red were taken at several temperatures between 30 and 300 K. For these measurements, the sample was pumped into the $^3P_2$ level, near 450 nm. Following excitation, the Pr ion underwent a fast nonradiative decay to the $^1D_2$ level. At each temperature, we took three spectra in the range from 590 to 620 nm: one spectrum for σ-polarized emission, one for π-polarized emission, and one with no polarizer. Sample results of these spectra at 90, 150, and 300 K are shown in

Can. J. Chem. Downloaded from www.nrcresearchpress.com by University of Electronic and Science Techonology of China on 09/18/12
For personal use only.

Fig. 2. Crystal field levels of the $^1D_2$ and $^3H_4$ manifolds of Pr^{3+} in YPO_4. Energy values are taken from Moune et al.[3]

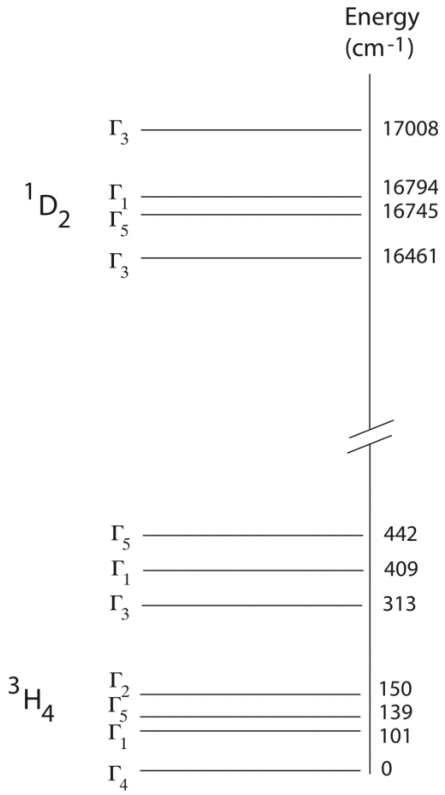

Figs. 3, 4, and 5, respectively. We note that as the temperature increases, the upper levels of the manifold become populated; consequently, more lines appear in the spectrum. The lines also broaden as temperature increases.

Before turning our attention to the luminescence spectra, we note that the crystals had some small cracks and other scattering centers in its bulk. The sides of the crystal, through which the luminescence was observed, were mostly smooth but not polished, and so scattered some of the emitted light. Because of this scattering, the σ-polarized spectra contain small amounts of π-polarized emission, and vice versa. The spectra in Figs. 3–5 all show the effects of these scattering centers.

Figures 3–5 exhibit four prominent lines between 595 and 605 nm, as seen in the emission spectra without the polarizer. In the σ-polarized spectra the lines at 597.2 and 600.4 nm dominate, whereas the lines at 595.5 and 602.2 nm are suppressed. In the π-polarized spectra the opposite occurs: the lines at 595.5 and 602.2 nm dominate, whereas the lines at 597.2 and 600.4 nm are suppressed. Comparing the emission spectra for different polarizations and knowing the energies of each transition (see Fig. 2), it is straightforward to assign transitions to the various lines. The assignments, shown in Figs. 3–5 and in Table 1, are in good agreement with those given by Reid and Moos.[4]

The response of the system to pulsed excitation was measured by monitoring emission from the $^3P_0$ level (at 500 nm) and the $^1D_2$ level (at 613 nm). For these measurements, excitation was into the $^3P_2$ level near 450 nm. The $^3P_0$ decay curve was a pure exponential with a lifetime of

Fig. 3. Luminescence spectrum of YPO_4:Pr (0.1%) at 90 K for (*a*) no polarizer in the optical path, (*b*) σ-polarized emission, and (*c*) π-polarized emission. Excitation was into the $^3P_2$ level near 450 nm.

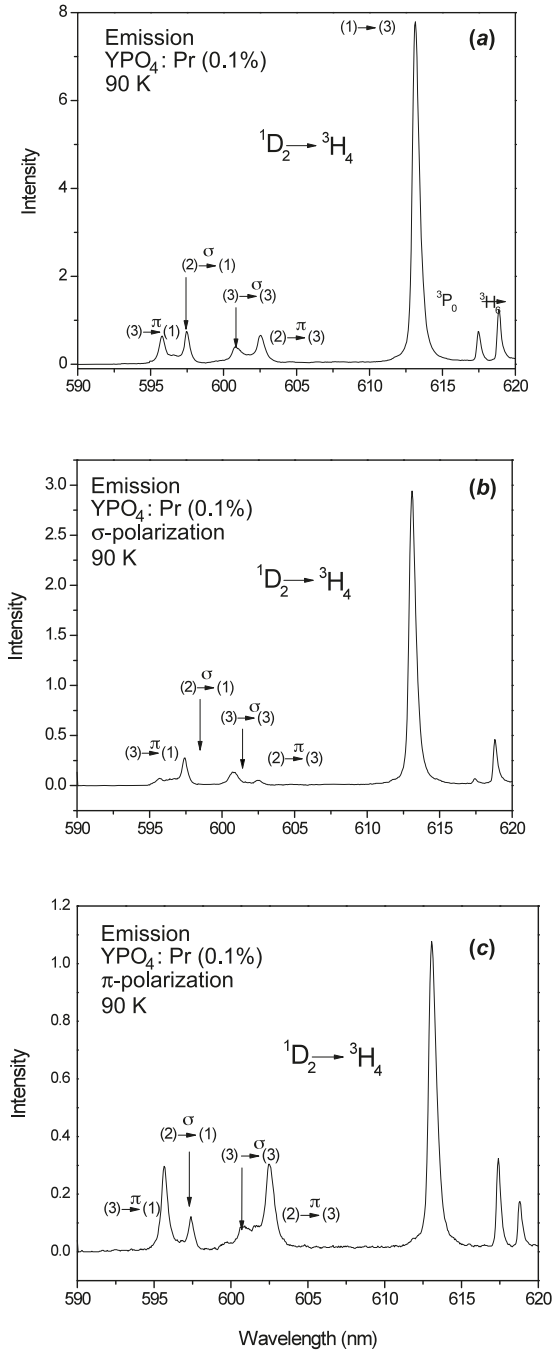

0.65 μs at 30 K and 0.62 μs at 300 K, in general agreement with previous work.[3] Decay curves of the $^1D_2$ level were recorded at temperatures between 28 and 300 K. Plots of sample decay curves at 28 and 150 K are shown in Fig. 6. All of the decay curves were very nearly exponential. They displayed a slight nonexponential behavior only for the first 50 μs or so. The lifetime values were determined by taking the inverse of the slope of the ln(intensity) vs time curves at times >100 μs. Figure 7 shows the $^1D_2$ lifetime at temperatures between 30 and 300 K.

Can. J. Chem. Downloaded from www.nrcresearchpress.com by University of Electronic and Science Techonology of China on 09/18/12
For personal use only.

Fig. 4. Luminescence spectrum of YPO_4:Pr (0.1%) at 150 K for (*a*) no polarizer in the optical path, (*b*) σ-polarized emission, and (*c*) π-polarized emission. Excitation was into the $^3P_2$ level near 450 nm.

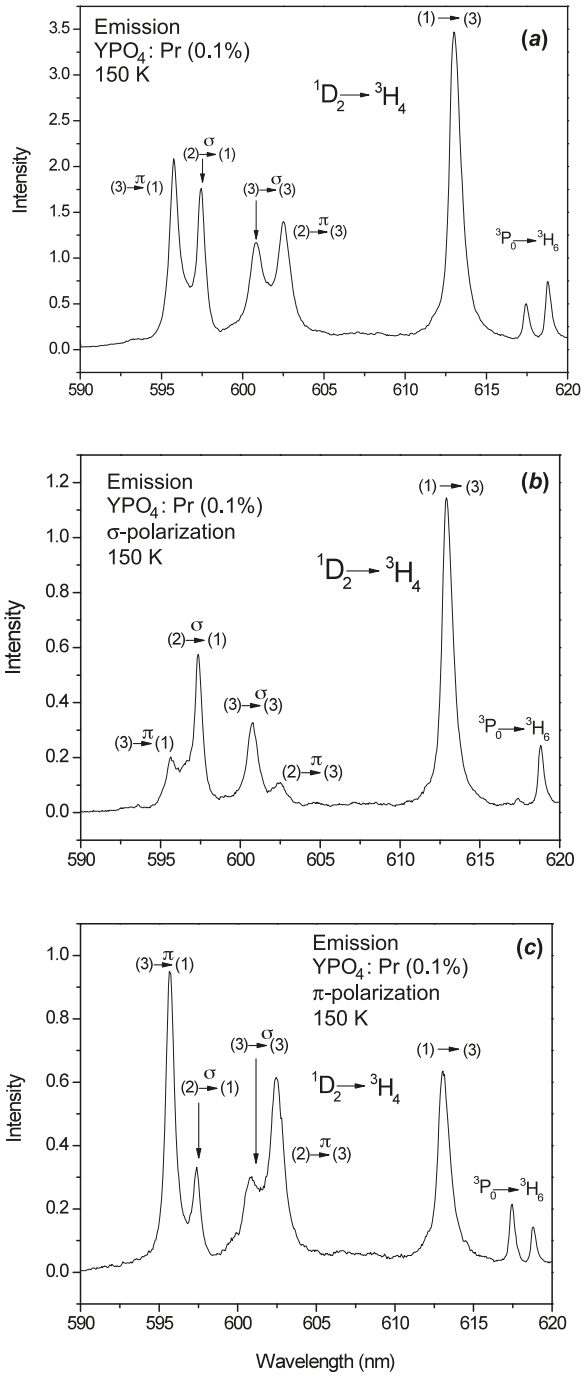

Fig. 5. Luminescence spectrum of YPO_4:Pr (0.1%) at 300 K for (*a*) no polarizer in the optical path, (*b*) σ-polarized emission, and (*c*) π-polarized emission. Excitation was into the $^3P_2$ level near 450 nm.

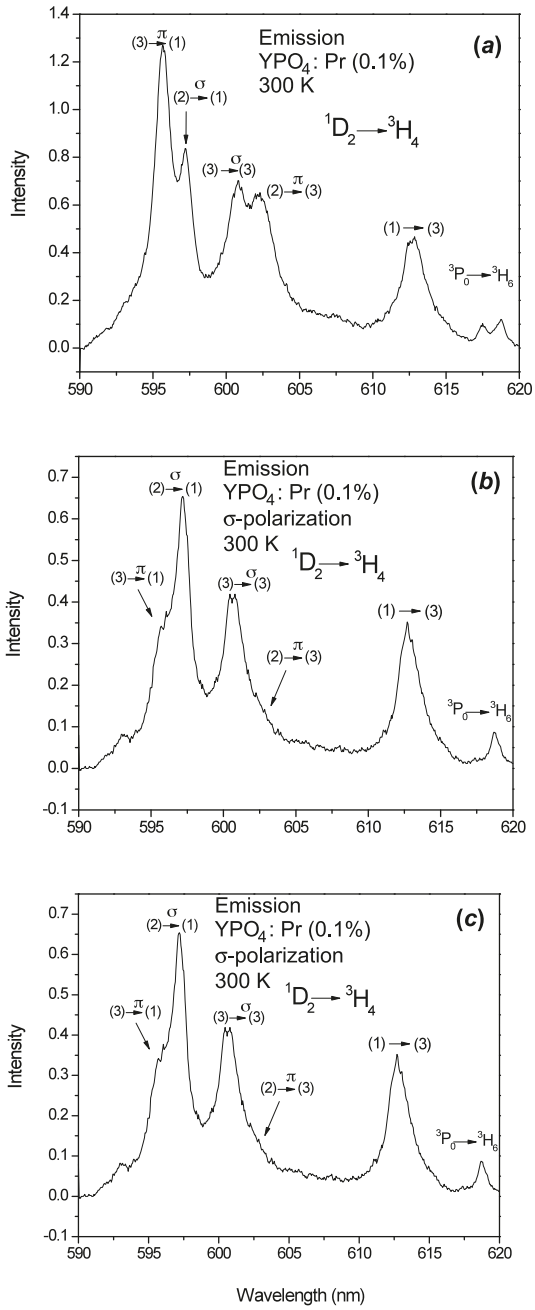

Discussion

The decay of the $^1D_2$ level of Pr^{3+} in YPO_4 is governed by three processes: radiative decay, multiphonon relaxation, and energy transfer via a cross-relaxation to the $^1D_2$. These three processes are shown in Fig. 1. The cross-relaxation process tends to quench the luminescence from the $^1D_2$ level and introduces a nonexponential component into the decay curve. The process becomes more probable as the concentration of Pr increases and can sometimes act as the dominant

Table 1. $^1D_2 \rightarrow {}^3H_4$ transitions and selection rules.

Initial $^1D_2$ level	Final $^3H_4$ level	Energy (cm^{-1})	Wavelength (nm)	Polarization
(1) Γ_3	(3) Γ_5	16 322	612.7	σ
(2) Γ_5	(1) Γ_4	16 745	597.2	σ
(2) Γ_5	(2) Γ_1	16 644	600.8	σ
(2) Γ_5	(3) Γ_5	16 606	602.2	π
(3) Γ_1	(1) Γ_4	16 794	595.5	π
(3) Γ_1	(3) Γ_5	16 655	600.4	σ

Can. J. Chem. Downloaded from www.nrcresearchpress.com by University of Electronic and Science Techonology of China on 09/18/12
For personal use only.

Fig. 6. Decay curves of the $^1D_2$ level at 28 and 150 K.

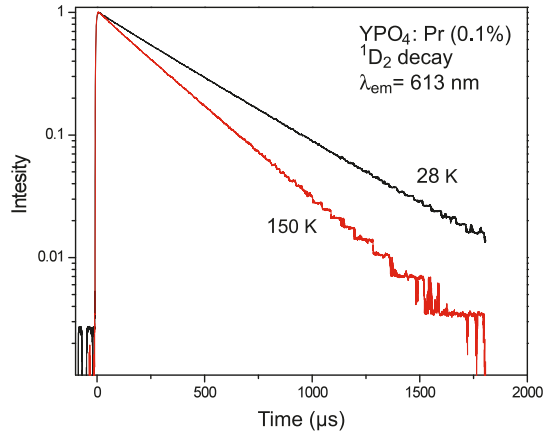

Fig. 7. Calculated and experimental lifetimes of the $^1D_2$ level versus temperature.

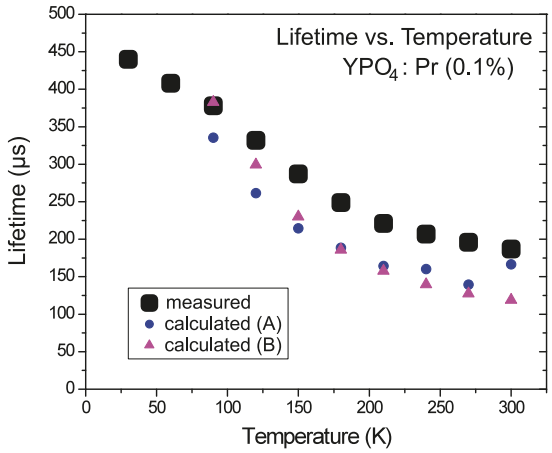

Table 2. Fractional population of $^1D_2$ levels with temperature.

	Fractional population (*f*)			
Temp. (K)	$^1D_2$(1)	$^1D_2$(2)*	$^1D_2$(3)	$^1D_2$(4)
30	1.000	0.000	0.000	0.000
60	0.998	0.002	0.000	0.000
90	0.975	0.020	0.005	0.000
120	0.922	0.060	0.0166	0.001
150	0.852	0.110	0.034	0.004
180	0.779	0.158	0.053	0.010
210	0.712	0.201	0.071	0.016
240	0.653	0.235	0.0874	0.024
270	0.604	0.263	0.101	0.032
300	0.562	0.285	0.113	0.040

*The $^1D_2$(2) level is doubly degenerate. All other levels have a degeneracy of 1.

decay process. In such systems the decay curve is highly nonexponential. In a system with Pr ions doped to a low level, however, it contributes only very little to the decay, as only those atoms near one another are likely to undergo such a process. The low doping concentration and the very nearly exponential shape of the decay patterns at all temperatures suggest that though some cross-relaxation is likely occurring in this sample, it can be neglected to a good approximation. Thus, the lifetimes plotted in Fig. 7 most closely represent the lifetime of Pr ions that are isolated from one another.

We note that the measured lifetime of 440 μs in the 0.1% sample at low temperature represents a much longer lifetime than that reported elsewhere. The $^1D_2$ lifetime has been measured at low temperatures by other workers and was found to be as short at 70 μs[11] and as long as 225 μs.[3] Judd–Ofelt calculations have also been referred to in the literature, and the calculated value of the lifetime of the $^1D_2$ level was 490 μs, close to the lifetime we observed.[12] Though we offer no specific reason as to why the low-temperature lifetime differs so widely sample to sample, it is sometimes the case that during crystal growth there can be centers formed that contribute to the nonradiative decay. The fact that our measured lifetime is greater than that of others leads us to believe that 440 μs is a more accurate value of the lifetime of an isolated Pr ion in YPO_4 in the absence of any unwanted centers.

As shown in Fig. 7, we observed a decrease in the $^1D_2$ lifetime as the temperature increases. This behavior is consistent with the observations of others. The fact that the lifetime decreases from ~440 μs at 30 K to 187 μs at 300 K suggests the possibility of multiphonon relaxation to the $^1G_4$ level as a high probability decay channel. Other workers have seen similar decreases in the lifetime with temperature, though there is no agreement as to the process responsible. Work by Reed and Moos[4] attributes the decrease in lifetime to an increase in the multiphonon decay rate as temperature increases. They constructed a model that allowed for phonons of different frequencies to bridge the gap to the $^1G_4$. Moune et al.[3] were inclined to the same conclusion. Zheng and Meltzer,[12] using Judd–Ofelt calculations of the radiative rate and a measured decay time, estimated the nonradiative decay rate to be 4.4×10^3 s^{-1} and pointed to multiphonon decay as the nonradiative mechanism. Naik et al.,[5] on the other hand, estimated the multiphonon decay rate to be negligible compared with the radiative decay. They noted that the energy gap between the $^1D_2$ and the next lowest $^1G_4$ level was 6500 cm^{-1}, and since it would take seven phonons to bridge the gap, such a process was unlikely. They concluded that the decrease in the lifetime as temperature increases was due to the increase in the rate of decay via cross-relaxation. Here we propose a different simpler mechanism to explain the temperature dependence of the $^1D_2$ level.

Before beginning our analysis, we calculated the temperature dependence of the population of the various levels of the $^1D_2$ manifold between 30 and 300 K. Using the energies of the levels of the $^1D_2$ manifold shown in Fig. 2, we calculated the fractional occupancy of each level at various temperatures. We noted that the Γ_5 crystal field level $^1D_2$ level was doubly degenerate, whereas the other levels were singly degenerate. We assumed that the $^1D_2$ manifold was thermalized, so that the fractional populations were determined by the Boltzmann distribution according to

$$[1] \qquad f_i(T) = \frac{g_i e^{-\Delta E_i/kT}}{\sum_i g_i e^{-\Delta E_i/kT}}$$

where f_i is the fraction of ions in the *i*th level of the $^1D_2$ manifold, T is the temperature, g_i is the degeneracy of the

Can. J. Chem. Downloaded from www.nrcresearchpress.com by University of Electronic and Science Techonology of China on 09/18/12
For personal use only.

Table 3. Line intensity and lifetime versus temperature data.

	Line intensity			Lifetime (μs)			
Temp. (K)	A_1 ($^1D_2(1)$)	A_2 ($^1D_2(2)$)	A_3 ($^1D_2(3)$)	τ_2	τ_3	τ (A)	τ (B)
90	126	19.7	18.2	58	14	335	383
120	112	45.7	46.6	70	19	261	299
150	85.3	58.4	61.5	83	24	214	230
180	82.4	79.4	85.6	93	29	189	185
210	58.9	75.1	88.1	97	30	164	157
240	46.0	69.3	78.1	105	35	160	139
270	28.5	50.0	58.7	109	36	140	127
300	29.5	50.0	58.8	132	44	166	118

Note: A_i is the area under the emission lines associated with transitions from the ith level of the $^1D_2$ manifold and is proportional to the number of photons collected at the detector, τ_i is the "radiative lifetime" associated with the ith level of the $^1D_2$ manifold, and τ is the lifetime of the $^1D_2$ level.

ith level of the $^1D_2$ manifold, and $e^{-\Delta E_i/kT}$ is the Boltzmann factor. The results are shown in Table 2.

Considering the results of Table 2 together with the luminescence spectra at various temperatures, we notice a process that may account, in part or in whole, for the decrease in the lifetime at temperature increases. Though the spectrum is not shown, at 30 K the emission originates completely from the lowest energy level of the $^1D_2$ manifold, and a single line at 612.8 nm dominates the spectrum. At 90 K (Fig. 3*a*), additional lines appear that represent transitions originating from the next two highest excited $^1D_2$ levels (Γ_5 and Γ_1). By integrating the area under the various lines in Fig. 3*a*, we conclude that the lines associated with the higher $^1D_2$ levels account for approximately one-quarter of the emission intensity at 90 K. According to Table 2, however, only about 2% of the Pr ions reside in these higher energy states at 90 K. At 150 K (Fig. 4*a*), >50% of the $^1D_2$ emission intensity originates from these upper levels, though only about 15% of the Pr ions occupy those upper $^1D_2$ levels. These results are possible only if the radiative decay rates of the upper $^1D_2$ levels are higher than that of the lowest level. These observations suggest that as temperature increases and the higher energy states are populated, the $^1D_2$ lifetime should decrease because the radiative decay rates of these upper levels of the $^1D_2$ manifold are higher than the radiative rate of the lowest level of the manifold. Let us follow this lead more carefully, as we attempt to quantify how much of the decrease in the $^1D_2$ lifetime might be due to the thermal occupation of the higher $^1D_2$ levels.

In our analysis, we will be using luminescence data to estimate the ratio of the intensity of emission from the lowest level to the intensity of emission from the upper energy levels. An exact treatment would require us to consider all emission lines from the $^1D_2$ level to all lower energy states. This was not practical experimentally for us, since many of the emission lines fall outside of the range of the photomultiplier, and because our system is not corrected to give meaningful relative intensity values. Thus, we make the following two assumptions. The first assumption is that the $^1D_2 \rightarrow {}^3H_4$ emission is the dominant radiative decay channel, so that a reasonable estimate of the relative emission from the various $^1D_2$ levels can be obtained simply by observing transitions between these two manifolds. The second assumption is that the response of our system is reasonably flat over the range of wavelengths between 590 and 620 nm, where the bulk of the $^1D_2 \rightarrow {}^3H_4$ emissions occur. Though neither of these assumptions is completely valid, it is known that the $^1D_2$ level is as a strong emitter in the red and that in many systems the $^1D_2 \rightarrow {}^3H_4$ transitions dominate the emission spectrum. According to our observations, the lines corresponding to $^1D_2 \rightarrow {}^3H_4$ emission are much stronger than lines representing transitions to other lower levels, at least for emission lines from 600 to 850 nm. Our second assumption is validated by the fact that we are examining the luminescence in a rather narrow wavelength range, roughly between 593 and 615 nm.

Using the luminescence spectra of the $^1D_2 \rightarrow {}^3H_4$ emission at various temperatures, we first plotted the luminescence data as a function of energy instead of wavelength. We then fit the spectra to a sum of Lorentzian peaks and found the area under the various peaks. (This was done using the Origin software program in which the data were plotted.) This gives a value that is proportional to the total energy under each peak. We then divided that number by the photon energy for each peak to obtain a value that is proportional to the number of photons emitted by the various lines. As we move from 30 to 300 K, we go from a situation where the emission is from only one level ($^1D_2(1)$) to where the emission originates from up to four levels: $^1D_2(1)$, $^1D_2(2)$, $^1D_2(3)$, and $^1D_2(4)$). The uppermost $^1D_2(4)$ level was negligibly populated for most temperatures (only 4% at 300 K), so we did not consider this an important contributor to the emission. Emission from this level is neglected in the following treatment, representing yet another approximation. The emission lines we focused on are the five lines shown in Figs. 3–5. Specifically, they are the following lines: 612.8 nm from $^1D_2(1)$, 602.2 and 597.2 nm from $^1D_2(2)$, and 600.8 and 595.5 nm from $^1D_2(3)$. Other transitions do occur in that same spectral region between 590 and 615 nm, but most are weak and it was impossible to discern all the peaks. We limited our analysis to these transitions because they appeared to be considerably stronger than the other emission lines.

At 30 and 60 K, the area under the peaks owing to the $^1D_2(2)$ and $^1D_2(3)$ levels were too small to be considered reliable, so our estimates of the relative fraction of photons emitted from the various levels begin at 90 K and continues

Can. J. Chem. Downloaded from www.nrcresearchpress.com by University of Electronic and Science Techonology of China on 09/18/12
For personal use only.

through 300 K. The results of these calculations are shown in Table 3.

To relate these data to the temperature dependence of the lifetime, we define the following terms:

N_i is the number of Pr ions in the ith level of the $^1D_2$ manifold.

N is the total number of Pr ions in the $^1D_2$ manifold.

$f_i = N_i/N$ is the fraction of ions in the ith $^1D_2$ level. These are given in Table 2.

τ_i is the "radiative lifetime" associated with the ith level of the $^1D_2$ manifold, i.e., $1/\tau_i$ is the probability per unit time that a Pr ion in the ith level undergoes radiative decay to a lower level.

τ is the lifetime of the $^1D_2$ level.

A_i is the area under the emission lines associated with transitions from the ith level of the $^1D_2$ manifold and is proportional to the number of photons collected at the detector.

The number of photons emitted per unit time by the ith $^1D_2$ level is given by N_i/τ_i. Thus, the ratio of the number of photons per unit time emitted from the ith level to that emitted from the jth level is

$$[2] \qquad \frac{A_i}{A_j} = \frac{N_i/\tau_i}{N_j/\tau_j} = \frac{f_i\tau_j}{f_j\tau_i}$$

The A_i are known from the experimental data (see Table 3), and the f_i are given in Table 2. We assume that τ_1 = 440 ms, the lifetime of the $^1D_2$ level at low temperature, so we can use eq. 2 to find the lifetime associated with the ith level.

$$[3] \qquad \tau_i = \frac{A_1 f_i}{A_i f_1}\tau_1$$

The values of τ_i can be calculated at each temperature. The results are shown in Table 3. The data show significant variation in the inherent radiative lifetime of each of the upper levels, which is perhaps unsurprising given the assumptions involved. One would expect that inherent lifetime to be nearly temperature-independent, especially if there are no nonradiative processes. The average value of these lifetimes are τ_2 = 92 μs and τ_3 = 28 μs.

Again under the assumption that the $^1D_2$ level is thermalized, τ is given by:

$$[4] \qquad \frac{1}{\tau} = \sum_i \frac{f_i(T)}{\tau_i}$$

Values of τ as a function of temperature are shown in Fig. 7 and in Table 3. The results labeled "calculated (A)" in Fig. 7 were calculated using the lifetime values associated with different temperatures, as given in Table 3. The results labeled "calculated (B)" in Fig. 7 were calculated using the average lifetimes of the $^1D_2(2)$ and $^1D_2(3)$ level. For both calculated curves, the temperature dependence of the lifetime as determined from the luminescence data decreases with increasing temperature. Although the calculated results do not follow the experimentally measured lifetimes precisely, the match is reasonably good considering the assumptions involved. Our results give too large an estimate of the radiative transition rates from the upper levels, so that the predicted lifetimes are shorter than the measured lifetimes. We speculate this can be largely attributed to the fact that not all the transitions from the $^1D_2$ manifold were monitored.

Given these results, we conclude that the temperature dependence of the $^1D_2$ levels of Pr between 30 and 300 K can be adequately explained by the fact that the upper levels within the $^1D_2$ manifold have a radiative decay rate that is higher than that of the lowest $^1D_2$ level. We see no evidence to indicate that nonradiative decay owing to multiphonon relaxation is taking place, so that at least in low-doped systems, the emission from the $^1D_2$ should be very efficient.

Conclusions

The decay from the $^1D_2$ level of Pr in YPO_4 was considered in some detail. At low temperatures we find a lifetime of 440 μs, which is roughly twice as long as that reported previously. Using polarization emission spectra at various temperatures, we were able to identify the most prominent transitions from the $^1D_2$ level. By monitoring these main emission lines of the $^1D_2 \rightarrow {}^3H_4$ transition, we estimated the lifetime of each of the upper $^1D_2$ levels. Using this data and knowing the thermal distribution of ions among the energy levels of the $^1D_2$ manifold, we were able to estimate the temperature dependence of the lifetime of the $^1D_2$ level and compare it with the experimentally measured values. The reasonable fit between the experimental and calculated values of the lifetime allow us to conclude that, contrary to the conclusion of previous workers, there is no significant contribution of multiphonon relaxation to the lifetime of the $^1D_2$ level.

Acknowledgement

We are grateful to have been invited to submit a contribution to this special publication in honor of Professor Scaiano.

References

(1) Koepke, C.; Wisiewski, K.; Dyl, D.; Grinberg, M.; Malinowski, M. *Opt. Mater.* **2006** *28* (1-2), 137. doi:10.1016/j.optmat.2004.10.035.

(2) Boutinaud, P.; Mahiou, R.; Cavalli, E.; Bettinelli, M. *J. Lumin.* **2007** *122–123*, 430. doi:10.1016/j.jlumin.2006.01.198.

(3) Moune, O. K.; Faucher, M. D.; Edelstein, N. *J. Lumin.* **2002** *96* (1), 51. doi:10.1016/S0022-2313(01)00211-3.

(4) Reed, E. D.; Moos, H. W. *Phys. Rev. B* **1973** *8* (3), 980. doi:10.1103/PhysRevB.8.980.

(5) Naik, R. C.; Karanjikar, N. P.; Razvi, M. A. N. *J. Lumin.* **1992** *54* (3), 139. doi:10.1016/0022-2313(92)90001-P.

(6) Mazurak, Z. G.; Van Vliet, J. P. M.; Blasse, G. *J. Solid State Chem.* **1987** *68*, 227. doi:10.1016/0022-4596(87)90307-0.

(7) Özen, G.; Forte, O.; Di Bartolo, B.; Collins, J. M. *J. Appl. Phys.* **2007** *102* (2), 023110. doi:10.1063/1.2753685.

(8) Özen, G.; Forte, O.; Di Bartolo, B.; Collins, J. *J. Lumin.* **2007** *125* (1-2), 223. doi:10.1016/j.jlumin.2006.08.033.

(9) Feigelson, R. S. *J. Am. Ceram. Soc.* **1964** *47* (5), 257. doi:10.1111/j.1151-2916.1964.tb14409.x.

(10) Milligan, W. O.; Mullica, D. F.; Beall, G. W.; Boatner, L. A. *Inorg. Chim. Acta* **1982** *60* (2), 39. doi:10.1016/S0020-1693(00)91148-4.

(11) Lian, R.; Yin, M.; Zhang, W.; Lou, L.; Krupa, J. C. *J. Alloy. Comp.* **2000** *311* (1), 97. doi:10.1016/S0925-8388(00)00858-6.

(12) Zheng, H.; Meltzer, R. *J. Lumin.* **2007** *122–123*, 478. doi:10.1016/j.jlumin.2006.01.211.

Can. J. Chem. Downloaded from www.nrcresearchpress.com by University of Electronic and Science Techonology of China on 09/18/12
For personal use only.

A Förster resonance energy transfer (FRET) approach for enhancing fluorescence contrast in phase-separated membranes

Daniel M. Carter Ramirez, Jason Ding, Jack Guan, Dusan Vobornik, Anna Carnini, William W. Ogilvie, Zygmunt J. Jakubek, and Linda J. Johnston

Abstract: The partitioning of the dye-labeled lipid probe, NBD-DHPE (1,2-dipalmitoyl-*sn*-glycero-3-phosphoethanolamine-*N*-(7-nitro-2-1,3-benzoxadiazol-4-yl) (ammonium salt)), was examined by fluorescence microscopy in phase-separated lipid bilayers with mixtures of coexisting liquid-ordered and fluid phases. This probe shows slightly higher fluorescence intensity in the ordered domains but undergoes a contrast reversal to give a more strongly fluorescent fluid phase in the presence of >0.2% Texas red-DHPE (TR-DHPE). The change in contrast is shown to result from Förster resonance energy transfer between the NBD donor and TR acceptor in the fluid phase, which has a TR concentration that is approximately 3 times higher than in the domains. An alternate approach using a nitroxide-substituted lipid that partitions into the fluid phase as a quencher, was also examined as a means to enhance the contrast; however, the quencher modified the behaviour of the bilayer. The energy transfer method for enhancing the contrast between ordered and fluid phases was used to examine the morphology of enzyme-treated bilayers.

Key words: fluorescence microscopy, lipid bilayers, vesicles, ceramide.

Résumé : Faisant appel à la microscopie de fluorescence, on a étudié la partition de la sonde de lipide marquée d'un colorant, la 1,2-dipalmitoyl-*sn*-glycero-3-phosphoethanolamine-*N*-(7-nitro-2-1,3-benzoxadiazol-4-yl, NBD-DHPE, dans des bicouches de lipides séparés par phases coexistentes de fluide ou de liquide ordonné. Cette sonde présente une intensité de fluorescence qui n'est que légèrement supérieure dans le domaine ordonné, elle subit un renversement de contraste qui conduit à une phase fluide beaucoup plus fluorescente en présence de plus de 0,2 % de Texas Rouge-DHPE (TR-DHPE). On a démontré que le changement de contraste résulte d'un transfert d'énergie de résonance de Förster entre le donneur NBD et l'accepteur TR dans la phase fluide qui comporte une concentration de TR qui est approximativement 3 fois plus élevée que dans les autres domaines. Dans le but d'obtenir une augmentation du contraste, on a fait appel à une autre approche impliquant un lipide substitué par un groupe nitroxyde qui se partitionne entre la phase fluide comme désactivant; toutefois, le désactivant a modifié le comportement de la bicouche. La méthode d'énergie de transfert pour augmenter le contraste entre les phases fluides et ordonnées a donc été utilisée pour examiner la morphologie des bicouches traitées par un enzyme.

Mots-clés : microscopie de fluorescence, bicouches de lipide, vésicules, céramide.

[Traduit par la Rédaction]

Introduction

The compartmentalization of the plasma membrane into functional microdomains provides an important mechanism for regulating biological processes. Lipid or membrane rafts are defined as small, dynamic, heterogeneous microdomains that are enriched in cholesterol, sphingolipids, and certain proteins.[1–5] They are believed to exist in a liquid-ordered (L_o) phase that is surrounded by the bulk fluid or liquid-disordered (L_d) membrane. Rafts are postulated to have an important functional role in modulating cell signaling by spatial and temporal control of the organization of membrane proteins. The direct visualization of rafts in cell membranes is challenging because of their small size (10–200 nm, below the optical diffraction limit) and their relatively short lifetime.[6] These limitations have prompted many studies of lipid-phase behavior in model membranes such as small unilamellar vesicles, giant unilamellar vesicles, and supported lipid bilayers. Coexisting liquid phases have been observed for a variety of lipid mixtures

Received 22 June 2010. Accepted 30 July 2010. Published on the NRC Research Press Web site at canjchem.nrc.ca on 7 March 2011.

This article is part of a Special Issue dedicated to Professor J. C. Scaiano.

D.M. Carter Ramirez. Steacie Institute for Molecular Sciences, National Research Council Canada, Ottawa, K1A 0R6 ON, Canada; Department of Chemistry, University of Ottawa, Ottawa, ON K1N 6N5, Canada.
J. Ding, J. Guan, D. Vobornik, A. Carnini, Z.J. Jakubek, and L.J. Johnston.[1] Steacie Institute for Molecular Sciences, National Research Council Canada, Ottawa, K1A 0R6 ON, Canada.
W.W. Ogilvie. Department of Chemistry, University of Ottawa, Ottawa, ON K1N 6N5, Canada.

[1]Corresponding author (e-mail: Linda.Johnston@nrc-cnrc.gc.ca).

Can. J. Chem. Downloaded from www.nrcresearchpress.com by University of Electronic and Science Techonology of China on 09/18/12
For personal use only.

Can. J. Chem. Downloaded from www.nrcresearchpress.com by University of Electronic and Science Techonology of China on 09/18/12
For personal use only.

Scheme 1.

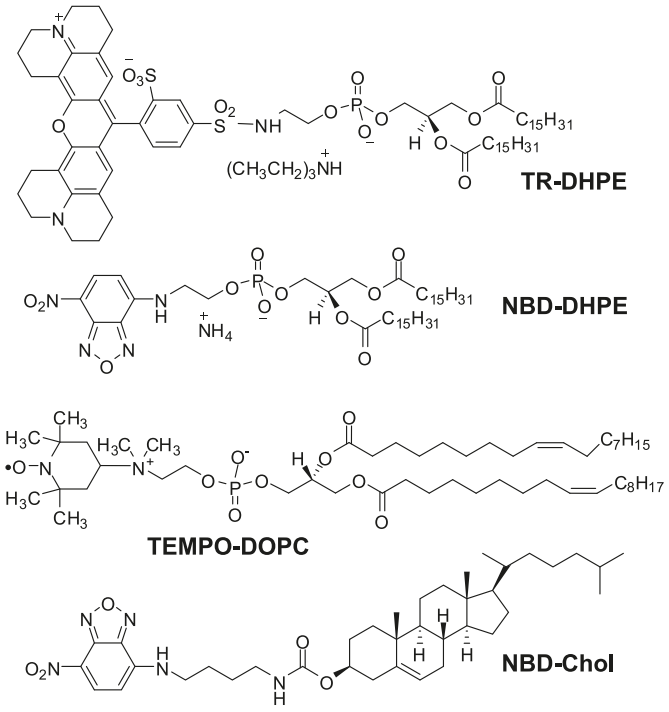

with at least three components, a low melting unsaturated phospholipid, a high melting saturated phosphatidylcholine or sphingomyelin, and cholesterol (Chol),[7–9] thus confirming one of the key concepts of the lipid raft hypothesis.

Despite the widespread use of fluorescence microscopy to study coexisting L_d and L_o phase separation in supported membranes and in giant unilamellar vesicles, there are relatively few dyes or dye-labeled lipids that can be used to selectively label the L_o phase. For example, the partitioning of more than 25 different fluorophores was assessed by fluorescence microscopy in giant unilamellar vesicles using a standard protocol for two different ternary lipid mixtures.[10] This study examined phospholipid probes with both saturated and unsaturated acyl chains and with fluorophores attached to either the acyl chain or polar headgroup. Based on relative fluorescence intensities, all fluorophore-labeled phospholipids partitioned more strongly into the disordered phase, including several headgroup-labeled lipids with saturated acyl chains that would be expected to cause the least disturbance to lipid packing in the L_o phase.[10] Although cholestatrienol partitioned into the L_o phase, other studies have demonstrated that dye-labeled cholesterol analogs show slight preferences for either L_o or L_d phases, depending on the fluorophore polarity and the method and location (hydroxyl vs alkyl chain) of its attachment to the sterol.[11–14] Several aromatic hydrocarbons show stronger fluorescence in the L_o phase, whereas dialkylcarbocyanine dyes have a preference for either the L_o or L_d phase, depending on the chain length and saturation or unsaturation of the hydrocarbon chain of the dye and the lipid composition for DOPC/SM/Chol (dioleolylphosphatidylcholine/sphingomyelin/cholesterol) and DOPC/DSPC (distearoylphosphatidylcholine)/Chol mixtures. Despite the clear preference of most lipid probes to partition into L_d phases in model membranes, NBD-DHPE (1,2-dipalmitoyl-*sn*-glycero-3-phosphoethanolamine-*N*-(7-nitro-2-1,3-benzoxadiazol-4-yl); headgroup labeled) partitions strongly into L_o domains in vesicles (POPC (1-palmitoyl-2-oleoyl-*sn*-glycerophosphocholine)/C_{16}-SM/Chol, K_p (L_o/L_d partition coefficient) = 3.7)) and fluoresces more strongly in the L_o phase in supported planar bilayers prepared from POPC / brain SM / Chol mixtures.[15,16] Interestingly, this probe has also been reported to partition into the L_o phase in giant plasma membrane vesicles, although many other common lipid probes partition into the L_d phase in this system.[17]

As part of our investigations of the enzymatic generation of ceramide in bilayers with coexisting L_o and L_d phases, we had attempted to use NBD-DHPE to label L_o domains in supported bilayers prepared from DOPC/ESM (egg sphingomyelin)/Chol mixtures. Although this probe showed a slight preference for partitioning into the disordered phase based on relative fluorescence intensity measurements, we observed that a combination of NBD-DHPE and Texas red-DHPE (TR-DHPE) resulted in stronger NBD fluorescence in L_o domains. Here, we show that this apparent reversal of contrast for NBD-DHPE is caused by Förster resonance energy transfer (FRET) between NBD-DHPE and TR-DHPE in the fluid phase. TR-DHPE partitions strongly into the L_d phase, leading to efficient FRET, as expected from the strong overlap of donor NBD emission with absorption of the TR acceptor. Energy transfer was characterized in detail using a combination of fluorescence microscopy experiments for supported bilayers and measurements of FRET efficiencies based on donor fluorescence lifetimes in vesicle solution. We also examined an alternate approach using a nitroxide quencher, TEMPO-DOPC (1,2-dioleoylphosphatidyl-*N*,*N*-dimethyl-*N*-(2,2,6,6-tetramethyl-1-oxyl-piperidinyl)-ethanolamine), that partitions strongly into the disordered phase, to enhance the contrast for NBD in the L_o domains. Finally, we demonstrate that the double labeling strategy can be used to visualize the complex morphologies obtained during enzyme restructuring of supported membranes

Experimental section

Materials

DOPC, ESM (chicken), Chol, TEMPO-DOPC, and *N*-NBD-DHPE were purchased from Avanti Polar Lipids and were used as received. Texas red 1,2-dihexadecanoyl-*sn*-glycero-3-phosphoethanolamine triethylammonium salt (TR-DHPE) was obtained from Invitrogen. NBD-Chol was synthesized as described previously.[13] Sphingomyelinase (SMase) isolated from *Staphylococcus aureus* was obtained from Sigma-Aldrich. All aqueous solutions were prepared using 18.3 MΩ/cm Milli-Q water. SMase buffer: 125 mmol/L NaCl, 10 mmol/L $CaCl_2$, 2 mmol/L $MgCl_2$, and 10 mmol/L HEPES (4-(2-hydroxyethyl)-1-piperazineethanesulfonic acid), pH 7.4. Structures of the lipid probes are shown in Scheme 1.

Preparation of supported bilayers

Small unilamellar vesicles (SUVs) were prepared as described previously.[18] Briefly, chloroform solutions of phospholipids and dye-labeled lipids were mixed in the appropriate ratios and the lipid films obtained after evaporating the solvent were hydrated in water. The samples were

Can. J. Chem. Downloaded from www.nrcresearchpress.com by University of Electronic and Science Techonology of China on 09/18/12
For personal use only.

then sonicated in a bath sonicator to clarity to form SUVs with a final lipid concentration of 0.5 mg/mL. All vesicle solutions were sonicated at temperatures above the melting temperature (T_m) of the constituent lipids and were used immediately or stored at 4 °C for up to 1 week prior to use.

Planar supported bilayers were formed via vesicle fusion. Vesicle solution (60 μL) and 750 μL $CaCl_2$ (15 mmol/L) were added to freshly cleaved mica (15–25 μm thick for fluorescence imaging) clamped in a liquid cell. After incubation at 45 °C for 60 min, bilayers were gradually cooled to room temperature over a period of 2 h, and then washed with Milli-Q water to remove unattached vesicles before imaging.

Atomic force microscopy

Atomic force microscopy (AFM) images were obtained on a PicoSPM atomic force microscope (Molecular Imaging) in MAC mode using magnetic coated silicon tips with spring constants of ~0.5 N/m and resonance frequencies between 8 and 35 kHz in aqueous solutions. Either a 30 μm × 30 μm or 5 μm × 5 μm scanner was used with a scan rate between 0.7 and 1.3 Hz. All images shown are flattened raw data. Two independently prepared samples were imaged for each bilayer composition, and several areas were scanned for each sample. Domain heights were measured as the difference between the condensed-phase domains and the fluid phase.

Fluorescence microscopy

Fluorescence images of bilayers were measured in a total internal reflection fluorescence (TIRF) mode on an Olympus IX81 microscope equipped with a high- resolution charge-coupled device (CCD) camera (CoolSNAP, Photometrics) and a 60×/1.45 NA Plan Apochromat TIRF objective. Fluorescence was excited with a 488 nm Ar ion laser (NBD-labeled probes) or a 543 nm Kr ion laser beam (TR-DHPE). NBD and TR fluorescence were recorded through FF01-536/40 and FF01-624/40 emission filters (Semrock), respectively. For comparison of the effects of laser polarization, images were recorded using TIRF and epifluorescence geometries; the linearly polarized emission from the laser results in ~70% axial polarization for TIRF as compared with in-plane polarized excitation for epifluorescence. For SMase treatment, the bilayers were washed with SMase buffer and imaged. The effect of enzyme on the bilayer was followed in time by imaging the same area before and after the addition of buffered enzyme solution at room temperature.

The fluorescence intensity analysis was done using ImagePro software (MediaCybernetics). The intensities of adjacent L_d fluid phase and L_o domains were measured from intensity cross sections of the area of interest. These values were corrected for background fluorescence before calculating the L_d/L_o intensity ratio (I_{L_o}/I_{L_d}). The background fluorescence count was obtained by either completely bleaching an area immediately adjacent to the area of interest or by using a bilayer defect in the region of interest. Care was taken to ensure that background, domain, and fluid-phase intensities were measured within a small area (2–4 μm) with uniform excitation intensity to minimize effects owing to variation in excitation intensity across the field of view. A minimum of 10 corrected I_{L_o}/I_{L_d} values were collected per region (~100 μm^2), and multiple samples were measured for each experiment to check for reproducibility.

Fluorescence spectroscopy

Absorption spectra were measured with a Cary 5000 UV–vis–NIR spectrophotometer (Varian, Inc.) at 22 °C using a 1 cm path length quartz cuvette. Emission spectra and fluorescence lifetimes were recorded at 22 °C using a Fluorolog Tau-3 (Horiba Jobin Yvon) spectrofluorometer. Fluorescence quantum yields for TR-DHPE in vesicle solutions were measured with reference to rhodamine 101 ($\Phi = 1.0$)[19] at an excitation wavelength of 550 nm and absorbance < 0.2. Fluorescence lifetimes were measured using the frequency domain method with modulation frequencies in the 2–80 MHz range.

Results and discussion

Fluorescence microscopy of supported bilayers

Figure 1 illustrates a representative fluorescence image of a supported lipid bilayer prepared from DOPC/ESM/Chol (2:2:1) vesicles containing 0.3 mol% NBD-DHPE. The small slightly darker domains are analogous to those observed in previous fluorescence microscopy studies of similar supported bilayers using TR-DHPE to visualize phase separation; AFM showed that the dye-excluded domains were thicker than the surrounding membranes, consistent with assignment to a cholesterol- and sphingomyelin-enriched liquid-ordered phase.[20] Contrary to our expectations based on literature data for POPC mixtures,[15,16] NBD-DHPE has a slight preference for the L_d phase, based on relative fluorescence intensities. However, bilayers containing both NBD-DHPE and TR-DHPE showed an apparent reversal in contrast for the NBD channel, as illustrated in Figs. 1B and 1C. In this case, the NBD channel indicates significantly stronger fluorescence in the domains, whereas TR-DHPE shows a strong preference for the L_d phase, as previously observed. Qualitatively similar results were obtained for DOPC/ESM/Chol (1:1:1) bilayers; bilayers with NBD alone showed slightly darker domains, and the contrast was reversed for bilayers prepared with a mixture of 0.5 mol% NBD-DHPE and 0.3 mol% TR-DHPE. A change from the apparent L_d preference of the probe was also observed for Oregon green in the presence of TR-DHPE in 2:2:1 DOPC/ESM/Chol bilayers.

The change in intensity for NBD-DHPE in the L_o and L_d phases was examined as a function of TR-DHPE concentration ([TR-DHPE]). Bilayers containing 0.1 mol% TR-DHPE showed similar images (data not shown) to that for NBD-DHPE alone (Fig. 1A). However, the contrast is reversed at higher dye loadings (≥0.2 mol%). A matched experiment (same excitation intensity and exposure time) for bilayers containing 0, 0.2, and 0.5 mol% TR-DHPE is presented in Fig. 2. Note that the images in Fig. 2 are all displayed on a fixed intensity scale so that the NBD-DHPE image appears to have lower contrast compared with that shown in Fig. 1. The overall intensity for NBD fluorescence decreases significantly in the L_d phase at 0.5 mol% TR-DHPE as shown in Fig. 2D. The large decrease in NBD intensity (to ~24% of the initial value) in the L_d phase contrasts with the relatively modest decrease (to ~80% of the initial value) for the L_o

Can. J. Chem. Downloaded from www.nrcresearchpress.com by University of Electronic and Science Techonology of China on 09/18/12
For personal use only.

Fig. 1. Fluorescence images for dioleolylphosphatidylcholine (DOPC)/egg sphingomyelin (ESM)/cholesterol (Chol) (2:2:1 molar ratio) bilayers labeled with (A) 0.5% 1,2-dipalmitoyl-*sn*-glycero-3-phosphoethanolamine-*N*-(7-nitro-2-1,3-benzoxadiazol-4-yl (NBD-DHPE) and (B) and (C) 0.3% NBD-DHPE plus 0.3% Texas red 1,2-dihexadecanoyl-*sn*-glycero-3-phosphoethanolamine triethylammonium salt (TR-DHPE). (B) and (C) show NBD and TR channels, respectively.

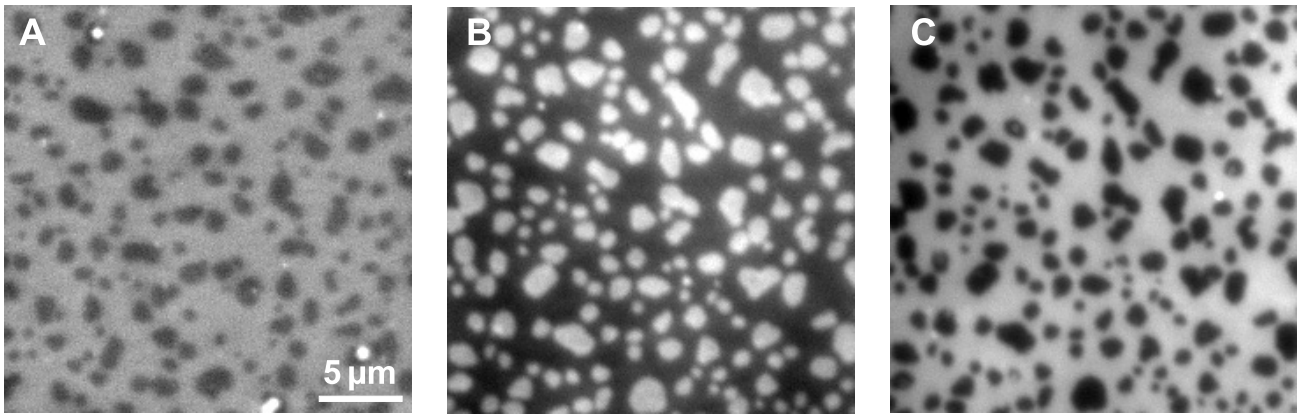

Fig. 2. Fluorescence images for dioleolylphosphatidylcholine (DOPC)/egg sphingomyelin (ESM)/cholesterol (Chol) bilayers labeled with 0.5% 1,2-dipalmitoyl-*sn*-glycero-3-phosphoethanolamine-*N*-(7-nitro-2-1,3-benzoxadiazol-4-yl (NBD-DHPE) and (A) 0 mol% Texas red 1,2-dihexadecanoyl-*sn*-glycero-3-phosphoethanolamine triethylammonium salt (TR-DHPE), (B) 0.2 mol% TR-DHPE, and (C) 0.5 mol%. All three images are displayed on the same intensity scale. The column charts in (D) and (E) illustrate the change in NBD intensities for the L_o and L_d phases and the L_d/L_o intensity ratios, respectively, as a function of [TR-DHPE].

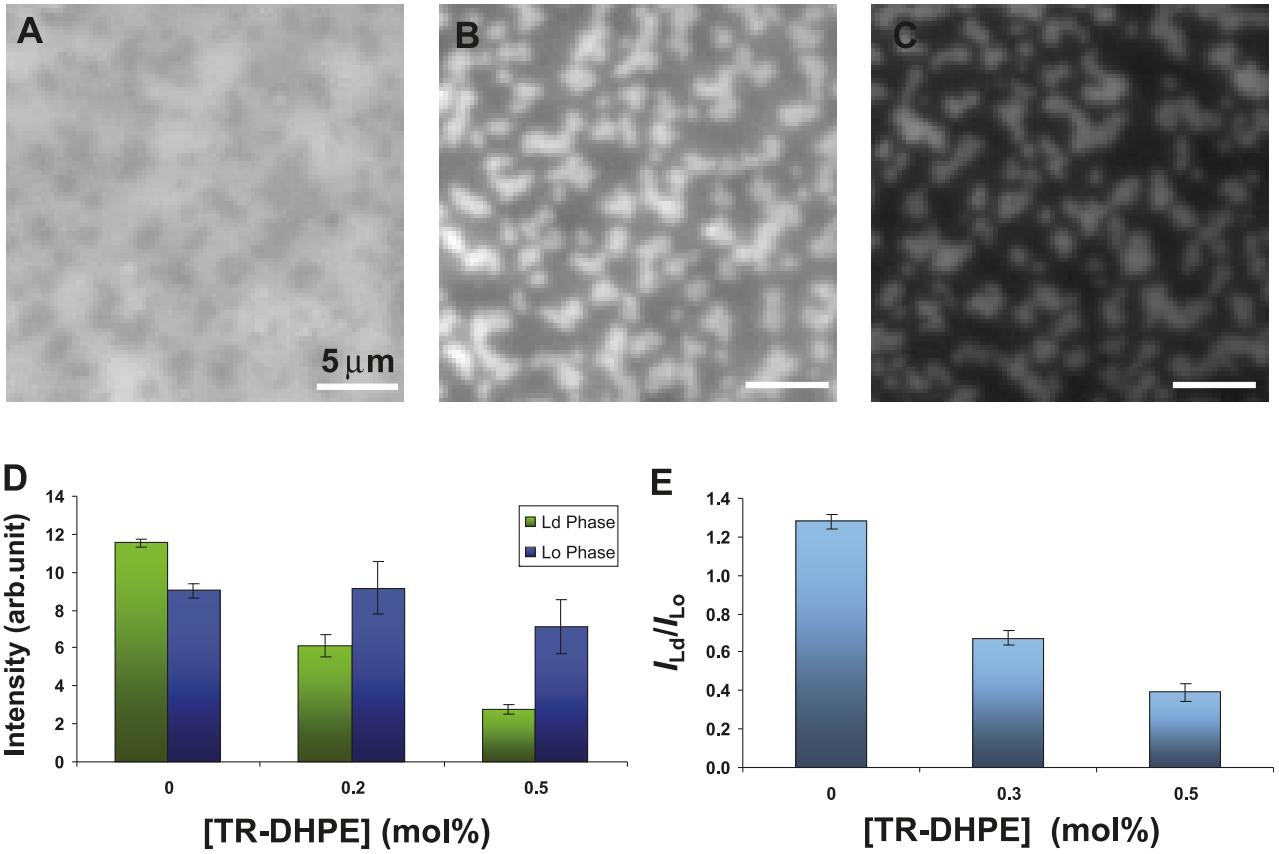

domains. The variation in the relative intensities of the L_o and L_d phases are displayed in Fig. 2E.

One possible explanation for the reversal in contrast for NBD in the presence of TR-DHPE is that FRET from NBD (donor) to TR (acceptor) occurs with a much higher efficiency in the fluid phase as compared with the ordered domains for the DOPC/ESM/Chol bilayers. This explanation is consistent with both the strong overlap of donor NBD emission with absorption of the TR acceptor and pronounced reduction in NBD emission in the L_d phase with increasing [TR-DHPE]. More efficient FRET in the L_d phase requires either a more favorable relative orientation of the transition

Can. J. Chem. Downloaded from www.nrcresearchpress.com by University of Electronic and Science Techonology of China on 09/18/12
For personal use only.

dipoles of the donor and acceptor in this phase or a significantly higher concentration of TR. Several additional experiments with DOPC/ESM/Chol bilayers and vesicles labeled with only TR-DHPE were carried out to investigate this in more detail.

First, images of bilayers with [TR-DHPE] between 0.01 and 1 mol% all showed significantly stronger fluorescence from the L_d phase, providing qualitative evidence for a higher probe concentration in this phase. The relative fluorescence intensity ratios for several concentrations are shown in Fig. 3A and indicate that the I_{L_d}/I_{L_o} ratio is ~2.7 for probe concentrations below ~0.2 mol%, but shows a modest decrease at higher concentrations (to 2.2 at 1 mol%). The fluorescence intensity ratios do not give a direct measure of the partition coefficient (K_p) between the two phases and, thus, cannot be directly related to the ratio of concentrations in L_o and L_d phases. Changes in quantum yield in the two lipid phases, differences in self-quenching between the two phases, and effects of probe orientation on the absorption efficiency all contribute to the measured intensity ratios. Fluorescence quantum yields were measured for several concentrations of TR-DHPE in DOPC, DOPC/Chol (2:1), and ESM/Chol (2:1) vesicles for comparison with the fluorescence microscopy results and to test for the effect of lipid composition on fluorescence efficiency. The data are shown in Fig. 3B and indicate that the fluorescence quantum yield at low [TR-DHPE] is the same (Φ = 0.6) within experimental error for DOPC and ESM/Chol and is only slightly higher for DOPC/Chol (Φ = 0.66). Comparison of quantum yields at 0.2, 0.5, and 1 mol% TR for each of the vesicle compositions shows a decrease in quantum yield with increased concentration for vesicles containing Chol, with self-quenching increasing with increased lipid order (DOPC < DOPC/Chol < ESM/Chol). Assuming that results in vesicles can be extrapolated to supported bilayers, the modest changes in quantum yield and the low self-quenching indicate that the fluorescence intensity ratio for the supported bilayers at the lowest [TR-DHPE] do not reflect differences in fluorescence efficiency or self-quenching between the two phases. Finally, images obtained with in-plane and axial polarization for the excitation laser had the same I_{L_d}/I_{L_o} ratio within experimental error; this indicates that the transition dipole moment for TR must be oriented similarly in the two phases, since in-plane polarization will favor excitation of fluorophores with dipoles oriented parallel to the membrane surface, whereas axial polarization will preferentially excite molecules oriented perpendicular to the membrane. Thus, we conclude that the concentration of TR-DHPE is approximately 3 times higher in the L_d phase than in the L_o domains.

FRET in vesicle solution

FRET between NBD-DHPE and TR-DHPE in vesicle solution was investigated by measuring NBD-DHPE lifetime distributions in the frequency domain.[21] First, the fluorescence lifetime of NBD-DHPE was evaluated in methanol solution and in DOPC, DOPC/Chol, and ESM/Chol vesicles. In methanol, the fluorescence intensity decay fits well to a single exponential function, with a lifetime of 6.2 ns. By contrast, NBD decays in vesicle solution were clearly not single exponential but gave adequate fits to a Lorentzian

Fig. 3. (A) I_{L_d}/I_{L_o} ratios for dioleolylphosphatidylcholine (DOPC) / egg sphingomyelin (ESM) / cholesterol (Chol) bilayers containing variable concentrations of Texas red 1,2-dihexadecanoyl-*sn*-glycero-3-phosphoethanolamine triethylammonium salt (TR-DHPE). (B) The dependence of TR-DHPE fluorescence quantum yield on concentration in dioleolylphosphatidylcholine (DOPC), DOPC/Chol, and ESM/Chol vesicles.

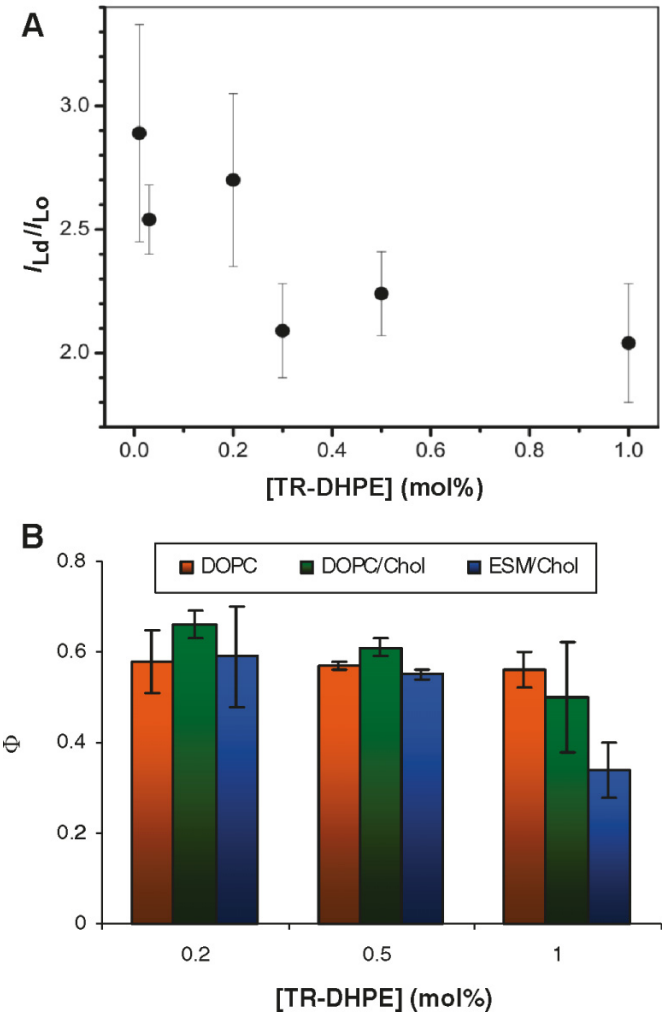

lifetime distribution. Fits with a Gaussian lifetime distribution were also statistically acceptable. The amplitude-weighted lifetimes were 6.9, 7.4, and 9.5 ns in DOPC, DOPC/Chol, and ESM/Chol vesicles, respectively, longer than the lifetime measured in methanol. These data are consistent with the increased quantum yields with increasing bilayer order: quantum yields of 0.18, 0.16 and 0.26 for ~0.5 mol% NBD-DHPE in DOPC, DOPC/Chol, and ESM/Chol vesicles, respectively.[13] The increased quantum yields reflect a less polar environment, which is related to the positioning of the fluorophore in the polar head group region of the bilayers; the longer lifetimes and increased quantum yields indicate a decrease in the nonradiative rate constant in more ordered environments.

The non-single-exponential decay kinetics and the amplitude-weighted lifetimes are consistent with previous fluorescence data for several NBD-phospholipid probes (head group labeled) in vesicle solution.[22–24] For example,

Can. J. Chem. Downloaded from www.nrcresearchpress.com by University of Electronic and Science Techonology of China on 09/18/12
For personal use only.

fluorescence decays with long and short components were measured for *N*-(7-nitrobenz-2-oxa-1,3-diazol-4-yl)-dimyristoylphosphatidylethanolamine (NBD-DMPE) in dimyristoylphosphatidylcholine (DMPC) vesicles with 0–0.4 mol fraction Chol (10–12 ns and 1.9–2.2 ns)[23] and for NBD-DHPE in dipalmitoylphosphatidylglycerol (DPPG) vesicles (6.0 and 12.6 ns).[24] Similarly, lifetimes of 9.2–10.5 ns were measured for NBD-DHPE in POPC/SM/Chol mixtures with varying fractions of L_o phase.[22] By contrast, monoexponential decay kinetics with a lifetime of 7.9 ns were reported in an earlier study for NBD-DHPE in egg phosphatidylcholine (PC) vesicles.[25] The differences in probe structure and concentration and lipid environment account for the variation in lifetimes for the various NBD-labeled lipids. There is no evidence for changes in emission properties that would be indicative of probe aggregation.

Figure 4A shows fluorescence spectra obtained by 450 nm excitation of 0.5 mol% NBD-DHPE in DOPC vesicles with 0, 0.1, 0.5, and 0.85 mol% [TR-DHPE], clearly illustrating energy transfer from the NBD donor to TR acceptor with efficiency increasing with increasing TR fractional concentration. The fluorescence lifetime for NBD in DOPC vesicles was measured as a function of TR-DHPE concentration using the frequency-domain method and modeled with a Lorentzian distribution function. The resulting decay curves and lifetime distributions are shown in Figs. S1 and S2 in the Supplementary data. For each distribution we calculated the amplitude-weighted lifetime, which is proportional to the total NBD fluorescence and which, therefore, we could subsequently use to calculate energy transfer efficiencies (E) as a function of the TR fractional concentration ($E = 1 - \frac{\bar{\tau}_{DA}}{\bar{\tau}_D}$, where $\bar{\tau}_{DA}$ is the amplitude-weighted lifetime for the donor in the presence of the acceptor and $\bar{\tau}_D$ is the amplitude-weighted lifetime for the donor in the absence of acceptor. The amplitude-weighted lifetimes and FRET efficiencies are shown in Table 1. FRET efficiencies are also plotted against the TR fractional concentration in Fig. 4B. Energy transfer occurs with similar efficiency in cholesterol mixtures, based on the comparison of measured values of 0.36 and 0.29 FRET for 0.3 mol% TR in DOPC/Chol and ESM/Chol vesicles, respectively, compared with 0.30 FRET for DOPC (see Fig. 4B and Table 1) at the same TR concentration.

The NBD to TR energy transfer efficiencies measured in DOPC vesicle membranes were compared with values calculated assuming a random distribution of acceptors in the membrane (see Fig. 4B, solid and broken lines).[26] The solid line represents energy transfer efficiencies calculated with a Förster distance of R_0 = 42.7 Å, which, in turn, was calculated using a quantum yield of NBD in DOPC equal to 0.18, a refractive index of donor and acceptor environment equal to 1.33, an overlap integral obtained from measured absorption and emission intensities of TR and NBD in DOPC, respectively, and assuming the orientation factor κ^2 = 2/3, which corresponds to transition dipole moments randomized in three dimensions. As seen in Fig. 4B, the calculated efficiencies are systematically smaller than the measured values. A possible reason for this disagreement could be underestimation of κ^2. In fact, our preliminary observations of NBD and TR interactions in supported bilayers indicate that κ^2 should be >2/3 as orientation randomization

Fig. 4. (A) Fluorescence spectra measured after 450 nm excitation of 1,2-dipalmitoyl-*sn*-glycero-3-phosphoethanolamine-*N*-(7-nitro-2-1,3-benzoxadiazol-4-yl (NBD-DHPE) in dioleolylphosphatidylcholine (DOPC) vesicles containing various concentrations of Texas red 1,2-dihexadecanoyl-*sn*-glycero-3-phosphoethanolamine triethylammonium salt [TR-DHPE]. (B) Förster resonance energy transfer (FRET) efficiency as a function of [TR-DHPE] in DOPC vesicles (●). The error bars indicate maximum error. The solid and broken lines represent calculated energy transfer efficiencies with Förster distances (R_0) of 42.7 and 48 Å, respectively, assuming random acceptor distribution.

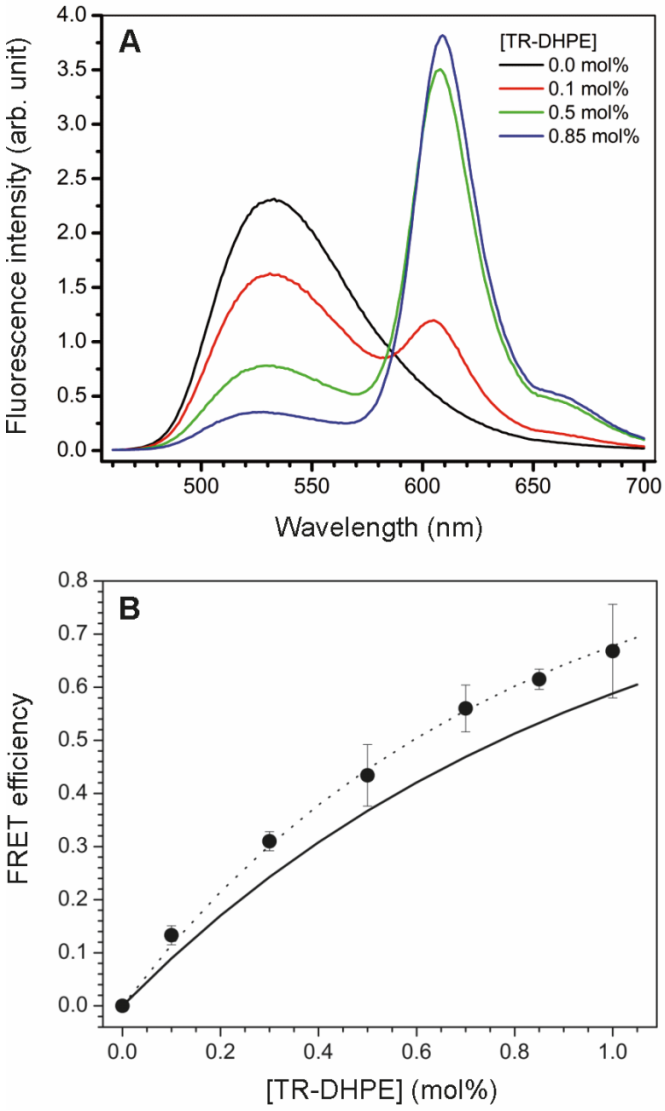

of the transition dipole moments of both NBD and TR results in nonvanishing components along the direction normal to the bilayers.[27] As shown in Fig. 4B (broken line), should the Förster distance be somewhat longer, $R_0 \approx 48$ Å, the calculated efficiencies would agree with the observation very well. This longer value of R_0 could be calculated using $\kappa^2 \approx 1.35$. A κ^2 significantly >1 indicates a large contribution from energy transfer between dyes in opposite leaflets of the bilayer.

As shown in Table 1, the widths of the Lorentzian lifetime distributions do not vary systematically with TR fractional

Can. J. Chem. Downloaded from www.nrcresearchpress.com by University of Electronic and Science Techonology of China on 09/18/12
For personal use only.

Table 1. NBD to TR resonance energy transfer in dioleolylphosphatidylcholine (DOPC) vesicles as a function of TR fractional concentration.

TR concentration (mol%)	Amplitude-weighted lifetime (error) (ns)	FRET efficiency (error)	Lorentzian distribution mode value (ns)	Lorentzian distribution width (ns)
0.0	6.9 (0.12)	0.0	7.1	1.8
0.1	6.0 (0.06)	0.13 (0.024)	6.1	2.2
0.3	4.7 (0.09)	0.31 (0.025)	4.6	2.1
0.5	3.9 (0.39)	0.43 (0.067)	3.5	1.7
0.7	3.0 (0.30)	0.56 (0.051)	2.7	1.6
0.85	2.6 (0.12)	0.62 (0.024)	2.1	2.1
1.0	2.3 (0.60)	0.67 (0.093)	1.2	3.0

Note: NBD, 7-nitro-2,1,3-benzoxadiazole; TR, Texas red; FRET, Förster resonance energy transfer.

Fig. 5. (A), (B), and (C) Fluorescence and (D) and (E) AFM images comparing the effect of Texas red 1,2-dihexadecanoyl-*sn*-glycero-3-phosphoethanolamine triethylammonium salt (TR-DHPE) and 1,2-dioleoylphosphatidyl-*N*,*N*-dimethyl-*N*-(2,2,6,6-tetramethyl-1-oxyl-piperidinyl)-ethanolamine (TEMPO-DOPC) on NBD fluorescence in DOPC / egg sphingomyelin (ESM) / cholesterol (Chol) bilayers containing 0.5 mol% 1,2-dipalmitoyl-*sn*-glycero-3-phosphoethanolamine-*N*-(7-nitro-2-1,3-benzoxadiazol-4-yl (NBD-DHPE). (A) 0.3 mol% TR-DHPE, (B) 3 mol% TEMPO-DOPC, (C) 6 mol% TEMPO-DOPC, (D) 0.3 mol% TR-DHPE, (E) 6 mol% TEMPO-DOPC.

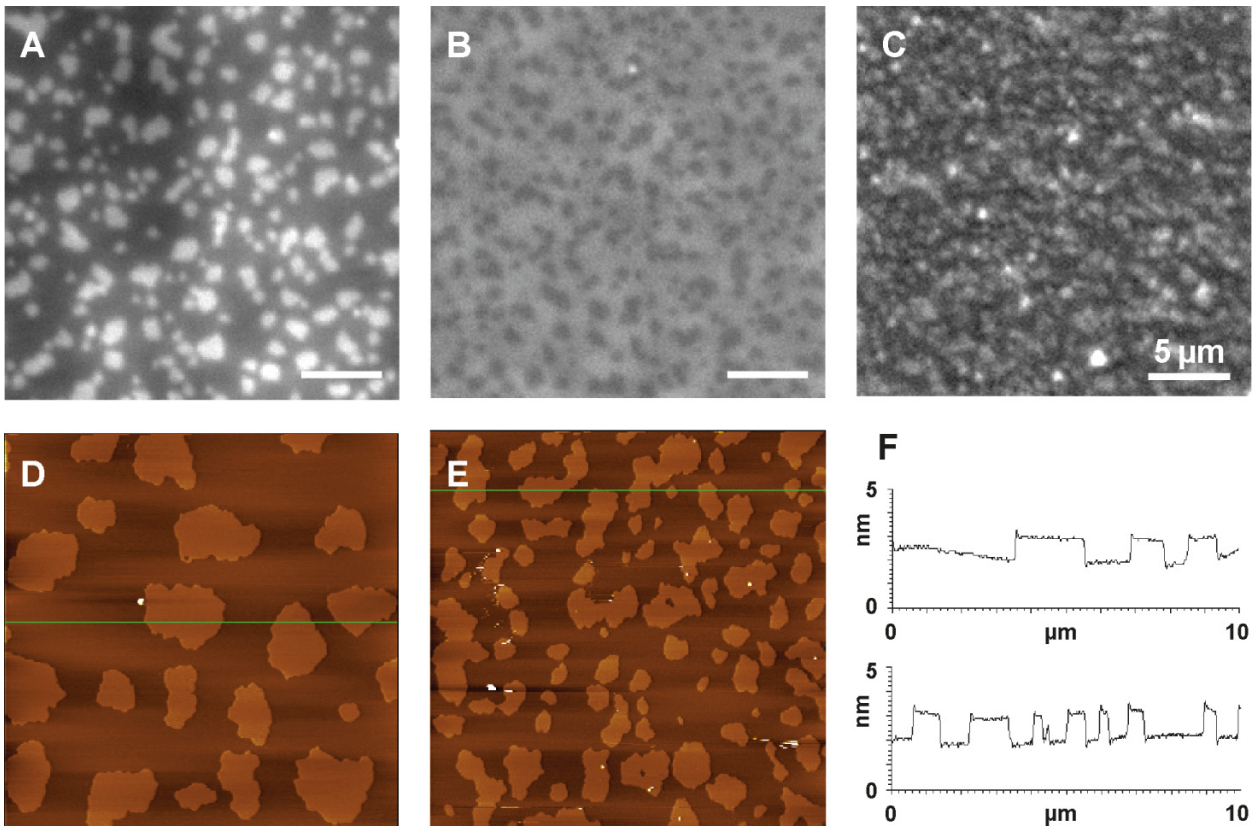

concentration and are approximately equal to or only slightly greater than the width for 0.0 mol% TR. This suggests that the distributions are primarily defined by variation in the NBD environment rather than by a distribution of NBD-TR energy transfer distances.

Fluorescence quenching by TEMPO-DOPC in supported bilayers

To test whether the I_{L_d}/I_{L_o} ratio for NBD-DHPE could be tuned using a nonluminescent quencher, bilayers containing NBD-DHPE and variable concentrations of TEMPO-DOPC (Scheme 1) were examined by fluorescence microscopy. Several nitroxide-labeled unsaturated phosphatidylcholines have been shown to localize in disordered-membrane phases and have been used in fluorescence quenching assays to assess phase separation in multicomponent vesicles.[28,29] Figure 5 shows fluorescence images for bilayers labeled with 0.5 mol% NBD-DHPE and containing either 0.3 mol% TR-DHPE or 3 or 6 mol% TEMPO-DOPC; a fraction of the DOPC has been replaced by TEMPO-DOPC in the latter two mixtures while keeping the ESM/Chol ratio constant. With 3 mol% TEMPO-DOPC, the domains are still visible but the contrast between L_o and L_d is lower than in the absence of TEMPO-DOPC. The addition of 3 mol% TEMPO-DOPC also

Fig. 6. Fluorescence time course for a dioleolylphosphatidylcholine (DOPC)/egg sphingomyelin (ESM)/(Chol) (7:9:4) bilayer labeled with 0.5% NBD-Chol and 0.2% Texas red 1,2-dihexadecanoyl-*sn*-glycero-3-phosphoethanolamine triethylammonium salt (TR-DHPE) and treated with 0.5 U sphingomyelinase (SMase) in a final volume of 1.5 mL. (A) Before SMase addition, (B) 3 min after SMase addition, (C) 9 min after SMase addition, and (D) 16 min after SMase addition.

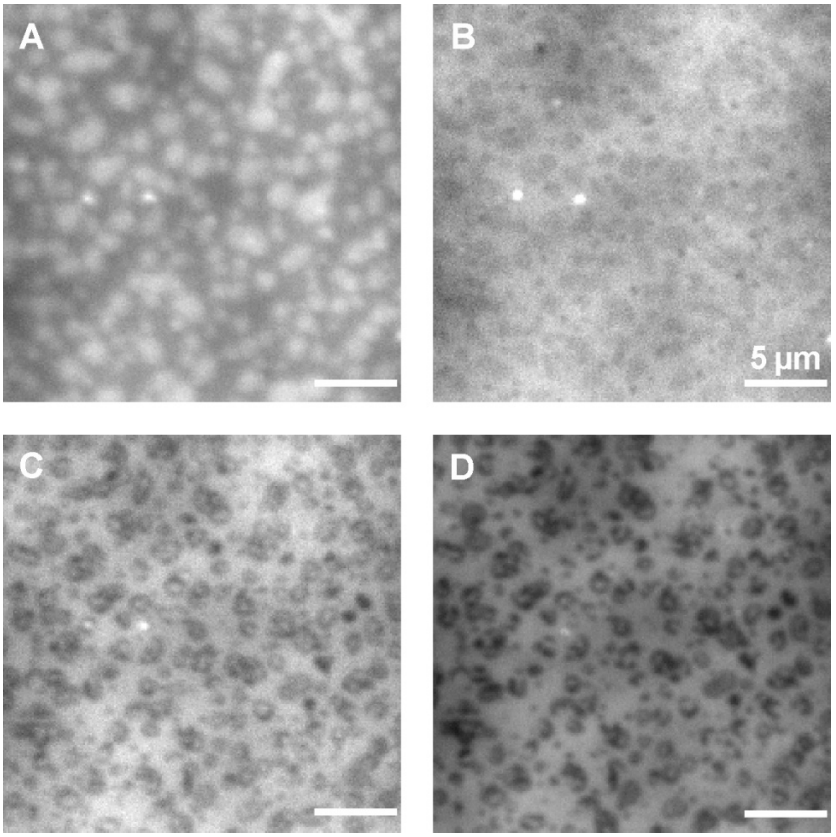

Can. J. Chem. Downloaded from www.nrcresearchpress.com by University of Electronic and Science Techonology of China on 09/18/12
For personal use only.

modifies the domain size and morphology, suggesting that it may not be completely excluded from the L_o phase. At higher TEMPO concentrations, the bilayer morphology is further modified by the TEMPO with smaller and more irregular-shaped domains detected by AFM and with a slight increase in the height difference between the domain and surrounding fluid phase (0.8–1.0 nm and 1.0–1.2 nm for 0 and 6 mol% TEMPO, respectively). However, the domains are still visible in fluorescence images and are now brighter than the fluid phase, indicating more efficient quenching of NBD by TEMPO-DOPC in the L_d phase than in the domains. The relatively high concentration of TEMPO required to see the same contrast reversal achieved with low [TR-DHPE] and the significant effects of TEMPO on the bilayer morphology indicate that TEMPO quenching is not a generally useful strategy for fluorescence microscopy.

Contrast-enhanced imaging to follow the dynamics of enzyme-mediated bilayer restructuring

Our previous studies have used correlated fluorescence and AFM to characterize morphological changes in supported bilayers of DOPC/ESM/Chol following in situ enzymatic generation of ceramide.[13,20,30] Ceramide is a small hydrophobic sphingolipid that has been implicated in the regulation of lipid raft-associated signaling processes; the enzymatic hydrolysis of sphingomyelin by sphingomyelinases (SMases) is a physiologically important pathway for generating ceramide.[31] The high spatial resolution of AFM coupled with the superior temporal resolution of fluorescence microscopy provides detailed information on the complex membrane restructuring that occurs. These changes include the formation of heterogeneous L_o domains with ceramide-enriched subdomains, a new dye-excluded membrane phase, and occasional defects.[20] A novel NBD-labeled cholesterol probe (NBD-Chol; Scheme 1) with a carbamate linker was synthesized and shown to partition more strongly into the L_o phase than a commercially available ester-linked probe;[13] NBD-Chol was used to identify regions of a highly ordered, cholesterol-depleted phase in SMase-treated bilayers and to show that cholesterol is depleted from the raft-like domains following ceramide generation.[13] However, the NBD-Chol partitioned almost equally between ordered- and disordered-membrane phases and did not adequately resolve the heterogeneity in ceramide-containing domains that can be observed by AFM. Here, we show that a labeling strategy using a NBD-Chol/TR-DHPE FRET pair has some advantages for resolving the complex changes that occur during enzymatic generation of ceramide in supported bilayers.

Figure 6 illustrates a representative time course experiment recording the evolution of a DOPC/ESM/Chol (7:9:4) supported bilayer following SMase treatment. The bilayer has been labeled with 0.5% NBD-Chol and 0.2% TR-DHPE, and incubated with 0.33 U/mL of enzyme. Figure 6A shows the bilayer before enzyme addition. The L_o

Can. J. Chem. Downloaded from www.nrcresearchpress.com by University of Electronic and Science Techonology of China on 09/18/12
For personal use only.

domains appear bright relative to the L_d phase; this is in contrast to bilayers labeled with NBD-Chol alone for which the fluid phase is brighter, but is consistent with contrast reversal owing to FRET, as described above for NBD-DHPE and TR-DHPE in membranes of similar composition. In an image (Fig. 6B) of the same sample region taken 3 min after SMase addition, the domains now appear slightly darker than the surrounding membrane. Control experiments confirmed that this change was not due to accelerated NBD photobleaching in the domain relative to the fluid phase. In our previous work, we reported that as ceramide is generated in the domains, NBD-Chol is gradually ejected from these features into the fluid phase.[13] The domain darkening observed here is consistent with this earlier observation. Recorded 9 min after enzyme addition, Fig. 6C reveals domains that exhibit two levels of fluorescence intensity. Although the features retain their overall rounded shape and can be matched to domains in the initial untreated bilayer, they now appear as dark rings enclosing bright regions at their centers. Over time, these rings continue to darken and thicken, and the bright regions at the domain centers decrease in size (see Fig. 6D, 16 min; note that the intensities are weaker in both phases owing to probe bleaching).

Based on previous correlated fluorescence–AFM imaging of similar SMase-treated bilayers, the dark border and bright central regions that appear in the domains correspond to a raised, fencelike gel-phase perimeter and a liquid-ordered core that is lower in height. The taller gel-phase regions have been assigned to ceramide-enriched regions that are depleted in cholesterol,[18,32] and so should exclude a probe for cholesterol. The dark domain perimeters in Figs. 6C and 6D show that this is in fact the case with the NBD-Chol. The domain centers remain bright indicating that they retain the probe and therefore also a significant cholesterol content, consistent with previous AFM results.[13] Such heterogeneity within domains was not observed by fluorescence with the NBD-Chol probe in the absence of TR-DHPE, illustrating the advantage of the FRET method for enhancing fluorescence contrast.

Conclusions

The probe NBD-DHPE shows stronger fluorescence in the fluid phase in DOPC/ESM/Chol mixtures, but contrast reversal to give more strongly fluorescent liquid-ordered domains is observed in the presence of >0.2% TR-DHPE. This observation is explained by the occurrence of efficient FRET between NBD and TR in the fluid phase, consistent estimates of a threefold higher concentration of TR-DHPE in the L_d phase relative to the L_o domains, and with a detailed study of fluorescence lifetimes for NBD-DHPE in the presence of 0.0–1.0 mol% TR-DHPE in homogeneous DOPC vesicles. FRET efficiencies of ~0.30 at 0.3 mol% TR were measured for vesicles of several different compositions. The utility of the FRET approach for enhancing contrast between phases in complex lipid mixtures was demonstrated by imaging bilayers during enzyme-mediated bilayer restructuring. Labeling the bilayers with an NBD-TR combination allowed us to resolve domain heterogeneity owing to ceramide-enriched subdomains that was not evident when using either of the two dyes independently.

FRET methodologies have been used to detect and characterize phase separation in a variety of lipid mixtures of varying complexity and quantitative approaches have been devised to determine phase boundaries, probe partition coefficients, and domain size.[33] However, energy transfer between donor and acceptor fluorophores, as examined here, has not been utilized as a means for improving fluorescence contrast or visualizing liquid-ordered domains for which most lipid probes show a relatively low partition coefficient. It is important to note that significant FRET efficiencies are measured even at the relatively low dye concentration of 0.2%. Similar (or higher) concentrations are widely used in fluorescence microscopy studies of both supported membranes and giant unilamellar vesicles (GUVs), frequently in double labeling experiments with dyes that have a significant overlap of donor emission and acceptor absorption. Thus, it is important to ensure that results for the partitioning of components into a specific phase in doubly labeled membranes are correctly interpreted and do not reflect a FRET component.

Supplementary data

Supplementary data are available with this article through the journal Web site (www.nrcresearchpress.com/cjc).

Acknowledgments

We thank Drs. M. Chen and Z. Lu for imaging assistance. J.G. was the recipient of a 2009 Reactive Intermediates Student Exchange (RISE) Summer Research Award and D.M.C.R. of an Ontario Graduate Scholarship. L.J.J. and W.W.O. gratefully acknowledge financial support from the Natural Sciences and Engineering Research Council of Canada (NSERC).

References

(1) Edidin, M. *Annu. Rev. Biophys. Biomol. Struct.* **2003**, *32* (1), 257. doi:10.1146/annurev.biophys.32.110601.142439.
(2) Jacobson, K.; Mouritsen, O. G.; Anderson, R. G. W. *Nat. Cell Biol.* **2007**, *9* (1), 7. doi:10.1038/ncb0107-7.
(3) Pike, L. J. *J. Lipid Res.* **2006**, *47* (7), 1597. doi:10.1194/jlr.E600002-JLR200.
(4) Simons, K.; Ikonen, E. *Nature* **1997**, *387* (6633), 569. doi:10.1038/42408.
(5) Simons, K.; Vaz, W. L. *Annu. Rev. Biophys. Biomol. Struct.* **2004**, *33* (1), 269. doi:10.1146/annurev.biophys.32.110601.141803.
(6) Lagerholm, B. C.; Weinreb, G. E.; Jacobson, K.; Thompson, N. L. *Annu. Rev. Phys. Chem.* **2005**, *56* (1), 309. doi:10.1146/annurev.physchem.56.092503.141211.
(7) Heberle, F. A.; Buboltz, J. T.; Stringer, D.; Feigenson, G. W. *Biochim. Biophys. Acta,* Mol. Cell Res. **2005**, *1746* (3), 186. doi:10.1016/j.bbamcr.2005.05.008.
(8) London, E. *Biochim. Biophys. Acta*, Mol. Cell Res. **2005**, *1746* (3), 203. doi:10.1016/j.bbamcr.2005.09.002.
(9) Veatch, S. L.; Keller, S. L. *Biochim. Biophys. Acta*, Mol. Cell Res. **2005**, *1746* (3), 172. doi:10.1016/j.bbamcr.2005.06.010.
(10) Baumgart, T.; Hunt, G.; Farkas, E. R.; Webb, W. W.; Feigenson, G. W. *Biochim. Biophys. Acta*, Biomembr. **2007**, *1768* (9), 2182. doi:10.1016/j.bbamem.2007.05.012.
(11) Ariola, F. S.; Li, Z.; Cornejo, C.; Bittman, R.; Heikal, A. A.

Biophys. J. **2009**, *96* (7), 2696. doi:10.1016/j.bpj.2008.12.3922.
(12) Chiantia, S.; Ries, J.; Chwastek, G.; Carrer, D.; Li, Z.; Bittman, R.; Schwille, P. *Biochim. Biophys. Acta*, Biomembr. **2008**, *1778* (5), 1356. doi:10.1016/j.bbamem.2008.02.008.
(13) Carter Ramirez, D. M.; Ogilvie, W. W.; Johnston, L. J. *Biochim. Biophys. Acta*, Biomembr. **2010**, *1798* (3), 558. doi:10.1016/j.bbamem.2009.12.005.
(14) Shaw, J. E.; Epand, R. F.; Epand, R. M.; Li, Z.; Bittman, R.; Yip, C. M. *Biophys. J.* **2006**, *90* (6), 2170. doi:10.1529/biophysj.105.073510.
(15) Dietrich, C.; Bagatolli, L. A.; Volovyk, Z. N.; Thompson, N. L.; Levi, M.; Jacobson, K.; Gratton, E. *Biophys. J.* **2001**, *80* (3), 1417. doi:10.1016/S0006-3495(01)76114-0.
(16) Silva, L. C.; de Almeida, R. F. M.; Castro, B. M.; Fedorov, A.; Prieto, M. *Biophys. J.* **2007**, *92* (2), 502. doi:10.1529/biophysj.106.091876.
(17) Sengupta, P.; Hammond, A.; Holowka, D.; Baird, B. *Biochim. Biophys. Acta*, Biomembr. **2008**, *1778* (1), 20. doi:10.1016/j.bbamem.2007.08.028.
(18) Ira; Johnston, L. J. *Langmuir* **2006**, *22* (26), 11284. doi:10.1021/la061636s.
(19) Karstens, T.; Kobs, K. *J. Phys. Chem.* **1980**, *84* (14), 1871. doi:10.1021/j100451a030.
(20) Ira; Zou, S.; Carter Ramirez, D. M.; Vanderlip, S.; Ogilvie, W.; Jakubek, Z. J.; Johnston, L. J. *J. Struct. Biol.* **2009**, *168* (1), 78. doi:10.1016/j.jsb.2009.03.014.
(21) Lakowicz, J. R. *Principles of Fluorescence Spectroscopy,* 3rd ed.; Springer: New York, 2006.
(22) de Almeida, R. F. M.; Loura, L. M. S.; Fedorov, A.; Prieto, M. *J. Mol. Biol.* **2005**, *346* (4), 1109. doi:10.1016/j.jmb.2004.12.026.
(23) Loura, L. M. S.; Federov, A.; Prieto, M. *Biophys. J.* **2001**, *80* (2), 776. doi:10.1016/S0006-3495(01)76057-2.
(24) Duportail, G.; Merola, F.; Lianos, P. *J. Photochem. Photobiol. Chem.* **1995**, *89* (2), 135. doi:10.1016/1010-6030(95)04045-H.
(25) Mazeres, S.; Schram, V.; Tocanne, J.-F.; Lopez, A. *Biophys. J.* **1996**, *71* (1), 327. doi:10.1016/S0006-3495(96)79228-7.
(26) Wolber, P. K.; Hudson, B. C. *Biophys. J.* **1979**, *28* (2), 197. doi:10.1016/S0006-3495(79)85171-1.
(27) Dale, R. E.; Eisinger, J.; Blumberg, W. E. *Biophys. J.* **1979**, *26* (2), 161. doi:10.1016/S0006-3495(79)85243-1.
(28) Megha; London, E. *J. Biol. Chem.* **2004**, *279* (11), 9997. doi:10.1074/jbc.M309992200.
(29) Silvius, J. R. *Biophys. J.* **2003**, *85* (2), 1034. doi:10.1016/S0006-3495(03)74542-1.
(30) Ira; Johnston, L. J. *Biochim. Biophys. Acta, Biomembr.* **2008**, *1778* (1), 185. doi:10.1016/j.bbamem.2007.09.021.
(31) Goñi, F. M.; Alonso, A. *Biochim. Biophys. Acta*, Biomembr. **2009**, *1788* (1), 169. doi:10.1016/j.bbamem.2008.09.002.
(32) Chiantia, S.; Kahya, N.; Ries, J.; Schwille, P. *Biophys. J.* **2006**, *90* (12), 4500. doi:10.1529/biophysj.106.081026.
(33) Loura, L. M. S.; de Almeida, R. F. M.; Silva, L. C.; Prieto, M. *Biochim. Biophys. Acta*, Biomembr. **2009**, *1788* (1), 209. doi:10.1016/j.bbamem.2008.10.012.

Can. J. Chem. Downloaded from www.nrcresearchpress.com by University of Electronic and Science Techonology of China on 09/18/12
For personal use only.

Excited state intramolecular proton transfer in 1-hydroxypyrene

Matthew Lukeman, Misty-Dawn Burns, and Peter Wan

Can. J. Chem. Downloaded from www.nrcresearchpress.com by Xi'an Jiaotong University on 09/19/12
For personal use only.

Abstract: 1-Hydroxypyrene (**1**) shows unusual acid–base chemistry in its singlet excited state. Whereas most hydroxyarenes experience a marked enhancement in their acidity when excited, and rapidly deprotonate to give the corresponding phenolate anion, this is not an important pathway for **1**, despite theoretical predictions that **1** should experience enhanced acidity as well. In this work, we demonstrate that **1** undergoes a competing excited state intramolecular proton transfer from the OH to carbon atoms at the 3, 6, and 8 positions of the pyrene ring to give quinone methide intermediates. When the reaction is carried out in D_2O, reversion of these quinone methides to starting material results in replacement of the ring hydrogens with deuterium, providing a convenient handle to follow the reaction with NMR spectroscopy and mass spectrometry. The quantum yield for the reaction is 0.025 and appears to not be strongly dependent on the water content when aqueous acetonitrile solutions are used. 1-(2-Hydroxyphenyl)pyrene (**19**) was prepared and studied and shows similar reactivity to **1**.

Key words: 1-pyrenol, 1-hydroxypyrene, excited state intramolecular proton transfer, quinone methide, photoprotonation, photochemistry.

Résumé : Dans son état excité singulet, le 1-hydroxypyrène (**1**) présente une chimie acide–base inhabituelle. La plupart des hydroxyarènes présentent une augmentation marquée de leur acidité dans leur état excité et ils se déprotonent rapidement pour conduire à l'anion phénolate correspondant; ce n'est pas une voie importante pour **1** même si les prédictions théoriques indiquent que **1** devrait aussi voir son acidité augmentée. Dans ce travail, on démontre que dans son état excité **1** subit aussi une réaction compétitive de transfert intramoléculaire de proton à partir du groupe OH vers les atomes de carbone dans les positions 3, 6 et 8 du noyau pyrène qui conduisent à des intermédiaires quinone-méthides. Quand on effectue la réaction dans du D_2O, la réversion de ces quinone-méthides vers le produit de départ conduit au remplacement des atomes d'hydrogène du cycle par du deutérium qui fournit un moyen utile de suivre la réaction à l'aide de la spectroscopie RMN et de la spectrométrie de masse. Le rendement quantique pour la réaction est de 0.025 et il ne semble pas dépendre beaucoup du contenu d'eau lorsqu'on utilise des solutions aqueuses d'acétonitrile. On a aussi préparé et étudié la réaction du 1-(2-hydroxyphényl)pyrène (**19**) et il présente la même réactivité que le **1**.

Mots-clés : 1-pyrénol, 1-hydroxypyrène, transfert intramoléculaire de proton dans l'état excité, quinone-méthides, photoprotonation, photochimie.

[Traduit par la Rédaction]

Introduction

It is well-known that a large variety of aromatic alcohols experience enhanced acidity when excited to S_1.[1] For example, the hydroxyl group of 2-naphthol increases in acidity by nearly 7 orders of magnitude on excitation from its ground state ($pK_a(S_0) \approx 9.5$) to its first excited state ($pK_a(S_1) \approx 2.8$). The enhancement of acidity on excitation is even more pronounced for 1-naphthol, whose pK_a changes from 9.2 in the ground state to 0.4 in S_1.[2] Excited phenols will usually deprotonate adiabatically within picoseconds in water via a process known as excited state proton transfer (ESPT), and observation of fluorescence emission from the resultant excited-state phenolate is generally taken as a diagnostic sign of ESPT.

The excited-state acidity of 1-hydroxypyrene (**1**) has been a source of interest because unlike most other phenols, it is difficult to discern the existence of ESPT from fluorescence spectroscopy. Milosavljevic and Thomas[3] used Förster cycle calculations to predict that **1** should possess a $pK_a(S_1)$ value of 4.5, indicating that ESPT in neutral water should be thermodynamically favourable. They then explored the photophysics of **1** in water and concluded that "no discernable equilibrium exists between the excited state [of **1**] and its excited ionic forms", which is at variance with the Förster cycle predictions. This prompted the authors to question the validity of Förster cycle calculations, and indeed the "concepts of acidity of excited states". By comparing steady-state emission spectraof **1** in pH 4–7 unbuffered water with those in low pH (<2) solution, Kombarova and Il'ichev[4]

Received 31 May 2010. Accepted 28 November 2010. Published on the NRC Research Press Web site at canjchem.nrc.ca on 5 March 2011.

This article is part of a Special Issue dedicated to Professor J. C. Scaiano.

M. Lukeman[1] and M.-D. Burns. Department of Chemistry, 6 University Avenue, Acadia University, NS B4P 2R6, Canada.
P. Wan. Department of Chemistry, Box 3065, University of Victoria, BC V8W 3V6, Canada.

[1]Corresponding author (e-mail: matthew.lukeman@acadiau.ca).

Can. J. Chem. Downloaded from www.nrcresearchpress.com by Xi'an Jiaotong University on 09/19/12
For personal use only.

were able to detect emission from the pyrenolate arising from ESPT, although only a small fraction of the excited phenol appears to dissociate. Using time-resolved fluorescence data, the authors are able to confirm that the pyrenolate emission indeed arises from excited-state dissociation of the pyrenol hydroxyl group, and they estimate a $pK_a(S_1)$ of 3.8 for **1**, which is in good agreement with the value obtained by the Förster cycle calculations. However, the calculated rate constant for ESPT was only 4×10^6 s^{-1}, which is exceptionally slow for a proton transfer reaction. For comparison, pyranine, the 3,6,8-trisulfonated derivative of **1**, undergoes ESPT to water with a rate constant $>10^{10}$ s^{-1}.[5]

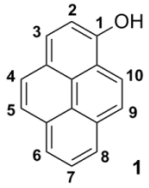

Over the past decade, we have shown that several simple aromatic alcohols can undergo efficient excited state intramolecular proton transfer (ESIPT) from the OH group to aromatic carbon atoms to yield quinone methide (QM) intermediates. For example, ESIPT in 1-naphthol (**2**) from the hydroxyl group to the 5 or 8 position leads to formation of QMs **3** or **4**, which then undergo reverse proton transfer to refurnish starting material (eq. [1]).[6] Evidence for the ESIPT pathway was provided by monitoring deuterium incorporation at the 5 and 8 positions (when the solvent contained D_2O), and by nanosecond laser flash photolysis (LFP) studies that allowed direct observation of QM **3**. Whereas ESIPT in **2** requires water to mediate the proton transfer, an intrinsic or "direct" ESIPT that does not require water was discovered to be available for 2-phenylphenol (**5**) to give QM **6** (eq. [2]).[7] Since these discoveries, we have also found that similar ESIPT processes can occur in naphthylphenols[8] and hydroxyphenylanthracenes,[9] and in these cases, products in addition to deuterium-labeled starting material were obtained. Irradiation of **7**–**9** resulted in ESIPT from the OH to the 7′ carbon atom on the attached naphthalene ring to give quinone methides **10**–**12**, which underwent electrocyclic ring closure to give benzopyran products **13**–**15** (eq. [3]).[8] ESIPT from the OH to the 10 position of **16** gave QM **17**, which reacted with water to give the isolable hydration product **18** (eq. [4]).[9] Discovery of these elementary photochemical pathways in these relatively simple aromatic alcohols piqued our curiosity as to whether a similar process might be available for **1**, which would shed some light on its apparently anomalous ESPT behavior and may help explain why ESPT to water (to yield $\mathbf{1}^-$) is inefficient. In addition, biaryl derivative **19** was prepared and examined for ESIPT reactivity via possible deuterium exchange, photocyclization, or photohydration. We present results that indicate that ESIPT can occur in **1** and **19** from the OH to the 3, 6, and 8 positions of the pyrene ring in both compounds to give rise to QM intermediates, which undergo exclusive reverse proton transfer to give starting material (labeled with deuterium when D_2O is used).

[1]

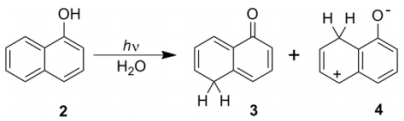

[2]

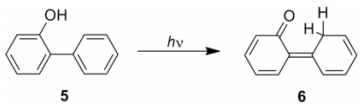

[3]

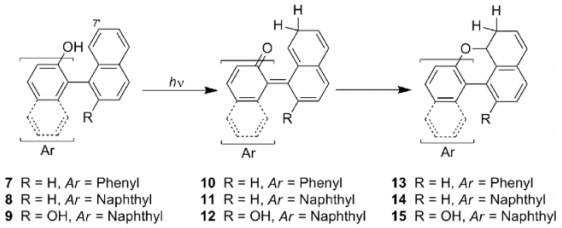

[4]

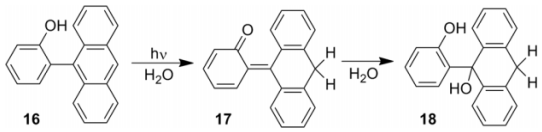

Experimental

General

All fine chemicals were purchased from Sigma-Aldrich Canada and used as received. Solvents were purchased as spec. grade or better, acetonitrile was dried over CaH_2 and distilled prior to use, and water was distilled and deionized. ^{1}H NMR spectra were recorded on a Bruker AVANCE 500 MHz instrument. MS were recorded on a Kratos Concept H spectrometer (EI). UV–vis were recorded on a Varian CARY 50 or CARY 100 spectrometer.

Materials

1-(2′-Hydroxyphenyl)pyrene (19)

1-Bromopyrene (1.00 g, 3.56 mmol), *o*-methoxyphenylboronic acid (0.684 g, 4.5 mmol), K_2CO_3 (4 g), $Pd(PPh_3)_4$ (0.20 g), and DME (50 mL, N_2 purged prior to addition) were combined and refluxed under N_2 for 20 h and allowed to cool. Sixty millilitres of 1 mol/L NaOH were added to the reaction mixture, which was then extracted with two portions of CH_2Cl_2 totaling 70 mL. The combined organics were dried with $MgSO_4$, filtered, and the solvent was removed by rotary evaporation. The crude 1-(2′-methoxyphenyl)pyrene was redissolved in 40 mL of diethyl ether, which was passed through a 1 cm plug of silica gel and a 2 cm plug of celite to remove catalyst. The silica and celite were flushed with an additional 100 mL of diethyl ether, and solvent was removed from the combined ethers by rotary evaporation. The resulting material was redissolved in 50 mL of CH_2Cl_2 and placed in an ice bath. To this cooled solution was added a solution of BBr_3 (10 mmol) in CH_2Cl_2 (60 mL) via a dropping funnel over a period of 30 min, after which the mixture was allowed to stir for 1 h. The reaction was quenched by the addition of 100 mL of H_2O, 10 mL of 10% HCl, and 10 mL of brine. The organic layer was removed and the aqueous layer was washed with an additional 30 mL of CH_2Cl_2. The organics were combined, dried with $MgSO_4$, filtered, and the solvent was removed by rotary evaporation. The resulting solid was recrystallized from methanol to yield **19** as white crystals. ^{1}H NMR (500 MHz,

Can. J. Chem. Downloaded from www.nrcresearchpress.com by Xi'an Jiaotong University on 09/19/12
For personal use only.

$CDCl_3$, ppm) δ: 4.842 (1H, s, OH), 7.118 (1H, ddd, J = 7.4, 7.4, 1.2 Hz), 7.128 (1H, dd, J = 8.4, 1.2 Hz), 7.387 (1H, dd, J = 7.4, 1.6 Hz), 7.423 (1H, ddd, J = 8.4, 7.4, 1.6 Hz), 7.894 (1H, d, J = 9.2 Hz), 7.984 (1H, d, J = 7.8 Hz), 8.032 (1H, t, J = 7.6 Hz), 8.053 (1H, d, J = 9.2 Hz), 8.108 (1H, d, J = 8.9 Hz), 8.135 (1H, d, J = 8.9 Hz), 8.190 (1H, dd, J = 7.6, 0.9 Hz), 8.224 (1H, d, J = 7.6, 0.9 Hz), 8.267 (1H, d, J = 7.8 Hz). ^{13}C NMR (125 MHz, $CDCl_3$) δ: 115.68, 120.72, 124.67, 124.69, 125.05, 125.21, 125.38, 125.52, 126.29, 126.81, 127.27, 128.02, 128.26, 128.37, 129.37, 129.66, 130.96, 131.03, 131.33, 131.42, 131.60, 153.25.

1-Methoxypyrene

To a 10 mL flask was added **1** (35 mg, 0.16 mmol), DMSO (10 mL), crushed KOH (1 g), and methyl iodide (2.85 g, 20 mmol). The mixture was stirred at room temperature for 16 h and then diluted by the addition of 50 mL of water to dissolve remaining KOH. The resulting mixture was extracted with 50 mL of CH_2Cl_2, and the organic layer was washed with 1 mol/L NaOH (50 mL) and water (2 × 150 mL), and then dried over $MgSO_4$, and the solvent was removed by rotary evaporation. The crude reaction mixture was purified by preparatory TLC (1000 μm silica gel) using 15:85 *v*/*v* ether–hexanes as the elutant, and yielded **20** as a white solid (90% yield). ^{1}H NMR (500 MHz, acetone-d_6, ppm) δ: 4.189 (3H, s, OCH_3), 7.706 (1H, d, J = 8.4 Hz), 7.935 (1H, d, J = 9.0 Hz), 7.990 (1H, t, J = 7.6 Hz), 8.025 (1H, d, J = 9.0 Hz), 8.097 (1H, d, J = 9.2 Hz), 8.152 (1H, dd, J = 7.6, 0.9 Hz), 8.173 (1H, dd, J = 7.6, 0.9 Hz), 8.208 (1H, d, J = 8.4 Hz), 8.425 (1H, d, J = 9.2 Hz). the ^{1}H NMR datamatches a previous report.[10] ^{13}C NMR (125 MHz, acetone-d_6) δ: 56.67, 109.43, 120.90, 121.97, 125.12, 125.27, 125.79, 126.16, 126.57, 126.84, 127.21, 127.24, 128.30, 132.69, 132.82, 154.70.

Product studies

Solutions were prepared in a quartz reaction vessel and purged with argon or oxygen for 10 min prior to and continuously during irradiation in a Rayonet RPR 100 or Luz-Chem LZC-Org photochemical reactor using 350 nm lamps. The photolysate was extracted with CH_2Cl_2, dried with anhyd $MgSO_4$, and solvent was removed under reduced pressure, and the resulting material analyzed by ^{1}H NMR spectroscopy and MS. For quantum yields, four such runs were carried out for each of **1** and **5** (both in D_2O–CH_3CN (1:9) solution), and the total amount of deuterium incorporation was determined based on peak integrations in the respective ^{1}H NMR spectra. Quantum yields were calculated according to eq. [5]:

$$[5] \qquad \Phi_{\mathbf{1}} = \Phi_{\mathbf{5}} \frac{\%\mathrm{conv}(\mathbf{1})}{\%\mathrm{conv}(\mathbf{5})}$$

where $\Phi_{\mathbf{1}}$ and $\Phi_{\mathbf{5}}$ are the quantum yields of the deuterium incorporation of **1** and **5**, respectively, and %conv(**1**) and %conv(**5**) are the percents of conversion as measured by ^{1}H NMR. The reported quantum yields are the average of the four runs.

Fluorescence and laser flash photolysis measurements

Solutions for fluorescence spectroscopy were purged with argon for 5 min before analysis. Spectra were obtained using a Photon Technology International (PTI) A-1010 Quanta-Master luminescence spectrometer. All transient absorption spectra and lifetimes were obtained using a Nd:YAG laser (Spectra Physics Quanta-Ray, GCR, <30 mJ/pulse) with a pulse duration of ~10 ns and an excitation wavelength of 355 nm. Flow cells were used (7 mm path length) and solutions were purged with nitrogen or oxygen for 10 min prior to excitation. Solution concentrations were adjusted to achieve an optical density of 0.3 at the excitation wavelength.

Results and discussion

Our primary evidence for the ESIPT pathway in **2** came from the observation of H–D exchange at the 5 and 8 positions when the substrate was irradiated in D_2O–CH_3CN solvent mixtures.[6] The same strategy was employed for **1** in an attempt to observe the deuterated products that would arise if a similar ESIPT process as that of **2** was available for **1**. Irradiation of **1** in D_2O–CH_3CN (1:1, *v*/*v*) (~5 × 10^{-4} mol/L, 16 × 350 nm lamps, argon saturated, 2 h) gave starting material with deuterium incorporated at the 3 position (7%), and to the 6 and 8 positions (34% for both positions combined) to give **1**-*3D*, **1**-*6D*, and **1**-*8D*, respectively (eq. [6]). The deuterium exchange is evident in the ^{1}H NMR spectrum (Fig. 1) where irradiation led to a decrease in the areas of the peaks at 8.10, 8.12, and 8.14 ppm assigned to the protons at the 3, 6, and 8 positions, respectively.[11] A broad doublet is observed to grow in under the doublet of doublets at 7.96 ppm assigned to the proton at the 7 position. This reduced coupling is consistent with deuterium incorporation at one of the adjacent sites. Similarly, a small broad singlet has grown in under the doublet at 7.62 ppm assigned to the 2 position, consistent with a lesser amount of deuterium incorporation at the 3 position. The overall extent of exchange was confirmed by MS, which showed a distribution of 65.8% undeuterated, 29.8% monodeuterated, and 4.2% dideuterated starting material, giving an overall deuterium exchange of 39% (NMR measurements indicate a total of 41%). No other photoproducts were observed in the photolysate. Irradiation of 1-methoxypyrene, the methyl ether of **1**, under the same conditions led to no observable deuterium incorporation by NMR, confirming that the reaction requires the OH functional group, consistent with an ESIPT mechanism.

[6]

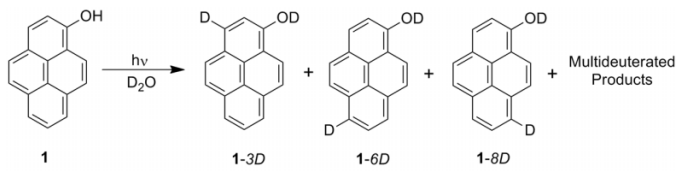

Fig. 1. [1]H NMR spectrum (500 MHz) of **1** before (bottom) and after (top) irradiation in D_2O–CH_3CN (1:1; 2 h), showing decreases in the areas of the peaks at 8.14, 8.12, and 7.99 ppm assigned to ring protons at the 8, 6, and 3 positions, respectively.

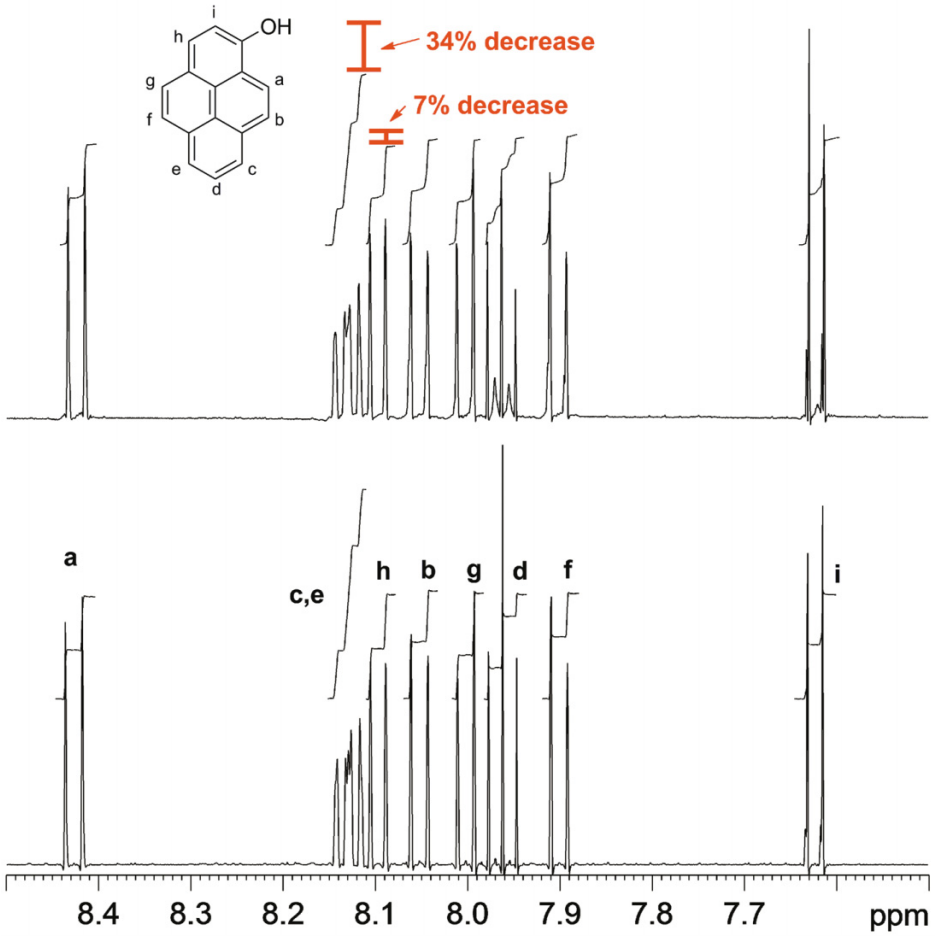

Fig. 2. Plot of the sum of the % deuterium exchange at the 3, 6, and 8 positions of **1** as a function of [D_2O] (in CH_3CN) as determined by MS.

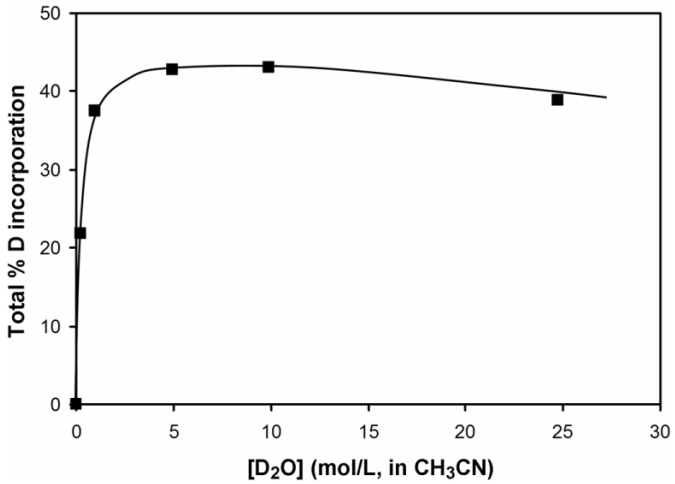

By irradiating solutions of **2** in CH_3CN containing varying amounts of D_2O and analyzing the photolysate by [1]H NMR, it was found that the ESIPT efficiency for this compound relied heavily on the composition of the solvent mixture.[6] Only residual reaction was observed at D_2O concentrations less than ~2 mol/L. Also, less water was apparently required for ESIPT to the 8 position than for ESIPT to the 5 position, which we rationalized to be a consequence of the different distances between the acidic OH and aromatic ring sites; the closer the phenol OH is to the site that receives the proton, the less water is required to mediate the proton transfer. To probe the dependence on water of the deuterium exchange reaction of **1**, irradiations were carried out in which the concentration of D_2O (in CH_3CN) was varied. The photolysate (after evaporation in vacuo) was examined by [1]H NMR and MS for deuterium incorporation at aromatic ring positions, and the total deuterium exchange at the three positions (as determined by MS) is presented in Fig. 2. Very different behaviour is observed for this derivative than was observed for **2** when the D_2O content is lowered: the total deuterium exchange did not decrease significantly until very small D_2O concentrations were reached, suggesting that very little water (or possibly none at all) is required to mediate the process. An intrinsic ESIPT (such as that observed for **5**)[7] seems unlikely, since the hydroxyl functionality is located a significant distance from the sites of deuterium exchange, particularly the 6 and 8 positions, preventing the ground-state hydrogen bonding interaction that is thought to be a prerequisite.

Can. J. Chem. Downloaded from www.nrcresearchpress.com by Xi'an Jiaotong University on 09/19/12
For personal use only.

Can. J. Chem. Downloaded from www.nrcresearchpress.com by Xi'an Jiaotong University on 09/19/12
For personal use only.

Fig. 3. ^{1}H NMR spectra (500 MHz), 7.8–8.3 ppm region, of **19** before (bottom) and after (top) irradiation in D_2O–CH_3CN (1:1; 30 min), highlighting the changes in peaks at 7.98 and 8.03 ppm that are consistent with loss of vicinal coupling with adjacent hydrogens because of deuterium exchange. Resonances owing to the phenolic ring appear between 7.0 and 7.5 ppm and are not included in this figure.

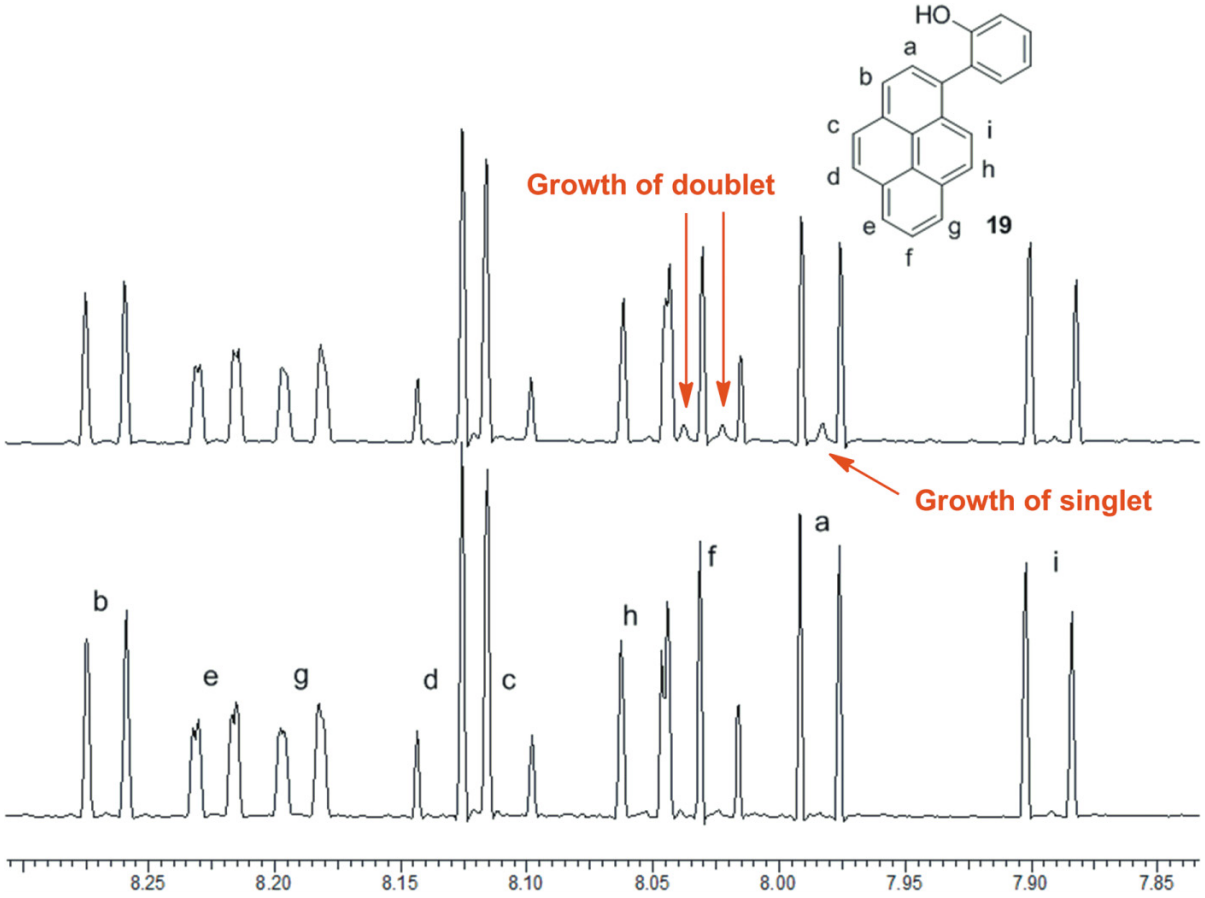

The relative extents of deuterium exchange at the 3, 6, and 8 positions were monitored by ^{1}H NMR at the different D_2O concentrations. If the deuterium exchange reaction is the result of a water-mediated ESIPT, deuterium incorporation at the 3 position should require far less water (or D_2O) than at the 6 and 8 positions, because of the smaller distance between the 3 position and the OH moiety that the water would have to span. The efficiency of exchange at the 6 and 8 positions was expected to show a much stronger dependence on D_2O concentration with significantly larger D_2O concentrations needed. The ratio of deuterium exchange at the 3 position to the 6 and 8 positions was completely unchanged as the D_2O content of the solution was reduced. This result argues against a water-mediated ESIPT such as that observed for **2**,[6] indicating water is likely not acting as a "bridge" to mediate the proton (deuteron) transfer.

The quantum yield of deuterium exchange for **1** was measured by ^{1}H NMR in CH_3CN–D_2O (9:1, *v*:*v*) solutions using the deuterium exchange reaction of **5** as a secondary reference standard.[7b] The quantum yield for exchange was measured to be 0.021 at the 6 or 8 positions and 0.004 for the 3 position, for a total quantum yield of deuterium incorporation at any one of these sites of 0.025. This value is somewhat lower than the other examples of ESIPT to aromatic carbon reported by us.[6–9] The ESIPT is expected to be more than twice as efficient in CH_3CN–H_2O (9:1, *v*/*v*), assuming a primary isotope effect of 2 or greater.

Irradiation of **19** was carried out in a similar manner as for **1** in D_2O–CH_3CN (1:1, *v*/*v*) (~5 × 10^{-4} mol/L, 16 × 350 nm lamps, argon saturated, 30 min), and the photolysate was examined by ^{1}H NMR spectroscopy (peak assignments were made with the aid of COSY and NOESY NMR spectra, included in the Supplementary data). Deuterium exchange was observed at the 3, 6, and 8 positions of the pyrene ring, the same positions as observed for **1**. The ^{1}H NMR spectra of **19** before and after irradiation are shown in Fig. 3. The areas of the peaks at 8.27, 8.22, and 8.19 ppm are reduced following irradiation, consistent with replacement of the hydrogens at these positions with deuterium. A broad singlet is observed to have grown beneath the doublet at 7.98, which is assigned to the proton on carbon 2 of the pyrene ring, which is consistent with loss of coupling to the adjacent proton (Fig. 3). Similarly, a doublet has grown beneath the triplet at 8.03 ppm, consistent with loss of coupling to an adjacent proton at position 6 or 8. The overall quantum yield for exchange of these three sites is similar to that of **1**. No other products, such as photocyclization or photohydration products, were observed, indicating that this derivative does not show chemistry similar to **7**, **8**, **9**, or **16**.

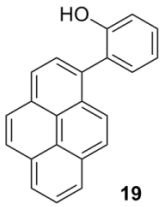

19

Fluorescence measurements

Fluorescence spectroscopy was used to study **1** to confirm the lack of significant observable emission from the pyrenolate (**1**$^-$) that would result from an adiabatic ESPT to water. Excitation of **1** (λ_{ex} = 345 nm) in neat CH_3CN or in neat water gave strong and structured emission with maxima at 383, 405, and 427 nm. Excitation of an authentic sample of **1**$^-$ (formed by dissolving **1** in 0.01 mol/L NaOH solution, λ_{ex} = 400 nm) gave strong, broad, and unstructured fluorescence emission at 450 nm. The fluorescence yield of **1** was not noticeably diminished on moving from CH_3CN to water, and no phenolate emission was observed under neutral conditions, confirming that ESPT to water is at best a very minor pathway for **1** under these conditions. These observations mirror previous fluorescence studies carried out for **1** by others.[3,4]

Solutions of **1** in water with the same concentration as those employed in the product studies (~5 × 10^4 mol/L) were also examined by fluorescence spectroscopy to monitor for excimer formation. No long wavelength band assignable to excimer emission was observed at these concentrations, indicating that excimer formation does not contribute to the observed photochemistry.

Nanosecond laser Fflash photolysis (LFP)

Milosavljevic and Thomas[4] studied the photophysics of **1** using LFP in cyclohexane, methanol, and methanol–NaOH. In cyclohexane and methanol solutions, three transients were observed and assigned to the triplet excited state of **1** (^{3}**1***, λ_{max} = 430 nm), the radical cation of **1** (**1**$^{\bullet+}$, λ_{max} = 515 nm), and the pyrenyloxyl radical (**PyO**$^\bullet$, λ_{max} = 430 nm). In methanol, the solvated electron that accompanies formation of **1**$^{\bullet+}$ is also observed, and its yield was observed to vary with the square of the laser power, indicating that the solvated electron (and the accompanying radicals **1**$^{\bullet+}$ and **PyO**$^\bullet$) are formed via a two-photon process and are therefore not likely to be important species at low light intensities such as those used in the product studies in this work. The pyrenolate anion (generated by deprotonating **1** with NaOH in methanol) was also studied and gave ^{3}**1***, **PyO**$^\bullet$, and solvated electrons (via a one-photon process), but no **1**$^{\bullet+}$. No data was reported in aqueous solution, which is the relevant solvent for the deuterium exchange reaction that we report in the present work. An ESIPT reaction to the 3, 6, and 8 positions of **1** would give QM intermediates **20**–**22**, respectively (eq. [7]). QMs **20** and **22** are non-Kekule structures, and thus were expected to have short lifetimes that would be inaccessible by LFP.[12] QM **21** was anticipated to have a much longer lifetime, and so we made an attempt to detect it with LFP. LFP of a solution of **1** in CH_3CN–H_2O (1:1), nitrogen purged, gave rise to a transient absorption with maxima at 440 and 510 nm. The signal at 510 nm was assigned to the radical cation (**1**$^{\bullet+}$), which was previously reported in methanol.[3] This transient completely decayed within ~3 μs to leave a long-lived transient with λ_{max} = 440 nm, whose absorption profile and lifetime strongly resemble that of **PyO**$^\bullet$ reported in methanol solution.[3] **PyO**$^\bullet$ can presumably be readily generated by deprotonation of **1**$^{\bullet+}$, which in turn can be generated by photoejection of an electron. In our experiments, the solvated electron was not visible, so laser power dependence studies were not carried out. No additional transients were observed, so direct evidence for the formation of QMs **20**–**22** in this solvent could not be obtained by this method. Our inability to detect these species likely stems from their low quantum yield of formation, although it is also possible that they are too short-lived for the time resolution of the instrumentation (i.e., τ < 20 ns).

Scheme 1.

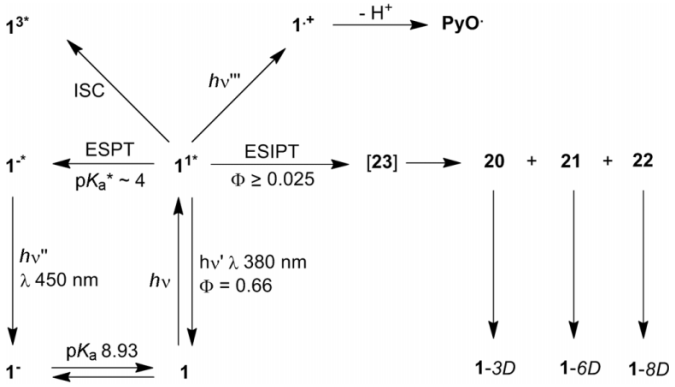

[7]

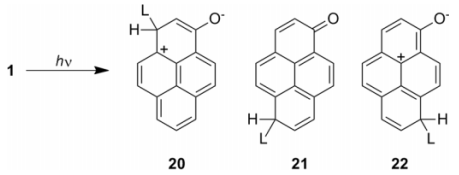

20 21 22

Mechanism

The relevant photophysical and photochemical processes for **1** in aqueous solution are summarized in Scheme 1. Excitation of **1** produces the singlet excited state (^{1}**1***), which has a lifetime of approximately 16 ns.[4] The dominant relaxation pathway for this excited state is fluorescence emission (Φ_F ~ 0.66)[12] at 380 nm.[3] A small fraction of the singlet excited state undergoes ESPT of the phenolic OH to the solvent (water) adiabatically to give the pyrenolate anion in its singlet excited state (**1**$^{-*}$), which has a lifetime of 3 ns,[4] and returns to the ground-state pyrenolate anion (**1**$^-$) via fluorescence emission with λ_{max} 450 nm. The triplet state of **1** (^{3}**1***) is observed in LFP experiments and absorbs at 430 nm.[3] The radical cation (**1**$^{\bullet+}$) and pyrenoxyl radicals (**PyO**$^\bullet$) are also observed in LFP experiments and are proposed to arise via two-photon processes that are only relevant under conditions of high photon flux (i.e., under laser irradiation), as was the case for these transients previously reported in cyclohexane and methanol.[4]

In addition to these photophysical properties that have been previously reported for **1** in water and in other solvents,

Can. J. Chem. Downloaded from www.nrcresearchpress.com by Xi'an Jiaotong University on 09/19/12
For personal use only.

Can. J. Chem. Downloaded from www.nrcresearchpress.com by Xi'an Jiaotong University on 09/19/12
For personal use only.

we propose an additional deactivation pathway that is available to $^1\mathbf{1}^*$ in water that is an ESIPT from the OH to carbon atoms on the pyrene ring to give quinone methides **20**–**22**, which revert to **1** via reverse proton transfer (resulting in deuterium labeling when the solvent is D_2O). Classification of the observed deuterium exchange reaction as an ESIPT process is consistent with recent literature on related compounds[6–9] and is supported by the absence of deuterium incorporation observed for the methyl ether analogue under the same conditions. An unexpected dependence on water content was observed with very little or no water required to mediate the proton transfer between the OH and the 3, 6, and 8 positions. Such behaviour was only previously observed for 2-phenylphenol and 2,2′-bisphenol that have an intrinsic ESIPT mechanism available to them because of the close proximity of the phenolic OH to the site of exchange.[7] An intrinsic ESIPT from the OH to the 6 or 8 positions would be difficult to envisage for **1** because of their considerable distance from the OH. Also of interest is that the ratio of exchange efficiencies for the three sites remains constant over wide variations of D_2O concentration, suggesting the formation of **20**–**22** from the excited state of **1** is independent of the degree of aqueous solvation of the excited state. A possible mechanism to account for these observations involves the existence of an intermediate prior to QM formation that is common to all three QMs that are formed (**20**–**22**). One such possibility involves an initial proton transfer occurring from the OH to the pyrene π system to form a ''protonated π complex'' such as **23**. This proton transfer might occur without solvent assistance or with the help of a small amount of a hydroxylic solvent. The acidic proton in **23** may then rearrange to form **20**–**22** via a solvent-independent process. The relative efficiencies for protonation at these three sites would simply be a function of the electron density at each position and the mobility of the proton. It would be expected that the most favourable destination of the proton in an intermediate such as **23** would be the oxygen atom, an overall process that would not lead to observable deuterium incorporation. If this is the case, the quantum yield of this initial ESIPT would be considerably higher than the quantum yield of deuterium exchange ($\Phi = 0.025$) ESIPT from the OH to one of the central (ipso) carbons might also be possible, and would give rise to QM intermediates **24** or **25**, which could undergo reverse proton transfer to regenerate starting material (without deuterium labeling) or rearrange to QMs **20**–**22**. The exact nature, and indeed the existence of an intermediate prior to QM formation, remains speculative at the moment, and the relatively low efficiency of these processes complicates their study via time-resolved absorption techniques, especially in light of the strong signals produced by the other absorbing transient species.

The deuterium exchange reaction of **19** is proposed to proceed via a related pathway — ESIPT from the phenol to the pyrene ring gives QMs that undergo reverse proton transfer to regenerate starting material, labeled with deuterium when D_2O is used in place of H_2O as the solvent. The same positions in **1** and **19** undergo exchange, indicating that the regiochemistry of the ESIPT is controlled solely by the electronics of the 1-substituted pyrene ring in S_1 and that the 3, 6, and 8 positions are the sites with the highest electron density in S_1. This is an interesting result, given that when the 3, 6, and 8 positions of **1** are substituted with the electron-withdrawing sulfonate groups (to make pyranine), ESPT to water becomes rapid ($\tau = 87$ ps)[5] and the acidity in S_1 becomes much greater ($pK_a(S_1) = 0.4–1.4$).[14] The substitution pattern of the sulfonate groups in pyranine is ideal for promoting photoacidity considering the localization electron density on the 3, 6, and 8 carbons in S_1. Tolbert et al.[2a] successfully employed the strategy of substituting aromatic carbon–hydrogen bonds of phenols with electron-withdrawing groups at positions that are electron-rich in S_1 to create phenols with very low values of $pK_a(S_1)$, a class of compounds known as ''super photoacids''. The lack of photocyclization or photohydration products for **19** (or **1** in fact) similar to those observed on irradiation of **7**–**9** and **16** is probably a consequence of the high resonance energy associated with the cyclic array of 14 π electrons that make up the periphery of the pyrene ring,[15] since photocyclization or photohydration would necessarily disrupt this aromaticity.

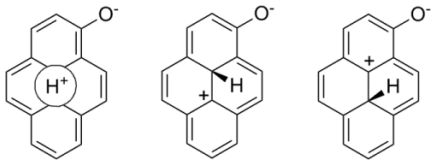

23 **24** **25**

The discovery of this ESIPT pathway provides additional evidence that **1** becomes more strongly acidic in S_1, supporting earlier findings based on fluorescence spectroscopy[4] and Forster calculations.[3] However, the ESIPT is not particularly efficient ($\Phi = 0.025$), especially when compared with fluorescence ($\Phi_F = 0.66$),[12] the dominant photophysical process from S_1. The ESIPT pathway has a similar efficiency to ESPT to water, indicating that it is a major photoprototropic reaction of **1** and provides a competitive pathway that would reduce the yield of $\mathbf{1}^{-*}$. Discovery of this ESIPT reaction and the related process for **19** provides further evidence that ESIPT is a very general reaction for hydroxyaromatic compounds and that this process must be considered in any serious investigation of the photophysics of hydroxyarenes.

Supplementary data

Supplementary data are available with this article through the journal Web site (www.nrcresearchpress.com/cjc).

References

(1) (a) Weller, A.; In *Progress in Reaction Kinetics;* Pergamon Press: London, 1961; Vol. 1, p 187.; (b) Martynov, I. Yu.; Demyashkevich, A. B.; Uzhinov, B. M.; Kuz'min, M. G. *Usp. Khim.* **1977** *46*, 3.

(2) (a) Tolbert, L. M.; Solntsev, K. M. *Acc. Chem. Res.* **2002** *35* (1), 19. doi:10.1021/ar990109f.; (b) Webb, S. P.; Philips, L. A.; Yeh, S. W.; Tolbert, L. M.; Clark, J. H. *J. Phys. Chem.* **1986** *90* (21), 5154. doi:10.1021/j100412a053.

(3) Milosavljevic, B. H.; Thomas, J. K. *Photochem. Photobiol. Sci.* **2002** *1* (2), 100. doi:10.1039/b107925e.

(4) Kombarova, S. V.; Il'ichev, Y. V. *Langmuir* **2004** *20* (15), 6158. doi:10.1021/la049585r.

(5) Tran-Thi, T.-H.; Gustavsson, T.; Prayer, C.; Pommeret, S.; Hynes, J. T. *Chem. Phys. Lett.* **2000** *329* (5-6), 421. doi:10.1016/S0009-2614(00)01037-X.
(6) Lukeman, M.; Veale, D.; Wan, P.; Munasinghe, V. R. N.; Corrie, J. E. T. *Can. J. Chem.* **2004** *82* (2), 240. doi:10.1139/v03-184.
(7) (a) Lukeman, M.; Wan, P. *Chem. Commun. (Camb.)* **2001** (11): 1004. doi:10.1039/b100817j.; (b) Lukeman, M.; Wan, P. *J. Am. Chem. Soc.* **2002** *124* (32), 9458. doi:10.1021/ja0267831.
(8) (a) Lukeman, M.; Wan, P. *J. Am. Chem. Soc.* **2003** *125* (5), 1164. doi:10.1021/ja029376y.; (b) Flegel, M.; Lukeman, M.; Wan, P. *Can. J. Chem.* **2008** *86* (2), 161. doi:10.1139/V07-143.
(9) Flegel, M.; Lukeman, M.; Huck, L.; Wan, P. *J. Am. Chem. Soc.* **2004** *126* (25), 7890. doi:10.1021/ja039078g.
(10) Wunder, T.; Marr, J.; Kremer, S.; Sterner, O.; Anke, H. *Arch. Microbiol.* **1997** *167* (5), 310. doi:10.1007/s002030050449.
(11) Peak assignments were made using COSY and NOESY spectra of 1 (available in the Supplementary data) and agree with an earlier report. Cerniglia, C. E.; Kelly, D. W.; Freeman, J. P.; Miller, D. W. *Chem. Biol. Interact.* **1986** *57* (2), 203. doi:10.1016/0009-2797(86)90038-4.
(12) These expectations are based on our past experience with Kekule and non-Kekule QM intermediates. For example, QM **3** is readily detectable with ns LFP, however, non-Kekule QM **4** was not (ref. 6).
(13) Ivanec-Goranina, R.; Kulys, J. *Cent. Eur. J. Biol.* **2008** *3* (3), 224. doi:10.2478/s11535-008-0021-x.
(14) (a) Valeur, B.; Weber, G. *Photochem. Photobiol.* **1977** *25* (5), 441. doi:10.1111/j.1751-1097.1977.tb09168.x.; (b) Pines, E.; Huppert, D.; Agmon, N. *J. Chem. Phys.* **1988** *88* (9), 5620. doi:10.1063/1.454572.
(15) Wu, J. I.; Dobrowolski, M. A.; Cyrański, M. K.; Merner, B. L.; Bodwell, G. J.; Mo, Y.; Schleyer, P. R. *Mol. Phys.* **2009** *107* (8), 1177. doi:10.1080/00268970902784918.

Can. J. Chem. Downloaded from www.nrcresearchpress.com by Xi'an Jiaotong University on 09/19/12
For personal use only.

Antineuroinflammatory constituents from the root extract of *Paris verticillata*

Ki Hyun Kim, Kyu Ha Lee, Ho Kyung Kim, Eunjung Moon, Sung-Hoon Kim, Sun Yeou Kim, Kyung Ran Kim, and Kang Ro Lee

Can. J. Chem. Downloaded from www.nrcresearchpress.com by Xi'an Jiaotong University on 09/19/12
For personal use only.

Abstract: Two new cyclopropanoic fatty acid glycosides, named parisveroside A (**1**) and parisveroside B (**2**), were isolated from a MeOH extract of the roots of *Paris verticillata* (Liliaceae) together with three other known compounds, salicin (**3**), 3-(β-D-glucopyranosyloxymethyl)-2-(4-hydroxy-3-methoxyphenyl)-5-(3-hydroxypropyl)-7-methoxy-(2*R*,3*S*)-dihydrobenzofuran (**4**), and allantoin (**5**). Their structures were elucidated on the basis of spectroscopic data, including 1D and 2D NMR, HR-FAB-MS, and chemical evidence. To investigate the antineuroinflammatory effects of the isolated compounds (**1**–**5**), nitric oxide (NO) production was evaluated in the lipopolysaccharide-activated microglia cell line, BV-2. Compounds **2** and **4** significantly inhibited NO production with IC_{50} values of 74.8 and 60.5 μmol/L, respectively.

Key words: Paris verticillata, Liliaceae, fatty acid glycosides, parisveroside A, parisveroside B, neuroinflammation.

Résumé : Utilisant comme produit de départ le mélange obtenu par extraction des racines de *Paris verticillata* (Liliacée) à l'aide de méthanol, on a isolé deux nouveaux glycosides dérivés de l'acide gras cyclopropanoïque, soit le parisvéroside A (**1**) et le parisvéroside B (**2**), ainsi que trois autres produits connus, la salicine (**3**), le 3-(β-D-glucopyranosyloxyméthyl)-2-(4-hydroxy-3-méthoxyphényl)-5-(3-hydroxypropyl)-7-méthoxy-(2*R*,3*S*)-dihydrobenzofurane (**4**) et l'allantoïne (**5**). On a élucidé les structures en se basant sur des preuves chimiques et des données spectroscopiques, dont celles des RMN 1D et 2D et de la spectrométrie de masse à haute résolution avec bombardement avec des atomes rapides (SM-HR-BAR). Pour étudier les effets anti-neuroinflammatoires des composés isolés, on a évalué la production d'oxyde d'azote (NO) dans des cellules BV-2 de la lignée cellulaire de microglie activée par un lipopolysaccharide. Les composés **2** et **4** inhibent d'une façon significative la production de NO avec des valeurs de IC_{50} de 74,8 et 60,5 μmol/L respectivement.

Mots-clés : Paris verticillata, Liliacée, glycosides d'acides gras, parisvéroside A, parisvéroside B, neuroinflammation.

Introduction

The genus *Paris* consists of less than two dozen herbaceous plants that have 4- to 11-merous flowers.[1] Some *Paris* species are used in traditional Chinese medicine for their analgesic and anticoagulant properties, most notably as an ingredient of Yunnan Baiyao.[2] In Korea, the perennial herb *Paris verticillata* (Liliaceae) is widely distributed in valleys and its root has been used as a Korean traditional medicine against asthma, boils, and chronic bronchitis.[3] Few phytochemical and biological investigations on this plant have been previously conducted. The presence of several constituents, including saponins, sterols, and flavonoids, was reported from the aerial parts of *P. verticillata*.[4] In our continuing search for bioactive constituents from Korean medicinal plants, we investigated a MeOH extract from the roots of *P. verticillata*, which is in use as traditional medicine. The investigation led to the isolation of a phenolic amide, phenolics, and pyrrolizidine alkaloids with cytotoxic activity.[5,6] In our continuing investigation of bioactive constituents from the roots of *P. verticillata*, we further isolated two new cyclopropanoic fatty acid glycosides, named parisveroside A (**1**) and parisveroside B (**2**), together with three previously reported compounds (**3**–**5**). Compounds **3**–**5** were characterized for the first time from this plant. Here, we also investigated the antineuroinflammatory effects of isolated compounds (**1**–**5**) in lipopolysaccharide (LPS)-activated BV-2 cells, a microglia cell line.

Results and discussion

The 80% MeOH extract of the roots of *P. verticillata* was subjected to repeated column chromatography on silica gel to afford two new cyclopropanoic fatty acid glycosides (**1**–**2**), together with three known compounds (**3**–**5**) (Fig. 1). Their structures were elucidated by 1D and 2D NMR and HR-FAB-MS and compared with published data.

Parisveroside A (**1**) was isolated as a colorless gum with a molecular formula of $C_{17}H_{30}O_8$ on the basis of the $[M + H]^+$ peak at *m*/*z* 363.2021 (calcd. for $C_{17}H_{31}O_8$: 363.2019) in the

Received 24 August 2010. Accepted 18 November 2010. Published on the NRC Research Press Web site at canjchem.nrc.ca on 16 February 2011.

K.H. Kim, K.H. Lee, H.K. Kim, K.R. Kim, and K.R. Lee.[1] Natural Products Laboratory, School of Pharmacy, Sungkyunkwan University, Suwon 440-746, Korea.
E. Moon and S.Y. Kim. Graduate School of East-West Medical Science, Kyung Hee University, No. 1 Seocheon-dong, Gihung-gu, Yongin-city, Gyeonggi-do 446-701, Korea.
S.-H. Kim. Cancer preventive Material Development Research center, Kyung Hee University, Seoul 151-742, Korea.

[1]Corresponding author (e-mail: krlee@skku.ac.kr).

Can. J. Chem. Downloaded from www.nrcresearchpress.com by Xi'an Jiaotong University on 09/19/12
For personal use only.

Fig. 1. Chemical structures of compounds **1**–**5**.

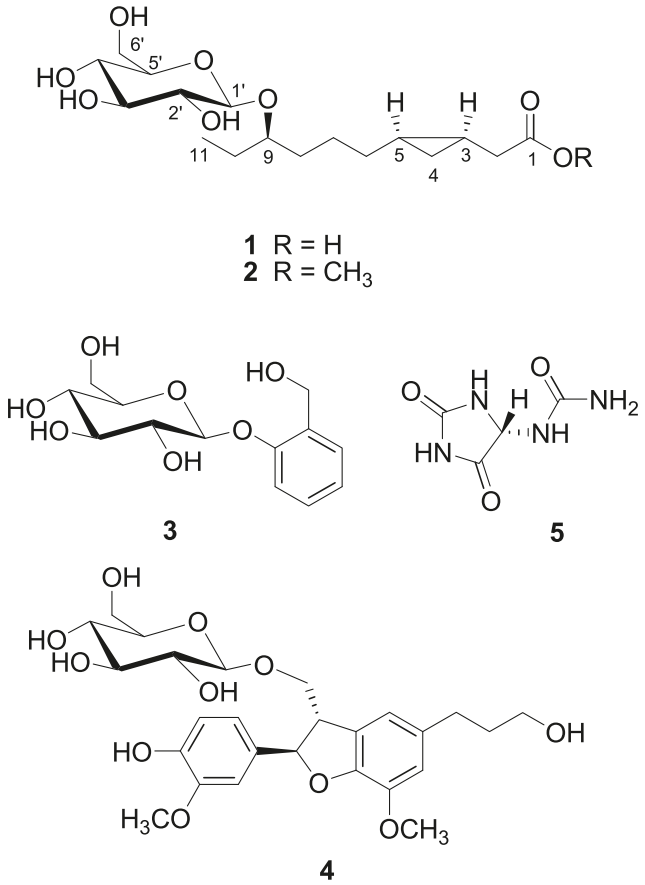

Fig. 2. Key ^{1}H–^{1}H COSY and HMBC correlations of **1**.

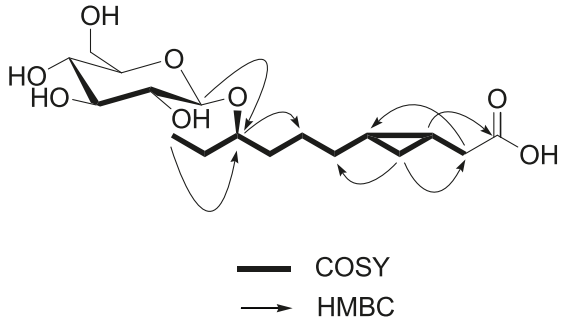

HR-FAB-MS. The IR spectrum of **1** indicated the presence of hydroxyl groups (3390 cm^{-1}) and a carbonyl group (1698 cm^{-1}). The ^{1}H NMR spectrum of **1** showed an anomeric proton at δ 4.34 (1H, d, J = 8.0 Hz, H-1′), which is a characteristic signal for a β-glucopyranosyl unit, and six oxygenated protons attributed to a sugar at δ 3.86–3.26. It also displayed signals for one methyl at δ 0.93 (3H, t, J = 6.5 Hz, H-11), 10 methylenes at δ 2.34–2.24 (2H, m, H-2), 1.62–1.33 (8H, m, H-6, 7, 8, 10), and one oxygenated methine at δ 3.75 (1H, m, H-9), as well as a cyclopropane ring at δ 1.08 (1H, m, H-3), 0.82 (1H, m, H-5), 0.73 (1H, m, H-4a), and –0.11 (1H, q, J = 5.5 Hz, H-4b). The ^{13}C NMR and DEPT spectra of **1** showed signals of 11 carbons of an aglycone attributable to one methyl, six methylenes, three methines (one oxygenated), and one quaternary carbon (carboxyl), along with signals for a β-glucopyranosyl unit (δ 102.3, 77.0, 76.5, 74.1, 70.6, and 61.7). These data suggested that compound **1** was a glycosidic fatty acid with a cyclopropane ring.[7,8] The glucose unit obtained after hydrolysis gave a positive optical rotation, $[\alpha]_D^{25}$ +48.6 (c 0.05, H_2O), indicating that it was D-glucose.

The proton and protonated carbon NMR signals of **1** were assigned unambiguously by the HSQC experiment. The cyclopropanoic fatty acid was further confirmed by the ^{1}H–^{1}H COSY correlations from H-2 to H-11 and the HMBC correlations H-2/C-5, H-3/C-1, H-4/C-2, 6, H-9/C-7, and H-11/C-9 (Fig. 2), together with their chemical shift values. The HMBC correlation of the anomeric proton H-1′ (δ 4.34) with C-9 (δ 80.7) indicated that the β-D-glucopyranosyl unit is located at C-9. The stereochemistry, including the absolute configuration at C-9, was established by a combination of analyses, including correlations in the NOESY experiment and the modified Mosher's method.[9] The proton signals for cyclopropylmethylene at δ 0.73 and –0.11 revealed the presence of a cis-1,2-disubstituted cyclopropane ring.[7,8] In the trans form, there are no signals for the cyclopropane proton above δ 0. The *cis*-cyclopropylmethine protons were also confirmed by the NOESY correlation H-3/H-5. On enzymatic hydrolysis of **1** with β-glucosidase, a new fatty acid, 9-hydroxy-*cis*-cascarillic acid (**1a**) was obtained. Compound **1a** was treated with (+)- and (–)-α-methoxy-α-trifluoromethylphenyl acetyl (MTPA) chlorides in NMR tubes to afford (*R*)-MTPA ester (**1r**) and (*S*)-MTPA ester (**1s**), respectively.[9] Diagnostic ^{1}H NMR chemical-shift differences between the MTPA esters of **1** ($\Delta\delta = \delta_S - \delta_R$) (Fig. 3) indicated the 9*R* configuration of **1**. Thus, the structure of **1** was determined as 9*R*-(β-D-glucopyranosyloxy)-*cis*-cascarillic acid, and it was named parisveroside A (Fig. 1).

Parisveroside B (**2**) was isolated as a colorless gum. Its molecular formula was determined to be $C_{18}H_{32}O_8$ from the $[M + Na]^+$ peak at m/z 399.2012 (calcd. for $C_{18}H_{32}NaO_8$: 399.1995) in the HR-FAB-MS spectrum. Its IR spectrum revealed similar absorption bands to **1**. The ^{1}H and ^{13}C NMR spectra of **2** were almost identical to those of **1**, except for the resonance of one additional methoxy signal. On the basis of the ^{1}H–^{1}H COSY and HSQC spectra, all protons and carbons could be assigned. The HMBC correlation between the methoxy proton at δ 3.69 and C-1 at δ 174.9 indicated that the methoxy group was located at C-1. Enzymatic hydrolysis of **2** yielded a new fatty acid, methyl-9-hydroxy-*cis*-cascarillate (**2a**) and glucose as the sugar component, having a β-D-configuration from the ^{1}H and ^{13}C NMR data and optical rotation analysis. The glycosidic linkage was determined from the HMBC correlation H-1′/C-9. The stereochemistry of **2** was assigned to be the same as that of **1** on the basis of the comparison of the NMR data and optical rotation values: $[\alpha]_D^{25}$ +26.6 (c 0.10, MeOH) of **2** with those of **1**. Thus, the structure of **2** was determined as methyl-9*R*-(β-D-glucopyranosyloxy)-*cis*-cascarillate, and it was named parisveroside B (Fig. 1).

Three other known compounds obtained in this investigation were identified as salicin (**3**),[10] 3-(β-D-glucopyranosyloxymethyl)-2-(4-hydroxy-3-methoxyphenyl)-5-(3-hydroxypropyl)-7-methoxy-(2*R*,3*S*)-dihydrobenzofuran (**4**),[11] and allantoin (**5**)[12] by comparison of their spectroscopic data with those published in the literature (Fig. 1). The known compounds **3**–**5** are reported from this plant source for the first time.

Fig. 3. Δδ Values ($\delta_S - \delta_R$) in ppm of the two α-methoxy-α-trifluoromethylphenyl acetyl (MTPA) esters derived from **1a**.

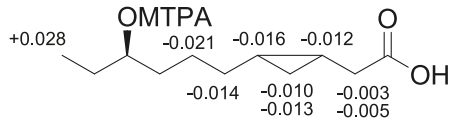

Microglia, the unique population of central nervous system resident immune cells, have been implicated in the pathogenesis of a variety of neurodegenerative diseases including Parkinson's disease and Alzheimer's disease.[13,14] Excessive production of nitric oxide (NO) and proinflammatory cytokines from activated microglia play an important role in neurodegenerative disorders. Therefore, regulation of the microglial activation will be an important strategy to prevent the progressive damage of the neurodegenerative diseases. Here, the antineuroinflammatory activities of the isolated compounds (**1**–**5**) were evaluated by assessing NO production in the BV-2 cells. BV-2 cells were pretreated with or without compounds **1**–**5** for 30 min prior to the addition of LPS (100 ng/mL). As shown in Fig. 4, compounds **2** and **4** significantly inhibited the NO production in LPS-stimulated BV-2 cells. Among tested compounds, compound **4** was the most potent. Pretreatment of BV-2 cells with compound **4** inhibited LPS-induced NO production in a dose-dependent manner with an IC_{50} value of 60.5 μmol/L. It revealed effective ratios of 23.9% ± 5.7%, 30.2% ± 6.2%, and 44.9% ± 3.5% at concentrations of 10, 20, and 50 μmol/L, respectively, in comparison with the control. The IC_{50} value of compound **2** was also 74.8 μmol/L. On the other hand, none of the compounds showed any cytotoxicity at concentrations used in the present study (data not shown).

Microglial cell activation plays a key role in mediating inflammatory processes in the CNS, which are associated with various neurodegenerative diseases. NO is one of the main proinflammatory mediators produced by activated microglia.[15] Therefore, compounds **2** and **4** from *P. verticillata* might be of therapeutic interest with respect to the treatment of neurodegenerative disease mediated by neuroinflammation.

Experimental

General experimental procedures

Optical rotations were measured on a Jasco P-1020 polarimeter in MeOH or $CHCl_3$. IR spectra were recorded on a Bruker IFS-66/S FT-IR spectrometer. FAB and HR-FAB mass spectra were obtained on a JEOL JMS700 mass spectrometer. NMR spectra, including ^1H–^1H COSY, HSQC, HMBC, and NOESY experiments, were recorded on a Varian UNITY INOVA 500 NMR spectrometer operating at 500 MHz (^1H) and 125 MHz (^{13}C) with chemical shifts given in ppm (δ). Preparative HPLC was conducted using a Gilson 306 pump with a Shodex refractive index detector and an Apollo silica 5 μ column (250 mm × 10 mm). Silica gel 60 (Merck, 70–230 mesh and 230–400 mesh) and RP-C_{18} silica gel (Merck, 230–400 mesh) were used for column chromatography (CC). Merck precoated silica gel F_{254} plates and RP-18 F_{254s} plates were used for TLC. Spots were detected on TLC under UV light or by heating after spraying with 10% H_2SO_4 in C_2H_5OH (*v*/*v*).

Plant material

The roots of *P. verticillata* were collected at Mount O-Dae, Gangwon Province, Korea, in August 2002, and the plants were identified by one of the authors (K.R.L.). A voucher specimen (SKKU 2002-08) was deposited in the herbarium of the School of Pharmacy, Sungkyunkwan University, Suwon, Korea.

Extraction and isolation

The roots of *P. verticillata* (1.5 kg) were extracted using 80% aq MeOH at room temperature over a period of 3 days three times. The solvent was evaporated under reduced pressure to give a crude extract (180 g). The crude extract was dissolved in distilled water (800 mL) and successively extracted with *n*-hexane, CH_2Cl_2, EtOAc, and *n*-BuOH to provide *n*-hexane (5.2 g), CH_2Cl_2 (3.5 g), EtOAc (4.4 g), and *n*-BuOH extracts (20 g). The EtOAc-soluble fraction (4.4 g) was subjected to normal-phase CC over a silica gel using $CHCl_3$–MeOH of increasing polarity (5:1–1:1) to give five fractions (E1–E5). Fraction E3 (1.2 g) was subjected to reversed-phase CC over a RP-C_{18} silica gel using MeOH–H_2O (2:3) to provide four subfractions (E31–E34). Subfraction E33 (120 mg) was separated by preparative normal-phase HPLC using a solvent system of *n*-hexane–$CHCl_3$–MeOH (3:5:1) over 30 min at a flow rate of 2.0 mL/min (Apollo silica 5 μ column; Shodex refractive index detector) to obtain parisveroside B (**2**, 7 mg). The *n*-BuOH-soluble fraction (10 g) was subjected to CC over HP-20 resin using 100% H_2O and 100% MeOH to give two fractions (B1, 100% H_2O, and B2, 100% MeOH). The B1 fraction (2 g) was washed using MeOH and recrystallized to give allantoin (**5**, 200 mg). The B2 fraction (3 g) was subjected to normal-phase CC over silica gel using $CHCl_3$–MeOH–H_2O (10:10:0.5) to give six fractions (B21–B26). The B21 fraction (180 mg) was further separated using silica gel CC with $CHCl_3$–MeOH–H_2O (10:4:0.5) and purified by preparative normal-phase HPLC using a solvent system of $CHCl_3$–MeOH–H_2O (9:4:0.5) to afford salicin (**3**, 6 mg) and 3-(β-D-glucopyranosyloxymethyl)-2-(4-hydroxy-3-methoxyphenyl)-5-(3-hydroxypropyl)-7-methoxy-dihydrobenzofuran (**4**, 4 mg). The B22 fraction (70 mg) was purified using silica gel CC with $CHCl_3$–MeOH–H_2O (9:4:0.5) to yield parisveroside B (**1**, 5 mg).

Parisveroside A (1)

Colorless gum; $[\alpha]_D^{25}$ +36.5 (*c* 0.05, MeOH). IR (KBr, cm^{-1}) ν_{max}: 3390, 2949, 1698, 1522, 1450, 1026, 674. ^1H NMR (CD_3OD, 500 MHz) δ: 4.34 (1H, d, *J* = 8.0 Hz, H-1′), 3.86 (1H, dd, *J* = 11.0, 1.0 Hz, H-6′a), 3.77 (1H, dd, *J* = 11.0, 3.5 Hz, H-6′b), 3.75 (1H, m, H-9), 3.46–3.35 (3H, m, H-2′, 3′, 4′), 3.26 (1H, m, H-5′), 2.34–2.24 (2H, m, H-2), 1.62–1.58 (4H, m, H-8, 10), 1.43–1.33 (4H, m, H-6, 7), 1.08 (1H, m, H-3), 0.93 (3H, t, *J* = 6.5 Hz, H-11), 0.82 (1H, m, H-5), 0.73 (1H, m, H-4a), –0.11 (1H, q, *J* = 5.5 Hz, H-4b). ^{13}C NMR (CD_3OD, 125 MHz) δ: 177.5 (C-1), 102.3 (C-1′), 80.7 (C-9), 77.0 (C-3′), 76.5 (C-5′), 74.1 (C-2′), 70.6 (C-4′), 61.7 (C-6′), 34.1 (C-2), 33.1 (C-8), 28.8 (C-6), 27.4 (C-10), 25.2 (C-7), 15.4 (C-5), 11.7 (C-3), 10.2 (C-4), 8.8 (C-11). HR-FAB-MS *m*/*z* 363.2021 $[M + H]^+$ (calcd. for $C_{17}H_{31}O_8$: 336.2019).

Can. J. Chem. Downloaded from www.nrcresearchpress.com by Xi'an Jiaotong University on 09/19/12
For personal use only.

Fig. 4. Inhibitory effects of compounds **1**–**5** on nitric oxide (NO) production in lipopolysaccharide (LPS)-activatied BV-2 cells.

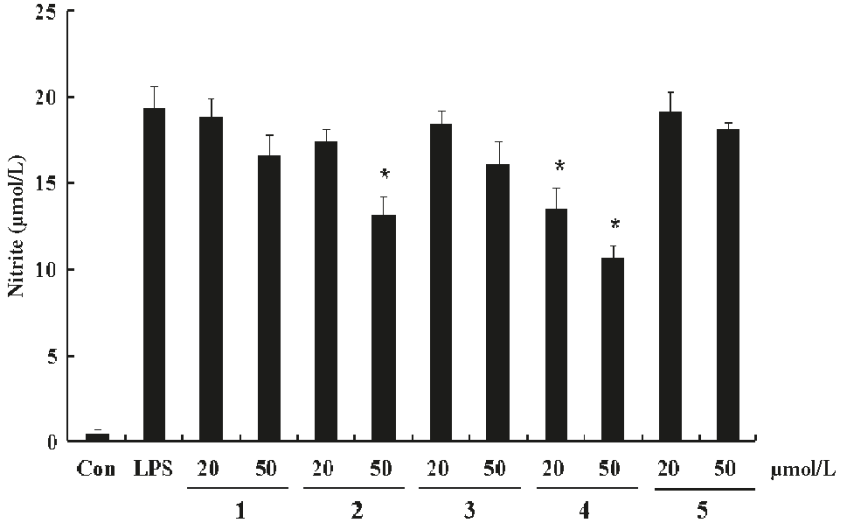

Can. J. Chem. Downloaded from www.nrcresearchpress.com by Xi'an Jiaotong University on 09/19/12
For personal use only.

Parisveroside B (2)

Colorless gum; $[\alpha]_D^{25}$ +26.6 (*c* 0.10, MeOH). IR (KBr, cm^{-1}) ν_{max}: 3395, 2948, 1702, 1515, 1455, 1026, 674. ^1H NMR (CD_3OD, 500 MHz) δ: 4.33 (1H, d, *J* = 8.0 Hz, H-1′), 3.86 (1H, dd, *J* = 11.5, 1.5 Hz, H-6′a), 3.69 (3H, s, OCH_3), 3.68 (1H, dd, *J* = 11.5, 3.5 Hz, H-6′b), 3.65 (1H, m, H-9), 3.38–3.33 (3H, m, H-2′, 3′, 4′), 3.25 (1H, m, H-5′), 2.39–2.30 (2H, m, H-2), 1.64–1.56 (4H, m, H-8, 10), 1.50–1.35 (4H, m, H-6, 7), 1.08 (1H, m, H-3), 0.93 (3H, t, *J* = 6.5 Hz, H-11), 0.83 (1H, m, H-5), 0.73 (1H, m, H-4a), –0.10 (1H, q, *J* = 5.5 Hz, H-4b). ^{13}C NMR (CD_3OD, 125 MHz) δ: 174.9 (C-1), 102.4 (C-1′), 80.7 (C-9), 77.1 (C-3′), 76.6 (C-5′), 74.2 (C-2′), 70.7 (C-4′), 61.8 (C-6′), 50.9 (OCH_3), 33.3 (C-2), 33.1 (C-8), 28.8 (C-6), 27.5 (C-10), 25.1 (C-7), 15.4 (C-5), 11.4 (C-3), 10.2 (C-4), 8.9 (C-11). HR-FAB-MS *m/z* 399.2012 $[M + Na]^+$ (calcd. for $C_{18}H_{32}NaO_8$: 399.1995).

Enzymatic hydrolysis of 1 and 2

Compounds **1** and **2** (3 mg each) were dissolved in H_2O (3 mL) and β-glucosidase (emulsin, 9 mg) was added to the solution and kept at 37 °C for 3 days, in each case. The reaction mixtures were extracted with $CHCl_3$, and the aqueous phases compared with an authentic sugar sample using co-TLC (MeCN–H_2O, 6:1, R_f 0.33 for glucose). Identification of D-glucose in the aqueous layer was carried out by comparing the optical rotation of the liberated glucose ($[\alpha]_D^{25}$ +48.6 (*c* 0.05, H_2O) from **1** and $[\alpha]_D^{25}$ +45.3 (*c* 0.05, H_2O) from **2**) with that of an authentic sample of D-glucose.[16] The $CHCl_3$ layers of **1** and **2** were followed by purification on a silica gel Waters Sep-Pak Vac 6cc ($CHCl_3$–MeOH, 15:1) to afford new compounds **1a** (1.4 mg) and **2a** (1.1 mg). **1a**: colorless gum; $[\alpha]_D^{25}$ –12.5 (*c* 0.04, $CHCl_3$). ^1H NMR (C_5D_5N, 500 MHz) δ: 3.95 (1H, m, H-9), 2.62–2.48 (2H, m, H-2), 1.64–1.57 (4H, m, H-8, 10), 1.30 (2H, m, H-7), 1.24 (2H, m, H-6), 1.17 (1H, m, H-3), 1.06 (3H, t, *J* = 6.5 Hz, H-11), 0.85 (1H, m, H-5), 0.76 (1H, m, H-4a), –0.03 (1H, q, *J* = 5.5 Hz, H-4b). HR-FAB-MS *m/z* 201.1485 $[M + H]^+$ (calcd. for $C_{11}H_{21}O_3$: 201.1491). **2a**: colorless gum; $[\alpha]_D^{25}$ –20.7 (*c* 0.03, $CHCl_3$). ^1H NMR (C_5D_5N, 500 MHz) δ: 3.91 (1H, m, H-9), 3.70 (3H, s, OCH_3), 2.65–2.47 (2H, m, H-2), 1.65–1.58 (4H, m, H-8, 10), 1.28 (2H, m, H-7), 1.23 (2H, m, H-6), 1.19 (1H, m, H-3), 1.05 (3H, t, *J* = 6.5 Hz, H-11), 0.87 (1H, m, H-5), 0.77 (1H, m, H-4a), –0.01 (1H, q, *J* = 5.5 Hz, H-4b). HR-FAB-MS *m/z* 215.1652 $[M + H]^+$ (calcd. for $C_{12}H_{23}O_3$: 215.1647).

Preparation of the Mosher ester derivatives of 1a

Compound **1a** (0.7 mg) was transferred to a clean and completely dry NMR tube. Deuterated pyridine (0.7 mL) and (*S*)-(+)-α-methoxy-α-(trifluoromethyl)phenylacetyl chloride, (*S*)-MTPA-Cl, (5 μL) were added immediately to the NMR tube and then the NMR tube was shaken carefully to mix the sample and (*S*)-MTPA-Cl evenly. The reaction NMR tube was then permitted to stand at room temperature overnight. The completed reaction afforded the (*R*)-MTPA ester derivative (**1r**) of **1a**. The (*S*)-MTPA ester derivative (**1s**) of **1a** was obtained in the same manner as described for **1r**. The ^1H NMR spectra for **1r** and **1s** were directly measured with the reaction NMR tubes. **1s**: ^1H NMR (C_5D_5N, 500 MHz) δ: 5.184 (1H, m, H-9), 2.537 (1H, m, H-2a), 2.485 (1H, m, H-2b), 1.762–1.559 (4H, m, H-8, 10), 1.257 (2H, m, H-7), 1.200 (2H, m, H-6), 1.156 (1H, m, H-3), 1.042 (3H, t, *J* = 6.5 Hz, H-11), 0.801 (1H, m, H-5), 0.686 (1H, m, H-4a), –0.078 (1H, q, *J* = 5.5 Hz, H-4b). **1r**: ^1H NMR (C_5D_5N, 500 MHz) δ: 5.192 (1H, m, H-9), 2.540 (1H, m, H-2a), 2.490 (1H, m, H-2b), 1.772–1.560 (4H, m, H-8, 10), 1.278 (2H, m, H-7), 1.214 (2H, m, H-6), 1.168 (1H, m, H-3), 1.014 (3H, t, *J* = 6.5 Hz, H-11), 0.817 (1H, m, H-5), 0.696 (1H, m, H-4a), –0.065 (1H, q, *J* = 5.5 Hz, H-4b).

Measurement of NO production and cell viability

The BV-2 mouse microglial cell line was maintained in Dulbecco's modified Eagle medium (DMEM) supplemented with 5% fetal bovine serum (FBS) and 1% penicillin–streptomycin (PS). To measure NO production, BV-2 cells were plated into a 96 well plate (3×10^4 cells/well) and treated with 100 ng/mL LPS in the presence or absence of chrysin for 24 h. Nitrite, a soluble oxidation product of NO, was measured in the culture media using the Griess reaction. The supernatant (50 μL) was harvested and mixed with an equal volume of Griess reagent (1% sulfanilamide and 0.1% *N*-1-napthylethylenediamine dihydrochloride in 5% phos-

phoric acid). After 10 min, the absorbance at 540 nm was measured using a microplate reader. Sodium nitrite was used as a standard to calculate the NO_2^- concentration. Cell viability was assessed by a 3-[4,5-dimethylthiazol-2-yl]-2,5-diphenyl-tetrazolium bromide (MTT) assay.[17] N^G-Monomethyl-L-arginine (L-NMMA, Sigma-Aldrich), a well-known NOS inhibitor, was tested as a positive control. The IC_{50} value for the positive control, L-NMMA, was 18.0 μmol/L.

Acknowledgements

The authors would like to thank Mr. Do Kyun Kim, Dr. Eun Jung Bang, and Dr. Jung Ju Seo at the Korea Basic Science Institute for the NMR and MS spectra measurements. This work was supported by a Korea Science and Engineering Foundation (KOSEF) Grant funded by the Korean Government Ministry of Education, Science, and Technology (MEST) (No. 2009-0063466).

References

(1) Farmer, S. B.; Schilling, E. E. *Syst. Bot.* **2002**, *27*, 674.
(2) Liu, H.; Huang, Y.; Wang, Q.; Zhang, T.; Song, Y. *Planta Med.* **2006**, *72* (9), 835. doi:10.1055/s-2006-946637.
(3) Ahn, D. K. *Illustrated Book of Korean Medicinal Herbs;* Kyo-Hak Pub.: Seoul, 1998; p 107.
(4) Nakano, K.; Murakami, K.; Nohara, T.; Tominatsu, T.; Kawasaki, T. *Chem. Pharm. Bull. (Tokyo)* **1981**, *29*, 1445.
(5) Lee, K. H.; Yang, M. C.; Kim, K. H.; Kwon, H. C.; Choi, S. U.; Lee, K. R. *Molecules* **2008**, *13* (1), 41. doi:10.3390/molecules13010041.
(6) Kim, K. H.; Lee, K. H.; Choi, S. U.; Kim, K. R.; Lee, K. R. *Heterocycles* **2010**, *81* (6), 1493. doi:10.3987/COM-10-11942.
(7) Wilson, S. R.; Prodan, K. A. *Tetrahedron Lett.* **1976**, *17* (47), 4231. doi:10.1016/0040-4039(76)80081-0.
(8) Jiao, Y.; Yoshihara, T.; Ishikun, S.; Uchino, H.; Ichihara, A. *Tetrahedron Lett.* **1996**, *37* (7), 1039. doi:10.1016/0040-4039(95)02342-9.
(9) Su, B. N.; Park, E. J.; Mbwambo, Z. H.; Santarsiero, B. D.; Mesecar, A. D.; Fong, H. H. S.; Pezzuto, J. M.; Kinghorn, A. D. *J. Nat. Prod.* **2002**, *65* (9), 1278. doi:10.1021/np0202475.
(10) Khatoon, F.; Khabiruddin, M.; Ansari, W. H. *Phytochemistry* **1988**, *27* (9), 3010. doi:10.1016/0031-9422(88)80716-7.
(11) Kikuzaki, H.; Kayano, S.; Fukutsuka, N.; Aoki, A.; Kasamatsu, K.; Yamasaki, Y.; Mitani, T.; Nakatani, N. *J. Agric. Food Chem.* **2004**, *52* (2), 344. doi:10.1021/jf034954v.
(12) Yin, F.; Hu, L.; Pan, R. *Chem. Pharm. Bull. (Tokyo)* **2004**, *52* (12), 1440. doi:10.1248/cpb.52.1440.
(13) Wilms, H.; Zecca, L.; Rosenstiel, P.; Sievers, J.; Deuschl, G.; Lucius, R. *Curr. Pharm. Des.* **2007**, *13* (18), 1925. doi:10.2174/138161207780858429.
(14) McGeer, P. L.; McGeer, E. G. *Brain Res. Brain Res. Rev.* **1995**, *21* (2), 195. doi:10.1016/0165-0173(95)00011-9.
(15) Iadecola, C. *Trends Neurosci.* **1997**, *20* (3), 132. doi:10.1016/S0166-2236(96)10074-6.
(16) Kim, K. H.; Choi, S. U.; Lee, K. R. *J. Nat. Prod.* **2009**, *72* (6), 1121. doi:10.1021/np900101t.
(17) Sargent, J. M.; Taylor, C. G. *Br. J. Cancer* **1989**, *60*, 206.

Can. J. Chem. Downloaded from www.nrcresearchpress.com by Xi'an Jiaotong University on 09/19/12
For personal use only.

The use of a silica-based heat sink to "uncouple" the matrix-assisted laser desorption/ionization (MALDI) mechanism

E. Lourantos, O.M. Ramirez II, A.E. Giannakopulos, K.A. Beran, Peter J. Derrick, and S. Bashir

Can. J. Chem. Downloaded from www.nrcresearchpress.com by Xi'an Jiaotong University on 09/19/12
For personal use only.

Abstract: The relationships between ion yield(s) as a function of desorption alone and (or) ionization was investigated using two model systems. In the first model system, a carbohydrate (2,3,6-tri-*O*-methyl-β-cyclodextrin, TMBCD), which could be directly laser desorbed, was analyzed with and without a silicon-based heat sink compound (HSC). The HSC allowed heat to pass through but obstructed the flow of charge. In the second model system, a peptide (substance P), which ccould not be laser desorbed, was analyzed under similar conditions. The ion yield of TMBCD under either system of heat conductivity was similar, whereas the ion yield of the peptide with the heat sink was negligible. Compounds that are predominately cationized either in the gas phase or preformed in solution give an ion yield that is not dependent upon the surface conditions, whereas compounds that are not ordinarily cationized are affected by the emission of electrons from the metal surface.

Key words: heat sink, matrix-assisted laser desorption (MALD), matrix-assisted laser desorption/ionization (MALDI), electron emission.

Résumé : Faisant appel à deux systèmes modèles, on a étudié les relations entre les rendements ioniques en fonction de la désorption seule et (ou) de l'ionisation. Dans le premier système modèle, on a analysé un hydrate de carbone, la 2,3,6-tri-*O*-méthyl-β-cyclodextrine, TMBCD, qui peut être désorbée avec et sans composé dissipateur thermique (CDT) à base de silicone. Le CDT permet la libre circulation de la chaleur, mais obstrue les déplacements de la charge. Dans le deuxième système modèle, on a analysé dans les mêmes conditions un peptide (substance P) qui ne peut pas être désorbé par le laser. Le rendement ionique en TMBCD est semblable quel que soit le système de conductivité thermique alors que le rendement ionique du peptide avec le dissipateur thermique est négligeable. Les composés qui sont d'une façon prédominante cationisés en phase gazeuse ou préformés en solution donnent un rendement ionique qui ne dépend pas des conditions superficielles alors que les composés qui ne sont habituellement pas cationisés sont affectés par l'émission d'électrons par la surface métallique.

Mots-clés : dissipateur thermique, désorption laser assistée par la matrice (DLAM), désorption/ionisation assistée par la matrice (DILAM), émission d'électron.

[Traduit par la Rédaction]

Introduction

Matrix-assisted laser desorption/ionization (MALDI) has become an important analytical technique in the study of a range of compounds,[1] including peptides[2,3] and synthetic polymers,[4,5] from which accurate end-group analysis and molecular weight determination, including both whole mass and sequence information, can be obtained.[6–11] Recently, Spengler et al.[12] reported that fragment analysis of a variety of compounds generated by the MALDI process can allow linkage information to be obtained by post-source delay (PSD), whereas others have extended this to in-source decay (ISD),[13] electron-capture dissociation,[14] or terminal sequenc-

Received 15 February 2010. Accepted 11 October 2010. Published on the NRC Research Press Web site at canjchem.nrc.ca on 1 March 2011.

Dedicated to R. E. Marcotte (Texas A&M-Kingsville).

E. Lourantos, A.E. Giannakopulos,[1] P.J. Derrick,[2] and S. Bashir.[3] Institute of Mass Spectrometry, University of Warwick, Coventry CV4 7AL, UK.
O.M. Ramirez II and K.A. Beran.[4] Department of Physical Sciences, The University of Texas of the Permian Basin, 4901 E. University Blvd., Odessa, TX 79762, USA.

[1]Present address: ThermoFisher Scientific, Hanna-Kunath-Str. 11, 28199 Bremen, Germany.
[2]Present address: Massey University, Institute of Fundamental Sciences, Science Towers B4, Turitea Site, Palmerston North Campus, Private Bag 11222, Palmerston North 5301, New Zealand.
[3]Present address: Chemical Biology Research Group (CBRG), Department of Chemistry, Texas A&M-Kingsville, MSC 161, 700 University Blvd., Kingsville, TX 78363, USA.
[4]Corresponding author (e-mail: beran_k@utpb.edu).

Can. J. Chem. Downloaded from www.nrcresearchpress.com by Xi'an Jiaotong University on 09/19/12
For personal use only.

ing[15], thereby furthering the utility of the MALDI technique.[16]

Since Karas and Hillenkamp's[17] initial report on MALDI, the physio-chemical processes that underlie the MALDI process are still not entirely known.[18] There are a number of models that attempt to explain the MALDI process. Vertes et al.[19] proposed a mechanical expansion model in which the matrix, following laser irradiation, converts its electronic excitation energy via radiationless transitions into vibrational energy that causes the matrix to expand. This rapid expansion leads to the sublimation of the matrix, which aids in the desorption of the analyte molecules.[19] Additionally, the laser interacts with the MALDI matrix and also with the metal probe tip, which would therefore pass heat back into the sample by conduction.[20] Several processes may contribute to the expansion and ionization of a laser-induced plume, including the thermal-spike model as proposed by Vertes and Gijbels,[21,22] in which a bottleneck in energy transfer is created from the hot matrix molecules to the analyte molecules by a *mismatch* in vibrational coupling. A pressure-pulse model, which has also been described,[23] is derived from plasma desorption. A pressure gradient is created perpendicular to the surface by energy deposition, resulting in molecular ejection by momentum transfer.[24] Analysis of the physical laser–matter interaction zone suggests that the excitation profile is essentially two-dimensional,[20] based on the penetration depth (85 nm) of a typical nitrogen laser.

There are a variety of additional desorption/ionization mechanisms[25–41] that have been postulated to account for the MALD/MALDI phenomena. The "ionization" theory[25] is based on a two-step ionization process in which the primary ionization refers to the production of ions directly from neutral molecules and mainly produces excited analyte molecules after the laser shot.[26] The secondary ionization process occurs through the collision of excited matrix molecules with each other and analyte molecules during the expansion of the plume. The "multi-photon excitation" theory[27] considers that the matrix molecule is directly ionized by the laser pulse. Typical ionization potentials of a matrix in the solid state are in the range of 8–10 eV.[28] Taking into consideration that photons of two commonly used UV lasers have 3.68 eV (for nitrogen) and 4.66 eV (for Nd:YAG),[29] it is understood that two or three photons are required to produce an excited matrix molecule.[30] Two photons, though, appear in most cases to contribute insufficient energy to overcome the ionization potential (IP) and a three-photon mechanism does not seem plausible under the low laser irradiation used in MALDI.[27] "Excited state proton transfer (ESPT)" theory[31,32] proposes an intramolecular proton transfer after a single photon excitation.[42] However, salicylic acid and salicylamide are matrices known to have ESPT behavior, but 2,5-dihydroxybenzoic acid (2,5-DHB), which is widely used and complies with the IP requirement, is not efficient in ESPT, nor are other matrices. "Energy pooling"[25] suggests a model in which more than one excited matrix molecule is required to excite an analyte molecule. The two excited matrix molecules collide with each other to produce a radical anion[43] or cation. The hypothesis is that in the laser fluences available in MALDI, it is more likely that a second photon will not interact with the same matrix molecule as the first photon, but the one next to it. So a matrix ion should be produced from two or more not fully excited matrix molecules. The "crystal size and analyte incorporation" theory[33] suggests that there is no universal explanation for the processes under MALDI. The authors experimented by changing sample preparation, sample deposition, and droplet drying rate methods as well as laser parameters. The results of these variations were significantly different depending on crystal size, analyte–matrix incorporation, and laser fluence. Finally, the "desorption"[34] step in the MALDI process is just as important as the ionization process. Desorption is believed to be a combination of thermal contribution and photomechanical stress, as well as Coulombic forces from the applied potential to the "early" charged particles that underline this process. Desorption is highly dependent upon the heat that is transferred to the sample as well as the laser fluence, the laser spot, and the duration of the pulse. In addition, desorption is influenced by the size and the density of the matrix–analyte crystals. Other theories propose that ablation from hydrodynamic pressure increases under the laser pulse;[35] ablation is caused by spallation under strong mechanical stress;[36] ablation is caused by phase explosion;[37] thermal desorption of individual molecules;[38] and layer by layer sublimation.[39] A more appealing theory, however, is the formation of big clusters that are ejected from the surface with high velocities owing to phase explosion.[40] Phase explosion occurs in the sample when the rate of laser energy deposition exceeds that of the phase transitions by melting, evaporating, or sublimating the system, producing high-energy electrons[41] and both positive and negative ions.[44]

In this paper, we investigate the effect of a heat sink compound (HSC) on the MALDI process. The HSC is used in electronics to allow high thermal conduction while eliminating electrical contact, thereby safeguarding electrical components from excessive heat damage (cf. Table S1 in the Supplementary data). The heat sink would thereby "short circuit" the MALD process if local heating is the major mechanism. Although the heat sink has a macroscopic impact on the MALD process, it also exhibits microscopic effects in that the heat transfer and electrical conductivity are separated. This separation is based on the design of the layered surface; metal surface – heat sink – matrix/analyte. Consequently, the laser photons most likely interact with only the matrix–analyte layer. Additionally, heat conduction from the metal MALDI slide to the sample would be unaffected, but electrical contact would be prohibited.

Experimental method

A general experimental design is summarized in the following section followed by a description of various instrument parameters to assess standard errors in the measurement of the time-of-flight of substance P (Sub P; Error and standard deviation measurement section), the effect of shielding section, followed by a description of chemicals utilized, with an overview of the sample preparation method. An alternative "masking" technique is also described for comparison, with a section summarizing the various techniques.

Can. J. Chem. Downloaded from www.nrcresearchpress.com by Xi'an Jiaotong University on 09/19/12
For personal use only.

Scheme 1. Schematic of the experimental design illustrating the various formulations, use of atomic force and optical microscopy for visual or morphological examination, and mass spectrometry to determine ion yields.

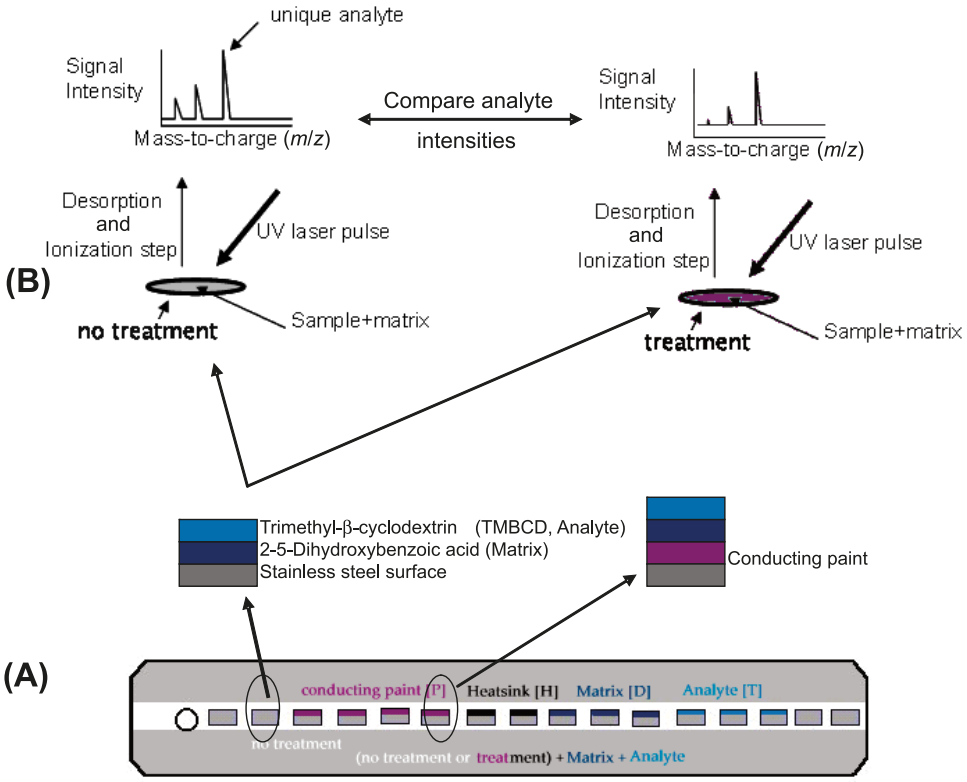

Experimental design

The rationale for the layering was that the effect of "no treatment" (–HSC, summarizing MALDI) to "treatment" (+HSC, summarizing LDI, MALD, or MALDI) would give an indication of which parameters were paramount. Comparison of the different formulations that comprise the application of the heat sink (H), or the conducting paint (P), or the heat sink followed by conducting paint (H + P), would give an indication of whether MALD or MALDI was more important and whether this was analyte specific for analytes that are predominately protonated ($C_{63}H_{98}N_{18}O_{13}S$, Sub P) or cationized (2,3,6-tri-*O*-methyl-β-cyclodextrin). A number of instrument parameters were adjusted to obtain the highest ion intensity and then applied to experiments in which the heat sink was utilized. These adjustments are described in the Supplementary data (cf. *Adjustment of Instrument Parameters*) including three-dimensional profiling of the surface to determine surface roughness (cf. *Surface Profiling Procedure*).

Error and standard deviation measurement

Standard errors for the flight times were determined to evaluate the presence of a voltage lag owing to the application of the heat sink. These results are summarized in Tables S2 and S3 in the Supplementary data in full. Briefly, no lag was observed, confirming earlier calculations that indicated that the voltage drop, if any, would be a fraction of the applied extraction of 20 kV (also see *Expressions used to determine ion flight time in the Kratos III MALDI-TOF mass spectrometer*, *Expression used to determine signal-to-noise ratio*, and *MALDI reproducibility and accuracy assessment* in the Supplementary data for equations used to determine flight times).

Shielding effect measurement

To determine whether the "surface-shielding" effect could result in a change in the analyte peak intensity, a number of analytical systems were compared and are presented in the work-flow process as illustrated in Scheme 1. Comparison of the analyte peak intensity under normal conditions (no treatment, –HSC) to conditions in which the heat sink had been applied (treatment, +HSC) indicated a diminished analyte peak intensity. A follow-up experiment was performed to determine whether the results could be reversed by use of a conductive additive. The role of the conductive layer is twofold: (*i*) to supply an ample amount of charge to the system and (*ii*) to separate the effects of charge and temperature. The conductive layer enables us to short circuit the effect of the heat sink (+HSC), and restores the analyte peak intensities to almost 100% of their initial readings.

General chemicals and layering procedure

The peptides, solvents, and chemicals, unless otherwise stated, were analytical purity grade purchased from Sigma-Aldrich (Dorset, UK). The matrices (Fig. S2 for the respective structures), α-cyano-4-hydroxy-cinnamnic acid (CHCA),[45] 2,5-dihydroxybenzoic acid (2,5-DHB[46]), and analytes, trimethyl-β-cyclodextrin (TMBCD, $C_{63}H_{112}O_{35}$, average molecular mass = 1429.54 Da) and Sub P ($C_{63}H_{98}N_{18}O_{13}S$, average molecular mass = 1347.63 Da)

Table 1. Summary of the experimental conditions.

System annotation	Sequence of layering	Experimental condition (evaluation of desorption (MALD) or ionization (MALDI) or a combination thereof (group I–IV))
T	Stainless steel – TMBCD	LDI
H + D	Stainless steel – matrix	LDI
H + T	Stainless steel – heat sink – TMBCD	LDI
H + P + T	Stainless steel – heat sink – conducting paint – TMBCD	LDI
D + T	Stainless steel – matrix – TMBCD	Matrix-assisted laser desorptionionization (group I)
H + D	Stainless steel – heat sink – matrix	Matrix-assisted laser desorption/ionization (MALD)
H + P + D	Stainless steel – heat sink – conducting paint	Matrix-assisted laser desorption/ionization (MALDI)
P + D + T	Stainless steel – conducting paint – matrix – TMBCD	Matrix-assisted laser desorption/ionization (group II)
H + D + T	Stainless steel – heat sink – matrix – TMBCD	Matrix-assisted laser desorption/ionization (group III)
H + P + D + T	Stainless steel – heat sink – conducting paint – matrix – TMBCD	Matrix-assisted laser desorption/ionization (group IV)

Note: TMBCD, trimethyl-β-cyclodextrin; LDI, laser desorption ionization.

Scheme 2. Schematic of the work flow illustrating how the heat sink compound would be used to determine the mode of sample ionization (preformed ions vs ions formed during secondary reactions in the gas phase).

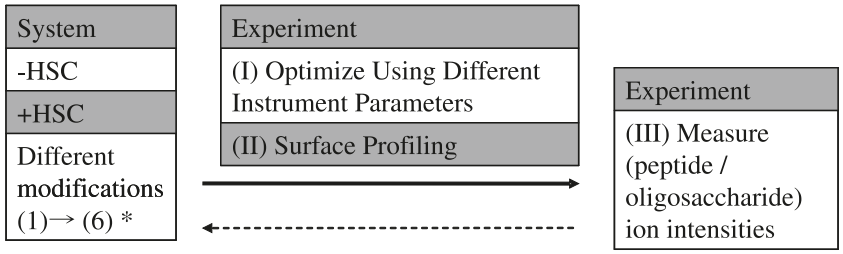

(*cf. Table 3, Scheme 2, Supplemental Tables 2 and 3, and Supplemental Figure 1)

were purchased from Sigma-Aldrich and were used with no further purification. CHCA was chosen as a matrix because of the good analyte-to-noise ratio that it provides when used with peptides and its high IP potential.[47] Three additional peptides were initially used for the calibration of the instrument. Bradykinin fragment 1-5 ($C_{27}H_{40}N_8O_6$, MW = 572.66), Sub P fragment 1-7 ($C_{41}H_{65}N_{13}O_{10}$, MW = 900.04), and Alytesin ($C_{68}H_{106}N_{22}O_{17}S$, MW = 1535.77). Only Bradykinin 1-5 and Sub P 1-7 were further analysed in the series of experiments (see Supplemental spectra (SS) 1–14 presented in the Supplementary data for some representative MALDI-TOF spectra).

The HSC was manufactured by Dow Corning (CD340 (CAS – 6850-01-127-6826) and is a nonmelting silicone (optimum temperature 200 °C) with high thermal conductivity (0.42 W/m·K) and a high dielectric strength (21 kV/mm), Midland, Michigan). The HSC was dissolved in tetrahydrofuran (THF). The matrix (0.1 mol/L CHCA or 2,5-DHB) was dissolved in acetonitrile–water (1:1 *v*/*v*). The sample consisted of 0.5 μL HSC that was air-dried and upon which 0.5 μL of CHCA (or 2,5-DHB) was added and dried. To this bilayer a 0.5 μL aliquot of analyte (TMBCD or Sub P) was added and dried in a stream of nitrogen. Cations were not added. The ratio of matrix:analyte was 1:1000–3000.

In preparing the peptide samples for deposition via masking and spraying, the peptides were diluted separately in water. The resulting concentration was 0.1 μmol/L. The matrix was diluted in a water–methanol (1:1 *v*/*v*) solution until precipitation occurred. Both the peptide samples and the matrix were stored below –20 °C. A droplet of 1 μL of the peptide solution was deposited on the target and dried under a flow of air at room temperature. A droplet of 1 μL of the matrix solution was deposited on the same target and dried in the same way.

The peptides were analysed under several laser powers above the threshold to achieve the best analyte-to-noise ratio. At a power of 101 (arbitrary units), the best analyte-to-noise ratio was achieved for both peptides on a simple steel substrate with no modifications. Higher analyte-to-noise ratios were observed for the insulators at higher laser powers. For the normal substrate at powers of 112, there were signs of fragmentation and consequently reduced peptide peaks.

Sample preparation method: overview

The general preparative approach used is illustrated in Scheme 2, and the various formulations utilized are summarized in Table 1. Briefly, the following three systems were evaluated: (*a*) determination of the protonated or sodiated pseudomolecular ion under laser desorption/ionization (LDI) conditions on stainless steel that has (*i*) not been modified, (*ii*) has been modified with an HSC, and (*iii*) has been modified with a bilayer of HSC followed by a conducting paint; (*b*) determination of the protonated or sodiated pseudomolecular ion under MALDI conditions on stainless steel that has not been modified in the same manner as for the LDI system; and (*c*) repeating the process in system (*b*) with a number of experimental permutations. In each case, one component of the sample was deposited (0.5 μL) and allowed to dry before the next component was deposited.

Can. J. Chem. Downloaded from www.nrcresearchpress.com by Xi'an Jiaotong University on 09/19/12
For personal use only.

Can. J. Chem. Downloaded from www.nrcresearchpress.com by Xi'an Jiaotong University on 09/19/12
For personal use only.

Chemicals used for the masking procedure

The green-coloured polyvinylchloride (PVC) nonconductive tape (Wilco) was purchased from Wilkinson, Chatsworth, California, and the transparent tape was purchased from Niceday (purchased from Viking-Direct, Leicester, UK). Dow Corning 340 silicon HSC (white) and Electrolube silver conductive paint were purchased from RS Components, Ltd. (Corby, Northants, UK). The electron-capture compound,[48] trifluoromethylundecafluoro-cyclohexane ($C_6F_{11}CF_3$),[49] also known as perfluoromethylcyclohexane (PFMC), reagent[50]) was purchased from Sigma-Aldrich and was of technical grade. PFMC is a highly volatile liquid with high dielectric strength that captures free electrons by collision. The most commonly used electron-capture compound is sulfur hexafluoride (SF_6), but it could not be used in this experiment because it is in the gas phase at room temperature and the application of it in the MALDI-TOF (Kratos) mass spectrometer, or on a target exposed in an open room, would not be plausible.

The slides for the MALDI-TOF (Kratos IV) mass spectrometer were purchased from Kratos Analytical (Manchester, UK). They are stainless steel substrates with 20 separate target locations. The SIMair Focus airbrush with a 0.2 mm nozzle tip was purchased from Ziggy Art (Coventry, UK). The air was pumped from a 10 mol/L compressor (Air Products PLC, Crewe, Cheshire, UK). The semisolid state of the silicon HSC meant that its surface was distorted by the touch of a light brush applying the silver paint. This problem was overcome by the use of an airbrush. Another application involved the spraying of the electron-capture compound directly onto the substrate surface.

Masking procedure

To prepare the modified slides, the heat sink layer (mask) was created from transparent tape, which restrained the silicon-based semifluid paste that was subsequently applied to the surface of the slide with a metal spatula. With the use of a microscopic slide, the excess silicon was removed and the surface of the layer was smoothed. The length, width, and thickness of the layer were adjusted from the mask. A continuous layer of 2 cm $\times$ 6 mm tape was applied to the slide and was cut to fit on the targets precisely. A silver paint mask, similar to the heat sink, was also constructed. The paint was sprayed with the airbrush over the layers. The paint was applied in such a way that it was touching the edges of the metal substrate to create an electric field.

Every slide was modified in a different way, taking into account the limitations and the special handling that each of the materials required because of those limitations. This resulted in differences in the thickness of the layers, which could have affected the resulting spectra. (cf. Table S4 for a summary of the measurements of individual and combined layers). The target was considered to be flat (average of the low and high points) for the calculations, but the actual morphology is as shown in Fig. S3, which is slightly concave.

Sample preparation: summary

1. Both peptides were analyzed on a normal slide and the six modified slides (see Supplementary data, Fig. S1, for pictorial depcitions of the modified slides) at laser power 101 with CHCA as the matrix.
2. Both peptides were analyzed on modified slides (1) and (4) at laser power 106 with CHCA matrix.
3. Both peptides were analyzed on modified slide (2) at laser power 112 with CHCA matrix.

Analogously, the following control experiments were also conducted.

1. CHCA matrix was analyzed on a normal slide at several laser powers with no peptide. The experiment took place to verify the purity of the matrix and identify any unknown peaks.
2. 2,5-DHB matrix was analyzed on a normal slide with and without peptides. The experiment took place to identify any unknown peaks in comparison with the results from CHCA matrix.
3. Both peptides were analyzed on a normal slide at several laser powers with no matrix. The experiment took place to certify that neither peptide has any absorbance at the wavelength of the laser pulse, verifying that nonmatrix-assisted LDI was not occurring. No peaks were observed.
4. An additional modified slide was created. The slide carried a single layer of continuous PVC tape. The purpose of this control experiment was to observe if and how the electrical field was influenced by a layer of nonconductive material and if the was any relationship to the amount applied. The measurements on this slide were compared with the ones from the modified slide (2). No significant differences were observed. (Also see Figs. S4 and S5, which are bar graphs summarizing the measured ion intensities under different surface modification conditions).

Results and discussion

Experimental rationale

In this paper the model presented examines two parameters that could possibly affect desorption and ionization processes; they are the electron and thermal contributions induced by the laser pulse. In the model discussed, the energy pooling and multi-photon theories have been adopted and modified by introducing an additional energy parameter. Taking into consideration that the IP of the matrix cannot be overcome by one or two photons, it is necessary to take into account the energy given from the photoelectrons produced at the surface of the substrate after the laser pulse. Even though the normal stainless steel substrate does not have a significant photoelectron emission under the laser pulse in MALDI, the metal undergoes reduction when in contact with the matrix–analyte system.[51] Free electrons are possibly created in two processes of MALDI. Firstly, electrons may be produced after the laser pulse from the substrate surface. Secondly, electrons could be produced during ionization owing to collision between excited matrix molecules and matrix or analyte molecules.[52] This project examines the plausibility of a free electron[41] from the substrate surface and single or multiple photon co-excitation of the matrix.[26]

The thermal contribution parameter is considered to be necessary and is expected to have a significant influence in MALDI. There are many indications that a thermal factor is

Can. J. Chem. Downloaded from www.nrcresearchpress.com by Xi'an Jiaotong University on 09/19/12
For personal use only.

Table 2. Data for the sodiated form of trimethyl-β-cyclodextrin (TMBCD+Na), protonated substance P ($C_{63}H_{98}N_{18}O_{13}S$, Sub P), and α-cyano-4-hydroxy-cinnamnic acid (Matrix) pseudomolecular peak intensities without the heat sink compound (–HSC) and with the heat sink compound (+HSC), normalized and not normalized (in arbitrary units).

	Pseudomolecular peak intensity (mean ± SD; arb. units)			Mean ± SD (arb. units)	
Treatment	(A) Matrix	(B) TMBCD (MALDI)	(C) TMBCD (LDI)	(D) Ratio of TMBCD:Matrix ((B):(A))*	(E) Ratio of (TMBCD–HSC):(TMBCD+HSC) (B:b)
TMBCD–HSC	8562.17±122.55	154804.00±33672.6	431.00	18.08±27.48	2.31±1.67
	(a) Matrix†	(b) TMBCD (MALDI)	(c) TMBCD (LDI)*	(d) Ratio TMBCD:Matrix ((b):(a))*	(e) Ratio of (TMBCD/Matrix–HSC):(TMBCD/Matrix+HSC) (D:d)
TMBCD+HSC	3945.50±2533.42	67044.75±20184.52		16.99±7.97	1.06±3.45
Sub P–HSC	(F) Matrix	(G) Sub P (MALDI)	(H) Sub P (LDI)*	(I) Ratio Sub P : Matrix ((G):(F))*	(J) Ratio of (Sub P–HSC):(Sub P+HSC) (G:g)
	2969.00±372.81	59070.00±1506.14		19.89±4.04	191.58±7.19
Sub P+HSC	(f) Matrix†	(g) Sub P (MALDI)†	(h) Sub P (LDI)*	(i) Ratio Sub P : Matrix ((b):(a))*	(j) Ratio of (Sub P / Matrix–HSC) : (Sub P / Matrix+HSC) (I:i)
	2058.33±1121.89	308.33±209.38		0.15±0.19	132.79±21.66

Note: LDI, laser desorption/ionization; MALDI, matrix-assisted laser desorption/ionization Analysis of variance (ANOVA) indicates all comparisons were significant at the 95% confidence level including the ad hoc Scheffé's test, unless indicated. Capital letters: without HSC; lower case letters: with HSC.

*Not attempted (insignificant data for a statistical comparison).

†Not significant.

responsible for a thermally induced ionization. This is based on a sample being rapidly heated during desorption, then rapidly cooled during plume expansion, and then heated again owing to collisions between molecules. This makes a thermal contribution during ionization extremely unlikely. Thus, thermal contribution effects will be taken into account mainly for the desorption process.

To evaluate the validity of these considerations one needs to isolate the thermal and electron contribution to the sample. Different insulating, conductive and semiconductive materials were used to facilitate these conditions. Specially modified targets were produced that (*i*) allow thermal diffusion to the substrate and electron production, (*ii*) allow thermal diffusion but prohibit electron production, and (*iii*) prohibit both thermal diffusion to the substrate and electron production. The values of thermal and electrical conductivity were relatively different among the materials used; therefore, the variability of the applied conditions on the slides is taken into account. This process was continued until all of the layers of the sample were deposited (as shown in Fig. S1. Also see Supplemental spectra (SS) 1–14 for some representative MALDI-TOF spectra).

Results

The peak intensity of the protonated form of CHCA (nominal mass 190 Da, matrix species), Sub P (nominal mass 1348 Da, analyte species), and the sodiated form of trimethyl-β-cyclodextrin (TMBCD+Na, nominal mass 1430 Da, analyte species) were measured either under LDI or MALDI conditions. The peak intensities (in mV) were normalized to the analyte (analyte peak / matrix peak) such that any variations in the spectra would be taken into account (and plotted in arbitrary units, arb units). Table 2 shows the relationship between the peak intensity of the matrix and the analyte with (+HSC) and without (–HSC) the heat sink compound.

Table 2 shows that the TMBCD pseudomolecular peak intensity is ~56.69% (general expression 1: 100 – [(+HSC value]/(–HSC value)]100] or, for this example, 100 – [(column b)/(column B)]100) more intense without the HSC than with the HSC under MALDI conditions (Table 2, column E). This is reflected in the ratio of the analyte peak without the HSC compared with the ratio with the HSC. The peaks were then normalized where the analyte peak intensity was divided by the matrix peak, such that any ionization factors were cancelled out (Table 2, columns D and d). The normalized peak difference drops from 53.92% to ~6.03% (see general expression 1). The relationship between the matrix peak intensity without the heat sink (Table 2, column A) to the corresponding peak with the heat sink (Table 2, column a) is also shown. The matrix peak is ~53.92% (see general expression 1) higher without the HSC than with the HSC. It can also be noted that TMBCD can be laser desorbed (Table 2, column C). The pseudomolecular peak intensities of TMBCD without and with the heat sink under MALDI conditions relative to the corresponding measurements under LDI conditions are 99.72% (general expression 2: 100 – [(LDI value)/(MALDI value)]100 or, for this example, 100 – [(C)/(B)]100) (Table 2, column B vs column C) higher under MALDI conditions (i.e., $MALDI_{HSC–TMBCD} >> LDI_{HSC–TMBCD}$) and 99.36% (see gen-

Can. J. Chem. Downloaded from www.nrcresearchpress.com by Xi'an Jiaotong University on 09/19/12
For personal use only.

Table 3. Accuracy, statistical analysis, and reproducibility data for the instrument employed in this study.

Table A. Kratos MALDI-TOF mass spectrometer III data.

Target	Laser power	*%T*	Noise (%; mean±SD)	Analyte peak intensity (%; mean±SD)	Analyte to noise ratio (mean±SD)	Peak error (%; mean±SD of *m*/*z* shifting)	Peak width (mm; mean±SD)	Total No. of spectrums used
Normal slide			1.00±0.00	100.00±0.00	100.00±0.00	0.22±1.38	0.48±0.19	10(10)
Ag + PVC(targets)			1.53±0.66	100.00±0.00	65.22±28.07	0.36±0.31	0.21±0.05	9(9)
Ag + PVC(broad)			1.00±0.00	100.00±0.00	100.00±0.00	0.31±1.31	0.24±0.05	10(10)
Ag + Si	101	11.64	6.37±3.36	95.08±12.04	14.93±8.11	0.20±0.46	0.17±0.05	6(6)
Si			8.00±2.61	60.70±40.55	7.59±5.64	0.26±1.35	0.69±0.24	4(11)
PVC(targets)			4.33±5.27	94.44±17.23	21.81±26.84	0.26±1.80	0.18±0.07	10(10)
Ag			1.00±0.00	99.75±0.79	99.75±0.79	0.19±1.54	0.68±0.20	10(10)
Si	106	13	5.07±4.23	97.03±23.50	17.18±15.07	0.25±0.73	0.21±0.04	9(9)
Ag + Si			1.00±0.00	100.00±0.00	100.00±0.00	0.30±1.41	0.36±0.24	7(7)
PVC(targets)	112	6	1.49±0.81	100.00±0.00	67.11±36.48	0.14±0.76	0.18±0.08	10(10)

Table B. Kratos MALDI-TOF mass spectrometer IV data.

Target	Laser power	*%T*	Noise (%; mean±SD)	Analyte peak intensity (%; mean±SD)	Analyte to noise ratio (mean±SD)	Peak error (%; mean±SD of *m*/*z* shifting)	Peak width (mm; mean±SD)	Total No. of spectrums used
Normal slide			1.00±0.00	95.15±13.72	95.15±13.72	0.18±0.92	0.81±0.22	8(8)
Ag + PVC(targets)			1.08±0.09	98.77±3.89	91.45±8.43	0.11±0.88	0.39±0.10	10(10)
Ag + PVC(broad)			1.23±0.31	99.29±1.89	80.81±20.45	0.13±1.19	0.58±0.21	7(7)
Ag + Si	101	11.64	5.12±3.26	87.58±21.29	17.12±11.67	0.08±1.09	0.83±0.24	12(12)
Si			6.70±4.27	80.42±28.73	12.00±8.77	0.29±3.63	0.41±0.25	9(10)
PVC(targets)			3.63±3.38	77.01±26.78	21.21±21.09	0.25±1.99	0.55±0.31	10(10)
Ag			1.00±0.00	88.39±16.02	88.39±16.02	0.26±2.75	0.79±0.21	10(10)
Si	106	13.00	3.23±2.86	84.86±20.09	26.27±24.08	0.09±0.38	0.72±0.28	10(10)
Ag + Si			1.14±0.26	97.46±17.78	85.28±24.87	0.08±0.90	0.59±0.23	7(7)
PVC(targets)	112	16.00	1.26±0.47	71.61±34.41	57.04±34.74	0.13±1.54	0.47±0.23	9(10)

Note: *%T*, percent transmission. Analysis of variance (ANOVA) indicates all comparisons were significant at the 95% confidence level and for the ad hoc Scheffé's test, except where indicated.

Can. J. Chem. Downloaded from www.nrcresearchpress.com by Xi'an Jiaotong University on 09/19/12
For personal use only.

Fig. 1. (A) MALDI-TOF mass spectrum of the protonated sodiated forms of trimethyl-β-cyclodextrin (TMBCD) with α-cyano-4-hydroxycinnamic acid (CHCA) as the matrix (upper spectrum). The matrix-to-trimethyl-β-cyclodextrin ratio was 1500:1 and ~100 laser shouts were summed. A 0.5 μL aliquot of matrix (0.1 mol/L in acetonitrile) was deposited onto a stainless steel slide and allowed to dry. Once dry, 0.5 μL of peptide (dissolved in acetonitrile–water (2:1) with 0.01% trifluoroacetic acid) was deposited and allowed to dry. The mass spectrum is annotated as (CHCA + TMBCD). (B) MALDI-TOF mass spectrum of the protonated sodiated forms of TMBCD with CHCA as the matrix (lower spectrum). The matrix-to-trimethyl-β-cyclodextrin ratio was 1500:1 and ~100 laser shouts were summed. A 0.5 μL aliquot of matrix (0.1 mol/L in acetonitrile) was deposited onto a heat sink compound (+HSC) that had previously (using a stock solution of 1 mg/mL in tetrahydrofuran) been applied onto a stainless steel slide and allowed to dry. Once dry, 0.5 μL of peptide (dissolved in acetonitrile–water (2:1) with 0.01% trifluoroacetic acid) was deposited and allowed to dry. The mass spectrum is annotated as (HSC + CHCA + TMBCD).

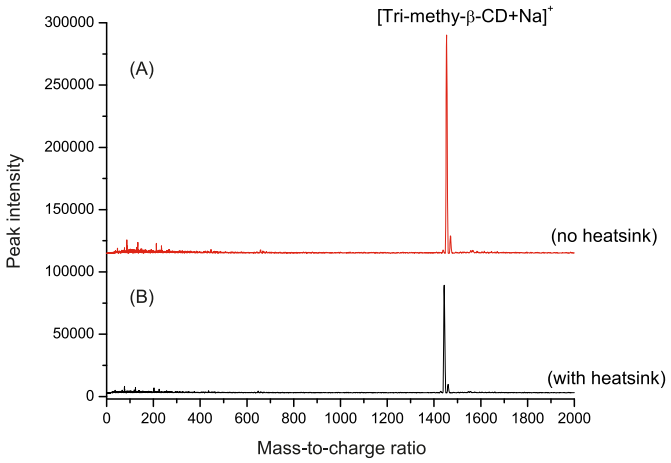

Fig. 2. (A) MALDI-TOF mass spectrum of the protonated form of substance P (Sub P) with α-cyano-4-hydroxycinnamic acid (CHCA) as the matrix. The matrix-to-Sub P ratio was 1000:1 and ~100 laser shouts were summed. A 0.5 μL aliquot of matrix (0.1 mol/L in acetonitrile) was deposited onto a stainless steel slide and allowed to dry. Once dry, 0.5 μL of peptide (dissolved in acetonitrile–water (2:1) with 0.01% trifluoroacetic acid) was deposited and allowed to dry. The mass spectrum was annotated as (CHCA + Sub P) [A]. (B) MALDI-TOF mass spectrum of the protonated form of Sub P with CHCA as the matrix. The matrix-to-Sub P ratio was 1000:1 and ~100 laser shouts were summed. A 0.5 μL aliquot of matrix (0.1 mol/L in acetonitrile) was deposited onto a heat sink compound (+HSC) that had previously (using a stock solution of 1 mg/mL in tetrahydrofuran) been applied onto a stainless steel slide and allowed to dry. Once dry, 0.5 μL of peptide (dissolved in acetonitrile–water (2:1) with 0.01% trifluoroacetic acid) was deposited and allowed to dry. The mass spectrum was annotated as (HSC + CHCA + Sub P) [B].

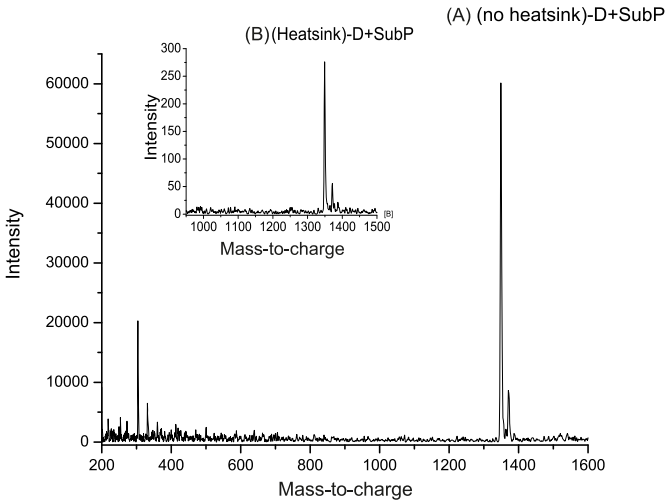

eral expression 2) (Table 2, column b vs column C) with the heat sink, respectively (i.e., $MALDI_{HSC+TMBCD} >> LDI_{HSC-TMBCD}$). The comparisons were also subjected to an analysis of variance and an ad hoc Sheffé's test pairwise comparison at the 95% confidence level,[53] and were mostly insignificant (the insignificant pairwise comparisons are noted in Tables 2 and 3). The accuracy and reproducibility of the instrument is presented in Table 3. The data in Table 3A were obtained on the Kratos MALDI-TOF mass spectrometer III and the data in Table 3B were collected on the Kratos MALDI-TOF mass spectrometer IV. The effect of the heat sink upon the MALD process will be discussed shortly.

For Sub P we see a more pronounced difference between the peak intensities with and without the HSC. The Sub P peak intensity without the HSC is 99.48% higher than with the HSC (Table 2, column G vs column g). Although there seemed to be no difference with and without the HSC for TMBCD, (Table 2, column e), we see a 190-fold difference in the relative peak intensities of Sub P and +HSC vs –HSC (Table 2, column J). It can be seen that the heat sink may influence the desorption process under MALDI conditions (i.e., the MALD process) in this case (Table 2, column J, as opposed to MALDI (or Table 2, column e). When the peak intensities are normalized, this difference decreases from 99.5% to 99.25% (Table 2, column I vs column i). The peak ratio drops from 190-fold (Table 2, column J) to ~130-fold (Table 2, column j), a drop of 30.37% . Also, Sub P cannot be laser desorbed (Table 2, column H) irrespective of the surface treatment (Table 2, column h). On the contrary, TMBCD can be laser desorbed (Table 2, column C), even though the signal intensity with the HSC was almost negligible (Table 2, column c), indicating that the molecule was potentially desorbed or ions had preformed prior to desorption.

Figure 1 is a MALDI-TOF mass spectrum of the sodiated form of TMBCD without (Fig. 1*a*) and with the HSC (Fig. 1*b*). For clarification, the mass spectrometer software integrates the peaks in mV; however, upon conversion of the data into an *x*–*y* table and subsequently graphed, the *y* axis is plotted in arb units, whereas the *x* axis maintains its charge-to-mass units. Analysis of the spectra did not reveal any major peaks <100 Da. The main matrix species observed were the protonated matrix (which was greatly diminished with the heat sink), the dehydrated matrix species (exhibiting a loss of 18 Da), and the matrix dimer, which has also been observed for liquid matrices.[54] Comparison of the matrix peaks obtained from the untreated (stainless steel) and treated (stainless steel with HSC) indicated that the application of the heat sink does not drastically affect the frag-

Can. J. Chem. Downloaded from www.nrcresearchpress.com by Xi'an Jiaotong University on 09/19/12
For personal use only.

mentation pattern of the matrix,[55] except that the intensity of some species was diminished for a surface treated with a HSC. Figure 2 depicts the corresponding MALDI-TOF mass spectra of the protonated form of Sub P without (Fig. 2*a*) and with the heat sinks (Fig. 2*b*). Comparison of Figs. 2*a* and 2*b* (and columns A and a in Table 2) illustrate a decrease in the intensity of the matrix peak for the matrix – heat sink bilayer. This phenomenon is similar to the MALDI suppression effect, in which low-mass matrix-ion peaks are suppressed.[20] However, in Fig. 2 the matrix peaks (and columns F and f in Table 2) are seen and thus are not totally diminished, indicating that the matrix suppression may partly be dependent upon the analyte species that is characterized.[56] Alternatively, there may be a different physical process occurring that results in lower intensity matrix peaks that are commonly observed under matrix suppression conditions.

In summary, the main utility of applying the HSC is to facilitate efficient heat transport between the analyte crystals and the surface, although the thermal conductivity of HSC is less than that of stainless steel (Table S1); however, comparisons of the same peptide under both conditions gave different ion intensities (cf. Tables 2 and 3 and Figs. S4 and S5) indicating a role for the heat sink.

The rationale for the use of the HSC is to determine if heat conductance from the metal slide to the matrix is a major pathway in the MALD process. If the contribution of metal-to-matrix or metal-to-analyte heating was minimal in the overall desorption of the matrix or analyte, then it can be expected that no difference should be seen in the –HSC vs +HSC system. This was not the case. The heat sink is thought to operate as a capacitor, storing charge. Consequently, if the pressure–pulse model is used to describe the MALD process, the desorption of the matrix–analyte system will occur only if an inordinately large number of collision events create the molecular momentum necessary for the desorption process to take place.[57] The model predicts that the number of molecules varies as a function of molecular mass (assuming a constant binding energy), which can be described by a power function ($f(M^{5/3})$, where M = molecular mass).[58] Soft expansion of the matrix by low-energy secondary electron excitation may be partially blocked by the heat sink.[59] Additional experiments using an electron donor in the Fourier transform ion cyclotron resonance (FTICR) mass spectrometer were conducted that support our conclusion[60] that photoelectrons are also involved in the ionization process.[3,47,61] Therefore, if the MALD process is dominant, and not the heat conduction from the metal to the matrix, then the result may be observed as two contradictory trends. In cases where MALD is more efficient, more ions would be generated, leading to an increase in the molecular ion signal intensity even though a larger standard deviation may be expected owing to uneven layering resulting in varied flight times (cf. *Error and Standard Deviation Measurement* and *MALDI reproducibility and accuracy assessment* in the Supplementary data). This deviation can be compensated for by the reflectron, (assuming the kinetic energy is not too dispersed for the ion of the same mass-to-charge ratio[62]), which can be negligible if the sample layers are thin. The other process ion generation (i.e., the ionization of the neutral matrix through thermal induction from the metal slide) through heat conduction in this scenario would generate zero ions and the overall sum may decrease in spite of the improved efficiency of the MALD process.

Our preliminary thickness measurement indicates that all layers are <50 μm thick (cf. *Surface Profiling Procedure* in the Supplementary data). These observations can lead to a number of possible conclusions (i.e., the change in analyte signal intensity as a function of heat sink deposition could be due to mechanisms (*a*) or (*b*) as follows), which describe how heat sink deposition can affect the analyte signal intensity. Plausible conclusions can be summarized as (*a*) a large voltage drop owing to the possible "capacitance"-related voltage drop attributed to the heat sink, thus, resulting in delayed ionizations, and (*b*) formation of meta-stable peaks,[63] owing to incomplete extraction and acceleration. However, the (*b*) phenomenon was not observed.

The calculation of the voltage drop in the presence of the HSC utilizes equations commonly seen in any traditional university physics course.[64] The parallel-plate capacitor consists of plates that possess dimensions of 2.0 mm × 100 μm that are separated by a distance of 5.0 mm, and exhibit a surface charge density (σ) of 3.5×10^{-5} C/m^2. Based on the 20 kV accelerating voltage of the Kratos III, the capacitance of the system in a vacuum is calculated using

$$[1] \qquad C_0 = \frac{\varepsilon_0 A}{d}$$

where ε_0 is permittivity in a vacuum, A is the area of the plates, and d is the distance separating the plates. Without the HSC, the capacitance of the system was 3.54×10^{-16} F. Therefore, in the absence of an insulator the charge carried by the capacitor was calculated ($Q = VC_0$, where V = 20 kV) to be $Q = 7.1 \times 10^{-12}$ C. The insertion of the heat sink (+HSC) into the system creates a bilayer capacitor that can be addressed mathematically as two capacitors in series, such that

$$[2] \qquad \frac{1}{C_{eq}} = \frac{1}{C_{vac}} + \frac{1}{C_{+HSC}}$$

where C_{eq} is the equivalent capacitance, C_{vac} is the capacitance in a vacuum, and C_{+HSC} is the capacitance of the system including the HSC. The value for C_{vac} was determined as above, except that d = 0.00495 m and C_{+HSC} was calculated using

$$[3] \qquad C_{+HSC} = \frac{\kappa \varepsilon_o A}{d}$$

where κ is the dielectric constant (κ = 5, Dow Corning product information) and $d = 50 \times 10^{-6}$ m (see text). The resulting C_{eq} corresponds to an increase of ~0.85% of the initial capacitance of the system. Assuming that the charge of the system remains constant, the potential difference between the plates owing to the insertion of heat sink (+HSC) is calculated to be 199 kV. Consequently, we predict the voltage drop to be on the order of $\sim 1.0 \times 10^2$ V (a decrease of 0.50% in the effective accelerating voltage), which we deem as being negligible. Alternatively, if the voltage is not fixed, it can be concluded ($Q = VC_0$) that as the capacitance increases, so does the charge, which in turn will give greater ion yield for the measured analyte ion intensities. However,

Can. J. Chem. Downloaded from www.nrcresearchpress.com by Xi'an Jiaotong University on 09/19/12
For personal use only.

this phenomenon was not observed because the measured intensities of both analytes under regular MALDI conditions were higher than the intensities with the heat sink or under LDI conditions, emphasizing the importance of the heat transfer and energy transfer processes involved in MALDI.

An initial look into the analysis of the charge and photon excitation effects focuses on the space charge effect. The space charge effect is the consequence of the mutual repulsion (owing to Coulombic forces) between particles of similar charge and, in our case, mostly influences the nonconductive material. It is based on the principle that static electricity is generated by unbalancing the molecular construction of relatively nonconductive insulators, such as plastics and paper. If one considers that a static electric field is created on the nonconductive material from the laser pulse, then the similarly charged ion beam can be repulsed and consequently defocused.[65]

To assess if the target is still "in focus" one needs to calculate the beam waist of the laser beam (cf. Fig. S6). Beam waist is the location along the propagation direction where the beam radius has a minimum, which in theory is located at $x = 0$ and is normal to the substrate in MALDI experiments where the laser beam is ideally focused.

For Gaussian beams: the governing equations of a Gaussian beam are the e^{-2} radius $w(x)$ eq. [4] and the wave front curvature $R(x)$ eq. [5].

$$[4] \qquad w(x) = w_0^2\left[1 + \left(\frac{\lambda x}{\pi w_0^2}\right)^2\right]$$

$$[5] \qquad R(x) = x\left[1 + \left(\frac{\pi w_0^2}{\lambda x}\right)^2\right]$$

where λ is the laser wavelength, x is the distance from the source, w_0^2 is the radius of the beam waist at $x = 0$, and $2w_0$ is the beam waist. The beam waist at $x = 0$ (focal point) was calculated using eq. [6].

$$[6] \qquad 2w_0 = \left(\frac{4\lambda}{\pi}\right)\left(\frac{F}{D}\right)$$

where $F(S_2)$ is the focal length (4 cm) and D is the diameter of the beam illuminated on the lens (1 cm). Therefore, $2w_0 = 1.72$ μm. Equation [6] is valid only when the depth of focusing (DOF) is smaller than the focal length. DOF was calculated using eq. [7].

$$[7] \qquad \mathrm{DOF} = \left(\frac{8\lambda}{\pi}\right)\left(\frac{F}{D}\right)^2$$

Therefore, DOF = 13.7 μm.

It was observed that the beam waist is really small compared with the thickness of the layers; therefore, one may assume that the results are affected. However, in laser beam profile measurements carried out on a laser used in a MALDI-TOF (Kratos IV) mass spectrometer, it was shown that the laser beam of the LSI lasers is not Gaussian in profile. The beam was TEM_{mn} (transverse electromagnetic mode, where $m, n \neq 0$; Gaussian beams are TEM_{00}) shaped, which increases the beam waist significantly. From the indices, m refers to the number of intensity minima in the direction of the electric field oscillation and n refers to the number of minima in the direction of the magnetic field oscillation.[24] At $x = 0$, the beam waist is approximately equal to the diameter of the laser pulse, which is estimated to be 100 μm.

For a real beam, the concept of M^2, which is known as the propagation constant, is introduced to describe the relationship between a real beam and an ideal Gaussian beam. M^2 was calculated using eq. [8].[25]

$$[8] \qquad d = M^2\left(\frac{4\lambda}{\pi}\right)\left(\frac{F}{D}\right) \Leftrightarrow M^2$$

where d is the the diameter of the laser beam ($\approx$100 μm) or the real beam waist at $x = 0$. Therefore, $M^2 = 58.26$. The real beam waist (W_0) is given by eq. [9].

$$[9] \qquad 2W_0 = M^2 2w_0$$

Therefore, $2W_0 \approx 100$ μm. Now, eq. [4] becomes eq. [10] for a real beam.

$$[10] \qquad W(x) = W_0^2 + M^4\left(\frac{\lambda x}{\pi W_0}\right)^2$$

The comparison of $W(x)$ (eq. [10]) and $w(x)$ (eq. [4]) can be clearly seen (Figs. S7 and S8 in the Supplementary data). To evaluate the importance of these calculations, one must take into consideration the 45° angle of the laser beam to the target. The Gaussian beam waist is very narrow and can be easily defocused even with a small change in thickness to which the slides have been subjected (cf. Figs. S6–S8). The real beam waist for $x = 115$ μm presents a beam waist $W(x) = 104.05$ μm, which shows that the beam is slightly defocused but still within the beam waist; therefore, no significant result alteration should be expected.

The third control experiment (see the Sample preparation: summary section) utilized tape on the targets and a continuous layer of tape on targets that were analyzed under the same conditions. The results from both slides were similar. In theory, the slide with the continuous layer should present increasing electric field phenomena with the increase of the shots on the layer.[66] Furthermore, comparison of the results from the heat sink and the PVC tape on target slides shows that the analyte-to-noise ratio for PVC was higher than that of the silicon (Si) (cf. Figs. S4 and S5). Taking into account the thickness of each layer, one can see that the PVC layer is double in thickness. That should mean a higher space-to-charge ratio because the target comes closer to both the focal lens and the plate with the 20 kV potential (the potential difference increases when the same potential is applied in a smaller space). The experiments that took place prove that a significant charge-to-space ratio did not take place.

It is also necessary to evaluate the applicability of the proposition made in the Introduction that electron contribution by collisions with matrix molecules, after one- or two-photon excitation, completes the primary ionization process.[27] The calculation will take place for a nitrogen laser with photon energy 3.68 eV[25] and a matrix molecule with IP = 10 eV. Since 10 eV IP is considered to be high, and the nitrogen photon laser energy low, the calculations should

Can. J. Chem. Downloaded from www.nrcresearchpress.com by Xi'an Jiaotong University on 09/19/12
For personal use only.

Table 4. Data for trimethyl-β-cyclodextrin and 2,5-dihydroxybenzoic acid pseudomolecular peak intensities with conductive paint (P + D + T) and with the heat sink compound + paint (H + P + D + T) in arbitrary units.

Treatment group	Sample composition	TMBCD intensity (mean±SD)	Ratio of TMBCD:Matrix (mean±SD)
I	D+T	83904.75±33770.36	7.50±4.43
II	P+D+T	44092.00±19989.14	7.07±5.71
III	H+D+T*	6164.00±3539.78	262.30±122.10
IV	H+P+D+T*	29768.25±11817.88	3.82±1.44
$(analyte/matrix)_{control}$:$(analyte/matrix)_{paint}$ (I:II)			1.06
$(analyte/matrix)_{heatsink}$:$(analyte/matrix)_{heatsink+paint}$ (III/IV)			37.11
$(analyte/matrix)_{heatsink}$:$(analyte/matrix)_{paint}$ (III/II)			68.75
$(analyte/matrix)_{heatsink+paint}$:$(analyte/matrix)_{paint}$ (IV/II)			0.54

Note: D = protonated 2,5-dihydroxybenzoic acid (2,5-DHB, $[M + H]^+$, 155.4 Da, and dehydrated 2,5-DHB $[M - 18]^+$, 138.2 Da); T = protonated 2,3,6-tri-*O*-methyl-β-cyclodextrin (TMBCD, $[M + H]^+$, 1430.6 Da); H = heat sink compound (HSC; Dow Corning 097); P = conductive paint (Ag-based). Analysis of variance (ANOVA) indicates all comparisons were significant at the 95% confidence level and for the ad hoc Scheffé's test, except where indicated.

*Not significant.

Fig. 3. Representation of the "normalized" signal intensity of the protonated sodiated forms of trimethyl-β-cyclodextrin (TMBCD) under matrix-assisted laser desorption/ionization conditions (MALDI) without (TMBCD/Matrix–HSC) and with (TMBCD/Matrix+HSC) the heat sink compound (HSC). A minimum of 10 experiments were conducted, and the mean peak intensity with the corresponding standard deviation was calculated.

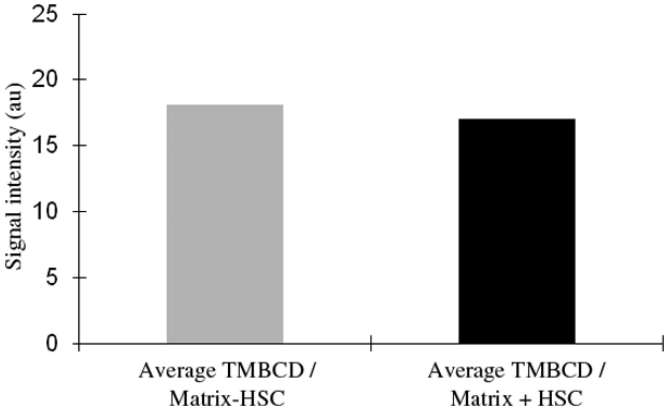

Fig. 4. Representation of the "normalized" signal intensity of the protonated forms of substance P ($C_{63}H_{98}N_{18}O_{13}S$, Sub P) under matrix-assisted laser desorption/ionization (MALDI) conditions without (Sub P/Matrix–HSC) and with (Sub P/Matrix+HSC) the heat sink compound (HSC). A minimum of 10 experiments were conducted, and the mean peak intensity with the corresponding standard deviation was calculated. The values were also calculated for the protonated sodiated forms, which were within 5% of the values determined for the protonated form. This observation is based on the fact that Sub P is predominately in the protonated form.

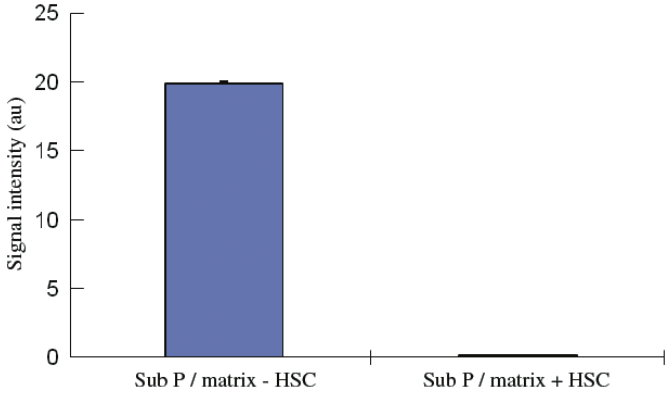

cover a large range of lasers and matrices.[67] The potential is considered to increase linearly with distance from the substrate until it reaches 20 kV. The distance between the plates is 5 mm, and the elementary charge of an electron is 1.6×10^{-19} C. To excite a matrix molecule, the additional required energy is 10 eV – 3.68 eV = 6.32 eV. Therefore, an electron needs to obtain an energy of at least 6.32 eV. The distance from the target surface that the electron must be to be located in the potential difference of 6.32 eV is given by eq. [11]

$$[11] \qquad \text{Distance} = \frac{H\text{NP}}{\text{FP}} = \frac{5 \times 6.3}{20} = 1.57$$

giving Distance = 1.57 μm, where H is the distance (in mm) between the plates, NP is the needed potential (in V) in calculated distance, and FP is the final potential (in kV) applied in distance H. But this begs the question as to whether or not the electron can be removed from the surface.[41,47,60,61] Between the positively charged metal targets, the electron-attracting Coulombic force exists. To overcome those forces, work must be consumed. The work needed is given by eq. [12].

$$[12] \qquad W = \text{NP}q$$

where W is the work required to remove the charge (q). This gives $W = 6.3\ \text{V} \times 1.6 \times 10^{-19}\ \text{C} = 1.08 \times 10^{-18}$ J.

In the case of the two-photon single electron excitation,[68] the same calculation employed with the previous case predicts the additional energy needed, 10 eV – 2×3.68 eV = 2.64 eV from eqs. [11] and 12, where the Distance = 0.59 μm and $W = 4.22 \times 10^{-19}$ J. Several other combinations could exist with one or two photons and one or more

Can. J. Chem. Downloaded from www.nrcresearchpress.com by Xi'an Jiaotong University on 09/19/12
For personal use only.

electrons. The work needed for the electrons to travel at this distance is negligible when compared with the rapid expansion of the plume from 200 m/s to ultrasonic velocities depending on the molecule (ion or neutral).[69] It can therefore be said that electrons can travel the distance required for contribution in the matrix excitation, which in turn would present a different threshold for analyte desorption or dissociation.[70]

Also, no delayed flight times were observed and the standard deviation[53] was within the range observed for samples under normal conditions, suggesting that the layers were not too thick or uneven to cause defocusing of the laser (data not shown). The defocusing process would be attributed to the short focal distance, which creates a shallow field depth. Therefore, if the target is not exactly positioned at the laser focal point, a decrease in peak intensity would be observed. In the follow-up experiment, TMBCD (T) was used as the analyte because it was shown (in this study) to possess a large desorption cross section relative to Sub P, which would also presumably be observed under IR MALDI conditions.[63] The ratio of the signal intensity to analyte intensity is shown in Table 4.

It can be seen by comparing the ratio of the analyte signal peak to the matrix signal peak that there is very little difference (7.50 vs 7.07 arb units, $P > 0.05$) in having metal slide – matrix – analyte (Table 4, group I) vs metal slide – conductive paint – matrix – analyte (Table 4, group II), where the paint acts as a second control (P + D + T). Comparing this with the system with the heat sink (Table 4, group III), we see a 37-fold (from approximately 7 to 260 arb units, $P < 0.05$) increase in the ratio of the analyte–matrix peak (Table 4, group III vs group II). Comparing this (Table 4, group II) to the composite system with the heat sink, followed by conducting paint coating (Table 4, group IV), we see a drop in the ratio to ~54% (3.82 vs 7.07 arb units, $P < 0.05$) of the initial group II value, indicating that the "charging and shielding" effect of the heat sink is not significant enough to account for the reductions in signal intensity observed for Sub P. The reductions seen for TMBCD are less than what is seen in this experiment, indicating that this is a maximum value. Therefore, the largest drop in peak intensity, which can account for the charging effect of the heat sink, is at best 54%.

Discussion

The heat sink could allow heat conduction from the metal surface of the slide to the MALDI matrix, but would not allow any charge conduction. Any excited matrix molecules formed at the heat sink – matrix interface would "experience" a lower extraction potential (set at +20 kV) than a system without the heat sink. This may lead to a lowering of the matrix peak intensity, although our calculations indicate any voltage drop is on the order of 100 V and the defocusing of the ion beam to be minimal at best. The difference in matrix peak intensities, therefore, cannot be accounted for entirely by the heat sink – matrix interactions alone, in that the thermal conductivities are too low in comparison with stainless steel. For TMBCD, no difference was observed (Fig. 3). We have determined that TMBCD can itself be minimally desorbed (Table 2, column C). Consequently, when TMBCD is the analyte the majority of the molecules undergo desorption partly by laser desorption and by MALDI processes, such as matrix sublimation,[19] pressure–pulse model,[23] or by soft expansion by secondary electrons.[38] The heat sink may interact with these secondary electrons,[41] thereby minimizing their influence in the MALD process[71] and leading to a lowering of peak signal intensity.

In the system where Sub P is the analyte, the contributions to MALD by matrix sublimation may not in itself be sufficient to cause all the molecules to desorb (Fig. 4). In this system, contributions from soft expansion by secondary electrons may also be required in the MALD processes to yield efficient desorption. When TMBCD is the analyte, matrix sublimation may be a MALD pathway, which in itself is sufficient to cause the majority of analyte molecules to desorb. However, when Sub P is the analyte, this pathway may be insufficient and an alternative pathway concurrent to, or consecutive to, matrix sublimation may be required to cause efficient desorption. The heat sink would interfere with this pathway and limit the efficiency of desorption compared with the system without the heat sink. If there is a contributory pathway via heat conduction from the metal slide in the Sub P system, it is insufficient to cause desorption.

In the experiment carried out to test this idea, it could be seen that the drop in signal intensity solely owing to shielding of the heat sink was 54%. That was based on comparing the analyte–matrix ratios of (P + D + T, or group II in Table 4) and comparing them with the corresponding system with the heat sink (H + P + D +T, or group IV in Table 4). If one were to look at total analyte (TMBCD) signal intensity, then the ratio ((H + P + D + T)/(P + D + T)) drops to 32.5%. The drop in signal intensity cannot be totally accounted for by heat-sink shielding, and the follow-up experiment would tend to support that observation. It is therefore more likely that the drop can be attributed to "blocking or short-circuiting" one of the MALD pathways. Recently, Allwood et al.[72] proposed that more than one mechanism may play an important part in the MALD process, both thermal and photoprocesses, which may have different contributions to the phenomenological event of MALD. If both matrix sublimation and soft expansion (the so-called "popcorn" model),[58] are processes that contribute to MALD, it can be seen that inhibiting one system may affect the desorption yield. In the TMBCD case, laser(s) desorption and matrix sublimation processes are sufficient to desorb the majority of the molecules. Additionally, the presence of the heat sink was observed to have a negligible effect on the desorption yield (Fig. 3). Sub P, which does not undergo laser desorption, shows a marked difference in the presence and absence of the heat sink (Fig. 4). It seems unlikely that metal–matrix heat conduction plays a major role because Sub P peak intensity varies according to the presence or absence of the heat sink and, as previously stated, the thermal conductivities of the heat sink are less than that of stainless steel (cf. Table S1 in the Supplementary data). It can also be assumed that the bulk of the laser energy is absorbed by the (<100) monolayers; therefore, is seems likely that direct interaction with the heat sink is minimal because of the two-dimensional nature of laser desorption.[20] Additionally, slow heat diffusion in solid organic samples,[73] owing to a mismatch

Can. J. Chem. Downloaded from www.nrcresearchpress.com by Xi'an Jiaotong University on 09/19/12
For personal use only.

in the time scale in the sample heating desorption/ionization in MALDI, leads to minimal direct heat dissipation via conduction. On the contrary, the laser-induced conductive thermal heating depth is much greater than radiative absorption heating depth (defined as $1/a$, where a is the absorption cross section, which for pure silicon is $\sim 1 \times 10^6$ cm^{-1})[74] at the end of the laser pulse. The temperature difference can be estimated to be 142 K ($\Delta T_{surface} = \frac{2I}{K}\sqrt{\frac{\kappa t}{\pi}}$, where I is the laser irradiance that is determined from the measured fluence (F) and laser pulse time (ns); ($F/t \sim 15 \times 10^{-3}$ mJ/cm^2 / 3×10^{-9} s = 5 MW/cm^2) and K is the thermal conductivity (0.42 WK cm^{-1} (see Table S1), and κ is the thermal diffusivity = $K/C_p \sim 0.42/2 = 0.21$ cm^{-1}, where C_p is the specific heat capacity estimated to be 2 J/K/cm^3 for pure silicon).[75] The temperature is sufficient for the evaporation or decomposition of the physioabsorbed solvent molecules surrounding the analytes, leading to emission of preformed ions at a threshold temperature, which is easily within reach of the HSC relative to pure silicon.

Conclusion

In summary, there are strong indications that emissions of photoelectrons close to the surface enhance the ion yield and improves the reproducibility of the resulting spectra.[67] Photoelectrons could provide the additional energy to overcome the ionization potential of the matrix without significantly influencing the ion yield, since the attractive Coulombic forces (between substrate and photoelectrons) increase with a decrease in the distance and attract the electrons back to the surface. Even if the forces exerted by the expanding plume are higher than the attractive Coulombic force, the photon and photoelectron co-excitation of the matrix is not excluded.[25] Further enhancement of the photoemission phenomenon can be attributed to the topology of the heat sink layer. The uneven surface can lead to the creation of electron-holes that under certain conditions can lead to photoemission. This photoemission may also enhance the ionization process through the generation of radical species that have been observed in our and other studies. The uneven layering of the heat sink can aid in the recycling of new analyte species post-UV radiation, which has been observed under SALDI conditions.[76] Under SALDI-like conditions local charge separation at the surface could be increased. This charge separation could indicate desorption of preformed analyte ions (e.g., highly charged ions) by restricting ion-to-ion recombination in the early formation of the desorption plume. The charge separation on the uneven surface could be facilitated by the electric field of the laser pulse, (in tandem with local surface heating). The phenomena of local heating and charge separation has also been observed by surface-enhanced Raman spectroscopy for other surfaces[77] where the local electric field component can lead to ion emission.[78] Thermal diffusion, on the other hand, provides insufficient thermal contribution to the matrix–analyte system. Consequently, since the MALD process occurs only partially, a subsequent decrease in the ion yield is anticipated and in fact observed.[79] There is no indication that the thermal contribution directly influences the ionization.

The TMBCD ions can exist based on solution thermodynamics.[20] In the case of Sub P, ionization processes involving cluster ejection and breakdown result in a singly charged protonated peptide[80] in the selvedge region,[81] or in the gas-phase reactions with or without solvation[30]; however, some analytes in either the monomeric or multimeric form[45] may be analyzed via charge-transfer processes from the matrix.[40,82] It can be thought of as a multistep process, in which solvent evaporation is followed by ion desolvation and eventually ion desorption of the preformed ions. This is a phenomenon that has been observed for other surface desorption techniques.[83]

Another parameter to take into account is the substrate surface and its mechanical characteristics. The HSC facilitated thermal diffusion but may also have influenced the mechanical stress and pressure increase during desorption, since its semisolid state would absorb more stress than a solid target. This can also be supported by the differences in thermal conductivities (see Table S1 presented in the Supplementary data section for conductivity data), in that stainless steel and silver metal or alloy have higher values of thermal conductivity than the heat sink, but the ion yields are not decreased as would be expected, which indicates that even though thermal diffusion takes place there are other processes occurring that compensate for the decrease in thermal transfer to the sample. Another mechanism for ionization is cation attachment,[26] which is characterized by the carbohydrate that is preferentially sodiated. Under these conditions, the preformed ions may negate any analyte yield reduction[81] that may result from the interaction of the heat sink.

The present results for MALD from a regular metal surface and from a composite with an intervening heat sink material (allowing for electrical conductance but no heat transfer) indicates that the measured ion yield is highly analyte-dependant. When the analyte was a carbohydrate, the differences in measured ion yield for the sodiated species were similar, although greater yields were measured under regular MALDI-TOF conditions, strongly indicating that the ions were formed in solution (via a physioadsorbed solvent)[84] or were preformed in bulk solution prior to desorption.[85] Conversely, with Sub P a negligible ion yield was detected for the protonated peptide, indicating that the fraction of preformed ions was negligible and that the peptide absorbed on the surface as a neutral species with subsequent protonation either at the surface or in the gas phase with a solvating environment. The solvating medium can possibly be described as highly charged state clusters in which ion desorption is assisted via local charge pair separation, desolvation, and laser-induced heating that is assisted by localized electric fields promoted by some intrinsic proton source (e.g., acid, either from the matrix species, the acidic side group, or the free acid). This ion separation would be aided by electron emission from the lower surfaces, or "active sites", in which the analyte is turned over and exposes a fresh analyte between laser pulses. A side indicator would be the population of the radical cation of the matrix [M$^{\bullet+}$], which was observed (under MALDI-TOF and FTICR conditions, data not shown, although no radical analyte was observed under the current conditions of the experiment. Other instrument parameters were investigated to determine whether the measured differences in the ion yields were dependent upon instrumental effects. It was shown that the effect of voltage drop, beam width, or surface profile (affecting the kinetic

energy spread) were not adequately significant to account for the differences. In addition, many of the differences observed with the peptide could be mitigated by the addition of electron capture agents (lowering ion intensities) or silver (increasing ion intensities) indicating that the affect of the heat sink was to decouple the desorption and ionization events under MALDI-TOF conditions. For optimal ion yields, an acidic environment, an uneven surface, and localized heating are the necessary prerequisites.

Supplementary data

Supplementary data for this article are available on the journal Web site (canjchem.nrc.ca).

Acknowledgements

SB would like to thank I. Herbert, B. Thomas, and T. Jenkins of Courtaulds Corporate Technology for their support and Professor T. Wood (State University of New York at Buffalo) for his comments. SB would also like to acknowledge financial support from the Engineering and Physical Sciences Research Council (EPSRC), the Welch Foundation, and National Institutes of Health / Research Infrastructure in Minority Institutions (NIH/RIMI) No. 5 PMD000216-02. KAB would like to thank The University of Texas of the Permian Basin (UTPB) Stars Grant Program, the UTPB Faculty Development Fund for Academic Excellence, and the Robert A. Welch Foundation Inc. (AW-0013) for their support of this investigation.

References

(1) Karas, M.; Bachmann, D.; Bahr, U.; Hillenkamp, F. *Int. J. Mass Spectrom. Ion Process.* **1987**, *78*, 53. doi:10.1016/0168-1176(87)87041-6.

(2) Chan, T.-W. D.; Colburn, A. W.; Derrick, P. J. *Org. Mass Spectrom.* **1992**, *27* (1), 53. doi:10.1002/oms.1210270114.

(3) Wysocki, V. H.; Resing, K. A.; Zhang, Q.; Cheng, G. *Methods* **2005**, *35* (3), 211. doi:10.1016/j.ymeth.2004.08.013.

(4) Montaudo, M. S.; Garozzo, D.; Montaudo, M. S.; Puglisi, C.; Samperi, F. *Macromolecules* **1995**, *28* (24), 7983. doi:10.1021/ma00128a003.

(5) Crecelius, A. C.; Baumgaertel, A.; Schubert, U. S. *J. Mass Spectrom.* **2009**, *44* (9), 1277. doi:10.1002/jms.1623.

(6) Huberty, M. C.; Vath, J. E.; Yu, W.; Martin, S. A. *Anal. Chem.* **1993**, *65* (20), 2791. doi:10.1021/ac00068a015.

(7) Juhasz, P.; Costello, C. E.; Biemann, K. *J. Am. Soc. Mass Spectrom.* **1993**, *4* (5), 399. doi:10.1016/1044-0305(93)85005-I.

(8) Garozzo, D.; Spina, E.; Sturiale, L.; Montaudo, G.; Rizzo, R.; Daolio, S. *Rapid Commun. Mass Spectrom.* **1994**, *8* (5), 358. doi:10.1002/rcm.1290080503.

(9) Garrozzo, D.; Impallomeni, G.; Spina, E.; Sturiale, L.; Zanetti, F. *Rapid Commun. Mass Spectrom.* **1995**, *9* (10), 937. doi:10.1002/rcm.1290091014.

(10) Tang, K.; Allman, S. L.; Chen, C. H. *Rapid Commun. Mass Spectrom.* **1992**, *6* (6), 365. doi:10.1002/rcm.1290060602.

(11) Merrigan, T. L.; Hunniford, C. A.; Timson, D. J.; Catney, M.; McCullough, R. W. *Biochem. Soc. Trans.* **2009**, *37* (4), 905. doi:10.1042/BST0370905.

(12) Spengler, B.; Kirsch, D.; Kaufmann, R.; Lemoine, J. *J. Mass Spectrom.* **1994**, *30*, 782.

(13) Köcher, T.; Engström, A.; Zubarev, R. A. *Anal. Chem.* **2005**, *77* (1), 172. doi:10.1021/ac0489115.

(14) Yin, H.; Chacon, A.; Porter, N. A.; Masterson, D. S. *J. Am. Soc. Mass Spectrom.* **2007**, *18* (5), 807. doi:10.1016/j.jasms.2007.01.004.

(15) Suckau, D.; Resemann, A. *Anal. Chem.* **2003**, *75* (21), 5817. doi:10.1021/ac034362b.

(16) Becker, J. S.; Jakubowski, N. *Chem. Soc. Rev.* **2009**, *38* (7), 1969. doi:10.1039/b618635c.

(17) Karas, M.; Hillenkamp, F. *Anal. Chem.* **1988**, *60* (20), 2299. doi:10.1021/ac00171a028.

(18) Knochenmuss, R.; Zhigilei, L. V. *J. Phys. Chem. B* **2005**, *109* (48), 22947. doi:10.1021/jp052945e.

(19) Vertes, A.; Gijbels, R.; Levine, R. D. *Rapid Commun. Mass Spectrom.* **1990**, *4* (6), 228. doi:10.1002/rcm.1290040613.

(20) Chan, T.-W. D. Matrix-assisted Ultraviolet Laser Desorption/Ionisation Mass Spectrometry of Macromolecules; Ph.D. Thesis, Chapter 4, The University of Warwick, Coventry, UK, 1992.

(21) Vertes, A.; Gijbels, R. *Chem. Phys. Lett.* **1990**, *171* (4), 284. doi:10.1016/0009-2614(90)85365-J.

(22) Vertes, A.; Gijbels, R. *Scanning Microsc.* **1991**, *5*, 317.

(23) Johnson, R. E.; Sundqvist, B. U. R.; Ens, W. *Rapid Commun. Mass Spectrom.* **1991**, *5* (11), 574. doi:10.1002/rcm.1290051116.

(24) Sundqvist, B. U. R. *Anal. Chim. Acta* **1991**, *247* (2), 265. doi:10.1016/S0003-2670(00)83822-2.

(25) Zenobi, R.; Knochenmuss, R. *Mass Spectrom. Rev.* **1998**, *17* (5), 337. doi:10.1002/(SICI)1098-2787(1998)17:5<337::AID-MAS2>3.0.CO;2-S.

(26) Knochenmuss, R.; Zenobi, R. *Chem. Rev.* **2003**, *103* (2), 441. doi:10.1021/cr0103773.

(27) Karbach, V.; Knochenmuss, R. *Rapid Commun. Mass Spectrom.* **1998**, *12* (14), 968. doi:10.1002/(SICI)1097-0231(19980731)12:14<968::AID-RCM255>3.0.CO;2-4.

(28) Mormann, M.; Bashir, S.; Derrick, P. J.; Kuck, D. *J. Am. Soc. Mass Spectrom.* **2000**, *11* (6), 544. doi:10.1016/S1044-0305(00)00112-4.

(29) Karas, M.; Kruger, R. *Chem. Rev.* **2003**, *103* (2), 427. doi:10.1021/cr010376a.

(30) Knochenmuss, R. *Analyst (Lond.)* **2006**, *131* (9), 966. doi:10.1039/b605646f.

(31) Karas, M.; Bachmann, D.; Hillenkamp, F. *Anal. Chem.* **1985**, *57* (14), 2935. doi:10.1021/ac00291a042.

(32) Krause, J.; Stoeckli, M.; Schlunegger, U. P. *Rapid Commun. Mass Spectrom.* **1996**, *10* (15), 1927. doi:10.1002/(SICI)1097-0231(199612)10:15<1927::AID-RCM709>3.0.CO;2-V.

(33) Glückmann, M.; Pfenninger, A.; Krüger, R.; Theirolf, M.; Karasa, M.; Horneffer, V.; Hillenkamp, F.; Strupat, K. *Int. J. Mass Spectrom.* **2001**, *210–211*, 121.

(34) Dreisewerd, K. *Chem. Rev.* **2003**, *103* (2), 395. doi:10.1021/cr010375i.

(35) Vertes, A.; Juhasz, P.; De Wolf, M.; Gijbels, R. *Int. J. Mass Spectrom. Ion Process.* **1989**, *94* (1-2), 63. doi:10.1016/0168-1176(89)80060-6.

(36) Jackson, S. N.; Kim, J.-K.; Laboy, J. L.; Murray, K. K. *Rapid Commun. Mass Spectrom.* **2006**, *20* (8), 1299. doi:10.1002/rcm.2443.

(37) Vertes, A.; Juhasz, P.; Balazs, L.; Gijbels, R. *Microbeam Anal.* **1989**, *1989*, 273.

(38) Ehring, H.; Costa, C.; Demirev, P. A.; Sundqvist, B. U. R. *Rapid Commun. Mass Spectrom.* **1996**, *10* (7), 821. doi:10.1002/(SICI)1097-0231(199605)10:7<821::AID-RCM566>3.0.CO;2-A.

(39) Hankin, J. A.; Barkley, R. M.; Murphy, R. C. *J. Am. Soc.*

Can. J. Chem. Downloaded from www.nrcresearchpress.com by Xi'an Jiaotong University on 09/19/12
For personal use only.

Can. J. Chem. Downloaded from www.nrcresearchpress.com by Xi'an Jiaotong University on 09/19/12
For personal use only.

Mass Spectrom. **2007**, *18* (9), 1646. doi:10.1016/j.jasms.2007.06.010.
(40) Karas, M.; Glückmann, M.; Schäfer, J. *J. Mass Spectrom.* **2000**, *35* (1), 1. doi:10.1002/(SICI)1096-9888(200001)35:1<1::AID-JMS904>3.0.CO;2-0 .
(41) Dashtiev, M.; Frankevich, V.; Zenobi, R. *J. Phys. Chem. A* **2006**, *110* (3), 926. doi:10.1021/jp053343y.
(42) Raczyńska, E. D.; Gal, J. F.; Maria, P. C.; Zientara, K.; Szelag, M. *Anal. Bioanal. Chem.* **2007**, *389* (5), 1365. doi:10.1007/s00216-007-1508-4.
(43) Fung, Y. M.; Adams, C. M.; Zubarev, R. A. *J. Am. Chem. Soc.* **2009**, *131* (29), 9977. doi:10.1021/ja8087407.
(44) Liu, B. H.; Lee, Y. T.; Wang, Y. S. *J. Am. Soc. Mass Spectrom.* **2009**, *20* (6), 1078. doi:10.1016/j.jasms.2009.02.012.
(45) Fournier, I.; Brunot, A.; Tabet, J. C.; Bolbach, G. *J. Mass Spectrom.* **2005**, *40* (1), 50. doi:10.1002/jms.772.
(46) Karas, M.; Ehring, H.; Nordhoff, E.; Stahl, B.; Strupat, K.; Hillenkamp, F.; Grehl, M.; Krebs, B. *Org. Mass Spectrom.* **1993**, *28* (12), 1476. doi:10.1002/oms.1210281219.
(47) Frankevich, V.; Zhang, J.; Dashtiev, M.; Zenobi, R. *Rapid Commun. Mass Spectrom.* **2003**, *17* (20), 2343. doi:10.1002/rcm.1194.
(48) Asundi, R. K.; Craggs, J. D. *Proc. Phys. Soc.* **1964**, *83* (4), 611. doi:10.1088/0370-1328/83/4/314.
(49) Lagemann, R. T.; Evans, J. S.; McMillan, D. R. *J. Am. Chem. Soc.* **1948**, *70* (9), 2996. doi:10.1021/ja01189a048.
(50) Grimsrud, E. P.; Chowdhury, S.; Kebarle, P. *J. Chem. Phys.* **1985**, *83* (3), 1059. doi:10.1063/1.449468.
(51) Knochenmuss, R. *Anal. Chem.* **2004**, *76* (11), 3179. doi:10.1021/ac035501s.
(52) Ehring, H.; Karas, M.; Hillenkamp, F. *Org. Mass Spectrom.* **1992**, *27* (4), 472. doi:10.1002/oms.1210270419.
(53) Jaccard, J.; Becker, M. A.; Wood, G. *Psychol. Bull.* **1984**, *96* (3), 589. doi:10.1037/0033-2909.96.3.589.
(54) Przybylski, C.; Gonnet, F.; Bonnaffé, D.; Hersant, Y.; Lortat-Jacob, H.; Daniel, R. *Glycobiology* **2009**, *20* (2), 224. doi:10.1093/glycob/cwp169.
(55) Moon, J. H.; Yoon, S. H.; Kim, M. S. *J. Phys. Chem. B* **2009**, *113* (7), 2071. doi:10.1021/jp810077e.
(56) Lou, X.; van Dongen, J. L.; Vekemans, J. A.; Meijer, E. W. *Rapid Commun. Mass Spectrom.* **2009**, *23* (19), 3077. doi:10.1002/rcm.4224.
(57) Tang, H. W.; Ng, K. M.; Lu, W.; Che, C. M. *Anal. Chem.* **2009**, *81* (12), 4720. doi:10.1021/ac8026367.
(58) Williams, P.; Sundqvist, B. U. R. *Phys. Rev. Lett.* **1987**, *58* (10), 1031. doi:10.1103/PhysRevLett.58.1031.
(59) Kosevich, M. V.; Chagovets, V. V.; Shmigol, I. V.; Snegir, S. V.; Boryak, O. A.; Orlov, V. V.; Shelkovsky, V. S.; Pokrovskiy, V. A.; Gomory, A. *J. Mass Spectrom.* **2008**, *43* (10), 1402. doi:10.1002/jms.1421.
(60) Frankevich, V.; Zenobi, R. *Rapid Commun. Mass Spectrom.* **2001**, *15* (21), 2035. doi:10.1002/rcm.474.
(61) Frankevich, V. E.; Zhang, J.; Friess, S. D.; Dashtiev, M.; Zenobi, R. *Anal. Chem.* **2003**, *75* (22), 6063. doi:10.1021/ac034436j.
(62) Cotter, R. J.; Gardner, B. D.; Iltchenko, S.; English, R. D. *Anal. Chem.* **2004**, *76* (7), 1976. doi:10.1021/ac0349431.
(63) Berkout, V. D. *Anal. Chem.* **2006**, *78* (9), 3055. doi:10.1021/ac060069a.
(64) Young, H. D.; Freedman, R. A. *University Physics with Modern Physics with Mastering Physics;* 11th ed., Chapter 24; New York: Addison Wesley, 2003.
(65) Whittal, R. M.; Russon, L. M.; Weinberger, S. R.; Li, L. *Anal. Chem.* **1997**, *69* (11), 2147. doi:10.1021/ac961151g.
(66) Knochenmuss, R.; McCombie, G.; Faderl, M. *J. Phys. Chem. A* **2006**, *110* (47), 12728. doi:10.1021/jp064760t.
(67) Stevenson, E.; Breuker, K.; Zenobi, R. *J. Mass Spectrom.* **2000**, *35* (8), 1035. doi:10.1002/1096-9888(200008)35:8<1035::AID-JMS34>3.0.CO;2-V.
(68) Bökelmann, V.; Spengler, B.; Kaufmann, R. *Eur. Mass Spectrom.* **1995**, *1* (1), 81. doi:10.1255/ejms.163.
(69) Chan, T.-W. D.; Thomas, I.; Colburn, A. W.; Derrick, P. J. *Chem. Phys. Lett.* **1994**, *222* (6), 579. doi:10.1016/0009-2614(94)00385-8.
(70) Penn, S. G.; Cancilla, M. T.; Lebrilla, C. B. *Anal. Chem.* **1996**, *68* (14), 2331. doi:10.1021/ac960155i.
(71) Knochenmuss, R.; Dubois, F.; Dale, M. J.; Zenobi, R. *Rapid Commun. Mass Spectrom.* **1996**, *10* (8), 871. doi:10.1002/(SICI)1097-0231(19960610)10:8<871::AID-RCM559>3.0.CO;2-R.
(72) Allwood, D. A.; Dyer, P. E.; Dreyfus, R. W. *Appl. Surf. Sci.* **1997**, *11*, 499.
(73) Koubenakis, A.; Frankevich, V.; Zhang, J.; Zenobi, R. *J. Phys. Chem. A* **2004**, *108* (13), 2405. doi:10.1021/jp037811k.
(74) Kruse, R. A.; Li, X.; Bohn, P. W.; Sweedler, J. V. *Anal. Chem.* **2001**, *73* (15), 3639. doi:10.1021/ac010317x.
(75) Lide, D. R. Ed.; *Handbook of Chemistry and Physics;* 90th ed., Section 4; Boca Raton: CRC Press, Boca Raton, FL, 2009.
(76) Kraft, P.; Alimpiev, S.; Dratz, E.; Sunner, J. *J. Am. Soc. Mass Spectrom.* **1998**, *9* (9), 912. doi:10.1016/S1044-0305(98)00063-4.
(77) Garrell, R. L. *Anal. Chem.* **1989**, *61* (6), 401A. doi:10.1021/ac00181a001.
(78) Bermond, J. M.; Lenoir, M.; Prulhiére, J. P.; Drechsler, M. *Surf. Sci.* **1974**, *42* (1), 306. doi:10.1016/0039-6028(74)90018-1.
(79) Beavis, R. C. *Org. Mass Spectrom.* **1992**, *27* (8), 864. doi:10.1002/oms.1210270804.
(80) Erb, W. J. *Exploration of the Fundamentals of Matrix Assisted Laser Desorption/Ionization Time-of-Flight Mass Spectrometry;* Ph.D. Thesis, Chapter 2; Drexel University, Philadelphia, PA, 2007.
(81) Knochenmuss, R.; Stortelder, A.; Breuker, K.; Zenobi, R. *J. Mass Spectrom.* **2000**, *35* (11), 1237. doi:10.1002/1096-9888(200011)35:11<1237::AID-JMS74>3.0.CO;2-O.
(82) McCombie, G.; Knochenmuss, R. *J. Am. Soc. Mass Spectrom.* **2006**, *17* (5), 737. doi:10.1016/j.jasms.2006.02.005.
(83) Sunner, J.; Dratz, E.; Chen, Y.-C. *Anal. Chem.* **1995**, *67* (23), 4335. doi:10.1021/ac00119a021.
(84) Cooks, R. G.; Busch, K. L. *Int. J. Mass Spectrom. Ion Process.* **1983**, *53*, 111. doi:10.1016/0020-7381(83)85106-7.
(85) Day, R. J.; Unger, S. E.; Cooks, R. G. *Anal. Chem.* **1980**, *52* (4), 557. doi:10.1021/ac50054a002.

Flavanone glucuronides from the leaves of *Garcinia prainiana*

Saranyoo Klaiklay, Yaowapa Sukpondma, Vatcharin Rukachaisirikul, Nongporn Hutadilok-Towatana, and Kanokphorn Chareonrat

Can. J. Chem. Downloaded from www.nrcresearchpress.com by Xi'an Jiaotong University on 09/19/12
For personal use only.

Abstract: Phytochemical investigation of *Garcinia prainiana*'s leaves led to the isolation of prainianonide (**1**), a new flavanone glucuronide, together with six known compounds: (2*S*)-eriodictyol 7-*O*-β-D-glucuronide (**2**), naringenin 7-*O*-β-D-glucuronide (**3**), (–)-GB-1a (**4**), (+)-morelloflavone (**5**), amenthoflavone (**6**), and friedelin (**7**). Their structures were elucidated by spectroscopic methods. The absolute configuration of **1** was determined by circular dichroism spectroscopy. Compounds **4** and **5** showed significant antioxidant activity.

Key words: Garcinia prainiana, Guttiferae, flavanone glucuronide, biflavonoid, antioxidant.

Résumé : Une étude phytochimique des feuilles de *Garcinia prainiana* a permis d'isoler le prainianonide (**1**), un nouveau glucuronide de flavanone ainsi que six nouveaux composés : le 7-*O*-β-D-glucuronide du (2*S*)-ériodictyol (**2**), le 7-*O*-β-D-glucuronide du de la naringénine (**3**), le (–)-GB-1a (**4**), la (+)-morelloflavone (**5**), l'amenthoflavone (**6**) et la friedéline (**7**). Leurs structures ont été élucidées par des méthodes spectroscopiques. La configuration absolue du composé **1** a été déterminée par spectroscopie de dichroïsme circulaire. Les composés **4** et **5** présentent une activité antioxydante significative.

Mots-clés : Garcinia prainiana, Guttiferae, glucuronide de flavanone, biflavonoïde, antioxydant.

[Traduit par la Rédaction]

Introduction

Plants in the genus *Garcinia* are known to be a rich source of bioactive compounds such as xanthones,[1–3] biflavonoids,[4,5] benzophenones,[5] benzoquinones,[6] and triterpenes.[7,8] Some of them have shown a wide range of biological activities including antibacterial,[1,6] antifungal,[9] antioxidant,[3,10] and cytotoxic[5,11] effects. In our ongoing effort to search for biologically active substances from *Garcinia* plants, we found that the crude methanol extract from the leaves of *G. prainiana* showed significant antioxidant activity. *Garcinia prainiana*, locally named Chu-pu, is distributed in the southern part of Thailand. This plant is a small tree with a berrylike fruit. Its ripe fruits are edible and used for lowering blood pressure.[12] In this paper, we describe the isolation and structural elucidation of one new flavanone glucuronide together with six known compounds and their antioxidant activity.

Results and discussion

The crude methanol extract from the leaves of *G. prainiana* was subjected to chromatographic techniques to yield one new flavanone glucuronide, prainianonide (**1**), as well as two known flavanone glucuronides, (2*S*)-eriodictyol 7-*O*-β-D-glucuronide (**2**)[13] and naringenin 7-*O*-β-D-glucuronide (**3**),[14] three biflavonoids, (–)-GB-1a (**4**),[15] (+)-morelloflavone (**5**),[16] and amenthoflavone (**6**),[17] and friedelin (**7**) (Chart 1).[18] The structure of **1** was determined by analysis of one- and two-dimensional NMR spectroscopic data, while the known compounds were identified by comparison of the NMR data, especially ^{1}H and ^{13}C NMR data, with previously reported data (see Supplementary data). The absolute configurations of **1** and **2** were assigned by circular dichroism (CD) spectroscopy. This is the first report on the isolation of a flavanone glucuronide from the genus *Garcinia*.

Prainianonide (**1**) was isolated as a pale yellow gum. Its molecular formula, $C_{22}H_{22}O_{11}$, was deduced by high-resolution electron impact mass spectrometry (HR-EI-MS) (*m*/*z* 462.1144 $[M]^+$ (calcd. 462.1162)). The UV spectrum showed characteristic absorption bands of a flavanone chromophore at 283 and 337 nm.[19] The IR spectrum showed absorption bands for a hydroxyl group (3422 cm^{-1}), an ester carbonyl group (1716 cm^{-1}), and a flavanone carbonyl group (1644 cm^{-1}). The ^{1}H NMR spectrum (Table 1) displayed AA′BB′ signals at δ 7.33 and 6.82 (2H each, d, J = 8.4 Hz), two meta-coupled signals at δ 6.16 and 6.17 (1H each, brs), an oxymethine proton signal at δ 5.39 (1H, dd, J = 13.2, 2.7 Hz), and methylene proton signals at δ 3.18 (1H, dd, J = 17.1, 13.2 Hz) and 2.75 (1H, dd, J = 17.1, 2.4 Hz). These data indicated that **1** had a 4′,5,7-trihydroxyflavanone

Received 6 August 2010. Accepted 22 November 2010. Published on the NRC Research Press Web site at canjchem.nrc.ca on 11 March 2011.

S. Klaiklay, Y. Sukpondma,[1] and V. Rukachaisirikul. Department of Chemistry and Center for Innovation in Chemistry, Faculty of Science, Prince of Songkla University, Hat Yai 90112, Thailand.
N. Hutadilok-Towatana. Department of Biochemistry, Faculty of Science, Prince of Songkla University, Hat Yai 90112, Thailand.
K. Chareonrat. Srinagarindra The Princess Mother School Phuket, Phuket 83000, Thailand.

[1]Corresponding author (e-mail: yaowapa.suk@psu.ac.th).

Can. J. Chem. Downloaded from www.nrcresearchpress.com by Xi'an Jiaotong University on 09/19/12
For personal use only.

Chart 1.

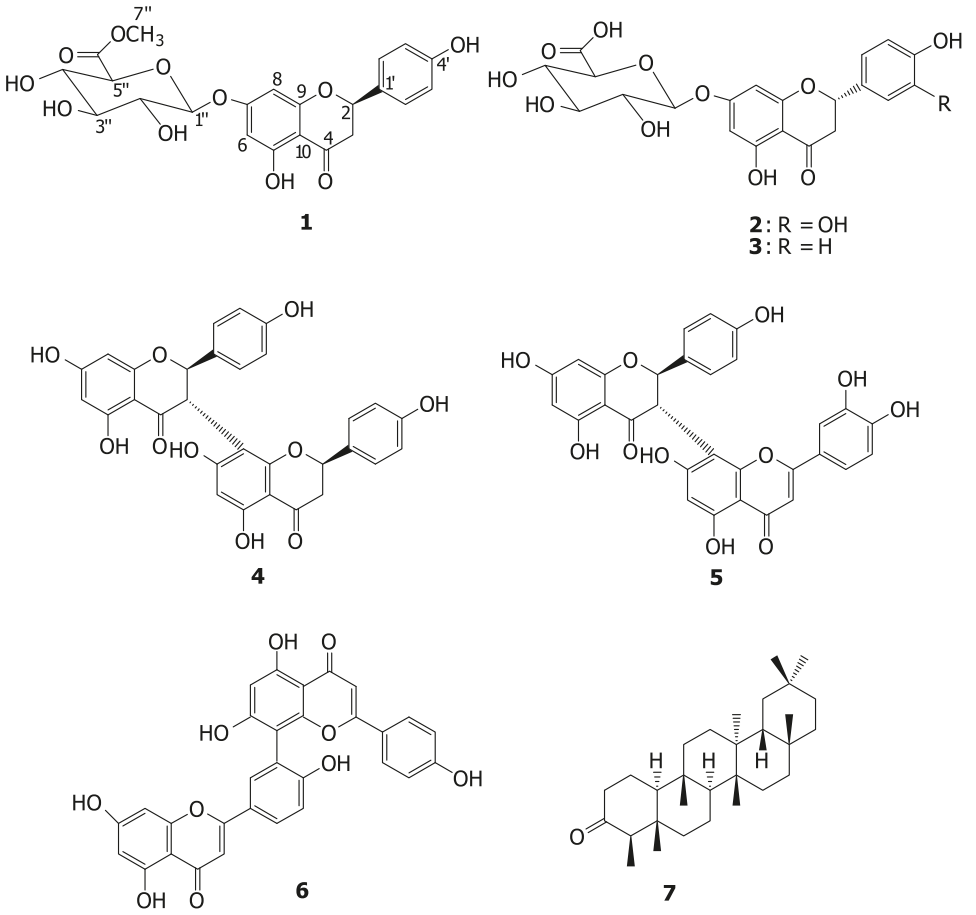

skeleton.[20] In addition, the ^{1}H NMR data (Table 1) showed signals of a sugar unit (δ 5.07 (1H, d, J = 7.2 Hz), 4.09 (1H, d, J = 9.6 Hz), 3.60 (1H, t, J = 9.6 Hz), 3.49 (1H, dd, J = 9.6, 7.2 Hz), 3.47 (1H, t, J = 9.6 Hz)) and a methoxyl signal at δ 3.76 (3H, s). The ^{13}C NMR spectrum (Table 1) showed the presence of one ester carbonyl carbon (δ 169.4). A heteronuclear multiple bond correlation (HMBC) between the methoxy protons (δ 3.76) and the ester carbonyl carbon (δ 169.4) indicated the presence of a methyl ester group. This methyl ester group was connected to C-5″ (δ 75.2) of a sugar moiety, which was determined by HMBC of H-5″ (δ 4.09) / C-6″ (δ 169.4). From these results, the sugar moiety was identified as a methyl ester of glucuronic acid.[13] The anomeric proton of the glucuronic acid at δ 5.07 with a large coupling constant of 7.2 Hz implied that this unit must have a β-glucuronide form.[13] Irradiation of H-5″ affected signal intensities of both H-1″ (δ 5.07) and H-3″ (δ 3.47), supporting the assigned stereochemistry of the glucuronide unit. A cross peak in the HMBC spectrum between H-1″ of the glucuronide unit and C-7 (δ 165.1) of the flavanone skeleton indicated the attachment of the glucuronide unit to the 7-hydroxyl group of the flavanone moiety. The absolute configuration of **1** was assigned by CD spectroscopy. Its CD spectrum showed positive Cotton effects (249 (Δε –5.84), 290 (Δε +2.35) nm), indicating that the absolute configuration of the 2-position is an *R* orientation, which was supported by comparison with positive (252 (Δε –1.00), 292 (Δε +3.66) nm) and negative Cotton effects (250

Table 1. ^{1}H and ^{13}C NMR spectral data of **1** in CD_3OD and major correlations.

Position	δ_H, mult, J (in Hz)	δ_C	HMBC
2	5.39, dd, 13.2, 2.7	79.3	C-4, C-9, C-2′,6′
3	3.18, dd, 17.1, 13.2	42.8	C-10, C-1′
	2.75, dd, 17.1, 2.4		
4		197.2	
5		163.6	
6	6.17, brs	96.5	C-8, C-10
7		165.1	
8	6.16, brs	95.4	C-6, C-10
9		163.2	
10		103.7	
1′		129.4	
2′, 6′	7.33, d, 8.4	127.7	C-2, C-4′
3′, 5′	6.82, d, 8.4	114.9	C-1′, C-4′
4′		157.7	
1″	5.07, d, 7.2	99.6	C-7
2″	3.49, dd, 9.6, 7.2	75.6	C-3″, C-4″
3″	3.47, t, 9.6	72.9	C-1″, C-2″, C-4″
4″	3.60, t, 9.6	71.4	C-2″
5″	4.09, d, 9.6	75.2	C-1″, C-4″, C-6″
6″		169.4	
7″	3.76, s	51.5	C-6″

Can. J. Chem. Downloaded from www.nrcresearchpress.com by Xi'an Jiaotong University on 09/19/12
For personal use only.

(Δε +1.43), 293 (Δε –3.48) nm) of (2*R*)-eriodictyol 7-*O*-β-D-glucuronide and (2*S*)-eriodictyol 7-*O*-β-D-glucuronide (**2**), respectively.[13] Therefore, **1** was characterized as (2*R*)-4,5-dihydroxyflavanone 7-*O*-β-glucuronide methyl ester, a new flavanone glucuronide.

Compounds **1**–**6** were examined for their antioxidant activity against DPPH (diphenylpicrylhydrazyl) radicals, while compound **7** was not tested owing to the lack of phenolic moiety. Compounds **4** and **5** showed higher radical scavenging potency than the standard (butylated hydroxyanisole), with IC_{50} values (concentration required to reduce DPPH radicals by 50%) of 148 and 72 μmol/L, respectively (Table 2). Compound **2** was much less active, with an IC_{50} value of 841 μmol/L. The radical trapping potency of morelloflavone (**5**), which was twofold higher than that of GB-1a (**4**), was mainly due to the presence of *ortho*-dihydroxy groups in its B ring, a structural feature required for effective radical scavenging.[21] Compound **5**, however, has been shown to be a potent antioxidant in various studies.[22,23] In comparison with the biflavonoids (**4** and **5**), the flavanone glucuronide (**2**) seemed to be a poor scavenger. As the 5,7-dihydroxy moiety in the A ring is known to have a strong influence on the total antioxidant activity of flavonoids,[21] thus blocking the 7-position by glycosylation and containing only a single hydroxyl substituent at position 5 in the A ring, compound **2** became an ineffective hydrogen donor in this chemical arrangement.

Table 2. Antioxidant activity of compounds **1**–**6**.

	DPPH•
Compound	IC_{50} (μmol/L)
1	—[a]
2	841
3	—[a]
4	148
5	72
6	—[a]
BHA[b]	167

[a]Inactive.
[b]Butylated hydroxyanisole.

Experimental

General

The infrared (IR) spectra were recorded neat using a PerkinElmer 783 FTS165 FTIR spectrometer. The ultraviolet (UV) absorption spectra were measured on a SHIMADZU UV-160A spectrophotometer. ^1H and ^{13}C NMR spectra were recorded on a 300 MHz Bruker FTNMR Ultra Shield spectrometer in deuterochloroform solution with tetramethylsilane as an internal standard. The EI and HR-EI mass spectra were obtained on a MAT 95 XL mass spectrometer (Thermofinnigan). Optical rotation was measured on a JASCO P-1020 polarimeter. CD spectra were recorded on a JASCO J-810 spectropolarimeter. Thin-layer chromatography was performed on silica gel 60 GF_{254} (Merck). Column chromatography (CC) was carried out on Sephadex LH-20, silica gel (Merck) type 60 (230–400 mesh ASTM) or type 100 (70–230 mesh ASTM), or reverse phase C-18 silica gel. Light petroleum had a bp of 40–60 °C.

Plant material

The leaves of *G. prainiana* were collected in Narathiwat Province, Thailand. The voucher specimens (K.Maneenoon2010-001-003) were deposited in the Herbarium at the Department of Biology, Faculty of Science, Prince of Songkla University, Hat Yai, Songkhla, Thailand.

Extraction and isolation

The leaves of *G. prainiana* (0.80 kg), cut into small segments, were extracted with MeOH three times over a period of 7 days at room temperature. After filtration, the filtrate was evaporated to dryness under reduced pressure to give a crude methanol extract as a dark brown gum (56.2 g). The resulting residue was subjected to CC over Sephadex LH-20 with MeOH to afford four fractions (G1–G4). Fraction G3 (1.01 g) was dissolved with CH_2Cl_2 to provide soluble (G3D) and insoluble (G3N) fractions. Fraction G3D (399.6 mg) was subjected to CC over silica gel with a gradient of CH_2Cl_2/petroleum ether (1:1) to provide **7** (73.4 mg). Fraction G4 (2.7 g) was subjected to CC over reverse phase silica gel with a gradient of MeOH/H_2O (1:1) to provide five subfractions (G4A–G4E). Subfraction G4A (260.2 mg) was chromatographed using CC over reverse phase silica gel with a gradient of MeOH/H_2O (1:4) to produce **2** (14.1 mg). Subfraction G4B (31.2 mg) was separated by CC over reverse phase silica gel with a gradient of MeOH/H_2O (2:3) to provide four subfractions (G4B1–G4B4). Subfraction G4B1 (15.6 mg) was further subjected to CC over reverse phase silica gel with a gradient of MeOH/H_2O (1:4) to provide **3** (4.3 mg). Subfractions G4B3 (25.9 mg) and G4B4 (34.7 mg) were chromatographed using CC over Sephadex LH-20 with MeOH/CH_2Cl_2 to produce **1** (3.9 mg) and **4** (8.7 mg), respectively. Subfraction G4D (69.5 mg) was purified by CC over reverse phase silica gel with a gradient of MeOH/H_2O (6:4) to afford **5** (25.3 mg). Subfraction G4E (67.1 mg) was subjected to CC over reverse phase silica gel with a gradient of MeOH/H_2O (6:4) followed by CC over Sephadex LH-20 using MeOH/CH_2Cl_2 to produce **6** (4.0 mg).

Prainianonide (1)

Pale yellow gum. $[\alpha]_D^{26}$ –26.0° (*c* 0.20, MeOH). UV (MeOH) (nm, log ε): 337 (2.14), 283 (3.63), 224 (3.81). FTIR (neat, cm^{-1}): 3422, 1716, 1644. CD (MeOH) (nm, Δε): 249 (–5.84), 290 (+2.35). ^1H NMR (300 MHz, CD_3OD) and ^{13}C NMR (75 MHz, CD_3OD) data: see Table 1. EI-MS *m*/*z*: 462 $[M]^+$ (3), 272 (100), 254 (7), 179 (27), 166 (36), 153 (86), 120 (57), 107 (23). HR-EI-MS *m*/*z*: 462.1144 $[M]^+$ (calcd. for $C_{22}H_{22}O_{11}$: 462.1162).

Determination of antioxidant activity

DPPH radical scavenging assay

The DPPH radical scavenging assay was carried out in triplicate, based on the method used by Hutadilok-Towatana et al.[24] BHA (butylated hydroxyanisole), a positive control, gave an IC_{50} value of 167 μmol/L. The DPPH radical scav-

enging ability was calculated based on the concentration of sample required to reduce DPPH radicals by 50% (IC_{50}).

Supplementary data

Supplementary data are available with the article through the journal Web site (www.nrcresearchpress.com/cjc).

Acknowledgements

V.R. thanks the Commission on Higher Education and the Thailand Research Fund (TRF) for the TRF Research-Team Promotion Grant (No. RTA5180007). S.K. thanks the Center for Innovation in Chemistry and K.C. thanks the Science, Mathematics and Technology Excellence Development Project; the Teacher Professional Development Project for scholarships. Finally, Y.S. is grateful to Dr. Katesarin Maneenoon for collecting the plant, Assistant Professor Dr. Tiengthong Thongpanchang for recording CD spectra, and the Graduate School, Prince of Songkla University, for partial support.

References

(1) Rukachaisirikul, V.; Kaewnok, W.; Koysomboon, S.; Phongpaichit, S.; Taylor, W. C. *Tetrahedron* **2000**, *56* (43), 8539. doi:10.1016/S0040-4020(00)00778-X.

(2) Rukachaisirikul, V.; Painuphong, P.; Sukpondma, Y.; Koysomboon, S.; Sawangchote, P.; Taylor, W. C. *J. Nat. Prod.* **2003**, *66* (7), 933. doi:10.1021/np030080v.

(3) Rukachaisirikul, V.; Naklue, W.; Phongpaichit, S.; Towatana, N. H.; Maneenoon, K. *Tetrahedron* **2006**, *62* (36), 8578. doi:10.1016/j.tet.2006.06.059.

(4) Parveen, M.; Ilyas, M.; Mushfiq, M.; Busudan, O. A.; Muhaisen, H. M. H. *Nat. Prod. Res.* **2004**, *18* (3), 269. doi:10.1080/14786410310001620574.

(5) Yang, H.; Figueroa, M.; To, S.; Baggett, S.; Jiang, B.; Basile, M. J.; Weinstein, I. B.; Kennelly, E. J. *J. Agric. Food Chem.* **2010**, *58* (8), 4749. doi:10.1021/jf9046094.

(6) Rukachaisirikul, V.; Trisuwan, K.; Sukpondma, Y.; Phongpaichit, S. *Arch. Pharm. Res.* **2008**, *31* (1), 17. doi:10.1007/s12272-008-1114-9.

(7) Rukachaisirikul, V.; Pailee, P.; Hiranrat, A.; Tuchinda, P.; Yoosook, C.; Kasisit, J.; Taylor, W. C.; Reutrakul, V. *Planta Med.* **2003**, *69* (12), 1141. doi:10.1055/s-2003-818006.

(8) Rukachaisirikul, V.; Saelim, S.; Karnsomchoke, P.; Phongpaichit, S. *J. Nat. Prod.* **2005**, *68* (8), 1222. doi:10.1021/np050131j.

(9) Mackeen, M. M.; Ali, A. M.; Lajis, N. H.; Kawazu, K.; Kikuzaki, H.; Nakatani, N. *Z. Naturforsch.* **2002**, *57c* (3/4), 291.

(10) Panthong, K.; Hutadilok-Towatana, N.; Panthong, A. *Can. J. Chem.* **2009**, *87* (11), 1636. doi:10.1139/V09-123.

(11) Suksamrarn, S.; Komutiban, O.; Ratananukul, P.; Chimnoi, N.; Lartpornmatulee, N.; Suksamrarn, A. *Chem. Pharm. Bull. (Tokyo)* **2006**, *54* (3), 301. doi:10.1248/cpb.54.301.

(12) Whitmore, T. C. *Tree Flora of Malaya;* Wing Tai Cheung Printing Co. Ltd.: Hong Kong, 1972; Vol. 2, pp 220.

(13) Matsuda, H.; Morikawa, T.; Toguchida, I.; Harima, S.; Yoshikawa, M. *Chem. Pharm. Bull. (Tokyo)* **2002**, *50* (7), 972. doi:10.1248/cpb.50.972.

(14) Yoshimura, M.; Sano, A.; Kamei, J.-I.; Obata, A. *J. Agric. Food Chem.* **2009**, *57* (14), 6432. doi:10.1021/jf901137x.

(15) Terashima, K.; Kondo, Y.; Aqil, M.; Waziri, M.; Niwa, M. *Heterocycles* **1999**, *50* (1), 283. doi:10.3987/COM-98-S(H)40.

(16) Li, X.-C.; Joshi, A. S.; Tan, B.; Elsohly, H. N.; Walker, L. A.; Zjawiony, J. K.; Ferreira, D. *Tetrahedron* **2002**, *58* (43), 8709. doi:10.1016/S0040-4020(02)01096-7.

(17) Gonçalez, E.; Felicio, J. D.; Pinto, M. M. *Braz. J. Med. Biol. Res.* **2001**, *34* (11), 1453. doi:10.1590/S0100-879X2001001100013.

(18) LeFevre, J.; McNeill, K. I.; Moore, J. L. *J. Chem. Educ.* **2001**, *78* (4), 535. doi:10.1021/ed078p535.

(19) Cui, C.-B.; Tezuka, Y.; Kikuchi, T.; Nakano, H.; Tamaoki, T.; Park, J.-H. *Chem. Pharm. Bull. (Tokyo)* **1990**, *38* (12), 3218.

(20) Jeon, S. H.; Chun, W.; Choi, Y. J.; Kwon, Y. S. *Arch. Pharm. Res.* **2008**, *31* (8), 978. doi:10.1007/s12272-001-1255-9.

(21) Rice-Evans, C. A.; Miller, N. J.; Paganga, G. *Free Radic. Biol. Med.* **1996**, *20* (7), 933. doi:10.1016/0891-5849(95)02227-9.

(22) Sanz, M. J.; Ferrandiz, M. L.; Cejudo, M.; Terencio, M. C.; Gil, B.; Bustos, G.; Ubeda, A.; Gunasegaran, R.; Alcaraz, M. J. *Xenobiotica* **1994**, *24* (7), 689. doi:10.3109/00498259409043270.

(23) Hutadilok-Towatana, N.; Kongkachuay, S.; Mahabusarakam, W. *Nat. Prod. Res.* **2007**, *21* (7), 655. doi:10.1080/14786410701371256.

(24) Hutadilok-Towatana, N.; Chaiyamutti, P.; Panthong, K.; Mahabusarakam, W.; Rukachaisirikul, V. *Pharm. Biol* **2006**, *44* (3), 221. doi:10.1080/13880200600685592.

Can. J. Chem. Downloaded from www.nrcresearchpress.com by Xi'an Jiaotong University on 09/19/12
For personal use only.

Metallacarboranes for the labelling of DNA — Synthesis of oligonucleotides bearing a 3,3′-iron-1,2,1′,2′-dicarbollide complex

Agnieszka B. Olejniczak

Can. J. Chem. Downloaded from www.nrcresearchpress.com by Xi'an Jiaotong University on 09/19/12
For personal use only.

Abstract: The present work reports the efficient synthesis of oligonucleotides bearing metallacarborane complexes containing iron (3,3′-iron-1,2,1′,2′-dicarbollide) on a solid support via the H-phosphonate method. This versatile methodology can be applied to the synthesis of DNA oligomers bearing various metallacarborane units.

Key words: metallacarborane, oligonucleotide, modified oligonucleotide, H-phosphonate chemistry.

Résumé : Dans ce travail, on rapporte la synthèse efficace d'oligonucléotides portant des métallacarboranes contenant du fer (3,3′-fer-1,2,1′2′-dicarbollide) sur un support solide en faisant appel à la méthode du H-phosphonate. Cette méthodologie versatile peut être appliquée à la synthèse d'oligomères de l'ADN portant diverses unités métallacarboranes.

Mots-clés : métallacarborane, oligonucléotide, oligonucléotide modifié, chimie du H-phosphonate.

[Traduit par la Rédaction]

Introduction

Metal- and metalloid-containing nucleic acids exhibit a wide range of biological and physicochemical activities, some of which have been employed in molecular medicine, diagnostics, and technology, providing a variety of advantages. The applications of metal-labelled nucleic acids include electrochemically detectable probes, fluorescent probes, artificial "chemical nucleases", probes for DNA-mediated electron transfer, and "molecular wires" in bioelectrochemical devices.[1,2] Among several types of nucleic acid modifications with metals, two general classes can be distinguished. In the first class, metal ions form a complex directly with DNA; in the second class, the metal is attached to the DNA as part of a metal carrier, usually a metal complex or a metallo-organic substituent.[2]

We have focused on the second class of metal-containing DNAs, using metallacarboranes as the metal carriers. Metallacarboranes are a family of metallocene-type complexes consisting of at least one carborane cage and one or more metal atoms. Carborane clusters are versatile and efficient ligands for metals such as Co, Fe, Ni, Cr, Mn, Re, Au, Cu, Ir, and Pt and can be used to incorporate a wide variety of other metals with different properties into nucleic acids, nucleic acid components, and other biomolecules.[3,4]

The rationale for this study of the synthesis of DNA oligomers labelled with a metal complex bearing iron was the potential use of this type of modification as redox-active probes for electrochemical DNA detection and the central component of DNA biosensors. The number of metal complexes tested for this purpose is limited, with the best-known example being ferrocene, a metallocene-type complex.[5,6] The only other examples of a nucleoside–metallocene conjugate reported so far are nucleoside–metallacarborane modifications.[2] In the present work, a metallacarborane label containing iron was selected because of its analogy to ferrocene and because of the favorable electrochemical characteristics of iron. The study of metallacarborane redox labels bearing other metals is ongoing in our laboratory.

Results and discussion

A modified nucleoside derivative of 2′-deoxyadenosine was used as a monomer. 5′-*O*-Dimethoxytrityl-6-*N*-{5-[(3,3′-iron-1,2,1′,2′-dicarbollide)-8-yl]-3-oxa-pentoxy}-2′-deoxyadenosine (**6**) was obtained as described (Scheme 1).[7]

Briefly, the 5′- and 3′-hydroxyl groups of 2′-deoxyadenosine (**1**) were protected. For that purpose, *tert*-butyldimethylsilyl (TBDMS) protection was used for both hydroxyl groups, providing 3′,5′-*O*,*O*-di(*tert*-butyldimethylsilyl)-2′-deoxyadenosine (**2**).[8] In the second step, **2** was activated with a 2.5-fold molar excess of sodium hydride and then treated with a 1.5-fold molar excess of the 8-dioxane-(3,3′-iron-1,2,1′,2′-dicarbollide) adduct [8-O(CH_2CH_2)$_2$O-1,2-$C_2B_9H_{10}$-3,3′-Fe-1′,2′-$C_2B_9H_{11}$] (**3**).[7,9] Compound **3**[10] can be easily prepared from 3,3′-iron-1,2,1′,2′-dicarbollide[11] and dioxane. In the third step, the TBDMS protective groups in **4** were removed with tetrabutylammonium fluoride (TBAF), providing the metallacarborane–nucleoside conjugate 6-*N*-{5-[(3,3′-iron-1,2,1′,2′-dicarbollide)-8-yl]-3-oxa-pentoxy}-2′-deoxyadenosine (^{BEFeC}A, **5**). Finally, the 5′-hydroxyl group in **5** was protected with a dimethoxytrityl group (DMT) under standard conditions,[12] yielding 5′-*O*-dimethoxytrityl 6-*N*-{5-

Received 25 August 2010. Accepted 30 November 2010. Published on the NRC Research Press Web site at canjchem.nrc.ca on 17 March 2011.

A.B. Olejniczak. Laboratory of Molecular Virology and Biological Chemistry, Institute for Medical Biology of the Polish Academy of Sciences, 106 Lodowa Street, 93-232 Łódź, Poland (e-mail: aolejniczak@cbm.pan.pl).

Scheme 1. (i) TBDMSCl, DMF, imidazole. (ii) NaH/toluene, **3**, 70 °C. (iii) TBAF/THF. (iv) DMTCl, pyridine. (v) PCl_3, imidazole, Et_3N, CH_2Cl_2, –40 °C.

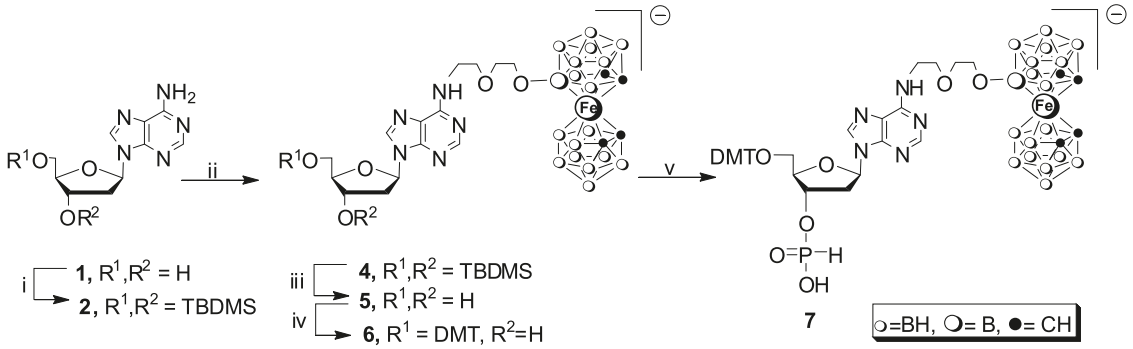

Scheme 2. (i) Detritylation: 3% DCA in CH_2Cl_2. (ii) Coupling: unmodified monomers, phosphoramidite chemistry. (iii) Oxidation: 0.1 mol/L I_2 in THF/pyridine/H_2O (13:6:1); capping: 1 mol/L $(CH_3CO)_2O$ in THF/pyridine (1:8) and 0.5 mol/L DMAP in THF. (iv) Coupling: modified monomer **7**, H-phosphonate chemistry. (v) Oxidation: 10% H_2O in CCl_4, triethylamine, *N*-methylimidazole (9.0:0.5:0.5). (vi) Cleavage from the support: 30% NH_3 aq., 1 h, RT. (vii) Base deprotection: 30% NH_3 aq., 2 h, 50 °C.

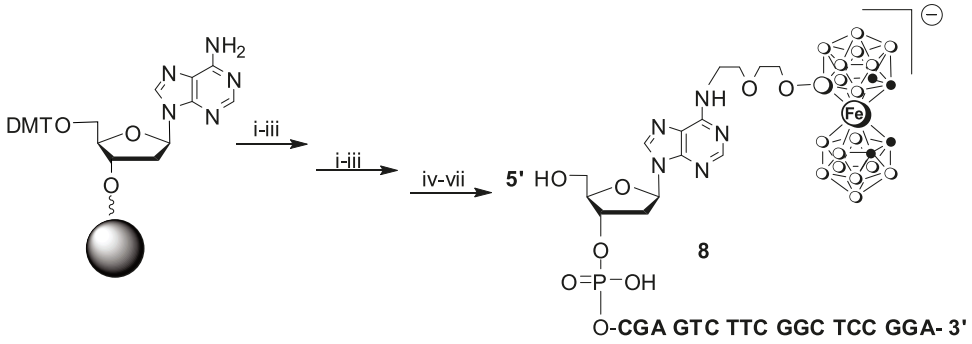

[(3,3′-iron-1,2,1′,2′-dicarbollide)-8-yl]-3-oxa-pentoxy}-2′-deoxyadenosine (**6**).

A sequence complementary to a fragment of the UL55 gene of human cytomegalovirus was selected as a model oligonucleotide. The modified oligomer containing the 3,3′-iron-1,2,1′,2′-dicarbollide at the 5′ end, ^{BEFeC}ACGAGTCTTCGGCTCCGGA-3′, was prepared by solid-phase synthesis (Scheme 2).

The unmodified part of the oligonucleotide was synthesized using phosphoramidite chemistry, a β-cyanoethyl cycle,[13] and an automated DNA synthesizer. A manual step and H-phosphonate chemistry were used to add the modified monomer bearing the (3,3′-iron-1,2,1′,2′-dicarbollide)-8-yl group.[7,14] Phosphoramidite chemistry was originally designed for the incorporation of conjugate **5** into an oligonucleotide according to the methodology developed by us for the analogous modification with cobalt.[15] Unfortunately, the phosphitylation of **6** with (β-cyanoethoxy)(*N*,*N*-diisopropylamino)chlorophosphine under standard conditions proved to be more challenging than expected and the reaction produced several unidentified phosphorus-containing products. Therefore, H-phosphonate chemistry, which has been used previously for the solution-phase synthesis of metallacarborane-containing dinucleotides,[7] was employed.

The key intermediate, 5′-*O*-dimethoxytrityl 6-*N*-{5-[(3,3′-iron-1,2,1′,2′-dicarbollide)-8-yl]-3-oxa-pentoxy}-2′-deoxyadenosine 3′-*O*-(H-phosphonate) (**7**), was obtained using the PCl_3–triazole method.[16] After cooling a solution of imidazole, triethylamine, and phosphorus trichloride in methylene chloride to –40 °C, a solution of **6** in the same solvent was added. After the reaction was complete, a solution of triethylammonium bicarbonate (TEAB) buffer was added, and the mixture was allowed to warm to room temperature. After a standard work-up, the product was isolated by silica gel column chromatography.

The modified oligonucleotide **8** was prepared as follows. After completion of the synthesis of the unmodified part of the oligonucleotide, the column was detached from the DNA synthesizer and the oligomer was manually detritylated.

H-phosphonate-modified **7** was dissolved in a mixture of anhydrous pyridine–acetonitrile, activated with pivaloyl chloride (PvCl), and then applied to the column. The coupling step was repeated three times, and each coupling reaction was performed for 10 min. Owing to the limited stability of **7** bearing the 3,3′-iron-1,2,1′,2′-dicarbollide modification in the presence of the PvCl present in the solution containing pyridine, a fresh solution of the activated monomer was prepared for each subsequent coupling reaction. The final oxidation step was performed using an oxidizing solution containing 10% H_2O in CCl_4, triethylamine, and *N*-methylimidazole.[14] Cleavage of the completed oligomer from the support was performed according to the standard procedure. The deprotection with 30% aqueous ammonia solution was shortened to 2 h at 50 °C without any adverse effect on the deprotection efficacy. Deprotected metalated oligonucleotide **8** was characterized by reverse-phase HPLC

Can. J. Chem. Downloaded from www.nrcresearchpress.com by Xi'an Jiaotong University on 09/19/12
For personal use only.

Fig. 1. MALDI-TOF for modified oligonucleotide **8** bearing a metallacarborane group.

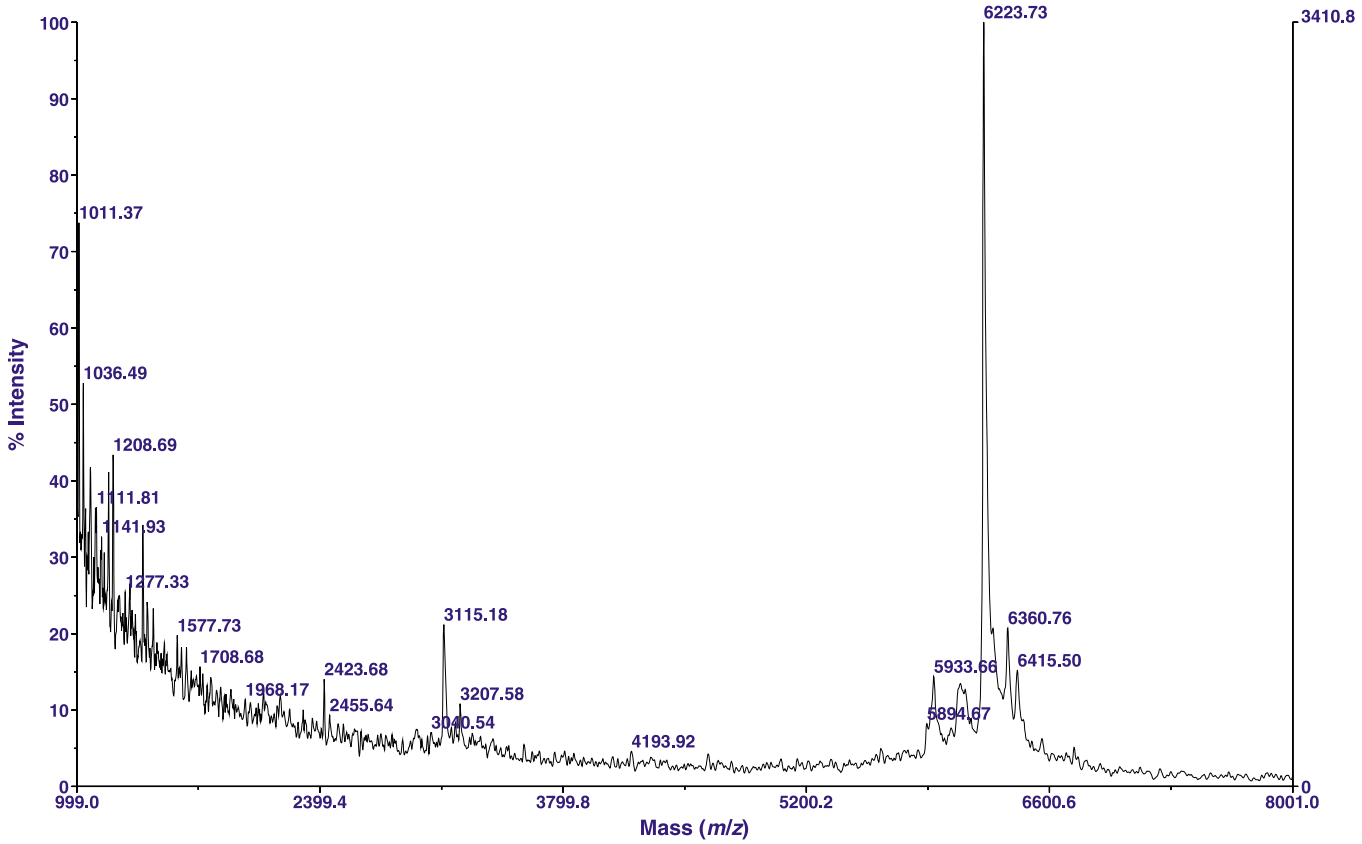

(RP-HPLC), MALDI-TOF (Fig. 1), and UV spectrophotometry.

Because of the presence of the amphiphilic metallacarborane group, oligonucleotide **8** showed highly increased lipophilicity as measured by the retention time on the RP-HPLC column. The usefulness and diagnostic value of UV spectra in the case of nucleoside conjugates bearing metallacarboranes should be noted. UV detection during HPLC analysis can be conducted at λ = 268 nm (for oligonucleotides) and at λ = 310 nm, the characteristic wavelength for the metallacarborane modification.

Enzymatic digestion of oligomer **8** with snake venom phosphodiesterase (CVPD) was performed. RP-HPLC analysis of the digestion products showed the presence of unmodified nucleosides at the expected ratio and modified nucleoside **5** (Fig. 2).

The purity of oligomer **8** was confirmed additionally by electrophoresis using 20% polyacrylamide gel containing 7 mol/L urea (PAGE) (Fig. 3). The PAGE analysis showed the expected diagnostic spot corresponding to the modified oligonucleotide **8**.

In summary, we have developed a new type of modified oligonucleotide bearing a metallacarborane complex containing iron. The usefulness of the H-phosphonate method for the synthesis of DNA oligomers bearing metallacarborane modifications on a solid support was shown. Enzymatic digestion of the modified oligonucleotide **8** fully confirmed the expected nucleoside composition and presence of the metallacarborane modification. This study expands the available range of metallacarborane-modified oligonucleotides and opens the way for further design and use of novel biopharmaceuticals and molecular probes bearing metallacarborane complexes.

Experimental section

2′-*O*-Deoxyadenosine was purchased from Pharma Waldhof GmbH. *tert*-Butyldimethylsilyl chloride was obtained from ABCR GmbH & Co. KG, 1 mol/L tetrabutylammonium fluoride solution in THF was from Sigma-Aldrich (Steinheim, Germany), and dimethoxytrityl chloride was from Avocado Research Chemicals. Imidazole was purchased from Merck, phosphorus trichloride was from Sigma-Aldrich, and pivaloyl chloride was from Fluka Chemie AG. Crude dried venom from *Crotalus atrox* (EC 3.1.4.1) was purchased from Sigma-Aldrich. Column chromatography was performed on 230–400-mesh silica gel obtained from Sigma-Aldrich. A reverse-phase Econosil C18 column (5 µm, 4.6 mm × 250 mm) was obtained from Alltech Associates, Inc. Thin-layer chromatography was performed on silica gel F254 plates purchased from Sigma-Aldrich. All solvents were of the highest available quality. CPG (500 Å pore size) 0.2 µmol columns loaded with the DMT-on, base-protected, unmodified oligonucleotide 5′-CGAGTCTTCGGCTCCGGA-3′ were obtained from Genomed. Acrylamide and urea were purchased from Serva (Heidelberg, Germany).

Matrix-assisted laser desorption ionization time-of-flight (MALDI-TOF) mass spectra were obtained on a Voyager-Elite mass spectrometer (PerSeptive Biosystems, Framing-

Can. J. Chem. Downloaded from www.nrcresearchpress.com by Xi'an Jiaotong University on 09/19/12
For personal use only.

Fig. 2. Enzymatic digestion (CVPD) of oligonucleotide 5′-^{BEFeC}ACGAGTCTTCGGCTCCGGA-3′ (**8**): (*a*) oligonucleotide **8**, (*b*) 6-*N*-{5-[(3,3′-iron-1,2,1′,2′-dicarbollide)-8-yl]-3-oxa-pentoxy}-2′-deoxyadenosine (**5**) (^{BEFeC}A), (*c*) products of oligonucleotide **8** digestion.

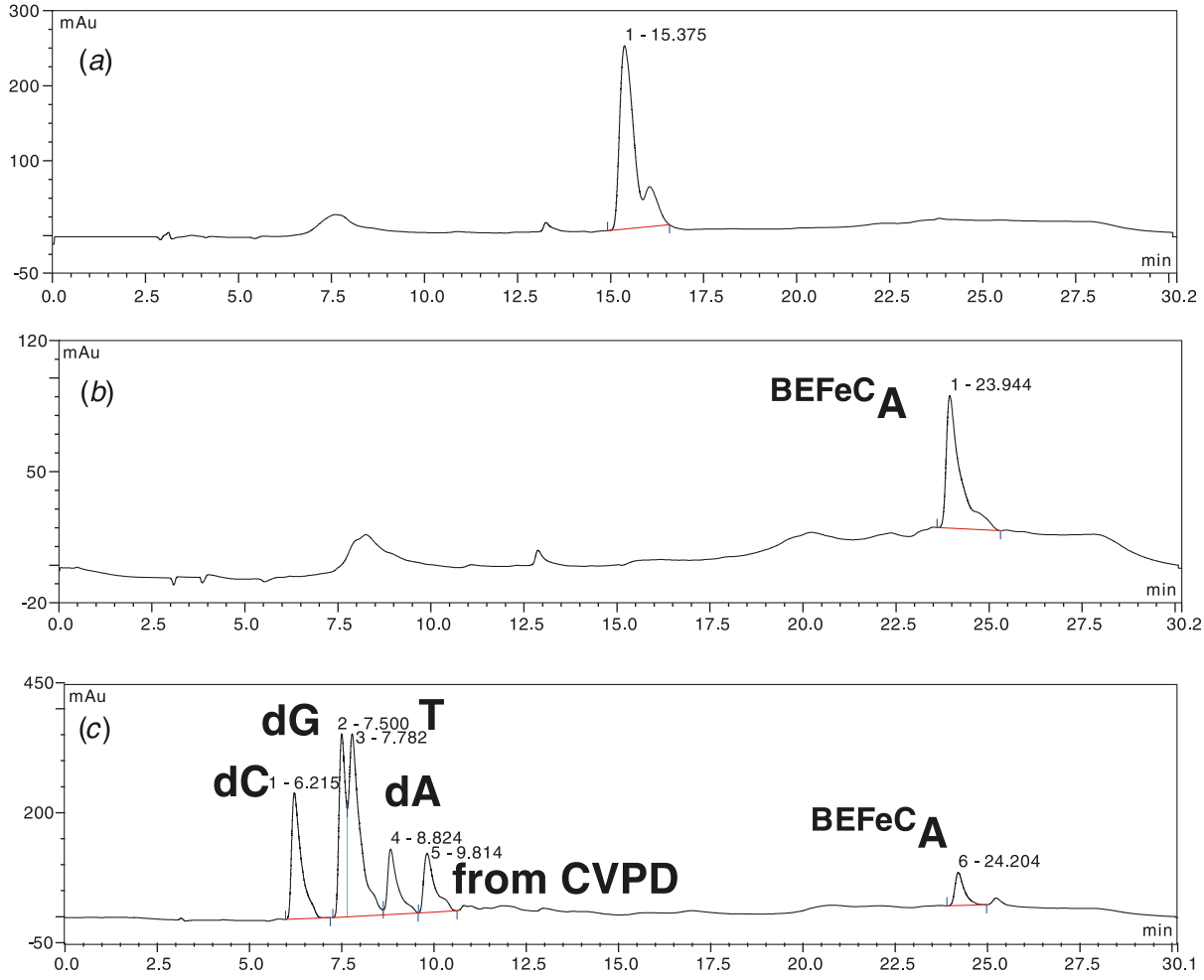

ham, Massachusetts, USA). The ratio of 3-hydroxypicolinic acid to diammonium citrate was 8:1. The masses are those of the negative ions.

UV spectroscopy measurements were performed on a GBC Cintra 10 UV–vis spectrometer (Dandenong, Australia). Samples were dissolved in purified deionized water. The measurements were performed at ambient temperature.

RP-HPLC analysis and purification were performed using a Hewlett-Packard 1050 system equipped with a UV detector and an Alltech Econosil C18 column (5 μm, 4.6 mm × 250 mm). UV detection was conducted at λ = 268 nm and λ = 310 nm. The flow rate was 1 mL/min. All analyses were performed at ambient temperature.

Polyacrylamide gel electrophoresis was performed using a Sigma-Aldrich apparatus for vertical electrophoresis. Stains-All staining dye for slab gels was purchased from Sigma-Aldrich.

Synthesis of the nonadecanucleotide ^{BEFeC}ACGAGTCTTCGGCTCCGGA-3′ bearing a (3,3′-iron-1,2,1′,2′-dicarbollide) modification

The unmodified part of the oligonucleotide was synthesized using an ABI 3900 DNA synthesizer. A column loaded with controlled pore glass functionalized with 5′-*O*-dimethoxytrityl-6*N*-benzoyl-2′-deoxyadenosine (0.2 μmol) was used as the solid support. Elongation of the oligomer was performed using a standard 0.2 μmol-scale β-cyanoethyl DNA synthesis cycle without changing the condensation time. The coupling of the modified monomer **7** using H-phosphonate chemistry and the oxidation step were performed manually. After completion of the synthesis of the unmodified part of the oligonucleotide, the column was detached from the DNA synthesizer. The oligomer was next detritylated manually with 3% dichloroacetic acid (DCA) in dichloromethane (2 × 5 mL). The column was then washed with dichloromethane (10 mL) followed by pyridine–acetonitrile (1:3 *v*/*v*, 4 mL) and was dried using an argon stream (10 min). Monomer **7** (5 mg) (0.005 mmol) was co-evaporated twice with anhydrous pyridine under reduced pressure. Next, **7** was dissolved in a mixture of anhydrous pyridine–acetonitrile (1:3 *v*/*v*, 40 μL), to which was added PvCl (1.8 μL) in pyridine–acetonitrile (1:3 *v*/*v*, 40 μL). A solution of activated **7** was applied to the column, and the coupling reaction was allowed to proceed for 10 min. The coupling step was repeated three times, each time with a freshly prepared solution of activated **7**. The column was then washed with pyridine–acetonitrile (1:3 *v*/*v*, 4 mL) and dried with a stream of argon. The oxidation step was performed using an oxidizing solution containing

Can. J. Chem. Downloaded from www.nrcresearchpress.com by Xi'an Jiaotong University on 09/19/12
For personal use only.

Can. J. Chem. Downloaded from www.nrcresearchpress.com by Xi'an Jiaotong University on 09/19/12
For personal use only.

Fig. 3. PAGE analysis of modified oligonucleotide **8**; 20% polyacrylamide denaturing gel containing 7 mol/L urea. The oligonucleotide sample was visualized by staining with Stains-All.

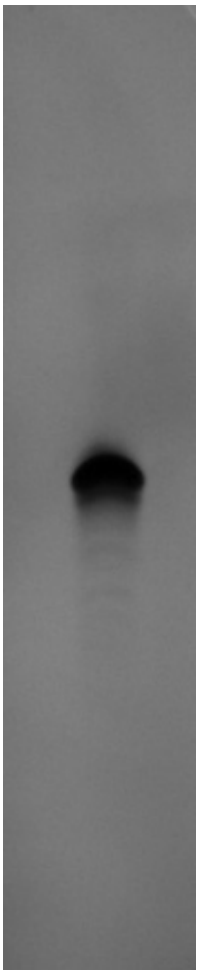

10% H_2O in CCl_4, triethylamine, and *N*-methylimidazole (9.0:0.5:0.5) for 35 min. The column was washed with pyridine–acetonitrile (1:3 *v*/*v*, 4 mL) and dried with a stream of argon. The oligonucleotide was then cleaved from the support with 30% aqueous ammonia (1 mL) at ambient temperature for 1 h. The deprotection of the bases was achieved by incubation of the oligonucleotide solution at 50 °C for 2 h. The solution of base-deprotected, DMT-on oligonucleotide was degassed with a stream of argon, evaporated to dryness under vacuum, and then redissolved in water, yielding crude product with an optical density of 23.5 units (ODU) at 260 nm. The crude DMT-on oligomer was purified by RP-HPLC. For each run, 5 ODU of the DMT-on oligonucleotide was used. The following conditions were used for the RP-HPLC purification of the DMT-on oligonucleotide: 0 min 100% A, 20 min from 0% D to 100% D, 5 min 100% D, and 5 min from 100% D to 0% D. Buffer A contained 0.1 mol/L TEAB (triethylammonium bicarbonate) (pH 7.0) in a mixture of acetonitrile and water (2:98, *v*/*v*), and buffer D contained 0.1 mol/L TEAB (pH 7.0) in a mixture of acetonitrile and water (40:60, *v*/*v*). The flow rate was 1 mL/min. UV detection was conducted at λ = 268 nm. The fractions containing the desired product were collected, and the buffer was evaporated under vacuum. The residue was co-evaporated with 95% ethanol to remove the TEAB, and then detritylation was performed using 80% acetic acid (1 mL) at ambient temperature for 20 min, yielding crude **8**. Next, the acetic acid solution was evaporated to dryness under vacuum, and the completely deprotected **8** was purified by RP-HPLC. The same HPLC conditions as described above for the DMT-on oligomer were used for the purification and analysis of the completely deprotected oligonucleotide **8**. The fractions containing the desired product were collected, and the buffer was evaporated under vacuum. The residue was co-evaporated with 95% ethanol to remove the buffer. The oligonucleotide was redissolved in water and lyophilised. Yield: 10.2 ODU (A_{260}). UV (H_2O) λ_{min}: 235 nm; λ_{max}: 264 nm. RP-HPLC Rt: 15.4 min. MALDI-TOF MS *m/z* (%): 6223.73 [M+12] (100%); calcd. for $C_{192}H_{261}B_{18}FeN_{71}O_{115}P_{18}$: 6211.32 (100%).

Enzymatic digestion of 8 with snake venom phosphodiesterase

Tris–HCl buffer (100 mmol/L containing $MgCl_2$ (20 mmol/L)) was added to an aqueous solution of oligonucleotide **8** (0.75 ODU, 40.5 μL). The resulting solution was treated with 1.9×10^{-2} units (15 μL) of phosphodiesterase (crude dried venom from *Crotalus atrox* dissolved in water) and incubated at 38 °C. After 10 and 20 min, aliquots were withdrawn, heated at 80 °C, and then stored at –70 °C prior to analysis by RP-HPLC.

PAGE analysis

The sample of modified oligonucleotide **8** (0.2 ODU in 7 μL formamide containing bromophenol blue and xylene cyanol) was analyzed by electrophoresis using 20% polyacrylamide denaturing gel containing urea (7 mol/L) for 5 h at 500 V. The sample was visualized by staining with Stains-All.

Acknowledgements

This work was supported in part by grant K152/H03/2007/09 from the Polish Ministry of Science and Higher Education and by an internal grant from the Institute for Medical Biology PAS. I thank Dr. Bohumir Grüner, Institute of Inorganic Chemistry, Academy of Sciences of the Czech Republic, for providing a sample of compound **3**. I thank Dr. Magda Janicka (Centre of Molecular and Macromolecular Studies PAS) for PAGE analysis of the modified oligonucleotide **8**.

References

(1) *Macromolecules Containing Metal and Metal-Like Elements*; Abd-El-Aziz, A. S.; Carraher, C. E., Jr.; Pittman, C. U., Jr.; Sheats, J. E.; Zeldin, M., Eds.; John Wiley and Sons: Hoboken, NJ, 2004; Vol. 3.

(2) Lesnikowski, Z. J. *Curr. Org. Chem.* **2007**, *11* (4), 355. doi:10.2174/138527207780059358.

(3) Grimes, R. N. *Coord. Chem. Rev.* **2000**, *200–202* (1), 773. doi:10.1016/S0010-8545(00)00262-9.

(4) Corsini, M.; de Biani, F. F.; Zanello, P. *Coord. Chem. Rev.* **2006**, *250* (11–12), 1351. doi:10.1016/j.ccr.2005.12.009.

(5) Zatsepin, T. S.; Andreev, S. Y.; Hianik, T.; Oretskaya, T. S. *Russ. Chem. Rev.* **2003**, *72* (6), 537. doi:10.1070/RC2003v072n06ABEH000807.

(6) van Staveren, D. R.; Metzler-Nolte, N. *Chem. Rev.* **2004**, *104* (12), 5931. doi:10.1021/cr0101510.
(7) Olejniczak, A. B.; Mucha, P.; Grüner, B.; Lesnikowski, Z. J. *Organometallics* **2007**, *26* (14), 3272. doi:10.1021/om070102z.
(8) Ogilvie, K. K. *Can. J. Chem.* **1973**, *51* (22), 3799. doi:10.1139/v73-569.
(9) Wojtczak, B. A.; Olejniczak, A. B.; Lesnikowski, Z. J. Nucleoside Modification with Boron Clusters and Their Metal Complexes. In *Current Protocols in Nucleic Acid Chemistry*; S.L. Beaucage, D.E. Bergstrom, P. Herdewijn, A. Matsuda, Eds.; John Wiley & Sons, Inc.: USA, 2009; pp 1–26.
(10) Plešek, J.; Grüner, B.; Macháček, J.; Císařová, I.; Čáslavský, J. *J. Organomet. Chem.* **2007**, *692* (22), 4801. doi:10.1016/j.jorganchem.2007.07.026.
(11) Hawthorne, M. F.; Young, D. C.; Wegner, P. A. *J. Am. Chem. Soc.* **1965**, *87* (8), 1818. doi:10.1021/ja01086a053.
(12) Schaller, H.; Weimann, B.; Lerch, B.; Khorana, H. G. *J. Am. Chem. Soc.* **1963**, *85*(23), 3821. doi:10.1021/ja00906a021.
(13) Beaucage, S. L. Oligodeoxyribonucleotides Synthesis, Phosphoramidite Approach. In *Methods in Molecular Biology*; S. Agrawal, Ed.; Humana Press Inc.: Totowa, NJ, 1993; Vol. 20, Protocols for Oligonucleotides and Analogs, Synthesis and Properties, pp 33–61.
(14) Sinha, N. D.; Striepeke, S. Oligonucleotides with Reporter Groups Attached to the 5′-Terminus. In *Oligonucleotides and Analogues: A Practical Approach*; F. Eckstein, Ed.; IRL Press at Oxford University Press: New York, 1991; pp 185–210.
(15) Olejniczak, A. B.; Plesek, J.; Kriz, O.; Lesnikowski, Z. J. *Angew. Chem. Int. Ed. Engl.* **2003**, *42* (46), 5740. doi:10.1002/anie.200352505.
(16) Stawiński, J.; Strömberg, R. Di- and Oligonucleotide Synthesis using H-Phosphonate Chemistry. In *Methods in Molecular Biology*; P. Herdewijn, Ed.; Humana Press Inc.: Totowa, NJ, 2005; Vol. 288, Oligonucleotide Synthesis: Methods and Applications, pp 81–100.

Can. J. Chem. Downloaded from www.nrcresearchpress.com by Xi'an Jiaotong University on 09/19/12
For personal use only.

A PEG_{1000}-DAIL[$CdCl_3$]–toluene temperature-dependent biphasic system that regulates homogeneously catalyzed C–O coupling of organic halides with phenols and alcohols under ligand-free conditions

Yu Lin Hu, Xiao Yun Ma, and Ming Lu

Can. J. Chem. Downloaded from www.nrcresearchpress.com by Xi'an Jiaotong University on 09/19/12
For personal use only.

Abstract: An efficient, experimentally simple, and convenient procedure for the C–O coupling of organic halides with phenols and alcohols in a PEG_{1000}-DAIL[$CdCl_3$]–toluene temperature-dependent biphasic system has been developed. The product can be easily isolated by a simple decantation, and the catalytic system can be recycled and reused without loss of catalytic activity.

Key words: C–O coupling, organic halide, ionic liquid, thermoregulated ionic liquid biphasic system.

Résumé : On a mis au point une méthode commode, efficace et expérimentalement simple de faire un couplage C–O d'halogénures organiques avec des phénols et des alcools dans un système biophysique PEG_{1000}-DAIL[$CdCl_3$]–toluène qui varie avec la température. Les produits peuvent être facilement isolés par une simple décantation et le système catalytique peut être recyclé et réutilisé dans perte d'activité catalytique.

Mots-clés : couplage C–O, halogénure organique, liquide ionique, système biphasique de liquide ionique soumis à une thermorégulation.

[Traduit par la Rédaction]

Introduction

The carbon–oxygen bond-forming reaction is one of the most fundamental transformations because of the large number of applications of the resulting compounds (ethers) in organic, pharmaceutical, and polymer chemistry.[1,2] The usual synthetic methods for such a conversion include the Williamson ether synthesis,[3,4] Ullmann coupling,[5,6] palladium-catalyzed couplings of aryl halides,[7–10] C–O couplings of arylboronic acids with phenols,[11,12] iron-catalyzed couplings,[13,14] and other coupling reactions.[15–17] However, these protocols, are generally associated with one or more disadvantages, such as long reaction times, high reaction temperatures, high catalyst loading, tedious work-up procedures, poor substrate scope, moisture sensitivity, costly metal catalysts, difficulty of catalyst recovery, and environmental toxicity. To overcome these limitations, some significant modifications have been made for the Ullmann ether synthesis during the past few years. It has been observed that certain additives, such as 8-hydroxyquinoline,[18] *N*,*N*-dimethyl glycine,[19] 1-naphthoic acid,[20] 2,2,6,6-tetramethylheptane-3,5-dione,[21] tripod ligands,[22] Schiff base,[23] PPAMP,[24] triphenylphosphine,[25] neocuproine,[26] nitrogen-based multidentate ligands,[27] phosphorus dendrimer ligands,[28] and some copper(I) complexes,[29] can accelerate the rate of the reactions, and therefore, the reactions can be performed under milder conditions. Whilst these remarkable advances in the field of Ullmann coupling are exceedingly beneficial, most of the reactions still require long reaction times of more than 24 h, elevated reaction temperatures, and high catalyst loading, and entail difficulties in recycling of the catalyst. Therefore, the introduction of new and environmentally benign procedures that address these drawbacks continues to be of value and interest.

The room-temperature ionic liquid, a kind of environmentally friendly solvent and catalyst because of its adjustable physical and chemical properties, got broad attention from scholars in various fields such as synthesis, catalysis, separation, and electrochemistry.[30,31] In view of both the advantages and disadvantages of homogeneous and heterogeneous catalysis, and to improve catalyst recovery, some novel temperature-dependent ionic liquid biphasic catalytic systems have been reported recently,[32–34] and in our research project group, Luo and co-workers very recently reported a new PEG_{1000}-based dicationic ionic liquid (PEG_{1000}-DAIL) exhibiting temperature-dependent phase behavior with toluene, and applied it successfully in a one-pot synthesis of

Received 6 July 2010. Accepted 30 November 2010. Published on the NRC Research Press Web site at canjchem.nrc.ca on 18 March 2011.

Y.L. Hu, X.Y. Ma, and M. Lu.[1] College of Chemical Engineering, Nanjing University of Science and Technology, Nanjing 210094, P. R. China.

[1]Corresponding author (e-mail: luming1963@163.com).

Scheme 1. Carbon–oxygen coupling of organic halides with phenols and alcohols.

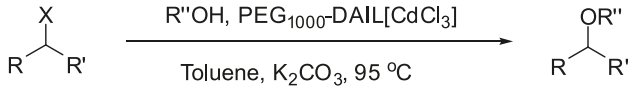

R, R'' = aryls, alkyls; R' = H, aryls, alkyls

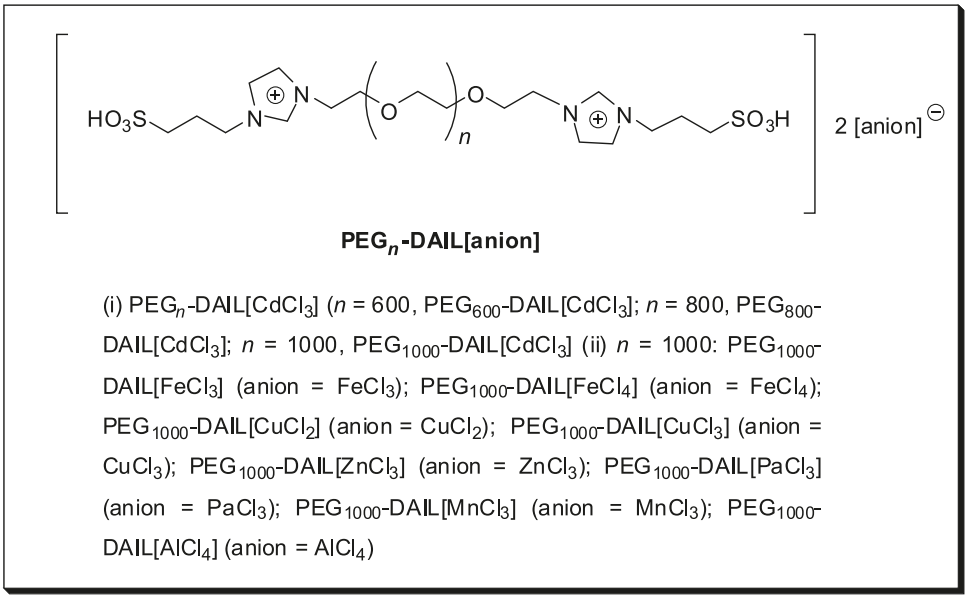

PEG$_n$-DAIL[anion]

(i) PEG$_n$-DAIL[$CdCl_3$] (n = 600, PEG$_{600}$-DAIL[$CdCl_3$]; n = 800, PEG$_{800}$-DAIL[$CdCl_3$]; n = 1000, PEG$_{1000}$-DAIL[$CdCl_3$]) (ii) n = 1000: PEG$_{1000}$-DAIL[$FeCl_3$] (anion = $FeCl_3$); PEG$_{1000}$-DAIL[$FeCl_4$] (anion = $FeCl_4$); PEG$_{1000}$-DAIL[$CuCl_2$] (anion = $CuCl_2$); PEG$_{1000}$-DAIL[$CuCl_3$] (anion = $CuCl_3$); PEG$_{1000}$-DAIL[$ZnCl_3$] (anion = $ZnCl_3$); PEG$_{1000}$-DAIL[$PaCl_3$] (anion = $PaCl_3$); PEG$_{1000}$-DAIL[$MnCl_3$] (anion = $MnCl_3$); PEG$_{1000}$-DAIL[$AlCl_4$] (anion = $AlCl_4$)

Can. J. Chem. Downloaded from www.nrcresearchpress.com by Xi'an Jiaotong University on 09/19/12
For personal use only.

benzopyrans.[35] They found that the ionic liquid showed some advantages such as high conversions and selectivity, stability at high temperatures, and reusability in the reaction, and it provides a novel route for the separation and recycling of catalysts. Herein, we report a convenient and efficient procedure for the C–O coupling of organic halides with both phenols and alcohols to synthesize aryl ethers catalyzed by PEG$_{1000}$-based dicationic ionic liquid (PEG$_{1000}$-DAIL[$CdCl_3$]) under ligand-free conditions (Scheme 1).

Results and discussion

The investigation was initiated by using the coupling of 4-iodonitrobenzene with phenol as a model reaction (Table 1). At first, catalysts of different types of ionic liquids were tested in this model reaction (Table 1, entries 1–11) with K_2CO_3 as base, and the results showed that PEG$_{1000}$-DAIL[$CdCl_3$] demonstrated the best performance (Table 1, entry 3). No product was detected in the absence of ionic liquid as a catalyst (Table 1, entry 12). For comparison on the efficiency of different bases in the couplings (Table 1, entries 3 and 14–18), both K_2CO_3 and Cs_2CO_3 were found to be effective bases for this aryl ether formation (Table 1, entries 3 and 15). Other bases, including K_3PO_4, Na_2CO_3, and some organic bases such as Et_3N and pyridine, gave lower yields (Table 1, entries 14 and 16–18). The bases had a large effect on the reaction and were crucial for achieving high yields because a much lower yield (65%) was obtained in the absence of a base (Table 1, entry 13). Therefore, the combination of less expensive base K_2CO_3 and PEG$_{1000}$-DAIL[$CdCl_3$] was chosen as the optimal condition for further exploration.

In addition, the catalytic system could be typically recovered and reused for subsequent reactions with no appreciable decrease in yields and reaction rates (Fig. 1). The recycling process involved the removal of the top oil layer (toluene, containing product) by decantation. The bottom aqueous layer (PEG$_{1000}$-DAIL[$CdCl_3$]) was concentrated under vacuum and then filtered. Fresh substrates and toluene were then recharged with the residual PEG$_{1000}$-DAIL[$CdCl_3$] and the mixture was heated to react once again.

With these optimized reaction conditions in hand, we employed a variety of organic halides in an attempt to synthesize different aryl ethers, as shown in Table 2. Various types of aryl, benzylic, allylic, and aliphatic halides were successfully converted to the corresponding ethers with phenol (Table 2, entries 1–24), whereas the aliphatic halides were less reactive, and higher reaction temperature and longer reaction time were needed to reach good yields (Table 2, entries 16 and 17). Aryl halides with electron-withdrawing substituents (Table 2, entries 6–10, 12, 13, and 15) were more reactive than those with or without electron-donating substituents (Table 2, entries 1–5, 11, and 14). It was also observed that the reactions were faster with benzylic and allylic halides (Table 2, entries 18–24) than with aryl halides (Table 2, entries 1–15). Moreover, the halogen sources greatly influenced the reaction. Taking aryl halides as an example, the reaction activity decreased in the order iodobenzene > bromobenzene > chlorobenzene (Table 2, entries 1, 11, and 14). In addition, to examine a greater range of hydroxy substrates to better illustrate the scope and limitations of this protocol, we investigated the reactions with phenols and alcohols using 4-iodonitrobenzene as a representative organic halide (Table 2, entries 25–30). The experimental

Can. J. Chem. Downloaded from www.nrcresearchpress.com by Xi'an Jiaotong University on 09/19/12
For personal use only.

Table 1. Optimization studies for the coupling of 4-iodonitrobenzene with phenol.

Entry	Ionic liquid	Base	Time (h)	Yield (%)[a]
1	PEG_{600}-DAIL[$CdCl_3$]	K_2CO_3	8	87
2	PEG_{800}-DAIL[$CdCl_3$]	K_2CO_3	8	92
3	PEG_{1000}-DAIL[$CdCl_3$]	K_2CO_3	8	95
4	PEG_{1000}-DAIL[$FeCl_3$]	K_2CO_3	8	82
5	PEG_{1000}-DAIL[$FeCl_4$]	K_2CO_3	8	91
6	PEG_{1000}-DAIL[$CuCl_2$]	K_2CO_3	8	84
7	PEG_{1000}-DAIL[$CuCl_3$]	K_2CO_3	8	81
8	PEG_{1000}-DAIL[$ZnCl_3$]	K_2CO_3	8	89
9	PEG_{1000}-DAIL[$PdCl_3$]	K_2CO_3	8	86
10	PEG_{1000}-DAIL[$MnCl_3$]	K_2CO_3	8	74
11	PEG_{1000}-DAIL[$AlCl_4$]	K_2CO_3	8	71
12	—	K_2CO_3	24	0
13	PEG_{1000}-DAIL[$CdCl_3$]	—	14	65
14	PEG_{1000}-DAIL[$CdCl_3$]	K_3PO_4	8	88
15	PEG_{1000}-DAIL[$CdCl_3$]	Cs_2CO_3	8	94
16	PEG_{1000}-DAIL[$CdCl_3$]	Na_2CO_3	8	85
17	PEG_{1000}-DAIL[$CdCl_3$]	Et_3N	8	76
18	PEG_{1000}-DAIL[$CdCl_3$]	Pyridine	8	81

Note: DAIL, dicationic ionic liquid. The reactions were carried out with 4-iodonitrobenzene (2.4 mmol), phenol (2 mmol), base (2 mmol), and ionic liquid (0.4 mmol) in toluene (5 mL) at 95 °C.

[a]Isolated yield.

Fig. 1. Repeating reactions using recovered PEG_{1000}-DAIL[$CdCl_3$]. DAIL, dicationic ionic liquid.

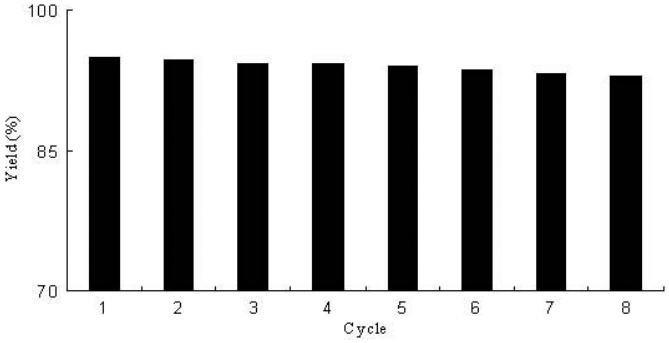

results indicated that substituents on the phenol ring have a great influence on the reaction. For example, substitution of a methyl or methoxy group at the position of phenol incurs a reduction in both yield and reaction rate (Table 2, entries 25 and 26). Finally, the reactions are faster with phenols (Table 2, entries 25–28) than with alcohols (Table 2, entries 29 and 30).

The excellent reaction results of the catalytic system suggest that the coupling among organic halides, phenols, or alcohols, K_2CO_3, toluene, and PEG_{1000}-DAIL[$CdCl_3$] has a particular catalytic process, which is schematically depicted in Fig. 2. Before the coupling, there exists an obvious biphasic system, and the bottom layer consists of PEG_{1000}-DAIL[$CdCl_3$] and K_2CO_3, and the top layer consists of toluene and substrates. During the process of coupling, the biphasic system disappears and a homogeneous reaction medium is formed. After the completion of the reaction, a complete phase separation is formed again after being cooled to room temperature. The next process involves the removal of the oil layer by decantation; the bottom aqueous layer is concentrated by removing the water produced in the reaction under vacuum and then filtered. Fresh substrates and toluene are then recharged to the recovered PEG_{1000}-DAIL[$CdCl_3$] and then recycled. The PEG_{1000}-DAIL[$CdCl_3$] plays a very important role in the coupling process to locally concentrate the reacting species by exhibiting a temperature-dependent phase behavior with methylcyclohexane (i.e., the thermoregulated biphasic behavior of monophase under high temperature and biphase under room temperature), which leads to a large increase in the effective reactant concentration and excellent results of the coupling.

Conclusion

In conclusion, we have developed an experimentally simple and efficient protocol for the C–O coupling of organic halides with phenols and alcohols in a PEG_{1000}-DAIL[$CdCl_3$]–toluene temperature-dependent biphasic system. A wide range of aryl, benzylic, allylic, and aliphatic halides were found to be applicable to the catalytic system. Advantages of our procedure include simplicity of operation, high yields, easy isolation of products, good thermoregulated biphasic behavior of the ionic liquid, and excellent recyclability of the catalyst. Efforts to define the coupling mechanism and expand the utility of the environmentally benign catalytic system to other organic synthesis are currently under study in our laboratory.

Experimental

All the chemicals were obtained from commercial sources without any pretreatment. All reagents were of analytical grade. The ionic liquids were synthesized according to liter-

Can. J. Chem. Downloaded from www.nrcresearchpress.com by Xi'an Jiaotong University on 09/19/12
For personal use only.

Table 2. Catalytic coupling of various organic halides.

Entry	Organic halides	R_3OH	Time (h)	Products and yields (%)[a]
1	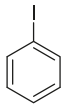	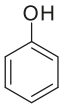	11	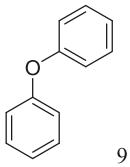 **1** 91
2	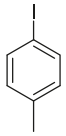	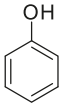	14	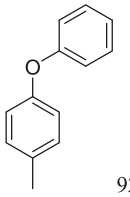 **2** 92
3	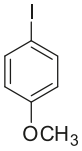	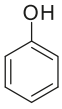	14	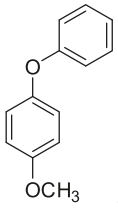 **3** 89
4	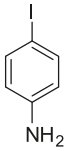	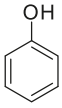	14	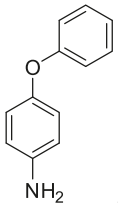 **4** 87
5	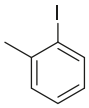	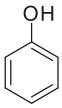	14	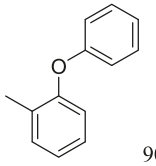 **5** 90
6	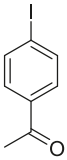	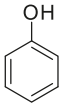	8	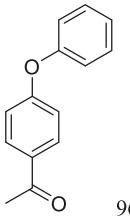 **6** 96

ature procedures.[30,35] ^{1}H NMR spectra were recorded on a Bruker 400 MHz spectrometer using $CDCl_3$ as the solvent with tetramethylsilane (TMS) as an internal standard. High-performance liquid chromatography (HPLC) experiments were performed on a liquid chromatograph (Dionex Softron GmbH, America), consisting of a pump (P680) and UV–vis light detector (UVD) system (170U). Elemental analyses were performed on a Vario EL III instrument (Elmentar Analysen Systeme GmbH, Germany).

General procedure for coupling reactions

To a stirred solution of organic halide (2.4 mmol), R_3OH

Can. J. Chem. Downloaded from www.nrcresearchpress.com by Xi'an Jiaotong University on 09/19/12
For personal use only.

Table 2. (*continued*).

Entry	Organic halides	R_3OH	Time (h)	Products and yields (%)[a]
7	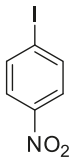	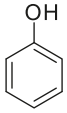	8	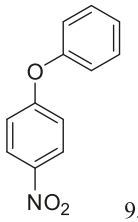 95 **7**
8	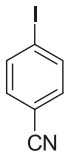	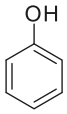	8	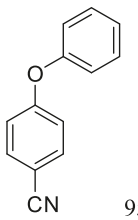 95 **8**
9	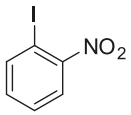	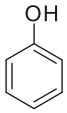	8	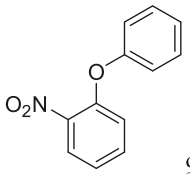 94 **9**
10	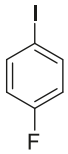	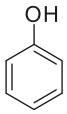	8	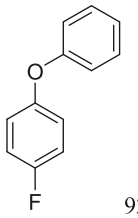 92 **10**
11	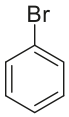	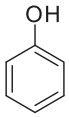	14	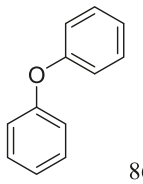 86 **11**
12	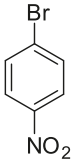	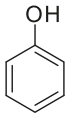	10	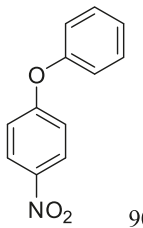 90 **12**

(2 mmol), and PEG_{1000}-DAIL[$CdCl_3$] (0.4 mmol) in toluene (5 mL) was added K_2CO_3 (2 mmol). Stirring was continued at 95 °C for an appropriate time, the reaction progress being monitored by HPLC. Upon completion, the mixture was cooled to room temperature. The organic phase was separated by decantation and then rinsed with water (3 × 10 mL) and dried with anhydrous sodium sulfate. The crude mixture was purified by column chromatography on silica

Table 2. (*continued*).

Entry	Organic halides	R_3OH	Time (h)	Products and yields (%)[a]
13	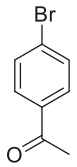	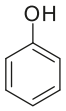	10	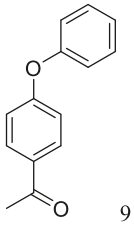 91 **13**
14	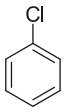	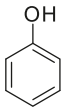	18	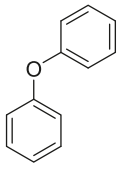 82 **14**
15	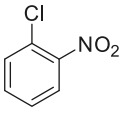	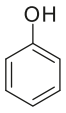	14	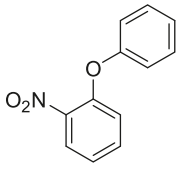 89 **15**
16	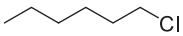	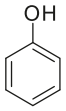	24[b]	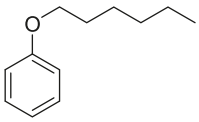 81 **16**
17	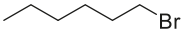	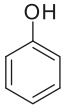	24[b]	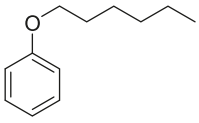 84 **17**
18	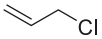	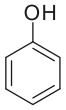	7	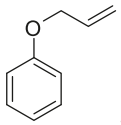 89 **18**

gel to afford the product with high purity. The next run was performed under identical reaction conditions. All the products were confirmed by ^{1}H NMR or elemental analysis or compared with their authentic samples.

Spectral data of selected products

1-Methyl-4-phenoxybenzene (2)

^{1}H NMR (400 MHz, $CDCl_3$) δ: 2.31 (s, CH_3, 3H), 6.89–7.01 (m, Ar-H, 4H), 7.05–7.09 (m, Ar-H, 1H), 7.12–7.16 (m, Ar-H, 2H), 7.29–7.35 (m, Ar-H, 2H). Anal. calcd for $C_{13}H_{12}O$: C 84.73, H 6.56, O 8.69; found: C 84.75, H 6.57, O 8.68.

1-Methoxy-4-phenoxybenzene (3)

^{1}H NMR (400 MHz, $CDCl_3$) δ: 3.78 (s, CH_3, 3H), 6.86–6.93 (m, Ar-H, 2H), 6.96–7.02 (m, Ar-H, 4H), 7.05–7.11 (m, Ar-H, 1H), 7.27–7.33 (m, Ar-H, 2H). Anal. calcd for $C_{13}H_{12}O_2$: C 77.95, H 6.04, O 15.99; found: C 77.98, H 6.04, O 15.98.

1-Nitro-4-phenoxybenzene (7)

^{1}H NMR (400 MHz, $CDCl_3$) δ: 6.93–6.97 (m, Ar-H, 2H), 7.01–7.05 (m, Ar-H, 2H), 7.24–7.27 (m, Ar-H, 1H), 7.47–7.54 (m, Ar-H, 2H), 8.11–8.16 (m, Ar-H, 2H). Anal. calcd for $C_{12}H_9NO_3$: C 66.94, H 4.23, N 6.50, O 22.32; found: C 66.97. H 4.22. N 6.51. O 22.30.

Can. J. Chem. Downloaded from www.nrcresearchpress.com by Xi'an Jiaotong University on 09/19/12
For personal use only.

Can. J. Chem. Downloaded from www.nrcresearchpress.com by Xi'an Jiaotong University on 09/19/12
For personal use only.

Table 2. (*continued*).

Entry	Organic halides	R_3OH	Time (h)	Products and yields (%)[a]
19	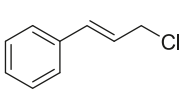	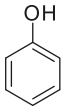	7	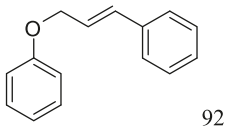 92 **19**
20	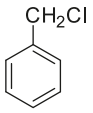	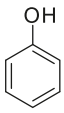	7	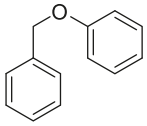 94 **20**
21	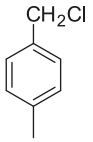	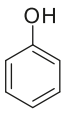	7	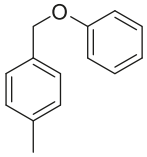 96 **21**
22	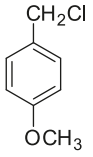	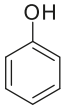	7	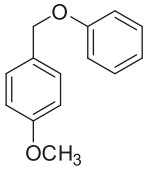 97 **22**
23	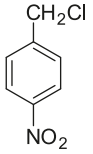	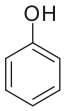	9	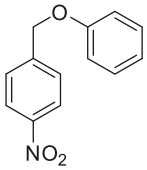 90 **23**
24	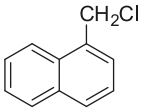	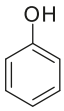	7	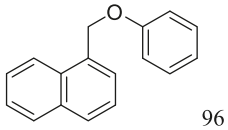 96 **24**

4-Phenoxybenzonitrile (8)

^{1}H NMR (400 MHz, $CDCl_3$) δ: 6.89–6.93 (m, Ar-H, 2H), 6.97–7.01 (m, Ar-H, 2H), 7.17–7.21 (m, Ar-H, 1H), 7.34–7.38 (m, Ar-H, 2H), 7.71–7.76 (m, Ar-H, 2H). Anal. calcd for $C_{13}H_9NO$: C 79.96, H 4.66, N 7.17, O 8.21; found: C 79.98, H 4.65, N 7.17, O 8.20.

1-Methyl-4-(phenoxymethyl)benzene (21)

^{1}H NMR (400 MHz, $CDCl_3$) δ: 2.32 (s, CH_3, 3H), 5.13 (s, CH_2, 2H), 6.92–7.03 (m, Ar-H, 3H), 7.08–7.17 (m, Ar-H, 4H), 7.27–7.34 (m, Ar-H, 2H). Anal. calcd for $C_{14}H_{14}O$: C 84.77, H 7.13, O 8.09; found: C 84.81, H 7.12, O 8.07.

1-Methoxy-4-(phenoxymethyl)benzene (22)

^{1}H NMR (400 MHz, $CDCl_3$) δ: 3.81 (s, CH_3, 3H), 5.12 (s, CH_2, 2H), 6.89–7.06 (m, Ar-H, 7H), 7.29–7.35 (m, Ar-H, 2H). Anal. calcd for $C_{14}H_{14}O_2$: C 78.46, H 6.59, O 14.94; found: C 78.48, H 6.59, O 14.93.

1-Methoxy-4-(4-nitrophenoxy)benzene (26)

^{1}H NMR (400 MHz, $CDCl_3$) δ: 3.81 (s, CH_3, 3H), 6.94–6.97 (m, Ar-H, 2H), 7.16–7.19 (m, Ar-H, 2H), 7.38–7.42 (m, Ar-H, 2H), 8.14–8.18 (m, Ar-H, 2H). Anal. calcd for $C_{13}H_{11}NO_4$: C 63.63, H 4.52, N 5.71, O 26.12; found: C 63.67, H 4.52, N 5.71, O 26.10.

1-(Cyclohexyloxy)-4-nitrobenzene (29)

^{1}H NMR (400 MHz, $CDCl_3$) δ: 1.32 (m, CH_2, 2H), 1.46 (m, CH_2, 4H), 1.87 (m, CH_2, 4H), 3.72 (m, CH, 1H), 7.32–7.38 (m, Ar-H, 2H), 8.12–8.16 (m, Ar-H, 2H). Anal. calcd

Table 2. (*concluded*).

Entry	Organic halides	R_3OH	Time (h)	Products and yields (%)[a]
25	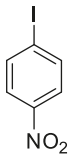	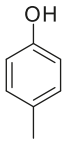	14	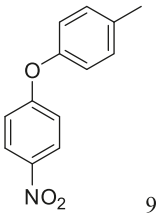 **25** 91
26	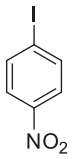	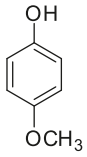	14	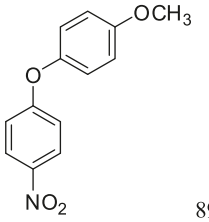 **26** 89
27	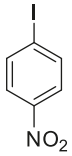	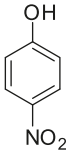	8	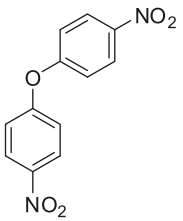 **27** 98
28	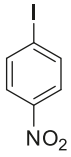	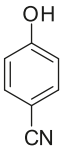	8	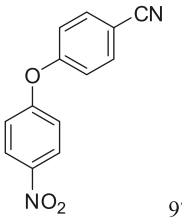 **28** 97
29	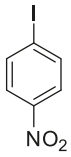	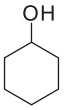	24[c]	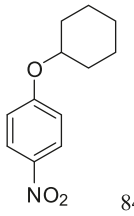 **29** 84
30	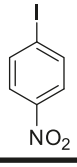	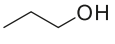	24[c]	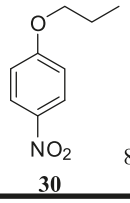 **30** 82

Note: Unless otherwise noted, the reactions were carried out with organic halide (2.4 mmol), R_3OH (2 mmol), K_2CO_3 (2 mmol), PEG_{1000}-DAIL[$CdCl_3$] (0.4 mmol), in toluene (5 mL) at 95 °C.

[a] Isolated yield.

[b] The reaction was carried out at 105 °C.

Can. J. Chem. Downloaded from www.nrcresearchpress.com by Xi'an Jiaotong University on 09/19/12
For personal use only.

Fig. 2. Thermoregulated ionic liquid biphase catalytic process for the C–O coupling.

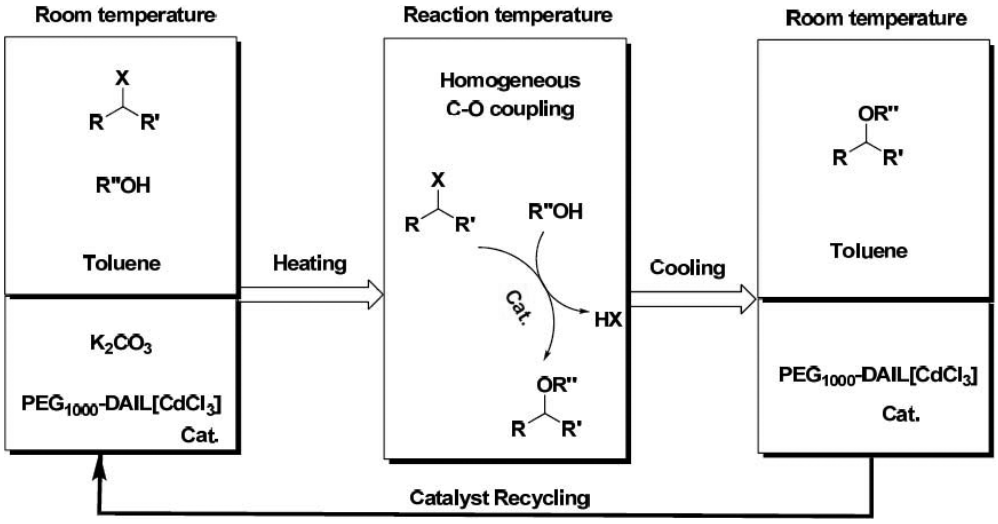

for $C_{12}H_{15}NO_3$: C 65.10, H 6.83, N 6.34, O 21.71; found: C 65.14, H 6.83, N 6.33, O 21.69.

Acknowledgements

We thank the National Basic Research Program (973) of China (grant No. 613740101) and the Natural Science Foundation of Jiangsu Province for support of this research.

References

(1) Sawyer, J. S. *Tetrahedron* **2000**, *56*, 5045. doi:10.1016/S0040-4020(00)00257-X.
(2) Buckingham, J. *Dictionary of Natural Products;* University Press: Cambridge, MA, 1994.
(3) Hassner, A.; Stumer, C. *Organic Synthesis Based on Name Reactions and Unnamed Reactions;* Pergamon: Kidlington, 1994.
(4) Paul, S.; Gupta, M. *Tetrahedron Lett.* **2004**, *45* (48), 8825. doi:10.1016/j.tetlet.2004.10.009.
(5) Lindley, J. *Tetrahedron* **1984**, *40* (9), 1433. doi:10.1016/S0040-4020(01)91791-0.
(6) Hassan, J.; Sévignon, M.; Gozzi, C.; Schulz, E.; Lemaire, M. *Chem. Rev.* **2002**, *102* (5), 1359. doi:10.1021/cr000664r. PMID:11996540.
(7) Kataoka, N.; Shelby, Q.; Stambuli, J. P.; Hartwig, J. F. *J. Org. Chem.* **2002**, *67* (16), 5553. doi:10.1021/jo025732j. PMID:12153253.
(8) Vorogushin, A. V.; Huang, X.; Buchwald, S. L. *J. Am. Chem. Soc.* **2005**, *127* (22), 8146. doi:10.1021/ja050471r. PMID:15926842.
(9) Ikawa, T.; Barder, T. E.; Biscoe, M. R.; Buchwald, S. L. *J. Am. Chem. Soc.* **2007**, *129* (43), 13001. doi:10.1021/ja0717414. PMID:17918833.
(10) Milton, E. J.; Fuentes, J. A.; Clarke, M. L. *Org. Biomol. Chem.* **2009**, *7* (12), 2645. doi:10.1039/b907784g. PMID:19503941.
(11) Evans, D. A.; Katz, J. L.; West, T. R. *Tetrahedron Lett.* **1998**, *39*, 2937. doi:10.1016/S0040-4039(98)00502-4.
(12) Chan, D. M. T.; Monaco, K. L.; Wang, R. P.; Winters, M. P. *Tetrahedron Lett.* **1998**, *39* (19), 2933. doi:10.1016/S0040-4039(98)00503-6.
(13) Bistri, O.; Correa, A.; Bolm, C. *Angew. Chem. Int. Ed.* **2008**, *47* (3), 586. doi:10.1002/anie.200704018.
(14) Namboodiri, V. V.; Polshettiwar, V.; Varma, R. S. *Tetrahedron Lett.* **2007**, *48* (50), 8839. doi:10.1016/j.tetlet.2007.10.068.
(15) Mann, G.; Hartwig, J. F. *J. Org. Chem.* **1997**, *62* (16), 5413. doi:10.1021/jo970453v.
(16) Robinson, M. W. C.; Buckle, R.; Mabbett, I.; Grant, G. M.; Graham, A. E. *Tetrahedron Lett.* **2007**, *48* (27), 4723. doi:10.1016/j.tetlet.2007.05.010.
(17) Benyahya, S.; Monnier, F.; Taillefer, M.; Man, M. W. C.; Bied, C.; Ouazzani, F. *Adv. Synth. Catal.* **2008**, *350* (14-15), 2205. doi:10.1002/adsc.200800360.
(18) Fagan, P. J.; Hauptman, E.; Shapiro, R.; Casalnuovo, A. *J. Am. Chem. Soc.* **2000**, *122* (21), 5043. doi:10.1021/ja000094c.
(19) Cai, Q.; Zou, B.; Ma, D. *Angew. Chem. Int. Ed.* **2006**, *45* (8), 1276. doi:10.1002/anie.200503538.
(20) Marcoux, J. F.; Doye, S.; Buchwald, S. L. *J. Am. Chem. Soc.* **1997**, *119* (43), 10539. doi:10.1021/ja971901j.
(21) Buck, E.; Song, Z. J.; Tschaen, D.; Dormer, P. G.; Volante, R. P.; Reider, P. J. *Org. Lett.* **2002**, *4* (9), 1623. doi:10.1021/ol025839t. PMID:11975644.
(22) Chen, Y. J.; Chen, H. H. *Org. Lett.* **2006**, *8* (24), 5609. doi:10.1021/ol062339h. PMID:17107084.
(23) Cristau, H. J.; Cellier, P. P.; Hamada, S.; Spindler, J. F.; Taillefer, M. *Org. Lett.* **2004**, *6* (6), 913. doi:10.1021/ol036290g. PMID:15012063.
(24) Rao, H.; Jin, Y.; Fu, H.; Jiang, Y.; Zhao, Y. *Chem. Eur. J.* **2006**, *12* (13), 3636. doi:10.1002/chem.200501473.
(25) Gujadhur, R. K.; Venkataraman, D. *Synth. Commun.* **2001**, *31* (18), 2865. doi:10.1081/SCC-100105338.
(26) Gujadhur, R. K.; Bates, C. G.; Venkataraman, D. *Org. Lett.* **2001**, *3* (26), 4315. doi:10.1021/ol0170105. PMID:11784206.
(27) Ouali, A.; Spindler, J. F.; Jutand, A. C.; Taillefer, M. *Adv. Synth. Catal.* **2007**, *349* (11-12), 1906. doi:10.1002/adsc.200600628.
(28) Ouali, A.; Laurent, R.; Caminade, A. M.; Majoral, J. P.; Taillefer, M. *J. Am. Chem. Soc.* **2006**, *128* (50), 15990. doi:10.1021/ja066505s. PMID:17165724.
(29) Naidu, A. B.; Jaseer, E. A.; Sekar, G. *J. Org. Chem.* **2009**, *74* (10), 3675. doi:10.1021/jo900438e. PMID:19361190.
(30) Zhang, S. J.; Lu, X. M. *Ionic Liquids: From Fundamental*

Can. J. Chem. Downloaded from www.nrcresearchpress.com by Xi'an Jiaotong University on 09/19/12
For personal use only.

Research to Industrial Applications; Science Press: Beijing, 2006.
(31) Kumar, A.; Rao, M. S.; Ahmad, I.; Khungar, B. *Can. J. Chem.* **2009**, *87* (6), 714. doi:10.1139/V09-049.
(32) Cole, A. C.; Jensen, J. L.; Ntai, I.; Tran, K. L. T.; Weaver, K. J.; Forbes, D. C.; Davis, J. H., Jr. *J. Am. Chem. Soc.* **2002**, *124* (21), 5962. doi:10.1021/ja026290w. PMID: 12022828.
(33) Tan, B.; Jiang, J. Y.; Wang, Y. H.; Wei, L.; Chen, D. J.; Jin, Z. L. *Appl. Organomet. Chem.* **2008**, *22* (11), 620. doi:10.1002/aoc.1431.
(34) Leng, Y.; Wang, J.; Zhu, D. R.; Ren, X. Q.; Ge, H. Q.; Shen, L. *Angew. Chem. Int. Ed.* **2009**, *48* (1), 168. doi:10.1002/anie.200803567.
(35) Zhi, H. Z.; Lü, C. X.; Zhang, Q.; Luo, J. *Chem. Commun. (Camb.)* **2009**, (20): 2878. doi:10.1039/b822481a. PMID: 19436896.

Can. J. Chem. Downloaded from www.nrcresearchpress.com by Xi'an Jiaotong University on 09/19/12
For personal use only.

Far-red absorbing azodipyrrin dyes — Synthesis, X-ray crystallographic, and spectral characterization of 1,9-diazodipyrrins and their metal complexes

Yan Li and David Dolphin

Can. J. Chem. Downloaded from www.nrcresearchpress.com by Xi'an Jiaotong University on 09/19/12
For personal use only.

Abstract: A series of novel 1,9-diazodipyrrins (**4**) were readily synthesized by reacting aryldiazonium salts with 5-aryldipyrromethanes under both acidic and basic conditions. The zinc complex of 1,9-diphenylazodipyrrin (**5aZn**) was confirmed by X-ray crystallographic analysis, and 1,9-diazodipyrrins and their zinc and nickel complexes (**5M**) were characterized by ^{1}H and ^{13}C NMR, IR, UV–vis, and MS. All of the metal complexes absorb almost all colours of the rainbow; the absorption maximums are >650 nm and the half-band widths are over 100 nm. The fluorescence of the zinc complexes of 1,9-diphenylazodipyrrin (**5aZn**) and 1,9-di(2-iodophenylazo)dipyrrin (**5cZn**) were also explored.

Key words: dipyrrin, dipyrromethane, azo dye, boron-dipyrromethene (BODIPY), fluorescence.

Résumé : On a facilement réalisé la synthèse d'une série de nouvelles 1,9-diazodipyrrines (**4**) en faisant réagir des sels d'aryldiazonium avec des 5-aryldipyrrométhanes dans des conditions acides ou basiques. On a confirmé la structure du complexe de zinc de la 1,9-diphénylazodipyrrine (**5aZn**) par diffraction des rayons-X alors que les 1,9-diazodipyrrines et leurs complexes avec le zinc et le nickel (**5M**) ont été caractérisés par leurs spectres RMN du ^{1}H et du ^{13}C, leurs spectres IR, UV–vis et leurs spectres de masse. Tous les complexes métalliques absorbent pratiquement toutes les couleurs de l'arc-en-ciel; les maxima d'absorption sont supérieurs à 650 nm et les largeurs des bandes à demi-hauteur s'etalent sur 100 nm. On a aussi examiné la fluorescence des complexes de zinc de la 1,9-diphénylazodipyrrine (**5aZn**) et de la 1,9-di(2-iodophénylazo)dipyrrine (**5cZn**).

Mots-clés : dipyrrine, dipyrrométhane, colorant azo, bore-dipyrrométhène (BODIPY), fluorescence.

[Traduit par la Rédaction]

Introduction

Dipyrrins are well-known as important building blocks in supramolecular chemistry and as subunits of porphyrins (Fig. 1).[1] Owing to the fluorescent characteristics of their BF_2 complexes (boron-dipyrromethene (BODIPY) dyes), publications related to dipyrrins have increased dramatically during the past two decades.[2] In comparison with their bridged nitrogen analogues, azadipyrromethenes,[3] dipyrrins have smaller absorption maxima, which has limited their potential use as photosensitizers for photodynamic therapy.[4] The design and synthesis of dipyrrin derivatives with longer wavelength absorption has been a challenge in this field. Nucleophilic substitutions and catalyzed coupling reactions on 1,9-dichloro-BODIPY have been adapted to produce BODIPYs with greater absorption maxima (**1**), but their absorption maxima are still <620 nm.[5,6] Until now, among the numerous known dipyrrin derivatives, only a few 1,9-distyryldipyrrin-BF_2 (**2**)[7] and rigid 1,5,9-triaryldipyrrin-BF_2 (**3**)[8] complexes with strong electron-donating substituents (OR and NR_2) have absorption maxima >650 nm. Herein, we report the synthesis, X-ray crystallographic, and spectral characterization of novel 1,9-diazodipyrrins (**4**) and their zinc and nickel complexes (**5M**).

Results and discussion

Synthesis of 1,9-diazodipyrrins

In our initial studies, we employed the use of dipyrromethanes[9] to react with diazonium salts to form the desired 1,9-diazodipyrrins. Unfortunately, the reaction of dipyrromethanes with phenyldiazonium chloride did not afford 2,2′-di(phenylazo)dipyrromethane (**6**) but rather 2,5-diphenylazopyrrole (**7**) was isolated in a 61% yield (Scheme 1). This is the same product that would result from reacting diazonium salts with pyrrole.[10] The degradation reactions between dipyrromethanes and aryldiazonium salts leading to monopyrrollic products are known in the literature and can be assumed to be the result of the strong electrophilic nature of pyrrole.[11,12] Depraetere and Dehaen[12] reported the structure

Received 3 August 2010. Accepted 30 November 2010. Published on the NRC Research Press Web site at canjchem.nrc.ca on 18 March 2011.

Y. Li and D. Dolphin.[1] Department of Chemistry, The University of British Columbia, 2036 Main Mall, Vancouver, BC V6T 1Z1, Canada.

[1]Corresponding author (e-mail: david.dolphin@ubc.ca).

Can. J. Chem. Downloaded from www.nrcresearchpress.com by Xi'an Jiaotong University on 09/19/12
For personal use only.

Fig. 1. Structures of dipyrrin–BF_2 (**1**), distyryldipyrrin–BF_2 (**2**), and the rigid 1,5,9-triaryldipyrrin–BF_2 (**3**) complexes, and 1,9-diazodipyrrins (**4**) and their metal complexes (**5M**).

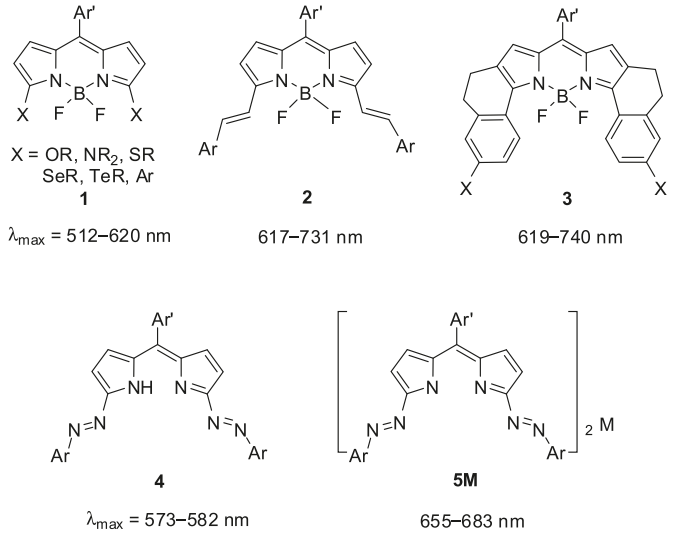

Scheme 1. The reaction between a dipyrromethane and phenyldiazonium chloride.

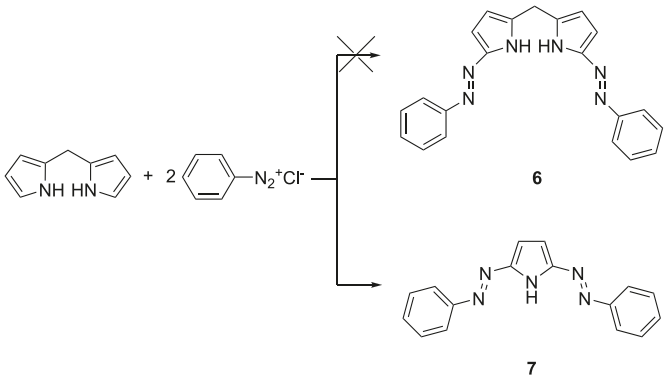

of 1,9-diphenylazo-5,5-dipropyl-dipyrromethane in 2003, but did not provide any supporting analytical data.

While dipyrrins are relatively electron deficient, they can also act as nucleophiles in the presence of Lewis acids to form porphyrins.[13] This characteristic prompted us to investigate the reaction between 5-phenyldipyrrin and phenyldiazonium salt (Scheme 2). 5-Phenyldipyrrin was readily prepared by the reaction of trimethyl orthobenzoate with pyrrole and an excess of dichloroacetic acid.[14] The phenyldiazonium salt was formed by reacting aniline with sodium nitrite – aqueous dichloroacetic acid at temperatures <5 °C.[10] After neutralization with triethylamine and treatment with 0.5 equiv. of 5-phenyldipyrrin in methanol, a red mixture was formed. Chromatography on a silica gel column provided a small amount of purple product that was identified as 1,9-diazodipyrrin **4a** by NMR and MS. When an acidic solution of the phenyldiazonium salt was added directly to the methanol solution of 5-phenyldipyrrin, the same purple compound was isolated in a 15% yield. Further reaction of **4a** with zinc acetylacetonate provided the complex **5aZn**. With the growth of diffraction-quality crystals of **5aZn** by the slow evaporation of a dichloromethane–hexane solution

Scheme 2. The reaction between 5-phenyldipyrrin and phenyldiazonium dichloroacetic salt.

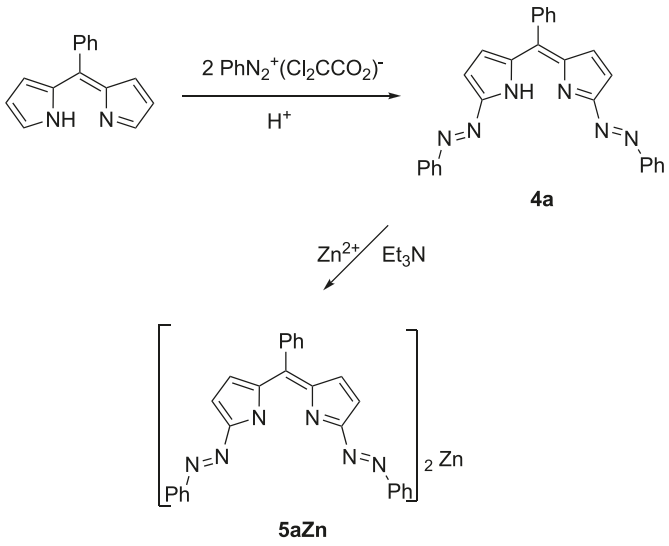

Fig. 2. ORTEP view of **5aZn** (hydrogen atoms are not shown).

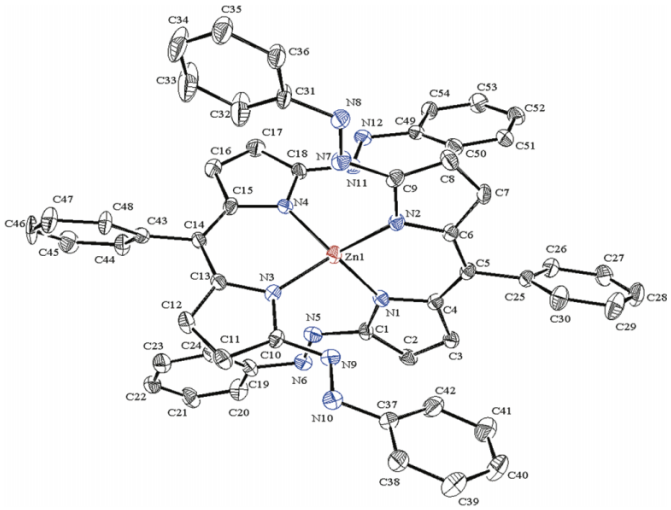

at –5 °C, the structure of complex **5aZn** was confirmed by X-ray crystallographic analysis (Fig. 2; also see the Supplementary data).

With the confirmed structure of the 1,9-diazodipyrrin in hand, we turned our attention to exploration of an alternate synthetic method to improve the yield of 1,9-diazodipyrrins. Interestingly, in contrast to the dipyrromethane, 5-(4-iodophenyl)dipyrromethane[15] was found to react with phenyldiazonium chloride under basic conditions to form 1,9-di(phenylazo)-5-(4-iodophenyl)dipyrromethane (**6d**) (route 1 in Scheme 3). When air was bubbled into an ethyl acetate solution of **6d** for several hours, **6d** was converted into 1,9-(diphenylazo)-5-(4-iodophenyl)dipyrrin (**4d**). Following this method, the reaction of 5-(2,4,6-trimethoxyphenyl)dipyrromethane[16] with phenyldiazonium chloride afforded 1,9-(diphenylazo)-5-(2,4,6-trimethoxyphenyl)dipyrrin (**4e**) in a moderate yield. Furthermore, when the reactions between 5-phenyldipyrrin with aryldiazonium dichloroacetic salts were carried out under acidic conditions, 1,9-diazodipyrrins (**4b**:

Can. J. Chem. Downloaded from www.nrcresearchpress.com by Xi'an Jiaotong University on 09/19/12
For personal use only.

Scheme 3. Synthesis of 1,9-diazodipyrrin complexes starting from 5-aryldipyrromethane and aryldiazonium dichloroacetic salt.

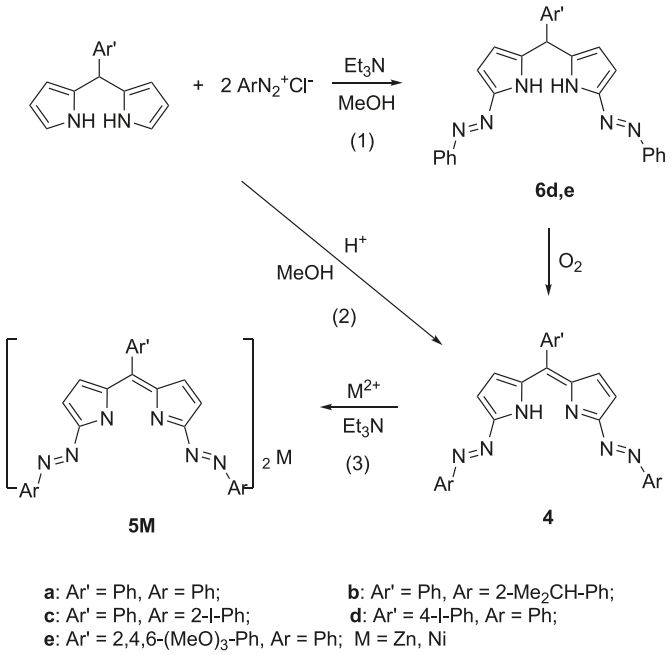

Ar′ = Ph, Ar = 2-Me_2CH-Ph; **4c**: Ar′ = Ph, Ar = 2-I-Ph) were formed directly in a one-pot synthesis (route 2 in Scheme 3). All of the 1,9-diazodipyrrins (**4**) reacted with a zinc salt to form complexes (**5aZn**, **5bZn**, **5cZn**, **5dZn**, and **5eZn**) and **4a** reacted with nickel acetate to form the nickel complex **5aNi** (route 3 in Scheme 3). Whereas complexes **5aZn**, **5aNi**, **5bZn**, **5cZn**, and **5dZn** are fully characterized by NMR, MS, and UV–vis spectra, complex **5eZn** was unstable even when stored at low temperature.

X-ray crystal structure of 5aZn

The structure of **5aZn** was determined by X-ray crystallography and is shown in Fig. 2. Data were collected at –170.0 ± 0.1 °C with maximum 2θ values of 45.1° on a Bruker APEX II diffractometer with graphite-monochromated Mo Kα radiation. The structures were solved by direct methods.[17] The material crystallizes with one disordered phenyl ring (C43–C48), which was modeled in two orientations with restraints to maintain the hexagonal character of the phenyl ring. All refinements were performed using the SHELXL-97[18] via the WinGX[19] interface. Crystal data and structure refinements are summarized in Table 1, and selected bond lengths and angles are listed in Table 2.

Complex **5aZn** has a tetrahedral structure around the central zinc ion. The Zn–N(pyrrole) bond distances are 1.983(4), 1.984(4), 1.981(4), and 1.981(4) Å, respectively, but the N–Zn–N angles within the same diazodipyrrin ligand (92.2(2)° and 91.8(2)°) are smaller than those between two ligands (116.2(2)°, 117.5(2)°, 123.4(2)°, and 117.8(2)°). **5aZn** exhibits N=N bond distances between 1.262 and 1.265 Å, which are slightly longer than that of free 2-phenylazopyrrole (1.253(2) Å) and shorter than those of 2,5-diazopyrroles (1.283–1.293 Å).[10]

Figure 3 shows the top and side view representations of **5aZn**. Whereas 2,5-diazopyrroles have the trans–cis form for their N=N–C(pyrrole) configurations,[10] all N=N–C(pyrrole) configurations in structure **5aZn** are in the trans–trans form as a result of the coordination to the central zinc ion. The diazodipyrrin ligands are slightly distorted, where the dihedral angles between the dipyrrin planes and phenyl planes are 18° and 16° for the ligand of C5 and 19° and 23° for the ligand of C14, respectively. The 5-phenyl groups are not perpendicular to their dipyrrin planes, thus, not parallel to the dipyrrin planes of the other ligands. The 5-phenyl group C25–C30 has angles of 63° to the parent dipyrrin plane and 33° to that of the other ligand; the 5-phenyl group C43–C48 has angles of 63° and 56° to the parent dipyrrin

Table 1. Crystal data and structure refinements for **5aZn**.

Formula	$C_{60}H_{52}N_{12}Zn$
M_w	1006.51
Crystal system	Orthorhombic
Space group	*Pbca* (No. 61)
a (Å)	10.0893(3)
b (Å)	20.2261(7)
c (Å)	50.323(2)
α (°)	90
β (°)	90
γ (°)	90
V (Å^3)	10 269.2(6)
Z	8
D_c (g/cm^3)	1.302
μ (cm^{-1})	5.31
Unique (R_{int} = 0.075)	6791
Reflection/parameter ratio	9.20
*R*1; *wR*2	0.116; 0.120
GoF	1.12
No. of obs. data ($I > 2\sigma(I)$)	4340
*R*1; *wR*2	0.063; 0.104

Table 2. Selected bond distances and angles for **5aZn**.

Bond distances (Å)	
N—N	1.264(5), 1.265(5), 1.262(5), 1.264(5)
N(azo)—C(pyrrole)	1.403(6), 1.399(6), 1.401(6), 1.398(6)
N(azo)—C(phenyl)	1.444(6), 1.431(6), 1.417(6), 1.425(6)
Zn—N	1.983(4), 1.984(4), 1.981(4), 1.981(4)
Bond angles (°)	
N–N–C(pyrrole)	112.6(4), 113.2(4), 113.4(4), 113.9(4)
N–N–C(phenyl)	112.8(4), 113.5(4), 113.0(4), 111.8(4)
N(1)–Zn–N(2,3,4)	92.2(2), 116.2(2), 117.5(2)
N(2)–Zn–N(3,4)	123.4(2), 117.8(2)
N(3)–Zn–N(4)	91.8(2)
C–N–N–C	176.8(4), 174.8(4), 177.1(4), 178.1(4)

Fig. 3. Top and side views of **5aZn** (hydrogen atoms are not shown).

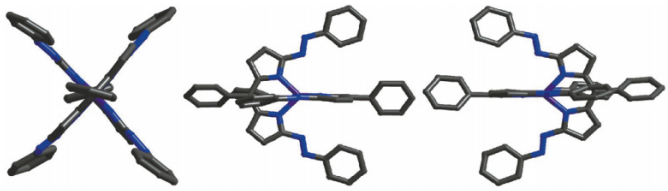

Can. J. Chem. Downloaded from www.nrcresearchpress.com by Xi'an Jiaotong University on 09/19/12
For personal use only.

plane and 33° and 29° to that of the other ligand, respectively. Furthermore, the mean deviations of carbon and nitrogen atoms from the π-delocalized skeletons of the diazodipyrrin ligands are 0.14 and 0.16 Å, respectively.

^{1}H NMR spectra

1,9-Diazodipyrrin (**4a** and **4c**–**4e**) and their complexes (**5aZn**, **5aNi**, **5cZn**, and **5dZn**) exhibit symmetric proton signals in their ^{1}H NMR spectra, but the bulky *ortho*-isopropyl substituents of **4b** and **5bZn** distort their ligand planes and result in distinct proton signals for the two arylazo and two pyrrole groups.

^{1}H NMR spectra were generated at various temperatures between 25 and –80 °C for **4a**, **5aZn**, and **5cZn**, and their pyrrolic proton signals are shown in Fig. 4. Azo dyes have cis and trans isomers, which exist in an equilibrium specific to the solvent and temperature. Upon decreasing the temperature, the equilibrium between the cis and trans isomers shifts toward the cis isomer.[20] The planar 1,9-diazodipyrrin **4a** has two pyrrolic proton signals at 7.05 and 6.78 ppm at room temperature. No significant change was observed for the chemical shift difference of the two pyrrolic protons (0.27 ppm) from 25 to –80 °C (0.25 ppm). This suggests the phenylazo groups have little influence on the pyrrolic proton signals in the same 1,9-diazodipyrrin ligand regardless of whether the cis or trans configuration dominates. However, the chemical shift difference of two pyrrolic protons of **5aZn** increases from 0.00 ppm at 25 °C to 0.31 ppm at –80 °C. This phenomenon suggests that the trans–trans form of the N=N–C(pyrrole) configuration in structure **5aZn** at room temperature shifts toward the cis–trans form at –80 °C, so that the phenylazo group is further away from the pyrrolic groups in an adjacent 1,9-diazodipyrrin ligand and has less influence on their pyrrolic proton signals. Interestingly, the chemical shift difference of the two pyrrolic protons of **5cZn** shows little change from 0.28 ppm at 25 °C to 0.31 ppm at –80 °C. This may be explained by the large radius of the iodo substituent at the ortho position of the –N=N–, which restricts the azo cis/trans isomerization.

UV–vis spectra

Table 3 lists the UV–vis absorption data of **4** and complexes **5M**. Figure 5 shows the UV–vis absorption spectra of **4a**, **5aZn**, and **5aNi**. **4a** has its visible absorption maximum at 528 nm and a half-band width of 119 nm that reflects the overlap of absorptions between the arylazo and dipyrrin chromophores. Complexation with the zinc ion in **5aZn** shifts the absorption maximum bathochromically and forms two distinct and sharper absorptions at 613 and 659 nm with a total half-band width of 108 nm. The absorption on the blue side should be attributed to the azo chromophore as it is less affected by the metal ion; correspondingly, the lower energy absorption can be assigned to the dipyrrin chromophore. With the introduction of the iodo atom, the corresponding absorptions of **5cZn** shift further to 631 and 683 nm. In contrast, complexation with nickel in **5aNi** shifts the absorption maximum to 655 nm and produces a half-band width of 155 nm. As the analogue of **4a**, the 1,9-distyryldipyrrin–BF_2 complex has its absorption maximum at 630 nm.[21]

Fig. 4. The partial ^{1}H NMR spectra of **4a**, **5aZn**, and **5cZn** at temperatures between 25 and –80 °C.

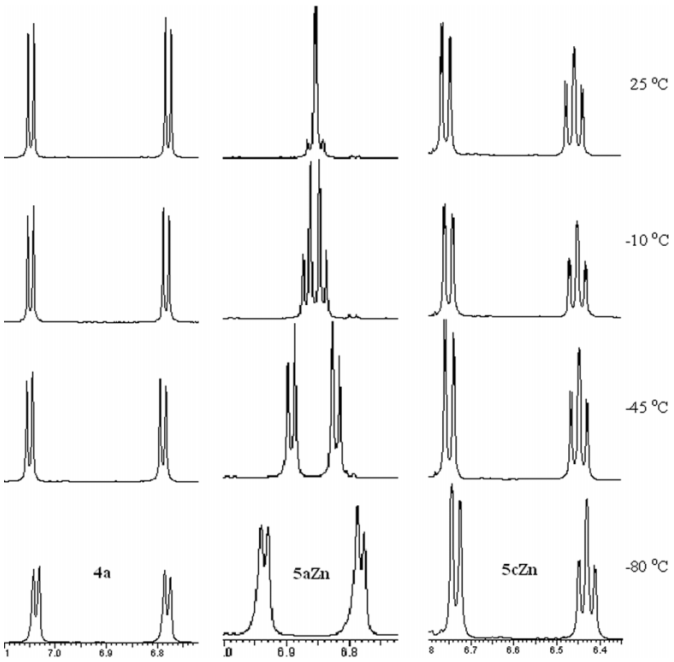

Table 3. The UV–vis absorption data of 1,9-diazodipyrrins (**4**) and their complexes (**5M**) in $CHCl_3$.

Compd.	λ_{max} (log ε) (nm)	Half-band width (nm)
4a	574 (4.47)	119
4b	580 (4.49)	136
4c	582 (4.52)	149
4d	573 (4.50)	130
4e	573 (4.54)	144
5aZn	613 (4.61), 659 (4.67)	108
5aNi	655 (4.62)	155
5bZn	615 (4.66), 674 (4.68)	136
5cZn	631 (4.80), 683 (4.83)	122
5dZn	615 (4.63), 662 (4.67)	128
5eZn	628, 674	128

Fluorescence

Since the zinc complexes of dipyrrins are reported to be fluorescent,[22] the fluorescence of complexes **5aZn** and **5cZn** were examined at room temperature. When **5aZn** was excited at a wavelength of 630 nm, a weak but noticeable emission was detected with a maximum wavelength of 690 nm (Fig. 6). Complex **5eZn** might have better emission because of the restricted rotation of the bulky 5-(2,4,6-trimethoxy)phenyl group,[22,23] but it decomposed during the detection process. Interestingly, **5cZn**, which is stable, did not fluoresce when excited at 650 nm, which is consistent with the heavy atom effect of the iodines.[4,24]

Conclusion

In this work, we report the facile synthesis of 1,9-diazodipyrrins and select metal complexes as novel dipyrrin and azo dye derivatives. Along with only a few 1,9-distyryldipyrrin–BF_2 and rigid 1,5,9-triaryldipyrrin–BF_2 complexes

Can. J. Chem. Downloaded from www.nrcresearchpress.com by Xi'an Jiaotong University on 09/19/12
For personal use only.

Fig. 5. Absorption spectra of **4a** (black line) and complexes **5aZn** (purple line) and **5aNi** (blue line) in chloroform.

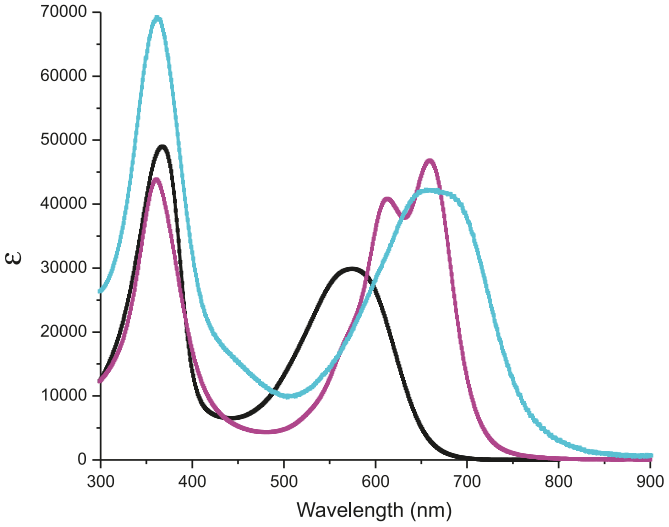

Fig. 6. Fluorescence spectrum of **5aZn** in chloroform with excitation at 630 nm.

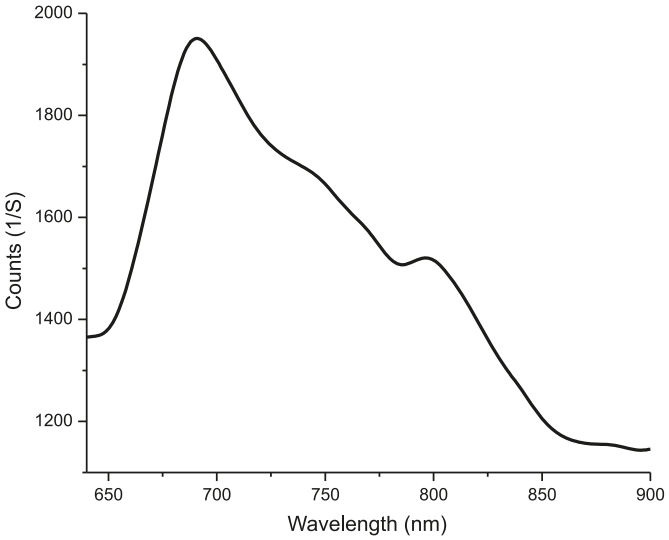

with strong electron-donating substituents, these compounds constitute a rare group of dipyrrin derivatives with absorption maxima >650 nm, an important feature for potential photodynamic therapy (PDT) agents. As well, initial studies show the **5aZn** complex exhibits weak fluoresence. Future work entails the introduction of π-conjugated substituents (SR, OR, I, Br, and NO_2) to the two ortho positions of the arylazo group to restrict cis/trans isomerization of the –N=N– bond. These changes, as well as complexation with BF_2, should enhance fluorescence efficiency.

Experimental

All starting materials, reagents, and solvents were commercially available and used as received. Column chromatography was performed using 230–400 mesh silica gel. Melting points are uncorrected. ^{1}H and ^{13}C NMR spectra were recorded in $CDCl_3$ with a 400 MHz spectrometer (J in Hz); the chemical shifts (δ, ppm) are quoted relative to the residual nondeuterated solvent ($CHCl_3$). UV–vis spectra were measured in $CHCl_3$. IR spectra were measured as solid samples and N=N stretching vibrations were designated referring to the literature.[25] Mass spectra were measured using ESI and MALDI-TOF.

General procedure for the preparation of 1,9-diazodipyrrins 4a–4c

To a suspension of the aromatic amine (4.0 mmol) in water (8 mL) was added dichloroacetic acid (12 mmol, 1.0 mL). The solution was cooled and kept at 0–5 °C in an ice bath and diazotized by addition of a solution of sodium nitrite (4.1 mmol, 0.283 g) in water (3 mL), followed by stirring for 30 min at 0–5 °C. To a solution of the dipyrrin (2 mmol) and dichloroacetic acid (2 mmol, 0.17 mL) in methanol (80 mL) was slowly added a solution of the diazonium salt at 0–5 °C. The resulting mixture was stirred for 5 h and then evaporated under vacuum to dryness. The residues were purified by column chromatography, eluting with a gradient mixture of ethyl acetate and hexane (1:20 to 1:10) for **4a** and dichloromethane and hexane (2:3) for **4b** and **4c**.

1,9-Diphenylazo-5-phenyldipyrrin (4a)

Yield: 42%; mp 133–134 °C. UV–vis (1.05×10^{-5} mol/L, CH_2Cl_2) λ_{max} (log ε): 367 (4.69), 574 (4.47). IR (N=N, cm^{-1}) ν: 1053. ^{1}H NMR ($CDCl_3$) δ: 13.05 (b, 1H), 8.04 (d, 4H, J = 6.9), 7.59–7.52 (m, 11H), 7.04 (d, 2H, J = 4.7), 6.76 (d, 2H, J = 4.4). ^{13}C NMR ($CDCl_3$) δ: 163.4, 153.6, 143.1, 143.0, 136.4, 131.9, 131.3, 130.6, 129.6, 129.4, 128.1, 123.6, 115.2. ESI MS $(M + H)^+$ m/z: 429. Anal. calcd for $C_{27}H_{20}N_6 \cdot 1/4C_6H_{14}$ (solvent of crystallization determined by NMR): C 76.06, H 5.26, N 18.67; found: C 76.07, H 4.89, N 18.62.

1,9-Di(2-isopropylphenylazo)-5-phenyldipyrrin (4b)

Yield: 34%; mp 123–124 °C. UV–vis (1.13×10^{-5} mol/L, $CHCl_3$) λ_{max}: 372 (4.66), 580 (4.49). IR (N=N, cm^{-1}) ν: 1038. ^{1}H NMR (CD_2Cl_2) δ: 13.20 (b, 1H), 7.81 (d, 2H, J = 8.0), 7.59–7.48 (m, 9H), 7.33–7.28 (m, 2H), 7.04 (d, 2H, J = 4.5), 6.78 (d, 2H, J = 4.5), 4.23–4.16 (m, 2H), 1.39 (s, 6H), 1.38 (s, 6H). ^{13}C NMR (CD_2Cl_2) δ: 164.0, 150.8, 150.0, 143.3, 136.7, 132.8, 131.6, 130.7, 130.0, 128.5, 127.2, 126.8, 126.4, 116.1, 115.6, 28.5, 24.3. ESI MS $(M + H)^+$ m/z: 513.4. Anal. calcd for $C_{33}H_{32}N_6$: C 77.31, H 6.29, N 16.39; found: C 77.35, H 6.58, N 16.26.

1,9-Di(2-iodophenylazo)-5-phenyldipyrrin (4c)

Yield: 38%; mp 159–160 °C. UV–vis (9.9×10^{-6} mol/L, $CHCl_3$) λ_{max}: 376 (4.63), 582 (4.52). IR (N=N, cm^{-1}) ν: 1065. ^{1}H NMR (CD_2Cl_2) δ: 13.3 (1H), 8.08 (d, 2H, J = 8.0), 7.80 (d, 2H, J = 6.8), 7.59–7.53 (m, 5H), 7.50–7.47 (m, 2H), 7.24–7.21 (m, 2H), 7.10 (d, 2H, J = 4.6), 6.79 (m, 2H, J = 4.5). ^{13}C NMR (CD_2Cl_2) δ: 163.4, 152.2, 144.2, 143.7, 140.7, 136.3, 133.7, 131.6, 131.0, 130.2, 129.6, 128.6, 117.6, 117.3, 105.0. ESI MS $(M + H)^+$ m/z: 681.1. Anal. calcd for $C_{27}H_{18}I_2N_6$: C 47.67, H 2.67, N 12.35; found: C 47.92, H 2.81, N 12.00.

General procedure for the preparation of 1,9-diazodipyrrins 4d and 4e

To a suspension of the aromatic amine (4.0 mmol) in

Can. J. Chem. Downloaded from www.nrcresearchpress.com by Xi'an Jiaotong University on 09/19/12
For personal use only.

water (8 mL) was added dichloroacetic acid (12 mmol, 1.0 mL). The solution was cooled and kept at 0–5 °C in an ice bath and diazotized by addition of a solution of sodium nitrite (4.1 mmol, 0.283 g) in water (3 mL), followed by stirring for 30 min at 0–5 °C. To a solution of the dipyrrin (2 mmol) and triethylamine (25 mmol, 3.5 mL) in methanol (80 mL) was slowly added a solution of the diazonium salt at 0–5 °C. The resulting mixture was stirred for 5 h and then evaporated under vacuum to dryness. The residues were dissolved in ethyl acetate and washed with water. Air was bubbled into the organic phase for 4 h and then evaporated and purified by column chromatography, eluting with a mixture of ethyl acetate and hexane (1:20).

1,9-Diphenylazo-5-(4-iodophenyl)dipyrrin (4d)

Yield: 43%; mp 164–166 °C. UV–vis (1.03×10^{-5} mol/L, $CHCl_3$) λ_{max}: 372 (4.63), 573 (4.50). IR (N=N, cm^{-1}) ν: 1044. ^1H NMR (CD_2Cl_2) δ: 8.06 (d, 4H, J = 6.8), 7.91 (d, 2H, J = 8.3), 7.64–7.57 (m, 6H), 7.35 (d, 2H, J = 8.3), 7.07 (d, 2H, J = 4.4), 6.77 (d, 2H, J = 4.4). ^{13}C NMR (CD_2Cl_2) δ: 163.3, 153.4, 142.7, 137.4, 135.7, 132.8, 132.1, 130.2, 129.4, 129.2, 123.4, 122.1, 115.6. ESI MS $(M + H)^+$ m/z: 555.2. Anal. calcd for $C_{27}H_{19}IN_6 \cdot 2/5C_6H_{14}$ (solvent of crystallization determined by NMR): C 59.97, H 4.21, N 14.27; found: C 60.24, H 3.78, N 14.09.

1,9-Diphenylazo-5-(2,4,6-trimethoxyphenyl)dipyrrin (4e)

Yield: 40%; mp 180–181 °C. UV–vis (1.06×10^{-5} mol/L, $CHCl_3$) λ_{max}: 351 (4.60), 573 (4.54). IR (N=N, cm^{-1}) ν: 1050. ^1H NMR (CD_2Cl_2) δ: 12.78 (b, 1H), 8.04 (d, 4H, J = 7.4), 7.59 (t, 4H, J = 7.5), 7.54 (t, 2H, J = 7.2), 6.99 (d, 2H, J = 4.5), 6.69 (d, 2H, J = 4.4), 6.30 (s, 2H), 3.92 (s, 3H), 3.74 (s, 6H). ^{13}C NMR (CD_2Cl_2) δ: 162.2, 162.0, 158.9, 152.9, 143.8, 136.1, 131.2, 128.8, 128.7, 122.7, 114.8, 105.3, 90.1, 55.5, 55.0. ESI MS $(M + H)^+$ m/z: 519.4. Anal. calcd for $C_{30}H_{26}N_6O_3 \cdot 1/5C_6H_{14}$ (solvent of crystallization determined by NMR): C 69.94, H 5.42, N 15.68; found: C 69.78, H 5.33, N 15.33.

General procedure for the preparation of zinc complexes of 1,9-diazodipyrrins (5Zn)

The solution of 1,9-diazodipyrrin (0.06 mmol), zinc acetylacetonate hydrate (0.03 mmol, 8 mg), and triethylamine (0.2 mmol, 28 μL) in dry dichloromethane (30 mL) was refluxed for 1 h and then evaporated under vacuum to dryness. The residue was purified by column chromatography, eluting with a mixture of ethyl acetate and hexane (1:20) for **5aZn**, **5dZn**, and **5eZn** and dichloromethane and hexane (2:3) for **5bZn** and **5cZn**.

Zinc complex of 1,9-diphenylazo-5-phenyldipyrrin (5aZn)

Yield: 90%. UV–vis (1.03×10^{-5} mol/L, CH_2Cl_2) λ_{max} (log ε): 361 (4.64), 613 (4.61), 659 (4.67). IR (N=N, cm^{-1}) ν: 1043. ^1H NMR ($CDCl_3$) δ: 7.56 (t, 1H, J = 7.4), 7.50 (t, 2H, J = 7.5), 7.43 (dd, 6H, J = 7.6, 1.3), 7.32 (t, 2H, J = 7.2), 7.25 (t, 4H, J = 7.55), 6.83 (d, 2H, J = 4.5), 6.79 (d, 2H, J = 4.5). ^{13}C NMR ($CDCl_3$) δ: 166.4, 153.8, 149.4, 143.2, 138.4, 133.9, 131.4, 131.0, 129.2, 129.0, 127.6, 123.3, 111.8. MALDI-TOF MS $(M)^+$ m/z: 918. Anal. calcd for $C_{54}H_{38}N_{12}Zn \cdot 1/2H_2O \cdot 1/2C_6H_{14}$ (solvents of crystallization determined by NMR): C 70.40, H 4.77, N 17.28; found: C 70.08, H 4.62, N 16.90.

Zinc complex of 1,9-di(2-isopropylphenylazo)-5-phenyldipyrrin (5bZn)

Yield: 88%. UV–vis (1.06×10^{-5} mol/L, $CHCl_3$) λ_{max} (log ε): 367 (4.66), 615 (4.66), 674 (4.68). IR (N=N, cm^{-1}) ν: 1047. ^1H NMR (CD_2Cl_2) δ: 7.67–7.59 (m, 10H), 7.34–7.31 (m, 8H), 7.02 (d, 4H, J = 8.0), 6.95–6.88 (m, 8H), 6.79 (d, 4H, J = 4.5), 3.93–3.86 (m, 4H), 1.19 (s, 12H), 1.17 (s, 12H). ^{13}C NMR (CD_2Cl_2) δ: 167.4, 150.7, 149.0, 148.6, 142.8, 138.2, 133.9, 131.7, 131.4, 129.3, 127.7, 126.4, 126.2, 115.1, 108.4, 27.6, 23.6. ESI MS $(M + H)^+$ m/z: 1087.8. Anal. calcd for $C_{66}H_{62}N_{12}Zn \cdot 2/3C_6H_{14}$ (solvent of crystallization determined by NMR): C 73.36, H 6.27, N 14.67; found: C 73.53, H 6.22, N 14.68.

Zinc complex of 1,9-di(2-iodophenylazo)-5-phenyldipyrrin (5cZn)

Yield: 92%. UV–vis (1.50×10^{-5} mol/L, $CHCl_3$) λ_{max} (log ε): 370 (4.69), 631 (4.80), 683 (4.83). IR (N=N, cm^{-1}) ν: 1051. ^1H NMR (CD_2Cl_2) δ: 7.93–7.92 (dd, 2H, J = 7.0, 2.0), 7.66–7.57 (m, 10H), 7.15–7.12 (dt, 4H, J = 8.1, 1.3), 7.08–7.04 (m, 4H), 6.94–6.93 (dd, 2H, J = 6.4, 2.5), 6.91–6.88 (q, 4H, J = 9.9), 6.76–6.75 (dd, 4H, J = 8.0, 1.4), 6.47–6.44 (dt, 4H, J = 7.9, 1.5). ^{13}C NMR (CD_2Cl_2) δ: 167.1, 153.0, 144.0, 140.4, 139.4, 134.8, 132.9, 131.8, 129.9, 128.3, 120.2, 117.7, 115.1, 110.4, 103.9. MALDI-TOF MS m/z: 1421.8. Anal. calcd for $C_{54}H_{34}I_4N_{12}Zn \cdot 1/2CH_2Cl_2$ (solvents of crystallization determined by NMR): C 44.64, H 2.41, N 11.46; found: C 44.23, H 2.63, N 11.42.

Zinc complex of 1,9-diphenylazo-5-(4-iodophenyl)dipyrrin (5dZn)

Yield: 85%. UV–vis (9.42×10^{-6} mol/L, $CHCl_3$) λ_{max} (log ε): 369 (4.68), 615 (4.63), 662 (4.67). IR (N=N, cm^{-1}) ν: 1040. ^1H NMR (CD_2Cl_2) δ: 7.90 (d, 4H, J = 8.6), 7.42 (d, 8H, J = 7.1), 7.38 (t, 4H, J = 7.3), 7.29 (t, 8H, J = 7.7), 7.19 (d, 4H, J = 8.4), 6.89 (d, 4H, J = 4.6), 6.83 (d, 4H, J = 4.4). ^{13}C NMR (CD_2Cl_2) δ: 166.9, 154.1, 148.5, 143.2, 138.1, 137.3, 134.2, 133.4, 131.8, 129.5, 123.5, 112.6, 95.9. ESI MS $(M + H)^+$ m/z: 1171.1. Anal. calcd for $C_{54}H_{36}I_2N_{12}Zn \cdot 4/7C_6H_{14}$ (solvent of crystallization determined by NMR): C 56.47, H 3.63, N 13.76; found: C 56.01, H 3.62, N 13.38.

Zinc complex of 1,9-diphenylazo-5-(2,4,6-trimethoxyphenyl)dipyrrin (5eZn)

Yield: 76%. UV–vis ($CHCl_3$) λ_{max}: 356, 628, 674. IR (N=N, cm^{-1}) ν: 1048. MALDI-TOF MS $(M + H)^+$ m/z: 1099.4.

Preparation of the nickel complex of 1,9-diphenylazo-5-phenyldipyrrin (5aNi)

A solution of **4a** (0.06 mmol, 25.7 mg), nickel acetate tetrahydrate (0.03 mmol, 7.5 mg), and triethylamine (0.2 mmol, 28 μL) in dry dichloromethane (30 mL) was refluxed for 1 h and then evaporated under vacuum to dryness. The residue was purified by column chromatography, eluting with a mixture of ethyl acetate and hexane (1:20) to give the product. Yield: 92%. UV–vis (1.10×10^{-5} mol/L, $CHCl_3$) λ_{max} (log ε): 361 (4.84), 655 (4.62). IR

(N=N, cm^{-1}) ν: 1054. ^1H NMR (CD_2Cl_2) δ: 7.64 (9H), 7.50 (4H), 6.89 (6H). ^{13}C NMR ($CDCl_3$) δ: 170.0, 146.1, 141.8, 138.1, 132.9, 131.3, 130.0, 129.7, 129.1, 128.7, 122.9, 121.7, 104.2. ESI MS $(M + Na)^+$ *m/z*: 935.3. Anal. calcd for $C_{54}H_{38}N_{12}Ni \cdot 1/2H_2O$: C 70.29, H 4.26, N 18.22; found: C 70.11, H 4.24, N 17.93.

Supplementary data

Supplementary data (^1H NMR, ^{13}C NMR, and UV–vis spectra) are available with this article through the journal Web site (www.nrcresearchpress.com/cjc). CCDC 784639 contains the X-ray data in CIF format for this manuscript. These data can be obtained, free of charge, via http://www.ccdc.cam.ac.uk/conts/retrieving.html (or from the Cambridge Crystallographic Data Centre, 12 Union Road, Cambridge CB2 1EZ, UK; fax +44 1223 336033; or deposit@ccdc.cam.ac.uk).

Acknowledgement

This work was supported by QLT Inc., Vancouver, British Columbia, and the Natural Sciences and Engineering Research Council of Canada (NSERC). We thank the NMR, Mass Spectroscopy, and Elemental Analysis labs of the Chemistry Department at the University of British Columbia, Vancouver, British Columbia.

References

(1) Wood, T. E.; Thompson, A. *Chem. Rev.* **2007**, *107* (5), 1831. doi:10.1021/cr050052c.

(2) (a) Loudet, A.; Burgess, K. *Chem. Rev.* **2007**, *107* (11), 4891. doi:10.1021/cr078381n.; (b) Ulrich, G.; Ziessel, R.; Harriman, A. *Angew. Chem.* **2008**, *47* (7), 1184. doi:10.1002/anie.200702070.

(3) Li, Y.; Dolphin, D.; Patrick, B. O. *Tetrahedron Lett.* **2010**, *51* (5), 811. doi:10.1016/j.tetlet.2009.12.003.

(4) Yogo, T.; Urano, Y.; Ishitsuka, Y.; Maniwa, F.; Nagano, T. *J. Am. Chem. Soc.* **2005**, *127* (35), 12162. doi:10.1021/ja0528533.

(5) (a) Rohand, T.; Baruah, M.; Qin, W.; Boens, N.; Dehaen, W. *Chem. Commun. (Camb.)* **2006**, 266. doi:10.1039/b512756d.; (b) Dilek, O.; Bane, S. L. *Tetrahedron Lett.* **2008**, *49* (8), 1413. doi:10.1016/j.tetlet.2007.12.052.; (c) Li, L.; Nguyen, B.; Burgess, K. *Bioorg. Med. Chem. Lett.* **2008**, *18* (10), 3112. doi:10.1016/j.bmcl.2007.10.103.; (d) Han, J.; Gonzalez, O.; Aguilar-Aguilar, A.; Pena-Cabrera, E.; Burgess, K. *Org. Biomol. Chem.* **2009**, *7* (1), 34. doi:10.1039/b818390b.; (e) Qin, W.; Leen, V.; Dehaen, W.; Cui, J.; Xu, C.; Tang, X.; Liu, W.; Rohand, T.; Beljonne, D.; Averbeke, B. V.; Clifford, J. N.; Driesen, K.; Binnemans, K.; Auweraer, M. V.; Boens, N. *J. Phys. Chem. C* **2009**, *113* (27), 11731. doi:10.1021/jp9017822.; (f) Fron, E.; Coutiño-Gonzalez, E.; Pandey, L.; Sliwa, M.; Van der Auweraer, M.; De Schryver, F. C.; Thomas, J.; Dong, Z.; Leen, V.; Smet, M.; Dehaen, W.; Vosch, T. *New J. Chem.* **2009**, *33* (7), 1490. doi:10.1039/b900786e.

(6) Rohand, T.; Qin, W.; Boens, N.; Dehaen, W. *Eur. J. Org. Chem.* **2006**, *2006* (20), 4658. doi:10.1002/ejoc.200600531.

(7) (a) Yu, Y.-H.; Descalzo, A. B.; Shen, Z.; Rohr, H.; Liu, Q.; Wang, Y.-W.; Spieles, M.; Li, Y.-Z.; Rurack, K.; You, X.-Z. *Chem. Asian J.* **2006**, *1* (1–2), 176. doi:10.1002/asia.200600042.; (b) Zheng, Q.; Xu, G.; Prasad, P. N. *Chem. Eur. J.* **2008**, *14* (19), 5812. doi:10.1002/chem.200800309.; (c) Barin, G.; Yilmaz, M. D.; Akkaya, E. U. *Tetrahedron Lett.* **2009**, *50* (15), 1738. doi:10.1016/j.tetlet.2009.01.141.; (d) Diring, S.; Puntoriero, F.; Nastasi, F.; Campagna, S.; Ziessel, R. *J. Am. Chem. Soc.* **2009**, *131* (17), 6108. doi:10.1021/ja9015364.; (e) Guliyev, R.; Coskun, A.; Akkaya, E. U. *J. Am. Chem. Soc.* **2009**, *131* (25), 9007. doi:10.1021/ja902584a.

(8) (a) Chen, J.; Burghart, A.; Derecskei-Kovacs, A.; Burgess, K. *J. Org. Chem.* **2000**, *65* (10), 2900. doi:10.1021/jo991927o.; (b) Mei, Y.; Bentley, P. A.; Wang, W. *Tetrahedron Lett.* **2006**, *47* (14), 2447. doi:10.1016/j.tetlet.2006.01.091.

(9) Littler, B. J.; Miller, M. A.; Hung, C.-H.; Wagner, R. W.; O'Shea, D. F.; Boyle, P. D.; Lindsey, J. S. *J. Org. Chem.* **1999**, *64* (4), 1391. doi:10.1021/jo982015+.

(10) Li, Y.; Patrick, B. O.; Dolphin, D. *J. Org. Chem.* **2009**, *74* (15), 5237. doi:10.1021/jo9003019.

(11) (a) Treibs, A.; Derra-Scherer, H. *Liebigs Ann. Chem.* **1954**, *589* (3), 196. doi:10.1002/jlac.19545890306.; (b) Treibs, A.; Fritz, G. *Liebigs Ann. Chem.* **1958**, *611* (1), 162. doi:10.1002/jlac.19586110117.; (c) Butler, A. R.; Shepherd, P. T. *J. Chem. Soc., Perkin Trans. 2* **1980**, *113*. doi:10.1039/P29800000113.

(12) Depraetere, S.; Dehaen, W. *Tetrahedron Lett.* **2003**, *44* (2), 345. doi:10.1016/S0040-4039(02)02521-2.

(13) Yon-Hin, P.; Scott, A. I. *Tetrahedron Lett.* **1991**, *32* (34), 4231. doi:10.1016/S0040-4039(00)92135-X.

(14) Reese, C. B.; Yan, H. *Tetrahedron Lett.* **2001**, *42* (32), 5545. doi:10.1016/S0040-4039(01)01031-0.

(15) Lee, C.-H.; Lindsey, J. S. *Tetrahedron* **1994**, *50* (39), 11427. doi:10.1016/S0040-4020(01)89282-6.

(16) Milanesio, M. E.; Moran, F. S.; Ines Yslas, E.; Gabriela Alvarez, M.; Rivarola, V.; Durantini, E. N. *Bioorg. Med. Chem.* **2001**, *9* (8), 1943. doi:10.1016/S0968-0896(01)00138-9.

(17) Altomare, A.; Burla, M. C.; Camalli, M.; Cascarano, G. L.; Giacovazzo, C.; Guagliardi, A.; Moliterni, A. G. G.; Polidori, G.; Spagna, R. *J. Appl. Cryst.* **1999**, *32* (1), 115. doi:10.1107/S0021889898007717.

(18) *SHELXTL,* version 5.1; Bruker AXS Inc.: Madison, WI, 1997.

(19) Farrugia, L. J. *J. Appl. Cryst.* **1999**, *32* (4), 837. doi:10.1107/S0021889899006020.

(20) Brode, W. R.; Gould, J. H.; Wyman, G. M. *J. Am. Chem. Soc.* **1953**, *75* (8), 1856. doi:10.1021/ja01104a022.

(21) Rurack, K.; Kollmannsberger, M.; Daub, J. *N. J. Chem.* **2001**, *25* (2), 289. doi:10.1039/b007379m.

(22) Sazanovich, I. V.; Kirmaier, C.; Hindin, E.; Yu, L.; Bocian, D. F.; Lindsey, J. S.; Holten, D. *J. Am. Chem. Soc.* **2004**, *126* (9), 2664. doi:10.1021/ja038763k.

(23) Thoi, V. S.; Stork, J. R.; Magde, D.; Cohen, S. M. *Inorg. Chem.* **2006**, *45* (26), 10688. doi:10.1021/ic061581h.

(24) Killoran, J.; Allen, L.; Gallagher, J. F.; Gallagher, W. M.; O'Shea, D. F. *Chem. Commun. (Camb.)* **2002**, 1862. doi:10.1039/b204317c.

(25) Zemskov, A. V.; Rodionova, G. N.; Tuchin, Yu. G.; Karpov, V. V. *J. Appl. Spectrosc.* **1988**, *49* (4), 1020. doi:10.1007/BF00657220.

Can. J. Chem. Downloaded from www.nrcresearchpress.com by Xi'an Jiaotong University on 09/19/12
For personal use only.

The synthesis of the 8-*C*-substituted 2,6-diamino-9-[2-(phosphonomethoxy)ethyl]purine (PMEDAP) derivatives by diverse cross-coupling reactions

Ondřej Sedláček, Petra Břehová, Radek Pohl, Antonín Holý, and Zlatko Janeba

Can. J. Chem. Downloaded from www.nrcresearchpress.com by Xi'an Jiaotong University on 09/19/12
For personal use only.

Abstract: Diisopropyl 8-bromo-2,6-diamino-9-[2-(phosphonomethoxy)ethyl]purine was used as a starting material for the synthesis of the 8-*C*-substituted 2,6-diamino-9-[2-(phosphonomethoxy)ethyl]purine (PMEDAP) analogues. A systematic screening of diverse cross-coupling reactions was carried out. Stille, Suzuki–Miyaura, Negishi, and Sonogashira cross-couplings, as well as Pd-catalysed reactions with trialkylaluminiums, were employed for the introduction of various alkyl, alkenyl, alkynyl, aryl, and hetaryl substituents to the C-8 position of the 2,6-diaminopurine moiety. In contrast to the potent parent compound PMEDAP, which exhibits potent antiretroviral and antitumor activity, none of the sixteen newly synthesized 8-*C*-substituted analogues of PMEDAP showed any specific antiviral activity.

Key words: acyclic nucleoside phosphonates, PMEDAP, cross-coupling, antiviral, antitumor.

Résumé : On a réalisé la synthèse d'analogues substitués en 8-*C* de la 2,6-diamino-9-[2-(phosphonométhoxy)éthyl]purine (PMEDAP) en utilisant le dérivé diisopropyle de la 8-bromo-2,6-diamino-9-[2-(phosphonométhoxy)éthyl]purine comme produit de départ. On a effectué une évaluation systématique de diverses réactions de couplages croisés. On a utilisé les couplages croisés de Stille, Suzuki–Miyaura, Negishi et Sonogashira ainsi que les réactions catalysées par le palladium avec des dérivés de type trialkylaluminium pour effectuer l'introduction de substituants alkyle, alkényle, alkynyle, aryle et hétaryle dans la position C-8 de la portion 2,6-aminopurine. Par opposition au composé fondamental PMEDAP qui présente une activité antirétrovirale et antitumorale importante, aucun des seize nouveaux analogues de synthèse du PMEDAP portant un substituant en position C-8 ne présente d'activité antivirale spécifique.

Mots-clés : phosphonates de nucléoside acycliques, PMEDAP, couplage-croisé, antiviral, antitumoral.

[Traduit par la Rédaction]

Introduction

Acyclic nucleoside phosphonates[1] (ANPs) are nucleotide analogues with a wide range of biological activities, especially antiviral,[2] antiparasitic,[3] cytostatic,[4] and immunomodulatory.[5] Extensive structure–activity relationship (SAR) studies of ANPs have been conducted to increase their potential for biological properties, leading to potential drug candidates and approved drugs.[2c,6]

Analogues with a 2,6-diaminopurine (DAP) base occupy a special place among ANPs, as their antiviral activity and potency is comparable to that of their adenine counterparts.[2c] For its remarkable biological and therapeutic properties, 2,6-diamino-9-[2-(phosphonomethoxy)ethyl]purine (PMEDAP) constitutes an attractive candidate for the treatment of both retrovirus and herpesvirus infections.[2c] Furthermore, N^6-substituted PMEDAP derivatives, and especially N^6-cyclopropyl-PMEDAP, possess promising cytostatic and tumour-cell differentiation-inducing properties.[7] A novel prodrug of the cytostatic agent 9-[2-(phosphonomethoxy)ethyl]guanine (PMEG), GS-9219, has potential for the treatment of non-Hodgkin lymphoma (NHL).[8] It has been shown that the N^6-substituted PMEDAP derivatives act as prodrugs of PMEG,[7] and that the enzymes that catalyse their conversion to PMEG are human abacavir monophosphate (hABC-MP) deaminase[9] and the recently identified N^6-methyl-AMP aminohydrolase.[10]

The SAR studies of ANPs involve various modifications of the phosphonate moiety, of the aliphatic linker, and of the purine and pyrimidine bases. A C-8 position of the purine ring is a clear option for the base modification of the purine derivatives. A number of ANPs substituted at the C-8 position of the purine have previously been prepared by nucleophilic substitution from the corresponding 8-bromopurine derivatives.[11] Various cross-coupling techniques have recently been developed for the syntheses of purines bearing carbon substituents at the C-8 position,[12] although the cross-coupling reactions were studied more extensively at the C-6 position of the purine moiety.[13]

Within the SAR studies of ANPs and also from the synthetic point of view, we decided to prepare a series of PMEDAP derivatives substituted at the C-8 position of the purine

Received 12 October 2010. Accepted 17 December 2010. Published on the NRC Research Press Web site at canjchem.nrc.ca on 18 March 2011.

O. Sedláček, P. Břehová, R. Pohl, A. Holý, and Z. Janeba.[1] Institute of Organic Chemistry and Biochemistry, Academy of Sciences of the Czech Republic, Flemingovo nám. 2, CZ-166 10 Prague 6, Czech Republic.

[1]Corresponding author (e-mail: janeba@uochb.cas.cz).

Can. J. Chem. Downloaded from www.nrcresearchpress.com by Xi'an Jiaotong University on 09/19/12
For personal use only.

Table 1. Stille cross-coupling to produce compounds **2** (reagents: Method A: $Pd(PPh_3)_4$, NMP, 100 °C; Method B: Pd_2dba_3, $AsPh_3$, NMP, 100 °C); deprotection to produce compounds **3** (reagents: $(CH_3)_3SiBr$, CH_3CN, room temperature).

Entry	R	R–M	Product	Yield[a] (%)	Product	Yield[a] (%)
1[b]	Me –	Me_4Sn	**2a**	17	**3a**	67
2[b]	Et –	Et_4Sn	**2b**	22	**3b**	81
3[b]		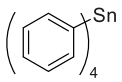	**2c**	39	**3c**	78
4[b]		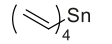	**2d**	43	**3d**	—
5[c]		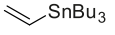	**2d**	84	**3d**	69
6[b]		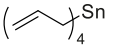	**2e**	8	**3e**	—
7[c]		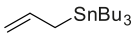	**2e**	50	**3e**	68
8[c]		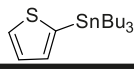	**2f**	59	**3f**	75

[a] Isolated yields.
[b] Method A.
[c] Method B.

Scheme 1. General synthesis of 8-*C*-substituted 2,6-diamino-9-[2-(phosphonomethoxy)ethyl]purine (PMEDAP) derivatives. Reagents: (*i*) R–M, Pd catalyst, solvent; (ii) $(CH_3)_3SiBr$, CH_3CN, room temperature.

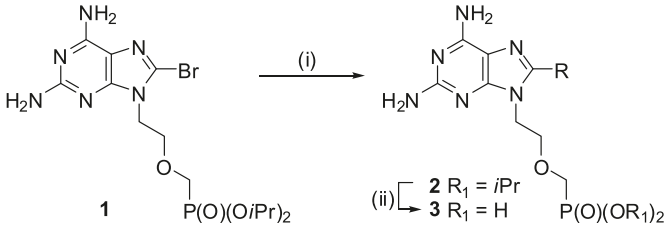

moiety with carbon substituents using various cross-coupling reactions. Since some ANPs substituted at the C-8 position of the purine moiety displayed pronounced biological properties (antiviral and immunomodulatory),[14] the antiviral activity of the final C-8 modified PMEDAP analogues has been evaluated.

Results and discussion

Diisopropyl 8-bromo-2,6-diamino-9-[2-(phosphonomethoxy)ethyl]purine (**1**, Scheme 1) was prepared by alkylation of 2,6-diaminopurine with 2-[(diisopropoxyphosphoryl)methoxy]ethyl chloride followed by bromination with the bromine solution in a DMF/CCl_4 mixture according to the previously described procedure.[15]

At first, a series of 8-alkyl- and 8-aryl-substituted PMEDAP derivatives were prepared by Stille cross-coupling[16] of **1** with tetraalkyl and alkyltributyl stannanes under a catalysis of $Pd(PPh_3)_4$ in NMP (1-methyl-2-pyrrolidone) (Scheme 1 and Table 1). Cross-coupling with more reactive unsaturated stannanes (phenyl and vinyl) proceeded in short reaction times (2 h) at 100 °C and yielded the desired 8-substituted products (**2c** and **2d**) in ~40% yields (Table 1, entries 3 and 4). On the other hand, saturat7ed stannanes afforded only low yields of the 8-substituted products **2a** (17%; Table 1, entry 1) and **2b** (22%; Table 1, entry 2). It was caused by the lower reactivity of aliphatic stannanes and by the undesirable deprotection of diisopropyl esters by alkylstannanes (good Lewis acids) at higher temperatures (>100 °C) during longer reaction times. When more reactive alkyltributyl stannanes and the Pd_2dba_3/Ph_3As catalytic system[17] were used, compounds **2d**, **2e**, and **2f** were obtained in 84%, 50%, and 59% yields, respectively (Table 1, entries 5, 7, and 8). Compounds **2a**–**2f** were deprotected by the standard procedure (Me_3SiBr, CH_3CN, room temperature (rt)) to yield phosphonic acids **3a**–**3f** (Scheme 1 and Table 1).

Suzuki–Miyaura[18] cross-coupling was used for the introduction of various aryl, hetaryl, and alkenyl substituents to the C-8 position of the 2,6-diaminopurine moiety (Scheme 1 and Table 2).[19] The 8-bromo derivative **1** reacted smoothly with aryl-, hetaryl- and alkenylboronic acids. The reaction was catalysed with $Pd(PPh_3)_4$ (5 mol%) and potassium carbonate was used as a base. To improve the solubility of potassium carbonate, a mixture of DMF and water was used as a solvent. The corresponding 8-substituted derivatives **2c** and **2g**–**2k** were obtained in very good yields (65%–79%; Table 2) and the subsequent removal of the ester groups yielded free phosphonic acids **3g**–**3k** (Scheme 1 and Table 2).

The third approach used for the introduction of the *C*-substituent to the C-8 position of the purine ring was Negishi cross-coupling employing alkylzinc halides (Scheme 1 and Table 3).[20] The reactions with benzyl-, allyl-, trifluoromethyl-, and cyclopropylzinc halides in DMF were catalysed with $Pd(PPh_3)_4$ at 50 °C and gave the products **2l**–**2n** in satisfactory 49%–71% yields (Table 3). The starting benzyl- and allylzinc bromides were obtained by transmetalation of the appropriate organomagnesium Grignard reagent with $ZnBr_2$ in THF. Trifluoromethylzinc iodide was prepared by the sonication of trifluoromethyl iodide in THF with activated zinc on cooling. Finally, cyclopropylzinc chloride was prepared by lithiation of cyclopropyl bromide with *n*-BuLi

Table 2. Suzuki–Miyaura cross-coupling to produce compounds **2** (reagents: $RB(OH)_2$, $Pd(PPh_3)_4$, K_2CO_3, DMF/H_2O, 90 °C, 2–4 h); deprotection to produce compounds **3** (reagents: $(CH_3)_3SiBr$, CH_3CN, room temperature).

Entry	R	R–M	Product	Yield[a] (%)	Product	Yield[a] (%)
1		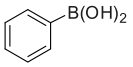	**2c**	72	**3c**	78
2	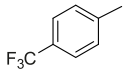	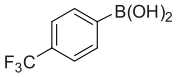	**2g**	68	**3g**	82
3	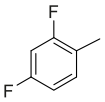	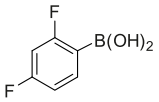	**2h**	76	**3h**	84
4		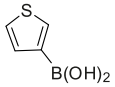	**2i**	64	**3i**	76
5	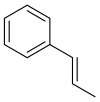	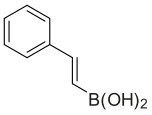	**2j**	79	**3j**	65
6		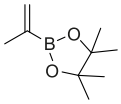	**2k**	65	**3k**	69

[a] Isolated yields.

Table 3. Negishi cross-coupling to produce compounds **2** (reagents: (*i*) $Pd(PPh_3)_4$, DMF, 50 °C; (*ii*) Pd_2dba_3/dppf, THF, 50 °C); deprotection to produce compounds **3** (reagents: $(CH_3)_3SiBr$, CH_3CN, room temperature).

Entry	R	R–M	Product	Yield[a] (%)	Product	Yield[a] (%)
1[b]	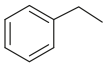	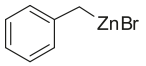	**2l**	71	**3l**	82
2[b]			**2e**	64	**3e**	68
3[b]	F_3C-	F_3C-ZnI	**2m**	55	**3m**	81
4[b]			**2n**	49	**3n**	74
5[b]	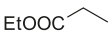	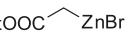	**2o**	57	—	—
6[c]	$NC-$	$Zn(CN)_2$	**2p**	81	**3p**	65

[a] Isolated yields.
[b] Using $Pd(PPh_3)_4$.
[c] Using Pd_2dba_3.

followed by transmetalation with $ZnBr_2$. Ethyl (2,6-diaminopurine-8-yl)acetate **2o** was prepared by Negishi cross-coupling of **1** with the Reformatsky reagent $BrZnCH_2COOEt$ prepared in situ by the sonication of 2-bromoethyl acetate with zinc in THF. In this case, the best yield of 57% was obtained using the catalytic system Pd_2dba_3/dppf (diphenylphosphinoferrocene) (Table 3, entry 5).[21] The coupling with zinc cyanide proceeded well under the catalysis of the Pd_2dba_3/dppf catalytic system and gave the 8-cyano derivative **2p** in an 81% yield (Table 3, entry 6), whereas the reaction using $Pd(PPh_3)_4$ as a catalyst gave an unsatisfactory 27% yield (data not shown).[22] The compounds **2l**–**2n** and **2p** were deprotected by the standard procedure to afford free phosphonic acids **3l**–**3n** and **3p** (Scheme 1 and Table 3). Compound **2o** is unstable under the reaction conditions and decomposes.

Trialkylaluminium was used for the introduction of the methyl and ethyl substituents. The reaction in THF was catalysed by $Pd(PPh_3)_4$ and proceeded smoothly to give the desired products **2a** and **2b** in 54% and 48% yields, respectively (Scheme 1 and Table 4).[23] This method proved to be more suitable for the introduction of a simple alkyl substituent to the C-8 position of the purine moiety than Stille cross-coupling with tetraalkyl stannanes.

The ethynyl group can be introduced by Sonogashira cross-coupling of compounds **1** with trimethylsilylacetylene. The reaction was performed under standard conditions ($PdCl_2(PPh_3)_4$, CuI, Et_3N, DMF) and gave the product **4** in a 67% yield (Scheme 2).[24] Free phosphonic acid **5** was obtained in a 31% yield after the removal of the TMS group with methanolic ammonia followed by the standard deprotection of the phosphonate moiety (Me_3SiBr, CH_3CN). The

Can. J. Chem. Downloaded from www.nrcresearchpress.com by Xi'an Jiaotong University on 09/19/12
For personal use only.

Table 4. The reaction with trialkylaluminium reagents to produce compounds **2** (reagents: R_3Al, $Pd(PPh_3)_4$, THF, reflux); deprotection to produce compounds **3** (reagents: $(CH_3)_3SiBr$, CH_3CN, room temperature).

Entry	R	R–M	Product	Yield[a] (%)	Product	Yield[a] (%)
1	Me–	Me_3Al	**2a**	54	**3a**	67
2	Et–	Et_3Al	**2b**	48	**3b**	81

[a]Isolated yields.

Scheme 2. Sonogashira cross-coupling of **1** with trimethylsilylacetylene. Reagents: (*i*) $PdCl_2(PPh_3)_2$, CuI, Et_3N, DMF, room temperature; (ii) NH_3, CH_3OH, r.t.; (iii) $(CH_3)_3SiBr$, CH_3CN, rt.

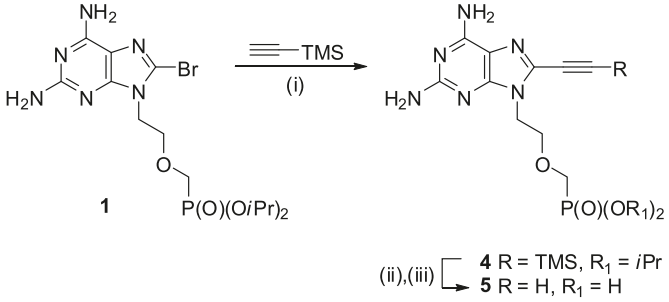

final step was conducted at 0 °C owing to the instability of the ethynyl group under the reaction conditions.

All final compounds **3a**–**3n**, **3p**, and **5** were tested for cytostatic and antiviral activities. Although certain C-8 substituted purine nucleotide analogues are known to exhibit pronounced antiviral activity, none of the C-8 substituted PMEDAP derivatives prepared displayed any appreciable biological activity. Nevertheless, this work constitutes an important partial result of a broader SAR study of acyclic nucleoside phosphonates, compounds of an enormous medicinal importance.

Conclusions

In conclusion, various cross-coupling reactions of diisopropyl 8-bromo-2,6-diamino-9-[2-(phosphonomethoxy)ethyl]purine (**1**) with diverse types of organometallic reagents were employed for the preparation of a series of 2,6-diamino-8-*C*-substituted purine derivatives. Although various Pd-catalysed cross-coupling reactions on halopurines have appeared in the literature over the last decade or so, this work first describes a comprehensive and systematic study of various cross-coupling methods on 8-bromopurine derivatives. Stille and Suzuki cross-coupling reactions of stannanes and boronic acids, respectively, were used for the introduction of aryl, hetaryl, and alkenyl substituents. Alkylzinc halides and trialkylaluminium reagents were used for the introduction of suitable alkyl groups. Sonogashira cross-coupling was efficiently used for the preparation of the 8-ethynylpurine derivative **4**. All of the organometallic reagents used tolerated the presence of the unprotected amino group at the C-2 position of the purine ring well. The cleavage of the phosphonate esters **2a**–**2n**, **2p**, and **4** with Me_3SiBr/MeCN afforded the target acyclic nucleotide analogues **3a**–**3n**, **3p**, and **5**. The deprotection of the compound **2o** was not successful owing to its instability under the reaction conditions. All 16 of the final compounds **3a**–**3n**, **3p**, and **5** were tested for cytostatic and antiviral activities, but none of them displayed any appreciable activity against the viruses tested. It can be concluded that the substitution at the C-8 position of a PMEDAP analogue with the *C*-substituents leads to the loss of biological activity of the potent parent compound.

Experimental

General

The solvents were dried by standard procedures. Tetrahydrofuran (THF) was freshly distilled from sodium/benzophenone under argon. The NMR spectra were recorded with Bruker Avance 500 (500 MHz for ^1H and 125.8 MHz for ^{13}C) and Bruker Avance 400 (^1H at 400, ^{13}C at 100.6 MHz) spectrometers in $CDCl_3$, DMSO-d_6, or D_2O. The chemical shifts (in ppm, δ scale) were referenced to TMS (for the ^1H NMR spectra in $CDCl_3$) and (or) to the solvent signal ($CDCl_3$ δ = 7.26 ppm for the ^1H NMR and δ = 77.0 ppm for the ^{13}C NMR; DMSO-d_6 for the ^1H NMR δ = 2.5 ppm and for the ^{13}C NMR δ = 39.7). The chemical shifts in D_2O were referenced to 1,4-dioxane for ^1H NMR δ = 3.75 and for ^{13}C NMR δ = 67.19. The melting points were determined on a Büchi melting point B-545 apparatus and are uncorrected. The TLC was performed on plates of Kieselgel 60 F254 (Merck). The mass spectra were measured on a ZAB-EQ (VG Analytical) spectrometer using FAB (ionization by Xe, accelerating voltage 8 kV, glycerol matrix) or on a LCQ classic spectrometer using electrospray ionization (ESI). Preparative HPLC purification was performed on a column packed with 10 μm C_{18} reversed phase (Luna) (250 mm × 21 mm.

Stille cross-coupling with organostannanes

Method A (general procedure)

8-Bromopurine **1** (475 mg, 1 mmol) and $Pd(PPh_3)_4$ (58 mg, 0.05 mmol) in NMP (4 mL) were treated with the appropriate stannane (3 mmol) under an argon atmosphere, and the reaction mixture was heated at 100 °C until the complete consumption of the starting material (monitored by TLC). The solvent was evaporated under reduced pressure and the residue was taken to EtOAc and washed with brine and EDTA and dried over $MgSO_4$. The product was purified by column chromatography (SiO_2; EtOAc/acetone/EtOH/H_2O, 18:3:1:1) and crystallized from EtOH.

Method B (general procedure)

8-Bromopurine **1** (475 mg, 1 mmol), Pd_2dba_3 (23 mg, 0.025 mmol) and $AsPh_3$ (31 mg, 0.1 mmol) in NMP (4 mL) were treated with the appropriate stannane (3 mmol) under an argon atmosphere, and the reaction mixture was heated at 100 °C until the complete consumption of the starting ma-

Can. J. Chem. Downloaded from www.nrcresearchpress.com by Xi'an Jiaotong University on 09/19/12
For personal use only.

Can. J. Chem. Downloaded from www.nrcresearchpress.com by Xi'an Jiaotong University on 09/19/12
For personal use only.

terial (monitored by TLC). The solvent was evaporated under reduced pressure and the residue was taken to EtOAc and washed with brine and EDTA and dried over $MgSO_4$. The product was purified by column chromatography (SiO_2; EtOAc/acetone/EtOH/H_2O, 18:3:1:1) and crystallized from EtOH.

Diisopropyl 2,6-diamino-8-methyl-9-[2-(phosphonomethoxy)ethyl]purine (2a)

Method A afforded a colourless crystalline product; yield: 70 mg (17%); mp 162–164 °C. ^{1}H NMR (500 MHz, $CDCl_3$) δ: 1.23 and 1.28 (2 × d, J_{vic} = 6.2, 12H, $(CH_3)_2CH$), 2.52 (s, 3H, CH_3-8), 3.68 (d, $J_{H,P}$ = 8.5, 2H, CH_2P), 3.88 (t, J_{vic} = 5.3, 2H, CH_2O), 4.18 (t, J_{vic} = 5.3, 2H, CH_2N), 4.65 (dh, $J_{H,P}$ = 7.6, J_{vic} = 6.2, 2H $(CH_3)_2CH$), 4.73 (bs, 2H, NH_2-2), 5.45 (bs, 2H, NH_2-6) ppm. ^{13}C NMR (125.8 MHz, $CDCl_3$): 14.06 (CH_3-8), 23.84 and 23.96 (d, $J_{C,P}$ = 4, $(CH_3)_2CH$), 42.34 (CH_2N), 65.98 (d, $J_{C,P}$ = 168, CH_2P), 71.02 (d, $J_{C,P}$ = 7, $(CH_3)_2CH$), 71.35 (d, $J_{C,P}$ = 4, CH_2O), 112.98 (C-5), 147.60 (C-8), 153.08 (C-4), 154.69 (C-6), 159.1 (C-2). MS (FAB) *m/z* (%): 387 (100) $[M + H]^+$. Anal. calcd for $C_{15}H_{27}N_6O_4P$ (386.4): C 46.63, H 7.04, N 21.75; found: C 46.52, H 7.12, N 21.71.

Diisopropyl 2,6-diamino-8-ethyl-9-[2-(phosphonomethoxy)ethyl]purine (2b)

Method A gave a colourless crystalline product; yield: 93 mg (22%); mp 169–171 °C. ^{1}H NMR (400 MHz, DMSO-d_6) δ: 1.13 and 1.17 (2 × d, J_{vic} = 6.2, 12H, $(CH_3)_2CH$), 1.26 (t, J_{vic} = 7.5, 3H, CH_3CH_2), 2.78 (q, J_{vic} = 7.5, 2H, CH_3CH_2), 3.72 (d, $J_{H,P}$ = 8.4, 2H, CH_2P), 3.76 (t, J_{vic} = 5.3, 2H, CH_2O), 4.09 (t, J_{vic} = 5.3, 2H, CH_2N), 4.48 (dh, $J_{H,P}$ = 7.7, J_{vic} = 6.2, 2H, $(CH_3)_2CH$), 5.81 (bs, 2H, NH_2-2), 6.65 (bs, 2H, NH_2-6) ppm. ^{13}C NMR (100.6 MHz, DMSO-d_6) δ: 11.44 (CH_3CH_2), 20.09 (CH_3CH_2), 23.75 and 23.90 (d, $J_{C,P}$ = 4, $(CH_3)_2CH$), 41.55 (CH_2N), 65.02 (d, $J_{C,P}$ = 164, CH_2P), 70.29 (d, $J_{C,P}$ = 6, $(CH_3)_2CH$), 78.84 (d, $J_{C,P}$ = 12, CH_2O), 111.80 (C-5), 150.27 (C-8), 152.96 (C-4), 154.82 (C-6), 156.01 (C-2) ppm. MS (FAB) *m/z* (%): 401 (100) $[M + H]^+$. Anal. calcd for $C_{16}H_{29}N_6O_4P$ (400.4): C 47.99, H 7.30, N 20.99; found: C 48.14, H 7.26, N 21.09.

Diisopropyl 2,6-diamino-8-phenyl-9-[2-(phosphonomethoxy)ethyl]purine (2c)

Method A afforded a pale yellow oil; yield: 174 mg (39%). ^{1}H NMR (500 MHz, $CDCl_3$) δ: 1.18 and 1.28 (2 × d, J_{vic} = 6.2, 12H, $(CH_3)_2CH$), 3.68 (d, $J_{H,P}$ = 8.5, 2H, CH_2P), 3.98 (t, J_{vic} = 5.6, 2H, CH_2O), 4.29 (t, J_{vic} = 5.6, 2H, CH_2N), 4.63 (dh, $J_{H,P}$ = 7.7, J_{vic} = 6.2, 2H, $(CH_3)_2CH$), 5.17 (bs, 2H, NH_2-2), 6.23 (bs, 2H, NH_2-6), 7.44–7.50 (m, 3H, H-m,p-Ph), 7.78 (m, 2H, H-o-Ph) ppm. ^{13}C NMR (125.8 MHz, $CDCl_3$) δ: 23.71 and 23.88 (d, $J_{C,P}$ = 4, $(CH_3)_2CH$), 43.08 (CH_2N), 65.74 (d, $J_{C,P}$ = 167, CH_2P), 70.43 (d, $J_{C,P}$ = 12, CH_2O), 70.98 (d, $J_{C,P}$ = 7, $(CH_3)_2CH$), 113.80 (C-5), 128.59 (CH-m-Ph), 129.30 (CH-o-Ph), 129.94 (C-i-Ph) 148.94 (C-8), 153.42 (C-4), 155.70 (C-6), 159.59 (C-2) ppm. MS (FAB) *m/z* (%): 471 (22) $[M + Na]^+$, 449 (100) $[M + H]^+$. Anal. calcd for $C_{20}H_{29}N_6O_4P$ (448.4): C 53.57, H 6.52, N 18.74; found: C 53.71, H 6.43, N 18.72.

Diisopropyl 2,6-diamino-8-vinyl-9-[2-(phosphonomethoxy)ethyl]purine (2d)

Method A afforded a pale yellow crystalline product; yield: 171 mg (43%); mp 179–181 °C. Method B gave yellowish crystals; yield: 334 mg (84%); mp 179 °C. ^{1}H NMR (500 MHz, $CDCl_3$) δ: 1.23 and 1.28 (2 × d, J_{vic} = 6.2, 12H, $(CH_3)_2CH$), 3.70 (d, $J_{H,P}$ = 8.3, 2H, CH_2P), 3.88 (t, J_{vic} = 5.2, 2H, CH_2O), 4.25 (t, J_{vic} = 5.2, 2H, CH_2N), 4.66 (dh, $J_{H,P}$ = 7.6, J_{vic} = 6.2, 2H, $(CH_3)_2CH$), 5.14 (bs, 2H, NH_2-2), 5.51 (d, J_{cis} = 4.5, 1H, CH_2-2′$_{trans}$) 6.08 (bs, 2H, NH_2-6), 6.30 (d, J_{trans} = 17.5, 1H, CH_2-2′$_{cis}$), 6.78 (dd, J_{trans} = 17.5, J_{cis} = 4.5, 1H, CH-1′) ppm. ^{13}C NMR (125.8 MHz, $CDCl_3$) δ: 23.80 and 23.90 (d, $J_{C,P}$ = 4, $(CH_3)_2CH$), 41.82 (CH_2N), 65.96 (d, $J_{C,P}$ = 167, CH_2P), 71.04 (d, $J_{C,P}$ = 7, $(CH_3)_2CH$), 71,32 (d, $J_{C,P}$ = 11, CH_2O), 113.79 (C-5), 120.68 (C-2′), 123.51 (C-1′), 146.22 (C-8), 152.76 (C-4), 155.64 (C-6), 159.77 (C-2) ppm. MS (FAB) *m/z* (%): 399 (100) $[M + H]^+$. Anal. calcd for $C_{16}H_{27}N_6O_4P$ (398.4): C 48.24, H 6.83, N 21.09; found: C 48.20, H 6.92, N 21.27.

Diisopropyl 8-allyl-2,6-diamino-9-[2-(phosphonomethoxy)ethyl]purine (2e)

Method A afforded a white crystalline product; yield: 33 mg (8%); mp 185–187 °C. Method B afforded white crystals; yield: 206 mg (50%); mp 186–188 °C. ^{1}H NMR (500 MHz, $CDCl_3$) δ: 1.20 and 1.27 (2 × d, J_{vic} = 6.2, 12H, $(CH_3)_2CH$), 3.38 (d, J_{vic} = 6.3, 2H, CH_2-1′), 3.65 (d, $J_{H,P}$ = 8.5, 2H, CH_2P), 3.89 (t, J_{vic} = 5.5, 2H, CH_2O), 4.27 (t, J_{vic} = 5.5, 2H, CH_2N), 4.65 (dh, $J_{H,P}$ = 7.6, J_{vic} = 6.2, 2H, $(CH_3)_2CH$), 5.21 (bs, 2H, NH_2-2), 5.28 (dq, $J_{3'cis,1'} = J_{gem}$ = 1.5, J_{cis} = 8.1, 1H, CH_2-3′$_{trans}$), 5.35 (dq, $J_{3'cis,1'} = J_{gem}$ = 1.5, J_{trans} = 17.2, 1H, CH_2-3′$_{cis}$), 6.11 (bs, 2H, NH_2-6), 6.05 (ddt, J_{trans} = 17.2, J_{cis} = 8.1, J_{vic} = 6.3, 2H, CH-2′) ppm. ^{13}C NMR (125.8 MHz, $CDCl_3$) δ: 23.78 and 23.88 (d, $J_{C,P}$ = 4, $(CH_3)_2CH$), 40.33 (C-1′), 41.76 (CH_2N), 66.15 (d, $J_{C,P}$ = 168, CH_2P), 71.22 (d, $J_{C,P}$ = 7, $(CH_3)_2CH$), 71,39 (d, $J_{C,P}$ = 10, CH_2O), 113.79 (C-5), 116.46 (C-3′), 138.21 (C-2′), 148.65 (C-8), 151.72 (C-4), 156.39 (C-6), 159.54 (C-2) ppm. MS (ESI): *m/z* (%): 435 (45) $[M + Na]^+$, 413 (100) $[M + H]^+$. Anal. calcd for $C_{17}H_{29}N_6O_4P$ (412.4): C 49.51, H 7.09, N 20.38; found: C 49.56, H 7.13, N 20.25.

Diisopropyl 2,6-diamino-8-(thien-2-yl)-9-[2-(phosphonomethoxy)ethyl]purine (2f)

Method B gave a pale yellow oil; yield: 268 mg (59%). ^{1}H NMR (500 MHz, $CDCl_3$) δ: 1.19 and 1.25 (2 × d, J_{vic} = 6.2, 12H, $(CH_3)_2CH$), 3.73 (d, $J_{H,P}$ = 8.5, 2H, CH_2P), 4.01 (t, J_{vic} = 5.5, 2H, CH_2O), 4.42 (t, J_{vic} = 5.5, 2H, CH_2N), 4.63 (dh, $J_{H,P}$ = 7.6, J_{vic} = 6.2, 2H, $(CH_3)_2CH$), 5.31 (bs, 2H, NH_2-2), 6.36 (bs, 2H, NH_2-6), 7.13 (dd, $J_{4',5'}$ = 5.1, $J_{4',3'}$ = 3.7, 1H, H-4), 7.44 (dd, $J_{5',4'}$ = 5.1, $J_{5',3'}$ = 0.8, 1H, H-5′), 7.69 (dd, $J_{3',4'}$ = 3.7, $J_{3',5'}$ = 0.8, 1H, H-3′) ppm. ^{13}C NMR (125.8 MHz, $CDCl_3$) δ: 23.60 and 23.75 (d, $J_{C,P}$ = 4, $(CH_3)_2CH$), 42.91 (CH_2N), 65.73 (d, $J_{C,P}$ = 167, CH_2P), 70.64 (d, $J_{C,P}$ = 12, CH_2O), 70.97 (d, $J_{C,P}$ = 7, $(CH_3)_2CH$), 113.55 (C-5), 127.60 (CH-5′), 127.65 (CH-4′), 128.07 (CH-3′), 131.64 (CH-2′), 142,7 (C-8), 153.34 (C-4), 155.38 (C-6), 159.59 (C-2) ppm. MS (ESI) *m/z* (%): 477 (35) $[M + Na]^+$,

Can. J. Chem. Downloaded from www.nrcresearchpress.com by Xi'an Jiaotong University on 09/19/12
For personal use only.

455 (100) $[M + H]^+$. Anal. calcd for $C_{18}H_{27}N_6O_4PS$ (454.4): C 47.57, H 5.99, N 18.49; found: C 47.68, H 6.03, N 18.31.

Suzuki–Miyaura cross-coupling with boronic acids

Method C (general procedure)

$Pd(PPh_3)_4$ (58 mg, 0.05 mmol) was added to a mixture of 8-bromopurine **1** (475 mg, 1 mmol), boronic acid (3 mmol) and K_2CO_3 (331 mg, 3 mmol) in a DMF/H_2O mixture (4:1, 10 mL) under an argon atmosphere. The mixture was heated at 90 °C for 4 h. The solvents were evaporated, and the residue in EtOAc was washed with H_2O and dried over $MgSO_4$. The product was isolated by column chromatography (SiO_2; EtOAc/acetone/EtOH/H_2O, 18:3:1:1).

Diisopropyl 2,6-diamino-8-phenyl-9-[2-(phosphonomethoxy)ethyl]purine (2c)

Method C afforded **2c** as a yellowish oil; yield: 321 mg (72%).

Diisopropyl 2,6-diamino-8-[4-(trifluoromethyl)phenyl]-9-[2-(phosphonomethoxy)ethyl]purine (2g)

Method C afforded a colourless oil; yield: 351 mg (68%). ^{1}H NMR (500 MHz, $CDCl_3$) δ: 1.17 and 1.25 (2 × d, J_{vic} = 6.3, 12H, $(CH_3)_2CH$), 3.68 (d, $J_{H,P}$ = 8.6, 2H, CH_2P), 4.04 (t, J_{vic} = 5.3, 2H, CH_2O), 4.29 (t, J_{vic} = 5.3, 2H, CH_2N), 4.63 (dh, $J_{H,P}$ = 7.6, J_{vic} = 6.3, 2H, $(CH_3)_2CH$), 4.73 (bs, 2H, NH_2-2), 5.38 (bs, 2H, NH_2-6), 7.75 (d, J = 8.1, 2H, H-3′, H-5′), 8.00 (d, J = 8.1, 2H, H-2′, H-6′) ppm. ^{13}C NMR (125.8 MHz, $CDCl_3$) δ: 23.38 and 23.74 (d, $J_{C,P}$ = 4.2 $(CH_3)_2CH$), 42.89 (CH_2N), 65.85 (d, $J_{C,P}$ = 162, CH_2P), 70.21 (d, $J_{C,P}$ = 12, CH_2O), 70.84 (d, $J_{C,P}$ = 7, $(CH_3)_2CH$), 112.73 (C-5), 126.79 (CH-m-Ph), 127.60 (CH-o-Ph), 130.57 (CF_3), 131.59 (CH-i-Ph), 153.96 (C-8), 157.43 (C-4), 158.94 (C-6), 162.87 (C-2) ppm. MS (ESI) *m*/*z* (%): 539 (25) $[M + Na]^+$, 517 (100) $[M + H]^+$. Anal. calcd for $C_{21}H_{28}F_3N_6O_4P$ (516.4) calcd.: C 48.84, H 5.46, N 16.27; found: C 49.01, H 5.39, N 16.31.

Diisopropyl 2,6-diamino-8-(2,4-difluorophenyl)-9-[2-(phosphonomethoxy)ethyl]purine (2h)

Method C afforded a colourless oil; yield: 367 mg (76%). ^{1}H NMR (500 MHz, $CDCl_3$) δ: 1.17 and 1.25 (2 × d, J_{vic} = 6.3, 12H, $(CH_3)_2CH$), 3.58 (d, $J_{H,P}$ = 8.6, 2H, CH_2P), 3.84 (t, J_{vic} = 5.3, 2H, CH_2O), 4.17 (t, J_{vic} = 5.8, 2H, CH_2N), 4.60 (dh, $J_{H,P}$ = 7.8, J_{vic} = 6.3, 2H, $(CH_3)_2CH$), 4.72 (bs, 2H, NH_2-2), 5.35 (bs, 2H, NH_2-6), 6.96 (ddd, $J_{3',F}$ = 8.3, $J_{3',5'}$ = 1.5, $J_{3',F}$ = 8.1, 1H, H-3′), 7.04 (ddd, $J_{5',F}$ = 8.3, $J_{5',6'}$ = 7.5, $J_{3',5'}$ = 1.5, 1H, H-5′), 7.70 (ddd, $J_{5',6'}$ = 7.5, $J_{6',F}$ = 5.0, $J_{6',F}$ = 5.0, 1H, H-6′) ppm. ^{13}C NMR (125.8 MHz, $CDCl_3$) δ: 23.47 and 23.94 (d, $J_{C,P}$ = 4.3 $(CH_3)_2CH$), 43.15 (CH_2N), 65.43 (d, $J_{C,P}$ = 162, CH_2P), 70.74 (d, $J_{C,P}$ = 13, CH_2O), 71.30 (d, $J_{C,P}$ = 7, $(CH_3)_2CH$), 102.74 (C-3′), 112.32 (C-5), 113.68 (C-5′), 119.65 (C-1′), 132.78 (C-6′), 154.58 (C-8), 156.47 (C-4), 156.59 (C-6), 159.49 (C-2′), 162.75 (C-4′), 163.29 (C-2) ppm. MS (ESI): *m*/*z* (%): 507 (30) $[M + Na]^+$, 485 (100) $[M + H]^+$. Anal. calcd for $C_{20}H_{27}F_2N_6O_4P$ (484.5): C 49.59, H 5.62, N 17.35; found: C 49.65, H 5.51, N 17.38.

Diisopropyl 2,6-diamino-8-(thien-3-yl)-9-[2-(phosphonomethoxy)ethyl]purine (2i)

Method C gave a colourless oil; yield: 290 mg (64%). ^{1}H NMR (500 MHz, $CDCl_3$) δ: 1.17 and 1.26 (2 × d, J_{vic} = 6.2, 12H, $(CH_3)_2CH$), 3.57 (d, $J_{H,P}$ = 8.7, 2H, CH_2P), 3.96 (t, J_{vic} = 5.6, 2H, CH_2O), 4.34 (t, J_{vic} = 5.6, 2H, CH_2N), 4.58 (dh, $J_{H,P}$ = 7.4, J_{vic} = 6.2, 2H, $(CH_3)_2CH$), 4.85 (bs, 2H, NH_2-2), 5.51 (bs, 2H, NH_2-6), 7.22 (dd, $J_{5',4'}$ = 7.5, $J_{5',1'}$ = 1.5, 1H, H-5′), 7.74 (dd, $J_{4',5'}$ = 7.5, $J_{4',1'}$ = 2.9, 1H, H-4′), 8.01 (ddd, $J_{5',6'}$ = 2.9, $J_{2',4'}$ = 5.0, $J_{2',5'}$ = 1.5, 1H, H-2′) ppm. ^{13}C NMR (125.8 MHz, $CDCl_3$) δ: 23.17 and 23.64 (d, $J_{C,P}$ = 4.2 $(CH_3)_2CH$), 42.95 (CH_2N), 66.21 (d, $J_{C,P}$ = 165, CH_2P), 70.26 (d, $J_{C,P}$ = 12, CH_2O), 71.35 (d, $J_{C,P}$ = 7, $(CH_3)_2CH$), 113.47 (C-5), 126.38 (C-2′), 127.60 (C-4′), 128.19 (C-5′), 135.51 (C-1′), 154.28 (C-8), 157.74 (C-4), 160.19 (C-6), 164.86 (C-2) ppm. MS (ESI): *m*/*z* (%): 477 (38) $[M + Na]^+$, 455 (100) $[M + H]^+$ Anal. calcd for $C_{18}H_{27}F_2N_6O_4PS$ (454.4): C 47.57, H 5.99, N 18.49; found: C 47.63, H 6.06, N 18.37.

Diisopropyl 2,6-diamino-8-(2-phenylvinyl)-9-[2-(phosphonomethoxy)ethyl]purine (2j)

Method C gave a colourless oil; yield: 374 mg (79%). ^{1}H NMR (500 MHz, $CDCl_3$) δ: 1.19 and 1.24 (2 × d, J_{vic} = 6.4, 12H, $(CH_3)_2CH$), 3.64 (d, $J_{H,P}$ = 8.7, 2H, CH_2P), 4.02 (t, J_{vic} = 5.5, 2H, CH_2O), 4.30 (t, J_{vic} = 5.5, 2H, CH_2N), 4.63 (dh, $J_{H,P}$ = 7.4, J_{vic} = 6.4, 2H, $(CH_3)_2CH$), 5.22 (bs, 2H, NH_2-2), 6.32 (bs, 2H, NH_2-6), 6.91 (d, J_{trans} = 15.2, 1H, H-2′), 6.99 (d, J_{trans} = 15.2, 1H, H-1′), 7.44–7.51 (m, 3H, H-m, p-Ph), 7.82 (m, 2H, H-o-Ph) ppm. ^{13}C NMR (125.8 MHz, $CDCl_3$) δ: 23.52 and 23.74 (d, $J_{C,P}$ = 4.0 $(CH_3)_2CH$), 42.72 (CH_2N), 66.47 (d, $J_{C,P}$ = 165, CH_2P), 71.24 (d, $J_{C,P}$ = 12, CH_2O), 72.69 (d, $J_{C,P}$ = 7, $(CH_3)_2CH$), 112.73 (C-1′), 113.63 (C-5), 128.21 (CH-m-Ph), 129.57 (CH-o-Ph), 131.20 (C-i-Ph), 134.63 (C-2′), 152.97 (C-8), 153.68 (C-4), 156.92 (C-6), 160.01 (C-2) ppm. MS (ESI): *m*/*z* (%): 497 (25) $[M + Na]^+$, 475 (100) $[M + H]^+$. Anal. calcd for $C_{22}H_{31}N_6O_4P$ (474.5): C 55.69, H 6.59, N 17.71; found: C 55.81, H 6.63, N 17.67.

Diisopropyl 2,6-diamino-8-(propene-2-yl)-9-[2-(phosphonomethoxy)ethyl]purine (2k)

Method C afforded a colourless crystalline product; yield: 283 mg (65%); mp 196–198 °C. ^{1}H NMR (500 MHz, $CDCl_3$) δ: 1.20 and 1.25 (2 × d, J_{vic} = 6.4, 12H, $(CH_3)_2CH$), 2.45 (s, 3H, CH_3-8), 3.70 (d, $J_{H,P}$ = 8.6, 2H, CH_2P), 4.0 (t, J_{vic} = 5.5, 2H, CH_2O), 4.37 (t, J_{vic} = 5.5, 2H, CH_2N), 4.68 (dh, $J_{H,P}$ = 7.4, J_{vic} = 6.4, 2H, $(CH_3)_2CH$), 5.31 (bs, 2H, NH_2-2), 5.49 and 5.51 (2 × s, 2H, CH_2-2′), 6.32 (bs, 2H, NH_2-6) ppm. ^{13}C NMR (125.8 MHz, $CDCl_3$) δ: 22.27 (CH3–8), 23.27 and 23.45 (d, $J_{C,P}$ = 4.0 $(CH_3)_2CH$), 42.82 (CH_2N), 64.87 (d, $J_{C,P}$ = 168, CH_2P), 66.52 (d, $J_{C,P}$ = 7, $(CH_3)_2CH$), 70.91 (d, $J_{C,P}$ = 8, CH_2O), 113.03 (C-5), 119.26 (C-2′), 134.44 (C-1′), 149.01 (C-8), 153.19 (C-4), 155.65 (C-6), 159.72 (C-2) ppm. MS (ESI) *m*/*z* (%): 435 (55) $[M + Na]^+$, 413 (100) $[M + H]^+$. Anal. calcd for $C_{17}H_{29}N_6O_4P$ (412.4): C 49.51, H 7.09, N 20.38; found: C 49.39, H 7.01, N 20.52.

Negishi cross-coupling

Diisopropyl 2,6-diamino-8-benzyl-9-[2-(phosphonomethoxy)ethyl]purine (2l)

Benzylbromide (855 mg, 784 μL, 5 mmol) was added to magnesium turnings in THF (5 mL) and activated with io-

Can. J. Chem. Downloaded from www.nrcresearchpress.com by Xi'an Jiaotong University on 09/19/12
For personal use only.

dine under an argon atmosphere. The reaction mixture was stirred at rt until the complete consumption of magnesium, cooled to –78 °C, and a solution of $ZnCl_2$ in THF (1 mol/L, 5 mL, 5 mmol) was added. The resulting mixture was stirred at rt for 1 h and subsequently added to the solution of compound **1** (475 mg, 1 mmol) and $Pd(PPh_3)_4$ (58 mg, 0.05 mmol) in dry DMF (5 mL), and the mixture was stirred at rt for 3 h. The solvent was evaporated and the residue in EtOAc was washed with water and the solvent was evaporated. The crude product was purified by column chromatography (SiO_2, EtOAc/acetone/EtOH/H_2O, 18:3:1:1) and crystallized from EtOH to give **2l** (328 mg, 71%) as colourless crystals; mp 185–187 °C. MS (ESI): *m/z* (%): 485 (100) $[M + Na]^+$. ^1H NMR (500 MHz, $CDCl_3$) δ: 1.17 and 1.26 (2 × d, J_{vic} = 6.4, 12H, $(CH_3)_2CH$), 3.63 (d, $J_{H,P}$ = 8.6, 2H, CH_2P), 4.01 (s, 2H, H-1′), 4.05 (t, J_{vic} = 5.5, 2H, CH_2O), 4.31 (t, J_{vic} = 5.5, 2H, CH_2N), 4.60 (dh, $J_{H,P}$ = 7.8, J_{vic} = 6.4, 2H, $(CH_3)_2CH$), 5.25 (bs, 2H, NH_2-2), 6.38 (bs, 2H, NH_2-6), 7.34–7.42 (m, 3H, H-o,p-Ph), 7.58 (m, 2H, H-m-Ph) ppm. ^{13}C NMR (125.8 MHz, $CDCl_3$) δ: 23.52 and 23.68 (d, $J_{C,P}$ = 4.0 $(CH_3)_2CH$), 32.11 (CH_2-1′), 43.72 (CH_2N), 66.82 (d, $J_{C,P}$ = 164, CH_2P), 71.92 (d, $J_{C,P}$ = 11, CH_2O), 72.08 (d, $J_{C,P}$ = 7, $(CH_3)_2CH$), 113.37 (C-5), 128.53 (CH-m-Ph), 128.97 (CH-o-Ph), 134.74 (C-i-Ph), 150.12 (C-8), 153.82 (C-4), 156.92 (C-6), 161.35 (C-2) ppm. MS (ESI) *m/z* (%): 485 (100) $[M + Na]^+$. Anal. calcd for $C_{21}H_{31}N_6O_4P$ (462.5): C 54.54, H 6.76, N 18.17; found: C 54.63, H 6.62, N 18.10.

Diisopropyl 8-allyl-2,6-diamino-9-[2-(phosphonomethoxy)ethyl]purine (2e)

1,2-Dibromoethane (15 μL, 0.1 mmol) was added to a zinc (326 mg, 5 mmol) suspension in THF (2 mL) under an argon atmosphere, and the resulting mixture was sonicated for 15 min. Allylbromide (105 μL, 1.2 mmol) in DMF (1.5 mL) was added and the mixture was sonicated for a further 45 min. After zinc sedimentation, the supernatant was added to a mixture of compound **1** (475 mg, 1 mmol) and $Pd(PPh_3)_4$ (58 mg, 0.05 mmol) in dry DMF (5 mL) under an argon atmosphere. The reaction mixture was stirred at rt for 2 h. The solvent was evaporated and the residue in EtOAc was washed with water and the solvent was evaporated. The crude product was purified by column chromatography (SiO_2, EtOAc/acetone/EtOH/H_2O, 18:3:1:1) and crystallized from EtOH to give **2e** (263 mg, 64%) as colourless crystals.

Diisopropyl 2,6-diamino-8-trifluoromethyl-9-[2-(phosphonomethoxy)ethyl]purine (2m)

1,2-Dibromomethane (15 μL, 0.1 mmol) was added to a zinc suspension (326 mg, 5 mmol) in dry THF (2 mL) under an argon atmosphere, and the mixture was sonicated for 15 min, cooled to –78 °C, and trifluoromethyl iodide (105 μL, 1.2 mmol) was added. The resulting mixture was sonicated and cooled until the complete dissolution of zinc (30 min). The solution was then added to compound **1** (475 mg, 1 mmol) and $Pd(PPh_3)_4$ (58 mg, 0.05 mmol) in dry DMF (5 mL), and the reaction mixture was stirred at rt for 2 h. The solvent was removed and the residue in EtOAc was washed with H_2O and the solvent was evaporated. The crude product was purified by column chromatography (SiO_2, EtOAc/acetone/EtOH/H_2O, 18:3:1:1) to give **2m** (212 mg, 55%) as a colourless solid. ^1H NMR (500 MHz, $CDCl_3$) δ: 1.23 and 1.29 (2 × d, J_{vic} = 6.3, 12H, $(CH_3)_2CH$), 3.43 (d, $J_{H,P}$ = 8.5, 2H, CH_2P), 3.81 (t, J_{vic} = 5.4, 2H, CH_2O), 4.13 (t, J_{vic} = 5.4, 2H, CH_2N), 4.36 (dh, $J_{H,P}$ = 7.6, J_{vic} = 6.3, 2H $(CH_3)_2CH$), 4.64 (bs, 2H, NH_2-2), 5.38 (bs, 2H, NH_2-6) ppm. ^{13}C NMR (125.8 MHz, $CDCl_3$) δ: 23.75 and 23.92 (d, $J_{C,P}$ = 4.0, $(CH_3)_2CH$), 41.47 (CH_2N), 64.01 (d, $J_{C,P}$ = 164, CH_2P), 71.89 (d, $J_{C,P}$ = 7.0, $(CH_3)_2CH$), 72.04 (d, $J_{C,P}$ = 4.0, CH_2O), 113.93 (C-5), 117.85 (CF_3), 148.76 (C-8), 152.95 (C-4), 154.90 (C-6), 160.37 (C-2). MS (ESI) *m/z* (%): 463 (25) $[M + Na]^+$, 441 (100) $[M + H]^+$. Anal. calcd for $C_{15}H_{24}F_3N_6O_4P$ (440.4): C 40.91, H 5.49, N 19.08; found: C 41.02, H 4.38, N 19.05.

Diisopropyl 8-cyclopropyl-2,6-diamino-9-[2-(phosphonomethoxy)ethyl]purine (2n)

n-BuLi (2 mol/L solution in hexanes, 1.2 mL, 3 mmol) was added to cyclopropyl bromide (362 mg, 242 μL, 3 mmol) in THF (4 mL) at –78 °C under an argon atmosphere and stirred at –78 °C for 15 min. Anhydrous $ZnCl_2$ in THF (1 mol/L solution, 3 mL, 3 mmol) was added, and the mixture was stirred at rt for 1 h. The resulting mixture was added to compound **1** (475 mg, 1 mmol) and $Pd(PPh_3)_4$ (58 mg, 0.05 mmol) in dry DMF (5 mL), and the reaction mixture was stirred at rt for 2 h. The solvent was evaporated and the residue in EtOAc was washed with water and the solvent was evaporated. The crude product was purified by column chromatography (SiO_2, EtOAc/acetone/EtOH/H_2O, 18:3:1:1) and crystallized from EtOH to give **2n** (200 mg, 49%) as colourless crystals, mp 178–180 °C. ^1H NMR (500 MHz, $CDCl_3$) δ: 1.11 (d, J_{vic} = 7.2, 4H, H-2′,3′), 1.18 and 1.24 (2 × d, J_{vic} = 6.2, 12H, $(CH_3)_2CH$), 1.59 (d, J_{vic} = 7.2, 1H, CH-1′), 3.60 (d, $J_{H,P}$ = 8.5, 2H, CH_2P), 4.12 (t, J_{vic} = 5.3, 2H, CH_2O), 4.40 (t, J_{vic} = 5.3, 2H, CH_2N), 4.53 (dh, $J_{H,P}$ = 7.7, J_{vic} = 6.2, 2H $(CH_3)_2CH$), 4.98 (bs, 2H, NH_2-2), 5.56 (bs, 2H, NH_2-6) ppm. ^{13}C NMR (125.8 MHz, $CDCl_3$) δ: 3.69 (C-1′), 8.24 (C-2′,3′), 23.56 and 23.74 (d, $J_{C,P}$ = 4.0, $(CH_3)_2CH$), 41.48 (CH_2N), 66.03 (d, $J_{C,P}$ = 167, CH_2P), 70.59 (d, $J_{C,P}$ = 12.0, CH_2O), 71.36 (d, $J_{C,P}$ = 7.0, $(CH_3)_2CH$), 113.89 (C-5), 134.58 (C-8), 152.91 (C-4), 155.78 (C-6), 163.04 (C-2). MS (ESI) *m/z* (%): 435 (60) $[M + Na]^+$, 413 (100) $[M + H]^+$. Anal, calcd for $C_{17}H_{29}N_6O_4P$ (412.4): C 49.51, H 7.09, N 20.38; found: C 49.71, H 6.98, N 20.34.

Diisopropyl 2,6-diamino-8-(2-ethoxy-2-oxoethyl)-9-[2-(phosphonomethoxy)ethyl]purine (2o)

1,2-Dibromomethane (15 μL, 0.1 mmol) was added to a zinc (326 mg, 5 mmol) suspension in freshly distilled THF (2 mL) under an argon atmosphere, and the mixture was sonicated for 15 min. Ethyl 2-bromoacetate (654 μL, 4 mmol) in dry DMF (2 mL) was added and the mixture was sonicated for 45 min. After zinc decantation, the supernatant was added to a mixture of compound **1** (475 mg, 1 mmol) and $Pd(PPh_3)_4$ (58 mg, 0.05 mmol) in dry DMF (5 mL) under an argon atmosphere. The reaction mixture was stirred at rt for 3 h. The solvent was evaporated and the residue in EtOAc was washed with water and the solvent was evaporated. The crude product was purified by column chromatography (SiO_2, EtOAc/acetone/EtOH/H_2O, 18:3:1:1) to give **2o**

Can. J. Chem. Downloaded from www.nrcresearchpress.com by Xi'an Jiaotong University on 09/19/12
For personal use only.

(260 mg, 57%) as a colourless solid. ^{1}H NMR (500 MHz, $CDCl_3$) δ: 1.18 and 1.26 (2 × d, J_{vic} = 6.5, 12H, $(CH_3)_2CH$), 1.29 (t, J_{vic} = 8.0, 3H, CH_2CH_3), 3.51 (s, 2H, CH-1′), 3.63 (d, $J_{H,P}$ = 8.6, 2H, CH_2P), 4.05 (t, J_{vic} = 5.6, 2H, CH_2O), 4.12 (q, J_{vic} = 8.0, 2H, CH_2CH_3), 4.35 (t, J_{vic} = 5.6, 2H, CH_2N), 4.57 (dh, $J_{H,P}$ = 7.6, J_{vic} = 6.5, 2H $(CH_3)_2CH$), 5.32 (bs, 2H, NH_2-2), 6.45 (bs, 2H, NH_2-6) ppm. ^{13}C NMR (125.8 MHz, $CDCl_3$) δ: 16.17 (CH_2CH_3), 23.43 and 23.56 (d, $J_{C,P}$ = 4.0, $(CH_3)_2CH$), 34.74 (CH_2-1′), 43.12 (CH_2N), 61.27 (CH_2CH_3), 66.38 (d, $J_{C,P}$ = 164, CH_2P), 71.42 (d, $J_{C,P}$ = 12.0, CH_2O), 72.61 (d, $J_{C,P}$ = 7.0, $(CH_3)_2CH$), 112.99 (C-5), 149.28 (C-8), 152.35 (C-4), 155.92 (C-6), 161.76 (C-2) ppm. MS (ESI) *m/z* (%): 471 (100) $[M + Na]^+$, 459 (85) $[M + H]^+$. Anal. calcd for $C_{18}H_{31}N_6O_6P$ (458.4): C 47.16, H 6.82, N 18.33; found: C 47.25, H 6.73, N 18.15.

Diisopropyl 8-cyano-2,6-diamino-9-[2-(phosphonomethoxy)ethyl]purine (2p)

Compound **1** (400 mg, 0.84 mmol), $Zn(CN)_2$ (295 mg, 2.5 mmol), Pd_2dba_3 (87 mg, 0.15 mmol), and dppf (92 mg, 0.16 mmol) in dry NMP (5 mL) were stirred under an argon atmosphere for 3 h. The solvent was evaporated and the residue suspended in $CHCl_3$ (30 mL), filtered through Celite, and washed with water (3 × 20 mL). The organics were dried over $MgSO_4$, purified by column chromatography (SiO_2, EtOAc/acetone/EtOH/H_2O, 18:3:1:1), and crystallized from EtOH to give **2p** (260 mg, 81%) as a white crystalline product, mp 164–166 °C. ^{1}H NMR (500 MHz, MeOD) δ: 1.19 and 1.24 (2 × d, J_{vic} = 6.2, 12H, $(CH_3)_2CH$), 3.78 (d, $J_{H,P}$ = 8.3, 2H, CH_2P), 3.92 (t, J_{vic} = 5.0, 2H, CH_2O), 4.34 (t, J_{vic} = 5.0, 2H, CH_2N), 4.55 (dh, $J_{H,P}$ = 7.4, J_{vic} = 6.2, 2H $(CH_3)_2CH$), 4.73 (bs, 2H, NH_2-2), 5.45 (bs, 2H, NH_2-6) ppm. ^{13}C NMR (125.8 MHz, $CDCl_3$) δ: 23.86 and 23.98 (d, $J_{C,P}$ = 4.0, $(CH_3)_2CH$), 43.20 (CH_2N), 64.67 (d, $J_{C,P}$ = 141, CH_2P), 69.28 (d, $J_{C,P}$ = 7.0, $(CH_3)_2CH$), 72.36 (d, $J_{C,P}$ = 5.0, CH_2O), 111.43 (C-5), 113.24 (CN), 129.62 (C-8), 154.93 (C-4), 156.74 (C-6), 162.15 (C-2) ppm. MS (ESI) *m/z* (%): 420 (100) $[M + Na]^+$, 398 (91) $[M + H]^+$. Anal. calcd for $C_{15}H_{24}N_7O_4P$ (397.4): C 45.34, H 6.09, N 24.67; found: C 45.48, H 6.04, N 24.31.

Reactions with trialkylaluminum reagents

Method D (general procedure)

Trialkylaluminum (3 mmol) was added to smixture of 8-bromopurine **1** (475 mg, 1 mmol) and $Pd(PPh_3)_4$ (58 mg, 0.05 mmol) in THF (5 mL) under an argon atmosphere and the reaction mixture was stirred at reflux for 5 h. The solvent was evaporated, washed with brine and saturated aqueous EDTA solution, and dried over $MgSO_4$. The crude product was purified by column chromatography (SiO_2, EtOAc/acetone/EtOH/H_2O, 18:3:1:1) and crystallized from EtOH.

Diisopropyl 2,6-diamino-8-methyl-9-[2-(phosphonomethoxy)ethyl]purine (2a)

Treatment of **1** with trimethylaluminum using Method D afforded **2a** as colourless crystals; yield: 221 mg (54%).

Diisopropyl 2,6-diamino-8-ethyl-9-[2-(phosphonomethoxy)ethyl]purine (2b)

Treatment of **1** with triethylaluminum using Method D gave **2b** as colourless crystals; yield: 203 mg (48%).

Deprotection of Diisopropyl esters 2 to free phosphonic acids 3

Method E (general procedure)

Diisopropylesters **2a**–**2p** (0.5 mmol) in CH_3CN (10 mL) were treated with Me_3SiBr (2 mL, 15.2 mmol), and the reaction mixture was stirred at rt overnight. The volatiles were removed under reduced pressure, the residue was co-distilled with toluene (5 mL) and TEAB (tetrabutylammonium bicarbonate, 0.5 mol/L, 2 mL) was added and the solvent was evaporated. The residue in H_2O (5 mL) was applied onto a column of Dowex 50 × 8 (H^+). The column was washed with water and the product was eluted with 2.5% aqueous ammonia. The crude product was then applied to a column of Dowex 1 × 2 (AcO^-), the column was then washed with water, and the product was eluted with a linear gradient of AcOH (0–2 mol/L). The product-containing fractions were evaporated and co-distilled with water (2 × 10 mL), and the crude product was crystallized from the H_2O/EtOH mixture.

2,6-Diamino-8-methyl-9-[2-(phosphonomethoxy)ethyl]purine (3a)

Method E afforded a colourless solid; yield: 67%; mp > 250 °C. ^{1}H NMR (500 MHz, D_2O) δ: 2.45 (s, 3H, CH_3-8), 3.26 (d, $J_{H,P}$ = 8.6, 2H, CH_2P), 3.85 (t, J_{vic} = 5.2, 2H, CH_2O), 4.11 (t, J_{vic} = 5.2, 2H, CH_2N) ppm. ^{13}C NMR (125.8 MHz, D_2O) δ: 15.66 (CH_3-8), 44.99 (CH_2N), 70.29 (d, $J_{C,P}$ = 155, CH_2P), 73.27 (d, $J_{C,P}$ = 4.0, CH_2O), 112.98 (C-5), 152.62 (C-8), 154.05 (C-4), 155.30 (C-6), 159.75 (C-2) ppm. MS (ESI) *m/z* (%): 303 (100) $[M + H]^+$. Anal. calcd for $C_9H_{15}N_6O_4P$ (302.2): C 35.77, H 5.00, N 27.81; found: C 35.82, H 4.92, N 27.95.

2,6-Diamino-8-ethyl-9-[2-(phosphonomethoxy)ethyl]purine (3b)

Method E afforded a colourless solid; yield: 81%; mp > 250 °C. ^{1}H NMR (500 MHz, D_2O) δ: 1.32 (t, J_{vic} = 7.5, 3H, CH_3CH_2), 2.84 (q, J_{vic} = 7.5, 2H, CH_3CH_2), 3.50 (d, $J_{H,P}$ = 8.3, 2H, CH_2P), 3.84 (t, J_{vic} = 5.7, 2H, CH_2O), 4.16 (t, J_{vic} = 5.7, 2H, CH_2N) ppm. ^{13}C NMR (125.8 MHz, D_2O) δ: 13.09 (CH_3CH_2), 22.83 (CH3CH_2), 44.61 (CH_2N), 70.58 (d, $J_{C,P}$ = 152, CH_2P), 72.89 (d, $J_{C,P}$ = 10.0, CH_2O), 114.12 (C-5), 154.67 (C-4), 156.73 (C-8), 157.22 (C-6), 161.68 (C-2) ppm. MS (ESI) *m/z* (%): 317 (100) $[M + H]^+$. Anal. calcd for $C_{10}H_{17}N_6O_4P$ (316.2): C 37.98, H 5.42, N 26.57; found: C 38.12, H 5.48, N 26.41.

2,6-Diamino-8-phenyl-9-[2-(phosphonomethoxy)ethyl]purine (3c)

Method E afforded a colourless solid; yield: 78%; mp > 250 °C. ^{1}H NMR (400 MHz, D_2O) δ: 3.65 (d, $J_{H,P}$ = 8.4, 2H, CH_2P), 4.00 (t, J_{vic} = 5.6, 2H, CH_2O), 4.18 (t, J_{vic} = 5.6, 2H, CH_2N), 7.48–7.53 (m, 3H, H-m, p-Ph), 7.81 (m, 2H, H-o-Ph) ppm. ^{13}C NMR (125.8 MHz, D_2O) δ: 43.15 (CH_2N), 71.47 (d, $J_{C,P}$ = 151, CH_2P), 72.34 (d, $J_{C,P}$ = 12.0, CH_2O), 113.75 (C-5), 128.51 (CH-m-Ph), 129.26 (CH-o-Ph), 129.29 (C-i-Ph), 149.07 (C-8), 153.16 (C-4), 155.23 (C-6),

Can. J. Chem. Downloaded from www.nrcresearchpress.com by Xi'an Jiaotong University on 09/19/12
For personal use only.

158.03 (C-2) ppm. MS (ESI) *m/z* (%): 365 (100) $[M + H]^+$. Anal. calcd for $C_{14}H_{17}N_6O_4P$ (364.3): C 46.16, H 4.70, N 23.07; found: C 46.29, H 4.72, N 3.04.

2,6-Diamino-8-vinyl-9-[2-(phosphonomethoxy)ethyl]purine (3d)

Method E gave a colourless solid; yield: 69%; mp > 250 °C. ^{1}H NMR (400 MHz, D_2O) δ: 3.78 (d, $J_{H,P}$ = 8.3, 2H, CH_2P), 3.86 (t, J_{vic} = 5.2, 2H, CH_2O), 4.24 (t, J_{vic} = 5.2, 2H, CH_2N), 5.48 (d, J_{cis} = 4.8, 1H, CH_2-2′trans), 6.33 (d, J_{trans} = 17.1, 1H, CH_2-2′cis), 6.70 (dd, J_{trans} = 17.1, J_{cis} = 4.8, 1H, CH-1′) ppm. ^{13}C NMR (125.8 MHz, D_2O) δ: 41.80 (CH_2N), 72.22 (d, $J_{C,P}$ = 157, CH_2P), 72.42 (d, $J_{C,P}$ = 11.0, CH_2O), 113.65 (C-5), 120.63 (C-2′), 123.29 (C-1′), 146.07 (C-8), 152.61 (C-4), 154.96 (C-6), 159.73 (C-2) ppm. MS (ESI) *m/z* (%): 337 (30) $[M + Na]^+$, 315 (100) $[M + H]^+$. Anal. calcd for $C_{10}H_{15}N_6O_4P$ (314.2): C 38.22, H 4.81, N 26.74; found: C 38.36, H 4.78, N 26.75.

2,6-Diamino-8-allyl-9-[2-(phosphonomethoxy)ethyl]purine (3e)

Method E afforded a colourless solid; yield: 68%; mp > 250 °C. ^{1}H NMR (400 MHz, D_2O) δ: 3.35 (d, J_{vic} = 6.3, 2H, CH_2-1′), 3.72 (d, $J_{H,P}$ = 8.4, 2H, CH_2P), 3.86 (t, J_{vic} = 5.4, 2H, CH_2O), 4.26 (t, J_{vic} = 5.4, 2H, CH_2N), 5.30 (dq, $J_{3'cis1'}$ = J_{gem} = 1.4, J_{trans} = 17.7, 1H, CH_2-3′cis), 6.02 (ddt, J_{trans} = 17.7, J_{cis} = 8.3, J_{vic} = 6.3, 1H, CH-2′) ppm. ^{13}C NMR (125.8 MHz, D_2O) δ: 40.15 (C-1′), 41.59 (CH_2N), 69.11 (d, $J_{C,P}$ = 155, CH_2P), 71.84 (d, $J_{C,P}$ = 10.0, CH_2O), 113.74 (C-5), 116.45 (C-3′), 138.26 (C-2′), 148.64 (C-8), 151.72 (C-4), 156.27 (C-6), 159.53 (C-2) ppm. MS (ESI) *m/z* (%): 351 (10) $[M + Na]^+$, 329 (100) $[M + H]^+$. Anal. calcd for $C_{11}H_{17}N_6O_4P$ (328.2): C 40.25, H 5.22, N 25.60; found: C 40.15, H 5.19, N 25.64.

2,6-Diamino-8-(thien-2-yl)-9-[2-(phosphonomethoxy)ethyl]purine (3f)

Method E gave a pale yellow solid; yield: 75%; mp > 250 °C. ^{1}H NMR (400 MHz, D_2O) δ: 3.71 (d, $J_{H,P}$ = 8.5, 2H, CH_2P), 3.99 (t, J_{vic} = 5.5, 2H, CH_2O), 4.41 (t, J_{vic} = 5.5, 2H, CH_2N), 7.13 (dd, $J_{4',5'}$ = 5.0, $J_{4',3'}$ = 3.7, 1H, H-4′), 7.39 (dd, $J_{5',4'}$ = 5.0, $J_{5',3'}$ = 0.7, 1H, H-5′), 7.62 (dd, $J_{3',4'}$ = 3.7, $J_{3',5'}$ = 0.7, 1H, H-3′) ppm. ^{13}C NMR (125.8 MHz, D_2O) δ: 41.35 (CH_2N), 69.72 (d, $J_{C,P}$ = 156, CH_2P), 70.62 (d, $J_{C,P}$ = 10.0, CH_2O), 113.51 (C-5), 127.52 (CH-5′), 127.52 (CH-4′), 128.04 (CH-3′), 131.25 (CH-2′), 141.22 (C-8), 153.95 (C-4), 155.36 (C-6), 159.50 (C-2) ppm. MS (ESI) *m/z* (%): 371 (100) $[M + H]^+$. Anal. calcd for $C_{12}H_{15}N_6O_4PS$ (370.3): C 38.92, H 4.08, N 22.69; found: C 39.20, H 4.15, N 22.74.

2,6-Diamino-8-[4-(trifluoromethyl)phenyl]-9-[2-(phosphonomethoxy)ethyl]purine (3g)

Method E afforded a colourless solid; yield: 82%; mp > 250 °C. ^{1}H NMR (500 MHz, $CDCl_3$) δ: 3.70 (d, $J_{H,P}$ = 8.6, 2H, CH_2P), 4.12 (t, J_{vic} = 5.7, 2H, CH_2O), 4.36 (t, J_{vic} = 5.7, 2H, CH_2N), 4.51 (bs, 2H, NH_2-2), 5.68 (bs, 2H, NH_2-6), 7.56 (d, J = 8.2, 2H, H-3′,5′), 8.01 (d, J = 8.2, 2H, H-2′,6′) ppm. ^{13}C NMR (125.8 MHz, D_2O) δ: 42.92 (CH_2N), 65.73 (d, $J_{C,P}$ = 166, CH_2P), 70.36 (d, $J_{C,P}$ = 12.0, CH_2O), 112.95 (C-5), 126.32 (CH-m-PH), 127.53 (CH-o-Ph), 131.22 (CF_3), 132.18 (C-i-Ph), 154.23 (C-8), 157.47 (C-4), 159.01 (C-6), 162.73 (C-2) ppm. MS (ESI) *m/z* (%): 455 (100) $[M + Na]^+$.

2,6-Diamino-8-(2,4-difluorophenyl)-9-[2-(phosphonomethoxy)ethyl]purine (3h)

Method E gave a colourless solid; yield: 84%; mp > 250 °C. ^{1}H NMR (500 MHz, D_2O) δ: 3.61 (d, $J_{H,P}$ = 8.6, 2H, CH_2P), 3.86 (t, J_{vic} = 5.7, 2H, CH_2O), 4.22 (t, J_{vic} = 5.7, 2H, CH_2N), 4.59 (bs, 2H, NH_2-2), 5.68 (bs, 2H, NH_2-6), 6.91 (ddd, $J_{3',F}$ = 8.2, $J_{3',F}$ = 8.0, $J_{3',5'}$) = 1.5, 1H, H-3′), 7.04 (ddd, $J_{5',F}$ = 8.2, $J_{5',6'}$ = 7.6, $J_{3',5'}$ = 1.5, 1H, H-5′), 7.72 (ddd, $J_{5',6'}$ = 7.6, $J_{6',F}$ = 5.0, 1H, H-6) ppm. ^{13}C NMR (125.8 MHz, D_2O) δ: 43.45 (CH_2N), 65.18 (d, $J_{C,P}$ = 167, CH_2P), 70.94 (d, $J_{C,P}$ = 13.0, CH_2O), 102.63 (C-3′), 112.07 (C-5), 114.23 (C-5′), 119.69 (C-1′), 132.85 (C-6′), 154.90 (C-8), 156.67 (C-4), 157.82 (C-6), 159.91 (C-2′), 162.36 (C-4′), 162.99 (C-2) ppm. MS (ESI) *m/z* (%): 401 (100) $[M + H]^+$.

2,6-Diamino-8-(thien-3-yl)-9-[2-(phosphonomethoxy)ethyl]purine (3i)

Method E afforded a colourless solid; yield: 76%; mp > 250 °C. ^{1}H NMR (400 MHz, D_2O) δ: 3.62 (d, $J_{H,P}$ = 8.7, 2H, CH_2P), 3.96 (t, J_{vic} = 5.6, 2H, CH_2O), 4.34 (t, J_{vic} = 5.6, 2H, CH_2N), 4.85 (bs, 2H, NH_2-2), 5.51 (bs, 2H, NH_2-6), 7.22 (dd, $J_{5',4'}$ = 7.5, $J_{5',2'}$ = 1.5, 1H, H-5′), 7.74 (dd, $J_{4',5'}$ = 7.5, $J_{4',2'}$ = 2.9, 1H, H-4′), 8.01 (dd, $J_{2',4'}$ = 5.0, $J_{2',5'}$ = 1.5, H-2′) ppm. ^{13}C NMR (125.8 MHz, D_2O) δ: 42.95 (CH_2N), 66.21 (d, $J_{C,P}$ = 165, CH_2P), 70.26 (d, $J_{C,P}$ = 12.0, CH_2O), 113.47 (C-5), 126.38 (C-2′), 127.60 (C-4′), 128.19 (C-5′), 135.51 (C-1′), 154.28 (C-8), 157.74 (C-4), 160.19 (C-6), 164.86 (C-2) ppm. MS (ESI) *m/z* (%): 371 (100) $[M + H]^+$.

2,6-Diamino-8-(2-phenylvinyl)-9-[2-(phosphonomethoxy)ethyl]purine (3j)

Method E gave a colourless solid; yield: 65%; mp > 250 °C. ^{1}H NMR (500 MHz, D_2O) δ: 3.59 (d, $J_{H,P}$ = 8.5, 2H, CH_2P), 4.08 (t, J_{vic} = 5.7, 2H, CH_2O), 4.34 (t, J_{vic} = 5.7, 2H, CH_2N), 5.36 (bs, 2H, NH_2-2), 6.44 (bs, 2H, NH_2-6), 6.89 (d, J_{trans} = 15.5, 1H, H-2′), 7.04 (d, J_{trans} = 15.5, 1H, H-1′), 7.44–7.51 (m, 3H, H-m, p-Ph), 7.83 (m, 2H, H-o-Ph) ppm. ^{13}C NMR (125.8 MHz, D_2O) δ: 42.15 (CH_2N), 66.32 (d, $J_{C,P}$ = 161, CH_2P), 71.65 (d, $J_{C,P}$ = 12.0, CH_2O), 112.92 (C-1′), 114.07 (C-5), 128.39 (CH-m-Ph), 130.22 (CH-o-Ph), 131.21 (C-i-Ph), 134.58 (C-2′), 153.06 (C-8), 153.80 (C-4), 157.19 (C-6), 160.25 (C-2) ppm. MS (ESI) *m/z* (%): 391 (100) $[M + H]^+$.

2,6-Diamino-8-(propene-2-yl)-9-[2-(phosphonomethoxy)ethyl]purine (3k)

Method E gave a pale yellow solid; yield: 69%; mp > 250 °C. ^{1}H NMR (400 MHz, D_2O) δ: 2.42 (s, 3H, CH_3-8), 3.71 (d, $J_{H,P}$ = 8.6, 2H, CH_2P), 4.19 (t, J_{vic} = 5.6, 2H, CH_2O), 4.35 (t, J_{vic} = 5.6, 2H, CH_2N), 5.41 and 5.45 (2 × s, 2H, CH_2-2′) ppm. ^{13}C NMR (125.8 MHz, D_2O) δ: 22.19 (CH_3-8), 42.97 (CH_2N), 70.87 (d, $J_{C,P}$ = 8.0, CH_2O), 71.47 (d, $J_{C,P}$ = 153, CH_2P), 112.85 (C-5), 119.23 (C-2′), 134.41 (C-1′), 148.73 (C-8), 153.16 (C-4), 155.61 (C-6), 159.70 (C-2) ppm. MS (ESI) *m/z* (%): 350 (5) $[M + Na]^+$, 329 (100) $[M + H]^+$.

2,6-Diamino-8-(benzyl)-9-[2-(phosphonomethoxy)ethyl]purine (3l)

Method E afforded a pale yellow solid; yield: 82%; mp > 250 °C. ^{1}H NMR (500 MHz, D_2O) δ: 3.58 (d, $J_{H,P}$ = 8.3, 2H, CH_2P), 4.04 (s, 2H, H-1′), 4.00 (t, J_{vic} = 5.8, 2H, CH_2O), 4.36 (t, J_{vic} = 5.8, 2H, CH_2N), 5.22 (bs, 2H, NH_2-

Can. J. Chem. Downloaded from www.nrcresearchpress.com by Xi'an Jiaotong University on 09/19/12
For personal use only.

2), 6.49 (bs, 2H, NH_2-6), 7.35–7.44 (m, 3H, H-o, p-Ph), 7.59 (m, 2H, H-m-Ph) ppm. ^{13}C NMR (125.8 MHz, D_2O) δ: 32.46 (CH_2-1′), 43.15 (CH_2N), 67.23 (d, $J_{C,P}$ = 167, CH_2P), 72.59 (d, $J_{C,P}$ = 11.0, CH_2O), 113.32 (C-5), 128.45 (CH-m-Ph), 129.03 (CH-o-Ph), 134.56 (C-i-Ph), 150.88 (C-8), 154.27 (C-4), 156.13 (C-6), 159.90 (C-2) ppm. MS (ESI) *m/z* (%): 379 (100) $[M + H]^+$.

2,6-Diamino-8-(trifluoromethyl)-9-[2-(phosphonomethoxy)ethyl]purine (3m)

Method E gave a colourless solid; yield: 81%; mp > 250 °C. ^{1}H NMR (500 MHz, D_2O) δ: 3.48 (d, $J_{H,P}$ = 8.2, 2H, CH_2P), 3.78 (t, J_{vic} = 5.4, 2H, CH_2O), 4.40 (t, J_{vic} = 5.4, 2H, CH_2N), 4.68 (bs, 2H, NH_2-2), 5.32 (bs, 2H, NH_2-6) ppm. ^{13}C NMR (125.8 MHz, D_2O) δ: 41.48 (CH_2N), 64.12 (d, $J_{C,P}$ = 165, CH_2P), 72.02 (d, $J_{C,P}$ = 4.0, CH_2O), 114.78 (C-5), 117.91 (CF_3), 148.54 (C-8), 153.06 (C-4), 155.32 (C-6), 160.26 (C-2) ppm. MS (ESI) *m/z* (%): 357 (100) $[M + H]^+$. Anal. calcd for $C_9H_{12}F_3N_6O_4P$ (356.2): C 30.35, H 3.40, N 23.59; found: C 30.51, H 3.34, N 23.51.

2,6-Diamino-8-(cyclopropyl)-9-[2-(phosphonomethoxy)ethyl]purine (3n)

Method E afforded a colourless solid; yield: 74%; mp > 250 °C. ^{1}H NMR (500 MHz, D_2O) δ: 1.13 (d, J_{vic} = 7.1, 4H, H-2′,3′), 1.61 (d, J_{vic} = 7.1, 1H, CH-1′), 3.58 (d, $J_{H,P}$ = 8.4, 2H, CH_2P), 4.10 (t, J_{vic} = 5.5, 2H, CH_2O), 4.45 (t, J_{vic} = 5.5, 2H, CH_2N), 5.04 (bs, 2H, NH_2-2), 5.51 (bs, 2H, NH_2-6) ppm. ^{13}C NMR (125.8 MHz, D_2O) δ: = 3.63 (C-1′), 8.27 (C-2′,3′), 41.38 (CH_2N), 66.12 (d, $J_{C,P}$ = 161, CH_2P), 70.47 (d, $J_{C,P}$ = 12.0, CH_2O), 113.24 (C-5), 134.63 (C-8), 152.74 (C-4), 156.72 (C-6), 163.89 (C-2) ppm. MS (ESI) *m/z* (%): 351 (50) $[M + Na]^+$, 329 (100) $[M + H]^+$.

2,6-Diamino-8-(cyano)-9-[2-(phosphonomethoxy)ethyl]purine (3p)

Method E gave a colourless solid; yield: 65%; mp > 250 °C. MS (ESI): *m/z* (%): 314 (100) $[M + H]^+$. ^{1}H NMR (500 MHz, D_2O) δ: 3.82 (d, $J_{H,P}$ = 8.4, 2H, CH_2P), 3.84 (t, J_{vic} = 5.3, 2H, CH_2O), 4.38 (t, J_{vic} = 5.3, 2H, CH_2N), 4.62 (bs, 2H, NH_2-2), 5.48 (bs, 2H, NH_2-6) ppm. ^{13}C NMR (125.8 MHz, D_2O) δ: 43.96 (CH_2N), 64.50 (d, $J_{C,P}$ = 131, CH_2P), 73.03 (d, $J_{C,P}$ = 5.0, CH_2O), 111.96 (C-5), 113.22 (CN), 130.75 (C-8), 154.24 (C-4), 156.48 (C-6), 162.27 (C-2) ppm. MS (ESI) *m/z* (%): 314 (100) $[M + H]^+$.

Diisopropyl 2,6-diamino-8-[(2-trimethylsilyl)ethynyl]-9-[2-(phosphonomethoxy)ethyl]purine (4)

Triethylamine (0.2 mL, 1.5 mmol) was added to amixture of the compound **1** (475 mg, 1 mmol), CuI (10 mg, 0.05 mmol), and $Pd(PPh_3)_2Cl_2$ (35 mg, 0.05 mmol) in dry DMF (4 mL) under an argon atmosphere at rt, and the resulting mixture was stirred for 15 min at rt. Trimethylsilylacetylene (160 μL, 1.15 mmol) in THF (1 mL) was added and the reaction mixture was stirred at rt for 3 h. The solvent was evaporated and the residue in EtOAc was washed with water and dried over $MgSO_4$. The crude product was purified by column chromatography (SiO_2, EtOAc/acetone/EtOH/H_2O, 18:3:1:1) and crystallized form EtOH to give **4** (350 mg, 67%) as a pale yellow crystalline product; mp 146–148 °C. ^{1}H NMR (500 MHz, $CDCl_3$) δ: 0.30 (s, 9H, CH_3Si), 1.24 and 1.28 (2 × d, J_{vic} = 6.2, 12H, (CH_3)$_2$CH), 3.77 (d, $J_{H,P}$ = 8.6, 2H, CH_2P), 3.98 (t, J_{vic} = 5.8, 2H, CH_2O), 4.31 (t, J_{vic} = 5.8, 2H, CH_2N), 4.48 (dh, $J_{H,P}$ = 7.6, J_{vic} = 6.2, 2H (CH_3)$_2$C*H*), 5.73 (bs, 2H, NH_2-2), 7.28 (bs, 2H, NH_2-6) ppm. ^{13}C NMR (125.8 MHz, $CDCl_3$) δ: –0.48 (CH_3Si), 23.86 and 24.00 (d, $J_{C,P}$ = 4.0, (CH_3)$_2$CH), 42.36 (CH_2N), 65.73 (d, $J_{C,P}$ = 167, CH_2P), 70.28 (d, $J_{C,P}$ = 11.0, CH_2O), 71.13 (d, $J_{C,P}$ = 7.0, (CH_3)$_2$*C*H), 93.26 (C-1′), 101.53 (C-2′), 114.06 (C-5), 131.93 (C-8), 151.84 (C-4), 155.65 (C-6), 160.43 (C-2) ppm. MS (ESI) *m/z* (%): 469 (100) $[M + Na]^+$. Anal. calcd for $C_{19}H_{33}N_6O_4PSi$ (468.6): C 48.70, H 7.10, N 17.94; found: C 48.75, H 7.00, N 18.06.

2,6-Diamino-8-(ethynyl)-9-[2-(phosphonomethoxy)ethyl]purine (5)

Compound **4** (261 mg, 0.5 mmol) was stirred in methanolic ammonia (10 mol/L, 5 mL) at rt overnight. The volatiles were evaporated and the crude product was recrystallized from an EtOAc – light petroleum (1:1) mixture to give 197 mg (94%) of 8-ethylnyl derivative as a colourless crystalline product; mp 192–194 °C. ^{1}H NMR (500 MHz, $CDCl_3$) δ: 1.23 and 1.28 (2 × d, J_{vic} = 6.2, 12H, (CH_3)$_2$CH), 3.41 (s, 1H, CH-2′), 3.75 (d, $J_{H,P}$ = 8.5, 2H, CH_2P), 3.97 (t, J_{vic} = 5.8, 2H, CH_2O), 4.33 (t, J_{vic} = 5.8, 2H, CH_2N), 4.48 (dh, $J_{H,P}$ = 7.6, J_{vic} = 6.2, 2H (CH_3)$_2$C*H*), 4.82 (bs, 2H, NH_2-2), 5.48 (bs, 2H, NH_2-6) ppm. ^{13}C NMR (125.8 MHz, $CDCl_3$) δ: 23.88 and 24.00 (d, $J_{C,P}$ = 4.0, (CH_3)$_2$CH), 42.57 (CH_2N), 65.83 (d, $J_{C,P}$ = 167, CH_2P), 70.40 (d, $J_{C,P}$ = 11.0, CH_2O), 71.15 (d, $J_{C,P}$ = 7.0, (CH_3)$_2$*C*H), 73.30 (C-1′), 82.66 (C-2′), 114.20 (C-5), 131.25 (C-8), 151.91 (C-4), 155.71 (C-6), 160.60 (C-2) ppm. MS (ESI) *m/z* (%): 397 (100) $[M + H]^+$. Anal. calcd for $C_{16}H_{25}N_6O_4P$ (396.4): C 48.48, H 6.36, N 21.20; found: C 48.42, H 6.45, N 21.27.

Deprotected 8-ethynylpurine derivative **5** was prepared by GP3, isolated by preparative HPLC (eluted with 1% MeOH in H_2O), and crystallized from an EtOH/H_2O mixture to give pale yellow crystals; yield: 31%; mp > 250 °C. ^{1}H NMR (500 MHz, D_2O) δ: 3.64 (d, $J_{H,P}$ = 8.4, 2H, CH_2P), 3.94 (t, J_{vic} = 5.0, 2H, CH_2O), 4.08 (bs, 1H, CH-2′), 4.29 (t, J_{vic} = 5.0, 2H, CH_2N) ppm. ^{13}C NMR (125.8 MHz, D_2O) δ: 45.48 (CH_2N), 69.76 (d, $J_{C,P}$ = 156, CH_2P), 72.82 (d, $J_{C,P}$ = 10.0, CH_2O), 74.28 (C-1′), 88.30 (C-2′), 114.96 (C-5), 134.94 (C-8), 153.12 (C-4), 157.53 (C-6), 161.99 (C-2) ppm. MS (ESI) *m/z* (%): 313 (100) $[M + H]^+$. Anal. calcd for $C_{10}H_{13}N_6O_4P$ (312.2): C 38.47, H 4.20, N 26.92; found: C 38.42, H 4.26, N 27.04.

Acknowledgments

This study was performed as a part of research project OZ40550506 of the Institute of Organic Chemistry and Biochemistry, Academy of Sciences of the Czech Republic, Prague. It was supported by the Centre for New Antivirals and Antineoplastics 1M0508 by the Ministry of Education, Youth, and Sports of the Czech Republic and by the Gilead Sciences and IOCB Research Centre, Prague, Czech Republic.

References

(1) De Clercq, E.; Holý, A.; Rosenberg, I.; Sakuma, T.; Balzarini, J.; Maudgal, P. C. *Nature* **1986** *323* (6087), 464. doi:10.1038/323464a0.

Can. J. Chem. Downloaded from www.nrcresearchpress.com by Xi'an Jiaotong University on 09/19/12
For personal use only.

(2) (a) Holý, A. *Curr. Pharm. Des.* **2003** *9* (31), 2567. doi:10.2174/1381612033453668.; (b) Holý, A. *Antiviral Res.* **2006** *71* (2-3), 248. doi:10.1016/j.antiviral.2006.06.002.; (c) De Clercq, E. *Antiviral Res.* **2007** *75* (1), 1. doi:10.1016/j.antiviral.2006.10.006.

(3) (a) Smeijsters, L. J. J. W.; Franssen, F. F. J.; Naesens, L.; de Vries, E.; Holý, A.; Balzarini, J.; De Clercq, E.; Overdulve, J. P. *Int. J. Antimicrob. Agents* **1999** *12* (1), 53. doi:10.1016/S0924-8579(99)00003-5.; (b) Keough, D. T.; Hocková, D.; Holý, A.; Naesens, L. M. J.; Skinner-Adams, T. S.; de Jersey, J.; Guddat, L. W. *J. Med. Chem.* **2009** *52* (14), 4391. doi:10.1021/jm900267n.; (c) Hocková, D.; Holý, A.; Masojídková, M.; Keough, D. T.; de Jersey, J.; Guddat, L. W. *Bioorg. Med. Chem.* **2009** *17* (17), 6218. doi:10.1016/j.bmc.2009.07.044.

(4) Zídek, Z.; Potměšil, P.; Holý, A. *Toxicol. Appl. Pharmacol.* **2003** *192* (3), 246. doi:10.1016/S0041-008X(03)00215-1.

(5) (a) Zídek, Z.; Franková, D.; Holý, A. *Int. J. Immunopharmacol.* **2000** *22* (12), 1121. doi:10.1016/S0192-0561(00)00068-0.; (b) Zídek, Z.; Potměšil, P.; Kmoníčková, E.; Holý, A. *Eur. J. Pharmacol.* **2003** *475* (1-3), 149. doi:10.1016/S0014-2999(03)02110-1.; (c) Potměšil, P.; Krečmerová, M.; Kmoníčková, E.; Holý, A.; Zídek, Z. *Eur. J. Pharmacol.* **2006** *540* (1-3), 191. doi:10.1016/j.ejphar.2006.04.018.

(6) De Clercq, E.; Holý, A. *Nat. Rev. Drug Discov.* **2005** *4* (11), 928. doi:10.1038/nrd1877.

(7) (a) Hatse, S.; Naesens, L.; De Clercq, E.; Balzarini, J. *Biochem. Pharmacol.* **1999** *58* (2), 311. doi:10.1016/S0006-2952(99)00091-X.; (b) Holý, A.; Votruba, I.; Tloušťová, E.; Masojídková, M. *Collect. Czech. Chem. Commun.* **2001** *66* (10), 1545. doi:10.1135/cccc20011545.

(8) Reiser, H.; Wang, J.; Chong, L.; Watkins, W. J.; Ray, A. S.; Shibata, R.; Birkus, G.; Cihlar, T.; Wu, S.; Li, B.; Liu, X.; Henne, I. N.; Wolfgang, G. H. I.; Desai, M.; Rhodes, G. R.; Fridland, A.; Lee, W. A.; Plunkett, W.; Vail, D.; Thamm, D. H.; Jeraj, R.; Tumas, D. B. *Clin. Cancer Res.* **2008** *14* (9), 2824. doi:10.1158/1078-0432.CCR-07-2061.

(9) Schinkmanová, M.; Votruba, I.; Shibata, R.; Han, B.; Liu, X.; Cihlar, T.; Holý, A. *Collect. Czech. Chem. Commun.* **2008** *73* (2), 275. doi:10.1135/cccc20080275.

(10) Schinkmanová, M.; Votruba, I.; Holý, A. *Biochem. Pharmacol.* **2006** *71* (9), 1370. doi:10.1016/j.bcp.2006.01.013.

(11) (a) Janeba, Z.; Holý, A.; Votavová, H.; Masojídková, M. *Collect. Czech. Chem. Commun.* **1996** *61* (3), 442. doi:10.1135/cccc19960442.; (b) Janeba, Z.; Holý, A.; Masojídková, M. *Collect. Czech. Chem. Commun.* **2000** *65* (7), 1126. doi:10.1135/cccc20001126.; (c) Janeba, Z.; Holý, A.; Masojídková, M. *Collect. Czech. Chem. Commun.* **2000** *65* (11), 1698. doi:10.1135/cccc20001698.; (d) Janeba, Z.; Holý, A.; Masojídková, M. *Collect. Czech. Chem. Commun.* **2001** *66* (3), 517. doi:10.1135/cccc20010517.; (e) Janeba, Z.; Holý, A.; Masojídková, M. *Collect. Czech. Chem. Commun.* **2001** *66* (9), 1393. doi:10.1135/cccc20011393.; (f) Janeba, Z.; Holý, A. *Nucleosides Nucleotides Nucleic Acids* **2001** *20* (4-7), 1103 doi:10.1081/NCN-100002498.; (g) Janeba, Z.; Masojídková, M.; Holý, A. *Collect. Czech. Chem. Commun.* **2010** *75* (3), 371. doi:10.1135/cccc2009569.

(12) (a) Tu, C.; Keane, C.; Eaton, B. E. *Nucleosides Nucleotides Nucleic Acids* **1995** *14* (8), 1631. doi:10.1080/15257779508009745.; (b) Hocek, M. *Eur. J. Org. Chem.* **2003** *2003* (2), 245. doi:10.1002/ejoc.200390025.; (c) Hocek, M.; Hocková, D.; Štambaský, J. *Collect. Czech. Chem. Commun.* **2003** *68* (5), 837. doi:10.1135/cccc20030837.; (d) Andrei, M.; Bjørnstad, V.; Langli, G.; Rømming, C.; Klaveness, J.; Taskén, K.; Undheim, K. *Org. Biomol. Chem.* **2007** *5* (13), 2070. doi:10.1039/b702403g.

(13) (a) Gundersen, L.-L.; Grand, A.; Pilawa, B.; Jensen, G. W.; Møller, I. L.; Nielsen, R. I.; Olsen, C. E.; Rosendahl, C. N.; Haugg, M.; Trabesinger-Rüf, N.; Weinhold, E. G. *Acta Chem. Scand.* **1996** *50*, 462. doi:10.3891/acta.chem.scand.50-0462.; (b) Hocek, M.; Holý, A.; Votruba, I.; Dvořáková, H. *Collect. Czech. Chem. Commun.* **2001** *66* (3), 483. doi:10.1135/cccc20010483.; (c) Hocek, M.; Holý, A.; Dvořáková, H. *Collect. Czech. Chem. Commun.* **2002** *67* (3), 325. doi:10.1135/cccc20020325.

(14) Janeba, Z.; Holý, A.; Balzarini, J. De Clercq. Unpublished results.

(15) Holý, A.; Günter, J.; Dvořáková, H.; Masojídková, M.; Andrei, G.; Snoeck, R.; Balzarini, J.; De Clercq, E. *J. Med. Chem.* **1999** *42* (12), 2064. doi:10.1021/jm9811256.

(16) Stille, J. K. *Pure Appl. Chem.* **1985** *57* (12), 1771. doi:10.1351/pac198557121771.

(17) Farina, V.; Krishnan, B. *J. Am. Chem. Soc.* **1991** *113* (25), 9585. doi:10.1021/ja00025a025.

(18) (a) Suzuki, A. *Pure Appl. Chem.* **1994** *66* (2), 213. doi:10.1351/pac199466020213.; (b) Miyaura, N.; Suzuki, A. *Chem. Rev.* **1995** *95* (7), 2457. doi:10.1021/cr00039a007.

(19) (a) Havelková, M.; Hocek, M.; Česnek, M.; Dvořák, D. *Synlett 1999* (7), 1145. doi:10.1055/s-1999-2753.; (b) Havelková, M.; Dvořák, D.; Hocek, M. *Synthesis 2001* (11), 1704. doi:10.1055/s-2001-16765.; (c) Čapek, P.; Vrábel, M.; Hasník, Z.; Pohl, R.; Hocek, M. *Synthesis* **2006** *20*, 3515; (d) Čapek, P.; Pohl, R.; Hocek, M. *Org. Biomol. Chem.* **2006** *4* (11), 2278. doi:10.1039/b604010a.

(20) (a) Hocek, M.; Masojídková, M.; Holý, A. *Collect. Czech. Chem. Commun.* **1997** *62* (1), 136. doi:10.1135/cccc19970136.; (b) Česnek, M.; Hocek, M.; Holý, A. *Collect. Czech. Chem. Commun.* **2000** *65* (8), 1357. doi:10.1135/cccc20001357.; (c) Šilhár, P.; Pohl, R.; Votruba, I.; Hocek, M. *Org. Lett.* **2004** *6* (19), 3225. doi:10.1021/ol049059r.; (d) Čapek, P.; Pohl, R.; Hocek, M. *J. Org. Chem.* **2004** *69* (23), 7985. doi:10.1021/jo048812r.

(21) Hasník, Z.; Šilhár, P.; Hocek, M. *Tetrahedron Lett.* **2007** *48* (32), 5589. doi:10.1016/j.tetlet.2007.06.053.

(22) (a) Doláková, P.; Masojídková, M.; Holý, A. *Heterocycles* **2007** *71* (5), 1107. doi:10.3987/COM-07-11014.; (b) Gundersen, L.-L.; Bechgaard, K.; Bechgaard, K.; Songstad, J.; Leskelä, M.; Polamo, M.; Homsi, M. N.; Kuske, F. K. H.; Haugg, M.; Trabesinger-Rüf, N.; Weinhold, E. G. *Acta Chem. Scand.* **1996** *50*, 58. doi:10.3891/acta.chem.scand.50-0058.

(23) (a) Hirota, K.; Kitade, Y.; Kanbe, Y.; Maki, Y. *J. Org. Chem.* **1992** *57* (19), 5268. doi:10.1021/jo00045a051.; (b) Hocek, M.; Dvořáková, H. *J. Org. Chem.* **2003** *68* (14), 5773. doi:10.1021/jo034351i.

(24) (a) Nauš, P.; Votruba, I.; Hocek, M. *Collect. Czech. Chem. Commun.* **2004** *69* (10), 1955. doi:10.1135/cccc20041955.; (b) Hocková, D.; Holý, A.; Masojídková, M.; Votruba, I. *Tetrahedron* **2004** *60* (23), 4983. doi:10.1016/j.tet.2004.04.035.; (c) Hocková, D.; Masojídková, M.; Holý, A. *Collect. Czech. Chem. Commun.* **2005** *70* (2), 247. doi:10.1135/cccc20050247.; (d) Janeba, Z.; Balzarini, J.; Andrei, G.; Snoeck, R.; De Clercq, E.; Robins, M. J. *Can. J. Chem.* **2006** *84* (4), 580. doi:10.1139/V06-041.

Flexible and rigid core molecules in the synthesis of poly(lactic acid) star polymers

Mitchell R. Perry and Michael P. Shaver

Can. J. Chem. Downloaded from www.nrcresearchpress.com by Xi'an Jiaotong University on 09/19/12
For personal use only.

Abstract: This study presents the synthesis and physical characterization of a series of structurally well-defined star-shaped poly(lactic acids). Polymer stars are prepared from a series of multifunctional alcohol cores including flexible polyols pentaerythritol and dipentaerythritol (four-armed and six-armed cores, respectively) and rigid substituted arenes tri(hydroxymethyl)benzene and hexa(hydroxymethyl)benzene. Utilizing a tin(II) octanoate catalyst, arms of 10 monomer units long are built from *rac*-lactide and L-lactide to form atactic and isotactic star polymers. Polymers were subsequently characterized by means of NMR spectroscopy, gel permeation chromatography, differential scanning calorimetry, and thermogravimetric analysis. Our results support previous work that suggests that the length of the individual arms, not the total molecular weight, correlates to physical characteristics including glass, melt, crystallization, and decomposition temperatures. In addition, differences between core molecules suggest that the chemical nature of the core can significantly alter the physical properties of the star polymer. Trends in crystallization and glass transition temperatures relative to the core used merit further study and correlate closest to the molecular weight and the number of arms emanating from the star core. It is also clear that the rigidity provided by aromatic cores has a significant effect on the melting temperatures of these macromolecules.

Key words: Polymer star, lactide, poly(lactic acid), ring opening polymerization.

Résumé : On a réalisé la synthèse et effectué la caractérisation physique d'une série d'acides poly(lactique) bien définie et en forme étoilée. Les polymères étoilés ont été préparés à partir d'une série l'alcools de base multifonctionnels, dont les polyols flexibles pentaérythritol et dipentaérythritol (respectivement les alcools de base à quatre et à six branches) et des arènes substitués rigides, tels le tri(hydroxyméthyl)benzène et l'hexa(hydroxyméthyl)benzène. Faisant appel à l'octanoate de zinc comme catalyseur et les *rac*-lactide et L-lactide comme monomères, on prépare des bras comportant 10 unités monomères de longueur dans les formes atactique et isotactique des polymères étoilés. On a subséquemment caractérisé ces polymères par spectroscopie RMN, par chromatographie par perméation de gel, par calorimétrie à balayage différentiel et par analyse thermogravimétrique. Les résultats obtenus sont en accord avec ceux obtenus antérieurement d'après lesquels c'est avec le nombre total de bras individuels, et non le poids moléculaire total, qu'il existe une corrélation avec les caractéristiques physiques, dont les températures de transition vitreuse, de fonte, de cristallisation et de décomposition. De plus, les différences entre les molécules de base suggèrent que la nature chimique de la base peut altérer les propriétés physiques d'un polymère étoilé d'une façon significative. Les tendances dans les températures de cristallisation et de transition vitreuse par rapport à celles des molécules de base méritent des études ultérieures et donne la meilleure corrélation avec le poids moléculaire et le nombre de bras émanant de la base étoilée. Il est aussi clair que la rigidité fournit par les molécules de base aromatiques provoque un effet significatif sur les températures de fusion de ces macromolécules.

Mots-clés : polymèrer étoilé, lactide, acide poly(lactique), polymérisation par ouverture de cycle.

[Traduit par la Rédaction]

Introduction

Poly(lactic acid) (PLA) has become an essential green material as it is derived from renewable feedstocks, is biodegradable and bioassimilable, and has found many niche applications across a broad sweep of commercial fields.[1] Of particular interest is the role these and other aliphatic polyesters have to play in the biomedical industry.[2] Whereas linear PLA homo- and co-polymers have been used in sutures and stents since 1960,[3] the physical properties of the macromolecules can be refined by incorporating PLA into more complex macrostructures like polymer stars[4] and brushes.[5] In particular, PLA polymer stars have found utility as matrices for controlled-release drug delivery and other biomedical applications.[6]

The core-first approach dominates star polymer synthesis for PLA, where a multifunctional initiator promotes the ring-opening polymerization of the lactide monomer from alcohol or amine functionalities. When catalyzed by tin(II) octanoate ($Sn(Oct)_2$), the reaction transforms *rac*- or L-lactide into atactic PLA (a-PLA) and isotactic PLA (L-PLA) stars,

Received 19 October 2010. Accepted 6 December 2010. Published on the NRC Research Press Web site at canjchem.nrc.ca on 19 March 2011.

M.R. Perry and M.P. Shaver.[1] Department of Chemistry, University of Prince Edward Island, 550 University Avenue, Charlottetown, PE C1A 4P3, Canada.

[1]Corresponding author (e-mail: mshaver@upei.ca).

Can. J. Chem. Downloaded from www.nrcresearchpress.com by Xi'an Jiaotong University on 09/19/12
For personal use only.

respectively. Previous studies have focused on the role of molecular weight[7] or polymer tacticity[8] in shaping polymer properties, whereas others have examined the incorporation of PLA stars into miktoarm[9–11] and dendritic frameworks[12–14] or examined the application of these materials in self assembly and drug delivery.[15,16] The initiator is also a key differentiator between polymer stars. A diverse array of simple multifunctional polyols have been used as initiators for PLA polymer stars[4] including three-armed stars prepared from trimethylolpropane and glycerol; four-armed stars from pentaerythritol, ditrimethylolpropane, and erythritol; five-armed stars from xylitol; six-armed stars from dipentaerythritol, inositol, and sorbitol; and eight-armed stars from tripentaerythritol. Less clear is the effect of these cores on polymer star synthesis or properties, but some key trends have been observed. The macromolecular structure dependence of thermal properties were investigated for three- to six-armed L-PLA stars.[17] Increasing molecular weights of six-armed sorbitol polymers correlated to concomitant increases in thermal decomposition (T_d) and melting (T_m) temperatures, a trend exacerbated by the different reactivities between primary and secondary alcohol functionalities in the sorbitol core. For polymer stars with similar theoretical absolute molecular weights ($M_{n,th}$), structures with fewer arms exhibited higher T_m values, suggesting that physical properties correlate with the length of the polymer arm emanating from the star core rather than the absolute molecular weight of the star.[17]

There is a surprising lack of chemical diversity in the choice of simple discrete initiators for this ring-opening polymerization because of an expected focus on flexible sugar alcohols. Cores with more rigidity include β-cyclodextrins,[18] modified perylenes,[19] hexahydroxytriphenylene,[20] and dibenzoylmethane- and bipyridine-ligated metal complexes.[21] Whereas these cores impart photochemical, spectroscopic, and supramolecular properties to the stars, no correlation between core structure and properties has been made.

In this vein we endeavoured to develop synthetic methodologies to prepare three-, four-, and six-armed star polymers of *rac*- and L-lactide with variable core structures with a focus on simple rigid cores. Specifically, we targeted PLA stars built from 1,3,5-tri(hydroxymethyl)benzene (THMB, **1**), hexa(hydroxymethyl)benzene (HHMB, **2**), pentaerythritol (PE, **3**), and dipentaerythritol (DPE, **4**) (Fig. 1) and characterized the star polymers with gel permeation chromatography (GPC), ^{1}H NMR spectroscopy, thermogravimetric analysis (TGA), and differential scanning calorimetry (DSC).

Experimental

Materials

HPLC-grade toluene, THF, methanol, and dichloromethane were purchased from Fisher Scientific and deuterated solvents were purchased from Cambridge Isotopes. Anhydrous toluene was obtained by passing the solvent through an Innovative Technologies solvent purification system consisting of columns of alumina and a copper catalyst. Anhydrous solvents were tested with addition of a toluene solution of sodium benzophenone ketyl prior to use. $Sn(Oct)_2$ was purchased from Sigma-Aldrich Chemical Co. and distilled prior to use. Dipentaerythritol and pentaerythritol were purchased from Sigma-Aldrich Chemical Co. and purified by recrystallization from methanol and vacuum sublimation three times, respectively, before being dried in vacuo for 48 h prior to use. 1,4-Dioxane was dried over CaH_2 and distilled prior to use. Benzene-1,3,5-tricarboxylic acid (98%) was purchased from Sigma-Aldrich Chemical Co. and used as received. The monomers *rac*- and L-lactide were purchased from PURAC Biomaterials and purified by three successive vacuum sublimations of the material prior to use.

Fig. 1. Core molecules for poly(lactic acid) star polymers.

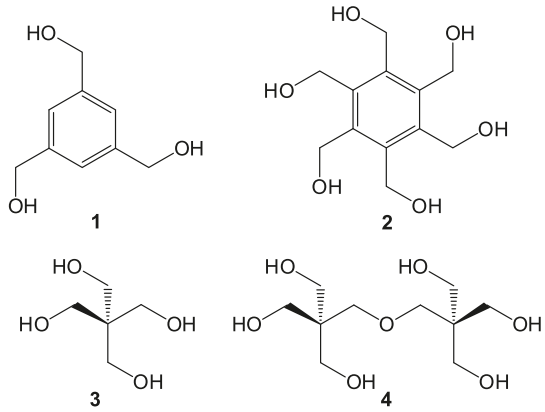

General considerations

All experiments involving moisture- and air-sensitive compounds and catalysts were performed under a nitrogen atmosphere using an MBraun LABmaster sp. glovebox system equipped with a –35 °C freezer and [H_2O] and [O_2] analyzers. GPC was carried out in THF (flow rate: 1 mL min^{-1}) at 50 °C with a Polymer Labs PL–GPC 50 Plus integrated GPC system using three 300 mm × 7.5 mm Resipore columns. Polystyrene standards were used for calibration and corrected for PLA.[22] ^{1}H NMR spectra were recorded with a Bruker Avance spectrometer (300 MHz) in $CDCl_3$ or D_2O. TGA was performed on a TA instruments TGA Q500 under an inert nitrogen atmosphere with a flow rate of 60 mL min^{-1} and a heating rate of 10 °C min^{-1}. DSC was performed on a TA instruments DSC Q100 using a heating rate of 5 °C min^{-1} and a flow rate of 50 mL min^{-1}. Guelph Analytical Laboratories conducted the CHN elemental analyses.

Core syntheses

1,3,5-Tri(hydroxymethyl)benzene

This procedure was modified from an existing literature procedure.[23] In a glovebox, lithium aluminum hydride (2.505 g, 6.60 mmol) was added to a 250 mL round bottom Schlenk flask and suspended in 10 mL of anhydrous THF. The vessel was sealed and removed from the glovebox. Trimethyl 1,3,5-benzene-tricarboxylate (5.002 g, 1.98 mmol) was dissolved in 50 mL of anhydrous THF in a 250 mL Schlenk tube. The carboxylate solution was added via cannula dropwise to the $LiAlH_4$, and the dark grey lithium

Can. J. Chem. Downloaded from www.nrcresearchpress.com by Xi'an Jiaotong University on 09/19/12
For personal use only.

suspension turned to a deep orange colour that quickly dissipated. Upon completion of the carboxylate addition, the mixture was a deep green colour. The mixture was allowed to reflux for 5 h after which the vessel was cooled in an ice–water bath and stirred. Three solutions (5 mL H_2O, 5 mL 15% (*w*/*w*) NaOH in H_2O, and 15 mL H_2O) were sequentially added in a dropwise fashion to quench any remaining $LiAlH_4$ and hydrolyze the Al salts. Filtration and washing with three 20 mL portions of THF provided a colourless filtrate. Organics were removed under reduced pressure, yielding a colourless crude oil in 92% yield. Purification of this material by recrystallization from ethyl acetate and column chromatography gave an analytically pure white powder (0.934 g, 0.56 mol, 28.2%). Improved yields were obtained by forgoing recrystallization and purifiying the material by silica gel column chromatography. ^{1}H NMR data (300 MHz, MeOD, 298 K) δ: 7.25 (s, 3H, Ar*H*), 4.60 (s, 6H, ArCH_2). ^{13}C NMR data (75 MHz, MeOD, 298 K) δ: 141.41 (s, *Ar*-CH_2), 126.00 (s, *Ar*-H), 64.04 (s, *C*H_2). Elemental anal. calcd (%): C 65.27, H 7.19, N 0.00; found (%): C 65.41, H 7.22, N 0.00.

Hexa(hydroxymethyl)benzene

This synthesis was modified from an existing literature procedure.[24] In a glovebox, 2-butyne-1,4-diol (6.008 g, 6.98 mmol) was dissolved using 50 mL anhydrous dioxane in a 250 mL round bottom flask. Cyclopentadienylcobalt dicarbonyl (2.06 g, 1.05 mmol) was added, along with 50 mL dioxane, to a 500 mL Strauss flask, to which the alkyne solution was added in a dropwise fashion. The vessel was sealed and removed from the glovebox where it was left to react in a 130 °C oil bath for 4 days. The formation of an orange precipitate was evident after 1 day. After the allotted reaction time, the mixture was filtered using a fine glass filter frit, the solid was collected, washed three times using 25 mL THF, and dried in vacuo (3.73 g, 1.44 mmol, 62.0%). ^{1}H NMR data (300 MHz, d_6-DMSO, 298 K) δ: 4.86 (s, 6H, ArCH_2), 4.69 (s, 12H, O*H*). ^{13}C NMR data (75 MHz, d_6-DMSO, 298 K) δ: 138.79 (s, Ar), 56.75 (s, *C*H_2). Elemental anal. calcd (%): C 55.81, H 7.02, N 0.00; found (%): C 56.06, H 6.88, N 0.00.

Polymerization experiments

Polymerization procedures were modified from previously reported protocols.[25] All polymerization reactions were performed in sealed 25 mL round bottom ampoules under an inert atmosphere, at 125 °C, with a molar ratio of monomer – alcohol functionality – catalyst of 10:1:0.04. The catalyst employed in each instance was $Sn(Oct)_2$. Monomers employed included *rac*-lactide and L-lactide and core initiators **1**–**4**. Experiments were also conducted with a benzyl alcohol initiator to prepare a standard material for comparative purposes. The reaction proceeded for ~8 h and was then quenched with 10 mL of a 9:1 *v*/*v* solution of CH_2Cl_2–MeOH for 30 min at room temperature. The resulting mixture was precipitated from cold methanol, collected via filtration, washed with 50 mL H_2O and 50 mL MeOH, and dried in vacuo prior to analysis.

For example, *rac*-lactide (0.545 g, 3.86 mmol) and hexa(hydroxymethyl)benzene (0.0162 g, 6.83 mmol) were added to a dry 25 mL round bottom ampoule equipped with a magnetic stirring bar. The ampoule was connected to a Schlenk line, sealed, and evacuated for 10 min before being filled with N_2. This evacuation/refill procedure was repeated three times. A 7.33 mmol/L $Sn(Oct)_2$ solution in toluene (2.1 mL, 6.24 mg, 0.0154 mmol) was syringed into the vessel that was then sealed and put under vacuum to remove the toluene. The ampoule was then placed into a preheated oil bath at 125 °C for 8 h. After the allotted time, the vessel was cooled to room temperature, opened to the atmosphere, and quenched with 10 mL of a 9:1 *v*/*v* solution of CH_2Cl_2 and methanol. The solution was stirred for 30 min and then added dropwise to 100 mL of cold methanol to precipitate the polymer. The resultant white polymer was collected via filtration, washed with 50 mL MeOH and 50 mL H_2O, and dried in vacuo for 12 h. Monomer conversion was determined gravimetrically to be 89.7% (0.5033 g).

Table 1. Polymer data for atactic and isotactic poly(lactic acid) (PLA) stars.

Initiator	Monomer	% Conv.	$M_{n,GPC}$	$M_{n,th}$	PDI
1	*rac*-LA	68.4	5023	4488	1.23
1	L-LA	76.9	3490	4506	1.32
2	*rac*-LA	89.7	13787	8030	1.22
2	L-LA	98.8	8944	8845	1.51
3	*rac*-LA	78.2	4642	5707	1.20
3	L-LA	86.3	5920	5905	1.16
4	*rac*-LA	86.7	9899	7723	1.21
4	L-LA	78.7	8452	7011	1.18

Note: PDI, polydispersity index; $M_{n,GPC}$, molecular weight as determined by size exclusion chromatography; $M_{n,th}$, theoretical absolute molecular weight.

Table 2. Differential scanning calorimetry (DSC) and thermogravimetric analysis (TGA) thermal data for poly(lactic acid) (PLA) stars.

Star	T_g (°C)	T_c (°C)	T_m (°C)	T_d (°C)	X_c (%)
1-*r*	42.14	—	—	228.39	—
1-L	41.16	86.99	130.60, 138.43	235.35	29.1
2-*r*	45.25	—	—	234.35	—
2-L	49.72	93.33	148.14, 159.25	242.35	27.0
3-*r*	40.48	—	—	218.14	—
3-L	43.67	99.63	121.10, 135.42	232.39	17.5
4-*r*	45.72	—	—	227.75	—
4-L	49.21	84.38	125.41, 139.35	256.16	27.3

Note: T_g, glass transition temperature; T_c, crystallization transition temperature; T_m, melting transition temperature; T_d, onset temperature for polymer decomposition; and X_c,percent crystallinity of the star samples.

Results and discussion

Core and polymer synthesis

Whereas PE and DPE are commercially available polyols, the rigid THMB and HHMB cores had to be synthesized. The reduction of 1,3,5-benzene-tricarboxylate with excess lithium aluminum hydride provided the crude desired aromatic **1** in high yields. Purification substantially lowered

Fig. 2. Differential scanning calorimetry (DSC) profile for hexa(hydroxymethyl)benzene (HHMB) poly(lactic acid) (PLA) star **2-L**.

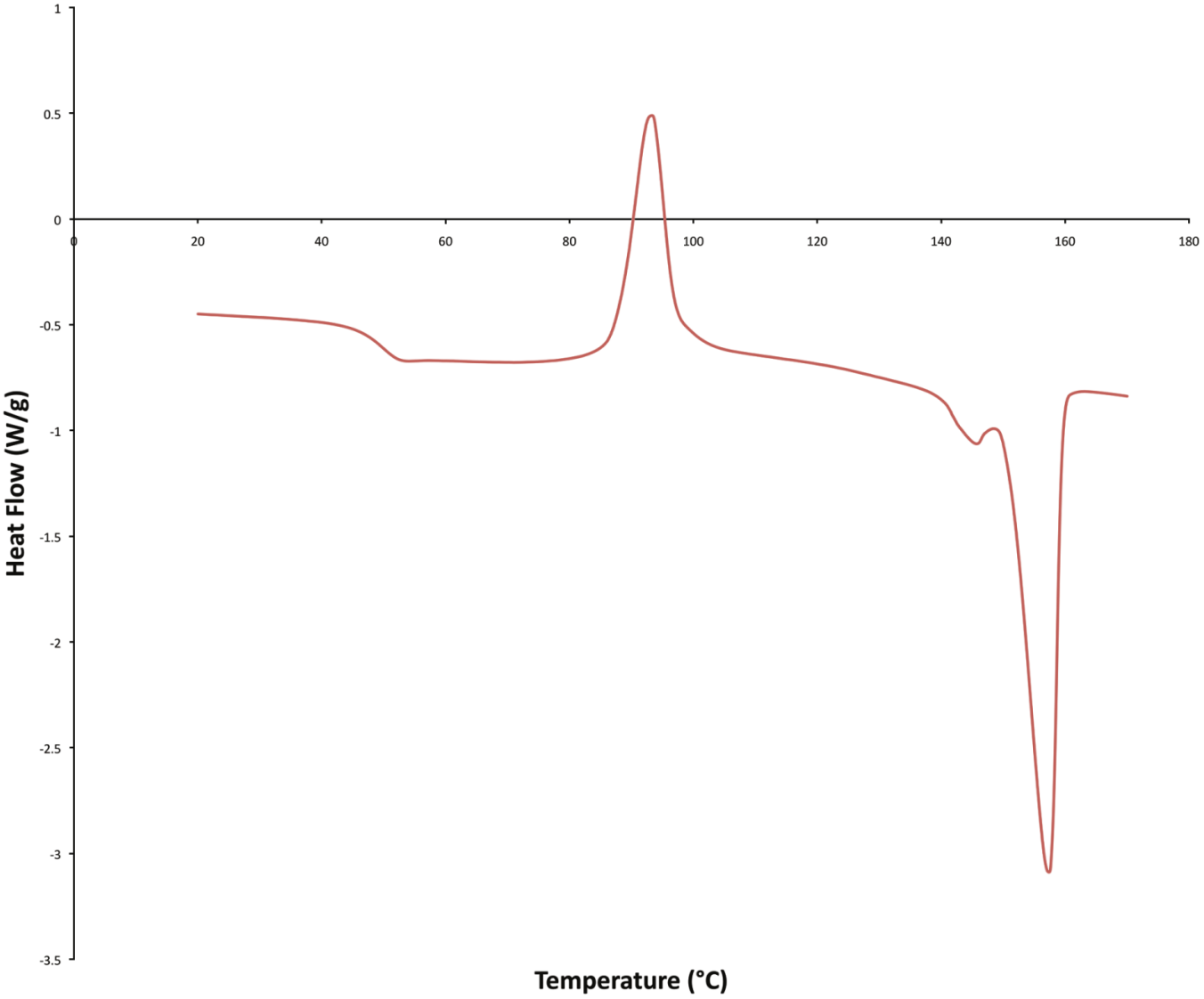

Can. J. Chem. Downloaded from www.nrcresearchpress.com by Xi'an Jiaotong University on 09/19/12
For personal use only.

yields, but enough product was isolated from this effort that optimization of this step was not pursued. For the hexa-substituted core initiator, the $CpCo(CO)_2$ catalyzed cyclotrimerization of 2-butyne-1,4-diol afforded **2** in moderate yields. Attempts to synthesize **1** via a cobalt-catalyzed cyclotrimerization of 1-propyn-3-ol were unsuccessful, accessing a mixture of aromatic isomers with various substitution patterns arising from head-to-tail additions and an insoluble polymeric material resulting from thermal polymerization of the propargyl alcohol. These reactions are shown in eqs. [1] and [2], respectively.

[1]

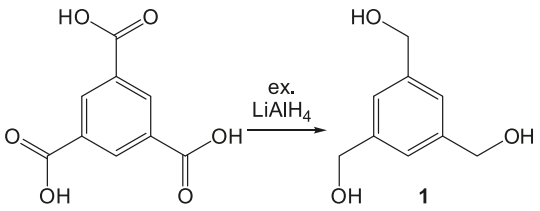

[2]

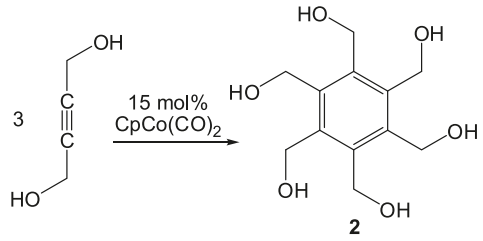

PLA stars with 10 monomer units per alcohol functionality were synthesized. Oligomeric arm lengths were chosen because their low overall molecular weights accentuate the structural differences.[4] A molar ratio corresponding to 0.04 $Sn(Oct)_2$ units and 10 lactide monomer units per alcohol functionality was used (ie. 0.25:1:60 using one DPE molecule). Higher catalyst loadings, up to the one catalyst unit per growing arm expected for living ring-opening polymerizations, gave consistent bimodal product distributions. This suggests self-initiation behavior by the $Sn(Oct)_2$ or a reaction impurity while also increasing the propensity for

Can. J. Chem. Downloaded from www.nrcresearchpress.com by Xi'an Jiaotong University on 09/19/12
For personal use only.

Fig. 3. Thermogravimetric analysis (TGA) profile for **2-r** (gray line) and **2-L** (black line).

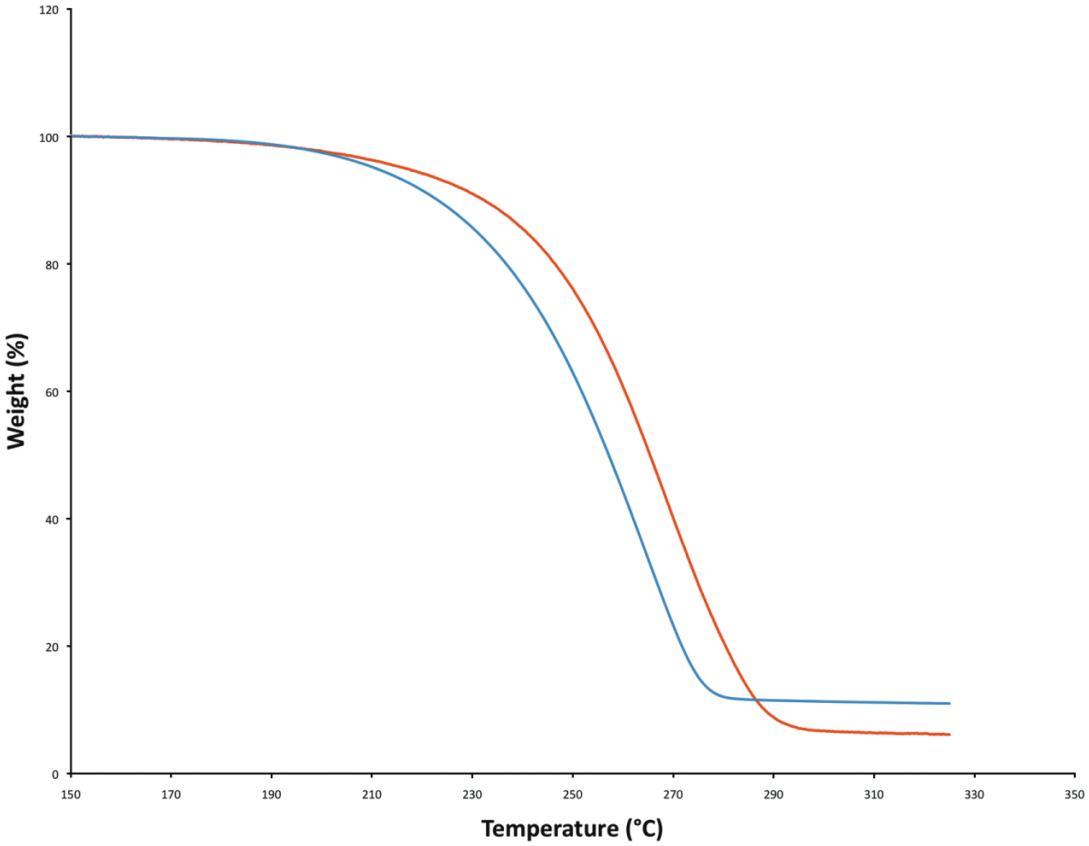

transesterification reactions leading to reduced molecular weights for long reaction times. Additionally, the efficacy of low catalyst loadings suggests some immortal behavior for the tin catalyst under these reaction conditions.[26] As an example, the synthesis of the resultant star polymer for an HHMB core is shown in eq. [3].

[3]

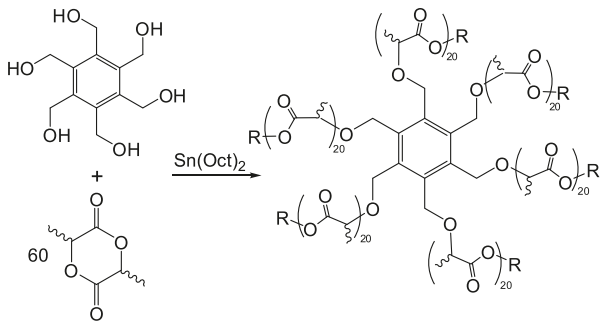

^{1}H NMR analysis in $CDCl_3$ of the resultant PLA macromolecules shows that all alcohol functionalities associated with the parent core molecules disappear, suggesting activation of all arms in the formation of the star polymers. In addition, each sample exhibits a shift in the methylene (CH_2) resonances towards higher ppm owing to the deshielded environment of the polymer chain. For example, HHMB-initiated PLA displays the loss of the O*H* peak present at 4.86 ppm and shifts the CH_2 peak from 4.69 to 5.16 ppm. Because of peak overlap, end-group analysis of the terminal alcohol functionalities after polymer isolation could not assist in further polymer characterization, although the uniformity of the spectral resonances is suggestive of arms of similar lengths. Characterization by GPC is collected in Table 1. Percent conversions, measured gravimetrically, are shown along with the determined polydispersity and molecular weight values calculated relative to polystyrene standards and corrected for linear PLA, but remain uncorrected for the differences in star hydrodynamic volumes. Polymerization times of 8 h were chosen as shorter reaction times and led to inefficient initiation and broadened polydispersities, whereas reaction times of 24 h led to significant transesterification.

Low to moderate polydispersities (PDIs) imply good control over the polymerization reactions. Slightly higher PDIs for aromatic initiators **1** and **2** may be due to longer initiation times, as expected from comparative benzyl alcohol and isopropanol initiations of linear PLA.[1] Deviations from expected molecular weights are likely due to significant differences in effective hydrodynamic volume between linear and star-shaped polymers, affecting size-exclusion chromatographic techniques,[4] with six-armed stars built from **2** and **4** showing, as expected, the highest M_n deviations.

Physical properties of polymer stars

The six polymer stars in question were then characterized by TGA and DSC to assess the effect of core initiator on polymer properties. These data are collected in Table 2. T_g, T_c, and T_m values refer to glass, crystallization, and melting transitions, respectively, whereas T_d refers to the onset temperature for polymer decomposition and X_c refers to the percent crystallinity of the star samples.

Can. J. Chem. Downloaded from www.nrcresearchpress.com by Xi'an Jiaotong University on 09/19/12
For personal use only.

The variation of core initiator was shown to influence the chemical properties of the resulting polymeric material in both atactic and isotactic PLA. Differences in T_g depended predominantly on the number of polymer arms, not the core molecule. Additionally, differences in T_g may also be due to changes in molecular weight between the different samples.[25] In the case of initiators **2**, **3**, and **4**, the isotactic samples exhibited higher T_g values than their atactic partners. Owing to the lower molecular weights ($M_{n,th}$ = 4.5 vs 5.8–8.8 kDa), the stars formed from initiator **1** do not follow this trend. For samples of the same or similar molecular weight and number of arms little difference is observed in comparing rigid to flexible cores. While we expected the rigidity present in the aromatic initiator to restrict the movement of the polymer arms and potentially prevent energy distribution throughout the macromolecule, the low energy process associated with the glass transition is unaffected. Similarly, crystallization characteristics observed for stereoregular stars derived from L-lactide (T_c and X_c) are unaffected by core rigidity. Crystallization temperatures appear to have an inverse relationship to percent crystallinity, with THMB-derived samples exhibiting a low T_c and the highest X_c, whereas PE-derived samples had the highest T_c and the lowest X_c.

As expected, melting signals were only observed for isotactic polymer stars.[4] In agreement with previous work, the presence of two melting points is characteristic of semicrystalline PLA.[27] Here, clear differences exist between rigid and flexible core initiators: **1** and **2** possess the two highest T_m values, suggesting increased order and rigidity throughout the star. The thermal stability imparted by the rigid core is especially apparent when comparing two six-armed polymer stars of similar molecular weights, with an increase of ~20 °C in the T_m for the hexa-substituted benzene versus the flexible dipentaerythritol. Comparing **1** with **2** and **3** with **4** also shows that a greater number of arms in PLA star polymers may induce higher melting temperatures, but this trend may be an artifact of molecular weight differences between the samples. A representative DSC profile for sample **2-L** is shown in Fig. 2.

Finally, thermal stability was measured by TGA and reported as the onset temperature (T_d) of rapid thermal decomposition. In each case, the isotactic samples showed higher thermal stability, as high as a 25 °C difference for DPE stars. Six-armed stars also possessed higher decomposition points, but few obvious trends existed between the nature of the initiating core and the thermal stability. For aromatic rigid cores, drawn out decomposition profiles were observed, with larger decomposition ranges noted in both isotactic and atactic samples with cores **1** and **2**. Two representative TGA profiles are shown in Fig. 3 for HHMB-initiated atactic (black line) and isotactic (gray line) star polymers. Small weight percentages that remain intact in each case may be due to persistence of the HHMB core, as pure HHMB has a T_d of ~320 °C.

Current efforts are focused on expanding the range of rigid and flexible polymer cores to other numbers of arms, including three-armed flexible, four-armed rigid, and five-armed flexible and rigid cores based upon hydroxybenzyl and polyol frameworks.

Conclusions

Eight PLA polymer stars were prepared from four multifunctional core initiators. Whereas good control over the reaction, in general, is offered by the $Sn(Oct)_2$ catalyst, the benzyl functionalities in hexa- and tri-(hydroxymethyl)benzene initiators are more challenging to initiate and lead to minor deviations from ideal living characteristics. Physical properties of the stars correlate well with established markers including molecular weight and the number of polymer arms. A striking effect of the rigidity of the core was noted in the melting temperatures of the star polymers, with increased core rigidity correlating with higher T_m values. Efforts to examine whether the core initiator has an effect on polymer degradation and to expand the range of core initiators accessible for star polymer synthesis continue.

Acknowledgement

We thank the Natural Sciences and Engineering Research Council of Canada (NSERC) and the University of Prince Edward Island (UPEI), Charlottetown, for financial support, the Canada Foundation for Innovation and the Atlantic Canada Opportunities Agency for infrastructure, and Dr. R. Bissessur, UPEI, for access to TGA and DSC instrumentation.

References

(1) Becker, J. M.; Pounder, R. J.; Dove, A. P. *Macromol. Rapid Commun.* **2010** *31* (22), 1923. doi:10.1002/marc.201000088.
(2) (a) Alexis, F. *Polym. Int.* **2005** *54* (1), 36. doi:10.1002/pi.1697.; (b) Mecerreyes, D.; Jérôme, R.; Dubois, P. *Adv. Polym. Sci.* **1999** *147* (9), 1. doi:10.1007/3-540-49196-1_1.
(3) Reed, A. M.; Gilding, D. K. *Polymer (Guildf.)* **1981** *22* (4), 494. doi:10.1016/0032-3861(81)90168-3.
(4) Cameron, D. J. A.; Shaver, M. P. *Chem. Soc. Rev.* **2011**, in press.
(5) Ouchi, T.; Ohya, Y. *J. Polym. Sci. A* **2004** *42* (3), 453. doi:10.1002/pola.10848.
(6) (a) Zou, T.; Li, S.-L.; Cheng, S.-X.; Zhang, X.-Z.; Zhuo, R.-X. *J. Biomed. Mater. Res. A* **2007** *83A* (3), 696 doi:10.1002/jbm.a.31303.; (b) Breitenbach, A.; Li, Y. X.; Kissel, T. *J. Control. Release* **2000** *64* (1–3), 167. doi:10.1016/S0168-3659(99)00134-0.
(7) Zhao, Y. L.; Cai, Q.; Jiang, J.; Shuai, X. T.; Bei, J. Z.; Chen, C. F.; Xi, F. *Polymer (Guildf.)* **2002** *43* (22), 5819. doi:10.1016/S0032-3861(02)00529-3.
(8) Stanford, M. J.; Dove, A. P. *Chem. Soc. Rev.* **2010** *39* (2), 486. doi:10.1039/b815104k.
(9) Klok, H. A.; Becker, S.; Schuch, F.; Pakula, T.; Mullen, K. *Macromol. Biosci.* **2003** *3* (12), 729. doi:10.1002/mabi.200300023.
(10) Gorczynski, L.; Chen, J.; Fraser, C. L. *J. Am. Chem. Soc.* **2005** *127* (43), 14956. doi:10.1021/ja0530927.
(11) Bender, L.; Corbin, P. S.; Fraser, C. L.; Metcalf, D. H.; Richardson, F. S.; Thomas, E. L.; Urbas, A. M. *J. Am. Chem. Soc.* **2002** *124* (29), 8526. doi:10.1021/ja0261269.
(12) Sosnik, A.; Leung, B. M.; Sefton, M. V. *Biomed. Mater. Res. Part A* **2008** *86A* (2), 339. doi:10.1002/jbm.a.31594.
(13) Choi, Y. K.; Bae, Y. H.; Kim, S. W. *Macromolecules* **1998** *31* (25), 8766. doi:10.1021/ma981069i.
(14) Hiemstra, C.; Zhong, Z.; Li, L.; Dijkstra, P. J.; Feijen, J.

Biomacromolecules **2006** *7* (10), 2790. doi:10.1021/bm060630e.
(15) Kim, E. S.; Kim, B. C.; Kim, S. H. *J. Polym. Sci. B, Polym. Phys.* **2004** *42* (6), 939. doi:10.1002/polb.10685.
(16) Sobczak, M.; Witkowska, E.; Olędzka, E.; Kolodziejski, W. *Molecules* **2008** *13* (1), 96. doi:10.3390/molecules13010096.
(17) (a) Hao, Q.; Li, F.; Li, Q.; Li, Y.; Jia, L.; Yang, J.; Fang, Q.; Cao, A. *Biomacromolecules* **2005** *6* (4), 2236. doi:10.1021/bm050213m.; (b) Lee, J. S.; Choo, D. J.; Kim, S. H.; Kim, Y. H. *Polym. (Korea)* **1998** *22* (6), 880.
(18) Adeli, M.; Zarnegar, Z.; Kabiri, R. *Eur. Polym. J.* **2008** *44* (7), 1921. doi:10.1016/j.eurpolymj.2008.03.028.
(19) Klok, H. A.; Becker, S.; Schuch, F.; Pakula, T.; Mullen, K. *Macromol. Biosci.* **2003** *3* (12), 729. doi:10.1002/mabi.200300023.
(20) Yu, X.; Tang, X.; Pan, C. *Polymer (Guildf.)* **2005** *46* (24), 11149. doi:10.1016/j.polymer.2005.08.075.
(21) (a) Gorczynski, L.; Chen, J.; Fraser, C. L. *J. Am. Chem. Soc.* **2005** *127* (43), 14956. doi:10.1021/ja0530927.; (b) Fiore, G. L.; Klinkenberg, J. L.; Fraser, C. L. *Macromolecules* **2008** *41* (23), 9397. doi:10.1021/ma801721q.; (c) Corbin, P. S.; Webb, M. P.; McAlvin, J. E.; Fraser, C. L. *Biomacromolecules* **2001** *2* (1), 223. doi:10.1021/bm005621z.; (d) Smith, A. P.; Fraser, C. L. *Macromolecules* **2003** *36* (15), 5520. doi:10.1021/ma025697i.
(22) Kowalski, A.; Duda, A.; Penczek, S. *Macromolecules* **1998** *31* (7), 2114. doi:10.1021/ma971737k.
(23) Díez-Barra, E.; García-Martínez, J. C.; Merino, S.; del Rey, R.; Rodríguez-López, J.; Sánchez-Verdú, P.; Tejeda, J. *J. Org. Chem.* **2001** *66* (17), 5664. doi:10.1021/jo015764r.
(24) (a) Agenet, N.; Gandon, V.; Vollhardt, K. P. C.; Malacria, M.; Aubert, C. *J. Am. Chem. Soc.* **2007** *129* (28), 8860. doi:10.1021/ja072208r.; (b) Sigman, M. S.; Fatland, A. W.; Eaton, B. E. *J. Am. Chem. Soc.* **1998** *120* (20), 5130. doi:10.1021/ja9807284.
(25) Shaver, M. P.; Cameron, D. J. A. *Biomacromolecules* **2010** *11* (12), 3673. doi:10.1021/bm101140d.
(26) Inoue, S. *J. Polym. Sci. A Polym. Chem.* **2000** *38* (16), 2861. doi:10.1002/1099-0518(20000815)38:16<2861::AID-POLA20>3.0.CO;2-1.
(27) Cohn, D.; Younes, H.; Marom, G. *Polymer (Guildf.)* **1987** *28* (12), 2018. doi:10.1016/0032-3861(87)90035-8.

Can. J. Chem. Downloaded from www.nrcresearchpress.com by Xi'an Jiaotong University on 09/19/12
For personal use only.

One-pot domino synthesis of polyvicinalamine monomers

Cem B. Kilic and Alpay Taralp

Can. J. Chem. Downloaded from www.nrcresearchpress.com by Xi'an Jiaotong University on 09/19/12
For personal use only.

Abstract: Imidazole was generated in situ via a domino reaction between glyoxal, formaldehyde, and two units of aqueous ammonia. Aqueous bicarbonate and a carboxylic anhydride or dialkyl dicarbonate were added, yielding the corresponding *N*,*N*′-diacyl or *N*,*N*′-dicarbalkoxy-2-hydroxyimidazoline. A Bamberger ring cleavage ensued, affording *cis*-1,2-di(acetamido)-ethene, *cis*-1,2-di(propylamido)ethene, *cis*-1,2-di(ethoxyamido)ethene, *cis*-1,2-di(*tert*-butoxyamido)ethene, or *cis*-1,2-di(benz-amido)ethene as easily isolable solids. The convenience and generality offered by this one-pot approach implied a cost-effective route to the routine synthesis of oligo- and polyvicinalamine precursors.

Key words: Bamberger ring cleavage, domino reaction, one-pot reaction, multicomponent reaction, polyvicinalamine monomers.

Résumé : On a généré de l'imidazole par une réaction de type domino in situ entre le glyoxal, le formaldéhyde et deux unités d'ammoniac aqueux. L'addition de bicarbonate aqueux et d'un anhydride carboxylique ou d'un dicarbonate de dialkyle conduit à la formation de la *N*,*N*′-diacyl- ou *N*,*N*′-dicarbalkoxy-2-hydroxyimidazoline correspondante. Il s'ensuit une réaction de clivage de cycle de Bamberger qui permet d'isoler facilement le *cis*-1,2-di(acétamido)éthène, le *cis*-1,2-di(propylamido)éthène, le *cis*-1,2-di(éthoxyamido)éthène, le *cis*-1,2-di(*tert*-butoxyamido)éthène ou le *cis*-1,2-di(benzamido)éthène sous la forme de solides. La facilité et la généralité offerte par cette approche monotope implique une voie efficace du point de vue des coûts en vue de la synthèse de routine de précurseurs d'amines oligo- et polyvicinales.

Mots-clés : clivage de cycle de Bamberger, réaction de type domino, réaction monotope, réaction à plusieurs composants, amine vicinale.

[Traduit par la Rédaction]

Introduction

Polyamines have received much interest in view of their high amino group content, multi-interaction modes, facile tailorability, and widespread applicability in products ranging from commodity chemicals for pulp processing or water treatment to specialty chemicals intended for use in pharmacy and biotechnology.[1–3]

Recently, oligo- and polyvicinalamines with an impressive 1:1 nitrogen–carbon ratio were prepared (Scheme 1). Of the three approaches portrayed (Scheme 2), the monomers utilized have been based on butenedioic acid, *cis*-1,2-diamidoethene, and 1,3-diacetyl-4-imidazolin-2-one.[1–13] The use of commercial butenedioic acid-type monomers (Scheme 2, top left) introduces inconveniences related to halogenation, corrosion control, and waste management. The use of *cis*-1,2-diamidoethene monomers (Scheme 2, top right) permits a relatively simpler, greener industrial process. Still, neither approach has enabled the formation of high molecular weight polyvicinalamines.[2–5] The polymerization of 1,3-diacetyl-4-imidazolin-2-one (Scheme 2, bottom left) has yielded comparatively higher molecular weight materials.[2,4] This last monomer, a cyclic analogue of *cis*-1,2-di(acetamido)ethene (**1a**, entry 1 in Table 1), is

Scheme 1. Polyamine featuring a 1:1 nitrogen–carbon ratio.

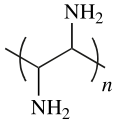

Scheme 2. Monomers used to prepare oligo- and polyvicinalamines: butenedioic acid and derivatives (top, left), *cis*-1,2-diamidoethene (top, right), and 1,3-diacetyl-4-imidazolin-2-one (bottom, left).

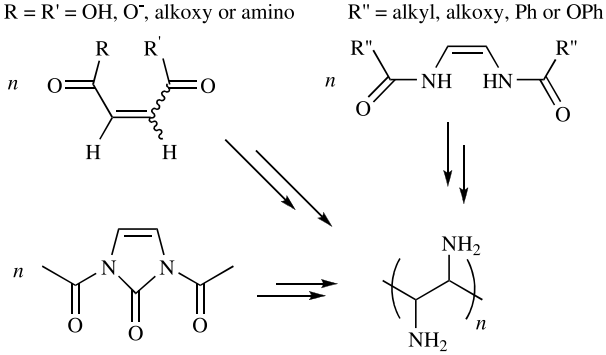

Received 13 August 2010. Accepted 15 December 2010. Published on the NRC Research Press Web site at canjchem.nrc.ca on 25 March 2011.

C.B. Kilic and A. Taralp.[1] Faculty of Engineering and Natural Sciences, Sabanci University, Tuzla 34956 Istanbul, Turkey.

[1]Corresponding author (e-mail: taralp@sabanciuniv.edu).

Table 1. Reaction of in situ-generated imidazole with activating agents in alkaline media (products: *cis*-1,2-di(acetamido)ethene (**1a**), *cis*-1,2-di(ethoxyamido)ethene (**2a**), *cis*-1,2-di(*tert*-butoxyamido)ethene (**3a**), *cis*-1,2-di(benzamido)ethene (**4a**), and *cis*-1,2-di(propylamido)ethene (**5a**)).

Entry	Acylating/alkoxyformylating agent	Product	Time (h)	Solvent	Yield[a] (%)	Yield[b] (%)
1	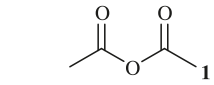 **1**	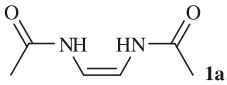 **1a**	13	H_2O/EtOAc	35	53.8 (80)[c]
2	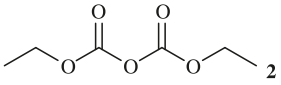 **2**	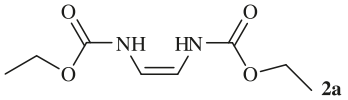 **2a**	12	H_2O/EtOAc	22.4	34.5 (60)[d]
3	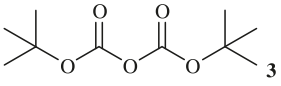 **3**	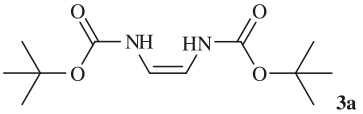 **3a**	30	H_2O/1,4-Dioxane	28.7	44.1[e]
4	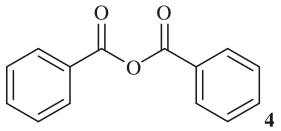 **4**	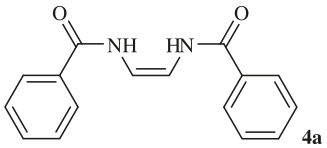 **4a**	12.5	H_2O/1,4-Dioxane	14.7	22.6 (10, 43)[f]
5	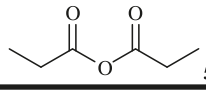 **5**	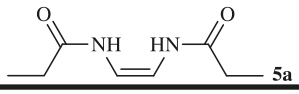 **5a**	12	H_2O/EtOAc	39.2	60.3[e]

[a] Yields were calculated with respect to glyoxal as limiting reagent.
[b] Yields with respect to in-situ-generated imidazole were estimated after determining a 65% yield by ^{1}H NMR. Parentheses indicate literature yields.
[c] Literature yield with imidazole as starting material and limiting reagent.[1]
[d] Literature yield with imidazole as starting material and limiting reagent, and ethylchloroformate as ethoxyformylating agent.[2]
[e] No literature preparation was available for comparative purposes.
[f] Literature yields with imidazole as starting material and limiting reagent, and benzoyl chloride as benzoylating agent.[2,10]

Can. J. Chem. Downloaded from www.nrcresearchpress.com by Xi'an Jiaotong University on 09/19/12
For personal use only.

highly reactive by virtue of the ring structure, which limits steric clutter about the double bond, and the acetyl groups, which overcome limitations inherent to polymerizing 4-imidazolin-2-one.[3] Still, the high hydrolytic stability of the polymeric intermediate formed demands harsh conditions to generate the free polyvicinalamine.[3]

Some other factors, which influence the production feasibility of these polyamines, include the cost and commercial availability of the starting materials. Whereas the butenedioic acid-based monomers are readily available, the *cis*-1,2-diamidoethene monomers are inevitably prepared using commercial imidazole. An even more inconvenient starting material, 1,3-diacetyl-4-imidazolin-2-one, is prepared from 4-imidazolin-2-one, a synthon that is commercially unavailable.[5] Interestingly, the related monomer 1,3-diethoxy-4-imidazolin-2-one has been prepared directly from *cis*-1,2-di(ethoxyamido)ethene (**2a**, entry 2 in Table 1) by treatment with phosgene.[4] As this route bypassed 4-imidazolin-2-one, it seemed reasonable to assume that a suitable source of imidazole, prepared very cost effectively, could serve as a raw material of both the *cis*-1,2-diamidoethene type monomers and heterocyclic variants such as 1,3-diacetyl-4-imidazolin-2-one. This prospect was also attractive in that it seemed extendable to the preparation and conversion of 4-substituted and 4,5-disubstituted imidazoles.

In this work, a simple approach was envisaged to generate and utilize imidazole, affording the *cis*-1,2-diamidoethene monomers. The rationale was to prepare imidazole in situ via a domino synthesis,[7,13,14] and to continue directly with a Bamberger reaction (Schemes 3 and 4).[1] As implied, a key advantage of this approach was to bypass the inconveniences normally associated with isolating imidazole.[7,13] Integrating the two processes into a one-pot strategy appeared technically feasible, given that each reaction has traditionally been conducted in aqueous media. In a typical in-house procedure (Scheme 3), a small excess of ammonia and stoichiometric amounts of glyoxal and formaldehyde, were heated in a slightly oversized vessel, yielding imidazole. Unlike the classic 3 h domino synthesis,[7] the generation of imidazole was restricted to 1 h; time-course trials confirmed that the yields of *cis*-1,2-di(acetamido)ethene (**1a**, entry 1 in Table 1) were not improved by further incubation. The conditions to achieve ring cleavage were subsequently established in the same pot by modifying the solvent system and temperature. The workup was facilitated by spontaneous crystallization or selective organic-phase partitioning of the *cis*-1,2-diamidoethene products. Recrystallization was conceivably optional, as the "crude" lyophilized products revealed a purity, which implied their suitability as monomers.[1,2]

Results and discussion

The one-pot process proved easy to implement and amenable to a broad selection of acylating agents (**1**–**5**, Table 1). The yields, while modest, were offset by the extremely cheap starting materials and ease of product isolation. The

Scheme 3. One-pot domino reaction scheme to afford *cis*-1,2-di(alkylamido)ethene, *cis*-1,2-di(alkoxyamido)ethene, and *cis*-1,2-di(benzamido)ethene from commodity materials.

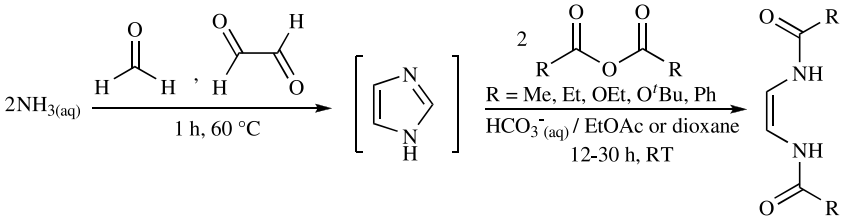

Scheme 4. Bamberger ring cleavage pathway in aqueous bicarbonate. Imidazole is activated via carboxylic anhydride or dialkyl dicarbonate.[1] The *N*,*N*′-diacyl or *N*,*N*-dicarbalkoxy imidazolium species formed is attacked by hydroxide at the C-2 center, affording an *N*,*N*′-diacyl or *N*,*N*′-dicarbalkoxy-2-hydroxyimidazoline. Ring fission ensues, producing a *cis*-1,2-diamido-*N*-formylethene. Hydrolytic *N*-deformylation follows, yielding the end product.

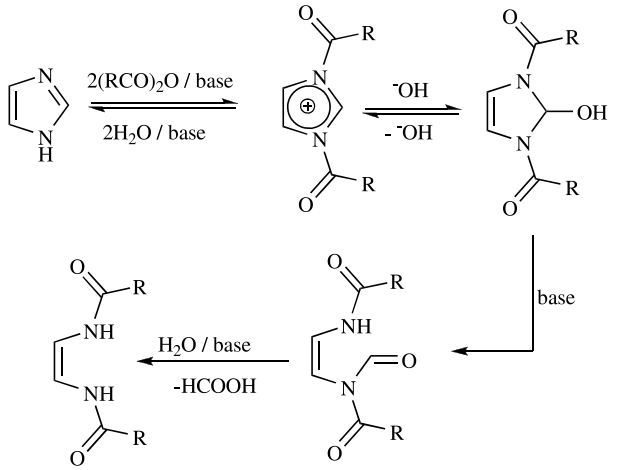

facility of the overall process was best illustrated by the example of acetic anhydride (**1**, entry 1 in Table 1), which upon gradual addition smoothly afforded **1a** via spontaneous crystallization.[1] The process was readily upscaled to 30 L, further implying its industrial merit. The approach also served to confirm the general utility of acid anhydrides, as all work on the Bamberger reaction had been focused, until recently,[1] on the use of benzoyl chloride, alkyl and aryl chloroformates, and **2**.[2,6,8–11] This validation was particularly encouraging, as one of the two reported attempts to prepare a *cis*-1,2-di(alkylamido)ethene, specifically **1a**, had failed using **1**.[12] Lastly, the stereo-electronic diversity among **1a**–**5a** (Table 1) was attractive, as it could potentially serve to extend the utility of this monomer class. For instance, a copolymer prepared from **1a**, **2a**, and **3a** could likely be prompted to selectively deblock under the appropriate conditions.

Prior studies[6,9] on the Bamberger reaction provided a mechanistic basis to relate product yield to the conversion of a 2-hydroxyimidazoline intermediate. As shown in Scheme 4, ring fission is initially prompted by the stepwise *N*,*N*′-diacylation or *N*,*N*′-dialkoxy formylation of imidazole in aqueous base, forming an activated imidazolium species. Hydroxide attack ensues at the C-2 carbon, reversibly forming a *N*,*N*′-diacyl or *N*,*N*′-dicarbalkoxy-2-hydroxy-imidazoline. A general or specific base-catalyzed cleavage of the ring follows, yielding a *cis*-1,2-diamido-*N*-formylethene. The formyl group is hydrolyzed via base catalysis, affording the *cis*-1,2-diamidoethene product. Hydrolytic pathways are also known to resist the activation of imidazole. These act to quench reagents and to hydrolyze any *N*-substituted and *N*,*N*′-disubstituted imidazoles. By probing the interaction of imidazole and **2** at low concentrations, Grace et al.[6] described a kinetic scenario, characterizable by the rapid accumulation of 2-hydroxy-*N*,*N*′-dicarbethoxyimidazoline, the slow cleavage of the ring, and the pH-dependent and typically rate-determining deformylation of the carbon at position C-2. As all reactants of the current study were utilized at much higher initial concentrations, it was safe to conclude that the *N*,*N*′-disubstituted 2-hydroxyimidazoline intermediate derived from each of **1**–**5** would be rapidly formed. In the mechanistic assessment of Grace et al.,[6] it was also clear that given enough time, the yield of *cis*-1,2-di(ethoxyamido)ethene would not reflect the deformylation rate of *cis*-1,2-diethoxyamido-*N*-formylethene. Rather, it would reflect the committed conversion of 2-hydroxy-*N*,*N*′-dicarbethoxyimidazoline to *cis*-1,2-diethoxyamido-*N*-formylethene. Thus, achieving a good yield ultimately rested on establishing an extended and sufficiently high steady-state concentration of the imidazoline, a task realized by discouraging hydrolytic deactivation and optimizing the availability of **2**. A similar kinetic view applied to the current work. Namely, the yield of each of **1a**–**5a** (Table 1) reflected the extent to which an effective and prolonged conversion of the corresponding *N*,*N*′-disubstituted 2-hydroxyimidazoline could be realized. Hence, the yield discrepancies amongst **1a**–**5a** not only reflected inherent stereoelectronic differences acting along the reaction coordinate, but presumably also some variations related to the addition of **1**–**5**. The literature yields (in parentheses in Table 1) were generally superior to the corresponding in-house process. No attempt was made to derive insight from this discrepancy, as the protocols differed notably.[2]

From a practical viewpoint, the yields were generally improved by both strong stirring, which served to disperse **1**–**5**, and by the moderately prolonged addition of sufficient **1**–**5**, which prompted the steady *N*,*N*′-diacylation or *N*,*N*′-dicarbalkoxylation of imidazole (Scheme 4). While the influence of pH on the course of the reaction had not been systematically characterized at large reactant concentrations, the Bamberger reaction was reported to proceed best within the pH range of 6–7.[6] Increasing the alkalinity further was discouraged, as the half-life of the *N*,*N*′-diacyl or *N*,*N*′-dicarbalkoxy imidazolium species would drop accordingly, detracting from the accumulation and turnover of the corresponding 2-hydroxyimidazoline. Still, the findings obtained

Can. J. Chem. Downloaded from www.nrcresearchpress.com by Xi'an Jiaotong University on 09/19/12
For personal use only.

herein using alkaline bicarbonate implied a rather flexible working pH range of reaction.

As a final point, the elusive *cis*-1,2-di(formamido)ethene was targeted in view of its potential to serve as an easily polymerizable monomer.[1] Just as with prior attempts, however, no product was isolated when formic acetic anhydride was added to the in situ-generated imidazole or to commercially produced imidazole as per the established method.[1] The fact that imidazole was recovered unchanged was attributed to the high accessibility and electropositive nature of the formyl carbonyl center, which presumably served to speed the hydrolytic deactivation of reagent and formylated imidazole species.

To summarize, several *cis*-1,2-diamidoethene monomers were prepared by manipulating glyoxal, formaldehyde, ammonia, and an acylating agent in one pot. The process precluded the purification of intermediates, the deployment of relatively expensive or volatile compounds like imidazole and chloroformate, and any laborious workup. The fact that an industrially applicable end product was prepared and readily isolable, following a four-component transformation in the presence of many potentially interfering by-products,[7] further attested to the facility and robustness of this strategy. Finally, whereas *cis*-1,2-diamidoethene can serve as a monomer, this class of compound may also be converted to the corresponding *N*,*N*′-disubstituted 4-imidazolin-2-one heterocycle,[4] which is known to have a much greater propensity to polymerize.[3] All in all, it would appear that the cost efficiency and conveniences imparted by this one-pot approach could promote the routine preparation and use of oligo- and polyvicinalamines.

Can. J. Chem. Downloaded from www.nrcresearchpress.com by Xi'an Jiaotong University on 09/19/12
For personal use only.

Experimental

Technical grade starting materials were obtained from local suppliers and were used without further purification.

Typical experimental procedure

To a stirred solution of ammonium hydroxide (6.0 g, 22–25 wt%), a mixture of glyoxal (4.35 g, 30.0 mmol, 40 wt%) and formaldehyde (2.25 mL, 30.2 mmol, 37 wt%) was cautiously added. The mixture was allowed to stir (60 °C, 1 h), generating imidazole. Subsequently, distilled water (150.0 mL), ethylacetate (30.0 mL), and sodium bicarbonate (25.0 g) were added to the reaction. Acetic anhydride (12.0 mL, 127.0 mmol, 4.23 equiv with respect to glyoxal) was slowly added (30 min) under vigorous stirring during which time effervescence was noted. The reaction vessel was lightly capped after **1** was fully added and stirring was continued (13 h, room temperature (RT)) to promote full deformylation. The precipitated solid was recovered by filtration, washed with distilled water (3 × 5.0 mL), optionally triturated in distilled water (20.0 mL, 80 °C, 15–30 min), and lyophilized to yield **1a** (1.50 g, 35% with respect to glyoxal) as a white solid. Di-*tert*-butyl dicarbonate (**3**) was gently warmed prior to use and administered dropwise as in the case of acetic anhydride. Unlike **1**–**3** and **5**, benzoic anhydride (**4**) was finely pulverized and added in one shot. For **3a** and **4a**, 1,4-dioxane (75.0 mL) was used in place of ethylacetate (Entries 3–4). Precipitation of **4a** (Entry 4) was facilitated by adding water (250 mL) during the workup. Product **5a** (Entry 5) was directly isolated by evaporating the ethylacetate layer. To ascertain the in situ yield of imidazole, an aliquot of the domino reaction (48.0 μL) was dissolved in deuterium oxide (600 μL) spiked with sodium acetate (24.0 μg). The sample was immediately analyzed using ^{1}H NMR (RT, D_2O/DHO presaturation, 10 s interpulse delay, and 256 scans). The signal corresponding to the three C–H protons of imidazole was compared with the three protons of acetate, permitting a yield calculation of the former compound.

Parameters used for characterization

NMR: Inova 500; ATR-FTIR: Bruker Equinox 55; GC–MS: gas chromatography, Agilent 6890N; GC column: J&W, DB5, 30 m, i.d. = 0.25 mm; film thickness: 0.25 μm; carrier gas: He; injection: 50 ng / 1 μL MeOH; injection temp.: 270 °C; aux. temp.: 240 °C; temp. progr.: 100/5–5–260; mass spectrometry: Sensi-TOF, Five Technologies, Munich; mass range: 40–500 amu; ionization energy: 70 eV; DSC: Netzsch 204 Phoenix; temp. ramp rate: 5 K/min; atmosphere: N_2. A chemical shift of 2.5 ppm (^{1}H NMR) and 39.4 ppm (^{13}C NMR) was applied to reference DMSO-d_6.[15] The melting onset temperature (T_{onset}) was estimated from the DSC profile as per ASTM standard test procedure E794.[16] The peak melting temperature (T_m) was obtained by direct inspection. Both values have been expressed for clarity. In **1a**–**5a**, the TLC runs showed one spot under UV light. All GC–MS profiles yielded one peak.

Entry 1

R_f: 0.06 (EtOAc); mp (recrys. EtOH): T_{onset} = 134.8 °C, T_m = 136.3 °C, lit. value[1] not reported. IR (neat) ν: 3301 (w), 3211 (w), 3051 (w), 1708 (w), 1676 (m), 1637 (m), 1560 (m), 1356 (m), 1274 (m), 1164 (s), 1039 (m), 997 (m), 744 (m), 668 (s). ^{1}H NMR (500 MHz, DMSO-d_6) δ: 1.95 (s, 3H), 5.99 (m, 1H), 9.27 (d, 1H). ^{13}C NMR (125.725 MHz, DMSO-d_6) δ: 22.61, 105.04, 166.13. GC–MS *m*/*e*: 142 M^+. MS ($C_6H_{10}N_2O_2$) calcd: 142.16; found: 142.09. Anal. calcd: C 50.69, H 7.09, N 19.71; found: C 48.61, H 7.25, N 18.60.

Entry 2

R_f: 0.58 (EtOAc); mp (recrys. EtOH): T_{onset} = 141.3 °C, T_m = 143.7 °C (lit.[11] mp 139–141 °C). IR (neat) ν: 3338 (w), 3316 (w), 3229 (w), 2976 (w), 1724 (m), 1668 (m), 1525 (s), 1455 (m), 1367 (m), 1308 (m), 1241 (s), 1149 (s), 1081 (s), 870 (m), 765 (m), 718 (s), 675 (m). ^{1}H NMR (500 MHz, DMSO-d_6) δ: 1.19 (t, 3H), 4.06 (q, 2H), 5.69 (m, 1H), 8.78 (d, 1H). ^{13}C NMR (125.725 MHz, DMSO-d_6) δ: 14.31, 60.38, 105.24, 153.18. GC–MS *m*/*e*: 202 M^+. MS ($C_8H_{14}N_2O_4$) calcd: 202.21; found: 202.12. Anal. calcd: C 47.52, H 6.98, N 13.85; found: C 47.23, H 6.76;, N 13.62.

Entry 3

R_f: 0.66 (EtOAc); mp (recrys. EtOH): T_{onset} = 221.9 °C, T_m = 223.7 °C. IR (neat) ν: 3340 (w), 3255 (w), 3226 (w), 2975 (w), 1723 (m), 1692 (s), 1525 (s), 1454 (w), 1367 (m), 1307 (m), 1239 (s), 1146 (s), 1080 (s), 869 (m), 772 (m), 717 (s), 676 (m). ^{1}H NMR (500 MHz, DMSO-d_6) δ: 1.41 (s, 9H), 5.61 (m, 1H), 8.59 (d, 1H). ^{13}C NMR (125.725 MHz, DMSO-d_6) δ: 27.92, 78.94, 104.75, 152.29.

GC–MS *m*/*e*: 258 M^+. MS ($C_{12}H_{22}N_2O_4$) calcd: 258.31; found: 258.23. Anal. calcd: C 55.80, H 8.58, N 10.84; found: C 54.25, H 3.78, N 7.18.

Entry 4

R_f: 0.48 (EtOAc); mp (recrys. EtOH): T_{onset} = 204.7 °C, T_m = 207.8 °C (lit.[11] mp 212–213 °C). IR (neat) ν: 3322 (w), 3265 (w), 3057 (w), 1697 (m), 1670 (m), 1619 (m), 1515 (s), 1487 (s), 1316 (m), 1275 s), 1259 (s), 1175 (s), 1147 (m), 1075 (w), 921 (m), 802 (m), 693 (s). ^{1}H NMR (500 MHz, DMSO-d_6) δ: 6.40 (m, 1H), 7.52–7.64 (m, 2H), 7.89–7.94 (m, 3H), 10.10 (d, 1H). ^{13}C NMR (125.725 MHz, DMSO-d_6) δ: 106.69, 127.17, 128.42, 131.94, 133.79, 163.81. GC–MS *m*/*e*: 266 M^+. MS ($C_{16}H_{14}N_2O_2$) calcd: 266.29; found: 265.88. Anal. calcd: C 72.17, H 5.30, N 10.52; found: C 53.04, H 7.53, N 15.32.

Entry 5

R_f: 0.23 (EtOAc); mp (recrys. EtOH): T_{onset} = 138.4 °C, T_m = 139.6 °C. IR (neat) ν: 3316 (w), 3199 (w), 2982 (w), 1706 (m), 1687 (m), 1635 (m), 1549 (s), 1507 (s), 1457 (s), 1420 (m), 1375 (m), 1280 (w), 1239 (m), 1202 (s), 1163 (s), 1085 (m), 1029 (m), 940 (w), 758 (s), 646 (m). ^{1}H NMR (500 MHz, DMSO-d_6) δ: 1.04 (t, 3H), 2.12 (q, 2H), 6.00 (m, 1H), 9.26 (d, 1H). ^{13}C NMR (125.725 MHz, DMSO-d_6) δ: 9.41, 28.46, 104.99, 169.86. GC–MS *m*/*e*: 170 M^+. MS ($C_8H_{14}N_2O_2$) calcd: 170.21; found: 170.13. Anal. calcd: C 56.45, H 8.29, N 16.46; found: C 54.49, H 7.87, N 10.19.

Acknowledgments

The authors acknowledge B. Yıldız of Sabancı University (SU), Istanbul, Turkey, and M. Wiesheu, A. Friess, and M. Çölhan of the Technical University of Munich (TUM) for technical help; H. Parlar of TUM for supporting the MS tests and elemental analyses, M. Manyas of the SU Information Center for procuring literature, and C. Ow Yang of SU and E. Alberico of the Consiglio Nazionale Delle Richerche (CNR)-Sassari, Italy, for comments.

References

(1) Chang, H. T.; Charmot, D.; Zard, S. W. O. Patent 2005/041900, 2005.
(2) Dyllick-Brenzinnger, R.; Steuerle, U.; Braig, V. W. O. Patent 2004/013207, 2004.
(3) Klapper, M.; Hamciuc, C.; Dyllick-Brenzinger, R.; Müllen, K. *Angew. Chem. Int. Ed.* **2003** *42* (38), 4687. doi:10.1002/anie.200351500.
(4) Kundu, N. R. Synthesis, Characterization & Chemical Modification of a Novel Cationic Polyelectrolyte Poly(methylene amine). Ph.D. Thesis, Johannes Gutenberg-Universität Mainz, Germany, 2007.
(5) Haines, D. R.; Leonard, N. J.; Wiemer, D. F. *J. Org. Chem.* **1982** *47* (3), 474. doi:10.1021/jo00342a020.
(6) Grace, M. E.; Loosemore, M. J.; Semmel, M. L.; Pratt, R. F. *J. Am. Chem. Soc.* **1980** *102* (22), 6784. doi:10.1021/ja00542a020.
(7) Mesch, W. US Patent 4,719,309, 1988.
(8) Bamberger, E. *Justus Liebigs Ann.* **1893** 273, 342–363, 267–269.
(9) Loosemore, M. J.; Pratt, R. F. *FEBS Lett.* **1976** *72* (1), 155. doi:10.1016/0014-5793(76)80834-4.
(10) Morkovnik, A. S.; Khrustalev, V. N. *Russ. Chem. Bull.* **1998** *47* (8), 1550. doi:10.1007/BF02495608.
(11) Babad, E.; Ben-Ishai, D. *J. Heterocycl. Chem.* **1969** *6* (2), 235. doi:10.1002/jhet.5570060215.
(12) Hoffmann, K. *Imidazole and Its Derivatives;* Interscience Publishers: New York, 1953; Part I, p 48.
(13) Arduengo, A. J.; Gentry, F. P.; Taverkere, P. K.; Simmons, H. E. US Patent 6,177,575, 2001.
(14) As described previously (Tietze, L. F. *Chem. Rev.* **1996,** 96, 115–136), a domino reaction entails the formation of at least two bonds with the proviso that the reaction conditions are not altered, additional reagents are not added, and at least one transformation yields a functionality that also enters the reaction.
(15) Macomber, R. S. *A Complete Introduction to Modern NMR Spectroscopy;* Wiley: New York, 1998.
(16) American Society of Testing and Materials. *ASTM E754, Standard Test Methods for Melting and Crystallization Temperatures by DSC;* Annual Book of ASTM Standards, 14.02; ASTM International: West Conshohocken, PA, 1994.

Can. J. Chem. Downloaded from www.nrcresearchpress.com by Xi'an Jiaotong University on 09/19/12
For personal use only.

The detection of ruthenium chloride clusters by laser desorption ionization-mass spectrometry of $RuCl_3 \cdot 3H_2O$

Alexander G. Boncheff and Mario A. Monteiro

Can. J. Chem. Downloaded from www.nrcresearchpress.com by Xi'an Jiaotong University on 09/19/12
For personal use only.

Abstract: The production of gas-phase singly charged ruthenium chloride anionic complexes by laser desorption ionization of $RuCl_3 \cdot 3H_2O$ is reported. The $[Ru_xCl_y]^-$ clusters could only be detected in the absence of the matrix component in the negative mode. The cluster compositions observed were $[RuCl_4]^-$, $[RuCl_5]^-$, $[Ru_2Cl_6]^-$, $[Ru_2Cl_7]^-$, $[Ru_3Cl_9]^-$, $[Ru_4Cl_{11}]^-$, and $[Ru_5Cl_{12}]^-$. With the aid of density functional theory calculations, we proposed feasible structures for each ruthenium chloride cluster, in which Ru–Ru bonds and Cl bridges were a common characteristic.

Key words: ruthenium, laser desorption ionization, metal clusters, $RuCl_3 \cdot 3H_2O$, density functional theory, mass spectrometry.

Résumé : Faisant appel à la technique d'ionisation par désorption au laser du $RuCl_3 \cdot 3H_2O$, on a réalisé la production en phase gazeuse de complexes anioniques du chlorure de ruthénium portant une seule charge. Dans le mode négatif, on ne peut détecter la présence des agrégats de $[Ru_xCl_y]^-$ qu'en l'absence de la composante matricielle. On a pu observer les cations de composition $[RuCl_4]^-$, $[RuCl_5]^-$, $[Ru_2Cl_6]^-$, $[Ru_2Cl_7]^-$, $[Ru_3Cl_9]^-$, $[Ru_4Cl_{11}]^-$ et $[Ru_5Cl_{12}]^-$. En se basant sur des calculs selon la théorie de la fonctionnelle de la densité, on propose des structures plausibles pour chacun des agrégats de chlorure de ruthénium dans lesquels des liaisons Ru–Ru et des ponts Cl sont des caractéristiques communes.

Mots-clés : ruthénium, ionisation par désorption au laser, agrégats métalliques, $RuCl_3 \cdot 3H_2O$, théorie de la fonctionnelle de la densité, spectrométrie de masse.

[Traduit par la Rédaction]

Introduction

Part of our research program focuses on the development of new methods for the structural characterization of complex bacterial polysaccharides (PSs). We envisaged that the coupling of ruthenium to PSs, especially those expressing amine moieties, may help us obtain less convoluted NMR spectra of the PSs and possibly yield compounds suitable for crystallographic analysis. The coordination of monosaccharide units to transition metals, especially those of the platinum group, is well-documented.[1] Other investigations into the mechanisms of coordination, with characterization of the resulting products, have also been carried out with metals such as iron,[2] platinum,[3] palladium,[3] and copper.[4] X-ray crystallography and spectroscopic data has shown that monosaccharides coordinate to the metal through vicinal hydroxyl or amine functional groups.

For comparison with the matrix-assisted laser desorption ionization – time of flight – mass spectrometry (MALDI-TOF-MS) spectra of putative products from reactions in which $RuCl_3 \cdot 3H_2O$ was a starting material, a MALDI-TOF-MS spectrum of $RuCl_3 \cdot 3H_2O$ was sought. The results afforded by the MALDI-TOF-MS and LDI-TOF-MS experiments carried out on $RuCl_3 \cdot 3H_2O$ are described.

Materials and methods

Mass spectrometry

For MALDI-TOF-MS, $RuCl_3 \cdot 3H_2O$ was mixed directly with a matrix solution composed of 2 mg of 3,4-dihydroxybenzoic acid in 20% of ethanol. An analyte–matrix 1:2 ratio (*v*/*v*) and 1 μL was spotted on the MALDI sample target and allowed to dry at room temperature. For LDI-TOF-MS, a few crystals of analyte were deposited on the sample target and gently pressed toward the target. The analyses were performed using a MALDI-TOF-MS instrument (model Reflex III, Bruker) equipped with a 337 nm nitrogen laser. Samples were analyzed in reflectron and negative ion modes. Ion sources 1 and 2 were held at 20 and 16.35 kV, respectively. The guiding lens voltage was set at 9.75 kV. The reflector detection gain was set at 5.3 with pulsed ion extraction at 200 ns. The nitrogen laser power was set to the minimum level necessary to generate a reasonable signal and avoid possible degradation of analytes. Typically, 15% of laser energy was used, which was calculated to be 4 mJ. In the case of high laser energy experiments, 45% of laser energy was used, which equalled 12.5 mJ. The pulse duration was 9 Hz, the spot size was 2 mm, and the calculated energy density was 100 μJ/0.1 mm^2. A two-point external calibration was

Received 16 September 2010. Accepted 1 December 2010. Published on the NRC Research Press Web site at canjchem.nrc.ca on 24 March 2011.

A.G. Boncheff and M.A. Monteiro.[1] Department of Chemistry, University of Guelph, Guelph, ON N1G 2W1, Canada.

[1]Corresponding author (e-mail: monteiro@uoguelph.ca).

Fig. 1. Laser desorption ionization – time of flight – mass spectrometry (LDI-TOF-MS) spectrum of $RuCl_3 \cdot 3H_2O$ (negative mode).

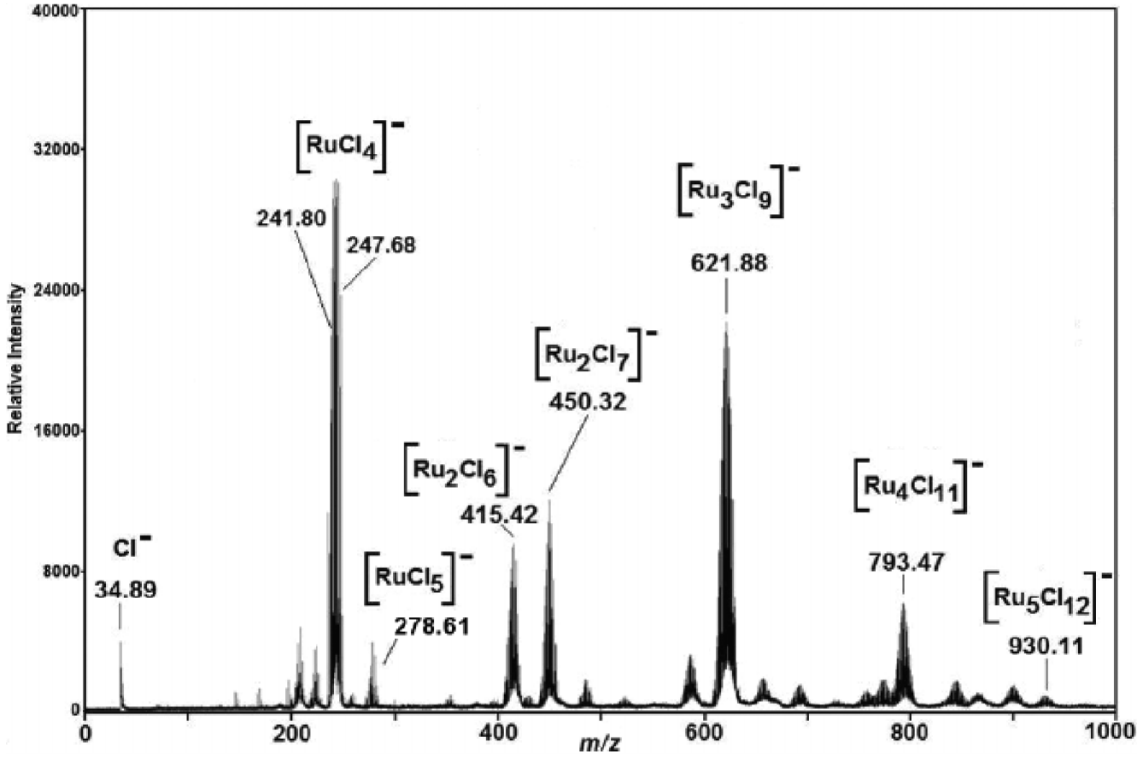

Can. J. Chem. Downloaded from www.nrcresearchpress.com by Xi'an Jiaotong University on 09/19/12
For personal use only.

performed, using the $[M - H]^{-1}$ (153.01 Da) and $[2M - H]^{-2}$ (447.12 Da) peaks of dehydroxybenzoic acid and the dimer of sinapinic acid, respectively, prepared in acetonitrile–water solution (10 pmol/μL). Ruthenium(III) trichloride trihydrate was purchased from Pressure Chemicals (Pittsburgh, Pennsylvania).

Computations

All geometry optimization and vibrational frequency analysis density functional theory (DFT) calculations were performed using Gaussian09.[5] All calculations used the PBE0 exchange-correlation functional[6] with a dual basis set; SDD[7] was used for the Ru atoms and 6–311G(2d) was used for the Cl atoms. The composition of molecular orbitals and overlap population analysis, to determine bond orders and bonding of all species, were calculated using AOMix.[8,9]

Results and discussion

Our first attempt, using a matrix solution of 3,4-dihydroxybenzoic acid in 20% of ethanol, yielded no easily understood *m/z* ions, and no ions representative of the molecular weight of $RuCl_3 \cdot 3H_2O$ or related species were observed. Subsequently, we attempted the same experiment with no matrix (LDI-TOF-MS). The LDI-TOF-MS experiment in the negative mode also showed no *m/z* ions attributable to $RuCl_3 \cdot 3H_2O$ or associated residues, but afforded a series of low and high *m/z* ions of defined compositions with an isotope pattern that suggested the presence of ruthenium- and chloride-containing species (Fig. 1).

The most intense *m/z* ion at 243.69 was attributed to a complex containing one Ru atom and four Cl atoms, $[RuCl_4]^-$. Dominant species containing two Ru atoms were observed at *m/z* 415.42 for $[Ru_2Cl_6]^-$ and at *m/z* 450.32 for $[Ru_2Cl_7]^-$. Two other intense ions containing three and four Ru atoms were observed at *m/z* 621.88 for $[Ru_3Cl_9]^-$ and at 793.47 for $[Ru_4Cl_{11}]^-$. Although of low intensity, *m/z* ions attributable to $[RuCl_5]^-$ and $[Ru_5Cl_{12}]^-$ complexes were also observed at *m/z* 278.61 and 930.11, respectively. Computer-generated isotopic distribution profiles for the described compositions matched the observed experimental data (Fig. 2). However, that of $[RuCl_4]^-$ suggested that this *m/z* peak could also contain $[RuCl_3{:}2OH]^-$. Within the limits of detection, no other higher mass ions were observed.

Based on computational studies, a structure is proposed for each cluster, and, in particular, we suggest cyclic conformations for the larger complexes, $[Ru_3Cl_9]^-$, $[Ru_4Cl_{11}]^-$, and $[Ru_5Cl_{12}]^-$. Figure 3 shows the proposed cluster structures with their respective total energy values. DFT calculations showed that the proposed noncyclic structures of $[RuCl_4]^-$ and $[Ru_2Cl_6]^-$ favoured a planar and tetrahedral-like geometry, respectively (Fig. 3). As $[RuCl_4]^-$ and $[Ru_2Cl_6]^-$ are both doublet species, an unrestricted PBE0 method was used for the calculations, with the S^2 values for $[RuCl_4]^-$ and $[Ru_2Cl_6]^-$ being 0.7503 and 0.7547, respectively, after annihilation of the first-order spin contaminant. A square pyramidal geometry was attributed to the $[RuCl_5]^-$, a closed shell singlet species with an S^2 value of 0.0000.

The proposed $[Ru_2Cl_7]^-$ cluster contains two Ru atoms bonded together with a single bond and three chloride bridges (Fig. 3). Two terminal chlorides extended from each Ru atom. As a singlet species, the $[Ru_2Cl_7]^-$ cluster optimization had an S^2 value of 0.0000.

For the $[Ru_3Cl_9]^-$ complex, one of the most intense *m/z* ions, the structure is composed of a series of three-membered

Can. J. Chem. Downloaded from www.nrcresearchpress.com by Xi'an Jiaotong University on 09/19/12
For personal use only.

Fig. 2. Mass spectral profile of the isotopic pattern of $[Ru_2Cl_6]^-$ (top) and $[Ru_3Cl_9]^-$ (bottom). The experimental spectrum is at the left and the computed isotopic pattern is at the right.

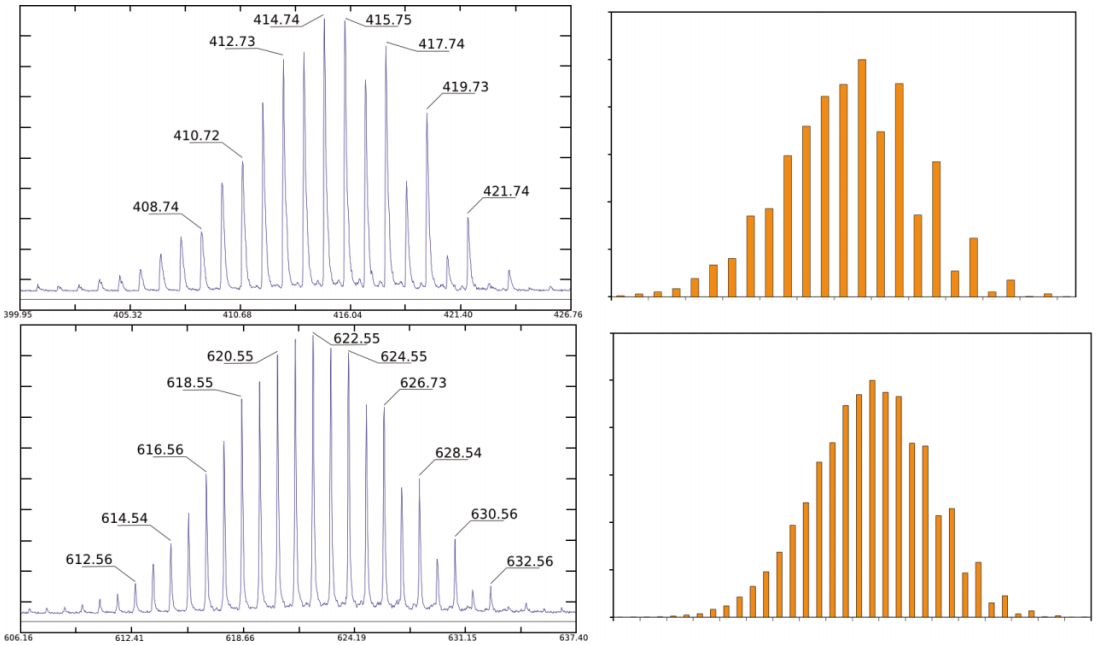

rings lying on a single plane (Fig. 3). The proposed structure of the $[Ru_3Cl_9]^-$ cluster bares a strong resemblance to the DFT geometry optimizations of $[Re_3(\mu\text{-}Cl)_3Cl_9]^{-3}$ described by Psaroudakis et al.[10] Both molecules contain a three-membered ring of metal atoms with each metal atom being connected to two in-plane bridging chlorides and two out-of-plane terminal chlorides. The optimization of the $[Ru_3Cl_9]^-$ cluster gave an S^2 value of 0.0000 (singlet species).

For the $[Ru_4Cl_{11}]^-$ cluster, we first envisaged a bicyclo[3.3.1]nonane-like structure; however, a molecular orbital overlap population analysis to determine bonding suggested the cyclic structure presented in (Fig. 3). As a singlet species, the $[Ru_4Cl_{11}]^-$ cluster optimization had an S^2 value of 0.0000. For $[Ru_5Cl_{12}]^-$, we hypothesized a tetracyclic[3.3.3.1.1]tridecane-like structure, in which all Ru atoms were connected to each other through Cl bridges. However, the computational calculations afforded the structure shown in Fig. 3. To obtain convergence, the optimization and frequency calculations on the $[Ru_5Cl_{12}]^-$ cluster were performed with loose convergence criteria (1×10^{-6}) for the self-consistent field (SCF) energy. The optimization showed that $[Ru_5Cl_{12}]^-$ is a highly symmetric molecule with Ru atoms in both planar and tetrahedral configurations. An S^2 value of 0.9106 resulted for this unrestricted calculation and one virtual frequency was reported from the vibrational analysis. Geometry optimization and vibrational analysis of the neutral $[Ru_5Cl_{12}]$ cluster was also performed and was successful under the default convergence criteria with no virtual frequencies reported. A comparison between the optimized neutral $[Ru_5Cl_{12}]$ and anionic $[Ru_5Cl_{12}]^-$ clusters showed they were visually similar. The observed difficulties in the convergence of the anionic $[Ru_5Cl_{12}]^-$ cluster under default criteria is thought to arise from the highly delocalized HOMO, which contains the unpaired electron for this doublet species. Except for $[Ru_5Cl_{12}]^-$, no imaginary frequencies were reported for the optimized geometries, indicating that an energy minimum was reached for the aforementioned cases.

We suggest that the cyclic $[Ru_3Cl_9]^-$, $[Ru_4Cl_{11}]^-$ and $[Ru_5Cl_{12}]^-$ clusters may be in part formed through intranucleophilic substitutions in the gas phase, and, to some extent, the presence of *m/z* 35 $[Cl^-]$ in the LDI-TOF-MS spectrum (Fig. 1) lends support to this hypothesis. In addition to the structures shown in Fig. 3, other structural arrangements for $[Ru_2Cl_7]^-$, $[Ru_3Cl_9]^-$, and $[Ru_4Cl_{11}]^-$ were also observed to minimize, but at higher total energies (Fig. 4).

As mentioned, we suggested that the *m/z* ions at 622.30 and 794.30 corresponded to cyclic clusters of $[Ru_3Cl_9]^-$ and $[Ru_4Cl_{11}]^-$, respectively; but, the possibility exists that these *m/z* ions could be adduct compounds in the form of $[Ru_3Cl_8 + Cl]^-$ and $[Ru_4Cl_{10} + Cl]^-$. Similarly, $[RuCl_5]^-$ could exist in the form of a $[RuCl_4 + Cl]^-$ adduct. However, neutral clusters of $[RuCl_4]$, $[Ru_3Cl_8]$, and $[Ru_4Cl_{10}]$ were not converged in the SCF during optimization. Thus, we suggest that there is a low probability that these adductlike clusters exist. In the proposed structures (Figs. 3 and 4), there were no data that would suggest the presence of double or triple bonds between the Ru atoms.

Neighbouring the high-intensity *m/z* ions, ions of much lower intensity could be observed that differed by *m/z* 35. These could be generated by loss of Cl atoms from the described clusters or could represent other species. Although of very low intensity, other ions at *m/z* 208.77, 224.72, 278.64, 844.12, and 874.51 might be attributed to $[RuCl_3]^-$, $[RuCl_3{:}OH]^-$, $[RuCl_4{:}2OH]^-$, $[Ru_4Cl_{10}{:}OH]^-$, and $[Ru_5Cl_9{:}2OH]^-$, respectively.

Conclusions

We have shown that gas-phase Ru_xCl_y clusters may be synthesized by the laser ablation of $RuCl_3{\cdot}3H_2O$ in the

Fig. 3. Optimized ruthenium chloride cluster structures.

Formula and Total Energy (kJ/mol)	Cluster Model	Cluster Structure
$[RuCl_4]^-$ $E = -5.0811 \times 10^6$	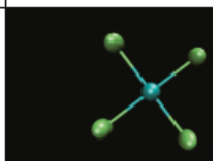	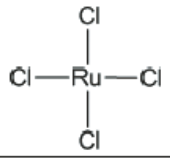
$[RuCl_5]^-$ $E = -6.2892 \times 10^6$	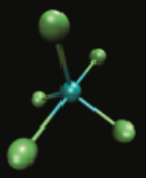	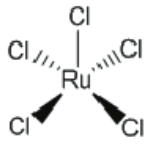
$[Ru_2Cl_6]^-$ $E = -7.7464 \times 10^6$	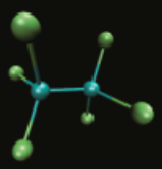	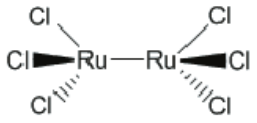
$[Ru_2Cl_7]^-$ $E = -8.9543 \times 10^6$	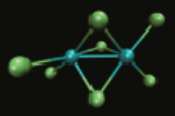	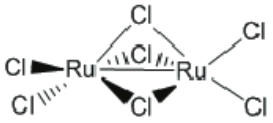
$[Ru_3Cl_9]^-$ $E = -1.1612 \times 10^7$		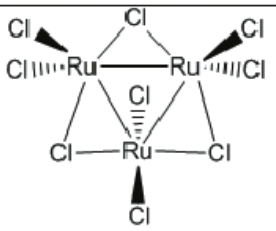
$[Ru_4Cl_{11}]^-$ $E = -1.4285 \times 10^7$	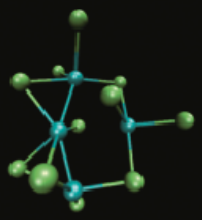	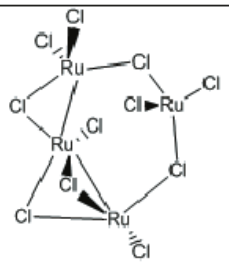
$[Ru_5Cl_{12}]^-$ $E = -1.5742 \times 10^7$	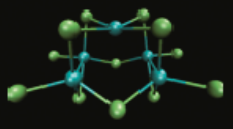	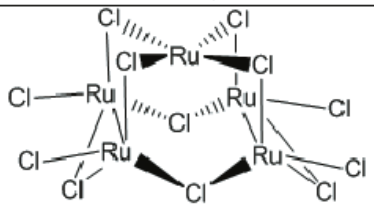

negative ion mode. Based on computational calculations, Figs. 3 and 4 show proposed structures for the ruthenium chloride clusters. However, other structural isomers may be possible. Cluster formation was found to be inhibited when 3,4-dihydroxybenzoic acid was used as the matrix. The MS data showed that the Ru–Cl ratio decreases as the number of Ru atoms increase and that the higher order clusters contain a mixed oxidation state. Other examples of cluster formations by LDI containing various transition metals have been described.[11–13] Also, a wide range of metal clusters have

Can. J. Chem. Downloaded from www.nrcresearchpress.com by Xi'an Jiaotong University on 09/19/12
For personal use only.

Can. J. Chem. Downloaded from www.nrcresearchpress.com by Xi'an Jiaotong University on 09/19/12
For personal use only.

Fig. 4. Optimized ruthenium chloride cluster structures with higher total energies.

Formula and Total Energy (kJ/mol)	Cluster Structure	
$[Ru_2Cl_7]^-$ **1.** E = -8.954323x10^6 **2.** E = -8.954208x10^6	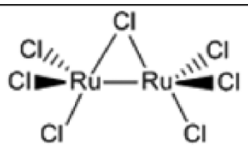 **1**	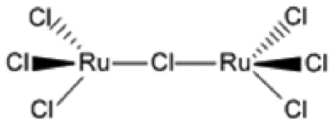 **2**
$[Ru_3Cl_9]^-$ **1.** E = -1.161929x10^7 **2.** E = -1.161946x10^7	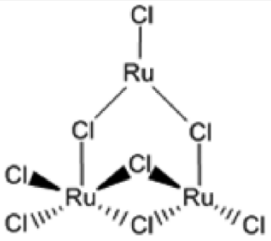 **1**	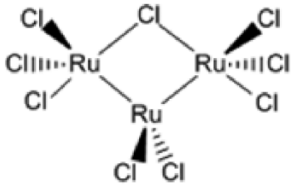 **2**
$[Ru_4Cl_{11}]^-$ E = -1.4284x10^7	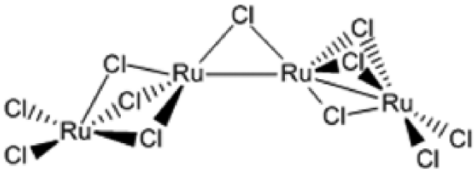	

been produced by LDI of metal oxides, metal phosphides, metal chalcogenides, and metal carbonyls.[11] Similarly to the results obtained here, it has been reported that the use of a matrix prevented the formation of these types of metal-containing clusters.[11,12] Large rhenium chloride clusters have also been observed to be generated by LDI of rhenium trichloride,[12] with cluster formation only being afforded under negative mode ionization.[12]

Although reports describing the production of gas-phase transition-metal clusters are typically limited to laser ablation methods, work by Wang and Wang[14] showed that electrospray ionization (ESI) of alkali and alkali – earth metal halide solutions lead to the generation of various metal cluster dianions. However, they were unable to observe cluster formation from metal halide solutions of any of the 3d transition-metal elements. Although gas-phase clusters may not have a solution or solid-state counterpart, O'Hair and Khairallah[13] produced gas-phase metal clusters in a MALDI-TOF-MS apparatus that could be employed as catalysts, and thus the ruthenium chloride clusters described in this work could prove to be useful chemical compounds.

Acknowledgement

This work was funded by Natural Sciences and Engineering Research Council of Canada (NSERC).

References

(1) Allscher, T.; Klüfers, P.; Mayer, P. *Glycoscience* **2008** (4): 1077. doi:10.1007/978-3-540-30429-6_24.

(2) Geetha, K.; Raghavan, M. S. S.; Kulshreshtha, S. K.; Sasikala, R.; Rao, C. P. *Carbohydr. Res.* **1995** *271* (2), 163. doi:10.1016/0008-6215(95)00050-4.

(3) Schwarz, T.; Heß, D.; Klüfers, P. *Dalton Trans.* **2010** *39* (23), 5544. doi:10.1039/c002711a.

(4) Striegler, S.; Dittel, M. *Inorg. Chem.* **2005** *44* (8), 2728. doi:10.1021/ic048724p.

(5) Frisch, M. J.; Trucks, G. W.; Schlegel, H. B.; Scuseria, G. E.; Robb, M. A.; Cheeseman, J. R.; Scalmani, G.; Barone, V.; Mennucci, B.; Petersson, G. A.; Nakatsuji, H.; Caricato, M.; Li, X.; Hratchian, H. P.; Izmaylov, A. F.; Bloino, J.; Zheng, G.; Sonnenberg, J. L.; Hada, M.; Ehara, M.; Toyota, K.; Fukuda, R.; Hasegawa, J.; Ishida, M.; Nakajima, T.; Honda, Y.; Kitao, O.; Nakai, H.; Vreven, T.; Montgomery, J. A., Jr.; Peralta, J. E.; Ogliaro, F.; Bearpark, M.; Heyd, J. J.; Brothers, E.; Kudin, K. N.; Staroverov, V. N.; Kobayashi, R.; Normand, J.; Raghavachari, K.; Rendell, A.; Burant, J. C.; Iyengar, S. S.; Tomasi, J.; Cossi, M.; Rega, N.; Millam, J. M.; Klene, M.; Knox, J. E.; Cross, J. B.; Bakken, V.; Adamo, C.; Jaramillo, J.; Gomperts, R.; Stratmann, R. E.; Yazyev, O.; Austin, A. J.; Cammi, R.; Pomelli, C.; Ochterski, J. W.; Martin, R. L.; Morokuma, K.; Zakrzewski, V. G.; Voth, G. A.; Salvador, P.; Dannenberg, J. J.; Dapprich, S.; Daniels, A. D.; Farkas, O.; Foresman, J. B.; Ortiz, J. V.; Cioslowski, J.; Fox, D. J. *Gaussian 09,* Revision A.02; Gaussian, Inc.: Wallingford, CT, 2009.

(6) Adamo, C.; Barone, V. *J. Chem. Phys.* **1999** *110* (13), 6158. doi:10.1063/1.478522.

(7) Andrae, D.; Häyβermann, U.; Dolg, M.; Stoll, H.; Preuβ, H. *Theor. Chem. Acc.* **1990** *77* (2), 123. doi:10.1007/BF01114537.

(8) Gorelsky, S. I. *AOMix: Program for Molecular Orbital Analysis,* version 6.4; University of Ottawa; Ottawa, ON, 2010. http://www.sg-chem.net.
(9) Gorelsky, S. I.; Lever, A. B. P. *J. Organomet. Chem.* **2001** *635* (1–2), 187. doi:10.1016/S0022-328X(01)01079-8.
(10) Psaroudakis, N.; Mertis, K.; Liakos, D. G.; Simandiras, E. D. *Chem. Phys. Lett.* **2003** *369* (3–4), 490. doi:10.1016/S0009-2614(02)02045-6.
(11) McIndoe, J. S. *Trans. Met. Chem. (Weinh.)* **2003** *28* (1), 122. doi:10.1023/A:1022515104991.
(12) Dopke, N. C.; Treichel, P. M.; Vestling, M. M. *Inorg. Chem.* **1998** *37* (6), 1272. doi:10.1021/ic971220p.
(13) O'Hair, R. A. J.; Khairallah, G. N. *J. Cluster Sci.* **2004** *15* (3), 331. doi:10.1023/B:JOCL.0000041199.40945.e3.
(14) Wang, X. B.; Wang, L. S. *Phys. Rev. Lett.* **1999** *83* (17), 3402. doi:10.1103/PhysRevLett.83.3402.

Can. J. Chem. Downloaded from www.nrcresearchpress.com by Xi'an Jiaotong University on 09/19/12
For personal use only.

Development of a solid-phase extraction – spectrofluorimetric method for trace glutathione determination

Ke-Jing Huang, Cong-Hui Han, Ying-Ying Wu, Chao-Qun Han, De-Jun Niu, Zhi-Wei Wu, and Ya-Ping Xue

Can. J. Chem. Downloaded from www.nrcresearchpress.com by Xi'an Jiaotong University on 09/19/12
For personal use only.

Abstract: A simple and efficient solid-phase extraction – spectrofluorimetric method has been developed to determine glutathione (GSH). Fluorescent probe *N*-(4,4-difluoro-5,7-dimethyl-4-bora-3a,4a-diaza-*s*-indacene-3-yl)methyl)iodoacetamide (BODIPY Fl-C_1-IA) was used as the derivatization reagent. The procedure was based on a BODIPY Fl-C_1-IA selective reaction with GSH to form the highly fluorescent product BODIPY Fl-C_1-IA–GSH, using a solid-phase extraction column and spectrofluorimetric determination. The variables affecting analytical performance were studied and optimized. The calibration graph using the preconcentration system for GSH was linear over the range of 1–200 nmol/L with a limit of detection of 0.05 nmol/L (signal-to-noise ratio = 3). The relative standard deviation for six replicate determinations of GSH at the 100 nmol/L concentration level was 3.9%. The method was applied to water samples and average recoveries between 87.5% and 111.5% were obtained for spiked samples.

Key words: spectrofluorimetry, glutathione, solid-phase extraction, *N*-(4,4-difluoro-5,7-dimethyl-4-bora-3a,4a-diaza-*s*-indacene-3-yl)methyl)iodoacetami-de.

Résumé : On a développé une méthode simple et efficace d'extractoin spectrofluorimétrique en phase solide pour déterminer le glutathion (GSH). On a utilisé la sonde fluorescente *N*-(4,4-difluoro-5,7-diméthyl-4-bora-3a,4a-diaza-*s*-indacène-3-yl)méthyl)iodoacétamide (BODIPY F1-C_1-1A) comme réactif pour obtenir des dérivés. La méthode repose sur le fait que le BODIPY F1-C_1-1A donne une réaction sélective avec le GSH conduisant à la formation du produit hautement fluorescent BODIPY F1-C_1-1A–GSH qui peut être isolé par extraction en phase solide sur colonne et soumis à une détermination spectrofluorimétrique. On a étudié et optimisé les variables qui affectent la performance analytique. Le graphique de calibration à l'aide du système de préconcentration du GSH est linéaire sur la plage de 1 à 200 nmol/L, avec une limite de détection de 0,05 nmol/L (rapport signal à bruit = 3). La déviation relative standard pour six déterminations de GSH en duplicata, à un niveau de concentration de 100 nmol/L, est de 3,9 %. On a appliqué la méthode à des échantillons d'eau et on a obtenu des taux de récupérations moyens variant de 87,5 % à 111,5 % pour les échantillons ensemencés.

Mots-clés : spectrofluorimétrie, glutathion, extraction en phase solide, *N*-(4,4-difluoro-5,7-diméthyl-4-bora-3a,4a-diaza-*s*-indacène-3-yl)méthyl)iodoacétamide.

[Traduit par la Rédaction]

Introduction

The tripeptide glutathione (L-γ-glutamyl-L-cysteine-glycine, GSH) is the most abundant low molecular mass thiol in the cells of many organisms.[1] It is the major compound containing the –SH group produced by animals, plants, phytoplankton, and bacteria.[2,3] GSH is recognized as a key physiological antioxidant that not only detoxifies reactive oxygen species directly, but also enhances the functional ability of other crucial antioxidants such as vitamins E and C.[4,5] Many studies have pointed out the importance of GSH homeostasis during human diseases or intoxication by toxins, particularly in the liver,[6–9] kidney,[10] and the central nervous system.[11] Therefore, the quantitative measurement of low levels of GSH is desirable.

Currently available methods for determining GSH are generally based on chromatography and immunoassays. For example, Griffith[12] reported the determination of the total glutathione content in mouse plasma with an enzymatic recycling assay based on glutathione reductase; Guo et al.[13] developed a high-performance liquid chromatographic method based on a derivatizing reagent, 1,3,5,7-tetramethyl-8-phenyl-(4-iodoacetamido)difluoroboradiaza-*s*-indacene, for measuring low molecular weight thiol-containing compounds, including GSH, coenzyme A, *N*-acetylcysteine, cysteine, homocysteine, and 6-mercaptopurine in human plasma

Received 3 November 2010. Accepted 16 December 2010. Published on the NRC Research Press Web site at canjchem.nrc.ca on 24 March 2011.

K.-J. Huang,[1] C.-H. Han, Y.-Y. Wu, D.-J. Niu, Z.-W. Wu, and Y.-P. Xue. College of Chemistry and Chemical Engineering, Xinyang Normal University, Xinyang 464000, P. R. China.
C.-Q. Han. College of Chemistry and Chemical Engineering, Xuchang University, Xuchang 461000, P. R. China.

[1]Corresponding author (e-mail: kejinghuang@163.com).

Can. J. Chem. Downloaded from www.nrcresearchpress.com by Xi'an Jiaotong University on 09/19/12
For personal use only.

samples; Sakhi et al.[14] reported the detection of glutathione in human plasma using a two-dimensional chromatographic system with parallel porous graphitized carbon columns coupled with fluorescence and coulometric electrochemical detection; Guo et al.[15] developed a spectrofluorimetric method for the determination of GSH in human blood and pig liver based on a fluorescence probe (1,3,5,7-tetramethyl-8-phenyl-(2-maleimide)-difluoroboradiaza-*s*-indacene).
Although these methods are currently available for GSH determination, most of them are time-consuming, complicated, and inconvenient to operate. Therefore, a rapid, selective, and sensitive method for the analysis of GSH is still desired.

In the spectrofluorimetric method, GSH is either chemically reactive or a catalyst for several types of chemical reactions on products, with a subsequent effect on the fluorescence properties (development, inhibition, or enhancement) in either a direct or an indirect way. Difluoroboradiaza-*s*-indacenes (BODIPY, Fig. 1*a*) are a class of highly rigidized and polymethine-like fluorescent dyes that have found numerous applications in biochemistry and molecular biology because of their high extinction coefficients, high fluorescence quantum efficiency, and stability in light. *N*-(4,4-Difluoro-5,7-dimethyl-4-bora-3a,4a-diaza-*s*-indacene-3-yl)methyl)iodoacetamide (BODIPY Fl-C_1-IA) has been used for derivation and determination of GSH. It has almost no fluorescence before it reacts with thiols. When it reacts with GSH to produce BODIPY Fl-C_1-IA–GSH, the fluorescence of the fluorophore is strongly increased. This gives it good sensitivity and selectivity in the determination of GSH. Compared with other GSH derivatization reagents,[16,17] BODIPY Fl-C_1-IA exhibits the highest fluorescence enhancement. Therefore, it is favorable for the determination of trace GSH in real samples.

Direct determination of GSH at low concentration in complex matrices is often difficult because of the insufficient sensitivity of this technique as well as the matrix interferences occurring in real samples. So a pretreatment step for sample enrichment and cleanup is necessary. Solid-phase extraction (SPE) is usually used to purify various samples and preconcentrate the analytes to improve the analytical sensitivity because of its advantages in simplicity, rapidness, and less consumption of organic solvents.[18–21] However, to the best of our knowledge, there is no report on the application of SPE coupled with spectrofluorimetry to determine GSH in environmental waters.

In this paper, a method for the detection and quantification of GSH using BODIPY Fl-C_1-IA derivatization followed by SPE and spectrofluorimetry is presented. The derivatization conditions and the parameters affecting the SPE procedure are discussed and optimized. The proposed method permits the analysis and quantification of GSH in different water samples using a simple spectrofluorimetric method.

Experimental

Apparatus

All fluorescence measurements were performed using a Cary Eclipse fluorescence spectrophotometer (Varian) with 1 cm path length quartz cells. Both the instrument excitation and emission slits were adjusted to 5 nm. The pH value of the solution was measured using a pHS-3C meter (Shanghai Leici Equipment Factory, China). A Waters OAsis MCX (SPE) cartridge column (3 mL) was purchased from Waters Corporation.

Fig. 1. (*a*) The structure of difluoroboradiaza-*s*-indacene (BODIPY) and (*b*) the derivatization reaction of *N*-(4,4-difluoro-5,7-dimethyl-4-bora-3a,4a-diaza-*s*-indacene-3-yl)methyl)iodoacetamide (BODIPY Fl-C_1-IA) and thiols.

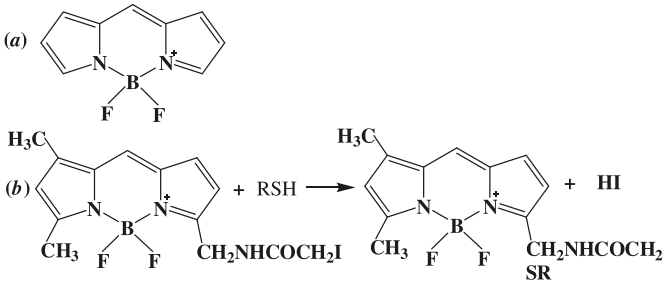

Reagents

BODIPY Fl-C_1-IA was purchased from Sigma-Aldrich (St. Louis, Missouri), and a 5×10^{-3} mol/L stock solution was prepared with pretreated acetonitrile (dried with P_2O_5). GSH was purchased from Shanghai Chemicals (Shanghai, China). A 1.0×10^{-3} mol/L standard solution of GSH was prepared with water daily. Dilution of these stock solutions to appropriate concentrations was performed before use. KH_2PO_4–$Na_2B_4O_7$ buffer solution was obtained by mixing 0.1 mol/L KH_2PO_4 solution and 0.05 mol/L $Na_2B_4O_7$ solution to the required pH. $Na_2B_4O_7$–H_3BO_3–KCl was obtained by mixing 0.05 mol/L $Na_2B_4O_7$, 0.20 mol/L H_3BO_3, and 0.20 mol/L KCl solutions to the required pH. Unless otherwise specified, all reagents were of analytical reagent grade and used without further purification, and all solutions were prepared from double-distilled water

Sample preparation

Three water samples were selected for validating the developed method. These include tap, rain, and Shi River waters. Tap water was collected from our own laboratory after flowing for 10 min. The rain and Shi River water samples were collected from the city of XinYang in Henan Province (China).

General procedure

Derivative procedure

Twenty microlitres of BODIPY Fl-C_1-IA (5×10^{-5} mol/L), 20 μL H_3BO_3–KCl–Na_2CO_3 buffer (pH 9.0), and an appropriate volume of GSH solution were transferred into a 1 mL tube. Then the well-mixed solution was incubated at 35 °C for 35 min, and the derivatization (Fig. 1*b*) was completed.

Solid-phase extraction

A SPE column was first preconditioned by methanol and water. The appropriate volume of sample solutions was passed through the cartridge by an injector. Subsequently, analytes retained on the SPE column were eluted with an optimal volume of acetone. The eluate was evaporated under a stream of nitrogen at 40 °C, and the residue was reconstituted

Can. J. Chem. Downloaded from www.nrcresearchpress.com by Xi'an Jiaotong University on 09/19/12
For personal use only.

Fig. 2. Fluorescence spectra of *N*-(4,4-difluoro-5,7-dimethyl-4-bora-3a,4a-diaza-*s*-indacene-3-yl)methyl)iodoacetamide (BODIPY Fl-C_1-IA) and BODIPY Fl-C_1-IA – glutathione (GSH). BODIPY Fl-C_1-IA (solid line) and BODIPY Fl-C_1-IA–GSH (dashed line). Fluorescence intensities: $C_{\text{BODIPY Fl-C1-IA}} = 3.3 \times 10^{-6}$ mol/L and $C_{\text{BODIPY Fl-C1-IA-GSH}} = 6.7 \times 10^{-7}$ mol/L. Spectral bandpass: 5 and 5 nm for excitation and emission spectra, respectively.

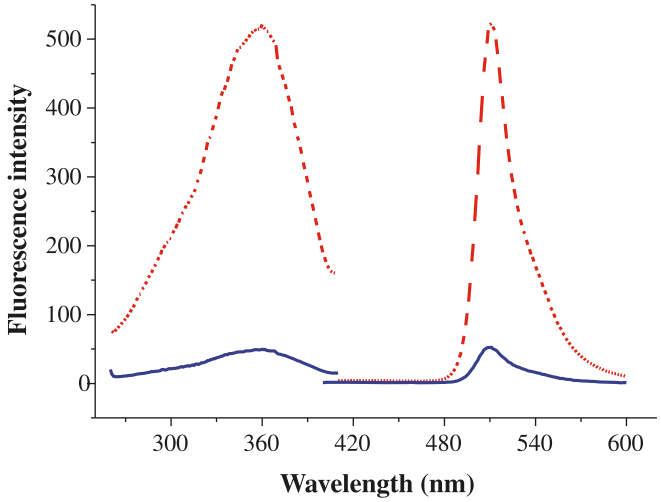

with 300 μL of water. Finally, 250 μL of the resultant solution was measured at excitation wavelength (λ_{ex})/emission wavelength (λ_{em}) = 360/510 nm.

Results and discussion

Fluorescence characteristics

The fluorescence spectra of BODIPY Fl-C_1-IA and its derivatization product BODIPY Fl-C_1-IA–GSH are shown in Fig. 2. The maximum excitation wavelength for BODIPY Fl-C_1-IA–GSH was at 360 nm and the maximum emission wavelength was at 510 nm. The fluorescent characteristics of BODIPY Fl-C1-IA and other reagents are compared in Table 1. The results show that the fluorescent characteristics of BODIPY Fl-C1-IA are comparable to those probes, especially for the photostability of the derivatization product.

The experiments showed that the fluorescence intensity of BODIPY Fl-C_1-IA–GSH at $\lambda_{ex}/\lambda_{em}$ = 360/510 nm could be stable for at least 24 h at room temperature with a change of 5%, which was long enough to complete the determination of GSH. The experimental results indicated that BODIPY Fl-C_1-IA–GSH had excellent stability. The adding sequence of buffer, BODIPY Fl-C_1-IA, and GSH solutions had no evident influence on the fluorescence signal.

Optimization of derivatization

The chemical structure of BODIPY Fl-C_1-IA and its reaction with thiols are shown in Fig. 1*b*. To achieve the maximum derivatization yield, the derivatization conditions including the buffer type, pH of the buffer, the volume of the buffer, the concentration of BODIPY Fl-C_1-IA, the reaction temperature, and the reaction time were carefully optimized.

The effect of the buffer on the derivatization was studied. Three different buffers (H_3BO_3–KCl–Na_2CO_3, $Na_2B_4O_7$–H_3BO_3–KCl, and KH_2PO_4–$Na_2B_4O_7$) were tested at a pH range of 7.50–9.50 (Fig. 3*a*). The maximum signal was achieved at pH 8.50 in H_3BO_3–KCl–Na_2CO_3 buffer, which is suitable for further study. The influence of the buffer amount was also estimated. The signal of the derivatives reached the maximum at 20 μL of H_3BO_3–KCl–Na_2CO_3 buffer (pH 8.50) (Fig. 3*b*). Thus, 20 μL of H_3BO_3–KCl–Na_2CO_3 buffer (pH 8.50) was selected in the derivatization reaction.

The effect of BODIPY Fl-C_1-IA concentration was evaluated in the concentration range of 1.7×10^{-6} to 7.5×10^{-6} mol/L (Fig. 3*c*). It was observed that the maximum and the constant fluorescence intensities were obtained with a concentration between 3.3×10^{-6} and 7.5×10^{-6} mol/L. Then, 3.3×10^{-6} mol/L of the reagent was selected.

The effect of the temperature on derivatization yield was also studied in the range of 20–55 °C (Fig. 3*d*). The results show that the fluorescence intensity reached a maximum at 35 °C. Therefore, 35 °C was selected as the optimum temperature value for the derivatization.

With respect to the reaction time, optimization was performed in the range of 25–50 min (Fig. 3*e*). The results show that fluorescence intensity reached its maximum and was invariable when the reaction time was 35 min. Thus, 35 min was selected for this work.

Optimization of SPE conditions

The goal of the present study was to use the SPE method coupled with spectrofluorimetry to sensitively determine GSH. To obtain the maximum enrichment yield, the type of eluent, its volume, and the extraction time were carefully optimized.

Effect of type of the eluent

Choosing the most suitable eluent was important for SPE. Desorption of the analyte from the SPE column was investigated using different kinds of organic solvents including acetone, methanol, acetonitrile, and ethanol. The experimental results show that the desorption ability of acetonitrile and acetone was better than that of methanol and ethanol (Fig. 4*a*). However, boiling point and toxicity of acetone were lower than that of acetonitrile, and the time of extraction process was shortened with acetone. Therefore, acetone was selected for the elution of analytes from the SPE column.

Effect of the volume of the eluent

During a SPE procedure, the volume of eluent is an essential factor that can affect the enrichment performance. The effect of acetone volume was evaluated in the range of 200–500 μL. As shown in Fig. 4*b*, the fluorescence intensity of the derivative increased along with acetone volume in the range of 200–300 μL and then remained constant when the volume was continuously enhanced. Therefore, 300 μL of acetone was selected for further study.

Effect of extraction time

SPE is a type of equilibrium extraction, and the optimal extraction efficiency is achieved when equilibrium is established. Hence, extraction time is one of the most important parameters in the extraction process, which is regarded as the interval time between entering sample solutions and

Table 1. Comparison of the characters of different reagents.

Reagents	Derivatization time (min)	Derivatization temp. (°C)	$\lambda_{ex}/\lambda_{em}$	Derivative photostability	Ref.
TMPAB-I	20	45	500/510	Not given	13
TMPAB-*o*-M	5	37	507/520	90 min	15
mBBr	40	60	390/470	120 min	18
SBD-BF	30	25	385/515	Room temperature, stable for 90 min	22
MCB	10	Not given	370/478	6–8 h	23
FM	15	37	345/400	1 week at 0 °C in the dark	24
MMPB	25	35	299/355	3 h	25
BODIPY Fl-C_1-IA	35	35	360/510	Room temperature, 24 h	This work

Note: λ_{ex}, excitation wavelength; λ_{em}, emission wavelength; SBD-BF, 5-bromo-7-fluorobenzo-2-oxa-1,3-diazole-4-sulphonate; TMPAB-I, 1,3,5,7-tetramethyl-8-phenyl-(4-iodoacetamido)difluoroboradiaza-*s*-indacene; MCB, monochlorobimane; FM, fluorescein-5-maleimide; TMPAB-*o*-M, 1,3,5,7-tetramethyl-8-phenyl-(2-maleimide)-difluoroboradiaza-*s*-indacene; MMPB, 5-maleimidyl-2-(*m*-methylphenyl)benzoxazole; mBBr, monobromobimane; and BODIPY Fl-C_1-IA, *N*-(4,4-difluoro-5,7-dimethyl-4-bora-3a,4a-diaza-*s*-indacene-3-yl)methyl)iodoacetamide.

Fig. 3. Optimization of derivatization conditions. (*a*) Buffer pH. (*b*) The volume of buffer. (*c*) Derivatization reagent concentration. (*d*) Reaction temperature. (*e*) Reaction time. H_3BO_3–KCl–Na_2CO_3 (■), KH_2PO_4–$Na_2B_4O_7$ (●), $Na_2B_4O_7$–H_3BO_3–KCl (▲).

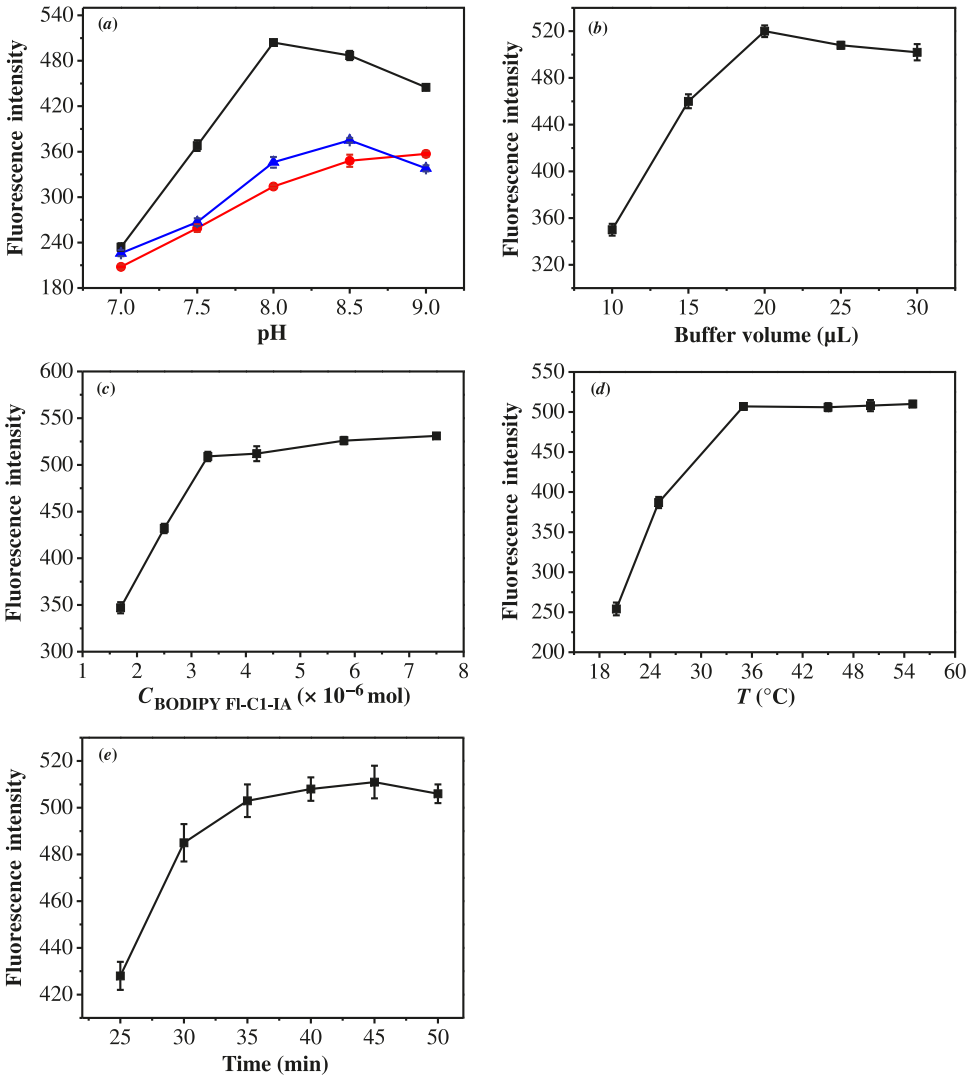

Can. J. Chem. Downloaded from www.nrcresearchpress.com by Xi'an Jiaotong University on 09/19/12
For personal use only.

Can. J. Chem. Downloaded from www.nrcresearchpress.com by Xi'an Jiaotong University on 09/19/12
For personal use only.

Fig. 4. Optimization of extraction conditions. (*a*) The type of eluent. (*b*) Acetone volume. (*c*) Extraction time. Conditions: thiol concentration: 6.7×10^{-8} mol/L.

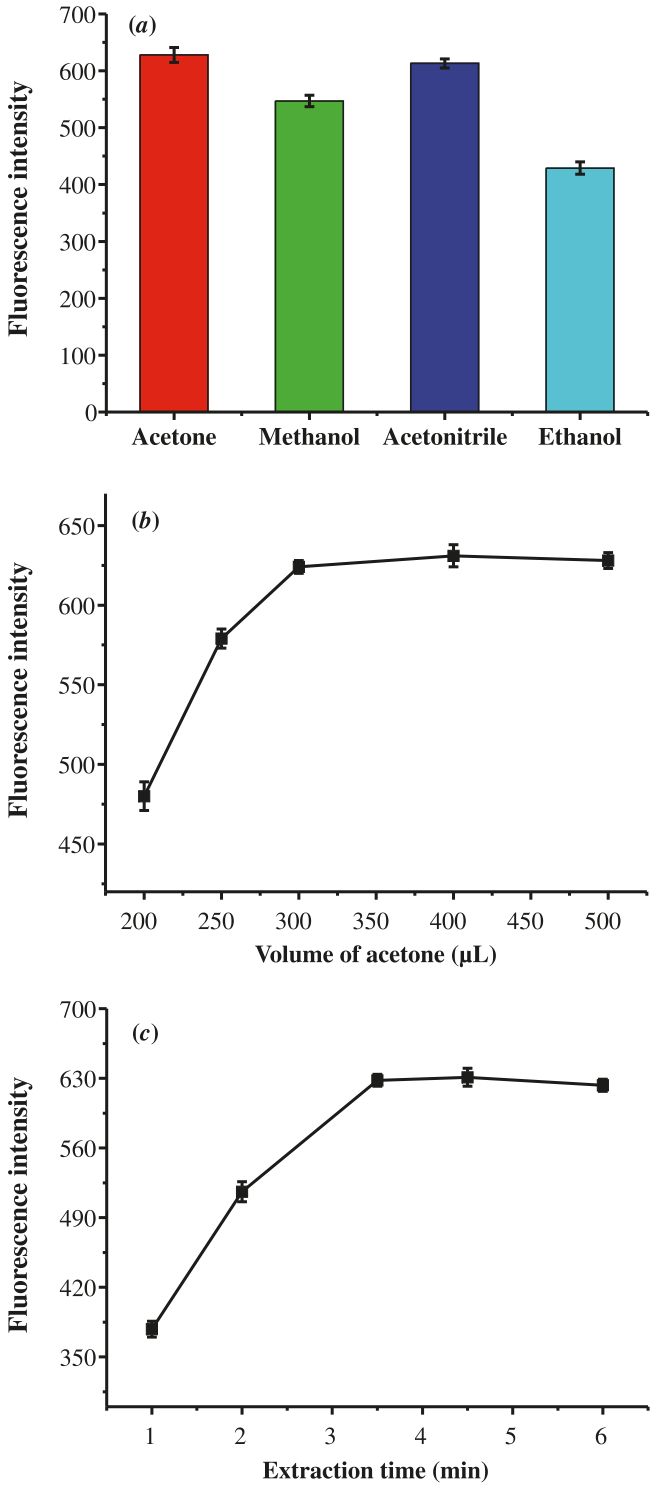

before washing. The effect of extraction time on extraction efficiency was researched in the range of 1–6 min (Fig. 4*c*). The fluorescence intensity of the derivative increased along with extraction time in the range of 1–3.5 min and then remained constant when the time was continuously lengthened. Thus, 3.5 min was selected as the extraction time.

Table 2. Effect of interfering substances on the relative fluorescence intensity ($C_{GSH} = 6.8 \times 10^{-8}$ mol L^{-1} and $C_{BODIPY\ Fl\text{-}C1\text{-}IA} = 1.7 \times 10^{-7}$ mol L^{-1}).

Interfering substances	Mole ratio (ion or amino acid : GSH)	Change in fluorescence intensity (%)
K^+	100	–2.6
Na^+	200	1.7
Ag^+	30	–4.7
NH_4^+	80	–2.4
Mn^{2+}	100	2.1
Ba^{2+}	120	–1.9
Co^{2+}	80	–3.4
Cu^{2+}	300	1.3
Ni^{2+}	50	–3.5
Pb^{2+}	8	–4.1
Zn^{2+}	8	–1.6
Ca^{2+}	100	–3.4
Sr^{2+}	10	–2.8
Cr^{3+}	15	–3.1
Fe^{3+}	60	–2.7
F^-	80	–3.2
Cl^-	100	–2.6
NO_3^-	200	–3.7
CH_3COO^-	50	–3.1
CO_3^{2-}	30	–4.4
SO_4^{2-}	150	–3.8
Glycine	500	–1.9
Glutamic acid	100	–3.7
Alanine	80	–4.2
Tryptophan	100	–2.6
Cysteine	1	4.5
L-Ascorbic acid	80	2.8

Note: GSH, L-γ-glutamyl-L-cysteineglycine; BODIPY Fl-C_1-IA, *N*-(4,4-difluoro-5,7-dimethyl-4-bora-3a,4a-diaza-*s*-indacene-3-yl)methyl)iodoacetamide.

Interference

Under the above selective conditions, the effects of some coexisting substances on the determination of GSH (6.7×10^{-8} mol/L) were investigated. The results are shown in Table 2 (relative error ≤±5%). The interference study of common metal ions and inorganic anions existing at high levels showed that the presence of these ions had a negligible interference to the determination. This indicates that the proposed method has good selectivity.

Analytical curve, sensitivity, and precision

Under optimum conditions, a calibration graph was constructed. Table 3 shows the analytical characteristics of the method. The calibration graph was linear between 1 and 200 nmol/L, with a correlation coefficient of 0.996. The limit of detection, calculated as three times the standard deviation (SD) of the blank signal, was 0.05 nmol/L for the preconcentration sample solution. The relative SD (RSD) resulting from the analysis of six replicates was 3.9%. These values were better than that for the spectrofluorimetry without SPE procedure in water (Table 3).

Table 3. Analytical characteristics of the method.

Analytical parameters	Without preconcentration	With preconcentration
Linear range (nmol/L)	60–7000	1–200
Regression equation[a]	$Y = 0.8736X + 10.439$	$Y = 3.3601X + 132.06$
Detection limit[b] (nmol/L)	4	0.05
Correlation coefficient	0.992	0.996
Relative RSD	2.4	3.9

Note: RSD, relative standard deviation.

[a]X is the concentration of the mercapto compounds (nmol/L) and Y is the fluorescence intensity of the mercapto compound derivatives.

[b]Calculated as three times the SD of the blank signal.

Table 4. Analytical results for the samples.

Samples	GSH added (μmol/L)	GSH found (μmol/L)	Recovery (%)	RSD (%)
Tap water	0	0		
	0.4	0.43	107.5	3.6
	2	1.94	97	4.9
	20	20.18	100.9	2.7
Shi River water	0	0		
	0.4	0.38	95	5.2
	2	1.85	92.5	3.8
	20	17.64	88.2	2.6
Rain water	0	0		
	0.4	0.35	87.5	5.5
	2	2.23	111.5	3.7
	20	20.69	103.4	3.2

Note: GSH, L-γ-glutamyl-L-cysteineglycine; RSD, relative standard deviation.

Can. J. Chem. Downloaded from www.nrcresearchpress.com by Xi'an Jiaotong University on 09/19/12
For personal use only.

Sample analysis

The proposed method was applied for the determination of GSH in water samples. GSH concentrations in different water samples were measured according to the methods mentioned in the General procedure section. The results are summarized in Table 4. No GSH was found in three water samples. The accuracy of the sample analysis was validated by spiking a known amount of standard GSH with the sample and calculating its recovery. Recoveries were obtained from 87.5% to 111.5% with a satisfactory RSD of 2.6%–5.5%, which verifyed the feasibility and reliability of the present method.

Conclusions

The proposed method outlined the successful development and application of SPE combed with spectrofluorimetry for the sensitive determination of GSH in environmental water samples. It permited the analysis and quantification of GSH at nmol/L levels in different water samples with a simple and low-cost spectrofluorimetric method. This methodology offers a simple, rapid, sensitive, and inexpensive alternative to other separation–preconcentration techniques with the concomitant benefits from the use of SPE (safety, cost, high separation yield, versatility, and nonpolluting aspect). The proposed method gave low LOD, good RSD, and recovery of the GSH from its initial matrix without previous treatment. The method was verified with real samples and applied satisfactory to the determination of GSH in different water samples.

Acknowledgments

This work was supported by the National Natural Science Foundation of China (20805040), the Program for Science &Technology Innovation Talents in Universities of Henan Province (2010HASTIT025), and the Excellent Youth Foundation of the He'nan Scientific Committee (104100510020).

References

(1) Wang, L. Y.; Wang, L.; Xia, T. T.; Bian, G. R.; Dong, L.; Tang, Z. X.; Wang, F. *Spectrochim. Acta A Mol. Biomol. Spectrosc.* **2005** *61* (11–12), 2533. doi:10.1016/j.saa.2004.07.041.

(2) Ahner, B. A.; Wei, L.; Oleson, J. R.; Ogura, N. *Mar. Ecol. Prog. Ser.* **2002** *232*, 93. doi:10.3354/meps232093.

(3) Noctor, G.; Foyer, C. H. *Annu. Rev. Plant Physiol. Plant Mol. Biol.* **1998** *49* (1), 249. doi:10.1146/annurev.arplant.49.1.249.

(4) Sen, C. K.; Packer, L. *Am. J. Clin. Nutr.* **2000** *72* (2), 653.

(5) Głowacki, R.; Bald, E. *J. Chromatogr. B Analyt. Technol. Biomed. Life Sci.* **2009** *877* (28), 3400. doi:10.1016/j.jchromb.2009.06.012.

(6) Zhao, P.; Slattery, J. T. *Drug Metab. Dispos.* **2002** *30* (12), 1413. doi:10.1124/dmd.30.12.1413.

(7) Zhao, P.; Kalhorn, T. F.; Slattery, J. T. *Hepatology* **2002** *36* (2), 326. doi:10.1053/jhep.2002.34943.

(8) DeLeve, L. D. *Hepatology* **1996** *24* (4), 830. doi:10.1002/hep.510240414.

(9) Lieber, C. S. *Alcohol* **2004** *34* (1), 9. doi:10.1016/j.alcohol.2004.07.008.

(10) Santangelo, F.; Witko-Sarsat, V.; Drüeke, T.; Descamps-Latscha,

B. *Nephrol. Dial. Transplant.* **2004** *19* (8), 1951. doi:10.1093/ndt/gfh266.
(11) Hsu, M.; Srinivas, B.; Kumar, J.; Subramanian, R.; Andersen, J. *J. Neurochem.* **2005** *92* (5), 1091. doi:10.1111/j.1471-4159.2004.02929.x.
(12) Griffith, O. W. *Anal. Biochem.* **1980** *106* (1), 207. doi:10.1016/0003-2697(80)90139-6.
(13) Guo, X. F.; Wang, H.; Guo, Y. H.; Zhang, Z. X.; Zhang, H. S. *J. Chromatogr. A* **2009** *1216* (18), 3874. doi:10.1016/j.chroma.2009.02.083.
(14) Sakhi, A. K.; Russnes, K. M.; Smeland, S.; Blomhoff, R.; Gundersen, T. E. *J. Chromatogr. A* **2006** *1104* (1–2), 179. doi:10.1016/j.chroma.2005.11.129.
(15) Guo, X. F.; Wang, H.; Guo, Y. H.; Zhang, H. S. *Anal. Chim. Acta* **2009** *633* (1), 71. doi:10.1016/j.aca.2008.11.028.
(16) Kosower, N. S.; Kosower, E. M.; Newton, G. L.; Ranney, H. M. *Proc. Natl. Acad. Sci. U.S.A.* **1979** *76* (7), 3382. doi:10.1073/pnas.76.7.3382.
(17) Langmuir, M. E.; Yang, J. R.; Moussa, A. M.; Laura, R.; LeCompte, K. A. *Tetrahedron Lett.* **1995** *36* (23), 3989. doi:10.1016/0040-4039(95)00695-9.
(18) Tang, D.; Shafer, M. M.; Vang, K.; Karner, D. A.; Armstrong, D. E. *J. Chromatogr. A* **2003** *998* (1–2), 31. doi:10.1016/S0021-9673(03)00639-3.
(19) Sánchez-Rojas, F.; Bosch-Ojeda, C.; Cano-Pavón, J. M. *Chromatographia* **2009** *69* (Suppl. 1), 79. doi:10.1365/s10337-008-0687-2.
(20) Jiang, T. H.; Zhao, L. X.; Chu, B. L.; Feng, Q. Z.; Yan, W.; Lin, J. M. *Talanta* **2009** *78* (2), 442. doi:10.1016/j.talanta.2008.11.047.
(21) Pan, M. F.; Wang, J. P.; Fang, G. Z.; Tang, W. W.; Wang, S. *J. Chromatogr. B Analyt. Technol. Biomed. Life Sci.* **2010** *878* (19), 1531. doi:10.1016/j.jchromb.2010.04.004.
(22) Cevasco, G.; Piatek, A. M.; Scapolla, C.; Thea, S. *J. Chromatogr. A* **2010** *1217* (14), 2158. doi:10.1016/j.chroma.2010.02.012.
(23) Raththagala, M.; Root, P. D.; Spence, D. M. *Anal. Chem.* **2006** *78* (24), 8556. doi:10.1021/ac061163u.
(24) Chassaing, C.; Gonin, J.; Wilcox, C. S.; Wainer, I. W. *J. Chromatogr. B Analyt. Technol. Biomed. Life Sci.* **1999** *735* (2), 219. doi:10.1016/S0378-4347(99)00425-9.
(25) Liang, S. C.; Wang, H.; Zhang, Z. M.; Zhang, X.; Zhang, H. S. *Anal. Chim. Acta* **2002** *451* (2), 211. doi:10.1016/S0003-2670(01)01409-X.

Can. J. Chem. Downloaded from www.nrcresearchpress.com by Xi'an Jiaotong University on 09/19/12
For personal use only.

Computer study of absorption of oxygen and ozone molecules by water clusters with Cl^- and Br^-

Alexander Y. Galashev

Can. J. Chem. Downloaded from www.nrcresearchpress.com by Xi'an Jiaotong University on 09/19/12
For personal use only.

Abstract: Infrared absorption and Raman spectra were calculated by using the molecular dynamics method for water clusters with chlorine and bromine ions in a medium of water and either ozone or oxygen molecules. The intensity of IR absorption spectra of clusters with absorbed oxygen increased and that of clusters with absorbed ozone decreased as the number of chlorine ions grew. When Br^- were present in the system the inverse behaviour was observed. An increase in the number of ions weakened the intensity of the Raman spectra when either oxygen or ozone was absorbed; for ozone this weakening was more noticeable. A stronger reduction of the integrated intensity of the Raman spectrum with an increase in the number of Br^- was observed in the presence of ozone molecules in the system. Cl^- ions caused an amplification of the emission power of the IR radiation for both systems in the presence of oxygen and ozone, and Br^- strengthened the emission of IR radiation for systems containing ozone, and weakened it for systems with oxygen molecules.

Key words: absorption, chlorine and bromine ions, IR and Raman spectra, oxygen, ozone, water clusters.

Résumé : Faisant appel à la méthode de la dynamique moléculaire, on a calculé les spectres d'absorption IR et Raman d'agrégats d'eau avec des ions chlorure et bromure dans un milieu aqueux contenant des molécules d'ozone ou d'oxygène. L'intensité des spectres d'absorption IR des agrégats comportant de l'oxygène absorbé augmente alors que celle des agrégats comportant de l'ozone absorbé diminue avec une augmentation du nombre d'ions chlorures. Dans les systèmes comportant des ions bromures, on a observé un comportement inverse de cette amplitude. En présence d'oxygène ou d'ozone absorbé, une augmentation du nombre d'ions chlorures diminue l'intensité des spectres Raman; avec l'ozone, cette diminution est plus importante. Une réduction encore plus forte de l'intensité intégrée du spectre Raman est observée avec une augmentation du nombre d'ions bromures, en présence de molécules d'ozone dans le système. Les ions chlorures provoquent une amplification de la puissance de l'émission du rayonnement IR pour les deux systèmes en présence d'oxygène ou d'ozone et les ions bromures augmentent l'émission du rayonnement IR des systèmes contenant d'ozone alors que les molécules d'oxygène l'affaiblissent.

Mots-clés : absorption, ions chlorures et bromures, spectres IR et Raman, oxygène, ozone, agrégats d'eau.

[Traduit par la Rédaction]

Introduction

The stratospheric ozone (O_3) layer contains 90% of the atmosphere's ozone and thus is responsible for the majority of the absorption of solar UV radiation. Halogen atoms are released by the degradation of long-lived halocarbon species (CH_3Cl, $CFCl_3$, CH_3Br, etc.), which are emitted either naturally or anthropogenically in the troposphere and then transported into the stratosphere. Halogen atoms (X = F, Cl, Br, or I), which are released in the degradation processes, react quickly with O_3 to form halogen oxides. In addition, halogen atoms can react with O_2 by association reactions to form halogen peroxide radicals. These radicals are unstable and dissociate by the reverse of their formation reaction, therefore, under atmospheric conditions the XO_2 species exist in equilibrium with X and O_2. The stability of XO_2 decreases in the series F > Cl > Br > I. One of the main causes of formation of the ozone hole is the increase in stratospheric chlorine and bromine levels because of the release of man-made chlorofluorocarbons (CFCs) such as CF_3Cl and CF_2Cl_2. The ClO dimer plays a major part in the catalytic destruction of ozone occurring in the polar lower stratosphere during wintertime, which leads to the formation of the ozone hole over Antarctica. On the other hand, BrO is lost by BrCl production. The behaviour of halogen oxides in the stratosphere is strongly influenced by the chemistry of temporary reservoir species containing chlorine and bromine. The combined Br–Cl catalytic cycles are very efficient in depleting ozone, and can therefore cause equal or even larger ozone destruction than chlorine alone in the lower stratosphere. Although there are significant human sources of Br, the contemporary abundance of total stratospheric Br is only ~0.5% of that of Cl.[1] Owing to the much shorter atmospheric lifetimes of iodine-containing compounds (e.g., CH_3I emitted from the oceans) compared with

Received 1 May 2010. Accepted 7 December 2010. Published on the NRC Research Press Web site at canjchem.nrc.ca on 28 March 2011.

A.Y. Galashev. Institute of Industrial Ecology, Ural Division, Russian Academy of Sciences, Sofia Kovalevskaya Str, 20a, GSP-594, Yekaterinburg 620219, Russia (e-mail: galashev@ecko.uran.ru).

Can. J. Chem. Downloaded from www.nrcresearchpress.com by Xi'an Jiaotong University on 09/19/12
For personal use only.

their Cl^-- and Br^--containing analogues, iodine does not reach the stratosphere in significant quantities.

In the chemistry of atmospheric particles, halogen activation, which describes the liberation of halogen containing components from sea salt particles, must be considered. These components undergo subsequent photolysis to release exceedingly reactive Cl and Br atoms. Photochemical reactions in clouds occur in the liquid phase with the participation of $HO^\bullet$ and $HO_2^\bullet$ radicals and other oxidizing components (H_2O_2 or O_3) supplied from the gas phase. Dense small aggregates of molecules are conventionally called clusters. Water clusters are present in clouds and can also exist in a cloudless atmosphere.[2] Atoms and molecules in the atmosphere experience ionization from the action of cosmic rays, from the radiation of radioactive rocks, and from radon in the air itself. The ionization of molecules releases electrons. Chlorine and bromine atoms easily attract free electrons to produce negatively charged ions. Chlorine or bromine ions interact with ozone and split it into oxygen molecules and atoms (possibly into three oxygen atoms). This reaction is facilitated by the presence of water. In other words, the reaction has its highest rate on the surfaces of water clusters. Fast chlorine or bromine ions are the first to reach the surface of water clusters.

The purpose of this work was to study the interaction of halide-containing electrically charged water clusters with ozone and oxygen molecules, and to determine the character of the changes in the dielectric properties of these aggregates that occur as a result of such interactions.

Model

Water is among the most studied of chemicals, owing in part to its ubiquity and its necessity for all life. In addition to these "natural" reasons, water is an interesting compound because it has unique physical properties and is a model hydrogen-bonded liquid. Most of the available water interaction potentials are parameterized to reproduce the thermodynamic and structural properties of bulk water. The polarizable model allows us to examine the changes in the dipole moment of the individual water molecules as a function of their environment. This can provide insight into many body effects in water clusters at a molecular level. Dang and Chang[3] developed a polarizable potential model for water that behaves reasonably well with changes in the environment (i.e., for clusters, liquid, and liquid–vapor). The simulation of water clusters was performed using a modified transferable intermolecular potential 4 points (TIP4P) interaction potential for water and the rigid four-centre model of the H_2O molecule.[4] The modification of the interaction potential for water by Dang and Chang[3] concerned variation of the parameters of the Lennard–Jones part of the potential and localization of negative charge. As a result, the value of the permanent dipole moment for the water molecule is taken to be equal to its experimentally obtained value of 1.848 D. The geometry of this molecule corresponds to the experimentally obtained parameters of the molecule in the gas phase: r_{OH} = 0.09572 nm and angle HOH = 104.5°.[5] Fixed charges (q_H = 0.519e and q_M = –1.038e, where e is electronic charge) are assigned to H atoms and to a point M lying on the bisector of angle HOH at a distance of 0.0215 nm from the oxygen atom. The values of the charges and the position of point M are selected so as to reproduce the experimentally obtained values of the dipole and quadrupole moments[6,7] as well as the ab initio calculated energy of the dimer and the typical distances in the dimer.[8]

The total interaction energy of the system can be written as

$$[1] \qquad U_{tot} = U_{pair} + U_{pol}$$

where the pairwise additive part of the potential is the sum of the Lennard–Jones and Coulomb interactions,

$$[2] \qquad U_{pair} = \sum_i \sum_j \left\{ 4\varepsilon^{(LJ)} \left[\left(\frac{\sigma_{ij}^{(LJ)}}{r_{ij}} \right)^{12} - \left(\frac{\sigma_{ij}^{(LJ)}}{r_{ij}} \right)^{6} \right] + \frac{q_i q_j}{r_{ij}} \right\}$$

Here r_{ij} is the distance between sites i and j, q is the charge, and $\sigma^{(LJ)}$ and $\varepsilon^{(LJ)}$ are the Lennard–Jones parameters.

The nonadditive polarization energy is given by

$$[3] \qquad U_{pol} = -\frac{1}{2} \sum_i \mathbf{d}_i \cdot \mathbf{E}_i$$

where $\mathbf{d}_i$ is the induced dipole moment at the centre of mass of the ith molecule, $\mathbf{E}_i$ is the total electric field at this centre, and $\mathbf{E}_i^0$ is the electric field at site i produced by the fixed charges in the system,

$$[4] \qquad \mathbf{E}_i^0 = \sum_{j \neq i} \frac{q_j \mathbf{r}_{ij}}{r_{ij}^3}$$

where $\mathbf{r}_{ij}$ is the vector from the centre of mass of the jth molecule to the centre of mass of the ith molecule,

$$[5] \qquad \mathbf{d}_i = \alpha_i \mathbf{E}_i$$

where α_i is the atomic polarizability and

$$[6] \qquad \mathbf{E}_i = \mathbf{E}_i^0 + \sum_{j \neq i} \mathbf{T}_{ij} \cdot d_j$$

where $\mathbf{T}_{ij}$ is the dipole tensor,

$$[7] \qquad \mathbf{T}_{ij} = \frac{1}{|r_{ij}|^3} (3\hat{\mathbf{r}}_{ij}\hat{\mathbf{r}}_{ij} - \mathbf{1})$$

where $\hat{\mathbf{r}}_{ij} = \mathbf{r}_{ij}/r_{ij}$ is the unit vector and $\mathbf{1}$ is the 3 × 3 unit tensor.

The stabilization of short-range order in water clusters is largely attained because of the short-range Lennard–Jones potential with the centre of interaction ascribed to the oxygen atom. Related to point M, in addition to the electric charge, is the polarizability, which is required for the description of nonadditive polarization energy. The standard iterative procedure is used at every time step for calculating induced dipole moments.[3] The accuracy of determination of $\mathbf{d}_i$ was in the range 1×10^{-5} to 1×10^{-4} D.

The additive part of the oxygen–oxygen and oxygen–water interactions is described by an atom–atom potential calculated by the Gordon–Kim approximation with the application of the spherical average of electronic densities,[9,10]

Can. J. Chem. Downloaded from www.nrcresearchpress.com by Xi'an Jiaotong University on 09/19/12
For personal use only.

$$[8] \qquad \Phi(r_{ij}) = b_i b_j \exp[-(c_i + c_j)r_{ij}] - a_i a_j r_{ij}^{-6} + \frac{q_i q_j}{r_{ij}}$$

where the parameters a_i, b_i, and c_i of the potential describing these interactions were borrowed from Spackman.[9,10] The $q_+ = 0.19e$ positive charge was set on the central atom of the O_3 molecule and the $q_- = -0.095e$ negative charge on each of its side atoms.[11] The O_3 molecule was electrically neutral as a whole. Atoms in the O_2 molecule had no electric charges.

The Coulomb interaction of Cl^- and Br^- ions with water was determined by their electric charge ($q = -1e$, where e is the elementary charge unit). The ion–H_2O non-Coulomb interaction was included as a Lennard–Jones Cl^-–O or Br^-–O interaction with the parameters from refs. 11 and 12. We also considered atom–atom interaction between Cl^- or Br^- ions described by eq. [8] with the parameters from ref. 10. The nonadditive contribution to interactions between water, oxygen, ozone, chlorine, and bromine was caused by polarization and was taken into account in calculations according to eqs. [3]–[7].

Here, we consider flexible models of molecules. Flexibility was created using the procedure developed in terms of Hamilton dynamics in refs. 13 and 14. Let us consider a diatomic molecule and let atoms a and b in it be separated by the distance

$$[9] \qquad R = \| \mathbf{r}_a - \mathbf{r}_b \|$$

where $\mathbf{r}_a$ and $\mathbf{r}_b$ are the vectors that determine the positions of the atoms. Let $\mathbf{v}_a$ and $\mathbf{v}_b$ be the corresponding velocities and let the reduced mass have the form

$$[10] \qquad \mu = \frac{m_a m_b}{m_a + m_b}$$

The size of the molecule consisting of atoms a and b is determined by the equality of the total potential force $\mathbf{f}(\mathbf{R}) = -\frac{\partial \mathbf{r}}{\partial R} \bigtriangledown \Phi(\mathbf{r})$ to the centrifugal force $-\mu R\omega^2$, that is,

$$[11] \qquad -\mu R\omega^2 - \mathbf{f}(\mathbf{r})\frac{\partial \mathbf{r}}{\partial R} = 0$$

where vector $\mathbf{R} = \mathbf{r}_a - \mathbf{r}_b$, $\mathbf{r}$ is the vector determining distance from atoms a or b up to the external centre interacting with them, and $\omega = \| \mathbf{v}_a - \mathbf{v}_b \| /R$ is the angular velocity. The minimization of contributions to the potential energy U of each generalized coordinate yields

$$[12] \qquad \frac{\partial}{\partial q_i} U(\mathbf{r}, \mathbf{v}) = \frac{\partial}{\partial R_i}\left[\frac{1}{2}\mu_i R_i^2 \omega_i^2 + \Phi(\mathbf{r})\right] = 0$$

This method is applicable to molecules with arbitrary compositions.[15] The use of the flexible model of molecules allowed us to expand the range of frequencies under study.

The simulation of the interaction of $(Cl^-)_i(H_2O)_{50-i}$ or $(Br^-)_i(H_2O)_{50-i}$ clusters with a gas medium containing iH_2O molecules and six O_2 or O_3 molecules began with creating the configuration of the equilibrium cluster of water $(H_2O)_{50}$ with the kinetic energy corresponding to 250 K in the molecular dynamics calculations. The positions of Cl^- or Br^- in the cluster were determined using a system of coordinates fixed at the centre of mass of the cluster. The cluster was approximated by a sphere and water molecules situated most closely to the coordinate axes from this sphere were found. These molecules (their number was from one to six) were displaced outside along the coordinate axes through distances of 0.6–0.7 nm from the former positions of their centres of mass, into which Cl^- or Br^- were introduced. The number of ions equaled the number of displaced molecules. The interaction of the newly formed $(Cl^-)_i(H_2O)_{50-i}$ or $(Br^-)_i(H_2O)_{50-i}$ cluster with water and O_2 or O_3 molecules was studied in an ensemble with an external thermostat[16] at 250 K. The cutoff radius for intermolecular interactions was 0.9 nm in our model. Six O_2 or O_3 molecules were situated predominantly on the lower side of the cluster. The fairly compact arrangement of these molecules facilitated studies of their influence on the behavior of Cl^- or Br^-. The time instant at which ions were incorporated into the water cluster and O_2 (or O_3) molecules approached this aggregate was taken as time $t = 0$. The calculation of spectral characteristics started with time instant $10^5\Delta t$ (1 ps), where Δt is the integration time step, and the complete duration of the calculation was $2.5 \times 10^6 \Delta t$ time steps.

The Gear method[17] of the fourth order was used for determining the trajectories of the centres of mass of the molecules. The integration time step was 10^{-17} s. The Rodriguez–Hamilton parameters[18] were used to derive the analytical solution of equations of motion for molecular rotation, and the scheme of integration of the equations of motion in the presence of rotations corresponded to the approach suggested by Sonnenschein.[19]

Dielectric propeties

It was assumed that a cluster containing i molecules of oxygen or ozone and n molecules of water has the statistical weight

$$[13] \qquad W_{i,n} = \frac{N_{i,n}}{N_{i,\Sigma}} \quad i = 1, ..., n$$

where $N_{i,n}$ is the number of clusters with i molecules (ions) of impurity and n molecules of water per 1 cm^3 and $N_{i,\Sigma} = \sum_{i=1}^{n} N_{i,n}$. The value of $N_{i,n}$ was estimated as follows. We considered the case of the scattering of nonpolarized light where the molecular free path l is much less than the wavelength of light λ. The extinction (attenuation) coefficient η of the incident beam may be determined on the one hand by the Rayleigh formula[20] and on the other hand in terms of the scattering coefficient ρ[21] in the approximation of the scattering at an angle of 90°. In view of the fact that η is $\alpha + \rho$, where α is the absorbance, we have

$$[14] \qquad N_{i,n} = \frac{2\omega^4}{3\pi c^4}\frac{(\sqrt{\varepsilon} - 1)^2}{\alpha}\left(1 - \frac{3}{16\pi}\right)$$

Here c is the velocity of light, ε is the permittivity of the medium, and ω is the incident wave frequency. The spectral characteristics of the systems were calculated in view of the adopted statistical weights $W_{i,n}$. The procedure of forming the systems of clusters provided for the uniform distribution of these formations and is valid at a low concentration of clusters, which means that they do not interact with one

Can. J. Chem. Downloaded from www.nrcresearchpress.com by Xi'an Jiaotong University on 09/19/12
For personal use only.

another. The average value of the concentrations of the clusters of each type in the systems under investigation was 12–13 orders of magnitude lower than the Loschmidt number.

The total dipole moment of the cluster $\mathbf{d}_{cl}$ was calculated by the formula

$$[15] \qquad \mathbf{d}_{cl}(t) = q_+^{(k)} \sum_{i=1}^{N_{tot1}} \mathbf{r}_i(t) + q_-^{(k)} \sum_{j=1}^{N_{tot2}} \mathbf{r}_j(t)$$

where $\mathbf{r}_i(t)$ is the vector indicating the location of nucleus i or point M at the instant of time t, q is the electric charge located at the centre under consideration, the index k specifies the type of nucleus (or point M), the subscript + relates to the nucleus carrying a positive electric charge, the subscript – to the nucleus carrying a negative charge, and N_{tot1} and N_{tot2} are the numbers of positively and negatively charged nuclei in the cluster, respectively.

The permittivity $\varepsilon(\omega)$ as a function of frequency is given by the complex quantity $\varepsilon(\omega) = \varepsilon'(\omega) - i\varepsilon''(\omega)$ (where ε' is the real part and ε'' is the imaginary part of permittivity), which was determined using the equation[22,23]

$$[16] \qquad \frac{\varepsilon(\omega) - 1}{\varepsilon - 1} = -\int_0^\infty \exp(-i\omega t)\frac{\mathrm{d}F}{\mathrm{d}t}\mathrm{d}t = 1 - i\omega\int_0^\infty \exp(-i\omega t)F(t)\mathrm{d}t$$

where the function $F(t)$ is the normalized autocorrelation function of the total dipole moment of the cluster,

$$[17] \qquad F(t) = \frac{\langle \mathbf{d}_{cl}(t)\cdot\mathbf{d}_{cl}(0)\rangle}{\langle \mathbf{d}_{cl}^2\rangle}$$

The cross section of IR radiation absorption is given by

$$[18] \qquad \sigma(\omega) = \frac{2}{\varepsilon_v c\hbar n}\omega\tanh\left(\frac{\hbar\omega}{2kT}\right)\mathrm{Re}\int_0^\infty \mathrm{d}t e^{i\omega t}\langle \mathbf{d}_{cl}(t)\cdot\mathbf{d}_{cl}(0)\rangle$$

where ε_v is the permittivity of the vacuum, $\hbar = h/2\pi$, h is Planck's constant, and n is the refractive index.

The Raman and IR spectra of the clusters were calculated via the autocorrelation functions of polarizability and dipole moment, respectively. A polar molecule is characterized by a permanent (gas phase) dipole moment $\mathbf{d}_{i,0}$ and polarizability tensor $\boldsymbol{\alpha}_{i,0}$. Interaction with neighbouring molecules creates the induced dipole moment and polarizability of molecule i. Each model molecule was treated as a polarizable point dipole situated in the centre of mass of the molecule. The $\mathbf{d}_i$ dipole moment of molecule i and its polarizability α_i are related because of molecule interactions with the environment.[24]

$$[19] \qquad \mathbf{d}_i = \mathbf{d}_{i,0} + \boldsymbol{\alpha}_{i,0}\sum_{j\neq 1}\mathbf{T}_{ij}\mathbf{d}_j$$

$$[20] \qquad \boldsymbol{\alpha}_i = \boldsymbol{\alpha}_{i,0} + \boldsymbol{\alpha}_{i,0}\sum_{j\neq 1}\mathbf{T}_{ij}\boldsymbol{\alpha}_j$$

We used the anisotropic gas-phase polarizability tensor $\boldsymbol{\alpha}_{xx,yy,zz} = \{1.495, 1.626, 1.286\}$ Å^3 for the water molecule.[24] O_3 and O_2 molecules were characterized by the isotropic experimental polarizability values 2.85 and 0.793 Å^3, respectively.[25] The atomic polarizabilities for Cl^- (3.25 Å^3) and Br^- (3.1 Å^3) were taken from ref. 25.

Equations [19] and [20] for $\mathbf{d}_i$ and $\boldsymbol{\alpha}$ were solved by inverting the matrix and using the $\mathbf{d}_{i,0}$ and $\mathbf{a}_{i,0}$ values on the right-hand side.

For depolarized light, the Raman spectrum is given by the equation[24]

$$[21] \qquad J(\omega) = \frac{\omega}{(\omega_L - \omega)^4}(1 - \mathrm{e}^{-\hbar\omega/kT})\,\mathrm{Re}\int_0^\infty \mathrm{d}t e^{i\omega t}\langle \Pi_{xz}(t)\Pi_{xz}(0)\rangle$$

where

$$[22] \qquad \Pi(t) \equiv \sum_{j=1}^{N}[\boldsymbol{\alpha}_j(t) - \langle\boldsymbol{\alpha}_j\rangle]$$

where ω_L is the exciting laser frequency, Π_{xz} is the xz component of $\Pi(t)$, the x axis is directed along the molecular dipole, and xy is the molecular plane. Simulations were performed for ω_L = 19 436.3 cm^{-1} (the argon laser green line, λ = 514.5 nm).

In liquid water the interaction of Cl^- and Br^- with H_2O molecules is limited to the electrostatic attraction of water dipoles to anions. In a small water cluster Cl^- and Br^- experience mutual repulsion and cannot be held close to water molecules for long. We performed calculations for six $(Cl^-)_i(H_2O)_{50-i}$ + iH_2O + $6O_2$, systems and six $(Cl^-)_i(H_2O)_{50-i}$ + iH_2O + $6O_3$ systems, with i = 1–6. The same calculations were carried out for the corresponding systems containing Br^-. Systems with i = 1–6 are denoted by I–VI in the presence of oxygen and by VII–XII in the presence of ozone. We put one stroke at the number of the system containing Cl^- and two strokes at the system number including Br^-. The criterion for the addition of O_3 or O_2 molecules to a water cluster was the establishment of $r_{o-o} \leq$ 0.35 nm distances.

The frequency dispersion of permittivity defines the frequency dependence of dielectric loss $P(\omega)$ in accordance with the expression[21]

$$[23] \qquad P = \frac{\varepsilon'' < E^2 > \omega}{4\pi}$$

where $< E^2 >$ is the average value of the square of the electric field strength and ω is the frequency of the emitted electromagnetic wave.

Motions with a frequency of <1200 cm^{-1} correspond to the liberation of molecules and those with a frequency >1200 cm^{-1} largely describe intramolecular vibrations.[26]

Results and discussion

Chlorine-containing systems

Because of Coulomb repulsion from negatively charged oxygen ions and mutual repulsion, the Cl^- in $(Cl^-)_i(H_2O)_{50-i}$ clusters rushed to the outside of the cluster. The ions leaving a cluster pushed water molecules apart. This and the interaction with the environment molecules (H_2O and either O_2 or O_3) heated the $(Cl^-)_i(H_2O)_{50-i}$ + iH_2O + $6O_3$ (or $6O_2$) system.

Can. J. Chem. Downloaded from www.nrcresearchpress.com by Xi'an Jiaotong University on 09/19/12
For personal use only.

The strongest heating, to 311 K (at time $t \sim 3$ ps), was observed when the cluster of water with six chlorine atoms was surrounded by O_3 molecules. The algorithm that we used allowed for the decomposition of O_3 molecules with energies of 1.3 eV or higher. This energy is sufficient for splitting an ozone molecule surrounded by water molecules. However, in reality there was no decomposition of ozone. As a rule, in 2 ps, that is by the time that $t = 5$ ps, the system was cooled because of velocity scaling and reached its initial temperature of ~250 K. Two Cl^- leave the $(Cl^-)_6(H_2O)_{44}$ cluster in both O_2- and O_3-containing systems by the time $t = 1.2$ ps (Fig. 1). One of the Cl^- hit an O_2 molecule (Fig. 1A). In the same system with ozone, two ions directly interacted with O_3 molecules (one of these ions interacted with two O_3 molecules at once), one ion was "bound" to a water molecule, and one ion was almost free (Fig. 1B). By $t = 2.8$ ps all Cl^- ions had left the cluster and, conversely, O_3 molecules had approached it. Clusters with four and two Cl^- lost these ions in 2.8 and 2.2 ps, respectively. A similar interaction picture was observed when O_2 rather than O_3 molecules approached the cluster. The system was then free of ions in 2.8 ps (six Cl^-), 2.4 ps (four Cl^-), and 2.2 ps (two Cl^-).

The IR absorption spectra are determined by the behaviour of the autocorrelation function of the total $\mathbf{d}_{cl}$ of a cluster. When O_2 molecules without permanent dipole moments are added to a water cluster, they weakly influence the $\mathbf{d}_{cl}$ value determined by the aqueous component of the cluster. For this reason, the perturbation force introduced by Cl^- is approximately proportional to the number of ions (N_{Cl^-}). The integral intensities of the IR absorption spectra (I_{tot}s) therefore grow as N_{Cl^-} increases (Fig. 2A). The opposite situation arises if O_3 molecules are absorbed. When O_3 molecules, whose permanent dipole moment (0.12 D) is lower than that of water, are added to a cluster they create additional "beats" during the evolution of the $\mathbf{d}_{cl}$ value.

The action of Cl^- on the cluster strengthens these oscillations with different frequencies and phases. The larger the number of Cl^- in the cluster, the stronger the beats created by the O_3 molecules. As a result, the ability of the system to absorb IR radiation decreases (I_{tot} decreases) as the number of ions increases (Fig. 2B). The I_{tot} values for systems I′–VI′ increase nonmonotonically and those for systems VII′–XII′ decrease as the number of Cl^- grows. The I_{tot} ratios are 1:0.80:1.22:1.10:2.83:1.83 for systems I′–VI′ and 1:1.04:0.86:0.79:0.99:0.94 for systems VII′–XII′. In all cases the absorption peak is in the vicinity of the frequency $\omega = 960 \pm 20$ cm^{-1}. The main absorption of liquid water is observed at 690 cm^{-1},[27] and that of ozone–oxygen gas mixtures in the vicinity of 996 cm^{-1}.[28]

The Raman spectra of aqueous systems containing oxygen or ozone are differ more than the IR spectra (Fig. 3). The Rayleigh line at $\omega = 0$ is excluded from the spectra. The positions of the first peaks coincide (26 cm^{-1}), but there is no correspondence between the other peaks. In addition, the integral intensities of Raman spectra are noticeably higher with oxygen than with ozone in aqueous systems. The Raman spectrum for liquid water is characterized by low-frequency peaks at 60 cm^{-1} as well as by a peak near 170 cm^{-1}.[29] The peak at 60 cm^{-1} is caused by the bending of hydrogen bonds between water molecules; the peak at

Fig. 1. Configurations of systems $(Cl^-)_6(H_2O)_{44}$+ $6H_2O$+ 6X at time $t = 1.2$ ps. (A) X = O_2. (B) X = O_3. Coordinates of the molecules are presented in nm.

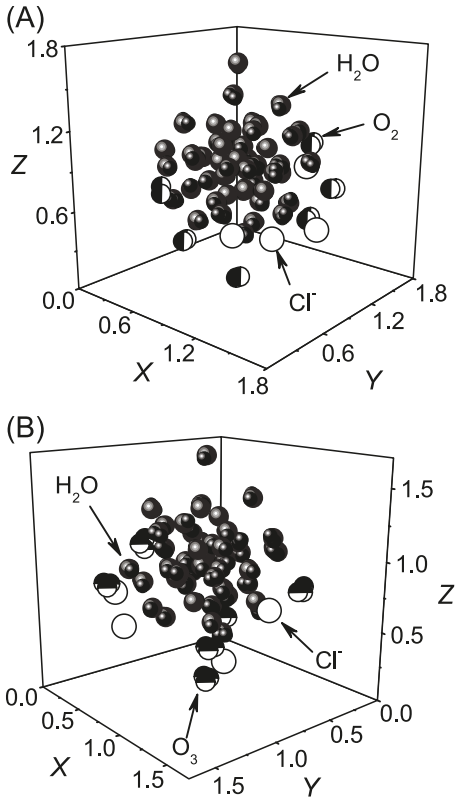

Fig. 2. IR absorption spectra of systems with (A) oxygen and (B) ozone: (1) systems I′ and VII′, (2) III′ and IX′, (3) VI′ and XII′, (4) $\sigma(\omega)$ function of bulk liquid water, experimental,[27] and (4′) experimental spectrum of an $O_2 + O_3$ mixture of gases.[28]

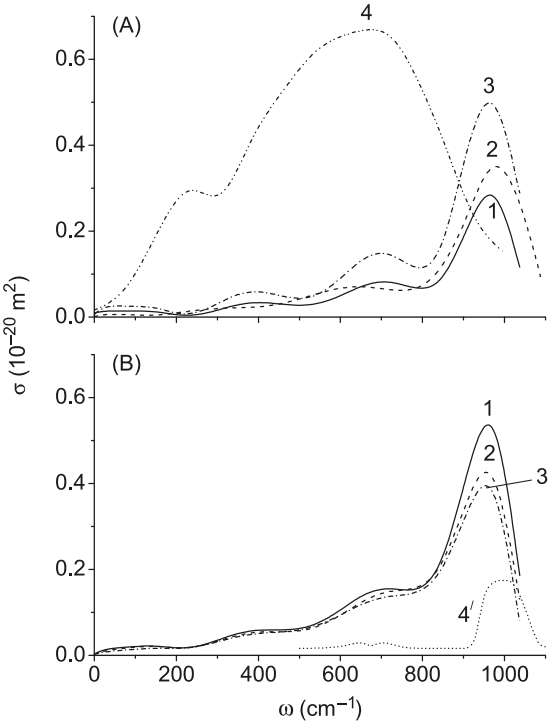

Can. J. Chem. Downloaded from www.nrcresearchpress.com by Xi'an Jiaotong University on 09/19/12
For personal use only.

Fig. 3. Raman spectra of systems with (A) oxygen and (B) ozone: (1) systems I′ and VII′, (2) III′ and IX′, (3) VI′ and XII′, (4) liquid water experimental,[29] and (4') a solution of OClO in water, experimental.[30]

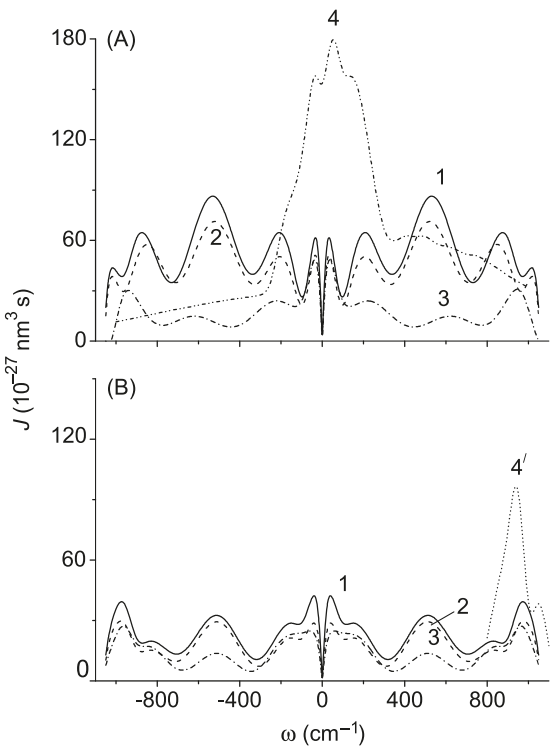

170 cm^{-1} appears because of bond stretching.[24] The position of the newly formed last peak at 950 cm^{-1} in the spectrum of the system with six O_2 molecules and six Cl^- is close to the position of the peak in the Raman spectrum of an aqueous solution of chlorine dioxide (945 cm^{-1}) determined experimentally.[30] The peak observed in femtosecond measurements of a solution of OClO in water was assigned to a fundamental transition to a new energy level with symmetrical dilatation of the OClO molecule.

A study of the photolysis of OClO in aqueous solution showed the possibility of separation of dielectric relaxation related to solvent (water) libration modes and mechanical solvation caused by low-frequency translational motion.[31] The mechanical response of a solvent is usually provided by one or two molecules in its first solvation shell. According to the computer simulation results, 80% of water solvation that follows OClO photoexcitation occurred during a 2×10^{-14} s time interval, whereas the remaining 20% of the response was diffusive in nature and could be observed on a picosecond time scale.[31]

Two characteristic times can also be identified for excitation related to the removal of Cl^- from a water cluster. A short time interval (~3 ps) corresponds to the excitation or interaction of ions with water and O_3 (or O_2) molecules. The dielectric relaxation interval is ~10 ps. During this time, the cluster "forgets" the value and direction of its dipole moment at time $t = 0$. The dissociation of the free O_3 molecule (in the vacuum) usually occurs when energy of 4–5.5 eV is imparted to it. Chlorine ions moving out of the cluster do not possess such energy. For this reason, we did not observe the decomposition of ozone molecules.

As the strength and duration of perturbation caused by the "bombardment" of molecules (H_2O and O_3 or O_2) by Cl^- increased, the integral intensity of the IR absorption spectrum decreased in the presence of ozone and increased with the addition of oxygen. The main absorption frequency remained constant. The Raman spectra substantially changed their shape and intensity when absorbed oxygen was replaced with ozone. Irrespective of the number of Cl^- initially contained in a water cluster and the molecules it absorbs (O_3 or O_2), the main Raman spectrum frequency remains unchanged. The absorption of ozone causes a more rapid decrease in the intensity of Raman spectra compared with the absorption of oxygen.

IR emission $P(\omega)$ spectra for oxygen-containing systems are characterized by the presence of a principal band in the $800 \le \omega \le 1000$ cm^{-1} frequency range (Fig. 4A). The integral intensity (I_{rad}) of the emission spectra of the systems under consideration increased significantly in the presence of Cl^-. The ratio of I_{rad} values for the $P(\omega)$ spectra of the $(O_2)_6(H_2O)_{50}$ cluster and systems II′, IV′, and VI′ is 1:1.45:1.09:1.70. The intensity of IR radiation emission by the $(O_3)_6(H_2O)_{50}$ cluster increases as a result of the action of chlorine ions (Fig. 4A). The ratio of I_{rad} in the $P(\omega)$ spectra of the $(O_3)_6(H_2O)_{50}$ cluster and systems VIII′, X′, and XII′ is 1:1.34:1.16:1.07. In the presence of ions, Cl^- displacement of the main maximum of the $P(\omega)$ spectrum in the area of low frequencies occurs more strongly for the systems containing oxygen. The increase in the number of Cl^- acting on the cluster results in a better resolution of the second and third peaks of the $P(\omega)$ spectrum.

Bromine-containing systems

Differences in the behaviour of Br^- in water clusters, when interacting with O_2 or O_3 molecules, can appear because of their greater weight than that of Cl^- (m_{Br}/m_{Cl} = 2.25). Configurations of the $6Br^-(H_2O)_{44}$+ $6H_2O$ + 6X cluster systems, obtained up to t = 25 ps, are shown in Fig. 5. Here, X refers to O_2 molecules (Fig. 5A) or O_3 molecules (Fig. 5B). In both cases six free water molecules have joined the $6Br^-(H_2O)_{44}$ cluster. Three of six Br^- have abandoned the cluster in the presence of oxygen in the system. One of these ions is depicted in the bottom part of Fig. 5A. Three O_2 molecules also evaporated with the left ions that left the cluster, while three other molecules of oxygen joined the cluster. The effect of the presence of ozone molecules produced a different result. All six O_3 molecules were adsorbed by cluster. Thus, six Br^- have left the cluster surface, but they have are not at such a great distance that we could consider them as evaporated ones. We consider ions or molecules for which non-Coulomb interaction with other molecules vanishes at a distance of 0.9 nm as evaporated ones. These types of ions or molecules do not come back to the cluster.

Frequencies and intensities of normal vibrations are defined by the weight and kind of atoms, the bonding force, and the spatial arrangement of the atoms (lengths and corners of the bond). Absorbed ions change the cluster structure and influence the intensity of the IR spectrum and to a smaller degree the intensity of the Raman spectrum.

Absorption IR spectra of some systems containing bromine are depicted in Fig. 6. The addition of six O_2 molecules

Can. J. Chem. Downloaded from www.nrcresearchpress.com by Xi'an Jiaotong University on 09/19/12
For personal use only.

Fig. 4. IR emission spectra of systems $(Cl^-)_i(H_2O)_{50-i} + iH_2O + 6X$ for (A) X = O_2 and (B) X = O_3. (1) i = 2, (2) i = 4, (3) i = 6, (4) the $P(\omega)$ function of the $(O_3)_6(H_2O)_{50}$ cluster.

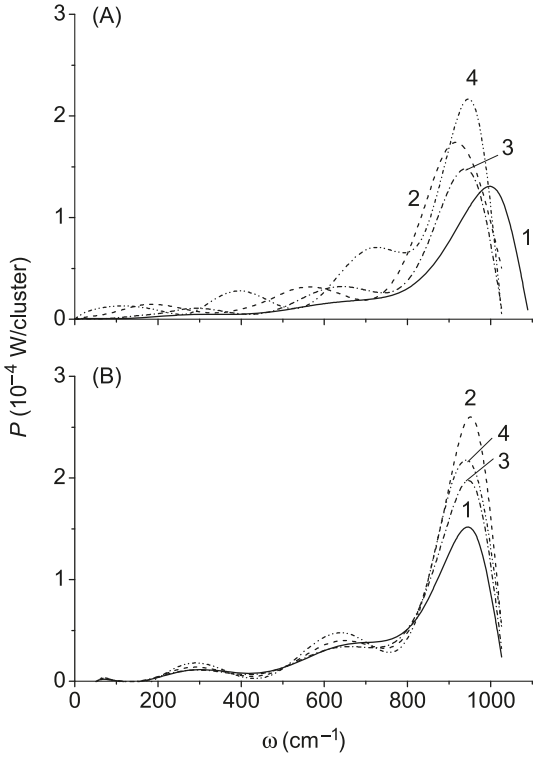

to the $(H_2O)_{50}$ cluster resulted in an increase of the integrated I_{tot} of IR radiation absorption by a factor of 2.3. However, if a water cluster initially absorbed Br^- ions (at the equivalent desorption of water molecules), then such an amplification of I_{tot} value was not observed, and the I_{tot} magnitude in the presence of four or more Br^- and the absorption of oxygen, decreases. The position of the main peak of the IR spectrum of the dispersed water system with molecular oxygen did not change, and the next highest intensity peak is deformed into a shoulder. The location of the basic peak shifted (by ~100 cm^{-1}) in the of low-frequency area with respect to the position of the main peak of an experimental IR spectrum of liquid bulk water.[27] Localization of the minimum between two peaks of the $\sigma(\omega)$ spectra of the cluster systems falls within an interval of the maximal intensity of an experimental IR spectrum of gaseous bromine hydride,[32] and the fast rise in spectrum intensity of the systems under consideration corresponds to the position of the main maximum of an experimental IR spectrum of a gaseous $O_2 + O_3$ mix.[28]

Opposite transformations of the $\sigma(\omega)$ spectrum occur with a change in the number of Br^- in the cluster with ozone present in the system. The addition of O_3 molecules to the cluster gives a reduction in the I_{tot} magnitude by a factor of 7.3. This decrease is less observed with the growth of the number of Br^- in the cluster. In other words, adsorption of ozone follows the increase of the I_{tot} values if the water cluster consistently attaches Br^-. Therefore, with two Br^- the intensity of the IR spectrum on adsorption of ozone decreases by a factor of 2.1, and when four Br^- are in the cluster the I_{tot} magnitude is reduced by only a factor of 1.07.

Fig. 5. Configurations of the systems $(Br^-)_i(H_2O)_{44} + 6H_2O + 6X$ corresponding to time (t) = 25 ps: (A) X = O_2 and (B) X = O_3. Coordinates of the molecules are presented in nanometers.

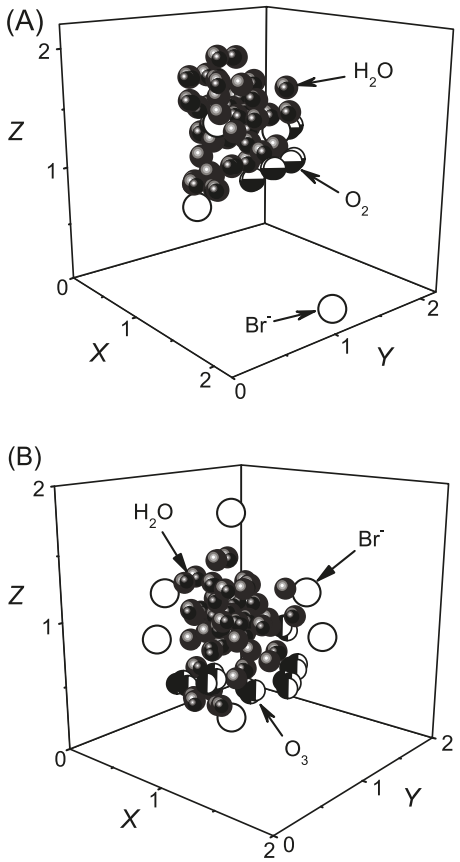

The increase of intensity of the $\sigma(\omega)$ spectra stops when the number of Br^- ions exceeds four.

The position of the main peak of the IR spectrum hardly changes and approximately corresponds to the frequency 3300 cm^{-1} during the change of the number of Br^- within a cluster. Here (as well as in the presence of oxygen in the system), a red shift of the position of the main maximum of the spectrum concerning localization of the basic peak of the experimental IR spectrum of liquid water was observed. The minimum dividing peak of the $\sigma(\omega)$ spectra of the cluster systems falls into an area of the greatest intensity of the IR spectrum of gaseous bromine hydride. The fast increase in intensities of the $\sigma(\omega)$ spectra of these systems occurs in the frequency range where the peak of the IR spectrum of gaseous ozone[33] is located.

Nonpolar O_2 molecules create a "dilution" effect owing to the decrease in the total dipole moment magnitude. The Br^- perturb an internal electric field of the cluster, accelerating the attenuation of the autocorrelation function of $\mathbf{d}_{cl}$ magnitude. As a result the intensity of the IR spectrum decreases with an increase in the number of bromine ions. The grouped polar O_3 molecules create a poorly varying electric field that orders the dipole moments of the water molecules. As a result the $\mathbf{d}_{cl}$ magnitude is increased, and the intensity of the IR spectrum grows with the increase in the number of Br^- in the system. Amplification of the perturbation owing to the addition to the cluster of more than

Can. J. Chem. Downloaded from www.nrcresearchpress.com by Xi'an Jiaotong University on 09/19/12
For personal use only.

Fig. 6. IR absorption spectra for systems $(Br^-)_i(H_2O)_{50-i} + iH_2O + 6X$: (A) X = O_2 and (B) X = O_3. (1) $i = 0$. (2) $i = 2$. (3) $i = 4$. (4) $i = 6$. For (A): (5) the $\sigma(\omega)$ function of bulk liquid water, experiment;[27] (6) experimental spectrum of an $O_2 + O_3$ mixture of gases;[28] and (7) $\sigma(\omega)$ of gaseous HBR, experiment.[32] For (B): (5) the $\sigma(\omega)$ function of the $(H_2O)_{50}$ cluster and (6) the experimental spectrum of gaseous O_3.[33]

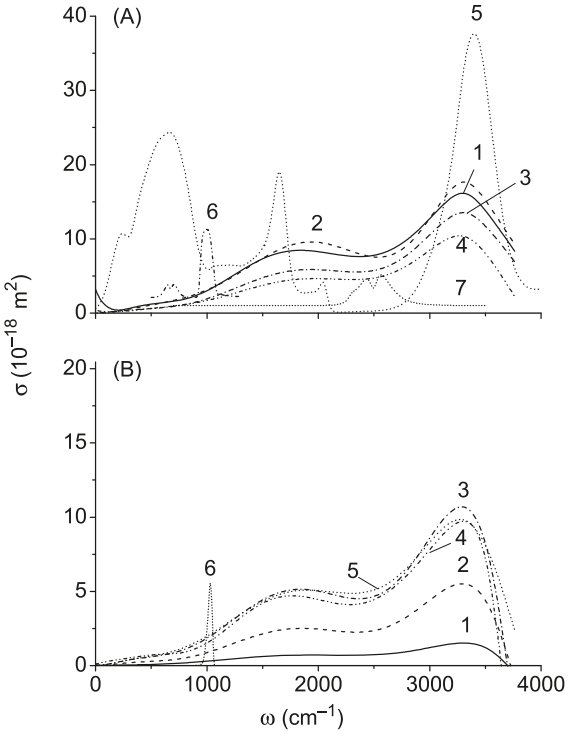

Fig. 7. Raman spectra of the $(Br^-)_i(H_2O)_{50-i} + iH_2O + 6X$ systems: (A) X = O_2 and (B) X = O_3. (1) $i = 0$. (2) $i = 6$. For (A): (3) liquid water at 293 K, experiment[34] and (4) the Br_2 clathrate hydrates at 266 K, experiment.[35] For (B): (3) the $(H_2O)_{50}$ cluster and (4) gaseous O_3, experiment.[36]

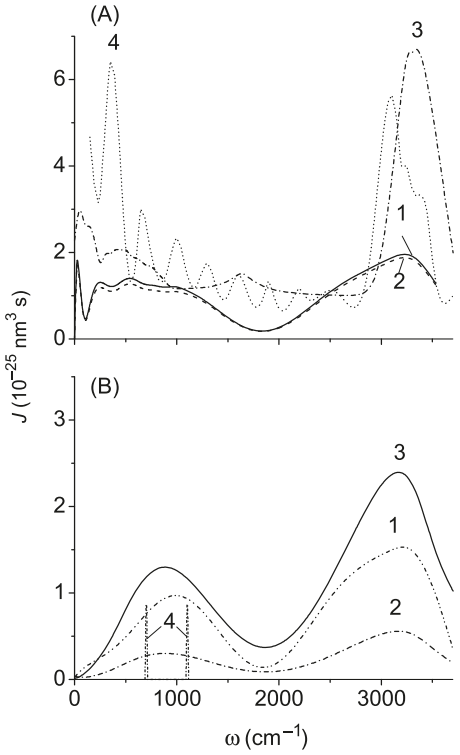

four Br^- results in faster attenuation of the autocorrelation function of the $\mathbf{d}_{cl}$. As a consequence, the intensity of the IR spectrum in an aqueous–ozone system at $i = 4$ starts to lessen.

Raman spectra for bromine-containing systems (I″, VI″, VII″, and XII″) are shown in Fig. 7. Adsorption of six oxygen molecules resulted in an increase in the integrated intensity of the Raman spectrum (J_{tot}) for the $(H_2O)_{50}$ cluster by a factor of 1.6. In the presence of oxygen, the $J(\omega)$ spectrum poorly changed the intensity and the shape with variation in the number of Br^- in a cluster. When absorption of six Br^- by the aqueous–oxygen system occurred, the J_{tot} magnitude decreased by only 7.1%. In the systems containing up to six Br^-, a red shift of the basic peak at ~110 cm^{-1} relative to the main peak in the experimental Raman spectrum of liquid water[34] was observed. This peak has blue shift on quantity ~130 cm^{-1} with respect to the localization of the expressed peak in the similar experimental spectrum of the Br_2 clathrate hydrates.[35] The addition of six ozone molecules resulted in a decrease in the J_{tot} of the Raman spectrum for the $(H_2O)_{50}$ cluster by a factor of 1.5. The quantity of Br^- within the clusters is essentially reflected in the shape of the $J(\omega)$ spectra of the cluster systems containing ozone. $J(\omega)$ spectra considerably reduced the intensity with an increase in the number of Br^-. The J_{tot} magnitude of the aqueous–ozone system in the presence of six Br^- is lower by a factor of 4.3 than the J_{tot} value of this system in the absence of Br^-.

Red and blue (~170 and 20 cm^{-1}, respectively) shifts of the maximum position of the Raman spectra of cluster systems with respect to the corresponding peaks of the experimental spectra for water and bromine clathrate hydrates were observed. The position of the first (less intense) peak in the $J(\omega)$ spectra of cluster systems containing ozone lies in the interval between the two peaks of the experimental spectrum of gaseous ozone.[36]

The average polarizability per molecule ($\bar{\alpha}$) goes down in comparison with the designated α magnitude for water clusters with the addition of nonpolar molecules having a lower α (0.793 Å^3) than the α magnitude for molecules of liquid water (1.49 Å^3). In this case the presence of bromine ions exerts a weak influence on chaotization of the dipole moments of water molecules. Thus, fluctuations of α magnitude and behaviour of the appropriate correlation function poorly change. It results in minor alterations of the Raman spectrum at a variation in the number of Br^- in the system. Another situation arises for the systems containing ozone. The polar molecules of ozone have a higher polarizability (α = 2.7 Å^3) than water molecules. Therefore, the $\bar{\alpha}$ magnitude in the ozone system is higher than α for the water cluster. Disordering of the dipole moments was amplified with an increase in the number of Br^- and the polarizability values were smoothly reduced. Fluctuations of the α magnitude were lower than those for systems with oxygen. As a result, the intensities of the $J(\omega)$ spectra for the systems containing ozone was reduced with an increase in the number of Br^-.

Adsorption of molecules of both oxygen and ozone by the $(H_2O)_{50}$ cluster strengthens the integrated intensities of the emission spectra of IR radiation (P_{tot}). As a result of the

Can. J. Chem. Downloaded from www.nrcresearchpress.com by Xi'an Jiaotong University on 09/19/12
For personal use only.

Fig. 8. IR emission spectra of systems $(Br^-)_i(H_2O)_{50-i}+ iH_2O + 6X$. (A) X = O_2, and (B) X = O_3 (1) i = 0. (2) i = 2. (3) i = 4. (4) i = 6. (5) The $P(\omega)$ function of the $(H_2O)_{50}$ cluster.

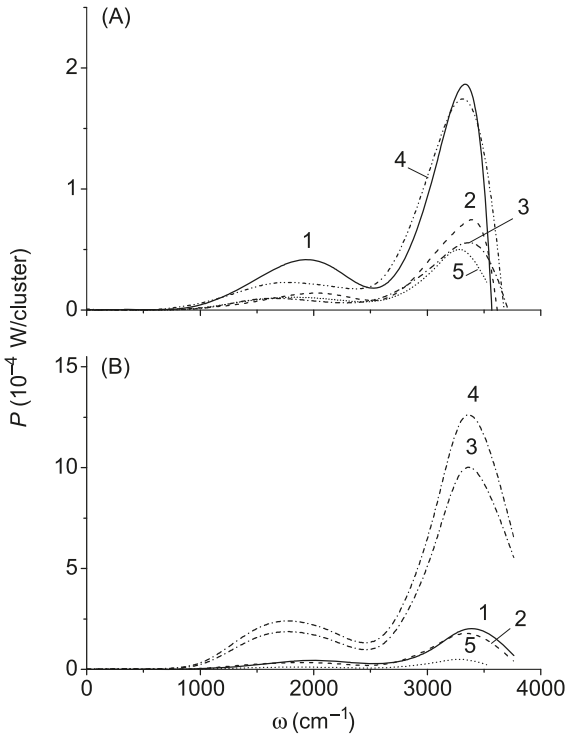

addition of six O_2 molecules, the P_{tot} magnitude increased by a factor of 3.8, and with the addition of six O_3 molecules to the cluster by a factor of 4.1 (Fig. 8). Emission spectra of cluster systems essentially change in intensity with a variation of the number of Br^- in the cluster. As a rule, the intensities of emission spectra are reduced in the presence of oxygen in the system and grows when the clusters adsorb ozone. For example, with six Br^- the $P(\omega)$ spectrum P_{tot} was reduced by a factor of 1.1 on adsorption of oxygen and it was increased by a factor of 6.4 when ozone joins. When bromine ions are added into an oxygen-containing system, the main peak of the emission spectrum, on average, is displaced by 20 cm^{-1} aside high frequencies. But addition of Br^- into ozone-containing systems results in a shift of the main peak up to 35 cm^{-1} aside low frequencies. The maximal reduction of the intensities of emission spectra for systems with oxygen occured in the presence of four Br^- in the cluster, and the maximal increase of this characteristic was observed for systems with ozone in the presence of six Br^- in the aggregate.

Conclusion

Ozone depletion occurs when the natural balance between the production and destruction of stratospheric ozone is tipped in favour of destruction. Although natural phenomena can cause temporary ozone loss, chlorine and bromine released from man-made compounds such as CFCs are now accepted as the main cause of this depletion. Emissions of CFCs have accounted for roughly 80% of total stratospheric ozone depletion. CFCs are photolyzed by UV radiation that breaks the weakest bond, usually a C–Cl or C–Br bond. Naturally occurring chlorine has the same effect on the ozone layer, but has a shorter life span in the atmosphere.

The present work demonstrates that water clusters are capable of adsorbing ozone and of detaining its molecules on the cluster surface over a significant time. Clusters consisting of polar molecules can hold Cl^- and Br^-. Thus, on the surface of a water cluster favourable conditions are created for the reaction of chlorine or bromine with ozone to proceed, which results in the destruction of the latter. The time that Br^- remain in water clusters is at least 10 times more than the time that Cl^- remain. Therefore, bromine ions destroy ozone more effectively. The intensities of IR absorption spectra essentially increase as the number of Br^- per cluster increases. Raman spectra of dispersed aqueous–ozone systems considerably reduce intensities with an increase in the number of Br^- contained in them. Emission spectra of IR radiation essentially have an increase in their intensities only at significant concentrations of Br^- in clusters.

In summary, the more massive Br^- are held in water clusters much longer than Cl^-, allowing the addition of ozone molecules to the cluster. At the same time absorption of oxygen molecules, as a rule, leads to evaporation of some of the Br^- from the cluster and to a loss of some oxygen molecules from its environment.

Acknowledgement

This work was financially supported by the Russian Foundation for Basic Research (project No. 08-08-00136-a).

References

(1) Schauffler, S. M.; Atlas, E. L.; Flocke, F.; Lueb, R. A.; Stroud, V.; Travnicek, W. *Geophys. Res. Lett.* **1998**, *25* (3), 317. doi:10.1029/98GL00040.
(2) Daniel, J. S.; Solomon, S.; Sanders, R. W.; Portmann, R. W.; Miller, D. C. J.; Madsen, W. *J. Geophys. Res.* **1999**, *104* (D14), 16785. doi:10.1029/1999JD900220.
(3) Dang, L. X.; Chang, T.-M. *J. Chem. Phys.* **1997**, *106* (19), 8149. doi:10.1063/1.473820.
(4) Galashev, A. Y.; Rakhmanova, O. R. J. *Struct. Chem.* **2005**, *46* (4), 626. doi:10.1007/s10947-006-0180-4.
(5) Benedict, W. S.; Gailar, N.; Plyler, E. K. *J. Chem. Phys.* **1956**, *24* (6), 1139. doi:10.1063/1.1742731.
(6) Xantheas, S. *J. Chem. Phys.* **1996**, *104* (21), 8821. doi:10.1063/1.471605.
(7) Feller, D.; Dixon, D. A. J. *J. Chem. Phys.* **1996**, *100*, 2993. doi:10.1021/jp952860l.
(8) Smith, D. E.; Dang, L. X. *J. Chem. Phys.* **1994**, *100* (5), 3757. doi:10.1063/1.466363.
(9) Spackman, M. A. *J. Chem. Phys.* **1986**, *85* (11), 6579. doi:10.1063/1.451440.
(10) Spackman, M. A. *J. Chem. Phys.* **1986**, *85* (11), 6587. doi:10.1063/1.451441.
(11) Hunt, S. W.; Roeselova, M.; Wang, W.; Wingen, L. M.; Knipping, E. M.; Tobias, D. J.; Dabdub, D.; Finlayson-Pitts, B. J. *J. Phys. Chem. A* **2004**, *108* (52), 11559. doi:10.1021/jp0467346.
(12) Perera, L.; Berkowitz, M. L. *J. Chem. Phys.* **1991**, *95* (3), 1954. doi:10.1063/1.460992.
(13) Lemberg, H. L.; Stillinger, F. H. *J. Chem. Phys.* **1975**, *62* (5), 1677. doi:10.1063/1.430718.

(14) Rahman, A.; Stillinger, F. H.; Lemberg, H. L. *J. Chem. Phys.* **1975**, *63* (12), 5223. doi:10.1063/1.431307.
(15) Saint-Martin, H.; Hess, B.; Berendsen, H. J. C. *J. Chem. Phys.* **2004**, *120* (23), 11133. doi:10.1063/1.1747927.
(16) Berendsen, H. J. C.; Postma, J. P. M.; van Gunsteren, W. F.; DiNola, A.; Haak, J. R. *J. Chem. Phys.* **1984**, *81* (8), 3684. doi:10.1063/1.448118.
(17) Haile, J. M. *Molecular dynamics simulation. Elementary methods;* John Wiley & Sons: New York, 1992.
(18) Koshlyakov, V. N. *Zadachi dinamiki tverdogo tela i prikladnoi teorii giroskopov (Problems in Dynamics of Solid and Applied Theory of Gyroscopes);* Nauka: Moscow, 1985.
(19) Sonnenschein, R. *J. Comp. Phys.* **1985**, *59*, 347. doi:10.1016/0021-9991(85)90151-2.
(20) Landau L. D.; Lifshitz E. M. *Electrodinamica sploshnykh sred (Electrodynamics of Continuous Media);* Vol. 8; Nauka: Moscow, 1982.
(21) Prokhorov, A. M., Ed. *Fizicheskaya entsiklopediya;* Vol. 1. (Physical Encyclopedia); Sovetskaya Entsiklopediya: Moscow, 1988.
(22) Bresme, F. *J. Chem. Phys.* **2001**, *115* (16), 7564. doi:10.1063/1.1407288.
(23) Neumann, M. *J. Chem. Phys.* **1985**, *82* (12), 5663. doi:10.1063/1.448553.
(24) Bosma, W. B.; Fried, L. E.; Mukamel, S. *J. Chem. Phys.* **1993**, *98* (6), 4413. doi:10.1063/1.465001.
(25) Nikol'skii, B. P., Ed. *The Chemist's Manual;* Vol. 1; Khimiya: Leningrad, 1971.
(26) Stern, H. A.; Berne, B. J. *J. Chem. Phys.* **2001**, *115* (16), 7622. doi:10.1063/1.1407287.
(27) Goggin, P. L.; Carr, C. In *Water and Aqueous Solutions;* Neilson G.W., Enderby J.E. Eds.; Vol. 37; Adam Hilger: Bristol, Boston, 1986.
(28) Potapova, G. F.; Klochikhin, V. L.; Putilov, A. V.; Kasatkin, E. V.; Kozlova, N. V. In *Proceedings of the 1st All-Russian Conference on Ozone and Other Ecological Pure Oxidants;* Science and Technology, Moskow State University: Moscow, 2005.
(29) Murphy, W. F. *J. Chem. Phys.* **1977**, *67* (12), 5877. doi:10.1063/1.434794.
(30) Reid, P. J. *Acc. Chem. Res.* **2001**, *34* (9), 691. doi:10.1021/ar010064u.
(31) Brooksby, C.; Prezhdo, O. V.; Reid, P. J. *J. Chem. Phys.* **2003**, *118* (10), 4563. doi:10.1063/1.1545097.
(32) Kozintzev, V. I.; Belov, M. L.; Gorodnichev, V. A.; Fedotov, Yu. V. *Lazernyi optiko-akusticheskii analis mnogokomponentnyh gazovyh smesei. (Laser Optical Accoustic Analysis of Multicomponent Gas Mixtures);* N.E. Bauman Press of the Moskow State Technical University: Moscow, 2003.
(33) Upschulte, B. L.; Green, B. D.; Blumberg, W. A.; Lipson, S. J. *J. Phys. Chem.* **1994**, *98* (9), 2328. doi:10.1021/j100060a021.
(34) Vallée, P.; Lafait, J.; Ghomi, M.; Jouanne, M.; Morhange, J. F. *J. Mol. Struct.* **2003**, *651–653*, 371. doi:10.1016/S0022-2860(02)00653-1.
(35) Goldschleger, I. U.; Kerenskaya, G.; Janda, K. C.; Apkarian, V. A. *J. Phys. Chem. A* **2008**, *112* (5), 787. doi:10.1021/jp077562q.
(36) Andrews, L.; Spiker, R. C., Jr. *J. Phys. Chem.* **1972**, *76* (22), 3208. doi:10.1021/j100666a018.

Can. J. Chem. Downloaded from www.nrcresearchpress.com by Xi'an Jiaotong University on 09/19/12
For personal use only.

AWARD LECTURE / CONFÉRENCE D'HONNEUR

Dauben–Michno oxidative transposition of allylic cyanohydrins — Enantiomeric switch of (–)-carvone to (+)-carvone*

Jason R. Hudlicky, Lukas Werner, Vladislav Semak, Razvan Simionescu, and Tomas Hudlicky

Can. J. Chem. Downloaded from www.nrcresearchpress.com by 80.58.250.72 on 09/16/12
For personal use only.

Abstract: Allylic cyanohydrins were subjected to Dauben–Michno oxidation at low temperatures to provide β-cyanoenones in good to excellent yields. The potential of this oxidative transposition as a means of an enantiomeric switch of enones containing a latent plane of symmetry was tested by conversion of (–)-carvone to its enantiomer.

Key words: Dauben–Michno reaction, oxidative 1,3-transposition of allylic alcohols, cyanoenones, enantiomeric switch of carvone.

Résumé : On a soumis des cyanohydrines allyliques à une oxydation de Dauben–Michno, à basse température, pour obtenir des β-cyanoénones avec des rendements allant de bons à excellents. Dans le but d'évaluer le potentiel de cette transposition oxydante comme méthode de réaliser une transposition énantiomère dans les énones contenant un plan de symétrie latent, on a transformer la (–)-carvone en son énantiomère.

Mots-clés : réaction de Dauben–Michno, transposition oxydante 1,3 d'alcools allyliques, cyanoénones, transposition énantiomère de la carvone.

[Traduit par la Rédaction]

Introduction

The Dauben–Michno oxidation constitutes a reliable protocol for oxidative transposition of tertiary allylic alcohols substituted with electron-donating groups.[1,2] The reaction proceeds by a [3,3] sigmatropic rearrangement of the initially formed chromate ester followed by further oxidation of the rearranged chromate ester to the final enone. The process is analogous to the well-known chromium(VI) oxidations of olefins to enones that proceed via an ene reaction of the chromium oxide followed by oxidation. The initially formed chromate ester is either oxidized to an enone or undergoes [3,3] sigmatropic rearrangement prior to the final oxidation. Thus, mixtures of regioisomeric enones are frequently encountered in the oxidation of cyclic olefins.[3,4] Because only one product can arise from the rearrangement of a tertiary allylic alcohol, the Dauben–Michno reaction does not suffer from regiochemical issues. Although well-documented for allylic alcohols flanked by electron-donating groups, this reaction has not been reported for allylic alcohols substituted with esters or nitriles. To our knowledge the first example of such oxidation was the conversion of allylic alcohol **1** to enone **2** during our recently completed synthesis of oseltamivir (**3**) (Tamiflu), Fig. 1.[5]

To establish whether the reaction is general for allylic alcohols substituted with other electron-withdrawing groups we investigated a series of cyanohydrins as means of synthesis of β-cyanoenones. In this paper we report the results of this investigation, along with a procedure for an enantiomeric switch of (–)-carvone to (+)-carvone.

Results and discussion

We began the investigation with a series of cyclic enones (Table 1, entries 1–3) and their conversion to cyanohydrins following a recently published procedure that uses proline catalysis for the formation of the intermediate trimethylsilyl ethers of cyanohydrins.[6] Following the hydrolysis, the free cyanohydrins were obtained in essentially quantitative yield and used without purification in the Dauben–Michno oxidation. The proline-catalyzed protocol is exceedingly efficient and cleanly affords the cyanohydrins, thus obviating any

Received 13 November 2010. Accepted 14 January 2011. Published at www.nrcresearchpress.com/cjc on 21 April 2011.

J.R. Hudlicky, L. Werner, V. Semak, R. Simionescu, and T. Hudlicky. Department of Chemistry and Centre for Biotechnology, Brock University, 500 Glenridge Avenue, St. Catharines, ON L2S 3A1, Canada.

Corresponding author: T. Hudlicky (e-mail: thudlicky@brocku.ca).

*Based on the 2010 Bader Award Lecture.

Fig. 1. Dauben–Michno oxidation of α-hydroxybutenoate.

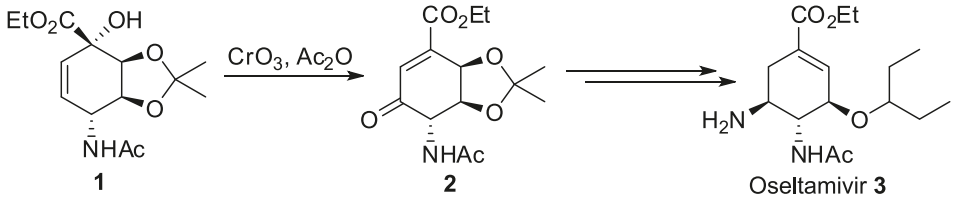

Fig. 2. Proposed enantiomeric switch of (–)-carvone via Dauben–Michno oxidation.

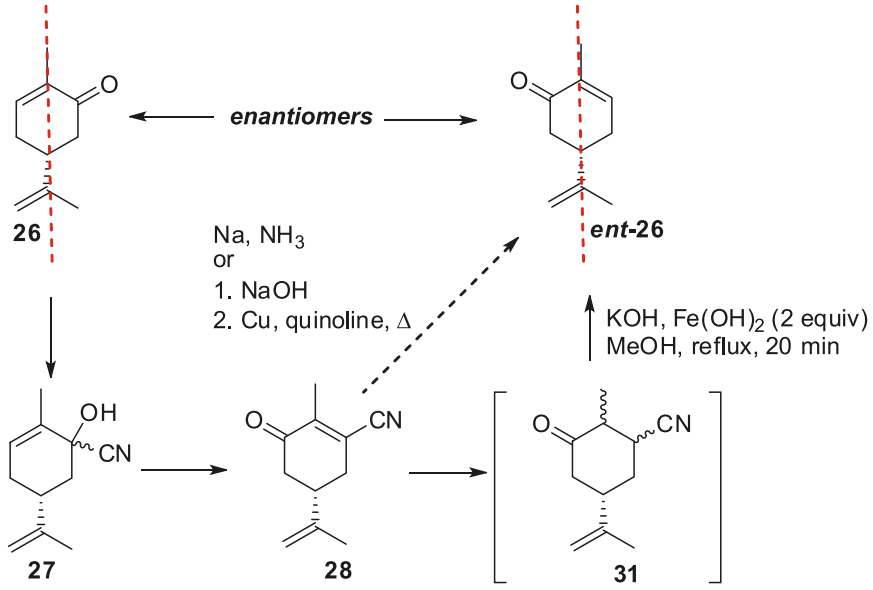

separation issues prior to subsequent reactions. In the case of cyclopentenone, the cyanohydrin was obtained in 60% yield at the expense of the competing 1,4-addition of the cyanide to the enone. Similarly, cyanohydrins were obtained from methylvinyl ketone (Table 1, entry 4), 3-penten-2-one (Table 1, entry 5), 4-phenylbutenone (Table 1, entry 6), acetophenone (Table 1, entry 7), and (–)-carvone (Table 1, entry 8).

The Dauben–Michno procedure required the treatment of CrO_3 with acetic anhydride at 80 °C before cooling and addition of the cyanohydrin at or below 0 °C. The best results were obtained by performing the oxidation below 0 °C to avoid competing reactions at the site of the double bond that may result from the generation of peroxyacetic acid during the reaction. Such competition is absent when the oxidation is performed at –40 °C or below. The yields of transposed cyanoenones were in the range of 70%–80% except in the case of cyclopentenone, where the conversion was excellent and essentially quantitative (vide NMR); however, the volatility of the product contributed to low isolated yields (Table 1).

With acyclic enones the results were different; in the case of methylvinyl ketone the corresponding unsaturated aldehyde **15** (a consequence of the oxidation of a primary chromate ester formed by the sigmatropic rearrangement) was isolated as a mixture of *Z*- and *E*-isomers in the ratio of 7:1. (Note: On repetition of these experiments at higher temperatures or on a larger scale only the *Z*-isomer was detected.) The volatility of the product made the accurate determination of yield difficult. It was somewhat surprising that little or no over-oxidation took place whether 1 equiv or up to 3 equiv of the oxidant were used. We did not detect the corresponding acid even after careful repetition of the experiments; however, over-oxidation of an aldehyde to an acid requires the formation of a hydrate, which cannot take place under the conditions of the reaction. If the corresponding acid is desired, a simple dilution of the reaction with water and addition of an additional equivalent of chromium oxide should provide the corresponding carboxylic acid in high yield.

With pent-3-en-2-one (**16**) the corresponding cyanohydrin **17** was isolated in 76% yield and rearranged cleanly to the β-cyanoenone **18** in 84% yield (66% over two steps); only the *Z*-isomer **18a** was observed. In the case of 4-phenylbutenone (**19**), the rearrangement of the corresponding cyanohydrin **20** produced only traces of the transposed enone **21**, and the major product isolated was benzaldehyde (**22**). The formation of benzaldehyde may be rationalized by the oxidative cleavage of the intermediate 1,2-chromate diester formed from the styrene double bond in competition with the Dauben–Michno reaction.

For acetophenone (**23**) and the oxidation of its cyanohydrin **24**, only the formation of an intractable polymer was observed at prolonged reaction times or at higher temperatures. The cyanohydrin derived from acetophenone was still present in the reaction mixture after 16 h at room temperature. We expected the Dauben–Michno to proceed with disruption of aromaticity to provide **25**, in analogy with reported cases of reactivity of this type;[7] however, attempts at trapping intermediates of type **25** with external dienophiles such as maleic anhydride proved unsuccessful.

The oxidative 1,3-transposition could, in principle, be used

Can. J. Chem. Downloaded from www.nrcresearchpress.com by 80.58.250.72 on 09/16/12
For personal use only.

Table 1. Dauben–Michno oxidation of cyanohydrins.

Entry	Enone	Cyanohydrin	Product(s) (%)
1	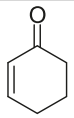 **4**	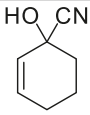 **5**	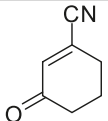 **6** (79)[a]
2	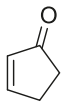 **7**	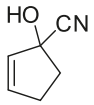 **8** (60)[b]	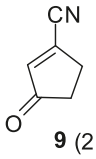 **9** (25%)[c] (93%)[d]
3	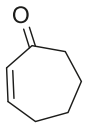 **10**	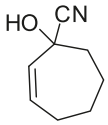 **11**	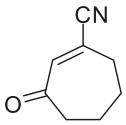 **12** (81)[a]
4	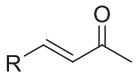 **13** R = H	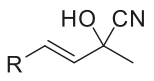 **14** R = H (67%)[d]	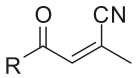 (Z:E = 7:1) 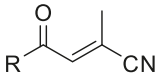 **15a** R = H **(Z-)** **15b** R = H **(E-)** (43)[a,c]
5	**16** R = Me	**17** R = Me (78%)	**18a** R = Me (84%)(66%)[a] **18b** R = Me
6	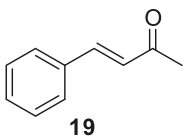 **19**	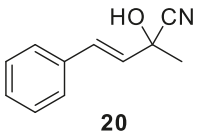 **20**	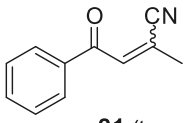 **21** (trace) 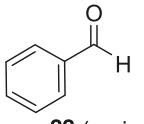 **22** (major)
7	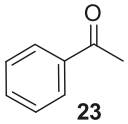 **23**	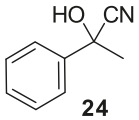 **24**	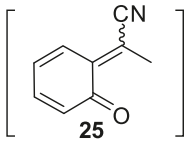 polymer **25**
8	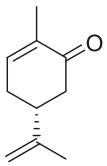 **26**	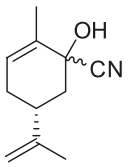 **27**	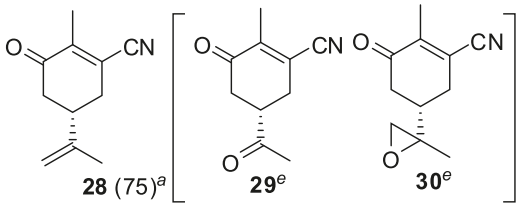 **28** (75)[a] **29**[e] **30**[e]

[a]Isolated yield over two steps.
[b]Yield of 1,2-adduct, 1,4-adduct of cyanide was observed during the cyanohydrin synthesis.
[c]Isolated yield, product is volatile and losses occur on evaporation.
[d]Product content as estimated by NMR.
[e]Formed only in reactions above 0 °C.

to provide enantiomers of homochiral enones that contain a latent plane of symmetry, as shown in Fig. 2 with carvone. To test this idea we applied the Dauben–Michno protocol to carvone with the expectation that further manipulations of the β-cyanoenone **28** would lead to the formation of *ent*-carvone, as depicted in Fig. 2.

The Dauben–Michno oxidation of cyanohydrin **27** derived from carvone provided the corresponding β-cyanoenone **28** in 75% yield. At 0–4 °C, considerable amount of side products, such as the methyl ketone **29** and epoxide **30**, were isolated. The former compound is likely a result of the oxidative cleavage of the 1,2-diol, formed by the addition of CrO_3 to the isopropylidine double bond, whereas the latter is probably formed by epoxidation mediated by peroxyacetic acid generated by in situ oxidation of acetic acid. When the reaction was performed at –40 to –50 °C, only oxidative rearrangement took place, and no side products arising from over-oxidation were observed.

Can. J. Chem. Downloaded from www.nrcresearchpress.com by 80.58.250.72 on 09/16/12
For personal use only.

Fig. 3. Synthesis of *ent*-dihydrocarvone from enone **28**.

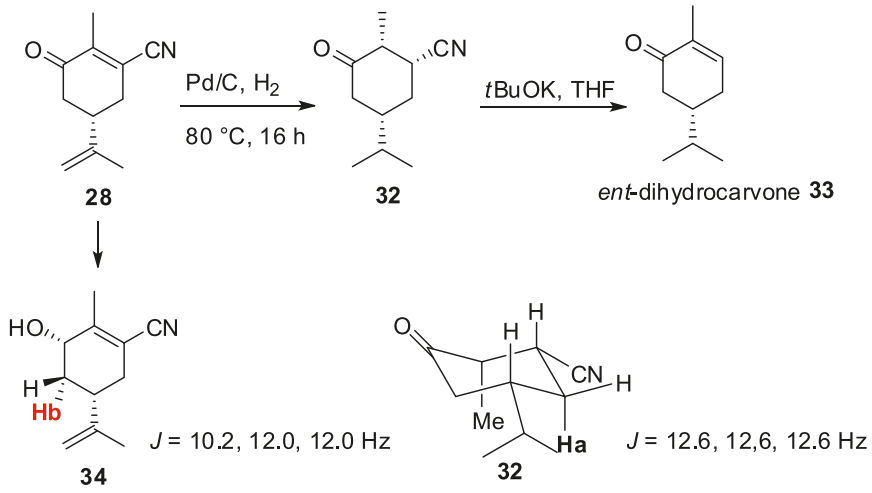

Fig. 4. Enantiomeric switch of (–)-carvone.

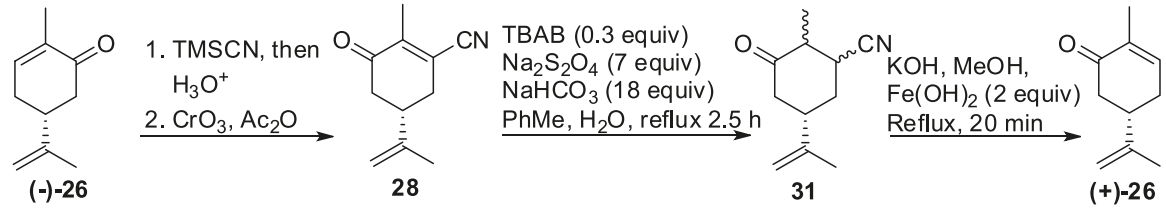

Fig. 5. Djerassi's assignment of diastereomeric dihydrocyanocarvone **31**.

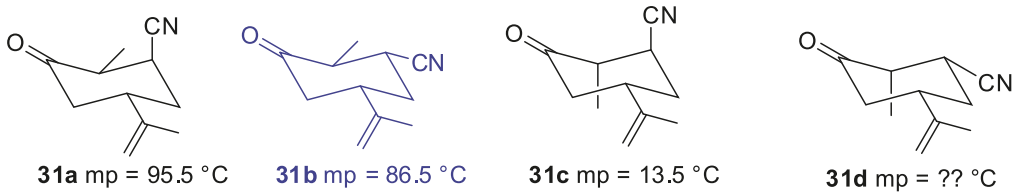

The proof of principle for the enantiomeric switch was demonstrated on a small scale by the conversion of cyanoenone **28** to the fully saturated β-cyano ketone **32** as shown in Fig. 3. Hydrogenation of **28** at 1 atm (1 atm = 101.325 kPa) produced ketone **32** (34% yield), whose structure was assigned by the analysis of coupling constants of H_a, as shown in Fig. 3.

The low yield of the hydrogenation was attributed to the formation of a by-product (2-methyl-3-cyano-5-isopropylphenol) resulting from full aromatization under the conditions of the hydrogenation. Treatment of **32** with *t*-BuOK in THF provided *ent*-dihydrocarvone (**33**). Enone **28** was also reduced under Luche conditions to the allylic alcohol **34** in anticipation of a possible rhodium-catalyzed isomerization[8] ($RhCl_3$, EtOH) to the saturated ketone **31**; however, this isomerization proved unsuccessful. The stereochemistry assignment of **34** was evident from the large coupling constants of the axial H_b, as shown in Fig. 3.

For the direct conversion of cyanoenone **28** to *ent*-carvone (**26**) several methods were investigated, among them hydrolysis to the corresponding acid and thermal decarboxylation,[9] and Birch reduction,[10] as shown in Fig. 2. Neither method proved very efficient in our hands.

The enantiomeric switch of carvone was accomplished in two steps via a reduction–elimination sequence as shown in Fig. 4. The cyanoenone **28** was reduced with sodium dithionite[11] to a mixture of the saturated cyanoketones **31**. All four diastereomers of **31** are known compounds, generated over the years in investigations of various reactions of enones[12–14] that utilized carvone as a convenient starting material. The major product from the dithionite reduction turned out to be the diastereomer **31b** (Fig. 5), as evidenced by melting point as well as by detailed NMR analysis.

In the early 1900s Lapworth[15–17] studied the addition of cyanide to *ent*-carvone and isolated two diastereomers of **31**, one from the reaction of potassium cyanide in ethanol, water, and acetic acid conducted at room temperature, and the other from a reaction performed in refluxing ethanol without acetic acid. (These two compounds would later be identified as **31a** and **31b**, respectively; Fig. 5) When Djerassi et al.[18] repeated Lapworth's experiments in 1963 with (–)-carvone, they found that the physical constants of the two diastereomers matched Lapworth's results. They then studied the equilibration of the two isomers and isolated a third when **31a** was treated with *p*-TsOH in EtOAc at room temperature for 1 week. The third isomer, a much lower melting compound, was later assigned as structure **31c**, Fig. 4.

Can. J. Chem. Downloaded from www.nrcresearchpress.com by 80.58.250.72 on 09/16/12
For personal use only.

Fig. 6. Assignment of stereochemistry of **31b** by NMR methods. (A) Resolution enhanced ^{1}H spectrum. (B) Resolution enhanced ^{1}H spectrum selectively decoupled from H7 methyl.

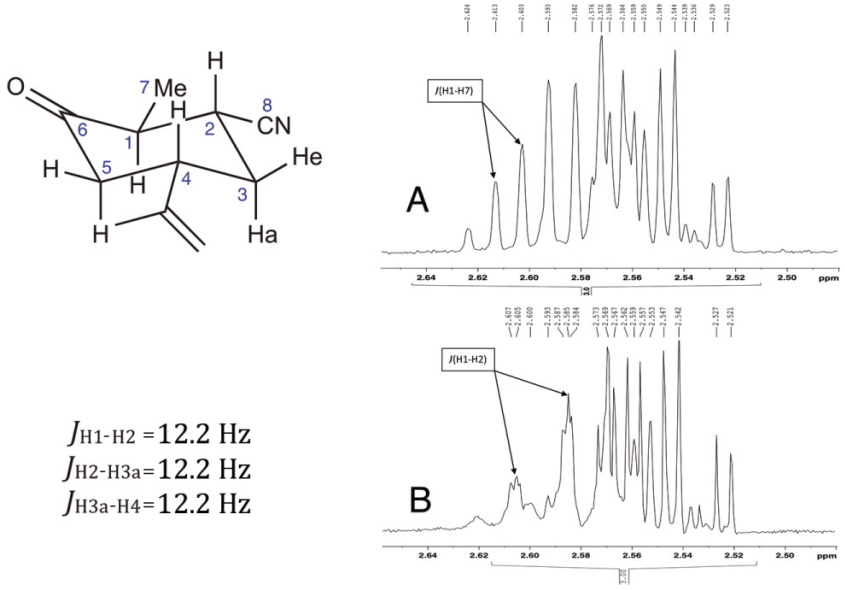

Fig. 7. Attempted Dauben–Michno synthesis of (+)-carvone from (–)-carvol **35**.

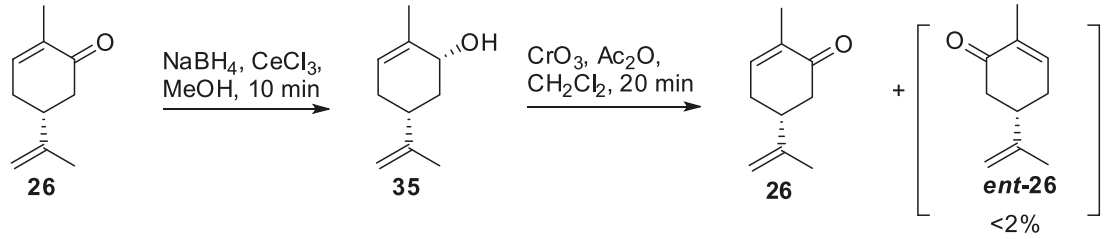

Attempted equilibration of **31b** was unsuccessful save for a trace amount of a new compound tentatively assigned as **31d**. Djerassi et al.[18] assigned the stereochemistry of the four diastereomers of **31** by use of detailed conformational analysis and optical rotary dispersion. In addition, they proved by simple yet ingenious experiments that the equilibration of **31a** occurs at C-2 and not at C-3 by conversion of nitriles to benzamides and equilibration of C-2 positions. The stereochemistry of **31b** was evident by matching the melting point with the compound identified by Djerassi et al.[18]

The assignment of **31b** by NMR methods proved to be nontrivial because of overlapping signals of the key protons and required the dispersion field of a 600 MHz spectrometer with advanced methods to separate the overlapping signals. The assignment of stereochemistry is shown in Fig. 6. In the normal proton spectrum, the six protons from the ring are all grouped at 1.9–2.6 ppm with one proton at 2.03 ppm, a multiplet at 2.37 ppm corresponding to three protons, and another multiplet at 2.57 ppm also corresponding to three protons. The proton at 2.03 ppm shows a d–d–d splitting pattern with three equal coupling constants (J = 12.2 Hz). Given the ring structure of cyclohexane there is only one possible case for the assignment of this proton, H3a. It is the only possible case with two large vicinal couplings (axial–axial) and one large geminal coupling. This also establishes that protons H4a and H2a are axial protons, implying that both the CN group and the propylene are in equatorial positions on the ring.

For the assignment of the H1 proton two-dimensional NMR methods had to be employed. From the H–C HSQC and COSY spectra, the locations of the other ring protons were determined. H1, H5, (H2a or H4a) are grouped at 2.6 ppm and H5 and H3e (H4a or H2a) are grouped at 2.37 ppm. H1 is identified from the coupling to the H7 methyl group in the COSY spectrum as being located on the left side of the multiplet, as shown in Fig. 6A. To increase spectral resolution, Gaussian line broadening was employed with a shift of 0.5 and a line-broadening factor of –1 Hz. From the proton spectrum a coupling constant of 6.2 Hz, corresponding to the vicinal coupling of H1 to H7 protons, was determined. This coupling alone would generate a quartet splitting pattern for H1. However, a more complicated pattern is observed for H1, therefore, the coupling H1 to H2 cannot be extracted directly from the proton 1-D NMR spectrum.

A homonuclear proton experiment was employed to measure the H1–H2 vicinal coupling constant. A proton spectrum was acquired selectively decoupling the H7 methyl group protons at 1.30 ppm from H1. As a result the H1 coupling pattern was simplified and reduced to H1–H2 vicinal coupling, as shown in Fig. 6B. By overlapping the normal proton spectrum with the selectively decoupled spectrum, the H1–H2 coupling constant of 12.2 Hz was extracted. This corresponds to an axial position for H1, confirming that the C-1 methyl group occupies an equatorial position. At this point the right side of the 2.57 ppm multiplet can be assigned as

Can. J. Chem. Downloaded from www.nrcresearchpress.com by 80.58.250.72 on 09/16/12
For personal use only.

Can. J. Chem. Downloaded from www.nrcresearchpress.com by 80.58.250.72 on 09/16/12
For personal use only.

H2a showing the d–d–d pattern expected for H2a, as H4a would generate a d–d–d–d pattern. As this spectral assignment for **31b** would, of course, not have been possible in the 1960s, one must admire the brilliant deductive logic employed by Djerassi et al.[18] in accurately assigning all four diastereomers of **31**.

In preliminary experiments the treatment of **31b** with NaOEt in ethanol provided (+)-carvone, identical in all respects to (–)-carvone except for the sign of optical rotation, thus accomplishing the intended enantiomeric switch. Under these conditions, however, the yields of carvone were low (~35%) at the expense of condensation products. The conditions that employ $Fe(OH)_2$ (shown in Fig. 4) provided the much improved yield of 79% for (+)-carvone.

Finally, we subjected carvol (**35**), obtained by Luche reduction of carvone according to literature protocol,[19] to the Dauben–Michno conditions at –50 °C to investigate the possibility of competition between chromate ester re-oxidation to (–)-carvone versus the Dauben–Michno transposition–oxidation to (+)-carvone (Fig. 7). The rate-determining step in chromium(VI) oxidation of alcohols is the collapse of the chromate ester[20] and not its formation. We speculated that at low temperature, the sigmatropic rearrangement of the initially formed chromate ester required for the transposition may compete with the oxidation even for secondary allylic alcohols.

If the transition state of the [3,3] rearrangement is not symmetrical along the latent plane of symmetry in carvone, then the Dauben–Michno protocol applied to carvol would provide the enantiomer directly. The initial experiment, performed at –55 °C, indeed provided a scalemic mixture of carvone with an optical rotation lower than that of the (–)-enantiomer, indicating that the two processes may indeed compete.

We performed three experiments at different temperatures (–55, –78, and –100 °C) and noted some decrease in the value of rotation for the (–)-enantiomer. However, verification of true *er* by HPLC (Daicel Chiralcel OB-H; flow = 0.6 mL/min (hexane–*i*-PrOH, 95:5; retention time for (*R*)-(–)-carvone = 9.56 min and for (*R*)-(–)-carvone = 10.41 min)[21] provided at best an indication of an ~1%–2% increase in the (+)-enantiomer. Thus, no conclusion can be drawn from these experiments. For now, the three-step high-yielding protocol for the enantiomeric switch via Dauben–Michno oxidation of cyanohydrins should suffice.

Conclusions

We have developed a reliable procedure for the conversion of enones to the corresponding β-cyanoenones with the attendant 1,3-functional transposition of the carbonyl group of the original enone. The possibility of using this transposition to generate enantiomers of enones that possess a latent plane of symmetry was tested and reduced to practice with the enantiomeric switch of (–)-carvone. Future attention should be given to a more detailed study of the Dauben–Michno oxidation of other allylic alcohols, including secondary ones, and the dependence of the outcome of such oxidation on conformational bias and stereochemical features of the substrates.

Experimental section

General procedure for the synthesis of cyanohydrins[6]

To a vial charged with the lithium salt of L-proline (0.1 mmol) was added the enone (1.0 mmol) followed by trimethylsilyl cyanide (1.0 mmol, 133 μL). After the suspension was stirred at room temperature for 12 h, an additional portion of trimethylsilyl cyanide (1.0 mmol, 133 μL) was added, and the reaction mixture was subsequently stirred for another 12 h. Upon completion, THF (2 mL) and 1 mol/L aq HCl (2 mL) were added, and the resulting solution was stirred for 1 h. Following the hydrolysis, the reaction mixture was washed with diethyl ether (30 mL) and water (5 mL), and the aqueous layer was re-extracted with diethyl ether (2 × 15 mL). The combined organic layers were dried over magnesium sulfate with a spatula tip of sodium bicarbonate, then filtered and concentrated under reduced pressure to afford the essentially pure cyanohydrin, which was used without further purification.

General procedure for the Dauben–Michno oxidations[5]

Acetic anhydride (5.3 mmol, 0.5 mL) was added to a vial charged with chromium(VI) oxide (2.5 mmol). The mixture was stirred at 80 °C until complete dissolution (5 min). After cooling to room temperature, the solution was diluted with dichloromethane (2 mL) and added dropwise to a solution of cyanohydrin (1.0 mmol) in dichloromethane (3 mL) at 4 °C. The resulting solution was stirred for 10 min before addition of ethanol (3 mL). The solution was allowed to stir for 30 min at room temperature before concentration under reduced pressure and co-evaporated with toluene. The crude mixture was passed through a column of silica gel using dichloromethane as a solvent to yield β-cyanoenone.

1-Hydroxycyclohex-2-enecarbonitrile (5)[6,22]

^{1}H (300 MHz, $CDCl_3$) δ: 6.03–6.09 (m, 1H), 5.79 (d, 1H, J = 9.9 Hz), 1.79–2.21 (m, 6H).

3-Oxocyclohex-1-enecarbonitrile (6)[23,24]

^{1}H (300 MHz, $CDCl_3$) δ: 6.53 (s, 1H), 2.50–2.59 (m, 4H), 2.10–2.19 (m, 2H).

1-Hydroxycyclopent-2-enecarbonitrile (8)

^{1}H (300 MHz, $CDCl_3$) δ: 6.17 (dt, 1H, J= 2.3, 5.4 Hz), 5.82 (dt, 1H, J = 2.0, 5.4 Hz), 2.14–2.59 (m, 5H). ^{13}C (75 MHz, $CDCl_3$) δ: 138.81, 130.74, 120.88, 67.91, 31.01, 25.52. A by-product of this reaction was the 1,4-adduct, 3-oxocyclopentanecarbonitrile:[25] ^{1}H (300 MHz, $CDCl_3$) δ: 3.15–3.25 (m, 1H), 2.42–2.67 (m, 4H), 2.24–2.36 (m, 2H).

3-Oxocyclopent-1-enecarbonitrile (9)[26]

^{1}H (300 MHz, $CDCl_3$) δ: 6.74 (s, 1H), 2.58–2.91 (m, 2H), 2.53 (t, 2H, J = 4.8 Hz). ^{13}C (75 MHz, $CDCl_3$) δ: 206.24, 143.45, 143.04, 114.81, 34.10, 30.20.

1-Hydroxycyclohept-2-enecarbonitrile (11)

^{1}H (300 MHz, $CDCl_3$) δ: 5.99 (ddd, 1H, J = 6.3, 6.3, 11.4 Hz), 5.68 (ddd, 1H, J = 1.2, 1.2, 11.7 Hz), 3.65 (bs, 1H), 2.19–2.25 (m, 1H), 1.82–2.07 (m, 6H), 1.70–1.75 (m, 1H). ^{13}C (75 MHz, $CDCl_3$) δ: 135.04, 133.16, 120.55, 71.39, 39.28, 27.50, 26.18, 25.21.

Can. J. Chem. Downloaded from www.nrcresearchpress.com by 80.58.250.72 on 09/16/12
For personal use only.

3-Oxocyclohept-1-enecarbonitrile (12)[27]

^{1}H (300 MHz, $CDCl_3$) δ: 6.56 (s, 1H), 2.63–2.67 (m, 4H), 1.82–1.93 (m, 4H). ^{13}C (300 MHz, $CDCl_3$) δ: 201.17, 142.81, 127.36, 118.95, 42.96, 32.14, 25.36, 21.14.

2-Hydroxy-2-methylbut-3-enenitrile (14)

^{1}H (300 MHz, $CDCl_3$) δ: 5.95 (dd, 1H, J = 10.2, 17.1 Hz), 5.67 (d, 1H, J = 16.8 Hz), 5.35 (d, 1H, J = 10.2 Hz), 1.67 (s, 3H). ^{13}C (300 MHz, k$CDCl_3$) δ: 137.49, 120.45, 116.77, 68.76, 28.06.

(Z)-2-Methyl-4-oxobut-2-enenitrile (15a) *(major)*

IR (film, cm^{-1}) ν: 2925, 2222, 1688, 1618, 1448, 1381, 1227, 1171, 1095, 1041, 1019, 861, 787, 665. ^{1}H (300 MHz, $CDCl_3$) δ: 10.02 (d, 1H, J = 7.8 Hz), 6.52 (dq, 1H, J = 1.5, 7.8 Hz), 2.25 (d, 3H, J = 1.5 Hz). ^{13}C (300 MHz, $CDCl_3$) δ: 189.62, 141.64, 129.26, 115.41, 21.68. MS (EI+) *m/z* % 94 (M^+ – H): 83 (15), 68 (63), 52 (29), 44 (100).

(E)-2-Methyl-4-oxobut-2-enenitrile (15b) *(minor)*

IR (film, cm^{-1}) ν: 2925, 2222, 1688, 1618, 1448, 1381, 1227, 1171, 1095, 1041, 1019, 861, 787, 665. ^{1}H (300 MHz, $CDCl_3$) δ: 10.07 (d, 1H, J = 7.8 Hz), 6.52 (dq, 1H, J = 1.5, 7.8 Hz), 2.38 (d, 3H, J = 1.5 Hz). ^{13}C (300 MHz, $CDCl_3$) δ: 189.62, 141.64, 129.26, 115.41, 21.68. MS (EI+) *m/z* % 94 (M^+ – H): 83 (15), 68 (63), 52 (29), 44 (100).

(E)-2-Hydroxy-2-methyl-3-pentenenitrile (17)

R_F = 0.76 (hexanes–EtOAc, 5:1). ^{1}H NMR (300 MHz, $CDCl_3$, ppm) δ: 6.10 (dq, J = 15.3, 6.6 Hz, 1H), 5.55 (dd, J = 15.4, 1.7 Hz, 1H), 3.08 (brs, 1H), 1.76 (dd, J = 6.6, 1.7 Hz, 3H), 1.64 (s, 3H); –OH signal confirmed by D_2O exchange. ^{13}C NMR (75 MHz, $CDCl_3$, ppm) δ: 130.81, 129.02, 120.80, 68.42, 28.27, 17.26; NMR data are in agreement with those previously reported.[28]

(Z)-2-Methyl-4-oxopent-2-enenitrile (18)

R_F = 0.15 (hexanes–EtOAc, 5:1); mp 37–38 °C (white crystals, pentane–Et_2O). IR (KBr, cm^{-1}) ν: 2359, 1732, 1637, 1385. ^{1}H NMR (600 MHz, $CDCl_3$, ppm) δ: 6.60 (d, J = 1.5 Hz, 1H), 2.39 (s, 3H), 2.16 (d, J = 1.5 Hz, 3H). ^{13}C NMR (151 MHz, $CDCl_3$, ppm) δ: 194.25, 140.10, 119.64, 117.12, 30.06, 22.18. MS (+EI) *m/z* (%): 109 (22), 94 (100), 66 (15), 43 (40). HRMS (+EI) calcd for C_6H_7NO: 109.05276; found: 109.05246.

1-Hydroxy-2-methyl-5-(prop-1-en-2-yl)cyclohex-2-enecarbonitrile (27)

^{1}H (300 MHz, $CDCl_3$) δ: 5.70 (dd, 1H, J = 1.2, 3.0 Hz), 4.79 (d, 2H, J = 12.3 Hz), 3.24 (bs, 1H), 2.49–1.90 (m, 5H), 1.86 (s, 3H), 1.74 (s, 3H). ^{13}C (300 MHz, $CDCl_3$) δ: 146.85, 131.76, 128.40, 121.09, 110.18, 70.21, 41.27, 38.96, 30.67, 20.57, 17.01.

β-Cyanocarvone (28)

To a solution of crude cyanohydrin **27** (352 mg, 1.99 mmol) in dichloromethane (3 mL) cooled to –55 °C was added a solution of CrO_3 (499 mg, 4.99 mmol) and Ac_2O (2 mL) in dichloromethane (6 mL). After 30 min the reaction was quenched by the addition of methanol (10 mL) and allowed to warm to room temperature. The mixture was then concentrated and co-evaporated three times with toluene (10 mL). Chromatography of the residue (silica, 20 mL; dichloromethane–hexane, 1:1) afforded enone **28** as a light yellow solid; yield: 260 mg (75%). R_F = 0.6 (dichloromethane–hexane, 1:1). $[\alpha]_D^{20}$ = 82.8 (*c* 1, $CHCl_3$); mp 25–26 °C (neat). IR (KBr, cm^{-1}) ν: 3747, 30.85, 2970, 2925, 2218, 1688, 1648, 1439, 1383, 1318, 1295, 1140, 1108, 1070, 900. ^{1}H NMR ($CDCl_3$, 300 MHz) δ: 4.81 (s, 1H), 4.72 (s, 1H), 2.73–2.53 (m, 3 H), 2.45 (ddq, 1H, J = 3 × 2.4, 12.3, 17.4 Hz), 2.37 (dd, 1H, J= 12.9, 16.2 Hz), 2.00 (dd, 3H, J = 1.8, 2.4 Hz), 1.70 (s, 3H). ^{13}C NMR ($CDCl_3$, 75 MHz) δ: 196.66, 146.31, 144.74, 124.58, 116.95, 111.86, 42.60, 41.26, 33.07, 20.40, 14.86. MS (+FBA) *m/z* (%): 176 (100). HRMS could not be obtained; the compound proved to be too labile. Structure was confirmed by HRMS after reduction of the keto group.

Oxidation of 27 at elevated temperature

To a solution of crude cyanohydrin **27** (235 mg, 1.33 mmol) in dichloromethane (5 mL) cooled to 0 °C was added a solution of CrO_3 (332 mg, 3.33 mmol) and Ac_2O (0.78 mL) in dichloromethane (2.5 mL). After 20 min at 0 °C a new portion of CrO_3 (332 mg, 3.33 mmol) and Ac_2O (0.78 mL) in dichloromethane (2.5 mL) was added. After an additional 70 min, the reaction was quenched by the addition of ethanol (2 mL) and allowed to warm to room temperature over 45 min. The mixture was then concentrated. Chromatography of the residue (silica, 25 mL; Et_2O–hexane, 1:1) afforded diketone **29** (yield: 17.6 mg), epoxide **30** (yield: 73.2 mg), and a mixed fraction (yield: 61 mg).

5-Acetyl-2-methyl-3-oxocyclohex-1-enecarbonitrile (29)

$[\alpha]_D^{20}$ = 25.1 (*c* 1, $CHCl_3$). IR (film, cm^{-1}) ν: 3022, 2964, 2220, 1685, 1416, 1358, 1314, 1265, 1216, 1104, 752, 668, 629. ^{1}H (600 MHz, $CDCl_3$) δ: 3.23 (dddd, 1H, J = 4.2, 7.2, 10.5, 10.5 Hz), 2.82–2.78 (m, 3H), 2.65 (dd, 1H, J = 11.4, 16.8 Hz), 2.25 (s, 3H), 2.10 (s, 3H). ^{13}C (600 MHz, $CDCl_3$) δ: 205.98, 194.49, 146.66, 122.89, 116.56, 46.69, 38.99, 29.71, 27.88, 14.97. MS (EI+) *m/z* % 177 (M^+): 135 (45), 107 (6), 79 (7), 43 (100), HRMS calcd for $C_{10}H_{11}NO_2$: 177.1998; found: 177.0790.

2-Methyl-5-(2-methyloxiran-2-yl)-3-oxocyclohex-1-enecarbonitrile (30)

$[\alpha]_D^{20}$ = 57.5 (*c* 1, $CHCl_3$). IR (film, cm^{-1}) ν: 2927, 2218, 1686, 1436, 1386, 1313, 1140, 1070, 894, 820, 682, 622. ^{1}H (300 MHz, $CDCl_3$) δ: 2.70 (dd, 1H, J = 4.1, 14.2 Hz), 2.66–2.57 (m, 3H), 2.50–2.43 (m, 1H), 2.33–2.26 (m, 1H), 2.26–2.14 (m, 1H), 2.04 (s, 3H), 1.32 (d, 3H, J = 8.4 Hz). ^{13}C (300 MHz, $CDCl_3$) δ: 195.81, 146.45, 124.28, 116.78, 57.39, 52.64, 40.13, 39.41, 29.85, 18.82, 14.87. MS (EI+) *m/z* % 176 (M^+ – CH_3): 148 (51), 134 (100), 122 (53), 58 (81), 43 (96). HRMS calcd for $C_{11}H_{13}NO_2$: 191.2264; found: 176.0712.

(1R,2R,5S)-2-Methyl-3-oxo-5-(prop-1-en-2-yl) cyclohexanecarbonitrile (32)

A solution of enone **28** (0.1g, 0.57 mmol) with Pd/C (20 mg, 10%) in ethanol (3 mL, 95%) was hydrogenated in

Can. J. Chem. Downloaded from www.nrcresearchpress.com by 80.58.250.72 on 09/16/12
For personal use only.

an H_2 atmosphere at 80 °C for 16 h. The reaction mixture was then filtered through Celite and concentrated. Chromatography (silica, 8 mL; dichloromethane–hexane, 1:1) of crude product afforded 35 mg (34%) of fully saturated ketone **32** as a white solid. The remaining mass balance consisted of fully aromatized material identified as 2-methyl-3-cyano-5-isopropylphenol. R_F = 0.5 (dichloromethane–hexane, 1:1). $[\alpha]_D^{20}$ = –49.26 (*c* 1, $CHCl_3$); mp 77 °C (hexane). IR (KBr, cm^{-1}) *v*: 3412, 2979, 2959, 2938, 2916, 2874, 2241, 1713, 1477, 1469, 1448, 1429, 1381, 1369, 1346, 1313, 1245, 1231, 1218, 1147, 1076, 870, 628. ^{1}H NMR ($CDCl_3$, 300 MHz) δ: 2.58–2.44 (m, 3 H), 2.27 (dddd, 1H, *J* = 2.4, 2.7, 2.7, 13.5 Hz), 2.14 (dd, 1H, *J* =13.2, 12.9 Hz), 1.81 (ddd, 1H, *J* = 12.6, 12.6, 12.6 Hz), 1.63 (dd, 1H, *J* = 12.6, 14.1 Hz), 1.61 (m, 1H), 1.25 (d, 3H, *J* = 6.0 Hz), 0.93 (d, 3H, *J* = 6.6 Hz), 0.92 (d, 3H, *J* = 5.4 Hz). ^{13}C NMR ($CDCl_3$, 75 MHz) δ: 207.54, 120.28, 46.35, 44.53, 43.71, 36.13, 32.78, 32.36, 19.28, 19.06, 12.71. MS (+EI) *m/z* (%): 179 (100). HRMS (+EI) calcd for $C_{11}H_{17}N_1O_1$: 179.13101; found: 179.13136.

(3S,5S)-3-Hydroxy-2-methyl-5-(prop-1-en-2-yl)cyclohex-1-enecarbonitrile (34)

To the cooled (4 °C) solution of enone **28** (50 mg, 29 mmol) in methanol (2 mL) was added $CeCl_3{\cdot}7H_2O$ (106 mg, 29 mmol). After 5 min of stirring, $NaBH_4$ (11 mg, 29 mmol) was added portionwise. After an additional 10 min stirring, the reaction was quenched by the addition of a citric acid solution (0.5 mL, 5% *w*/*w*) and concentrated. The residue was dissolved in dichloromethane (25 mL) and washed with citric acid (5 mL, 5% *w*/*w*). The aqueous layer was re-extracted with additional dichloromethane (5 mL), the combined organic layers were dried over $MgSO_4$, and then concentrated to yield essentially pure product. Chromatography (silica, 5 mL, dichloromethane) yielded 48 mg (95%) of the allylic alcohol **34** as a colourless oil. R_F = 0.2 (dichloromethane). $[\alpha]_D^{20}$ = 40.42 (*c* 1, $CHCl_3$). IR (KBr, cm^{-1}) *v*: 3446, 3084, 2926, 2859, 2215, 1646, 1441, 1378, 1288, 1261, 1071, 1056, 1025, 895. ^{1}H NMR ($CDCl_3$, 300 MHz) δ: 4.81 (s, 1H), 4.76 (s, 1H), 4.24 (m, 1H), 2.36–2.13 (m, 5 H), 2.11 (s, 3H), 1.75 (s, 3H), 1.55 (ddd, 1H, *J* = 10.2, 12.0, 12.0 Hz). ^{13}C NMR ($CDCl_3$, 75 MHz) δ: 154.69, 146.75, 118.34, 110.52, 108.08, 70.25, 39.28, 36.62, 32.71, 20.43, 18.33. MS (+EI) *m/z* (%): 177 (3), 159 (100), 144 (33), 134 (59). HRMS (+EI) calcd for $C_{11}H_{15}N_1O_1$: 177.11536; found: 177.11525. HRMS (+EI) calcd for $C_{11}H_{13}N_1$: 159.10480; found: 159.10496.

Reduction of 28 to 31a, 31b, and 31c

To a round-bottomed flask containing water (5 mL) and tetrabutylammonium bromide (100 mg, 0.3 mmol) was added a solution of enone **28** (175 mg, 1.0 mmol) in toluene (5 mL). The emulsion was degassed in an ultrasonic bath for 20 min. A condenser was attached, and the system was flushed with nitrogen. Sodium bicarbonate (1.52 g, 18 mmol) was added, and the reaction mixture was heated to reflux. Sodium dithionite (7 × 200 mg, 85%, 6.95 mmol) was added in seven portions over 2 h. After an additional 30 min of stirring at reflux, the reaction mixture was allowed to cool to room temperature. The reaction mixture was diluted with CH_2Cl_2 (50 mL) and water (10 mL). The aqueous layer was extracted with CH_2Cl_2 (3 × 30 mL). The combined organic extracts were washed with 0.5 N HCl (5 mL), then water (5 mL), and dried over magnesium sulfate. After filtration and evaporation of the solvent, the crude mixture was purified via flash column chromatography (EtOAc in hexanes, 10%–25%) to yield 145 mg (82%) of the mixture consisting of three of the four isomers of cyanoketone **31**. This mixture was suitable for use in the elimination to (+)-carvone.

Identification of isomers 31a, 31b, and 31c

To a round-bottomed flask containing water (60 mL), sodium bicarbonate (4.31 g, 51.30 mmol), and tetrabutylammonium bromide (275 mg, 0.855 mmol) was added a solution of enone **28** (500 mg, 2.85 mmol) in toluene (60 mL). The reaction mixture was heated to reflux, and sodium dithionite (6 × 875 mg, 4.28 mmol) was added in six portions over 3 h. After an additional 1 h of stirring at reflux, the reaction mixture was allowed to cool to room temperature. The organic layer was separated from the aqueous layer and then dried over magnesium sulfate. After filtration and evaporation of solvent, the crude mixture was purified via flash column chromatography (hexane – diethyl ether, 7:1) to provide 75 mg (15%) of saturated ketone **31b** as a white solid. Further separation provided the remaining isomers **31a** and **31c**.

(1S,2S,5S)-2-Methyl-3-oxo-5-(prop-1-en-2-yl) cyclohexanecarbonitrile (31a)

R_F = 0.17 (hexanes–EtOAc, 5:1). ^{1}H NMR (300 MHz, $CDCl_3$, ppm) δ: 4.86 (s, 1H), 4.80 (s, 1H), 3.34 (dt, *J* = 6.0, 3.7 Hz, 1H), 2.86–2.72 (m, 1H), 2.66–2.47 (m, 2H), 2.36–2.18 (m, 2H), 2.05–1.86 (m, 1H), 1.77 (s, 3H), 1.25 (d, *J* = 6.6 Hz, 3H).

^{1}H NMR data are in agreement with the literature.[14]

(1R,2S,5S)-2-Methyl-3-oxo-5-(prop-1-en-2-yl) cyclohexanecarbonitrile (31b)

White solid. R_F = 0.42 (hexane – ethyl acetate, 5:1). $[\alpha]_D^{20}$ = –56 (*c* 1, $CHCl_3$). mp 82–84 °C (first crystallization: hexanes – diethyl ether; second crystallization: mp 85–86 °C (lit.[18] mp 86.5). IR ($CHCl_3$, cm^{-1}) *v*: 2244, 1719, 1648, 1452, 901. ^{1}H NMR ($CDCl_3$, 600 MHz, ppm) δ: 4.85 (s, 1H), 4.78 (s, 1H), 2.61–2.52 (m, 3 H), 2.40–2.36 (m, 3H), 2.01 (ddd, 1H, *J* = 10.9, 11.9, 12.4 Hz), 1.75 (s, 3H), 1.28 (d, 3H, *J* = 6.4 Hz). ^{13}C NMR ($CDCl_3$, 150 MHz, ppm) δ: 206.66, 145.27, 119.98, 111.30, 46.28, 44.14, 36.00, 34.25, 20.23, 12.67. MS (+EI) *m/z* (%): 177 (12), 95 (55), 82 (54), 68 (100), 67 (74), 41 (41). HRMS (+EI) calcd for $C_{11}H_{15}NO$: 177.11536; found: 177.11509.

(1S,2R,5S)-2-Methyl-3-oxo-5-(prop-1-en-2-yl) cyclohexanecarbonitrile (31c)

Viscous oil; assignment is tentative (**31c** has a mp of 13 °C). IR (KBr, cm^{-1}) *v*: 2359, 1650, 1385, 1088. ^{1}H NMR (600 MHz, $CDCl_3$, ppm) δ: 4.87 (s, 1H), 4.79 (s, 1H), 3.14 (td, *J* = 5.1, 2.5 Hz, 1H), 2.64 (t, *J* = 12.8 Hz, 1H), 2.40 (dt, *J* = 12.8, 2.3 Hz, 1H), 1.87–1.80 (m, 1H), 1.78 (s, 1H), 1.61–1.49 (m, 1H), 1.45 (d, *J* = 6.8 Hz, 1H). MS (+EI) *m/z* (%): 177 (27), 95 (72), 82 (52), 69 (29), 68 (100), 67 (70), 41 (42).; HRMS (+EI) calcd for $C_{11}H_{15}NO$: 177.11536; found: 177.11498.

Can. J. Chem. Downloaded from www.nrcresearchpress.com by 80.58.250.72 on 09/16/12
For personal use only.

ent-Carvone

The mixture of saturated ketones **31a**, **31b**, and **31c** obtained (445 mg, 2.5 mmol) was dissolved in MeOH (15 mL). The solution was degassed in an ultrasonic bath for 5 min (to avoid oxidation of Fe(II) by air). A condenser was attached, and $FeSO_4 \cdot 7H_2O$ (1.39 g, 5.0 mmol) was added. KOH (2.25 g, 35 mmol, 10 + 4 equiv) was added to a vigorously stirred suspension to generate $Fe(OH)_2$. The reaction flask was placed in a preheated oil bath, and the mixture heated at reflux for 20 min. The resulting dark black mixture was quickly cooled to room temperature and diluted with EtOAc (100 mL) and water (10 mL). The organic layer was washed with 0.2 N HCl (3 × 10 mL) and dried over magnesium sulfate. After filtration and evaporation of solvent, the crude product was filtered through a short pad of silica gel (eluted with 10% EtOAc in hexanes) to yield *S*-(+)-carvone (296 mg, 79%).

S-(+)-Carvone

$[\alpha]_D^{19} = +54.2$ (*c* 1, $CHCl_3$). ^1H NMR (300 MHz, $CDCl_3$) δ: 6.82–6.65 (m, 1H), 4.80 (s, 1H), 4.75 (s, 1H), 2.78–2.51 (m, 2H), 2.51–2.37 (m, 1H), 2.37–2.19 (m, 2H), 1.85–1.76 (m, 3H), 1.75 (s, 3H). (Commercially available (+)-carvone is 96% optically pure; (–)-carvone is 98% optically pure).

Acknowledgements

The authors are grateful to the following agencies for financial support of this work: Natural Sciences and Engineering Research Council of Canada (NSERC) (Idea to Innovation and Discovery Grants); Canada Research Chair Program; Canada Foundation for Innovation (CFI); Research Corporation; Noramco, Inc.; TDC Research, Inc.; TDC Research Foundation; and Brock University, St. Catharines, Ontario. Thanks are also due to the Ministry of Education (Spain) for fellowships to V.S. (AP2006-03468ESTANCIA-2010). The authors thank K. Ridolfo for preliminary experiments performed as part of his fourth-year Honours Thesis, Spring 2010.

References

(1) Luzzio, F. A. *Org. React.* **1998**, *53*, 1.
(2) Dauben, W. G.; Michno, D. M. *J. Org. Chem.* **1977** *42* (4), 682. doi:10.1021/jo00424a023.
(3) Hudlicky, M. *Oxidations in Organic Chemistry*; ACS Monograph 186; American Chemical Society: Washington, DC, 1990; pp 86–87.
(4) Wender, P. A.; Eissenstat, M. A.; Filosa, M. P. *J. Am. Chem. Soc.* **1979** *101* (8), 2196. doi:10.1021/ja00502a042.
(5) Werner, L.; Machara, A.; Hudlicky, T. *Adv. Synth. Catal.* **2010** *352* (1), 195. doi:10.1002/adsc.200900844.
(6) Shen, Z.-L.; Ji, S.-J. *Synth. Commun.* **2009** *39* (5), 775. doi:10.1080/00397910802431149.
(7) Wenkert, E.; Hudlicky, T. *Synth. Commun.* **1977** *7* (8), 541. doi:10.1080/00397917709409274.
(8) [Review:]van der Drift, R. C.; Bouwman, E.; Drent, E. *J. Organomet. Chem.* **2002** *650* (1–2), 1. doi:10.1016/S0022-328X(02)01150-6.
(9) Arnold, R. T.; Elmer, O. C.; Dodson, R. M. *J. Am. Chem. Soc.* **1950** *72* (10), 4359. doi:10.1021/ja01166a007.
(10) Marshall, J. A.; Bierenbaum, R. *J. Org. Chem.* **1977** *42* (20), 3309. doi:10.1021/jo00440a029.
(11) For reduction of enones with sodium dithionite see: Louis-Andre, O.; Gelbard, G. *Tetrahedron Lett.* **1985** *26* (7), 831. doi:10.1016/S0040-4039(00)61940-8.
(12) Cocker, W.; Grayson, D. H.; Shannon, P. V. R. *J. Chem. Soc. Perkin Trans.* **1995** *1* (9), 1153. doi:10.1039/p19950001153.
(13) Verstegen-Haaksma, A. A.; Swarts, H. J.; Jansen, B. J. M.; de Groot, A. *Tetrahedron* **1994** *50* (33), 10073. doi:10.1016/S0040-4020(01)89623-X.
(14) Lagriffoul, P.-H.; Tadros, Z.; Taillades, J.; Commeeyras, A. *J. Chem. Soc. Perkin Trans.* **1992**, *2*, 1279. doi:10.1039/P29920001279.
(15) Lapworth, A. *J. Chem. Soc.* **1906** *89*, 945.
(16) Lapworth, A. *J. Chem. Soc.* **1906** *89*, 1819.
(17) Lapworth, A.; Steele, V. *J. Chem. Soc.* **1911**, *99*, 1877.
(18) Djerassi, C.; Schneider, R. A.; Vorbrueggen, H.; Allinger, N. L. *J. Org. Chem.* **1963** *28* (6), 1632. doi:10.1021/jo01041a049.
(19) Valeev, R. F.; Vostrikov, N. S.; Miftakhov, M. S. *Russ. J. Org. Chem.* **2009** *45* (6), 810. doi:10.1134/S1070428009060025.
(20) Lee, D. G.; Downey, W. L.; Maass, R. M. *Can. J. Chem.* **1968** *46* (3), 441. doi:10.1139/v68-070.
(21) Hareau, G. P.-J.; Koiwa, M.; Hikichi, S.; Sato, F. *J. Am. Chem. Soc.* **1999** *121* (15), 3640. doi:10.1021/ja9843122.
(22) Wada, M.; Takahashi, T.; Domae, T.; Fukuma, T.; Miyoshi, N.; Smith, K. *Tetrahedron: Asymmetry* **1997** *8* (23), 3939. doi:10.1016/S0957-4166(97)00570-3.
(23) Cronyn, M. W.; Goodrich, J. E. *J. Am. Chem. Soc.* **1952** *74* (13), 3331. doi:10.1021/ja01133a034.
(24) Zhao, Y.; Yeung, Y.-Y. *Org. Lett.* **2010**, *12* (9), 2128. doi:10.1021/ol100603q.
(25) Farcasiu, D.; Schleyer, P. V. R.; Ledlie, D. B. *J. Org. Chem.* **1973** *38* (20), 3455. doi:10.1021/jo00960a002.
(26) Zimmerman, H. E.; Pasteris, R. J. *J. Org. Chem.* **1980** *45* (24), 4864. doi:10.1021/jo01312a013.
(27) Mease, R. C.; Hirsch, J. A. *J. Org. Chem.* **1984** *49* (16), 2925. doi:10.1021/jo00190a017.
(28) Kirsten, C. N.; Herm, M.; Schrader, T. H. *J. Org. Chem.* **1997** *62* (20), 6882. doi:10.1021/jo970854a.

NaZSM-5-catalyzed dimethyl carbonate synthesis via the transesterification of ethylene carbonate with methanol

Zhen-Zhen Yang, Xiao-Yong Dou, Fang Wu, and Liang-Nian He

Can. J. Chem. Downloaded from www.nrcresearchpress.com by Xi'an Jiaotong University on 09/19/12
For personal use only.

Abstract: NaZSM-5 zeolite was found to be an efficient heterogeneous catalyst for the synthesis of dimethyl carbonate (DMC), which can serve as a building block, an additive to fuel oil, and an electrolyte in batteries, via the transesterification of ethylene carbonate (EC) with methanol. Notably, 77% DMC yield and 97% selectivity were achieved under mild reaction conditions. Furthermore, the effects of various reaction parameters such as catalyst loading, reaction time, and methanol/EC molar ratio on the catalytic performance were investigated in detail. This protocol was found to be applicable to a variety of alcohols, producing the corresponding dialkyl carbonates with moderate yields and selectivities. Moreover, the catalyst can be recovered by simple filtration with retention of catalytic activity; a stable crystal configuration and a slight alteration of its superficial structure were observed by X-ray diffraction and BET measurements.

Key words: ethylene carbonate, zeolite, transesterification, dimethyl carbonate.

Résumé : On a trouvé que la zéolite NaZSM-5 est un catalyseur hétérogène efficace pour la synthèse, par le biais d'une transestérification du carbonate d'éthylène (CE) avec du méthanol. du carbonate de diméthyle (CDM) qui peut être utilisé produit de départ en synthèse, comme additif pour les huiles à chauffage et comme électrolyse dans les batteries. Il est remarquable que le rendement de 77 % en CDM avec une sélectivité de 97 % ait été obtenu dans des conditions réactionnelles douces. De plus, on a étudié en détail les effets de divers paramètres réactionnels, comme la charge de catalyseur, le temps de réaction et le rapport molaire méthanol/CE. On a trouvé que ce protocole peut être appliquer à une variété d'alcools conduisant à la production des carbonates de dialkyle correspondants, avec des rendements et des sélectivités modérées. De plus, le catalyseur peut être récupéré par simple filtration avec rétention de son activité catalytique; des mesures de BET et de diffraction des rayons-X indiquent que la configuration cristalline est stable, mais qu'elle subit de légères altérations de sa structure superficielle.

Mots-clés : carbonate d'éthylène, zéolite, transestérification, carbonate de diméthyle.

[Traduit par la Rédaction]

Introduction

Dimethyl carbonate has been drawing much attention as a safe, non-corrosive, and environmentally friendly building block for the production of polycarbonate and other chemicals.[1] Most promisingly, DMC could be of interest as an additive to fuel oil owing to a high octane number, reducing particulate emission from diesel engines.[2] In addition, it has been used as an electrolyte in lithium batteries owing to its high dielectric constant.[3] Therefore, the development of green and efficient DMC production technology and investigation of its fuel properties have attracted much more attention in the oil and chemical industries. From the viewpoint of green chemistry, the two-step transesterification process (steps 1 and 2) utilizing CO_2 as a raw material, as illustrated in Scheme 1, is more promising than other commercial processes[4] including methanolysis of phosgene, carbon monoxide–nitrite process, and gas-phase oxidative carbonylation of methanol using toxic, corrosive, flammable, and explosive gases.

In past decades, numerous homogeneous catalysts have been developed for the transesterification of alkylene carbonates with methanol, such as alkali metals,[5] quaternary ammonium salts,[6] and ionic liquids.[7] However, these catalysts are difficult to recover from the reaction mixture in homogeneous catalysis. In this context, easily recovered heterogeneous catalysts would be more desirable. Indeed, the transesterification reaction also proceeds very efficiently with heterogeneous catalysts including molecular sieves,[8] basic metal oxides,[9] metal cyanides,[10] basic salts,[11] dawsonites,[12] hydrotalcites,[13] smectites,[14] basic anion-exchange resin,[15] functionalized chitosan,[16] and silica.[17] Although great advances have been seen,[5–17] most catalytic processes suffer from low catalytic activity, and high reaction temperature and (or) the use of expensive metallic compounds are often required. So development of efficient, cost-effective, and easily recycled catalysts for DMC synthesis is still highly desired.

In the framework of our continuous effort to synthesize organic carbonates from CO_2,[16,18,19] we would like to report herein that DMC synthesis via a transesterification reaction of ethylene carbonate (EC) and methanol was achieved by

Received 4 July 2010. Accepted 15 February 2011. Published at www.nrcresearchpress.com/cjc on 15 April 2011.

Z.-Z. Yang, X.-Y. Dou, F. Wu, and L.-N. He. State Key Laboratory and Institute of Elemento-Organic Chemistry, Nankai University, Tianjin 300071, China.

Corresponding author: L.-N. He (e-mail: heln@nankai.edu.cn).

Can. J. Chem. Downloaded from www.nrcresearchpress.com by Xi'an Jiaotong University on 09/19/12
For personal use only.

Scheme 1. (1) Cyclic carbonate synthesis via a coupling reaction of epoxide with CO_2. (2) Dimethyl carbonate (DMC) synthesis via the transesterification of a cyclic carbonate with methanol.

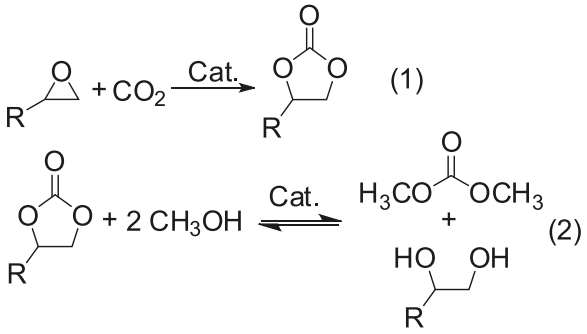

Table 1. Synthesis of dimethyl carbonate (DMC) via transesterification of ethylene carbonate (EC) with methanol catalyzed by various bases.

Entry	Catalyst	Yield of DMC (%)[a]	Selectivity of DMC (%)[a]
1	—	5	—
2	NaZSM-5[b]	77	97
3	NaOH	71	83
4	K_2CO_3	68	77
5	CH_3ONa	71	85
6	MgO	74	94
7	*n*-Bu_3N	19	40
8	Et_3N	64	80
9	TMG[c]	72	85
10	ZnO	3	11
11	Al_2O_3	5	29

Note: Reaction conditions were EC (30 mmol), methanol (240 mmol), catalyst (0.25 g for solid catalyst; 5 mol% relative to EC for homogeneous catalyst), 70 °C, 3 h.

[a]Determined by GC using biphenyl as internal standard.

[b]NaZSM-5 zeolite (Si/Al = 38, surface area = 281 m^2/g, pore size = 0.66 nm), supplied by Catalyst Plant of Nankai University, was calcined in air at 500 °C for 3 h.

[c]TMG, tetramethylguanidine.

employing a commercially available NaZSM-5 zeolite as an efficient and recyclable catalyst. Perfect catalyst performance in this process was obtained under mild conditions.

Results and discussion

In the initial study, the transesterification of EC with methanol was conducted in the presence of various homogeneous organic and inorganic bases. Experiments were carried out under identical operating conditions (Table 1). A small amount of DMC could be detected even without any catalyst (entry 1), but basic catalysts could greatly improve the reaction (entries 2–6, 8–9). In particular, NaZSM-5 zeolite (entry 2) showed higher catalytic activity than alkali metal compounds (NaOH, K_2CO_3, CH_3ONa; entries 3–5), an alkali earth metal oxide (MgO; entry 6), and organic bases such as tributylamine, triethylamine, and tetramethylguanidine (entries 7–9). A transition metal oxide (ZnO) and aluminum oxide (entries 10 and 11) also showed much lower activity than NaZSM-5 zeolite. It is worth mentioning that 2-hydroxyethyl methyl carbonate (HEMC), regarded as the intermediate of

Fig. 1. (*a*) Formation of 2-hydroxyethyl methyl carbonate. (*b*) ^1H NMR spectrum of the reaction mixture after removing DMC and MeOH under reduced pressure. (*c*) ^{13}C NMR spectrum of the mixture.

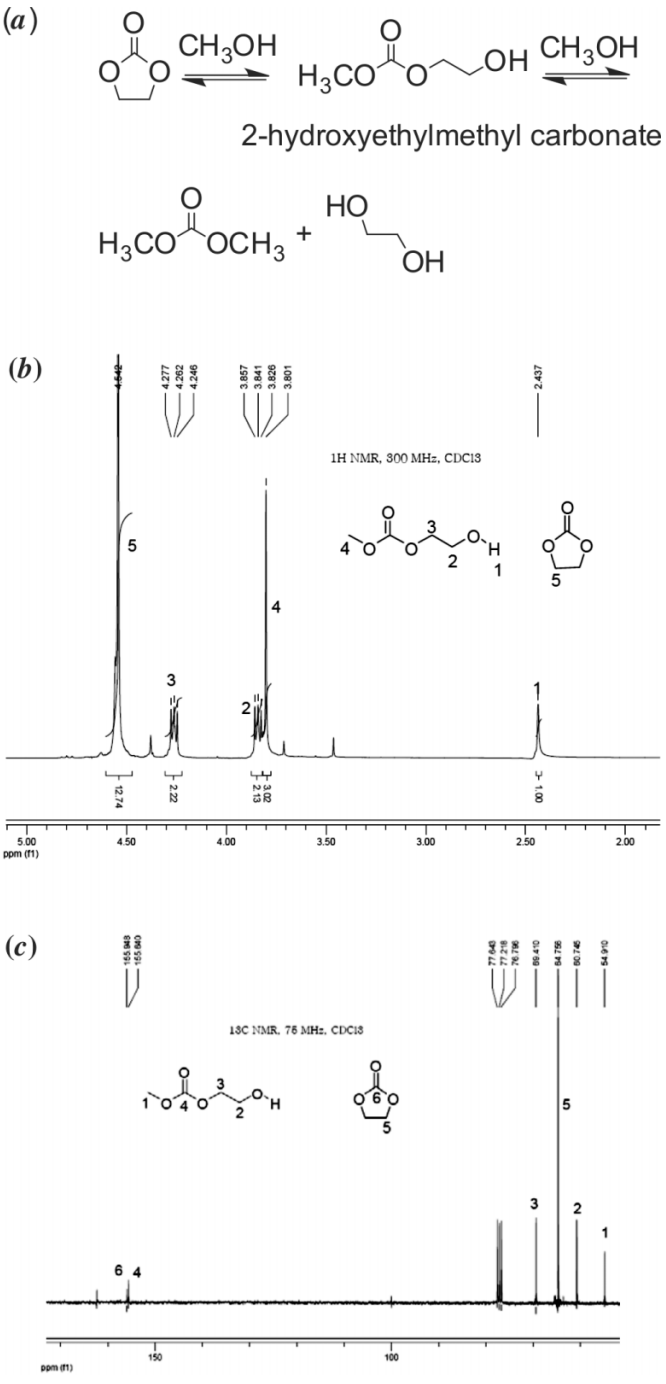

DMC formation (Fig. 1*a*),[7b] was detected by ^1H NMR (Fig. 1*b*) and ^{13}C NMR (Fig. 1*c*). A 77% DMC yield with 97% selectivity was attained by using NaZSM-5 as the catalyst at 70 °C for 3 h.

Subsequently, the influence of catalyst loading on DMC yield and selectivity was investigated under otherwise identical reaction conditions. As shown in Fig. 2, the catalyst amount had a considerable influence on DMC yield. It is worth noting that lower catalyst loadings such as 0.1 g and

Can. J. Chem. Downloaded from www.nrcresearchpress.com by Xi'an Jiaotong University on 09/19/12
For personal use only.

Fig. 2. Influence of catalyst loading on DMC yield and selectivity using NaZSM-5 as catalyst. Reaction conditions: EC (30 mmol), methanol (240 mmol), 70 °C, 3 h.

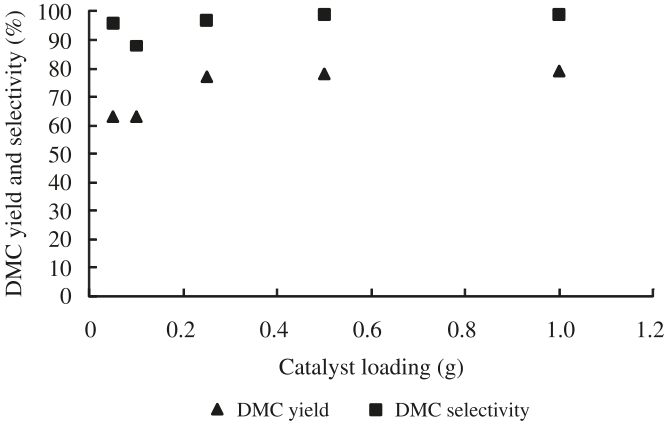

Fig. 3. Effect of reaction time on DMC yield and selectivity using NaZSM-5 as catalyst. Reaction conditions: EC (30 mmol), methanol (240 mmol), NaZSM-5 (0.25 g), 70 °C.

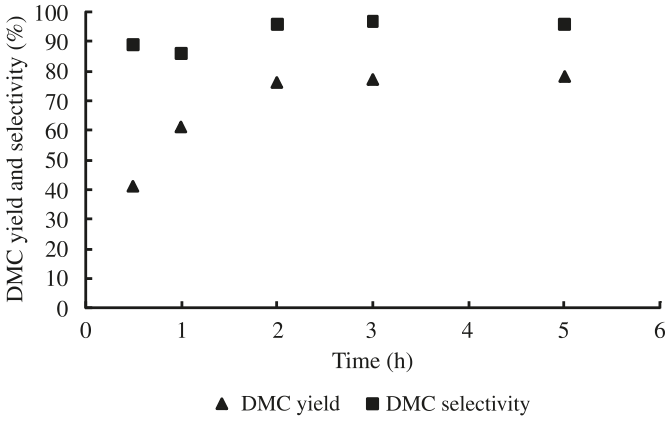

0.05 g gave lower DMC yield and selectivity, probably owing to facile formation of HEMC at low catalyst concentration, whereas higher catalyst loadings would be required for further transesterification of HEMC with methanol to form DMC. A 77% yield and 97% selectivity of DMC were obtained at 0.25 g of catalyst loading. However, further increasing the catalyst loading to 0.5 g and 1 g produced almost no change in DMC yield and selectivity. Therefore, a catalyst loading of 0.25 g is enough for this transformation within 3 h.

The dependence of DMC yield and selectivity on reaction time was also evaluated. It was found that the reaction time had a strong influence on the yield and selectivity of DMC. As shown in Fig. 3, the reaction rate was fast at the initial stage and remained almost invariant after 2 h. This hints that the transesterification reaction reached equilibrium after approximately 2 h under the reaction conditions. Notably, the selectivity of DMC was slightly lower within the first hour of reaction, probably owing to the facile formation of HEMC at the initial stage, whereas a longer reaction time led to further transesterification of HEMC with methanol for DMC formation. Therefore, we conclude that a reaction time of 2 h is appropriate for DMC synthesis under the reaction conditions used in this study.

The influence of the methanol/EC ratio on the reaction outcome was investigated under identical reaction conditions. As shown in Fig. 4, the methanol/EC ratio had a significant impact on the transesterification reaction. As the molar ratio of methanol/EC varied from 4:1 to 16:1, both DMC yield and selectivity increased gradually, presumably because of the reversible nature of the transesterification step.[18] In addition, much lower selectivity of DMC with a 4:1 molar ratio of methanol/EC was probably due to the prior formation of HEMC. Nevertheless, further increasing the methanol/EC molar ratio to 30 did not result in a significant change, probably owing to a dilution effect, which would cause a low concentration of EC in the vicinity of the catalyst and retard the interaction between EC and the catalyst. To overcome the thermodynamic limitation of the transesterification and to realize the complete conversion of EC, the reaction was continued for another hour after it reached equilibrium and the

Fig. 4. The dependence of DMC yield and selectivity on the methanol/EC ratio using NaZSM-5 as catalyst. Reaction conditions: EC (30 mmol), catalyst loading (0.25 g), 70 °C, 3 h.

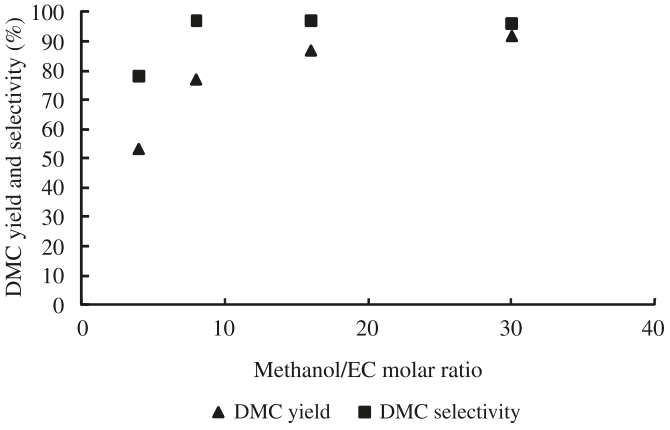

product was simultaneously removed through distillation under atmosphere pressure. Indeed, EC was completely converted to DMC with a methanol/EC molar ratio of 30:1, as determined by GC analysis.

Various alcohols including methanol, ethanol, and propan-2-ol were also tested for the synthesis of dialkyl carbonates (DACs) through the present process for the transesterification of various alcohols with EC and propylene carbonate (PC). As shown in Table 2, the yield and selectivity of DACs decreased with increasing alkyl chain length of alcohols (entries 1–3, 4–6) and increasing steric hindrance of alkylene carbonates (entry 1 vs. 4, 2 vs. 5, 3 vs. 6).[15] The reaction of EC with methanol under the reaction conditions gave 77% yield and 97% selectivity of DMC (entry 1). The reactivity decreased sharply when the substrate changed from EC to PC, while the selectivity remained high (entry 1 vs. 4). This is due to the steric effect of the bulky methyl group in PC as compared with symmetrical EC. Moreover, the reactions with ethanol and propan-2-ol appeared to be more sluggish (entry 1 vs. 2–3). It was observed that an increase in the number of carbon atoms of the alcohol led to a decrease in the yield and selectivity of the DAC, presumably because of increasing steric hindrance. On the other hand, ethoxylate

Can. J. Chem. Downloaded from www.nrcresearchpress.com by Xi'an Jiaotong University on 09/19/12
For personal use only.

Table 2. Process for dialkyl carbonate (DAC) synthesis using different alcohols.

Entry	Alcohol	Alkylene carbonate	Yield of DAC (%)[a]	Selectivity of DAC (%)[a]
1	MeOH	EC	77	97
2	EtOH	EC	20	45
3	^{i}PrOH	EC	3	20
4	MeOH	PC	39	91
5	EtOH	PC	3	75
6	^{i}PrOH	PC	Trace	Trace
7[b]	^{i}PrOH	PC	35	96
8[b]	MeOH	PC	63	90
9[c]	MeOH	EC	75	98
10[d]	MeOH	EC	71	96

Note: Reaction conditions were EC (30 mmol), alcohol (240 mmol), NaZSM-5 (0.25 g), 70 °C, 3 h.

[a]Determined by GC.

[b]NaOH (5 mol% relative to EC) was used as a catalyst instead of NaZSM-5.

[c]Recovered catalyst, second run.

[d]Recovered catalyst, third run.

and propan-2-ol anions were more difficult to form in comparison with methanol, probably because of the electronic effect. It is worth mentioning that ZSM-5 zeolite contains straight channels, and a large substrate like ^{i}PrOH almost loses reactivity (entry 6), presumably owing to diffusional restriction as previously reported.[20] The pore diffusion limitation induced by the large molecular size of the reactants could play an important role in the transesterification reaction when using a zeolite catalyst. Furthermore, comparison of heterogeneous catalysis with its homogenous counterpart (entry 1, Table 2 vs. entry 3, Table 1; entry 6 vs. 7, Table 2; entry 4 vs. 8, Table 2) also supports this hypothesis.

To better understand the present catalysis, both fresh catalyst and recovered catalyst were characterized using X-ray diffraction (XRD) and BET.[21] The solid catalyst can be easily recovered from the reaction mixture simply by filtration, washing with methanol, and drying at 60 °C. As shown in Fig. 5, the XRD patterns of the fresh catalyst and the recovered catalyst did not show appreciable differences, indicating the stable crystal configuration of the catalyst. In addition, based on the BET measurement, the surface area and the pore size of the zeolite changed from 281 m^2/g, 0.66 nm to 273 m^2/g, 0.66 nm, indicating slight changes of the catalyst superficial structure after reaction. To further test catalyst reusability, the reaction was carried out under the same conditions (30 mmol EC, 240 mmol methanol, reaction temperature 70 °C, reaction time 3 h) with the recovered NaZSM-5. The solid catalyst was found to be recyclable and showed retention of activity in 3 recycles (entries 9 and 10, Table 2).

Experimental section

Chemical reagents

Methanol (99.5%) was purified using magnesium and stored under a nitrogen atmosphere. Other reagents were of analytical grade and were used without further purification.

Fig. 5. X-ray diffraction pattern of fresh (*a*) and recovered (*b*) catalyst.

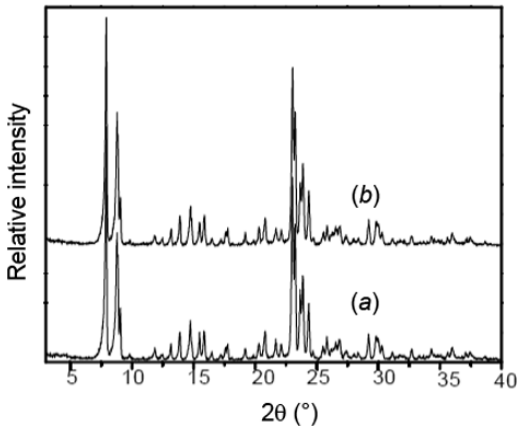

Characterization

The crystalline phase of the as-prepared sample was characterized at room temperature by X-ray diffraction using a Rigaku D/MAX-2500 powder diffractometer in a 2θ range from 3° to 40° equipped with graphite-monochromatized Cu Kα radiation (λ = 1.541874 Å). The powder samples were mounted on a silicon plate for X-ray measurement. Pore size distributions, BET surface areas, and pore volumes were measured by nitrogen adsorption/desorption at –196 °C using a BELSORP-mini gas adsorption analyzer (BEL Japan, Inc.) according to the standard IUPAC recommendations. Prior to measurement, the sample was degassed for 3 h at 300 °C to 0.1 Pa. The specific surface area, S_{BET}, was calculated by applying the BET equation.[21] Average pore diameter was estimated by the average method from the relation $4V_p/S_{BET}$, where V_p is the total pore volume (at $P/P_0 = 0.975$). Pore width distribution over the mesopore range was generated by Barrett–Joyner–Halenda (BJH) analysis of the adsorption branches and the average pore width was also estimated from the BJH distribution.

The analysis of products was performed with a gas chromatograph (Shimadzu 2014 chromatograph) equipped with a capillary column (RTX-5, 30 m × 0.25 mm) using a flame ionization detector. The intermediate was characterized by NMR spectra recorded on a Bruker 300 MHz spectrometer in $CDCl_3$. ^{1}H and ^{13}C NMR chemical shifts (δ) in ppm are downfield from tetramethylsilane ($CDCl_3$: $\delta_C = 77.0$ ppm; residual $CHCl_3$ in $CDCl_3$: $\delta_H = 7.26$ ppm).

Typical procedure for DMC synthesis via transesterification of EC with methanol

A mixture of ethylene carbonate (2 mL, 30 mmol), methanol (9.7 mL, 240 mmol), NaZSM-5 (0.25 g), and biphenyl (60 mg, an internal standard for GC analysis) was added to a 50 mL flask and refluxed for 3 h. The vessel was then cooled to room temperature. The products were analyzed by GC and further identified by GC-MS (HP G1800A) by comparing retention times and fragmentation patterns with those of authentic samples.

Conclusions

Commercially available NaZSM-5 zeolite was found to be

Can. J. Chem. Downloaded from www.nrcresearchpress.com by Xi'an Jiaotong University on 09/19/12
For personal use only.

a highly efficient catalyst for DMC synthesis through the transesterification reaction of EC with methanol under mild reaction conditions. A 77% yield and 97% selectivity of DMC were obtained under optimal reaction conditions. It is worth mentioning that EC was completely converted to DMC when the product was simultaneously removed through distillation under atmospheric pressure. This catalytic system can be used with various alcohols and alkylene carbonates, obtaining the corresponding dialkyl carbonates. Variation of catalytic activity towards different substrates is correlated with steric effect, electronic effect, and pore diffusion limitation of the NaZSM-5 zeolite. In addition, the catalyst can be recovered by simple filtration with retention of catalytic activity. These characteristics make it an ideal catalyst system for DMC production in terms of green process and potential industrial applications. Further applications of NaZSM-5 zeolite towards other reactions are currently under investigation in our laboratory.

Acknowledgements

We gratefully acknowledge the National Natural Science Foundation of China (No. 20672054, 20872073), the 111 project (B06005), and the Committee of Science and Technology of Tianjin for financial support.

References

(1) Fujita, S.-i.; Bhanage, B. M.; Ikushima, Y.; Arai, M. *Green Chem.* **2001** *3* (2), 87. doi:10.1039/b100363l.

(2) Pacheco, M. A.; Marshall, C. L. *Energy Fuels* **1997** *11* (1), 2. doi:10.1021/ef9600974.

(3) Wei, T.; Wang, M.; Wei, W.; Sun, Y.; Zhong, B. *Green Chem.* **2003** *5* (3), 343. doi:10.1039/b210716n.

(4) (a) Jessop, P. G.; Ikariya, P. T.; Noyori, R. *Chem. Rev.* **1999** *99* (2), 475. doi:10.1021/cr970037a.; (b) Sakakura, T.; Kohno, K. *Chem. Commun. (Camb.)* **2009** (11): 1312. doi:10.1039/b819997c.

(5) Han, M. S.; Lee, B. G.; Ahn, B. S.; Park, K. Y.; Hong, S. I. *React. Kinet. Catal. Lett.* **2001** *73* (1), 33. doi:10.1023/A:1013904317108.

(6) Jeong, E.-S.; Kim, K.-H.; Park, D.-W.; Park, S.-W.; Lee, J.-W. *React. Kinet. Catal. Lett.* **2005** *86* (2), 241. doi:10.1007/s11144-005-0318-y.

(7) (a) Ju, H. Y.; Manju, M. D.; Park, D. W.; Choe, Y.; Park, S.-W. *React. Kinet. Catal. Lett.* **2007** *90* (1), 3. doi:10.1007/s11144-007-4965-z.; (b) Yang, Z.-Z.; He, L.-N.; Dou, X.-Y.; Chanfreau, S. *Tetrahedron Lett.* **2010** *51* (21), 2931. doi:10.1016/j.tetlet.2010.03.114.

(8) Tatsumi, T.; Watanabe, Y.; Koyano, K. A. *Chem. Commun. (Camb.)* **1996** (19): 2281. doi:10.1039/cc9960002281.

(9) (a) Abimanyu, H.; Kim, C. S.; Ahn, B. S.; Yoo, K. S. *Catal. Lett.* **2007** *118* (1–2), 30. doi:10.1007/s10562-007-9091-z.; (b) Wei, T.; Wang, M. H.; Wei, W.; Sun, Y. H.; Zhong, B. *Fuel Process. Technol.* **2003** *83* (1–3), 175. doi:10.1016/S0378-3820(03)00065-1.; (c) Wang, H.; Wang, M. H.; Liu, S. G.; Zhao, N.; Wei, W.; Sun, Y. H. *J. Mol. Catal. Chem.* **2006** *258* (1–2), 308. doi:10.1016/j.molcata.2006.05.050.; (d) Wang, H.; Wang, M. H.; Zhang, W. Y.; Zhao, N.; Wei, W.; Sun, Y. H. *Catal. Today* **2006** *115* (1–4), 107. doi:10.1016/j.cattod.2006.02.031.; (e) Wang, H.; Wang, M. H.; Zhao, N.; Wei, W.; Sun, Y. H. *Catal. Lett.* **2005** *105* (3–4), 253. doi:10.1007/s10562-005-8699-0.

(10) Srivastava, R.; Srinivas, D.; Ratnasamy, P. *J. Catal.* **2006** *241* (1), 34. doi:10.1016/j.jcat.2006.04.002.

(11) (a) De Filippis, P.; Scarsella, M.; Borgianni, C.; Pochetti, F. *Energy Fuels* **2006** *20* (1), 17. doi:10.1021/ef050142k.; (b) Cui, H. Y.; Wang, T.; Wang, F. J.; Gu, C. R.; Wang, P. L.; Dai, Y. Y. *J. Supercrit. Fluids* **2004** *30* (1), 63. doi:10.1016/S0896-8446(03)00164-5.; (c) Sankar, M.; Nair, C. M.; Murty, K.; Manikandan, P. *Appl. Catal. A Gen.* **2006** *312*, 108. doi:10.1016/j.apcata.2006.06.034.

(12) (a) Stoica, G.; Abelló, S.; Pérez-Ramírez, J. *ChemSusChem* **2009** *2* (4), 301. doi:10.1002/cssc.200800195.; (b) Stoica, G.; Abelló, S.; Pérez-Ramírez, J. *Appl. Catal. A Gen.* **2009** *365* (2), 252. doi:10.1016/j.apcata.2009.06.022.

(13) Watanabe, Y.; Tatsumi, T. *Microporous Mesoporous Mater.* **1998** *22* (1–3), 399. doi:10.1016/S1387-1811(98)00099-7.

(14) (a) Bhanage, B. M.; Fujita, S.; Ikushima, Y.; Torii, K.; Arai, M. *Green Chem.* **2003** *5* (1), 71. doi:10.1039/b207750g.; (b) Bhanage, B. M.; Fujita, S.; He, Y. F.; Ikushima, Y.; Shirai, M.; Torii, K.; Arai, M. *Catal. Lett.* **2002** *83* (3–4), 137. doi:10.1023/A:1021065409888.; (c) Fujita, S. I.; Bhanage, B. M.; Aoki, D.; Ochiai, Y.; Iwasa, N.; Arai, M. *Appl. Catal. A Gen*. **2006** *313* (2), 151. doi:10.1016/j.apcata.2006.07.018.

(15) Dhuri, S. M.; Mahajani, V. V. *J. Chem. Technol. Biotechnol.* **2006** *81* (1), 62. doi:10.1002/jctb.1358.

(16) Zhao, Y.; He, L. N.; Zhuang, Y. Y.; Wang, J. *Chin. Chem. Lett.* **2008** *19* (3), 286. doi:10.1016/j.cclet.2007.12.033.

(17) Feng, X. J.; Lu, X. B.; He, R. *Appl. Catal. A Gen.* **2004** *272* (1–2), 347.

(18) (a) Tian, J. S.; Miao, C. X.; Wang, J. Q.; Cai, F.; Du, Y.; Zhao, Y.; He, L. N. *Green Chem.* **2007** *9* (6), 566. doi:10.1039/b614259a.; (b) Wang, J. Q.; Yue, X. D.; Cai, F.; He, L. N. *Catal. Commun.* **2007** *8* (2), 167. doi:10.1016/j.catcom.2006.05.049.; (c) Wang, J. Q.; Kong, D. L.; Chen, J. Y.; Cai, F.; He, L. N. *J. Mol. Catal. Chem.* **2006** *249* (1–2), 143. doi:10.1016/j.molcata.2006.01.008.

(19) (a) Tian, J. S.; Wang, J. Q.; Chen, J. Y.; Fan, J. G.; Cai, F.; He, L. N. *Appl. Catal. A Gen.* **2006** *301* (2), 215. . doi:10.1016/j.apcata.2005.12.002.; (b) Miao, C. X.; Wang, J. Q.; Wu, Y.; Du, Y.; He, L. N. *ChemSusChem* **2008** *1* (3), 236. doi:10.1002/cssc.200700133.; (c) Dou, X. Y.; Wang, J. Q.; Du, Y.; Wang, E.; He, L. N. *Synlett* **2007** (19): 3058; (d) Du, Y.; Cai, F.; Kong, D. L.; He, L. N. *Green Chem.* **2005** *7* (7), 518. doi:10.1039/b500074b.; (e) Du, Y.; He, L. N.; Kong, D. L. *Catal. Commun.* **2008** *9* (8), 1754. doi:10.1016/j.catcom.2008.02.004.; (f) Wang, J. L.; Wang, J. Q.; He, L. N.; Dou, X. Y.; Wu, F. *Green Chem.* **2008** *10* (11), 1218. doi:10.1039/b807108j.; (g) He, L. N.; Wang, J. Q.; Wang, J. L. *Pure Appl. Chem.* **2009** *81* (11), 2069. doi:10.1351/PAC-CON-08-10-22.; (h) Du, Y.; Wu, Y.; Liu, A. H.; He, L. N. *J. Org. Chem.* **2008** *73* (12), 4709. doi:10.1021/jo800269v.; (i) Du, Y.; Wang, J.-Q.; Chen, J.-Y.; Cai, F.; Tian, J.-S.; Kong, D.-L.; He, L.-N. *Tetrahedron Lett.* **2006** *47* (8), 1271. doi:10.1016/j.tetlet.2005.12.077.

(20) Thomas, B.; Prathapan, S.; Sugunan, S. *Appl. Catal. A Gen.* **2004** *277* (1–2), 247.

(21) Brunauer, S.; Emmett, P. H.; Teller, E. *J. Am. Chem. Soc.* **1938** *60* (2), 309. doi:10.1021/ja01269a023.

Biaryl crosslinkers. I. Crosslinking of a bisazidobiaryl with poly(3-hexylthiophene)

Jaya Lohani, V.R. Balakrishnan, Manoj Gaur, P. Raghunathan, and S.V. Eswaran

Abstract: A new biaryl-based bisazide has been used to crosslink poly(3-hexylthiophene), a conducting polymer useful for organic electronics. Crosslinking was monitored using infrared spectroscopy and film morphology was studied using scanning electron microscopy. Hole mobility studies of the devices prepared from pristine and crosslinked polymer show an increase in hole mobility of one order of magnitude for the latter devices.

Key words: crosslinkers, 2D NMR, bisazide, poly(3-hexylthiophene), hole mobility.

Résumé : On a utilisé un nouveau biazide à base de biaryle pour effectuer une réticulation du poly(3-hexylthiophène), un polymère conducteur utile en électronique organique. On a suivi la réticulation par spectroscopie infrarouge et on a étudié la morphologie du film par microscopie électronique à balayage. Des études de mobilité du trou sur des dispositifs préparés à partir de polymère vierge et réticulé ont permis de démontrer que la mobilité du trou est d'un ordre de grandeur plus grande pour les dispositifs à base de polymère réticulé.

Mots-clés : coupleur de réticulation, RMN-2D, bisazide, poly(3-hexylthiophène), mobilité du trou.

[Traduit par la Rédaction]

Can. J. Chem. Downloaded from www.nrcresearchpress.com by Xi'an Jiaotong University on 09/19/12
For personal use only.

Introduction

Polythiophenes and their derivatives, especially poly(3-alkylthiophenes), have been investigated extensively owing to their relatively good environmental stability[1,2] and interesting electrical and electronic properties.[3] Among this class of polythiophenes, poly(3-hexylthiophene) (P3HT) is the most widely studied material because of its good film-forming properties, strong absorption, and high hole mobilities, making it one of the foremost candidates for large-area device applications. P3HT has been used for fabrication of photovoltaic devices,[4–8] memory devices,[9] and thin-film transistors,[10,11] for lithographic purposes,[12–14] and for biosensors.[15,16] Polymer-based diodes are typically fabricated using a "vertical stack architecture" in which the active polymer material is sandwiched between two electrodes having a desired difference in work function.[17] Hole mobility is an important parameter, especially for photovoltaic applications. Hole mobilities of regioregular polythiophene (Fig. 1) as calculated by the space charge limited current (SCLC) method are of the order of 10^{-5} cm^2 V^{-1} s^{-1}.[18–22] However, field-effect mobilities in the range of 0.1 to 1 cm^2 V^{-1} s^{-1} have been achieved using highly ordered films.[23]

To use conducting polymers in organic electronics, materials with good hole mobilities are required. Only a few methods are available to increase the hole mobility. Besides synthesizing new materials, some of the approaches employed in this respect involve increasing molecular weight and decreasing polydispersivity,[24,25] introducing conjugated bridges in the polymer backbone,[26] doping,[27] and using high-boiling solvents.[28]

Recently, we have shown the use of a biaryl natural product as a material for device fabrication.[29] In this paper, we report the synthesis and use of a new biaryl-based bisazide to crosslink P3HT. Hole mobility studies of devices fabricated using pristine and crosslinked polymer were carried out using the SCLC method, and film morphology was studied using scanning electron microscopy (SEM).

Materials and methods

Chemicals and solvents were purchased from Merck or S.D. Fine-Chem Ltd. Regioregular P3HT was purchased from Spectrochem Pvt. Ltd. and used without additional purification. Reactions were monitored by thin-layer chromatography on fluorescent indicator coated plates purchased from Merck. Purification of compounds was done by column chromatography over silica gel (60 to 120 mesh) with a gradient elution using hexane with increasing proportions of ethyl acetate. Melting points were measured on an electrothermal melting-point apparatus and are uncorrected. IR spectra were recorded on a Spectrum BX series spectrophotometer using KBr. ^1H and ^{13}C NMR spectra were recorded on a Bruker AVANCE 300 MHz spectrometer and 2D NMR spectra were recorded on a Bruker 400 MHz instrument. TMS was used as the internal standard in all cases. Mass spectra were recorded on a Waters Microanalysis LCT mass spectrometer (model No. KC455). Film thickness was measured by a

Received 19 February 2010. Accepted 9 November 2010. Published at www.nrcresearchpress.com/cjc on 15 April 2011.

J. Lohani and V.R. Balakrishnan. Solid State Physics Laboratory, Lucknow Road, Delhi 110054, India.
M. Gaur and S. Eswaran. St. Stephen's College, University of Delhi, Delhi 110007, India.
P. Raghunathan. National Brain Research Centre, Manesar 122050, India.

Corresponding author: S.V. Eswaran (e-mail: sv.eswaran@gmail.com).

Fig. 1. Structure of head-to-tail regioregular P3HT.

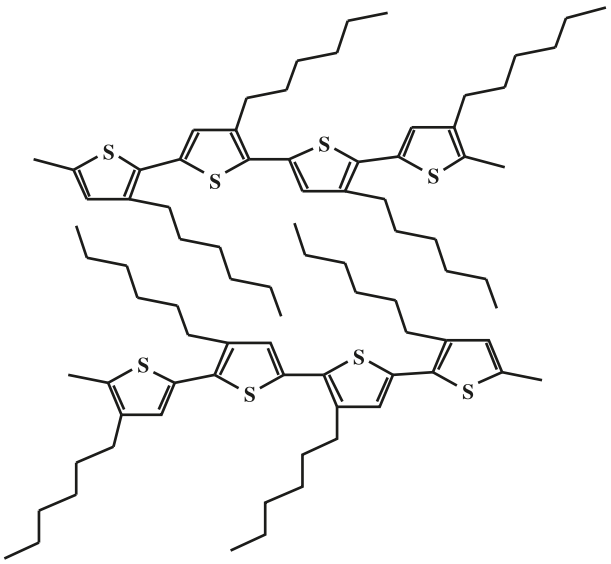

SENTECH SE 500 ellipsometer. SEM investigations were carried out on a LEO 1430 instrument using films coated over indium tin oxide (ITO) coated glass.

Device fabrication

Devices were prepared on glass substrates coated with a thin layer of ITO, which were patterned by an etching process using a mixture of HNO_3–HCl–H_2O in a 1:12:12 ratio. The coated and etched substrates were cleaned by a standard wet process with detergent, followed by boiling acetone, isopropanol, and deionized water, with sonication at each step. Solutions of regioregular P3HT in chlorobenzene (2 wt %) were spin-coated at 2000 rpm, resulting in films with a thickness of about 175 nm. The solutions were prepared with different concentrations of the crosslinker and were filtered through a 0.2 μm pore size PTFE membrane syringe filter before spin coating. The solvent was removed in vacuo and metallic electrode contacts were formed by thermal evaporation of the metal, aluminum (~200 nm), in a vacuum coating unit using a base pressure of 2×10^{-6} mbar (1 bar = 100 kPa) in the evaporation chamber and a deposition rate of >1 Å s^{-1} over the film through a shadow mask. To avoid any doping by oxygen, the devices were kept in vacuum till measurements were done. Current–voltage (I–V) characteristics were recorded under normal class 10 000 clean room environmental conditions (temperature 25 °C and relative humidity ~45% to 50%) using a Keithley 2410 SourceMeter.

Results and discussion

Figure 2 shows the reaction sequence used to synthesize the crosslinker. 1,2,4-Trimethoxybenzene **(I)** was synthesized by Thiele's acetylation of *p*-benzoquinone followed by methylation with dimethyl sulfate in aqueous alkali. Lithiation of 1,2,4-trimethoxybenzene using *n*-butyllithium in diethyl ether gave the lithium salt, which on subsequent iodination gave compound **II**. The iodo-derivative, on Ullmann coupling in the presence of activated copper, yielded **III**, which on further nitration gave the corresponding dinitro compound (**IV**). The dinitro derivative, on reduction with stannous chloride in HCl, gave the corresponding diamino derivative **(V)**, which on diazotization followed by displacement by sodium azide yielded the crosslinker **(VI)**.

2D NMR studies of 2,2′,3,3′,6,6′-hexamethoxy-5,5′-dinitrobiphenyl (IV)

Previously we reported an aromatic nitro ipso substitution leading to a molecule belonging to a rare space group, $P4_2$.[30] Synthesis of compound **IV** was taken up to determine whether it too would belong to the rare space group $P4_2$. 2D NMR studies were then undertaken to establish its structure. The nuclear Overhauser effect (NOE) spectrum (see Fig. S1 in the Supplementary data) of the compound shows that the assignment from ^{1}H-3 at δ 7.59 corresponds to a peak at δ 3.94 (CH_3-10), indicating this methyl is ortho to C-3. In this NOE spectrum, cross peaks are observed between CH_3-8 at δ 3.77 and both of the other methyl groups, i.e., CH_3-10 at δ 3.94 and CH_3-14 at δ 3.62. ^{13}C NMR assignments from heteronuclear multiple bond coherence (HMBC) spectra (Fig. 3) were based on the magnitude of the observed coupling constants for C-4 (5.93 Hz) and C-6 (none resolved). However, it cannot be ruled out that these assignments could be reversed. The signal for C-4 appears at 137.7 ppm. From this, C-6 can be calculated and placed as being extremely shielded at 88.9 ppm. The observance of a four-bond coupling ($^4J_{HC}$) only for CH_3-8 may be the result of this being the only methyl group with the OCH_3 aligned in the plane with the aromatic ring. The other two methoxy groups exhibit an angle of ~125° from the plane of the ring. Complete NMR assignments for the compound are given in Table 1.

Crosslinking with poly(3-hexylthiophene)

In regioregular P3HT, inter-chain interactions are enhanced by π-stacking of the polymer chains, and the formation of a lamellar stacking of the polymer chains with good π-orbital overlap between neighboring chains is promoted by the regular arrangement of the alkyl side chain in P3HT.[18] With better control of the structural order, the efficiency of charge transport is expected to improve with stronger π–π interactions. This π-overlap can be further improved by crosslinking the polymer chains, which in turn will improve the electronic communication between them. For this purpose a biaryl-based bisazide was synthesized and crosslinked with the polymer. Crosslinking was achieved in a Rayonet photoreactor fitted with eight UV tubes (λ = 254 nm) of 12 W each. To avoid the effect of heat, the fan of the instrument was kept on during the experiment. Photolysis of the azide generates highly reactive nitrenes that can insert into a single bond (C–H) or double bond (thiophene ring) of the polymer. IR spectroscopy was used as a tool to determine the progress of crosslinking in the polymer film. The disappearance of the characteristic peak (20 min) for the azide group at ~2100 cm^{-1} in the IR spectrum indicated the completion of crosslinking (Fig. 4).

To determine the effect of crosslinking on the hole mobility of P3HT, devices with a glass/ITO/polymer/Al structure were prepared. Pristine P3HT films were prepared from a 2 wt % solution of polymer in chlorobenzene after stirring for 24 h in the dark. For the crosslinking experiments, the crosslinker was mixed in an appropriate ratio, namely 10 or

Can. J. Chem. Downloaded from www.nrcresearchpress.com by Xi'an Jiaotong University on 09/19/12
For personal use only.

Can. J. Chem. Downloaded from www.nrcresearchpress.com by Xi'an Jiaotong University on 09/19/12
For personal use only.

Fig. 2. Synthesis of a new biaryl-based crosslinker.

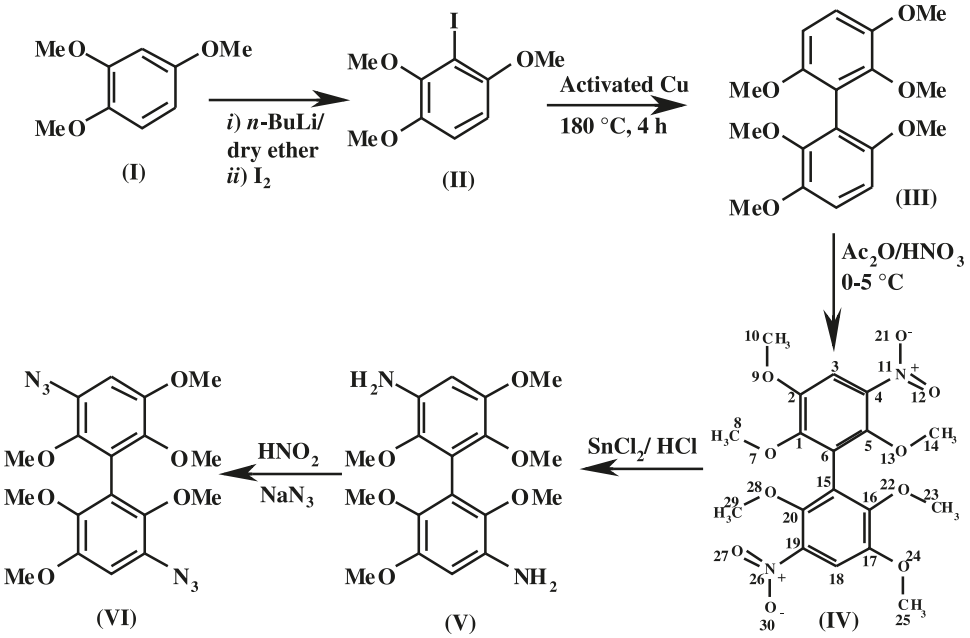

Fig. 3. HMBC spectrum of compound **IV**. In the expanded inset view appearing as the inner box, the $^{2}J_{HC}$ and $^{3}J_{HC}$ values are optimized for digital resolution of 4 Hz (black) and 2.5 Hz (red), respectively.

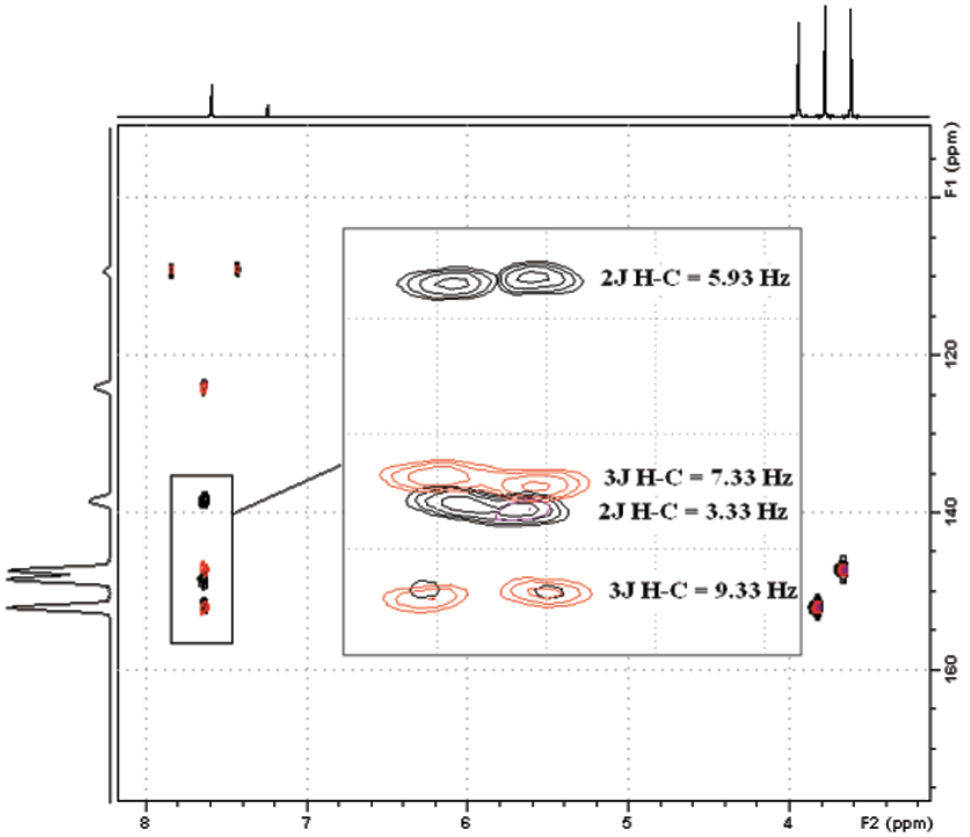

20 wt % of the polymer. The prepared films were protected from light until crosslinking was complete. As a control, pristine P3HT films were also studied after being subjected to similar conditions. The hole mobility can be described by the Mott and Gurney model of space charge limited current, considering the current flow in the trap-free limit.[31] Figure 5 shows a linear rise in current with voltage and a subsequent transition at high voltages to the region towards V^2 dependence. The field-independent mobility, μ, can be calculated by applying Child's Law,

Can. J. Chem. Downloaded from www.nrcresearchpress.com by Xi'an Jiaotong University on 09/19/12
For personal use only.

Table 1. NMR assignments for compound **IV**.

Position	^{1}H NMR	^{13}C NMR	NOESY	HMBC
1/16		151.9		3, 8
2/17		148.3		3, 10
3/18	7.59	109	10, 14	10
4/19		138.3		3
5/20		147		3, 14
6/15		124		3
8/23	3.77	61.1	10, 14	
10/25	3.94	56.2	8	
14/29	3.62	62.2	8	

Fig. 4. IR spectrum of the P3HT film before (upper trace) and after (lower trace) crosslinking with 20 wt % crosslinker (disappearance of the azide is shown by the arrow).

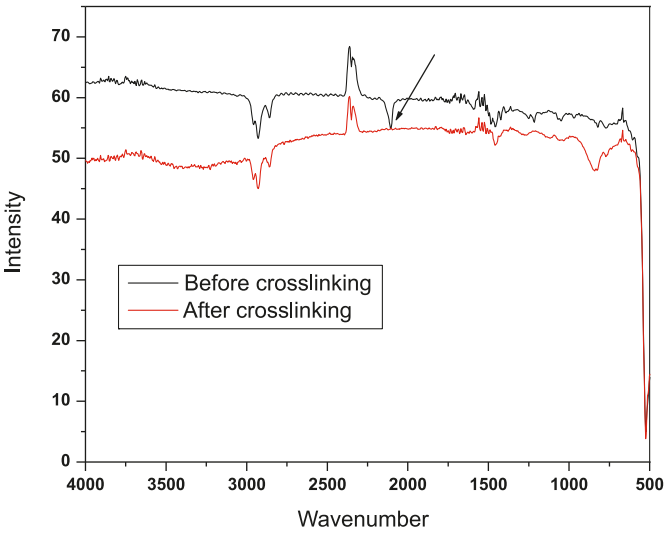

$$[1] \qquad J = \frac{9}{8}\mu\varepsilon\varepsilon_0\frac{V^2}{d^3}$$

where J is the current density, μ is the free carrier hole mobility, ε is the dielectric constant (taken to be 3), ε_0 is the permittivity in a vacuum, V is the applied voltage, and d is the film thickness. The hole mobility was calculated from the intercept of the corresponding lines on the axis of current density. Using the above J–V relationship, the SCLC mobility (Fig. 5) of P3HT and the blank was calculated to be of the order of $\sim 10^{-5}$ cm^2 V^{-1} s^{-1}, which is in accordance with values reported earlier.[18–22] Hole mobility values for the crosslinked polymer, as compared with pristine P3HT (4.5×10^{-5} cm^2 V^{-1} s^{-1}), increased by an order of magnitude of one, reaching 5×10^{-4} cm^2 V^{-1} s^{-1} and 3×10^{-4} cm^2 V^{-1} s^{-1} for devices fabricated after crosslinking with 10 wt % and 20 wt % crosslinker, respectively. A slight decrease in hole mobility was observed in devices fabricated using pristine P3HT exposed to UV as a control. The increase in hole mobility after crosslinking may be a result of better molecular ordering due to better π-overlap of the polymer chains. When a higher concentration of crosslinker is used, there is formation of an amorphous region due to twisting and bending of the polymer chains, resulting in a decrease in hole mobility.

Fig. 5. Comparison of current–voltage characteristics of the glass/ITO/polymer/Al devices. (*a*) Semi-log plot and (*b*) logarithmic plot. The hole mobilities were found to be 4.5×10^{-5} cm^2 V^{-1} s^{-1} for P3HT, 2×10^{-5} cm^2 V^{-1} s^{-1} for UV-exposed P3HT, 5×10^{-4} cm^2 V^{-1} s^{-1} for 10 wt % crosslinker, and 3×10^{-4} cm^2 V^{-1} s^{-1} for 20 wt % crosslinker.

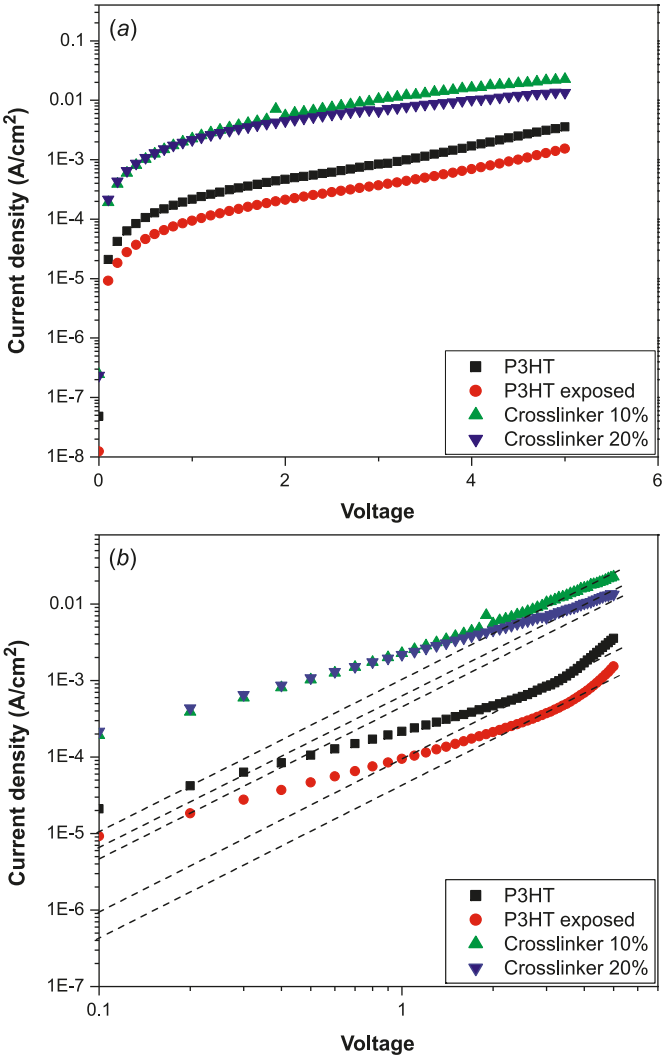

The film morphology was studied using SEM. Film morphology for P3HT, both pristine and exposed, is smooth (Figs. 6*a* and 6*b*). After crosslinking a change in film morphology is seen. Films with a crosslinker concentration of 10 wt % show granular morphology (Fig. 6*c*) and those with a higher crosslinker concentration show fibrous structure (Fig. 6*d*), possibly due to excessive crosslinking.

To conclude, a new biaryl-based bisazide has been synthesized and evaluated as a crosslinker. Devices fabricated using crosslinked P3HT show an increase in hole mobility, as determined by the SCLC method, by a factor of one order of magnitude. This study could be useful for fabrication of devices, especially thin-film transistors and solar cells.

Supplementary data

Supplementary data (the NOE spectrum along with synthe-

Fig. 6. SEM images of the films before crosslinking (*a*, pristine P3HT; *b*, pristine P3HT exposed to UV radiation) and after crosslinking (*c*, 10 wt % crosslinker; *d*, 20 wt % crosslinker).

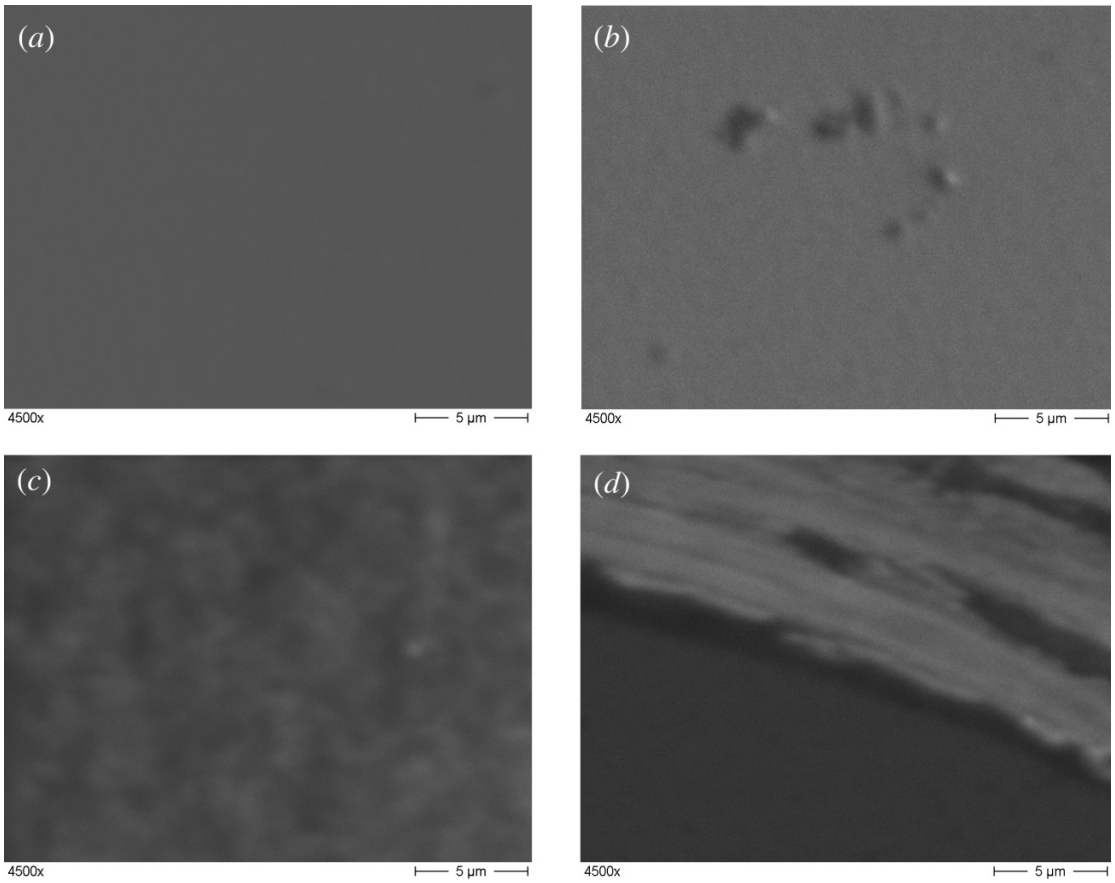

Can. J. Chem. Downloaded from www.nrcresearchpress.com by Xi'an Jiaotong University on 09/19/12
For personal use only.

sis and characterization data) are available with the article through the journal Web site (www.nrcresearchpress.com/cjc).

Acknowledgements

We thank The Principal, St. Stephen's College, Delhi, and the Director, Solid State Physics Laboratory, Delhi, for providing facilities. We thank the Defence Research Development Organisation and University Grants Commission, Government of India, New Delhi, for the grant of research projects. Mr. Manoj Gaur is thanked for preparing the crosslinker. We thank Prof. Amitabha Sarkar, IACS, Kolkata, for help in synthesis and characterization of compounds and Dr. Russell Hopson, Brown University, USA, for recording the NMR spectra. We thank Prof. David Cane, Brown University, USA, for the assistance received during a St. Stephen's College – Brown University exchange visit by one of us (S.V.E.).

References

(1) Groenendaal, L.; Jonas, F.; Freitag, D.; Pielartzik, H.; Reynolds, J. R. *Adv. Mater.* **2000** *12* (7), 481. doi:10.1002/(SICI)1521-4095(200004)12:7<481::AID-ADMA481>3.0.CO;2-C.

(2) Chen, S. A.; Ni, J. M. *Macromolecules* **1992** *25* (23), 6081. doi:10.1021/ma00049a001.

(3) Yildiz, U. H.; Sahin, E.; Akhmedov, I. M.; Tanyeli, C.; Toppare, L. A. *J. Polym. Sci. A Polym. Chem.* **2006** *44* (7), 2215. doi:10.1002/pola.21337.

(4) Fritz, K. P.; Guenes, S.; Luther, J.; Kumar, S.; Sariciftci, N. S.; Scholes, G. D. *J. Photochem. Photobiol. Chem.* **2008** *195* (1), 39. doi:10.1016/j.jphotochem.2007.09.004.

(5) Ko, C.-J.; Lin, Y.-K.; Chen, F.-C. *Adv. Mater.* **2007** *19*, 3520. doi:10.1002/adma.200700741.

(6) Li, G.; Shrotriya, V.; Yao, Y.; Huang, J.; Yang, Y. *J. Mater. Chem.* **2007** *17* (30), 3126. doi:10.1039/b703075b.

(7) Na, S.-I.; Kim, S.-S.; Jo, J.; Lee, K.-S.; Park, S.-J.; Kim, D.-Y. *J. Photochem. Photobiol. A Chem.* **2008** *194* (2–3), 161. doi:10.1016/j.jphotochem.2007.08.003.

(8) Kroon, R.; Lenes, M.; Hummelen, J. C.; Blom, P. W. M.; de Boer, B. *Polym. Rev.* **2008** *48* (3), 531. doi:10.1080/15583720802231833.

(9) Kaneto, K.; Mori, K.; Morita, T.; Takashima, W. *Jpn. J. Appl. Phys.* **2008** *47* (2), 1382. doi:10.1143/JJAP.47.1382.

(10) Balocco, C.; Majewski, L. A.; Song, A. M. *Org. Electron.* **2006** *7* (6), 500. doi:10.1016/j.orgel.2006.07.009.

(11) Jia, H.; Gross, E. K.; Wallace, R. M.; Gnade, B. *Org. Electron.* **2007** *8* (1), 44. doi:10.1016/j.orgel.2006.10.009.

(12) Abdou, M. S. A.; Diaz-Guijada, G. A.; Arroyo, M. I.; Holdcroft, S. *Chem. Mater.* **1991** *3* (6), 1003. doi:10.1021/cm00018a009.

(13) Balocco, V.; Jones, A. G.; Kingsley, J. M.; Chan, J. R.; Huang, X. Q.; Song, A. M. *Jpn. J. Appl. Phys.* **2006** *45* (3B), 2095. doi:10.1143/JJAP.45.2095.

(14) Lowe, J.; Holdcroft, S. *Macromolecules* **1995** *28* (13), 4608. doi:10.1021/ma00117a035.

(15) Singhal, R.; Chaubey, A.; Kaneto, K.; Takashima, W.; Malhotra, B. D. *Biotechnol. Bioeng.* **2004** *85* (3), 277. doi:10.1002/bit.10869.
(16) Arya, S. K.; Solanki, P. R.; Singh, S. P.; Kaneto, K.; Pandey, M. K.; Datta, M.; Malhotra, B. D. *Biosens. Bioelectron.* **2007** *22* (11), 2516. doi:10.1016/j.bios.2006.10.011.
(17) Andersson, P.; Robinson, N. D.; Berggren, M. *Synth. Met.* **2005** *150* (3), 217. doi:10.1016/j.synthmet.2004.06.035.
(18) Grecu, S.; Roggenbuck, M.; Opitz, A.; Brütting, W. *Org. Electron.* **2006** *7* (5), 276. doi:10.1016/j.orgel.2006.03.005.
(19) Kumar, P.; Chand, S.; Dwivedi, S.; Kamalasanan, M. N. *Appl. Phys. Lett.* **2007** *90* (2), 023501. doi:10.1063/1.2431466.
(20) Goh, C.; Kline, R. J.; McGehee, M. D.; Kadnikova, E. N.; Fréchet, J. M. J. *Appl. Phys. Lett.* **2005** *86* (12), 122110. doi:10.1063/1.1891301.
(21) Song, M. Y.; Kim, J. K.; Kim, K. J.; Kim, D. Y. *Synth. Met.* **2003** *137* (1–3), 1389. doi:10.1016/S0379-6779(02)01154-2.
(22) Chiguvare, Z.; Dyakonov, V. *Phys. Rev. B* **2004** *70* (23), 235207. doi:10.1103/PhysRevB.70.235207.
(23) Schön, J. H.; Kloc, Ch.; Fichou, D.; Batlogg, B. *Phys. Rev. B* **2001** *64* (3), 035209. doi:10.1103/PhysRevB.64.035209.
(24) Miyakoshi, R.; Yokoyama, A.; Yokozawa, T. *Macromol. Rapid Commun.* **2004** *25* (19), 1663. doi:10.1002/marc.200400281.
(25) Schilinsky, P.; Asawapirom, U.; Scherf, U.; Biele, M.; Brabec, C. *Chem. Mater.* **2005** *17* (8), 2175. doi:10.1021/cm047811c.
(26) Zhou, E.; Tan, Z.; Yang, Y.; Huo, L.; Zou, Y.; Yang, C.; Li, Y. *Macromolecules* **2007** *40* (6), 1831. doi:10.1021/ma062633p.
(27) Ma, L.; Lee, W. H.; Park, Y. D.; Kim, J. S.; Lee, H. S.; Cho, K. *Appl. Phys. Lett.* **2008** *92* (6), 063310. doi:10.1063/1.2883927.
(28) Chang, J.-F.; Sun, B.; Breiby, D. W.; Nielsen, M. M.; Solling, T. I.; Giles, M.; McCulloch, I.; Sirringhaus, H. *Chem. Mater.* **2004** *16* (23), 4772. doi:10.1021/cm049617w.
(29) Gaur, M.; Lohani, J.; Balakrishnan, V. R.; Raghunathan, P.; Eswaran, S. V. *Bull. Korean Chem. Soc.* **2009** *30* (12), 2895. doi:10.5012/bkcs.2009.30.12.2895.
(30) Sharma, M.; Gaur, M.; Eswaran, S. V. *J. Indian Chem. Soc.* **2005** *82*, 1129.
(31) Rashmi; Kapoor, A. K.; Kumar, U.; Balakrishnan, V. R.; Basu, P. K. *Pramana* **2007** *68* (3), 489. doi:10.1007/s12043-007-0052-2.

Can. J. Chem. Downloaded from www.nrcresearchpress.com by Xi'an Jiaotong University on 09/19/12
For personal use only.

Silica-supported barium chloride (SiO_2–$BaCl_2$) — Efficient and heterogeneous catalyst for the environmentally friendly preparation of *N*,*N*′-alkylidene bisamides under solvent-free conditions

Mohammad Reza Mohammad Shafiee

Can. J. Chem. Downloaded from www.nrcresearchpress.com by Xi'an Jiaotong University on 09/19/12
For personal use only.

Abstract: A series of *N*,*N*′-alkylidene bisamides were prepared via a green and environmentally friendly synthetic protocol from the reaction of phenyl acetylene or hex-1-yne, aromatic aldehyde, and benzamide or acetamide. Silica-supported barium chloride (SiO_2–$BaCl_2$) catalyzes the process of the reaction. The prepared catalysts were characterized by X-ray diffraction, and the products were obtained with high conversions and yields.

Key words: SiO_2–$BaCl_2$, heterogeneous catalyst, environmentally friendly synthesis, *N*,*N*′-alkylidene bisamides.

Résumé : On a préparé une série de *N*,*N*′-alkylidène bisamides par un protocole de synthèse écologique impliquant la réaction du phénylacétylène ou de l'hex-1-yne, d'un aldéhyde aromatique et du benzamide ou de l'acétamide. Du chlorure de baryum déposé sur de la silice (SiO_2–$BaCl_2$) catalyse la réaction. Les catalyseurs préparés ont été caractérisés par diffraction des rayons-X et les produits ont été obtenus avec des taux de conversion et des rendements élevés.

Mots-clés : SiO_2–$BaCl_2$, catalyse hétérogène, synthèse écologique, *N*,*N*′-alkylidène bisamides.

[Traduit par la Rédaction]

Introduction

The development of simple, efficient, and environmentally benign chemical processes or methodologies for widely used pharmacophores from readily available reagents and catalysts are the major challenges for chemists throughout the world.[1] To plan and manage chemical reactions with "green" experimental protocol is an enormous challenge that chemists have to confront to improve the quality of the environment for present and future generations.[2] Over the past, chemists have been aware of the environmental implications of their chemistry. Nowadays, they are trying to develop new synthetic methods, reaction conditions, and uses of chemicals that reduce risks to humans and the environment. Organic solvents are high on the list of damaging chemicals because they are employed in huge amounts and are usually volatile liquids that are difficult to store.[3]

One important aspect of clean technology is the use of environmentally friendly catalysts — typically a solid catalyst that can be recovered easily when the reaction is complete. Heterogeneous organic reactions have proven useful to chemists in the laboratory as well as in an industrial context. These reactions are affected by the reagents immobilized on the porous solid supports and have advantages over the conventional solution-phase reactions because of the good dispersion of active reagent sites, associated selectivity, and easier work-up.[3]

Compounds bearing amide and bisamide groups are important intermediates in organic synthesis, since these groups can be easily transformed into other functionalities (such as *gem*-diaminoalkyl and aminoalkyl groups) and are of considerable interest in the synthesis of pharmacological materials such as peptidomimetic compounds.[4] Therefore, preparation of amides has attracted considerable attention in the past and in recent years.

The common approach for the synthesis of bisamides is the direct reaction of aldehydes with the corresponding amides or nitriles.[5–10]

In this paper various acidic catalysts such as sulfuric acid (85%; also as solvent),[5] sulfonic acid,[6] triflic acid,[8] sulfamic acid,[10a] or chlorosulfonic acid[10b] were examined.

Considering that most of the organic reagents involved in fine chemical synthesis are sensitive to harsh conditions, it is desirable to choose catalysts that can catalyze organic transformations under mild conditions.

The aim of the present protocol was to summarize the data for the one-pot preparation of *N*,*N*′-alkylidene bisamide derivatives in high yield using a three-component condensation of an alkyne, aromatic aldehydes, and amides in the presence

Received 3 October 2010. Accepted 12 January 2011. Published at www.nrcresearchpress.com/cjc on 16 May 2011.

M.R.M. Mohammad Shafiee. Faculty of Sciences, Islamic Azad University – Najafabad Branch, Najafabad, Esfahan, Iran.

Corresponding author: M.R. Mohammad Shafiee (e-mail: mohammadreza.mohammadshafiee@gmail.com).

PROOF/ÉPREUVE

Scheme 1.

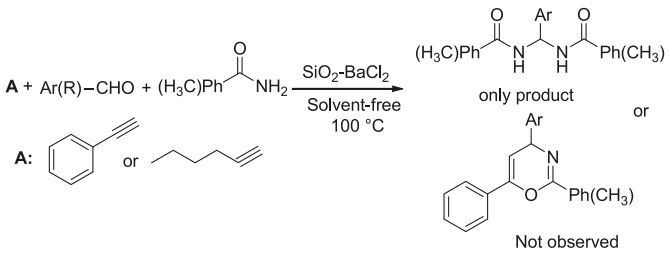

of silica-supported barium chloride (SiO_2–$BaCl_2$) as the catalyst under thermal, solvent-free conditions (Scheme 1).

Results and discussion

Hung et al.[11] reported that the condensation of phenyl acetylene, aromatic aldehyde, and urea with acetic acid / trifluoroacetic acid as the catalyst and acetonitrile as the solvent lead to the formation of 4*H*-[1,3]oxazines. In continuation of this theme, we are trying to develop new synthetic methods, reaction conditions, and uses of heterogeneous catalysts that reduce risks to humans and the environment. Thus, the reaction of phenyl acetylene, benzaldehydes, and benzamide in the presence of a catalytic amount of SiO_2–$BaCl_2$ as the catalyst under thermal, solvent-free conditions was investigated (Scheme 1). As can be seen from Scheme 1 we did not observe 2-phenyl(methyl)-4*H*-1,3-oxazine derivatives, and a series of *N*,*N*′-alkylidene bisamides formed.

Within our plan to investigate the structures of bisamide and needing an alkyne or a catalyst for the formation of bisamides, the reaction including benzaldehyde, benzamide, and a catalytic amount of SiO_2–$BaCl_2$ under heating at 100 °C failed to give the correlative product in the absence of phenyl acetylene, which indicated that phenyl acetylene plays an important role in the reaction (Scheme 2). Chromatographic studies (TLC) confirmed that the alkyne was completely disappearing when the product was formed.

As a result the mentioned reaction failed to give any products in the absence of the catalyst.

To improve the yield and optimize the reaction conditions, the reaction was carried out using phenyl acetylene, benzaldehyde, and benzamide in the presence of SiO_2–$BaCl_2$ as the catalyst (Scheme 3). Initially, the effect of temperature on the rate of the reaction was investigated (Table 1). At 80 °C, the reaction proceeded smoothly and almost complete conversion of the product was observed. A further increase in temperature to 100 °C increased the rate of the reaction. Therefore, the reaction temperature was kept at 100 °C (giving a short reaction time and high yield).

We then tried to optimize the amount of catalyst for this reaction. It should be noted that 0.025 g of SiO_2–$BaCl_2$ was efficient enough to catalyze the reaction, and increasing the amount of catalyst did not significantly improve the yield (Table 1). Finally, an optimimal set of conditions was achieved using 0.025 g of SiO_2–$BaCl_2$ as the catalyst and 100 °C. The results are summarized in Table 1.

Using these optimized reaction conditions, the scope and efficiency of these procedures were explored for the synthesis of a wide variety of substituted bisamides (Scheme 1). The results are summarized in Table 2.

Scheme 2.

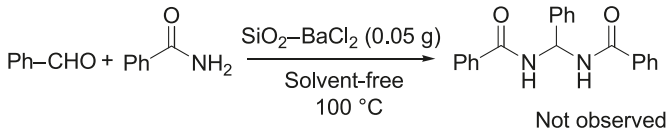

Scheme 3.

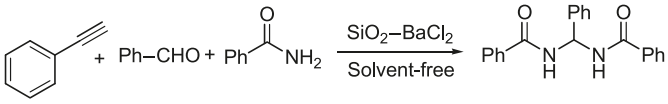

As expected, this reaction proceeded smoothly, and the desired products were obtained in good to excellent yields. A series of aromatic aldehydes with either electron-donating or electron-withdrawing groups attaching to aromatic rings were investigated (Table 1, entries 1–9). However, when aromatic aldehydes with electron-withdrawing groups (such as nitro-) were reactants, the reaction time was shorter than that with electron-donating groups (such as methoxy-). Although meta- and para-substituted aromatic aldehydes gave good results, ortho-substituted aromatic aldehydes (such as 2-nitrobenzadehyde) gave lower yields and longer reaction times because of the steric effects. These good results were also obtained in the case of the hex-1-yne (Table 1, entries 14 and 15).

As a result the reaction of butyraldehyde with phenyl acetylene and benzamide failed to give any product (Table 1, entry 10).

Encouraged by the results obtained with benzamide, we turned our attention to acetamide (Table 1). As shown in Table 1, the reactions of phenyl acetylene and aryl aldehyde with acetamide under the mentioned reaction conditions progressed smoothly but with longer reaction times, and the desired products were obtained in good yields. (Table 1, entries 11 and 12). However, ortho-substituted aromatic aldehydes (such as 2-nitrobenzadehyde) failed to give any product (Table 1, entry 13).

To explain the formation of bisamides via the one-pot multicomponent reaction, we have proposed a plausible reaction mechanism, which is illustrated in Scheme 4. Firstly, the interaction of aldehyde with an empty π orbital of the Lewis acid occurs to form a cation intermediate. Therefore, the formation of **A** resulting from the cyclocondensation of an activated aldehyde with phenyl acetylene is established. The second step is the addition of amide to **A** to yield β-amido ketones (**B**) that protonate and convert to the bisamide as the product by an attack of the amide (Scheme 4).

Conclusion

In conclusion, a rapid and environmentally benign protocol for the preparation of *N*,*N*′-alkylidene bisamides in a one-pot procedure wasn developed. The work-up procedure is very clear-cut; that is, the products were isolated and purified by simple filtration and crystallization from aqueous ethanol (or diethyl ether). Our protocol avoids the use of dry media during the reaction process, making it superior to the reactions that use solvent.

Can. J. Chem. Downloaded from www.nrcresearchpress.com by Xi'an Jiaotong University on 09/19/12
For personal use only.

Table 1. Preparation of *N*,*N*′-alkylidene bisamide derivatives.

Entry	Aldehyde	Amide	Alkyne	Time (min)	Yield (%)[a]	mp (°C) [lit. mp][ref]
1	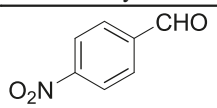	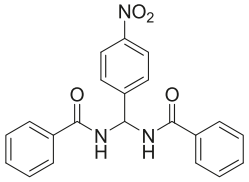	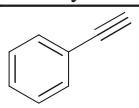	90	91	260–262 [265–267][5d]
2	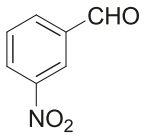	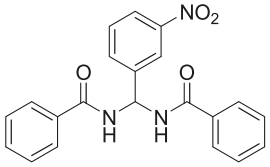	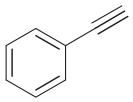	100	79	235–237
3	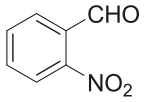	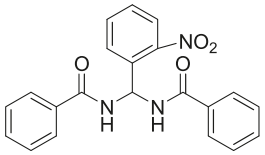	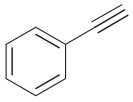	230	71	256–258
4	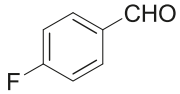	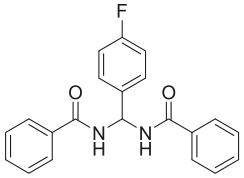	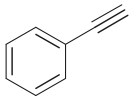	160	85	203–205
5	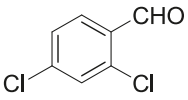	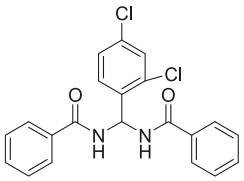	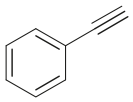	150	89	195–197 [190–192][5e]
6	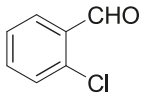	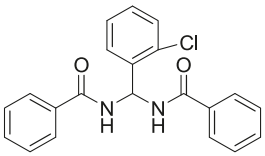	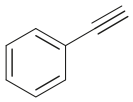	130	69	242–244
7	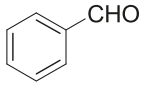	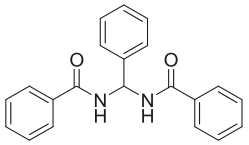	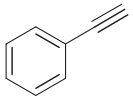	120	74	236–238 [237–238][5d]
8	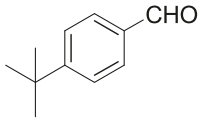	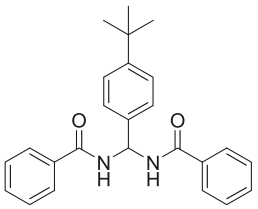	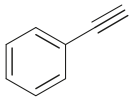	310	67	212–214
9	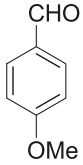	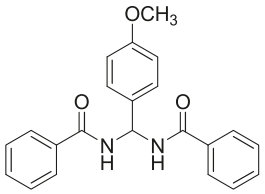	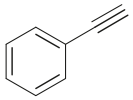	300	71	227–229 [232–234][5d]

Can. J. Chem. Downloaded from www.nrcresearchpress.com by Xi'an Jiaotong University on 09/19/12
For personal use only.

PROOF/ÉPREUVE

Can. J. Chem. Downloaded from www.nrcresearchpress.com by Xi'an Jiaotong University on 09/19/12
For personal use only.

Table 1. (*concluded*).

Entry	Aldehyde	Amide	Alkyne	Time (min)	Yield (%)[a]	mp (°C) [lit. mp][ref]
10	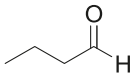	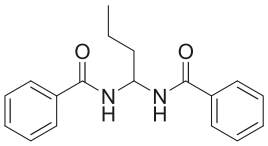	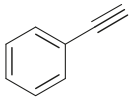	240	—	—
11	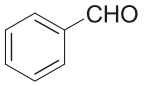	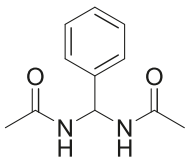	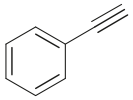	360	69	251–253
12	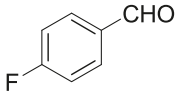	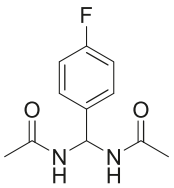	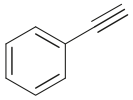	280	76	257–259
13	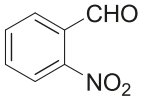	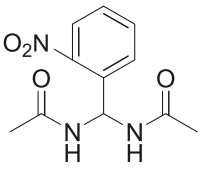	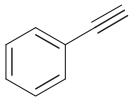	300	—	—
14	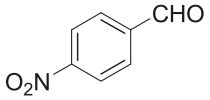	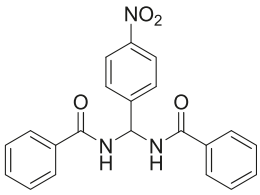	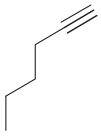	60	82	244–246
15	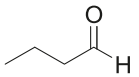	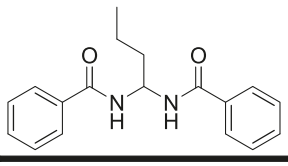	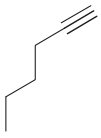	10	76	210–212

[a]Isolated yields.

Table 2. Optimization amount of SiO_2–$BaCl_2$ and reaction temperatures.

Entry	Catalyst (g)	*T* (°C)	Time (min)	Yield (%)[a]
1	0.025	rt	300	—
2	0.025	80	450	55
3	0.1	100	180	62
4	0.05	100	170	73
5	0.025	100	120	74
6	0.01	100	160	60

Note: rt, room temperature.

[a]Isolated yield (based on phenyl acetylene (1 mmol), benzaldehyde (1.1 mmol), and benzamide (2.5 mmol)).

Experimental

All reagents were purchased from Merck and Sigma-Aldrich and used without further purification. All yields refer to isolated products after purification based on the amount of aldehyde. Products were characterized by comparison of spectroscopic data (IR and ^{1}H NMR spectra) and melting points with authentic samples. The NMR spectra were recorded on a Bruker Avance DPX 300 MHz instrument. The

Scheme 4. Proposed mechanism for the formation of *N*,*N*′-alkylidene bisamides.

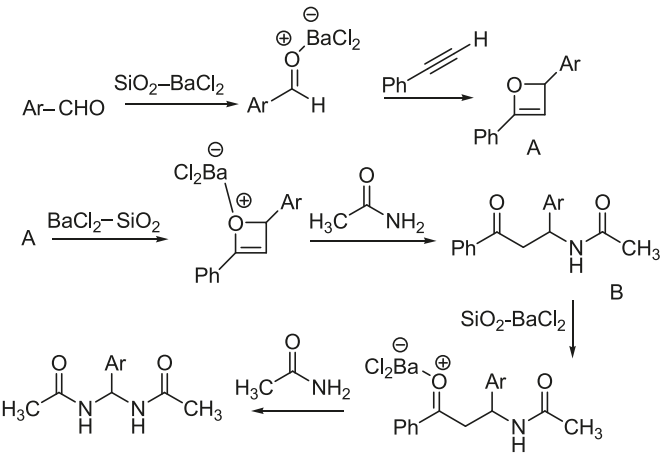

Can. J. Chem. Downloaded from www.nrcresearchpress.com by Xi'an Jiaotong University on 09/19/12
For personal use only.

spectra were measured in DMSO-d_6 relative to TMS (0.00 ppm). IR spectra were recorded on a PerkinElmer 781 spectrophotometer. Melting points were determined in open capillaries with a BUCHI 510 melting point apparatus. TLC was performed on silica gel polygram SIL G/UV 254 plates.

Preparation of SiO_2–$BaCl_2$

In a 250 mL flask, barium chloride dihydrate ($BaCl_2 \cdot 2H_2O$, 1 g) was dissolved in water (50 mL) and silica gel (10 g) (Silica gel 60 for column chromatography, 230 mesh) was added to this mixture, which was vigorously stirred under rotary evaporation until the water was completely evaporated. This powder was kept in an oven at 100 °C for 1 h to give the active catalyst.

X-ray diffraction (XRD)

Powder X-ray diffraction measurements were performed using a D_8 Advance diffractometer made by Bruker AXS, Germany. Scans were taken with a 2θ step size of 0.02 and a counting time of 1.0 s using a Cu Kα radiation source generated at 40 kV and 30 mA. Specimens for XRD were prepared by compaction into a glass-backed aluminum sample holder. Data were collected over a 2 u range from 48° to 70°, and phases were identified by matching experimental patterns to entries in the Diffract^{plus} version 6.0 indexing software. The fresh catalyst was characterized by XRD and its pattern is presented in Fig. 1. As shown in Fig. 1, the actual phases were silicon oxide (silica) – SiO_2 (cubic) and $BaCl_2$.

General procedure for the synthesis of *N*,*N*′-alkylidene bisamides

To a mixture of aryl aldehyde (1.1 mmol), benzamide or acetamide (2.5 mmol), and phenyl acetylene or hex-1-yne (1 mmol) was added SiO_2–$BaCl_2$ (0.025 g) and the mixture was heated at 100 °C in an oil bath for the appropriate time (Table 1). The progress of the reaction was monitored by TLC. After completion of the reaction, the mass was cooled to 25 °C, and the mixture was dissolved in boiling ethanol. The catalyst was removed by simple filtration. The solvent was concentrated and the solid product was purified by a recrystallization procedure in the appropriate solvent (ethanol 40% or diethyl ether).

All products were characterized by IR, ^{1}H NMR, and ^{13}C NMR spectra.

N-Benzoylamino(4-nitrophenyl)methyl benzamide (Table 1, entry 1)

IR (KBr, cm^{-1}): 3264, 3085, 3028, 2963, 1650, 1633, 1608, 1579, 1548, 1486, 1345, 1295, 1277, 1201, 1143, 1083, 1055, 875, 852, 794, 718, 695. ^{1}H NMR (300 MHz, DMSO-d_6, ppm) δ: 7.08 (t, J = 7.3 Hz, 1H), 7.47–7.60 (m, 6H), 7.75 (d, J = 8.6 Hz, 2H), 7.93 (d, J = 7.1 Hz, 4H), 8.26 (d, J = 8.7 Hz, 2H), 9.22 (d, J = 7.4 Hz, 2H). ^{13}C NMR (75 MHz, DMSO-d_6, ppm) δ: 59.4, 124.4, 128.5, 128.9, 129.2, 132.6, 134.4, 147.9, 148.4, 166.8. Anal. calcd for $C_{21}H_{17}N_3O_4$ (%): C 67.19, H 4.56, N 11.19; found: C 67.36, H 4.60, N 11.26.

N-Benzoylamino(3-nitrophenyl)methyl benzamide (Table 1, entry 2)

IR (KBr, cm^{-1}): 3313, 3259, 3086, 2969, 1649, 1602, 1581, 1534, 1505, 1340, 1271, 1211, 1140, 1054, 873, 736, 716. ^{1}H NMR (300 MHz, DMSO-d_6, ppm) δ: 7.11 (t, J = 7.3 Hz, 1H), 7.47–7.60 (m, 6H), 7.71 (t, J = 7.9 Hz, 1H), 7.94–7.96 (m, 5H), 8.21 (d, J = 8.1 Hz, 2H), 8.36 (s1, H), 9.27 (d, J = 7.3 Hz, 2H). ^{13}C NMR (75 MHz, DMSO-d_6, ppm) δ: 59.5, 122.3, 123.6, 128.5, 129.2, 130.8, 132.6, 134.4, 134.6, 143.3, 148.7, 166.8. Anal. calcd for $C_{21}H_{17}N_3O_4$ (%): C 67.19, H 4.56, N 11.19; found: C 67.32, H 4.65, N 11.29.

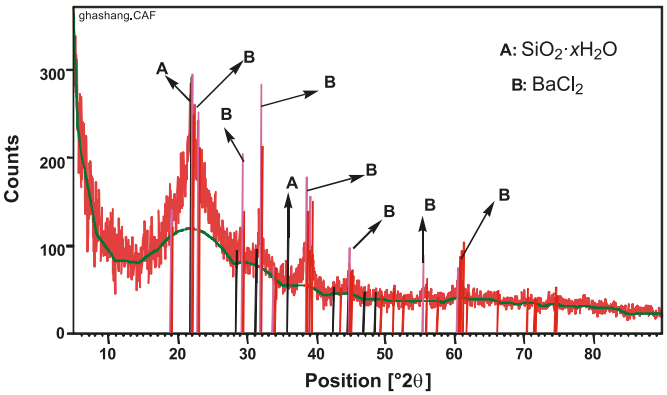

Fig. 1. X-ray diffraction (XRD) pattern of SiO_2–$BaCl_2$.

N-Benzoylamino(2-nitrophenyl)methyl benzamide (Table 1, entry 3)

IR (KBr, cm^{-1}): 3275, 3073, 3030, 1648, 1610, 1531, 1481, 1347, 1274, 1189, 1146, 1086, 1059, 854, 796, 703. ^{1}H NMR (300 MHz, DMSO-d_6, ppm) δ: 7.41–7.61 (m, 8H), 7.76–7.81 (m, 2H), 7.91 (d, J = 7.0 Hz, 4H), 7.98 (d, J = 8.1 Hz, 1H), 9.19 (d, J = 6.9 Hz, 2H). ^{13}C NMR (75 MHz, DMSO-d_6, ppm) δ: 56.7, 125.3, 128.6, 129.1, 129.7, 130.1, 132.5, 133.9, 134.4, 134.6, 149.4, 166.9. Anal calcd for $C_{21}H_{17}N_3O_4$ (%): C 67.19, H 4.56, N 11.19; found: C 67.26, H 4.63, N 11.24.

N-Benzoylamino(4-fluorophenyl)methyl benzamide (Table 1, entry 4)

IR (KBr, cm^{-1}): 3277, 3065, 3026, 1643, 1521, 1480, 1350, 1275, 1141, 1072, 1037, 800, 753, 699. ^{1}H NMR (300 MHz, DMSO-d_6, ppm) δ: 7.19 (t, J = 6.9 Hz, 1H), 7.36–7.69 (m, 10H), 7.94 (d, J = 7.2 Hz, 4H), 9.11 (d, J = 7.0 Hz, 2H). ^{13}C NMR (75 MHz, DMSO-d_6, ppm) δ: 58.1, 127.9, 128.2, 128.5, 129.0, 129.3, 129.6, 130.3, 130.4, 132.4, 133.4, 134.7, 138.2, 166.6. Anal. calcd for $C_{21}H_{17}FN_2O_2$ (%): C 72.40, H 4.92, N 8.04; found: C 72.49, H 4.98, N 8.11.

N-Benzoylamino(2,4-dichlorophenyl)methyl benzamide (Table 1, entry 5)

IR (KBr, cm^{-1}): 3290, 3214, 3066, 3028, 1639, 1602, 1579, 1543, 1514, 1364, 1330, 1261, 1145, 1078, 1043, 860, 827, 744, 698. ^{1}H NMR (300 MHz, DMSO-d_6, ppm) δ: 7.14 (t, J = 6.8 Hz, 1H), 7.45–7.68 (m, 9H), 7.93 (d, J = 7.1 Hz, 4H), 9.13 (d, J = 6.8 Hz, 2H). ^{13}C NMR (75 MHz, DMSO-d_6, ppm) δ: 57.9, 128.0, 128.5, 129.1, 129.7, 130.7, 132.4, 134.1, 134.4, 134.6, 137.4, 166.7. Anal. calcd for $C_{21}H_{16}Cl_2N_2O_2$ (%): C 63.17, H 4.04, N 7.02; found: C 63.19, H 4.08, N 7.05.

PROOF/ÉPREUVE

Can. J. Chem. Downloaded from www.nrcresearchpress.com by Xi'an Jiaotong University on 09/19/12
For personal use only.

_N_-Benzoylamino(2-chlorophenyl)methyl benzamide (Table 1, entry 6)

IR (KBr, cm^{-1}): 3280, 3092, 1649, 1547, 1506, 1343, 1274, 1228, 1146, 1062, 830, 790, 703. ^1H NMR (300 MHz, DMSO-d_6, ppm) δ: 7.01 (t, J = 7.5 Hz, 1H), 7.18–7.24 (m, 2H), 7.46–7.59 (m, 8H), 7.91 (d, J = 7.1 Hz, 4H), 9.05 (d, J = 7.6 Hz, 2H). ^{13}C NMR (75 MHz, DMSO-d_6, ppm) δ: 58.1, 117.3, 117.7, 128.3, 129.2, 129.5, 129.8, 132.5, 134.6, 137.5, 164.1, 166.5. Anal. calcd for $C_{21}H_{17}ClN_2O_2$ (%): C 69.14, H 4.70, N 7.68: found: C 69.19, H 4.81, N 7.72.

_N_-Benzoylamino(phenyl)methyl benzamide (Table 1, entry 7)

IR (KBr, cm^{-1}): 3285, 3088, 1651, 1543, 1497, 1342, 1269, 1137, 1047, 875, 802, 702. ^1H NMR (300 MHz, DMSO-d_6, ppm) δ: 7.05 (t, J = 7.7 Hz, 1H), 7.29–7.58 (m, 11H), 7.92 (d, J = 7.1 Hz, 4H), 9.03 (d, J = 7.7 Hz, 2H). ^{13}C NMR (75 MHz, DMSO-d_6, ppm) δ: 59.6, 127.4, 128.4, 128.5, 129.2, 132.5, 134.7, 141.1, 166.5. Anal. calcd for $C_{21}H_{18}N_2O_2$ (%): C 76.34, H 5.49, N 8.48; found: C 76.39, H 5.55, N 8.51.

_N_-Benzoylamino(4-(1,1-dimethylethyl)phenyl)methyl benzamide (Table 1, entry 8)

IR (KBr, cm^{-1}): 3271, 3060, 2965, 1646, 1601, 1579, 1555, 1511, 1352, 1271, 1136, 1075, 871, 833, 710. ^1H NMR (300 MHz, DMSO-d_6, ppm) δ: 1.29 (s, 9H), 7.03 (t, J = 7.6 Hz, 1H), 7.36–7.58 (m, 10H), 7.93 (d, J = 7.8 Hz, 4H), 9.02 (d, J = 7.7 Hz, 2H). ^{13}C NMR (75 MHz, DMSO-d_6, ppm) δ: 32.0, 35.1, 59.4, 125.9, 127.1, 128.1, 128.4, 129.2, 132.4, 134.7, 138.3, 166.4. Anal. calcd for $C_{25}H_{26}N_2O_2$ (%): C 77.69, H 6.78, N 7.25; found: C 77.80, H 6.89, N 7.29.

_N_-Benzoylamino(4-methoxyphenyl)methyl benzamide (Table 1, entry 9)

IR (KBr, cm^{-1}): 3273, 3068, 2958, 1648, 1546, 1511, 1280, 1249, 1177, 1065, 815, 765, 703. ^1H NMR (300 MHz, DMSO-d_6, ppm) δ: 3.74 (s, 3H), 6.93–6.99 (m, 3H), 7.39–7.55 (m, 8H), 7.91 (d, J = 7.3 Hz, 4H), 8.97 (d, J = 7.3 Hz, 2H). ^{13}C NMR (75 MHz, DMSO-d_6, ppm) δ: 56.0, 59.3, 114.5, 128.3, 128.6, 129.2, 132.4, 133.3, 134.8, 159.7, 166.3. Anal. calcd for $C_{22}H_{20}N_2O_3$ (%): C 73.32, H 5.59, N 7.77; found: C 73.37, H 5.65, N 7.89.

_N_-Acetylamino(phenyl)methyl acetamide (Table 1, entry 11)

IR (KBr, cm^{-1}): 3278, 3119, 3060, 3029, 2932, 1663, 1563, 1517, 1371, 1273, 1094, 848, 749, 696. ^1H NMR (300 MHz, DMSO-d_6, ppm) δ: 1.86 (s, 6H), 6.52 (t, J = 7.8 Hz, 1H), 7.26–7.38 (m, 5H), 8.57 (d, J = 7.8 Hz, 2H). ^{13}C NMR (75 MHz, DMSO-d_6, ppm) δ: 23.3, 58.1, 127.2, 128.4, 129.1, 141.4, 169.4. Anal. calcd for $C_{11}H_{14}N_2O_2$ (%): C 64.06, H 6.84, N 13.58; found: C 64.16, H 6.91, N 13.66.

_N_-Acetylamino(4-fluorophenyl)methyl acetamide (Table 1, entry 12)

IR (KBr, cm^{-1}): 3276, 3124, 3016, 2957, 1665, 1555, 1515, 1369, 1237, 1093, 1028, 861, 823. ^1H NMR (300 MHz, DMSO-d_6, ppm) δ: 1.86 (s, 6H), 6.48 (t, J = 7.7 Hz, 1H), 7.19 (t, J = 8.8 Hz, 2H), 7.32–7.37 (dd, J = 5.6, 8.4 Hz, 2H), 8.53 (d, J = 7.7 Hz, 2H). ^{13}C NMR (75 MHz, DMSO-d_6, ppm) δ: 23.3, 57.6, 115.7, 116.0, 129.2, 129.3, 137.5, 137.6, 160.8, 164.0, 169.4. Anal. calcd for $C_{11}H_{13}FN_2O_2$ (%): C 58.92, H 5.84, N 12.49: found: C 59.01, H 5.95, N 12.56.

_N_-Acetylamino(4-nitrophenyl)methyl acetamide (Table 1, entry 14)

IR (KBr, cm^{-1}): 3270, 3116, 2999, 2949, 1670, 1605, 1563, 1518, 1353, 1273, 1089, 1017, 852, 825, 772. ^1H NMR (300 MHz, DMSO-d_6, ppm) δ: 1.88 (s, 6H), 6.56 (t, J = 7.7 Hz, 1H), 7.58 (d, J = 8.4 Hz, 2H), 8.23 (d, J = 8.5 Hz, 2H), 8.71 (d, J = 7.6 Hz, 2H). ^{13}C NMR (75 MHz, DMSO-d_6, ppm) δ: 23.3, 57.8, 124.3, 128.6, 147.8, 148.7, 169.7. Anal. calcd for $C_{11}H_{13}N_3O_4$ (%): C 52.59, H 5.22, N 16.73; found: C 52.63, H 5.30, N 16.83.

_N_-Benzoylamino butyl benzamide (Table 1, entry 15)

IR (KBr, cm^{-1}): 3237, 3106, 2966, 2927, 1648, 1557, 1518, 1483, 1365, 1333, 1288, 1134, 1079, 1053, 995, 844, 809, 764. ^1H NMR (300 MHz, DMSO-d_6, ppm) δ: 0.93 (t, J = 7.3 Hz, 3H), 1.37 (six, J = 7.4 Hz, 2H), 1.82 (q, J = 7.6 Hz, 2H), 5.88 (quin, J = 7.4 Hz, 1H), 7.43–7.55 (m, 6H), 7.86 (d, J = 7.0 Hz, 4H), 8.57 (d, J = 7.6 Hz, 2H). ^{13}C NMR (75 MHz, DMSO-d_6, ppm) δ: 14.5, 19.3, 37.2, 57.7, 128.2, 129.1, 132.2, 135.1, 166.4. Anal. calcd for $C_{18}H_{20}N_2O_2$ (%): C 72.95, H 6.80, N 9.45; found: C 73.00, H 6.89, N 9.55.

Acknowledgments

We are thankful to the Islamic Azad University – Najafabad Branch Research Council for partial support of this research.

References

(1) (a) Bannwarth, W.; Hinzen, B. *Combinatorial Chemistry: From Theory to Application;* Wiley/VCH: Weinheim, 2006; (b) Laszlo, P. *Preparative Chemistry Using Supported Reagents;* Academic Press, Inc.: San Diego, 1987; (c) Smith, K. *Solid Supports and Catalyst in Organic Synthesis;* Ellis Horwood: Chichester, UK, 1992.

(2) (a) Corma, A. *Curr. Opin. Solid State Mater. Sci.* **1997** *2* (1), 63. doi:10.1016/S1359-0286(97)80107-6;; (b) Tanaka, K.; Kaupp, G. *Solvent-free Organic Synthesis;* Wiley-VCH: Weinheim, 2009.

(3) (a) Varma, R. S. *Green Chem.* **1999** *1* (1), 43. doi:10.1039/a808223e;; (b) Anastasas, P. T.; Warner, J. C. *Green Chemistry: Theory and Practice;* Oxford University Press: New York, 1988; (c) Shaterian, H. R.; Ghashang, M.; Feyzi, M. *Appl. Catal. A Gen.* **2008** *345* (2), 128. doi:10.1016/j.apcata.2008.04.032;; (d) Shaterian, H. R.; Ghashang, M.; Hassankhani, A. *Dyes Pigments* **2008** *76* (2), 564. doi:10.1016/j.dyepig.2006.11.004.

(4) (a) Dingermann, T. Steinhilber, D.; Folkers, G. In *Molecular Biology in Medicinal Chemistry;* Wiley-VCH: Weinheim, 2004; (b) Shen, A. Y.; Tsai, C. T.; Chen, C. L. *Eur. J. Med. Chem.* **1999** *34* (10), 877. doi:10.1016/S0223-5234(99)00204-4;; (c) Shaterian, H. R.; Hosseinian, A.; Ghashang, M. *Can. J. Chem.* **2008** *86* (5), 376. doi:10.1139/V08-013.

(5) Magat, E. E.; Faris, B. F.; Reith, J. E.; Salisbury, L. F. *J. Am. Chem. Soc.* **1951** *73* (3), 1028. doi:10.1021/ja01147a042.

(6) Zhu, S.; Xu, G.; Chu, Q.; Xu, Y.; Qui, C. *J. Fluor. Chem.* **1999** *93* (1), 69. doi:10.1016/S0022-1139(98)00286-3.
(7) Pernak, J.; Błazej, M.; Józef, W. *Synthesis* **1994** *1994* (12), 1415. doi:10.1055/s-1994-25705.
(8) Herrera Fernández, A.; Martínez Alvarez, R.; Morales Abajo, T. *Synthesis* **1996** *1996* (11), 1299. doi:10.1055/s-1996-4385.
(9) Selvam, N. P.; Saranya, S.; Perumal, P. T. *Can. J. Chem.* **2008** *86* (1), 32. doi:10.1139/V07-134.
(10) (a) Anary-Abbasinejad, M.; Mosslemin, M.; Hassanabadi, A.; Safa, S. T. *Synth. Commun.* **2010** *40* (15), 2209. doi:10.1080/00397910903219617;; (b) Anary-Abbasinejad, M.; Mosslemin, M. H.; Hassanabadi, A. *J Chem. Res.* **2009** *2009* (4), 218. doi:10.3184/030823409X435937.
(11) Huang, S.; Pan, Y.; Zhu, Y.; Wu, A. *Org. Lett.* **2005** *7* (17), 3797. doi:10.1021/ol051458e.

Can. J. Chem. Downloaded from www.nrcresearchpress.com by Xi'an Jiaotong University on 09/19/12
For personal use only.

PROOF/ÉPREUVE

Sensing hazardous metal ions using a fluoroionophore calix[4]arene species containing two 8-oxyquinoline groups

Izilda A. Bagatin, Koiti Araki, and Henrique E. Toma

Can. J. Chem. Downloaded from www.nrcresearchpress.com by Xi'an Jiaotong University on 09/19/12
For personal use only.

Abstract: The interaction of a calix[4]arene-based species containing two 8-oxyquinoline chromophore pendants with hazardous metal ions has been investigated using optical absorption and fluorimetric techniques. In the presence of Hg^{2+}, Cd^{2+}, and Pb^{2+} ions, there is only a small decrease of the calixarene absorption band at 283 nm. The main changes are associated with the absorption band of the 8-oxyquinoline group at 315 nm, undergoing a systematic bathochromic shift to above 350 nm. In addition, a systematic decrease of the oxyquinoline emission at λ_{em} = 392 nm (λ_{exc} = 315 nm) has been observed. These observations are consistent with the coordination of the metal ions to the quinoline groups attached to the calixarene ligand, providing a useful fluoroinophore species for analytical purposes.

Key words: 8-oxyquinoline, calix[4]arene, hazardous metal ions.

Résumé : Faisant appel aux techniques d'absorption optique et fluorimétrique, on a étudié les réactions d'interaction entre des ions métalliques dangereux et des espèces à base de calix[4]arène contenant deux chromophores pendants 8-oxyquinoléine. En présence des ions Hg^{2+}, Cd^{2+} et Pb^{2+}, on n'observe qu'une faible diminution de la bande l'absorption du calixarène à 283 nm. Les principaux changements sont associés à la bande d'absorption du groupe 8-oxyquinoléine à 315 nm qui subit un déplacement bathochrome systématique au-dessus de 350 nm. De plus, on observe une diminution systématique de l'émission de l'oxyquinoléine à $\lambda_{ém}$ = 392 nm (λ_{exc} = 315 nm). Ces observations sont en accord avec une coordination des ions métalliques par les groupes quinoléines attachés au ligand calixarène, fournissant une espèce fluoroionophore pour des besoins analytiques.

Mots-clés : 8-oxyquinoléine, calix[4]arène, ions métalliques dangereux.

[Traduit par la Rédaction]

Introduction

Ionophores are becoming important selective agents for the detection and extraction of hazardous metal ions, allowing many applications in environmental chemistry and biology.[1] Recently, a new chemosensor species that signals Hg^{2+}, Cu^{2+}, and Zn^{2+} ions in acetonitrile has been published.[2] In particular, functionalized calixarenes have been extensively employed in molecular recognition of metal ions, because of their unique structural features. They can be chemically modified in the upper or lower rim positions, providing suitable architectures exhibiting improved solubility in organic solvents, and binding ability and selectivity for guest molecules or ions.[3] In fact, most analytical publications on calixarenes have focused on the extraction of alkali ions,[4] actinides, lanthanides,[5] and hazardous metals, including toxic metals from nuclear waste. Calixarenes bearing a crown-6 group[6] can selectively extract Hg^{2+} and Pb^{2+} ions, whereas those involving a crown-5 group are able to extract smaller cations, such as Zn^{2+} and Cd^{2+}. Successful extraction of Hg^{2+}, Ag^{+}, Pd^{2+}, and Au^{3+} ions has been performed[7] using the 25,26,27,28-(2-*N*,*N*-dimethyldithiocarbamoylethoxy)calix[4]arene and 25,26,27,28-(2-methylthioethoxy)calix[4]arene species. On the other hand, a high Ba^{2+} selectivity has been reported for calix[4]arene-1,2-crown-4 ethers[8] in the competitive extraction of alkaline earth metal cations.

The chemical characteristics of calixarenes can be conveniently exploited in combination with analytical techniques such as chromatography, spectrophotometry, spectrofluorimetry, and atomic absorption spectrometry for the determination of metal ions. In particular, it has been reported that spectrofluorimetry using fluorescent probes exhibits many advantages in terms of sensitivity and selectivity in the detection of metal ions such as Cr(VI),[9] Tl(I), and Cs(I).[10]

To extend the use of calix[4]arenes as fluorescent probes, we have successfully attached hydroxyquinoline groups to lower rim positions leading to species **1** (5,11,17,23-tetra(*tert*-

Received 25 November 2010. Accepted 29 January 2011. Published at www.nrcresearchpress.com/cjc on 19 April 2011.

I.A. Bagatin. Instituto de Ciências Ambientais, Químicas e Farmacêuticas, Depto de Ciências Exatas e da Terra, Universidade Federal de São Paulo, Rua Prof. Arthur Riedel, 275, CEP 09972-270 Diadema, SP, Brazil.
K. Araki and H.E. Toma. Instituto de Química, Universidade de São Paulo, Cx. P.: 26077, CEP 05513-970 São Paulo, SP, Brazil.

Corresponding author: I.A. Bagatin (e-mail: ibagatin@unifesp.br and ibagatin@gmail.com).

Can. J. Chem. Downloaded from www.nrcresearchpress.com by Xi'an Jiaotong University on 09/19/12
For personal use only.

Fig. 1. Complexation scheme of Hg^{2+}, Pb^{2+}, and Cd^{2+} by ligand **1** (5,11,17,23-tetra(*tert*-butyl)-25,27-bis[(quinoline-8-oxy)propyloxy]-26,28-dihydroxy-calix[4]arene).

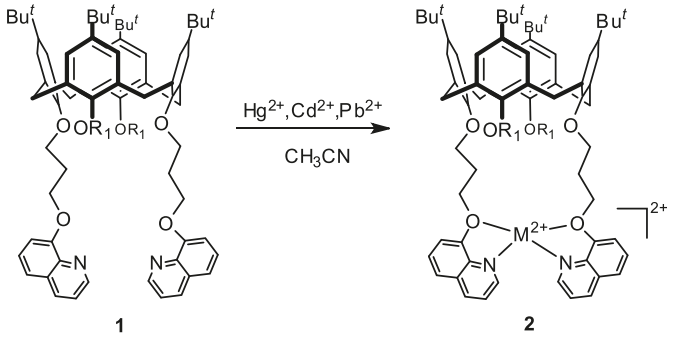

butyl)-25,27-bis[(quinoline-8-oxy)propyloxy]-26,28-dihydroxy-calix[4]arene)[11,12] (Fig. 1). It should be noticed that hydroxyquinoline (HQ) has been extensively used in the form of [Al $(HQ)_3$] complexes in commercial organic light-emitting devices because of its high luminescent properties. As a matter of fact, we have already shown that species **1** exhibits a remarkable performance in tunable light-emitting devices.[13] However, when attached to the calix[4]arene species, in addition to their luminescent role, the hydroxyquinoline groups also allow the selective binding of metal ions,[12,13] giving rise to many interesting applications as fluoroionophore agents. This type of application has not yet been explored for the detection of the hazardous Hg^{2+}, Pb^{2+}, and Cd^{2+} metal ions. For this reason, the investigation of this new relevant aspect is dealt with in this paper.

Experimental

General

Electronic spectra were recorded on a Hewlett-Packard model 8453 diode array spectrophotometer. Photoluminescence spectra were recorded on a Photon Technology International (PTI) fluorescence spectrophotometer equipped with a xenon pulsed lamp, using 1 cm quartz cells, at room temperature.

The solvents employed for the syntheses were dried, freshly distilled, and kept under nitrogen. TLC was performed on alumina plates (neutral Al_2O_3 60 F_{254}).

Species **1** was synthesized as previously described.[11,12]

The solutions of metal ions were prepared from their corresponding nitrate or chloride salts. The acid solution of HCl was freshly prepared with milliQ water (18.2 mΩ cm at 298 K). All reagents and solvents were purchased from Merck (Darmstadt, Germany).

Analytical procedure

For the determination of the acid dissociation constant of **1**, a 1×10^{-5} mol dm^{-3} solution was prepared in previously deaerated CH_3CN–H_2O (1:1 *v/v*) mixed solvent. The formal pH was varied, in the range of 6.00 to 3.30, by adding small aliquots (μL) of 1×10^{-3} mol dm^{-3} HCl directly into the spectrophotometric quartz cell.

Fig. 2. (*a*) Spectral variation for ligand **1** as a function of pH in CH_3CN–H_2O (1:1 *v/v*). (*b*) Sigmoidal plots of intensity as a function of pH at $\lambda = 253$ nm. $R^2 = 0.99$.

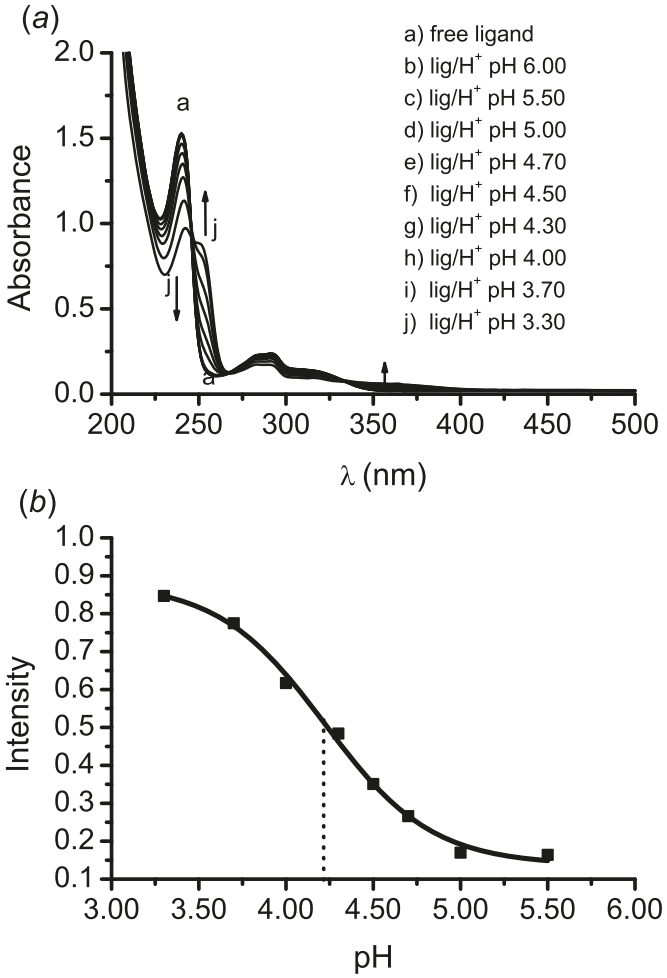

Stoichiometry and determination of the formation constants

For the evaluation of the composition and equilibrium constants of the complexes, the experiments were carried out in deaerated acetonitrile. By starting with a solution containing 1×10^{-5} mol dm^{-3} of **1**, and varying the concentrations of the Hg^{2+}, Pb^{2+}, and Cd^{2+} ions, as expressed in terms of the metal–ligand ratios: 0.3:1, 0.6:1, 1:1, 1.5:1, 2:1, 3:1, 5:1, 8:1, 10:1, 12:1, 15:1, 18:1, and 20:1. The solutions were monitored by means of absorption and fluorescence measurements. The binding constants were calculated using the data corresponding to $[M]/[L] \geq 3$. Nonlinear regression analysis using the simplex minimization method and Benesi–Hildebrand and Scatchard methods[14] were used for the determination of the binding constants.

Results and discussion

The oxyquinoline–calixarene species (ligand **1**) exhibits characteristic absorption bands at 283 and 292 nm (ε = 38 000 cm^{-1} mol^{-1} dm^3, for both bands) ascribed to $\pi \rightarrow \pi^*$ transitions in the calixarene groups, and at 320 nm (ε = 20 000 cm^{-1} mol^{-1} dm^3) ascribed to $\pi \rightarrow \pi^*$ transitions in the

Can. J. Chem. Downloaded from www.nrcresearchpress.com by Xi'an Jiaotong University on 09/19/12
For personal use only.

Fig. 3. (*a*) Linear logarithmic plot of ligand **1** as a function of pH, $R = 0.99$. (*b*) Variation of the emission intensity of **1** as a function of pH.

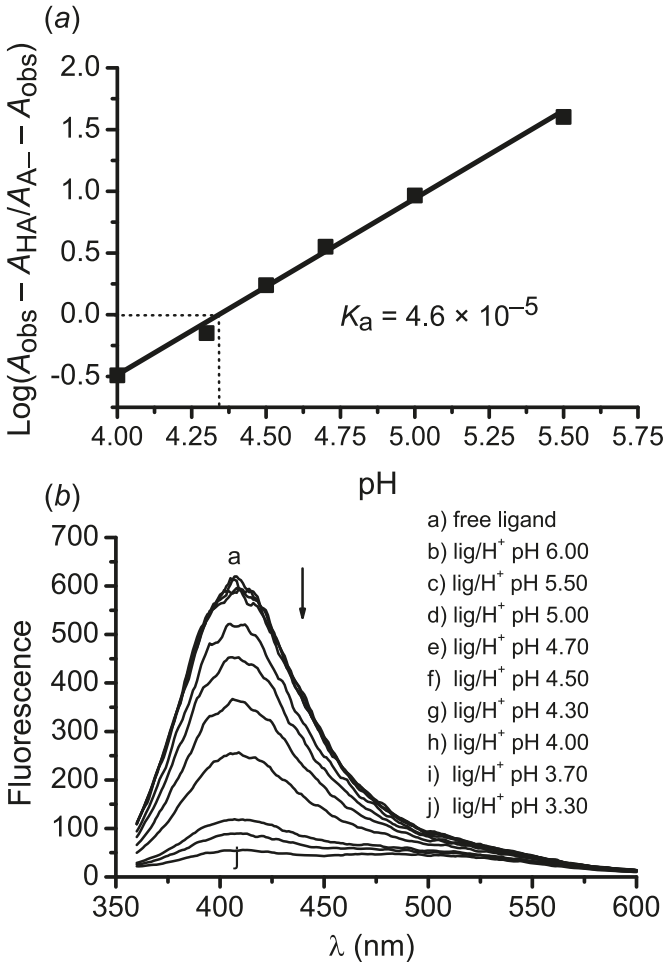

8-oxyquinoline groups. Fluorescence emission is observed at 392 nm ($\lambda_{exc} = 315$ nm) associated with the 8-oxyquinoline group. The emission quantum yield of **1** was previously determined in acetonitrile as $\phi_{q313} = 0.039$,[11] which is one order of magnitude higher than that of the 8-hydroxyquinoline group[15] ($\phi = 0.0038$). It was observed that the substitution of the –OH group by $–OCH_3$ in the quinoline group increases the quantum yield of this group.[16] In the absence of metal ions, this species exists predominantly in neutral form. In acidic $CH_3CN–H_2O$ (1:1 *v*/*v*) solutions, (pH range 3.30–6.00), the quinoline nitrogen atom is protonated (Fig. 2*a*) according to a well-behaved equilibrium process, exhibiting well-defined isosbestic points in the absorption spectra. The plot of intensity versus pH (Fig. 2*b*) shows a typical sigmoidal curve. For a monoprotonated species, the plots of log $[(A - A_{HA})/(A_A - A)]$ (where A is the absorbance, A_{HA} is the absorbance of all protonated ligand, and A_A is the absorbance of nonprotonated ligand) vs pH are expected to be linear, with a unitary slope; however, as shown in Fig. 3*a*, the observed slope is practically 2, indicating simultaneous protonation of the two quinoline groups in **1**. The pK_a was calculated as 4.34 (±0.05) ($K_a = 4.6 \times 10^{-5}$ mol^{-1} dm^3) ($\lambda = 353$ nm), and is consistent to the p$K_a = 4.9$ observed for the *N*-pyridine

Fig. 4. Titration of ligand **1** with Hg^{2+} in acetonitrile. (*a*) Evolution of the absorption spectrum as a function of Hg^{2+} concentration. (*b*) Plot of ΔAbs, where ΔAbs is Absorbance – initial Absorbance, as a function of $[Hg^{2+}]$ at $\lambda = 350$ nm. $R^2 = 0.97$. Instrumental artifact (*).

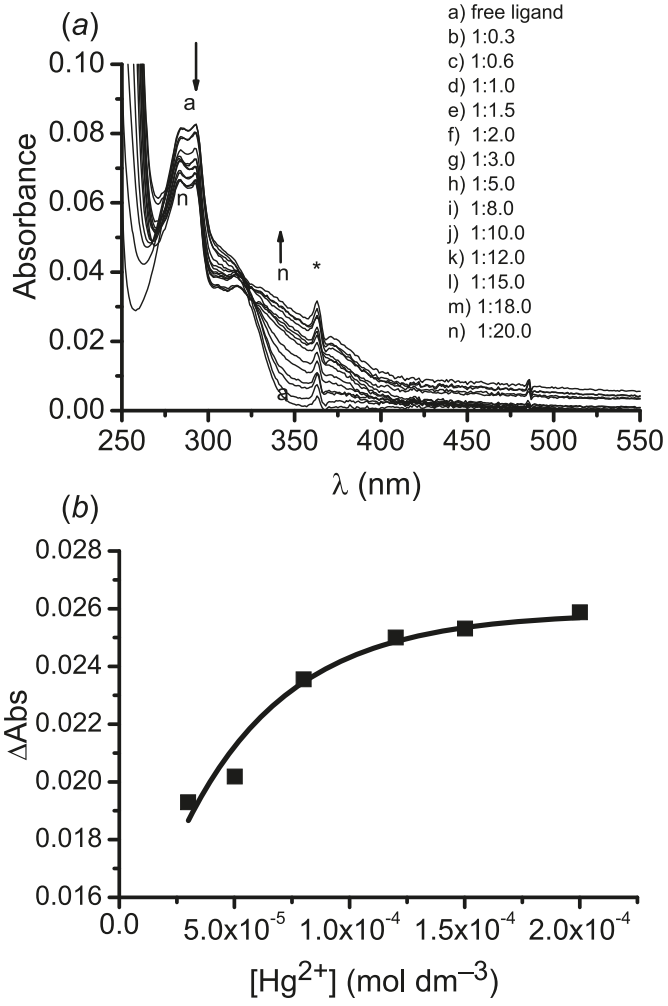

ring[17] in 8-hydroxyquinoline; the difference reflects the replacement of –OH by the –OR group (R = $CH_2CH_2CH_2$calix) in ligand **1**.

Calculation of the charge-transfer excited state pK_a* for this ligand was carried out by using eq. [1][18,19]

$$[1] \qquad pK_a^* = pK_a(gs) + 2.86(\nu_1 - \nu_2)/2.303\,RT$$

where pK_a(gs) is the ground-state pK_a, ν_1 is the frequency in wavenumbers of the charge-transfer absorption maxima band of the unprotonated form, ν_2 is the frequency of the corresponding absorption in the protonated form, $R = 1.9872$ cal mol^{-1} K^{-1} (1 cal = 4.184 J), and 2.86 is a conversion factor to energy. The calculated pK_a* of **1** was 11.50, indicating a basicity increase of seven orders of magnitude with respect to the ground-state p$K_a = 4.34$.

Protonation of **1** can also be monitored by the decrease of the emission band at 410 nm upon excitation at 315 nm, as shown in Fig. 3*b*. The pK_a calculated in this way is consistent with that obtained spectrophotometrically (p$K_a = 4.25$).

The interaction of hazardous metal ions with ligand **1** has

Can. J. Chem. Downloaded from www.nrcresearchpress.com by Xi'an Jiaotong University on 09/19/12
For personal use only.

Fig. 5. (*a*) Evolution of the emission spectrum of ligand **1** with increasing concentrations of Hg^{2+} at λ_{em} = 392 nm. (*b*) Plot of F_0/F vs [Hg^{2+}], R = 0.98.

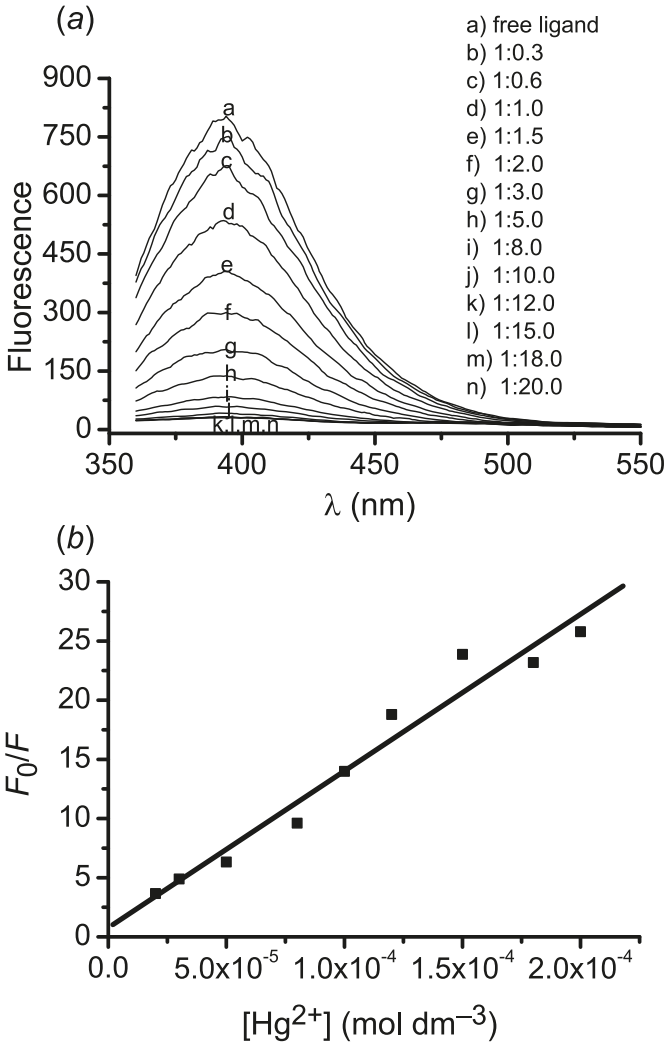

Fig. 6. Titration of ligand **1** with Pb^{2+} in acetonitrile. (*a*) Evolution of the absorption spectrum as a function of Pb^{2+} concentrations, (*b*) Plot of ΔAbs, where ΔAbs is Absorbance – initial Absorbance, as a function of [Pb^{2+}] at λ = 350 nm. R^2 = 0.94.

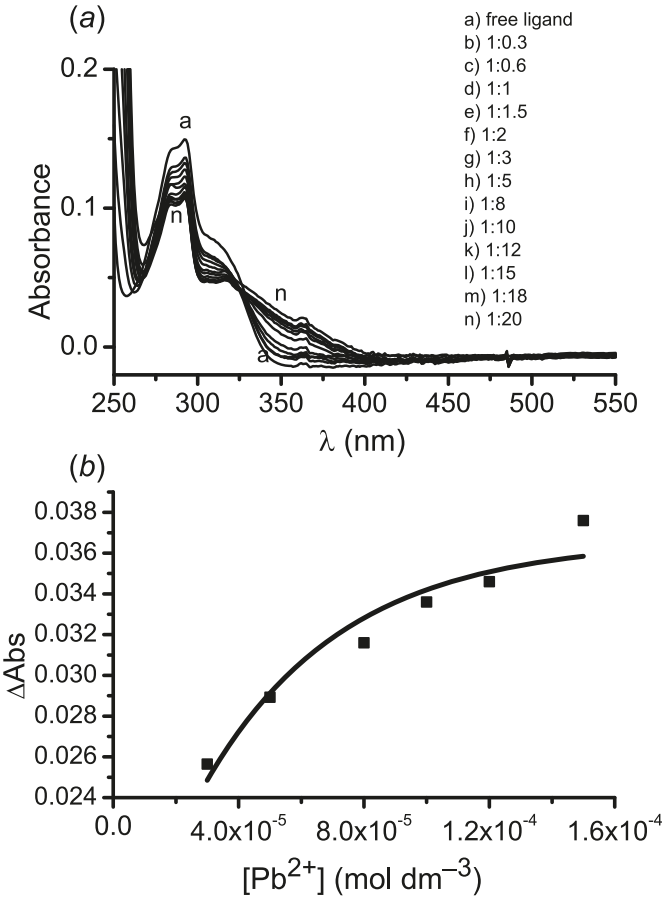

been investigated in acetonitrile, by monitoring the changes in the UV–vis absorption spectra and in the corresponding fluorescence spectra.

In the presence of Hg^{2+} ions, there is only a small decrease of absorbance in the region of the calixarene band (283 nm; Fig. 4*a*). The main changes are associated with the absorption band of the 8-oxyquinoline group at 315 nm, which undergoes a systematic bathochromic shift to about 350 nm, generating an isosbestic point at 322 nm. This result is consistent with the selective binding of the Hg^{2+} ions to the 8-oxyquinoline chromophore.

The titration plot, monitoring ΔAbs vs the concentration of metal ion ([M]), is shown in Fig. 4*b*. It was treated by nonlinear regression analysis, yielding a good fitting for a 1:1 stoichiometry, according to eq. [2]

$$[2] \qquad \Delta A = \frac{L K_{11} \Delta\varepsilon [M]}{1 + K_{11}[M]}$$

where $\Delta A = A_t - A_0$, A_t is the total absorbance, L = ligand, M = metal ion ([M] = [Mt], where [M] >> [L] and [Mt] = total concentration of metal ion), $\Delta\varepsilon$ = molar absorptivity ($\Delta\varepsilon = \varepsilon - \varepsilon_M - \varepsilon_L$, where ε = molar absorptivity of complex, ε_M = molar absorptivity of metal ion, and ε_L = molar absorptivity of ligand), and K_{11} = binding constant.

The calculated binding constant for the Hg^{2+} ions was K_{11} = 6.4 (±0.70) × 10^4 mol dm^{-3}. Similarly, the binding constant was also calculated based on the Benesi–Hildebrand method, assuming a 1:1 stoichiometry, yielding K_{11} = 7.3 (±0.7) × 10^4 mol dm^{-3}, and also by the Scatchard method, yielding K_{11} = 3.1 (±0.5) × 10^4 mol dm^{-3}. The Scatchard method led to a binding constant of the same magnitude as the preceding methods, but yielded a smaller absolute value because of the larger oscillation of R^2 = 0.76 associated with the experimental data.

The binding of the Hg^{2+} ions to the oxyquinoline–calixarene species was also monitored by the changes in the emission profiles, as shown in Fig. 5*a*. One can see that there is a systematic decrease of the luminescence of free ligand **1** at 392 nm. This fact contrasts with the results previously reported for the binding of ligand **1** to Zn^{2+} ions.[12] In this case, a new emission band has been observed at 440 nm, ascribed to the Zn^{2+}-coordinated ligand **1** complex. The lack of this band in the corresponding Hg^{2+} complex indicates that the metal ion is acting as a powerful quencher, in contrast with the Zn^{2+} ions.

In this case, the binding constants can be evaluated from

Can. J. Chem. Downloaded from www.nrcresearchpress.com by Xi'an Jiaotong University on 09/19/12
For personal use only.

Fig. 7. (*a*) Evolution of the emission spectrum of ligand **1** with increasing concentrations of Pb^{2+} at λ_{em} = 392 nm. (*b*) Plot of F_0/F (where F_0 is the fluorescence in the absence of metal ion and F is the fluorescence) vs [Pb^{2+}], R = 0.99.

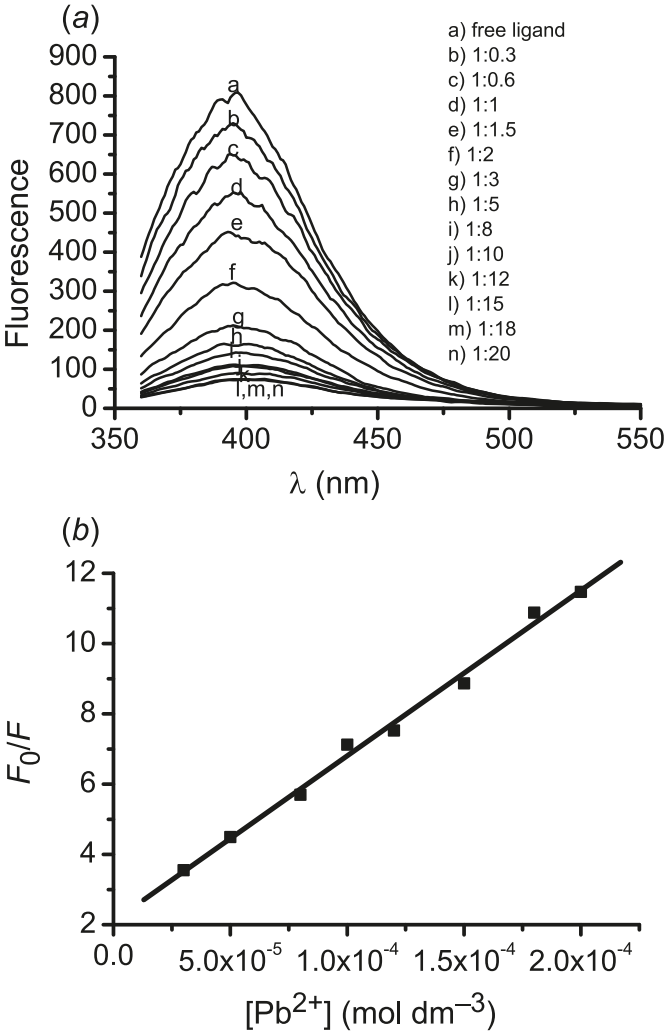

the fluorescence data according to the Stern–Volmer equation (eq. [3]),

$$[3] \qquad \frac{F_0}{F} = 1 + K_{11}[\mathrm{M}]$$

where F_0 = fluorescence in the absence of metal ion, F = fluorescence, and K_{11} = Stern–Volmer constant. Under the conditions of [M] >> [L], the plot of F_0/F vs [M] was linear, as shown in Fig. 5*b*, yielding K_{11} = 13.2 (±0.8) × 10^4 mol dm^{-3}. The equilibrium constant based on the Stern–Volmer plot is two times higher than that determined spectrophotometrically. Presumably, this constant should also involve additional contributions of outer sphere or collisional complexes generated with Hg^{2+} ions, which are effective in suppressing the fluorescence of the ligand, but leading to minor changes in the absorption spectra.

Similar experiments have been carried for Pb^{2+} ions, as shown in Figs. 6 and 7. The changes observed in the absorption and emission spectra, as a function of the amount of

Fig. 8. Titration of ligand **1** with Cd^{2+} in acetonitrile. (*a*) Evolution of the absorption spectrum as a function of Cd^{2+} concentrations. (*b*) Plot of ΔAbs, where ΔAbs is Absorbance – initial Absorbance, as a function of [Cd^{2+}] at λ = 350 nm, R^2 = 0.96.

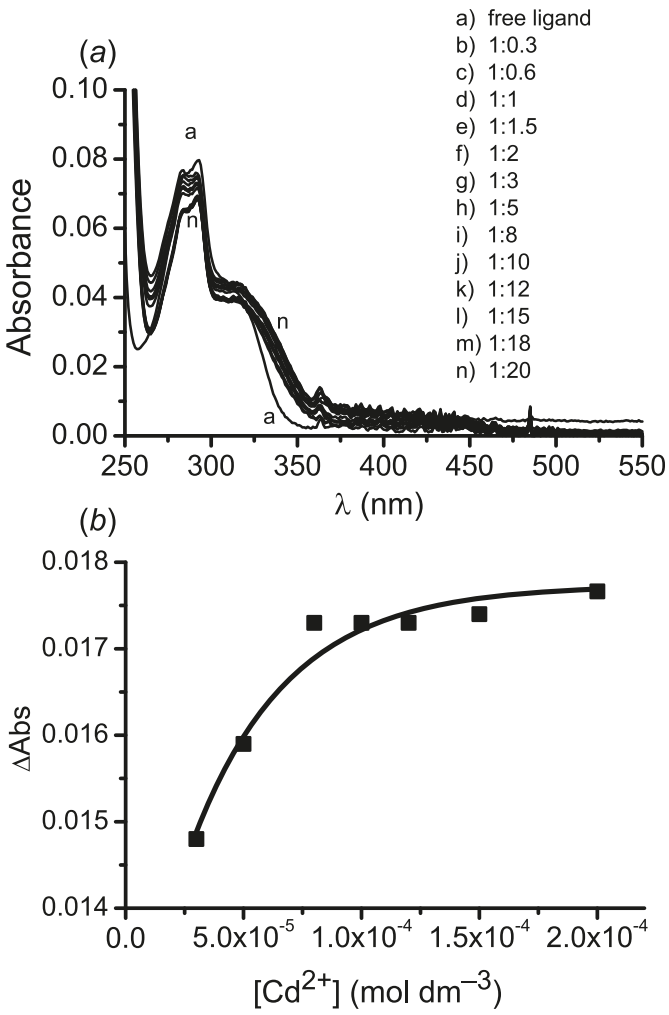

Pb^{2+} ions, are very similar to those found in the case of the Hg^{2+} ions. The corresponding binding constants are collected in Table 1, for comparison purposes. In this case, however, a good agreement can be observed for the absorption and fluorescence data, indicating negligible quenching from the outer-sphere complexes.

In the case of the Cd^{2+} ions, the results shown in Figs. 8 and 9 depart from those observed for the Hg^{2+} and Pb^{2+} ions, and resemble those previously reported for Zn^{2+} ions. The estimated binding constants based on the spectrophotometric data were in the range of 11.6 × 10^4 to 13.8 × 10^4 mol dm^{-3}. The binding of the Cd^{2+} ions leads only to a partial quenching of the oxyquinoline emission at 392 nm, leading to a less intense emission band of the Cd^{2+}-coordinated species at 440 nm, as for the Zn^{2+} system.[12] In this case, the calculation of the equilibrium constant from the Stern–Volmer plots is no longer valid.

Conclusion

The fluoroionophore species **1** provides an interesting optical sensor for the determination of Hg^{2+}, Cd^{2+}, and Pb^{2+}

Table 1. Binding constants for Zn^{2+}, Cd^{2+}, Hg^{2+}, and Pb^{2+} ions with the calix[4]arene ligand **1**.

		Methods		
Ions	Simplex minimization (mol dm^{-3})	Benesi–Hildebrand (mol dm^{-3})	Scatchard (mol dm^{-3})	Stern–Volmer (mol dm^{-3})
Zn^{2+a}	7.8 (±1.5)×10^4	4.6 (±0.1)×10^4	4.9 (±0.9)×10^4	—
Cd^{2+}	13.8 (±1.4)×10^4	11.6 (±0.4)×10^4	13.0 (±1.2)×10^4	
Hg^{2+}	6.4 (±0.7)×10^4	7.3 (±0.7)×10^4	3.1 (±0.5)×10^4	13.2 (±0.8)×10^4
Pb^{2+}	5.2 (±0.9)×10^4	9.4 (±0.3)×10^4	5.8 (±0.9)×10^4	4.7 (±0.2)×10^4

[a]Constants calculated from the data of ref. 12.

Can. J. Chem. Downloaded from www.nrcresearchpress.com by Xi'an Jiaotong University on 09/19/12
For personal use only.

Fig. 9. (*a*) Evolution of the emission spectrum of ligand **1** with increasing concentrations of Cd^{2+} at λ_{em} = 392 nm. (*b*) Plot of F_0/F (where F_0 is the fluorescence in the absence of metal ion and F is the fluorescence) vs [Cd^{2+}], R = 0.98.

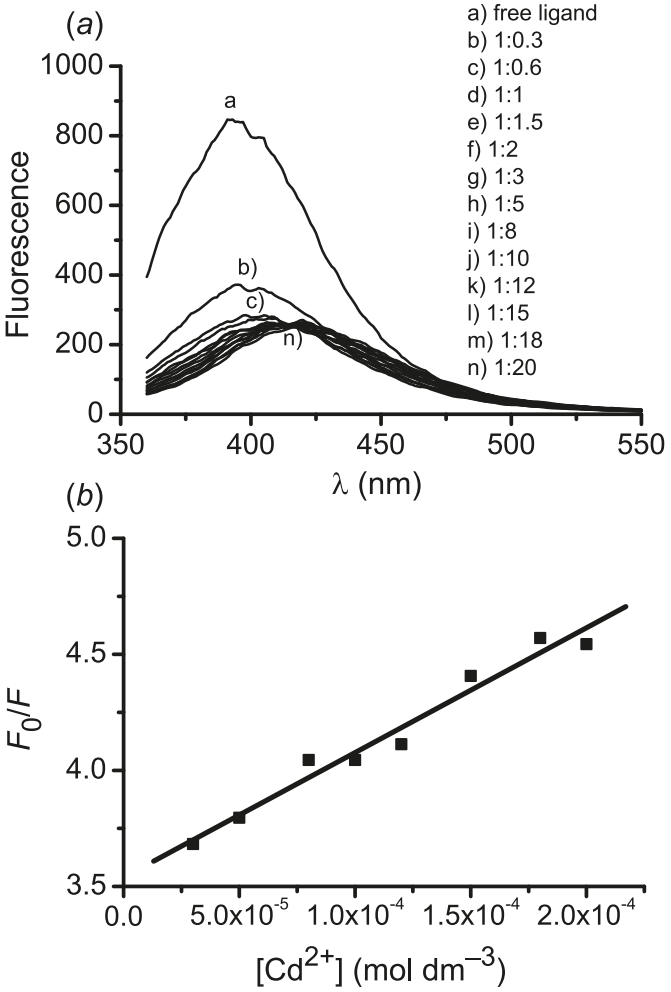

ions. The complexation reaction is consistent with a 1:1 metal–ligand stoichiometry, involving the coordination of the hazardous metal ions to the oxyquinoline group. The good stability and reproducible performance of system **1** are important qualities of this fluoroionophore ligand, which, in addition to the selective recognition of metals, can also allow further applications in extraction procedures.

Acknowledgements

Financial support from Rede de Nanotecnologia Molecular e de Interfaces – Conselho Nacional de Desenvolvimento Cientifico e Tecnológico (Renami-CNPq) as well as from Fundação de Amparo a Pesquisa do Estado de São Paulo (Fapesp) is gratefully acknowledged.

References

(1) Valeur, B.; Leray, I. *Coord. Chem. Rev.* **2000** *205* (1), 3. doi:10.1016/S0010-8545(00)00246-0.
(2) Nisar Ahamed, B.; Ravikumar, I.; Ghosh, P. *N. J. Chem.* **2009** *33* (9), 1825. doi:10.1039/b9nj00204a.
(3) Shinkai, S. *Tetrahedron* **1993** *49*, 8933. doi:10.1016/S0040-4020(01)91215-3.
(4) Burgard, M.; Yaftian, M. R.; Jeunesse, C.; Bagatin, I. A.; Matt, D. *J. Incl. Phenom. Macrocycl. Chem.* **2000** *38* (1/4), 413. doi:10.1023/A:1008192012881.
(5) Matulková, I.; Rohovec, J. *Polyhedron* **2005** *24* (2), 311. doi:10.1016/j.poly.2004.11.008.
(6) Dung, N. T. K.; Ludwig, R. *N. J. Chem.* **1999** *23* (6), 603. doi:10.1039/a809771b.
(7) Yordanov, A. T.; Roundhill, D. M. *Inorg. Chim. Acta* **1998** *270* (1–2), 216. doi:10.1016/S0020-1693(97)05843-X.
(8) Tu, C.; Surowiec, K.; Bartsch, R. A. *Tetrahedron* **2007** *63* (19), 4184. doi:10.1016/j.tet.2007.02.105.
(9) Xiang, Y.; Mei, L.; Li, N.; Tong, A. *Anal. Chim. Acta* **2007** *581* (1), 132. doi:10.1016/j.aca.2006.08.006.
(10) Roper, E. D.; Talanov, V. S.; Gorbunova, M. G.; Bartsch, R. A.; Talanova, G. G. *Anal. Chem.* **2007** *79* (5), 1983. doi:10.1021/ac061387c.
(11) Bagatin, I. A.; Toma, H. E. *N. J. Chem.* **2000** *24* (11), 841. doi:10.1039/b005127f.
(12) Bagatin, I. A.; de Souza, E. S.; Ito, A. S.; Toma, H. E. *Inorg. Chem. Commun.* **2003** *6* (3), 288. doi:10.1016/S1387-7003(02)00756-6.
(13) Legnani, C.; Reyes, R.; Cremona, M.; Bagatin, I. A.; Toma, H. E. *Appl. Phys. Lett.* **2004** *85* (1), 10. doi:10.1063/1.1767274.
(14) Connors, K. A. In *Binding Constants — The Measurement of Molecular Complex Stability;* John Wiley & Sons: New York, 1987; Chapter 4.
(15) Bardez, E.; Devol, I.; Larrey, B.; Valeur, B. *J. Phys. Chem. B* **1997** *101* (39), 7786. doi:10.1021/jp971293u.
(16) Goldman, M.; Wehry, E. L. *Anal. Chem.* **1970** *42* (11), 1178. doi:10.1021/ac60293a045.
(17) Smith, G.; Thomasson, J. H.; White, J. M. *Aust. J. Chem.* **1999** *52* (4), 317. doi:10.1071/C98127.
(18) Toma, H. E.; Stadler, E. *Inorg. Chem.* **1985** *24* (19), 3085. doi:10.1021/ic00213a045.
(19) Jackson, G.; Porter, G. *Proc. R. Soc. Lond. A Math. Phys. Sci.* **1961** *260* (1300), 13. doi:10.1098/rspa.1961.0010.

Partition coefficients of disparlure at hydrophobic/aqueous interfaces: A comparative experimental and theoretical study

Sarah Reimer, Christa Van Klei, Yang Yu, Erika Plettner, and Noham Weinberg

Can. J. Chem. Downloaded from www.nrcresearchpress.com by Xi'an Jiaotong University on 09/19/12
For personal use only.

Abstract: The gypsy moth, *Lymantria dispar*, uses pheromones, such as (+)-disparlure, for communication. These pheromones are detected by the sensitive antennae of the male moth and travel through their aqueous environment to the sensory neuron, possibly with assistance from pheromone binding proteins (PBPs). The hydrophobicity of disparlure, which is of primary importance for its interactions with PBPs, can be measured by its partition coefficients. These coefficients for heptane/water and chloroform/water interfaces were obtained in this work experimentally and using molecular dynamics (MD) simulations. The agreement between the experimental and calculated values validates the choice of the force field parameters, which can thus be used in future MD simulations of the PBP–pheromone interactions.

Key words: gypsy moth, disparlure, partition coefficients, hydrophobicity, epoxide, OPLS parameters, molecular dynamics simulations.

Résumé : La lymantride spongieuse, mite gitane, *Lymantria dispar*, fait appel à des phéromones, tel le (+)-disparlure, pour ses communications. Ces phéromones sont détectées par des antennes sensibles des lymantrides mâles et elles circulent dans leur environnement aqueux vers le neurone sensoriel, peut-être avec l'aide de protéines fixatrices de phéromones (PFP). Le caractère hydrophobe du disparlure qui est d'importance capitale pour ses interactions avec les PFP peut être mesuré par ses coefficients de partition. Dans ce travail, on a mesuré expérimentalement ces coefficients pour les systèmes heptane/eau et chloroforme/eau et on les a aussi calculés par la méthode de la dynamique moléculaire (DM). L'accord entre les valeurs calculées et celles obtenues expérimentalement valide le choix des paramètres de champ de force qui pourront être utilisés dans des simulations ultérieures de DM des interactions PFP/phéromone.

Mots-clés : lymantride spongieuse, disparlure, coefficients de partition, caractère hydrophobe, époxyde, paramètres des potentiels optimisés pour des simulations de liquides, simulations de dynamiques moléculaires.

[Traduit par la Rédaction]

Introduction

(7*R*,8*S*)-*cis*-7,8-Epoxy-2-methyloctadecane (**1**) is the main sex pheromone of the gypsy moth, *Lymantria dispar*.[1]

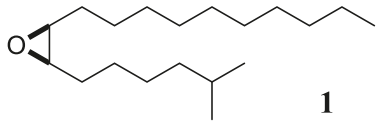

1

This pheromone, commonly known as (+)-disparlure, is released by the female moth and detected by the very sensitive antennae of the male. These antennae are covered with hollow sensory hairs, which contain the target olfactory nerve cells (see Fig. 1). The pheromone is thought to access the interior of the hair through a system of pore tubules.[2] Inside the hair is an aqueous protein-rich environment containing pheromone-binding proteins (PBPs),[3] one possible role of which is to transport hydrophobic molecules, such as disparlure, through the aqueous environment to the receptors of the olfactory nerve cell,[4] where the pheromone itself is believed to activate the receptors.[5] A study with expressed odorant receptors[6] has shown that the receptors can be activated by direct addition of pheromone to the incubation medium. In contrast, another recent study has proposed that a conformer of the PBP–pheromone complex plays a role in activating the receptor,[7] and other studies have suggested that the PBP–pheromone complex works in conjunction with the sensory neuron membrane protein in regulating the ion conductance of the olfactory nerve cell.[8]

The hydrophobicity of disparlure must be of primary importance in its interactions with PBPs. Experimental studies of these interactions and their kinetics have recently been reported.[9] Further insight could be achieved through molecular modeling and molecular dynamics (MD) simulations. With

Received 20 October 2010. Accepted 21 January 2011. Published at www.nrcresearchpress.com/cjc on 20 April 2011.

S. Reimer and C. Van Klei. Department of Chemistry, University of the Fraser Valley, Abbotsford, BC V2S 7M8, Canada.
Y. Yu and E. Plettner. Department of Chemistry, Simon Fraser University, Burnaby, BC V5A 1S6, Canada.
N. Weinberg. Department of Chemistry, University of the Fraser Valley, Abbotsford, BC V2S 7M8, Canada; Department of Chemistry, Simon Fraser University, Burnaby, BC V5A 1S6, Canada.

Corresponding authors: E. Plettner (e-mail: plettner@sfu.ca) and N. Weinberg (email: noham.weinberg@ufv.ca).

Fig. 1. The suggested route[2] disparlure takes through the sensillum lymph on its way to the olfactory nerve. A moth antenna (A) is highly branched, and the branches are covered with sensory hairs (sensilla). The sensilla are hollow cuticular structures that are innervated by a few olfactory neurons (1 in panel B). The cuticle of the hair (4) is traversed by pores (5). The dendrite of an olfactory neuron (3) protrudes into the space of the hair and is bathed by an electrolyte, the sensillum lymph (panel C). The sensillum lymph contains the pheromone-binding protein (triangles) and ions (Na^+, K^+, Cl^-, phosphate). The dendritic membrane (8) houses the olfactory receptors (7) and the sensory neuron membrane protein (6). The figure is from Gong et al.,[9] reproduced with kind permission of Chemistry & Biology, © 2009 Elsevier.

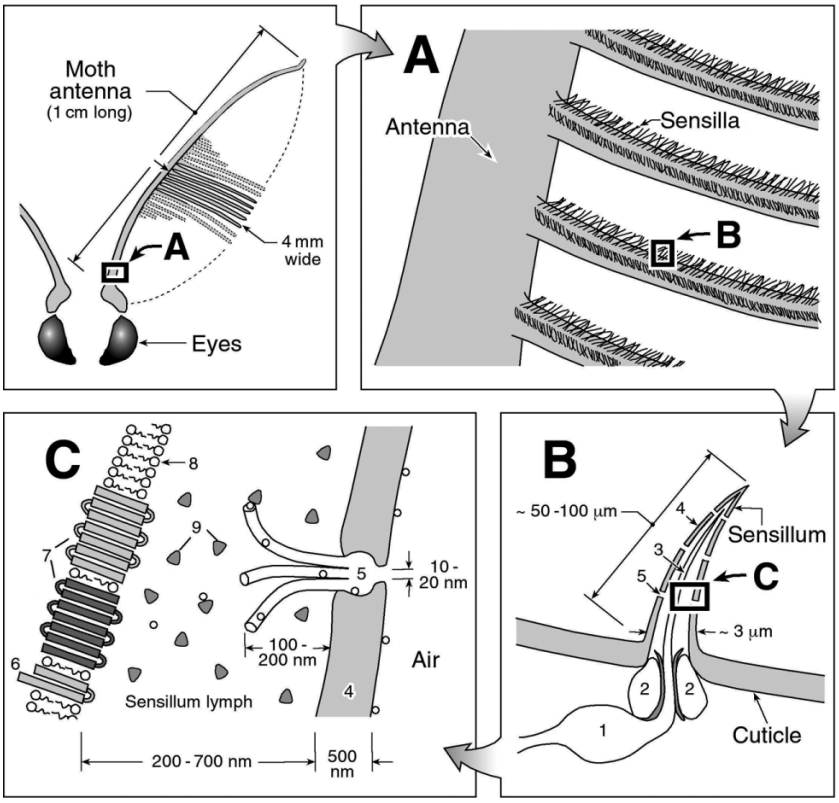

Can. J. Chem. Downloaded from www.nrcresearchpress.com by Xi'an Jiaotong University on 09/19/12
For personal use only.

recent advances in computer technology, MD has become an excellent companion and a viable alternative to often costly and difficult experiments.[10] The quality of the MD results depends on the quality of the force field used in the simulations. The OPLS (optimized potentials for liquid simulations) force field[11] is often used to study reactions and processes in solutions. Unfortunately, to the best of our knowledge, the epoxy ring parameters have never been reported in the literature. In the present work we propose such parameters and test their quality in describing hydrophobic properties of disparlure. For that purpose, we have measured experimentally the partition coefficients of racemic disparlure at *n*-heptane/water and chloroform/water interfaces (*n*-heptane and chloroform were chosen because of their different hydrophobicities) and compared the experimental results with the MD values calculated using the augmented OPLS parameters.

Experimental procedures

Synthesis and purification of disparlure

Racemic disparlure, (±)-*cis*-7,8-epoxy-2-methyloctadecane, was prepared by *meta*-chloroperoxybenzoic acid epoxidation of (*Z*)-2-methyl-7-octadecene, which was obtained in 96:4 diastereoselectivity by partial hydrogenation of 2-methyl-7-octadecyne using Lindlar's catalyst under a hydrogen atmosphere. The 2-methyl-7-octadecyne was synthesized by an acetylide coupling reaction between 1-dodecyne and 1-bromo-5-methylhexane using *n*-butyllithium as a base and tetramethylethylenediamine as a co-solvent in tetrahydrofuran under gentle reflux. This three-step synthesis gave an overall yield of 17% (limiting reagent 1-bromo-5-methylhexane) with high *cis*-epoxide configuration (96%; see ^{1}H NMR spectra of (*Z*)-2-methyl-7-octadecene[12] and the racemic disparlure, Supplementary data). Also, the method avoided using carcinogenic hexamethylphosphoramide during the acetylide coupling reaction.

The *cis*- and *trans*-disparlure were easily distinguished by ^{1}H NMR. H-7 and H-8[13] of *cis*-disparlure showed a multiplet signal at δ 2.90 ppm, whereas in *trans*-disparlure these two methine protons gave a broad triplet at δ 2.38 ppm.[12] However, the signals of H-7 and H-8 of (*Z*)- and (*E*)-2-methyl-7-octadecene overlapped at δ 5.30 ppm[13] and therefore could not be used to distinguish these two isomers. The *Z* and *E* alkene isomers and the *cis* and *trans* disparlure isomers also ran at different retention times in gas chromatography with an SPB-5 (Supelco) column.

Determination of partition coefficients

The purest available organic solvent (2.00 mL heptane or chloroform, HPLC grade) and 2.00 mL of double-distilled water were pipetted into a 4 mL glass vial using 2.00 mL glass pipettes. The system was allowed to equilibrate for 20 min. Then 2.0 μL of purified racemic disparlure was

Can. J. Chem. Downloaded from www.nrcresearchpress.com by Xi'an Jiaotong University on 09/19/12
For personal use only.

added to the organic phase using a 10 μL glass syringe from a 50 mg mL^{-1} stock solution in distilled *n*-hexane. Once the disparlure was added, the vial was capped and the system was equilibrated for 30 min before a sample was extracted from each phase.[14] A portion (0.40 mL) of the organic phase was removed from the incubation mixture, using a 2.00 mL glass pipette, and added to a 1 mL glass vial with 4 μL of 1.3 mg mL^{-1} *n*-hexadecane in distilled *n*-hexane, as an internal standard, and ~10 mg Na_2SO_4. The internal standard was added to compensate for evaporation. It was allowed to dry for 1 min before the volume was measured using a 100 μL glass syringe. An aliquot (1 μL) of the organic sample was analyzed using gas chromatography mass spectrometry (GC-MS). Spectra were recorded on a Varian Saturn 2000 mass spectrometer coupled to a CP 300 gas chromatograph equipped with an SPB-5 GC column (Supelco, 30 m, 0.25 mm i.d., 0.25 μm film). MS conditions were as follows: collection period, 4–14 min; *m/z* range, 50–500; ionization mode, electron impact; ion preparation technique, selected ion storage (49–501 *m/z*). For analysis of the aqueous layer, 0.50 mL was retrieved from the aqueous phase of the incubation system with a 0.50 mL glass pipette. Internal standard (0.20 mL of 9.6 μg mL^{-1} *n*-hexadecane in distilled ethyl acetate/hexane (1:1)) was added to the extract in a silicon-coated glass vial, the vial was shaken, and the organic layer was removed using a 100 μL glass syringe (Hamilton). The extraction was repeated with another 0.20 mL of solvent with internal standard. The two organic phases were pooled and dried in a 1 mL glass vial with ~10 mg Na_2SO_4 for 1 min, and the volume was measured using a 100 μL glass syringe. An aliquot (1 μL) was analyzed using GC. All experiments were performed at 25 °C. The partition coefficient P was calculated as the ratio of the disparlure concentrations in organic solvent (C_s) and the aqueous phase (C_w): $P = C_s/C_w$.

Molecular dynamics calculations

MD simulations were performed using the GROMACS program suite[15] at a constant temperature of 298 K (Berendsen thermostat, $\tau_T = 0.01$ ps), a constant pressure of 100 kPa (Berendsen barostat, $\tau_P = 0.1$ ps), and periodic boundary conditions[10] for the systems containing a single molecule of disparlure in solvents that consisted of either 320 molecules of *n*-heptane, 375 molecules of chloroform, or 2500 molecules of water. The 1 ns MD trajectories were obtained by leap-frog integration with a step size of 1 fs. The total interaction energy of the system was calculated as the sum of five terms:[11]

$$[1] \quad U = U_{\text{bond}} + U_{\text{angle}} + U_{\text{torsion}} + U_{\text{Coulomb}} + U_{\text{LJ}}$$

The first three terms represent the intramolecular energy associated with bond stretching, angle bending, and torsions:

$$[2] \quad U_{\text{bond}} = \sum_{\text{bonds}} \frac{1}{2} k_r (r - r_0)^2$$

$$[3] \quad U_{\text{angle}} = \sum_{\text{angles}} \frac{1}{2} k_\theta (\theta - \theta_0)^2$$

$$U_{\text{torsions}} = \sum_{\text{dihedrals}} \sum_{n=0}^{3} C_n (\cos \phi)^n$$

No cross-terms were taken into account. The intermolecular and through-space intramolecular interactions were described by the pairwise Coulomb potential

$$[4] \quad U_{\text{Coulomb}} = \sum_{\text{atom pairs}} K \frac{q_i q_j}{r_{ij}}$$

representing charge–charge electrostatic interactions and the Lennard Jones (LJ) potential

$$[5] \quad U_{\text{LJ}} = \sum_{\text{atom pairs}} 4\varepsilon_{ij} \left[\left(\frac{\sigma_{ij}}{r_{ij}} \right)^{12} - \left(\frac{\sigma_{ij}}{r_{ij}} \right)^{6} \right]$$

representing van der Waals interactions. Standard combination rules were used for the LJ parameters ε and σ:

$$[6] \quad \varepsilon_{ij} = \sqrt{\varepsilon_i \varepsilon_j}$$

$$[7] \quad \sigma_{ij} = \frac{1}{2}(\sigma_i + \sigma_j)$$

The particle mesh Ewald method[16] was used to calculate coulombic energy, with $r_{\text{coul}} = 1.4$ nm. The LJ cutoff radius was 1.4 nm.

OPLS parameters[11,17] were used for disparlure, *n*-heptane, and chloroform, and the SPC model[18] was used for water. The atomic, bond, and angle parameters for the epoxy group of disparlure were missing from the standard OPLS set and thus we augmented the set with the parameters listed in Table 1. The atomic (non-bonded) parameters for the epoxy group were assumed to be the same as the corresponding OPLS parameters for ether.[19] The values of r_0 and θ_0 were obtained by B3LYP/6-31G(d,p) geometry optimization using Gaussian 03.[20] The bond and angle force constants, k, as well as all torsion parameters were assumed to be the same as the OPLS parameters for cyclopropane.[19]

The Gibbs energies of solvation of disparlure in water (ΔG_w) and organic solvent (ΔG_s) were found by thermodynamic integration.[10] To avoid singularities at small values of the scaling parameter λ, the solvent–disparlure interaction U_{sd} was scaled as λ^n:[21]

$$[8] \quad U(\lambda) = U_{\text{solvent}} + U_{\text{disparlure}} + \lambda^n U_{\text{sd}}$$

For $n = 9$, the convergence was achieved with 40-point integration. Each point was obtained by averaging over a 1 ns trajectory. The partition coefficients P were then calculated as

$$[9] \quad P = \exp\left(\frac{\Delta G_w - \Delta G_s}{RT} \right)$$

Results and discussion

The values of the logarithms of the partition coefficients calculated for (+)-disparlure (**1**) at chloroform/water and *n*-heptane/water interfaces are compared with the experimentally obtained values in Table 2 and demonstrate a very good fit. As expected, disparlure appears to prefer *n*-heptane to chloroform, and either organic solvent to water. This is consistent with the structure of the pheromone, which is dominated

Can. J. Chem. Downloaded from www.nrcresearchpress.com by Xi'an Jiaotong University on 09/19/12
For personal use only.

Table 1. Atomic, bond, and angle parameters for the epoxy group of disparlure.

(A) Atomic parameters (eqs. [3] and [4])			
Atom	q (au)	σ (nm)	ε (kJ mol^{-1})
O	–0.40	0.29	0.586
H	0.03	0.25	0.12552
C	0.17	0.35	0.276144
(B) Bond parameters (eq. [1])			
Bond	r_0 (nm)	k_r (kJ mol^{-1} nm^{-2})	
OC	0.14304	217 568	
CC	0.14691	217 568	
CH	0.10899	284 512	
(C) Angle parameters (eq. [2])			
Angle	θ_0 (°)	k_θ (kJ mol^{-1} rad^{-2})	
COC	61.798	251.04	
CCO	59.104	251.04	
HCO	117.2	313.8	
HCC	117.2	313.8	

Table 2. Calculated and experimental log P for disparlure at hydrophobic/aqueous interfaces.

	log P	
Interface	Calculated	Experimental
Chloroform/water	3.1	3.4±0.3
n-Heptane/water	3.9	3.8±0.2

by two long hydrocarbon chains. However, the impact of the more polar epoxy group cannot be ignored. Thus, *n*-nonane, with fewer than half the number of carbon atoms of disparlure, appears to be much more hydrophobic, with a log P value at the chloroform/water interface of 6.57.[22]

The reported results validate the parameter set listed in Table 1 as a reliable tool for assessing the hydrophobic properties of disparlure. The high hydrophobicity of the pheromone seems to imply that PBPs may indeed play an important role in the transport of disparlure through the aqueous environment of the antenna lymph to the olfactory nerve dendrite. However, our preliminary calculations suggest that diffusion of disparlure in water is fast enough to allow the independent migration of this pheromone through aqueous medium, which is consistent with observations made with expressed receptors.[7] This result is in agreement with the experimental fact that the diffusion constants of such hydrophobic molecules as toluene, cyclohexane, and propene in dilute aqueous solutions are comparable to those of hydrophilic methanol.[23] Further experimental and computational studies are therefore needed to obtain a definitive answer to the question of disparlure transport and the role of PBPs in it.

Supplementary data

Supplementary data are available with the article through the journal Web site (www.nrcresearchpress.com/cjc).

Acknowledgements

Financial support of the Natural Sciences and Engineering Council of Canada (NSERC) is gratefully acknowledged (Discovery grant No. 222923 and Strategic grant No. STGP351045 to E.P., and Discovery grant No. 184086 to N.W.). This research has been enabled by the use of WestGrid computing resources, which are funded in part by the Canada Foundation for Innovation, Alberta Innovation and Science, B.C. Advanced Education, and the participating research institutions. WestGrid equipment is provided by IBM, Hewlett Packard, and SGI.

References

(1) (a) Cardé, R. T.; Doane, C. C.; Baker, T. C.; Iwaki, S.; Marumo, S. *Environ. Entomol.* **1977** *6*, 768; (b) Hansen, K. *Physiol. Entomol.* **1984** *9* (1), 9. doi:10.1111/j.1365-3032.1984.tb00676.x; (c) Grant, G. G.; Langevin, D.; Liska, J.; Kapitola, P.; Chong, J. M. *Naturwissenschaften* **1996** *83*, 328.

(2) Steinbrecht, R. A. *Int. J. Insect Morphol. Embryol.* **1997** *26* (3–4), 229. doi:10.1016/S0020-7322(97)00024-X.

(3) Vogt, R. G.; Riddiford, L. M. *Nature* **1981** *293* (5828), 161. doi:10.1038/293161a0.

(4) Prestwich, G. D. *Bioorg. Med. Chem.* **1996** *4* (3), 505. doi:10.1016/0968-0896(96)00033-8.

(5) (a) Sato, K.; Pellegrino, M.; Nakagawa, T.; Nakagawa, T.; Vosshall, L.; Touhara, K. *Nature* **2008** *452* (7190), 1002. doi:10.1038/nature06850; (b) Wicher, D.; Schäfer, R.; Bauernfeind, R.; Stensmyr, M. C.; Heller, R.; Heinemann, S. H.; Hansson, B. S. *Nature* **2008** *452* (7190), 1007. doi:10.1038/nature06861.

(6) Nakagawa, T.; Sakurai, T.; Nishioka, T.; Touhara, K. *Science* **2005** *307* (5715), 1638. doi:10.1126/science.1106267.

(7) Laughlin, J. D.; Ha, T. S.; Jones, D. N. M.; Smith, D. P. *Cell* **2008** *133* (7), 1255. doi:10.1016/j.cell.2008.04.046.

(8) (a) Benton, R.; Vannice, K. S.; Vosshall, L. B. *Nature* **2007** *450* (7167), 289. doi:10.1038/nature06328; (b) Jin, X.; Ha, T. S.; Smith, D. P. *Proc. Natl. Acad. Sci. U.S.A.* **2008** *105* (31), 10996. doi:10.1073/pnas.0803309105.

(9) Gong, Y.; Pace, T. C. S.; Castillo, C.; Bohne, C.; O'Neill, M.A.; Plettner, E. *Chem. Biol.* **2009** *16* (2), 162. doi:10.1016/j.chembiol.2009.01.005.

(10) (a) Leach, A. R. *Molecular Modelling: Principles and Applications*; Longman: Singapore, 1996; (b) Allen, M. P.; Tildesley, D. J. *Computer Simulation of Liquids*; Oxford University Press: New York, 1989.

(11) Jorgensen, W. L.; Maxwell, D. S.; Tirado-Rives, J. *J. Am. Chem. Soc.* **1996** *118* (45), 11225. doi:10.1021/ja9621760.

(12) Pirkle, W. H.; Rinaldi, P. L. *J. Org. Chem.* **1979** *44* (7), 1025. doi:10.1021/jo01321a001.

(13) Prestwich, G. D.; Graham, S. M.; Kuo, J. W.; Vogt, R. G. *J. Am. Chem. Soc.* **1989** *111* (2), 636. doi:10.1021/ja00184a035.

(14) Our earlier studies revealed that the aqueous mixture stabilized within 30 min of addition of the ethanolic stock solution of disparlure. See Plettner, E.; Lazar, J.; Prestwich, E. G.; Prestwich, G. D. *Biochemistry* **2000** *39* (30), 8953. doi:10.1021/bi000461x.

(15) (a) Berendsen, H. J. C.; van der Spoel, D.; van Drunen, R. *Comput. Phys. Commun.* **1995** *91* (1–3), 43. doi:10.1016/0010-4655(95)00042-E; (b) Lindahl, E.; Hess, B.; van der Spoel, D. *J. Mol. Model.* **2001** *7*, 306; (c) Van Der Spoel, D.; Lindahl, E.; Hess, B.; Groenhof, G.; Mark, A. E.; Berendsen, H. J. C. *J. Comput. Chem.* **2005** *26* (16), 1701. doi:10.1002/jcc.20291; (d) Hess, B.; Kutzner, C.; van der Spoel, D.; Lindahl, E. *J. Chem. Theory Comput.* **2008** *4* (3), 435. doi:10.1021/ct700301q.

(16) (a) Darden, T.; York, D.; Pedersen, L. *J. Chem. Phys.* **1993** *98*

(12), 10089. doi:10.1063/1.464397; (b) Essmann, U.; Perera, L.; Berkowitz, M. L.; Darden, T.; Lee, H.; Pedersen, L. G. *J. Chem. Phys.* **1995** *103* (19), 8577. doi:10.1063/1.470117.

(17) Jorgensen, W. L.; Briggs, J. M.; Contreras, M. L. *J. Phys. Chem.* **1990** *94* (4), 1683. doi:10.1021/j100367a084.

(18) Berendsen, H. J. C.; Postma, J. P. M.; van Gunsteren, W. F.; Hermans, J. Interaction Model for Water in Relation to Protein Hydration. In *Intermolecular Forces*; B. Pullman, Ed.; Reidel Publishing Company: Dordrecht, 1981; pp 331–342.

(19) A similar approach has been previously employed to extend the MM2 parameter set for epoxides. See Podlogar, B. L.; Raber, D. J. *J. Org. Chem.* **1989** *54* (21), 5032. doi:10.1021/jo00282a016.

(20) Frisch, M. J.; Trucks, G. W.; Schlegel, H. B.; Scuseria, G. E.; Robb, M. A.; Cheeseman, J. R.; Montgomery, J. A., Jr.; Vreven, T.; Kudin, K. N.; Burant, J. C.; Millam, J. M.; Iyengar, S. S.; Tomasi, J.; Barone, V.; Mennucci, B.; Cossi, M.; Scalmani, G.; Rega, N.; Petersson, G. A.; Nakatsuji, H.; Hada, M.; Ehara, M.; Toyota, K.; Fukuda, R.; Hasegawa, J.; Ishida, M.; Nakajima, T.; Honda, Y.; Kitao, O.; Nakai, H.; Klene, M.; Li, X.; Knox, J. E.; Hratchian, H. P.; Cross, J. B.; Bakken, V.; Adamo, C.; Jaramillo, J.; Gomperts, R.; Stratmann, R. E.; Yazyev, O.; Austin, A. J.; Cammi, R.; Pomelli, C.; Ochterski, J. W.; Ayala, P. Y.; Morokuma, K.; Voth, G. A.; Salvador, P.; Dannenberg, J. J.; Zakrzewski, V. G.; Dapprich, S.; Daniels, A. D.; Strain, M. C.; Farkas, O.; Malick, D. K.; Rabuck, A. D.; Raghavachari, K.; Foresman, J. B.; Ortiz, J. V.; Cui, Q.; Baboul, A. G.; Clifford, S.; Cioslowski, J.; Stefanov, B. B.; Liu, G.; Liashenko, A.; Piskorz, P.; Komaromi, I.; Martin, R. L.; Fox, D. J.; Keith, T.; Al-Laham, M. A.; Peng, C. Y.; Nanayakkara, A.; Challacombe, M.; Gill, P. M. W.; Johnson, B.; Chen, W.; Wong, M. W.; Gonzalez, C.; Pople, J. A. *Gaussian 03*, revision B.02; Gaussian, Inc.: Wallingford, Conn., 2004.

(21) (a) Mezei, M.; Beveridge, D. L. *Ann. N.Y. Acad. Sci.* **1986** *482*, 1. doi:10.1111/j.1749-6632.1986.tb20933.x; (b) see also Pitera, J. W.; van Gunsteren, W. F. *Mol. Simul.* **2002** *28* (1–2), 45 and references therein. doi:10.1080/08927020211973.

(22) Sprunger, L. M.; Achi, S. S.; Acree, W. E., Jr; Abraham, M. H.; Leo, A. J.; Hoekman, D. *Fluid Phase Equilib.* **2009** *281* (2), 144. doi:10.1016/j.fluid.2009.04.012.

(23) Lide, D. R.; Haynes, W. M., Eds. *CRC Handbook of Chemistry and Physics*, 90th ed.; CRC Press: Boca Raton, Fla., 2009.

Can. J. Chem. Downloaded from www.nrcresearchpress.com by Xi'an Jiaotong University on 09/19/12
For personal use only.

Chemical bond and hardness of M-,W-type hexagonal barium ferrites

Zhiping Li and Faming Gao

Abstract: Using the chemical bond theory of dielectric description, the chemical bond parameters of the M-, W-type hexagonal barium ferrites were calculated. The hardness of $BaFe_{12}O_{19}$ and $BaFe_{18}O_{27}$ were calculated. The calculated hardness of $BaFe_{12}O_{19}$ is 5.9 GPa, which is in agreement with the experimental values. The calculated hardness of planes parallel to the *c* axis of $BaFe_{18}O_{27}$ is 5.5 GPa, which is smaller than that of $BaFe_{12}O_{19}$.

PACS Nos: 62.20.Qp, 71.10.2w

Key words: bonding, hardness, ferrites.

Résumé : Faisant appel à la théorie de la liaison chimique de la description diélectrique, on a calculé les paramètres de la liaison chimique des ferrites de baryum de type-M et W. On a calculé la dureté du $BaFe_{12}O_{19}$ et du $BaFe_{18}O_{27}$. La dureté calculée du $BaFe_{12}O_{19}$ est de 5,9 GPa, qui est en accord avec les valeurs expérimentales. La dureté des plans parallèles à l'axe *c* du $BaFe_{18}O_{27}$ est de 5,5 GPa qui est inférieure à celle du $BaFe_{12}O_{19}$.

Mots-clés : liaison, dureté, ferrites.

[Traduit par la Rédaction]

Can. J. Chem. Downloaded from www.nrcresearchpress.com by Xi'an Jiaotong University on 09/19/12
For personal use only.

Introduction

Ferrite materials are particularly excellent in wear resistance and chemical stability. Therefore, the protective layer on the surface of medium is dispensable, leading to a great advantage for high-density recording.[1–3] The best known of these structures is the hexagonal M structure of $BaFe_{12}O_{19}$, an isotype to the mineral magnetoplunbite, which is built up from the S block with a spinel structure and Ba^{2+} containing a R block perpendicular to the *c* axis and alternating in the *c* direction. The W-type hexaferrite $BaFe_{18}O_{27}$ has a structure that is closely related to that of M. The R block is identical to that in M, but the spinel block is thicker. This makes the Fe_2-W structure more complicated, resulting in seven nonequivalent sites for the Fe^{2+} and Fe^{3+} ions. To understand their high mechanical hardness and chemical stability, we studied the origin of their hardness by using chemical bond theory.

Theory and calculations

According to the chemical bond theory for complex crystals,[4,5] the "crystal formula," and is a combination of subformulas of chemical bonds. Because any chemical bond is binary, the bond subformula is therefore also binary, and Levine's[6] model may be reasonably applied to calculate these binary bond subformulas.

The subformula of any kind of chemical bond A–B in the multibond crystal $A_aB_bD_dG_g\ldots$ can be expressed by the following formula

$$[1] \qquad \left[\frac{N(\mathrm{B}-\mathrm{A})a}{N_{\mathrm{CA}}}\right]\mathrm{A}\left[\frac{N(\mathrm{A}-\mathrm{B})b}{N_{\mathrm{CB}}}\right]\mathrm{B}$$

where A, B, D, G,… represent different elements or different sites of the same element in the crystal formula, *a*, *b*, *d*, *g*,… represent numbers of the corresponding element, *N*(B–A) represents the number of B ions in the coordination group of the A ion, *N*(A–B) represents the number of A ions in the coordination group of the B ion, N_{CA} represents the nearest coordination number of the A ion, and N_{CB} represents the nearest coordination number of the B ion.

The macroscopic linear susceptibility χ can be resolved into the contributions χ^{μ} from the various types of bonds or from the various binary crystals

$$[2] \qquad \chi = \varepsilon - 1 = \sum_{\mu} F^{\mu}\chi^{\mu} = \sum_{\mu} N_{\mathrm{b}}^{\mu}\chi_{\mathrm{b}}^{\mu}$$

where ε is the dielectric constant, χ^{μ} is the total macroscopic susceptibility of a binary crystal composed of only one type of μ bond, F^{μ} is the fraction of the binary crystal composed within the actual crystal complex, χ_{b}^{μ} is the susceptibility of a single bond of type μ in the corresponding binary crystal, and N_{b}^{μ} is the number of bonds per cubic centimetre.

$$[3] \qquad \chi^{\mu} = (4\pi)^{-1}[(h\Omega_{\mathrm{p}}^{\mu})^2/(E_{\mathrm{g}}^{\mu})^2]$$

where E_{g}^{μ} is the average energy gap for the type μ bond, $\Omega_{\mathrm{p}}^{\mu}$ is the plasma frequency obtained from the numbers of valence electrons of type μ per cubic centimetre (N_{e}^{μ}), using

Received 17 February 2010. Accepted 2 December 2010. Published at www.nrcresearchpress.com/cjc on 26 April 2011.

Z. Li and F. Gao. Key Laboratory of Applied Chemistry, Yanshan University, Qinhuangdao 066004, China.

Corresponding author: Faming Gao (e-mail: gfm0827@sina.com).

Can. J. Chem. Downloaded from www.nrcresearchpress.com by Xi'an Jiaotong University on 09/19/12
For personal use only.

Table 1. Chemical bond parameters for $BaFe_{12}O_{19}$.

Bond type	Cation site	Anion site	N_e^μ	k_F^μ	E_h^μ	C^μ	f_c^μ	χ^μ	H_v^μ(GPa)
BaO(3)	2d	6h	0.063	1.231	2.717	14.899	0.033	0.157	1.199
BaO(5)	2d	$12k_2$	0.068	1.263	2.914	11.519	0.060	0.468	1.398
Fe(1)O(4)	2a	$12k_1$	0.604	2.615	7.123	13.504	0.218	3.378	17.688
Fe(2)O(1)	2b	4e	0.797	2.868	5.048	11.037	0.173	7.429	14.293
Fe(2)O(3)	2b	6h	0.502	2.459	8.539	11.306	0.363	3.235	22.277
Fe(3)O(2)	$4f_1$	4f	0.712	2.762	8.153	7.415	0.547	8.062	33.429
Fe(3)O(4)	$4f_1$	$12k_1$	1.186	3.275	8.153	10.381	0.382	9.500	38.594
Fe(4)O(3)	$4f_2$	6h	0.724	2.778	6.517	19.551	0.100	2.156	15.867
Fe(4)O(5)	$4f_2$	$12k_2$	0.422	2.320	7.404	10.124	0.349	3.474	16.921
Fe(5)O(1)	12k	4e	0.412	2.302	7.257	9.924	0.349	3.532	16.322
Fe(5)O(2)	12k	4f	0.528	2.500	6.371	12.052	0.218	3.717	14.464
Fe(5)O(4)	12k	$12k_1$	0.341	2.161	6.208	9.417	0.303	3.451	11.652
Fe(5)O(5)	12k	$12k_2$	1.006	3.100	7.761	18.216	0.154	3.385	25.092

Note: N_e^μ is the number of valence electrons of type μ per cubic centimetre, k_F^μ is the Fermi wavenumber of the valence electron, E_h^μ is the homopolar part of the average energy gap, C^μ is the heteropolar part of the average energy gap, f_c^μ is the covalency of a chemical bond, χ^μ is the total macroscopic susceptibility of a binary crystal composed of only one type of μ bond, and H_v^μ (in GPa) are the calculated Vickers hardness for pseudobinary crystals.

Table 2. Chemical bond parameters for $BaFe_{18}O_{27}$.

Bond type	Cation site	Anion site	N_e^μ	k_F^μ	E_h^μ	C^μ	f_c^μ	χ^μ	H_v^μ
BaO(4)	2b	6h	0.058	1.197	2.708	15.372	0.030	0.284	1.127
BaO(7)	2b	12k	0.063	1.229	2.894	11.809	0.057	0.396	1.315
Fe(1)O(3)	2d	4f	0.724	2.777	4.972	11.276	0.163	6.490	13.048
Fe(1)O(4)	2d	6h	0.465	2.397	8.551	11.588	0.352	2.868	20.922
Fe(2)O(5)	$4f_3$	12k	0.571	2.566	7.248	13.727	0.218	3.014	17.336
Fe(2)O(6)	$4f_3$	12k	0.176	1.732	6.782	3.739	0.766	3.675	14.217
Fe(3)O(2)	6g	4f	0.516	2.482	6.668	12.961	0.209	3.137	14.749
Fe(3)O(6)	6g	12k	0.523	2.493	6.741	13.096	0.210	3.113	15.063
Fe(4)O(1)	4e	4e	0.684	2.726	8.415	7.860	0.534	7.046	33.077
Fe(4)O(6)	4e	12k	1.082	3.175	8.058	10.606	0.366	8.459	35.203
Fe(5)O(2)	$4f_1$	4f	0.642	2.668	7.974	7.463	0.533	7.359	30.011
Fe(5)O(5)	$4f_1$	12k	1.070	3.164	7.985	10.502	0.366	8.529	34.626
Fe(6)O(4)	$4f_2$	6h	0.659	2.692	6.432	19.629	0.097	1.929	14.655
Fe(6)O(7)	$4f_2$	12k	0.388	2.256	7.385	10.264	0.339	3.118	15.769
Fe(7)O(1)	12k	4e	0.492	2.442	6.409	12.444	0.210	3.248	13.749
Fe(7)O(3)	12k	4f	0.384	2.249	7.303	10.178	0.340	3.137	15.505
Fe(7)O(5)	12k	12k	0.315	2.105	6.201	8.579	0.343	3.626	11.578
Fe(7)O(7)	12k	12k	0.933	2.023	7.781	9.054	0.425	9.089	33.038

Note: N_e^μ is the number of valence electrons of type μ per cubic centimetre, k_F^μ is the Fermi wavenumber of the valence electron, E_h^μ is the homopolar part of the average energy gap, C^μ is the heteropolar part of the average energy gap, f_c^μ is the covalency of a chemical bond, χ^μ is the total macroscopic susceptibility of a binary crystal composed of only one type of μ bond, and H_v^μ (in GPa) are the calculated Vickers hardness for pseudobinary crystals.

$$[4] \qquad (h\Omega_p^\mu)^2 = (4\Pi N_e^\mu e^2/m)D^\mu A^\mu$$

where D^μ and A^μ are the correction factors for the order of unity and m is the electron mass. N_e^μ is expressed as follows

$$[5] \qquad \begin{aligned} N_e^\mu &= (n_e^\mu)^*/v_b^\mu \\ (n_e^\mu)^* &= [(Z_A^\mu)^*/N_{CA}^\mu + (Z_B^\mu)^*/N_{CB}^\mu] \\ (k_F^\mu)^3 &= 3\Pi^2 N_e^\mu \end{aligned}$$

where $(n_e^\mu)^*$ is the number of effective valence electrons per μ bond, $(Z_A^\mu)^*$ is the number of effective valence electrons of the A ion, k_F^μ is the Fermi wavenumber of the valence electron, and v_b^μ is the bond volume,

$$[6] \qquad v_b^\mu = (d^\mu)^3/\sum_\nu [(d^\nu)^3 N_b^\nu]$$

where d^μ is the bond length. According to the Phillips – Van Vechten theory, the E_g^μ for every μ bond can be separated into homopolar (E_h^μ) and heteropolar (C^μ) parts.

$$[7] \qquad (E_g^\mu)^2 = (E_h^\mu)^2 + (C^\mu)^2$$

The ionicity and covalency of any type of chemical bond is defined as follows

Can. J. Chem. Downloaded from www.nrcresearchpress.com by Xi'an Jiaotong University on 09/19/12
For personal use only.

$$[8]\quad \begin{aligned} f_i^\mu &= (C^\mu)^2/(E_g^\mu)^2 \\ f_c^\mu &= (E_h^\mu)^2/(E_h^\mu)^2 \end{aligned}$$

where

$$[9]\quad E_h^\mu = 39.74/(d^\mu)^{2.48} \quad \text{(eV)}$$

For any binary crystal AB_n-type compounds, the heteropolar C^μ part is defined as

$$[10]\quad C^\mu = 14.4b^\mu[(Z_A^\mu) + \Delta Z_A^\mu - n(Z_B^\mu)]e^{-k_s^\mu r_0^\mu}/r_0^\mu \quad \text{(eV)}$$

where

$$[11]\quad \begin{aligned} r_0^\mu &= d^\mu/2 \\ k_s^\mu &= (4k_F^\mu/\Pi a_B)^{1/2} \end{aligned}$$

where a_B is the Bohr radius, n is the ratio of element B to element A in the subformula, ΔZ_A^μ is the correction factor for d electron effects such as the crystal field stable energy and the Janh–Teller effect, etc.,[7] and b^μ is proportional to the square of the average coordination number N_c^μ

$$[12]\quad \begin{aligned} b^\mu &= \beta(N_c^\mu)^2 \\ N_c^\mu &= N_{CA}^\mu/(1+n) + nN_{CB}^\mu/(1+n) \end{aligned}$$

where b^μ depends on a given crystal structure. If the dielectric constant of the crystal is known, the value of β can be deduced by using the above equations. The bond parameters of a crystal for which the dielectric constant is not known may also be estimated by using the β value of its isostructural crystals.

Results and discussion

The crystal structure data of $BaFe_{12}O_{19}$ and $BaFe_{18}O_{27}$ are taken from refs. 8 and 9. In the hexagonal structure of $BaFe_{12}O_{19}$, the Fe^{3+} ions occupy five different crystallographic sites. Three of the Fe^{3+} sites are octahedral (12k, 4f2, and 2a), one is tetrahedral (4f1), and one is trigonal bipyramidal (2b). In the hexagonal structure of $BaFe_{18}O_{27}$, the Fe^{3+} ions occupy seven different crystallographic sites. According to their detailed structural data and eq. [1], we can write their bond-valence equations as

$$[13]\quad \begin{aligned} BaFe_{12}O_{19} &= BaFe(1)Fe(2)Fe(3)_2Fe(4)_2Fe(5)_6O(1)_2O(2)_2O(3)_3O(4)_6O(5)_6 \\ &= 1/2BaO(3)_{12/5} + 1/2BaO(5)_3 + Fe(1)O(4)_{3/2} + 2/5Fe(2)O(1)_{5/4} + \\ &\quad 3/5Fe(2)O(3) + 1/2Fe(3)O(2) + 3/2Fe(3)O(4) + Fe(4)O(3)_{6/5} + \\ &\quad Fe(4)O(5)_{3/2} + Fe(5)O(1)_{3/2} + Fe(5)O(2)_{3/2} + Fe(5)O(4)_{3/2} + Fe(5)O(5)_{3/2} \end{aligned}$$

$$\begin{aligned} BaFe_{18}O_{27} &= BaFe(1)Fe(2)_2Fe(3)_3Fe(4)_2Fe(5)_2Fe(6)_2Fe(7)_6O(1)_2O(2)_2O(3)_2O(4)_3O(5)_6O(6)_6O(7)_6 \\ &= 1/2BaO(4)_{12/5} + 1/2BaO(7)_3 + 2/5Fe(1)O(3)_{5/4} + 3/5Fe(1)O(4) + Fe(2)O(5)_{3/2} + \\ &\quad Fe(2)O(6)_{3/2} + Fe(3)O(2)_{3/2} + 2Fe(3)O(6)_{3/2} + 1/2Fe(4)O(1) + 3/2Fe(4)O(6) + \\ &\quad 1/2Fe(5)O(2) + 3/2Fe(5)O(5) + Fe(6)O(4)_{6/5} + Fe(6)O(7)_{3/2} + Fe(7)O(1)_{3/2} + \\ &\quad Fe(7)O(3)_{3/2} + 2Fe(7)O(5)_{3/2} + 2Fe(7)O(7)_{3/2} \end{aligned}$$

Using the $\beta = 0.097$ for the isostructrual crystal $LaMgAl_{11}O_{19}$,[10] the chemical bond parameters for each type of chemical bond were calculated, and are listed in Tables 1 and 2.

Using the obtained chemical bond parameters we can calculate the hardness of $BaFe_{12}O_{19}$ and $BaFe_{18}O_{27}$ crystals. The average hardness H_v of complex crystals may be calculated by a geometric average of the hardness of the pseudobinary compound composed of a μ-type bond as follows:[10]

$$[14]\quad H_v = [\prod_{\mu}^{\mu}(H_v^\mu)^{n^\mu}]^{1/\Sigma n^\mu}$$

$$[15]\quad H_v^\mu = 350(N_e^\mu)^{2/3}e^{-1.191f_i^\mu}/(d^\mu)^{2.5}$$

where n^μ is the number of type-μ bonds within the actual crystal complex.

From Fig. 1, we observe the layer structure along the c axis in the $BaFe_{12}O_{19}$ and $BaFe_{18}O_{27}$ crystals. There are three different bonding layers along the c axis in $BaFe_{12}O_{19}$: (I), (II), and (III). In the (I) layer, Fe(1) and Fe(3) are contained. Thus, the hardness of the (I) layer should equal the geometric average of the hardness of the pseudobinary compounds $Fe(1)O(4)_{3/2}$, Fe(2)O(3), Fe(3)O(2), and Fe(3)O(4). In the (II) layer, Fe(5) is only contained. The hardness of the (II) layer should equal the geometric average of the hardness of the pseudobinary compounds $Fe(5)O(1)_{3/2}$, $Fe(5)O(2)_{3/2}$, $Fe(5)O(4)_{3/2}$, and $Fe(5)O(5)_{3/2}$. In the (III) layer, there are Fe(2), Fe(4), and Ba ions. So the hardness of the (III) layer should equal the geometric average of the hardness of the pseudobinary compounds $BaO(3)_{12/5}$, $BaO(5)_3$, $Fe(2)O(1)_{5/4}$, Fe(2)O(3), $Fe(4)O(3)_{6/5}$, and $Fe(4)O(5)_{3/2}$. Using eq. [13], the calculated hardness of the (I) layer, (II) layer, and (III) layer areas are 27.1, 16.5, and 5.9 GPa, respectively. Therefore, the (III) layer area could be the easiest slip area, and plays a determinative role in the hardness of planes parallel to the c axis. In other words, the calculated hardness of planes parallel to the c axis of $BaFe_{12}O_{19}$ should be 5.9 GPa, which is in good agreement with the experimental value of 6.0 GPa.[3]

Fig. 1. (*a*) Crystal structure of $BaFe_{12}O_{19}$. (*b*) Crystal structure of $BaFe_{18}O_{27}$.

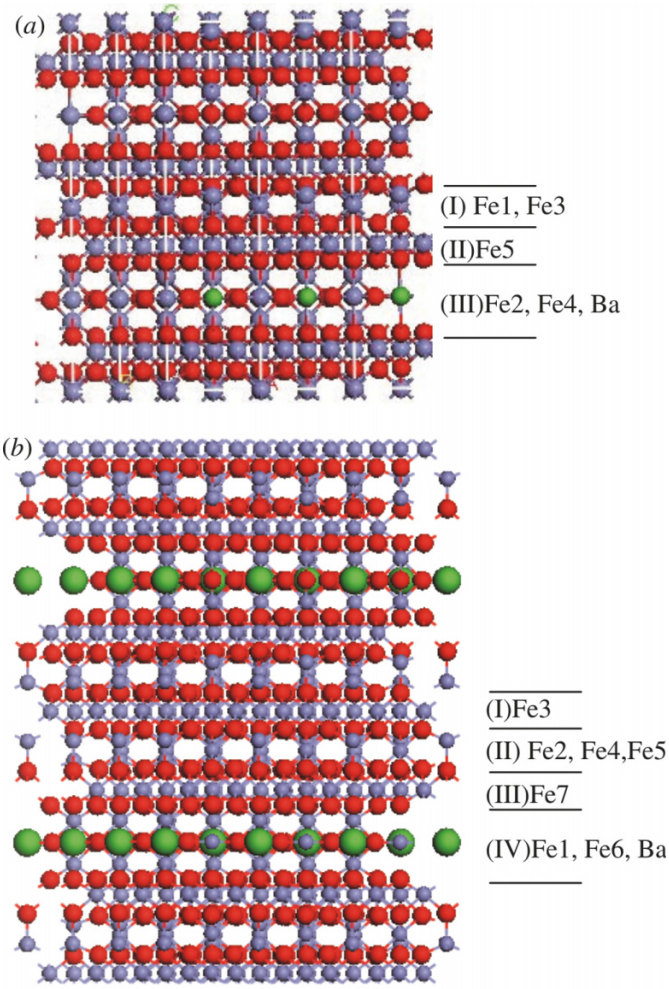

In $BaFe_{18}O_{27}$, there are four different bonding layers along the *c* axis: (I), (II), (III), and (IV). In the (I) layer, Fe(3) is only contained. Thus, the hardness of the (I) layer should equal the geometric average of the hardness of the pseudobinary compounds $Fe(3)O(2)_{3/2}$ and $Fe(3)O(6)_{3/2}$. In the (II) layer, Fe(2), Fe(4), and Fe(5) are contained. The hardness of the (II) layer should equal the geometric average of the hardness of pseudobinary compounds $Fe(2)O(5)_{3/2}$, $Fe(2)O(6)_{3/2}$, Fe(4)O(1), Fe(4)O(6), Fe(5)O(2), and Fe(5)O(5). In the (III) layer, Fe(7) is contained. The hardness of the (III) layer should equal the geometric average of the hardness of pseudobinary compounds $Fe(7)O(1)_{3/2}$, $Fe(7)O(3)_{3/2}$, $Fe(7)O(5)_{3/2}$, and $Fe(7)O(7)_{3/2}$. In the (IV) ayer, there are Fe(1), Fe(6), and Ba ions. So the hardness of the (IV) layer should equal the geometric average of the hardness of pseudobinary compounds $BaO(4)_{12/5}$, $BaO(7)_3$, $Fe(1)O(3)_{5/4}$, Fe(1)O(3), $Fe(6)O(4)_{6/5}$, and $Fe(6)O(7)_{3/2}$. Using eq. [13], the calculated hardness of the (I) layer, (II) layer, (III) layer, and (IV) layer areas are 15.0, 24.4, 17.7, and 5.5 GPa, respectively. Therefore, the (IV) layer area could be the easiest slip area, and plays a determinative role in the hardness of the planes parallel to the *c* axis. In other words, the calculated hardness of the planes parallel to the *c* axis of $BaFe_{18}O_{27}$ should be 5.5 GPa.

Conclusion

Using the chemical bond theory of dielectric description, the chemical bond parameters of M-, W-type hexagonal barium ferrites were calculated. The hardness of $BaFe_{12}O_{19}$ and $BaFe_{18}O_{27}$ were calculated. The calculated hardness of $BaFe_{12}O_{19}$ is 5.9 GPa, which is in agreement with the experimental value. The calculated hardness of the planes parallel to the *c* axis of $BaFe_{18}O_{27}$ is 5.5 GPa, which is less than that of $BaFe_{12}O_{19}$.

References

(1) Fritzsche, J.; Kramer, R. B. G.; Moshchalkov, V. V. *Phys. Rev. B* **2009** *80* (9), 094514. doi:10.1103/PhysRevB.80.094514.
(2) Sharma, R.; Agarwala, R.C.; Agarwal, V. *J. Nano Res.* **2008** *2*, 91. doi:10.4028/www.scientific.net/JNanoR.2.91.
(3) Matsumoto, M.; Morisako, A.; Takei, S. *J. Alloys Compd.* **2001** *326* (1–2), 215. doi:10.1016/S0925-8388(01)01280-4.
(4) Xue, D. F.; Zhang, S. Y. *Appl. Phys. Lett.* **1997** *70* (8), 943. doi:10.1063/1.118448.
(5) Zhang, S. Y. *Chin. J. Chem. Phys.* **1991** *4*, 109.
(6) Levine, B. F. *J. Chem. Phys.* **1973** *59*, 1463. doi:10.1063/1.1680204.
(7) Gao, F. M.; Zhang, S. Y. *Chin. J. Inorg. Chem.* **2000** *16*, 751.
(8) Obradors, X.; Collomb, A.; Pernet, M.; Samaras, D.; Joubert, J. C. *J. Solid State Chem.* **1985** *56* (2), 171. doi:10.1016/0022-4596(85)90054-4.
(9) Braun, P. J. *Philips Res. Rep.* **1957** *12*, 491.
(10) Gao, F. M.; Gao, L. H. *J. Superhard Mater.* **2010** *32* (3), 148. doi:10.3103/S1063457610030020.

Can. J. Chem. Downloaded from www.nrcresearchpress.com by Xi'an Jiaotong University on 09/19/12
For personal use only.

Postsynthetic modification of an imine-based microporous organic network

Phillip A. Kerneghan, Shira D. Halperin, David L. Bryce, and Kenneth E. Maly

Abstract: A highly cross-linked microporous organic network with imine linkers was prepared by condensation of tetrakis(4-aminophenyl)methane with terephthaldehyde. Gas adsorption studies indicate that the material exhibits permanent microporosity, and guest exchange experiments demonstrate that small molecules can diffuse into the network. Postsynthetic modification of this microporous network was achieved by treatment with borane in THF, which reduced the imine groups to the corresponding amines as shown by IR and ^{13}C CP-MAS solid-state NMR spectroscopy. The resulting material showed enhanced resistance to acidic hydrolysis compared with the imine precursor, and retained its ability to absorb guest molecules. The amine network was amenable to further postsynthetic modifications. Specifically, acetylation of this network using acetic anhydride was demonstrated.

Key words: imines, synthesis, microporous polymers, postsynthetic modification.

Résumé : On a préparé un réseau organique microporeux très réticulé à l'aide de coupleurs imines par condensation du tétrakis(4-aminophényl)méthane avec du téréphtaldéhyde. Des études d'adsorption de gaz indiquent que le matériau comporte une microporosité permanente alors que des expériences d'échange de molécule invitée démontrent que les petites molécules peuvent diffuser dans le réseau. On a réalisé des modifications postsynthétiques de ce réseau microporeux par un traitement avec du borane dans le THF qui a permis de réduire les groupes imines en amines correspondantes, tel que démontré par la spectroscopie infrarouge et la RMN du ^{13}C à l'état solide dans le mode de la rotation à l'angle magique avec polarisation croisée (RAM-PC). Le matériau qui en résulte présente une résistance accrue à l'hydrolyse acide par comparaison avec le précurseur imine et il conserve sa facilité à absorber des molécules invitées. Le réseau amine peut être amené à d'autres modifications postsynthétiques. On a démontré, en particulier, la possibilité d'acyler ce réseau à l'aide d'anhydride acétique.

Mots-clés : imines, synthèse, polymères microporeux, modification postsynthétique.

[Traduit par la Rédaction]

Can. J. Chem. Downloaded from www.nrcresearchpress.com by Xi'an Jiaotong University on 09/19/12
For personal use only.

Introduction

Microporous solids are an important class of materials because their small pore sizes and high surface area make them potentially useful for chemical separation, catalysis, or gas storage.[1] Metal–organic frameworks (MOFs), which are crystalline three-dimensional coordination polymers, have been extensively studied, and show large surface areas and well-defined channels and pores.[2] In addition to coordination polymers, recent studies have focused on covalently linked microporous solids derived entirely from organic building blocks.[3] These materials, which include highly cross-linked polymers,[4] polymers of intrinsic microporosity (PIMs),[5] other amorphous polymers,[6] and covalent organic frameworks (COFs),[7] also exhibit large surface areas that make them potentially suitable for applications.

An important challenge in the field of microporous solids is the control of the properties of these materials, and, in particular, the incorporation of specific functional groups into the materials. The incorporation of any desired functionality into microporous solids often requires that desired groups be attached to the molecular building blocks prior to network formation and that these groups be compatible with the reaction conditions for network formation. An alternative strategy for incorporating desired functional groups involves covalent "postsynthetic" modification of the microporous material. Covalent postsynthetic modification of a porous coordination polymer was first reported by Seo et al.,[8] who showed that a network bearing uncoordinated and exposed pyridine groups could be methylated using iodomethane. More recently, Cohen and co-workers[9,10] demonstrated that covalent postsynthetic modification of MOFs can be used effectively to incorporate functionality into these microporous solids while maintaining a desired network topology. Similarly, postsynthetic modification of a permeable organic hydrogen-bonded network by reaction of thiols with exposed allyl groups has also been demonstrated.[11] Although postsynthetic modification of polymers such as polyolefins is well-established,[12] comparable postsynthetic transformations of organic microporous materials has not been reported, in part because many microporous polymers do not have the requisite functional groups for further reactions. In other cases, microporous

Received 15 November 2010. Accepted 21 January 2011. Published at www.nrcresearchpress.com/cjc on 26 April 2011.

P.A. Kerneghan, S.D. Halperin, and K.E. Maly. Wilfrid Laurier University, 75 University Ave. W, Waterloo, ON N2L 3C5, Canada.
D.L. Bryce. Department of Chemistry and Centre for Catalysis Research and Innovation, University of Ottawa, 10 Marie Curie Pvt, Ottawa, ON K1N 6N5, Canada.

Corresponding author: K.E. Maly (e-mail: kmaly@wlu.ca).

Scheme 1.

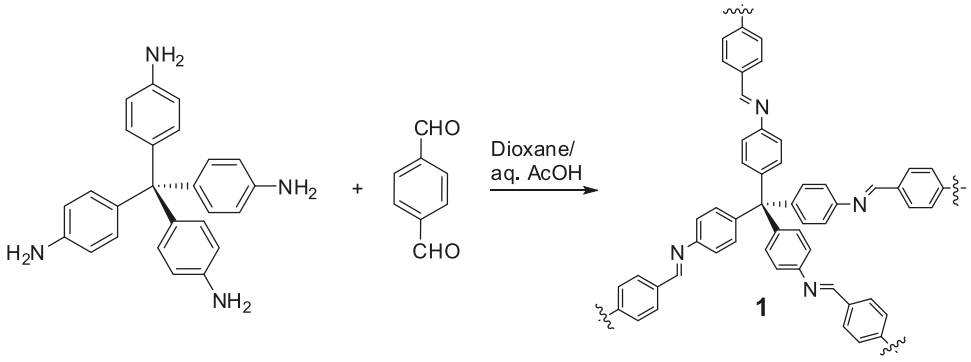

Fig. 1. Infrared spectra of imine network **1**, amine network **2**, and acetylated network **3**.

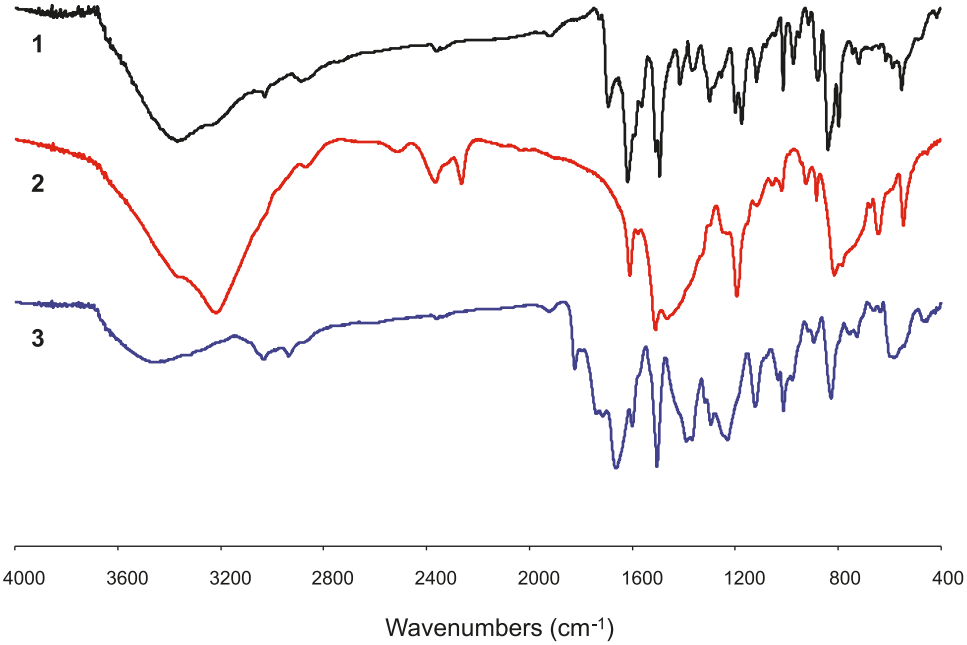

organic solids such as COFs are linked by readily hydrolyzed groups such as boroxines or boronates that make them sensitive to further synthetic transformations. Postsynthetic modification of microporous organic materials therefore requires networks that are robust enough to withstand further reaction conditions, as well as functional groups that are accessible to reagents that can diffuse into the porous network.

Recently, Yaghi and co-workers[7d] introduced a new class of COFs based on imine linking groups. Schwab et al.[13] also used Schiff base formation for the preparation of microporous polymer networks. The presence of imine groups as linkers for organic microporous materials presents a unique opportunity for postsynthetic modification of the organic framework by reduction of these imines to the corresponding amines. Although imines are susceptible to hydrolysis, the corresponding amine networks are expected to display increased chemical stability. Moreover, the amine groups provide a functional handle for further synthetic transformations. Such an approach could provide access to new microporous organic solids with diverse functionality and controllable properties. Herein we report the postsynthetic modification of an imine-based microporous network by reduction and show that it can produce a network with enhanced resistance to hydrolysis. We also demonstrate that the reduced network can undergo further synthetic transformations, such as acetylation of the amino groups.

Results and discussion

Imine network **1** was prepared as outlined in Scheme 1 using terephthaldehyde and tetrakis(4-aminophenyl)methane[14] under solvothermal conditions in a mixture of dioxane and aqueous acetic acid, as described by Yaghi and co-workers.[7d]

The formation of the imine network was confirmed by IR spectroscopy (Fig. 1) and ^{13}C CP-MAS solid-state NMR spectroscopy (Fig. 2); the results are consistent with the previously reported data[7d] as well as the spectroscopic data from model compounds (See Supplementary data). Further investigation by powder X-ray diffraction showed that in contrast to Yaghi's[7d] crystalline and multiply interpenetrated COF, network **1** diffracted very weakly, showing broad reflections consistent with largely amorphous material (see Supplementary data). Despite the amorphous nature of **1**, nitrogen adsorption studies showed a sharp uptake at low pressure, indicating that the material was indeed microporous (Fig. 3).

Can. J. Chem. Downloaded from www.nrcresearchpress.com by Xi'an Jiaotong University on 09/19/12
For personal use only.

Can. J. Chem. Downloaded from www.nrcresearchpress.com by Xi'an Jiaotong University on 09/19/12
For personal use only.

Fig. 2. ^{13}C CP-MAS spectra of imine network **1**, reduced network **2**, and acetylated network **3**. Signals marked with * indicate spinning side bands, and the two signals marked with # for the spectrum of **2** correspond to included THF.

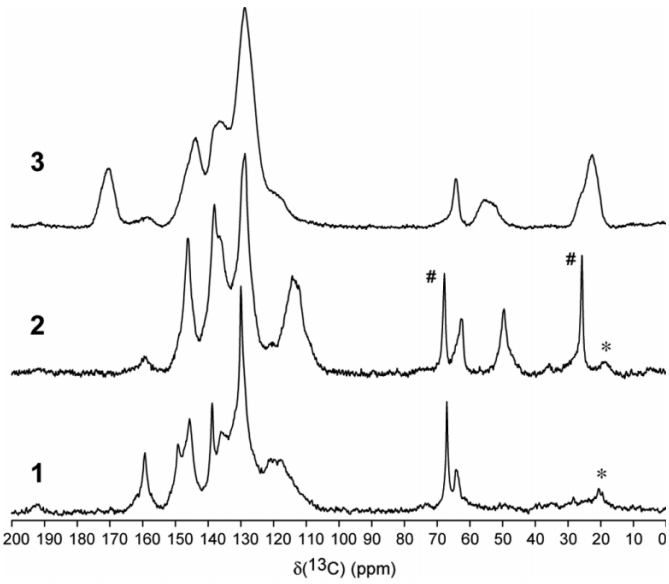

Fig. 3. Nitrogen adsorption isotherm for **1** measured at 77 K.

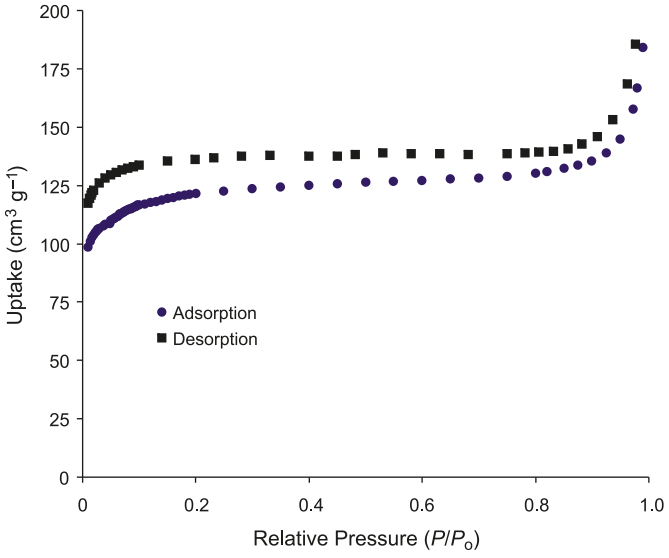

From the adsorption data, the Brunauer–Emmett–Teller (BET) surface area was determined to be 416 m^2/g. This value is significantly lower than that reported by Yaghi and co-workers (1360 m^2/g)[7d], but is comparable to some other microporous networks. We attribute these differences in the properties of our material compared with Yaghi's to the sensitivity of COF network formation to slight variations in the reaction conditions. It is noteworthy that some hysteresis is observed in comparing the adsorption and desorption isotherms. This observation is consistent with the results of Yaghi and co-workers[7d] and indicates some flexibility of the framework. Thermogravimetric analysis of **1** solvated with THF showed ~7% mass loss below 100 °C, corresponding to the loss of the solvent (Fig. 4), with substantial mass loss above 450 °C, corresponding to decomposition of the network.

Fig. 4. Thermogravimetric analysis traces of **1** with THF, activated, and resolvated with THF.

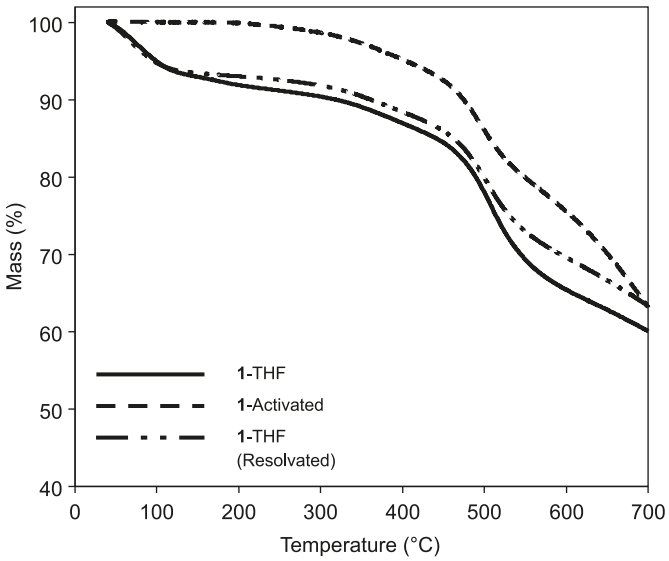

Subsequent activation by heating at 100 °C under vacuum overnight, followed by resolvation with THF showed a similar uptake compared with the original solvated network, providing further support for the porosity of the material and evidence that it can take up small molecules. Further solvent-exchange experiments and subsequent analysis by TGA showed that the guest molecules can be exchanged (see Supplementary data). These thermal analysis experiments demonstrate that **1** is permeable to guest molecules, and therefore may be suitable for postsynthetic modification by allowing reactants to diffuse into the porous network.

Network **1** was suspended in anhydrous THF and treated with an excess of borane–THF (Scheme 2). After standing for 24 h, the solid was collected and washed with water, followed by THF. The IR spectrum of **2** showed a substantial attenuation of the C=N stretching band at 1615 cm^{-1} and a concomitant increase in the N–H stretching band at ~3200 cm^{-1} (Fig. 1). These results are consistent with the reduction of the imine linkages of **1** to the corresponding amines. Further confirmation of the reduction was provided by ^{13}C CP-MAS spectroscopy, which showed a disappearance of the signal at 159 ppm and the appearance of a signal at 50 ppm, corresponding to the benzylic carbon of the reduced product (Fig. 2). Based on integration of the aromatic region and comparison with the remaining imine signal, the conversion is estimated to be ~83%. These chemical shifts are consistent with those of *N*-benzylideneaniline and the corresponding *N*-benzylaniline model compounds (see Supplementary data). These results, which show reduction of the imines, indicate that the reducing agent is able to penetrate the porous network and react with interior imine sites.

Nitrogen adsorption measurements on **2** show showed negligible uptake and gave a BET surface area of 10 m^2/g, indicating that the material no longer exhibited microporosity (see Supplementary data). We attribute this observation to the increased flexibility of the network upon reduction, allowing it to collapse upon evacuation. Thermogravimetric analysis showed that reduced network **2** shows comparable thermal stability to **1** with substantial decomposition at

Scheme 2.

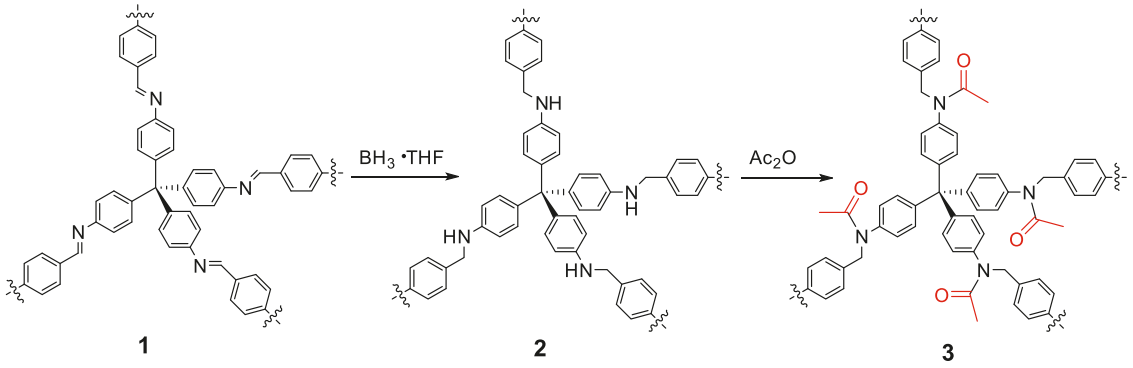

Fig. 5. Thermogravimetric analysis traces of **2** with THF, activated, and resolvated with THF.

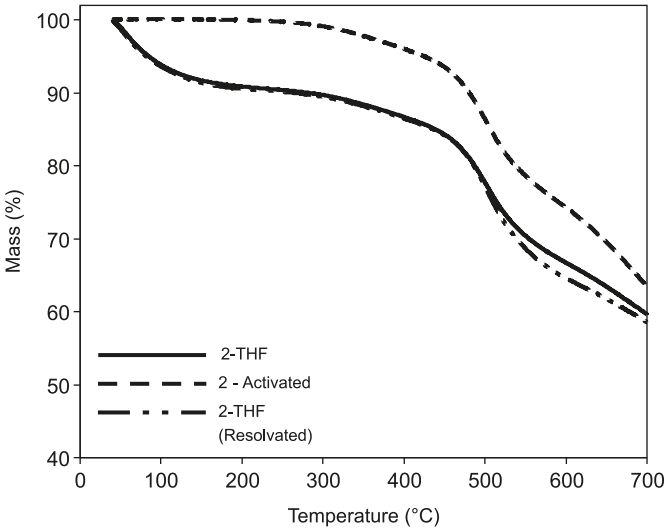

temperatures >400 °C. Activation resulted in complete loss of solvent, as demonstrated by TGA, and subsequent resolvation showed solvent uptake very similar to the original solvated material, suggesting that although **2** does not exhibit permanent microporosity, it retains its ability to uptake guest molecules (Fig. 5). The stability of networks **1** and **2** to acidic hydrolysis was evaluated by heating at reflux in 2 mol/L HCl. Imine network **1** is readily hydrolyzed to its corresponding starting materials, as shown by dissolution of the material after only a few minutes of gentle heating. In contrast, network **2** remained insoluble after heating at reflux for 3 h.

The IR spectrum of the material recovered after acid digestion of **2** shows a very broad N–H stretching band that is characteristic of ammonium salts (see Supplementary data), suggesting that **2** has been protonated and that these materials may ultimately be used to prepare novel permeable ionic networks.

The amine groups present in **2** not only increase the chemical stability of the network, but also provide an opportunity for further synthetic transformations. To demonstrate that subsequent postsynthetic transformations are possible, we decided to explore acetylation using acetic anhydride. Network **2** was immersed in acetic anhydride, and allowed to stand at room temperature overnight to ensure complete exchange of the solvent for acetic anhydride. The reaction mixture was subsequently heated at 100 °C in a sealed tube for 24 h. After cooling to room temperature, the solid was collected by filtration and washed thoroughly with THF to yield acetylated network **3**. Evidence for acetylation was provided by IR spectroscopy, which showed a substantial decrease in the intensity of the N–H stretching band and the appearance of a band at 1658 cm^{-1}, which is consistent with the amide C=O stretching. It is noteworthy that the observed C=O stretching is not consistent with the absorbance bands of either acetic acid (1714 cm^{-1}) or remaining acetic anhydride (1755 cm^{-1}), providing evidence for amide formation. The ^{13}C CP-MAS NMR spectrum of **3** shows a change in the aromatic region of the spectrum, as well as the diagnostic appearance of two new signals at 22 and 170 ppm, which are consistent with the incorporation of acetamide methyl and carbonyl carbons, respectively, into the structure. Indeed, these signals are consistent with the solution ^{13}C NMR spectrum of model compound *N*-benzyl-*N*-phenylacetamide (see Supplementary data.)

In summary, we have demonstrated postsynthetic modification of a microporous organic network for the first time. Network **2**, prepared by reduction of imine **1**, loses its permanent microporosity, presumably because the framework is more flexible and collapses upon removal of guests. However, **2** retains high thermal stability and the ability to uptake guest molecules, and also shows enhanced resistance to acid hydrolysis, suggesting that this may ultimately provide a route to more chemically robust microporous organic solids. In addition, we have shown that further synthetic transformations are possible, which may offer an approach for preparing new microporous organic solids with controlled properties for potential applications in gas storage, molecular separations, and heterogeneous catalysis.

Experimental

General

All starting materials and solvents were obtained from commercial sources and used without purification, unless otherwise specified. Anhydrous and oxygen-free THF was dispensed from a custom-built solvent purifier that used purification columns packed with activated alumina and supported copper catalyst (Glasscontour, Irvine, California). Tetrakis(4-aminophenyl)methane was prepared according to published procedures and recrystallized from DMSO–H_2O prior to use,[14] and terephthaldehyde (99%) was purchased

Can. J. Chem. Downloaded from www.nrcresearchpress.com by Xi'an Jiaotong University on 09/19/12
For personal use only.

Can. J. Chem. Downloaded from www.nrcresearchpress.com by Xi'an Jiaotong University on 09/19/12
For personal use only.

from Sigma-Aldrich and recrystallized from water prior to use. IR spectra were recorded as KBr disks using a PerkinElmer Spectrum BX FT-IR spectrometer.

Samples for ^{13}C CP-MAS NMR spectroscopy were ground into fine powders and packed into 4 mm o.d. zirconia rotors. NMR spectra were acquired with high-power proton decoupling at 9.4 T ($\nu_0(^{13}C)$ = 100.6 MHz) using a Bruker Avance III console and a 4 mm triple-resonance Bruker MAS NMR probe. The magic angle was set by maximizing the number of rotational echoes in a ^{79}Br MAS NMR experiment on powdered KBr. Carbon-13 CP-MAS NMR pulse calibrations and chemical shift referencing were performed using adamantane (δ = 38.55 ppm for the high-frequency peak, relative to the primary standard TMS). Ninety degree ^1H pulse widths were 3.45 μs, contact pulses were 1.5 or 2.0 ms, acquisition times were 40–50 ms, and recycle delays were 20–50 s. Approximately 1000 to 2000 scans were averaged for each of the COF samples. MAS rates were chosen to eliminate the overlap of spinning sidebands with resonances of interest, and ranged from 11 111 to 13 600 Hz. FIDs were processed with zero-filling, 15–20 Hz exponential apodization, and Fourier transformation.

Gas adsorption isotherms were measured volumetrically using a Micromeritics ASAP 2010 automated adsorption analyzer. Samples were degassed at room temperature for 7 h prior to measurement. A liquid nitrogen bath (77 K) was used for the N_2 isotherms. The N_2 gas used was UHP grade. Brunauer–Emmett–Teller (BET) method was used to determine the specific surface areas (ABET, $m^2\ g^{-1}$) using the adsorption data over 0.05–0.20 relative pressure (P/P_0).

Synthesis of network 1[7d]

A pyrex glass tube with a 6 mm i.d. and an 8 mm o.d. was charged with tetrakis(4-aminophenyl)methane (20 mg, 0.052 mmol), terephthaldehyde (12 mg, 0.089 mmol), and a mixture of dioxane (0.8 mL) and 2 mol/L AcOH (0.2 mL). The tube was flash-frozen in liquid nitrogen, evacuated to a pressure of 150 mTorr (1 Torr = 133.322 Pa), and flame-sealed at a length of 12 cm. The contents of the tube were allowed to warm to room temperature and then heated at 100 °C for 72 h. The yellow solid formed was collected via filtration and washed repeatedly with THF. The yellow precipitate was collected and dried under vacuum at 100 °C for 24 h to evacuate the pores of all solvent guest molecules. Yield: 48 mg.

Synthesis of network 2

An oven-dried flask was charged with **1** (104 mg) and purged with N_2(g) for 15 min. Borane–THF (15 mL, 1 mol/L) was then added to the flask and the mixture was allowed to stir for 24 h at room temperature. The solid was collected by filtration and washed with THF to yield 97 mg of **2** as a beige solid.

Synthesis of network 3

Network **2** (96 mg) was submerged in Ac_2O for 18 h to allow Ac_2O to exchange into the pores of the network. This mixture was then placed into a sealed glass tube, heated to 100 °C, and stirred for 24 h. The solid was collected via filtration, washed with THF, and submerged in THF for 24 h to remove any remaining Ac_2O. The solid was collected via filtration and washed with THF to give **3** (109 mg) as a beige solid.

Supplementary data

Supplementary data (synthesis and characterization, details of spectroscopic characterization, powder X-ray diffraction studies, characterization of model compounds, and representative thermogravimetric analysis) are available with the article through the journal Web site (www.nrcresearchpress.com/cjc).

Acknowledgments

We are grateful to the Natural Sciences and Engineering Research Council of Canada (NSERC), the Canada Foundation for Innovation, the Ontario Research Fund, and Wilfrid Laurier University, Waterloo, Ontario, for financial support. We are also grateful to Dr. T. Maris for powder X-ray diffraction studies and to Drs. S. Lang and J. Ripmeester for assistance with the gas adsorption studies.

References

(1) (a) Davis, M. E. *Nature* **2002** *417* (6891), 813. doi:10.1038/nature00785; (b) Morris, R. E.; Wheatley, P. S. *Angew. Chem. Int. Ed.* **2008** *47* (27), 4966. doi:10.1002/anie.200703934.

(2) For a recent review, see Long, J. R.; Yaghi, O. M. *Chem. Soc. Rev.* **2009** *38* (5), 1213. doi:10.1039/b903811f.

(3) For a recent review, see Maly, K. E. J. *Mater. Chem.* **2009** *19* (13), 1781. doi:10.1039/b816089a.

(4) (a) Germain, J.; Hradil, J.; Fréchet, J. M. J.; Svec, F. *Chem. Mater.* **2006** *18* (18), 4430. doi:10.1021/cm061186p; (b) Germain, J.; Fréchet, J. M. J.; Svec, F. *J. Mater. Chem.* **2007** *17* (47), 4989. doi:10.1039/b711509a.

(5) (a) McKeown, N. B.; Budd, P. M. *Chem. Soc. Rev.* **2006** *35* (8), 675. doi:10.1039/b600349d; (b) Budd, P. M.; Butler, A.; Selbie, J.; Mahmood, K.; McKeown, N. B.; Ghanem, B.; Msayib, K.; Book, D.; Walton, A. *Phys. Chem. Chem. Phys.* **2007** *9* (15), 1802. doi:10.1039/b618053a; (c) Ghanem, B. S.; Msayib, K. J.; McKeown, N. B.; Harris, K. D. M.; Pan, Z.; Budd, P. M.; Butler, A.; Selbie, J.; Book, D.; Walton, A. *Chem. Commun. (Camb.)* **2007** (1): 67. doi:10.1039/b614214a; (d) Ghanem, B. S.; McKeown, N. B.; Budd, P. M.; Fritsch, D. *Macromolecules* **2008** *41* (5), 1640. doi:10.1021/ma071846r.

(6) (a) Weber, J.; Antonietti, M.; Thomas, A. *Macromolecules* **2007** *40* (4), 1299. doi:10.1021/ma062598m; (b) Thomas, A.; Goettmann, F.; Antonietti, M. *Chem. Mater.* **2008** *20* (3), 738. doi:10.1021/cm702126j; (c) Weber, J.; Antonietti, M.; Thomas, A. *Macromolecules* **2008** *41* (8), 2880. doi:10.1021/ma702495r; (d) Jiang, J. X.; Su, F.; Trewin, A.; Wood, C. D.; Campbell, N. L.; Niu, H.; Dickinson, C.; Ganin, A. Y.; Rosseinsky, M. J.; Khimyak, Y. Z.; Cooper, A. I. *Angew. Chem. Int. Ed.* **2007** *46* (45), 8574. doi:10.1002/anie.200701595; (e) Jiang, J.-X.; Su, F.; Trewin, A.; Wood, C. D.; Niu, H.; Jones, J. T. A.; Khimyak, Y. Z.; Cooper, A. I. *J. Am. Chem. Soc.* **2008** *130* (24), 7710. doi:10.1021/ja8010176; (f) Farha, O. K.; Spokoyny, A. M.; Hauser, B. G.; Bae, Y.-S.; Brown, S. E.; Snurr, R. Q.; Mirkin, C. A.; Hupp, J. T. *Chem. Mater.* **2009** *21* (14), 3033. doi:10.1021/cm901280w.

(7) (a) Côté, A. P.; Benin, A. I.; Ockwig, N. W.; O'Keeffe, M.; Matzger, A. J.; Yaghi, O. M. *Science* **2005** *310* (5751), 1166. doi:10.1126/science.1120411; (b) Côté, A. P.; El-Kaderi, H. M.; Furukawa, H.; Hunt, J. R.; Yaghi, O. M. *J. Am. Chem. Soc.* **2007** *129* (43), 12914. doi:10.1021/ja0751781; (c) El-Kaderi,

H. M.; Hunt, J. R.; Mendoza-Cortes, J. L.; Côté, A. P.; Taylor, R. E.; O'Keeffe, M.; Yaghi, O. M. *Science* **2007** *316* (5822), 268. doi:10.1126/science.1139915; (d) Uribe-Romo, F. J.; Hunt, J. R.; Furukawa, H.; Klock, C.; O'Keeffe, M.; Yaghi, O. M. *J. Am. Chem. Soc.* **2009** *131* (13), 4570. doi:10.1021/ja8096256; (e) Tilford, R. W.; Gemmill, W. R.; zur Loye, H. C.; Lavigne, J. J. *Chem. Mater.* **2006** *18* (22), 5296. doi:10.1021/cm061177g; (f) Tilford, R. W.; Mugavero, S. J.; Pellechia, P. J.; Lavigne, J. J. *Adv. Mater. (Deerfield Beach Fla.)* **2008** *20*, 2741. doi:10.1022/adma.200800030.

(8) Kim, K.; Seo, J. S.; Whang, D.; Lee, H.; Jun, S. I.; Oh, J.; Jeon, Y. J. *Nature* **2000** *404* (6781), 982. doi:10.1038/35010088.

(9) For a recent review, see Wang, Z. Q.; Cohen, S. M. *Chem. Soc. Rev.* **2009** *38* (5), 1315. doi:10.1039/b802258p.

(10) (a) Wang, Z. Q.; Cohen, S. M. *J. Am. Chem. Soc.* **2007** *129* (41), 12368. doi:10.1021/ja074366o; (b) Tanabe, K. K.; Wang, Z. Q.; Cohen, S. M. *J. Am. Chem. Soc.* **2008** *130* (26), 8508. doi:10.1021/ja801848j; (c) Wang, Z. Q.; Cohen, S. M. *Angew. Chem. Int. Ed.* **2008** *47* (25), 4699. doi:10.1002/anie.200800686; (d) Jones, S. C.; Bauer, C. A. *J. Am. Chem. Soc.* **2009** *131* (35), 12516. doi:10.1021/ja900893p.

(11) Brunet, P.; Demers, E.; Maris, T.; Enright, G. D.; Wuest, J. D. *Angew. Chem. Int. Ed.* **2003** *42* (43), 5303. doi:10.1002/anie.200352252.

(12) Boaen, N. K.; Hillmyer, M. A. *Chem. Soc. Rev.* **2005** *34* (3), 267. doi:10.1039/b311405h.

(13) Schwab, M. G.; Fassbender, B.; Spiess, H. W.; Thomas, A.; Feng, X. L.; Müllen, K. *J. Am. Chem. Soc.* **2009** *131* (21), 7216. doi:10.1021/ja902116f.

(14) Ganesan, P.; Yang, X. N.; Loos, J.; Savenije, T. J.; Abellon, R. D.; Zuilhof, H.; Sudholter, E. J. R. *J. Am. Chem. Soc.* **2005** *127* (42), 14530. doi:10.1021/ja053689m.

Can. J. Chem. Downloaded from www.nrcresearchpress.com by Xi'an Jiaotong University on 09/19/12
For personal use only.

Copper and chromium oxide nanocomposite catalysts for simultaneous elimination of CO and oxygenate VOCs in toxic gas emissions

Tanya Tsoncheva, Krasimir Ivanov, and Dimitar Dimitrov

Can. J. Chem. Downloaded from www.nrcresearchpress.com by Xi'an Jiaotong University on 09/19/12
For personal use only.

Abstract: Copper and chromium oxide nanocomposite materials with different Cu/Cr ratios were prepared by impregnation of a conventional silica support with toluene solutions of the corresponding acetylacetonate precursors and characterized by X-ray diffraction, Fourier transform infrared spectroscopy, UV–vis spectroscopy, X-ray photoelectron spectroscopy, and temperature-programmed reduction–thermogravimetric methods. Their catalytic behaviour in the total oxidation of CO and different oxygenate VOCs (methanol, dimethyl ether, and ethyl acetate) was tested. The relation between the phase composition and catalytic properties of the materials was also analyzed. It was established that materials with a 1:2 CuO/Cr_2O_3 molar ratio exhibit high catalytic activity for dimethyl ether oxidation, those with 2:1 and 1:1 ratios are suitable for CO and methanol oxidation, respectively, and both of the latter, but at much higher temperatures, are good for ethyl acetate elimination. A catalyst with an optimal composition of 1:1 (mol/mol) CuO/Cr_2O_3, working in a reactor with three temperature zones of 490–500 K, 570–580 K, and 620–630 K, is proposed for the effective simultaneous elimination of CO, methanol, ethyl acetate, and dimethyl ether in toxic emissions.

Key words: copper chromium oxide nanocomposites, total oxidation, CO, methanol, dimethyl ether, ethyl acetate.

Résumé : On a préparé des matériaux nanocomposites d'oxydes de cuivre et de chrome, avec divers rapports Cu/Cr, en procédant à l'imprégnation d'un support de silice conventionnel avec une solution de toluène des précurseurs acétylacétonates correspondants et on les a caractérisés par des méthodes de diffraction des rayons-X, de spectroscopie infrarouge à transformée de Fourier, UV-visible, de spectroscopie photoélectronique des rayons-X et par thermogravimétrie par réduction thermoprogrammée. On a évalué leur comportement catalytique pour l'oxydation totale du CO et de divers composés organiques volatils oxygénés (méthanol, oxyde de diméthyle, acétate de méthyle). On discute de la relation entre la composition de la phase et les propriétés catalytiques des échantillons. Il a été établi que les matériaux comportant un rapport molaire de 1 : 2 de CuO/Cr_2O_3 présentent l'activité catalytique la plus élevée pour l'oxydation de l'oxyde de diméthyle et que ceux avec des rapports de 2 : 1 et 1 : 1 sont appropriés pour l'oxydation respectivement du CO et du méthanol alors que les deux sont bons, à des températures beaucoup plus élevées, pour l'élimination de l'acétate d'éthyle. Pour l'élimination simultanée efficace du CO, du méthanol et de l'acétate d'éthyle d'émissions toxiques, on propose l'utilisation du catalyseur de composition optimale, avec un rapport molaire de 1 : 1 de CuO/Cr_2O_3, opérant dans un réacteur comportant trois zones de température à 490–500 K, 570–580 K et 620–630 K.

Mots-clés : nanocomposites d'oxydes de cuivre et de chrome, oxydation totale, CO, méthanol, oxyde de diméthyle, acétate d'éthyle.

[Traduit par la Rédaction]

Introduction

In the last decades, CO and volatile organic compounds (VOCs), generally emitted from automotive devices and a variety of industrial processes, have been a subject of strong monitoring and legislation. Catalytic incineration has been reported as one of the most appropriate methods for their elimination, but the development of highly effective catalysts for stationary and mobile installations is still a matter of intensive investigation.[1–6] This problem is more complicated by the fact that real emissions are often a mixture of different toxic compounds (CO, alcohols, aldehydes, esters, ethers, hydrocarbons etc.). Noble metals have been reported as typical catalysts for VOC elimination, but they are costly and have low stability in the presence of chloride compounds. Transition metal oxide materials are a cheaper alternative to noble metals and recently much attention has been paid to the development of supported catalysts, using a paired metal oxide system as the active ingredient.[7] The possibility of specific interaction between the loaded metal oxides as well as between them and the support provides a great potential for development of materials with tunable composition and variable catalytic properties. A copper and chromium oxide combination has been considered one of the most effective

Received 30 March 2010. Accepted 18 February 2011. Published at www.nrcresearchpress.com/cjc on 25 April 2011.

T. Tsoncheva. Institute of Organic Chemistry with Centre of Phytochemistry, Bulgarian Academy of Sciences, Sofia, Bulgaria.
K. Ivanov and D. Dimitrov. Department of Chemistry, Agricultural University, Plovdiv, Bulgaria.

Corresponding author: T. Tsoncheva (e-mail: tsoncheva@orgchm.bas.bg).

Can. J. Chem. Downloaded from www.nrcresearchpress.com by Xi'an Jiaotong University on 09/19/12
For personal use only.

non-precious metal catalysts for CO oxidation,[8–12] but its behaviour in VOC incineration is less studied.[11,13,14] Moreover, the mechanism of the catalytic processes and the role of different active ingredients have often been subjects of intensive discussion. The Mars–van Krevelen mechanism, including release of oxygen from the metal oxide lattice and its further recovery from the oxidized agent,[15] is usually reported for hydrocarbon oxidation, while both the Langmuir–Hinshelwood mechanism, involving adsorption of CO molecules and oxygen atoms,[9,16] and the Mars–van Krevelen mechanism[17,18] have been discussed for CO oxidation. For monocomponent chromium materials supported on silica, formation of surface-grafted chromium-containing species as well as crystalline Cr_2O_3 has been observed.[19] Higher catalytic activity in total oxidation of organic compounds has been reported for the latter. It was assumed that the complete oxidation of ethyl acetate is determined by the efficiency of the redox cycle of surface Cr(III) → Cr(IV) ions.[20] For monocomponent copper oxide materials supported on silica, higher catalytic activity for methane oxidation was observed for isolated copper species than for interacting copper species.[21] In the case of bi-component copper–chromium materials, copper species are usually reported as the main active centers for CO oxidation, while the role of chromium is thought to be limited copper reduction via formation of $CuCr_2O_4$.[22] It was reported also that Cu(II) species and higher chromium content in copper–chromium materials favour deep oxidation of methanol to CO_2, while metallic Cu generates active sites for the partial oxidation of methanol.[14] In contrast, a decrease in the rate of CO oxidation with increasing copper oxidation state was found in other studies.[9,23,24] A mechanism of CO oxidation where the catalyst surface was considered as a thin layer of Cu_2O and oxygen vacancies, allowing CO adsorption on exposed Cu(I) sites or on the Cu_2O/Cu interface, was proposed.[16] Formation of a mixture of CuO, $CuCr_2O_4$, and $Cu_2Cr_2O_4$ compounds was considered for catalysts with higher activity in CO and propene oxidation.[11,12] Higher catalytic activity of $CuCr_2O_4$ in comparison with CuO in CO oxidation has also been demonstrated.[9] The observed synergetic effect of copper–chromium systems during CO oxidation has been associated with facilitated electron transfer between the components with stabilization of Cr(VI) and Cu(I) ions[25] and with increased metal oxide dispersion via formation of mixed copper–chromium oxides.[11] It was also suggested that chromium particles suppress copper aggregation by acting as a barrier between the copper particles ("barrier restricting" effect).[25]

The aim of the present paper is to investigate the effect of the composition of copper and chromium oxide nanocomposites supported on conventional silica on their catalytic behaviour in the total oxidation of CO and various oxygenate VOCs (alcohols, ethers, esters). CO, methanol, and dimethyl ether (DME) are used as model compounds, as they are the most important pollutants emitted during formaline production. For comparison, oxidation of ethyl acetate, which is a typically emitted pollutant in the printing industry and generally reported as one of the most difficult to oxidize among VOCs, is also studied. Special attention is paid to optimization of the catalyst composition for the simultaneous elimination of a mixture of different model pollutants.

Experimental

Materials

Conventional SiO_2 (Cab-O-sil M-5, Aldrich) with a BET surface area of 202 m^2/g was used as a support. Copper (Cu/silica) and chromium (Cr/silica) oxides were loaded using the incipient wetness impregnation technique from the corresponding acetylacetonate precursors in toluene. Bi-component materials were prepared by simultaneous deposition of precursors in the desired ratio using the same procedure. After impregnation the samples were dried and the precursors were decomposed in air at 773 K for 2 h. Samples with a total metal oxide loading of 10 wt % were prepared. The CuO/Cr_2O_3 molar ratio in bi-component materials was 1:1 for 1Cu1Cr/silica, 1:2 for 1Cu2Cr/silica, and 2:1 for 2Cu1Cr/silica.

Methods of investigation

Powder X-ray diffraction (XRD) was carried out on a STADI P diffractometer (STOE & Cie GmbH) configured in transmission geometry and equipped with a germanium primary monochromator (Johann-type) and a linear position sensitive detector (Cu $K\alpha_1$ radiation, 40 kV, 30 mA). For data processing the software WinX^{POW} v. 1.10 (STOE & Cie GmbH) was used. The UV–vis spectra were recorded on the powder samples using a PerkinElmer Lambda 900 UV/VIS/NIR spectrometer equipped with a diffuse reflectance unit. X-ray photoelectron spectroscopy (XPS) measurements were performed with a Physical Electronics Quantum 2000 instrument equipped with a monochromatic Al Kα X-ray source. An operating power of 25 W was used with a spot diameter of 100 μm. An electron flood gun and a low-energy ion gun were used for charge compensation. The detector was positioned at an angle of 45° in relation to the sample surface. The low and high resolutions of pass energy in spectral acquisition were 117.4 and 23.5 eV, respectively. Surface concentrations were determined with MultiPak 6.1 software (Physical Electronics), using peak areas to give surface concentrations in atom percent. The binding energies were referenced to that of the Si 2p signal of silica at 103.5 eV. In Ar^+ ion sputtering, a focused beam with a current of 50 μA, a raster area of 2 mm × 2 mm, and an acceleration voltage of 4 kV was used.

The TPR–TG (temperature-programmed reduction–thermogravimetric) analyses were performed in a Setaram TG92 instrument. Typically, 40 mg of the sample was placed in a microbalance crucible and heated in a flow of 50 vol % H_2 in Ar (100 cm^3/min) up to 773 K at 5 K/min with a final hold of 1 h.

Catalytic experiments

CO, DME, and methanol oxidation was studied under isothermal conditions using 0.5 mL catalyst diluted with 0.5 mL pumice. A flow mixture of 2.0 wt % CO in air, flow velocity of 20 000 h^{-1}, and contact time of 0.18 s were used in CO oxidation experiments. A mixture of 1 wt % DME in air, flow velocity of 20 000 h^{-1}, and contact time of 0.18 s were used in DME oxidation experiments. For methanol oxidation experiments, 2 wt % methanol in air, a flow velocity of 20 000 h^{-1}, and a contact time of 0.18 s were used. Ethyl acetate oxidation was performed with 0.5 mL catalyst and a

Can. J. Chem. Downloaded from www.nrcresearchpress.com by Xi'an Jiaotong University on 09/19/12
For personal use only.

Fig. 1. XRD patterns of copper- and chromium-modified silica.

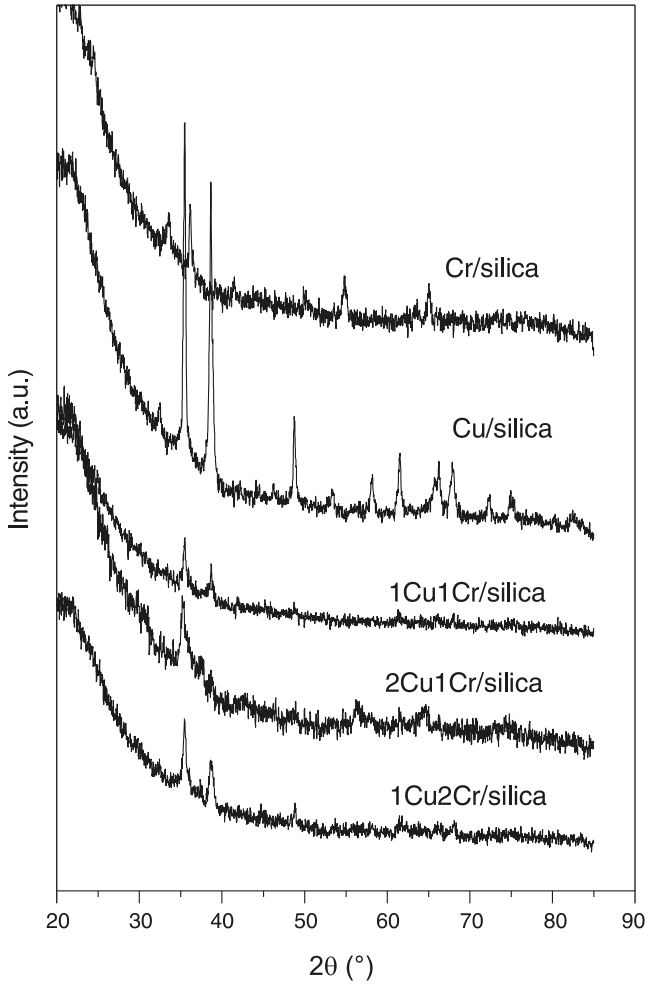

mixture of 1.21 wt % ethyl acetate in air under an isothermal or temperature-programmed regime.

Before the catalytic experiments the samples were pretreated in air at 773 K for 2 h. Gas chromatography analyses were done on a Varian 3700 apparatus using carbon-based calibration. The activation energy was determined using the Arrhenius equation. According to this equation, the slope of a plot of $\ln k$ versus $1/T$ is $-E_a/R$, where k is the rate constant, E_a is the activation energy, R is the ideal gas constant, and T is the temperature.

Results and discussion

Physicochemical characterization

In Fig. 1 are presented XRD patterns for all modified silica materials, and the corresponding data of phase composition are listed in Table 1. In the case of monocomponent materials, intense and well-defined reflections of CuO (powder diffraction file (PDF) 80-0076) are registered in the XRD pattern of Cu/silica, while wider and less intense reflections corresponding to Cr_2O_3 (PDF 85-0730) are observed in the case of Cr/silica. The average particle size, calculated by Scherer formulae, is about 35 and 26 nm for Cu/silica and Cr/silica, respectively, indicating relatively high dispersion of the loaded metal oxide nanoparticles. A mixture of CuO and

Table 1. XRD data for all copper and chromium modifications, including phase composition, average particle size (D), and relative proportion of each component.

Sample	Phase composition	D (nm)	wt %
Cu/silica	CuO	35	100
Cr/silica	Cr_2O_3	26	100
1Cu1Cr/silica	CuO	17	79
	Cr_2O_3	11	21
2Cu1Cr/silica	CuO	16	17
	$CuCr_2O_4$	12	83
1Cu2Cr/silica	CuO	15	44
	Cr_2O_3	12	56

Cr_2O_3 metal oxide phases is registered for 1Cu1Cr/silica and 1Cu2Cr/silica. We should point out the increased metal oxide dispersion in both cases in comparison with the corresponding monocomponent samples (Table 1). It is interesting to mention also the higher CuO/Cr_2O_3 ratio elucidated on the basis of XRD reflections as compared with the expected ratio (see Experimental section). We ascribe this observation to the formation of copper- and chromium-containing species with higher dispersion, which could not be detected by the XRD method. The phase composition of the sample with higher copper content (2Cu1Cr/silica) differs significantly from that of the other bi-component materials (Table 1). Here a new $CuCr_2O_4$ phase (PDF 88-0110) with an average particle size of about 12 nm is predominantly registered.

To describe the loaded metal oxide species more precisely, various spectroscopic methods were applied. Fourier transform infrared spectra of all modifications represent all absorption bands typical of silica skeletons (not shown). The intense broad band centered at about 3400 cm^{-1} is typically assigned to hydrogen-bonded vicinal pairs of silanol groups.[26] The decrease in the intensity of this band for modified materials in comparison with the parent ones indicates the existence of interactions between the loaded metal oxide species and the surface silanol groups. The high intensity of the band at about 1050 cm^{-1}, which is more pronounced in the case of Cr/silica and 1Cu2Cr/silica samples, is probably due to stretching vibrations of the terminal Cr=O group in polymeric hexavalent chromia species.[25] The bands at 571 and 624 cm^{-1} in the spectra of Cr/silica could be ascribed to crystalline Cr_2O_3 nanoparticles.[27] The relatively high intensity of the band at about 600 cm^{-1} for Cr/silica and the broadening of this band for the bi-component materials could be due to the presence of amorphous, highly dispersed Cr_2O_3 species,[27] which seem to be more abundant in the case of the latter materials.

The presence of various chromium-containing species is also confirmed by XPS spectra. The Cr $2p_{3/2}$ peaks in the spectra (the one for 1Cu1Cr/silica is presented in Fig. 2*a*) could be fitted to two components with binding energies of approximately 576.3 and 579.6 eV, which generally are attributed to Cr(III)- and Cr(VI)-containing species, respectively.[19,28–32] At the same time, the Cu $2p_{3/2}$ peak (Fig. 2*b*) is positioned at about 933 eV, with a shake-up satellite peak between ~940–945 eV and ~960–965 eV, which could be attributed to Cu(II) ions in different environments.[14,33]

Selected UV–vis spectra of copper- and chromium-modified

Can. J. Chem. Downloaded from www.nrcresearchpress.com by Xi'an Jiaotong University on 09/19/12
For personal use only.

Fig. 2. Cr 2p and Cu 2p signals for the 1Cu1Cr/silica modification.

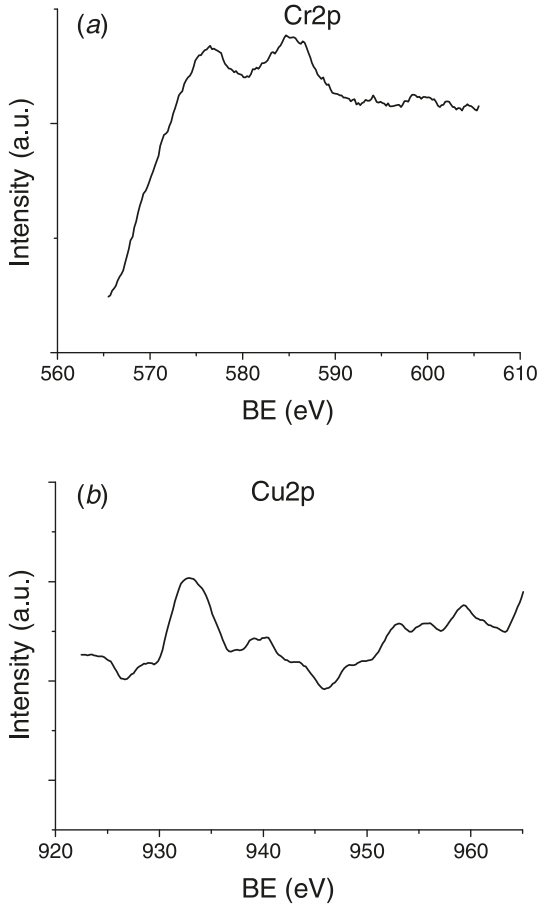

Fig. 3. UV–vis spectra of selected copper- and chromium-modified silica materials. *R*, reflectance.

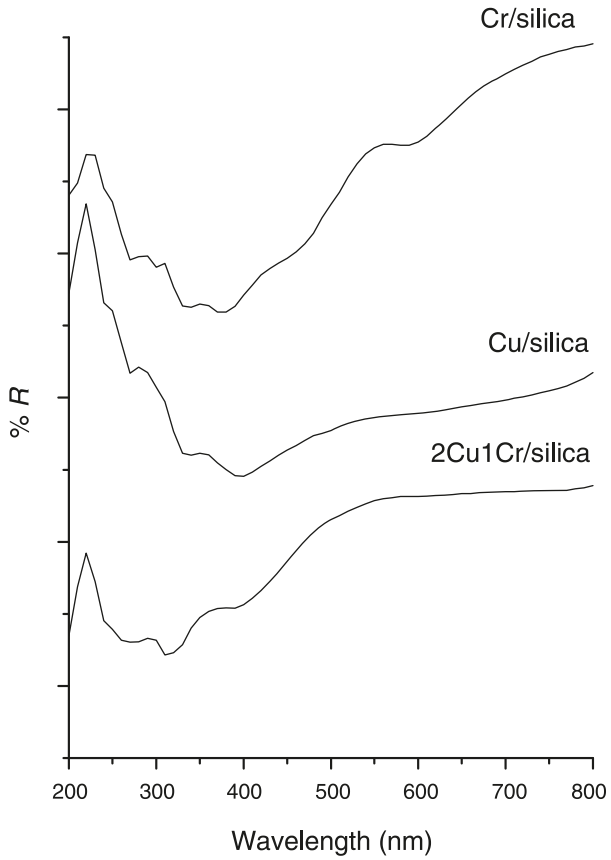

silica materials are shown in Fig. 3. The spectrum of Cr/silica presents bands at approximately 260–280, 370–380, and 470 nm, which could be assigned to O → Cr(VI) charge transfer (CT) in mono- and polychromate species, respectively.[30,34–37] The absorption at about 300, 450, and 600 nm is generally ascribed to transitions of Cr(III) ions in octahedral coordination in Cr_2O_3.[34–37] The spectrum of Cu/silica consists of absorption bands in the 230–265 nm and 330–390 nm regions. The first band could be attributed to CT transitions between surface oxygen and isolated Cu(II) ions and the second one originates from Cu-O-Cu clusters in a highly dispersed state.[38] The broad band centered at 670–750 nm is usually assigned to d-d transitions of Cu(II) in octahedral coordination in CuO.[38] The spectra of bi-component materials represent superposition of the spectra of both monocomponent materials. Taking into account the XRD data (see above), we ascribe the observed increase of absorption at about 270 nm and 330 nm for all bi-component materials to the formation of highly dispersed chromium- and copper-containing species, probably interacting with each other.[38]

Temperature-programmed reduction–differential thermogravimetric (TPR–DTG) profiles of all copper- and chromium-modified silica materials are presented in Fig. 4. The main reduction peak for Cu/silica is centered at 484 K and the registered mass loss corresponds to about 68% reduction of CuO to Cu. In agreement with the UV–vis data, the observed result could be attributed to the presence of finely dispersed, difficult to reduce copper oxide species strongly interacting with the silica support. In comparison, no significant mass loss was observed for the Cr/silica sample, indicating negligible reduction transformations of the active ingredient in this case, most probably due to the predominant presence of Cr_2O_3 nanocrystallites. The TPR profiles for all bi-component materials are characterized by broader reduction peaks, and in some cases these peaks are shifted to higher temperatures. A new high-temperature peak at about 656 K is registered in the case of the 2Cu1Cr/silica sample. At the same time, the observed mass loss for all bi-component materials is about 15%–22% lower than that expected for the corresponding mechanical mixtures of bulk copper and chromium oxides. In accordance with the spectroscopic and XRD data (see above), we assign this effect to increased dispersion of copper and chromium species and to step-wise reduction of $CuCr_2O_4$ species.[11,12]

Catalytic study

CO oxidation

Data for CO oxidation on various samples with increasing temperature are presented in Fig. 5*a*. All modifications exhibit catalytic activity above 423 K and CO_2 is the only registered carbon-containing product in the whole investigated temperature interval. Higher catalytic activity is observed for the monocomponent copper modification than for the chromium one. Among the bi-component materials, higher activity is registered only for the 2Cu1Cr/silica sample, where the

Can. J. Chem. Downloaded from www.nrcresearchpress.com by Xi'an Jiaotong University on 09/19/12
For personal use only.

Fig. 4. TPR–DTG profiles of copper and chromium oxide modifications.

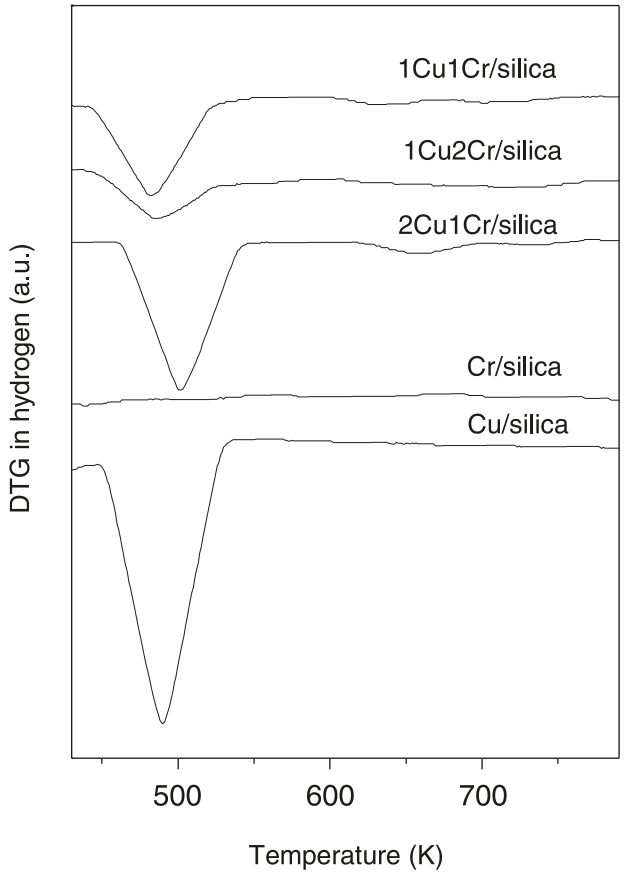

conversion curve is shifted to the lower temperatures by about 50 K in comparison with that of Cu/silica. These observations are supported by the calculated turnover frequency (TOF) values (Table 2), as the highest TOF was found for 2Cu1Cr/silica. We should also emphasize the lower values of the activation energy (E_a) for this sample (5 kcal/mol) in comparison with Cu/silica (9 kcal/mol), which could be attributed to the presence of different catalytic active sites in these materials. In accordance with the XRD data (Table 1, Fig. 1), the observed higher activity of 2Cu1Cr/silica is probably due to the formation of $CuCr_2O_4$ spinel nanoparticles, and this assumption correlates well with the data reported in other studies.[9,12] On the other hand, it seems that the increased dispersion of copper and chromium oxide nanoparticles, which is observed mainly for 1Cu2Cr/silica and 1Cu1Cr/silica, does not significantly improve the catalytic activity (Table 2). Taking into account the TPR–DTG data (Fig. 4), we suggest that the formation of Cu(I) ions, stabilized in a $Cu_xCr_yO_4$ spinel structure, facilitates the catalytic process via better CO adsorption.[24]

Methanol oxidation

Figure 5*b* illustrates total oxidation of methanol under the same experimental conditions. Here, the catalytic activity was observed above 473–523 K and again CO_2 is the only registered product. Copper and chromium monocomponent materials exhibit similar but lower catalytic activity in comparison with all bi-component materials. We draw attention to the high activity of 1Cu1Cr/silica. Here, the conversion curve was shifted to the lower temperatures by about 100 K, and the calculated TOF is 3–4 times higher than that for the other samples (Table 2). Taking into account the physicochemical data (see above), this extremely high catalytic activity could not be ascribed simply to the increased dispersion of the metal oxide nanoparticles or to the formation of new mixed oxide compounds. In our opinion, the observed synergetic effect can be assigned to the formation of a new type of catalytic active site at the copper and chromium species interface. We propose a mechanism consisting of methanol dehydrogenation on the chromium species with the formation of surface methoxide intermediates[39,40] and their further transformation to CO_2 via formation of carbonate intermediates by oxygen insertion from the copper oxide species.[39]

DME oxidation

The temperature dependencies of DME total oxidation are shown in Fig. 5*c*. As can be seen, DME oxidation occurs at a much higher temperature in comparison with CO and methanol oxidation (Figs. 5*a*, 5*b*). Moreover, the conversion curve of Cu/silica is shifted to higher temperatures in comparison with that of Cr/silica, indicating its lower catalytic activity. The calculated values of E_a for both materials are 26 and 20 kcal/mol, respectively, which could be evidence for changes in the mechanism of DME oxidation on these materials. We assume the facilitated DME oxidation on Cr/silica to be a complex step-wise process of DME hydration to methanol on the Cr_2O_3 species[41] and its further oxidation to CO_2 via the mechanism described for methanol oxidation (see above).

As a whole, all bi-component materials exhibit higher catalytic activity than the corresponding monocomponent ones, which is also well demonstrated by TOF values, presented in Table 2. No significant increase in catalytic activity is observed for 2Cu1Cr/silica, where CuO and $CuCr_2O_4$ are the main registered phases (Fig. 1, Table 1). At the same time, the catalytic activity of bi-component systems increases with chromia content. These results provide further evidence of the important role of chromia species in DME oxidation. Thus, the higher catalytic activity of bi-component materials could be related both to the increased dispersion of copper and chromium oxide species and to the appearance of a synergetic effect at the interface of copper and chromium oxide nanoparticles.

Ethyl acetate (EA) oxidation

The conversion curves of EA oxidation versus temperature for all modified materials are shown in Fig. 5*d*. Like DME oxidation, EA oxidation occurs at higher temperatures (above 500 K). Ethanol, acetaldehyde, and acetic acid are registered as by-products below 570 K. The shifting of the conversion curves with the temperature (Fig. 5*d*) and the calculated TOF values (Table 2) strongly indicate that Cr/silica has the lowest activity and the bi-component materials with copper content have increased catalytic activity. The similarity in the course of the conversion curves for various materials reveals the similarity in the mechanism of EA oxidation, which according to Gandhe et al.[42] includes hydrolysis of EA to acetic acid and ethanol and further oxidation to acetaldehyde with the participation of oxygen from the solid. According to the

Can. J. Chem. Downloaded from www.nrcresearchpress.com by Xi'an Jiaotong University on 09/19/12
For personal use only.

Fig. 5. Temperature dependencies of CO (*a*), methanol (*b*), DME (*c*), and EA (*d*) oxidation for various silica modifications.

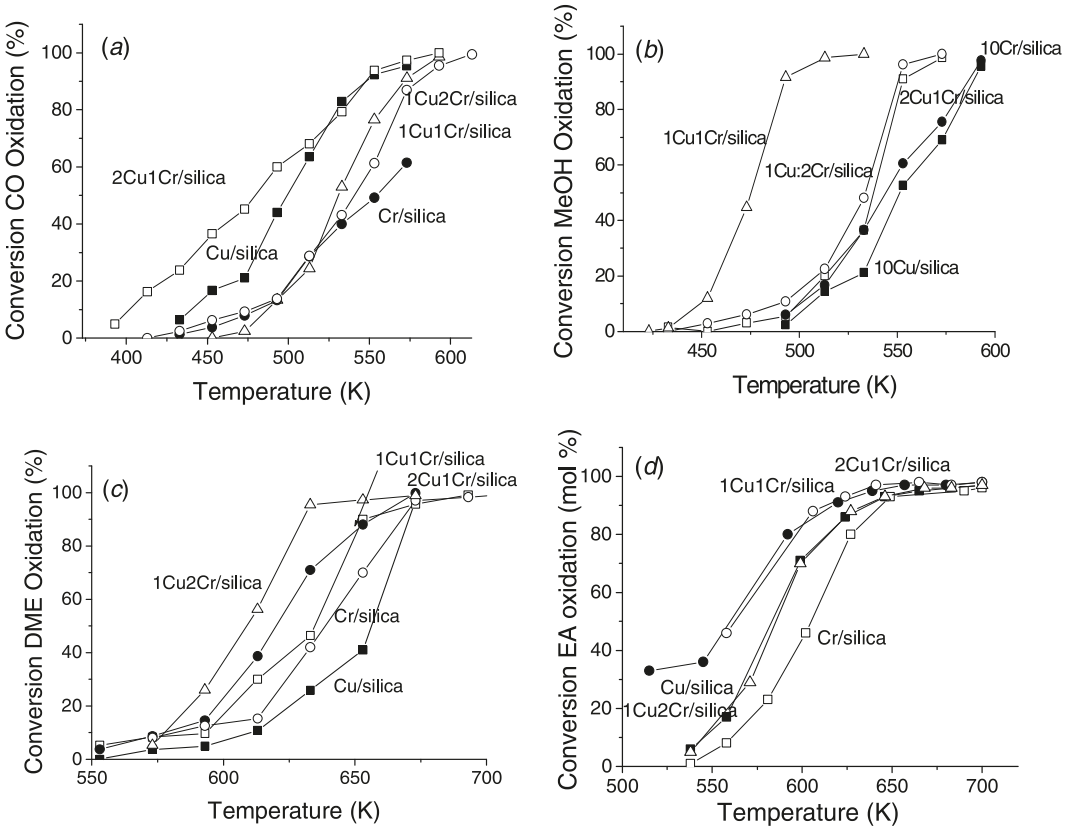

Table 2. TOF (conversion per metal site) for total oxidation of CO, methanol, DME, and ethyl acetate over various samples at selected temperatures.

Sample	CO (473 K)	Methanol (523 K)	DME (613 K)	Ethyl acetate (576 K)
Cu/silica	5.57	4.58	2.92	10.61
Cr/silica	2.02	6.73	9.62	4.81
1Cu1Cr/silica	0.62	25.60	14.51	16.84
2Cu1Cr/silica	11.78	7.38	11.78	15.96
1Cu2Cr/silica	3.59	9.12	17.74	9.25

Table 3. The lowest temperature (K) at which 90% conversion is achieved for various reactions and catalyst compositions.

Sample	CO	Methanol	DME	Ethyl acetate
Cr/silica	604	586	655	645
Cu/silica	549	590	670	639
1Cu1Cr/silica	573	492	630	619
2Cu1Cr/silica	549	552	633	619
1Cu2Cr/silica	560	550	627	639

XRD data (Fig. 1, Table 1), the increased activity of the bicomponent materials could be mainly related to the increased dispersion of chromium and copper metal oxide nanoparticles and also to the formation of spinel $CuCr_2O_4$ species (sample 2Cu1Cr/silica).

Therefore, catalysts with different copper/chromium ratios seem to be suitable for oxidation of CO and various oxygenate VOCs with high efficiency. However, under real industrial conditions, when toxic gas emissions represent a mixture of different oxygenates, the problem of their simultaneous elimination becomes much more complex. A catalyst for the deep oxidation of each component, working at relatively low temperature with high catalytic activity and selectivity, is needed. Obviously, optimization of the catalyst composition and its working regime requires detailed investigation of the formation of the active ingredients and their role in catalysis. It could be expected that the final phase composition of the samples is strongly affected not only by the initial Cu/Cr ratio but also by the reaction medium as well. Analyzing the relation between the sample composition and the temperature at which 90% conversion is achieved for each component (Fig. 5, Table 3), we propose 1Cu1Cr/silica (CuO/Cr_2O_3 in a 1:1 molar ratio) as the most effective catalyst for simultaneous elimination of a complex mixture of CO, methanol, DME, and EA. However, a reactor with a temperature layer gradient with at least three temperature zones (490–500 K, 570–580 K, and 620–630 K) seems to be most effective in this case.

Conclusion

Higher dispersion is observed for all silica-supported bicomponent copper–chromium materials in comparison with the corresponding monocomponent ones. The final phase composition of the samples (a mixture of CuO, Cr_2O_3, and (or) $CuCr_2O_4$), which significantly affects their catalytic behaviour in CO, methanol, DME and ethyl acetate oxidation, is strongly affected by the Cu/Cr ratio. The materials with a 1:2 molar ratio of CuO/Cr_2O_3 exhibit high catalytic activity for deep oxidation of DME, while those with 2:1 and 1:1

Can. J. Chem. Downloaded from www.nrcresearchpress.com by Xi'an Jiaotong University on 09/19/12
For personal use only.

ratios are suitable for total oxidation of CO and methanol, respectively, and both of the latter, but at much higher temperatures, are good for EA elimination. The effective simultaneous elimination of CO, methanol, ethyl acetate, and dimethyl ether in toxic gas emissions seems to be facilitated by a catalyst with an optimal composition of 1:1 CuO/Cr_2O_3 (mol:mol) and a reactor with a temperature layer gradient consisting of three temperature zones of 490–500 K, 570–580 K, and 620–630 K.

Acknowledgements

Financial support by the Bulgarian Academy of Sciences, Ministry of Education and Science (projects BYX-305/07 and DO-02-295) is gratefully acknowledged. Prof. T. Tsoncheva thanks Dr. L. Ivanova for help with catalytic experiments and sample modifications and Prof. M. Froeba and Dr. Daniela Paneva for XRD analysis.

References

(1) Armor, N. *Res. Chem. Intermed.* **1998** *24* (2), 105. doi:10.1163/156856798X00690.
(2) Guczi, L.; Borkó, L.; Schay, Z.; Bazin, D.; Mizukami, F. *Catal. Today* **2001** *65* (1), 51. doi:10.1016/S0920-5861(00)00544-7.
(3) Yang, H.-C.; Cho, Y.-J.; Eun, H.-C.; Kim, E.-H. *Chemosphere* **2008** *73* (1), S311. doi:10.1016/j.chemosphere.2008.03.045.
(4) Kim, S. K.; Kim, K. H.; Ihm, S. K. *Chemosphere* **2007** *68* (2), 287. doi:10.1016/j.chemosphere.2006.12.080.
(5) Orlov, A.; Klinowski, J. *Chemosphere* **2009** *74* (2), 344. doi:10.1016/j.chemosphere.2008.08.049.
(6) Tahir, S. F.; Koh, C. A. *Chemosphere* **1997** *34* (8), 1787. doi:10.1016/S0045-6535(97)00034-9.
(7) Peluso, M. A.; Pronsato, E.; Sambeth, J. E.; Thomas, H. J.; Busca, G. *Appl. Catal. B* **2008** *78* (1–2), 73. doi:10.1016/j.apcatb.2007.09.002.
(8) Severino, F.; Brito, J.; Carias, O.; Laine, J. *J. Catal.* **1986** *102* (1), 172. doi:10.1016/0021-9517(86)90151-X.
(9) Severino, F.; Brito, J. L.; Laine, J.; Fierro, J. L. G.; López Agudo, A. *J. Catal.* **1998** *177* (1), 82. doi:10.1006/jcat.1998.2094.
(10) Stegenga, S.; van Soest, R.; Kapteijn, F.; Moulijn, J. A. *Appl. Catal. B* **1993** *2* (4), 257. doi:10.1016/0926-3373(93)80001-T.
(11) Chien, C. C.; Chuang, W. P.; Huang, T.-J. *Appl. Catal. A Gen.* **1995** *131* (1), 73. doi:10.1016/0926-860X(95)00136-0.
(12) Pantaleo, G.; Liotta, L. F.; Venezia, A. M.; Deganello, G.; Ezzo, E. M.; El Kherbawi, M. A.; Atia, H. *Mater. Chem. Phys.* **2009** *114* (2–3), 604. doi:10.1016/j.matchemphys.2008.10.006.
(13) Spasova, I.; Ivanov, G.; Georgescu, V.; Mehandjiev, D. *J. Univ. Chem. Technol. Metallurgy* **2006** *41*, 225.
(14) Wang, Z.; Xi, J.; Wang, W.; Lu, G. *J. Mol. Catal. Chem.* **2003** *191* (1), 123. doi:10.1016/S1381-1169(02)00352-7.
(15) Wachs, I. E. *Catal. Today* **2005** *100* (1–2), 79. doi:10.1016/j.cattod.2004.12.019.
(16) Choi, K. I.; Vannice, M. A. *J. Catal.* **1991** *131* (1), 22. doi:10.1016/0021-9517(91)90320-4.
(17) Delimaris, D.; Ioannides, T. *Appl. Catal. B* **2008** *84* (1–2), 303. doi:10.1016/j.apcatb.2008.04.006.
(18) Águila, G.; Gracia, F.; Cortés, J.; Araya, P. *Appl. Catal. B* **2007** *77* (3–4), 325. doi:10.1016/j.apcatb.2007.08.002.
(19) Pradier, C. M.; Rodrigues, F.; Marcus, P.; Landau, M. V.; Kaliya, M. L.; Gutman, A.; Herskowitz, M. *Appl. Catal. B* **2000** *27* (2), 73. doi:10.1016/S0926-3373(00)00142-9.
(20) Rotter, H.; Landau, M. V.; Carrera, M.; Goldfarb, D.; Herskowitz, M. *Appl. Catal. B* **2004** *47* (2), 111. doi:10.1016/j.apcatb.2003.08.006.
(21) Park, P.; Ledford, J. *Appl. Catal. B* **1998** *15* (3–4), 221. doi:10.1016/S0926-3373(98)80008-8.
(22) Huang, T.; Lee, K.; Yang, H.; Dow, W. *Appl. Catal. A Gen.* **1998** *174* (1–2), 199. doi:10.1016/S0926-860X(98)00193-8.
(23) Jernigan, G. G.; Somorjai, G. A. *J. Catal.* **1994** *147* (2), 567. doi:10.1006/jcat.1994.1173.
(24) Monnier, J. R.; Hanrahan, M. J.; Apai, G. *J. Catal.* **1985** *92* (1), 119. doi:10.1016/0021-9517(85)90241-6.
(25) Wojciechowska, M.; Haber, J.; Łomnicki, S.; Stoch, J. *J. Mol. Catal. Chem.* **1999** *141* (1–3), 155. doi:10.1016/S1381-1169(98)00259-3.
(26) Samanta, S.; Mal, N. K.; Bhaumik, A. *J. Mol. Catal. Chem.* **2005** *236* (1–2), 7. doi:10.1016/j.molcata.2005.04.005.
(27) Steger, W. E.; Landmesser, H.; Boettcher, U.; Schubert, E. *J. Mol. Struct.* **1990** *217*, 341. doi:10.1016/0022-2860(90)80373-R.
(28) Liotta, L. F.; Venezia, A. M.; Pantaleo, G.; Deganello, G.; Gruttadauria, M.; Noto, R. *Catal. Today* **2004** *91–92*, 231. doi:10.1016/j.cattod.2004.03.050.
(29) Liu, B.; Terano, M. *J. Mol. Catal. Chem.* **2001** *172* (1–2), 227. doi:10.1016/S1381-1169(01)00121-2.
(30) Moriceau, P.; Grzybowska, B.; Gengembre, L.; Barbaux, Y. *Appl. Catal. A Gen.* **2000** *199* (1), 73. doi:10.1016/S0926-860X(99)00538-4.
(31) Hakuli, A.; Kytokivi, A.; Krause, A. O. I.; Suntola, T. *J. Catal.* **1996** *161* (1), 393. doi:10.1006/jcat.1996.0197.
(32) Zhao, X.; Wang, X. *Catal. Commun.* **2006** *7* (9), 633. doi:10.1016/j.catcom.2006.02.005.
(33) Moulder, J. F.; Stickle, W. F.; Sobol, P. E.; Bomben, K. D.; Chastain, J., Eds. *Handbook of X-ray Photoelectron Spectroscopy*; Perkin-Elmer: Eden Prairie, Minn., 1992.
(34) Michorczyk, P.; Ogonowski, J.; Kustrowski, P.; Chmielarz, L. *Appl. Catal. A Gen.* **2008** *349* (1–2), 62. doi:10.1016/j.apcata.2008.07.008.
(35) Liu, L.; Li, H.; Zhang, Y. *Catal. Commun.* **2007** *8* (3), 565. doi:10.1016/j.catcom.2006.08.005.
(36) Shao, Y.; Wang, L.; Zhang, J.; Anpo, M. *Microporous Mesoporous Mater.* **2008** *109* (1–3), 271. doi:10.1016/j.micromeso.2007.05.001.
(37) Zhang, L.; Zhao, Y.; Dai, H.; He, H.; Au, C. T. *Catal. Today* **2008** *131* (1–4), 42. doi:10.1016/j.cattod.2007.10.017.
(38) Chmielarz, L.; Kustrowski, P.; Dziembaj, R.; Cool, P.; Vansant, E. F. *Appl. Catal. B* **2006** *62* (3–4), 369. doi:10.1016/j.apcatb.2005.09.004.
(39) Derossi, S.; Ferraris, G.; Fremiotti, S.; Garrone, E.; Ghiotti, G.; Campa, M. C.; Indovina, V. *J. Catal.* **1994** *148* (1), 36. doi:10.1006/jcat.1994.1183.
(40) Barteau, M. A. *Chem. Rev.* **1996** *96* (4), 1413. doi:10.1021/cr950222t.
(41) Badmaev, S. D.; Belyaev, V. D.; Volkova, G. G.; Paukshtis, E. A.; Sobyanin, V. A. *React. Kinet. Catal. Lett.* **2007** *90* (1), 197. doi:10.1007/s11144-007-5081-9.
(42) Gandhe, A. R.; Rebello, J. S.; Figueiredo, J. L.; Fernandes, J. B. *Appl. Catal. B* **2006** *72* (1–2), 129. doi:10.1016/j.apcatb.2006.10.017.

Antibiotic-inspired zinc oxide with morphology-dependent photocatalytic activity

Shuyan Gao, Xiaoxia Jia, Zhengdao Li, Yanli Chen, and Kai Jiang

Abstract: ZnO materials with different morphologies (hexahedron, coneflowerlike, cauliflowerlike, and nanorods) have been synthesized via a bioinspired method, which is effective and facile for the controlled synthesis of ZnO. Zinc acetate and ammonia were used as growth precursors, and ampicillin was used as the morphology-directing agent. X-ray diffraction (XRD) data showed that the obtained ZnO with different morphologies displayed different crystal growth habits. Photodegradation of Orange G was used as a model reaction to test the photocatalytic activity of ZnO samples. Different morphologies exhibited different activities to Orange G degradation. The cauliflowerlike ZnO sample showed the best photocatalytic performance compared with the others. The influence of the morphology-directing agent and pH on the morphology of ZnO samples and the effect of the morphologies on the photocatalytic activity are tentatively discussed.

Key words: bioinspired method, formation mechanism, ZnO, morphologies, nanostructures, photocatalytic activity.

Résumé : Faisant appel à une méthode d'inspiration biologique, on a effectué la synthèse de divers matériaux à base de ZnO, avec des morphologies différentes (en forme d'hexaèdre, d'échinacée, de chou-fleur ou de nanobâtonnet); c'est une méthode efficace et facile d'effectuer des synthèses contrôlées de ZnO. On a utilisé de l'acétate de zinc et de l'ammoniac comme précurseurs de croissance et l'ampicilline comme agent pour orienter la morphologie. Des données de diffraction des rayons X (DRX) montrent que les ZnO obtenus avec diverses morphologies présentes des habitudes de croissance cristalline différentes. On a utilisé la photodégradation du colorant Orange G comme modèle réactionnel pour évaluer l'activité photocatalytique des échantillons de ZnO. Les diverses morphologies présentent des activités différentes vis-à-vis de la dégradation de l'Orange G. L'échantillon de ZnO en forme de chou-fleur présente une meilleure activité photocatalytique que les autres. On discute d'une façon préliminaire de l'influence de l'agent d'orientation de la morphologie et du pH sur la morphologie des échantillons de ZnO et de l'effet des morphologies sur l'activité photocatalytique.

Mots-clés : méthode d'inspiration biologique, mécanisme de formation, ZnO, morphologies, nanostructures, activité photocatalytique.

[Traduit par la Rédaction]

Can. J. Chem. Downloaded from www.nrcresearchpress.com by Xi'an Jiaotong University on 09/19/12
For personal use only.

Introduction

Zinc oxide (ZnO) is a direct, wide band-gap semiconductor material with many promising properties for blue/UV optoelectronics, transparent electronics, spintronic devices, and sensor applications.[1–6] Recently, a number of nanostructured ZnO materials with morphologies such as rods, belts, cables, combs, wires, tetrapods, and hierarchical nanostructures with high symmetries have been synthesized.[7–13] Nevertheless, the synthesis methods to obtain controlled nanostructures often involve tedious processes.[14] Generally, morphology control in metal oxide nanostructures requires chemical methods using highly alkaline solutions,[15,16] or physical methods performed at high temperatures.[17–19]

It is well-known that the photocatalytic properties of ZnO are related primarily to the amount of surface catalytically active sites, which depend on (*i*) the surface area of the catalyst, (*ii*) the mass of the catalyst, or (*iii*) the number of surface OH groups on a photocatalyst. Other factors affecting degradation rates include structural properties (such as phase composition, crystalline quality, particle size, size distribution, and band-gap energy) and various parameters including temperature, pH, initial concentration of the pollutant, light intensity, the reactor geometry, agglomeration, stirring, etc.[20] Therefore, the morphology of one catalyst, which determines both surface area and the structural properties mentioned above, plays a key role in catalytic activity.[21–23] To tailor electronic, optical, and catalytic properties of ZnO, much effort has been made to control its structure.[24–31] However, much more research is still needed in this area. Controlling the morphologies of nanomaterials via green methods is of great interest in many fields. Herein, we recently developed a bioinspired method to synthesize ZnO materials with different morphologies (hexahedron, coneflowerlike, cauliflowerlike, and nanorods) and investigated the influence of the morphology-directing agent and pH on the morphology and the effect of the morphologies on the photocatalytic activity. In this paper, biomolecule ampicillin was used as the morphology-directing agent to synthesize ZnO.

Received 25 October 2010. Accepted 22 December 2010. Published at www.nrcresearchpress.com/cjc on 12 May 2011.

S. Gao, X. Jia, Z. Li, Y. Chen, and K. Jiang. College of Chemistry and Environmental Science, Henan Normal University, 46 Jianshe street, Xinxiang, 453007, Henan, P. R. China.

Corresponding author: S. Gao (e-mail: shuyangao@htu.cn).

Table 1. Methods for the preparation of ZnO nanostructures with different morphologies.

Sample	$Zn(Ac)_2 \cdot 2H_2O$ (mL)	Ammonia (mL)	Ampicillin (mL)	pH
1	30	0.2	3	10.95
2	30	0.2	2	10.96
3	30	0.4	2	11.10
4	30	1.2	2	11.34

Can. J. Chem. Downloaded from www.nrcresearchpress.com by Xi'an Jiaotong University on 09/19/12
For personal use only.

Experimental section

Preparation of pure ZnO

Ampicillin trihydrate ($C_{16}H_{19}N_3O_4S \cdot 3H_2O$) was purchased from Zhengzhou Biosail Biotechnology Co. Ltd., and all other analytical grade chemicals were supplied by Beijing Chemicals Co. Ltd. and used as received. The synthesis procedure for ZnO is quite straightforward. Briefly, a 25.4 mmol/L aqueous solution of ampicillin (calculated by the repeating unit) and 5.0 mmol/L of zinc acetate dihydrate were mixed with agitation in a beaker. Then, a 28 wt% aqueous solution of ammonia was added dropwise to the above mixture. The resulting solution was transferred into a 50 mL Teflon-lined autoclave and heated at 373 K for 7 h. When the reactions were completed, the precipitates were collected, washed with deionized water and ethanol several times, and finally dried in air. The detailed methods for preparing samples 1–4 are listed in Table 1.

Sample characterizations

The phase and purity of the sample was determined by X-ray diffraction (XRD) on a Bruker D8A X-ray diffractionmeter with Cu Kα radiation ($\lambda = 0.154\,056$ nm). The morphologies of the as-prepared samples were observed by a field emission scanning electron microscope (FESEM, Hitachi S-4800). The surface property of all as-prepared samples was determined by X-ray photoelectron spectroscopy (XPS) measurements using a PerkinElmer PHI 5600ci X-ray source (1486.6 eV). The C 1sESCA System, with a monochromatized Al Kα peak of hydrocarbon contamination was used as an internal reference (284.5 eV). Raman spectra were recorded on a Raman 960 FT-Raman spectrometer using a laser beam with an excitation wavelength of 1064 nm and a resolution of 8 cm^{-1}.

Photocatalytic test

Orange G (OG; formula, $C_{16}H_{10}N_2O_7S_2Na_2$; molecular weight, 452), a widely used anionic azo dye, was employed as a representative dye pollutant to evaluate the photocatalytic performance of ZnO samples. A cylindrical photoreactor surrounded by a circulating water jacket to cool the reaction solution was used and the UV light was provided by a 250 W high-pressure fluorescent Hg lamp (Institute of Electrical Light Source, Beijing; the strongest emission at 365 nm). For a typical procedure, a mixture of 100 mL of a 10 ppm aqueous solution of OG and 100 mg of each ZnO photocatalyst was agitated in the dark for 1 h in the photoreactor to ensure establishment of an adsorption equilibrium of the dye on the surface of the catalyst. After the initiation of the reaction by irradiation of the reactor, 5 mL samples of the suspension were withdrawn at regular intervals and were immediately centrifuged and then filtered to remove the catalyst particles completely. The degradation of OG was determined by measuring the absorbance of the solution samples on a TU-1810 UV–vis spectrophotometer (Beijing Purkinje General Instrument Co., Ltd.).

Crystal structure and microstructure of the as-prepared ZnO samples

FESEM images

Figure 1 shows the FESEM images of the samples obtained under different preparation conditions. Sample 1 (Fig. 1a) displays a hexagonal structure. The planes on each crystal are smooth. The height of the hexahedron is ~1 μm, and the side length of the hexagonal face is ~3 μm. A few hexahedrons were joined across the basal plane. Figure 1b is coneflowerlike assembled by seven or eight cones in all directions. Figure 1c has well-defined cauliflowerlike microstructures, assembled by many densely arranged nanosheets as "petals". ZnO nanorods with uniform diameters of ~100 nm were obtained, with an open cavity at the end (Fig. 1d). These show that the preparation conditions have an evident effect on the product morphologies, which can in turn guide the fabrication technologies to service materials synthesis.

It is well-known that shape control of the crystals can be achieved by manipulating the growth kinetics.[32–34] First, ZnO nuclei generally evolve into nanorods by preferential *c*-axis ([001] direction) oriented growth. Second, when the crystal growth along the [001] direction is suppressed, a hexahedron can be obtained because of the growth along the sixfold symmetric directions, which are normal to the [001] direction.[35] Third, petal-interlaced growth results in a cauliflower. Connecting all the "petal" frameworks leads to a larger piece of cauliflower. Finally, cone-interlaced growth results in a coneflower. Therefore, the synthetic conditions therein favour the structure control. Based on the above observations, the schematic illustration of the formation process of the obtained different ZnO microstructures is presented in Fig. 2.

XRD patterns

Typical XRD patterns of all four samples are shown in Fig. 3 to investigate the phase purity. All of the diffraction peaks from the samples corresponded to those of wurtzite-structure ZnO (The Joint Committee on Powder Diffraction Standards (JCPDS): 36-1451; *a*, 3.249 Å; *c*, 5.206 Å) with high crystallinity. No impurity peaks were observed for the other impurities such as $Zn(OH)_2$. Interestingly, compared with the XRD patterns of samples a and d, the intensity of

Fig. 1. Field emission scanning electron microscope (FESEM) images of ZnO samples. Images (a)–(d) correspond to samples 1–4, respectively.

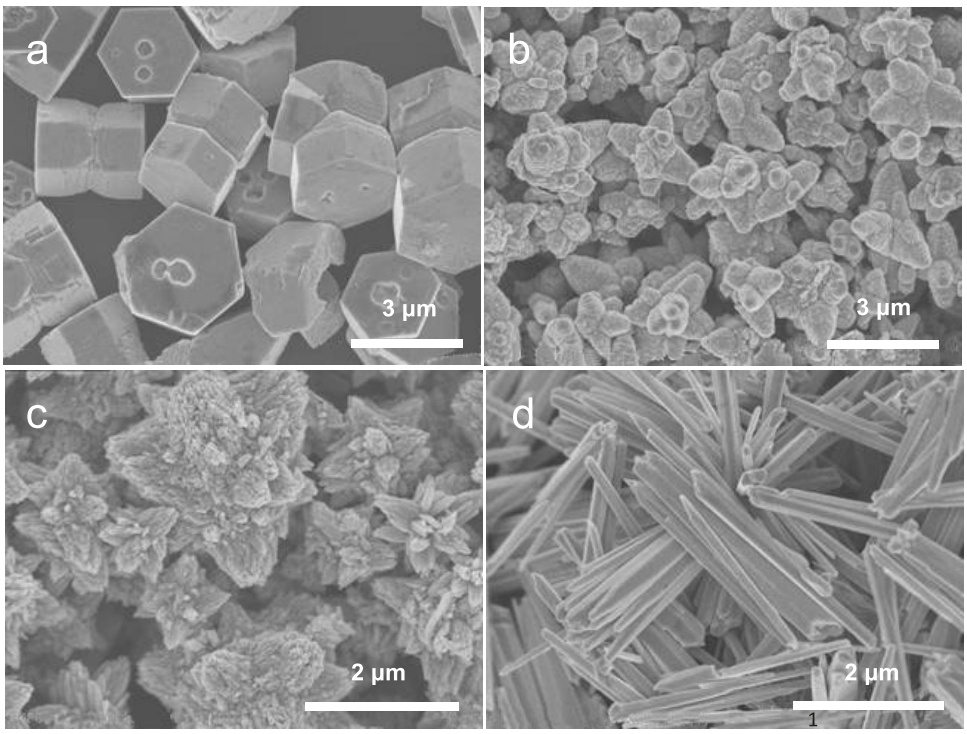

Fig. 2. Schematic graph of the shape-selective synthesis of ZnO with different morphologies: hexahedron, coneflower, cauliflower, and nanorods.

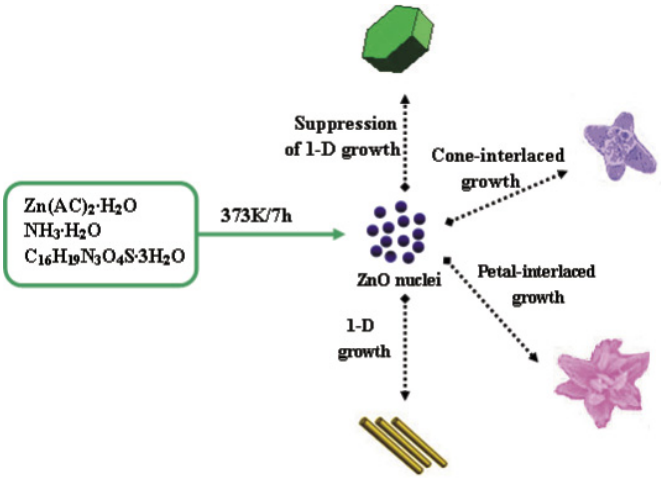

Fig. 3. X-ray diffraction (XRD) patterns of ZnO obtained at different conditions ((a)–(d) correspond to samples 1–4, respectively).

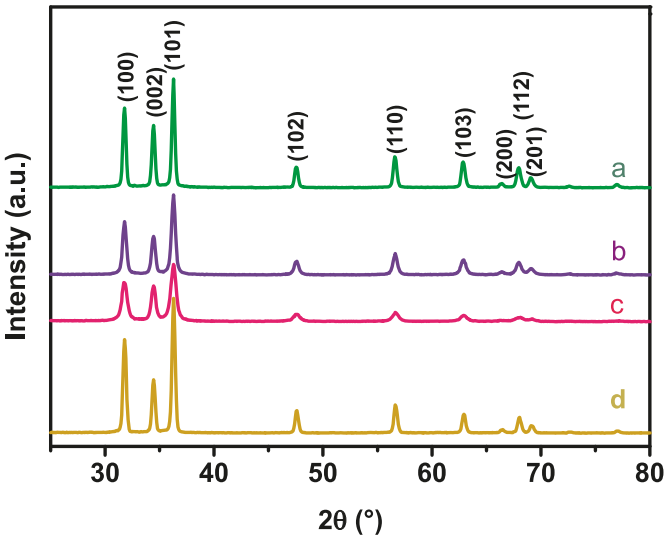

the (002) peak in the patterns of the ZnO coneflower (sample b) and the cauliflower (sample c) is relatively weaker.

Raman spectroscopy

Raman scattering is very sensitive to the lattice microstructure. Phonon frequencies and scattering intensities determined by Raman spectroscopy can lead to conclusions concerning microscopic parameters such as bonding and structure as well as deviations from the ideal crystalline counterpart.[36] ZnO belongs to the wurtzite space group. On the basis of group theory, the correlation of the site group to the factor group is constructed in Table 2.

There are eight sets of optical phonon modes at the Γ point of the Brillouin zone in single-crystalline ZnO, in which the $A_1 + E_1 + 2E_2$ modes are Raman-active and expected in Raman spectra. Moreover, the A_1 and E_1 are polar and hence split into transverse optical (TO) and longitudinal optical (LO) phonon components. Figure 4 shows a typical Raman spectrum of the sample. The sharp, strong Raman peak at 438 cm^{-1} is attributed to the ZnO nonpolar optical phonon (E_2) modes,[37] which is one of the characteristic peaks of wurtzite ZnO.[38,39] The less prominent peak at 381 cm^{-1} corresponds to the A_1(TO) mode, which is caused by the

Can. J. Chem. Downloaded from www.nrcresearchpress.com by Xi'an Jiaotong University on 09/19/12
For personal use only.

Can. J. Chem. Downloaded from www.nrcresearchpress.com by Xi'an Jiaotong University on 09/19/12
For personal use only.

Table 2. Correlation of the site group to the factor group of ZnO.

Site group C_{3v}	Correlation	Factor group C_{3v}
A_1		A_1
		A_2
		B_1
E		B_2
		E_1
A_2		E_2

$\Gamma = A_1 + A_2 + B_1 + B_2 + E_1 + E_2$

Fig. 4. Room-temperature Raman spectrum of ZnO samples: (a) hexahedron, (b) coneflowerlike, (c) cauliflowerlike, and (d) nanorods.

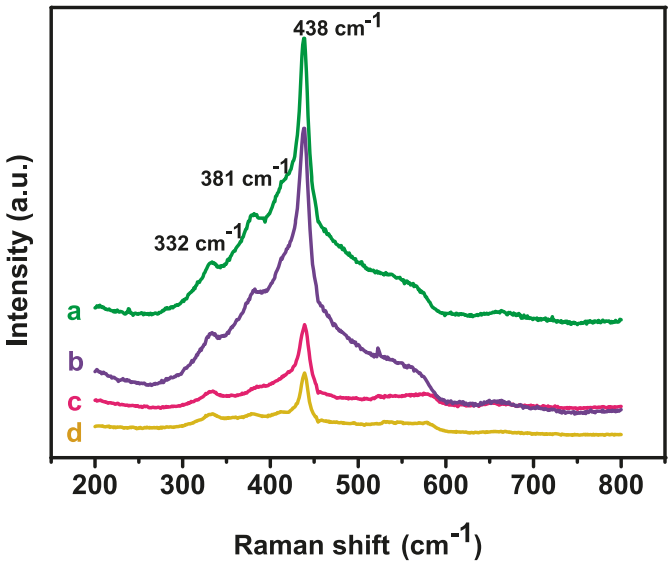

formation of oxygen vacancies, zinc interstitials, and a free carrier in ZnO[40], and indicates that a few defects exist in the sample, which is in agreement with the XPS results. The bands at 332 cm^{-1} are assigned to A1 s-order overtones.

XPS characterizations

The surface components and chemical states of the as-prepared ZnO samples were investigated by XPS analysis, and the corresponding results are shown in Fig. 5. Figure 5a shows the scan survey spectra for the representative ZnO sample. All of the peaks on the curve can be ascribed to Zn, O, and C elements and no peaks of other elements were observed. The presence of C mainly comes from the hydrocarbon contaminants that commonly exist for XPS. Therefore, it can be concluded that the sample is composed of Zn and O only, which is in agreement with the XRD results. A strong peak at ~1022.6 eV can be attributed to Zn 2p3/2 (Fig. 5b), which is slightly larger than the value 1022.0 eV of Zn in the bulk ZnO. This indicates that Zn is in the 2+ valence state within an oxygen-deficient environment. The curve-fitting patterns of O1s are shown in Fig. 5c. The hollow circles denote the original data, and the solid lines represent the fitted

Fig. 5. (a) A representative X-ray photoelectron spectroscopy (XPS) survey spectrum of a ZnO sample. XPS full spectra of (b) Zn 2p3/2 and (c) O1s.

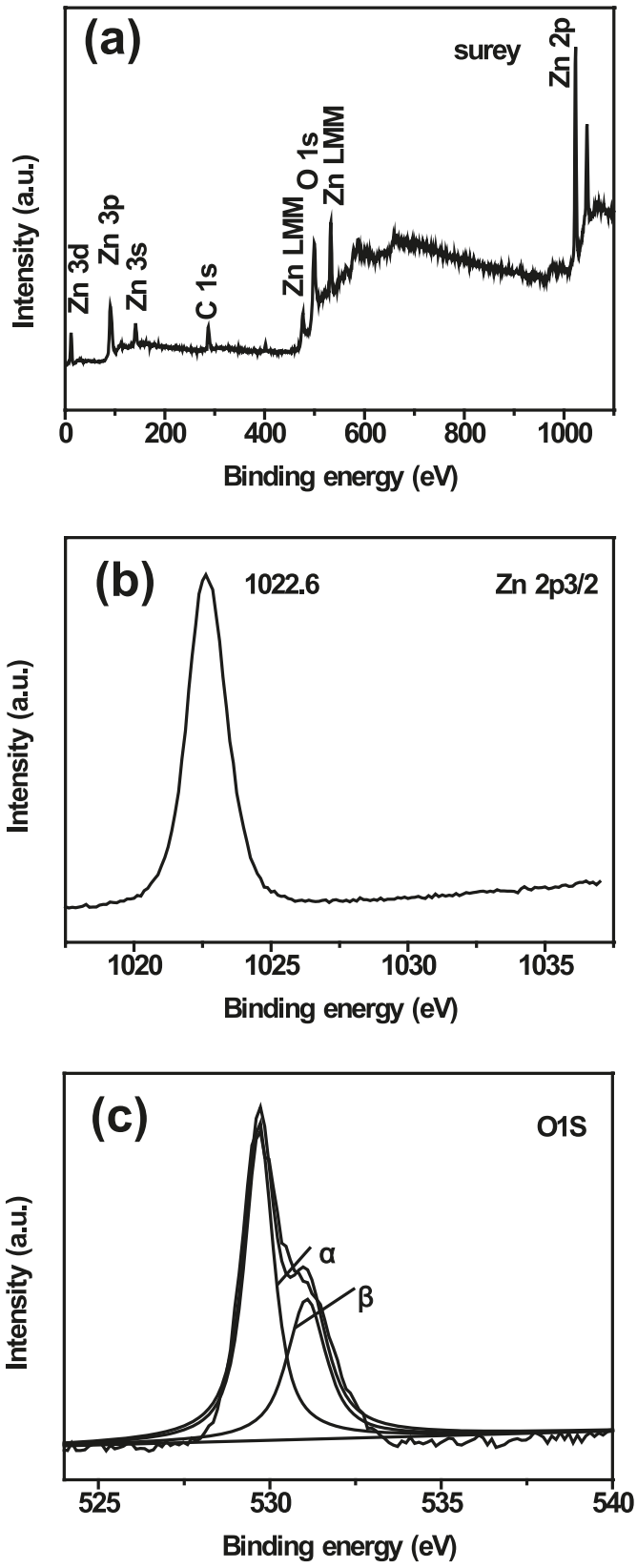

Can. J. Chem. Downloaded from www.nrcresearchpress.com by Xi'an Jiaotong University on 09/19/12
For personal use only.

curves and the deconvoluted individual peaks of the two different oxygen species present on the surface. The deconvoluted peak marked with "α" is closely associated with the lattice oxygen (O_L) of ZnO and its position is at ~529.7 eV, while the other peak marked with "β" is attributed to the oxygen of surface hydroxyl (OH) and its position is at ~531.1 eV.

OG photodegradation

ZnO has been used as a photocatalyst for the photodegradation of water pollutants, the photoreduction of halogenated benzene derivatives, the photoreduction of toxic metal ions, and photocatalytic water splitting. To understand the relationship between the structure and photocatalytic performance of ZnO samples, the photocatalytic activities of as-synthesized ZnO with different morphologies were studied using OG degradation as a model system. The UV–vis absorption spectra and degradation profile of all of the ZnO samples are shown in Fig. 6.

Figure 6a shows the UV–vis absorption spectra of OG in the presence of cauliflowerlike ZnO as the photocatalyst. It can be seen that the absorbance peaks at 331 and 477 nm were reduced significantly, indicating the degradation of the dye molecules. To demonstrate the morphology-induced enhancement of the photocatalytic performance of ZnO, a further experiment was performed using other samples as photocatalysts for the photodegradation of OG under the same conditions. The results of the OG degradation in a series of experimental conditions are summarized in Fig. 6b. The time-dependent photoactive performance of ZnO catalysts for phenol degradation was recorded. Degradation (y axis) is defined as $(C/C_0) \times 100\%$, and the x axis is reaction time (min), in which C_0 and C are the initial concentration after the equilibrium adsorption and the reaction concentration of OG, respectively. As can be clearly seen in Fig. 6b, the residual concentration of the OG aqueous solution at 100 min UV irradiation is as follows: ZnO coneflower (22.0%), cauliflower (5.2%), hexahedron (14.4%), and nanorods (12.5%). After 100 min of irradiation, the OG in aqueous solution was almost completely eliminated by the cauliflowerlike ZnO sample. These observations demonstrate that the photocatalytic activity depends on the morphology of the ZnO samples, which are decided on by their growth behaviors.

Reaction mechanism

Reaction mechanism of ZnO

In the ammonia system solution, the growth process of ZnO nanocrystals at room temperature is as follows:

$$[1] \quad NH_3{\cdot}H_2O \rightarrow NH_4^+ + OH^-$$

$$[2] \quad Zn^{2+} + NH_3{\cdot}H_2O \rightarrow [Zn(NH_3)_4]^{2+} + H_2O$$

$$[3] \quad [Zn(NH_3)_4]^{2+} \rightarrow [Zn(OH)_n]^{(n-2)-} \rightarrow ZnO$$

Thereinto, $n = 2$ or 4. At room temperature, in the saturated solution of $Zn^{2+}/NH_3{\cdot}H_2O$, Zn is mainly in the form of

Fig. 6. (a) The time-dependent UV–vis absorbance spectra of Orange G (OG) in the presence of ZnO with a cauliflowerlikepattern. (b) The reaction concentration of OG (C) / the initial concentration after the equilibrium adsorption (C_o) vs time curves of the photodegradation of OG in the presence of four kinds of samples.

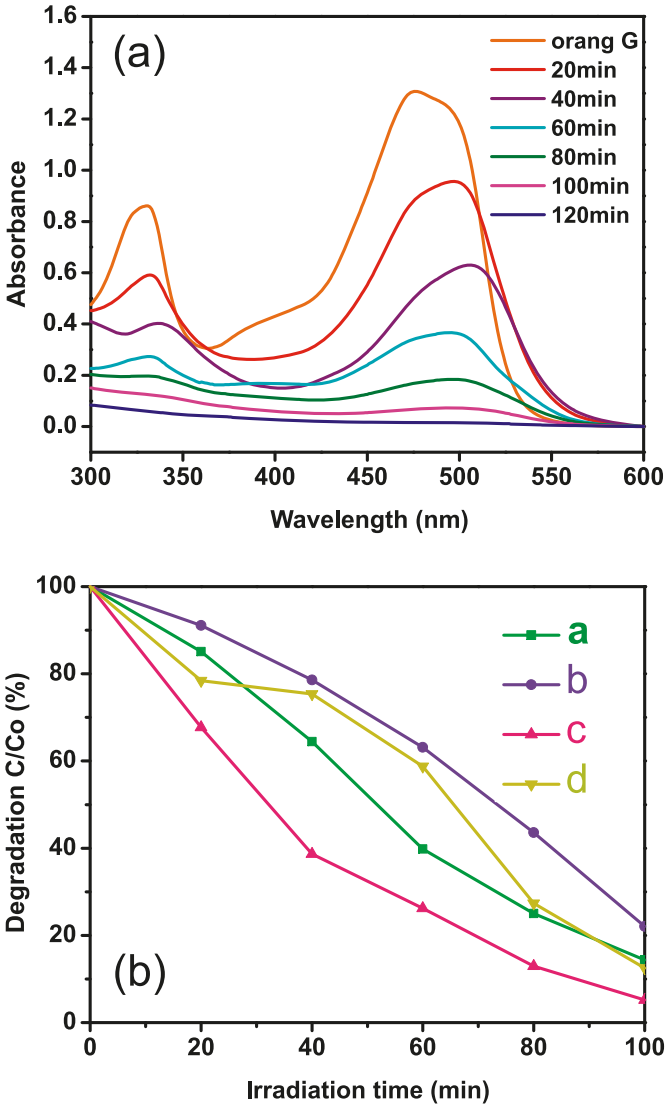

$[Zn(NH_3)_4]^{2+}$ and $[Zn(OH)_n]^{(n-2)-}$. When the temperature increases, $[Zn(NH_3)_4]^{2+}$ begins to decompose and forms saturated liquid, and the content of the hydroxy-aggregates $[Zn(OH)_n]^{(n-2)-}$ in zinc solution exceeds its saturation. Hence, $[Zn(OH)_n]^{(n-2)-}$ forms ZnO after dehydration. The whole process is shown in eqs. [1]–[3].[41]. The supersaturated degree of solution is expressed by the supersaturation, which refers to the ratio of quality and degree that is over the saturation of solution. As the layer of crystal seed and the product of growth are the same composition, and the lattice matches well, ZnO gives priority to heterogeneous nucleation between the substrate and the electrolyte interface, and prefers to epitaxialy grow along the c-axis polar surface, which has a relatively high surface energy. When the supersaturation of the solution is too large, $[Zn(OH)_n]^{(n-2)-}$ easily undergoes polymerization through dehydration, and homogeneous nucleation precipitation occurs as follows:

Can. J. Chem. Downloaded from www.nrcresearchpress.com by Xi'an Jiaotong University on 09/19/12
For personal use only.

[4] $$2[Zn(OH)_n]^{(n-2)^-} \rightarrow [Zn_2O(OH)_{2n-2}]^{(2n-4)^-} + H_2O$$

[5] $$[Zn_{x+1}O_x(OH)_{(x+1)n-2x}]^{(x+1)n-2(x+1)^-} + [Zn(OH)_n]^{(n-2)^-}] \rightarrow [Zn_{x+2}O_{x+1}(OH)_{(x+2)n-2(x+1)}]^{(x+2)n-2(x+2)^-} + H_2O$$

The subscript x represents the number of Zn^{2+} in the congeries. When the congeries are large enough, ZnO sediment begins to separate out.

Formation mechanisms of different morphologies

According to the FESEM observations, different amounts of ampicillin lead to different morphologies. First, the theory of Israelachvili[42] tells us that (*i*) surfactants will spontaneously form aggregates when their concentration is above a certain "critical" value and (*ii*) the aggregate morphology depends on the well-known packing parameter P

[6] $$P = v/I_c a_o$$

where v and I_c are the volume and chain length of the hydrophobic group, respectively, and a_o is the cross-sectional area of the headgroup dictated by the electrostatic repulsion between adjacent headgroups in the associates. Alternatively, reducing the electrostatic repulsion between adjacent headgroups can increase P. pH, temperature, and salinity[43] can all alter the electrostatic repulsion and thus the aggregation morphology. At the high pH value, only a few vesicles are formed. With the decrease of pH value, more and bigger vesicles are formed, and the vesicle diameter increases with the decrease of pH value at a fixed surfactant concentration. In our experiment, when the amount of ampicillin is the same, particles more easily aggregate with a decrease in pH value, and petals and cones can easily self-assemble to cauliflower and coneflower, respectively, whereas nanorods cannot further self-assemble into a hierarchical microstructure. Why cannot hexahedron further self-assemble into a hierarchical microstructure? The formation of a hexahedron rests with too much ampicillin (3 mL, pH 10.95), which is a morphology-directing agent. The steric hindrance effect with a larger volume should cause the rejection of the micelle and influence the micelle aggregates.[44] These phenomena indicate that different pH values and relative amount of morphology-directing agent will result in dissimilar morphologies of the product and the formation of diverse and novel assemblies of the ZnO nanostructures. More studies and work are underway to further understand the mechanisms for the assembly process induced by this new driving action.

Influence of the morphologies on the catalytic performance of the ZnO samples

In terms of the previously proposed mechanism for the photocatalytic degradation for organic dye,[45,46] which occurs by an indirect pathway involving hydroxyl radicals as the oxidizing intermediate as follows:

[7] $$ZnO + h\upsilon \rightarrow ZnO(e_{CB}^- + h_{VB}^+)$$

[8] $$H_2O + h_{VB}^+ \rightarrow H^+ + \cdot OH$$

Scheme 1. The charge separation process and the photocatalytic mechanism of ZnO samples under UV irradiation.

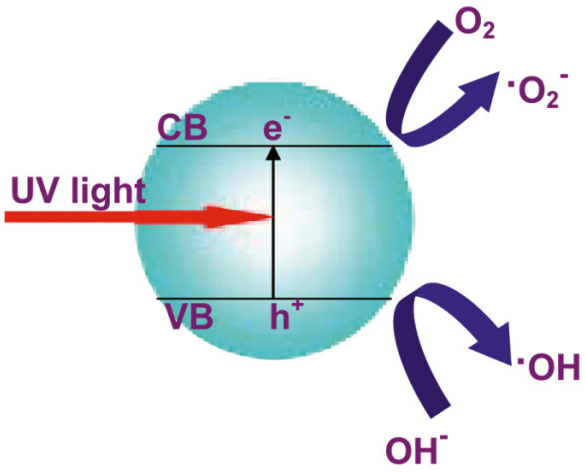

[9] $$\text{Dye} + \cdot OH \rightarrow \text{Oxidation products}$$

The conduction-band electrons (e_{CB}^-) and valence-band holes (h_{VB}^+) are generated on the surfaces of ZnO nanostructures when they are illuminated by UV light with an energy greater than the band-gap energy. Holes can react with water adhering to the surfaces of ZnO nanostructures to form highly reactive hydroxyl radicals (·OH), which have a powerful oxidation ability to degrade organic dye. The charge separation process and the photocatalytic mechanism of ZnO samples under UV irradiation are shown in Scheme 1.

Usually, a high specific surface area has a beneficial effect on the activity for catalysts. Thus, the morphologies of ZnO catalysts play an important role in the photocatalytic activity.[47,48] According to the above photocatalytic results, cauliflower > hexahedron > nanorod > coneflower ZnO, which may be attributed to their special structural features. The size of the surface areas of ZnO samples is cauliflower > hexahedron > nanorod, which can be roughly judged from the FESEM images. Cauliflower is assembled by many densely arranged nanosheets, hexahedron is suppressed 1-D growth, and nanorod is 1-D growth. The surface photochemical reaction of OG degradation occurs in the sequence of dispersion, diffusion, adsorption, surface reaction, and final desorption, and each of these elementary processes affects the surface reaction rate. The large surface area and capacious interspaces in the cauliflowerlike ZnO nanostructures offer more opportunity for the diffusion and mass transportation of OG molecules and hydroxyl radicals in the photochemical reaction of OG degradation. However, the photocatalytic activity of the coneflower is inferior, probably because the photocatalytic activity of ZnO is also strongly dependent on the surface orientation of the nanocrystals, which could result in orientation-dependent charge-transfer processes, and the type and concentration of oxygen vacancies on the surface, which needs to be verified by further work.

Conclusion

In this work, biomolecule ampicillin was used as a morphology-directing agent for the first time to construct ZnO without any metal catalysts under ambient conditions. This demonstrates that the bioinspired green method is an

efficient approach for the preparation of ZnO with different morphologies. ZnO samples with different morphologies exhibited different activities to OG degradation probably because of the morphology and growth habit. The underlying formation mechanism and catalytic mechanism were discussed. The as-synthesized ZnO samples are also expected to be useful for other applications such as gas sensing. Moreover, this work further hints that this green and economical approach can be extended to synthesize other metal oxide materials with a novel morphology.

Acknowledgement

The authors are grateful to the National Natural Science Foundation of China (No. 21071047), the Henan Provincial Natural Science Foundation of China (092300410196), and the Natural Science Foundation of Educational Department of Henan Province (2008A150014).

References

(1) Hwang, D.-K.; Kang, S.-H.; Lim, J.-H.; Yang, E.-J.; Oh, J. Y.; Yang, J.-H.; Park, S.-J. *Appl. Phys. Lett.* **2005** *86*, 222101. doi:10.1063/1.1940736.
(2) Hoffman, R.; Norris, B.; Wager, J. F. *Appl. Phys. Lett.* **2003** *82* (5), 733. doi:10.1063/1.1542677.
(3) Li, Y.; Cai, W.; Duan, G.; Cao, B.; Sun, F.; Lu, F. *J. Colloid Interface Sci.* **2005** *287* (2), 634. doi:10.1016/j.jcis.2005.02.010.
(4) Jones, A.; Jones, T. A.; Mann, B.; Firth, J. *Sens. Actuators B Chem.* **1984** *5* (1), 75. doi:10.1016/0250-6874(84)87008-0.
(5) Choi, J.; Choi, G. *Sens. Actuators B Chem.* **2000** *69* (1-2), 120. doi:10.1016/S0925-4005(00)00519-0.
(6) Kassis, A.; Saad, M. *Sol. Energy Mater. Sol. Cells* **2003** *80* (4), 491. doi:10.1016/j.solmat.2003.07.003.
(7) Huang, M. H.; Mao, S.; Feick, H.; Yan, H.; Wu, Y. Y.; Kind, H.; Weber, E.; Russo, R.; Yang, P. D. *Science* **2001** *292* (5523), 1897. doi:10.1126/science.1060367.
(8) Pan, Z. W.; Dai, Z.; Wang, Z. L. *Science* **2001** *291* (5510), 1947. doi:10.1126/science.1058120.
(9) Dai, Y.; Zhang, Y.; Li, Q. K.; Nan, C. W. *Chem. Phys. Lett.* **2002** *358* (1–2), 83. doi:10.1016/S0009-2614(02)00582-1.
(10) Tian, Z. R.; Voigt, J.; Liu, J.; McKenzie, B.; McDermott, M. J.; Rodriguez, M. A.; Konishi, H.; Xu, H. F. *Nat. Mater.* **2003** *2* (12), 821. doi:10.1038/nmat1014.
(11) Peng, W.; Qu, S.; Cong, G.; Wang, Z. *Cryst. Growth Des.* **2006** *6* (6), 1518. doi:10.1021/cg0505261.
(12) Cho, S.; Jung, S. H.; Jang, J. W.; Oh, E.; Lee, K. H. *Cryst. Growth Des.* **2008** *8* (12), 4553. doi:10.1021/cg800593q.
(13) Cheng, C.; Xin, R.; Leng, Y.; Yu, D.; Wang, N. *Inorg. Chem.* **2008** *47* (17), 7868. doi:10.1021/ic8005234.
(14) Murray, C. B.; Norris, D. J.; Bawendi, M. G. *J. Am. Chem. Soc.* **1993** *115* (19), 8706. doi:10.1021/ja00072a025.
(15) Du, G. H.; Chen, Q.; Che, R. C.; Yuan, Z. Y.; Peng, L. M. *Appl. Phys. Lett.* **2001** *79* (22), 3702. doi:10.1063/1.1423403.
(16) Yan, T.; Liu, X. L.; Wang, N. R.; Chen, J. F. *J. Cryst. Growth* **2005** *281* (2–4), 669. doi:10.1016/j.jcrysgro.2005.04.078.
(17) Wang, Y. G.; Yuen, C.; Lau, S. P.; Yu, S. F.; Tay, B. K. *Chem. Phys. Lett.* **2003** *377* (3–4), 329. doi:10.1016/S0009-2614(03)01191-6.
(18) Li, S. Y.; Lin, P.; Lee, C. Y.; Tseng, T. Y. *J. Appl. Phys.* **2004** *95* (7), 3711. doi:10.1063/1.1655685.
(19) Han, X.; Wang, G.; Wang, Q.; Cao, L.; Liu, R.; Zou, B.; Hou, J. G. *Appl. Phys. Lett.* **2005** *86*, 223106. doi:10.1063/1.1941477.
(20) Kolen'ko, Yu. V.; Cheragulov, B. R.; Kunst, M. *Appl. Catal. B* **2004** *54*, 51. doi:10.1016/j.apcatb.2004.06.006.
(21) Chhor, K.; Bocquet, J. F.; Colbeau-justin, C. *Mater. Chem. Phys.* **2004** *86* (1), 123. doi:10.1016/j.matchemphys.2004.02.023.
(22) Du, Y. K.; Rabani, J. *J. Phys. Chem. B* **2003** *107* (43), 11970. doi:10.1021/jp035491z.
(23) Madhugiri, S.; Sun, B.; Smirniotis, P. G.; Ferraris, J. P.; Balkus, K. J., Jr. *Microporous Mesoporous Mater.* **2004** *69* (1–2), 77. doi:10.1016/j.micromeso.2003.12.023.
(24) Wang, D.; Song, C. *J. Phys. Chem. B* **2005** *109* (26), 12697. doi:10.1021/jp0506134.
(25) Huang, H.; Yang, S.; Gong, J.; Liu, H.; Duan, J.; Zhao, X.; Zhang, R.; Liu, Y.; Liu, Y. *J. Phys. Chem. B* **2005** *109* (44), 20746. doi:10.1021/jp054239j.
(26) Zhang, J.; Sun, L.; Yin, J.; Su, H.; Liao, C.; Yan, C. *Chem. Mater.* **2002** *14* (10), 4172. doi:10.1021/cm020077h.
(27) Djurišić, A. B.; Leung, Y. H. *Small* **2006** *2* (8–9), 944. doi:10.1002/smll.200600134.
(28) Yan, X.; Li, Z.; Zou, C.; Li, S.; Yang, J.; Chen, R.; Han, J.; Gao, W. *J. Phys. Chem. C* **2010** *114* (3), 1436. doi:10.1021/jp908101z.
(29) Han, X. G.; He, H. Z.; Kuang, Q.; Zhou, X.; Zhang, X. H.; Xu, T.; Xie, Z. X.; Zheng, L. S. *J. Phys. Chem. C* **2009** *113* (2), 584. doi:10.1021/jp808233e.
(30) Na, J. S.; Gong, B.; Scarel, G.; Parsons, G. N. *ACS Nano* **2009** *3* (10), 3191. doi:10.1021/nn900702e.
(31) Pauporté, T.; Bataille, G.; Joulaud, L.; Vermersch, F. J. *J. Phys. Chem. C* **2010** *114* (1), 194. doi:10.1021/jp9087145.
(32) Peng, X.; Manna, L.; Yang, W.; Wickham, J.; Scher, E.; Kadavanich, A.; Alivisatos, A. P. *Nature* **2000** *404* (6773), 59. doi:10.1038/35003535.
(33) Li, B. X.; Jing, M.; Rong, G. X.; Xu, Y.; Xie, Y. *Eur. J. Inorg. Chem.* **2006** No. 21, 4349. doi:10.1002/ejic.200600412.
(34) Zhang, D. F.; Sun, L. D.; Zhang, J.; Yan, Z. G.; Yan, C. H. *Cryst. Growth Des.* **2008** *8* (10), 3609. doi:10.1021/cg800143x.
(35) Jung, S.-H.; Oh, E.; Lee, K.-H.; Yang, Y.; Park, C. G.; Park, W.; Jeong, S.-H. *Cryst. Growth Des.* **2008** *8* (1), 265. doi:10.1021/cg070296l.
(36) Wang, R.-P.; Zhou, G.-W.; Liu, Y.-L.; Pan, S.-H.; Zhang, H.-Z.; Yu, D.-P.; Zhang, Z. *Phys. Rev. B* **2000** *61* (24), 16827. doi:10.1103/PhysRevB.61.16827.
(37) Damen, T. C.; Porto, S. P.; Tell, B. *Phys. Rev.* **1966** *142* (2), 570. doi:10.1103/PhysRev.142.570.
(38) Xu, C. K.; Xu, G. D.; Liu, Y. K.; Wang, G. H. *Solid State Commun.* **2002** *122* (3–4), 175. doi:10.1016/S0038-1098(02)00114-X.
(39) Li, Z.; Xiong, Y.; Xie, Y. *Inorg. Chem.* **2003** *42* (24), 8105. doi:10.1021/ic034029q.
(40) Callender, R. H.; Sussman, S. S.; Selders, M.; Chang, R. K. *Phys. Rev. B* **1973** *7* (8), 3788. doi:10.1103/PhysRevB.7.3788.
(41) Peterson, R. B.; Fields, C. L.; Gregg, B. A. *Langmuir* **2004** *20* (12), 5114. doi:10.1021/la049683c.
(42) Israelachvili, J. N. *Intermolecular and Surface Forces;* 2nd ed.; Academic Press: New York, 1992.
(43) Zhai, L. M.; Zhao, M.; Sun, D. J.; Hao, J. C.; Zhang, L. J. *J. Phys. Chem. B* **2005** *109* (12), 5627. doi:10.1021/jp044596e.
(44) Liu, Y.; Chu, Y.; Zhuo, Y. J.; Li, M. Y.; Li, L. L.; Dong, L. H. *Cryst. Growth Des.* **2007** *7* (3), 467. doi:10.1021/cg060480r.
(45) Hoffmann, M. R.; Martin, S. T.; Choi, D. W.; Bahnemann, D. W. *Chem. Res.* **1995** *95* (1), 69. doi:10.1021/cr00033a004.
(46) Yatmaz, H. C.; Akyol, A.; Bayramoglu, M. *Ind. Eng. Chem. Res.* **2004** *43* (19), 6035. doi:10.1021/ie049921z.

Can. J. Chem. Downloaded from www.nrcresearchpress.com by Xi'an Jiaotong University on 09/19/12
For personal use only.

(47) Li, G. R.; Hu, T.; Pan, G. L.; Yan, T. Y.; Gao, X. P.; Zhu, H. Y. *J. Phys. Chem. C* **2008** *112* (31), 11859. doi:10.1021/jp8038626.

(48) Lu, F.; Cai, W.; Zhang, Y. *Adv. Funct. Mater.* **2008** *18* (7), 1047. doi:10.1002/adfm.200700973.

Can. J. Chem. Downloaded from www.nrcresearchpress.com by Xi'an Jiaotong University on 09/19/12
For personal use only.

Modeling of ^{13}C NMR chemical shifts of benzene derivatives using the RC–PC–ANN method: A comparative study of original molecular descriptors and multivariate image analysis descriptors

Zahra Garkani-Nejad and Marziyeh Poshteh-Shirani

Can. J. Chem. Downloaded from www.nrcresearchpress.com by Xi'an Jiaotong University on 09/19/12
For personal use only.

Abstract: The primary goal of a quantitative structure–property relationship study is to identify a set of structurally based numerical descriptors that can be mathematically linked to a property of interest. In this work, two main groups of descriptors have been used to predict ^{13}C NMR chemical shifts of ipso, ortho, meta, and para positions in a series of 113 monosubstituted benzenes. First, two groups of descriptors — original molecular descriptors (constitutional, topological, electronic, and geometrical) and multivariate image analysis (MIA) descriptors — were calculated. Then, calculated descriptors were subjected to principal component analysis and the most significant principal components were extracted. Finally, more correlated principal components were used as inputs of artificial neural networks. The results obtained using the rank correlation–principal component–artificial neural network (RC–PC–ANN) modeling method show high ability to predict ^{13}C NMR chemical shifts. Also, comparison of the results indicates that MIA descriptors show better ability to predict ^{13}C NMR chemical shifts than the original molecular descriptors.

Key words: multivariate image analysis (MIA), quantitative structure–property relationship (QSPR), principal component–artificial neural network (PC–ANN), ^{13}C NMR chemical shift, monosubstituted benzenes.

Résumé : Le but principal d'une étude de relation quantitative structure-propriété est d'identifier un ensemble des descripteurs numériques à base de structure que peuvent être liés d'une façon mathématique à une propriété intéressante. Dans ce travail, deux groupes principaux de descripteurs pour prédire les déplacements chimiques, en RMN du ^{13}C, des positions ipso, ortho, méta et para dans une série de 113 dérivés monosubstitués du benzène. Dans un premier temps, on a calculé deux groupes de descripteurs, incluant des descripteurs moléculaires originaux (constitutionnels, topologiques, électroniques et géométriques) et on a procédé à une analyse d'image multivariable (AIM). Dans un deuxième temps, on a soumis les descripteurs calculés à une analyse du composant principal et on en a extrait les composants principaux les plus significatifs. Enfin, on a utilisé d'autres composants principaux apparentés comme données pour des réseaux neuraux artificiels. Les résultats obtenus à l'aide de la méthode modelage par corrélation des rangs de Spearman avec un composant principal appliqué à un réseau neural artificiel (« CR-CP-RNA ») montrent une grande habilité à prédire les déplacements chimiques en RMN du ^{13}C. De plus une comparaison des résultats indique que les descripteurs d'AIM possèdent une plus grande habilité à prédire les déplacements chimiques en RMN du ^{13}C que les descripteurs moléculaires originaux.

Mots-clés : analyse d'image multivariable (AIM), relation quantitative structure-propriété (RQSP), composant principal appliqué à un réseau neural artificiel (« CP-RNA »), déplacement chimique en RMN du ^{13}C, benzènes monosubstitués.

[Traduit par la Rédaction]

Introduction

At the present time the methods of studying quantitative structure–property relationships are increasingly developed in various areas of chemistry, biology, and pharmacy. Quantitative structure–activity/structure–property relationship (QSAR/QSPR) studies, one of the most important areas in chemometrics, give information that is useful for molecular design and medicinal chemistry.[1–4] QSAR/QSPR models are mathematical equations relating chemical structure to a wide variety of physical, chemical, biological, and technological properties. In general, development of a QSPR model involves three steps: structural encoding, feature selection, and model building. Structural encoding involves the use of numerical descriptors to encode the structural features of a compound. Feature selection is then employed to determine which subset of the descriptors indicates the best relation with the property of interest. Models built from the best subset

Received 20 November 2010. Accepted 12 February 2011. Published at www.nrcresearchpress.com/cjc on 3 May 2011.

Z. Garkani-Nejad and M. Poshteh-Shirani. Chemistry Department, Faculty of Science, Vali-e-Asr University, Rafsanjan, Iran.

Corresponding author: Z. Garkani-Nejad (e-mail: garakani@vru.ac.ir).

Can. J. Chem. Downloaded from www.nrcresearchpress.com by Xi'an Jiaotong University on 09/19/12
For personal use only.

Table 1. Structure of monosubstituted benzenes and experimental ^{13}C NMR chemical shifts (ppm) for four positions.

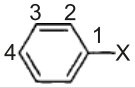

No.	Substituent X	C-1	C-2	C-3	C-4
1	–H	128.5	128.5	128.5	128.5
2	$–CH_3$	137.7	129.5	128.4	125.5
3	$–CH_2CH_3$	140.2	127.9	128.4	125.7
4	$–CH_2CH_2CH_3$	138.8	128.3	128.6	125.8
5	$–CH(CH_3)_2$	148.7	126.3	128.2	125.7
6	$–CH_2CH_2CH_2CH_3$	139.4	128.3	128.3	125.7
7	$–C(CH_3)_3$	147.1	125.2	128.1	125.4
8	–cyclopropyl	143.6	125.2	127.9	124.9
9	–cyclopentyl	146.3	127	128.1	125.6
10	–cyclohexyl	144.8	126.7	128.2	125.7
11	–1-adamantyl	150.7	125.6	128.0	125.4
12	$–CH_2F$	137.0	127.8	128.9	129.0
13	$–CF_3$	131.0	125.3	128.8	131.8
14	$–CH_2Cl$	137.8	128.8	128.7	128.5
15	$–CHCl_2$	140.4	126.1	128.6	129.7
16	$–CCl_3$	144.8	126.8	128.4	130.3
17	$–CH_2Br$	138.0	129.2	128.8	128.7
18	$–CH_2I$	139.0	128.5	128.5	128.5
19	$–CH_2OH$	140.9	127.3	128.7	127.4
20	$–CH_2OCH_3$	137.2	127.6	128.4	127.6
21	$–CH_2NH_2$	143.4	127.1	128.3	126.5
22	$–CH_2NHCH_3$	141.1	128.2	128.2	126.7
23	$–CH_2N(CH_3)_2$	136.3	129.0	128.2	127.0
24	$–CH_2NO_2$	130.7	130.7	130.7	129.7
25	$–CH_2CN$	130.1	129.0	127.7	127.8
26	$–CH_2SH$	141.0	127.9	128.5	126.9
27	$–CH_2SCH_3$	138.3	128.9	128.4	126.9
28	$–CH_2S(O)CH_3$	129.3	130	128.9	128.3
29	$–CH_2SO_2CH_3$	128.4	130.6	129.1	129.1
30	$–CH_2CHO$	135.9	129.8	129.0	127.4
31	$–CH_2COCH_3$	134.3	129.3	128.6	126.9
32	$–CH_2COOH$	135.0	129.9	128.9	127.3
33	$–CH=CH_2$	137.4	126.2	128.4	127.7
34	$–C(CH_3)=CH_2$	141.1	125.4	128.1	127.3
35	–C≡CH	122.3	132.1	128.1	128.2
36	–phenyl	136.6	127.4	129.0	127.4
37	–2-pyridyl	139.7	127.1	129.0	127.1
38	–4-pyridyl	138.1	126.9	129.0	129
39	–F	162.1	115.5	130.1	124.1
40	–Cl	133.8	128.9	129.9	126.6
41	–Br	123.1	131.8	130.7	127.5
42	–I	97.3	137.4	130.1	127.4
43	–OH	157.3	115.7	129.9	121.1
44	$–OCH_3$	162.0	114.1	129.5	125.3
45	$–OCH=CH_2$	156.7	117	129.2	122.7
46	–O-phenyl	156.1	117.3	128.2	121.6
47	$–OCOCH_3$	150.9	121.4	128.9	125.3
48	$–OSi(CH_3)_3$	155.3	120.1	129.4	121.4
49	$–OPO(O\text{-phenyl})_2$	150.4	120.1	129.7	125.5
50	–OCN	153.5	115.8	131.1	127.5
51	$–NH_2$	146.7	115.1	129.3	118.5
52	$–NHCH_3$	143.5	112.3	129.3	116.9
53	$–N(CH_3)_2$	144.5	113.1	129.4	118.0
54	–NH-phenyl	143.2	117.9	129.4	118.0
55	$–N(phenyl)_2$	141.6	121.5	129.4	122.9
56	$–NH_3^+$	128.6	122.7	130.7	130.7
57	$–NH_2^+CH(CH_3)_2$	134.0	124.4	129.6	129.2

Table 1 (*concluded*).

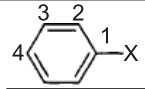

No.	Substituent X	C-1	C-2	C-3	C-4
58	$–N^+(CH_3)_3$	148.0	121.2	131.0	130.9
59	$–N(O)(CH_3)_2$	154.7	120.1	129.3	129.1
60	$–NHCOCH_3$	138.2	120.4	128.7	124.1
61	–NHOH	150.0	115.4	126.3	123.2
62	$–NHNH_2$	151.3	112.0	129.0	118.9
63	$–N(NO)CH_3$	142.2	119.1	129.4	127.2
64	–N=CH-phenyl	153.2	122.0	129.8	127.0
65	$–N=NCH_3$	150.7	122.3	129.0	127.0
66	–NO	165.9	120.9	129.3	135.6
67	$–NO_2$	148.9	123.6	129.4	134.6
68	–CN	112.5	132.0	129.2	132.8
69	–NCO	133.6	124.8	129.6	125.7
70	–NCS	131.5	125.8	129.8	127.5
71	$–N^+≡N$	115.8	134.5	134.2	144.5
72	–SH	132.5	129.2	128.8	125.3
73	$–SCH_3$	138.5	126.6	128.7	124.9
74	$–SC(CH_3)_3$	133.0	137.5	128.2	128.5
75	$–S(CH_3)_2^+$	127.5	131.6	130.7	134.8
76	$–SCH=CH_2$	134.3	130.5	128.7	126.7
77	–S-phenyl	135.8	131.0	129.1	127.0
78	–S-S-phenyl	136.0	127.2	129.3	127.4
79	$–S(O)CH_3$	146.1	123.5	129.6	130.9
80	$–SO_2CH_3$	140.8	127.1	129.3	133.6
81	$–SO_2OH$	143.5	126.3	129.8	132.3
82	$–SO_2OCH_3$	134.9	127.9	130.0	134.4
83	$–SO_2F$	133.1	128.5	130.0	136.0
84	$–SO_2Cl$	144.1	126.8	129.7	135.3
85	$–SO_2NH_2$	139.3	125.5	128.8	131.7
86	–SCN	124.8	131.0	130.7	130.7
87	–CHO	136.7	129.7	129.0	134.3
88	$–COCH_3$	137.4	128.6	128.4	132.9
89	$–COCF_3$	122.9	130.3	129.2	135.2
90	–COC≡CH	135.9	129.5	128.5	134.4
91	–CO-phenyl	137.8	130.1	128.2	132.2
92	–COOH	130.6	130.1	128.4	133.7
93	$–COOCH_3$	130.5	129.7	128.4	132.8
94	$–CONH_2$	133.5	127.3	128.6	131.9
95	$–CON(CH_3)_2$	134.5	127	128.3	129.5
96	–COF	132.7	130.1	127.8	133.8
97	–COCl	133.2	131.2	128.8	135.1
98	–COSH	134.7	127.9	128.7	133.9
99	$–CH=NCH_3$	137.3	129.0	128.6	130.8
100	$–CSH_2\text{-phenyl}$	147.2	129.5	127.9	130.9
101	$–CSH_2\text{-(1-piperidyl)}$	143.5	125.4	128.3	128.3
102	$–SiH_3$	128.0	135.8	128.1	129.8
103	$–SiH_2CH_3$	133.3	134.8	128.0	129.5
104	$–Si(CH_3)_3$	140.1	133.4	127.8	128.9
105	$–Si(phenyl)_3$	134.3	136.4	127.9	129.6
106	$–SiCl_3$	131.5	133.1	128.6	132.7
107	$–P(CH_3)_2$	142.1	130.1	127.9	127.5
108	$–P(phenyl)_2$	137.4	133.7	128.5	128.6
109	$–PO(CH_3)_2$	131.0	129.6	128.6	131.5
110	$–PO(OH)_2$	126.6	132.1	130.0	134.1
111	$–PO(OCH_2CH_3)_2$	130.1	132.1	128.3	131.9
112	$–PS(CH_3)_2$	135.2	130.5	128.7	131.4
113	$–PS(OCH_2CH_3)_2$	134.6	131.3	128.1	131.9

Fig. 1. 2D images and the unfolding step of the 113 chemical structures to give the X-matrix. The arrow in the structure indicates the coordinates of a pixel in common among the whole series of compounds, used in the 2D alignment step.

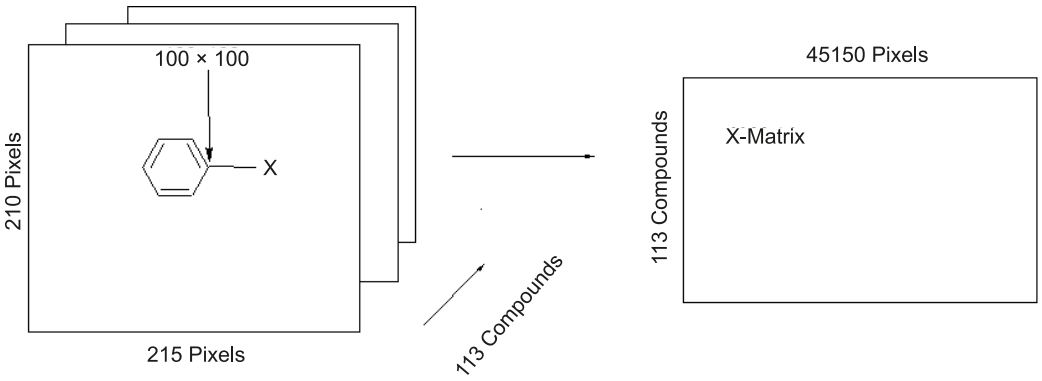

Table 2. CR–PCR models for C1–C4 positions of monosubstituted benzenes using PCs extracted from original molecular descriptors.

Position	Model
Ipso	$138.627(\pm0.694) + 0.460(\pm0.131)C_2 + 0.625(\pm0.203)C_3 - 1.463(\pm0.278)C_7 - 1.509\ (\pm0.378)C_9 + 1.179(\pm0.462)C_{12} - 2.868(\pm0.947)C_{27} - 3.884(\pm1.216)C_{32} + 3.295\ (\pm1.299)C_{34} + 21.199(\pm7.830)C_{76}$
Ortho	$126.691(\pm0.367) - 0.289(\pm0.070)C_2 - 0.623(\pm0.108)C_3 + 0.657(\pm0.147)C_7 + 1.221(\pm0.200)C_9$
Meta	$128.950(\pm0.064) + 0.147(\pm0.022)C_5 + 0.117(\pm0.025)C_6 + 0.141(\pm0.026)C_7 + 0.116(\pm0.035)C_9$
Para	$128.458(\pm0.275) - 0.531(\pm0.052)C_2 + 0.591(\pm0.110)C_7$

Table 3. CR–PCR models for C1–C4 positions of monosubstituted benzenes using PCs extracted from MIA descriptors.

Position	Model
Ipso	$138.627(\pm0.718) + 0.298(\pm0.111)C_3 - 0.682(\pm0.277)C_{27} - 0.731(\pm0.322)C_{36} + 0.893(\pm0.395)C_{52} + 0.988(\pm0.397)C_{53} - 1.344(\pm0.459)C_{64} + 1.281(\pm0.537)C_{76} - 1.369(\pm0.547)C_{78} - 1.258(\pm0.570)C_{81} + 1.297(\pm0.587)C_{82} + 1.504(\pm0.627)C_{87} + 1.524(\pm0.672)C_{91} - 1.912(\pm0.733)C_{95} - 2.566(\pm0.748)C_{96} - 2.644(\pm0.966)C_{108}$
Ortho	$126.691(\pm0.386) - 0.170(\pm0.60)C_3 + 0.212(\pm0.096)C_{10} + 0.305(\pm0.135)C_{21} - 0.384(\pm0.144)C_{25} + 0.318(\pm149)C_{27} - 0.380(\pm0.152)C_{29} + 0.573(\pm0.171)C_{35} + 0.569(\pm0.173)C_{36} + 0.578(\pm0.268)C_{71} - 0.745(\pm0.293)C_{77} + 0.772(\pm0.294)C_{78} + 0.773(\pm0.306)C_{81} - 0.773(\pm0.315)C_{82} + 1.005(\pm0.394)C_{95} + 1.021(\pm0.518)C_{108}$
Meta	$128.950(\pm0.069) + 0.034(\pm0.013)C_5 - 0.051(\pm0.017)C_{10} - 0.049(\pm0.020)C_{14} - 0.044(\pm0.022)C_{18} + 0.059(\pm0.023)C_{20} - 0.065(\pm0.026)C_{26} + 0.067(\pm0.026)C_{27} - 0.099(\pm0.029)C_{33} + 0.074(\pm0.032)C_{39} + 0.069(\pm0.034)C_{44} + 0.068(\pm0.035)C_{46} + 0.103(\pm0.042)C_{61} + 0.098(\pm0.043)C_{63} + 0.119(\pm0.053)C_{79} - 0.117(\pm0.054)C_{80}$
Para	$128.958(\pm0.307) - 0.068(\pm0.027)C_1 - 0.157(\pm0.068)C_7 - 0.243(\pm0.074)C_9 - 0.285(\pm0.094)C_{17} - 0.268(\pm0.099)C_{16} + 0.233(\pm0.103)C_{20} + 0.317(\pm0.118)C_{27} + 0.442(\pm0.136)C_{35} + 0.386\ (\pm0.143)C_{39} - 0.356(\pm0.149)C_{40} + 0.422(\pm0.193)C_{61} + 0.456(\pm0.230)C_{75} - 0.479(\pm0.236)C_{76} - 0.500(\pm0.244)C_{79} - 0.686(\pm0.313)C_{94}$

of descriptors form a direct link between descriptors and the property of interest. Finally, validation determines the level of the model's predictive capabilities for unknown compounds.

The most frequently applied computational methods for QSPR are based on 3D or multidimensional approaches,[5–11] which provide information about the relation between physicochemical parameters and the property of interest. A 2D image-based methodology has recently been developed (MIA-QSPR, multivariate image analysis applied to QSPR),[12,13] which avoids conformational screening and 3D alignment steps. MIA-QSPR has also been shown to be nicely predictive with some operational advantages.

Geladi and Esbensen[14] have demonstrated that image analysis may provide useful information in chemistry, though the descriptors do not have a direct physicochemical meaning, since they are binaries. In MIA-QSPR studies, images (2D chemical structures) have been shown to contain chemical information,[12,13] allowing the correlation of chemical structures and properties.

Goodarzi et al. have reported a QSPR study of the ^{13}C NMR chemical shifts of methoxy flavonol derivatives using the MIA-QSPR method.[15] They revealed that the predictive ability of MIA descriptors is comparable or even superior to that of the well-known gauge-included atomic orbital procedure for ^{13}C NMR chemical shift calculation. Garkani-Nejad and Poshteh-Shirani have used the MIA-QSPR method to predict ^{13}C NMR chemical shifts of naphthalene derivatives.[16] The obtained results indicated high predictive ability of MIA descriptors in predicting ^{13}C NMR chemical shifts of naphthalene derivatives.

The main aim of the present work was to reveal the capabilities of the rank correlation–principal component–artificial neural network (RC–PC–ANN) modeling method in predicting ^{13}C NMR chemical shifts of a series of 113 monosubstituted benzenes using two kinds of descriptors: original

Can. J. Chem. Downloaded from www.nrcresearchpress.com by Xi'an Jiaotong University on 09/19/12
For personal use only.

Can. J. Chem. Downloaded from www.nrcresearchpress.com by Xi'an Jiaotong University on 09/19/12
For personal use only.

Table 4. Calculated values of ^{13}C NMR chemical shifts (ppm) using the RC–PC–ANN method based on original molecular descriptors for all carbon positions: training, validation, and test sets.

No.	Substituent X	C-1	C-2	C-3	C-4
Training					
1	–H	130.77	128.54	128.50	128.61
2	$–CH_3$	144.90	129.50	128.44	122.31
3	$–CH_2CH_3$	134.64	128.76	128.30	124.56
4	$–CH_2CH_2CH_3$	140.20	129.52	128.28	125.16
6	$–CH_2CH_2CH_2CH_3$	139.85	129.58	128.28	126.44
7	$–C(CH_3)_3$	142.36	125.32	128.37	125.16
8	–cyclopropyl	143.79	125.31	128.43	123.18
10	–cyclohexyl	144.79	126.70	128.37	127.42
11	–1-adamantyl	145.38	125.60	128.55	122.90
12	$–CH_2F$	142.51	128.35	128.52	127.33
13	$–CF_3$	139.14	125.28	128.87	132.63
15	$–CHCl_2$	141.35	125.49	128.99	132.23
16	$–CCl_3$	146.07	126.74	128.40	132.60
17	$–CH_2Br$	138.43	128.73	128.74	129.06
18	$–CH_2I$	137.53	129.28	129.05	129.12
19	$–CH_2OH$	140.93	128.23	128.43	127.43
21	$–CH_2NH_2$	136.76	127.10	128.50	126.96
25	$–CH_2CN$	141.68	129.27	128.61	126.80
26	$–CH_2SH$	137.10	128.29	128.46	127.52
27	$–CH_2SCH_3$	138.78	129.30	128.38	126.98
28	$–CH_2S(O)CH_3$	134.01	129.36	128.70	128.21
31	$–CH_2COCH_3$	143.34	129.55	128.36	128.58
32	$–CH_2COOH$	135.63	129.51	128.50	131.38
35	–C≡CH	122.04	129.35	128.45	126.39
39	–F	142.86	115.50	130.10	122.29
40	–Cl	134.78	128.09	129.65	126.82
41	–Br	123.11	128.39	130.47	128.56
43	–OH	153.63	115.18	129.90	121.23
45	$–OCH=CH_2$	156.87	119.54	128.86	124.65
46	–O-phenyl	151.65	117.30	129.67	120.61
47	$–OCOCH_3$	146.26	119.70	128.87	127.81
48	$–OSi(CH_3)_3$	151.17	119.45	129.40	124.75
49	$–OPO(O\text{-phenyl})_2$	147.79	119.76	129.70	125.29
50	–OCN	149.70	118.99	130.83	128.26
51	$–NH_2$	151.84	115.06	129.30	120.53
53	$–N(CH_3)_2$	149.10	113.03	129.40	120.20
54	–NH-phenyl	147.96	117.90	129.26	118.80
55	$–N(phenyl)_2$	147.08	121.52	129.33	122.78
56	$–NH_3^+$	134.14	122.70	130.70	129.51
57	$–NH_2^+CH(CH_3)_2$	133.33	129.50	129.59	129.73
58	$–N^+(CH_3)_3$	136.65	126.78	131.00	131.97
60	$–NHCOCH_3$	138.31	119.59	129.12	126.68
61	–NHOH	152.47	115.16	126.24	124.32
62	$–NHNH_2$	153.31	112.84	129.16	123.85
64	–N=CH-phenyl	156.51	119.71	128.76	128.33
65	$–N=NCH_3$	147.51	129.32	128.72	127.46
66	–NO	156.92	127.54	128.84	131.69
67	$–NO_2$	150.51	123.84	128.88	132.44
68	–CN	127.19	128.90	128.93	128.11
69	–NCO	135.44	124.80	129.04	127.93
71	$–N^+≡N$	119.60	134.31	134.18	143.96
72	–SH	138.54	129.29	128.73	125.94
74	$–SC(CH_3)_3$	133.15	128.93	128.61	127.88
75	$–S(CH_3)_2^+$	130.46	130.85	130.84	132.48
76	$–SCH=CH_2$	133.75	128.53	128.70	127.42
78	–S-S-phenyl	137.85	129.24	129.06	128.29
81	$–SO_2OH$	144.52	128.17	129.33	132.67
83	$–SO_2F$	138.80	128.18	129.64	136.00
84	$–SO_2Cl$	137.25	128.21	130.01	135.30
85	$–SO_2NH_2$	141.86	128.19	129.57	132.67
86	–SCN	128.93	126.59	130.07	129.68
89	$–COCF_3$	123.48	129.18	128.86	132.66
90	–COC≡CH	130.74	129.40	128.33	132.30
91	–CO-phenyl	137.02	129.55	128.39	126.38
92	–COOH	133.85	128.48	128.38	132.51
93	$–COOCH_3$	131.50	129.37	128.30	132.41
94	$–CONH_2$	128.46	126.91	128.46	132.38
96	–COF	135.14	127.83	128.47	132.52
97	–COCl	136.80	131.20	128.51	132.51
99	$–CH=NCH_3$	141.22	129.42	128.38	127.12
100	$–CSH_2$-phenyl	143.13	129.50	128.61	128.88
101	$–CSH_2$-(1-piperidyl)	145.58	125.40	128.53	128.74
104	$–Si(CH_3)_3$	137.92	133.67	128.36	132.44
105	$–Si(phenyl)_3$	136.67	136.09	127.99	125.37
106	$–SiCl_3$	131.81	134.78	128.60	132.67
108	$–P(phenyl)_2$	139.23	133.66	128.85	129.83
109	$–PO(CH_3)_2$	139.08	129.02	128.34	132.67
110	$–PO(OH)_2$	131.61	128.42	128.71	132.67
111	$–PO(OCH_2CH_3)_2$	131.31	132.32	129.00	132.67
112	$–PS(CH_3)_2$	137.13	128.32	128.36	132.67
113	$–PS(OCH_2CH_3)_2$	135.35	131.30	128.34	132.67
Validation					
5	$–CH(CH_3)_2$	139.53	126.32	128.20	125.75
14	$–CH_2Cl$	137.10	128.85	128.70	128.50
23	$–CH_2N(CH_3)_2$	133.69	128.96	128.20	127.00
24	$–CH_2NO_2$	131.78	130.21	130.70	129.75
30	$–CH_2CHO$	132.87	129.73	129.00	127.40
36	–phenyl	133.43	127.36	129.00	127.39
37	–2-pyridyl	138.17	127.10	130.70	127.10
38	–4-pyridyl	137.34	126.73	130.70	128.98
42	–I	96.90	136.38	130.70	127.41
63	$–N(NO)CH_3$	140.25	119.07	130.70	127.22
70	–NCS	128.28	125.92	129.80	127.50
73	$–SCH_3$	139.63	130.25	128.70	124.91
87	–CHO	135.77	129.81	129.00	133.19
88	$–COCH_3$	136.32	128.67	128.40	131.37
95	$–CON(CH_3)_2$	132.84	127.10	128.30	131.36
103	$–SiH_2CH_3$	137.91	131.39	128.00	129.46
Test					
9	–cyclopentyl	143.84	128.16	128.10	125.62
20	$–CH_2OCH_3$	136.52	128.15	128.19	127.11
22	$–CH_2NHCH_3$	137.34	128.15	128.23	126.81
29	$–CH_2SO_2CH_3$	124.95	128.12	129.10	129.22
33	$–CH=CH_2$	134.98	128.15	128.38	127.58
34	$–C(CH_3)=CH_2$	141.08	128.15	128.26	127.53
44	$–OCH_3$	156.50	114.21	129.49	125.37
52	$–NHCH_3$	144.57	112.02	129.30	116.91
59	$–N(O)(CH_3)_2$	154.18	119.95	129.31	128.67
77	–S-phenyl	131.75	128.15	129.10	127.04
79	$–S(O)CH_3$	144.01	123.10	129.60	132.34
80	$–SO_2CH_3$	139.73	127.30	129.30	132.40
82	$–SO_2OCH_3$	134.99	127.09	130.00	134.40
98	–COSH	132.02	127.83	128.70	132.19
102	$–SiH_3$	128.19	135.79	128.10	129.72
107	$–P(CH_3)_2$	139.46	129.02	127.93	127.64

Can. J. Chem. Downloaded from www.nrcresearchpress.com by Xi'an Jiaotong University on 09/19/12
For personal use only.

Table 5. Calculated values of ^{13}C NMR chemical shifts (ppm) using the RC–PC–ANN method based on MIA descriptors for all carbon positions: training, validation, and test sets.

No.	Substituent X	C-1	C-2	C-3	C-4
Training					
1	–H	128.64	129.48	128.66	128.28
2	$–CH_3$	143.43	129.42	128.22	125.31
3	$–CH_2CH_3$	137.86	127.79	128.42	125.79
4	$–CH_2CH_2CH_3$	140.30	128.93	128.55	125.93
6	$–CH_2CH_2CH_2CH_3$	136.20	128.80	128.05	127.35
7	$–C(CH_3)_3$	150.40	123.66	128.03	124.93
8	–cyclopropyl	141.98	126.97	127.81	125.45
10	–cyclohexyl	147.67	127.65	128.25	125.61
11	–1-adamantyl	148.03	125.25	128.02	126.66
12	$–CH_2F$	132.34	127.83	129.08	128.67
13	$–CF_3$	134.16	125.95	128.94	130.94
15	$–CHCl_2$	141.55	129.37	128.33	129.58
16	$–CCl_3$	138.09	126.53	128.42	129.44
17	$–CH_2Br$	136.52	129.62	128.62	128.96
18	$–CH_2I$	136.10	129.04	128.39	128.57
19	$–CH_2OH$	142.10	127.87	128.70	127.10
21	$–CH_2NH_2$	142.01	128.02	128.26	126.33
25	$–CH_2CN$	129.74	128.14	127.72	127.87
26	$–CH_2SH$	141.08	127.82	128.52	127.15
27	$–CH_2SCH_3$	140.73	129.40	128.41	127.27
28	$–CH_2S(O)CH_3$	134.06	128.75	128.98	128.21
31	$–CH_2COCH_3$	131.35	129.81	128.44	127.02
32	$–CH_2COOH$	128.69	128.32	129.00	127.27
35	–C≡CH	123.75	131.40	128.18	128.73
39	–F	158.59	115.21	129.71	123.33
40	–Cl	135.37	128.35	129.98	126.74
41	–Br	128.02	130.36	130.19	127.86
43	–OH	154.16	115.47	129.98	121.06
45	$–OCH=CH_2$	145.89	116.58	129.07	122.34
46	–O-phenyl	155.84	117.78	128.18	121.56
47	$–OCOCH_3$	142.60	126.41	128.86	125.76
48	$–OSi(CH_3)_3$	155.30	120.38	129.54	121.53
49	$–OPO(O\text{-phenyl})_2$	145.62	123.16	129.55	124.04
50	–OCN	151.82	116.70	131.12	128.03
51	$–NH_2$	146.77	115.10	129.30	119.17
53	$–N(CH_3)_2$	145.27	111.75	129.49	118.92
54	–NH-phenyl	139.53	120.92	129.49	117.85
55	$–N(phenyl)_2$	137.70	121.68	129.41	122.61
56	$–NH_3^+$	131.57	123.83	130.74	130.49
57	$–NH_2^+CH(CH_3)_2$	133.52	125.96	129.39	129.64
58	$–N^+(CH_3)_3$	140.98	121.20	131.00	130.08
60	$–NHCOCH_3$	140.27	121.62	128.76	124.12
61	–NHOH	149.95	115.20	126.36	122.72
62	$–NHNH_2$	151.35	112.83	129.03	118.77
64	–N=CH-phenyl	158.37	121.11	129.44	127.32
65	$–N=NCH_3$	143.43	126.10	129.04	124.87
66	–NO	159.06	122.15	129.21	136.28
67	$–NO_2$	148.15	124.59	129.39	134.66
68	–CN	115.95	132.18	128.99	130.90
69	–NCO	135.16	124.88	129.54	124.50
71	$–N^+≡N$	111.49	133.62	133.75	142.15
72	–SH	129.47	128.27	128.81	125.38
74	$–SC(CH_3)_3$	134.27	136.88	128.14	128.80
75	$–S(CH_3)_2^+$	128.94	130.72	130.67	134.74
76	$–SCH=CH_2$	134.21	129.93	128.64	127.02
78	–S-S-phenyl	136.55	127.47	129.21	128.21
81	$–SO_2OH$	137.19	125.63	129.85	131.68
83	$–SO_2F$	133.74	129.72	130.14	136.44
84	$–SO_2Cl$	142.98	126.23	129.75	135.74
85	$–SO_2NH_2$	139.05	127.57	128.79	132.29
86	–SCN	123.97	128.93	130.80	130.62
89	$–COCF_3$	129.87	129.41	129.22	135.43
90	–COC≡CH	136.88	129.46	128.50	134.16
91	–CO-phenyl	142.13	129.78	128.16	132.21
92	–COOH	132.37	130.13	128.51	133.30
93	$–COOCH_3$	137.27	129.49	128.57	132.47
94	$–CONH_2$	133.92	127.81	128.54	131.40
96	–COF	134.89	127.73	127.64	132.03
97	–COCl	132.94	129.20	128.80	134.90
99	$–CH=NCH_3$	142.24	129.63	128.60	130.45
100	$–CSH_2$-phenyl	144.82	129.05	127.86	130.95
101	$–CSH_2$-(1-piperidyl)	146.27	125.91	128.24	128.05
104	$–Si(CH_3)_3$	138.54	133.34	127.83	129.26
105	$–Si(phenyl)_3$	137.75	135.16	128.27	129.97
106	$–SiCl_3$	133.81	134.07	128.58	132.86
108	$–P(phenyl)_2$	140.55	133.88	128.49	129.02
109	$–PO(CH_3)_2$	131.81	129.86	129.03	132.29
110	$–PO(OH)_2$	127.40	128.61	129.96	134.04
111	$–PO(OCH_2CH_3)_2$	127.84	128.10	128.37	131.42
112	$–PS(CH_3)_2$	138.03	132.24	128.72	131.68
113	$–PS(OCH_2CH_3)_2$	140.34	129.72	128.71	131.54
Validation					
5	$–CH(CH_3)_2$	148.39	126.10	128.20	125.71
14	$–CH_2Cl$	137.52	128.94	128.69	128.03
23	$–CH_2N(CH_3)_2$	135.13	126.63	128.19	126.87
24	$–CH_2NO_2$	129.76	130.83	130.60	129.65
30	$–CH_2CHO$	134.66	128.42	128.98	127.54
36	–phenyl	138.02	127.07	128.96	127.33
37	–2-pyridyl	138.48	125.44	128.97	127.14
38	–4-pyridyl	137.40	127.48	128.97	129.12
42	–I	96.85	136.27	130.07	127.35
63	$–N(NO)CH_3$	141.65	118.95	129.38	127.12
70	–NCS	129.01	124.36	129.78	127.61
73	$–SCH_3$	137.91	127.67	128.67	125.39
87	–CHO	136.84	127.26	128.99	134.11
88	$–COCH_3$	136.33	127.79	128.41	132.83
95	$–CON(CH_3)_2$	133.50	126.72	128.29	129.69
103	$–SiH_2CH_3$	134.99	132.96	127.99	129.58
Test					
9	–cyclopentyl	144.12	127.61	128.09	125.39
20	$–CH_2OCH_3$	134.31	127.82	128.42	127.48
22	$–CH_2NHCH_3$	141.16	128.34	128.18	126.76
29	$–CH_2SO_2CH_3$	125.87	131.49	129.08	129.12
33	$–CH=CH_2$	138.50	126.24	128.41	127.79
34	$–C(CH_3)=CH_2$	139.316	125.77	128.08	127.27
44	$–OCH_3$	161.33	114.06	129.49	125.34
52	$–NHCH_3$	142.10	112.96	129.27	116.63
59	$–N(O)(CH_3)_2$	154.10	120.21	129.29	129.14
77	–S-phenyl	131.02	131.57	129.06	126.99
79	$–S(O)CH_3$	143.04	123.42	129.58	130.84
80	$–SO_2CH_3$	139.51	131.33	129.29	133.59
82	$–SO_2OCH_3$	131.24	126.66	129.92	134.19
98	–COSH	133.20	128.11	128.71	133.78
102	$–SiH_3$	127.83	131.49	128.11	129.51
107	$–P(CH_3)_2$	138.87	130.34	127.90	127.52

Table 6. Statistical parameters for RC–PC–ANN models based on original molecular descriptors and MIA descriptors.

		C-1		C-2		C-3		C-4	
Method	Set	R^2	SE	R^2	SE	R^2	SE	R^2	SE
RC–PC–ANN (original)	Training	0.761	3.997	0.853	1.978	0.842	0.376	0.821	1.785
	Validation	0.931	2.784	0.894	1.196	0.655	0.647	0.924	0.626
	Test	0.956	1.827	0.946	1.413	0.989	0.071	0.975	0.661
RC–PC–ANN (MIA)	Training	0.871	3.242	0.935	1.332	0.976	0.155	0.982	0.613
	Validation	0.991	1.043	0.933	1.007	0.999	0.016	0.993	0.196
	Test	0.973	1.566	0.927	1.625	0.999	0.019	0.999	0.127
ChemDraw	All	0.903	3.239	0.942	1.286	0.328	0.815	0.831	1.540

Can. J. Chem. Downloaded from www.nrcresearchpress.com by Xi'an Jiaotong University on 09/19/12
For personal use only.

molecular descriptors and MIA descriptors. The results obtained using the two kinds of descriptors were compared.

Experimental

Data set

The ^{13}C NMR chemical shifts of 113 monosubstituted benzenes (in ppm relative to TMS) for ipso, ortho, meta, and para positions were obtained from the literature.[17] During this study, attention was paid to collecting ^{13}C NMR chemical shift data under similar experimental conditions. The chemical structures of the different substituted compounds used in this study and their ^{13}C NMR chemical shifts are shown in Table 1.

Descriptors

Original molecular descriptors

All structures were generated with HyperChem software (version 7) and optimized by the AM1 semi-empirical method.[18] The selection and calculation of the structural descriptors as numerically encoded parameters is regarded as an essential step in every QSPR study. In this work, some QSPR descriptors were calculated using the HyperChem package. Then the HyperChem files were transferred into Dragon software[19] to calculate different kinds of descriptors. Constitutional, topological, and geometrical descriptors calculated with Dragon software have been successfully used in various QSPR studies.[20,21] Also, MOPAC software[22] was used to calculate electronic and quantum chemical descriptors. Then, descriptors with constant or almost constant values for all molecules were eliminated. In addition, pairs of variables with a correlation coefficient greater than 0.90 were classified as intercorrelated and only one of them was considered in developing the models. A total of 146 descriptors were considered for further investigations.

Multivariate image analysis (MIA) descriptors

The structures of studied compounds (Table 1) were systematically drawn in ACD/ChemSketch[23] and saved in PaintStar[24] as bitmap files. The bitmap windows were cut to a 215 × 210 pixels size to minimize memory and the drawn molecules were systematically fixed in a given coordinate by a common point among them. For instance, position 1 (Fig. 1) was manually fixed at the 100 × 100 pixels coordinate. Each 2D image was read and converted into binaries (double array in MATLAB[25]). Each image of 215 × 210 pixels was unfolded to a 1 × 45 150 pixels row and then the 113 images were grouped to form a 113 × 45 150 pixels matrix (Fig. 1). Columns with zero variance were removed to minimize memory, reducing the size of matrices to 113 × 817 pixels.

Principal component regressions

In QSAR/QSPR studies, a regression model of the form $y = Xb + e$ may be used to describe a set of predictor variables (X) with a predicted variable (y) by means of a regression vector (b). However, the collinearity that often exists between independent variables creates a severe problem in certain types of mathematical treatments such as matrix inversion.[26] A better predictive model can be obtained by orthogonalization of the variables by means of principal component analysis (PCA), and the consequent method is called principal component regression (PCR).[27–29] To reduce the dimensionality of the independent variable space, a limited number of principal components (PCs) are used. Selection of significant and informative PCs is the main problem in almost all PCA-based calibration methods.[30–32] Different methods have been used to select the significant PCs for calibration purposes. In the simplest and most common one, the factors are ranked in order of decreasing eigenvalue and introduced into the calibration model one after the other. In another method, called correlation ranking, the factors are ranked by their correlation coefficient with the property to be correlated (a dependent variable).[32] Better results are often achieved by this method. Therefore, in this study, the correlation ranking method was used to select significant PCs obtained from original molecular descriptors and MIA descriptors.

In the present work, the first PCA was carried out on two data matrices using Minitab.[33] After acquiring PCs, PCR analysis including correlation ranking (CR–PCR) was employed. In the CR–PCR procedure, the PCs were entered into the PCR model consecutively based on their decreasing correlation with the ^{13}C NMR chemical shifts. The coefficient of determination $R^2 \geq 0.5$ was used to select the optimum number of factors in the PCR models. The obtained models are summarized in Tables 2 and 3 for original molecular descriptors and MIA descriptors, respectively. In all CR–PCR equations, the factor with the highest correlation with the ^{13}C NMR chemical shift is considered the most significant and, subsequently, the factors are introduced into the calibration model until $R^2 \geq 0.5$ is achieved. PCs with higher correlations have greater information about the variation in the ^{13}C NMR chemical shifts.

Artificial neural network modeling

Because of the complexity of the relationships between the

Can. J. Chem. Downloaded from www.nrcresearchpress.com by Xi'an Jiaotong University on 09/19/12
For personal use only.

Table 7. ^{13}C NMR chemical shifts (ppm) calculated using ChemDraw.

No.	Substituent X	C-1	C-2	C-3	C-4
1	–H	128.5	128.5	128.5	128.5
2	$–CH_3$	138.4	129.0	128.6	125.7
3	$–CH_2CH_3$	144.3	127.7	128.6	125.9
4	$–CH_2CH_2CH_3$	142.0	128.1	128.8	126.0
5	$–CH(CH_3)_2$	148.4	126.1	128.4	125.9
6	$–CH_2CH_2CH_2CH_3$	142.6	128.1	128.5	125.9
7	$–C(CH_3)_3$	151.3	125.0	128.3	125.6
8	–cyclopropyl	145.8	125.0	128.1	125.1
9	–cyclopentyl	148.5	126.8	128.3	125.8
10	–cyclohexyl	147.0	126.5	128.4	125.9
11	–1-adamantyl	147.7	126.5	128.4	125.9
12	$–CH_2F$	137.0	127.6	129.1	129.2
13	$–CF_3$	131.0	125.1	129.0	132.0
14	$–CH_2Cl$	137.8	128.6	128.9	128.7
15	$–CHCl_2$	140.4	125.9	128.8	129.9
16	$–CCl_3$	144.0	126.6	128.6	130.5
17	$–CH_2Br$	138.0	129.0	129.0	128.9
18	$–CH_2I$	139.1	128.3	128.7	127.8
19	$–CH_2OH$	141.2	127.1	128.9	127.6
20	$–CH_2OCH_3$	137.5	127.4	128.6	127.8
21	$–CH_2NH_2$	143.3	126.9	128.5	126.7
22	$–CH_2NHCH_3$	140.2	127.9	128.5	127.0
23	$–CH_2N(CH_3)_2$	138.6	128.8	128.4	127.2
24	$–CH_2NO_2$	130.7	129.4	130.9	129.9
25	$–CH_2CN$	131.3	128.8	127.9	128.0
26	$–CH_2SH$	139.6	127.7	128.7	127.1
27	$–CH_2SCH_3$	138.8	128.7	128.6	127.1
28	$–CH_2S(O)CH_3$	130.7	131.6	129.1	128.5
29	$–CH_2SO_2CH_3$	128.5	132.3	129.3	129.3
30	$–CH_2CHO$	131.9	129.6	129.2	127.6
31	$–CH_2COCH_3$	134.0	129.1	128.8	127.1
32	$–CH_2COOH$	134.7	129.7	129.1	127.5
33	$–CH=CH_2$	137.9	128.5	128.6	127.9
34	$–C(CH_3)=CH_2$	141.1	126.4	128.6	127.9
35	–C≡CH	122.7	132.3	128.3	128.4
36	–phenyl	140.8	127.9	129.2	127.6
37	–2-pyridyl	139.0	127.6	129.2	127.3
38	–4-pyridyl	142.3	127.4	129.2	129.2
39	–F	162.9	115.5	130.3	124.3
40	–Cl	134.3	128.8	130.1	126.8
41	–Br	123.1	131.6	130.9	127.7
42	–I	94.3	137.6	130.3	127.6
43	–OH	158.5	115.9	130.1	121.3
44	$–OCH_3$	160.6	114.3	129.7	121.0
45	$–OCH=CH_2$	157.6	117.2	129.4	122.9
46	–O-phenyl	157.0	118.9	128.4	121.8
47	$–OCOCH_3$	151.3	121.6	129.1	125.5
48	$–OSi(CH_3)_3$	156.4	120.1	129.6	121.6
49	$–OPO(O\text{-phenyl})_2$	150.2	120.3	130.1	121.3
50	–OCN	153.8	116.0	131.3	127.7
51	$–NH_2$	148.4	115.0	129.5	122.4
52	$–NHCH_3$	150.0	113.5	129.5	120.8
53	$–N(CH_3)_2$	151.1	114.3	129.6	121.9
54	–NH-phenyl	142.4	120.6	129.6	121.9
55	$–N(phenyl)_2$	145.9	125.7	129.6	126.8
56	$–NH_3^+$	134.1	121.2	130.5	128.7
57	$–NH_2^+CH(CH_3)_2$	138.0	121.2	130.5	128.7
58	$–N^+(CH_3)_3$	146.4	121.2	130.5	128.7
59	$–N(O)(CH_3)_2$	150.0	116.6	126.5	127.1
60	$–NHCOCH_3$	138.5	121.6	128.9	128.0
61	–NHOH	153.5	114.5	130.0	127.1
62	$–NHNH_2$	153.0	113.2	129.2	122.8
63	$–N(NO)CH_3$	142.5	118.9	129.5	131.0
64	–N=CH-phenyl	152.0	122.3	130.0	127.2
65	$–N=NCH_3$	150.9	122.6	129.2	125.7
66	–NO	168.3	121.1	129.5	135.7
67	$–NO_2$	147.9	123.9	129.6	134.8
68	–CN	112.6	132.2	129.4	133.0
69	–NCO	133.6	125.1	129.8	125.9
70	–NCS	131.5	126.1	130.0	127.7
71	$–N^+≡N$	114.0	131.5	132.8	135.2
72	–SH	130.7	129.4	129.0	125.5
73	$–SCH_3$	139.4	126.8	128.9	125.1
74	$–SC(CH_3)_3$	133.8	140.2	128.4	128.7
75	$–S(CH_3)_2^+$	143.3	125.4	128.7	128.7
76	$–SCH=CH_2$	135.1	129.4	129.0	125.5
77	–S-phenyl	135.7	131.2	129.3	127.2
78	–S-S-phenyl	136.0	127.2	129.0	125.5
79	$–S(O)CH_3$	145.7	124.1	129.8	131.1
80	$–SO_2CH_3$	141.0	128.3	129.7	133.7
81	$–SO_2OH$	145.5	128.1	130.0	132.5
82	$–SO_2OCH_3$	147.4	129.7	130.2	134.6
83	$–SO_2F$	131.9	127.9	130.2	136.2
84	$-SO_2Cl$	144.1	126.8	129.9	135.5
85	$–SO_2NH_2$	143.7	127.3	129.0	131.9
86	–SCN	124.8	131.2	130.9	130.9
87	–CHO	136.9	129.9	129.2	134.5
88	$–COCH_3$	136.7	128.8	128.6	133.1
89	$–COCF_3$	123.4	130.5	129.4	135.4
90	–COC≡CH	135.1	128.9	129.2	134.5
91	–CO-phenyl	138.4	130.3	128.4	132.4
92	–COOH	130.2	130.3	128.6	133.9
93	$–COOCH_3$	130.1	129.9	128.6	133.0
94	$–CONH_2$	134.2	127.5	128.8	132.1
95	$–CON(CH_3)_2$	135.2	127.2	128.5	129.7
96	–COF	132.8	129.9	129.2	134.5
97	–COCl	133.2	131.4	129.0	135.3
98	–COSH	134.7	128.1	128.9	134.1
99	$–CH=NCH_3$	136.4	129.2	128.8	131.0
100	$–CSH_2$-phenyl	137.1	127.7	128.7	127.1
101	$–CSH_2$-(1-piperidyl)	136.9	127.7	128.7	127.1
102	$–SiH_3$	128.0	135.8	129.5	130.0
103	$–SiH_2CH_3$	133.0	134.8	135.3	130.0
104	$–Si(CH_3)_3$	140.1	133.4	129.2	129.1
105	$–Si(phenyl)_3$	134.3	136.4	129.5	130.0
106	$–SiCl_3$	131.9	134.0	129.5	130.0
107	$–P(CH_3)_2$	142.1	131.4	128.1	127.7
108	$–P(phenyl)_2$	137.1	133.7	128.7	128.8
109	$–PO(CH_3)_2$	135.0	129.6	128.8	134.2
110	$–PO(OH)_2$	139.1	126.9	128.8	134.2
111	$–PO(OCH_2CH_3)_2$	134.2	129.4	128.5	134.6
112	$–PS(CH_3)_2$	128.5	131.2	128.7	131.2
113	$–PS(OCH_2CH_3)_2$	128.5	131.2	128.7	131.2

Table 7 (*concluded*).

activity and properties of the molecules and the structures, nonlinear modeling methods are often used to model the structure–activity and structure–property relationships. Artificial neural networks (ANNs) as nonparametric nonlinear modeling techniques have attracted increasing interest in re-

Can. J. Chem. Downloaded from www.nrcresearchpress.com by Xi'an Jiaotong University on 09/19/12
For personal use only.

cent years.[34,35] Multilayer feed-forward neural networks trained with back-propagation learning algorithms have become increasingly popular.[34–37] The flexibility of ANN for discovering a more complex relationship has resulted in this method finding wide application in QSAR/QSPR studies (reviewed by Duch et al.[38]).

The principal component–artificial neural network (PC–ANN) was proposed by Gemperline et al. to improve the training speed and decrease the overall calibration error.[39] PC–ANN combines the PCA with ANN and models the nonlinear relationships between the PCs and the dependent variable.

A feed-forward neural network with a back-propagation of error algorithm was constructed to model the structure–property relationship. Our network had an input layer, a hidden layer, and an output layer. The input vectors were the set of PCs selected by correlation ranking (Tables 2 and 3). The number of nodes in the input layer depended on the number of PCs introduced to the network. The number of nodes in the hidden layer was optimized through the learning procedure. There was only one node in the output layer. The data set was separated into three subsets: a training set including 71 compounds, a validation set including 16 compounds, and a test set including 16 compounds. The training, validation, and test data sets were used to optimize the network performance. The training set was used for model generation, the test set was used to control the overtraining, and the validation set was used to evaluate the generated model. The ANN program was coded in MATLAB 7.1 for Windows.[25] The network was then trained using the training set by the back-propagation strategy for optimization of the weight values. The proper number of nodes in the hidden layer was determined by training the network with different numbers of nodes in the hidden layer. The standard error (SE) measures how good the outputs are in comparison with the target values. It should be noted that for evaluating the overfitting, the training of the network for the prediction of ^{13}C NMR chemical shifts must stop when the SE of the test set begins to increase while the SE of the training set continues to decrease. Therefore, training of the network was stopped when overtraining began.

The results obtained using the RC–PC–ANN method for PCs extracted from original molecular descriptors and MIA descriptors are shown in Tables 4 and 5.

Results and discussion

Table 1 lists the structures of monosubstituted benzenes used in this study and their corresponding experimental ^{13}C NMR chemical shift values for four different positions: ipso, ortho, meta, and para. After elimination of the constants and one of the collinear descriptors, 146 original molecular descriptors and 817 MIA descriptors remained. After the application of PCA to the two descriptor data matrices, 112 PCs were extracted for each group of descriptors. Then, separate PCR models were obtained for each position (ipso, ortho, meta, and para). The models obtained by the correlation ranking procedure are shown in Tables 2 and 3. The QSPR models for all positions resulted in high statistical qualities. Comparison of these models indicates that the number of PCs is lower for the original molecular descriptors than for the MIA descriptors. This shows that the PCs obtained from

Fig. 2. Plots of experimental ^{13}C chemical shifts of monosubstituted benzenes against values calculated using RC–PC–ANN models based on original molecular descriptors for C1–C4 (*a–d*, respectively).

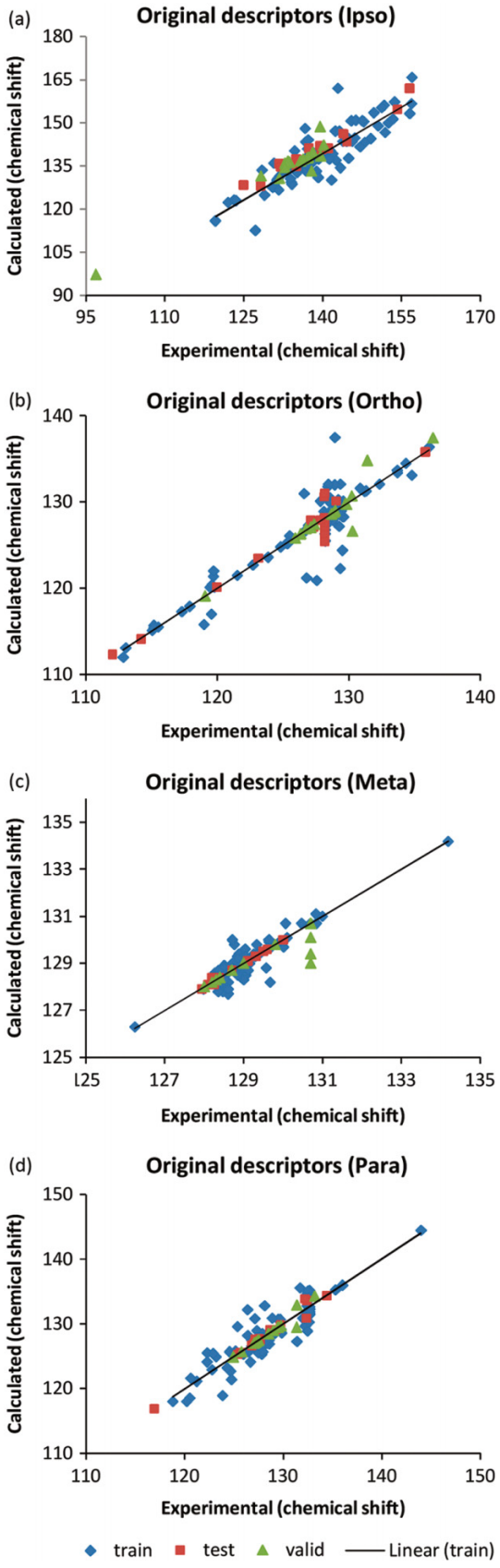

Can. J. Chem. Downloaded from www.nrcresearchpress.com by Xi'an Jiaotong University on 09/19/12
For personal use only.

Fig. 3. Plots of experimental ^{13}C chemical shifts of monosubstituted benzenes against values calculated using RC–PC–ANN models based on MIA descriptors for C1–C4 (*a–d*, respectively).

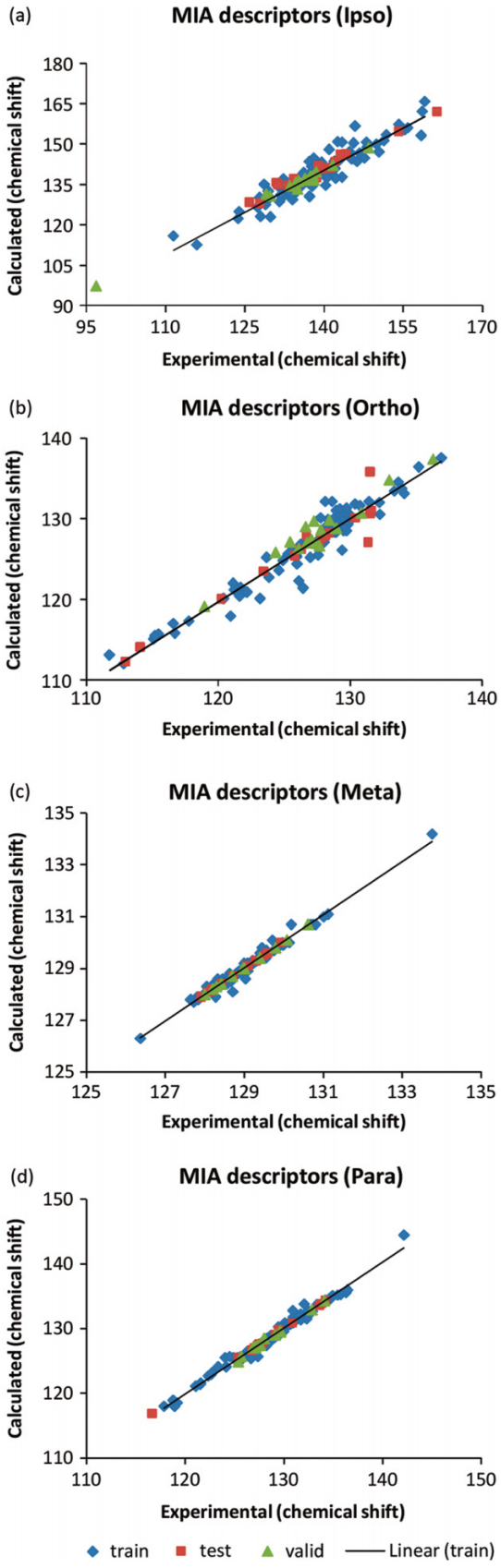

the original molecular descriptors provide greater information about the variations of ^{13}C NMR chemical shifts.

To increase the ability of the obtained models to predict ^{13}C NMR chemical shifts, a nonlinear modeling method was employed. Typically, superior models can be found using ANNs because they implement nonlinear relationships and because they have more adjustable parameters than linear models. Therefore, in this study we used ANN as the nonlinear model. Correlation ranking was used to select the most relevant set of PCs as inputs of the ANN. The results of the RC–PC–ANN method are presented in Tables 4 and 5 for the training, validation, and test sets, respectively.

For comparison, R^2 and SE values of RC–PC–ANN models for original molecular descriptors and MIA descriptors are summarized in Table 6. As can be seen from this table, the QSPR models obtained from the two main groups of descriptors indicate good performance for different carbon positions and could predict the ^{13}C NMR chemical shifts of the related molecules with low error. Also, comparison of the results indicates that the RC–PC–ANN models based on PCs extracted from the MIA descriptors are more accurate and show better predictive ability than the RC–PC–ANN models based on PCs extracted from the original molecular descriptors.

Finally, ^{13}C NMR chemical shifts of the studied compounds were calculated using ChemDraw;[40] these values are shown in Table 7. Also, statistical parameters of these values are indicated in Table 6.

The results obtained in the present work indicate that though MIA descriptors do not have a direct physicochemical meaning, they may provide useful information and are capable of predicting the ^{13}C NMR chemical shifts of studied compounds with a good predictive ability.

Plots of experimental ^{13}C NMR chemical shifts versus those calculated using RC–PC–ANN modeling methods for ipso, ortho, meta, and para positions are shown in Figs. 2*a*–2*d* for the original molecular descriptors and Figs. 3*a*–3*d* for the MIA descriptors.

Conclusion

The QSPR modeling of ^{13}C NMR chemical shifts of monosubstituted benzenes was studied using the RC–PC–ANN method. A comparison was made between the original molecular descriptors and MIA descriptors. The results showed that both groups of descriptors are capable of predicting ^{13}C NMR chemical shifts of benzene derivatives. Also, it was found that RC–PC–ANN models based on PCs extracted from MIA descriptors are more accurate and show better predictive ability than RC–PC–ANN models based on PCs extracted from original molecular descriptors.

Acknowledgements

Support of this work by Vali-e-Asr University is acknowledged.

References

(1) Garkani-Nejad, Z.; Ahmadi-Roudi, B. *Eur. J. Med. Chem.* **2010** *45* (2), 719. doi:10.1016/j.ejmech.2009.11.019.
(2) Jalali-Heravi, M.; Garkani-Nejad, Z.; Kyani, A. *QSAR Comb. Sci.* **2008** *27* (2), 137. doi:10.1002/qsar.200510205.

Can. J. Chem. Downloaded from www.nrcresearchpress.com by Xi'an Jiaotong University on 09/19/12
For personal use only.

(3) Gedeck, P.; Lewis, R. A. *Curr. Opin. Drug Discov. Devel.* **2008** *11*, 569.
(4) Freitas, M. P. *Curr. Comput. Aided Drug Des.* **2007** *3* (4), 235. doi:10.2174/157340907782799408.
(5) Schweitzer, R. C.; Small, G. W. *J. Chem. Inf. Comput. Sci.* **1997** *37*, 249.
(6) Cramer, R. D.; Patterson, D. E.; Bunce, J. D. *J. Am. Chem. Soc.* **1988** *110* (18), 5959. doi:10.1021/ja00226a005.
(7) Klebe, G.; Abraham, U.; Mietzner, T. *J. Med. Chem.* **1994** *37* (24), 4130. doi:10.1021/jm00050a010.
(8) Jalali-Heravi, M.; Garkani-Nejad, Z. *J. Chromatogr. A* **2002** *950* (1–2), 183. doi:10.1016/S0021-9673(02)00054-7.
(9) Jalali-Heravi, M.; Garkani-Nejad, Z. *J. Chromatogr. A* **2002** *971* (1–2), 207. doi:10.1016/S0021-9673(02)01043-9.
(10) Vedani, A.; Dobler, M. *J. Med. Chem.* **2002** *45* (11), 2139. doi:10.1021/jm011005p.
(11) Vedani, A.; Dobler, M.; Lill, M. A. *J. Med. Chem.* **2005** *48* (11), 3700. doi:10.1021/jm050185q.
(12) Freitas, M. P.; Brown, S. D.; Martins, J. A. *J. Mol. Struct.* **2005** *738* (1–3), 149. doi:10.1016/j.molstruc.2004.11.065.
(13) Freitas, M. P. *Org. Biomol. Chem.* **2006** *4* (6), 1154. doi:10.1039/b516396j.
(14) Geladi, P.; Esbensen, K. *J. Chemom.* **1989** *3* (2), 419. doi:10.1002/cem.1180030209.
(15) Goodarzi, M.; Freitas, M. P.; Ramalho, T. C. *Spectrochim. Acta A Mol. Biomol. Spectrosc.* **2009** *74* (2), 563. doi:10.1016/j.saa.2009.07.003.
(16) Garkani-Nejad, Z.; Poshteh-Shirani, M. *Talanta* **2010** *83* (1), 225. doi:10.1016/j.talanta.2010.09.012.
(17) Pretsch, E.; Bühlmann, P.; Affolter, C. *Structure Determination of Organic Compounds*: *Tables of Spectral Data*; Springer: Berlin, 2000; pp 97–99.
(18) *HyperChem*, version 7.0; Hypercube, Inc.: Gainesville, Fla., 2002.
(19) Todeschini, R.; Consonni, V.; Mauri, A.; Pavan, M. *DRAGON* (software for the calculation of molecular descriptors), version 3; Dipartimento di Scienze dell'Ambiente e del Territorio, Università degli Studi di Milano–Bicocca, and Talete srl: Milan, 2003. Available from http://www.disat.unimib.it/chm/Dragon.htm.
(20) Lü, W. J.; Chen, Y. L.; Ma, W. P.; Zhang, X. Y.; Luan, F.; Liu, M. C.; Chen, X. G.; Hu, Z. D. *Eur. J. Med. Chem.* **2008** *43* (3), 569. doi:10.1016/j.ejmech.2007.04.011.
(21) Turabekova, A.; Rasulev, B. F. A.; Levkovich, M. G.; Abdullaev, N. D.; Leszczynski, J. *Comput. Biol. Chem.* **2008** *32* (2), 88. doi:10.1016/j.compbiolchem.2007.10.003.
(22) Stewart, J.J.P. *MOPAC: A Semiempirical Molecular Orbital Program*, version 6; US Air Force Academy: Colorado Springs, Colo., 1990.
(23) *ACD/ChemSketch*, version 11.02; Advanced Chemistry Development Inc.: Toronto, Ont., 2008.
(24) *PaintStar*, version 2.70; 2003. Available from http://paintstar.en.softonic.com.
(25) *MATLAB*, version 7.1; MathWorks, Inc.: Natick, Mass., 2005. Available from www.mathworks.com.
(26) Montgomery, D. C.; Peck, E. A. *Introduction to Linear Regression Analysis*; Wiley: New York, 1982.
(27) Jolliffe, I. T. *Principal Component Analysis*; Springer, New York, 1986.
(28) Kalivas, J. H.; Lang, P. M. *Mathematical Analysis of Spectral Orthogonality*; Marcel Dekker: New York, 1994.
(29) Puchwein, G. *Anal. Chem.* **1988** *60* (6), 569. doi:10.1021/ac00157a015.
(30) Xie, Y. L.; Kalivas, J. H. *Anal. Chim. Acta* **1997** *348* (1–3), 19. doi:10.1016/S0003-2670(97)00035-4.
(31) Sutter, J. M.; Kalivas, J. H.; Lang, P. M. *J. Chemometr.* **1992** *6* (4), 217. doi:10.1002/cem.1180060406.
(32) Sun, J. *J. Chemom.* **1995** *9* (1), 21. doi:10.1002/cem.1180090104.
(33) *Minitab*, version 15.1; Minitab Inc.: State College, Pa., 2008. Available from www.minitab.com.
(34) Chen, H. F. *Anal. Chim. Acta* **2008** *609* (1), 24. doi:10.1016/j.aca.2008.01.003.
(35) Garkani-Nejad, Z. *Chromatographia* **2009** *70* (5–6), 869. doi:10.1365/s10337-009-1241-6.
(36) Garkani-Nejad, Z. *J. Chromatogr. Sci.* **2010** *48*, 317.
(37) Manallack, D. T.; Tehan, B. G.; Gancia, E.; Hudson, B. D.; Ford, M. G.; Livingstone, D. J.; Whitley, D. C.; Pitt, W. R. *J. Chem. Inf. Comput. Sci.* **2003** *43*, 674.
(38) Duch, W.; Swaminathan, K.; Meller, J. *Curr. Pharm. Des.* **2007** *13* (14), 1497. doi:10.2174/138161207780765954.
(39) Gemperline, P. J.; Long, J. R.; Gregoriou, V. G. *Anal. Chem.* **1991** *63* (20), 2313. doi:10.1021/ac00020a022.
(40) *ChemDraw*, version 11; CambridgeSoft: Cambridge, Mass., 2008. Available from www.cambridgesoft.com.

Functionalizing poly(cyclic olefins) using copper-catalyzed azide–alkyne "click" reactions

Robert J. Faragher, Craig S. McKay, Xuyen D. Hoa, Barbara Prikrylova, Gregory P. Lopinski, Daniel Figeys, Teodor Veres, and John P. Pezacki

Can. J. Chem. Downloaded from www.nrcresearchpress.com by Xi'an Jiaotong University on 09/19/12
For personal use only.

Abstract: A robust method for functionalizing poly(cyclic olefin) surfaces comprised of Zeonor 1060R was developed. These surfaces were first oxidized using two separate methods, ozonolysis and oxygen plasma treatment, to increase their hydrophilic properties and produce carboxylic acids on the surface. The resulting acids enabled direct amide coupling with various amines containing azide or alkyne moieties onto the surface. These modified surfaces were further functionalized via copper-catalyzed azide–alkyne cycloadditions (CuAAC) on the surface and the method was optimized for this material. Surface modifications were characterized by water contact angle measurements, fluorescence microscopy, atomic force microscopy, and X-ray photoelectron spectroscopy. Our data demonstrates a robust method for generating "clickable" Zeonor 1060R surfaces as demonstrated through attachment and subsequent detection of a triazole-linked fluorophore. The method developed enables the systematic modification of any poly(cyclic olefin) surface for functionalization using the click reaction.

Key words: "click" chemistry, Zeonor, ozone, oxygen plasma.

Résumé : On a mis au point une méthode puissante pour fonctionnaliser les surfaces de poly(oléfines cycliques), dont le Zeonor 1060R. Afin d'augmenter leurs propriétés hydrophiles et de produire des acides carboxyliques à leur surfaces, on a procédé dans une première étape à l'oxydation de ces surfaces à l'aide de deux méthodes distinctes, l'ozonolyse et un traitement à l'aide d'un plasma d'oxygène. Les acides qui en résultent permettent de réaliser un couplage amide direct avec diverses amines contenant des portions azoture ou alcyne à leur surface. On a soumis ces surfaces modifiées à d'autres fonctionnalisations par le biais de cycloadditions azoture–alcyne catalysées par le cuivre (AACCu) sur la surface et on a optimisé la méthode pour ce matériau. Les modifications de la surface ont été caractérisées par des mesures de l'angle de contact avec l'eau, par microscopie de fluorescence, par microscopie des forces atomiques et par spectroscopie photoélectronique des rayons X. Les données démontrent qu'il s'agit d'une méthode puissante pour générer des surfaces de Zeonor 1060R cliquables tel que démontré en attachant, puis en détectant un fluorophore lié par un triazole. La méthode développé permet une modification systématique de toute surface de poly(oléfines cycliques) en vue d'une fonctionnalisation à l'aide d'une réaction par cliquage.

Mots-clés : chimie par cliquage, Zeonor, ozone, plasma d'oxygène.

[Traduit par la Rédaction]

Introduction

Microcrofluidic technologies are used in the fields of medical diagnostics, drug discovery, genomics, and proteomics for providing rapid, reliable, sensitive, and simultaneous processing and detection of many different analytes present in a biological mixture.[1–6] There is increased interest in developing plastic microfluidic- and microarray-based technologies for modification of surfaces and immobilization of biomolecules onto the surfaces. Amorphous thermoplastics, specifically Zeonor and Zeonex, have attracted a great deal of attention in recent years owing to their favorable chemical

Received 22 October 2010. Accepted 25 January 2011. Published at www.nrcresearchpress.com/cjc on 10 May 2011.

R.J. Faragher and C.S. McKay. Steacie Institute for Molecular Sciences, National Research Council of Canada, 100 Sussex Dr., Ottawa, ON K1A 0R6, Canada; Chemistry Department, University of Ottawa, 10 Marie-Curie, Ottawa, ON K1N 6N5, Canada.
X.H. Hoa and T. Veres. Industrial Materials Institute, National Research Council of Canada, 75 de Mortagne, Boucherville, QC J4B 6Y4, Canada.
B. Prikrylova. Chemistry Department, University of Ottawa, 10 Marie-Curie, Ottawa, ON K1N 6N5, Canada.
G.P. Lopinski. Steacie Institute for Molecular Sciences, National Research Council of Canada, 100 Sussex Dr., Ottawa, ON K1A 0R6, Canada.
D. Figeys. Department of Biochemistry, Microbiology and Immunology, Faculty of Medicine, University of Ottawa, 451 Smyth Road, Ottawa, ON K1H 8M5, Canada.
J.P. Pezacki. Steacie Institute for Molecular Sciences, National Research Council of Canada, 100 Sussex Dr., Ottawa, ON K1A 0R6, Canada; Chemistry Department, University of Ottawa, 10 Marie-Curie, Ottawa, ON K1N 6N5, Canada; Department of Biochemistry, Microbiology and Immunology, Faculty of Medicine, University of Ottawa, 451 Smyth Road, Ottawa, ON K1H 8M5, Canada.

Corresponding authors: J.P. Pezacki (email: John.Pezacki@nrc-cnrc.gc.ca) and T. Veres (e-mail: Teodor.Veres@nrc-cnrc.gc.ca)

Can. J. Chem. Downloaded from www.nrcresearchpress.com by Xi'an Jiaotong University on 09/19/12
For personal use only.

properties such as high transition temperature, low fluorescence background, high transparency, resistance to organic solvents, low water uptake, and moldability.[7–11] From a commercial point of view, Zeonor and Zeonex materials exhibit other desirable properties such as low cost, micromachining abilities, and mass producibility.[11] Surface functionalization on plastic surfaces represents a simple, robust, and industrially scalable alternative to conventional inorganic substrates such as silica, glass, silicon nitride, and epoxy-based polymers.[10]

Poly(cyclic olefins) are typically hydrophobic, comprised purely of hydrocarbons with no functional groups amenable for covalent functionalization. These Zeonor surfaces can be rendered hydrophilic via photografting,[12] oxygen plasma,[13–15] or ozonolysis.[16] Poly(cyclic olefin) Zeonor materials have been successfully employed for DNA immobilization,[15] purification of nucleic acids,[17] microarrays,[16] and immunoassays.[18,19] In these examples, hydrophilic Zeonor surfaces were functionalized via 1-ethyl-3-(3-dimethylaminopropyl) carbodiimide (EDC) – *N*-hydroxysuccinimide (NHS) mediated couplings of surface carboxylic acids with terminal amino groups[15–17] or through Schiff's base formations from (3-aminopropyl)triethoxysilane (APTES)-functionalized surface amino groups with terminal aldehydes.[19] These coupling procedures for functionalizing oxidized surfaces are typically hampered by lack of specificity, difficulty introducing the functional groups at a range of pH, or low yields.

In our search for versatile chemistry and functional groups to modify Zeonor surfaces, naturally we were attracted to Sharpless's "click" chemistry,[20] particularly the copper-catalyzed azide–alkyne cycloaddition (CuAAC).[21] Azides and alkynes are convenient to introduce, are mutually reactive, and show extraordinary tolerance to other functionality. Furthermore, the regioselective Cu(I) catalyst used in CuAAC reactions is tolerant to solvent and pH, and the triazole products are formed irreversibly and often quantitatively. Although the CuAAC reaction has been employed for functionalizing other polymers[22] and surfaces,[23,24] to our knowledge this is the first report of CuAAC reactions on the surface of a poly(cyclic olefin) leading to a "clickable" surface.

Herein we describe CuAAC reactions on commerically available Zeonor 1060R surfaces that were first oxidized by plasma or ozone treatment. Covalent modification of oxidized plastic surfaces with either azide or alkyne groups enables specific and efficient modular functionalization of Zeonor 1060R surfaces with virtually any organic monolayer. This method presents a distinct advantage for fabricating different devices and for processing and evaluating biological samples because click chemistry is uniform and reproducible regardless of what functional groups are incorporated onto the surface.

Results and discussion

Surface modification

Several approaches are available that allow the hydrophilization of cyclic olefin polymer and copolymer surfaces. Oxygen plasma treatment is rather aggressive and significantly increases the hydrophilicity of the surface through the introduction of numerous polar groups, such as hydroxyl and carboxylic acids. Carboxylic acids offer an efficient means to connect other molecules to the surface via amide or ester bond-forming reactions. Oxygenation of these surfaces via oxygen plasma treatment has been shown not to result in deleterious effects on biological compatibility,[16] providing opportunities for experimentation and analysis directly on the plastic surface. Oxygen plasma is a robust method for modifying poly(cyclic olefin) surfaces, but for use on an industrial scale, it will require specialized equipment that is appropriate for large manufacturing facilities only. Alternatively, ozone treatment of cycloolefin polymer surfaces is known to generate hydroxyls, esters, ketones, and carboxylic acid groups on the surface.[16] Whereas the mechanism for this process is not precisely known, studies have shown the presence of intermediates containing hydroperoxides, hydrotrioxides, and peroxyl radicals that generate the various functional groups.[25,26] It has been demonstrated that aggressive oxygen plasma or UV–ozone treatment of plastic surfaces dramatically alters the surface topography and background fluorescence.[16] Simple ozone treatment of plastic surfaces has been shown not to increase background fluorescence as required for fluorescence studies,[16] as well as being an economical, industrially scalable, and environmentally friendly alternative.

We chose an amide bond to append the clickable group for its chemical stability and general ease of formation from a surface carboxylic acid, amine, and carbodiimide coupling agent.[16] Solvent compatibility was a major factor to consider and negated numerous reactions from surface functionalization. For example, reacting the polymeric surface with highly reactive intermediates such as free radicals,[27] nitrenes,[28–30] or carbenes[31,32] is an effective method to attach molecules through C–H insertion, but these reactions are typically carried out within hydrocarbon solvents systems that are not compatible with the Zeonor scaffold. Generally, polar aprotic and polar protic solvents provide optimal surface compatibility. Several carbodiimides are available and effective at generating the desired amide bond, but since Zeonor is hydrocarbon-based, we wanted to avoid reagents derived from aromatic or hydrocarbon side chains from being embedded within the surface. For that reason, we chose EDC because it is water-soluble and known to be compatible with Zeonor coupling procedures.[16] Generally, immobilization of the clickable functionality was accomplished by standard NHS–EDC coupling of oxidized Zeonor surface carboxylic acids with a primary amine containing the azide or alkyne functionality. Control reactions demonstrated that neither the NHS group nor the amine could be attached without the presence of EDC (X-ray photoelectron spectroscopy (XPS) data not shown).

After exploring possible linking reagents for establishing the azide moiety onto the surface, a short, easily synthesized linker azido-propyl amine **1** was chosen.[33] Preparation of the azide-terminated surface was performed as depicted in Scheme 1 and surface incorporation of the azide was confirmed through XPS, described in more detail (vide infra). To test the feasibility of the click reaction on the poly(cyclic olefin) surface, a small clickable tag **2**,[34] possessing a trifluoro carboxamide group was synthesized and used for monitoring the CuAAC reaction by XPS. The trifluoromethyl group is rarely present or incorporated into Zeonor or most other molecules and was ideally suited for demonstrating

Scheme 1. Preparation of alkyne-terminated Zeonor 1060R and subsequent copper(I)-catalyzed [3 + 2] azide–alkyne cycloaddition.

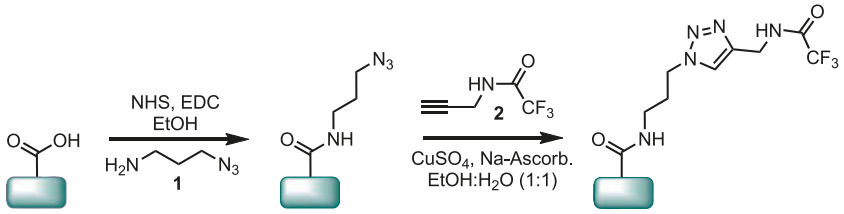

CuAAC reactions on the surface. Any fluorine present on the surface results from reactions of the alkyne and azide directly; this is supported because there was no fluorine incorporation in the absence of copper catalyst. This shows that the copper catalyst was indeed required and that nonspecific adsorption did not occur between the oxidized Zeonor surface and **2**.

There have been reports of catalytic rate enhancements and copper(I) stabilizing effects for CuAAC reactions when conducted in the presence of tris((1-benzyl-1*H*-1,2,3-triazol-4-yl) methyl)amine (TBTA),[35] sulfonated bathophenanthroline (SBP),[36] and tris(2-benzimidazolylmethyl)amine[37,38] ligands. We conducted CuAAC reactions on the surface using stoichiometric equivalents of $CuSO_4$ in the absence of these heterocyclic ligands, since it was found that some of the ligands induced nonuniform surface functionalization as measured by XPS (data not shown). We found that aqueous ethanol in the presence of Cu(I) was an effective medium for direct [3 + 2] cycloadditions on the surface.

After functionalizing the oxidized Zeonor surface with the azide linker **1**, we investigated the immobilization of an alkyne onto the polymer (cyclic olefin) surface to determine if there were surface compatibility issues or reaction preferences between the azide or alkyne moieties. It was not known how the polymer would tolerate a purely hydrocarbon-based linker or how this would affect the [3 + 2] cycloaddition, since the oxidized poly(cyclic olefin) surface is essentially hydrocarbons imparted with oxygen functional groups from either ozone or oxygen plasma oxidation. Using NHS–EDC conditions for coupling **1** to the oxidized surface, we reacted propargyl amine **3** and propargyl tetraethylene glycol amine **4**.[39] It is well-known that pegylated surfaces have greater biocompatibility and increased water solubility, and can inhibit surface-induced denaturation of biomolecules.[40] Zeonor plates were functionalized using both native and ozonated surfaces that were exposed to either **3** or **4** in the presence of NHS–EDC. Incorporation of **3** or **4** terminal alkyne groups was monitored through XPS measurements of signals arising from nitrogen. XPS spectra for surfaces functionalized with **3** or **4** were found to exhibit the expected elemental compositions for the respective reactions. To further confirm click functionalization, we conducted the reaction of **3** and **4** terminated surfaces with derivative **5** (Scheme 2). The resulting fluorine signal in the XPS spectra clearly demonstrated successful CuAAC reactions on the surface.

Contact angle measurements

Poly(cyclic olefins) with unmodified surfaces exhibit a high contact angle (>90°). These pristine surfaces have poor surface wettability, rendering them hydrophilic requires high energy modifications. It is well-established that ozone or oxygen plasma treatments generate various polar functional groups on the surface (e.g., alcohols, ethers, carboxylic acids, ketones, hydroperoxides, or peroxides)[11] and impart a great degree of wettability onto the surface. It was found that ozone treatments of the plastic surface provided a marginal improvement based on contact angles, a decrease to 50°–55°, which was maintained for up to 2 weeks without any change.[41] It is known that oxygenated plastic surfaces rearrange from their treated polar morphology back to a form resembling their original state.[42] The exact mechanism for this rearrangement is not known, but is thought to proceed through incorporation of the polar groups within the polymer.[43–45] Samples treated with oxygen plasma showed the greatest contact angle decrease, reaching essentially 0° with a 15 min exposure. A 5 or 10 min exposure to oxygen plasma provided contact angles of 5°. It was noted that prolonged exposure times resulted in significant alterations of the surface topography and distorted the optical properties of the surface. Since these alterations were undesired, a shorter reaction time was used to preserve the necessary optical properties of Zeonor.

Upon surface oxidation, the Zeonor plates were converted into the azide- and alkyne-terminated surfaces, as described in Schemes 1 and 2, prior to measuring surface contact angles (see Table 1). The measured contact angles from Table 1 show that there is a significant difference between the advancing and receding contact angles, where advancing is the largest possible angle and receding is the smallest angle from the sample. Differences between the advancing and receding contact angles, or the hysteresis, can be used to describe characteristics about the surface.[46] Contact angles from freshly oxygenated samples were found to be <5° for oxygen plasma treatment and about 55° for ozone treatment. From these reference points, functionalization of the surface with the different alkyl and pegylated linkers was found to influence the resulting contact angles for the samples. As shown in Table 1, both oxygenation methods and ensuing surface chemistry were found to significantly decrease the receding contact angle, indicating an enhanced wettability of the surface. Substantial differences in oxygen plasma-treated surfaces were found between initial treatment with the plasma and the functionalization of the clickable surface. This is expected to some degree because the functional groups being attached (mostly alkyl or perfluoroalkyl groups) are more hydrophobic than the expected functional groups present after oxidation, such as carboxylic acids that would be ionized at neutral pH. A possible contributing factor may also be the scission of the polymer during the oxidation process, resulting in highly oxygenated defects on the surface. Initial contact angle measurements would include surfaces that might contain microscopic defects, and upon solution-based functionalization the small defects and (or) the washing away of

Can. J. Chem. Downloaded from www.nrcresearchpress.com by Xi'an Jiaotong University on 09/19/12
For personal use only.

Scheme 2. Preparation of azide-terminated Zeonor 1060R surfaces and subsequent copper(I)-catalyzed [3 + 2] azide–alkyne cycloaddition.

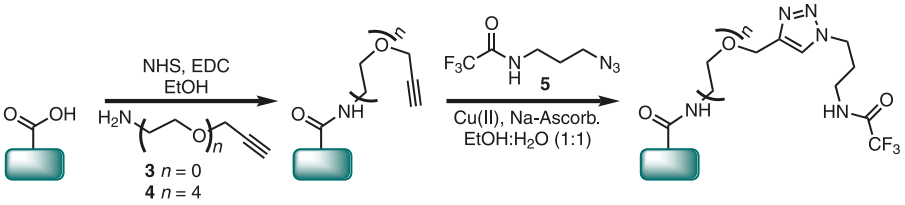

Table 1. Contact angle measurements for azide- and alkyne-terminated Zeonor 1060R surfaces before and after copper-mediated [3 + 2] cycloadditions (CA = contact angle, adv. = advancing and rec. = receding).

Entry	Terminated surface	Oxygen source	Ca[a] (adv.)	Ca[a] (rec.)
1	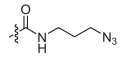	O_3	73.0	21.9
2		O_3	77.7	25.1
3		O_2	72.8	20.5
4	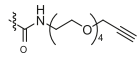	O_3	82.4	15.5
5	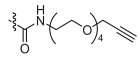	O_2	65.7	17.8
6	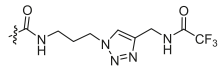	O_3	72.2	42.4
7	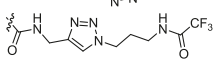	O_3	81.5	41.0

[a]Values are an average of five measurements for each plate and generally have a standard deviation of 1°–2° for the advancing contact angle and a deviation of 2°–5° for the receding contact angle.

fragments might contribute to a greater change in contact angle and a more hydrophobic surface.[11]

Contact angles for surfaces functionalized with **4** (Table 1, entries 4 and 5) were found to possess the smallest receding contact angles, for both oxygen plasma and ozone treatments; this result was expected because pegylated derivatives are useful for increasing water solubility. Ozone-treated surfaces possessing either alkyne or azide motifs appended via hydrocarbon linkers (Table 1, entries 1–3) were found to exhibit the greater receding contact angles. In comparing entries 2 and 3 in Table 1, there is a significant difference between oxygen plasma and ozone treatment on surfaces terminated with **3**. Entries 6 and 7 demonstrate that once the CuAAC reaction has been carried out, a significant increase in receding contact angle occurred because of the hydrophobic nature of the linker.

Surface hysteresis can be influenced by a number of factors including surface roughness, chemical heterogeneity, surface deformation, surface configurational change, and adsorption and desorption. Surface roughness and deformation of the samples were found to have little influence on the contact angles based on AFM (results not shown), since the average deviation on surfaces was determined to be 90 Å. Oxygenated Zeonor surfaces are known to revert to their original surface environment over time through molecular reorganization,[47] but reorganization will not occur once surface functional groups are converted to the corresponding amides. Chemical heterogeneity, where the surface functionalization randomly occurs across the surface, may have some contribution to the observed hysteresis because it is known that ozonolysis produces some chemical heterogeneity on the surface.[16]

Surface functionalization by CuAAC and XPS

To unequivocally prove that the surfaces were functionalized through amide bond formation and not by nonspecific binding, a series of experiments were measured by XPS. For all samples, the binding energy (BE) was calibrated to 285 eV for the C1s signal. The XPS spectrum for native Zeonor surface (Fig. 1*a*) displays a predominant peak from C1s (98.78%; Table 1, entry 1) and a small O1s signal (1.22%; Table 1, entry 1). XPS analysis of surfaces treated by ozonolysis demonstrated that a significant degree of oxygenation had occurred (Fig. 1*b*), where the elemental oxygen on the surface rose to 11.43% (Table 2, entry 2). Determining an effective surface coverage of oxygen from the XPS data requires knowledge of the inelastic mean free path for C1s photoelectrons in Zeonor. In the absence of this quantity, a value of ~3.5 nm can be assumed based on calculations for other polymers such as polystyrene and PMMA.[48] Using this value along with the density of Zeonor (1 g/cm^3), and assuming that all the oxygen is incorporated at the surface of the polymer, the observed oxygen signal corresponds to ~1.25 oxygen atoms per surface carbon atom. NHS–EDC coupling of **1** to the surface resulted in a signal for N1s (Fig. 1*c*). The observation of a N1s peak clearly indicated that the azide had been covalently attached to the surface via an amide linkage, since control experiments conducted in the absence of NHS–EDC found that nonspecific binding of **1** did not occur (data not shown). The percentage of nitrogen was shown to increase on the surface to 6.44% (Table 3, entry 3). Since each grafted azide will contribute four nitrogen atoms, the observed nitrogen signal corresponds to a surface coverage of ~0.1 ML (~10% of a monolayer) of azide groups. Having an azide grafted to ~10% of surface carbons is a useful amount in terms of immobilizing probe biomolecules on the surface.

After subjecting the azide-terminated surface to CuAAC reaction with fluorinated alkyne **2**, the XPS spectrum (Fig. 1*d*) showed incorporation of fluorine (2.72%; Table 3, entry 4) at a BE of 686 eV and of copper at a BE of 932 eV. Control experiments without the presence of copper did not provide a signal from fluorine, which indicated that nonspecific adsorption of **2** had not occurred on the surface and, as well, that copper was indeed necessary for the CuAAC reaction (data not shown).

Analogously, modification of the ozone-treated Zeonor 1060R surface with alkyne **3** and subsequent CuAAC reaction with **4** were analyzed by XPS (Fig. 2). XPS spectra were obtained for the alkyne-terminated surface (Fig. 2*a*)

Can. J. Chem. Downloaded from www.nrcresearchpress.com by Xi'an Jiaotong University on 09/19/12
For personal use only.

Can. J. Chem. Downloaded from www.nrcresearchpress.com by Xi'an Jiaotong University on 09/19/12
For personal use only.

Fig. 1. X-ray photoelectron spectroscopy (XPS) analysis of Zeonor 1060R oxidation followed by functionalization with **1** and copper-catalyzed azide–alkyne cycloaddition (CuAAC) reaction with **2**. (*a*) Native Zeonor 1060R. (*b*) Ozone-treated Zeonor 1060R. (*c*) **1**-Terminated surface. (*d*) CuAAC reaction of **1**-terminated surface with **2**.

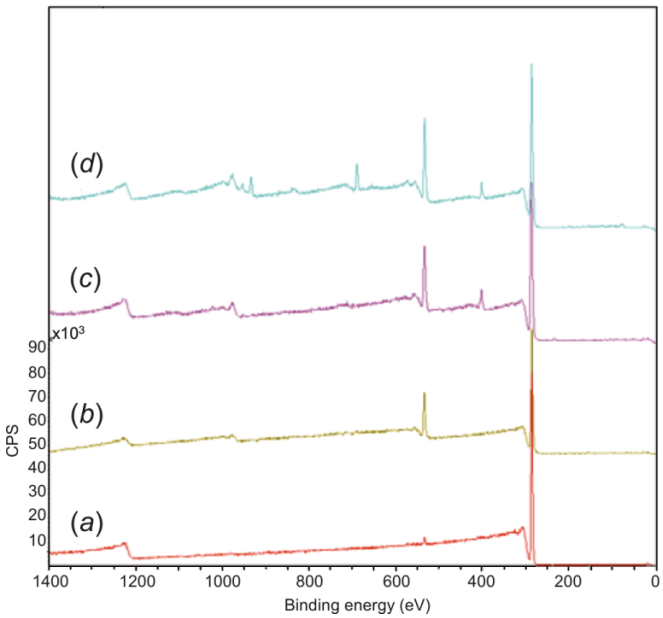

Table 2. X-ray photoelectron spectroscopy (XPS) analysis of the azide- and alkyne-terminated Zeonor surfaces before and after performing copper-catalyzed azide–alkyne cycloaddition (CuAAC) reactions.

Entry	Terminated surface	C–O ratio	C–N ratio	O–N ratio	N–F ratio
1	**1** (before)	7.1	12.8	1.8	na
2	**1** (after)	6.1	15.0	2.4	1.9
3	**3** (before)	6.1	26.8	4.4	na
4	**3** (after)	5.1	19.4	3.8	2.2

and triazole-linked surface (Fig. 2*b*). NHS–EDC coupling with **3** resulted in 3.10% nitrogen incorporation (Table 3, entry 5) with a BE of ca. 400 eV. As expected, the peak intensity of the N1s signal for the alkyne-terminated surface was much lower than for the previous azide-terminated surface, since there was only one nitrogen being incorporated, not four. The fact that the nitrogen signal is only two times higher (and not four) for the azide is likely due to the fact that some of the observed nitrogen signal arises from unreacted NHS-activated groups on the surface. CuAAC of the alkyne-terminated Zeonor 1060R surface with fluorinated azide **5** was confirmed with the incorporation of fluorine (1.88%; Table 3, entry 6) at a BE of 686 eV. As in Fig. 1*d*, some copper catalyst remains on the surface as indicated by the 931 eV feature. Nitrogen features around 400 eV represented an increase of nitrogen from the formation of the triazole cycloadduct. The copper feature at 931eV could be minimized by washing the surface with an ethanol–imidazole solution (Fig. 2*c*). Control experiments conducted in the absence of CuSO4 – sodium ascorbate did not show nonspecific adsorption of **5** onto the surface.

Additional analysis of the surfaces that underwent click reactions was performed to compare the different ratios of incorporated elements (Table 2). Investigating either azide **1** or alkyne **3** terminated surfaces before and after click reactions provides information regarding CuAAC reaction efficiency on the surface. Under ideal conditions, where incorporation of the CF_3 label results from triazole formation, N and F should be found in a 5:3 ratio. The observed N–F ratios for reactions of **1** and **3** terminated surfaces with **5** were found to be 1.9 and 2.2, respectively (Table 2, entries 2 and 4), which are quite close to the expected value. This close correspondence between expected and measured N–F ratios indicates that the CuAAC coupling reactions proceed quite efficiently with most of the initial azide or alkyne groups leading to triazole formation. Coupling with the azide-terminated surface yields a slightly greater amount of fluorine incorporation suggesting a greater overall grafting efficiency for this route. The expected O–N ratios for **1**-and **3**-terminated surfaces are 0.25 and 1, respectively. Upon triazole formation, the ratio should change to 0.4. The observed O–N ratios for the initial azide and alkyne surfaces are significantly larger than expected. The azide-terminated surface exhibits 14% of the expected nitrogen content, whereas the alkyne-terminated surface has 22% of the expected nitrogen (assuming all of the initial oxygen is the form of acid groups). Several factors contribute to the excess oxygen (or lower nitrogen content): not all oxygen induced by the ozone treatment is in the form of carboxylic acids; it is likely that not all carboxylic acids are NHS activated; and finally not all NHS-activated acids lead to amide formation. Unreacted NHS activated groups yield a O–N ratio of 4. Because the initial surfaces have excess oxygen, it is not surprising that the surfaces after CuAAC reaction also exhibit larger O–N ratios than expected. However, the trends upon triazole formation are as expected with coupling to the azide surface increasing the O–N ratio, whereas coupling to the alkyne surface decreases the O–N ratio. The observed C–N and C–O ratios are also clearly larger than expected based on the grafted molecules alone, since much of the carbon signal comes from several layers of "bulk" Zeonor. However, the changes after the CuACC reaction are in accord with expectations, with the C–N ratio increasing upon coupling to the azide-terminated surface and decreasing upon addition to the alkyne.

CuAAC reactions of alkyne-terminated cycloolefin polymer surfaces with tetramethylrhodamine azide

Having demonstrated CuAAC reactions on the surface of alkyne- or azide-terminated Zeonor surfaces using fluorinated chemical handles, we wanted to investigate the generation of a thin fluorescent film by reacting alkyne-terminated Zeonor surfaces with a fluorescent chemical handle (Fig. 3), tetramethylrhodamine azide (TAMRA-N_3).[49] We also wanted to evaluate the dependence of alkyne linker length and whether the presence of a TBTA ligand would result in more efficient CuAAC reactions within shorter timeframes.

As expected, **3**- and **4**-terminated Zeonor 1060R surfaces underwent CuAAC reactions with TAMRA-N_3, and the course of the reaction was monitored by fluorescence. After 1 h of reaction, a significant increase in fluorescence on the surface was observed for both alkyne-terminated surfaces, indicating successful formation of the 1,4-substituted triazole

Can. J. Chem. Downloaded from www.nrcresearchpress.com by Xi'an Jiaotong University on 09/19/12
For personal use only.

Table 3. Elemental composition percentages of Zeonor 1060R, ozone-treated Zeonor 1060R, and **1**-and **3**-terminated surfaces before and after copper-catalyzed azide–alkyne cycloaddition (CuAAC) with **2** and **5**, respectively.

			Elemental composition (%)[a]			
Entry	Terminated surface	Oxidant	C1s	O1s	N1s	F1s
1	Native	na	98.78	1.22	0	0
2	Oxidized	O_3	88.17	11.43	0	0
3	**1** (before)	O_3	82.25	11.66	6.44	0
4	**1** (after)	O_3	79.10	12.88	5.28	2.72
5	**3** (before)	O_3	82.94	13.65	3.10	0
6	**3** (after)	O_3	78.42	15.37	4.05	1.88

[a]Values were determined by background subtraction and applying a sensitivity-factor correction using the Casa XPS software. Values represent the average of at least three measurements from two independent samples.

Fig. 2. X-ray photoelectron spectroscopy (XPS) analysis of surface modification through ozonolysis and functionalization with **3** followed by copper-catalyzed azide–alkyne cycloaddition (CuAAc) with **5**. (*a*) Functionalization through EDC–NHS and **3**. (*b*) CuAAC reaction of **3**-terminated surface with **5**. (*c*) Removal of copper through ethanol–imidazole washing.

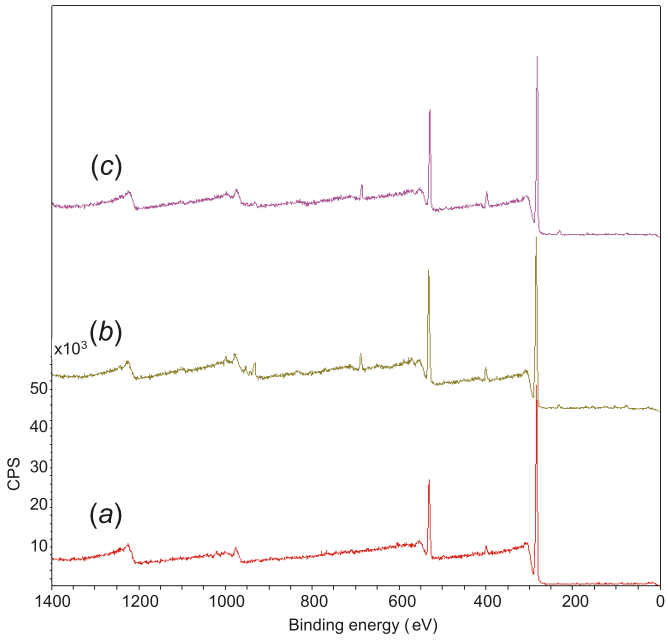

Fig. 3. Generation of a fluorescent thin film on **3**- and **4**-terminated Zeonor surfaces via copper-catalyzed azide–alkyne cycloaddition (CuAAC) reactions with tetramethylrhodamine azide (TAMRA-N_3).

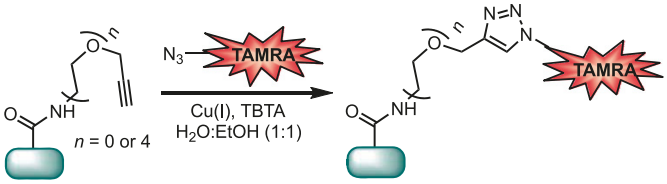

product (Fig. 4, lanes 2 and 3). The negative controls after 1 h of reaction (Fig. 4, lanes 4 and 5) and 20 h of reaction (Fig. 4, lanes 8 and 9) resulted in negligible increases in fluorescence, indicating minimal nonspecific binding of

Fig. 4. Fluorescence from copper-catalyzed azide–alkyne cycloaddition (CuAAC) reactions of **3**- and **4**-terminated surfaces with tetramethylrhodamine azide (TAMRA-N_3).

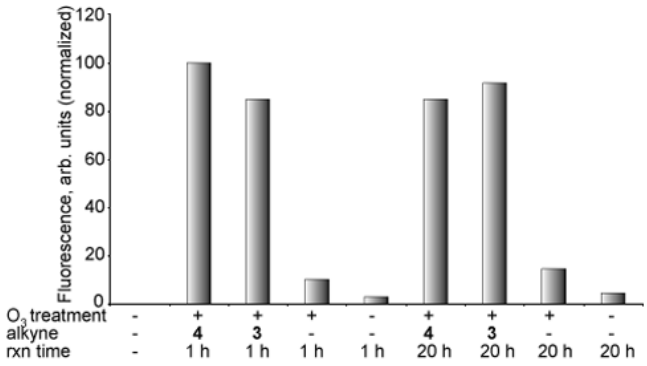

TAMRA-N_3 to the surface. This background fluorescence could be minimized by washing the surface with KOH–EtOH solution.

After 20 h of CuAAC reaction, fluorescence signals from reactions of **3**- and **4**-terminated surfaces displayed the expected changes owing to successful functionalization (Fig. 4, lanes 6 and 7), whereas the negative controls demonstrated a small increase of nonspecific binding of TAMRA-N_3 to the surface (Fig. 4, entries 8 and 9). Based on the fluorescence experiments, **3**- and **4**-terminated Zeonor surfaces underwent successful CuAAC reactions within 1 h in the presence of TBTA. The added pegylated linker length of **4** displayed slightly more efficient CuAAC reactions in the 1 h reaction times; this can likely be attributed to the added flexibility and solubility of this alkyne linker under the CuAAC reaction conditions.

Conclusion

We investigated the oxidation of Zeonor 1060R surfaces using both ozone and oxygen plasma and found both techniques to provide viable routes for attaching the unique azide or alkyne clickable groups via amide couplings. From our data, ozone and oxygen plasma were comparable in binding efficacy for identical amines, and ozone would be the preferred choice based on convenience and cost. Zeonor surfaces were found to support a clickable surface that reacted in

aqueous ethanol for either azide or alkyne moieties, but azide surfaces were found to be ideal based on yields estimated by multiple XPS experiments. Fluorescence experiments with TAMRA-N3 provided a visual means of monitoring the CuAAC reactions of **3** and **4** on the oxidized Zeonor 1060R surface. With these proof-of-principle approaches that we have shown for clickable surfaces, it is now possible to apply modular chemistry to incorporate numerous different reporter groups onto Zeonor-based slides or devices. We are currently conducting such experiments and the results will be reported in due course.

Can. J. Chem. Downloaded from www.nrcresearchpress.com by Xi'an Jiaotong University on 09/19/12
For personal use only.

Materials and methods

Materials

Zeonor 1060R pellets were obtained from Zeon Chemical (Louisville, Kentucky). The plates weree formed by injection moulding using a Boy 30A injection tool (Dr. Boy GmbH & Co. KG, Germany) at a temperature of 250–260 °C, an injection speed of 40 mm/s, and a pressure of 132 bar (1 bar = 100 kPa). All chemicals were purchased from Sigma-Aldrich and were used without further purification. The following reagents were prepared according to literature procedures: 3-azidopropylamine (**1**),[33,34] *N*-trifluoroacetylpropargylamine (**2**),[50,51] 3,6,9,12-tetraoxopentadec-14-yn-1-amine (**4**),[39] 1-azido-3-(trifluoroacetamido)propane (**5**),[34] and TAMRA-N_3.[49]

XPS

The XPS analyses were performed using a PHI 5500 XPS instrument with a monochromated Al Kα source at an angle 45° from the wafer normal. (The X-ray source is Al 1486.6 eV mono at 350.0 W.) The PHI model 10-360 precision energy analyzer consists of an input lens, a spherical capacitor analyzer (SCA), and a detector. All experimental data were obtained within a vacuum of 10^{-9} Torr (1 Torr = 133.322 Pa). Quantitative analysis of the spectra reported in Tables 2 and 3 was carried out using CasaXPS version 2.3.14.

Preparation of Zeonor 1060R plates

Ozone treatment of Zeonor 1060R plates

Surfaces of Zeonor 1060R were treated for 1 h in an OZO-2VTT (O_3 Zomax, Canada) ozone generator that produces 3% ozone (by weight).

Oxygen plasma treatment of the Zeonor 1060R plates

Plates were exposed to an oxygen plasma (Plasma-lab 80Plus, Oxford Instruments, UK) for 10 min at a pressure of 100 mTorr, a gas flow of 20 cm^3/min, and a power of 200 W.

Contact angle measurements

Advancing and receding contact angle measurements were obtained from a Ramé-Hart Instrument Co. goniometer (model 200-F1, Netcong, New Jersey) using deionized water as the probe liquid.

General procedure for azide–alkyne functionalization of oxygenated Zeonor 1060R

To a 50 mL round bottom flask were added EtOH (30 mL), NHS (158 mg, 1.37 mmol), and EDC–HCl (570 mg, 2.74 mmol), and the mixture was stirred until a homogeneous solution was obtained. Then, oxygenated Zeonor 1060R was introduced into the solution and stirring was continued for 2 h, after which time the samples were removed and washed with EtOH (two times) and dried under purified nitrogen. The samples were then added to a solution containing either azide (**1**) or alkyne (**3** or **4**) in DMSO (30 mL) and stirred for 16 h. After 16 h, samples were removed and washed with EtOH and again dried under a stream of nitrogen gas.

General procedure for CuAAC reactions on the plastic surface

In a 20 mL screw cap vial were added EtOH (5 mL), dH_2O (5 mL), and $CuSO_4{\cdot}5H_2O$ (2.2 mg, 0.088 mmol) and the vial was covered with aluminum foil and cooled to 0 °C. Sodium ascorbate (3 equiv, 5.0 mg, 0.252 mmol) was added and the solution was stirred for 20 min, at which time either **2** or **5** was added followed by the functionalized plastic surface. After stirring overnight, samples were washed with EtOH, H_2O, and EtOH and dried with purified nitrogen or argon. Samples were examined by XPS. Samples were placed into a solution of imidazole in EtOH (0.11 mol/L (113 mg, 1.66 mmol in 15 mL)) for 30 min, followed by two successive EtOH washes and then dried with purified nitrogen. Samples were re-examined by XPS to confirm the presence or absence of copper.

General procedure for CuAAC reactions of alkyne-terminated surfaces with TAMRA-N_3

In a 20 mL screw cap vial in the dark was added 10 mL of EtOH–H_2O (1:1), the solution was cooled to 0 °C, and then 0.5 mL of a $CuSO_4{\cdot}5H_2O$ solution (3.8 mg in 4.0 mL of water) and 0.5 mL of a sodium ascorbate solution (30.7 mg in 4 mL of water) were added. The solution was stirred for 20 min at which time 0.25 mL of a TBTA solution (16.2 mg in 2.0 mL DMSO) and 0.25 mL of TAMRA-N_3[49] (3.9 mg in 4.0 mL EtOH) were added, followed by a Zeonor plate (**3**-terminated, **4**-terminated, ozone treated, and native Zeonor 1060R). After the desired reaction time, the plates were removed, then briefly washed for 2 min with a freshly prepared solution of KOH in EtOH, then washed with EtOH, H_2O, and EtOH, and then dried with purified nitrogen. Plates were scanned for fluorescence using the Typhoon 9410 (GE Healthcare, Piscataway, New Jersey) and analyzed using ImageJ software.

Acknowledgements

This work has been generously supported by funding from Genome Canada and the Genomics and Health Initiative of the National Research Council of Canada. The authors thank Dr. J. Hulse and Dr. D. Kennedy for helpful discussions, and Dr. Z. He and Ms. S. Moisa for XPS assistance.

References

(1) Wang, J. *Nucleic Acids Res.* **2000** *28* (16), 3011. doi:10.1093/nar/28.16.3011.

Can. J. Chem. Downloaded from www.nrcresearchpress.com by Xi'an Jiaotong University on 09/19/12
For personal use only.

(2) Southern, E.; Mir, K.; Shchepinov, M. *Nat. Genet.* **1999** *21*, 5. doi:10.1038/4429.
(3) Ramsay, G. *Nat. Biotechnol.* **1998** *16* (1), 40. doi:10.1038/nbt0198-40.
(4) Nallur, G.; Marrero, R.; Luo, C.; Krishna, R. M.; Bechtel, P. E.; Shao, W.; Ray, M.; Wiltshire, S.; Fang, L.; Huang, H.; Liu, C.-G.; Sun, L.; Sawyer, J. R.; Kingsmore, S. F.; Schweitzer, B.; Xia, J. Protein and Nucleic Acid Detection by Rolling Circle Amplification on Gel-based Microarrays. In *Biomedical Microdevices;* Springer: Netherlands, 2003; pp 115–123.
(5) Kusnezow, W.; Hoheisel, J. D. *J. Mol. Recognit.* **2003** *16* (4), 165. doi:10.1002/jmr.625.
(6) Cutler, P. *Proteomics* **2003** *3* (1), 3. doi:10.1002/pmic.200390007.
(7) Henares, T. G.; Mizutani, F.; Hisamoto, H. *Anal. Chim. Acta* **2008** *611* (1), 17. doi:10.1016/j.aca.2008.01.064.
(8) Becker, H.; Gartner, C. *Anal. Bioanal. Chem.* **2008** *390* (1), 89. doi:10.1007/s00216-007-1692-2.
(9) Shin, J. Y.; Park, J. Y.; Liu, C.; He, J.; Kim, S. C. *Pure Appl. Chem.* **2005** *77* (5), 801. doi:10.1351/pac200577050801.
(10) Raj, J.; Herzog, G.; Manning, M.; Volcke, C.; MacCraith, B. D.; Ballantyne, S.; Thompson, M.; Arrigan, D. W. M. *Biosens. Bioelectron.* **2009** *24* (8), 2654. doi:10.1016/j.bios.2009.01.026.
(11) Zhao, Z.; Peytavi, R.; Diaz-Quijada, G. A.; Picard, F. J.; Huletsky, A.; Leblanc, E.; Frenette, J.; Boivin, G.; Veres, T.; Dumoulin, M. M.; Bergeron, M. G. *J. Clin. Microbiol.* **2008** *46* (11), 3752. doi:10.1128/JCM.00377-08.
(12) Stachowiak, T. B.; Mair, D. A.; Holden, T. G.; Lee, L. J.; Svec, F.; Fréchet, J. M. J. *J. Sep. Sci.* **2007** *30* (7), 1088. doi:10.1002/jssc.200600515.
(13) Larsson, A.; Liedberg, B. *Langmuir* **2007** *23* (22), 11319. doi:10.1021/la700729q.
(14) Larsson, A.; Ekblad, T.; Andersson, O.; Liedberg, B. *Biomacromolecules* **2007** *8* (1), 287. doi:10.1021/bm060685g.
(15) Laib, S.; MacCraith, B. D. *Anal. Chem.* **2007** *79* (16), 6264. doi:10.1021/ac062420y.
(16) Diaz-Quijada, G. A.; Peytavi, R.; Nantel, A.; Roy, E.; Bergeron, M. G.; Dumoulin, M. M.; Veres, T. *Lab Chip* **2007** *7* (7), 856. doi:10.1039/b700322f.
(17) Liu, Y.; Cady, N.; Batt, C. *Biomed. Microdevices* **2007** *9* (5), 769. doi:10.1007/s10544-007-9088-9.
(18) Bhattacharyya, A.; Klapperich, C. *Biomed. Microdevices* **2007** *9* (2), 245. doi:10.1007/s10544-006-9026-2.
(19) Jönsson, C.; Aronsson, M.; Rundstrom, G.; Pettersson, C.; Mendel-Hartvig, I.; Bakker, J.; Martinsson, E.; Liedberg, B.; MacCraith, B.; Ohman, O.; Melin, J. *Lab Chip* **2008** *8* (7), 1191. doi:10.1039/b800297e.
(20) Kolb, H. C.; Finn, M. G.; Sharpless, K. B. *Angew. Chem. Int. Ed.* **2001** *40* (11), 2004. doi:10.1002/1521-3773(20010601)40:11<2004::AID-ANIE2004>3.0.CO;2-5.
(21) Rostovtsev, V. V.; Green, L. G.; Fokin, V. V.; Sharpless, K. B. *Angew. Chem. Int. Ed.* **2002** *41* (14), 2596. doi:10.1002/1521-3773(20020715)41:14<2596::AID-ANIE2596>3.0.CO;2-4.
(22) Fazio, F.; Bryan, M. C.; Blixt, O.; Paulson, J. C.; Wong, C.-H. *J. Am. Chem. Soc.* **2002** *124* (48), 14397. doi:10.1021/ja020887u.
(23) Collman, J. P.; Devaraj, N. K.; Chidsey, C. E. D. *Langmuir* **2004** *20* (4), 1051. doi:10.1021/la0362977.
(24) Collman, J. P.; Devaraj, N. K.; Eberspacher, T. P. A.; Chidsey, C. E. D. *Langmuir* **2006** *22* (6), 2457. doi:10.1021/la052947q.
(25) Yamauchi, J.; Yamaoka, A.; Ikemoto, K.; Matsui, T. *Bull. Chem. Soc. Jpn.* **1991** *64* (4), 1173. doi:10.1246/bcsj.64.1173.
(26) Giamalva, D. H.; Church, D. F.; Pryor, W. A. *J. Org. Chem.* **1988** *53* (15), 3429. doi:10.1021/jo00250a005.
(27) Rohr, T.; Ogletree, D.; Svec, F.; Fréchet, J. *Adv. Funct. Mater.* **2003** *13* (4), 264. doi:10.1002/adfm.200304229.
(28) Schnapp, K. A.; Platz, M. S. *Bioconjug. Chem.* **1993** *4* (2), 178. doi:10.1021/bc00020a011.
(29) Schnapp, K. A.; Poe, R.; Leyva, E.; Soundararajan, N.; Platz, M. S. *Bioconjug. Chem.* **1993** *4* (2), 172. doi:10.1021/bc00020a010.
(30) Keana, J. F. W.; Cai, S. X. *J. Org. Chem.* **1990** *55* (11), 3640. doi:10.1021/jo00298a048.
(31) Kramer, W.; Schneider, S. *J. Lipid Res.* **1989** *30* (8), 1281.
(32) Bergmann, K. E.; Carlson, K. E.; Katzenellenbogen, J. A. *Bioconjug. Chem.* **1994** *5* (2), 141. doi:10.1021/bc00026a006.
(33) Lampkins, A. J.; O'Neil, E. J.; Smith, B. D. *J. Org. Chem.* **2008** *73* (16), 6053. doi:10.1021/jo8011336.
(34) Carboni, B.; Benalil, A.; Vaultier, M. *J. Org. Chem.* **1993** *58* (14), 3736. doi:10.1021/jo00066a028.
(35) Chan, T. R.; Hilgraf, R.; Sharpless, K. B.; Fokin, V. V. *Org. Lett.* **2004** *6* (17), 2853. doi:10.1021/ol0493094.
(36) Gupta, S. S.; Kuzelka, J.; Singh, P.; Lewis, W. G.; Manchester, M.; Finn, M. G. *Bioconjug. Chem.* **2005** *16* (6), 1572. doi:10.1021/bc050147l.
(37) Rodionov, V. O.; Presolski, S. I.; Díaz Díaz, D.; Fokin, V. V.; Finn, M. G. *J. Am. Chem. Soc.* **2007** *129* (42), 12705. doi:10.1021/ja072679d.
(38) Rodionov, V. O.; Presolski, S. I.; Gardinier, S.; Lim, Y.-H.; Finn, M. G. *J. Am. Chem. Soc.* **2007** *129* (42), 12696. doi:10.1021/ja072678l.
(39) Polito, L.; Monti, D.; Caneva, E.; Delnevo, E.; Russo, G.; Prosperi, D. *Chem. Commun. (Camb.)* **2008** (5), 621. doi:10.1039/b716113a.
(40) Alauzun, J. G.; Fortuna, J. N.; Sheardown, H.; Gonzaga, F.; Brook, M. A. *J. Mater. Chem.* **2009** *19* (28), 5033. doi:10.1039/b904396a.
(41) Chai, J.; Lu, F.; Li, B.; Kwok, D. Y. *Langmuir* **2004** *20* (25), 10919. doi:10.1021/la048947s.
(42) Beaulieu, I.; Geissler, M.; Mauzeroll, J. *Langmuir* **2009** *25* (12), 7169. doi:10.1021/la9001972.
(43) Wilson, D. J.; Williams, R. L.; Pond, R. C. *Surf. Interface Anal.* **2001** *31* (5), 397. doi:10.1002/sia.1066.
(44) Chatelier, R. C.; Xie, X.; Gengenbach, T. R.; Griesser, H. J. *Langmuir* **1995** *11* (7), 2585. doi:10.1021/la00007a043.
(45) Chatelier, R. C.; Xie, X.; Gengenbach, T. R.; Griesser, H. J. *Langmuir* **1995** *11* (7), 2576. doi:10.1021/la00007a042.
(46) Wang, J.-H.; Claesson, P. M.; Parker, J. L.; Yasuda, H. *Langmuir* **1994** *10* (10), 3887. doi:10.1021/la00022a080.
(47) Gaudioso, J.; Craighead, H. G. *J. Chromatogr. A* **2002** *971* (1–2), 249. doi:10.1016/S0021-9673(02)00843-9.
(48) Tanuma, S.; Powell, C. J.; Penn, D. R. *Surf. Interface Anal.* **1994** *21* (3), 165. doi:10.1002/sia.740210302.
(49) Speers, A. E.; Cravatt, B. F. *Chem. Biol.* **2004** *11* (4), 535. doi:10.1016/j.chembiol.2004.03.012.
(50) Trybulski, E. J.; Zhang, J.; Kramss, R. H.; Mangano, R. M. *J. Med. Chem.* **1993** *36* (23), 3533. doi:10.1021/jm00075a007.
(51) Orain, D.; Mattes, H. *Synlett* **2005** *2005* (19), 3008. doi:10.1055/s-2005-921902.

Synthesis of phenylacetic acid regioisomers possessing an N-substituted 1,2-dihydropyrid-2-one pharmacophore — Evaluation as inhibitors of cyclooxygenases and 5-lipoxygenase

Gang Yu, Morshed A. Chowdhury, Zhangjian Huang, Khaled R. A. Abdellatif, and Edward E. Knaus

Can. J. Chem. Downloaded from www.nrcresearchpress.com by Xi'an Jiaotong University on 09/19/12
For personal use only.

Abstract: The Suzuki–Miyaura cross-coupling reaction provides a useful method for the synthesis of methyl 2-(2-chloropyridyl or 2-methoxypyridyl)phenylacetates. The 2-chloropyridyl or 2-methoxypyridyl ring system can be readily elaborated to N-substituted (OH, Me, CHF_2, H) 1,2-dihydropyrid-2-one ring systems that are useful synthons for use in bioorganic and medicinal chemistry applications.

Key words: Suzuki–Miyaura cross-coupling reaction, 1,2-dihydropyrid-2-ones, cyclooxygenase (COX) and 5-lipoxygenase (5-LOX) inhibition.

Résumé : La réaction de couplage croisé de Suzuki–Miyaura est une méthode utile pour la synthèse d'esters 2-(2-chloropyridyl)- ou de 2-(méthoxypyridyl)phénylacétates. Ce système cyclique, portant des groupes 2-chloropyridyle ou 2-méthoxypyridyle, peut facilement être transformé en systèmes cycliques à base de 1,2-dihydropyrid-2-one N-substituée (OH, Me, CHF_2, H), des synthons utiles dans des applications de chimie bioorganique ou médicinale.

Mots-clés : réaction de couplage croisé de Suzuki–Miyaura, 1,2-dihydropyrid-2-ones, inhibition de la cyclooxygénase (COX) et de la 5-lipoxygénase (5-LOX).

[Traduit par la Rédaction]

Introduction

Biotransformation of arachidonic acid gives rise to prostaglandin and leukotriene inflammatory mediators that are produced via their respective cyclooxygenase (COX) and lipoxygenase (LOX) pathways.[1] Dual inhibition of the LOX and COX enzymatic pathways[2] provides a rational approach for the design of superior anti-inflammatory agents with a better safety profile relative to ulcerogenic nonsteroidal anti-inflammatory drugs (NSAIDs) or selective COX-2 inhibitors that increase the incidence of adverse cardiovascular thrombotic effects.[3,4] The most successful effort to develop 5-LOX inhibitors was focused on *N*-hydroxyureas such as zileuton (**1**, see structure in Fig. 1), which is believed to chelate iron present in the 5-LOX enzyme.[5,6] In earlier studies, we showed that linear acetylenes possessing cyclic hydroxamic acid, *N*-hydroxy-1,2-dihydropyrid-2-one (**2**),[7] or *N*-difluoromethyl-1,2-dihydropyrid-2-one (**3**,[8] **4**[9]) 5-LOX pharmacophores exhibited dual COX and 5-LOX inhibitory activities. In a continuation of our ongoing program to design novel anti-inflammatory agents and acquire additional structure–activity relationship data, we now describe the synthesis of a group of arylacetic acids possessing an N-substituted (OH, Me, CHF_2, H) 1,2-dihydropyrid-2-one moiety, and their evaluation as inhibitors of the COX-1, COX-2, and 5-LOX enzymes.

Results and discussion

Reaction of methyl 2-iodophenylacetate (**5**)[9] with a 4- or 5-pyridineboronic acid (**6a**–**6c**) using a Suzuki–Miyaura[10,11] cross-coupling reaction in the presence of the tetrakis(triphenylphosphine)palladium (0) catalyst and 2 mol/L aqueous sodium carbonate furnished the respective diaryl products **7a**–**7c** in good yields (58%–77%) (Scheme 1). Oxidation of **7a** and **7c** using *m*-chloroperbenzoic acid (*m*-CPBA) in dichloromethane afforded the target methyl 2-(1-oxido-2-chloropyridin-4-yl)phenylacetate (**8a**, 42%) or methyl 2-(1-oxido-2-methoxypyridin-5-yl)phenylacetate (**8c**, 59%). Hydrolysis of the methyl ester **8a** using 2 N sodium hydroxide at reflux for 24 h afforded the target phenylacetic acid product **9a** in 41% yield. Reaction of the *N*-oxide **8c** with acetyl chloride at reflux, and then methanolysis, afforded the *N*-hydroxy-1,2-dihydropyrid-2-one **9c** in 96% yield.[12] Subsequent depro-

Received 3 November 2010. Accepted 22 February 2011. Published at www.nrcresearchpress.com/cjc on 3 May 2011.

G. Yu,* M.A. Chowdhury, Z. Huang, K.R.A. Abdellatif, and E.E. Knaus. Faculty of Pharmacy and Pharmaceutical Sciences, University of Alberta, Edmonton, AB T6G 2N8, Canada.

Corresponding author: Edward E. Knaus (e-mail: eknaus@pharmacy.ualberta.ca).

*Present address: Jiangsu Academy Agricultural Sciences, Nanjing, Jiangsu, 210014, China.

Can. J. Chem. Downloaded from www.nrcresearchpress.com by Xi'an Jiaotong University on 09/19/12
For personal use only.

Fig. 1. Structures of the iron-chelating 5-LOX inhibitor zileuton (**1**) and dual inhibitors of the COX and LOX enzymes that possess an *N*-hydroxy-1,2-dihydropyrid-2-one (**2**) or *N*-difluoromethyl-1,2-dihydropyrid-2-one (**3**, **4**) 5-LOX pharmacophore.

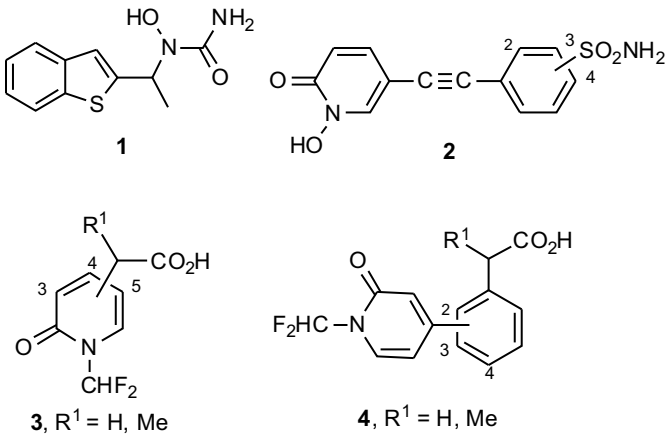

tection of the methyl ester group present in **9c** using lithium hydroxide in MeOH and tetrahydrofuran (THF) at reflux temperature afforded the target phenylacetic acid product **10c** in 74% yield.

The 2-chloropyridine compounds **7a** and **7b** were converted to their respective *N*-methylpyridinium methylsulfate salts (**11a** and **11b**) upon reaction with dimethyl sulfate at reflux in acetonitrile (see Scheme 2).[13] Subsequent treatment of the salts **11a** and **11b** with 2 N aqueous lithium hydroxide at reflux proceeded smoothly, resulting in simultaneous hydrolysis of the methyl ester and conversion of the *N*-methyl-2-chloropyridinium ring to an *N*-methyl-1,2-dihydropyrid-2-one ring, to furnish the corresponding target products **12a** and **12b** in 70%–89% yield.[14] Alternatively, reaction of the 2-chloropyridyl compound **7b** with $FSO_2CF_2CO_2H$[15] in the presence of $NaHCO_3$ afforded the *N*-difluoromethyl-1,2-dihydropyrid-2-one product **13** in 53% yield. Selective hydrolysis of the methyl ester group in **13** using 2 N LiOH in a MeOH–THF–H_2O (1:1:1, *v*/*v*/*v*) solvent system afforded the phenylacetic acid product **14**.[14] In contrast, hydrolysis of **13** under more basic reaction conditions using aqueous 2 N NaOH and a longer reaction time of 5 h resulted in concomitant cleavage of the methyl ester substituent and removal of the *N*-difluoromethyl substituent to afford 2-(2-oxo-1,2-dihydropyridin-5-yl)phenylacetic acid (**15**) in 65% yield.

The *N*-hydroxy-1,2-dihydropyrid-2-one cyclic hydroxamic acid mimetics **9a** and **10c** were designed with the expectation[7] that they would act as iron chelators to inhibit the 5-LOX enzyme. Although the C-5 regioisomer **10c** did exhibit weak COX-2 inhibition (IC_{50} = 10.1 μmol/L), **9a** and **10c** were both inactive as inhibitors of the 5-LOX enzyme (see data in Table 1). Similar enzyme inhibition studies showed that the C-4 (**12a**) and C-5 (**12b**) *N*-methyl-1,2-dihydropyrid-2-one regioisomers were inactive as inhibitors of the 5-LOX and COX-2 enzymes (IC_{50} > 100 μmol/L), but the C-4 regioisomer **12a** exhibited weak inhibition (IC_{50} = 52.4 μmol/L) of the COX-1 enzyme. In spite of its weak in vitro COX-1 inhibitory activity, **12a** showed good in vivo anti-inflammatory activity in a rat model, where a 45% reduction in inflammation was observed for a 100 mg/kg oral dose relative to the reference drug ibuprofen, which furnished a 50% reduction in inflammation for a 67 mg/kg oral dose. The structurally related *N*-difluoromethyl-1,2-dihydropyrid-2-one **14** and 1,2-dihydropyrid-2-one **15** compounds, which failed to inhibit the COX-1 and 5-LOX enzymes (IC_{50} > 100 μmol/L), showed weak inhibition of the COX-2 enzyme relative to the reference drugs aspirin and ibuprofen. In view of their weak COX-2 inhibitory potency and failure to inhibit 5-LOX, the anti-inflammatory activities for **14** and **15** were not determined. These enzyme inhibition structure–activity data show that none of the compounds investigated in this study exhibited the desired dual inhibition of the COX-2 and 5-LOX enzymes.

Scheme 1. Synthesis of *N*-hydroxy-1,2-dihydropyrid-2-one derivatives of phenylacetic acid. Reagents and conditions: (*a*) $Pd(PPh_3)_4$, 2 mol/L Na_2CO_3 (**6a** and **6b**, reflux in THF for 16 h; **6c**, reflux in 1,4-dioxane for 4 h); (*b*) *m*-CPBA, CH_2Cl_2, 25 °C, 48 h; (*c*) 2 N NaOH, reflux, 24 h (**8a**); (*d*) (*i*) AcCl, reflux, 1 h, (*ii*) MeOH, 25 °C, 16 h (**8c**); (*e*) 2 N LiOH, MeOH–THF–H_2O (1:1:1, *v*/*v*/*v*), reflux, 3 h.

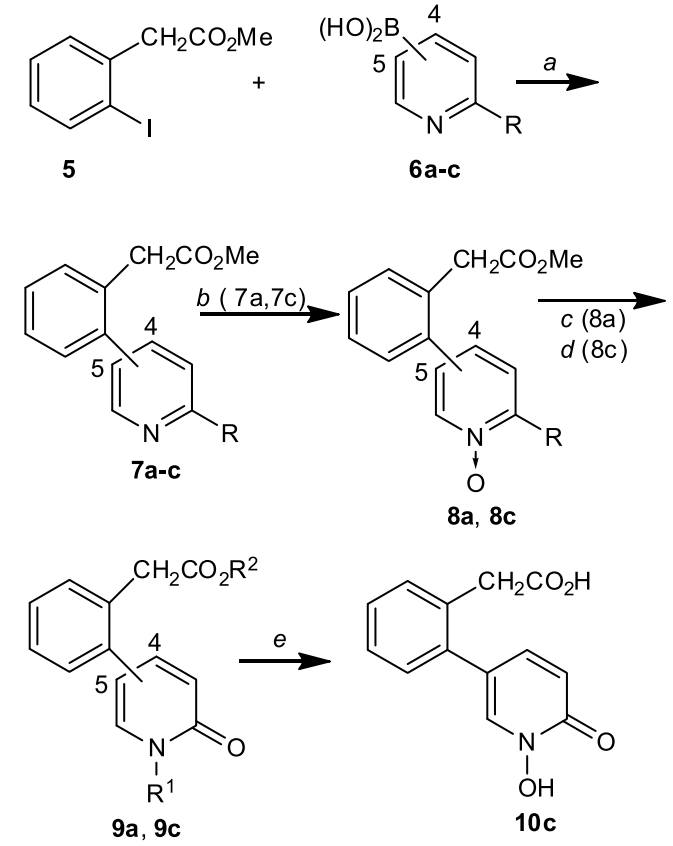

6-8a; 4-isomer, R = Cl
6-7b; 5-isomer, R = Cl
6-8c; 5-isomer, R = OMe
9a; 4-isomer, R^1 = OH, R^2 = H
9c; 5-isomer, R^1 = OH, R^2 = Me

Conclusion

The Suzuki–Miyaura cross-coupling reaction of methyl 2-iodophenylacetate with a 2-chloro- or 2-methoxypyridine-

Can. J. Chem. Downloaded from www.nrcresearchpress.com by Xi'an Jiaotong University on 09/19/12
For personal use only.

Scheme 2. Synthesis of N-substituted (Me, CHF_2, H) 1,2-dihydropyrid-2-one derivatives of phenylacetic acid. Reagents and conditions: (*a*) Me_2SO_4, MeCN, reflux, 6 h; (*b*) 2 N LiOH, MeOH–THF–H_2O (1:1:1, *v*/*v*/*v*), reflux, 2 h; (*c*) $FSO_2CF_2CO_2H$, MeCN, $NaHCO_3$, reflux under argon, 12 h; (*d*) 2 N NaOH, reflux, 5 h.

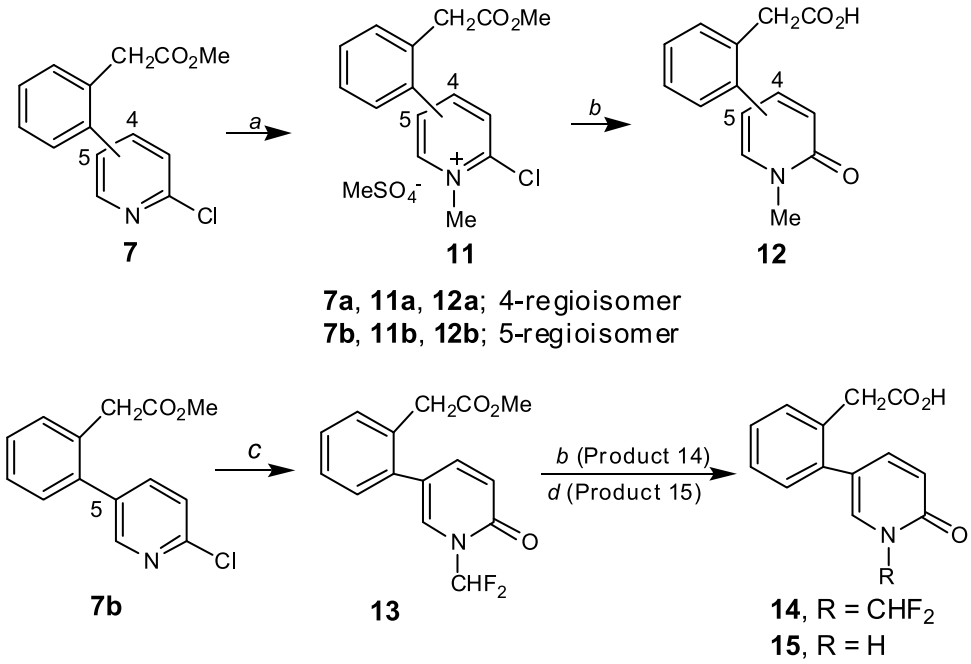

Table 1. In vitro COX-1, COX-2, and 5-LOX enzyme inhibition data for N-substituted (OH, Me, CHF_2, H) 1,2-dihydropyrid-2-one derivatives of phenylacetic acid.

Entry	Compound	COX-1 IC_{50} (μmol/L)[a]	COX-2 IC_{50} (μmol/L)[a]	5-LOX IC_{50} (μmol/L)[b]
1	**9a**	—	—	>100
2	**10c**	>100	10.1	>100
3	**12a**	52.4	>100	>100
4	**12b**	>100	>100	>100
5	**14**	>100	187	>100
6	**15**	>100	18.2	>100
7	Aspirin	0.2	2.4[c]	—
8	Ibuprofen	2.9	1.1[c]	—
9	Zileuton	—	—	1.1

[a]The in vitro test compound concentration required to produce 50% inhibition of ovine COX-1 or human recombinant COX-2. The result (IC_{50}, μmol/L) is the mean of two determinations acquired using an enzyme immunoassay kit (catalog No. 560131, Cayman Chemicals Inc., Ann Arbor, Michigan), and the deviation from the mean is <10% of the mean value.

[b]The in vitro test compound concentration required to produce 50% inhibition of potato 5-LOX (Cayman Chemicals Inc. catalog No. 60401). The result (IC_{50}, μmol/L) is the mean of two determinations acquired using a LOX assay kit (catalog No. 760700, Cayman Chemicals Inc.), and the deviation from the mean is <10% of the mean value.

[c]Data taken from a previous report (ref. 16). COX-2 inhibition was determined using ovine COX-2.

boronic acid provides a useful method for the synthesis of methyl 2-(pyridinyl)phenylacetates. The 2-chloropyridyl and 2-methoxypyridyl ring systems present in this group of compounds can be readily elaborated to *N*-hydroxy-1,2-dihydropyrid-2-one (a cyclic hydroxamic acid), *N*-methyl-1,2-dihydropyrid-2-one, and 1,2-dihydropyrid-2-one ring systems that may serve as useful synthons in bioorganic and medicinal chemistry applications.

Experimental

Instrumentation, analysis, and starting material

Melting points were determined on a Thomas Hoover capillary apparatus and are uncorrected. IR spectra were recorded as films on NaCl plates using a Nicolet 550 Series II Magna FT–IR spectrometer. ^1H NMR spectra were measured on a Bruker AM-300 spectrometer in $CDCl_3$ or DMSO-d_6 with TMS as the internal standard. Compounds **7**–**8**, **9c**, **10c**, **11**, and **13** showed a single spot on Macherey–Nagel Polygram Sil G/UV254 silica gel plates (0.2 mm) using a low, medium, or highly polar solvent system; no residue remained after combustion, indicative of high purity. Microanalyses for all other compounds were performed for C, H, and N (Micro Analytical Service Laboratory, Department of Chemistry, University of Alberta) and were within 0.4% of theoretical values. Silica gel column chromatography was performed using Merck silica gel 60 ASTM (70–230 mesh). All reagents were purchased from the Sigma-Aldrich Chemical Company (Milwaukee, Wisconsin), with the exception of 2-chloropyridine-4-boronic acid, purchased from Combi-Blocks Inc., and were used without further purification.

General Suzuki–Miyaura cross-coupling synthesis of 7a–7c

Methyl 2-iodophenylacetate (**5**, 1.20 g, 4.35 mmol) and a pyridineboronic acid (**6a**–**6c**, 4.35 mmol) were dissolved in a polar solvent (THF, 50 mL for **6a** and **6b** or 1,4-dioxane, 50 mL for **6c**). Aqueous 2 mol/L Na_2CO_3 (6.5 mL, 13.05 mmol) and then $Pd(PPh_3)_4$ (115 mg, 0.10 mmol) were added. The reaction was allowed to proceed at reflux under argon (16 h for **6a** and **6b** and 4 h for **6c**) and then cooled to 25 °C; water (50 mL) was added, and the mixture was extracted with EtOAc (3 × 50 mL). The combined EtOAc extracts were washed with water (2 × 30 mL), the organic

Can. J. Chem. Downloaded from www.nrcresearchpress.com by Xi'an Jiaotong University on 09/19/12
For personal use only.

fraction was dried ($MgSO_4$), and the solvent was removed in vacuo. The residue obtained was purified by silica gel column chromatography using hexanes–EtOAc (3:1, *v*/*v*) as eluent to afford the respective products **7a**–**7c**. Some spectroscopic data for **7a**–**7c** are listed below.

Methyl 2-(2-chloropyridin-4-yl)phenylacetate (7a)

Yield, 74%; yellow oil. IR (film): 2920, 1736, 1536 cm^{-1}. ^1H NMR ($CDCl_3$) δ: 3.72 (s, 2H, C*H*$_2$), 3.73 (s, 3H, O*Me*), 7.39–7.55 (overlapping multiplets, 6H total, phenyl H-3, H-4, H-5, H-6, pyridyl H-3, H-5), 8.44 (d, J = 5.5 Hz, 1H, pyridyl H-6). ^{13}C NMR ($CDCl_3$) δ: 41.0, 52.2, 120.5, 122.1, 125.8, 128.0, 129.5, 130.6, 135.1, 137.2, 150.0, 151.2, 152.2, 171.5.

Methyl 2-(2-chloropyridin-5-yl)phenylacetate (7b)

Yield, 58%; pale yellow oil. IR (film): 2918, 1734, 1590 cm^{-1}. ^1H NMR ($CDCl_3$) δ: 3.56 (s, 2H, C*H*$_2$), 3.64 (s, 3H, O*Me*), 7.24 (d, J = 6.1 Hz, 1H, phenyl H-6), 7.36–7.41 (overlapping multiplets, 3H, phenyl H-3, H-4, H-5), 7.37 (d, J = 8.5 Hz, 1H, pyridyl H-3), 7.68 (dd, J = 8.5, 2.4 Hz, 1H, pyridyl H-4), 8.37 (d, J = 2.4 Hz, 1H, pyridyl H-6). ^{13}C NMR ($CDCl_3$) δ: 38.6, 52.1, 123.7, 127.6, 128.7, 130.3, 130.7, 132.1, 135.6, 137.3, 139.5, 149.7, 150.5, 171.7.

Methyl 2-(2-methoxypyridin-5-yl)phenylacetate (7c)

Yield, 77%; pale yellow syrup. IR (film): 2919, 1736, 1086 cm^{-1}. ^1H NMR ($CDCl_3$) δ: 3.60 (s, 2H, C*H*$_2$), 3.65 (s, 3H, O*Me*), 3.99 (s, 3H, pyridyl-O*Me*), 6.80 (d, J = 8.5 Hz, 1H, pyridyl H-3), 7.23–7.39 (overlapping multiplets, 4H total, phenyl H-3, H-4, H-5, H-6), 7.57 (dd, J = 8.5, 1.8 Hz, 1H, pyridyl H-4), 8.12 (d, J = 1.8 Hz, 1H, pyridyl H-6). ^{13}C NMR ($CDCl_3$) δ: 38.7, 52.0, 53.5, 110.2, 127.2, 127.4, 127.9, 129.7, 130.4, 132.3, 138.7, 139.6, 146.6, 163.3, 172.0.

General procedure for the synthesis of methyl 2-(1-oxido-2-chloropyridin-4-yl)phenylacetate (8a) and methyl 2-(1-oxido-2-methoxypyridin-5-yl)phenylacetate (8c)

m-Chloroperoxybenzoic acid (77% maximum purity) (12 mmol) was added to a stirred solution of a pyridine (**7a** or **7c**, 3.0 mmol) in CH_2Cl_2 (30 mL), and the reaction was allowed to proceed with stirring at 25 °C for 48 h. The solvent was washed with a saturated solution of aqueous $NaHCO_3$ (2 × 20 mL), then washed with water (40 mL) and brine, and the organic fraction was dried ($MgSO_4$). Removal of the solvent from the organic fraction in vacuo gave a residue that was purified by silica gel column chromatography using methanol–EtOAc (10:1, *v*/*v*) as eluent to afford the respective product **8a** or **8c**. Some physical and spectroscopic data for **8a** and **8c** are listed below.

Methyl 2-(1-oxido-2-chloropyridin-4-yl)phenylacetate (8a)

Yield, 42%; pale yellow oil. IR (film): 3060, 3030, 2955, 1741, 1461, 1267 cm^{-1}. ^1H NMR ($CDCl_3$) δ: 3.59 (s, 2H, C*H*$_2$), 3.69 (s, 3H, O*Me*), 7.26 (dd, J = 6.7, 2.4 Hz, 1H, pyridyl H-5), 7.27–7.55 (overlapping multiplets, 4H total, phenyl H-3, H-4, H-5, H-6), 7.55 (d, J = 2.4 Hz, 1H, pyridyl H-3), 8.40 (d, J = 6.7 Hz, 1H, pyridyl H-6). ^{13}C NMR ($CDCl_3$) δ: 38.5, 52.3, 124.7, 127.6, 127.9, 129.3, 129.5, 131.1, 131.5, 137.1, 139.5, 139.9, 141.6, 171.5.

Methyl 2-(1-oxido-2-methoxypyridin-5-yl)phenylacetate (8c)

Yield, 59%; pale yellow oil. IR (film): 2961, 1740, 1438, 1257 cm^{-1}. ^1H NMR ($CDCl_3$) δ: 3.58 (s, 2H, C*H*$_2$), 3.67 (s, 3H, O*Me*), 4.14 (s, 3H, pyridyl-O*Me*), 6.96 (d, J = 8.5 Hz, 1H, pyridyl H-3), 7.23–7.39 (overlapping multiplets, 4H total, phenyl H-3, H-4, H-5, H-6), 7.32 (dd, J = 8.5, 1.8 Hz, 1H, pyridyl H-4), 8.29 (d, J = 1.8 Hz, 1H, pyridyl H-6). ^{13}C NMR ($CDCl_3$) δ: 38.5, 52.2, 57.4, 107.3, 127.7, 128.8, 129.0, 130.1, 130.8, 132.1, 136.0, 139.9, 157.8, 171.6.

2-(1-Hydroxy-2-oxo-1,2-dihydropridin-4-yl)phenylacetic acid (9a)

A mixture of methyl 2-(1-oxido-2-chloropyridin-4-yl)phenylacetate (**8a**, 0.75 mmol) and 2 N NaOH (3.0 mL, 6.0 mmol) was refluxed for 24 h. The reaction mixture was cooled to 25 °C and washed with CH_2Cl_2 (30 mL). The water phase was then acidified to pH 2 by addition of 3 N hydrochloric acid prior to extraction with EtOAc (3 × 50 mL). The combined EtOAc extracts were washed with water and then brine, the organic fraction was dried ($MgSO_4$), and the solvent was removed in vacuo. The crude product was purified by flash silica gel column chromatography using EtOAc–MeOH (9:1, *v*/*v*) as eluent to furnish **9a** in a 41% yield as an off-white solid, mp >335 °C. IR (film): 3084, 3018, 2922, 1722, 1651, 1575, 1229 cm^{-1}. ^1H NMR (DMSO-d_6) δ: 3.56 (s, 2H, C*H*$_2$), 6.63 (dd, J = 6.7, 1.8 Hz, pyridone H-5), 6.85 (dd, J = 6.7, 1.8 Hz, 1H, pyridone H-3), 7.18–7.34 (overlapping multiplets, 4H total, phenyl H-3, H-4, H-5, H-6), 8.02 (d, J = 6.7 Hz, 1H, pyridone H-6), 8.65 (br s, 2H, NO*H* and COO*H*). Anal. Calcd for $C_{13}H_{11}NO_4 \cdot 1/8H_2O$: C, 63.03; H, 4.55; N, 5.65. Found: C, 63.21; H, 4.64; N, 5.62.

Methyl 2-(1-hydroxy-2-oxo-1,2-dihydropridin-5-yl) phenylacetate (9c)

Acetyl chloride (5 mL) was added to methyl 2-(1-oxido-2-methoxypyridin-5-yl)phenylacetate (**8c,** 82 mg, 0.30 mmol) and the reaction was allowed to proceed at reflux for 1 h. The reaction mixture was cooled to 25 °C, and excess acetyl chloride was removed in vacuo. The residue was dissolved in methanol prior to stirring at 25 °C for 16 h. Methanol was removed in vacuo to afford **9c**; yield, 96%; pale yellow oil. IR (film): 3026, 2961, 2921, 1746, 1656, 1582, 1168 cm^{-1}. ^1H NMR ($CDCl_3$) δ: 3.61 (s, 2H, C*H*$_2$), 3.68 (s, 3H, O*Me*), 6.87 (d, J = 9.1 Hz, 1H, pyridyl H-3), 7.23–7.37 (overlapping multiplets, 4H total, phenyl H-3, H-4, H-5, H-6), 7.49 (dd, J = 9.1, 2.4 Hz, 1H, pyridyl H-4), 7.90 (d, J = 2.4 Hz, 1H, pyridyl H-6), 8.67 (br s, 1H, *N*-O*H*). ^{13}C NMR ($CDCl_3$) δ: 38.7, 52.2, 116.8, 119.8, 127.7, 128.7, 130.4, 130.6, 130.7, 132.4, 136.3, 139.5, 156.7, 171.9.

2-(1-Hydroxy-2-oxo-1,2-dihydropridin-5-yl)phenylacetic acid (10c)

A mixture of **9c** (0.75 mmol) and 2 N LiOH (3.0 mL, 6.0 mmol) in THF (3.0 mL) and MeOH (3.0 mL) was stirred at reflux temperature for 3 h. The reaction mixture was cooled to 25 °C and washed with CH_2Cl_2 (30 mL). The water phase was acidified to pH 2 by addition of 3 N hydrochloric acid prior to extraction with EtOAc (3 × 50 mL). The combined EtOAc extracts were washed with water and then brine, the organic fraction was dried ($MgSO_4$), and the solvent was removed in vacuo. The crude product was purified

Can. J. Chem. Downloaded from www.nrcresearchpress.com by Xi'an Jiaotong University on 09/19/12
For personal use only.

by flash silica gel column chromatography using EtOAc–MeOH (9:1, *v*/*v*) as eluent to yield **10c**; yield, 74%; pale yellow solid, mp 147–149 °C. IR (film): 3081, 3041, 2924, 2859, 1703, 1663, 1562 cm^{-1}. ^1H NMR (DMSO-d_6) δ: 3.70 (s, 2H, CH_2), 6.57 (d, J = 6.7 Hz, pyridone H-3), 7.24–7.39 (overlapping multiplets, 5H total, phenyl H-3, H-4, H-5, H-6 and pyridone H-4), 7.88 (d, J = 2.4 Hz, 1H, pyridone H-6), 12.22 (br s, 2H, NO*H* and COO*H*). Anal. Calcd for $C_{13}H_{11}NO_4 \cdot 1/10H_2O$: C, 63.21; H, 4.57; N, 5.67. Found: C, 63.25; H, 4.55; N, 5.61.

General procedure for the synthesis of 2-(1-methyl-2-oxo-1,2-dihydropyridyl)phenylacetic acids (12a–12b)

Dimethyl sulfate (420 mg, 3.33 mmol) in MeCN (10 mL) was added to a solution of **7a** or **7b** (290 mg, 1.11 mmol) in MeCN (10 mL). The mixture was stirred at reflux for 6 h. Removal of excess dimethyl sulfate and MeCN in vacuo afforded the respective 1-methylpyridinium methylsulfate salt **11a** or **11b**. Compound **11a**, ^1H NMR (DMSO-d_6) δ: 3.62 (s, 3H, *Me*SO_4^-), 3.67 (s, 2H, CH_2), 3.68 (s, 3H, O*Me*), 4.53 (s, 3H, N*Me*), 7.41–7.47 (overlapping multiplets, 4H total, phenyl H-3, H-4, H-5, H-6), 7.98 (dd, J = 6.7, 1.8 Hz, 1H, pyridyl H-5), 8.09 (d, J = 1.8 Hz, 1H, pyridyl H-3), 9.19 (d, J = 6.7 Hz, 1H, pyridyl H-6). Compound **11b**, ^1H NMR (DMSO-d_6) δ: 3.65 (s, 3H, O*Me*), 3.67 (s, 3H, *Me*SO_4^-), 3.68 (s, 2H, CH_2), 4.46 (s, 3H, N*Me*), 7.34–7.50 (overlapping multiplets, 4H total, phenyl H-3, H-4, H-5, H-6), 8.07 (d, J = 8.5, Hz, 1H, pyridyl H-3), 8.48 (dd, J = 8.5, 1.8 Hz, 1H, pyridyl H-4), 9.12 (d, J = 1.8 Hz, 1H, pyridyl H-6). A solution of the 1-methylpyridinium methylsulfate **11a** or **11b** in THF (3.0 mL) and MeOH (3.0 mL) was added to 2 N LiOH (3.0 mL, 6.0 mmol), and the mixture was stirred at reflux temperature for 2 h. The reaction mixture was cooled to 25 °C and washed with CH_2Cl_2 (30 mL). The water phase was then acidified to pH 4 by addition of 3 N hydrochloric acid prior to extraction with EtOAc (3 × 50 mL). The combined EtOAc extracts were washed with water and then brine, the organic fraction was dried ($MgSO_4$), and the solvent was removed in vacuo. The crude product was purified by flash silica gel column chromatography using EtOAc–MeOH (9:1, *v*/*v*) to yield the respective product **12a** or **12b**. Some physical and spectral data of **12a** and **12b** are listed below.

2-(1-Methyl-2-oxo-1,2-dihydropridin-4-yl)phenylacetic acid (12a)

Yield, 89%; off-white solid, mp 182–184 °C. IR (film): 3068, 2943, 1723, 1658, 1558 cm^{-1}. ^1H NMR ($CDCl_3$ + DMSO-d_6) δ: 3.52 (s, 3H, N*Me*), 3.53 (s, 2H, CH_2), 6.22 (dd, J = 6.7, 1.8 Hz, 1H, pyridone H-5), 6.52 (d, J = 1.8 Hz, 1H, pyridone H-3), 7.15–7.33 (overlapping multiplets, 5H total, phenyl H-3, H-4, H-5, H-6, pyridone H-6), 9.98 (br s, 1H, COO*H*). Anal. Calcd for $C_{14}H_{13}NO_3$: C, 69.12; H, 5.39; N, 5.76. Found: C, 68.64; H, 5.42; N, 5.66.

2-(1-Methyl-2-oxo-1,2-dihydropridin-5-yl)phenylacetic acid (12b)

Yield, 70%; pale yellow solid, mp 171–173 °C. IR (film): 3075, 2941, 1719, 1659, 1564 cm^{-1}. ^1H NMR ($CDCl_3$ + DMSO-d_6) δ: 3.47 (s, 3H, N*Me*), 3.48 (s, 2H, CH_2), 6.46 (d, J = 9.2 Hz, 1H, pyridone H-3), 7.12–7.28 (overlapping multiplets, 4H total, phenyl H-3, H-4, H-5, H-6), 7.34 (dd, J = 9.2, 2.4 Hz, 1H, pyridone H-4), 7.46 (d, J = 1.8 Hz, 1H, pyridone H-6), 10.1 (br s, 1H, COO*H*). Anal. Calcd for $C_{14}H_{13}NO_3$: C, 69.12; H, 5.39; N, 5.76. Found: C, 68.78; H, 5.51; N, 5.55.

Methyl 4-(1-difluoromethyl-2-oxo-1,2-dihydropyridin-5-yl) phenylacetate (13)

To a solution of **7b** (522 mg, 2.0 mmol) in acetonitrile (15 mL) was added $FSO_2CF_2CO_2H$ (1.12 g, 6.0 mmol) followed by $NaHCO_3$ (186 mg, 2.2 mmol). This mixture was heated at reflux under argon for 12 h and cooled to 25 °C; a saturated solution of aqueous $NaHCO_3$ (40 mL) was added and the mixture was extracted with CH_2Cl_2 (3 × 40 mL). The organic fraction was washed with water (50 mL) and then brine, and the organic fraction was dried ($MgSO_4$). Removal of the solvent from the organic fraction in vacuo afforded **13** in 53% yield; pale yellow oil. IR (film): 3010, 2966, 1744, 1694, 1619, 1153 cm^{-1}. ^1H NMR ($CDCl_3$) δ: 3.60 (s, 2H, CH_2), 3.67 (s, 3H, O*Me*), 6.61 (d, J = 9.1 Hz, 1H, pyridone H-3), 7.23–7.39 (overlapping multiplets, 4H, phenyl H-3, H-4, H-5, H-6), 7.43 (dd, J = 9.1, 2.4 Hz, 1H, pyridone H-4), 7.48 (d, J = 2.4 Hz, 1H, pyridone H-6), 7.74 (t, J = 60.4 Hz, 1H, C*H*F_2). ^{13}C NMR ($CDCl_3$) δ: 38.7, 52.2, 107.5 (t, J = 250 Hz), 120.4, 121.1, 127.8, 128.5, 128.8, 130.0, 130.8, 132.4, 136.3, 143.3, 160.2, 171.8.

2-(1-Difluoromethyl-2-oxo-1,2-dihydropyridin-5-yl) phenylacetic acid (14)

A mixture of methyl 2-(1-difluoromethyl-2-oxo-1,2-dihydropyridin-5-yl)phenylacetate (**13**, 0.75 mmol) and 2 N LiOH (3.0 mL, 6.0 mmol) in THF (3.0 mL) and MeOH (3.0 mL) was stirred at reflux temperature for 2 h. The reaction mixture was cooled to 25 °C and washed with CH_2Cl_2 (30 mL). The water phase was then acidified to pH 2 by addition of 3 N hydrochloric acid prior to extraction with EtOAc (3 × 50 mL). The combined EtOAc extracts were washed with water and then brine, the organic fraction was dried ($MgSO_4$), and the solvent was removed in vacuo. The crude product was purified by flash silica gel column chromatography using EtOAc–MeOH (9:1, *v*/*v*) as eluent to furnish **14** in 90% yield; pale yellow gum. IR (film): 3063, 2948, 1737, 1692, 1592, 1152 cm^{-1}. ^1H NMR ($CDCl_3$) δ: 3.64 (s, 2H, CH_2), 6.68 (dd, J = 7.3, 1.8 Hz, 1H, pyridone H-3), 7.25–7.42 (overlapping multiplets, 4H total, phenyl H-3, H-4, H-5, H-6), 7.47 (dd, J = 7.3, 2.4 Hz, 1H, pyridone H-4), 7.56 (d, J = 2.4 Hz, 1H, pyridone H-6), 7.75 (t, J = 60.4 Hz, 1H, C*H*F_2), 10.2 (br s, 1H, COO*H*). Anal. Calcd for $C_{14}H_{11}F_2NO_3$: C, 60.22; H, 3.97; N, 5.02. Found: C, 59.94; H, 4.30; N, 4.79.

2-(2-Oxo-1,2-dihydropyridin-5-yl)phenylacetic acid (15)

A mixture of **13** (0.75 mmol) and 2 N NaOH (3.0 mL, 6.0 mmol) was heated at reflux for 5 h. The reaction mixture was cooled to 25 °C and washed with CH_2Cl_2 (30 mL). The water phase was then acidified to pH 2 by addition of 3 N hydrochloric acid prior to extraction with EtOAc (3 × 50 mL). The combined EtOAc extracts were washed with water and then brine, the organic fraction was dried ($MgSO_4$), and the solvent was removed in vacuo. The crude product was purified by flash silica gel column chromatography using EtOAc–MeOH (9:1, *v*/*v*) as eluent to afford **15**;

yield, 56%; pale yellow solid, mp 242–244 °C. IR (film): 3060, 2981, 1663, 1614 cm^{-1}. ^1H NMR (DMSO-d_6) δ: 3.46 (s, 2H, CH_2), 6.43 (d, J = 9.1 Hz, 1H, pyridone H-3), 7.18–7.33 (overlapping multiplets, 5H total, phenyl H-3, H-4, H-5, H-6 and pyridone H-6), 7.38 (dd, J = 9.1, 2.4 Hz, 1H, pyridone H-4), 7.60 (s, 1H, N*H*), 10.1 (br s, 1H, COO*H*). Anal. Calcd for $C_{13}H_{11}NO_3$: C, 68.11; H, 4.84; N, 6.11. Found: C, 68.23; H, 4.86; N, 5.98.

Cyclooxygenase inhibition assays

The ability of the test compounds listed in Table 1 to inhibit ovine COX-1 and human recombinant COX-2 (IC_{50} value, μmol/L) were determined using an enzyme immunoassay kit (catalog No. 560131, Cayman Chemical, Ann Arbor, Michigan, USA) according to our previously reported method.[17]

5-Lipoxygenase inhibition assay

The ability of the test compounds listed in Table 1 to inhibit potato 5-LOX (catalog No. 60401, Cayman Chemical, Ann Arbor, Michigan, USA) (IC_{50} values, μmol/L) were determined using an enzyme immunoassay kit (catalog No. 760700, Cayman Chemical) according to our previously reported method.[18]

Acknowledgements

We are grateful to the Canadian Institutes of Health Research (CIHR) for financial support of this research (MOP-14712).

References

(1) Funk, C. D. *Science* **2001** *294* (5548), 1871. doi:10.1126/science.294.5548.1871.
(2) Praveen Rao, P. N.; Chen, Q.-H.; Knaus, E. E. *J. Med. Chem.* **2006** *49* (5), 1668 and references cited therein. doi:10.1021/jm0510474.
(3) Scheen, A. J. *Rev. Med. Liege* **2004** *59*, 565.
(4) Dogné, J.-M.; Supuran, C. T.; Pratico, D. *J. Med. Chem.* **2005** *48* (7), 2251. doi:10.1021/jm0402059.
(5) Muri, E. M. F.; Nieto, M. J.; Sindelar, R. D.; Williamson, J. S. *Curr. Med. Chem.* **2002** *9*, 1631.
(6) Carter, G. W.; Young, P. R.; Albert, D. H.; Bouska, J.; Dyer, R.; Bell, R. L.; Summers, J. B.; Brooks, D. W. *J. Pharmacol. Exp. Ther.* **1991** *256*, 929.
(7) Chowdhury, M. A.; Chen, H.; Abdellatif, K. R. A.; Dong, Y.; Petruk, K. C.; Knaus, E. E. *Bioorg. Med. Chem. Lett.* **2008** *18* (14), 4195. doi:10.1016/j.bmcl.2008.05.071.
(8) Yu, G.; Praveen Rao, P. N.; Chowdhury, M. A.; Abdellatif, K. R. A.; Dong, Y.; Das, D.; Velázquez, C. A.; Suresh, M. A.; Knaus, E. E. *Bioorg. Med. Chem. Lett.* **2010** *20* (7), 2168. doi:10.1016/j.bmcl.2010.02.040.
(9) Yu, G.; Chowdhury, M. A.; Abdellatif, K. R. A.; Dong, Y.; Praveen Rao, P. N.; Das, D.; Velázquez, C. A.; Suresh, M. A.; Knaus, E. E. *Bioorg. Med. Chem. Lett.* **2010** *20* (3), 896. doi:10.1016/j.bmcl.2009.12.073.
(10) Miyaura, N.; Suzuki, A. *Chem. Rev.* **1995** *95* (7), 2457. doi:10.1021/cr00039a007.
(11) Stanforth, S. P. *Tetrahedron* **1998** *54* (3–4), 263. doi:10.1016/S0040-4020(97)10233-2.
(12) Chowdhury, M. A.; Abdellatif, K. R.; Dong, Y.; Das, D.; Suresh, M. R.; Knaus, E. E. *Bioorg. Med. Chem. Lett.* **2008** *18* (23), 6138. doi:10.1016/j.bmcl.2008.10.009.
(13) Franceschin, M.; Frasca, S.; Alvino, A.; Bianco, A. *Lett. Org. Chem.* **2007** *4* (2), 86. doi:10.2174/157017807780414217.
(14) Chowdhury, M. A.; Abdellatif, K. R.; Dong, Y.; Das, D.; Yu, G.; Velázquez, C. A.; Suresh, M. R.; Knaus, E. E. *Bioorg. Med. Chem. Lett.* **2009** *19* (24), 6855. doi:10.1016/j.bmcl.2009.10.083.
(15) Ando, M.; Sato, N.; Nagase, T.; Nagai, K.; Ishikawa, S.; Takahasi, H.; Ohtake, N.; Ito, J.; Hirayama, M.; Mitobe, Y.; Iwaasa, H.; Gomori, A.; Matsushita, H.; Tadano, K.; Fujino, N.; Tanaka, S.; Ohe, T.; Ishihara, A.; Kanatani, A.; Fukaimi, T. *Bioorg. Med. Chem.* **2009** *17* (16), 6106. doi:10.1016/j.bmc.2009.05.069.
(16) Velázquez, C.; Praveen Rao, P. N.; Knaus, E. E. *J. Med. Chem.* **2005** *48* (12), 4061. doi:10.1021/jm050211k .
(17) Rao, P. N. P.; Amini, M.; Li, H.; Habeeb, A. G.; Knaus, E. E. *J. Med. Chem.* **2003** *46* (23), 4872. doi:10.1021/jm0302391.
(18) Chowdhury, M. A.; Abdellatif, K. R. A.; Dong, Y.; Das, D.; Suresh, M. R.; Knaus, E. E. *Bioorg. Med. Chem. Lett.* **2008** *18* (23), 6138. doi:10.1016/j.bmcl.2008.10.009.

Can. J. Chem. Downloaded from www.nrcresearchpress.com by Xi'an Jiaotong University on 09/19/12
For personal use only.

One-pot synthesis of tetrahydrobenzo[*a*]xanthen-11-one derivatives catalyzed by ruthenium chloride hydrate as a homogeneous catalyst

Khalil Tabatabaeian, Alireza Khorshidi, Manouchehr Mamaghani, Ali Dadashi, and Milad Khoshnood Jalali

Can. J. Chem. Downloaded from www.nrcresearchpress.com by Xi'an Jiaotong University on 09/19/12
For personal use only.

Abstract: Three-component cyclocondensation of β-naphthol, aldehydes, and 5,5-dimethylcyclohexane-1,3-dione (dimedone) was catalyzed efficiently by ruthenium chloride hydrate under mild reaction conditions to afford 12-aryl or alkyl-8,9,10,12-tetrahydrobenzo[*a*]xanthen-11-one derivatives in good to excellent yields.

Key words: ruthenium, one-pot synthesis, tetrahydrobenzo[*a*]xanthen-11-one.

Résumé : La cyclocondensation à trois composants du β-naphtol, d'aldéhydes et de 5,5-diméthylcyclohexane-1,3-dione (dimédone) est catalysée d'une façon efficace par l'hydrate du chlorure de ruthénium, dans des conditions douces, pour conduire à la formation de dérivés 12-aryl- ou 12-alkyl- de la 8,9,10,12-tétrahydrobenzo[*a*]xanthén-11-one, avec des rendements allant de bons à excellents.

Mots-clés : ruthénium, synthèse monotope, tétrahydrobenzo[*a*]xanthén-11-one.

[Traduit par la Rédaction]

Introduction

In recent years, multicomponent reactions (MCRs) have attracted great attention from research groups working in medicinal chemistry, drug discovery, and materials science as they furnish the desired products in a single operation without isolating the intermediates. Simple procedures, facile execution, atom economy, and high selectivity are among the described advantages of multicomponent reactions.[1–5]

Developing ways to synthesize xanthenes and benzoxanthenes has been of considerable interest because these compounds possess antiviral,[6] antibacterial,[7] and anti-inflammatory properties.[8] Such compounds are also utilized for antagonism of the paralyzing action of zoxazolamine,[9] and can also be employed as dyes,[10] as pH-sensitive fluorescent materials for the visualization of biomolecules,[11] and in cancer therapy.[12] In addition, these heterocyclic compounds are structural key units in several natural products.[13] Xanthone derivatives are also found abundantly in a variety of natural products and exhibit various biological properties.[14,15] Synthetic tetrahydrobenzo[*a*]xanthen-11-ones have been prepared through three-component reaction of β-naphthol, aldehydes, and 1,3-dicarbonyl compounds in the presence of catalysts such as $BF_3{\cdot}Et_2O$,[16] $NaHSO_4{\cdot}SiO_2$,[17] strontium triflate ($Sr(OTf)_2$),[18] *p*-toluenesulfonic acid (pTSA),[19] indium trichloride ($InCl_3$),[20] phosphorous pentoxide (P_2O_5),[20] I_2,[21] tetrabutylammonium fluoride (TBAF),[22] HBF_4-SiO_2,[23] dodecatungstophosphoric acid ($H_3PW_{12}O_{40}$),[24] ceric ammonium nitrate (CAN),[25] 2,4,6-trichloro-1,3,5-triazine (TCT),[26] and $HClO_4$-SiO_2.[27] Several of these methodologies, however, suffer from severe drawbacks including long reaction times and toxic solvents,[16–18,22] the use of expensive reagents,[19] drastic conditions for catalyst preparation,[27] the use of a toxic catalyst,[21] and the requirement of a large or stoichiometric amount of catalysts.[20] Therefore, to avoid these limitations, the discovery of a new and efficient catalyst for preparation of these important molecules is of prime interest.

Recently, we have been involved in the study of the catalytic activity of ruthenium towards organic reactions such as the condensation of indoles and aldehydes,[28] oxidation of aromatic and heteroaromatic compounds,[29] double-conjugate 1,4-addition to enones,[30] nucleophilic addition to epoxides,[31] oxidative trimerization of indoles,[32] and Michael addition of indoles to hormone steroids.[33] As a matter of fact, many organic transformations that involve ruthenium species as catalyst are known and well-documented.[34–36] In continuation of our investigation in this context, hereby, we introduce a simple and efficient method for the synthesis of tetrahydrobenzo [*a*]xanthen-11-ones from one-pot condensation of β-naphthol, aldehydes, and dimedone in the presence of ruthenium chloride hydrate under mild reaction conditions.

Results and discussion

Typical results of the ruthenium-catalyzed cyclocondensation of β-naphthol, aldehydes, and 5,5-dimethylcyclohexane-1,3-dione are shown in Table 1. In an optimized procedure, with respect to the catalyst concentration, choice of solvent,

Received 6 November 2010. Accepted 15 February 2011. Published at www.nrcresearchpress.com/cjc on 5 May 2011.

K. Tabatabaeian, A. Khorshidi, M. Mamaghani, A. Dadashi, and M.K. Jalali. Department of Chemistry, Faculty of Sciences, University of Guilan, P. O. Box 41335-1914, Iran.

Corresponding author: K. Tabatabaeian (e-mail: Taba@guilan.ac.ir).

Table 1. $RuCl_3 \cdot nH_2O$ catalyzed synthesis of 12-aryl or alkyl-8,9,10,12-tetrahydrobenzo[*a*]xanthen-11-ones.

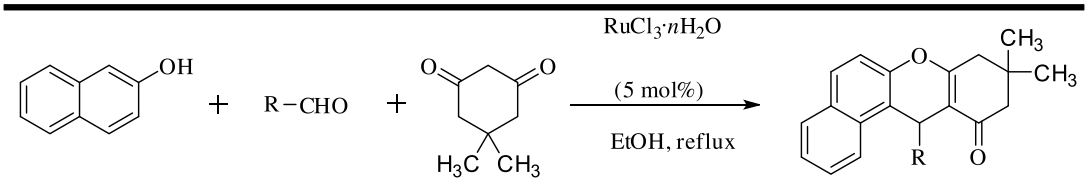

1 **2** **3** **(4a – 4m)**

Entry	R	Time (min)	Product	Yield (%)[a]	Mp (°C) Found	Mp (°C) Reported
1	C_6H_5	30	**4a**	88[b]	148–151	149–150
2	4-$NO_2C_6H_4$	30	**4b**	92[b]	177–180	178–180
3	3-$NO_2C_6H_4$	35	**4c**	86[b]	169–171	168–170
4	4-ClC_6H_4	30	**4d**	92[b]	187–189	188–189
5	2-ClC_6H_4	45	**4e**	86[b]	177–180	179–180
6	2,4-$Cl_2C_6H_3$	35	**4f**	85[b]	178–181	178–180
7	4-$CH_3C_6H_4$	50	**4g**	88[b]	175–177	176–177
8	4-OHC_6H_4	55	**4h**	85[b]	151–153	151–152
9	4-$OCH_3C_6H_4$	55	**4i**	86[b]	206–208	206–207
10	2-OH-3-$OCH_3C_6H_3$	45	**4j**	84[b]	214–216	213–215
11	3,4-$(CH_3O)_2C_6H_3$	50	**4k**	82	201–204	—
12	4-SCH_3-C_6H_4	50	**4l**	86	209–211	—
13	$(CH_3)_2CH$	70	**4m**	75[b]	116–119	116–117

Note: All products were characterized by ^1H NMR, ^{13}C NMR, and IR data.

[a]Isolated yields.

[b]Identified by comparison with authentic samples.[21, 20, 17, 27]

Can. J. Chem. Downloaded from www.nrcresearchpress.com by Xi'an Jiaotong University on 09/19/12
For personal use only.

temperature, and time, the treatment of benzaldehyde (1 mmol), β-naphthol (1 mmol), and dimedone (1.2 mmol) in the presence of $RuCl_3 \cdot nH_2O$ catalyst (5 mol%) in ethanol (2.5 mL) at 80 °C for 30 min gave the corresponding tetrahydrobenzo[*a*]xanthen-11-one as a precipitate, which was easily purified (see Experimental) (product **4a**, 88% yield).

To evaluate the generality of the process, we also examined the reaction of β-naphthol and 5,5-dimethylcyclohexane-1,3-dione with a variety of aromatic aldehydes (Table 1, entries 2–12). Both aromatic aldehydes bearing electron-withdrawing and electron-donating groups afforded corresponding tetrahydrobenzo[*a*]xanthen-11-one derivatives in high yields (82%–92%). It is also noteworthy that the electronic properties of the aromatic ring have an effect on the time of this nucleophilic addition reaction. Aromatic aldehydes with electron-withdrawing groups reacted, somehow, faster than the aromatic aldehydes with electron-donating groups. An aliphatic aldehyde (Table 1, entry 13), however, showed a longer reaction time and lower yield. Although the precise mechanism of the reaction awaits further studies, a plausible mechanism for this transformation, which rationalizes the formation of products, is outlined in Scheme 1. By referring to the literature,[16,17] we proposed that after prior activation of the carbonyl group of aldehyde by Ru^{III} (intermediate **1**), nucleophilic attack from C_1 of β-naphthol provides an *ortho*-quinone methide intermediate (*o*-QM, intermediate **2**). After subsequent attack of dimedone to the *o*-QM and loss of water, intermediate **3** undergoes dehydration to afford the desired product **4**.

A comparison between the present results and other reported methods in this context is shown in Table 2.

As it is shown, operational simplicity and higher efficiency of our protocol covers the expensive cost of ruthenium chloride hydrate. Moreover, reusability of the catalyst was also studied to minimize costs and inorganic waste. As it is shown in Table 3, after four times, the reused catalyst showed only a 4% decrease in the yield of desired product.

To improve efficiency, we carried out this reaction under microwave irradiation. As it is shown in Table 4, this method affords the desired products in excellent yields in rather short times.

Conclusion

In brief, we have reported a convenient synthesis of tetrahydrobenzo[*a*]xanthen-11-ones by using $RuCl_3 \cdot nH_2O$ as a homogeneous catalyst. The unique feature of the reaction is that the corresponding tetrahydrobenzo[*a*]xanthen-11-ones are insoluble in the reaction solvent and this leads to an easy workup along with high yields (75%–92%). In all cases, simple filtration of the reaction mixture and rinsing with cold ethanol provided spectroscopically pure products. Several merits, such as efficiency, mild reaction conditions, short reaction times, high yields of products, easy workup procedure, low catalyst loading, reusability of the catalyst, and use of ethanol as an eco-friendly solvent, make this protocol a useful and attractive process for the synthesis of tetrahydrobenzo [*a*]xanthen-11-ones.

Experimental

General

All products were characterized by spectroscopic data (IR, ^1H NMR, ^{13}C NMR). IR spectra were recorded on a Shimadzu

Scheme 1. Proposed mechanistic pathway for the formation of tetrahydrobenzo[*a*]xanthen-11-one derivatives under ruthenium catalysis.

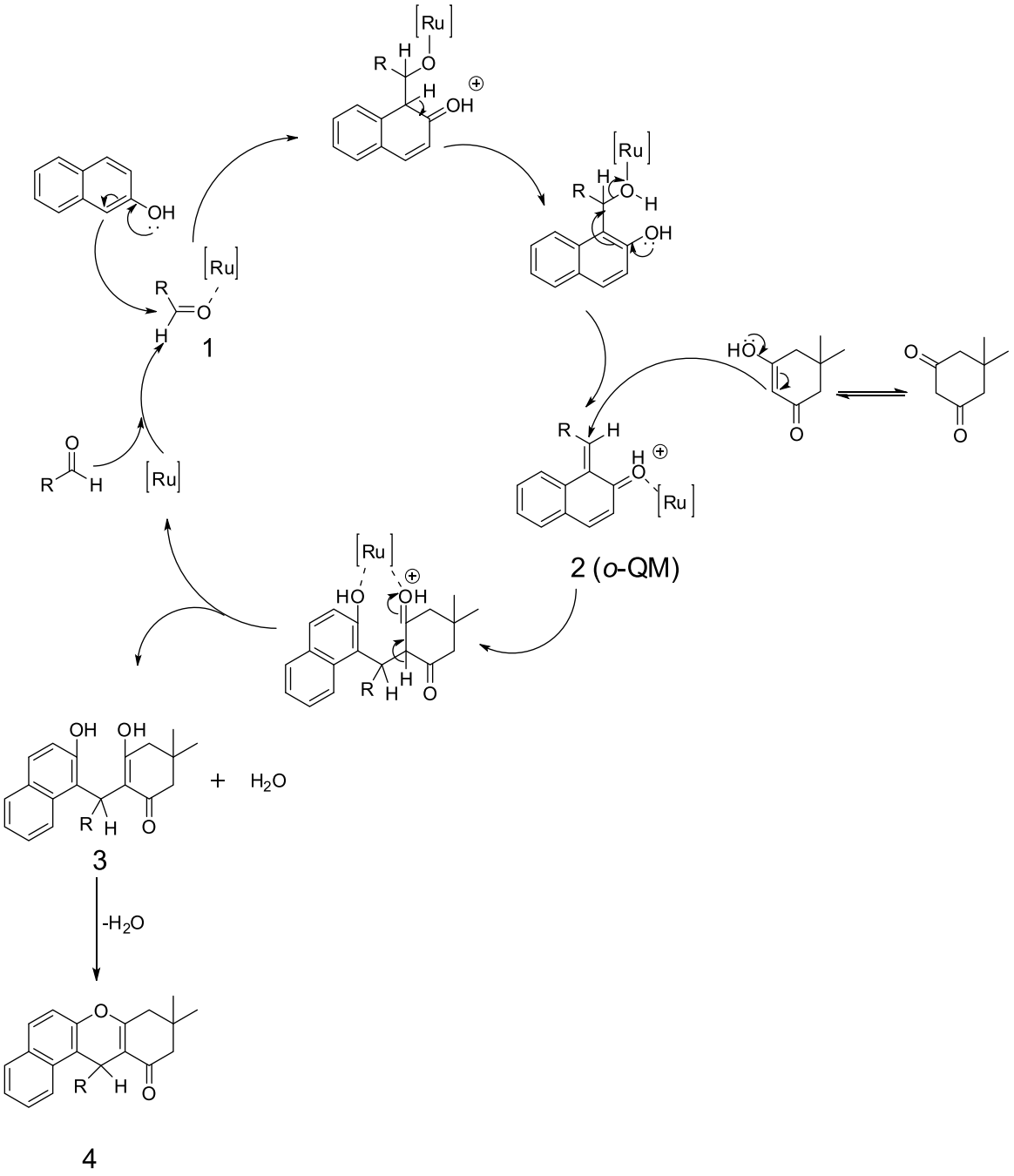

Can. J. Chem. Downloaded from www.nrcresearchpress.com by Xi'an Jiaotong University on 09/19/12
For personal use only.

FTIR-8400S spectrophotometer. ^{1}H NMR spectra were measured on a Bruker DRX-400 Avance spectrometer. ^{13}C NMR spectra were obtained on a Bruker DRX-100 Avance spectrometer. Chemical shifts of ^{1}H and ^{13}C NMR spectra were expressed in parts per million downfield from trimethylsilane (TMS) as the internal standard. Melting points were measured on a BÜCHI Melting Point B-540 and are uncorrected.

Elemental analyses were made by a Carlo-Erba EA1110 CNNO-S analyzer and agreed with the calculated values. Microwave irradiation was performed in a LBP125 microwave oven.

Materials

All the reagents were purchased from Merck and used without further purification.

Typical experimental procedure

To a mixture of β-naphthol (144.17 mg, 1 mmol), benzaldehyde (106.13 mg, 1 mmol), and dimedone (168.22 mg, 1.2 mmol) in ethanol (2.5 mL), $RuCl_3 \cdot nH_2O$ (10.71 mg, 0.05 mmol) was added and the mixture was refluxed in an oil bath at 80 °C for 30 min, which yielded a precipitate. The progress of the reaction was monitored by thin-layer chromatography (TLC). After completion of the reaction, as

Table 2. Comparison of our results with those obtained by other groups in the reaction of β-naphthol, benzaldehyde, and dimedone.

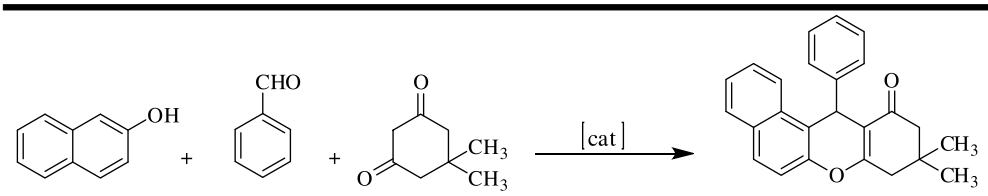

Entry	Catalyst	Concentration of catalyst (mol %)	Solvent	Temperature (°C)	Time (min)	Yield (%)	References
1	$NaHSO_4{\cdot}SiO_2$	56	$ClCH_2CH_2Cl$	80	240	87	17
2	$Sr(OTf)_2$	10	$ClCH_2CH_2Cl$	80	300	85	18
3	pTSA	10	[bmim]BF_4	80	180	90	19
4	$InCl_3$	30	—	120	30	84	20
5	P_2O_5	20	—	120	40	76	20
6	I_2	10	—	60	75	90	21
7	HBF_4-SiO_2	10	—	80	65	91	23
8	$H_3PW_{12}O_{40}$	5	—	60	70	86	24
9	TCT	5	—	80	50	90	26
10	$HClO_4$-SiO_2	5	—	80	72	89	27
11	$RuCl_3{\cdot}nH_2O$	5	C_2H_5OH	80	30	88	—

Table 3. Reusability of the catalyst in the reaction of β-naphthol, benzaldehyde, and dimedone in the presence of $RuCl_3{\cdot}nH_2O$ (5 mol%).

Run No.	Yield (%)
1	88
2	88
3	86
4	84

Table 4. Ru^{III}-catalyzed synthesis of tetrahydrobenzo[*a*]xanthen-11-one derivatives under microwave irradiation.

Entry	R	Time (min)	Product	Yield (%)
1	C_6H_5	4	**4a**	88
2	4-$NO_2C_6H_4$	2	**4b**	90
3	4-ClC_6H_4	3	**4d**	93
4	4-$CH_3C_6H_4$	5	**4g**	87
5	$(CH_3)_2CH$	7	**4m**	78

indicated by TLC, the precipitate was filtered off and rinsed with cold ethanol. The solid was dried under vacuum to afford the desired compound in pure form (311.78 mg, 88%). The same procedure was also used for the other products listed in Table 1. To reuse the catalyst, after filtration, substrates were added into solution and the same procedure was repeated. For microwave reactions, irradiation was conducted in an open vessel at 50 °C in a 500 W microwave oven (Table 4).

12-(3,4-Dimethoxyphenyl)-9,9-dimethyl-8,9,10,12-tetrahydrobenzo[*a*]xanthen-11-one (4k)

Solid; mp 201–204 °C. IR (KBr, cm^{-1}) ν: 3070, 2960, 1644, 1590, 1371, 1260, 1220, 1140, 1020, 817. ^1H NMR (400 MHz, $CDCl_3$, 25 °C, ppm) δ: 7.93 (d, 1H, J = 8.8 Hz), 7.78 (d, 1H, J = 8.0 Hz), 7.62 (d, 1H, J = 8.4 Hz), 7.48 (t, 1H, J = 7.2 Hz), 7.36 (t, 1H, J = 7.2 Hz), 7.18 (d, 1H, J = 8.8 Hz), 6.69 (d, 1H, J = 7.6 Hz), 6.59 (d, 1H, J = 7.6 Hz), 6.50 (s, 1H), 5.64 (s, 1H), 3.68 (s, 3H), 3.57 (s, 3H), 2.54 (s, 2H), 2.42 (d, 1H, J = 16.4 Hz), 2.27 (d, 1H, J = 16.4 Hz), 1.09 (s, 3H), 0.98 (s, 3H). ^{13}C NMR (100 MHz, $CDCl_3$, 25 °C, ppm) δ: 196.2, 162.8, 153.6, 142.1, 136.0, 133.5, 130.2, 129.0, 128.2, 127.1, 126.8, 125.4, 124.3, 123.5, 116.9, 116.4, 115.8, 113.2, 112.4, 53.7, 53.4, 49.6, 40.2, 32.7, 31.2, 27.8, 26.0. Anal. calcd. for $C_{27}H_{26}O_4$: C 78.24, H 6.32; found: C 78.25, H 6.34.

9,9-Dimethyl-12-(4-methylthiophenyl)-8,9,10,12-tetrahydrobenzo[*a*]xanthen-11-one (4l)

Solid; mp 209–211 °C. IR (KBr, cm^{-1}) ν : 3050, 2960, 1642, 1593, 1372, 1220, 1180, 1020, 800. ^1H NMR (400 MHz, $CDCl_3$, 25 °C, ppm) δ: 7.93 (d, 1H, J = 8.4 Hz), 7.78 (d, 1H, J = 8.0 Hz), 7.62 (d, 1H, J = 8.8 Hz), 7.52 (t, 1H, J = 7.2 Hz), 7.41 (t, 1H, J = 7.2 Hz), 7.19 (d, 1H, J = 8.4 Hz), 7.08 (d, 2H, J = 7.6 Hz), 6.98 (d, 2H, J = 7.6 Hz), 5.66 (s, 1H), 2.56 (s, 2H), 2.50 (s, 3H), 2.38 (d, 1H, J = 16.4 Hz), 2.28 (d, 1H, J = 16.4 Hz), 1.12 (s, 3H), 0.98 (s, 3H). ^{13}C NMR (100 MHz, $CDCl_3$, 25 °C, ppm) δ: 196.7, 163.2, 154.1, 147.2, 136.2, 133.7, 132.1, 131.8, 130.1, 129.4, 127.9, 126.3, 124.3, 123.5, 117.8, 116.2, 113.7, 50.6, 40.8, 33.9, 31.9, 28.3, 26.6, 25.4. Anal. calcd. for $C_{26}H_{24}O_2S$: C 77.97, H 6.04; found: C 77.98, H 6.05.

Acknowledgement

Partial support of this work by the Research Council of the University of Guilan is gratefully acknowledged.

References

(1) Arndtsen, B. A. *Chem. Eur. J.* **2009**, *15* (2), 302. doi:10.1002/chem.200800767.
(2) Shestopalov, A. M.; Shestopalov, A. A.; Rodinovskaya, L. A. *Synthesis* **2008**, *2008* (1), 1. doi:10.1055/s-2007-990942.
(3) Balme, G.; Bouyssi, D.; Monteiro, N. In *Multicomponent*

Can. J. Chem. Downloaded from www.nrcresearchpress.com by Xi'an Jiaotong University on 09/19/12
For personal use only.

Can. J. Chem. Downloaded from www.nrcresearchpress.com by Xi'an Jiaotong University on 09/19/12
For personal use only.

Reactions; Zhu, J., Bienaymé, H., Eds.; Wiley-VCH: Weinheim, Germany, 2005; pp 224–276.
(4) Montgomery, J. *Angew. Chem. Int. Ed.* **2004**, *43* (30), 3890. doi:10.1002/anie.200300634.
(5) von Wangelin, A. J.; Neumann, H.; Gördes, D.; Klaus, S.; Strübing, D.; Beller, M. *Chem. Eur. J.* **2003**, *9* (18), 4286. doi:10.1002/chem.200305048.
(6) Hideo, T. Jpn. Tokkyo. Koho. JP 56005480, 1981; *Chem. Abstr.* 1981, 95, 80922.
(7) Lambert, R. W.; Martin, J. A.; Merrett, J. H.; Parkes, K. E. B.; Thomas, G. J. PCT Int. Appl. WO 9706178, 1997; *Chem. Abstr.* 1997, 126, 212377.
(8) Poupelin, J. P.; Saint-Rut, G.; Foussard-Blanpin, O.; Narcisse, G.; Uchida-Ernouf, G.; Lacroix, R. *Eur. J. Med. Chem.* **1978**, *13*, 67.
(9) Saint-Ruf, G.; Huynh-Trong-Hieu, ; Poupelin, J.-P. *Naturwissenschaften* **1975**, *62* (12), 584. doi:10.1007/BF01166986.
(10) Encinas, M. V.; Rufs, A. M.; Bertolotti, S. G.; Previtali, C. M. *Polymer (Guildf.)* **2009**, *50* (13), 2762. doi:10.1016/j.polymer.2009.04.024.
(11) Buehler, C. A.; Cooper, D. E.; Scrudder, E. O. *J. Org. Chem.* **1943**, *8* (4), 316. doi:10.1021/jo01192a003.
(12) Koeller, K. M.; Haggarty, S. J.; Perkins, B. D.; Leykin, I.; Wong, J. C.; Kao, M. C. J.; Schreiber, S. L. *Chem. Biol.* **2003**, *10* (5), 397. doi:10.1016/S1074-5521(03)00093-0.
(13) Alcantara-Licudine, J. P.; Kawate, M. K.; Li, Q. X. *J. Agric. Food Chem.* **1997**, *45* (3), 766. doi:10.1021/jf960372k.
(14) Urbain, A.; Marston, A.; Grilo, L. S.; Bravo, J.; Purev, O.; Purevsuren, B.; Batsuren, D.; Reist, M.; Carrupt, P.-A.; Hostettmann, K. *J. Nat. Prod.* **2008**, *71* (5), 895. doi:10.1021/np070690l.
(15) Isakovic, A.; Jankovic, T.; Harhaji, L.; Kostic-Rajacic, S.; Nikolic, Z.; Vajs, V.; Trajkovic, V. *Bioorg. Med. Chem.* **2008**, *16* (10), 5683. doi:10.1016/j.bmc.2008.03.069.
(16) Mashraqui, S. H.; Patil, M. B.; Mistry, H. D.; Ghadigaonkar, S.; Meetsma, A. *Chem. Lett.* **2004**, *33* (8), 1058. doi:10.1246/cl.2004.1058.
(17) Das, B.; Laxminarayana, K.; Krishnaiah, M.; Srinivas, Y. *Synlett* **2007**, *2007* (20), 3107. doi:10.1055/s-2007-990922.
(18) Li, J.; Tang, W.; Lu, L.; Su, W. *Tetrahedron Lett.* **2008**, *49* (50), 7117. doi:10.1016/j.tetlet.2008.09.129.
(19) Khurana, J. M.; Magoo, D. *Tetrahedron Lett.* **2009**, *50* (33), 4777. doi:10.1016/j.tetlet.2009.06.029.
(20) Nandi, G. C.; Samai, S.; Kumar, R.; Singh, M. S. *Tetrahedron* **2009**, *65* (34), 7129. doi:10.1016/j.tet.2009.06.024.
(21) Wang, R.-Z.; Zhang, L.-F.; Cui, Z.-S. *Synth. Commun.* **2009**, *39* (12), 2101. doi:10.1080/00397910802638511.
(22) Gao, S.; Tsai, C. H.; Yao, C.-F. *Synlett* **2009**, *2009* (6), 949. doi:10.1055/s-0028-1088214.
(23) Zhang, Z.-H.; Wang, H.-J.; Ren, X.-Q.; Zhang, Y.-Y. *Monatsh. Chem.* **2009**, *140* (12), 1481. doi:10.1007/s00706-009-0204-9.
(24) Wang, H.-J.; Ren, X.-Q.; Zhang, Y.-Y.; Zhang, Z.-H. *J. Braz. Chem. Soc.* **2009**, *20* (10), 1939. doi:10.1590/S0103-50532009001000025.
(25) Kumar, A.; Sharma, S.; Maurya, R. A.; Sarkar, J. *J. Comb. Chem.* **2010**, *12* (1), 20. doi:10.1021/cc900143h.
(26) Zhang, Z.-H.; Zhang, P.; Yang, S.-H.; Wang, H.-J.; Deng, J. *J. Chem. Sci.* **2010**, *122* (3), 427. doi:10.1007/s12039-010-0049-0.
(27) Mo, L.-P.; Chen, H.-L. *J. Chin. Chem. Soc.* **2010**, *57* (2), 157.
(28) Tabatabaeian, K.; Mamaghani, M.; Mahmoodi, N. O.; Khorshidi, A. *Can. J. Chem.* **2006**, *84* (11), 1541. doi:10.1139/V06-159.
(29) Tabatabaeian, K.; Mamaghani, M.; Mahmoodi, N. O.; Khorshidi, A. *Catal. Commun.* **2008**, *9* (3), 416. doi:10.1016/j.catcom.2007.07.024.
(30) Tabatabaeian, K.; Mamaghani, M.; Mahmoodi, N. O.; Khorshidi, A. *J. Mol. Catal. Chem.* **2007**, *270* (1–2), 112. doi:10.1016/j.molcata.2007.01.038.
(31) Tabatabaeian, K.; Mamaghani, M.; Mahmoodi, N. O.; Khorshidi, A. *Tetrahedron Lett.* **2008**, *49* (9), 1450. doi:10.1016/j.tetlet.2008.01.001.
(32) Tabatabaeian, K.; Mamaghani, M.; Mahmoodi, N. O.; Khorshidi, A. *Can. J. Chem.* **2009**, *87* (9), 1213. doi:10.1139/V09-098.
(33) Tabatabaeian, K.; Mamaghani, M.; Mahmoodi, N. O.; Khorshidi, A. *Synth. Commun.* **2010**, *40* (11), 1677. doi:10.1080/00397910903161678.
(34) Murahashi, S.-I., Ed. *Ruthenium in Organic Synthesis;* Wiley-VCH: New York, 2004.
(35) Bruneau, C., Dixneuf, P. H.,Eds. *Ruthenium Catalysts and Fine Chemistry;* Springer: Berlin, 2004.
(36) Murai, S., Ed. *Activation of Unreactive Bonds and Organic Synthesis;* Springer: Berlin, 1999.

Interaction of 5-aminosalicylic acid with nitrous acid: formation of the diazonium derivative and nitric oxide release

C. López-Alarcón, E. Lissi, P. Hoffmann, J. Mella, C.D. Pessoa-Mahana, H. Speisky, M. Möller, G. Ferrer-Sueta, and A. Denicola

Can. J. Chem. Downloaded from www.nrcresearchpress.com by Xi'an Jiaotong University on 09/19/12
For personal use only.

Abstract: The reaction of 5-aminosalicylic acid (5-ASA) with nitrous acid has been studied at low pH under conditions that simulate a gastric environment. The course of the reaction was followed by UV–visible and fluorescence spectroscopy and the products were analyzed by high performance liquid chromatography (HPLC) with UV–visible and mass spectroscopic detectors. In addition, the formation of nitric oxide (NO) was estimated electrochemically. 5-ASA was readily consumed in a process catalyzed by chloride and thiocyanate, whose rate is first order in 5-ASA and second order in nitrous acid. 2-Hydroxy-5-diazonium benzoic acid (diazonium derivative) and NO were detected as products of the reaction. From the NO formation profiles, it is concluded that NO is produced as a minor product in a process parallel to the path that leads to generation of the diazonium derivative. While the formation of NO could be beneficial for the protection of the stomach, the generation of the diazonium derivative could be considered a potentially toxic process.

Key words: 5-aminosalicylic acid, mesalazine, nitrous acid, nitrite, diazonium derivative, nitric oxide.

Résumé : On a étudié la réaction de l'acide 5-aminosalicylique (5-AAS) avec l'acide nitreux, à un pH faible, dans des conditions qui simulent un environnement gastrique. On a suivi l'évolution de la réaction par spectroscopies UV-visible et de fluorescence et on a analysé les produits par chromatographie liquide à haute performance (CLHP) avec des détecteurs par spectroscopie UV-visible et de masse. De plus, on a fait appel à une méthode électrochimique pour évaluer la formation d'oxyde nitrique (NO). L'acide 5-aminosalicylique est rapidement consommé dans un processus catalysé par les ions chlorure et thiocyanate et pour lequel la vitesse est du premier ordre en 5-AAS et du second ordre en acide nitreux. On a détecté de l'acide 2-hydroxy-5-diazoniumbenzoïque (dérivé diazonium) et du NO comme produis de la réaction. D'après les profils de formation du NO, on en conclut que le NO se forme comme produit mineur dans un processus parallèle à la voie qui conduit à la formation du dérivé diazonium. Alors que la formation du NO pourrait être bénéfique pour la protection de l'estomac, la formation du dérivé diazonium peut être considérée comme un processus potentiellement toxique.

Mots-clés : acide 5-aminosalicylique, mésalazine, acide nitreux, nitrite, dérivé diazonium, oxyde nitrique.

[Traduit par la Rédaction]

Introduction

Chronic inflammatory bowel pathologies such as ulcerative colitis and Crohn's disease cause inflammatory changes and ulcers of different types in the gastrointestinal mucosa.[1] 5-Aminosalicylic acid (5-ASA), the active moiety of azosalicylic drugs such as sulfasalazine and olsalazine, is currently used in the treatment of these pathologies and in the maintenance of their clinical remission.[2–4] The mechanism of action of 5-ASA has been related to the inhibition of the production of mediators of the lipooxygenase and cyclo-oxygenase pathways as well as platelet activating factor, which are elevated in the colonic tissue of patients with inflammatory bowel disease.[4] In addition, 5-ASA inhibits the production of interleukin and other cytokines, including tumor necrosis factor alpha.[4]

Besides the inhibition of inflammatory pathways, 5-ASA has additional protective effects, being an efficient scavenger of peroxyl radicals and a highly effective molecule in protecting membranes against lipid peroxidation.[5–8] Furthermore, after its oxidation by peroxyl radicals, 5-ASA can be regenerated by endogenous compounds such as ascorbic acid, cysteine, and glutathione.[9] In addition, 5-ASA delays the

Received 9 December 2010. Accepted 4 March 2011. Published at www.nrcresearchpress.com/cjc on 3 May 2011.

C. López-Alarcón, J. Mella, and C.D. Pessoa-Mahana. Departamento de Farmacia, Facultad de Química, Pontificia Universidad Católica de Chile, C.P. 782 0436, Santiago, Chile.
E. Lissi. Facultad de Química y Biología, Universidad de Santiago de Chile, Santiago, Chile.
P. Hoffmann. UMR/CNRS 5068, Université Paul Sabatier, Toulouse, France.
H. Speisky. Instituto de Nutrición y Tecnología de los Alimentos, Universidad de Chile, Santiago, Chile.
M. Möller, G. Ferrer-Sueta, and A. Denicola. Laboratorio de Fisicoquímica Biológica, Facultad de Ciencias, and Center for Free Radical and Biomedical Research, Universidad de la República, Montevideo 11400, Uruguay.

Corresponding author: C. López-Alarcón (e-mail: clopezr@uc.cl).

Can. J. Chem. Downloaded from www.nrcresearchpress.com by Xi'an Jiaotong University on 09/19/12
For personal use only.

oxidation of low density lipoprotein[10] and reacts with hypochlorous acid,[11] singlet oxygen,[12] and hydroxyl radicals.[13,14]

The beneficial action of 5-ASA in the treatment of bowel diseases is exerted from the luminal side. For this reason, different pharmaceutical formulations (e.g., Salofalk, Pentasa, Asacol) have been developed to allow orally ingested 5-ASA to reach the inflamed distal intestine without being absorbed and (or) decomposed in the stomach. Nevertheless, it has been shown, using in vitro dissolution tests, that a fraction of 5-ASA can be released from Pentasa tablets even at low pH (1.2).[15]

Owing to the reactivity of 5-ASA towards oxidants, it appears to be a potential substrate of nitrite in acidic medium. The steady-state concentration of nitrite in the human body is regulated by different sources, with ingested nitrate being the most important nutritional source of nitrite. Nitrate derived from foods such as green leaves, cereals, and meat is reduced by commensal bacteria in the oral cavity, generating high nitrite concentrations in saliva (1–2 mmol L^{-1}) and the stomach.[16–18] In stomach conditions, nitrite (pK_a = 3.2–3.4) is present as nitrous acid (eq. [1]) in equilibrium with nitrogen oxides, according to eqs. [2]–[5]:[19]

$$[1] \quad NO_2^- + H^+ \rightleftharpoons HNO_2$$

$$[2] \quad HNO_2 + H^+ \rightleftharpoons NO^+ + H_2O$$

$$[3] \quad 2HNO_2 \rightleftharpoons N_2O_3 + H_2O$$

$$[4] \quad N_2O_3 \rightleftharpoons NO + NO_2$$

$$[5] \quad HNO_2 + H^+ + X^- \rightleftharpoons NOX + H_2O$$

where X^- corresponds to a thiocyanate or chloride ion.

Thus, nitrite in the gastric environment (or its derived nitrogen species) could react with xeno- or endobiotics that, depending on their structure, could generate nitroso, nitro, or nitrosamine derivatives.[19–21] In particular, nitrosamines (generated from the interaction of nitrous acid with amines) have been directly related to an increased carcinogenic risk.[22] Many drugs with an amine moiety in their structure could form nitrosamine compounds by their interaction with acidic nitrite.[22]

Nonetheless, the interaction of nitrite with xenobiotics does not always lead to toxic metabolites (nitrosamines), as in some cases this interaction is associated with the release of nitric oxide (NO), thus contributing to vasodilation, mucosal blood flow, and mucus thickness.[23–26] It has been shown that the interaction of ascorbic acid[23] and phenols such as chlorogenic acid,[24] quercetin,[24,25] and caffeic acid[26] with nitrite in stomach conditions leads to NO release. Furthermore, it has been reported both in vitro and in vivo that foods and beverages such as wine,[26,27] apple extracts,[28] and coffee melanoidins[29] generate NO from their interaction with nitrite in acidic medium.

Considering that 5-ASA, a drug whose chemical structure has an aromatic amine and a phenol group, is partially released from Pentasa tablets in simulated gastric medium, in the present work a systematic study of the reaction between 5-ASA and nitrite in acidic conditions (nitrous acid) was performed. The time course of decomposition and the formation of reaction products were studied both by spectroscopic techniques (UV–visible and fluorescence) and by high performance liquid chromatography (HPLC), with diode array (DAD) and mass spectroscopy (MS) detection. In addition, the generation of NO during the reaction was evaluated by an electrochemical technique.

Experimental

Chemicals

5-Aminosalicylic acid (5-ASA), diethylenetriaminepentaacetic acid (DTPA), sodium nitrite, resorcinol, quercetin, catechol, pyrogallol, phloretin, and sodium hydrosulfite were purchased from Sigma-Aldrich (St. Louis, Missouri, USA). Potassium sulfate and potassium thiocyanate (KSCN) were purchased from Applichem (Darmstadt, Germany). Potassium iodide was supplied by Acros Organics (New Jersey, USA).

Solutions

Unless otherwise indicated, experiments were carried out in simulated gastric fluid (SGF), consisting of sodium chloride (34 mmol L^{-1}) adjusted to pH 2.0 with concentrated hydrochloric acid. Stock solutions of 5-ASA (10 mmol L^{-1}) were prepared daily in DMSO. Stock solutions of nitrite (10 mmol L^{-1}) and KSCN (10 mmol L^{-1}) were prepared daily in double-distilled water.

UV–visible and fluorescence studies

The reaction mixture, containing 5-ASA (1–300 μmol L^{-1}) and nitrite (10–500 μmol L^{-1}) in SGF, was incubated at 25 °C in the thermostated cuvette of either a Hewlett Packard 8453 (Palo Alto, California, USA) or a Varian Cary 50 (Mulgrave, Victoria, Australia) UV–visible spectrophotometer. A similar procedure was carried out to follow the reaction by fluorescence, except the reaction mixture was incubated in the thermostated cuvette of a PerkinElmer LS-55 spectrofluorimeter (Beaconsfield, UK). Fluorescence measurements were carried out using 303 nm and 430 nm as the excitation and emission wavelengths, respectively. During the reaction of 5-ASA with nitrous acid, no significant changes in the shape of the fluorescence band of 5-ASA were observed. Also, control 5-ASA solutions, incubated in the absence of nitrous acid, revealed no changes in the initial absorbance or fluorescence intensity. The addition of DTPA (0.1 mmol L^{-1}) to SGF had no effect on the reactions. Therefore, no special precautions were taken against transition metal ion contamination in the water and salts used for the preparation of SGF. In some experiments, a 5-ASA (500 μmol L^{-1}) plus nitrite (500 μmol L^{-1}) solution was incubated in SGF at 25 °C, and at different times (15, 40, and 60 min) aliquots of 100 μL were taken and added to 2.9 mL of either SGF, phosphate buffer (pH 7.0), or NaOH (0.1 N). UV–visible spectra of these solutions were registered (pH was rigorously controlled after the addition of aliquots). In addition, in the experiments carried out at pH 7.0, the effect of sodium hydrosulfite (100 μmol L^{-1}) on the UV–visible spectra was evaluated. Reaction order and rate constant determinations were conducted in acidic medium (either SGF or $HClO_4$) with $[5\text{-ASA}]_0$ = 50 μmol L^{-1} and variable concentrations of $NaNO_2$ (0.65–50 mmol L^{-1}), NaCl ($[Cl^-]_0$ = 0–1.8 mol L^{-1}),

and KSCN (0–2 mmol L^{-1}), following the absorbance increase at 340 nm.

The reaction of the final product of the reaction between 5-ASA and nitrous acid (in SGF) with phenols was carried out at alkaline (pH = 12) or neutral (pH = 7.3) pH. Briefly, the diazonium product was obtained by incubating a solution of 5-ASA (5 mmol L^{-1}) plus nitrite (10 mmol L^{-1}) in SGF at 25 °C for 30 min. The solution was diluted 20-fold and an aliquot was added to a solution containing phenols (0.2–1.0 mmol L^{-1}) in NaOH (20 mmol L^{-1}). The time course of the reaction was followed by the changes in the UV–vis spectra up to 3 h.

Electrochemical detection of NO

NO release was followed using an ISO–NO electrode (WPI, Inc., Sarasota, Florida, USA) under nitrogen atmosphere at 25 °C. Solutions of KI–H_2SO_4 (0.1 mol L^{-1}) plus nitrite (0.7–10 μmol L^{-1}) were used to calibrate the electrode. Working solutions containing 5-ASA (5 μmol L^{-1} – 1 mmol L^{-1}) in SGF were incubated in a thermostated cell. After stabilization of the baseline, a nitrite bolus (20–200 μmol L^{-1}) was added. In some experiments, 5-ASA (50 μmol L^{-1}) was co-incubated with KSCN (200 μmol L^{-1}) before nitrite addition.

HPLC studies

Time course of the reaction of 5-ASA with nitrous acid followed by HPLC–DAD

Chromatograms were obtained using a PerkinElmer HPLC system (pump 410) equipped with a Supelco C-18 column (25 cm × 4.6 mm) and a diode array detector (PerkinElmer 235C). A 95:5 mixture of phosphate (KH_2PO_4, 0.1 mol L^{-1}, adjusted to pH 4.4 with orthophosphoric acid) and methanol was used as the mobile phase. The flow rate was 1.0 mL min^{-1}. Solutions of 5-ASA (50–100 μmol L^{-1}) were incubated in the absence and presence of nitrite (100–200 μmol L^{-1}) in SGF. At different times, aliquots were taken through an autosampler system (PerkinElmer ISS 200) and immediately injected into the HPLC system. The reaction was followed at 220, 305, and 340 nm. All experiments were carried out in duplicate or triplicate.

HPLC–MS studies

HPLC measurements were performed using an 1100 Series liquid chromatograph (Agilent Technologies) coupled to an ion trap mass spectrometer (Esquire 4000, Bruker Daltonics, Inc., Massachusetts, USA). MS analyses were performed in the positive electrospray ionization mode with a desolvation temperature of 325 °C. A C-18 chromatography column (150 mm × 4.6 mm, Luna, Phenomenex Inc., Torrance, California, USA) was used. A 95:5 mixture of 0.1% acetic acid and methanol was used as the mobile phase and the flow rate was 1.0 mL min^{-1}. Briefly, 20 μL of the samples, 5-ASA (50 μmol L^{-1}) in the absence or presence of nitrite (200 μmol L^{-1}) in SFG, were injected into the HPLC–MS system at different reaction times. All experiments were carried out in duplicate or triplicate.

Fig. 1. Decay of the fluorescence of 5-ASA induced by nitrite in acidic medium. 5-ASA (50 μmol L^{-1}) was incubated in simulated gastric fluid (SGF) at 25 °C in the presence of the following concentrations of nitrite: 20 μmol L^{-1} (◇), 50 μmol L^{-1} (▽), 75 μmol L^{-1} (□), and 150 μmol L^{-1} (○). The excitation and emission wavelengths were 303 nm and 430 nm, respectively.

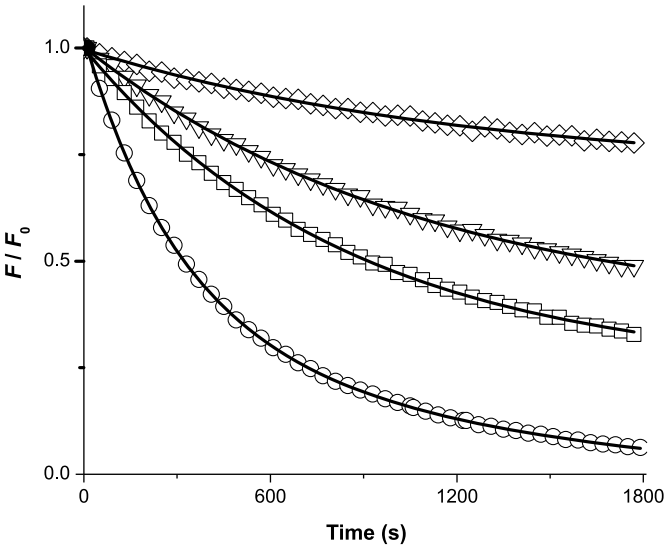

Results

UV–visible and fluorometric studies

Exposure of 5-ASA to nitrite in SGF (nitrous acid) led to a progressive decrease in its fluorescence intensity, as shown in Fig. 1. The data depicted in this figure imply that 5-ASA (50 μmol L^{-1}) reacts efficiently with nitrous acid. In fact, nearly 68% of 5-ASA was consumed after 20 min of reaction with nitrous acid (75 μmol L^{-1}). The UV–visible spectrum of 5-ASA was recorded as a function of time to further assess the characteristics of its reaction with nitrous acid. The results obtained with 50 μmol L^{-1} 5-ASA and 200 μmol L^{-1} nitrous acid are presented in Fig. 2A. As can be seen in this figure, a significant increase in the absorbance at λ = 303 nm with time was observed. This increase was due to the presence of a new strong band at λ = 340 nm, the wavelength that was chosen to follow the time course of the reaction. Typical results (presented in Fig. 2B) show that the addition of increasing concentrations of nitrite (10–500 μmol L^{-1}) to a 5-ASA solution (50 μmol L^{-1}) in SGF leads to higher rates of the absorbance increases in a nitrite concentration dependent way. The absorbance at 340 nm reaches a plateau at nearly 0.86 absorbance units (AU), which is clearly evident at the highest nitrite concentration employed (500 μmol L^{-1}), where the plateau is reached after approximately 20 min of reaction.

Considering that chloride can act as a nitrosonium carrier, the reaction was also studied in perchloric acid ($HClO_4$) solution (Fig. 3). As shown in Fig. 3A, the time course of the absorbance at 340 nm corresponding to the reaction of 5-ASA (50 μmol L^{-1}) with an excess of nitrite in $HClO_4$ (0.65 mol L^{-1}) follows pseudo-first-order kinetics, adjusting in all cases to a mono-exponential function. Pseudo-first-order rate constants were obtained from these data and plotted

Can. J. Chem. Downloaded from www.nrcresearchpress.com by Xi'an Jiaotong University on 09/19/12
For personal use only.

Can. J. Chem. Downloaded from www.nrcresearchpress.com by Xi'an Jiaotong University on 09/19/12
For personal use only.

Fig. 2. Kinetics of the reaction of 5-ASA with nitrite followed by UV–visible spectroscopy. (A) Changes in the UV–visible spectra of 5-ASA during the reaction with nitrous acid. 5-ASA (50 μmol L^{-1}) was incubated with nitrite (200 μmol L^{-1}) in SGF at 25 °C. Lines a–n are the spectra taken every 3 min from 0 to 42 min of incubation. (B) Kinetic profiles (followed at λ = 340 nm) of the reaction of 5-ASA with nitrous acid. 5-ASA (50 μmol L^{-1}) was incubated in SGF with the following concentrations of nitrite: 10 μmol L^{-1} (△), 50 μmol L^{-1} (◇), 100 μmol L^{-1} (▽), 200 μmol L^{-1} (□), and 500 μmol L^{-1} (○).

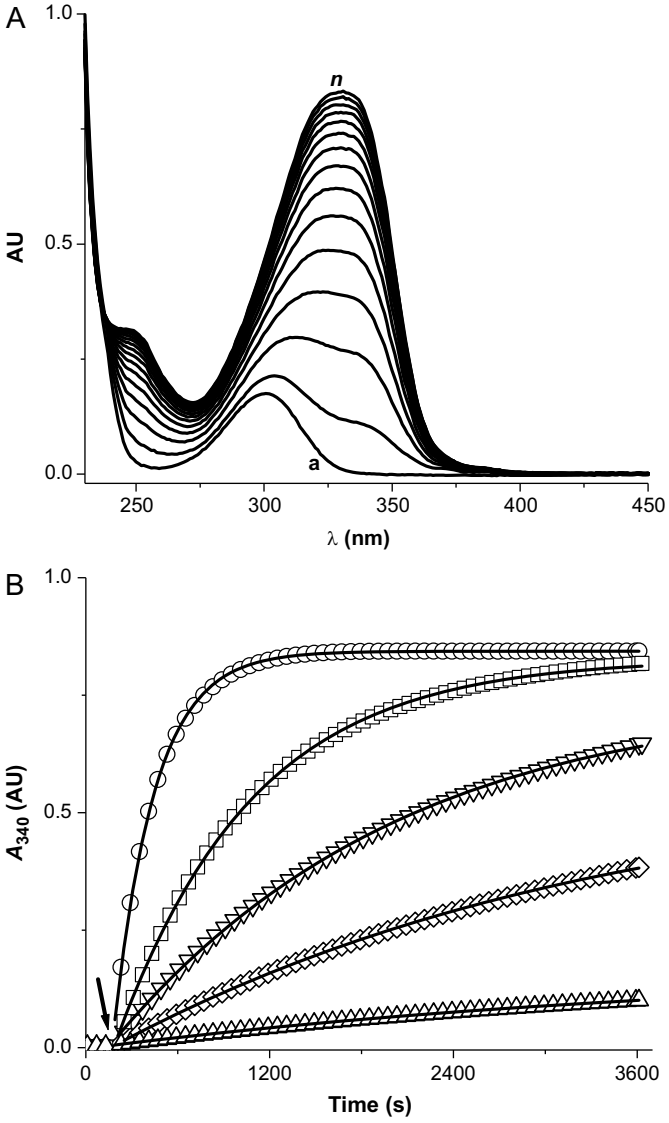

Fig. 3. Kinetic parameters of the 5-ASA–nitrous acid reaction. (A) First-order linearization of the absorbance units at λ = 340 nm associated with the time course of the reaction. 5-ASA (50 μmol L^{-1}) was incubated in 0.65 mol L^{-1} $HClO_4$ with an excess of nitrite ([nitrite] = 2.5 (line a), 3.9 (line b), 12.5 (line c), 16.7 (line d), and 43 mmol L^{-1} (line e)). Data were adjusted to a monoexponential equation (A = Amp × e^{-kt} + A_∞), where amplitude (Amp) is the difference of the absorbance at zero time and the absorbance at infinity ($A_0 - A_\infty$). (B) Dependence of the pseudo-first-order rate constant for 5-ASA consumption on the nitrite concentration. The points were fitted to a second-order polynomial function. Best fit values: k_{obs} = 1.54[NO_2^-] + 146[NO_2^-]^2.

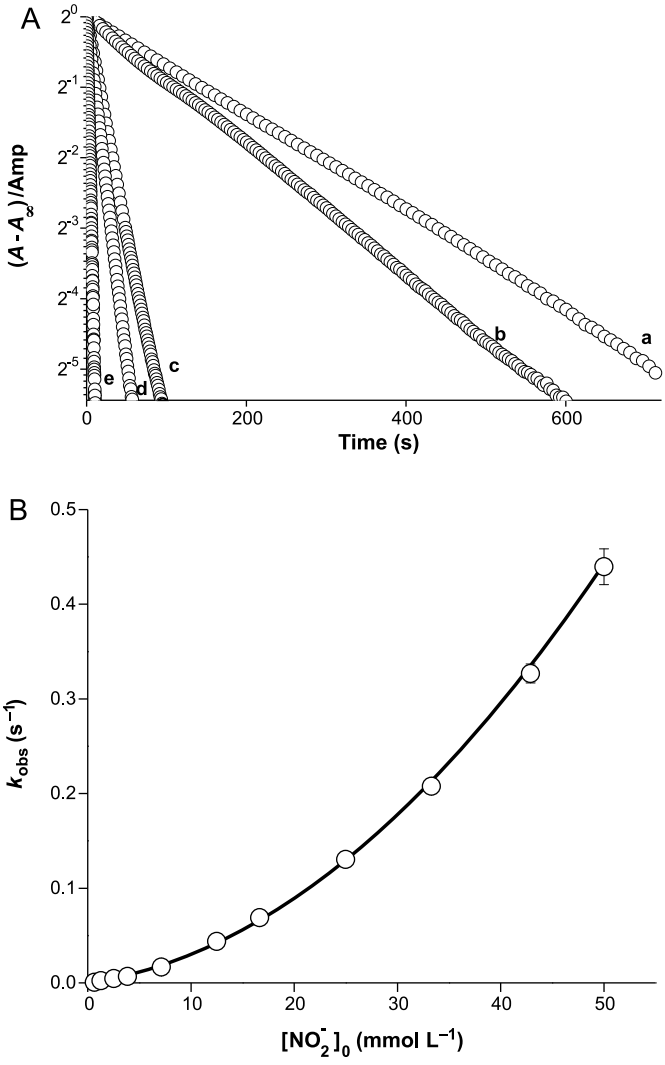

against the total nitrite concentration (Fig. 3B). In agreement with previous knowledge of amine nitrosation reactions,[30] the data depicted in Fig. 3B show a second-order polynomial dependence. These data indicate parallel reactions that are first- and second-order in nitrous acid with rate constants (under these conditions) of 1.5 L mol^{-1} s^{-1} and 146 L^2 mol^{-2} s^{-1}, respectively. This implies similar contributions of both processes at 10 mmol L^{-1} nitrous acid.

In view of the catalytic activity of chloride and thiocyanate (SCN^-) in nitrosation reactions, the reaction of 5-ASA with nitrous acid was studied in the presence of both nitrosonium carriers (in $HClO_4$). The results depicted in Fig. 4 show that the reaction was first-order in each nitrosonium carrier (chloride or SCN^-). As expected, SCN^- (k = 136 L mol^{-1} s^{-1}) was a better catalyst than chloride (k = 0.39 L mol^{-1} s^{-1}).[30]

The influence of the pH of the medium on the initial rate of reaction (assessed from the time courses at 340 nm) and the UV–visible spectra of the product(s) was studied. As shown in Fig. 5, the dependence of the initial rate of reaction on pH follows the trend expected for a single-ionization process. The data were adjusted to the Henderson–Hasselbach equation, obtaining a pK_a of 3.6. This value is very close to that of nitrous acid, suggesting that the reactive species is the

Can. J. Chem. Downloaded from www.nrcresearchpress.com by Xi'an Jiaotong University on 09/19/12
For personal use only.

Fig. 4. Effect of chloride and thiocyanate on the 5-ASA–nitrous acid reaction. (A) Dependence of the observed reaction rate constant (k_{obs}, s^{-1}) on the initial chloride (Cl^-) concentration. $[5\text{-ASA}]_0$ = 50 μmol L^{-1}; $[HClO_4]$ = 0.65 mol L^{-1}; $[NO_2^-]_0$ = 16.7 mmol L^{-1}. (B) Dependence of the observed reaction rate constant (k_{obs}, s^{-1}) on the initial thiocyanate (SCN^-) concentration. $[5\text{-ASA}]_0$ = 25 μmol L^{-1}; $[HClO_4]$ = 10 mmol L^{-1}; $[NO_2^-]_0$ = 1 mmol L^{-1}. Best linear fits: $k_{obs} = 0.37[Cl^-] + 0.04$ and $k_{obs} = 145[SCN^-] + 0.008$.

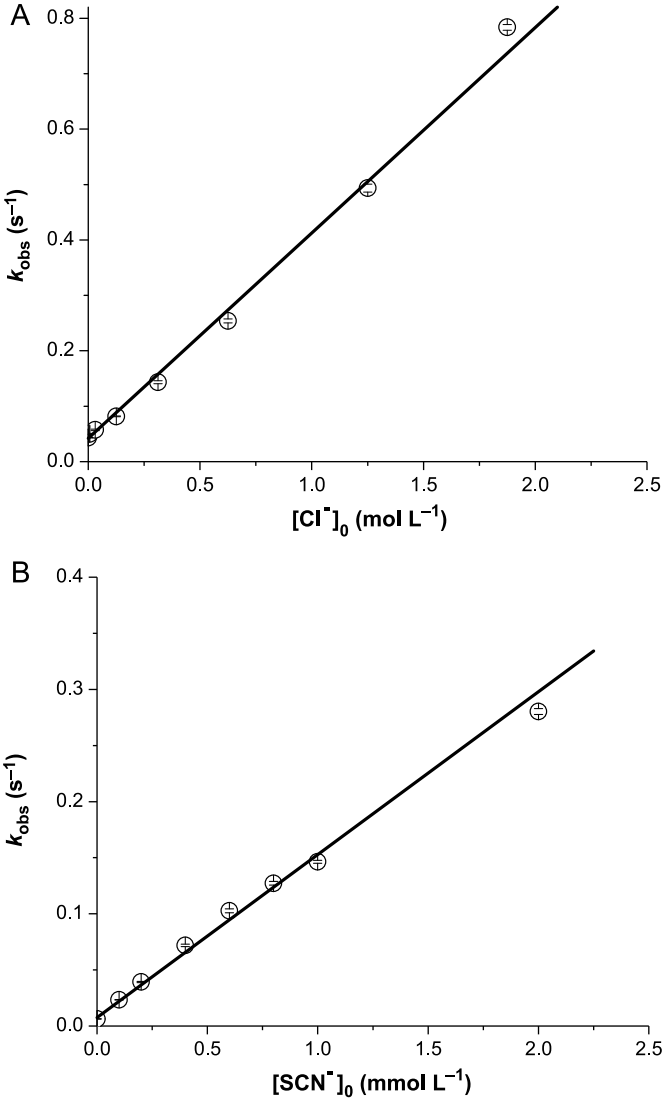

monoprotonated acid (nitrous acid) and that there is no relevant role for other species, such as nitrite (NO_2^-) or $H_2NO_2^+$. The UV–vis spectra of the products of the reaction (obtained by incubating 5-ASA (500 μmol L^{-1}) plus nitrite (500 μmol L^{-1}) in SGF for 40 min) were studied in SGF, phosphate buffer (pH = 7.0), and 0.1 mol L^{-1} NaOH. As shown in Fig. 6, the maximum wavelength in SGF (330 nm, line a) was displaced to 355 nm at pH 7.0 (line b). Similar results were obtained in 0.1 mol L^{-1} NaOH (data not shown). In addition, the maximum absorption band of the spectrum obtained at pH 7.0 shifted to 332 nm when sodium hydrosulfite (100 μmol L^{-1}) was added to the solution (dashed line in Fig. 6). These results imply that the product generated at pH 2.0 and absorbing at 340 nm shifts its absorption to 355 nm at neutral pH.

Fig. 5. Influence of pH on the initial rate of the 5-ASA–nitrous acid reaction. 5-ASA (50 μmol L^{-1}) was incubated with nitrite (1 mmol L^{-1}) at 25 °C. The pH of the medium (SGF, acetic acid/sodium acetate buffer, K_2HPO_4, or phosphate buffer) was adjusted with HCl or NaOH. The time course of the reaction was followed at 340 nm.

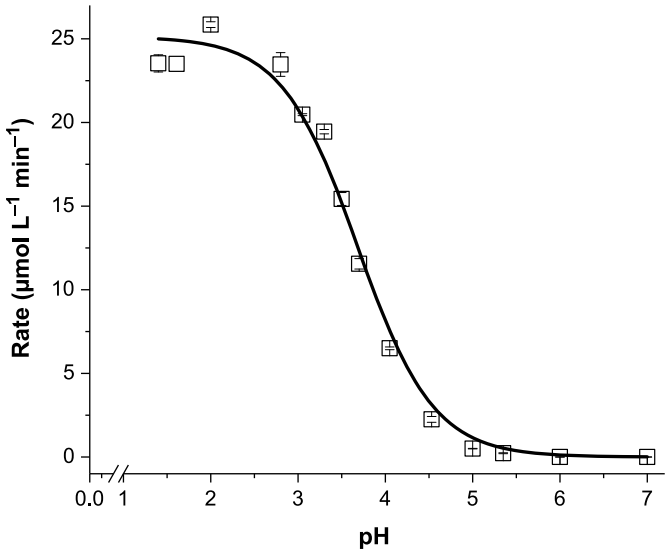

Fig. 6. Effect of pH and sodium hydrosulfite on the UV–visible spectra obtained after the reaction of 5-ASA with nitrous acid. 5-ASA (500 μmol L^{-1}) was incubated with nitrite (500 μmol L^{-1}) at 25 °C in SGF for 1 h. Afterwards, 100 μL of the solution was added to 2.9 mL of SGF (curve a) or phosphate buffer at pH 7.0 (curve b). Dashed line: solution of curve b plus sodium hydrosulfite (100 μmol L^{-1}).

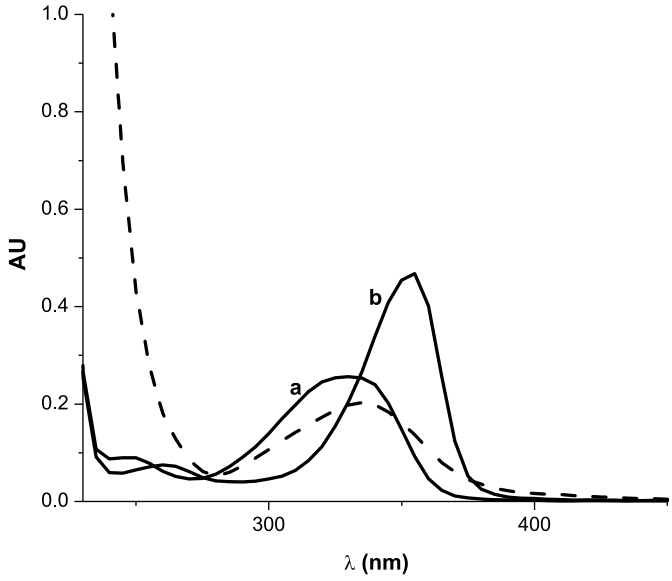

At this pH the product can be reduced by sodium hydrosulfite.

Electrochemical detection of nitric oxide (NO)

Figure 7 shows the time course of the production of NO during the reaction of 5-ASA with nitrite in SGF. The release of NO was studied in the presence of an excess of nitrite or 5-ASA. A steady-state concentration of NO was observed

Can. J. Chem. Downloaded from www.nrcresearchpress.com by Xi'an Jiaotong University on 09/19/12
For personal use only.

Fig. 7. Production of NO during the reaction of 5-ASA with nitrous acid. Time course of the production of NO upon addition of 200 μmol L^{-1} nitrite (arrow) in the absence (line a) and presence of 5-ASA: 10 μmol L^{-1} (line b), 50 μmol L^{-1} (line c), and 1 mmol L^{-1} (line d). The solutions were incubated in SGF at 25 °C.

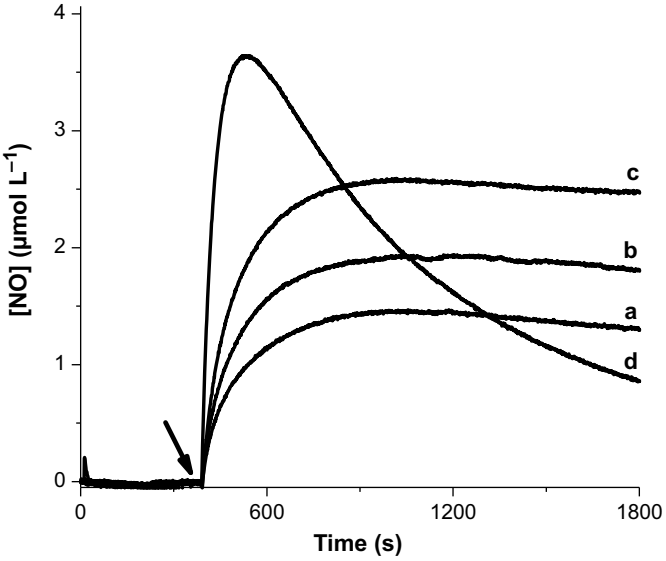

when 5-ASA (10 and 50 μmol L^{-1}) was incubated with excess nitrite (200 μmol L^{-1}). This steady-state concentration was higher than that observed in the absence of 5-ASA (1.5 μmol L^{-1}) and was dependent on the 5-ASA concentration. The maximum NO concentrations were near 1.9 and 2.6 μmol L^{-1} for 10 and 50 μmol L^{-1} 5-ASA, respectively (Fig. 7). Interestingly, the steady state of NO was registered after 12 min of reaction, at which time 5-ASA is still reacting with nitrous acid, as can be observed in Fig. 2. This, and the maximum rate observed at zero reaction time (Fig. 7), implies that the release of NO is due to a direct reaction between 5-ASA and nitrous acid, without the formation of long-lived intermediates. In addition, the initial rate of NO formation increased linearly with 5-ASA concentration, suggesting its formation with first-order kinetics in 5-ASA. The steady-state concentration of NO observed in Fig. 7 at low 5-ASA concentrations suggests that NO is being generated and consumed at similar rates. A different behavior of NO release was observed in the excess 5-ASA condition. When 250 μmol L^{-1} – 1 mmol L^{-1} 5-ASA was incubated with 200 μmol L^{-1} nitrite, a clear decrease in NO concentration was observed after the maximum NO concentration had been reached. After the maximum NO concentration is reached, the slope becomes dependent on the 5-ASA concentration, being maximal at the highest 5-ASA concentration used (1 mmol L^{-1}). This could indicate NO consumption by 5-ASA or by the initial products.[31–33] In fact, it is well known that NO and (or) its nitrosating derivatives can react with aromatic amines, in particular with aminosalicylates.[33]

Since thiocyanate (SCN^-) acts as a nitrosonium carrier[19,30] and is a normal salivary component reaching physiological concentrations close to 1 mmol L^{-1} in the stomach,[34] we investigated a possible effect of SCN^- on NO formation during the reaction of 5-ASA and nitrite in SGF. For this purpose, a nitrite bolus (200 μmol L^{-1} final concentration) was added to

Fig. 8. Time course of the reaction of 5-ASA with nitrous acid followed by HPLC. 5-ASA (50 μmol L^{-1}) was incubated with nitrite (200 μmol L^{-1}) in SGF. (A) Chromatograms obtained from the reaction of 5-ASA plus nitrite at different incubation times. Line a, 0 min; line b, 5 min; and line c, 50 min. (B) Dependence of the area of the chromatographic peaks at 4.3 min (○) and 7.5 min (◇) on the incubation time.

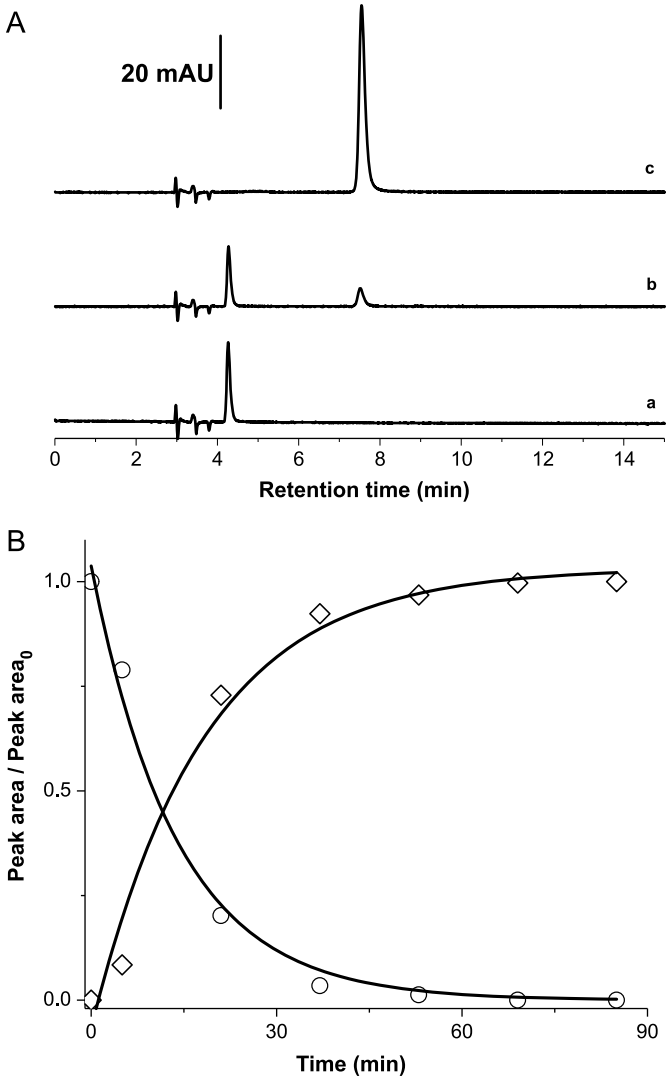

a solution of 5-ASA (1 mmol L^{-1}) plus KSCN (200 μmol L^{-1}) in SFG. The results showed that the presence of KSCN increased the maximum NO concentration from 3.6 to 4.8 μmol L^{-1} (data not shown). These results could be explained by the formation of NOSCN, a species that has been implicated as a nitrosating agent[19] able to generate NO in the presence of reductants such as ascorbic acid.[28,34]

Independently of the experimental conditions employed (excess of either nitrite or 5-ASA, or presence of KSCN), it is remarkable that under our experimental conditions the yield of the detected NO in the system is small. In fact, at the time at which the maximum NO concentration is observed (at 1 mmol L^{-1} 5-ASA), all the limiting reactant (nitrous acid, HNO_2) has been consumed. This implies that approx. 200 μmol L^{-1} nitrite in SGF produces less than

Fig. 9. Extracted mass spectrum (HPLC–MS) obtained during the reaction of 5-ASA and nitrous acid. 5-ASA (50 μmol L^{-1}) was incubated with nitrite (200 μmol L^{-1}) in SGF. After 10 min an aliquot of the reaction mixture was injected into the HPLC–MS system. (A) Mass spectrum of the HPLC–MS peak (2.8 min) corresponding to 5-ASA. (B) Mass spectrum of the HPLC–MS peak (6.6 min) corresponding to the final product of the reaction.

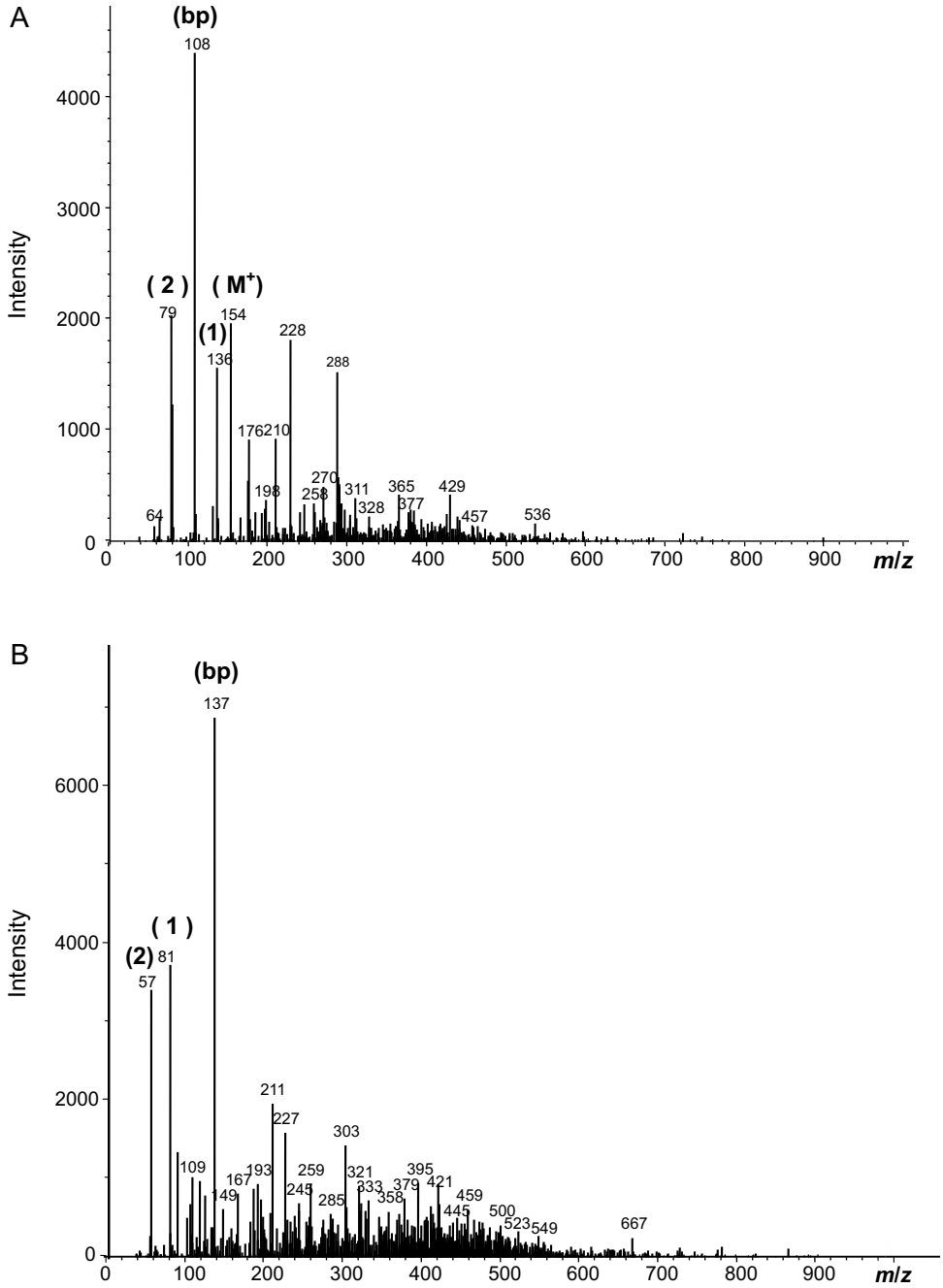

3.6 μmol L^{-1} NO (in the absence of KSCN), rendering a yield of less than 2%. In this context, it is important to consider that NO is formed with a very fast initial rate, implying that the NO is generated as a primary product, probably in parallel with the main reaction of 5-ASA and nitrous acid. In fact, the initial slope of NO release is 6 times lower than the initial slope of 5-ASA consumption assessed by fluorescence.

Studies aimed at characterizing the final product(s) of the 5-ASA–nitrous acid reaction

To characterize the product(s) generated during the reaction of 5-ASA and nitrous acid, HPLC measurements were carried out. Solutions of 5-ASA (50–100 μmol L^{-1}) plus nitrite (100–200 μmol L^{-1}) were incubated in SGF and injected into the HPLC system at different reaction times. As can be seen in Fig. 8A, 5-ASA (50 μmol L^{-1}) in the absence of nitrous acid showed a single chromatographic peak with a retention time of 4.3 min. When nitrite was added to a 5-ASA solution in SGF, in parallel with a decrease of the peak at 4.3 min, a new peak at 7.5 min was registered (line b in Fig. 8A). The intensity of both peaks was dependent on the incubation time and after 60 min of reaction, only the peak

Can. J. Chem. Downloaded from www.nrcresearchpress.com by Xi'an Jiaotong University on 09/19/12
For personal use only.

Can. J. Chem. Downloaded from www.nrcresearchpress.com by Xi'an Jiaotong University on 09/19/12
For personal use only.

Fig. 10. Time course of the reaction between the final product of the 5-ASA–nitrous acid reaction (diazonium derivative) and resorcinol. The diazonium product was obtained by incubating a solution containing 5-ASA (5 mmol L^{-1}) and nitrite (10 mmol L^{-1}) in SGF at 25 °C for 30 min. Afterwards, the solution was diluted 20-fold. An aliquot of this solution was added to a solution containing resorcinol (250 μmol L^{-1}) in NaOH (20 mmol L^{-1}). The time course of the reaction was followed by the changes in UV–visible spectra registered in the range 250–700 nm. Lines a–i represent spectra taken every 3 min. Inset: time course of the reaction followed at 355 nm (□) and 466 nm (○).

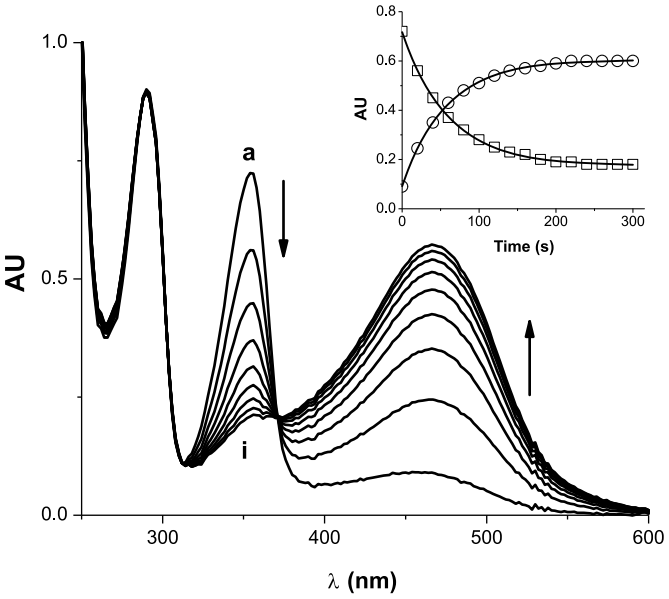

at 7.5 min was detected. The time course of the reaction assessed by HPLC (Fig. 8B) is similar to the kinetic profiles registered by UV–visible or fluorescence spectroscopy. These results showed that only one product is formed in the main reaction of 5-ASA with nitrous acid. To identify this product, HPLC–MS studies were carried out. For this purpose, a solution containing 5-ASA (50 μmol L^{-1}) plus nitrite (200 μmol L^{-1}) was incubated for 30 min in SGF and injected into the HPLC–MS system. The registered HPLC–MS chromatograms showed two chromatographic peaks at 2.8 and 6.6 min (data not shown). The mass spectrum of the peak at 2.8 min is in agreement with the structure of 5-ASA (Fig. 9A), according to the following fragmentation pattern: ion molecular peak (M^+) of 5-ASA, m/z = 154; base peak (bp), m/z = 108, corresponding to the loss of the C-1 substituent (COOH) of 5-ASA; peak (1), m/z = 136, related to the loss of the amine group of 5-ASA; peak (2), m/z = 79, related to the loss of C-1, C-2, and C-5 substituents.

The fragmentation pattern of the peak detected at 6.6 min (product of the reaction) is shown in Fig. 9B and gave the following ions: base peak (bp) with m/z = 137, corresponding to the loss of the N_2^+ fragment; peak (1) with m/z = 81 and peak (2) with m/z = 57, according with the fragmentation pattern of salicylic acid.[35]

The analysis of this fragmentation pattern indicated the formation of the diazonium derivative (2-hydroxy-5-diazonium benzoic acid) as a product of the reaction of 5-ASA and nitrous acid. To corroborate this finding, we assayed a number of reactions expected from a diazonium compound with phenols. A solution containing the final product of the reaction between 5-ASA (5 mmol L^{-1}) and nitrite (10 mmol L^{-1}) in SGF was diluted 20-fold and mixed with a solution of resorcinol in 20 mmol L^{-1} NaOH (pH = 12) or 50 mmol L^{-1} Tris buffer (pH 7.3). Figure 10 shows the changes in the UV–visible spectra upon the reaction of the diazonium derivative of 5-ASA (2-hydroxy-5-diazonium benzoic acid, approx. 25 μmol L^{-1}) with resorcinol (250 μmol L^{-1}) at pH 12. As can be seen in this figure, in the presence of resorcinol a clear decrease in the absorbance at 355 nm (associated with the diazonium derivative) was observed. In parallel with this decrease, a new absorption band at 466 nm was generated. This band can be associated with the formation of diazo derivatives.[36] This behavior, observed in the first 30 min of incubation (see inset of Fig. 10), was characterized by the presence of a neat isosbestic point at 370 nm. In addition, UV–visible studies allowed us to postulate that the final product of the reaction between 5-ASA and nitrous acid (diazonium derivative) also reacts with phenols such as phloretin, catechol, pyrogallol, and quercetin at pH 7.3 (data not shown).

Discussion

The interaction of xenobiotics with nitrite in acidic media (nitrous acid) and the possible release of NO during the reaction is currently a matter of study[20–28,37,38] Here, we investigated the interaction of 5-ASA, a drug widely employed in the treatment of bowel diseases, with nitrous acid. The structure of 5-ASA (Scheme 1), characterized by an aromatic amine and a hydroxyl group, makes 5-ASA a plausible substrate to react with nitrous acid. In fact, our findings demonstrate that 5-ASA reacts efficiently with nitrous acid to form the diazonium derivative (2-hydroxy-5-diazonium benzoic acid). In addition, NO was detected as a minor product of the reaction (~16% of the consumed 5-ASA). This value is higher than the yield estimated from the maximum NO concentration observed in Fig. 7 (2% of the initial nitrous acid concentration). This difference is due to the consumption of the NO formed by 5-ASA or its derivatives.

The reaction of 5-ASA and nitrous acid was evidenced by the decrease of 5-ASA fluorescence and by the generation of new bands in the UV–visible spectrum (Figs. 1 and 2, respectively). The reaction was dependent on the pH of the medium in a way that indicated a single-ionization process with a pK_a of 3.6 (Fig. 5). This pK_a value is very close to that of nitrous acid, implying that nitrous acid is a necessary precursor in the reaction. The reaction order, first in 5-ASA and first and second in nitrous acid (Fig. 3), points to a classical nitrosation reaction, which in the case of primary amines is followed by a rapid dehydration to yield the diazonium compound. In addition, the results presented in Fig. 4 demonstrate that the reaction is catalyzed by chloride and thiocyanate in similar ways, as has been reported for others compounds containing amine moieties.[19]

The UV–visible spectrum obtained after the reaction between 5-ASA and nitrous acid was dependent on the pH of the medium (Fig. 6). The maximum band of the UV–visible spectrum was displaced from 340 nm to 355 nm when the pH changed from 2.0 to 7.0. Also, the addition of sodium hydrosulfite (dithionite) to the solution at pH 7.0 shifted the

Scheme 1.

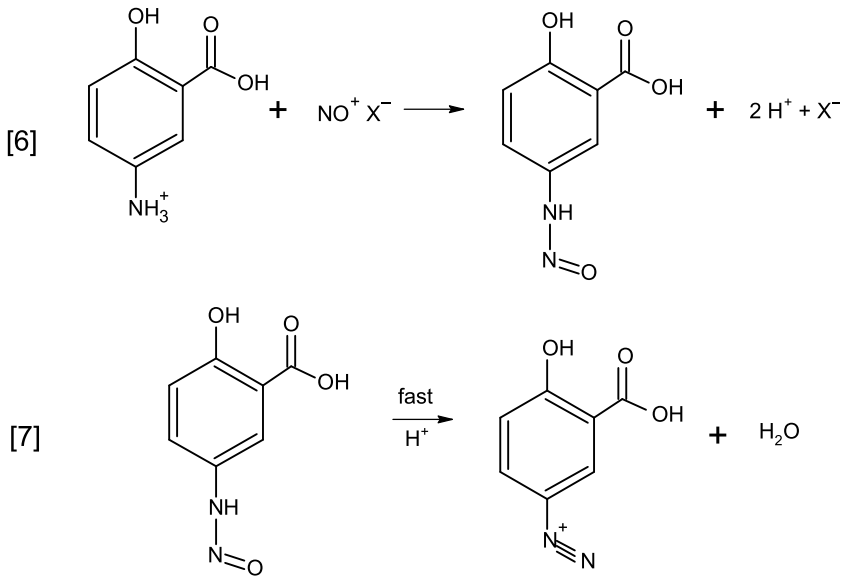

absorbance maximum to 332 nm. The latter could be explained by the known reductive effect of hydrosulfite on azo compounds.[39]

The present data reveal that in addition to 2-hydroxy-5-diazonium benzoic acid, NO was generated (as a minor product) during the reaction of 5-ASA and nitrous acid in SGF (Fig. 7). The kinetic profiles of NO release indicate that NO (at low concentration) was formed as a primary product, probably in a minor parallel reaction. Similar NO concentrations have been detected in the reaction of phenols such as caffeic acid and coumaric acid with nitrite in SGF.[26] However, even low concentrations of NO could be significant, giving some protection to the stomach and probably contributing to vasodilation, mucosal blood flow, and mucus thickness.[23–26] In this context, an NO-releasing 5-ASA derivative has been proposed as a plausible alternative with improved efficacy in the treatment of bowel disease.[40]

From the obtained results, we propose that 2-hydroxy-5-diazonium benzoic acid and NO are formed through parallel mechanisms, according to Scheme 1 and Scheme 2. 5-ASA would react with nitrous acid to form 2-hydroxy-5-diazonium benzoic acid (Scheme 1) as the main product and in a parallel way (minor) to form NO (Scheme 2). As low NO concentrations were detected during the reaction, the final product(s) generated by the NO pathway were probably not detected in the HPLC experiments.

As eq. [6] shows (Scheme 1), the first step of the reaction is the formation of the *N*-nitrosamine derivative to form the diazonium salt (eq. [7]), as expected for the reaction between primary aromatic amines and nitrosonium carriers.[19,30] In this context, a methodology based on the formation of diazonium salts from the reaction of 5-ASA with nitrous acid has recently been proposed as a simple assay to estimate 5-ASA concentration in pharmaceutical formulations.[41]

The mixed first- and second-order kinetics in nitrous acid arises from the identity of the NOX species. In the absence of external nitrosonium carriers the reaction proceeds via HNO_2 and N_2O_3, which can be interpreted as nitrosonium hydroxide and nitrosonium nitrite, respectively. The generation of these nitrosating species (eqs. [1] and [3]) implies first- and second-order kinetics in nitrous acid, respectively.[19] In the presence of chloride and thiocyanate, additional NOX species are present that catalyze reaction [6].

NO is in turn produced by a combination of reactions. Acidic nitrite is in equilibrium with N_2O_3 via eq. [3], and N_2O_3 is in equilibrium with NO and NO_2 (eq. [4]). This equilibrium is displaced to the left ($K = 2 \times 10^{-5}$),[42] but $\cdot NO_2$ also has an alternative escape route via dimerization and dismutation:[43]

$$[8] \qquad 2\cdot NO_2 \rightleftharpoons N_2O_4 + H_2O \rightarrow NO_2^- + NO_3^- + 2H^+$$

Reaction [8] would displace equilibrium [4] to the right, thus explaining the spontaneous NO evolution in the absence of 5-ASA (Fig. 7, trace a). Two additional possibilities appear likely, both involving the reduction of intermediates. First, 5-ASA or 2-hydroxy-5-diazonium benzoic acid (or both) could be oxidized by $\cdot NO_2$, a strong oxidant known to react quickly with aminophenols (eq. [9] in Scheme 2). The reaction would not produce NO directly but would sequester NO_2 from equilibrium [4], thus making more NO available for detection. Alternatively, either aromatic substrate could react with NO^+ (or NOX), which is also a strong one-electron oxidant with a redox potential ($E°$) of 1.24 V (eq. [10] in Scheme 2). This reaction has been proposed to explain how phenols such as caffeic acid and coumaric acid (among others) generate NO in their interaction with nitrite in stomach conditions.[26]

Additionally, the fact that thiocyanate increases NO production indicates that reaction [10] is occurring and its rate depends on the identity of NOX. This does not rule out the possibility of reaction [9] occurring concomitantly. Nevertheless, the reactions proposed in Scheme 2 imply that final products corresponding to the oxidation of 5-ASA should be generated. However, these products were not detected in our HPLC studies. Furthermore, we estimate that the initial rate of NO formation represents close to 16% of the consumption

Can. J. Chem. Downloaded from www.nrcresearchpress.com by Xi'an Jiaotong University on 09/19/12
For personal use only.

Scheme 2.

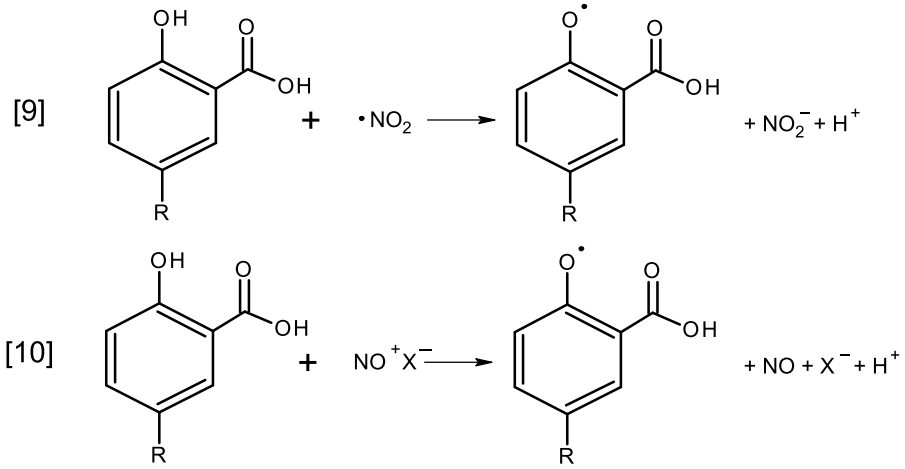

of 5-ASA, leading to concentrations of the final products in the micromolar range.

The detected diazonium derivative (Fig. 9) would be stable under stomach conditions, but upon neutralization of the medium (as in the small intestine or at alkaline pH) would be able to react with phenols to form diazocompounds.[44,45] Our results showed that the diazonium derivative generated from the reaction of 5-ASA with nitrite in SGF reacted with resorcinol, giving the characteristic visible absorption band of diazo derivatives (Fig. 10).

Conclusion

The present in vitro studies indicate that 5-ASA reacts with nitrous acid, generating the diazonium derivative as the main product with minor amounts of nitric oxide. While the formation of nitric oxide could be beneficial for the protection of the stomach, the generation of the diazonium salt could be considered a potentially toxic process.

Acknowledgments

This work was supported by FONDECYT (No. 1100659), Vicerrectoría Adjunta de Investigación y Desarrollo (VRAID), Pontificia Universidad Católica de Chile, and CSIC (Universidad de la República, Uruguay).

References

(1) Williams, J. W.; Shepherd, N. A. *Surgery* **2005** *23*, 346.
(2) Kozuch, P. L.; Hanauer, S. B. *World J. Gastroenterol.* **2008** *14* (3), 354. doi:10.3748/wjg.14.354.
(3) Lakatos, P. L.; Lakatos, L. *Pharmacol. Res.* **2008** *58* (3–4), 190. doi:10.1016/j.phrs.2008.08.003.
(4) Desreumaux, P.; Ghosh, S. *Aliment. Pharmacol. Ther.* **2006** *24* (s1), 2. doi:10.1111/j.1365-2036.2006.03069.x.
(5) Dinis, T.; Madeira, V.; Almeida, L. *Arch. Biochem. Biophys.* **1994** *315* (1), 161. doi:10.1006/abbi.1994.1485.
(6) Pearson, D.; Jourd'heuil, D.; Meddings, J. *Free Radic. Biol. Med.* **1996** *21* (3), 367. doi:10.1016/0891-5849(96)00031-7.
(7) Kanski, J.; Lauderback, C.; Butterfield, D. A. *Neurochem. Res.* **2001** *26* (1), 23. doi:10.1023/A:1007620330168.
(8) Gonçalves, E.; Almeida, L. M.; Dinis, T. C. P. *Free Radic. Res.* **1998** *29* (1), 53. doi:10.1080/10715769800300071.
(9) López-Alarcón, C.; Rocco, C.; Lissi, E.; Carrasco, C.; Squella, J. A.; Nuñez-Vergara, L. J.; Speisky, H. *Pharm. Res.* **2005** *22* (10), 1642. doi:10.1007/s11095-005-6948-y.
(10) López-Alarcón, C.; Speisky, H.; Lissi, E. *Biol. Res.* **2007** *40* (2), 155. doi:10.4067/S0716-97602007000200006.
(11) Liu, Z. C.; McClelland, R. A.; Uetrecht, J. P. *Drug Metab. Dispos.* **1995** *23*, 246.
(12) Yppolito, R.; Pappano, N.; Debattista, N.; Miskoski, S.; Bertolotti, S. G.; García, N. A. *Redox Rep.* **2002** *7* (4), 229. doi:10.1179/135100002125000613.
(13) Kumarathasan, P.; Vincent, R.; Goegan, P.; Potvin, M.; Guenette, J. *Biochem. Cell Biol.* **2001** *79* (1), 33. doi:10.1139/bcb-79-1-33.
(14) Joshi, R.; Kumar, S.; Unnikrishnan, M.; Mukherjee, T. *Free Radic. Res.* **2005** *39* (11), 1163. doi:10.1080/10715760500177880.
(15) Fadda, H. M.; Mohamed, M. A.; Basit, A. W. *Int. J. Pharm.* **2008** *360* (1–2), 171. doi:10.1016/j.ijpharm.2008.04.035.
(16) Gorelik, S.; Kohen, R.; Ligumsky, M.; Kanner, J. *Arch. Biochem. Biophys.* **2007** *458* (2), 236. doi:10.1016/j.abb.2006.12.006.
(17) Pannala, A. S.; Mani, A. R.; Spencer, J. P.; Skinner, V.; Bruckdorfer, K. R.; Moore, K. P.; Rice-Evans, C. A. *Free Radic. Biol. Med.* **2003** *34* (5), 576. doi:10.1016/S0891-5849(02)01353-9.
(18) Bryan, N. S. *Free Radic. Biol. Med.* **2006** *41* (5), 691. doi:10.1016/j.freeradbiomed.2006.05.019.
(19) Williams, D. L. H. *Nitrosation Reactions and the Chemistry of Nitric Oxide*; Elsevier: Amsterdam, 2004.
(20) Dubois, M.; Bailly, F.; Mbemba, G.; Mouscadet, J. F.; Debyser, Z.; Witvrouw, M.; Cotelle, P. *J. Med. Chem.* **2008** *51* (8), 2575. doi:10.1021/jm7011134.
(21) Pannala, A. S.; Mani, A. R.; Rice-Evans, C. A.; Moore, K. P. *Free Radic. Biol. Med.* **2006** *41* (6), 896. doi:10.1016/j.freeradbiomed.2006.05.010.
(22) Brambilla, G.; Martelli, A. *Mutat. Res.* **2007** *635* (1), 17. doi:10.1016/j.mrrev.2006.09.003.
(23) Weitzberg, E.; Lundberg, J. O. *Nitric Oxide* **1998** *2* (1), 1. doi:10.1006/niox.1997.0162.
(24) Takahama, U.; Oniki, T.; Hirota, S. *J. Agric. Food Chem.* **2002** *50* (15), 4317. doi:10.1021/jf011697q.
(25) Takahama, U.; Yamamoto, A.; Hirota, S.; Oniki, T. *J. Agric. Food Chem.* **2003** *51* (20), 6014. doi:10.1021/jf021253+.

Can. J. Chem. Downloaded from www.nrcresearchpress.com by Xi'an Jiaotong University on 09/19/12
For personal use only.

(26) Gago, B.; Lundberg, J. O.; Barbosa, R. M.; Laranjinha, J. *Free Radic. Biol. Med.* **2007** *43* (9), 1233. doi:10.1016/j.freeradbiomed.2007.06.007.
(27) Takahama, U.; Tanaka, M.; Hirota, S. *Free Radic. Res.* **2010** *44* (3), 293. doi:10.3109/10715760903486057.
(28) Peri, L.; Pietraforte, D.; Scorza, G.; Napolitano, A.; Fogliano, V.; Minetti, M. *Free Radic. Biol. Med.* **2005** *39* (5), 668. doi:10.1016/j.freeradbiomed.2005.04.021.
(29) Takahama, U.; Hirota, S. *J. Agric. Food Chem.* **2008** *56* (12), 4736. doi:10.1021/jf703660k.
(30) Turney, T. A.; Wright, G. A. *Chem. Rev.* **1959** *59* (3), 497. doi:10.1021/cr50027a004.
(31) Pallapies, D.; Peskar, B. A.; Peskar, B. M. *Eur. J. Pharmacol.* **1995** *282* (1–3), 145. doi:10.1016/0014-2999(95)00305-5.
(32) Reynolds, P. D.; Middleton, S. J.; Shorthouse, M.; Hunter, J. O. *Aliment. Pharmacol. Ther.* **1995** *9* (5), 491. doi:10.1111/j.1365-2036.1995.tb00411.x.
(33) Grisham, M. B.; Miles, A. M. *Biochem. Pharmacol.* **1994** *47* (10), 1897. doi:10.1016/0006-2952(94)90320-4.
(34) Takahama, U.; Hirota, S.; Oniki, T. *Chem. Res. Toxicol.* **2006** *19* (8), 1066. doi:10.1021/tx060038a.
(35) Spectral Database for Organic Compounds, SDBS. http://riodb01.ibase.aist.go.jp/sdbs/cgi-bin/direct_frame_top.cgi.
(36) Whitlock, L. R.; Siggia, S.; Smola, J. E. *Anal. Chem.* **1972** *44* (3), 532. doi:10.1021/ac60311a021.
(37) Pietraforte, D.; Brambilla, G.; Camerini, S.; Scorza, G.; Peri, L.; Loizzo, A.; Crescenzi, M.; Minetti, M. *Free Radic. Biol. Med.* **2008** *45* (2), 124. doi:10.1016/j.freeradbiomed.2008.03.018.
(38) Takahama, U.; Tanaka, M.; Hirota, S. *Plant Foods Hum. Nutr.* **2010** *65* (1), 1. doi:10.1007/s11130-009-0144-x.
(39) Sydnes, L. K.; Elmi, S.; Heggen, P.; Holmelid, B.; Malthe-Soerensen, D. *ChemInform* **2007** *38* (45), 63. doi:10.1002/chin.200745064.
(40) Wallace, J. L. *Dig. Liver Dis.* **2003** *35*, S35. doi:10.1016/S1590-8658(03)00050-1.
(41) Rafael, J. A.; Jabor, J. R.; Casagrande, R.; Georgetti, S. R.; Borin, M. F.; Fonseca, M. *Rev. Bras. Cienc. Farm.* **2007** *43* (1), 97. doi:10.1590/S1516-93322007000100012.
(42) Graetzel, M.; Taniguchi, S.; Henglein, A. *Ber. Bunsenges. Phys. Chem.* **1970** *74*, 488.
(43) Treinin, A.; Hayon, E. *J. Am. Chem. Soc.* **1970** *92* (20), 5821. doi:10.1021/ja00723a001.
(44) Cassano, R.; Trombino, S.; Cilea, A.; Ferrarelli, T.; Muzzalupo, R.; Picci, N. *Chem. Pharm. Bull. (Tokyo)* **2010** *58* (1), 103. doi:10.1248/cpb.58.103.
(45) Carceller, E.; Salas, J.; Merlos, M.; Giral, M.; Ferrando, R.; Escamilla, I.; Ramis, J.; García-Rafanell, J.; Forn, J. *J. Med. Chem.* **2001** *44* (18), 3001. doi:10.1021/jm010852p.

Can. J. Chem. Downloaded from www.nrcresearchpress.com by Xi'an Jiaotong University on 09/19/12
For personal use only.

Amine and thiazole substituted γ-butyrolactones from naturally occurring limonene

Pushpinder Kaur, Pralay Das, Abha Chaudhary, and Bikram Singh

Abstract: Substituted γ-butyrolactones are important structural motifs in several natural products and pharmaceuticals. In this paper, we report the synthesis of novel γ-butyrolactone amine and thiazole derivatives from naturally occurring limonene. Regioselective bromination followed by nucleophilic substitution with different amines and thiourea gave desired products in moderate yield.

Key words: regioselectivity, bromination, amination, thiazole, γ-butyrolactone.

Résumé : Les γ-butyrolactones substituées sont d'importants motifs structuraux dans plusieurs produits naturels et pharmaceutiques. Dans ce travail, on a synthétisé de nouveaux dérivés amine et thiazole de la γ-butyrolactone à partir du limonène qu'on peut obtenir de sources naturelles. La bromation régiosélective, suivie d'une substitution nucléophile avec diverses amines et thiourées permet d'obtenir les produits désirés avec des rendements modérés.

Mots-clés : régiosélectivité, bromation, amination, thiazole, γ-butyrolactone.

[Traduit par la Rédaction]

Can. J. Chem. Downloaded from www.nrcresearchpress.com by Xi'an Jiaotong University on 09/19/12
For personal use only.

Introduction

The amine derivatives of γ-butyrolactone are important motifs found in several biologically active natural products and pharmaceuticals. These structural units are very common in antiallergic,[1] antineoplastic,[2] and antifungal[3] compounds, in antimalarial alkaloids[4] and gastroprotective drugs,[5] and in new inhibitors of phosphodiesterase and HIV-1 protease.[6] Moreover, these amino derivatives have been used as building blocks of other important molecules.[7]

In recent years, significant attention has been focused on the synthesis of amine derivatives of γ-butyrolactone. Different research groups have started with an α-halo-γ-butyrolactone derivative and a C-protected amino acid in the presence of base,[8] oxazolone with α-haloketones in the presence of potassium bicarbonate and a phase transfer reagent,[9] aza-Michael-type addition using $NsONHCO_2Et$,[10] and amino hydroxylation of diesters.[11] Roos and Effenberger first prepared amino alcohols and then proceeded with stepwise amino protection, ozonolysis, and oxidation.[12] All the research groups have either synthesized N-protected derivatives or used starting materials that contain nitrogen functionality. Also, they have prepared amine derivatives substituted in the lactone ring. In our case, a new type of butyrolactone derivative (**3**) having a side chain with a carbonyl group has been synthesized from naturally occurring limonene (**1**).

Thiazole and its derivatives are very useful compounds in various fields of chemistry including medicine and agriculture. For example, the thiazolium ring present in vitamin B_1 serves as an electron sink, and its coenzyme form is important for the decarboxylation of α-keto acids.[13] This heterocyclic system has found broad application in drug development for the treatment of several diseases.[14] To the best of our knowledge, γ-butyrolactones with different substituted amine and thiazole moieties are very rare entries in organic synthesis. In the last few years we have been engaged in the development of limonene to γ-butyrolactone chemistry. Herein we report the regioselective bromination of the side chain of **3** followed by nucleophilic substitution with different amines and thiourea. Amide and sulfonamide derivatives of thiazolobutyrolactone have also been synthesized.

Results and discussion

Limonene (**1**) was isolated from citrus peel essential oil (extracted with a Clevenger apparatus) using column chromatography. Limonene was identified by gas chromatography – mass spectrometry and with the reference sample procured from Sigma-Aldrich (Germany). α-Terpineol (**2**) was prepared by selective oxymercuration-demercuration of the external double bond in limonene (Scheme 1). α-Terpineol was subjected to oxidative cleavage using different oxidizing agents such as CrO_3,[15] $KMnO_4$,[16] and $RuCl_3$.[17] $RuCl_3$–$NaIO_4$ was found to be the best oxidizing agent, giving the highest yield of **3**.

We were interested in introducing amine and sulfur atoms in the side chain of **3** to enhance its activity. But when **3** was treated with primary amine, ring opening was taking place. So we decided to first introduce a halogen atom in the side chain and then carry out the substitution with different amines.

The α-halogenation of carbonyl compounds is the step for introducing a heteroatom, generating a stabilized carbon radical

Received 25 June 2010. Accepted 10 January 2011. Published at www.nrcresearchpress.com/cjc on 24 May 2011.

P. Kaur, P. Das, A. Chaudhary, and B. Singh. Natural Plant Products Division, Institute of Himalayan Bioresource Technology, Palampur (H.P.) 176061, India.

Corresponding author: B. Singh (e-mail: bikram_npp@rediffmail.com).

Scheme 1. Synthesis of γ-butyrolactone (**3**) from limonene.

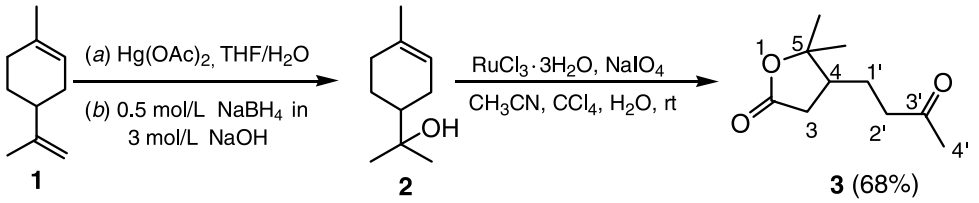

or carbanion and providing conjugation to carbonyl groups. Aldehydes and ketones can be halogenated at the α-position with bromine, chlorine, and iodine. Various α-bromination methods for carbonyl compounds have been reported, including the basic method using Br_2, *N*-bromosuccinimide, dioxane/dibromide, and a hexamethylenetetramine–bromine complex under microwave irradiation.[15]

For unsymmetrical ketones the preferred order of halogenation is typically CH > CH_2 > CH_3, but mixtures are frequently encountered.[18] In basic conditions the reaction goes through an enolate mechanism where the C-4′ group is attacked preferably over the C-2′ group to stabilize the enolate (Scheme 1). With acid catalysts, the reaction goes through enol formation, and for enol stabilization an internal carbon (C-2′) is brominated rather than the terminal C-4′ (Scheme 1). The quantity of brominating reagent is an important factor in controlling consecutive bromination at the same position.[18] The purpose of the catalyst is to provide a small amount of enol or enolate. The reaction can also be carried out without addition of catalyst, as traces of catalyst are always present and these are enough to catalyze enol formation.

We have developed a milder, selective, and controlled bromination of **3** at the C-2′ position. In this procedure, 1 mol/L Br_2 in dichloromethane (DCM) was added dropwise to **3** in a 1:1 ratio at room temperature. In situ formation of **4** was monitored and identified by thin layer chromatography (TLC) and liquid chromatography – mass spectrometry (LC-MS). Bis-brominated product was observed with increasing molar concentrations of bromine in DCM. The molar ratio (1:1) is an important factor for selective monobromination at the C-2′ position. Isolation of **4** is very difficult owing to the unstable C–Br bond under moist and basic conditions. After the addition of bromine the reaction mixture was immediately dried on a rotary evaporator to remove unreacted bromine and HBr produced under the reaction conditions.

Bromo-substituted γ-butyrolactone (**4**) was used for amination reactions without further purification. Compounds **5a**–**5g** were prepared (Table 1) through selective bromination and nucleophilic substitution by different amines in a consecutive manner at the C-2′ position of **4**. Aminations of **4** using primary aliphatic amines like cyclohexylamine, benzylamine, and ethylenediamine occurred very rapidly with the γ-butyrolactone ring, and ring-substituted products (A and B) were observed simultaneously as major by-products along with the expected minor product C (Scheme 2). The mixture of products was observed by TLC and LC-MS.

For steric reasons, *tert*-butylamine (entry 3) and isopropylamine (entry 9) remained unreacted even on addition of higher equivalents of amine for a longer time. Primary aromatic amines such as aniline and *p*-toluidine (entries 1 and 2) participated in selective bromine substitution and produced **5a** and **5b** in 58% and 61% yield, respectively.

Primary aromatic amines are less reactive than primary aliphatic amines and the expected products were formed in greater quantity (entry 1, 58%; entry 2, 61%) than the ring-opened product. It is clear from the results that the bromine substitution rate is much faster than the rate of ring cleavage of the γ-butyrolactone **4**.

Secondary amines were found to be more suitable and selective for aminations of **4**. No ring cleavage product was observed. The reactions were carried out with acyclic as well as cyclic (five- and six-member) amines. Compound **5c** was obtained in good yield (84%) by the reaction of diethylamine (entry 4) with **4**.

Using morpholine and piperidine (entries 5 and 6), the yields obtained for **5d** and **5e** were 69% and 63%, respectively. For piperazine (entry 7) there was the possibility of substitution by both nitrogen atoms, but as one equivalent of **4** and one equivalent of piperazine were used, only monosubstituted product was obtained. The yield obtained with pyrrolidine (entry 8) was less than that obtained with six-member cyclic amines.

Intermediate **4** was further used for the synthesis of another heterocyclic molecule containing both sulfur and nitrogen atoms by Hantzsch thiazole synthesis (Scheme 3). In this reaction, **4** was refluxed with thiourea to give the thiazole-containing butyrolactone derivative **6** in 68% yield.

As the thiazole derivative **6** contains a free amino group in its skeleton, it can be further substituted to introduce other functional groups that can lead to enhanced biological activity. Therefore, we substituted the amino group of **6** with different amides and sulfonamides (Scheme 4). Acetyl and benzyl amide derivatives (**6a** and **6b**) were prepared by refluxing **6** with one equivalent of acetyl or benzoyl chloride, respectively, in the presence of a catalytic amount of pyridine. Product **6** was refluxed with the acid chlorides of acetic acid, benzoic acid, and *p*-toluenesulfonic acid in the presence of pyridine to yield **6a** (72%), **6b** (68%), and **6c** (75%), as shown in Scheme 4.

Conclusion

In summary, methods to introduce a diverse set of amino groups onto γ-butyrolactone have been developed. The key intermediate for all of these transformations is γ-butyrolactone bromide derivative **4**, obtained from γ-butyrolactone derivative **3** in a selective bromination reaction. To this intermediate were introduced a variety of substituted amines to produce amino-functionalized γ-butyrolactones.

Experimental section

General

All reactions were conducted using oven-dried glassware.

Can. J. Chem. Downloaded from www.nrcresearchpress.com by Xi'an Jiaotong University on 09/19/12
For personal use only.

Can. J. Chem. Downloaded from www.nrcresearchpress.com by Xi'an Jiaotong University on 09/19/12
For personal use only.

Table 1. Selective aminations of γ-butyrolactone bromo derivative **4**.

Entry	Intermediate	Amine	Time (min) / temp. (°C)	Product[a]		Overall yield[b]
1	**4**	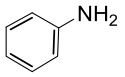	20/55	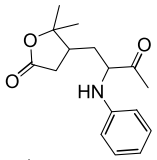	**5a**	58%
2	**4**	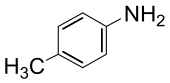	20/60	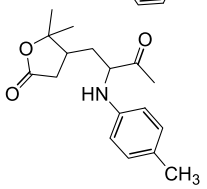	**5b**	61%
3	**4**		30/60	No reaction		—
4	**4**	$HN(C_2H_5)_2$	15/55	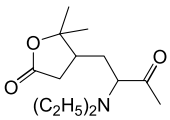	**5c**	84%
5	**4**	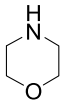	20/50	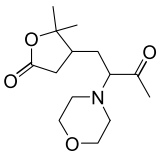	**5d**	69%
6	**4**		20/50	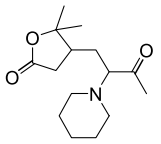	**5e**	63%
7	**4**	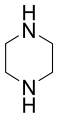	30/50	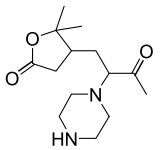	**5f**	62%
8	**4**		20/50	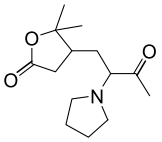	**5g**	53%
9	**4**		30/60	No reaction		—

[a]All products were characterized by IR, ^{1}H NMR, ^{13}C NMR, and HRMS (ESI) spectral data.
[b]Isolated yields were calculated from **4**.

Commercial-grade reagents were used without further purification. Solvents were dried and distilled following usual protocols. Column chromatography was carried out using silica gel (60–120 mesh). TLC was performed on aluminum-backed plates coated with silica gel 60 with F_{254} indicator.

The ^{1}H NMR and ^{13}C NMR spectra were recorded with a 300 MHz spectrometer using $CDCl_3$. ^{1}H NMR chemical shifts are expressed in parts per million (δ) relative to $CHCl_3$ (δ = 7.26); ^{13}C NMR chemical shifts are expressed in parts per million (δ) relative to the $CDCl_3$ resonance (δ = 77.0). High-resolution mass spectra (HRMS) were obtained using positive electrospray ionization (*m*/*z* values are given). Infrared spectra were recorded as thin films on sodium chloride plates. Optical rotation was measured with a HORIBA SEPA-300 polarimeter.

Synthesis of dihydro-5,5-dimethyl-4-(3-oxobutyl)furan-2(3*H*)-one (3)

To 20 mL of water, $NaIO_4$ (56.39 g, 0.263 mmol) followed by acetonitrile (10 mL) and carbon tetrachloride (10 mL) was

Can. J. Chem. Downloaded from www.nrcresearchpress.com by Xi'an Jiaotong University on 09/19/12
For personal use only.

added and stirred for 5 min. $RuCl_3 \cdot 3H_2O$ (1.299 mmol) was added and stirred for 10 min. To the reaction mixture, **2** (10 g, 0.064 mmol) was added dropwise at 0 °C. It was stirred at 0 °C for 20 min and then at room temperature for 5–6 h until the reaction was complete. The reaction mixture was partitioned with water and ethyl acetate in a separatory funnel and the water layer was washed with ethyl acetate (3 × 30 mL). The combined ethyl acetate layer was dried over sodium sulfate. The solvent was evaporated under vacuum to give **3**, which was purified by column chromatography over silica gel using hexane – ethyl acetate (41:9), providing **3** as an oily liquid (8 g, 68%). $[\alpha]_D^{27}$ –43.2° (c = 0.01, MeOH). R_f 0.65 (1:1 hexane – ethyl acetate). IR ($CHCl_3$) υ_{max} (cm^{-1}): 1781, 1722, 1549, 1251, 1004, 977. ^1H NMR (300 MHz, $CDCl_3$, δ): 2.48–2.40 (m, 1H), 2.37–2.35 (m, 2H), 2.20–2.15 (m, 1H), 2.10–2.07 (m, 1H), 2.05 (s, 3H), 1.65–1.60 (m, 1H), 1.45–1.35 (m, 1H), 1.30 (s, 3H), 1.13 (s, 3H). ^{13}C NMR (75 MHz, $CDCl_3$, δ): 207.2 (1C), 174.9 (1C), 86.4 (1C), 44.8 (1C), 41.8 (1C), 34.1 (1C), 29.7 (1C), 27.1 (1C), 22.9 (1C), 21.6 (1C). HRMS (ESI) data (*m/z*): $[M + H]^+$ calcd. for $C_{10}H_{17}O_3$, 185.2402; found, 185.2402.

Representative procedure for the synthesis of dihydro-5,5-dimethyl-4-(2-(phenyl amino)-3-oxobutyl)furan-2(3*H*)-one (5a)

To compound **3** (200 mg, 1.08 mmol) dissolved in 1 mL dichloromethane, 0.1 mL of 1 mol/L Br_2 in dichloromethane was added dropwise and stirred at room temperature for 5 min. The completion of the reaction was monitored by TLC and LC-MS. The reaction mixture was dried in a rotary evaporator to remove extra bromine and HBr present in the reaction mixture. To the resulting brominated product, aniline (1.08 mmol) and 1–2 drops of triethylamine were added and stirred at 55–60 °C in a water bath. After the completion of the reaction, the reaction mixture was extracted with ethyl acetate. The ethyl acetate layer was washed with a minimum amount of $NaHCO_3$ solution and then with water. It was dried over sodium sulfate and concentrated in a rotary evaporator. Purification was performed by silica gel column chromatography using hexane : ethyl acetate (95:5 to 80:20) to give **5a** as an oily liquid (173 mg, 58%); $[\alpha]_D^{27}$ +61.7° (c = 0.01, MeOH). R_f 0.90 (1:1 hexane – ethyl acetate). IR ($CHCl_3$) υ_{max} (cm^{-1}): 3622, 3018, 2975, 1758, 1712, 1513, 1476, 1420, 1229, 1046, 723. ^1H NMR (300 MHz, $CDCl_3$, δ): 7.20–6.53 (m, 5H), 3.98 (br s, NH), 2.62–2.54 (dd, J = 8.05, 7.08 Hz, 1H), 2.50–2.43 (m, 1H), 2.32–2.28 (m, 1H), 2.23–2.19 (m, 1H), 2.16 (s, 3H), 1.80–1.78 (m, 1H), 1.54–1.49 (m, 1H), 1.45 (s, 3H), 1.26 (s, 3H). ^{13}C NMR (75 MHz, $CDCl_3$, δ): 207.2 (1C), 175.0 (1C), 146.2 (1C), 129.6 (2C), 118.7 (1C), 113.2 (1C), 86.7–85.9 (1C), 62.4–61.8 (1C), 45.2 (1C), 42.6–41.8 (1C), 34.8–35.1 (1C), 31.4–31.2 (1C), 30.0–29.7 (1C), 27.4–26.3 (1C), 23.3–21.9 (1C). HRMS (ESI) data (*m/z*): $[M + H]^+$ calcd. for $C_{16}H_{22}NO_3$, 276.3508; found, 276.1692.

Dihydro-5,5-dimethyl-4-(2-(*p*-tolylamino)-3-oxobutyl) furan-2(3*H*)-one (5b)

The compound was purified by column chromatography over silica gel using hexane – ethyl acetate (41:9), providing **5b** as an oily liquid (191 mg, 61%). R_f 0.53 (1:1 hexane – ethyl acetate). IR ($CHCl_3$) υ_{max} (cm^{-1}): 3622, 3018, 2975, 1759, 1722, 1513, 1476, 1420, 1229, 1046, 723. ^1H NMR (300 MHz, $CDCl_3$, δ): 6.98 (d, J = 7.87, 2H), 6.49 (d, J = 7.87, 2H), 3.91 (br s, NH), 2.74–2.53 (m, 1H), 2.49–2.42 (m, 1H), 2.40–2.31 (m, 2H), 2.22 (s, 3H), 2.18–2.12 (m, 3H), 1.69–1.84 (m, 1H), 1.44–1.36 (m, 4H), 1.26–1.24 (s, 3H). ^{13}C NMR (75 MHz, $CDCl_3$, δ): 209.9 (1C), 175.2 (1C), 144.1–143.9 (1C), 129.9–129.2 (3C), 113.2–113.1 (2C), 86.6–86.3 (1C), 62.6–62.0 (1C), 45.0 (1C), 42.6–41.6 (1C), 35.0–34.7 (1C), 31.2–31.0 (1C), 27.2–27.0 (1C), 21.9–21.7 (1C), 20.2 (1C). HRMS (ESI) data (*m/z*): $[M + H]^+$ calcd. for $C_{17}H_{24}NO_3$, 290.3774; found, 290.3773.

Dihydro-5,5-dimethyl-4-(2-(diethylamino)-3-oxobutyl) furan-2(3*H*)-one (5c)

The compound was purified by column chromatography over silica gel using hexane – ethyl acetate (17:3), providing **5c** as an oily liquid (231 mg, 84%). R_f 0.50 (1:1 hexane – ethyl acetate). IR ($CHCl_3$) υ_{max} (cm^{-1}): 3616, 3019, 2975, 2400, 1756, 1720, 1514, 1417, 1203, 1046, 928. ^1H NMR (300 MHz, $CDCl_3$, δ): 2.77–2.61 (m, 2H), 2.57–2.51 (m, 2H), 2.46–2.39 (m, 2H), 2.30–2.28 (m, 1H), 2.28 (s, 3H), 1.82–1.77 (m, 1H), 1.72–1.60 (m, 1H), 1.51 (s, 3H), 1.33 (s, 3H), 1.27–1.13 (m, 6H). ^{13}C NMR (75 MHz, $CDCl_3$, δ): 201.2 (1C), 174.9 (1C), 86.9–86.4 (1C), 60.6 (1C), 52.6–51.0 (2C), 45.4–42.1 (1C), 35.1–34.3 (1C), 33.7 (1C), 32.7 (1C), 27.7–27.1 (1C), 23.5–22.1 (1C), 14.4 (2C). HRMS (ESI) data (*m/z*): $[M + H]^+$ calcd. for $C_{14}H_{26}NO_3$, 256.3611; found, 256.3689.

Dihydro-5,5-dimethyl-4-(2-morpholino-3-oxobutyl)furan-2 (3*H*)-one (5d)

The compound was purified by column chromatography over silica gel using hexane – ethyl acetate (8:17), providing **5d** as an oily liquid (200 mg, 69%). $[\alpha]_D^{27}$ –46.4° (c = 0.01, MeOH). R_f 0.19 (1:1 hexane – ethyl acetate). IR ($CHCl_3$) υ_{max} (cm^{-1}): 3616, 3019, 2975, 2400, 1758, 1720, 1514, 1423, 1217, 1046, 1031, 928. ^1H NMR (300 MHz, $CDCl_3$, δ): 3.70–3.69 (4H), 3.13–2.97 (1H), 2.63–2.59 (3H), 2.52–2.51 (3H), 2.33–2.29 (1H), 2.25–2.21 (s, 3H), 2.18–2.17 (1H), 1.90–1.70 (1H), 1.46 (s, 3H), 1.26 (s 3H). ^{13}C NMR (75 MHz, $CDCl_3$, δ): 210.5 (1C), 175.2 (1C), 85.6 (1C), 71.3 (1C), 66.3–66.1 (2C), 49.0–48.8 (2C), 42.1–41.8 (1C), 33.8 (1C), 28.6 (1C), 27.5 (1C), 26.4 (1C), 20.9 (1C). HRMS (ESI) data (*m/z*): $[M + H]^+$ calcd. for $C_{14}H_{24}NO_3$, 270.3447; found, 270.3448.

Dihydro-5,5-dimethyl-4-(2-(piperidin-1-yl-3-oxobutyl) furan-2(3*H*)-one (5e)

The compound was purified by column chromatography over silica gel using hexane – ethyl acetate (8:17), providing **5e** as an oily liquid (182 mg, 63%). $[\alpha]_D^{27}$ –55.3° (c = 0.01, MeOH). R_f 0.50 (hexane – ethyl acetate, 1:1). IR ($CHCl_3$) υ_{max} (cm^{-1}): 3620, 3089, 2975, 2400, 1759, 1730, 1519, 1423, 1227, 1046, 928. ^1H NMR (300 MHz, $CDCl_3$, δ): 2.75–2.46 (m, 4H), 2.32 (s, 3H), 2.25–2.09 (m, 4H), 1.75–1.71 (m, 1H), 1.55–1.36 (m, 10H), 1.20 (s, 3H). ^{13}C NMR (75 MHz, $CDCl_3$, δ): 208.7–207.6 (1C), 175.5–174.9 (1C), 86.9–86.4 (1C), 71.4 (1C), 52.5–51.2 (2C), 43.7–42.1 (1C), 35.2–34.3 (1C), 32.7 (1C), 29.9–29.2 (1C), 27.7–27.3 (1C), 26.1–25.6 (2C), 25.1–24.9 (1C), 22.8–22.2 (1C). HRMS

Scheme 2. Ring-substituted products obtained with cyclohexylamine.

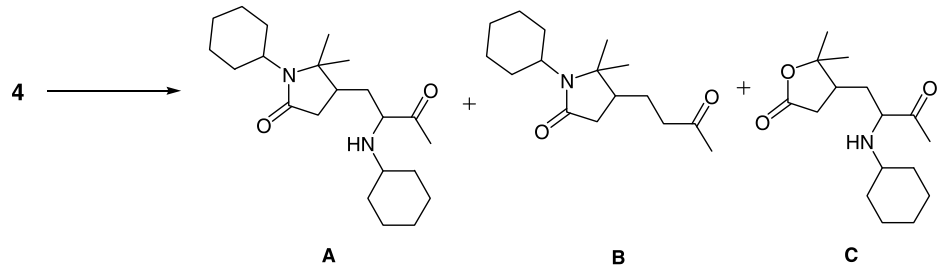

Scheme 3. Synthesis of amine and thiazole derivatives from **3**.

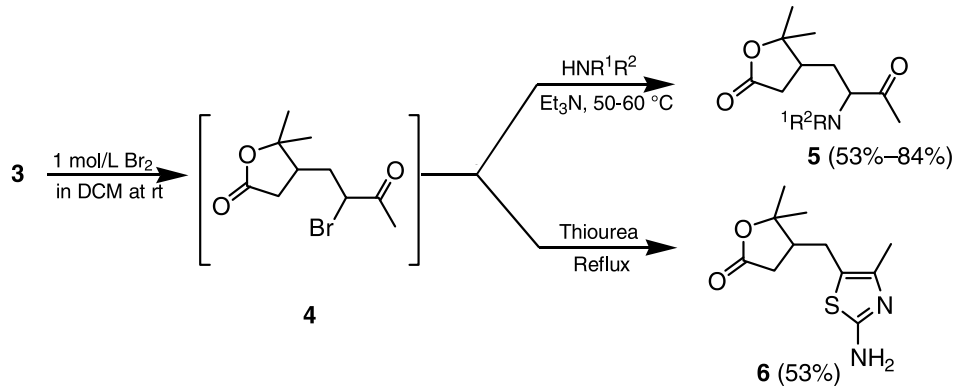

Scheme 4. Synthesis of amide and sulfonamide derivatives of **6**.

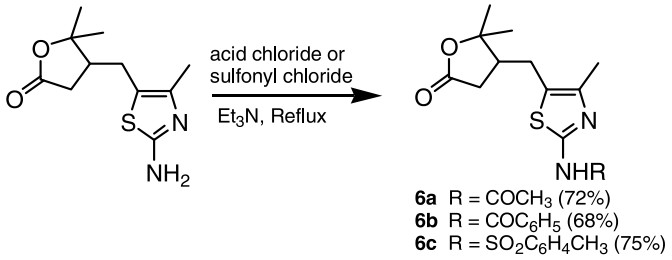

(ESI) data (*m/z*): $[M + H]^+$ calcd. for $C_{15}H_{25}NO_3$, 268.3719; found, 268.3718.

Dihydro-5,5-dimethyl-4-(2-(piperazin-1-yl-3-oxobutyl) furan-2(3*H*)-one (5f)

The compound was purified by column chromatography over silica gel using hexane – ethyl acetate (8:17), providing **5f** as an oily liquid (180 mg, 62%). $[\alpha]_D^{27}$ –65.9° (c = 0.01, MeOH). R_f 0.44 (9:1 hexane – ethyl acetate). IR ($CHCl_3$) υ_{max} (cm^{-1}): 3620, 3288, 3089, 2975, 2400, 1759, 1730, 1519, 1423, 1227, 1046, 928. ^1H NMR (300 MHz, $CDCl_3$, δ): 2.95–2.92 (m, 1H), 2.53–2.43 (m, 5H), 2.22–2.03 (m, 9H), 1.77–1.60 (m, 1H), 1.55–1.44 (m, 1H), 1.37 (s, 3H), 1.17 (s, 3H). ^{13}C NMR (75 MHz, $CDCl_3$, δ): 208.4 (1C), 175.6 (1C), 87.2–86.9 (1C), 72.0–71.2 (1C), 62.0 (2C), 50.4–49.9 (2C), 43.4–43.2 (1C), 35.2–35.0 (1C), 30.3–29.0 (1C), 27.7–27.4 (1C), 25.4–24.8 (1C), 22.3–22.2 (1C). HRMS (ESI) data (*m/z*): $[M + H]^+$ calcd. for $C_{14}H_{26}NO_3$, 269.3600; found, 269.3597.

Dihydro-5,5-dimethyl-4-(2-(pyrrolidine-1-yl-3-oxobutyl) furan-2(3*H*)-one (5g)

The compound was purified by column chromatography over silica gel using hexane – ethyl acetate (8:17), providing **5g** as an oily liquid (145 mg, 53%). $[\alpha]_D^{27}$ –38.3° (c = 0.01, MeOH). R_f 0.11 (hexane – ethyl acetate, 1:1). IR ($CHCl_3$) υ_{max} (cm^{-1}): 3619, 3018, 2975, 2400, 1758, 1720, 1520, 1218, 1046, 928. ^1H NMR (300 MHz, $CDCl_3$, δ): 2.89–2.83 (m, 1H), 2.66–2.58 (m, 3H), 2.51–2.35 (m, 3H), 2.30–2.26 (m, 1H), 2.18 (s, 3H), 2.02–1.98 (m, 2H), 1.85–1.78 (m, 3H), 1.65 (m, 1H), 1.45 (s, 3H), 1.26 (s, 3H). ^{13}C NMR (75 MHz, $CDCl_3$, δ): 208.6 (1C), 174.1–173.5 (1C), 85.4–85.2 (1C), 71.2 (1C), 49.9–48.8 (2C), 41.8–41.4 (1C), 40.7–40.3 (1C), 34.2–33.5 (1C), 26.3–25.9 (1C), 25.8–25.2 (2C), 22.7–22.4 (1C), 21.2–20.8 (1C). HRMS (ESI) data (*m/z*): $[M + H]^+$ calcd. for $C_{14}H_{24}NO_3$, 254.3453; found, 254.3531.

4-(2-Amino-4-methyl-thiazol-5-ylmethyl)-5,5-dimethyl-dihydro-furan-2-one (6)

Thiourea (82.6 mg, 1.08 mmol) was dissolved in 20 mL of distilled water with heating in a round-bottomed flask equipped with a reflux condenser. Compound **4** (200 mg, 1.08 mmol) dissolved in 2 mL of methanol was added dropwise to the thiourea solution and the reaction mixture was refluxed till the reaction was complete. The reaction mixture was cooled and made alkaline with a saturated solution of $NaHCO_3$ and extracted with ethyl acetate. The ethyl acetate layer was washed twice with distilled water, dried over Na_2SO_4, and concentrated in a rotary evaporator. Purification was performed by recrystallization with hot dichloromethane to give **6**. Crystalline powder (137.4 mg, 68%); mp 152–

Can. J. Chem. Downloaded from www.nrcresearchpress.com by Xi'an Jiaotong University on 09/19/12
For personal use only.

154 °C; $[\alpha]_D^{27}$ –44.3° (c = 0.01, MeOH). R_f 0.18 (ethyl acetate). ^{1}H NMR (300 MHz, $CDCl_3$, δ): 2.76–2.70 (m, 1H), 2.65–2.51 (m, 2H), 2.44–2.28 (m, 2H), 2.09 (s, 3H), 1.43 (s, 3H), 1.33 (s, 3H). ^{13}C NMR (75 MHz, $CDCl_3$, δ): 175.0 (1C), 165.0 (1C), 143.3 (1C), 116.6 (1C), 86.1 (1C), 47.2 (1C), 34.7 (1C), 27.4 (1C), 26.2 (1C), 21.8 (1C), 14.6 (1C). HRMS (ESI) data (m/z): $[M + H]^+$ calcd. for $C_{11}H_{17}N_2O_2S$, 241.1011; found, 241.3394.

N-[5-(2,2-Dimethyl-5-oxo-tetrahydro-furan-3-ylmethyl)-4-methyl-thiazol-2-yl]-acetamide (6a)

The compound was purified by recrystallization with hot dichloromethane to give **6a**. Crystalline powder (84.5 mg, 72%), mp 203–204 °C. R_f 0.59 (ethyl acetate). ^{1}H NMR (300 MHz, $CDCl_3$, δ): 2.87–2.81 (m, 1H), 2.71–2.59 (m, 2H), 2.38–2.30 (m, 2H), 2.25 (s, 3H), 2.24 (s, 3H), 1.46 (s, 3H), 1.37 (s, 3H). ^{13}C NMR (75 MHz, $CDCl_3$, δ): 175.0 (1C), 168.3 (1C), 156.6 (1C), 141.7 (1C), 122.6 (1C), 86.4 (1C), 47.7 (1C), 35.2 (1C), 27.9 (1C), 26.6 (1C), 23.5 (1C), 22.4 (1C), 15.0 (1C). HRMS (ESI) data (m/z): $[M + H]^+$ calcd. for $C_{14}H_{23}N_2O_3S$, 283.3666; found, 283.3683.

N-[5-(2,2-Dimethyl-5-oxo-tetrahydro-furan-3-ylmethyl)-4-methyl-thiazol-2-yl]-4-methyl-benzenesulfonamide (6c)

The compound was purified by recrystallization with hot dichloromethane to give **6c**. Crystalline powder (123.1 mg, 75%), mp 245–247 °C. R_f 0.51 (ethyl acetate). ^{1}H NMR (300 MHz, $CDCl_3$, δ): 7.75 (d, J = 7.5 Hz, 2H), 7.25 (d, J = 7.9 Hz), 2.68–2.63 (m, 1H), 2.60–2.58 (m, 2H), 2.41 (s, 3H), 2.36–2.27 (m, 2H), 2.24 (s, 3H), 1.45 (s, 3H), 1.33 (s, 3H). ^{13}C NMR (75 MHz, $CDCl_3$, δ): 174.3 (1C), 168.5 (1C), 155.6 (1C), 143.2 (1C), 138.6 (1C), 130.3 (1C), 129.5 (2C), 126.7 (2C), 85.8 (1C), 46.4 (1C), 34.8 (1C), 27.7 (1C), 26.6 (1C), 22.2 (1C), 21.7 (1C), 11.9 (1C). HRMS (ESI) data (m/z): $[M + H]^+$ calcd. for $C_{19}H_{27}N_2O_4S_2$, 395.5162; found, 395.5187.

Acknowledgments

The authors are grateful to Dr. P.S. Ahuja, Director, IHBT (CSIR), Palampur, for providing required facilities. Financial assistance to Pushpinder Kaur (JRF) and Abha Chaudhary (SRF) from CSIR, New Delhi, India, is gratefully acknowledged. The authors also thank Mr. Rajeev Chaudhary for providing IR spectra.

References

(1) (a) Yokomatsu, T.; Yuasa, Y.; Kano, S.; Shibuya, S. *Heterocycles* **1991** *32* (12), 2315. doi:10.3987/COM-91-5880; (b) Casey, M.; Manage, A. C.; Murphy, P. J. *Tetrahedron Lett.* **1992** *33* (7), 965. doi:10.1016/S0040-4039(00)91589-2.

(2) Sinha, S. C.; Keinan, E. *J. Am. Chem. Soc.* **1993** *115* (11), 4891. doi:10.1021/ja00064a060.

(3) (a) Harding, K. E.; Nam, D. *Tetrahedron Lett.* **1988** *29* (31), 3793. doi:10.1016/S0040-4039(00)82116-4; (b) Wakamiya, T.; Shiba, T.; Kaneko, T. *Bull. Chem. Soc. Jpn.* **1972** *45* (12), 3668. doi:10.1246/bcsj.45.3668; (c) Teshima, T.; Ando, T.; Shiba, T. *Bull. Chem. Soc. Jpn.* **1980** *53* (4), 1191. doi:10.1246/bcsj.53.1191.

(4) Barringer, D. F.; Berkelhammer, G.; Wayne, R. S. *J. Org. Chem.* **1973** *38* (10), 1937. doi:10.1021/jo00950a033.

(5) (a) Shimojima, Y.; Hayashi, H.; Ooka, T.; Shibukawa, M.; Iitaka, Y. *Tetrahedron* **1984** *40* (13), 2519. doi:10.1016/S0040-4020(01)83504-3; (b) Shimojima, Y.; Shirai, T.; Baba, T.; Hayashi, H. *J. Med. Chem.* **1985** *28* (1), 3. doi:10.1021/jm00379a002.

(6) Askin, D.; Wallace, M. A.; Vacca, J. P.; Reamer, R. A.; Volante, R. P.; Shinkai, I. *J. Org. Chem.* **1992** *57* (10), 2771. doi:10.1021/jo00036a004.

(7) Smith, A. B., III; Liu, H.; Hirschmann, R. *Org. Lett.* **2000** *2* (14), 2037. doi:10.1021/ol0059293.

(8) Hasegawa, H.; Shioiri, N.; Narita, C.; Katori, T. US Patent 4,876,359, October 24, 1989.

(9) Cannella, R.; Clerici, F.; Gelmi, M. L.; Penso, M.; Pocar, D. *J. Org. Chem.* **1996** *61*, 1854. doi:10.1021/jo951213n.

(10) Capuzzi, M.; Gambacorta, A.; Gasperi, T.; Loreto, M. A.; Tardella, P. A. *Eur. J. Org. Chem.* **2006** *2006* (22), 5076. doi:10.1002/ejoc.200600540.

(11) Samarat, A.; Amri, H.; Landais, Y. *Tetrahedron* **2004** *60* (40), 8949. doi:10.1016/j.tet.2004.07.012.

(12) Roos, J.; Effenberger, F. *Tetrahedron Asymmetry* **2002** *13* (17), 1855. doi:10.1016/S0957-4166(02)00437-8.

(13) Harwood, H. J. *Chem. Rev.* **1962** *62* (2), 99. doi:10.1021/cr60216a002.

(14) Juneja, S. K.; Choudhary, D.; Paul, S.; Gupta, R. *Synth. Commun.* **2006** *36* (19), 2877. doi:10.1080/00397910600770714.

(15) Decorzant, R.; Vial, C.; Näf, F.; Whitesides, G.M. *Tetrahedron* **1987** *43* (8), 1871. doi:10.1016/S0040-4020(01)81499-X.

(16) Gray, C. A.; Davies-Coleman, M. T.; Rivett, D. E. A. *Tetrahedron* **2003** *59* (2), 165. doi:10.1016/S0040-4020(02)01481-3.

(17) Feddouli, A.; Itto, M. Y. A.; Ali, M. A.; Hasnaoui, A.; Riahi, A. *Synth. Commun.* **2006** *36* (23), 3617. doi:10.1080/00397910600943709.

(18) March, J. *Advanced Organic Chemistry: Reactions, Mechanisms and Structure*, 4th ed.; Wiley: New York, 2003; p 588.

Can. J. Chem. Downloaded from www.nrcresearchpress.com by Xi'an Jiaotong University on 09/19/12
For personal use only.

A simple and efficient copper-catalyzed amination of aryl halides by aqueous ammonia in water

Yefeng Zhu and Yunyang Wei

Abstract: The copper(I) iodide/1,4-bis(2-hydroxy-3,5-di-*tert*-butylbenzyl)piperazine (CuI–L2) system catalyzed the cross-coupling reactions between aryl halides and aqueous ammonia in water to produce primary aromatic amines in good yields. The protocol was simple and efficient, avoiding the need for inert atmosphere, additional base, or other additives.

Key words: copper, catalysis, cross coupling, water chemistry, aqueous ammonia, primary arylamine.

Résumé : Le système iodure de cuivre(I)/1,4-bis(2-hydroxy-3,5-di-*tert*-butylbenzyl)pipérazine (CuI–L2) catalyse les réactions de couplages croisées entre les halogénures d'aryles et une solution aqueuse d'ammoniaque pour conduire à la formation d'amines aromatiques primaires avec de bons rendements. Le protocole est simple et efficace, il ne nécessite pas d'atmosphère inerte, de base additionnelle ou d'autres additifs.

Mots-clés : cuivre, catalyse, couplage croisé, chimie dans l'eau, solution aqueuse d'ammoniaque, arylamine primaire.

[Traduit par la Rédaction]

Can. J. Chem. Downloaded from www.nrcresearchpress.com by Xi'an Jiaotong University on 09/19/12
For personal use only.

Introduction

Ammonia is an attractive source of nitrogen in organic synthesis owing to its great abundance and low cost.[1] In recent years, the palladium- or copper-catalyzed coupling of aryl halides with ammonia has attracted increasing attention because of the value of primary aromatic amines in the preparation of natural products, agrochemicals, dyes, polymers, and medicinal compounds.[2] While palladium catalysts developed by Buchwald and Hartwig[3] proved most useful for this reaction, less progress has been achieved with copper catalysts. Recently, Kim and Chang[4] reported a proline-derived copper complex catalyzed arylation of ammonium chloride or aqueous ammonia with aryl iodides. Following these pioneering works, a lot of catalytic systems have been reported,[5] such as CuI/diketone ligands,[5a] CuI/2-pyridinyl-β-ketone ligands,[5b] CuI/4-hydroxy-L-proline,[5c] etc. Furthermore, Rao et al.[6a] also introduced a ligand-free copper-catalyzed arylation of aqueous ammonia with aromatic boronic acids at room temperature. These reactions are generally performed in organic solvents, which lead to environmental problems.[7] It is highly desirable to find a procedure to carry out these coupling reactions in cheap, nontoxic, and nonflammable "green" solvents. Obviously, water is the most cheap and environmentally benign solvent.[8] However, to the best of our knowledge, there are only a few well-established methods to effectively synthesize anilines from aryl halides and aqueous ammonia in water.[9] More recently, Wu et al.[9b] reported the coupling reactions of aryl halides with aqueous ammonia by a sulfonato–Cu(salen) complex in water, but an additional base was essential.

We have identified Mannich bases[10] (Fig. 1) as efficient ligands for the Cu-catalyzed N-arylation of imidazoles in water.[11] We now report a ligand-assisted copper(I)-catalyzed method for the coupling of aryl halides with aqueous ammonia in water. This method utilizes inexpensive CuI as the catalyst and simple synthesized Mannich bases as ligands and tolerates a wide range of functional groups. Inert atmosphere and additional base were not needed. The use of aqueous ammonia makes the reaction easier to handle than the cases where gaseous ammonia or ammonia in organic solvent was used.

Results and discussion

We initially selected iodobenzene as a model substrate for optimization of the reaction conditions. The standardized protocol was carried out by using iodobenzene (1 equiv.), CuI (10 mol%), L2 (10 mol%), and aqueous ammonia (2 mL) in water at 120 °C for 12 h. The results are summarized in Table 1.

It can be seen from Table 1 that the CuI–L combination successfully promoted the coupling reaction with yields from 75% to 90% (Table 1, entries 1–4), whereas no product was detected without the ligand under similar conditions (Table 1, entry 5). Among the ligands used, 1,4-bis(2-hydroxy-3,5-di-*tert*-butylbenzyl)piperazine (L2) displayed the best catalytic activity (Table 1, entry 2). Thus, L2 was chosen as the ligand for further optimization of the reaction conditions. Different copper sources have also been examined, the catalysis by CuI, CuCl, and $CuSO_4$ with L2 afforded the aniline product in good yields of 90%, 85%, and 87%, respectively (Table 1, entries 2, 7, and 8, respectively). However, the use of the $CuCl_2$–L2 combination resulted in a moderate yield of 51% (Table 1, entry 9). It must be pointed out that in the absence of copper catalysis, no aniline derivative was obtained

Received 10 November 2010. Accepted 15 February 2011. Published at www.nrcresearchpress.com/cjc on 22 June 2011.

Y. Zhu and Y. Wei. School of Chemical Engineering, Nanjing University of Science and Technology, Nanjing 210094, China.

Corresponding author: Yunyang Wei (e-mail: ywei@mail.njust.edu.cn).

Fig. 1. Structures of Mannich bases **L1**–**L4**.

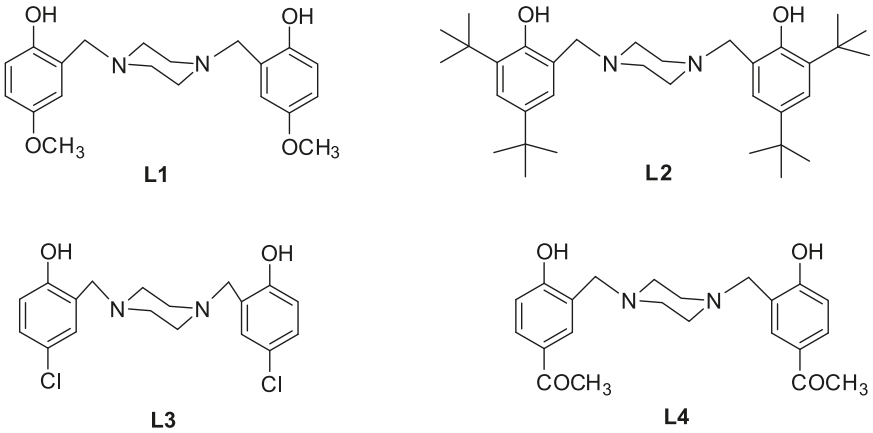

Table 1. Results of amination of iodobenzene with aqueous ammonia in water.

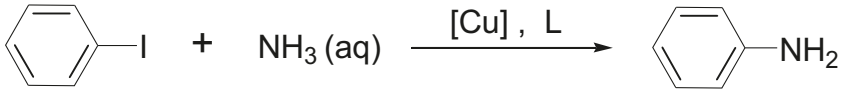

Entry	Cu	Ligand	NH_3(aq) (mL)	Yield (%)[a]
1	CuI	L1	2	75
2	CuI	L2	2	90
3	CuI	L3	2	80
4	CuI	L4	2	78
5	CuI		2	0
6		L2	2	0
7	CuCl	L2	2	85
8	$CuSO_4$	L2	2	87
9	$CuCl_2$	L2	2	51
10	CuI	L2	1	57
11	CuI	L2	3	91
12	CuI	L2	1	32[b]
13	CuI	L2	2	70[c]
14	CuI	L2	2	<5[d]

Note: Unless otherwise noted, the reactions were carried out with iodobenzene (1 mmol), 25%–28% aqueous ammonia (2 mL) at 120 °C for 12 h.

[a]Isolated yields.

[b]H_2O (1 mL) was added.

[c]Reaction time was 8 h.

[d]Reaction temperature was 100 °C.

(Table 1, entry 6). Further investigation revealed that 2 mL aqueous ammonia was needed for the reaction to take place. When we decreased the amount or the concentration of aqueous ammonia, the reaction rate decreased (Table 1, entries 10–12). In addition, a lower temperature decelerated the reaction rate and led to a lower yield (Table 1, entry 14). In summary, the proper conditions for amination of aryl halides by aqueous ammonia in water consist of the combination of CuI (10 mol %), L2 (10 mol %), and aqueous ammonia (2 mL) at 120 °C for 12 h in air.

With this practical procedure in hand, we explored the scope of this reaction and screened a wide range of aryl iodides and bromides. As shown in Table 2, most of the aryl iodides with either electron-donating or electron-withdrawing substituents afforded aniline derivatives in water in excellent yields, and the highest yield was obtained by using 4-iodoacetophenone. However, when the highly activated 4-nitroiodobeneze was used, a slightly lower yield (61%; Table 2, entry 3) was obtained because of the formation of a small amount of unidentified byproduct.

Next, we were intrigued by the possibility of using aryl bromides as coupling partners, which are less reactive substrates but of much greater interest for industrial applications. It can be seen from Table 2 that all the electron-deficient aryl bromides afforded the aniline products with excellent yields ranging from 72% to 92% under the optimized conditions (Table 2, entries 5–9). The reactions with the electron-rich aryl bromides were slower, but the products could be isolated in good yields by extending the reaction time to 24 h (Table 2, entries 10–14). It is noteworthy that the catalytic system displayed a great tolerance for multiple groups including the nitro, acetyl, and ether groups. However, the steric hin-

Can. J. Chem. Downloaded from www.nrcresearchpress.com by Xi'an Jiaotong University on 09/19/12
For personal use only.

Can. J. Chem. Downloaded from www.nrcresearchpress.com by Xi'an Jiaotong University on 09/19/12
For personal use only.

Table 2. CuI–L2 catalyzed amination of aryl halides with aqueous ammonia in water.

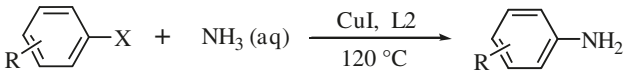

Entry	ArX	ArNH2	Yield (%)[a]
1	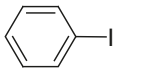	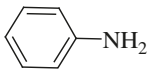	90
2	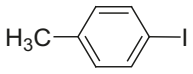	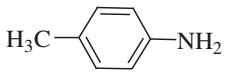	85
3	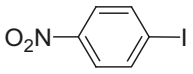	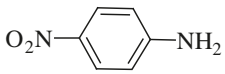	61
4	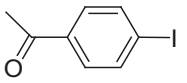	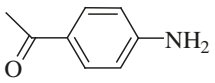	95
5	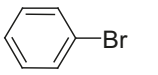	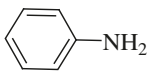	85
6	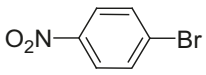	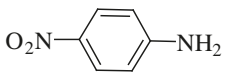	90
7	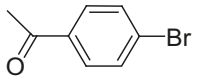	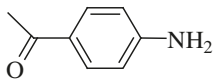	92
8	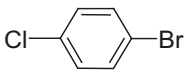	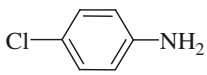	72
9	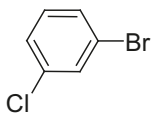	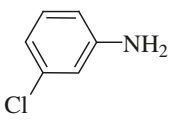	85
10	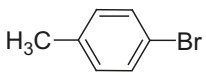	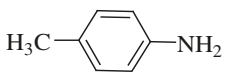	85[b]
11	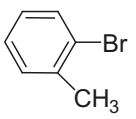	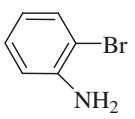	27[b]
12	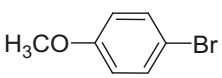	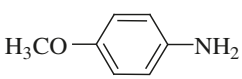	83[b]
13	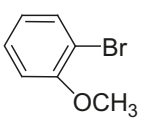	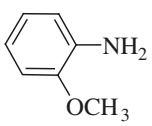	85[b]
14	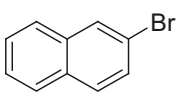	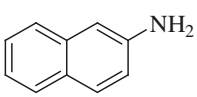	88[b]
15	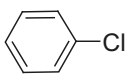	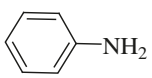	0
16	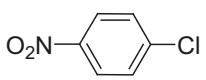	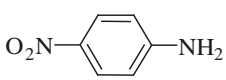	<5[b]

Note: Reaction conditions: aryl halides (1 mmol), 25%–28% aqueous ammonia (2 mL), CuI (10 mmol%), L2 (10 mmol%), 120 °C, 12 h.

[a]Isolated yield.

[b]Reaction time was 24 h.

Can. J. Chem. Downloaded from www.nrcresearchpress.com by Xi'an Jiaotong University on 09/19/12
For personal use only.

drance has a huge influence on the coupling reaction. When 2-methylbromobenzene was aminated with this catalytic system, only a 27% isolated yield was obtained (Table 2, entry 11). Fortunately, when the reaction was performed with *o*-methoxybromobenzene, the corresponding *o*-methoxyaniline was obtained in an 85% isolated yield (Table 2, entry 13). Furthermore, attempts to use chlorobenzene as an aryl source failed (Table 2, entry 15). When 4-nitrochlorobenzene, an activated aryl chloride, was used as the arylating agent, only a 5% yield of the corresponding coupling product was detected (Table 2, entry 16).

Conclusion

In summary, we have developed a ligand-assisted copper (I)-catalyzed method for coupling aryl halides with aqueous ammonia in water. This protocol avoids the use of toxic organic solvents and eliminates the need for an inert atmosphere, additional base, or other additives, which greatly facilitates operations. Excellent yields are obtained with a wide range of aryl bromides and aryl iodides as substrates in the catalytic system.

Experimental

General method

All reactions were carried out in a Teflon septum screw-capped tube under air atmosphere. All chemicals were obtained from a commercial source (Sinopharm Chemical Reagent Company, Ltd., Shanghai, China, and Aladdin Reagent, Shanghai, China) and used without further purification. Ligands L1–L4 were synthesized according to the literature.[10] Column chromatography was performed on silica 200–300 mesh. ^{1}H NMR and ^{13}C NMR spectra was recorded on a Bruker Avance 300, 400, or 500 and 125 spectrometer at ambient temperature in $CDCl_3$ or DMSO-d_6. Chemical shifts are reported in parts per million relative to TMS.

Typical procedure for the coupling

Aryl halides (1 mmol), CuI (0.1 mmol), 1,4-bis(2-hydroxy-3,5-di-*tert*-butylbenzyl)piperazine (0.1 mmol), and aqueous ammonia (2 mL) were added to a Teflon septum screw-capped tube. The reaction mixture was stirred at 120 °C for 12 h and then cooled to room temperature and extracted with ethyl acetate. The organic layer was then dried with anhydrous Na_2SO_4, and the solvent was removed under reduced pressure. The aniline product was finally obtained by column chromatography on silica gel.

1,4-Bis(2-hydroxy-5-methoxybenzyl)piperazine (L1)

White solid; mp (recrystallization in methanol) 184–186 °C (lit. value[10a] mp 184–186 °C). ^{1}H NMR (300 MHz, $CDCl_3$) δ: 2.40–2.90 (m, 8H), 3.69 (s, 4H), 3.72 (s, 6H), 6.57–6.76 (m, 6H), 10.25 (br s, 2H). ^{13}C NMR (125 MHz, $CDCl_3$) δ: 151.7, 150.2, 120.4, 115.6, 113.6, 112.9, 60.2, 54.8, 51.2. MS (ESI, *m*/*z*): 359 [M$^+$].

*1,4-Bis(2-hydroxy-3,5-di-*tert*-butylbenzyl)piperazine (L2)*

White solid; mp (recrystallization in methanol) 258–260 °C (lit. value[10b] mp > 250 °C). ^{1}H NMR (300 MHz, $CDCl_3$) δ: 1.31 (s, 18H), 1.43 (s, 18H), 2.39–2.90 (m, 8H), 3.72 (s, 4H), 6.84–7.27 (m, 4H), 10.75 (br s, 2H). ^{13}C NMR (125 MHz, $CDCl_3$) δ: 153.1, 139.8, 134.6, 122.6, 122.2, 119.3, 61.0, 51.2, 33.9, 33.2, 30.7, 28.6. MS (ESI, *m*/*z*): 523 [M$^+$].

1,4-Bis(2-hydroxy-5-chlorobenzyl)piperazine (L3)

White solid; mp (recrystallization in methanol) 243–246 °C (lit. value[10a] mp 243–245 °C). ^{1}H NMR (300 MHz, $CDCl_3$) δ: 2.48–2.78 (m, 8H), 3.70 (s, 4H), 6.77 (d, J = 8.6 Hz, 2H), 6.98 (d, J = 2.2 Hz, 2H), 7.15 (dd, J = 8.6, 2.2 Hz, 2H). ^{13}C NMR (125 MHz, DMSO-d_6) δ: 154.9, 128.2, 127.2, 124.2, 121.7, 116.3, 56.7, 51.6. MS (ESI, *m*/*z*): 368 [M$^+$].

1,4-Bis(2-hydroxy-5-acetylbenzyl)piperazine (L4)

White solid; mp (recrystallization in methanol) 222–223 °C. ^{1}H NMR (300 MHz, $CDCl_3$) δ: 2.54 (s, 6H), 2.67–2.86 (m, 8H), 3.81 (s, 4H), 6.86 (d, J = 8.5 Hz, 2H), 7.68 (s, 2H), 7.83 (dd, J = 8.6, 2.0 Hz, 2H). ^{13}C NMR (125 MHz, $CDCl_3$) δ: 195.7, 161.4, 129.5, 128.5, 128.3, 119.4, 115.1, 59.8, 51.1, 25.2. MS (ESI, *m*/*z*): 383 [M$^+$]. Elemental anal. calcd. (%): C 68.75, H 7.15, N 7.06; theoretical: C 69.09, H 6.85, N 7.32.

Aniline[9a]

Pale yellow oil. ^{1}H NMR (500 MHz, $CDCl_3$) δ: 7.24–7.28 (m, 2H), 6.87–6.88 (m, 1H), 6.75–6.86 (m, 2H), 3.66 (s, 2H). ^{13}C NMR (125 MHz, $CDCl_3$) δ: 145.7, 128.5, 117.6, 114.3, 19.6.

4-Toluidine[9a]

Slight yellow solid; mp (recrystallization in methanol) 43–45 °C (lit. value[12a] mp 43–44 °C). ^{1}H NMR (500 MHz, $CDCl_3$) δ: 6.99 (d, J = 10.0 Hz, 2H), 6.63 (d, J = 10.0 Hz, 2H), 3.46 (s, 2H), 2.26 (s, 3H). ^{13}C NMR (125 MHz, DMSO-d_6) δ: 145.5, 128.7, 123.4, 113.5.

4-Nitroaniline[9b]

Yellow solid; mp (recrystallization in methanol) 148–149 °C (lit. value[12b] mp 146–149 °C). ^{1}H NMR (500 MHz, $CDCl_3$) δ: 8.09 (d, J = 10.0 Hz, 2H), 6.64 (d, J = 10.0 Hz, 2H), 4.40 (s, 2H). ^{13}C NMR (125 MHz, DMSO-d_6) δ: 155.2, 135.1, 125.6, 111.8.

4-Aminoacetophenone[9b]

Slight yellow solid; mp (recrystallization in methanol) 105–106 °C (lit. value[12c] mp 103–105 °C). ^{1}H NMR (500 MHz, $CDCl_3$) δ: 7.82 (d, J = 5.0 Hz, 2H), 6.66 (d, J = 5.0 Hz, 2H), 4.22 (s, 2H), 2.51 (s, 3H). ^{13}C NMR (125 MHz, DMSO-d_6) δ: 194.5, 153.1, 130.1, 124.4, 112.0, 25.3.

4-Chloroaniline[9b]

Pale white solid; mp (recrystallization in methanol) 69–71 °C (lit. value[12b] mp 69–72 °C). ^{1}H NMR (500 MHz, $CDCl_3$) δ: 7.12 (d, J = 10.0 Hz, 2H), 6.62 (d, J = 10.0 Hz, 2H), 3.65 (s, 2H). ^{13}C NMR (125 MHz, DMSO-d_6) δ: 147.1, 128.0, 118.2, 114.7.

3-Chloroaniline[6]

Slight yellow oil. ^{1}H NMR (400 MHz, $CDCl_3$) δ: 7.02–7.06 (m, 1H), 6.65–6.71 (m, 2H), 6.52–6.54 (m, 1H), 3. 63 (s, 2H). ^{13}C NMR (125 MHz, $CDCl_3$) δ: 146.9, 133.8, 129.5, 117.4, 114.0, 112.4.

Can. J. Chem. Downloaded from www.nrcresearchpress.com by Xi'an Jiaotong University on 09/19/12
For personal use only.

***2-Toluidine*[9b]**

Colorless oil. ^{1}H NMR (500 MHz, $CDCl_3$) δ: 7.09–7.12 (m, 2H), 6.72–6.80 (m, 2H), 3.59 (s, 2H), 2.23 (s, 3H). ^{13}C NMR (125 MHz, $CDCl_3$) δ: 143.8, 129.6, 126.2, 121.5, 117.8, 114.1, 16.5.

***4-Methoxyaniline*[9b]**

Pale white solid; mp (recrystallization in methanol) 54–56 °C (lit. value[12a] mp 57 °C). ^{1}H NMR (400 MHz, $CDCl_3$) δ: 6.72–6.74 (m, 2H), 6.62–6.65 (m, 2H), 3.73 (s, 3H), 2.92 (s, 2H). ^{13}C NMR (125 MHz, DMSO-d_6) δ: 150.2, 141.8, 114.2, 114.1, 54.7.

***2-Methoxyaniline*[9b]**

Slight yellow oil. ^{1}H NMR (500 MHz, $CDCl_3$) δ: 6.85–6.88 (m, 2H), 6.76–6.81 (m, 2H), 3.90 (s, 3H), 3.75 (s, 2H). ^{13}C NMR (125 MHz, $CDCl_3$) δ: 146.4, 135.4, 120.2, 117.5, 114.1, 109.6, 54.5.

***β-Aminonaphthalene*[6]**

Dark brown solid; mp (recrystallization in methanol) 109–111 °C (lit. value[12a] mp 107–109 °C). ^{1}H NMR (400 MHz, $CDCl_3$) δ: 7.51–7.63 (m, 3H), 7.27–7.31 (m, 1H), 7.13–7.19 (m,1H), 6.86–6.92 (m, 2H), 3.76 (s, 2H). ^{13}C NMR (125 MHz, DMSO-d_6) δ: 146.1, 134.5, 128.0, 127.0, 125.8, 125.3, 124.5, 120.3, 117.9, 105.3.

Supplementary data

Supplementary data for this article (^{1}H NMR and ^{13}C NMR spectra for all products) are available on the journal Web site (www.nrcresearchpress.com/cjc).

Acknowledgements

We are grateful to Nanjing University of Science and Technology for financial support.

References

(1) Roundhill, D. M. *Chem. Rev.* **1992**, *92* (1), 1. doi:10.1021/cr00009a001.

(2) (a) Weissermel, K.; Arpe, H. J. *Industry Organic Chemistry;* Wiley-VCH: Weinheim, 1997; (b) Lawrence, S. A. *Amines: Synthesis, Properties and Application;* Cambridge University Press: Cambridge, 2004.

(3) (a) Shen, Q.; Hartwig, J. F. *J. Am. Chem. Soc.* **2006**, *128* (31), 10028. doi:10.1021/ja064005t; (b) Surry, D. S.; Buchwald, S. L. *J. Am. Chem. Soc.* **2007**, *129* (34), 10354. doi:10.1021/ja074681a; (c) Willis, M. C. *Angew. Chem.* **2007**, *119* (19), 3470. doi:10.1002/ange.200605071; (d) Willis, M. C. *Angew. Chem. Int. Ed.* **2007**, *46* (19), 3402. doi:10.1002/anie.200605071; (e) Schulz, T.; Torborg, C.; Enthaler, S.; Schäffner, B.; Dumrath, A.; Spannenberg, A.; Neumann, H.; Börner, A.; Beller, M. *Chem. Eur. J.* **2009**, *15* (18), 4528. doi:10.1002/chem.200802678; (f) Vo, G. D.; Hartwig, J. F. *J. Am. Chem. Soc.* **2009**, *131* (31), 11049. doi:10.1021/ja903049z; (g) Lundgren, R. J.; Peters, B. D.; Alsabeh, P. G.; Stradiotto, M. *Angew. Chem. Int. Ed.* **2010**, *49* (24), 4170. doi:10.1002/anie.201000526.

(4) Kim, J.; Chang, S. *Chem. Commun. (Camb.)* **2008**, *2008* (26), 3052. doi:10.1039/b804637a.

(5) (a) Xia, N.; Taillefer, M. *Angew. Chem. Int. Ed.* **2009**, *48* (2), 337. doi:10.1002/anie.200802569; (b) Wang, D. P.; Cai, Q.; Ding, K. *Adv. Synth. Catal.* **2009**, *351* (11–12), 1722. doi:10.1002/adsc.200900327; (c) Jiang, L.; Lu, X.; Zhang, H.; Jiang, Y.; Ma, D. *J. Org. Chem.* **2009**, *74* (12), 4542. doi:10.1021/jo9006738; (d) Yang, C. T.; Fu, Y.; Huang, Y. B.; Yi, J.; Guo, Q. X.; Liu, L. *Angew. Chem. Int. Ed.* **2009**, *48* (40), 7398. doi:10.1002/anie.200903158; (e) Lang, F.; Zewge, D.; Houpis, I. N.; Volante, R. P. *Tetrahedron Lett.* **2001**, *42* (19), 3251. doi:10.1016/S0040-4039(01)00458-0; (f) Wu, X. F.; Darcel, C. *Eur. J. Org. Chem.* **2009**, *2009* (28), 4753. doi:10.1002/ejoc.200900588; (g) Taillefer, M.; Xia, N. Fr 07 0682, 2007; (h) Taillefer, M.; Xia, N. PTC 051701, 2008; (i) Gaillard, S.; Elmkaddem, M. K.; Fischmeister, C.; Thomas, C. M.; Renaud, J. L. *Tetrahedron Lett.* **2008**, *49* (21), 3471. doi:10.1016/j.tetlet.2008.03.096; (j) Elmkaddem, M. K.; Fischmeister, C.; Thomas, C. M.; Renaud, J. L. *Chem. Commun. (Camb.)* **2010**, *46* (6), 925. doi:10.1039/b916569j; (k) Ntaganda, R.; Dhudshia, B.; Macdonald, C. L. B.; Thadani, A. N. *Chem. Commun. (Camb.)* **2008**, *2008* (46), 6200. doi:10.1039/b815757j; (l) Guo, Z.; Guo, J.; Song, Y.; Wang, L.; Zou, G. *Appl. Organomet. Chem.* **2009**, *23* (4), 150. doi:10.1002/aoc.1485.

(6) Rao, H.; Fu, H.; Jiang, Y.; Zhao, Y. *Angew. Chem. Int. Ed.* **2009**, *48* (6), 1114. doi:10.1002/anie.200805424.

(7) (a) Sheldon, R. A. *Green Chem.* **2005**, *7* (5), 267. doi:10.1039/b418069k; (b) Capello, C.; Fischer, U.; Hungerbühler, K. *Green Chem.* **2007**, *9* (9), 927. doi:10.1039/b617536h.

(8) (a) Li, C. J. *Chem. Rev.* **2005**, *105* (8), 3095. doi:10.1021/cr030009u; (b) Blackmond, D. G.; Armstrong, A.; Coombe, V.; Wells, A. *Angew. Chem. Int. Ed.* **2007**, *46* (21), 3798. doi:10.1002/anie.200604952; (c) Minakata, S.; Komatsu, M. *Chem. Rev.* **2009**, *109* (2), 711. doi:10.1021/cr8003955; (d) Narayan, S.; Muldoon, J.; Finn, M. G.; Fokin, V. V.; Kolb, H. C.; Sharpless, K. B. *Angew. Chem. Int. Ed.* **2005**, *44* (21), 3275. doi:10.1002/anie.200462883.

(9) (a) Xu, H.; Wolf, C. *Chem. Commun. (Camb.)* **2009**, *2009* (21), 3035. doi:10.1039/b904188e; (b) Wu, Z.; Jiang, Z.; Wu, D.; Xiang, H.; Zhou, X. *Eur. J. Org. Chem.* **2010**, *2010* (10), 1854. doi:10.1002/ejoc.201000060.

(10) (a) Hodgkin, J. H. *J. Polym. Sci. Part A: Polym. Chem.* **1986**, *24* (11), 3117. doi:10.1002/pola.1986.080241136; (b) Mohanty, S.; Suresh, D.; Balakrishna, M. S.; Mague, J. T. *Tetrahedron* **2008**, *64* (1), 240. doi:10.1016/j.tet.2007.10.081.

(11) Zhu, Y.; Shi, Y.; Wei, Y. *Monatsh. Chem.* **2010**, *141* (9), 1009. doi:10.1007/s00706-010-0363-8.

(12) (a) Wallace, R. G.; Barker, J. M.; Wood, M. L. *Synthesis* **1990**, *1990* (12), 1143. doi:10.1055/s-1990-27117; (b) Maddani, M. R.; Moorthy, S. K.; Prabhu, K. R. *Tetrahedron* **2010**, *66* (1), 329. doi:10.1016/j.tet.2009.10.093; (c) Norman, J. J.; Heggie, R. M.; Larose, J. B. *Can. J. Chem.* **1962**, *40* (8), 1547. doi:10.1139/v62-233.

Quasi-classical trajectory study of the O(^{1}D) + HF reaction dynamics on 1^{1}A′ potential energy surface

Juan Zhao

Can. J. Chem. Downloaded from www.nrcresearchpress.com by Xi'an Jiaotong University on 09/19/12
For personal use only.

Abstract: The quasi-classical trajectory (QCT) calculations for the title reaction were carried out using the recently developed, accurate potential energy surface (PES) of the $1^1A'$ singlet state of the OHF system The integral cross section and the product rotational alignment factor $\langle P_2(\mathbf{j}' \cdot \mathbf{k})\rangle$ were calculated as a function of collision energy. In addition, I discovered the effect of isotopic substitution on stereodynamics for the title reaction, and the influence of the rotation excitation of the reagent on stereodynamics is also presented. Both the scalar and vector properties of the reaction $O(^1D) + HF \rightarrow OH + F$ (^2P) are studied in this paper. It was found that the reaction is mainly controlled by an indirect reaction mechanism, and that the deep noncollinear insertion HOF well has a great impact on the dynamics of the reaction. The conclusions drawn in this paper will draw from references to similar reactions, and provide a theoretical foundation for related experiments.

Key words: scalar and vector properties, O + HF reaction, isotope effect, rotation excitation of the reagent, quasi-classical trajectory.

Résumé : On a effectué des calculs de trajectoire quasi-classique (TQC) pour la réaction mentionnée dans le titre en faisant appel à la surface d'énergie potentielle (SEP) précise développée récemment de l'état singulet $1^1A'$ du système OHF. On a calculé la section droite intégrale et le facteur d'alignement rotationnel du produit $\langle P_2(\mathbf{j}' \cdot \mathbf{k})\rangle$ en fonction de l'énergie de collision. De plus, on a découvert un effet de substitution isotopique pour la réaction mentionnée dans le titre et on présente aussi l'influence de l'excitation de rotation du réactif sur la stéréodynamique. Dans ce travail, on étudie aussi les propriétés scalaires et les propriétés vectorielles de la réaction $O(^1D) + HF \rightarrow OH + F(^2P)$. On a trouvé que la réaction est principalement contrôlée par un mécanisme réactionnel indirect et que l'important puits d'insertion non colinéaire du HOF affecte beaucoup la dynamique de la réaction. Les conclusions tirées de ce travail serviront de référence à des réactions semblables et fourniront des bases théoriques pour des expériences apparentées.

Mots-clés : propriétés scalaires et vectorielles, réaction OHF, effet isotopique, rotation et excitation du réactif, trajectoire quasi-classique.

[Traduit par la Rédaction]

Introduction

Recently, the reactions of atomic oxygen with hydrogen halides (HX, where X refers to halogens) have received considerable attention for their importance in the studies of molecular reaction dynamics.[1–5] By disentangling the relative contributions in high-resolution angular and velocity distribution measurements at different collision energies, the dynamics of both O(^{3}P) and O(^{1}D) reactions have been investigated, and the effect of electronic excitation on the reaction dynamics of atomic oxygen and the possible role of intersystem crossing between triplet and singlet potential energy surfaces have also been explored directly. Examples of these studies include the reactions of O(^{1}D) with hydrogen halides (HF, HCl, HBr, and HI) to give the halogen oxides (FO, ClO, BrO, and IO),[1,3,6–9] and the reaction of O(^{1}D) with CF_3Br to give BrO,[10] etc. The halogenated compounds are currently of interest and the subject ofrecent studies, owing to their abundance in nature and their importance for human health and environmental protection.[11–30]

Among the halogenated compounds, the OHF system is considered to be one of the model systems for open shell reactions because of its relatively simple electronic structure. There have been several recent reports on the accurate potential energy surfaces (PESs) of the OHF reactive system. In 2004, based on multireference configuration interaction (MRCI) electronic calculations, Gómez-Carrasco et al.[12] fitted 8069 ab initio points, and obtained a high quality global PES for the ground triplet state of the OHF reactive system. Running the quasi-classical trajectory (QCT) calculations in this PES for the F + HO reaction, they[12] got similar results that are in good agreement with existing kinetic and dynamic experiments. In addition, using the aug-cc-pVTZ extended basis sets of Dunning[13,14] for the ab initio calculations, Gómez-Carrasco et al.[15] obtained a new global PES of the ground $^3A''$ adiabatic electronic state. Based on this PES, they performed the wave packet (WP) and QCT calculations for the reactive collision F + OH, and found that the reaction presented a dynamic barrier, essentially due to the zero-point energy (ZPE) for the bending vibration near the saddle point

Received 26 December 2010. Accepted 1 March 2011. Published at www.nrcresearchpress.com/cjc on 22 June 2011.

J. Zhao. School of Pharmaceutical Science and Technology, Dalian University of Technology, Dalian, 116024, China.

E-mail for correspondence: zhjuan2002@126.com.

Can. J. Chem. Downloaded from www.nrcresearchpress.com by Xi'an Jiaotong University on 09/19/12
For personal use only.

that determines two different reaction mechanisms.[15] In the same year, González-Sánchez et al.[16] reported a quantum WP study on the reagent **k**–**j** vector correlations for the reaction of F + OH on the $1^3A''$ state and the rate constants at nearly room temperature. Later, on the global three-dimensional adiabatic PESs for the excited $2^3A''$ and $1^3A'$ triplet states of the OHF system, Gómez-Carrasco et al.[17] studied the reaction dynamics of $F(^2P) + OH(^2\Pi) \rightarrow O(^3P) + HF(^1\Sigma^+)$ using a WP treatment within a centrifugal sudden approach. In 2007, they calculated the angle-resolved photodetachment spectra for the first five adiabatic singlet states $2^1A'$, $3^1A'$, $1^1A''$, $1^1A'$, and $2^1A''$ of the OHF system,[18] and calculated about 20 000 MRCI single point energies for the $O(^1D) + HF \rightarrow OH + F(^2P)$ reaction and obtained the highly accurate $1^1A'$ PES.[19] The minimum energy path of $1^1A'$ PES is shown in Fig. 1.[19] In the figure, *s* is defined as the sum of the displacements d*s* between two consecutive points of the surface, in terms of the three internuclear distances. By convention, *s* is positive (negative) from the saddle point toward O + HF (OH + F) channel, being $s = 0$ at the saddle point for the PES. Thus the sign of *s* distinguishes both chemical channels. In Fig. 1, one can see a very deep well in the product channel, which is the most noteworthy characteristic of this PES. This deep well locates the F + HO channel with energy $V \approx 2.111$ eV (including ZPE). In addition, there is a shallow well (energy of 0.323 eV) located at the O + HF channel, and the transition state of the PES has an energy of 0.375 eV over the F + HO channel. Based on this PES, Gómez-Carrasco et al.[19] investigated the dynamic and kinetic properties of reaction $O(^1D) + HF \rightarrow OH + F(^2P)$ using quantum WP and QCT methods, and the results agreed well with each other. More recently, Chu[20] has studied the chemical stereodynamics of reactions H/D + FO → OH/OD + F, HF/DF + O using three PESs of the $1^1A'$, $1^3A'$, and $1^3A''$ states by the time-dependent quantum WP and QCT method, and Zhao et al.[21] have investigated the H + OF → OH + F, HF + O reaction stereodynamics on $1^3A'$ PES using the QCT method.

To date, our work has mainly focused on the scalar and vector properties of the reactions based on $1^3A''$ PES of OHF system,[22–27] and only one paper has reported the effect of reagent vibration on the stereodynamics of the reaction $O(^1D) + HF \rightarrow OH + F(^2P)$ based on $1^1A'$ PES.[28] For a better understanding of the dynamic properties of the $O(^1D) + HF$ reaction on $1^1A'$ PES with a very deep well in the product channel, I have studied not only the scalar (vector) properties, but also its isotope variant, using QCT.

Theoretical method

The QCT calculation method used here is the same as used in other studies.[29–34] Classic Hamilton's equations are numerically integrated in three dimensions. First, I have calculated the integral cross section and the product rotational alignment factor. Setting the initial rovibrational conditions of the HF reagent to be $v = 0$, $j = 0$, the collision energy was chosen from 0.02 to 0.6 eV; second, I have studied the effect of isotope substitution O + HF/DF/TF ($v = 0$, $j = 0$) on stereodynamics at the different collision energies; and third, I have investigated the effect of rotation excitation O + HF ($v = 0$, $j = 1, 2, 3$) on the product polarization at the same collision energy. For each reaction, a batch of 10 000 trajectories was run, the integration step size in the trajectories was chosen to be 0.1 fs, and the initial distance from the O atom to the center of mass of HF was 20.0 Å, which can guarantee conservation of the total energy and angular momentum.

Fig. 1. Global minimum-energy path for the three-dimensional ground single state $1^1A'$ for $O(^1D) + HF > OH + F(^2P)$ reaction. (From Gómez-Carrasco et al.[19], reproduced with the kind permission of Chemical Physics Letters © Elsevier 2007).

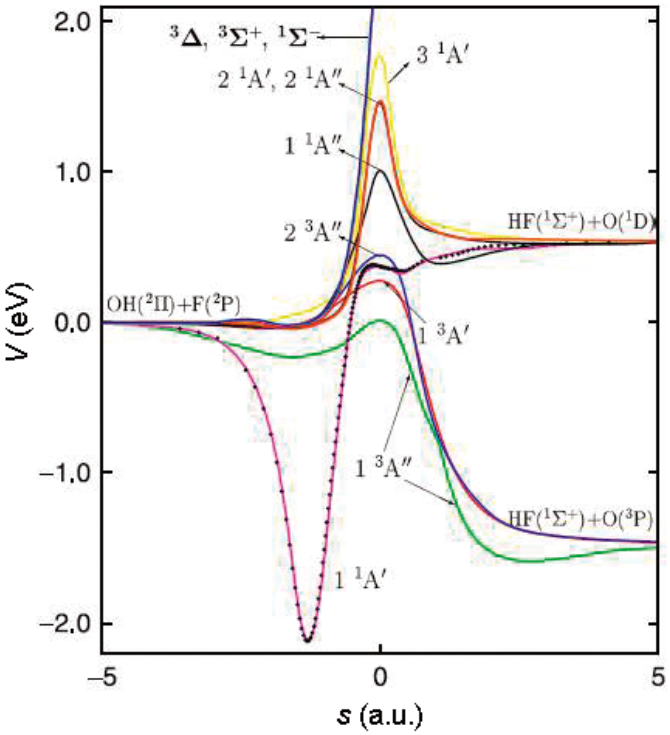

I have used standard product rotational polarization theory,[23–40] but I only summarize the details relevant to the present work. The QCT calculation was performed in the center-of-mass (CM) frame where the reagent relative velocity vector **k** is parallel to the *z* axis, and the *x*–*z* plane is the scattering plane containing the initial and final relative velocity vectors, **k** and **k**′. The angle θ_t is the so-called scattering angle between the reagent relative velocity and the product relative velocity. θ_r and ϕ_r are the polar and azimuthal angles of the final rotational angular momentum **j**′.

The $P(\theta_r)$ distribution describes the $\mathbf{k} - \mathbf{j}'$ vector correlation with $\mathbf{j}' \cdot \mathbf{k} = \cos\theta_r$, it can be expanded in a series of Legendre polynomials,

$$[1] \qquad P(\theta_r) = 2\sum_k k(2k+1)a_0(k)P_k(\cos\theta_r)$$

the expanding coefficients $a_0(k) = \int_0^\pi P(\theta_r)P_k(\cos\theta_r)\sin\theta_r d\theta_r = \langle P_k(\cos\theta_r)\rangle$ are called orientation (*k* is odd) and alignment (*k* is even) parameters, and *k* is the integer to ensure the convergent results of $P(\theta_r)$. Because only the rotational alignment of the product is measured in most experiments, in this study we mainly discuss the average rotational alignment factor $\langle P_2(\mathbf{j}' \cdot \mathbf{k})\rangle$.

The dihedral angle distribution function $P(\phi_r)$ describing the $\mathbf{k} - \mathbf{k}' - \mathbf{j}'$ correlation can be expanded in a Fourier series as

Can. J. Chem. Downloaded from www.nrcresearchpress.com by Xi'an Jiaotong University on 09/19/12
For personal use only.

$$[2] \qquad P(\phi_{jr}) = \frac{1}{2\pi}(1 + \sum_{\text{even},n\geq 2} a_n \cos n\phi_r + \sum_{\text{odd},n\geq 1} b_n \sin n\phi_r)$$

where $a_n = 2\langle \cos n\phi_r \rangle$ and $b_n = 2\langle \sin n\phi_r \rangle$. Using θ_r and ϕ_r to define the direction of $\mathbf{j}'$, the space distribution of the product's rotation angular momentum can be written as

$$[3] \qquad P(\theta_r, \phi_r) = \frac{1}{4\pi}\sum_{kq}[k]a_q^k C_{kq}(\theta_r, \phi_r)$$

$$= \frac{1}{4\pi}\sum_{k}\sum_{q\geq 0}(a_{q\pm}^k \cos q\phi_r - a_{q\mp}^k i \sin q\phi_r)C_{kq}(\theta_r, 0)$$

where $a_{q\pm}^k = 2\langle C_{k|q|}(\theta_r, 0)\cos q\theta_r \rangle$ (k is even) and $a_{q\mp}^k = 2i\langle C_{k|q|}(\theta_r, 0)\sin q\theta_r \rangle$ (k is odd).

In this calculation, $P(\theta_r)$, $P(\phi_r)$, and $P(\theta_r, \phi_r)$ are expanded up to $k = 18$, $n = 24$, and $k = 7$, respectively, which shows a good convergence.

Results and discussion

The dynamics of reaction O + HF OH + F

The QCT reaction probability as a function of collision energy for $O(^1D) + HF \rightarrow OH + F(^2P)$ ($J = 0$) reaction has been reported by Gómez–Carrasco et al.,[19] and the QCT result is in good accord with the WP result.

Figure 2 shows the QCT results of the integral reaction cross section. It is clear that the value of integral cross section is very large at the low collision energies, and rapidly decreases with increase in relative translational energy. The biggest impact parameter b_{max} at different collision energies is shown in Table 1. As can be seen in Table 1, b_{max} is large and rapidly decreases when the collision energy is <0.1 eV, but is small and decreases very slowly when the collision energy is >0.1 eV. Considering the integral cross section and b_{max}, it can be concluded that the value of orbital angular momentum, **L**, plays an important role in the reaction. Additionally, there is a shallow well in the reagent channel and no barrier in the reaction profile, which also affects the integral reaction cross section, as shown in Fig. 2.

To further investigate the dynamics of this reaction, I have also studied the vector properties of the title reaction. Figure 3 shows the dependence of the product rotational alignment factor $\langle P_2(\mathbf{j}' \cdot \mathbf{k}) \rangle$ on the collision energy. It can be seen from this figure that the value of $\langle P_2(\mathbf{j}' \cdot \mathbf{k}) \rangle$ is about –0.1 in the whole collision energy range, which indicates that there are weak product rotational alignments, and the degree of alignment is almost invariant when the collision energy increases. This could be due to the heavy–light–heavy (H–L–H) mass combination: much angular momentum transfers from the reagent orbit to the product orbit, $\mathbf{L} - \mathbf{L}'$, and little to rotation. Instead, in my calculations, the rotation number, j', of product molecule OH is large, which is shown in Fig. 4. It is easy to figure out that the rotational excitation of the product is quite strong, with the most probable population appearing at a high rotation number. The distribution changes towards higher j' value while the translational energy of the reactant increases. That is to say, much more energy goes into rotation than into translation, which is consistent with the result reported in by Gómez-Carrasco et al.[19] In that paper, the authors have ascribed their result to the noncollinear deep insertion well in the product channel. In view of my work, the reason for weak product rotational alignment can also be the deep well, which induces the complex to rotate for a long time. In Fig. 5, the internuclear distances of OH, HF, and OF as a function of propagation time are shown. It can be observed from this figure that the life of the "complex" is very long, whether the collision energy is low (0.02 eV) or

Fig. 2. The quasi-classical-trajectory-computed reaction cross sections as a function of collision energy in this study.

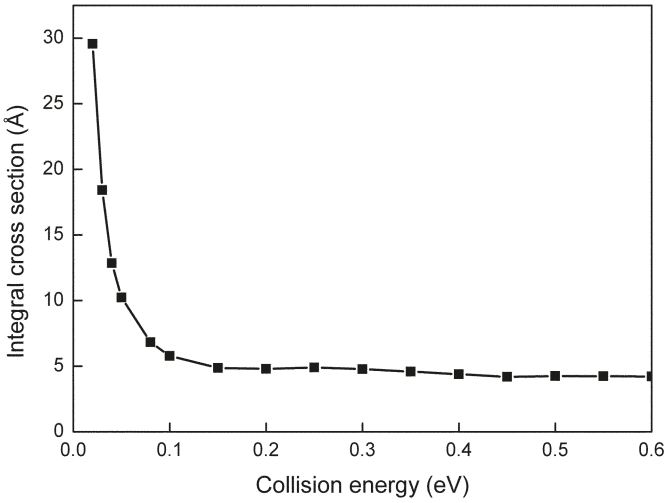

Table 1. The value of b_{max} at different collision energies for the reaction $O(^1D) + HF \rightarrow OH + F(^2P)$.

E_C (eV)	b_{max} (Å)	E_C (eV)	b_{max} (Å)
0.02	6.42	0.25	2.42
0.03	5.60	0.3	2.39
0.04	4.60	0.35	2.29
0.05	4.00	0.4	2.26
0.08	3.15	0.45	2.24
0.1	2.95	0.5	2.18
0.15	2.73	0.55	2.17
0.2	2.55	0.6	2.18

Fig. 3. The product rotational alignment factor of O + HF → OH + F reaction as a function of collision energy.

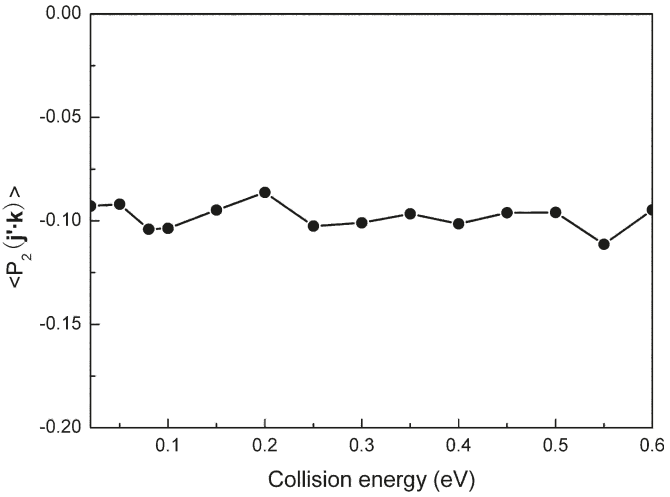

Can. J. Chem. Downloaded from www.nrcresearchpress.com by Xi'an Jiaotong University on 09/19/12
For personal use only.

Fig. 4. The rotational distribution of OH for the title reaction at different initial collision energies.

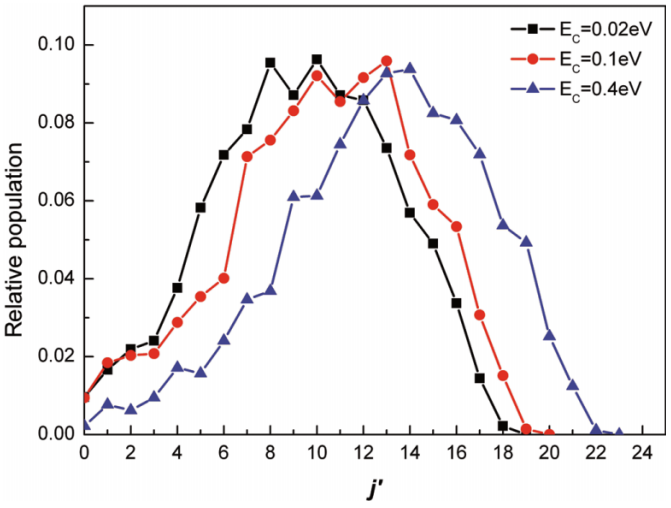

Fig. 5. Internuclear distances of OH, HF, and OF as a function of propagation time at (*a*) E_c = 0.02 eV and (*b*) E_c = 0.6 eV. Unbroken lines, the internuclear distances of OH; dashed lines, the internuclear distances of HF; dotted lines, the internuclear distances of OF.

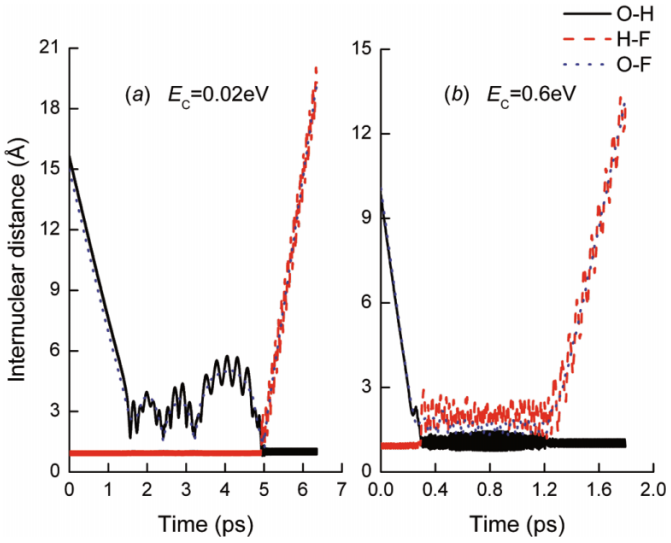

high (0.6 eV). Hence it is not difficult to conclude that this reaction is mainly controlled by an indirect reaction mechanism.

The dynamics of reactions O + HF/DF/TF ($v = 0, j = 0$) → OH/OD/OT + F

In this section, I consider the isotopic effect of the reactions O + HF/DF/TF (v = 0, j = 0) → OH/OD/OT + F at different collision energies, on dynamics.

Figures 6*a*–6*c* represent the differential cross sections (DCSs), which reflect the angular distribution for the reactions O + HF/DF/TF (v = 0, j = 0) → OH/OD/OT + F at the collision energy of 0.1 eV, 0.3 eV, and 0.5 eV. As is seen in Figs. 6*a*–6*c*, at the different collision energies, the reaction O + HF/DF/TF is dominated by strongly forward–backward scattering; at the same collision energy, forward scattering is always stronger than backward scattering. When the collision energy increases, the backward scattering becomes stronger

Fig. 6. The angular distributions for O + H/DF/TF (v = 0, j = 0) → OH/OD/OT + F reactions.

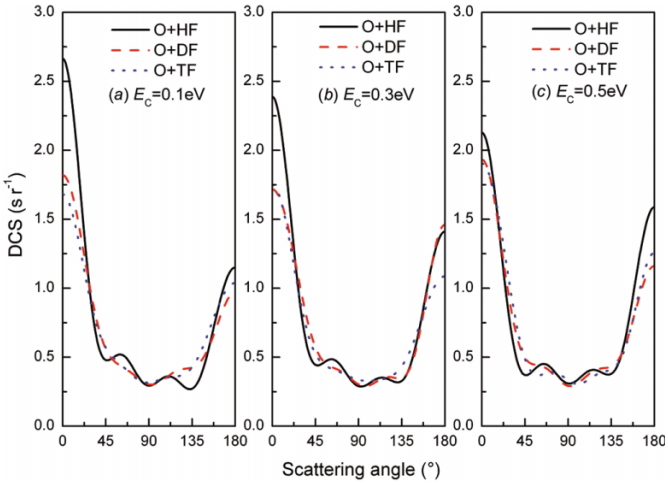

and the products trend to forward–backward symmetrical scattering. The reason for these results may be the two wells in PES, and that the title reaction is mainly controlled by an indirect reaction mechanism. Increase in collision energy speeds up the complex rotation, which makes the products trend to forward–backward symmetrical scattering. At the same collision energy, when the target molecule HF is substituted by DF and TF, the same qualitative markedly forward–backward distribution is given. These results are consistent those discussed by Gómez-Carrasco et al.[19] Of course, if hydrogen is substituted by its deuterium (tritium) isotope, there appears to be some divergence among the three DCSs for each collision energy, i.e., the trend of forward–backward scattering becomes weaker. It is obvious that the relative velocity of the product molecule of the O+DF/TF → OD/OT + F reaction is lower at the same initial collision energy, which may make forward–backward scattering weaker.

From the above statements, it is not clear what the isotopic effect is on the scalar properties of the title reaction, at the same collision energy. To consider isotopic effect fully, we have studied the isotopic effect on vector properties. Figures 7 and 8 show the distributions of $P(\theta_r)$ and $P(\phi_r)$ of the reactions O + HF/DF/TF → OH/OD/OT + F at collision energies of 0.1 eV and 0.4 eV, respectively. In Figs. 7*a* and 7*b*, it is clear that the peaks of $P(\theta_r)$ are at $\theta_r = 90°$ and are symmetric around 90°, which indicates that the product rotational angular momentum vector is strongly aligned along a direction at right angles to the relative velocity direction, and one can conclude that the three reactions are mainly governed by the "in plane" mechanism. Obviously, there is a discrepancy among the three $P(\theta_r)$ distributions after H is substituted by D and T. For E_c = 0.1 eV, the peak of the $P(\theta_r)$ distribution becomes lower and lower, which indicates that the product molecule alignment becomes weaker and weaker. According to other studies (Zhao et al.,[24] Wang and He,[30] and Wang et al.,[32]) $P(\theta_r)$ is sensitive to two factors: the character of the PES, and the mass factor (i.e., $\cos^2\beta = m_A m_c/(m_A + m_B)(m_B + m_C)$ for the reaction A + BC → AB + C). With respect to adiabatic approximation, the influence of isotopic substitution on the PES is not considered here. Therefore, the difference in the $P(\theta_r)$ distribution is probably attributable to the difference

Can. J. Chem. Downloaded from www.nrcresearchpress.com by Xi'an Jiaotong University on 09/19/12
For personal use only.

Fig. 7. The distribution of $P(\theta_r)$ for the product molecule from the reaction O + HF/DF/TF → OH/OD/OT + F.

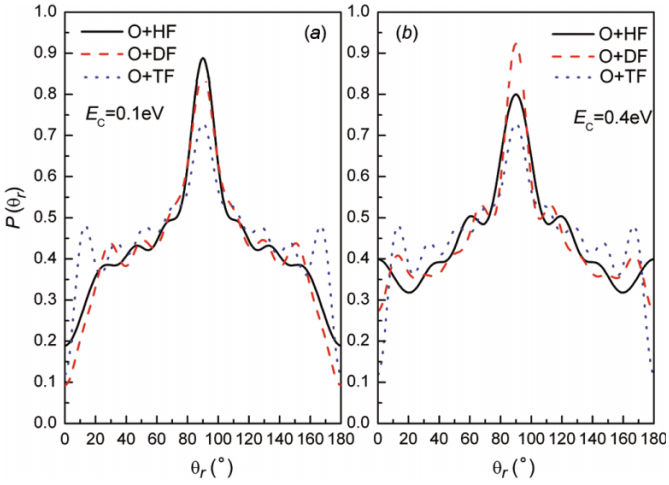

Fig. 8. The distribution of $P(\phi_r)$ for the product molecule from the reaction O + HF/DF/TF → OH/OD/OT + F.

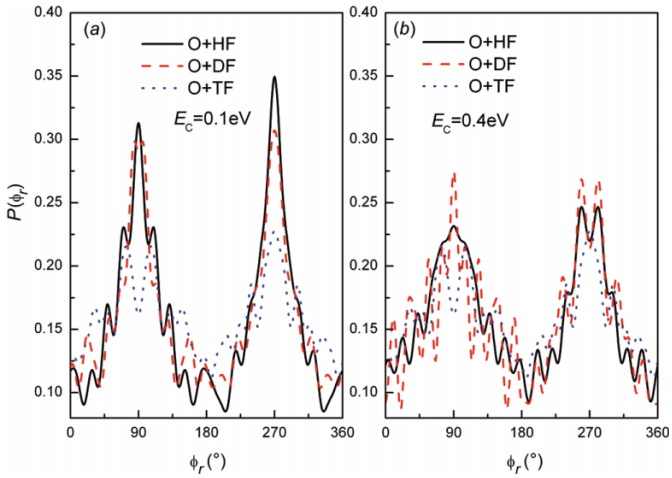

in the mass factor among the reactions O + HF/DF/TF → OH/OD/O, the values for mass factor being 0.893, 0.803, and 0.726, respectively. From Fig. 7*a*, it can be seen that that larger the mass factor, the stronger the product molecule alignment. To achieve a much clearer understanding of the isotopic effect, I have also calculated the $P(\theta_r)$ distribution at the higher collision energy, 0.4 eV, and presented it in Fig. 7*b*. As is shown in Fig. 7*b*, the result is different from the one in Fig. 7*a*. In Fig. 7*b*, the peak of the $P(\theta_r)$ distribution for O + HF is lower than that for O + DF, while higher than that for O + TF, which indicates that the degree of alignment of OH is weaker than that of OD, while stronger than that of OT. The calculations show that the isotopic effect on $P(\theta_r)$ distribution is irregular for our reactions at different collision energies. Although the O + HF/DF/TF reactions are occurring on the same PES, considering the most salient feature of $1^1A'$ PES, the very deep noncollinear insertion HOF well, we can attribute the results for $P(\theta_r)$ to this well, which may make $P(\theta_r)$ vary in relation to changes in mass factor.

Similarly, the dihedral angle distributions $P(\phi_r)$ describing the $\mathbf{k} - \mathbf{k}' - \mathbf{j}'$ correlations for E_c = 0.1 eV and 0.4 eV are depicted in Figs. 8*a* and 8*b*. The $P(\phi_r)$ tends to be asymmetric with respect to the $\mathbf{k} - \mathbf{k}'$ scattering plane, directly reflecting the polarization of angular moment. As is seen in Figs. 8*a* and 8*b*, the main peaks of six $P(\phi_r)$ distributions all appear at ϕ_r = 90° and 270°, which indicates that the rotational angular momentum vectors of the product molecule are mainly aligned along the *y*-axis in the CM frame, and the isotope effect on $P(\phi_r)$ distribution is noticeable for the same collision energy. Seen in Fig. 8*a*, the peaks of $P(\phi_r)$ at ϕ_r = 270° are slightly higher than the ones at ϕ_r = 90°, which indicates that the rotational angular momentum vector of the product molecule OH/OD/OT is not only aligned, but also slightly oriented along the negative *y*-axis. In addition, it can be seen that the product molecule orientation becomes weaker after H is substituted by D and T, and that the orientation of the OT molecule is the weakest. However, for E_c = 0.4 eV in Fig. 8*b*, the trend of $P(\phi_r)$ is inconsistent when H is substituted by D and T. For O + HF/TF → OH/OT + F reactions, the product rotational angular momentum is oriented along the negative *y*-axis, whereas, for O+DF → OD + F, the product rotational angular momentum is oriented along the positive *y*-axis. As stated previously, the isotope effect on $P(\phi_r)$ distribution is also irregular. Other studies (Zhao et al.,[24] Lin et al.,[39] Chu et al., [40] Han et al.,[41] and Li et al.[42]) have shown that the difference in orientation is due to the different harmonic ZPE of the reactant molecules HF (DF/TF). For our reactions, however, the reason for the irregular isotope effect on $P(\phi_r)$ is not the difference in ZPE, but rather because of the particular character of $1^1A'$ PES, the deep well.

Fig. 9. The distribution of $P(\theta_r)$ for the product molecule from the reaction O + HF (v = 0, j = 1, 2, 3) → OH + F at E_c = 0.4 eV.

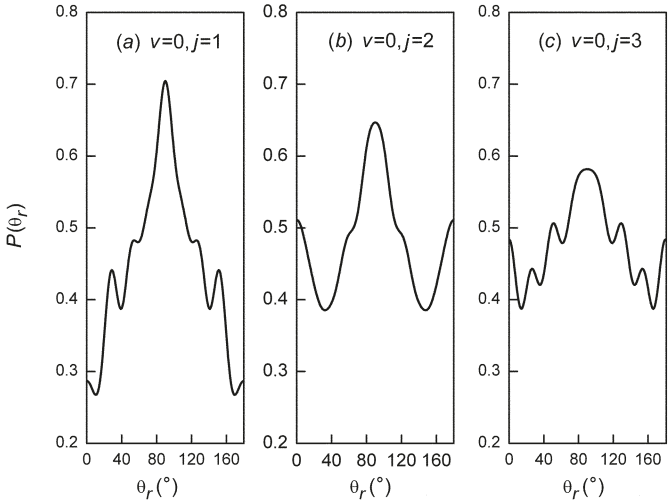

The stereodynamics of reactions O + HF (v = 0, j = 1, 2, 3) → OH + F

In this section, I have studied the effect of reagent rotational excitation on the stereodynamics of the O + HF → OH + F reaction. Figures 9 and 10 show the distributions of $P(\theta_r)$ and $P(\phi_r)$ for the reaction O + HF (v = 0, j = 1, 2, 3) → OH + F, respectively.

In Fig. 9, it is clear that the peak of $P(\theta_r)$ distribution becomes lower with the increase of rotational quantum number, which indicates that the larger the rotational quantum number, the weaker the degree of alignment of OH. This result is different from the findings of Meng et al.,[23] where the reaction

Fig. 10. The distribution of $P(\phi_r)$ for the product molecule from the reaction O + HF ($v = 0$, $j = 1, 2, 3$) → OH + F at $E_c = 0.4$ eV.

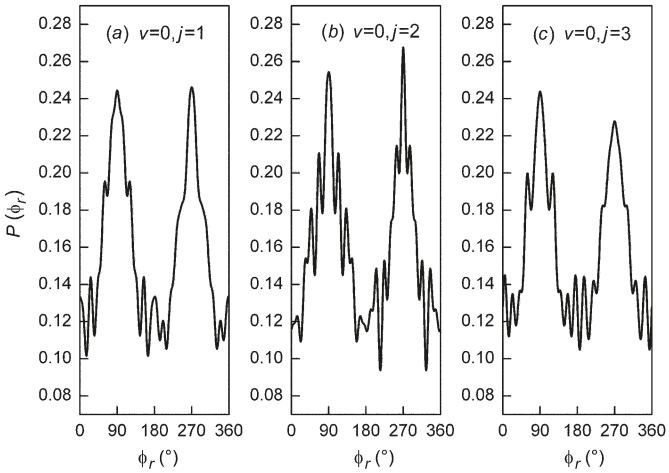

H + FO ($v = 0$, $j = 1, 2, 3$) → HO + F proceeds to $1^3A''$ PES. The reason for this discrepancy may be the difference between $1^1A'$ and $1^3A''$ PESs. For the reaction H + FO ($v = 0$, $j = 1, 2, 3$), there is a barrier in the $1^3A''$ PES; while for the reaction O + HF ($v = 0$, $j = 1, 2, 3$) based on $1^1A'$ PES, there is no barrier other than a deep well in the product channel.

From Fig. 10, which shows the $P(\phi_r)$ distribution, one can find that for the reaction O + HF ($v = 0$, $j = 1$), $\mathbf{j}'$ has no evident orientation, but for $j = 2$, $\mathbf{j}'$ tends to be oriented along the negative direction of the y-axis, and for $j = 3$, $\mathbf{j}'$ tends to be oriented along the positive direction of the y-axis. In both latter cases, the degree of orientation is very weak. That is to say, the reagent rotational excitation influences the orientation of the products, but the impact is not great. The reason for this is the deep noncollinear insertion HOF well in the PES. Whether or not the reagent rotational quantum number is large, the complex will rotate for a long time in the well, and the product molecule OH will not have a predictable rotational orientation.

Conclusion

This paper has presented a QCT study of the scalar and vector properties of the $O(^1D) + HF$ reaction, and discussed the effect of isotope substitution as well as the influence of the rotation excitation of the reagent on stereodynamics for the title reaction. Owing to the deep noncollinear insertion HOF well and the barrierless exoergic reaction profile, some interesting results have been obtained: the reaction cross section rapidly decreases with increasing relative translational energy and then flattens out, the angular momentum polarization of the product molecule is weak, the angular distribution of products is markedly forward–backward, and both the effects of isotope substitution on stereodynamics and the reagent rotation excitation on stereodynamics are indistinctive. These conclusions could also be applied to similar reactions (e.g., $O(^3P) + HCl$),[43] and provide a theoretical foundation for related experiments.

References

(1) Balucani, N.; Beneventi, L.; Casavecchia, P.; Volpi, G. G. *Chem. Phys. Lett.* **1991** *180* (1–2), 34. doi:10.1016/0009-2614(91)87112-O.
(2) Han, K. L.; He, G. Z. *J. Photochem. Photobiol. Photochem. Rev.* **2007** *8* (2), 55. doi:10.1016/j.jphotochemrev.2007.03.002.
(3) Takacs, G. A.; Glass, G. P. *J. Phys. Chem.* **1973** *77* (9), 1182. doi:10.1021/j100628a020.
(4) Balucani, N.; Casavecchia, P.; Stranges, D.; Volpi, G. G. *Chem. Phys. Lett.* **1993** *211* (4–5), 469. doi:10.1016/0009-2614(93)87092-H.
(5) Alagia, M.; Aquilanti, V.; Ascenzi, D.; Balucani, N.; Cappelletti, D.; Cartechini, L.; Casavecchia, P.; Pirani, F.; Sanchini, G.; Volpi, G. G. *Isr. J. Chem.* **1997** *37* (3–4), 329.
(6) Balucani, N.; Beneventi, L.; Casavecchia, P.; Volpi, G. G.; Kruus, E. J.; Sloan, J. J. *Can. J. Chem.* **1994** *72* (3), 888. doi:10.1139/v94-116.
(7) Alagia, M.; Balucani, N.; Casavecchia, P.; Volpi, G. G. *J. Phys. Chem. A* **1997** *101* (36), 6455. doi:10.1021/jp970697j.
(8) Alagia, M.; Balucani, N.; Casavecchia, P.; Stranges, D.; Volpi, G. G. *J. Chem. Soc., Faraday Trans.* **1995** *91* (4), 575. doi:10.1039/ft9959100575.
(9) Singleton, D. L.; Cvetanovi, R. J. *Int. J. Chem. Kinet.* **1981** *13* (9), 945. doi:10.1002/kin.550130916.
(10) Alagia, M.; Balucani, N.; Casavecchia, P.; Laganà, A.; Ochoa de Aspuru, G.; van Kleef, E. H.; Volpi, G. G.; Lendvay, G. *Chem. Phys. Lett.* **1996** *258* (3–4), 323. doi:10.1016/0009-2614(96)00810-X.
(11) González-Sánchez, L.; Gómez-Carrasco, S.; Aguado, A.; Paniagua, M.; Hernández, M. L.; Alvariño, J. M.; Roncero, O. *J. Chem. Phys.* **2004** *121* (1), 309. doi:10.1063/1.1756581.
(12) Gómez-Carrasco, S.; González-Sánchez, L.; Aguado, A. *Chem. Phys. Lett.* **2004** *383* (1–2), 25. doi:10.1016/j.cplett.2003.10.142.
(13) Dunning, T. H., Jr. *J. Chem. Phys.* **1989** *90* (2), 1007. doi:10.1063/1.456153.
(14) Kendall, R. A.; Dunning, T. H., Jr.; Harrison, R. J. *J. Chem. Phys.* **1992** *96* (9), 6796. doi:10.1063/1.462569.
(15) Gómez-Carrasco, S.; González-Sánchez, L.; Aguado, A.; Roncero, O.; Alvariño, J. M.; Hernández, M. L.; Paniagua, M. *J. Chem. Phys.* **2004** *121* (10), 4605. doi:10.1063/1.1780168.
(16) González-Sánchez, L.; Gómez-Carrasco, S.; Aguado, A.; Paniagua, M.; Hernández, M. L.; Alvariño, J. M.; Roncero, O. *Mol. Phys.* **2004** *102* (21–22), 2381. doi:10.1080/00268970412331318831.
(17) Gómez-Carrasco, S.; Roncero, O.; González-Sánchez, L.; Hernández, M. L.; Alvariño, J. M.; Paniagua, M.; Aguado, A. *J. Chem. Phys.* **2005** *123* (11), 114310. doi:10.1063/1.2046669.
(18) Gómez-Carrasco, S.; Aguado, A.; Paniagua, M.; Roncero, O. *J. Photochem. Photobiol. A.* **2007** *190* (2–3), 145. doi:10.1016/j.jphotochem.2007.01.027.
(19) Gómez-Carrasco, S.; Hernández, M. L.; Alvariño, J. M. *Chem. Phys. Lett.* **2007** *435* (4–6), 188. doi:10.1016/j.cplett.2006.12.073.
(20) Chu, T.-S. *J. Comput. Chem.* **2010** *31* (7), 1385. doi:10.1022/jcc.21423.
(21) Zhao, D.; Zhang, T.-Y.; Chu, T.S. *Can. J. Chem.* **2010** *88* (9), 893. doi:10.1139/V10-063.
(22) Zhao, J.; Xu, Y.; Yue, D.G.; Meng, Q.-T. *Chem. Phys. Lett.* **2009** *471* (1–3), 160. doi:10.1016/j.cplett.2009.02.007.
(23) Meng, Q.T.; Zhao, J.; Xu, Y.; Yue, D.G. *Chem. Phys.* **2009** *362* (1–2), 65. doi:10.1016/j.chemphys.2009.06.009.
(24) Zhao, J.; Xu, Y.; Meng, Q.T. *J. Phys. B* **2009** *42* (16), 165006. doi:10.1088/0953-4075/42/16/165006.

Can. J. Chem. Downloaded from www.nrcresearchpress.com by Xi'an Jiaotong University on 09/19/12
For personal use only.

(25) Zhao, J.; Xu, Y.; Meng, Q.-T. *Can. J. Phys.* **2009** *87* (12), 1247. doi:10.1139/P09-074.
(26) Zhao, J.; Xu, Y.; Zhao, X.; Meng, Q.-T. *Sci. China Chem.* **2010** *53* (4), 927. doi:10.1007/s11426-010-0043-x.
(27) Zhao, J.; Xu, Y.; Meng, Q.-T. *Chin. Phys. B* **2010** *19* (6), 063403. doi:10.1088/1674-1056/19/6/063403.
(28) Xu, Y.; Zhao, J.; Yue, D.-G.; Liu, H.; Zheng, X.-Y.; Meng, Q.-T. *Chin. Phys. B.* **2009** *18* (12), 5308. doi:10.1088/1674-1056/18/12/032.
(29) Han, K.-L.; He, G.-Z.; Lou, N.-Q. *J. Chem. Phys.* **1996** *105* (19), 8699. doi:10.1063/1.472651.
(30) Wang, M.-L.; Han, K.-L.; He, G.-Z. *J. Phys. Chem. A* **1998** *102* (50), 10204. doi:10.1021/jp981738u.
(31) Chen, M.-D.; Han, K.-L.; Lou, N.-Q. *J. Chem. Phys.* **2003** *118* (10), 4463. doi:10.1063/1.1545112.
(32) Wang, M.-L.; Han, K.-L.; He, G.-Z. *J. Chem. Phys.* **1998** *109* (13), 5446. doi:10.1063/1.476522.
(33) Chen, M.-D.; Han, K.-L.; Lou, N.-Q. *Chem. Phys. Lett.* **2002** *357* (5–6), 483. doi:10.1016/S0009-2614(02)00585-7.
(34) Zhang, X.; Han, K.-L. *Int. J. Quantum Chem.* **2006** *106* (8), 1815. doi:10.1002/qua.20929.
(35) Han, K.-L.; Zheng, X.-G.; Sun, B.-F.; He, G.-Z.; Zhang, R.-Q. *Chem. Phys. Lett.* **1991** *181* (5), 474. doi:10.1016/0009-2614(91)90383-K.
(36) Ju, L.-P.; Han, K.-L.; Zhang, J.Z.H. *J. Comput. Chem.* **2009** *30* (2), 305. doi:10.1002/jcc.21032.
(37) Zhang, H.; Zhu, R.-S.; Wang, G.-J.; Han, K.-L.; He, G.-Z.; Lou, N.-Q. *J. Chem. Phys.* **1999** *110* (6), 2922. doi:10.1063/1.477935.
(38) Chu, T.-S.; Han, K.-L. *Phys. Chem. Chem. Phys.* **2008** *10* (18), 2431. doi:10.1039/b715180b.
(39) Lin, S.-Y.; Han, K.-L.; Zhang, J. Z. H. *Chem. Phys. Lett.* **2000** *324* (1–3), 122. doi:10.1016/S0009-2614(00)00590-X.
(40) Chu, T.-S.; Zhang, Y.; Han, K.-L. *Int. Rev. Phys. Chem.* **2006** *25* (1), 201. doi:10.1080/01442350600677929.
(41) Han, K.-L.; He, G.-Z.; Lou, N.-Q. *Chin. J. Chem. Phys.* **1989** *2* (5), 323 .
(42) Li, R.-J.; Han, K.-L.; Li, F.-E.; Lu, R.-C.; He, G.-Z.; Lou, N.-Q. *Chem. Phys. Lett.* **1994** *220* (3–5), 281. doi:10.1016/0009-2614(94)00174-X.
(43) Ramachandran, B. *J. Chem. Phys.* **2000** *112* (8), 3680. doi:10.1063/1.480520.

Can. J. Chem. Downloaded from www.nrcresearchpress.com by Xi'an Jiaotong University on 09/19/12
For personal use only.

Fast computation of DFT nuclear gradient with multiresolution*

Nicholas J. Russ, Chun-min Chang, and Jing Kong

Abstract: We present an efficient algorithm for evaluating the exchange-correlation contribution to the nuclear gradients of density-functional theory calculation within the local spin-density approximation. The algorithm is an extension of the multiresolution exchange-correlation (mrXC) method, which treats smooth and compact parts of the electron density separately. The nuclear gradient of the smooth density is calculated on the even-spaced grid while the compact part of the density is handled on the normal atom-centered grid (ACG). The overall formulism is still formally based on the ACG, and thus does not change the results of the existing ACG-based algorithms for all-electron density-functional theory (DFT) calculations. The variation of the positions and weights of ACG owing to the nuclear perturbation is also handled rigorously. Benchmark calculations with different basis sets and sizes of ACG show that mrXC reduces the computational cost by several times without loss of accuracy. It also lessens the impact on the CPU time when the size of the ACG is increased.

Key words: density-functional theory, exchange-correlation, planewaves, quantum chemistry.

Résumé : On a développé un algorithme efficace pour évaluer la contribution échange-corrélation aux gradients nucléaires pour des calculs selon la théorie de la fonctionnelle de la densité, dans les limites de l'approximation de la densité de spin locale. L'algorithme est une extension de la méthode de l'échange-corrélation à multirésolution (ECmr) qui traite séparément des parties lisses et compactes de la densité électronique. Le gradient nucléaire de la densité lisse est calculé sur une grille à espaces réguliers alors que la partie compacte de la densité est traitée sur la grille normale centrée sur l'atome (GCA). Le formalisme global est malgré tout basé sur une grille normale centrée sur l'atome et ne change donc par les résultats des algorithmes existants basés sur les GCA pour les calculs selon la TFD pour tous les électrons. La variation des positions et des poids de la GCA due à une perturbation nucléaire est traitée d'une façon rigoureuse. Des calculs repères avec divers ensembles de base et diverses tailles de GCA montrent que la méthode ECmr réduit de beaucoup les coûts de calcul sans perte de précision. Elle réduit aussi l'impact que pourrait avoir une augmentation de la taille de la GCA sur le temps requis de l'unité centrale.

Mots-clés : théorie de la fonctionnelle de la densité (TFD), échange-corrélation, ondes planes, chimie quantique.

Can. J. Chem. Downloaded from www.nrcresearchpress.com by Xi'an Jiaotong University on 09/19/12
For personal use only.

Introduction

Numerical integration of the exchange-correlation (XC) terms is one of the major bottlenecks in a density-functional theory (DFT) calculation. We have recently devised a novel scheme called multiresolution XC (mrXC) and showed its ability to speed up the calculation of the energy with local spin density approximation (LSDA) by three to five times.[1,2] The essence of mrXC is to divide the XC terms into *smooth* (low resolution) and *compact* (high resolution) categories, and treat the former more efficiently. In this paper, we will present the mrXC algorithm for the calculation of analytical gradients of the LSDA energy with respect to the nuclear coordinates, which is fundamental to nearly all types of applications.

Tremendous progress has been made to enhance the performance of DFT since the 1990s, with most of the effort on the reduction of the computational cost for Coulomb and Hartree–Fock (HF) exchange interactions. One of the most recent examples is the development of the Fourier transform Coulomb (FTC) method,[3] of which we have made a new implementation in combination with other latest efficient Coulomb algorithms.[4] FTC replaces the most expensive part of the Coulomb interaction, namely the computation of four-index electronic repulsive integrals of diffuse basis functions with small exponents, with an accurate numerical evaluation using planewaves as the auxiliary basis. The computational cost of FTC scales as $O(N^2)$ with respect to the size of the basis set and as $O(V \log V)$ with respect to the size of the molecule (V), versus $O(N^4)$ and $O(V^2)$, respectively, for the conventional approach. Prior to FTC, the most efficient way of calculating the Coulomb energy was the combination of the continuous fast multipole method (CFMM) and the J-engine method. CFMM[5] is the first linear-scaling method for the calculation of Coulomb interaction, which reduces the computational cost of the calculation of Coulomb interaction among the well-separated Gaussians from quadratic scaling to linear. The J-engine technology[6] that reduced the calculation time of the Coulomb interaction in short range by 5–10 fold was developed some time later. We showed that FTC ac-

Received 1 October 2010. Accepted 20 January 2011. Published at www.nrcresearchpress.com/cjc on 23 June 2011.

N.J. Russ, C.-M. Chang, and J. Kong. Q-Chem Inc, 5001 Baum Blvd, Pittsburgh, PA 15213, USA.

Corresponding author: Jing Kong (e-mail: jkong@q-chem.com).

**This article is dedicated to Dr. Russell J. Boyd for his distinguished career in chemical research.*

Can. J. Chem. Downloaded from www.nrcresearchpress.com by Xi'an Jiaotong University on 09/19/12
For personal use only.

celerates the Coulomb calculation further, by up to six times, by replacing the most time-consuming part of the J-engine calculation of the integrals containing three and four diffuse basis functions with an efficient numerical integration. The combination of FTC, CFMM, and J-engine represents the state-of-the-art in accurate Coulomb calculation with Gaussian basis functions while maintaining rigorous control of the error. Other efficient but approximating methods exist, such as the resolution-of-the-identity scheme that has been shown to have significant errors in total energy, but small errors in relative energy.[7] Much progress has also been made for the linear-scaling calculation of HF exchange,[8,9] required for hybrid DFT methods.

The other computational bottleneck besides the Coulomb and HF exchange energies, is the XC energy, and its share of the computational cost of a DFT calculation has increased significantly with the improvement of the performance of the others. A typical numerical quadrature for XC is the superposition of atom-centered grids (ACGs).[10] In such a grid, the density of the grid points is very high near nuclei because the electron density changes rapidly in this region, and becomes increasingly lower away from the nucleus as the electron density changes more slowly. While this is necessary for functions with high resolutions such as compact basis functions, it is not necessary for smooth functions with low resolutions. FTC has shown that accurate and efficient numerical integration can be done on a quite sparse even-spaced cubic grid (ESCG) for quantities related to smooth functions. It is, however, impossible to mix the ACG and the ESCG directly without loss of accuracy because the XC functional has a complicated nonlinear dependency on the total electron density that cannot be separated into smooth and compact terms without significant approximation. MrXC overcomes this difficulty by the introduction of two fast transformations between the ESCG and the ACG, which ensures accuracy while maintaining maximum efficiency.

Algorithm

An LSDA functional, f, is a nonlinear function of electron spin densities ρ_α and ρ_β. The integration of f yields the XC energy, and is done numerically on an ACG grid in a standard DFT calculation:

$$[1] \qquad E_{\mathrm{XC}} = \sum_i w_i f[\rho_\alpha(\bar{r}_i), \rho_\beta(\bar{r}_i)] \equiv \sum_i \varepsilon_{\mathrm{XC}}(i)$$

where i is the index for each point on the ACG, and w_i is the weight for that point. The computation of the density is as follows:

$$[2] \qquad \rho_{\sigma i} \equiv \rho_\sigma(\bar{r}_i) = \sum_{\mu\nu} P^\sigma_{\mu\nu}\phi_\mu(\bar{r}_i)\phi_\nu(\bar{r}_i) \equiv \sum_{\mu\nu} P^\sigma_{\mu\nu}\phi_{\mu\nu}(\bar{r}_i), \qquad \sigma = (\alpha, \beta)$$

in which $\mathbf{P}^\sigma$ is the spin density matrix and ϕ_μ and ϕ_ν are atomic basis functions. We use the two-indexed symbol $\phi_{\mu\nu}$ to denote the product of two basis functions or the basis function pair (BFP). The contribution of the XC energy to the nuclear gradient of the total DFT energy is to take the derivative of the XC energy with respect to the nuclear coordinates while the density matrix remains constant.[11] Denoting it as $E^{\bar{A}}_{\mathrm{XC}}$ with $\bar{A}$ being the coordinates of atom A, one obtains from eq. [1] through chain rule:

$$[3] \qquad E^{\bar{A}}_{\mathrm{XC}} \equiv \frac{\partial E_{\mathrm{XC}}}{\partial \bar{A}}\Big|_{\mathbf{P}} = \sum_i \left[w_i (f_i^{\rho_\alpha}\rho^{\bar{A}}_{\alpha i} + f_i^{\rho_\beta}\rho^{\bar{A}}_{\beta i}) + w_i^{\bar{A}} f_i \right] \equiv \sum_i \varepsilon^{\bar{A}}_{\mathrm{XC}}(i)$$

with the following definitions:

$$[4] \qquad f_i \equiv f[\rho_\alpha(\bar{r}_i), \rho_\beta(\bar{r}_i)], \qquad f_i^{\rho_\sigma} \equiv \frac{\partial f_i}{\partial \rho_\sigma}$$
$$\rho^{\bar{A}}_{\sigma i} \equiv \sum_{\mu\nu} P^\sigma_{\mu\nu} \frac{d}{d\bar{A}}[\phi_{\mu\nu}(\bar{r}_i)], \qquad \sigma = (\alpha, \beta)$$

The nuclear gradient of a BFP on the ACG has two components. One is the derivative of each basis function with respect to its atomic position, or the *explicit* nuclear derivative. The other is the derivative of each ACG point with respect to the position of the atom that originates the point, or the *implicit* nuclear derivative. Those two derivatives, denoted as $\rho^{(\bar{A})}_{\sigma i}$ and $\rho^{[\bar{A}]}_{\sigma i}$, respectively, are defined below:

$$[5] \qquad \rho^{\bar{A}}_{\sigma i} = \sum_{\mu\nu} \left(P^\sigma_{\mu\nu} \frac{\partial \phi_{\mu\nu}(\bar{r}_i)}{\partial \bar{A}} + P^\sigma_{\mu\nu} \frac{\partial \bar{r}_i}{\partial \bar{A}} \cdot \frac{\partial \phi_{\mu\nu}(\bar{r}_i)}{\partial \bar{r}_i} \right) \equiv \rho^{(\bar{A})}_{\sigma i} + \rho^{[\bar{A}]}_{\sigma i}$$

The evaluation of eq. [3] is dominated by calculating the nuclear gradient of the electron density, $\rho_{\sigma i\bar{A}}$, as it involves loops over BFPs and atomic coordinates at each ACG point. The calculation of the nuclear gradient of the weight involves only the loop over the atomic coordinates. The electron density value at each ACG point required for the calculation of the derivative of the functional, $f_i^{\rho_\sigma}$, is identical to the last iteration of SCF, which precedes the nuclear gradient calculation.

In the context of mrXC, the electron spin density is separated into smooth and compact parts, with the calculation of the smooth part done on an ESCG, while the compact part is calculated directly on the ACG. The motivation for an ESCG comes from two observations. First, the calculation associated with the smooth part of the density is the computational bottleneck with the ACG as it has large spatial extent and covers many more grid points than the compact part of the density. Second, the ESCG has been used for DFT calculations with pseudopotentials with high efficiency. In a calculation with pseudopotentials, only the smooth part of the density is optimized, and the Coulomb and XC terms are calculated on the ESCG. This procedure has been applied successfully for the studies of solids, especially when combined with Car–Perrilleno-type of molecular dynamics.[12] Efforts have been made to combine the ACG and the ESCG for the full electron calculation by separated integrations.[13] This scheme however involves significant approximation and numerical imprecision, as the XC functional is not a linear function of density. By contrast, mrXC keeps the integration formally on the ACG and thus maintains the full accuracy. The actual calculation associated with smooth density is done on the ESCG for the time-consuming components,

Can. J. Chem. Downloaded from www.nrcresearchpress.com by Xi'an Jiaotong University on 09/19/12
For personal use only.

namely the density and the XC matrix elements. The values calculated on the ESCG are projected onto the ACG grid through accurate interpolations.

The mrXC algorithm classifies each BFP as either smooth or compact. A smooth pair meets the condition that its value at any point in space can be interpolated accurately from those on an ESCG within a tight tolerance:

$$[6] \qquad \widetilde{\phi}_{\mu\nu i} = \sum_{\overline{m}} C_{i\overline{m}} \widetilde{\phi}_{\mu\nu}, \qquad \overline{m} \equiv (m_x, m_y, m_z)$$

In the above equation, $\overline{m}$ is a 3-dimensional index for the points on the ESCG, and $C_{i\overline{m}}$ the interpolation coefficient. $C_{i\overline{m}}$ is a function of the position of the point i and the positions of a small number of ESCG points surrounding that point. The sparsity of $C_{i\overline{m}}$ allows for very fast transformation of numerical values between the two grids. We use a tilde (~) to denote a smooth function and a caret (^) to denote a compact function. It then follows that the smooth density $\widetilde{\rho}$ on the ACG can be calculated as

$$[7] \qquad \widetilde{\rho}_{\sigma i} = \sum_{\overline{m}} C_{i\overline{m}} \widetilde{\rho}_{\sigma\overline{m}}$$

and its explicit nuclear gradient as

$$[8] \qquad \widetilde{\rho}^{(\overline{A})}_{\sigma i} = \sum_{\overline{m}} C_{i\overline{m}} \widetilde{\rho}^{\overline{A}}_{\sigma\overline{m}}, \ \widetilde{\rho}^{(\overline{A})}_{\sigma i} = \sum_{\overline{m}} C^{\overline{A}}_{i\overline{m}} \widetilde{\rho}_{\sigma\overline{m}}$$

Two ESCGs with different grid densities are used in the calculation of the smooth density for the XC energy with mrXC. First, the smooth density is calculated on the less dense grid that is sufficiently accurate for a Fourier expansion of the density. Then, it undergoes a Fourier transform to the more dense ESCG. The latter allows an accurate local interpolation onto an ACG using eqs. [6] and [7]. One could follow the same procedure to produce the nuclear gradient of the smooth density on the ACG, which would be accurate. However, it will not be efficient as it will require many Fourier transformations, owing to the number of nuclear perturbations involved. Instead, one would wish to calculate directly on the coarse ESCG grid the nuclear gradient of E_{XC} contributed from the nuclear gradient of the smooth density. This can be achieved through a reverse interpolation by combining eqs. [7] and [3] for the contribution of the explicit nuclear derivative of the smooth density to E_{XC}:

$$\begin{aligned}[9] \qquad \widetilde{E}^{(\overline{A})}_{\mathrm{XC}} &\equiv \sum_i w_i (f_i^{\rho_\alpha} \widetilde{\rho}^{(\overline{A})}_{\alpha i} + f_i^{\rho_\beta} \widetilde{\rho}^{(\overline{A})}_{\beta i}) \\ &= \sum_i \sum_{\overline{m}} w_i (f_i^{\rho_\alpha} C_{i\overline{m}} \widetilde{\rho}^{\overline{A}}_{\alpha\overline{m}} + f_i^{\rho_\beta} C_{i\overline{m}} \widetilde{\rho}^{\overline{A}}_{\beta\overline{m}}) \\ &\equiv \sum_{\overline{m}} [(\sum_i w_i f_i^{\rho_\alpha} C_{i\overline{m}}) \widetilde{\rho}^{\overline{A}}_{\alpha\overline{m}} + (\sum_i w_i f_i^{\rho_\beta} C_{i\overline{m}}) \widetilde{\rho}^{\overline{A}}_{\beta\overline{m}}] \\ &\equiv \sum_{\overline{m}} (\widetilde{f}^{\rho_\alpha}_{\overline{m}} \widetilde{\rho}^{\overline{A}}_{\alpha\overline{m}} + \widetilde{f}^{\rho_\beta}_{\overline{m}} \widetilde{\rho}^{\overline{A}}_{\beta\overline{m}}) \end{aligned}$$

In the above equation, evaluation of $\widetilde{f}^{\rho_\sigma}_{m}$ takes little time, as only a few neighboring points of the ESCG are involved in the interpolation of each ACG point. We should also note that $\widetilde{f}^{\rho_\alpha}$ is not equal to f^{ρ_α} on the ESCG. The latter is a function of total electron spin densities, which include the smooth and compact parts.

In a DFT energy calculation with mrXC,[1] the smooth density is first calculated on an ESCG that is less dense than the one needed for the local interpolation, i.e., eq. [9]. Such a transformation between two ESCGs can be expressed as

$$[10] \qquad \widetilde{\rho}_{\sigma m} = \sum_{|k_{\bar{j}}| \le \frac{1}{2} D_m} \widetilde{\rho}_\sigma(k_{\bar{j}}) \, \mathrm{e}^{2\pi i k_{\bar{j}} \cdot r_{\overline{m}}} = \sum_{|k_{\bar{j}}| \le \frac{1}{2} D_n} \widetilde{\rho}_\sigma(k_{\bar{j}}) \mathrm{e}^{2\pi i k_{\bar{j}} \cdot r_{\bar{n}}},$$

$$k_{\overline{j+1}} - k_{\bar{j}} = (L_x^{-1}, L_y^{-1}, L_z^{-1})$$

In the above equation, D_m and D_n are the grid densities of the dense and coarse ESCGs, respectively, L_x, L_y, and L_z the dimensions of the ESCG. $\widetilde{\rho}_\sigma(\overline{k})$ is the Fourier transformation of the smooth density calculated on the coarse ESCG according to eq. [2]:

$$[11] \qquad \widetilde{\rho}_\sigma(k_{\bar{j}}) = \sum_{\bar{n}} \widetilde{\rho}_{\sigma\bar{n}} \, \mathrm{e}^{-2\pi i k_{\bar{j}} \cdot r_{\bar{n}}}$$

The computation of the density on an ESCG (eq. [2]) involves a loop over BFPs and is computationally more expensive than the fast Fourier transformations (FFTs) required in eqs. [10] and [11]. The transformation from the coarse grid to the dense grid, shown in eq. [10], provides a significant gain in efficiency as the number of the ESCG points, and thus the computational cost of the smooth density on the grid, scale cubically with respect to the grid density. A BFP is judged as smooth when it is represented on the coarse grid within a tight threshold of error, a scheme developed and implemented by Fusti-Molnar in Q-Chem Program:[14]

$$[12] \qquad 1 - \frac{\int_{-\frac{1}{2}D_n}^{\frac{1}{2}D_n} |\widetilde{\phi}_{\mu\nu}(\overline{k})| d^3k}{\int_{-\infty}^{\infty} |\widetilde{\phi}_{\mu\nu}(\overline{k})| d^3k} < \text{threshold}$$

This screening process takes little CPU time as it is done analytically for each BFP.

To apply mrXC for the calculation nuclear gradient, it is evident from the first few equations that one needs to obtain $\widetilde{\rho}_{\sigma m\overline{A}}$ on the dense ESCG. While one can do so with the same procedure as above starting from $\widetilde{\rho}_{\sigma n\overline{A}}$ on the coarse ESCG, it would require one FFT for each atomic coordinate within the molecular framework. We will instead calculate $\widetilde{E}^{\overline{A}}_{\mathrm{XC}}$ directly on the coarse ESCG by the following reformulation with the help of eqs. [9] and [10]:

$$\begin{aligned}[13] \qquad \sum_{\overline{m}} \widetilde{f}^{\rho_\sigma}_{\overline{m}} \widetilde{\rho}^{\overline{A}}_{\sigma\overline{m}} &= \sum_{|k_{\bar{j}}| \le \frac{1}{2} D_m} \widetilde{\rho}^{\overline{A}}_\sigma(k_{\bar{j}}) \sum_{\overline{m}} \widetilde{f}^{\rho_\sigma}_{\overline{m}} \mathrm{e}^{2\pi i k_{\bar{j}} \cdot r_{\overline{m}}} \\ &\equiv \sum_{|k_{\bar{j}}| \le \frac{1}{2} D_m} \widetilde{\rho}^{\overline{A}}_\sigma(k_{\bar{j}}) \widetilde{f}^{\rho_\sigma}(k_{\bar{j}}) \\ &= \sum_{\bar{n}} \widetilde{\rho}^{\overline{A}}_{\sigma\bar{n}} \sum_{|k_{\bar{j}}| \le \frac{1}{2} D_n} \widetilde{f}^{\rho_\sigma}(k_{\bar{j}}) \mathrm{e}^{-2\pi i k_{\bar{j}} \cdot r_{\bar{n}}} \\ &\equiv \sum_{\bar{n}} \widetilde{\rho}_{\sigma\bar{n}} \widetilde{f}^{\rho_\sigma}_{\bar{n}} \end{aligned}$$

with the following:

$$[14] \qquad \widetilde{\rho}^{\overline{A}}_{\sigma n} = \sum_{\mu\nu} P^\sigma_{\mu\nu} \phi^{\overline{A}}_{\mu\nu n}, \qquad \widetilde{\rho}^{\overline{A}}_\sigma(\overline{k}_j) = \sum \widetilde{\rho}^{\overline{A}}_{\sigma n} \mathrm{e}^{-2\pi i \overline{k}_j \cdot \overline{r}_n}$$

Equation [13] leads to the calculation of the contribution

Can. J. Chem. Downloaded from www.nrcresearchpress.com by Xi'an Jiaotong University on 09/19/12
For personal use only.

of the explicit nuclear derivative of the smooth density to the XC energy gradient as follows:

$$[15]\qquad \widetilde{E}_{\mathrm{XC}}^{(\overline{A})} = \sum_n (\widetilde{f}_n^{\rho_\alpha}\widetilde{\rho}_{\alpha n}^{\overline{A}} + \widetilde{f}_n^{\rho_\beta}\widetilde{\rho}_{\beta n}^{\overline{A}}) = \sum_n \sum_{\mu\nu} (\widetilde{f}_n^{\rho_\alpha} P_{\mu\nu}^{\alpha} + \widetilde{f}_n^{\rho_\beta} P_{\mu\nu}^{\beta}) \phi_{\mu\nu n}^{\overline{A}}$$

We should note that the formulism in eq. [15] resembles the calculation of nuclear gradients of Coulomb energy with FTC if one replaces $(\widetilde{f}_n^{\rho_\alpha} P_{\mu\nu}^{\alpha} + \widetilde{f}_n^{\rho_\beta} P_{\mu\nu}^{\beta})$ with the Coulomb potential. Thus, further reduction of CPU time can be realized when these two methods are applied in concert.

We have shown hitherto how to apply mrXC to the calculation of the nuclear gradient of the DFT energy without the consideration of perturbations of ACG points with the atoms. This perturbation arises when the ACG point is centered on the perturbing atom and accounts for a small but numerically significant correction. In the current Q-Chem Program, such a correction is done through a simple procedure utilizing translational invariance of the nuclear gradients of a molecule. When an ACG point is centered on atom A, its contribution to the nuclear gradient of XC energy is calculated as

$$[16]\qquad E_{\mathrm{XC}}^{\overline{A}}(i) = -\sum_{B\neq A} E_{\mathrm{XC}}^{\overline{B}}(i), \qquad i \in A$$

This formulism is, however, not applicable to mrXC as it requires the nuclear gradient of the smooth density at every ACG point, which we have intentionally avoided. Instead, we start from eq. [5] and recognize that $\frac{\partial \overline{r}_i}{\partial \overline{A}}$ is the identity matrix when i is originated from A and zero otherwise, which leads the following expression for this correction from each spin:

$$[17]\qquad w_i f_i^{\rho_\sigma} \rho_{\sigma i}^{[\overline{A}]} = w_i f_i^{\rho_\sigma} \sum_{\mu\nu} P_{\mu\nu}^{\sigma} \frac{\partial \phi_{\mu\nu}(\overline{r}_i)}{\partial \overline{r}_i} \equiv w_i f_i^{\rho_\sigma} \nabla \rho_{\sigma i}, \qquad i \in A$$

We use ∇ to denote the partial derivative with respect to the electronic coordinate $\overline{r}_i$.

Finally, we arrive at the expression of the mrXC contribution to the nuclear gradients as

$$[18]\qquad E_{\mathrm{XC}}^{\overline{A}} = \widetilde{E}_{\mathrm{XC}}^{(\overline{A})} + \sum_{i\in A}\Big(w_i f_i^{\rho_\alpha} (\nabla \widetilde{\rho}_{\alpha i} + \nabla \widehat{\rho}_{\alpha i}) + w_i f_i^{\rho_\beta} (\nabla \widetilde{\rho}_{\alpha i} + \nabla \widehat{\rho}_{\alpha i}) \Big) + \sum_i \Big(w_i f_i^{\rho_\alpha} \widehat{\rho}_{\alpha i}^{(\overline{A})} + w_i f_i^{\rho_\beta} \widehat{\rho}_{\beta i}^{(\overline{A})} + w_i^{\overline{A}} f_i \Big)$$

with the nonsmooth density, $\widehat{\rho}$, and its nuclear derivatives calculated directly on the ACG.

Performance of mrXC

We have implemented the above algorithm to calculate mrXC energy gradients within the quantum chemistry package Q-Chem.[14] Its performance is tested with the DFT energy and gradient calculations using two different basis sets and two choices of ACG. Taxol ($C_{47}NO_{14}H_{51}$), a natural cancer drug with a globular structure, was chosen as the test molecule. The two sizes of ACG are SG-1[15] and unpruned (100, 302) grid. SG-1 is a pruned (50, 94) grid with about 3000 points per atom. The (100, 302) grid has 100 radial points,[16] and 302 angular points,[17] resulting in 30 200 points per atom. The accuracy of the former is considered moderate, and accuracy of the latter is high. The threshold of the smoothness is set at 10^{-6}, and the grid densities of the coarse and fine ESCGs are 3.8 and 5.7, respectively. The benchmarks are run on a 2.5 GHz quad-core Pentium processor.

Table 1 lists the results of the calculations. The third column shows the percentage of BFPs that are classified by mrXC as smooth. The fourth column shows the accuracy of mrXC in total DFT energy with the error per atom listed in the parentheses. The mean-absolute-errors (MAEs) and the maximum errors of the nuclear gradient with mrXC are listed in columns five and six. The errors are calculated using the full ACG calculations as the reference. One can see that mrXC classifies more than 90% of BFPs as smooth but yields errors less than one micro-Hartree (10^{-6} au) per atom in total energy, and about 10^{-5} au in gradient. These errors are well within the tolerance of numerical precision for a typical DFT calculation.

The calculation associated with smooth BFPs can be done more efficiently on the ESCG than on the ACG. Column seven in Table 1 shows the CPU time directly on the ACG, with and without mrXC, for the computation of the electron density and its nuclear gradients. Column eight in Table 1 shows the CPU time for the same computation on the ESCG. The calculation of these two quantities takes the vast majority of the CPU (>95%) for the calculation of the nuclear gradient of the XC energy. One can see that it only took 12 s to do the calculation with smooth BFPs with SG-1 grid and 6–311G(df,pd) basis, in comparison with 357 s (405 – 48) that it takes on the ACG for the same calculation. The transformation steps — FFT and divided-difference — between the ACG and ESCG take a relatively small amount of CPU time and are listed in column nine. From those numbers, we can calculate the speedups mrXC provides, and they are listed in Table 1, column 10. As one can see, mrXC provides speed-up of 6–10 times for the gradient part of the calculation. Further gain of efficiency can be achieved when the calculation on the ESCG is combined with the Coulomb calculation with FTC, and thus becomes "free." The speedups for this scenario are listed in Table 1, column 11.

Table 1 also lists the results with different basis sets and sizes of ACG. One can see from the numbers that there is more efficient gain with cc-pVTZ basis than with 6–311G (df,pd). This is due to the fact that the former has more functions in the valence region than the latter. Smooth BFPs are more likely formed with those valence basis functions than core functions as the former have smaller exponents. MrXC also provides better performance gain as the grid size increases, because the computational cost on ACG increases with the ACG grid size, but the cost on the ESCG remains unchanged. By reducing the workload on the ACG, mrXC minimizes the impact of enlarging the ACG on CPU time. A large ACG is often desirable due to increased accuracy, and has even been shown necessary for a numerically reliable description of intermolecular interactions.[18]

Can. J. Chem. Downloaded from www.nrcresearchpress.com by Xi'an Jiaotong University on 09/19/12
For personal use only.

Table 1. The performance of mrXC for the calculation of the nuclear gradients of taxol with LSDA functional.

Basis (no. of BFs)	Method	Compact BFPs (%)	Error in energy (micro-Hartree)	Error in gradient (au)		CPU time (s)			Speed-up	
				MAE	Max.	ACG	ESG	Interpolation		with FTC
ACG SG-1										
6–311G(df,pd)	ACG only					405				
2111	MrXC	10.00	37.79 (0.33)	6.36E-06	6.21E-05	48	12	6	6.19	7.58
cc-pVTZ	ACG only					698				
2574	MrXC	8.60	8.27 (0.07)	3.09E-06	2.77E-05	72	28	6	6.59	8.96
ACG (100, 302)										
6–311G(df,pd)	ACG only					2715				
	MrXC	10.00	49.34 (0.44)	1.19E-06	1.38E-05	265	12	34	8.73	9.08
cc-pVTZ	ACG only					5204				
	MrXC	8.60	13.20 (0.12)	7.68E-07	7.36E-06	424	28	29	10.83	11.50

Note: The numbers in parenthesese in the 4th column (Error in energy) are errors per atom. MrXC, multiresolution exchange-correlation method; LSDA, local spin density approximation; ACG, atom-centered grid; BF, basis function; BFP, basis function pair; MAE, mean absolute error; ESG, even-spaced grid; FTC, Fourier transform Coulomb method; SG-1, pruned grid (50, 94) with ca. 3000 points per atom.

Conclusions

We have shown how to seamlessly combine the ESCG and the ACG for the numerical integration of the nuclear gradient of the XC part of the DFT energy with LSDA functionals. The algorithm is the extension of the mrXC method, which treats the smooth and the compact parts of the electron density separately. The nuclear gradient of the smooth density is calculated on the ESCG, while the compact part of the density is handled on the ACG. The overall technique is still formally based on the ACG, and thus does not change the results of the existing ACG-based algorithms for all-electron DFT calculations. The variation of the positions and weights of ACG owing to the nuclear perturbation is also handled rigorously. The benchmark calculations on the drug molecule taxol with different basis sets and sizes of ACG show that mrXC reduces the computational cost without loss of accuracy. MrXC also lessens the impact of increase in the size of the ACG on the CPU time. We are working on extending the method to all common types of DFT functionals.

Acknowledgement

This work received financial support from National Institutes of Health with Grant GM073408. All of the authors wish to thank Dr. Gan, Dr. Proynov, and Dr. Shao for helpful discussions. J.K. wishes to thank Dr. Boyd for the wonderful experience as a graduate student at Dalhousie University in Halifax.

References

(1) Kong, J.; Brown, S. T.; Fusti-Molnar, L. *J. Chem. Phys.* **2006** *124* (9), 094109. doi:10.1063/1.2173244.

(2) Brown, S. T.; Fusti-Molnar, L.; Kong, J. *Chem. Phys. Lett.* **2006** *418* (4–6), 490. doi:10.1016/j.cplett.2005.10.098.

(3) Füsti-Molnár, L.; Pulay, P. *J. Chem. Phys.* **2002** *117* (17), 7827. doi:10.1063/1.1510121.

(4) Füsti-Molnár, L.; Kong, J. *J. Chem. Phys.* **2005** *122* (7), 074108. doi:10.1063/1.1849168.

(5) White, C. A.; Johnson, B. G.; Gill, P. M. W.; Head-Gordon, M. *Chem. Phys. Lett.* **1996** *253* (3–4), 268. doi:10.1016/0009-2614(96)00175-3.

(6) Shao, Y.; Head-Gordon, M. *Chem. Phys. Lett.* **2000** *323* (5–6), 425. doi:10.1016/S0009-2614(00)00524-8.

(7) Dunlap, B. I.; Connolly, J. W. D.; Sabin, J. R. *J. Chem. Phys.* **1979** *71* (8), 3396. doi:10.1063/1.438728.

(8) Ochsenfeld, C.; White, C. A.; Head-Gordon, M. *J. Chem. Phys.* **1998** *109* (5), 1663. doi:10.1063/1.476741.

(9) Polly, R.; Werner, H. J.; Manby, F. R.; Knowles, P. J. *Mol. Phys.* **2004** *102* (21–22), 2311. doi:10.1080/00268970420002748O1.

(10) Becke, A. D. *J. Chem. Phys.* **1988** *88* (4), 2547. doi:10.1063/1.454033.

(11) Pulay, P. *Mol. Phys.* **1969** *17* (2), 197. doi:10.1080/00268976900100941.

(12) Kresse, G.; Furthmüller, J. *Phys. Rev. B* **1996** *54* (16), 11169. doi:10.1103/PhysRevB.54.11169.

(13) VandeVondele, J.; Iannuzzi, J.; Hutter, X. *Lect. Notes Phys.* **2006** *703*, 287. doi:10.1007/3-540-35273-2_8.

(14) Shao, Y.; Molnar, L. F.; Jung, Y.; Kussmann, J.; Ochsenfeld, C.; Brown, S. T.; Gilbert, A. T. B.; Slipchenko, L. V.; Levchenko, S. V.; O'Neill, D. P.; DiStasio, R. A., Jr; Lochan, R. C.; Wang, T.; Beran, G. J. O.; Besley, N. A.; Herbert, J. M.;

Yeh Lin, C.; Van Voorhis, T.; Hung Chien, S.; Sodt, A.; Steele, R. P.; Rassolov, V. A.; Maslen, P. E.; Korambath, P. P.; Adamson, R. D.; Austin, B.; Baker, J.; Byrd, E. F. C.; Dachsel, H.; Doerksen, R. J.; Dreuw, A.; Dunietz, B. D.; Dutoi, A. D.; Furlani, T. R.; Gwaltney, S. R.; Heyden, A.; Hirata, S.; Hsu, C.-P.; Kedziora, G.; Khalliulin, R. Z.; Klunzinger, P.; Lee, A. M.; Lee, M. S.; Liang, W. Z.; Lotan, I.; Nair, N.; Peters, B.; Proynov, E. I.; Pieniazek, P. A.; Min Rhee, Y.; Ritchie, J.; Rosta, E.; David Sherrill, C.; Simmonett, A. C.; Subotnik, J. E.; Lee Woodcock, H., III; Zhang, W.; Bell, A. T.; Chakraborty, A. K.; Chipman, D. M.; Keil, F. J.; Warshel, A.; Hehre, W. J.; Schaefer, H. F., III; Kong, J.; Krylov, A. I.; Gill, P. M. W.; Head-Gordon, M. *Phys. Chem. Chem. Phys.* **2006** *8* (27), 3172 . doi:10.1039/b517914a.

(15) Gill, P. M. W.; Johnson, B. G.; Pople, J. A. *Chem. Phys. Lett.* **1993** *209* (5–6), 506. doi:10.1016/0009-2614(93)80125-9.

(16) Murray, C. W.; Handy, N. C.; Laming, G. J. *Mol. Phys.* **1993** *78* (4), 997. doi:10.1080/00268979300100651.

(17) Lebedev, V. I.; Skorokhodov, A. L. *Russ. Acad. Sci. Dokl. Math.* **1992** *45*, 587.

(18) Johnson, E. R.; Becke, A. D.; Sherrill, C. D.; Dilabio, G. A. *J. Chem. Phys.* **2009** *131* (3), 034111. doi:10.1063/1.3177061.

Can. J. Chem. Downloaded from www.nrcresearchpress.com by Xi'an Jiaotong University on 09/19/12
For personal use only.

Silica-supported methanesulfonic acid — An efficient solid Brønsted acid catalyst for the Pechmann reaction in the presence of higher *n*-alkanes

J. Joshi, M.K. Mishra, and M. Srinivasarao

Can. J. Chem. Downloaded from www.nrcresearchpress.com by Xi'an Jiaotong University on 09/19/12
For personal use only.

Abstract: A cost-effective and efficient solid Brønsted acid catalyst was synthesized by loading methanesulfonic acid (MSA) on silica and was used for the acid-catalyzed Pechmann reaction to test the catalytic activity and its reusability. Derivatives of 4-methylcoumarin were synthesized in good yields within short reaction times in the presence of environmentally friendly higher *n*-alkanes as solvents. The regeneration study of the spent catalyst showed satisfactory results.

Key words: silica supported solid acids, methanesulfonic acid, Brønsted acidity, Pechmann reaction, derivatives of 4-methylcoumarin.

Résumé : On a synthétisé un catalyseur acide de Brønsted efficace et rentable d'un point de vue coût en recouvrant de la silice avec de l'acide méthanesulfonique (AMS) et on l'a utilisé catalyseur acide pour la réaction de Pechmann dans le but d'évaluer son activité catalytique et la possibilité de le réutiliser. On a synthétisé des dérivés de la 4-méthylcoumarine avec de bons rendements, avec des temps de réaction relativement courts, dans des solvants à base d'alcanes supérieurs écologiques. L'étude de régénération du catalyseur utilisé a donné des résultats satisfaisants.

Mots-clés : acides solides supportés par de la silice, acide méthanesulfonique, acidité de Brønsted, réaction de Pechman, dérivés de la 4-méthylcoumarine.

[Traduit par la Rédaction]

Introduction

Methanesulfonic acid (CH_3SO_3H; MSA) is a strong Brønsted acid ($pK_a = -1.9$) and has been reported as a potential acid catalyst for various acid-catalyzed reactions.[1–3] MSA is very cheap, has a lower tendency to oxidize organic compounds, is far less corrosive and toxic than widely used fluoro-substituted alkanesulfonic acids, like triflic acid and 1,1,2,2-tetrafluoroethanesulfonic acid, and the mineral acids. The problems associated with recovery and reuse of MSA from homogeneous conditions makes its application limited. To overcome these problems, a supported form of MSA could be the best alternative. The supported fluoro-substituted alkanesulfonic acids (triflic acid, 1,1,2,2-tetrafluoroethanesulfonic acid, etc.) have been synthesized and used for various acid-catalyzed organic transformations.[4–10] However, supported MSA, which could be a cost-effective and eco-friendly solid acid catalyst, and an attractive alternative to supported fluoro-substituted alkanesulfonic acids for acid-catalyzed transformations, has not been reported in the literature. The present work was aimed at developing silica-supported MSA as a cost-effective, eco-friendly, and reusable solid acid catalyst. The synthesized catalyst was used for the Pechmann reaction to synthesize derivatives of 4-methylcoumarin.

Coumarins are heterocyclic natural products finding applications as pharmacologically and biologically active compounds.[11,12] Coumarins are usually synthesized by acid-catalyzed Pechmann reaction of activated phenols and α-keto esters[13] using homogeneous Brønsted[14–16] and Lewis[17,18] acid catalysts. It is to be noted that the homogeneous acids are corrosive, required in excess, and nonreusable, sometimes result in the formation of side products, and generate acidic waste. Various solid acid catalysts such as Amberlyst ion-exchange resins,[19] zeolites,[20] montmorillonite K-10,[21] sulfated zirconia,[22] benzylsulfonic acid functionalized mesoporous Zr-TMS,[23] metal ion-exchanged ZAPO-5,[24] W/ZrO_2,[25] Nafion resin / silica nanocomposites,[26] polyaniline sulfate salt,[27] etc., have been found to be the best alternatives to homogeneous acids. However, most of the solid acids require either a longer reaction time[20–25,27] or a higher reaction temperature[22,24,27] to achieve maximum yield. The syntheses using some of the solid acids are not cost-effective because of either tedious methods of synthesizing the catalysts[27] or the use of large amounts of catalysts.[19,20,26] In addition, the solid acid catalyzed Pechmann reactions are usually carried out using nonpolar solvents like tetrahydrofuran (THF), toluene, etc.,[19,20] which are volatile, hazardous, and nonrecoverable. To the best of our knowledge, there is no report

Received 4 September 2010. Accepted 4 February 2011. Published at www.nrcresearchpress.com/cjc on 23 June 2011.

J. Joshi, M. Mishra, and M. Srinivasarao. Department of Chemical Engineering and Shah-Schulman Center for Surface Science and Nanotechnology, Faculty of Technology, Dharmsinh Desai University, College Road, Nadiad – 387 001, Gujarat, India.

Corresponding author: M.K. Mishra (e-mail: manishorgch@gmail.com).

Can. J. Chem. Downloaded from www.nrcresearchpress.com by Xi'an Jiaotong University on 09/19/12
For personal use only.

available on the application of higher *n*-alkanes as nonpolar solvents in heterogeneous catalysis. Hence, an attempt was also made in the present work to use higher *n*-alkanes as environmentally friendly nonpolar solvents for Pechmann reactions.

Experimental

Chemicals

Tetraethylorthosilicate, ethyl acetoacetate, and pyrogallol were procured from s.d. Fine Chemicals, India. Hydrochloric acid, methanol, *n*-hexadecylamine (HDA), resorcinol, nitrobenzene, petroleum ether, *n*-butylamine, and acetonitrile were from Merck, USA. *n*-Octadecane, *n*-hexadecane, *n*-dodecane, phloroglucinol, methoxyphenol, and *m*-cresol were procured from National Chemicals, India. Methanesulfonic acid was procured from Loba Chemie, India.

Synthesis of silica-supported methanesulfonic acid (SiO_2–MSA) solid acid catalyst

The silica support was synthesized by hydrolysis of tetraethylorthosilicate (TEOS) using HDA as the template. The pH of the TEOS (20 g) and methanol (50 mL) solution was adjusted in the range of 2–3 by adding a few drops of concentrated hydrochloric acid. Water (7.2 mL) was then added to the acidic TEOS solution with stirring and the solution was kept for 30 min. The HDA solution, prepared by dissolving HDA (2.4 g, 0.01 mol) in methanol (50 mL), was added to the TEOS solution with vigorous stirring and the solution was aged for 5 days at room temperature. The gel was filtered and washed with methanol to remove surfactant template, which was confirmed by FT-IR analysis of the dried silica. The gel was dried at room temperature for 24 h and then at 120 °C for 12 h. To load a nominal amount of MSA (~1 mmol MSA / g of silica) on the silica support, 10 g of dried silica gel was treated with MSA solution (5 mL of MSA in 50 mLof carbon tetrachloride) at room temperature with stirring for 24 h. The gel was filtered and washed with methanol and then with petroleum ether to remove free MSA. The gel was dried at room temperature for 24 h and later at 120 °C for 6 h.

Characterization of SiO_2–MSA catalyst

The catalyst was characterized by N_2 adsorption–desorption isotherm, FT-IR, FT-IR of the pyridine-adsorbed sample, potentiometric titration, thermal analysis (TGA-DTA), and CHNS/O elemental analysis. The Brunauer–Emmett–Teller (BET) surface area and average pore diameter of the samples were measured by N_2 adsorption–desorption isotherm studies using a Quantachrome NOVA 1000e surface area analyzer. The sample was degassed under vacuum at 120 °C for 4 h prior to adsorption measurement, to evacuate the physisorbed moisture. The surface area was determined by using the BET equation, and the average pore diameter of the samples was measured by the Barrett, Joyner, and Halenda method (BJH).[28] The loading of MSA over the silica support was confirmed by FT-IR study using a FT-IR spectrophotometer (Shimadzu IRPrestige-21) with a diffuse reflectance scanning disc technique by mixing the sample with dried KBr (in a 1:20 wt ratio) in the range of 400–4000 cm^{-1} with a resolution of 4 cm^{-1}. The type of surface acidity (Brønsted or Lewis) in the samples was characterized by FT-IR study of the pyridine-adsorbed samples. For this the sample (0.2 g) was activated at 120 °C for 2 h. The activated sample was cooled in a desiccator under vacuum and was exposed to pyridine (25 mL) vapor for 12 h. The pyridine-adsorbed sample was degassed under vacuum for 15 min to remove physically adsorbed pyridine from the sample. The FT-IR spectra of the samples adsorbed with pyridine (mixed with KBr in a 1:20 wt ratio) were recorded in the range of 400–4000 cm^{-1}. The amount of acidity and the strength of the acid sites in the samples were measured by potentiometric titration.[8] The sample (0.05 g) was suspended in acetonitrile and stirred for 3 h. The suspension was titrated with 0.05 N *n*-butylamine in acetonitrile at 0.05 mL/min. The electrode potential variation was measured using a potentiometric titrator (Chemito, India). The TGA-DTA of the samples was carried out by a Shimadzu DTG-60H, by heating the sample in the range of 50–1000 °C with a heating rate of 10 °C/min under nitrogen flow (30 cm^3/min). The amount of MSA loaded on the silica was calculated from the TGA results (W_{MSA}) using the following equation:[8]

$$[1] \qquad W_{MSA} = (W_{SiO-MSA})/FW_{MSA}$$

where $W_{SiO-MSA}$ = weight loss (mg/g) of SiO_2–MSA catalyst from 25 to 500 °C, W_{SiO} = weight loss (mg/g) of SiO_2 support from 25 to 500 °C, and FW_{MSA} = molecular weight of CH_3SO_3H. Percentage of sulfur in the catalysts was also analyzed by CHNS/O elemental analysis (PerkinElmer 2400) to estimate the amount of methanesulfonic acid loaded on the silica.

Catalytic activity of SiO_2–MSA for synthesis of 4-methylcoumarin derivatives by the Pechmann reaction

The derivatives of 4-methylcoumarin were synthesized by the SiO_2–MSA catalyzed Pechmann reaction of a phenol (resorcinol, phloroglucinol, pyrogallol, *m*-methylphenol, *m*-methoxyphenol, or phenol) and ethyl acetoacetate (Scheme 1). The reaction was carried out by adding preactivated (at 120 °C for 1 h) catalyst to the mixture of phenol and ethyl acetoacetate, with or without solvent, at constant temperature under stirring. After the completion of reaction, the reaction mixture was cooled and methanol (~10 mL) was added to dissolve the product. The reaction mixture was filtered to separate the catalyst and the product was crystallized by cooling the filtrate.

Characterization of the products

The products were recrystallized in ethanol–water (95:1) solution and the isolated yields were calculated. The products were characterized by melting point and by FT-IR and ^1H NMR spectroscopy, and the data were matched with those reported in the literature. Melting points were measured by a melting point apparatus (Choudhary Instruments, India) and are uncorrected. Infrared spectra were recorded on a FT-IR spectrophotometer (Shimadzu IRPrestige-21) in KBr with transmittance in cm^{-1}. ^1H NMR spectra were determined on a NMR spectrometer (Bruker Avance DPX, 200 MHz) as dimethyl sulfoxide (DMSO-d_6) solutions. Chemical shifts (δ) were expressed in ppm downfield from the internal standard tetramethylsilane.

Scheme 1. SiO_2 – methanesulfonic acid (MSA) catalyzed Pechmann reaction of phenols and ethyl acetoacetate to synthesize derivatives of 4-methylcoumarin.

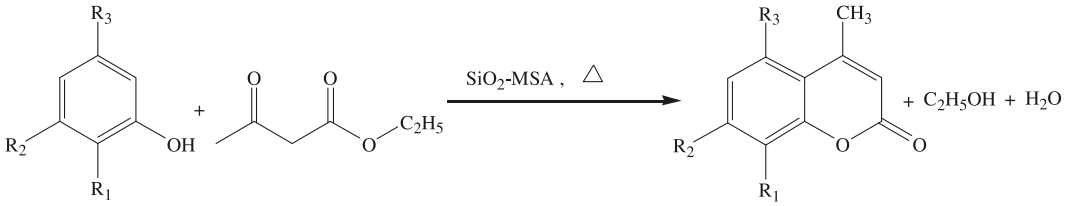

Resorcinol; R_1=R_3=-H, R_2=-OH
Phloroglucinol; R_1=-H, R_2=R_3=-OH
Pyrogallol; R_1=R_2=-OH, R_3=-H
m-Methoxy phenol; R_1=R_3=-H, R_2=-OCH_3
m-Methyl phenol; R_1=R_3=-H, R_2=-CH_3
Phenol; R_1=R_2=R_2=H

Table 1. Physicochemical and catalytic properties of SiO_2 support and SiO_2 – methanesulfonic acid (MSA) catalyst.

			Type of acid site[a]		Loading of MSA (μmol/g)			
Sample	S_{BET} (m^2/g)	D_P (Å)	Brønsted acidity band area (A/cm)	Lewis acidity band area (A/cm)	N_{MSA}[b]	W_{MSA}[c]	Acid site (μmol *n*-butylamine / g)[d]	Yield of 7-hydroxy-4-methylcoumarin (wt %)[e]
SiO_2 support	373	31	—	—	—	—	—	0
SiO_2–MSA	362	31	5.3	Nil	1000	1200	1200	94

Note: S_{BET}, BET surface area; D_P, average pore diameter; N_{MSA}, the amount of MSA loaded on silica calculated from the sulfur content; W_{MSA}, amount of MSA loaded on silica calculated from TGA analysis.

[a]IR study of pyridine-adsorbed sample.

[b]Calculated from sulfur wt % obtained by CHNS/O analysis.

[c]By TGA analysis.

[d]By potentiometric titration with *n*-butylamine.

[e]Resorcinol (10 mmol), ethyl acetoacetate (20 mmol), catalyst (0.25 g), 160 °C, 12 h.

Can. J. Chem. Downloaded from www.nrcresearchpress.com by Xi'an Jiaotong University on 09/19/12
For personal use only.

7-Hydroxy-4-methylcoumarin

mp: 185–190 °C (lit.[25] mp 188 °C). FT-IR (KBr, cm^{-1}): 3159 (ν_{OH}), 1674 ($\nu_{C=O}$). ^{1}H NMR (DMSO-d_6) δ: 10.54 (s, 1H, –OH), 7.56 (d, 1H, Ar–H), 6.79 (d, 1H, Ar–H), 6.72 (s, 1H, Ar–H), 6.12 (s, 1H, –C=CH–), 2.36 (s, 3H, $–CH_3$).

5,7-Dihydroxy-4-methylcoumarin

mp: 283–285 °C (lit.[29] mp 284–285 °C). FT-IR (KBr, cm^{-1}): 3159 (ν_{OH}), 1670 ($\nu_{C=O}$). ^{1}H NMR (DMSO-d_6) δ: 10.5 (s, 1H, –OH), 10.3 (s, 1H, –OH), 6.3 (s, 1H, Ar–H), 6.2 (s, 1H, Ar–H), 5.9 (s, 1H, –C=CH–), 2.5 (s, 3H, $–CH_3$).

7,8-Dihydroxy-4-methylcoumarin

mp: 242–245 °C (lit.[30] mp 242–244 °C). FT-IR (KBr, cm^{-1}): 3231 (ν_{OH}), 1648 ($\nu_{C=O}$). ^{1}H NMR (DMSO-d_6) δ: 10.0 (s, 1H, –OH), 9.4 (s, 1H, –OH), 7.1 (d, 1H, Ar–H), 6.8 (d, 1H, Ar–H), 6.1 (s, 1H, –C=CH–), 2.3 (s, 3H, $–CH_3$).

Results and discussion

Characterization of SiO_2–MSA

The physicochemical characteristics of the silica and the supported catalyst are given in Table 1. The average pore diameter for the samples was 31 Å. The SiO_2–MSA had a slightly lesser BET surface area (362 m^2/g) compared with the silica support (373 m^2/g), which is attributed to the loading of MSA on the silica surface (Table 1).

The FT-IR spectrum (Fig. 1) of SiO_2 exhibits a broad band in the range of 2800–3750 cm^{-1} ($\nu_{O–H}$, for –OH groups of silica and adsorbed water) including small peaks at 3650 ($\nu_{O–H}$, for free silanols ≡Si–OH) and 1630 cm^{-1} ($\delta_{O–H}$, for adsorbed water). In the FT-IR spectrum of SiO_2–MSA the peak for silanols (3650 cm^{-1}) disappeared and the broadness of the band in the –OH region increased. This spectral change indicates that MSA is bonded with free silanols of silica by the reaction of MSA and silanols. A similar observation was also reported for silica-supported triflic acid.[4] The FT-IR spectrum of SiO_2–MSA shows a peak at 1337 cm^{-1} for the $\nu_{S=O}$ stretching mode of the $–SO_3H$ group and a small peak at 1425 cm^{-1} for the $\delta_{C–H}$ bending mode of the $–CH_3$ group.[31] A peak for SO_2 deformation was found at 554 cm^{-1}. The FT-IR spectrum of pyridine-adsorbed catalyst (Fig. 2) shows peaks at 1489, 1554, 1620, and 1635 cm^{-1}. The peak at 1554 cm^{-1} is a characteristic peak of adsorbed pyridine on Brønsted acid sites, showing the presence of a significant amount of Brønsted acidity. There is no peak in the range of 1440–1450 cm^{-1} for adsorbed pyridine on Lewis sites. Thus, the catalyst has predominantly Brønsted acidity showing 5.3 A/cm peak area of the band at 1554 cm^{-1} (Table 1). The reaction of the $–SO_3H$ group of MSA and silanols results in

Scheme 2. Interaction of methanesulfonic acid (MSA) with the silanol of silica and generation of Brønsted acid sites.

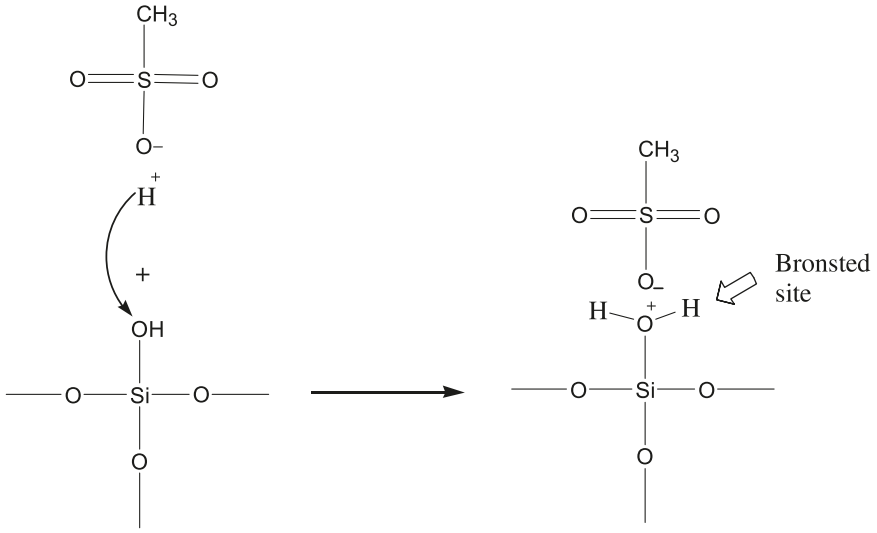

Fig. 1. FT-IR spectra of silica support and SiO_2 – methanesulfonic acid (MSA) catalyst.

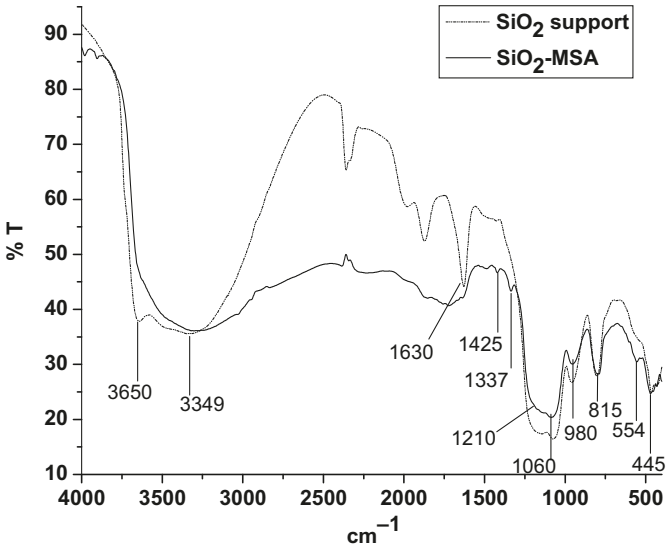

Fig. 2. FT-IR spectrum of pyridine adsorbed SiO_2 – methanesulfonic acid (MSA) catalyst.

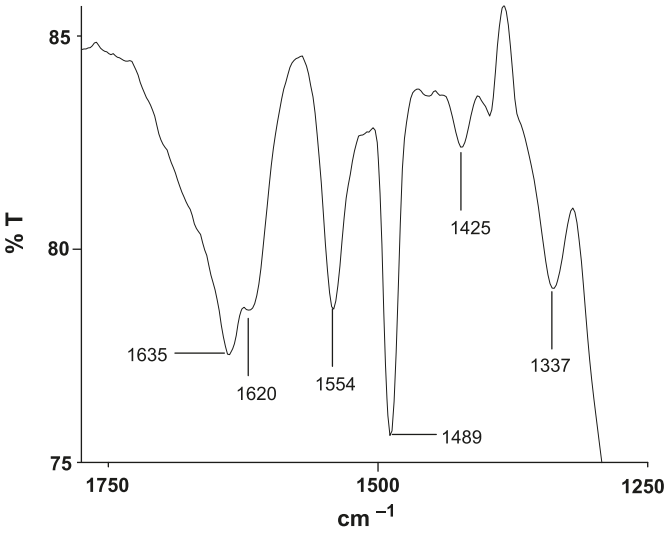

formation of protonated silanols, which hold methanesulfonate ions on the silica surface (Scheme 2). The protonated silanols bonded with methanesulfonate ions on the silica surface act as Brønsted acid sites.

The initial electrode potential (E_i), obtained by potentiometric titration with *n*-butylamine, indicates that the catalyst possesses very strong acid sites (E_i = 612 mV)[25] compared with those of the silica support (Fig. 3). The total number of acid sites in the catalyst was found to be 1200 mmol *n*-butylamine / g of catalyst (Table 1).

TGA-DTA profiles of SiO_2 support and SiO_2–MSA catalyst are given in Figs. 4*a* and 4*b* showing two-stage weight loss in SiO_2–MSA. The weight loss that occurred from 50 to 150 °C corresponds to the removal of adsorbed water. The second stage weight loss in the range of 300–450 °C is attributed to the decomposition of loaded MSA. The amount of MSA loaded on silica, calculated from TGA analysis (W_{MSA}),[8] was 1200 μmol/g (Table 1). The amount of MSA loaded over silica (N_{MSA}), calculated from the sulfur content (3.2 wt %, obtained from CHNS/O elemental analysis), corresponds to 1000 μmol/g (Table 1), which is in close agreement with W_{MSA}.

The characterization results confirmed that a significant amount of MSA was loaded over silica by surface reaction of MSA with silanols, generating predominantly Brønsted acidity. This catalyst can be used as a solid Brønsted acid for acid-catalyzed reactions.

Catalytic activity of SiO_2–MSA for the Pechmann reaction to synthesize 4-methylcoumarin derivatives and the effect of reaction parameters

SiO_2–MSA catalyst was found to be active for the Pechmann reaction giving 94% yield of 7-hydroxy-4-methylcoumarin at 160 °C after 12 h (Table 1). No product formation was observed with pure silica without loading MSA. The reaction temperature was optimized by carrying out the reaction in

Can. J. Chem. Downloaded from www.nrcresearchpress.com by Xi'an Jiaotong University on 09/19/12
For personal use only.

Can. J. Chem. Downloaded from www.nrcresearchpress.com by Xi'an Jiaotong University on 09/19/12
For personal use only.

Fig. 3. Potentiometric titration curves of SiO_2 – methanesulfonic acid (MSA) catalyst and SiO_2 support.

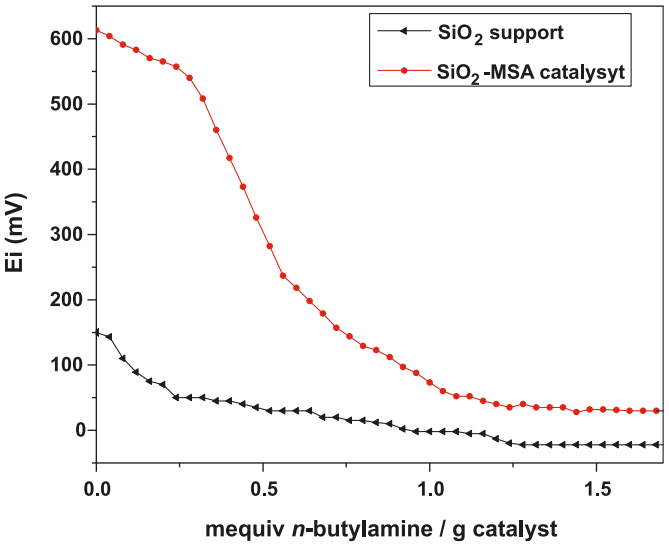

Fig. 4. TGA-DTA profile of (*a*) silica support and (*b*) SiO_2 – methanesulfonic acid (MSA) catalyst.

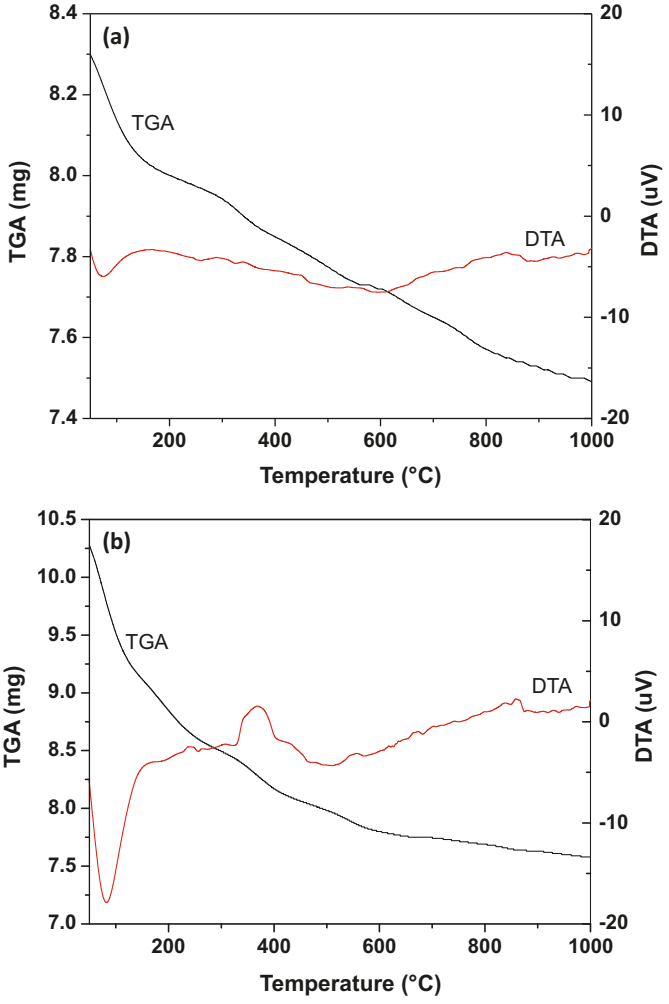

Fig. 5. Yield (wt %) of 7-hydroxy-4-methylcoumarin at different catalyst loading (6.5–1.3 wt %). (Reaction conditions: resorcinol – ethyl acetoacetate molar ratio = 2, 0.25 g catalyst, 160 °C, 12 h)

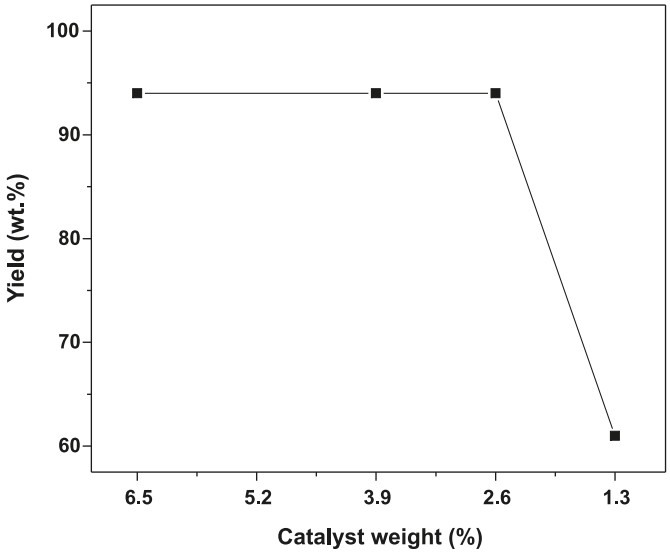

Fig. 6. Yield (wt %) of 7-hydroxy-4-methylcoumarin with time in solvent-free conditions and in the presence of various solvents. (Reaction conditions: 10 mmol resorcinol, 20 mmol ethyl acetoacetate, 3 mL solvent, 0.25 g catalyst, 160 °C)

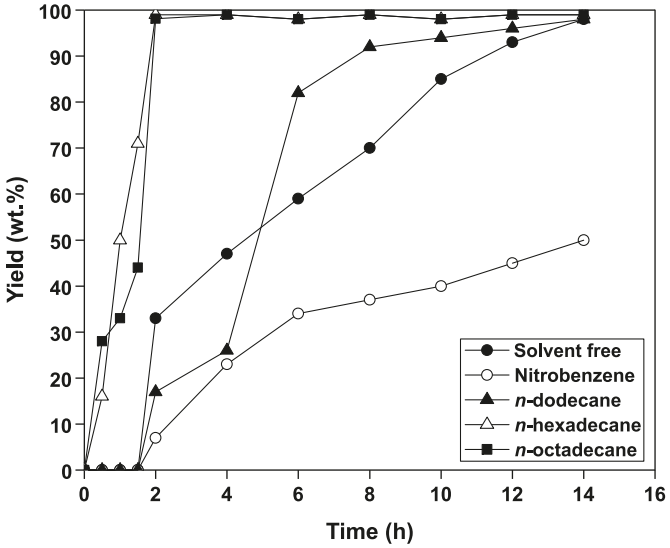

the range of 90–180 °C keeping all other parameters the same (see Supplementary data, Fig. S1). The maximum yield of 7-hydroxy-4-methylcoumarin (94%) was obtained after 12 h at 160 °C. The yield was observed to be slightly decreased (90% after 12 h) at 180 °C. Therefore, 160 °C was selected as the optimized reaction temperature.

To demonstrate the efficiency of the catalyst, the reaction was carried out by varying the catalyst loading (6.5, 3.9, 2.6, and 1.3 wt %) under similar reaction conditions. The yield of 7-hydroxy-4-methylcoumarin was observed to be steady (94%) up to a catalyst loading of 2.6 wt % (Fig. 5). It shows that the catalyst is very efficient and required in only a small quantity to achieve the maximum yield. However, the reaction kinetics were affected by the catalyst loading. It was

Table 2. The reaction conditions and yield of 7-hydroxy-4-methylcoumarin reported with various solid acid catalysts and SiO_2 – methanesulfonic acid (MSA) catalyst.

Sample No.	Solid acid	Reaction temp. (°C)	Reaction time (h)	Solvent	Yield (wt %)	Ref.
1	Amberlyst ion-exchange resins	Reflux temp.	2	Toluene	95	19
2	Zeolite	120 / Reflux temp.	4	None/toluene	77–80	20
3	Montmorillonite				96	21
	K-10	150	4	None		
	K-10	Reflux temp.	8	Toluene	94	
	KSF	150	5	None	88	
	KSF	Reflux temp.	10	Toluene	90	
4	SO_4/ZrO_2	170	3–24	None	91	22
5	Benzylsulfonic acid functionalized mesoporous Zr–TMS	150	20	None	86	23
6	Metal (Ga^{3+}, In^{3+}, La^{3+}, and Ce^{3+}) ion-exchanged ZAPO-5	175	6	None	90	24
7	W/ZrO_2	Reflux temp.	6	Toluene	80	25
8	Nafion resin / silica nanocomposites	Reflux temp.	2	Toluene	80–97	26
9	Polyaniline sulfate salt	150/170	6	None	72	27
10	SiO_2–MSA catalyst	160	2	*n*-Hexadecane/*n*-octadecane	99	—

Can. J. Chem. Downloaded from www.nrcresearchpress.com by Xi'an Jiaotong University on 09/19/12
For personal use only.

also observed that the higher the catalyst amount, the faster the initial rate (see Supplementary data, Fig. S2.

Nitrobenzene and higher *n*-alkanes (*n*-dodecane, *n*-hexadecane, and *n*-octadecane) were used as polar and nonpolar solvents, respectively, to study the effect of solvent on SiO_2–MSA catalyzed synthesis of 7-hydroxy-4-methylcoumarin. In nitrobenzene, the yield was significantly reduced (50% after 14 h) compared with the yield (94% after 14 h) obtained in solvent-free synthesis (Fig. 6). The lesser yield in the polar medium has been attributed to cleavage of the product[19] and the reduction in the number of available active sites owing to bonding of nitrobenzene molecules with active sites.[22] Nonpolar solvents such as toluene, cumene, THF, etc.,[19,20] have been widely used for synthesis of 7-hydroxy-4-methylcoumarin and toluene has been found to be one of the best nonpolar solvents.[19] However, toluene is a hazardous, nonseparable, nonreusable, and volatile aromatic, which limits its high-temperature applications. In the present work, higher *n*-alkanes (*n*-dodecane, *n*-hexadecane, and *n*-octadecane) were used as nonpolar solvents, which are nonhazardous, less volatile, and easily recoverable. The higher *n*-alkanes improved the activity of the catalyst by decreasing the reaction time (2–8 h) to achieve a maximum yield (>94%). *n*-Hexadecane and *n*-octadecane were more effective than *n*-dodecane, giving the maximum yield within 2 h. The enhanced activity of the catalyst in higher *n*-alkanes may be attributed to the higher nonpolar nature of the medium and the insolubility of reactant molecules in *n*-alkanes, which drives polar reactant molecules towards the catalyst surface for adsorption and chemical reaction. As the chain length of the *n*-alkane chain is increased, the reaction time to achieve maximum yield of the product was observed to be reduced as it enhances the catalytic activity of the SiO_2–MSA. This effect was explained on the basis of increasing nonpolar behavior of the *n*-alkanes with increasing chain length. The longer chain *n*-alkane molecules (*n*-hexadecane and *n*-octadecane) have strong van der Waals interactions, which does not allow the polar reactant molecules to stay in the bulk of the solvent. This forces the reactant molecules to come out from the bulk of *n*-alkane towards the catalyst surface, facilitating the adsorption of the reactant molecules on the catalyst surface for the reaction. It appears that the bulk diffusion of the reactants from solvent to catalyst surface and the surface adsorption are made easier by higher *n*-alkanes. After the surface reaction, the product (7-hydroxy-4-methylcoumarin) formed on the surface is desorbed and tends to come into the *n*-alkane (the nonpolar solvent) as the solubility of the product is significant in the nonpolar solvent. The solubilization of product in *n*-alkane facilitates the removal (desorption) of the product molecules from the catalyst surface, making surface sites free, as well as the bulk diffusion of the product molecules from the catalyst surface to the bulk of the solvent. The lesser yield in the polar medium (nitrobenzene) may also be attributed to the higher solubility of the polar reactants in the solvent, which reduces the bulk diffusion rate of the reactant molecules from solvent to catalyst surface.

The yield of 7-hydroxy-4-methylcoumarin and the reaction conditions reported with the other solid acid catalysts were compared with the SiO_2–MSA catalyst (Table 2). It can be observed that SiO_2–MSA in the presence of higher *n*-alkanes as solvents gives the highest yield (99%) in the shortest time (2 h) at relatively lower temperature in comparison with the other catalysts.

The SiO_2–SA catalyst showed significant activity for the synthesis of derivatives of 4-methylcoumarin (Table 3). However, the activated phenols (resorcinol, phloroglucinol, and pyrogallol) were found to be more reactive, giving 99%, 78%, and 70% yields of the corresponding coumarin derivatives. No product formation was observed under the given reaction conditions with less reactive phenols (*m*-methoxyphenol, *m*-methylphenol, and phenol). The reactivity of various phenols for the Pechmann reaction has already been reported.[12]

Regeneration study of spent SiO_2–MSA

The spent catalyst, recovered from the reaction mixture (in *n*-octadecane) was regenerated by washing with methanol

Can. J. Chem. Downloaded from www.nrcresearchpress.com by Xi'an Jiaotong University on 09/19/12
For personal use only.

Table 3. Yield (wt %) of 4-methylcoumarin derivatives synthesized by the Pechmann reaction using SiO_2 – methanesulfonic acid (MSA) catalyst.

Phenol	4-Methyl coumarin derivative	Isolated yield (wt%)[a]
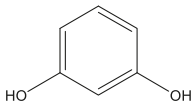 Resorcinol	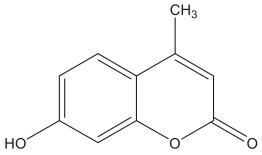 7-hydroxy 4-methyl coumarin	99
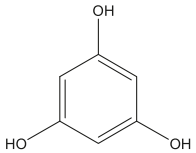 Phloroglucinol	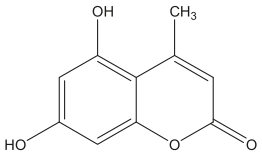 5,7-dihydroxy4-methyl coumarin	78
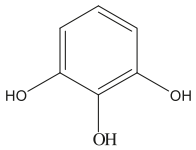 Pyrogallol	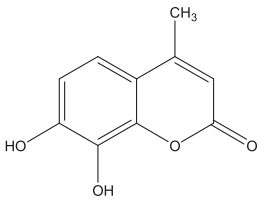 7,8-dihydroxy4-methyl coumarin	70
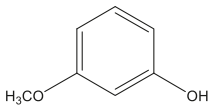 *m*-methoxy phenol	Not obtained	—
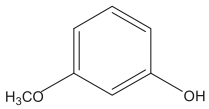 *m*-methyl phenol	Not obtained	—
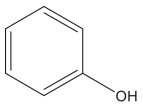 Phenol	Not obtained	—

[a]Phenol substrate (10 mmol), ethyl acetoacetate (20 mmol), *n*-octadecane (3 mL; solvent), catalyst (0.25 g), 160 °C, 2 h.

(2 × 10 mL) then with petroleum ether (10 mL), followed by drying at 120 °C for 2 h (see Supplementary data, Fig. S3). The regenerated catalyst was reused for three cycles under similar reaction conditions as with fresh catalyst. The regenerated catalysts showed similar activity to fresh catalyst giving 94%–96% yield (Table 4). The CHNS/O elemental analysis of regenerated catalyst showed a slight loss of MSA, giving 984 μmol MSA/g catalyst (Table 4).

In conclusion, a cost-effective, efficient, and reusable SiO_2–MSA solid acid catalyst was synthesized and used for the synthesis of 4-methylcoumarin derivatives by the Pechmann reaction. The higher *n*-alkanes were used as nonpolar solvents for the Pechmann reaction and found to be the best alternative to conventional nonpolar solvents.

Table 4. Regeneration study of spent SiO_2 – methanesulfonic acid (MSA) catalyst.

Reaction cycle	Yield (wt %) of 7-hydroxy-4-methylcoumarin[a]	Amount of MSA (N_{MSA}, μmol/g)[b]
Fresh catalyst	99	1000
I	97	—
II	96	—
III	94	984

[a]Phenol substrate (10 mmol), ethyl acetoacetate (20 mmol), *n*-octadecane (3 mL, solvent), catalyst (0.25 g), 160 °C, 2 h.

[b]Calculated from sulfur wt % obtained by CHNS/O analysis.

Supplementary data

Supplementary data are available with the article through the journal Web site (www.nrcresearchpress.com/cjc).

Acknowledgement

The authors are thankful to H.M. Desai, Vice-Chancellor, Dharmsinh Desai University (DDU), Gujarat, India, for providing necessary facilities and Professor D.O. Shah, Founding Director, Shah-Schulman Center for Surface Science and Nanotechnology (SSCSSN), DDU, for valuable technical discussions. They are also thankful to Shimadzu Application Lab, Mumbai, for thermal analysis and to CSMCRI, Bhavnagar, for NMR analysis.

References

(1) Ge, F.-Y.; Yan, X.-L.; Yan, F.-Y.; Pan, H.-Y.; Chen, L.-G. *J. Fluoresc.* **2005** *15* (6), 829. doi:10.1007/s10895-005-0016-1.
(2) Luong, B. X.; Petre, A. L.; Hoelderich, W. F.; Commarieu, A.; Laffitte, J.-A.; Espeillac, M.; Souchet, J.-C. *J. Catal.* **2004** *226* (2), 301. doi:10.1016/j.jcat.2004.05.025.
(3) Zinin, A. I.; Malysheva, N. N.; Shpirt, A. M.; Torgov, V. I.; Kononov, L. O. *Carbohydr. Res.* **2007** *342* (3–4), 627. doi:10.1016/j.carres.2006.10.009.
(4) de Angelis, A.; Flego, C.; Ingallina, P.; Montanari, L.; Clerici, M. G.; Carati, C.; Perego, C. *Catal. Today* **2001** *65* (2–4), 363. doi:10.1016/S0920-5861(00)00592-7.
(5) Chidambaram, M.; Curulla-Ferre, D.; Singh, A. P.; Anderson, B. G. *J. Catal.* **2003** *220* (2), 442. doi:10.1016/S0021-9517(03)00282-3.
(6) Pizzio, L. R. *Mater. Lett.* **2006** *60* (29–30), 3931. doi:10.1016/j.matlet.2006.07.190.
(7) Bennardi, D. O.; Romanelli, G. P.; Autino, J. C.; Pizzio, L. R. *Appl. Catal., A: Gen.* **2007** *324*, 62. doi:10.1016/j.apcata.2007.03.009.
(8) Bennardi, D. O.; Romanelli, G. P.; Autino, J. C.; Pizzio, L. R. *Catal. Commun.* **2009** *10* (5), 576. doi:10.1016/j.catcom.2008.10.040.
(9) Díez, V. K.; Apesteguía, C. R.; Di Cosimo, J. I. *Catal. Today* **2010** *149* (3–4), 267. doi:10.1016/j.cattod.2009.09.016.
(10) Harmer, M. A.; Junk, C.; Rostovtsev, V.; Carcani, L. G.; Vickery, J.; Schnepp, Z. *Green Chem.* **2007** *9* (1), 30. doi:10.1039/b607428f.
(11) Murray, R. D. H.; Mendez, J.; Brown, S. A. *The Natural Coumarins: Occurrence, Chemistry and Biochemistry;* Wiley: New York, 1982.
(12) Tyagi, Y. K.; Kumar, A.; Raj, H. G.; Vohra, P.; Gupta, G.; Kumari, R.; Kumar, P.; Gupta, R. K. *Eur. J. Med. Chem.* **2005** *40* (4), 413. doi:10.1016/j.ejmech.2004.09.002.
(13) Von Pechmann, H.; Duisberg, C. *Ber. Dtsch. Chem. Ges.* **1883** *16* (2), 2119. doi:10.1002/cber.188301602117.
(14) Russell, A.; Frye, J. R. *Org. Synth.* **1941** *21*, 22.
(15) Woods, L. L.; Sapp, J. *J. Org. Chem.* **1962** *27* (10), 3703. doi:10.1021/jo01057a519.
(16) Sugino, T.; Tanaka, K. *Chem. Lett.* **2001** *30* (2), 110. doi:10.1246/cl.2001.110.
(17) Smitha, G.; Sanjeeva Reddy, Ch. *Synth. Commun.* **2004** *34* (21), 3997. doi:10.1081/SCC-200034821.
(18) Wang, L.; Xia, J.; Tian, H.; Qian, C.; Ma, Y. *Int. J. Chem. B* **2003** *42*, 2097.
(19) Sabou, R.; Hoelderich, W. F.; Ramprasad, D.; Weinand, R. *J. Catal.* **2005** *232* (1), 34. doi:10.1016/j.jcat.2005.02.002.
(20) Hoefnagel, A. J.; Gunnewegh, E. A.; Downing, R. S.; van Bekkum, H. *J. Chem. Soc. Chem. Commun.* **1995** (2): 225. doi:10.1039/c39950000225.
(21) Li, T.-S.; Zhang, Z.-H.; Yang, F.; Fu, C.-G. *J. Chem. Res. (S)* **1998**, 38. doi:10.1039/a703694i.
(22) Tyagi, B.; Mishra, M. K.; Jasra, R. V. *J. Mol. Catal. A: Chem.* **2007** *276* (1–2), 47. doi:10.1016/j.molcata.2007.06.003.
(23) Selvakumar, S.; Chidambaram, M.; Singh, A. P. *Catal. Commun.* **2007** *8* (5), 777. doi:10.1016/j.catcom.2006.08.039.
(24) Gopalakrishnan, S.; Viswanathan, K. R.; Vishnu Priya, S.; Herbert Mabel, J.; Palanichamy, M.; Murugesan, V. *Microporous Mesoporous Mater.* **2009** *118* (1–3), 523. doi:10.1016/j.micromeso.2008.09.030.
(25) Reddy, B. M.; Reddy, V. R.; Giridhar, D. *Synth. Commun.* **2001** *31* (23), 3603. doi:10.1081/SCC-100107007.
(26) Laufer, M. C.; Hausmann, H.; Hölderich, W. F. *J. Catal.* **2003** *218* (2), 315. doi:10.1016/S0021-9517(03)00073-3.
(27) Palaniappan, S.; Shekhar, R. C. *J. Mol. Catal. A: Chem.* **2004** *209* (1–2), 117. doi:10.1016/j.molcata.2003.08.006.
(28) Gregg, S. J.; Sing, K. S. W. *Adsorption Surface Area and Porosity,* 2nd ed.; Academic Press: New York, 1982.
(29) Khandekar, A. C.; Khadilkar, B. M. *Synlett 2002* (01), 0152. doi:10.1055/s-2002-19332.
(30) Sharma, G. V. M.; Reddy, J. J.; Lakshmi, P. S.; Krishna, P. R. *Tetrahedron Lett.* **2005** *46* (36), 6119. doi:10.1016/j.tetlet.2005.06.166.
(31) Kemp, W. *Organic Spectroscopy,* 2nd ed.; ELBS/Macmillan: London, 1987.

Can. J. Chem. Downloaded from www.nrcresearchpress.com by Xi'an Jiaotong University on 09/19/12
For personal use only.

Density functional theory (DFT) calculations on the structures and stabilities of $[C_nO_{2n+1}]^{2-}$ and $[C_nO_{2n+1}]X_2$ polycarbonates containing chainlike $(CO_2)_n$ units (n = 2–6; X = H or Li)

Pablo J. Bruna, Friedrich Grein, and Jack Passmore

Can. J. Chem. Downloaded from www.nrcresearchpress.com by Xi'an Jiaotong University on 09/19/12
For personal use only.

Abstract: The structures and stabilities of chainlike $(CO_2)_n$ (n = 2–6) polycarbonates, where adjacent C atoms are linked by C–O–C bonds, were investigated at the density functional theory (DFT) level (B3PW91/6–311G(2d,p)), including dicarboxylic dianions, $[C_nO_{2n+1}]^{2-}$, and the corresponding acids, $[C_nO_{2n+1}]H_2$, and Li salts, $[C_nO_{2n+1}]Li_2$. At equilibrium, the most stable systems have C_s, C_2, or C_{2v} symmetries. In the gas phase, these dianions are generally metastable with respect to spontaneous ejection of one electron, yet in the presence of counterions they become stabilized, for example, as $[C_nO_{2n+1}]^{2-}(Li^+)_2$ ion pairs. $[C_nO_{2n+1}]^{2-}$ linkages are also stabilized as dicarboxylic acids, $[C_nO_{2n+1}]H_2$; we find the latter to have equilibrium conformations of higher symmetry than previously reported in the literature. To the best of our knowledge, none of the $[C_nO_{2n+1}]X_2$ (X = Li or H) compounds with $n \geq 2$ have been reported in the experimental literature (albeit, the alkyl esters $C_2O_5R_2$ and $C_3O_7R_2$ are commercially available). All CO bonds in $C_2O_5X_2$ to $C_6O_{13}X_2$ have single- to double-bond character (≈140–118 pm), indicating that the $[C_nO_{2n+1}]$ moieties are held together by strong chemical forces (in contrast to the weakly bound complexes $(CO_2)_n$ and $(CO_2)_n^-$, $n > 1$). Vibrational frequencies were calculated to ensure all conformations were true minima. The IR and Raman intensities show that the high intensity C=O stretching modes (1750 ± 100 cm^{-1}) will help in the spectral characterization of these compounds. Solvation calculations using the polarizable continuum model (PCM) find that $C_2O_5^{2-}$ can be formed via $CO_3^{2-} + CO_2$ as well as $CO_3^- + CO_2^-$, each reaction having $\Delta G^{298} < 0$ in practically all solvents. This result confirms the experimentally observed large solubility of CO_2(g) in molten carbonates, CO_3M_2 (M = Li, Na, or K). In contrast, starting with $n = 2$, the reactions $[C_nO_{2n+1}]^{2-} + CO_2$ do not proceed spontaneously in any solvent ($\Delta G^{298} > 0$).

Key words: dicarboxylic acids, Li salts, equilibrium geometries, vibrational frequencies, density functional theory, solvent effects.

Résumé : Opérant au niveau (B3PW91/6–311G(2d,p)) de la théorie de la fonctionnelle de la densité (TFD), on a étudié les structures et les stabilités des polycarbonates $(CO_2)_n$ (n = 2–6) similaires à des chaînes dans lesquels les atomes de carbone sont liés par des liaisons C–O–C, ainsi que les dianions dicarboxylates $[C_nO_{2n+1}]^{2-}$ et les acides correspondants $[C_nO_{2n+1}]H_2$ et les sels de lithium $(C_nO_{2n+1}]Li_2$. À l'équilibre, les systèmes les plus stables présentent des symétries C_S, C_2 ou C_{2v}. En phase gazeuse, ces dianions sont généralement métastables par rapport à l'éjection spontanée d'un électron; toutefois, en présence de contre-ions, ils sont stabilisés, par exemple sous la forme de paires d'ions $[C_nO_{2n+1}]^{2-}(Li^+)_2$. Les liaisons $[C_nO_{2n+1}]^{2-}$ sont aussi stabilisées sous la forme d'acides dicarboxyliques $[C_nO_{2n+1}]H_2$; on a trouvé que ces derniers possèdent des conformations d'équilibre de symétrie plus élevée que celles rapportées antérieurement dans la littérature. Au meilleur de nos connaissances, aucun des composés $[C_nO_{2n+1}]X_2$ (X = Li ou H) avec $n \geq 2$ n'a été rapporté dans la littérature (même si les esters portant des groupes alkyles, $C_2O_5R_2$ et $C_3O_7R_2$ sont disponibles commercialement). Toutes les liaisons CO des composés allant de $C_2O_5X_2$ à $C_6H_{13}X_2$ possèdent des caractères allant de simple à double liaison (≈ 140 à 118 pm) indiquant que les portions $[C_nO_{2n+1}]$ sont liées entre elles par de fortes forces chimiques (en opposition aux complexes faiblement liés des entités $(CO_2)_n$ et $(CO_2)_n^-$, $n > 1$). On a calculé les fréquences vibrationnelles afin de s'assurer que toutes les conformations sont de véritables minima. Les intensités des spectres IR et Raman montrent l'intensité élevée des modes d'élongation C=O (1750 ± 100 cm^{-1}) sera très utile pour une caractérisation spéciale de ces composés. Des calculs de solvatation à l'aide du modèle du continuum polarisable (MCP) montrent que le $C_2O_5^{2-}$ peut être formé aussi bien par $CO_3^{2-} + CO_2$ que par $CO_3^- + CO_2^-$, le ΔG^{298} pour chaque réaction dans chaque solvant étant inférieur à zéro. Ces calculs confirment la grande solubilité observée expérimentalement du CO_2(g) dans les carbonates fondus CO_3M_2 (M = Li, Na ou K). Par ailleurs, à partir de $n = 2$, les réactions des $[C_nO_{2n+1}]^{2-} + CO_2$ ne peuvent se produire spontanément dans aucun solvant ($\Delta G^{298} > 0$).

Received 17 January 2011. Accepted 10 February 2011. Published at www.nrcresearchpress.com/cjc on 23 June 2011.

P.J. Bruna, F. Grein, and J. Passmore. Department of Chemistry and Centre for Laser, Atomic and Molecular Sciences, University of New Brunswick, PO Box 4400, Fredericton, NB E3B 5A3, Canada.

Corresponding author: P.J. Bruna (e-mail: fg01@unb.ca).

Mots-clés : acides dicarboxyliques, sels de lithium, géométries en équilibre, fréquences vibrationnelles, théorie de la fonctionnelle de la densité, effets de solvant.

[Traduit par la Rédaction]

Can. J. Chem. Downloaded from www.nrcresearchpress.com by Xi'an Jiaotong University on 09/19/12
For personal use only.

Introduction

The ground state of gaseous $CO_2(X^1\Sigma_g^+)$ has a charge density distribution where C is partially positive and both O centres are negative.[1–4] Linear CO_2 is able to accommodate one or two electrons in excess to form bent anions CO_2^- and CO_2^{2-}. Although the latter are unstable in the gas phase, they are stabilized by counterions, e.g., as in the crystals $[CO_2^-]M^+$ and $[CO_2^{2-}](M^+)_2$, M = alkali metal.[5–8]

The positively charged C in CO_2 behaves as an electrophilic agent, avid for electron pairs.[1–4] Typical examples of CO_2-attack reactions are (*i*) at the N lone pair of NH_3 to form urea (HCO_2NH_2); (*ii*) at the N atom of amines to form carbamic acid or derivatives ($RNH_2 + CO_2 \rightarrow RNHCO_2H$), a process widely used at an industrial scale for CO_2(g) capture; (*iii*) in aqueous solutions at the O centre of OH^- to form bicarbonate (HCO_3^-); and (*iv*) in solids at the negatively charged O^{2-} centre in crystalline oxides (e.g., CaO or Li_2O) to form stable carbonates (CO_3Ca or CO_3Li_2, respectively) widely found in nature.

In all the above reactions, CO_2 plays a passive role, since they actually take place owing to the presence of strongly nucleophilic centres (NH_3, RNH_2, OH^-, or O^{2-}) that attract, or bind, CO_2(g) molecules. Indeed, neutral clusters $(CO_2)_n$ are weakly bound van der Waals complexes[9] of little relevance in chemistry. Experimental[10] and theoretical[11] studies have found that gaseous $(CO_2)_n^-$ is more stable than gaseous $(CO_2)_n$ ($n > 1$). The anionic clusters have either $CO_2^-(CO_2)_{n-1}$ or $(C_2O_4)^-(CO_2)_{n-2}$ structures where CO_2^- or $C_2O_4^-$ are "solvated" by $(CO_2)_x$ molecules, i.e., C–O–C bonds are not formed. However, under extreme conditions ($P = 40$ GPa and $T = 1800$ K), a new and extended solid phase of $(CO_2)_n$ with a polymeric, quartz-like structure called CO_2-V was synthesized by Iota et al.,[12] who assigned an intense band at 790 cm^{-1} to the symmetric stretching of a C–O–[C] single bond.

At this point, one interesting question can be put forward: what simple starting *nucleophilic* moiety X that by successive addition of CO_2s will form $X(CO_2)_n$ with strong CO bonds throughout? More precisely, one expects all *R*(CO)s and ν(CO) in $X(CO_2)_n$ to be close to those measured for standard single and double CO bonds. A positive answer to this question can be inferred right away, as several experimental works have dealt with stable polycarbonate esters (odourless liquids at room temperature), e.g., CO_3X_2,[13,14] $C_2O_5X_2$,[15,16] and $C_3O_7H_2$[15,17–19] (X = alkyl group or H). The next member, $C_4O_9H_2$, is only briefly mentioned in one patent citation.[20] These esters (of mono-, di-, tri-, and tetra-carbonic acids) have the structures shown in Scheme 1.

As seen above, the formation of stabilized chainlike $(CO_2)_n$ units with alternating double C=O and single C–O–C bonds is evident. To the best of our knowledge, nothing has been reported experimentally on similar compounds such as polycarbonic acids, $[C_nO_{2n+1}]H_2$, or alkalipolycarbonates, $[C_nO_{2n+1}]M_2$, except for the simple representatives, CO_3H_2 and CO_3M_2 (M = Li, Na,…).[21,22] No X-ray studies have been reported for any solid system with $n \geq 2$; however, IR–Raman spectra in the liquid phase have been recorded for esters such as $CO_3(CH_3)_2$[23] and $C_2O_5(CH_3)_2$.[24]

From the theoretical side, we are aware of the existence of three papers dealing with chainlike $(CO_2)_n$ systems. The first study, carried out by Lewars[25] at the AM1 and HF/3–21G levels, reported structures, vibrational frequencies, and stabilities for the (mostly of low symmetry C_1) acyclic dicarboxylic acids, $HO(CO_2)_nH$ with $n = 2–6$ (equivalent to our $[C_nO_{2n+1}]H_2$ series). In the second article, also by Lewars,[26] the $HO(CO_2)_nH$ ($n = 2–4$) compounds were reinvestigated at a higher level of computation (B3LYP/6–31G(d)); their possible decomposition mechanisms were also briefly discussed. The third study, done by Frapper and Saillard[27] at the B3LYP/6–31G(d,p) level, focused on the structures and energetics of $[C_nO_{2n-1}]H_2$ molecules from HC_2O_3H to HC_5O_9H. Each member of this series was derived from the corresponding dicarboxylic acid by replacing the two terminal OH groups by one H atom each. In summary, these theoretical studies found the CO_2 chains (alternating C=O and C–O–C bonds) to have standard double and single CO bonds, i.e., the investigated structures are held together by relatively strong chemical bonds.

The information available on $[C_nO_{2n+1}]^{2-}$ dianions is practically restricted to carbonate CO_3^{2-}. Indeed, the next member, $C_2O_5^{2-}$ (dicarbonate or pyrocarbonate), seems to be the only one of this family to have been mentioned in the literature. Claes et al.[28,29] studied the solubility and solvation of CO_2(g) in a molten eutectic mixture of $CO_3Li_2/CO_3Na_2/CO_3K_2$ at 973 K. They found CO_2(g) to be extremely soluble, well beyond what is expected from Henry's law (physical absorption). The authors concluded that chemical absorption was taking place, most probably $CO_3^{2-}{}_{molten} + CO_2(g) \rightarrow C_2O_5^{2-}{}_{molten}$. Because they could not prove the formation of $C_2O_5^{2-}$ directly (via vibrational or NMR spectroscopy, for example), QCISD/6–31+G(d) calculations[29] were carried out to gain insight about the reaction energetics. The calculated values for ΔH^{973} and ΔG^{973} (–223 and –119 kJ/mol, respectively) indicate favourable gas-phase energetics, and solvation should not hinder the formation of the postulated $C_2O_5^{2-}$ in the molten mixture. Furthermore, another article[30] reported crossover ^{13}C NMR experiments between [^{13}C] and [^{18}O] carbonates in aqueous solutions of CO_3Na_2. The complex kinetic problem was interpreted as giving evidence for the existence of the equilibrium $CO_3^{2-} + CO_2 \leftrightarrow C_2O_5^{2-}$ under these experimental conditions.

The main goal of this work was to study the structures and energetics of $[C_nO_{2n+1}]X_2$ compounds having polymeric $(CO_2)_n$ chains ($n = 2–6$). The species investigated included the free dianions $[C_nO_{2n+1}]^{2-}$ and two classes of neutral molecules, namely those with ionic bonding, $[C_nO_{2n+1}]Li_2$, and

Scheme 1.

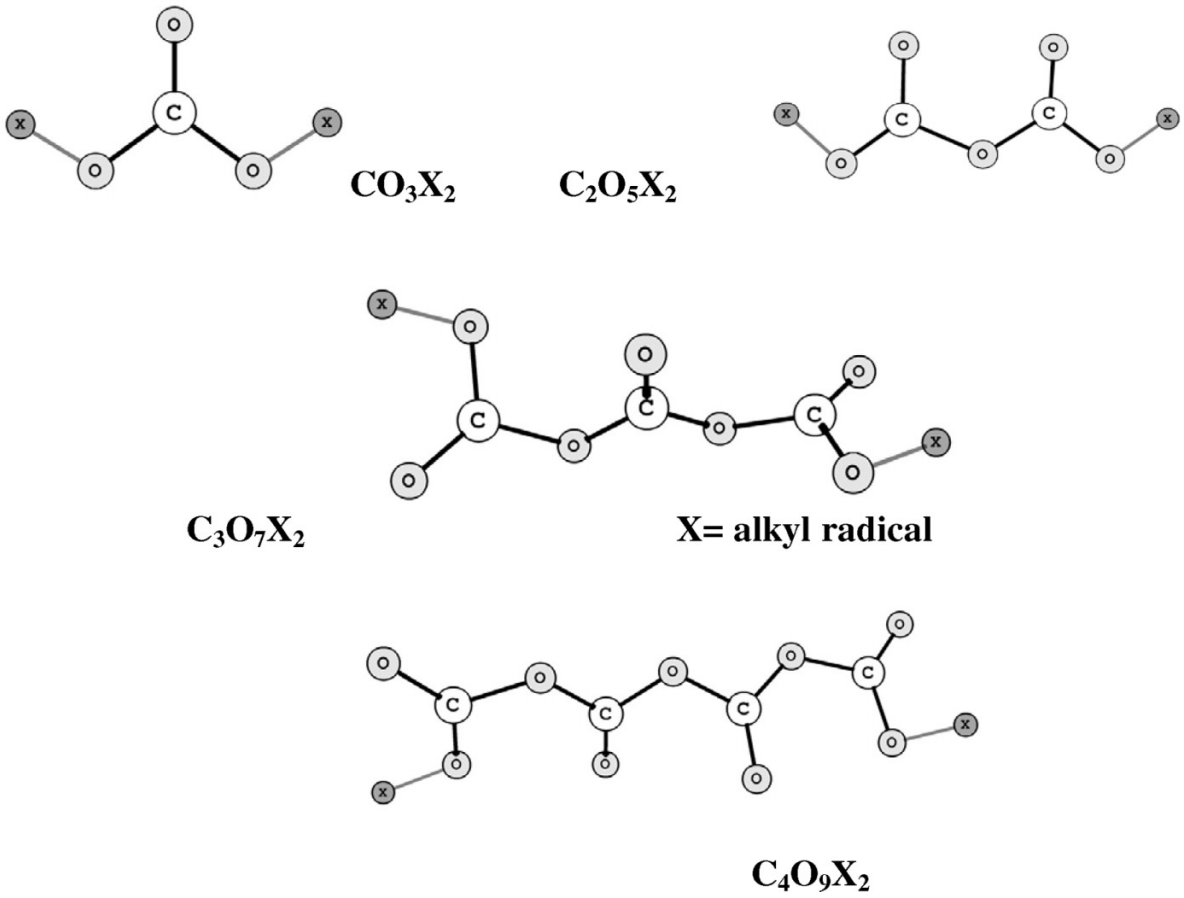

Can. J. Chem. Downloaded from www.nrcresearchpress.com by Xi'an Jiaotong University on 09/19/12
For personal use only.

others with terminal COOH groups, the dicarboxylic acids $[C_nO_{2n+1}]H_2$. From the start, we focused on systems having C_s, C_2, and C_{2v} symmetries. Vibrational frequencies are reported to assist the experimental characterization of these novel compounds. Finally, the energetics of $[C_nO_{2n+1}]^{2-}$ species in different solvents were analyzed using the polarizable continuum model (PCM).

Technical details

All calculations were carried out with Gaussian 03;[31] auxiliary software helped to visualize structures and vibrational frequencies (ChemCraft).[32] The theoretical method employed was the B3PW91 model of density functional theory (DFT); two basis sets were used, 6–311G(2d,p) for all systems, as well as 6–311++G(2d,p) for neutral molecules. As explained in the following, some comparative calculations were carried out using other methods (B3LYP and CCSD(T)) and basis sets.

Vibrational frequencies were systematically calculated to ensure that all geometry-optimized structures were true minima; the frequencies reported here are those directly calculated with Gaussian 03[31] (i.e., no scaling factors). Vast experience from the literature indicates that the equilibrium geometries and frequencies in the solid state are, in general, satisfactorily mimicked by ab initio calculations on the gas-phase species as long as the basis sets are compact (without semidiffuse atomic orbitals (AOs),[33] as done here).

Thermodynamic properties like enthalpy (ΔH^{298}) and Gibbs free energy (ΔG^{298}) were taken from the Gaussian 03[31] outputs. Reaction energies (ΔH^{298} and ΔG^{298}) were derived by combining data in the gas phase with the corresponding solvation energies in different solvents. The solvent calculations were carried out using the PCM method.[34]

Results and discussion

Equilibrium geometries and ν(CO) stretching frequencies

A standard procedure to identify newly synthesized compounds is to record IR and Raman vibrational spectra. This procedure is relevant as long as strongly absorbing chromophoric groups exist inside the whole molecule, and the vibrational spectrum is not too congested (which usually happens below 900 cm^{-1} because of the superposition of bending, rocking, and torsional modes). Intense bands should appear at ν(C=O) $\approx$ 1750 $\pm$ 50 cm^{-1} and ν(C–O) $\approx$ 1350 $\pm$ 50 cm^{-1}.[35] In a carboxylic C(=O)OH group, the ν(C–OH)-stretch and δ(COH)-bending modes are heavily coupled;[35] this group also strongly absorbs at ν(OH) $\approx$ 3700 $\pm$ 100 cm^{-1}. The situation is even more complex for dicarboxylic acids because of the in- and out-of-phase couplings between pairs of terminal C=O, C–OH, and OH bonds.[35]

The R(CO) distances and frequencies in CO_2^{m-} and CO_3^{m-} (m = 0, 1, or 2) species, which are the basic units of the more complex $[C_nO_m]^{2-}(X^+)_2$ oligomers, are discussed in the next sections. The same information on reference compounds

Can. J. Chem. Downloaded from www.nrcresearchpress.com by Xi'an Jiaotong University on 09/19/12
For personal use only.

with single and double CO bonds and the novel $[C_nO_{2n+1}]X_2$ systems is presented afterwards.

CO_2^{m-} series (m = 0, 1, or 2)

The calculated data are displayed in Table 1. CO_2 is linear in its $X^1\Sigma_g^+$ ($4\sigma_g^2 3\sigma_u^2 1\pi_u^4 1\pi_g^4$) ground state. The $2\pi_u$ lowest unoccupied molecular orbital (LUMO) is CO antibonding; the addition of up to two electrons increases R(CO) and lowers ν(CO), i.e., electron attachment results in the CO bond being shifted from a double to a single bond. The equilibrium geometry changes from linear ($D_{\infty h}$) for CO_2 to bent (C_{2v}) for $CO_2^-(X^2A_1)$ and $CO_2^{2-}(X^1A_1)$. Note that gaseous CO_2^- and CO_2^{2-} are unstable upon electron detachment, but they stabilize in solutions and crystals (spatial confinement keeps the extra electrons bound). The experimentally known properties of CO_2^- and CO_2^{2-} mostly stem from studies on $CO_2^-M^+$ and $CO_2^-(M^+)_2$ crystals, with M = alkali atom.[5–8]

In going from CO_2 (linear) to CO_2^- to CO_2^{-2} (bent), the data in Table 1 show that R(CO) increases stepwise by about 8 pm, from ~116 to 124 to 132 pm. In several discussions to follow, these R(CO) distances will be considered as simple representatives of the bond character: a double bond with $R \approx 116$–120 pm, a strong single bond (or a mixed double and single bond) with $R \approx 125$–130 pm, and a weak single bond with $R \approx 130$–140 pm (definitively well below 150 pm).

Such bond elongation results from the successive addition of one electron to the $6a_1$ molecular orbital (MO) (correlating with the $2\pi_u$-LUMO of CO_2). Taking z as the symmetry axis in C_{2v} symmetry, the in-plane $6a_1$ MO is mainly p_z(C), with minor contributions from ($p_z(O^1) + p_z(O^2)$); note that $6a_1$ is CO antibonding but O–O bonding (leading to bent CO_2^- and CO_2^{2-}). These geometrical trends give valuable clues about the bonding strength of a newly formed C′–O bond when an extra *linear* O′–C′–O′ molecule combines with a terminal O_t atom of $[C_nO_m]^{2-}$ to form $[C_{n+1}O_{m+2}]$.$^{2-}$ More precisely, a strong bond is obtained only when (*i*) the attached O′–C′–O′ group becomes *bent*, indicating its share of the negative charge in excess and (*ii*) the new C′–O_t single bond has R(CO) << 150 pm.

The increase in CO distance is accompanied by a total decrease of ≈1200 cm^{-1} in the asymmetrical ν(CO) stretch, from ~2440 (CO_2) to 1730 (CO_2^-) to 1230 cm^{-1} (CO_2^{2-}), in line with the change from double to single bond along the series. Contrastingly, the symmetric ν(CO) stretch decreases by only ≈150 cm^{-1} between CO_2 and CO_2^{2-}. Worth noting is the small increase in the bending frequency δ(OCO), <50 cm^{-1}, in passing from linear CO_2 to the strongly bent CO_2^{2-} ($\alpha \approx 116°$). Interestingly, the two ν(C–O)s in CO_2^{2-} are found to be accidentally degenerate (≈1230 cm^{-1}).

The intensity data (in square brackets, Table 1) show that the IR spectra are dominated by the intense asymmetric ν(C–O) mode in all three CO_2 species. In the bent anions, all vibrational bands have significant Raman intensities, albeit with stretching modes dominating.

Thus, a given CO_2 moiety within $[C_nO_{2n+1}]$ is generally expected to give rise to three characteristic IR absorption bands, near 1700 (ν_{as}(CO)), 1300 (ν_s(CO)), and 750 cm^{-1} (δ_{bend}(OCO)). The low-frequency mode may be superimposed by other low-lying vibrational motions.

CO_3^{m-} series (m = 0, 1, or 2)

These planar species are studied for a common D_{3h} geometry, with z being the threefold perpendicular symmetry axis. Two MOs composed *exclusively* by p AOs on the oxygen atoms are relevant: 1e″ (out-of-plane $p_z(p_\pi)$ AOs) and $1a_2'$ (in-plane MO made up of p_x,p_y(p_σ) contributions). In neutral CO_3, 1e″ and $1a_2'$ are, respectively, the highest occupied molecular orbital (HOMO) and LUMO, i.e., the latter becomes successively singly and doubly occupied in CO_3^- and CO_3^{2-}.

A R(CO) = 124.5 pm in CO_3 is almost as large as R(CO) = 123.9 pm in CO_2^-. Electron attachment slightly increases R(CO) by ~6 pm between CO_3 and CO_3^{2-}. Interestingly, CO_2^{2-} and CO_3^{2-} are found to have quite similar values of R(CO) (≈131 pm) and $\alpha(CO_2)$ (≈120°). In general, the ν(CO) stretching frequencies in CO_2 and CO_2^- are invariably larger (from 200 to 500 cm^{-1}) than in CO_3 and CO_3^-. When comparing the CO_2^{2-} and CO_3^{2-} dianions, one notes that the asymmetric ν(CO) mode in CO_3^{2-} is ~200 cm^{-1} larger than in CO_2^{2-}, where the opposite situation holds for the symmetric ν(CO) (Table 1). The bending frequency in CO_3 is less than one-half the CO_2 value (≈300 cm^{-1} vs 680 cm^{-1}), but they are not too much apart in CO_3^{2-} and CO_2^{2-} (≈675 cm^{-1} vs 725 cm^{-1}).

Single- and double-CO bond compounds as reference

A comparison between experimental and theoretical ν(CO) s for known single- and double-CO bond compounds allows us to get insight about the accuracy of the B3PW91/6–311G (2d,p) method. Four compounds were selected: (*i*) dimethyl ether $(H_3C)_2O$, with two single C–O bonds; (*ii*) acetic anhydride $(H_3C–C=O)_2O$, with two C–O and C=O bonds each; (*iii*) oxalic acid $C_2O_4H_2$, the simplest dicarboxylic compound with two CO_2^- groups; and (*iv*) ethylene oxide C_2H_2O, an epoxy compound with a C–O–C ring. Relevant data are listed in Table 2.

Dimethyl ether has large R(C–O)s of 140.3 pm, resulting in relatively low stretching frequencies of 1210 and 960 cm^{-1}. Our unscaled frequencies agree with previous calculations,[36] both being about 4% higher than the experimental data.[37,38]

Acetic anhydride (C_2 symmetry) is a prime example of the $[C_nO_{2n+1}]X_2$ species: two C=O bonds interconnected via a C–O–C bridge. A short R(C=O) = 119.0 pm compares with R = 115.9 pm in CO_2 (Table 1). We calculated two close lying ν(C=O)s at 1898 and 1828 cm^{-1} (Table 2). Experimentally,[39] these bands lie at ≈1837 and 1779 cm^{-1} (about 4% lower than our DFT data).

The two single R(C–O)s in acetic anhydride (139.0 pm) are even larger than in CO_2^{2-} (131.9 pm, Table 1). The symmetric O–C(–O) mode of the anhydride is placed at 1235 cm^{-1}, in agreement with experiments (1230 cm^{-1}).[39] The asymmetric counterpart lies ~100 cm^{-1} lower (≈1150 cm^{-1}), in a region where mixing with other modes is prevalent (Table 2).

For oxalic acid ($C_2O_4H_2$, C_{2h}), two close-lying frequencies (1867 and 1842 cm^{-1}, Table 2) are the out- and in-phase coupling between C=O bonds; only one of these modes is IR or Raman active. The ν(C–O) and δ(COH) motions are strongly coupled; these four bands lie in the 1450–1200 cm^{-1} region. Our calculated frequencies are ~5% larger than the experimental values.[40]

In ethylene oxide with R(C–O) = 142.2 pm (indeed, a rather long single bond) we calculated the ν(C–O)s at 1312

Can. J. Chem. Downloaded from www.nrcresearchpress.com by Xi'an Jiaotong University on 09/19/12
For personal use only.

Table 1. Equilibrium geometries, vibrational frequencies (relative absorption intensities), and relative energies (ΔE) for CO_2^{m-} and CO_3^{m-} species (m = 0, 1, 2); B3PW91/6–311(2d,p) data.

Parameter	$CO_2(D_{\infty h})\cdots(1b_1)^2(4b_2)^2$	$CO_2^-(C_{2v})\cdots(4b_2)^2(6a_1)^2$	$CO_2^{2-}(C_{2v})\cdots(4b_2)^2(6a_1)^2$	$CO_3(D_{3h})^*\cdots(1e'')^2$	$CO_3^-(D_{3h})^*\cdots(1e'')^2(1a_2')$	$CO_3^{2-}(D_{3h})\cdots(1e'')^2(1a_2')^2$
R (pm)	115.9	123.9	131.9	124.5	126.8	130.3
α (°)	180.0	134.5	116.1	120.0	120.0	120.0
Mulliken C/O	0.58/–0.29	0.08/–0.54	–0.47/–0.78	0.63/–0.21	0.56/–0.52	0.46/–0.82
ν(CO) (str, asym)	2443 (σ_u) [1.00, 0]	1727 (b_2) [1.00, 0.64]	1227 (b_2) [1.00, 1.00]	1955 (e′) [0.19, 0.57]	1315 (e′) [0.04, 0.27]	1445 (e′) [1.00, 0.08]
ν(CO) (str, sym)	1376 (σ_g) [0, 1.00]	1340 (a_1) [0.03, 1.00]	1233 (a_1) [0.11, 0.58]	1154 (a_1') [0, 1.00]	1110 (a_1') [0, 1.00]	1027 (a_1') [0, 1.00]
δOCO (bend)	678 (π_u) [0.05, 0]	739 (a_1) [0.02, 0.30]	725 (a_1) [≈0, 0.55]			
CO_3 (out of plane)				775 (a_2'') [1.00, 0]	847 (a_2'') [0.95, 0]	896 (a_2'') [0.03, 0]
ΔE (kJ/mol; (eV))	0.0 (0.0)	109.6 (1.14)	888.6 (9.21)	0.0 (0.0)	–379.7 (–3.94)	96.4 (1.00)

Note: Energies (au): –188.568053 (CO_2), –188.526330 (CO_2^-), –188.229527 (CO_2^{2-}), –263.604232 (CO_3), –263.771417 (CO_3^-), and –263.590024 (CO_3^{2-}). Values in square brackets are relative intensities: IR and Raman (first and second entries, respectively).

*Fixed D_{3h} symmetry for comparison purposes.

and 871 cm^{-1}, with the latter demonstrating how low a single bond ν(C–O) can be shifted in a particular molecule. In fact, the bending mode δ(C–O–C) in this strained ring lies even higher (910 cm^{-1}). The theoretical values are slightly larger than those in the literature[41] (cf. Table 2).

In summary, our directly calculated frequencies for the various types of CO bonds at the B3PW91/6–311G(2d,p) level overestimate the experimental (gas phase) results by no more than 5%, and the same accuracy is expected for the vibrational data presented in the following for the new molecules.

Novel compounds with C_2O_5 to C_6O_{13} chainlike units

Table 3 lists CO distances and relevant frequencies for $[C_nO_{2n+1}]^{2-}$, $[C_nO_{2n+1}]Li_2$, and $[C_nO_{2n+1}]H_2$ species containing C_nO_{2n+1} units from C_2O_5 to C_4O_9 and Table 4 gives the same information for those with C_5O_{11} and C_6O_{13} chains. All systems are assumed to be in the gas phase. The different structures are shown in Figs. 1–5. Detailed information on the calculated geometries, vibrational frequencies, and IR–Raman intensities can be found in the Supplementary data.

All Li polycarbonates $[C_nO_{2n+1}]Li_2$ exhibit ion-pair structures already in the gas phase, i.e., the metal Li centres are mostly positively charged and the $[C_nO_{2n+1}]$ units carry up to two negative charges in excess. In fact, M^+ counterions stabilize the intrinsically unstable $[C_nO_{2n+1}]^{2-}$ fragment in the gas phase. The third compound of each group is a dicarboxylic acid, $[C_nO_{2n+1}]H_2$; because both C=O and O–H bonds are highly polarized (all having $O^{\delta-}$), their IR intensities are expected to be strong.

The parameter $p = 3n$ (first column in Tables 3 and 4) gives quick information about the total number of CO bonds, or equivalently, the total number of ν(CO) modes expected (starting with $p = 6$ for C_2O_5 and up to $p = 18$ for C_6O_{13}). Clearly, CO_2 addition increases the total number of CO bonds (or corresponding stretch frequencies) by three: two terminal COs plus the newly formed single CO bond.

In Tables 3 and 4, the R(C=O) and R(C–O) columns list R distances up to and beyond 125 pm, respectively (R = 125 pm is taken here as the upper limit for a double bond). Each R(CO) is followed by an [n] number counting how many times such a distance appears in the molecule. In both tables, those R values out of range in the dianions (i.e., with *too large* CO bonds) are italicized; they are associated with the outermost single C–O bonds connecting terminal CO_2 groups to the main (inner) frame.

As mentioned, there are as many ν(CO) stretching frequencies as CO bonds (i.e., p in total). The assignment of such ν(CO)s, experimentally and theoretically, is straightforward as long as they do not mix heavily with other normal modes (of the same symmetry). According to the literature,[35] double-bond ν(C=O)s typically lie in the 1700–1900 cm^{-1} region, whereas single-bond ν(C–O)s appear at lower frequencies, from 1500 to 900 cm^{-1}. Fortunately, CO bonds are strong IR–Raman absorbers and their contributions to the vibrational spectra are easily identifiable. Actually, that is true for the higher frequency part of the spectrum: for these systems, there are no other normal modes absorbing in the same 1700–1900 cm^{-1} region as the ν(C=O) motion characteristically does. Particularly for long chains with $n \geq 3$, the characterization of C–O single bonds (1350–800 cm^{-1}) is more complex for several reasons: (*i*) the number of ν(C–O–C)

Can. J. Chem. Downloaded from www.nrcresearchpress.com by Xi'an Jiaotong University on 09/19/12
For personal use only.

Table 2. Bond distances R(CO), stretching frequencies ν(CO), and relative absorption intensities for compounds with single and double CO bonds (B3PW91/6–311G(2d,p) data).

Compound	Ref.	R(CO) (pm)	ν(CO) (cm^{-1})	IR	Raman
$H_3C–O–CH_3$ dimethyl ether (C_{2v}) (two single CO bonds)	TW	140.3 (C–O–(C))	1209 $(b_2)_a$	1.00	0.04
			960 $(a_1)_s$	0.31	1.00
	32		1282 (b_2)	1.00	≈0.05
			963 (a_1)	0.30	1.00
	33		1178 (b_2)	1.00	
			931 (a_1)	≈0.30	
	34*	141.3	1189/1173 (b_2)	1.00	
			931/ 926 (a_1)	0.32	
$H_3C–C(O)–O–C(O)–CH_3$ acetic anhydride (C_2) (two single and two double CO bonds)	TW	119.0 (C=O)	1911 $(a)_s$	0.46	1.00
			1842 $(b)_a$	0.15	0.34
		139.0 (C–O–(C))	1237 (a)	0.004	0.12
			1155 (b)	1.00	0.02
			99 (b)	0.42	0.06
			913 (b)	0.08	0.04
	35	(C=O)	1837 (a)	s	
			1779 (b)	s	
		(C–O–(C))	1230 (a)	w	
			1135 (b)	vs	
			1002 (b)	S (CH_3)	
			904 (b)	m	
HOOC–COOH oxalic acid (C_{2h}) (two single and two double CO bonds)	TW†	120.1 (C=O)	1867 (b_u)	0.61	0
			1842 (a_g)	0	1.00
		131.9 (C–OH)	1456 (a_g)	0	0.05
			1346 (b_u)	1.00	0
			1230 (a_g)	0	0.44
			1218 (b_u)	0.01	0
	36†		1817 (b_u)		
			1800 (a_g)		
			1423 (a_g)		
			1329 (b_u)		
			1195 (a_g)		
			1255 (b_u)		
$(C_2H_4)O$ ethylene oxide (C_{2v}) (C–O–C ring)	TW	142.2 (146.1, R(CC))	1312 (a_1)	0.24	1.00
			910 (a_1)	1.00	0.37
			871 (b_2)	0.19	0.14
	37		1272 (a_1)	s	
			876 (a_1)	vs	
			842 (b_2)	s	

Note: TW = this work.

*Experimental/calculated frequencies. The band at 1189/1173 cm^{-1} is reassigned here to ν(C–O) instead of CH_3 torsion (b_2) in the original paper.

†6–311++G(2d,p) basis. The last four frequencies are mixtures of ν(C–OH) and δ(COH). Because of H bonding, the ν(O–H)s lie at lower frequencies (cm^{-1}): 3657 (b_u) / 3654 (a_g) (TW) vs 3472 (b_u) / unknown (a_g), where subscripts a and s stand for asymmetric and symmetric stretching mode, respectively.[40]

frequencies lying close together, which is equal to $2(n - 1)$, increases rapidly, from just 2 in C_2O_5 to 6 in C_4O_9 to 10 in C_6O_{13}. These internal motions couple together to give in-phase and out-of-phase resultants; (*ii*) in the case of the dicarboxylic acids $C_nO_{2n+1}H_2$, there exist differences between the ν(C–O)s for inner C–O–C links versus ν(C–O)s for terminal C–OH groups (with unlike absorption patterns as well); and (*iii*) mixing with other normal modes (mostly bending motions). For example, the δ(COC) and δ(OCO) bending modes in $C_nO_{2n+1}^{2-}$ and $C_nO_{2n+1}Li_2$ lie at 1000–800 cm^{-1}, so they can mix with the low-lying ν(C=O)s in the same region. In summary, the best candidates for IR characterization of the present compounds is via all available double-bond ν(C=O)s.

Analysis of the data in Tables 3 and 4 lead to the following observations: (*i*) For either the R(C=O) or R(C–O) column, the equilibrium distance invariably decreases from D^{2-} to DLi_2 to DH_2, with D standing for a general $[C_nO_{2n+1}]$ fragment. This trend is more noticeable for single C–O bonds, particularly as n increases from $n = 2$ to 6. Furthermore, $C_3O_7^{2-}$ has a short R(C–O) of 133.1 pm and a large R(C–O) of 153.9 pm, with the latter lying well above 145 pm, which is perhaps an acceptable upper bound for a (relatively weak) single bond. However, in passing from $C_3O_7^{2-}$ to

Can. J. Chem. Downloaded from www.nrcresearchpress.com by Xi'an Jiaotong University on 09/19/12
For personal use only.

Table 3. *R*(CO) distances and frequencies (mostly ν(CO) stretchings) for $C_nO_{2n+1}^{2-}$ and $C_nO_{2n+1}X_2$ species (X = Li or H; n = 2, 3, or 4) (B3PW91(6–311G(2d,p) data).

					Frequencies	
p*	Species	Symmetry	*R*(C=O) (pm)†	*r*(C–O)† (pm)	High (>1600 cm^{-1})	Low (<1500 cm^{-1})‡
6	$C_2O_5^{2-}$	C_2	124.1[2], 125.0[2]	142.9[2]	1765, 1732	1395, 1256, 935, 915, [850, 811, 725, 692, …
	$C_2O_5Li_2$	C_2	<125.5>[4]	137.2 [2]	1687, 1643	1490, 1328, 1091, 975, [870, 818, 781, 731, …
	$C_2O_5H_2$§	C_s	118.0[1]	130.6[1] (C–OH)	1973, 1784	1516, 1441, 1237, 1196, [1050, 865, 865, 797, 769, 707, 640, 582, …
			121.5[1]	132.2[1]		
				133.1[1] (C–O–C)		
				143.6[1]		
9	$C_3O_7^{2-}$	C_2	121.7[1], 122.3[4]	133.1[2], *153.9*[2]	1890, 1883, 1756	1405, 1321, 1201, 1064, 870, 855, […]
	$C_3O_7Li_2$	C_{2v}	119.8[1], 124.5[4]	133.8[2], 140.9[2]	1835, 1720, 1713	1450, 1409, 1235, 1111, 985, 946, [897, 842 773, 750, 700, 639, 597, 583, …
	$C_3O_7H_2$§	C_{2v}	117.6[2]	130.5[2](C–OH)	1995, 1981, 1724	1477, 1465, 1348, 1209, 1179, 1092, [903, 827, 814, 778, 772, 751, 738, 723, …
			122.5[1]			
				132.0[2](O–C–O)		
				144.9[2](C–O–C)		
12	$C_4O_9^{2-}{}_2$	C	120.7[2], 120.8[2], 129.5[2]	139.5[2], *165.7*[2]	1998, 1996, 1840	1387, 1344, 1280, 1169, 1059, 955, 859, 834, [794, 766, 722, 709, 690, 652, …
					1782	
	$C_4O_9Li_2$	C_2	118.4[2], 124.5[4]	134.3[2], 137.0[2]	1936, 1866, 1717	1414, 1413, 1284, 1141, 1110, 1003, 970, 947, [873, 863, 790, 781, 773, 739, 682, 664, …
				140.1[2]	1716	
	$C_4O_9H_2$§	C_2	117.6[2], 120.0[2]	130.4[2], 132.1[2]	1992, 1987, 1855	1475, 1474, 1362, 1253, 1199, 1166, 1109, 983, [863, 857, 824, 823, 802, 778, 763, 754, …
				136.2[2], 145.1[2]	1784	

*p = number of CO bonds.

†Values in square brackets reflect the number of CO bonds with the same *R*. Unusually large *R*(C–O)s in the dianions are italicized.

‡The first p frequencies owing to CO bonds are separated from the rest by an opening square bracket.

§ν(OH) frequencies (cm^{-1}): 3810 and 3253 ($C_2O_5H_2$), 3430 and 3388 ($C_3O_7H_2$), and 3362 and 3355 ($C_4O_9H_2$). The lower values (<<3800 cm^{-1}) in $C_2O_5H_2$, $C_3O_7H_2$, and $C_4O_9H_2$ are due to hydrogen bonding (see Figs. 1–3).

Can. J. Chem. Downloaded from www.nrcresearchpress.com by Xi'an Jiaotong University on 09/19/12
For personal use only.

Table 4. *R*(CO) distances and frequencies (mostly ν(CO) stretching) for $C_nO_{2n+1}^{2-}$ and $C_nO_{2n+1}X_2$ species (X = Li or H; n = 5 or 6) (B3PW91/6–311G(2d,p) data).

					Frequencies	
p*	Species	Symmetry	*R*(C=O) (pm)†	*R*(C–O) (pm)†	High (>1600 cm^{-1})	Low (<1500 cm^{-1})‡
15	$C_5O_{11}^{2-}$	C_2	120.3[1]	124.7[2], 134.1[2]	2305, 2305, 1847	1388, 1344, 1335, 1314, 1169, 1073, 893, 874
			121.6[2]	*147.5*[2], *218.8*[2]	1829, 1791	824, 813, [772, 747, 697, 689, 687, 591, 590
			117.2[4]			552, 547, 500, 315, …
	$C_5O_{11}Li_2$	C_2	117.9[1]	133.7[2], 136.1[2]	1960, 1902, 1861	1412, 1410, 1300, 1240, 1138, 1084, 1024, 971
			118.3[2]	137.8[2], 140.7[2]	1727, 1726	954, 946, 878, [862, 828, 780, 776, 755, 735
			124.4[4]			715, 676, 632, 600, 576, …
	$C_5O_{11}H_2$§	C_2	117.5[1]	130.4[2], 132.2[2]	1987, 1986, 1952	1475, 1473, 1328, 1322, 1210, 1200, 1130, 1107
			117.7[2]	136.2[2], 136.6[2]	1823, 1808	1001, 971, [886, 844, 822, 796, 794, 780, 773
			120.0[2]	144.9[2]		770, 743, 734, 706, 673, …
18	$C_6O_{13}^{2-}$‖	C_2	<116.1>[4] out	130.5[2] C_2O_5	<2419>[2] (CO_2)	1387, 1368, 1368,1352, 1276, 1152, 1081, 967
			<121.8>[4] mid	138.9[2] C_2O_5	<1910>[2] (CO_2^-)	862, 855, 791, 776, [743, 727, 718, 701, 665
			120.1[2] C_2O_5	*156.7*[2] mid	1864, 1802	619, 603, 595, 561, 530, 513, 344, …
				286.0 [2] out		
	$C_6O_{13}Li_2$	C_2	<118.1>[4]	133.6[2], 135.0[2]	1946, 1925, 1923	1401, 1400, 1298, 1251, 1172, 1136, 1056, 1038
			<124.3>[4]	136.8[2], 139.0[2]	1871, 1732, 1732	997, 979, 944, 930, [866, 840, 829, 808, 787, 786
				140.7[2]		753, 737, 725, 666, 655, 636, …
	$C_6O_{13}H_2$§	C_2	117.6[2]	132.8[2], 135.2[2]	1968, 1963, 1946	1399, 1399, 1289, 1254, 1228, 1212, 1153, 1136
			118.0[2]	135.5[2], 136.6[2]	1885, 1885, 1877	1046, 1045, 998, 979, [919, 911, 861, 825, 791, 778
			118.5[2]	138.0[2], 138.1[2]		772,759, 736, 719, 682, 658, 606, 584, …

*p = number of CO bonds.

†Values in square brackets reflect the number of CO bonds with the same *R*. Unusually large *R*(C–O)s in the dianions are italicized.

‡The first p frequencies owing to CO bonds are separated from the rest by an opening square bracket.

§ν(OH) frequencies (cm^{-1}): 3406 and 3403 ($C_5O_{11}H_2$) and 3817 and 3817 ($C_6O_{13}H_2$). The lower values in $C_5O_{11}H_2$ are due to hydrogen bonding (Fig. 4).

‖This dianion consists of a central C_2O_5 unit plus a pair of two weakly attached CO_2 groups (middle (mid), outer (out)), with quite short *R*(C=O)s and very large *R*(CO)s. The $C_6O_{13}X_2$ species, however, have normal *R*(CO)s throughout (see data above and Fig. 5).

Published by NRC Research Press

Can. J. Chem. Downloaded from www.nrcresearchpress.com by Xi'an Jiaotong University on 09/19/12
For personal use only.

Fig. 1. Equilibrium geometries of $C_2O_5^{2-}$, $C_2O_5Li_2$, and $C_2O_5H_2$.

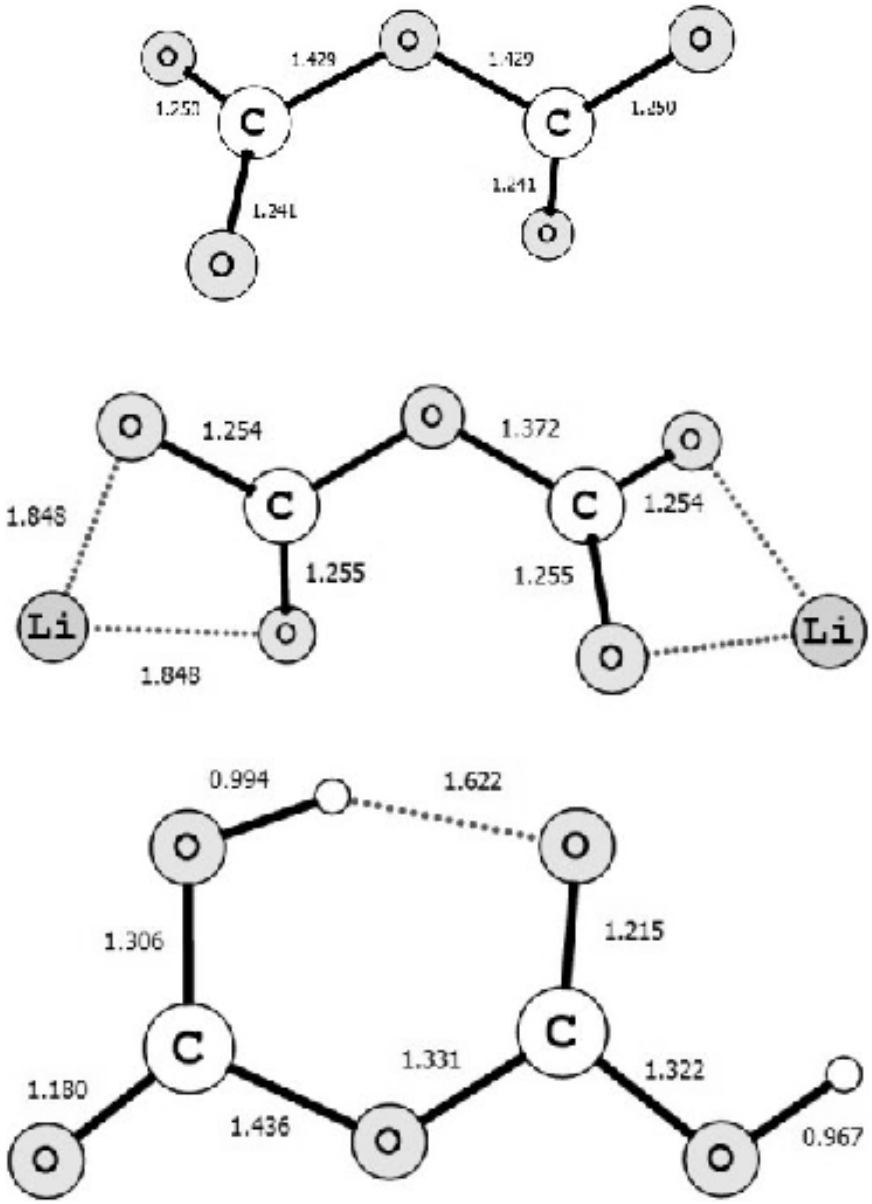

$C_3O_7Li_2$, the two most elongated *R*(C–O)s in the Li salt, at 133.8 and 140.9 pm, can be considered normal distances (Table 3). Clearly, the formation of ion pairs [i.e., $(C_3O_7)^{2-}(Li^+)_2$] already in the gas phase helps to shrink and stabilize the electronic charge distribution of the otherwise spatially expanded and metastable isolated $C_3O_7^{2-}$. Further, in passing to the corresponding acid $C_3O_7H_2$, all six single C–O bonds (132.7–138.2 pm) are even shorter than in the ion pair $C_3O_7Li_2$, which points out that the formation of two covalent OH bonds is a rather effective mechanism for stabilizing the dianionic core. (*ii*) In connection with point (*i*), as the dianion cluster becomes bigger and bigger, the aforementioned large *R*(C–O)s become anomalously larger and larger, about 166, 219, and 278 pm for $C_4O_9^{2-}$, $C_5O_{11}^{2-}$, and $C_6O_{13}^{2-}$, respectively. In reality, these dianions are extremely weakly bound with respect to the liberation of CO_2. However, the corresponding Li salts contain a more compact dianionic unit with all C–O bonds being shorter than 145 pm (Tables 3 and 4). (*iii*) Regarding the ν(CO)s, the theoretical values are collected in two sets, with frequencies above 1600 cm^{-1} and below 1500 cm^{-1}, respectively. The structure of the high-frequency region is simple: it contains as many ν(C=O)s as the number of C atoms (from $n = 2$ to 6), all of them appearing as strong IR bands. For the weakly bound $C_5O_{11}^{2-}$ and $C_6O_{13}^{2-}$, our calculations find extremely high ν(CO)s at $\approx$2350 cm^{-1}. This anomaly is easy to explain: the two terminal CO_2 groups share very little of the negative charge so they essentially retain a neutral CO_2 character (quasilinear frame, short *R* and high ν(CO), as shown in Table 1 for isolated CO_2).

The low ν(CO)s region (<500 cm^{-1}) is less helpful for structure determinations because of mixings with several low-lying normal modes, as pointed out earlier. In Tables 3 and 4, each low-frequency region lists *all* calculated values in decreasing order, without distinction between stretching, bending, or rocking modes. Since we expected ($p - n$) CO-

Can. J. Chem. Downloaded from www.nrcresearchpress.com by Xi'an Jiaotong University on 09/19/12
For personal use only.

Fig. 2. Equilibrium geometries of $C_3O_7^{2-}$, $C_3O_7Li_2$, and $C_3O_7H_2$.

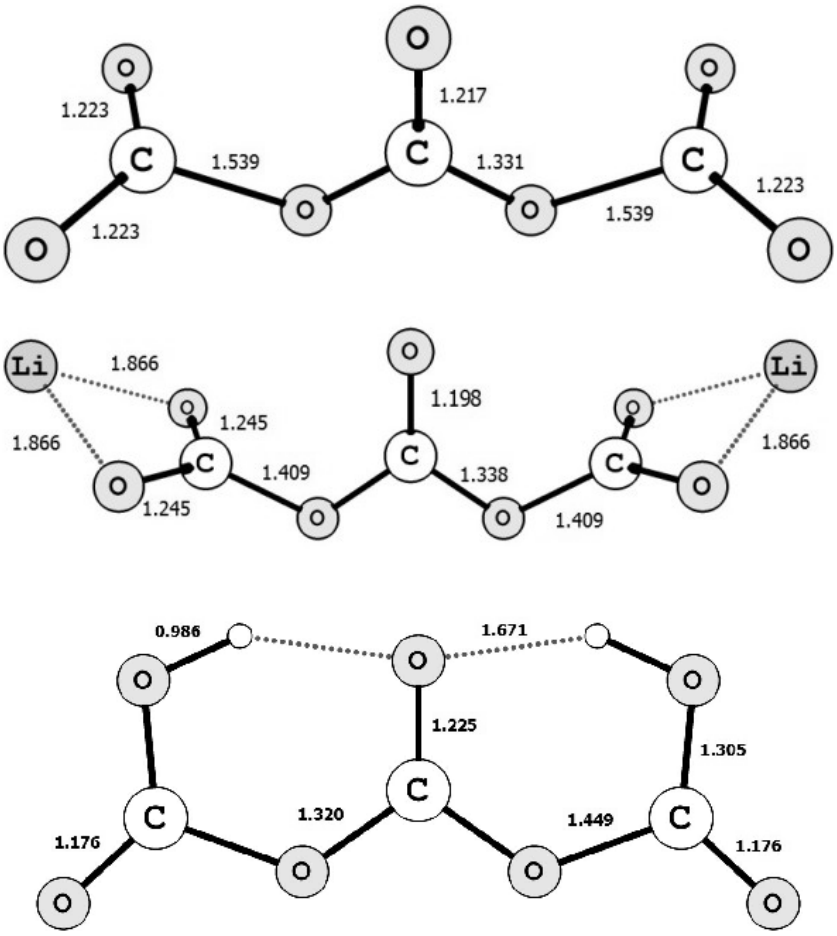

Fig. 3. Equilibrium geometries of $C_4O_9^{2-}$, $C_4O_9Li_2$, and $C_4O_9H_2$.

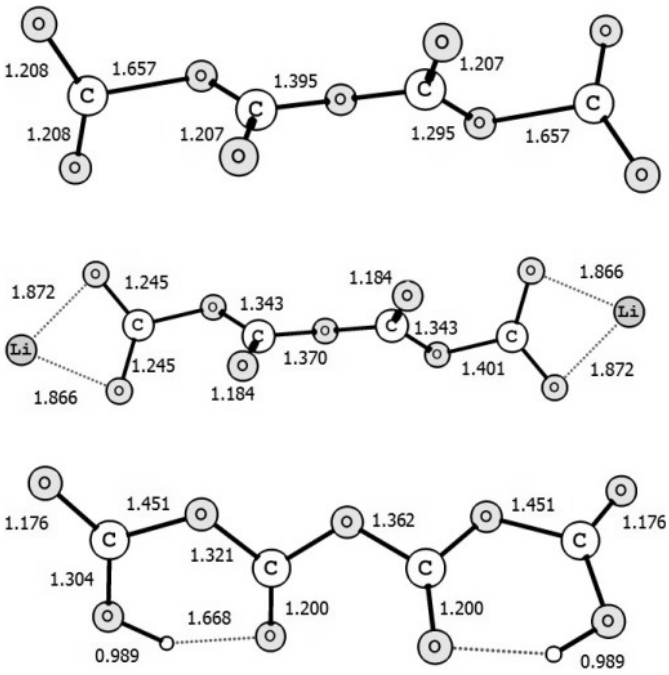

Fig. 4. Equilibrium geometries of $C_5O_{11}^{2-}$, $C_5O_{11}Li_2$, and $C_5O_{11}H_2$.

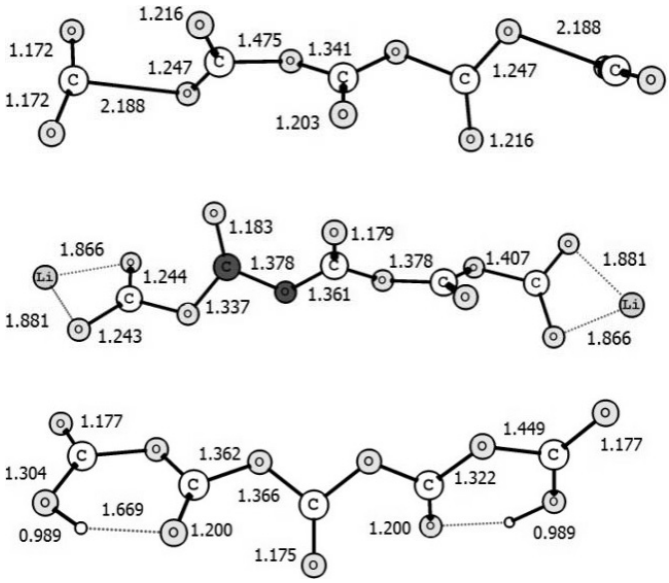

Can. J. Chem. Downloaded from www.nrcresearchpress.com by Xi'an Jiaotong University on 09/19/12
For personal use only.

Fig. 5. Equilibrium geometries of $C_6O_{13}^{2-}$, $C_6O_{13}Li_2$, and $C_6O_{13}H_2$.

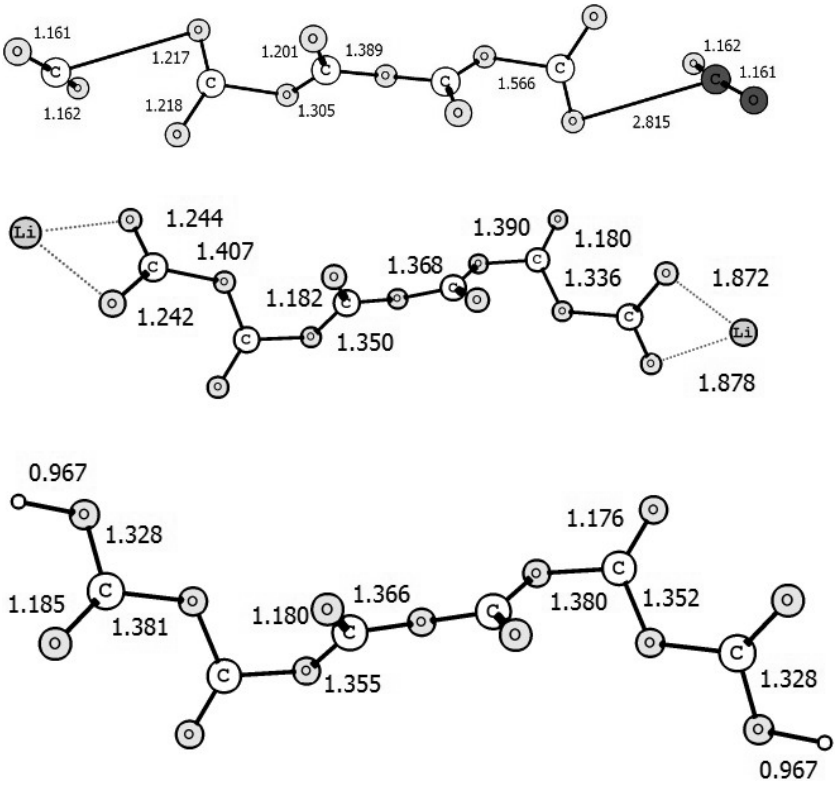

stretching modes in total in this region, we counted the number of modes and marked the (arbitrary) boundary with a left square bracket ([).

Relative stabilities upon CO_2 uptake

Calibration reaction — $CO_3X_2 + CO_2 \rightarrow C_2O_5X_2$ (X = Li or H)

Table 5 lists the gas-phase reaction energy (ΔE_{rxn}) for $CO_3X_2 + CO_2 \rightarrow C_2O_5X_2$ (X = Li or H) and $CO_3^{2-} + CO_2 \rightarrow C_2O_5^{2-}$ as calculated with DFT (B3PW91 and B3LYP) and ab initio (MP4SDTQ and CCSD(T)) methods. Four basis sets were used: cc-pVTZ, 6–311G(2d,p), 6–311++G(2d,p), and 6–311++G(3df,p), labeled from A to D. Note that ΔE_{rxn} is the difference between directly calculated total electronic energies (no zero-point corrections); all electrons are correlated with DFT, but only valence electrons are correlated with the ab initio methods.

Carbon dioxide capture by CO_3X_2 (which is found to be *endothermic* for X = Li and H) depends weakly on the composition of the basis set. For the Li series, the DFT data with B (6–311G(2d,p)) differ by not more than 1 kJ/mol from those obtained with the extended set D (6–311++G(3df,p)). For the H series, however, the endothermicity increases by 7.5 ± 1 kJ/mol in passing from B to C (6–311++G(2d,p)), suggesting the compact basis B does not properly describe the mostly covalent but $C^{\delta-}H^{\delta+}$ polarized bonds in both carbonic and dicarbonic acids. In that regard, the existence in the gas phase of well-defined ion pairs $CO_3^{2-}(Li^+)_2$ and $C_2O_5^{2-}(Li^+)_2$ is consistent with the little influence diffuse functions have on their ΔE_{rxn}s.

For the Li compounds, the median $<\Delta E_{rxn}>$ amounts to 42.9 and 52.5 kJ/mol with B3PW91 and B3LYP, respectively, whereas for the H series, the corresponding values are 56.9 and 65.3 kJ/mol. This comparison indicates that the predicted $<\Delta E_{rxn}>$s are about 9 ± 1 kJ/mol larger with B3LYP than with B3LYP, but not necessarily more accurate. In fact, ab initio calculations at the coupled-cluster level CCSD(T) (and correlating valence electrons only) lead to $<\Delta E_{rxn}>$s that generally lie between both DFT sets (and much closer to the lower B3PW91 values).

The situation is different for isolated dianions because of their unbound character *with respect to spontaneous electron detachment*. The reaction $CO_3^{2-} + CO_2 \rightarrow C_2O_5^{2-}$ is found to be largely *exothermic* ($|\Delta E_{rxn}| \geq 200$ kJ/mol), but the actual value depends strongly on the composition of the basis set. With basis C (i.e., adding a semidiffuse subset *sp* to basis B), we find that ΔE_{rxn} changes from –295 to –231 kJ/mol with B3PW91 or from –291 to –224 kJ/mol with B3LYP (on average, a 22% decrease). As seen in Table 5, a similar degree of destabilization is found with the valence-only CCSD(T) treatment.

In summary, this brief comparison between methods and basis sets indicates that reasonable descriptions are expected to be obtained with (*i*) B3PW91 and basis B for the $C_nO_mLi_2$ series, (*ii*) B3PW91 and basis C for the carbonic acids $C_nO_mH_2$, and (*iii*) the average value between the possibly extreme B3PW91 results calculated with bases B and C.

General energetics for $C_nO_m^{2-} + CO_2 \rightarrow C_{n+1}O_{m+2}^{2-}$

Table 6 summarizes thermodynamic data for CO_2 uptake by several dianions, starting with O^{2-} to form CO_3^{2-} and end-

Table 5. Reaction energy (ΔE_{rxn}, kJ/mol), for CO_2 uptake by CO_3Li_2, CO_3H_2, and CO_3^{2-} using different methods and basis sets.

Reaction	Basis	B3PW91	B3LYP	MP4SDTQ	CCSD(T)
$CO_3Li_2 + CO_2 \rightarrow C_2O_5Li_2$	A	43.2	52.6	48.3	39.4
	B	42.6	51.9	43.2	49.2
	C	43.3	53.2	54.7	45.7
	D	42.5	52.3		
$CO_3H_2 + CO_2 \rightarrow C_2O_5H_2$	A	56.2	64.3	62.2	
	B	53.2	60.5	69.4	54.5
	C	59.6	68.7	72.0	
	D	58.5	67.7		
$CO_3^{2-} + CO_2 \rightarrow C_2O_5^{2-}$	A	–302.2	–271.2	–275.5	–281.5
	B	–294.9	–290.8	–285.7	–291.5
	C	–231.3	–224.4	–219.2	–229.8
	D	–231.4	–222.3	–222.2	

Note: All species are in the gas phase. Basis sets: A, cc-pVTZ; B, 6–311G(2d,p); C, 6–311++G(2d,p); and D, 6–311++G(3df,p). DFT: all electrons correlated; CCSD(T) and MP4SDTQ: frozen core approximation.

Can. J. Chem. Downloaded from www.nrcresearchpress.com by Xi'an Jiaotong University on 09/19/12
For personal use only.

ing with the most complex case studied here, $C_5O_{11}^{2-} + CO_2 \rightarrow C_6O_{13}^{2-}$. The tabulated properties comprise changes in internal energy, ΔE_{rxn} (0 K), as well as enthalpy (H), entropy (S), and Gibbs free (G) energies at normal conditions (T = 298 K and P = 1 atm (1 atm = 101.325 kPa)). The calculations were carried out with the standard B3PW91/6–311G (2d,p) method as codified in Gaussian 03;[31] the corresponding H, S, and G data were obtained from vibrational frequency calculations at the optimized geometries. Note that $|\Delta H^{298}|$ and $|\Delta E_{rxn}|$ differ by <10 kJ/mol. Similar information for the general neutral reactions $C_nO_mX_2 + CO_2 \rightarrow C_{n+1}O_{m+2}X_2$ (X = H, Li, Na, or K) is discussed elsewhere.[42]

Gas-phase results

As seen in Table 6, CO_2 uptake in the gas phase from the simplest (O^{2-}) to the most complex dianion ($C_2O_{11}^{2-}$) is exothermic throughout, from an impressive ΔH^{298} of –1075.5 kJ/mol for the first case to a modest –21 kJ/mol in the last one (sixth reaction). Quite interestingly, the decrease in ΔS for each uptake reaction (a *disorder* → *order* reorganization owing to volume contraction) remains more or less constant along the whole series with a median of 35 ± 6 kJ/mol for $-(T\Delta S)^{298}$.

According to the ΔG (= ($\Delta H - T\Delta S$)) data in Table 6, in the gas phase only the first four uptake reactions can proceed forward as written: ΔS is unfavourable for all six, but only for the last two does this outweigh the favourable ΔH (<0) to give a positive ΔG.

For the general reaction $[C_nO_{2n+1}]^{2-} + CO_2 \rightarrow [C_{n+1}O_{2n+3}]^{2-}$, two single C–O bonds are gained and one C=O broken. In a rather simple model, ΔE_{rxn} ($\approx \Delta H_{rxn}$) can be assumed to result from three contributions: bonds gained ($\Delta E < 0$) + bonds broken ($\Delta E > 0$) + charge delocalization (ΔE_d). Taking 358 and 805 kJ/mol for C–O and C=O, respectively, as reference bond dissociation energies,[43] it follows that $\Delta E_d \approx \Delta E_{rxn} = -89$ (kJ/mol). Using the data in Table 6, one obtains $\Delta E_d \approx$ –1166, –384, and –219 kJ/mol for CO_2 uptake by O^{2-}, CO_3^{2-}, and $C_2O_5^{2-}$, respectively. Clearly, delocalization of the negative charge in excess ($2e^-$) decreases in passing from O^{2-} to CO_3^{2-} to $C_2O_5^{2-}$, as the corresponding molecular volumes increase in the same order. Further, formation of $C_4O_9^{2-}$, $C_5O_{11}^{2-}$, and $C_6O_{13}^{2-}$ is accompanied by ΔE_d values of approx. –147, –121, and –117 kJ/mol, respectively.

Solvent results

It is well-known experimentally that dianions, which are unstable (upon electron detachment) in the gas phase, become stabilized when spatially confined, as in solutions or crystals. Thus, our gas-phase results have been supplemented by others taking account solvent effects as calculated with the PCM of Tomasi et al.[34] Five different solvents were selected, with dielectric constants from 7.58 (THF) to 78.39 (water), which should give a broad picture about changes in ΔG under different conditions (solvents). The free-energy change, ΔG_X, in a given solvent (X) is given by the relationship

$$\Delta G_X = \Delta G_{gas} + [\Delta G_X(\text{solvation, products}) - \Delta G_X(\text{solvation, reactants})]$$

The theoretical treatment becomes physically more realistic when considering solvation effects, whereby dianions are generally stabilized upon electron detachment, and thus these solvation calculations are more realistic for the description of reaction energies. Now, only the first two model reactions in Table 6 are predicted to take place at room temperature (independent of the solvent), that is for the processes $O^{2-} + CO_2 \rightarrow CO_3^{2-}$ and $CO_3^{2-} + CO_2 \rightarrow C_2O_5^{2-}$ (see the following, however). Equivalently, in liquid media O^{2-} is able to capture two CO_2 molecules to form the symmetrical dianion $[O_2C–O–CO_2]^{2-}$. At this point, the following comments are worth noting. First, the nature of the counterions present in solution is of great relevance for the overall reaction mechanism. Although this topic will be discussed in more detail in future articles,[42] one example should clarify our statement: assuming that Li_2O is well soluble in solvent X to give O^{2-} and Li^+ ions, the uptake reaction $O^{2-} + CO_2 \rightarrow CO_3^{2-}$ concurs with another thermodynamically favoured reaction, i.e., the formation of ion pairs, $CO_3^{2-} + Li^+ \rightarrow CO_3Li^-$. Thus, a formal uptake of a second CO_2 by O^{2-} may be hampered by the presence of such a stable CO_3Li^- intermediate (Note: this point is indirectly supported by the endothermicity of the

Can. J. Chem. Downloaded from www.nrcresearchpress.com by Xi'an Jiaotong University on 09/19/12
For personal use only.

Table 6. Energetics (kJ/mol) for reactions forming $[C_nO_{2n+1}]^{2-}$ dianions in gas and selected solvents (B3PW91/6–311(2d,p) data).

		ΔE_{rxn}*	ΔH^{298}	$-(T\Delta S)^{298}$	$-G^{298}$					
Reactants	Products	Gas	Gas	Gas	Gas	THF	Acetone	Acetonitrile	DMSO	Water
$O^{2-} + CO_2$	CO_3^{2-}	–1076.7	–1075.5	32.9	–1042.6	–643.0	–605.7	–596.5	–597.0	–590.7
$CO_3^{2-} + CO_2$	$C_2O_5^{2-}$	–294.9	–290.8	36.7	–254.1	–76.6	–58.4	–54.1	–49.1	–52.3
$C_2O_5^{2-} + CO_2$	$C_3O_7^{2-}$	–129.9	–126.3	40.3	–86.0	25.8	37.0	40.0	42.6	42.5
$C_3O_7^{2-} + CO_2$	$C_4O_9^{2-}$	–57.8	–54.5	40.6	–13.9	69.3	78.2	80.2	79.1	82.2
$C_4O_9^{2-} + CO_2$	$C_5O_{11}^{2-}$	–32.1	–31.6	31.7	0.1	29.5	29.1	28.5	28.9	27.8
$C_5O_{11}^{2-} + CO_2$	$C_6O_{13}^{2-}$	–28.1	–21.0	28.1	7.1	40.0	43.0	43.5	44.2	42.5
$O^- + CO_2^-$	CO_3^{2-}	–10.4	–1.9	45.3	43.4	–328.5	–365.7	–375.2	–380.9	–382.2
$O + CO_2^{2-}$	CO_3^{2-}	–801.7	–789.5	45.4	–744.1	–687.4	–682.3	–681.0	–684.0	–677.7
$CO_3^- + CO_2^-$	$C_2O_5^{2-}$	71.7	87.0	47.8	134.9	–167.6	–197.4	–205.4	–206.0	–212.5
$CO_3^{2-} + 2CO_2$	$C_3O_7^{2-}$	–424.8	–417.1	77.0	–340.1	–50.8	–21.4	–14.1	–6.5	–9.8

Note: Dielectric constants: 7.38 (THF), 20.7 (acetone), 36.64 (acetonitrile), 46.7 (DMSO), and 78.39 (water), as listed in Gaussian 03.[31]

* ΔE_{rxn} is the energy difference between surface minima (i.e., without any type of corrections).

gas-phase reaction $CO_3Li_2 + CO_2 \rightarrow C_2O_5Li_2$ discussed earlier). Second, aprotic solvents should be considered for experimentally studying the first two reactions in Table 6. When protic solvents are used (e.g., water), the reaction $CO_3^{2-} + CO_2 \rightarrow C_2O_5^{2-}$ may not be observed because of the dominance of the solute–solvent interaction, $CO_3^{2-} + H_2O \rightarrow CO_3H^- + OH^-$. Under these conditions, a second uptake of another CO_2 molecule will preferably form CO_3H^- via the reaction $CO_2 + OH^- \rightarrow CO_3H^-$. Third, the reactions $O^{2-} + CO_2 \rightarrow CO_3^{2-}$ and $CO_3^{2-} + CO_2 \rightarrow C_2O_5^{2-}$ are not just of academic interest. Electrochemical studies carried out in molten salts[28] have discussed the occurrence of the reaction $O^{2-} + CO_2 \rightarrow CO_3^{2-}$ at the electrode surface. Also, it was experimentally found that molten CO_3M_2 salts (M = Li, Na, or K) near 1000 K, indeed an aprotic solvent itself, absorbed a large amount of CO_2(gas), possibly owing to the process $CO_3^{2-}{}_{molten} + CO_{2\ gas} \rightarrow C_2O_5^{2-}{}_{molten}$. Indeed, our ΔG calculations for different solvents indicate the reaction above proceeds as written at normal temperatures.

The last four rows in Table 6 are devoted to reactions of general interest. Those involving monoanions, $O^{2-} + CO_2 \rightarrow CO_3^{2-}$ and $CO_3^{2-} + CO_2 \rightarrow C_2O_5^{2-}$, are not favoured in the gas phase ($\Delta G > 0$) because of the Coulomb repulsion between singly charged reactants. However, the solvent calculations provide a different view: formation of CO_3^{2-} or $C_2O_5^{2-}$ should proceed to a large extent, but with reservations, depending on the type of both the solvent (aprotic or not) and counterion present.

Polycarbonic acids, $C_2O_5H_2$, $C_3O_7H_2$, and $C_4O_9H_2$ — High versus low symmetry

As stated earlier, the only works known to us dealing with polycarbonic acids $C_nO_{2n+1}H_2$ (n = 2–6) are the two theoretical studies carried out by Lewars.[25,26] In the 1996 paper,[25] his main results (energetics, equilibrium geometries, and vibrational frequencies) were obtained at a low level of theory (HF/3–21G). In the second article from 2008,[26] an improved treatment was used (B3LYP/6–31G(d)); Lewars stated that the $C_nO_{2n+1}H_2$ geometries shown in both articles were not necessarily the lowest energy conformations. In fact, the isomers previously reported[25,26] *have different equilibrium geometries* (C_1 symmetry, in general) *than those found in this work* (C_s, C_2, or C_{2v}), and it is therefore of interest to reinvestigate some of Lewars polycarbonic acids at the B3PW91/6–311G(2d,p) level. Three acid isomers were chosen: $C_2O_5H_2$ (**3a**), $C_3O_7H_2$ (**3b**), and $C_4O_9H_2$ (**3c**), with Lewars'[25] labelling in parentheses (ref. 25 does not report all equilibrium parameters, so the reoptimization procedure was started using trial geometries after visual inspection of the figures in this reference). Apart from the simple case of $C_2O_5H_2$, it could be that our optimized **3b** and **3c** isomers do not have *exactly* the same spatial conformation as in the original paper, but that is not a substantial drawback as the results below will show. The presently optimized "look-alike" **3a**, **3b**, and **3c** geometries are depicted in Fig. 6, which also includes a third $C_3O_7H_2$ isomer called **3b′** (not reported in ref. 25); according to our calculations, all these species are stationary minima (no imaginary frequencies).

$C_2O_5H_2$ (3a)

Seven different rotational isomers of $C_2O_5H_2$ (dicarbonic

Fig. 6. Equilibrium geometries calculated in this work for low-symmetry (C_1) isomers, including $C_2O_5H_2$ (**3a**), $C_3O_7H_2$ (**3b**), and $C_4O_9H_2$ (**3c**), as reported in ref. 25. $C_3O_7H_2$ (**3b′**) is a new isomer optimized in this work.

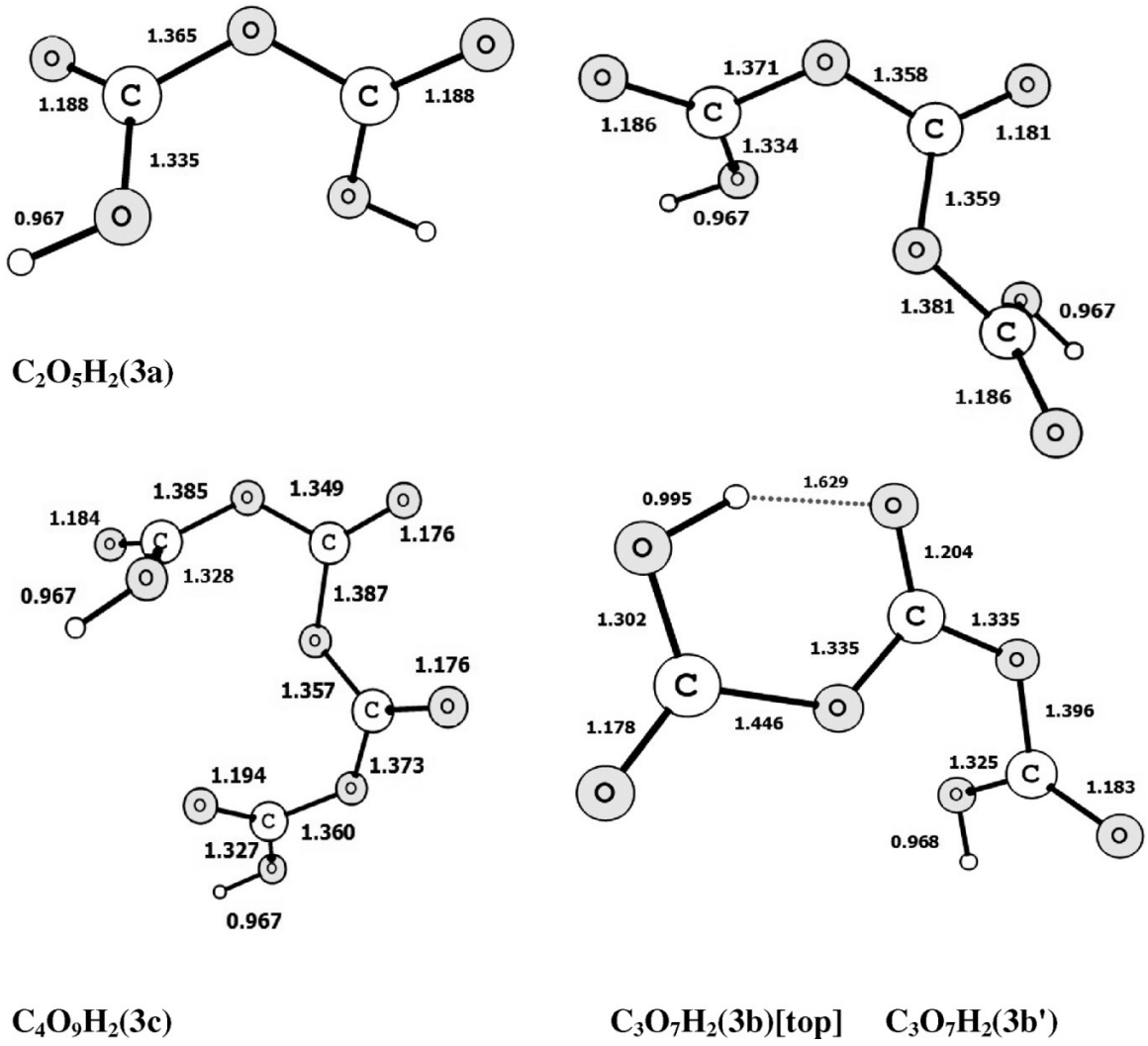

acid) were studied; details of their properties will be the subject of a future article.[42] As discussed previously, we found the most stable $C_2O_5H_2$ conformation to have a planar geometry (C_s), with one H-atom bridge bonded to a carbonyl O atom (dashed lines in Fig. 1) and the second H at a cis position relative to the same O. Energetically, the next isomer, also of C_s symmetry and with the second H at a trans position (not shown in Fig. 6), lies just 2 kJ/mol higher (with both bases B and C: Table 5).

None of the seven isomers look like the $C_2O_5H_2$ (**3a**) species discussed by Lewars.[25] Our calculations find a C_2 structure for **3a** (Fig. 6), in visual agreement with refs. 25 and 26; interestingly, the new CO and OH distances differ by <1 pm from the older ones. The energetics, however, is quite different: the present $C_2O_5H_2$ (**3a**) species lies $\Delta E \approx 28$ kJ/mol above the most stable (C_s) conformation found here (Table 3 and Fig. 1). Basis C, with semidiffuse AOs, leads to $\Delta E \approx 26$ kJ/mol. Taking these findings into account, a ΔE_{rxn} of ≈83 kJ/mol calculated by Lewars[26] for the (gas phase) process $C_2O_5H_2 \rightarrow 2CO_2 + H_2O$ appears to have been overestimated by about 27 kJ/mol.

$C_3O_7H_2$ (3b)

In ref. 25, the C_1 isomer $C_3O_7H_2$ (**3b**) relates to $C_2O_5H_2$ (**3a**) by replacing one H by CO_2H (i.e., the geometry of the C_2O_5 unit is practically the same in both $C_3O_7H_2$ (**3b**) and $C_2O_5H_2$ (**3a**)). Our simulation of **3b** (Fig. 6) reproduces such features; also, the R(CO) distances are close to those given in ref. 25. But again, our calculated relative energies do not support the previous assignment: the present C_1 isomer $C_3O_7H_2$ (**3b**) lies ≈30 kJ/mol higher than the minimum C_{2v} structure assigned here for $C_3O_7H_2$ (Table 3 and Fig. 2). Note that our optimal C_{2v} isomer is strongly stabilized because of the formation of two H bonds relative to the central carbonyl oxygen (Fig. 2).

The new isomer $C_3O_7H_2$ (**3b′**) of C_1 symmetry (Fig. 6) is derived from our $C_3O_7H_2$ (C_{2v}) minimum by keeping one H bond intact and rotating the remaining $-OCO_2H$ to destroy the C_{2v} symmetry. The stabilizing effect of the H bond is clear: the **3b′** isomer lies ≈10 kJ/mol above our most stable C_{2v} conformation (two H bonds), but ~20 kJ/mol lower than the previous $C_3O_7H_2$ (**3b**) structure[25] with no H bonds (the same applies to the 4-CO_2 conformation shown in ref. 26).

Can. J. Chem. Downloaded from www.nrcresearchpress.com by Xi'an Jiaotong University on 09/19/12
For personal use only.

Can. J. Chem. Downloaded from www.nrcresearchpress.com by Xi'an Jiaotong University on 09/19/12
For personal use only.

$C_4O_9H_2$ (3c)

Our simulation of this nonsymmetric (C_1) isomer also has R(CO)s similar to those given by Lewars,[25] but the B3PW91/6–311G(2d,p) calculations find $C_4O_9H_2$ (**3c**) to be less stable, by ~30 kcal/mol (1 cal = 4.184 J), than the minimum C_2 structure assigned here to $C_4O_9H_2$ (Table 3 and Fig. 4).

In summary, geometry reoptimizations of the first $C_nO_{2n+1}H_2$ acids (n = 2, 3, or 4) support the findings that our high-symmetry polycarbonic acids are more stable than those of low symmetry previously reported.[25,26] Since the energy gaps between them lie well above 10 kJ/mol, it is quite improbable that other (C_1) isomers not scanned here may be more stable than our recommended high-symmetry structures. However, a note of caution: the spatially more compact, low symmetry **3a**–**3c** isomers (and similar higher species (n = 5 or 6) studied earlier[25,26]) may play a more relevant role when dealing with *solid* $C_nO_{2n+1}H_2$ systems than the present gas-phase simulations would suggest.

Another point worth noting regarding the equilibrium geometries is as follows: although not so obviously emerging from the (two-dimensional) structures shown in Figs. 2–6, the relative positions of consecutive C=O groups can be seen as generating helicoid-like frameworks (such a behaviour is more clearly discernible by the acyclic isomers depicted in Fig. 11.1 of ref. 26).

Summary and concluding remarks

This study finds a positive answer to the question posed in the Introduction: the dianion CO_3^{2-} is a simple nucleophilic system that can successively bind several CO_2s to form $CO_3^{2-}(CO_2)_n$ compounds with strong CO bonds throughout. Indeed, one factor contributing to the stability of these systems is delocalization of the extra electronic charge upon an increase in molecular size. Stabilization is additionally attained by capping both terminal $-COO^-$ groups by counterions (forming ion pairs) or H atoms (forming polycarbonate – dicarboxylic acids).

Our B3PW91/6–311G(2d,p) study on $[C_nO_{2n+1}]^{2-}$ and $[C_nO_{2n+1}]X_2$ (X = Li or H), with n = 2–6, finds several (C_s, C_2, C_{2v}) species containing chainlike $[C_nO_{2n+1}]$ moieties to be structurally stable, as pointed out by standard single and double CO bond distances and real frequencies throughout. (No attempts were made to calculate dissociation barriers of the present compounds, but the existence of relatively short C–O bonds, and correspondingly high stretching frequencies, would suggest the existence of sizeable dissociation barriers. See also ref. 26.) Similar findings regarding bond distances and frequencies were reported by Lewars[25,26] for dicarboxylic acids $[C_nO_{2n+1}]H_2$ (n = 2–6), and by Frapper and Saillard[27] for $[C_nO_{2n-1}]H_2$ (n = 2–5) molecules with fixed trans O′=C–O–C=O′ units. In general, the higher symmetry compounds studied here are more stable than those discussed in refs. 25 and 26.

Although the gaseous dianions are unstable upon electron detachment, this study shows that they stabilize in the presence of Li^+ ions, without substantial changes in their geometrical structures for n = 2, 3, or 4 (the same feature holds for $[C_nO_{2n+1}]X_2$, X = Na or K).[42] The reported geometries, frequencies, and IR–Raman intensities should help in the future characterization of these $[C_nO_{2n+1}]X_2$ ionic crystals.

To the best of our knowledge, none of these chainlike CO_2 compounds have been synthesized in the laboratory, although $C_2O_5X_2$ and $C_3O_7X_2$ esters are well-known commercially available liquid compounds at room temperature and widely used in biochemistry studies and the food industry.[13–19] We hope experimental chemists will be able to find ways to replace these X–alkyls groups by X = H or alkali-metal to synthesize some of the compounds presented here. Indeed, as is also pointed out by Lewars,[26] these CO_2 chainlike compounds could be potential candidates for high-energy density materials, as, for example, $C_nO_{2n+1}H_2$ compounds decompose *exothermically* into $nCO_2 + H_2O$ products, but they are locally stable because of the existence of substantial dissociation barriers.

In general, as the index n increases, the bond distances in $[C_nO_{2n+1}]X_2$ (X = Li or H) approximately approach three characteristic <R(CO)> values: (*i*) 118 (±1), (*ii*) 122 (±2), and (*ii*) 136 (±4) pm. By comparing these R values with the information in Tables 1 and 2, the short distances in group (*i*) can be associated with a C=O double bond (e.g., R = 115.9 and 119.0 pm in CO_2 and acetic anhydride, respectively). The intermediate R values (group (*ii*)) are close to R(CO) = 123.9 pm in CO_2^-, which can be considered a weakly CO double bond. Finally, the group (*iii*) values (132–140 pm) may be roughly correlated with the (singlelike) bonds in CO_3^{2-} (130.3 pm) and CO_2^{2-} (131.9 pm), to the extreme case of $O(CH_3)_2$ with R(CO) = 140.3 pm. Clearly, the various CO bonds in all present neutral $[C_nO_{2n+1}]X_2$ compounds are strong. The situation is somewhat less clear-cut for the isolated higher dianions (n = 5 or 6) where anomalously larger R(CO) distances are predicted (>145 pm and up to ≈280 pm; Tables 3 and 4). Clearly, the presence of X^+ counterions, or the formation of OH bonds, strongly stabilizes such floppy dianionic structures in the gas phase.

Our vibrational calculations indicate that the strong absorptions owing to C=O double bonds should help in the experimental characterization of these species, noting that $[C_nO_{2n+1}]X_2$ has as many C=O bonds as C atoms. On the other hand, C–O stretching modes associated with the C–O–C groups appear at lower frequencies and have moderately high intensities (Supplementary data). They lie in a congested area, owing to the larger number of C–O–C bonds as well as their mixing with other modes (e.g., δ(C–O–C) bending in all species as well as ν(C–OH) and δ(COH) modes in dicarboxylic acids).

Recently, spectroscopic studies[44] have been able to analyze the rovibrational spectrum of gas-phase carbonic acid (CO_3H_2) after many years of having been declared as nonexistent by traditional chemistry textbooks, which is close to the truth when dealing with the overall reaction $CO_2(g) + H_2O(l) \leftrightarrow CO_3H_2(aq)$, since the concentration of the latter has been estimated to be small.[45] According to the literature,[46] gaseous carbonic acid may play a relevant role in astrophysics, mostly in those regions where CO_2 and ice (water) are abundant, as, for example, in comets and, particularly, the planet Mars. Under those conditions, it could be possible that dicarbonic acid ($C_2O_5H_2$) also exists.

Our solvation calculations find that the CO_2 uptake reactions by O^{2-} and CO_3^{2-} (to form CO_3^{2-} and $C_2O_5^{2-}$, respec-

tively) are the only ones to proceed spontaneously ($\Delta G < 0$) in any type of solvent, although protic solvents should be avoided. These theoretical results agree with the experimental observations that CO_3Li_2(molten), for example, is an optimal absorber of CO_2(g). As well, it is also possible that the formation of solid polycarbonates $C_nO_{2n+1}R_2$ (R = large-size group) can be used for large-scale CO_2(g) uptake, which is a topic under current investigation in our laboratory.[42]

Supplementary data

Supplementary data (B3PW91/G–311G(2d,p) total energies, equilibrium geometries, and vibrational frequencies (including IR and Raman intensities) for the compounds discussed in the text) are available with the journal article through the journal Web site (www.nrcresearchpress.com/cjc).

Acknowledgment

The authors thank the Natural Sciences and Engineering Research Council of Canada (NSERC) for financial support, via Discovery (F.G.) and Strategic (J.P.) Grants. The Atlantic Computational Excellence Network (ACEnet) is also gratefully acknowledged for providing the computer time essential for carrying out this study.

References

(1) Baba, T.; Takeuchi, M.; Nakai, H. *Chem. Phys. Lett.* **2006**, *424* (1–3), 193. doi:10.1016/j.cplett.2006.03.098.
(2) Nelson, M. R.; Borkman, R. F. *J. Phys. Chem. A* **1998**, *102* (40), 7860. doi:10.1021/jp981824u.
(3) Teague, C. M.; Dai, S.; Jian, D.-e. *J. Phys. Chem. A* **2010**, *114* (43), 11761. doi:10.1021/jp1056072.
(4) Jhon, Y. H.; Shim, J.-G.; Kim, J.-H.; Lee, J. H.; Jang, K.-R.; Kim, J. *J. Phys. Chem. A* **2010**, *114* (49), 12907. doi:10.1021/jp105914c.
(5) Kafafi, Z. H.; Hauge, R. H.; Billups, W. E.; Margrave, J. L. *J. Am. Chem. Soc.* **1983** *105*, (12), 3886. doi:10.1021/ja00350a025.
(6) Kafafi, Z. H.; Hauge, R. H.; Billups, W. E.; Margrave, J. L. *Inorg. Chem.* **1984**, *23* (2), 177. doi:10.1021/ic00170a013.
(7) Manceron, L.; Loutellier, A.; Perchard, J. P. *J. Mol. Struct. (Theochem)* **1985**, *129*, 115.
(8) Ramondo, F.; Sanna, N.; Bencivenni, L. *Chem. Phys. Lett.* **1991**, *180* (4), 369. doi:10.1016/0009-2614(91)90336-8.
(9) Takeuchi, H. *J. Phys. Chem. A* **2008**, *112* (33), 7492, and refs. cited therein. doi:10.1021/jp802872p.
(10) Shin, J.-W.; Hammer, N. I.; Johnson, M. A.; Schneider, H.; Glöβ, A.; Weber, J. M. *J. Phys. Chem. A* **2005**, *109* (14), 3146. doi:10.1021/jp050092k.
(11) Fleischman, S. H.; Jordan, K. D. *J. Phys. Chem.* **1987**, *91* (6), 1300. doi:10.1021/j100290a006.
(12) Iota, V.; Yoo, C. S.; Cynn, H. *Science* **1999**, *283* (5407), 1510. doi:10.1126/science.283.5407.1510.
(13) Bilde, M.; Møgelberg, T. E.; Sehested, J.; Nielsen, O. J.; Wallington, T. J.; Hurley, M. D.; Japar, S. M.; Dill, M.; Orkin, V. L.; Buckley, T. J.; Huie, R. E.; Kurylo, M. J. *J. Phys. Chem. A* **1997**, *101* (19), 3514. doi:10.1021/jp961664r.
(14) Kozlova, S. A.; Emel'yanenko, V. N.; Georgieva, M.; Verevkin, S. P.; Chernyak, Y.; Schäffner, B.; Börner, A. *J. Chem. Thermodyn.* **2008**, *40* (7), 1136. doi:10.1016/j.jct.2008.02.012.
(15) Pope, B. M.; Sheu, S.-J.; Stanley, R. L.; Tarbel, D. S.; Yamamoto, Y. *J. Org. Chem.* **1978**, *43* (12), 2410. doi:10.1021/jo00406a023.
(16) Greener, B.; Walton, P. H. *J. Chem. Soc., Dalton Trans.* **1997**, 3733. doi:10.1039/a705144a.
(17) Dean, C. S.; Tarbell, D. S. *J. Org. Chem.* **1971**, *36* (9), 1180. doi:10.1021/jo00808a003.
(18) Henke, S. L.; Hadad, C. M.; Morgan, K. M.; Wiberg, K. B.; Wasserman, H. H. *J. Org. Chem.* **1993**, *58* (10), 2830. doi:10.1021/jo00062a029.
(19) Nagai, A.; Sato, D.; Ishikawa, J.; Ochiai, B.; Kudo, H.; Endo, T. *Macromolecules* **2004**, *37* (7), 2332. doi:10.1021/ma0498464.
(20) Pastre, J., Mueller, U., Schubert, M., Kiener, C., Teich, F., Poplow, F. *Patent No. WO 2007101797*, 2007. C4O9H2, CAS number: 177962-75-3.
(21) Kumar, P. P.; Kalinichev, A. G.; Kirkpatrick, R. J. *J. Chem. Phys.* **2007**, *126* (20), 204315. doi:10.1063/1.2741552.
(22) (a) Ramondo, F.; Bencivenni, L. *J. Mol. Struct.* **1990**, *221* (1–2), 169. doi:10.1016/0022-2860(90)80400-E;; (b) Ramondo, F.; Bencivenni, L.; Sanna, N.; Cesaro, S. N. *J. Mol. Struct. THEOCHEM* **1992**, *253*, 121. doi:10.1016/0166-1280(92)87102-6.
(23) KatonJ. E.; , CohenM. D. *Can. J. Chem.***1975**1378.
(24) Lang, P. L.; Katon, J. E. *J. Mol. Struct.* **1988**, *172*, 113. doi:10.1016/0022-2860(88)87010-8.
(25) Lewars, E. *J. Mol. Struct. THEOCHEM* **1996**, *363* (1), 1. doi:10.1016/0166-1280(95)04420-5.
(26) Lewars, E. *Modeling Marvels: Computational Anticipation of Novel Molecules;* Springer Verlag: Amsterdam, 2008.
(27) Frapper, G.; Saillard, J.-Y. *J. Am. Chem. Soc.* **2000**, *122* (22), 5367. doi:10.1021/ja9935714.
(28) Claes, P.; Moyaux, D.; Peeters, D. *Eur. J. Inorg. Chem.* **1999**, *1999* (4), 583. doi:10.1002/(SICI)1099-0682(199904)1999:4<583::AID-EJIC583>3.0.CO;2-Y.
(29) Claes, P.; Moyaux, D.; Peeters, D. *Eur. J. Inorg. Chem.* **1999**, 589.
(30) Zeller, K.-P.; Schuler, P.; Haiss, P. *Eur. J. Inorg. Chem.* **2005**, *2005* (1), 168. doi:10.1002/ejic.200400445.
(31) Frisch, M. J.; Trucks, G. W.; Schlegel, H. B.; Scuseria, G. E.; Robb, M. A.; Cheeseman, J. R.; Montgomery, J. A., Jr.; Vreven, T.; Kudin, K. N.; Burant, J. C.; Millam, J. M.; Iyengar, S. S.; Tomasi, J.; Barone, V.; Mennucci, B.; Cossi, M.; Scalmani, G.; Rega, N.; Petersson, G. A.; Nakatsuji, H.; Hada, M.; Ehara, M.; Toyota, K.; Fukuda, R.; Hasegawa, J.; Ishida, M.; Nakajima, T.; Honda, Y.; Kitao, O.; Nakai, H.; Klene, M.; Li, X.; Knox, J. E.; Hratchian, H. P.; Cross, J. B.; Adamo, C.; Jaramillo, J.; Gomperts, R.; Stratmann, R. E.; Yazyev, O.; Austin, A. J.; Cammi, R.; Pomelli, C.; Ochterski, J. W.; Ayala, P. Y.; Morokuma, K.; Voth, G. A.; Salvador, P.; Dannenberg, J. J.; Zakrzewski, V. G.; Dapprich, S.; Daniels, A. D.; Strain, M. C.; Farkas, O.; Malick, D. K.; Rabuck, A. D.; Raghavachari, K.; Foresman, J. B.; Ortiz, J. V.; Cui, Q.; Baboul, A. G.; Clifford, S.; Cioslowski, J.; Stefanov, B. B.; Liu, G.; Liashenko, A.; Piskorz, P.; Komaromi, I.; Martin, R. L.; Fox, D. J.; Keith, T.; Al-Laham, M. A.; Peng, C. Y.; Nanayakkara, A.; Challacombe, M.; Gill, P. M. W.; Johnson, B.; Chen, W.; Wong, M. W.; Gonzalez, C.; Pople, J. A. *Gaussian 03,* Revision-B.04; Gaussian Inc.: Pittsburgh, PA, 2003.
(32) Zhurko, G. A.; Zhurko, D. A. ChemCraft. http://www.chemcraftprog.org.
(33) Sommerfeld, T. *J. Phys. Chem. A* **2000**, *104* (38), 8806. doi:10.1021/jp0017590.

Can. J. Chem. Downloaded from www.nrcresearchpress.com by Xi'an Jiaotong University on 09/19/12
For personal use only.

(34) Tomasi, J.; Mennucci, B.; Cammi, R. *Chem. Rev.* **2005**, *105* (8), 2999. doi:10.1021/cr9904009.
(35) Bellamy, L. J. *The Infra-Red Spectra of Complex Molecules,* 3rd ed.; Chapman and Hall: London, 1975.
(36) Hameka, H. F. *J. Mol. Struct. THEOCHEM* **1991**, *226* (3–4), 241. doi:10.1016/0166-1280(91)85005-R.
(37) Blom, C. E.; Altona, C.; Oskam, A. *Mol. Phys.* **1977**, *34* (2), 557. doi:10.1080/00268977700101901.
(38) Asselin, P.; Soulard, P.; Alikhani, M. E.; Perchard, J. P. *Chem. Phys.* **1999**, *249* (1), 73. doi:10.1016/S0301-0104(99)00251-7.
(39) Mirone, P.; Fortunato, B.; Canziani, P. *J. Mol. Struct.* **1970**, *5* (4), 283. doi:10.1016/0022-2860(70)80031-X.
(40) Redington, R. L.; Redington, T. E. *J. Mol. Struct.: THEOCHEM* **1978**, *48*, 165.
(41) Thompson, H. W.; Cave, W. T. *Trans. Faraday Soc.* **1951**, *47*, 946. doi:10.1039/tf9514700946.
(42) Unpublished results of this laboratory.
(43) Johnson, D. A. *Some Thermodynamic Aspects of Inorganic Chemistry,* 2nd ed.; Cambridge UK: Cambridge, 1982.
(44) Mori, T.; Suma, K.; Sumiyoshi, Y.; Endo, Y. *J. Chem. Phys.* **2009**, *130* (20), 204308. doi:10.1063/1.3141405.
(45) Adamczyk, K.; Prémont-Schwarz, M.; Pines, D.; Pines, E.; Nibbering, E. T. J. *Science* **2009**, *326* (5960), 1690, and refs. cited therein. doi:10.1126/science.1180060.
(46) Hage, W.; Liedl, K. R.; Hallbrucker, A.; Mayer, E. *Science* **1998**, *279* (5355), 1332. doi:10.1126/science.279.5355.1332.

Can. J. Chem. Downloaded from www.nrcresearchpress.com by Xi'an Jiaotong University on 09/19/12
For personal use only.

Synthesis, Rietveld refinement of crystal structure, electron diffraction, and electrical transport properties of $Ba_2(Ca_{1-x-y}Fe_xNb_y)(Nb_{1-z}Fe_z)O_{6-\delta}$ double perovskites

Wang Hay Kan, Trang T. Trinh, Tobias Fürstenhaupt, and Venkataraman Thangadurai

Can. J. Chem. Downloaded from www.nrcresearchpress.com by Xi'an Jiaotong University on 09/19/12
For personal use only.

Abstract: We report the synthesis, crystal structure, and electrochemical properties of new Fe-doped $Ba_2(Ca_{1-x-y}Fe_xNb_y)(Nb_{1-z}Fe_z)O_{6-\delta}$ (Fe–BCN). The Fe–BCN was synthesized by a solid-state method in air using corresponding metal oxides and salts at elevated temperature. All of the observed powder X-ray diffraction (PXRD) peaks of the investigated Fe–BCN were indexed as cubic *Fm*-3*m* (space group No. 225) double perovskite-type structure with cell constants $a \sim 8.4$ Å and is consistent with selected area electron diffraction (SAED). Rietveld analysis suggested the distribution of Fe was at both *4a* and *4b* sites, supported the proposed chemical formula $Ba_2(Ca_{1-x-y}Fe_xNb_y)(Nb_{1-z}Fe_z)O_{6-\delta}$. This was further verified by bond valence sum (BVS) analysis of the cations. The Fe–BCN showed superior chemical stability in pure CO_2 and boiling H_2O confirmed by PXRD and FTIR. The electrical conductivity was determined by AC impedance spectroscopy. Among the samples investigated, $Ba_2(Ca_{0.79}Fe_{0.21})(Nb_{0.71}Fe_{0.29})O_{6-\delta}$ showed the highest total (bulk + grain-boundary) conductivity of 1.1×10^{-2} S cm^{-1} in humidified (3%) N_2 at 600 °C with activation energy of 0.43 eV in the temperature range 200–800 °C.

Key words: protonic conductors, perovskites, Fe–BCNs, mixed ionic and electronic conductors (MIECs), solid oxide fuel cells (SOFCs), anodes, Rietveld refinement, AC impedance spectroscopy, selected area electron diffraction (SAED), powder X-ray diffraction (PXRD).

Résumé : On a effectué la synthèse, déterminé la structure cristalline et mesuré les propriétés électrochimiques de nouveaux $Ba_2(Ca_{1-x-y}Fe_xNb_y)O_{6-\delta}$ dopés au fer (Fe–BCN). Les Fe–BCN ont été synthétisés par une méthode à l'état solide, dans l'air, en utilisant les oxydes et des sels des métaux correspondants, à des températures élevées. Toutes les raies des spectres de diffraction des rayons-X de poudres (DRXP) des Fe–BCN étudiés ont été indexées comme des structures cubiques *Fm-3m* (groupe d'espace No. 225) de type perovskite double avec des constantes de maille de $\alpha \sim 8{,}4$ Å qui est en accord avec la diffraction électronique d'une surface choisie (DESC). Une analyse de Rietveld suggère que la distribution du Fe se fait tant sur les sites *4a* que *4b* qui est en accord avec la formule chimique proposée $Ba_2(Ca_{1-x-y}Fe_xNb_y)O_{6-\delta}$. Cette hypothèse a aussi été confirmée par une analyse de la somme des valences de liaison (SVL) des cations. La stabilité chimique supérieure du Fe–BCN dans le CO_2 pur et dans l'eau bouillante a été confirmée par DRXP et par infrarouge à transformée de Fourier (IR-TF). On a déterminé la conductivité électrique par spectroscopie d'impédance en courant alternatif (CA). Parmi les échantillons étudiés, le $Ba_2(Ca_{0,79}Fe_{0,21})(Nb_{0,71}Fe_{0,29})O_{6-\delta}$ présente la conductivité totale (ensemble + limite des grains) la plus élevée, $1{,}1 \times 10^{-2}$ S cm^{-1}, dans de l'azote humidifié (3 %), à 600 °C, avec une énergie d'activation de 0,43 eV dans la plage de température allant de 200 à 800 °C.

Mots-clés : conducteurs protoniques, perovskite, Fe–BCN, conducteurs mixtes ionique et électronique (CMIE), piles à combustible à oxyde solide (PCOS), anodes, affinement de Rietveld, spectroscopie d'impédance à courant alternatif, diffraction électronique d'une surface choisie (DESC), diffraction des rayons X de poudres (DRXP).

[Traduit par la Rédaction]

Introduction

Proton conduction in the perovskite-type (ABO_3 A = divalent or trivalent metal ions; B = trivalent or tetravalent metal ions) oxide was pioneered by Iwahara et al.[1] in 1981. The acceptor-doped $SrCe_{0.95}Yb_{0.05}O_{3-\delta}$ compound exhibited an appreciably high proton conductivity of 5×10^{-2} S cm^{-1} at 800 °C in humidified H_2.[1] The proton conduction arises because of the partial occupation of oxide vacancy sites ($V_O^{\bullet\bullet}$) by H_2O; the subsequent formation of hydroxyl protons ($OH_O^{\bullet}$) and can be described using Kröger–Vink notation:[2,3]

$$[1] \qquad H_2O + V_O^{\bullet\bullet} + O_O^{x} \rightarrow 2OH_O^{\bullet}$$

Received 4 November 2010. Accepted 2 March 2011. Published at www.nrcresearchpress.com/cjc on 23 June 2011.

W.H. Kan, T.T. Trinh, T. Fürstenhaupt, and V. Thangadurai. Department of Chemistry, University of Calgary, 2500 University Dr. NW, Calgary, AB T2N 1N4, Canada.

Corresponding author: Venkataraman Thangadurai (e-mail: vthangad@ucalgary.ca).

Fig. 1. Powder X-ray diffraction (PXRD) Rietveld refinement plots of (*a*) $Ba_2Ca_{0.67}Fe_{0.33}NbO_{6-\delta}$ (**I**), (*b*) $Ba_2(Ca_{0.67}Fe_{0.165}Nb_{0.165})(Nb)O_{6-\delta}$ (**II**), (*c*) $Ba_2(Ca_{0.79}Fe_{0.16}Nb_{0.05})(Nb)O_{6-\delta}$ (**III**), (*d*) $Ba_2(Ca_{0.79}Fe_{0.21})(Nb_{0.98}Fe_{0.02})O_{6-\delta}$ (**IV**), and (*e*) $Ba_2(Ca_{0.79}Fe_{0.21})(Nb_{0.71}Fe_{0.29})O_{6-\delta}$ (**V**) using the *Fm*-3*m* (No. 225) space group.

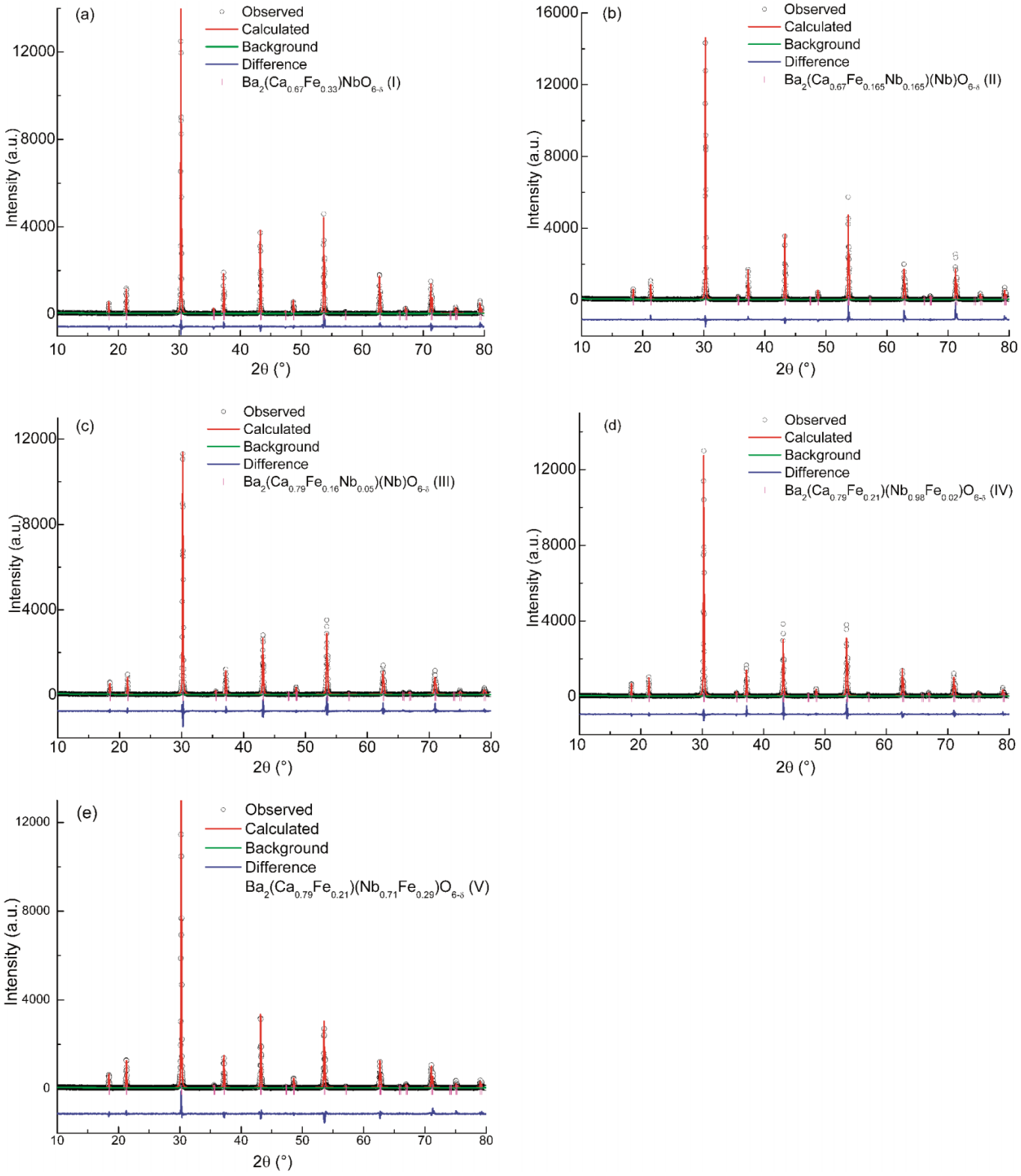

Can. J. Chem. Downloaded from www.nrcresearchpress.com by Xi'an Jiaotong University on 09/19/12
For personal use only.

Can. J. Chem. Downloaded from www.nrcresearchpress.com by Xi'an Jiaotong University on 09/19/12
For personal use only.

where O_O^x represents the lattice oxygen in the perovskite lattices. The hydroxyl protons are highly mobile and can hop from one O^{2-} ion site to the adjacent site through the Grotthuss mechanism.[4] Commonly, AC impedance and DC polarization methods were used to measure the proton conductivity,[5] and neutron diffraction (ND),[6] Fourier transform infrared (FTIR) spectroscopy, and thermogravimetry (TG) were employed to characterize the crystal structure and chemical stability.[7] Among the perovskite-type oxides, rare-earth-doped $BaCeO_3$ was found to be chemically unstable in CO_2 or H_2O at elevated temperatures,[8,9] whereas B-site ordered double perovskite $Ba_3Ca_{1+x}Nb_{2-x}O_{9-\delta}$ (BCN) showed superior chemical tolerance.[10,11]

Recently, we investigated the effect of Ta substitution for Nb in BCN on proton conductivity and chemical stability under pure CO_2 and boiling H_2O.[12] Among the double perovskites reported in the literature, $Ba_3Ca_{1.18}Nb_{1.82}O_{9-\delta}$ (BCN18), is one of the most representative compounds because of its high proton conductivity of 1.8×10^{-2} S cm^{-1} at 600 °C in humidified atmospheres.[11,13] In the present work, an attempt was made to convert the proton-conducting BCN into mixed proton and electronic conductors (MPECs) through the partial substitution of Ca and Nb by transition metal ions, such as Fe, at low oxygen partial pressures (pO_2), for application as anodes for solid oxide fuel cells (SOFCs).

Experimental section

Synthesis

All Fe–BCNs were prepared by the solid-state method in air using stoichiometric amounts of ACS grade $Ba(NO_3)_2$ (99+%, Alfa Aesar), $CaCO_3$ (99%, Fisher Scientific Company), Nb_2O_5 (99.5%, Alfa Aesar), and Fe_2O_3 (98+%, Alfa Aesar). The precursors were ball-milled (Pulverisette, Fritsch, Germany) in 2-propanol using ZrO_2 balls for 6 h at 200 rpm and then dried in an oven at 100 °C. Subsequently, it was calcinated at 900 °C for 14 h at a 5–10 °C/min ramp rate in a clean alumina crucible. The resultant powdery samples were first ball-milled for another 6 h and then pressed into pellets (~1 cm in diameter and ~2 cm long) using isostatic pressure (1.2×10^8 Pa for ~2 min). The pellets were finally sintered at 1300–1500 °C for 14 h in air.

Characterization

Solid phases were identified by powder X-ray diffraction (PXRD) (Bruker D8 Advance powder X-ray diffractometer Cu Kα, 40 kV, 40 mA) from $2\theta = 10°$ to 80° at a count rate of 15 s per step of 0.02° at room temperature. The PXRD was refined by the Rietveld method using the GSAS package with the EXPGUS interface.[14] Background, scale factors, zero-point positions, cell parameters, atomic positions, and profile coefficients for the Pseudo-Voight/FCJ asymmetric peak-shape function were refined until the convergence was achieved. The displacement parameters (temperature factors) for the *4a* and *4b* sites were not refined meaningfully, possibly because of the disorder. Alternatively, the parameter for *4a* was fixed to $U_{iso} = 0.015$ Å^2 and *4b* was fixed to $U_{iso} = 0.01$ Å^2. Those values are comparable to Ca and Nb atoms in other perovskites in the literature.[15,16] Bond lengths were obtained with the DISAGL Version Win32 crystal structure distance and angle program in the GSAS packet on XRD data sets.[14] Bond valence sums (BVS) of cations were calculated with the Bond Valence Calculator Version 2.[17,18]

Fig. 2. Idealized structure of Fe-doped $Ba_2(Ca_{0.67}Fe_{0.33})(Nb)O_{6-\delta}$.

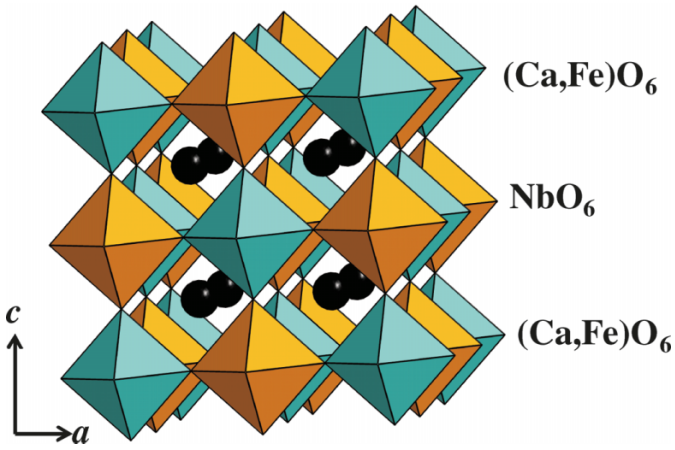

A Philips XL 30 conventional scanning electron microscope equipped with an energy dispersive X-ray spectrometer (EDX) was used to study the morphology of the investigated Fe–BCN. Images were recorded at 20 kV with a secondary electron detector. Selected area electron diffraction (SAED) was performed on a FEI Tecnai F20 FEG-TEM (FEI, Eindhoven, The Netherlands) equipped with a Gatan imaging filter and a Gatan 860 GIF 2001 CCD of 1024 pixel × 1024 pixel resolution. Ex-situ PXRD, FTIR, and SEM were used to access the chemical stability of the samples in pure CO_2 at 800 °C for 14–20 h and boiling H_2O for at least 72 h. Prior to the FTIR measurements, samples were grounded with dried KBr and pressed into pellets. The pellets were measured in a NEXUS 470 FTTR spectrometer.

The sintered pellets were cut into smaller pellets (1.5 mm thickness and ~10 mm in diameter) for the electrical conductivity measurements using AC impedance spectroscopy (Solartron Electrochemical Impedance Spectroscopy; SI model No. 1260, 100 mV, 0.01 Hz to 7 MHz). The pellets were painted with Pt paste (LP A88-11S, Heraeus Inc., Germany) on both sides at room temperature and subsequently heated to 900 °C for 1 h to remove the organic binders. The pellets were connected with Pt wires using spring-loaded contact. The temperatures of the electrochemical cells were controlled by a Barnstead tubular furnace (model No. 21100) in a range of 200–800 °C. The cells were stabilized at constant temperature for 1 h prior to each AC impedance measurement and were made upon heating and cooling cycles to ensure the reproducibility.

Results and discussion

Structural analysis

The parent phase $Ba_3CaNb_2O_9$ was found to exhibit as hexagonal *P-3m1* (space group No. 164) with 1:2 ordering on B sites (*1b* and *2d*),[11,19] as cubic *Fm-3m* (space group No. 225) with 1:1 ordering on B sites (*4a* and *4b*),[19,20] and as B-site disordered simple cubic *Pm3m* (space group No. 221) structures.[21] We indexed all diffraction peaks of Fe–BCN

Table 1. Comparison of Rietveld refinement results of $Ba_2(Ca_{1-x-y}Fe_xNb_y)(Nb_{1-z}Fe_z)O_{6-\delta}$ using *Fm*-3*m* (No. 225) as the space group for all structural models.

Compound	Atom	Wyckoff notation	*x*, *y*, *z*	U_{iso} (100 Å^2)	Occupancy
$Ba_2(Ca_{0.67}Fe_{0.33})(Nb)O_{5.67}$	Ba	*8c*	0.25, 0.25, 0.25	0.63(5)	1
	Ca	*4a*	0, 0, 0	1.5	0.67
Fm-3m; a = 8.37402(8) Å	Fe	*4a*	0, 0, 0	1.5	0.33
$_wR_p$: 10.33, R_p: 7.48, χ^2: 2.02	Nb	*4b*	0.5, 0.5, 0.5	2.4(1)	1
	O	*24e*	0.2462(7), 0, 0	3.6(2)	0.945
$Ba_2(Ca_{0.67}Fe_{0.165}Nb_{0.165})(Nb)O_{5.83}$	Ba	*8c*	0.25, 0.25, 0.25	0.16(5)	1
	Ca	*4a*	0, 0, 0	1.5	0.67
Fm-3m; a = 8.3785(3) Å	Fe	*4a*	0, 0, 0	1.5	0.167
$_wR_p$: 12.56, R_p: 9.38, χ^2: 2.219	Nb	*4a*	0, 0, 0	1.5	0.167
	Nb	*4b*	0.5, 0.5, 0.5	1	1
	O	*24e*	0.2586(7), 0, 0	3.0(2)	0.972
$Ba_2(Ca_{0.79}\ Fe_{0.16}Nb_{0.05})(Nb)O_{5.65}$	Ba	*8c*	0.25, 0.25, 0.25	0.46(6)	1
	Ca	*4a*	0, 0, 0	1.5	0.787
Fm-3m; a = 8.4186(2) Å	Fe	*4a*	0, 0, 0	1.5	0.167
$_wR_p$: 13.26, R_p: 10.79, χ^2: 2.319	Nb	*4a*	0, 0, 0	1.5	0.047
	Nb	*4b*	0.5, 0.5, 0.5	1	1
	O	*24e*	0.2556(9), 0, 0	3.4(3)	0.942
$Ba_2(Ca_{0.79}\ Fe_{0.21})(Nb_{0.98}Fe_{0.02})O_{5.59}$	Ba	*8c*	0.25, 0.25, 0.25	1.22(6)	1
	Ca	*4a*	0, 0, 0	1.5	0.787
Fm-3m; a = 8.4160(1) Å	Fe	*4a*	0, 0, 0	1.5	0.213
$_wR_p$: 12.31, R_p: 9.65, χ^2: 2.144	Fe	*4b*	0.5, 0.5, 0.5	1.5(1)	0.02
	Nb	*4b*	0.5, 0.5, 0.5	1.5(1)	0.98
	O	*24e*	0.2556(9), 0, 0	3.0(2)	0.931
$Ba_2(Ca_{0.79}Fe_{0.21})(Nb_{0.71}Fe_{0.29})O_{5.3}$	Ba	*8c*	0.25, 0.25, 0.25	2.68(4)	1
	Ca	*4a*	0, 0, 0	1.5	0.787
Fm-3m; a = 8.40444(4) Å	Fe	*4a*	0, 0, 0	1.5	0.213
$_wR_p$: 13.14, R_p: 10.18, χ^2: 2.162	Fe	*4b*	0.5, 0.5, 0.5	2.8(1)	0.287
	Nb	*4b*	0.5, 0.5, 0.5	2.8(1)	0.713
	O	*24e*	0.2736(9), 0, 0	2.1(3)	0.887

Can. J. Chem. Downloaded from www.nrcresearchpress.com by Xi'an Jiaotong University on 09/19/12
For personal use only.

based on the *Fm-3m* space group, and the atomic positions of the Fe dopant were further analyzed by Rietveld analysis (Fig. 1). A structural model was constructed in which the lower charge cations (Ca^{2+} and Fe^{3+}) were mainly located on the *4a* site and the higher charged cations (Nb^{5+}) were on *4b* site (Fig. 2).[19,22,23] The detailed structural models and the corresponding refinement results are summarized in Table 1. The proposed structural models were supported by good fits (R_p) on the refinements. The structural models were further verified by BVS (Table S1; see Supplementary data) and SAED (Fig. 3). BVS calculations for cations on the specific positions in *Fm-3m* were found to be in good agreement with the assigned normal oxidation states of the cations. The small discrepancy can be explained by the presence of covalent character on the bonding in the Fe–BCN, which is opposite to the pure ionic assumption used in the BVS. Brown[24] also pointed out that many highly symmetric double perovskites in the ICSD database were not verified commonly by BVS. Shown in Fig. S1 (see Supplementary data) are the typical SEM images of Fe-doped BCN. All the investigated samples showed uniform contrast and support the absence of a potential second phase. SEM analysis was mainly used to determine the elemental analysis by energy dispersive spectroscopy (EDS) and confirmed the formulas of all Fe–BCN (Table 2) (Fig. S2; see Supplementary data).

Chemical stability

The chemical stability of the investigated Fe–BCN was accessed in pure CO_2 at 800 °C for 14–20 h and boiling H_2O for 72 h. PXRD showed that the double perovskite structure of $Ba_2(Ca_{0.67}Fe_{0.33})(Nb)O_{6-\delta}$ (**I**) was well maintained upon the chemical stability tests (Fig. 4). Furthermore, carbonate and hydroxyl groups were not observed from the FTIR spectra (Fig. 5). All other Fe–BCN (Supplementary data Figs. S3–S5) were also found to be chemically stable under the same environments, except for $Ba_2(Ca_{0.79}Fe_{0.21})(Nb_{0.71}Fe_{0.29})O_{6-\delta}$ (**V**), where additional peaks were observed after the chemical treatments (Supplementary data Fig. S6). The degradation mechanism was not clear to us but it could be similar to the $Ba(Co,Fe,Nb)O_{3-\delta}$ system.[25] In fact many barium containing oxides, such as barium cerates and rare earth-doped barium cerates, are reactive with CO_2 and H_2O.[26,27] Substitution of a small amount of foreign ions into the lattice is one of the most effective and common methods to improve the stability and performance.[28,29]

Electrical properties

AC impedance plots of $Ba_2(Ca_{0.67}Fe_{0.167}Nb_{0.167})(Nb)O_{6-\delta}$ (**II**) at 300 °C in air are shown in Fig. 6. The semicircles can be interpreted as different regions of a ceramic such as bulk, grain–boundary, and electrolyte–electrode, based upon

Can. J. Chem. Downloaded from www.nrcresearchpress.com by Xi'an Jiaotong University on 09/19/12
For personal use only.

Fig. 3. Typical grains of $Ba_2(Ca_{0.67}Fe_{0.33})(Nb)O_{6-\delta}$ (**I**) are shown in (*a*) TEM and (*b*) HRTEM images. The corresponding selected area electron diffraction (SAED) in (*c*) was measured where all Debye rings can be indexed on a cubic structure with a double perovskite cell constant. The corresponding data for $Ba_2(Ca_{0.67}Fe_{0.165}Nb_{0.165})(Nb)O_{6-\delta}$ (**II**), $Ba_2(Ca_{0.79}Fe_{0.16}Nb_{0.05})(Nb)O_{6-\delta}$ (**III**), $Ba_2(Ca_{0.79}Fe_{0.21})(Nb_{0.98}Fe_{0.02})O_{6-\delta}$ (**IV**), and $Ba_2(Ca_{0.79}Fe_{0.21})(Nb_{0.71}Fe_{0.29})O_{6-\delta}$ (**V**) are shown in (*d*)–(*f*), (*g*)–(*i*), (*j*)–(*l*) and (*m*)–(*o*), respectively.

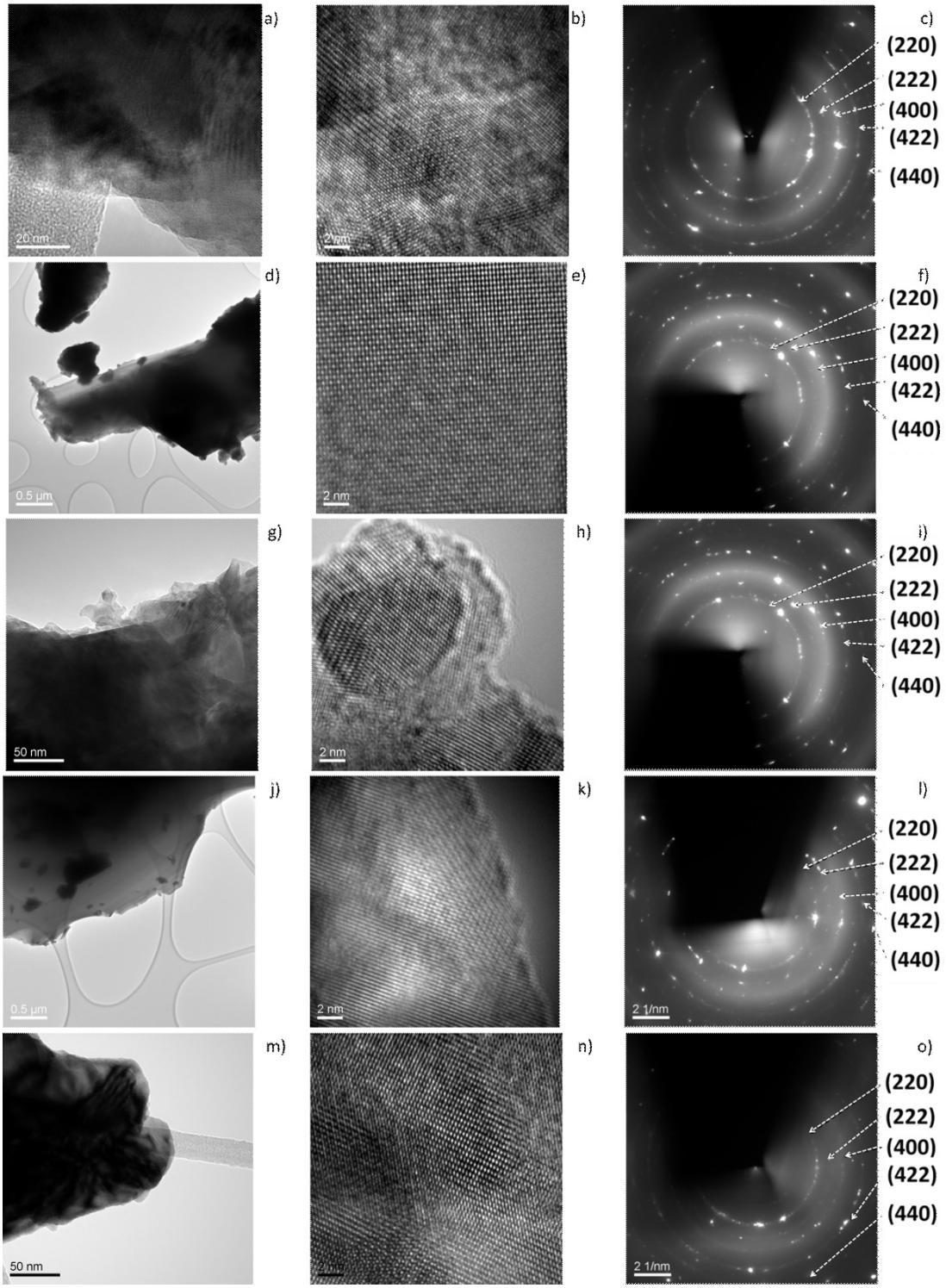

the corresponding capacitance (C) and resistance (R) values that can be obtained using the equation[30]

$$[2] \qquad \omega_{max} RC = 1$$

where $\omega = 2\pi F$ (F is the linear frequency). Commonly, impedance plots are analyzed using the equivalent circuits and fitting parameters that consist of R and CPE (constant phase element). The impedance of CPE can be expressed as[31,32]

Can. J. Chem. Downloaded from www.nrcresearchpress.com by Xi'an Jiaotong University on 09/19/12
For personal use only.

Table 2. Elemental analysis of Fe–BCN by energy dispersive X-ray spectroscopy.

Compound	Ba	Ca	Fe	Nb
$Ba_2(Ca_{0.67}Fe_{0.33})(Nb)O_{5.67}$ (I)				
Measured atom ratio	6.60	2.04	1	3.01
Expected atom ratio	6.06	2.03	1	3.03
$Ba_2(Ca_{0.67}\ Fe_{0.165}Nb_{0.165})(Nb)O_{5.83}$ (II)				
Measured atom ratio	13.59	3.97	1	7.50
Expected atom ratio	12.12	4.06	1	7.06
$Ba_2(Ca_{0.79}\ Fe_{0.16}Nb_{0.05})(Nb)O_{5.65}$ (III)				
Measured atom ratio	12.52	4.24	1	6.33
Expected atom ratio	12.50	4.94	1	6.56
$Ba_2(Ca_{0.79}Fe_{0.21})(Nb_{0.98}Fe_{0.02})O_{5.59}$ (IV)				
Measured atom ratio	8.96	3.23	1	5.15
Expected atom ratio	8.70	3.43	1	4.26
$Ba_2(Ca_{0.79}Fe_{0.21})(Nb_{0.71}Fe_{0.29})O_{5.3}$ (V)				
Measured atom ratio	4.09	1.46	1	1.30
Expected atom ratio	4.00	1.58	1	1.42

Fig. 4. Powder X-ray diffraction (PXRD) patterns of $Ba_2(Ca_{0.67}Fe_{0.33})(Nb)O_{6-\delta}$ (**I**) sintered at 1500 °C for 14 h: (*a*) as-prepared sample, (*b*) post-treatment of the as-prepared sample in 100% CO_2 for 14 h, and (*c*) post-treatment of the as-prepared sample in boiling H_2O for 72 h.

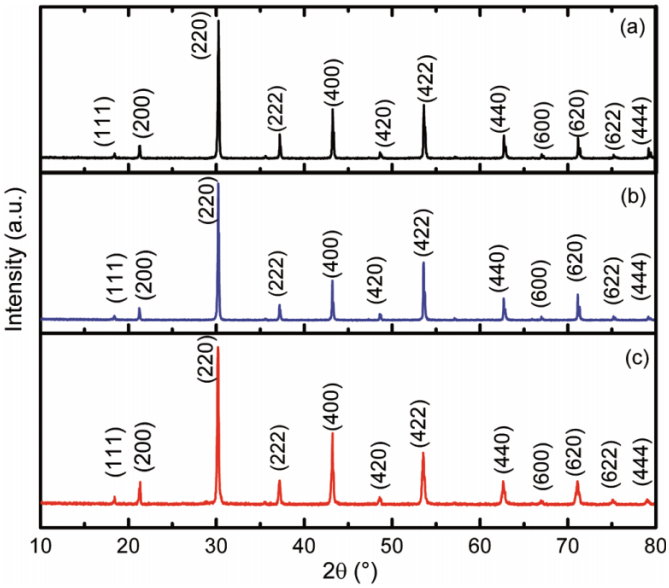

$$[3] \qquad Z_{CPE} = \frac{1}{Q(j\omega)^n}$$

where Q is the pseudo-capacitance, $j = \sqrt{1}$, and n is the empirical constant that can be any arbitrary value between 0 and 1. The actual capacitance can be calculated by[30,31,33,34]

$$[4] \qquad C = R^{\frac{1-n}{n}} Q^{\frac{1}{n}}$$

The fitting AC impedance analysis (Table 3) of the sample in air indicated that the capacitances for the high- and low-frequency semicircles were in the order of 10^{-11} and 10^{-6} F, respectively, which are characteristic values for the bulk and grain–boundary effects in ceramic materials.[30] Since all Fe–BCN were well-sintered (>90% theoretical density), the impedance owing to the grain–boundary was found to be less significant (roughly a one-sixth contribution to the total)

Fig. 5. FTIR spectra of $Ba_2(Ca_{0.67}Fe_{0.33})(Nb)O_{6-\delta}$ (**I**): (*a*) as-prepared, (*b*) post-treatment of the as-prepared sample in 100% CO_2 for 14 h, and (*c*) post-treatment of the as-prepared sample in boiling H_2O for 72 h. The C=O vibration band around 1700 cm^{-1} and the O–H vibration at 3500 cm^{-1} were not observed under experimental conditions.

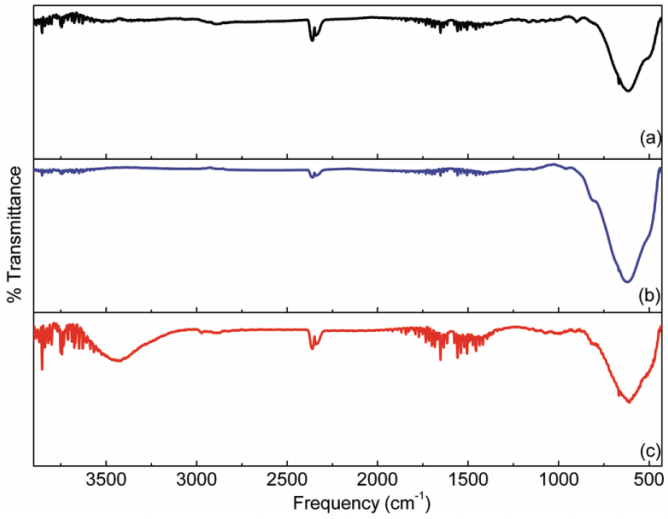

Fig. 6. Typical electrochemical impedance plot with equivalent circuits fitting of $Ba_2(Ca_{0.67}Fe_{0.165}Nb_{0.165})(Nb)O_{6-\delta}$ (**II**) at 300 °C in air and N_2 + 3% H_2O. The equivalent circuits used to fit the experimental data are shown in top right corner. The solid line passing through data points represents the best-fit line. Inset shows expanded view of high frequency region of impedance plot.

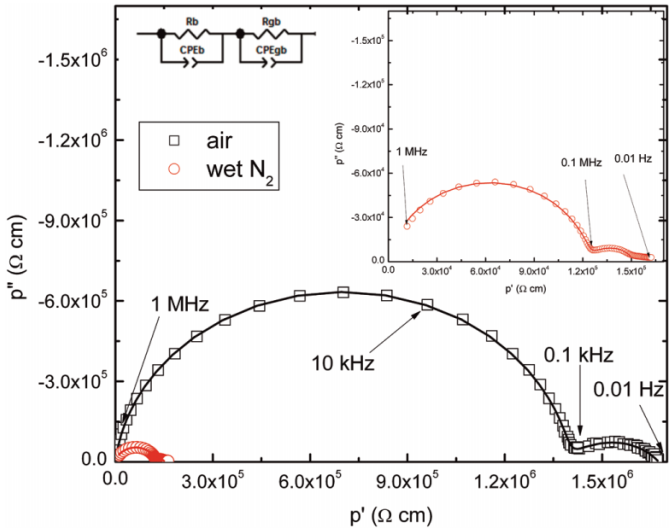

even at 300 °C. At a high-temperature regime (500–800 °C), the semicircles were highly deformed and overlapped; hence, separation of the bulk and grain–boundary contributions was not possible. Alternatively, the low-frequency intercept was used as total impedance, which included bulk and grain–boundary impedances. Such consideration was widely used in our group and in other groups.[31,32,35] Therefore, the total conductivities (bulk and grain–boundary) were used to study the doping effect on all Fe–BCN.

The Arrhenius plots for the total electrical conductivities of all Fe–BCNs, including $Ba_2(Ca_{0.67}Fe_{0.33})(Nb)O_{6-\delta}$ (**I**),

Can. J. Chem. Downloaded from www.nrcresearchpress.com by Xi'an Jiaotong University on 09/19/12
For personal use only.

Table 3. AC impedance fitting parameters for $Ba_2(Ca_{0.67}Fe_{0.33})(Nb)O_{6-\delta}$ (**I**) and $Ba_2(Ca_{0.67}Fe_{0.165}Nb_{0.165})(Nb)O_{6-\delta}$ (**II**) at 300 °C in air and wet (3% H_2O) N_2 using equivalent circuits and electrical conductivity and activation energy.

Compound	Medium	R_b (Ω)	Q_b (F)	C_b (F)	n	R_{gb} (Ω)	Q_{gb} (F)	C_{gb} (F)	n
$Ba_2(Ca_{0.67}Fe_{0.33})(Nb)O_{6-\delta}$ (**I**)	Air	4.1×10^5	5.0×10^{-11}	2.5×10^{-11}	0.94	8.3×10^4	1.2×10^{-6}	2.6×10^{-7}	0.60
	Wet N_2	3.7×10^4	8.1×10^{-11}	2.0×10^{-12}	0.90	8.2×10^3	4.1×10^{-7}	3.9×10^{-8}	0.71
$Ba_2(Ca_{0.67}Fe_{0.165}Nb_{0.165})(Nb)O_{6-\delta}$ (**II**)	Air	6.7×10^3	2.4×10^{-10}	2.8×10^{-11}	0.86	2.1×10^3	5.3×10^{-8}	2.7×10^{-8}	0.93
	Wet N_2	9.1×10^3	2.1×10^{-10}	1.7×10^{-12}	0.84	8.8×10^3	7.9×10^{-8}	2.0×10^{-8}	0.84

Note: n, empirical constant; R_b, bulk resistance; Q_b, bulk pseudo-capacitance; C_b, bulk capacitance; R_{gb}, grain–boundary resistance; Q_{gb}, grain–boundary pseudo-capacitance; C_{gb}, grain–boundary capacitance.

Fig. 7. The Arrhenius plot of $Ba_2(Ca_{0.67}Fe_{0.33})(Nb)O_{6-\delta}$ (**I**), $Ba_2(Ca_{0.67}Fe_{0.165}Nb_{0.165})(Nb)O_{6-\delta}$ (**II**), $Ba_2(Ca_{0.79}Fe_{0.16}Nb_{0.05})(Nb)O_{6-\delta}$ (**III**), $Ba_2(Ca_{0.79}Fe_{0.21})(Nb_{0.98}Fe_{0.02})O_{6-\delta}$ (**IV**), and $Ba_2(Ca_{0.79}Fe_{0.21})(Nb_{0.71}Fe_{0.29})O_{6-\delta}$ (**V**) in air and hydrated N_2.

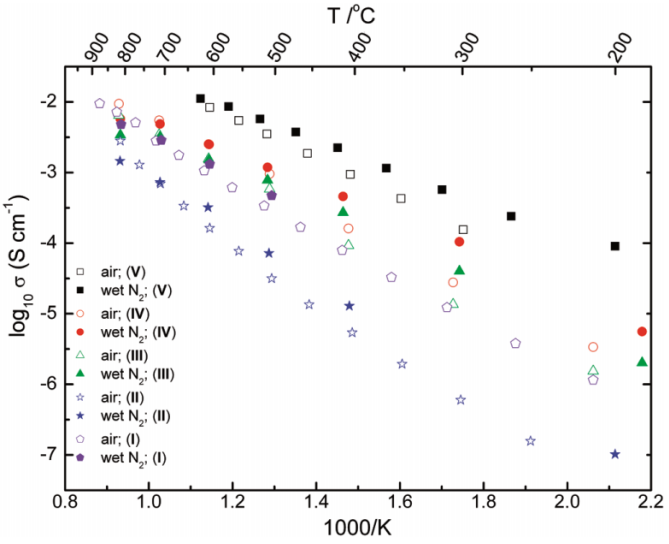

Fig. 8. Electrical conductivity of $Ba_2(Ca_{0.67}Fe_{0.33})(Nb)O_{6-\delta}$ (**I**) in air, dry N_2, dry H_2, N_2 + 3% H_2O, and H_2 + 3% H_2O.

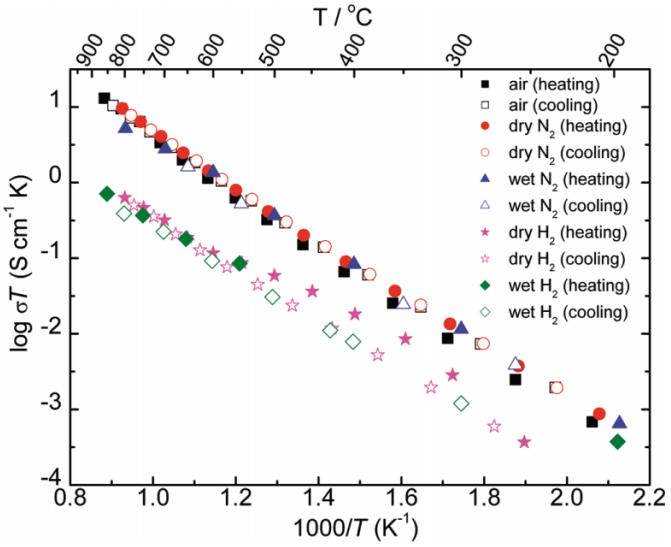

$Ba_2(Ca_{0.67}Fe_{0.165}Nb_{0.165})(Nb)O_{6-\delta}$ (**II**), $Ba_2(Ca_{0.79}Fe_{0.16}Nb_{0.05})(Nb)O_{6-\delta}$ (**III**), $Ba_2(Ca_{0.79}Fe_{0.21})(Nb_{0.98}Fe_{0.02})O_{6-\delta}$ (**IV**), and $Ba_2(Ca_{0.79}Fe_{0.21})(Nb_{0.71}Fe_{0.29})O_{6-\delta}$ (**V**), in air and hydrated N_2 are shown in Fig. 7. Interestingly, the conductivity of **IV** and **V** were found to be higher than that of **I**, **II**, and **III** in both air and hydrated N_2. The increase in electrical conductivity in wet N_2 may appear because of proton conduction. In wet N_2, the activation energies of all Fe–BCNs were found to be ~0.5 eV (200–800 °C). Typically, ceramic proton conductors exhibit smaller activation energies (ca. 0.3–0.6 eV) than that of oxide ion electrolytes (ca. 0.9 eV) and electron-holes (ca. 0.8 eV).[8,36,37] A slight variation in activation energy can be anticipated with different structures and dopant levels. Furthermore, additional electronic carriers could be created under the low oxygen partial pressure (pO_2) because

Can. J. Chem. Downloaded from www.nrcresearchpress.com by Xi'an Jiaotong University on 09/19/12
For personal use only.

of the reduction of Fe and Nb in Fe–BCN at elevated temperatures.

To study the effect of electrical conduction at low pO_2 (in fuel H_2), compound **I** was chosen as a case study. The Arrhenius plot of **I** in air, wet N_2, wet H_2, and dry H_2 are shown in Fig. 8. Surprisingly, the conductivities in wet and dry H_2 were lower than those for wet N_2 and air. The origin of the dramatic reduction in conductivity could be attributed to the formation electron-holes ($h^\bullet$) according to the proposed defect equilibrium reaction:

$$[5] \qquad V_O^{\bullet\bullet} + 0.5O_2 \Leftrightarrow O_O^x + 2h^\bullet$$

The detail analysis on the oxidation states of the Fe ions in Fe–BCN is important for understanding the electronic properties and the amount of oxygen vacancy in the lattices. A combination of TGA and Mössbauer spectroscopy studies will be conducted in the future to understand the electrical properties of Fe–BCN in H_2.

Conclusions

Our preliminary studies on the non-stoichiometric ordered double perovskites $Ba_2(Ca_{1-x-y}Fe_xNb_y)(Nb_{1-z}Fe_z)O_{6-\delta}$ (Fe–BCN) indicate all the prepared compounds exhibited cubic *Fm*-3*m* with cell constant $a \sim 8.4$ Å. Fe–BCN showed good chemical stability in CO_2 at elevated temperatures and in boiling water. The highest total (bulk + grain–boundary) conductivities of 2.23×10^{-3} and 1.11×10^{-2} S cm^{-1} in hydrated N_2 at 400 and 600 °C, respectively, with an activation energy of 0.43 eV (200–800 °C) were found for $Ba_2(Ca_{0.79}Fe_{0.21})(Nb_{0.71}Fe_{0.29})O_{6-\delta}$.

Supplementary data

Supplementary data are available with the article through the journal Web site (www.nrcresearchpress.com/cjc).

Acknowledgments

This research was supported through funding to the NSERC Solid Oxide Fuel Cell Canada Strategic Research Network from the Natural Sciences and Engineering Research Council of Canada (NSERC) and other sponsors (www.sofccanada.com). The authors also would like to thank NSERC for funding through the Research Tools and Instruments and Infrastructure grants (RTI) (cat. 1) and the Canada Foundation for Innovation (CFI) for their financial support. We also thank Professor V.I. Birss at the Department of Chemistry, University of Calgary, Calgary, Alberta, for useful discussions.

References

(1) Iwahara, I.; Esaka, T.; Uchida, H.; Maeda, N. *Solid State Ion.* **1981** *3–4*, 359. doi:10.1016/0167-2738(81)90113-2.
(2) Stotz, S.; Wagner, C. *Ber. Bunsenges Phys. Chem.* **1966** *70*, 781.
(3) Shores, D. A.; Rapp, R. A. *J. Electrochem. Soc.* **1972** *119* (3), 300. doi:10.1149/1.2404190.
(4) Agmon, N. *Chem. Phys. Lett.* **1995** *244* (5–6), 456. doi:10.1016/0009-2614(95)00905-J.
(5) Balachandran, U.; Ma, B.; Maiya, P. S.; Mieville, R. L.; Dusek, J. T.; Picciolo, J. J.; Guan, J.; Dorris, S. E.; Liu, M. *Solid State Ion.* **1998** *108* (1–4), 363. doi:10.1016/S0167-2738(98)00064-2.
(6) Tadokoro, Y.; Shan, Y. J.; Nakamura, T.; Nakamura, S. *Solid State Ion.* **1998** *108* (1–4), 261. doi:10.1016/S0167-2738(98)00048-4.
(7) Glerup, M.; Poulsen, F. W.; Berg, R. W. *Solid State Ion.* **2002** *148* (1–2), 83. doi:10.1016/S0167-2738(02)00048-6.
(8) Fabbri, E.; D'Epifanio, A.; Di Bartolomeo, E.; Licoccia, S.; Traversa, E. *Solid State Ion.* **2008** *179* (15–16), 558. doi:10.1016/j.ssi.2008.04.002.
(9) Zakowsky, B.; Williamson, S.; Irvine, J. T. S. *Solid State Ion.* **2005** *176* (39–40), 3019. doi:10.1016/j.ssi.2005.09.040.
(10) Liang, K. C.; Nowick, A. S. *Solid State Ion.* **1993** *61* (1–3), 77. doi:10.1016/0167-2738(93)90337-3.
(11) Liang, K. C.; Du, Y.; Nowick, A. S. *Solid State Ion.* **1994** *69* (2), 117. doi:10.1016/0167-2738(94)90399-9.
(12) Bhella, S. S.; Thangadurai, V. *J. Power Sources* **2009** *186* (2), 311. doi:10.1016/j.jpowsour.2008.09.110.
(13) Du, Y.; Nowick, A. S. *Solid State Ion.* **1996** *91* (1–2), 85. doi:10.1016/S0167-2738(96)00409-2.
(14) Toby, B. H. *J. Appl. Crystallogr.* **2001** *34* (2), 210. doi:10.1107/S0021889801002242.
(15) Sosnowska, I.; Przenioso, R.; Schäfer, W.; Kockelmann, W.; Hempelmann, R.; Wysocki, K. *J. Alloy Comp.* **2001** *328* (1–2), 226. doi:10.1016/S0925-8388(01)01299-3.
(16) Levin, I.; Chan, J. Y.; Geyer, R. G.; Maslar, J. E.; Vanderah, T. A. *J. Solid State Chem.* **2001** *156* (1), 122. doi:10.1006/jssc.2000.8971.
(17) Brown, I. D.; Altermat, D. *Acta Crystallogr.* **1985** *B41*, 244. doi:10.1107/S0108768185002063.
(18) Hormillosa, C.; Healy, S.; Stephen, T.; Brown, I. D. *Bond Valence Calculator* Version 2.0; 1993. www.ccp14.ac.uk/ccp/web-mirrors/i_d_brown/valence.exe.
(19) Nowick, A. S.; Du, Y.; Liang, K. C. *Solid State Ion.* **1999** *125* (1–4), 303. doi:10.1016/S0167-2738(99)00189-7.
(20) Sosnowska, I.; Schofer, W.; Przenioslo, R.; Lind, K.; Hempelmann, R. *Physica B* **2000** *276–278* (1–3), 864. doi:10.1016/S0921-4526(99)01313-7.
(21) Galasso, F. S. *High Modulus Fibers and Composites;* Gordon and Breach: London, 1990.
(22) Davies, P. K.; Wu, H.; Borisevich, A. Y.; Molodetsky, I. E.; Farber, L. *Annu. Rev. Mater. Res.* **2008** *38* (1), 369. doi:10.1146/annurev.matsci.37.052506.084356.
(23) Anderson, M. T.; Greenwood, K. B.; Taylor, G. A.; Poeppelmeier, K. R. *Prog. Solid State Chem.* **1993** *22* (3), 197. doi:10.1016/0079-6786(93)90004-B.
(24) Brown, I. D. McMaster University, Hamilton, ON. Personal communication, 2010.
(25) Yi, J.; Schroeder, M.; Weirich, T.; Mayer, J. *Chem. Mater.* **2010** *22* (23), 6246. doi:10.1021/cm101665r.
(26) Bhide, S. V.; Virkar, A. V. *J. Electrochem. Soc.* **1999** *146* (6), 2038. doi:10.1149/1.1391888.
(27) Bhella, S. S.; Furstenhaupt, T.; Thangadurai, V. *J. Alloy Comp.* **2010** *503* (1), L5. doi:10.1016/j.jallcom.2010.04.239.
(28) Matsumoto, H.; Kawasaki, Y.; Ito, N.; Enoki, M.; Ishihara, T. *Electrochem. Solid-State Lett.* **2007** *10* (4), B77. doi:10.1149/1.2458743.
(29) Bi, L.; Tao, Z.; Liu, C.; Sun, W.; Wang, H.; Liu, W. *J. Membr. Sci.* **2009** *336* (1–2), 1. doi:10.1016/j.memsci.2009.03.042.
(30) Irvine, J. T. S.; Sinclair, D. C.; West, A. R. *Adv. Mater. (Deerfield Beach Fla.)* **1990** *2* (3), 132. doi:10.1002/adma.19900020304.
(31) Li, Q.; Thangadurai, V. *Fuel Cells (Weinh.)* **2009** *9*, 686. doi:doi:10.1002/fuce.200900044.

(32) Li, Q.; Thangadurai, V. *J. Mater. Chem.* **2010** *20* (37), 7970. doi:10.1039/c0jm01324b.
(33) Hijalmarsson, P.; Søgaard, M.; Mogensen, M. *Solid State Ion.* **2009** *180* (26–27), 1395. doi:10.1016/j.ssi.2009.08.007.
(34) Chinarro, E.; Jurado, J. R.; Figueiredo, F. M.; Frade, J. R. *Solid State Ion.* **2003** *160* (1–2), 161. doi:10.1016/S0167-2738(03)00151-6.
(35) Peng, R.; Wu, T.; Liu, W.; Liu, X.; Meng, G. *J. Mater. Chem.* **2010** *20* (30), 6218. doi:10.1039/c0jm00350f.
(36) Fabbri, E.; Pergolesi, D.; Traversa, E. *Chem. Soc. Rev.* **2010** *39* (11), 4355. . doi:10.1039/b902343g.
(37) Slade, R. C. T.; Singh, N. *Solid State Ion.* **1991** *46* (1–2), 111. doi:10.1016/0167-2738(91)90137-Z.

Can. J. Chem. Downloaded from www.nrcresearchpress.com by Xi'an Jiaotong University on 09/19/12
For personal use only.

Application of cetyltrimethylammonium bromide – graphene modified electrode for sensitive determination of caffeine

Jun-Yong Sun, Ke-Jing Huang, Shuai-Yun Wei, and Zhi-Wei Wu

Can. J. Chem. Downloaded from www.nrcresearchpress.com by Xi'an Jiaotong University on 09/19/12
For personal use only.

Abstract: An electrochemical sensor based on a cationic surfactant cetyltrimethylammonium bromide (CTAB) – dispersed graphene (Gr) system for sensitive detection of caffeine is presented. The electrochemical behavior of caffeine on the modified glassy carbon electrode was investigated by cyclic voltammetry and differential pulse voltammetry. The results showed that the modified electrode exhibited good electrocatalytic activity to the oxidation of caffeine. Under the optimized experimental conditions, caffeine was detected in the concentration range from 0.3 to 100 μmol L^{-1} with a detection limit of 91 nmol L^{-1} at a signal-to-noise ratio = 3. The biosensor exhibited some advantages over other electrochemical sensors, such as long-term stability, satisfactory recovery (98.1%–102.3%), and good reproducibility (RSD = 5.1%). The practical application of the developed method was verified in soft-drink sample analysis.

Key words: caffeine, cetyltrimethylammonium bromide, graphene, electrochemical sensor.

Résumé : On a mis au point un senseur électrochimique, à base d'un système formé de l'agent de surface bromure de cétyltriméthylammonium (BCMA) dispersé sur du graphène, comme détecteur sensible de la caféine. On a étudié les comportements électrochimiques de la caféine sur une électrode de carbone vitreuse modifiée par voltampérométrie cyclique et par voltampérométrie pulsée différentielle. Les résultats montrent que l'électrode modifiée présente une bonne activé catalytique pour l'oxydation de la caféine. Dans des conditions expérimentales optimisées, il est possible de détecter de la caféine dans la plage de concentration allant de 0,3 à 100 μmol L^{-1}, avec une limite de détection de 91 nmol L^{-1}, pour un rapport de signal à bruit égal à 3. Le biosenseur présente quelques avantages, telle sa stabilité à long terme, une récupération satisfaisante (98,1 % à 102,3 %) et une bonne reproductibilité (déviation standard de la reproductibilité = 5,1 %). On a vérifié l'application pratique de la méthode développée par l'analyse d'échantillons de liqueurs douces.

Mots-clés : caffeine, bromure de cétyltriméthylammonium, graphène, senseur électrochimique.

[Traduit par la Rédaction]

Introduction

Caffeine (3,7-dihydro-1,3,7-trimethyl-1*H*-purine-2,6-dione) is an active alkaloid. It has some important physiological effects, such as stimulating gastric acid secretion, diuresis, and the central nervous system.[1,2] However, it can cause adverse mutation effects when excessively consumed,[3] including inhibition of DNA repair and cyclic AMP phosphodiesterase activity,[4] resulting in the occurrence of cancer and heart diseases.[5] Therefore, the determination (quantification) of caffeine has great significance for both biosciences and clinical diagnosis, and even criminology.

Several techniques have been developed for the determination of caffeine, including HPLC,[6] UV spectrophotometry,[7] mass spectroscopy,[8] capillary electrophoresis, and gas chromatography.[9–12] Although these methods are sensitive, complicated instruments and time-consuming sample pretreatment are required. Compared with these methods, an electrochemical technique is attractive due to its high sensitivity, inherent simplicity, miniaturization, and low cost, and thus some electrochemical methods have been developed for the determination of caffeine.[13–15] One key area of electrochemical sensor research is in the use of various materials with nanoparticle-like physical and chemical properties, because they provide a large surface area and improve the biocompatibility, stability, and immobilization of biomolecules on the electrode surface.[16,17]

Graphene (Gr), a single layer of carbon atoms in a closely packed honeycomb two-dimensional lattice, is a novel and fascinating carbon material. Recently, it has attracted considerable attention from both the experimental and theoretical scientific communities owing to its many unique and excellent properties.[18–20] It exhibits extremely high thermal conductivity, good mechanical strength, high mobility of charge carriers, high specific surface area, quantum hall effect, and outstanding electric conductivity.[21–23] Much research effort has been put into exploring the fascinating possibilities for applications with Gr, such as the fabrication of various electrical devices, e.g., batteries,[24] field-effect transistors,[25] ultra-

Received 4 January 2011. Accepted 6 March 2011. Published at www.nrcresearchpress.com/cjc on 23 June 2011.

J.-Y. Sun, K.-J. Huang, S.-Y. Wei, and Z.-W. Wu. College of Chemistry and Chemical Engineering, Xinyang Normal University, Xinyang 464000, P.R. China.

Corresponding author: Ke-Jing Huang (e-mail: kejinghuang@163.com).

Can. J. Chem. Downloaded from www.nrcresearchpress.com by Xi'an Jiaotong University on 09/19/12
For personal use only.

sensitive sensors,[26] electromechanical resonators,[27] and electrochemical biosensors.[28] Some studies have demonstrated that Gr possesses excellent electrochemical catalytic activity, and should be considered as a modified material for a novel electrode with excellent performance.

Herein, a simple and sensitive method for the determination of caffeine was developed based on the surfactant cetyltrimethylammonium bromide (CTAB) dispersed Gr system modified glassy carbon electrode (GCE). The surfactant is a special compound with amphiphilic groups, which has been widely used in electroanalytical chemistry. It can improve the peak shape and sensitivity, and possesses antifouling capacity via inhibiting direct contact of the substrates with the electrode surfaces.[29–31] Gr is easier to disperse in a surfactant solution. This can improve the dispersion and homogeneity of the Gr. The CTAB–Gr composite film was characterized with electrochemical methods. Based on the unique properties of graphene, the fabricated modified electrode facilitated the electron transfer of caffeine, resulting in the increase of oxidation signals. The method proved to be simple, reliable, and inexpensive for the determination of caffeine in the soft-drink samples at low levels.

Experimental

Reagents

Caffeine was purchased from Beijing Shuanghuan Weije Reagent Co. (Beijing, China), and the stock solution of caffeine (1.0×10^{-2} mol L^{-1}) was prepared with doubly distilled water, and diluted with 0.01 mol L^{-1} H_2SO_4 (pH 2.0) before use. CTAB was purchased from Jing Wei Chemical Co., Ltd (Shanghai, China). The Gr used in this study was synthesized according to the reported method of Hummers et al.[32] Ultrapure water (18.2 MΩ) was obtained from a Milli-Q water purification system and used throughout. All other reagents were of analytical reagent grade and used as received.

Instrumentation

Electrochemical measurements were carried out at a CHI660D electrochemistry workstation (CH Instrumental Co., ShangHai, China). A conventional 3-electrode system was employed, including a bare glassy carbon electrode (GCE) (d = 3 mm) and the modified GCE as working electrode, a platinum wire as a counter electrode and a saturated calomel reference electrode as the reference electrode. All the pH values were measured using a PHS-3C precision pH meter (Leici Devices Factory of Shanghai, China).

Preparation of modified electrode

For electrode preparation, 2 mg of graphene was dispersed in 1 mL of DMF using an ultrasonic bath to give a black suspension. CTAB–Gr suspension was accomplished as follows: 2.0 mg CTAB and 2.0 mg Gr were sonicated in 1.0 mL doubly distilled water for about 2 h. Before modification, the GCE was polished to a mirror-like surface with 0.3 and 0.05 μm alumina slurry, then washed successively with ultrapure water, anhydrous alcohol, and ultrapure water in an ultrasonic bath and dried in blowing N_2. The cleaned GC electrode was treated by dropping 5 μL of CTAB–Gr suspension and then dried in air. The obtained electrodes were noted as CTAB–Gr/GCE. For contrast, the CTAB/GCE and Gr/GCE was prepared with the same procedure, but without Gr and CTAB, respectively.

Fig. 1. Cyclic voltammograms of (*a*) the CTAB–Gr modified GCE, (*b*) Gr modified GCE, (*c*) CTAB modified GCE, and (*d*) the bare GCE in a medium containing 2.0×10^{-5} mol L^{-1} caffeine in 0.01 mol L^{-1} H_2SO_4 (pH 2.0); scan rate 100 mV s^{-1}.

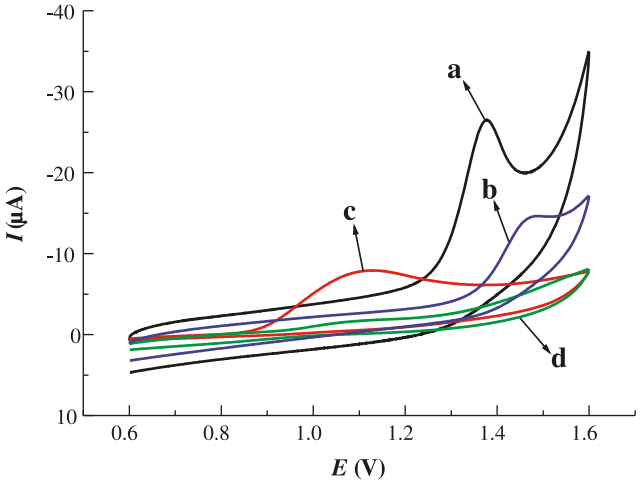

Results and discussion

Electrochemical response of the CTAB–Gr/GCE electrode to caffeine

The effective surface areas of different modified electrodes were obtained by cyclic voltammetry (CV) with 1 mmol L^{-1} $K_3Fe(CN)_6$ as a probe at different scan rates. For a reversible process, the following equation applies:

$$[1] \qquad i_p = 2.69 \times 10^5 A n^{3/2} D^{1/2} c \upsilon^{1/2}$$

where i_p refers to the peak current, and A is the electrode area (cm^2). For 1 mmol L^{-1} $K_3Fe(CN)_6$, n = 1, $D = 7.6 \times 10^{-6}$ cm^2 s^{-1} (0.1 mol L^{-1} KCl), where n is the number of electrons transferred, D is the diffusion coefficient, c is the concentration of $K_3Fe(CN)_6$, and υ is the scan rate.[33] The surface areas of the bare GCE and CTAB–Gr/GCE electrodes were calculated from the slope of the i_p versus $\upsilon^{1/2}$ plot to be 0.054 cm^2 and 0.168 cm^2, respectively.

Fig. 1 shows the cyclic voltammograms (CVs) of 2.0×10^{-5} mol L^{-1} caffeine in 0.01 mol L^{-1} H_2SO_4 (pH 2.0) on the CTAB–Gr modified GCE (Fig. 1*a*), Gr modified GCE (Fig. 1*b*), CTAB modified GCE (Fig. 1*c*), and the bare GCE (Fig. 1*d*) at a scan rate of 100 mV s^{-1}, respectively. No anodic peak of caffeine was observed at the bare GCE. Compared with the Gr/GCE, the anodic peak potentials at the CTAB–Gr/GCE and CTAB/GCE shifted negatively to 1.378 and 1.112 V, respectively, indicating an electrocatalytic oxidation process. The oxidation peak current significantly increased at the modified electrodes, especially the CTAB–Gr/GCE, indicating enhanced electrocatalytic activity towards the oxidation of caffeine. By adding caffeine, the enhancement of the current density obtained using CTAB–Gr/GCE was about 9.6 times higher than that achieved at the bare GCE. Obviously, the CTAB–Gr composite film exhibited enhanced electrocatalytic activity towards the oxidation of caffeine. This performance can be ascribed to CTAB, which

Can. J. Chem. Downloaded from www.nrcresearchpress.com by Xi'an Jiaotong University on 09/19/12
For personal use only.

Fig. 2. Cyclic voltammograms of the CTAB–Gr modified GCE in the presence of 2.0×10^{-5} mol L^{-1} caffeine in 0.01 mol L^{-1} different supporting electrolytes ($a \rightarrow d$): H_2SO_4, HNO_3, HCl, CH_3COOH; scan rate 100 mV s^{-1}.

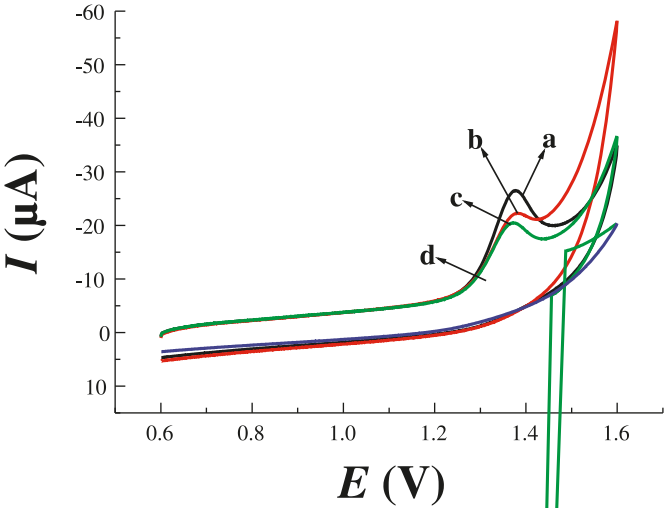

Fig. 3. Cyclic voltammograms of the CTAB-Gr modified GCE in the presence of 2.0×10^{-5} mol L^{-1} caffeine with different pH of 0.01 mol L^{-1} H_2SO_4 mediums ($a \rightarrow f$): 0.5, 1.0, 1.5, 2.0, 2.5, 3.0; scan rate 100 mV s^{-1}. Insert: plot pf pH versus oxidation peak current.

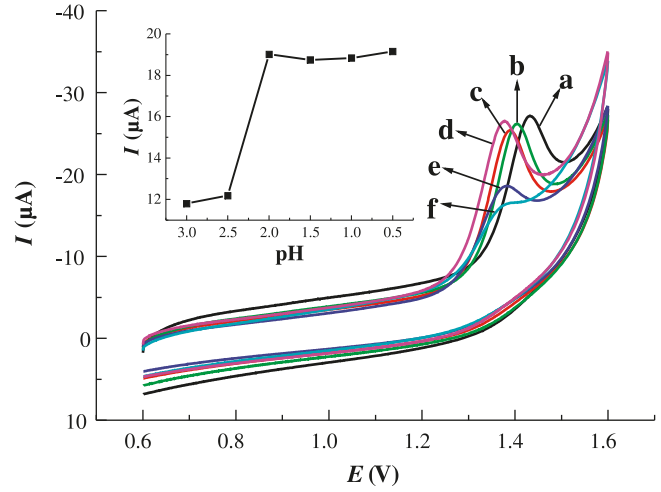

acts as a good substrate for Gr deposition on the electrode, as well as the unique characters of Gr. This composite film greatly increased the effective surface of the electrode and therefore enhanced the peak current of caffeine.

Effect of electrolytes and pH on sensor response

A number of different electrolyte solutions influence the electrochemical behavior of caffeine. Electrolyte solutions including H_2SO_4, HNO_3, CH_3COOH, and HCl are typically used in electrochemical analysis, especially in the electrochemical oxidation of caffeine.[34–37] To investigate the effect of the supporting electrolyte system on the sensor response, CV measurements of the CTAB–Gr/GCE in the presence of 2.0×10^{-5} mol L^{-1} caffeine were carried out in 0.01 mol L^{-1} H_2SO_4, HNO_3, CH_3COOH, and HCl, respectively, as depicted in Fig. 2. The highest current response was obtained in 0.01 mol L^{-1} H_2SO_4. Thus 0.01 mol L^{-1} H_2SO_4 was chosen.

Fig. 4. Cyclic voltammograms of CTAB–Gr modified GCE in the presence of 2.0×10^{-5} mol L^{-1} caffeine at different scan rate: (*a*) 20, (*b*) 100, (*c*) 180, (*d*) 260, (*e*) 340, (*f*) 420, (*g*) 500 mV s^{-1}, respectively. Insert: plot of i_p versus $\upsilon^{1/2}$.

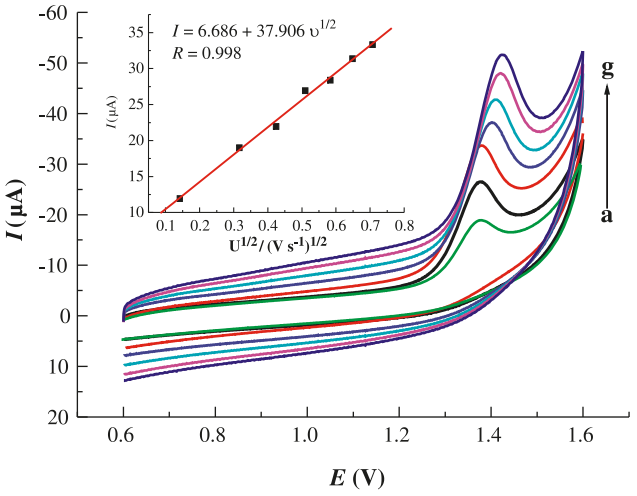

Fig. 5. Differential pulse voltammograms of CTAB–Gr modified GCE in different concentrations of caffeine ($a \rightarrow h$): 5.0×10^{-7}, 1.0×10^{-6}, 2.0×10^{-6}, 5.0×10^{-6}, 8.0×10^{-6}, 3.0×10^{-5}, 7.0×10^{-5}, 1.0×10^{-4} mol L^{-1}. Insert: plot of i_p versus $c_{caffeine}$.

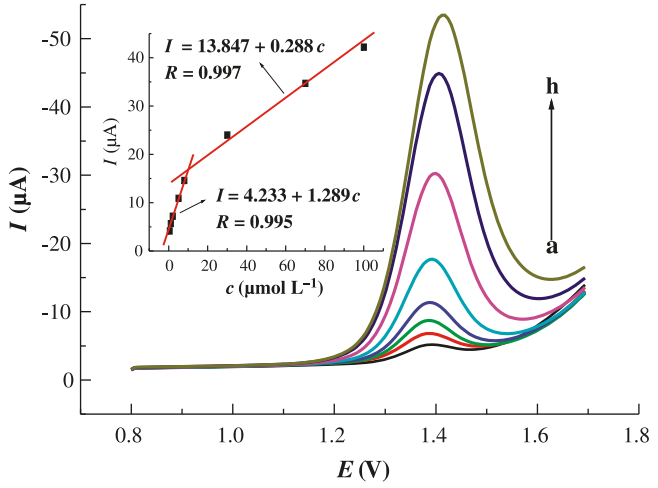

The effect of buffer pH on the electrooxidation of caffeine was investigated in the pH range 0.5–3.0. As shown in Fig. 3, the peak potential decreases with increasing pH. In addition, the peak current changed little in the pH range from 0.5 to 2.0, while it noticeably decreases at a higher pH. Therefore, pH 2.0 was chosen for the subsequent analytical experiments.

Effect of the amount of CTAB–Gr suspension

Generally speaking, the thickness of the CTAB–Gr film on GCE surface, which was determined by the amount of CTAB–Gr suspension, affected the reponse of the analytes to current. The results showed that the oxidation peak currents of caffeine reached the maximum when 5 μL of CTAB–Gr

Table 1. Comparison with other electrochemical methods for determination of caffeine.

Methods/reagent(s) used	Analytical ranges (μmol L^{-1})	LODs (μmol L^{-1})	References
Nafion – BDD electrode	0.2–12	0.1	34
Graphite pencil electrode	Up to 2574.8	47.4	35
Nafion – ruthenium oxide pyrochlore CME*	5.0–200	2.0	36
ALP†	1–10	0.08	37
CTAB–Gr/GCE‡	0.3–100	0.091	This paper

*Nafion® – ruthenium-oxide pyrochlore ($Pb_2Ru_{2-x}Pb_xO_{7-y}$) chemically modified electrode (CME).
†Alkaline phosphatase.

Can. J. Chem. Downloaded from www.nrcresearchpress.com by Xi'an Jiaotong University on 09/19/12
For personal use only.

suspension was used. The oxidation peak currents of caffeine decreased when the amount of CTAB–Gr suspension was less or higher than 5 μL. So for this study, 5 μL of CTAB–Gr suspension was selected for fabrication of the sensors.

Effect of scan rate

To obtain the kinetic parameters of caffeine redox at CTAB–Gr/GCE, the scan rate effect was investigated by cyclic voltammetry (Fig. 4). Only oxidation peaks were observed, indicating that the oxidation of caffeine was a totally irreversible electrode process. Along with the increase of the scan rate, the oxidation peak currents of caffeine increased gradually, and the relationship of the oxidation peak current with the square root of the scan rate were established with linear regression equations as I (μA) = 6.686 + 37.906 $\upsilon^{1/2}$ (R = 0.998) in the range of 20 to 350 mV s^{-1}, which indicated that the electrooxidation of caffeine was a diffusion-controlled process. With increasing scan rate, the anodic peak potential at the CTAB–Gr/GCE slightly shifted positively. For an irreversible system, at a higher scan rate the relationship between E_{pa} (absolute potential at the oxidation peak) and ln υ should submit to the equation:[38]

$$E_{pa} = (E + RT)/(1 - \alpha)nF \times \{0.78 + \ln(D_R^{1/2}/K^0) + \ln[(1 - \alpha)nF\upsilon/RT]^{1/2}\}$$

In this work, the linear regression equation was expressed as follows: $E = 1.441 + 0.0279 \ln \upsilon$ (E is absolute potential in V, υ is in V s^{-1}, and R = 0.997), thus $RT/2(1 - \alpha)nF$ = 0.0279, where T is absolute temperature (K), α is the electron transfer coefficient, and nF is the number of electrons × Faraday constant). Letting n = 2,[1,35] α was estimated to be 0.77.

Determination of caffeine at the CTAB–Gr/GCE

Differential pulse voltammetry (DPV) is often used to make electrochemical measurements, owing to its high sensitivity and rejection of background current. The preparatory experiments were performed to choose the best parameters, such as pulse increment, pulse amplitude, pulse width, and pulse period. The optimized conditions were recorded as follows: pulse increment was 6 mV, pulse amplitude was 49 mV, pulse width was 20 ms, and pulse period was 60 ms.

Under the optimized conditions, the variation of peak currents with different concentrations of caffeine was measured by DPV (Fig. 5). The peak currents of caffeine were linearly related to the concentration over the range of 3.0 × 10^{-7} to 8.0 × 10^{-6} mol L^{-1} and 8.0 × 10^{-6} to 1.0 × 10^{-4} mol L^{-1}, and the regression equations were I (μA) = 4.233 + 1.289 c (μmol L^{-1}) (R = 0.995) and I (μA) = 13.847 + 0.288 c (μmol L^{-1}) (R = 0.997), respectively. According to the following equation: LOD = 3.3 × ($s_{y/x}/b$),[39] where $s_{y/x}$ is the residual standard deviation, and b is the slope of the calibration plot, the limit of detection was calculated to be 9.1 × 10^{-8} mol L^{-1} (signal-to-noise ratio = 3). A comparison of the different electrochemical methods for the determination of caffeine is summarized in Table 1. The method for the determination of caffeine proposed herein shows high sensitivity and a wide linear range, and is suitable to be the most commonly used analytical method for detecting low concentrations of caffeine.

Table 2. Interference effects of some compounds on caffeine sensor response.

Interferent	Current (μA)*	Current (μA)†	Difference of current ratio‡ (%)
Glucose	19.61	19.67	0.32
Glycine	—	19.89	1.42
Citric acid	—	19.36	–1.27
Sucrose	—	19.34	–1.35
Fructose	—	19.85	1.21
Aminoacetic acid	—	20.08	2.41
L-Tyrosine	—	20.26	3.31
Catechin	—	20.05	2.26

*Anodal peak current responses after sensors incubated with 2.0 × 10^{-5} mol L^{-1} caffeine without the interference (I_a).
†Anodal peak current responses after sensors incubated with 2.0 × 10^{-5} mol L^{-1} caffeine with the interference (I_b).
‡Difference of current ratio = $(I_b - I_a)/I_a$.

Stability and reproducibility of the CTAB–Gr/GCE

To examine the stability and repeatability of the developed method, the direct electrochemistry of CTAB–Gr/GCE was investigated by CV. The peak current of CTAB–Gr/GCE stayed almost unchanged when the electrode undergone successive potential scans between 600 and 1500 mV in the presence of 2.0 × 10^{-5} mol L^{-1} caffeine in 0.01 mol L^{-1} H_2SO_4. After 100 cycles of potential scanning, the anodic peak current decreased by 4.9%. When storing in a refrigerator (4 °C) for 20 days, 95.1% of its initial current response was obtained, indicating that the CTAB–Gr/GCE has long-term stability. Moreover, under the same preparing conditions, the relative standard deviation (RSD) of the peak current was 5.1% for 5 different CTAB–Gr/GCEs. This indicated good reproducibility for the method of construction of the sensor.

Table 3. Analysis of caffeine in real samples by the UV–vis spectroscopic, present sensor and HPLC methods ($n = 4$).

Sample	Caffeine (mg mL^{-1})		
	Test sensor*	UV–vis†	HPLC
Coca Cola	0.0995±0.004	0.103±0.0051	0.0991±0.005
Pepsi Cola	0.109±0.0051	0.11±0.0046	0.106±0.0049
Energy drink	0.189±0.008	0.187±0.009	0.19±0.008
Instant coffee	0.135±0.01	0.137±0.009	0.1349±0.008
Commercial coffee sample 1	0.176±0.003	0.1744±0.0019	0.1767±0.002
Commercial coffee sample 2	0.175±0.003	0.1768±0.0029	0.1756±0.0028

*Electrochemical sensor based on cationic surfactant cetyltrimethylammonium-bromide- dispersed graphene system.
†Measured using UV–vis absorption spectroscopy at 290 nm.

Table 4. Determination results of caffeine in spiked cola beverage ($n = 5$).

Added (mol L^{-1})	Expected (mol L^{-1})	Found (mol L^{-1})	Average recovery (%)	Ref. value (mol L^{-1})*	Ref. value (mol L^{-1})†
0.0	—	2.0×10^{-5}	—	2.06×10^{-5}	1.99×10^{-5}
1.0×10^{-5}	3.0×10^{-5}	3.07×10^{-5}	102.3		
8.0×10^{-6}	2.8×10^{-5}	2.84×10^{-5}	101.4		
5.0×10^{-6}	2.5×10^{-5}	2.49×10^{-5}	99.6		
1.0×10^{-6}	2.1×10^{-5}	2.06×10^{-5}	98.1		

*Measured using UV–vis absorption spectroscopy at 290 nm.
†Measured using HPLC.

Interference

We investigated interference from glucose, glycine, citric acid, sucrose, fructose, aminoacetic acid, L-tyrosine, and catechin, which may be present in the soft-drink samples. The electrochemical sensor was separately exposed to two different incubating solutions of 20 μmol L^{-1} caffeine: one with interference and the other without. The results were shown in Table 2, which indicated that the selectivity of the as-prepared sensor was acceptable within experimental error.

Analysis of real samples

To evaluate the validity of the proposed method, CTAB–Gr/GCE was applied to determine the caffeine content of the soft-drink samples. Table 3 shows a comparison of the detection performance of sensor developed here and the other methods. Data were presented as the average of 4 trial replicates ± SD. The results are in agreement with the value achieved by using UV–vis spectrophotometry and HPLC, as well as the regulation of I (μA) = 13.847 + 0.288 c (μmol L^{-1}) ($R = 0.997$). According to the results, it was obvious that caffeine in the soft-drink samples could be measured using the present sensor.

To test the reliability of the measurements, a standard addition method was adopted to determine the caffeine levels in cola beverage samples spiked with caffeine standard solution. The results are listed in Table 4. The recoveries were in the range of 98.1%–102.3%. It was in accordance with the result obtained by using UV–vis absorption spectrophotometry and HPLC, which indicated good accuracy of the developed method.

Conclusions

In this work, a novel electrochemical sensor was fabricated based on a CTAB–Gr/GCE modified GCE for the sensitive determination of caffeine. The developed sensor shows an excellent electrocatalytic activity towards the oxidation of caffeine. The CTAB–Gr/GCE obviously improves the sensitivity of the electrode towarts caffeine, and has a low detection limit. The results were attributed to the specific characteristics of Gr. The developed biosensor exhibited a wide linear detection range, acceptable reproducibility, high sensitivity, long-term stability, and a low detection limit. The proposed method was further used for the detection of caffeine in soft-drink samples with satisfactory results. This work demonstrated that the proposed CTAB–Gr modification was highly useful for bioelectrochemical and biosensing applications.

Acknowledgments

This work was supported by the National Natural Science Foundation of China (20805040), Program for Science and Technology Innovation Talents in the Universities of Henan Province (2010HASTIT025), and Excellent Youth Foundation of Henan Scientific Committee (104100510020).

References

(1) Spataru, N.; Sarada, B. V.; Tryk, D. A.; Fujishima, A. *Electroanalysis* **2002** *14* (11), 721. doi:10.1002/1521-4109(200206)14:11<721::AID-ELAN721>3.0.CO;2-1.
(2) Pizzariello, A.; Švorc, J.; Stred'ansky, M.; Miertuš, S. *J. Sci. Food Agric.* **1999** *79* (8), 1136. doi:10.1002/(SICI)1097-0010(199906)79:8<1136::AID-JSFA337>3.0.CO;2-4.
(3) Pons, F. W.; Muller, P. *Mutagenesis* **1990** *5* (2), 173. doi:10.1093/mutage/5.2.173.
(4) Blecher, R.; Lingens, F. *Hoppe Seylers Z. Physiol. Chem.* **1977** *358* (2), 807. doi:10.1515/bchm2.1977.358.2.807.
(5) Kalmar, J. M.; Cafarelli, E. *J. Appl. Physiol.* **1999** *87* (2), 801.

Can. J. Chem. Downloaded from www.nrcresearchpress.com by Xi'an Jiaotong University on 09/19/12
For personal use only.

Can. J. Chem. Downloaded from www.nrcresearchpress.com by Xi'an Jiaotong University on 09/19/12
For personal use only.

(6) Arinobu, T.; Hattori, H.; Kumazawa, T.; Lee, X. P.; Mizutani, Y.; Katase, T.; Kojima, S.; Omori, T.; Kaneko, R.; Ishii, A.; Seno, H. *Forensic Tox.* **2009** *27* (1), 1. doi:10.1007/s11419-008-0058-6.
(7) Alpdogan, G.; Karabina, K.; Sungur, S. *Turk. J. Chem.* **2002** *26*, 295.
(8) Statheropoulos, M.; Samargadi, E.; Tzamtzis, N.; Geogakopoulous, C. *Anal. Chim. Acta* **1996** *113*, 292.
(9) Verenitch, S. S.; Mazumder, A. *Anal. Bioanal. Chem.* **2008** *391* (7), 2635. doi:10.1007/s00216-008-2174-x.
(10) Emre, D.; Özaltin, N. *J. Chromatogr B* **2007** *847* (2), 126. doi:10.1016/j.jchromb.2006.09.036.
(11) Chen, Z.; Zhang, L.; Chen, G. *J. Chromatogr A* **2008** *1193* (1–2), 178. doi:10.1016/j.chroma.2008.04.032.
(12) El-Hady, D. A.; El-Maali, N. A. *Talanta* **2008** *76* (1), 138. doi:10.1016/j.talanta.2008.02.026.
(13) Sadik, O. A.; Land, W. H.; Wang, J. *Electroanalysis* **2003** *15* (14), 1149. doi:10.1002/elan.200390140.
(14) Safavi, A.; Maleki, N.; Shams, E.; Shahbaazi, H. R. *Electroanalysis* **2002** *14* (13), 929. doi:10.1002/1521-4109(200207)14:13<929::AID-ELAN929>3.0.CO;2-W.
(15) Desimoni, E.; Brunetti, B.; Bacchella, R. *Electroanalysis* **2002** *14* (6), 459. doi:10.1002/1521-4109(200203)14:6<459::AID-ELAN459>3.0.CO;2-D.
(16) Li, J.; Wu, Z.; Wang, H.; Shen, G.; Yu, R. *Sens. Actuators B Chem.* **2005** *110* (2), 327. doi:10.1016/j.snb.2005.02.011.
(17) Moulton, S. E.; Barisci, J. N.; Bath, A.; Stella, R.; Wallace, G. G. *Langmuir* **2005** *21* (1), 316. doi:10.1021/la0487242.
(18) Wang, Y.; Li, Y. M.; Tang, L. H.; Lu, J.; Li, J. H. *Electrochem. Commun.* **2009** *11* (4), 889. doi:10.1016/j.elecom.2009.02.013.
(19) Shan, C. S.; Yang, H. F.; Song, J. F.; Han, D. X.; Ivaska, A.; Niu, L. *Anal. Chem.* **2009** *81* (6), 2378. doi:10.1021/ac802193c.
(20) Xu, Y.; Bai, H.; Lu, G.; Li, C.; Shi, G. *J. Am. Chem. Soc.* **2008** *130* (18), 5856. doi:10.1021/ja800745y.
(21) Li, D.; Müller, M. B.; Gilje, S.; Kaner, R. B.; Wallace, G. G. *Nat. Nanotechnol.* **2008** *3* (2), 101. doi:10.1038/nnano.2007.451.
(22) Geim, A. K.; Novoselov, K. S. *Nat. Mater.* **2007** *6* (3), 183. doi:10.1038/nmat1849.
(23) Park, S.; Ruoff, R. S. *Nat. Nanotechnol.* **2009** *4* (4), 217. doi:10.1038/nnano.2009.58.
(24) Cassagneau, T.; Fendler, J. H. *Adv. Mater. (Deerfield Beach Fla.)* **1998** *10* (11), 877. doi:10.1002/(SICI)1521-4095(199808)10:11<877::AID-ADMA877>3.0.CO;2-1.
(25) Gilje, S.; Han, S.; Wang, M.; Wang, K. L.; Kaner, R. B. *Nano Lett.* **2007** *7* (11), 3394. doi:10.1021/nl0717715.
(26) Schedin, F.; Geim, A. K.; Morozov, S. V.; Hill, E. W.; Blake, P.; Katsnelson, M. I.; Novoselov, K. S. *Nat. Mater.* **2007** *6* (9), 652. doi:10.1038/nmat1967.
(27) Bunch, J. S.; van der Zande, A. M.; Verbridge, S. S.; Frank, I. W.; Tanenbaum, D. M.; Parpia, J. M.; Craighead, H. G.; McEuen, P. L. *Science* **2007** *315* (5811), 490. doi:10.1126/science.1136836.
(28) Fu, C. L.; Yang, W. S.; Chen, X.; Evans, D. G. *Electrochem. Commun.* **2009** *11* (5), 997. doi:10.1016/j.elecom.2009.02.042.
(29) Rama, H. S.; Prasad Kumar, D. *Colloids Surf. A Physicochem. Eng. Asp.* **1998** *142* (1), 41. doi:10.1016/S0927-7757(98)00384-7.
(30) Hu, C.; Dang, X.; Hu, S. *J. Electroanal. Chem.* **2004** *572* (1), 161. doi:10.1016/j.jelechem.2004.06.009.
(31) Hu, C.; He, Q.; Li, Q.; Hu, S. *Anal. Sci.* **2004** *20* (7), 1049. doi:10.2116/analsci.20.1049.
(32) Hummers, W.; Offeman, R. *J. Am. Chem. Soc.* **1958** *80* (6), 1339. doi:10.1021/ja01539a017.
(33) Bard, A. J.; Fanlkner, L. R. *Electrochemical Methods Fundamentals and Applications;* Wiley: New York, 1980; p 258.
(34) Martínez-Huitle, C. A.; Suely Fernandes, N.; Ferro, S.; De Battisti, A.; Quiroz, M. A. *Diamond Related Materials* **2010** *19* (10), 1188. doi:10.1016/j.diamond.2010.05.004.
(35) Ly, S. Y.; Jung, Y. S.; Kim, M. H.; Han, I. K.; Jung, W. W.; Kim, H. S. *Mikrochim. Acta* **2004** *146* (3–4), 207. doi:10.1007/s00604-004-0209-3.
(36) Zen, J. M.; Ting, Y. S.; Shih, Y. *Analyst (Lond.)* **1998** *123* (5), 1145. doi:10.1039/a708360b.
(37) Akyilmaz, E.; Turemis, M. *Electrochim. Acta* **2010** *55* (18), 5195. doi:10.1016/j.electacta.2010.04.038.
(38) Zhang, Z.; Wang, E. *Electrochemical Principles and Methods;* Science Press: Beijing, 2000; p 242.
(39) Desimoni, E.; Brunetti, B.; Cattaneo, R. *Ann. Chim.* **2004** *94* (7–8), 555. doi:10.1002/adic.200490069.

Étude DFT (« density functional theory ») des réactions d'addition de l'ozone sur les doubles liaisons des terpènes : limonène, β-phellandrène et terpinolène

Sameh Ayadi et Manef Abderrabba

Can. J. Chem. Downloaded from www.nrcresearchpress.com by Xi'an Jiaotong University on 09/19/12
For personal use only.

Résumé : Dans ce travail, nous avons réalisé une étude théorique concernant les réactions d'addition de l'ozone sur les doubles liaisons des molécules des terpènes tels que le terpinolène **1**, le β-phellandrène **2** et le limonène **3**. En nous basant sur la méthode de calcul DFT (« density functional theory ») avec la base standard 6–31G(d) et les deux fonctionnelles BPW91 et B3LYP, nous avons discuté, du point de vue thermodynamique et orbitalaire, la possibilité et la stéréosélectivité de ces réactions. Les états de transition des réactions entre la molécule de l'ozone et les molécules des terpènes **1**, **2** et **3** ont été déterminés.

Mots-clés : terpènes, limonène, β-phellandrène, terpinolène, méthode DFT (density functional theory).

Abstract: In this work, we conducted a theoretical study on the addition reactions between ozone and double bonds of terpene molecules such as terpinolene **1**, β-phellandrene **2**, and limonene **3**. Based on the DFT (density functional theory) calculation method with the standard basis set 6–31G(d) and the two functional bases such as BPW91 and B3LYP, we discuss, from thermodynamic and orbital points of view, the possibility and the stereoselectivity of these reactions. The transition states of reactions between the ozone molecule and the terpene molecules **1**, **2**, and **3** have been calculated and discussed.

Key words: terpenes, limonene, β-phellandrene, terpinolene, DFT (density functional theory) method.

[Journal translation]

Introduction

Les terpènes sont des hydrocarbures de formule brute $(C_5H_8)_n$. Ces hydrocarbures se trouvent généralement dans les végétaux. Plusieurs études expérimentales et théoriques ont été réalisées sur l'ozonolyse des molécules des terpènes.[1–3] Les réactions des terpènes avec l'ozone ont pour première étape l'addition d'ozone sur la double liaison. Ce qui entraîne la formation d'un intermédiaire appelé le molozonide. Ce molozonide s'ouvre pour conduire à la formation d'un composé carbonylé et d'un intermédiaire biradicalaire dit de Criegee.[3] Ensuite par réarrangement interne de l'intermédiaire de Criegee, on observe la formation des composés tels que des aldéhydes, des cétones et des acides carboxyliques. À titre d'exemples, ces différentes étapes se trouvent dans la réaction de l'α-pinène avec l'ozone.[2]

Nous avons trouvé intéressant d'effectuer une étude théorique sur les réactions d'addition de l'ozone sur les doubles liaisons des molécules de terpènes. Pour mettre cette étude en évidence, nous avons choisi des molécules de terpènes de formule brute $C_{10}H_{16}$ qui possèdent chacune deux doubles liaisons, une première double liaison C1=C2 se trouve à l'extérieur du cycle à 6 carbones et une deuxième double liaison C3=C4 se trouve dans le cycle (fig. 1). Ces molécules sont appelées le terpinolène **1**, le β-phellandrène **2**, le limonène **3**.

Figure 1.

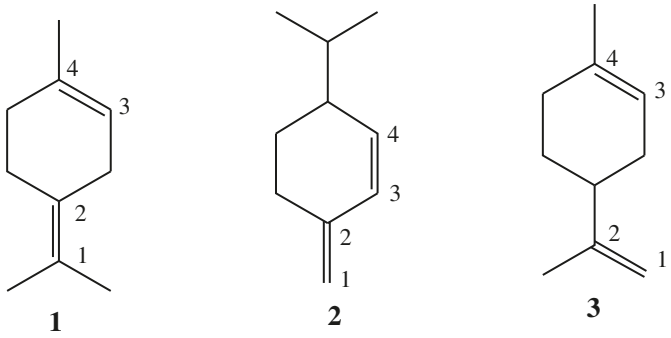

Dans ce travail, nous avons comparé la réactivité de ces deux doubles liaisons C1=C2 et C3=C4 appartenant à une même molécule de terpène vis-à-vis de la molécule de l'ozone **4** (fig. 2). Dans chaque cas de ces réactions, nous avons vérifié que ces réactions sont sous le contrôle des orbitales frontières. Enfin, nous avons étudié du point de vue thermo-

Reçu le 17 décembre 2010. Acceptée le 27 février 2011. Publié au www.nrcresearchpress.com/cjc, le 23 juin 2011.

S. Ayadi et M. Abderrabba. Unité de recherche physico-chimie moléculaire, Institut préparatoire aux études scientifiques et techniques (IPEST), B.P. 51, 2070 la Marsa, Tunisie.

Auteur correspondant : Sameh Ayadi (courriel : sameh_ayadi2003@yahoo.fr).

Figure 2.

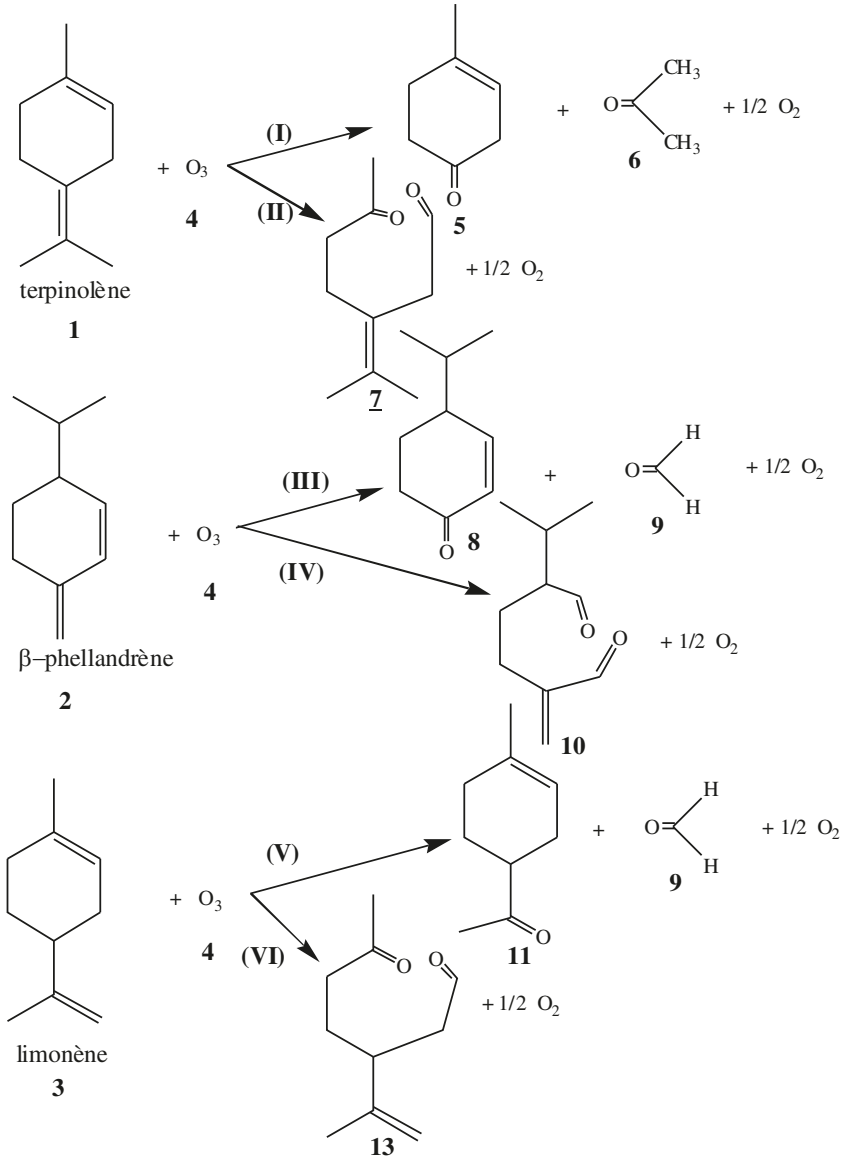

dynamique et cinétique la possibilité et la stéréosélectivité de ces réactions.

Les méthodes de calcul

Cette étude a été réalisée en utilisant le programme GAUSSIAN 03.[4] Les calculs ont été effectués au niveau DFT (« density functional theory ») avec la base standard 6–31G(d). Nous avons utilisé deux types de fonctionnelles : une de type GGA tels que BPW91[5,6] et l'autre de type hybride tels que B3LYP.[5,7] En effet, il a été établi que cette méthode de calcul DFT est une des plus performantes pour ce type de molécules organiques.[8] Les calculs de fréquences vibrationnelles harmoniques ont été exécutés pour vérifier la nature des points stationnaires. Dans le cas d'absence de fréquence imaginaire, les points fixes sont classés comme des minima. Pour chaque état de transition, nous avons trouvé une seule fréquence imaginaire.[9] Afin de nous assurer que les états de transition sont corrects, nous avons déterminé (l'IRC « intrinsic reaction coordinate ») à chaque état de transition de réaction.[10]

Résultat et discussion

Étude thermodynamique

Nous avons étudié du point de vue thermodynamique la possibilité et la stéréosélectivité des réactions d'additions de l'ozone **4** sur les molécules de terpène tels que le terpinolène **1**, le β-phellandrène **2**, le limonène **3** (fig. 2). Dans le but de comparer la réactivité de ces molécules de terpènes vis-à-vis de la molécule de l'ozone **4**, nous avons déterminé dans les conditions standard de température et de pression (T = 298,15 K; P = 1 atm (1 atm = 101,325 kPa)) les variations d'énergie réactionnelle ΔEr, les variations d'enthalpie réactionnelle ΔHr, les variations d'enthalpie libre réactionnelle ΔGr et le ZPE (« zero point energy ») qui correspond aux réactions I, II, III, IV, V et VI.

Comme le montre le tableau 1, les variations d'enthalpie

Can. J. Chem. Downloaded from www.nrcresearchpress.com by Xi'an Jiaotong University on 09/19/12
For personal use only.

Can. J. Chem. Downloaded from www.nrcresearchpress.com by Xi'an Jiaotong University on 09/19/12
For personal use only.

Tableau 1. Valeurs calculées (kcal mol^{-1}) des variations d'énergie réactionnelle ΔEr, des variations d'enthalpie libre réactionnelle ΔGr, des variations d'enthalpie réactionnelle ΔHr et le ZPE.

Réactions	Produits	ΔEr	ΔEr + ZPE	ΔHr	ΔGr
B3LYP/6–31G(d)					
I	**5** + **6** + 1/2O_2	–111,691	–111,823	–111,392	–117,983
II	**7** + 1/2O_2	–102,893	–103,921	–103,195	–98,604
III	**8** + **9** + 1/2O_2	–96,672	–97,296	–96,387	–102,091
IV	**10** + 1/2O_2	–96,604	–97,187	–96,378	–91,613
V	**11** + **12** + 1/2O_2	–102,324	–103,406	–102,626	–103,526
VI	**13** + 1/2O_2	–98,257	–98,873	–97, 958	–97,748
BPW91/6–31G(d)					
I	**5** + **6** + 1/2O_2	–141,497	–141,633	–141,248	–147,524
II	**7** + 1/2O_2	–132,995	–133,772	–133,083	–128,447
III	**8** + **9** + 1/2O_2	–126,776	–127,235	–126,337	–131,957
IV	**10** + 1/2O_2	–126,534	–127,073	–126,215	–121,246
V	**11** + **12** + 1/2O_2	–132,271	–133,294	–132,437	–133,338
VI	**13** + 1/2O_2	–128,357	–128,834	–127,815	–127,586

libre réactionnelle ΔGr sont toutes négatives, par conséquent ces réactions sont possibles et favorisées thermodynamiquement. De plus, nous avons remarqué que les valeurs de la variation d'enthalpie libre réactionnelle ΔGr qui correspond aux réactions I, III et V sont respectivement supérieures en valeur absolue aux valeurs de la variation d'enthalpie libre réactionnelle qui correspond aux réactions II, IV et VI. Ce qui nous a permis de dire que les réactions I, III et V sont respectivement plus stables thermodynamiquement que les réactions II, IV et VI. Par conséquent, les doubles liaisons de type C1=C2 des molécules des terpènes **1**, **2** et **3** sont respectivement plus réactives que les doubles liaisons de type C3=C4 appartenant à ces mêmes molécules. De plus, nous avons remarqué que la réaction I est plus favorisée thermodynamiquement que les autres réactions II, III, IV, V et VI, puisque nous avons trouvé une valeur d'enthalpie libre réactionnelle plus importante en valeur absolue que celle qui correspond aux réactions II, III, IV, V et VI.

De la même manière, nous avons trouvé que les valeurs de la variation de l'énergie ΔEr qui correspondent aux réactions I, III et V sont respectivement supérieures en valeur absolue aux valeurs de la variation de l'énergie ΔEr qui correspondent aux réactions II, IV et VI. Ce qui confirme de nouveau que la liaison C1=C2 des molécules des terpènes **1**, **2** et **3** est plus réactive que la double liaison C3=C4 de ces mêmes molécules de terpènes. Par conséquent, les réactions I, III et V sont respectivement plus stables thermodynamiquement que les réactions II, IV et VI.

Étude des orbitales frontières

Nous avons déterminé les énergies de la LUMO (moléculaires inoccupées les moins élevés) et de la HOMO (moléculaires occupées les plus élevés) de l'ozone **4** ainsi que les énergies de la LUMO et de la HOMO des molécules des terpènes tels que le terpinolène **1**, le β-phellandrène **2**, le limonène **3** (voir tableau 2). D'après la théorie des orbitales frontières, lors de l'intéraction entre deux molécules, les orbitales frontières à considérer sont la HOMO de l'une et la LUMO de l'autre, choisies de telle sorte que l'écart énergétique ΔE qui les sépare soit le plus faible possible.[11] Comme le montre la fig. 3, le diagramme orbitalaire donne une bonne

Tableau 2. Les énergies (eV) de la moléculaires inoccupées les moins élevés (LUMO) et de la moléculaires occupées les plus élevés (HOMO) des molécules des terpènes **1**, **2** et **3** et de la molécule de l'ozone **4**.

Produit	LUMO	HOMO	μ^{12}	η^{12}	ω^{12}
B3LYP/6–31G(d)					
O_3	–5,024	–9,121	–7,072	4,096	6,105
1	0,894	–5,875	–2,490	6,769	0,458
2	–0,357	–5,831	–3,094	5,474	0,874
3	0,764	–6,139	–2,687	6,903	0,523
BPW91/6–31G(d)					
O_3	–5,830	–7,489	–6,659	1,659	13,367
1	0,014	–4,965	–2,475	4,979	0,615
2	–1,183	–5,019	–3,101	3,836	1,253
3	–0,143	–5,218	–2,681	5,074	0,708

indication qualitative quant à la réactivité de notre système. Nous avons remarqué que l'intéraction principale se fait entre l'énergie de la LUMO de l'ozone et l'énergie de la HOMO des molécules des terpènes **1**, **2** et **3**, puisque nous avons observé un recouvrement favorable entre les orbitales de la LUMO de l'ozone et les orbitales de la HOMO de ces molécules **1**, **2** et **3**. De plus, nous avons remarqué que la variation d'énergie ΔE entre la LUMO de l'ozone **4** et la HOMO de terpinolène **1** est inférieure à la variation d'énergie ΔE entre la LUMO de l'ozone **4** et la HOMO de limonène **3**. Ce qui explique bien que la réaction entre l'ozone **4** et le terpinolène **1** est plus favorisée que dans le cas des réactions entre l'ozone **4** et le limonène **3**.

Nous avons par la suite déterminé les valeurs de l'électrophilicité global $\omega = \mu^2/(2\eta)^{12}$ de ces molécules de terpènes **1**, **2** et **3** (tableau 2). Pour déterminer cet électrophilicité, nous avons calculé le potentiel chimique ($\mu \approx (E_{HOMO} + E_{LUMO})/2$) qui est une valeur négative[12] et la dureté chimique $\eta \approx (E_{LUMO} - E_{HOMO})^{12}$ pour ces molécules.

Comme le montre le tableau 2, nous avons trouvé une valeur importante de l'électrophilicité pour la molécule de l'ozone **4** (ω = 6,105°; au niveau de calcul B3LYP/6–31G(d)). Par contre, les valeurs de l'électrophilicité des molécules de terpènes **1**, **2** et **3** sont moins importantes que celle de l'ozone

Figure 3. Diagramme orbitalaire des molécules des terpènes **1**, **2** et **3** et la molécule de l'ozone **4**. Énergies en eV, la valeur de l'isocontour = (0,002 unités atomiques).

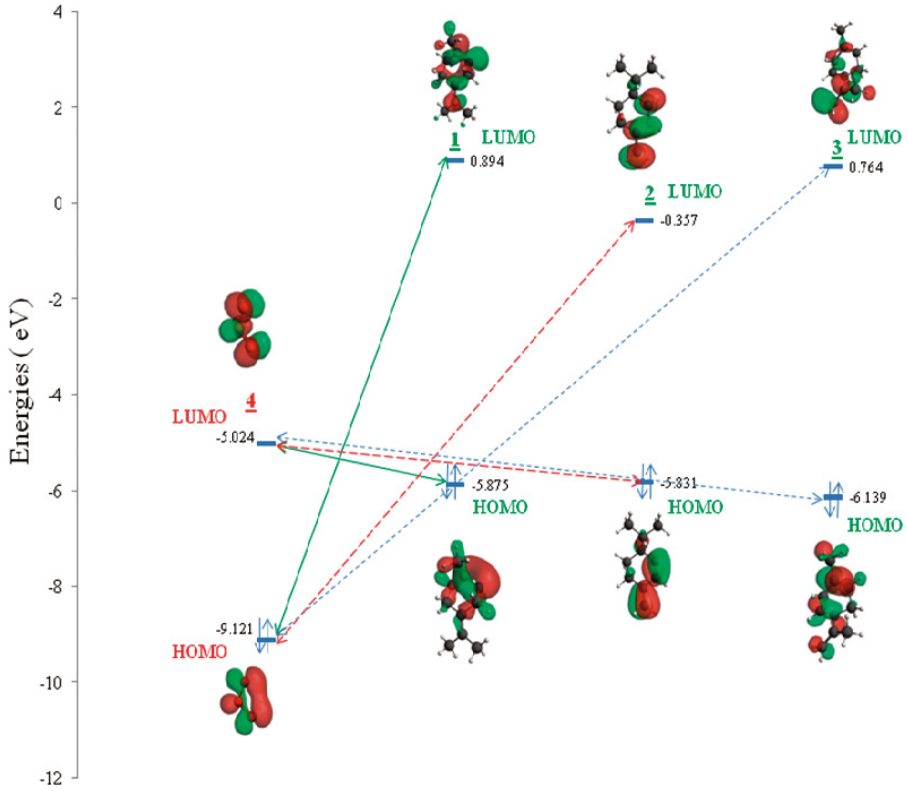

4. De plus, la valeur de l'électrophilicité du terpinolène **1** est moins importante que la valeur de l'électrophilicité du limonène **3** qui est moins importante que celle du β-phellandrène **2**.

Ces résultats, nous ont permis de dire que la réaction d'addition de l'ozone **4** sur le terpinolène **1** est plus favorisée que la réaction entre l'ozone **4** et le limonène **3**, qui est plus favorisée que la réaction entre l'ozone **4** et le β-phellandrène **2**. Ces résultats confirment bien les résultats trouvés précédemment par l'étude thermodynamique.

Calcul des états de transition

Nous avons optimisé les états de transition de la réaction d'addition de l'ozone **4** sur le terpinolène **1**. Nous avons obtenu quatre conformations des états de transitions **5***(endo), **5***(exo), **7***(endo) et **7***(exo) : Les états de transitions **5*** (endo) et **5***(exo) obtenus respectivement avec une approche de l'ozone en endo de la double liaison C1=C2 de la molécule de terpinolène **1** et avec une approche de l'ozone en exo de la double liaison C1=C2 de terpinolène **1**; Les états de transitions **7***(endo) et **7***(exo) obtenus respectivement avec une approche de l'ozone en endo de la double liaison C3=C4 de terpinolène **1** et avec une approche de l'ozone en exo de la double liaison C3=C4 de terpinolène **1** (fig. 4).

Les calculs théoriques montrent que la formation des composés (**5** + **6**) est favorisée par rapport à la formation du composé **7** (fig. 4). En utilisant les méthodes de calculs DFT/B3LYP et DFT/BPW91 avec la base standard 6–31G(d), nous avons trouvé pour la formation du composé **7** une grande énergie d'activation respectivement de 3,57 et 8,36 kcal mol^{-1} aux niveaux du calcul cités précédemment. Ces valeurs sont plus grandes que celles trouvées pour les états de transition conduisant à la formation des composés (**5** + **6**) (tableau 3). Ce qui confirme de nouveau que la double liaison C1=C2 de la molécule du terpinolène **1** est plus réactive que la double liaison C3=C4 de cette même molécule **1**. De la même manière, nous avons optimisé les états de transition des réactions d'addition de l'ozone **4** sur les molécules de β-phellandrène **2** et de limonène **3**. Comme le montre le tableau 3, nous avons obtenu quatre conformations des états de transitions dans chaque cas de ces réactions. Nous avons obtenu les états de transitions **8***(endo) et **8***(exo) respectivement par une approche de l'ozone **4** en endo et en exo de la liaison C1=C2 du β-phellandrène **2**. Les états de transitions **10***(endo) et **10***(exo) sont obtenus respectivement par une approche de l'ozone **4** en endo et en exo de la liaison C3=C4 du β-phellandrène **2**. Nous avons aussi obtenu les états de transitions **11***(endo) et **11***(exo) respectivement par une approche de l'ozone **4** en endo et en exo de la liaison C1=C2 de la molécule du limonène **3**. Nous avons obtenu les états de transitions **13***(endo) et **13***(exo) respectivement par une approche de l'ozone **4** en endo et en exo de la liaison C3=C4 de la molécule du limonène **3**. Comme le montre le tableau 3, nous avons remarqué que la valeur de l'énergie de l'état de transition **5***(endo) est moins importante que les valeurs des états de transitions qui correspondent aux **8***(endo) et **11***(endo). Ce qui explique que la formation du composé **5** est plus favorisée que la formation des composés **8** et **11**. Nous avons aussi remarqué que dans chaque cas de ces réactions, les états de transitions de la forme endo sont toujours inférieurs aux états de transitions de la forme exo. De plus les valeurs des états de transitions **8***(endo) et **8***(exo) sont inférieures à celles des états de transitions **10***(endo)

Can. J. Chem. Downloaded from www.nrcresearchpress.com by Xi'an Jiaotong University on 09/19/12
For personal use only.

Can. J. Chem. Downloaded from www.nrcresearchpress.com by Xi'an Jiaotong University on 09/19/12
For personal use only.

Figure 4. Profil énergétique des réactions conduisant aux composés **7** et (**5** + **6**); B3LYP/6–31G* (énergie en kcal mol^{-1}).

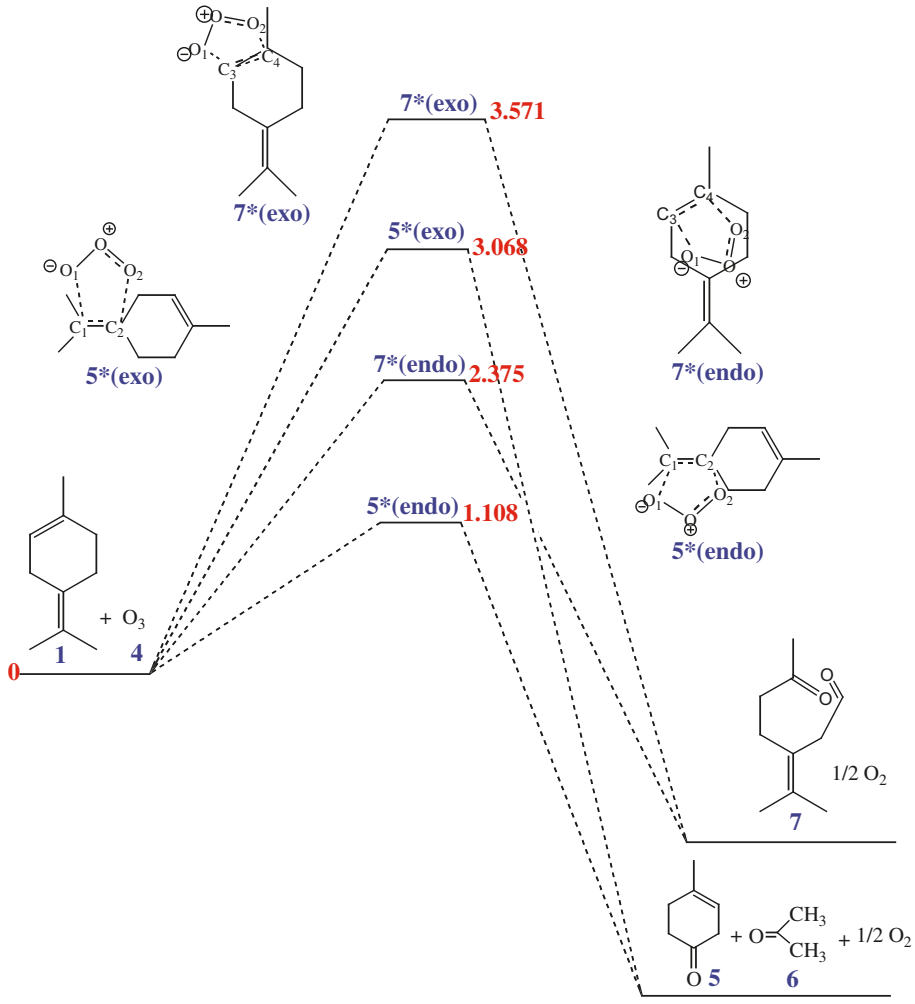

Tableau 3. Énergies relatives *E** (kcal mol^{-1}) des états de transition par rapport aux énergies des réactifs (calculées avec la méthode DFT/B3LYP et DFT/BPW91).

	*E** (kcal mol^{-1})	
Produit	B3LYP/6–31G(d)	BPW91/6–31G(d)
1		
4		
5*(endo)	1,108	5,491
5*(enxo)	3,068	7,864
7*(endo)	2,375	7,117
7*(exo)	3,571	8,368
2		
4		
8*(endo)	1,456	6,263
8*(enxo)	3,392	8,121
10*(endo)	2,667	7,482
10*(exo)	3,918	8,725
3		
4		
11*(endo)	1,513	6,314
11*(enxo)	3,468	8,267
13*(endo)	2,731	7,531
13*(exo)	3,989	8,799

et **10***(exo). Les valeurs des états de transitions **11***(endo) et **11***(exo) sont aussi inférieures à celles des valeurs des états de transitions **13***(endo) et **13***(exo). Ceci confirme bien que la double liaison C1=C2 des molécules **1**, **2** et **3** est respectivement plus réactive que la double liaison C3=C4 de ces mêmes molécules vis-à-vis de la molécule de l'ozone **4**.

Nous avons comparé nos résultats théoriques avec des études antérieures.[3,13] Ces études ont été réalisées sur l'oxydation des flavonoïdes et l'ozonolyse du limonène. Nous avons remarqué que nos résultats sont très proches des résultats trouvées par Jiang et al.[3]

La géométrie des états de transition **5***(endo) et **7***(exo) est présentée sur la fig. 5.

Nous avons comparé les longueurs de liaisons en formation; on constate que la liaison C_2–O_2 est plus courte que la liaison C_1–O_1. Nous avons aussi trouvé que les longueurs de liaisons en formation C_4–O_2 sont plus courtes que les liaisons C_3–O_1 (tableau 4). Ces distances sont assez proches de celle trouvée par Jiang et al.[3] pour la réaction entre l'ozone **4** et le limonène **3**.

Conclusion

Dans ce travail, nous avons étudié théoriquement les réactions d'addition de l'ozone **4** sur les deux doubles liaisons C1=C2 et C3=C4 appartenant à une même molécule de ter-

Can. J. Chem. Downloaded from www.nrcresearchpress.com by Xi'an Jiaotong University on 09/19/12
For personal use only.

Figure 5. Géométrie des états de transition de la formation des composés **5***(endo) et **7***(exo).

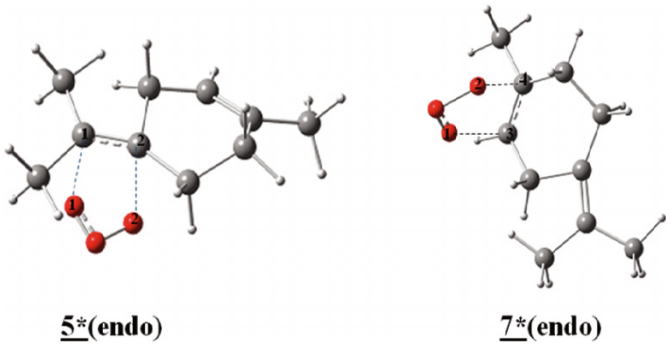

Tableau 4. Longueurs des liaisons en formation C_1–O_1, C_2–O_2, C_3–O_1 et C_4–O_2 dans l'état de transition des réactions d'addition de l'ozone **4** sur les molécules des terpènes **1**, **2** et **3** dans les deux approches endo et exo (Å).

Produit	C_1–O_1	C_2–O_2	C_3–O_1	C_4–O_2
B3LYP/6–31G(d)				
5*(endo)	2,406	2,276		
5* (enxo)	2,523	2,424		
7*(endo)			2,318	2,309
7*(exo)			2,351	2,304
8*(endo)	2,314	2,274		
8*(enxo)	2,511	2,401		
10*(endo)			2,371	2,316
10*(exo)			2,398	2,364
11*(endo)	2,410	2,275		
11*(enxo)	2,520	2,419		
13*(endo)			2,317	2,294
13*(exo)			2,349	2,301
BWP91/6–31G(d)				
5*(endo)	2,394	2,269		
5*(enxo)	2,511	2,415		
7*(endo)			2,311	2,291
7*(exo)			2,342	2,286
8*(endo)	2,227	2,197		
8*(enxo)	2,490	2,387		
10*(endo)			2,290	2,235
10*(exo)			2,312	2,268
11*(endo)	2,351	2,284		
11*(enxo)	2,498	2,420		
13*(endo)			2,297	2,286
13*(exo)			2,321	2,257

pène, tels que le terpinolène **1**, le β-phellandrène **2** et le limonène **3**.

Les résultats de calculs théoriques par les méthodes DFT/B3LYP et DFT/BPW91 avec la base standard 6–31G(d) montrent que ces réactions sont possibles et favorisées thermodynamiquement. De plus, nous avons trouvé que la réaction entre l'ozone **4** et le terpinolène **1** est plus stable thermodynamiquement que les réactions entre l'ozone **4** et les autres molécules de terpène, tels que le β-phellandrène **2** et le limonène **3**.

Les résultats théoriques montrent aussi que dans chaque cas des molécules de terpènes **1**, **2** et **3**, la double liaison C1=C2 est toujours plus réactive que la double liaison C3=C4 vis-à-vis de la molécule de l'ozone **4**. Les calculs des états de transition montrent que les produits cinétiques des réactions d'addition de l'ozone 4 sur les molécules **1**, **2** et **3** sont les produits provenant de l'addition de l'ozone **4** sur la double liaison C1=C2 et non pas les produits provenant de l'addition de l'ozone **4** sur la double liaison C3=C4. De plus, pour chaque molécule des terpènes **1**, **2** et **3**, les produits provenant par une approche de l'ozone **4** en endo de la double liaison C1=C2 sont plus favorisés que ceux obtenus par une approche en exo de l'ozone sur la double liaison C1=C2.

Bibliographie

(1) Mathis, C.; Ourisson, G. *Phytochemistry* **1964** *3* (1), 115. doi:10.1016/S0031-9422(00)84003-0.

(2) Pathak, R. K.; Presto, A. A.; Lane, T. E.; Stanier, C. O.; Donahue, N. M.; Pandis, S. N. *Atmos. Chem. Phys. Discuss.* **2007** *7* (1), 1941. doi:10.5194/acpd-7-1941-2007.

(3) Jiang, L.; Wang, W.; Xu, Y. *Chem. Phys.* **2010** *368* (3), 108. doi:10.1016/j.chemphys.2010.01.003.

(4) Frisch, M. J.; Trucks, G. W.; Schlegel, H. B.; Scuseria, G. E.; Robb, M. A.; Cheeseman, J. R.; Montgomery, J. A., Jr.; Vreven, T.; Kudin, K. N.; Burant, J. C.; Millam, J. M.; Iyengar, S. S.; Tomasi, J.; Barone, V.; Mennucci, B.; Cossi, M.; Scalmani, G.; Rega, N.; Peterson, G. A.; Nakatsuji, H.; Hada, M.; Ehara, M.; Toyota, K.; Fukuda, R.; Hasegawa, J.; Ishida, M.; Nakajima, T.; Honda, Y.; Kitao, O.; Nakai, H.; Klene, M.; Li, X.; Knox, J. E.; Hratchian, H. P.; Cross, J. B.; Adamo, C.; Jaramillo, J.; Gomperts, R.; Stratmann, R. E.; Yazyev, O.; Austin, A. J.; Cammi, R.; Pomelli, C.; Ochterski, J. W.; Ayala, P. Y.; Morokuma, K.; Voth, G. A.; Salvador, P.; Dannenberg, J. J.; Zakrzewski, V. G.; Dapprich, S.; Daniels, A. D.; Strain, M. C.; Farkas, O.; Malick, D. K.; Rabuck, A. D.; Raghavachari, K.; Foresman, J. B.; Ortiz, J. V.; Cui, Q.; Baboul, A. G.; Clifford, S.; Cioslowski, J.; Stefanov, B. B.; Liu, G.; Liashenko, A.; Piskorz, P.; Komaromi, I.; Martin, R. L.; Fox, D. J.; Keith, T.; Al-Laham, M. A.; Peng, C. Y.; Nanayakkara, A.; Challacombe, M.; Gill, P. M. W.; Johnson, B.; Chem, W.; Wong, M. W.; Gonzalez, C.; Pople, J. A. *Gaussian 03, Revision A.1;* Gaussian, Inc., Pittsburgh PA, 2003.

(5) (a) Becke, A. D. *J. Chem. Phys.* **1993** *98* (7), 5648. doi:10.1063/1.464913;; (b) Becke, A. D. *J. Chem. Phys.* **1993** *98* (7), 5648. doi:10.1063/1.464913;; (c) Stephens, P. J.; Devlin, F. J.; Chabalowski, C. F.; Frisch, P. J. *J. Phys. Chem.* **1994** *98* (45), 11623. doi:10.1021/j100096a001.

(6) Perdew, J. P.; Burke, K.; Wang, Y. *Phys. Rev. B* **1996** *54* (23), 16533. doi:10.1103/PhysRevB.54.16533.

(7) Lee, C.; Yang, W.; Parr, R. G. *Phys. Rev. B* **1988** *37* (2), 785. doi:10.1103/PhysRevB.37.785.

(8) Goldstein, E.; Beno, B.; Houk, N. K. *J. Am. Chem. Soc.* **1996** *118* (25), 6036. doi:10.1021/ja9601494.

(9) Schlegel, H. B. *J. Comput. Chem.* **1982** *3* (2), 214. doi:10.1002/jcc.540030212.

(10) (a) Gonzalez, C.; Schlegel, H. B. *J. Chem. Phys.* **1989** *90* (4), 2154. doi:10.1063/1.456010;; (b) Gonzalez, C.; Schlegel, H. B. *J. Chem. Phys.* **1990** *94* (14), 5523. doi:10.1021/j100377a021.

(11) J. Louis. *Rivial; élements de chimie quantique à l'usage des chimistes;* C.N.R.S éditions, 1994.

(12) Domingo, L. R.; Aurell, M. J.; Perez, P.; Contreras, R. R. *J. Phys. Chem. A* **2002** *106* (29), 6871. doi:10.1021/jp020715j.

(13) Fiorucci, S.; Golebiowski, J.; Cabrol-Bass, D.; Antonczak, S. *ChemPhysChem* **2004** *5* (11), 1726. doi:10.1002/cphc.200400186.

AWARD LECTURE / CONFÉRENCE D'HONNEUR

Chemoenzymatic total synthesis of *ent*-neopinone and formal total synthesis of *ent*-codeinone from β-bromoethylbenzene*

Jan Duchek, T. Graeme Piercy, Jacqueline Gilmet, and Tomas Hudlicky

Can. J. Chem. Downloaded from www.nrcresearchpress.com by 80.58.250.72 on 09/16/12
For personal use only.

Abstract: Formal total synthesis of *ent*-codeinone and *ent*-codeine was accomplished via the total synthesis of *ent*-neopinone attained in 14 steps from β-bromoethylbenzene. The key steps included (*i*) enzymatic dihydroxylation of β-bromoethylbenzene with *E. coli* JM109 (pDTG601a), an organism that overexpresses toluene dioxygenase, (*ii*) a Heck reaction to establish C-13 stereogenic center, (*iii*) aldol condensation, and (*iv*) 1,6-conjugate addition of the ethylamino side chain to C-9. Several other modes of construction of the C-9 and C-14 centers were also investigated: Mannich cyclization, and aza-Prins reaction. The synthesis of *ent*-codeinone was formalized by intersecting Fukuyama's recently published approach. Experimental and spectral data are provided for all new compounds.

Key words: synthesis of morphine alkaloids, *ent*-codeinone synthesis, *ent*-neopinone synthesis, enzymatic dihydroxylation of aromatics, Heck reaction.

Résumé : On a réalisé une synthèse totale formelle de l'*ent*-codéinone et de l'*ent*-codéine par le biais d'une synthèse totale de l'*ent*-néopinone qui a été obtenue en quatorze étapes à partir du β-bromoéthylbenzène. Les étapes clés comportent (*i*) une dihydroxylation enzymatique du β-bromoéthylbenzène à l'aide d'*E. coli* JM109 (pDTG601a), un organisme qui imite la dioxygénase du toluène, (*ii*) une réaction de Heck pour établir le centre stéréogénique en C-13, (*iii*) une condensation aldolique et (*iv*) une addition 1,6-conjuguée de la chaîne latérale éthylamino sur le site C-9. On a aussi examiné plusieurs autres modes de construction des centres C-9 et C-14, dont une cyclisation de Mannich et une réaction aza-Prins. La synthèse de l'*ent*-codéinone a été formalisée en procédant à une intersection avec la méthode de Fukuyama publiée récemment. Les données expérimentales et spectrales pour tous les nouveaux produits.

Mots-clés : synthèse d'alcaloïdes de la morphine, synthèse de l'*ent*-codéinone, synthèse de l'*ent*-néopinone, dihydroxylation enzymatique de produits aromatiques, réaction de Heck.

[Traduit par la Rédaction]

Introduction

There has not been a shortage of interest in new synthetic approaches to morphine (**1**) in the last decade. The most recent review, published in 2011,[1] summarized all published syntheses of morphine and its congeners (there were nine syntheses in total, including the most recent synthesis of codeine (**2**)[2]), (Fig. 1), since the last major review on this topic, which appeared in 2005.[3] Altogether, more than 25 total and formal syntheses of the opiate alkaloids have been reported since the first milestone total synthesis by Gates in 1952.[4,5]

Given the rich chemical[6–8] as well as societal[9–11] history of morphine and the impact that this molecule has had on the human condition, it should not be surprising that the interest in designing a practical synthesis of this unique compound has not waned. Two hundred years after its isolation by Serturner,[12,13] chemists are still designing new and imaginative routes to this challenging molecule.[14–19]

In 2009 we published the enantiodivergent synthesis of codeine that originated in the enzymatically derived *cis*-diol **3** produced from β-bromoethylbenzene by the whole-cell fermentation with the recombinant organism *E. coli* JM109 (pDTG601a), capable of over-expressing toluene dioxygenase.[20] In that particular approach, a series of Heck reactions and a hydroamination were used to complete the synthesis of codeine (**1**) and its enantiomer.[21,22] One of the advanced intermediates used in that synthesis was aldehyde **5**.

This aldehyde was also easily converted to a homologue **6**

Received 15 February 2011. Accepted 5 April 2011. Published at www.nrcresearchpress.com/cjc on 23 June 2011.

J. Duchek, T.G. Piercy, J. Gilmet, and T. Hudlicky. Chemistry Department and Centre for Biotechnology, Brock University, 500 Glenridge Avenue, St. Catharines, ON L2S 3A1, Canada.

Corresponding author: Tomas Hudlicky (e-mail: thudlicky@brocku.ca).

*Based on the 2010 Bader Award Lecture.

Fig. 1. Chemoenzymatic approach to *ent*-codeine via toluene dioxygenase-mediated dihydroxylation of β-bromoethylbenzene.

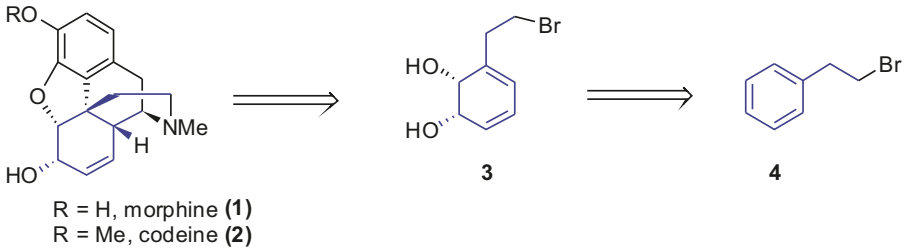

Fig. 2. Three approaches to *ent*-codeine synthesis from protected aldehyde **6**.

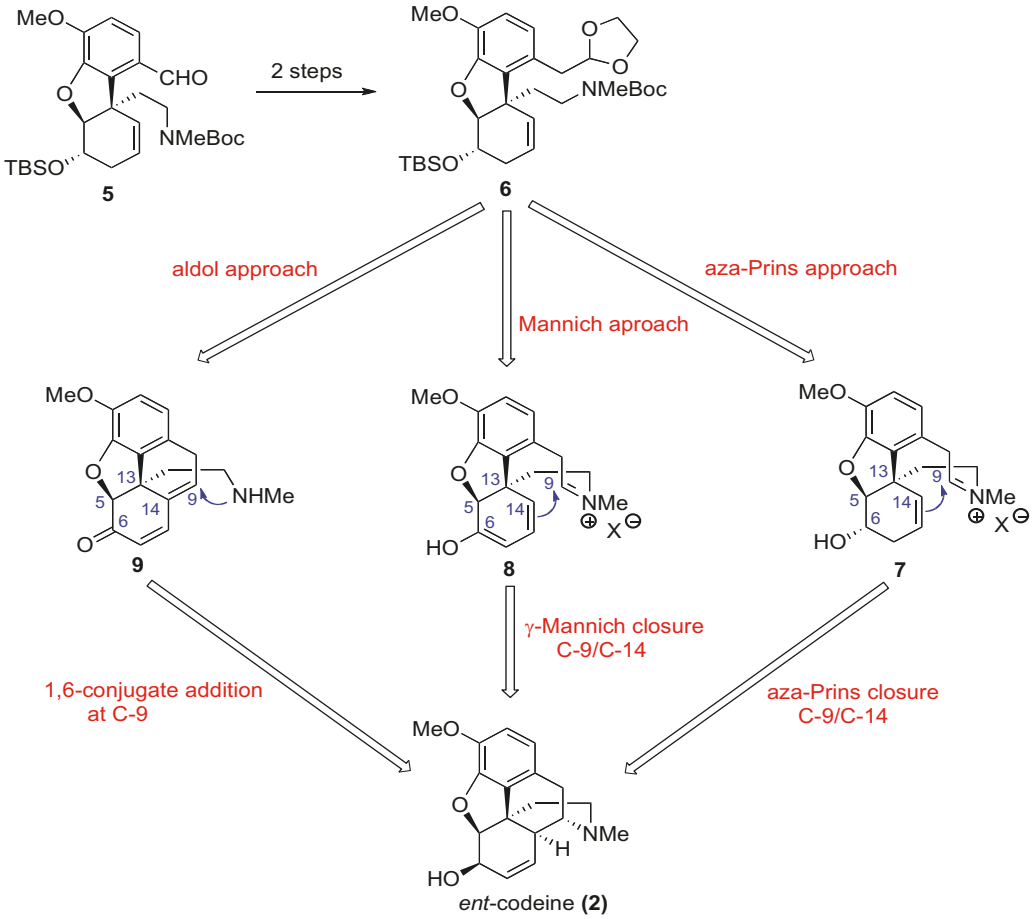

Can. J. Chem. Downloaded from www.nrcresearchpress.com by 80.58.250.72 on 09/16/12
For personal use only.

via a Wittig reaction and transketalization. We envisioned three different approaches, shown in Fig. 2, emanating from this compound, which was prepared on intermediate scale in eight steps from diol **3**.

In the first approach we considered a C-9 and C-14 closure by an aza-Prins reaction of the iminium salt **7** derived from the condensation of the ethylamino side chain with the masked aldehyde in **6**. Similarly, the oxidized version of this compound, enone **8** (depicted in its enolized form in Fig. 2), was expected to undergo a γ-Mannich closure to the iminium species. The third approach assumed the formation of the dienone **9** from the aldehyde and the C-ring enone, to be followed by a 1,6-conjugate addition of the amine at C-9, which closure would yield the more energetically favored enone. This type of strategy was used by Fuchs to access the natural enantiomer of morphine.[23–26] In this paper, we report the outcome of these approaches and the total synthesis of *ent*-neopinone, as well as formal total synthesis of *ent*-codeinone and *ent*-codeine via the intermediate dienone **9**.[27]

Results and discussion

The inspiration for the approach to codeine depicted in Fig. 2 came from Wiesner's zizanoic acid synthesis published in 1972.[28] In one of his many ingenious solutions to the synthetic problems of that particular era, he conceived the construction of tricyclic enone **12**, the key intermediate in his synthesis of zizanoic acids, from the β,γ-deconjugated enone

Can. J. Chem. Downloaded from www.nrcresearchpress.com by 80.58.250.72 on 09/16/12
For personal use only.

Scheme 1. Reagents and conditions: (*i*) NBS, $CHCl_3$, reflux, 68%; (*ii*) MOM-Cl, *i*Pr_2NEt, CH_2Cl_2, 4 °C; (*iii*) $ClPh_3PCH_2OCH_3$, *t*BuLi, THF, –78 °C to 4 °C; (*iv*) $(CH_2OH)_2$, *p*TsOH, THF, reflux, 76% from **14**; (*v*) *E. coli* JM109 (pDTG601a), 10–15 g L^{-1} h^{-1}; (*vi*) potassium azodicarboxylate, AcOH, MeOH, 0 °C, 83%; (*vii*) 2,2-dimethoxypropane, acetone, *p*TsOH, 80%; (*viii*) NH_2Me, K_2CO_3, THF, sealed tube, 90%; (*ix*) 3 mol L^{-1} HCl, EtOH; (x) Boc_2O, $NaHCO_3$, EtOH, 72% (2 steps); (*xi*) TBSCl, imidazole, CH_2Cl_2, –78 °C to 25 °C, 80%–88%.

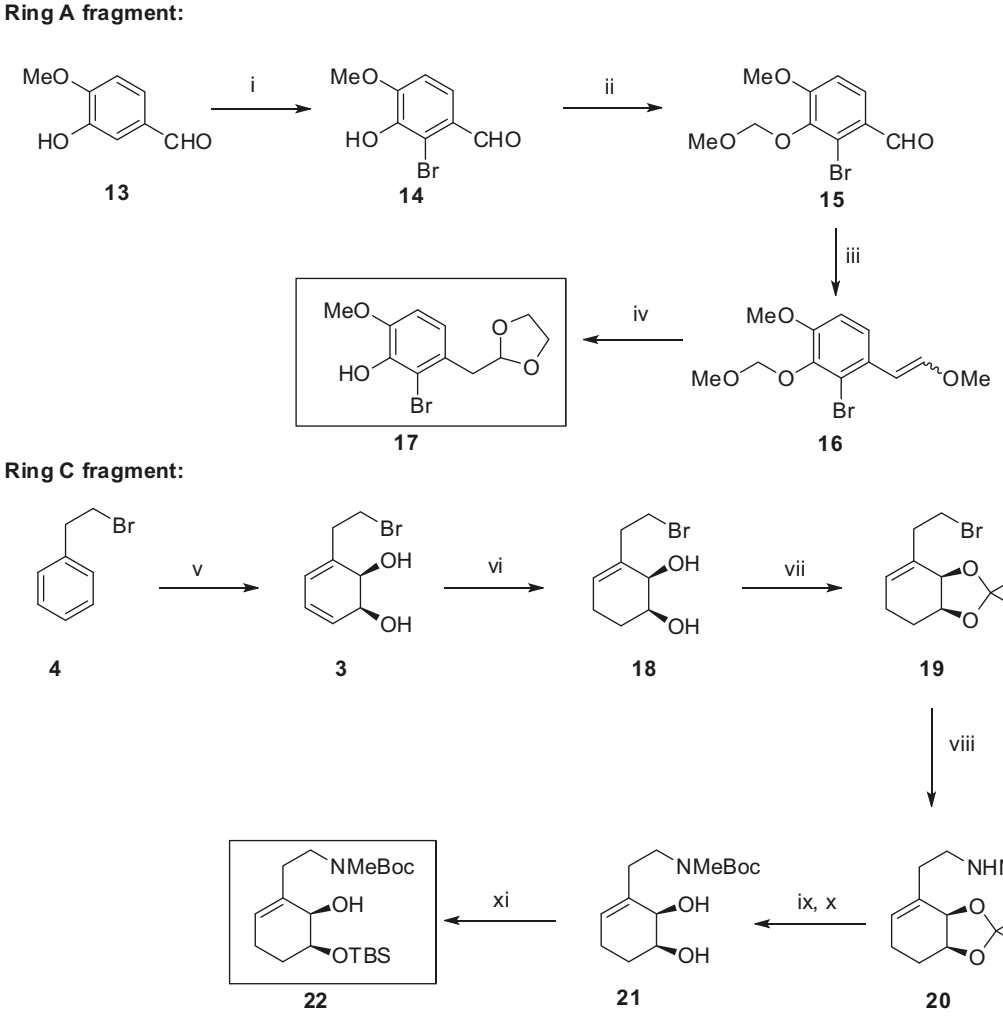

10 under both acid- and base-catalyzed conditions, as shown in Fig. 3 in an abbreviated manner.

Whereas the stereochemical outcome of these closures differed slightly depending on the conditions of the reaction, the mechanism of the closure could be interpreted in a number of ways, each of which would lead to the same product.[29,30] Thus, whether the closures proceeded via equilibrating aldol reactions in the enolized version **11**, the Prins reaction in **10**, or an ene reaction between the aldehyde and the olefin in **10**, in each case the final outcome would be enone **12**.

When we noticed the similarity in connectivity of the two asterisked carbons in **12** (Fig. 3) with C-9 and C-14 of the morphine skeleton, we saw the opportunity to explore the reactive options of intermediates such as **7** and **8**, whose functional disposition closely resembles the compounds used by Wiesner.[28]

The synthesis of the key protected aldehyde **6** required the connection of ring A and ring C fragments via Mitsunobu reaction, followed by Heck cyclization, to establish the C-13 stereogenic center. The synthesis of both fragments, adopted from our previous synthesis of codeine and its enantiomer,

Fig. 3. Wiesner's strategy toward the construction of a tricyclic core of zizanoic acid.

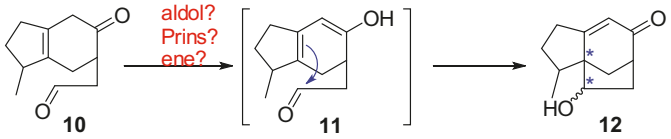

proceeded at medium scale as shown in Scheme 1 and was subjected to a moderate degree of optimization.

The A-ring derives from the isovanillin (**13**), which was brominated with *N*-bromo-succinimide (NBS) to provide bromoisovanillin **14**. Subsequent protection of the hydroxy group as its MOM ether furnished **15**, which was converted to the enol ether **16** by a Wittig reaction using the ylide generated from (methoxymethyl)triphenylphosphonium chloride. Treatment of the resulting crude mixture of (*E*)- and (*Z*)-enol ethers with ethylene glycol under acidic conditions furnished phenol **17** in 48% overall yield from **13**.

The synthesis of the intermediate comprising the C-ring started from (2-bromoethyl)benzene (**4**), which was converted

Scheme 2. Reagents and conditions: (*i*) DIAD, Bu_3P, THF, 0 °C to 25 °C, 76% (10 g scale); (*ii*) $Pd_2(dba)_3$, $(tBu)_3P$, K_2CO_3, toluene, 110 °C, 85%–95%; (*iii*) TBAF, THF, –78 °C to 25 °C, 83%–85%.

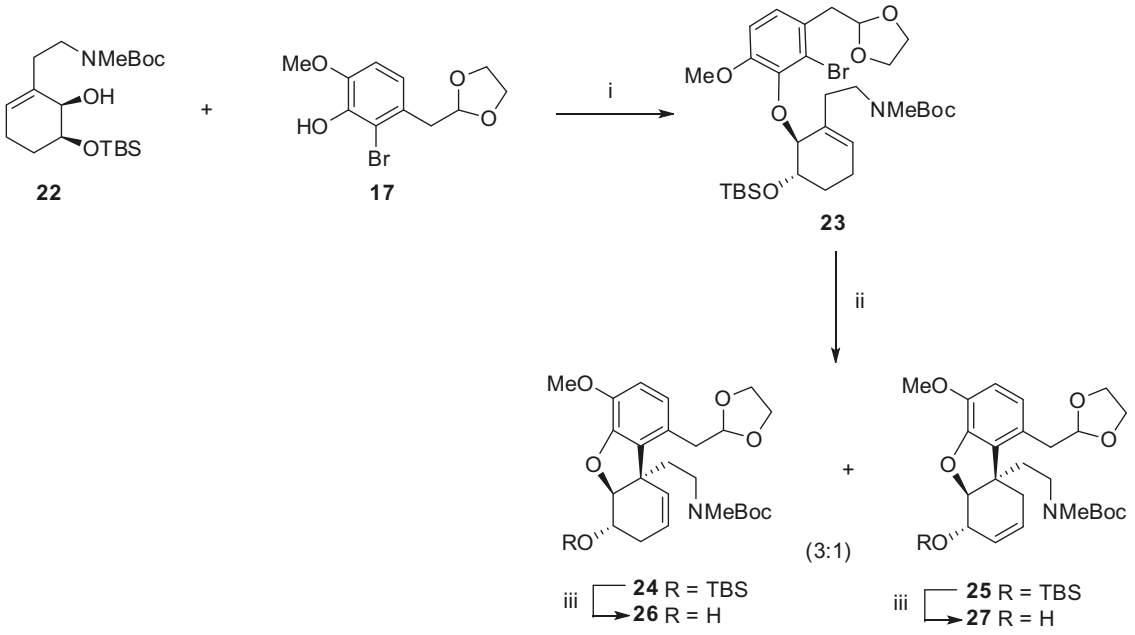

to diol **3** by microbial dihydroxylation using *E. coli* JM109 (pDGT601A) in space-time yields of 10–15 $g\,L^{-1}\,h^{-1}$ on 15 L fermentor scale, as described previously.[21] Diimide reduction of the sterically less hindered double bond led to diol **18**, whose protection as its isopropylidene ketal gave **19**. Substitution of the bromine by $MeNH_2$ provided the methyl amine **20**. This was followed by the removal of the isopropylidene group and protection of the secondary amine as its Boc carbamate to afford diol **21**, whose regioselective silylation provided the key ring C fragment **22** in 31% overall yield from **3**. This optimized route to fragment **22** is more robust than the one we reported in the context of an earlier total synthesis of codeine.[22]

Following the preparation of the two fragments **17** and **22**, their union was accomplished by the Mitsunobu reaction, as shown in Scheme 2, to provide the aryl ether **23** in yields in the range of 76%–85% and on a maximum scale of 10 g. By-products from the large-scale Mitsunobu coupling isolated by chromatography included phenol **17** (8%) and its silylated derivative (4%). The latter compound likely resulted from the trans-silylation of the free phenol by the TBS ether **22** and (or) the product **23**.

To set the C-13 quarternary center, the aryl ether **23** was subjected to an intramolecular Heck coupling using $Pd_2(dba)_3$ with tri-*tert*-butylphosphine and K_2CO_3 in toluene[31–33] to provide an inseparable mixture of homoallylic and allylic TBS ethers **24** and **25** in an approximate 5:1 ratio and in 86% combined yield.[34] The minor allylic alcohol **25** is likely the product of palladium-mediated isomerization of the double bond (**24** → **25**). The mixture of **24** and **25** was treated with TBAF in THF to furnish alcohols **26** and **27**, respectively, which were separated by chromatography.

The two regioisomeric alcohols **26** and **27** obtained on desilylation were oxidized with IBX to the key intermediates ketone **28** and its conjugated isomer **29**, respectively (Scheme 3), which under either acidic or basic conditions should provide the same dienolate or dienolate anion to be tested in various cyclization schemes.

Treatment of the crude ketone **28** or enone **29** with trifluoroacetic acid resulted in a clean conversion to the [3.3.1] bicyclic adduct **30**, formed in 45%–55% yield over the two steps, and without the expected condensation of the secondary amine with the masked aldehyde as shown in Scheme 3. This was a disappointing turn of events, as it appeared that the conjugate addition of the free secondary amine occurred much faster than the formation of the required iminium species.

The precursors to the aza-Prins and Mannich cyclizations were generated from the protected aldehyde derivative **26** or, in the earlier approach, also from the enol ether equivalent **33**,[35] synthesized from aldehyde **5** by a Wittig reaction. Thus the enamine **32** was generated by treatment of **31** with trifluoroacetic acid, as shown in Scheme 4. Treatment of alcohol **26** with trifluoroacetic acid in CH_2Cl_2 resulted in a mixture of secondary amine **31** (49%–65%) and enamine **32** (10%–21%) in an approximate 3:1 ratio. Secondary amine **31** was smoothly converted to enamine **32** with treatment of oxalic acid in water, with a yield of 88%.

The cyclic enamine **32** was a minor product in the TFA-mediated deprotection of **26,** but was the exclusive product in the corresponding deprotection of **33** with TFA. The cyclic enamine proved reasonably stable to storage and manipulation. Reduction of **32** with cyanoborohydride provided amine **34**, and served to confirm the structure of the enamine.

With these results we turned to the investigations of the cyclizations proposed in Fig. 2. The summary of our attempts, most of which proved unsuccessful, is shown in Scheme 5.

Enamine **32** was subjected to Lewis-acid-catalyzed cyclizations to attempt the C-9/C-14 closure via the aza-Prins reaction of the iminium ion **7** (Scheme 5). All attempts resulted only in the recovery of the starting material and traces of

Can. J. Chem. Downloaded from www.nrcresearchpress.com by 80.58.250.72 on 09/16/12
For personal use only.

Scheme 3. Reagents and conditions: (*i*) IBX, AcOEt, reflux; (*ii*) TFA, CH_2Cl_2, 45%–55% (2 steps).

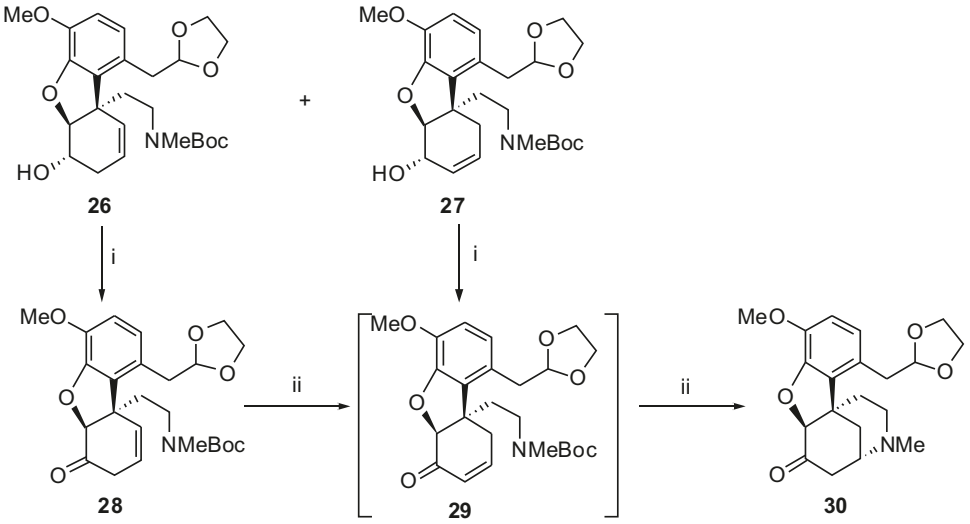

Scheme 4. Reagents and conditions: (*i*) TFA, CH_2Cl_2, 49%–65% of **31**, 10%–21% of **32**; (*ii*) oxalic acid, H_2O, 45 °C, 88%; (*iii*) TFA, CH_2Cl_2, 0 °C to 25 °C; (*iv*) $NaBH_3CN$, AcOH, MeOH, 0 °C to 25 °C, 41% (from **33**).

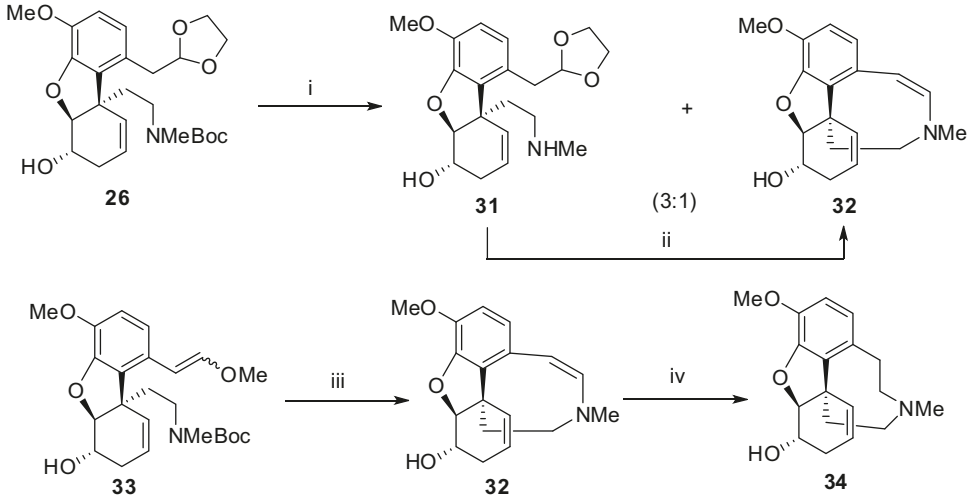

minor products that were not further identified. The presence of *ent*-isocodeine **35** (or its neopine isomer, with the olefin at C-8/C-14) was not detected by either TLC or HPLC analysis.

As mentioned above, the attempted generation of **8**, the precursor for the Mannich cyclization, failed and only the [3.3.1]bicyclic adduct **30** was formed, presumably via the α,β-conjugated isomer generated under the reaction conditions.

We were not able to produce intermediates, such as **36** or **38,** required for the enolized enone-iminium species **8** (Scheme 5) essential for the Mannich reaction. In addition, any attempts to establish an equilibrium between **39** and **38** also failed.

The free aldehyde **39** was obtained by treating **30** with aqueous oxalic acid at 40 °C (88%–92% yield), Fig. 4. Interestingly, when the hydrolysis was conducted with HCl in aqueous acetonitrile at pH 1 and 40 °C, a mixture of **39** and **40** was obtained in various ratios depending on the reaction time. When we subjected aldehyde **39** to HCl in aqueous acetonitrile, it was cleanly converted to **40** over 20 h. Benzaldehyde **40** exhibits a typical downfield shift of the CHO and aromatic CH signals in the ^{1}H-NMR spectrum, found at 9.91 ppm (CHO) and at 7.43 and 6.91 ppm (Ar CH), while the same signals of **39** resonate upfield, at 9.70 ppm (CHO) and at 6.79 and 6.66 ppm (Ar CH). We were interested in whether this "demethylenation" could be applied to other substrates, and therefore subjected the structurally related phenol **17** (Fig. 4) to the same conditions. Treatment of phenol **17** with aqueous oxalic acid at 40 °C afforded a mixture of homobenzaldehyde **41** and benzaldehyde **14** in a 3:1 ratio, while the reaction in aqueous acetonitrile in the presence of HCl afforded benzaldehyde **14** as the major product (**41/14,** 1:3.5). These results suggested that in addition to apparent solvent effects, there must be another factor affecting the outcome of this reaction. Indeed, degassing the HCl–H_2O–MeCN mixture, prior to the addition of phenol **17**, and stirring at 40 °C led to homobenzaldehyde **41** as the major product, accompanied by traces of **14**. When these reaction conditions (degassed HCl–H_2O–MeCN) were applied to the acetal cleavage in **30**, we isolated homobenzaldehyde **39** as the major product, with only traces of **40**. The proposed

Can. J. Chem. Downloaded from www.nrcresearchpress.com by 80.58.250.72 on 09/16/12
For personal use only.

Fig. 4. Generation of byproducts during the hydrolysis of acetals **30** and **17**.

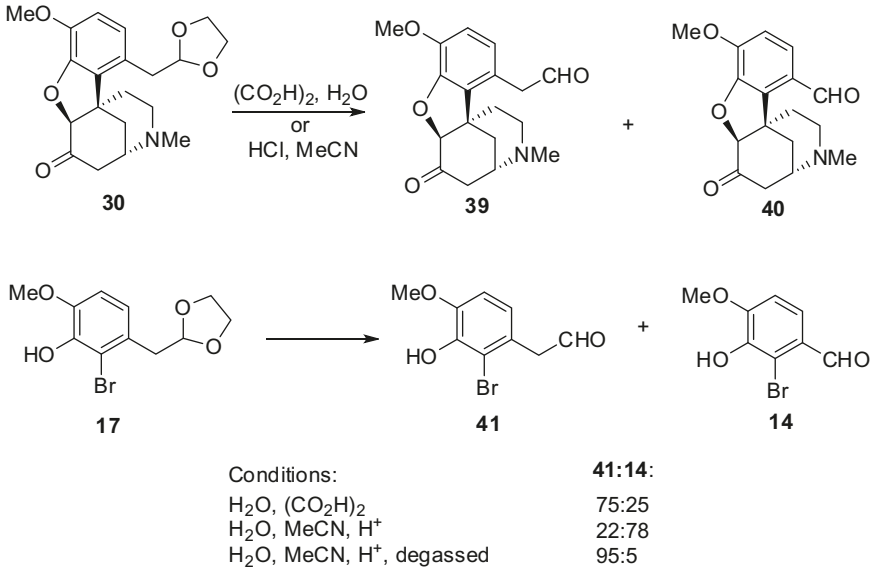

mechanism for the formation of benzaldehyde **40** is shown in Fig. 5. We speculate that in the presence of oxygen (Option A) the transformation likely involves an oxidation at the benzylic position leading to intermediate **42**, which is then converted, via **43**, to hydroperoxide **44**. Fragmentation of **44** then leads to benzaldehyde **40** and formic acid. The fact that trace amounts of benzaldehydes **40** and **14** were present even in the degassed oxygen-free reaction mixtures led us to propose an alternative mechanism shown in option B. This pathway would assume the formation of the acetonitrile adduct **47** from the readily enolisable **39** via the enol form **46**, followed by the formation of epoxide **48**. Opening of the oxirane ring with water generates **49** and the retro aldol reaction then leads to **40**. This option is indeed highly speculative as we did not isolate **51**, an expected by-product of this pathway, during the initial experiments. However, further studies of this transformation are warranted to assess both the mechanism as well as potential general utility.

Returning to the synthesis of *ent*-codeinone, we expected that base-catalyzed treatment of **39** would generate the desired dienone **9**, while acid catalysis would ultimately lead to the dienolate-iminium species **8**, as indicated in Scheme 5; however, neither of these attempts led to appreciable concentrations of the enone or dienone species. The presence of *ent*-codeinone or *ent*-neopinone **37** was not detected in the reaction mixtures. We were unable to solve the functional incompatibility issues between the hydrolysis of the acetal and the deprotection of the Boc group.

To test the feasibility of formation of dienone **9** (Scheme 5) we exchanged the Boc group in **26** for a more robust acetyl group in **52** (Scheme 6). Deprotection of **26** with TFA provided the secondary amine **31** whose acetylation gave **52**. Oxidation of **52** with IBX provided the deconjugated enone **53**, whose treatment under acidic conditions led to the formation of the inseparable mixture of diastereomeric alcohols **54** in 22% in a 1:1 ratio. The IR spectrum exhibited two bands corresponding to the OH groups. Presence of a sharp band at 3606 cm^{-1} and a broad band at 3386 cm^{-1} suggested that one diastereoisomer possessed free OH while the OH group of the other diastereoisomer participated in hydrogen bonding. This was supported also by the ^1H NMR spectrum in which only one diastereoisomer displayed two rotameric sets of signals, typical for amides. We assumed that the α-hydroxy diastereoisomer of **54**, the isomer having the OH and NMeAc groups on the same face, forms an intramolecular hydrogen bond favoring one of the rotamers. Isolation of **54** validated the aldol approach as the alcohols **54** would be convertible to the required dienone of type **9**.

As our work was nearing completion, Fukuyama[36] reported a conceptually identical approach to the natural enantiomer of morphine, using a derivative of type **54** bearing a DNS protecting group on the nitrogen atom, so we have decided to formalize our synthesis. Thus the problem of aldol cyclization and the ultimate 1,6-addition of the ethylamino side chain was solved in a similar way as was done in Fukuyama's synthesis. *ent*-Neopinone was prepared as shown in Scheme 7.

After generating the DNS protected amine **55**, we subjected it to the sequence used in the Fukuyama's synthesis, namely hydrolysis of the acetal with aqueous trifluoroacetic acid, intramolecular aldol reaction, and mesylation of the resulting hydroxy group. The repetition of the aforementioned sequence with the ethylene glycol acetal **55** provided lower yields than those reported for the route utilizing the dimethoxy acetal. The robust nature of the acetal in **56** required longer reaction times to generate the free aldehyde that would undergo the aldol reaction whose product was isolated as the mesylate **57**. The use of 1.2 equiv of MsCl and 1.5 equiv of Hünig's base (Fukuyama's conditions) in the reaction following the aldol closure led to isolation of **57** in only 6% yield from **55**. We speculated that traces of ethylene glycol present in the reaction mixture contributed to the low yield. Performing the mesylation with large excess of both MsCl (4.5 equiv) and Hünig's base (5 equiv) led directly to in situ elimination and a mixture of **58** and **59** was obtained in 42% and 13% yield, respectively, over the two steps from

Can. J. Chem. Downloaded from www.nrcresearchpress.com by 80.58.250.72 on 09/16/12
For personal use only.

Scheme 5. Reagents and conditions: (*i*) various Brønsted and Lewis acids; (*ii*) TFA, CH_2Cl_2, 56% from **26**; (*iii*) oxalic acid, 45 °C, 68%–75% (crude).

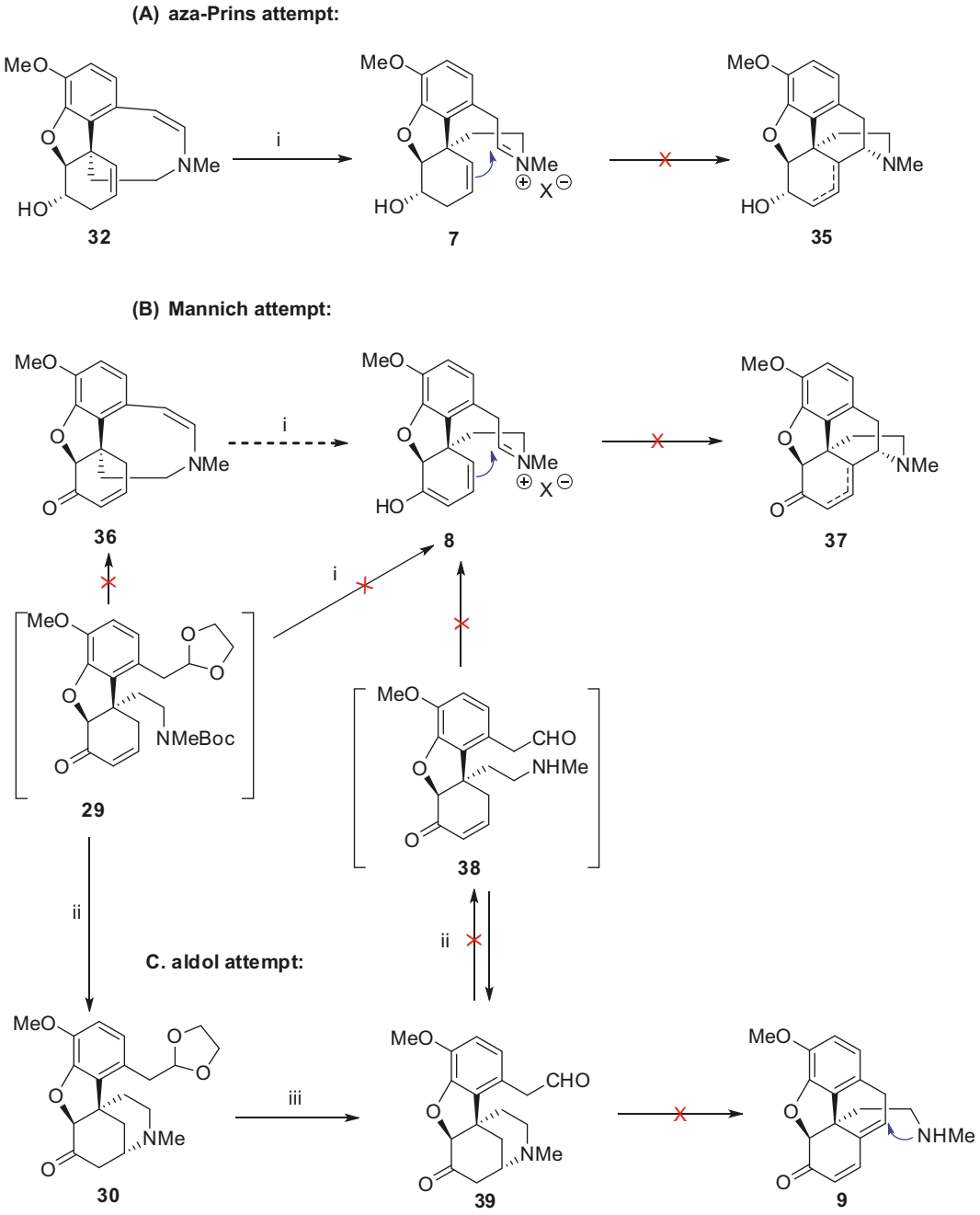

Can. J. Chem. Downloaded from www.nrcresearchpress.com by 80.58.250.72 on 09/16/12
For personal use only.

55. Enantiomers of both **57** and **58** have been converted via neopinone and codeinone to (–)-codeine by Fukuyama,[36] thus their attainment completed the formal synthesis.

The desired dienone **58** was separated and treated with thioglycolic acid in the presence of triethylamine. NMR and TLC analysis of the reaction mixture confirmed the formation of *ent*-neopinone (**61**) accompanied by a small amount of *ent*-codeinone (**60**). For the purpose of direct comparison, a sample of neopinone was prepared from thebaine according to Rapoport's procedure,[37] and matched with the product of this reaction. Fukuyama[36] reported isomerization of neopinone obtained from the cyclization to codeinone followed by reduction of the latter to codeine. Thus the attainment of *ent*-neopinone also formalizes the synthesis of *ent*-codeinone and *ent*-codeine.

To ensure that the low yields obtained from acetal **55** were indeed the function of the robust protecting group, we decided to repeat the chemistry with Fukuyama's acetal, generated by treatment of **55** with *p*TsOH in MeOH at reflux (Scheme 8). Oxidation of **62** with IBX in AcOEt at 80 °C afforded ketone **63** having optical rotation of +25.5°, opposite to that of *ent*-**63** (–24.2°).[36] Treatment of **63** with aqueous trifluoroacetic acid, followed by mesylation afforded mesylate **57** in 28% and dienone **58** in 24% yield from **62**. The cyclization of **63** indeed provided higher yields of **57** and **58** than the corresponding reaction of the acetal **56**.

Fig. 5. Proposed mechanism for the formation of benzaldehyde **40**.

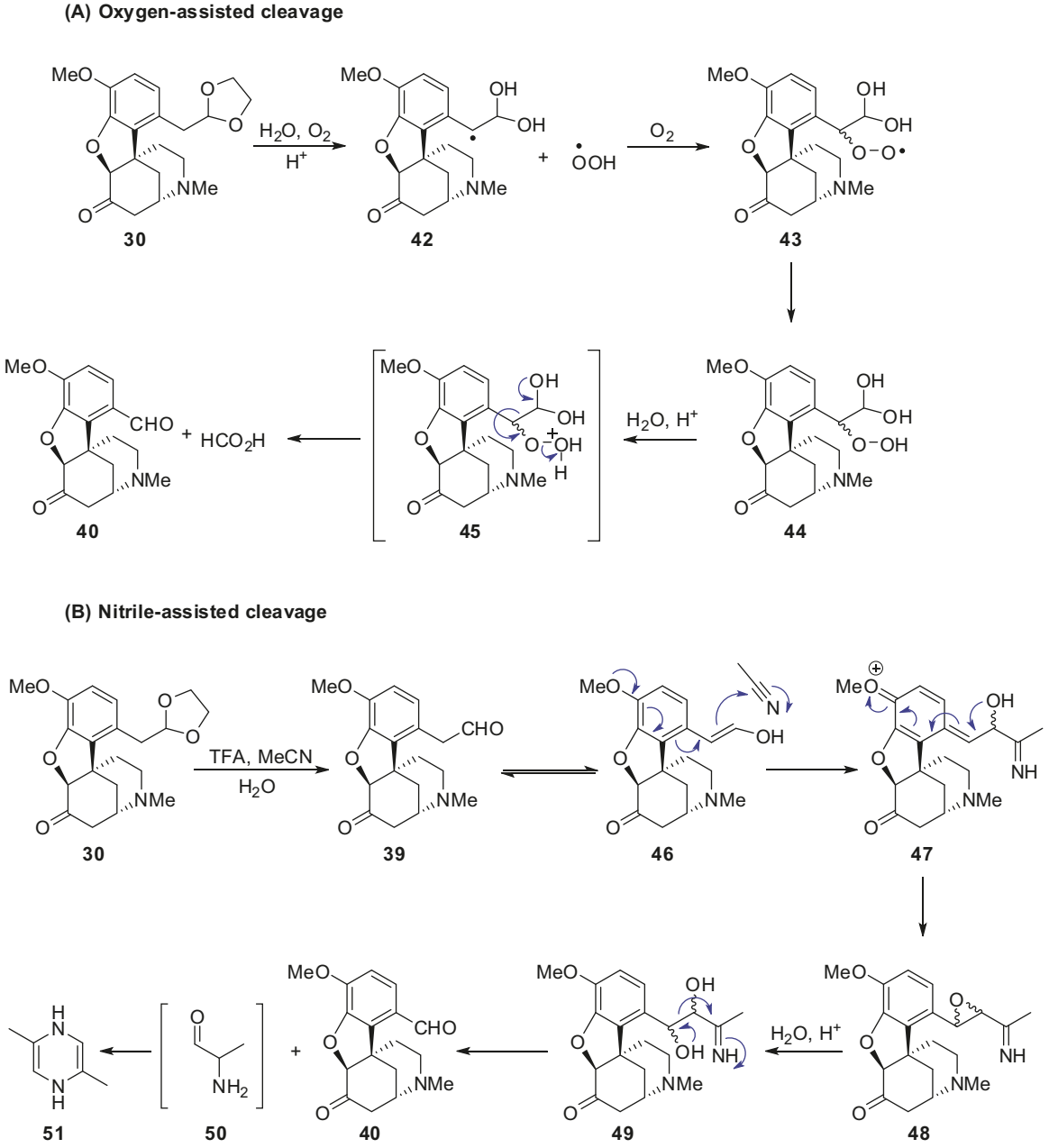

Scheme 6. Reagents and conditions: (*i*) (*a*) AcCl, Et_3N, CH_2Cl_2, (*b*) MeONa, MeOH, 87%; (*ii*) **52**, IBX, AcOEt, 80 °C; (*iii*) 50% aqueous TFA, toluene, 50 °C, 22% from **52**.

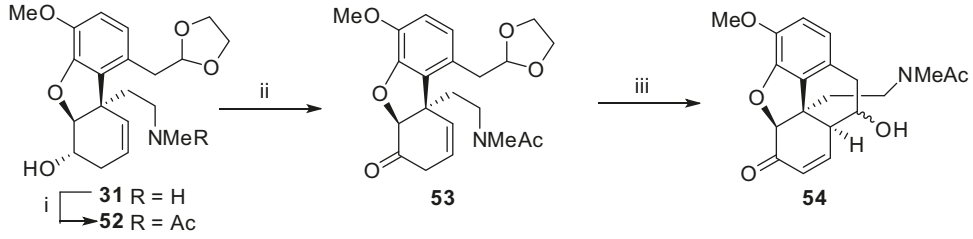

Can. J. Chem. Downloaded from www.nrcresearchpress.com by 80.58.250.72 on 09/16/12
For personal use only.

Scheme 7. Reagents and conditions: (*i*) 2,4-dinitrobenzenesulfonyl chloride, *i*Pr$_2$NEt, CH_2Cl_2 (51%); (*ii*) IBX, AcOEt, 80 °C; (*iii*) (*a*) 50% aqueous TFA, toluene, 50 °C, (*b*) MsCl (4.5 equiv), *i*Pr$_2$NEt (5 equiv), CH_2Cl_2, 0 °C (42% of **58** from **55**, 13% of **59** from **55**); (*iv*) thioglycolic acid, *i*Pr$_2$NEt, CH_2Cl_2, 0 °C .

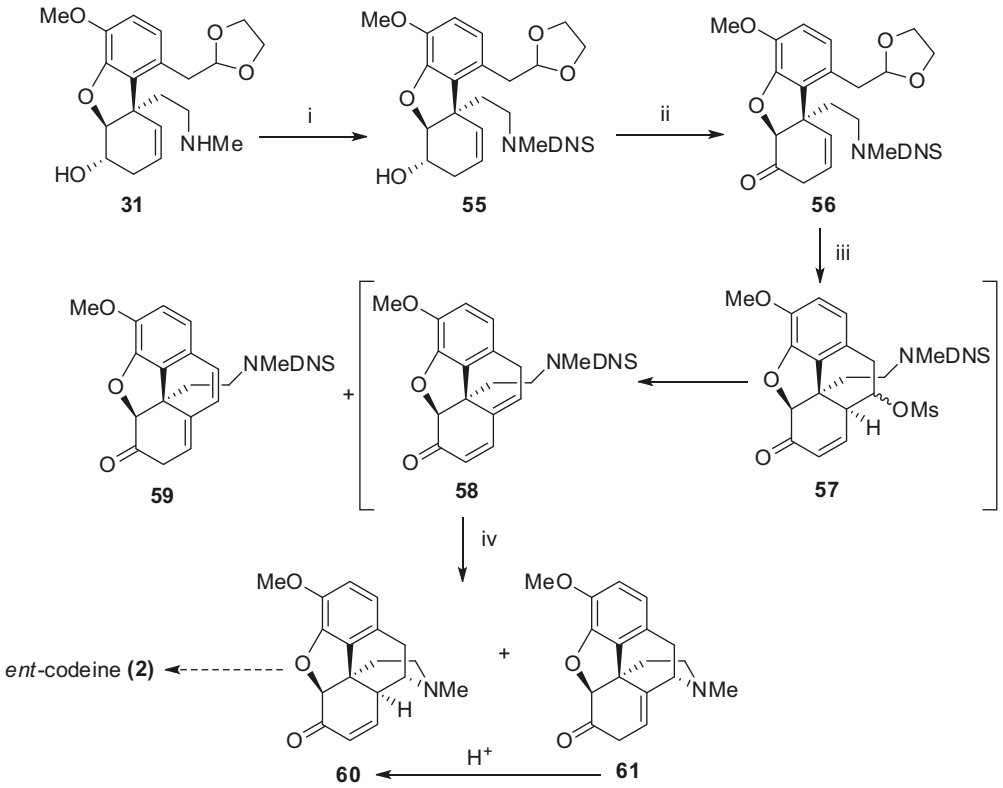

Scheme 8. Reagents and conditions: (*i*) MeOH, *p*TsOH, reflux (86%); (*ii*) IBX, AcOEt, 80 °C; (*iii*) 50% aqueous TFA, toluene, 50 °C; MsCl *i*Pr$_2$NEt, CH_2Cl_2, 0 °C (24% of **58** from **62**, 28% of **57** from **62**); (*iv*) thioglycolic acid, *i*Pr$_2$NEt, CH_2Cl_2, 0 °C.

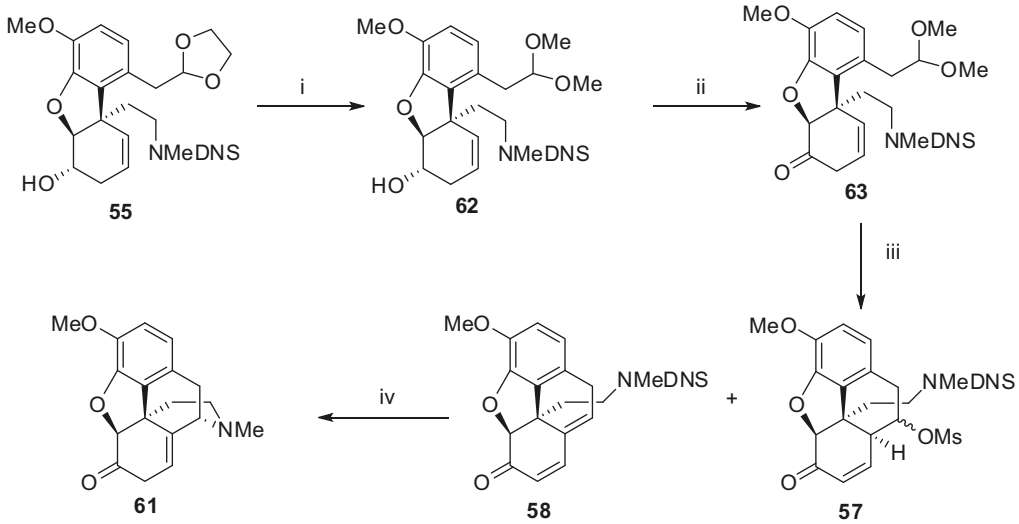

Treatment of the mixture of **57** and **58** with thioglycolic acid and Hünig's base, as reported by Fukuyama,[36] afforded a full conversion to *ent*-neopinone (**61**), matched with authentic samples.

Conclusions

ent-Neopinone was synthesized from β-bromoethyl benzene in 14 steps via enzymatic dihydroxylation, Heck closure to establish the C-13 stereogenic center, and 1,6-conjugate addition of the ethylamono side chain to C-9 of the dienone **9**, obtained by aldol cyclization. Attempts at intramolecular Mannich cyclizations or aza-Prins cyclizations to iminium species derived from enamines of type **32** or **36** proved unsuccessful. The synthesis of *ent*-neopinone by the route described also constitutes a formal synthesis of *ent*-codeinone and *ent*-codeine.

Can. J. Chem. Downloaded from www.nrcresearchpress.com by 80.58.250.72 on 09/16/12
For personal use only.

Can. J. Chem. Downloaded from www.nrcresearchpress.com by 80.58.250.72 on 09/16/12
For personal use only.

Experimental section

General

Reactions were carried out under inert atmosphere in oven-dried glassware unless stated otherwise. Solvents were distilled: CH_2Cl_2, DMF, iPr$_2$NEt, and pyridine from CaH_2; MeOH from magnesium methoxide; THF from Na/benzophenone; toluene from Na. Qualitative TLC was done with precoated silica gel aluminium sheets (EMD silica gel 60 F_{254}); detection by UV or by spraying with "CAM" solution (5 g of $(NH_4)_6Mo_7O_{24}\cdot 4H_2O$, 1 g of $Ce(SO_4)_2$, 100 mL of 10% H_2SO_4) or 0.5% aqueous $KMnO_4$ solution followed by heating. Column chromatography was performed using silica gel SiliaFlash P60 from Silicycle (40–66 μm). Optical rotation was measured in a 1 dm cell at 20–25 °C and 589 nm; concentration c in g 100 mL^{-1}. IR spectra were recorded as ca. 2% solutions in $CHCl_3$ or as a thin film. ^{1}H NMR and ^{13}C NMR spectra were recorded at 300 or 600 MHz and 75 or 150 MHz, respectively, and were calibrated to the solvent signal or tetramethylsilane; the chemical shifts are reported in ppm. Mass spectra were recorded on Kratos/MsI Concept 1S mass spectrometer at Brock University. Combustion analyses were performed by Atlantic Microlabs, Norcross, Georgia, USA.

*2-(2,2-Dimethyl-3a,6,7,7a-tetrahydrobenzo[d][1,3]dioxol-4-yl)-*N*-methylethanamine (20)*

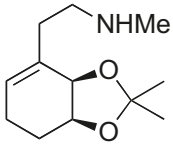

20

A solution of diol **18**[22] (45.2 g, 204.5 mmol) in acetone (400 mL) was treated with 2,2,-dimethoxypropane (37.6 mL, 306.8 mmol) and *p*TsOH. The reaction was stirred for 4 h at room temperature, whereupon the solvent was evaporated. The residue was diluted with H_2O (50 mL) and extracted with CH_2Cl_2 (3 × 200 mL). The combined organic layers were washed with saturated aqueous Na_2CO_3 solution (2 × 20 mL), and brine, then dried (Na_2SO_4), filtered, and evaporated to yield bromide **19** (46.1 g) as a clear colorless oil, which was used without further purification. Bromide **19** (10.05 g, 38.3 mmol) was dissolved in THF (35 mL) and transferred to a 200 mL thick-walled reaction vessel containing K_2CO_3 (2.64 g, 19.1 mmol) and a magnetic stirring bar. The reaction vessel was cooled to –40 °C, and the solution was saturated with methylamine by passing gaseous methylamine from a lecture bottle through the solution for 15 min. The reaction vessel was sealed, and the mixture was stirred at 25 °C for 18 h. The mixture was cooled to –40 °C before the vessel was opened. Potassium salts were removed by filtration and rinsed with CH_2Cl_2. The solvent was evaporated to obtain amine **20** (7.56 g, 94%), which was used without further purification. R_f (AcOEt/MeOH/aqueous NH_3, 7:3:1) 0.3; Mp 143–147 °C (oxalate salt); $[\alpha]_D^{24}$ = 25.8 (c 1, MeOH); IR (film): ν 3324 (w), 2983 (s), 2932 (s), 2844 (s), 2790 (m), 1674 (m), 1563 (w), 1443 (m), 1367 (s), 1242 (s), 1221 (s), 1156 (m), 1077 (s), 1030 (s), 869 (m) cm^{-1}; ^{1}H NMR ($CDCl_3$, 300 MHz): δ 5.63 (s, 1H); 4.34 (d, J = 5.5 Hz, 1H), 4.27 (td, J = 5.8, 3.2 Hz, 1H), 2.78–2.72 (m, 2H), 2.41 (s, 3H), 2.38–2.31 (m, 1H), 2.25 (q, J = 7.4 Hz, 1H), 2.14 (dddd, J = 9.0, 7.3, 3.9, 1.7 Hz, 1H), 1.91 (t, J = 5.3 Hz, 1H), 1.86–1.79 (m, 1H), 1.75–1.69 (m, 1H), 1.48 (s, 1H), 1.36 (s, 6H); ^{13}C NMR ($CDCl_3$, 150 MHz): δ 133.97, 126.58, 108.24, 73.64, 73.47, 49.81, 36.32, 34.28, 27.91, 26.46, 25.56, 20.80; LRMS-EI (*m*/*z*): M$^+$ 196 (3), 153 (14), 136 (5), 44 (100); anal. calcd. for $C_{12}H_{21}NO_2\cdot(COOH)_2$: C, 55.80; H, 7.69; found C, 55.75; H, 7.66.

tert-*Butyl 2-((5*S*,6*R*)-5,6-dihydroxycyclohex-1-enyl)ethyl (methyl)carbamate (21)*

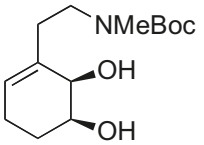

21

A solution of acetonide **20** (7.02 g, 33.2 mmol) in EtOH (40 mL) and H_2O (4 mL) was treated with 3 mol L^{-1} HCl (16.6 mL, 49.8 mmol). The reaction mixture was stirred for 4 h, treated with $NaHCO_3$ (42 g, 498 mmol), and stirred vigorously for 1 h. Then Boc anhydride (10.9 g, 49.8 mmol) was added, reaction mixture was stirred for additional 4 h, filtered, and evaporated. The residue was diluted with H_2O (25 mL) and extracted with CH_2Cl_2 (3 × 20 mL). The combined organic layers were washed with saturated aqueous NH_4Cl solution (2 × 10 mL), brine, dried (Na_2SO_4), filtered, and evaporated. Flash column chromatography (hexanes/AcOEt, 6:1 → 1:2) afforded **21** (6.48 g, 72%) as a colorless oil. R_f (hexanes/AcOEt, 1:1) 0.20; $[\alpha]_D^{23}$ = –95.5° (c 0.75, $CHCl_3$); IR (film): ν 3394 (s), 2975 (s), 2931 (s), 1674 (s), 1483 (s), 1353 (s), 1397 (s), 1366 (s), 1308 (m), 1247 (m), 1220 (m), 1160 (s), 1075 (m), 1053 (m), 989 (m), 945 (w), 919 (w) cm^{-1}; ^{1}H NMR ($CDCl_3$, 300 MHz): 5.43 (s, 1H), 4.87 (s, 1H), 3.96 (s, 2H), 3.56 (s, 1H), 2.99 (d, J = 8.8 Hz, 1H), 2.91 (s, 1H), 2.86 (s, 3H), 2.42–2.30 (m, 1H), 2.18 (d, J = 13.4 Hz, 1H), 2.03 (s, 2H), 1.74–1.63 (m, 1H), 1.60–1.45 (m, 1H), 1.43 (s, 9H); ^{13}C NMR ($CDCl_3$, 150 MHz): 157.0, 133.9, 128.8, 79.9, 70.0, 69.8, 48.3, 34.8, 34.0, 28.3, 25.4, 24.8; LRMS-EI (*m*/*z*): M$^+$ 271 (1), 197 (3), 171 (1), 153 (9), 144 (29), 110 (23), 88 (16), 57 (88), 44 (100); HRMS-EI (*m*/*z*): M$^+$ calcd. for $C_{14}H_{25}NO_4$: 271.1784, found 271.1796.

tert-*Butyl 2-((5*S*,6*R*)-5-(*tert*-butyldimethylsilyloxy)-6-hydroxycyclohex-1-enyl)ethyl(methyl)carbamate (22)*

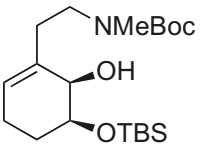

22

A solution of carbamate **21** (7.76 g, 28.6 mmol) and imidazole (3.89 g, 57.2 mmol) in CH_2Cl_2 (50 mL) was treated

Can. J. Chem. Downloaded from www.nrcresearchpress.com by 80.58.250.72 on 09/16/12
For personal use only.

with TBSCl (4.75 g, 31.5 mmol) at –78 °C, the reaction mixture was left to warm slowly to 25 °C overnight and treated with saturated aqueous NH_4Cl solution (15 mL). After extraction with CH_2Cl_2 (3 × 100 mL), the combined organic layers were washed with saturated aqueous $NaHCO_3$ solution (20 mL), brine (20 mL), dried ($MgSO_4$), filtered, and evaporated. Flash column chromatography (hexanes/AcOEt, 3:1) afforded **22** (8.54 g, 77%) as a clear colorless oil. R_f (CH_2Cl_2/AcOEt, 96:4) 0.47; $[\alpha]_D^{24}$ = –22.6 (*c* 0.5, $CHCl_3$); IR (film): ν 3556 (w), 3475 (w), 2953 (s), 2857 (s), 1692 (s), 1472 (s), 1392 (s), 1253 (s), 1085 (s) cm^{-1}; ^1H NMR ($CDCl_3$, 600 MHz, mixture of rotamers): δ 5.54 (s, 1H), 5.52 (s, 1H), 3.98 (s, 1H), 3.90 (s, 1H), 3.79 (s, 1H), 3.77 (s, 1H), 3.26–3.20 (m, 2H), 2.85 (s, 3H), 2.82 (s, 3H), 2.39–2.32 (m, 2H), 2.30–2.23 (m, 2H), 2.13 (br s, 2H),1.98 (br s, 2H) 1.80–1.72 (m, 2H),1.54 (s, 2H),1.44 (s,18H), 0.9 (s,18H), 0.11 (s, 6H), 0.10 (s, 6H); ^{13}C NMR ($CDCl_3$, 150 MHz): δ 155.7, 134.8, 126.6, 79.0, 71.0, 68.8, 48.4, 47.2, 34.1, 33.3, 32.8, 28.4, 25.8, 25.4, 25.3, 24.3, 24.1, 18.1, –4.4, –4.8; LRMS-EI (*m*/*z*): M^+ 228 (21), 197 (21), 136 (12), 74 (22), 73 (15), 57 (63), 44 (100); HRMS-EI (*m*/*z*): [M-57]$^+$ calcd. for $C_{12}H_{30}NO_4Si$: 328.1944, found 328.1946; anal. calcd for $C_{20}H_{39}NO_4Si$: C, 62.10, H,10.22; found C, 62.29, H,10.19.

2-Bromo-3-(1,3-dioxolan-2-ylmethyl)-6-methoxyphenol (17)

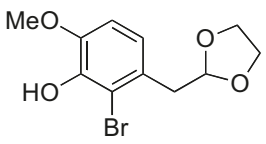

17

A solution of bromoisovanillin **14** (10.0g, 43.4 mmol) in CH_2Cl_2 (300 mL) was cooled to 0 °C and treated with *i*Pr_2-NEt (15.1 mL, 86.7 mmol) and MOM-Cl (4.94 mL, 65.1 mmol). Reaction mixture was stirred for 3 h while the light yellow solution turned clear. The reaction mixture was diluted with H_2O (100 mL), the layers were separated and the aqueous layer was extracted with AcOEt (3 × 40 mL). The combined organic layers were washed with brine, dried ($MgSO_4$), filtered, and evaporated to yield crude **15** as a light yellow/brown solid (12.2 g) which was used without further purification. R_f (hexanes/AcOEt, 1:1) 0.69.

A solution of $Ph_3P^+CH_2OCH_3Cl^-$ (23.1 g, 67.2 mmol) in THF (125 mL) was cooled to –78 °C, treated with *t*BuLi (35.9 mL, 61.1 mmol) dropwise over 10 min, and stirred for 15 min. The solution was warmed to 0 °C and treated with crude **15** (16.3 g, 61.1 mmol) in THF (17 mL) dropwise over 5 min while the deep orange solution turned to a deep yellow suspension. The suspension was refluxed for 3.5 h, cooled to 25 °C, diluted with AcOEt (100 mL), and washed with H_2O (100 mL). The aqueous layer was extracted with AcOEt (3 × 50 mL) and the combined organic layers were washed with brine, dried ($MgSO_4$), filtered, and evaporated to yield crude **16** as a yellow solid (30.8 g) which was used without further purification.

A solution of crude **16** (32.2 g, 106 mmol) in THF (300 mL) was treated with *p*TsOH (10.1 g, 53.0 mmol), ethylene glycol (29.6 mL, 530.3 mmol), and refluxed for 2 h. Reaction mixture was cooled to 25 °C, concentrated, diluted with AcOEt (150 mL), and washed with H_2O (2 × 20 mL). Organic layer was washed with brine, dried ($MgSO_4$), filtered, and evaporated. The residue was dissolved in CH_2Cl_2 (100 mL) and extracted with 0.5 mol L^{-1} NaOH (3 × 10 mL). The combined aqueous layers were neutralized with 1 mol L^{-1} HCl to pH 7 and extracted with AcOEt (3 × 15 mL). Combined organic layers were washed saturated aqueous $NaHSO_3$ solution (5 × 15 mL), and brine, then dried ($MgSO_4$), filtered, and evaporated to yield **17** (16.2 g, 76% from **14**) as a light yellow solid. Sample for analysis was recrystallized from AcOEt/hexanes. R_f (hexanes/AcOEt, 1:1) 0.59; Mp 118–120 °C (AcOEt/hexanes); IR ($CHCl_3$): ν 3370 (w), 2959 (w), 2892 (w), 1607 (w), 1577 (w), 1490 (s), 1465 (w), 1441 (m), 1404 (w), 1362 (w), 1336 (w), 1283 (s), 1232 (m), 1199 (w), 1169 (w), 1130 (m), 1034 (s), 986 (w), 942 (w), 820 (w), 802 (w) cm^{-1}; ^1H NMR ($CDCl_3$, 300 MHz): 6.88 (d, *J* = 8.3 Hz, Ar H), 6.79 (d, *J* = 8.3 Hz, 1H), 5.95 (s, exchange with D_2O, 1H), 5.12 (t, *J* = 4.9 Hz, 1H), 4.03–3.80 (m, 4H), 3.89 (s, 3H), 3.09 (d, *J* = 4.9 Hz, 1H); ^{13}C NMR ($CDCl_3$, 150 MHz): δ 145.97, 143.20, 128.86, 111.36, 122.13, 109.66, 103.51, 65.05, 56.41, 40.17; LRMS-EI (*m*/*z*): M^+ 289 (1), 73 (100), 45 (14); HRMS-EI (*m*/*z*): M^+ calcd. for $C_{11}H_{13}BrO_4$: 287.9997, found 287.9994; anal. calcd. for $C_{11}H_{13}BrO_4$: C, 45.70, H, 4.53; found: C, 45.99, H, 4.47.

tert-*Butyl 2-((5′S,6′S)-6′-(3″-((1,3-dioxolan-2-yl)methyl)-2″-bromo-6″-methoxyphenoxy)-5′-*(tert-*butyldimethylsilyloxy) cyclohex-1′-enyl)ethyl(methyl)carbamate (23)*

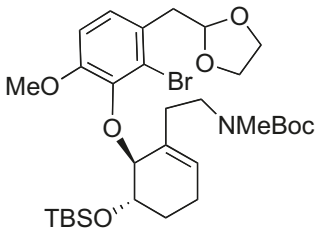

23

An orange solution of DIAD (7 mL, 35.6 mmol) in degassed THF (45 mL) was cooled to –10 °C and treated with PBu_3 (9.5 mL, 38.5 mmol) at one portion. The resulting pale yellow solution was stirred for 25 min at –10 °C and cannulated during 35 min into a chilled (4 °C) solution of alcohol **22** (10.6 g, 27.4 mmol) and phenol **17** (8.7 g, 30.2 mmol) in degassed THF (90 mL). The mixture was allowed to reach 25 °C, stirred for 12 h, and evaporated. The residue was adsorbed on silica gel and subjected to chromatography (hexanes/AcOEt, 8:1) obtaining **23** (13.8 g, 76%) and recovered phenol **17** (664 mg, 8%). Data for **23**: Yellow oil; R_f (hexanes/AcOEt, 2:1) 0.75; $[\alpha]_D^{20}$ = + 43.7 (*c* 0.125, $CHCl_3$); IR ($CHCl_3$): ν 3294 (w), 2930 (s), 2857 (m), 1736 (w), 1697 (s), 1594 (w), 1482 (s), 1441 (m), 1393 (m), 1365 (m), 1293 (m), 1252 (s), 1171 (s), 1137 (s), 1105 (m), 1085 (m), 1035 (s),

Can. J. Chem. Downloaded from www.nrcresearchpress.com by 80.58.250.72 on 09/16/12
For personal use only.

1007 (m), 943 (w) cm^{-1}; ^1H NMR ($CDCl_3$, 600 MHz, two rotamers): 7.04 (d, J = 8.3 Hz, 1H), 6.83 (d, J = 8.3 Hz, 1H), 5.80, 5.77 (2 br. s, 1H), 5.06 (t, J = 4.9 Hz, 1H), 4.48 (br. s, 1H), 4.00–3.92 (m, 3H), 3.87–3.78 (m, 2H), 3.83 (s, 3H), 3.55 (br. s, 0.4H), 3.41 (br. s, 0.6H), 3.22–3.15 (m, 1H), 3.13 (dd, J = 14.0, 4.5 Hz, 1H), 3.07 (dd, J = 14.0, 5.3 Hz, 1H), 2.81 (br. s, 3H), 2.52 (br. s, 0.4 H), 2.46 (br. s, 0.6H), 2.42–2.35 (m, 1H), 2.25–2.13 (m, 2H), 2.02–1.94 (m, 1H), 1.67–1.60 (m, 1H), 1.44 (s, 9H), 0.72 (s, 9H), –0.18, –0.21 (2 s, 6H); ^{13}C NMR ($CDCl_3$, 150 MHz, 2 rotamers): 155.93, 155.74, 152.00, 144.55, 131.39, 129.17, 121.33, 131.39, 126.16, 111.14, 103.51, 79.84, 79.60, 79.05, 67.50, 65.00, 55.78, 49.08, 48.30, 40.58, 35.25, 35.10, 33.70, 32.85, 28.60, 25.77, 25.29, 20.83, 18.13, –5.09; LRMS-EI (*m*/*z*): M^+ 656 (1), 368 (8), 312 (45), 268 (39), 237 (52), 180 (8), 136 (28), 105 (10), 73 (100), 57 (58), 44 (35); HRMS-EI (*m*/*z*): M^+ calcd. for $C_{31}H_{51}BrNO_7Si$: 656.2540, found 656.2595; anal. calcd. for $C_{31}H_{51}BrNO_7Si$: C, 56.70; H, 7.67; found C, 56.95; H, 7.77.

tert-*Butyl 2-((5aS,6S,9aR)-1-((1,3-dioxolan-2-yl)methyl)-6-(*tert-*butyldimethyl-silyloxy)-4-methoxy-5a,6,7,9a-tetrahydrodibenzo[*b,d*]furan-9a-yl)ethyl(methyl)-carbamate (24) and* tert-*butyl 2-((5aS,6S,9aR)-1-((1,3-dioxolan-2-yl) methyl)-6-(*tert-*butyldimethylsilyloxy)-4-methoxy-5a,6,9,9a-tetrahydrodibenzo[*b,d*]furan-9a-yl)ethyl(methyl)carbamate (25)

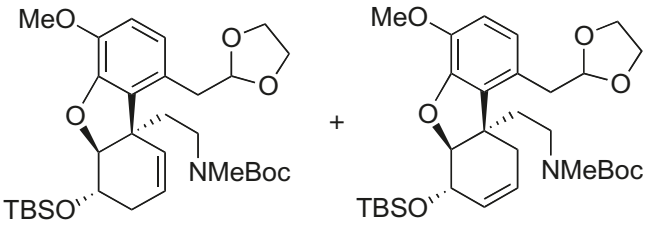

24 **25**

A solution of **23** (6.38 g, 9.7 mmol) in degassed toluene (60 mL) was treated with K_2CO_3 (2.01 g, 14.6 mmol), $Pd_2(dba)_3$ (888 mg, 0.97 mmol), and t-Bu_3P (393 mg, 1.94 mmol), immersed in a preheated oil bath (110 °C), and stirred for 16 h. The reaction mixture was filtered through a plug of Celite (washing with CH_2Cl_2) and evaporated. Flash column chromatography (hexanes/AcOEt, 4:1) afforded an inseparable mixture of **24** and **25** (**24/25** ≈ 5:1, 4.82 g, 86%) as a brown oil. R_f (hexanes/AcOEt, 2:1) 0.59; $[\alpha]_D^{20}$ = +34.8 (*c* 1.00, $CHCl_3$); IR ($CHCl_3$): ν 3010 (w), 2956 (m), 2931 (m), 2895 (w), 2857 (w), 1730 (w), 1683 (m), 1626 (w), 1584 (w), 1506 (m), 1482 (w), 1472 (w), 1438 (w), 1401 (w), 1394 (w), 1367 (w), 1321 (w), 1282 (w), 1258 (m), 1221 (s), 1216 (s), 1213 (s), 1210 (s), 1155 (m), 1127 (m), 1048 (w), 1009 (w) cm^{-1}; ^1H NMR ($CDCl_3$, 300 MHz): δ 6.78 (d, J = 8.3 Hz, 1H), 6.72 (d, J = 8.3 Hz, 1H), 6.01–5.97 (m, 1H), 5.73–5.68 (m, 1H), 5.05 (m, 1H), 4.45 (m, 1H), 4.01 (m, 2H), 3.90–3.86 (m, 3H), 3.82 (s, 3H), 3.07 (m, 1H), 3.00–2.88 (m, 2H), 2.77 (s, 3H), 2.28–2.18 (m, 1H), 2.13–1.95 (m, 1H), 1.92–1.83 (m, 2H), 1.57 (m, 2H), 1.43 (s, 9H), 0.89 (s, 9H), 0.13 (s, 3H), 0.01 (s, 3H); ^{13}C NMR ($CDCl_3$, 150 MHz): δ 155.5, 146.1, 143.9, 132.3, 129.4, 124.8, 123.1, 111.7, 104.7, 104.5, 89.8, 79.4, 68.4, 65.0, 64.9, 55.8, 51.4, 45.2, 37.5, 36.3, 35.4, 34.2, 30.8, 29.7, 28.4, 25.8, 25.7, 18.1; LRMS-EI (*m*/*z*): 310 (7), 237 (1), 184 (10), 139 (4), 91 (22), 73 (66), 57 (80), 43 (100); HRMS-EI (*m*/*z*): M^+ calcd. for $C_{31}H_{49}NO_7Si$: 575.3278, found 575.3276.

tert-*Butyl 2-((5aS,6S,9aR)-1-((1,3-dioxolan-2-yl)methyl)-6-hydroxy-4-methoxy-5a,6,7,9a tetrahydrodibenzo[*b,d*]furan-9a-yl)ethyl(methyl)carbamate (26) and* tert-*butyl 2-((5aS,6S,9aR)-1-((1,3-dioxolan-2-yl)methyl)-6-hydroxy-4-methoxy-5a,6,9,9a-tetrahydrodibenzo[*b,d*]furan-9a-yl)ethyl (methyl)carbamate (27)

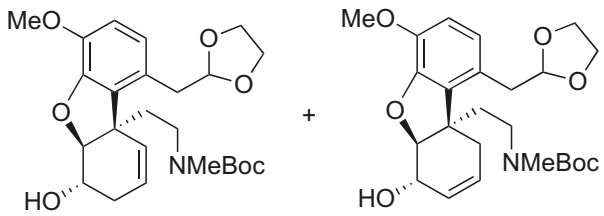

26 **27**

A solution of **24** and **25** (**24/25** ≈ 5:1, 4.818 g, 8.34 mmol) in THF (50 mL) was cooled to 0 °C and treated with a 1.0 mol L^{-1} solution of TBAF in THF (12.6 mL, 12.6 mmol). The mixture was stirred for 16 h at 25 °C, diluted with AcOEt (40 mL), and washed with H_2O (25 mL). The aqueous layer was extracted with AcOEt (3 × 45 mL) and the combined organic layers were washed with brine, dried (Na_2SO_4), filtered, and evaporated. Flash column chromatography (hexanes/AcOEt, 4:1 → 1:1) afforded **27** (593 mg, 15%) as a light yellow foam and **26** (3.14 g, 82%) as a light yellow foam.

Data for ***26***

R_f (hexanes/AcOEt, 1:2) 0.26; $[\alpha]_D^{20}$ +9.5 (*c* 3.2, $CHCl_3$); IR (film): ν 3629 (m), 3018 (s), 1732 (m), 1683 (s), 1625 (w), 1584 (w), 1507 (m), 1400 (m), 1367 (m), 1318 (w) 1280 (m), 1216 (s), 1156 (m), 1097 (m), 1047 (m), 978 (w) cm^{-1}; ^1H NMR ($CDCl_3$, 300 MHz, 2 rotamers): δ 6.81 (d, J = 8.3 Hz, 1H), 6.74 (d, J = 8.3 Hz, 1H), 6.03 (dd, J = 9.8, 1.5 Hz, 1H), 5.78 (ddd, J = 9.8, 5.7, 2.3 Hz, 1H), 5.04 (dd, J = 6.0, 3.8 Hz, 1H), 4.55–4.37 (br. s, 1H), 4.05–3.95 (m, 2H), 3.90–3.80 (m, 2H); 3.85 (s, 3H), 3.47–3.20 (m, 1H), 3.06 (dd, J = 14.3, 3.4 Hz, 1H), 2.94–2.82 (m, 1H), 2.89 (dd, J = 14.3, 6.0 Hz, 1H), 2.77 (s, 3H), 2.45–2.30 (m, 1H), 2.19–2.03 (m, 1H), 2.03–1.78 (m, 2H), 1.43 (s, 9H); ^{13}C NMR ($CDCl_3$, 150 MHz): δ 155.61, 145.76, 144.18, 129.29, 125.10, 129.49, 124.66, 123.92, 111.80, 104.67, 90.64, 90.12, 79.67, 68.18, 65.10, 65.06, 56.03, 51.84, 36.59, 34.41, 29.41, 28.61; LRMS-EI (*m*/*z*): M^+ 461 (6), 388 (3), 340 (8), 285 (16), 271 (6), 241 (2), 213 (8), 142 (31), 103 (20), 84 (31), 73 (100), 57 (81); HRMS-EI (*m*/*z*): M^+ calcd. for $C_{25}H_{35}NO_7$: 461.2414, found 461.2414; Anal. calcd. for $C_{25}H_{35}NO_7$: C, 65.06; H, 7.64; found C, 64.94; H, 7.67.

Can. J. Chem. Downloaded from www.nrcresearchpress.com by 80.58.250.72 on 09/16/12
For personal use only.

Data for ***27***

R_f (hexanes/AcOEt, 1:2) 0.58; $[\alpha]_D^{20}$ = +11.7 (*c* 1.00, $CHCl_3$); IR ($CHCl_3$): ν 3596 (w), 3024 (w), 3010 (m), 2979 (m), 2935 (m), 2895 (m), 2840 (w), 1729 (w), 1683 (s), 1626 (w), 1585 (w), 1507 (s), 1482 (m), 1463 (m), 1453 (m), 1436 (m), 1401 (m), 1367 (m), 1344 (w), 1320 (w), 1282 (m), 1167 (s), 1154 (s), 1097 (m), 1047 (m), 1020 (m), 987 (m) cm^{-1}; ^1H NMR ($CDCl_3$, 600 MHz, 2 rotamers): δ 6.85 (d, *J* = 8.4 Hz, 1H), 6.75 (d, *J* = 8.4 Hz, 1H), 5.94 (br. s, 1H), 5.89 (br. s, 1H), 5.07 (br. s, 1H), 4.36 (br. d, *J* = 6.4 Hz, 1H), 4.30–4.25 (m, 1H), 4.02–3.95 (m, 2H), 3.90–3.80 (m, 2H), 3.85 (s, 3H), 3.24 (ddd, *J* = 13.9, 12.3, 4.0 Hz, 1H), 2.98 (dd, *J* = 14.4, 4.3 Hz, 1H), 2.96–2.90 (m, 1H), 2.84–2.60 (m, 3H), 2.46 (d, *J* = 15.1 Hz, 1H), 2.15–2.00 (m, 1H), 1.92–1.77 (m, 1H), 1.41 (s, 3H); ^{13}C NMR ($CDCl_3$, 150 MHz, 2 rotamers): δ 155.56, 146.94, 143.37, 131,75, 124.85, 130.52, 127.49, 123.41, 111.62, 104.76, 92.96, 79.65, 70.39, 65.09, 65.01, 55.93, 48.60, 45.48, 40.08, 35.64, 35.48, 34.43, 28.58; LRMS-FAB (*m*/*z*): $[M+H]^+$ 462 (7), 344 (38), 285 (17), 241 (9), 159 (7), 103 (36), 73 (100), 57 (73); HRMS-FAB (*m*/*z*): $[M+H]^+$ calcd. for $C_{25}H_{36}NO_7$: 462.2492, found: 462.2428.

tert-*Butyl 2-((5a*S*,6*S*,9a*R*)-1-((1,3-dioxolan-2-yl)methyl)-6-hydroxy-4-methoxy-5a,6,7,9a-tetrahydrodibenzo[*b,d*]furan-9a-yl)ethyl(methyl)carbamate (28)

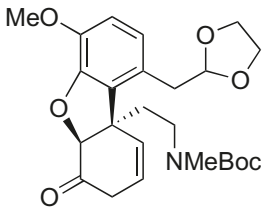

28

A solution of **26** (499 mg, 1.081 mmol) in AcOEt (20 mL) was treated with IBX (457 mg, 1.632 mmol), the resulting suspension was stirred for 6 h at 80 °C, and cooled to 0 °C. Filtration through Celite (washing with cold AcOEt) afforded crude **28** (601 mg), which was used in the next step without further purification. R_f (hexanes/AcOEt, 1:1) 0.35; IR ($CHCl_3$): ν 3025 (w), 3010 (m), 2979 (m), 2934 (m), 2894 (w), 2840 (w), 1736 (m), 1683 (s), 1627 (w), 1583 (w), 1508 (m), 1481 (m), 1462 (m), 1454 (m), 1428 (m), 1399 (m), 1367 (m), 1319 (w), 1283 (s), 1168 (s), 1154 (s), 1092 (w), 1078 (w), 1042 (m), 1017 (m), 984 (w), 944 (w), 909 (w) cm^{-1}; ^1H NMR ($CDCl_3$, 300 MHz): δ 6.84 (d, *J* = 8.3 Hz, 1H), 6.76 (d, *J* = 8.3 Hz, 1H), 6.03 (br. s, 1H), 5.81 (dt, *J* = 9.8, 3.8 Hz, 1H), 5.03 (br. t, *J* ≈ 4.5 Hz, 1H), 4.99 (br. s, 0.33H), 4.75 (br. s, 0.66H), 4.03–3.94 (m, 2H), 3.94–3.80 (m, 2H), 3.87 (s, 3H), 3.30–2.87 (m, 6H), 2.81 (s, 3H), 2.23–2.02 (m, 2H), 1.44 (s, 9H); ^{13}C NMR ($CDCl_3$, 150 MHz, 2 rotamers): δ 146.90, 143.96, 129.75, 129.40, 124.56, 124.16, 124.16, 123.64, 112.49, 104.57, 87.81, 87.47, 79.93, 65.08, 56.24, 45.34, 44.83, 37.64, 37.20, 36.43, 34.40, 34.44, 28.58; LRMS-FAB (*m*/*z*): M^+ 459 (1), 85 (67), 83 (100), 73 (81), 57 (27), 47 (19), 44 (22), 41 (18); HRMS-EI (*m*/*z*): M^+ calcd. for $C_{25}H_{33}NO_7$: 459.2257, found 459.2252.

tert-*Butyl 2-((5a*S*,9a*S*)-1-((1,3-dioxolan-2-yl)methyl)-4-methoxy-6-oxo-5a,6,9,9a-tetrahydrodibenzo[*b,d*]furan-9a-yl)ethyl(methyl)carbamate (29)

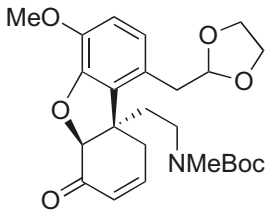

29

A solution of alcohol **27** (229 mg, 0.496 mmol) in DMF (10 mL) was cooled to 0 °C and treated with IBX (139 mg, 0.496 mmol). The reaction mixture was stirred for 16 h at 25 °C, diluted with H_2O (4 mL), and the layers were separated. The aqueous layer was extracted with $CHCl_3$ (3 × 8 mL). The combined organic layers were washed with brine, dried (Na_2SO_4), filtered, and evaporated. Flash column chromatography (hexanes/AcOEt, 3:1 → 1.5:1) afforded **27** (12 mg, 5%) as a light yellow foam and **29** (159 mg, 70%) as a light yellow oil. R_f (hexanes/AcOEt, 1:2) 0.32; $[\alpha]_D^{20}$ = +91.3° (*c* 1.415, $CHCl_3$); IR (film): ν 2979 (w), 1685 (s), 1625 (w), 1507 (m), 1393 (w), 1366 (w), 1284 (w), 1148 (m), 1044 (w) cm^{-1}; ^1H NMR ($CDCl_3$, 300 MHz): δ 6.92 (m, 1H), 6.82 (d, *J* = 8.4, 1H), 6.73 (d, *J* = 8.4, 1H), 6.20 (d, *J* = 9.6, 1H), 5.05 (t, *J* = 4.5, 1H), 4.66 (br s, 1H), 3.98–3.88 (m, 2H), 3.87–3.79 (m, 6H), 3.34–3.24 (m, 1H), 3.17–3.03 (m, 1H), 3.03–2.94 (m, 2H), 2.88–2.82 (m, 1H), 2.77 (s, 4H), 2.15–2.09 (m, 2H), 1.42 (s, 9H); ^{13}C NMR ($CDCl_3$, 150 MHz): δ 155.36, 148.63, 147.28, 143.69, 128.96, 124.57, 124.04, 112.52, 104.55, 86.31, 79.80, 65.03, 64.97, 60.39, 56.05, 49.62, 45.23, 38.45, 35.77, 34.27, 28.45, 21.05, 14.20; LRMS-EI (*m*/*z*): M^+ 386(2), 359(12), 301(21), 257(14), 216(5), 190(4), 149(4), 103(7), 84(20), 73(100), 57 (33), 43(82); HRMS-EI (*m*/*z*): M^+ calcd. for $C_{25}H_{33}NO_7$: 459.2257, found 459.2260.

(4*S*, 6a*S*, 11b*R*)-11-(1,3-Dioxolan-2-ylmethyl)-8-methoxy-3-methyl-2,3,4,5-tetra-hydro-1*H*-4,11b-methano[1]benzofuro[3,2-*d*]azocin-6-one (30)

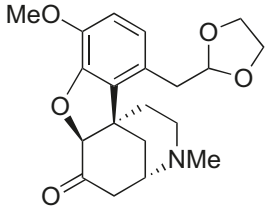

30

A solution of crude **28** (theoretical content 1.081 mmol) in CH_2Cl_2 (8 mL) was treated with TFA (2 mL), the mixture was stirred for 1 h, and poured into saturated aqueous Na_2CO_3 solution (30 mL) containing solid Na_2CO_3 (6 g). The biphasic mixture was stirred for 10 min (effervescence), diluted with CH_2Cl_2 (30 mL), and the layers were separated. The aqueous layer was extracted with CH_2Cl_2 (3 × 30 mL).

Can. J. Chem. Downloaded from www.nrcresearchpress.com by 80.58.250.72 on 09/16/12
For personal use only.

The combined organic layers were washed with brine (40 mL), dried (Na_2SO_4), and evaporated. Flash column chromatography (AcOEt/MeOH, 6:1) afforded **30** (217 mg, 56% from **26**) as a brown foam. R_f ($CHCl_3$/MeOH/aqueous NH_3, 92:8:1) 0.52; IR ($CHCl_3$): ν 3021 (m), 3011 (m), 2959 (m), 2935 (m), 2893 (m), 2794 (w), 1727 (s), 1628 (w), 1584 (w), 1508 (s), 1475 (w), 1462 (w), 1452 (m), 1452 (m), 1437 (m), 1401 (m), 1377 (w), 1359 (w), 1340 (w), 1283 (s), 1267 (m), 1167 (m), 1142 (s), 1115 (s), 1017 (s), 990 (m), 951 (w), 944 (w), 924 (w) cm^{-1}; ^1H NMR ($CDCl_3$, 300 MHz): δ 6.82 (d, J = 8.5 Hz, 1H), 6.73 (d, J = 8.5 Hz, 1H), 5.02 (t, J = 4.8 Hz, 1H), 4.72 (s, 1H), 4.00–3.90 (m, 2H), 3.90–3.79 (m, 2H), 3.83 (s, 3H); 3.51 (m, 1H), 3.01 (dd, J = 14.5, 4.7 Hz, 1H), 2.97 (dd, J = 14.5, 5.1 Hz, 1H), 2.96–2.85 (m, 1H), 2.71–2.55 (m, 2H), 2.50–2.30 (m, 2H), 2.34 (s, 3H), 1.85 (br. d, J = 12.9 Hz, 1H), 1.70 (dt, J = 13.2, 2.8 Hz, 1H); ^{13}C NMR ($CDCl_3$, 75 MHz): δ 205.76, 147.02, 143.69, 131.30, 124.72, 124.13, 111.98, 104.81, 89.16, 65.09, 55.98, 49.39, 46.92, 42.96, 36.28, 35.67, 34.25; LRMS-EI (*m*/*z*): 290 (18), 288 (18), 217 (21), 215 (22), 74 (11), 73 (100), 45 (41); HR MS-EI (*m*/*z*): M^+ calcd. for $C_{20}H_{25}NO_5$: 359.1733, found 359.1740. Anal. calcd. for $C_{20}H_{25}NO_5$: C, 66.83; H, 7.01; found C, 66.83; H, 7.02.

(4S,4aS,9bR)-9-((1,3-Dioxolan-2-yl)methyl)-6-methoxy-9b-(2-(methylamino)ethyl)-3,4,4a,9b-tetrahydrodibenzo[b,d]furan-4-ol (31) and (4aS,5S,8aR,E)-3-methoxy-11-methyl-4a,5,6,9,10,11-hexahydrobenzo[2,3]benzo-furo[3,4-de]azocin-5-ol (32)

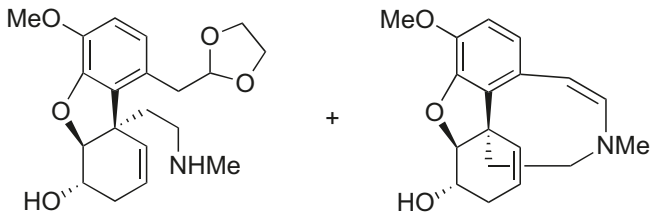

31 **32**

A solution of carbamate **26** (514 mg, 1.13 mmol) in CH_2Cl_2 (1 mL) was cooled to 0 °C and treated with TFA (0.25 mL) over 10 min. The mixture was stirred for 15 min, concentrated, diluted with saturated aqueous Na_2CO_3 solution (3 mL), and extracted with CH_2Cl_2 (3 × 5 mL). The combined organic layers were washed with brine (5 mL), dried ($MgSO_4$), and evaporated. Flash column chromatography (CH_2Cl_2/MeOH/aqueous NH_3, 100:10:1) afforded secondary amine **31** (202 mg, 0.559 mmol, 49%) and enamine **32** (34 mg, 10%).

*Data for **31***

Colorless oil; R_f (CH_2Cl_2/MeOH/aqueous NH_3, 100:10:1) 0.33; $[\alpha]_D^{20}$ = +22.8 (*c* 0.875, $CHCl_3$); IR ($CHCl_3$): ν 3588 (w), 3027 (w), 2936 (m), 1624 (m), 1582 (m), 1506 (s), 1438 (m), 1280 (s), 1131 (s), 1099 (s), 1043 (s), 975 (s) cm^{-1}; ^1H NMR ($CDCl_3$, 600 MHz): δ 6.80 (d, J = 8.4 Hz, 1H), 6.72 (d, J = 8.4 Hz, 1H), 6.00 (d, J = 9.6 Hz, 1H), 5.04 (dd, J = 5.4, 4.2 Hz, 1H), 4.65 (d, J = 6.0 Hz, 1H), 4.04–4.00 (m, 3H), 3.88–3.85 (m, 2H), 3.03 (dd, J = 14.4, 5.4 Hz, 1H), 2.92 (dd, J = 14.4, 5.4 Hz, 1H), 2.78–2.71 (m, 1H), 2.60–2.54 (m, 1H), 2.38 (s, 1H), 2.31 (d, J = 1.8 Hz, 1H), 2.15–2.12 (m, 2H), 2.02–2.00 (m, 1H); ^{13}C NMR ($CDCl_3$, 150 MHz): δ 145.87, 143.71, 133.12, 129.68, 125.15, 124.54, 123.50, 111.33, 104.53, 89.46, 66.77, 64.94, 64.92, 55.82, 47.70, 41.46, 39.19, 36.82, 36.24, 35.87, 28.74; LRMS-FAB (*m*/*z*): $[M + H]^+$ 362 (100), 73 (45), 59 (32), 45 (12), 44 (40); HRMS-EI (*m*/*z*): M^+ calcd. for $C_{20}H_{27}NO_5$: 361.1889, found 361.1891. Anal. calcd. for $C_{20}H_{27}NO_5$: C, 66.46; H, 7.53; found C, 66.17; H, 7.56.

*Data for **32***

Ocre solid; R_f (CH_2Cl_2/MeOH/aqueous NH_3, 100:10:1) 0.57; IR ($CHCl_3$): ν 3593 (w), 3027 (w), 3008 (m), 2958 (m), 2932 (m), 2854 (w), 2801 (w), 1723 (w), 1690 (w), 1666 (w), 1627 (s), 1572 (w), 1503 (s), 1464 (m), 1438 (m), 1427 (m), 1415 (m), 1380 (m), 1339 (w), 1285 (s), 1263 (s), 1160 (m), 1103 (s), 1087 (s), 1074 (m), 1055 (s), 1020 (m), 1005 (m), 976 (w), 968 (w), 955 (w), 908 (w) cm^{-1}. ^1H NMR ($CDCl_3$, 300 MHz): δ 6.66 (d, J = 8.5 Hz, 1H), 6.58 (d, J = 8.5 Hz, 1H), 6.53 (dd, J = 10.2, 3.0 Hz, 1H), 5.75 (d, J = 9.4 Hz, 1H), 5.64 (ddd, J ≈ 10.2, 6.4, 1.9 Hz, 1H), 4.88 (d, J = 9.4 Hz, 1H), 4.30 (d, J = 9.0 Hz, 1H), 3.85 (s, 3H), 3.82–3.69 (m, 1H), 3.61 (ddd, J = 15.1, 12.8, 3.4 Hz, 1H), 2.87 (s, 3H), 2.87 (s, 3H), 2.82–2.67 (m, 1H), 2.36 (dt, J = 16.6, 6.0 Hz, 1H), 2.10 (ddd, J ≈ 10.9, 2.3 Hz, 1H), 1.86 (dt, J = 13.0, 4.3 Hz, 1H), 1.51 (dt, J ≈ 13.6, 2.6 Hz, 1H); ^{13}C NMR ($CDCl_3$, 150 MHz): δ 145.30, 142.94, 137.41, 129.80, 129.04, 127.48, 122.83, 121.36, 111.45, 94.96, 93.82, 68.66, 55.97, 52.88, 48.47, 42.19, 30.92, 29.39; LRMS-FAB (*m*/*z*): $[M + H]^+$ 300 (23), M^+ 299 (54), $[M - OMe]^+$ 268 (12), 136 (23), 91 (20), 73 (100), 69 (26), 57 (57), 55 (42), 44 (30), 43 (43), 41 (37); HRMS-FAB (*m*/*z*): M^+ calcd. for $C_{18}H_{21}NO_3$: 299.1521, found 299.1523.

(E)- and (Z)-tert-Butyl 2-((5aS,6S,9aR)-6-hydroxy-4-methoxy-1-(2-methoxyvinyl)-5a,6,7,9a-tetrahydrodibenzo[b,d]furan-9a-yl)ethyl(methyl)carbamate (33)

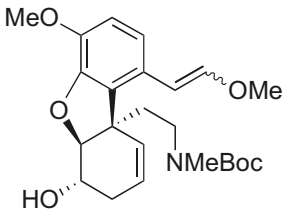

33

TBS-protected derivative of the enol ether **33** was prepared from aldehyde **5** by a Wittig reaction with (methoxymethyl) triphenyl-phosphonium chloride as previously described.[35] The TBS ether (384 mg, 0.704 mmol) was dissolved in THF (6 mL) at 0 °C, and then TBAF (1.0 mol L^{-1} in THF, 775 μL, 0.775 mmol) was added. The reaction mixture was stirred at 25 °C for 3 h. A second portion of TBAF (352 μL, 0.352 mmol) was added at 25 °C and the reaction was stirred for 2 h, diluted with H_2O (10 mL) and extracted with CH_2Cl_2 (3 × 15 mL). The combined organic layers were washed with brine and dried (Na_2SO_4). Flash column chromatography (AcOEt/hexanes, 1:9 → 1:4 → 1:1) afforded **33** (mixture of *E* and *Z* isomers, 225 mg, 74%) as an oil. R_f (hexanes/AcOEt, 1:1) 0.2; IR (film): ν 3426 (m), 2933 (s), 1682 (s),

Can. J. Chem. Downloaded from www.nrcresearchpress.com by 80.58.250.72 on 09/16/12
For personal use only.

1572 (m), 1504 (s), 1483 (s), 1423 (s), 1399 (s), 1366 (s), 1282 (s), 1215 (s), 1156 (s), 1098 (s), 1046 (s), 1012 (s), 882 (m) cm^{-1}. ^1H NMR ($CDCl_3$, 300 MHz, mixture of 2 diastereoisomers): δ 6.79–6.65 (m, 3H), 6.20–6.05 (m, 1H), 5.85–5.70 (m, 1H), 4.70–4.25 (m, 1H), 4.00–3.80 (m, 5H), 3.76 (d, J = 3.6 Hz, 1H), 3.71 (s, 3H), 3.60–3.10 (m, 2H), 3.00–2.50 (m, 7H), 2.50–2.30 (m, 2H), 2.20–1.70 (m, 6H), 1.45 (s, 12H), 1.01–0.80 (m, 2H); ^{13}C NMR ($CDCl_3$, 75 MHz, mixture of 2 diastereoisomers): δ 155.51, 149.27, 147.60, 145.70, 145.52, 143.73, 143.43, 143.09, 130.10, 129.18, 127.59, 125.36, 124.69, 124.58, 124.42, 123.05, 119.26, 111.74, 111.68, 111.28, 111.22, 101.53, 101.31, 96.13, 90.30, 89.64, 79.48, 78.07, 77.25, 77.04, 68.21, 67.81, 60.65, 60.61, 57.00, 56.09, 55.96, 55.89, 55.86, 53.45, 51.39, 51.33, 48.42, 45.21, 44.76, 37.14, 36.64, 36.10, 34.30, 31.95, 29.75, 29.38, 28.97, 28.46, 24.70, 22.72, 14.15, 13.74, 1.04. LRMS-EI (*m/z*): M^+ 142 (25), 84 (100), 71 (28), 57 (43), 43 (88); HRMS-EI (*m/z*): M^+ calcd. for $C_{24}H_{33}NO_6$: 431.2308, found 431.2308.

(4aS,5S,8aR)-3-Methoxy-11-methyl-4a,5,6,9,10,11,12,13-octahydrobenzo[2,3]benzofuro[3,4-de]azocin-5-ol (34)

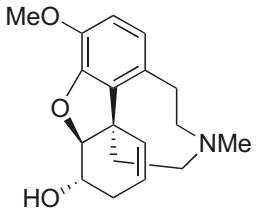

34

Enol ether **33** (146 mg, 0.34 mmol) was dissolved in a 4/1 mixture of CH_2Cl_2 and TFA (0.5 mL) at 0 °C. The reaction mixture was warmed to 25 °C and stirred overnight before being treated with cold saturated aqueous $NaHCO_3$ solution (2 mL) and extracted with $CHCl_3$ (3 × 4 mL). The combined organic layers were dried (Na_2SO_4) and evaporated. The resulting enamine **32** was dissolved in dry MeOH (0.3 mL) and treated with $NaBH_3CN$ (7 mg, 0.11 mmol) and AcOH (19 μL, 0.34 mmol) at 0 °C. The reaction mixture was warmed to 25 °C, stirred overnight and treated with cold saturated aqueous $NaHCO_3$ solution (2 mL). Methanol was evaporated and the aqueous residue was extracted with $CHCl_3$ (3 × 3 mL) and dried ($NaSO_4$). Flash column chromatography (CH_2Cl_2/AcOEt, 4:1) afforded amine **34** (42 mg, 41%) as a colorless oil. R_f (CH_2Cl_2/AcOEt, 96:4) 0.49; ^1H NMR ($CDCl_3$, 600 MHz): δ 6.71 (d, J = 8.1 Hz, 1H), 6.59 (d, J = 8.1 Hz, 1H), 5.74–5.68 (m, 1H), 4.32 (m, 1H), 4.00–4.93 (m, 1H), 3.87 (s, 3H), 3.13–3.05 (m, 1H), 2.85–2.76 (m, 1H), 2.74–2.65 (m, 1H), 2.59–2.52 (m, 2H), 2.46–2.38 (m, 2H), 2.31 (s, 3H), 2.17–2.11 (m, 1H), 2.01–1.96 (m, 1H), 1.83–1.75 (m, 1H), 1.32–1.25 (m, 2H); ^{13}C NMR ($CDCl_3$, 150 MHz): δ 145.54, 143.79, 132.20, 129.65, 122.74, 122.09, 111.18, 96.13, 67.48, 60.51, 55.79, 52.60, 47.51, 42.29, 33.06, 29.22; LRMS-EI (*m/z*): M^+ 42 (27), 43 (50), 44 (27), 57 (38), 58 (56), 70 (100), 71 (27), 83 (22), 149 (49), 179 (62), 301 (41); HRMS-EI (*m/z*): M^+ calcd. for $C_{18}H_{23}NO_3$: 301.1678, found 301.1678.

[(4S,6aS,11bR)-8-Methoxy-3-methyl-6-oxo-2,3,4,5,6,6a-hexahydro-1H-4,11b-methano[1]benzofuro[3,2-d]azocin-11-yl]acetaldehyde (39)

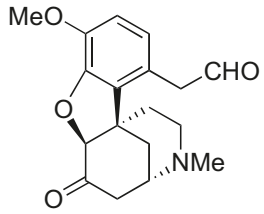

39

A mixture of **30** (231 mg, 0.643) and oxalic acid (159 mg, 1.766 mmol) in H_2O (6 mL) was stirred at 40 °C for 13 h, cooled to 25 °C, poured into saturated aqueous $NaHCO_3$ solution (15 mL), and extracted with $CHCl_3$ (3 × 15 mL). The combined organic layers were washed with brine (15 mL), dried ($MgSO_4$), and evaporated to get crude aldehyde **39** (227 mg) that was used without further purification. A sample was purified by flash column chromatography ($CHCl_3$/MeOH/aqueous NH_3, 92:8:1). Colorless oil; R_f ($CHCl_3$/MeOH/aqueous NH_3, 92:8:1) 0.52; ^1H NMR ($CDCl_3$, 600 MHz, crude): δ 9.70 (br t, J = 1.9 Hz, 1H), 6.79 (d, J = 8.3 Hz, 1H), 6.66 (d, J = 8.3 Hz, 1H), 4.76 (s, 1H), 3.86 (s, 3H), 3.78 (dd, J = 17.0, 1.9 Hz, 1H), 3.72 (dd, J = 17.0, 1.9 Hz, 1H), 3.53–3.48 (m, 1H), 2.96–2.91 (m, 1H); 2.68 (d, J = 17.4 Hz, 1H), 2.50–2.30 (m, 3H), 2.35 (s, 3H), 2.19 (br d, J = 12.8 Hz, 1H), 1.89–1.84 (m, 1H), 1.71 (dt, $J \approx$ 12.8, 2.3 Hz, 1H); LRMS-EI *(m/z)*: M+ 315 (3), $[M\text{-}OH]^+$ 298 (21), $[M\text{-}H_2O]^+$ 297 (100), 282 (11), 229 (18), 214 (20), 188 (10), 43 (11), 42 (14); HRMS-EI *(m/z)*: M^+ calcd. for $C_{18}H_{21}NO_4$: 315.1471, found 315.1469.

(4S,6aS,11bR)-8-Methoxy-3-methyl-6-oxo-2,3,4,5,6,6a-hexahydro-1H-4,11b-methano[1]benzofuro[3,2-d]azocine-11-carbaldehyde (40)

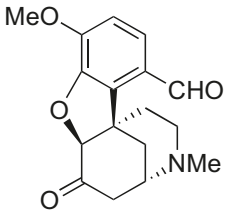

40

A solution of crude aldehyde **39** (4 mg) in MeCN (0.2 mL) and H_2O (0.2 mL) was treated with concentrated HCl until the pH reached 1, the mixture was stirred at 40 °C for 22 h, cooled to 25 °C, poured into saturated aqueous $NaHCO_3$ solution (5 mL), and extracted with $CHCl_3$ (4 × 5 mL). The combined organic layers were washed with brine (5 mL), dried ($MgSO_4$), and evaporated to furnish crude **40** (4 mg). A pure sample was obtained by flash column chromatography (AcOEt/MeOH, 7:1 → 5:1). R_f (AcOEt/MeOH, 5:1) 0.33; IR ($CHCl_3$): ν 3027 (w), 3012 (w), 2963 (m), 2964 (m), 2845 (w), 2789 (w), 2745 (w), 1726 (s), 1691 (s), 1615 (s), 1574 (m), 1507 (m), 1447 (m), 1438 (m), 1410 (w), 1377 (w), 1340 (w), 1293 (s), 1270 (m), 1260 (m), 1169 (m), 1144 (m), 1117 (m), 1102 (m), 1066 (w), 1054 (w), 1017 (m), 981 (w), 953 (w), 927 (w) cm^{-1}; ^1H NMR ($CDCl_3$,

Can. J. Chem. Downloaded from www.nrcresearchpress.com by 80.58.250.72 on 09/16/12
For personal use only.

300 MHz): δ 9.91 (s, 1H), 7.43 (d, J = 8.3 Hz, 1H), 6.91 (d, J = 8.3 Hz, 1H), 4.93 (s, 1H), 3.95 (s, 3H), 3.51–3.46 (m, 1H), 3.05 (td, J = 12.5, 5.3 Hz, 1H), 2.95 (br dd, $J \approx$ 12.8, 4.2 Hz 1H), 2.85 (br d, $J \approx$12.1 Hz, 1H), 2.67 (br d, $J \approx$ 17.4 Hz, 1H); 2.53 (br t, $J \approx$ 11.3 Hz, 1H); 2.42 (dd, J = 17.0, 8.7 Hz, 1H), 2.37 (s, 3H), 1.70 (br d, $J \approx$ 12.8 Hz, 1H), 1.54 (br dt, $J \approx$ 12.8, 2.6 Hz, 1H); ^{13}C NMR ($CDCl_3$, 150 MHz): δ 206.07, 190.54, 150.03, 148.00, 132.57, 126.45, 131.08, 110.88, 90.22, 56.17, 55.76, 50.45, 46.38, 43.10, 34.34, 34.18; LRMS-EI (*m/z*): M^+ 301 (23), 273 (23), 272 (20), 258 (34), 231 (29), 230 (72), 215 (40), 167 (30), 150 (26), 149 (100), 112 (21), 83 (28), 71 (36), 70 (84), 69 (20), 57 (52), 55 (26), 44 (41), 43 (49), 41 (31); HRMS-EI (*m/z*): M^+ calcd. for $C_{17}H_{19}NO_4$: 301.1314, found 301.1310.

N*-(2-((5a**S**,6**S**,9a**R**)-1-((1,3-Dioxolan-2-yl)methyl)-6-hydroxy-4-methoxy-5a,6,7,9a-tetrahydrodibenzo[b,d]furan-9a-yl)ethyl)-N-*methylacetamide (52)

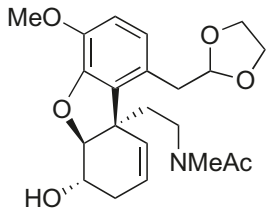

52

A solution of **31** (21 mg, 0.058 mmol) in CH_2Cl_2 (1.5 mL) and pyridine (0.1 mL, 1.239 mmol) was treated with AcCl (25 μL, 0.352 mmol) at 4 °C. The suspension was stirred 2.5 h at 4 °C and 1 h at 25 °C, diluted with CH_2Cl_2 (10 mL) and washed with 1 mol L^{-1} HCl (6 mL), saturated aqueous $NaHCO_3$ solution (6 mL), and brine (6 mL), dried ($MgSO_4$), and evaporated. The crude diacetate was pure, based on ^{1}H NMR spectrum, and was used directly in the next step. A solution of crude diacetate in 0.12 mol L^{-1} solution of MeONa in MeOH was stirred for 4 h and treated with DOWEX 50WX8–100(H^+ form). Filtration, evaporation, and liquid chromatography (AcOEt/MeOH, 5:1) afforded **52** (20 mg, 87%) as a colorless oil. R_f (CH_2Cl_2/MeOH/aqueous, NH_3 100:10:1) 0.51; $[\alpha]_D^{20}$ +17.5 (*c* 1.00, $CHCl_3$); IR ($CHCl_3$): ν 3593 (w), 3024 (w), 3010 (m), 2937 (m), 2896 (w), 2841 (w), 1732 (w), 1633 (s), 1584 (w), 1507 (m), 1463 (w), 1439 (m), 1428 (m), 1402 (m), 1379 (w), 1362 (w), 1315 (w), 1280 (m), 1262 (m), 1255 (m), 1167 (w), 1130 (m), 1091 (m), 1049 (m), 1017 (m), 980 (w), 944 (w), 909 (w) cm^{-1}; ^{1}H NMR ($CDCl_3$, 300 MHz, 2 rotamers): δ 6.85–6.69 (m, 2H), 6.04 (br s, 0.6H), 6.01 (br s, 0.4H), 5.85–5.72 (m, 1H), 5.08–4.99 (m, 1H), 4.56–4.49 (m, 0.6H), 4.35 (d, J = 8.5 Hz, 0.4H), 4.03–3.79 (m, 1H), 7H), 3.65–3.59 (m, 0.6H), 3.40–3.26 (m, 1.4H), 3.10–2.78 (m, 6H), 2.47–2.29 (m, 1H), 2.21–1.78 (m, 3H), 2.00 (s, 1.7H), 1.95 (1.3H). ^{13}C NMR ($CDCl_3$, 150 MHz, 2 rotamers): δ 170.49, 170.39, 145.76, 145.59, 144.14, 144.06, 132.52, 131.73, 129.19, 128.91, 125.58, 125.18, 124.74, 124.53, 124.17, 123.77, 111.90, 111.72, 104.62, 104.60, 90.75, 90.05, 67.90, 67.86, 65.11, 65.05, 56.02, 55.97, 55.95, 51.74, 51.65, 46.84, 44.10, 38.39, 36.51, 36.48, 36.46, 36.37, 33.41, 21.94, 21.06; LRMS-EI (*m/z*): M^+ 403 (1.1), 122 (18), 102 (18), 101 (27), 100 (16), 86 (11), 85 (16), 83 (23), 80 (100), 73 (35), 44 (14), 43 (50); HRMS-EI (*m/z*): M^+ calcd. for $C_{22}H_{29}NO_6$: 403.1995, found 403.2000.

N*-(2-((5a**S**,9a**R**)-1-((1,3-Dioxolan-2-yl)methyl)-4-methoxy-6-oxo-5a,6,7,9a-tetrahydrodibenzo[b,d]furan-9a-yl)ethyl)-N-*methylacetamide (53)

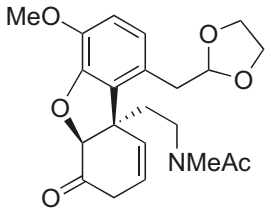

53

A suspension of **52** (30 mg, 0.074 mmol) and IBX (31 mg, 0.11 mmol) in AcOEt (2 mL) was stirred at 80 °C for 4 h, cooled to 25 °C, filtered through Celite (washing with AcOEt), and evaporated to get crude ketone **53** (15 mg) which was used in the next step without further purification. R_f (AcOEt/MeOH, 10:1) 0.30.

N-*(2-((2S**,2a^1**R**,5a**S**)-2-Hydroxy-7-methoxy-5-oxo-1,2,2a,2a1,5,5a-hexahydrophenanthro[4,5-bcd]furan-2a1-yl)ethyl)*-N-*methylacetamide (54)***

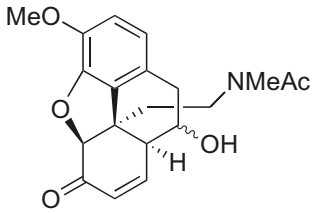

54

A solution of crude ketone **53** (15 mg, 0.037 mmol) in toluene (1 mL) was treated with 50% aqueous TFA (0.3 mL), the mixture was stirred at 50 °C for 4 h, concentrated, and the residue extracted with CH_2Cl_2 (3 × 15 mL). The combined organic layers were washed with saturated aqueous $NaHCO_3$ solution (1 × 2 mL), brine (1 × 2 mL), dried ($MgSO_4$), filtered, and evaporated. Flash column chromatography (CH_2Cl_2/MeOH/aqueous NH_3, 92:8:1) afforded a mixture of alcohols **54** (3 mg, 22% from **52**). R_f (AcOEt/MeOH, 5:1) 0.33; IR ($CHCl_3$): ν 3606 (w), 3386 (w), 3021 (w), 3006 (w), 2934 (w), 1799 (w), 1730 (w), 1686 (m), 1631 (s), 1508 (m), 1453 (m), 1439 (m), 1413 (m), 1363 (w), 1283 (m), 1265 (m), 1159 (w), 1092 (w), 1035 (m), 908 (m) cm^{-1}; ^{1}H NMR ($CDCl_3$, 600 MHz, 1/1 mixture of 2 diastereoisomers): δ 7.13 (dd, J = 10.8, 3.0 Hz, 0.5H), 7.07 (dd, J = 10.2, 4.2 Hz, 0.5H), 7.01 (dd, J = 10.4, 4.0 Hz, 1H), 6.75–6.60 (m, 1H), 6.19 (dd, J = 10.8, 3.0 Hz, 0.5H), 6.14 (dd, J = 10.2, 1.9 Hz, 0.5H), 6.10 (dd, J = 10.4, 2.1 Hz, 1H), 4.82 (s, 1H), 4.78, 4.76 (2s, 1H), 3.88, 3.85 (2s, 3H), 3.87 (s, 3H), 3.83–3.72 (m, 2H), 3.20–2.75 (m, 12H), 2.10–2.00 (10H); LRMS-EI (*m/z*): M^+ 357 (3), 304 (13), 303 (17), 257 (22), 251 (10), 240 (14), 239 (23), 227 (19), 211 (10), 115 (10), 101 (67), 100 (61), 87 (10), 86 (81), 84 (61), 75 (25), 73 (68), 58 (30), 57 (19), 56 (13), 55 (13), 51 (11), 49 (26), 47 (31), 45 (18),

Can. J. Chem. Downloaded from www.nrcresearchpress.com by 80.58.250.72 on 09/16/12
For personal use only.

44 (100), 43 (68), 42 (24), 41 (13); HRMS-EI (*m/z*): M^+ calcd. for $C_{20}H_{23}NO_5$: 357.1576, found 357.1571.

N-*(2-((5aS,6S,9aR)-1-((1,3-Dioxolan-2-yl)methyl)-6-hydroxy-4-methoxy-5a,6,7,9a-tetrahydrodibenzo[b,d]furan-9a-yl)ethyl)*-N-*methyl-2,4-dinitrobenzenesulfonamide (55)*

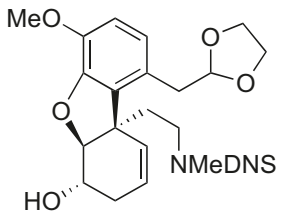

55

A solution of secondary amine **31** (61 mg, 0.169 mmol) in CH_2Cl_2 (1.5 mL) was treated with *i*Pr_2NEt (35 μL, 0.203 mmol) and dinitrobezenesulfonyl chloride (49.6 mg, 0.186 mmol) and stirred for 20 min. The reaction mixture treated with water (1 mL) and extracted with CH_2Cl_2 (3 × 10 mL). The combined organic layers were washed with saturated aqueous Na_2CO_3 solution and brine, dried ($MgSO_4$), filtered, and evaporated. Flash column chromatography (hexanes/AcOEt, 1:1) afforded sulfonamide **55** (51 mg, 51%) as a yellow oil. R_f (hexanes/AcOEt, 1:1) 0.35; $[\alpha]_D^{20}$ = +8.34° (*c* 1.0, $CHCl_3$); IR ($CHCl_3$): ν 3592 (w), 3029 (w), 2983 (w), 2893 (w), 1731 (w), 1556 (s), 1541 (s), 1366 (s), 1351 (s), 1279 (m), 1165 (s), 1131 (m), 1049 (s), 946 (m) cm^{-1}; ^1H NMR ($CDCl_3$, 600 MHz): δ 8.47 (dd, *J* = 6.6., 2.2 Hz, 1H), 8.45 (d, *J* = 2.4 Hz, 1H), 8.10 (d, *J* = 8.5 Hz, 1H), 6.86 (d, *J* = 8.4 Hz, 1H), 6.79 (d, *J* = 8.4 Hz, 1H), 6.04 (dd, *J* = 10.1, 1.7 Hz, 1H), 5.86–5.83 (m, 1H), 5.05 (dd, *J* = 6.3, 3.5, 1H), 4.39 (d, *J* = 8.4, 1H), 4.03 (ddd, *J* = 15.5, 10.1, 7.4, 2H), 3.92–3.85 (m, 3H), 3.87 (s, 3H), 3.41–3.35 (m, 1H), 3.01 (dd, *J* = 14.5, 3.5, 1H), 2.96–2.91 (m, 1H), 2.93 (s, 3H), 2.89 (dd, *J* = 14.5, 6.4, 1H), 2.40 (dt, *J* = 17.4, 5.4, 1H), 2.16–2.11 (m, 2H), 1.99 (td, *J* = 12.1, 4.7, 1H); ^{13}C NMR ($CDCl_3$, 75 MHz): δ 149.60, 148.05, 145.46, 144.07, 137.93, 132.58, 131.61, 128.47, 126.03, 125.72, 124.60, 124.03, 119.72, 111.80, 104.39, 90.24, 67.77, 64.99, 64.94, 55.87, 51.50, 46.38, 37.64, 36.33, 29.31; LRMS-EI (*m/z*): M^+ 591 (12), 147 (16), 136 (24), 91 (14), 89 (14), 77 (13), 73 (100); HRMS-EI (*m/z*): M^+ cald. for $C_{26}H_{29}N_3O_{11}S$: 591.1507, found 591.1522.

N-*(2-((5aS,9aR)-1-((1,3-Dioxolan-2-yl)methyl)-4-methoxy-6-oxo-5a,6,7,9a-tetrahydrodibenzo[b,d]furan-9a-yl)ethyl)*-N-*methyl-2,4-dinitrobenzenesulfonamide (56)*

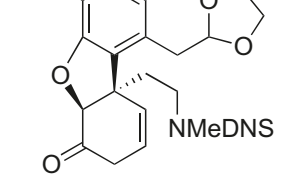

56

A suspension of alcohol **55** (64 mg, 0.11 mmol) and IBX (45 mg, 0.16 mmol) in AcOEt (3 mL) was stirred at 80 °C for 4 h, cooled to 25 °C, and filtered through Celite (washing with AcOEt) affording crude **56** (60 mg), which was used without further purification. R_f (hexanes/AcOEt, 1:1) 0.23; IR ($CHCl_3$): ν 3101 (w), 3032 (w), 2981 (w), 2893 (w), 1738 (m), 1556 (s), 1541 (s), 1508 (m), 1366 (s), 1351 (s), 1283 (m), 1164 (s), 1131 (m), 1044 (m), 908 (s) cm^{-1}; ^1H NMR ($CDCl_3$, 600 MHz): δ 8.49 (dd, *J* = 8.6, 1.9 Hz, 1H); 8.44 (d, *J* = 1.9 Hz, 1H), 8.15 (d, *J* = 8.6 Hz, 1H), 6.85 (d, *J* = 8.4 Hz, 1H), 6.77 (d, *J* = 8.4 Hz, 1H), 6.03 (d, *J* = 9.9 Hz, 1H), 5.87 (ddd, *J* = 10.0, 3.9, 3.9 Hz, 1H), 5.02 (dd, *J* = 5.6, 4.1, 1H), 4.81 (s, 1H); 4.00–3.96 (m, 2H), 3.92–3.84 (m, 2H), 3.87 (s, 3H), 3.40–3.35 (m, 1H), 3.09 (ddd, *J* = 19.31, 3.86, 1.99, 1H), 3.07–3.02 (m, 2H), 2.96–2.93 (m, 1H), 2.94 (s, 3H), 2.30–2.22 (m, 2H); ^{13}C NMR ($CDCl_3$, 150 MHz): δ 203.68, 149.70, 148.09, 146.74, 143.84, 137.65, 132.65, 129.82, 128.73, 126.17, 124.71, 124.53, 124.12, 119.77, 112.67, 104.37, 87.68, 64.99, 64.97, 57.38, 56.17, 46.37, 37.30, 36.86, 36.14, 35.05; LRMS-EI (*m/z*): M^+ 591 (12), 147 (16), 136 (24), 91 (14), 89 (14), 77 (13), 73 (100); HRMS-EI (*m/z*): M^+ calcd. for $C_{26}H_{29}N_3O_{11}S$: 591.1507, found 591.1522.

(2a²R,6aS,9aS)-5-Methoxy-2a²-(2-(N-methyl-2,4-dinitrophenylsulfonamido)ethyl)-7-oxo-1,2,2a²,6a,7,9a-hexahydrophenanthro[4,5-bcd]furan-1-yl methanesulfonate (57)

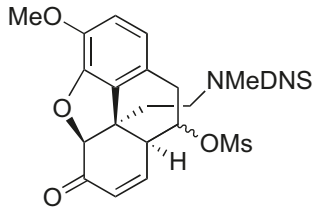

57

A solution of crude **56** (15 mg, 0.025 mmol) in toluene (1 mL) was treated with 50% aqueous TFA (0.14 mL) and the biphasic mixture was stirred at 50 °C for 2 h. The volatiles were removed in vacuo, the residue was dissolved in CH_2Cl_2 (1 mL) and treated with *i*Pr_2NEt (5 μL, 0.038 mmol) and MsCl (2.4 μL, 0.031 mmol) at 0 °C. The mixture was stirred for 30 min at 0 °C, treated with saturated aqueous NH_4Cl solution (1 mL) and extracted with CH_2Cl (3 × 5 mL). The combined organic layers were washed with brine, dried (Na_2SO_4), filtered, and evaporated. Flash column chromatography ($CHCl_3$/EtOAc, 3:1) afforded **57** (1 mg, 6% from **55**). The ^1H NMR spectrum was identical to one reported in the literature.[36]

R_f (hexanes/AcOEt, 1:3) 0.51; ^1H NMR ($CDCl_3$, 600 MHz): δ 8.49–8.44 (m, 2H); 8.08 (d, *J* = 8.4 Hz, 1H), 6.90 (dd, *J* = 10.3, 4.0 Hz, 1H), 6.77 (d, *J* = 8.6 Hz, 1H), 6.73 (d, *J* = 8.6 Hz, 1H), 6.20 (dd, *J* = 10.6, 2.3 Hz, 1H), 4.86 (s, 1H), 3.88 (s, 3H), 3.51–3.43 (m, 1H), 3.23–3.18 (m, 1H), 3.16 (s, 3H), 3.16 (s, 1H), 3.12–3.09 (m, 1H), 2.94 (s, 3H), 2.89–2.87 (m, 1H), 2.26–2.18 (m, 2H).

Can. J. Chem. Downloaded from www.nrcresearchpress.com by 80.58.250.72 on 09/16/12
For personal use only.

N-*(2-((2a[1]*R*,5a*S*)-7-Methoxy-5-oxo-1,2a1,5,5a-tetrahydrophenanthro[4,5-bcd]furan-2a1-yl)ethyl)*-N-*methyl-2,4-dinitrobenzenesulfonamide (58) and* N-*(2-((2a[1]*R*,5a*S*)-7-methoxy-5-oxo-2a1,4,5,5a-tetrahydrophenanthro[4,5-bcd]furan-2a1-yl)ethyl)*-N-*methyl-2,4-dinitrobenzenesulfonamide (59)*

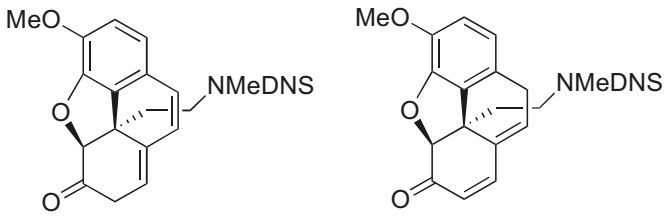

59 **58**

A solution of crude **56** (10 mg, 0.017 mmol) in toluene (1 mL) was treated with 50% aqueous TFA (0.1 mL), and the biphasic mixture was stirred at 50 °C for 2 h. The volatiles were removed in vacuo, the residue was dissolved in CH_2Cl_2 (1 mL), cooled to 0 °C, treated with *i*Pr_2NEt (12 μL, 0.085 mmol) and MsCl (5 μL, 0.077 mmol), and stirred for 30 min. The reaction mixture was treated with saturated aqueous NH_4Cl solution (1 mL) and extracted with CH_2Cl_2 (3 × 5 mL). The combined organic layers were washed with brine, dried (Na_2SO_4), filtered, and evaporated. Flash column chromatography ($CHCl_3$/AcOEt, 3:1) afforded **58** (3 mg, 33% from **55**) and a mixture of **58/59** ≈ 1:1.5 (2 mg, 22% from **55**).

*Data for **58***

R_f ($CHCl_3$/AcOEt, 2:1) 0.47; IR ($CHCl_3$): ν 3101 (w), 3026 (w), 3012 (w), 2961 (w), 2930 (w), 1784 (w), 1730 (m), 1686 (m), 1641(w), 1604 (w), 1556 (s), 1541 (s), 1506 (m), 1455 (w), 1440 (w), 1367 (s), 1350 (s), 1265 (m), 1235 (m), 1162 (s), 1102 (s), 1046 (m), 1008 (m), 963 (w), 950 (w), 905 (w) cm^{-1}; ^1H NMR ($CDCl_3$, 600 MHz): δ 8.47–8.43 (m, 1H), 8.07 (d, *J* = 7.9 Hz, 1H), 7.26 (1H overlapped with a signal of residual $CHCl_3$), 6.75 (d, *J* = 7.9 Hz, 1H), 6.71 (d, *J* = 7.9 Hz, 1H), 6.40 (d, *J* = 7.2 Hz, 1H), 5.98 (d, *J* = 10.2 Hz, 1H), 4.99 (s, 1H), 3.87 (s, 3H), 3.59 (d, *J* = 20.0 Hz, 1H), 3.46–3.38 (m, 2H), 3.14–3.07 (m, 1H), 2.91 (s, 3H), 2.19 (td, *J* ≈ 12.1, 4.9 Hz, 1H), 2.11 (td, *J* ≈ 12.1, 3.8 Hz, 1H); ^{13}C NMR ($CDCl_3$, 150 MHz): δ 193.43, 149.89, 148.26, 145.34, 143.24, 139.20, 137.70, 131.26, 126.36, 143.96, 133.51, 131.26, 126.22, 120.51, 119.93, 113.95, 125.28, 86.86, 56.84, 47.91, 46.70, 37.67, 35.28, 30.65; LRMS-EI (*m/z*): M^+ 527 (9), 266 (32), 252 (22), 251 (56), 250 (21), 240 (65), 239 (55), 238 (62), 235 (26), 231 (21), 225 (54), 223 (54), 211 (25), 168 (44), 152 (24), 139 (41), 76 (42), 75 (50), 74 (27), 64 (100), 63 (34), 51 (42), 45 (44), 44 (85); HRMS-EI (*m/z*): M^+ calcd. for $C_{24}H_{21}N_3O_9S$: 527.0998, found 527.1018.

*Data for **59***

R_f ($CHCl_3$/AcOEt, 2:1) 0.53; ^1H NMR ($CDCl_3$, 600 MHz, mixture of **58/59** ≈ 1:1.3): δ 8.50–8.43 (m, overlapped with signals of **58**, 2H), 8.14 (d, *J* = 9.1 Hz, 1H), 6.74 (d, *J* = 9.1 Hz, 1H), 6.69 (d, *J* = 9.1 Hz, 1H), 6.45 (d, *J* = 9.1 Hz, 1H), 6.17 (d, *J* = 9.1 Hz, 1H), 5.77 (d, *J* = 7.2 Hz, 1H), 5.28 (s, 1H), 3.91 (s, 3H), 3.48–3.36 (m, overlapped with signals of **58**, 2H), 3.30–3.20 (m, 1H); 2.92 (dd, *J* = 16.2, 7.2 Hz, partially overlapped with a signal of MeN of **58**, 1H), 2.89 (s, 3H), 2.22–2.07 (m, overlapped with signals of **58**, 2H).

N-*(2-((5a*S*,6*S*,9a*R*)-1-(2,2-Dimethoxyethyl)-4-methoxy-6-oxo-5a,6,7,9a-tetrahydrodibenzo[b,d]furan-9a-yl)ethyl)*-N-*methyl-2,4-dinitrobenzenesulfonamide (62)*

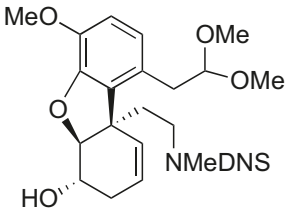

62

A solution of **55** (42 mg, 0.071 mmol) and *p*TsOH (6 mg, 0.035 mmol) in MeOH was refluxed for 3 d, cooled to 25 °C, treated with with saturated aqueous Na_2CO_3 solution (2 mL), and extracted with CH_2Cl_2 (3 × 10 mL). The combined organic layers were washed with brine, dried (Na_2SO_4), filtered, and evaporated. Flash column chromatography (hexanes/AcOEt, 1:3) afforded dimethyl acetal **62** (36 mg, 86%) as a yellow oil whose ^1H NMR spectrum was identical to that of its enantiomer reported in the literature.[36]

N-*(2-((5a*S*,9a*R*)-1-(2,2-Dimethoxyethyl)-4-methoxy-6-oxo-5a,6,7,9a-tetrahydrodibenzo[b,d]furan-9a-yl)ethyl)*-N-*methyl-2,4-dinitrobenzenesulfonamide (63)*

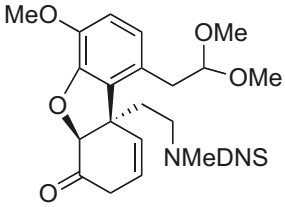

63

A suspension of dimethyl acetal **62** (36 mg, 0.061 mmol) and IBX (25 mg, 0.91 mmol) in AcOEt (2 mL) was stirred at 80 °C for 3 h. The reaction mixture was cooled to 25 °C and filtered through Celite (washing with AcOEt) affording crude ketone **63** (33 mg, 91%) as a yellow oil which was used in the next step without further purification. R_f (hexanes/AcOEt, 1:1) 0.35; $[\alpha]_D^{20}$ = +25.5° (*c* 1.0, $CHCl_3$); IR ($CHCl_3$): 2982 (w), 2936 (w), 1731 (s), 1556 (m), 1541 (m), 1507 (w), 1374 (m), 1351 (m), 1267 (m), 1164 (m), 1046 (s), 908 (s) cm^{-1}; ^1H NMR ($CDCl_3$, 300 MHz): δ 8.49 (dd, *J* = 8.6, 2.2 Hz, 1H), 8.44 (d, *J* = 2.0 Hz, 1H), 8.14 (d, *J* = 8.6 Hz, 1H), 6.79 (d, *J* = 8.6 Hz, 1H), 6.76 (d, *J* = 8.6 Hz, 1H), 6.03 (br d, *J* = 10.0 Hz, 1H), 5.87 (ddd, *J* = 10.0, 3.9, 3.9 Hz 1H), 4.82 (s, 1H), 4.50 (t, *J* = 5.3 Hz, 1H), 3.88 (s, 3H), 3.35 (s, 3H), 3.32 (s, 3H), 3.34 (m, 1H), 3.17–3.01 (m, 3H); 2.94 (s, 3H); 2.86–2.83 (m, 1H); 2.27–2.20 (m, 2H); ^{13}C NMR ($CDCl_3$, 75 MHz): δ 203.85, 149.77, 146.81, 143.79, 137.75, 132.77, 129.90, 128.96, 126.29, 125.15, 124.60,

Can. J. Chem. Downloaded from www.nrcresearchpress.com by 80.58.250.72 on 09/16/12
For personal use only.

124.47, 119.90, 112.77, 105.60, 87.72, 57.59, 56.29, 54.43, 53.70, 46.50, 37.43, 36.77, 35.99, 35.14; LRMS-EI (*m*/*z*): M^+ 591 (1), 327 (3), 270 (9), 248 (100), 231 (55), 227 (10), 203 (19), 187 (5), 167 (25), 163 (7) 149 (72), 128 (69), 127 (51), 122 (38.9), 105 (57); HRMS-EI (*m*/*z*): M^+ calcd. for $C_{26}H_{29}N_3O_{11}S$: 591.1523, found 591.1531.

N-*(2-((2a[1]*R*,5a*S*)-7-Methoxy-5-oxo-1,2a1,5,5a-tetrahydrophenanthro[4,5-*bcd*]furan-2a1-yl)ethyl)*-N-*methyl-2,4-dinitrobenzenesulfonamide (58) and (2a[2]*R*,6a*S*,9a*S*)-5-methoxy-2a[2]-(2-(*N*-methyl-2,4-dinitrophenylsulfonamido)ethyl)-7-oxo-1,2,2a[2],6a,7,9a-hexahydrophenanthro[4,5-*bcd*]furan-1-yl methanesulfonate (57)

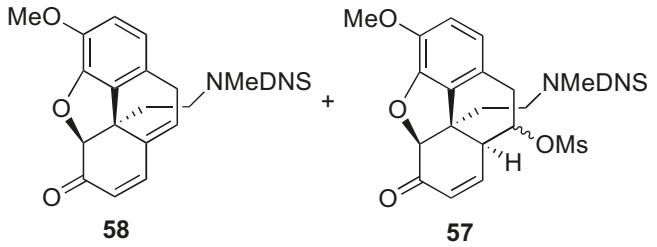

A solution of **63** (13 mg, 0.022 mmol), 50% aqueous trifluoroacetic acid (0.12 mL) in toluene was heated to 50 °C for 2 h, cooled to 25 °C and concentrated. The volatiles were removed in vacuo, the residue was dissolved in CH_2Cl_2 (1 mL) and treated with *i*Pr_2NEt (6 μL, 0.034 mmol) and MsCl (2 μL, 0.031 mmol) at 0 °C. The mixture was stirred for 30 min at 0 °C, treated with saturated aqueous NH_4Cl solution (1 mL) and extracted with CH_2Cl (3 × 7 mL). The combined organic layers were washed with brine, dried (Na_2SO_4), filtered, and evaporated. Flash column chromatography (hexanes/AcOEt, 1:1) afforded **57** (3.6 mg, 28% from **62**) and **58** (3.6 mg, 24% from **62**). The ^{1}H NMR spectrum of **57** was identical to that reported in the literature for its enantiomer.[36]

ent-*Neopinone (61)*

A solution of **57** and **58** (6 mg, 0.01 mmol), *i*Pr_2NEt (5.25 μL, 0.03 mmol) and thioglycolic acid (1 μL, 0.014 mmol) in CH_2Cl_2 was stirred at 0 °C for 30 min, treated with saturated aqueous Na_2CO_3 and stirred for 30 min at 25 °C. The solution was extracted with CH_2Cl_2 (3 × 7 mL) and the combined organic layers were washed with brine, dried (Na_2SO_4), filtered, and evaporated. The product was matched with a sample of neopinone standard.[37] R_f (CH_2Cl_2/EtOH, 85:15) 0.4.

Acknowledgements

The authors are grateful to the following agencies for financial support of this work: Noramco, Inc., Natural Sciences and Engineering Research Council of Canada (NSERC) (Idea to Innovation and Discovery Grants); Canada Research Chair Program, Canada Foundation for Innovation (CFI), Research Corporation, TDC Research, Inc., TDC Research Foundation, and Brock University. One of us (J.D.) is grateful to the Swiss National Foundation for a postdoctoral fellowship.

References

(1) Rinner, U.; Hudlicky, T. *Top. Curr. Chem.* **2011**, in press. doi:10.1007/128_2011_133.
(2) Erhard, T.; Ehrlich, G.; Metz, P. *Angew. Chem. Int. Ed.* **2011** *50* (17), 3892. doi:10.1002/anie.201007448.
(3) Zezula, J.; Hudlicky, T. *Synlett* **2005** 388.
(4) Gates, M.; Tschudi, G. *J. Am. Chem. Soc.* **1952** *74* (4), 1109. doi:10.1021/ja01124a538.
(5) Gates, M.; Tschudi, G. *J. Am. Chem. Soc.* **1956** *78* (7), 1380. doi:10.1021/ja01588a033.
(6) Holmes, H. L. The morphine alkaloid. In *The Alkaloids, Chemistry and Physiology;* Manske, R. H. F; Holmes, H. L., Eds.; Academic Press Inc.: New York, 1952; Vol. 2, pp 1–159.
(7) Butora, G.; Hudlicky, T. The Story of Morphine Structure Elucidation: One Hundred Years of Deductive Reasoning. In *Organic Synthesis: Theory and Applications;* Hudlicky, T., Ed.; JAI Press: Stamford, 1998; Vol. 4, pp 1–51.
(8) Gulland, J. M.; Robinson, R. *Mem. Proc. Manchester Lit. Phil. Soc.* **1925** *69*, 79.
(9) Kapoor, L. D. *Opium Poppy: botany, chemistry, and pharmacology;* The Haworth Press: New York, 1995; pp. 1–326.
(10) Bryant, R. J. *Chem. Ind.* **1988** *5*, 146.
(11) Booth, M. *Opium: A History;* St. Martin's Press: New York, 1998.
(12) Sertürner, F. W. *Tromsdorf J. Pharm.* **1806** *14*, 47.
(13) Sertürner, F. W. *Gilbert's. Ann. Phys.* **1817** *25*, 56.
(14) Taber, D. F.; Neubert, T. D.; Schlecht, M. F. *Strategies and Tactics in Organic Synthesis;* Harmata, M., Ed.; Elsevier; Amsterdam: 2004; Vol. 5, pp 353–389.
(15) Blakemore, P. R.; White, J. D. *Chem. Commun. (Camb.)* **2002** (11): 1159. doi:10.1039/b111551k.
(16) Novak, B. H.; Hudlicky, T.; Reed, J. W.; Mulzer, J.; Trauner, D. *Curr. Org. Chem.* **2000** *4* (3), 343. doi:10.2174/1385272003376292.
(17) Hudlicky, T.; Butora, G.; Fearnley, S. P.; Gum, A. G.; Stabile, M. R. A historical perspective of morphine syntheses; In *Studies Natural Products Chemistry;* Atta-ur-Rahman, Ed.; Elsevier: Amsterdam, 1996; Vol. 18, pp 43–154.
(18) Waldman, H. *Organic Synthesis Highlights* **1995** *II*, 407.
(19) Maier, M. *Organic Synthesis Highlights* **1995** *II*, 357. doi:10.1002/9783527619948.ch38.
(20) Zylstra, G. J.; Gibson, D. T. *J. Biol. Chem.* **1989** *264*, 14940.
(21) Omori, A. T.; Finn, K. J.; Leisch, H.; Carroll, R. J.; Hudlicky, T. *Synlett* **2007** 2859.
(22) Leisch, H.; Omori, A. T.; Finn, K. J.; Gilmet, J.; Bissett, T.; Ilceski, D.; Hudlický, T. *Tetrahedron* **2009** *65* (47), 9862. doi:10.1016/j.tet.2009.09.052.
(23) Toth, J. E.; Fuchs, P. L. *J. Org. Chem.* **1987** *52* (3), 473. doi:10.1021/jo00379a038.
(24) Toth, J. E.; Fuchs, P. L. *J. Org. Chem.* **1986** *51* (13), 2594. doi:10.1021/jo00363a037.
(25) Hamann, P. R.; Toth, J. E.; Fuchs, P. L. *J. Org. Chem.* **1984** *49* (20), 3865. doi:10.1021/jo00194a051.
(26) Toth, J. E.; Hamann, P. R.; Fuchs, P. L. *J. Org. Chem.* **1988** *53* (20), 4694. doi:10.1021/jo00255a008.
(27) As this project was nearing completion in late 2010 a report by Fukuyama appeared describing a conceptually identical approach also via dienone of type **9** (see ref. 36).
(28) Deljac, A.; MacKay, W. D.; Pan, C. S. J.; Wiesner, K. J.; Wiesner, K. *Can. J. Chem.* **1972** *50* (5), 726. doi:10.1139/v72-111.
(29) For definition of the term "redundant operation" see: Hudlicky,

T.; Reed, J. W. *The Way of Synthesis;* VCH: Meinhein, 2007; pp 107–109.
(30) Hudlicky, T. *Chem. Rev.* **1996** *96* (1), 3. doi:10.1021/cr950012g.
(31) Littke, A. F.; Fu, G. C. *J. Am. Chem. Soc.* **2001** *123* (29), 6989. doi:10.1021/ja010988c.
(32) Littke, A. F.; Fu, G. C. *J. Org. Chem.* **1999** *64* (1), 10. doi:10.1021/jo9820059.
(33) Christmann, U.; Vilar, R. *Angew. Chem. Int. Ed.* **2005** *44* (3), 366. doi:10.1002/anie.200461189.
(34) In our earlier synthesis of codeine (ref. 22), intermediate **5**, Fig. 2, was prepared in 82% yield by an intramolecular Heck coupling using $Pd(OAc)_2$, 1,1′-bis(diphenylphosphino)ferrocene (dppf) and Ag_2CO_3 in boiling toluene. In that reaction the isomerization of the double bond was not observed. These conditions, however, when used for the cyclization of **23** to **24**, led to low yields and formation of side-products. Optimization of this reaction (**23** → **24**) revealed that Fu's conditions (see refs. 31 and 32) using $Pd_2(dba)_3$, $(t\text{Bu})_3\text{P}$, and K_2CO_3 in boiling toluene were superior to other methods and led reproducibly to high yields. The reaction proceeds faster in boiling *m*-xylene; $Pd(OAc)_2$ and $Cs_2(CO)_3$ can be used instead of $Pd_2(dba)_3$ and K_2CO_3, respectively, while use of Ag_2CO_3 leads to a formation of side products. Starting aldehydes used in the formation of **5** and **24** are both electronically and sterically very different. The reaction leading to **5** and promoted by Ag_2CO_3 likely follows a cationic Heck mechanism, which appears to be unfavorable for the cyclization of **23**. The cyclization of **23** to **24** with $(t\text{Bu})_3\text{P}$ likely involves the formation of the monophosphine complex $[Pd(Pt\text{Bu})_3]$. For the detailed discussion of the reactivity of such monoligated palladium complexes see ref. 33 and refs. quoted there.
(35) Gilmet, J. Enantiodivergent chemoenzymatic synthesis of balanol and approaches to the synthesis of (+)-Codeine. M.Sc. Thesis, Brock University, St. Catharines, Ont., 2009.
(36) Koizumi, H.; Yokoshima, S.; Fukuyama, T. *Chem. Asian J.* **2010** *5* (10), 2192. doi:10.1002/asia.201000458.
(37) Barber, R. B.; Rapoport, H. *J. Med. Chem.* **1976** *19* (10), 1175. doi:10.1021/jm00232a002.

Can. J. Chem. Downloaded from www.nrcresearchpress.com by 80.58.250.72 on 09/16/12
For personal use only.

REVIEW / SYNTHÈSE

Improvements in MR imaging of solids through gradient waveform optimization

Marco L.H. Gruwel, Peter Latta, and Boguslaw Tomanek

Can. J. Chem. Downloaded from www.nrcresearchpress.com by Xi'an Jiaotong University on 09/19/12
For personal use only.

Abstract: Magnetic resonance imaging (MRI) is known to provide a useful approach for the exploration of the chemistry and dynamics of a wide range of soft condensed materials. However, its application to solids has been limited to those materials with relatively narrow resonances. The time needed to obtain an image of a solid with a given resolution and signal-to-noise ratio (SNR) is directly proportional to the line width of the resonance. For MRI to become practical for the imaging of solids it will have to rely on the development and use of MR sequences that avoid the issues raised by line broadening of the resonance. In this paper we review the latest contributions towards MR imaging of solids from our laboratory, in particular, applications using optimized gradient waveforms. Acoustic noise reduction and SNR improvement obtained with modifications of the standard single-point imaging sequence are presented and discussed using examples.

Key words: MRI, solids, gradient shape, gradient ramp, sound pressure, signal-to-noise ratio.

Résumé : L'imagerie par résonance magnétique (IRM) est connue comme une approche utile pour explorer la chimie et la dynamique d'un grand nombre de matériaux condensés et mous. Toutefois, son application aux solides a été limitée aux matériaux avec des résonances relativement étroites. Le temps requis pour obtenir une image d'un solide avec une résolution et un rapport de signal à bruit (RSB) donnés est directement proportionnel à la largeur de la raie de résonance. Pour que l'IRM devienne pratique dans la production d'images de solides, il faudra développer et utilise des séquences de résonance magnétique qui éviteront les problèmes liés à l'élargissement des raies de résonance. Dans ce travail, on présente une revue des plus récentes contributions de notre laboratoire à l'IRM des solides, en particulier aux applications utilisées pour optimiser le gradient des formes des ondes. On présente la réduction acoustique du bruit et l'amélioration du rapport signal à bruit obtenues par modifications de la séquence d'imagerie habituelle avec point localisé et on en discute à l'aide d'exemples.

Mots-clés : imagerie par résonance magnétique (IRM), solides, gradient de forme, gradient de forme, pression du son, rapport signal à bruit.

[Traduit par la Rédaction]

Introduction

Over the last decades magnetic resonance imaging (MRI) has become a major diagnostic tool in medicine and biomedical research. Nearly all applications involve the study of ^{1}H magnetization in soft water-containing tissues. Within these soft tissues, water mobility is more or less unrestricted, resulting in a typically narrow ^{1}H resonance and a corresponding long transverse relaxation time (T_2). Thus, the Hamiltonian best describing these spin systems consists of one major contribution, the Zeeman interaction.[1] Perturbations to the Hamiltonian usually do not have to be considered unless measurements are performed near interfaces, where susceptibility effects from metal parts or air can be large.[2] Because of this high degree of water mobility, spatial information can be obtained using frequency encoding techniques.[3] However, in solid materials the line width of the resonance is perturbed by large anisotropic interactions (approximately in the order of a few kHz), therefore, frequency encoding techniques result in images with poor resolution and sensitivity.

Although many different experimental approaches have been used to reduce unwanted line broadening, standard NMR line-narrowing techniques such as CPMAS, multipulse sequences, etc.,[4,5] require additional attention to spatially dependent gradient interactions modulating image

Received 23 September 2010. Accepted 21 January 2011. Published at www.nrcresearchpress.com/cjc on 6 July 2011.

M.L.H. Gruwel and B. Tomanek. NRC-CNRC Institute for Biodiagnostics, 435 Ellice Avenue, Winnipeg, MB R3B 1Y6 Canada.
P. Latta. NRC-CNRC Institute for Biodiagnostics, 435 Ellice Avenue, Winnipeg, MB R3B 1Y6 Canada; Slovak Academy of Sciences, Institute for Measurement Science, Dúbravská cesta 9, SK-84219 Bratislava, Slovakia.

Corresponding author: Marco L.H. Gruwel (e-mail: marco.gruwel@nrc-cnrc.gc.ca).

This article is part of a Special Issue dedicated to Professor Roderick E. Wasylishen. We are pleased to contribute this paper to the Special Issue recognizing the scientific career of Rod Wasylishen, particularly for his contributions to solid-state magnetic resonance.

Can. J. Chem. Downloaded from www.nrcresearchpress.com by Xi'an Jiaotong University on 09/19/12
For personal use only.

Fig. 1. (A) Single point imaging (SPI) sequence showing RF and gradient sections. During RF excitation the gradient is kept stable (interval *P*) while a single datum point is collected at an encoding time t_p. One set of encoding gradients is shown and up to three gradients can be used to perform 3D spatial encoding. The time intervals *R* and *P* represent the gradient ramp and plateau time, respectively. (B) As in (A), except sinusoidal gradient ramps were used.

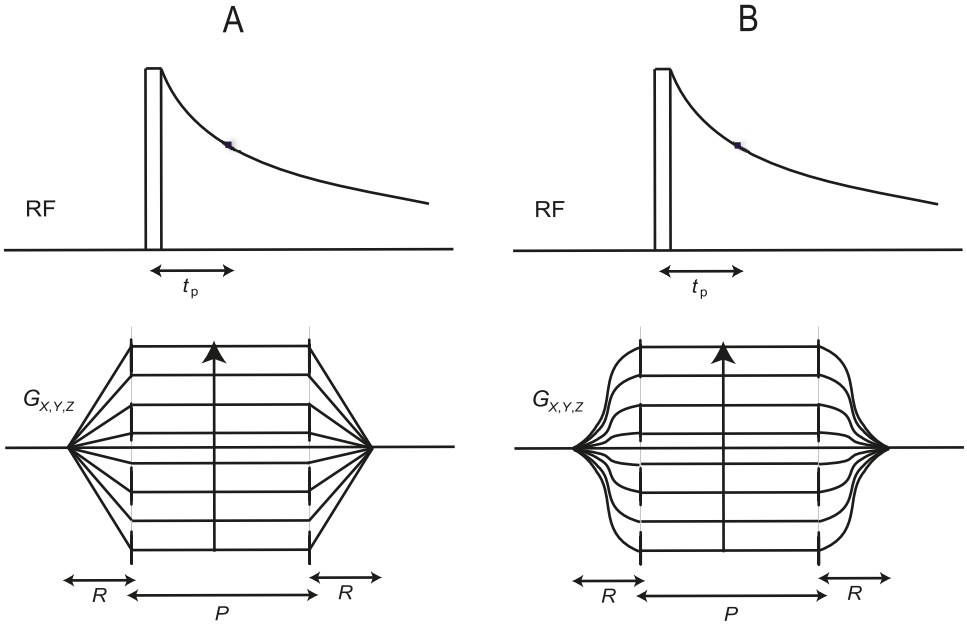

resolution. Also, these techniques are not suitable for larger objects and in vivo MR imaging of, for example, human bones or teeth. Emid and Creyghton[6] proposed a spatial encoding technique based on pure phase encoding in combination with the collection of one point of the free induction decay after RF excitation, the so-called single point imaging (SPI) technique. As only one point of the NMR signal is collected, any convoluting effects from time-dependent perturbations such as the chemical shift, quadrupolar effect, etc., will not be observed in the acquired data. Resolution and sensitivity of the image will thus only be determined by the strength of the applied gradient.[7] In general, when the gradient switching time becomes longer than the longitudinal relaxation (T_2*) of the sample, SPI will provide a superior signal-to-noise ratio (SNR) compared with frequency-encoding techniques. The only drawback of the SPI pure phase-encoding technique is the replacement of a single line of frequency-encoded data with individual phase-encode steps, each requiring a relaxation delay. However, for many solids spin-lattice relaxation times (T_1) are relatively short, allowing fast repetition of the phase-encode steps without the risk of signal saturation. As an example we will show images of human teeth in which the water T_1 is relatively short vide infra.

A typical SPI experiment consists of three gradients, one for each spatial dimension, as shown in Fig. 1A. As soon as the ramped gradient has reached its plateau value, a RF pulse is applied and after an encoding time interval t_p (~50–400 μs) a single datum point is collected. After the gradients are ramped down and sufficient time for T_1 relaxation is given, the experiment can be repeated. Typically repetition times range from 1 to 20 ms. The signal intensity *S* from the spin density ρ of a voxel in an SPI image acquired with a repetition time TR is given by[8]

$$[1] \qquad S_{SPI}(t_p) = \rho \exp\left(-\frac{t_p}{T_2^*}\right)\left[\frac{1-\exp\left(-\frac{TR}{T_1}\right)}{1-\cos\alpha\,\exp\left(-\frac{TR}{T_1}\right)}\sin\alpha\right]$$

where α is the RF flip angle. Thus, $S_{SPI}(t_p)$ has an optimum for $\cos\alpha = \exp\left(-\frac{TR}{T_1}\right)$. Transverse and longitudinal weighting of the image can be introduced through careful selection of t_p and TR. For comparison, the signal intensity in a standard frequency-encoded spin-echo experiment can be described by

$$[2] \qquad S_{SE}(TE) = \rho \exp\left(-\frac{TE}{T_2}\right)\left[1-\exp\left(\frac{TR}{T_1}\right)\right]$$

with TE defining the echo time, and assuming that diffusion can be ignored. Thus, in the case where TR is long and (or) the RF flip angle α is small:

$$[3] \qquad S_{SPI}(t_p) = \rho \exp\left(-\frac{t_p}{T_2^*}\right)$$

resulting in a T_2* weighted spin-density image in SPI. Frequency-encoding experiments use typical echo times of ~10 ms, whereas SPI-encoding times typically are ~100 μs. Gravina and Cory[7] discuss these differences in more detail.

In general, MRI experiments generate acoustic noise owing to the rapid switching of the magnetic field ($\frac{dB}{dt}$) in the gradient coils, inducing strong Lorentz's forces causing mechanical vibrations in the gradient coils and cryostat. SPI, with its high gradient duty cycle and relatively long experiment time, can cause dangerous levels of mechanical vibrations. This, of course, sets a limit on the speed of the data acquisition and could severely hamper SPI applications on medical MRI systems because of acoustic noise exposure limits set by

Can. J. Chem. Downloaded from www.nrcresearchpress.com by Xi'an Jiaotong University on 09/19/12
For personal use only.

regulatory bodies. To improve the efficiency of the SPI sequence and significantly reduce the mechanical vibrations, the single point ramped imaging with the T_1 enhancement (SPRITE) technique was introduced[9] followed by later modifications.[10–12] SPRITE uses gradual gradient switching (step-function-like), avoiding large gradient ramps between successive phase-encoding steps. However, because of the large currents flowing through the gradient coils, overheating can become an issue for long experiments. Additional cooling delays will need to be introduced into the experiment to avoid equipment damage.[13]

Recently, we introduced an SPI modification different from SPRITE, using a sinusoidal gradient ramp that efficiently attenuates acoustic noise and at the same time has a lower power deposition into the gradient set.[14] In a second modification we introduced SPI/VTI, an SPI modification using a variable phase-encoding time,[15] introducing a substantial gain in SNR. Combining SPI/VTI with the use of soft shaped gradients resulted in an efficient pulse sequence for high-resolution solid-state MRI. These methods are described in detail in the following.

Theory

Acoustic noise reduction

Gradient coils in MR scanners have been observed to show a linear response to applied gradient pulses.[16] Each gradient coil in each MR scanner can thus be characterized by its corresponding frequency response function (FRF).[14,16] The product of the FRF and the frequency spectrum of the gradient pulse determines the frequency output of the gradient set. The FRF of a gradient coil can be determined as the Fourier transform of its response to a frequency-limited sinc-shaped gradient pulse. This type of excitation can be achieved using a 10 ms long 40-lobed sinc pulse that has a flat frequency spectrum in the human audible, most sensitive frequency range of 0–4000 Hz. Figure 2 shows the typical FRFs for a transverse gradient coil (Fig. 2A) and the longitudinal coil (Fig. 2B).

The gradient pulse program for SPI is straightforward and can be described as a train of trapezoids with amplitude A, ramp time R, a plateau duration P, and a repetition time TR (see Fig. 1A). Assuming these phase encode gradients are an even periodical function, the gradient train $G(t)$ can be written as a Fourier series:[17]

$$[4] \qquad G(t) = \frac{a_0}{2} + \sum_{n=1}^{\infty} a_n \cos\left(nt\frac{2\pi}{\mathrm{TR}}\right)$$

$$[5] \qquad a_n = \frac{2}{\mathrm{TR}}\int_0^{\mathrm{TR}} G(t)\,\cos\left(nt\frac{2\pi}{\mathrm{TR}}\right)\mathrm{d}t, \quad \text{with } n = 0, 1, 2, \ldots$$

where a_n (n = 0, 1, 2, ...) are the expansion coefficients of the Fourier series. Expressions for the coefficients a_n for the specific case of linear and sinusoidally ramped gradients was presented by Latta et al.[14] Each coefficient a_n corresponds to a frequency $f_n = \frac{n}{\mathrm{TR}}$. The spectral power (sound pressure level, SPL) for a specific gradient pulse can now be calculated for various combinations of $\frac{R}{\mathrm{TR}}$ and $\frac{P}{\mathrm{TR}}$. It has been shown that the power of the fundamental frequency, corresponding to $f_1 = (\mathrm{TR})^{-1}$, is relatively insensitive to changes in $\frac{R}{\mathrm{TR}}$ and $\frac{P}{\mathrm{TR}}$. However, for the remaining frequencies a minimum value in the total power can be obtained.[14] Moving the fundamental frequency to the low-frequency range of the FRF of the gradient set by fixing $\mathrm{TR} > f_{\mathrm{R}}^{-1}$, with f_{R} the cut-off frequency in the FRF, audible acoustic noise is significantly reduced. In addition, choosing sufficiently long P and R values adds to the total accomplished acoustic noise reduction.

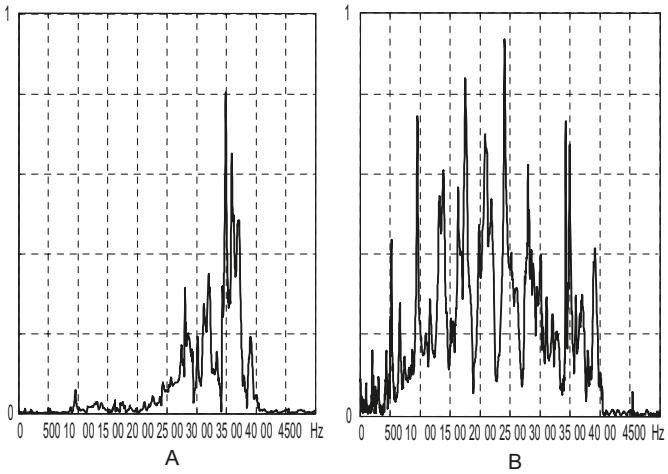

Fig. 2. (A) Frequency response function (FRF) of a transverse gradient coil. (B) FRF of the longitudinal gradient coil. Both spectra were obtained on the 11.7 T wide bore vertical bore system. The FRF magnitudes were scaled to 1 a.u. The transverse gradients show a typical reduced response for the low-frequency region up to ~800 Hz, whereas this is absent for the longitudinal coil. However, the sound pressure level for the longitudinal coil is ~18 dB (in C mode), below that of the transverse coils.

SNR optimization

When imaging an object with MR, data is collected in k-space (the spatial frequency domain). After acquisition the data is Fourier-transformed to obtain a map of the spin-density distribution. The spatial frequency vector in the raw-data map is given by the product of the gradient vector ($\boldsymbol{G}$) and the encoding time t_{p}:

$$[6] \qquad \boldsymbol{k} = \frac{\gamma_H \boldsymbol{G} t_{\mathrm{p}}}{2\pi}$$

Here, $\boldsymbol{G}$, is kept constant during t_{p} and the position in k-space is thus determined by the product of the gradient vector and the encoding time. During the standard SPI experiment, k-space is traversed by changing the gradient vector while leaving the encoding time constant. The SPI/VTI method traverses k-space differently than an SPI experiment, introducing a variable encoding time[15] (Fig. 3). To obtain the same spatial frequency mapping we introduced a scaling constant that ensures encoding with the same spatial frequencies, however, with additional enhancement in the spin-density mapping, resulting in an increase in SNR. In short, the rescaled parameters are

$$[7] \qquad t_{\mathrm{p}} = cT_{\mathrm{p}}$$

Fig. 3. (A) Single point imaging (SPI) / VTI pulse diagram, showing the variable encoding delay t_p. Close to the centre of k-space (t_p) varies as follows: $T_D < t_p < T_p$ (where T_D is the minimal encoding time possible and T_p is the maximum phase encoding time. (B) The SPI experiment, with a constant t_p, displays a constant signal amplitude (solid line); the SPI/VTI experiment shows a larger signal amplitude for $T_D < t_p < T_p$, close to the centre of k-space, while reducing at the extremities of k-space to the value obtained in the SPI experiment (broken line).

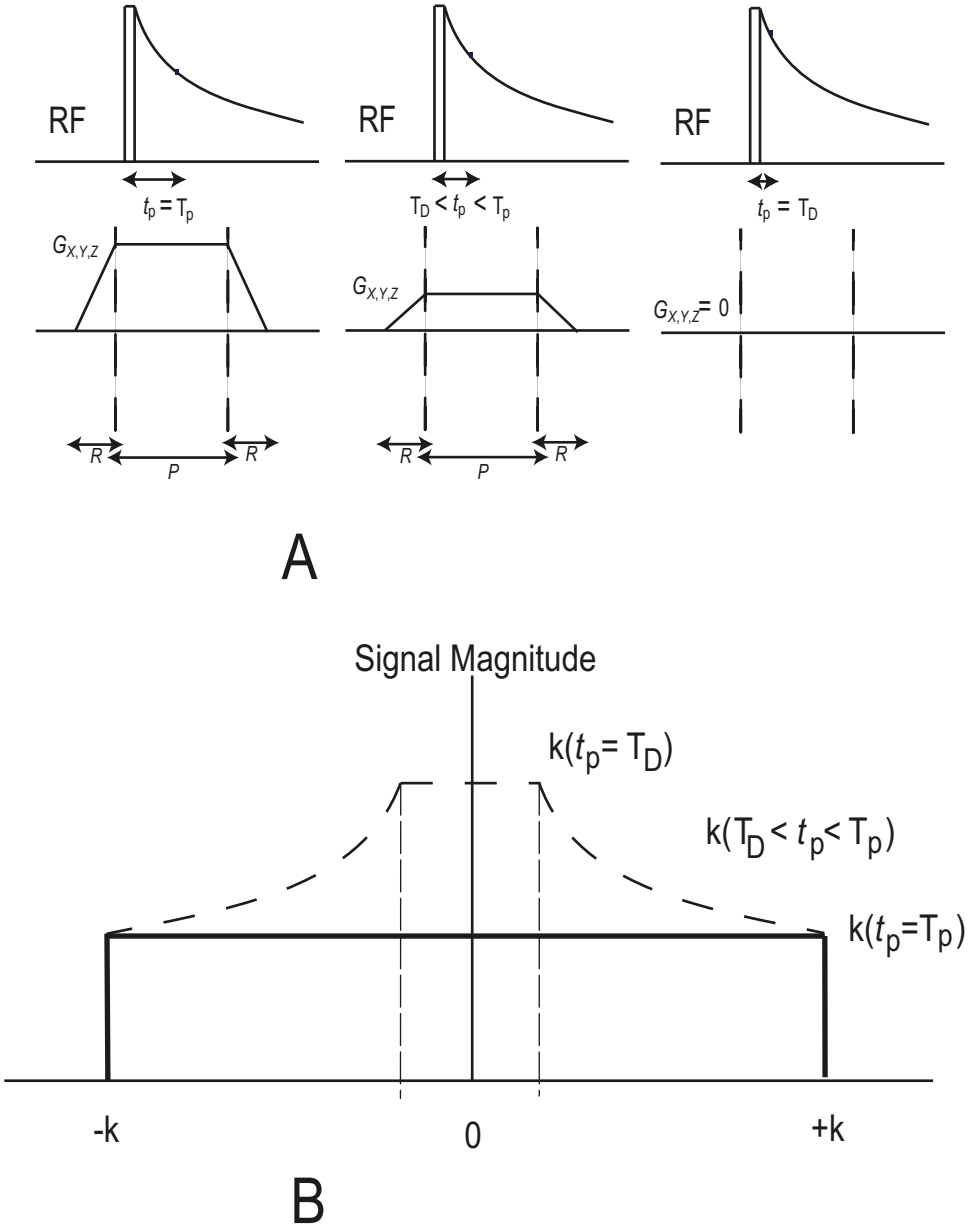

Can. J. Chem. Downloaded from www.nrcresearchpress.com by Xi'an Jiaotong University on 09/19/12
For personal use only.

$$[8] \qquad G_i' = \frac{1}{c} G_i, \quad \text{with } i = x, y, z$$

where c is the scaling constant, T_p is the phase encode interval, G_i' is the rescaled gradient magnitude, and G_i is the original gradient magnitude.

This allows for the variation of t_p; $T_D < t_p < T_p$, where T_D represents the minimal encoding time possible set by hardware limitations. The sensitivity, defined as SNR per unit time, of SPI and SPI/VTI can be compared as both sequences use the same bandwidth and thus have an identical noise level per measurement.[7] Comparing the total signal amplitude for the two sequences in one phase-encode cycle we obtained:[15]

$$[9] \qquad \frac{S_{SPI}}{S_{SPI/VTI}} = \frac{1}{T_p}\left[(T_D + {T_2}^*)e^{\frac{(T_D - T_p)}{{T_2}^*}} - {T_2}^*\right]$$

A phase-encode interval $T_p = \frac{{T_2}^*}{2}$ provides the optimal sensitivity for SPI.[7] However, for this ratio, the maximal gain in sensitivity using SPI/VTI would be 1.28 for $\frac{T_D}{T_p} = 0.2$. However, with increasing $\frac{T_p}{{T_2}^*}$ sensitivity enhancements by a factor of 3–4 can easily be achieved.[15] Thus, using SPI/VTI becomes beneficial when experimental limitations prevent the selection of a sufficiently short T_p. The ratio $\frac{T_D}{T_p}$ can be used to control image resolution, which in turn can be affected be-

Fig. 4. Top and bottom rows represent two different orientations of a human tooth. Data was collected with the silent 3D single point imaging (SPI) sequence (see text) and reconstructed according to Šrámek et al.[18] (A) Surface reconstruction, (B) volume reconstruction, and (C) object reconstruction, with particular attention to the area with high water content (caries), indicated in the crown area.

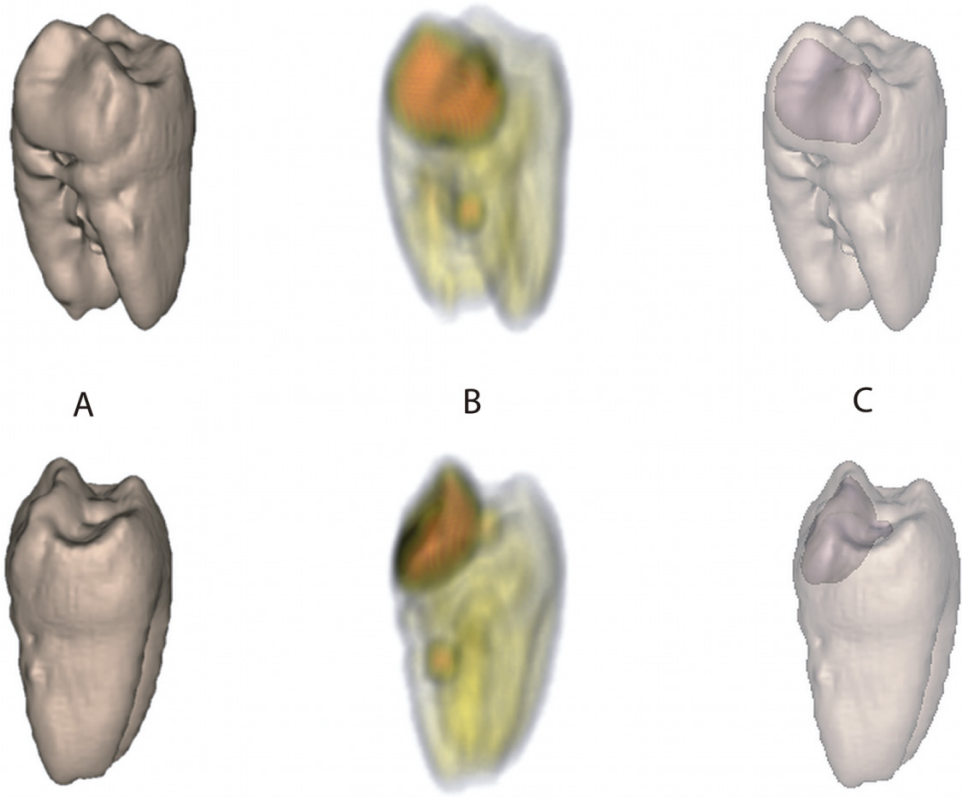

Fig. 5. Maximum intensity projections[17] of the same tooth shown in Fig. 4. The two orientations shown in the top and bottom row of Fig. 4 correspond to (A) and (B), respectively.

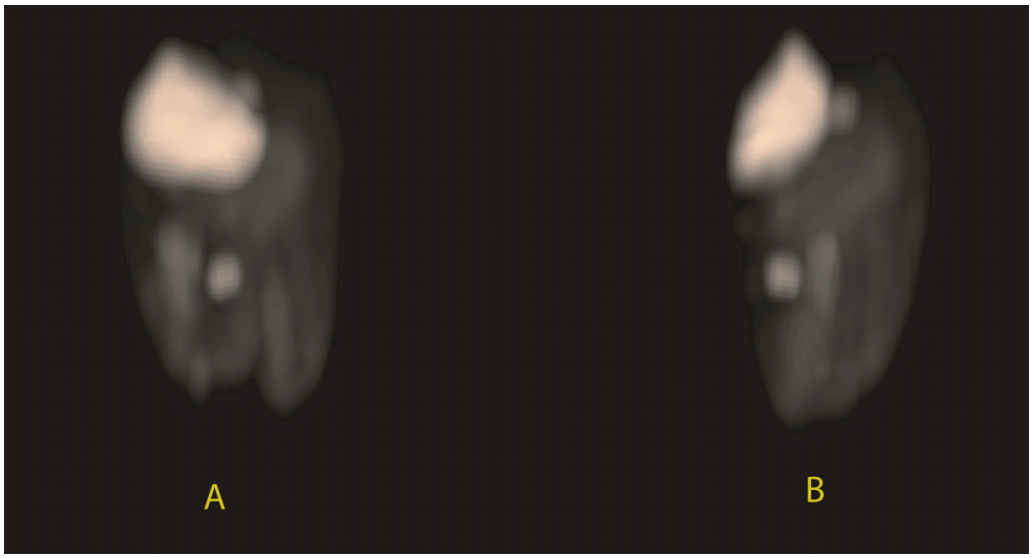

Can. J. Chem. Downloaded from www.nrcresearchpress.com by Xi'an Jiaotong University on 09/19/12
For personal use only.

cause of the influence of T_2* related line broadening as SPI/VTI uses a variable encoding delay.

Experimental

The new methods were tested on human teeth and rubber stoppers. All MRI experiments were performed on an Avance DRX Bruker console (Bruker, Karlsruhe, Germany) using a 72 mm self-shielded gradient system SGRAD 123/72/S (o.d./i.d.) (Magnex, UK) installed in a vertical bore, 11.7 T magnet (Magnex, UK). Acoustic noise was measured using a Bruel and Kjær (Nærum, Denmark) 2238 Mediator sound level meter equipped with a prepolarized free-field condenser microphone type 4188. For all measurements the microphone was centred 20 cm deep into the magnet and connected to

Fig. 6. Images of a phantom using different pulse sequences. Each image represents a slice in the phantom acquired at exactly the same position, using the following parameters: (A) 3D single point imaging (SPI), encoding time (t_p) = 270 μs, repetition time (TR) = 10 ms. (B) 3D-SPI/VTI, 30 μs ≤ t_p ≤ 120 μs, TR = 10 ms. (C) 3D gradient echo, echo time (TE) = 4 ms, TR = 40 ms. (D) 3D spin-echo, TE = 15 ms, TR = 1000 ms. All data were acquired with a matrix size of 64 × 64 × 8 and a field of view (FOV) of 11 × 11 × 25 mm^3. These images show that SPI/VTI is not sensitive for susceptibility artifacts despite the variable encoding time used in the phase encoding. The phantom consists of a cylinder of water containing an air bubble (visible at top in the images) and two smaller cylinders with different diameters and thicknesses placed at the bottom.

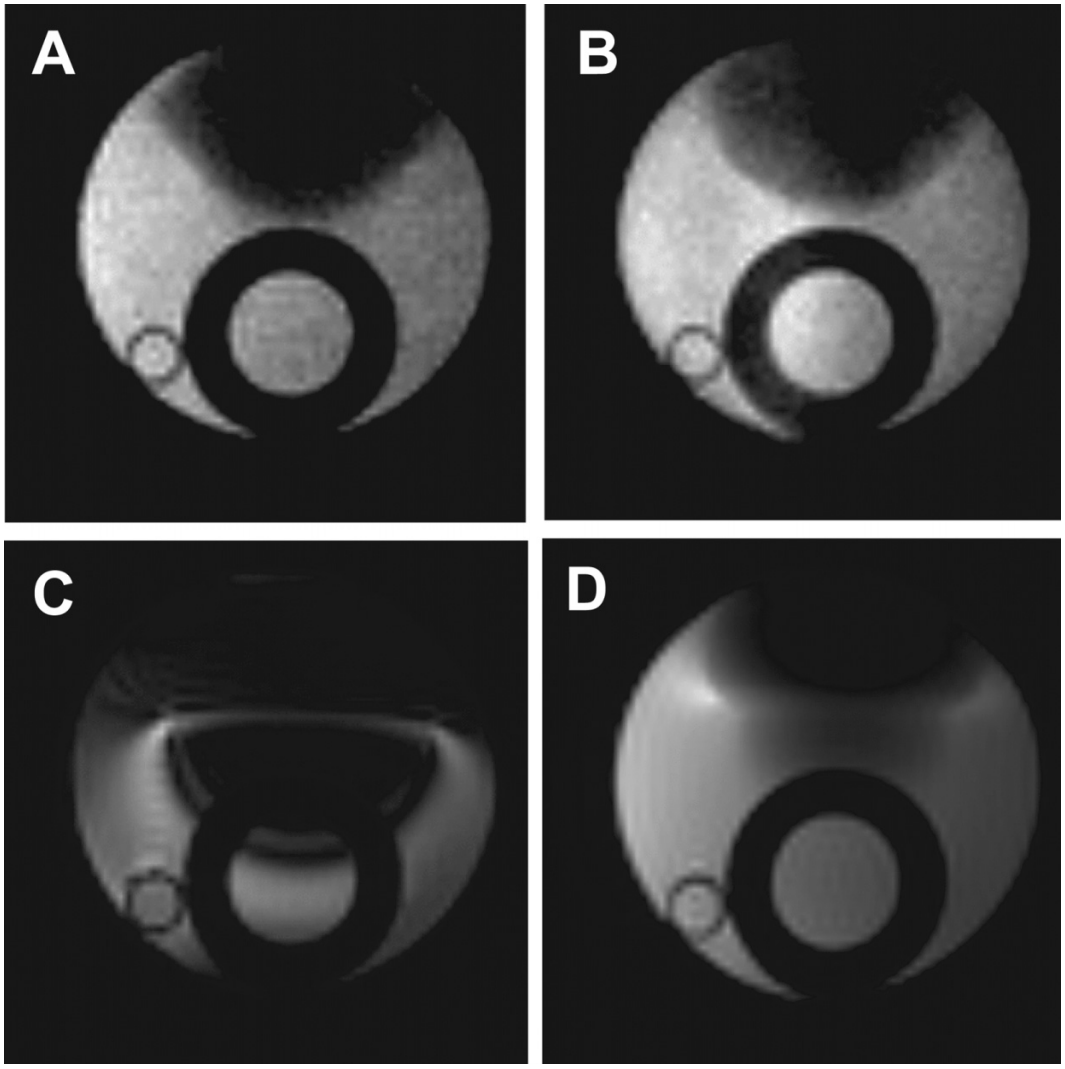

Can. J. Chem. Downloaded from www.nrcresearchpress.com by Xi'an Jiaotong University on 09/19/12
For personal use only.

the sound meter by a double-shielded cable. In all acoustic measurements the mean equivalent SPL was recorded (as defined by IEC 1672) and the results were obtained in both C and A modes. The latter takes into account the physiological characteristics of human hearing.

Experiments were performed using a home-built probe containing a Helmholtz RF coil tuned to 500 MHz for ^{1}H imaging and an orthogonally positioned three-turn RF solenoid tuned to 202 MHz for ^{31}P experiments. The sample chamber had a diameter of 12 mm (i.d.) and a length of 12 mm.

^{1}H images were obtained using a data matrix of 96 × 96 × 32 with a field of view (FOV) of 3 × 3 × 4 cm^3. Unless mentioned otherwise, SPI experiments used a detection time of t_p = 125 μs in combination with a 10 μs excitation pulse and a repetition time of 15 ms. The gradients were sinusoidally shaped with a ramp time of 1.0 ms for optimal acoustic noise reduction (Fig. 1B). The resulting total experiment time was 80 min.

Teeth were obtained with consent from University of Manitoba Faculty of Dentistry, Winnipeg, Manitoba, patients. After sterilization, samples were stored in distilled water while refrigerated. Prior to an MRI experiment a tooth was removed from the container, blotted dry with tissue paper, and acclimatized to room temperature. Teeth used in this study did not contain living dental pulp.

Results and discussion

Using the simple modification of gradient shape adjustment as shown in Fig. 1B, SPI experiments can be made effectively silent for the 3D measurement of teeth. Restricting the TR of the experiment to values set by the flat part in the

Fig. 7. Single point imaging (SPI) images with a resolution of 64 × 64 × 16 points, encoding time (t_p) = 120 μs and a total acquisition time of 11 min; signal-to-noise ratio (SNR) = 8.25. (B) SPI/VTI with a resolution of 64 × 64 × 16 points, 40 μs ≤ t_p ≤ 120 μs and a total acquisition time of 11 min; SNR = 32.6. All other parameters were kept identical using the same maximal gradient amplitude. (A) and (B) Central slice of the 3D experiment. (C) and (D) A zoomed detail of the object, indicated by the square in (A). The SPI/VTI (B) sequence exhibits an ~4× higher SNR compared with SPI (A).

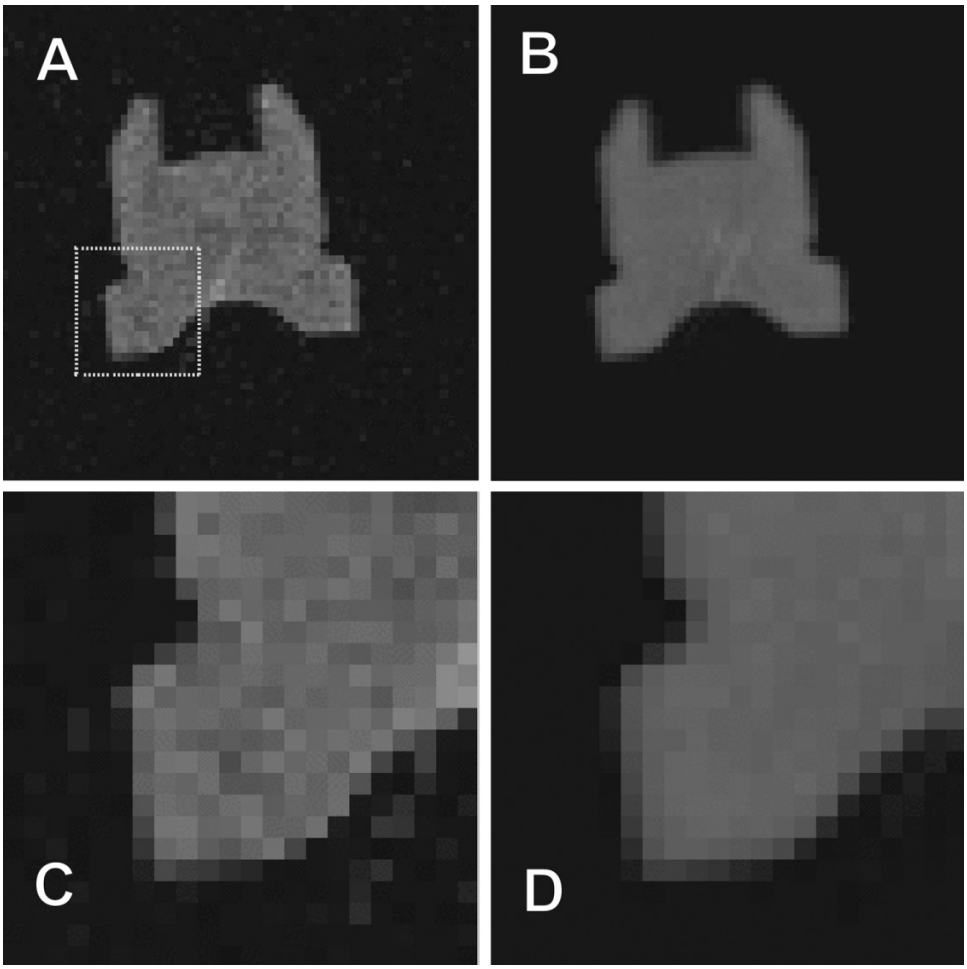

Can. J. Chem. Downloaded from www.nrcresearchpress.com by Xi'an Jiaotong University on 09/19/12
For personal use only.

FRF in Fig. 2A, containing frequencies up to ~800 Hz; TR > 800^{-1} s, will result in significant modulation of the fundamental acoustic frequency. Excellent acoustic noise suppression was achieved for the 11.7 T gradient system when the R = 175 μs linear gradient ramps were replaced by a 1 ms sinusoidal slope while keeping the duration of the gradient at P = 0.4 ms and TR = 15 ms. These parameters resulted in an approximate sound pressure level of ~68 dB, close to the background value (measured in A scale) in the laboratory.

SPI with shaped gradients also significantly reduced the power deposition into the gradient system compared with SPRITE.[9] The ratio of power deposition for the two sequences can be calculated as[14]

$$[10] \qquad \frac{\mathbf{P}_{\text{ShapedSPI}}}{\mathbf{P}_{\text{SPRITE}}} = \frac{0.625R + P}{\text{TR}}$$

where $\mathbf{P}_{\text{ShapedSPI}}$ and $\mathbf{P}_{\text{SPRITE}}$ represent the power deposited by the shaped SPI and the SPRITE sequences, respectively. For a gradient ramp time R = 1 ms, a plateau time P = 0.4 ms, and a repetition time TR = 15 ms, a reduction by a factor of 15 can be obtained. Of course, SPRITE was designed for samples with smaller T_1 values, allowing for a shorter TR.

SPI was used to obtain 3D maps of the mobile proton distribution in teeth, shown in Figs. 4 and 5. Most of the observed signal will arise from water; however, a small negligible fraction of the signal arises from proteins. Intact teeth (no caries) show T_1 relaxation with a relaxation constant of ~500 ms.[19–21] T_2 relaxation is bi-exponential, arising from water in dentin tubules and in enamel. Water in the latter compartment is more restricted in mobility and thus has a shorter relaxation time. In Fig. 4B, which shows a volume reconstruction of the SPI data, the root canals can clearly be observed. Roots are mainly composed of dentin and show a higher water content. Also visible in Figs. 4B and 4C are the areas with tooth decay. Caries makes enamel porous, allowing the absorption of water, hence providing a larger proton density on the SPI images. SPI can be used as an analytical tool to study both tooth surface as well as volume. Images can be used to provide detailed 3D information on roots that can be used to construct accurate inner root canal fixations for tooth restoration purposes. Figure 5 shows a gray scale

image of the tooth, reconstructing the proton spin density in a maximum intensity projection.

Figure 6 shows the effect of susceptibility changes at the air–water interface. Images of a water phantom filled with an air bubble were obtained with SPI, SPI/VTI, gradient echo, and spin echo sequences (see Fig. 6 for details). The reconstructed images reveal that despite severe inhomogeneity artifacts observed in the gradient and, to a lesser extend, spin echo acquisition, no artifacts were detected for the SPI/VTI acquisition when compared with the SPI image, which is known to be artifact free. The influence of the variable time encoding in the SPI/VTI sequence did not significantly affect image resolution.[15] In vivo applications of SPI are being developed, especially with an increasing number of people having bones replaced (hip, knee, etc.).[22] These applications would benefit from the use of SPI/VTI and (or) silent SPI.

The use of the SPI/VTI sequence was demonstrated by imaging a small object made of soft rubber with $T_2^* = 73 \pm 4$ μs. Figure 7 shows the results comparing the central slice of 3D SPI (Figs. 7A and 7C) experiment with that of the SPT/VTI (Figs. 7B and 7D) experiment. Both experiments were performed with the same data matrix ($64 \times 64 \times 16$), gradient strengths, 1 average, FOV = $20 \times 20 \times 20$ mm^3 and a 32° RF pulse. The SPI/VTI experiment, with 40 μs ≤ 120 μs, resulted in an SNR of 32.6, whereas the SPI experiment, with $t_p = 120$ μs, only resulted in an SNR of 8.25. The finer details of the images (see Figs. 7C and 7D)) show that the SPI/VTI acquisition, despite the partial filtration effect owing to the variable encoding time, is capable of reproducing the geometric details of the object while providing substantial SNR enhancement compared with SPI.

Conclusions

In summary, two modifications of the SPI sequence were discussed and tested experimentally. The first modification was based on a general reduction of the SPL of SPI, associated with the fast switching of encoding gradients. Shaped gradients were shown to significantly reduce acoustic noise while offering an attractive alternative to the SPRITE sequence, reducing the overall power deposition into the gradient set of the magnet. The second modification was based on a reduction of signal attenuation during the phase-encoding period (SPI/VTI sequence), using a variable reduction of the encoding time. Used on materials with short T_2^* values, the SPI/VTI sequence showed a significant increase in SNR with minimal distortions owing to susceptibility effects.

Acknowledgements

We would like to thank M. Šrámek for his help with the data reconstruction of teeth images and S. Volotovskyy for his help constructing RF coils. M.L.H.G. would like to thank R. Wasylishen for introducing him to the art of solid-state NMR, and last but not least, V. Wasylishen for stimulating discussions and generous hospitality. “A man is a success if he gets up in the morning and gets to bed at night, and in between he does what he wants to do.” Bob Dylan.

References

(1) Kuhn, W. *Angew. Chem. Int. Ed. Engl.* **1990** *29* (1), 1. doi:10.1002/anie.199000013.
(2) McKinstry, R. C., III; Jarrett, D. Y. *AJR Am. J. Roentgenol.* **2002** *182*, 532.
(3) Callaghan, P. T. *Principles of Nuclear Magnetic Resonance Microscopy;* Clarendon Press: Oxford, UK, 1991.
(4) Cory, D. G. Three-Dimensional NMR Imaging of Solids. In *Magnetic Resonance Microscopy;* Blümich B.; Kuhn W., Eds.; VCH: Weinheim, Germany, 1992; pp 49–58.
(5) Harris, R. K.; Wasylishen, R. E.; Duer, M. J., Eds. *NMR Crystallography;* Wiley: Chichester, UK, 2009.
(6) Emid, S.; Creyghton, J. H. N. *Physica B* **1985** *128* (1), 81. doi:10.1016/0378-4363(85)90087-7.
(7) Gavina, S.; Cory, D. J. *J. Magn. Reson. B.* **1994** *104* (1), 53. doi:10.1006/jmrb.1994.1052.
(8) Ernst, R. R.; Bodenhausen, G.; Wokaun, A. *Principles of Nuclear Magnetic Resonance in One and Two Dimensions;* Oxford University Press: Oxford, UK, 1987.
(9) Balcom, B. J.; Macgregor, R. P.; Beyea, S. D.; Green, D. P.; Armstrong, R. L.; Bremner, T. W. *J. Magn. Reson.* **1996** *123* (1), 131. doi:10.1006/jmra.1996.0225.
(10) Mastikhin, I. V.; Balcom, B. J.; Prado, P. J.; Kennedy, C. B. *J. Magn. Reson.* **1999** *136* (2), 159. doi:10.1006/jmre.1998.1612.
(11) Romanzetti, S.; Halse, M.; Kaffanke, J.; Zilles, K.; Balcom, B. J.; Shah, N. J. *J. Magn. Reson.* **2006** *179* (1), 64. doi:10.1016/j.jmr.2005.11.007.
(12) Halse, M.; Rioux, J.; Romanzetti, S.; Kaffanke, J.; MacMillan, B.; Mastikhin, I.; Shah, N. J.; Aubanel, E.; Balcom, B. J. *J. Magn. Reson.* **2004** *169* (1), 102. doi:10.1016/j.jmr.2004.04.008.
(13) Beyea, S. D.; Altobelli, S. A.; Mondy, L. A. *J. Magn. Reson.* **2003** *161* (2), 198. doi:10.1016/S1090-7807(02)00172-6.
(14) Latta, P.; Gruwel, M. L. H.; Edie, E.; Šrámek, M.; Tomanek, B. *J. Magn. Reson.* **2004** *170* (2), 177. doi:10.1016/j.jmr.2004.06.012.
(15) Latta, P.; Gruwel, M. L. H.; Volotovskyy, V.; Weber, M. H.; Tomanek, B. *Magn. Reson. Imaging* **2008** *26* (1), 109. doi:10.1016/j.mri.2007.05.004.
(16) Hedeen, R. A.; Edelstein, W. A. *Magn. Reson. Med.* **1997** *37* (1), 7. doi:10.1002/mrm.1910370103.
(17) Tuma, J. J.; Walsh, R. A. *Engineering Mathematics Handbook;* McGraw-Hill: New York, 1997.
(18) Šrámek, M.; Kaufman, A. *IEEE Trans. Vis. Comput. Graph.* **2000** *6* (3), 236. doi:10.1109/2945.879785.
(19) Schreiner, L. J.; Cameron, I. G.; Funduk, N.; Miljkovic, L.; Pintar, M. M.; Kydon, D. N. *Biophys. J.* **1991** *59* (3), 629. doi:10.1016/S0006-3495(91)82278-0.
(20) Funduk, N.; Kydon, D. N.; Schreiner, L. J.; Peemoeller, H.; Miljkovic, L.; Pintar, M. M. *Magn. Reson. Med.* **1984** *1* (1), 66. doi:10.1002/mrm.1910010108.
(21) Gruwel, M. L. H.; Latta, P.; Tanasiewicz, M.; Volotovskyy, V.; Šrámek, M.; Tomanek, B. *Appl. Phys., A Mater. Sci. Process.* **2007** *88* (4), 763. doi:10.1007/s00339-007-4066-x.
(22) Ramos-Cabrer, P.; van Duynhoven, J. P. M.; Van der Toorn, A.; Nicolay, K. *Magn. Reson. Imaging* **2004** *22* (8), 1097. doi:10.1016/j.mri.2004.01.061.

Can. J. Chem. Downloaded from www.nrcresearchpress.com by Xi'an Jiaotong University on 09/19/12
For personal use only.

Measurement and calculation of ^{13}C chemical shift tensors in α-glucose and α-glucose monohydrate

Darren H. Brouwer, Kevin P. Langendoen, and Quentin Ferrant

Can. J. Chem. Downloaded from www.nrcresearchpress.com by Xi'an Jiaotong University on 09/19/12
For personal use only.

Abstract: The ^{13}C chemical shift tensors of two crystalline forms of glucose (α-glucose and α-glucose·H_2O) were determined from one-dimensional (1D) and two-dimensional (2D) solid-state nuclear magnetic resonance (NMR) spectroscopy experiments. The experimental values determined from 1D and 2D methods are in very good agreement. Quantum chemical calculations were also carried out using the gauge-including projector augmented wave (GIPAW) method for plane-wave density functional theory (DFT) as implemented in the CAmbridge Serial Total Energy Package (CASTEP). The calculated ^{13}C chemical shifts were found to be in excellent agreement with experimental values for crystal structures that had their hydrogen atoms optimized and after an appropriate calibration was applied to convert calculated chemical shieldings into chemical shifts. The work presented here lays an important foundation for future solid-state NMR and quantum chemical calculation investigations of the various crystalline forms of cellulose.

Key words: NMR crystallography, carbohydrates, cellulose, quantum chemical calculations, crystal structure.

Résumé : On a déterminé les tenseurs des déplacements chimiques du ^{13}C de deux formes cristallines du glucose (α-glucose et α-glucose·H_2O) à partir des valeurs obtenues par résonance magnétique nucléaire (RMN) monodimensionnelle (1D) et bidimensionnelle (2D), à l'état solide. Les valeurs expérimentales obtenues par les méthodes 1D et 2D sont en très bon accord. On a aussi effectué des calculs de chimie quantique en faisant appel à une onde améliorée par un opérateur de projection comportant une jauge de la théorie de la fonctionnelle de la densité (« GIPAW-DFT ») avec une onde plane telle, qu'appliquée dans le « CAmbridge Serial Total Energy Package (CASTEP) ». On a trouvé que les valeurs calculées pour les déplacements chimiques du ^{13}C sont en excellent accord avec les valeurs expérimentales pour des structures cristallines pour lesquelles les atomes d'hydrogène avaient été optimisés et après qu'une calibration appropriée a été appliquée pour convertir les déplacements chimiques calculés en déplacements chimiques. Le présent travail pose une fondation importante pour des études futures de RMN à l'état solide et pour des calculs de chimie quantique de diverses formes cristallines de la cellulose.

Mots-clés : cristallographie par RMN, hydrates de carbone, cellulose, calculs de chimie quantique, structure cristalline.

[Traduit par la Rédaction]

Introduction

The detailed characterization of the structure of cellulose, the most abundant biopolymer on earth, has presented numerous challenges due mainly to its fibrous nature and multiplicity of crystalline forms. Two of the most important contributions to the understanding of the structure of cellulose have come from solid-state NMR spectroscopy and neutron and X-ray fibre diffraction experiments. The solid-state ^{13}C NMR work of Atalla and Vanderhart revealed that native celluloses consist of two crystalline forms, referred to as cellulose I_α and cellulose I_β, and that these two forms can coexist in the same sample of cellulose.[1] Langan, Nishiyama, and Chanzy have reported structures of various crystalline forms of cellulose derived from X-ray and neutron diffraction data collected on carefully aligned fibres of cellulose.[2–4] While these structures are considered to be the best structural models for the various forms of cellulose, there may still be a place for further study of the structures. The fact that diffraction data were collected on fibre samples places a limitation on the accuracy of the derived structures.

Solid-state NMR spectroscopy may provide an opportunity to probe the structures of cellulose in greater detail. Recent advances in solid-state NMR techniques and quantum chemical calculation methods for solids have expanded the opportunities for solid-state NMR spectroscopy to provide structural information for materials whose structures are difficult to characterize. Broadly referred to as "NMR crystallography",[5] innovative and creative ways of integrating solid-state NMR data with quantum chemical calculations and diffraction experiments have led to significant achievements in the structural characterization of inorganic[6–12] and organic solids.[13–22]

However, before jumping right in to applying NMR crys-

Received 1 November 2010. Accepted 17 January 2011. Published at www.nrcresearchpress.com/cjc on 3 May 2011.

D.H. Brouwer, K.P. Langendoen, and Q. Ferrant. Chemistry Department, Redeemer University College, Ancaster, ON L9K 1J4, Canada.

Corresponding author: D.H. Brouwer (e-mail: dbrouwer@redeemer.ca).

This article is part of a Special Issue dedicated to Professor Roderick E. Wasylishen.

Can. J. Chem. Downloaded from www.nrcresearchpress.com by Xi'an Jiaotong University on 09/19/12
For personal use only.

tallography approaches to the structures of cellulose, it is important to do some foundational work on model compounds to gain confidence that such an approach will be successful. In this paper, we present solid-state NMR experiments and quantum chemical calculations for two crystalline forms of glucose: α-glucose and α-glucose·H_2O. Since glucose is the monomer from which cellulose is built, these structures are appropriate model systems to test and develop an NMR crystallography approach.

Chemical shielding tensors are particularly sensitive probes of the local structure around a nucleus. The ability to reliably measure and calculate these tensors provides a powerful combination for testing structural models and even refining structures. We have previously shown how measurements and quantum chemical calculations of ^{29}Si tensors in zeolites can be integrated into an NMR crystallography structure determination process for zeolite crystal structures.[10–12,23] We hope to extend these successes to other materials such as cellulose. The work presented here on measuring and calculating ^{13}C tensors for α-glucose and α-glucose·H_2O is a first step in that direction.

Intermolecular O–H···O hydrogen bonds play a key role in the organization of all of the glucose and cellulose structures. Therefore, it is very important to consider the full three-dimensional periodicity of the crystal structures in any quantum chemical calculations of NMR properties, rather than simply treating the glucose molecules or monomers as isolated units. Recent developments in quantum chemical calculations for solids, most notably the gauge-including projector augmented wave (GIPAW) approach[24–26] for density functional theory (DFT) implemented in the CAmbridge Serial Total Energy Package (CASTEP) program,[27] now allow for accurate calculations of NMR properties on actual crystal structures, rather than molecular fragments or clusters extracted from a crystal structure. The successes and limitations of this method for performing calculations on organic molecular crystals have recently been reviewed.[18,28]

In this paper we present one-dimensional (1D) and two-dimensional (2D) solid-state NMR experiments for measuring ^{13}C chemical shift tensors in α-glucose and α-glucose·H_2O and demonstrate that GIPAW DFT quantum chemical calculations can accurately reproduce these experimental NMR measurements, providing us with the confidence needed for future NMR crystallography studies on the more complicated crystal structures of cellulose.

Experimental

Samples

The α-glucose·H_2O sample in this work was ^{13}C-enriched at every carbon site to a level of 6%. A sample of [6% $^{13}C_6$] D-(+)-glucose was purchased from Sigma-Aldrich and dissolved in a minimum amount of hot water, after which the water was slowly evaporated at room temperature over several days. Anhydrous α-glucose was prepared at ^{13}C natural abundance by heating a sample of α-glucose·H_2O (with ^{13}C natural abundance) at approximately 70 °C overnight under vacuum. The cellulose sample was bio-synthesized by growing *Acetobacter xylinum* (ATCC 23769) bacterial cultures at 30 °C in sterile Hestrin and Schramm medium[29] with glucose as the carbon source. After 20 days, the cellulose pellicle was extracted, washed, and blended with 1 mol/L NaOH. The resulting slurry was centrifuged and the supernatant was decanted. This was followed by two additional cycles of resuspension in water and centrifugation.

Solid-state NMR

Experiments were carried out on a Bruker Avance 200 MHz spectrometer operating at a magnetic field strength of 4.7 T (50.42 MHz ^{13}C Larmour frequency) using a wide-bore double-resonance 7 mm MAS NMR probe. Samples filled the entire 7 mm rotors. The ^{13}C chemical shifts were referenced by setting the low-field ^{13}C resonance for a sample of adamantane to 38.84 ppm. ^{13}C cross-polarization/magic-angle spinning (CP MAS) spectra were collected with moderate MAS frequencies (4 kHz) for spectra with only isotropic resonances and slow MAS frequencies (285 Hz and 275 Hz for α-glucose·H_2O and α-glucose, respectively) for spectra with spinning sideband manifolds. All 1D spectra were acquired with a recycle delay of 20 s, 4 ms of cross-polarization from protons, and SPINAL-64 decoupling[30] during acquisition with a radio frequency (rf) field strength of 83 kHz. A modified version[23] of the 2D 4π-pulse chemical shift anisotropy (CSA) recoupling sequence[31] was used in this work, which correlates quasi-static powder line shapes to the isotropic chemical shifts. These quasi-static powder line shapes have the same shape as static powder line shapes but are narrowed by a scaling factor of 0.393 and have their centers of gravity at zero frequency in the indirect dimension. Composite 90_x–180_y–90_x recoupling pulses were employed, since the sensitivity of the CSA-recoupled line shapes to errors in the rf amplitude of the recoupling pulses has been shown to be dramatically reduced compared with using regular 180° pulses.[23] The pulse sequence was implemented with ^{13}C 90° and 180° pulses of 6 and 12 μs, respectively. The experiments were carried out at a spinning frequency of 2000 Hz and employed 4 ms of cross-polarization from protons, a recycle delay of 5 s, a continuous-wave ^{1}H decoupling rf field strength of approximately 100 kHz during the CSA recoupling period, and 83 kHz SPINAL-64 ^{1}H decoupling during the acquisition period. Twelve t_1 increments, each with two spectra, were acquired with 64 scans for α-glucose·H_2O and 320 scans for α-glucose. The displayed experimental and simulated quasi-static CSA-recoupled line shapes have the frequency axis scaled using a pulse sequence scaling factor of 0.393.

Spectrum fitting

To estimate ^{13}C chemical shift tensors from experimental data, spectrum fitting of the slow MAS spectra and CSA-recoupled line shapes was carried out according to the protocols described previously.[23] The Herzfeld–Berger convention[32] for quantifying the chemical tensor was employed in which the three principal components of the CS tensor, $\delta_{11} \geq \delta_{22} \geq \delta_{33}$, are expressed in terms of the isotropic chemical shift $\delta_{iso} = (\delta_{11} + \delta_{22} + \delta_{33})/3$, which is observed in MAS experiments, the span $\Omega = \delta_{11} - \delta_{33}$, which describes the breadth of the tensor, and the skew $\kappa = (3\delta_{22} - \delta_{iso})/\Omega$, which describes the asymmetry of the tensor. To find the values of Ω and κ giving the best fit to the experimental data, a series of simulations were carried out using SIMPSON[33] over a range of values for Ω and κ. Contour plots of χ^2 (sum of

Can. J. Chem. Downloaded from www.nrcresearchpress.com by Xi'an Jiaotong University on 09/19/12
For personal use only.

the squares of the differences between experimental and simulated data) as a function of Ω and κ were constructed to locate the values of Ω and κ giving the χ^2 minimum, χ^2_{min}. The uncertainties in Ω and κ were estimated from the values of Ω and κ with $\chi^2 = 2\chi^2_{min}$. The uncertainties of δ_{11}, δ_{22}, and δ_{33} were determined from the widest possible ranges of their values given the uncertainties in δ_{iso}, Ω, and κ.

Quantum chemical calculations

Plane-wave DFT calculations of nuclear magnetic shielding tensors were performed using the NMR module of the CASTEP code[27] that employs the GIPAW algorithm[24–26] and is a part of the Accelrys Materials Studio simulation and modeling package.[34] The Perdew–Burke–Ernzerhof (PBE) functional was used with the generalized gradient approximation for all calculations.[35] On-the-fly pseudopotentials were used as supplied in Materials Studio. All calculations were performed on primitive cells using the cell parameters and atomic coordinates from the X-ray diffraction structure of α-glucose·H_2O,[36] the neutron diffraction structure of α-glucose,[37] and structures of both in which the hydrogen positions were optimized with the CASTEP program (with the unit cell parameters fixed to those measured by diffraction). The NMR calculations and geometry optimizations of hydrogen positions were carried out at the "fine" level with basis set cutoff energies of 550 eV and *k*-point spacing of 0.05 $Å^{-1}$. The geometry optimization was performed using the PBE functional and the same Monkhorst–Pack *k*-point grid spacings and cutoff energies as in corresponding single point energy calculations. Convergence tolerance parameters in geometry optimization were set as follows: energy, 10^{-5} eV/atom; maximum force, 0.03 eV/A; maximum stress, 0.05 GPa; maximum displacement, 10^{-3} Å.

Results and discussion

Crystal structures

The crystal structures for α-glucose·H_2O[36] and α-glucose[37] have been determined previously from single-crystal X-ray and neutron diffraction data, respectively. The structure of a single glucose molecule and the packing of the two-crystal structures are shown in Fig. 1. α-Glucose·H_2O crystallizes in the $P2_1$ space group with a unit cell volume of 430.674 $Å^3$, which contains two symmetry-related glucose and two symmetry-related water molecules, while α-glucose crystallizes in the $P2_12_12_1$ space group with a large unit cell of 765.919 $Å^3$ containing four symmetry-related glucose molecules. The molecules pack together with a large degree of intermolecular O–H···O hydrogen bonding involving the -OH groups of the glucose molecules and also involving the water molecules in the case of α-glucose·H_2O.

Solid-state NMR spectroscopy

The asymmetric unit of each material contains a single glucose molecule and this fact is confirmed in the ^{13}C CP MAS spectra of α-glucose·H_2O (Fig. 2*a*) and α-glucose (Fig. 2*b*), which each consist of six peaks corresponding to the six carbon sites. The spectra are clearly different, yet the isotropic chemical shifts are for the most part quite similar between the two materials. The main exception is C6, which has a greater orientational degree of freedom than the other

Fig. 1. (*a*) Glucose molecule with carbon numbering scheme indicated. (*b*) Crystal structure of α-glucose·H_2O. (*c*) Crystal structure of α-glucose. Carbon, oxygen, and hydrogen atoms are represented by dark, medium, and light grey shading, respectively, while intermolecular hydrogen bonds are indicated by dotted lines.

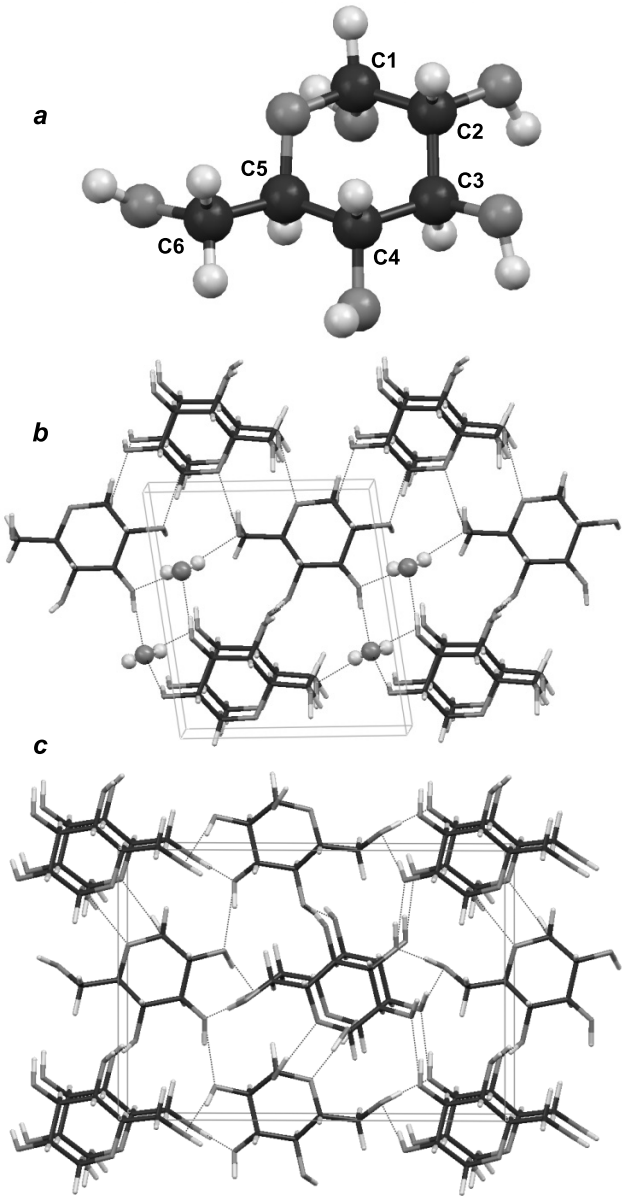

carbons in the glucopyranose ring. The peaks are very narrow, indicating very crystalline and well-ordered materials. The peaks are labeled according to the peak assignments worked out previously in selective ^{13}C labeling experiments.[38]

Figure 2*c* presents a ^{13}C CP MAS spectrum of bacterial cellulose for comparison. C1 and C4 are at significantly different shifts owing to the 1,4-glycosidic linkage that exists between joined neighbouring glucose moieties in the cellulose polymer chains. The chemical shifts of the other carbons remain in the same general regions. The peaks in the cellulose spectrum are not nearly as sharp and simple as those in the glucose spectra. The complexity of the spectrum is due mainly to the existence of two crystalline forms of cellulose[1]

Can. J. Chem. Downloaded from www.nrcresearchpress.com by Xi'an Jiaotong University on 09/19/12
For personal use only.

Fig. 2. ^{13}C CP MAS NMR spectra of (*a*) α-glucose·H_2O, (*b*) α-glucose, and (*c*) bacterial cellulose.

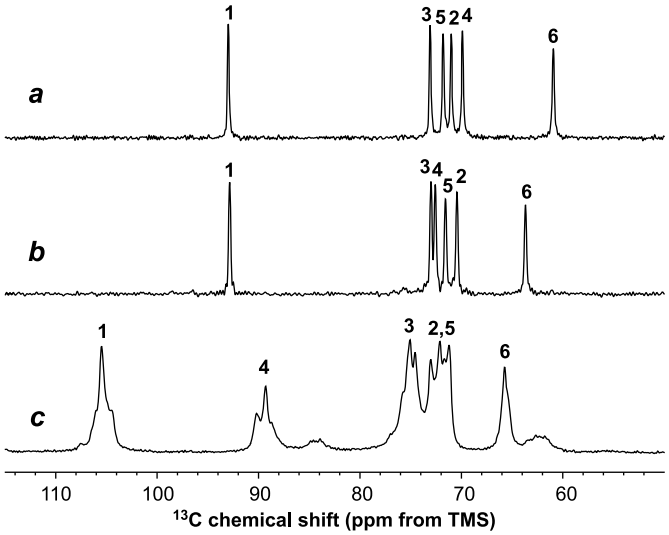

(I_α and I_β), which each consist of two glucose units in their asymmetric units,[3,4] and the presence of non-crystalline cellulose. Each labeled peak is actually a superposition of at least four peaks, which leads to the complex line shapes. The cellulose spectrum is presented here as a comparison with the much simpler glucose spectra to demonstrate that the measurement of ^{13}C chemical shift tensors of cellulose requires more sophisticated NMR experiments than just simply collecting a spectrum at a slow MAS frequency and analyzing the spinning sideband profile.

A straightforward approach to measuring the six ^{13}C chemical tensors in the two glucose samples is to analyze the spinning sideband manifolds in ^{13}C CP MAS spectra collected at slow MAS frequencies. Figures 3 and S1 (see Supplementary data) show the slow MAS spectra for α-glucose·H_2O and α-glucose, respectively, along with the individual spinning sideband manifolds for each carbon site. The spinning frequencies were carefully chosen to ensure that there was no overlap of the peaks and that the spinning was sufficiently slow so that enough spinning sidebands would be present. The relative simplicity of the glucose spectra allows for such an approach, whereas the complexity of the cellulose spectrum means that a sufficiently slow MAS frequency does not exist such that peak overlap is avoided.

A more sophisticated approach is to perform a 2D experiment in which the chemical shift tensor is recoupled by a series of carefully timed pulses synchronized with the rotation of the sample about the magic angle. While there are a variety of approaches to measuring chemical shift tensors in complex spectra using 2D methods,[39–47] we have chosen to employ a composite-pulse version of the 4π CSA recoupling experiment introduced by Tycko et al.[31] This modified pulse sequence was highly successful for measuring small ^{29}Si chemical shift tensors in zeolites at ultrahigh magnetic fields.[23] The resulting spectra give quasi-static powder patterns in the indirect dimension that are each correlated to the isotropic chemical shift in the direct dimension. The 2D spectra for α-glucose·H_2O and α-glucose are presented in Figs. 4 and S2 (see Supplementary data), respectively. In each case, six distinct scaled powder patterns are obtained

Fig. 3. (*a*, *b*) Experimental ^{13}C CP MAS NMR spectra of α-glucose·H_2O obtained using MAS spinning frequencies of (*a*) 4000 Hz (8 scans) and (*b*) 285 Hz (200 scans) with recycle delays of 20 s. (*c*) Simulated 285 Hz MAS spectrum composed of (*d*) individual simulated spinning sideband patterns for each carbon site. The arrows indicate the isotropic peaks. Corresponding data for α-glucose are presented in Fig. S1 in the Supplementary data.

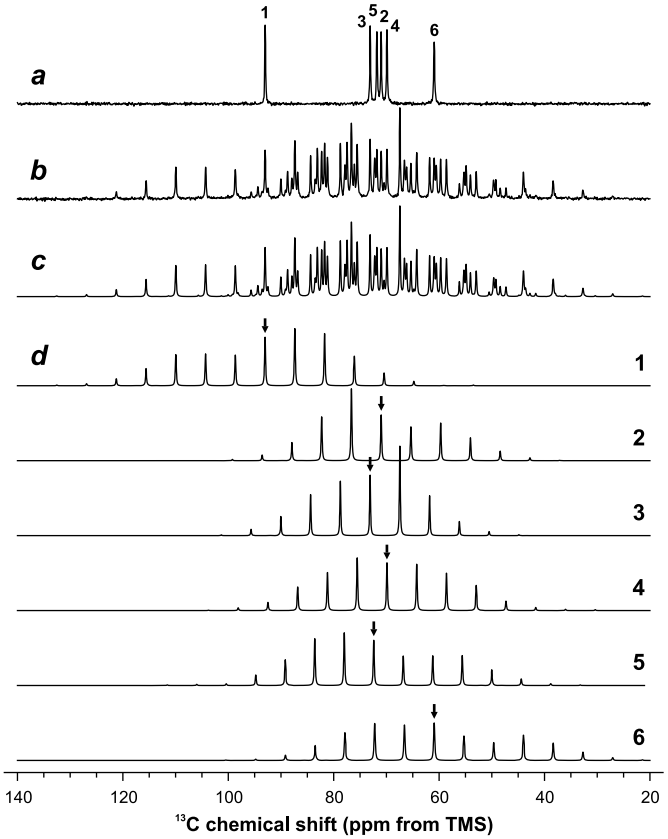

from which the principal components of the ^{13}C chemical shifts tensors can be estimated.

The intention here is to examine the reliability of this 2D method in comparison with analyzing spinning sideband manifolds for the two simple glucose samples, so that further studies involving the ^{13}C chemical shift tensors of the more complicated cellulose sample can be done with confidence. To that end, the spinning sideband manifolds obtained in the slow MAS spectra and the quasi-static powder patterns obtained in the 2D experiments were analyzed and compared. In each case, a series of simulations were performed as a function of the span Ω and skew κ of the chemical shift tensors and compared with the experimental data to map out a contour plot not only to identify the values of Ω and κ that give the best fit in each case, but also to estimate their uncertainties. Figure 5 presents these contour plots for each carbon site, for each experimental method, and for each glucose sample. These plots show that the two methods are in agreement within their estimated uncertainties. The plots also reveal that the uncertainties estimated from the spinning sideband manifolds are considerably less than those estimated from the 2D recoupling spectra. Not unexpectedly, the uncertainties for the ^{13}C-enriched sample (α-glucose·H_2O) are noticeably less for both methods.

Can. J. Chem. Downloaded from www.nrcresearchpress.com by Xi'an Jiaotong University on 09/19/12
For personal use only.

Fig. 4. (*a*) 2D ^{13}C CSA recoupling spectrum for α-glucose·H_2O. (*b*) Experimental (solid lines) and best-fit simulated (dashed lines) pseudo-static CSA-recoupled line shapes for the indicated carbon sites extracted from the 2D spectrum. Corresponding data for α-glucose are presented in Fig. S2 in the Supplementary data.

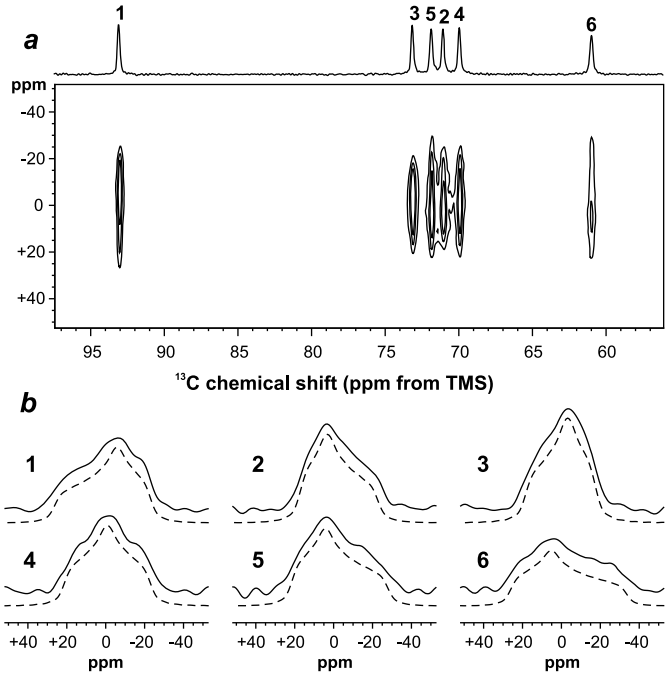

Fig. 5. Contour plots of χ^2 from which the best-fit values of Ω and κ and their uncertainties were estimated for each carbon site in (*a*) α-glucose·H_2O and (*b*) α-glucose. The solid contours indicate the χ^2 surfaces near the minima obtained from the analysis of the spinning sideband manifolds in Figs. 3 and S1, while the dashed contours indicate those obtained from the analysis of the recoupled pseudo-static powder patterns in Figs. 4 and S2. The contours are at multiples of $\sqrt{2}$ and 2 of the minimum χ^2 value for each carbon site and method. The plus symbols indicate the quantum chemical calculated Ω and κ values for each carbon site. The experimental and calculated values are listed in Tables S1 and S2 in the Supplementary data.

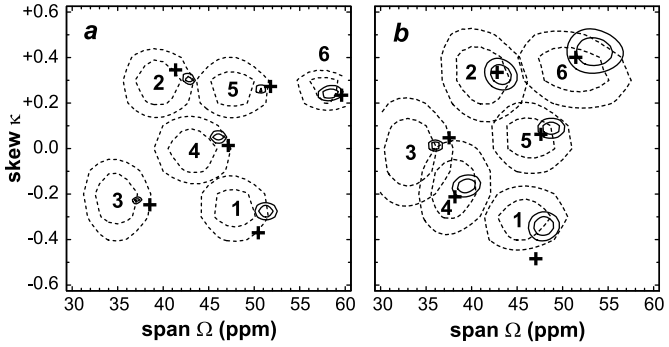

Figure 6 also provides a comparison of the two methods in which the span and skew obtained from each method are compared. The span values seem to be systematically slightly underestimated in the 2D experiment (Fig. 6*a*), while the skew values agree very well between the two methods (Fig. 6*b*). The difference in span values likely results from the fact that, based on simulations of the pulse sequence,[23]

Fig. 6. Comparison of (*a*) the span Ω and (*b*) the skew κ values determined from the CSA recoupling experiment with those determined by analysis of the spinning sideband manifolds in the slow MAS experiments. The black circles and grey squares represent the values obtained for α-glucose·H_2O and α-glucose, respectively.

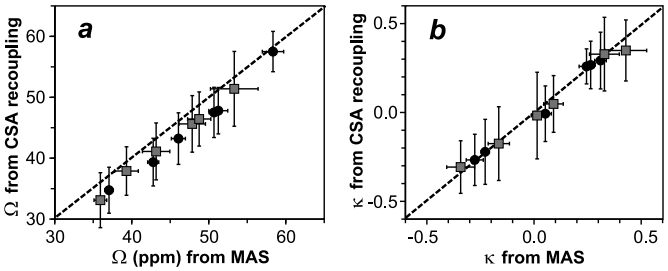

any error in the recoupling pulses tends to decrease the observed span in the 2D recoupling experiment. Overall, however, these results do indicate that the 2D recoupling approach can be employed with confidence for situations that are considerably more complex than the glucose spectra presented here, such as cellulose.

Quantum chemical calculations

Quantum chemical calculations of ^{13}C chemical shielding tensors were carried out on the as-published α-glucose·H_2O crystal structure determined from X-ray diffraction data. In Fig. 7*a* the principal components (σ_{11}, σ_{22}, σ_{33}) of the six calculated ^{13}C chemical shielding tensors are plotted against the corresponding principal components (δ_{11}, δ_{22}, δ_{33}) of the ^{13}C chemical shift tensors determined experimentally from the spinning sideband profiles in the slow MAS spectrum. While there is a clear linear correlation between the calculated and experimental values, there remains a significant degree of scatter (the root-mean-square deviation, RMSD, is 2.8 ppm) and, most noticeably, the slope of the line of best fit (–1.358) is quite a bit steeper than the expected slope of –1.

The hydrogen atom positions in α-glucose·H_2O were then optimized and the ^{13}C chemical shielding tensors were recalculated. Figure 7*b* shows the substantial improvement in the agreement between calculated shieldings and experimental shifts, with the RMSD improving to 1.0 ppm. This improvement is a reflection of the fact that X-ray diffraction data do not provide H atom positions to a sufficiently high accuracy owing to the low X-ray scattering ability of hydrogens.

Similarly, quantum chemical calculations of ^{13}C chemical shielding tensors were carried out on the α-glucose structure before (Fig. 7*c*) and after (Fig. 7*d*) optimization of H atom positions. However, in this case the published crystal structure for α-glucose was determined from neutron diffraction data and the H atom positions have a high degree of accuracy. Consequently, optimization of the H atom positions does not improve agreement between calculated and experimental NMR parameters, with the RMSD being 0.9 ppm before and after optimization.

Notice that for both α-glucose·H_2O (Fig. 7*b*) and α-glucose (Fig. 7*d*), the slopes of the lines still deviate noticeably from the expected slope of –1. For the H-optimized structures, the lines of best fit are $\sigma = -1.149\delta + 179.6$ ppm for α-glucose·H_2O and $\sigma = -1.123\delta + 178.0$ ppm for α-glucose (see Table 1). If the data for both structures are pooled, the

Can. J. Chem. Downloaded from www.nrcresearchpress.com by Xi'an Jiaotong University on 09/19/12
For personal use only.

Fig. 7. Comparison of the principal components (σ_{11}, σ_{22}, σ_{33}) of the chemical shielding tensors for each carbon site calculated using CASTEP with the principal components (δ_{11}, δ_{22}, δ_{33}) of the chemical shift tensors measured experimentally from the spinning sideband manifolds in slow MAS spectra. The chemical shielding tensors in *a* and *b* were calculated from the published X-ray diffraction structure of α-glucose·H_2O[36] (*a*) before and (*b*) after geometry optimization of the H positions, while those in *c* and *d* were calculated from the neutron diffraction structure of α-glucose[37] (*c*) before and (*d*) after geometry optimization of the H positions. The dashed lines indicate the best fits with the slope fixed to –1. In *a* and *c* the solid lines indicate the line of best fit, while in *b* and *d* each solid line corresponds to the equation $\sigma = -1.139\delta + 177.9$ ppm[48] (see text).

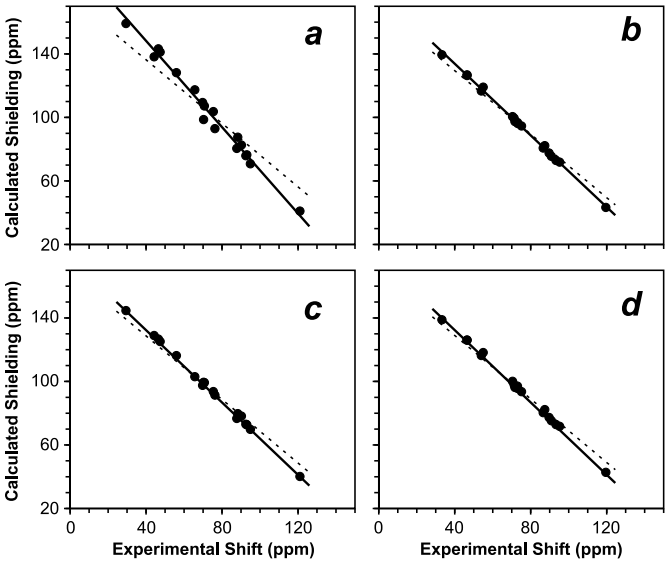

Table 1. Results of linear least-squares fitting of the relationship between calculated chemical shielding and experimental chemical shifts in Fig. 7.

Structure	Slope	Intercept	RMSD
α-Glucose·H_2O			
XRD structure	–1.358	202.6	2.8
H-optimized	–1.149	179.6	1.0
α-Glucose			
Neutron structure	–1.128	178.9	0.9
H-optimized	–1.123	178.0	0.9

line of best fit for all the data is $\sigma = -1.137\delta + 178.9$ ppm with an overall RMSD of 1.0 ppm.

Johnston and co-workers recently reported the exact same phenomenon in a very detailed study of GIPAW DFT calculations of ^{13}C shielding tensors in carbohydrate crystal structures.[48] A set of 10 carbohydrates with the highest quality crystal structures and solid-state NMR data were examined; each of the structures examined was determined from single-crystal neutron diffraction and the ^{13}C chemical shift tensors were all determined from single-crystal NMR experiments. Calculations of the ^{13}C chemical shielding tensors were performed under the same conditions as those reported in this work (using CASTEP at the "fine" level of calculation after optimizing the hydrogen atom positions). For the entire set of ^{13}C tensors from all of the structures, the relationship between calculated shieldings and experimental shifts was found to be $\sigma = -1.139\delta + 177.9$ ppm with an overall RMSD of 1.88 ppm.

Fig. 8. Comparison of experimental and calculated ^{13}C isotropic chemical shifts for (*a*) α-glucose·H_2O and (*b*) α-glucose. The relationship $\sigma = -1.139\delta + 177.9$ ppm[48] was used to convert calculated chemical shieldings to chemical shifts.

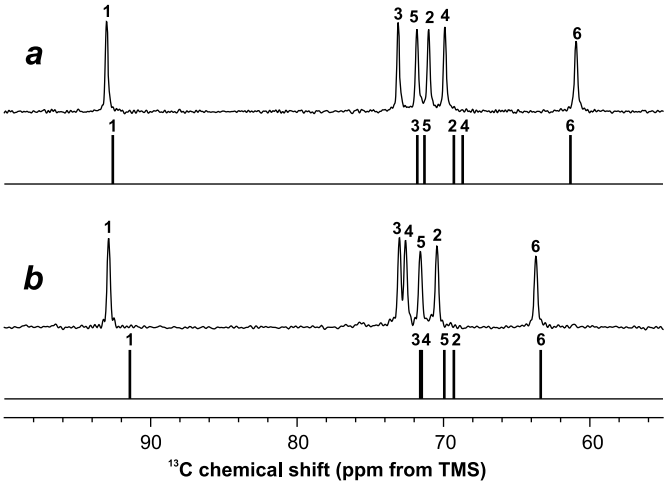

The results presented here for α-glucose·H_2O and α-glucose are entirely consistent with this larger data set. As shown in Figs. 7*b* and 7*d*, both sets of data are very well fit by the relationship derived from this larger high-quality data set. The RMSDs of the data points from this line are 1.3 and 1.5 ppm for α-glucose·H_2O and α-glucose, respectively.

Therefore, the relationship $\sigma = -1.139\delta + 177.9$ ppm found by Johnston and co-workers can reliably be used as a "calibration curve" for carbohydrates to convert calculated chemical shieldings into chemical shifts to make comparisons with experimental measurements of chemical shifts. These calculated principal components of the chemical shift tensors are listed in Tables S1 and S2 (see Supplementary data). In Fig. 8 the experimental and calculated isotropic chemical shifts are compared visually. In Fig. 5 the calculated Ω and κ for each ^{13}C tensor have been added for comparison purposes to the contour plots for the two experimental determinations of the chemical shift tensors. Additionally, the calculated principal components of the ^{13}C chemical shift tensors are compared in Fig. 9 with those determined experimentally by the two methods (along with estimates of their experimental uncertainties). In each of these representations, the agreement between calculated and experimental chemical shifts is shown to be quite remarkable. Therefore, we have confidence that measurements and calculations of ^{13}C chemical shift tensors hold promise to be valuable tools for future work in probing the crystal structures of cellulose in greater detail.

Johnston and co-workers[48] suggested two main reasons for the deviation of the slope from –1. The first is that the calculations assume a static molecule where temperature effects and zero-point energy corrections are neglected. Dumez and Pickard recently reported calculations that attempt to account for motional effects.[49] Although there is improved agreement when this is done, there is still a deviation from a slope of –1. The second suggested reason is that there are systematic

Can. J. Chem. Downloaded from www.nrcresearchpress.com by Xi'an Jiaotong University on 09/19/12
For personal use only.

Fig. 9. Comparison of principal components (δ_{11}, δ_{22}, δ_{33}) of the ^{13}C chemical shift tensors for (*a*) α-glucose·H_2O and (*b*) α-glucose calculated using CASTEP (filled diamonds) with those obtained from spinning sideband manifolds in slow MAS experiments (open circles) and those obtained from 2D CSA recoupling experiments (open squares). The relationship $\sigma = -1.139\delta + 177.9$ ppm[48] was used to convert calculated chemical shieldings to chemical shifts.

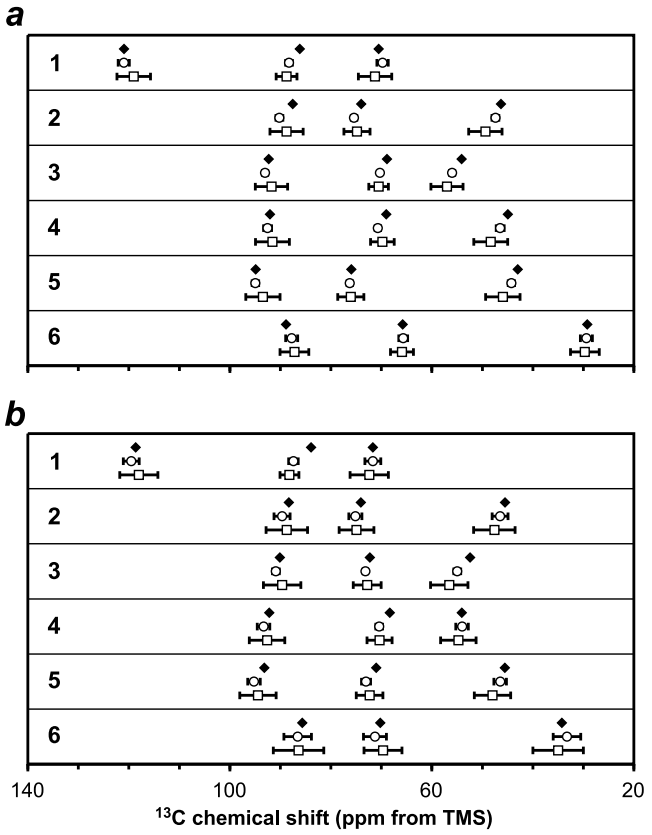

errors in the quantum chemical calculation method itself, related to the calculation of the paramagnetic contribution to the chemical shielding, which stem from the fact that it is difficult for existing exchange-correlation functionals to reproduce dynamic polarization in low electron density regions.[48] Nonetheless, with an appropriate calibration curve that relates chemical shieldings and chemical shifts, highly accurate calculations of chemical shift tensors can be still be performed.

Conclusions

The work presented here lays an important foundation for future solid-state NMR and quantum chemical calculation investigations of the various crystalline forms of cellulose. Using two crystalline forms of glucose, the monomer from which cellulose is constructed, we have established two important points. First, it has been demonstrated that the principal components of the ^{13}C chemical shift tensors in systems with complicated spectra (such as cellulose) can be reliably measured with the 2D recoupling experiment used here. The ^{13}C chemical shift tensors determined from spinning sideband manifolds and 2D recoupling spectra for α-glucose·H_2O and α-glucose are in good agreement, although higher uncertainties are to be expected for tensors determined from 2D recoupling experiments. Second, this work on glucose crystal structures demonstrates that quantum chemical calculations of ^{13}C chemical shift tensors are very accurate if two important precautions are taken. The crystal structure must have highly accurate atomic positions, especially hydrogen atom positions, which can be achieved by using a neutron diffraction structure or by performing a geometry optimization of hydrogen atom positions. The second precaution is that an appropriate conversion between calculated chemical shielding and chemical shifts must be applied. This work confirms the "calibration" for this conversion, as the results are very consistent with previous work on other carbohydrate crystal structures.[48]

With the confidence to accurately measure and calculate ^{13}C chemical shift tensors, it will be possible to evaluate the existing structural models for the various forms of crystalline cellulose[2–4] by comparing experimentally measured and quantum chemical calculated chemical shift tensors. For example, these experiments could potentially adjudicate between two reported structures of cellulose I_α.[4,50] Should neither of these structural models show consistency between calculated and experimental chemical shifts, CASTEP calculations also provide the ability to perform geometry optimizations of the structures which may, in the end, lead to more accurate structural models of cellulose. This would be a significant achievement in the field of NMR crystallography.

Supplementary data

Supplementary data (Figs. S1 and S2, Tables S1 and S2) are available with the article through the journal Web site (www.nrcresearchpress.com/cjc).

Acknowledgements

Access to the 200 MHz solid-state NMR spectrometer was provided by the National Research Council Canada. Access to CASTEP software was provided by the National Ultra-high-field NMR Facility for Solids (http://nmr900.ca). We thank Victor Terskikh for assistance with NMR experiments and quantum chemical calculations. We thank the Natural Sciences and Engineering Research Council of Canada for research support in the form of a Discovery Grant (D.H.B.) and an undergraduate student research award (Q.F.).

References

(1) Atalla, R. J.; Vanderhart, D. L. *Science* **1984** *223* (4633), 283. doi:10.1126/science.223.4633.283.
(2) Langan, P.; Nishiyama, Y.; Chanzy, H. *J. Am. Chem. Soc.* **1999** *121* (43), 9940. doi:10.1021/ja9916254.
(3) Nishiyama, Y.; Langan, P.; Chanzy, H. *J. Am. Chem. Soc.* **2002** *124* (31), 9074. doi:10.1021/ja0257319.
(4) Nishiyama, Y.; Sugiyama, J.; Chanzy, H.; Langan, P. *J. Am. Chem. Soc.* **2003** *125* (47), 14300. doi:10.1021/ja037055w.
(5) *NMR Crystallography*; Harris, R. K., Wasylishen, R. E., Duer, M. J., Eds.; John Wiley and Sons Ltd.: Chichester, 2009.
(6) Dutour, J.; Guillou, N.; Huguenard, C.; Taulelle, F.; Mellot-Draznieks, C.; Ferey, G. *Solid State Sci.* **2004** *6* (10), 1059. doi:10.1016/j.solidstatesciences.2004.07.031.
(7) Hedin, N.; Graf, R.; Christiansen, S. C.; Gervais, C.; Hayward, R. C.; Eckert, J.; Chmelka, B. F. *J. Am. Chem. Soc.* **2004** *126* (30), 9425. doi:10.1021/ja040030s.
(8) Brouwer, D. H.; Darton, R. J.; Morris, R. E.; Levitt, M. H.

J. Am. Chem. Soc. **2005** *127* (29), 10365. doi:10.1021/ja052306h.
(9) Fyfe, C. A.; Brouwer, D. H. *J. Am. Chem. Soc.* **2006** *128* (36), 11860. doi:10.1021/ja060744y.
(10) Brouwer, D. H. *J. Am. Chem. Soc.* **2008** *130* (20), 6306. doi:10.1021/ja800227f.
(11) Brouwer, D. H. *J. Magn. Reson.* **2008** *194* (1), 136. doi:10.1016/j.jmr.2008.06.020.
(12) Brouwer, D. H.; Moudrakovski, I. L.; Darton, R. J.; Morris, R. E. *Magn. Reson. Chem.* **2010** *48* (S1), S113. doi:10.1002/mrc.2642.
(13) Elena, B.; Emsley, L. *J. Am. Chem. Soc.* **2005** *127* (25), 9140. doi:10.1021/ja051208t.
(14) Elena, B.; Pintacuda, G.; Mifsud, N.; Emsley, L. *J. Am. Chem. Soc.* **2006** *128* (29), 9555. doi:10.1021/ja062353p.
(15) Pickard, C. J.; Salager, E.; Pintacuda, G.; Elena, B.; Emsley, L. *J. Am. Chem. Soc.* **2007** *129* (29), 8932. doi:10.1021/ja071829h.
(16) Salager, E.; Stein, R. S.; Pickard, C. J.; Elena, B.; Emsley, L. *Phys. Chem. Chem. Phys.* **2009** *11* (15), 2610. doi:10.1039/b821018g.
(17) Salager, E.; Day, G. M.; Stein, R. S.; Pickard, C. J.; Elena, B.; Emsley, L. *J. Am. Chem. Soc.* **2010** *132* (8), 2564. doi:10.1021/ja909449k.
(18) Harris, R. K.; Hodgkinson, P.; Pickard, C. J.; Yates, J. R.; Zorin, V. *Magn. Reson. Chem.* **2007** *45* (S1), S174. doi:10.1002/mrc.2132.
(19) Harris, R. K.; Cadars, S.; Emsley, L.; Yates, J. R.; Pickard, C. J.; Jetti, R. K. R.; Griesser, U. J. *Phys. Chem. Chem. Phys.* **2007** *9* (3), 360. doi:10.1039/b614318k.
(20) Harris, R. K. *Solid State Sci.* **2004** *6* (10), 1025. doi:10.1016/j.solidstatesciences.2004.03.040.
(21) Harper, J. K.; Grant, D. M.; Zhang, Y.; Lee, P. L.; Von Dreele, R. *J. Am. Chem. Soc.* **2006** *128* (5), 1547. doi:10.1021/ja055570j.
(22) Harper, J. K.; Doebbler, J. A.; Jacques, E.; Grant, D. M.; Von Dreele, R. B. *J. Am. Chem. Soc.* **2010** *132* (9), 2928. doi:10.1021/ja907671p.
(23) Brouwer, D. H.; Enright, G. D. *J. Am. Chem. Soc.* **2008** *130* (10), 3095. doi:10.1021/ja077430a.
(24) Pickard, C. J.; Mauri, F. *Phys. Rev. B* **2001** *63* (24), 245101. doi:10.1103/PhysRevB.63.245101.
(25) Yates, J. R.; Pickard, C. J.; Mauri, F. *Phys. Rev. B* **2007** *76* (2), 024401. doi:10.1103/PhysRevB.76.024401.
(26) Yates, J. R.; Pickard, C. J. Computation of Magnetic Resonance Parameters for Crystalline Systems: Principles. In *NMR Crystallography*; Harris, R. K., Wasylishen, R. E., Duer, M. J., Eds.; John Wiley and Sons: Chichester, 2009; pp 29–40.
(27) Clark, S. J.; Segall, M. D.; Pickard, C. J.; Hasnip, P. J.; Probert, M. I. J.; Refson, K.; Payne, M. C. *Z. Kristallogr.* **2005** *220* (5–6), 567. doi:10.1524/zkri.220.5.567.65075.
(28) Harris, R. K.; Hodgkinson, P.; Pickard, C. J.; Yates, J. R.; Zorin, V. Chemical Shift Computations for Crystalline Molecular Systems: Practice. In *NMR Crystallography*; Harris, R. K., Wasylishen, R. E., Duer, M. J., Eds.; John Wiley and Sons: Chichester, 2009; pp 81–97.
(29) Hestrin, S.; Schramm, M. *Biochem. J.* **1954** *58*, 345.
(30) Fung, B. M.; Khitrin, A. K.; Ermolaev, K. *J. Magn. Reson.* **2000** *142* (1), 97. doi:10.1006/jmre.1999.1896.
(31) Tycko, R.; Dabbagh, G.; Mirau, P. A. *J. Magn. Reson.* **1989** *85*, 265.
(32) Herzfeld, J.; Berger, A. E. *J. Chem. Phys.* **1980** *73* (12), 6021. doi:10.1063/1.440136.
(33) Bak, M.; Rasmussen, J. T.; Nielsen, N. C. *J. Magn. Reson.* **2000** *147* (2), 296. doi:10.1006/jmre.2000.2179.
(34) *Materials Studio*, version 4.4. Accelrys. Available from http://accelrys.com.
(35) Perdew, J. P.; Burke, K.; Ernzerhof, M. *Phys. Rev. Lett.* **1996** *77* (18), 3865. doi:10.1103/PhysRevLett.77.3865.
(36) Hough, E.; Neidle, S.; Rogers, D.; Troughton, P. G. H. *Acta Crystallogr.* **1973** *B29*, 365.
(37) Brown, G. M.; Levy, H. A. *Acta Crystallogr.* **1979** *B35*, 656.
(38) Pfeffer, P. E.; Hicks, K. B.; Frey, M. H.; Opella, S. J.; Earl, W. L. *J. Carb. Chem.* **1984** *3* (2), 197. doi:10.1080/07328308408058815.
(39) Frydman, L.; Chingas, G. C.; Lee, Y. K.; Grandinetti, P. J.; Eastman, M. A.; Barrall, G. A.; Pines, A. *J. Chem. Phys.* **1992** *97* (7), 4800. doi:10.1063/1.463860.
(40) Gan, Z. *J. Am. Chem. Soc.* **1992** *114* (21), 8307. doi:10.1021/ja00047a062.
(41) Hu, J. Z.; Orendt, A. M.; Alderman, D. W.; Pugmire, R. J.; Ye, C.; Grant, D. M. *Solid State Nucl. Magn. Reson.* **1994** *3* (4), 181. doi:10.1016/0926-2040(94)90039-6.
(42) Antzutkin, O. N.; Shekar, S. C.; Levitt, M. H. *J. Magn. Reson. A* **1995** *115* (1), 7. doi:10.1006/jmra.1995.1142.
(43) Crockford, C.; Geen, H.; Titman, J. J. *Chem. Phys. Lett.* **2001** *344* (3–4), 367. doi:10.1016/S0009-2614(01)00820-X.
(44) Gullion, T. *J. Magn. Reson.* **1989** *85*, 614.
(45) Orr, R. M.; Duer, M. J.; Ashbrook, S. E. *J. Magn. Reson.* **2005** *174* (2), 301. doi:10.1016/j.jmr.2005.03.001.
(46) Bax, A.; Szeverenyi, N. M.; Maciel, G. E. *J. Magn. Reson.* **1983** *51*, 400.
(47) Liu, S. F.; Mao, J. D.; Schmidt-Rohr, K. *J. Magn. Reson.* **2002** *155* (1), 15. doi:10.1006/jmre.2002.2503.
(48) Johnston, J. C.; Iuliucci, R. J.; Facelli, J. C.; Fitzgerald, G.; Mueller, K. T. *J. Chem. Phys.* **2009** *131* (14), 144503. doi:10.1063/1.3225270.
(49) Dumez, J.-N.; Pickard, C. J. *J. Chem. Phys.* **2009** *130* (10), 104701. doi:10.1063/1.3081630.
(50) Witter, R.; Sternberg, U.; Hesse, S.; Kondo, T.; Koch, F. T.; Ulrich, A. S. *Macromolecules* **2006** *39* (18), 6125. doi:10.1021/ma052439n.

Can. J. Chem. Downloaded from www.nrcresearchpress.com by Xi'an Jiaotong University on 09/19/12
For personal use only.

Zero-mode TEM parallel-plate resonator for high-resolution thin film magnetic resonance imaging

Ziheng Zhang, Andrew E. Marble, Rodney P. MacGregor, Jonathan Martin, Haijiang Wang, and Bruce J. Balcom

Can. J. Chem. Downloaded from www.nrcresearchpress.com by Xi'an Jiaotong University on 09/19/12
For personal use only.

Abstract: A parallel-plate radio frequency resonator has been designed for high-resolution thin film magnetic resonance imaging. The $\mathbf{B}_1$ field produced by the resonator was evaluated through experiment and numerical simulation. The resonator, composed of two conductive plates sandwiching the sample, generates a uniform $\mathbf{B}_1$ field parallel to the plates. This feature renders the resonator largely immune to radio frequency screening from conductive layers parallel to the sample. The resonator is custom fabricated according to the dimensions of the sample, yielding a high filling factor. The radio frequency probe is shown to facilitate high-sensitivity depth profiling of thin films. Three variations on the basic design are examined. Since the intention is to employ these resonators for functional studies of membranes, we introduce perforations in the parallel plates to permit mass transfer in and out of the thin films under study. One-dimensional depth profiles of Nafion 117 are presented with and without the addition of additional plates of conductive material. One-dimensional depth profiles of Nafion 1110 and a two-dimensional image of Nafion 117 in an operating fuel cell, which was integrated into the radio frequency circuit, are also illustrated.

Key words: RF coil, parallel plate, zero-mode transverse electric and magnetic (TEM), Nafion, fuel cell.

Résumé : On a développé un résonateur de radiofréquence à plaques parallèles pour l'imagerie de résonance magnétique à haute résolution de films minces. On a évalué le champ $\mathbf{B}_1$ produit par le résonateur par le biais d'une expérience et d'une simulation numérique. Le résonateur, qui est composé de deux plaques conductrices maintenant l'échantillon en sandwich, génère un champ $\mathbf{B}_1$ uniforme, parallèle aux plaques. Cette caractéristique fait que le résonateur est grandement protégé de l'effet d'écran de radiofréquence des couches conductrices parallèles à l'échantillon. Le résonateur a été fabriqué sur mesure, d'après les dimensions de l'échantillon, ce qui lui assure un facteur de remplissage élevé. On a démontré que la sonde de radiofréquence facilite une grande sensibilité dans la détermination du profil en profondeur des films minces. On a examiné trois variations sur le modèle de base. Puisque l'intention est d'utiliser ces résonateurs pour des études fonctionnelles de membranes, on a introduit des perforations dans les plaques parallèles afin de permettre des transferts de masse à partir de et vers les films minces étudiés. On présente les profils de profondeur unidimensionnelle du Nafion 117, avec et sans addition de plaques additionnelles de matériel conducteur. On illustre aussi les profils de profondeur unidimensionnelle du Nafion 1110 et une image bidimensionnelle du Nafion 117 dans une pile à combustible opérationnelle intégrée dans un circuit de radiofréquence.

Mots-clés : bobine RF, plaque parallèle, mode électrotransversal (MET) zéro, Nafion, pile à combustible.

[Traduit par la Rédaction]

Introduction

In high-resolution magnetic resonance imaging (MRI), selecting a suitable resonator is of great significance in determining the final signal-to-noise ratio (SNR).[1] The surface coil, due to its strong $\mathbf{B}_1$ field strength, is often a natural selection for this purpose.[2,3] However, the sensitivity of the surface coil decreases rapidly with distance.

In previous high-resolution imaging of thin films, we positioned a surface coil directly below the thin film sample.[4] The $\mathbf{B}_1$ field is thus perpendicular to the plane of the film. However, in many practical thin film devices, for example,

Received 1 November 2010. Accepted 9 January 2011. Published at www.nrcresearchpress.com/cjc on 3 May 2011.

Z. Zhang[†], **R.P. MacGregor, and B.J. Balcom.** MRI Centre, Department of Physics, University of New Brunswick, Fredericton, NB E3B 5A3, Canada.
A.E. Marble.[‡] Department of Electrical Engineering, P.O. Box 4400, University of New Brunswick, Fredericton, NB E3B 5A3, Canada.
J. Martin and H. Wang. Institute for Fuel Cell Innovation, National Research Council of Canada, Vancouver, BC V6T 1W5, Canada.

Corresponding author: B.J. Balcom (e-mail: bjb@unb.ca).

This article is part of a Special Issue dedicated to Professor Roderick E. Wasylishen.

[†]Present address: Department of Diagnostic Radiology, Yale University School of Medicine, P.O. Box 208043, New Haven, CT 06520-8043, USA.
[‡]Present address: Department of Systems and Computer Engineering, 1125 Colonel By Drive, Carleton University, Ottawa, ON K1S 5B6, Canada.

Can. J. Chem. Downloaded from www.nrcresearchpress.com by Xi'an Jiaotong University on 09/19/12
For personal use only.

fuel cells and batteries, the thin layer of interest is sandwiched between conductive electrodes. In these cases the radio frequency (RF) excitation of a surface coil will be shielded from the thin film. Moving to lower RF will increase the skin depth and potentially permit better excitation, but this is not an appealing strategy. A better choice, which we explore in this paper, is to introduce a $\mathbf{B}_1$ field oriented parallel to the plane of the thin film while still orthogonal to $\mathbf{B}_0$. A surface coil is clearly not appropriate for this application, while the use of a standard volume coil will incur a substantial filling factor penalty.

Parallel-plate resonators have been employed in many scientific areas,[5,6] but their use is relatively new for thin film MRI. Zhang et al. have employed a type of parallel-plate resonator to study liquid crystal properties in both bulk and constrained thin film capillaries[7] and have undertaken chemical shift resolved velocity mapping in microfluidic systems.[8] A similar RF coil has been developed for MRI histology by Meadowcroft et al.[9] The Meadowcroft design was not intended to be part of a functioning electrochemical device and does not permit mass transport through the resonator plates, contrary to the current design.

For thin film MRI, in this study we present a zero-mode transverse electric and magnetic (TEM)[10] parallel-plate resonator, which uses two parallel conductive plates to sandwich the sample. This approach avoids the RF shielding problem, as the plates are in the same orientation as the conductors in the sample, and the resultant $\mathbf{B}_1$ field is parallel to the plane of the membrane being imaged. A homogeneous current distribution on the plates will lead to a homogeneous $\mathbf{B}_1$ field distribution. In addition, such a resonator will structurally confine the sample and maintain its geometrical shape with controlled pressure if the sample is morphologically sensitive to its environment. The parallel-plate resonator features high sensitivity, because the excitation volume will structurally match the sample size, yielding a high filling factor.

We compare the experimental $\mathbf{B}_1$ field distribution with the results of numerical simulations for different plate assemblies. We also present the results of high-resolution depth imaging of Nafion 117 membranes with graphite plates of different thicknesses inserted inside the parallel-plate resonator. Testing with graphite plates adjacent to the resonator is critical in regards to use of the parallel-plate resonator for studies of electrochemical cells, for example a fuel cell. The graphite plates provide mechanical support and an electrical connection to the remainder of the electrochemical cell.

As the resonator is immediately adjacent to the sample, it will distort the $\mathbf{B}_0$ field and introduce artifacts into a frequency-encoded image if the plate material's magnetic susceptibility differs substantially from that of the sample. Pure phase-encoding methods were implemented in all measurements because they are free from distortions due to $\mathbf{B}_0$ inhomogeneity, susceptibility variations, and chemical shift.[11,12] Two-dimensional centric-scan SPRITE imaging was employed to visualize the $\mathbf{B}_1$ field distribution generated by the parallel-plate resonator. Double half *k*-space (DHK) spin echo (SE) single point imaging (SPI)[4,13] was employed to acquire high-resolution water content profiles of Nafion samples. Both techniques are centric-scan MRI methods, with an extended recovery time preceding each $k = 0$ RF pulse to permit full recovery of longitudinal magnetization, M_z, and are thus immune to T_1-contrast.[14–16]

The application of MRI methods to study water content and water transport in Nafion proton electrolyte membrane fuel cells was pioneered by Tsushima[17,18] and Wasylishen.[19,20] This new parallel-plate resonator aims to improve the limited MRI sensitivity of conventional RF probes that hinders sensitivity and limits resolution. To demonstrate its capabilities, an image was acquired of water in the membrane layer of an operating fuel cell. The fuel cell design requires that the layer be sandwiched between conductive plates during operation. The new resonator design, combined with the DHK SE SPI method, allows high-resolution (less than 10 μm) 1D images with SNR > 40 to be acquired in 90 s. Information about the structure and function of an operating fuel cell may be inferred from such high-quality results.

The current paper is intended as background justification and explanation of the RF probe employed in our recent MRI study of an operational fuel cell.[21]

Theory

RF circuit with an integrated parallel-plate transmission line

A schematic diagram of the parallel-plate resonator is presented in Fig. 1. The parallel plates sandwich the thin film sample and are bolted together as illustrated. The $\mathbf{B}_1$ field from a plate curls around the flowing current. Therefore, the fields from both plates add along *x* in the gap between them and cancel outside. If the thin film sample is layered with conductive material, the cross section seen by $\mathbf{B}_1$ is small and there is therefore minimal interference from the conductor.

The parallel plates chiefly represent a distributed inductance, but there will be a substantial capacitive component for closely spaced plates. The inductance is tuned to resonance with a fixed capacitor, C_m, and a standard matching circuit, as shown in the figure.

Numerical simulation

A design with perforated plates, allowing mass transport through the resonator to the sample, was required. Changes in the field due to the plate geometry were first studied through simulation. The longest dimension of the resonator was ~9 cm and as a result only the TEM00 mode will be excited at the 100 MHz operating frequency. This mode will have the same field pattern as for a static current flowing in the plates, allowing static methods to be used in modeling the probe.

The current distribution in the plates was simulated by modeling each plate as a grid of vanishingly small, equal resistors. Assuming the current enters the plate at a single point and leaves it at a second point, the current distribution in the resistor grid is obtained by numerically solving Kirchoff's voltage and current laws. The corresponding magnetic field was calculated from the current distribution using the Biot–Savart law.

Can. J. Chem. Downloaded from www.nrcresearchpress.com by Xi'an Jiaotong University on 09/19/12
For personal use only.

Fig. 1. (*a*) Schematic of a zero-mode parallel-plate resonator. The sample membrane was sandwiched between the plates. (*b*) Simplified diagram of the parallel-plate resonator for numerical simulation. (*c*) Three different designs for the top plate of the resonator, which were separately employed for numerical simulation and experimental visualization of the $\mathbf{B}_1$ field distribution. The bottom plate of the resonator was solid in all three cases.

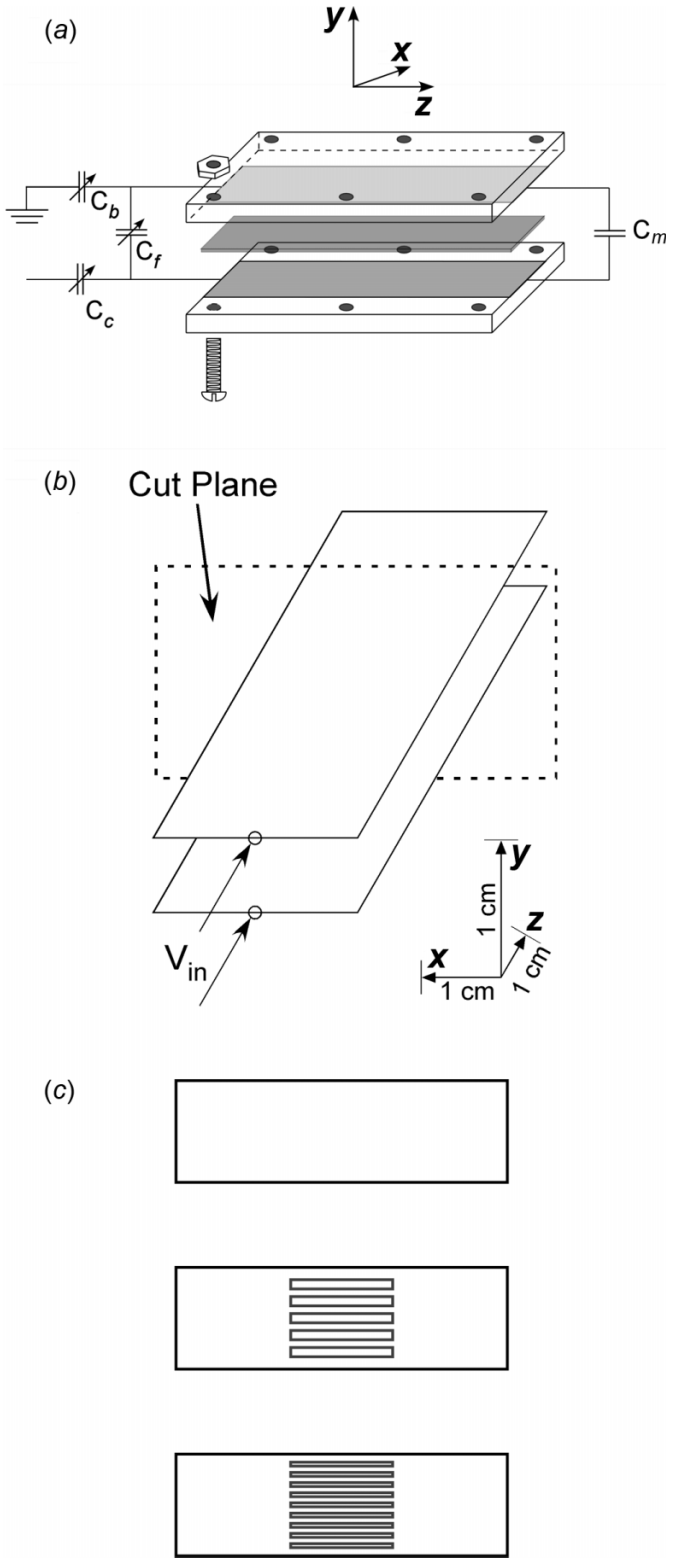

Results and discussion

Numerical simulation with experimental examination in three cases

Three cases, illustrated in Figs. 2–4, were investigated through simulations and imaging experiments. The figures show current and magnetic field distributions and imaging results for the cases of a solid top plate, a top plate with several large longitudinal slits, and a top plate with a large number of smaller slits cut to permit mass transport. The plate geometry for the three cases is illustrated in Fig. 1*c*. The bottom plate was solid in each case. Plot (*a*) of each figure shows the simulated current distribution in the top plate. Plot (*b*) is a 2D magnetic resonance image of a silicone rubber film sample acquired with the chosen parallel-plate resonator. The local image intensity reflects the $\mathbf{B}_1$ field strength, which is expected to be proportional to the local current intensity in the plates. Plot (*c*) is the simulated magnetic field in a cut-plane, as illustrated in Fig. 1*b*, along *x* through the center of the resonator. The position of the plates is indicated by the horizontal lines. Plot (*d*) is a 1D MRI profile from a 2D image along *x* of the rubber phantom, arbitrarily selected from plot (*b*) around the middle region of the parallel-plate resonator. The length scale of the simulations is arbitrary but has been selected to show the features of the field–current distribution.

Figure 2*a* illustrates that for the solid plate, there is a small region close to the current feed point where the current is not uniform. The current quickly becomes uniform in the central region of the plate. This is reflected experimentally in Fig. 2*b*. The image acquisition parameters are such that the signal intensity is proportional to the magnetic field $\mathbf{B}_1$. With the exception of the feed points, which have a higher current density, the signal intensity is uniform throughout the image. The uniformity of the field between the plates is clear from Fig. 2*c* and is confirmed by the uniform profile in Fig. 2*d*.

Figure 3*a* depicts the current distribution for a plate with several large slits. The current in each remaining "rung" is equal and reasonably uniform. The current distribution away from the slits is not substantially changed from that of the solid plate. In Fig. 3*b*, gaps in the signal appear in the position of the slots and the signal over the rungs is higher than that over the surrounding plate, owing to the higher current density. In Fig. 3*c*, the effect of the slits in the top plate is pronounced: the field between the plates varies by ~50%, depending on the position. The variation decreases closer to the bottom plate. This manifests as a series of peaks and troughs in the profile (Fig. 3*d*).

The results for the case of many smaller slits, Fig. 4, are comparable to those in Fig. 3. However, the effect of the smaller slits is less pronounced than for the previous case. This is expected, as it is well known that the extent of a disturbance in a magnetic field will occur on the length scale of the feature creating the perturbation.[22] Thus, many smaller slits is a better choice.

High-resolution depth imaging with and without integrated graphite plates

A primary goal of the parallel-plate resonator design was robust behavior in the presence of conductive layers adjacent to the sample. With this in mind, depth profiles through thin

Can. J. Chem. Downloaded from www.nrcresearchpress.com by Xi'an Jiaotong University on 09/19/12
For personal use only.

Fig. 2. (*a*) Calculated current distribution in a parallel-plate resonator with a solid top plate. (*b*) 2D lateral image of a rubber sheet phantom, to illustrate the $\mathbf{B}_1$ field distribution. The sensitivity of the probe at the current input was pronounced. The dashed line illustrates the slice position of figure (*d*). (*c*) $\mathbf{B}_1$ field distribution in the cross section. The position of the conductive plates is indicated by the white horizontal lines. The grayscale levels in (*a*), (*b*), and (*c*) for current, magnetic resonance image intensity, and $\mathbf{B}_1$ field strength are all plotted in arbitrary units, with white corresponding to the highest relative intensity. (*d*) A profile across the short axis of the 2D image. The image intensity between the plates is homogeneous.

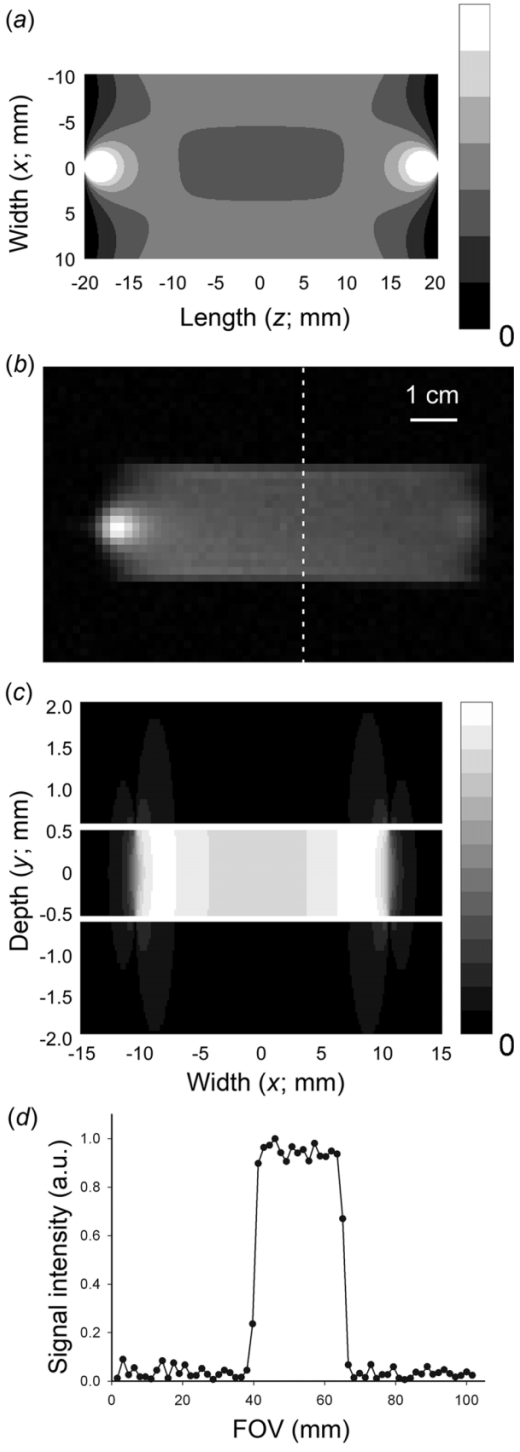

Fig. 3. (*a*) Current distribution for a plate with several large slits. (*b*) The corresponding 2D image of the rubber phantom. The dashed line illustrates the slice position of figure (*d*). (*c*) The calculated magnetic field. The grayscale levels in (*a*), (*b*), and (*c*) for current, magnetic resonance image intensity, and $\mathbf{B}_1$ field strength are all plotted in arbitrary units, with white corresponding to the highest relative intensity. (*d*) The profile across the short axis of image (*b*), by averaging the profiles located in the area where slots exist. Because of the finite image resolution, the peaks on the profile are not of the same intensity.

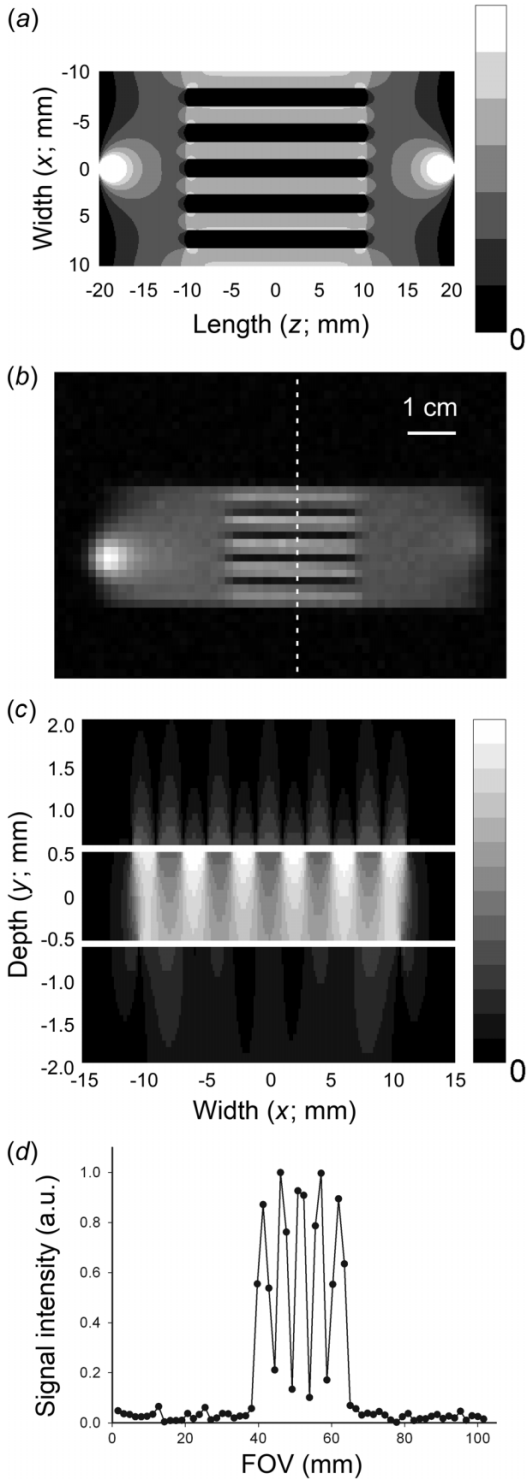

Can. J. Chem. Downloaded from www.nrcresearchpress.com by Xi'an Jiaotong University on 09/19/12
For personal use only.

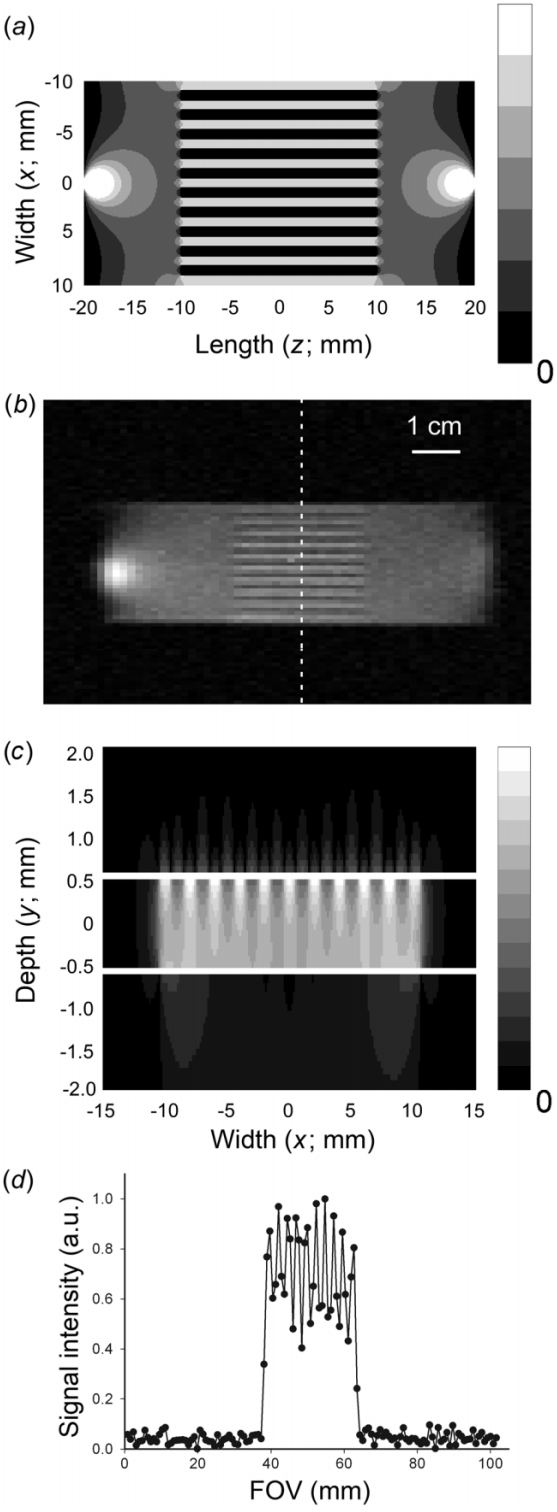

Fig. 4. (*a*) Current distribution for a plate with many small slits. (*b*) Corresponding magnetic resonance image. The dashed line illustrates the slice position of figure (*d*). The resolution of (*b*) in direction *x* was doubled, compared with Fig. 3*b*. (*c*) The $\mathbf{B}_1$ magnetic field distribution between the electrodes (figure from Zhang et al.,[21] reproduced with permission of *Journal of Magnetic Resonance*, © 2008 Elsevier). The grayscale levels in (*a*), (*b*), and (*c*) for current, magnetic resonance image intensity, and $\mathbf{B}_1$ field strength are all plotted in arbitrary units, with white corresponding to the highest relative intensity. (*d*) The averaged profile across the short axis of image (*b*), processed in the same way as in Fig. 3*d*.

films were obtained with and without the presence of conductive graphite plates.

High-resolution 1D depth profile of Nafion 117

A high-resolution depth profile of a fully hydrated Nafion 117 film, approximately 200 μm thick, was obtained with the parallel-plate resonator. The DHK SE SPI technique developed by Ouriadov et al.[4] was employed, with the result shown in Fig. 5*a*. The image was acquired in ~90 s with an SNR better than 40. The blurred edges of the profile indicate a degradation of the true image resolution compared with the nominal resolution, 4.5 μm. This occurs because of a mismatch between the encoding gradient direction and the axis normal to the sample plane.[4]

Depth profiles of Nafion 117 with graphite plates inserted

In a functional fuel cell, a thin membrane is sandwiched between conductive electrodes. Imaging water in this layer in situ requires the ability to tolerate the presence of conductive plates on either side of the membrane.

The previous depth-imaging experiments were repeated with a graphite plate inserted on either side of the sample to explore the effect of the conductive materials on the probe system. Two pieces of 0.254 cm thick graphite sheet were used to sandwich the Nafion 117 layer, and the resultant 1D depth profile is shown in Fig. 5*b*. Thicker (0.635 cm) graphite plates were then inserted, yielding the resulting profile shown in Fig. 5*c*. The nominal spatial resolution of both profiles, with the graphite plates, was approximately 5.5 μm.

The graphite plates degrade the performance of the parallel-plate resonator, as indicated by the decreased SNR and the increased blurring observed. Decreased SNR is due to higher resistive losses as the $\mathbf{B}_1$ field induces currents in the conductive graphite. In addition, the distance between the plates is increased substantially in the presence of the graphite, which decreases the filling factor.[23,24] The additional graphite plates will increase the probe resistance without substantially changing its inductance, therefore decreasing the quality (Q) factor, according to $Q = \omega_0 L/R$. If there is electrical contact between the probe plates and the conductive insert, some current will flow through the graphite and may contribute to the probe sensitivity. However, because the conductivity of graphite is approximately 100 times less than that of copper, according to Ohm's law, the amount of the current in the graphite plates will be quite small.

The corresponding Q value, SNR, and 90° pulse length of these three cases (no graphite, thin graphite layer, and thick graphite layer) are reported in Table 1. Notice that while the Q and SNR decrease as graphite is added, the pulse width changes minimally, indicating that the $\mathbf{B}_1$ strength is little affected by the presence of the conductors.

1D depth imaging and 2D lateral imaging of Nafion in an operating fuel cell

This parallel-plate resonator concept was developed specifically for the study of operating proton electrolyte membrane (PEM) fuel cells.[21] The water distribution within the PEM is a critical parameter in fuel cell operation, and an ongoing

Can. J. Chem. Downloaded from www.nrcresearchpress.com by Xi'an Jiaotong University on 09/19/12
For personal use only.

Fig. 5. (*a*) Depth profile of a static, fully hydrated Nafion 117 film. The image was derived from the first echo. (*b* and *c*) Similar depth profiles of water content across Nafion 117 film, with 2.54 mm and 6.35 mm graphite plates sandwiching the membrane, respectively. The SNR and the resolution were degraded compared with (*a*).

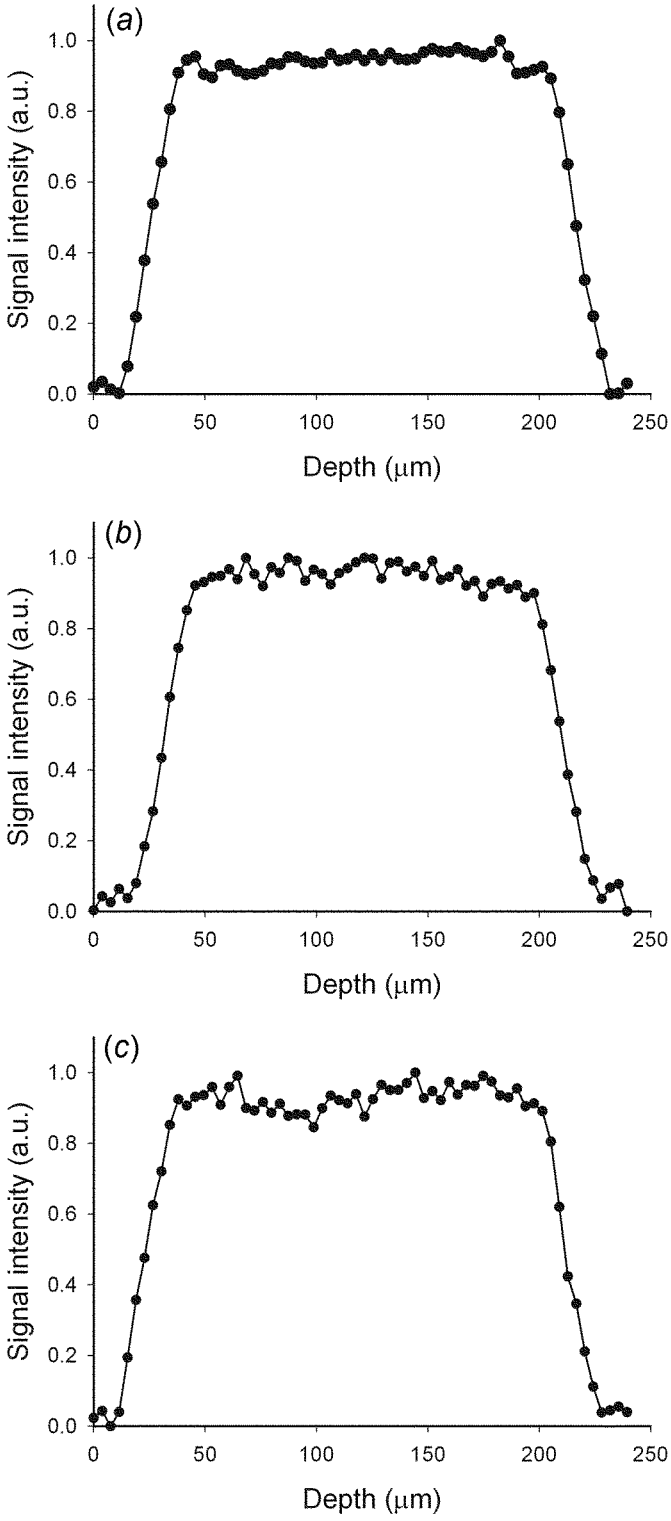

challenge is to obtain quantitative water maps within an operating cell. At the heart of a typical fuel cell is the membrane electrode assembly (MEA), which is a PEM (in this case, Nafion 1110) sandwiched between two conductive gas diffusion electrodes, which represent the catalyst-sprayed gas diffusion layers. The MEA is held by two conductive plates, perforated to allow the ingress of water, hydrogen, and oxygen.[25,26] The presence of the metal electrodes has previously hindered attempts to image operating fuel cells using MRI.[27]

Table 1. Quality (*Q*) factor, signal-to-noise ratio (SNR), and 90° pulse length for a Nafion 117 sample in the parallel-plate resonator.

	SNR	*Q* factor	90° pulse length (μs)
No graphite	41	115	10.5
Thin graphite (2.54 mm thick)	26	70	12.5
Thick graphite (6.35 mm thick)	15	52	13.5

A homemade operating fuel cell was designed following the schematic shown in Fig. 6*a*. The electrodes of the homemade fuel cell were made of gold-plated printed circuit (PC) boards, with slots cut in the surface to allow gas flow. The Nafion layer, sandwiched by two catalyst-sprayed gas diffusion layers, is held between the electrodes. This assembly was tightened by brass bolts to a desired pressure and sealed with homemade Teflon O-rings. As shown in Fig. 6*a*, this assembly was then connected with capacitors to complete the RF circuit and achieve probe tuning and matching. The capacitors block DC currents and thus do not affect the operation of the fuel cell. A 3 Ω carbon resistor was directly connected with the electrodes of the cell as the electrical load of the fuel cell. This resistor was located inside the magnet bore to reduce the external RF noise introduced to the experiment. In this design, the parallel plates of the RF resonator also function as electrodes of the fuel cell. The cell operated for 7 h, at which point several 1D depth profiles of the water content in Nafion during quasi-steady-state operation and a 2D lateral image of water in Nafion were acquired.

Four 1D 128-pixel profiles are illustrated in Fig. 6*b*, with the anode on the left side of the profiles and the cathode on the right side. During operation, the chemical reaction at the cathode generates water as a byproduct. Condensed water adjacent to the Nafion layer in the flow channels could introduce undesired signal into the water content profiles.[28] However, as illustrated in Fig. 4*c*, with small slots applied as flow channels, the $\mathbf{B}_1$ field beside the slots is approximately 10 times less than that beside the intact plate. In addition, the $\mathbf{B}_1$ fields inside the gas channels are very small and will not efficiently excite the water or vapor in the channels.[21] As a result, water content serves as a marker for chemical activity in the cell. We estimate the edges of the Nafion layer to be at 230 μm and 520 μm. The poor edge definition is due to sample misalignment with the imaging axis and potentially due to nonlinearity of the Nafion surface. An apparent peak is observed close to the cathode side, as predicted. The signal then decreases and levels out near the center of the profile. Near the anode, the signal intensity decreases once again. Less water is anticipated near the anode. All the above observations agree with our common understanding of an operational fuel cell.[25,26] MRI results of this type, however, offer the prospect of quantifiable studies.

In the 2D image shown in Fig. 6*c*, a generally uniform water signal intensity was observed. The slightly higher signal inten-

Can. J. Chem. Downloaded from www.nrcresearchpress.com by Xi'an Jiaotong University on 09/19/12
For personal use only.

Fig. 6. (*a*) Schematic of a homemade operating fuel cell combined into the RF probe circuit (figure from Zhang et al.,[21] reproduced with permission of *Journal of Magnetic Resonance*, © 2008 Elsevier). Outer load (⊗) and tuning capacitors are connected to complete the DC circuit for fuel cell operation and the high-frequency AC circuit for RF resonance. The outlets of the reactant gases, H_2 and air, are marked, while the inlet connections are on the left side but not shown. Grooves, as shown by discrete lines, are machined on two G10 fiberglass substrates, which support the PC boards, to generate paths for gas flow. (*b*) Four 1D depth profiles of water, acquired during quasi-steady-state operation of the cell. Each profile is from the first echo. Experiments (●), (○), (▼), and (▽) correspond to experimental times of 3.4, 3.6, 3.8, and 4.0 h, respectively. (*c*) Lateral 2D image, acquired with 2D SE SPI, of the operating fuel cell. The dashed lines indicate the position of the flow inlets/outlets on the left and right sides of the image. The flow inlets are illustrated in (*a*).

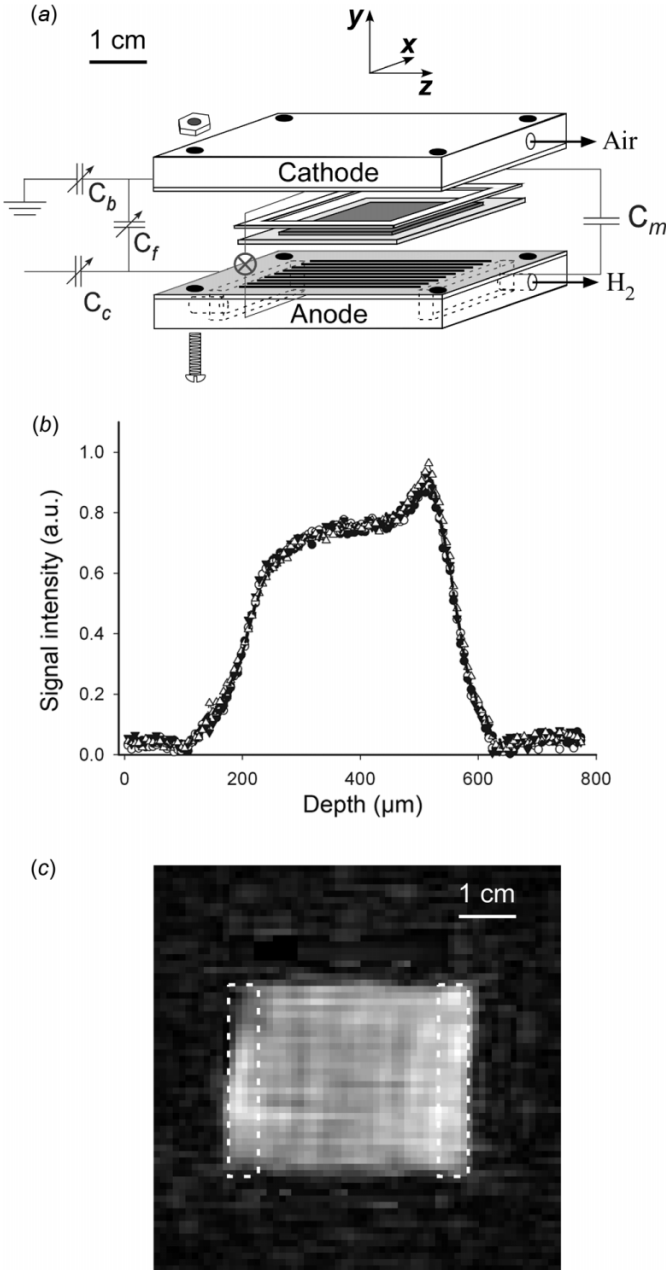

sity to the left and right suggests that water vapor in the humidified reactant gases may have condensed at the flow inlets.

The 2D image also confirms the essentially uniform excitation of this parallel-plate resonator. No pattern due to the perforated electrodes is observed in the image. The signal in this case is averaged over the depth of the Nafion. One-dimensional depth profiles of course do not reveal information about lateral variation in water content.

The parallel-plate resonator employed for this experiment used 30 slits, each 0.5 mm wide, to allow gas to flow to the membrane. The size of the slots was empirically determined through balancing the $\mathbf{B}_1$ uniformity in the lateral plane with the efficiency of feeding the reactant gases. As discussed above, because of the large number of small slits the spatial variation of signal intensity is minimal. In the 1D images, averaging over the lateral extent of the Nafion yields a smooth image with no manifestation of the slots employed for mass transport through the plates.

Conclusion

A novel parallel-plate RF resonator was investigated through experiment and simulation. The RF probe has an inherently high filling factor, which permits high-SNR imaging.

The parallel-plate resonator allows high-resolution depth imaging of thin films and can be employed in a fully functioning fuel cell. The presence of auxiliary conductive materials does not significantly degrade the performance of the probe.

Experimental

Design of the parallel-plate resonators and homemade operating fuel cell

Figure 1*a* shows the geometry of a typical parallel-plate resonator. Two pieces of 2.54 cm wide, 7.62 cm long copper tape were affixed to two pieces of G10 fiberglass substrate, 5.08 cm wide and 7.62 cm long, purchased from McMaster (Cleveland, Ohio). The phantom employed in the $\mathbf{B}_1$ field visualization measurements, a 381 μm thick silicone rubber sheet purchased from AAA-ACME (Tempe, Arizona), was cut to the same size as the copper tape.

The top plates with slots employed in the imaging measurements were made of PC board and were of the same size as the bottom copper tape. The slots were all cut 2.54 cm long, with a width of 2.38 mm for the larger ones and 0.79 mm for the smaller ones.

Each plate of the homemade operating fuel cell, 5 cm long and 4 cm wide, consists of a gold-plated PC board and the substrate to which it is affixed. Thirty slots, 3 cm long, 0.5 mm wide, and 0.5 mm deep, were cut and homogeneously distributed in a 3 cm × 3 cm area on the PC board, 1.59 mm in thickness. The substrate, 9.53 mm thick G10 fiberglass, was fabricated following the discrete line shown in Fig. 6*a* to construct a path for flow. Each gas-diffusion electrode was cut into a 3.2 cm × 3.2 cm square, and the Nafion was cut into a 3.5 cm × 3.5 cm square.

Nafion and its preparation

The sample films, Nafion 117, 178 μm thick, and Nafion

Can. J. Chem. Downloaded from www.nrcresearchpress.com by Xi'an Jiaotong University on 09/19/12
For personal use only.

1110, 250 μm thick, were purchased from Ion Power (New Castle, Delaware). The Nafion films were cut to desired sizes (2.03 cm × 6.10 cm for Nafion 117 and 2.54 cm × 2.54 cm for Nafion 1110) and pretreated by heating in ~3–5 wt % H_2O_2 solution at 80 °C for 1 h. The sample was then rinsed in deionized water at 80 °C for 1 h and then heated in 0.5 mol/L H_2SO_4 at 80 °C for 1 h. The sample was finally cleaned by prolonged heating in deionized water at 80 °C for 1 h to remove any possible chemical residues. The basic procedure was based on the work of Jalani et al.[29] and Moore and Martin.[30]

MRI details

The 2D DHK SPRITE and DHK SE SPI experiments were implemented on a Nalorac (Martinex, California) 2.4 T 32 cm i.d. horizontal-bore superconducting magnet. A water-cooled 7.5 cm i.d. gradient set driven by a Techron (Elkhart, Indiana) 8710 amplifier, which provided maximum gradients of 100 Gauss/cm, was employed for all experiments. The imaging console was a Tecmag (Houston, Texas) Apollo in all cases.

The homemade RF probes, driven by a 2 kW AMT (Brea, California) 3445 RF amplifier, were respectively custom-built single-channel parallel plate probes and an operating fuel cell style resonator. They were tuned to 100 MHz with three tuning capacitors, C_f, C_c, and C_b, in a standard series-parallel tank circuit. The fixed capacitor, C_m, illustrated in Fig. 1*a* and Fig. 6*a*, was 1000 pF.

In the 2D DHK SPRITE measurement, the encoding time, t_p, was 150 μs. The flip angle was 4.3° with a pulse duration of 0.5 μs. The dwell time was 4 μs with a repetition time of 2 ms. The 90° pulse length was 10.5 μs in all three cases.

Nafion 117, a form of perfluorosulfonic acid, is a hydrophilic ionic polymer with measured ^{1}H relaxation times that are reasonably long (T_1, 100 ms; T_2, 13 ms[31,32]) and ideally suited to these measurements.

In DHK SE SPI and 2D SE SPI measurements, the repetition time was maintained at 500 ms, a period approximately equal to $5T_1$. The encoding time, t_p, was 2.2 ms and the echo time was 5.5 ms. Dwell times were set to 200 μs to narrow the filter width in all measurements.

In high-resolution depth imaging measurements, the Nafion film cannot be exactly positioned at the origin of the gradient G_y. Experimental profiles therefore wrap around the field of view (FOV) and are translated into the center of the FOV for display and subsequent data processing.

Matrices of 64 points by 64 points were collected for most of the 2D lateral images, with one exception, a 64 by 128 *k*-space matrix employed in measurement of the $\mathbf{B}_1$ distribution with the presence of small slits in the top plate. For 1D depth images, 64 *k*-space points were collected. In the 2D DHK SPRITE measurements, 4 signal averages were accumulated for each profile, with an acquisition time of 30 min. In the DHK SE SPI measurements, the acquisition time was 90 s with 4 signal averages. Four averages, with a 2 h acquisition time, were acquired for 2D SE SPI measurement.

In the operational fuel cell measurement, the nominal resolution for the 1D depth image (Fig. 6*b*) is approximately 6 μm with an 800 μm FOV. The 2D lateral image (Fig. 6*c*) had a resolution of approximately 1.2 mm × 1.2 mm, with a FOV of 7.5 cm × 7.5 cm. No filtering or zero-filling was applied prior to Fourier transform for all the measurements. The SNR of the two experiments was, respectively, 40 and 15.

Acknowledgements

B.J.B. thanks NSERC of Canada for operating and equipment grants. B.J.B. also thanks the Canada Chairs program for a Research Chair in MRI of Materials (2002–2016). The MRI Centre was supported through an NSERC Major Resources Support award. We thank M. Olive and B. Titus for fabricating the plates and the frame of the probe.

References

(1) Callaghan, P. T. *Principles of Nuclear Magnetic Resonance Microscopy*; Clarendon Press: Oxford, 1991.
(2) Blumich, B. *NMR Imaging of Materials*; Clarendon Press: Oxford, 2000.
(3) McDonald, P. J. *Prog. Nucl. Magn. Reson. Spectrosc.* **1997** *30* (1–2), 69. doi:10.1016/S0079-6565(96)01035-7.
(4) Ouriadov, A. V.; MacGregor, R. P.; Balcom, B. J. *J. Magn. Reson.* **2004** *169* (1), 174. doi:10.1016/j.jmr.2004.04.015.
(5) Reible, S. A.; Wilker, C. W. *IEEE Trans. Magn.* **1991** *27* (2), 2813. doi:10.1109/20.133794.
(6) Talanov, V. V.; Mercaldo, L. V.; Anlage, S. M.; Claassen, J. H. *Rev. Sci. Instrum.* **2000** *71* (5), 2136. doi:10.1063/1.1150596.
(7) Zhang, J.; MacGregor, R. P.; Balcom, B. J. *Chem. Phys. Lett.* **2008** *461* (1–3), 106. doi:10.1016/j.cplett.2008.06.090.
(8) Zhang, J.; Balcom, B. J. *Magn. Reson. Imaging* **2010** *28* (6), 826. doi:10.1016/j.mri.2010.03.033.
(9) Meadowcroft, M. D.; Zhang, S.; Liu, W.; Park, B. S.; Connor, J. R.; Collins, C. M.; Smith, M. B.; Yang, Q. X. *Magn. Reson. Med.* **2007** *57* (5), 835. doi:10.1002/mrm.21213.
(10) Collin, R. E. *Field Theory of Guided Waves*; IEEE Press: New York, 1991; Chapter 3.
(11) Balcom, B. J.; MacGregor, R. P.; Beyea, S. D.; Green, D. P.; Armstrong, R. L.; Bremner, T. W. *J. Magn. Reson.* **1996** *123* (1), 131. doi:10.1006/jmra.1996.0225.
(12) Gravina, S.; Cory, D. G. *J. Magn. Reson. B.* **1994** *104* (1), 53. doi:10.1006/jmrb.1994.1052.
(13) Zhang, Z.; Marble, A. E.; MacMillan, B.; Promislow, K.; Martin, J.; Wang, H.; Balcom, B. J. *J. Magn. Reson.* **2008** *194* (2), 245. doi:10.1016/j.jmr.2008.07.011.
(14) Mastikhin, I. V.; Balcom, B. J.; Prado, P. J.; Kennedy, C. B. *J. Magn. Reson.* **1999** *136* (2), 159. doi:10.1006/jmre.1998.1612.
(15) Halse, M.; Rioux, J.; Romanzetti, S.; Kaffanke, J.; MacMillan, B.; Mastikhin, I.; Shah, N. J.; Aubanel, E.; Balcom, B. J. *J. Magn. Reson.* **2004** *169* (1), 102. doi:10.1016/j.jmr.2004.04.008.
(16) Zhang, Z.; Ouriadov, A. V.; Willson, C.; Balcom, B. J. *J. Magn. Reson.* **2005** *176* (2), 215. doi:10.1016/j.jmr.2005.06.009.
(17) Teranishi, K.; Tsushima, S.; Hirai, S. *Therm. Sci. Eng.* **2002** *10*, 59.
(18) Shim, J.; Tsushima, S.; Hirai, S. *ECS Trans.* **2009** *25*, 523. doi:10.1149/1.3210602.
(19) Feindel, K. W.; LaRocque, L. P.-A.; Starke, D.; Bergens, S. H.; Wasylishen, R. E. *J. Am. Chem. Soc.* **2004** *126* (37), 11436. doi:10.1021/ja0461116.
(20) Wang, M.; Feindel, K. W.; Bergens, S. H.; Wasylishen, R. E. *J. Power Sources* **2010** *195* (21), 7316. doi:10.1016/j.jpowsour.2010.05.029.
(21) Zhang, Z.; Martin, J.; Wu, J.; Wang, H.; Promislow, K.;

Balcom, B. J. *J. Magn. Reson.* **2008** *193* (2), 259. doi:10.1016/j.jmr.2008.05.005.
(22) Lupu, M.; Briguet, A.; Mispelter, J. *NMR Probeheads: For Biophysical and Biomedical Experiments*; Imperial College Press: London, 2006; Chapter 7.
(23) Hoult, D. I.; Richards, R. E. *J. Magn. Reson.* **1976** *24*, 71.
(24) Hoult, D. I. *Prog. Nucl. Magn. Reson. Spectrosc.* **1978** *12* (1), 41. doi:10.1016/0079-6565(78)80002-8.
(25) Wielstich, W.; Gasteiger, H. A.; Lamm, A. *Handbook of Fuel Cells: Fundamentals, Technology and Applications*; John Wiley & Sons: New York, 2003.
(26) Hoogers, G. *Fuel Cell Technology Handbook*; CRC Press: New York, 2000.
(27) Zhang, Z.; Balcom, B. J. Magnetic Resonance Imaging. In *Handbook of PEM Fuel Cell Durability*; Wong, H., Yuan, Y., and Li, H., Eds.; Taylor and Francis: Oxford, UK, 2011.
(28) Dunbar, Z. W.; Masel, R. I. *J. Power Sources* **2008** *182* (1), 76. doi:10.1016/j.jpowsour.2008.03.057.
(29) Jalani, N. H.; Choi, P.; Datta, R. *J. Membr. Sci.* **2005** *254* (1–2), 31. doi:10.1016/j.memsci.2004.12.020.
(30) Moore, R. B., III; Martin, C. R. *Macromolecules* **1988** *21* (5), 1334. doi:10.1021/ma00183a025.
(31) MacMillan, B.; Sharp, A. R.; Armstrong, R. L. *Polymer (Guildf.)* **1999** *40* (10), 2481. doi:10.1016/S0032-3861(98)00483-2.
(32) MacMillan, B.; Sharp, A. R.; Armstrong, R. L. *Polymer (Guildf.)* **1999** *40* (10), 2471. doi:10.1016/S0032-3861(98)00484-4.

Can. J. Chem. Downloaded from www.nrcresearchpress.com by Xi'an Jiaotong University on 09/19/12
For personal use only.

A multinuclear solid-state magnetic resonance and GIPAW DFT study of anhydrous calcium chloride and its hydrates

Cory M. Widdifield and David L. Bryce

Can. J. Chem. Downloaded from www.nrcresearchpress.com by Xi'an Jiaotong University on 09/19/12
For personal use only.

Abstract: The group 2 metal halides and corresponding metal halide hydrates serve as useful model systems for understanding the relationship between the electric field gradient (EFG) and chemical shift (CS) tensors at the halogen nuclei and the local molecular and electronic structure. Here, we present a $^{35/37}$Cl and ^{43}Ca solid-state nuclear magnetic resonance (SSNMR) study of $CaCl_2$. The ^{35}Cl nuclear quadrupole coupling constant, 8.82(8) MHz, and the isotropic chlorine CS, 105(8) ppm (with respect to dilute NaCl(aq)), are different from the values reported previously for this compound, as well as those reported for $CaCl_2{\cdot}2H_2O$. Chlorine-35 SSNMR spectra are also presented for $CaCl_2{\cdot}6H_2O$, and when taken in concert, the SSNMR observations for $CaCl_2$, $CaCl_2{\cdot}2H_2O$, and $CaCl_2{\cdot}6H_2O$ clearly demonstrate the sensitivity of the chlorine EFG and CS tensors to the local symmetry and to changes in the hydration state. For example, the value of δ_{iso} decreases with increasing hydration. Gauge-including projector-augmented wave (GIPAW) density functional theory (DFT) calculations are used to substantiate the experimental SSNMR findings, to rule out the presence of other hydrates in our samples, to refine the hydrogen positions in $CaCl_2{\cdot}2H_2O$, and to explore the isostructural relationship between $CaCl_2$ and $CaBr_2$. Finally, the ^{43}Ca CS tensor span is measured to be 31(5) ppm for anhydrous $CaCl_2$, which represents only the fifth CS tensor span measurement for calcium.

Key words: solid-state NMR, chlorine, ^{35}Cl, ^{37}Cl, ^{43}Ca, $CaCl_2$, polymorphism, hydrates, C_Q, chemical shift anisotropy (CSA), electric field gradient.

Résumé : Les halogénures des métaux du groupe 2 et les hydrates d'halogénures métalliques sont des systèmes modèles qui permettent comprendre la relation entre le gradient du champ électrique (GCE) et les tenseurs du déplacement chimique (DC) au niveau du noyau d'halogène et la structure électronique et moléculaire locale. Dans ce travail, on présente les résultats d'une étude de résonance magnétique nucléaire à l'état solide (RMN-ES) du $^{35/37}$Cl et ^{43}Ca du $CaCl_2$. Les valeurs de la constante de couplage quadripolaire nucléaire du ^{35}Cl, 8,82(8) MHz, et le DC isotrope du chlore, 105(8) ppm [par rapport au NaCl(aq) dilué], sont différentes de celles rapportées pour ce composé ainsi que les valeurs rapportés pour le $CaCl_2{\cdot}2H_2O$. Les spectres RMN-ES du ^{35}Cl sont aussi presentés pour le $CaCl_2{\cdot}6H_2O$ et, lorsqu'on les compare, les observations relatives aux spectres RMN-ES du $CaCl_2$, du $CaCl_2{\cdot}2H_2O$ et du $CaCl_2{\cdot}6H_2O$ démontrent clairement la sensibilité du GCE du chlore et des tenseurs du DC sur la symétrie locale et aux changements dans l'état d'hydratation. Par exemple, les valeurs de δ_{iso} diminuent avec une augmentation de l'hydratation. On a fait appel à des calculs selon la théorie de la fonctionnelle de la densité en utilisant une onde améliorée par un opérateur de projection comportant une jauge (« GIPAW-DFT ») pour corroborer les observations faites par RMN-ES, pour éliminer la présence d'autres hydrates dans nos échantillons, pour affiner les positions des atomes d'hydrogène dans le $CaCl_2{\cdot}2H_2O$ et pour explorer la relation isostructurale entre le $CaCl_2$ et $CaBr_2$. Enfin, on a établi que la portée du tenseur de DC du ^{43}Ca est de 31(5) ppm pour le $CaCl_2$ anhydre, ce qui représente seulement la cinquième valeur mesurée pour l'anisotropie du tenseur du DC du calcium.

Mots-clés : RMN à l'état solide, chlore, ^{35}Cl, ^{37}Cl, ^{43}Ca, $CaCl_2$, polymorphie, hydrates, C_Q, anisotropie du déplacement chimique (ADC), gradient du champ électrique.

[Traduit par la Rédaction]

Introduction

Solid-state nuclear magnetic resonance (SSNMR) spectroscopy is an important tool that is used to characterize structure and dynamics within a range of chemical systems. Recent developments in SSNMR[1,2] have extended its applicability to a number of "exotic" nuclei. To obtain a more complete picture of a given solid-state system, however, it is

Received 2 November 2010. Accepted 22 December 2010. Published at www.nrcresearchpress.com/cjc on 3 May 2011.

C.M. Widdifield and D.L. Bryce. Department of Chemistry and Centre for Catalysis Research and Innovation, University of Ottawa, 10 Marie Curie Private, Ottawa, ON K1N 6N5, Canada.

Corresponding author: D.L. Bryce (e-mail: dbryce@uottawa.ca).

This article is part of a Special Issue dedicated to Professor Roderick E. Wasylishen in honour of his outstanding contributions to NMR spectroscopy, to chemistry in Canada, and to the training of NMR spectroscopists.

Can. J. Chem. Downloaded from www.nrcresearchpress.com by Xi'an Jiaotong University on 09/19/12
For personal use only.

often desirable to complement SSNMR data with information acquired using other methods. Recently, density functional theory (DFT) methods have been paired with ultrasoft pseudopotentials[3] and the gauge-including projector-augmented wave (GIPAW) formalism[4] to calculate magnetic shielding and electric field gradient (EFG) tensors at the nuclei in solid materials.[4–6] These tensors are important SSNMR observables, and a number of recent studies have illustrated that magnetic shielding and EFG tensor calculations using GIPAW DFT can provide additional insights in the study of a variety of chemical systems.[7–17]

There is an increasing interest in "NMR crystallography", which pertains to obtaining molecular-level and crystal structure information for solid materials using SSNMR data.[18] Although there have been a number of exciting recent advances in this area of research,[6,19–25] one cannot currently convert SSNMR data into a unique solid-state structure in a completely generalized manner. With a small amount of a priori knowledge, however, NMR crystallography methods have been applied to solve and refine the structures related to certain classes of materials, such as zeolites,[26–28] which are sometimes subject to crystal twinning and typically do not possess enough long-range order to produce crystals that would be considered suitable for X-ray diffraction (XRD) studies. With the aid of computational modeling, SSNMR data acquired for spin-1/2 nuclei have been used to solve or refine structures of organic molecules such as β-L-aspartyl-L-alanine[6] and thymol.[22] We have recently contributed to this area by exploiting quadrupolar nuclei (i.e., nuclear spin quantum number, $I > 1/2$); for example, $^{79/81}$Br SSNMR data have been complemented with GIPAW DFT computations to refine the structure of the simple salt $MgBr_2$.[29] This work showed the pronounced sensitivity of the $^{79/81}$Br EFG tensor to minute structural changes. Quadrupolar nuclei possess a quadrupole moment (Q) which couples with the EFG at the nucleus to produce characteristic SSNMR spectral line shapes. These line shapes can usually be modeled using analytical simulation software, such as that developed by Wasylishen and co-workers, which treats this "quadrupolar interaction" (QI) as a second-order perturbation to the Zeeman states (the magnitude of which depends on the nuclear quadrupole coupling constant, C_Q, and the quadrupole asymmetry parameter, η_Q).[30] Owing to the presence of the QI, SSNMR experiments using these probe nuclei should be able to offer additional structural restraints, relative to spin-1/2 nuclei.

A recent focus of our research group has been SSNMR spectroscopy of the quadrupolar halogen nuclides ($^{35/37}$Cl, $^{79/81}$Br, and ^{127}I).[12,14,29,31–37] We have observed that the NMR spectra of these nuclei are very sensitive to the EFG produced by the ions and molecules of the surrounding environment. There exist two NMR-active chlorine nuclides (^{35}Cl and ^{37}Cl), both of which are quadrupolar ($I(^{35/37}\text{Cl}) = 3/2$) and of moderately high abundance (75.779(46)% for ^{35}Cl, 24.221(46)% for ^{37}Cl).[38] The Q associated with these nuclei are moderate ($Q(^{35}\text{Cl}) = -81.65(80)$ mb; $Q(^{37}\text{Cl}) = -64.35(64)$ mb);[39] however, their magnetogyric ratios (γ) are rather low (below that of ^{15}N). Probe ringing and second-order QI line shape broadening are both reduced by performing the SSNMR experiments in as high an applied magnetic field ($\mathbf{B}_0$) as available. A variety of chlorine environments have been probed using $^{35/37}$Cl SSNMR spectroscopy at "ultrahigh" $\mathbf{B}_0$, including (*i*) group 4 organometallic[40,41] and group 13 inorganic materials,[31] (*ii*) amino acid hydrochlorides,[34,36] (*iii*) ionic liquids,[42,43] (*iv*) group 2 metal chlorides,[44] and (*v*) pharmaceutical hydrochlorides.[45] As a result of these recent studies, a number of trends in the halogen SSNMR parameters have been observed and rationalized. For example, for the group 2 metal halides studied to date, it has been observed that sample hydration will (*i*) generally result in a decrease in the halogen isotropic chemical shift (CS) and (*ii*) nearly always lead to a decrease in the halogen C_Q value.[12,14,44] It was also noted, however, that the currently available ^{35}Cl SSNMR data collected for $CaCl_2$ indicate that this system does not follow the latter trend;[46] rather, the data suggest that upon hydration the C_Q value increases substantially. We therefore sought to carry out additional NMR studies on $CaCl_2$, which included multiple $\mathbf{B}_0$ data acquisition and modern quantum chemical calculations, to confirm or refute the prior ^{35}Cl SSNMR data.

We present here the results of ^{35}Cl SSNMR measurements for $CaCl_2$ and $CaCl_2{\cdot}6H_2O$. The ^{37}Cl and ^{43}Ca SSNMR spectra of anhydrous $CaCl_2$ are also discussed. The results of GIPAW DFT computations on $CaCl_2$ and its known crystalline hydrates (i.e., $CaCl_2{\cdot}2H_2O$, ($\alpha/\beta/\gamma$)–$CaCl_2{\cdot}4H_2O$, and $CaCl_2{\cdot}6H_2O$) are discussed in an attempt to understand the prior ^{35}Cl SSNMR measurements for $CaCl_2$, to refine the hydrogen positions for $CaCl_2{\cdot}2H_2O$, and to complement our experimental SSNMR data.

Experimental

Sample preparation

$CaCl_2$ (99.99%) and $CaCl_2{\cdot}6H_2O$ (98%) were purchased from Sigma-Aldrich and received as powders. Sample purity for both compounds was confirmed by the manufacturer (see the Supplementary data, Additional Experimental). As $CaCl_2$ is hygroscopic, it was stored and prepared for use under either dry N_2 or Ar. $CaCl_2{\cdot}6H_2O$ was handled for short periods of time in a low humidity atmosphere to avoid further hydration. Prior to SSNMR experiments, the samples were powdered and then tightly packed into either 4 mm or 7 mm o.d. Bruker magic-angle spinning (MAS) ZrO_2 rotors.

Solid-state $^{35/37}$Cl and ^{43}Ca NMR

Data were acquired at the National Ultrahigh-field NMR Facility for Solids in Ottawa and at the University of Ottawa. Experiments at the Ultrahigh-field Facility used a standard-bore Bruker AVANCE II spectrometer, which operates at $\mathbf{B}_0 = 21.1$ T ($\nu_0(^1\text{H}) \approx 900.08$ MHz). For $^{35/37}$Cl SSNMR experiments at 21.1 T ($\nu_0(^{35}\text{Cl}) = 88.189$ MHz; $\nu_0(^{37}\text{Cl}) = 73.408$ MHz), home-built static probes (single-channel 7 mm or 4 mm HX) were used. Calcium-43 SSNMR experiments at the same field ($\nu_0(^{43}\text{Ca}) = 60.575$ MHz) employed a single-channel 7 mm Bruker MAS probe. Experiments performed at the University of Ottawa used a wide-bore Bruker AVANCE spectrometer, which operates at $\mathbf{B}_0 = 11.75$ T ($\nu_0(^1\text{H}) \approx 500.13$ MHz). All ^{35}Cl SSNMR experiments at 11.75 T ($\nu_0(^{35}\text{Cl}) = 49.002$ MHz) used a 4 mm Bruker HX MAS probe. The $^{35/37}$Cl SSNMR spectra were referenced to 0.1 mol/dm^3 NaCl in D_2O at 0 ppm[47] using solid KCl as a secondary reference ($\delta_{iso}(\text{KCl(s)}) = 8.54$ ppm).[32] Calcium-

Can. J. Chem. Downloaded from www.nrcresearchpress.com by Xi'an Jiaotong University on 09/19/12
For personal use only.

43 SSNMR spectra were referenced to a 2 mol/dm^3 aqueous solution of $CaCl_2$ (δ_{iso} = 0 ppm).[48] Chlorine and calcium pulse widths were established using the $^{35/37}$Cl and ^{43}Ca SSNMR signals of solid KCl and saturated $CaCl_2$ (aq), respectively. Central transition (CT) selective (i.e., "solid $\pi/2$") pulse widths were determined by scaling the $\pi/2$ pulse widths measured for the above standards by $1/(I + 1/2)$ (i.e., 1/2 for $^{35/37}$Cl and 1/4 for ^{43}Ca). All $^{35/37}$Cl SSNMR signals were acquired using the Solomon (i.e., "solid") echo (i.e., $\pi/2$–τ_1–$\pi/2$–τ_2–*acq*)[49–51] pulse sequence. Typical $^{35/37}$Cl SSNMR experimental parameters were as follows: CT-selective $\pi/2$ pulse width = 2.4–3.2 μs; spectral window = 200–1000 kHz; τ_1 = 27.5–50 μs; and 512–2048 complex time-domain data points. All ^{43}Ca SSNMR signals were acquired using a single-pulse experiment (typical parameters: CT-selective $\pi/2$ ~1.0 μs; spectral window = 20 kHz; 512–1024 complex time-domain data points). The pulse delays used, as well as the number of scans required for the collection of the spectra, may be found in the figure captions and the Supplementary data (Table S1). For ^{35}Cl SSNMR experiments on $CaCl_2$ at 11.75 T, variable offset cumulative spectrum (VOCS)[52,53] data acquisition was used (offset = 110 kHz). After VOCS data acquisition, each component spectrum was processed as usual and combined in the frequency domain by co-addition. For $CaCl_2 \cdot 6H_2O$, continuous-wave ^{1}H decoupling was tested at both applied fields ($\nu_1(^1H)$ ~50 kHz at 11.75 T and ~85 kHz at 21.1 T). For additional experimental details, see the Supplementary data, Table S1. Observed spectra were modeled using WSolids1, an analytical simulation software package developed by Eichele and Wasylishen.[54]

Quantum chemical calculations

GIPAW DFT calculations employed CASTEP-NMR (v. 4.1) software,[4,5,55,56] while the input files were generated using Materials Studio (v. 3.2.0.0) (Accelrys). Computations used either ultrasoft[3] or "on-the-fly" pseudopotentials and the generalized gradient approximation. Further details pertaining to the relevant on-the-fly pseudopotentials may be found in the Supplementary data, Table S2. All geometry optimizations were carried out using the exchange-correlation (XC) functional of Perdew, Burke, and Ernzerhof (PBE),[57,58] while the EFG and magnetic shielding tensor parameters were calculated using either the PBE XC functional or the XC functional of Perdew and Wang (PW91).[59–63] Computed chlorine magnetic shielding tensor elements (σ_{ij}) were transformed into CS tensor elements (δ_{ij}) using the following procedure: the chlorine isotropic magnetic shielding value (σ_{iso}) for NaCl was determined using a plane-wave cutoff energy (E_{cut}) of 1200 eV, a 4 × 4 × 4 Monkhorst–Pack *k*-point grid,[64] and the same XC functional as the sample of interest. Using the above calculated σ_{iso} value and the known chlorine chemical shift of solid NaCl relative to 0.1 mol/dm^3 NaCl in D_2O (i.e., δ_{iso}(NaCl(s)) = –41.11 ppm),[32] the σ_{iso} value for 0.1 mol/dm^3 NaCl in D_2O could be calculated; hence, all computed σ_{ij} values could be placed on an experimental δ scale. The E_{cut} and *k*-point grid used for the GIPAW DFT calculations on each system are in the footnotes to Tables 1 and 2. For computed structure energies, structure references, optimized structure parameters, the pseudopotentials used, and additional computational details, see the Supplementary data, Tables S2 and S3.

Results and discussion

Experimental $^{35/37}$Cl and ^{43}Ca SSNMR observations and analysis for $CaCl_2$

The ^{35}Cl EFG tensor parameters reported previously[46] for $CaCl_2$ appeared to be inconsistent with the trends observed for other group 2 metal halides,[12,44] prompting us to reinvestigate this system using SSNMR spectroscopy. Chlorine-35 SSNMR spectra were obtained for $CaCl_2$ at two applied fields ($\mathbf{B}_0$ = 11.75 and 21.1 T), and analytical modeling of all observed line shapes resulted in identical EFG and CS tensor parameters (Fig. 1). Additional ^{37}Cl SSNMR experiments were performed at 21.1 T, and the spectra were modeled using the same parameters as those for the ^{35}Cl SSNMR line shapes, after appropriate scaling of C_Q by the $Q(^{37}Cl)/Q(^{35}Cl)$ ratio of 0.788 (Fig. 2). Extracted parameters are summarized in Table 1. It is immediately clear that the observed $^{35/37}$Cl SSNMR line shapes and EFG tensor parameters are inconsistent with the prior literature account for $CaCl_2$.[46]

The presently measured $C_Q(^{35}Cl)$ value of 8.82(8) MHz is more than twice as large as the values observed for other anhydrous and hydrated group 2 metal chlorides.[44,46,69] This is primarily attributed to the arrangement of the Ca^{2+} ions within the first coordination sphere of each chloride, which forms a distorted trigonal plane.[65] Our measured $\eta_Q(^{35/37}Cl)$ value of 0.383(15) confirms the absence of high-symmetry rotational axes (i.e., C_n where $n > 2$), in support of the local symmetry for this site determined using XRD data, which is *m*.[65] The observed chlorine chemical shift value (δ_{iso} = 105 ± 8 ppm, or 146 ppm with respect to solid NaCl) is deshielded by 36 ppm relative to $CaCl_2 \cdot 2H_2O$, which is consistent with the general trend observed for halogen chemical shift values upon hydration in group 2 metal halides.[12]

Experiments at 21.1 T were essential to characterize chlorine chemical shift anisotropy (CSA) and non-coincident EFG and CS tensor principal axis systems (PASs) in this sample. The prior ^{35}Cl SSNMR study on $CaCl_2$ was carried out under MAS conditions only and CSA information was not reported.[46] Our measured chemical shift tensor span of 135 ± 15 ppm is by far the largest measured for a group 2 metal chloride system (72 ppm for $CaCl_2 \cdot 2H_2O$ being the second largest reported to date).[44] The span value measured by modeling the ^{35}Cl SSNMR spectrum is identical to the one extracted from the ^{37}Cl SSNMR signal at 21.1 T (Fig. 2). As expected, the ^{35}Cl SSNMR line shape of $CaCl_2$ acquired at 11.75 T was not particularly sensitive to CSA effects, as nearly all the broadening could be attributed to the QI.[70] The measured Euler angle values (these angles describe the relative orientation of the EFG and CS tensor PASs) for $CaCl_2$ (i.e., $\alpha = 90° \pm 20°$, $\beta = 90° \pm 5°$, $\gamma = 0° \pm 5°$) are consistent with the presence of mirror plane symmetry at the chloride anion, in agreement with prior X-ray data.[65]

Natural abundance ^{43}Ca SSNMR experiments were also performed at $\mathbf{B}_0$ = 21.1 T to more completely characterize the sample. The resonance observed in the ^{43}Ca MAS SSNMR spectrum (Fig. 3*e*) of $CaCl_2$ (i.e., δ_{peak} = 54.1 ± 0.2 ppm relative to 2 mol/dm^3 $CaCl_2$(aq)) cannot, unfortunately, be rigorously compared with that reported previously

Can. J. Chem. Downloaded from www.nrcresearchpress.com by Xi'an Jiaotong University on 09/19/12
For personal use only.

Table 1. Experimental and GIPAW DFT-computed $^{35/37}$Cl EFG and chemical shift tensor parameters.

Experimental or computed	Site label	$C_Q(^{35}Cl)$ (MHz)[a]	η_Q	Ω (ppm)	κ	δ_{iso} (ppm)[b]	α (°)	β (°)	γ (°)	Notes
Anhydrous $CaCl_2$[c]										
Experimental	—	2.1(1)	0.7(1)	—	—	122(5)	—	—	—	Ref. 46
Experimental	—	8.82(8)	0.383(15)	135(15)	0.0(3)	105(8)	90(20)	90(5)	0(5)	This study; $C_Q(^{37}Cl)$ = 6.96(7) MHz
Computed	—	9.66	0.419	200.9	0.12	179.0	90.0	89.7	0.0	X-ray structure from ref. 65
$CaCl_2 \cdot 2H_2O$[d]										
Experimental	—	4.26(3)	0.75(3)	72(15)	0.6(2)	69(2)	90(10)	82(5)	0(20)	Ref. 44
Computed	—	6.69	0.04	141.4	0.36	114.0	—	—	—	Ref. 44; non-optimized H positions
Computed	—	4.43	0.520	140.7	0.49	109.3	118.3	80.8	2.7	This study; optimized H positions
α–$CaCl_2 \cdot 4H_2O$[e]										
Computed	Cl(1)	–3.70	0.405	73.6	0.39	76.1	15.4	1.4	18.8	Optimized H positions
Computed	Cl(2)	5.97	0.944	77.9	–0.47	78.7	118.1	77.3	178.1	Optimized H positions
β–$CaCl_2 \cdot 4H_2O$[f]										
Computed	Cl(1)	–3.75	0.947	123.5	0.70	92.9	183.1	3.2	269.3	Optimized H positions
Computed	Cl(2)	2.16	0.828	83.6	0.59	78.9	135.5	73.6	199.5	Optimized H positions
Computed	Cl(3)	3.97	0.776	125.6	0.45	104.6	65.3	82.6	357.7	Optimized H positions
γ–$CaCl_2 \cdot 4H_2O$[g]										
Computed	—	3.59	0.149	77.1	0.12	48.5	111.1	47.7	190.6	Optimized H positions
$CaCl_2 \cdot 6H_2O$[c]										
Experimental	—	4.33(3)	<0.01	40(8)	–1	57(3)	N/A	90(7)	0(8)	—
Computed	—	5.48	0.000	46.4	–1	43.3	N/A	90.0	0.3	Neutron structure from ref. 66

Note: Measurement errors are within parentheses and parameters are defined as follows: $C_Q = eQV_{33}/h$; $\eta_Q = (V_{11} - V_{22})/V_{33}$, where $|V_{11}| \leq |V_{22}| \leq |V_{33}|$; $\Omega \approx \delta_{11} - \delta_{33}$; $\kappa \approx 3(\delta_{22} - \delta_{iso})/\Omega$; $\delta_{iso} = (\delta_{11} + \delta_{22} + \delta_{33})/3$, where $\delta_{33} \leq \delta_{22} \leq \delta_{11}$; and α, β, and γ describe the relative orientation between the EFG and CS tensor principal axis systems, which are disclosed here using the "ZYZ" convention[67] and generated using EFGShield.[68] All calculated results in this table used the PBE XC functional. Additional computational results and details can be found in the Supplementary data, Tables S2–S4. N/A, not applicable.

[a]While C_Q may take any real value, $|C_Q|$ is measured experimentally. Experimental signs are attributed based upon the GIPAW DFT results.

[b]Experimental chlorine chemical shifts are relative to 0.1 mol/dm^3 NaCl in D_2O ($\delta_{iso}(^{35/37}Cl) = 0$ ppm) and were established using solid KCl as a secondary reference ($\delta_{iso}(^{35/37}Cl) = 8.54$ ppm). For the computational reference, NaCl(s), $\sigma_{iso}(^{35/37}Cl)$ was calculated to be 975.06 ppm (4 × 4 × 4 *k*-point grid and E_{cut} = 1200 eV). Additional details can be found in the Experimental section.

[c]Calculations for this compound used a 4 × 4 × 6 *k*-point grid and E_{cut} = 800 eV.

[d]For the current study, calculations for this compound used a 4 × 3 × 2 *k*-point grid. Optimization of the hydrogen atomic positions used E_{cut} = 500 eV, and EFG and CS tensor parameter calculations used E_{cut} = 600 eV.

[e]Calculations for this compound used a 4 × 4 × 3 *k*-point grid and E_{cut} = 650 eV.

[f]Calculations for this compound used a 3 × 2 × 2 *k*-point grid and E_{cut} = 500 eV.

[g]Calculations for this compound used a 4 × 3 × 3 *k*-point grid and E_{cut} = 650 eV.

Table 2. Experimental and GIPAW DFT-computed ^{43}Ca EFG and chemical shift tensor parameters for $CaCl_2$.

Experimental or computed	$C_Q(^{43}Ca)$ (MHz)[a]	η_Q	Ω (ppm)	κ	δ_{iso} (ppm)[b]	α (°)	β (°)	γ (°)	Notes
Experimental	–0.95(20)	0.7(2)	31(5)	–0.5(3)	54.8(5)	90.0[c]	90.0[c]	0.0[c]	—
Computed[d]	–0.98	0.541	52.7	–0.24	—[e]	90.0	89.4	0.0	X-ray structure from ref. 65

Note: Measurement errors are within parentheses. Parameter definitions can be found in the footnotes to Table 1. All calculated results in this table used the PBE XC functional. Additional computational results and details can be found in the Supplementary data, Tables S2, S3, and S5.

[a]While C_Q may take any real value, $|C_Q|$ is measured experimentally using SSNMR. Experimental signs are attributed based upon the GIPAW DFT results.

[b]Experimental calcium chemical shifts are relative to dilute $CaCl_2$(aq) ($\delta_{iso}(^{43}Ca) = 0$ ppm) and were established using 2 mol/dm^3 $CaCl_2$(aq), which possesses an identical calcium CS as the primary standard.

[c]Value assigned as a result of crystal symmetry and GIPAW DFT results.

[d]Calculations for $CaCl_2$ used a 4 × 4 × 6 k-point grid and E_{cut} = 800 eV.

[e]Computed isotropic calcium magnetic shielding value: 1048.85 ppm.

Can. J. Chem. Downloaded from www.nrcresearchpress.com by Xi'an Jiaotong University on 09/19/12
For personal use only.

Fig. 1. Analytical simulations (*a*, *b*, *c*, *e*), experimental static Solomon echo (*d*), and experimental static VOCS Solomon echo (*f*) ^{35}Cl SSNMR spectra of powdered $CaCl_2$, acquired at (*d*) $\mathbf{B}_0$ = 21.1 T (ν_0 = 88.189 MHz) and (*f*) $\mathbf{B}_0$ = 11.75 T (ν_0 = 49.002 MHz). In (*a*), the principal axis system orientations of the EFG and CS tensor frames are assumed to be equivalent (i.e., $\alpha = \beta = \gamma = 0°$), while in (*b*), CSA effects are ignored (i.e., Ω = 0 ppm). The best-fit spectra presented in (*c*) and (*e*) are simulated with the parameters given in Table 1. For (*d*), an optimized pulse delay of 10.0 s was used and 400 transients were collected, while for (*f*), a pulse delay of 1.0 s was used and 40 000 transients were collected for each of 6 transmitter frequencies (offset value used: 110 kHz).

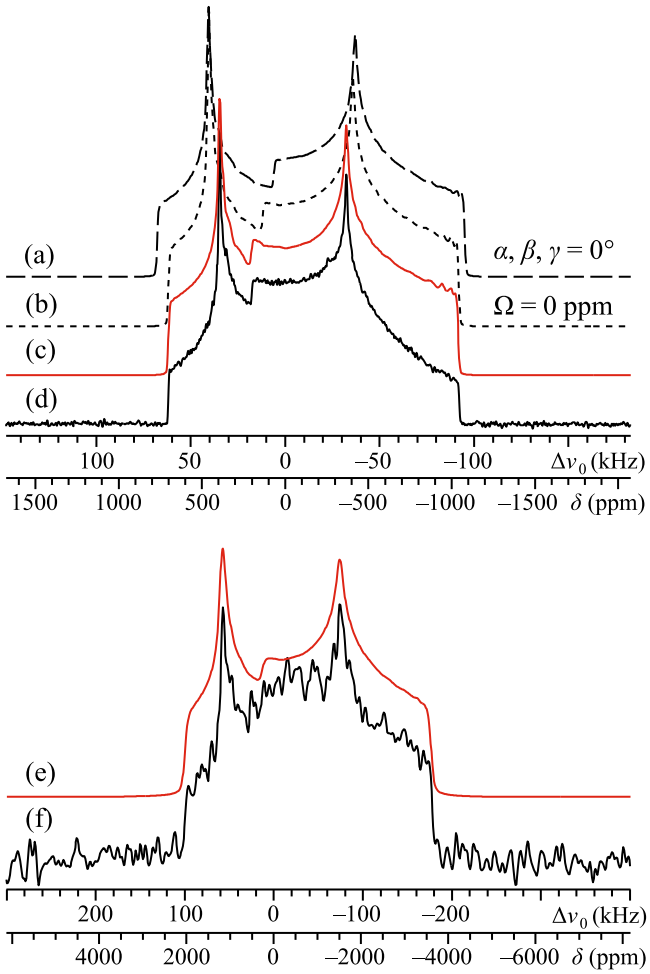

Fig. 2. Analytical simulation (*a*) and experimental static Solomon echo ^{37}Cl SSNMR spectrum (*b*) of powdered $CaCl_2$, acquired at $\mathbf{B}_0$ = 21.1 T (ν_0 = 73.408 MHz). A pulse delay of 10.0 s was used and 960 transients were collected.

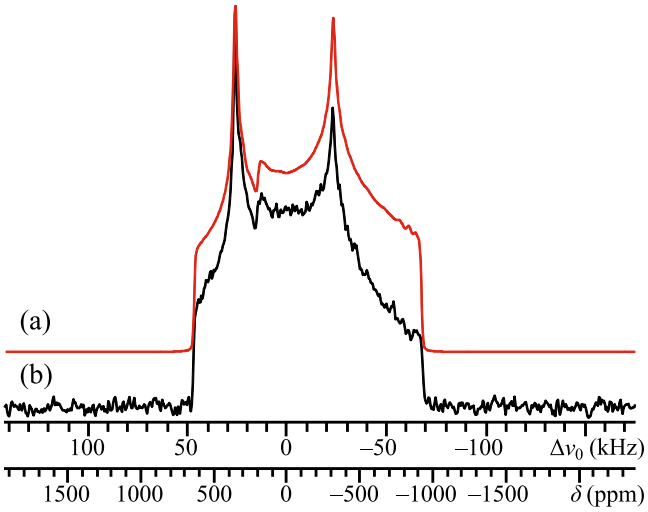

by Lin et al. (δ_{peak} = 53.1 ± 2.0 ppm relative to saturated $CaCl_2$(aq)).[71] This is because the reference standard used in the earlier account (i.e., "saturated" $CaCl_2$(aq)) shows a highly variable resonance position that depends on the preparation method (approx. ±10 ppm).[48,72] Analytical modeling of the ^{43}Ca MAS SSNMR line shape was used to establish approximate ^{43}Ca EFG tensor parameters as well as the isotropic calcium CS for $CaCl_2$: $C_Q(^{43}Ca)$ = –0.95 ± 0.20 MHz, η_Q = 0.7 ± 0.2, and δ_{iso} = 54.8 ± 0.5 ppm, where the sign of C_Q is based upon the results of GIPAW DFT computations (*vide infra*). Calcium-43 SSNMR experiments were also carried out under stationary conditions (Fig. 3*b*) and the parameters measured from the ^{43}Ca MAS NMR spectrum were used to estimate the static line shape broadening that could be attributed to the ^{43}Ca QI (Fig. 3*c*). It is clear that the QI does not dominate the line shape for this sample under static conditions at 21.1 T and that additional line broadening due to calcium CSA is present. Analytical line shape modeling of the static ^{43}Ca SSNMR spectrum allows us to report a calcium CS tensor span of 31 ± 5 ppm (Fig. 3*a*), which represents the fifth measurement of calcium CSA in the literature[73] and the first where oxygen atoms are not coordinated to the calcium. The calcium CS tensor span for $CaCl_2$ is moderate, as calcium CS tensor spans range

Can. J. Chem. Downloaded from www.nrcresearchpress.com by Xi'an Jiaotong University on 09/19/12
For personal use only.

Fig. 3. Analytical simulations (*a*, *c*, *d*) and experimental single-pulse (*b*, *e*) ^{43}Ca SSNMR spectra of powdered $CaCl_2$, acquired at $\mathbf{B}_0$ = 21.1 T (ν_0 = 60.575 MHz) under (*a*, *b*, *c*) static and (*d*, *e*) MAS conditions. In (*c*), the effects due to calcium CSA are ignored (i.e., Ω = 0 ppm), while the simulation in (*a*) includes calcium CSA. The spectrum in (*e*) was acquired using a MAS frequency of 4 kHz. The experimental pulse delay for both (*b*) and (*e*) was 5.0 s. The spectrum in (*b*) is the result of the collection of 25 648 transients, while the spectrum in (*e*) is the result of the collection of 4313 transients.

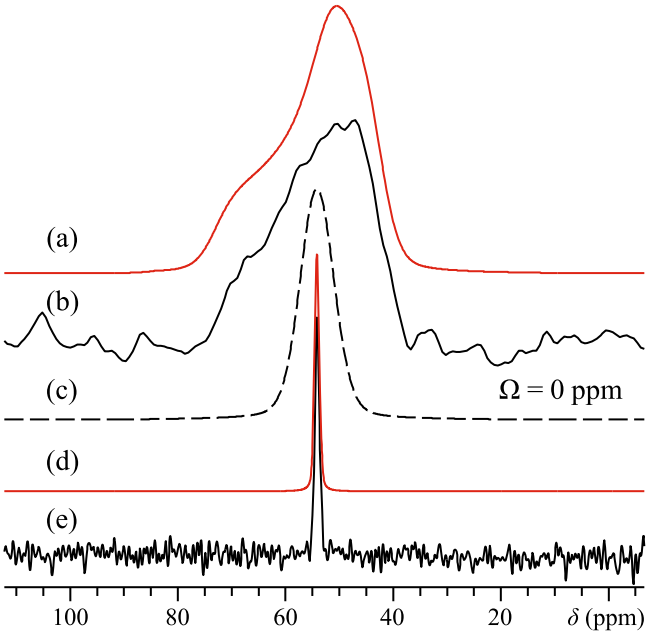

from 8 ± 2 ppm in the calcite polymorph of $CaCO_3$ to 70 ± 20 ppm in the vaterite polymorph of $CaCO_3$.[72] The remaining calcium SSNMR parameters for $CaCl_2$ are summarized in Table 2.

$CaCl_2$·6H_2O and other hydrates

It is well known that $CaCl_2$ is a strongly hygroscopic material, and as such it is widely used as a desiccant. In this section, we discuss the known experimental data for $CaCl_2$ and selected hydrates to ensure that the spectral data above have been correctly interpreted. We have characterized $CaCl_2$·6H_2O using ^{35}Cl SSNMR experiments at 11.75 and 21.1 T (Figs. 4 and 5), and analytical line shape modeling of both spectra yields identical parameters, which are summarized in Table 1.

Our discussion of the $^{35/37}$Cl SSNMR data for the $CaCl_2$ hydrates begins by noting that $^{35/37}$Cl SSNMR data were recently reported for $CaCl_2$·2H_2O[44] and that this dihydrate possesses distinctly different EFG and CS tensor parameters compared with anhydrous $CaCl_2$ (Table 1). To the best of our knowledge, two other hydrated forms of $CaCl_2$ are stable under typical laboratory conditions: α–$CaCl_2$·4H_2O[74] and $CaCl_2$·6H_2O.[66] Additional polymorphic forms of the tetrahydrate (β–$CaCl_2$·4H_2O[75] and γ–$CaCl_2$·4H_2O[76]) may be prepared under normal conditions but appear to slowly convert to the α-form.[77] As the hexahydrate is commercially available in a highly pure form, ^{35}Cl SSNMR experiments were carried out on this material.

By observing the ^{35}Cl SSNMR line shapes associated with

Fig. 4. Analytical simulations (*a*, *c*) and experimental static Solomon echo (*b*, *d*) ^{35}Cl SSNMR spectra of powdered $CaCl_2$·6H_2O, acquired at $\mathbf{B}_0$ = 11.75 T. The spectrum in (*b*) did not employ proton decoupling during signal acquisition, while the spectrum in (*d*) was acquired using proton decoupling. The simulation parameters used in (*a*) and (*c*) are identical, except for the addition of 1000 Hz of dipolar broadening in (*a*) ($\alpha^d = \beta^d = 0°$, inferred from the neutron crystal structure), due to the expected ^{1}H–^{35}Cl distances of ~2.27 Å. The experimental pulse delay for both (*b*) and (*d*) was 3.0 s. The spectrum in (*b*) is the result of the collection of 16 000 transients, while the spectrum in (*d*) is the result of the collection of 5616 transients.

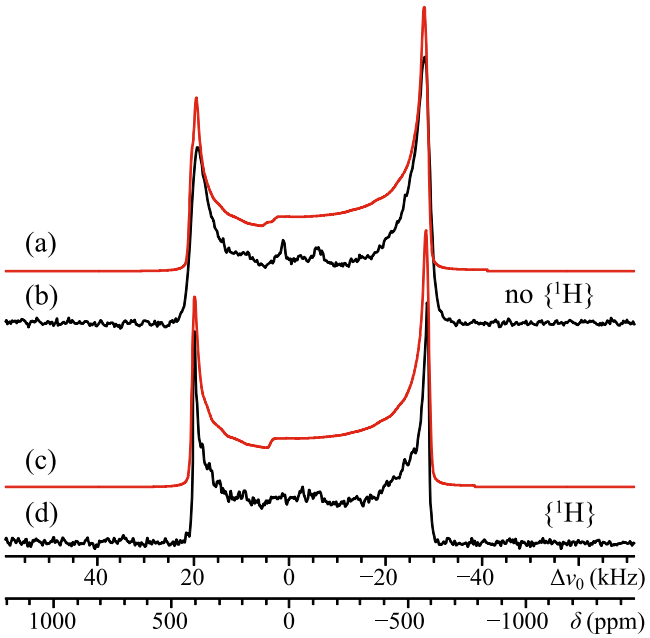

$CaCl_2$·6H_2O (Figs. 4 and 5), it is clear that $CaCl_2$·6H_2O possesses a distinct line shape with respect to both anhydrous $CaCl_2$ and $CaCl_2$·2H_2O. The measured ^{35}Cl EFG tensor parameters (C_Q(^{35}Cl) = 4.33 ± 0.03 MHz, η_Q < 0.01) strongly suggest that each chloride anion in $CaCl_2$·6H_2O is located on a C_3 (or higher) rotational axis. The smaller value of C_Q (^{35}Cl) for this sample is consistent with earlier observations for group 2 metal halides, which nearly always exhibit smaller halogen C_Q values upon hydration.[12] It is also important to note that $CaCl_2$·2H_2O and all the polymorphs of $CaCl_2$·4H_2O place the chloride anions at positions lacking any local symmetry elements and hence the axial ^{35}Cl EFG observed is unique to the hexahydrate. We also see a clear broadening of the discontinuities in Fig. 4*b* when ^{1}H decoupling is not applied, which indicates that the sample is hydrated.

The observed chlorine chemical shift for $CaCl_2$·6H_2O (δ_{iso} = 57 ± 3 ppm) is smaller than that of both $CaCl_2$ and $CaCl_2$·2H_2O, which is in agreement with earlier observations that the halogen shift value decreases (i.e., shielding increases) upon increasing hydration.[12] The observed ^{35}Cl SSNMR line shape of $CaCl_2$·6H_2O was best modeled when CSA effects were included (Ω = 40 ± 8 ppm, κ = –1; also see Fig. 5). The observed chlorine Ω value is quite similar to that measured for other group 2 metal chloride hydrates.[44] Based on the above discussion, it is clear that our anhydrous

Can. J. Chem. Downloaded from www.nrcresearchpress.com by Xi'an Jiaotong University on 09/19/12
For personal use only.

Fig. 5. Analytical simulations (*a*, *b*) and experimental static Solomon echo (*c*) ^{35}Cl{^{1}H} SSNMR spectra of powdered $CaCl_2·6H_2O$, acquired at $\mathbf{B}_0$ = 21.1 T. The spectrum in (*b*) is the best fit to the experimental spectrum, while the spectrum in (*a*) does not include chlorine CSA (i.e., Ω = 0 ppm). A pulse delay of 5.0 s was used and 272 transients were collected.

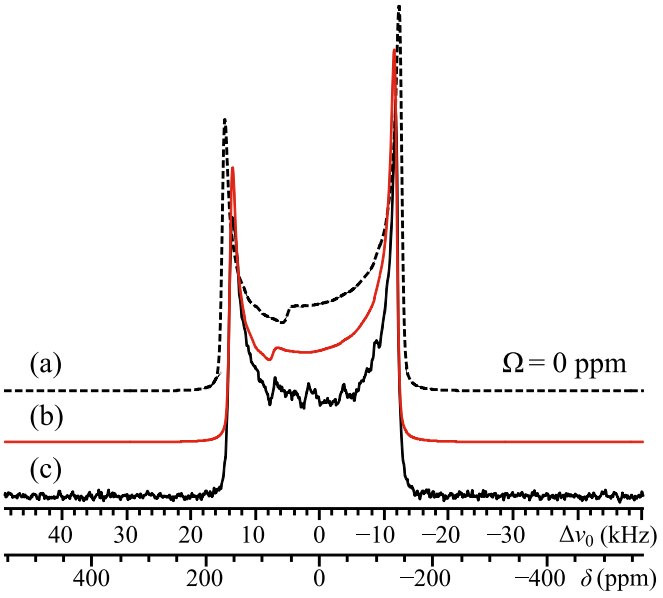

$CaCl_2$ sample cannot be $CaCl_2·2H_2O$ or $CaCl_2·6H_2O$, and it is very unlikely to be a $CaCl_2·4H_2O$ polymorph, owing to the observed large positive chlorine chemical shift value, the large C_Q(^{35}Cl) value, and the mirror site symmetry implied by the EFG and CS tensor interplay observed in the $^{35/37}$Cl SSNMR spectra of $CaCl_2$.

Quantum chemical computations

GIPAW DFT quantum chemical calculations were carried out using the accepted crystal structures of $CaCl_2$,[65] $CaCl_2·2H_2O$,[78] α–$CaCl_2·4H_2O$,[74] β–$CaCl_2·4H_2O$,[75] γ–$CaCl_2·4H_2O$,[76] and $CaCl_2·6H_2O$,[66] although for the hydrates (except $CaCl_2·6H_2O$, whose structure was solved using neutron diffraction data) the H positions were optimized computationally (*vide infra*). The computed ^{35}Cl EFG and chlorine CS tensor parameters are presented in Table 1, while more detailed computational results can be found in the Supplementary data, Table S4.

Agreement between experimental and GIPAW DFT-computed chlorine CS and EFG tensor parameters

For nearly all of the relevant $^{35/37}$Cl NMR tensor parameters, excellent agreement between experimental observations and GIPAW DFT computations is seen for $CaCl_2$ and $CaCl_2·6H_2O$. The calculated C_Q(^{35}Cl) values for these compounds are slightly overestimated relative to the experiment (~1 MHz), which appears to be a general feature for chloride anions when using this computational method and pseudopotential.[79] In addition, while there is a lack of quantitative agreement between the quantum chemical and experimental δ_{iso} values, the pertinent experimental trend is reproduced computationally (i.e., as hydration increases, δ_{iso} decreases). The quantitative disagreement in δ_{iso} extends to the computational reference standard used in this study (i.e., NaCl(s)). According to the absolute shielding scale established by Gee et al.,[80] the experimental absolute shielding at the chlorine nuclei in solid NaCl is 1015 ± 4 ppm, while the present GIPAW DFT calculations provide a value of 975.06 ppm. Our data therefore suggest the presence of a systematic error in the calculation of σ_{iso} values using the GIPAW DFT method and the current pseudopotential. We note that all calculated shift values reported in Table 1 used the computational shielding standard (i.e., σ_{iso}(NaCl) = 975.06 ppm).

There is also clear disagreement between the chlorine quantum chemical results for $CaCl_2$ and the earlier ^{35}Cl MAS NMR experimental observation:[46] for example, the computed C_Q(^{35}Cl) is too large by roughly a factor of 4. Therefore, the quantum chemical result for $CaCl_2$ provides independent evidence that the earlier ^{35}Cl MAS NMR experimental measurements were either not correctly interpreted or were inadvertently carried out on a material other than $CaCl_2$. The GIPAW DFT result for $CaCl_2·6H_2O$ confirms the local symmetry (i.e., C_3) for the chloride anions, as η_Q = 0.0 and κ = –1.0. It is also rather interesting to note the quantitative agreement between the calculated and experimental Euler angle values for $CaCl_2$ and $CaCl_2·6H_2O$.

While there typically exists very good agreement between experimental and computational values for the $^{35/37}$Cl EFG and magnetic shielding tensors in $CaCl_2$ and $CaCl_2·6H_2O$, relatively poor agreement was observed for $CaCl_2·2H_2O$ in a previous study.[44] Inspection of the source data for the accepted crystal structure of $CaCl_2·2H_2O$ reveals that the structure was generated using X-ray diffraction data, rather than neutron diffraction data, and hence the hydrogen positions are not precisely known. Out of all the group 2 metal chloride hydrates where ^{35}Cl or ^{37}Cl SSNMR data are available, $CaCl_2·2H_2O$ represents the only structure for which neutron diffraction data are unavailable. The H positions in $CaCl_2·2H_2O$ were therefore optimized using the GIPAW DFT method. Subsequent GIPAW DFT calculation of the EFG and magnetic shielding tensor parameters using this optimized structure yields markedly different tensor parameters as compared with the prior study (Table 1). Relative to the earlier computational results, there is a decrease in the computed C_Q(^{35}Cl) by about 34% (6.69 MHz to 4.43 MHz) and a substantial increase in η_Q (0.04 to 0.520). Both of these significant changes result in better agreement between the experimental and computed EFG tensor parameter values.

GIPAW DFT-computed chlorine EFG and CS tensor parameters for $CaCl_2·4H_2O$ polymorphs

Good agreement between the observed and computed $^{35/37}$Cl NMR tensor data was seen for the compounds above; hence, we explored whether GIPAW DFT computations would predict that chlorine SSNMR experiments could be used to differentiate between the α, β, and γ polymorphs of $CaCl_2·4H_2O$. The differentiation of polymorphs using chlorine SSNMR has been demonstrated previously for chlorine-containing pharmaceuticals,[45] and as seen in Table 1, these experiments should also be able to distinguish the polymorphs of $CaCl_2·4H_2O$. Each polymorph should present a different number of magnetically unique chloride sites (ranging from 1 to 3). In addition, there exists significant disparity in the other relevant NMR parameters (notably η_Q, which

Can. J. Chem. Downloaded from www.nrcresearchpress.com by Xi'an Jiaotong University on 09/19/12
For personal use only.

ranges from 0.149 in γ–$CaCl_2{\cdot}4H_2O$ to above 0.776 for all three sites in β–$CaCl_2{\cdot}4H_2O$).

Are $CaCl_2$ and $CaBr_2$ isostructural?

Based on prior XRD data, the ambient-condition structures of both $CaCl_2$ and $CaBr_2$ belong to the same space group and place the halogen anions at the same Wyckoff positions.[65,81] The absolute $C_Q(^{81}Br)$ value for $CaBr_2$ is the largest amongst the group 2 metal bromides ($C_Q(^{81}Br) = 62.8 \pm 0.4$ MHz).[14] At the same time, the previously measured $C_Q(^{35}Cl)$ value for $CaCl_2$ was among the smallest measured relative to other group 2 metal chlorides ($C_Q(^{35}Cl) = 2.1$ MHz).[46] The above sections have provided ample evidence that the earlier report was in error, likely because of the formation of a $CaCl_2$ hydrate or the neglect to acquire spectral data using VOCS (or equivalent) methods. In addition, we now have reliable $C_Q(^{35/37}Cl)$ measurements for $CaCl_2$.

It was recently shown by Wu and Terskikh[82] that for a series of isostructural compounds, a linear relationship exists between the measured C_Q values and the quantity $Q(1 - \gamma_\infty)/V$, where γ_∞ is the Sternheimer antishielding factor[83–86] and V is the unit cell volume. This finding has been extended by observations made for the $^{35/37}Cl$,[44,46,69] $^{79/81}Br$,[14,29] and ^{127}I[12] nuclides within several isostructural series of group 2 metal halides and selected hydrates thereof. This linear relationship between C_Q and $Q(1 - \gamma_\infty)/V$ is therefore useful for both confirming and predicting isostructural series within classes of analogous compounds. Although enough data do not exist in this case to construct a meaningful plot of $C_Q(X)$ vs. $Q(1 - \gamma_\infty)/V$, we can compare the respective $C_Q(^{81}Br)/C_Q(^{35}Cl)$ and $[Q_{81Br}(1 - \gamma_{\infty(Br)})/V]/[Q_{35Cl}(1 - \gamma_{\infty\ (Cl)})/V]$ ratios, which should be equivalent according to the above model if these two compounds are isostructural. Using the experimental SSNMR data for $CaCl_2$ and $CaBr_2$, the $C_Q(^{81}Br)/C_Q(^{35}Cl)$ ratio is ~7.12. Using additional known information, with the volume of the unit cells established using X-ray diffraction,[65,81] the $[Q_{81Br}(1 - \gamma_{\infty(Br)})/V]/[Q_{35Cl}(1 - \gamma_{\infty(Cl)})/V]$ ratio is calculated to be 5.19 (a 31.4% difference). This percent difference is comparable to what has been calculated previously for pairs of group 2 metal halide compounds that are understood to be isostructural; in fact, for the isostructural group 2 metal chlorides and bromides studied to date, it is observed that $C_Q(^{81}Br)/C_Q(^{35}Cl)$ ratios range between 6.30 and 7.08, while the calculated $[Q_{81Br}(1 - \gamma_{\infty(Br)})/V]/[Q_{35Cl}(1 - \gamma_{\infty(Cl)})/V]$ ratios for the same systems vary between 5.48 and 5.64.[12] A likely contributor to the disagreement between the calculated $[Q_{81Br}(1 - \gamma_{\infty(Br)})/V]/[Q_{35Cl}(1 - \gamma_{\infty(Cl)})/V]$ ratios and the experimental $C_Q(^{81}Br)/C_Q(^{35}Cl)$ ratios is the uncertainty associated with the γ_∞ values: these values for the quadrupolar halogens are not known to high precision, unlike the group 1 metal atom γ_∞ values used in the study by Wu and Terskikh.[82] At this time it is noted that, using the accepted structures for $CaCl_2$ and $CaBr_2$, the GIPAW DFT-calculated $C_Q(^{81}Br)/C_Q(^{35}Cl)$ ratio is ~7.16, which is in excellent agreement with our experimental observations (a difference of 0.56%).

Likewise, upon consideration of the fine details associated with the $CaCl_2$ and $CaBr_2$ crystal structures, two points are clear: (*i*) the structure of $CaCl_2$ is rather old (1935), and (*ii*) the placement of the halogen anions is, in fact, not equivalent for the two structures (in $CaBr_2$ the bromide is at $x/a = 0.2636 \pm 0.0029$, $y/b = 0.3417 \pm 0.0026$, $z/c = 0$, whereas in $CaCl_2$ the chloride is at $x/a = 0.275 \pm 0.08$, $y/b = 0.325 \pm 0.08$, $z/c = 0$). It is therefore probable that this discrepancy in the halide positions within their respective crystalline lattices would contribute to the difference between the $[Q_{81Br}(1 - \gamma_{\infty(Br)})/V]/[Q_{35Cl}(1 - \gamma_{\infty(Cl)})/V]$ ratio and the $C_Q(^{81}Br)/C_Q(^{35}Cl)$ ratio. Indeed, it has been demonstrated recently that very small displacements of the halide anion (typically < 0.05 Å) can dramatically alter the calculated halogen C_Q value for several similar systems.[12,29] Therefore, while it is clear that the $C_Q/[Q(1 - \gamma_\infty)/V]$ relationship appears to be of general use for group 2 metal halides, the precision of the halogen γ_∞ values is a limiting factor and the compounds must be rigorously isostructural to obtain exactly equal ratios.

Conclusions

Solid-state $^{35/37}Cl$ NMR experiments are sensitive probes of the local structure of inorganic materials and have allowed for differentiation between the hydrates of $CaCl_2$. By performing chlorine SSNMR experiments in two applied magnetic fields, both the EFG and CS tensor parameters could be accurately measured in $CaCl_2$ and $CaCl_2{\cdot}6H_2O$. The measurement of these tensor parameters allowed us to correct the ^{35}Cl SSNMR literature data for $CaCl_2$ and illustrate that this species conforms to the established quadrupolar halogen NMR trends for group 2 metal halide systems (i.e., that both the halogen C_Q value and the halogen chemical shift will decrease upon hydration). GIPAW DFT quantum chemical calculations have provided complementary data for the $CaCl_2$ hydrates where experimental SSNMR data exist and predict that $^{35/37}Cl$ SSNMR experiments should be able to distinguish the three known polymorphs of $CaCl_2{\cdot}4H_2O$. It is seen that optimization of the H positions for $CaCl_2{\cdot}2H_2O$, whose structure has been determined using X-ray diffraction data, is necessary to obtain good agreement between the quantum chemical and experimental EFG tensor parameter values. By carrying out ^{43}Ca SSNMR experiments at ultrahigh $\mathbf{B}_0$ (i.e., 21.1 T), we have been able to measure the fifth calcium CS tensor anisotropy, which is expected to prove useful in future SSNMR studies that correlate calcium CS tensor information to local structure and symmetry in other calcium-containing materials. Lastly, although it has been demonstrated that comparing $C_Q/[Q(1 - \gamma_\infty)/V]$ ratios can provide evidence that a series of compounds are isostructural when using group 1 metal nuclei as probes, additional problems (i.e., uncertainty in halogen γ_∞ values and a requirement that the compounds be rigorously isostructural) present themselves when the quadrupolar halogen nuclei are used.

Supplementary data

Supplementary data, including detailed $^{35/37}Cl$ and ^{43}Ca SSNMR experimental data acquisition parameters, GIPAW DFT quantum chemical calculations (pseudopotential files used, structure energies, structure references, crystal structure parameters used, and additional information), and GIPAW DFT-computed $^{35/37}Cl$ and ^{43}Ca EFG and magnetic shielding

tensor parameters, are available with the article through the journal Web site (www.nrcresearchpress.com/cjc).

Acknowledgements

D.L.B. would like to express his gratitude to Prof. Rod Wasylishen for his training and guidance throughout the years in the field of solid-state NMR spectroscopy and quantum chemistry. D.L.B. thanks the Natural Sciences and Engineering Research Council (NSERC) of Canada for funding. C.M.W. thanks NSERC for an Alexander Graham Bell CGS D2 scholarship. We are grateful to Dr. Victor Terskikh and Dr. Eric Ye for technical support. Access to the 900 MHz NMR spectrometer was provided by the National Ultrahigh-field NMR Facility for Solids (Ottawa, Canada), a national research facility funded by the Canada Foundation for Innovation, the Ontario Innovation Trust, Recherche Québec, the National Research Council Canada, and Bruker Biospin and managed by the University of Ottawa (http://nmr900.ca). NSERC is acknowledged for a Major Resources Support grant.

References

(1) Lesage, A. *Phys. Chem. Chem. Phys.* **2009** *11* (32), 6876. doi:10.1039/b907733m.
(2) Ashbrook, S. E. *Phys. Chem. Chem. Phys.* **2009** *11* (32), 6892. doi:10.1039/b907183k.
(3) Vanderbilt, D. *Phys. Rev. B* **1990** *41* (11), 7892. doi:10.1103/PhysRevB.41.7892.
(4) Pickard, C. J.; Mauri, F. *Phys. Rev. B* **2001** *63* (24), 245101. doi:10.1103/PhysRevB.63.245101.
(5) Profeta, M.; Mauri, F.; Pickard, C. J. *J. Am. Chem. Soc.* **2003** *125* (2), 541. doi:10.1021/ja027124r.
(6) Pickard, C. J.; Salager, E.; Pintacuda, G.; Elena, B.; Emsley, L. *J. Am. Chem. Soc.* **2007** *129* (29), 8932. doi:10.1021/ja071829h.
(7) Johnston, K. E.; Tang, C. C.; Parker, J. E.; Knight, K. S.; Lightfoot, P.; Ashbrook, S. E. *J. Am. Chem. Soc.* **2010** *132* (25), 8732. doi:10.1021/ja101860r.
(8) Moudrakovski, I. L.; Alizadeh, R.; Beaudoin, J. J. *Phys. Chem. Chem. Phys.* **2010** *12* (26), 6961. doi:10.1039/c000353k.
(9) Hamaed, H.; Ye, E.; Udachin, K.; Schurko, R. W. *J. Phys. Chem. B* **2010** *114* (18), 6014. doi:10.1021/jp102026m.
(10) Middlemiss, D. S.; Blanc, F.; Pickard, C. J.; Grey, C. P. *J. Magn. Reson.* **2010** *204* (1), 1. doi:10.1016/j.jmr.2010.01.004.
(11) Sutrisno, A.; Hanson, M. A.; Rupar, P. A.; Terskikh, V. V.; Baines, K. M.; Huang, Y. *Chem. Commun. (Camb.)* **2010** *46* (16), 2817. doi:10.1039/b926071d.
(12) Widdifield, C. M.; Bryce, D. L. *J. Phys. Chem. A* **2010** *114* (40), 10810. doi:10.1021/jp108237x.
(13) Hanna, J. V.; Pike, K. J.; Charpentier, T.; Kemp, T. F.; Smith, M. E.; Lucier, B. E. G.; Schurko, R. W.; Cahill, L. S. *Chem.–Eur. J.* **2010** *16* (10), 3222. doi:10.1002/chem.200901581.
(14) Widdifield, C. M.; Bryce, D. L. *J. Phys. Chem. A* **2010** *114* (5), 2102. doi:10.1021/jp909106j.
(15) Moudrakovski, I.; Lang, S.; Patchkovskii, S.; Ripmeester, J. *J. Phys. Chem. A* **2010** *114* (1), 309. doi:10.1021/jp908206c.
(16) Kibalchenko, M.; Yates, J. R.; Massobrio, C.; Pasquarello, A. *Phys. Rev. B* **2010** *82* (2), 020202(R). doi:10.1103/PhysRevB.82.020202.
(17) Truflandier, L. A.; Boucher, F.; Payen, C.; Hajjar, R.; Millot, Y.; Bonhomme, C.; Steunou, N. *J. Am. Chem. Soc.* **2010** *132* (13), 4653. doi:10.1021/ja908973y.
(18) Harris, R. K. Crystallography & NMR: an Overview. In *NMR Crystallography*; Harris, R. K., Wasylishen, R. E., and Duer, M. J., Eds.; John Wiley & Sons: Chichester, UK, 2009; p 3.
(19) Webber, A. L.; Emsley, L.; Claramunt, R. M.; Brown, S. P. *J. Phys. Chem. A* **2010** *114* (38), 10435. doi:10.1021/jp104901j.
(20) Webber, A. L.; Elena, B.; Griffin, J. M.; Yates, J. R.; Pham, T. N.; Mauri, F.; Pickard, C. J.; Gil, A. M.; Stein, R.; Lesage, A.; Emsley, L.; Brown, S. P. *Phys. Chem. Chem. Phys.* **2010** *12* (26), 6970. doi:10.1039/c001290d.
(21) Ganapathy, S.; Sengupta, S.; Wawrzyniak, P. K.; Huber, V.; Buda, F.; Baumeister, U.; Würthner, F.; de Groot, H. J. M. *Proc. Natl. Acad. Sci. U.S.A.* **2009** *106* (28), 11472. doi:10.1073/pnas.0811872106.
(22) Salager, E.; Stein, R. S.; Pickard, C. J.; Elena, B.; Emsley, L. *Phys. Chem. Chem. Phys.* **2009** *11* (15), 2610. doi:10.1039/b821018g.
(23) Seyfarth, L.; Senker, J. *Phys. Chem. Chem. Phys.* **2009** *11* (18), 3522. doi:10.1039/b819319c.
(24) Ashbrook, S. E.; Cutajar, M.; Pickard, C. J.; Walton, R. I.; Wimperis, S. *Phys. Chem. Chem. Phys.* **2008** *10* (37), 5754. doi:10.1039/b805681a.
(25) Harris, R. K.; Hodgkinson, P.; Pickard, C. J.; Yates, J. R.; Zorin, V. *Magn. Reson. Chem.* **2007** *45* (S1), S174. doi:10.1002/mrc.2132.
(26) Brouwer, D. H. *J. Magn. Reson.* **2008** *194* (1), 136. doi:10.1016/j.jmr.2008.06.020.
(27) Brouwer, D. H. *J. Am. Chem. Soc.* **2008** *130* (20), 6306. doi:10.1021/ja800227f.
(28) Brouwer, D. H.; Kristiansen, P. E.; Fyfe, C. A.; Levitt, M. H. *J. Am. Chem. Soc.* **2005** *127* (2), 542. doi:10.1021/ja043228l.
(29) Widdifield, C. M.; Bryce, D. L. *Phys. Chem. Chem. Phys.* **2009** *11* (33), 7120. doi:10.1039/b911448n.
(30) Power, W. P.; Wasylishen, R. E.; Mooibroek, S.; Pettitt, B. A.; Danchura, W. *J. Phys. Chem.* **1990** *94* (2), 591. doi:10.1021/j100365a019.
(31) Chapman, R. P.; Bryce, D. L. *Phys. Chem. Chem. Phys.* **2009** *11* (32), 6987. doi:10.1039/b906627f.
(32) Chapman, R. P.; Widdifield, C. M.; Bryce, D. L. *Prog. Nucl. Magn. Reson. Spectrosc.* **2009** *55* (3), 215. doi:10.1016/j.pnmrs.2009.05.001.
(33) Widdifield, C. M.; Chapman, R. P.; Bryce, D. L. Chlorine, Bromine, and Iodine Solid-State NMR Spectroscopy. In *Annual Reports on NMR Spectroscopy*; Webb, G.A., Ed.; Elsevier Ltd.: Oxford, UK, 2009; Vol. 66, pp 195–326. doi:10.1016/S0066-4103(08)00405-5.
(34) Chapman, R. P.; Bryce, D. L. *Phys. Chem. Chem. Phys.* **2007** *9* (47), 6219. doi:10.1039/b712688c.
(35) Bryce, D. L.; Sward, G. D. *J. Phys. Chem. B* **2006** *110* (51), 26461. doi:10.1021/jp065878c.
(36) Bryce, D. L.; Sward, G. D.; Adiga, S. *J. Am. Chem. Soc.* **2006** *128* (6), 2121. doi:10.1021/ja057253i.
(37) Bryce, D. L.; Sward, G. D. *Magn. Reson. Chem.* **2006** *44* (4), 409. doi:10.1002/mrc.1741.
(38) Coplen, T. B.; Böhlke, J. K.; De Bièvre, P.; Ding, T.; Holden, N. E.; Hopple, J. A.; Krouse, H. R.; Lamberty, A.; Peiser, H. S.; Révész, K.; Rieder, S. E.; Rosman, K. J. R.; Roth, E.; Taylor, P. D. P.; Vocke, R. D., Jr; Xiao, Y. K. *Pure Appl. Chem.* **2002** *74* (10), 1987. doi:10.1351/pac200274101987.
(39) Pyykkö, P. *Mol. Phys.* **2008** *106* (16–18), 1965. doi:10.1080/00268970802018367.
(40) Rossini, A. J.; Mills, R. W.; Briscoe, G. A.; Norton, E. L.;

Can. J. Chem. Downloaded from www.nrcresearchpress.com by Xi'an Jiaotong University on 09/19/12
For personal use only.

Geier, S. J.; Hung, I.; Zheng, S.; Autschbach, J.; Schurko, R. W. *J. Am. Chem. Soc.* **2009** *131* (9), 3317. doi:10.1021/ja808390a.
(41) Hung, I.; Shetty, K.; Ellis, P. D.; Brey, W. W.; Gan, Z. *Solid State Nucl. Magn. Reson.* **2009** *36* (4), 159. doi:10.1016/j.ssnmr.2009.10.001.
(42) Gordon, P. G.; Brouwer, D. H.; Ripmeester, J. A. *J. Phys. Chem. A* **2008** *112* (49), 12527. doi:10.1021/jp808524h.
(43) Gordon, P. G.; Brouwer, D. H.; Ripmeester, J. A. *ChemPhysChem* **2010** *11* (1), 260. doi:10.1002/cphc.200900624.
(44) Bryce, D. L.; Bultz, E. B. *Chem.–Eur. J.* **2007** *13* (17), 4786. doi:10.1002/chem.200700056.
(45) Hamaed, H.; Pawlowski, J. M.; Cooper, B. F. T.; Fu, R.; Eichhorn, S. H.; Schurko, R. W. *J. Am. Chem. Soc.* **2008** *130* (33), 11056. doi:10.1021/ja802486q.
(46) Sandland, T. O.; Du, L. S.; Stebbins, J. F.; Webster, J. D. *Geochim. Cosmochim. Acta* **2004** *68* (24), 5059. doi:10.1016/j.gca.2004.07.017.
(47) Harris, R. K.; Becker, E. D.; Cabral De Menezes, S. M.; Granger, P.; Hoffman, R. E.; Zilm, K. W. *Pure Appl. Chem.* **2008** *80* (1), 59. doi:10.1351/pac200880010059.
(48) Gervais, C.; Laurencin, D.; Wong, A.; Pourpoint, F.; Labram, J.; Woodward, B.; Howes, A. P.; Pike, K. J.; Dupree, R.; Mauri, F.; Bonhomme, C.; Smith, M. E. *Chem. Phys. Lett.* **2008** *464* (1–3), 42. doi:10.1016/j.cplett.2008.09.004.
(49) Solomon, I. *Phys. Rev.* **1958** *110* (1), 61. doi:10.1103/PhysRev.110.61.
(50) Weisman, I. D.; Bennett, L. H. *Phys. Rev.* **1969** *181* (3), 1341. doi:10.1103/PhysRev.181.1341.
(51) Kunwar, A. C.; Turner, G. L.; Oldfield, E. *J. Magn. Reson.* **1986** *69*, 124. doi:10.1016/0022-2364(86)90224-6.
(52) Massiot, D.; Farnan, I.; Gautier, N.; Trumeau, D.; Trokiner, A.; Coutures, J. P. *Solid State Nucl. Magn. Reson.* **1995** *4* (4), 241. doi:10.1016/0926-2040(95)00002-8.
(53) Medek, A.; Frydman, V.; Frydman, L. *J. Phys. Chem. A* **1999** *103* (25), 4830. doi:10.1021/jp990410d.
(54) Eichele, K.; Wasylishen, R. E. *WSolids1: Solid-State NMR Spectrum Simulation Package,* ver. 1.19.11; Universität Tübingen: Tübingen, 2009.
(55) Clark, S. J.; Segall, M. D.; Pickard, C. J.; Hasnip, P. J.; Probert, M. I. J.; Refson, K.; Payne, M. C. *Z. Kristallogr.* **2005** *220* (5–6), 567. doi:10.1524/zkri.220.5.567.65075.
(56) Yates, J. R.; Pickard, C. J.; Mauri, F. *Phys. Rev. B* **2007** *76* (2), 024401. doi:10.1103/PhysRevB.76.024401.
(57) Perdew, J. P.; Burke, K.; Ernzerhof, M. *Phys. Rev. Lett.* **1996** *77* (18), 3865. doi:10.1103/PhysRevLett.77.3865.
(58) Perdew, J. P.; Burke, K.; Ernzerhof, M. *Phys. Rev. Lett.* **1997** *78* (7), 1396. doi:10.1103/PhysRevLett.78.1396.
(59) Perdew, J. P. Unified Theory of Exchange and Correlation Beyond the Local Density Approximation. In *Electronic Structure of Solids '91: Proceedings of the 75th WE-Heraeus-Seminar*; Ziesche, P., Eschrig, H., Eds.; Akademie Verlag: Berlin, 1991; p 11.
(60) Perdew, J. P.; Chevary, J. A.; Vosko, S. H.; Jackson, K. A.; Pederson, M. R.; Singh, D. J.; Fiolhais, C. *Phys. Rev. B* **1992** *46* (11), 6671. doi:10.1103/PhysRevB.46.6671.
(61) Perdew, J. P.; Chevary, J. A.; Vosko, S. H.; Jackson, K. A.; Pederson, M. R.; Singh, D. J.; Fiolhais, C. *Phys. Rev. B* **1993** *48* (7), 4978. doi:10.1103/PhysRevB.48.4978.2.
(62) Perdew, J. P.; Burke, K.; Wang, Y. *Phys. Rev. B* **1996** *54* (23), 16533. doi:10.1103/PhysRevB.54.16533.
(63) Burke, K.; Perdew, J. P.; Wang, Y. Derivation of a Generalized Gradient Approximation: the PW91 Density Functional. In *Electronic Density Functional Theory: Recent Progress and New Directions*; Dobson, J. F., Vignale, G., and Das, M. P., Eds.; Plenum: New York, 1998.
(64) Monkhorst, H. J.; Pack, J. D. *Phys. Rev. B* **1976** *13* (12), 5188. doi:10.1103/PhysRevB.13.5188.
(65) van Bever, A. K.; Nieuwenkamp, W. *Z. Kristallogr.* **1935** *90*, 374.
(66) Agron, P. A.; Busing, W. R. *Acta Crystallogr. C* **1986** *C42* (2), 141. doi:10.1107/S0108270186097007.
(67) Arfken, G. B.; Weber, H. J. *Mathematical Methods for Physicists*, 6th ed. Academic Press: New York, 2005; p 202.
(68) Adiga, S.; Aebi, D.; Bryce, D. L. *Can. J. Chem.* **2007** *85* (7–8), 496. doi:10.1139/v07-069.
(69) Stebbins, J. F.; Du, L. S. *Am. Mineral.* **2002** *87* (2–3), 359.
(70) MacKenzie, K. J. D.; Smith, M. E. *Multinuclear Solid-State NMR of Inorganic Materials*; Pergamon: Amsterdam, 2002.
(71) Lin, Z.; Smith, M. E.; Sowrey, F. E.; Newport, R. J. *Phys. Rev. B* **2004** *69* (22), 224107. doi:10.1103/PhysRevB.69.224107.
(72) Bryce, D. L.; Bultz, E. B.; Aebi, D. *J. Am. Chem. Soc.* **2008** *130* (29), 9282. doi:10.1021/ja8017253.
(73) Bryce, D. L. *Dalton Trans.* **2010** *39* (37), 8593. doi:10.1039/c0dt00416b.
(74) Leclaire, A.; Borel, M. M. *Acta Crystallogr. B* **1979** *B35* (3), 585. doi:10.1107/S0567740879004209.
(75) Leclaire, A.; Borel, M. M. *Acta Crystallogr. B* **1978** *B34* (3), 900. doi:10.1107/S0567740878004288.
(76) Leclaire, A.; Borel, M. M.; Monier, J. C. *Acta Crystallogr. B* **1980** *B36* (11), 2757. doi:10.1107/S0567740880009909.
(77) Shepelev, A. I.; Lyashenko, M. N.; Druzhinin, I. G. *Dokl. Akad. Nauk SSSR* **1950** *75*, 379.
(78) Leclaire, A.; Borel, M. M. *Acta Crystallogr. B* **1977** *B33* (5), 1608. doi:10.1107/S0567740877006645.
(79) Chapman, R. P.; Hiscock, J. R.; Gale, P. A.; Bryce, D. L. *Can. J. Chem.* **2011** *89*. This issue.
(80) Gee, M.; Wasylishen, R. E.; Laaksonen, A. *J. Phys. Chem. A* **1999** *103* (50), 10805. doi:10.1021/jp9925841.
(81) Brackett, E. B.; Brackett, T. E.; Sass, R. L. *J. Inorg. Nucl. Chem.* **1963** *25* (10), 1295. doi:10.1016/0022-1902(63)80396-6.
(82) Wu, G.; Terskikh, V. *J. Phys. Chem. A* **2008** *112* (41), 10359. doi:10.1021/jp8064739.
(83) Sternheimer, R. *Phys. Rev.* **1950** *80* (1), 102. doi:10.1103/PhysRev.80.102.2.
(84) Sternheimer, R. *Phys. Rev.* **1951** *84* (2), 244. doi:10.1103/PhysRev.84.244.
(85) Sternheimer, R. *Phys. Rev.* **1954** *95* (3), 736. doi:10.1103/PhysRev.95.736.
(86) Lucken, E. A. C. Sternheimer Shielding. In *Nuclear Quadrupole Coupling Constants*; Academic Press: London, 1969; p 79.

Can. J. Chem. Downloaded from www.nrcresearchpress.com by Xi'an Jiaotong University on 09/19/12
For personal use only.

Exact calculation of the response of a quadrupolar nucleus to radio frequency irradiation

T. Leigh Spencer, Gillian R. Goward, and Alex D. Bain

Can. J. Chem. Downloaded from www.nrcresearchpress.com by Xi'an Jiaotong University on 09/19/12
For personal use only.

Abstract: The effect of a pulse in NMR is usually considered as a rotation of the frame of reference of the spin system. For spins-1/2, this concept is an important and very useful tool. The assumption behind this concept is that while the radio frequency irradiation is on, this term dominates all other interactions. Although this is usually true for spins-1/2, typical interactions for a quadrupolar nucleus can be very large and the assumption is no longer valid. The full solution is complex, but two extreme cases are already solved. If the quadrupole interaction is very small, then the assumption is valid and the pulse does act like a rotation of the frame of reference. At the other extreme, if the interaction is large and the spin, I, is half-integral, then the central transition remains relatively narrow and can be treated as a fictitious spin-1/2. The pulse then acts as a rotation, but with a scaling factor of $I + 1/2$. This paper treats the general case, where no approximations are made. The effects can be observed in a nutation experiment, in which the observed signal is plotted as a function of pulse width, in a simple one-pulse experiment. If the pulse acts as a rotation, then the nutation plot will be a sine wave, but otherwise it will be a sum of sinusoids. This is true even for a single-crystal sample with a single quadrupolar coupling. If the sample is a powder, then the nutation plot will be a sum of many sinusoids, since the quadrupole coupling will vary with the powder average. This paper sketches out the theory of these effects based on a full and exact description of a quadrupolar system and illustrates it with some nutation spectra of ^{23}Na in a powdered sample of sodium nitrate.

Key words: NMR, quadrupolar nuclei, nutation spectra, radio frequency interactions, spin-3/2, spin operators.

Résumé : L'effet d'une pulsation en RMN et généralement considéré comme une rotation du système de référence du système de spin. Pour les spins 1/2, ce concept est un outil important et très utile. L'hypothèse derrière ce concept est que lorsque l'irradiation par une radiofréquence est appliquée, ce terme domine toutes les autres interactions. Même s'il est généralement vrai que pour les spins 1/2, les interactions typiques pour un noyau quadripolaire peuvent être assez importantes et l'hypothèse n'est plus valide. La solution totale est complexe, mais deux cas extrêmes ont déjà été résolus. Si l'interaction quadripolaire est très faible, l'hypothèse est alors valide et la pulsation agit comme une rotation du système de référence. À l'autre extrême, si l'interaction est grande et que le spin, I, n'est pas un nombre entier, la transition centrale demeure alors étroite et elle peut être traitée comme un spin 1/2 fictif. La pulsation agit alors comme une rotation, mais elle comporte un facteur d'étalement de $I + 1/2$. Dans ce travail, on traite du cas général pour lequel aucune approximation n'est faite. Les effets peuvent être observés dans une expérience de nutation au cours de laquelle on trace un graphique du signal observé en fonction de la largeur de la pulsation exercée dans une expérience simple à une pulsation. Si la pulsation agit comme une rotation, le graphique de la nutation sera une onde sinusoïdale simple, autrement il sera la somme de sinusoïdes. Ceci est vrai pour un échantillon de cristal unique avec un couplage quadripolaire simple. Si l'échantillon est une poudre, le graphique de la nutation sera la somme de plusieurs sinusoïdes puisque le couplage quadripolaire variera avec la moyenne de la poudre. Le présent travail esquisse la théorie de ces effets en se basant sur une description complète et exacte d'un système quadripolaire et il les illustre à l'aide de spectres de nutation du ^{23}Na dans un échantillon en poudre de nitrate de sodium.

Mots-clés : RMN, noyau quadripolaire, spectres de nutation, interactions avec des radiofréquences, spin 3/2, opérateurs de spin.

[Traduit par la Rédaction]

Introduction

In most fields of NMR, a common assumption is that the pulses are "hard" and that they act like a rotation of the frame of reference. This arises from the assumption that the radio frequency (rf) magnetic field dominates all the other interactions.[1–4] This is equivalent to assuming that there is no other evolution during the pulse — it effectively has zero length, yet has a finite flip angle; hence, the common parlance of 90° pulses, etc. This is usually a valid assumption for spins-1/2, but for quadrupolar nuclei it fails because

Received 1 November 2010. Accepted 13 December 2010. Published at www.nrcresearchpress.com/cjc on 3 May 2011.

T.L. Spencer, G.R. Goward, and A.D. Bain. Department of Chemistry and Chemical Biology, McMaster University, 1280 Main Street West, Hamilton, ON L8S 4M1, Canada.

Corresponding author: A.D. Bain (e-mail: bain@mcmaster.ca).

This article is part of a Special Issue dedicated to Professor Roderick E. Wasylishen.

Can. J. Chem. Downloaded from www.nrcresearchpress.com by Xi'an Jiaotong University on 09/19/12
For personal use only.

quadrupole couplings can be several megahertz. Solutions of this problem are available for very large and very small (with respect to the rf) quadrupole couplings, but a general solution is more complicated. In this paper, we give some preliminary discussion of the theory, based on an exact solution (no perturbation theory) of the quadrupole system without rf irradiation. The specific results may well be familiar to the reader, but the approach is very general[5] and more systematic than standard methods. This paper represents a test and a validation of these methods.

Nutation plots

One manifestation of the rotation character is that a plot of signal against pulse width gives a sine wave. This plot, called a nutation plot, usually forms the basis for pulse power calibrations and rf homogeneity tests. Even when this hard pulse approximation is not fully justified, the rotation picture is remarkably successful, and it pervades almost all NMR. Since rf fields are typically 40 kHz or so, the approximation is often acceptable for spins-1/2 in solution. Few spin interactions in this case are of that size. Offsets from resonance can approach that magnitude, so that both precession and rf interactions occur during the pulse but the pulse is still well approximated by a rotation around a tilted effective rf field.[2,3,6–8]

Quadrupolar nuclei, on the other hand, have much larger interactions, so the hard pulse approximation is much more difficult to justify. For example, one consequence of this failure is that a single pulse can create substantial multiple-quantum coherence, as in the original multiple-quantum magic-angle spinning experiment.[9] Similarly, the selection rules break down and multiple-quantum and overtone spectra can be observed.[10–13] Even though this breakdown complicates the spin dynamics, it also gives us an easily manipulated experimental parameter (the pulse width) with which to probe the system. To study the effects of pulses on quadrupolar systems, we must look at the simultaneous interaction of rf and quadrupole coupling in more detail.

A good way of probing the effects of a general quadrupole interaction is to study the nutation plots.[14–18] Quadrupolar systems with large interactions can give very broad spectra, but nuclei with half-integral spins have a central transition (from m_z of –1/2 to +1/2) which remains sharp even in the presence of large quadrupole couplings (>1 MHz).[19,20] This central transition is perturbed only to second order in the quadrupole coupling,[21] so it is much narrower than the satellites, whose width is directly proportional to the quadrupole coupling. The nutation experiment in this case usually involves the intensity of the central transition as a function of pulse width.

There are two easily treated extremes: the quadrupole coupling is very much bigger or very much smaller than the rf field. In both these cases, the nutation plot still has a sinusoidal form, but the nutation frequencies differ. For small quadrupolar coupling, the hard pulse approximation applies and all the transitions are affected equally: the spin acts like a spin-1/2. For large couplings, the central transition is essentially isolated and can be treated as a fictitious spin-1/2 system. The nutation plot is again sinusoidal, but the period is reduced (the nutation frequency is increased) by a factor of $I + 1/2$, where I is the nuclear spin.

Theory

The intermediate case is more complicated and forms the subject of this paper. A number of solutions have already been published for spin-3/2.[22–29] Since spin-3/2 is a small finite system, the calculations are not particularly difficult. Straightforward numerical density matrix manipulations[30,31] can be peformed, either with the density matrix as a matrix in Hilbert space,[1] as in eq. [1],

$$[1] \qquad \hat{\rho}(t) = \exp(-i\hat{H}t)\hat{\rho}(0)\exp(i\hat{H}t)$$

or with the density matrix as a vector in Liouville space under the influence of $\boldsymbol{L}$, the Liouvillian,[32,33] as in eq. [2].

$$[2] \qquad \rho(t) = \exp(-iLt)\rho(0)$$

Solutions that are clear and meet our intuitions are more elusive — we are very attached to the rotation and vector picture of a pulse, even though it does not apply here. If the hard pulse approximation applies to a weakly coupled system of spins-1/2, the product operator formalism[34] gives an excellent description of the time evolution. This has become the standard way of describing pulse sequences, but for strongly coupled or quadrupolar nuclei, the calculations are less clear. On the other hand, if a transition is relatively isolated because the interactions are large, then the evolution can be treated as a fictitious spin-1/2 and described by single transition operators.[35,36] However, this creates an overcomplete basis — more operators than the dimensionality of the system — so a full treatment is clumsy. In the present case, neither is appropriate. All transitions are potentially involved simultaneously, even though it is only the central transition that is measured. We must expect that the result could be complicated.

The various solutions must agree, since they are all exact, but there is virtue in solving a problem in a number of different ways. Simple numerical integration will simulate the experiments, but it tends not to provide much insight into mechanisms. Provided approximations are made, then explicit formulae can often be derived for the evolution of the system. This gives us a functional form which we can manipulate analytically. In this paper, we present a new solution based on a recently published exact description of a quadrupolar system.[13,37] The present approach is exact, but the full solution is too complicated to present algebraically. However, its structure is quite simple and it is clear where approximations can be made to give explicit formulae.

Analogy to NQR

As with all NMR experiments, the system is described by the density matrix, which evolves in time according to the Liouville–von Neumann equation. The solution to this equation is given in eqs. [1] and [2]. For a single quadrupolar spin, the total Liouvillian includes terms from the Zeeman interaction, the quadrupole coupling, and the effect of the rf irradiation. The rf is treated in the laboratory frame of reference rotating at the transmitter frequency, so the Zeeman term is zero, or reduced to a small offset from resonance.

Can. J. Chem. Downloaded from www.nrcresearchpress.com by Xi'an Jiaotong University on 09/19/12
For personal use only.

This means that we only deal with the quadrupole and rf terms.

In the pure quadrupole interaction, the energy of a spin state is proportional to the *square* of the z component of the spin angular momentum, so the levels with z component $\pm 1/2$ are degenerate, as are the other pairs of corresponding levels. This is shown schematically in Fig. 1 for the spin-3/2 with just a quadrupole interaction. There are two energies, which are separated by $e^2qQ/2$, the frequency at which nuclear quadrupole resonance (NQR) absorption appears.[38]

Note that we are not using the usual frame of reference for NQR. There, the convention is that the principal axes of the electric field gradient tensor define the frame. For a powder sample, then, the rf field will have a powder distribution, with respect to the field gradient. In our calculation, we use the laboratory frame, in which the z axis is defined by the Zeeman interaction and the rf is in the xy plane. In either case, the relative orientation of the rf and the quadrupole interaction will define the ratio of the sizes of these two, and it will be different for each crystallite in the powder.

A magnetic field will lift this degeneracy of the levels. If a small static field is applied in the laboratory frame, this mixes the $\pm 1/2$ states strongly, since they differ by only one unit of angular momentum and there is a direct matrix element between them. The $\pm 3/2$ states are less affected.[38]

Since there are four spin states, there are six possible coherences with nonzero resonance frequency. In the NQR spectrum, there are four transitions close to the NQR frequency.[38] Two are allowed transitions, $-1/2 \rightarrow -3/2$ and $+1/2 \rightarrow +3/2$ (transitions *1* and *2* in Fig. 1), where the z component changes by one unit. Since the $\pm 1/2$ states are strongly mixed, the formally forbidden transitions $-1/2 \rightarrow +3/2$ and $+1/2 \rightarrow -3/2$ (transitions *3* and *4* in Fig. 1) also have substantial transition probabilities. There are clearly analogies with the AB system of two spins-1/2. The other two coherences are the low-frequency (zero, if the magnetic field is zero) coherences $-1/2 \rightarrow +1/2$ and $-3/2 \rightarrow +3/2$ (transitions *5* and *6* in Fig. 1).

This is the pattern of frequencies when the Zeeman interaction is much smaller than the quadrupole and we are doing NQR. As the Zeeman interaction increases and comes to dominate, we change to the regime of quadrupole-perturbed NMR, and the correlation of the coherences is given in Fig. 2. While the rf is on, even in a large magnetic field, the interaction of rf with a quadrupole system still belongs in the NQR regime, since the rotating frame reduces the Zeeman interaction. It is still useful to keep the NMR situation in mind, however.

For the calculation we are doing, the Liouvillian has three terms: $\boldsymbol{L}_z$, the Zeeman term, $\boldsymbol{L}_q$, the quadrupole term, and $\boldsymbol{L}_{rf}$, the term describing the rf. We have formulae for the matrix elements of all these terms,[5,37] so eq. [2] gives an exact solution for any set of parameters. In practical terms, valid approximations such as neglecting the Zeeman term (because of the transformation to the rotating frame of reference) can be easily imposed. If we assume that the electric field gradient tensor is cylindrical, then the Liouvillian is further simplified and we can extract explicit formulae. For the purposes here, we will use the numerical solution to the exact equation. Future work will explore approximations and algebraic solutions.

Fig. 1. Schematic energy-level diagram of a spin-3/2 in a small magnetic field. Six transitions are possible amongst the four energy levels: there are two formally allowed transitions, *1* and *2*, and two formally forbidden transitions, *3* and *4*. These are the transitions that would be observed in a Zeeman-perturbed NQR spectrum. The final two transitions, *5* and *6*, are low-frequency ones.

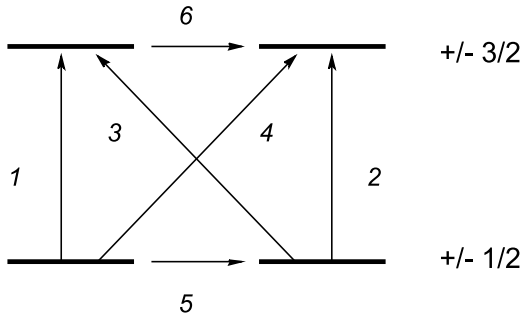

Fig. 2. Schematic energy levels of a spin-3/2 in zero applied magnetic field (left) and high field (right). The splittings are nominal and not to scale.

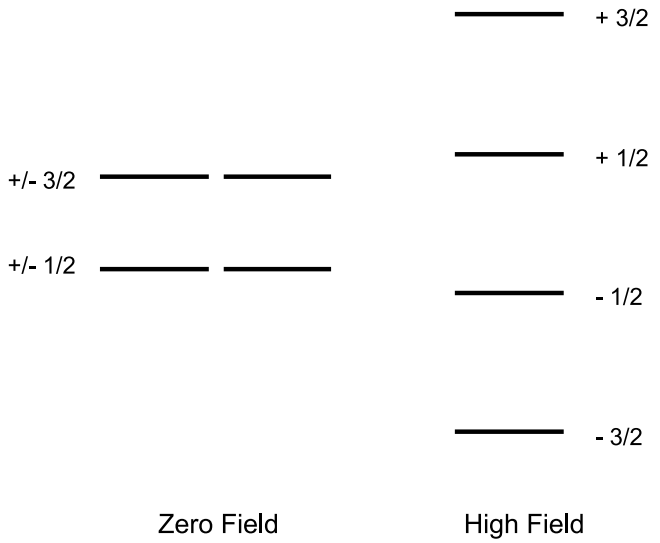

Experimental

NMR spectra were acquired on a Bruker Avance I 500 MHz spectrometer using a standard 2.5 mm MAS probe. The samples were not spinning, and all spectra were acquired at ambient temperature. Sodium nitrate was purchased from Sigma-Aldrich and used without further purification. The sample was ground in a mortar and pestle and put into a standard 2.5 mm rotor.

The magnetic field associated with the rf was determined from measurements of a 90° pulse on a solution of sodium nitrate in water. For each spectrum of the solid sample, 64 acquisitions were made with a delay time of 40 s between pulses. The full spectral width was 500 kHz, and 4K points were acquired in the time domain.

The simulations for a given quadrupole coupling were done with a specifically written program in the C language. No attempt was made to make the code numerically efficient, since the goal was to implement the theory clearly. Source code is available from A. D. Bain on request. The signal for

Can. J. Chem. Downloaded from www.nrcresearchpress.com by Xi'an Jiaotong University on 09/19/12
For personal use only.

a powder sample was then simulated by doing a powder average over the orientation and the quadrupole coupling using the Zaremba–Conroy–Wolfsberg method.[39,40] For a system with approximately 1000 powder average points and 256 points along the nutation plot, the calculations took approximately 30 s on an Intel-based personal computer running at 1.5 GHz with 512 MB of RAM.

Results and discussion

Figure 3 shows the plot of signal intensity of the central transition of the ^{23}Na spectrum of sodium nitrate as a function of pulse width. The data points are the solid circles and the smooth curve shows the simulation. No adjustable parameters were used in the simulation other than a slight adjustment of the rf field strength to improve the fit. This discrepancy may have been caused by small differences in the probe tuning between the liquid solution (used to calibrate the rf field) and the solid sample. The quadrupole parameters for sodium in sodium nitrate were fixed at values from the literature (e^2qQ = 335 kHz, η = 0).[23,41–43] The quadrupole coupling could be verified, since the signal/noise ratio was good enough to see the edges of the powder pattern of the satellite transitions.

Since there are six possible coherences for a spin-3/2, any time evolution can be written as a sum of six oscillations, although a selection rule reduces this to four. Even for a crystal with a single quadrupole coupling, the nutation plot will not be a simple sinusoid (Fig. 4), but rather a sum of them. The frequencies of these oscillations are given by the eigenvalues of the Liouvillian. This is always true, but the question is how much does each oscillation contribute to the observed signal?

In the extreme limits, a single term dominates. For $\gamma B_1 >> e^2qQ$ (hard pulse), the dependence on pulse width is sinusoidal with a nutation frequency of γB_1. At the other extreme (large quadrupole coupling), a spin-3/2 shows a sinusoidal dependence, but now with a nutation frequency of $2\gamma B_1$, obeying the $I + 1/2$ rule. In the intermediate range, even though there is a single quadrupole coupling, the signal is a sum of sinusoidal terms, each with substantial contributions.

A powder sample will have a range of quadrupole couplings, depending on the orientation of the crystallite in the magnetic field. If the rf field is comparable to the quadrupole coupling, then there will be signals at the edges of the powder pattern where the quadrupole coupling dominates, but there will also be crystallites close to the magic angle for which the rf is the major term. This means that not only does a single crystallite have a time evolution made up of a sum of sine waves, but the powder average will contribute many more frequencies to the total evolution. Figure 5 shows a number of simulated nutation plots for a number of orientations of the crystal.

This means that for a powder sample, the central transition will not show a sinusoidal nutation plot, except in extreme cases. All of the sinusoids will start out together, so the signal will initially increase in an apparent sine wave with increasing pulse width. As the nominal flip angle (for a sample with no quadrupole interaction) approaches 90°, the oscillations will grow out of phase with each other and start to cancel. This leads to the occasional phenomenon of never

Fig. 3. Experimental nutation plot for the central transition in the ^{23}Na spectrum of a powder sample of sodium nitrate. The solid circles represent measured data, and the line represents the simulation. No adjustable parameters were used in the simulation.

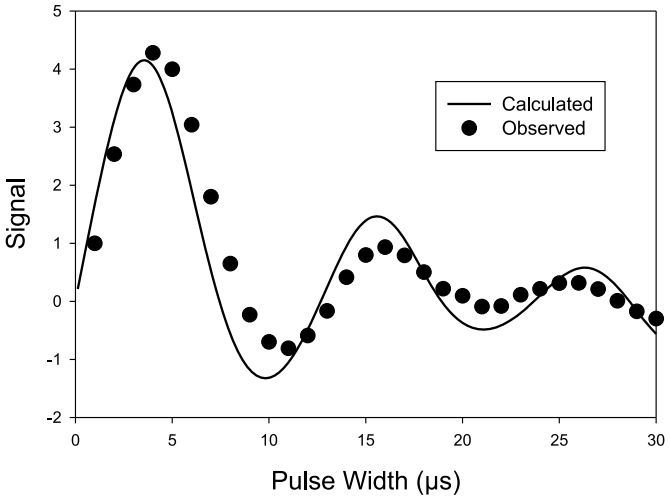

Fig. 4. Simulation of a ^{23}Na nutation plot for a single crystal of sodium nitrate oriented at an angle of 140° with the z axis in the laboratory frame — the frame in which the rf magnetic field is in the xy plane. The parameters used were γB_1 = 200 kHz, e^2qQ = 337 kHz, and η = 0. The curve is a sum of up to six sinusoids with different frequencies and scale factors.

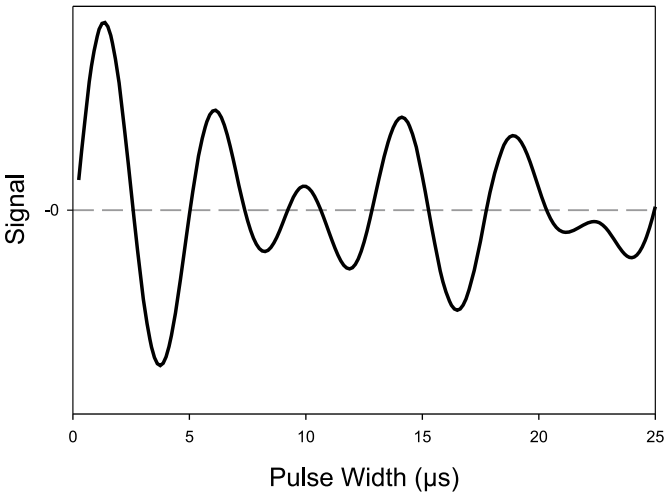

getting an inversion in a nutation plot of a powder sample — the parameters are such that the signal stays positive and just dies away.

Figure 3 shows the correspondence between theory and experiment for the ^{23}Na spectrum of powdered sodium nitrate. No adjustable parameters were used in the theoretical calculation. The match between the experimental data and the simulations is good, but not perfect. We think that the discrepancies are long pulse widths that may be due to poor rf homogeneity in the probe, and experiments to provide a more rigorous test of the theory are under way.

This discussion is in the time domain — the width of the pulse is the independent variable. Many nutation experiments take the Fourier transform of these data to create a nutation

Fig. 5. Simulations of single-crystal ^{23}Na nutation plots for a number of different orientations of a sodium nitrate crystal. The orientation with respect to the laboratory frame is given in the legend. The parameters used were $\gamma B_1 = 200$ kHz, $e^2qQ = 337$ kHz, and $\eta = 0$. The full powder pattern will be an average over all such plots, representing all orientations with appropriate weightings.

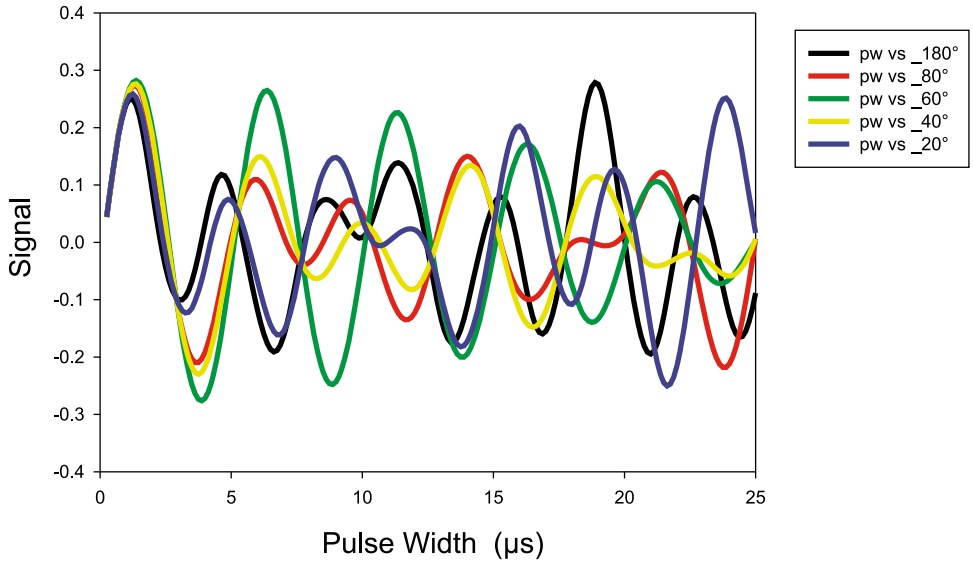

spectrum. The time domain and the frequency domain are equivalent, of course. The arguments above show that for a spin-3/2, a single crystal will have a nutation spectrum with four frequencies (of various intensities) in it. When averaged over a powder, there will be a complete range of frequencies, leading to a broad nutation spectrum with some maxima and other features. These frequencies are important in setting up matching curves for cross-polarization with quadrupolar nuclei.[44] Both the time domain and the frequency domain will give poorly resolved data, so it is up to the user to choose which presentation provides more insight.

Finally, Fig. 1 suggests why multiple-quantum coherence can be created by a single pulse. The transition from –3/2 → +3/2 is a low-frequency transition for a quadrupolar nucleus in a very small magnetic field, even though it is triple-quantum coherence at high field. It is therefore well within the range of the relatively weak rf pulse. After the rf is switched off, the system reverts to the NMR regime (Fig. 2) and the coherence created in the NQR situation will evolve as triple-quantum coherence with the attendant advantages. We aim to follow this qualitative explanation more quantitatively in future work.

Conclusions

We have presented a clear and rigorous picture of nutation behaviour for a quadrupolar spin. The calculation makes no approximations and is applicable to any spin. Its major application will be to half-integral rather than integral spins, but both can be treated. The nutation plot will be a sum of sinusoids, even for a single crystal with one quadrupole coupling. A powder sample will show an almost continuous range of nutation frequencies. The results of the calculation agree well with experimental nutation plots of the ^{23}Na spectrum of a powder sample of sodium nitrate.

Acknowledgements

Alex Bain and Gillian Goward are grateful to the Natural Sciences and Engineering Research Council of Canada (NSERC) for financial support. We also thank Dr. Bob Berno for technical assistance.

References

(1) Ernst, R. R.; Bodenhausen, G.; Wokaun, A. *Principles of Nuclear Magnetic Resonance in One and Two Dimensions*; Clarendon Press: Oxford, 1987.
(2) Levitt, M. H. *Spin Dynamics*; John Wiley: Chichester, 2001.
(3) Keeler, J. *Understanding NMR Spectroscopy*; John Wiley and Sons: New York, 2005.
(4) Duer, M. J. *Introduction to Solid-State NMR Spectroscopy*; Blackwell: Oxford, 2004.
(5) Bain, A. D.; Berno, B. *Prog. Nucl. Magn. Reson. Spectrosc.*, in press. doi:10.1016/j.pnmrs.2010.12.002.
(6) Warren, W. S. *J. Chem. Phys.* **1984** *81* (12), 5437. doi:10.1063/1.447644.
(7) Gregory, R. M.; Bain, A. D. *Concepts Magn. Reson.* **2009** *34A* (6), 305. doi:10.1002/cmr.a.20147.
(8) Bain, A. D.; Anand, C. K.; Nie, Z. *J. Magn. Reson.* **2010** *206* (2), 227. doi:10.1016/j.jmr.2010.07.012.
(9) Medek, A.; Harwood, J. S.; Frydman, L. *J. Am. Chem. Soc.* **1995** *117* (51), 12779. doi:10.1021/ja00156a015.
(10) Tycko, R.; Opella, S. J. *J. Am. Chem. Soc.* **1986** *108* (12), 3531. doi:10.1021/ja00272a071.
(11) Tycko, R.; Opella, S. J. *J. Chem. Phys.* **1987** *86* (4), 1761. doi:10.1063/1.452176.
(12) Eles, P. T.; Michal, C. A. *Chem. Phys. Lett.* **2003** *376* (3–4), 268. doi:10.1016/S0009-2614(03)00969-2.
(13) Khasawneh, M.; Hartman, J. S.; Bain, A. D. *Mol. Phys.* **2004** *102* (9–10), 975. doi:10.1080/00268970410001717304.
(14) Samoson, A.; Lippmaa, E. *Phys. Rev. B* **1983** *28* (11), 6567. doi:10.1103/PhysRevB.28.6567.
(15) Samoson, A.; Lippmaa, E. *Chem. Phys. Lett.* **1983** *100* (3), 205. doi:10.1016/0009-2614(83)87276-5.
(16) Kentgens, A. P. M.; Lemmens, J. J. M.; Geurts, F. M. M.; Veeman, W. S. *J. Magn. Reson.* **1987** *71*, 62.
(17) Kentgens, A. P. M. *Prog. Nucl. Magn. Reson. Spectrosc.* **1998** *32* (2), 141. doi:10.1016/S0079-6565(98)00015-6.

Can. J. Chem. Downloaded from www.nrcresearchpress.com by Xi'an Jiaotong University on 09/19/12
For personal use only.

(18) Harbison, G. S.; Slokenbergs, A.; Barbara, T. M. *J. Chem. Phys.* **1989** *90* (10), 5292. doi:10.1063/1.456433.
(19) Slichter, C. P. *Principles of Magnetic Resonance*, 3rd ed.; Springer-Verlag: Berlin, 1989.
(20) Baugher, J. F.; Taylor, P. C.; Oja, T.; Bray, P. J. *J. Chem. Phys.* **1969** *50* (11), 4914. doi:10.1063/1.1670988.
(21) Bain, A. D. *J. Magn. Reson.* **2006** *179* (2), 308. doi:10.1016/j.jmr.2006.01.007.
(22) Man, P. P. *J. Magn. Reson.* **1986** *67*, 78.
(23) Pandey, L.; Towta, S.; Hughes, D. G. *J. Chem. Phys.* **1986** *85* (12), 6923. doi:10.1063/1.451378.
(24) Janssen, R.; Veeman, W. S. *J. Chem. Soc., Faraday Trans.* **1988** *84* (11), 3747. doi:10.1039/f19888403747.
(25) van der Mijden, J. A. M.; Janssen, R.; Veeman, W. S. *Mol. Phys.* **1990** *69* (1), 53. doi:10.1080/00268979000100041.
(26) Man, P. P. *Mol. Phys.* **1993** *78* (2), 307. doi:10.1080/00268979300100251.
(27) Man, P. P.; Tougne, P. *Mol. Phys.* **1994** *83* (5), 997. doi:10.1080/00268979400101721.
(28) Ageev, S. Z.; Sanctuary, B. C. *Chem. Phys. Lett.* **1996** *255* (1–3), 71. doi:10.1016/0009-2614(96)00334-X.
(29) Ageev, S. Z.; Sanctuary, B. C. *Mol. Phys.* **1995** *84* (5), 835. doi:10.1080/00268979500100591.
(30) Bak, M.; Rasmussen, J. T.; Nielsen, N. C. *J. Magn. Reson.* **2000** *147* (2), 296. doi:10.1006/jmre.2000.2179.
(31) Veshtort, M.; Griffin, R. G. *J. Magn. Reson.* **2006** *178* (2), 248. doi:10.1016/j.jmr.2005.07.018.
(32) Fano, U. Liouville Representation of Quantum Mechanics with Application to Relaxation Processes. In *Lectures on the Many-Body Problem*; Caianiello, E. R., Ed.; Academic Press: New York, 1964; Vol. 2, p. 217.
(33) Bain, A. D. *Prog. Nucl. Magn. Reson. Spectrosc.* **1988** *20* (3), 295. doi:10.1016/0079-6565(88)80004-9.
(34) Sørensen, O. W.; Eich, G. W.; Levitt, M. H.; Bodenhausen, G.; Ernst, R. R. *Prog. Nucl. Magn. Reson. Spectrosc.* **1984** *16*, 163. doi:10.1016/0079-6565(84)80005-9.
(35) Vega, S.; Pines, A. *J. Chem. Phys.* **1977** *66* (12), 5624. doi:10.1063/1.433884.
(36) Wokaun, A.; Ernst, R. R. *J. Chem. Phys.* **1977** *67* (4), 1752. doi:10.1063/1.435038.
(37) Bain, A. D. *Mol. Phys.* **2003** *101* (21), 3163. doi:10.1080/00268970310001626298.
(38) Das, T. P.; Hahn, E. L. *Nuclear Quadrupole Resonance Spectroscopy*; Academic Press: New York, 1958.
(39) Conroy, H. *J. Chem. Phys.* **1967** *47* (12), 5307. doi:10.1063/1.1701795.
(40) Cheng, V. B.; Suzukawa, H. H.; Wolfsberg, M. *J. Chem. Phys.* **1973** *59* (8), 3992. doi:10.1063/1.1680590.
(41) Andrew, E. R.; Eades, R. G.; Hennel, J. W.; Hughes, D. G. *Proc. Phys. Soc.* **1962** *79* (5), 954. doi:10.1088/0370-1328/79/5/306.
(42) Jakobsen, H. J.; Skibsted, J.; Bildsoe, H.; Nielsen, N. C. *J. Magn. Reson.* **1989** *85*, 173.
(43) Nielsen, N. C.; Bildsoe, H.; Jakobsen, H. J. *J. Magn. Reson.* **1992** *97*, 149.
(44) Ashbrook, S. E.; Wimperis, S. *Mol. Phys.* **2000** *98* (1), 1. doi:10.1080/00268970009483265.

Can. J. Chem. Downloaded from www.nrcresearchpress.com by Xi'an Jiaotong University on 09/19/12
For personal use only.

NMR crystallography — Three polymorphs of phenobarbital

Anuji Abraham, David C. Apperley, Thomas Gelbrich, Robin K. Harris, and Ulrich J. Griesser

Can. J. Chem. Downloaded from www.nrcresearchpress.com by Xi'an Jiaotong University on 09/19/12
For personal use only.

Abstract: The NMR spectra of polymorphs I, II, and III of the pharmaceutical drug compound phenobarbital are discussed in relation to the crystal structures. Whilst some features can be explained by inspection of the structures, others require more detailed work. In this paper, shielding computations for the ^{13}C, ^{15}N, and ^{1}H nuclei using crystallographic repetition (with optimization of the positions of all atoms) are presented. These have enabled the majority of the signals to be assigned with some confidence and several features of NMR crystallography are illuminated. In particular, resonances have been attributed separately for the three independent molecules of form I (and also for form II). Moreover, the chemically equivalent but crystallographically distinct nuclei forming the two halves of the phenyl ring (and likewise of the heteronuclear ring) have been distinguished and a structural conformational motif attached to the ^{15}N chemical shifts revealed. The small differences between the spectra of forms I and II (which have very closely related crystal structures) are well-reproduced. The value of computations for establishing precise assignments of signals to crystallographic sites of atoms is emphasised. Conversely, the work provides a good test of the accuracy of computations for crystalline materials.

Key words: NMR crystallography, phenobarbital, polymorphism, shielding computation, assignment of signals.

Résumé : On discute des spectres RMN des polymorphes I, II et III du phénobarbital, un composé médicamenteux, en relation avec leurs structures cristallines. Alors que certaines caractéristiques peuvent être expliquées par l'examen des structures, d'autres demandent un travail plus détaillé. Dans ce travail, on rapporte des calculs de blindage des noyaux ^{13}C, ^{15}N et ^{1}H à l'aide de répétitions cristallographiques (avec optimisation des positions de tous les atomes). Ces résultats ont permis d'attribué pratiquement tous les signaux avec un certain degré de confiance et plusieurs caractéristiques de la cristallographie par RMN sont mis en lumière. En particulier, les résonances ont pu être attribuées séparément pour les molécules indépendantes de la forme I (ainsi que de la forme II). De plus, on a pu établir une distinction entre les noyaux chimiquement équivalents, mais distincts d'un point de vue cristallographique, des deux moitiés du noyau phényle (de même que pour le noyau hétéronucléaire) et mettre en évidence un motif conformationnel attaché aux déplacements chimiques du ^{15}N. Les petites différences entre les spectres des formes I et II (dont les structures cristallines sont très semblables) sont bien reproduites. On met en relief la valeur des calculs dans l'établissement d'attributions précises de signaux à des sites cristallographiques d'atomes. Et en conséquence, ce travail fournit un bon test de la précision des calculs pour des matériaux cristallins.

Mots-clés : cristallographie par RMN, phénobarbital, polymorphisme, calcul de blindage, attribution de signaux.

[Traduit par la Rédaction]

Introduction

Phenobarbital (5-ethyl-5-phenyl-2,4,6(1*H*,3*H*,5*H*)-pyrimidinetrione), $C_{12}H_{12}N_2O_3$, is a well-known barbiturate drug, which is still in clinical use nearly a century after first being put on the market. It has the molecular structure given on the right, together with the atomic numbering used for the NMR spectra and for the reported crystal structure of polymorph III (although it needs to be noted that the numbering for the other two crystal forms is not entirely consistent).

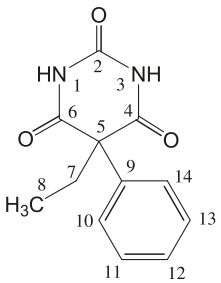

Received 13 October 2010. Accepted 22 December 2010. Published at www.nrcresearchpress.com/cjc on 5 July 2011.

A. Abraham, D.C. Apperley, and R.K. Harris. Department of Chemistry, University of Durham, South Road, Durham City DH1 3LE, UK.
T. Gelbrich and U.J. Griesser. Institute of Pharmacy, University of Innsbruck, Innrain 52c, 6020 Innsbruck, Austria.

Corresponding author: R.K. Harris (e-mail r.k.harris@durham.ac.uk)

This article is part of a Special Issue dedicated to Professor Roderick E. Wasylishen.

Can. J. Chem. Downloaded from www.nrcresearchpress.com by Xi'an Jiaotong University on 09/19/12
For personal use only.

The characteristics of eleven polymorphs of phenobarbital, including six metastable forms that crystallize only in the presence of other barbiturates, have been reviewed recently.[1,2] New crystal-structure determinations of the most stable forms (I, II, and III) were presented (see the Cambridge Structural Database[3] CCDC codes PHBARB07–09), as were the high-resolution ^{13}C and ^{15}N solid-state NMR spectra. However, the chemical shifts were not discussed in detail and, since no shielding computations were carried out, it was not possible to assign the chemical shifts to the different independent molecules in the asymmetric unit of forms I and II or to link the chemical shifts to crystallographic sites for any of the forms. The aim of the present paper is to investigate these aspects, so as to provide a complete relationship between chemical shifts and atomic positions, and to include, for the first time, solid-state proton MAS spectra.

The computations have been carried out with the CASTEP program, which uses the gauge-including projector augmented wave (GIPAW) method,[4–6] the successes and limitations of which have been recently reviewed for organic systems.[7]

The salient features of the crystal structures are as follows. Forms I (space group $P2_1/n$) and II ($P\bar{1}$) both contain three crystallographically independent molecules (denoted A, B, and C). The structures are built up from the same 2D packing fragments but differ in the symmetry operation, either a glide plane (I) or an inversion (II), between adjacent 2D building blocks.[1] Each of the two polymorphs exhibits two separate hydrogen-bonded patterns, a 1D chain formed by molecules of type C and a 2D network that is composed of molecules A and B (see Fig. 1). A-type molecules as well as C-type molecules are linked together in a similar fashion by strong N–H···O hydrogen bonds so that two independent 1D chains are generated. Additionally, B molecules act as bridges between adjacent A-type chains via two weaker N–H···O interactions, so that a 2D hydrogen-bonded network A + B is generated. Molecules of type B are hydrogen-bonded only through the nitrogen atoms, so none of the carbonyl groups are hydrogen-bonded. The crystal structure of form III (space group $P2_1/c$) contains a single type of molecule, which forms the same sort of 1D chain motif as those for the A-type and C-type molecules of polymorphs I and II (see Fig. 2). In each case the hydrogen bonds involve carbonyl groups at C4 and C6, but not C2. It is noteworthy that molecules forming the 1D motif can be related either by inversion symmetry (form I, C-type molecule; and form II, A- and C-type molecules) or glide symmetry (form I, A-type molecule) or by a 2_1 screw axis (form III). Thus, the two N–H···O bonds linking two adjacent molecules of the chain are either crystallographically equivalent (inversion) or are crystallographically independent (glide or 2_1).

All independent molecules adopt the same fundamental conformation in which the mean plane of the phenyl ring and one C5–C bond in the pyrimidinetrione ring deviate somewhat from being coplanar, and the corresponding C–C5–C9–C torsion angle lies between 7.8° and 27.6°. The molecules themselves are not symmetrical because the plane of the phenyl group is not perpendicular to the pyrimidinetrione plane in any of the systems, so the two sides of the pyrimidinetrione ring are nonequivalent in an NMR sense (see Fig. 3). We will refer to the carbonyl group and the

Fig. 1. The structure of phenobarbital form II, showing the three independent molecules and their hydrogen bonding. Top: the 2D hydrogen-bonded network composed of molecules A and B; bottom: the 1D chain of a C-type molecule. Hydrogen and oxygen atoms linked by N–H···O bonds are drawn as balls, and selected intermolecular distances are given in Å. Symmetry operations: (*i*) $x + 1, -y + 1, -z + 2$; (*ii*) $-x, -y + 1, -z + 1$; (*iii*) $x + 1, y, z$; (*iv*) $-x, -y + 2, -z$; (*v*) $-x + 1, -y + 2, -z + 1$.

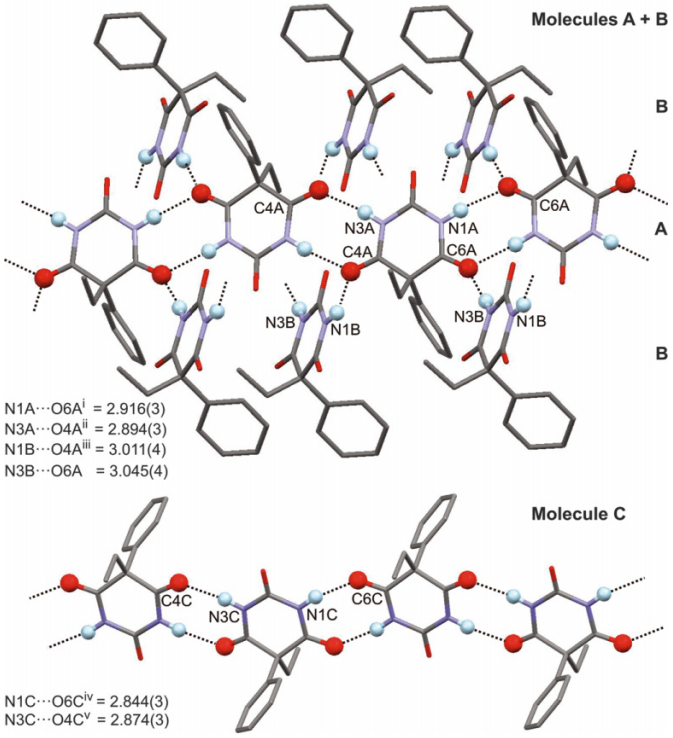

Fig. 2. The 1D hydrogen-bonded chain of phenobarbital form III. Hydrogen and oxygen atoms linked by N–H···O bonds are drawn as balls, and selected intermolecular distances are given in Å. Symmetry operations: (*i*) $-x + 2, y + 1/2, -z + 1/2$; (*ii*) $-x + 2, y - 1/2, -z + 1/2$.

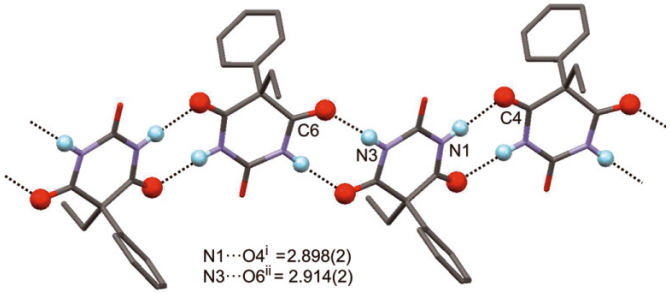

nitrogen atom on the right of Fig. 3, together with the corresponding ortho and meta phenyl carbons, as the "edge" atoms because of their proximity in the molecular projection shown. As a consequence of this situation, form III is expected to give two ^{15}N resonances and carbons C4 and C6 should give two ^{13}C signals. The spectra of forms I and II are predicted to be more complicated, with every nucleus giving three signals, so there should be six ^{15}N resonances. These predictions have been borne out in practice.[1] As mentioned above, the 1D NMR spectra leave a number of assignment

Can. J. Chem. Downloaded from www.nrcresearchpress.com by Xi'an Jiaotong University on 09/19/12
For personal use only.

Fig. 3. View of a molecule of phenobarbital showing the conformation of the phenyl ring in the crystal structures. The right-hand side is designated in the text as the "edge" side. Some atoms are labelled with crystal structure notation (as for form III).

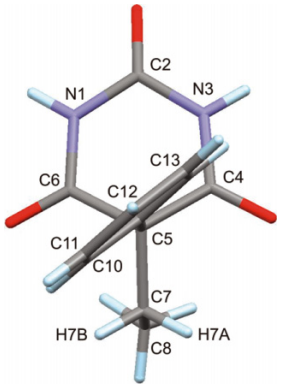

questions unanswered; for instance, it was not possible to assign the signals to the nuclei of the two sides of the phenyl ring or to the two sides of the pyrimidinetrione ring. It is also not feasible to assign the signals for forms II and III to the three independent molecules separately. Whilst more sophisticated NMR experiments might allow some of these questions to be addressed, only computational work is able to completely evaluate the relationship between chemical shifts and atomic positions, thus forming an essential link in NMR crystallography.

Experimental

Phenobarbital was available as a mixture of forms I and II (Mallinckrodt Chemical Works, USP XIII powder, USA). Phase-pure form I was prepared by annealing the commercial product at 160 °C for 2 h, and forms II and III by crystallization from hot ethanol and acetonitrile solutions, respectively.

The experimental details for the ^{13}C and ^{15}N spectra appear in ref. 1. The proton spectra were obtained at 400 MHz and ambient temperature using a Varian VNMRS spectrometer and a 4.0 mm o.d. pencil rotor, with magic-angle spinning at modest rate (12 kHz). A windowed phase-modulated Lee–Goldburg (PMLG) pulse sequence[8] was employed to obtain homonuclear dipolar-decoupled spectra, with 10.0 ms acquisition time, a recycle time of 10.0 s, 90° pulse angles (2.5 μs), and 32 FIDs. The experimental ^{13}C spectra[1] were referenced using the high-frequency signal for a replacement sample of adamantane (δ_C = 38.5 ppm). The experimental ^{15}N spectra[1] were referenced to the resonance of neat nitromethane via the nitrate signal of ammonium nitrate (δ_N = –5.1 ppm). The proton spectra were referenced indirectly[8] to the signal for tetramethylsilane via a spectrum of glycine obtained under exactly the same conditions. The scaling factor was obtained by adjusting the shift difference for glycine to its known value.

The GIPAW computations were carried out on the Hamilton supercomputer cluster at the University of Durham, Durham City, UK. For structures determined by X-ray diffraction (as in the present case), rather than by neutron diffraction, it is always necessary to optimize the positions of hydrogen atoms before the magnetic shieldings are computed, since otherwise all X–H distances are underestimated (diffraction of X-rays being caused by electron density, not atomic nuclei). However, we chose to optimize all atomic positions to still further improve the agreement between computed and experimental chemical shifts. The Perdew–Burke–Ernzerhof (PBE) functional was used, with 3 k-points and a cutoff energy of 600 eV for the geometry optimization stage, but 800 eV for the shielding calculations. Forms I, II, and III contain 12, 6, and 4 molecules per unit cell (348, 174, and 116 atoms per unit cell, respectively). The computation of form I was challenging for the Durham Hamilton facility. The full sets of computed isotropic shieldings are given in the Supplementary data. The ^{13}C shieldings (σ) were converted to chemical shifts[7] (δ) by equating the average shielding (σ_{ave}) with the average observed chemical shift (δ_{ave}) for forms II and III together and using the equation

$$[1] \qquad \delta = \sigma_{ave} + \delta_{ave} - \sigma$$

For form II, only the lines that were clearly assignable were used to obtain σ_{ave}. The nitrogen shieldings were similarly converted for forms II and III, treated together. However, because the low resolution in the proton spectrum prevented assignments of individual lines, the computed ^{1}H spectra (with a line width of 100 Hz) were simply adjusted in scale to give the best comparison to the experimental spectra. The computed ^{13}C and ^{15}N spectra were plotted with a line width of 30 Hz.

Results and discussion

Figures 4, 5, and 6 compare the experimental ^{13}C, ^{15}N, and ^{1}H MAS NMR spectra of forms II and III of phenobarbital. The signals assigned to C2 are substantially broadened by second-order effects arising from dipolar coupling to the two neighbouring ^{14}N nuclei, the C4/C6 signals being less affected because of the orientation of the electric field gradient at the single neighbouring ^{14}N nucleus. The spectra of forms I and II are remarkably similar[1] (though there are subtle differences in detail), so much of the discussion herein will focus on comparisons involving forms II and III. The ^{13}C and ^{15}N chemical shifts of all three forms are listed in full in ref. 1. Tables 1 and 2 of the present paper contain selected experimental ^{13}C data for forms II and III. Table 3 gives the ^{15}N shifts for forms II and III and Table 4 lists the ^{1}H shifts for all three forms (not reported previously), although resolution of the separate signals is not very high. Several features of the experimental results are of particular interest and require explanation in terms of the crystal structure:

- The number of ^{13}C and ^{15}N peaks observed clearly shows that there are three molecules in the asymmetric unit for forms I and II, but only one for form III.
- The most obvious difference in the ^{13}C spectra of forms I and II is that, for the methylene group, form I shows overlap of two of the resonances, to high frequency of the third, whereas form II has three clearly resolved peaks.
- The range of ^{15}N resonance frequencies is slightly smaller for form II (8.85 ppm) than for form I (9.51 ppm), and the second and third lines (from high frequency) are closer together for form I (separation 0.66 ppm) than for form II (1.28 ppm).

Can. J. Chem. Downloaded from www.nrcresearchpress.com by Xi'an Jiaotong University on 09/19/12
For personal use only.

Fig. 4. The $^{1}H \rightarrow {}^{13}C$ CPMAS spectra of forms II and III of phenobarbital. Top: high-frequency region; bottom: low-frequency region. In each case the simpler spectrum is that of form III. The signals in the 45–60 ppm region (marked with an asterisk) are spinning sidebands.

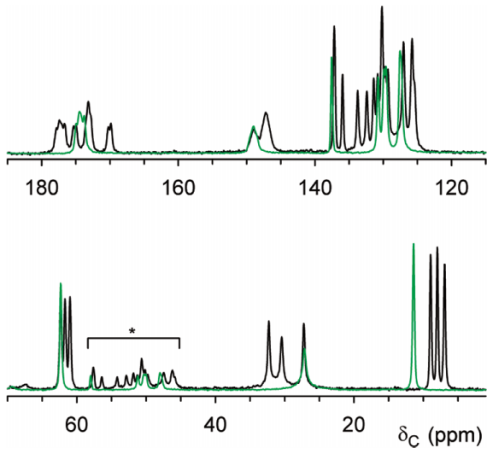

Fig. 5. The ^{15}N CPMAS spectra of forms II and III of phenobarbital. Top: form II; bottom: form III. In each case the experimental spectrum can be recognised by the noise level.

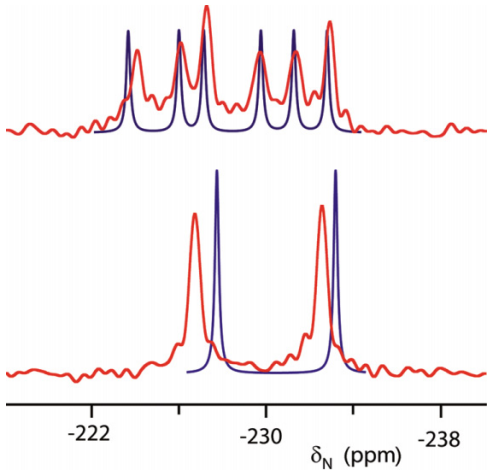

- The chemical shifts for some carbons of form III are almost identical to those of forms I and II.
- On the other hand, the methyl signal of form III is distinctly shifted from those of the other two forms.
- The range of CH carbon peaks is rather narrow for form III, in contrast with the situation for forms I and II.
- The six ^{15}N peaks for forms I and II appear to be created by a doubling of three peaks at an interval of ca. 5 ppm.
- Two of these six peaks are more intense than the other four, presumably because of more efficient cross polarization.
- The two ^{15}N peaks of form III lie close to the more intense resonances of forms I and II.
- The proton spectra all contain peaks at ca. 10 ppm, indicating hydrogen bonding.
- The proton spectra of forms I and II contain two signals in the range 1.5 to 3.0 ppm, typical of methylene protons, but such resonances are absent (presumably shifted to lower frequency) from the proton spectrum of form III.

Some of these facts are readily explained by the crystal structures. Thus, the nearly identical appearance of the spectra for forms I and II arises from the unusual similarity of the two structures. In all three cases the number of molecules in the asymmetric units derived from NMR is in agreement with the crystal structures. All the structures contain moderately strong N–H···O hydrogen bonding, which explains the high-frequency proton signals.

Fig. 6. The MAS proton spectra of forms II and III of phenobarbital. Top: form II; bottom,: form III. In each case the experimental spectrum can be recognised by the noise level. A Gaussian broadening of 0.010 s was used to plot the experimental spectra and a line width of 100 Hz was imposed for the computed spectra.

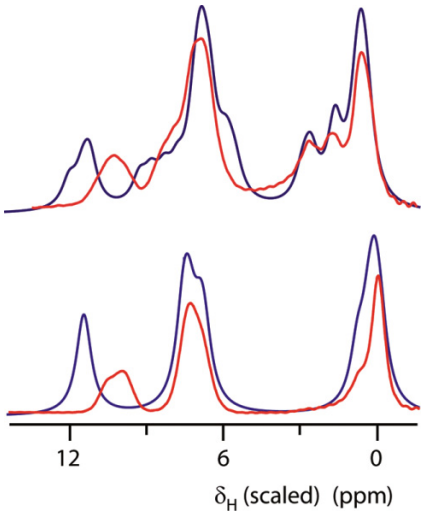

Other features cannot be readily explained merely by examination of the structures. Some speculations are, of course, possible. Thus, it can be noted that molecules A, B, and C in I and II differ somewhat in their conformation (in the rotation of the Ph ring about C5–C9); the single torsion angle for III is closer to 0° (where the Ph ring and C5–C4 would be coplanar) than in the other cases.

C–C5–C9–C torsion angles (°):

I: A = 27.6; B = 13.4; C = 15.8;
II: A = 22.3; B = 16.2; C = 12.8;
III: 7.8.

Such variations are sufficiently large to cause the magnitudes of the changes in ^{13}C chemical shifts observed experimentally. The spread of ^{15}N frequencies could arise from hydrogen-bonding differences, or from long-range effects of "ring currents" in the phenyl groups or of electric fields of the carbonyl groups.

However, other features do not have any obvious structural explanation and assignment of signals to atomic sites in the crystal structures is not straightforward. Thus, there is no simple experimental method to separately distinguish the signals arising from the three independent molecules for forms I and II. Whilst an INADEQUATE pulse sequence can, in principle, link signals arising from the same independent molecule, such an experiment would leave uncertain which molecule gives which signals. In any case, an INADEQUATE experiment is not feasible in practice for the present samples (especially for ^{15}N) without isotopic enrichment because of the inherently very low sensitivity. Other

Table 1. Carbon-13 resonances (in ppm) for phenobarbital forms II and III used to correlate experimental and adjusted computed chemical shifts.

Polymorph	Molecule	Assignment[a]	Expt. shift[b]	Comp. adj.[c]	Diff. adj.
Form II	A	Carbonyl C2	147.15	145.75	1.40
	B	Carbonyl C2	148.91	147.05	1.86
	C	Carbonyl C2	147.15	145.83	1.32
	A	Ipso	136.00	137.20	–1.20
	B	Ipso	137.17	138.11	–0.94
	C	ipso	137.17	137.93	–0.76
	A	Quaternary	61.68	64.21	–2.53
	B	Quaternary	61.00	62.78	–1.78
	C	Quaternary	62.37	64.48	–2.11
	A	Methylene	30.35	32.00	–1.65
	B	Methylene	32.21	34.59	–2.38
	C	Methylene	27.22	26.68	0.54
	A	Methyl	6.86	5.53	1.33
	B	Methyl	7.93	6.18	1.75
	C	Methyl	8.91	6.55	2.36
Form III		Carbonyl e	174.20	175.80	–1.60
		Carbonyl ne	174.20	173.98	0.22
		Carbonyl C2	149.01	147.24	1.77
		Ipso	137.56	138.81	–1.25
		Meta e	130.70	129.08	1.62
		Meta ne	129.92	130.10	–0.18
		Para	129.53	127.89	1.64
		Ortho e	127.57	127.68	–0.11
		Ortho ne	127.57	127.05	0.52
		Quaternary	62.27	64.86	–2.59
		Methylene	27.12	26.90	0.22
		Methyl	11.36	8.88	2.48
			93.82[d]	93.82[d]	1.60[e]

[a]e ≡ edge-on to the phenyl group; ne ≡ not edge-on to the phenyl group.
[b]The accuracy is only to one significant figure at best, but two figures are retained to give the data of column 6.
[c]Adjusted for slope and intercept according to corrected shift = (computed shift + 3.6097)/1.0385.
[d]Average.
[e]Root mean square deviation.

Can. J. Chem. Downloaded from www.nrcresearchpress.com by Xi'an Jiaotong University on 09/19/12
For personal use only.

experiments, such as DQ-CRAMPS are more sensitive but still do not give a direct relationship of signals to crystallographic sites. A further limitation of experiment is an inability to assign signals for chemically equivalent atoms (such as C4 and C6) to the structural positions. On the other hand, suitable computation, if accurate enough, should allow such assignments. Moreover, spectral simulation, if successful, should reproduce the observed special features indicated above. In some situations the assignments may then reveal simple structural explanations of those features that could be used, for example, to make assignments for related chemical systems.

First, one must establish that the computations are sufficiently accurate and robust to give confidence in the use of the data produced. The results of GIPAW computations (which involve use of crystallographic repetition of the unit cell) for ^{15}N for forms II and III are presented in Table 3. They match the experimental chemical shifts very well (see Fig. 5). The computed chemical shifts are plotted against the experimental values in Fig. 7 *assuming the orders of computed and experimental shifts for form II are the same*. It can be seen that a very satisfactory linear correlation is obtained. The two peaks for form III fall slightly below the line established for form II, which may be the result of globally equating average computed and experimental shifts rather than separately doing this for the two forms. Figures 5 and 7 show that the computed results are essentially valid and, thus, the linking of chemical shifts to crystallographic sites is robust. The computations allow the assignments of form II signals to the three independent molecules A, B, and C. Somewhat surprisingly, the signals for form III (which has a C-type chain) are close to those for molecule A of form II, not molecule C. The chemically equivalent nitrogens of each molecular type can now be assigned to the relevant structural positions. Overall, there is no correlation of the ^{15}N chemical shifts with the strength of the hydrogen bonds. However, the doubling, at an interval of ca. 5 ppm, of three signals for form II can now be seen to arise from the two nitrogens of each independent molecule N1 and N3 (Figs. 1 and 2). A close look at the crystal structure with this in mind reveals that the distinction can be traced to the conformation of the phenyl group (see Fig. 3). The high-frequency trio of signals arises for the nitrogens closer to one edge of the phenyl plane. An analogous assignment can be made for the signals of form III. This situation suggests that a major influence may be the ring current, since the nitrogens with the high-

Can. J. Chem. Downloaded from www.nrcresearchpress.com by Xi'an Jiaotong University on 09/19/12
For personal use only.

Table 2. Experimental and adjusted computed chemical shifts (in ppm) for the C4/C6 and aromatic carbons (except ipso carbons) for phenobarbital form II.

Assignment	Molecule	Expt. shift[a]	Comp. shift[b]	Difference
CO edge	A	177.41	179.23	–1.82
	B	169.87	171.75	–1.88
	C	173.20	174.67	–1.47
CO	A	177.41	177.38	0.03
	B	173.20	173.98	–0.78
	C	174.96	175.33	–0.37
ortho edge	A	125.76	126.17	–0.41
	B	127.02	127.23	–0.21
	C	125.40	124.83	0.57
meta edge	A	131.39	131.55	–0.16
	B	130.18	130.65	–0.47
	C	133.74	134.82	–1.08
para	A	132.41	131.97	0.44
	B	129.30	129.31	–0.01
	C	130.18	130.70	–0.52
meta	A	132.81	130.77	2.04
	B	127.02	126.77	0.25
	C	130.18	130.01	0.17
ortho	A	129.70	129.61	0.09
	B	127.02	126.77	0.25
	C	125.76	125.41	0.35

[a]The accuracy is only to one significant figure at best, but two figures are retained to give the data of column 5.

[b]Adjusted for slope and intercept according to corrected shift = (computed shift + 3.6097)/1.0385.

Table 3. Experimental and computed ^{15}N chemical shifts (in ppm) for phenobarbital forms II and III.

Polymorph	Molecule[a]	Expt. shift[b]	Comp. shift	Difference
Form II	A	–229.69	–230.00	0.31
	A e	–224.04	–223.15	–0.89
	B e	–227.24	–227.05	–0.19
	B	–232.89	–233.42	0.53
	C e	–226.02	–225.77	–0.25
	C	–231.33	–231.71	0.38
Form III		–232.56	–232.72	0.16
	e	–226.67	–226.58	–0.09

[a]e ≡ edge-on to the phenyl group.

[b]The accuracy is only to one significant figure at best, but two figures are retained to give the data of column 5.

frequency shifts are in the deshielding region of space, whereas the other nitrogens are in the shielding region. Whilst such a qualitative explanation may not be quantitatively satisfactory, there is no doubt about the structural assignments of the signals.

The computations also correctly reproduce the observed small differences between the ^{15}N spectra of forms I and II. Thus, the range of computed shifts is slightly smaller for form II (10.27 ppm) than for form I (11.25 ppm), and the separation of the second and third peaks is smaller for form I than for form II (0.66 vs 1.28 ppm)

The results of computation for the ^{13}C chemical shifts of forms II and III are also generally in excellent agreement with the observed spectra, although there are a few divergences in detail (see Figs. 8 and 9, which show the aliphatic region and the 120–150 ppm range, respectively). Thus, the following experimental features are reproduced by the computations (with special mention of comparisons between data for forms II and III, those for form I being generally very similar to those for form II):

- The C4/C6 signals for form III are near the middle of the range covered by form II peaks. However, in contrast to the ^{15}N results, there is no correlation of chemical shifts with the orientation of the phenyl ring.
- Hydrogen bonding has some influence; the C4/C6 signals for molecule A (which has both a strong and a weak hydrogen bond to C4 and to C6) are at the highest frequencies, whereas those for molecule B (which has no hydrogen bonds to C4 or C6) are at the lowest frequencies.

Can. J. Chem. Downloaded from www.nrcresearchpress.com by Xi'an Jiaotong University on 09/19/12
For personal use only.

Table 4. Experimental and computed ^{1}H chemical shifts for the three phenobarbital forms.

	Experimental shift (ppm)[a,b]		
Assignment	Form I	Form II	Form III
NH	9.9[c,d]	10.3[c,d]	10.0
NH	ca. 8.0 sh[e]	ca. 8.1 sh[e]	—
Aromatic	6.6	6.9	7.4
CH_2	2.4[f]	2.7[f]	ca. 0.8 sh
CH_2	1.5[f]	1.7[f]	—
CH_3	0.3	0.6	0.0

[a]The peaks are broad and tend to have unsymmetrical shapes arising from overlapping resonances.

[b]sh = shoulder.

[c]For molecules A and C.

[d]With a shoulder to high frequency.

[e]For molecules B.

[f]The computing shows that each of the three CH_2 groups for each form has one resonance at the higher shift and one at the lower.

Fig. 7. Plot of computed versus experimental ^{15}N chemical shifts for phenobarbital forms II and III. The two points falling below the straight line are for form III.

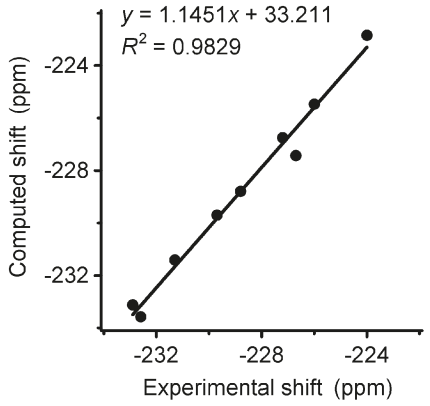

Fig. 8. Carbon-13 CPMAS spectra of forms II and III for the aliphatic region of phenobarbital. Top: form II; bottom: form III. In each case the experimental spectrum can be recognised by the noise level. The signals in the 45–60 ppm region for the experimental spectra (marked with an asterisk) are spinning sidebands.

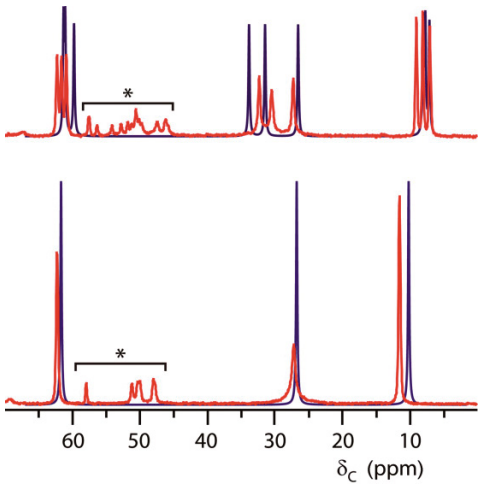

Fig. 9. Carbon-13 CPMAS spectra of forms II and III for the high-frequency region of phenobarbital. Top: form II; bottom: form III. In each case the experimental spectrum can be recognised by the noise level.

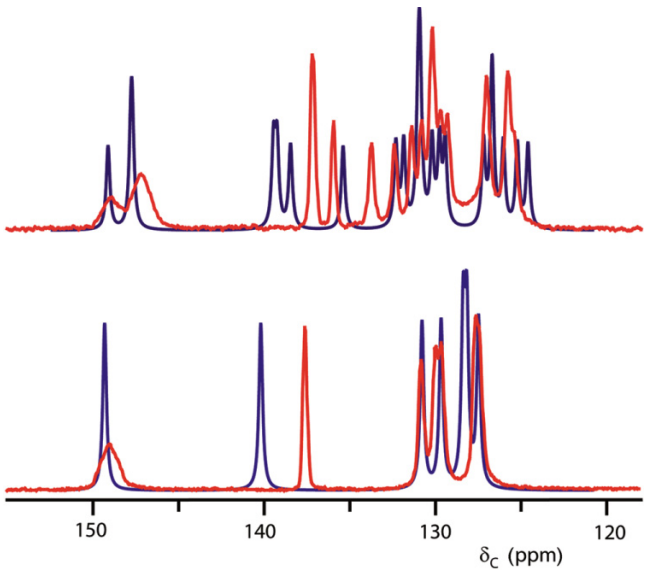

Fig. 10. Plot of computed versus experimental ^{13}C chemical shifts for phenobarbital forms II and III. Only resonances with reasonably certain assignments (15 for form II and 13 for form III) are used for the plot.

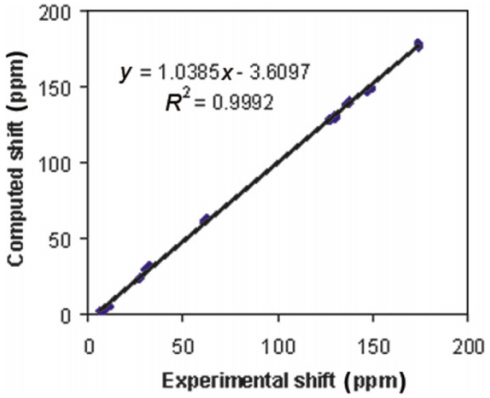

- The C2 signal for form III is very close to the high-frequency C2 peak for form II (which is for molecule B).
- The range of aromatic signals (excluding the ipso carbon) for form III is significantly narrower than that for form II.
- The CH_2 peak for form III is very close to the lowest frequency form II CH_2 signal (which is for molecule C).
- The CH_3 resonance of form III is substantially to high frequency of those for form II.

The computed ^{13}C chemical shifts for form III and some of those for form II (where assignments are reasonably certain, assuming the order of the computed resonances for the three independent molecules of form II is correct) are given in Table 1 and are plotted against the experimental values in Fig. 10. The correlation is excellent, but the slope deviates from the ideal value of unity (and thus the intercept is non-zero). To compare the data sensibly, the computed values given in Table 1 have been adjusted to give unit slope and zero intercept. The maximum deviation is 2.6 ppm. However,

Can. J. Chem. Downloaded from www.nrcresearchpress.com by Xi'an Jiaotong University on 09/19/12
For personal use only.

Fig. 11. The low-frequency regions of the observed and computer-simulated ^{13}C spectra for forms I and II of phenobarbital. Top to bottom: form I experimental; form I computed; form II computed; and form II experimental. The low-intensity signals in the 45–60 ppm region in the experimental spectra are spinning sidebands.

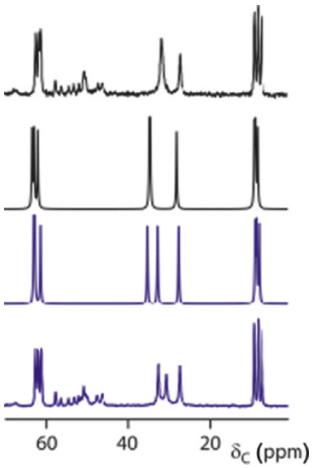

this understates the value of the computation, since if like is compared to like, i.e., if comparisons are made for particular types of carbon, the agreement is much better. In other words, there are consistent deviations for related carbons; for example, the four C2 carbons all have deviations between 1.3 and 1.9 ppm. This points out the particular value of applying GIPAW computations to restricted crystallographic aspects, especially comparison between polymorphs and between different molecules in asymmetric units, as has been emphasised before.[7]

Having established the ^{13}C correlation using the set of results in Table 1, it is of interest to compare computed and experimental data for the rest of the aromatic signals, which are in a much more crowded region of the spectra. This is done in Table 2, assuming the order of signals is the same for computed and experimental cases. This provides a tentative assignment of the resonances. The agreement is good, though not perfect, as is shown in Fig. 9. Most importantly, assignments can be made separately for the three independent molecules of forms I and II. Similarly, the two sides of the ring are distinguished (Tables 1 and 2), as they were for the ^{15}N resonances.

The computed ^{13}C spectrum for form I is, as expected, close to that of form II. Remarkably, the computing reproduces the only major experimental difference, namely, the closeness of the CH_2 signals for molecules A and B for form I (A to high frequency of B by 0.26 ppm), in contrast with the case for form II (A to low frequency of B by 2.69 ppm) — see Fig. 11. For the aromatic ^{13}C signals the largest computed differences (still small on an absolute scale, but significant) between forms I and II are for molecule A. This can be traced to the fact that this molecular chain has glide symmetry for form I (resulting in the phenyl groups being on the same side as viewed down the chain) in contrast to form II, which has inversion symmetry for chain A, so that the phenyl groups are on opposite sides of the chain from the same viewpoint (as is the case for all the remaining chains in all three forms) — see Fig. 10 of ref. 1.

The computed proton shifts also show very good correlation with the observed spectra (see Fig. 6). Thus, the lack of signals in the usual methylene region for form III is reproduced. The two CH_2 signals for forms I and II are shown to arise from the individual protons, all three independent molecules giving two resonances, 1.0–1.5 ppm apart, to high frequency of the methyl signal. In each case the lower frequency signal is from the proton on the "edge" side. For form III, the separation of the two methylene proton signals is also computed to be ca. 1.0 ppm (with the proton on the "edge" side at the lower frequency), but in this case the resonances straddle those for the methyl protons, thus, explaining why they are not clearly visible. The greater experimental separation between the methyl and aromatic protons for form III is also found for the computed spectra. The signals for the NH protons for form III and for molecules A and C of forms I and II are at similar high-frequency positions, but those for molecule B of forms I and II are ~3 ppm to lower frequency (and can be observed experimentally as a shoulder on the aromatic signals). This corresponds to the significantly weaker N–H···O hydrogen-bond strengths for molecule B.

Conclusions

Computations using the GIPAW approach have successfully simulated the ^{1}H, ^{13}C, and ^{15}N spectra of three polymorphs of phenobarbital, with the results closely matching the observed spectra. Therefore, full assignments of ^{13}C and ^{15}N signals have been made to atomic sites in the crystal structures and various features of the spectra can now be understood. The experimental proton spectra have been presented and these too are adequately explained by the computations.

Supplementary data

Supplementary data are available with the article through the journal Web site (www.nrcresearchpress.com/cjc).

Acknowledgements

We thank Drs. J.R. Yates and S.J. Clark for helpful comments on the GIPAW programming. T.G. is supported by the Lise Meitner Program of the Austrian Science Fund (FWF, LM 1135-N17). We are grateful to the UK Engineering and Physical Sciences Research Council (EPSRC) Solid-state NMR Research Service based at the University of Durham for the experimental spectra.

References

(1) Zencirci, N.; Gelbrich, T.; Apperley, D. C.; Harris, R. K.; Kahlenberg, V.; Griesser, U. J. *Cryst. Growth Des.* **2010** *10* (1), 302. doi:10.1021/cg901062n.

(2) Zencirci, N.; Gelbrich, T.; Kahlenberg, V.; Griesser, U. J. *Cryst. Growth Des.* **2009** *9* (8), 3444. doi:10.1021/cg801416a.

(3) Allen, F. H. *Acta Crystallogr. B* **2002** *58* (3), 380. doi:10.1107/S0108768102003890.

(4) Pickard, C. J.; Mauri, F. *Phys. Rev. B* **2001** *63* (24), 245101. doi:10.1103/PhysRevB.63.245101.

(5) Yates, J. R.; Pickard, C. J.; Mauri, F. *Phys. Rev. B* **2007** *76* (2), 024401. doi:10.1103/PhysRevB.76.024401.

(6) Yates, J. R.; Pickard, C. J. In *NMR Crystallography;* Harris, R.K.,

Wasylishen, R.E., Duer, M.J., Eds.; John Wiley & Sons Ltd.: Chichester, UK, 2009; Chapter 3, pp 29–40.
(7) (a) Harris, R. K.; Hodgkinson, P.; Pickard, C. J.; Yates, J. R.; Zorin, V. *Magn. Reson. Chem.* **2007** *45* (S1), S174. doi:10.1002/mrc.2132;; (b) Harris, R. K.; Wasylishen, R. E.; Duer, M. J., Eds. *NMR Crystallography;* John Wiley & Sons Ltd.: Chichester, 2009; revised and updated version of ref. 7a published as Chapter 7, pp 81–97.
(8) Vinogradov, E.; Madhu, P. K.; Vega, S. *Chem. Phys. Lett.* **2002** *354* (3–4), 193. doi:10.1016/S0009-2614(02)00060-X.

Can. J. Chem. Downloaded from www.nrcresearchpress.com by Xi'an Jiaotong University on 09/19/12
For personal use only.

Quadrupolar central transition (QCT) and ^{13}C NMR competition studies of metal ion binding to ovotransferrin

Jillian A. Saponja and Hans J. Vogel

Can. J. Chem. Downloaded from www.nrcresearchpress.com by Xi'an Jiaotong University on 09/19/12
For personal use only.

Abstract: The transferrins are a family of relatively large bilobal proteins that play a major role in the transport of Fe^{3+}, as well as several other physiological and nonphysiological metal ions. Transferrins can also act as antimicrobial agents, by tightly sequestering iron and making it unavailable for bacterial growth. Using a combination of quadrupolar central transition (QCT) metal ion NMR (^{27}Al, ^{45}Sc, ^{51}V, and ^{71}Ga) and ^{13}C NMR, the binding and displacement of a variety of metal ions to ovotransferrin was studied through direct metal ion competition experiments. The metal ions investigated (Al^{3+}, Co^{3+}, Fe^{3+}, Ga^{3+}, In^{3+}, Sc^{3+}, Y^{3+}, and VO_2^+) were of differing ionic radius and charge, thus allowing for an assessment of how these factors contribute to metal ion affinity. The competition for the N- and C-terminal metal ion binding sites on ovotransferrin was directly followed by metal ion QCT NMR. Moreover, ^{13}C NMR was used to study the two protein-bound synergistic anions (^{13}C-labeled carbonate), whose chemical shifts are distinct and dependent on the bound metal ion that is present in the binding sites. The observed order of decreasing affinity for the metal ions studied was $Fe^{3+} \approx In^{3+} \geq Sc^{3+} \geq Ga^{3+} > Al^{3+} > VO_2^+ > Y^{3+} \geq Co^{3+}$. These results illustrate how a combination of multinuclear solution NMR methods can provide unique insights into the ligand binding properties of larger metalloproteins.

Key words: quadrupolar central transition NMR, ^{13}C NMR, ovotransferrin, quadrupolar nuclei, metal ions, competition experiments.

Résumé : Les transferrines correspondent à une famille relativement grande de protéines bilobales qui jouent un rôle majeur dans le transport du Fe^{3+} ainsi que ceux de plusieurs autres ions métalliques physiologiques et non physiologiques. Les transferrines peuvent aussi agir comme agents antimicrobiens en séquestrant fortement le fer et en le rendant indisponible pour la croissance des bactéries. Faisant appel à une combinaison de RMN du ^{13}C et d'ions métalliques (^{27}Al, ^{45}Sc, ^{51}V et ^{71}Ga) de transition centrale quadripolaire (TCQ), on a étudié la fixation et le déplacement d'une variété d'ions métalliques vers l'ovotransferrine par le biais d'expériences de compétition directe entre les ions métalliques. Les ions métalliques étudiés (Al^{3+}, Co^{3+}, Fe^{3+}, Ga^{3+}, In^{3+}, Sc^{3+}, Y^{3+} et VO_2^+) possédaient des rayons ioniques et des charges différentes qui ont permis d'évaluer l'influence de ces facteurs sur l'affinité des ions métalliques. Les compétitions pour les sites de fixation en positions N- et C-terminales de l'ovotransferrine ont été suivies directement par RMN-TCQ des ions métalliques. De plus, on a utilisé la RMN du ^{13}C pour étudier les deux anions de synergie liés à la protéine (carbonate marqué au ^{13}C) dont les déplacements chimiques sont distincts et qui dépendent de l'ion métallique qui est présent sur les sites de fixation. L'ordre observé d'affinité décroissante pour les ions métalliques étudiés est $Fe^{3+} \approx In^{3+} \geq Sc^{3+} \geq Ga^{3+} > Al^{3+} > VO_2^+ > Y^{3+} \geq Co^{3+}$. Ces résultats illustrent comment une combinaison de méthodes de RMN multinucléaires en solution peut jeter une lumière unique sur les propriétés de fixation de ligands par des métalloprotéines plus volumineuses.

Mots-clés : RMN de transition centrale quadripolaire, RMN du ^{13}C, ovotransferrine, noyau quadripolaire, ions métalliques, expériences de compétition.

[Traduit par la Rédaction]

Introduction

The transferrins are a family of iron-binding proteins found in serum, milk, and other bodily fluid secretions. These large (~80 kDa) bilobal glycoproteins function in iron metabolism, where they primarily sequester and transport iron. It has also been reported that the high affinity binding of iron(III) to ovotransferrin, serum transferrin, and lactoferrin can give rise to an antimicrobial activity by withholding iron required for bacterial growth or biofilm formation.[1,2] All transferrin proteins are comprised of two lobes that each possess a high-affinity ferric iron-binding site that contains a unique binding motif where an additional anion (usually called the synergistic anion) is required for metal ion binding (for a

Received 2 November 2010. Accepted 11 January 2011. Published at www.nrcresearchpress.com/cjc on 3 June 2011.

J.A. Saponja and H.J. Vogel. Biochemistry Research Group, Department of Biological Sciences, University of Calgary, Calgary, AB T2N 1N4, Canada.

Corresponding author: Hans J. Vogel (e-mail: vogel@ucalgary.ca).

This article is part of a Special Issue dedicated to Professor Roderick E. Wasylishen.

Can. J. Chem. Downloaded from www.nrcresearchpress.com by Xi'an Jiaotong University on 09/19/12
For personal use only.

review see ref. 3). The three-dimensional structure of the protein and the organization of the two metal ion and synergistic anion binding sites are illustrated in Fig. 1. To satisfy the preference of Fe^{3+} for an octahedral coordination sphere, all the transferrins provide four ligands from the protein (1 Asp, 2 Tyr, and 1 His) and in vivo the synergistic anion carbonate provides two additional oxygen ligands.[4] However, several other anions, such as oxalate, can substitute for carbonate, and act as the synergistic anion in vitro.[5–7] Numerous high-resolution crystal structures for the various proteins of the transferrin family have been reported, and some common structural motifs for proteins involved in ferric iron and heme binding have emerged from these studies.[8]

In addition to binding iron(III) with very high affinity, the transferrins can bind a wide variety of metal ions, varying both in ionic radius and charge. Serum transferrin, the principal iron carrier in the mammalian circulatory system, is found to be only 30% saturated with iron in blood, leading to speculation that this protein can also play a significant role in the metabolic fate of other nonphysiological trivalent and divalent metal ions.[9] A complete understanding of how such a wide range of metal ions can be accommodated in the binding sites of the transferrins is still missing. It is clearly more complicated than simply being related to the ionic radius of the metal ion alone.[10–12] In fact, Sadler and co-workers[13] reported that the strength of metal binding to the transferrins correlates with the metal ion acidity. Several of the metal ions that have been found to bind to transferrin are of toxicological interest (e.g., aluminum), but some also have therapeutic and diagnostic uses. For example, the ^{111}In and ^{67}Ga isotopes are used as radiopharmaceuticals for the labeling of leukocytes and tumors.[14,15] Interestingly, unlike iron, some nonphysiological serum transferrin-bound metal ions are not deposited in bone marrow,[16] suggesting that the binding of these metal ions to the protein must affect its recognition by the transferrin receptor, probably through a conformational change.[17] Plutonium, for example, is known to bind to serum transferrin in blood, but it is not found in bone marrow reticulocytes.[18]

Competitive metal ion binding experiments provide a direct method for determining the relative metal ion affinity. Tan and Woodworth[19] previously compared the affinity of ovotransferrin (oTf) for a variety of transition metal ions using UV-difference spectroscopy to detect the preferential binding of certain metal ions over others. This study was the first to describe the binding and displacement of one metal ion by another. Cochran et al.[20] also observed Al^{3+}/Fe^{3+} competition for the two serum transferrin (sTf) binding sites, and their results enabled them to calculate the binding affinity for Al^{3+}. Displacement of oTf-bound Cd^{2+} by Fe^{3+} has been observed by ^{13}C NMR by studying the bound ^{13}C-labeled synergistic carbonate. The latter results indicate the potential of ^{13}C NMR spectroscopy to monitor metal ion substitution in the transferrins in aqueous solution.[6,21,22]

In addition to studying transferrin-bound isotopically labeled synergistic anions, such as carbonate and oxalate, by ^{13}C NMR, it is also possible to study the binding of several half-integer quadrupolar metal ions to the transferrins directly by quadrupolar central transition (QCT) NMR.[23–28] QCT NMR spectroscopy involves the specific detection of the 1/2 to –1/2 transition of quadrupolar metal ions that are bound to

Fig. 1. Overall fold of the hen ovotransferrin protein (A, PDB 1OVT) and the structures of the two metal ion binding sites of the two ferric binding sites (B, N lobe; and C, C lobe). The direct interactions to the metal ion are identical for the N lobe and the C lobe of the protein, suggesting that other features of the protein must govern their distinct preferences for larger and smaller trivalent metal ions. Fe^{3+} is drawn as an orange sphere, carbonate is coloured in green, and the ovotransferrin (oTf) residues that directly coordinate Fe^{3+} are shown as stick models. (B) and (C) illustrate the role of carbonate acting as the synergistic anion for metal ion binding in both sites.

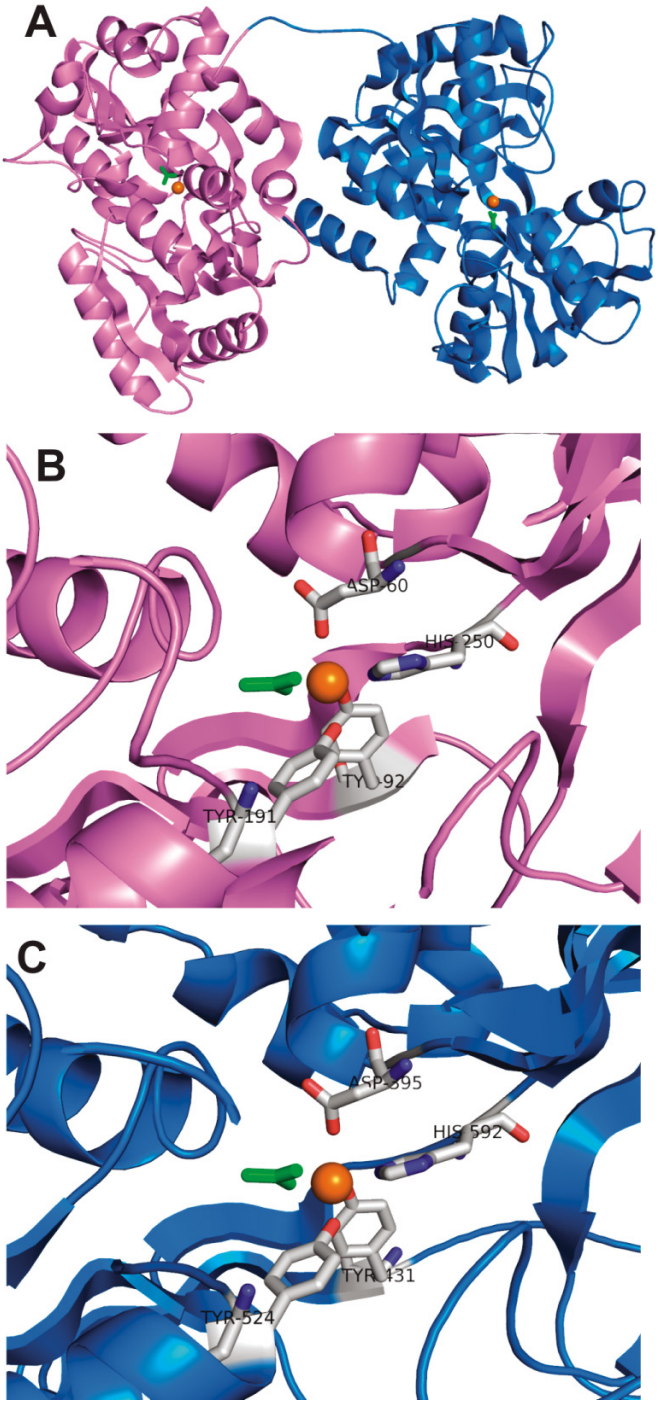

Can. J. Chem. Downloaded from www.nrcresearchpress.com by Xi'an Jiaotong University on 09/19/12
For personal use only.

Table 1. ^{13}C and quadrupolar central transition (QCT) NMR chemical shifts at 9.4 T of metal-bound ovotransferrin (oTf) with ^{13}C-labeled carbonate at 25 °C.

Metal ionic ion	Radius (Å)[a]	Binding site	^{13}C chemical shift (ppm)	QCT NMR nucleus	Chemical shift (ppm)
Al^{3+}	0.51	N	165.7	^{27}Al	–4.6
		C	165.5		–6.8
Ga^{3+}	0.62	N	166.1	^{71}Ga	–151
		C	165.9		–192
Co^{3+}	0.63	N	169.3	—	—
		C	168.8		
Fe^{3+}[b]	0.64				
Sc^{3+}	0.73	N	166.7	^{45}Sc	78.1
		C	166.6		66.0
In^{3+}	0.81		166.4	—	—
Y^{3+}	0.89	N	168.6	—	—
		C	168.2		
VO_2^{+}[c]		—	—	^{51}V	–534.5

Note: Data for Al^{3+}, Sc^{3+}, Ga^{3+} were obtained from Aramini and Vogel[25,38] and Aramini et al. 1994.[24] Data for VO_2^{+} were obtained from Saponja and Vogel.[28] Data for In^{3+}, Y^{3+}, and Co^{3+} were determined in this study.

[b] Fe^{3+} is paramagnetic, resulting in no NMR data.

[a] Ionic radii were taken from the *CRC Handbook of Chemistry and Physics*.[39]

[c] VO_2^{+} binds without a synergistic anion.

large proteins in aqueous solution. Under conditions of slow overall protein tumbling, as is the case for proteins with a similar size as oTF, this so-called central transition gives relatively narrow spectral lines that can be detected by NMR, whereas all the other transitions of half integer spin nuclei are too broad to be detected (for a brief summary of the relevant quadrupolar relaxation theory see ref. 29). QCT NMR can provide detailed information on the binding site symmetry and protein motions through the measurement of frequency-dependent chemical shifts and line widths (for reviews see refs. 29 and 30).

In this work, the relative affinities of oTf for Al^{3+}, Co^{3+}, Fe^{3+}, Ga^{3+}, In^{3+}, Sc^{3+}, Y^{3+}, and VO_2^{+} are evaluated through metal ion competition experiments that were followed by multinuclear NMR spectroscopy. Because of the extremely tight binding of Fe^{3+} to transferrin ($K_D = 10^{-21}$),[31] NMR spectroscopy cannot be used for direct binding experiments, necessitating the use of competition experiments. Moreover, transferrin-bound Fe^{3+} is paramagnetic and hence it cannot be observed directly by iron-57 NMR. Scandium(III) and yttrium(III) were included in this work because of their larger ionic radii, whereas aluminum(III) is much smaller than ferric iron (see Table 1). Despite its smaller ionic radius the coordination of Al^{3+} bound to oTf closely resembles that of iron (III).[32] The medically relevant metal ions, indium(III) and gallium(III), were included in this study to assess their affinities with respect to iron; gallium(III) has a similar ionic radius as ferric iron,[33] whereas indium(III) is somewhat larger. Also, the micronutrient cobalt(III) has been shown to bind to the transferrins,[34] and its binding was analyzed in this study as well because its ionic radius is very similar to that of ferric iron. Finally, serum transferrin is believed to be the major transporter of vanadate in physiological fluids,[35–37] and hence competition with VO_2^{+} binding was also examined. The metal ion competition for the two binding sites of ovotransferrin was monitored directly by ^{27}Al, ^{45}Sc, ^{71}Ga, and ^{51}V QCT NMR, and indirectly by ^{13}C NMR of the bound synergistic anion, using isotopically enriched $^{13}CO_3^{2-}$.

Methods and materials

Metal ion stock solutions of $ScCl_3$, $GaCl_3$, and $InCl_3$ were prepared by dissolving Sc_2O_3 (Sigma-Aldrich), Ga_2O_3 (Sigma-Aldrich), or In metal (Alfa Inorganics) in 12 mol/L HCl and evaporating to dryness. The residue was then carefully taken up in double distilled water to form the appropriate stock solution. Aluminum nitrate and yttrium chloride stock solutions were prepared by directly dissolving the metal salt (Sigma-Aldrich) in water. The vanadium stock solution was prepared as described by Butler and Eckert.[26] Nitrilotriacetic acid (NTA) solutions of Fe^{3+} or Sc^{3+} were prepared with a metal–chelate ratio of 1:2. All metal ion stock solutions were kept at an acidic pH to prevent hydrolysis.

Iron-free chicken oTf (also known as conalbumin) was purchased from Sigma-Aldrich. It was shown to be >95% pure by gel electrophoresis and was used without further purification. The protein concentration was determined on a Hitachi U-2000 spectrophotometer at 280 nm, using a molar extinction coefficient of 91 200 for the apo-protein.

The preparation of Co_2–oTf essentially followed the procedure of Zweier et al.,[22] except that the Co_2–oTf complex was put through a Biorad Econo-Pac 10DG desalting column equilibrated with 10 mmol/L NH_4HCO_3 to remove the excess carbonate and peroxide prior to freeze drying.

Samples for NMR spectroscopy were prepared by dissolving the lyophilized protein in 1.30 mL double distilled water and 0.50 mL D_2O. ^{13}C-labeled Na_2CO_3 (99%, MSD Isotopes, Montreal, Quebec) was added to a final concentration of 10 mmol/L. The pH was adjusted with small amounts of 1.0 mol/L KOD or 1.0 mol/L DCl and measured with a Fisher Accumet 805MP pH meter fitted with an Ingold Electronics 3.5 mm glass electrode.

The metal ion competition experiments were performed by the addition of a known amount of the competing metal ion

Can. J. Chem. Downloaded from www.nrcresearchpress.com by Xi'an Jiaotong University on 09/19/12
For personal use only.

to an oTf metal ion NMR sample, followed by pH adjustment and incubation at 20 °C for at least 12 h prior to acquisition of the NMR spectra.

NMR spectroscopy

NMR spectroscopy was performed on a Bruker widebore AM400 spectrometer equipped with a 10 mm broadband probe. All spectra were acquired at 25 °C. ^{13}C (100.6 MHz), ^{27}Al (104.3 MHz), ^{45}Sc (97.2 MHz), ^{51}V (105.2 MHz), and ^{71}Ga (122.0 MHz) NMR data were acquired and processed using parameters given elsewhere.[24,25,28,38] Chemical shifts were referenced to 0 ppm as follows: ^{13}C, TMS; ^{27}Al, 1.0 mol/L $Al(NO_3)_3$; ^{45}Sc, 1.0 mol/L $ScCl_3$; ^{51}V, $VOCl_3$; and ^{71}Ga, 1.0 mol/L $Ga(NO_3)_3$. ^{13}C NMR experiments with diamagnetic metal ions were acquired as described earlier.[28] ^{13}C NMR experiments on solutions containing iron(III) were performed as follows. Because of the paramagnetic relaxation caused by ferric iron, conditions were set up to allow complete relaxation of the signals of interest prior to the addition of iron to ensure that the spectra could be analyzed quantitatively. The T_1 of 100 mmol/L $Na_2{}^{13}CO_3$ (~15 s) was obtained using the method of inversion recovery. Acquisition parameters for ^{13}C NMR (100.63 MHz) of the iron-containing competitions were as follows: a pulse length (45°) of 7.5 ms, a sweep width of 25 kHz, an acquisition time of 0.3 s, and a relaxation delay of 37.7 s. The spectra for the iron(III)-containing samples were otherwise processed in the same manner as the other ^{13}C NMR experiments (e.g., Aramini and Vogel[38]).

Results

^{13}C NMR chemical shifts of bound $^{13}CO_3^{2-}$

The chemical shifts for ^{13}C-labeled CO_3^{2-} bound to oTf in the presence of various trivalent metal ions were determined by NMR spectroscopy (Table 1). Many of the peaks for the bound carbonate ions are well-resolved for the two binding sites of oTf. They are also distinct from the peak for free carbonate, and hence ^{13}C NMR can be used to follow the metal ion competition indirectly by observing the bound anion. The signals could be assigned to the N and C sites, respectively, by studying the individual isolated lobes of oTf, which can be obtained through limited proteolysis (data not shown; see, for example, Aramini and Vogel[40]). For most metal ions, the chemical shifts show small differences for the two sites, and hence the two binding sites of the protein can be distinguished for most of the metal ions.

Metal ion competitions with binding site preferences

^{13}C NMR spectra for a titration of Sc^{3+} into a solution of Ga_2–oTf containing ^{13}C-labeled carbonate are shown in Fig. 2. The spectra of the carbonyl region show that bound Sc^{3+}–anion signals ($Sc_2(^{13}CO_3)_2$oTf; δ_{Nlobe} = 166.74 ppm and δ_{Clobe} = 166.61 ppm) displace the bound gallium–anion signals (δ_N = 166.09 ppm and δ_C = 165.91 ppm) during the titration. The displacement of the gallium is not totally complete at two molar equivalents of scandium as shown by the small remaining peaks for bound gallium–carbonate (δ_N = 166.09 ppm). ^{45}Sc QCT NMR (Fig. 2) also provides similar results in which two overlapping signals corresponding to oTf-bound scandium appear during the titration; they also indicate a stepwise binding mechanism wherein the C-lobe site of oTf is filled first by the scandium ions. The broad peak that appears upfield from the protein-bound scandium signals is free scandium, which is not bound to the metal ion binding sites of the protein. A separate titration experiment showed that gallium is unable to displace oTf-bound scandium (data not shown).

The displacement of aluminum by scandium follows a distinctive site order as well. Figure 3 shows this titration as detected through three different NMR-active nuclei. The ^{13}C NMR spectra show a drastic decrease in intensity for the bound aluminum–anion signal corresponding to the C-lobe binding site after the addition of 1 equiv of scandium; at the same time a new signal corresponding to $Sc_2(^{13}CO_3)_2$oTf appears. No $Al_2(^{13}CO_3)_2$oTf signal is seen after the addition of 2 equiv of scandium, indicating that scandium has a much higher affinity for oTf than aluminum. Complete displacement of Al^{3+} by Sc^{3+} was also observed via ^{27}Al and ^{45}Sc QCT NMR. Also, the QCT NMR spectra show that aluminum is preferentially displaced by scandium in the C lobe of the protein. At 1 equiv of scandium, it is apparent from both the ^{27}Al and ^{45}Sc QCT NMR spectra that the C lobe has significantly more scandium bound than the N lobe. At 2 equiv of Sc^{3+}, no bound Al^{3+} is seen by ^{27}Al NMR; thus, aluminum has been completely displaced from the protein. The small sharp signal seen at –7 ppm arises from a transmitter spike lying near the centre of the spectrum.

In a previous ^{51}V NMR study,[28] the displacement of VO_2^+ from oTf by aluminum was already noted. As expected, ^{27}Al QCT NMR demonstrated that aluminum(III) is capable of displacing the bound vanadate from the protein (Fig. 4). However, the displacement of vanadate is not complete after the addition of 2 equiv of Al^{3+}, with some VO_2^+ remaining bound in the C-lobe site. Unexpectedly, VO_2^+ showed a higher binding affinity than yttrium under our experimental conditions, as evidenced by the disappearance of the bound carbonate signals in the ^{13}C NMR spectra and the appearance of oTf-bound vanadate by ^{51}V QCT NMR (data not shown). The yttrium(III) was preferentially displaced from the N-lobe site, and only a small amount of yttrium(III) remained bound in the C-lobe site at the end of the titration.

Displacement of oTf-bound yttrium(III) by aluminum(III) also showed a similar pattern to what was observed for vanadate. Figure 5 depicts the displacement of Y^{3+} by Al^{3+}. In the ^{13}C NMR spectra, the signal for the N-lobe $Y_2(^{13}CO_3)_2$oTf dramatically decreases in intensity and is absent when 2 equiv of Al^{3+} were added. In contrast, the ^{13}C signal corresponding to the C lobe only begins to decrease in intensity when 2 equiv were added, indicating that the N lobe is completely exchanged before aluminum is able to dislodge yttrium from the C site. This slow displacement at the C site was also observed by ^{27}Al QCT NMR; only when 2 equiv of Al^{3+} were added is a small signal seen for the C lobe of oTf (δ = –6.5 ppm). Even at an excess of aluminum, the intensity of the C-lobe signal is only slightly increased.

Displacement of bound yttrium by gallium also exhibited a slight site preference. Inspection of the ^{13}C NMR spectra of the competition showed the two bound carbonate signals for $Y_2(^{13}CO_3)_2$oTf decrease at different rates (Fig. 6), with the signal corresponding to the N-lobe site decreasing slightly

Fig. 2. Ga_2–ovotransferrin (oTf, 0.98 mmol/L) and $^{13}CO_3^{2-}$ (10 mmol/L, pH 7.5) back-titration with Sc^{3+}. ^{13}C NMR spectrum of the expanded carbonyl region, 20 000 scans; ^{45}Sc quadrupolar central transition (QCT) NMR, 1 000 000 scans.

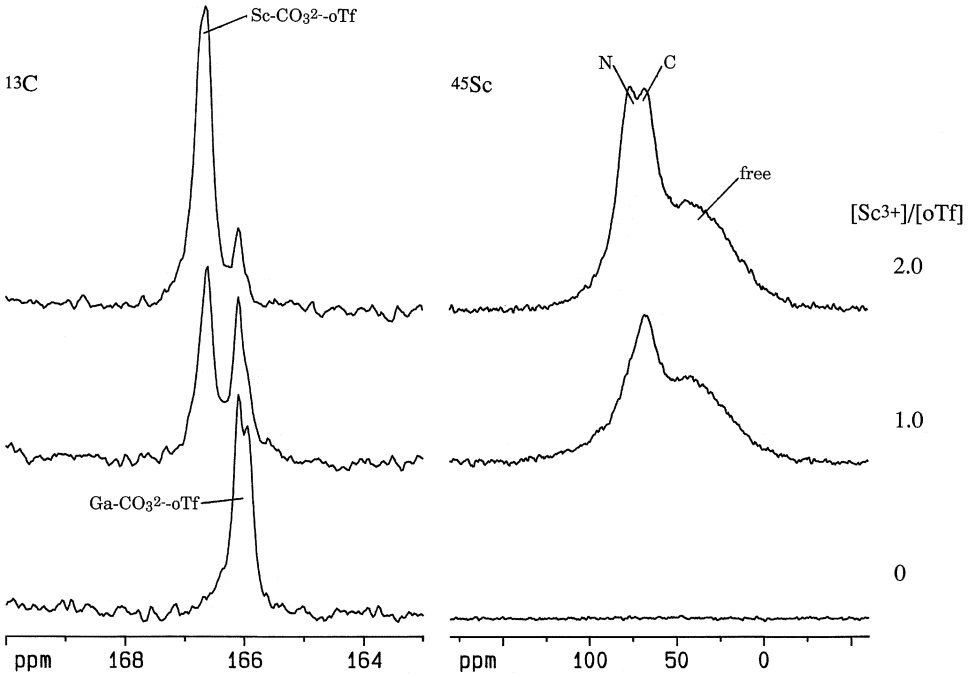

Fig. 3. Al_2–ovotransferrin (oTf, 0.98 mmol/L, pH 7.6) with 10 mmol/L $^{13}CO_3^{2-}$ back-titrated with Sc^{3+}. ^{13}C NMR spectrum, 20 000 scans; ^{45}Sc quadrupolar central transition (QCT) NMR spectrum, 1 000 000 scans; and ^{27}Al QCT NMR spectrum, 150 000 scans.

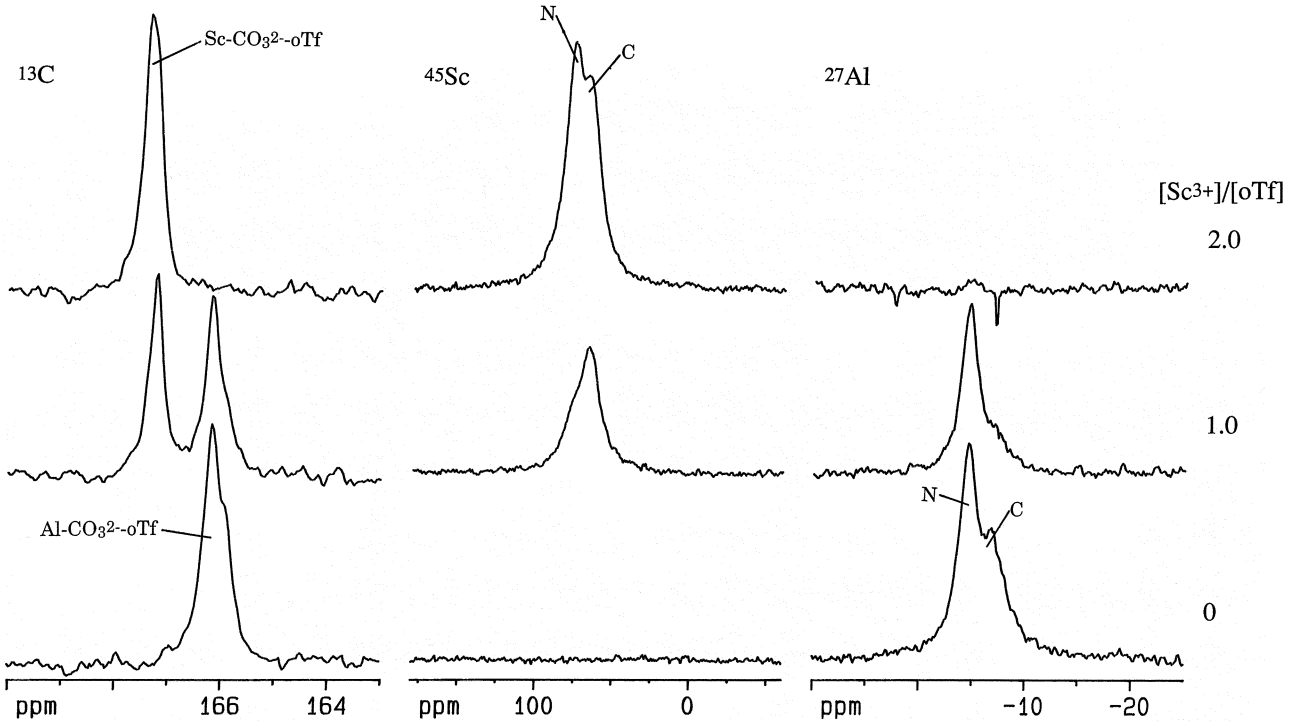

faster. Unfortunately, the two gallium–carbonate signals are overlapped at this magnetic field strength, so the occupancy of individual sites with gallium by ^{13}C NMR could not be followed. In the ^{71}Ga NMR spectra, a single broad signal corresponding to the N-lobe binding site is observed and increases in intensity during the titration. At 2 equiv of Ga^{3+} a slightly upfield broader signal (C-lobe site) can be resolved. The titration was almost complete at 2 equiv.

Metal ion competitions with no site preference

Titration of gallium into a solution of $Al_2(^{13}CO_3)_2$oTf induces the displacement of Al^{3+} from the protein. The ^{13}C chemical

Can. J. Chem. Downloaded from www.nrcresearchpress.com by Xi'an Jiaotong University on 09/19/12
For personal use only.

Fig. 4. $V(V)_2$–ovotransferrin (oTf, 1.04 mmol/L, pH 7.5) with 10 mmol/L $^{13}CO_3^{2-}$ back-titrated with Al^{3+}. ^{13}C NMR spectrum, 20 000 scans; ^{27}Al quadrupolar central transition (QCT) NMR spectrum, 150 000 scans; and ^{51}V QCT NMR spectrum, 150 000 scans.

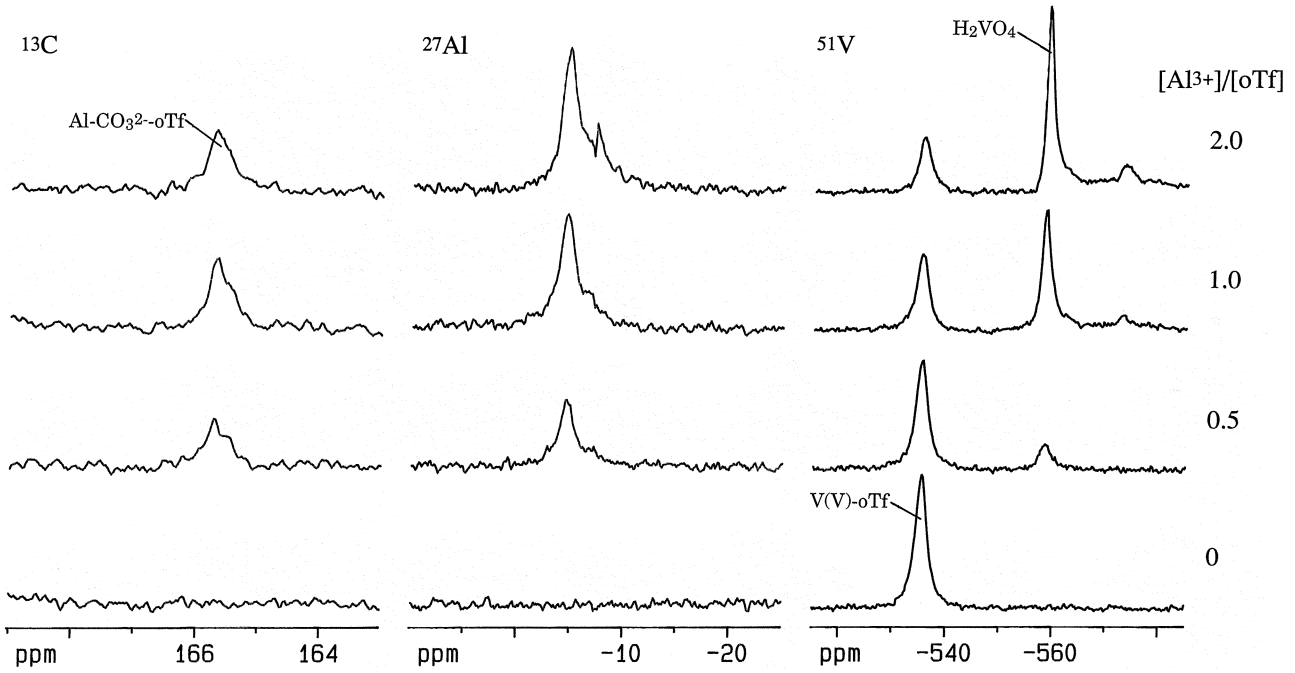

Fig. 5. Y_2–ovotransferrin (oTf, 1.1 mmol/L, pH 7.5) with 10 mmol/L $^{13}CO_3^{2-}$ back-titrated with Al^{3+}. ^{13}C NMR spectrum, 20 000 scans; and ^{27}Al quadrupolar central transition (QCT) NMR spectrum, 150 000 scans. The broad peaks in the ^{13}C NMR spectra arise from the background natural abundance signals of the protein.

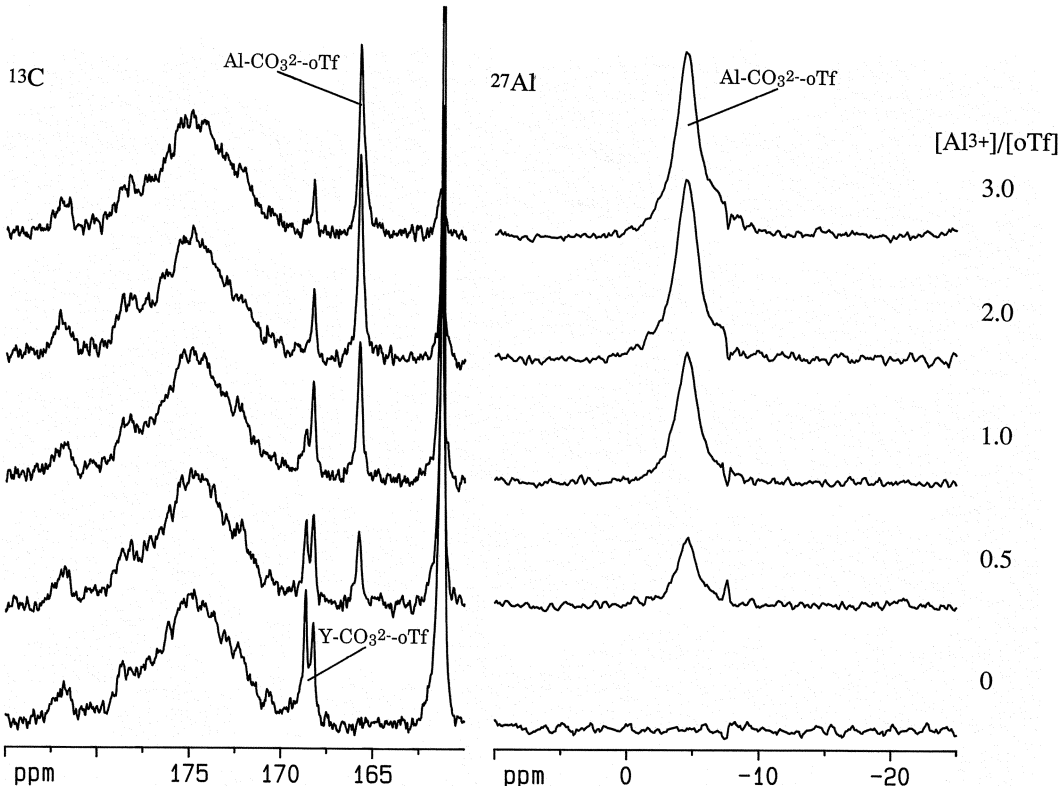

shifts of the bound anion in the presence of Ga^{3+} and Al^{3+} have quite similar chemical shifts (see Table 1), and hence ^{13}C NMR did not provide information on their competition. ^{27}Al QCT NMR showed a decrease in the bound aluminum signals as gallium(III) was added to the protein (data not shown). The displacement of Al^{3+} is only nearly complete

Can. J. Chem. Downloaded from www.nrcresearchpress.com by Xi'an Jiaotong University on 09/19/12
For personal use only.

Can. J. Chem. Downloaded from www.nrcresearchpress.com by Xi'an Jiaotong University on 09/19/12
For personal use only.

Fig. 6. Y_2–ovotransferrin (oTf, 1.02 mmol/L, pH 7.5) back-titrated with Ga^{3+} in the presence of 10 mmol/L $^{13}CO_3^{2-}$. ^{13}C NMR spectrum, 17 500 scans; and ^{71}Ga quadrupolar central transition (QCT) NMR spectrum, 1 480 000 scans. The broad peaks in the ^{13}C NMR spectra arise from the background natural abundance signals of the protein.

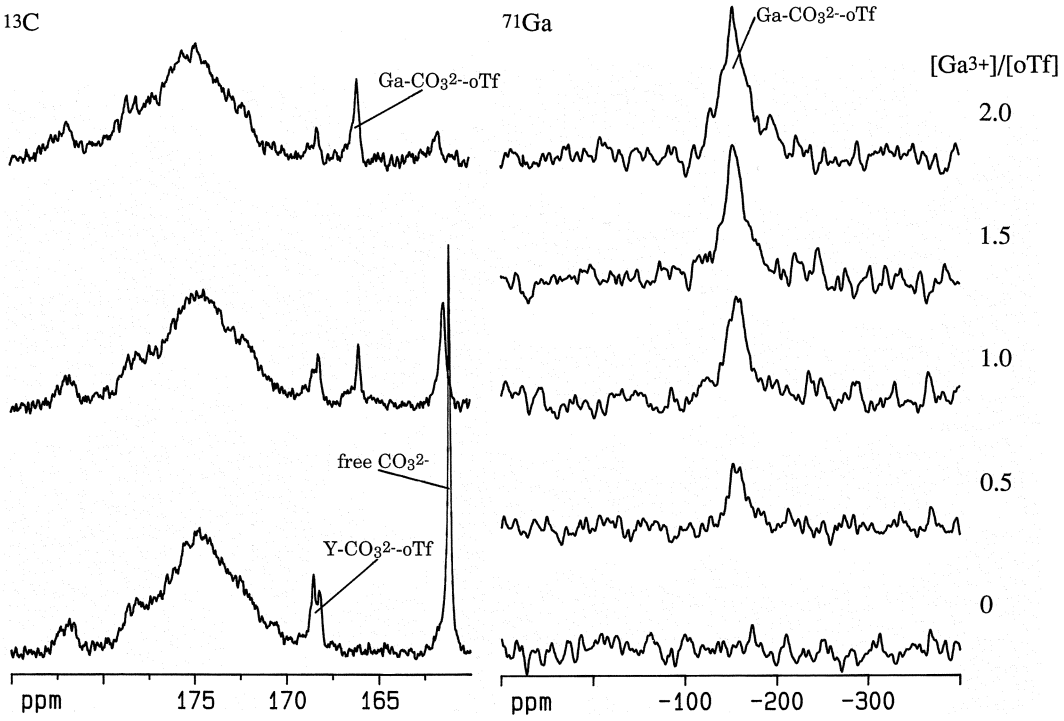

when 3 equiv of gallium are added, with aluminum being displaced at an equal rate from both binding sites.

The relative affinities of oTf for Al^{3+} and Co^{3+} were also tested. Displacement of Co^{3+} was observed via both ^{13}C and ^{27}Al NMR (data not shown). The intensities of the ^{13}C NMR signals of $Co_2(^{13}CO_3)_2$oTf decreased and a new signal corresponding to $Al_2(^{13}CO_3)_2$oTf appeared with increasing intensity after the addition of 0.5 equiv of aluminum. Signal intensities, in both the ^{13}C and ^{27}Al spectra did not appear to change after 1 equiv of Al^{3+} was added. Furthermore, at equimolar concentrations of cobalt and aluminum, a significant amount of cobalt still remained bound to the protein. Thus, nonspecific displacement of Co^{3+} and binding of Al^{3+} was observed.

Competition experiments between cobalt(III) and yttrium (III) provided ambiguous results. Titration of Y^{3+} into Co_2–oTf yielded little information by ^{13}C NMR because of overlapping signals. Addition of YCl_3 to the solution of Co_2–oTf also resulted in the precipitation of the $^{13}CO_3^{2-}$ present, causing the free carbonate signal to broaden and decrease severely in intensity, thus likely affecting the availability of yttrium to bind to the protein. A small, partly obscured, signal around 168 ppm appeared during the titration, which corresponds to the known chemical shift of $(Y^{3+})_2$oTf$(^{13}CO_3)_2$, suggesting that some yttrium was able to bind to the protein.

Metal in competitions involving higher affinity metal ions

Previous studies have indicated that a chelator, such as NTA, is required for the binding of higher affinity metal ions to occur at a reasonable rate.[14,31] Therefore, NTA was added to the competition experiments involving Fe^{3+}, Sc^{3+}, and In^{3+} in an attempt to achieve equilibrium within the 12 h incubation period used.

Indium(III) was competed with scandium(III) to assess the affinity of scandium, whose binding constants have not been reported for any of the transferrins. $In(NTA)_2$ was added to a solution of $Sc_2(^{13}CO_3)_2$oTf and this titration was followed by ^{45}Sc NMR (Fig. 7) and revealed the gradual displacement of scandium from the protein. Because of the signal overlap of free $ScCl_3$ (δ = 60.2 ppm) and Sc_2–oTf, it was impossible to determine if any site-specific displacement had occurred. Integration of the N-lobe signal (δ = 78.1 ppm) during the titration showed that ~40% of the scandium is displaced from the N lobe of the protein when an equal amount of indium is added.

Competition experiments involving iron(III) are more difficult to study by NMR because of the paramagnetic properties of this metal ion. The ^{13}C NMR signals for $Fe_2(^{13}CO_3)_2$oTf cannot be observed because they are broadened beyond detection. The competition experiments involving iron(III) with scandium or indium had surprising results. When $Fe(NTA)_2$ was back-titrated into a sample containing Sc_2oTf, an immediate dark red colour appeared, characteristic of iron binding to the protein. Furthermore, release of bound scandium was observed via ^{45}Sc QCT NMR and by ^{13}C NMR, where a reduction in signal area of the bound $^{13}CO_3^{2-}$ was seen. Notably, after the addition of 2 equiv of Fe^{3+}, some scandium remained bound (data not shown).

Displacement of indium by iron was also examined in the presence and absence of NTA. Titration of $Fe(NTA)_2$ into $In_2(^{13}CO_3)_2$oTf in the presence of NTA caused the formation of a red colour, characteristic of the formation of Fe_2oTf,

Can. J. Chem. Downloaded from www.nrcresearchpress.com by Xi'an Jiaotong University on 09/19/12
For personal use only.

Fig. 7. Sc_2–ovotransferrin (oTf, 1.1 mmol/L, pH 7.5) back-titrated with $In(NTA)_2$ in the presence of 10 mmol/L $^{13}CO_3^{2-}$. ^{45}Sc quadrupolar central transition (QCT) NMR spectrum, 900 000 scans.

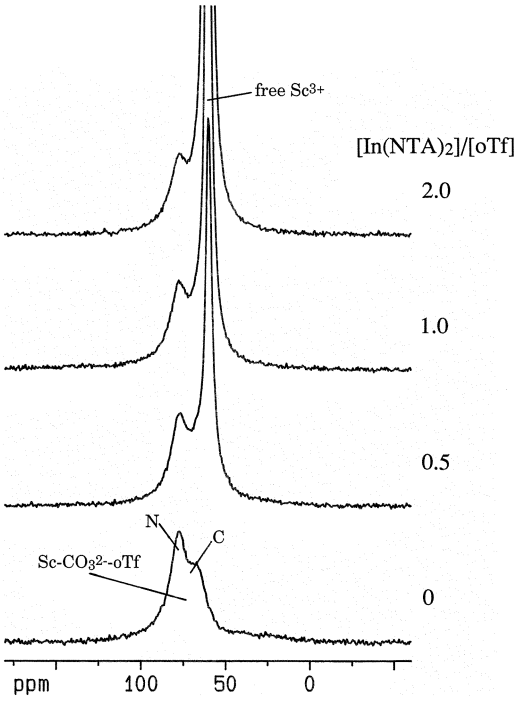

whereas addition of $Fe(NO_3)_3$ resulted in the protein solution having an orange colour similar to the ferric nitrate. Surprisingly, no decrease in the $In_2(^{13}CO_3)_2$oTf ^{13}C NMR signal was observed during the addition of either $Fe(NTA)_2$ or $Fe(NO_3)_3$ (not shown). Similarly, ^{13}C NMR of the reverse titration failed to show the appearance of a $In_2(^{13}CO_3)_2$oTf signal.

Discussion

A combined NMR spectroscopy approach allowed us to observe the competition between Al^{3+}, Co^{3+}, Fe^{3+}, Ga^{3+}, In^{3+}, Sc^{3+}, Y^{3+}, and VO_2^+ for the two ferric iron binding sites of oTf in a straightforward and qualitative manner. Metal ion QCT NMR and ^{13}C NMR of the bound synergistic anion allowed for the observation of the binding and displacement of metal ions either directly or indirectly by observing the bound carbonate. This combined approach offers several advantages: the ratios of the competing metal ions that are bound to the protein can be observed, and differences between the two binding sites can often be detected. The observed order of decreasing affinity for the metal ions studied was $Fe^{3+} \approx In^{3+} \geq Sc^{3+} \geq Ga^{3+} > Al^{3+} > VO_2^+ > Y^{3+} \geq Co^{3+}$.

Ichimura et al.[41] noted that aluminum has a higher affinity for the N-lobe site of oTf, and this behaviour is also observed in our NMR experiments. When aluminum displaced a lower affinity metal ion, such as yttrium or vanadate, binding of aluminum occurred preferentially at the N-lobe site. Displacement of aluminum by scandium occurred more rapidly at the C-lobe site, suggesting that aluminum is bound more tightly at the N site. Unexpectedly, this site preference was not observed when gallium displaced aluminum. This can be explained by the observation that gallium also has a preference for the N-lobe site.[24] From the competition experiments, gallium was shown to displace the lower affinity yttrium from this site; as well, gallium itself was displaced more slowly from this site by scandium. Scandium clearly exhibited a preference for the C lobe of the protein. Ichimura et al.[41] reported that Al^{3+}, Co^{2+}, Cu^{2+}, and Fe^{3+} all bind with higher preference to the N site, whereas the lanthanides with a larger ionic radius all bind to the C site with higher affinity, suggesting that the two binding sites have different size preferences. Additionally, Yamamura et al.[42] also reported that the lanthanides exhibited a higher affinity for the C site. Taken together with our results, this supports the notion that the ferric binding site in the N lobe of oTf is more suited for smaller ions, whereas the C-lobe site is better able to accommodate larger ions. Consistent with this, the relatively large Bi^{3+} ion (1.03 Å) also has been shown to bind preferentially to the C lobe of transferrin.[43] However, protein structure analysis of the iron-saturated oTf does not show any major differences between the sites located in the N and C lobes (see Fig. 1). The first coordination sphere is essentially the same in both lobes, and hence these differences must be caused by more distal parts of the protein. We also note that in biological experiments gallium(III) is often used as a direct substitute for iron(III), because it is not redox active and has the same ionic radius. Our data clearly show that Ga^{3+} binds much weaker than Fe^{3+} to oTf and probably to other transferrins as well. Similar results have been reported for the bacterial ferric binding protein FBP.[44]

The metal ions that were found to be at the weak end of the affinity series were VO_2^+, yttrium(III), and cobalt(III). The weak affinity for Co^{3+} when compared with Fe^{3+} was somewhat surprising, considering that both have similar ionic radii and both have a preference for the octahedral geometry found in the oTf binding sites. The weak affinity for cobalt (III) observed here is possibly due to its solution chemistry. $Co(III)_2$oTf is prepared by the oxidation of Co(II) by peroxide.[22] The standard reduction potential for cobalt is such that any Co(III) released from the protein is reduced to Co(II), which in turn has a rather low affinity for oTf.[19] In addition, the formation of insoluble cobalt–carbonate can occur. The appearance of paramagnetic Co(II) was actually observed in our cobalt–yttrium and cobalt–aluminum competition experiments; the free carbonate signal in these ^{13}C spectra was observed to broaden and decrease severely in intensity, indicating the presence of a paramagnetic moiety.

The displacement of yttrium by all metal ions, except possibly cobalt, is attributed to two factors. Yttrium is the largest metal ion that was studied in this series (Table 1) and therefore its large ionic radius may put it at a steric disadvantage. Secondly, yttrium forms highly insoluble carbonate complexes and therefore the amount of available free yttrium is likely to be low, thus giving other more soluble metal ions a competitive advantage.

Vanadate exhibited a higher binding affinity than yttrium and cobalt, but not aluminum. The oxo ligands of VO_2^+ have been found to be ideally suited for coordinating the ligands in the anion binding site of serum transferrin, thus overcoming the need for the simultaneous binding of the synergistic anion.[28,45,46] Therefore, the ability of vanadate to displace yttrium and cobalt is believed to be due to the fact that VO_2^+ does not require an anion and thus it is not dependent

Can. J. Chem. Downloaded from www.nrcresearchpress.com by Xi'an Jiaotong University on 09/19/12
For personal use only.

on the available carbonate in solution, which poses a significant problem with yttrium (see above). Harris and Carrano[47] found that gallium was able to displace vanadate from serum transferrin to some extent, suggesting that the affinities were similar. Since gallium was found in the competition experiments to displace aluminum from oTf, it is likely that the high rate of hydrolysis of gallium caused the incomplete displacement of vanadate by this metal ion in our experiments.

The ability of scandium to displace gallium was at first surprising to us, since gallium has an ionic radius more similar to that of ferric iron. This higher binding affinity of scandium correlates with earlier findings in which oTf-bound scandium was found to have a lower electric field gradient (eq_{ionic}) than bound gallium.[24,25] These results directly showed that the symmetry of the ligand environment in the binding site is higher in the presence of scandium, and this could possibly contribute to the higher binding affinity for this metal ion over gallium.

Competition experiments involving higher affinity metal ions (Fe^{3+}, In^{3+}, and Sc^{3+}) were not as straightforward as those involving the lower affinity metal ions. In this work, the dividing point between the low-affinity and the high-affinity metal ions appeared to be gallium. Competitions between any two of the metals higher in the series than gallium resulted in the inability of one metal to displace a significant amount of the other at an equal concentration. This was probably due to the slow off-rates of these metal ions under our experimental conditions preventing equilibrium from being reached during the 12 h incubation period. In an attempt to accelerate this process, the iron–indium competitions were performed with and without NTA for comparison. Direct observation of the colour of the oTf solutions indicated that some ferric oTf complex was formed, but no displacement of indium was observed by ^{13}C NMR. Evans and Ogwang,[48] using UV spectroscopy, also found that ferric-NTA was unable to displace indium from oTf. Although the observed colour change of the solution suggests the binding of some iron, it may be that the protein was not fully saturated. Aside from this, indium was found to displace some scandium from the protein, indicating that the observed binding affinity of scandium falls between that of indium and gallium.

It should be noted that NTA was not added to competition experiments involving metal ions that had a lower affinity than that of scandium to exclude the possibility that the presence of NTA would bias the outcome. For example, NTA has previously been shown to interfere with the binding of gallium and zinc to serum transferrin.[15,49] Indeed, NTA has also been shown to bind as a ligand to the protein-bound metal ion in partial protein fragments of duck ovotransferrin.[50] Thus, the presence of NTA could give rise to potentially confounding results when studying the lower affinity metal ions.

Overall, our results demonstrate that the combination of QCT NMR and ^{13}C NMR spectroscopy offers a valuable alternative approach to observe the binding of metal ions to the transferrins. The approach used here has the advantage of directly detecting metal ions that are otherwise spectroscopically silent; moreover, in many cases it was possible to observe site-specific effects that are not easily detectable by optical spectroscopy methods. This work could be further extended by studying the binding of spin 1/2 metal nuclei, such as Cd^{2+} and Tl^{3+} to oTf, which have been studied by cadmium-113 and thallium-205 NMR, respectively.[6,51] Understanding the affinities of proteins for metal ions is a complex issue because of their different solution chemistries, and thus many factors must be taken into account when observing the displacement of one metal ion over another. The order of the binding affinities found here is not unlike the observations of others using different methods,[13–15,19,41,52] indicating that our approach provides a viable and reliable method for assessing metal ion affinity. It should be noted that Li et al.[13] reported a different order for gallium and scandium than we observed; however, these authors studied human serum transferrin rather than ovotransferrin and this likely could have influenced the outcome. In future studies the same multinuclear NMR approach could be used to study other metalloproteins. However, the simultaneous binding of the synergistic anion is a unique property of the transferrins and hence ^{13}C NMR may not be as conveniently done for other proteins. On the other hand, the high concentrations of free carbonate in solution caused precipitations in some of our experiments and such complications would be avoided with soluble proteins. Whereas direct solution-state QCT NMR of protein-bound diamagnetic metal ions in other large metalloproteins would be possible, analogous indirect ^{13}C NMR work would require biosynthetic stable isotope labeling of the metal-liganding amino acid residues in these proteins.

Acknowledgments

This research was supported by an operating grant from the Medical Research Council (MRC) of Canada. H.J.V. is a Scientist of the Alberta Heritage Foundation for Medical Research (AHFMR). J.A.S. was the recipient of an AHFMR studentship. We thank Dr. D. McIntyre for spectrometer maintenance and Dr. J. Aramini for his insights, encouragement, and suggestions in the course of this research. We also wish to think B. Chu for editorial assistance. The AM400 NMR spectrometer was purchased with funds provided by AHFMR.

References

(1) Arnold, R. R.; Cole, M. F.; Mcghee, J. R. *Science* **1977** *197* (4300), 263. doi:10.1126/science.327545.
(2) Singh, P. K.; Parsek, M. R.; Greenberg, E. P.; Welsh, M. J. *Nature* **2002** *417* (6888), 552. doi:10.1038/417552a.
(3) Harris, D. C.; Aisen, P. *Physical Biochemistry of the Transferrins;* VCH Publishers: New York, 1989; p 241.
(4) Lambert, L. A.; Perri, H.; Halbrooks, P. J.; Mason, A. B. *Comp. Biochem. Physiol. B Biochem. Mol. Biol.* **2005** *142* (2), 129. doi:10.1016/j.cbpb.2005.07.007.
(5) Schlabach, M. R.; Bates, G. W. *J. Biol. Chem.* **1975** *250*, 2182.
(6) Sola, M. *Eur. J. Biochem.* **1990** *194* (2), 349. doi:10.1111/j.1432-1033.1990.tb15625.x.
(7) Zak, O.; Ikuta, K.; Aisen, P. *Biochemistry* **2002** *41* (23), 7416. doi:10.1021/bi0160258.
(8) Baker, H. M.; Anderson, B. F.; Baker, E. N. *Proc. Natl. Acad. Sci. U.S.A.* **2003** *100* (7), 3579. doi:10.1073/pnas.0637295100.
(9) Chasteen, N. D. *Coord. Chem. Rev.* **1977** *22* (1–2), 1. doi:10.1016/S0010-8545(00)80432-4.
(10) Harris, W. R. *Inorg. Chem.* **1986** *25* (12), 2041. doi:10.1021/ic00232a026.
(11) Harris, W. R.; Chen, Y. *Inorg. Chem.* **1992** *31* (24), 5001. doi:10.1021/ic00050a017.

(12) Harris, W. R.; Madsen, L. J. *Biochemistry* **1988** *27* (1), 284. doi:10.1021/bi00401a043.
(13) Li, H. Y.; Sadler, P. J.; Sun, H. Z. *Eur. J. Biochem.* **1996** *242* (2), 387. doi:10.1111/j.1432-1033.1996.0387r.x.
(14) Harris, W. R.; Chen, Y.; Wein, K. *Inorg. Chem.* **1994** *33* (22), 4991. doi:10.1021/ic00100a024.
(15) Harris, W. R.; Pecoraro, V. L. *Biochemistry* **1983** *22* (2), 292. doi:10.1021/bi00271a010.
(16) Durbin, P. W. *Health Phys.* **1962** *8* (6), 665. doi:10.1097/00004032-196212000-00015.
(17) Grossmann, J. G.; Neu, M.; Evans, R. W.; Lindley, P. F.; Appel, H.; Hasnain, S. S. *J. Mol. Biol.* **1993** *229* (3), 585. doi:10.1006/jmbi.1993.1063.
(18) Duffield, J. R.; Taylor, D. M. *Inorg. Chim. Acta* **1987** *140*, 365. doi:10.1016/S0020-1693(00)81125-1.
(19) Tan, A. T.; Woodworth, R. C. *Biochemistry* **1969** *8* (9), 3711. doi:10.1021/bi00837a033.
(20) Cochran, M.; Coates, J.; Neoh, S. *FEBS Lett.* **1984** *176* (1), 129. doi:10.1016/0014-5793(84)80926-6.
(21) Bertini, I.; Luchinat, C.; Messori, L.; Scozzafava, A.; Pellacani, G. C.; Sola, M. *Inorg. Chem.* **1986** *25* (11), 1782. doi:10.1021/ic00231a013.
(22) Zweier, J. L.; Wooten, J. B.; Cohen, J. S. *Biochemistry* **1981** *20* (12), 3505. doi:10.1021/bi00515a031.
(23) Aramini, J. M.; Germann, M. W.; Vogel, H. J. *J. Am. Chem. Soc.* **1993** *115* (21), 9750. doi:10.1021/ja00074a048.
(24) Aramini, J. M.; Mcintyre, D. D.; Vogel, H. J. *J. Am. Chem. Soc.* **1994** *116* (25), 11506. doi:10.1021/ja00104a034.
(25) Aramini, J. M.; Vogel, H. J. *J. Am. Chem. Soc.* **1994** *116* (5), 1988. doi:10.1021/ja00084a044.
(26) Butler, A.; Eckert, H. *J. Am. Chem. Soc.* **1989** *111* (8), 2802. doi:10.1021/ja00190a010.
(27) Germann, M. W.; Aramini, J. M.; Vogel, H. J. *J. Am. Chem. Soc.* **1994** *116* (15), 6971. doi:10.1021/ja00094a076.
(28) Saponja, J. A.; Vogel, H. J. *J. Inorg. Biochem.* **1996** *62* (4), 253. doi:10.1016/0162-0134(95)00159-X.
(29) Aramini, J. M.; Vogel, H. J. *Biochem. Cell Biol.* **1998** *76* (2–3), 210. doi:10.1139/o98-037.
(30) Aramini, J. M.; Saponja, J. A.; Vogel, H. J. *Coord. Chem. Rev.* **1996** *149*, 193.
(31) Aisen, P.; Leibman, A.; Zweier, J. *J. Biol. Chem.* **1978** *253*, 1930.
(32) Mizutani, K.; Mikami, B.; Aibara, S.; Hirose, M. *Acta Crystallogr. D Biol. Crystallogr.* **2005** *61* (12), 1636. doi:10.1107/S090744490503266X.
(33) Li, Y. Q.; Liu, B.; Ge, Z. J.; Yang, B. S. *J. Photochem. Photobiol. B* **2008** *91* (2–3), 137. doi:10.1016/j.jphotobiol.2008.03.001.
(34) Smith, T. A. D. *Bioorg. Med. Chem.* **2005** *13* (14), 4576. doi:10.1016/j.bmc.2005.04.052.
(35) Chasteen, N. D.; Grady, J. K.; Holloway, C. E. *Inorg. Chem.* **1986** *25* (16), 2754. doi:10.1021/ic00236a021.
(36) Harris, W. R.; Friedman, S. B.; Silberman, D. *J. Inorg. Biochem.* **1984** *20* (2), 157. doi:10.1016/0162-0134(84)80015-X.
(37) Sabbioni, E.; Marafante, E. *Bioinorg. Chem.* **1978** *9* (5), 389. doi:10.1016/S0006-3061(00)80148-9.
(38) Aramini, J. M.; Vogel, H. J. *J. Am. Chem. Soc.* **1993** *115* (1), 245. doi:10.1021/ja00054a035.
(39) Weast, R. C.; Lide, D. R. *CRC Handbook of Chemistry and Physics*, 70th edition; CRC Press: Boca Raton, FL, 1989.
(40) Aramini, J. M.; Vogel, H. J. *J. Magn. Reson. B.* **1996** *110* (2), 182. doi:10.1006/jmrb.1996.0028.
(41) Ichimura, K.; Kihara, H.; Yamamura, T.; Satake, K. *J. Biochem.* **1989** *106*, 50.
(42) Yamamura, T.; Ichimura, K.; Tsuda, T.; Hayashi, A.; Taniguchi, T.; Toi, R.; Kihara, H.; Satake, K. *Nippon Kagaku Kaishi* **1988** 452.
(43) Li, H.; Sadler, P. J.; Sun, H. *J. Biol. Chem.* **1996** *271* (16), 9483. doi:10.1074/jbc.271.16.9483.
(44) Weaver, K. D.; Heymann, J. J.; Mehta, A.; Roulhac, P. L.; Anderson, D. S.; Nowalk, A. J.; Adhikari, P.; Mietzner, T. A.; Fitzgerald, M. C.; Crumbliss, A. L. *J. Biol. Inorg. Chem.* **2008** *13* (6), 887. doi:10.1007/s00775-008-0376-5.
(45) Butler, A.; Carrano, C. J. *Coord. Chem. Rev.* **1991** *109* (1), 61. doi:10.1016/0010-8545(91)80002-U.
(46) Smith, C. A.; Ainscough, E. W.; Brodie, A. M. *J. Chem. Soc., Dalton Trans.* **1995** (7): 1121. doi:10.1039/dt9950001121.
(47) Harris, W. R.; Carrano, C. J. *J. Inorg. Biochem.* **1984** *22* (3), 201. doi:10.1016/0162-0134(84)80029-X.
(48) Evans, R. W.; Ogwang, W. *Biochem. Soc. Trans.* **1988** *16*, 833.
(49) Harris, W. R. *Biochemistry* **1983** *22* (16), 3920. doi:10.1021/bi00285a030.
(50) Kuser, P.; Hall, D. R.; Haw, M. L.; Neu, M.; Evans, R. W.; Lindley, P. F. *Acta Crystallogr. D Biol. Crystallogr.* **2002** *58* (5), 777. doi:10.1107/S0907444902003724.
(51) Aramini, J. M.; Krygsman, P. H.; Vogel, H. J. *Biochemistry* **1994** *33* (11), 3304. doi:10.1021/bi00177a022.
(52) Harris, W. R.; Sheldon, J. *Inorg. Chem.* **1990** *29* (1), 119. doi:10.1021/ic00326a024.

Can. J. Chem. Downloaded from www.nrcresearchpress.com by Xi'an Jiaotong University on 09/19/12
For personal use only.

A ZORA-DFT and NLMO study of the one-bond fluorine–X indirect nuclear spin-spin coupling tensors for various VSEPR geometries

Frédéric A. Perras and David L. Bryce

Can. J. Chem. Downloaded from www.nrcresearchpress.com by Xi'an Jiaotong University on 09/19/12
For personal use only.

Abstract: Zeroth-order regular approximation (ZORA) density functional theory (DFT) calculations of one-bond X–^{19}F indirect nuclear spin-spin coupling (**J**) tensors were performed on a series of fluorine-containing compounds covering several valence shell electron pair repulsion (VSEPR) theory geometries for which **J**, by symmetry, is not required to be axially symmetric. The calculations show that the antisymmetric components of **J** are only of the same order of magnitude as the principal components of the symmetric **J**-coupling tensor for a few geometries, and that in cases of approximate axial symmetry along the bond, **J** remains nearly axially symmetric with its unique component along the bond. In general, different species having the same nominal geometry tend to have similar tensor orientations, magnitudes of anisotropy of **J** relative to the isotropic coupling constant, as well as the same dominant contributions from the different coupling mechanisms. Structures are also systematically modified to determine how the tensor components depend on geometrical parameters. The isotropic coupling constants are subsequently interpreted using a natural localized molecular orbital (NLMO) approach. Our results could prove to be useful for future experimental characterizations of **J** tensors in systems having symmetry properties that do not force **J** to be axially symmetric or coincident with the dipolar coupling tensor.

Key words: nuclear magnetic resonance, *J* coupling, ZORA-DFT calculations, natural localized molecular orbitals.

Résumé : Des calculs de théorie de la fonctionnelle de la densité (DFT) de couplage spin-spin nucléaire indirect (**J**) X–^{19}F d'une liaison employant l'approximation régulière d'ordre zéro (ZORA) ont été effectués sur une série de composés du fluore couvrant plusieurs géométries de la théorie de la répulsion des paires électroniques de la couche de valence (RPECV) ayant une symétrie pour laquelle **J** n'est pas forcément axialement symétrique. Les calculs démontrent que les composants antisymétriques de **J** sont seulement du même ordre de magnitude que les composants du tenseur de couplage **J** symétrique pour très peu de géométries et que dans les situations de symétrie approximativement axiale le long de la liaison, **J** est axialement symétrique. En général, différentes espèces ayant la même géométrie ont des orientations de tenseur similaires, des anisotropies de **J** du même ordre de grandeur, par rapport à la constante de couplage isotropique, ainsi que les mêmes mécanismes de couplage dominants. Les structures ont par la suite été modifiées afin de déterminer la dépendance des composants principaux de **J** par rapport à la géométrie. Ces données sont ensuite reliées aux orbitales moléculaires en employant une approche d'orbitales moléculaires localisées naturelles (NLMO) pour investiguer les constantes de couplage isotropiques. Nos résultats pourraient être utiles dans la caractérisation complète de tenseurs **J** pour des systèmes ayant des symétries qui ne nécessite pas que **J** soit axialement symétrique ou coïncident avec le tenseur de couplage dipolaire.

Mots-clés : résonance magnétique nucléaire, calculs ZORA-DFT, couplage *J*, orbitales moléculaires localisées naturelles.

[Traduit par la Rédaction]

Introduction

Solid-state nuclear magnetic resonance (SSNMR) spectroscopy has become one of the prime methods for the characterization of solid materials. A wealth of information can be extracted from NMR spectra that can be used to refine or solve the solid-state structures of compounds that are difficult to crystallize or that lack long-range order.[1] The dipolar coupling interaction is commonly used in structure determinations, since its magnitude (R_{DD}) depends on the motionally averaged inverse cube of the internuclear distance ($\langle r_{1,2}^{-3} \rangle$):

$$[1] \qquad R_{DD} = \left(\frac{\mu_0}{4\pi}\right)\left(\frac{\gamma_1\gamma_2\hbar}{2\pi}\right)\langle r_{1,2}^{-3}\rangle$$

where μ_0 is the magnetic constant, γ_1 and γ_2 are the magnetogyric ratios of the two nuclei, and $\hbar$ is the reduced Planck's constant.

Several experiments have been designed for the measure-

Received 30 September 2010. Accepted 19 November 2010. Published at www.nrcresearchpress.com/cjc on 3 June 2011.

F.A. Perras and D.L. Bryce. Department of Chemistry and Centre for Catalysis Research and Innovation, University of Ottawa, 10 Marie Curie Private, Ottawa, ON K1N 6N5, Canada.

Corresponding author: D.L. Bryce (e-mail: dbryce@uottawa.ca).

This article is part of a Special Issue dedicated to Professor Roderick E. Wasylishen in honour of his outstanding contributions to NMR spectroscopy, to chemistry in Canada, and to the training of NMR spectroscopists.

Can. J. Chem. Downloaded from www.nrcresearchpress.com by Xi'an Jiaotong University on 09/19/12
For personal use only.

ment of dipolar coupling constants for homonuclear spin systems[2–5] as well as heteronuclear spin systems.[6–8] In all these cases an effective dipolar coupling constant is measured that has a contribution from the anisotropy of the indirect nuclear spin-spin coupling tensor, ΔJ. The effective dipolar coupling constant, R_{eff}, is often represented as follows when one assumes that **J** is axially symmetric and coincident with the dipolar coupling tensor, **D**:[9,10]

$$[2] \qquad R_{\text{eff}} = R_{\text{DD}} - \Delta J/3$$

where the anisotropy of **J** is

$$[3] \qquad \Delta J = J_{33} - (J_{11} + J_{22})/2$$

and the principal components of the **J** tensor are ordered as $|J_{33} - J_{iso}| \geq |J_{11} - J_{iso}| \geq |J_{22} - J_{iso}|$. Often, the strategy for determining ΔJ from SSNMR spectra is to compare the measured value of R_{eff} with the direct dipolar coupling constant calculated on the basis of the atomic coordinates extracted using diffraction data. This can lead to an overestimation of the anisotropy of **J**, since the dipolar coupling constant reflects the average bond distance resulting from molecular vibrations and librations.[10,11] Programs have been developed that take vibrations into account when calculating dipolar coupling constants using the harmonic oscillator[12] or anharmonic oscillator[13] models. Even so, there is still the general issue that **J** is neither required to be axially symmetric nor coincident with **D**, unless symmetry dictates this to be the case.[14–17] It has been shown theoretically that if ΔJ is significant relative to R_{DD} in cases where **J** is noncoincident with **D** or where **J** is non-axially symmetric, there can be pronounced changes in the line shapes associated with stationary powder samples.[18] In these cases, simulations must take into account the asymmetry of **J**, which is

$$[4] \qquad \eta_J = (J_{22} - J_{11})/(J_{33} - J_{\text{iso}})$$

where η_J is the asymmetry parameter, and can take values ranging from 0 to 1. An asymmetry parameter of 0 means the tensor is axially symmetric. **J** also has an antisymmetric component that has never been observed experimentally. Nonetheless, guidelines on how it could be measured have been published.[19–21] The antisymmetric **J** tensor is defined as follows:

$$[5] \qquad \mathbf{J}^{\text{antisym}} = (\mathbf{J} - \mathbf{J}^{\text{t}})/2$$

where $\mathbf{J}^t$ denotes the transpose of **J**.

The original theory for indirect nuclear spin-spin coupling was developed by Ramsey.[22] Generally, one nucleus polarizes the electronic network, which can be detected by neighbouring nuclei. There are two general classes of coupling mechanisms: electron-spin mechanisms and orbital-current mechanisms labelled spin-orbit (SO). The first electron-spin mechanism, known as Fermi-contact (FC), results from the magnetic interaction between the nucleus and an electron that has a finite probability of being located at the nucleus. This mechanism is purely isotropic and is the dominating mechanism in cases where s orbitals dominate bonding as is typically the case for hydrogen. The magnetic interaction between the nuclear spin and the dipole moment of an electron located elsewhere around the nucleus is labelled spin-dipolar (SD). The effects of FC can also be detected through the SD mechanism and vice versa. This leads to a nonzero cross-term between the two that is symmetric, anisotropic, and traceless. Analogously to magnetic shielding, the SO term can be partitioned into two submechanisms. There is a diamagnetic spin-orbital term (DSO), which is often negligible, and a paramagnetic spin-orbital term (PSO), which is often the dominant term in couplings between atoms where the s orbitals contribute little to bonding (e.g., fluorine).[23,24] When relativistic spin-orbit coupling is included, there is also the introduction of cross-terms between the PSO and the electron-spin coupling mechanisms.[25,26]

Autschbach[27–29] introduced a method for the analysis of isotropic *J*-coupling constants with respect to natural localized molecular orbitals (NLMOs) and other types of localized orbitals in general (relativistic and nonrelativistic) density functional computations. This approach is of great use to better understand isotropic coupling constants and their variation as a function of geometry. NLMOs, as opposed to the more common canonical orbitals,[30] are intuitive as they can be partitioned into contributions that represent bonds, lone pairs, and core orbitals. In this study, the complete one-bond **J**-coupling tensors are computed using the zeroth-order regular approximation (ZORA) DFT method for a series of neutral fluorine-containing compounds covering several valence shell electron pair repulsion (VSEPR) geometries that could yield significant **J** tensor asymmetries. Previous studies of some of these fluorine–X indirect nuclear spin-spin coupling tensors, from Wasylishen and co-workers,[31,32] mostly focused on the performance of the calculations relative to experimental data. In this paper, we focus on determining when large asymmetries and antisymmetric components are to be expected as well as when the assumptions that **J** is axially symmetric and coincident with **D** are well-founded, as the use of these assumptions could lead to a false interpretation of experimental data.[18,19] Additionally, the structures are systematically modified from their gas-phase geometries to see how **J** correlates with these changes, and this information is related to the NLMOs that contribute the most to the coupling.

Computational details

The structural models used for the calculations were built in Gaussview using previously published gas-phase structures. The structures of OF_2,[33] PF_3,[34] PF_5,[35] ClF_3,[36] and BrF_3[37] were determined using microwave spectroscopy. The structure for SF_2 was taken from a previous ab initio study by Irikura[38] in which calculated heats of formation were compared with thermochemical data. The structure of NF_3 was taken from a high level ab initio optimized geometry.[39] The structures of AsF_5,[40] BF_3,[41] AlF_3,[42] and SF_4[43] were determined using electron diffraction, and the structure of BrF_5 was determined by a joint electron diffraction and microwave spectroscopy study.[44] The structure of ClF_5 was determined using a joint Raman and IR spectroscopic analysis,[45] whereas the structures of SeF_4[46] and XeF_4 were determined by IR spectroscopy.[47]

The indirect nuclear spin-spin coupling tensors were calculated using the CPL program,[25,26,48,49] which is part of the Amsterdam density functional (ADF) software package.[50–52] Scalar and SO relativistic effects[53] were included using

Can. J. Chem. Downloaded from www.nrcresearchpress.com by Xi'an Jiaotong University on 09/19/12
For personal use only.

ZORA.[54] In the ZORA formalism, only the sum of the coupling tensors arising from FC, SD, and their cross-term is given. This tensor is reported as FC + SD. All calculations used the same all-electron ZORA triple zeta doubly polarized basis sets (ZORA/TZ2P). The local density approximation (LDA) of Vosko–Wilk–Nusair[55] (VWN) was used along with the generalized gradient approximation (GGA) of Becke88[56] and Perdew86.[57,58] It was shown that the quality of the results improve significantly in pure DFT calculations of **J** when LDA and GGA are implemented in succession.[59,60] The integration keyword was set to 6.0 and an SCF convergence of 10^{-7} was used for the spin-spin coupling calculations. Previous fluorine–X indirect nuclear spin-spin coupling calculations using the same computational methodology produced results in near-quantitative agreement with experiment.[31,32] Recent studies on the calculation of indirect nuclear spin-spin coupling tensors using the ZORA formalism have shown that these approach quantitative agreement with experiment even for heavy atoms.[61]

The calculated data were then analyzed using a modified version of the program EFGShield[62] that was altered to analyze the indirect nuclear spin-spin coupling information from the ADF output files. For the gas-phase geometries, the output files were critically analyzed to select the NLMOs with large contributions to the isotropic J coupling. Only the sum of the Lewis and non-Lewis terms is reported. The natural bonding orbitals (NBOs) and NLMOs[27–29,63] were calculated using NBO 5.0[64] and were visualized using the program adfview from the ADF package.

Results and discussion

The following results are organized in terms of geometry. In general, two compounds of each geometry were selected. The complete **J**-coupling tensor information, including symmetric and antisymmetric tensor components, is organized by coupling mechanism in Tables 1–8. The tensor orientations are reported in terms of two Euler angles (α and β) that describe the relative orientation of the principal axis systems (PAS) of **J** and **D**. The angle β is that between J_{33} and D_{33} (i.e., the bond axis) and α is the angle between J_{11} and the projection of D_{33} onto the plane formed by J_{11} and J_{22}.[65] If β is close to zero, then the assumption that **J** is coincident with **D** is valid. The results from the NLMO analysis are then discussed and are related to the geometry modifications and main coupling mechanisms for each geometry. Only the NLMOs having a contribution to the isotropic coupling constant of at least an order of magnitude larger than the remaining NLMOs were considered. Depictions of these NLMOs, as well as figures plotting the change in ΔJ and η_J as a function of bond angles are included in the Supplementary data. When possible, the calculated isotropic coupling constants are compared with experimental data. In these cases, the sign of the experimental coupling constants is taken from the calculations.

Bent geometry

To study the **J** tensors of bent molecules, the one-bond **J** (^{19}F, ^{17}O) coupling tensor of OF_2 was calculated along with the one-bond **J**(^{33}S, ^{19}F) coupling tensor of SF_2. The results are given in Table 1. Although these molecules are of C_{2v} point symmetry, the symmetry along the bond is C_s, and **J** therefore has five independent components. Even though the isotropic coupling constants are moderate, the anisotropy of **J** is approximately 5 (OF_2) to 12 (SF_2) times larger than J_{iso}. The asymmetry parameters of **J**(X, ^{19}F) in these compounds are fairly large (0.49 and 0.32), which is to be expected as they have low symmetry along the bond. It is also interesting to note that J_{33} is nearly perpendicular to the bond and it is J_{11} that lies nearly along the bond for both OF_2 and SF_2. The one-bond **J**(^{19}F, ^{17}O) coupling tensor for OF_2 was previously calculated using multiconfigurational self-consistent field (MCSCF) methods[66] and similar results were obtained, although the ZORA method yields a larger value for ΔJ. The PSO mechanism is the main contributor to the J coupling for OF_2, but the analogous one-bond coupling in SF_2 is dominated by the FC + SD mechanism. In both cases, the asymmetry of **J** originates almost entirely from the FC + SD cross-term.

Calculations were also carried out using structures in which the bond angle was incremented to determine how **J** responds to these geometry modifications. Figure 1 presents the change in the principal components of **J**(^{19}F, ^{17}O) for OF_2, and it can be seen that the magnitude of the anisotropy and the asymmetry of **J** increase as the bond angle is increased relative to the experimental geometry (Figs. S19 and S20 of the Supplementary data). The fact that the asymmetry of **J** increases with the bond angle in the range of realistic bond angles is consistent with the data for SF_2 (having a bond angle of 99.2° compared with 103.07° for OF_2) in which the **J**-coupling tensor has a smaller asymmetry parameter. The dominance of the PSO mechanism for OF_2 can be rationalized by looking at the NLMOs responsible for the coupling (Fig. 2). The coupling is dominated by p-type lone pairs on the oxygen and fluorines; in the context of Ramsey's equations, these orbitals are expected to largely contribute via the PSO and SD mechanisms. The orbitals responsible for the J coupling in SF_2 have significant s character (Fig. 2), which is consistent with the increased importance of the FC + SD mechanism for the isotropic coupling constant. Even though the anisotropy of **J** for SF_2 is dominated by the PSO mechanism, this cannot be currently explained using the NLMOs, since only their contribution to J_{iso} is given from the calculations. The value of $J(^{17}O, ^{19}F)_{iso}$ in OF_2 is known from solution studies to be (–)300 ± 30 Hz.[67] However, the computational value from this study (–265.6 Hz) is farther away from the experimental value than the previous MCSCF value of –309 Hz.[66]

Trigonal pyramidal geometry

In the case of trigonal pyramidal geometry, the one-bond **J**(^{19}F, ^{14}N) coupling tensor of NF_3 as well as the one-bond **J**(^{31}P, ^{19}F) coupling tensor of PF_3 were calculated. Even though these molecules belong to the C_{3v} point group, the symmetry along the individual bonds is C_s and **J** should have five independent components. The isotropic coupling constants are slightly larger than the anisotropy of **J** in both cases and the FC + SD mechanism dominates the total **J**-coupling tensor in NF_3 (Table 2). In the case of PF_3, the PSO mechanism dominates the anisotropy of **J** with a ΔJ of 547.1 Hz, whereas the FC + SD tensor has a ΔJ of only 196.1 Hz. The experimental isotropic ^{31}P–^{19}F coupling con-

Table 1. One-bond X–^{19}F **J**-coupling tensor parameters of bent compounds.

Compound	Tensor	J_{iso} (Hz)	ΔJ (Hz)	η_J	β (°)	α (°)	$\lvert J_{xz}\rvert$ (Hz)[a]
OF_2	Total	–265.6	–1298.6	0.49	83.2	0	130.1
	DSO	–0.4	–14.2	0.01	0.8	0	0.2
	PSO	–204.3	–1280.4	0.21	84.8	0	99.8
	FC + SD	–60.9	222.0	0.66	18.7	90	30.5
SF_2	Total	–57.4	709.8	0.32	85.2	0	48.0
	DSO	0.1	9.3	0.01	0.4	0	0.1
	PSO	32.6	719.2	0.15	86.2	0	41.3
	FC + SD	–90.1	–69.2	0.99	20.3	90	6.6

Note: $\Delta J = J_{33} - (J_{11} + J_{22})/2$; $\eta_J = (J_{22} - J_{11})/(J_{33} - J_{iso})$; DSO, diamagnetic spin orbital; PSO, paramagnetic spin orbital; FC + SD, Fermi contact and spin dipolar; and α and β, Euler angles.

[a]The antisymmetric tensor components are given in the principal axis system (PAS) of the total **J**-coupling tensor (i.e., the z axis lies along J_{33}, the x axis lies along J_{11}, and the y axis lies perpendicular to the plane of the molecule along J_{22}). Under these conditions, J_{xy} and J_{yz} are forcibly zero.

Table 2. One-bond X–^{19}F **J**-coupling tensor parameters of trigonal pyramidal compounds.

Compound	Tensor	J_{iso} (Hz)	ΔJ (Hz)	η_J	β (°)	α (°)	$\lvert J_{xz}\rvert$ (Hz)[a]	$\lvert J_{yz}\rvert$ (Hz)
NF_3	Total	–164.4	–82.0	0.25	18.5	90	0	1.3
	DSO	0.3	7.4	0.01	1.1	90	0	0.1
	PSO	–20.2	–64.9	0.44	69.7	90	0	2.9
	FC + SD	–144.5	–106.6	0.84	18.3	0	0	1.8
PF_3	Total	–1468.5	521.5	0.41	5.8	0	21.9	0
	DSO	0.9	52.0	0.00	0.5	90	0.4	0
	PSO	–297.7	547.1	0.86	12.0	0	4.9	0
	FC + SD	–1171.7	196.1	0.10	62.0	0	16.5	0

Note: $\Delta J = J_{33} - (J_{11} + J_{22})/2$; $\eta_J = (J_{22} - J_{11})/(J_{33} - J_{iso})$; DSO, diamagnetic spin orbital; PSO, paramagnetic spin orbital; FC + SD, Fermi contact and spin dipolar; and α and β, Euler angles.

[a]The antisymmetric tensor components are given in the principal axis system (PAS) of the total **J**-coupling tensor, where J_{11} and J_{22} are the components perpendicular to the symmetry plane in NF_3 and PF_3, respectively. Under these conditions, J_{xy} is forcibly zero for both compounds, although J_{11} and J_{22} have changed orientations from one compound to the other; therefore, the nonzero antisymmetric component has also changed.

Table 3. One-bond X–^{19}F **J**-coupling tensor parameters of trigonal bipyramidal compounds.

Compound	Tensor	J_{iso} (Hz)	ΔJ (Hz)	η_J[a]	β (°)[b]
PF_5 axial	Total	–1288.7	1231.0	0	0
	DSO	1.8	51.1	0	0
	PSO	–156.5	320.8	0	0
	FC + SD	–1134.0	859.1	0	0
PF_5 equatorial	Total	–1544.8	1419.6	0.28	0
	DSO	1.8	54.9	0.02	0
	PSO	–194.5	409.9	0.95	0
	FC + SD	–1352.1	954.9	0.00	0
AsF_5 axial	Total	–1417.2	1483.8	0	0
	DSO	0.5	39.1	0	0
	PSO	–185.5	403.3	0	0
	FC + SD	–1232.3	1041.5	0	0
AsF_5 equatorial	Total	–1700.4	1498.9	0.18	0
	DSO	0.6	43.0	0.01	0
	PSO	–220.7	510.1	0.54	0
	FC + SD	–1480.3	945.7	0.01	0

Note: $\Delta J = J_{33} - (J_{11} + J_{22})/2$; $\eta_J = (J_{22} - J_{11})/(J_{33} - J_{iso})$; DSO, diamagnetic spin orbital; PSO, paramagnetic spin orbital; FC + SD, Fermi contact and spin dipolar; and β, Euler angle.

[a]The symmetry along the (P, As)–F bonds forces all of the antisymmetric components to be zero.

[b]Since J_{33} is along the bond axis, the Euler angle α is not defined.

Can. J. Chem. Downloaded from www.nrcresearchpress.com by Xi'an Jiaotong University on 09/19/12
For personal use only.

Table 4. One-bond X–^{19}F **J**-coupling tensor parameters of trigonal planar compounds.

Compound	Tensor	J_{iso} (Hz)	ΔJ (Hz)	η_J	β (°)[a]	α (°)[b]
BF_3	Total	–143.5	420.4	0.28	0	N/A
	DSO	1.2	32.1	0.05	0	N/A
	PSO	–40.9	–113.7	0.94	90	0
	FC + SD	–103.8	278.4	0.00	0	N/A
AlF_3	Total	–380.4	966.7	0.12	0	N/A
	DSO	0.4	25.7	0.02	0	N/A
	PSO	–90.4	287.9	0.39	0	N/A
	FC + SD	–290.4	653.1	0.01	0	N/A

Note: $\Delta J = J_{33} - (J_{11} + J_{22})/2$; $\eta_J = (J_{22} - J_{11})/(J_{33} - J_{iso})$; DSO, diamagnetic spin orbital; PSO, paramagnetic spin orbital; FC + SD, Fermi contact and spin dipolar; and α and β, Euler angles.

[a]The symmetry along the (B, Al)–F bonds forces all of the antisymmetric components to be zero.

[b]In cases where J_{33} is along the bond axis, α is not defined.

Table 5. One-bond X–^{19}F **J**-coupling tensor parameters of T-shaped compounds.

Compound	Tensor	J_{iso} (Hz)	ΔJ (Hz)	η_J	β (°)	α (°)	$\lvert J_{xz}\rvert$ (Hz)[a]
ClF_3 axial	Total	203.6	924.9	0.64	87.6	0	152.3
	DSO	0.2	10.9	0.02	0.4	0	0.1
	PSO	–6.6	790.3	0.32	81.1	0	116.7
	FC+SD	210.0	–315.4	0.30	15.2	0	35.7
ClF_3 equatorial	Total	219.8	1041.7	0.40	90	0	0
	DSO	0.2	13.2	0.03	90	0	0
	PSO	246.9	1051.2	0.08	0	N/A	0
	FC + SD	–27.4	174.8	0.97	90	0	0
BrF_3 axial	Total	863.1	4869.9	0.55	87.2	0	818.3
	DSO	0.4	55.6	0.01	0.2	0	0.2
	PSO	–254.6	4393.2	0.28	81.2	0	647.0
	FC + SD	1117.2	–1391.3	0.25	18.1	0	171.6
BrF_3 equatorial	Total	1674.4	5825.3	0.30	90	0	0
	DSO	0.5	65.0	0.01	0	N/A	0
	PSO	1276.1	5928.6	0.01	90	0	0
	FC + SD	397.9	936.1	0.85	90	0	0

Note: $\Delta J = J_{33} - (J_{11} + J_{22})/2$; $\eta_J = (J_{22} - J_{11})/(J_{33} - J_{iso})$; DSO, diamagnetic spin orbital; PSO, paramagnetic spin orbital; FC + SD, Fermi contact and spin dipolar; and α and β, Euler angles.

[a]The antisymmetric tensor components are given in the principal axis system (PAS) of the total **J**-coupling tensor with J_{22} being perpendicular to the plane of the molecule in all cases. For the axial fluorines the only nonzero component of the antisymmetric tensor is J_{xz}, whereas they are all zero for the equatorial fluorine.

stant of –1439 Hz,[68] which was measured in the nematic solvent *N*(*p*-ethoxybenzylidene)-*p*-butylaniline (EBBA), is close to the calculated value of –1468.5 Hz; solvent effects may be partly responsible for the small difference. For both NF_3 and PF_3, J_{33} is oriented at <20° from the bond axis, with the orientation of the other two components changing from one compound to the other. In Fig. 3, the dependence of the principal components of **J**(^{19}F, ^{14}N) on geometry are shown as all three F–N–F bond angles are changed simultaneously while maintaining the C_{3v} point symmetry of the molecule. The anisotropy and asymmetry parameters both depend strongly on geometry, increasing by 12.8% and 48.9%, respectively, following a decrease of the bond angle by only 1.6° from the experimental value (Figs. S21 and S22 of the Supplementary data). Interestingly, if the various contributions are examined, the asymmetry parameters for the PSO and FC + SD tensors are fairly constant with respect to geometrical changes, characterized by standard deviations of 0.03 and 0.05, respectively, but the orientation of the two contributing tensors relative to one another causes a large variation in the total **J**-coupling tensor. A previous computation of **J**(^{31}P, ^{19}F) for PF_3 using the ZORA-DFT method also gave a large asymmetry parameter of 0.876.[32]

For both NF_3 and PF_3, the contributing NLMOs are largely s and σ-type orbitals, which is consistent with a FC-dominated coupling (Figs. S2 and S3 of the Supplementary data). It is interesting to note that there are no symmetry requirements forcing the antisymmetric component J_{yz} to be zero but it remains very small at <2% of the value of the isotropic coupling constants. It is therefore unlikely that one could observe the antisymmetric components of **J** in a trigonal pyramidal compound as one of the requirements given in ref. 19 for the observation of $\mathbf{J}^{antisym}$ is that it must be of the same order of magnitude as that of the symmetric components of **J**.

Trigonal bipyramidal geometry

The one-bond **J**(^{31}P, ^{19}F) coupling tensors of PF_5 as well as the one-bond **J**(^{75}As, ^{19}F) coupling tensors of AsF_5 were studied. The calculated parameters are given in Table 3. These molecules are of D_{3h} symmetry, but the symmetry along the axial bond is C_{3v}. The **J**-coupling tensor between

Can. J. Chem. Downloaded from www.nrcresearchpress.com by Xi'an Jiaotong University on 09/19/12
For personal use only.

Can. J. Chem. Downloaded from www.nrcresearchpress.com by Xi'an Jiaotong University on 09/19/12
For personal use only.

Table 6. One-bond X–^{19}F **J**-coupling tensor parameters of square pyramidal compounds.

Compound	Tensor	J_{iso} (Hz)	ΔJ (Hz)	η_J	β (°)	α (°)[a]	$\lvert J_{xz}\rvert$ (Hz)[b]
ClF_5 axial	Total	–193.8	–233.1	0	0	N/A	0
	DSO	0.4	12.8	0	0	N/A	0
	PSO	–44.1	52.4	0	0	N/A	0
	FC + SD	–150.2	–298.3	0	0	N/A	0
ClF_5 equatorial	Total	120.1	–536.9	0.69	14.5	0	5.4
	DSO	0.3	10.6	0.01	0.4	90	0.1
	PSO	–68.7	120.9	0.13	22.3	0	37.8
	FC + SD	188.5	–607.8	0.54	9.4	0	32.4
BrF_5 axial	Total	–1063.8	261.2	0	0	N/A	0
	DSO	0.8	68.2	0	0	N/A	0
	PSO	–346.8	578.8	0	0	N/A	0
	FC + SD	–717.8	–385.8	0	0	N/A	0
BrF_5 equatorial	Total	375.6	–1604.1	0.55	12.6	0	42.1
	DSO	0.8	60.1	0.00	0.2	90	0.3
	PSO	–441.3	781.9	0.50	15.8	0	163.9
	FC + SD	816.1	–2224.2	0.47	3.7	0	122.1

Note: $\Delta J = J_{33} - (J_{11} + J_{22})/2$; $\eta_J = (J_{22} - J_{11})/(J_{33} - J_{iso})$; DSO, diamagnetic spin orbital; PSO, paramagnetic spin orbital; FC + SD, Fermi contact and spin dipolar; and α and β, Euler angles.

[a]When J_{33} is along the bond axis, the angle α is not defined.

[b]The antisymmetric tensor components are given in the principal axis system (PAS) of the total **J**-coupling tensor. For the equatorial coupling tensors, J_{33} is oriented along the X–F_{eq} bond vector and J_{11} is oriented along the X–F_{ax} bond vector. For the equatorial fluorines the only nonzero component of the antisymmetric tensor is J_{xz}, whereas they are all zero for the axial fluorine.

Table 7. One-bond X–^{19}F **J**-coupling tensor parameters of seesaw compounds.

Compound	Tensor	J_{iso} (Hz)	ΔJ (Hz)	η_J	β (°)	α (°)	$\lvert J_{xz}\rvert$ (Hz)[a]	$\lvert J_{yz}\rvert$ (Hz)
SF_4 axial	Total	–97.7	–185.8	0.08	15.1	0	31.2	0
	DSO	0.2	9.0	0.01	0.5	90	0.1	0
	PSO	–50.4	–131.6	0.10	66.1	0	40.2	0
	FC + SD	–47.6	–214.4	0.71	0.5	0	9.1	0
SF_4 equatorial	Total	–339.3	83.1	0.47	59.7	90	0	4.5
	DSO	0.3	10.9	0.02	0.4	90	0	0.1
	PSO	–55.6	93.3	0.57	11.1	90	0	1.5
	FC + SD	–283.9	–118.6	0.70	19.0	0	0	2.9
SeF_4 axial	Total	–210.7	–616.6	0.31	27.3	0	127.0	0
	DSO	0.4	40.6	0.00	0.3	90	0.2	0
	PSO	–360.0	–709.5	0.89	73.2	0	165.6	0
	FC + SD	148.9	–998.1	0.62	1.1	0	38.8	0
SeF_4 equatorial	Total	–1027.3	365.6	0.76	59.5	90	0	17.4
	DSO	0.4	47.6	0.01	0.2	90	0	0.1
	PSO	–355.1	661.7	0.56	6.8	90	0	6.5
	FC + SD	–672.7	–702.8	0.38	13.7	0	0	10.8

Note: $\Delta J = J_{33} - (J_{11} + J_{22})/2$; $\eta_J = (J_{22} - J_{11})/(J_{33} - J_{iso})$; DSO, diamagnetic spin orbital; PSO, paramagnetic spin orbital; FC + SD, Fermi contact and spin dipolar; and α and β, Euler angles.

[a]The antisymmetric tensor components are given in the principal axis system (PAS) of the total **J**-coupling tensor. For the equatorial sites in both molecules J_{11} is oriented perpendicular to the symmetry plane, and in the case of the axial sites J_{22} is the component perpendicular to the relevant symmetry plane. In all these cases, J_{xy} was forcibly zero.

each of the axial fluorines and the central atom should therefore have two independent **J**-coupling tensor components, whereas coupling to the equatorial fluorines would have three, as there is C_{2v} symmetry along these bonds. $\mathbf{J}^{antisym}$ must be null for all fluorine sites and J_{33} must be oriented along the bond. The asymmetry parameter of the **J**-coupling tensor between the central atom and the axial fluorine must also be null because of the C_{3v} symmetry.[20] In both cases it can be seen that the FC + SD mechanism dominates the isotropic J coupling, although the asymmetry in **J** for the equatorial sites originates almost entirely from the PSO mechanism. Only the average experimental one-bond isotropic coupling constant of PF_5 is known at (–)929 ± 1 Hz, which was measured in a gas-phase study.[69] This value is smaller than the calculated average isotropic coupling constant of –1442.4 Hz, which was noted previously by Feindel and Wasylishen[32] using the same computational method. The use of large basis sets with a high exponent in the core region could perhaps improve the calculations.[70] The F_{eq}–P–F_{ax} bond angles in PF_5 were varied to move the equatorial fluorines towards the axial sites while maintaining C_{3v} point symmetry for the molecule (Fig. 4). Figure 4 shows that the

Can. J. Chem. Downloaded from www.nrcresearchpress.com by Xi'an Jiaotong University on 09/19/12
For personal use only.

Table 8. One-bond ^{129}Xe–^{19}F **J**-coupling tensor parameters of XeF_4.

Tensor	J_{iso} (Hz)	ΔJ (Hz)	η_J	β (°)[a]	α (°)[b]
Total	–3279.2	–5295.5	0.11	90	0
DSO	–0.4	–81.9	0.01	0	N/A
PSO	–229.3	–5615.2	0.05	90	90
FC + SD	–3049.4	–643.1	0.13	90	0

Note: $\Delta J = J_{33} - (J_{11} + J_{22})/2$; $\eta_J = (J_{22} - J_{11})/(J_{33} - J_{iso})$; DSO, diamagnetic spin orbital; PSO, paramagnetic spin orbital; FC + SD, Fermi contact and spin dipolar; and α and β, Euler angles.

[a]When J_{33} is along the bond axis, the angle α is not defined.

[b]The symmetry along the Xe–F bond forces all of the antisymmetric components to be zero.

Fig. 1. Tensor components of the one-bond **J**(^{19}F, ^{17}O) coupling tensor of OF_2 as a function of the bond angle. The experimental bond angle is 103.07°.[33]

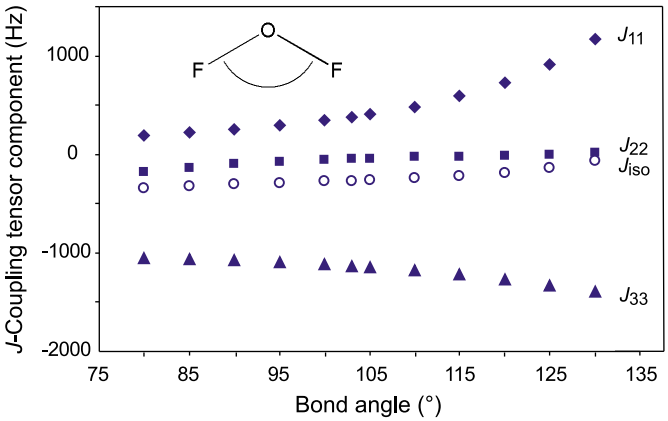

J(^{31}P, $^{19}F_{eq}$) coupling tensor parameters did not change substantially (Figs. S24 and S25 of the Supplementary data), but both the isotropic coupling constant and the anisotropy of **J**(^{31}P, $^{19}F_{ax}$) dramatically increased as the F_{ax}–P–F_{eq} bond angles were increased (Fig. S23 of the Supplementary data). The important NLMOs for the isotropic coupling constant seem to be a σ-bonding orbital, a lone pair on the fluorine atom, and a core orbital on the fluorine atom (Fig. S4 of the Supplementary data). The large change in J_{iso} as the F_{ax}–P–F_{eq} bond angles increase can be attributed to both the bonding orbital between phosphorus and the axial fluorine and the lone pair on the coupled fluorine, since the contributions to J_{iso} from these become more negative as the bond angle is increased. In the case of AsF_5, the bonding orbital between the two coupled nuclei is less important when compared with PF_5, and the bonding orbitals between the arsenic and fluorine atoms *not* directly implicated in the coupling become important (Figs. S6 and S7 of the Supplementary data). These orbitals extend farther out in space than those in PF_5 and give significant contributions to J_{iso}.

Trigonal planar geometry

In the case of trigonal planar geometry, the one-bond **J**(^{19}F, ^{11}B) tensor of BF_3 was calculated along with the one-bond **J**(^{27}Al, ^{19}F) tensor of AlF_3. Whereas these molecules have D_{3h} point symmetry, the symmetry along each bond is C_{2v}, forcing **J** to only have three independent tensor components. In both cases, the computed isotropic coupling constants of –143.5 and –380.4 Hz for BF_3 and AlF_3, respectively, are relatively small, and the anisotropy and asymmetry parameters are moderate: 420.4 Hz and 0.28, respectively, for BF_3. The antisymmetric components of **J** are all zero in this case because of the two mirror planes going through the bond axis.[20] Several geometry modifications were performed such as varying a single bond angle or

Fig. 2. Natural localized molecular orbitals (NLMOs) having the largest contributions to the isotropic oxygen–fluorine and sulfur–fluorine nuclear spin-spin coupling constants of OF_2 and SF_2, respectively. The percentage above the orbitals represents their contributions to the isotropic *J*-coupling constant.

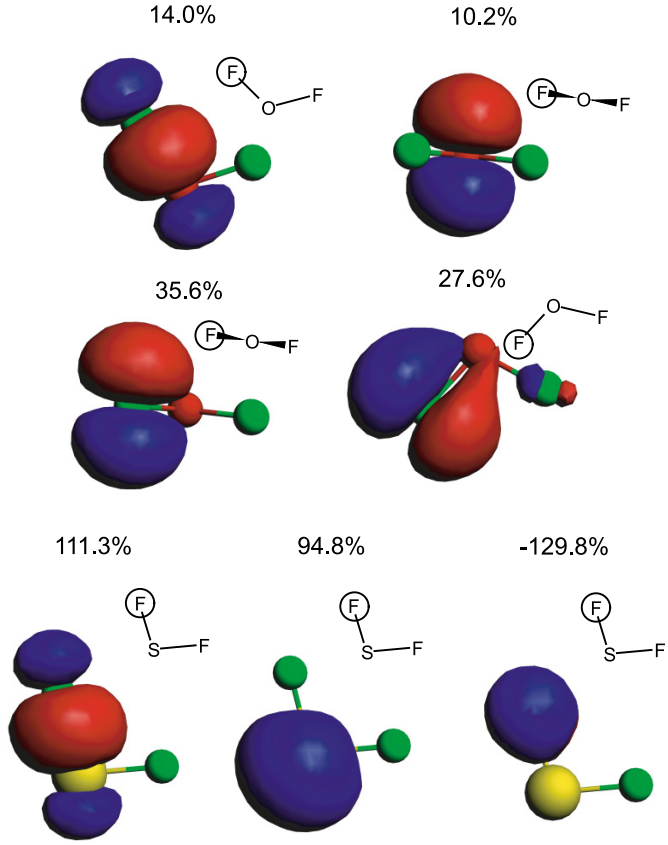

Fig. 3. Tensor components of the one-bond **J**(^{19}F, ^{14}N) coupling tensor of NF_3 as the bond angles are changed. All three angles are changed simultaneously to maintain the C_{3v} point symmetry of the molecule. The experimental bond angles are 101.6°.[39]

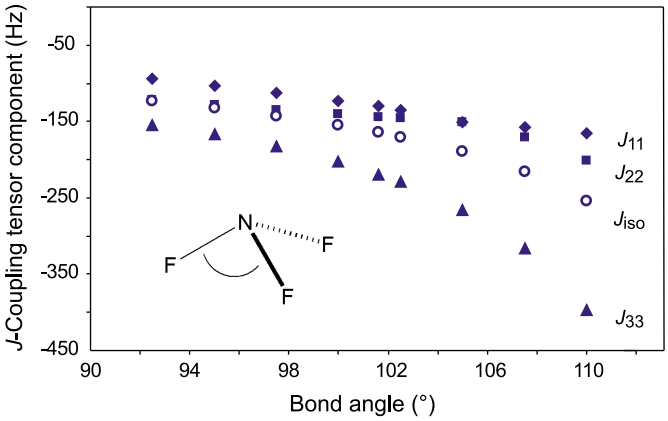

Can. J. Chem. Downloaded from www.nrcresearchpress.com by Xi'an Jiaotong University on 09/19/12
For personal use only.

Fig. 4. Tensor components of the one-bond **J**(^{31}P, ^{19}F) coupling tensors of PF_5 as a function bond angle. All three bond angles are changed simultaneously to maintain a C_{3v} point symmetry for this molecule. The solid symbol data points correspond to the **J**-coupling tensor components for the coupling to the axial fluorines, whereas the open symbol data points correspond to the tensor components for the coupling to the equatorial fluorines. The bond angles in the experimental geometry are 90°.[35]

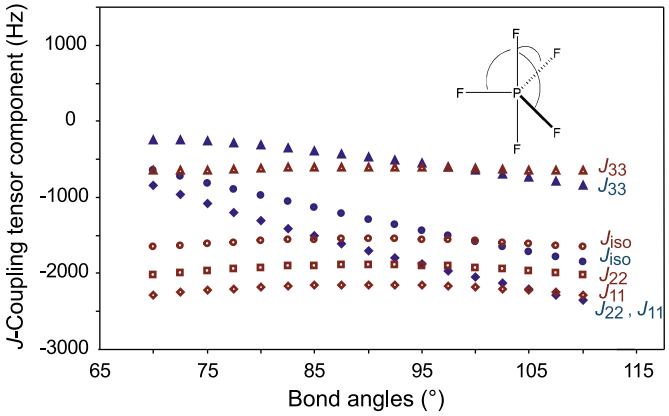

bending the fluorine atoms downwards while maintaining C_{3v} symmetry. The **J** tensor parameters remained relatively constant: the isotropic coupling constant changed by only 2.7 Hz after a bond angle was modified by 15°, which is consistent with the observation made in the case of the equatorial fluorines in PF_5. Again, the PSO mechanism dominates the asymmetry of **J**, but the magnitude of the total **J**-coupling tensor originates largely from the FC + SD mechanism, which is consistent with the picture provided by the most significant NLMOs that are of s type (Figs. S8 and S9 of the Supplementary data). In this case, as well, the PSO contribution is stronger for the heavier analogue, but the asymmetry parameter of the PSO tensor is smaller. These findings suggest that **J**-coupling tensor parameters for trigonal planar molecules could be more likely to agree with experimental data than other geometries, since they would be less sensitive to small deficiencies in the molecular structure and to molecular vibrations. However, Jackowski et al.[71] studied the ^{19}F–^{11}B indirect nuclear spin-spin coupling constant of BF_3 in the gas phase at various temperatures and pressures, from which an isotropic coupling constant of 16.4 Hz at zero pressure and 300 K could be extracted. This experimental value differs greatly from our calculated value of –143.5 Hz. Since FC is often the dominating coupling mechanism for the elements located in the first groups of the periodic table,[72] the use of basis sets optimized for *J* coupling would likely improve the computed value. Using the ZORA/QZ4P basis set, the anisotropy and asymmetry parameter values remained essentially constant (within 2.5%), although the magnitude of the isotropic coupling constant decreased by 35%, solely because of a change in the FC + SD tensor. Jackowski et al.[71] calculated an isotropic coupling constant of 19.277 Hz at the CCSD/TZsu3+2p1d level of theory. Still, a non-negligible discrepancy of 15% remains between the experimental value and their computed value, particularly given that the experimental value has been extrapolated to zero pressure. They emphasized the importance of the choice of basis set for the calculation of the FC contribution, although the PSO and DSO contributions were not sensitive to the choice of basis set and those values previously calculated are very similar to the values reported here. As ΔJ, η_J, and $\mathbf{J}^{antisym}$ do not depend on the pure Fermi-contact mechanism, these ZORA values are likely much more accurate than our computed value of J_{iso}.

T-shaped molecules

The one-bond **J**(^{35}Cl, ^{19}F) and **J**(^{81}Br, ^{19}F) coupling tensors were calculated for ClF_3 and BrF_3, respectively, and the data are summarized in Table 5. The symmetry along the equatorial bond is C_{2v} and therefore the **J**-coupling tensor between the equatorial fluorine and the central atom can have up to three independent components, whereas the axial fluorines may have five independent components, since the bond symmetry is C_s. In these compounds, for both the equatorial and axial sites, the anisotropy is three to six times larger than the isotropic coupling constant. The asymmetry parameter is also fairly large, ranging from 0.30 to 0.64. For the axial fluorines, the isotropic coupling constant is dominated by the FC + SD mechanism, whereas the PSO mechanism is the source of the sizeable anisotropy. In the case of the equatorial sites, PSO dominates both the isotropic coupling constant and the anisotropy, although FC + SD remains important and is the principal source of the asymmetry of **J**. The average isotropic *J*-coupling constant is known to be (+)260 Hz for liquid ClF_3.[73] The calculated isotropic *J*-coupling constant for ClF_3 from this study is in better agreement with the experimental data than the previous MCSCF study,[66] and is very similar to previous ZORA-DFT results.[31] The NLMO analysis reveals that the orbitals primarily responsible for the coupling, in all cases, are lone pairs on both the chlorine and the fluorine. In the case of the equatorial site, these orbitals resemble p orbitals, which explains the importance of the PSO mechanism, although the important NLMOs for BrF_3 are mostly s-type orbitals (Fig. 5; Figs. S11 and S12 of the Supplementary data). It is also important to note that J_{33} lies perpendicular to the bond, which is in agreement with previous computational studies of **J** for ClF_3 and BrF_3.[31,66] It is again noted that the non-Lewis terms from the NLMOs become more important with the larger atomic number as the lone-pair orbitals responsible for the coupling extend farther out in space. Interestingly, large antisymmetric tensor components of 152.3 and 818.3 Hz were calculated for the axial fluorines in ClF_3 and BrF_3, respectively (i.e., of the same order of magnitude as the isotropic *J*-coupling constant).

The F_{ax}–Cl–F_{eq} bond angles were incremented (Fig. S26 of the Supplementary data), but the tensor parameters for the axial site remained fairly constant: the isotropic coupling constant changed by only 4% after an increase of 10° in the bond angles (also see Figs. S27 and S28 of the Supplementary data). In the case of the equatorial F, both ΔJ and η_J increased as the bond angles were increased (Figs. S29 and S30 of the Supplementary data). It was also noticed that as the bonds were lengthened, both the anisotropy and the isotropic coupling constant increased.

Square pyramidal geometry

The one-bond **J**(^{35}Cl, ^{19}F) tensors of ClF_5 and the one-bond **J**(^{81}Br, ^{19}F) tensors of BrF_5 were calculated and are

Can. J. Chem. Downloaded from www.nrcresearchpress.com by Xi'an Jiaotong University on 09/19/12
For personal use only.

Fig. 5. Natural localized molecular orbitals (NLMOs) having the largest contributions to the isotropic chlorine–fluorine nuclear spin-spin coupling constant of ClF_3 for the axial fluorine (top) and the equatorial fluorine (bottom). The percentages above the orbitals represent their contributions to the isotropic *J*-coupling constant.

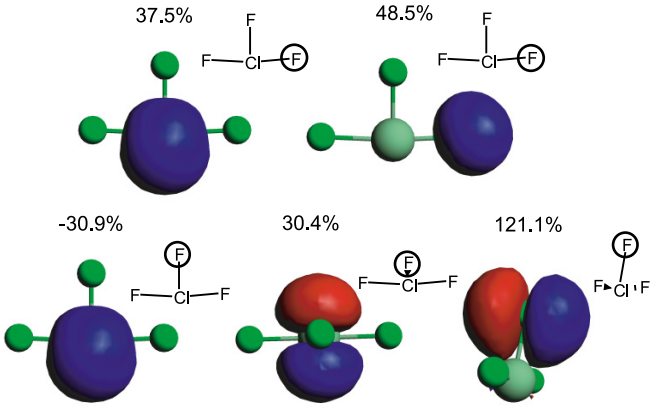

given in Table 6. Both these molecules, as well as the axial bonds, have C_{4v} symmetry; hence, the **J**-coupling tensor to the axial fluorine has two independent components, the asymmetry parameter is forcibly zero, and J_{33} orients along the bond. The **J**-coupling tensor between the central atom and each of the equatorial fluorines has five independent tensor components, as the symmetry along this bond is C_s. The ratio $\Delta J/J_{iso}$ for the axial fluorines is small when compared with the T-shaped molecules. In the case of the equatorial sites, the isotropic *J* couplings to the central atom (120.1 and 375.6 Hz for ClF_5 and BrF_5, respectively) are small when compared with the axial site and the T-shaped compounds discussed earlier. The anisotropy of **J** for the equatorial sites is, however, large when compared with the isotropic coupling constants, and J_{xz} remains small (5.4 and 42.1 Hz for ClF_5 and BrF_5, respectively).

The experimental isotropic $^{35}Cl–^{19}F_{ax}$ *J*-coupling constant was measured to be (–)192 Hz in liquid ClF_5, whereas the isotropic $^{35}Cl–^{19}F_{eq}$ *J*-coupling constant was estimated to be smaller than 20 Hz.[73] The calculated value of –193.8 Hz for the isotropic $^{35}Cl–^{19}F_{ax}$ *J*-coupling constant is in excellent agreement with the experimental value, whereas the calculated isotropic coupling constant to the equatorial fluorines (120.1 Hz) is much larger than experiment. A previous ZORA-DFT study of the **J**-coupling tensor of ClF_5 using the triple-polarized ADF ZORA V basis set predicted a much larger value for $J(^{35}Cl–^{19}F_{ax})_{iso}$ of –276 Hz, and a smaller value for $J(^{35}Cl–^{19}F_{eq})_{iso}$ of 69 Hz.[31] The FC + SD tensor does dominate **J**, although the PSO contribution is not negligible and the addition of the two tensors contributes to the nonzero asymmetry parameter of the total **J**-coupling tensor. From the plots in Fig. 6, which show the progression of the tensor components as the $F_{ax}–Cl–F_{eq}$ bond angles are changed (while maintaining the C_{4v} point symmetry of the molecule), it can be seen that the tensor components for both sites are extremely sensitive to those bond angles. J_{33} remains close to the bond (within 20°) as the angles are varied until it exchanges orientation with J_{11} when the bond angles are >95°. These large variations can be qualitatively understood by considering the contributions from the NLMOs. In the case of the coupling between chlorine and the axial fluorine, the bonding orbitals between the equatorial fluorines and the chlorine as well as the lone pairs on the equatorial fluorines contribute significantly to the coupling. The important NLMOs for the coupling between the axial fluorine and the chlorine are shown in Fig. 7. The change of J_{iso} owing to the contributions from all six important NLMOs can also be calculated and is outlined presently.

In Fig. 8, the one-bond $^{35}Cl–^{19}F_{ax}$ isotropic coupling constants owing to each NLMO are plotted as the bond angle is changed. The contributions to J_{iso} from most orbitals change in a similar fashion as the bond angle is increased. This change reflects the way J_{33} changes as the bond angle is increased, although the sign of the coupling varies. Overall, many of the contributions from the different NLMOs nearly cancel one another, and the behaviour of the isotropic *J*-coupling constant for the $^{35}Cl–^{19}F_{ax}$ spin pair is dominated by the s-type lone pair orbital on the chlorine.

For square pyramidal molecules, it is then expected that the calculation of **J**-coupling tensors would be particularly sensitive to geometry and to vibrational effects, as, for example, even a decrease of the bond angles by 5° relative to the experimental geometry causes a change in the asymmetry parameter of 0.33 and a decrease in ΔJ of 24.5% in the case of the $^{35}Cl–^{19}F_{eq}$ spin pair (Figs. S31–S33 of the Supplementary data).

Seesaw geometry

When considering the seesaw geometry, the one-bond $\mathbf{J}(^{33}S, ^{19}F)$ tensors of SF_4, as well as the one-bond $\mathbf{J}(^{77}Se, ^{19}F)$ coupling tensors of SeF_4, were calculated, and the data are given in Table 7. These molecules have C_{2v} symmetry, two nonequivalent fluorine sites, and the one-bond **J**-coupling tensors are restricted to five independent components for both sites as there is C_s symmetry along both bonds. In these cases, both sites are very different: the axial sites have small isotropic *J*-coupling constants (–97.7 Hz for SF_4 and –210.7 Hz for SeF_4), slightly larger ΔJ (–185.8 for SF_4 and 616.6 Hz for SeF_4), and antisymmetric **J** tensor components of the same order of magnitude as J_{iso}. The equatorial sites, on the other hand, have relatively large isotropic *J*-coupling constants (–339.3 Hz for SF_4 and –1027.3 Hz for SeF_4), but small values for ΔJ (83.1 Hz for SF_4 and 365.6 Hz for SeF_4) and $\mathbf{J}^{antisym}$ (4.5 Hz for SF_4 and 17.4 Hz for SeF_4). In all cases, contributions from the FC + SD and PSO mechanisms to the total **J**-coupling tensor are of the same order of magnitude, which is consistent with the fact that the important NLMOs have both s and p character (Figs. S15–S18 of the Supplementary data). It is important to note that the orientation of J_{33} does not appear to be reflective of any particular geometric feature (but its orientation remains constant from one compound to the other with β at 59.7° and 59.5° for the equatorial sites and 15.1° and 27.3° for the axial sites in SF_4 and SeF_4, respectively), whereas J_{11} has a predictable orientation perpendicular to the mirror plane. The small isotropic *J*-coupling constants in the case of the axial fluorines can be explained as follows: although many NLMOs contribute to the coupling, their contributions are of opposite signs and hence largely cancel one another. In the case of SeF_4, as the orbitals extend farther out in space, there are then more orbitals to contribute to the coupling, making the reduced coupling

Can. J. Chem. Downloaded from www.nrcresearchpress.com by Xi'an Jiaotong University on 09/19/12
For personal use only.

Fig. 6. Tensor components of the one-bond **J**(^{35}Cl, ^{19}F) coupling tensors of ClF_5 as a function of bond angle. These bond angles are changed simultaneously while maintaining a C_{4v} point symmetry for the molecule. The solid symbol data points correspond to the **J**-coupling tensor components for the coupling to the axial fluorine, whereas the open symbol data points correspond to the **J** tensor components for the coupling to the equatorial fluorines. The experimental bond angles are 90°.[45]

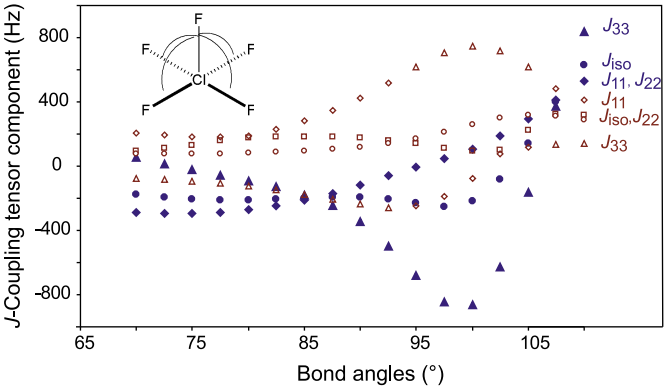

Fig. 7. Natural localized molecular orbitals (NLMOs) having the largest contributions to the isotropic chlorine–fluorine nuclear spin-spin coupling constant of ClF_5 (axial fluorine). The percentage above the orbitals represents their contributions to the isotropic *J*-coupling constant.

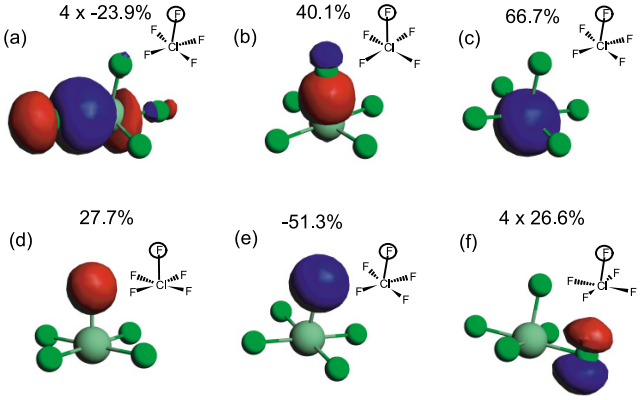

constant of -47.5×10^{20} N A^{-2} m^{-3} in SeF_4 larger in comparison with the reduced coupling constant of -39.1×10^{20} N A^{-2} m^{-3} in SF_4. This effect is consistent with the periodic trend that the reduced coupling constants become larger as the atomic number increases.[23,74] In Fig. 9, the principal components of **J**(^{33}S, ^{19}F) are shown as the axial bond angle is increased. The magnitude of the anisotropy for the axial site increases as the bond angle is increased (Fig. S35 of the Supplementary data), whereas it remains constant within 2.5 Hz in the case of the equatorial site (Fig. S37 of the Supplementary data). The asymmetry parameters for the axial and equatorial sites increase and decrease, respectively (Figs. S36 and S38 of the Supplementary data) with increasing bond angle. If we look at the separate contributions from the PSO and FC + SD mechanisms, we can see that the asymmetry parameters are fairly constant as the bond angle is changed, having standard deviations of 0.02 and 0.01, respectively (Fig. S36 of the Supplementary data), but the relative

Fig. 8. Variation of the contributions from various natural localized molecular orbitals (NLMOs) to the total ^{35}Cl–^{19}F$_{ax}$ isotropic *J*-coupling constant as the bond angles noted in Fig. 6 are changed. The orbitals shown are (*a*) the orbitals a (◆), the orbital b (▲), and the orbital c (■) from Fig. 7; (*b*) the orbital d (◆), the orbital e (▲), and the orbital f (■) from Fig. 7; and (*c*) the orbital c from Fig. 7 (◆), the sum of all other contributions (■), and the total isotropic coupling constants (▲).

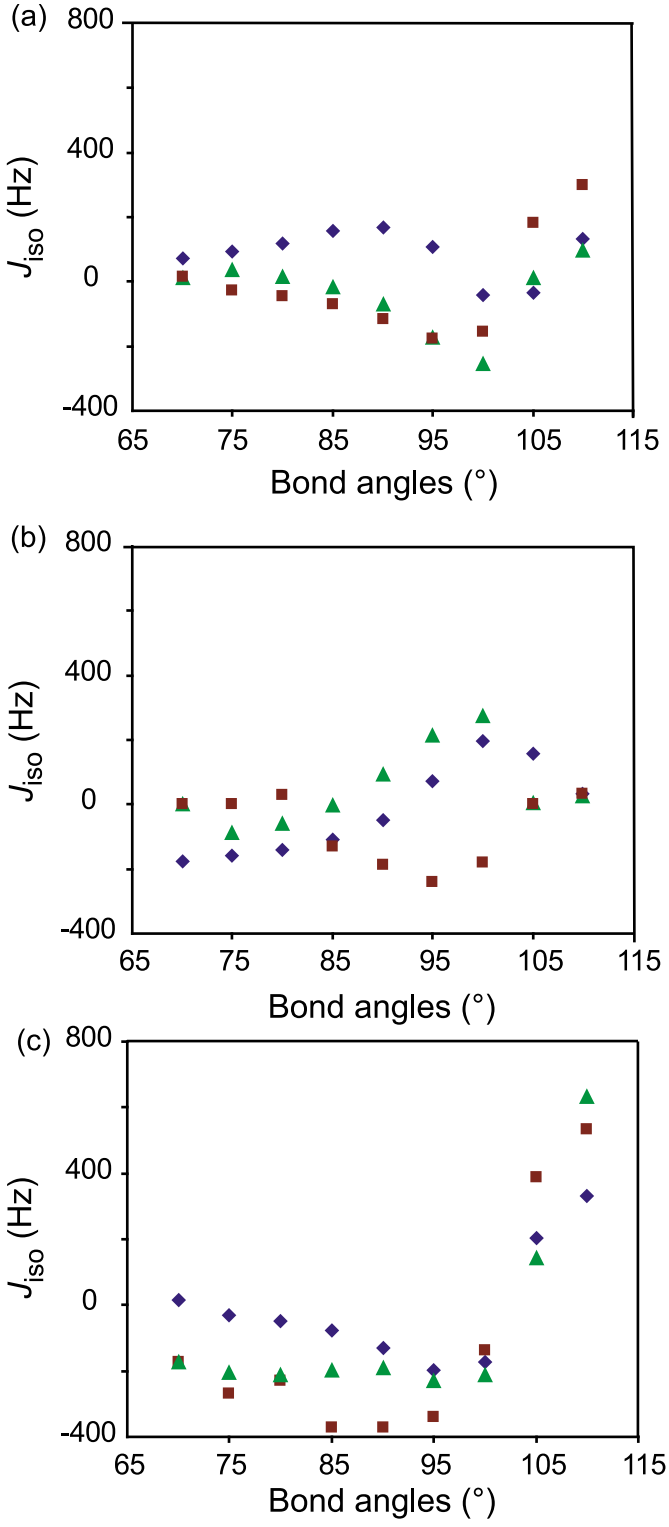

Can. J. Chem. Downloaded from www.nrcresearchpress.com by Xi'an Jiaotong University on 09/19/12
For personal use only.

Fig. 9. Tensor components of the one-bond **J**(^{33}S, ^{19}F) coupling tensors of SF_4 as a function of the axial bond angle shown in the top left corner. The solid symbol data points correspond to the **J**-coupling tensor components for the coupling to the equatorial fluorine, whereas the open symbol data points correspond to the tensor components for the coupling to the axial fluorines. The experimental bond angle is 176.8°.[43]

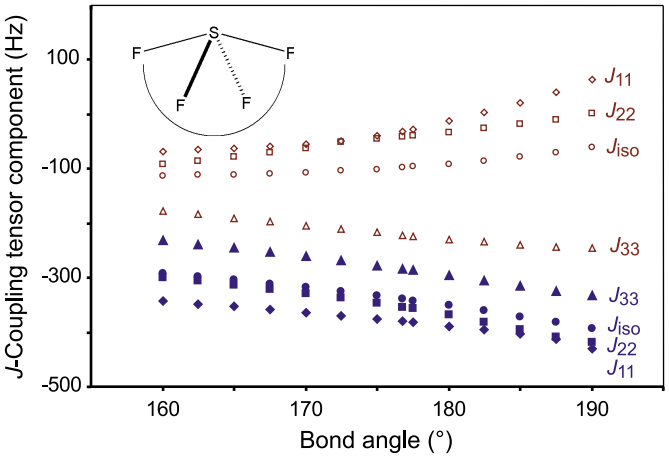

Fig. 10. Tensor components of the one-bond **J**(^{33}S, ^{19}F) coupling tensors of SF_4 as a function of the equatorial bond angle shown in the bottom left corner. The solid symbol data points correspond to the **J**-coupling tensor components for the coupling to the equatorial fluorine, whereas the open symbol data points correspond to the tensor components for the coupling to the axial fluorines. The experimental bond angle is 103.8°.[43]

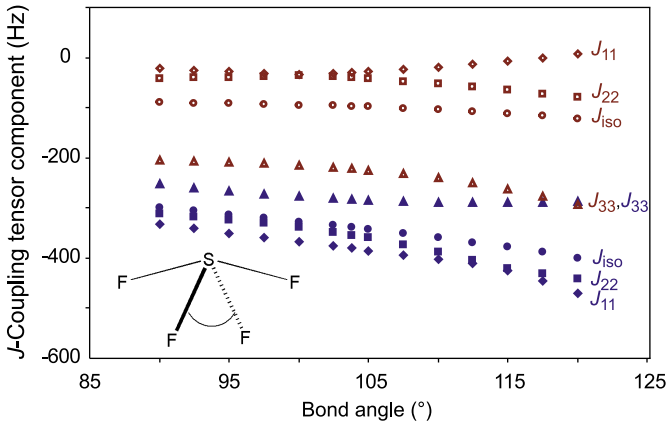

orientation of the two tensors varies, which in turn causes large variations in the asymmetry parameter of the total **J**-coupling tensor. The magnitude of the anisotropy becomes larger as the equatorial bond angle is increased for both sites (Fig. 10 and Figs. S39 and S41 of the Supplementary data). The asymmetry parameters of the PSO and FC + SD tensors for the equatorial fluorine atoms vary by only 0.3 as the equatorial bond angle is changed from 90° to 120° (Fig. S42 of the Supplementary data), although the total **J**-coupling tensor's asymmetry parameter varies significantly from 0.6 to 0 because the relative orientation of the two tensors changes. In the case of the axial sites, the asymmetry originates from the PSO term, whereas the FC + SD tensor has a relatively constant asymmetry parameter as the bond angle is varied, having a standard deviation of 0.006 over the range shown in Fig. S40 of the Supplementary data.

From solution NMR studies, the experimental ^{77}Se–^{19}F isotropic *J*-coupling constants are known to be (–)284 Hz for the axial fluorine and (–)1206 Hz for the equatorial fluorine.[75] These values are close to the values calculated here, which are –210.7 and –1027.3 Hz, respectively, but both coupling constants are underestimated.

Square planar geometry

For square planar geometry, the one-bond **J**(^{129}Xe, ^{19}F) coupling tensor of XeF_4 was studied. The symmetry along the Xe–F bond is C_{2v}, which restricts the number of allowed **J**-coupling tensor components to three.[20] The calculated **J** tensor parameters are given in Table 8. Interestingly, the computed isotropic *J*-coupling constant of –3279.2 Hz is mostly dominated by the FC + SD mechanism, although the anisotropy is dominated by the PSO mechanism. Multiple experimental values, ranging from (–)3801 to (–)3913 Hz have been published for the isotropic ^{129}Xe–^{19}F *J*-coupling constant of XeF_4,[76–80] which is solvent dependent. A previous ZORA-DFT study using the triple-polarized ADF ZORA V basis sets reported an isotropic coupling constant of –3925 Hz.[31] The responsible NLMOs in this case are shown in Fig. 11, and it is noticed that the largest contributions to the isotropic *J*-coupling constant are from s-type orbitals, which is consistent with a FC dominated coupling. Xenon is the heaviest element in this study, and a larger number of NLMOs have important contributions to the coupling: the six largest contributions noted here account for 87.8% of the total isotropic *J*-coupling constant. In the case of heavier elements, the orbitals extend farther out in space and therefore more orbitals have important contributions to the coupling.

To probe how sensitive the indirect nuclear spin-spin coupling tensor in XeF_4 is to geometrical changes, two opposite bond angles were changed simultaneously so as to maintain D_{2h} symmetry for the molecule. The variation in the tensor components as those angles are changed is shown in Fig. 12. The anisotropy remains fairly constant as the bond angles are changed, decreasing in magnitude by only 8% after a change of 20° in the bond angles, and the asymmetry parameter remains fairly small and ranges from 0.1 to 0.3. This is in agreement with the good fits obtained in the measurement of $\Delta J(^{31}P–^{195}Pt)$ in platinum–phosphine complexes using the approximations that **J** is axially symmetric and coincident with **D**.[81] This comparison is relevant because the platinum–phosphine complexes in that study have an approximate square planar geometry at the platinum site and a tetrahedral geometry at the phosphorus site.

Conclusions

The complete one-bond fluorine–X **J**-coupling tensors for a series of neutral fluorinated compounds belonging to several VSEPR geometry classes were calculated. It was noted that the tensor orientations for various molecules of the same geometry remain nearly identical, although in many cases J_{33} was not the tensor component closest to the internuclear bond vector. J_{33} remained nearly perpendicular to the bond vector in bent and T-shaped molecules, and was 59.7° and 59.5° from the bond vector for the equatorial sites and 15.1°

Fig. 11. Natural localized molecular orbitals (NLMOs) having the largest contributions to the isotropic xenon–fluorine nuclear spin-spin coupling constant of XeF_4. The percentage above the orbitals represents their contributions to the isotropic *J*-coupling constant.

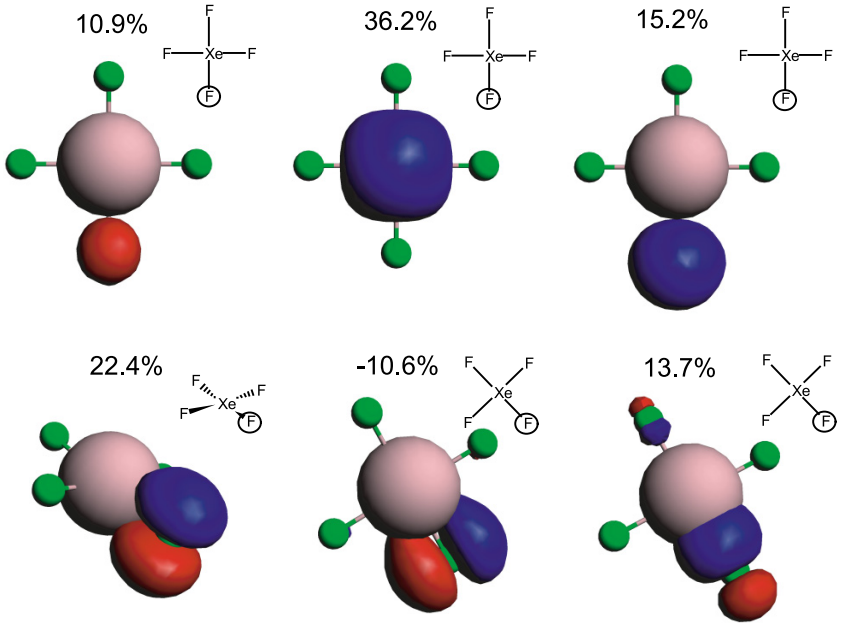

Fig. 12. Components of the one-bond $\mathbf{J}(^{129}Xe, ^{19}F)$ coupling tensors of XeF_4 as a function of the opposite bond angles. The two angles are changed simultaneously so as to maintain a D_{2h} point symmetry for the molecule. The experimental bond angle is 90°.[47]

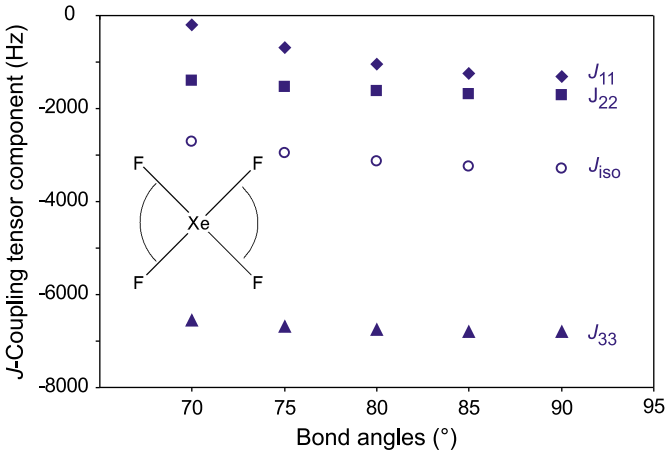

and 27.3° from the bond vector for the axial sites in SF_4 and SeF_4, respectively. In all other systems, **J** was nearly coincident with **D**. The use of NLMOs to filter the isotropic *J*-coupling constants in terms of their contributions from bonds and lone pairs proved to be useful in understanding the dominance of the PSO mechanism for bent, T-shaped, and seesaw molecules in which lone pairs in the form of p-like orbitals contributed significantly to the isotropic *J*-coupling constants.

It was also noted that when *J* coupling involved heavier atoms, a greater number of NLMOs contribute to J_{iso}. This is a result of these orbitals extending farther out in space and having larger non-Lewis contributions to J_{iso}. It could be pinpointed that the variations of $\mathbf{J}(^{35}Cl, ^{19}F_{ax})$ as the F_{ax}–Cl–F_{eq} bond angles were augmented were largely because of the s-type lone pair orbital on the chlorine, instead of the orbitals involving fluorine.

Assumptions that **J** is both coincident with **D** and axially symmetric are only truly valid in cases of near axial symmetry along the bond, as seen in mercury– and platinum–phosphine complexes.[18,81–86] Sizeable asymmetries were calculated for bent, trigonal pyramidal, T-shaped, and square pyramidal molecules. In other systems, the asymmetry parameter of **J** was fairly small and would therefore not greatly affect the NMR spectrum. It was determined that for bent molecules, the equatorial sites of T-shaped molecules, and square planar molecules the asymmetry originated from the FC + SD tensor, even though the anisotropy of **J** was dominated by the PSO mechanism. Conversely, in the case of trigonal planar and trigonal bipyramidal molecules, the anisotropy originated from the FC + SD mechanism, but the asymmetry of **J** largely depended on the PSO mechanism. In all other cases, both the FC + SD and the PSO mechanisms contributed to the anisotropy, but the asymmetry arose from the addition of the various tensors. Thus, in cases where many mechanisms contribute significantly to **J**, there can be an increase in the asymmetry because of the different orientations of multiple contributing tensor PASs.

Finally, large antisymmetric components were predicted only for particular *J*-coupling tensors in bent, T-shaped, and seesaw molecules. A successful experimental observation of $\mathbf{J}^{antisym}$ would then likely benefit from a spin pair in one of these geometries. The consistency of the calculated **J**-coupling tensor parameters and orientations when going from one system to another of the same geometry (e.g., ClF_3 to BrF_3) suggests that computational methods serve as valuable tools to assist in the experimental characterization of **J** for systems without approximate C_n (with $n > 2$) symmetry along the bond.

Supplementary data

Supplementary data (images of the most important NLMO

Can. J. Chem. Downloaded from www.nrcresearchpress.com by Xi'an Jiaotong University on 09/19/12
For personal use only.

contributions to J_{iso} for all molecules discussed and plots showing the variation of ΔJ and η_J as the geometries are modified) are available with the article on the journal Web site (www.nrcresearchpress.com/cjc).

Acknowledgements

D.L.B. thanks the Natural Sciences and Engineering Research Council of Canada (NSERC) for funding. F.A.P. thanks NSERC for a scholarship. D.L.B. thanks Dr. R. Wasylishen for his many contributions to the fundamental understanding of **J**-coupling tensors, which inspired this work. We are grateful to Dr. J. Autschbach for assistance with some of the technical aspects of this work.

References

(1) Harris, R. K.; Wasylishen, R. E.; Duer, M. J. *NMR Crystallography;* John Wiley & Sons: Chichester, UK, 2009.
(2) Tycko, R.; Dabbagh, G. *Chem. Phys. Lett.* **1990** *173* (5–6), 461. doi:10.1016/0009-2614(90)87235-J.
(3) Sun, B.-Q.; Costa, P. R.; Kocisko, D.; Lansbury, P. T., Jr; Griffin, R. G. *J. Chem. Phys.* **1995** *102* (2), 702. doi:10.1063/1.469182.
(4) Sodickson, D. K.; Levitt, M. H.; Vega, S.; Griffin, R. G. *J. Chem. Phys.* **1993** *98* (9), 6742. doi:10.1063/1.464766.
(5) Tycko, R. Dipolar Recoupling: Homonuclear. In *NMR Crystallography;* Harris, R. K.; Wasylishen, R. E.; Duer, M. J., Eds.; John Wiley & Sons: Chichester, UK, 2009; p 163.
(6) Shore, S. E.; Ansermet, J.-P.; Slichter, C. P.; Sinfelt, J. H. *Phys. Rev. Lett.* **1987** *58* (9), 953. doi:10.1103/PhysRevLett.58.953.
(7) Gullion, T.; Schaefer, J. *J. Magn. Reson.* **1989** *81* (1), 196. doi:10.1016/0022-2364(89)90280-1.
(8) Jaroniec, C. P. Dipolar Recoupling: Homonuclear. In *NMR Crystallography;* Harris, R. K.; Wasylishen, R. E.; Duer, M. J., Eds.; John Wiley & Sons: Chichester, UK, 2009; p 137.
(9) Wasylishen, R. E. Dipolar and Indirect Coupling Tensors in Solids. In *Encyclopedia of Nuclear Magnetic Resonance;* Grant, D. M.; Harris, R. K., Eds.; John Wiley & Sons: Chichester, 1996; pp 1685–1695.
(10) Vaara, J.; Jokisaari, J.; Wasylishen, R. E.; Bryce, D. L. *Prog. Nucl. Magn. Reson. Spectrosc.* **2002** *41* (3–4), 233. doi:10.1016/S0079-6565(02)00050-X.
(11) Snyder, L. C.; Meiboom, S. *J. Chem. Phys.* **1967** *47* (4), 1480. doi:10.1063/1.1712105.
(12) Sýkora, S.; Vogt, J.; Bösiger, H.; Diehl, P. *J. Magn. Reson.* **1979** *36* (1), 53. doi:10.1016/0022-2364(79)90214-2.
(13) Lounila, J.; Wasser, R.; Diehl, P. *Mol. Phys.* **1987** *62* (1), 19. doi:10.1080/00268978700102031.
(14) Nakatsuji, H.; Kato, H.; Morishima, I.; Yonezawa, T. *Chem. Phys. Lett.* **1970** *4* (10), 607. doi:10.1016/0009-2614(70)80096-3.
(15) Barfield, M. *Chem. Phys. Lett.* **1970** *4* (8), 518. doi:10.1016/0009-2614(70)85031-X.
(16) Buckingham, A. D.; Pyykkö, P.; Robert, J. B.; Wiesenfeld, L. *Mol. Phys.* **1982** *46* (1), 177. doi:10.1080/00268978200101171.
(17) Buckingham, A. D.; Love, I. *J. Magn. Reson.* **1970** *2* (3), 338. doi:10.1016/0022-2364(70)90104-6.
(18) Bryce, D. L.; Courchesne, N. M. D.; Perras, F. A. *Solid State Nucl. Magn. Reson.* **2009** *36* (4), 182. doi:10.1016/j.ssnmr.2009.11.004.
(19) Harris, K. J.; Bryce, D. L.; Wasylishen, R. E. *Can. J. Chem.* **2009** *87* (10), 1338. doi:10.1139/V09-089.
(20) Robert, J. B.; Wiesenfeld, L. *Phys. Rep.* **1982** *86* (7), 363. doi:10.1016/0370-1573(82)90164-8.
(21) Andrew, E. R.; Farnell, L. F. *Mol. Phys.* **1968** *15* (2), 157. doi:10.1080/00268976800100931.
(22) Ramsey, N. F. *Phys. Rev.* **1953** *91* (2), 303. doi:10.1103/PhysRev.91.303.
(23) Bryce, D. L.; Wasylishen, R. E.; Autschbach, J.; Ziegler, T. *J. Am. Chem. Soc.* **2002** *124* (17), 4894. doi:10.1021/ja012596b.
(24) Blizzard, A. C.; Santry, D. P. *Chem. Commun.* **1970** *1085*. doi:10.1039/C29700001085.
(25) Autschbach, J.; Ziegler, T. *J. Chem. Phys.* **2000** *113* (3), 936. doi:10.1063/1.481874.
(26) Autschbach, J.; Ziegler, T. *J. Chem. Phys.* **2000** *113* (21), 9410. doi:10.1063/1.1321310.
(27) Autschbach, J. *J. Chem. Phys.* **2007** *127* (12), 124106. doi:10.1063/1.2768363.
(28) Autschbach, J. *J. Chem. Phys.* **2008** *128* (16), 164112. doi:10.1063/1.2905235.
(29) Autschbach, J.; Le Guennic, B. *J. Chem. Educ.* **2007** *84* (1), 156. doi:10.1021/ed084p156.
(30) Pople, J. A.; Santry, D. P. *Mol. Phys.* **1964** *8* (1), 1. doi:10.1080/00268976400100011.
(31) Bryce, D. L.; Wasylishen, R. E. *Inorg. Chem.* **2002** *41* (12), 3091. doi:10.1021/ic020025u.
(32) Feindel, K. W.; Wasylishen, R. E. *Magn. Reson. Chem.* **2004** *42* (S1), S158. doi:10.1002/mrc.1453.
(33) Morino, Y.; Saito, S. *J. Mol. Spectrosc.* **1966** *19* (1–4), 435. doi:10.1016/0022-2852(66)90266-9.
(34) Hirota, E.; Morino, Y. *J. Mol. Spectrosc.* **1970** *33* (3), 460. doi:10.1016/0022-2852(70)90139-6.
(35) Styger, C.; Bauder, A. *J. Mol. Spectrosc.* **1991** *148* (2), 479. doi:10.1016/0022-2852(91)90403-W.
(36) Haubrich, S. T.; Roehrig, M. A.; Kukolich, S. G. *J. Chem. Phys.* **1990** *93* (1), 121. doi:10.1063/1.459611.
(37) Magnuson, D. W. *J. Chem. Phys.* **1957** *27* (1), 223. doi:10.1063/1.1743675.
(38) Irikura, K. K. *J. Chem. Phys.* **1995** *102* (13), 5357. doi:10.1063/1.469263.
(39) Grandinetti, F.; Hrušák, J.; Schröder, D.; Karrass, S.; Schwarz, H. *J. Am. Chem. Soc.* **1992** *114* (8), 2806. doi:10.1021/ja00034a007.
(40) Clippard, F. B., Jr; Bartell, L. S. *Inorg. Chem.* **1970** *9* (4), 805. doi:10.1021/ic50086a022.
(41) Kuchitsu, K.; Konaka, S. *J. Chem. Phys.* **1966** *45* (11), 4342. doi:10.1063/1.1727494.
(42) Utkin, A. N.; Girichev, G. V.; Giricheva, N. I.; Khaustov, S. V. *J. Struct. Chem.* **1986** *27* (2), 212. doi:10.1007/BF00751726.
(43) Kimura, K.; Bauer, S. H. *J. Chem. Phys.* **1963** *39* (12), 3172. doi:10.1063/1.1734179.
(44) Brier, P. N. *J. Mol. Struct.* **1991** *263* (1–2), 133. doi:10.1016/0022-2860(91)80061-8.
(45) Begun, G. M.; Fletcher, W. H.; Smith, D. F. *J. Chem. Phys.* **1965** *42* (6), 2236. doi:10.1063/1.1696273.
(46) Adams, C. J.; Downs, A. J. *Spectrochim. Acta, Part A* **1972** *28A* (10), 1841. doi:10.1016/0584-8539(72)80156-9.
(47) Claassen, H. H.; Chernick, C. L.; Malm, J. G. *J. Am. Chem. Soc.* **1963** *85* (13), 1927. doi:10.1021/ja00896a007.
(48) Dickson, R. M.; Ziegler, T. *J. Phys. Chem.* **1996** *100* (13), 5286. doi:10.1021/jp951930l.
(49) Khandogin, J.; Ziegler, T. *Spectrochim. Acta , Part A* **1999** *55* (3), 607. doi:10.1016/S1386-1425(98)00265-0.
(50) te Velde, G.; Bickelhaupt, F. M.; Baerends, E. J.; Fonseca Guerra, C.; Van Gisbergen, S. J. A.; Snijders, J. G.; Ziegler, T. *J. Comput. Chem.* **2001** *22* (9), 931. doi:10.1002/jcc.1056.

Can. J. Chem. Downloaded from www.nrcresearchpress.com by Xi'an Jiaotong University on 09/19/12
For personal use only.

(51) Fonseca Guerra, C.; Snijders, J. G.; te Velde, G.; Baerends, E. J. *Theor. Chem. Acc.* **1998** *99* (6), 391. doi:10.1007/s002140050353.
(52) Amsterdam Density Functional Software ADF2009.01. *SCM;* Theoretical Chemistry, Vrije Universiteit: Amsterdam, The Netherlands. http://www.scm.com/, 2010.
(53) Pyykkö, P. *Chem. Phys.* **1977** *22* (2), 289. doi:10.1016/0301-0104(77)87013-4.
(54) Autschbach, J. *J. Chem. Phys.* **2008** *129* (9), 094105. doi:10.1063/1.2969100.
(55) Vosko, S. H.; Wilk, L.; Nusair, M. *Can. J. Phys.* **1980** *58* (8), 1200. doi:10.1139/p80-159.
(56) Becke, A. D. *Phys. Rev. A* **1988** *38* (6), 3098. doi:10.1103/PhysRevA.38.3098.
(57) Perdew, J. P. *Phys. Rev. B* **1986** *33* (12), 8822. doi:10.1103/PhysRevB.33.8822.
(58) Perdew, J. P. *Phys. Rev. B* **1986** *34* (10), 7406. doi:10.1103/PhysRevB.34.7406.
(59) Sychrovský, V.; Gräfenstein, J.; Cremer, D. *J. Chem. Phys.* **2000** *113* (9), 3530. doi:10.1063/1.1286806.
(60) Helgaker, T.; Watson, M.; Handy, N. C. *J. Chem. Phys.* **2000** *113* (21), 9402. doi:10.1063/1.1321296.
(61) Moncho, S.; Autschbach, J. *J. Chem. Theory Comput.* **2010** *6* (1), 223. doi:10.1021/ct900535d.
(62) Adiga, S.; Aebi, D.; Bryce, D. L. *Can. J. Chem.* **2007** *85* (7–8), 496. doi:10.1139/V07-069.
(63) Wilkens, S. J.; Westler, W. M.; Markley, J. L.; Weinhold, F. *J. Am. Chem. Soc.* **2001** *123* (48), 12026. doi:10.1021/ja016284k.
(64) Glendening, E. D.; Badenhoop, J. K.; Reed, A. E.; Carpenter, J. E.; Bohmann, J. A.; Morales, C. M.; Weinhold, F. *NBO 5.0;* Theoretical Chemistry Institute, University of Wisconsin: Madison, WI. http://www.chem.wisc.edu/~nbo5, 2001.
(65) Eichele, K.; Wasylishen, R. E. *J. Magn. Reson. A* **1994** *106* (1), 46. doi:10.1006/jmra.1994.1005.
(66) Bryce, D. L.; Wasylishen, R. E. *J. Am. Chem. Soc.* **2000** *122* (45), 11236. doi:10.1021/ja0020431.
(67) Wasylishen, R. E.; Mooibroek, S.; Macdonald, J. B. *J. Chem. Phys.* **1984** *81* (3), 1057. doi:10.1063/1.447799.
(68) Zumbulyadis, N.; Dailey, B. P. *Mol. Phys.* **1973** *26* (3), 777. doi:10.1080/00268977300102081.
(69) Jameson, C. J.; Jameson, A. K.; Wille, S. *J. Phys. Chem.* **1979** *83* (26), 3372. doi:10.1021/j100489a012.
(70) Jaszuński, M. *Chem. Phys. Lett.* **2004** *385* (1–2), 122. doi:10.1016/j.cplett.2003.12.070.
(71) Jackowski, K.; Makulski, W.; Szyprowska, A.; Antušek, A.; Jaszuński, M. *Magn. Reson. Chem.* **2009** *47* (10), 857. doi:10.1002/mrc.2484.
(72) Bryce, D. L.; Wasylishen, R. E. *J. Am. Chem. Soc.* **2000** *122* (13), 3197. doi:10.1021/ja9942134.
(73) Alexandre, M.; Rigny, P. *Can. J. Chem.* **1974** *52* (21), 3676. doi:10.1139/v74-549.
(74) Jameson, C. J.; Gutowsky, H. S. *J. Chem. Phys.* **1969** *51* (7), 2790. doi:10.1063/1.1672415.
(75) Damerius, R.; Huppmann, P.; Lentz, D.; Seppelt, K. *J. Chem. Soc., Dalton Trans.* **1984** *2821*. doi:10.1039/DT9840002821.
(76) Schumacher, G. A.; Schrobilgen, G. J. *Inorg. Chem.* **1984** *23* (19), 2923. doi:10.1021/ic00187a005.
(77) Birchall, T.; Myers, R. D.; de Waard, H.; Schrobilgen, G. J. *Inorg. Chem.* **1982** *21* (3), 1068. doi:10.1021/ic00133a039.
(78) Schrobilgen, G. J.; Holloway, J. H.; Granger, P.; Brevard, C. *Inorg. Chem.* **1978** *17* (4), 980. doi:10.1021/ic50182a037.
(79) Schrobilgen, G. J. *Final Technical Report No. PL-TR-93-3007, Aug. 1993, Contract F04611-91-K-0004;* Phillips Laboratory, Propulsion Directorate, USAF Systems Command, Edwards Air Force Base, CA, 1993; Vol. 1, Part IV, pp 1–11.
(80) Christe, K. O.; Curtis, E. C.; Dixon, D. A.; Mercier, H. P.; Sanders, J. C. P.; Schrobilgen, G. J. *J. Am. Chem. Soc.* **1991** *113* (9), 3351. doi:10.1021/ja00009a021.
(81) Power, W. P.; Wasylishen, R. E. *Inorg. Chem.* **1992** *31* (11), 2176. doi:10.1021/ic00037a035.
(82) Penner, G. H.; Power, W. P.; Wasylishen, R. E. *Can. J. Chem.* **1988** *66* (8), 1821. doi:10.1139/v88-294.
(83) Power, W. P.; Lumsden, M. D.; Wasylishen, R. E. *J. Am. Chem. Soc.* **1991** *113* (22), 8257. doi:10.1021/ja00022a009.
(84) Lumsden, M. D.; Eichele, K.; Wasylishen, R. E.; Cameron, T. S.; Britten, J. F. *J. Am. Chem. Soc.* **1994** *116* (24), 11129. doi:10.1021/ja00103a030.
(85) Lumsden, M. D.; Wasylishen, R. E.; Britten, J. F. *J. Phys. Chem.* **1995** *99* (45), 16602. doi:10.1021/j100045a019.
(86) Power, W. P.; Lumsden, M. D.; Wasylishen, R. E. *Inorg. Chem.* **1991** *30* (15), 2997. doi:10.1021/ic00015a011.

Can. J. Chem. Downloaded from www.nrcresearchpress.com by Xi'an Jiaotong University on 09/19/12
For personal use only.

A natural abundance solid-state ^{25}Mg NMR study of layered magnesium phosphates

Jianfeng Zhu and Yining Huang

Can. J. Chem. Downloaded from www.nrcresearchpress.com by Xi'an Jiaotong University on 09/19/12
For personal use only.

Abstract: Natural abundance ^{25}Mg solid-state magic-angle spinning and static NMR spectra of several representative layered magnesium phosphates were acquired at 21.1 and 9.4 T by using quadrupolar echo and double-frequency sweep quadrupolar Carr–Purcell–Meiboom–Gill pulse sequences. The spectra were dominated by the second-order quadrupolar interaction. The electric field gradient tensor parameters were extracted from the spectra via spectral simulations. These parameters, such as the quadrupolar coupling constant (C_Q), appear to be sensitive to some parameters describing the distortion of the MgO_6 octahedron in the layer. The empirical relationships between C_Q and several structural parameters were established and used to obtain partial information on the Mg environment in a layered material ($MgHPO_4{\cdot}1.2H_2O$) with unknown structure. Theoretical calculations suggest that the C_Q values of the Mg sites are affected not only by the oxygen atoms in the first coordination sphere, but also by the spatial arrangements of the atoms in the second and third coordination spheres and beyond.

Key words: layered magnesium phosphates, ^{25}Mg NMR, quadrupolar echo, QCPMG.

Résumé : Opérant à 21,1 et 9,4 T, et faisant appel à l'écho quadripolaire et aux séquences pulsées quadripolaires à balayage à double fréquence de Carr-Purcell-Beiboom-Gill, on a mesuré les spectres RMN, statiques et en rotation à l'angle magique, en abondance naturelle du ^{25}Mg et à l'état solide de plusieurs phosphates de magnésium en couches représentatives. Les spectres sont dominés par l'interaction quadripolaire du deuxième ordre. On a extrait les paramètres du tenseur du gradient du champ électrique à partir des spectres en faisant appel à des simulations spectrales. Il semble que ces paramètres, telle la constante de couplage quadripolaire (C_Q), sont sensibles à certains paramètres qui décrivent la distorsion de l'octaèdre MgO_6 dans la couche. On a établis des relations empiriques entre la valeur de C_Q et plusieurs paramètres structuraux et on les a utilisés pour obtenir de l'information partielle sur l'environnement du Mg dans un matériau de ($MgHPO_4{\cdot}1,2H_2O$) de structure inconnue. Les calculs théoriques suggèrent que les valeurs de C_Q des sites de Mg ne sont pas uniquement affectées par les atomes d'oxygène de la première sphère de coordination, mais qu'ils le sont aussi par l'arrangement spatial des atomes, au moins dans les seconde et troisième sphères.

Mots-clés : phosphates de magnésium en couches, RMN du ^{25}Mg, écho quadripolaire, QCPMG.

[Traduit par la Rédaction]

Introduction

Layered metal phosphates (MPs) have potential applications as ion exchangers, ionic conductors, and catalysts because of their structural topologies and the properties of intercalation of various guest species. The structures of MPs are, in general, not very well-characterized owing to the fact that it is difficult to grow good single crystals suitable for X-ray diffraction. Recently, we applied solid-state NMR techniques to directly characterize the metal centre environments of several important MPs, including layered titanium phosphates,[1] niobium phosphates,[2] vanadium phosphates,[3] and zirconium phosphates.[4] The focus of this work is on the layered magnesium phosphates. Layered magnesium phosphates (MgPs) have proved useful in various processes of interest including removal of heavy metal ions from aqueous solutions,[5,6] removal of aqueous ammonium,[7] and catalysis of a variety of reactions.[8–11] These studies showed that the ion-exchange selectivity and catalytic activity of MgPs depend largely on their composition and structure. Therefore, detailed structure information regarding these layered materials is desired.

As mentioned earlier, because of the difficulty in the preparation of large single crystals for X-ray diffraction, most structures of this type of material have been determined from powder X-ray diffraction (XRD) data. Solid-state NMR is a complementary technique to X-ray diffraction. However, only a few ^{31}P MAS NMR studies[12,13] have been performed and ^{25}Mg solid-state NMR has never been used to directly probe the MgP-based materials. This is because ^{25}Mg ($I = 5/2$) has a low gyromagnetic ratio ($\gamma = -1.63890 \times 10^7$ rad T^{-1} s^{-1}) and a relatively low natural abundance (10.13%).[14] In addition, ^{25}Mg has a moderate quadrupole moment ($Q = -2.01 \times 10^{-29}$ m^2),[15] resulting in significant line broadening in the presence of an electric field gradient (EFG). The combination

Received 21 June 2010. Accepted 23 November 2010. Published at www.nrcresearchpress.com/cjc on 6 July 2011.

J. Zhu and Y. Huang. Department of Chemistry, The University of Western Ontario, London, ON N6A 5B7, Canada.

Corresponding author: Y. Huang (e-mail: yhuang@uwo.ca).

This article is part of a Special Issue dedicated to Professor Roderick E. Wasylishen to honour his outstanding contributions to Canadian chemistry.

Can. J. Chem. Downloaded from www.nrcresearchpress.com by Xi'an Jiaotong University on 09/19/12
For personal use only.

of these properties renders the observation of solid-state ^{25}Mg NMR spectra difficult. Despite the challenge, the feasibility of solid-state ^{25}Mg NMR was demonstrated by Dupree and Smith[16] who observed the MAS signals in several inorganic salts at 8.45 T. Since then, solid-state ^{25}Mg NMR has been performed on a variety of Mg-containing materials.[17–35] In recent years, a combination of ever higher magnetic fields and the development of sensitivity enhancement pulse sequences for low-γ quadrupolar nuclei such as quadrupolar Carr–Purcell–Meiboom–Gill (QCPMG) and related sequences[36–38] has made the observation of these low-γ quadrupolar nuclei much more practical.

In the present study, the local environments of the magnesium centres in several representative MgPs such as $NH_4MgPO_4{\cdot}H_2O$ (dittmarite), $[NH_3(CH_2)_2NH_3]_{0.5}[MgPO_4{\cdot}H_2O]$ (UiO-24-EN, UiO stands for University of Oslo), $[NH_3(CH_2)_4NH_3]_{0.5}[MgPO_4{\cdot}H_2O]$ (UiO-24-DAB), and $MgHPO_4{\cdot}1.2H_2O$ were directly probed using solid-state ^{25}Mg NMR. Magic-angle spinning (MAS) spectra were acquired first. Spinning the sample at the magic angle eliminates the effect of chemical shift anisotropy (CSA). The isotropic chemical shift (δ_{iso}) and the EFG parameters including the nuclear quadrupolar coupling constant (C_Q) and the asymmetry parameter (η_Q) can be extracted by simulating the MAS spectra. To examine the possible effect of the CSA, ^{25}Mg static echo or QCPMG spectra were then obtained. The experiments were carried out at two field strengths (9.4 and 21.1 T) to ensure the reliability of the extracted NMR parameters. Relationships between the NMR parameters and the structural properties were discussed. Correlations between C_Q and the distortion of the MgO_6 octahedron were established and used to obtain partial information on the Mg local structure in $MgHPO_4{\cdot}1.2H_2O$, a representative MgP with unknown structure. Theoretical calculations were also performed to assist in understanding the observed spectra.

Experimental

Synthesis

Dittmarite and UiO-24 compounds were synthesized using the method described by Fjellvåg and co-workers.[13] The procedure was as follows: $Mg_3(PO_4)_2{\cdot}8H_2O$, H_3PO_4 (85%), diamine, and water were mixed to form a homogeneous gel. The gel was then transferred into Teflon-lined steel autoclaves and heated at a specific temperature for 24 h; after the reaction, the autoclaves were quenched in cold water and the white precipitate was retrieved by filtration and air-dried. The use of ethylenediamine (EN) as a template yielded UiO-24-EN, while employing 1,4-diaminobutane (DAB) as the template produced dittmarite and UiO-24-DAB. The specific masses of each reactant and reaction temperatures are given in Table S1 of the Supplementary data.

$MgHPO_4{\cdot}1.2H_2O$ was synthesized hydrothermally in the presence of diethylamine (DEA).[39] The reaction mixture containing 5.0 g $MgAc_2{\cdot}4H_2O$, 2.69 g H_3PO_4, 0.908 g DEA, and 10.50 g H_2O was stirred until homogeneous and then transferred into a Teflon-lined steel autoclave and heated at 180 °C for 3 days under autogeneous pressure. The crystalline product was recovered by filtration and washing with water and then dried at room temperature.

The identity of the synthesized materials was confirmed by comparing the powder XRD patterns with those reported in the literature.[13,39] Powder XRD measurements were performed on a Rigaku rotating anode diffractometer (45 kV/160 mA) using graphite-monochromated Co Kα radiation with a wavelength of 1.7902 Å. The powder XRD patterns were recorded within the range $5° \leq 2\theta \leq 65°$ with a 10°/min step width and a 6 min count time.

NMR measurements

^{25}Mg NMR experiments were performed at two fields, 21.1 and 9.4 T, corresponding to the operating frequencies at 55.11 and 24.46 MHz, respectively. The experiments at 21.1 T were performed on a 900 MHz Bruker Avance II spectrometer at the National Ultrahigh-field NMR Facility for Solids in Ottawa, Ontario. The MAS spectra at a spinning rate of 5 kHz were obtained using the one-pulse sequence. The static spectra were acquired using the spin-echo pulse sequence with a $\pi/2$ refocusing pulse, i.e., ($\pi/2 - \tau - \pi/2 - \tau -$ acq), and the phase cycling developed by Oldfield and coworkers.[40] An interpulse delay time of 100 μs was used.

The experiments at 9.4 T were performed on a Varian Chemagnetics Infinityplus 400 WB spectrometer. A low-γ tuning box was used to tune the probe to the frequency range of ^{25}Mg. The MAS spectra at 9.4 T were obtained using the spin-echo pulse sequence to remove probe ring-down and acoustic ringing at the beginning of the free induction decays (FIDs). A $\pi/2$ pulse of 8.0 μs was calibrated on a 1.0 mol/L $MgCl_2$ aqueous solution, corresponding to a selective $\pi/2$ pulse width of 2.67 μs for central transition. A recycle delay of 5.0 s was used. Since the samples were spun at a rate of 10 kHz, the interpulse delay time was set to be 100 μs, synchronized with the spinning rate. The echo was collected prior to the echo maximum and shifted to ensure that the FIDs used in Fourier transformation began exactly at the echo maximum.

Because of the low sensitivity of ^{25}Mg at the low field of 9.4 T, the double-frequency-sweep (DFS) QCPMG pulse sequence,[41] was employed. The inter-pulse and inter-acquisition delays were $\tau_1 = \tau_2 = \tau_3 = \tau_4 = 30$ μs. The acquisition time (τ_a) for each echo was adjusted to obtain a spikelet separation ($1/\tau_a$) between 1000 and 2000 Hz in the frequency spectra for different samples. The number of Meiboom–Gill (MG) loops was set to 14. DFS was implemented using a converging amplitude-modulated pulse[42] with a starting frequency of 3.0 MHz and a final frequency of 400 kHz at a sweep-rate of 4333 MHz/s.

MAS probes of 5 and 7.5 mm were used for 9.4 and 21.1 T, respectively. ^{25}Mg chemical shifts were referenced to a 1.0 mol/L $MgCl_2$ aqueous solution ($\delta_{iso} = 0$ ppm). The spectral simulations were carried out using the WSOLIDS1 software package provided by Professor R.E. Wasylishen (University of Alberta, Edmonton, Alberta).

Calculations of the EFG tensors

The calculations of the ^{25}Mg EFG tensors in dittmarite and UiO-24 compounds were performed using the Gaussian 03 program[43] on a computer cluster.[44] To make the calculation practical, simplified molecular clusters containing the structural units of interest were examined. Two different model complexes, MgO_6H_{10} and $Mg_5P_4O_{32}H_{34}$, were examined for all three compounds. The model complexes were constructed according to the crystal structures of the MgPs determined by

Can. J. Chem. Downloaded from www.nrcresearchpress.com by Xi'an Jiaotong University on 09/19/12
For personal use only.

powder XRD[13] and no further optimization was performed. It should be noted that the limited accuracy of the powder XRD structures may affect the calculated NMR parameters. The clusters were terminated with OH groups to reduce the total charge to zero. This is an approach widely used in ab initio calculations of ^{27}Al EFG tensors in zeolites.[45–49] Terminal H atoms take the positions of P or Mg atoms, which are connected to the terminal O atoms. We also performed the calculations of the EFG parameters by placing the hydrogens at a shorter distance of 1 Å along the O–Mg vector. However, the agreement between calculated and observed values is poorer and, therefore, the data are not presented. Calculations were carried out using the restricted Hartree–Fock (RHF) method. Several researchers[50,51] have shown that this method yields EFG predictions superior to that of the hybrid density functional theory (DFT) with the B3LYP functional. To examine basis set dependence, various basis sets including 3–21G, 6–31G**, 6–31++G**, 6–311G**, and 6–311++G(2d,2p) were used.

The calculated EFGs (V_{XX}, V_{YY}, V_{ZZ}) were transferred to the quadrupolar coupling constant and asymmetry parameter according to the following definition: $|V_{XX}| \leq |V_{YY}| \leq |V_{ZZ}|$; $C_Q = (eV_{ZZ}Q/h)9.71736 \times 10^{21}$; and $\eta_Q = (V_{XX} - V_{YY})/V_{ZZ}$, where e is the electronic charge, Q is the nuclear quadrupolar moment ($Q(^{25}\text{Mg}) = -2.01 \times 10^{-29}$ m^2),[15] and h is Planck's constant. The constant 9.71736×10^{21} is used in the equation because V_{ZZ} is calculated in atomic units.

The EFG tensors were also calculated using the CASTEP code,[52] which has shown to be successful in calculating NMR parameters in a variety of systems,[53–61] including ^{25}Mg parameters in several inorganic salts.[20–22] This method employs the DFT approach to calculate the electronic structure of periodic solids by using a plane wave basis and pseudopotentials to describe the core electrons. The present calculations were performed by Dr. V. Terskikh (at the National Ultrahigh-field NMR Facility for Solids) using ultrasoft pseudopotentials generated from the "on-the-fly" method implemented within CASTEP. The generalized gradient approximations (GGA) PBE exchange-correlation functional was used. Plane wave cutoff energies of 550, 500, and 450 eV were applied for dittmarite, UiO-24-EN, and UiO-24-DAB, respectively. For integrations in reciprocal space, 4 × 3 × 5, 4 × 1 × 4, and 3 × 1 × 3 Monkhorst–Pack grids, corresponding to 12, 8, and 5 k-points, were used for dittmarite, UiO-24-EN, and UiO-24-DAB, respectively. Geometry optimization was performed on dittmarite prior to the calculation of the EFG tensors, but not for UiO-24-EN and UiO-24-DAB because of the large number of atoms in their unit cells. Note that small plane wave cutoff energies and k-points were used for UiO-24-EN and UiO-24-DAB also because of the large number of atoms in the unit cell, which may introduce errors to the calculated NMR parameters.

Results and discussion

Layered magnesium phosphate, $NH_4MgPO_4{\cdot}H_2O$, occurs naturally as mineral dittmarite. Its structure was solved from powder XRD data.[13] The structure is composed of magnesium layers separated by ammonium ions (Fig. 1A). Each MgO_6 octahedron is connected to four other MgO_6 octahedra and a PO_4 tetrahedron via corner-sharing oxygens and a

Fig. 1. Structures of (A) dittmarite, (B) UiO-24-EN, and (C) UiO-24-DAB. H atoms are omitted for clarity.

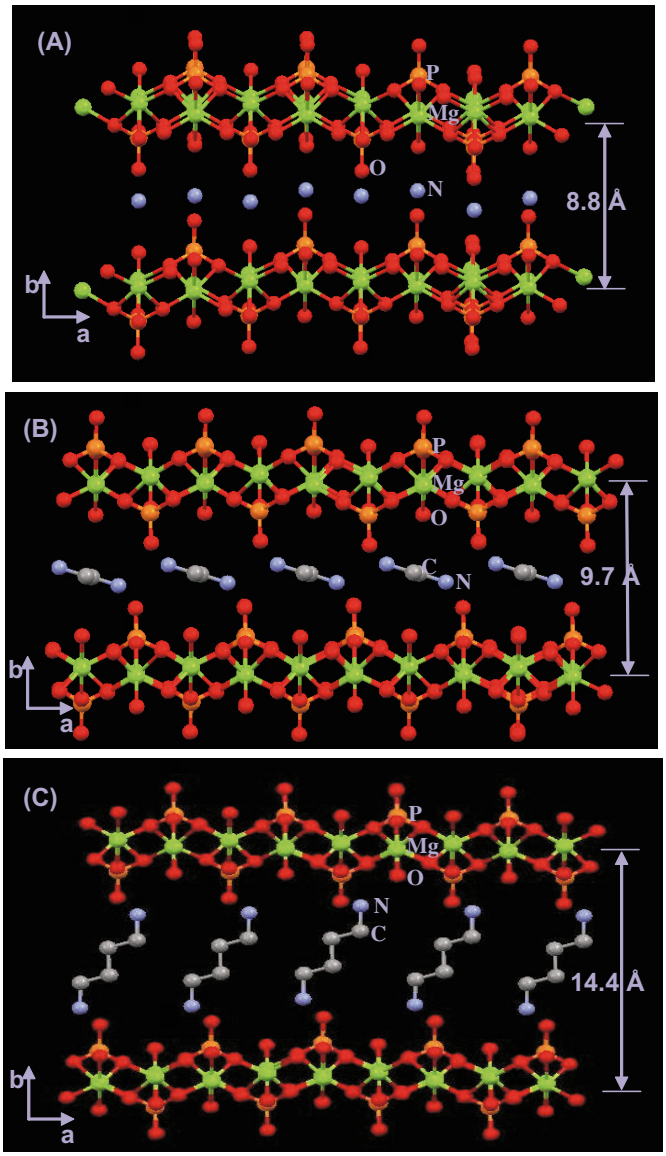

water molecule. The PO_4 tetrahedron is joined together with four MgO_6 octahedra by three corner- and edge-sharing oxygens. The fourth oxygen in the PO_4 tetrahedron points towards the interlayer space and is hydrogen bonded with four hydrogen atoms in four ammonium ions. The structures of $[NH_3(CH_2)_2NH_3]_{0.5}[MgPO_4{\cdot}H_2O]$ (UiO-24-EN) and $[NH_3(CH_2)_4NH_3]_{0.5}[MgPO_4{\cdot}H_2O]$ (UiO-24-DAB) are very similar to that of dittmarite except that the ammonium ions are replaced by organic templates; namely, EN and 1,4-diaminobutane (DAB) (Figs. 1B and 1C).[13] The introduction of organic templates causes the increase in the interlayer distances from 8.8 Å for dittmarite to 9.7 and 14.4 Å for UiO-24-EN and UiO-24-DAB, respectively. The significant difference in the interlayer distance between UiO-24-EN and UiO-24-DAB is because the EN molecules are oriented almost parallel to the inorganic magnesium phosphate layers (Fig. 1B), whereas the DAB molecules are tilted with respect to the layers (Fig. 1C). The insertion of organic templates also results in more distorted MgO_6 octahedra. The

Fig. 2. ^{25}Mg MAS (A) and (C) and static (B) and (D) NMR spectra of dittmarite at 21.1 and 9.4 T. Scans (8192 and 4096), corresponding to 11.4 and 5.7 h, were collected for the static and MAS spectra at 21.1 T, respectively. Scans (48 304 and 48 160), corresponding to 67.1 and 66.9 h, were collected for the static and MAS spectra at 9.4 T, respectively. A recycle delay of 5 s was used at both fields.

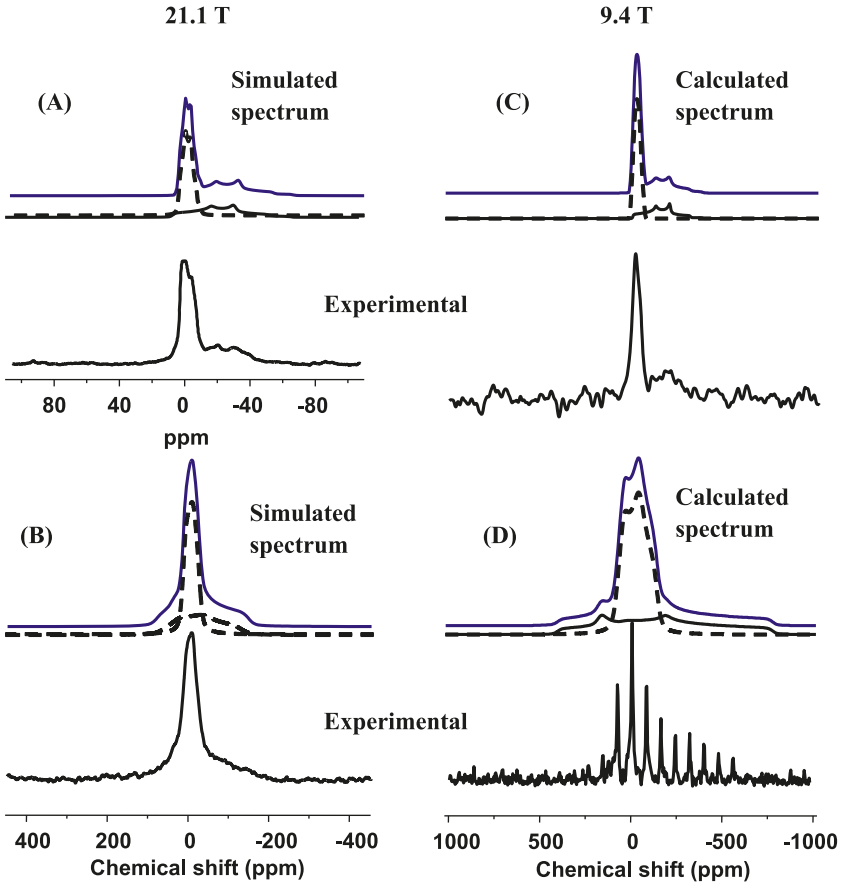

Can. J. Chem. Downloaded from www.nrcresearchpress.com by Xi'an Jiaotong University on 09/19/12
For personal use only.

powder XRD patterns of synthesized dittmarite, UiO-24-EN, and UiO-24-DAB are shown in Fig. S1 of the Supplementary data. The interlayer spaces estimated from the low angle diffractions are 8.71, 9.60, and 13.92 Å for dittmarite, UiO-24-EN, and UiO-24-DAB, respectively, consistent with those reported in the literature.[13] It is noted that there are several small peaks in the XRD pattern of dittmarite owing to an impurity. The identities of MgPs were also confirmed by ^{31}P MAS NMR spectra (not shown). ^{31}P signals at 6.8, 5.2, and 7.3 ppm were observed for dittmarite, UiO-24-EN, and UiO-24-DAB, respectively, in good agreement with the corresponding reported values of 6.2, 4.3, and 6.5 ppm.[13] The ^{31}P MAS spectrum of dittmarite also shows another signal at –1.0 ppm, which is probably due to the P in the impurity.

As mentioned previously, the insertion of organic templates results in a more distorted MgO_6 octahedron in UiO-24-EN and UiO-24-DAB compared with dittmarite, leading to a larger EFG at the Mg. The increase in EFG results in a larger quadrupolar interaction, which should be detected by solid-state ^{25}Mg NMR. ^{25}Mg MAS and static spectra of these three layered MgPs were recoded at 21.1 and 9.4 T. In all cases, the quadrupolar parameters were obtained and no CSA effects were observed.

Dittmarite

According to the crystal structure, there is only one Mg lattice site,[13] suggesting that there should be only one signal in the ^{25}Mg NMR spectrum. The ^{25}Mg MAS spectrum of dittmarite acquired at 21.1 T (Fig. 2A) shows two signals: a strong narrow peak and a weak pattern with a typical line shape owing to second-order quadrupolar interaction, indicating two different Mg environments. Based on the intensities of the signals and the proposed structure, the strong narrow peak is assigned to the Mg centre in the MgO_6 octahedra of dittmarite. The broad weak component is presumably due to the impurity noted in the XRD pattern. The spectrum can be well fitted (Fig. 2A) using the following parameters: δ_{iso} = 2 ppm, C_Q = 1.7 MHz, and η_Q = 0.5 for Mg in dittmarite; and δ_{iso} = 4 ppm, C_Q = 3.8 MHz, and η_Q = 0.6 for Mg in the impurity.

Similar to the MAS spectrum, two ^{25}Mg resonances were seen in the static-echo spectrum at 21.1 T (Fig. 2B), with a narrow peak superimposed on a weak broader pattern. The spectrum can be well-simulated using the same sets of quadrupolar parameters without CSA. To verify the parameters, ^{25}Mg spectra at a second field (9.4 T) were also acquired. The ^{25}Mg MAS spectrum at 9.4 T (Fig. 2C) also shows two Mg components. The strong signal can be fitted using the same set of parameters obtained from the simulation of the MAS spectrum at 21.1 T. It is difficult to accurately simulate the signal of the impurity because of its low intensity. The static DFS-QCPMG spectrum at 9.4 T is shown in Fig. 2D. The overall line shape is not well-defined owing to the fact that only a few spikelets were obtained after 3 days of data

Fig. 3. ^{25}Mg MAS (A) and (C) and static (B) and (D) NMR spectra of $[NH_3(CH_2)_4NH_3]_{0.5}[MgPO_4{\cdot}H_2O]$ (UiO-24-DAB) at 21.1 and 9.4 T. A recycle delay of 5 s was used at both fields. Scans (8192 and 2660), corresponding to 11.4 and 3.7 h, were collected for the static and MAS spectra at 21.1 T, respectively. Scans (49 728 and 21 248), corresponding to 69.1 and 29.5 h, were collected for the static and MAS spectra at 9.4 T, respectively.

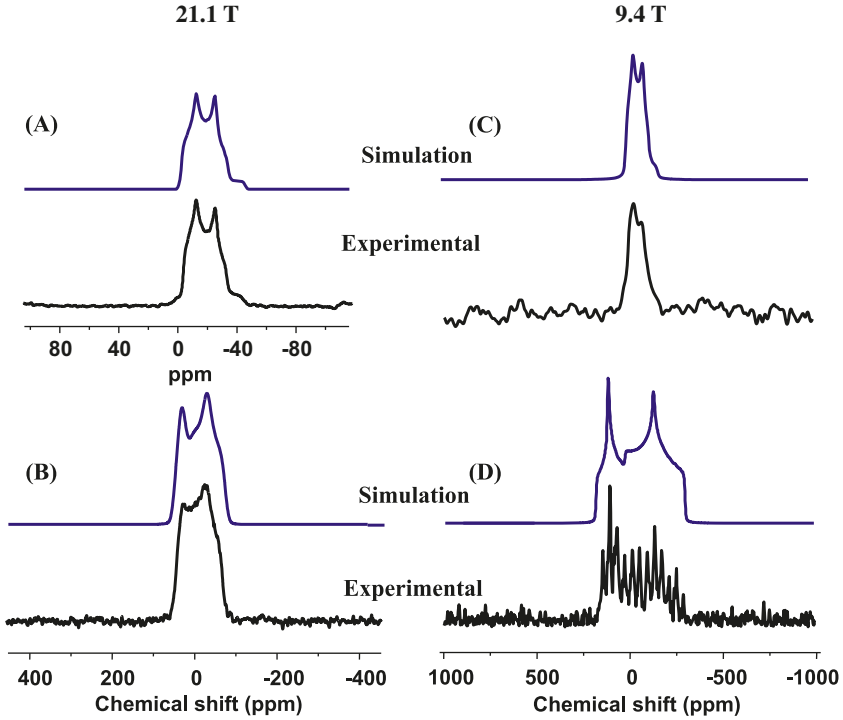

acquisition. To illustrate what is expected at 9.4 T, the spectra calculated by using the EFG parameters obtained from the 21.1 T spectra are shown in Figs. 2C and 2D.

Observing a small C_Q of 1.7 MHz is somewhat surprising because, although the variation in Mg–O bond length (2.024–2.211 Å) is not extremely large, the dispersion of the O–Mg–O bond angle in the MgO_6 octahedron is rather substantial, ranging from 67.33° to 101.93°. A possible explanation is that the spatial arrangement of the atoms beyond the oxygens in the first coordination sphere results in a charge distribution that partially cancels out the effect of the angle distortion in MgO_6, leading to an overall small C_Q value. The C_Q values of various inorganic magnesium salts[20–25] and magnesium silicates[18,19] reported in the literature also have similar magnitudes (<5 MHz). The value of η_Q is 0.5, implying that the EFG tensor is not axially symmetric, which is consist with the low site symmetry of the Mg site (C_s).

UiO-24-DAB

The crystal structure of UiO-24-DAB suggests that there exists only a single Mg site.[13] Indeed, the ^{25}Mg MAS spectrum at 21.1 T (Fig. 3A) shows only one signal with a typical line shape resulting from the second-order quadrupolar interaction. Fitting the MAS spectrum gives a single set of parameters: δ_{iso} = 2 ppm, C_Q = 2.7 MHz, and η_Q = 0.4, which can also be used to simulate the static-echo spectrum at 21.1 T (Fig. 3B) without CSA. ^{25}Mg MAS and static DFS-QCPMG spectra at a lower field of 9.4 T were also obtained. The same set of EFG parameters extracted from the spectra of 21.1 T can be used to well simulate the spectra of 9.4 T, confirming that these parameters are reliable. The spectra (Fig. 3) are broader than the corresponding ones of dittmarite (Fig. 2) because of a larger Mg C_Q in UiO-24-DAB.

Compared with dittmarite, the larger C_Q value of 2.7 MHz in UiO-24-DAB is probably due to a more distorted MgO_6 octahedron. The crystal structure of UiO-24-DAB, indeed, shows that the Mg–O bond lengths are more dispersed and that the O–Mg–O angles are more distorted[13]: the Mg–O bond lengths are in the range of 2.039–2.300 Å with a maximum difference of 0.261 Å, larger than that in dittmarite (0.187 Å); the O–Mg–O bond angles are in the range of 66.54°–101.37° with a maximum difference of 34.83°, also slightly larger than that in dittmarite (34.60°).

UiO-24-EN

There is also one Mg lattice site in UiO-24-EN.[13] Similarly, ^{25}Mg MAS and static spectra of this material were acquired at both 21.1 and 9.4 T (Fig. 4). The spectra are again dominated by the EFG as indicated by the observation that the signals, especially the static ones, exhibit typical line shapes owing to the second-order quadrupolar interactions. Furthermore, the resonance becomes much narrower at 21.1 T. The spectra of UiO-24-EN are broader than those of UiO-24-DAB, indicating a larger C_Q. Simulating the MAS spectra yields the following parameters: δ_{iso} = 4 ppm, C_Q = 3.3 MHz, and η_Q = 0.5. The static spectra can also be well fitted without the CSA. The larger EFG at the Mg can be attributed again to the more distorted MgO_6 octahedron. This is consistent with the crystal structure data[13] showing a large Mg–O bond length distribution from 2.006 to 2.360 Å and a large O–Mg–O bond angle range from 66.39° to 103.76°.

Can. J. Chem. Downloaded from www.nrcresearchpress.com by Xi'an Jiaotong University on 09/19/12
For personal use only.

Fig. 4. ^{25}Mg MAS (A) and (C) and static (B) and (D) NMR spectra of $[NH_3(CH_2)_2NH_3]_{0.5}[MgPO_4{\cdot}H_2O]$ (UiO-24-EN) at 21.1 and 9.4 T. A recycle delay of 5 s was used at both fields. Scans (8192 and 2284), corresponding to 11.4 and 3.2 h, were collected for the static and MAS spectra at 21.1 T, respectively. Scans (65 504 and 38 800), corresponding to 91.0 and 53.9 h, were collected for the static and MAS spectra at 9.4 T, respectively.

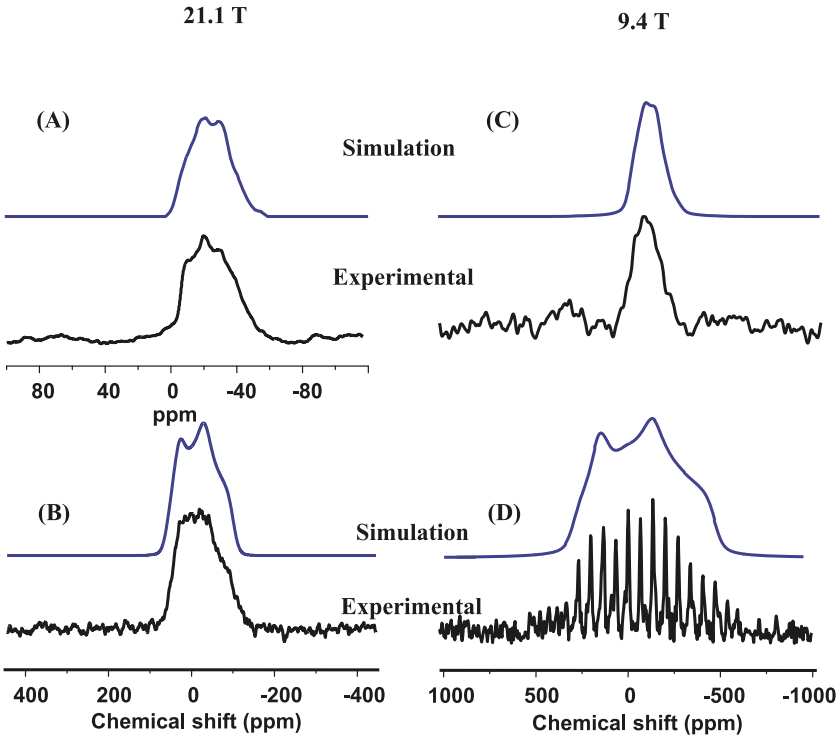

Can. J. Chem. Downloaded from www.nrcresearchpress.com by Xi'an Jiaotong University on 09/19/12
For personal use only.

Correlations between the C_Q and the distortion of MgO_6 octahedra

With insertion of the organic templates into the interlayer space of dittmarite, the MgO_6 octahedra become more distorted, resulting in larger C_Q values. In the literature, linear correlations between the C_Q values and the parameters describing the distortion of the metal–oxygen octahedron in MgO_6,[16,19] ZnO_6,[62] AlO_6,[63,64] TiO_6,[1,65,66] and ZrO_6[4] have been reported. Several parameters have been suggested for estimating the relative degree of distortion around an octahedral site. The simplest parameter characterizing the distortion of the octahedral bond angle is the angular distortion index (DI) of Baur[67] defined as

$$[1] \qquad \mathrm{DI} = (\sum |\Theta_i - \Theta_m|)/12\Theta_m \qquad (i = 1 - 12)$$

where Θ_i and Θ_m are the observed and undistorted bond angles, respectively. The other parameters are the shear strain (ψ) and the longitudinal strain (α) suggested by Ghose and Tsang,[68] defined as

$$[2] \qquad \psi = \sum |\tan(\Theta_i - \Theta_m)| \qquad (i = 1 - 12)$$

$$[3] \qquad \alpha = \sum |\ln(l_i/l_0)| \qquad (i = 1 - 6)$$

where l_0 is the "ideal" Mg–O bond length, a perfect octahedron with bond length l_0 having the same volume as the "real" octahedron.

The DI, ψ, and α values of the Mg sites in dittmarite, UiO-24-DAB, and UiO-24-EN were calculated from their crystal structures. The distortion parameters are compared with their NMR parameters in Table 1. The C_Q values follow the trend mentioned above, i.e., the more distorted site has a larger quadrupolar coupling constant. The isotropic shifts of different compounds differ only by several ppm, suggesting that δ_{iso} is not sensitive to the distortion of the MgO_6 octahedra.

To examine the relationship between C_Q and the degree of distortion in the MgO_6 octahedra, the four C_Q values (from the three compounds under investigation and the origin assuming C_Q is zero for a perfect MgO_6 octahedron) were plotted against the three distortion parameters. As shown in Figs. 5A and 5B, the data points in the plots of C_Q against the angular parameters (DI and ψ) are rather scattered. On the other hand, an approximate linear correlation between C_Q and α appears to exist (Fig. 5C).

$$[4] \qquad C_Q\,(\mathrm{MHz}) = 10.5 * \alpha - 0.08$$

Similar phenomena were reported by Smith and co-workers[21] for some Mg oxyanion compounds. Since both the angular and the bond length distortions contribute to the EFG and, consequently, the C_Q, a parameter reflecting the contributions from the distortion of both bond angle and bond length may give a better correlation with the C_Q. Here we simply use the product of the angular and bond length distortion parameters such as DI*α and ψ*α. Indeed, slightly better linear correlations were established when these new parameters were used (Figs. 5D and 5E).

Table 1. Fitting parameters of the ^{25}Mg spectra of magnesium phosphates (MgPs) and calculated [MgO_6] octahedra distortion parameters of MgPs from their structure data.

Compound	δ_{iso} (ppm)	C_Q (MHz)	η_Q	DI	Shear strain (ψ)	Longitudinal strain (α)
Dittmarite	2±1	1.7±0.1	0.5±0.1	0.0591	1.139	0.226
UiO-24-DAB	2±2	2.7±0.1	0.4±0.1	0.0620	1.197	0.232
UiO-24-EN	4±2	3.3±0.2	0.5±0.1	0.0651	1.259	0.301
$MgHPO_4{\cdot}1.2H_2O$	−1±2	3.5±0.2	0.6±0.1	0.0625	1.202	0.341

Note: δ_{iso}, isotropic chemical shift; C_Q, quadrupolar coupling constant; η_Q, asymmetry parameter; and DI, Baur's angular distortion index.

Can. J. Chem. Downloaded from www.nrcresearchpress.com by Xi'an Jiaotong University on 09/19/12
For personal use only.

Fig. 5. Correlation between (A) the quadrupolar coupling constant (C_Q) and angular DI, (B) C_Q and the shear strain (ψ), (C) C_Q and the longitudinal strain (α), and C_Q and a combination of angular and bond length distortion parameters (D) DI*α and (E) ψ*α.

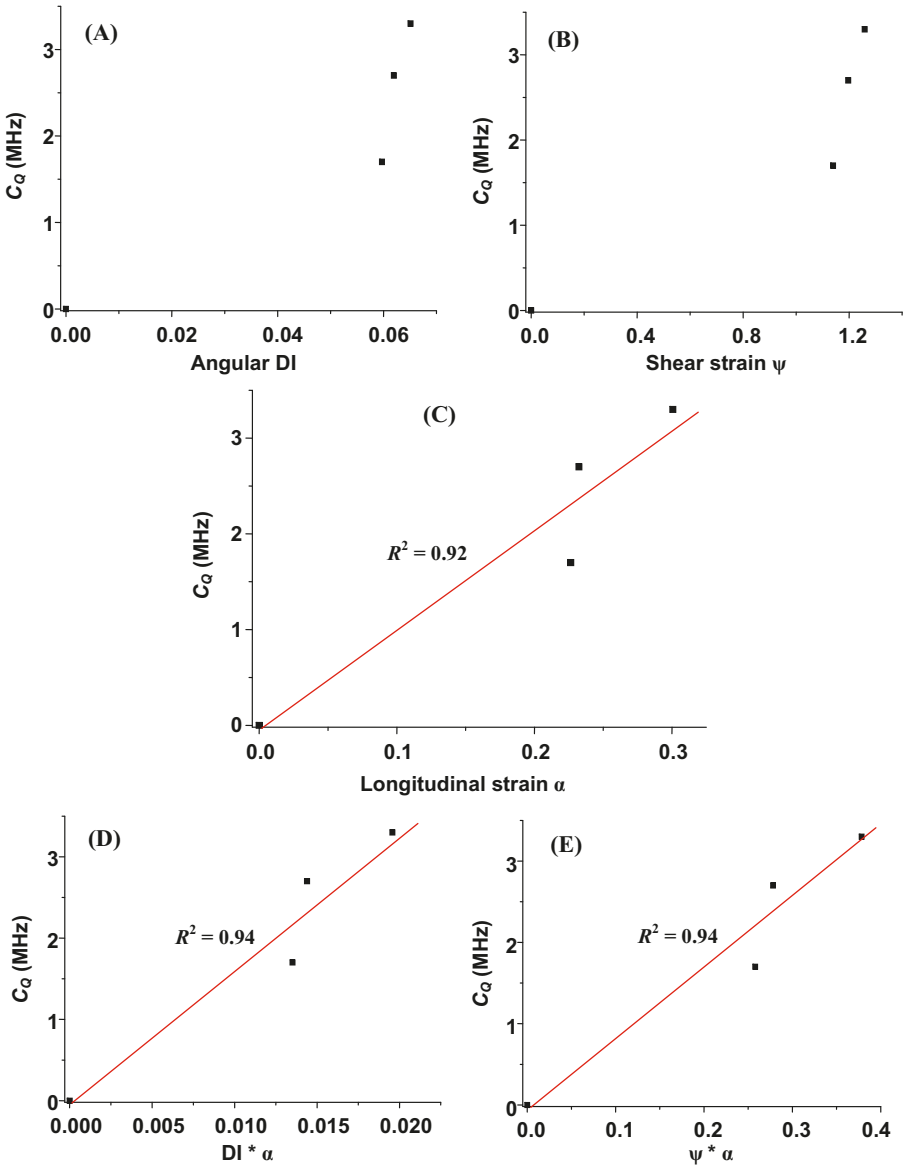

$$[5] \quad C_Q\,(\mathrm{MHz}) = 167.4{*}\mathrm{DI}{*}\alpha - 0.06$$

$$[6] \quad C_Q\,(\mathrm{MHz}) = 8.69{*}\psi{*}\alpha - 0.06$$

We wish to point out that these correlations should only be used as a guideline for estimating the parameters that describe the local environment around Mg in a material with unknown structure. This is because the structural parameters used to establish the correlations were derived from powder

Fig. 6. Clusters used in the ab initio calculations. (A) MgO_6H_{10} and (B) $Mg_5P_4O_{32}H_{34}$. H atoms in (B) are omitted for clarity.

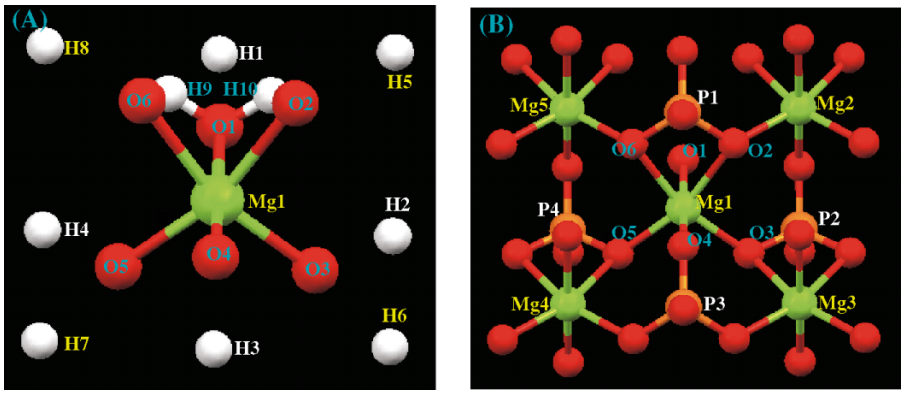

XRD data, which are much less reliable than those from single crystal work.

Theoretical calculations

To verify these empirical correlations, which are only based on four points, theoretical calculations were performed. The ab initio calculations were first carried out on a simple model compound, MgO_6H_{10} (Fig. 6A). The model consists of a MgO_6 octahedron and 10 H atoms connected to the 6 O atoms. The 10 H atoms are H1–H4 replacing P1–P4 (Fig. 6B), H5–H8 replacing Mg2–Mg5, and H9–H10 from the water molecule coordinated to Mg1. The calculation results (Fig. 7 and Table 2) are basis set dependent. However, the calculations do give the same trend as the experimental ones i.e., C_Q increases from dittmarite to UiO-24-DAB to UiO-24-EN with increasing distortion of the MgO_6 octahedra (Fig. 7), regardless of the basis sets used. The calculated trends are consistent with the empirical correlations between the C_Q and MgO_6 distortion parameters. However, all of the calculations overestimate the magnitude of the C_Q value for each compound. This is not completely unexpected, since the distortions of the MgO_6 octahedra are quite large and, therefore, should lead to large C_Q values. The reason why experimentally measured C_Q values are smaller might be due to the fact that the nature and the location of the atoms beyond the first coordination sphere also contribute to the C_Q, since the EFG is a long-range effect. It is possible that the spatial arrangements of the atoms in the second and third coordination spheres and even beyond affect the EFG in such a way that their contributions partially offset that from the distortion of the MgO_6 octahedron.

To verify this argument, the larger clusters with a composition of $Mg_5P_4O_{32}H_{34}$ (Fig. 6B) were truncated from the crystal structures. Indeed, smaller C_Q values (Table 2) that are in better agreement with the experimental ones were obtained. Among the basis sets used, the 6–31++G** basis set seemed to give overall the best predictions.

The Gaussian calculation results suggest that even larger clusters should be employed. This would, however, require much more expensive calculations. Alternatively, CASTEP,[52] a program able to calculate electronic properties of periodic structures, was applied. The results are also listed in Table 2. The calculations give the right trend, i.e., the C_Q values decrease in the order dittmarite < UiO-24-DAB < UiO-24-EN. However, the C_Q values calculated using the CASTEP are still overestimated. This is probably because the large number of atoms in unit cells limits the accuracy level of the calculation that can be performed. The fact that the model clusters used for calculation were built upon the structure derived from powder XRD data, which are not accurate enough, may also have led to the discrepancies between experimental and calculated C_Q values.

Fig. 7. Comparison of experimental and calculated quadrupolar coupling constant (C_Q) values of ^{25}Mg in dittmarite, $[NH_3(CH_2)_4NH_3]_{0.5}[MgPO_4{\cdot}H_2O]$ (UiO-24-DAB), and $[NH_3(CH_2)_2NH_3]_{0.5}[MgPO_4{\cdot}H_2O]$ (UiO-24-EN). The calculations were performed using the MgO_6H_{10} cluster with different basis sets.

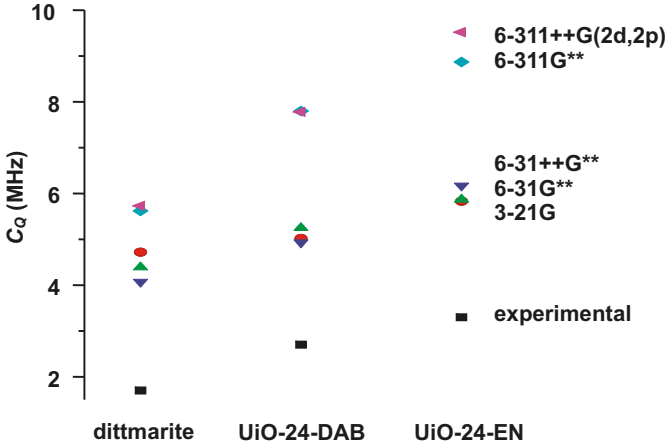

$MgHPO_4{\cdot}1.2H_2O$

The empirical relationships between C_Q and the structural parameters are useful. It allows one to extract, at least, partial information on the Mg local structure for the MgPs with unknown crystal structures, which is often the case for the MP derivatives. To illustrate this point, a layered acidic magnesium phosphate, $MgHPO_4{\cdot}1.2H_2O$,[39] was examined.

$MgHPO_4{\cdot}1.2H_2O$ was first synthesized in 1993 by Thomas and co-workers.[39] The special feature of this compound is that, unlike most layered magnesium phosphates, it undergoes reversible hydration up to 200 °C. The powder XRD pattern of the material synthesized in this study is shown in Fig. 8A. The number of reflections and their d spacing are exactly the same as those reported in the literature.[39,69] The pattern suggests that this material has an interlayer distance

Can. J. Chem. Downloaded from www.nrcresearchpress.com by Xi'an Jiaotong University on 09/19/12
For personal use only.

Can. J. Chem. Downloaded from www.nrcresearchpress.com by Xi'an Jiaotong University on 09/19/12
For personal use only.

Table 2. Calculated quadrupolar coupling constant (C_Q) and asymmetry parameter (η_Q) values of ^{25}Mg in dittmarite, $NH_3(CH_2)_4NH_3]_{0.5}[MgPO_4{\cdot}H_2O]$ (UiO-24-DAB), and $[NH_3(CH_2)_2NH_3]_{0.5}[MgPO_4{\cdot}H_2O]$ (UiO-24-EN0 using the clusters in Fig. 6. The CASTEP calculation results are also included.

		MgO_6H_{10}		$Mg_5P_4O_{32}H_{34}$	
Compound	Basis set	C_Q (MHz)	η_Q	C_Q (MHz)	η_Q
Dittmarite	3–21G	4.72	0.91	6.08	0.82
	6–31G**	4.39	0.78	2.36	0.48
	6–31++G**	4.07	0.79	2.26	0.39
	6–311G**	5.62	0.81	2.93	0.36
	6–311++G(2d,2p)	5.73	0.82	2.85	0.34
	CASTEP	—	—	2.8	0.68
	Experimental	—	—	1.7	0.5
UiO-24-DAB	3–21G	5.02	0.48	4.46	0.79
	6–31G**	5.25	0.55	1.76	0.49
	6–31++G**	4.93	0.49	1.93	0.39
	6–311G**	7.80	0.54	2.52	0.20
	6–311++G(2d,2p)	7.78	0.49	2.52	0.30
	CASTEP	—	—	4.6	0.99
	Experimental	—	—	2.7	0.4
UiO-24-EN	3–21G	5.83	0.92	9.37	0.16
	6–31G**	5.87	0.98	4.97	0.52
	6–31++G**	6.17	0.88	4.79	0.57
	6–311G**	8.87	0.96	6.52	0.58
	6–311++G(2d,2p)	9.52	0.83	6.58	0.56
	CASTEP	—	—	4.9	0.76
	Experimental	—	—	3.3	0.5

Fig. 8. (A) Powder X-ray diffraction (XRD) pattern of $MgHPO_4{\cdot}1.2H_2O$ and (B) and (D)^{25}Mg static NMR spectra and (C) MAS NMR spectra of Mg in $MgHPO_4{\cdot}1.2H_2O$ at (B) 9.4 and (C) and (D) 21.1 T. Recycle delays of 5 and 0.5 s were used for 21.1 and 9.4 T, respectively. Scans (8192 and 1400), corresponding to 11.4 and 1.9 h, were collected for the static and MAS spectra at 21.1 T, respectively. Scans (129 760), corresponding to 18.0 h, were collected for the static spectrum at 9.4 T. (* denotes spinning side bands.)

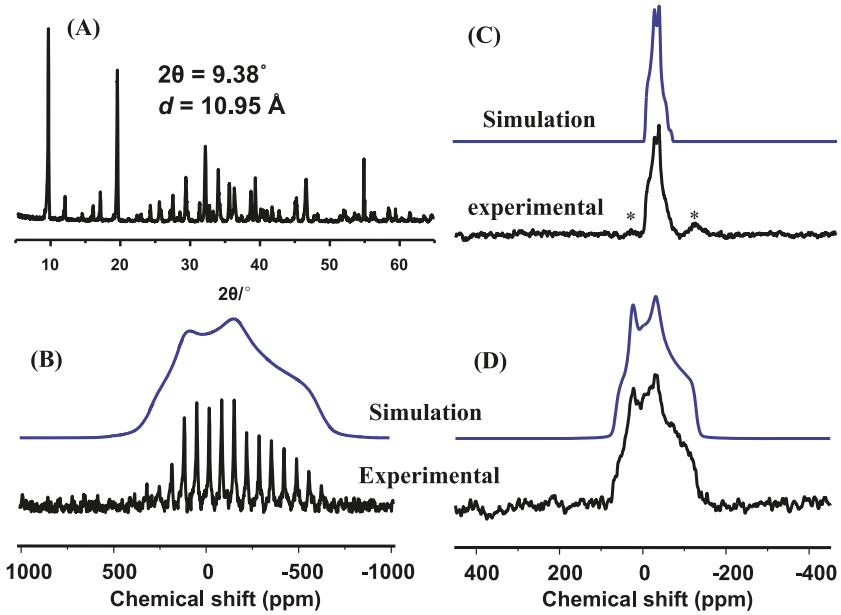

of 10.95 Å. Although the powder XRD data can be indexed on an orthorhombic cell, the crystal structure of this compound has yet to be solved. ^{31}P MAS NMR spectrum (Fig. S2 in the Supplementary data) shows that there are two crystallographically nonequivalent P sites with equal occupancy.

To characterize the local Mg environment in this material, the ^{25}Mg MAS spectrum at 21.1 T was first acquired (Fig. 8C). The spectrum shows a typical line shape owing to the second-order quadrupolar coupling and can be well fitted using a single set of parameters: $\delta_{iso} = -1$ ppm, $C_Q = 3.5$ MHz, and $\eta_Q = 0.6$, suggesting that there is only one Mg site. The static spectrum at 21.1 T also exhibits a typical

Can. J. Chem. Downloaded from www.nrcresearchpress.com by Xi'an Jiaotong University on 09/19/12
For personal use only.

quadrupolar line shape and can be well simulated using the above parameters without the CSA. The ^{25}Mg static DFS-QCPMG spectrum of $MgHPO_4 \cdot 1.2H_2O$ at 9.4 T was obtained and it can be well simulated by using the parameters extracted from the spectra at 21.1 T, confirming the reliability of these parameters. Using the C_Q value and eqs. [4]–[6], α, DI*α, and ψ*α are calculated to be 0.341, 0.0213, and 0.410, respectively. Further, using the α value derived from eq. [4], the angular DI and ψ were further calculated to be 0.0625 and 1.202. Comparing these distortion parameters with other MgPs discussed earlier (Table 1), the MgO_6 octahedron in $MgHPO_4 \cdot 1.2H_2O$ should have a larger bond length dispersion than all other three MgPs, whereas the angular distortion is similar to that of UiO-24-DAB.

Conclusions

In this work, ^{25}Mg MAS and static NMR spectra of several representative MgPs at two field strengths were acquired. The spectra are dominated by the second-order quadrupolar interaction. From the observed spectra, the quadrupolar parameters were extracted via spectral simulations. In this series of related layered MgPs, the C_Qs are sensitive to the distortion in the MgO_6 octahedron. Correlations between C_Q and the structural parameters reflecting the distortion such as α and its products with angular DI and ψ (DI*α, and ψ*α) were observed. Theoretical calculation results showed that the EFG and, therefore, the C_Q of the Mg site are not only determined by the distortion of the MgO_6 octahedron but also affected by the spatial arrangement of the atoms in the second and third coordination spheres. Solid-state ^{25}Mg NMR was used to obtain partial structural information on $MgHPO_4 \cdot 1.2H_2O$, which belongs to the same class of layered MgP, but the structure is unknown. The results show that this material only has a single Mg site and the MgO_6 octahedron has a large Mg–O bond length dispersion.

Supplementary data

Supplementary data are available with the article through the journal Web site (www.nrcresearchpress.com/cjc).

Acknowledgements

Y.H. acknowledges the financial support from the Natural Sciences and Engineering Research Council of Canada (NSERC) for a research grant and the Canadian Foundation for Innovation (CFI) for the equipment grants. Funding from the Canada Research Chair program is also gratefully acknowledged. Access to the 900 MHz NMR spectrometer was provided by the National Ultrahigh Field NMR Facility for Solids (Ottawa, Ontario), a national research facility funded by the CFI, the Ontario Innovation Trust, Recherche Québec, the National Research Council of Canada, and Bruker BioSpin, and managed by the University of Ottawa (http://nmr900.ca). The authors wish to thank Professor R.W. Schurko (University of Windsor, Windsor, Ontario) for providing the DFS-QCPMG pulse sequence and Professor R.E. Wasylishen (University of Alberta) for the WSOLIDS1 software. They also thank Drs. Terskikh, Pawsey, and Kirby for technical assistance in the NMR experiments.

References

(1) Zhu, J.; Trefiak, N.; Woo, T.; Huang, Y. *J. Phys. Chem. C* **2009** *113* (23), 10029. doi:10.1021/jp901235w.
(2) Zhu, J.; Huang, Y. *Inorg. Chem.* **2009** *48* (21), 10186. doi:10.1021/ic9011668.
(3) Zhu, J.; Huang, Y. *Langmuir* **2010** *26* (12), 10115. doi:10.1021/la100232s.
(4) Yan, Z.; Kirby, C. W.; Huang, Y. *J. Phys. Chem. C* **2008** *112* (23), 8575. doi:10.1021/jp711137c.
(5) Shul'ga, N. B.; Samusevich, V. V. *Russ. J. Appl. Chem.* **2002** *75* (3), 378. doi:10.1023/A:1016126301249.
(6) Shashkova, I. L.; Rat'ko, A. I.; Kitikova, N. V. *Coll. Surf. A* **1999** *160* (3), 207. doi:10.1016/S0927-7757(99)00193-4.
(7) Sugiyama, S.; Yokoyama, M.; Ishizuka, H.; Sotowa, K.-I.; Tomida, T.; Shigemoto, N. *J. Coll. Inter. Sci.* **2005** *292* (1), 133. doi:10.1016/j.jcis.2005.05.073.
(8) Aramendía, M. A.; Borau, V.; Jiménez, C.; Marinas, J. M.; Romero, F. J. *Catal. Lett.* **1999** *58* (1), 53. doi:10.1023/A:1019088708653.
(9) Aramendia, M. A.; Borau, V.; Jimenez, C. *J. Mol. Catal. A* **2002** *182–183*, 25. doi:10.1016/S1351-1169(01)00463-0.
(10) Sugiyama, S.; Kondo, N.; Satomi, K.; Hayashi, H.; Moffat, J. B. *J. Mol. Catal. A* **1995** *95* (1), 35. doi:10.1016/1381-1169(94)00160-X.
(11) Aramendía, M. A.; Borau, V.; Jiménez, C.; Marinas, J. M.; Romero, F. J. *React. Kinet. Catal. Lett.* **2000** *69* (2), 311. doi:10.1023/A:1005656001675.
(12) Kongshaug, K. O.; Fjellvag, H.; Lillerud, K. P. *Chem. Mater.* **1999** *11* (10), 2872. doi:10.1021/cm991056z.
(13) Kongshaug, K. O.; Fjellvåg, H.; Lillerud, K. P. *J. Mater. Chem.* **2000** *10* (8), 1915. doi:10.1039/b001715i.
(14) Mackenzie, K. J. D.; Smith, M. E. *Multinuclear Solid State NMR of Inorganic Materials;* Pergamon: Oxford, 2002.
(15) Pyykko, P. *Mol. Phys.* **2001** *99* (19), 1617. doi:10.1080/00268970110069010.
(16) Dupree, R.; Smith, M. E. *J. Chem. Soc. Chem. Commun.* **1988** (22), 1483. doi:10.1039/c39880001483.
(17) Bastow, T. J. *Chem. Phys. Lett.* **2002** *354* (1–2), 156. doi:10.1016/S0009-2614(02)00135-5.
(18) Fiske, P. S.; Stebbins, J. F. *Am. Mineral.* **1994** *79*, 848.
(19) MacKenzie, K. J. D.; Meinhold, R. H. *Am. Mineral.* **1997** *82*, 479.
(20) Pallister, P. J.; Moudrakovski, I. L.; Ripmeester, J. A. *Phys. Chem. Chem. Phys.* **2009** *11* (48), 11487. doi:10.1039/b916076k.
(21) Cahill, L. S.; Hanna, J. V.; Wong, A.; Freitas, J. C.; Yates, J. R.; Harris, R. K.; Smith, M. E. *Chemistry* **2009** *15* (38), 9785. doi:10.1002/chem.200900346.
(22) Widdifield, C. M.; Bryce, D. L. *Phys. Chem. Chem. Phys.* **2009** *11* (33), 7120. doi:10.1039/b911448n.
(23) Shimoda, K.; Nemoto, T.; Saito, K. *J. Phys. Chem. B* **2008** *112* (22), 6747. doi:10.1021/jp711417t.
(24) Davis, M. C.; Brouwer, W. J.; Wesolowski, D. J.; Anovitz, L. M.; Lipton, A. S.; Mueller, K. T. *Phys. Chem. Chem. Phys.* **2009** *11* (32), 7013. doi:10.1039/b907494e.
(25) Lipton, A. S.; Sears, J. A.; Ellis, P. D. *J. Magn. Reson.* **2001** *151* (1), 48. doi:10.1006/jmre.2001.2353.
(26) Wong, A.; Ida, R.; Mo, X.; Gan, Z.; Poh, J.; Wu, G. *J. Phys. Chem. A* **2006** *110* (33), 10084. doi:10.1021/jp061350w.
(27) Hung, I.; Schurko, R. W. *Solid State Nucl. Magn. Reson.* **2003** *24* (2–3), 78. doi:10.1016/S0926-2040(03)00050-X.
(28) Wu, G.; Wong, A.; Wang, S. *Can. J. Chem.* **2003** *81* (4), 275. doi:10.1139/v03-036.

Can. J. Chem. Downloaded from www.nrcresearchpress.com by Xi'an Jiaotong University on 09/19/12
For personal use only.

(29) Freitas, J. C.; Wong, A.; Smith, M. E. *Magn. Reson. Chem.* **2009** *47* (1), 9. doi:10.1002/mrc.2328.
(30) Lipton, A. S.; Heck, R. W.; Primak, S.; McNeill, D. R.; Wilson, D. M.; Ellis, P. D. *J. Am. Chem. Soc.* **2008** *130* (29), 9332. doi:10.1021/ja0776881.
(31) Grant, C. V.; Frydman, V.; Frydman, L. *J. Am. Chem. Soc.* **2000** *122* (47), 11743. doi:10.1021/ja003188v.
(32) Sham, S.; Wu, G. *Inorg. Chem.* **2000** *39* (1), 4. doi:10.1021/ic991060c.
(33) Zhu, J.; Lin, Z.; Yan, Z.; Huang, Y. *Chem. Phys. Lett.* **2008** *461* (4–6), 260. doi:10.1016/j.cplett.2008.07.030.
(34) Bastow, T. J.; Celotto, S. *Solid State Nucl. Magn. Reson.* **2009** *35* (4), 217. doi:10.1016/j.ssnmr.2009.02.002.
(35) Gan, Z.; Gor'kov, P. L.; Brey, W. W.; Sideris, P. J.; Grey, C. P. *J. Magn. Reson.* **2009** *200* (1), 2. doi:10.1016/j.jmr.2009.05.008.
(36) Larsen, F. H.; Jakobsen, H. J.; Ellis, P. D.; Nielsen, N. C. *J. Phys. Chem. A* **1997** *101* (46), 8597. doi:10.1021/jp971547b.
(37) Siegel, R.; Nakashima, T. T.; Wasylishen, R. E. *Chem. Phys. Lett.* **2004** *388* (4–6), 441. doi:10.1016/j.cplett.2004.03.047.
(38) Tang, J. A.; O'Dell, L. A.; Aguiar, P. M.; Lucier, B. E. G.; Sakellariou, D.; Schurko, R. W. *Chem. Phys. Lett.* **2008** *466* (4–6), 227. doi:10.1016/j.cplett.2008.10.044.
(39) Chen, J.; Natarajan, S.; Wright, P. A.; Jones, R. H.; Thomas, J. M.; Catlow, C. R. A.; Townsend, R. P. *J. Solid State Chem.* **1993** *103* (2), 519. doi:10.1006/jssc.1993.1130.
(40) Kunwar, A. C.; Turner, G. L.; Oldfield, E. *J. Magn. Reson.* **1986** *69*, 124.
(41) Schurko, R. W.; Hung, I.; Widdifield, C. M. *Chem. Phys. Lett.* **2003** *379* (1–2), 1. doi:10.1016/S0009-2614(03)01345-9.
(42) Kentgens, A. P. M.; Verhagen, R. *Chem. Phys. Lett.* **1999** *300* (3–4), 435. doi:10.1016/S0009-2614(98)01402-X.
(43) Frisch, M. J.; Trucks, G. W.; Schlegel, H. B.; Scuseria, G. E.; Robb, M. A.; Cheeseman, J. R.; Montgomery, J. A., Jr.; Vreven, T.; Kudin, K. N.; Burant, J. C.; Millam, J. M.; Iyengar, S. S.; Tomasi, J.; Barone, V.; Mennucci, B.; Cossi, M.; Scalmani, G.; Rega, N.; Petersson, G. A.; Nakatsuji, H.; Hada, M.; Ehara, M.; Toyota, K.; Fukuda, R.; Hasegawa, J.; Ishida, M.; Nakajima, T.; Honda, Y.; Kitao, O.; Nakai, H.; Klene, M.; Li, X.; Knox, J. E.; Hratchian, H. P.; Cross, J. B.; Bakken, V.; Adamo, C.; Jaramillo, J.; Gomperts, R.; Stratmann, R. E.; Yazyev, O.; Austin, A. J.; Cammi, R.; Pomelli, C.; Ochterski, J. W.; Ayala, P. Y.; Morokuma, K.; Voth, G. A.; Salvador, P.; Dannenberg, J. J.; Zakrzewski, V. G.; Dapprich, S.; Daniels, A. D.; Strain, M. C.; Farkas, O.; Malick, D. K.; Rabuck, A. D.; Raghavachari, K.; Foresman, J. B.; Ortiz, J. V.; Cui, Q.; Baboul, A. G.; Clifford, S.; Cioslowski, J.; Stefanov, B. B.; Liu, G.; Liashenko, A.; Piskorz, P.; Komaromi, I.; Martin, R. L.; Fox, D. J.; Keith, T.; Al-Laham, M. A.; Peng, C. Y.; Nanayakkara, A.; Challacombe, M.; Gill, P. M. W.; Johnson, B.; Chen, W.; Wong, M. W.; Gonzalez, C.; Pople, J. A. *Gaussian 03, Revision C.02;* Gaussian, Inc.: Wallingford, CT, 2004.
(44) Shared Hierarchial Academic Research Computing Network. https://www.sharcnet.ca/my/front/.
(45) Simperler, A.; Bell, R. G.; Philippou, A.; Anderson, M. W. *J. Phys. Chem. B* **2002** *106* (42), 10944. doi:10.1021/jp0257799.
(46) García-Serrano, L. A.; Zaragoza, I. P. *J. Mol. Catal. A* **2003** *200* (1–2), 205. doi:10.1016/S1381-1169(02)00680-5.
(47) Tielens, F.; Denayer, J. F. M.; Daems, I.; Baron, G. V.; Mortier, W. J.; Geerlings, P. *J. Phys. Chem. B* **2003** *107* (40), 11065. doi:10.1021/jp0223760.
(48) Bučko, T.; Hafner, J.; Benco, L. *J. Chem. Phys.* **2004** *120* (21), 10263. doi:10.1063/1.1737302.
(49) Soscún, H.; Castellano, O.; Hernandez, J. *J. Phys. Chem. B* **2004** *108* (18), 5620. doi:10.1021/jp036468g.
(50) Hung, I.; Schurko, R. W. *J. Phys. Chem. B* **2004** *108* (26), 9060. doi:10.1021/jp040270u.
(51) Moore, E. A.; Johnson, C.; Mortimer, M.; Wigglesworth, C. *Phys. Chem. Chem. Phys.* **2000** *2* (6), 1325. doi:10.1039/a909011h.
(52) Segall, M.; Lindan, P. J. D.; Probert, M. J.; Pickard, C. J.; Hasnip, P. J.; Clark, S. J.; Payne, M. C. *J. Phys. Condens. Matter* **2002** *14* (11), 2717. doi:10.1088/0953-8984/14/11/301.
(53) Benoit, M.; Profeta, M.; Mauri, F.; Pickard, C. J.; Tuckerman, M. E. *J. Phys. Chem. B* **2005** *109* (13), 6052. doi:10.1021/jp0492570.
(54) Zwanziger, J. W.; Shaw, J. L.; Werner-Zwanziger, U.; Aitken, B. G. *J. Phys. Chem. B* **2006** *110* (41), 20123. doi:10.1021/jp062432n.
(55) Zwanziger, J. W.; Werner-Zwanziger, U.; Shaw, J. L.; So, C. *Solid State Nucl. Magn. Reson.* **2006** *29* (1-3), 113. doi:10.1016/j.ssnmr.2005.09.010.
(56) Hart, R. T.; Zwanziger, J. W.; Werner-Zwanziger, U.; Yates, J. R. *J. Phys. Chem. A* **2005** *109* (33), 7636. doi:10.1021/jp052405h.
(57) Charpentier, T.; Ispas, S.; Profeta, M.; Mauri, F.; Pickard, C. J. *J. Phys. Chem. B* **2004** *108* (13), 4147. doi:10.1021/jp0367225.
(58) Ashbrook, S. E.; Le Pollès, L.; Gautier, R.; Pickard, C. J.; Walton, R. I. *Phys. Chem. Chem. Phys.* **2006** *8* (29), 3423. doi:10.1039/b604520k.
(59) Bryce, D. L.; Bultz, E. B. *Chemistry* **2007** *13* (17), 4786. doi:10.1002/chem.200700056.
(60) Harris, R. K.; Joyce, S. A.; Pickard, C. J.; Cadars, S.; Emsley, L. *Phys. Chem. Chem. Phys.* **2006** *8* (1), 137. doi:10.1039/b513392k.
(61) Mifsud, N.; Elena, B.; Pickard, C. J.; Lesage, A.; Emsley, L. *Phys. Chem. Chem. Phys.* **2006** *8* (29), 3418. doi:10.1039/b605227d.
(62) Sham, S.; Wu, G. *Can. J. Chem.* **1999** *77* (11), 1782. doi:10.1139/v99-154.
(63) Engelhardt, G.; Veeman, W. *J. Chem. Soc., Chem. Commun.* **1993** 622. doi:10.1039/C39930000622.
(64) Jansen, S. R.; Hintzen, H. T. *J. Phys. Chem. B* **1998** *102* (31), 5969. doi:10.1021/jp981224v.
(65) Padro, D.; Smith, M. E.; Dupree, R. *Solid State NMR* **2000** *15* (4), 231. doi:10.1016/S0926-2040(99)00061-2.
(66) Thomas, P. A.; Baldwin, A.; Dupree, R.; Blaha, P.; Schwarz, K.; Samoson, A.; Gan, Z. H. *J. Phys. Chem. B* **2004** *108* (14), 4324. doi:10.1021/jp037473n.
(67) Baur, W. H. *Acta Crystallogr.* **1974** *B30*, 1195.
(68) Ghose, S.; Tsang, T. *Am. Mineral.* **1973** *58*, 748.
(69) Bensalem, A.; Iyer, G.; Amar, S. *Mater. Res. Bull.* **1995** *30* (12), 1471. doi:10.1016/0025-5408(95)00168-9.

$[Pt@Pb_{12}]^{2-}$ — A challenging system for relativistic density functional theory calculations of ^{195}Pt and ^{207}Pb NMR parameters

Boris Le Guennic and Jochen Autschbach

Can. J. Chem. Downloaded from www.nrcresearchpress.com by Xi'an Jiaotong University on 09/19/12
For personal use only.

Abstract: We report computations of NMR chemical shifts and indirect spin-spin coupling constants (*J* couplings) for the $[Pt@Pb_{12}]^{2-}$ "superatom". The system is strongly influenced by relativistic effects. The Pt–Pb coupling constant is predicted to be negative, with its magnitude being in reasonable agreement with experiment. Pt and Pb chemical shifts also agree reasonably well with experiment. The Pb shielding tensor is strongly anisotropic, with a large deshielding principal component dominated by magnetic coupling between frontier orbitals of the cluster that resemble atomic g orbitals. The NMR parameters are sensitive to approximations made in the computations and require the inclusion of spin-orbit coupling in the theoretical model to achieve reliable results. Computing the NMR parameters of the compact $[Pt@Pb_{12}]^{2-}$ system with its many electrons proves to be a challenging test case for relativistic density functional methods.

Key words: NMR shielding, NMR indirect spin-spin coupling, relativistic quantum chemistry, density functional theory, superatoms.

Résumé : Les déplacements chimiques RMN ainsi que les constantes de couplage spin-spin indirectes (couplages *J*) ont été calculés pour le « super-atome » $[Pt@Pb_{12}]^{2-}$ pour lequel les effets relativistes jouent un rôle primordial. Il est ainsi proposé que la constante de couplage Pt–Pb est probablement négative, son amplitude étant en bon accord avec les résultats expérimentaux. De même, les déplacements chimiques tant du Pt que du Pd reproduisent raisonnablement les données expérimentales. Le tenseur de blindage du Pb est fortement anisotrope, avec une importante composante principal de déblindage dominée par le couplage magnétique entre les orbitales frontières du cluster ressemblant à des orbitales atomiques de type g. Les paramètres RMN sont fortement sensibles aux approximations faites dans les calculs. En particulier, la prise en compte du couplage spin-orbite dans le modèle théorique est indispensable pour obtenir des résultats fiables. Le calcul des paramètres RMN du système compact $[Pt@Pb_{12}]^{2-}$, avec ses nombreux électrons, s'est avéré représenter un défi pour les approches DFT relativistes.

Mots-clés : blindage RMN, couplage spin-spin indirect en RMN, chimie quantique relativiste, théorie de la fonctionnelle de la densité, super-atome.

Introduction

The past decade has seen intense research efforts directed at stable metal clusters that can be classified as artificial atoms or *superatoms* that are potential building blocks for nanoscale structures. This is particularly true for gold clusters because of the recent discovery of their fascinating optical, magnetic, and catalytic properties.[1–9] Among the various highly symmetrical geometries adopted by these systems, metal-encapsulated icosahedral gold clusters have been intensively studied both theoretically and experimentally.[10–19]

The closed-shell neutral WAu_{12} cluster may be singled out as a system where theoretical methods have been proven to be particularly useful to guide experimental efforts. Pyykkö and Runeberg[20] first predicted its existence and explained its stability by a synergy of aurophilic attraction and relativistic effects. This species was experimentally synthesized and characterized in the gas phase by Li et al.[10] a few months later. Pyykkö et al.[21] theoretically predicted a large selection of properties for this system, such as vibrational spectra, NMR chemical shifts, spin-spin and quadrupole coupling constants, and optical spectra. WAu_{12} was also used by Qiu et al.[12] as a benchmark molecule in the comparison of several computational approaches for the calculation of interatomic distances, atomization energies, energy gaps, and electron affinities. More recently, photoabsorption and catalytic properties were investigated on the basis of density functional theory (DFT),[16,22] and a DFT molecular dynamics study revealed surface melting of this cluster between ~100 and 200 °C.[23] Finally, Wang and co-workers[19,24] studied the binding energies of a single ligand on WAu_{12} and an isoelectronic series, whereas it was predicted that the metal-

Received 28 December 2010. Accepted 18 February 2011. Published at www.nrcresearchpress.com/cjc on 6 July 2011.

B. Le Guennic. Université de Lyon, Laboratoire de Chimie, Ecole Normale Supérieure de Lyon, CNRS, 46 allée d'Italie, F-69364 Lyon, France.
J. Autschbach. Department of Chemistry, University at Buffalo, State University of New York, Buffalo, NY 14260-3000, USA.

Corresponding author: Jochen Autschbach (e-mail: jochena@buffalo.edu).

This article is part of a Special Issue dedicated to Professor Roderick E. Wasylishen.

Can. J. Chem. Downloaded from www.nrcresearchpress.com by Xi'an Jiaotong University on 09/19/12
For personal use only.

surface-protected $W@Au_{12}(CO)_{12}$ molecule could exist also in the bulk.[25]

However, gold does not have a monopoly of forming ion-encapsulated icosahedral clusters. For instance, several ion-centered plumbaspharene clusters $[MPb_{12}]^x$ (M = Mg, Al, Co, Ni, Pd, Pt; $x = +1$, 0, –1, or –2) have been studied experimentally,[26–30] or predicted theoretically (M = Mg, Al, Sc, Sc, Ti, V, Cr, Mn, Fe, Co, Ni, Ga, In, Sr, Ba, Tl, Pb, Pu; $x = +1$ or 0).[31–36] Among these, one may focus on the inclusion compound $[Pt@Pb_{12}]^{2-}$ synthesized by oxidation of the $[Pb_9]^{4-}$ Zintl ion, since $[Pt@Pb_{12}]^{2-}$ is the only hitherto known Pt-centered bare-metal cluster.[28,29] This lead cluster was mainly characterized by energy-dispersive X-ray analysis and single crystal XRD. However, the present work is motivated by the reported experimental ^{207}Pb and ^{195}Pt NMR spectroscopy data. In particular, the measurement of a Pt–Pb coupling constant allows us to study this fascinating property theoretically, while being able to make a comparison with experimental data. Though there is a significant amount of literature related to ^{207}Pb and ^{195}Pt chemical shifts (see refs. 37–44 for pertinent reviews), measurements of Pb–Pt spin-spin coupling constants are rare. Indeed, since the first reported value of ^1J(Pt–Pb) in platinum–lead bonded compounds by Carr et al.,[45] and the observation of a small Pt–Pb coupling (^1J(Pt–Pb) = 274 Hz) in the ^{195}Pt NMR spectrum of a Pb(II)–Pt(II) complex by Balch et al.,[46] no further data has been published until the work of Esenturk et al.[28,29]

To our knowledge, among the quickly growing amount of works on first-principles relativistic calculations of transition-metal NMR properties (see refs. 44 and 47–53 for recent reviews), relatively few of them were devoted to the computation of ^{207}Pb NMR chemical shifts.[54–57] For early semiempirical calculations of Pb NMR chemical shifts see ref. 58. Calculations of spin-spin couplings of Pb to light nuclei have been addressed in several studies of "benchmark" type character,[59–66] but there are still no computational data on Pb – heavy metal couplings. Following pioneering work by Gilbert and Ziegler,[67] recent years have seen an increasing number of computational studies of Pt NMR parameters.[68–79] However, it remains very challenging to accurately predict Pt NMR parameters because of their strong sensitivity to geometry, solvent effects, relativistic effects, and related approximations in the computational model.[76–78]

The NMR parameters in $[Pt@Pb_{12}]^{2-}$ are particularly fascinating from a theoretical point of view because this system is composed entirely of two of the heaviest NMR active atoms. In the present work, the ^{207}Pb and ^{195}Pt chemical shifts as well as the Pt–Pb and Pb–Pb spin-spin coupling constants of $[Pt@Pb_{12}]^{2-}$ are computed and investigated using relativistic DFT. The results are discussed in comparison with experimental data.[28,29] The tensorial properties[80] of the nuclear magnetic shielding, in particular of Pb in $[Pt@Pb_{12}]^{2-}$, are also considered. We report a rather pronounced sensitivity of the computed data to the level of theory used. Our best theoretical estimates are in reasonable agreement with experimental data, indicating that $J(^{195}Pt–^{207}Pb)$, or J(Pt–Pb) in shorthand notation, is negative. The Pt nucleus inside the Pb cage has an isotropic shielding tensor with a comparatively small paramagnetic component. The Pb shielding tensors are strongly anisotropic. The calculations confirm the large deshielding (downfield shift) of the Pb nuclei relative to the $PbMe_4$ reference noted by the experimentalists that was tentatively attributed to s aromaticity in the Pb_{12} cage.[29]

Computational details

Relativistic DFT computations, based on the zeroth-order regular approximation (ZORA) Hamiltonian,[81] were carried out with 2004 and 2010 versions of the Amsterdam Density Functional (ADF) package.[82,83] The computations employed a modified version[84,85] of the code for the two-component relativistic computation of indirect nuclear spin-spin coupling constants originally developed by Autschbach and Ziegler[61,86] and a modified version[74,87] of the code developed by Wolff et al.[88] for the two-component relativistic computation of nuclear shielding constants. See refs. 68–70 for a more detailed description of the computational protocol. Time-dependent DFT (TDDFT) computations of singlet excitation energies employed the linear scaling code developed by van Gisbergen et al.[89] In all calculations, a distance cut-off parameter of 7.5 was employed to speed up the computations. Numerical integration accuracy parameters of 6.0 and 4.5 were assigned for the atomic cores and the remainder of the molecule, respectively, roughly indicating the number of significant figures for the electron density integration.

The Vosko–Wilk–Nusair (VWN)[90] local density approximation (LDA) functional was used in the geometry optimization and some computations of the NMR parameters. For comparison, the revised Perdew–Burke–Ernzerhof (PBE)[91–94] nonhybrid functional and the PBE0 hybrid density functional[95] (25% Hartree–Fock exchange) were applied in calculations of NMR chemical shifts and J-coupling constants. The geometry optimization was carried out in D_{5d} symmetry employing valence triple-ζ Slater-type atomic orbital (AO) basis sets with polarization functions (TZP). Inner shells up to, but not including 5spd and 6sp for Pt and Pb, were kept as frozen core. All electron Slater-type multiple-z basis sets with one (TZP), two (TZ2P), and for Pt four (QZ4P) sets of polarization functions, respectively, were used for the computations of NMR chemical shifts and spin-spin coupling constants as discussed in the Results section. In addition, for some of the J-coupling computations, the Pt and Pb TZ2P basis were augmented with an even-tempered set of 1s and 2p Slater functions with exponents α up to 10^4 as detailed in ref. 84. We denote this basis set as JCPL. Overall, the computations employed between 1580 and 2182 Cartesian Slater-type basis functions. Unless noted otherwise, the J-coupling computations employed a spherical Gaussian nuclear charge model to model effects from a finite nuclear volume.[85] The magnetogyric ratios used to convert calculated reduced spin-spin coupling constants K to J-coupling constants in units of Hz were 5.8385 and 5.5805 for Pt and Pb, respectively,[96] in units of 10^7 rad (T s)$^{-1}$. Solvent effects have been taken into account in a subset of the computations by using COSMO (conductor-like screening model)[97] as implemented in ADF.[98] The radii of the atomic spheres used in the COSMO calculations were 2.1 and 2.4 Å for Pt and Pb, respectively. The solvent used in the NMR experiments was DMF. Therefore, we used a value of 37 for the dielectric constant in the COSMO calculations.

Can. J. Chem. Downloaded from www.nrcresearchpress.com by Xi'an Jiaotong University on 09/19/12
For personal use only.

Results and discussion

Experimentally, $[Pt@Pb_{12}]^{2-}$ was found to have near-perfect I_h point symmetry. Because of the lack of support of this point symmetry group in the software version used for the geometry optimizations, the geometry optimization was carried out in D_{5d} symmetry, which is a subgroup of I_h. The optimized structure is shown in Fig. 1. Excellent agreement between the optimized and experimental geometries is obtained with average optimized distances of 3.051 Å (expt. 3.058 Å) and 3.209 Å (expt. 3.216 Å) for the Pt–Pb and Pb–Pb bonds, respectively. A comparatively large HOMO–LUMO gap of 1.97 eV is computed with COSMO/PBE/TZP, with a fivefold degenerate HOMO at –3.47 eV and a fourfold degenerate LUMO at –1.51 eV. Gas-phase calculations yielded a positive HOMO but the same frontier orbital degeneracy as the COSMO computations and a comparable value of 1.96 eV for the HOMO–LUMO gap. TDDFT computations with the PBE functional located a set of lowest energy allowed singlet transitions in the range of 2.7 to 3.2 eV both for gas-phase and COSMO computations (scalar ZORA, TZP). The absorption energy range is consistent with the intense reddish brown color reported in refs. 28 and 29.

Some of the scalar relativistic frontier orbitals are shown in Fig. 2. The triply degenerate HOMO-1 level exhibits distinct p-like superatom orbitals with inner nodes in the Pb_{12} cage. The HOMO and LUMO orbitals exhibit the shape and nodal structure of atomic g orbitals that, in a perfectly spherical atom and with equal populations, would be ninefold degenerate. In $[Pt@Pb_{12}]^{2-}$ these g-like orbitals are split into the fivefold degenerate HOMO (of H_g symmetry in the I_h point group[27]) and the fourfold degenerate LUMO (G_g). The orbital diagram in Fig. 1 indicates that these are linear combinations of Pb 6p AOs in the Pb_{12} cage. The frontier orbitals are seen to be comparable to those in the $AlPb^{+}_{12}$ superatom[27] albeit with a much smaller HOMO–LUMO gap in $[Pt@Pb_{12}]^{2-}$.

The calculated NMR chemical shifts for $[Pt@Pb_{12}]^{2-}$ are collected in Table 1. When assessing the Pt and Pb chemical shifts with respect to experiment, one should keep in mind that the calculation of the chemical shift involves the nuclear magnetic shielding σ of the probe and a reference nucleus:

$$[1] \qquad \delta = \frac{\sigma^{ref} - \sigma}{1 - \sigma^{ref}} \approx \sigma^{ref} - \sigma$$

The approximation is valid for small σ^{ref}. For convenience, we use the approximate form in this work. For heavy nuclei such as ^{195}Pt and ^{207}Pb neglecting the reference shielding in the denominator may lead to chemical shift changes on the order of 1%, which is much less than the variations of the chemical shifts with respect to approximations in the computational model.

Calculations with a hybrid functional (PBE0) turned out to be extremely demanding of computational resources and, in particular in conjunction with COSMO and spin-orbit (SO) coupling, suffered from very slow convergence. Therefore, a set of calculations was realized that allowed some extrapolations, with the PBE0 computations performed at an affordable level of theory. Given the definition of the chemical shift, eq. [1] systematic errors in the computations may cancel between probe and reference, or affect only one of the compounds in which case errors do not cancel. We refer the reader to a detailed discussion of the Pt shielding in the reference compound $[PtCl_6]^{2-}$ in solution;[73,76] the uncertainties in the Pt chemical shift from the reference may easily amount to several hundred ppm. The variations among the different calculations listed in Table 1 can be used to assess the overall accuracy limits of the computations.

Both the Pt and Pb chemical shift of $[Pt@Pb_{12}]^{2-}$ are sensitive to approximations in the computational model. The calculated values bracket the experimental data. The comparison of scalar relativistic computations with those that include SO coupling reveals large positive SO shielding contributions for the Pt nucleus both in the reference and in $[Pt@Pb_{12}]^{2-}$. The SO mechanism is much more pronounced in the $[PtCl_6]^{2-}$ reference, yielding a large net positive SO effect on the Pt chemical shift. For Pb, the SO effect on the shielding is also positive both in the reference and in $[Pt@Pb_{12}]^{2-}$, but here the magnitude for $[Pt@Pb_{12}]^{2-}$ dominates, leading to a net negative SO effect on the Pb shift. Switching the functional from PBE to the simpler VWN local density approximation has a comparatively small impact at the COSMO/SO level of theory. The net solvent effects on the chemical shifts do not exceed 300 ppm. This allows further comparisons based on gas-phase computations, which afforded faster SCF convergence. The comparison of the B1 with the B2 = TZP data shows that basis set effects are sizable for the Pb shift in the SO computations. Finally, there is a significant change in the chemical shifts when going from the "pure" PBE to the hybrid PBE0 functional at the scalar ZORA level. Unfortunately, full COSMO SO PBE0 computations with the large basis set B1 were not feasible for $[Pt@Pb_{12}]^{2-}$. Extrapolating the trends among the different computations, the Pb chemical shift expected for this level of theory likely exceeds the 3578 ppm obtained with the PBE nonhybrid functional. For Pt, the functional effect is also likely to increase the magnitude of the negative chemical shift. The chemical shifts obtained here at the highest level of theory that we were able to apply (PBE/SO/COSMO with the larger basis set) are smaller in magnitude than the experimental shifts, and therefore using a hybrid functional might offer some improvement both for Pt and Pb. However, SO effects must not be neglected.

The Pt shielding tensor in $[Pt@Pb_{12}]^{2-}$ is isotropic, as dictated by the highly symmetric icosahedral environment of the Pt atom. The data in Table 1 show that the Pt nucleus in the reference compound $[PtCl_6]^{2-}$ is particularly strongly deshielded while at the same time Pt in $[Pt@Pb_{12}]^{2-}$ is strongly shielded. Per eq. [1], this causes the Pt shift in $[Pt@Pb_{12}]^{2-}$ to be large and negative. The strong deshielding of Pt in $[PtCl_6]^{2-}$ was investigated in ref. 75; it is a result of a paramagnetic current density induced in the Pt 5d shell by the external magnetic field. Pyykkö et al.[21] reported large SO contributions to the ^{183}W chemical shifts in $W@Au_{12}$ and found an exceptionally strong shielding of the magnetic field inside the gold cage. By comparison, for the central Pt atom in $[Pt@Pb_{12}]^{2-}$ no particularly strong shielding from the Pb_{12} cage is noted. The atom-like (isotropic) diamagnetic shielding of Pt is on the order of 9300 ppm and partially compensated by paramagnetic shielding tensor contributions that are, however, much smaller than those in $[PtCl_6]^{2-}$. Therefore, the Pt shielding tensor in $[Pt@Pb_{12}]^{2-}$ is more similar to that of a free spherical non spin-polarized atom than the shielding tensor in

Can. J. Chem. Downloaded from www.nrcresearchpress.com by Xi'an Jiaotong University on 09/19/12
For personal use only.

Fig. 1. Left: Optimized icosahedral structure of $[Pt@Pb_{12}]^{2-}$. Right: Calculated scalar relativistic orbital energy diagram (conductor-like screening model (COSMO) / Perdew–Burke–Ernzerhof (PBE) / triple-ζ Slater-type atomic orbital (AO) basis set with polarization (TZP)).

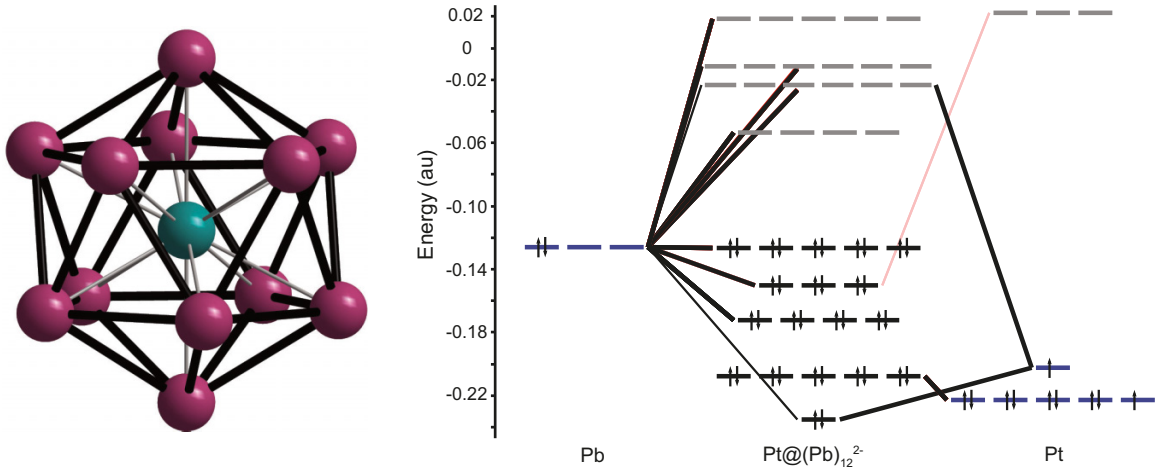

Fig. 2. Selected molecular orbitals (MOs) of $[Pt@Pb_{12}]^{2-}$ (scalar zeroth-order regular approximation (ZORA) conductor-like screening model (COSMO) / Perdew–Burke–Ernzerhof (PBE) / triple-ζ Slater-type atomic orbital (AO) basis set with polarization (TZP)). One of three degenerate HOMO-1 (p like), one of five degenerate HOMOs (g like), and one of four degenerate LUMOs (g like). Isosurfaces at ±0.003 au enclosing more than 95% of the electron density for the HOMO.

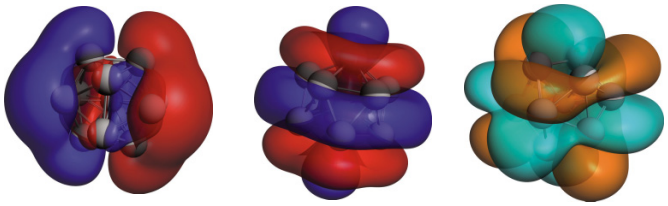

the reference compound. Paramagnetic contributions to the shielding tensor would be suppressed by symmetry for a spherical closed shell atom in the absence of SO coupling. The presence of sizable paramagnetic shielding terms demonstrate the impact of the deviation of the $[Pt@Pb_{12}]^{2-}$ superatom from spherical symmetry on the NMR shielding.

All computations confirm the atypical large positive chemical shift of the Pb nuclei in $[Pt@Pb_{12}]^{2-}$, which was already noted by the experimental group[28,29] who reported the synthesis and NMR spectra of $[Pt@Pb_{12}]^{2-}$. This large downfield shift of the NMR signal of Pb in $[Pt@Pb_{12}]^{2-}$ calls for a more detailed analysis. Owing to the tetrahedral Pb environment, the Pb shielding tensor in the reference compound $PbMe_4$ is isotropic, with a calculated diamagnetic shielding of 9941 ppm and a paramagnetic shielding of –5462 ppm, which is to a large extent compensated by a 3007 ppm SO shielding (COSMO/PBE/B1/SO). The shielding tensor of Pb in $[Pt@Pb_{12}]^{2-}$ has axial symmetry as depicted in Fig. 3, with a negative radial principal component σ_R and two positive degenerate orthoradial components σ_O. The anisotropy of the tensor is caused by the paramagnetic and SO mechanisms. The orthoradial components are on the order of $+10^4$ ppm, close to the diamagnetic shielding. The radial component is almost of the same magnitude but negative, with negative paramagnetic and SO "linear response" mechanisms reinforcing each other. An analysis[74,75] of the radial shielding tensor component in terms of contributions from individual MOs carried out within a SO computation indicated very large contributions from the HOMO level, with the bulk of the paramagnetic mechanism caused by matrix elements involving magnetic coupling between the HOMOs and LUMOs. The strong negative radial shielding tensor component calculated for Pb in $[Pt@Pb_{12}]^{2-}$ therefore supports the notion of σ aromaticity in the cluster[27,29] by which the magnetic field may induce particularly strong paramagnetic ring-current densities in the surface of the Pb_{12} cage. Per eq. [1] the large negative contributions in the shielding tensor of the Pb nuclei in $[Pt@Pb_{12}]^{2-}$ lead to a particularly large positive Pb chemical shift.

The Pt–Pb spin-spin coupling constants J(Pt–Pb) calculated at various levels of theory are collected in Table 2. The relative importance of different J-coupling mechanisms is similar for all calculations and therefore a detailed breakdown is not provided. The spin mechanism (Fermi-contact and, to a minor degree, spin-dipole) is negative and amounts to about 1.1 times the total coupling constant. This mechanism therefore dominates the coupling constant. It is to a small degree balanced by contributions from the orbital-current density mechanism. The diamagnetic contributions are smaller than 0.5 Hz and therefore they can safely be ignored. In Table 2 the basis set "LD" is a locally dense basis set of TZ2P quality where the high-exponent augmentation of the JCPL basis, required to calculate accurate spin-mechanism contributions, has only been used for selected atoms for which coupling constants were determined. The comparison with the full JCPL basis set for all atoms shows that, whereas the results are in good agreement across different theoretical levels, the differences cannot be completely ignored. The LD basis set is somewhat imbalanced, since the high-exponent augmentation not only affects the quality of the calculated coupling constants but also the extent to which relativistic effects in the ground-state electronic structure are described variationally both for core and valence orbitals. Thus, for a system like $[Pt@Pb_{12}]^{2-}$ the use of a locally dense basis set is not entirely satisfactory. We note in passing that larger differences between the LD and the full JCPL basis set results were obtained for

Can. J. Chem. Downloaded from www.nrcresearchpress.com by Xi'an Jiaotong University on 09/19/12
For personal use only.

Table 1. Calculated ^{195}Pt and ^{207}Pb nuclear magnetic shielding (σ) and chemical shifts (δ), in ppm.

	$[PtCl_6]^{2-}$	$PbMe_4$	$[Pt@Pb_{12}]^{2-}$		$[Pt@Pb_{12}]^{2-}$	
Computation[a]	σ (Pt)	σ (Pb)	σ (Pt)	σ (Pb)	δ (Pt)	δ (Pb)
COSMO						
PBE/B1/SC	–1752	4841	4773	400	–6524	4441
PBE/B1/SO	1852	7486	5588	3908	–3737	3578
VWN/B1/SO	1918	7407	5561	3664	–3643	3743
Gas phase						
PBE/B1/SC	–2049	4845	4639	554	–6688	4291
PBE/B1/SO	1566	7495	5510	4201	–3944	3294
PBE/B2/SC	–1257	4870	4940	739	–6197	4132
PBE/B2/SO	1686	7546	5552	4924	–3866	2622
PBE0/B2/SC	–2560	5073	5332	–94	–7893	5166

Note: Experimental chemical shifts for $[Pt@Pb_{12}]^{2-}$ as reported in refs. 28 and 29 are Pt = –4527 ppm (wrt. $[PtCl_6]^{2-}$) and Pb = +4741 ppm (wrt. $PbMe_4$).

[a]See the Computational details section for an explanation of the applied methods. COSMO, conductor-like screening model; ZORA, zeroth-order regular approximation; TZP, triple-ζ Slater-type atomic orbital (AO) basis set with polarization; PBE, Perdew–Burke–Ernzerhof; VWN, Vosko–Wilk–Nusair. B1 = QZ4P basis for Pt and TZ2P basis for Pb. B2 = TZP basis for Pt and Pb. SC = scalar ZORA, SO = spin-orbit ZORA.

Table 2. Calculated J(Pt–Pb) in Hz. Reduced coupling K in units of 10^{19} T^2/J.

Computation[a]	K(Pt–Pb)	J(Pt–Pb)
PBE/LD/SC	–6883	–3764
PBE/JCPL/SC	–6912	–3780
PBE/LD/SC/COSMO	–6513	–3561
PBE/LD/SC point nuc.	–8275	–4525
PBE/LD/SO	–7667	–4193
PBE/JCPL/SO	–7727	–4225
VWN/JCPL/SO/COSMO	–6279	–3434
PBE/JCPL/SO/COSMO	–7373	–4032
VWN/TZP/SC	–4180	–2286
PBE/TZP/SC	–5227	–2859
PBE0/TZP/SC	–5937	–3247

Note: Experimentally, $J(^{195}Pt–^{207}Pb)$ = 3440 Hz. PBE, Perdew–Burke–Ernzerhof; COSMO, conductor-like screening model; TZP, triple-ζ Slater-type atomic orbital (AO) basis set with polarization; VWN, Vosko–Wilk–Nusair.

[a]See the Computational details section for an explanation of the applied methods. LD = locally dense basis set where JCPL was used only for four atoms for which coupling constants were calculated, and TZ2P for the remaining atoms. JCPL = TZ2P augmented with high-exponent s and p basis functions. SC = scalar ZORA, SO = spin-orbit ZORA. Gaussian nuclear model applied except for "point nuc". The estimated uncertainty of K for PBE0 is ±10 because of slow convergence of the PSO mechanism. Gas-phase calculations unless the COSMO model is indicated.

Fig. 3. Graphical representation of the ^{207}Pb shielding tensor in $[Pt@Pb_{12}]^{2-}$ (conductor-like screening model (COSMO) / Perdew–Burke–Ernzerhof (PBE) / spin orbit (SO) with QZ4P(Pt)/TZ2P(Pb) basis). The plot indicates the tensor orientation as well as the relative magnitudes and signs of the principal components (dark gray / light gray = positive/negative). The diamagnetic contribution to the tensor is almost perfectly isotropic, but the paramagnetic +SO contributions are strongly anisotropic and overall negative, with a particularly large negative radial σ_R component in the direction of the Pb–Pt axis. Shielding tensor plot is as described in ref. 99.

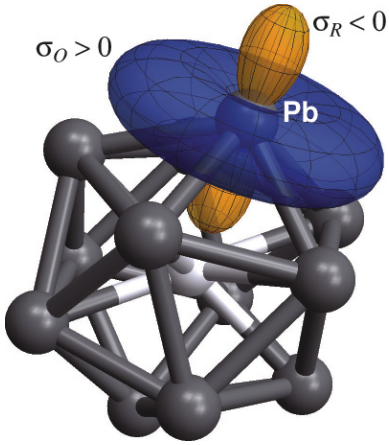

the two- and three-bond Pb–Pb coupling constants (vide infra).

Since J(Pt–Pb) is dominated by the spin mechanism, finite nucleus effects are pronounced; they reduce the magnitude of J(Pt–Pb) by as much as 16%. SO coupling increases the magnitude of J(Pt–Pb) by ~11%–12% (PBE). The simultaneous neglect of finite nucleus corrections and SO coupling therefore offers some error compensation for this system. The importance of augmenting the basis set with high-exponent basis functions in addition to those already present in the ZORA-optimized ADF basis sets is seen in the comparison of the TZP with the JCPL data, with JCPL yielding an over 30% increase in the coupling constant magnitude at the scalar ZORA PBE level of theory. The effects from the functional are also pronounced, with an increase of $|J|$ from VWN to PBE to PBE0 by ~40%. Solvent effects are seen to slightly reduce the coupling constant magnitude.

Since the magnetogyric ratios for ^{195}Pt and ^{207}Pb are both positive the reduced coupling and the J coupling have the same sign. The calculations consistently predict J(Pt–Pb) to be negative. It is well-recognized that it is difficult to experimentally determine the sign of coupling constants ^1J(Pb–M) where M is a metal nucleus because of the often strong

Can. J. Chem. Downloaded from www.nrcresearchpress.com by Xi'an Jiaotong University on 09/19/12
For personal use only.

polarizability and relative weakness of Pb–M bonds.[41] This situation is also partially explained by the lack of available experimental data. A comparison with similar platinum–tin compounds may be used to work around this problem. For instance, Wrackmeyer[41] proposed a positive sign for ^1J(Pt–Pb) in platinum–lead bonded compounds,[45] by considering data for comparable Pt–Sn complexes.[100] In the present case, because reasonable agreement with experiment is obtained for the heavy-metal chemical shifts as well as for the coupling constant magnitude, it is unlikely that the computations of the coupling constants predict the wrong sign. We therefore propose that $J(^{195}Pt–^{207}Pb)$ in $[Pt@Pb_{12}]^{2-}$ has a negative sign.

We have also calculated the Pb–Pb coupling constants, but owing to the lack of experimental data we forgo a detailed discussion. At the PBE/JCPL/SO/COSMO level of theory, using a Gaussian nuclear model, we have determined the reduced one-bond Pb–Pb coupling as 13 736, the two-bond coupling as –2235, and the three-bond coupling as 1639, in SI units of 10^{19} T^2/J.

Summary

Spin-orbit coupling causes important contributions to NMR parameters in $[Pt@Pb_{12}]^{2-}$ that may be considered as a "strongly relativistic" system because it is entirely composed of heavy atoms. The calculated NMR parameters proved to be somewhat sensitive to the computational model, but overall the agreement with experimental data for the highest affordable levels of theory is acceptable. Ideally, the computations should combine the gains in accuracy from including SO coupling, from using a hybrid functional, and from using a very flexible basis set with high-exponent augmentation for all atoms. The more affordable COSMO/PBE/B1/SO computational model appears to offer a good compromise. All calculations of $J(^{195}Pt–^{207}Pb)$ predicted this coupling constant to be negative. The Pb shielding tensor in $[Pt@Pb_{12}]^{2-}$ is strongly anisotropic. The large negative radial principal component calculated for the Pb shielding tensor is consistent with the proposed σ aromaticity in the Pb_{12} cage. The paramagnetic mechanism for the radial Pb shielding tensor component can, to a large extent, be attributed to magnetic coupling between g-orbital-like superatom HOMOs and LUMOs, resulting in a particularly strongly downfield shifted (deshielded) NMR resonance for the Pb nuclei in $[Pt@Pb_{12}]^{2-}$.

Acknowledgments

We thank the Center for Computational Research (CCR) at the University at Buffalo, Buffalo, New York, for continuing support of our research projects. This work has received financial support from the National Science Foundation (CHE 0447321 and 0952253).

References

(1) Schaaff, T. G.; Whetten, R. L. *J. Phys. Chem. B* **2000** *104* (12), 2630. doi:10.1021/jp993691y.
(2) Garzón, I. L.; Reyes-Nava, J. A.; Rodríguez-Hernández, J. I.; Sigal, I.; Beltrán, M.; Michaelian, K. *Phys. Rev. B* **2002** *66* (7), 073403. doi:10.1103/PhysRevB.66.073403.
(3) Li, J.; Zhai, H.-J.; Wang, L.-S. *Science* **2003** *299* (5608), 864. doi:10.1126/science.1079879.
(4) Schwerdtfeger, P. *Angew. Chem. Int. Ed.* **2003** *42* (17), 1892. doi:10.1002/anie.200201610.
(5) Daniel, M.-C.; Astruc, D. *Chem. Rev.* **2004** *104* (1), 293. doi:10.1021/cr030698+.
(6) Johansson, M. P.; Sundholm, D.; Vaara, J. *Angew. Chem. Int. Ed.* **2004** *43* (20), 2678. doi:10.1002/anie.200453986.
(7) Noguez, C.; Garzon, I. L. *Chem. Soc. Rev.* **2009** *38* (3), 757. doi:10.1039/b800404h.
(8) Yadav, B. D.; Kumar, V. *Appl. Phys. Lett.* **2010** *97* (13), 133701. doi:10.1063/1.3491269.
(9) Gao, Y.; Shao, N.; Pei, Y.; Zeng, X. C. *Nano Lett.* **2010** *10* (3), 1055. doi:10.1021/nl100017u.
(10) Li, X.; Kiran, B.; Li, J.; Zhai, H.-J.; Wang, L.-S. *Angew. Chem. Int. Ed.* **2002** *41* (24), 4786. doi:10.1002/anie.200290048.
(11) Zhai, H.-J.; Li, J.; Wang, L.-S. *J. Chem. Phys.* **2004** *121* (17), 8369. doi:10.1063/1.1799574.
(12) Qiu, Y.-X.; Wang, S.-G.; Schwarz, W. H. E. *Chem. Phys. Lett.* **2004** *397* (4–6), 374. doi:10.1016/j.cplett.2004.08.115.
(13) Wang, S.-Y.; Yu, J.-Z.; Mizuseki, H.; Sun, Q.; Wang, C.-Y.; Kawazoe, Y. *Phys. Rev. B* **2004** *70* (16), 165413. doi:10.1103/PhysRevB.70.165413.
(14) Gao, Y.; Bulusu, S.; Zeng, X. C. *ChemPhysChem* **2006** *7* (11), 2275. doi:10.1002/cphc.200600472.
(15) Graciani, J.; Oviedo, J.; Sanz, J. F. *J. Phys. Chem. B* **2006** *110* (23), 11600. doi:10.1021/jp057322f.
(16) Gao, Y.; Shao, N.; Bulusu, S.; Zeng, X. C. *J. Phys. Chem. C* **2008** *112* (22), 8234. doi:10.1021/jp801262v.
(17) Long, J.; Qiu, Y.-X.; Chen, X.-Y.; Wang, S.-G. *J. Phys. Chem. C* **2008** *112* (33), 12646. doi:10.1021/jp8033006.
(18) Stener, M.; Nardelli, A.; Fronzoni, G. *Chem. Phys. Lett.* **2008** *462* (4–6), 358. doi:10.1016/j.cplett.2008.08.010.
(19) Fu, Y.; Li, J.; Wang, S.-G. *J. Mol. Model.* **2010** *16* (1), 9. doi:10.1007/s00894-009-0517-y.
(20) Pyykkö, P.; Runeberg, N. *Angew. Chem. Int. Ed.* **2002** *41* (12), 2174. doi:10.1002/1521-3773(20020617)41:12<2174::AID-ANIE2174>3.0.CO;2-8.
(21) Autschbach, J.; Hess, B. A.; Johansson, P. A.; Neugebauer, J.; Patzschke, M.; Pyykkö, P.; Reiher, M.; Sundholm, D. *Phys. Chem. Chem. Phys.* **2004** *6* (1), 11. doi:10.1039/b310395a.
(22) Stener, M.; Nardelli, A.; Fronzoni, G. *J. Chem. Phys.* **2008** *128* (13), 134307. doi:10.1063/1.2884003.
(23) Manninen, K.; Pyykkö, P.; Häkkinen, H. *Phys. Chem. Chem. Phys.* **2005** *7* (10), 2208. doi:10.1039/b503656a.
(24) Li, J.; Qiu, Y.-X.; Wang, S.-G. *J. Phys. Chem. A* **2009** *113* (8), 1646. doi:10.1021/jp808403u.
(25) Johansson, M. P.; Pyykkö, P. *Chem. Commun. (Camb.)* **2010** *46* (21), 3762. doi:10.1039/c0cc00045k.
(26) Zhang, X.; Li, G.; Xing, X.; Zhao, X.; Tang, Z.; Gao, Z. *Rapid Commun. Mass Spectrom.* **2001** *15* (24), 2399. doi:10.1002/rcm.530.
(27) Neukermans, S.; Janssens, E.; Chen, Z. F.; Silverans, R. E.; Schleyer, P. R.; Lievens, P. *Phys. Rev. Lett.* **2004** *92* (16), 163401. doi:10.1103/PhysRevLett.92.163401.
(28) Esenturk, E. N.; Fettinger, J.; Lam, Y.-F.; Eichhorn, B. *Angew. Chem. Int. Ed.* **2004** *43* (16), 2132. doi:10.1002/anie.200353287.
(29) Esenturk, E. N.; Fettinger, J.; Eichhorn, B. *J. Am. Chem. Soc.* **2006** *128* (28), 9178. doi:10.1021/ja061842m.
(30) Schäfer, S.; Schäfer, R. *ChemPhysChem* **2008** *9* (13), 1925. doi:10.1002/cphc.200800264.
(31) Chen, D.-L.; Tian, W. Q.; Lu, W.-C.; Sun, C.-C. *J. Chem. Phys.* **2006** *124* (15), 154313. doi:10.1063/1.2189224.

Can. J. Chem. Downloaded from www.nrcresearchpress.com by Xi'an Jiaotong University on 09/19/12
For personal use only.

(32) Rajesh, C.; Majumder, C. *Chem. Phys. Lett.* **2006** *430* (1–3), 101. doi:10.1016/j.cplett.2006.08.117.
(33) Rajesh, C.; Majumder, C. *J. Chem. Phys.* **2008** *128* (2), 024308. doi:10.1063/1.2814166.
(34) Dognon, J.-P.; Clavaguéra, C.; Pyykkö, P. *Angew. Chem. Int. Ed.* **2007** *46* (9), 1427. doi:10.1002/anie.200604198.
(35) Dognon, J.-P.; Clavaguéra, C.; Pyykkö, P. *C. R. Chimie* **2010** *13* (6–7), 884. doi:10.1016/j.crci.2010.05.012.
(36) Chen, X.; Deng, K.; Liu, Y.; Tang, C.; Yuan, Y.; Hu, F.; Wu, H.; Huang, D.; Tan, W.; Wang, X. *Chem. Phys. Lett.* **2008** *462* (4–6), 275. doi:10.1016/j.cplett.2008.07.095.
(37) Pregosin, P. S. *Coord. Chem. Rev.* **1982** *44* (2), 247. doi:10.1016/S0010-8545(00)80523-8.
(38) Pregosin, P. S. *Annu. Rep. NMR Spectrosc.* **1986** *17*, 285. doi:10.1016/S0066-4103(08)60238-0.
(39) Pannell, K. H.; Rozell, J. M.; Cortez, S.; Kapoor, R. *Organometallics* **1990** *9* (4), 1322. doi:10.1021/om00118a070.
(40) Wrackmeyer, B.; Horchler, K. *Annu. Rep. NMR Spectrosc.* **1990** *22*, 249. doi:10.1016/S0066-4103(08)60257-4.
(41) Wrackmeyer, B. *Annu. Rep. NMR Spectrosc.* **2002** *47*, 1. doi:10.1016/S0066-4103(02)47037-8.
(42) Dybowski, C.; Neue, G. *Prog. Nucl. Magn. Reson. Spectrosc.* **2002** *41* (3–4), 153. doi:10.1016/S0079-6565(02)00005-5.
(43) Still, B. M.; Kumar, P. G. A.; Aldrich-Wright, J. R.; Price, W. S. *Chem. Soc. Rev.* **2007** *36* (4), 665. doi:10.1039/b606190g.
(44) Autschbach, J.; Zheng, S. *Annu. Rep. NMR Spectrosc.* **2009** *67*, 1. doi:10.1016/S0066-4103(09)06701-5.
(45) Carr, S.; Colton, R.; Dakternieks, D. *J. Organomet. Chem.* **1982** *240* (2), 143. doi:10.1016/S0022-328X(00)82508-5.
(46) Balch, A. L.; Fung, E. Y.; Nagle, J. K.; Olmstead, M. M.; Rowley, S. P. *Inorg. Chem.* **1993** *32* (15), 3295. doi:10.1021/ic00067a017.
(47) Autschbach, J.; Ziegler, T. Relativistic Computation of NMR shieldings and Spin-Spin Coupling Constants. In *Encyclopedia of Nuclear Magnetic Resonance;* Grant, D. M.; Harris, R. K., Eds.; John Wiley & Sons: Chichester, 2002; Vol. 9.
(48) Bühl, M. NMR of Transition Metal Compounds. In *Calculation of NMR and EPR Parameters. Theory and Applications;* Kaupp, M.; Bühl, M.; Malkin, V. G., Eds.; Wiley-VCH: Weinheim, 2004.
(49) Autschbach, J. The Calculation of NMR Parameters in Transition Metal Complexes. In *Principles and Applications of Density Functional Theory in Inorganic Chemistry I*; Vol. 112; Kaltsoyannis, N.; McGrady, J. E., Eds.; Springer: Heidelberg., 2004.
(50) Autschbach, J. Calculation of Heavy-Nucleus Chemical Shifts: Relativistic All-Electron Methods. In *Calculation of NMR and EPR Parameters. Theory and Applications;* Kaupp, M.; Bühl, M.; Malkin, V. G., Eds.; Wiley-VCH: Weinheim, 2004.
(51) Autschbach, J.; Ziegler, T. Relativistic Calculation of Spin-Spin Coupling Constants. In *Calculation of NMR and EPR Parameters. Theory and Applications;* Kaupp, M.; Bühl, M.; Malkin, V. G., Eds.; Wiley-VCH: Weinheim, 2004.
(52) Autschbach, J. *Coord. Chem. Rev.* **2007** *251* (13–14), 1796. doi:10.1016/j.ccr.2007.02.012.
(53) Bühl, M. *Annu. Rep. NMR Spectrosc.* **2008** *64*, 77. doi:10.1016/S0066-4103(08)00003-3.
(54) Rodriguez-Fortea, A.; Alemany, P.; Ziegler, T. *J. Phys. Chem. A* **1999** *103* (41), 8288. doi:10.1021/jp9912004.
(55) Lantto, P.; Romero, R. H.; Gómez, S. S.; Aucar, G. A.; Vaara, J. *J. Chem. Phys.* **2006** *125* (18), 184113. doi:10.1063/1.2378737.
(56) Briand, G. G.; Smith, A. D.; Schatte, G.; Rossini, A. J.; Schurko, R. W. *Inorg. Chem.* **2007** *46* (21), 8625. doi:10.1021/ic700738w.
(57) Dmitrenko, O.; Bai, S.; Dybowski, C. *Solid State Nucl. Magn. Reson.* **2008** *34* (3), 186. doi:10.1016/j.ssnmr.2008.08.003.
(58) Edlund, U.; Lejon, T.; Pyykkö, P.; Venkatachalam, T. K.; Buncel, E. *J. Am. Chem. Soc.* **1987** *109* (20), 5982. doi:10.1021/ja00254a015.
(59) Kirpekar, S.; Sauer, S. P. A. *Theor. Chem. Acc.* **1999** *103*, 146.
(60) Enevoldsen, T.; Visscher, L.; Saue, T.; Jensen, H. J. A.; Oddershede, J. *J. Chem. Phys.* **2000** *112* (8), 3493. doi:10.1063/1.480504.
(61) Autschbach, J.; Ziegler, T. *J. Chem. Phys.* **2000** *113* (3), 936. doi:10.1063/1.481874.
(62) Filatov, M.; Cremer, D. *J. Chem. Phys.* **2004** *120* (24), 11407. doi:10.1063/1.1752876.
(63) Oprea, C. I.; Rinkevicius, Z.; Vahtras, O.; Agren, H.; Ruud, K. *J. Chem. Phys.* **2005** *123* (1), 014101. doi:10.1063/1.1947190.
(64) Autschbach, J. *J. Chem. Phys.* **2007** *127* (12), 124106. doi:10.1063/1.2768363.
(65) Autschbach, J. *J. Chem. Phys.* **2008** *129* (9), 094105. doi:10.1063/1.2969100.
(66) Moncho, S.; Autschbach, J. *J. Chem. Theory Comput.* **2010** *6* (1), 223. doi:10.1021/ct900535d.
(67) Gilbert, T. M.; Ziegler, T. *J. Phys. Chem. A* **1999** *103* (37), 7535. doi:10.1021/jp992202r.
(68) Autschbach, J.; Le Guennic, B. *J. Am. Chem. Soc.* **2003** *125* (44), 13585. doi:10.1021/ja0368047.
(69) Autschbach, J.; Le Guennic, B. *Chem.-Eur. J.* **2004** *10* (10), 2581. doi:10.1002/chem.200305513.
(70) Le Guennic, B.; Matsumoto, K.; Autschbach, J. *Magn. Reson. Chem.* **2004** *42* (S1), S99. doi:10.1002/mrc.1450.
(71) Penka Fowe, E.; Belser, P.; Daul, C.; Chermette, H. *Phys. Chem. Chem. Phys.* **2005** *7* (8), 1732. doi:10.1039/b500574d.
(72) Koch, K. R.; Burger, M. R.; Kramer, J.; Westra, A. N. *Dalton Trans.* **2006** (27), 3277. doi:10.1039/b605182k.
(73) Sterzel, M.; Autschbach, J. *Inorg. Chem.* **2006** *45* (8), 3316. doi:10.1021/ic052143y.
(74) Autschbach, J. *J. Chem. Phys.* **2008** *128* (16), 164112. doi:10.1063/1.2905235.
(75) Autschbach, J.; Zheng, S. *Magn. Reson. Chem.* **2008** *46* (S1), S45. doi:10.1002/mrc.2289.
(76) Truflandier, L. A.; Autschbach, J. *J. Am. Chem. Soc.* **2010** *132* (10), 3472. doi:10.1021/ja9096863.
(77) Sutter, K.; Truflandier, L. A.; Autschbach, J. *ChemPhysChem* **2011** *12*, 1448. doi:10.1002/cphc201000997.
(78) Truflandier, L. A.; Sutter, K.; Autschbach, J. *Inorg. Chem.* **2011** *50*, 1723. doi:10.1021/ic1021746.
(79) Burger, M.; Kramer, J.; Chermette, H.; Koch, K. R. *Magn. Reson. Chem.* **2010** *48* (S1), S38. doi:10.1002/mrc.2607.
(80) Wasylishen, R. Characterization of NMR Tensors via Experiment and Theory. In *Calculation of NMR and EPR Parameters. Theory and Applications;* Kaupp, M.; Bühl, M.; Malkin, V. G., Eds.; Wiley-VCH: Weinheim, 2004.
(81) van Lenthe, E.; Baerends, E. J.; Snijders, J. G. *J. Chem. Phys.* **1993** *99* (6), 4597. doi:10.1063/1.466059.
(82) te Velde, G.; Bickelhaupt, F. M.; Baerends, E. J.; Fonseca Guerra, C.; van Gisbergen, S. J. A.; Snijders,

J. G.; Ziegler, T. *J. Comput. Chem.* **2001** *22* (9), 931. doi:10.1002/jcc.1056.
(83) Baerends, E. J.; Autschbach, J.; Bérces, A.; Bo, C.; Boerrigter, P. M.; Cavallo, L.; Chong, D. P.; Deng, L.; Dickson, R. M.; Ellis, D. E.; Fan, L.; Fischer, T. H.; Fonseca Guerra, C.; van Gisbergen, S. J. A.; Groeneveld, J. A.; Gritsenko, O. V.; Grüning, M.; Harris, F. E.; van den Hoek, P.; Jacobsen, H.; van Kessel, G.; Kootstra, F.; van Lenthe, E.; Osinga, V. P.; Patchkovskii, S.; Philipsen, P. H. T.; Post, D.; Pye, C. C.; Ravenek, W.; Ros, P.; Schipper, P. R. T.; Schreckenbach, G.; Snijders, J. G.; Sola, M.; Swart, M.; Swerhone, D.; te Velde, G.; Vernooijs, P.; Versluis, L.; Visser, O.; van Wezenbeek, E.; Wiesenekker, G.; Wolff, S. K.; Woo, T. K.; Ziegler, T. Amsterdam Density Functional, Theoretical Chemistry, Vrije Universiteit, Amsterdam. http://www.scm.com.
(84) (a) Autschbach, J. J. *Chem. Phys.* **2008** *129* 094105. doi:10.1063/1.2969100;; (b) Autschbach, J. J. *Chem. Phys.* **2009** *130*, 209901(Erratum). doi:10.1063/1.313724.
(85) Autschbach, J. *ChemPhysChem* **2009** *10* (13), 2274. doi:10.1002/cphc.200900271.
(86) Autschbach, J.; Ziegler, T. *J. Chem. Phys.* **2000** *113* (21), 9410. doi:10.1063/1.1321310.
(87) Autschbach, J.; Zurek, E. *J. Phys. Chem. A* **2003** *107* (24), 4967. doi:10.1021/jp0346559.
(88) Wolff, S. K.; Ziegler, T.; van Lenthe, E.; Baerends, E. J. *J. Chem. Phys.* **1999** *110* (16), 7689. doi:10.1063/1.478680.
(89) van Gisbergen, S. J. A.; Fonseca-Guerra, C.; Baerends, E. J. *J. Comput. Chem.* **2000** *21* (16), 1511. doi:10.1002/1096-987X(200012)21:16<1511::AID-JCC8>3.0.CO;2-C.
(90) Vosko, S. H.; Wilk, L.; Nusair, M. *Can. J. Phys.* **1980** *58* (8), 1200. doi:10.1139/p80-159.
(91) Perdew, J. P.; Burke, K.; Ernzerhof, M. *Phys. Rev. Lett.* **1996** *77* (18), 3865. doi:10.1103/PhysRevLett.77.3865.
(92) Zhang, Y.; Yang, W. *Phys. Rev. Lett.* **1998** *80* (4), 890. doi:10.1103/PhysRevLett.80.890.
(93) Perdew, J. P.; Burke, K.; Ernzerhof, M. *Phys. Rev. Lett.* **1998** *80* (4), 891. doi:10.1103/PhysRevLett.80.891.
(94) Hammer, B.; Hansen, L. B.; Norskov, J. K. *Phys. Rev. B* **1999** *59* (11), 7413. doi:10.1103/PhysRevB.59.7413.
(95) Adamo, C.; Barone, V. *Chem. Phys. Lett.* **1998** *298* (1–3), 113. doi:10.1016/S0009-2614(98)01201-9.
(96) WebElements. http://www.webelements.com.
(97) Klamt, A.; Schüürmann, G. *J. Chem. Soc., Perkin Trans. 2* **1993** (5), 799. doi:10.1039/p29930000799.
(98) Pye, C. C.; Ziegler, T. *Theor. Chem. Acc.* **1999** *101*, 396.
(99) Zurek, E.; Pickard, C.; Autschbach, J. *J. Phys. Chem. A* **2009** *113* (16), 4117. doi:10.1021/jp810523x.
(100) McFarlane, W.; Rees, N. H. *J. Chem. Soc., Dalton Trans.* **1990** (11): 3211. doi:10.1039/dt9900003211.

Can. J. Chem. Downloaded from www.nrcresearchpress.com by Xi'an Jiaotong University on 09/19/12
For personal use only.

A solid-state $^{35/37}$Cl NMR study of a chloride ion receptor and a GIPAW-DFT study of chlorine NMR interaction tensors in organic hydrochlorides

Rebecca P. Chapman, Jennifer R. Hiscock, Philip A. Gale, and David L. Bryce

Can. J. Chem. Downloaded from www.nrcresearchpress.com by Xi'an Jiaotong University on 09/19/12
For personal use only.

Abstract: The results of a $^{35/37}$Cl solid-state nuclear magnetic resonance (SSNMR) study of the 1-butyl-3-methylimidazolium chloride complex of *meso*-octamethylcalix[4]pyrrole (**1**) are reported. Line shapes obtained from magic-angle-spinning and stationary powder samples collected at 9.4 and 21.1 T are analyzed to provide the $^{35/37}$Cl quadrupolar tensor and chemical shift (CS) tensor and their relative orientation. The relatively high symmetry of the chloride ion coordination environment is manifested in the small value of the quadrupole coupling constant, $C_Q(^{35}Cl) = 1.0$ MHz. The isotropic chemical shift of 120 ppm (with respect to NaCl(s)) is at the upper edge of the typical range seen for organic hydrochlorides. Consideration of chemical shift anisotropy (span, $\Omega = 50$ ppm) and non-coincidence of the quadrupolar and CS tensors were essential to properly simulate the experimental spectra. The utility of gauge-including projector-augmented wave density functional theory (GIPAW-DFT) calculations of chlorine quadrupolar and CS tensors in organic chlorides was explored by validation against available benchmark experimental data for solid amino acid hydrochlorides. The calculations are shown to systematically overestimate the value of the ^{35}Cl quadrupole coupling constant. Additional calculations on various hydrated and solvated models of **1** are consistent with a structure in which solvent and water of hydration are absent.

Key words: solid-state NMR, octamethylcalix[4]pyrrole, quadrupolar coupling, chemical shift tensor, halogen NMR, solvates, ion binding, receptors.

Résumé : On rapporte les résultats d'une étude RMN à l'état solide (RMN-ES) du $^{35/37}$Cl du complexe du chlorure de 1-butyl-3-méthylimidazolium avec le *méso*-octaméthylcalix[4]pyrrole (**1**). On a analysé les formes des raies obtenues pour des échantillons de poudre à l'état stationnaire et à l'angle de rotation magique, à 9,4 et 21,1 T, pour en extraire le tenseur quadripolaire et le tenseur du déplacement chimique (DC) du $^{35/37}$Cl ainsi que leur orientation relative. La symétrie relativement élevée de l'environnement de coordination de l'ion chlorure se manifeste par la faible valeur de la constante de couplage quadripolaire, $C_Q(^{35}Cl) = 1{,}0$ MHz. Le déplacement chimique isotrope de 120 ppm (par rapport au NaCl) se trouve à la limite supérieure de la plage typique observée pour les chlorhydrates organiques. Une considération de l'anisotropie du déplacement chimique (portée, $\Omega = 50$ ppm) et de la non coïncidence des tenseurs quadripolaires et du déplacement chimique sont essentiels pour simuler correctement les spectres expérimentaux. L'utilité des calculs des tenseurs quadripolaires et du déplacement chimique du chlore, par la théorie de la fonctionnelle de la densité en utilisant une onde améliorée par un opérateur de projection et comportant une jauge (« GIPAW-DFT »), est vérifié en comparant avec les données expérimentales disponibles pour des chlorhydrates solides d'acides aminés. Il est démontré que les calculs surévaluent systématiquement la valeur de la constante de couplage quadripolaire du ^{35}Cl. Des calculs supplémentaires sur divers modèles hydratés et solvatés du composé **1** sont en accord avec une structure dans laquelle le solvant et l'eau d'hydratation sont absents.

Mots-clés : RMN à l'état solide, octaméthylcalix[4]pyrrole, couplage quadripolaire, tenseur du déplacement chimique, RMN des halogènes, produits solvatés, fixation d'ion, récepteurs.

[Traduit par la Rédaction]

Introduction

Calix[*n*]arene rings are metacyclophanes made up of aromatic units bridged with methylene links. These units have a hydrophobic wide rim and a hydrophilic narrow rim that encompass a cavity, making them ideal for encapsulating smaller guest molecules.[1,2] The rings can be functionalized to tune a variety of physical properties, such as their hydrophobicity, solubility, reactivity, etc. For example, conversion of calixarenes to esters greatly increases their solubility in organic solvents whereas sulfonation increases water solubility.[2]

Received 5 October 2010. Accepted 30 November 2010. Published at www.nrcresearchpress.com/cjc on 5 July 2011.

R.P. Chapman and D.L. Bryce. Department of Chemistry and Centre for Catalysis Research and Innovation, University of Ottawa, 10 Marie Curie Private, Ottawa, ON K1N 6N5, Canada.
J.R. Hiscock and P.A. Gale. School of Chemistry, University of Southampton, Southampton SO17 1BJ, UK.

Corresponding author: D.L. Bryce (e-mail: dbryce@uottawa.ca).

This article is part of a Special Issue dedicated to Professor Roderick E. Wasylishen in honour of his outstanding contributions to NMR spectroscopy, to chemistry in Canada, and to the training of NMR spectroscopists.

Scheme 1. Structure of *meso*-octamethylcalix[4]pyrrole.

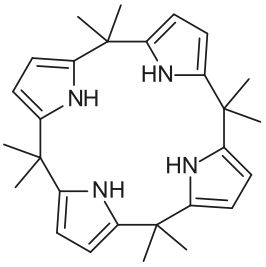

Calix[*n*]arene rings are known for their high melting points, generally around or over 250 °C, which was one of the initial features that drew interest to this family of compounds.[2] Given their tunability and thermal stability, calix[*n*]arene rings have been used for a wide range of applications including field effect transistors, biomimetic catalysts, nonlinear optic materials, potential drug carriers, and ion separators.[1–3] Calix[4]arenes are the most prevalent member of the calixarene family, with a great number of different functionalized rings having been produced. In the anion complexation arena, compounds containing pyrrole have been shown to be effective anion receptors.[4,5] Simple and easy-to-make macrocyclic polypyrroles such as *meso*-octamethylcalix[4]pyrrole, a known anion receptor and shown in Scheme 1, have been known since 1886,[6] but their anion complexation properties, only reported in 1996, together with salt binding properties, continue to be explored.[7–14] This compound can be regarded as a pyrrolic analogue of the calixarenes and has been found to adopt a cone conformation when complexed with a halide ion (including Cl^-) in the solid state.[8–11,14]

Solid-state nuclear magnetic resonance (SSNMR) spectroscopy has proven to be an effective method for the characterization of calixarene structure and complexation properties in the past.[15–18] Spectra of several different nuclei have been collected and analyzed in these studies, including both spin 1/2 (e.g., ^{1}H or ^{13}C) and quadrupolar nuclei (e.g., ^{2}H, ^{133}Cs, or ^{139}La).[15–19] Over the past decade, chlorine-35/37 SSNMR spectroscopy has become an increasingly popular method for studying the environments of chloride ions in a variety of organic and inorganic materials.[20,21] For example, Wasylishen and co-workers[22] studied a series of organic hydrochlorides in 2001 and found the magnitude of the nuclear quadrupole coupling constant to be related to the hydrogen bonding environment. The appeal of the technique stems from the sensitivity of chlorine NMR parameters to the local structural and electronic environment about the chlorine nucleus. Whereas some of the NMR properties of chlorine, primarily the moderately large quadrupole moments (Q) for both nuclides (–81.65 and –64.35 mb for ^{35}Cl and ^{37}Cl, respectively),[23] make collection of spectra difficult, the increasing availability of high magnetic field instruments and signal enhancement techniques have allowed chlorine SSNMR to become more routine.[21,24–29] Despite its slightly higher quadrupole moment, the higher natural abundance and higher resonance frequency of ^{35}Cl vs ^{37}Cl (75.53% and 39.2 MHz vs 24.47% and 32.6 MHz at 9.4 T) makes the former the more popular nucleus for study.

Often, computational studies can serve as a useful complement to SSNMR experiments, providing additional information and aiding analysis. While several commercial programs exist for the calculation of both electric field gradient (EFG) and magnetic shielding (MS) tensor properties, many are not ideal for solids as calculations are effectively carried out in the gas phase. The gauge-including projector-augmented wave density functional theory (GIPAW-DFT) method as implemented in the CASTEP program, however, is ideal for solids as it utilizes plane wave pseudopotentials and periodic boundary conditions, thus describing the system as an infinite crystal lattice.[30–32] The GIPAW-DFT method has proven useful in SSNMR studies of a wide variety of nuclei, including chlorine SSNMR studies.[21,27,33–41] However, the majority of materials included in the few studies for which GIPAW-DFT has been shown to be effective in the calculation of chlorine NMR parameters were inorganic systems.[27,40] Thus, a systematic study involving a large data set is beneficial to establish the reliability of the method for calculating chlorine NMR tensor parameters in organic chloride systems. The series of amino acid hydrochlorides is ideal for this type of study, as there exists high quality SSNMR data along with X-ray (or neutron) diffraction structures for 15 of these salts.[22,24–26]

Here, we present a $^{35/37}$Cl SSNMR study of the chloride ion receptor, 1-butyl-3-methylimidazolium chloride complex of *meso*-octamethylcalix[4]pyrrole (**1**), and establish the reliability of GIPAW-DFT calculations of chlorine NMR parameters for organic chloride compounds.

NMR tensor conventions

Presented here is a brief summary of the NMR tensor conventions used in the current study. A more complete description of the relevant theory of SSNMR spectroscopy of half-integer quadrupolar nuclei under the high-field approximation may be found in the literature.[42,43] In this study, only the spectrum owing to the $^{35/37}$Cl central transition (CT, $m_I = +1/2 \leftrightarrow -1/2$) was observed and all experiments are assumed to have been carried out under "high field" conditions as the Larmor frequency (ν_0) was much greater than the quadrupolar frequency, $\nu_Q = 3C_Q\sqrt{1 + (\eta_Q^2/3)}/[2I(2I-1)]$, where C_Q is the quadrupolar coupling constant and I is the nuclear spin quantum number. The spectral line shapes observed in this study are primarily due to anisotropic magnetic shielding and the quadrupolar interaction.

Nuclear magnetic shielding can be described by a second rank tensor ($\boldsymbol{\sigma}$) that, when expressed in its principal axis system (PAS), can be characterized by three eigenvalues, $\sigma_{33} \geq \sigma_{22} \geq \sigma_{11}$, and three corresponding eigenvectors. Experimentally, it is the chemical shift (CS) tensor ($\boldsymbol{\delta}$) that is measured and, similar to the MS tensor, its magnitude may also be represented by three eigenvalues, $\delta_{11} \geq \delta_{22} \geq \delta_{33}$. In the case of chlorine, it is possible to convert between the MS and CS tensors as an absolute shielding scale is available. For an infinitely dilute solution of aqueous NaCl, Wasylishen and co-workers[22] showed that σ_{iso}(ref) is 974 ppm.[44] Therefore,

$$[1] \qquad \delta_{iso} = \frac{974 \text{ ppm} - \sigma_{iso}}{1 - 974 \text{ ppm}}$$

In this study, the Maryland convention is used. Under this convention the CS tensor components are described using the span (Ω) and skew (κ), with the isotropic part simply equal

Can. J. Chem. Downloaded from www.nrcresearchpress.com by Xi'an Jiaotong University on 09/19/12
For personal use only.

to one-third the trace of the tensor ($\sigma_{iso} = (\sigma_{11} + \sigma_{22} + \sigma_{33})/3$; $\delta_{iso} = (\delta_{11} + \delta_{22} + \delta_{33})/3$).

$$[2] \qquad \Omega = \sigma_{33} - \sigma_{11} \approx \delta_{11} - \delta_{33}$$

$$[3] \qquad \kappa = \frac{3(\sigma_{iso} - \sigma_{22})}{\Omega} \approx \frac{3(\delta_{22} - \delta_{iso})}{\Omega}$$

Both ^{35}Cl and ^{37}Cl have nuclear spin quantum numbers of 3/2 and are therefore also affected by the nuclear quadrupole interaction (QI) between Q and the EFG at the nucleus. In its PAS, the EFG tensor may be diagonalized to yield three eigenvalues, which are ordered $|V_{33}| \geq |V_{22}| \geq |V_{11}|$. In this work, these eigenvalues are presented in terms of C_Q, which is related to the principal component of largest magnitude, and the asymmetry parameter (η_Q).

$$[4] \qquad C_Q = \frac{eV_{33}Q}{h}$$

$$[5] \qquad \eta_Q = \frac{V_{11} - V_{22}}{V_{33}}$$

where h is Planck's constant.

Because of the moderate quadrupole moment of both isotopes of chlorine it is often the case that observed line shapes are dominated by the QI. The breadth of the CT line shape of a stationary powdered sample owing to the QI depends on four parameters (C_Q, ν_0, I, and η_Q), as shown below.[45]

$$[6] \qquad \Delta\nu_{CT} = \left[\frac{3C_Q}{2I(2I-1)}\right]^2 \frac{(\eta_Q{}^2 + 22\eta_Q + 25)[I(I+1) - 3/4]}{144\nu_0}$$

The inverse proportionality between the CT line width and the Larmor frequency demonstrates why higher magnetic fields are advantageous for chlorine SSNMR studies: increasing B_0 increases ν_0, which results in an overall decrease in the second-order quadrupolar broadening of the CT. In addition, the effects of chemical shift anisotropy (CSA) increase at higher fields, allowing for them to be more easily observed. Generally, for both isotopes of chlorine, even in cases where the CSA can be easily observed, the spectrum obtained is usually still dominated by the QI and displays a typical second-order quadrupolar line shape.

The orientation of the EFG and CS tensors relative to one another can also be determined experimentally under favourable conditions. The relative orientation is described by three Euler angles.[42] The Arfken convention is used in this work, with the EFG PAS acting as the reference coordinate system.[46]

Experimental and computational details

Sample preparation

The 1-butyl-3-methylimidazolium chloride complex of *meso*-octamethylcalix[4]pyrrole (**1**) was prepared as described in ref. 7. The structure consists of a chloride ion bound to a *meso*-octamethylcalix[4]pyrrole ring and a 1-butyl-3-methylimidazolium group. The crystal structure described in ref. 7 also includes one dichloromethane and two water solvent molecules. Phase purity of the sample was confirmed by a ^{13}C CP/MAS NMR experiment collected with a spinning frequency of 8 kHz at 9.4 T. ^{13}C CP/MAS NMR of *meso*-octamethylcalix[4]pyrrole was also collected under the same conditions to ensure no free ligand was present in the sample. These spectra are included in the Supplementary data (Figs. S1 and S2).

The sample was also analyzed using thermogravimetric analysis (TGA) using a TA instruments 2960 SDT V3.0F unit in the temperature range of 25–593 °C, the outcome of which will be addressed in the Results and discussion section.

NMR spectroscopy

9.4 T

Chlorine-35/37 SSNMR experiments were carried out on a 400 MHz (B_0 = 9.4 T) Bruker Avance III spectrometer at the University of Ottawa, Ottawa, Ontario. A 4 mm Bruker HX MAS probe, tuned to 39.2 MHz (^{35}Cl) or 32.6 MHz (^{37}Cl), was used. Samples were ground into fine powders and packed into 4 mm o.d. zirconia rotors. Experimental setup and pulse calibrations were performed using solid NaCl or NH_4Cl, and all $^{35/37}$Cl NMR spectra were referenced to the $^{35/37}$Cl MAS centreband of solid NaCl at 0 ppm. The "solid" $\pi/2$ chlorine pulse was found by halving the nonselective $\pi/2$ pulse measured using solid NaCl or NH_4Cl, and was typically 2.3 and 2.4 μs for ^{35}Cl and ^{37}Cl, respectively. Recycle delays were 2 s. All spectra collected under stationary conditions used the $\pi/2 - \tau - \pi/2 - \tau -$ acquire echo sequence,[47–49] whereas MAS experiments used only a single pulse. Proton decoupling was applied during all experiments. To offset the effects of sample heating owing to fast spinning during MAS experiments, the environment of the sample was cooled to ~283 K (spectrometer VT setting) using liquid nitrogen boil-off.

21.1 T

Chlorine-35/37 SSNMR experiments were also performed on a 900 MHz (B_0 = 21.1 T) Bruker Avance II spectrometer at the National Ultrahigh-Field NMR Facility for Solids in Ottawa, Ontario. A 4 mm Bruker DVT MAS HX probe tuned to 88.2 MHz (^{35}Cl) or 73.4 (^{37}Cl) MHz was used for all experiments. Experimental setup, pulse calibration, and referencing were done using solid NaCl, as above. The pulse sequences used were identical to those used at 9.4 T, again with proton decoupling. The solid $\pi/2$ ^{35}Cl pulse was found to be 3.4 μs and a recycle delay of 2 s was used for all acquisitions. The same parameters were used for ^{37}Cl. All experiments, both static and MAS, were conducted with cooling to ~283 K (spectrometer VT setting).

Data processing and simulations

All NMR spectra were processed using Bruker's TopSpin 1.3. NMR spectra were simulated using the WSolids1 software package from the laboratory of R. Wasylishen,[50] which incorporates the space-tiling algorithm of Alderman et al.[51] Interpretations of the spectra were done within the high-field approximation and assumed a single magnetically unique site, in accord with the X-ray diffraction structure.[7] All stack plots presented were created using DMFit.[52]

GIPAW-DFT calculations

All quantum chemical calculations were carried out with

Can. J. Chem. Downloaded from www.nrcresearchpress.com by Xi'an Jiaotong University on 09/19/12
For personal use only.

Can. J. Chem. Downloaded from www.nrcresearchpress.com by Xi'an Jiaotong University on 09/19/12
For personal use only.

Fig. 1. (*a*), (*c*), and (*e*) Experimental and (*b*), (*d*), and (*f*) simulated solid-state ^{35}Cl (left and middle) and ^{37}Cl (right) magic-angle-spinning NMR spectra of **1** at 9.4 T (left) and 21.1 T (middle and right).

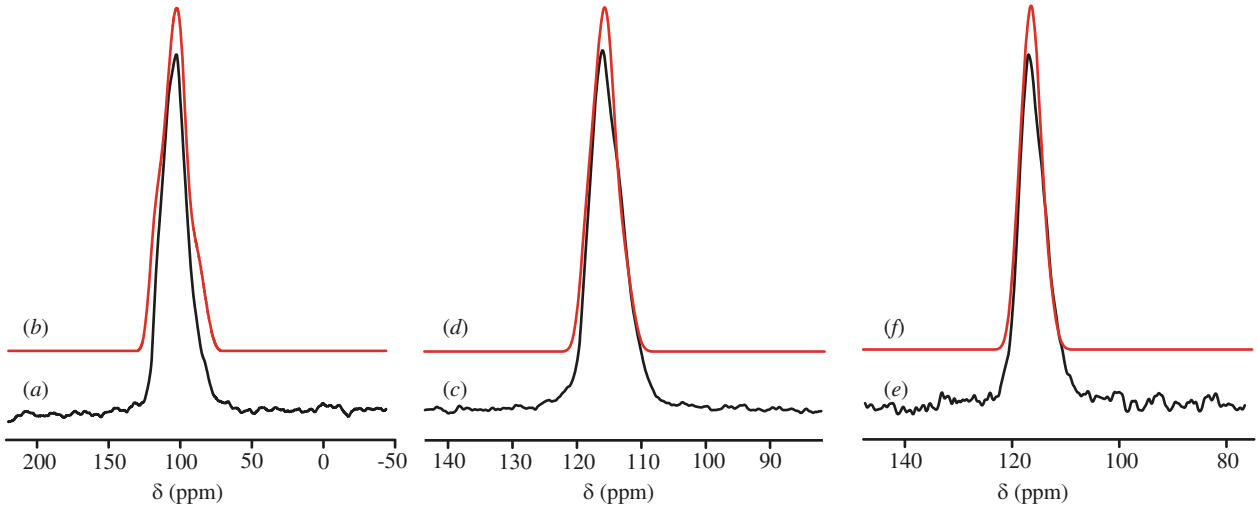

Table 1. Chlorine quadrupolar and chemical shift tensor data for *meso*-octamethylcalix[4]pyrrole 1-butyl-3-methyl imidazolium chloride (**1**).

$C_Q(^{35}Cl)$ (MHz)*	η_Q	δ_{iso} (ppm)†	Ω (ppm)	κ	α (°)	β (°)	γ (°)
1.0±0.1	0.7±0.1	120±10	50±5	0.4±0.4	15±30	27±20	60±15

Note: C_Q, quadrupolar coupling constant; η_Q, asymmetry parameter; δ_{iso}, isotropic chemical shift; Ω, chemical shift tensor span; κ, skew; α, β, γ, Euler angles.

*The ^{37}Cl quadrupolar coupling constant was identical to $C_Q(^{35}Cl) \times Q(^{37}Cl)/Q(^{35}Cl) = C_Q(^{35}Cl) \times 0.788$, where Q is the nuclear electric quadrupole moment.

†The ^{35}Cl chemical shift is with respect to solid sodium chloride at 0 ppm.

the CASTEP program using Materials Studio (version 3.2.0.0) and the PBE functional.[30,32] The planewave energy cutoffs and number of k-points used are included in the Supplementary Data, along with information about the chlorine on-the-fly pseudopotential. In the case of the models based on the available crystal structure of **1**, the highest energy cutoff that allowed for the calculations to complete was used. Calculations of the chlorine MS and EFG tensors used the atomic coordinates and unit cell parameters from the X-ray structure found in ref. 7 for **1** and the published structures for the amino acid hydrochlorides, listed below. Neutron diffraction structures were used for phenylalanine hydrochloride, valine hydrochloride, tyrosine hydrochloride, glutamic acid hydrochloride, lysine hydrochloride dihydrate, and glycine hydrochloride.[53–58] X-ray diffraction structures were used for arginine hydrochloride monohydrate, alanine hydrochloride, aspartic acid hydrochloride, cysteine hydrochloride monohydrate, methionine hydrochloride, proline hydrochloride, threonine hydrochloride, and tryptophan hydrochloride.[24,59–63] For histidine hydrochloride monohydrate, the neutron diffraction structure of Fuess et al.[64] was used; however, because of obvious typographical errors the *z* coordinate for C5 and the estimated position for H9 were taken from the X-ray structure of Donohue and Caron.[65] In cases where an X-ray structure was used, optimization of the proton positions was attempted, and in cases where this was computationally possible, the optimized structures were used for NMR calculations.

The EFG and MS tensors contained in the CASTEP output files were analyzed using a modified version of the EFG-Shield program (version 2.2).[46]

Results and discussion

Experimental results

The three MAS NMR spectra collected, and their corresponding spectral simulations, are presented in Fig. 1. The EFG tensor parameters and isotropic chemical shift were first extracted from the MAS NMR spectra, as CSA is averaged by the fast rotation of the sample. The quadrupolar and chemical shift tensor parameters for **1** are shown in Table 1. It is evident from the spectra that the QI at the chlorine nucleus in **1** is very small, as the MAS NMR line shapes are relatively featureless. The line width at half height is ~500 Hz for the ^{35}Cl NMR spectra collected at 21.1 T. The collection of the spectra at two fields and for two isotopes (^{35}Cl at 9.4 and 21.1 T and ^{37}Cl at 21.1 T) was useful to ensure the accuracy of the fits, as the same parameters were used to fit all three spectra (with the value of $C_Q(^{35}Cl)$ scaled by $Q(^{37}Cl)/Q(^{35}Cl) = 0.788$ to give the value of $C_Q(^{37}Cl)$). In addition, nutation spectroscopy was helpful to verify the accuracy of the obtained parameters (vide infra).

The ^{35}Cl quadrupolar coupling constant of 1.0 MHz is small in magnitude compared with most other organic chloride systems that have been studied to date with chlorine SSNMR.[20,21] This small $|C_Q(^{35}Cl)|$ is consistent with the low

Can. J. Chem. Downloaded from www.nrcresearchpress.com by Xi'an Jiaotong University on 09/19/12
For personal use only.

end of those observed in the study by Honda[66] on a series of *n*-alkylammonium chlorides, *n*-$C_xH_{(2x+1)}NH_3Cl$ (both deuterated and non-deuterated samples), in which the coupling constants observed were all between 1.0 and 1.5 MHz. In the *n*-$C_xH_{(2x+1)}NH_3Cl$ series, the chlorine lies on a high symmetry (C_4) axis, in contrast with **1**. In the case of the amino acid hydrochlorides, another comparable series of organic chlorides, the magnitude of $C_Q(^{35}Cl)$ ranges from 2.035 MHz in arginine hydrochloride monohydrate to 7.1 MHz in aspartic acid hydrochloride, demonstrating that the chloride ion in **1** sits at a site with a significantly smaller EFG compared with those systems.[21,24–26] This observation is consistent with the structure of the *meso*-octamethylcalix[4]pyrrole ring and the placement of the chloride ion within it. According to ref. 7, the chloride rests slightly above and close to the centre of the *meso*-octamethylcalix[4]pyrrole ring (in a cone conformation), nearly equidistant from the four amine groups of the arene ring that lie below. In addition, if we consider that the calix ring is lying directly "below" the chloride ion, then the 1-butyl-3-methyl imidazolium moiety lies directly above the chloride ion. Thus, the chloride ion interacts with six hydrogen atoms, which is more than most of the amino acid hydrochlorides.[24–26] The EFG η_Q determined from the fits has a value of 0.7, and hence the EFG tensor is non-axial. The accuracy of the parameters extracted from the fits was also confirmed with a nutation analysis,[67,68] which gave results that were consistent with the reported parameters (see Supplementary data, Fig. S3).

Shown in Figs. 2*a*–2*f* and 2*g*–2*l* are experimental and simulated ^{35}Cl NMR spectra of **1** collected at 9.4 and 21.1 T under stationary conditions. Figures 2*m*–2*n* present the ^{37}Cl experimental and simulated spectra at 21.1 T. As the EFG tensor parameters were known from the MAS experiments and nutation analysis, the static spectra were fit to extract the CS tensor parameters (Table 1). The collection of spectra of both isotopes at two fields was essential to ensure the accuracy of the extracted parameters. In addition, the small magnitude of $C_Q(^{35}Cl)$ resulted in the simulations being highly sensitive to slight changes in the magnitudes of the CS tensor parameters, giving further confidence in the values listed. Although small, the measured CS tensor span (50 ppm) is within the range observed for the amino acid hydrochlorides (26–129 ppm).[24–26] In addition, the chlorine chemical shift (120 ppm) is at the high end of those observed for the amino acid hydrochlorides (37–120 ppm).[24–26] The shift is within the range observed for the alkaline earth chloride hydrates, but lower than the range observed for other noncubic metal chlorides (e.g., $AlCl_3$).[20,21] The results clearly demonstrate that the EFG and CS tensors reflect different aspects of the chloride ion environment: whereas the EFG about the chlorine in **1** is relatively small compared with other organic hydrochloride systems, the isotropic chlorine CS and CS tensor span are not.

The experimental spectrum collected at 9.4 T under static conditions (Fig. 2*a*), has a line shape that approximately resembles that solely owing to a second-order quadrupolar interaction demonstrating, at this field, that the QI does dominate the spectrum despite the small magnitude of this interaction (shown by simulations in Figs. 2*d* and 2*f*). However, the effects of CSA are clearly observable as shown by the simulated spectrum in Fig. 2*d*, which assumes no CSA and is clearly not an ideal fit to the experimental spectrum. The QI is not the dominant interaction at 21.1 T (Figs. 2*g*–2*l*), as both the experimental and best-fit simulation spectra have line shapes that resemble the line shape observed for static spin-1/2 nuclei in powdered samples, for which CSA dictates the line shape. This is demonstrated in Figs. 2*j* and 2*l*, in which the simulation assuming no QI (*l*) is quite similar to the experimental line shape, whereas the experimental line shape that assumes no CSA (*j*) is a very poor fit. This type of CSA-dominated NMR spectrum is not typical for chlorine because of its moderately high Q value, and is a clear demonstration of the power of high field instruments to enhance the effects of CSA while reducing the effects of the QI.

Computational results

Meso-*octamethylcalix[4]pyrrole 1-butyl-3-methyl imidazolium chloride*

As an X-ray crystal structure is available for **1**·CH_2Cl_2·$2H_2O$,[7] complementary GIPAW-DFT calculations of the chlorine SSNMR parameters of that material were carried out. In addition, to assess the effects of slight changes to the chlorine environment on the NMR interaction tensors, five different models were used for calculations in which parts of the structure were removed to observe the effect that this would have. These models are shown in Fig. 3. All models employ the full X-ray crystal structure as a starting point: model (*a*) consists of the full X-ray crystal structure, including CH_2Cl_2 and water molecules; in model (*b*) the CH_2Cl_2 is removed; model (*c*) has only CH_2Cl_2 and no water molecules; model (*d*) has no CH_2Cl_2 or water molecules; and model (*e*) has only the *meso*-octamethylcalix[4]pyrrole ring and the chloride ion. It should be emphasized that the models used are only approximate, since no further optimization of the geometries were done. The results of the GIPAW-DFT calculations are shown in Table 2.

Inspection of the results in Table 2 reveals some interesting differences among the calculated NMR parameters for the five models. For example, the presence of the dichloromethane solvent molecule (models *a* and *c*) results in lower values of $|C_Q(^{35}Cl)|$, whereas the presence of water solvent molecules (models *a* and *b*) results in a much lower chlorine chemical shift, relative to models without it. Similarly, the CS tensor span only changes notably when water molecules are removed from the model structure. The results of the calculations on model *e* are quite interesting and further demonstrate an observation made on the basis of the experimental spectrum regarding the CS tensor span. Removal of the 1-butyl-3-methyl imidazolium group from model *d* (in addition to the solvent molecules) results in a structure with only the chloride ion lying slightly above and roughly in the centre of the *meso*-octamethylcalix[4]pyrrole ring. This results in an absence of chlorine–hydrogen bonds above the chloride ion, opposite to the calix ring. One may expect this structure to result in both a large value for $|C_Q(^{35}Cl)|$ and the CS tensor span; however, this is not what the calculations predict. Whereas both the CS tensor span and chlorine chemical shift jump significantly to 346 and 336 ppm, respectively, (much greater than those values in typical organic chloride systems) the value of $|C_Q(^{35}Cl)|$ does not rise signifi-

Fig. 2. (*a*), (*c*), and (*e*) Experimental and (*b*), (*d*), and (*f*) simulated solid-state ^{35}Cl NMR spectra of a stationary sample of *meso*-octamethylcalix[4]pyrrole 1-butyl-3-methyl imidazolium chloride (**1**) at 9.4 T. The best-fit simulation is shown in (*b*). The simulation assuming no chemical shift anisotropy (CSA) is shown in (*d*). The simulation assuming no quadrupole interaction (QI) is shown in (*f*). (*g*), (*i*), and (*k*) Experimental and (*h*), (*j*), and (*l*) simulated solid-state ^{35}Cl NMR spectra of a stationary sample of **1** at 21.1 T. The best-fit simulation is shown in (*h*). The simulation assuming no CSA is shown in (*j*). The simulation assuming no QI is shown in (*l*). (*m*) Experimental and (*n*) simulated solid-state ^{37}Cl NMR spectra of a stationary sample of **1** at 21.1 T. The best-fit simulation is shown in (*n*). (*o*) and (*q*) Experimental and (*p*) and (*r*) simulated solid-state ^{35}Cl NMR spectra of **1** at (*o*) and (*p*) 9.4 T and (*q*) and (*r*) 21.1 T, assuming a β angle of 90°.

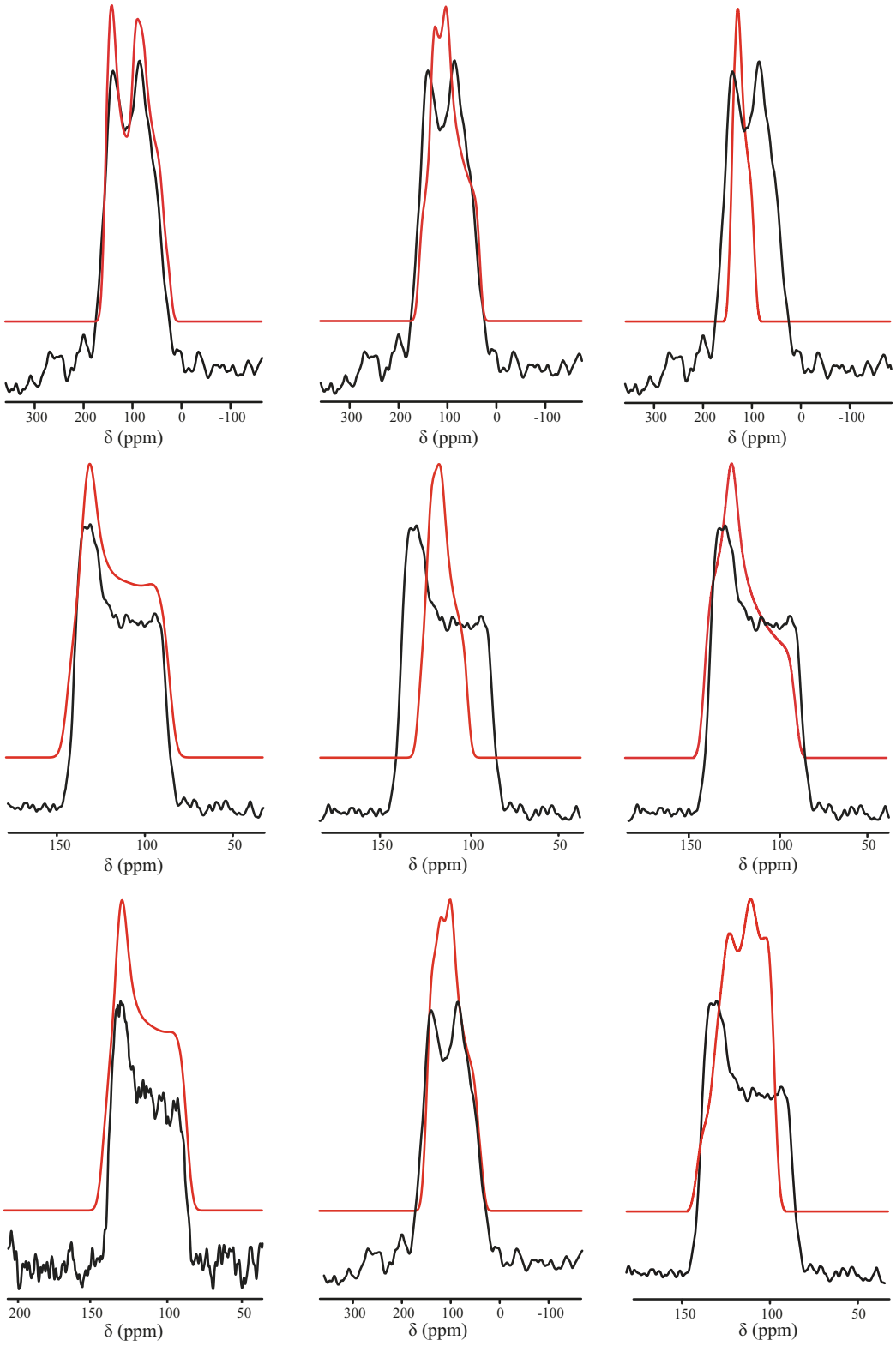

Can. J. Chem. Downloaded from www.nrcresearchpress.com by Xi'an Jiaotong University on 09/19/12
For personal use only.

Can. J. Chem. Downloaded from www.nrcresearchpress.com by Xi'an Jiaotong University on 09/19/12
For personal use only.

Fig. 3. Models, based on the crystal structure of *meso*-octamethylcalix[4]pyrrole 1-butyl-3-methyl imidazolium chloride (**1**), used for gauge-including projector-augmented wave density functional theory (GIPAW-DFT) calculations of chlorine quadrupolar and chemical shift tensor data. Model (*a*), **1**·CH_2Cl_2·$2H_2O$; model (*b*), **1**·$2H_2O$; model (*c*), **1**·CH_2Cl_2; model (*d*), **1**; and model (*e*), *meso*-octamethylcalix[4]pyrrole chloride only.

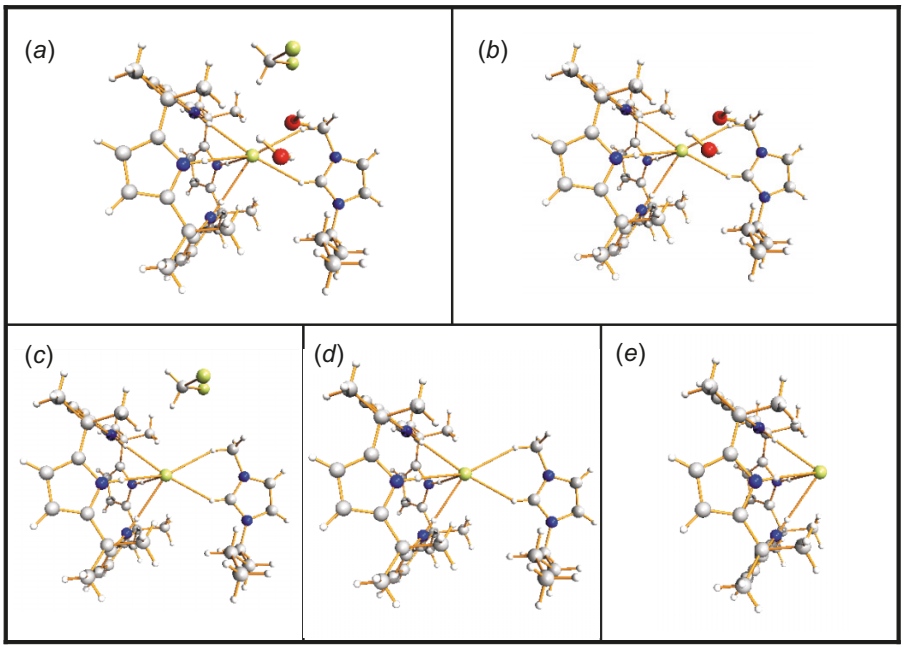

Table 2. Gauge-including projector-augmented wave density functional theory (GIPAW-DFT) calculated chlorine quadrupolar and chemical shift tensor data for various *meso*-octamethylcalix[4]pyrrole 1-butyl-3-methyl imidazolium chloride models.

Model*	$\lvert C_Q(^{35}Cl)\rvert$ (MHz)	η_Q	δ_{iso} (ppm)†	Ω (ppm)	κ	α (°)	β (°)	γ (°)
a	0.63	0.65	97.5	51	0.7	108	64	70
b	1.41	0.30	98.4	51	0.7	131	85	24
c‡	1.00	0.91	186	65	0.8	57	66	100
d‡	1.35	0.60	188	69	0.7	73	25	65
e‡	1.21	0.57	336	346	0.2	136	35	46

Note: C_Q, quadrupolar coupling constant; η_Q, asymmetry parameter; δ_{iso}, isotropic chemical shift; Ω, chemical shift tensor span; κ, skew; α, β, γ, Euler angles.

*Models are shown in Fig. 3.

†To convert from calculated shielding constants to chemical shifts, a shift of 45.37 ppm was used (for the conversion from solid to aqueous NaCl chemical shift scales) in addition to the absolute shielding conversion of 974 ppm.[44]

‡NMR calculation performed after the optimization of hydrogen positions.

cantly. In fact, the calculated value of 1.21 MHz is still lower than *all* the ^{35}Cl quadrupolar coupling constants observed for the amino acid hydrochloride salts and the calculated values for both models *b* and *d*. The large CS tensor span and chemical shift value calculated for model *e* demonstrate that the calix ring environment alone results in a significant amount of CSA. This result suggests that other chloride-containing calix[*n*]arene systems may also display measureable CSA and relatively high chlorine chemical shift values, even if the QI is small.

Comparison of the experimental NMR parameters from Table 1 with those from model *a* reveals a significant discrepancy. Specifically, the GIPAW-DFT calculations predict a β value close to 90°, which indicates non-coincidence of the largest components of the EFG and CS tensors. This result was *not* observed experimentally, as non-coincidence results in a very different line shape, as shown by Figs. 2*o*–2*r*. Only model *d* has a calculated β value that is consistent with the experimental value and the line shape observed. This observation suggests that the CH_2Cl_2 and water molecules were not part of the structure, and were likely lost as a result of the sample grinding prior to the NMR experiments. This is perhaps not surprising for CH_2Cl_2, as these molecules are simply solvates that were included in the structure during crystallization. Further confirmation was provided by a TGA analysis that showed, definitively, that there were no water or dichloromethane solvent molecules in the sample of **1** that was analyzed with SSNMR, as only one mass loss event occurred, at a temperature of ~265 °C (see Supplementary data, Fig. S4). This value is consistent with the melting point of a calix[4]arene system,[2] indicating that the calix ring is intact at temperatures lower than 265 °C. If water or dichlorome-

Can. J. Chem. Downloaded from www.nrcresearchpress.com by Xi'an Jiaotong University on 09/19/12
For personal use only.

Table 3. Gauge-including projector-augmented wave density functional theory (GIPAW-DFT) calculated and experimental ^{35}Cl quadrupolar and chemical shift data for amino acid hydrochloride salts for which X-ray structures are available.

Amino acid hydrochloride*	$\lvert C_Q(^{35}Cl)\rvert$ (MHz)	η_Q	δ_{iso} (ppm)†,‡	Ω (ppm)	κ	α, β, γ (°)
Alanine						
Calcd.§	8.45	0.775	146	75	0	16, 16, 86
Exp.	6.4±0.1	0.75±0.06	106±5	60±30	–0.3±0.5	90±15, 0±15, 0±15
Arginine						
Calcd.‖	2.45	0.197	51	44	–0.2	65, 71, 54
Exp.	2.035±0.020	0.98±0.02	91.5±1.0	57.5±3.0	0.27±0.10	85±15, 77.5±12.0, 30±30
Aspartic acid						
Calcd.§	10.31	0.396	149	91	–0.7	13, 18, 118
Exp.	7.1±0.1	0.42±0.05	102±5	75±30	–0.9±0.1	0±20, 30±20, 93±20
Cysteine						
Calcd.§	4.00	0.505	155	86	0.1	8, 6, 155
Exp.	3.92±0.01	0.47±0.02	104.2±0.5	66±10	0.12±0.12	155±20, 0±10, 0±20
Histidine						
Calcd.§	2.72	0.716	112	99	–0.5	158, 74, 173
Exp.	4.59±0.03	0.46±0.02	93±1	<150	na	na
Methionine						
Calcd.§	6.20	0.375	138	137	0.2	75, 13, 18
Eexp.	4.41±0.02	0.35±0.03	99±1	100±20	0.3±0.3	93±20, 163±15, 7±20
Proline						
Calcd.§	9.23	0.906	110	105	0.4	90, 88, 51
Exp.	4.50±0.05	0.63±0.05	37±5	63±5	–0.54±0.08	48±20, 69±3, 9±20
Threonine						
Calcd.§	12.21	0.849	149	133	0.2	110, 4, 18
Exp.	5.4±0.1	0.94±0.02	99±10	95±40	–0.2±0.5	95±15, 0±10, 0±15
Tryptophan						
Calcd.§	11.62	0.816	151	127	0.5	56, 7, 38
Exp.	5.05±0.04	0.86±0.03	105±1	72±5	0.1±0.1	90±15, 20±15, 2±20

Note: C_Q, quadrupolar coupling constant; η_Q, asymmetry parameter; δ_{iso}, isotropic chemical shift; Ω, chemical shift tensor span; κ, skew; α, β, γ, Euler angles. Experimental data are from refs. 24–26.

*Arginine, cysteine, and histidine hydrochloride salts are monohydrates.

†To convert from calculated shielding constants to chemical shifts, a shift of 45.37 ppm was used (for the conversion from solid to aqueous NaCl chemical shift scales) in addition to the absolute shielding conversion of 974 ppm.[44]

‡Experimental values are all with respect to solid NaCl at 0 ppm.

§NMR calculation performed after hydrogen atom positions were optimized using the method described in the Experimental section.

‖NMR calculation performed without hydrogen atom positions optimization.

thane were part of the structure, they would evaporate near their respective boiling points of 100 and 40 °C, resulting in multiple mass loss events in the TGA curve. To help verify that the sample maintained similar packing (and therefore unit cell parameters) upon loss of solvent molecules, a powder X-ray diffraction pattern was collected. The resulting pattern was consistent with the cell parameters of the parent compound (**1**·CH_2Cl_2·$2H_2O$), suggesting that the structure does not change significantly (Supplementary data Fig. S5). Furthermore, comparison of the ^{13}C CPMAS NMR spectrum of the free *meso*-octamethylcalix[4]pyrrole ligand with that of **1** (Supplementary data Figs. S1 and S2) shows that compound **1** has not decomposed into a mixture of free ligand and 1-butyl-3-methylimidazolium chloride. Comparison of the SSNMR tensor parameters calculated for model *d* with the experimental values listed in Table 1 shows relatively good agreement but overestimates $\lvert C_Q(^{35}Cl)\rvert$, Ω, and the chlorine chemical shift. The good agreement with model *d* further suggests that the cell parameters of the sample are likely similar to those of **1**·CH_2Cl_2·$2H_2O$. We next looked to determine if the overestimation computed for $\lvert C_Q(^{35}Cl)\rvert$, Ω, and δ_{iso} would be consistent with the results of GIPAW-DFT calculations for other organic chlorides.

Amino acid hydrochlorides

To determine whether these overestimations were inherent to GIPAW-DFT calculations of chlorine NMR parameters in organic hydrochlorides, a systematic computational study of the amino acid hydrochlorides was carried out. This also provided an opportunity to compare the results of GIPAW-DFT calculations with those carried out previously using a B3LYP or RHF level of theory and a cluster model,[24–26] as implemented in the Gaussian program.[69] The optimal method for determining chlorine SSNMR parameters using a cluster model has been determined previously to be B3LYP for CS tensor parameters and RHF for EFG tensor parameters (ideal basis sets were also determined).[25] This set of compounds is ideal as there is a large body of precise experimental chlorine SSNMR data,[24–26] in addition to published crystal structures.

Whereas the majority of the amino acid hydrochlorides have had their structures determined through X-ray diffraction, the availability of neutron diffraction structures for

Can. J. Chem. Downloaded from www.nrcresearchpress.com by Xi'an Jiaotong University on 09/19/12
For personal use only.

Table 4. Gauge-including projector-augmented wave density functional theory (GIPAW-DFT) calculated and experimental ^{35}Cl quadrupolar and chemical shift tensor data for amino acid hydrochloride salts for which neutron diffraction structures are available.

Amino acid hydrochloride*	$C_Q(^{35}Cl)$ (MHz)	η_Q	δ_{iso} (ppm)†,‡	Ω (ppm)	κ	α, β, γ (°)
Glutamic acid						
Calcd.	4.3	0.30	142	84	0.3	21, 79, 17
Exp.	3.61±0.01	0.65±0.02	102±1	66±15	0.0±0.3	9±20, 77±20, 6±20
Glycine						
Calcd.	8.14	0.80	133	110	0.3	123, 6, 142
Exp.	6.42±0.05	0.61±0.03	101±5	100±20	0.3±0.3	95±20, 0±20, 0±20
Lysine						
Calcd.	4.41	0.77	107	54	–0.2	70, 79, 8
Exp.	2.49±0.01	0.42±0.02	105±2	26±10	–0.4±0.4	0±20, 52±20, 0±20
Phenylalanine						
Calcd.	7.71	0.55	129	147	0.1	95, 12, 176
Exp.	6.08±0.05	0.52±0.03	96±5	129±20	0.26±0.25	91±20, 13±20, 10±20
Tyrosine						
Calcd.	3.27	0.35	142	129	–0.5	13, 39, 54
Exp.	2.23±0.02	0.72±0.03	94.7±0.5	<150	na	na
Valine						
Calcd.	7.96	0.55	128	149	0.1	83, 7, 14
Exp.	5.89±0.05	0.51±0.05	90±10	125±40	0.35±0.5	65±20, 0±20, 0±20

Note: C_Q, quadrupolar coupling constant; η_Q, asymmetry parameter; δ_{iso}, isotropic chemical shift; Ω, chemical shift tensor span; κ, skew; α, β, γ, Euler angles. Experimental data are from refs. 22 and 24–26.

*Lysine hydrochloride salt is a dihydrate.

†To convert from calculated shielding constants to chemical shifts, a shift of 45.37 ppm was used (for the conversion from solid to aqueous NaCl chemical shift scales) in addition to the absolute shielding conversion of 974 ppm.[44]

‡Experimental values are all with respect to solid NaCl.

some of these salts (those of glutamic acid, glycine, lysine, phenylalanine, tyrosine, and valine)[53–58] allowed for more complete testing of the accuracy of the calculations carried out using the GIPAW-DFT level of theory. From the neutron structures, the positions of all atoms (including hydrogens) in those amino acid hydrochlorides are known experimentally, meaning that any inaccuracy in the calculated NMR parameters compared with experiment may largely be attributed to deficiencies in the computational method. This is not true in the case where only X-ray structures are available, as incorrect placement of the hydrogen atoms may be the primary cause of inaccuracies relative to experiment.[25]

As the exact hydrogen atom positions are not known from X-ray structures, it is often standard to computationally optimize the proton positions prior to the NMR calculation, as was attempted above for all five models based on **1**. Therefore, we also chose to use the amino acid hydrochlorides to test the effect of optimizing the proton positions in GIPAW-DFT calculations, i.e., to determine if this would have a significant impact on the accuracy of the calculated NMR parameters. The calculated chlorine NMR parameters for the amino acid hydrochlorides for which there is an X-ray structure appear in Table 3, whereas those with a neutron structure appear in Table 4. In both these tables, the experimental data from the literature are included for comparison. As expected, hydrogen atom position optimization improved the accuracy of the calculations in most cases and confirm that, as with B3LYP and RHF calculations,[24–26] it is recommended to optimize proton positions in all cases for which they are not known exactly, provided it is computationally feasible.

A comparison of the experimental and calculated values of $C_Q(^{35}Cl)$ listed in Tables 3 and 4 clearly demonstrates that, even in cases where the full structure of the salt is known accurately, the quadrupolar coupling constant is significantly overestimated by GIPAW-DFT calculations. Shown in Fig. 4 is a graph of the experimental and calculated magnitudes of $C_Q(^{35}Cl)$ for 15 of the amino acid hydrochlorides. Eleven of the amino acids are represented by filled diamond symbols and four outliers appear as filled circle symbols. The data represented by the diamond symbols demonstrate that the experimental versus calculated values of $|C_Q(^{35}Cl)|$ can be fit by a linear equation, but also reveal a systematic overestimation by calculation. This overestimation is quantified by the line of best fit shown on Fig. 4: the slope of the line is 1.3203, the y intercept is 0.045 MHz, and the value of the correlation coefficient (R^2) is 0.9356. For three of the four outlier salts (those of proline, threonine, and tryptophan), the computed values of $|C_Q(^{35}Cl)|$ are more significantly overestimated compared with experiment. It is not known why these three amino acid hydrochlorides lie off the line of best fit, but it is clear that GIPAW-DFT calculations consistently overestimate the magnitude of the chlorine EFG in the vast majority of the amino acid hydrochlorides. The overestimation of this parameter is consistent with the results obtained from RHF calculations.[24–26]

The GIPAW-DFT results are consistent with those observed for **1**, where the calculated value of $|C_Q(^{35}Cl)|$ for model *d* was 1.35 MHz, a 35% overestimation of the experimental value (1.0 MHz). In fact, inclusion of the data point for **1** (1.0 MHz, 1.35 MHz) in Fig. 4 shows that the agreement between experiment and theory for **1** is completely

Can. J. Chem. Downloaded from www.nrcresearchpress.com by Xi'an Jiaotong University on 09/19/12
For personal use only.

Fig. 4. Comparison between the experimentally determined ^{35}Cl quadrupolar coupling constant (*x* axis) and the gauge-including projector-augmented wave density functional theory (GIPAW-DFT) calculated values (*y* axis) for the amino acid hydrochlorides. Data for 11 of the amino acid salts are presented as filled diamond symbols (♦) and that of the four outliers (not included in the fit) are shown as filled circle symbols (●). The equation for the line of best fit for the data represented by ♦ is y (MHz) = 1.3203x (MHz) + 0.045 MHz, with a R^2 value of 0.9356. The broken line represents the line $y = x$. Experimental data are from refs. 22 and 24–26. Also shown but not included in the line of best fit is the data point for *meso*-octamethylcalix[4]pyrrole 1-butyl-3-methyl imidazolium chloride (**1**), i.e., model (*d*) of Fig. 3 (■).

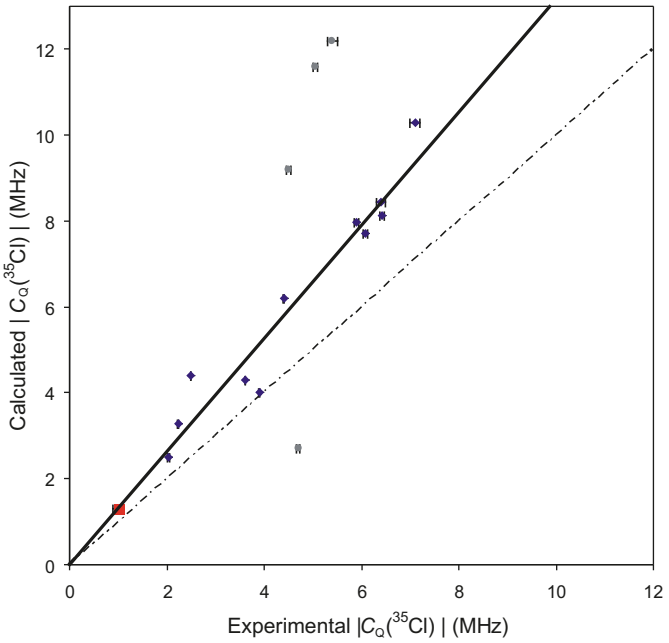

analogous to the agreement obtained for many of the amino acid hydrochlorides. These results further suggest that model *d* is representative of the compound analyzed experimentally, as the predicted |C_Q(^{35}Cl)| for the hydrated and solvated model *a* is actually *underestimated*, and therefore inconsistent with the correlations established between experimental and computed |C_Q(^{35}Cl)| values.

The trend observed for the CS tensor spans is similar to that observed for the chlorine quadrupolar coupling constants. Comparison of the calculated and experimental spans in Tables 3 and 4 again reveal consistent overestimation by calculation. Figure 5 displays these data graphically, with 11 of the amino acids shown as filled diamond symbols and two outliers shown as filled circle symbols. The data represented by the filled diamonds show a linear relationship and an overestimation by calculation, with the line of best fit having a slope of 0.9459, and a *y* intercept of 29.856 ppm. More telling, however, are the data presented in Fig. 6, where only the data points for those amino acid salts for which there is a crystal structure obtained from neutron diffraction are shown. The line of best fit has a slope of 0.9352, a *y* intercept of 25.299 ppm, and a correlation coefficient of 0.9771. These results differ from earlier B3LYP calculations, in which the trends in CS tensor span were not reproduced.[24–26] The present GIPAW-DFT results clearly reproduce the experimental trend, but indicate that even with accurate structures for the calculations, the value of Ω is overestimated. This overestimation is usually outside the error bounds of the experimental value. These results are perfectly consistent with the results for **1** (model *d*), as in that case the experimental value of 50 ppm was overestimated by 38% and predicted to be 69 ppm. As with the chlorine quadrupolar coupling constant, the data point for **1** using the calculation for model *d* (50 ppm, 69 ppm) is close to the line of best fit shown in Figs. 5 and 6.

Fig. 5. Comparison between the experimentally determined chlorine chemical shift (CS) tensor span (*x* axis) and the gauge-including projector-augmented wave density functional theory (GIPAW-DFT) calculated values (*y* axis) for all of the amino acid hydrochlorides for which experimental data are available. Data for 11 of the amino acid salts are presented as filled diamond symbols (♦) and that of the two outliers (not included in the fit) are shown as filled circle symbols (●). The equation for the line of best fit for the data represented by ♦ is y (ppm) = 0.9459x (ppm) + 29.856 ppm, with a R^2 value of 0.7878. The broken line represents the line $y = x$. Experimental data are from refs. 24–26. Also shown but not included in the line of best fit is the data point for *meso*-octamethylcalix[4]pyrrole 1-butyl-3-methyl imidazolium chloride (**1**), i.e., model (*d*) of Fig. 3 (■).

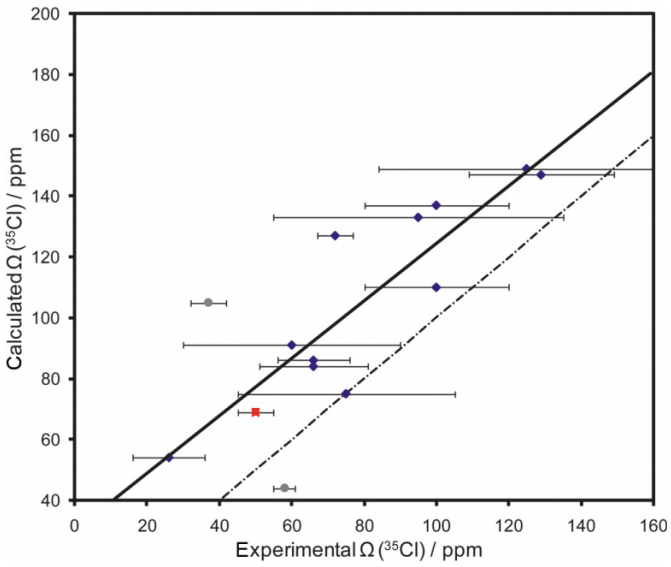

Similar to the CS tensor span, the calculated chlorine δ_{iso} values were significantly overestimated, usually by 30–50 ppm, in almost all cases. This demonstrates that all three components of the CS tensor are generally overestimated by calculation. Unfortunately, the same qualitative agreement between the experimental and calculated values that was observed for Ω was not observed for the chlorine δ_{iso}. These results differ significantly from those obtained with B3LYP calculations, where it was found that the chlorine chemical shifts are always underestimated by a significant margin. With B3LYP, the underestimation can be very significant, with some computed shifts for the amino acid salts being off by more than 70 ppm from experiment.[24–26] Although the calculated value of δ_{iso}(^{35}Cl) for **1** (188 ppm) was slightly more overestimated compared with the amino acid hydrochloride results, its calculated value is also consistent with the results for model *d* as the computation using model *a* results

Can. J. Chem. Downloaded from www.nrcresearchpress.com by Xi'an Jiaotong University on 09/19/12
For personal use only.

Fig. 6. Comparison between the experimentally determined chlorine chemical shift (CS) tensor span (*x* axis) and the gauge-including projector-augmented wave density functional theory (GIPAW-DFT) calculated values (*y* axis) for the amino acid hydrochlorides for which there are neutron diffraction structures (◆). The equation for the line of best fit is *y* (ppm) = 0.9352*x* (ppm) + 25.299 ppm, with a R^2 value of 0.9771. The broken line represents the line $y = x$. Experimental data are from refs. 24–26. Also shown but not included in the line of best fit is the data point for *meso*-octamethylcalix[4]pyrrole 1-butyl-3-methyl imidazolium chloride (**1**), i.e., model (*d*) of Fig. 3 (■).

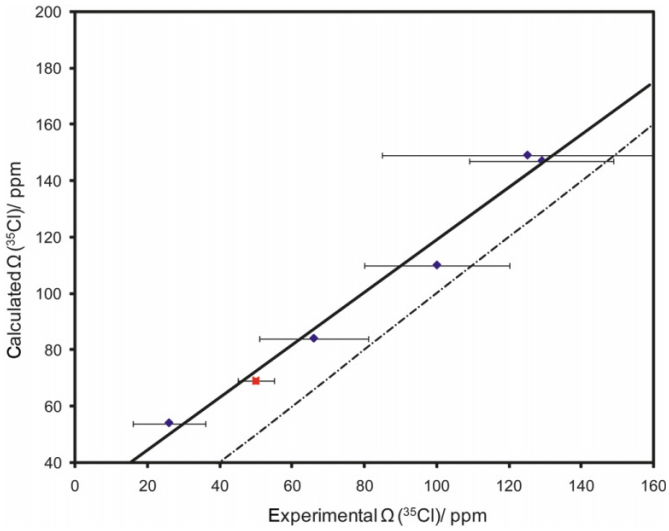

in an underestimation of the experimental chlorine chemical shift.

The series of GIPAW-DFT calculations of the chlorine SSNMR parameters of the amino acid hydrochlorides thus are consistent with those of compound **1**. The results demonstrate that with GIPAW-DFT calculations there is a consistent overestimation of the chlorine quadrupolar coupling constant, CS tensor span, and chlorine chemical shift compared with experiment for organic hydrochlorides.

Conclusions

Chlorine SSNMR was used to characterize the chloride ion receptor **1** at two magnetic field strengths. The EFG and CS tensor parameters, along with the relative orientation of the tensors, were extracted from simulations of the spectra collected. Interestingly, low-field spectra were clearly QI-dominated, whereas high-field spectra were CSA-dominated. The small $|C_Q(^{35}Cl)|$ observed (1.0 MHz) demonstrated that the EFG about the chloride was small because of a relatively symmetric environment. The chemical shift of 120 ppm (with respect to solid sodium chloride) is higher than typically observed for other organic chlorides. Inclusion of CSA and nonzero Euler angles were required to achieve quality fits to the experimental spectra. The CS tensor span is 50 ppm, which is within the range observed for other organic chlorides.

In addition, GIPAW-DFT calculations were carried out on a series of models based on the structure of **1** and those amino acid hydrochlorides for which there is both a known structure and chlorine SSNMR experimental data. These calculations systematically overestimate both $|C_Q(^{35}Cl)|$ and the CS tensor span and significantly overestimate the chlorine isotropic chemical shift in nearly all cases. Despite these problems, the GIPAW-DFT method is found to have more advantages than B3LYP or RHF calculations (e.g., the trend in CS tensor span is reproduced). The computational results for **1** were consistent with the loss of dichloromethane and water solvent molecules. The calculations also suggest that the NMR parameters of chloride ion receptors will be highly sensitive to slight changes in structure, such as the loss of solvent or water molecules. Overall, the computational benchmarks of this study will be useful in future chlorine NMR studies by aiding in the interpretation of the results of GIPAW-DFT calculations on similar systems.

Supplementary data

Supplementary data (information about the chlorine on-the-fly pseudopotential, carbon-13 CP/MAS NMR spectra, computational details, TGA curve, powder X-ray diffraction data, and nutation NMR data) are available with the article through the journal Web site (www.nrcresearchpress.com/cjc).

Acknowledgements

D.L.B. thanks the Natural Sciences and Engineering Research Council of Canada (NSERC) for funding, and Dr. R. Wasylishen for his instruction and guidance in the field of solid-state NMR spectroscopy of quadrupolar nuclei. R.P.C. thanks NSERC for a scholarship. We are grateful to Dr. V. Terskikh, Dr. E. Ye, Dr. G. Facey, Dr. T. Kell, and Dr. S. Letaief for technical support. Access to the 900 MHz NMR spectrometer was provided by the National Ultrahigh-Field NMR Facility for Solids, a national research facility funded by the Canada Foundation for Innovation, the Ontario Innovation Trust, Recherche Québec, the National Research Council Canada, and Bruker Biospin and managed by the University of Ottawa (www.nmr900.ca). NSERC is acknowledged for a Major Resources Support grant. P.A.G. and J.R.H. thank the EPSRC for support.

References

(1) Sliwa, W.; Kozlowski, C. In *Calixarenes and Resorcinarenes: Synthesis, Properties and Applications;* Wiley-VCH Verlag GmbH & Co. KGaA: Weinheim, Germany, 2009.
(2) Gutsche, C. D. In *Calixarenes: An Introduction;* Monographs in Supramolecular Chemistry; RSC Publishing: Cambridge, UK, 2008.
(3) Dibama, H. M.; Clarot, I.; Fontanay, S.; Salem, A. B.; Mourer, M.; Finance, C.; Duval, R. E.; Regnouf-de-Vains, J.-B. *Bioorg. Med. Chem. Lett.* **2009** *19* (10), 2679. doi:10.1016/j.bmcl.2009.03.139.
(4) Vega, I. E.D.; Gale, P. A.; Light, M. E.; Loeb, S. J. *Chem. Commun. (Camb.)* **2005** (39), 4913. doi:10.1039/b510506d.
(5) Evans, L. S.; Gale, P. A.; Light, M. E.; Quesada, R. *New J. Chem.* **2006** *30* (7), 1019. doi:10.1039/b603223k.
(6) Baeyer, A. *Ber. Dtsch. Chem. Ges.* **1886** *19* (2), 2184. doi:10.1002/cber.188601902121.
(7) Custelcean, R.; Delmau, L. H.; Moyer, B. A.; Sessler, J. L.; Cho, W.-S.; Gross, D.; Bates, G. W.; Brooks, S. J.; Light, M. E.; Gale, P. A. *Angew. Chem. Int. Ed.* **2005** *44* (17), 2537. doi:10.1002/anie.200462945.

Can. J. Chem. Downloaded from www.nrcresearchpress.com by Xi'an Jiaotong University on 09/19/12
For personal use only.

(8) Gale, P. A.; Sessler, J. L.; Král, V.; Lynch, V. *J. Am. Chem. Soc.* **1996** *118* (21), 5140. doi:10.1021/ja960307r.
(9) Sessler, J. L.; Andrievsky, A.; Gale, P. A.; Lynch, V. *Angew. Chem. Int. Ed. Engl.* **1996** *35* (23–24), 2782. doi:10.1002/anie.199627821.
(10) Camiolo, S.; Coles, S. J.; Gale, P. A.; Hursthouse, M. B.; Sessler, J. L. *Acta Crystallogr., Sect. E* **2001**, *E57* (9), o816. doi:10.1107/S1600536801012880.
(11) Woods, C. J.; Camiolo, S.; Light, M. E.; Coles, S. J.; Hursthouse, M. B.; King, M. A.; Gale, P. A.; Essex, J. W. *J. Am. Chem. Soc.* **2002** *124* (29), 8644. doi:10.1021/ja025572t.
(12) Sessler, J. L.; Gross, D. E.; Cho, W.-S.; Lynch, V. M.; Schmidtchen, F. P.; Bates, G. W.; Light, M. E.; Gale, P. A. *J. Am. Chem. Soc.* **2006** *128* (37), 12281. doi:10.1021/ja064012h.
(13) Bates, G. W.; Gale, P. A.; Light, M. E. *Supramol. Chem.* **2008** *20* (1–2), 23. doi:10.1080/10610270601089378.
(14) Gross, D. E.; Schmidtchen, F. P.; Antonius, W.; Gale, P. A.; Lynch, V. M.; Sessler, J. L. *Chem. Eur. J.* **2008** *14* (26), 7822. doi:10.1002/chem.200800899.
(15) Ripmeester, J. A.; Enright, G. D.; Ratcliffe, C. I.; Udachin, K. A.; Moudrakovski, I. L. *Chem. Commun. (Camb.)* **2006** (48): 4986. doi:10.1039/b605275d.
(16) Meier, U. C.; Detellier, C. *Dalton Trans.* **2003** (19): 4574. doi:10.1039/b307897n.
(17) Israëli, Y.; Bonal, C.; Detellier, C.; Morel, J.-P.; Morel-Desrosiers, N. *Can. J. Chem.* **2002** *80* (2), 163. doi:10.1139/v02-005.
(18) Meier, U. C.; Detellier, C. *J. Phys. Chem. A* **1999** *103* (20), 3825. doi:10.1021/jp9843609.
(19) Kuzmicz, R.; Kowalska, V.; Domagała, S.; Stachowicz, M.; Woźniak, K.; Kolodziejski, W. *J. Phys. Chem. B* **2010** *114* (32), 10311. doi:10.1021/jp1015565.
(20) Widdifield, C. M.; Chapman, R. P.; Bryce, D. L. *Chlorine, Bromine, and Iodine Solid-State NMR Spectroscopy;* Webb, G. A., Ed.; Annual Reports on Nuclear Magnetic Resonance Spectroscopy, 2009; Vol. 66, p 195.
(21) Chapman, R. P.; Widdifield, C. M.; Bryce, D. L. *Prog. Nucl. Magn. Reson. Spectrosc.* **2009** *55* (3), 215. doi:10.1016/j.pnmrs.2009.05.001.
(22) Bryce, D. L.; Gee, M.; Wasylishen, R. E. *J. Phys. Chem. A* **2001** *105* (45), 10413. doi:10.1021/jp011962a.
(23) Pyykkö, P. *Mol. Phys.* **2008** *106* (16–18), 1965. doi:10.1080/00268970802018367.
(24) Chapman, R. P.; Bryce, D. L. *Phys. Chem. Chem. Phys.* **2007** *9* (47), 6219. doi:10.1039/b712688c.
(25) Bryce, D. L.; Sward, G. D. *J. Phys. Chem. B* **2006** *110* (51), 26461. doi:10.1021/jp065878c.
(26) Bryce, D. L.; Sward, G. D.; Adiga, S. *J. Am. Chem. Soc.* **2006** *128* (6), 2121. doi:10.1021/ja057253i.
(27) Bryce, D. L.; Bultz, E. B. *Chem. Eur. J.* **2007** *13* (17), 4786. doi:10.1002/chem.200700056.
(28) Rossini, A. J.; Mills, R. W.; Briscoe, G. A.; Norton, E. L.; Geier, S. J.; Hung, I.; Zheng, S.; Autschbach, J.; Schurko, R. W. *J. Am. Chem. Soc.* **2009** *131* (9), 3317. doi:10.1021/ja808390a.
(29) Hamaed, H.; Pawlowski, J. M.; Cooper, B. F. T.; Fu, R.; Eichhorn, S. H.; Schurko, R. W. *J. Am. Chem. Soc.* **2008** *130* (33), 11056. doi:10.1021/ja802486q.
(30) Clark, S. J.; Segall, M. D.; Pickard, C. J.; Hasnip, P. J.; Probert, M. I. J.; Refson, K.; Payne, M. C. *Z. Kristallogr.* **2005** *220* (5–6), 567. doi:10.1524/zkri.220.5.567.65075.
(31) Pickard, C. J.; Mauri, F. *Phys. Rev. B* **2001** *63* (24), 245101. doi:10.1103/PhysRevB.63.245101.
(32) Segall, M. D.; Lindan, P. J. D.; Probert, M. J.; Pickard, C. J.; Hasnip, P. J.; Clark, S. J.; Payne, M. C. *J. Phys.: Condens. Matter* **2002** *14* (11), 2717. doi:10.1088/0953-8984/14/11/301.
(33) Ashbrook, S.E.; Berry, A. J.; Frost, D. J.; Gregorovic, A.; Pickard, C. J.; Readman, J. E.; Wimperis, S. *J. Am. Chem. Soc.* **2007** *129* (43), 13213. doi:10.1021/ja074428a.
(34) Choi, M.; Matsunaga, K.; Oba, F.; Tanaka, I. *J. Phys. Chem. C* **2009** *113* (9), 3869. doi:10.1021/jp810484j.
(35) Sutrisno, A.; Terskikh, V. V.; Huang, Y. *Chem. Commun. (Camb.)* **2009** (2), 186. doi:10.1039/b817017g.
(36) Joyce, S. A.; Yates, J. R.; Pickard, C. J.; Brown, S. P. *J. Am. Chem. Soc.* **2008** *130* (38), 12663. doi:10.1021/ja800419m.
(37) Jochum, M.; Werner-Zwanziger, U.; Zwanziger, J. W. *J. Chem. Phys.* **2008** *128* (5), 052304. doi:10.1063/1.2823130.
(38) Zurek, E.; Pickard, C. J.; Autschbach, J. *J. Phys. Chem. C* **2008** *112* (25), 9267. doi:10.1021/jp800873c.
(39) Wong, A.; Thurgood, G.; Dupree, R.; Smith, M. E. *Chem. Phys.* **2007** *337* (1–3), 144. doi:10.1016/j.chemphys.2007.07.007.
(40) Gervais, C.; Dupree, R.; Pike, K. J.; Bonhomme, C.; Profeta, M.; Pickard, C. J.; Mauri, F. *J. Phys. Chem. A* **2005** *109* (31), 6960. doi:10.1021/jp0513925.
(41) Widdifield, C. M.; Bryce, D. L. *J. Phys. Chem. A* **2010** *114* (5), 2102. doi:10.1021/jp909106j.
(42) Power, W. P.; Wasylishen, R. E.; Mooibroek, S.; Pettitt, B. A.; Danchura, W. *J. Phys. Chem.* **1990** *94* (2), 591. doi:10.1021/j100365a019.
(43) Wi, S.; Ashbrook, S. E.; Wimperis, S.; Frydman, L. *J. Chem. Phys.* **2003** *118* (7), 3131. doi:10.1063/1.1531998.
(44) Gee, M.; Wasylishen, R. E.; Laaksonen, A. *J. Phys. Chem. A* **1999** *103* (50), 10805. doi:10.1021/jp9925841.
(45) MacKenzie, K. J. D.; Smith, M. E. In *Multinuclear Solid-State NMR of Inorganic Materials;* Pergamon: Amsterdam, 2002.
(46) Adiga, S.; Aebi, D.; Bryce, D. L. *Can. J. Chem.* **2007** *85* (7–8), 496. doi:10.1139/v07-069.
(47) Solomon, I. *Phys. Rev.* **1958** *110* (1), 61. doi:10.1103/PhysRev.110.61.
(48) Weisman, I. D.; Bennett, L. H. *Phys. Rev.* **1969** *181* (3), 1341. doi:10.1103/PhysRev.181.1341.
(49) Kunwar, A. C.; Turner, G. L.; Oldfield, E. *J. Magn. Reson.* **1986** *69* (1), 124. doi:10.1016/0022-2364(86)90224-6.
(50) Eichele, K.; Wasylishen, R. E. *WSOLIDS NMR Simulation Package,* 1.17.30; Dalhousie University: Halifax, NS, 2001.
(51) Alderman, D. W.; Solum, M. S.; Grant, D. M. *J. Chem. Phys.* **1986**, *84* (7), 3717. doi:10.1063/1.450211.
(52) Massiot, D.; Fayon, F.; Capron, M.; King, I.; Le Calvé, S.; Alonso, B.; Durand, J.-O.; Bujoli, B.; Gan, Z.; Hoatson, G. *Magn. Reson. Chem.* **2002** *40* (1), 70. doi:10.1002/mrc.984.
(53) Al-Karaghouli, A. R.; Koetzle, T. F. *Acta Crystallogr., Sect. B* **1975**, *B31* (10), 2461. doi:10.1107/S0567740875007807.
(54) Koetzle, T. F.; Golic, L.; Lehmann, M. S.; Verbist, J. J.; Hamilton, W. C. *J. Chem. Phys.* **1974** *60* (12), 4690. doi:10.1063/1.1680969.
(55) Frey, M. N.; Koetzle, T. F.; Lehmann, M. S.; Hamilton, W. C. *J. Chem. Phys.* **1973** *58* (6), 2547. doi:10.1063/1.1679537.
(56) Sequeira, A.; Rajagopal, H.; Chidambaram, R. *Acta Crystallogr. Sect. B* **1972** *B28* (8), 2514. doi:10.1107/S0567740872006399.
(57) Bugayong, R. R.; Sequeira, A.; Chidambaram, R. *Acta Crystallogr. Sect. B* **1972** *B28* (11), 3214. doi:10.1107/S0567740872007769.
(58) Al-Karaghouli, A. R.; Cole, F. E.; Lehmann, M. S.; Miskell, C. F.; Verbist, J. J.; Koetzle, T. F. *J. Chem. Phys.* **1975** *63* (4), 1360. doi:10.1063/1.431523.
(59) Dow, J.; Jensen, L. H.; Mazumdar, S. K.; Srinivasan, R.;

Ramachandran, G. N. *Acta Crystallogr. Sect. B* **1970** *B26* (11), 1662. doi:10.1107/S0567740870004697.
(60) Di Blasio, B.; Pavone, V.; Pedone, C. *Cryst. Struct. Commun.* **1977** *6*, 745.
(61) Di Blasio, B.; Pavone, V.; Pedone, C. *Cryst. Struct. Commun.* **1977** *6*, 845.
(62) Mitsui, Y.; Tsuboi, M.; Iitaka, Y. *Acta Crystallogr. B* **1969** *B25* (11), 2182. doi:10.1107/S0567740869005449.
(63) Takigawa, T.; Ashida, T.; Sasada, Y.; Kakudo, M. *Bull. Chem. Soc. Jpn.* **1966** *39* (11), 2369. doi:10.1246/bcsj.39.2369.
(64) Fuess, H.; Hohlwein, D.; Mason, S. A. *Acta Crystallogr. Sect. B* **1977** *B33* (3), 654. doi:10.1107/S0567740877004415.
(65) Donohue, J.; Caron, A. *Acta Crystallogr.* **1964** *17* (9), 1178. doi:10.1107/S0365110X64003048.
(66) Honda, H. *Z. Naturforsch. A* **2003** *58a* (11), 623.
(67) Samoson, A.; Lippmaa, E. *Phys. Rev. B* **1983** *28* (11), 6567. doi:10.1103/PhysRevB.28.6567.
(68) Man, P. P. Introduction to the nutation NMR of quadrupole spins. http://www.pascal-man.com/presentation/nutation.shtml (accessed 2010).
(69) Frisch, M. J.; Trucks, G.; Schlegel, H. B.; Scuseria, G. E.; Robb, M. A.; Cheeseman, J. R.; Montgomery, J. A., Jr.; Vreven, T.; Kudin, K. N.; Burant, J. C.; Millam, J. M.; Iyengar, S. S.; Tomasi, J.; Barone, V.; Mennucci, B.; Cossi, M.; Scalmani, G.; Rega, N.; Petersson, G. A.; Nakatsuji, H.; Hada, M.; Ehara, M.; Toyota, K.; Fukuda, R.; Hasegawa, J.; Ishida, M.; Nakajima, T.; Honda, Y.; Kitao, O.; Nakai, H.; Klene, M.; Li, X.; Knox, J. E.; Hratchian, H. P.; Cross, J. B.; Bakken, V.; Adamno, C.; Jaramillo, J.; Gomperts, R.; Stratmann, R. E.; Yazyev, O.; Austin, A. J.; Cammi, R.; Pomelli, C.; Ochterski, J. W.; Ayala, P. Y.; Morokuma, K.; Voth, G. A.; Salvador, P.; Dannenberg, J. J.; Zakrzewski, V. G.; Dapprich, S.; Daniels, A. D.; Strain, M. C.; Farkas, O.; Malick, D. K.; Rabuck, A. D.; Raghavachari, K.; Foresman, J. B.; Ortiz, J. V.; Cui, Q.; Baboul, A. G.; Clifford, S.; Cioslowski, J.; Stefanov, B. B.; Liu, G.; Liashenko, A.; Piskorz, P.; Komaromi, I.; Martin, R. L.; Fox, D. J.; Keith, T.; Al-Laham, M. A.; Peng, C. Y.; Nanayakkara, A.; Challacombe, M.; Gill, P. M. W.; Johnson, B.; Chen, W.; Wong, M. W.; Gonzalez, C.; Pople, J. A. *Gaussian 03,* Revision C.02; Gaussian, Inc.: Wallingford, CT, 2004.

Can. J. Chem. Downloaded from www.nrcresearchpress.com by Xi'an Jiaotong University on 09/19/12
For personal use only.

Nuclear magnetic resonance and mass spectrometry studies of 2′,3′,5′-*O*-triacetylguanosine self-assembly in the presence of alkaline earth metal ions (Ca^{2+}, Sr^{2+}, Ba^{2+})

Irene C.M. Kwan, Yi-Min She, and Gang Wu

Can. J. Chem. Downloaded from www.nrcresearchpress.com by Xi'an Jiaotong University on 09/19/12
For personal use only.

Abstract: We report structural determination of cation-templated self-assembly of a guanosine derivative, 2′,3′,5′-*O*-triacetylguanosine (TAG), in the presence of three alkaline earth metal ions (Ca^{2+}, Sr^{2+}, and Ba^{2+}) in $CDCl_3$. Using a combination of nuclear magnetic resonance (NMR) and electrospray ionization mass spectrometry (ESI-MS) methods, we have found that TAG molecules form discrete octamers in the form of $[TAG]_8M^{2+}$ (M^{2+} = Ca^{2+}, Sr^{2+}, and Ba^{2+}), which is composed of two G-quartets and a sandwiched metal ion. We have determined the ability of the three alkaline earth metal ions to promote TAG self-assembly (relative binding affinity) to be $Sr^{2+} \gg Ba^{2+} > Ca^{2+}$. More importantly, we have used two-dimensional (2D) NMR methods to determine the structural details of $[TAG]_8Sr^{2+}$. In particular, we found that each octamer consists of an all-anti G-quartet stacking on top of an all-syn G-quartet in a tail-to-head fashion with a twist angle of 45° between the two G-quartets. This TAG octamer structure represents a unique case quite different from other lipophilic guanosine octamers reported in the literature.

Key words: nuclear magnetic resonance, mass spectrometry, self-assembly, guanosine (G), alkaline earth metal, G-quartet, structural elucidation.

Résumé : On a déterminer la structure d'un autoassemblage sur gabarit de cation d'un dérivé de la guanosine, 2′,3′,5′-*O*-triacétylguanosine (TAG), en présente de trois ions de métaux de terres alcalins (Ca^{2+}, Sr^{2+} et Ba^{2+}), dans du $CDCl_3$. Faisant appel à une combinaison des méthodes de résonance magnétique nucléaire (RMN) et de spectrométrie de masse avec ionisation par électronébulisation (SM-IEN), on a trouvé que les molécules de TAG forment des octamères individuels de la forme $[TAG]_8M^{2+}$ (M^{2+} = Ca^{2+}, Sr^{2+} et Ba^{2+}) qui se composent de deux quartets-G et d'un ion métallique en sandwich. On a déterminé que l'habilité relative des trois ions de métaux de terres alcalins à faire la promotion de l'autoassemblage du TAG (par rapport à l'affinité de fixation) est $Sr^{2+} \gg Ba^{2+} > Ca^{2+}$. En plus, on a fait appel à des méthodes de RMN bidimensionnelles (2D) pour déterminer les détails de la structure du $[TAG]_8Sr^{2+}$. On a trouvé, en particulier, que chaque octamère est formé d'un quartet-G complètement anti empilé sur un autre quartet-G complètement syn, d'une façon tête à queue, avec un angle de torsion de 45° entre les deux quartets-G. Cette structure de TAG octamère correspond à un cas unique différent des autres octamères de guanosine lipophiles rapportés dans la littérature.

Mots-clés : résonance magnétique nucléaire, spectrométrie de masse, autoassemblage, guanosine (G), métal de terre alcalin, quartet-G, élucidation de structure.

[Traduit par la Rédaction]

Introduction

Guanosine (G) is a biological molecule composed of a guanine nucleobase and a ribose ring (Scheme 1). Guanine is unique among nucleobases as its hydrogen-bond donors and acceptors are almost 90° to each other, making it possible to form a square-shaped, planar tetramer known as the G-quartet. It has been known for many years that G derivatives can self-assemble into G-quartets in the presence of certain cations,[1–4] except for just a few cases where cations are not required.[5–7] Within a G-quartet, Hoogsteen-type hydrogen bonds (O6···H–N1 and N7···H–N2; Scheme 2) are formed between the four guanine bases.[1] With assistance from certain cations, the disk-shaped G-quartets can stack on top of one another by ion–dipole and π–π interactions forming a rodlike structure in which the two adjacent G-quartets are separated by ~3.3 Å with a twist rotation ranging from 30° to 45°.[2–4] The most common mode of cation binding within the rodlike structure is the sandwich type where a cation is located at the centre between two G-quartets coordinating to eight carbonyl oxygen atoms (O6) in a square antiprism fasion.[8,9] Both ionic radius and charge of the cation are important for the formation and stability of the rodlike structure. In aqueous solution,

Received 1 November 2010. Accepted 11 December 2010. Published at www.nrcresearchpress.com/cjc on 5 July 2011.

I.C.M. Kwan, Y.-M. She, and G. Wu. Department of Chemistry, Queen's University, 90 Bader Lane, Kingston, ON K7L 3N6, Canada.

Corresponding author: G. Wu (e-mail: gang.wu@chem.queensu.ca).

This article is part of a Special Issue dedicated to Professor Roderick E. Wasylishen.

Scheme 1. Guanosine (R = H) and 2′,3′,5′-*O*-triacetylguanosine (R = acetyl).

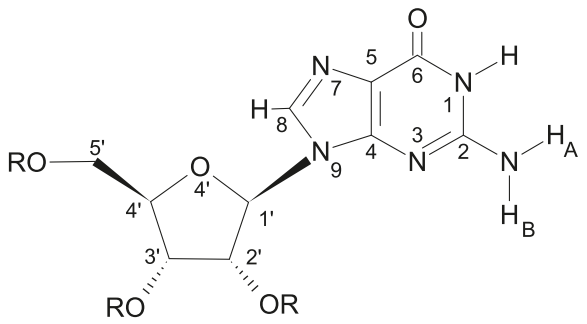

dehydration energy of the cation also plays a crucial role during the process.[2–4,9] Pinnavaia et al.[10] discovered that cations such as Li^+ and Cs^+ (ionic radius 0.92 and 1.69 Å, respectively) are not effective in promoting self-assembly of guanosine 5′-monophosphate (5′-GMP), whereas Na^+, K^+, and Rb^+ (ionic radius 1.18, 1.51, and 1.61 Å, respectively) are optimal for stable formation of the rodlike structure. The averaged $O_6 \cdots M^+$ distance in G self-assembled structures is 2.2–2.3 Å. Among monovalent alkali metal ions, K^+ has the strongest ability to promote 5′-GMP self-assembly followed by Na^+ and Rb^+. Using combined diffusion nuclear magnetic resonance (NMR) and dynamic light scattering methods, Wong et al.[11] showed that the length of the rodlike structure formed by 5′-GMP self-assembly can be on the order of several nanometers. For 5′-GMP, it is also known that cations are responsible for structural polymorphism. For example, in the presence of Na^+, Wu and Kwan[12] found that 5′-GMP self-assembles into a unique helix containing alternating C2′- and C3′-*endo* sugar puckering. In the presence of K^+ or Rb^+, on the other hand, the self-assembled structures of 5′-GMP in aqueous solution were quite complex as demonstrated by Walmsley and co-workers.[13,14] Studies on divalent cations (Ca^{2+}, Sr^{2+}, Ba^{2+}, Pb^{2+}) are less common. In general, a higher binding affinity is observed for these divalent cations compared with monovalent cations.[2,9,15] Moreover, as illustrated in Scheme 2, divalent cations are usually found at every other site to reduce electrostatic repulsion between positive charges.[9] Recently, we discovered that trivalent lanthanide metal ions can promote G-quartet formation in a new triple-decker mode of ion binding; see Scheme 2.[16]

Most previous studies were concerned with G self-assembly in aqueous solution because of potential therapeutic applications.[17–20] Folded G-rich DNA oligomers can prevent telomerase binding to the telomere, which in turn could prevent cancer formation as a result of natural cell death.[21] In comparison, G-quartet formation in organic solvents is less common.[2–4,9,22] In recent years, specially designed G-quartet motifs have been widely studied and used in applications of artificial ion channels and nanomaterials.[2–4,9,22–28] It remains a challenge to be able to synthesize homogenous and stable G self-assembled structures as many factors such as solvent, temperature, and concentration are at work. Because of its relevance to molecular biology and supramolecular chemistry, detailed information about G self-assembled structures can not only help us in the development of anticancer drugs and artificial ion channels, but also in molecular recognition in DNA that may enhance drug design.[27,29,30]

Although formation of G-quadruplexes with alkaline earth metal ions (Ca^{2+}, Sr^{2+}, and Ba^{2+}) has been previously documented in the literature,[15,26,31–40] there are very few cases where structural details are determined for the G-quadruplexes containing these metal ions in solution. In a previous study, we have used the Ca^{2+}-directed self-assembly of a simple lipophilic guanosine derivative, 2′,3′,5′-triacetylguanosine (TAG) as shown in Scheme 1, to obtain ^{43}Ca NMR signature.[41] In this work, we report a comprehensive NMR and electrospray ionization mass spectrometry (ESI-MS) study of TAG self-assembly in the presence of Ca^{2+}, Sr^{2+}, and Ba^{2+}. Our primary objective is to elucidate the structural details of TAG self-assemblies.

Experimental

Picrate salts

Picrate salts of Ca^{2+}, Sr^{2+}, and Ba^{2+} were synthesized by neutralizing picric acid (Sigma-Aldrich, 99+%) with $Ca(OH)_2$, $Sr(OH)_2$, and $Ba(OH)_2$, respectively. Crystalline picrate salts were obtained from aqueous solution. *WARNING:* Caution should be exercised when handling picric acid.

[TAG]M^{2+} complexes

2′,3′,5′-*O*-Triacetylguanosine (98%) was purchased from Sigma-Aldrich without further purification. [TAG]M^{2+} complexes were prepared using the following solvent–solvent extraction method described by Andrisano et al.[42] To 0.2 mmol of TAG (81 mg) suspended in $CHCl_3$ (cloudy solution) was added dropwise 1.6 mmol of picrate salt (i.e., $CaPic_2$, $SrPic_2$, $BaPic_2$) dissolved in H_2O (clear, yellow solution) with stirring. The two-phase solution was stirred until the organic phase became visually clear and yellow. The aqueous phase was then removed, and solid [TAG]M^{2+} complexes were obtained after the organic phase was dried in air.

NMR spectroscopy

All solution-state NMR spectra were recorded on a Bruker Avance 600 MHz spectrometer in $CDCl_3$. For ^1H NMR experiments, a π-pulse of 20 μs at a power level of 0 dB was used. Spectra were obtained at various temperatures achieved carefully by a Bruker BT-3000 unit.

Correlation spectroscopy (COSY)

Two-dimensional homonuclear shift correlation (^1H–^1H COSY) spectra were recorded at 15 °C using the pulse program COSYGPQF (XWinNMR, version 3.5, Bruker) on a Bruker Avance 600 MHz spectrometer. The data were collected using a 90° pulse of 10.0 μs and a relaxation delay of 1 s. The spectral width was 13 227 Hz on either dimension. One scan was collected. Final data matrix was 2048 ($F2$) × 256 ($F1$).

Diffusion-ordered spectroscopy (DOSY)

^1H diffusion experiments were carried out using the pulse sequence of longitudinal eddy current delay with bipolar-gradient pulses: LEDBPGP2s (XWinNMR, version 3.5, Bruker) on 1.0 mmol/L samples in $CDCl_3$. The pulse field gradient duration (δ) ranged from 1.0 to 2.0 ms, and the variable gradient strength (G) was changed from 5.75 to 5.8 mT/m. The diffusion period (Δ) was 50 ms. A total of 16 scans

Can. J. Chem. Downloaded from www.nrcresearchpress.com by Xi'an Jiaotong University on 09/19/12
For personal use only.

Scheme 2. A guanine (G)-quartet (left) and common modes of metal ion binding (right). Each bar represents a G-quartet.

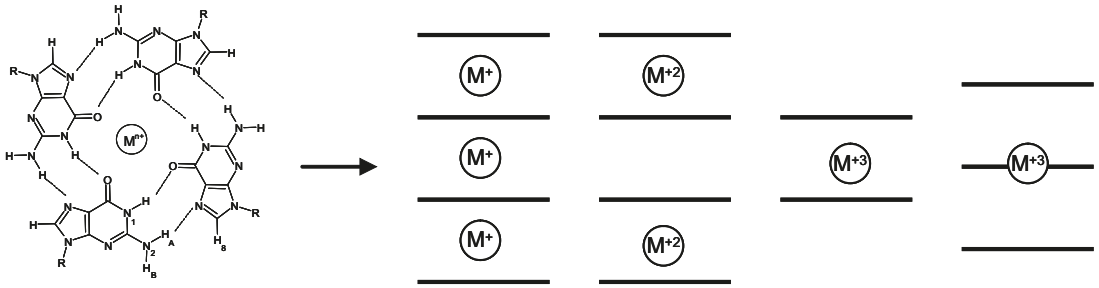

were collected for each of the 16 increment steps with a recycle delay of 5 s. The eddy current delay (t_e) was 5 ms, and the gradient recovery delay was 0.2 ms. All diffusion experiments were performed at 298.2 K. Calibration of the field gradient strength was performed by measuring the value of the translational diffusion coefficient (D_t) for the residual ^1H signal in D_2O (99.99% ^2H atom), where $D_t = 1.90 \times 10^{-9}$ m^2/s.[43] All diffusion coefficients were acquired using integration of the proton peaks to a single exponential decay, using the Simfit software (XWinNMR, version 3.5, Bruker).

Heteronuclear multiple bond correlation (HMBC)

Two-dimensional (2D) spectra of ^1H–^{13}C correlation through heteronuclear zero and double quantum coherence transfer were performed using the pulse program INV4GPLPLRND (XWinNMR, version 2.6, Bruker) at 11.7 T at room temperature. A low-pass J-filter was employed to suppress one-bond correlations. No ^{13}C decoupling was applied during acquisition. The long-range coupling delay was 100 ms. The 90° pulses were 10.0 μs and 13.4 μs for ^1H and ^{13}C nuclei, respectively, with a relaxation relay of 1 s. The spectral width was 10 965 Hz in the *F*2 dimension (^1H) and 27 667 Hz in the *F*1 dimension (^{13}C). A total of 48 scans were collected for each 946 increments of the *F*1 dimension. The final data matrix was 2048 (*F*2) × 1024 (*F*1).

Nuclear Overhauser enhancement spectroscopy (NOESY)

The 2D NOESY spectra were performed using the pulse program NOESYGPPH (XWinNMR, version 3.5, Bruker) with a mixing time (τ_{mix}) of 400 ms and the phase-sensitive TPPI mode. The data were collected using a 90° pulse of 10.0 μs and a relaxation delay of 3.0 s. A total of 8 scans were collected for each time increment. The final data matrix was 2048 (*F*2) × 1024 (*F*1).

Electrospray ionization (ESI) MS

ESI-MS spectra were recorded with an Applied Biosystems QSTAR XL quadrupole time-of-flight (QqTOF) mass spectrometer at positive ionization mode, and data were acquired using the Analyst QS 1.1 software (Applied Biosystems). Samples were dissolved in anhydrous nitromethane (CH_3NO_2) and injected with a syringe pump at a flow rate of 3.0 μL/min. The mass range of single MS measurements was set at *m*/*z* 300–5000. The declustering potential (DP) was 20 V. Subsequent tandem mass spectrometry (ESI-MS/MS) measurements were performed using nitrogen as the collision gas, and collision induced dissociation (CID) energy of 35–40 eV was applied to break down the octamers. The mass range of MS/MS measurements was set at *m*/*z* 0–4000. For spectral assignment, theoretical MS peaks were generated using Data Explorer version 4.0.0.0 (1997–2000) by Applied Biosystems.

Results and discussion

The ^1H NMR spectra of TAG–M^{2+} complexes in $CDCl_3$ are shown in Fig. 1, together with the ^1H spectrum of TAG in DMSO for comparison. In each of the ^1H NMR spectra for TAG–M^{2+} complexes, two sets of signals (in a 1:1 ratio) are observed for each proton compared with the corresponding signal in the spectrum of TAG in DMSO where TAG exists as monomers.[44] Of particular interest are the ^1H NMR signals from the imino (N^1H) and amino (N^2H_A and N^2H_B) groups. As indicated in Fig. 1, the single ^1H NMR signal of N^2H_2 observed for TAG in DMSO (at 6.3 ppm) splits into two well-separated signals, N^2H_A (at ~9–10 ppm) and N^2H_B (at ~5.2 ppm), upon extraction of Ca^{2+}, Sr^{2+}, and Ba^{2+} ions into $CDCl_3$. This suggests that N^2H_A is now involved in strong hydrogen bonding, thus considerably increasing the energy barrier for rotation about the C–N bond. At the same time, the observation of very sharp signals for N^1Hs in the range of 11.2–11.6 ppm suggests that this proton is also involved in strong hydrogen bonding. Using the integrated area of the picrate signal (indicated in Fig. 1) as a measure of the M^{2+} content (one M^{2+} per two Pic^-), we were able to determine that the ratio of TAG–M^{2+} is 8:1 for this hydrogen bonded structure. Of course, this stoichiometric ratio can be the result of many different structures, e.g., TAG_4–M^{2+}–TAG_4 octamers or TAG_4–M^{2+}–TAG_4–TAG_4–M^{2+}–TAG_4 hexadecamers or some kind of linear polymers known as G-ribbons; see Scheme 3.[2] To verify that the self-assembled structure is related to G-quartet formation, we obtained ^1H NOESY spectra for $[TAG]_8Ca^{2+}$, $[TAG]_8Sr^{2+}$, and $[TAG]_8Ba^{2+}$ species in $CDCl_3$ at 268 K. If TAG molecules form G-ribbons, the NOE cross peak formed between H8 and N^2H_A resonances in the NOESY spectrum would be less intense than that between H8 and N^1H resonances (see Scheme 3). As seen from Fig. 2, the NOE cross peaks between H8 and N^2H_A resonances are, in fact, stronger than those between H8 and N^1H resonances, providing definite proofs of G-quartet formation.

To further determine the size of the TAG self-assembly, we performed two types of experiments: diffusion-ordered spectroscopy (DOSY) NMR and electrospray ionization mass spectrometry (ESI-MS). DOSY allows the determination of the translational diffusion coefficient (D_t) of any molecular aggregate in solution, from which the size of the molecular aggregate can be inferred. According to the

Can. J. Chem. Downloaded from www.nrcresearchpress.com by Xi'an Jiaotong University on 09/19/12
For personal use only.

Can. J. Chem. Downloaded from www.nrcresearchpress.com by Xi'an Jiaotong University on 09/19/12
For personal use only.

Fig. 1. ^{1}H NMR spectra of TAG in DMSO and TAG–M^{2+} complexes in $CDCl_3$. All spectra were obtained at 268.2 K.

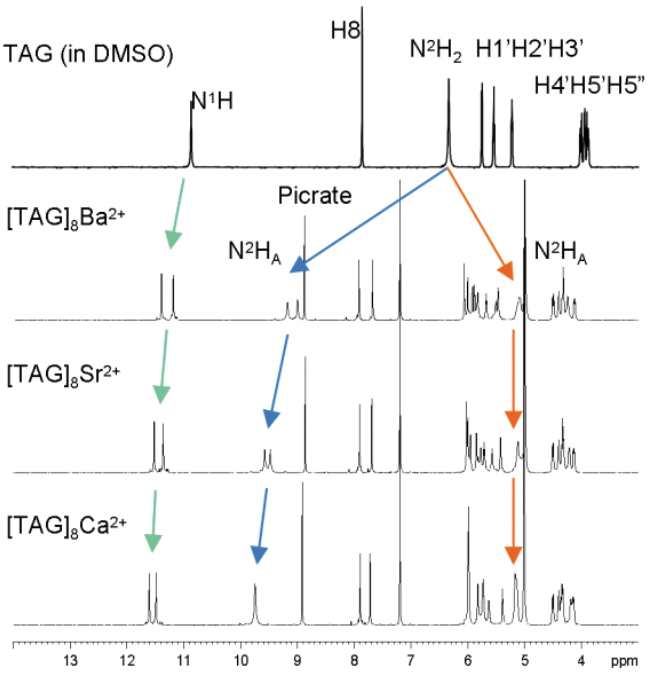

Scheme 3. (*a*) G-quartet, (*b*) G-ribbon A, and (*c*) G-ribbon B.

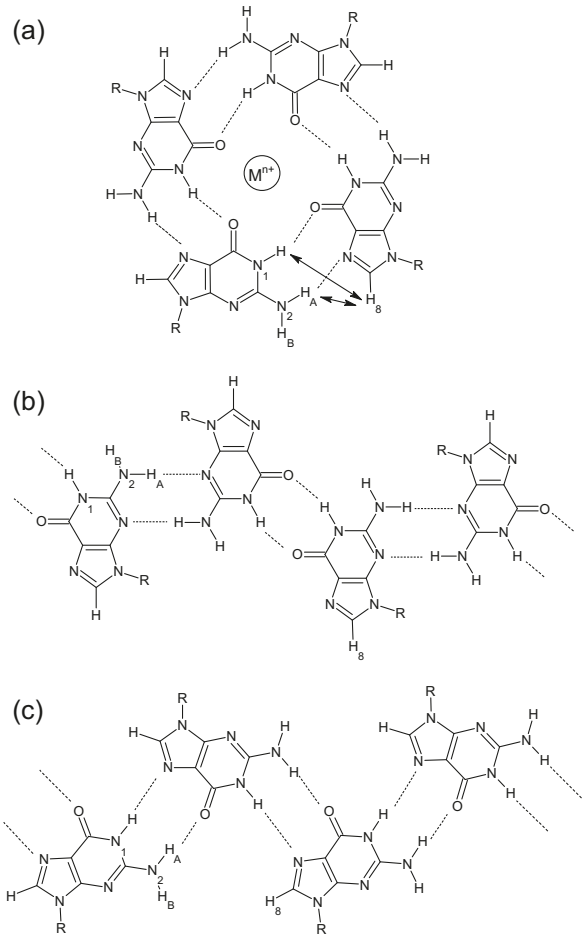

Fig. 2. A portion of the 2D NOESY spectrum of $[TAG]_8Sr^{2+}$ in $CDCl_3$ at 268.2 K. Cross peaks between N^2H_A and H8 resonances are highlighted in the broken box while those between N^1H and H8 resonances are enclosed in the unbroken box.

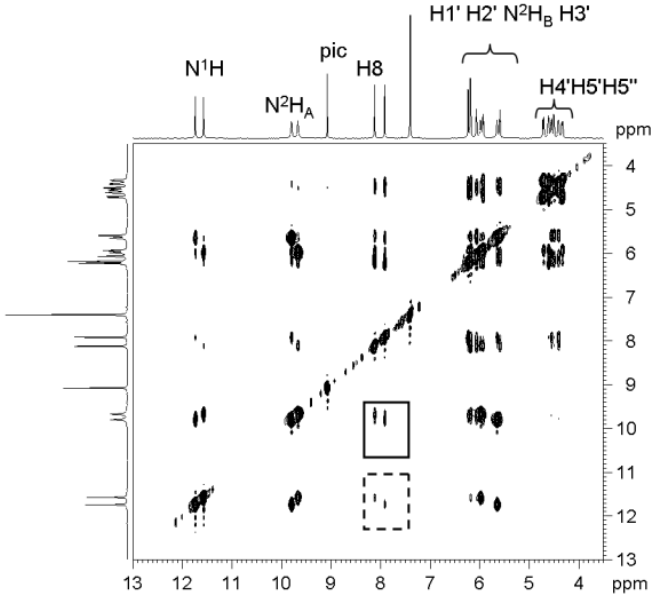

Stokes–Einstein equation, a sphere's diffusion coefficient is inversely related to the hydrodynamic radius and solvent viscosity: $D_t = kT/6\pi\eta R$, where k = Boltzmann constant, T = temperature, R = hydrodynamic radius, and η = solvent viscosity. In the DOSY experiments, dilute samples were prepared at 15 mmol/L and the sample temperature was carefully maintained at 298.2 K (±0.1 K) for solvent viscosity consistency. We have found two important pieces of information from the ^{1}H DOSY NMR experiments. First, the two sets of ^{1}H NMR signals mentioned earlier exhibit the same value of D_t, suggesting that they belong to the same self-assembled structure. Second, the D_t values measured for $[TAG]_8Ca^{2+}$, $[TAG]_8Sr^{2+}$, and $[TAG]_8Ba^{2+}$ are all very similar, ~3.9 ± 0.5 × 10^{-10} m^2/s, which is in agreement with a previously reported value for a G-octamer (D_t = 4.19 × 10^{-10} m^2/s).[45] In comparison, the value of D_t for TAG monomers measured under a similar condition in $CDCl_3$ is 7.0 × 10^{-10} m^2/s, and the D_t value for hexadecamers in the same solvent is 3.30 ± 0.07 × 10^{-10} m^2/s.[45] Therefore, we can conclude that TAG molecules exclusively form octamers in the presence of Ca^{2+}, Sr^{2+}, and Ba^{2+} in $CDCl_3$. We also note that, in the TAG systems, the value of D_t for the picrate anion is 5.4 ± 0.5 × 10^{-10} m^2/s, which is much larger than that of $[TAG]_8M^{2+}$. This suggests that the picrate anion is not involved in G-octamer formation.

To gain further evidence about the size of TAG self-assembly, we obtained ESI-MS and tandem MS (MS/MS) spectra for $[TAG]_8Ca^{2+}$, $[TAG]_8Sr^{2+}$, and $[TAG]_8Ba^{2+}$. ESI-MS allows molecular aggregates under study to be transferred from solution to the gas phase in a soft and smooth manner that is suitable for obtaining the sizes of both stable and short-lived molecules.[46] As seen in Fig. 3, positive mode (+)ESI-MS spectra allowed us to conclude that the self-assembled structures are exclusively octamers. Detailed isotopic pattern analyses of the MS spectra are given in the Supplementary data (Table

Can. J. Chem. Downloaded from www.nrcresearchpress.com by Xi'an Jiaotong University on 09/19/12
For personal use only.

Fig. 3. (+)ESI-MS spectrum of $[TAG]Sr^{2+}$ in nitromethane (top) and tandem (+)ESI-MS/MS spectrum of $[TAG]_8Sr^{2+}$ (bottom) at 1680.403 *m/z*. The asterisk (*) denotes the parent ion. M = monomeric TAG with 409.35 amu.

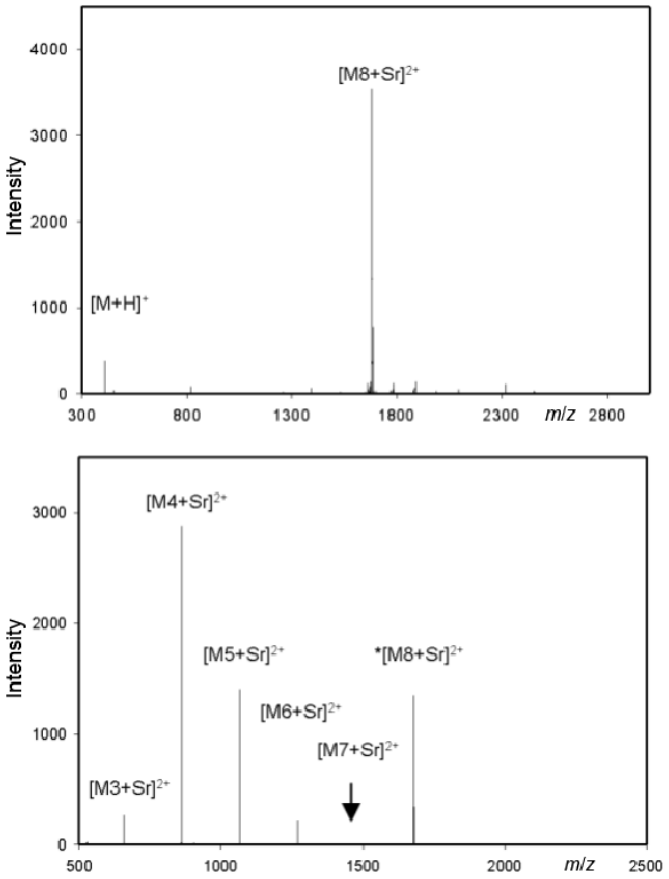

S1). Another important piece of information obtained from the ESI results is that the counter-ion picrate does not associate with any $[TAG]_8M^{2+}$ complexes under the current experimental conditions. Davis and co-workers[34] have previously reported that four picrate anions can "clamp" two G-octamers together to form a hexadecamer. In that case, a picrate anion utilizes the central phenoxide group and the two nitro groups in the ortho potions to link exocyclic amino N^2H_B protons from two G-quartets through hydrogen bonding. In the case of TAG, we did not observe any hexadecamer formation (vide infra). Discrete G-octamer formation has been previously seen in several other cases. For example, Marlow et al.[47] reported the first G-octamer formation in organic solvent from 3′,5′-didecanoyl-2′-deoxyguanosine promoted by K^+ ions. Shi et al.[48] observed that 5′-*tert*-butyl-dimethylsilyl-2′,3′-isopropylidene-guanosine can form G-octamers in the presence of Ba^{2+} and Sr^{2+}. Liu et al.[49] and Martić et al.[50] reported the G-octamer formation from N^2-modified guanosines.

Figure 4 shows a series of various-temperature (VT) ^1H NMR spectra for $[TAG]_8Sr^{2+}$ octamers to demonstrate its thermal stability. The fact that the ^1H NMR signals of the imino N^1H protons remain sharp at $\sim\delta = 11.6$ ppm suggests that integrity of the $[TAG]_8Sr^{2+}$ octamers do not break apart even at 323 K. It is also interesting to note that the amino protons N^2H_A and N^2H_B were not observed above room temperature because of severe line broadening from fast chemical exchange.

Fig. 4. ^1H NMR of $[TAG]_8Sr^{2+}$ complex at different temperatures in $CDCl_3$.

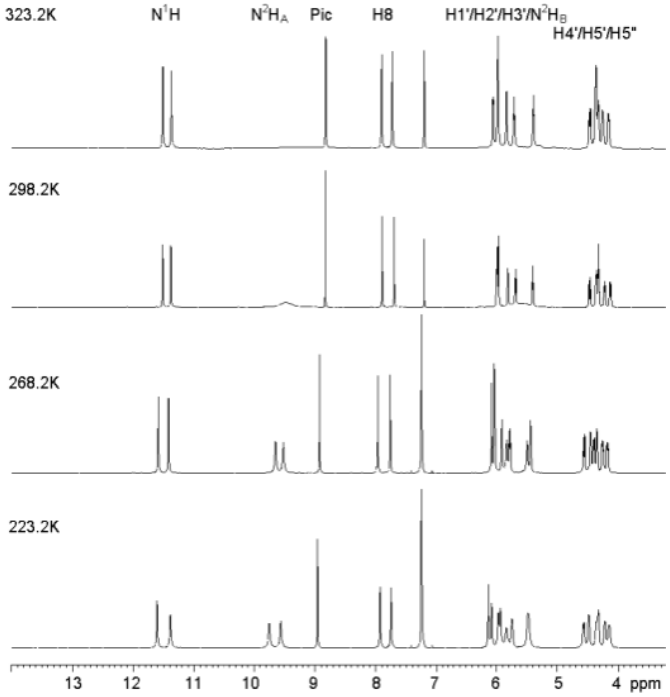

Although all three alkaline earth metal ions, Ca^{2+}, Sr^{2+}, and Ba^{2+}, are shown to be able to promote TAG self-assembly, the relative stabilities of $[TAG]_8Ca^{2+}$, $[TAG]_8Sr^{2+}$, and $[TAG]_8Ba^{2+}$ may be different. For example, their ionic radii are different (octa-coordinate ionic radius: Ca^{2+} 1.12 Å, Sr^{2+} 1.26 Å, and Ba^{2+} 1.42 Å).[51] To determine the relative binding affinity between the three metal ions, we performed a series of competitive extraction experiments. In each experiment, an equal molar mixture of two ions was used for the aqueous phase. The amount of each ion being extracted into the organic phase containing TAG can be monitored by ^1H NMR spectra. The results are shown in Fig. 5. For example, when Ca^{2+} or Ba^{2+} picrate salts (1:1) were used during extraction, the amount of $[TAG]_8Ba^{2+}$ formed in $CDCl_3$ is approximately eight times greater than that of $[TAG]_8Ca^{2+}$, suggesting that Ba^{2+} has a higher affinity than does Ca^{2+}. Similarly, when Ba^{2+} and Sr^{2+} were used, only $[TAG]_8Sr^{2+}$ can be found in $CDCl_3$. This indicates that Sr^{2+} has an even higher affinity than does Ba^{2+}. Using these simple experimental results, we can reach a qualitative conclusion that the relative binding affinity of TAG towards these three divalent cations is $Sr^{2+} \gg Ba^{2+} > Ca^{2+}$. We believe that this trend represents the true thermodynamic properties rather than kinetic effects, because extraction experiments performed over several days did not show any variation. This trend is indeed very common in G-quartet formation and has been documented in the literature for monovalent and divalent cations in biological G-quadruplexes systems.[2,9] Figure 5 also shows the result from an experiment where three kinds of $[TAG]_8M^{2+}$ octamers were first prepared separately in $CDCl_3$ and then mixed. We did not observe any change in the ^1H NMR spectrum of such a mixture for several months. This observation

Can. J. Chem. Downloaded from www.nrcresearchpress.com by Xi'an Jiaotong University on 09/19/12
For personal use only.

Fig. 5. ^{1}H NMR spectra of TAG–M^{2+} complexes obtained at 268.2 K from the "mixed" ion experiments. See the text for discussion.

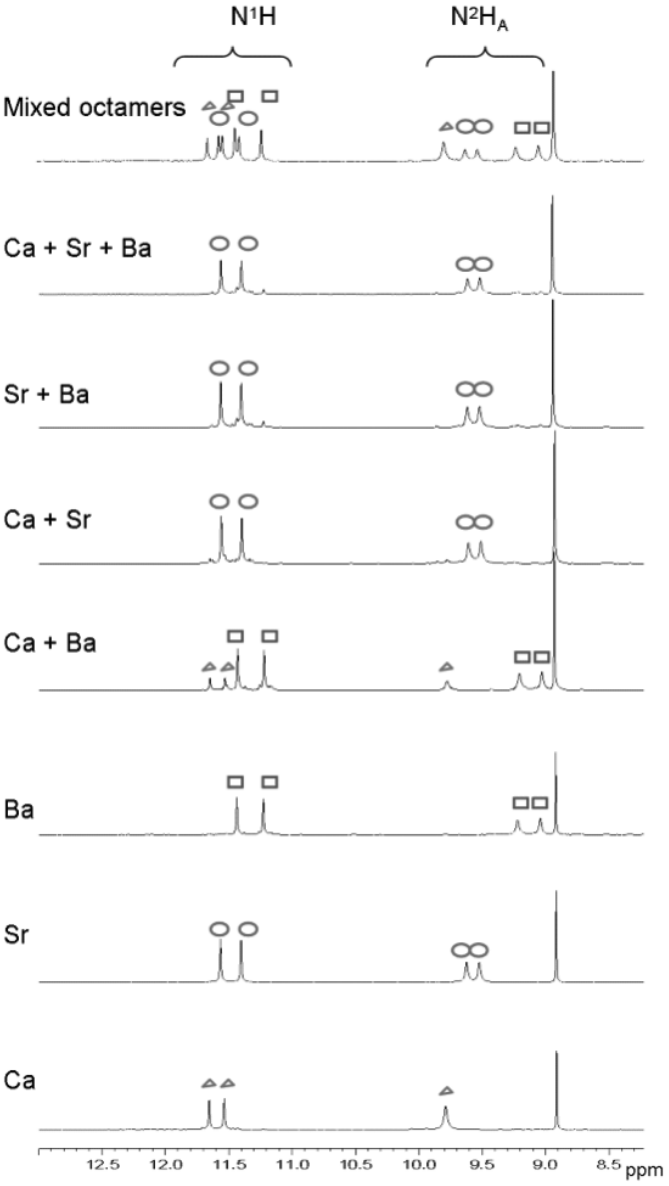

suggests that individual $[TAG]_8M^{2+}$ octamers do not stack on top of one another to form hexadecamers with mixed ions (e.g., $[TAG]_4$–Sr^{2+}–$[TAG]_4$–$[TAG]_4$–Ba^{2+}–$[TAG]_4$, etc.). This is in sharp contrast to the situations seen by Shi et al.[35] where hexadecamers with mixed ions are formed for 5′-*tert*-butyldimethylsilyl-2′,3′-isopropylidene-guanosine when the clamping anions are picrate and 2,5-dinitrophenolate.

Now we have established that, in $CDCl_3$, eight TAG molecules and one M^{2+} ion self-assemble into an octamer and that each octamer is composed of two structurally distinct TAG molecules in a 1:1 ratio. However, the structural details remain unknown with respect to the following aspects: (*i*) orientation of the guanine base with respect to the ribose ring (anti or syn conformers), (*ii*) intraquartet arrangement, and (*iii*) relative interquartet orientations within the octamer. Here, we decided to further investigate these structural features. To this end, we must first carry out complete spectral

Fig. 6. A region of the 2D COSY spectrum obtained for $[TAG]_8Sr^{2+}$ in $CDCl_3$ at 288.2 K revealing $^{3}J_{HH}$ relationships.

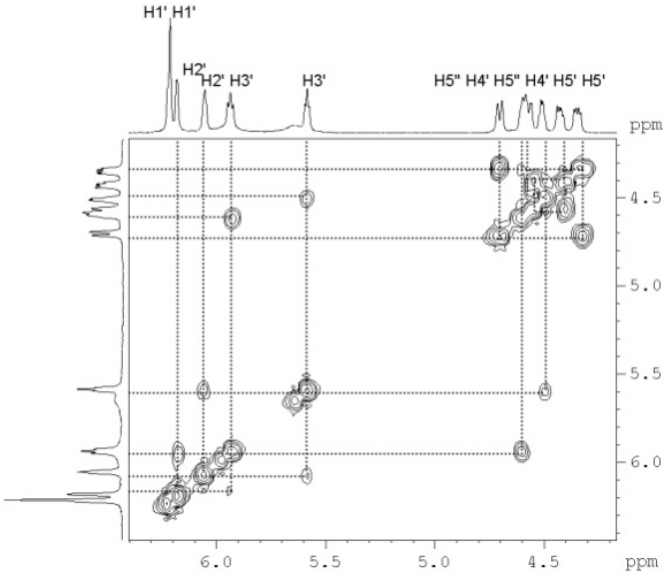

Fig. 7. Regions of the 2D NOESY spectrum for $[TAG]_8Sr^{2+}$ in $CDCl_3$ at 268.2 K showing the intra- and inter-quartet cross peaks (marked by green boxes) between H8 and sugar proton resonances. Red labels indicate the anti conformer and blue labels the syn conformer. Red arrows indicate intra- or inter-quartet NOE interactions. Colored lines link cross peaks from the same conformers.

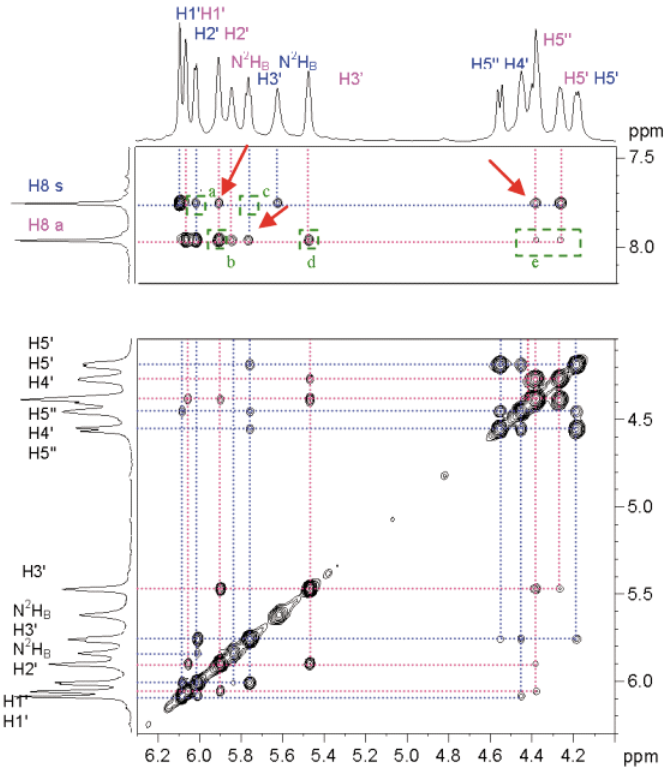

assignment. In the discussion that follows, we selected only $[TAG]_8Sr^{2+}$ for structural elucidation. In general, non-exchangeable protons (H1′/H2′/H3′/H4′/H5′/H5″) of the ribose ring were assigned using COSY, where $^{3}J_{HH}$ relationships were used (Fig. 6) along with NOESY (Fig. 7).

Scheme 4. NOE and $^3J_{CH}$ interactions in TAG used for spectral assignment.

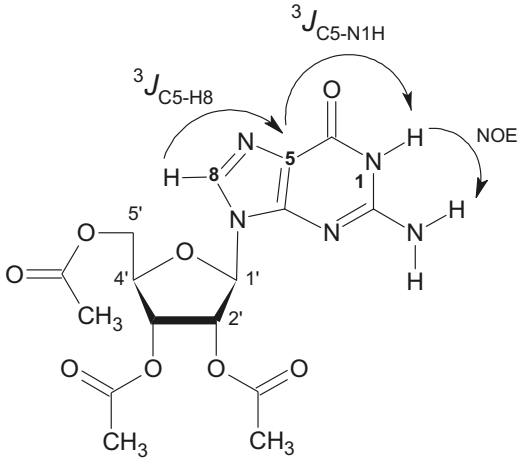

Fig. 8. A region of the ^{13}C–^1H HMBC spectrum obtained for $[TAG]_8Sr^{2+}$ in $CDCl_3$ at 298.2 K revealing correlation peaks due to $^3J_{C5–N1H}$ and $^3J_{C5–H8}$.

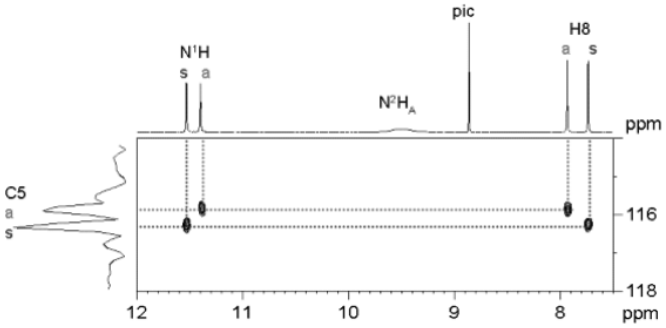

Fig. 9. A region of the 2D NOESY spectrum obtained for $[TAG]_8Sr^{2+}$ in $CDCl_3$ at 268.2 K showing the cross peaks of N^1H, N^2H_A, and N^2H_B resonances from either anti or syn molecules.

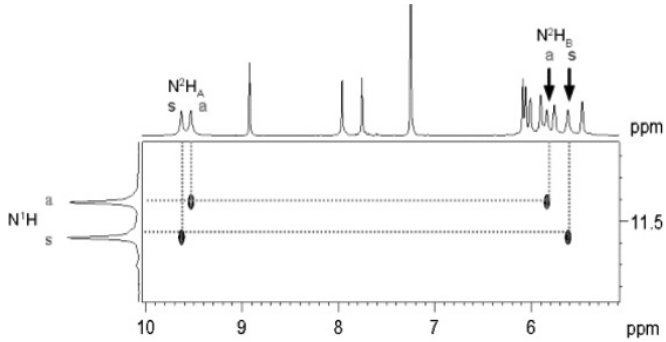

The exchangeable protons in the guanine base, N^1H, N^2H_A, and N^1H_B were located at δ = 11.6, 9.5, and 4.5 ppm, respectively.

The results from both COSY and NOESY experiments immediately reveal that the two sets of signals from TAG molecules are due to the presence of both anti and syn conformers. By definition, the anti conformation has an O4–C1′–N9–C4 torsion angle (χ) of 180° ± 90° while it is 0° ± 90° for the syn conformer.[52] As seen from Fig. 7, one of the H8 signals (δ = 7.75 ppm) exhibits a medium H8–H2′ NOE and no H8–H3′ cross peak (Fig. 7, boxes a and c). Thus, this H8 signal is from the syn conformer. In addition, NOE cross peaks between H8 and H4′, H5′, and H5″ were not observed for the syn conformer. On the other hand, the other H8 signal (δ = 7.96 ppm) has strong H8–H2′ and H8–H3′ NOEs (Fig. 7, boxes b and d), plus weak NOEs between H8 and H4′/H5″ and H5′ from the same molecule (Fig. 7, box e). These features are consistent with an anti conformation. The NOE cross peaks have almost the same intensity between H8 and H1′ protons from both conformers, suggesting that the distances between H8 and H1′ are very similar in both anti and syn conformers. This provides an approximate range for possible χ angles in both syn and anti monomers. In our case, the χ angle for the anti TAG conformer was determined to be in the "high-anti" region between –170° and –180°, while the syn conformation has a χ value between 60° and 70°. Observations of nucleosides in the syn conformer are rare because the C1′–N9 glycosidic bond is flexible and anti is preferred due to steric effect.[53] The syn conformers have been observed mostly in purines with C8 substituents that form intramolecular hydrogen bonding. In this case, the observation of equal population between syn and anti conformation further suggests that a divalent metal ion both templates and stabilizes the TAG octamer structure. As also shown in Fig. 7, several cross peaks (highlighted by arrows) were observed between anti and syn TAG molecules, which arise from either intra- or inter-quartet NOEs and will be further examined in a later section.

Next, while the assignment of the exchangeable imino N^1H and amino $N^2H_{A/B}$ protons is straightforward from NOESY, the connectivity between N^1H and H8 cannot reply on NOESY. Here, the standard technique is, as demonstrated by Phan,[54] a 2D HMBC experiment utilizing the two $^3J_{C–H}$ coupling constants between H8 and C5 and between N^1H and C5 (Scheme 4). As seen from Fig. 8, the HMBC experiment clearly shows the identity of the N^1H resonances. Having identified the N^1H resonances, $N^2H_{A/B}$ resonances were readily assigned using strong intraresidue NOE cross peaks due to their close proximity in space (~1.76 Å), as shown in Fig. 9. For amino N^2H protons, the anti conformer has chemical shifts at δ = 9.53 and 5.84 ppm, and the syn conformer has δ = 9.63 and 5.61 ppm. The large chemical shift difference ($\Delta\delta_{anti}$ = 3.69 ppm, $\Delta\delta_{syn}$ = 4.02 ppm) suggests that one of these amino protons is involved in strong hydrogen bonding as previously mentioned. A summary of the ^1H resonance assignment was given in Table 1.

Now, having anti and syn TAG molecules in a 1:1 ratio, there are still quite a few possible combinations to make two G-quartets within an octamer. As explained in detail by Davis and co-workers,[47] there are four possible combinations of conformer arrangement within the G-quartet. They are (*i*) all-syn, (*ii*) all-anti, (*iii*) alternating syn and anti, and (*iv*) adjacent syn and anti.[47] Because the bond distance of N^2H_A and H8 are within the NOE detection range (~3 Å), the cross peaks between these two protons can be used to determine the pattern of the G-quartets. All-anti or all-syn G-quartets would give strong NOEs between anti–anti and syn–syn signals, while alternating G-quartets would yield signals only between anti and syn conformers. Moreover, adjacent G-quartet arrangement would give four equal intensity cross peaks between all-anti and -syn signals.[43] The targeted spectral area for $[TAG]_8Sr^{2+}$ is shown in Fig. 10. The observed

Can. J. Chem. Downloaded from www.nrcresearchpress.com by Xi'an Jiaotong University on 09/19/12
For personal use only.

Table 1 . ^{1}H NMR resonance assignment for the ^{1}H NMR spectrum of $[TAG]_8Sr^{2+}$ in $CDCl_3$ at 268.2 K.

^{1}H	N^{1}H	N^{2}H$_A$	N^{2}H$_B$	H8	H1′	H2′	H3′	H4′	H5′[a]	H5″[a]
Syn	11.60	9.63	5.61	7.75	6.09	6.01	5.76	4.45	4.15	4.56
Anti	11.40	9.53	5.84	7.96	6.06	5.90	5.47	4.40	4.26	4.38

[a]Stereospecific assignment for H5′ and H5″ resonances was not performed.

Fig. 10. A region of the 2D NOESY spectrum obtained for $[TAG]_8Sr^{2+}$ in $CDCl_3$ at 268.2 K showing the cross peaks between N^{2}H$_A$ and H8 resonances.

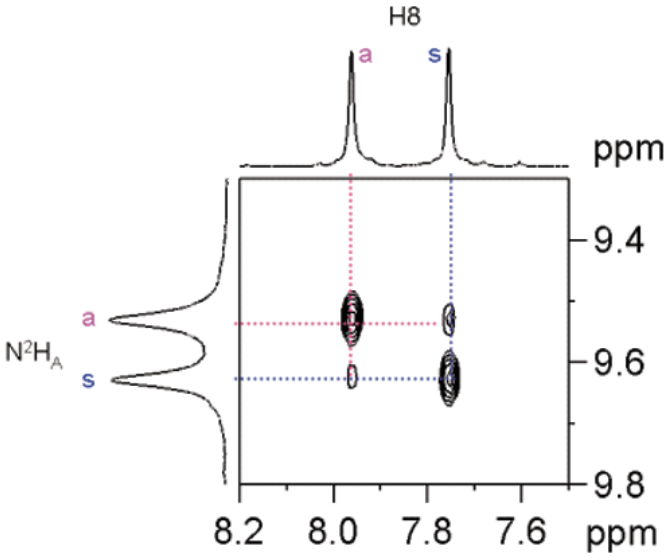

Fig. 11. A region of the 2D NOESY spectrum obtained for $[TAG]_8Sr^{2+}$ in $CDCl_3$ at 268.2 K showing interquartet cross peaks of the sugar rings. Red lines indicate the anti structure and blue lines indicate the syn structure. Red arrows indicate the presence or the lack of crucial intra- or inter-quartet interactions.

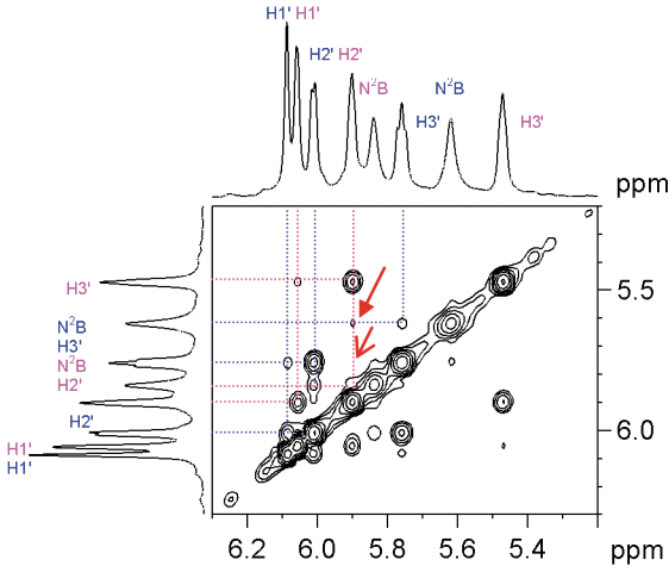

pattern within the NOE cross peaks suggests that the two G-quartets forming the $[TAG]_8Sr^{2+}$ octamer adopt an all-anti and all-syn conformation. On the other hand, the weak NOEs between anti and syn signals can be attributed to inter-quartet interactions within the octamer, which provides us with further information about the relative orientation between the two G-quartets as discussed later. We can now conclude that the $[TAG]_8Sr^{2+}$ octamer is composed of an all-anti G-quartet stacking on top of an all-syn G-quartet.

The next step of structure determination is to find the exact stacking orientation between the two G-quartets within $[TAG]_8Sr^{2+}$. In this regard, if the side of a G-quartet has a N^1–H···O–C6 hydrogen bond that has a clockwise rotation (from donor to acceptor), this side is defined as the "head" face; if the rotation was counterclockwise, the side is the "tail" face.[55] We used the NOE cross peaks from interquartet interactions, as shown in Figs. 7 and 11, to determine the interface between the two G-quartets in the $[TAG]_8Sr^{2+}$ octamer. Detailed NOESY assignment is given in the Supplementary data (Tables S2 and S3).

We have also built molecular models using basic units from the crystal structures of previously reported guanosine derivatives (see Table S3 in the Supplementary data).[56–58] These models include head–head, head–tail, tail–head, and tail–tail interface arrangements. In all these octamer models, the G-quartets were rotated 45° with respect to each other. This arrangement provides the least repulsion between the carbonyl oxygen atoms at the centre of the G-quartets and maximizes the π-stacking interaction between guanine bases. Using these models, theoretical interquartet NOE interactions were extracted and compared with the experimental NOEs. As reported in Table S2 in the Supplementary data, several important NOEs provided key information about the relative orientation of the two G-quartets in $[TAG]_8Sr^{2+}$. The signature NOE cross peaks included interactions between anti H8 and syn H2′/H3′. These interactions eliminated the head–tail and tail–tail structures because anti H8 and syn H2′ and H3′ are too far away in these models to be registered by NOESY (Table S3 in the Supplementary data). The other two models (head–head and tail–head) had orientations that allowed anti H8 to interact with syn H2′ and H3′. Furthermore, in order for H2′ from the anti conformer to be close enough to interact with the all-syn quartet underneath, the tail–head model is determined to be the most plausible solution (Table S3 in the Supplementary data). This model also explained the N^{2}H$_A$–H8 interquartet NOE interaction (Fig. 7) instead of the Hoogsteen-type hydrogen bond within a G-quartet. The interquartet NOEs arising from interactions of protons between the all-anti and the all-syn G-quartets also support the proposed twist angle of 45° about the octamer's central C_4 axis. As mentioned earlier, no NMR evidence was detected for further formation of a hexadecamer from two octamers. A plausible reason that hinders the hexadecamer formation from two $[TAG]_8Sr^{2+}$ octamers is related to how the two G-quartets are oriented within each octamer. We were quite confident that the stacking within each $[TAG]_8Sr^{2+}$ octamer is head(all-anti)-to-tail(all-syn), and the interoctamer interface is always a head(all-syn)-to-head(all-syn) symmetrical arrangement

Can. J. Chem. Downloaded from www.nrcresearchpress.com by Xi'an Jiaotong University on 09/19/12
For personal use only.

Can. J. Chem. Downloaded from www.nrcresearchpress.com by Xi'an Jiaotong University on 09/19/12
For personal use only.

Scheme 5. (*a*) A literature hexadecamer formed with two octamers and four clamping picrates. The head-to-head interoctamer interface is formed between all-syn G-quartets. Only one picrate is shown for clarity. (*b*) $[TAG]_8Sr^{2+}$ cannot form hexadecamers with a different interoctamer interface.

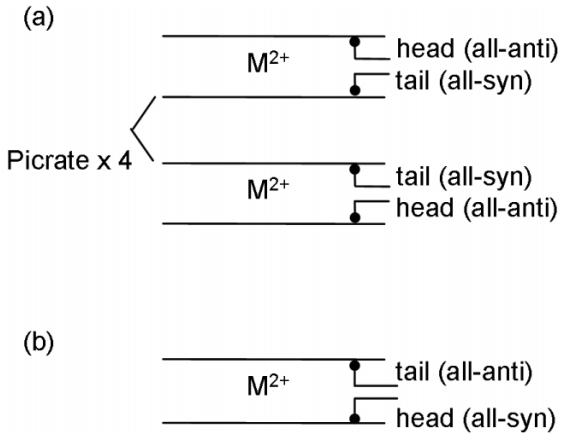

Fig. 12. An illustration of the $[TAG]_8Sr^{2+}$ octamer structure with an all-anti G-quartet stacking on top of an all-syn G-quartet in a tail–head fashion. The arrows indicate the N1–H···O=C6 hydrogen-bond rotation of each quartet's inner face (clockwise = head face).

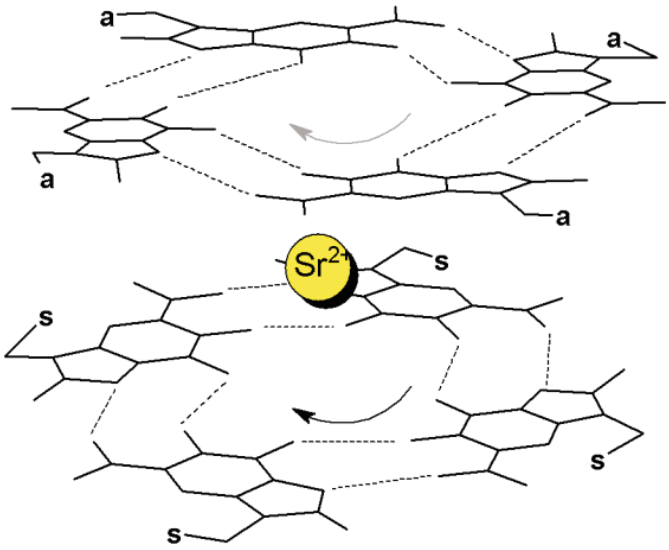

when hexadecamers are formed from two octamers.[2] In fact, the two octamers are related by a C_2 symmetry. In the case of $[TAG]_8Sr^{2+}$, the head-to-tail stacking is slightly different: two G-quartets in $[TAG]_8Sr^{2+}$ have a head(all-syn) stacking on top of a tail(all-anti). This may have prevented hexadecamer formation because of the steric repulsion from the remaining tail(all-syn) and head(all-anti) faces (Scheme 5). Besides, previously formed hexadecamers are comprised of octamers that are twisted 30° instead of 45° to each other.[48] The larger twist angle results in a larger separation between the exocyclic N^2H protons from the adjacent G-quartets, which may make them difficult to be clamped by a picrate anion. Our final structure for the $[TAG]_8Sr^{2+}$ octamer where the tail face of an all-anti G-quartet is stacked on the head face of an all-syn G-quartet is illustrated in Fig. 12. The similarity in the ^1H NMR spectra of $[TAG]_8Ba^{2+}$, $[TAG]_8Ca^{2+}$, and $[TAG]_8Sr^{2+}$ strongly suggests that all three octamers have the same structure.

Conclusion

In this study, we have used NMR and ESI-MS techniques to characterize the nature of $[TAG]M^{2+}$ complexes (M^{2+} = Ca^{2+}, Sr^{2+}, and Ba^{2+}). In all three cases, we observed formation of discrete TAG octamers composed of two G-quartets and a central M^{2+} ion. We also observed the following sequence for relative binding affinity towards $[TAG]_8$: $Sr^{2+} \gg Ba^{2+} > Ca^{2+}$. Using 2D NMR methods, we determined key structural details of the $[TAG]_8M^{2+}$ octamer. The octamer formation between TAG and alkaline earth metal ions represents a rather rare class of G-octamer structures and, hopefully, this new addition to the diverse family of G-quadruplex structures may bring some insights into the driving forces behind lipophilic G nucleoside self-assembly. It is possible that a controlled balance of monovalent and divalent cations can provide additional flexibility for making new G self-assembled structures. We are also currently investigating the possibility of using these simple G-octamer systems to obtain NMR spectral signatures for such exotic nuclei as ^{87}Sr and ^{137}Ba. It would also be of interest to investigate the impact of the chain length of the protecting groups and the nature of counteranions on the self-assembly.

Supplementary data

Supplementary data for this article are available on the journal Web sit (nrcresearchpress.com/cjc).

Acknowledgment

This work was supported by the Natural Sciences and Engineering Research Council of Canada (NSERC). I.C.M.K thanks NSERC for a Canada Graduate Scholarship. We also thank Ms. Jie Sui for assistance in MS sample preparation.

References

(1) Gellert, M.; Lipsett, M. N.; Davies, D. R. *Proc. Natl. Acad. Sci. U.S.A.* **1962**, *48* (12), 2013. doi:10.1073/pnas.48.12.2013.
(2) Davis, J. T. *Angew. Chem. Int. Ed.* **2004**, *43* (6), 668. doi:10.1002/anie.200300589.
(3) Davis, J. T.; Spada, G. P. *Chem. Soc. Rev.* **2007**, *36* (2), 296. doi:10.1039/b600282j.
(4) Lena, S.; Masiero, S.; Pieraccini, S.; Spada, G. P. *Chem. Eur. J.* **2009**, *15* (32), 7792. doi:10.1002/chem.200802506.
(5) Sessler, J. L.; Sathiosatham, M.; Doerr, K.; Lynch, V.; Abboud, K. A. *Angew. Chem. Int. Ed.* **2000**, *39* (7), 1300. doi:10.1002/(SICI)1521-3773(20000403)39:7<1300::AID-ANIE1300>3.0.CO;2-I.
(6) Kotch, F. W.; Sidorov, V.; Lam, Y.-F.; Kayser, K. J.; Li, H.; Kaucher, M. S.; Davis, J. T. *J. Am. Chem. Soc.* **2003**, *125* (49), 15140. doi:10.1021/ja0364165.
(7) Otero, R.; Schöck, M.; Molina, L. M.; Lægsgaard, E.; Stensgaard, I.; Hammer, B.; Besenbacher, F. *Angew. Chem. Int. Ed.* **2005**, *44* (15), 2270. doi:10.1002/anie.200461586.
(8) Phillips, K.; Dauter, Z.; Murchie, A. I. H.; Lilley, D. M. J.; Luisi, B. *J. Mol. Biol.* **1997**, *273* (1), 171. doi:10.1006/jmbi.1997.1292.

Can. J. Chem. Downloaded from www.nrcresearchpress.com by Xi'an Jiaotong University on 09/19/12
For personal use only.

(9) Hud, N. V.; Plavec, J. *Quadruplex Nucleic Acid;* Neidle, S., Balasubramanian, S., Eds.; RSC Publishing: Cambridge, UK, 2006; Chapter 4.
(10) Pinnavaia, T. J.; Marshall, C. L.; Mettler, C. M.; Fisk, C. L.; Miles, H. T.; Becker, E. D. *J. Am. Chem. Soc.* **1978**, *100* (11), 3625. doi:10.1021/ja00479a070.
(11) Wong, A.; Ida, R.; Spindler, L.; Wu, G. *J. Am. Chem. Soc.* **2005**, *127* (19), 6990. doi:10.1021/ja042794d.
(12) Wu, G.; Kwan, I. C. M. *J. Am. Chem. Soc.* **2009**, *131* (9), 3180. doi:10.1021/ja809258y.
(13) Walmsley, J. A.; Burnett, J. F. *Biochemistry* **1999**, *38* (42), 14063. doi:10.1021/bi9900370.
(14) Hightower, J. B.; Olmos, D. R.; Walmsley, J. A. *J. Phys. Chem. B* **2009**, *113* (36), 12214. doi:10.1021/jp904383y.
(15) Kankia, B. I.; Marky, L. A. *J. Am. Chem. Soc.* **2001**, *123* (44), 10799. doi:10.1021/ja010008o.
(16) Kwan, I. C. M.; She, Y.-M.; Wu, G. *Chem. Commun. (Camb.)* **2007**, 4286. doi:10.1039/b710299b.
(17) Sen, D.; Gilbert, W. *Nature* **1988**, *334* (6180), 364. doi:10.1038/334364a0.
(18) Sen, D.; Gilbert, W. *Nature* **1990**, *344* (6265), 410. doi:10.1038/344410a0.
(19) Sen, D.; Gilbert, W. *Biochemistry* **1992**, *31* (1), 65. doi:10.1021/bi00116a011.
(20) Balasubramanian, S.; Neidle, S. *Curr. Opin. Chem. Biol.* **2009**, *13* (3), 345. doi:10.1016/j.cbpa.2009.04.637.
(21) Hahn, W. C.; Stewart, S. A.; Brooks, M. W.; York, S. G.; Eaton, E.; Kurachi, A.; Beijersbergen, R. L.; Knoll, J. H. M.; Meyerson, M.; Weinberg, R. A. *Nat. Med.* **1999**, *5* (10), 1164. doi:10.1038/13495.
(22) Lena, S.; Masiero, S.; Pieraccini, S.; Spada, G. P. *Mini Rev. Org. Chem.* **2008**, *5* (4), 262. doi:10.2174/157019308786242205.
(23) Zhou, Y. F.; Morais-Cabral, J. H.; Kaufman, A.; MacKinnon, R. *Nature* **2001**, *414* (6859), 43. doi:10.1038/35102009.
(24) MacKinnon, R. *Angew. Chem. Int. Ed.* **2004**, *43* (33), 4265. doi:10.1002/anie.200400662.
(25) González-Rodríguez, D.; Janssen, P. G. A.; Martín-Rapún, R.; De Cat, I.; De Feyter, S.; Schenning, A. P. H. J.; Meijer, E. W. *J. Am. Chem. Soc.* **2010**, *132* (13), 4710. doi:10.1021/ja908537k.
(26) Shi, X.; Fettinger, J. C.; Davis, J. T. *J. Am. Chem. Soc.* **2001**, *123* (27), 6738. doi:10.1021/ja004330v.
(27) Mergny, J.-L.; Hélène, C. *Nat. Med.* **1998**, *4* (12), 1366. doi:10.1038/3949.
(28) Alberti, P.; Bourdoncle, A.; Saccà, B.; Lacroix, L.; Mergny, J.-L. *Org. Biomol. Chem.* **2006**, *4* (18), 3383. doi:10.1039/b605739j.
(29) Neidle, S.; Parkinson, G. *Nat. Rev. Drug Discov.* **2002**, *1* (5), 383. doi:10.1038/nrd793.
(30) Chen, Z.; Corey, D. R. *Adv. Cancer Res.* **2003**, *87*, 31. doi:10.1016/S0065-230X(03)87294-9.
(31) Chen, F.-M. *Biochemistry* **1992**, *31* (15), 3769. doi:10.1021/bi00130a006.
(32) Smirnov, I.; Shafer, R. H. *J. Mol. Biol.* **2000**, *296* (1), 1. doi:10.1006/jmbi.1999.3441.
(33) Kotch, F. W.; Fettinger, J. C.; Davis, J. T. *Org. Lett.* **2000**, *2* (21), 3277. doi:10.1021/ol0065120.
(34) Forman, S. L.; Fettinger, J. C.; Pieraccini, S.; Gottarelli, G.; Davis, J. T. *J. Am. Chem. Soc.* **2000**, *122* (17), 4060. doi:10.1021/ja9925148.
(35) Shi, X.; Mullaugh, K. M.; Fettinger, J. C.; Jiang, Y.; Hofstadler, S. A.; Davis, J. T. *J. Am. Chem. Soc.* **2003**, *125* (36), 10830. doi:10.1021/ja035267n.
(36) van Leeuwen, F. W. B.; Verboom, W.; Shi, X.; Davis, J. T.; Reinhoudt, D. N. *J. Am. Chem. Soc.* **2004**, *126* (50), 16575. doi:10.1021/ja0455650.
(37) Lee, M. P. H.; Parkinson, G. N.; Hazel, P.; Neidle, S. *J. Am. Chem. Soc.* **2007**, *129* (33), 10106. doi:10.1021/ja0740869.
(38) Pedroso, I. M.; Duarte, L. F.; Yanez, G.; Baker, A. M.; Fletcher, T. M. *Biochem. Biophys. Res. Commun.* **2007**, *358* (1), 298. doi:10.1016/j.bbrc.2007.04.126.
(39) Nikan, M.; Sherman, J. C. *J. Org. Chem.* **2009**, *74* (15), 5211. doi:10.1021/jo9001245.
(40) Miyoshi, D.; Nakao, A.; Toda, T.; Sugimoto, N. *FEBS Lett.* **2001**, *496* (2–3), 128. doi:10.1016/S0014-5793(01)02416-4.
(41) Kwan, I. C. M.; Wong, A.; She, Y.-M.; Smith, M. E.; Wu, G. *Chem. Commun. (Camb.)* **2008**, 682. doi:10.1039/b714803h.
(42) (a) Andrisano, V.; Gottarelli, G.; Masiero, S.; Heijne, E. H.; Pieraccini, S.; Spada, G. P. *Angew. Chem.* **1999**, *111* (16), 2543. doi:10.1002/(SICI)1521-3757(19990816)111:16<2543::AID-ANGE2543>3.0.CO;2-G;; (b) Andrisano, V.; Gottarelli, G.; Masiero, S.; Heijne, E. H.; Pieraccini, S.; Spada, G. P. *Angew. Chem. Int. Ed.* **1999**, *38* (16), 2386. doi:10.1002/(SICI)1521-3773(19990816)38:16<2386::AID-ANIE2386>3.0.CO;2-S.
(43) Van Geet, A. L. *Anal. Chem.* **1970**, *42* (6), 679. doi:10.1021/ac60288a022.
(44) West, R. T.; Garza, L. A., II; Winchester, W. R.; Walmsely, J. A. *Nucleic Acids Res.* **1994**, *22* (23), 5128. doi:10.1093/nar/22.23.5128.
(45) Kaucher, M. S.; Lam, Y.-F.; Peraccini, S.; Gottarelli, G.; Davis, J. T. *Chem. Eur. J.* **2005**, *11* (1), 164. doi:10.1002/chem.200400782.
(46) Enquist, P.-A.; Nilsson, P.; Sjöberg, P.; Larhed, M. *J. Org. Chem.* **2006**, *71* (23), 8779. doi:10.1021/jo061437d.
(47) Marlow, A. L.; Mezzina, E.; Spada, G. P.; Masiero, S.; Davis, J. T.; Gottarelli, G. *J. Org. Chem.* **1999**, *64* (14), 5116. doi:10.1021/jo9901440.
(48) Shi, X.; Fettinger, J. C.; Davis, J. T. *Angew. Chem. Int. Ed.* **2001**, *40* (15), 2827. doi:10.1002/1521-3773(20010803)40:15<2827::AID-ANIE2827>3.0.CO;2-1.
(49) Liu, X.; Kwan, I. C. M.; Wang, S.; Wu, G. *Org. Lett.* **2006**, *8* (17), 3685. doi:10.1021/ol061236w.
(50) Martić, S.; Liu, X.; Wang, S.; Wu, G. *Chem. Eur. J.* **2008**, *14* (4), 1196. doi:10.1002/chem.200701411.
(51) Shannon, R. D. *Acta Crystallogr. Sect. A* **1976**, *32* (5), 751. doi:10.1107/S0567739476001551.
(52) Neuhaus, D.; Williamson, M. *The Nuclear Overhauser Effect in Structural and Conformational Analysis;* VCH Publishers: New York, 1989.
(53) Davies, D. B. *Prog. Nucl. Magn. Reson. Spectrosc.* **1978**, *12* (3), 135. doi:10.1016/0079-6565(78)80006-5.
(54) (a) Phan, A. T. *J. Biomol. NMR* **2000**, *16* (2), 175. doi:10.1023/A:1008355231085;; (b) Phan, A. T. *J. Magn. Reson.* **2001**, *153* (2), 223. doi:10.1006/jmre.2001.2445.
(55) Smith, F. W.; Lau, F. W.; Feigon, J. *Proc. Natl. Acad. Sci. U.S.A.* **1994**, *91* (22), 10546. doi:10.1073/pnas.91.22.10546.
(56) Zimmerman, S. B. *J. Mol. Biol.* **1976**, *106* (3), 663. doi:10.1016/0022-2836(76)90257-6.
(57) Tougard, P.; Chantot, J.-F.; Guschlbauer, W. *Biochim. Biophys. Acta* **1973**, *308*, 9.
(58) Zimmerman, S. B.; Cohen, G. H.; Davies, D. R. *J. Mol. Biol.* **1975**, *92* (2), 181. doi:10.1016/0022-2836(75)90222-3.

Deposition of gold nanoparticles on organo-kaolinite — Application in electrocatalysis for carbon monoxide oxidation

Sadok Letaief, Wendy Pell, and Christian Detellier

Can. J. Chem. Downloaded from www.nrcresearchpress.com by Xi'an Jiaotong University on 09/19/12
For personal use only.

Abstract: The clay mineral kaolinite was used as support of gold nanoparticles for heterogeneous catalysis of oxidation reactions, particularly of carbon monoxide oxidation. The application of clay minerals in the preparation of new functional materials provides an alternative approach for the use of these abundant raw materials. To improve the physicochemical properties of kaolinite, as well as to ensure a strong immobilization of the adsorbed species, kaolinite was functionalized by grafting 2-amino-2-methyl-1,3-propanediol on the internal and external surfaces of the octahedral sheets by reaction with the aluminol groups. Gold nanoparticles were then deposited on the external surfaces of the fine particles of the functionalized kaolinite. The resulting gold kaolinite nanohybrid material was characterized by various physicochemical techniques. X-ray diffraction, X-ray photoelectron spectroscopy, transmission electron microscopy, and energy-dispersive X-ray spectrometry confirmed that gold was effectively reduced to the metallic state during adsorption onto the external surfaces of the modified kaolinite. The gold nanoparticles have a narrow size distribution: more than 88% are less than 4 nm in diameter. Gold nanoparticles deposited on kaolinite catalyze the electro-oxidation of carbon monoxide in alkaline solution at room temperature.

Key words: kaolinite, grafting, organoclay, nanohybrid materials, gold nanoparticles, carbon monoxide, oxidation.

Résumé : On a utilisé la kaolinite, une argile minérale, comme support pour des nanoparticules d'or pour la catalyse hétérogène de réactions d'oxydation, particulièrement l'oxydation du monoxyde de carbone. L'application des argiles minérales dans la préparation de nouveaux matériaux fonctionnels fournit une approche alternative à l'utilisation de ces matières premières abondantes. Afin d'améliorer les propriétés physico-chimiques de la kaolinite ainsi que pour s'assurer d'une immobilisation forte des substances adsorbées, on a procédé à une fonctionnalisation de la kaolinite en lui greffant du 2-amino-2-méthylpropane-1,3-diol sur ses surfaces internes et externes par réaction avec les groupes aluminol des couches octaédriques. Les nanoparticules d'or sont ensuite déposés sur les surfaces externes de fines particules de kaolinite fonctionnalisée. On a caractérisé le matériel nanohybride de kaolinite d'or qui en résulte par diverses techniques physico-chimiques. La diffraction des rayons-X, la spectroscopie photoélectronique des rayons-X, la microscopie électronique de transmission et la spectrométrie des rayons-X à dispersion d'énergie confirment que l'or est effectivement réduit à l'état métallique lors de son adsorption sur les surfaces extérieures de la kaolinite modifiée. La distribution des tailles des nanoparticules d'or est étroite : plus de 88 % ont un diamètre inférieur à 4 nm. Les nanoparticules d'or déposées sur la kaolinite catalysent l'électro-oxydation du monoxyde de carbone en solution alcaline, à la température ambiante.

Mots-clés : kaolinite, greffage, argile organique, matériaux nanohybrides, nanoparticules d'or, monoxyde de carbone, oxydation.

[Traduit par la Rédaction]

Introduction

The fascinating physicochemical properties of metallic nanoparticles, and particularly of gold nanoparticles (AuNP), lead to a large variety of applications, including the field of catalysis.[1,2] Gold nanoparticles were immobilized successfully on a variety of metal oxides, such as TiO_2, Fe_2O_3, CeO_2, and Al_2O_3,[3–5] as well as on other layered supports.[6] Their preparation is usually based on the method of deposition–precipitation, employing the most common gold precursor $HAuCl_4$. Although clay minerals are known to be useful catalytic supports, owing to their strong thermal and chemical stabilities, their use in the preparation of supported gold catalysts is scarce compared with metal oxides. Large gold nanoparticles with an average diameter ranging between 20 and 50 nm were deposited on laponite,[7] sepiolite,[8,9] and montmorillonite modified by polyethylenimine using $HAuCl_4 \cdot 3H_2O$ as precursor.[10] In 2009, Zhu et al.[11] prepared

Received 28 November 2010. Accepted 28 January 2011. Published at www.nrcresearchpress.com/cjc on 5 July 2011.

S. Letaief, W. Pell, and C. Detellier. Centre for Catalysis Research and Innovation and Department of Chemistry, University of Ottawa, 10 Marie Curie Private, Ottawa, ON K1N 6N5, Canada.

Corresponding author: Christian Detellier (e-mail: dete@uottawa.ca).

This article is part of a Special Issue dedicated to Professor Rod Wasylishen.

Can. J. Chem. Downloaded from www.nrcresearchpress.com by Xi'an Jiaotong University on 09/19/12
For personal use only.

small gold nanoparticles on the external surfaces of sepiolite and montmorillonite using $Au(en)_2Cl_3$ as precursor. They showed the usefulness of functionalizing sepiolite by a silane reagent such as aminopropyltriethoxysilane (APTES).[11] The mean diameters of the gold nanoparticles, supported both on sepiolite and on montmorillonite, were below 5 nm. More recently, Zhang et al.[12] deposited AuNP on commercial clay particles functionalized by APTES.

Kaolinite is one of the most abundant clay minerals found in nature. It is a 1:1 layered dioctahedral aluminosilicate[13–15] with a theoretical formula $Al_2Si_2O_5(OH)_4$ and a molecular weight of 258.10 g/mol, corresponding to an ideal composition of 46.55% SiO_2, 39.49% Al_2O_3, and 13.96% H_2O.[16] The kaolinite structure consists of a Si_2O_5 sheet bound on one side to a dioctahedral gibbsite-type layer through van der Waals interactions and hydrogen bonds. Although kaolinite is widely abundant in nature and is characterized by a much higher density of hydroxyl groups than clay minerals of the smectite group, its interlayer chemistry is much less developed in comparison with smectites. To access the aluminol groups, which are the prominent candidates for grafting reactions, kaolinite must be previously intercalated by small polar molecules like dimethylsulfoxide (DMSO) or urea.

The number of gold catalyzed reactions is extensive and varied including O_2 reduction,[17,18] the water gas shift reaction,[19] and selective oxidation of hydrocarbons,[20,21] as well as low temperature CO oxidation.[22,23] What makes gold an especially interesting catalyst is that its performance can be varied and tuned by varying the support material and (or) the catalyst loading. In the presence of O_2, H_2, and a gold catalyst supported on TiO_2, propylene was oxidized to propane, propylene oxide, and ultimately to CO_2, depending on the catalyst loading.[23,24] The optimization of the catalytic effectiveness has been linked to the role of the support material, to the Au oxidation state, to particle size and morphology, and to the operating conditions. An understanding of the catalytic process is important, as values in the literature for the rate of low temperature CO oxidation on similar catalysts vary by orders of magnitude.[23] In the study of CO oxidation, catalyst supports have been identified as active (generally reducible transition metal oxides) or inactive (typically Al_2O_3, SiO_2, and MgO).[25] It is not clear, however, if the activity of the Au catalyst is a direct reflection of the reducibility of the support, as catalysts prepared on Al_2O_3 have been found to show similar activities to those on TiO_2 supports. Furthermore, the catalytic activity can be significantly affected by operating conditions; it has been observed that the rate of CO oxidation at Au/TiO_2 was four times that at Au/Al_2O_3 surfaces at 298 K, but only twice as active at 273 K.[26]

In this work, carbon monoxide catalytic oxidation was obtained by gold nanoparticles (AuNP) supported on a modified kaolinite clay mineral. The preparation of the gold–clay nanoparticles was carried out by a wet chemical process using $Au(en)_2Cl_3$ salt as precursor.[11] Characterization results by X-ray diffraction (XRD) and X-ray photoelectron spectroscopy (XPS) confirmed the presence of metallic gold. High-resolution transmission electron microscopy (HRTEM) showed a homogeneous distribution of the gold nanoparticules with an average diameter of less than 5 nm.

Experimental

Materials

Well-crystallized Georgia kaolinite (KGa-1) was obtained from the Source Clay Minerals Repository, University of Missouri. 2-Amino-2-methyl-1,3-propanediol (AMPD), hydrogen tetrachloroaurate hydrate ($HAuCl_4 \cdot 3H_2O$), and ethylenediamine (en) pure grade were obtained from Sigma-Aldrich and were used without further purification.

Sample preparation

Kaolinite (K)

Kaolinite was purified using standard sedimentation techniques and the <2 μm fraction was used in the experiments.

Dimethyl sulfoxide (DMSO)–kaolinite intercalate (DMSO–K)

Kaolinite (10 g) was added to a mixture of 60 mL of DMSO and 5 mL of H_2O. The suspension was stirred continuously for 10 days with the temperature maintained at 80 °C, then it was allowed to cool to room temperature and stirred for a further 5 days. The resulting material was recuperated after two series of washing centrifugation using first dioxane (2 × 50 mL), then isopropanol (2 × 50 mL). The product was finally dried at 50 °C.

2-Amino-2-methyl-1,3-propanediol (AMPD)–kaolinite intercalate (AMPD–K)

The grafting of 2-amino-2-methyl-1,3-propanediol on kaolinite was performed under nitrogen at 180 °C over a 2 h period. In a typical set of experiments, 1 g of DMSO–K was mixed with 4 g of AMPD. The temperature of the mixture was then increased slowly from room temperature to 180 °C and maintained stable during 2 h. The resulting materials were recuperated after three series of centrifugation following washing with isopropanol (3 × 50 mL). The recovered solid sample was dried at 60 °C overnight, ground and suspended again in water and stirred for 72 h to remove the residual DMSO and intercalated, nongrafted, organic units from the sample.

Clay-supported gold nanoparticles (AuNP–AMPD–K)

The clay suspension was prepared by adding 0.5 g of modified kaolinite to 100 mL of distilled water. It was then dispersed by ultrasonic treatment for 10 min. To achieve 10 wt % of nominal gold loading, 0.050 g of $Au(en)_2Cl_3$ was dissolved in 50 mL of distilled water. The $Au(en)_2Cl_3$ solution was then added to the clay suspension. The mixture was maintained under stirring for 24 h at 60 °C. The colour of the suspension consisting of the gold precursor and of the modified kaolinite turned to dark violet. This colour change indicated that the gold precursor was autoreduced in situ to metallic gold in the presence of the modified kaolinite. The suspension was then filtered and the resulting solid was washed three times with water. The gold–clay nanohybrid materials were dried at 60 °C and stored for further characterization and application (Scheme 1). The reddish colouration of the resulting nanocomposites is a good indication that the gold nanoparticles exhibit a small diameter, in general between 5 and 20 nm.[27] The same procedure was applied using the nonmodified kaolinite and the kaolinite modified

Scheme 1. A schematic illustration of the preparation of gold nanoparticles deposited on the external surfaces of kaolinite.

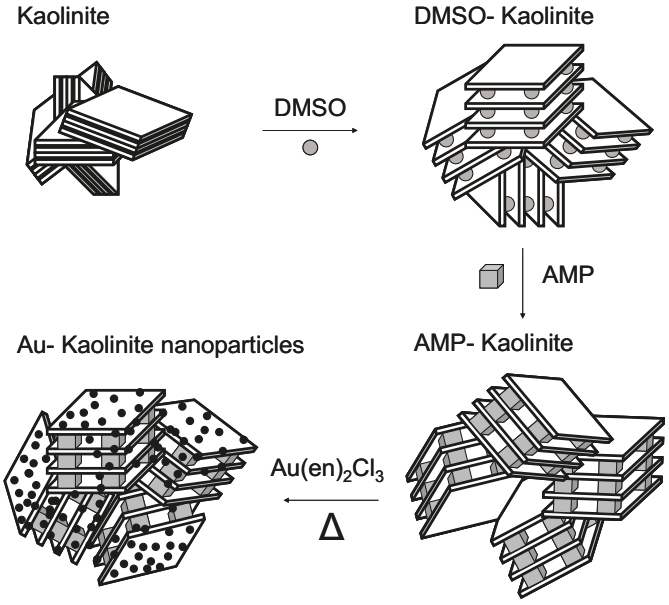

by intercalation of DMSO. In these cases, the gold precursor was reduced by adding a 0.1 mol/L $NaBH_4$ solution.

Catalytic test

Electrode preparation

Thin films of both the gold nanohybrid material and the AMPD–K support material were prepared by spin-coating on the surface of a glassy carbon electrode (GCE). The modified clay (10 mg; with and without inclusion of Au nanoparticles) was added quickly to 5 mL of 10 wt % dispersion of polystyrene in water and agitated for 10 min. The obtained suspension (1 mL) was spin-coated at 500 rpm for 10 min on the active surface of the GCE. The resulting organoclay-modified electrodes were dried at room temperature and used for electrochemical measurements without further treatment.

Cyclic voltammetry measurement

Electrochemical measurements were performed using a Princton Applied Research (PAR) VersaSTAT 3 potentiostat/galvanostat/frequency response analyzer and V3-Studio electrochemical software version 1.0.281 (2008) (PAR) employing a three compartment glass cell, a working-GCE spin-coated with gold nanohybrid material, a platinum gauze counter electrode, and a relative hydrogen electrode (RHE). The electrolyte was degassed with nitrogen prior to experiments, and subsequently saturated with carbon monoxide by bubbling with CO 99.3%. Nitrogen gas was bubbled through the cell during the measurements. Cyclic voltammograms were recorded over various potential ranges at 50 mV/s. Potential ranges were optimized to show the best response for each of the samples.

Characterization

X-ray diffraction (XRD) patterns were obtained with a Philips PW 3710 instrument equipped with a Ni filter and Cu Kα radiation (λ = 0.15418 nm) operating at 45 kV and 40 mA.

Differential thermal analyses (DTA) and thermal gravimetric analyses (TGA) were recorded on a SDT 2960 Simultaneous DSC-TGA instrument under N_2 flow (100 mL/min) with a heating rate of 10 °C/min.

The ^1H and ^{13}C NMR spectra in solution were recorded on a Bruker 400 MHz spectrometer. Solid-state ^{13}C NMR CP/MAS spectra were collected on a Bruker Avance 500 NMR spectrometer operating at 125.77 MHz. The ^{13}C chemical shifts were referenced to TMS at 0 ppm using the high frequency signal of adamantane at 38.4 ppm as a secondary standard.

Transmission and high-resolution transmission electron microscopic images were obtained on a JEOL JEM-2100F electron microscope. The powders were suspended in ethanol for about 10 min under ultrasonic treatment before depositing them on the carbon support.

XPS spectra of the gold nanoparticles deposited at the external surface of modified kaolinite were collected using a Kratos Axis Ultra DLD spectrometer, equipped with a standard Al Kα excitation source (1486.6 eV). The binding energy (BE) scale was calibrated by measuring C 1s peak from the surface contamination at 285.1 eV.

Results and discussion

X-ray diffraction

XRD diffractograms of pure kaolinite, of the precursor DMSO–kaolinite (DMSO–K), and of the organo-modified kaolinite (AMPD–K) before and after deposition of gold nanoparticles are presented in Fig. 1. The d_{001} spacing of kaolinite is 0.71 nm, and that of the DMSO–K intercalate is 1.10 nm (Figs. 1*a* and 1*b*).[28] The intercalation of DMSO into the interlamellar spaces of kaolinite is clearly observed by a shift of the 001 reflection to lower angles, owing to the keying of one of the DMSO methyl groups in the siloxane rings of the tetrahedral sheets.[29] After reaction with AMPD, the XRD pattern exhibits a well-developed 001 peak with a d_{001} spacing of 1.08 nm. There is, at this point, no evidence if the AMPD is intercalated, co-intercalated with DMSO, or grafted to the octahedral sheet, since no displacement of the 001 reflection to higher or lower angles upon displacement of DMSO was observed. To verify that AMPD is grafted to the octahedral sheet, the material was suspended in water and stirred for 72 h at room temperature. Intercalates of kaolinite are usually displaced by washing with water to recover the original kaolinite or to form a kaolinite hydrate.[30,31] However, in strong contrast, the grafted derivatives of kaolinite, resulting from esterification of the aluminol surfaces, are stable towards extensive washing.[31] The 001 reflection of the material obtained after treatment with water for 72 h is observed at 1.08 nm (Fig. 1*c*), and the intercalation ratio is still higher, which confirms that AMPD is grafted to the internal surfaces. An XRD diffractogram of the gold nanoparticles deposited on the grafted kaolinite (Au–AMPD–K) is given in Fig. 1*d*. The position of the 001 reflection (1.06 nm), as well as the characteristic peaks of kaolinite 001 (0.71 nm) and 060 (0.149 nm), remain at the same position. This indicates that the organic entities grafted into the interlayer space remain unaffected, and that the structure of kaolinite is not

Can. J. Chem. Downloaded from www.nrcresearchpress.com by Xi'an Jiaotong University on 09/19/12
For personal use only.

Can. J. Chem. Downloaded from www.nrcresearchpress.com by Xi'an Jiaotong University on 09/19/12
For personal use only.

Fig. 1. Powder X-ray diffractograms (2θ = 2°–70°) of (*a*) pristine kaolinite (K), (*b*) kaolinite intercalated by DMSO (DMSO–K), (*c*) kaolinite grafted by 2-amino-2-methyl-1,3-propanediol, and (*d*) kaolinite supported gold nanoparticles (AuNP–AMPD–K).

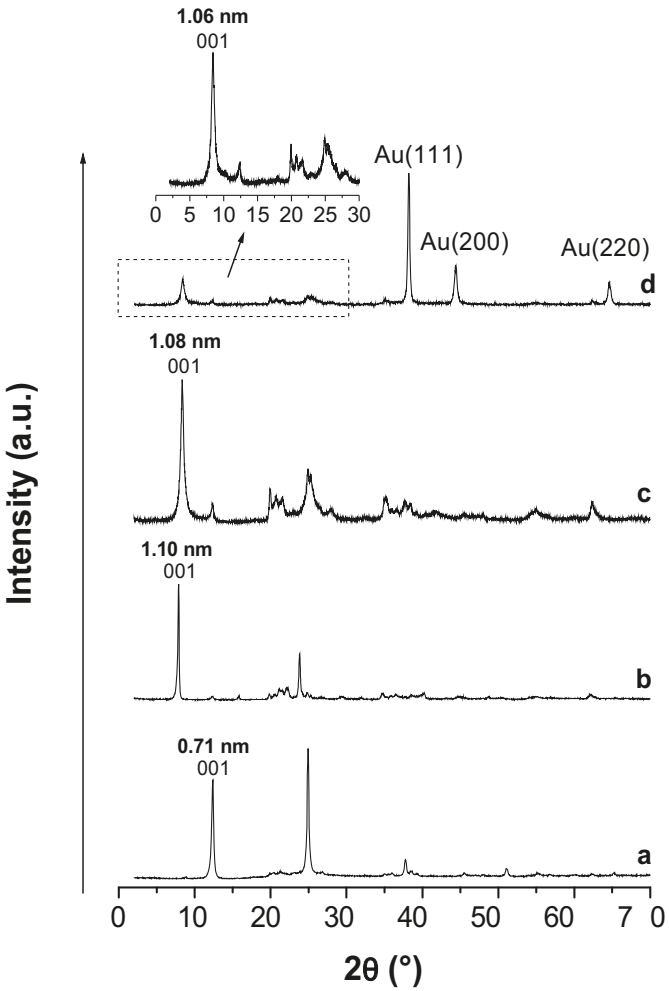

Fig. 2. ^{13}C CP/MAS NMR spectra of (*a*) kaolinite intercalated by DMSO (DMSO–K) and (*b*) kaolinite supported gold nanoparticles (AuNP–AMPD–K).

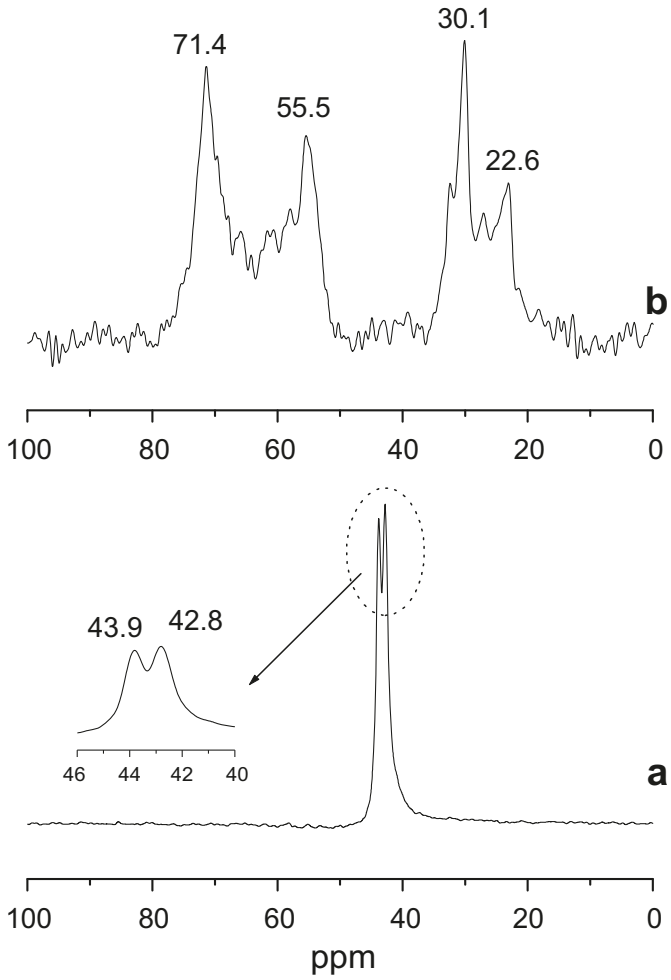

altered during the deposition process. In addition to the typical kaolinite diffraction peaks, three intense reflections at 38.2°, 44.5°, and 64.6° could be observed in the region of 2θ = 2°–70°. They correspond, respectively, to the (111), (200), and (220) reflection peaks of metallic gold. The presence of these peaks indicates that metallic gold particles have been successfully deposited on the modified kaolinite, using $Au(en)_2Cl_3$ as a precursor.

Nuclear magnetic resonance

The ^{13}C CP/MAS NMR spectra of the nanohybrid materials obtained by grafting AMPD onto kaolinite, then adsorbing gold nanoparticles onto the resulting surface, are shown in Fig. 2, along with a spectrum for the precursor DMSO–K. In DMSO–K, the two peaks characteristic of the asymmetric location of DMSO within the interlayer spaces of kaolinite are clearly observed at 43.9 and 42.8 ppm.[29] These peaks are absent in the spectrum of AMPD–K, confirming the complete removal of DMSO upon grafting of AMPD. For AMPD–K, the expected signals characterizing AMPD are observed with chemical shifts close to those observed in solution. To further test the chemical stability of the organo-modified kaolinite during the reaction of deposition of gold nanoparticles, the ^{13}C CP/MAS NMR spectra were recorded after deposition of gold. They are essentially identical to the one before decoration with gold, which confirms that the organo-kaolinite is not decomposed.

X-ray photoelectron spectroscopy

XPS was used to check the oxidation state of the gold nanoparticles deposited at the external surface of kaolinite. The XPS spectrum of the Au 4f region of the gold nanohybrid material is shown in Fig. 3. This region shows two peaks, owing to the Au $4f_{7/2}$ and Au $4f_{5/2}$ transitions. The Au $4f_{7/2}$ peak appears at a binding energy of 82.6 eV and the Au $4f_{5/2}$ peak appears at a binding energy of 86.0 eV. They correspond to the formation of gold in a metallic state.[32–34]

Transmission electron microscopy

Figure 4 displays TEM micrographs of unmodified kaolinite. Well-defined pseudohexagonal crystals could be observed. The average equivalent diameter of these crystals is about 100–500 nm. Figure 5 shows the micrograph of gold nanoparticles deposited on unmodified kaolinite. The existence of gold nanoparticles on the external surface of kaolin-

Can. J. Chem. Downloaded from www.nrcresearchpress.com by Xi'an Jiaotong University on 09/19/12
For personal use only.

Fig. 3. X-ray photoelectron spectra of gold nanoparticles deposited at the external surface of modified kaolinite, with amplification of the region Au 4f.

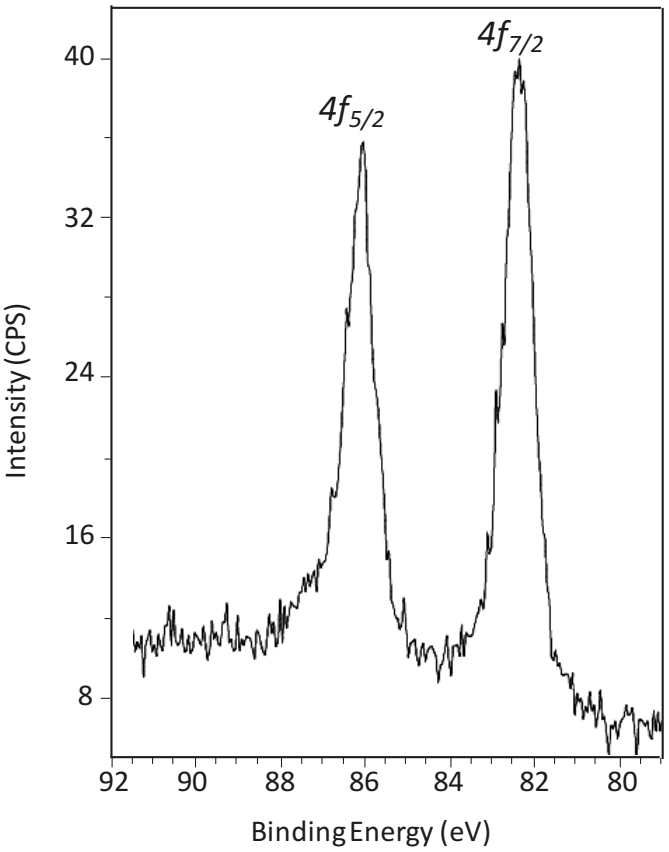

ite is supported by detection of dark spots and confirmed by in situ energy-dispersive X-ray spectrometry (EDXS) measurement. The gold loading is low and the gold particles are not homogenously dispersed throughout the kaolinite. This is evident in Fig. 5 in which large gold agglomerates having an average particle size on the order of 90 nm are clearly visible. TEM of gold nanoparticles prepared using DMSO–K as starting material are presented in Fig. 6. Regions of this micrograph are identical to pure kaolinite, which indicates that no gold was retained on the external surfaces. In other regions, the presence of gold nanoparticles with a broad size distribution could be observed (15–60 nm). TEM images as well as the particle size distribution of the gold nanoparticles prepared using AMPD–K as starting material are presented in Fig. 7. In this case, the Au nanoparticles cover all the surfaces of kaolinite. They are homogeneously scattered, not agglomerated, and characterized by a narrow size distribution (diameter $\leq$ 6 nm), with more than 88% of the resulting gold nanoparticles having diameters less than 4 nm. Several different regions within the sample were analyzed and no evidence of agglomeration of the gold nanoparticles was observed. Grafting of AMPD on the interlayer aluminol surfaces of kaolinite has a dramatic effect on the size of the gold nanoparticles. The same behaviour was observed in the preparation of Pd nanoparticles from reduction of $Pd(OAc)_2$ by ethanolamine ($HOCH_2CH_2NH_2$) at room temperature.[34] Similarly, it is expected that the two functions of AMPD are necessary for the formation of the nanoparticles. On one

Fig. 4. High-resolution micrograph of kaolinite showing single crystals.

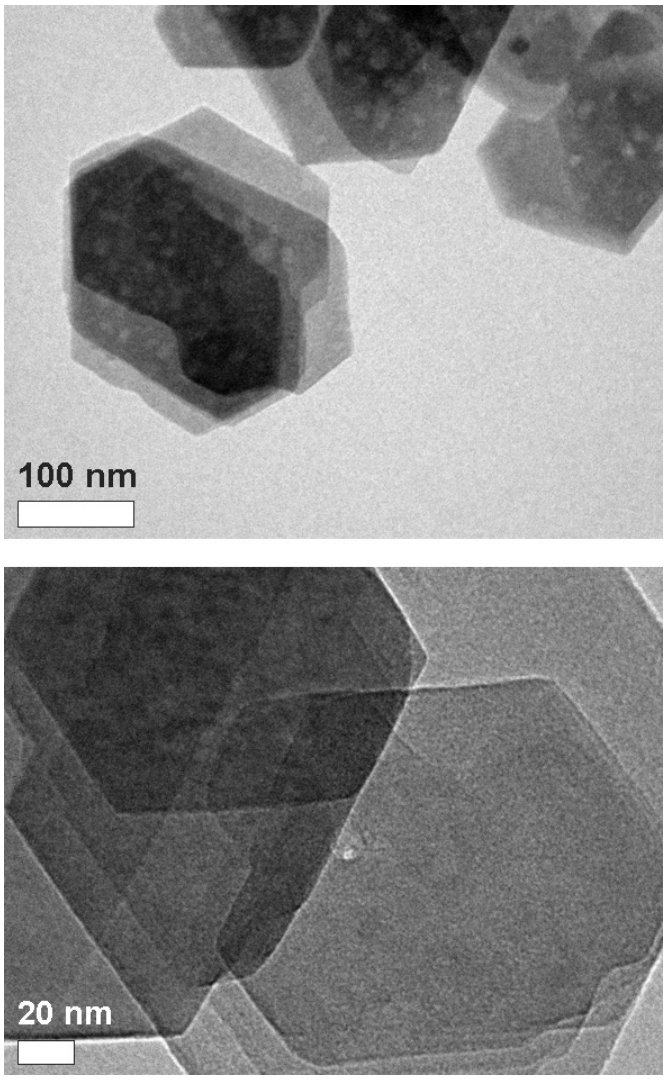

Fig. 5. TEM images of gold nanoparticles deposited at the external surface of pure kaolinite (K).

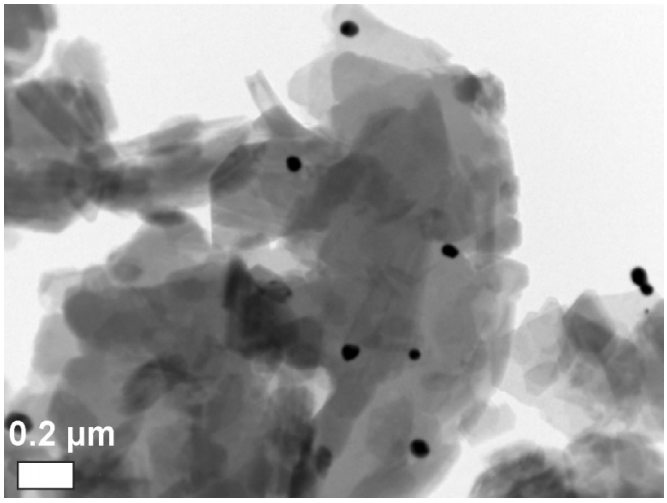

Can. J. Chem. Downloaded from www.nrcresearchpress.com by Xi'an Jiaotong University on 09/19/12
For personal use only.

Fig. 6. Top: HRTEM images of gold nanoparticles deposited at the external surface of kaolinite preintercalated with DMSO (DMSO–K). Bottom: Distribution of the gold nanoparticles.

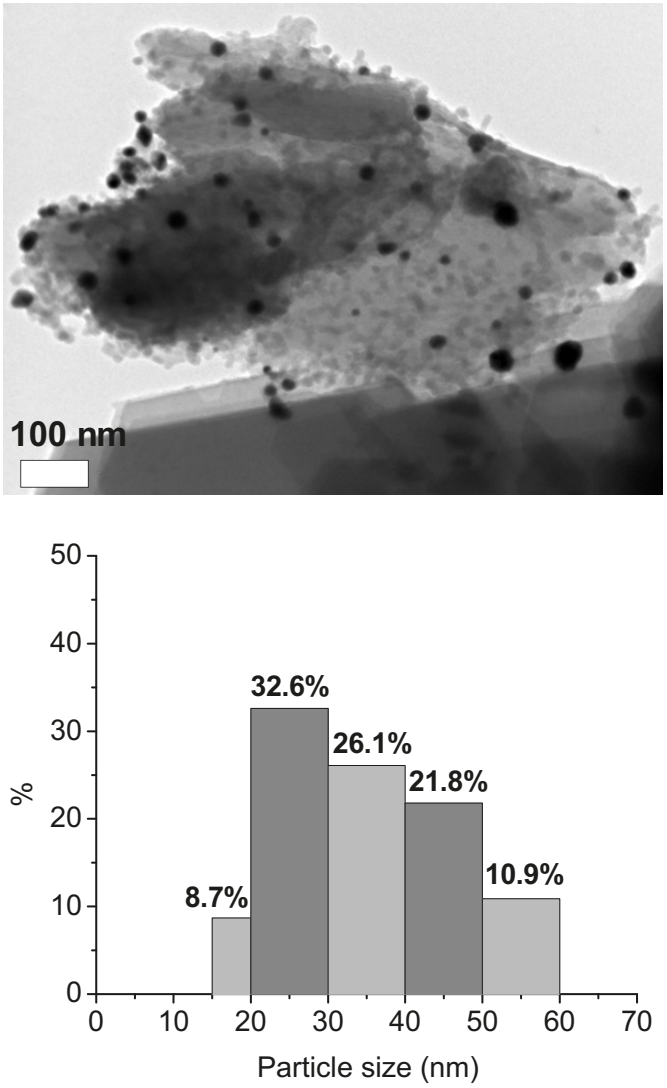

Fig. 7. Top: HRTEM images of gold nanoparticles deposited at the external surface of the organo-modified kaolinite (AMPD–K). Bottom: Distribution of the gold nanoparticles.

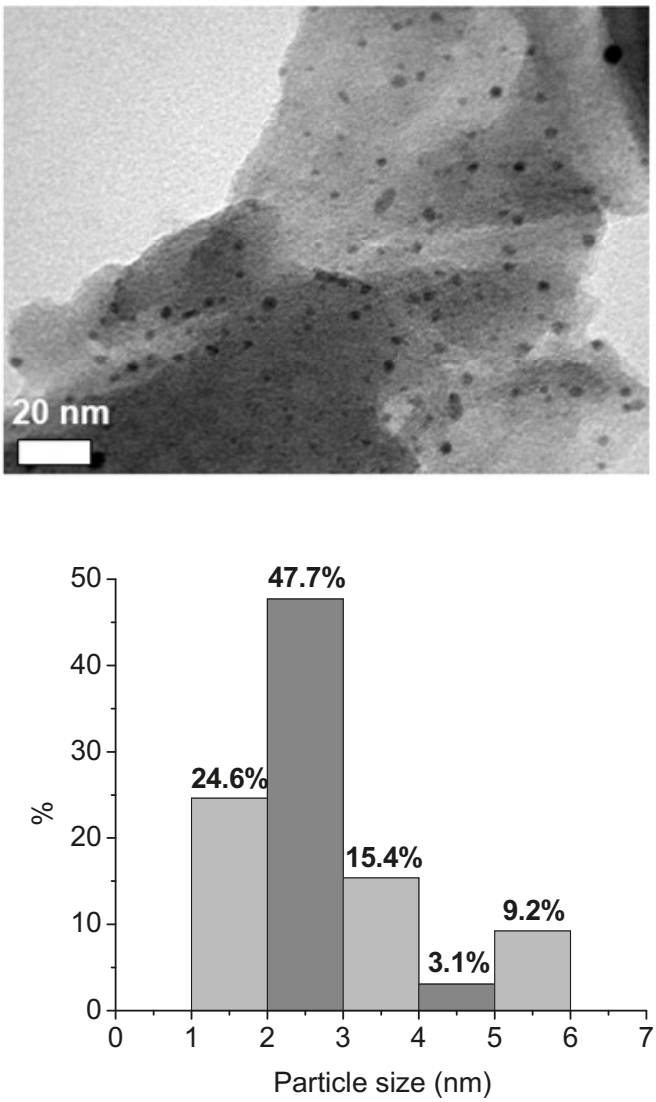

hand, the hydroxyl groups, which are not grafted to the aluminol surfaces, can serve as reducing agents. On the other hand, the amine groups protect gold nanoparticles from undesirable growth and aggregation via chemical interaction between Au and NH_2,[11,35–39] similarly to what has been reported in the case of Pd[35–38] and NH_2 interactions.[39–43]

Thermal gravimetric analyses

The thermal decomposition of the pristine kaolinite and of the resulting materials was studied by conventional thermal methods: TGA and DTA. In the case of kaolinite, two weight losses are observed (Fig. 8). The first weight loss observed below 60 °C corresponds to the loss of water adsorbed on the external surfaces. The second one observed around 518 °C is due to the dehydroxylation of kaolinite during the transformation of kaolinite to metakaolinite. In the case of AMPD–K, the TGA traces are mainly characterized by different weight losses. The first one at low temperature (below 100 °C) is due to the removal of water adsorbed on the external surfaces. The second one between 200 and 400 °C corresponds to the decomposition of the organic material. The third one observed at 427 °C is due to the dehydroxylation of kaolinite. Finally, the last one, observed around 560 °C, is due to the removal of remaining organic moieties. A significant decrease of the dehydroxylation temperature of AMPD–K (427 °C) compared with 518 °C for kaolinite was observed. This decrease of temperature is an indication that AMPD is grafted to the aluminol groups.[44] On the basis of the percentage of weight loss of water and organics leading to the formation of metakaolinite, the TGA data allow the calculation of the formula unit of AMPD–K as $Al_2Si_2O_5(OH)_4(AMPD)_{0.90}$. After deposition of AuNP, the evolution of the TGA curve of the Au–AMPD–K kaolinite is identical to the AMPD–K, indicating that the clay lattice was not modified during the reaction of deposition of the gold nanoparticles. Taking into account the total weight loss of AMPD–K and of Au–AMPD–K, one can calculate the amount of gold loaded on the nanohybrid material. It is close to 8.7%. The actual loading

Can. J. Chem. Downloaded from www.nrcresearchpress.com by Xi'an Jiaotong University on 09/19/12
For personal use only.

Fig. 8. Thermal gravimetric analysis patterns of (*a*) pure kaolinite (K), (*b*) kaolinite intercalated with DMSO (DMSO–K), (*c*) kaolinite grafted with 2-amino-2-methyl-1,3-propanediol (AMPD–K), and (*d*) kaolinite supported gold nanoparticles (AuNP–AMPD–K).

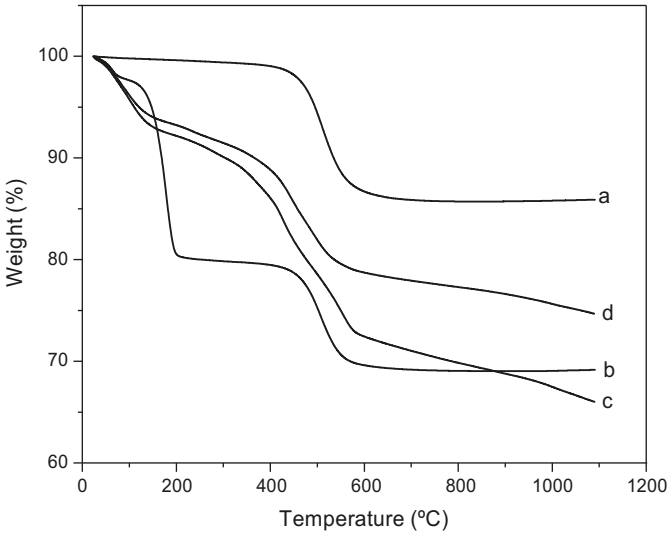

is marginally lower than that of the precursor materials (10%) indicating that a nominal portion of the gold precursor was displaced during washing.

Oxidation of carbon monoxide

Supported Au nanoparticles have been identified as suitable catalysts for carbon monoxide oxidation.[45,46] The use of kaolinite as a structural support of the gold nanocatalyst for CO oxidation was studied in a series of cyclic voltammetry experiments. Results are presented in Fig. 9 for (*a*) bare GCE, (*b*) kaolinite coated GCE without Au nanoparticles, and (*c*) Au–AMPD–K in the absence of carbon monoxide. No evidence of a faradic reaction is observed over the potential range of 0.8–1.4 V. In this potential region, only double layer charging at the electrode surface was observed. Above 1.4 V, oxygen evolution occurs at all electrodes. Similarly, in Fig. 10 the cyclic voltammograms are presented for the same electrodes in the presence of carbon monoxide. The CV response at the glassy carbon and kaolinite electrodes in the presence of carbon monoxide are identical to those in the absence of CO (compare with Fig. 9*b* and Fig. 10*a*). The Au–AMPD–K electrode shows markedly different response in the presence of CO. The potential was initially scanned from 0.9 V (RHE) in the positive direction to 1.7 V (RHE). Again, oxygen evolution was observed at potentials positive of 1.4 V; on the reversal of potential, a well-defined oxidation peak was observed in the potential range of 1.0–1.15 V (associated with oxidation of CO). This peak was found to increase upon repeated cycling into the oxygen evolution regime. Similar "activation" of supported Au catalysts has been reported in the literature.[32,47,48]

Conclusion

This work shows the potential of an abundant naturally occurring clay mineral, kaolinite, for the use in the development of novel advanced materials for heterogeneous catalysis of oxidation reactions. Kaolinite was intercalated by a bifunctional organic molecule, 2-amino-2-methyl-1,3-propanediol (AMPD), which was grafted on the internal and external surfaces of kaolinite fine particles. The hydroxyl functions have a dual function: (*i*) reacting with aluminol groups resulting in the grafting of the organic units and (*ii*) serving as reducing agent. The amino functions protect gold nanoparticles from undesirable growth and aggregation via chemical interaction between Au and NH_2. While the deposition of gold on unmodified kaolinite and on DMSO intercalated kaolinite lead to relatively large gold particles inhomogeneously dispersed on the solid, the situation was dramatically different in the case of the AMPD grafted kaolinite nanohybrid material, in which case gold nanoparticles were obtained with a narrow size distribution (diameter $\leq$ 6 nm) and with more than 88% of the resulting gold nanoparticles having diameters less than 4 nm. This material was coated on GCEs and studied in a

Fig. 9. Steady state cyclic voltammograms obtained at 50 mV s^{-1} at (*a*) the bare glassy carbon electrode (GCE) in 0.5 mol/L KOH, (*b*) the bare GCE coated with a thin film of purified kaolinite in 0.5 mol/L KOH, and (*c*) the bare GCE coated with a thin film of Au–AMPD–K in 0.5 mol/L KOH.

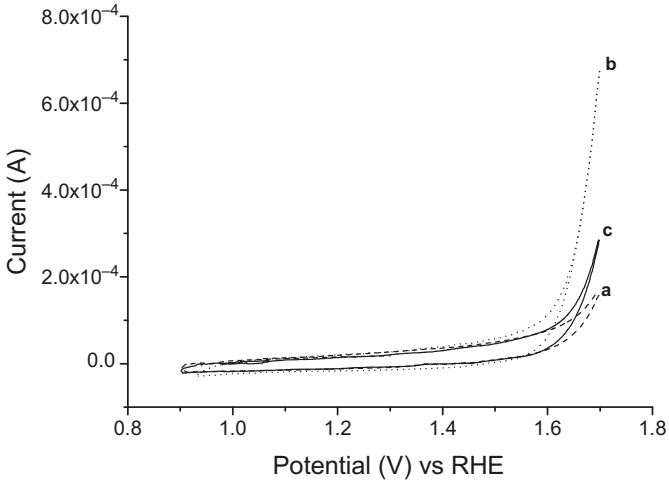

Fig. 10. Steady state cyclic voltammograms obtained at 50 mV s^{-1} at (*a*) the bare glassy carbon electrode (GCE) in 0.5 mol/L KOH in the presence of CO and (*b*) the bare GCE coated with a thin film of AuNP–AMPD–K in 0.5 mol/L KOH in the presence of CO.

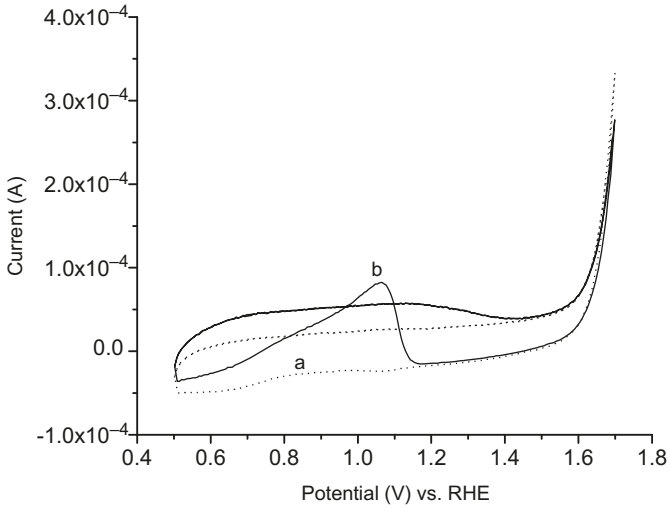

Can. J. Chem. Downloaded from www.nrcresearchpress.com by Xi'an Jiaotong University on 09/19/12
For personal use only.

series of cyclic voltammetry experiments, which showed a well-defined oxidation peak in the potential range of 1.0–1.15 V (associated with oxidation of CO).

Acknowledgements

This paper is in honour of the outstanding career contributions of Professor Rod Wasylishen to the chemical sciences in general and particularly to the field of nuclear magnetic resonance. This work was financially supported by a Discovery Grant of the Natural Sciences and Engineering Research Council of Canada (NSERC). The Canada Foundation for Innovation and the Ontario Research Fund are gratefully acknowledged for infrastructure grants to the Center for Catalysis Research and Innovation. Dr. Glenn A. Facey is thanked for recording the NMR spectra, Dr. Yun Liu for help in TEM microscopy measurements, and Dr. A. Mommers for the XPS measurements.

References

(1) (a) Hashmi, A. S. K. *Chem. Rev.* **2007**, *107* (7), 845. doi:10.1021/cr000436x;; (b) Daniel, M. C.; Astruc, D. *Chem. Rev.* **2004**, *104* (1), 293. doi:10.1021/cr030698+.

(2) Letaief, S.; Liu, Y.; Detellier, C. *Can. J. Chem.* **2011**, *89* (3), 280. doi:10.1139/V10-142.

(3) Okumura, M.; Nakamura, S.; Tsubota, S.; Nakamura, T.; Azuma, M.; Haruta, M. *Catal. Lett.* **1998**, *51* (1–2), 53. doi:10.1023/A:1019020614336.

(4) Chou, J.; Franklin, N. R.; Baeck, S. H.; Jaramillo, T. F.; McFarland, E. W. *Catal. Lett.* **2004**, *95* (3–4), 107. doi:10.1023/B:CATL.0000027282.20003.08.

(5) (a) Gluhoi, A. C.; Bogdanchikova, N.; Nieuwenhuys, B. E. *J. Catal.* **2005**, *229* (1), 154. doi:10.1016/j.jcat.2004.10.003;; (b) Thompson, D. T. *Top. Catal.* **2006**, *38* (4), 231. doi:10.1007/s11244-006-0021-x.

(6) (a) Ide, Y.; Fukuoka, A.; Ogawa, M. *Chem. Mater.* **2007**, *19* (5), 964. doi:10.1021/cm062117d;; (b) Ide, Y.; Matsuoka, M.; Ogawa, M. *J. Am. Chem. Soc.* **2010**, *132* (47), 16762. doi:10.1021/ja1083514.

(7) (a) Aihara, N.; Torigoe, K.; Esumi, K. *Langmuir* **1998**, *14* (17), 4945. doi:10.1021/la980370p;; (b) Nakamura, K.; Mori, Y. *J. Chem. Eng. Jpn.* **2001**, *34* (12), 1538. doi:10.1252/jcej.34.1538.

(8) Pecharromán, C.; Esteban-Cubillo, A.; Montero, I.; Moya, J. S.; Aguilar, E.; Santarén, J.; Alvarez, A. *J. Am. Ceram. Soc.* **2006**, *89* (10), 3043. doi:10.1111/j.1551-2916.2006.01190.x.

(9) Pecharromán, C.; Esteban-Cubillo, A.; Fernández, H.; Esteban-Tejeda, L.; Pina-Zapardiel, R.; Moya, J. S.; Solis, J.; Afonso, C. N. *Plasmonics* **2009**, *4* (4), 261. doi:10.1007/s11468-009-9101-7.

(10) Chen, C. C.; Kuo, P. L. *J. Colloid Interface Sci.* **2006**, *293* (1), 101. doi:10.1016/j.jcis.2005.06.051.

(11) Zhu, L.; Letaief, S.; Liu, Y.; Gervais, F.; Detellier, C. *Appl. Clay Sci.* **2009**, *43* (3–4), 439. doi:10.1016/j.clay.2008.10.004.

(12) Zhang, R.; Hummelgard, M.; Olin, H. *Langmuir* **2010**, *26* (8), 5823. doi:10.1021/la903747v.

(13) Newman, A. C. D.; Brown, G. The Chemical Constitution of Clays. In *Chemistry of Clays and Clay Minerals;* Newman, A. C. D., Ed.; Mineralogical Society: London, 1987.

(14) Bailey, S. W. *Hydrous Phyllosilicates;* American Mineralogical Society: Washington, DC, 1988**.**

(15) Bergaya, F.; Theng, B. K. G.; Lagaly, G. *Handbook of Clay Science;* Elsevier: Amsterdam, 2006.

(16) Grimshaw, R. W. *The Chemistry and Physics of Clays*, 4th ed.; Benn: London, 1971.

(17) Adžić, R. R.; Tripković, A. V.; Marković, N. M. *J. Electroanal. Chem. Interfacial Electrochem.* **1983**, *150* (1–2), 79. doi:10.1016/S0022-0728(83)80192-2.

(18) Lee, Y.; Loew, A.; Sun, S. *Chem. Mater.* **2010**, *22* (3), 755. doi:10.1021/cm9013046.

(19) Fu, Q.; Saltsbur, H.; Flytzani-Stephanopoulos, M. *Science* **2003**, *301* (5635), 935. doi:10.1126/science.1085721.

(20) Enache, D. I.; Edwards, J. K.; Landon, P.; Solsona-Espriu, B.; Carley, A. F.; Herzing, A. A.; Watanabe, M.; Kiely, C. J.; Knight, D. W.; Hutchings, G. J. *Science* **2006**, *311* (5759), 362. doi:10.1126/science.1120560.

(21) Hughes, M. D.; Xu, Y.-J.; Jenkins, P.; McMorn, P.; Landon, P.; Enache, D. I.; Carley, A. F.; Attard, G. A.; Hutchings, G. J.; King, F.; Stitt, E. H.; Johnston, P.; Griffin, K.; Kiely, C. J. *Nature* **2005**, *437* (7062), 1132. doi:10.1038/nature04190.

(22) Haruta, M.; Yamada, N.; Kobayashi, T.; Iijima, S. *J. Catal.* **1989**, *115* (2), 301. doi:10.1016/0021-9517(89)90034-1.

(23) Kung, M. C.; Davis, R. J.; Kung, H. H. *J. Phys. Chem. C* **2007**, *111* (32), 11767. doi:10.1021/jp072102i.

(24) Hayashi, T.; Tanaka, K.; Haruta, M. *J. Catal.* **1998**, *178* (2), 566. doi:10.1006/jcat.1998.2157.

(25) Schubert, M. M.; Hackenberg, S.; van Veen, A. C.; Muhler, M.; Plzak, V.; Behm, R. J. *J. Catal.* **2001**, *197* (1), 113. doi:10.1006/jcat.2000.3069.

(26) Calla, J. T.; Bore, M. T.; Datye, A. K.; Davis, R. J. *J. Catal.* **2006**, *238* (2), 458. doi:10.1016/j.jcat.2006.01.009.

(27) (a) Underwood, S.; Mulvaney, P. *Langmuir* **1994**, *10* (10), 3427. doi:10.1021/la00022a011;; (b) Link, S.; El-Sayed, M. A. *J. Phys. Chem. B* **1999**, *103* (40), 8410. doi:10.1021/jp9917648.

(28) (a) Letaief, S.; Detellier, C. *J. Mater. Chem.* **2005**, *15* (44), 4734. doi:10.1039/b511282f;; (b) Elbokl, T. A.; Detellier, C. *Can. J. Chem.* **2009**, *87* (1), 272. doi:10.1139/V08-142;; (c) Letaief, S.; Detellier, C. *J. Mater. Chem.* **2007**, *17* (15), 1476. doi:10.1039/b616922h;; (d) Tonlé, I. K.; Letaief, S.; Ngameni, E.; Detellier, C. *J. Mater. Chem.* **2009**, *19* (33), 5996. doi:10.1039/b907401e;; (e) Letaief, S.; Detellier, C. *Clays Clay Miner.* **2009**, *57* (5), 638. doi:10.1346/CCMN.2009.0570510.

(29) Hayashi, S. *Clays Clay Miner.* **1997**, *45* (5), 724. doi:10.1346/CCMN.1997.0450511.

(30) Tunney, J. J.; Detellier, C. *Clays Clay Miner.* **1994**, *42* (5), 552. doi:10.1346/CCMN.1994.0420506.

(31) Letaief, S.; Detellier, C. *Chem. Commun. (Camb.)* **2007**, 2613. doi:10.1039/b701235g.

(32) Jaramillo, T. F.; Baeck, S.; Cuenya, B. R.; McFarland, E. W. *J. Am. Chem. Soc.* **2003**, *125* (24), 7148. doi:10.1021/ja029800v.

(33) Wei, H.; Wang, E. *Nanotechnology* **2007**, *18* (29), 295603. doi:10.1088/0957-4484/18/29/295603.

(34) Casaletto, M. P.; Longo, A.; Martorana, A.; Prestianni, A.; Venezia, A. M. *Surf. Interface Anal.* **2006**, *38* (4), 215. doi:10.1002/sia.2180.

(35) Letaief, S.; Grant, S.; Detellier, C. *Appl. Clay Sci.* **2011**. In press.

(36) Wang, Z.; Zhang, Q.; Kuehner, D.; Ivaska, A.; Niu, L. *Green Chem.* **2008**, *10* (9), 907 . doi:10.1039/b806453a.

(37) Hu, J.; Wang, Z.; Li, J. *Sensors* **2007**, *7* (12), 3299. doi:10.3390/s7123299.

(38) Lee, S. H.; Bae, K. H.; Kim, S. H.; Lee, K. R.; Park, T. G. *Int. J. Pharm.* **2008**, *364* (1), 94. doi:10.1016/j.ijpharm.2008.07.027.

(39) Sainsbury, T.; Ikuno, T.; Okawa, D.; Pacile, D.; Frechet, J. M.; Zettl, A. *J. Phys. Chem. C* **2007**, *111* (35), 12992. doi:10.1021/jp072958n.

(40) Chen, F.; Zhong, Z.; Xu, X.-J.; Luo, J. *J. Mater. Sci.* **2005**, *40* (6), 1517 . doi:10.1007/s10853-005-0595-x.
(41) Garcia-Martinez, J.; Linares, N.; Sinibaldi, S.; Coronado, E.; Ribera, A. *Microporous Mesoporous Mater.* **2009**, *117* (1–2), 170. doi:10.1016/j.micromeso.2008.06.038.
(42) Okeya, S.; Sazaki, H.; Ogita, M.; Takemoto, T.; Onuki, Y.; Nakamura, Y.; Mohapatra, B. K.; Kawaguchi, S. *Bull. Chem. Soc. Jpn.* **1981**, *54* (7), 1978. doi:10.1246/bcsj.54.1978.
(43) Guin, D.; Baruwati, B.; Manorama, S. V. *Org. Lett.* **2007**, *9* (7), 1419. doi:10.1021/ol070290p.
(44) Letaief, S.; Detellier, C. *Can. J. Chem.* **2008**, *86* (1), 1. doi:10.1139/V07-130.
(45) Jia, C.-J.; Liu, Y.; Bongard, H.; Schüth, F. *J. Am. Chem. Soc.* **2010**, *132* (5), 1520. doi:10.1021/ja909351e.
(46) Koga, H.; Kitaoka, T.; Wariishi, H. *J. Mater. Chem.* **2009**, *19* (29), 5244. doi:10.1039/b905818d.
(47) Geng, D.; Lu, G. *J. Nanopart. Res.* **2007**, *9* (6), 1145. doi:10.1007/s11051-007-9210-1.
(48) Choudhary, T. V.; Goodman, D. W. *Top. Catal.* **2002**, *21* (1–3), 25. doi:10.1023/A:1020595713329.

Can. J. Chem. Downloaded from www.nrcresearchpress.com by Xi'an Jiaotong University on 09/19/12
For personal use only.

Investigation of the disorder of dibromo- and dichloromethane in their tri-*ortho*-thymotide clathrates using X-ray diffraction and solid-state ^{2}H NMR spectroscopy

Glenn A. Facey and Ilia Korobkov

Can. J. Chem. Downloaded from www.nrcresearchpress.com by Xi'an Jiaotong University on 09/19/12
For personal use only.

Abstract: The tri-*ortho*-thymotide (TOT) clathrates of dibromo- and dichloromethane were characterized by single crystal X-ray diffraction at 200 K and solid-state ^{2}H NMR spectroscopy as a function of temperature. The host structure was found to be typical of other cage-type TOT clathrates. The X-ray results showed a substantial amount of disorder among the guest molecules. In both clathrates, multiple guest molecule positions could be modeled. The heavy atoms of all the guest molecule positions lie approximately in the same plane, with some out-of-plane distortion. The guest molecules were of two different types in positions symmetric about the crystallographic twofold rotation axis: type A guests, with carbon atoms well removed from the crystallographic twofold axis, and type B guests, with carbon atoms very close to the twofold axis. The ^{2}H NMR spectra for the guests confirmed that the disorder was dynamic. The experimental results could be accounted for by the presence of three simultaneous types of molecular motion, all fast with respect to the ^{2}H quadrupolar interaction: (*i*) twofold molecular flips about the molecular C_2 symmetry axis, (*ii*) exchange between the type A and type B sites in a single plane, and (*iii*) a two-site libration of the plane containing the heavy atoms of the A and B guest sites with a temperature-dependent amplitude.

Key words: tri-*ortho*-thymotide, ^{2}H NMR, dibromomethane, dichloromethane, clathrate.

Résumé : On a caractérisé les clathrates de tri-*ortho*-thymotide (TOT) avec du dibromo- et du dichlorométhane en faisant appel à la diffraction des rayons-X sur un cristal unique à 200 K et par spectroscopie RMN du ^{2}H à l'état solide en fonction de la température. On a trouvé que la structure hôte est typique des autres clathrates TOT de type cage. Les résultats de la diffraction des rayons-X permettent d'observer une quantité importante de désordre parmi les molécules invitées. Dans les deux clathrates, il a été possible de faire des modèles de nombreuses positions des molécules invitées. Les atomes lourds de toutes les positions de la molécule sont approximativement dans le même plan, avec un peu de distorsion en dehors de ce plan. On a observé deux types différents de molécules invitées dans des positions symétriques autour de l'axe de rotation cristallographique binaire : les invitées de type A pour lesquelles les atomes de carbone sont éloignés de l'axe cristallographique binaire et les invitées de type B pour lesquelles les atomes de carbone sont très près de l'axe cristallographique binaire. Les spectres RMN du ^{2}H des molécules invitées confirment que le désordre est dynamique. Les résultats expérimentaux peuvent être expliqués par la présence de trois types simultanés de mouvements moléculaires, tous rapides par rapport à l'interaction ^{2}H quadripolaire : (*i*) des inversions moléculaires binaires autour de l'axe de symétrie moléculaire C_2, (*ii*) un échange entre les sites de type A et de type B dans un seul plan et (*iii*) une libration sur deux sites du plan contenant les atomes lourds des sites invités A et B avec une amplitude qui varie avec la température.

Mots-clés : tri-*ortho*-thymotide, RMN du ^{2}H, dibromométhane, dichlorométhane, clathrate.

[Traduit par la Rédaction]

Introduction

Inclusion compounds have generated a great deal of interest over the years for their applications in the pharmaceutical, agricultural, environmental, and food industries. Solid inclusion compounds consist of a host material and a guest material. There are several types, including those with ionic and neutral guest molecules. The hosts can be comprised of tunnels, cages, or both. Tri-*ortho*-thymotide (TOT, **1**) is the trimeric lactone of *ortho*-thymotic acid and is a versatile organic host material forming inclusion compounds with many guest molecules.[1–12] It is able to form both channel- and cage-type inclusion compounds.[13] In the solid state, the TOT molecules can adopt a helical conformation where two of the three carbonyl bonds in the macrocyclic ring point in

Received 26 October 2010. Accepted 28 November 2010. Published at www.nrcresearchpress.com/cjc on 7 July 2011.

G.A. Facey and I. Korobkov. Department of Chemistry, University of Ottawa, 10 Marie Curie Private, Ottawa, ON K1N 6N5, Canada.

Corresponding author: G.A. Facey (e-mail: gafacey@uottawa.ca)

This article is part of a Special Issue dedicated to Professor Roderick E. Wasylishen.

Can. J. Chem. Downloaded from www.nrcresearchpress.com by Xi'an Jiaotong University on 09/19/12
For personal use only.

one direction and the third points in the opposite direction. This conformation is present in the channel-type inclusion compounds. TOT molecules can also adopt propeller conformations where all three carbonyl groups point in the same direction. It is the propeller conformations of the host molecules that are present in the cage type inclusion compounds. It is primarily the guest molecule that determines the type of inclusion compound formed. Guests with an overall length exceeding ~9.5 Å will form channel type inclusion compounds, whereas those guests whose overall lengths are less than ~9.5 Å form cage type inclusion compounds, although there are a few exceptional cases where channel TOT inclusion compounds of small molecules are known.[10,11] The cages are comprised of eight TOT molecules and have been described as distorted ellipsoids with C_2 crystallographic symmetry.[12] The dimensions of the cages are ~7.0 Å × ~6.1 Å × ~5.2 Å and they are lined primarily with the methyl and isopropyl groups of the host with two carbonyl oxygens at one end. The propeller conformation of the TOT molecules forming the cage-type inclusion compounds can have either a left-hand or a right-hand pitch and therefore possess chirality. Furthermore, optical resolution of each of the two types of propellers is accomplished simply by recrystallization. Each TOT–guest crystal contains either all left-handed or all right-handed propellers. The presence of chiral host molecules leads to the void spaces also having chirality, making TOT cage-type inclusion compounds chirally selective towards racemic guests. This has generated a great deal of interest.[1–4,7,8,11,14–19] Also, the chiral TOT cages containing prochiral guest molecules render the prochiral groups of the guest diastereotopic and therefore nonequivalent.[20]

Guests trapped in confined spaces have the properties of neither their bulk material nor the bulk host material. It has been shown that for many inclusion compounds the guest molecules exhibit a great deal of dynamic behaviour, complicating the determination of the structure by single crystal X-ray diffraction methods. Sometimes the guest molecules cannot be located at all.[7] Dynamic disorder of the guest leads to smeared out electron density distributions, as the time scale of the diffraction experiment is hours compared with the wide range of much shorter motional correlation times for guest molecules. In such cases the refinement of the X-ray structure depends on modelling the disorder of the guest. There are cases where a guest molecule can undergo symmetric reorientations and this motion (by way of its symmetry) can go undetected by diffraction methods.[21] An example of this is the twofold reorientation of acetone in its TOT clathrate about its carbonyl bond.[22] Guest molecules can also exhibit static disorder, where the immobile rigid guest molecule can occupy a number of possible sites. As in the case of dynamic disorder, modelling is required in refining the X-ray structure. X-ray diffraction methods are unable to distinguish between dynamic and static disorder. Solid-state NMR spectroscopy, on the other hand, is very sensitive to dynamics on time scales of the same order as or shorter than the reciprocal of the span of the NMR interaction being observed. One of the proven methods for characterizing molecular motion is solid-state ^{2}H NMR spectroscopy. Using both X-ray diffraction and solid-state NMR techniques is essential for developing models to explain the observed disorder. In this work we employ both X-ray diffraction and wide line ^{2}H NMR spectroscopy to study the cage-type TOT–dibromomethane and TOT–dichloromethane inclusion compounds with the goal of characterizing the dynamic disorder of the guest molecules.

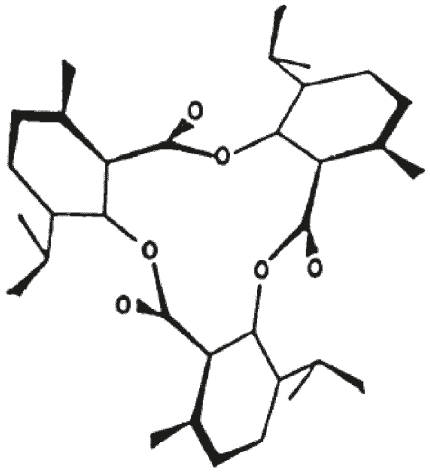

1

Background

Solid-state ^{2}H nuclear magnetic resonance spectroscopy (NMR) is an extremely sensitive technique for characterizing the molecular motion of molecules. ^{2}H is a spin $I = 1$ nucleus having three Zeeman energy levels perturbed by the electric quadrupolar interaction resulting in each crystallographically unique deuteron having two resonance frequencies. The separation between the resonances depends on the quadrupolar coupling constant ($\chi = e^2Qq/h$), where eQ is the electric quadrupole moment, eq is the electric field gradient at the nuclear site, and h is Planck's constant, and the orientation of the electric field gradient tensor ($\mathbf{V_{ij}}$) at the nuclear site with respect to the externally applied magnetic field. $\mathbf{V_{ij}}$ is traceless and symmetric. In its principal axis system, it is diagonal and characterized by its three principal components V_{xx}, V_{yy}, and V_{zz} ($|V_{zz}| > |V_{yy}| \geq |V_{xx}|$). For deuterons in C–D bonds the largest component, V_{zz}, lies along the C–D bond. In powdered samples, where all orientations of the electric field gradient tensor with respect to the magnetic field are represented, each unique deuteron will give rise to a powder pattern similar to the ones shown in Fig. 1. The spectra have a characteristic shape consisting of three pairs of features $\Delta\upsilon_{xx}$, $\Delta\upsilon_{yy}$, and $\Delta\upsilon_{zz}$, which are proportional to V_{xx}, V_{yy}, and V_{zz}, respectively. The asymmetry parameter (η) is defined by $(\Delta\upsilon_{yy} - \Delta\upsilon_{xx})/\Delta\upsilon_{zz}$ and can take on values between 0 and 1. When a molecular motion occurs on a time scale of the same order as $1/\chi$, the line shapes are distorted compared with those in Fig. 1 and contain a great deal of information about the mechanism and rate of the motion.[23] When a molecular motion is fast with respect to $1/\chi$, an averaged electric field gradient tensor ($\mathbf{a_{ij}}$) is produced. To calculate $\mathbf{a_{ij}}$, one must first define the components of each of the $\mathbf{V_{ij}}$ visited over the course of the motion in a common axis system defined by the axis of the molecular motion. The components of each $\mathbf{V_{ij}}$ are then expressed in terms of the Euler angles[24] α, β, and γ, relating them to the common axis system. The components of $\mathbf{a_{ij}}$ are calculated by taking

Can. J. Chem. Downloaded from www.nrcresearchpress.com by Xi'an Jiaotong University on 09/19/12
For personal use only.

Fig. 1. Examples of line shapes for ^{2}H NMR spectra for either rigid molecules or molecules undergoing motions fast with respect to the reciprocal quadrupolar coupling constant $1/\chi$. The separations between the features in the spectra ($\Delta\upsilon_{xx}$, $\Delta\upsilon_{yy}$, and $\Delta\upsilon_{zz}$) are proportional to the principal components of the electric field gradient tensor.

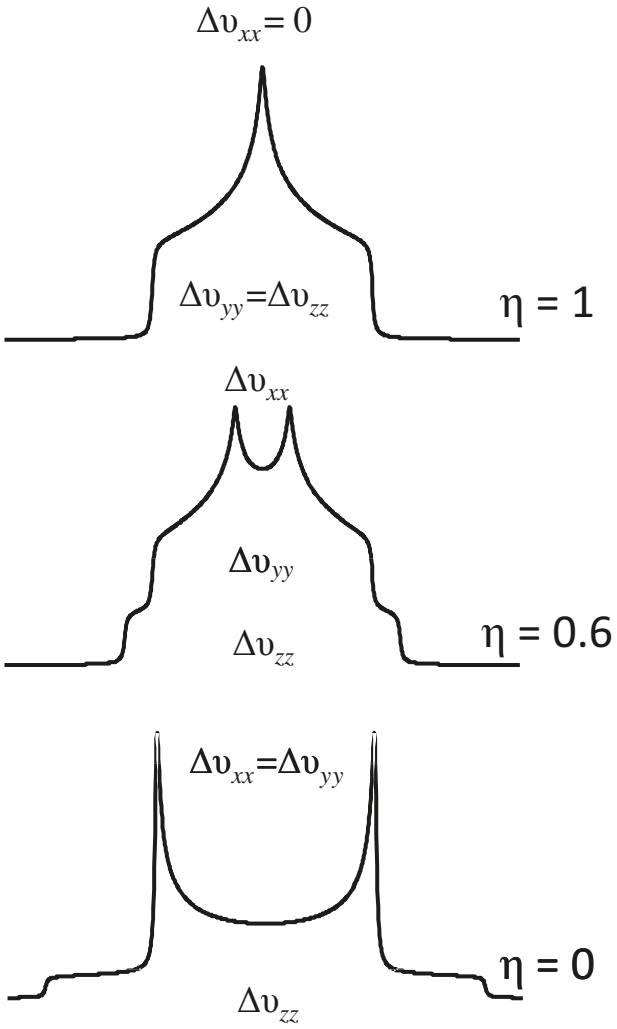

the population weighted average of each of the components of $\mathbf{V_{ij}}(\alpha, \beta, \gamma)$ visited over the course of the motion. The averaged tensor is then diagonalized, if necessary, yielding the three principal components a_{11}, a_{22}, and a_{33}. If the motion is symmetric $\mathbf{a_{ij}}$ will have one of its principal components along the axis of molecular rotation. The time-averaged ^{2}H NMR spectrum will be defined by $\mathbf{a_{ij}}$ rather than $\mathbf{V_{ij}}$; hence, the frequency separation between features in the averaged spectrum, $\Delta\upsilon'_{xx}$, $\Delta\upsilon'_{yy}$, and $\Delta\upsilon'_{zz}$, will be proportional to the principal components of $\mathbf{a_{ij}}$. The spectra will still retain the same general shapes as those depicted in Fig. 1. If more than one mode of fast molecular motion occurs, this averaging technique is applied in series. One first calculates $\mathbf{a_{ij}}$ as an average of $\mathbf{V_{ij}}(\alpha_1, \beta_1, \gamma_1)$ for the first motion and then $\mathbf{a_{ij}}'$ as an average of $\mathbf{a_{ij}}(\alpha_2, \beta_2, \gamma_2)$ for the second motion, etc.

Experimental section

TOT was purchased from Sigma-Aldrich and used without further purification. Dibromomethane-d_2 and dichloromethane-d_2 were purchased from CDN Isotopes (Pointe-Claire, Quebec) and used as received. The isotopic purities were reported to be 99.4% and 99.9%, respectively. The clathrates used for the ^{2}H NMR studies were prepared by dissolving TOT in CD_2Br_2 or CD_2Cl_2 and allowing for slow evaporation over the course of several days. The crystals of TOT–CH_2Br_2 and TOT–CH_2Cl_2 were grown by dissolving TOT in the respective solvent and allowing for slow evaporation.

The X-ray diffraction results for TOT–CH_2Cl_2 and TOT–CH_2Br_2 represent the best data sets obtained from several trials for each sample. The crystals were mounted on thin glass fibers using paraffin oil and cooled to 200.15 K. Data were collected on a Bruker AXS SMART single crystal diffractometer equipped with a sealed Mo tube source (wavelength 0.710 73 Å) APEX II CCD detector. Data for both samples were collected with a sequence of 0.5° ω scans at 0°, 120°, and 240° in φ. Initial unit cell parameters were determined from 60 data frames collected at the different sections of the Ewald sphere. Semiempirical absorption corrections based on equivalent reflections were applied.[25] Systematic absences in the diffraction data set and unit cell parameters were consistent with trigonal space group $P3_221$ for both TOT–CH_2Cl_2 and TOT–CH_2Br_2. Solutions in the centrosymmetric space groups yielded chemically reasonable and computationally stable results on refinement. The structures were solved by direct methods, completed with difference Fourier synthesis, and refined with full-matrix least-squares procedures based on F^2. All non-hydrogen atoms were refined with anisotropic displacement coefficients. All hydrogen atoms were treated as idealized contributions. All scattering factors are contained in several versions of the SHELXTL program library, with the latest version used being v.6.12.[26] Crystallographic data and selected data collection parameters are reported in Table 1.

The ^{2}H NMR data for the TOT–CD_2Br_2 clathrate were collected on a Bruker AVANCE III 200 operating at 30.7 MHz for ^{2}H using a 5 mm solenoid probe. The quadrupolar echo technique[27] was used with 90° pulses of 4.3 μs and an interpulse delay of 20 μs. The delay following the second pulse was set to 8 μs and the data were left-shifted to the top of the echo. A 1 MHz spectral width was employed and 1024 data points were collected. The recycle time was set to 2 s. Typically, 1024 scans were collected. The ^{2}H NMR data for the TOT–CD_2Cl_2 clathrate were collected on a Bruker AVANCE III 400 NMR spectrometer operating at 61.4 MHz for ^{2}H using a 10 mm solenoid probe. The quadrupolar echo technique was used with 90° pulses of 3.25 μs and an interpulse delay of 35 μs. The delay following the second pulse was set to 12 μs and the data were left-shifted to the top of the echo. A 1 MHz spectral width was employed and 1024 data points were collected. The recycle time was set to 2 s. Typically, between 3000 and 10 000 scans were collected and signal averaged. On both instruments, dry boil-off nitrogen gas was used to cool the sample and the temperature was regulated with the probe heater using the Bruker variable temperature control unit. All free induction decays were treated with 200 Hz of exponential line broadening before Fourier transformation. The Fourier transformed spectra were then symmetrized. All simulations of ^{2}H NMR spectra were performed using the online utility, NMR Weblab version 4.3.2.[28]

Can. J. Chem. Downloaded from www.nrcresearchpress.com by Xi'an Jiaotong University on 09/19/12
For personal use only.

Table 1. Crystallographic data and selected data collection parameters.

Parameter	TOT–CH_2Cl_2	TOT–CH_2Br_2
Empirical formula	$C_{33.42}H_{36.83}Cl_{0.83}O_6$	$C_{33.43}H_{36.86}Br_{0.86}O_6$
Formula weight	564.00	603.37
Crystal size (mm)	0.27×0.25×0.13	0.27×0.17×0.17
Crystal system	Trigonal	Trigonal
Space group	$P3_221$	$P3_221$
Z	6	6
a (Å)	13.3927(6)	13.4346(11)
b (Å)	13.3927(6)	13.4346(11)
c (Å)	29.9391(13)	29.998(3)
α (°)	90	90
β (°)	90	90
γ (°)	120	120
Volume (Å^3)	4650.6(4)	4688.9(7)
Calculated density (Mg/m^3)	1.208	1.282
Absorption coefficient (mm^{-1})	0.151	1.178
F(000)	1797	1893
Θ range for data collection (°)	1.88–28.30	1.88–28.32
Limiting indices	$h = \pm17$, $k = \pm14$, $l = \pm25$	$h = \pm17$, $k = \pm17$, $l = \pm33$
Reflections, collected/unique	35 155 / 7 653	71 763 / 7 689
R(int)	0.0402	0.0367
Completeness to Θ = 28.32	99.2%	98.9%
Max. and min. transmission	0.9807 and 0.9605	0.8249 and 0.7416
Data/restraints/parameters	7653/40/415	7689/15/442
Goodness-of-fit on F^2	1.006	1.008
Final R indices [$I > 2\sigma(I)$]	$R_1 = 0.0473$, $wR_2 = 0.1125$	$R_1 = 0.0397$, $wR_2 = 0.0973$
R indices (all data)	$R_1 = 0.0778$, $wR_2 = 0.1286$	$R_1 = 0.0565$, $wR_2 = 0.1058$
Absolute structure parameter	0.00(15)	–0.011(7)
Largest diff. peak and hole (e Å^{-3})	0.219 and –0.260	0.326 and –0.178

Note: TOT, tri-*ortho*-thymotide.

Results and discussion

A summary of the X-ray data for the TOT–CH_2Br_2 and TOT–CH_2Cl_2 2:1 clathrates is given in Table 1 with more details provided in the Supplementary data. The X-ray crystal structures of both clathrates are very similar to one another and to those determined previously for many of the cage-type clathrates. They have the same number of molecules in the unit cell and very similar cell constants. Unlike many of the other TOT clathrate structures reported in the 1980s, which were reported to crystallize in the space group $P3_121$, the TOT–CH_2Br_2 and TOT–CH_2Cl_2 clathrates both crystallized in the enantiomorphic space group $P3_221$. Refinement of the data for the TOT–CH_2Br_2 and TOT–CH_2Cl_2 clathrates was attempted in space group $P3_121$ in which the host structure could be refined satisfactorily; however, when the atoms for the guest species were introduced, the structure would not refine and it became clear that the $P3_221$ rather than the $P3_121$ space group was indeed correct. It may be possible that some of the unsuccessful attempts to locate guest molecules in TOT clathrates in the past are the result of refinements done in the wrong space group. This pair of space groups is also observed for the chiral structures of D- and L-α-quartz.[29,30] The only unusual feature of the host structures is that one of the three carbonyl oxygens in the macrocyclic ring exhibits a small degree of two-site disorder. It is unclear whether the disorder is static or dynamic in nature; however, it is common to the structures of both clathrates. The guest molecules were located in the cavities with occupancies of 0.92 and 0.84 for TOT–CH_2Br_2 and TOT–CH_2Cl_2, respectively. In the case of the CH_2Cl_2 clathrate, it was noticed that some of the guest was lost over time, and the crystal structure was determined immediately from a freshly prepared sample. The dihalomethane guest molecules showed a large degree of disorder as was also observed in the inclusion compound of CH_2Cl_2 with cryptophane-E.[31,32] The X-ray models for the guests are shown in Fig. 2. In the case of TOT–CH_2Br_2, six molecular sites were located. Of the six molecular sites, there are two types: sites with the central carbon atoms well removed from the crystallographic C_2 axis (type A sites, two molecules) and sites with the central carbon atoms nearly lying on the C_2 axis (type B sites, four molecules). To a first approximation the Br–C–Br planes of all the molecules are coincident; however, if viewed along the plane, it is evident that there are out-of-plane distortions. The X-ray model for the CH_2Cl_2 molecules is very similar to that of the CH_2Br_2 molecules except that four rather than six molecular sites could be identified: two molecules in type A sites and two molecules in type B sites. Two differences between the X-ray models for each of the guests in type A sites are, however, the degree of displacement of the carbon atoms from the crystallographic twofold axis, and the angle between the crystallographic twofold axis and the molecular twofold axis. These angles are approximately 95° and 60° for CH_2Br_2 and CH_2Cl_2, respectively. At 200 K, the X-ray model found populations of sites A and B (P_A and P_B) to be 0.232

Can. J. Chem. Downloaded from www.nrcresearchpress.com by Xi'an Jiaotong University on 09/19/12
For personal use only.

Fig. 2. The positions of the guest molecules determined from the X-ray diffraction data. (*a*) and (*b*) Dichloromethane. (*c*) and (*d*) Dibromomethane. The views in (*b*) and (*d*) are perpendicular to those in (*a*) and (*c*). The thin lines drawn in (*a*) and (*c*) are the crystallographic twofold axes. The grey spheres represent carbon. The colored spheres represent halogen atoms.

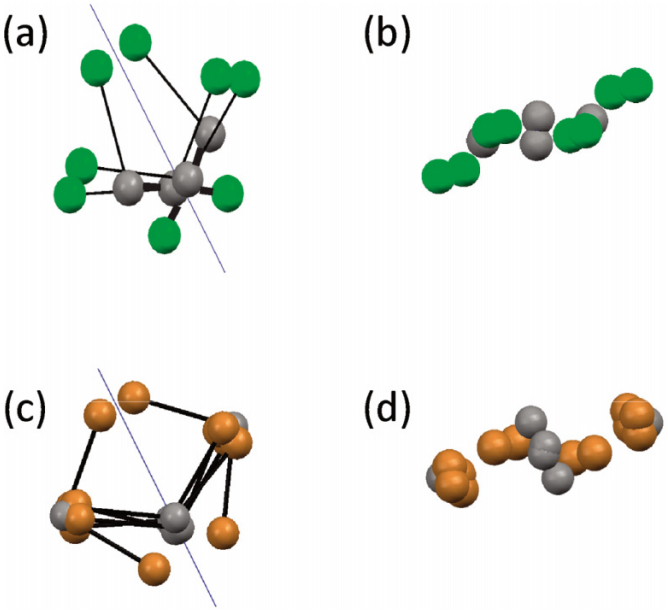

and 0.768, respectively, for TOT–CH_2Br_2 and 0.404 and 0.596, respectively, for TOT–CH_2Cl_2. One thing that is completely unclear from the X-ray data is whether or not the disorder of the guest molecules is static or dynamic in nature, or a combination of the two.

The solid-state ^{2}H NMR data collected as a function of temperature for the TOT–CH_2Br_2 clathrate are given in Table 2 and shown in Fig. 3*e*. In all of the spectra, the observed χ are much smaller than the range of those reported for the dihalomethanes (160–180 kHz),[33] indicating that the molecules are undergoing molecular motions on the submicrosecond time scale or faster. The line shapes are typical of those in the fast motion limit and were found not to vary with the echo times in the quadrupolar echo pulse sequence. Both χ and η vary with temperature. All of the spectra show a single powder pattern, indicating that all of the deuterons trace out the same trajectory over the course of their motions. In other words, all of the deuterons are identical in the time average. A plot of the frequency separations between the three features in the powder spectra is given in Fig. 4*a*.

The most obvious type of motion to account for the observed line narrowing, consistent with the X-ray model, is exchange between type A and type B sites. This involves both a translation and a rotation. Since ^{2}H NMR spectra are not sensitive to molecular translations, it is instructive to put all of the site A and site B molecules in a coordinate system where the central carbon atoms of each molecule are at the origin. In such a picture, the molecular rotations that affect the ^{2}H NMR spectra are more easily described. This is demonstrated in Fig. 5*c*. Ignoring the out-of-plane distortion (Fig. 5*d*), a simple picture is shown in Fig. 5*a*. In this picture, it is clear that the molecules in type A sites (labelled 1 and 3 in Fig. 5*a*) are related to molecules in type B sites (labelled 2 in Fig. 5*a*) by a simple rotation, the axis of which is perpendicular to the plane containing all of the C and Br atoms. The angle of rotation required to go from a type A site to a type B site is 95°. Based on the population ratios for sites A and B observed in the X-ray model at 200 K, and neglecting differences between the four type B sites, one might expect the potential energy coordinate for the required rotation from site A to site B to site A to be described by the simple symmetric three-site potential well shown in Fig. 6. Ignoring any out-of-plane motion, one would expect that the majority of the motional averaging in the ^{2}H NMR spectra can be accounted for by the rotation of the molecules between the A and B sites. If this is the case, each deuteron would move between the three sites on the surface of a cone of half angle $\beta = 35.5°$ assuming tetrahedral bond angles (see Fig. 5b). The rotation angle (γ) between the sites is 95°. The Euler angles relating the three $\mathbf{V_{ij}}$ tensors to the rotation axis are $\alpha = 0°$, $\beta = 35.5°$, and $\gamma = -95°$, 0°, and 95°. If this motion is fast with respect to $1/\chi$, a single averaged electric field gradient tensor will result with one component normal to the plane containing the C and Br atoms and the other two components in the plane. Using typical rigid values of χ and η of 170 kHz and 0, respectively,[33] the simulations of the ^{2}H NMR spectra are shown in Fig. 3*a* as a function of P_B with the assumption that the population of each of the A sites is equal. Clearly, these spectra are much broader than the experimental data in Fig. 3*e*. Even if one attempts to account for any dynamic disorder out of the C–Br plane of amplitude similar to that observed in the X-ray model, the degree of narrowing in the observed spectra cannot be accounted for.

The CH_2Br_2 molecules must be undergoing an additional mode of molecular motion. Furthermore, this additional mode of motion must be such that it is not detected by X-ray diffraction methods. One such motion is a twofold flip about the molecular C_2 symmetry axis similar to what has been reported for the TOT–acetone[22] and TOT–pyridine[21] clathrates. For the molecular twofold flips, the Euler angles relating the two $\mathbf{V_{ij}}$ to the rotation axis are $\alpha = 0°$, $\beta = 54.75°$, and $\gamma = 0°$ and 180°. The averaged tensor resulting from the twofold flips ($\mathbf{a_{ij}}$) will have one component perpendicular to the plane containing the C and Br atoms and the other two components in the plane. This averaged tensor is used as a starting point to compute the average tensor $\mathbf{a_{ij}}'$ resulting from both the twofold flips and the exchange among the type A and B sites. The Euler angles relating $\mathbf{a_{ij}}$ to the rotation axis for the site A to site B exchange are $\alpha = 0°$, $\beta = 0°$, and $\gamma = -95°$, 0°, and 95°. The averaged $\mathbf{a_{ij}}'$ resulting from both of these motions has a single component perpendicular to the plane containing the C and Br atoms, which remains unchanged compared with $\mathbf{a_{ij}}$, and two components in the plane. Simulations of the ^{2}H NMR spectra, assuming that the CH_2Br_2 molecules undergo both fast twofold flips and exchange between the type A and type B sites, are shown in Fig. 3*b* as a function of P_B with the assumption that the population of each of the A sites are equal. Although the spectra have a width of the same order as the experimental data, the line shapes are not a good fit. In the simulations η decreases as P_B decreases, whereas η in the observed spectra increases at higher temperatures where the population of the B sites is expected to decrease. The problem with this

Table 2. ^{2}H NMR Data for tri-*ortho*-thymotide (TOT) – TOT – CD_2X_2.

TOT–CD_2Br_2						TOT–CD_2Cl_2					
T (K)	$\Delta\upsilon_{xx}$ (kHz)[a]	$\Delta\upsilon_{yy}$ (kHz)[a]	$\Delta\upsilon_{zz}$ (kHz)[a]	P_B[c]	φ (°)[c]	T (K)	$\Delta\upsilon_{xx}$ (kHz)[b]	$\Delta\upsilon_{yy}$ (kHz)[b]	$\Delta\upsilon_{zz}$ (kHz)[b]	P_B[c]	φ (°)[c]
147	23.6	97.9	121.5	0.7650	23.0	137	51	65	116	0.3333	29
171	18.2	97.3	115.5	0.7575	32.5	180	35	73	108	0.3333	45
193	14.5	96.5	111.0	0.7525	38.1	220	26	73	99	0.3333	53
216	12.1	95.9	108.0	0.7480	41.3	260	19	70	89	0.3333	58
241	9.1	94.4	103.5	0.7355	45.8°	297	15	66	81	0.3333	61
271	7.9	89.6	97.5	0.6980	51.2						
293	6.2	86.8	93.0	0.6760	54.0						
327	5.3	83.2	88.5	0.6470	57.3						

Note: P_B = population of the B sites; φ = planar libration angle.
[a] ±1 kHz.
[b] ±2 kHz.
[c] From simulations.

Can. J. Chem. Downloaded from www.nrcresearchpress.com by Xi'an Jiaotong University on 09/19/12
For personal use only.

model is that it does not take into account the out-of-plane disorder observed in the X-ray model.

If the out-of-plane disorder is assumed to be dynamic, one simple way to model it may be as a two-site libration about one of the components of $\mathbf{a_{ij}}'$ in the plane containing the C and Br atoms. The averaged $\mathbf{a_{ij}}'$ resulting from both molecular twofold flips and the exchange between sites A and B is used as the starting point to compute the average tensor $\mathbf{a_{ij}}''$ resulting from the combination of all three motions. The Euler angles relating $\mathbf{a_{ij}}'$ to the librational axis of rotation are $\alpha = 0°$, $\beta = 90°$, and $\gamma = \pm 1/2\varphi$. Figure 3*c* shows simulations of the ^{2}H NMR spectra for molecules undergoing fast twofold flips about the molecular C_2 axis, a fast three-site exchange between type A and type B sites (with populations $P_A = 0.232$ and $P_B = 0.768$ as determined in the X-ray model) as well as a two-site libration of the plane containing all the C and Br atoms. The spectra were calculated as a function of φ. The libration angles were chosen such that the separation between the inner features of the simulations matched the experimental spectra. These data agree remarkably well with the experimental data; however, the simulated spectra do not take into account any possible temperature dependence of P_A and P_B. As a result, the simulations are somewhat broader than the experimental data. Since the axis of rotation resulting in the exchange between A and B sites and that of the rotation involved in the two-site out-of-plane libration are perpendicular, one would expect that one of the three frequency separations in the powder pattern would be constant as a function of temperature if P_A and P_B were invariant with temperature. From Fig. 4*a*, one can see that all three pairs of features in the observed spectra change with temperature. This indicates that the populations of the A and B sites must also change with temperature. Figure 3*d* shows simulations similar to those in Fig. 3*c*, except that both P_B and φ were adjusted to best fit the experimental spectra. P_B was chosen such that the frequency separation between the intermediate features of the simulated spectra ($\Delta\upsilon_{yy}$) matched the experimental data and then φ was chosen such that η matched that of the experimental spectrum. The results are shown in Table 2 and φ is plotted as a function of temperature in Fig. 7*a*. Since the population ratio P_A:P_B is expected to be determined by the Boltzmann distribution, one would expect a plot of $\ln(P_A/P_B)$ vs $1/T$ to be linear with slope = $-\Delta E/R$ and intercept = ln2, where ΔE is the energy difference between sites A and B. This plot is shown in Fig. 8. The high-temperature region of the plot seems to agree well with the Boltzmann model. The best fitting line with an intercept of ln2 is drawn in the figure. ΔE is 3.5 kJ /mol. At the lower temperatures the model breaks down. This may be due to the fact that, according to the X-ray model, there are in fact four nonequivalent type B sites rather than the one assumed in the simplified exchange model. As a result of the nonequivalent type B sites, at lower temperatures, one would expect the shape of the potential well to be more complicated and perhaps even temperature-dependent. The simplified potential energy picture in Fig. 6 is clearly not adequate to fully describe the in-plane motion over the entire temperature range. Nevertheless, the data strongly support the presence of three modes of molecular motion on a time scale fast with respect to $1/\chi$.

The uniqueness of the models for the dynamic disorder used to explain the spectroscopic results must always be examined. A number of other models were tested and found to be at least partially consistent with the NMR data. None, however, were consistent with the X-ray model. The three simultaneous modes of molecular motion described here were chosen based on their consistency with both the NMR and the X-ray data for the disorder. Although this is not proof that the models are a unique description of the data, the consistency with both the X-ray and NMR data demonstrates the credibility of the interpretation.

The solid-state ^{2}H NMR data collected as a function of temperature for the TOT–CD_2Cl_2 clathrate are given in Table 2 and shown in Fig. 9*d*. As with the TOT–CD_2Br_2 clathrate, all of the spectra exhibit an observed χ much smaller than that expected for the pure solid.[33] Again, the line shapes are typical of those in the fast motion limit and were found not to vary with the echo times in the quadrupolar echo pulse sequence. Both χ and η vary with temperature. All of the spectra show a single powder pattern indicating that all of the deuterons trace out the same trajectory over the course of their motions. A plot of the frequency separations between features in the spectra as a function of temperature is given in Fig. 4*b*. Unlike the case for the TOT–CD_2Br_2 clathrate, where the separation of all three pairs of features in the powder spectra varied with temperature, one pair of

Can. J. Chem. Downloaded from www.nrcresearchpress.com by Xi'an Jiaotong University on 09/19/12
For personal use only.

Fig. 3. Simulated and experimental ^{2}H NMR spectra for CD_2Br_2 in its tri-*ortho*-thymotide (TOT) clathrate. (*a*) Simulation of solid-state ^{2}H NMR spectra for a molecule exchanging between positions in the same plane separated by 95° as determined from the X-ray model. From bottom to top the populations ($1/2P_A$, P_B, $1/2P_A$) are as follows: (0, 1, 0), (0.05, 0.9, 0.05), (0.1, 0.8, 0.1), (0.15, 0.7, 0.15), (0.2, 0.6, 0.2), (0.25, 0.5, 0.25), (0.3, 0.4, 0.3), and (0.33, 0.33, 0.33). (*b*) Simulations under the same conditions as those in (*a*), except that in addition to the three-site exchange between the A and B sites in the plane, the molecules also undergo symmetric twofold flips about the bisector of the Br–C–Br bond. (*c*) Simulations of molecules undergoing twofold flips about the bisector of the Br–C–Br bond, a three-site exchange between A and B sites in the same plane (with populations 0.116, 0.768, and 0.116 as determined from the X-ray model), as well as a two-site libration of the plane of motion with libration angle (φ) from bottom to top: 22.5°, 31°, 36°, 38.5°, 42°, 42.7°, 44.5°, and 45.6°. (*d*) Same as for (*c*) except the spectra take into account the change in population among the three in-plane sites. From bottom to top the populations and libration angles ($1/2P_A$, P_B, φ) are as follows: (0.1175, 0.765, 23.0°), (0.12125, 0.7575, 32.5°), (0.12375, 0.7525, 38.05°), (0.126, 0.748, 41.3°), (0.13225, 0.7355, 45.8°), (0.151, 0.698, 51.2°), (0.162, 0.676, 54°), and (0.1765, 0.647, 57.3°). (*e*) Experimental ^{2}H NMR spectra for CD_2Br_2 in its TOT clathrate.

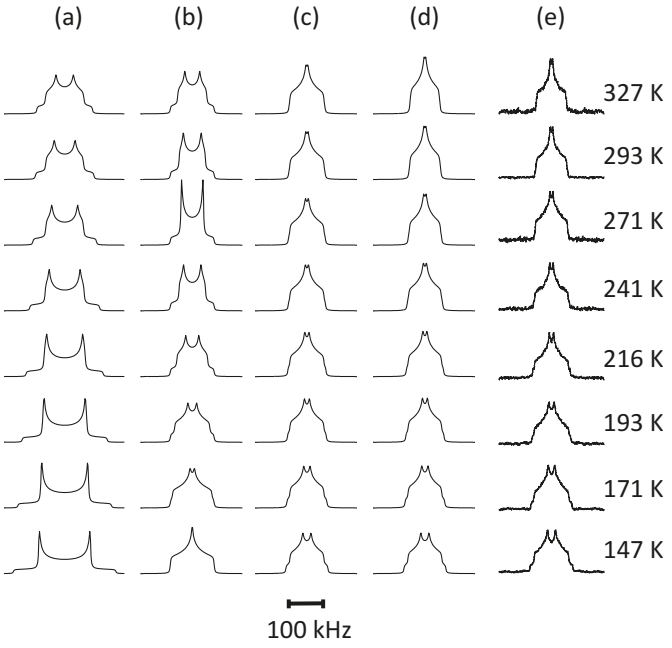

features in the ^{2}H spectrum of TOT–CD_2Cl_2 remains constant as a function of temperature. If we treat the motion of CD_2Cl_2 in a similar way to that of CD_2Br_2, then the populations of the A and B sites must be invariant with temperature. This can only be the case if ΔE is very close to zero and the populations of the A and B sites are equal to one another. This does not agree with the X-ray model that gives P_A and P_B equal to 0.404 and 0.596, respectively, at 200 K. The discrepancy may be due to the fact that the NMR data were collected on an older sample where some of the CD_2Cl_2 was lost to evaporation. The populations may vary with overall occupancy. This would account also for the reduced signal-to-noise ratio observed in the TOT–CD_2Cl_2 spectra in comparison to the TOT–CD_2Br_2 spectra.

Fig. 4. Plots of the frequency separation between the three pairs of features $\Delta\upsilon_{xx}$, $\Delta\upsilon_{yy}$, and $\Delta\upsilon_{zz}$ in the ^{2}H NMR spectra of (*a*) CD_2Br_2 and (*b*) CD_2Cl_2.

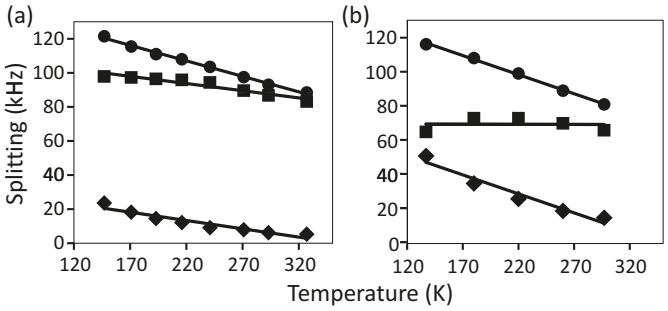

Fig. 5. Representations of the guest molecules after translating all molecules to have the central carbon atom at the origin. The grey spheres represent carbon. The colored spheres represent halogen atoms. (*a*) An idealized case showing two type A molecules (1 and 3) and one type B molecule (2) in the same plane. The molecules must rotate by an angle (γ) about an axis perpendicular to the heavy atom plane to go between A and B sites. (*b*) The positions of the deuterons over the course of the exchange between A and B sites. (*c*) The positions of the heavy atoms of the methylene bromide molecules in the tri-*ortho*-thymotide (TOT) clathrate from the X-ray model. The bonds have been omitted for clarity. (*d*) Same as for (*c*) viewed from the side. Note the out-of-plane distortion that is modeled with a two-site libration of angle φ (see text for details). (*e*) and (*f*) Similar to (*c*) and (*d*) for the TOT–dichloromethane clathrate.

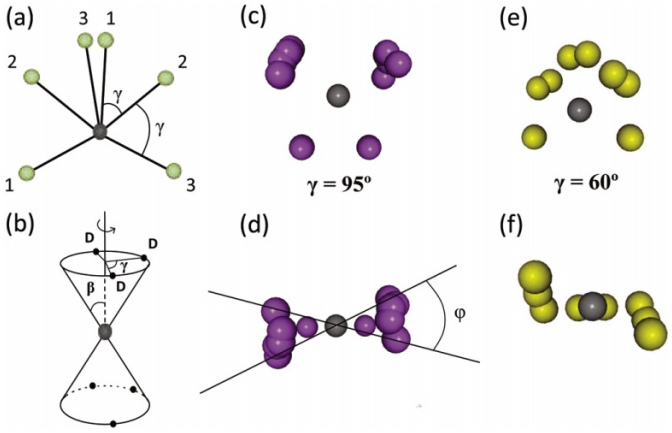

Fig. 6. Schematic representation of the potential energy on exchange between type A and type B sites.

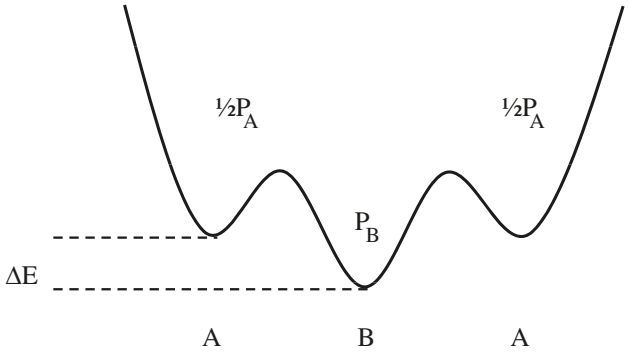

Can. J. Chem. Downloaded from www.nrcresearchpress.com by Xi'an Jiaotong University on 09/19/12
For personal use only.

Fig. 7. Plots of the two-site libration angle (φ) for the best fitting simulations versus temperature (see text for details). (*a*) CD_2Br_2. (*b*) CD_2Cl_2.

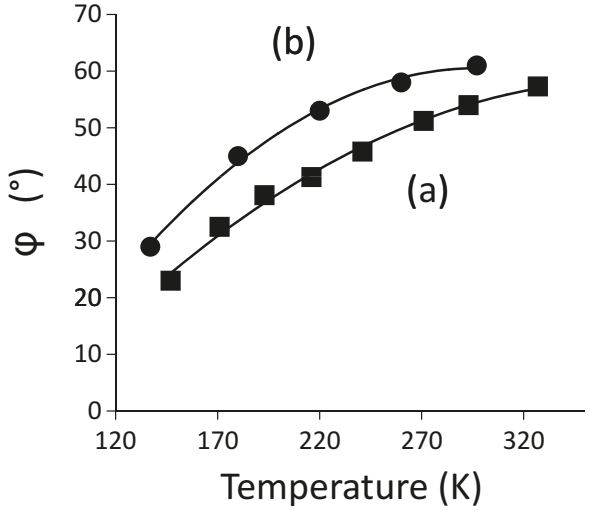

Fig. 8. Plot of $\ln(P_A/P_B)$ vs $1000/T$ for the tri-*ortho*-thymotide (TOT) – CD_2Br_2 clathrate derived from the best fitting simulations. The plot is expected to be linear with slope $-\Delta E/R$, where ΔE is the energy difference between sites A and B, and intercept ln2. This seems to be the case in the high-temperature region; however, the Boltzmann model breaks down at low temperatures. P_A is the population of site A and P_B is the population of site B.

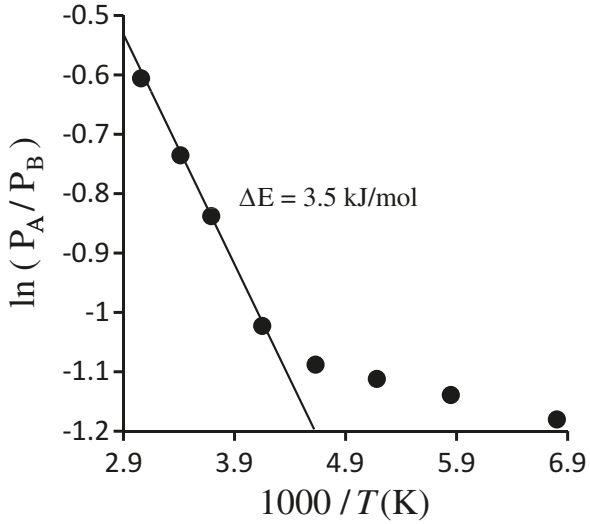

Simulations for the exchange between type A and type B sites were performed as a function of P_B with the assumption that the populations of the A sites are equal. The simulations were done with and without the assumption of a twofold flip about the molecular C_2 axis. The results are presented in Figs. 9*b* and 9*a*, respectively. In this case the in-plane angle of rotation (γ), on going from a type A site to a type B site, is 60° rather than 95°. In either case the agreement of the simulations with the experimental spectra is poor, presumably because the two-site out-of-plane libration has not been taken into account. Making the assumption that the populations of the A and B sites are equal, simulated spectra were calculated varying the out-of-plane φ for the best fit to the experimental

Fig. 9. Simulated and experimental ^2H NMR spectra for CD_2Cl_2 in its tri-*ortho*-thymotide (TOT) clathrate. (*a*) Simulation of solid-state ^2H NMR spectra for a molecule exchanging between positions in the same plane separated by 60° as determined from the X-ray model. From bottom to top the populations ($1/2P_A$, P_B, $1/2P_A$) are as follows: (0, 1, 0), (0.05, 0.9, 0.05), (0.1, 0.8, 0.1), (0.15, 0.7, 0.15), (0.2, 0.6, 0.2), (0.25, 0.5, 0.25), (0.3, 0.4, 0.3), and (0.33, 0.33, 0.33). (*b*) Simulations under the same conditions as those in (*a*), except that in addition to the three-site exchange between the A and B sites in the plane, the molecules also undergo symmetric twofold flips about the bisector of the Cl–C–Cl bond. (*c*) Simulations of molecules undergoing twofold flips about the bisector of the Cl–C–Cl bond, a three-site exchange between A and B sites in the same plane (with populations 0.333, 0.333, and 0.333) as well as a two-site libration of the plane of motion with libration angle (φ) from bottom to top: 29°, 45°, 53°, 58°, and 61°. (*d*) Experimental ^2H NMR spectra for CD_2Cl_2 in its TOT clathrate.

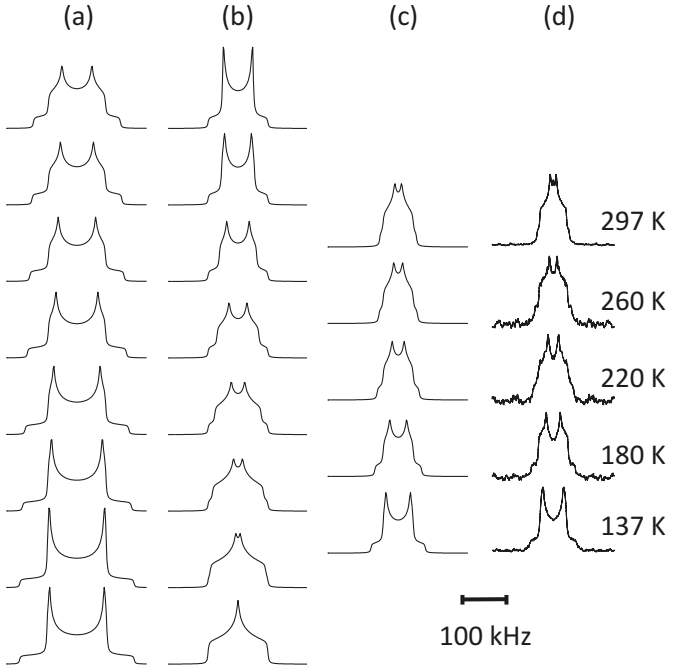

spectra. The libration angles used in the fits appear in Table 2 and are plotted in Fig. 7*b*. The out-of-plane φ for CD_2Cl_2 are larger than those for CD_2Br_2 as expected based on the reduced overall molecular volume of CD_2Cl_2 compared with CD_2Br_2 in a cavity of essentially the same size.

Conclusion

Solid-state ^2H NMR spectroscopy and single crystal X-ray diffraction were used to study the disorder of dibromomethane and dichloromethane in their tri-*ortho*-thymotide clathrates. The X-ray data showed a substantial amount of disorder. ^2H NMR data confirm that this disorder is dynamic rather than static in nature. For both guest molecules, the NMR results support three modes of molecular motion all on a time scale that is fast with respect to the quadrupolar interaction. The molecules undergo twofold flips about their molecular C_2 axes. They undergo both translation and rotation to exchange between two types of sites sharing a common plane containing all of the carbon and halogen atoms: A sites, with the central carbon atom well removed from the

twofold crystallographic axis, and B sites, with the central carbon atom lying very close to the crystallographic twofold axis. In addition, the plane containing the carbon and halogen atoms undergoes a two-site libration, the amplitude of which increases with temperature.

Supplementary data

The supplementary data are available with this article through the journal Web site (www.nrcresearchpress.com/cjc) or as CCDC 798035 (TOT–CH_2Cl_2) and 798036 (TOT–CH_2Br_2), which can be obtained, free of charge, via www.ccdc.cam.ac.uk/cgi-bin/catreq.cgi (or from the Cambridge Crystallographic Data Centre, 12 Union Road, Cambridge CB2 1EZ, UK (Fax: 44-1223-336033 or e-mail: deposit@ccdc.cam.ac.uk)).

References

(1) Allemand, J.; Gerdil, R. *Acta Crystallogr.* **1982** *B38*, 1473.
(2) Arad-Yellin, R.; Green, B. S.; Knossow, M.; Tsoucaris, G. *Tetrahedron Lett.* **1980** *21* (49), 387. doi:10.1016/S0040-4039(01)85481-2.
(3) Arad-Yellin, R.; Green, B. S.; Knossow, M.; Tsoucaris, G. *J. Am. Chem. Soc.* **1983** *105* (14), 4561. doi:10.1021/ja00352a010.
(4) Allemand, J.; Gerdil, R. *Acta Crystallogr. Sect. C. Cryst. Struct. Commun.* **1981** *10*, 33.
(5) Gerdil, R.; Frew, A. *J. Inclusion Phenom.* **1985** *3* (3), 335. doi:10.1007/BF00655734.
(6) Williams, D. J.; Lawton, D. *Tetrahedron Lett.* **1975** *16* (2), 111. doi:10.1016/S0040-4039(00)72484-1.
(7) Allemand, J.; Gerdil, R. *Acta Crystallogr.* **1982** *B38*, 2312.
(8) Siripitayananon, J.; Gerdil, R. *Acta Crystallogr.* **1988** *C45*, 768.
(9) Brunie, S.; Navaza, A.; Tsoucaris, G.; Declercq, P.; Germain, G. *Acta Crystallogr.* **1977** *B33*, 2645.
(10) Allemand, J.; Gerdil, R. *Acta Crystallogr.* **1983** *C39*, 260.
(11) Arad-Yellin, R.; Brunie, S.; Green, B. S.; Knossow, M.; Tsoucaris, G. *J. Am. Chem. Soc.* **1979** *101* (25), 7529. doi:10.1021/ja00519a012.
(12) Gerdil, R. *Top. Curr. Chem.* **1987** *140*, 71. doi:10.1007/BFb0003837.
(13) Lawton, D.; Powell, H. M. *J. Chem. Soc.* **1958** 2339. doi:10.1039/jr9580002339.
(14) Ripmeester, J. A.; Burlinson, N. E. *J. Am. Chem. Soc.* **1985** *107* (12), 3713. doi:10.1021/ja00298a049.
(15) Arad-Yellin, R.; Green, B. S.; Knossow, M. *J. Am. Chem. Soc.* **1980** *102* (3), 1157. doi:10.1021/ja00523a039.
(16) Gerdil, R.; Allemand, J. *Helv. Chim. Acta* **1980** *63* (6), 1750. doi:10.1002/hlca.19800630645.
(17) Facey, G. A.; Ripmeester, J. A. *J. Chem. Soc. Chem. Commun.* **1990** (22), 1585. doi:10.1039/c39900001585.
(18) Bishop, R.; Dance, I. *Top. Curr. Chem.* **1988** *149*, 161.
(19) Arad-Yellin, R.; Green, B. S.; Knossow, M.; Tsoucaris, G. In *Inclusion Compounds;* Atwood, J. L., Davies, J. E. D., MacNicol, D. D., Eds.; Academic Press: London, 1984; Vol. 3, Chapter 9.
(20) Facey, G. A.; Ripmeester, J. A. *Mol. Cryst. Liq. Cryst. (Phila. Pa.)* **1992** *211* (1), 167. doi:10.1080/10587259208025816.
(21) Facey, G. A.; Ratcliffe, C. I.; Ripmeester, J. A. *J. Phys. Chem.* **1995** *99* (32), 12249. doi:10.1021/j100032a030.
(22) Facey, G. A.; Ratcliffe, C. I.; Hynes, R.; Ripmeester, J. A. *J. Phys. Org. Chem.* **1992** *5* (10), 670. doi:10.1002/poc.610051009.
(23) Greenfield, M. S.; Ronemus, A. D.; Vold, R. L.; Vold, R. R.; Ellis, P. D.; Raidy, T. E. *J. Magn. Reson.* **1987** *72*, 89.
(24) Mathews, J.; Walker, R. R. *Mathematical Methods of Physics;* W.A. Benjamin: New York, 1965; p 374.
(25) Blessing, R. *Acta Crystallogr.* **1995** *A51*, 33.
(26) Sheldrick, G. M. *Acta Crystallogr.* **2008** *A64*, 112.
(27) Davis, J. H.; Jeffrey, K. R.; Bloom, M.; Valic, M. I.; Higgs, T. P. *Chem. Phys. Lett.* **1976** *42* (2), 390. doi:10.1016/0009-2614(76)80392-2.
(28) Macho, V.; Brombacher, L.; Spiess, H. W. *Appl. Magn. Reson.* **2001** *20* (3), 405. doi:10.1007/BF03162288.
(29) Saha, P.; Annamalai, N.; Bandyopadhyay, T. *Bull. Mater. Sci.* **1979** *1* (1), 14. doi:10.1007/BF02907456.
(30) Goodman, P.; Secomb, T. W. *Acta Crystallogr.* **1977** *A33*, 126.
(31) Tošner, Z.; Lang, J.; Sandström, D.; Petrov, O.; Kowalewski, J. *J. Phys. Chem. A* **2002** *106* (38), 8870. doi:10.1021/jp026066t.
(32) Petrov, O.; Tošner, Z.; Csöregh, I.; Kowalewski, J.; Sandström, D. *J. Phys. Chem. A* **2005** *109* (20), 4442. doi:10.1021/jp044884a.
(33) Kunwar, A. C.; Gutowsky, H. S.; Oldfield, E. *J. Magn. Reson.* **1985** *62*, 521.

Can. J. Chem. Downloaded from www.nrcresearchpress.com by Xi'an Jiaotong University on 09/19/12
For personal use only.

Solid-state ^{207}Pb nuclear magnetic resonance studies of adducts of 1,10-phenanthroline with lead(II) halides

Alicia Glatfelter, Shi Bai, Olga Dmitrenko, Dale L. Perry, Scott E. Van Bramer, and Cecil Dybowski

Can. J. Chem. Downloaded from www.nrcresearchpress.com by Xi'an Jiaotong University on 09/19/12
For personal use only.

Abstract: Experimental and predicted ^{207}Pb nuclear magnetic resonance (NMR) parameters of solid-state coordination complexes of lead(II) bromide, lead(II) iodide, and lead(II) chloride with 1,10-phenanthroline are reported. Structural and electronic differences between the 1:1 and 1:2 adducts are reflected by the NMR parameters. The NMR chemical shieldings of the isostructural complexes indicate that the electronic state of the lead(II) center depends on the number of ligands and the halogen anion. The NMR results suggest that the 1:2 adduct may be more stereochemically active than the 1:1 adduct.

Key words: 1,10-phenanthroline, lead(II) bromide, lead(II) iodide, ^{207}Pb NMR, solid-state NMR, density functional theory, zeroth-order regular approximation (ZORA).

Résumé : On rapporte les valeurs expérimentales et prédites pour les paramètres de résonance magnétique nucléaire (RMN) du ^{207}Pb de complexes de coordination à l'état solide du bromure de plomb(II), de l'iodure de plomb(II) et du chlorure de plomb(II) avec la 1,10-phénanthroline. Les différences structurales et électroniques entre les adduits 1 : 1 et 1 : 2 sont réfléchies par les paramètres de RMN. Les blindages chimiques en RMN des complexes isostructuraux indique que l'état électronique du noyau de plomb(II) dépend du nombre de ligands et de l'anion de l'halogène. Les résultats de la RMN suggèrent que l'adduit 1 : 2 peut être stéréochimiquement plus actif que l'adduit 1 : 1.

Mots-clés : 1,10-phénathroline, bromure de plomb(II), iodure de plomb(II), ^{207}Pb RMN, RMN à l'état solide, théorie de la fonctionnelle de la densité, approximation régulière d'ordre zéro ("ZORA").

[Traduit par la Rédaction]

Introduction

There has been a long interest in the roles of lead, its compounds, and lead-containing materials in the chemistry of electronic devices, optical sensors, and biological systems. Lead(II) oxide, PbO, for example, is a constituent at dopant concentrations of optical fibers used as radiation sensors,[1] while PbO_2 is used in nanocrystalline-based electrodes.[2] The electronic properties of the halides make them important components of devices such as layered semiconductors[3] and medical X-ray imaging detectors.[4] Materials such as lead(II) bromide, $PbBr_2$, exhibit complex crystal lattice physics.[5] The incorporation of lead into biological systems is a well-known cause for concern in poisoning, and its biological environment has been actively investigated.[6]

An organic molecule that has widespread application in chemistry and materials science is 1,10-phenanthroline, or *ortho*-phenanthroline. The electronic properties of this multiringed, nitrogen-containing aromatic chelating hydrocarbon can be tailored to provide materials that exhibit properties amenable to a wide array of uses. It is used, for example, in light-emitting devices (LEDs),[7] in luminescent probes for the study of micellar interactions,[8] in photosensitizers for nanocrystalline solar cells,[9] and in molecular-switching devices.[10] Because of the photoactivity of 1,10-phenanthroline and its complexes and materials, it has also been the focus of photochemical and photophysical studies.[11]

In this report, the ^{207}Pb nuclear magnetic resonance (NMR) spectroscopic parameters of a set of adducts of 1,10-phenanthroline in 1:1 and 1:2 ratios with lead halides are examined. Comparison of the experimental ^{207}Pb NMR results with density functional calculations of the NMR parameters shows that the chemical shift changes with structure mainly result from changes in the paramagnetic contributions to the chemical shielding. The NMR data indicate significant structural and electronic differences between the 1:1 and 1:2 PbX_2:1,10-phenanthroline adducts (X = Cl, Br, or I) and suggest that the 1:2 adducts are more stereochemically active than the 1:1 adducts.

Received 15 September 2010. Accepted 16 November 2010. Published at www.nrcresearchpress.com/cjc on 8 July 2011.

A. Glatfelter, S. Bai, O. Dmitrenko, and C. Dybowski. Department of Chemistry and Biochemistry, University of Delaware, Newark, DE 19716, USA.
D.L. Perry. Lawrence Berkeley National Laboratory, Berkeley, CA 94720, USA.
S.E. Van Bramer. Department of Chemistry, Widener University, Chester, PA 19013, USA.

Corresponding author: Cecil Dybowski (e-mail: dybowski@udel.edu).

This article is part of a Special Issue dedicated to Professor Roderick E. Wasylishen.

Can. J. Chem. Downloaded from www.nrcresearchpress.com by Xi'an Jiaotong University on 09/19/12
For personal use only.

Experimental methods

Synthesis

Reagent grade starting materials were purchased from Sigma-Aldrich and used without further purification. The synthetic procedure[12,13] is a modification of previously reported methods.[14–18] The 1:1 adducts were prepared by using equimolar amounts of PbX_2 (X = Cl, Br, or I) and 1,10-phenanthroline in ethanol in a sealed tube at 70 °C with a sidearm immersed in an ice–water bath. Over a period of 3 months, the product accumulated in the sidearm. The material was washed with ethanol and dried. The 1:2 adducts of 1,10-phenanthroline with $PbBr_2$ and PbI_2 were prepared from a suspension of the halide in ethanol with stirring while an eightfold excess of 1,10-phenanthroline was added. The reaction vessel was allowed to stand for 5 days while shielded from light. The product was filtered, washed with ethanol, and dried. $PbCl_2$ exhibits only the 1:1 adduct. The stoichiometries of the final materials were determined by elemental analyses (Table S1 in the Supplementary data) by Schwarzkopf Microanalytical Laboratories of Woodside, New York, and by single-crystal and powder X-ray diffraction. (Tables S2 and S3 in the Supplementary data).

NMR spectroscopy

NMR spectra were measured with a Bruker MSL-300 spectrometer at 295 (±1) K. ^{207}Pb NMR spectra of static powders were obtained at a nominal frequency of 62.601 MHz, using a spin-echo sequence, with proton decoupling.[19–23] The $\pi/2$ pulse width was 2.55 μs; the spacing between the pulses in the spin-echo experiment was 20 μs. Recycle delays of up to 2 min were used to allow recovery of magnetization. There were 3844 transients co-added for the sample of $PbCl_2$(1,10-phenanthroline), and 7022 scans were co-added for the other samples, so spectra were gathered over periods of 5–10 days. The sweep width for all spectra was 500 000 Hz. Spin-temperature alternation was applied with an inverting pulse applied on alternate acquisitions, with spectral subtraction. To minimize the effects of power drop away from the carrier, the offset in each case was optimized to place the carrier in the center of the powder line shape.

The crystal structures of the materials show only one chemical site for lead in each material, and the line shapes in the ^{207}Pb spectra of static powders represent the chemical shift dispersion of a single lead resonance, rather than multiple sites. The experimental powder spectra were fitted with an in-house program that accounts for effects of the spin-echo sequence and the measured drop-off of power away from the carrier frequency.[21] In fitting the spectra, idealized powder patterns were convoluted with a Gaussian function and an appropriate transfer function for the pulse sequence determined from the pulse widths and spacings.[21] By a simplex procedure we determined the optimal set of chemical shift and broadening parameters given in Table 1.

The lead spectra are referenced to the position of tetramethyllead ($\delta = 0$ ppm), with solid lead nitrate as a secondary standard ($\delta_{iso} = -3490.4$ ppm at 295 K).[19,23]

Computational methods

Calculations were performed on model clusters of PbX_2(1,10-phenanthroline) and PbX_2(1,10-phenanathroline)$_2$ generated from crystallographic data. We used the structures of the catena-(bis(m2-chloro))-(1,10-phenanthroline)-lead(II)) (Cambridge Structural Database (CSD) code RAQLEA), catena-(bis(m2-bromo))-(1,10-phenanthroline)-lead(II) (CSD code RAQLAW), and catena-(bis(m2-iodo))-(1,10-phenanthroline)-lead(II) (CSD code RAQKUP) drawn from the Cambridge Structural Database.[18] Crystallographic data for PbX_2(1,10-phenanthroline)$_2$, where X = Br, I, were determined at the University of Delaware, Newark, Delaware, and are reported in the Supplementary data, Table S2.[13]

Density functional theory (DFT) calculations of ^{207}Pb NMR parameters, using the zeroth-order regular approximation (ZORA), were performed with the Amsterdam Density Functional (ADF) program package.[25] NMR parameters were calculated with the associated NMR program module.[26–29] Core potentials were generated with the module DIRAC, and all atoms were treated without frozen cores or with partial frozen cores. The basis sets were triple-ζ Slater-type orbitals (STOs) including two polarization functions (TZ2P). The local density approximation (LDA)[30] and generalized gradient approximation (GGA) were both used in the calculations. The GGA was specified with Becke–Perdew (BP) exchange-correlation functions,[31,32] as well as with the set proposed by Perdew et al. (revBPE).[33,34] The calculation of the chemical shielding of $Pb(CH_3)_4$ was carried out using the reported experimental geometry (CSD code VADRAU).[35]

Results and discussion

Solid-state ^{207}Pb NMR spectroscopy

The ^{207}Pb NMR spectra of powders of the 1:1 and 1:2 adducts of $PbBr_2$ are shown in Fig. 1, and the spectra of the adducts of PbI_2 are shown in Fig. 2. The spectrum of $PbCl_2$(1,10-phenanthroline) is shown in Fig. 3. Table 1 gives the NMR parameters extracted from these spectra, in Mason's convention.[36] Included in Table 1 are NMR data for the parent halides from the literature.[35]

^{207}Pb NMR chemical shift parameters reflect local electronic structure at the lead site, and are strongly affected by crystal structure, electronegativity of atoms in the vicinity, and the presence of paramagnetic entities.[19–24,37–40] For these materials, there are not likely to be paramagnetic centers that would induce shifts. Certain general trends are evident in Table 1: (*i*) The isotropic shifts of the 1:1 adducts are deshielded relative to their parent salts. (*ii*) The isotropic shifts of the 1:2 adducts of $PbBr_2$ and PbI_2 are shielded relative to the corresponding 1:1 adducts. (*iii*) Comparison of the isotropic shifts of the 1:2 adducts of $PbBr_2$ and PbI_2 with their parent salts show that the former is deshielded but the latter is more shielded than its parent salt.

Subtler effects on the ^{207}Pb NMR properties are observed in Ω and κ. For example, the span of the 1:2 adduct of either $PbBr_2$ or PbI_2 is larger than the span of the corresponding 1:1 adduct (roughly by factors of 2 and 1.4, respectively). The spans of the 1:2 adducts of $PbBr_2$ and PbI_2 are similar and comparable to that of $PbCl_2$(1,10-phenanthroline).

The skews of the 1:1 adducts of $PbBr_2$ and PbI_2 are similar and nearly zero. The skews of the 1:2 adducts and that of the 1:1 adduct of $PbCl_2$ are much larger. A skew near zero implies that the three principal elements of the chemical shift

Can. J. Chem. Downloaded from www.nrcresearchpress.com by Xi'an Jiaotong University on 09/19/12
For personal use only.

Table 1. Experimental ^{207}Pb NMR parameters of adducts of 1,10-phenanthroline with lead halides in the solid state.

Compound	δ_{iso} (ppm)[a]	Ω (ppm)[a]	κ[a]	Gaussian width (kHz)
$PbCl_2$[b]	–1715	533	0.52	—
$PbCl_2$(1,10-phenanthroline)	–920	615	0.45	0.753
$PbBr_2$[b]	–981	699	0.58	—
$PbBr_2$(1,10-phenanthroline)	–642	323	0.02	2.713
$PbBr_2$(1,10-phenanthroline)$_2$	–875	655	0.62	2.511
PbI_2[b]	–29	<175[c]	—[c]	—
PbI_2(1,10-phenanthroline)	101	429	0.03	2.604
PbI_2(1,10-phenanthroline)$_2$	–156	618	0.29	3.372

Note: δ_{iso}, chemical shift; Ω, span; and κ, skew.

[a]The uncertainty in δ_{iso} is estimated to be ±5 ppm. The uncertainty in Ω is estimated to be ±10 ppm. The uncertainty in κ is approximately ±0.05.

[b]From Dybowski et al.[37]

[c]The span of PbI_2 may be as large as 175 ppm. In the original paper, line broadening prevented determination of the span and skew. The site symmetry in PbI_2 requires that κ be ±1.

Fig. 1. ^{207}Pb NMR spectra of $PbBr_2$(1,10-phenanthroline)$_n$ adducts. The shift scales are aligned to illustrate the magnitude of the shift. Grey lines indicate the fitted spectrum and the black lines indicate the experimental data.

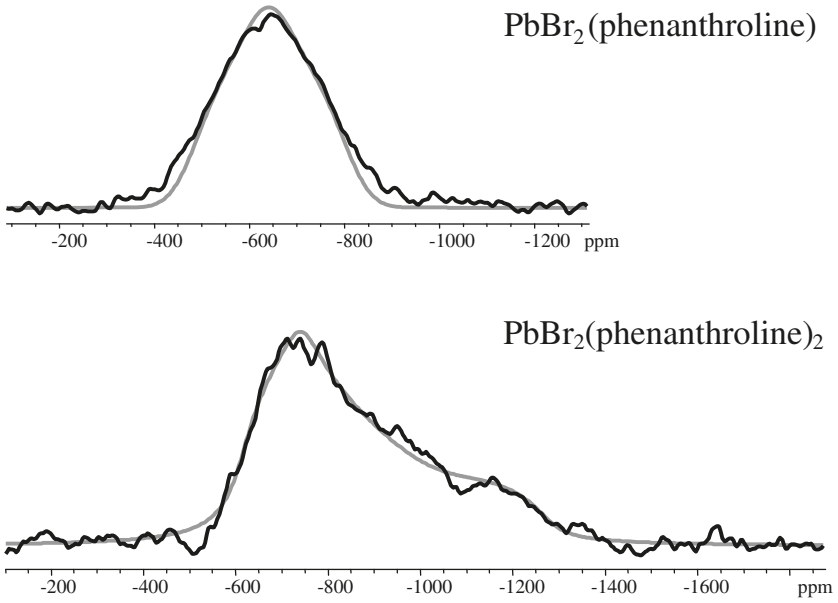

tensor are substantially different from each other. The fact that all skews are positive implies that, although the principal values of the tensors are all unique, the most strongly shielded principal element is the most nearly unique principal element of the chemical shift tensor in every case.

The isotropic ^{207}Pb chemical shifts of the complexes depend strongly on the anion partner, in a manner similar to the effect of anions on the isotropic shifts of pure salts.[37] If the notion that greater stereochemical activity correlates with isotropic shielding holds for solid-state complexes with different anions,[41,42] then the $PbBr_2$ adducts exhibit stronger stereochemical activity than the PbI_2 adducts, and the 1:1 adduct of $PbCl_2$ has an even stronger stereochemical activity.

Some experimental observations may be rationalized by correlation with structural differences (Fig. 4). For example, $PbBr_2$ has three bromine atoms at a distance of 0.2991 nm from the Pb center; all other Pb–Br distances are >0.32 nm. In the crystal structure of the 1:1 adduct, there are only two nearest-neighbor Pb–Br distances of 0.2997 nm, with other bromine atom distances being >0.31 nm. The 1:1 adducts of PbI_2 and $PbCl_2$ have similar structures to the 1:1 adduct of $PbBr_2$.[13] Thus, the fact that the isotropic shifts of the 1:1 complexes are deshielded relative to the salt is correlated with the fact that there are fewer anions in the near vicinity of the lead ion for the adducts.

The 1:2 adduct of $PbBr_2$ has two Pb–Br distances of 0.306 nm, similar to the 1:1 adduct, with other bromine centers farther away. In addition, it has four close contacts with nitrogens, Pb–N = 0.257 nm, compared with two close contacts for the 1:1 adduct. Its isotropic shift is shielded relative to the 1:1 adduct, which suggests that the additional nitrogens coordinating with Pb provide increased electronic density near the lead center. The isotropic shift of the 1:2 adduct of PbI_2 is shielded relative to the 1:1 adduct of PbI_2,

Fig. 2. ^{207}Pb NMR spectra of PbI_2(1,10-phenanthroline)$_n$ adducts. The shift scales are aligned to illustrate the magnitude of the shift. Grey lines indicate the fitted spectrum and the black lines indicate the experimental data.

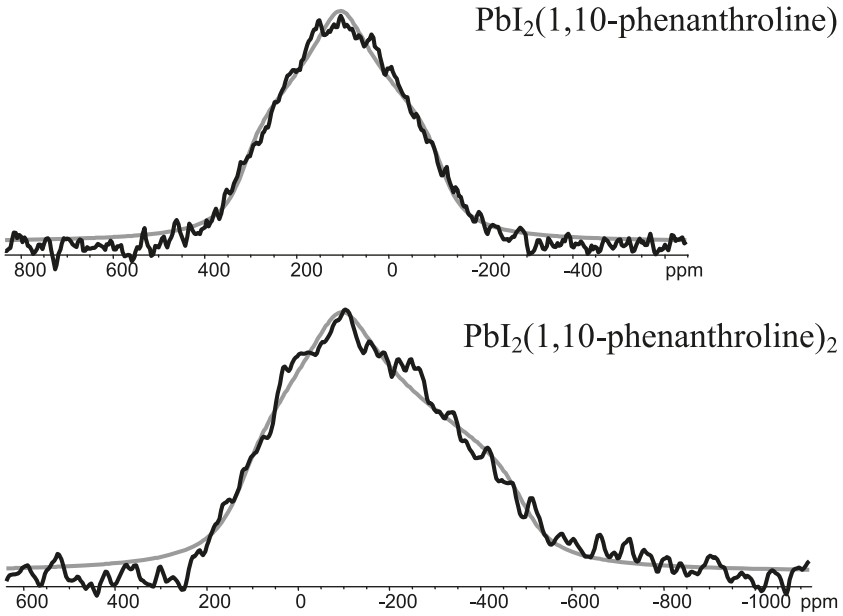

Fig. 3. ^{207}Pb NMR spectrum of $PbCl_2$(1,10-phenanthroline). Both the experimental spectrum (black line) and the fitted spectrum (grey line) are shown.

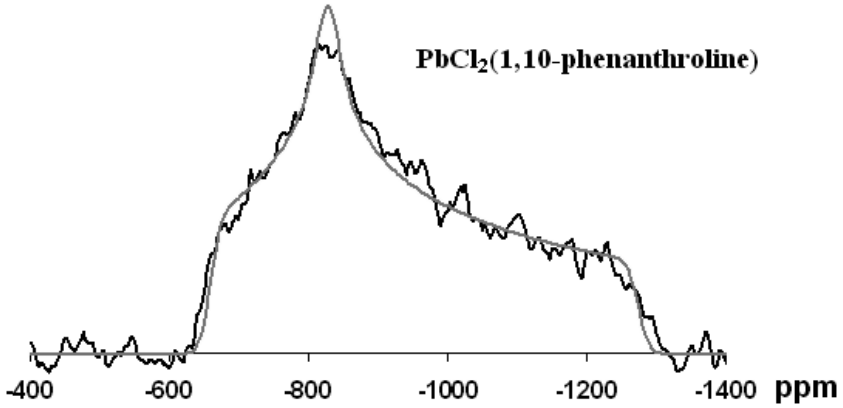

Fig. 4. Cluster models of (*a*) PbX_2(phenanthroline), X = Cl, Br, or I; and (*b*) PbX_2(phenanthroline)$_2$, X = Br or I.

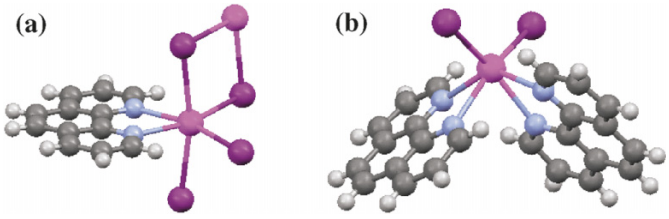

which is also consistent with increased electron density near the lead site.

A distinction between the iodide and bromide systems is that the 1:2 adduct of PbI_2 is shielded relative to PbI_2, in contrast to the behavior of the bromide system. This difference in the shifts may, however, be the result of the well-known structural difference between $PbBr_2$ and PbI_2, rather than a difference between the adducts, inasmuch as the anions are located somewhat differently in the crystal lattices of $PbBr_2$ and PbI_2.[35]

The span of each 1:2 adduct is larger than the span of the corresponding 1:1 adduct. This distinction between adducts correlates with the number of nitrogen centers coordinated with the lead center. This observation is similar to the reported dependence of ^{207}Pb chemical shift parameters on the number of oxygens with which it is coordinated, although in that case it was the isotropic chemical shift that was correlated with the oxygen number.[38]

The skews of the 1:1 adducts are almost zero, whereas the skews of the 1:2 adducts are not zero. This difference suggests that the local ^{207}Pb environment in the 1:2 adducts is tending more towards axial symmetry than the Pb environments in the 1:1 adducts. One might expect this result, given that the local environment of a 1:2 adduct contains four nitrogens at roughly equal distances from the Pb center, whereas the 1:1 adduct does not. As one can see from Fig. 4, the Pb site in the 1:1 adduct sits on a twofold axis. It coordinates with the nitrogens of the 1,10-phenanthroline in a pseudo-octahedral geometry. In the 1:2 adduct, the Pb center is coordinated with four nitrogens from two 1,10-phenanthroline

Can. J. Chem. Downloaded from www.nrcresearchpress.com by Xi'an Jiaotong University on 09/19/12
For personal use only.

Can. J. Chem. Downloaded from www.nrcresearchpress.com by Xi'an Jiaotong University on 09/19/12
For personal use only.

molecules and with two halogens. This situation is inherently less asymmetric than the Pb site in the 1:1 adducts.

The fitted line shapes require stronger broadening of the $PbBr_2$ and PbI_2 adduct spectra than does the spectrum of the $PbCl_2$ adduct. This observation is similar to the situation for the parent salts.[37] The origin of the broadening in these materials is likely to be unresolved coupling of the Pb nucleus to the quadrupolar nuclei. Although the Cl nucleus is quadrupolar, it is frequently seen to self-decouple, making the broadening of the Pb resonance in this material smaller.[44]

Prediction of ^{207}Pb NMR chemical shielding parameters of cluster models

To estimate the trends in chemical shielding, we have used cluster models based on crystallographic data (Fig. 4) to represent the local structures around the lead sites. The chemical shielding tensors of the target lead centers of the adducts and for tetramethyllead, $Pb(CH_3)_4$, calculated using the ADF set of programs with ZORA to include relativistic effects, are given in Table S4 in the Supplementary data. Figure 5 is a plot of the experimental principal values of the chemical shift tensors of the five adducts versus the calculated principal values of the chemical shielding tensors obtained from a calculation using the revBP-GGA and the triple-ζ basis that includes two polarization functions. As the plot shows, the calculations qualitatively reproduce the observed experimental trends in the chemical shift, but there are significant deviations from the general trend. The linear fit of the experimental principal values of the chemical shift tensors versus the calculated principal values has an intercept of 5652 ± 176 ppm and slope of -1.00 ± 0.26. A slope with a magnitude of one, although with a large uncertainty, indicates that the ADF calculations on these cluster models provide a reasonable prediction of the trends of chemical shielding for these materials. The intercept corresponds to the chemical shielding of the reference material, $Pb(CH_3)_4$. A calculation of the isotropic chemical shielding of $Pb(CH_3)_4$ with the same calculational procedure, however, gives a much lower value of 4857 ppm. The discrepancy may result from effects that are not considered at this level of calculation.

Similar comparisons (not shown) with the calculated values using the LDA and partial frozen cores (data in Table S1 in the Supplementary data) show substantially less correlation between the calculated values of the shielding and the experimental chemical shifts. To improve the correlation between experiment and calculation may require larger basis sets and perhaps better models than the small clusters used here. Calculation of the NMR parameters using periodic boundary conditions may better represent the electronic structure and, hence, produce closer agreement.[44] The NMR spans consistently obtained from the cluster calculations tend to be larger than the experimental spans.

An examination of the various predicted contributions to the chemical shieldings (Table S4 in the Supplementary data) show that the diamagnetic contribution is large and isotropic. However, it is essentially the same for all lead sites, regardless of the molecule. On the other hand, the value of the paramagnetic contribution to the chemical shielding is sensitive to the ligand partners and tends to be anisotropic. A similar result has been observed for lead ligated to substituted pyridines.[45] These calculations strongly suggest that the observed isotropic and anisotropic characteristics of the NMR spectrum reflect the paramagnetic contributions.

Fig. 5. Comparison of ^{207}Pb experimental chemical shift tensor principal values with calculated chemical shielding tensor elements for PbX_2(1,10-phenanthroline)$_n$, $n = 1$, 2 and X = Cl, Br, or I. The solid line is a linear fit to the data with the formula $\delta_{exp} = 5652 - 1.00\sigma_{calcd}$. The correlation coefficient (r) is 0.73081.

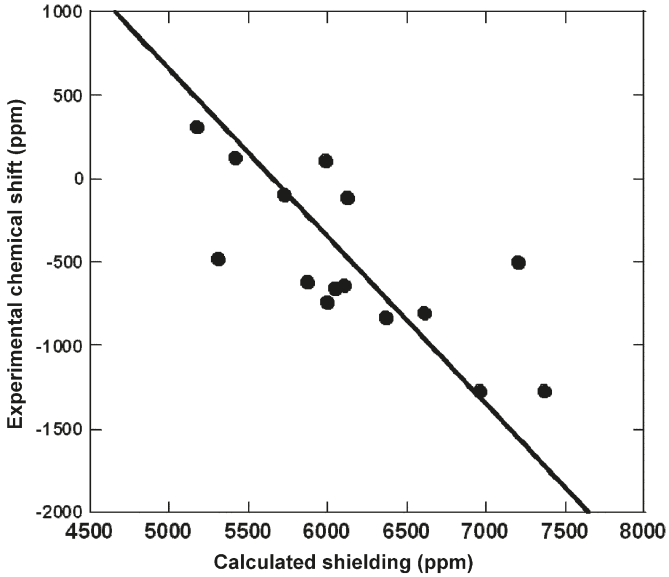

Conclusions

^{207}Pb NMR solid-state spectra of lead(II) halide complexes with 1,10-phenanthroline provide information on structure and bonding in 1:1 and 1:2 lead(II)–1,10-phenanthroline complexes. ^{207}Pb NMR chemical shifts show distinctive differences between the 1:2 and 1:1 adducts involving $PbBr_2$ and PbI_2. The isotropic chemical shift is significantly affected by the anion partner, but subtler effects are seen in the variation of the span and skew. In particular, the skew tends to be around zero for the 1:1 adducts. Broadening of the line shapes depends on the anion partner, perhaps suggesting unresolved coupling to the quadrupolar nuclei. Density functional calculations on cluster models of the complexes qualitatively reproduce some experimental trends. It is likely that the discrepancies represent neglect of the effects of neighboring groups in the solid, which would be included if a larger cluster or a periodic calculation were used.[43]

Supplementary data

Supplementary data for this article are available on the journal Web site (www.nrcresearchpress.com/cjc).

Acknowledgments

C.D. acknowledges the financial support of the Petroleum Research Fund of the American Chemical Society, Grant No. 33633-AC5, and the National Science Foundation under Grants CHE-0411790 and CHE-0956006. D.L.P. acknowledges support of the US Department of Energy under Contract No. DE-AC0205CH11231. We thank Professor A. Rheingold and Mr. G. Rossi for determining crystal structures of the 1:2 complexes.

This article is a contribution in honor of Professor Roderick Wasylishen. It is a great pleasure to recognize the contributions of Rod Wasylishen to chemistry, and particularly to NMR spectroscopy. In the 30 years I have known Rod, I have watched as he has explained and clarified many subtleties of the technology. I am pleased to be able not only to call him an esteemed colleague, but also a friend (C.D.).

References

(1) Qiu, S.; Sun, D.; Liao, Y.; Lai, S.; Wang, Z.; Qiao, X. In *Fiber Optic Sensors V,* Proceedings of the International Society of Optics and Photonics (SPIE), Beijing, China, 24 September 1996; K. D. Bennett; B. Y. Kim; Y. Liao, Eds.; SPIE: Bellingham, WA, 1996; Vol. 2895, pp 116–119. doi:10.1117/12.252170.

(2) Zhang, W.; Wan, F.; Gu, J.; Ai, S.; Ye, J.; Yamamoto, K.; Jin, L. *Chromatographia* **2004**, *59* (11–12), 677. doi:10.1365/s10337-004-0313-x.

(3) Adduci, F.; Catalano, I. M.; Cingolani, A.; Minafra, A. *Phys. Rev. B* **1977**, *15* (2), 926. doi:10.1103/PhysRevB.15.926.

(4) Moy, J.-P. *Nucl. Instrum. Methods Phys. Res. A* **2000**, *442* (1–3), 26. doi:10.1016/S0168-9002(99)01196-1.

(5) Iwanaga, M.; Watanabe, M.; Hayashi, T. *Phys. Rev. B* **2000**, *62* (16), 10766. doi:10.1103/PhysRevB.62.10766.

(6) Baird, C. *Environmental Chemistry;* W.H. Freeman and Company: New York, 1995.

(7) Guo, F.; Ma, D.; Wang, L.; Jing, X.; Wang, F. *Semicond. Sci. Technol.* **2005**, *20* (3), 310. doi:10.1088/0268-1242/20/3/010.

(8) Hackett, J.W.; Turro, C. *Inorg. Chem.* **1998**, *37* (8), 2039. doi:10.1021/ic970801b.

(9) Yanagida, M.; Singh, L.P.; Sayama, K.; Hara, K.; Katoh, R.; Islam, A.; Sugihara, H.; Arakawa, H.; Nazeeruddin, M.K.; Gratzel, M. *J. Chem. Soc., Dalton Trans.* **2000**, 2817. doi:10.1039/b002391o.

(10) Armaroli, N.; Eckert, J.-F.; Nierengarten, J.-F. *Chem. Commun. (Camb.)* **2000**, 2105. doi:10.1039/b006174n.

(11) Armaroli, N. *Chem. Soc. Rev.* **2001**, *30* (2), 113. doi:10.1039/b000703j.

(12) Glatfelter, A.; Dybowski, C.; Bai, S.; Perry, D.L. *Mater. Lett.* **2007**, *61* (2), 437. doi:10.1016/j.matlet.2006.04.076.

(13) Glatfelter, A. Ph.D. Dissertation, University of Delaware, Newark, DE, 2001.

(14) Harrowfield, J.M.; Miyamae, H.; Skelton, B.W.; Soudi, A.A.; White, A.H. *Aust. J. Chem.* **1996**, *49* (10), 1165, and references cited therein. doi:10.1071/CH9961165.

(15) Parr, J.; Ross, A. T.; Slawin, A. M. *Polyhedron* **1997**, *16* (16), 2765. doi:10.1016/S0277-5387(97)00033-8.

(16) Shimoni-Livny, L.; Glusker, J.P.; Bock, C.W. *Inorg. Chem.* **1998**, *37* (8), 1853, and refs. cited therein. doi:10.1021/ic970909r.

(17) Zhu, H.-G.; Xu, Y.; Yu, Z.; Wu, Q.-J.; Fun, H.-K.; You, X.-Z. *Polyhedron* **1999**, *18* (26), 3491. doi:10.1016/S0277-5387(99)00280-6.

(18) Bowmaker, G.A.; Harrowfield, J.M.; Miyamae, H.; Shand, T. M.; Skelton, B.W.; Soudi, A.A.; White, A.H. *Aust. J. Chem.* **1996**, *49* (10), 1089. doi:10.1071/CH9961089.

(19) Neue, G.; Dybowski, C.; Smith, M.L.; Barich, D.H. *Solid State Nucl. Magn. Reson.* **1994**, *3* (3), 115. doi:10.1016/0926-2040(94)90007-8.

(20) Neue, G.; Dybowski, C.; Smith, M.L.; Hepp, M. A.; Perry, D. L. *Solid State Nucl. Magn. Reson.* **1996**, *6* (3), 241. doi:10.1016/0926-2040(95)01225-7.

(21) Van Bramer, S.E.; Glatfelter, A.; Bai, S.; Dybowski, C.; Neue, G. *Concepts Magn. Reson.* **2002**, *14* (6), 365. doi:10.1002/cmr.10042.

(22) Neue, G.; Dybowski, C. *Solid State Nucl. Magn. Reson.* **1997**, *7* (4), 333. doi:10.1016/S0926-2040(96)01291-X.

(23) Beckmann, P.A.; Dybowski, C. *J. Magn. Reson.* **2000**, *146* (2), 379. doi:10.1006/jmre.2000.2171.

(24) Dybowski, C.; Neue, G. *Prog. Nucl. Magn. Reson. Spectrosc.* **2002**, *41* (3–4), 153. doi:10.1016/S0079-6565(02)00005-5.

(25) Baerends, E.J.; Autschbach, J.; Bérces, A.; Bickelhaupt, F.M.; Bo, C.; de Boeij, P.L.; Boerrigter, P.M.; Cavallo, L.; Chong, D. P.; Deng, L.; Dickson, R.M.; Ellis, D.E.; Fan, L.; Fischer, T.H.; Fonseca Guerra, C.; van Gisbergen, S.J.A.; Groeneveld, J.A.; Gritsenko, O.V.; Grüning, M.; Harris, F. E.; van den Hoek, P.; Jacob, C.R.; Jacobsen, H.; Jensen, L.; van Kessel, G.; Kootstra, F.; van Lenthe, E.; McCormack, D.A.; MIchalak, A.; Neugebauer, J.; Osinga, V.P.; Patchkovskii, S.; Philipsen, P. H.T.; Post, D.; Pye, C.C.; Ravenek, W.; Ros, P.; Schipper, P.R. T.; Schreckenbach, G.; Snijders, J.G.; Solà, M.; Swart, M.; Swerhone, D.; te Velde, G.; Vernooijs, P.; Versluis, L.; Visscher, L.; Visser, O.; Wang, F.; Wesolowski, T.A.; van Weezenbeek, E.; Wiesenekker, G.; Wolff, S.K.; Woo, T.K.; Yakovlev, A.L.; Ziegler, T. *Amsterdam Density Functional (ADF),* version 2006.01; Scientific Computing and Modelling: Vrije Universiteit, Amsterdam, the Netherlands, 2006.

(26) Schreckenbach, G.; Ziegler, T. *J. Phys. Chem.* **1995**, *99* (2), 606. doi:10.1021/j100002a024.

(27) Schreckenbach, G.; Ziegler, T. *Int. J. Quantum Chem.* **1996**, *60* (3), 753. doi:10.1002/(SICI)1097-461X(1996)60:3<753::AID-QUA4>3.0.CO;2-W.

(28) Schreckenbach, G.; Ziegler, T. *Int. J. Quantum Chem.* **1997**, *61* (6), 899. doi:10.1002/(SICI)1097-461X(1997)61:6<899::AID-QUA3>3.0.CO;2-R.

(29) (a) Wolff, S. K.; Ziegler, T. *J. Chem. Phys.* **1998**, *109* (3), 895. doi:10.1063/1.476630;; (b) Wolff, S. K.; Ziegler, T.; van Lenthe, E.; Baerends, E.J. *J. Chem. Phys.* **1999**, *110* (16), 7689. doi:10.1063/1.47880.

(30) Vosko, S.H.; Wilk, L.; Nusair, M. *Can. J. Phys.* **1980**, *58* (8), 1200. doi:10.1139/p80-159.

(31) Becke, A. *Phys. Rev. A* **1988**, *38* (6), 3098. doi:10.1103/PhysRevA.38.3098.

(32) Perdew, J. *Phys. Rev. B* **1986**, *33* (12), 8822. doi:10.1103/PhysRevB.33.8822.

(33) Perdew, J.; Burke, K.; Ernzerhof, M. *Phys. Rev. Lett.* **1996**, *77* (18), 3865. doi:10.1103/PhysRevLett.77.3865.

(34) Zhang, Y.; Yang, W. *Phys. Rev. Lett.* **1998**, *80* (4), 890. doi:10.1103/PhysRevLett.80.890.

(35) Oyamada, T.; Iijima, T.; Kimura, H. *Bull. Chem. Soc. Jpn.* **1971**, *44* (10), 2638. doi:10.1246/bcsj.44.2638.

(36) Mason, J. *Solid State Nucl. Magn. Reson.* **1993**, *2* (5), 285. doi:10.1016/0926-2040(93)90010-K.

(37) Dybowski, C.; Smith, M. L.; Hepp, M. A.; Gaffney, E. J.; Neue, G.; Perry, D. L. *Appl. Spectrosc.* **1998**, *52* (3), 426. doi:10.1366/0003702981943626.

(38) Nizam, M.; Allavena, M.; Bouteiller, Y.; Suits, B. H.; White, D. *J. Magn. Reson.* **1989**, *82* (3), 441. doi:10.1016/0022-2364(89)90080-2.

(39) Kye, Y.-S.; Connolly, S.; Herreros, B.; Harbison, G. S. *Main Group Met. Chem.* **1999**, *22*, 373.

(40) Fayon, F.; Farnan, I.; Bessada, C.; Coutures, J.; Massiot, D.; Coutures, J. P. *J. Am. Chem. Soc.* **1997**, *119* (29), 6837. doi:10.1021/ja963593f.

(41) Irwin, A. D.; Chandler, C. D.; Assink, R.; Hampden-Smith, M. J. *Inorg. Chem.* **1994**, *33* (6), 1005. doi:10.1021/ic00084a005.

(42) Katz, M. J.; Michaelis, V. K.; Aguiar, P. M.; Yson, R.; Lu, H.;

Can. J. Chem. Downloaded from www.nrcresearchpress.com by Xi'an Jiaotong University on 09/19/12
For personal use only.

Kaluarachchi, H.; Batchelor, R. J.; Schreckenbach, G.; Kroeker, S.; Patterson, H. H.; Leznoff, D. B. *Inorg. Chem.* **2008**, *47* (14), 6353. doi:10.1021/ic800425f.

(43) Alarcón, S. H.; Olivieri, A. C.; Carss, S. A.; Harris, R. K. *Angew. Chem. Int. Ed. Engl.* **1994**, *33* (15–16), 1624. doi:10.1002/anie.199416241.

(44) Skachkov, D.; Krykunov, M.; Kadantsev, E.; Ziegler, T. *J. Chem. Theory Comput.* **2010**, *6* (5), 1650. doi:10.1021/ct100046a.

(45) Briand, G. G.; Smith, A. D.; Schatte, G.; Rossini, A. J.; Schurko, R. W. *Inorg. Chem.* **2007**, *46* (21), 8625. doi:10.1021/ic700738w.

Can. J. Chem. Downloaded from www.nrcresearchpress.com by Xi'an Jiaotong University on 09/19/12
For personal use only.

Phosphorus-31 and vanadium-51 solid-state nuclear magnetic resonance spectroscopy of β-vanadyl phosphate — Effects of homo- and heteronuclear spin-spin, electrostatic, and paramagnetic interactions

Klaus Eichele and Arnd-Rüdiger Grimmer

Can. J. Chem. Downloaded from www.nrcresearchpress.com by Xi'an Jiaotong University on 09/19/12
For personal use only.

Abstract: Field-dependent ^{31}P solid-state NMR studies demonstrate that the line shape in spectra of β-$VOPO_4$ depends on ^{51}V–^{31}P direct and indirect spin-spin interactions (M_2 (^{51}V, ^{31}P) = 101(23) × 10^6 rad^2 s^{-2}, $^2J_{iso}$ (^{51}V, ^{31}P) = 48(5) Hz) and, to a lesser extent, on ^{31}P chemical shift anisotropy (δ_{iso} = –10.4(2), $\Omega = \delta_{11} - \delta_{33}$ = 22(2) ppm) and ^{31}P–^{31}P interactions (M_2 (^{31}P, ^{31}P) = 6.7(1) × 10^6 rad^2 s^{-2}). In contrast, homonuclear dipolar interactions play an important role for the field and spinning rate dependent ^{31}P spin-lattice relaxation via paramagnetic impurities (T_1 = 20–60 s). Vanadium-51 magic-angle spinning NMR spectra indicate a sizeable chemical shift anisotropy (δ_{iso} = –754(1), δ_{11} = –336(10), δ_{22} = –344(6), δ_{33} = –1581(8) ppm) and nuclear quadrupole interaction (χ = 1.5(1) MHz, η = 0.35(5)); the principal axis systems of both interactions are clearly not coincident, with an angle of 35(5)° between the greatest component of the electric field gradient tensor and δ_{33}.

Key words: solid-state NMR spectroscopy, ^{31}P NMR, ^{51}V NMR, spin-lattice relaxation, indirect nuclear spin-spin coupling, chemical shift anisotropy, electric field gradient tensor, vanadyl phosphate.

Résumé : Des études RMN du ^{31}P à l'état solide et dépendant du champ démontrent que la forme des raies dans les spectres du β-$VOPO_4$ dépend des interactions spin-spin directes et indirectes (M_2 (^{51}V, ^{31}P) = 101(23) × 10^6 rad^2 s^{-2}, $^2J_{iso}$ (^{51}V, ^{31}P) = 48(5) Hz) et, à un degré moindre, sur l'anisotropie du déplacement chimique du ^{31}P (δ_{iso} = –10,4(2); $\Omega = \delta_{11} - \delta_{23}$ = 22(2) ppm) et aux interactions ^{31}P–^{31}P (M_2 (^{31}P, ^{31}P) = 6,7(1) × 10^6 rad^2 s^{-2}). Par ailleurs, les interactions dipolaires homonucléaires jouent un rôle important pour la relaxation spin-réseau du ^{31}P qui varie avec le champ et la vitesse de rotation par le biais d'impuretés paramagnétiques (T_1 = 20–60 s). Les spectres RMN du vanadium à l'angle magique de rotation indiquent qu'il existe une anisotropie importante du déplacement chimique (δ_{iso} = –754(1), δ_{11} = –336(10), δ_{22} = –344(6), δ_{33} = –1581(8) ppm) et une interaction quadripolaire nucléaire (χ = 1,5(1) MHz, η = 0,35(5)); il est clair que les axes principaux des systèmes des deux interactions ne coïncident pas, avec un angle de 35(5)° entre la composante principale du tenseur du gradient de champ électrique et δ_{33}.

Mots-clés : spectroscopie RMN à l'état solide, RMN du ^{31}P, RMN du ^{51}V, relaxation spin-réseau, couplage spin-spin nucléaire indirect, anisotropie du déplacement chimique, tenseur du gradient de champ électrique, phosphate de vanadyle.

[Traduit par la Rédaction]

Introduction

Vanadium compounds are well-established ingredients in the modern synthesis of organic molecules,[1] where they most often take part in redox transformations, either stoichiometrically or catalytically. Amongst them, vanadyl phosphates (VPOs) found industrial applications as selective and efficient heterogeneous catalysts in the mild oxidation of alkanes or alkenes or in ammoxidation reactions.[2–4] One of the most striking reactions catalyzed by VPOs, dubbed the "Butox" process,[5] is the oxidation of *n*-butane to maleic acid anhydride, recognized as probably the most complex selective oxidation reaction used in industry.[2,6–8] In light of its technical importance, it is no surprise that a manifold of analytical methods, including theoretical investigations, has been employed to study partial aspects of this process such as the actual catalyst materials or the reaction mechanism.[6,9–11] The simultaneous presence of vanadium in oxidation states V(IV) and V(V) appears to be a key feature of active catalyst systems

Received 1 November 2010. Accepted 21 January 2011. Published at www.nrcresearchpress.com/cjc on 19 July 2011.

K. Eichele* and A.-R. Grimmer. Institut für Chemie, Humboldt-Universität zu Berlin, Brook-Taylor-Str. 2, D-12489, Berlin, Germany.

Corresponding author: Klaus Eichele (e-mail: Klaus.eichele@uni-tuebingen.de).

This article is part of a Special Issue dedicated to Professor Roderick E. Wasylishen.

*Present address: Institut für Anorganische Chemie, Universität Tübingen, Auf der Morgenstelle 18, 72076 Tübingen, Germany.

Can. J. Chem. Downloaded from www.nrcresearchpress.com by Xi'an Jiaotong University on 09/19/12
For personal use only.

containing $(VO)_2P_2O_7$ together with $VOPO_4$ phases.[12–14] Facile formation and interconversion of a number of crystalline V(IV) and V(V) phases are characteristics of the VPO system, and this has led to some confusion in the literature as to the actual nature of the active phase. A variety of different crystalline phases have been catalogued for the V(IV) and V(V) species, but often the identification is not straightforward, especially if amorphous materials are involved.[15–17] Further complications arise from the influence of the hydrocarbon, the different P:V ratios, the various methods used to obtain the precursor material that modify crystallinity and composition, and the residual proton content, factors all of which are known to affect the nature and performance of the catalyst material.[2,18–20]

Recently, the ability of $VOPO_4$ systems to form different 2D or 3D structures that can be interlayered with a wide variety of different molecules or ions[21–27] led to renewed interest regarding their potential use as cathode materials in lithium ion batteries.[28–33] Another, less apparent feature of VPO systems is the analogy of phosphate and vanadate, expressed for example in biological systems in certain enzymes (phosphatases or peroxidases),[34,35] or in materials where V(V) can potentially replace P(V),[36–38] such as in V_2O_5–P_2O_5 glasses that are of interest because of their electrical or optical properties.[39,40]

As part of our efforts to investigate the VPO system via solid-state NMR methods, the objective of the present study is the ^{31}P solid-state NMR characterization of β-$VOPO_4$ as a prototype of diamagnetic vanadyl phosphates. This is the most stable phase of $VOPO_4$, and its presence in catalyst systems has been detected by several groups.[9,41–46] The ^{31}P NMR properties of β-$VOPO_4$ have been investigated by other workers in the field, but the spectra were partly misinterpreted or obtained under conditions inappropriate to reveal NMR spectroscopic details.[13,14,47–49] Using ^{31}P spin-echo mapping, Li et al.[49] reported for a static powder sample of β-$VOPO_4$ a peak centered near 0 ppm, with a width of about 100 ppm (B_0 = 7.05 T), corresponding to ca. 12 kHz. They ascribed the observed width to chemical shift anisotropy. Using the same technique, Sananes et al.[48] observed a chemical shift of 0 ppm. Ben Abdelouahab et al.[47] reported line widths of around 500–600 Hz for the isotropic peak in ^{31}P MAS spectra of β-$VOPO_4$ and a chemical shift of –11.5 ppm. They stated that these widths essentially depend on the crystallinity of the sample, suggesting chemical shift dispersion as cause of broadening. Vedrine and co-workers[13,14] reported a "narrow" peak at –11.8 ppm from their ^{31}P MAS spectra. In contrast, we shall demonstrate that the striking line widths observed in ^{31}P NMR spectra of β-$VOPO_4$ are not due to chemical shift dispersion and chemical shift anisotropy.

The ^{51}V isotope, with a nuclear spin of 7/2 and a natural abundance of 99.8%, is another useful probe to study solid vanadium-containing compounds.[50] In their investigation of β-$VOPO_4$, Ben Abdelouahab et al.[47] also obtained the ^{51}V spectrum of a static powder sample and reported a narrow peak at –354 ppm, apparently in agreement with the octahedral coordination of vanadium. While our study was under way, Lapina et al.[51] and Hirschinger and co-workers[52] carried out detailed ^{51}V NMR investigations of vanadyl phosphates and reported considerable vanadium chemical shift anisotropies and nuclear quadrupolar coupling constants (1.451–1.990 MHz), in contrast to the findings of Ben Abdelouahab et al.[47] In our present investigation of β-$VOPO_4$, we also obtained ^{51}V MAS NMR spectra to resolve these discrepancies.

Experimental

Sample preparation and characterization

The β-polymorph of $VOPO_4$ has been prepared by the usual reaction of H_3PO_4 and V_2O_5.[53] The X-ray powder diffractogram of the reaction product showed 43 well-resolved reflections in the range of $10 \leq 2\theta \leq 50$. Seventeen of them were identical to corresponding lines of powder diffraction file No. 27-948,[54] based on the data of Bordes et al.[53] Another 23 lines of our diffractogram could also be assigned as lines owing to β-$VOPO_4$. Table 1 shows the results of a refinement of the unit cell data based on 40 reflections, the comparison with previous data[53,55] confirming the identity of β-$VOPO_4$. The three remaining weak lines were identical with lines of powder diffraction file No. 47-967, a hydrogen vanadium phosphate hydrate ($H_4V_3P_3O_{16.5}{\cdot}xH_2O$, indicating minor hydrolysis of β-$VOPO_4$ by atmospheric moisture.

NMR experiments

^{31}P and ^{51}V spectra were obtained at 161.98 and 105.25 MHz, respectively, using a Bruker MSL-400 spectrometer (B_0 = 9.4 T). Samples were packed into 4 mm o.d. zirconia rotors. ^{31}P spectra were also obtained at 81.03 MHz with Bruker MSL-200 and DSX-200 spectrometers, using 7 and 4 mm o.d. zirconia rotors, respectively. Phosphorus chemical shifts are referenced with respect to external 85% aqueous H_3PO_4, vanadium chemical shifts are referenced with respect to external neat $VOCl_3$. Spin-lattice relaxation times were obtained with the inversion recovery technique, using a composite pulse for the inversion.[56] Hahn spin-echo experiments employed the phase cycling of Rance and Byrd.[57] Vanadium-51 spectra were obtained after a single pulse with flip angles in the range 20°–30°, using a 0.7 μs pulse duration, corresponding to a "solution" 90° pulse width of 2.55 μs. Calculations of ^{31}P line shapes were carried out using HBA[58] and WSolids.[59] ^{51}V MAS spectra were calculated in the frequency domain using CSolids,[60] a program that takes into account first-order quadrupolar effects and chemical shift anisotropy as well as the relative orientation of both interactions. The calculation of spinning sideband intensities follows the approach of Herzfeld and Berger[61] and Olivieri[62] and incorporates the POWDER space-tiling and interpolation scheme.[63] Details on our implementation to compute NMR spectra under the combined influence of quadrupolar and chemical shift anisotropy interactions can be found in the literature.[64,65] In brief, the principal components of the chemical shift tensor are reported in the convention $\delta_{11} \geq \delta_{22} \geq \delta_{33}$, with an isotropic chemical shift of $\delta_{iso} = (\delta_{11} + \delta_{22} + \delta_{33})/3$, the span of the chemical shift tensor ($\Omega \approx \delta_{11} - \delta_{33}$), and the skew of the tensor ($\kappa = 3(\delta_{22} - \delta_{iso})/\Omega$), with possible values in the range from –1 to +1.[66] The span of the tensor is related to the Herzfeld–Berger parameter μ, via $\mu = \nu_L\Omega/\nu_r$, where ν_L is the Larmor frequency and ν_r is the spinning frequency.[61] The nuclear quadrupolar interaction is the interaction of the nuclear quadrupole moment (eQ) with the components of the electric field gradient (EFG) tensor about the nucleus (V_{ii}), where the components of the EFG

Can. J. Chem. Downloaded from www.nrcresearchpress.com by Xi'an Jiaotong University on 09/19/12
For personal use only.

Table 1. Unit cell data of β-$VOPO_4$.

Reference	*a* (Å)	*b* (Å)	*c* (Å)	Space group
Bordes et al.[53]	7.78	6.13	6.97	*Pbnm*
Gopal and Calvo[55]	7.770(3)	6.143(3)	6.965(3)	*Pnma*
This work	7.7866(7)	6.1331(5)	6.9694(6)	[a]

[a]Powder diffraction data do not permit the determination of the space group.

are ordered according to $|V_{ZZ}| \geq |V_{YY}| \geq |V_{XX}|$. This interaction is characterized by the nuclear quadrupolar coupling constant $\chi = eV_{ZZ}Q/h$ and the asymmetry parameter $\eta = (V_{XX} - V_{YY})/V_{ZZ}$. The relative orientations of the chemical shift and EFG tensor are expressed via the three Euler angles (α, β, and γ) that bring the EFG tensor into alignment with the CSA tensor by consecutive rotations in the *ZYZ* order.

Results and discussion

In the following sections, we shall describe first the structural features of β-$VOPO_4$, because of the intimate relationship between our NMR results and the structure of this system, followed by the ^{31}P and ^{51}V NMR results. ^{31}P NMR data encompass a detailed analysis of the line shapes of static and MAS samples, as well as spin-lattice relaxation data, whereas ^{51}V NMR results are limited to MAS spectra.

Crystal structure

The crystal structure of β-$VOPO_4$ has been described by Gopal and Calvo[55] as belonging to the orthorhombic system (Table 1). As indicated in Fig. 1, vanadium and phosphorus are located on crystallographic mirror planes and all phosphorus and vanadium sites are crystallographically equivalent, thus only one signal is expected in the ^{31}P or ^{51}V NMR spectra. The phosphorus nuclei of the phosphate tetrahedra are linked to four vanadium atoms via intervening oxygen bridges. Because of the crystallographic mirror plane, two of the four phosphorus–oxygen distances are equivalent (1.528 Å) and are not very different from the other P–O distances (1.519 and 1.540 Å). The O–P–O angles range from 107.6° to 110.6°, indicating a moderate distortion of the tetrahedron. However, the six oxygens surrounding vanadium form a severely distorted octahedral environment that is better described as a capped square pyramid. This is due to O4 that forms one short (1.566 Å) and one very long (2.591 Å) vanadium–oxygen contact. The basal square of oxygen atoms features V–O distances in the range from 1.849 to 1.902 Å. Vanadium is displaced from the basal oxygen plane by 0.366 Å toward the O4 atom with the shortest V–O distance, whereas the oxygen square pyramid is relatively regular with O···O distances of 2.605–2.705 Å; O···O distances involving the oxygen with the longest V–O distance are in the range of 2.847–2.981 Å. Thus, the environment of vanadium could still be described as octahedral.[67,68]

Phosphorus-31 NMR line width and line shape

Phosphorus-31 NMR spectra of static and magic-angle spinning powder samples of β-$VOPO_4$ obtained at 9.4 T are shown in Fig. 2. In agreement with the predictions from the crystal structure (vide supra), one peak is observed in the spectra. The spectrum of the static powder sample (Fig. 2*a*) exhibits a line shape that can be described rather well by a single Gaussian peak centered at –10.4 ppm and a full-width at half-maximum of 4780 Hz. Spinning the sample about the magic angle reduces this line width drastically (Fig. 2*b*). However, with a line width of 528 Hz, the peaks are still significantly broader than usually observed for crystalline phosphates of other metals (20–200 Hz).[69–76] We have observed comparable line widths on the order of 400–600 Hz in ^{31}P MAS spectra of other diamagnetic vanadyl orthophosphates,[77] hence, this seems to be a feature of this type of system. The line shapes in the MAS spectra are very close to Gaussian, but the wings of the peaks are even narrower than expected for a Gaussian line shape. In contrast, it is our experience[77] that ^{31}P MAS spectra frequently exhibit mixtures of Gaussian and Lorentzian line shapes.

Phosphorus-31 MAS spectra obtained at low spinning rates (1–2 kHz) show spinning sidebands of appreciable intensity (Fig. 3). Generally, spinning sidebands in ^{31}P MAS spectra arise from the presence of chemical shift anisotropy, i.e., the

Fig. 1. Essential part of the crystal structure of β-$VOPO_4$,[55] showing one PO_4 unit bridging four distorted VO_6 octahedra. Bond distances are indicated. There is a crystallographic mirror plane oriented horizontally and perpendicular to the paper plane, passing through phosphorus and bisecting the O1–P–O1 bond angle.

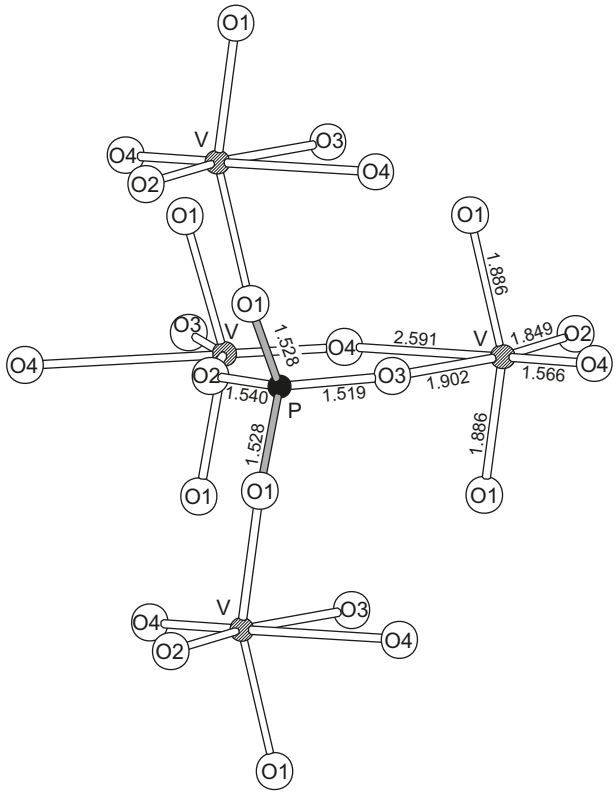

Can. J. Chem. Downloaded from www.nrcresearchpress.com by Xi'an Jiaotong University on 09/19/12
For personal use only.

Fig. 2. Solid-state ^{31}P NMR spectra of β-$VOPO_4$ powder samples obtained at 9.4 T. (*a*) Top trace: static sample, 16 scans, and a 200 s recycle delay. Bottom trace: MAS spectrum with a spinning rate of 3 kHz, 8 scans, and a recycle delay of 100 s. (*b*) Expansion of the MAS isotropic peak. Experimental points are represented by open circles, the best fits using Gaussian peaks of 4780 Hz (static) and 528 Hz (MAS) full-width at half height are indicated by solid lines.

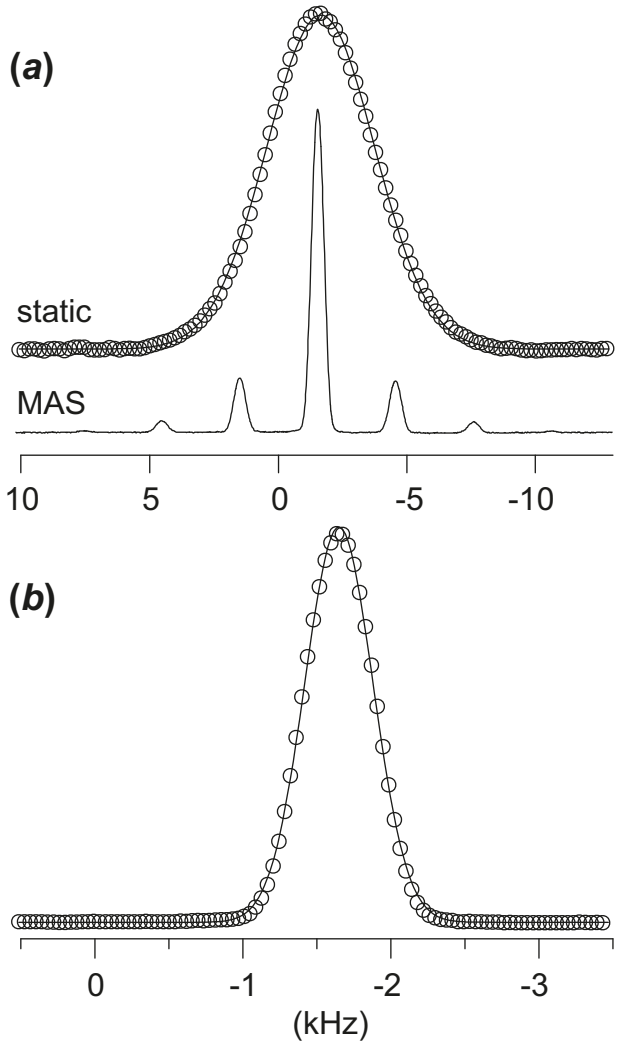

Fig. 3. Solid-state ^{31}P MAS NMR spectra of β-$VOPO_4$ at 9.4 T and a spinning rate of 1.2 kHz, 48 scans, and a recycle delay of 20 s. (*a*) Experimental (top) and calculated (middle) spectra normalized according to their respective total areas, together with the difference spectrum. (*b*) Contour lines representing the intensity ratios I_N/I_0 ($N = \pm1, \ldots, \pm4$) of spinning sidebands of order N. The solid circle represents the best fit at $\mu = 4.96$, $\kappa = 0.03$.

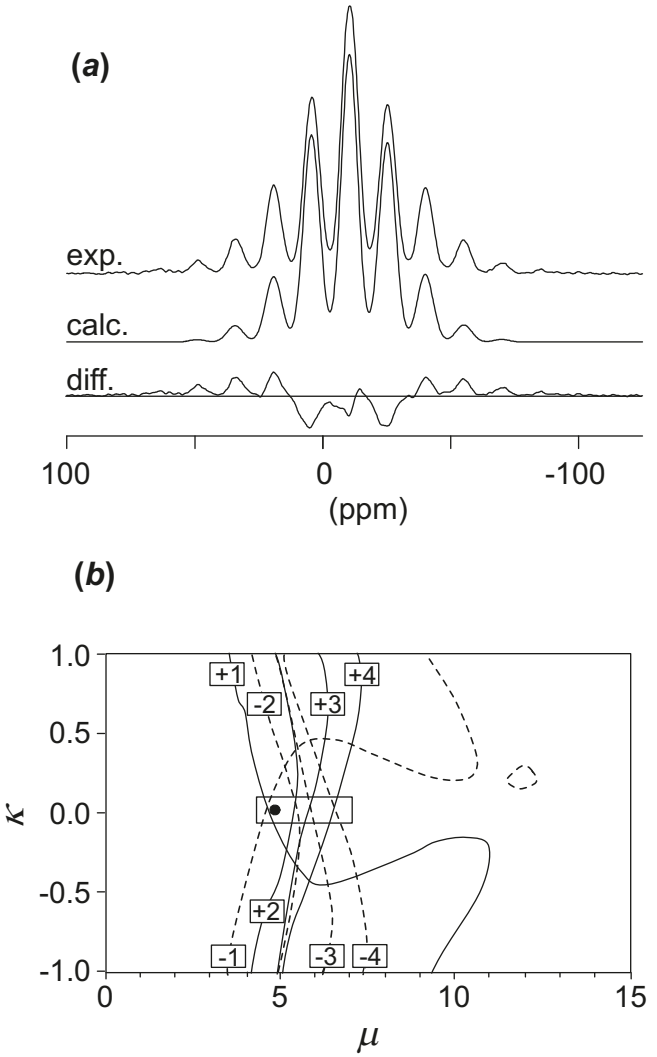

actual chemical shift of ^{31}P depends on the orientation of the crystallites with respect to the external magnetic field. Analysis of the spinning sideband intensities in ^{31}P MAS spectra of β-$VOPO_4$, according to the method of Herzfeld–Berger,[61] yields the following principal components of the phosphorus chemical shift tensor at 9.4 T: $\delta_{11} = 8(7)$, $\delta_{22} = -10(1)$, $\delta_{33} = -29(7)$ ppm, with an isotropic chemical shift of $\delta_{iso} = -10.4(2)$ ppm. This isotropic chemical shift is in good agreement with the chemical shifts reported by Ben Abdelouahab et al.[47] and Vedrine et al.[13] One measure of the magnitude of the chemical shift anisotropy is the span of the chemical shift tensor ($\Omega = 37$ ppm), whereas the symmetry can be characterized by the skew of the tensor ($\kappa = 0.03$).[66] However, the fit is not very satisfying and reveals systematic discrepancies between experimental and calculated intensities (Fig. 3*a*). If the intensities are normalized according to the total area of the spectrum, the experimental spectrum exhibits less intensity for the center peak and first-order spinning sidebands, whereas the other sidebands are more intense than anticipated. This problem of the regular Herzfeld–Berger analysis can also be visualized by looking at the contour plots of normalized spinning sideband intensities (Fig. 3*b*). The best fit ($\kappa = 0.03$, $\mu = 4.96$) lies close to the intersection of the contours of the first-order spinning sidebands because they contribute most of the spectral intensity, but the systematic spread in the intersections of contour lines is significant. Actually, for higher spinning rates the fit appears to be much better; this is, however, deceptive because under these conditions most of the spectral intensity is gathered in the center peak, the intensity of which is not sensitive to anisotropic interactions. The span of the phosphorus chemical shift tensor in β-$VOPO_4$ ($\Omega = 37$ ppm) obtained from the Herzfeld–Berger method is greater than usually observed for orthophosphates of the alkaline and earth alkaline metals, although

Can. J. Chem. Downloaded from www.nrcresearchpress.com by Xi'an Jiaotong University on 09/19/12
For personal use only.

Fig. 4. Field dependence of ^{31}P NMR spectra of β-$VOPO_4$ powder samples obtained under static conditions (*a*) and MAS with a spinning rate of 1.2 kHz (*b*) at 9.4 and 4.7 T. The spectra obtained at 9.4 T are shown as solid lines, overlapped by the broken lines of the 4.7 T spectra. Note that the MAS center peaks have the same line width at both applied magnetic fields.

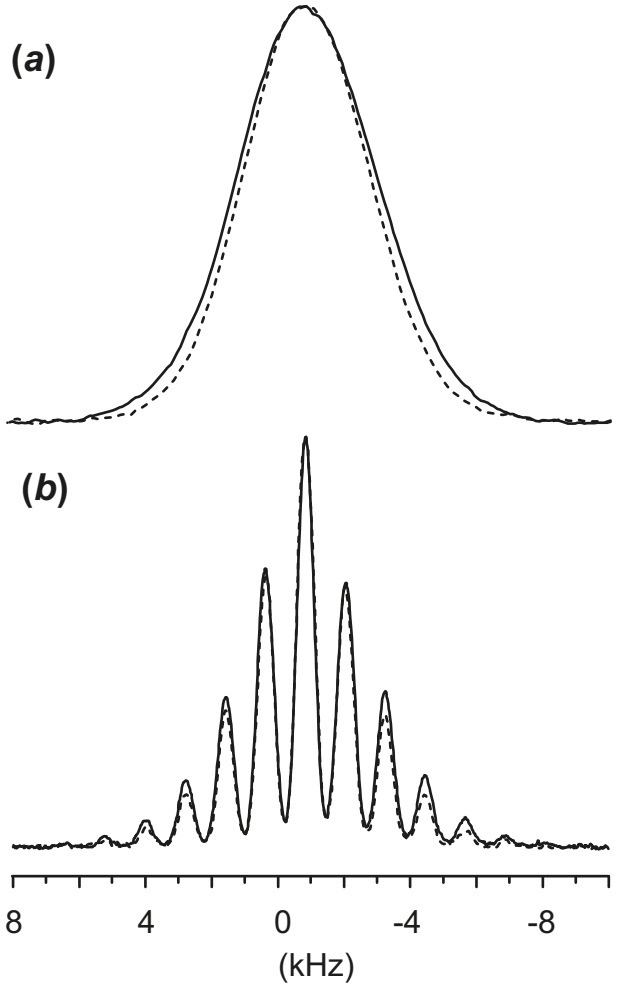

not outside the range observed for orthophosphates;[78–80] however, those cases with greater spans should be considered mixed oxides (e.g., Berlinite, $AlPO_4$, $\Omega = 110$ ppm)[81] rather than orthophosphates (vide infra). The value of 100 ppm reported by Li et al.[49] (vide supra) could be an artifact produced by the spin-echo mapping technique itself or indicate a different phase. The skew of the tensor ($\kappa = 0.03$), on the other hand, is in agreement with the relatively low point group symmetry (C_s) about phosphorus. Combined with the fact that the static powder pattern can be fitted rather well by a single Gaussian peak, these findings suggest that the spinning sideband intensities are not governed by a single chemical shift tensor or that additional interactions are responsible for the occurrence of spinning sidebands. Hence, application of a simple Herzfeld–Berger analysis seems inappropriate.

Initially, a low level of crystallinity of β-$VOPO_4$ appears to be the most likely explanation for the broad ^{31}P NMR peaks in spectra of static or MAS samples, also suggested by Ben Abdelouahab et al.[47] and in line with the observation that disorder is frequent in VPOs.[82] To elucidate the mechanisms potentially responsible for the line shapes observed in the ^{31}P NMR spectra, such as chemical shift dispersion, chemical shift anisotropy, homonuclear and heteronuclear spin-spin interactions, relaxation, or paramagnetic impurities, we have applied a variety of different NMR techniques.

Fig. 5. Center peak in the ^{31}P MAS NMR spectrum of a β-$VOPO_4$ powder sample obtained at 9.4 T. Experimental points are shown as open circles and the solid line represents a theoretical spectrum calculated for four equivalent vanadium nuclei indirect spin-spin coupled to the phosphorus nucleus, convoluted by a Gaussian peak of 70 Hz full-width at half height. This is a better fit than obtained using a pure Gaussian peak, cf. Fig. 2*b*. The bottom trace shows the unconvoluted theoretical spectrum.

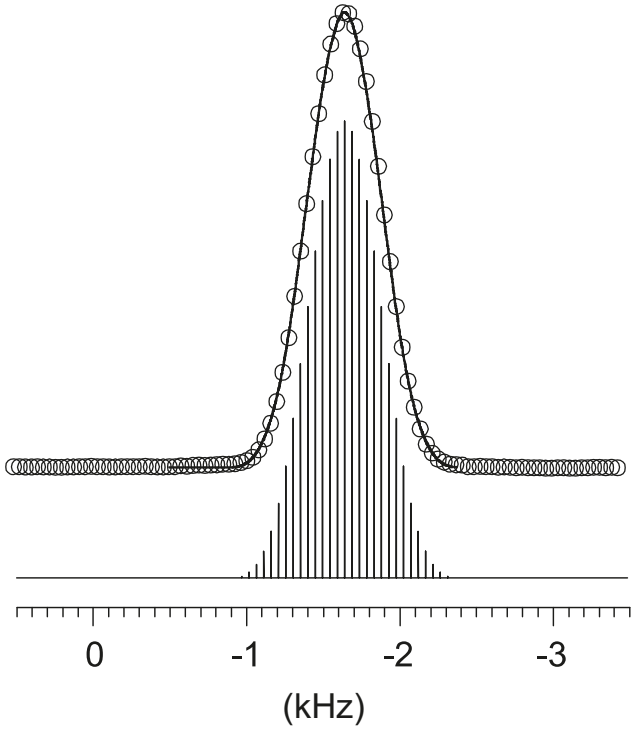

Table 2. Theoretical contributions of the homonuclear and heteronuclear dipolar second moments to the ^{31}P NMR line shape as function of the size of the spin system, calculated for a static powder sample of β-$VOPO_4$.

β-$VOPO_4$	Neighbors	10 Å	20 Å
Homonuclear			
No. of atoms	4	48	390
M_2 (10^6 rad^2 s^{-2})	2.596	8.932	9.244
Heteronuclear			
No. of atoms	4	53	401
M_2 (10^6 rad^2 s^{-2})	97.101	113.736	114.846
Sum			
M_2 (10^6 rad^2 s^{-2})	99.697	122.668	124.090

Magnetic field dependence

To study the contributions arising from chemical shift dispersion — as a consequence of disorder or lack of crystallinity — and chemical shift anisotropy, the field dependence of

Can. J. Chem. Downloaded from www.nrcresearchpress.com by Xi'an Jiaotong University on 09/19/12
For personal use only.

Table 3. Characteristic parameters describing the experimental ^{31}P NMR line shape of static powder samples of β-$VOPO_4$ at 9.4 and 4.7 T (standard deviations in units of least significant digits are given in parentheses).

Experimental	M_2 (10^6 rad^2 s^{-2})	T_2 (10^{-6} s)	σ (10^3 rad s^{-1})	$\Delta\nu_{1/2}$ (kHz)
9.4 T, FID (Gaussian)	156.4(14)	113.1(6)	12.52(6)	4.69(2)
9.4 T, spectrum (Gaussian)	160.0(9)	111.8(3)	12.65(4)	4.74(1)
9.4 T, spectrum[a]	157.9(102)	112.6(36)	12.56(41)	4.71(15)
4.7 T, FID (Gaussian)	127.2(24)	125.4(12)	11.28(11)	4.23(4)
4.7 T, spectrum (Gaussian)	131.4(9)	123.4(5)	11.46(4)	4.30(2)
4.7 T, spectrum[b]	131.1(9)	123.5(4)	11.45(4)	4.29(1)
Hahn spin echo	6.7(1)	547.3(40)	2.58(2)	0.97(1)
Solid echo	79.0(6)	159.1(57)	8.89(32)	3.33(12)
Mansfield sequence	123.3(132)	127.4(69)	11.10(60)	4.16(22)

[a] $M_4 = 7.64(137) \times 10^{16}$ rad^4 s^{-4}; $M_4{:}M_2^2 = 3.07$.
[b] $M_4 = 5.64(27) \times 10^{16}$ rad^4 s^{-4}; $M_4{:}M_2^2 = 3.28$.

Fig. 6. Phosphorus-31 NMR signal intensities of static powder samples of β-$VOPO_4$ as a function of time for different pulse experiments. Solid circles show the echo amplitudes of Hahn echo experiments, along with a fit assuming a Gaussian decay (solid line). This is to be compared with the broken lines calculated from the theoretical values of M_2 (P, P) for A_2 or AX spin systems. Also included is the decay of the free induction decay following a regular 90° pulse (solid diamonds), together with a Gaussian fit (solid line). This decay is slightly faster than calculated using the heteronuclear M_2 (V, P) value (broken line). The echo intensity decay in solid echo experiments is shown as open circles.

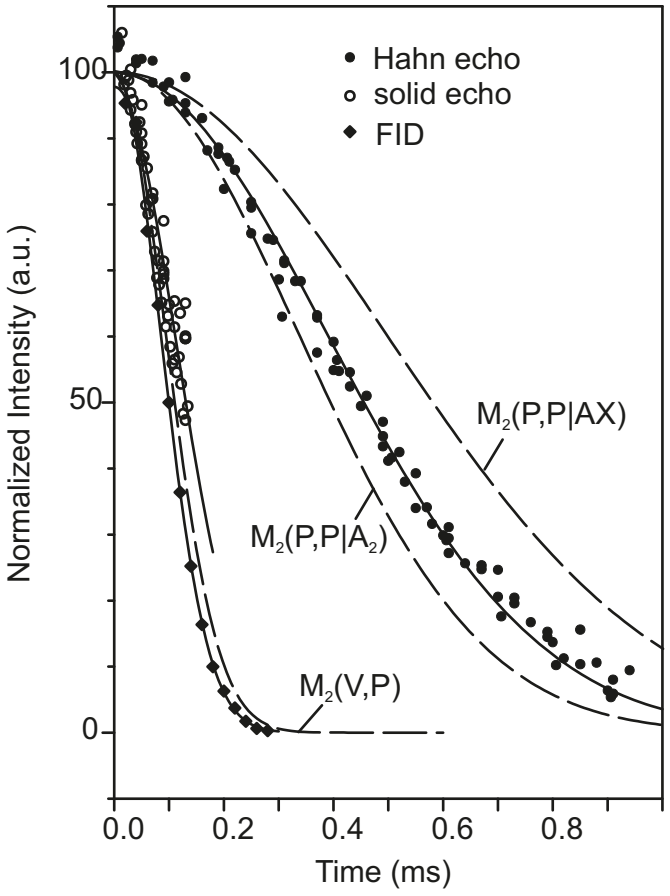

Fig. 7. Dependence of the initial gradient of ^{31}P NMR intensity at $t = 0$ on delay τ for a 90°–τ– 90°$_0$°–$acq(t)$ pulse sequence in a static powder sample of β-$VOPO_4$. The normalization factor A_0^{-1} is the inverse of the FID signal amplitude immediately following the first 90° pulse. The solid line represents the result from linear regression through the initial experimental points, shown as solid circles, whereas the broken line is the gradient calculated from the theoretical value of M_2 (V, P).

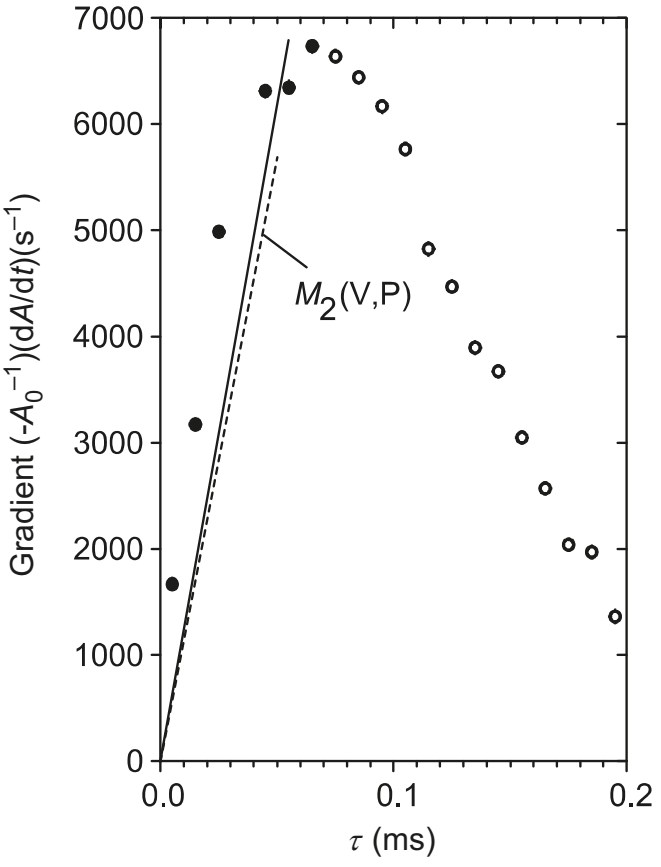

^{31}P spectra was studied at applied magnetic fields of 9.4 and 4.7 T. Spectra obtained for static and MAS samples at both fields are shown in Fig. 4. At 4.7 T, the spectrum of the static powder sample has a line width of 4320 Hz, i.e., about 460 Hz narrower than at 9.4 T. In contrast, the width of the center peak in the MAS spectra is basically independent of

Can. J. Chem. Downloaded from www.nrcresearchpress.com by Xi'an Jiaotong University on 09/19/12
For personal use only.

Table 4. Phosphorus-31 spin-lattice relaxation time (T_1) measured for a sample of β-$VOPO_4$ at different magnetic fields, spinning rates, and temperatures (standard deviations in units of the least significant digit are given in parentheses).

B_0 (T)	ν_R (kHz)	T_1 (s)	T_1' (s)	n
9.4	0	24.9(7)	25.7(2)	0.888(8)
	0, 330 K	20.5(5)	21.1(1)	0.885(7)
	1.2	19.9(4)	20.2(1)	0.910(7)
	2	20.7(9)	20.6(7)	0.912(35)
	5	31.2(10)	32.6(3)	0.880(8)
	10	53.3(21)	60.0(9)	0.852(8)
4.7	0	15.8(3)	16.0(1)	0.884(9)
	1.2	12.8(3)	12.8(1)	0.871(8)
	2	12.9(4)	13.3(1)	0.885(8)
	3	15.3(5)	15.9(1)	0.881(6)
	4	19.2(5)	19.8(2)	0.870(6)
	8	36.1(12)	37.5(3)	0.852(6)
	12	52.2(23)	56.2(7)	0.822(9)

Note: Measured at room temperature unless stated otherwise. Values of T_1 are the results of a mono-exponential, three-coefficient fit to the recovery curves, whereas the values of T_1' result from a fit to a stretched exponential, with the exponent n reported in the last column.

Fig. 8. Phosphorus-31 inversion recovery experiment on a static powder sample of β-$VOPO_4$ at 9.4 T. The broken line is a fit to a mono-exponential function using eq. [9] ($A = 0.943(9)$, $T_1 = 24.9(7)$ s, and $n = 1$) and the solid line is a fit to a stretched exponential ($A = 0.949(1)$, $T'_1 = 25.7(2)$ s, and $n = 0.888(8)$).

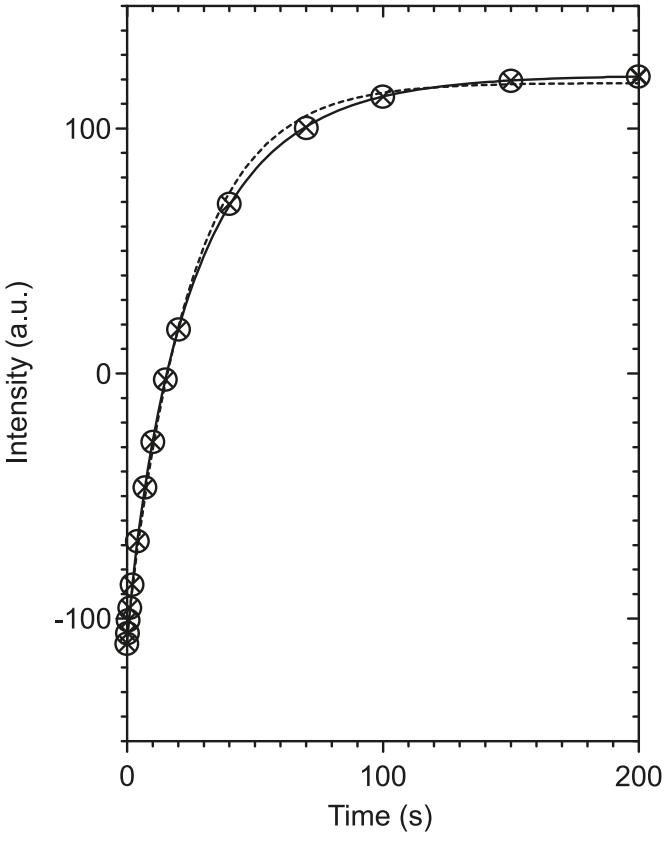

Fig. 9. Dependence of the ^{31}P spin lattice relaxation time (T_1) of a powder sample of β-$VOPO_4$ on spinning rate, magnetic field strength, and temperature. Lines connecting data points are merely guides for the eye.

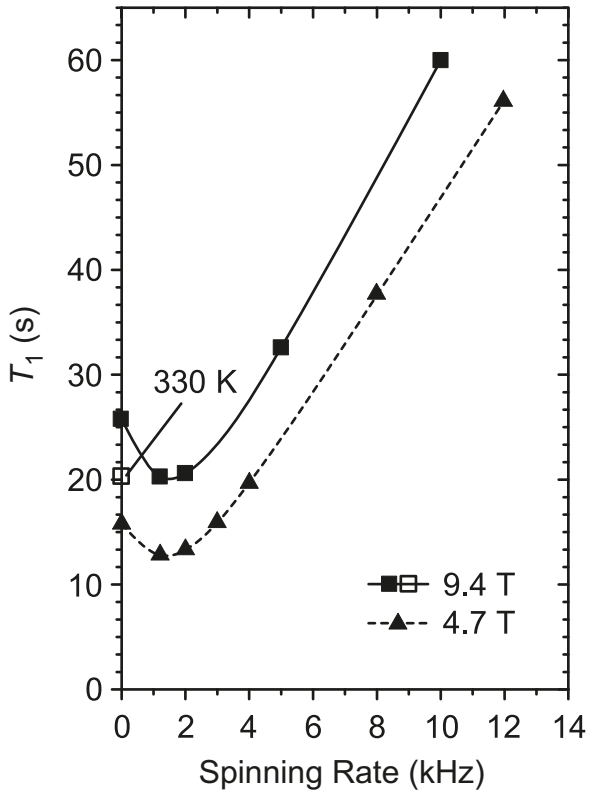

the magnetic field strength (506 Hz at 4.7 T). The lack of field dependence of the isotropic peak line width in the MAS spectra suggests that indirect spin-spin interactions between vanadium and phosphorus should be the cause of the line broadening observed for the isotropic peak, analogous to indium–phosphorus couplings in ^{31}P MAS spectra of indium phosphide.[83,84] The geometrical parameters (e.g., V–O and P–O distances) involving the four vanadium nuclei surrounding the phosphorus nucleus do not differ significantly from each other, hence we shall assume that ^{31}P is coupled to four equivalent ^{51}V nuclei ($I = 7/2$). Thus, the total spin of the four vanadium centers is $I_{max} = 4I = 14$, with a total number of components (i.e., the number of different states m_{Imax}) of $2I_{max} + 1 = 29$. There are $(2I + 1)^4 = 4096$ independent states of the four vanadium nuclear spins, the intensities of which are distributed according to the coefficients in the expansion of the polynomial $[\Sigma\, x^{(2I-q)}]^4$ ($q = 0,\ldots, 2I$) across the 29 different components, as demonstrated by the stick diagram in Fig. 5.[85,86] This stick diagram was calculated using a value of $^2J_{iso}(^{51}V, ^{31}P) = 48(5)$ Hz for the indirect spin-spin coupling constant. Convolution of this multiplet by a Gaussian peak of 70 Hz full-width at half-maximum results in a better representation of the experimental line shape than a mere Gaussian peak (Fig. 2*b*), especially in the wings of the peak. The value of 48 Hz should be considered as an upper limit because it was determined indirectly rather than from resolved splittings. However, given a recent ^{29}Si MAS NMR report on $^2J_{iso}(^{51}V, ^{29}Si) = 28$ Hz for a Si–O–V linkage, this value is not unreasonable.[87]

Can. J. Chem. Downloaded from www.nrcresearchpress.com by Xi'an Jiaotong University on 09/19/12
For personal use only.

Fig. 10. Vanadium-51 MAS spectrum of β-$VOPO_4$ obtained at 9.4 T with a spinning rate of 4.0 kHz. The top trace shows the experimental spectrum (400 scans and a 2 s recycle delay) and the bottom trace shows a spectrum calculated with the parameters given in the text.

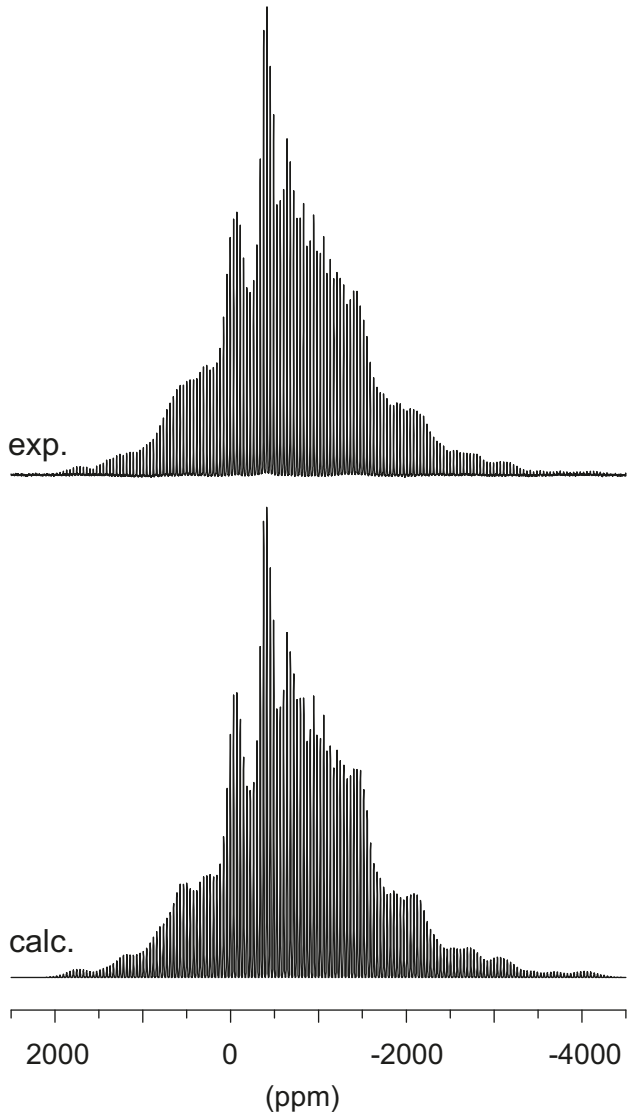

Potentially, there are other interactions that may influence the line width of the ^{31}P MAS spectra. The ^{51}V nucleus has a nuclear quadrupole moment and experiences a weak interaction with the electric field gradient about the vanadium nucleus (vide infra). Under such conditions, MAS will fail to completely average the phosphorus–vanadium direct dipolar coupling and to remove its effect on the ^{31}P MAS spectrum, leading to splitting or broadening of the isotropic MAS peaks. This phenomenon, also called residual dipolar coupling, has been amply studied for a variety of different spin systems.[88,89] The theoretical details shall not be reported here because the contributions from this effect to the ^{31}P MAS line width are negligibly small. From ^{51}V MAS NMR spectra, which show all possible ^{51}V transitions (vide infra), we can estimate the ^{51}V nuclear quadrupolar coupling constant to be 1.5 MHz. In combination with a dipolar coupling constant,

$$[1] \qquad R = \left(\frac{\mu_0}{4\pi}\right)\left(\frac{\gamma_I\gamma_S}{r_{IS}^3}\right)\left(\frac{\hbar}{2\pi}\right)$$

calculated from the crystal structure with r_{IS} between 3.173 and 3.334 Å, we can place an upper limit on the line width contribution from the residual dipolar coupling of <4 Hz at 9.4 T.

Because all phosphorus sites in β-$VOPO_4$ are crystallographically equivalent, all phosphorus nuclei have the same isotropic chemical shift. However, one half of the crystallographic sites are related by twofold screw axes to the other half, thus the chemical shift tensor principal axis systems of those sites will generally not be coincident.[90] In such cases, broadening or splitting may be observed in the MAS spectrum.[91] Such effects are generally dependent on the magnetic field strength and the spinning rate, but they were not observed in the present case.

Phosphorus-31 line shape of static powder sample

Via the field dependence of ^{31}P MAS NMR spectra we have demonstrated that the isotropic peak line width is dominated by the indirect vanadium–phosphorus spin-spin coupling. As shown above, the width of the static spectrum measured in Hz is also basically field independent (there is a 10% increase in width going from 4.7 to 9.4 T). Consequently, a Herzfeld–Berger analysis of the spinning sideband intensities at 4.7 T yields quite different chemical shift tensor principal components: δ_{11} = 26(13), δ_{22} = –10(2), δ_{33} = –48(13) ppm, $\Omega \approx 74$ ppm, and $\kappa = 0.03$, a clear indication that the Herzfeld–Berger analysis based on pure chemical shift anisotropy is inappropriate in this case. On the other hand, this suggests that homonuclear or heteronuclear dipolar couplings may play an important role:[92,93] if measured in ppm, the width of the spectrum should remain constant on going to twice the field if chemical shift anisotropy is the broadening mechanism; on the other hand, dipolar coupling as broadening mechanism will show a decrease of a factor of 0.5 on going to twice the magnetic field strength. In contrast to indirect spin-spin couplings, which are transmitted by the electrons of intervening bonds and are usually limited to nuclei in the immediate environment, dipolar couplings occur through space and, in principle, involve the total crystallite. The size of this spin system makes the detailed calculation of spectral line shapes an unsurmountable task. Because the resulting line shapes are generally featureless, the so-called moments of a spectrum are useful descriptors. The jth moment (M_j) for a line shape $f(\omega)$ is defined in angular frequency units as

$$[2] \qquad M_j = \int_{-\infty}^{\infty} (\omega - \langle\omega\rangle)^j f(\omega)\,\mathrm{d}\omega \Big/ \int_{-\infty}^{\infty} f(\omega)\,\mathrm{d}\omega$$

where the denominator is a normalizing factor and $\langle\omega\rangle$ is the mean angular frequency of the band

$$[3] \qquad \langle\omega\rangle = \int_{-\infty}^{\infty} \omega f(\omega)\,\mathrm{d}\omega \Big/ \int_{-\infty}^{\infty} f(\omega)\,\mathrm{d}\omega$$

The contribution to the second moment of a line shape resulting from homonuclear and heteronuclear dipolar couplings ($M_2(I, I)$ and $M_2(I, S)$) can be calculated from internuclear distances r_{ij} by Van Vleck theory,[94] which in the case of a polycrystalline material predicts[95,96]

Table 5. Vanadium-51 NMR parameters of β-$VOPO_4$ reported in the literature or obtained in the present study.

Parameter	Ben Abdelouahab et al.[47]	Lapina et al.[51]	Siegel et al.[52]	Nielsen[124]	Present work
δ_{iso} (ppm)	–354	–755	–735	–756	–754(1)[a]
Ω (ppm)	—	1227	1247	1247	1245(10)
κ	—	1.0	0.934	0.974	0.98(2)
η_σ	—	0	0.05	0.02(10)	0.02(2)
δ_{11} (ppm)	—	–346	–306	–335	–336(10)
δ_{22} (ppm)	—	–346	–346	–351	–344(6)
δ_{33} (ppm)	—	–1573	–1553	–1582	–1581(8)
$\alpha°$	—	6	90	82(10)	90(20)
$\beta°$	—	43	35	33(5)	35(5)
$\gamma°$	—	—	195	—	—[b]
χ (MHz)	—	1.990	1.451	1.52(2)	1.5(1)
η	—	0.59	0.44	0.37(3)	0.35(5)

[a]Corrected for second-order quadrupolar shift.

[b]Not defined for a basically axially symmetric chemical shift tensor. The tensor conventions used by Lapina et al. differs from ours, and we have converted them to meet our conventions.

$$[4] \qquad M_2(I,I) = \frac{3}{5} I(I+1)(2\pi)^2 \sum R_{ij}^2$$

$$[5] \qquad M_2(I,S) = \frac{4}{15} S(S+1)(2\pi)^2 \sum R_{ij}^2$$

where R_{ij} is the direct dipolar coupling constant between the two nuclei involved, as defined in eq. [1] and I, S are the nuclear spins. The sum runs over all relevant nuclei (j) in relation to the considered nucleus i. For the homonuclear case, eq. [4] is only strictly valid if the spins in the pair-wise summation behave as an A_2 spin system; otherwise, if the chemical shift difference becomes greater than the dipolar coupling, the spin system may behave similarly to a heteronuclear spin pair and eq. [5] should be used; a comparison of eqs. [4] and [5] shows that the second moment of an A_2 spin system is 9/4 times greater than that of an AX spin system. In Table 2, we have collected various second moments calculated from the structure of β-$VOPO_4$. It is evident that the dipolar second moment in ^{31}P NMR spectra of β-$VOPO_4$ depends mainly on the four nearest vanadium atoms; they contribute 78% of the total dipolar second moment. Basically, one can conclude that all NMR active nuclei within a sphere of 10 Å contribute significantly to M_2, and in the case of homonuclear dipolar interactions it is not sufficient to consider only the four nearest neighbors, because they contribute only 28% of the homonuclear dipolar M_2.

Experimentally, one can determine the second moment of the spectrum by evaluating eq. [2] directly (Table 3). However, in practice it is not so easy to obtain meaningful and reproducible second moments.[97,98] After we had developed a satisfactory protocol, we discovered that Hendrickson and Tabbey had already published a similar procedure.[98] In short, one starts to calculate M_2 with truncation limits too close to the mean angular frequency and this introduces a systematic error. Then, the truncation limits are gradually extended to both sides of the center, until they are far from the center and introduce appreciable random error. When M_2 is plotted as a function of truncation limits, the initial region of systematic errors shows a systematic increase of M_2 until a plateau is reached, afterwards the region of increasing random errors can be identified by increased scattering of the values of M_2. The final second moment is determined as an average of the values in the intermediate region, the plateau between the two extremes. The ratio M_4:M_2^2 is a useful measure whether an observed line shape is Gaussian; the ratio is 3 for a Gaussian and several orders of magnitude larger for a Lorentzian (in principle, the second and higher moments of a Lorentzian do not have a finite value).[99] As indicated by the ratios M_4:M_2^2 in Table 3 (3.07 at 9.4 T and 3.28 at 4.7 T), the experimental line shapes are very close to Gaussian line shapes. In such situations, it is much easier to obtain the second moment from a fit of the spectrum to a Gaussian peak or of the free induction decay to a Gaussian. The relations of the second moment to the variance of the distribution (i.e., the mean squared width), σ^2, the full-width at half-height (in Hz), $\Delta\nu_{1/2}$, or to the decay constant (in s), T_2, is given by

$$[6] \qquad M_2 = \sigma^2 = (2\ln 2)(\pi\Delta\nu_{1/2})^2 = \frac{2}{(T_2)^2}$$

In the present case, we found the fit of the spectrum to a Gaussian peak to be the most robust procedure, although all methods give consistent results. We also applied various pulse sequences to identify experimentally the different contributions to the second moment, i.e., homonuclear and heteronuclear couplings. The theory behind these sequences has been elaborated by previous workers,[100] thus, we shall focus on the essence of these methods. The results of these experiments are also given in Table 3 and visualized in Fig. 6.

Hahn echo sequence

One of the experiments that we have applied is the common 90°–τ/2–180°$_{0°}$–τ/2–*acq* sequence, which we shall call the Hahn echo sequence. The Hahn echo refocuses all interactions linear in the spin operators, such as chemical shift and heteronuclear dipolar interactions; thus, the decay of the echo intensity as a function of delay τ in a solid sample is, to a first approximation, determined by homonuclear dipolar interactions. In the case of β-$VOPO_4$, the decay of the echo intensity is of Gaussian type, characterized by an M_2 of 6.7(1) × 10^6 rad^2 s^{-2} (Table 3). In this fit, we have combined data obtained at 9.4 and 4.7 T. The experimental value compares reasonably well with the homonuclear second moment calculated from the crystal structure (9.2 × 10^6 rad^2 s^{-2}) shown in Table 2.

Can. J. Chem. Downloaded from www.nrcresearchpress.com by Xi'an Jiaotong University on 09/19/12
For personal use only.

Can. J. Chem. Downloaded from www.nrcresearchpress.com by Xi'an Jiaotong University on 09/19/12
For personal use only.

Several effects could be responsible for this reduction of the homonuclear M_2 compared with the value calculated from eq. [4]: (*i*) The dipolar coupling could be reduced by motion, not likely in such a rigid solid; (*ii*) indirect spin-spin coupling may also reduce M_2, also not likely for nuclear spins that are separated by four bonds; (*iii*) most likely is that eq. [4] is not strictly valid; this equation requires that the homonuclear spins in the pair-wise addition behave as an A_2 spin system. However, if the chemical shift difference in the spin pair is comparable to or greater than the dipolar interaction, the quantum mechanical "flip-flop" term may be quenched, and the spin system may behave similarly to a heteronuclear spin pair, where eq. [5] should be applied. The resulting value of M_2 is reduced by a factor of 4/9 and the spin echo intensity decays slower, as indicated in Fig. 6. In β-$VOPO_4$, at least two effects will cause instantaneous chemical shift differences: (*i*) crystallographically equivalent, but magnetically nonequivalent chemical shift tensors will have different instantaneous chemical shifts as a function of crystallite orientation; (*ii*) two coupled ^{31}P nuclei may be connected to ^{51}V nuclei in different spin states and the different heteronuclear ^{51}V–^{31}P dipolar and indirect couplings will act as chemical shift in this context. Our results on ^{31}P spin lattice relaxation in β-$VOPO_4$ (vide infra) also indicate that this effect is a likely explanation for the reduction of the homonuclear M_2 by partially quenching the flip-flop term.

Solid-echo sequence

The $90°$–$\tau/2$–$90°_{90°}$–$\tau/2$–*acq* sequence, referred to here as solid echo, refocuses interactions bilinear in the same type of spin, such as homonuclear dipolar or quadrupolar couplings. In cases where the homonuclear second moment is much greater than the heteronuclear interactions, a well-defined echo is produced; in contrast, if the heteronuclear interactions dominate, a solid echo will not occur. As the calculated values of M_2 owing to heteronuclear couplings indicate (Table 2), the latter situation is indeed met in the case of ^{31}P NMR spectra of β-$VOPO_4$. Additionally, the magnitude of heteronuclear dipolar couplings results in a fast decay of the signals such that the echoes have to be sampled after short delays, such that they are also affected by the recovery of the probe electronics (a situation that also affects the initial points of the FID). Overall, this results in large errors associated with this method, so that the outcome can be considered as a determination of the order of magnitude but not a quantitative determination of heteronuclear dipolar moments.

Mansfield sequence

Similar problems arise in the application of the $90°$–τ–$90°_{90°}$–*acq* sequence, suggested by Mansfield.[100] The application of this method should result in an echo-like signal, also called a cross-coupling transient, the initial slope of which depends on the heteronuclear M_2. However, as pointed out by other researchers,[100–103] this method suffers under several experimental problems. The major experimental problem is that the slope of the signal at $t = 0$ needs to be determined, the intensity of which is affected by the behavior of the electronics during the dead time of the receiver. The slope of the line through the first few points (Fig. 7) leads to an overestimation of the heteronuclear dipolar coupling, although if compared with the line calculated from the theoretical M_2 (V, P), the result does not appear unreasonable. At least, this method can serve as an indication of the order of magnitude of heteronuclear dipolar couplings, as in the case of the solid echo.

The average of the results from the solid echo and Mansfield sequence yields a heteronuclear dipolar M_2 (V, P) of $101(23) \times 10^6$ rad^2 s^{-2}, in decent agreement with the theoretical value (Table 2).

Phosphorus-31 chemical shift anisotropy

Evidently, the experimental second moments obtained from the FID or static spectrum, given in Table 3, are field dependent because of the contribution arising from chemical shift anisotropy. In the presence of both dipolar coupling and chemical shift anisotropy, the total second moment is given simply as sum of the individual moments,[104–106]

$$[7] \qquad M_2 = M_2^{\mathrm{D}} + M_2^{\mathrm{CSA}}$$

$$[8] \qquad M_2^{\mathrm{CSA}} = \frac{4}{45}\gamma^2 B_0^2[(\delta_{zz} - \delta_{xx})^2 + (\delta_{yy} - \delta_{xx})(\delta_{yy} - \delta_{zz})] = \frac{4}{45}\gamma^2 B_0^2(\delta_{\|} - \delta_{\perp})^2$$

In the special case of an axially symmetrical chemical shift tensor, the span of the chemical shift tensor can be obtained from the slope of M_2 vs B_0^2 plots. However, for systems lacking axial symmetry this is not possible, although one can put upper and lower limits on the span of the tensor.[106] Extrapolation of the second moments obtained at 9.4 and 4.7 T results in an intercept of $M_2 = 121.9 \times 10^6$ rad^2 s^{-2} ($\Delta\nu_{1/2} = 4137$ Hz), which compares favorably with the theoretical zero-field limit calculated in Table 2, $M_2 = 124.1 \times 10^6$ rad^2 s^{-2} ($\Delta\nu_{1/2} = 4175$ Hz). The slope is 0.43×10^6 rad^2 s^{-2} T^{-2}, corresponding to a lower limit of the span of 20 ppm and an upper limit of 23 ppm. This value is quite acceptable, given the small structural distortions of the PO_4 tetrahedron and compared to other orthophosphates (vide supra).[78]

Phosphorus-31 spin-lattice relaxation

Because the cause of the relatively broad ^{31}P peaks observed in the MAS spectra was initially not known, we also carried out measurements of ^{31}P spin-lattice relaxation times (T_1) using the inversion recovery experiment. It was not unreasonable to anticipate some contamination of β-$VOPO_4$ by paramagnetic V(IV) centers that may lead to short relaxation times and hence broad lines. However, as it turned out, the values of T_1 are on the order of tens of seconds (Table 4). For a particular sample, the measured T_1 values were reproducible over periods extending 1 year. However, the actual value of T_1 may vary from sample to sample because of different contents of paramagnetic vanadium centers. The inversion recovery of the ^{31}P NMR peak intensities of static or MAS samples of β-$VOPO_4$ is not mono-exponential (Fig. 8). Possible reasons for nonexponential behavior are a distribution of different T_1 values or a mixture of different relaxation mechanisms (e.g., spin diffusion). In such more general cases of relaxation, the stretched exponential law has been successfully used to fit the inversion recovery data to this equation,[107,108]

$$[9] \qquad I(\tau) = I_0\left\{1 - 2A\,\exp\left[-\left(\frac{\tau}{T_1'}\right)^n\right]\right\}$$

Can. J. Chem. Downloaded from www.nrcresearchpress.com by Xi'an Jiaotong University on 09/19/12
For personal use only.

Here, the magnetization I as a function of recovery time τ depends on the equilibrium magnetization I_0, the inversion efficiency A of the rf field (ideally, $A = 1$), and the time constant for nonexponential relaxation, denoted here as T_1' to distinguish it from the exponential time constant T_1 ($n = 1$).

According to Bloembergen,[109] two different relaxation mechanisms play a role in diamagnetic solids: relaxation by direct dipolar coupling with the electron spins of paramagnetic impurities[110] and, for nuclei far away from the electron spin, homonuclear spin diffusion.[111] The importance of both mechanisms can be studied by subjecting the sample to magic-angle spinning (Table 4 and Fig. 9).[112–114] Our data reveal a dramatic dependence of T_1 on the sample spinning rate, e.g., at 9.4 T ranging from 25.7 s for a static sample to 60 s for a sample spinning at 10 kHz. Because it is well-known that fast spinning causes frictional heating of the sample,[115–120] we also measured the T_1 of our static sample heated to 330 K (21.1 s), demonstrating that an increase in sample temperature causes a decrease in T_1, in contrast to the effect caused by increasing the spinning frequency. The spinning rate dependence of T_1 nicely illustrates two effects of homonuclear spin diffusion: (*i*) our Hahn spin-echo experiment on a static sample showed that the homonuclear dipolar interaction is sizeable, and the increase in T_1 with increasing spinning frequency demonstrates that the flip-flop interaction between neighboring ^{31}P nuclei becomes increasingly quenched; (*ii*) the small decrease in T_1 at moderate spinning rates (1–2 kHz) shows that the slow spinning actually enhances the flip-flop process by causing level crossing of the inhomogeneously broadened peaks,[121,122] i.e., two ^{31}P nuclei that have different resonance frequencies because of different local ^{51}V, ^{31}P dipolar interactions may experience the same resonance frequency due to the orientation dependence of the dipolar interaction during MAS.

Eventually, once homonuclear spin diffusion is quenched at high spinning rates, T_1 should become spinning rate independent and determined by the concentration of paramagnetic impurities.[114] For our sample of β-$VOPO_4$, ESR measurements confirmed the presence of a low amount of V(IV) centers. In systems where spin-lattice relaxation is diffusion limited, T_1 is proportional to $B_0^{1/2}$,[123] which is approximately true in the present case. There is also a slight decrease of n as T_1 increases, in line with the expectation that $n = 0.5$ for spin-diffusion limited relaxation.[108]

Vanadium-51 NMR spectroscopy

While the line shapes of the ^{31}P NMR spectra of β-$VOPO_4$ basically depend on heteronuclear ^{51}V–^{31}P spin-spin interactions, their contribution to ^{51}V spectra is smaller because of the much smaller spin of the ^{31}P nucleus.[38] Furthermore, they are dwarfed by the ^{51}V nuclear quadrupole interaction and chemical shift anisotropy that are greater by several orders of magnitude. A ^{51}V MAS NMR spectrum of β-$VOPO_4$ is shown in Fig. 10, together with a theoretical spectrum calculated using the parameters reported in Table 5 and compared with previous investigations. To first order, the line shape of the central transition depends only on the principal components of the ^{51}V chemical shift tensor, whereas the satellite transitions show the combined effect of quadrupolar coupling, chemical shift anisotropy, and the relative orientation of both interactions. If the quadrupolar interaction is much greater than the chemical shift anisotropy, it is relatively straightforward to analyze such spectra because central, and satellite transitions can be identified. In the present case, this is more difficult because χ and Ω are of similar magnitude and the individual subspectra cannot be identified, and the question of obtaining reasonable starting parameters arises. If second-order quadrupolar line shapes can be resolved or second-order quadrupolar shifts can be quantified via field-dependent studies, they can provide useful information on the quadrupolar interaction. However, the values in Table 5 indicate that at 9.4 T the second-order broadening contributes only 117 Hz and a shift of 55 Hz (≡0.5 ppm), both too small to aid in the analysis. At least, the observed line width (560 Hz) in the ^{51}V MAS spectra places an upper limit on χ of 4 MHz. It is much better to consider the separation between the outermost spinning sidebands (ca. 650 kHz) because this will correspond to six times the quadrupolar frequency ($6\nu_Q = 3\chi/7$), independent of η, and thus values of χ of 1.5–1.6 MHz.

The region at –412 ppm, corresponding to the region of highest intensity in the MAS spectrum (Fig. 10), also represents a very sharp feature in the spectrum of a static sample and is attributed to the central transition alone, i.e., arising from the perpendicular principal components of an axially symmetric chemical shift tensor. Closer analysis reveals $\delta_\perp = \delta_{11} = \delta_{22} = -340$ ppm, and, in combination with $\delta_{iso} = -754(1)$ ppm, results in $\delta_\parallel = \delta_{33} = -1582$ ppm. Using the parameters obtained at this point, the gross features of the envelope of spinning sidebands in ^{51}V MAS spectra were simulated using line shapes for static powder samples until a reasonable set of parameters was obtained. This is computationally much faster than the calculation of MAS spectra but will not reproduce the envelope exactly. Finally, the MAS spectra were simulated and the parameters modified in small steps until good agreement between calculated and experimental spectra was obtained. In contrast, we found it difficult to obtain decent spectra of static samples, as the initial loss of data points during the receiver dead time after a single pulse was too severe, whereas spin echo experiments produced spectral features that should not be present.

In their ^{51}V NMR study of β-$VOPO_4$, Ben Abdelouahab et al.[47] reported a narrow peak at –354 ppm in their ^{51}V spectrum of a static powder sample, supposedly in agreement with the octahedral coordination of vanadium. However, as indicated in our description above, we attribute this sharp feature to $\delta_\perp$ of the central transition, with the rest of the line shape lost during the receiver dead time. Later, Lapina et al.[51] reported a significant quadrupolar coupling constant of 1.990 MHz (Table 5), but the agreement between their experimental and calculated spectra is not overwhelming. Specifically, the third intensity maximum around 0 ppm in their and our experimental ^{51}V MAS spectra is clearly missing in their simulation. In 2004, Siegel et al.[52] reported the results of a detailed study of ^{51}V NMR spectra of α_{II}-, β-, and γ-$VOPO_4$ at three different external magnetic field strengths. As Table 5 demonstrates, our parameters obtained at 9.4 T are in close agreement with theirs, except for δ_{iso}. We also note, however, that their $\delta_{iso}(^{51}V)$ for α_{II}-$VOPO_4$ (–755 ppm) differs from the value reported by Lapina et al. (–776 ppm) and that also found by us (–778 ppm). Recently, we discovered that Nielsen[124] also investigated β-$VOPO_4$ in her Ph.D.

Can. J. Chem. Downloaded from www.nrcresearchpress.com by Xi'an Jiaotong University on 09/19/12
For personal use only.

thesis, with results very similar to our findings (Table 5). In concluding our discussion of literature data we note that Landsberger and Bray[40] studied the V_2O_5–P_2O_5 glass system using ^{51}V and found that values of χ increase from 1.0 to 1.5 MHz and $\sigma_{\|}$ decreases as the V_2O_5 content increases, whereas $\sigma_{\perp}$ is independent of the glass composition.

Jakobsen and co-workers[125] have thoroughly studied ^{51}V MAS NMR spectra of *ortho*- and *meta*-vanadates and have obtained excellent fits for their ^{51}V MAS spectra. Among the compounds studied, $NbOVO_4$ and $TaOVO_4$ are isostructural to β-$VOPO_4$ but with switched roles: vanadium now occupies the tetrahedral positions with dramatic consequences for the ^{51}V NMR spectra: χ is on the order of 1 MHz and Ω on the order of 100 ppm. The span of the ^{51}V chemical shift tensor in β-$VOPO_4$ is comparable to that in V_2O_5 (981–998 ppm),[50,126–129] indicating that the vanadyl–oxygen bond might be responsible for the chemical shift anisotropy because δ_{33} is the unique component of the almost axially symmetric chemical shift tensor and was found by ^{51}V single-crystal NMR on V_2O_5 to be close to the direction of this bond.[130] Interestingly, it was also found in this single-crystal NMR study that the principal axis systems of the electric field gradient and chemical shift tensors are markedly noncoincident ($\beta = 55°$). However, the presence of magnetically nonequivalent vanadium sites leaves a twofold ambiguity in assigning the direction of V_{ZZ} to a specific orientation in the distorted octahedral environment of vanadium.[128] A similar situation is evident for the ^{51}V nucleus in β-$VOPO_4$, as revealed by the data compiled in Table 5.

Conclusions

In summary, we have shown that the line shapes of the ^{31}P NMR spectra of β-$VOPO_4$ mostly depend on the heteronuclear ^{51}V, ^{31}P direct and indirect spin-spin interactions, as opposed to crystallinity or chemical shift anisotropy. The fact that indirect ^{51}V, ^{31}P spin-spin coupling can be detected indicates that communication between the nuclear spins via the intervening bonds takes place. While arguments have been brought forward that the vanadyl bond in vanadium oxides is a short ionic bond,[128] the observation of $^2J_{iso}(^{51}V, ^{31}P)$ hints towards covalent contributions to the vanadium–oxygen bond. This covalent contribution may also play a role in the transmission of spin density from vanadium to phosphorus in paramagnetic vanadyl phosphates.[11,131] Whereas homonuclear ^{31}P, ^{31}P interactions are less important for the ^{31}P NMR line shapes, they play an important role for the ^{31}P spin-lattice relaxation via paramagnetic impurities, as evidenced by the stretched exponential behavior of the inversion recovery and the spinning rate dependence of T_1.

The ^{51}V NMR spectra reveal a relatively large chemical shift anisotropy and quadrupolar coupling constant. It is expected that the orientation of the chemical shift tensor is similar to that in V_2O_5, i.e., the unique principal component of the (nearly) axially symmetric tensor is close to the direction of the vanadyl bond. Somewhat counterintuitively, the greatest component of the electric field gradient tensor is inclined at an angle of 35° with this direction, analogous to the situation found in V_2O_5. So far, theoretical methods have failed to rationalize this observation in V_2O_5,[128] however, successful theoretical calculations of ^{51}V electric field gradient tensors are just beginning to emerge.[132,133] It appears that the ^{51}V chemical shift anisotropy is a local property of the vanadyl group, whereas the ^{51}V nuclear quadrupolar interaction represents a long range property.

Acknowledgments

Financial support by the Deutsche Forschungsgemeinschaft (DFG) under project Gr 1516/1-2 is gratefully acknowledged. We acknowledge G.-U. Wolf (Institut für Angewandte Chemie Berlin-Adlershof e.V., Berlin) for his expert synthesis of β-$VOPO_4$. We thank Dr. A. Kretschmer (formerly of Humboldt-Universität zu Berlin) for some initial NMR measurements and Professor R.E. Wasylishen (University of Alberta, Edmonton, Alberta) for access to the MSL-200 and valuable discussions. K.E. thanks Professor A.C. Olivieri (Universidad Nacional de Rosario) for a listing of his program to calculate spinning sidebands of a spin-1/2 nucleus coupled to a spin–1 nucleus, and Dr. U.G. Nielsen for providing a copy of her Ph.D. thesis. We are grateful to an anonymous reviewer for his careful reading and thoughtful comments.

References

(1) Hirao, T. *Chem. Rev.* **1997** *97* (8), 2707. doi:10.1021/cr960014g.
(2) Centi, G.; Trifirò, F.; Ebner, J. R.; Franchetti, V. M. *Chem. Rev.* **1988** *88* (1), 55. doi:10.1021/cr00083a003.
(3) Centi, G. *Catal. Today* **1993** *16* (1), 5. doi:10.1016/0920-5861(93)85002-H.
(4) Narayana, K. V.; Martin, A.; Lücke, B.; Belmans, M.; Boers, F.; van Deynse, D. *Z. Anorg. Allg. Chem.* **2005** *631* (1), 25. doi:10.1002/zaac.200400246.
(5) Thorn, D. L.; Harlow, R. L.; Herron, N. *Inorg. Chem.* **1996** *35* (3), 547. doi:10.1021/ic950790r.
(6) Chen, B.; Munson, E. J. *J. Am. Chem. Soc.* **2002** *124* (8), 1638. doi:10.1021/ja010285v.
(7) Hodnett, B. K. *Catal. Rev., Sci. Eng.* **1985** *27* (3), 373. doi:10.1080/01614948508064740.
(8) Cavani, F.; Trifiró, F. In *Catalysis, A Specialist Periodical Report;* The Chemical Society: London, 1994; Vol. 11, pp 246–317.
(9) Coulston, G. W.; Thompson, E. A.; Herron, N. *J. Catal.* **1996** *163* (1), 122. doi:10.1006/jcat.1996.0311.
(10) Ritschl, F.; Fait, M.; Fiedler, K.; Köhler, J. E. H.; Kubias, B.; Meisel, M. *Z. Anorg. Allg. Chem.* **2002** *628* (6), 1385. doi:10.1002/1521-3749(200206)628:6<1385::AID-ZAAC1385>3.0.CO;2-1.
(11) Petit, S.; Borshch, S. A.; Robert, V. *J. Am. Chem. Soc.* **2003** *125* (13), 3959. doi:10.1021/ja0292602.
(12) Batis, N. H.; Batis, H.; Ghorbel, A.; Vedrine, J. C.; Volta, J. C. *J. Catal.* **1991** *128* (1), 248. doi:10.1016/0021-9517(91)90081-E.
(13) Vedrine, J. C.; Millet, J. M. M.; Volta, J. C. *Faraday Discuss. Chem. Soc.* **1989** *87*, 207. doi:10.1039/dc9898700207.
(14) Nagy, J. B.; Vedrine, J. C.; Krylov, O. V.; Centi, G.; Moffat, J. B.; Evans, J.; Pinnavaia, T. J.; van Santen, R. A.; Zecchina, A.; Ichikawa, M.; Sermon, P. A.; Baiker, A.; Bridge, M. E.; Spencer, M. S.; Dewing, J.; Conway, B. E.; Bond, G. C.; Datye, A. K. *Faraday Discuss. Chem. Soc.* **1989** *87*, 253. doi:10.1039/dc9898700253.
(15) Sananes, M. T.; Tuel, A. *Solid State Nucl. Magn. Reson.* **1996** *6* (2), 157. doi:10.1016/0926-2040(95)01215-X.

Can. J. Chem. Downloaded from www.nrcresearchpress.com by Xi'an Jiaotong University on 09/19/12
For personal use only.

(16) Zhang, Y.; Sneeden, R. P. A.; Volta, J. C. *Catal. Today* **1993** *16* (1), 39. doi:10.1016/0920-5861(93)85004-J.
(17) Bordes, E.; Courtine, P. *J. Chem. Soc. Chem. Commun.* **1985** (5), 294. doi:10.1039/c39850000294.
(18) Abon, M.; Bere, K. E.; Tuel, A.; Delichere, P. *J. Catal.* **1995** *156* (1), 28. doi:10.1006/jcat.1995.1228.
(19) Cavani, F.; Centi, G.; Trifirò, F. *J. Chem. Soc. Chem. Commun.* **1985** (8): 492. doi:10.1039/c39850000492.
(20) Sananes, M. T.; Hutchings, G. J.; Volta, J. C. *J. Catal.* **1995** *154* (2), 253. doi:10.1006/jcat.1995.1167.
(21) Ladwig, G. *Z. Anorg. Allg. Chem.* **1965** *338* (5–6), 266. doi:10.1002/zaac.19653380506.
(22) Zampronio, E. C.; Oliveira, H. P. *Mater. Res. Bull.* **2004** *39* (10), 1525. doi:10.1016/j.materresbull.2004.04.018.
(23) Melánová, K.; Beneš, L.; Zima, V.; Trchová, M.; Dybal, J. *Eur. J. Inorg. Chem.* **2004** *2004* (12), 2493. doi:10.1002/ejic.200300942.
(24) Johnson, J. W.; Jacobson, A. J.; Brody, J. F.; Rich, S. M. *Inorg. Chem.* **1982** *21* (10), 3820. doi:10.1021/ic00140a044.
(25) Antonio, M. R.; Barbour, R. L.; Blum, P. R. *Inorg. Chem.* **1987** *26* (8), 1235. doi:10.1021/ic00255a012.
(26) Chauvel, B.; Bondot, P.; de Roy, M.; Besse, J. P. *Solid State Ion.* **1993** *63–65*, 494. doi:10.1016/0167-2738(93)90150-2.
(27) Zhu, J.; Huang, Y. *Langmuir* **2010** *26* (12), 10115. doi:10.1021/la100232s.
(28) Grey, C. P.; Dupré, N. *Chem. Rev.* **2004** *104* (10), 4493. doi:10.1021/cr020734p.
(29) Whittingham, M. S. *Chem. Rev.* **2004** *104* (10), 4271. doi:10.1021/cr020731c.
(30) Dupré, N.; Wallez, G.; Gaubicher, J.; Quarton, M. *J. Solid State Chem.* **2004** *177* (8), 2896. doi:10.1016/j.jssc.2004.04.006.
(31) Yin, S.-C.; Grondey, H.; Strobel, P.; Huang, H.; Nazar, L. F. *J. Am. Chem. Soc.* **2003** *125* (2), 326. doi:10.1021/ja028973h.
(32) Dupré, N.; Gaubicher, J.; Angenault, J.; Wallez, G.; Quarton, M. *J. Power Sources* **2001** *97–98*, 532. doi:10.1016/S0378-7753(01)00534-1.
(33) Chauvel, A.; de Roy, M. E.; Besse, J. P.; Benarbia, A.; Legrouri, A.; Barroug, A. *Mater. Chem. Phys.* **1995** *40* (3), 207. doi:10.1016/0254-0584(95)01482-9.
(34) Plass, W. *Angew. Chem. Int. Ed. Engl.* **1999** *38* (7), 909. doi:10.1002/(SICI)1521-3773(19990401)38:7<909::AID-ANIE909>3.0.CO;2-S.
(35) Bühl, M.; Schurhammer, R.; Imhof, P. *J. Am. Chem. Soc.* **2004** *126* (10), 3310. doi:10.1021/ja039436f.
(36) Ninclaus, C.; Retoux, R.; Riou, D.; Férey, G. *J. Solid State Chem.* **1996** *122* (1), 139. doi:10.1006/jssc.1996.0093.
(37) Jordan, B. D.; Calvo, C. *Acta Crystallogr. B* **1976** *32* (10), 2899. doi:10.1107/S0567740876009163.
(38) Hudalla, C.; Eckert, H.; Dupree, R. *J. Phys. Chem.* **1996** *100* (39), 15986. doi:10.1021/jp960768z.
(39) Jordan, B.; Calvo, C. *Can. J. Chem.* **1973** *51* (16), 2621. doi:10.1139/v73-396.
(40) Landsberger, F. R.; Bray, P. J. *J. Chem. Phys.* **1970** *53*, 2757. doi:10.1063/1.1674400.
(41) Morselli, L.; Trifirò, F.; Urban, L. *J. Catal.* **1982** *75* (1), 112. doi:10.1016/0021-9517(82)90126-9.
(42) McCormick, R. L.; Alptekin, G. O.; Herring, A. M.; Ohno, T. R.; Dec, S. F. *J. Catal.* **1997** *172* (1), 160. doi:10.1006/jcat.1997.1840.
(43) Bordes, E.; Courtine, P. *J. Catal.* **1979** *57* (2), 236. doi:10.1016/0021-9517(79)90028-9.
(44) Moser, T. P.; Schrader, G. L. *J. Catal.* **1985** *92* (2), 216. doi:10.1016/0021-9517(85)90256-8.
(45) Moser, T. P.; Schrader, G. L. *J. Catal.* **1987** *104* (1), 99. doi:10.1016/0021-9517(87)90340-X.
(46) Nguyen, P. T.; Sleight, A. W.; Roberts, N.; Warren, W. W. *J. Solid State Chem.* **1996** *122* (2), 259. doi:10.1006/jssc.1996.0111.
(47) Ben Abdelouahab, F.; Olier, R.; Guilhaume, N.; Lefebvre, F.; Volta, J. C. *J. Catal.* **1992** *134* (1), 151. doi:10.1016/0021-9517(92)90218-7.
(48) Sananes, M. T.; Tuel, A.; Volta, J. C. *J. Catal.* **1994** *145* (2), 251. doi:10.1006/jcat.1994.1032.
(49) Li, J.; Lashier, M. E.; Schrader, G. L.; Gerstein, B. C. *Appl. Catal.* **1991** *73* (1), 83. doi:10.1016/0166-9834(91)85114-B.
(50) Lapina, O. B.; Mastikhin, V. M.; Shubin, A. A.; Krasilnikov, V. N.; Zamaraev, K. I. *Prog. Nucl. Magn. Reson. Spectrosc.* **1992** *24* (6), 457. doi:10.1016/0079-6565(92)80008-4.
(51) Lapina, O. B.; Khabibulin, D. F.; Shubin, A. A.; Bondareva, V. M. *J. Mol. Catal. Chem.* **2000** *162* (1–2), 381. doi:10.1016/S1381-1169(00)00305-8.
(52) Siegel, R.; Dupré, N.; Quarton, M.; Hirschinger, J. *Magn. Reson. Chem.* **2004** *42* (12), 1022. doi:10.1002/mrc.1485.
(53) Bordes, E.; Courtine, P.; Pannetier, G. *Ann. Chim. (Paris)* **1973** *8*, 105.
(54) *Powder Diffraction File;* International Centre for Diffraction Data: Newton Square, PA.
(55) Gopal, R.; Calvo, C. *J. Solid State Chem.* **1972** *5* (3), 432. doi:10.1016/0022-4596(72)90089-8.
(56) Freeman, R.; Kempsell, S. P.; Levitt, M. H. *J. Magn. Reson.* **1980** *38* (3), 453. doi:10.1016/0022-2364(80)90327-3.
(57) Rance, M.; Byrd, R. A. *J. Magn. Reson.* **1983** *52* (2), 221. doi:10.1016/0022-2364(83)90190-7.
(58) Eichele, K. *HBA,* Version 1.5.9; Tübingen, 2005.
(59) Eichele, K.; Wasylishen, R. E. *WSolids,* Version 2.0.21; Dalhousie University: Halifax, 2001.
(60) Eichele, K. *CSolids,* Version 1.4.12; Tübingen, 2002.
(61) Herzfeld, J.; Berger, A. E. *J. Chem. Phys.* **1980** *73* (12), 6021. doi:10.1063/1.440136.
(62) Olivieri, A. C. *Solid State Nucl. Magn. Reson.* **1997** *10* (1–2), 19. doi:10.1016/S0926-2040(97)00023-4.
(63) Alderman, D. W.; Solum, M. S.; Grant, D. M. *J. Chem. Phys.* **1986** *84* (7), 3717. doi:10.1063/1.450211.
(64) Eichele, K.; Lumsden, M. D.; Wasylishen, R. E. *J. Phys. Chem.* **1993** *97* (35), 8909. doi:10.1021/j100137a014.
(65) Eichele, K.; Wasylishen, R. E.; Nelson, J. H. *J. Phys. Chem. A* **1997** *101* (30), 5463. doi:10.1021/jp9712415.
(66) Jameson, C. J. *Solid State Nucl. Magn. Reson.* **1998** *11* (3–4), 265. doi:10.1016/S0926-2040(98)00029-0.
(67) Schindler, M.; Hawthorne, F. C.; Baur, W. H. *Chem. Mater.* **2000** *12* (5), 1248. doi:10.1021/cm990490y.
(68) Zavalij, P. Y.; Whittingham, M. S. *Acta Crystallogr. B* **1999** *55* (5), 627. doi:10.1107/S0108768199004000.
(69) Grimmer, A.-R.; Haubenreisser, U. *Chem. Phys. Lett.* **1983** *99* (5–6), 487. doi:10.1016/0009-2614(83)80180-8.
(70) Haubenreisser, U.; Scheler, G.; Grimmer, A.-R. *Z. Anorg. Allg. Chem.* **1986** *532* (1), 157. doi:10.1002/zaac.19865320122.
(71) Burlinson, N. E.; Dunell, B. A.; Ripmeester, J. A. *J. Magn. Reson.* **1986** *67* (2), 217. doi:10.1016/0022-2364(86)90430-0.
(72) Griffiths, L.; Root, A.; Harris, R. K.; Packer, K. J.; Chippendale, A. M.; Tromans, F. R. *J. Chem. Soc., Dalton Trans.* **1986** (10): 2247. doi:10.1039/dt9860002247.

Can. J. Chem. Downloaded from www.nrcresearchpress.com by Xi'an Jiaotong University on 09/19/12
For personal use only.

(73) Mudrakovskii, I. L.; Shmachkova, V. P.; Kotsarenko, N. S.; Mastikhin, V. M. *J. Phys. Chem. Solids* **1986** *47* (4), 335. doi:10.1016/0022-3697(86)90022-3.
(74) Jakeman, R. J. B.; Cheetham, A. K. *J. Am. Chem. Soc.* **1988** *110* (4), 1140. doi:10.1021/ja00212a023.
(75) Jäger, C.; Barth, S.; Feltz, A. *Chem. Phys. Lett.* **1988** *150* (5), 503. doi:10.1016/0009-2614(88)87237-3.
(76) Lagier, C. M.; Olivieri, A. C.; Apperley, D. C.; Harris, R. K. *Solid State Nucl. Magn. Reson.* **1992** *1* (4), 205. doi:10.1016/S0926-2040(10)80005-0.
(77) Grimmer, A.-R.; Eichele, K. Unpublished data.
(78) Duncan, T. M. *A Compilation of Chemical Shift Anisotropies;* The Farragut Press: Chicago, 1990.
(79) Hayashi, S.; Hayamizu, K. *Bull. Chem. Soc. Jpn.* **1989** *62* (10), 3061. doi:10.1246/bcsj.62.3061.
(80) Turner, G. L.; Smith, K. A.; Kirkpatrick, R. J.; Oldfield, E. *J. Magn. Reson.* **1986** *70* (3), 408. doi:10.1016/0022-2364(86)90129-0.
(81) Bleam, W. F.; Pfeffer, P. E.; Frye, J. S. *Phys. Chem. Miner.* **1989** *16*, 455. doi:10.1007/BF00197015.
(82) Hodnett, B. K. *Catal. Today* **1993** *16* (1), 131. doi:10.1016/0920-5861(93)85013-P.
(83) Adolphi, N. L.; Conradi, M. S.; Buhro, W. E. *J. Phys. Chem. Solids* **1992** *53* (8), 1073. doi:10.1016/0022-3697(92)90080-W.
(84) Tomaselli, M.; deGraw, D.; Yarger, J. L.; Augustine, M. P.; Pines, A. *Phys. Rev. B* **1998** *58* (13), 8627. doi:10.1103/PhysRevB.58.8627.
(85) Shaler, T. A. *J. Chem. Educ.* **1991** *68* (10), 853. doi:10.1021/ed068p853.
(86) Koster, D. F.; Jones, W. *J. Chem. Educ.* **1982** *59* (4), 289. doi:10.1021/ed059p289.
(87) Bonhomme, C.; Coelho, C.; Azaïs, T.; Bonhomme-Coury, L.; Babonneau, F.; Maquet, J.; Thouvenot, R. *Compt. Rend. Chim.* **2006** *9* (3–4), 466. doi:10.1016/j.crci.2005.06.028.
(88) Harris, R. K.; Olivieri, A. C. *Prog. Nucl. Magn. Reson. Spectrosc.* **1992** *24* (5), 435. doi:10.1016/0079-6565(92)80004-Y.
(89) Harris, R. K. In *Encyclopedia of Nuclear Magnetic Resonance;* Grant, D. M., Harris, R. K., Eds.; John Wiley & Sons: Chichester, UK, 1996; Vol. 5, pp 2909–2914.
(90) Haeberlen, U. In *Adv. Magn. Reson., Suppl.;* Waugh, J. S., Ed.; Academic Press: New York, 1976; Vol. 1, pp 1–468.
(91) Wu, G.; Eichele, K.; Wasylishen, R. E. In *Phosphorus-31 NMR Spectral Properties in Compound Characterization and Structural Analysis;* Quin, L. D., Verkade, J. G., Eds.; VCH Publishers, Inc.: New York, 1994; Chapter 33, pp 441–450.
(92) Eichele, K.; Wasylishen, R. E. *J. Phys. Chem.* **1994** *98* (12), 3108. doi:10.1021/j100063a012.
(93) Lagier, C. M.; Olivieri, A. C. *J. Magn. Reson.* **1997** *126* (1), 138. doi:10.1006/jmre.1997.1122.
(94) Van Vleck, J. H. *Phys. Rev.* **1948** *74* (9), 1168. doi:10.1103/PhysRev.74.1168.
(95) Lösche, A. *Kerninduktion;* VEB Deutscher Verlag der Wissenschaften: Berlin, Germany, 1957.
(96) Abragam, A. *The Principles of Nuclear Magnetism;* Clarendon Press: Oxford, 1961.
(97) Hughes, D. G. *J. Magn. Reson.* **1973** *11* (1), 83. doi:10.1016/0022-2364(73)90085-1.
(98) Hendrickson, J. R.; Tabbey, M. P. *J. Magn. Reson.* **1981** *43* (2), 282. doi:10.1016/0022-2364(81)90038-x.
(99) Powles, J. G.; Carazza, B. In *Magnetic Resonance: Proceedings of the International Symposium on Electron and Nuclear Magnetic Resonance 1969;* Coogan, C. K., Ham, N. S., Stuart, S. N., Pilbrow, J. R., Wilson, G. V. H., Eds.; Plenum Press: New York, 1970; pp 133–161.
(100) Mansfield, P. *Phys. Rev. A* **1965** *137* (3A), A961. doi:10.1103/PhysRev.137.A961.
(101) Boden, N.; Gibb, M.; Levine, Y. K.; Mortimer, M. *J. Magn. Reson.* **1974** *16* (3), 471. doi:10.1016/0022-2364(74)90231-5.
(102) Warren, W. W., Jr; Norberg, R. E. *Phys. Rev.* **1967** *154* (2), 277. doi:10.1103/PhysRev.154.277.
(103) Hutchins, D. K.; Day, S. M. *Phys. Rev.* **1969** *180* (2), 432. doi:10.1103/PhysRev.180.432.
(104) Bloembergen, N.; Rowland, T. J. *Acta Metall.* **1953** *1* (6), 731. doi:10.1016/0001-6160(53)90033-9.
(105) Blinc, R.; Pirkmajer, E.; Slivnik, J.; Zupancic, I. *J. Chem. Phys.* **1966** *45* (5), 1488. doi:10.1063/1.1727790.
(106) VanderHart, D. L.; Gutowsky, H. S. *J. Chem. Phys.* **1968** *49* (1), 261. doi:10.1063/1.1669820.
(107) Hartman, J. S.; Narayanan, A.; Wang, Y. X. *J. Am. Chem. Soc.* **1994** *116* (9), 4019. doi:10.1021/ja00088a041.
(108) Narayanan, A.; Hartman, J. S.; Bain, A. D. *J. Magn. Reson. A* **1995** *112* (1), 58. doi:10.1006/jmra.1995.1009.
(109) Bloembergen, N. *Physica* **1949** *15* (3-4), 386. doi:10.1016/0031-8914(49)90114-7.
(110) Bloembergen, N.; Purcell, E. M.; Pound, R. V. *Phys. Rev.* **1948** *73* (7), 679. doi:10.1103/PhysRev.73.679.
(111) Blumberg, W. E. *Phys. Rev.* **1960** *119* (1), 79. doi:10.1103/PhysRev.119.79.
(112) Kessemeier, H.; Norberg, R. E. *Phys. Rev.* **1967** *155* (2), 321. doi:10.1103/PhysRev.155.321.
(113) Hayashi, S. *Solid State Nucl. Magn. Reson.* **1994** *3* (6), 323. doi:10.1016/0926-2040(94)90016-7.
(114) Hayashi, S.; Akiba, E. *Solid State Nucl. Magn. Reson.* **1995** *4* (6), 331. doi:10.1016/0926-2040(95)00005-B.
(115) Bjorholm, T.; Jakobsen, H. J. *J. Magn. Reson.* **1989** *84*, 204. doi:10.1016/0022-2364(89)90020-6.
(116) Bielecki, A.; Burum, D. P. *J. Magn. Reson. A* **1995** *116* (2), 215. doi:10.1006/jmra.1995.0010.
(117) van Moorsel, G.-J. M. P.; van Eck, E. R. H.; Grey, C. P. *J. Magn. Reson. A* **1995** *113* (2), 159. doi:10.1006/jmra.1995.1075.
(118) van Gorkom, L. C. M.; Hook, J. M.; Logan, M. B.; Hanna, J. V.; Wasylishen, R. E. *Magn. Reson. Chem.* **1995** *33* (10), 791. doi:10.1002/mrc.1260331005.
(119) Grimmer, A.-R.; Kretschmer, A.; Cajipe, V. B. *Magn. Reson. Chem.* **1997** *35* (2), 86. doi:10.1002/(SICI)1097-458X(199702)35:2<86::AID-OMR34>3.0.CO;2-2.
(120) Langer, B.; Schnell, I.; Spiess, H. W.; Grimmer, A.-R. *J. Magn. Reson.* **1999** *138* (1), 182. doi:10.1006/jmre.1999.1717.
(121) Woessner, D. E.; Timken, H. K. C. *J. Magn. Reson.* **1990** *90* (2), 411. doi:10.1016/0022-2364(90)90151-x.
(122) Gan, Z.; Robyr, P.; Ernst, R. R. *Chem. Phys. Lett.* **1998** *283* (5–6), 262. doi:10.1016/S0009-2614(97)01233-5.
(123) Lowe, I. J.; Tse, D. *Phys. Rev.* **1968** *166* (2), 279. doi:10.1103/PhysRev.166.279.
(124) Nielsen, U. G. Solid-State ^{51}V NMR Studies of Vanadates and Vanadia-Based DeNO$_x$-Catalysts. Ph.D. Thesis, Aarhus Universitet, 2002.
(125) Skibsted, J.; Jacobsen, C. J. H.; Jakobsen, H. J. *Inorg. Chem.* **1998** *37* (12), 3083. doi:10.1021/ic971503h.
(126) Skibsted, J.; Nielsen, N. C.; Bildsøe, H.; Jakobsen, H. J. *Chem. Phys. Lett.* **1992** *188* (5–6), 405. doi:10.1016/0009-2614(92)80838-3.
(127) Fernandez, C.; Bodart, P.; Amoureux, J. P. *Solid State Nucl.*

Magn. Reson. **1994** *3* (2), 79. doi:10.1016/0926-2040(94)90026-4.
(128) Marichal, C.; Kempf, J.-Y.; Maigret, B.; Hirschinger, J. *Solid State Nucl. Magn. Reson.* **1997** *8* (1), 33. doi:10.1016/S0926-2040(96)01265-9.
(129) Eckert, H.; Wachs, I. E. *J. Phys. Chem.* **1989** *93* (18), 6796. doi:10.1021/j100355a043.
(130) Gornostansky, S. D.; Stager, C. V. *J. Chem. Phys.* **1967** *46*, 4959. doi:10.1063/1.1840660.
(131) Villeneuve, G.; Suh, K. S.; Amorós, P.; Casañ-Pastor, N.; Beltrán-Porter, D. *Chem. Mater.* **1992** *4* (1), 108. doi:10.1021/cm00019a023.
(132) Lo, A. Y. H.; Hanna, J. V.; Schurko, R. W. *Appl. Magn. Reson.* **2007** *32* (4), 691. doi:10.1007/s00723-007-0045-9.
(133) Pooransingh-Margolis, N.; Renirie, R.; Hasan, Z.; Wever, R.; Vega, A. J.; Polenova, T. *J. Am. Chem. Soc.* **2006** *128* (15), 5190. doi:10.1021/ja060480f.

Can. J. Chem. Downloaded from www.nrcresearchpress.com by Xi'an Jiaotong University on 09/19/12
For personal use only.

Phase transformation of calcium phosphates in the presence of glutamic acid

Tim W. T. Tsai, Wei-Ya Chen, Yao-Hung Tseng, and Jerry C. C. Chan

Can. J. Chem. Downloaded from www.nrcresearchpress.com by Xi'an Jiaotong University on 09/19/12
For personal use only.

Abstract: This work describes a phase-transformation pathway of calcium phosphate in the presence of glutamic acid. The route follows the order starting from amorphous calcium phosphate and brushite, then octacalcium phosphate (OCP), and finally hydroxyapatite (HAp). The preferred growth direction of the intermediate OCP and the final HAp phases lies along the *c* axis. On the basis of our scanning electron microscopy, X-ray powder diffraction, and ^{31}P solid-state NMR data, we suggest that the transformation is via the dissolution–reprecipitation process, which is facilitated in the presence of glutamic acid. The effect on the transformation kinetics is rationalized by the disruption of the water layer bound on the crystal surface.

Key words: biomineralization, octacalcium phosphate, calcium phosphate, HAp, NMR.

Résumé : Dans ce travail, on décrit une voie de transformation de phase du phosphate de calcium en présence d'acide glutamique. Cette voie suit un ordre partant du phosphate de calcium amorphe et de la brushite et passant par le phosphate d'octacalcium (POC) pour arriver finalement à l'hydroxyapatite (HAp). La direction de croissance préférée des phases du POC intermédiaire et de l'hydroxyapatite finale se trouve le long de l'axe *c*. Sur la base des données de microscopie électronique à balayage, de diffraction des rayons-X par des poudres et de RMN du ^{31}P à l'état solide, on suggère que la transformation se produit par le biais d'un processus de dissolution–reprécipitation qui est facilité par la présence d'acide glutamique. L'effet sur la cinétique de la transformation est rationalisé par la rupture de la couche d'eau liée à la surface cristalline.

Mots-clés : Biominéralisation, phosphate d'octacalcium, phosphate de calcium, hydroxyapatite (HAp), RMN.

[Traduit par la Rédaction]

Introduction

Biomineralization processes mainly occur at an organic–inorganic interface with the mediation of various biomolecules. However, questions of how these biomolecules control nucleation, growth, and morphology of inorganic minerals remain largely unanswered. The main challenge in this field is that it is difficult to characterize the interactions between two dissimilar organic and inorganic nanophases with atomic resolution. Nevertheless, the literature contains numerous studies of organic–inorganic interactions, which clearly reflects the importance of biomineralization.[1–6] The main constituent of biological hard tissue in vertebrates refers to poorly crystallized, nonstoichiometric carbonate-containing hydroxyapatite (HAp, $Ca_{10}(PO_4)_6(OH)_2$).[7,8] The formation mechanism of biological apatite is still under active debate.[9–11] Potential candidates for the precursor phase of biological apatite include octacalcium phosphate (OCP, $Ca_8H_2(PO_4)_6{\cdot}5H_2O$), amorphous calcium phosphate (ACP), poorly crystalline apatite, and dicalcium phosphate dihydrate (brushite, $CaHPO_4{\cdot}2H_2O$).[8] In particular, brushite has been proposed as an intermediate in the biomineralization processes of bone and dental caries.[8] On the other hand, the presence of a "central dark line" in tooth enamel supports the hypothesis of OCP being the precursor phase of biological apatite.[12] To shed more light on this intriguing issue, it is desirable to characterize the phase transformation of calcium phosphate in the presence of biomolecules.[13,14]

Graham and Brown suggested that the in situ transformation of OCP into HAp may proceed along routes such as hydrolysis of OCP, followed by HAp precipitation.[15] The transformation can be completed within 219 h under physiological conditions (pH 7.4 and 37 °C).[16] In general, the rate of transformation would increase with temperature. For example, the transformation could finish within 29 h at 70 °C and 12 h at 100 °C.[17–19] Furthermore, the pathway and the rate of transformation could be significantly altered by biomolecules.[18,20] In particular, it has been shown that in the presence of gelatin matrix, the transformation of OCP to HAp will occur via a single-crystal–single-crystal pathway.[20] Because the structure of macromolecules such as gelatin is difficult to characterize, it is of considerable interest to study the phase transformation of calcium phosphate in the presence of small molecules.

In our earlier work, we have prepared HAp crystallites in

Received 9 December 2010. Accepted 3 February 2011. Published at www.nrcresearchpress.com/cjc on 19 July 2011.

T.W.T. Tsai, W.-Y. Chen, Y.-H. Tseng, and J.C.C. Chan. Chemistry Department, National Taiwan University, Roosevelt Road, Taipei, Taiwan.

Corresponding author: Jerry C. C. Chan (e-mail: chanjcc@ntu.edu.tw).

This article is part of a Special Issue dedicated to Professor Roderick E. Wasylishen.

Can. J. Chem. Downloaded from www.nrcresearchpress.com by Xi'an Jiaotong University on 09/19/12
For personal use only.

the presence of glutaric acid, where we suggest that water molecules may play a prominent role in the interfacial interaction between glutaric acid and the HAp surface.[21] Here, we study the phase transformation of calcium phosphate in the presence of L-glutamic acid (Glu). We find that the transformation intermediates are in the order of brushite/ACP, OCP, and HAp. Furthermore, the transformation is likely to occur via the dissolution–reprecipitation pathway. Such process would be significantly slower in the absence of organic additives. We believe that the transient binding of Glu molecules onto the crystal surface would disrupt the structure of the water molecules bound on the crystal surface. Consequently, the dissolution–reprecipitation process required for the phase transformation is facilitated.

Experimental methods

Sample preparation

All chemicals were obtained from Acros, and used as received unless stated otherwise. $Ca(NO_3)_2{\cdot}4H_2O$ (0.572 g, 2.4 mmol) was dissolved in an aqueous solution of Glu (60 mL, 0.16 mol/L). The solution was adjusted to pH 6.0 using NaOH (3.1 mol/L) to ensure full dissolution of the reagents. Phosphate solution was prepared by dissolution of $NaH_2PO_4{\cdot}2H_2O$ (0.375 g, 2.4 mmol) in 60 mL water. The two solutions were mixed with vigorous stirring, and the mixture was adjusted to pH 6.00 ± 0.02. The mixture was sealed in an autoclave and heated to 150 °C for the desired periods. Subsequently, the white precipitates were collected by centrifugation (7000 rpm for 10 min), and washed three times with deionized water. The resulting pellets were lyophilized for at least 16 h and stored in a desiccator.

Sample characterization

X-ray diffraction (XRD) analysis was performed on a Philips X'pert diffractometer, using Cu Kα radiation (λ = 1.5418 Å). A JEOLJSM-6700F field emission scanning electron microscope operated at 10 kV provided SEM micrographs. Transmission electron microscopy (TEM) and selected-area electron diffraction (SAED) patterns were taken on Hitachi S-7100 and Philips FEI Tecnai 20 G2 instruments, operating at 75 kV. High-resolution TEM (HRTEM) images were collected on a FEI Tecnai G2 transmission electron microscope, operating at 200 kV.

All NMR experiments were carried out at ^{31}P and ^{1}H resonance frequencies of 121.5 MHz and 300.1 MHz, respectively, on a Bruker DSX300 NMR spectrometer equipped with a commercial 4 mm probe. The measurements were carried out at ambient temperature. The sample was confined to the middle one-third of the rotor volume using Teflon spacers. A commercially available pneumatic control unit limited variation in magic-angle spinning (MAS) frequency to ±3 Hz. Chemical shifts were externally referenced to 85% phosphoric acid for ^{31}P, and to TMS for ^{1}H spectra. The ^{31}P MAS spectra were measured at 10 kHz spin rate with a recycle delay of 610 s, with proton decoupling at 75 kHz using the scheme of two pulse phase modulation (TPPM).[22]

The ^{31}P double-quantum–single-quantum (DQ–SQ) correlation experiments were acquired using the finite-pulse radio frequency driven recoupling (fp-RFDR) technique at a MAS frequency of 10 kHz.[23–25] To prepare an identical initial spin system for each transient, a saturation comb was applied prior to the recycle delay (8 s). During the fp-RFDR recoupling period, the ^{31}P π pulses were set to 30 μs.[23] The π-pulse trains were phase-cycled following the XY-8 scheme.[26] The ^{31}P π/2 pulses flanking the fp-RFDR pulse blocks were set to 5 μs.[27] The DQ reconversion period was set equal to the excitation period. Continuous-wave and TPPM proton decouplings (70 kHz) were applied during the recoupling and t_2 acquisition periods, respectively. The tachometer signals for pulse-sequence synchronization were filtered with a home-built phase-locked loop circuit. We used the hypercomplex approach for quadrature detection in the F_1 dimension.[28] A z filter of 30 ms without proton decoupling was applied after the reconversion period. For each t_1 increment, 64 transients were accumulated and a total of 42 increments were done at steps of 300 μs. The two-dimensional (2D) ^{31}P spin diffusion experiment, based on the technique of radio-frequency-assisted diffusion (RAD),[29] was carried out with a mixing time of 300 ms. Other conditions were similar to those described in the ^{31}P DQ–SQ experiments.

Results and discussion

XRD

For convenience, all the samples are henceforth referred with reference to their aging times. Figure 1 shows the XRD patterns of some selected samples. The characteristic reflection peaks of brushite (Joint Committee for Powder Diffraction Studies, JCPDS 09–0077), OCP (JCPDS 44–0778), and HAp (JCPDS 24–0033) are at 2θ = 11.7°, 4.8°, and 10.8°, respectively. From the XRD patterns, the as-synthesized (0 min) sample is assigned to brushite, whereas the 30 min sample is a mixture of brushite and OCP. The characteristic reflection of brushite at 2θ = 11.7° becomes diminished in the 45 min sample, resulting in a major phase of OCP. In particular, the relative intensity of the (h00) peak of OCP is relatively strong and a significant attenuation of the (001) peak is rather apparent. This observation suggests a preferred orientation of the OCP crystals along the [001] direction. For the 60 min sample, the characteristic peak of HAp (2θ = 10.8°) becomes observable. Finally, the 250 min sample is assigned to pure HAp with very high crystallinity. The XRD data reported above are very similar to those obtained for glutaric acid (see the Supplementary data).[21] On the other hand, the XRD results of the samples prepared in the absence of Glu indicate that the transformation follows the same pathway, but at a significantly slower rate (see the Supplementary data). This interesting phenomenon has also been observed previously.[20] Furthermore, it has been speculated that trace amounts of monetite could form an intracrystalline mixture with OCP by direct precipitation of calcium phosphate or by hydrolysis of OCP.[30] However, the characteristic peak of monetite (JCPDS 09–0080) at 2θ = 13.1° is not found in our samples, although the solubility products of brushite and monetite are very similar under our pH condition.[31]

SEM

Figure 2 shows the SEM images of the 30, 45, 60, and 250 min samples. The image of the 0 min sample is quite similar to that of the 30 min sample, where the crystallites are poorly faceted rectangular plates (data not shown). The

Can. J. Chem. Downloaded from www.nrcresearchpress.com by Xi'an Jiaotong University on 09/19/12
For personal use only.

Fig. 1. XRD patterns measured for samples obtained at different reaction times.

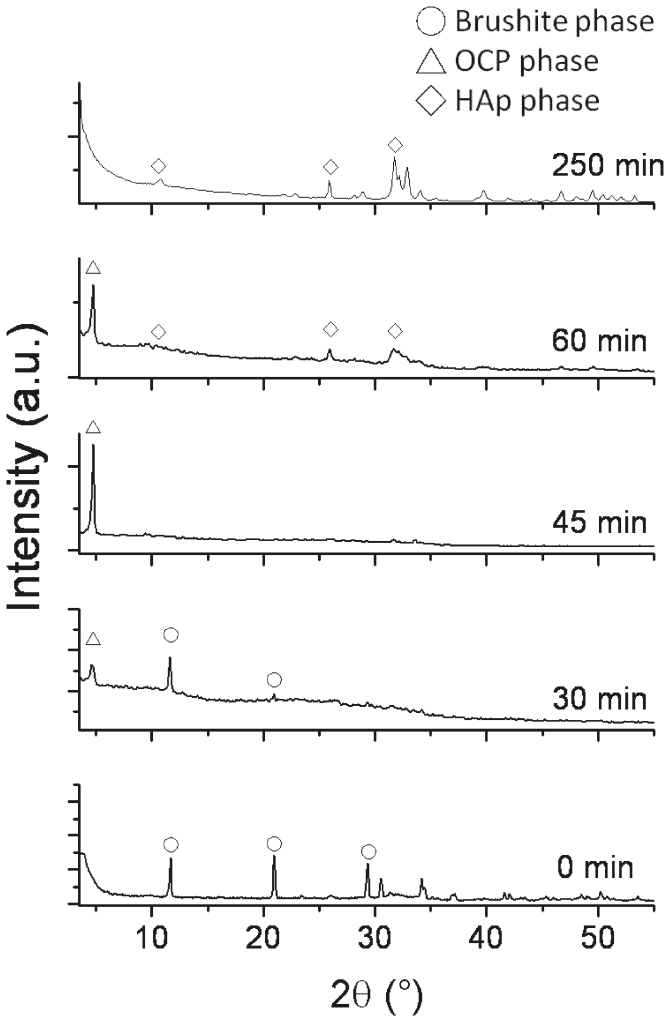

Fig. 2. SEM images of the samples collected at different reaction times: (*a*) 30 min, (*b*) 45 min, (*c*) 60 min, and (*d*) 250 min.

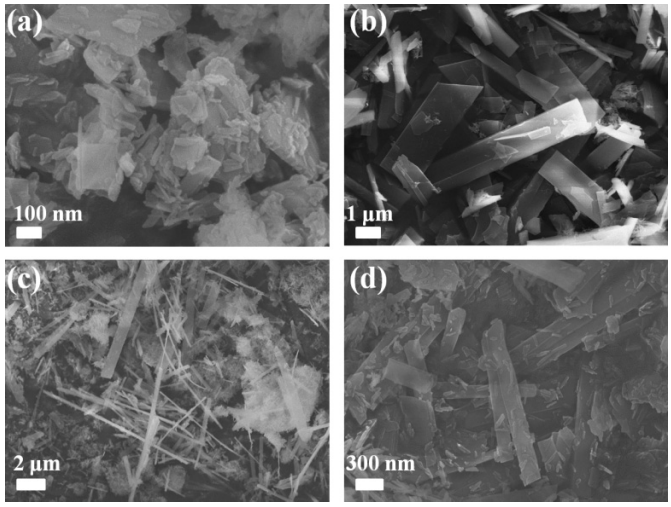

bladelike morphology of the 45 min sample is the characteristic of OCP. As the reaction proceeds to 60 min, the sample is dominated by needlelike crystallites. We attempt to ascribe

Fig. 3. TEM image measured for the 45 min sample. The bladelike morphology is typical for OCP. The inset shows the SAED pattern corresponding to the area marked by the circle in the main image. We assigned the SAED pattern to the reflections along the [110] zone axis of OCP.

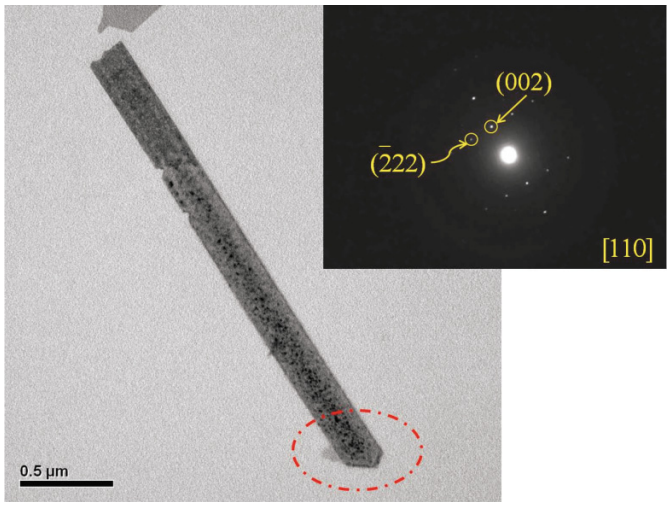

Fig. 4. HRTEM micrographs measured for the 45 min sample, which show an interplanar *d*-spacing of 0.346 nm. The inset shows the region for which we obtained the HRTEM image.

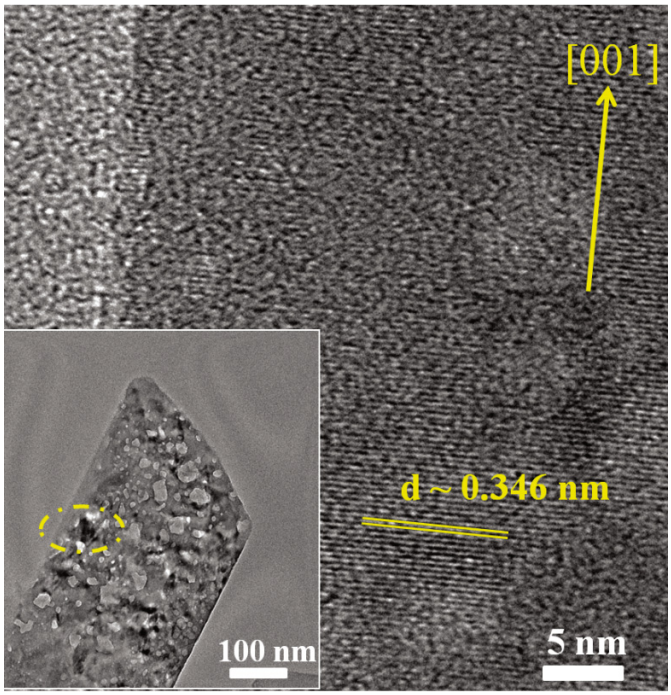

this phenomenon to the fragmentation of the OCP crystallites, which is presumably due to the mechanical stress stemming from the loss of water in OCP upon its transformation to HAp.[20] Furthermore, the XRD pattern of the 60 min sample supports the presence of a significant amount of OCP crystallites. Interestingly, those needlelike crystallites are not observed in the 250 min sample. Because of the distinctive difference in morphology between the 60 min sample (OCP + HAp) and the 250 min sample (HAp), the transformation is likely to occur via the dissolution–reprecipitation

Can. J. Chem. Downloaded from www.nrcresearchpress.com by Xi'an Jiaotong University on 09/19/12
For personal use only.

Fig. 5. TEM image measured for the 250 min sample. The inset shows the SAED pattern corresponding to the area marked by the circle. The SAED pattern is assigned to the reflections along the $[1\bar{1}0]$ zone axis of HAp.

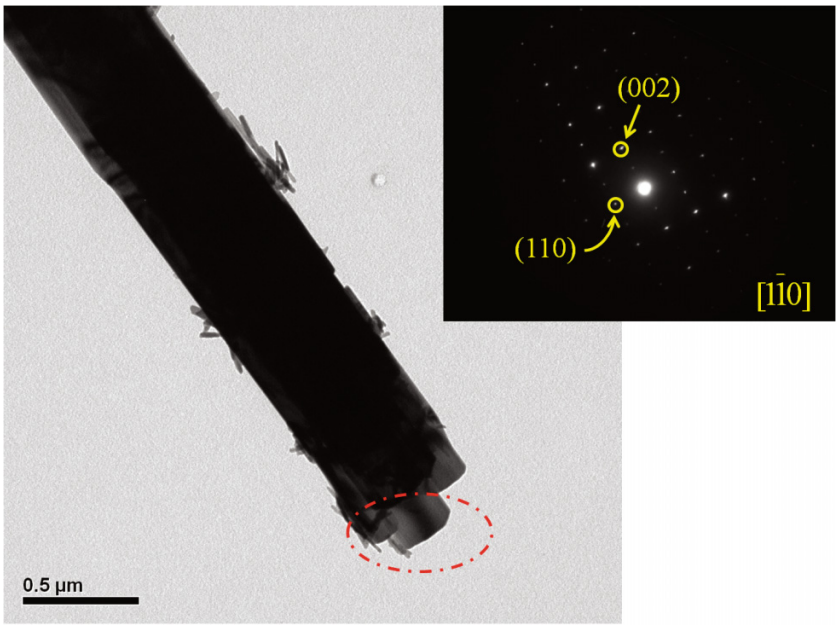

pathway. Nonetheless, we cannot rule out the possibility that some of the bladelike HAp crystallites found in the 250 min sample are transformed directly from OCP.[20]

TEM and HRTEM

Figure 3 shows a representative TEM image of the crystallites of the 45 min sample. The corresponding SAED pattern can be assigned to the reflections along the [110] zone axis of OCP crystal. The long edge of the bladelike crystallites lies along the *c* axis, which is in agreement with the XRD results. Figure 4 shows the HRTEM images of the 45 min sample, clearly demonstrating the OCP crystal to be single-crystalline. The lattice fringes ($d \sim 0.346$ nm) are assigned to the spacing of the (002) lattice planes. Together with the SAED pattern, we conclude that the OCP crystals prefer to grow along the [001] direction for our samples. The TEM image of the 250 min sample indicates that the sample contains aggregates of single-crystalline rodlike crystallites (Fig. 5). The SAED pattern shown in the figure can be assigned to the reflections along the $[1\bar{1}0]$ zone axis of HAp crystal. Furthermore, well-ordered lattice fringes with interplanar spacing corresponding to the (002) planes (~0.345 nm) are observed for the 250 min sample (see the Supplementary data). Thus, the preferred growth direction is the *c* axis for both the OCP and HAp crystallites. This observation is similar to the process without organic additives.[32,33]

^{31}P NMR

Figure 6 shows the ^{31}P MAS spectra measured for our sample series. The spectrum of the 0 min sample has a major peak at 1.3 ppm and a very broad shoulder at ~3 ppm. Because brushite has only one crystallographic site, the peak at 1.3 ppm is assigned to brushite,[34] whereas the shoulder is most likely due to ACP.[35] Note that the shoulder at 3 ppm cannot be due to HAp because the XRD pattern shows no characteristic peaks of HAp. The presence of ACP in the as-

Fig. 6. ^{31}P MAS spectra measured for the samples collected at different reaction times. The arrow indicates the peak of ACP.

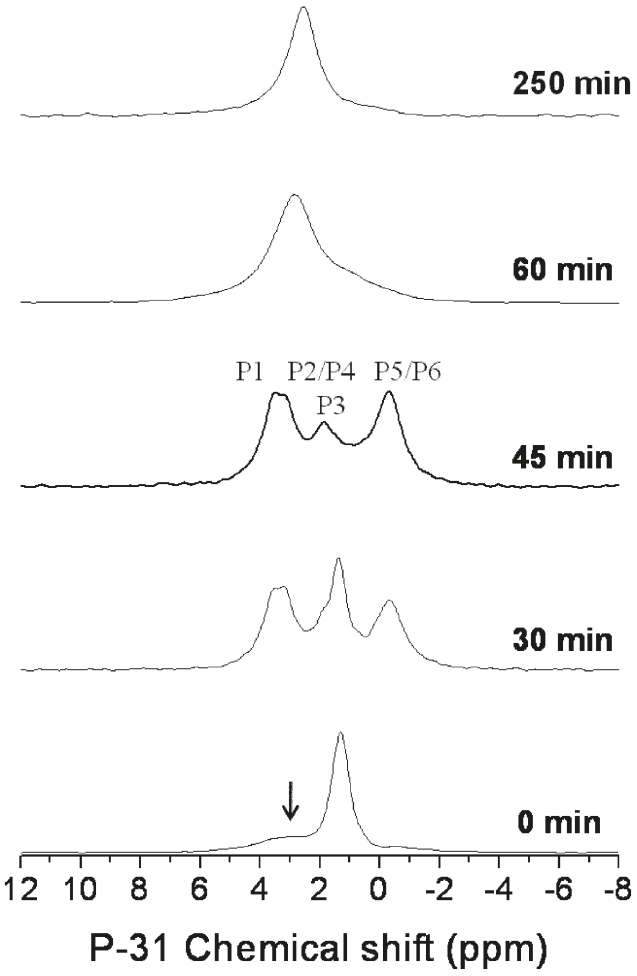

Can. J. Chem. Downloaded from www.nrcresearchpress.com by Xi'an Jiaotong University on 09/19/12
For personal use only.

Fig. 7. ^{31}P DQ–SQ correlation spectrum of the 30 min sample. The DQ excitation time was set to 3.2 ms. P_B denotes the signal of brushite.

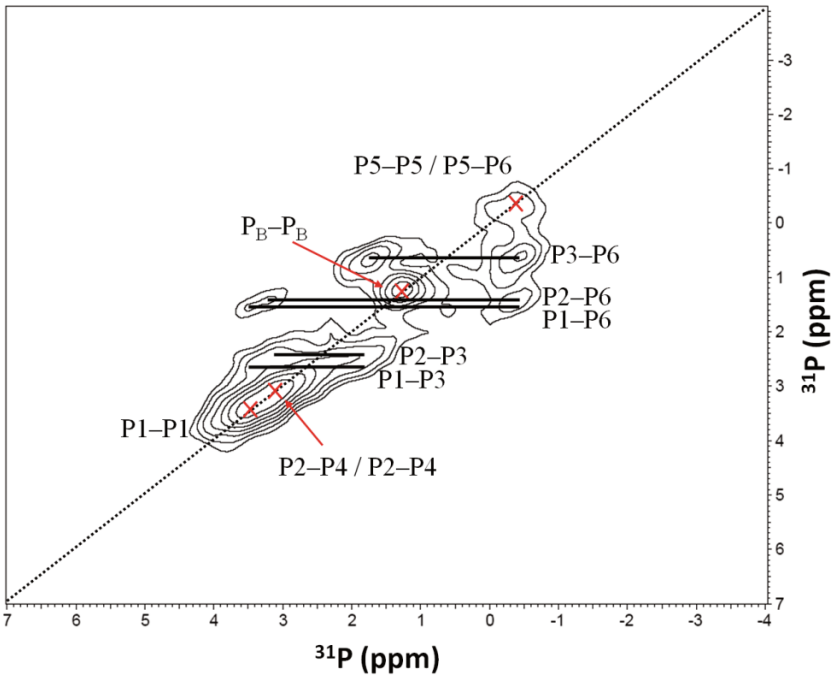

Fig. 8. ^{31}P–^{31}P RAD spectrum measured for the 30 min sample. The mixing time was 300 ms. The dashed lines show the chemical shift of the brushite peak.

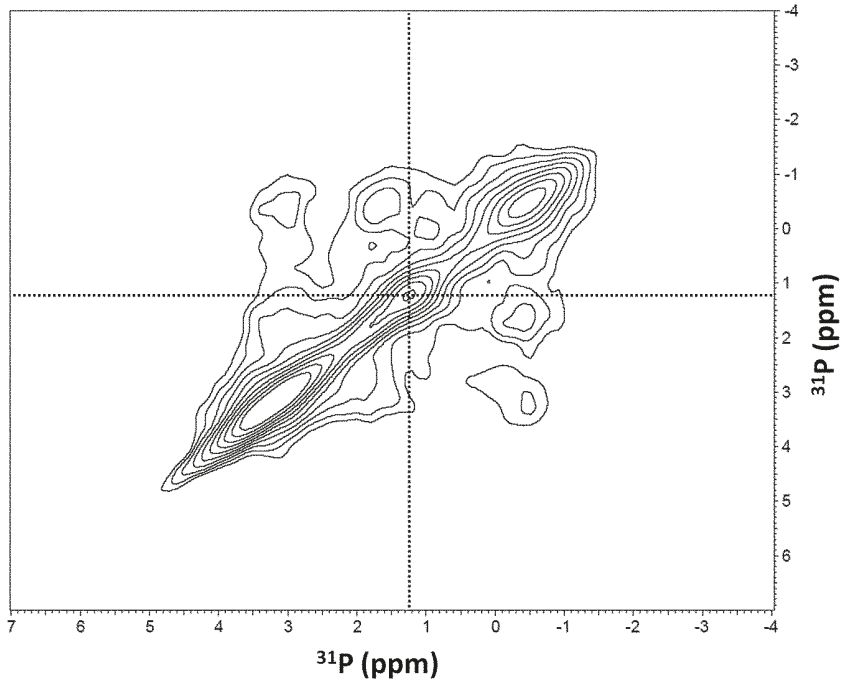

synthesized sample is expected because the precipitation of ACP would readily occur by rapid mixing of calcium and phosphate ions at pH 6.[36] For the 30 min sample, in addition to the peak of brushite, the characteristic peaks of OCP at –0.2, 2.0, 3.3, and 3.7 ppm become apparent. On the basis of their chemical shifts, these four peaks can be assigned to the crystallographic sites of P5/P6, P3, P2/P4, and P1, respectively.[37] As the reaction time increased to 45 min, the ^{31}P spectrum of the sample contains mainly the peaks of OCP but the crystallinity is relatively low. For the 60 min sample, the signal at 2.8 ppm is readily assigned to HAp. The line width at half maximum (LWHM) is ~182 Hz. The very minor shoulder at ~1 ppm may result from the relocation of the PO_4^{3-} ions of OCP.[19] From the XRD pattern, it has been shown that the 250 min sample is pure HAp with high crystallinity. Accordingly, the ^{31}P spectrum contains a single sharp peak at 2.6 ppm with LWHM equal to 102 Hz. Overall, the NMR data are consistent with the XRD results.

Can. J. Chem. Downloaded from www.nrcresearchpress.com by Xi'an Jiaotong University on 09/19/12
For personal use only.

For the 30 min sample, both the XRD pattern and the ^{31}P MAS spectrum indicate the presence of OCP and brushite. Figure 7 shows the ^{31}P DQ–SQ correlation spectrum of the 30 min sample. In addition to the eight sets of auto- and cross-correlation peaks assignable to OCP,[25] an auto-correlation peak at 1.3 ppm is also observed for brushite. To investigate the spatial proximity between the brushite and OCP phases, we measured the 2D ^{31}P spin-diffusion spectrum based on the RAD technique.[29] With a mixing time of 300 ms, it is evident that there is no cross peaks found between the signals of OCP and brushite (Fig. 8). Consequently, we conclude that the brushite and OCP crystallites exist in discrete phases.

Phase-transformation pathway

We have studied the phase-transformation pathway of calcium phosphates under hydrothermal conditions. The Ostwald-Lussac law states that the formation of the final crystalline phase is via a pathway passing through all other phases in order of decreasing solubility.[14,38] Accordingly, we found that ACP and brushite were formed initially. As the reaction proceeded further, crystallites of OCP were formed, and finally the HAp was formed. Surprisingly, this transformation process is accelerated in the presence of Glu. At the first glance, this observation is not consistent with the notion that organic additives usually would inhibit the growth of the crystal surface on which the organic molecules are bound. For example, it has been demonstrated that polyglutamate would considerably inhibit the transformation of OCP to HAp.[18,39,40] Nonetheless, a similar promoting effect of citrate ions for the transformation of brushite to HAp has been observed, which is attributed to the reduction in interfacial energies of brushite and HAp caused by citrate ions.[41]

Very recently, Hunter and co-workers suggest that the protein–surface interaction involves largely electrostatic interactions rather than arrays of complementary charges.[42] Also, it becomes evident that a considerable amount of water molecules is bound on mineral surface,[21,43,44] from which it may be surmised that the water layer must be disrupted before the detachment of ions (dissolution) or attachment of new ions (precipitation) could occur. Therefore, we suggest that the observed acceleration of the phase transformation is due to the electrostatic interaction between the Glu molecules and the crystal surface. That is, the water layer on the crystal surface is significantly altered by the Glu molecules when they are adsorbed to or detached from the surface. Consequently, both the processes of dissolution and precipitation of the crystal phase are facilitated. Although the electrostatic interaction is playing an important role as described above, the possibility exists that the difference in the kinetics between samples prepared with different organic molecules, such as aspartic, glutaric, and citric acids, could be rationalized by the difference in lattice matching.

Previously, it has been shown that the molecules of Glu prefer to adsorb onto the (001) face of HAp so that platelike crystallites of HAp are obtained at 37 °C.[32] In our case, however, the long axis of the HAp crystallites is along the (001) direction. A careful comparison of the experimental conditions shows that our samples were prepared at relatively high concentrations. Besides, at a temperature of 150 °C as in our case, the slight difference in the affinity of Glu to the different crystal facets may be overwhelmed by the thermal energy of the Glu molecules. This dramatic difference in the crystal habits reflects the complicated interplay of the thermodynamics and kinetics of the organic–inorganic interactions.[45]

Supplementary data

Supplementary data are available with the article through the journal Web site (www.nrcresearchpress.com/cjc).

Acknowledgments

We thank Dr. Jinhui Tao (Lawrence Berkeley National Laboratory, Berkeley, California) for his insightful comments. The authors express their gratitude toward the National Science Council for the financial support (Project No. NSC97-2628-M-002-014-MY3).

References

(1) Stupp, S. I.; Braun, P. V. *Science* **1997** *277* (5330), 1242. doi:10.1126/science.277.5330.1242.
(2) Estroff, L. A.; Hamilton, A. D. *Chem. Mater.* **2001** *13* (10), 3227. doi:10.1021/cm010110k.
(3) Meldrum, F. C. *Int. Mater. Rev.* **2003** *48* (3), 187. doi:10.1179/095066003225005836.
(4) Addadi, L.; Raz, S.; Weiner, S. *Adv. Mater. (Deerfield Beach Fla.)* **2003** *15* (12), 959. doi:10.1002/adma.200300381.
(5) Yu, S.-H.; Cölfen, H. *J. Mater. Chem.* **2004** *14* (14), 2124. doi:10.1039/b401420k.
(6) Wang, L. J.; Nancollas, G. H. *Chem. Rev.* **2008** *108* (11), 4628. doi:10.1021/cr0782574.
(7) LeGeros, R. Z. *Calcium Phosphates in Oral Biology and Medicine;* Karger: Basel, 1991; Vol. 15.
(8) Dorozhkin, S. V.; Epple, M. *Angew. Chem. Int. Ed.* **2002** *41* (17), 3130. doi:10.1002/1521-3773(20020902)41:17<3130::AID-ANIE3130>3.0.CO;2-1.
(9) Weiner, S. *Bone* **2006** *39* (3), 431. doi:10.1016/j.bone.2006.02.058.
(10) Grynpas, M. D.; Omelon, S. *Bone* **2007** *41* (2), 162. doi:10.1016/j.bone.2007.04.176.
(11) Rey, C.; Combes, C.; Drouet, C.; Glimcher, M. J. *Osteoporos. Int.* **2009** *20* (6), 1013. doi:10.1007/s00198-009-0860-y.
(12) Bodier-Houllé, P.; Steuer, P.; Voegel, J.-C.; Cuisinier, F. J. G. *Acta Crystallogr. D Biol. Crystallogr.* **1998** *54* (6), 1377. doi:10.1107/S0907444998005769.
(13) Weiner, S.; Addadi, L. *J. Mater. Chem.* **1997** *7* (5), 689. doi:10.1039/a604512j.
(14) Mann, S. *Biomineralization: Principles and Concepts in Bioinorganic Materials Chemistry;* Oxford University Press: New York, 2001.
(15) Graham, S.; Brown, P. W. *J. Cryst. Growth* **1996** *165* (1–2), 106. doi:10.1016/0022-0248(95)00994-9.
(16) Iijima, M.; Kamemizu, H.; Wakamatsu, N.; Goto, T.; Doi, Y.; Moriwaki, Y. *J. Cryst. Growth* **1997** *181* (1–2), 70. doi:10.1016/S0022-0248(97)00230-3.
(17) Nelson, D. G. A.; McLean, J. D. *Calcif. Tissue Int.* **1984** *36* (2), 219. doi:10.1007/BF02405321.
(18) Bigi, A.; Boanini, E.; Bracci, B.; Falini, G.; Rubini, K. *J. Inorg. Biochem.* **2003** *95* (4), 291. doi:10.1016/S0162-0134(03)00127-2.
(19) Tseng, Y. H.; Mou, C. Y.; Chan, J. C. C. *J. Am. Chem. Soc.* **2006** *128* (21), 6909. doi:10.1021/ja060336u.
(20) Zhan, J. H.; Tseng, Y. H.; Chan, J. C. C.; Mou, C. Y. *Adv. Funct. Mater.* **2005** *15* (12), 2005. doi:10.1002/adfm.200500274.

(21) Tseng, Y. H.; Mou, Y.; Chen, P. H.; Tsai, T. W. T.; Hsieh, C. I.; Mou, C. Y.; Chan, J. C. C. *Magn. Reson. Chem.* **2008** *46* (4), 330. doi:10.1002/mrc.2096.
(22) Bennett, A. E.; Rienstra, C. M.; Auger, M.; Lakshmi, K. V.; Griffin, R. G. *J. Chem. Phys.* **1995** *103* (16), 6951. doi:10.1063/1.470372.
(23) Ishii, Y. *J. Chem. Phys.* **2001** *114* (19), 8473. doi:10.1063/1.1359445.
(24) Oyler, N. A.; Tycko, R. *J. Phys. Chem. B* **2002** *106* (33), 8382. doi:10.1021/jp020906m.
(25) Tseng, Y. H.; Mou, Y.; Mou, C. Y.; Chan, J. C. C. *Solid State Nucl. Magn. Reson.* **2005** *27* (4), 266. doi:10.1016/j.ssnmr.2005.02.005.
(26) Gullion, T.; Baker, D. B.; Conradi, M. S. *J. Magn. Reson.* **1990** *89* (3), 479.
(27) Ishii, Y.; Balbach, J. J.; Tycko, R. *Chem. Phys.* **2001** *266* (2–3), 231. doi:10.1016/S0301-0104(01)00250-6.
(28) Ernst, R. R.; Bodenhausen, G.; Wokaun, A. *Principles of Nuclear Magnetic Resonance in One and Two Dimensions;* Clarendon Press: Oxford, UK, 1987.
(29) Morcombe, C. R.; Gaponenko, V.; Byrd, R. A.; Zilm, K. W. *J. Am. Chem. Soc.* **2004** *126* (23), 7196. doi:10.1021/ja047919t.
(30) Brown, W. E.; Smith, J. P.; Lehr, J. R.; Frazier, A. W. *Nature* **1962** *196* (4859), 1050. doi:10.1038/1961050a0.
(31) Heughebaert, J. C.; Nancollas, G. H. *J. Phys. Chem.* **1984** *88* (12), 2478. doi:10.1021/j150656a012.
(32) Pan, H. H.; Tao, J. H.; Xu, X. R.; Tang, R. K. *Langmuir* **2007** *23* (17), 8972. doi:10.1021/la700567r.
(33) Neira, I. S.; Kolen'ko, Y. V.; Lebedev, O. I.; Van Tendeloo, G.; Gupta, H. S.; Guitian, F.; Yoshimura, M. *Cryst. Growth Des.* **2009** *9* (1), 466. doi:10.1021/cg800738a.
(34) Aue, W. P.; Roufosse, A. H.; Glimcher, M. J.; Griffin, R. G. *Biochemistry* **1984** *23* (25), 6110. doi:10.1021/bi00320a032.
(35) Tropp, J.; Blumenthal, N. C.; Waugh, J. S. *J. Am. Chem. Soc.* **1983** *105* (1), 22. doi:10.1021/ja00339a006.
(36) Combes, C.; Rey, C. *Acta Biomater.* **2010** *6* (9), 3362. doi:10.1016/j.actbio.2010.02.017.
(37) Tseng, Y. H.; Zhan, J. H.; Lin, K. S. K.; Mou, C. Y.; Chan, J. C. C. *Solid State Nucl. Magn. Reson.* **2004** *26* (2), 99. doi:10.1016/j.ssnmr.2004.06.002.
(38) De Yoreo, J. J.; Vekilov, P. G. Principles of crystal nucleation and growth. In *Biomineralization;* Dove, P. M. D. J. J. W. S., Ed. Mineralogical Society of America: Washington, DC, 2003; Vol. 54, pp 57–93.
(39) Bigi, A.; Bracci, B.; Panzavolta, S.; Iliescu, M.; Plouet-Richard, M.; Werckmann, J.; Cam, D. *Cryst. Growth Des.* **2004** *4* (1), 141. doi:10.1021/cg034078d.
(40) Bigi, A.; Boanini, E.; Gazzano, M.; Rubini, K.; Torricelli, P. *Biomed. Mater. Eng.* **2004** *14* (4), 573.
(41) Jiang, W. G.; Chu, X. B.; Wang, B.; Pan, H. H.; Xu, X. R.; Tang, R. K. *J. Phys. Chem. B* **2009** *113* (31), 10838. doi:10.1021/jp904633f.
(42) Hunter, G. K.; O'Young, J.; Grohe, B.; Karttunen, M.; Goldberg, H. A. *Langmuir* **2010** *26* (24), 18639. doi:10.1021/la100401r.
(43) Wilson, E. E.; Awonusi, A.; Morris, M. D.; Kohn, D. H.; Tecklenburg, M. M. J.; Beck, L. W. *Biophys. J.* **2006** *90* (10), 3722. doi:10.1529/biophysj.105.070243.
(44) Best, S. M.; Duer, M. J.; Reid, D. G.; Wise, E. R.; Zou, S. *Magn. Reson. Chem.* **2008** *46* (4), 323. doi:10.1002/mrc.2168.
(45) Addadi, L.; Weiner, S. *Proc. Natl. Acad. Sci. U.S.A.* **1985** *82* (12), 4110. doi:10.1073/pnas.82.12.4110.

Can. J. Chem. Downloaded from www.nrcresearchpress.com by Xi'an Jiaotong University on 09/19/12
For personal use only.

Estimating internuclear distances between half-integer quadrupolar nuclei by central-transition double-quantum sideband NMR spectroscopy

Andreas Brinkmann and Mattias Edén

Can. J. Chem. Downloaded from www.nrcresearchpress.com by Xi'an Jiaotong University on 09/19/12
For personal use only.

Abstract: We demonstrate the estimation of homonuclear dipolar couplings, and thereby internuclear distances, between half-integer spin quadrupolar nuclei by central-transition (CT) double-quantum (2Q) sideband nuclear magnetic resonance (NMR) spectroscopy. It is shown that the rotor-encoded sideband amplitudes from CT 2Q coherences in the indirect dimension of the two-dimensional NMR spectrum are sensitive probes of the magnitude of the homonuclear dipolar coupling, but are significantly less affected by other NMR parameters such as the magnitudes and orientations of the electric field gradient tensors. Experimental results of employing the $R2_2^1R2_2^{-1}$ recoupling sequence to the ^{11}B spin pair of bis(catecholato)diboron resulted in an estimation of the internuclear B–B distance as (169.6 ± 3) pm, i.e., with a relative uncertainty of ±2%, and in excellent agreement with the distance of 167.8 pm determined by single-crystal X-ray diffraction.

Key words: solid-state NMR, quadrupolar nuclei, central transition, double-quantum coherence, sideband spectroscopy, distance estimation.

Résumé : Faisant appel à la spectroscopie de résonance magnétique nucléaire (RMN) à transition centrale (TC) avec une bande latérale à double quantum (2Q), on montre qu'il est possible d'évaluer les couplages dipolaires homonucléaires, et ainsi les distances internucléaires, entre des noyaux quadripolaires de spin une demie. On montre que les amplitudes des bandes latérales encodées par un rotor, obtenues à partir des cohérences de la TC 2Q dans la dimension indirecte de spectre RMN bidimensionnel, sont des sondes sensibles de l'amplitude de couplage dipolaire homonucléaire, mais qu'elles sont moins influencées par d'autres paramètres de la RMN, tel les amplitudes et les orientations des tenseurs du gradient du champ électrique. Les résultats expérimentaux obtenus en employant la séquence de recouplage $R2_2^1R2_2^{-1}$ à la paire de spin ^{11}B du bis(catécholato)dibore à permis de faire d'évaluer la distance internucléaire B–B à (169,6 ± 3) pm, c'est-à-dire avec une incertitude relative de ±2 %, et en excellent accord avec la distance de 167,8 pm déterminée par diffraction des rayons-X sur un cristal unique.

Mots-clés : RMN à l'état solide, noyau quadripolaire, transition centrale, cohérence à double quantum, spectroscopie des bandes latérales, évaluation de la distance.

[Traduit par la Rédaction]

Introduction

The utilization of through-space dipolar interactions is of pivotal importance for determining order, structure, and dynamics by solid-state nuclear magnetic resonance (NMR) spectroscopy.[1–3] The anisotropic (orientation-dependent) dipolar interactions may provide both geometric and interatomic distance-related structural information; the latter feature stems from the inverse cubic relationship between the separation (r_{jk}) of two NMR-active nuclei and their dipolar coupling constant (b_{jk}). Solid-state NMR experimentation is generally performed on powdered samples undergoing magic-angle spinning (MAS) to emphasize isotropic (orientation-independent) nuclear spin interactions by reducing, or even eliminating, the anisotropies. However, during one or several segments of the MAS NMR experiment, the effects of the dipolar interactions may temporarily be reactivated: this process is referred to as "dipolar recoupling" and is typically arranged by application of radio-frequency (rf) pulse sequences.[1–3]

This work exploits "homonuclear" dipolar interactions (i.e., couplings involving nuclei of the same type) among half-integer spin quadrupolar nuclei[4–20] for estimating internuclear distances. Half-integer spins dominate among all existing NMR-active nuclei; examples include ^{11}B, ^{17}O, ^{23}Na, ^{27}Al, and ^{43}Ca. Following the advent of high-resolution solid-state NMR techniques, to eliminate the broadening from second-order quadrupolar interactions of the central transitions

Received 1 November 2010. Accepted 25 January 2011. Published at www.nrcresearchpress.com/cjc on 28 July 2011.

A. Brinkmann. Steacie Institute for Molecular Sciences, National Research Council, 1200 Montreal Road, M-40, Ottawa, ON K1A 0R6, Canada.
M. Edén. Physical Chemistry Division, Department of Materials and Environmental Chemistry, Arrhenius Laboratory, Stockholm University, 106 91 Stockholm, Sweden.

Corresponding author: Andreas Brinkmann (e-mail: Andreas.Brinkmann@nrc-cnrc.gc.ca).

This article is part of a Special Issue dedicated to Professor Roderick E. Wasylishen.

Can. J. Chem. Downloaded from www.nrcresearchpress.com by Xi'an Jiaotong University on 09/19/12
For personal use only.

(CTs),[21–24] half-integer spins have become indispensable probes of local structure in widely diverse materials of technological and geological importance.[25–27]

An important subclass of recoupling methodology exploits dipolar interactions for generating double-quantum coherences (2QC) under MAS conditions.[2,3] Such recoupling techniques targeting the CTs of half-integer spins, i.e., employing rf fields that are weak compared with the quadrupolar frequency, have primarily been utilized in two-dimensional 2Q-1Q NMR correlation spectroscopy that reveals all pairs of spatially nearby homonuclear spins in the structure.[11,12,15,19] A double-quantum filtering (2QF) stage in a 2Q-1Q NMR experiment involves two events, one for creating 2QC from longitudinal magnetization and one for driving the reverse process.[2,3] Such "excitation" and "reconversion" intervals are often of equal duration: $\tau_{exc} = \tau_{rec}$ (Fig. 1*a*). They are interleaved by an evolution period (t_1), during which each 2QC acquires a phase factor involving the frequency sum of the two spin resonances within the pair. Each 2QC frequency, appearing along the indirect (ω_1) dimension of the 2D spectrum, becomes correlated with its two respective CT single-quantum coherence (1QC) frequencies along the direct (ω_2) spectral dimension.[11,12,15,19]

It is normally desirable to sample the t_1 evolution such that it is synchronized with the rotational period $\tau_r = 2\pi/\omega_r$ of the sample, where ω_r denotes the angular rotation frequency; then, all spinning sidebands fold onto the centre-band frequency. Besides improving signal-to-noise in the NMR spectrum and eliminating ambiguities in assigning the 2D NMR peaks, this avoids formation of intense sidebands along the 2QC dimension because of the orientation dependence of the (re)coupled dipolar Hamiltonian.[29–34] Such "rotor-encoded" spinning sidebands arise unless the 2QC excitation and reconversion processes are initiated at exactly the same rotor position. However, as the spinning-sideband amplitudes depend on the magnitudes of the anisotropic interaction tensors relative to the spinning frequency, they provide a vehicle to estimate dipolar coupling constants, and thereby internuclear distances, as introduced for spin-1/2 applications by Spiess and co-workers.[29–34] Here, we demonstrate the possibility of using such 2Q-1Q NMR correlation protocols for estimating internuclear distances between dipolar-coupled homonuclear half-integer spins. The dipolar recoupling and 2QC generation employed herein invokes symmetry-based pulse schemes,[3,35–41] as introduced by us for recoupling homonuclear quadrupolar spins,[15–17,19,42] under both MAS and double rotation (DOR)[21] conditions.

We present one of very few techniques for estimating homonuclear dipolar couplings among half-integer spin quadrupolar nuclei. Previous options include monitoring the 2QF signal buildup versus τ_{exc},[43] as is well-established for spin-1/2 applications,[2,3] or using magnetization transfers under a 2Q Hamiltonian[9,10] such as 2Q-HORROR.[35] In that case, one spectral dimension reveals a "Pake-like" pattern (whose width is proportional to b_{jk}) and may be implemented either as a 2D[10] or 3D[9] experiment, the latter incorporating triple-quantum MAS (3QMAS)[23] for improved NMR signal separation. Duer presented a strategy for homonuclear distance measurements by analyzing the spinning sideband formation originating from the evolution of triple-quantum coherences under homonuclear dipolar interactions in a 3QMAS experiment, coupled to multi-spin simulations based on the known crystal structure.[4] This approach did not invoke explicit dipolar recoupling but rather exploited spontaneous recoupling owing to the noncommutation of homonuclear dipolar and first-order quadrupolar interactions of half-integer spins.[4,8,44]

Fig. 1. (*a*) Radiofrequency pulse sequence to record two-dimensional homonuclear double-quantum correlation spectra on half-integer quadrupolar nuclei. The subscript "sel" indicates central-transition-selective pulses. A frequency sweep (FS) may be used to enhance the central transition population difference. The rotor-synchronized pulse sequence $R2_2^1R2_2^{-1}$ achieves homonuclear recoupling.[15] (*b*) Coherence transfer pathway diagram[28] for the *I* spins.

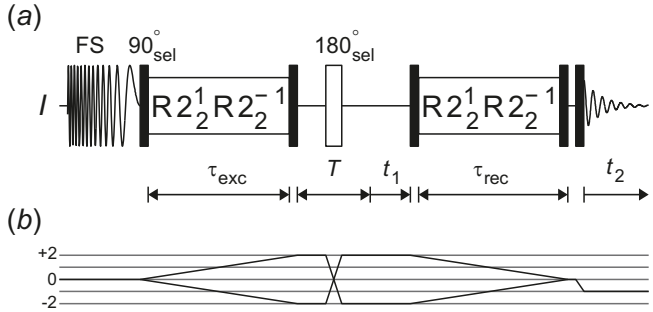

As isolated quadrupolar spin-pairs are rarely encountered, recoupling applications aiming at obtaining quantitative internuclear distances must generally consider large spin systems. To avoid such multi-spin effects and communicate the proof-of-principle, we here estimate the ^{11}B–^{11}B dipolar coupling and hence the internuclear B–B distance of the (isolated) pair of magnetically equivalent ^{11}B in the bis(catecholato)diboron molecule by 2Q-1Q correlation NMR spectroscopy. To support the analysis of the CT 2Q sideband NMR spectroscopy results, we calculated the ^{11}B chemical shift and quadrupolar tensors in bis(catecholato)diboron using gauge-including projector-augmented wave (GIPAW) density functional theory (DFT).[45] Our results are compared with those obtained by Weiss and Bryce[46] from various monoboronic acids and esters by DFT computations of isolated monomers and dimers.

Materials and methods

Solid-state NMR experiments

Figure 1 shows the pulse scheme used to obtain two-dimensional central-transition double-quantum (2D-CT-2Q) spectra of half-integer quadrupolar nuclei. At the start of the pulse sequence, the CT magnetization may optionally be enhanced;[13] possibilities include frequency sweeps as in Fig. 1*a*, encompassing double-frequency sweeps,[47] hyperbolic secant pulses,[48,49] and WURST single-frequency sweeps.[50] Other alternatives include the fast amplitude modulated (FAM)[51] and the equivalent rotor-assisted population transfer (RAPT) schemes,[52] or pulse shapes derived from optimal control theory.[53] The CT longitudinal magnetization is converted into homonuclear 2QC by a CT selective $R2_2^1R2_2^{-1}$ pulse sequence[15] of duration τ_{exc} that is bracketed by two CT 90° pulses; alternatively, for samples involving large spreads in resonance frequencies, it may be beneficial to employ the recoupling schemes of ref. 16. The 2QC are next subjected to a Hahn echo of total duration *T*,[15] adjusted so that the sum of

Can. J. Chem. Downloaded from www.nrcresearchpress.com by Xi'an Jiaotong University on 09/19/12
For personal use only.

the CT 90° pulses and T equals an even multiple of rotational periods (here, $2\tau_r$). The CT selective 180° refocusing pulse combined with phase cycling selects the coherence transfer pathway[28] shown in Fig. 1*b*.[12] After the subsequent evolution interval t_1, the 2QC are reconverted into longitudinal CT magnetization by a second $R2_2^1R2_2^{-1}$ block of duration τ_{rec}, which is also sandwiched by CT 90° pulses. Finally, observable CT transverse magnetization is created by a CT selective 90° read pulse.

A powdered sample of bis(catecholato)diboron (molecular structure shown in Fig. 2) was purchased from Sigma-Aldrich and used for all experiments. The experimental results shown in Figs. 3–6 were obtained at a ^{11}B Larmor frequency of –160.5 MHz in a static magnetic field of 11.75 T, by using a Bruker Advance-III console and a Varian 3.2 mm double-resonance standard-bore MAS probehead. The sample was rotated at a spinning frequency of 25 kHz, which corresponded to an rf nutation frequency of 6.25 kHz during dipolar recoupling, i.e., to a CT nutation frequency equal to half the MAS frequency,[15] as for the HORROR condition.[9,10,35] The selective 90° and 180° pulses operated at 9.0 kHz CT nutation frequency. All rf amplitudes were calibrated by complete 2D rf nutation experiments. To enhance the CT population difference, a single-frequency sweep was performed at the same rf field strength, by using a frequency offset and sweep bandwidths of 500 and 800 kHz, respectively, where the beginning and end of the sweep-pulse shape were attenuated by a $\sin^2$ and a $\cos^2$ function, respectively. The States-TPPI scheme was employed to obtain 2D pure absorption line shapes and to distinguish positive and negative 2Q coherences.[54,55]

Numerical spin dynamics simulations

All ^{11}B spin-pair simulations were performed using version 3.0.1 of the SIMPSON package.[56] The experimental parameters given in the preceding subsection were used, together with the experimentally estimated values of the ^{11}B quadrupolar coupling constant and asymmetry parameter listed in Table 1. In addition, the parameters of the CSA tensor and the orientation of the quadrupolar tensor were employed as obtained by GIPAW-DFT calculations (see Table 1). For all cases, powder averaging was accomplished by using a set of triplets of Euler angles, selected according to the ZCW scheme.[57–59] This set consisted of 1154 angles for simulating the CT 2Q build-up curves shown in Fig. 3, whereas the calculations of the CT 2Q sideband patterns displayed in Figs. 5 and 6 employed 6044 orientations. All pulses were taken explicitly into account in the simulations, except for the CT population enhancement and the 90° read pulse. The initial density operator and the detection operator were both set to represent CT z-magnetization. The CT 2QC were selected by setting all other elements in the density matrix to zero before and after the 180° spin-echo pulse. The CT 2Q sideband amplitudes were simulated by incrementing t_1 in 35 steps of duration $\tau_r/35$ and combining the results of the +2QC and –2QC time-dependent signal amplitudes to form the cosine and sine components required by the States procedure.[54] The resulting complex t_1 time signal was subjected to a complex Fourier transformation to obtain the integrated CT 2Q spinning sideband amplitudes.

Quantum chemical calculations

For the GIPAW-DFT calculations of the ^{11}B quadrupolar and chemical shift tensors in bis(catecholato)diboron, CASTEP[60] and CASTEP-NMR[45,61,62] (version 4.4) were used together with Accelrys' Materials Studio. The generalized gradient approximation with the Perdew–Burke–Ernzerhof exchange correlation functional[63] and "on-the-fly" pseudopotentials were chosen. The plane-wave cutoff energy was selected to be 550 eV and the k-point grid was set to $5 \times 2 \times 4$. Starting from the structure determined by single-crystal X-ray diffraction (XRD),[64] initially, only the proton positions were optimized, whereupon the NMR parameters were calculated.

Results and discussion

^{11}B NMR parameters in bis(catecholato)diboron

To use the full set of ^{11}B NMR parameters for bis(catecholato)diboron in the numerical simulations of the dipolar recoupling experiments, in a first step, we determined the ^{11}B isotropic shift, quadrupolar coupling constant $C_Q = e^2qQ/h$ and the quadrupolar asymmetry parameter η_Q experimentally; the results are shown in Table 1. In a second step, we derived the ^{11}B quadrupolar and chemical shift tensors in bis(catecholato)diboron by GIPAW-DFT calculations. Weiss and Bryce[46] recently reported ^{11}B NMR parameters in various monoboronic acids and esters by using DFT computations of isolated monomers and dimers. Since a crystal structure of bis(catecholato)diboron has been determined using single-crystal XRD,[64] we chose GIPAW-DFT calculations that explicitly account for the periodicity of the crystal.[45] The results of these computations are displayed in Table 1 and Fig. 2. Since the two boron sites in the bis(catecholato)diboron molecule are related by inversion symmetry through the centre of their internuclear vector, the chemical shift tensors, as well as quadrupolar tensors, are identical for both boron sites (magnitudes and orientations). The experimentally determined isotropic chemical shift and quadrupolar coupling constant of $\delta_{iso} = 28.6$ ppm and $C_Q = 2.71$ MHz, respectively, fall into the same range as that found for monoboronic esters,[46] whilst the present value $\eta_Q = 0.745$ is larger than those of the esters. Figure 2 shows the principle axis systems of the tensors, as obtained from GIPAW-DFT computations. The z principal axes of both tensors are approximately perpendicular to the molecular plane and the y axes are nearly collinear with the B–B bond. Whilst the calculated value $\eta_Q = 0.77$ is in good agreement with the experimentally determined one, the computed value $C_Q = 3.18$ MHz is significantly larger (by ≈0.5 MHz) than the experimentally measured value. In the Haeberlen notation[65] the calculated anisotropic chemical shift and asymmetry parameter are given by $(\delta_{aniso}, \eta) = (–22.6$ ppm, 0.67), which corresponds to a span and skew of $(\Omega, \kappa) = (41.5$ ppm, 0.27) in the Maryland notation.[65] We note that the calculated span is slightly higher than the largest one found in monoboronic acids,[46] whereas the skew is smaller.

Central-transition double-quantum NMR spectroscopy

A common approach to determine homonuclear dipolar couplings is to monitor the buildup of 2QC as a function of the excitation interval τ_{exc} of the recoupling sequence. This approach was launched by Mali et al.[12] in the present context

Table 1. ^{11}B NMR parameters of bis(catecholato)diboron as determined experimentally and by GIPAW-DFT calculations. The reported values of the anisotropic chemical shift (δ_{aniso}) and the asymmetry parameter (η) conform to the Haeberlen notation.[60]

	C_Q (MHz)	η_Q	Ω^Q_{PM} (°)	$\{\sigma_{xx}, \sigma_{yy}, \sigma_{zz}\}$ (ppm)	δ_{iso} (ppm)	δ_{aniso} (ppm)	η	Ω^{CSA}_{PM} (°)
Exptl.	2.71	0.745			28.6			
DFT	3.18	0.77	{–87.7, 89.8, 179.9}	{48.2, 63.4, 89.7}		–22.6	0.67	{–87.3, 85.8, –178.6}

Note: The Euler angles Ω^{Λ}_{PM} give the relative orientation of the principle axis system of the interaction tensor $\mathbf{\Lambda}$ and a molecule fixed frame with its z axis along the B–B internuclear vector and its x axis perpendicular to the O–B–O plane (compare Fig. 2). C_Q, quadrupolar coupling constant; η_Q, quadrupolar asymmetry parameter; $\{\sigma_{xx}, \sigma_{yy}, \sigma_{zz}\}$, principal components of the chemical shielding tensor; δ_{iso}, isotropic chemical shift.

Fig. 2. Molecular structure of bis(catecholato)diboron.[64] The principal axis system of the ^{11}B quadrupole coupling and chemical shift tensors as determined by CASTEP calculations are indicated in black and blue colors, respectively.

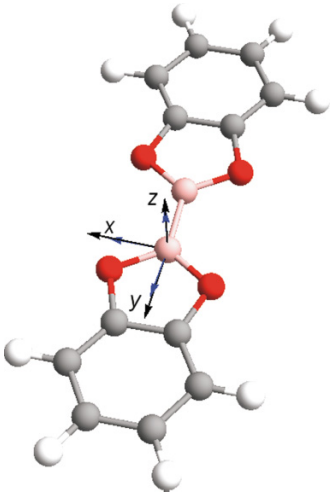

Fig. 3. ^{11}B double-quantum filtered efficiencies as a function of $\tau_{exc} = \tau_{rec}$ obtained in bis(catecholato)diboron using the pulse sequence shown in Fig. 1 at a spinning frequency of 25 kHz and an external field of 11.75 T. Experimental results are indicated by ■, whereas the outcome of numerical simulations for different homonuclear dipolar couplings constants $b_{jk}/2\pi$ are displayed as –2619 Hz (●), –3119 Hz (▲), and –2119 Hz (▼).

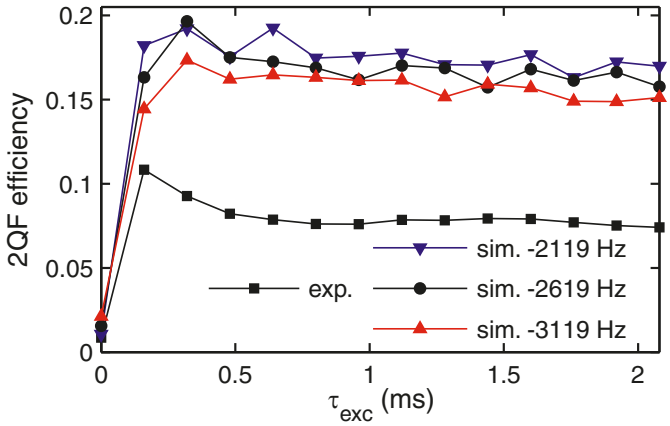

of distance estimations among half-integer spins. Figure 3 shows experimental and simulated ^{11}B two-spin 2QF efficiencies as a function of $\tau_{exc} = \tau_{rec}$, as determined in bis(catecholato)diboron by using the pulse sequence shown in Fig. 1 at a spinning frequency of 25 kHz and an external field of 11.75 T. Single-crystal XRD provided the B–B internuclear distance r_{jk} = 167.8 pm in the bis(catecholato)diboron molecule,[64] corresponding to a ^{11}B–^{11}B coupling constant of $b_{jk}/2\pi$ = –2619 Hz. The numerically simulated results in Fig. 3 account for the ^{11}B natural abundance of 80.1% that results in a probability of 64.2% to find a ^{11}B–^{11}B spin pair in an arbitrarily selected molecule. We achieved an experimental 2QF efficiency of 11%, whereas the simulation employing a ^{11}B–^{11}B dipolar coupling of –2619 Hz predicts a maximum 2QF efficiency of 20%. For comparison, Fig. 3 additionally displays the results of numerical simulations using dipolar couplings of –2119 and –3119 Hz. Minor variations of the ^{11}B 2QC dynamics were observed, despite the large difference between the dipolar couplings, which makes this approach an unfavourable choice if accurate determinations of large homonuclear dipolar couplings are desired. Significantly faster sample rotation would allow for finer sampling of the 2QC buildup, however, at the expense of requiring higher rf field strengths during recoupling: this compromises the CT selectivity of the pulses, while also leading to higher accumulation of rf errors during the 2Q-recoupling events. For the present experimental conditions, the problem of too coarse sampling of τ_{exc} prevails even for estimates of smaller couplings ($b_{jk} \approx 0.5$ kHz) and is accentuated further for homonuclear systems involving higher spin numbers (e.g., ^{27}Al) because of their accelerated 2QC excitation.[12,17]

Here we propose to instead utilize the spinning sidebands of the two-spin CT 2QC as a more favourable option for determining homonuclear dipolar couplings between half-integer quadrupolar nuclei. It offers particular advantages for measurements of strong dipolar interactions. In addition, whereas the efficiency of exciting CT 2QCs itself depends on the ability to employ CT-selective rf fields, the CT 2Q sideband patterns are significantly less influenced by this requirement. Although in the case of powdered samples, the rf fields may not be CT selective for all crystallite orientations at all time points, in practice this poses no serious limitation to the applicability of CT 2Q spectroscopy.[15–19]

Figure 4 shows the experimental ^{11}B 2D CT 2Q spectra of bis(catecholato)diboron, obtained by using the pulse sequence in Fig. 1 for three different intervals $\tau_{exc} = \tau_{rec}$ of 160, 320, and 480 μs at a spinning frequency of 25 kHz. The NMR spectra comprise strong rotor-encoded odd-order spinning sidebands in the indirect (2Q) dimension, analogous to the cases of coupled spin-1/2 nuclei or isolated quadrupolar spins, described by the group of Spiess.[29–34] If t_1 is incremented by a fraction of the rotational period under relatively fast MAS conditions, these sidebands mainly result from rotor encoding of the 2Q reconversion process. The rotor-encoded modulation of the 2QC gives rise solely to *odd-ordered*

Can. J. Chem. Downloaded from www.nrcresearchpress.com by Xi'an Jiaotong University on 09/19/12
For personal use only.

Fig. 4. Experimental two-dimensional ^{11}B central-transition (CT) double-quantum (2Q) spectra of bis(catecholato)diboron for different time intervals $\tau_{exc} = \tau_{rec}$: (*a*) 160 μs, (*b*) 320 μs, and (*c*) 480 μs.

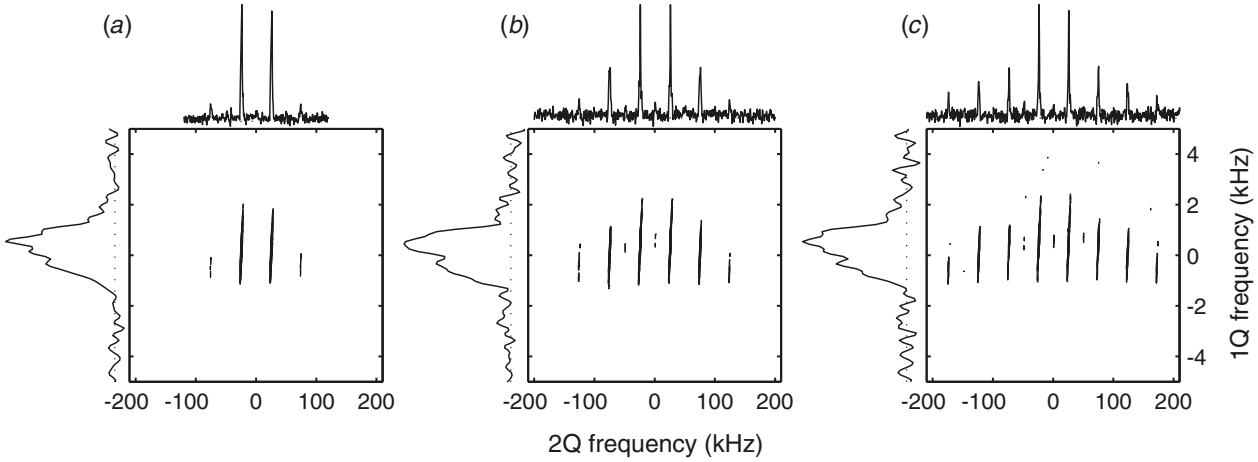

sidebands along the 2Q spectral dimension, even in scenarios devoid of 2QC evolution during t_1.[32,33] Ideally, the number and amplitudes of the sidebands depend only on the product $b_{jk}\tau_{rec}$ of the homonuclear dipolar coupling constant and the reconversion interval. On the other hand, the evolution of the 2QC under *all* noncommuting spin interactions during the t_1 interval produce conventional sidebands involving *all orders*, owing to the *rotor modulation* of the 2QC. The very small amplitudes of the even-order sidebands in the experimental spectra shown in Fig. 4 verify that hardly any rotor-modulated sidebands are present and that the rotor encoding of the 2Q reconversion process is indeed the predominant contribution to the odd-order sidebands. As expected,[29–34] a larger number of sidebands appear along the 2Q dimension of the 2D spectrum as the interval $\tau_{exc} = \tau_{rec}$ increases (Fig. 4).

The integrated amplitudes of the odd-ordered sidebands of the experimental ^{11}B 2D CT 2Q spectra of bis(catecholato)diboron are plotted in Figs. 5*a*, 5*c*, and 5*e* against the sideband order. For comparison, results of numerical simulations using the XRD distance-based ^{11}B–^{11}B dipolar coupling of $b_{jk}/2\pi = -2619$ Hz are presented in Figs. 5*b*, 5*d*, and 5*f*: the top row, (*a*) and (*b*), compares the experimental and simulated results for $\tau_{exc} = \tau_{rec} = 160$ μs; the middle row, (*c*) and (*d*), for 320 μs; and the bottom panel, (*e*) and (*f*), for 480 μs. It is evident that the experimental and simulated CT 2Q odd-order sideband amplitudes are similar overall, except from those of the ±1 sidebands that are more intense in the experiments relative to the simulations. However, the higher order (±3, ±5,…) sideband patterns are reproduced remarkably well. For internuclear distance measurements, we consequently suggest selecting $\tau_{exc} = \tau_{rec}$ sufficiently large, so that at least the ±3, ±5 and ±7 sidebands are present in the CT 2Q-1Q spectra.

To assess the sensitivity of the CT 2Q sideband pattern for the purpose of estimating the ^{11}B–^{11}B dipolar coupling b_{jk} and hence the B–B internuclear distance r_{jk}, we performed a series of numerical simulations for $\tau_{exc} = \tau_{rec} = 480$ μs by varying the dipolar coupling constants in steps of 20 Hz between –3619 and –1699 Hz. In each case we fitted one overall scaling factor of the complete sideband pattern by minimizing the sum-square deviation S between the simulated and experimental (±3, ±5, ±7, ±9) integrated sideband amplitudes. The 95% confidence interval was determined by the set of dipolar couplings for which $S \leq S_{min}\{1 + F^{0.05}_{1,6}/6\}$, where S_{min} is the sum-square deviation for the best fit and $F^{\alpha}(p_1,p_2)$ is the upper α probability point of the F distribution with p_1 and p_2 degrees of freedom.[66,67] We obtained a best fit

Fig. 5. Integrated odd-order CT 2Q spinning sideband amplitudes obtained in bis(catecholato)diboron for different time intervals $\tau_{exc} = \tau_{rec}$: (*a*) and (*b*) 160 μs, (*c*) and (*d*) 320 μs, and (*e*) and (*f*) 480 μs. The left column (*a*), (*c*), and (*e*) show experimental integrals, whereas the right column (*b*), (*d*), and (*f*) display numerically simulated sideband amplitudes for an ^{11}B–^{11}B dipolar coupling of $b_{jk}/2\pi = -2619$ Hz, which corresponds to an internuclear distance of 167.8 pm provided by single-crystal XRD.[64]

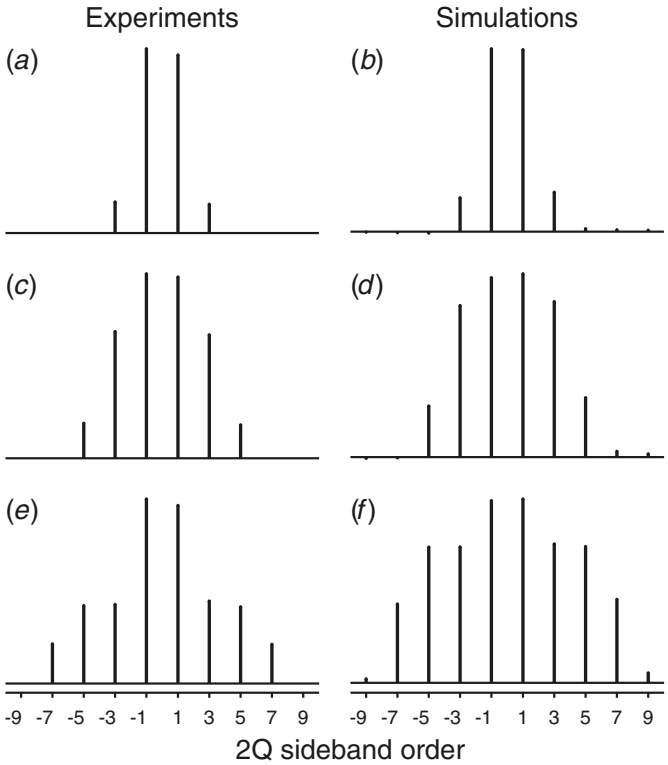

Can. J. Chem. Downloaded from www.nrcresearchpress.com by Xi'an Jiaotong University on 09/19/12
For personal use only.

Can. J. Chem. Downloaded from www.nrcresearchpress.com by Xi'an Jiaotong University on 09/19/12
For personal use only.

Fig. 6. Odd-order central-transition (CT) double-quantum (2Q) spinning sideband amplitudes obtained in bis(catecholato)diboron for $\tau_{exc} = \tau_{rec} = 480$ μs. Left column (*a*), (*c*), and (*e*): Blue/grey sticks depict the experimental integrals. Black sticks represent numerically simulated sideband amplitudes for different ^{11}B–^{11}B dipolar coupling constants $b_{jk}/2\pi$: (*a*) –2439 Hz, (*c*) –2579 Hz, and (*e*) –2699 Hz. Right column (*b*), (*d*), and (*f*): Simulated sideband amplitudes for $b_{jk}/2\pi = -2619$ Hz and different quadrupolar coupling constants C_Q: (*b*) 2.7 MHz, (*d*) 2.1 MHz, and (*f*) 3.5 MHz.

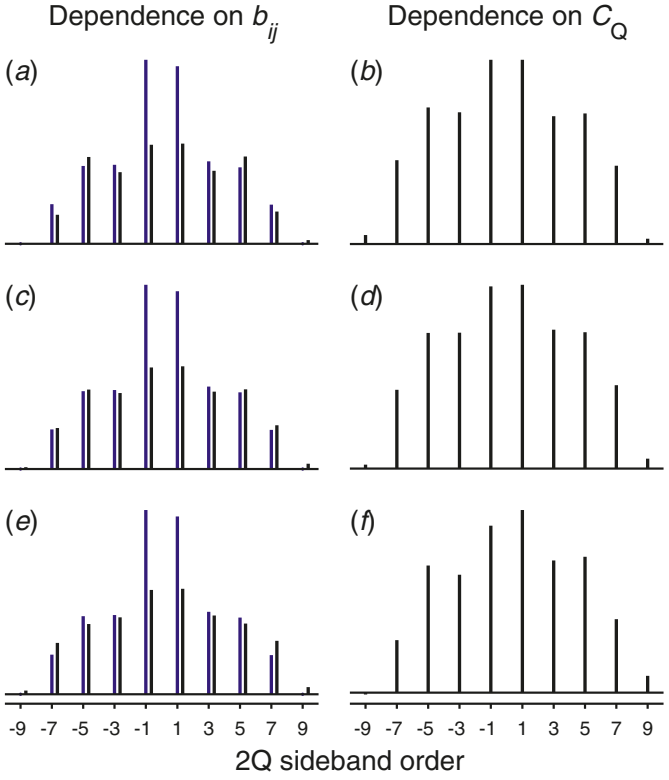

of –2579 (+70, –60) Hz for the ^{11}B–^{11}B dipolar coupling constant in bis(catecholato)diboron, which corresponds to a solid-state NMR-determined distance of 169.6 (+1.6, –1.3) ppm. These results are in excellent agreement with the values determined by X-ray diffraction, –2619 Hz and 167.8 pm, respectively. The best fit simulations of the CT 2Q sideband amplitudes are shown in Fig. 6*c* together with the experimental results.

In the right column of Fig. 6, the numerically simulated results from varying the quadrupolar coupling constant reveal very weak effects on the sideband amplitudes. This also applies if the quadruplar coupling constants of the two ^{11}B sites are different. Further, omitting the CSA interactions has even less bearing on the sideband patterns (data not shown). Numerical simulations (to be presented elsewhere) indicate that the quadrupolar coupling orientations, as well as the magnitude and orientation of the CSA tensor, only have relatively minor influences on the CT 2Q sideband pattern. However, because of these small effects, we conservatively state a final confidence interval for the estimation of the ^{11}B–^{11}B dipolar coupling constant in bis(catecholato)diboron that is twice the one found by the least-squares analysis. Therefore, we could reliably estimate the ^{11}B–^{11}B dipolar coupling constant as –2579 (+140, –120) Hz, corresponding to a solid-state NMR determined B–B distance of (169.6 ± 3) pm. Figures 6*a* and 6*e* show the experimental integrated CT 2Q sideband amplitudes together with the numerical simulations for the upper and lower bounds in the estimated dipolar coupling constant, i.e., –2439 and –2699 Hz, respectively. This confirms that the higher order (±3, ±5, …) sideband amplitudes clearly constitute sensitive measures of the homonuclear dipolar coupling. The relative uncertainty of our estimation is about ±5% in the ^{11}B–^{11}B dipolar coupling constant and about ±2% in the internuclear B–B distance.

Wi et al.[9,10] reported a recoupling-derived interatomic distance in the related bis(pinacolato)diboron complex, which also features two directly bonded boron atoms. Their approach utilized magnetization transfers under a 2Q dipolar Hamiltonian effected by the 2Q-HORROR technique[35] in the absence of 2QF. At the expense of significantly reduced NMR signal-to-noise, the explicit 2QF employed herein is advantageous for spin pairs where the recoupled isotope is not 100% naturally abundant (e.g., ^{11}B), as it ensures that only one pair of the targeted spins need to be considered in the numerical simulations involved in the distance analysis. Similar issues apply for Duer's 3QMAS-based strategy.[4] Besides this favorable feature of the present technique, we expect that its accuracy and resolution of the distance estimates provided will be at least as good as the methods presented in refs. 4, 10, and 43.

Concluding remarks

In this contribution, we have demonstrated that CT 2Q sideband NMR spectroscopy has great potential for estimating the internuclear distances between half-integer spin quadrupolar nuclei. We showed that for the ^{11}B spin pair of bis(catecholato)diboron, the amplitudes of higher odd-order (±3, ±5,…) double-quantum rotor-encoded spinning sidebands could be reproduced very well by numerical simulations and constitute sensitive probes of the homonuclear ^{11}B–^{11}B dipolar interaction. This resulted in an estimation of the ^{11}B–^{11}B dipolar coupling constant in bis(catecholato)diboron to –2579 (+140, –120) Hz (approx. ±5%), corresponding to an internuclear solid-state NMR-determined B–B distance of (169.6 ± 3) pm (approx. ±2%). This value is in excellent agreement with the single-crystal XRD-determined distance of 167.8 pm.[64] Our estimation of the uncertainties is conservative and takes into account that the exact size and orientation of the quadrupolar tensor has a weak influence on the CT 2Q sideband amplitudes. As a result, our approach is directly applicable for readily distinguishing between scenarios involving (for instance) single or double-bonded B–B motifs.[68]

Whereas the present work has provided one of very few examples of internuclear distance measurements in pairs of *directly* bonded quadrupolar spin-3/2 nuclei,[9,10] this approach is neither limited to strong dipolar couplings nor spin-3/2 systems. In a forthcoming publication we will present analytical expressions facilitating the 2Q spinning-sideband analysis and demonstrate the determination of much weaker homonuclear dipolar couplings among quadrupolar nuclei, such as ^{23}Na and ^{27}Al, in the more commonly encountered context of inorganic network materials. Further, extensions of this work for determining heteronuclear dipolar interactions

involving half-integer quadrupolar nuclei[34,69,70] are in progress in our laboratories.

Acknowledgments

The authors would like to thank G. Enright for confirming the X-ray structure of bis(catecholato)diboron and I. Moudrakovski, V. Terskikh, and C. Ratcliffe for helpful discussions. Access to CASTEP was provided by the National Ultrahigh-Field NMR Facility for Solids (Ottawa, Ontario), a national research facility funded by the Canada Foundation for Innovation, the Ontario Innovation Trust, Recherche Québec, the National Research Council Canada (NRC), and Bruker BioSpin and managed by the University of Ottawa (www.nmr900.ca). This work was supported by the National Research Council Canada, the Swedish Research Council (VR; contracts 2007-4967 and 2009-7551), and the Faculty of Natural Sciences at Stockholm University.

References

(1) Bennett, A. E.; Griffin, R. G.; Vega, S. In *NMR Basic Principles and Progress;* Diehl, P., Fluck, E., Gunther, H., Kosfield, R., Seelig, J., Eds.; Springer-Verlag: Berlin, 1994; pp 1–77.

(2) Dusold, S.; Sebald, A. *Ann. Rep. NMR Spectrosc.* **2000** *41*, 185. doi:10.1016/S0066-4103(00)41010-0.

(3) Levitt, M. H. Symmetry-Based Pulse Sequences in Magic-Angle Spinning Solid-State NMR. In *Encyclopedia of Nuclear Magnetic Resonance;* Grant, D. M., Harris, R. K., Eds.; Wiley: Chichester, UK, 2002; Vol. 9, pp 165–196.

(4) Duer, M. J. *Chem. Phys. Lett.* **1997** *277* (1–3), 167. doi:10.1016/S0009-2614(97)00929-9.

(5) Baldus, M.; Rovnyak, D.; Griffin, R. G. *J. Chem. Phys.* **2000** *112* (13), 5902. doi:10.1063/1.481187.

(6) Dowell, N. G.; Ashbrook, S. E.; McManus, J.; Wimperis, S. *J. Am. Chem. Soc.* **2001** *123* (33), 8135. doi:10.1021/ja010681d.

(7) Edén, M.; Grinshtein, J.; Frydman, L. *J. Am. Chem. Soc.* **2002** *124* (33), 9708. doi:10.1021/ja020534v.

(8) Edén, M.; Frydman, L. *J. Phys. Chem. B* **2003** *107* (51), 14598. doi:10.1021/jp035794t.

(9) Wi, S.; Heise, H.; Pines, A. *J. Am. Chem. Soc.* **2002** *124* (36), 10652. doi:10.1021/ja027043v.

(10) Wi, S.; Logan, J. W.; Sakellariou, D.; Walls, J. D.; Pines, A. *J. Chem. Phys.* **2002** *117* (15), 7024. doi:10.1063/1.1506907.

(11) Painter, A. J.; Duer, M. J. *J. Chem. Phys.* **2002** *116* (2), 710. doi:10.1063/1.1425831.

(12) Mali, G.; Fink, G.; Taulelle, F. *J. Chem. Phys.* **2004** *120* (6), 2835. doi:10.1063/1.1638741.

(13) Mali, G.; Kaučič, V. *J. Magn. Reson.* **2004** *171* (1), 48. doi:10.1016/j.jmr.2004.08.003.

(14) Edén, M.; Annersten, H.; Zazzi, Å. *Chem. Phys. Lett.* **2005** *410* (1–3), 24. doi:10.1016/j.cplett.2005.04.030.

(15) Edén, M.; Zhou, D.; Yu, J. *Chem. Phys. Lett.* **2006** *431* (4–6), 397. doi:10.1016/j.cplett.2006.09.081.

(16) Lo, A. Y. H.; Edén, M. *Phys. Chem. Chem. Phys.* **2008** *10* (44), 6635. doi:10.1039/b808295b.

(17) Brinkmann, A.; Kentgens, A. P. M.; Anupõld, T.; Samoson, A. *J. Chem. Phys.* **2008** *129* (17), 174507. doi:10.1063/1.3005395.

(18) Edén, M.; Lo, A. Y. H. *J. Magn. Reson.* **2009** *200* (2), 267. doi:10.1016/j.jmr.2009.07.007.

(19) Edén, M. *Solid State NMR* **2009** *36* (1), 1. doi:10.1016/j.ssnmr.2009.06.005.

(20) Wang, Q.; Hu, B.; Lafon, O.; Trébosc, J.; Deng, F.; Amoureux, J. P. *J. Magn. Reson.* **2009** *200* (2), 251. doi:10.1016/j.jmr.2009.07.009.

(21) Samoson, A.; Lippmaa, E.; Pines, A. *Mol. Phys.* **1988** *65* (4), 1013. doi:10.1080/00268978800101571.

(22) Mueller, K. T.; Sun, B. Q.; Chingas, G. C.; Zwanziger, J. W.; Terao, T.; Pines, A. *J. Magn. Reson.* **1990** *86*, 470.

(23) Frydman, L.; Harwood, J. S. *J. Am. Chem. Soc.* **1995** *117* (19), 5367. doi:10.1021/ja00124a023.

(24) Gan, Z. *J. Am. Chem. Soc.* **2000** *122* (13), 3242. doi:10.1021/ja9939791.

(25) Smith, M. E.; van Eck, E. R. H. *Prog. Nucl. Magn. Reson. Spectrosc.* **1999** *34* (2), 159. doi:10.1016/S0079-6565(98)00028-4.

(26) Ashbrook, S. E.; Duer, M. J. *Concepts Magn. Reson. A* **2006** *28*, 183. doi:10.1002/cmr.a.20053.

(27) Hanna, J. V.; Smith, M. E. *Solid State NMR* **2010** *38* (1), 1. doi:10.1016/j.ssnmr.2010.05.004.

(28) Bodenhausen, G.; Kogler, H.; Ernst, R. R. *J. Magn. Reson.* **1984** *58*, 370.

(29) Geen, H.; Titman, J. J.; Gottwald, J.; Spiess, H. W. *J. Magn. Reson. A* **1995** *114* (2), 264. doi:10.1006/jmra.1995.1137.

(30) Gottwald, J.; Demco, D. E.; Graf, R.; Spiess, H. W. *Chem. Phys. Lett.* **1995** *243* (3–4), 314. doi:10.1016/0009-2614(95)00872-2.

(31) Graf, R.; Demco, D. E.; Gottwald, J.; Hafner, S.; Spiess, H. W. *J. Chem. Phys.* **1997** *106* (3), 885. doi:10.1063/1.473169.

(32) Friedrich, U.; Schnell, I.; Brown, S. P.; Lupulescu, A.; Demco, D. E.; Spiess, H. W. *Mol. Phys.* **1998** *95* (6), 1209. doi:10.1080/00268979809483252.

(33) Schnell, I.; Spiess, H. W. *J. Magn. Reson.* **2001** *151* (2), 153. doi:10.1006/jmre.2001.2336.

(34) Lupulescu, A.; Brown, S. P.; Spiess, H. W. *J. Magn. Reson.* **2002** *154* (1), 101. doi:10.1006/jmre.2001.2464.

(35) Nielsen, N. C.; Bildsøe, H.; Jakobsen, H. J.; Levitt, M. H. *J. Chem. Phys.* **1994** *101* (3), 1805. doi:10.1063/1.467759.

(36) Lee, Y. K.; Kurur, N. D.; Helmle, M.; Johannessen, O. G.; Nielsen, N. C.; Levitt, M. H. *Chem. Phys. Lett.* **1995** *242* (3), 304. doi:10.1016/0009-2614(95)00741-L.

(37) Edén, M.; Levitt, M. H. *J. Chem. Phys.* **1999** *111* (4), 1511. doi:10.1063/1.479410.

(38) Brinkmann, A.; Edén, M.; Levitt, M. H. *J. Chem. Phys.* **2000** *112* (19), 8539. doi:10.1063/1.481458.

(39) Carravetta, M.; Edén, M.; Zhao, X.; Brinkmann, A.; Levitt, M. H. *Chem. Phys. Lett.* **2000** *321* (3–4), 205. doi:10.1016/S0009-2614(00)00340-7.

(40) Brinkmann, A.; Levitt, M. H. *J. Chem. Phys.* **2001** *115* (1), 357. doi:10.1063/1.1377031.

(41) Brinkmann, A.; Edén, M. *J. Chem. Phys.* **2004** *120* (24), 11726. doi:10.1063/1.1738102.

(42) Edén, M. *J. Magn. Reson.* **2010** *204* (1), 99. doi:10.1016/j.jmr.2010.02.007.

(43) Mali, G.; Kaučič, V.; Taulelle, F. *J. Chem. Phys.* **2008** *128* (20), 204503. doi:10.1063/1.2928809.

(44) Edén, M.; Frydman, L. *J. Chem. Phys.* **2001** *114* (9), 4116. doi:10.1063/1.1344886.

(45) Pickard, C. J.; Mauri, F. *Phys. Rev. B* **2001** *63* (24), 245101. doi:10.1103/PhysRevB.63.245101.

(46) Weiss, J. W. E.; Bryce, D. L. *J. Phys. Chem. A* **2010** *114* (15), 5119. doi:10.1021/jp101416k.

(47) Kentgens, A. P. M.; Verhagen, R. *Chem. Phys. Lett.* **1999** *300* (3–4), 435. doi:10.1016/S0009-2614(98)01402-X.

(48) Siegel, R.; Nakashima, T. T.; Wasylishen, R. E. *Chem. Phys. Lett.* **2004** *388* (4–6), 441. doi:10.1016/j.cplett.2004.03.047.

Can. J. Chem. Downloaded from www.nrcresearchpress.com by Xi'an Jiaotong University on 09/19/12
For personal use only.

(49) Siegel, R.; Nakashima, T. T.; Wasylishen, R. E. *J. Magn. Reson.* **2007** *184* (1), 85. doi:10.1016/j.jmr.2006.09.007.
(50) Hansen, M. R.; Brorson, M.; Bildsøe, H.; Skibsted, J.; Jakobsen, H. J. *J. Magn. Reson.* **2008** *190* (2), 316. doi:10.1016/j.jmr.2007.11.014.
(51) Madhu, P. K.; Goldbourt, A.; Frydman, L.; Vega, S. *J. Chem. Phys.* **2000** *112* (5), 2377. doi:10.1063/1.480804.
(52) Yao, Z.; Kwak, H.-T.; Sakellariou, D.; Emsley, L.; Grandinetti, P. J. *Chem. Phys. Lett.* **2000** *327* (1–2), 85. doi:10.1016/S0009-2614(00)00805-8.
(53) O'Dell, L. A.; Harris, K. J.; Schurko, R. W. *J. Magn. Reson.* **2010** *203* (1), 156. doi:10.1016/j.jmr.2009.12.016.
(54) States, D.; Haberkorn, R. A.; Ruben, D. J. *J. Magn. Reson.* **1982** *48*, 286.
(55) Marion, D.; Ikura, M.; Tschudin, R.; Bax, A. *J. Magn. Reson.* **1989** *85*, 393.
(56) Bak, M.; Nielsen, N. C. *J. Magn. Reson.* **2000** *147* (2), 296. doi:10.1006/jmre.2000.2179.
(57) Zaremba, S. K. *SIAM Rev.* **1968** *10* (3), 303. doi:10.1137/1010056.
(58) Conroy, H. *J. Chem. Phys.* **1967** *47* (12), 5307. doi:10.1063/1.1701795.
(59) Cheng, V. B.; Suzukawa, Jr., H. H.; Wolfsberg, M. *J. Chem. Phys.* **1973** *59* (8), 3992. doi:10.1063/1.1680590.
(60) Clark, S. J.; Segall, M. D.; Pickard, C. J.; Hasnip, P. J.; Probert, M. I. J.; Refson, K.; Payne, M. C. *Z. Kristallogr.* **2005** *220* (5–6), 567. doi:10.1524/zkri.220.5.567.65075.
(61) Yates, J. R.; Pickard, C. J.; Mauri, F. *Phys. Rev. B* **2007** *76* (2), 024401. doi:10.1103/PhysRevB.76.024401.
(62) Profeta, M.; Mauri, F.; Pickard, C. J. *J. Am. Chem. Soc.* **2003** *125* (2), 541. doi:10.1021/ja027124r.
(63) Perdew, J. P.; Burke, K.; Ernzerhof, M. *Phys. Rev. Lett.* **1996** *77* (18), 3865. doi:10.1103/PhysRevLett.77.3865.
(64) Clegg, W.; Elsegood, M. R. J.; Lawlor, F. J.; Norman, N. C.; Pickett, N. L.; Robins, E. G.; Scott, A. J.; Nguyen, P.; Taylor, N. J.; Marder, T. B. *Inorg. Chem.* **1998** *37* (20), 5289. doi:10.1021/ic9804317.
(65) Harris, R. K.; Becker, E. D.; Cabral de Menezes, S. M.; Granger, P.; Hoffman, R. E.; Zilm, K. W. *Pure Appl. Chem.* **2008** *80* (1), 59. doi:10.1351/pac200880010059.
(66) Seber, G. A. F.; Wild, C. J. *Nonlinear Regression;* Wiley Series in Probability and Statistics; Wiley-Interscience: Hoboken, NJ, 2003.
(67) Beale, E. M. L. *J. R. Stat. Soc., B* **1960** *22*, 41.
(68) Wang, Y.; Quillian, B.; Wei, P.; Wannere, C. S.; Xie, Y.; King, R. B.; Schaefer, H. F., III; von Ragué Schleyer, P.; Robinson, G. H. *J. Am. Chem. Soc.* **2007** *129* (41), 12412. doi:10.1021/ja075932i.
(69) Brinkmann, A.; Kentgens, A. P. M. *J. Phys. Chem. B* **2006** *110* (32), 16089. doi:10.1021/jp062809p.
(70) Brinkmann, A.; Kentgens, A. P. M. *J. Am. Chem. Soc.* **2006** *128* (46), 14758. doi:10.1021/ja065415k.

Can. J. Chem. Downloaded from www.nrcresearchpress.com by Xi'an Jiaotong University on 09/19/12
For personal use only.

Separation of nematic and smectic-A potential effects on solute ordering in a series of binary 6OCB–8OCB mixtures

E. Elliott Burnell, Ronald Y. Dong, Adrian C.J. Weber, Xuan Yang, and Anand Yethiraj

Can. J. Chem. Downloaded from www.nrcresearchpress.com by Xi'an Jiaotong University on 09/19/12
For personal use only.

Abstract: ^{1}H NMR and optical microscopy have been used to study four solutes dissolved in samples of a binary mixture of 4-*n*-hexyloxy-4′-cyanobiphenyl (6OCB) and 4-*n*-octyloxy-4′-cyanobiphenyl (8OCB) that are close to the region of the phase diagram where the smectic-A (SmA) and re-entrant nematic (RN) phases exist. Optical microscopy clearly indicates that one of the four studied samples shows the phase sequence of isotropic–nematic–SmA–RN. The derived solute order parameters were interpreted by means of two Maier–Saupe mechanisms in conjunction with the Kobayashi–McMillan theory in the case of the SmA phase. The novel feature of this study is that the nematic potential is extrapolated from the nematic to the SmA phase based on concentrations of the 6OCB–8OCB mixtures. The derived smectic order parameters for each of the studied solutes clearly show a maximum absolute magnitude near the centre of the SmA temperature range. The different partitioning of these solutes in the binary mixture is also discussed.

Key words: re-entrant nematic, smectic, nematic, NMR, optical microscopy, phase transition, order parameter.

Résumé : On a fait appel à la RMN du ^{1}H et à la microscopie optique pour étudier quatre solutés dissous dans des échantillons d'un mélange binaire de 4-hexyloxy-4′-*o*-cyanobiphényle (6OCB) et de 4-octyloxy-4′-*o*-cyanobiphényle (8OCB) qui sont près de la région du diagramme de phase dans laquelle les phase smectique-A (SmA) et nématique réentrante (NR) existent. La microscopie optique indique clairement qu'un des quatre échantillons étudiés présente une séquence de phase d'isotrope, nématique, smectique A et nématique réentrante. On a interprété les d'ordre de solutés qui en ont été dérivés à l'aide de deux mécanismes de Maier–Saupe en relation avec la théorie de Kobayashi–McMillan dans le cas de la phase smectique A. La caractéristique nouvelle de cette étude réside dans le fait que le potentiel nématique est extrapolé de la phase nématique à la phase SmA en se basant sur les concentrations des mélanges 6OCB–8OCB. Les paramètres d'ordre smectique dérivés pour chacun des solutés étudiés montre clairement la présence d'une amplitude absolue maximale près du centre de la plage de température smectique A. On discute aussi des diverses répartitions de ces solutions dans le mélange binaire.

Mots-clés : nématique réentrante, smectique, nématique, RMN, microscopie optique, transition de phase, paramètre d'ordre.

[Traduit par la Rédaction]

Introduction

Molecular orientational ordering in the nematic (N) phase, and in addition positional ordering in the case of smectic phases, is important to the basic understanding of liquid crystals (LCs).[1–4] Mean-field theories have been quite successfully applied for the qualitative understanding of this molecular ordering. However, careful quantitative studies of solutes in the N phase have indicated the existence of multiple ordering mechanisms (see ref. 5 and refs. therein). We have extended the study of molecular ordering to the smectic phase where nematic ordering remains but a new smectic order parameter is born.[6–10] Here we have uncovered unusual behaviour — while linear extrapolation of the nematic ordering potential into the smectic phase works well for some solutes, it does not for others. In this paper we study a LC system with a N – smectic A – (re-entrant) N phase sequence[8] where the smectic range is variable, allowing us to investigate this unusual behaviour quantitatively.

To investigate the mechanisms responsible for the anisotropic ordering of molecules in condensed mesophases, it is necessary to write down the relevant intermolecular potential(s). Though there are numerous different types of shape anisotropy in the

Received 18 November 2010. Accepted 21 January 2011. Published at www.nrcresearchpress.com/cjc on 4 August 2011.

E.E. Burnell, A.C. Weber, and X. Yang. Department of Chemistry, University of British Columbia, 2036 Main Mall, Vancouver, BC V6T 1Z1, Canada.
R.Y. Dong. Department of Physics and Astronomy, University of British Columbia, 6224 Agricultural Road, Vancouver, BC V6T 1Z1, Canada.
A. Yethiraj. Department of Physics and Physical Oceanography, Memorial University, St. John's, NL A1B 3X7, Canada.

Corresponding author: E.E. Burnell (e-mail: elliott.burnell@ubc.ca).

This article is part of a Special Issue dedicated to Professor Roderick E. Wasylishen.

Can. J. Chem. Downloaded from www.nrcresearchpress.com by Xi'an Jiaotong University on 09/19/12
For personal use only.

constituent molecules forming LCs, only the simplest kind, the rodlike mesogen, will be considered here. Even so, the molecules are usually composed of a rigid aromatic core, flanked by one or two flexible hydrocarbon chains. To a first approximation, it suffices to treat them as axially symmetric rods as is done in the Maier–Saupe (MS) nematic mean-field potential,[11,12] in which the dispersive energy is written in terms of a second Legendre polynomial $P_2(\cos\theta_L)$ with θ_L being the angle between the rod long axis and the nematic director **n**. In the smectic-A (SmA) phase, there is translational ordering as molecules tend to form layers. The director is along the layer normal. To extend the MS mean-field potential to the SmA phase, Kobayashi–McMillan (KM) theory[13–15] adds additional terms to account for a one-dimensional density wave in the direction of the layer normal, and for a coupling between the layering and the orientational potential. The MS–KM SmA potential contains, therefore, the two interaction prefactors τ_L' and κ_L' for the positional ordering and for its coupling to the orientational ordering, respectively. It is only in recent years that attempts have been made to determine these prefactors, as reported in the literature.[6–10,16,17]

Liquid crystals exhibiting smectic phases are invariably composed of large and flexible molecules that impose complexity in their ability to probe the intermolecular potential. One very successful approach to studying the anisotropic potential is to use small solute molecules as probes of the anisotropic environment. The size and shape of rigid solutes can be chosen to optimize their sensitivity to the orientational and (or) positional order. This has been most successful in conjunction with nuclear magnetic resonance (NMR) spectroscopy studies of the solutes.[3,18] In particular, in 2004 it was reported that the temperature dependence of the asymmetry in the orientational order parameters of solutes showed a distinct change on passing from the N to the SmA phase of a cyanobiphenyl.[6] The MS–KM theoretical approach was used to rationalize the dipolar couplings (or order parameters) of several solutes.

The experimental dipolar couplings of a solute can be used to obtain the independent second-rank order parameters, and since the number of independent order parameters equals the number of unknowns in the nematic potential, it is impossible to isolate the nematic and smectic mean-field potentials simply based on the available orientational order parameters. Thus, at a given temperature in the SmA phase, the number of unknowns in the SmA interaction Hamiltonian will always be two greater than the number of experimentally determined orientational order parameters, these unknowns being the nematic terms plus the two smectic prefactors. Crucial assumptions and approximations have to be made to make the problem solvable in terms of the smectic prefactors in the solute's smectic potential. To extract information on the KM potential from NMR experiments on the SmA phase, some details of the nematic potential in this phase must be known.

The effect of the smectic phase is clearly observed as a discontinuity in the slope at the N–SmA phase transition in plots of solute order parameter asymmetry versus quantities such as temperature, order parameter, or mean-field energy parameter. In the first attempts to utilize this observation it was assumed that the temperature behaviour of the asymmetry b_s of a molecular property tensor $\boldsymbol{\beta}_s$ for each solute in the N phase could be extrapolated to lower temperatures where the sample is in the SmA phase. In ref. 6 linear extrapolation of b_s vs $\beta_{s,xx}$ was used for two different solutes. Later, it was noted that such a linear procedure is not general, and could not, for example, be applied to the solute *ortho*-dichlorobenzene (odcb),[7] because for that solute the nematic points for b_s versus $\beta_{s,xx}$ are curved.

In an attempt to address the curvature problem, a binary mixture of 4-*n*-hexyloxy-4′-cyanobiphenyl (6OCB) – 4-*n*-octyloxy-4′-cyanobiphenyl (8OCB) was chosen because of its ability to form a re-entrant nematic (RN) phase at temperatures below the SmA phase. The hope was to see if the contiguity of behaviour between the two N phases would inform us about the validity of the extrapolation. A polynomial curve that went through all nematic points, including those in the RN phase, was drawn for odcb. When a reasonable value of ~0.3 is chosen for solute smectic–orientational order coupling κ', a successful global fit to all the temperatures can be carried out with the MS–KM potential.[8]

All these studies involved progressively improved strategies to extract meaningful values for solute smectic order parameters τ. To gauge the goodness of various approximations, let us consider the smectic order parameter values of *para*-dichlorobenzene (pdcb) (τ_{pdcb}) in the middle of the SmA phase in 8OCB and the 6OCB–8OCB mixture: –0.29,[6] –0.25,[7] and –0.35.[8] It is interesting to see that for this particular solute, the various τs are comparable, indicating the suitability of the KM mean-field potential at the molecular level.

However, there is a major difficulty with the studies above. If only one MS mechanism is responsible for the nematic potential, then the solute property anisotropy (b_s) should not show any temperature dependence. Thus, the observed temperature dependence of b_s indicates that two or more ordering mechanisms are operating in the N phase. In this regard, we note a recent study of eight solutes in seven N solvents (including a "magic mixture" for which there is evidence that solute orientational order arises from a single mechanism that involves only short-range size and shape interactions) demonstrated that solute orientational order can be rationalized to an excellent extent (agreement between experimental and calculated orientational order parameters to 5% and better) with the idea of two independent MS potentials, the so-called MSMS potential. In this potential the traceless β_{ii} ($i = x, y, z$) are solute properties that are taken to be different for the two mechanisms, but independent of temperature. The first mechanism is taken to be associated with short-range size and shape interactions (which is then the only mechanism in the magic mixture), and the second mechanism is taken to account for additional interactions in other N samples.[5]

The success of the MSMS approach in the N phase prompted us to extend its application over a wider nematic temperature range, and also to apply it to the SmA phase of two LCs.[9,10] The molecular β_{ii} properties for the two MS mechanisms were determined for each solute from joint fits to order parameters of these solutes in the nematic LCs *p*-ethoxybenzylidene-*p*′-*n*-butylaniline (EBBA), Merck ZLI-1132 (1132), a magic mixture of 55 wt% 1132 and 45 wt% EBBA, and at three temperatures in each of 4-*n*-octyl-4′-cyanobiphenyl (8CB) and 8OCB. These β_{ii} are then taken as molecular constants, and the MSMS potential was used in

Can. J. Chem. Downloaded from www.nrcresearchpress.com by Xi'an Jiaotong University on 09/19/12
For personal use only.

conjunction with the order parameters of 11 or 12 solutes to give $G_{L,ZZ}^{MS_1} \equiv G_1$ and $G_{L,ZZ}^{MS_2} \equiv G_2$ as the two fitting parameters for the nematic potential at each temperature studied in the N phase. It was then assumed that a plot of G_1 vs G_2, which is essentially linear in the N phase, can be extrapolated into the SmA phase, thus providing a description of the nematic potential in the SmA phase. In the SmA phase, a combined MSMS–KM theory is then applied to gain information on the solute prefactors τ_s', κ_1', and κ_2'. Note that the κ_i' account for coupling to the two nematic potentials and are LC properties.

This latest work tries to address two problems associated with earlier work: the need to incorporate two nematic mechanisms, and the extrapolation involving nonlinear results. However, extrapolation (of G_1) is still employed. In addition, to obtain a successful fit to all solute orientational order parameters obtained in the SmA phase, restrictions (upper limits) had to be placed on some τ_s' values.

For all the studies above, κ' (or κ_1') were chosen to be positive; the signs of the prefactors κ' and τ_s' are correlated in the smectic potential (a change of sign of all prefactors yields exactly the same result). Choosing κ' (or κ_1') > 0 is consistent with mechanism 1 being taken to be associated with size and shape interactions[5] that might be expected to lead to greater orientational order in the centre of the smectic layer. With the MSMS–KM approach, τ_{pdcb} in the middle of the SmA phase of 8OCB is ca. –0.18,[9,10] marginally lower than the values reported in the earlier studies.

The ability to detect, directly or indirectly, the location of solutes in layered phases is of increasing importance both because of the accessibility to this kind of information in large-scale simulations, as well as its biophysical relevance. In an attempt to better define the nematic potential in the SmA phase without the limitation imposed by extrapolation of the temperature dependence of nematic properties into the SmA phase, we again rely on the use of binary mixtures of 6OCB and 8OCB.[8] To this end, we have examined the NMR spectra of five solutes (1,3,5-trichlorobenzene (tcb), pdcb, odcb, *para*-bromobenzonitrile (pbbn), and phenylacetylene (phac)) dissolved in the same NMR tube for four different binary mixtures that are all close to the region in the phase diagram where a RN phase is observed; only one of the samples exhibits a stable SmA phase in microscopy studies. Although we still need to extrapolate nematic properties, it is now done as a function of small changes in LC composition, and no longer as a function of temperature.

Theory

For the solvent, the MS potential is given by:

$$[1] \qquad H_{N,L}(\theta_L) = -\nu_L S_L \left[\frac{3}{2}\cos^2(\theta_L) - \frac{1}{2}\right]$$

where S_L is the solvent order parameter, and ν_L governs the strength of the intermolecular interaction. The corresponding potential for a solute s (of symmetry sufficient that it has a maximum of two independent second-rank orientational order parameters) in an axially symmetric LC mean field can be written as

$$[2] \qquad H_{N,Ls}(\Omega_s) = -\frac{3}{4}G_{L,ZZ}\sum_{\gamma}\sum_{\delta}\cos(\theta_{s,\gamma})\cos(\theta_{s,\delta})\beta_{s,\gamma\delta}$$
$$= -\frac{3}{4}G_{L,ZZ}\beta_{s,zz}\left\{\left[\frac{3}{2}\cos^2(\theta_s) - \frac{1}{2}\right] + \frac{b_s}{2}\sin^2(\theta_s)\cos(2\phi_s)\right\}$$

where $\theta_{s,\gamma}$ is the angle between the molecular γ axis with respect to the nematic mean-field direction, $G_{L,ZZ}$ is proportional to S_L with Z being the mean-field symmetry axis, and θ_s and ϕ_s are the polar and azimuthal angles of the mean-field direction in the solute (xyz) axis system. Thus, $G_{L,ZZ}$ is the mean-field potential of the solvent, taken to be a purely LC property, and the tensor $\boldsymbol{\beta}_s$ is taken to be a purely molecular property. The asymmetry in this solute energy parameter $\beta_{s,ii}$ is given by

$$[3] \qquad b_s = \frac{\beta_{s,xx} - \beta_{s,yy}}{\beta_{s,zz}}$$

There are thus two unknown parameters ($G_{L,ZZ}$, $\beta_{s,zz}$, and b_s) needed to define the nematic potential. Solutes of lower symmetry may have up to five independent second-rank order parameters (or two principal order parameters plus three diagonalization angles): the number of unknowns in the potential equals the number of independent order parameters. Up to now only solutes with at most two unknown order parameters have been used in investigations of SmA phases.

The nematic order parameter S_L for the N solvent L can be evaluated using the MS potential $H_{N,L}(\theta_L)$ of eq. [1]:

$$[4] \qquad S_L = \frac{\int \sin(\theta_L)\mathrm{d}\theta_L\left[\frac{3}{2}\cos^2(\theta_L) - \frac{1}{2}\right]e^{-H_{N,L}(\theta_L)/k_BT}}{\int \sin(\theta_L)\mathrm{d}\theta_L e^{-H_{N,L}(\theta_L)/k_BT}}$$

Given the corresponding MS potential $H_{N,Ls}(\Omega_s)$ of eq. [2] for a solute in a LC, the $\gamma\delta$ components of the solute order parameters are given by

$$[5] \qquad S_{s,\gamma\delta} = \frac{\int \mathrm{d}\Omega_s\left[\frac{3}{2}\cos(\theta_{s,\gamma})\cos(\theta_{s,\delta}) - \frac{1}{2}\right]e^{-H_{N,Ls}(\Omega_s)/k_BT}}{\int \mathrm{d}\Omega_s e^{-H_{N,Ls}(\Omega_s)/k_BT}}$$

If we now assume that the nematic potential consists of two independent MS terms, the MSMS case, then the nematic potential for solute s and LC L is

$$[6] \qquad H_{N,Ls}(\Omega_s) = -\frac{3}{4}\sum_{i=1}^{2} G_{L,ZZ}(i)\beta_{s,zz}(i) \times \left\{\left[\frac{3}{2}\cos^2(\theta_s) - \frac{1}{2}\right] + \frac{b_s(i)}{2}\sin^2(\theta_s)\cos(2\phi_s)\right\}$$

$$[7] \qquad H_{N,Ls}(\Omega_s) = H_{MS_1} + H_{MS_2}$$

where $G_{L,ZZ}(1) \equiv G_1$ and $G_{L,ZZ}(2) \equiv G_2$ as used in the Introduction and $b_s(i)$ is still the solute energy asymmetry expressed according to eq. [3] with index i to distinguish the two different LC/solute interactions. $G_{L,ZZ}(i)\beta_{s,zz}(i)$ could be the short-range size and shape effects or longer range

Can. J. Chem. Downloaded from www.nrcresearchpress.com by Xi'an Jiaotong University on 09/19/12
For personal use only.

interactions such as that involving the LC average electric field gradient interacting with the solute quadrupole or the solute polarizability with the mean square electric field. We will use, in this study, the Hamiltonian of eq. [6] to evaluate solute order parameters $S_{s,\gamma\gamma}$ in the N phase based on eq. [5].

Following the success of the MSMS–KM theory in treating solutes in the SmA phases of 8CB and 8OCB, the smectic interaction potential is written as before,[9,10]

$$[8]\quad H_{A,Ls}(\Omega_s, Z) = H_{\mathrm{MS}_1}\left[1 + \kappa_1' \cos\left(\frac{2\pi Z}{d}\right)\right] + H_{\mathrm{MS}_2}\left[1 + \kappa_2' \cos\left(\frac{2\pi Z}{d}\right)\right] - \tau_s' \cos\left(\frac{2\pi Z}{d}\right) = H_N^{\mathrm{mod}}(1) + H_N^{\mathrm{mod}}(2) - \tau_s' \cos\left(\frac{2\pi Z}{d}\right)$$

where the prefactors κ_1' and κ_2' denote coupling between the nematic potential and the density wave for the two MS mechanisms (each κ' can in principle be temperature dependent), whereas the solute smectic prefactor $\tau_s' \equiv \tau'$ is the coupling strength for a solute to feel the smectic layering of the solvent molecules. The layer width is d and Z ($Z = 0$ in the centre of a layer) is along the layer normal. The observed orientational order parameters can be calculated based on this potential by the following expression,

$$[9]\quad S_{s,\gamma\gamma} = \frac{\int \mathrm{d}\Omega_s \int_0^d \left[\frac{3}{2}\cos^2(\theta_{s,\gamma}) - \frac{1}{2}\right] e^{-H_{A,Ls}(\Omega_s,Z)/k_\mathrm{B}T}\mathrm{d}Z}{\int \mathrm{d}\Omega_s \int_0^d e^{-H_{A,Ls}(\Omega_s,Z)/k_\mathrm{B}T}\mathrm{d}Z}$$

This would allow us to determine the prefactors in the smectic potential provided that one has prior knowledge of H_{MS_1} and H_{MS_2} at the temperature of interest in the SmA phase. Fortunately the $\beta_{s,\gamma\gamma}(1)$ and $\beta_{s,\gamma\gamma}(2)$ for the solutes studied have been carefully determined from studies of these solutes in several LCs including 8OCB[10] and can be taken as constants for the current binary mixtures of 8OCB–6OCB. However, the β values alone are not sufficient to give the nematic potential: one also must know the values of G_1 and G_2 at the desired temperature in the SmA phase. In this earlier study it was assumed that a plot of G_1 vs G_2 could be extrapolated from the N (where it is linear) into the SmA phase. In the present case, G_1 and G_2 have been obtained experimentally (vide infra).

Once the full smectic potential $H_{A,Ls}(\Omega_s,Z)$ is known, τ can be easily evaluated according to

$$[10]\quad \tau_s \equiv \tau = \frac{\int \mathrm{d}\Omega_s \int_0^d \cos\left(\frac{2\pi Z}{d}\right) e^{-H_{A,Ls}(\Omega_s,Z)/k_\mathrm{B}T}\mathrm{d}Z}{\int \mathrm{d}\Omega_s \int_0^d e^{-H_{A,Ls}(\Omega_s,Z)/k_\mathrm{B}T}\mathrm{d}Z}$$

The mixed order parameters (for κ coupling) can in principle be calculated for each solute, but there are many of them and they seem not to give any additional insight like the translational order parameter τ.

Experimental

The solutes odcb, phac, pdcb, pbbn, and tcb were dissolved into LCs 8OCB and 6OCB. Enough of each solute was mixed thoroughly in the isotropic phase to obtain 1 mol% per solute and a total of 4 g of each LC was prepared in this way. Both LCs were degassed and then kept in the N phase with the use of a warm water bath. To span the two-component 8OCB–6OCB phase diagram a series of samples were made with varying relative weight fraction ($w_{6\mathrm{OCB}}$) of the two LCs. In this way the solute concentrations were as equal as possible in all samples studied. Enough of each sample was made so that ^{1}H NMR and microscopy could be performed on the same sample. For NMR studies, each sample was thoroughly mixed, and part placed into a 5 mm o.d. NMR tube and the rest into a glass ampule, both being sealed under nitrogen. Ten samples were made of differing $w_{6\mathrm{OCB}}$. The compositions of those investigated were $w_{6\mathrm{OCB}} = 0.270$ (sample 4), 0.297 (sample 6), 0.301 (sample 7), and 0.318 (sample 8). The phase-transition sequence in each sample was independently monitored via cross-polarizer optical microscopy.

For microscopy studies, samples were prepared between No. 1 cover slips, using strips of No. 0 cover slips (~100 μm) as spacers. Samples were sealed using Norland epoxy NOA 68 and cured under a UV lamp. Samples for microscopy experiments were heated to the N phase and placed atop an aluminium baseplate with a circular window and inside an Instek HCS 61 hot stage, which was mounted on a Nikon Eclipse 80-i upright microscope equipped with crossable polarizing filters. White light transmission cross-polarizer micrographs were obtained using a Qimaging QICAM Fast 1394 12-bit monochrome camera. The hot-stage temperature was changed in a controlled slow ramp (2 °C/min), and images were acquired and saved to disk at 10 s intervals.

Samples for NMR experiments were heated to the N phase, mixed and then placed into a Bruker Avance 400 MHz NMR spectrometer magnet in which the director was oriented by the magnetic field along the field direction. With the temperature controlled by the Bruker air-flow system, spectra were acquired in 0.5 and 1 K steps throughout both N and SmA phases. The spectral parameters (dipolar couplings (D_{ij}) and chemical shifts (ω_i)) of the solutes were then obtained simultaneously and automatically with the use of a covariance matrix adaptation evolution strategy (CMA-ES)[9,19–21] for each LC mixture at each temperature. Figure 1 shows the NMR spectra of solutes in sample 4 at 339.5 K. The upper plot shows the experimental proton NMR spectrum, whereas the lower plot is a sum of the calculated spectra of the studied solutes. As seen from these, the calculated spectrum agrees very well with the experimental spectrum obtained at 400 MHz. The dipolar couplings obtained from the analysis, in conjunction with the solute geometries,[22–25] were then used to determine the solute order parameters, which are given in the Supplementary data. No corrections were made for molecular vibrations and other nonrigid effects.

Results and discussion

First, the phase sequence of the samples was verified by optical microscopy. Characterization of the phase-transition sequence by optical microscopy utilizes the dramatic differences in defect textures in the N and smectic phases. Sample 4 was the only one to exhibit an unambiguous I–N–SmA–RN phase sequence. Figure 2 shows cross-polarizer optical micrographs of sample 4 at different temperatures corresponding to N,

Fig. 1. [1]H NMR spectra of solutes in sample 4 at 339.5 K. The upper plot is of the experimental 400 MHz NMR spectrum and the bottom plot is a sum of the calculated spectra. The calculated spectra of the solutes from top to bottom are *ortho*-dichlorobenzene (odcb), phenylacetylene (phac), *para*-dichlorobenzene (pdcb), *para*-bromobenzonitrile (pbbn), and 1,3,5-trichlorobenzene (tcb), with the molecule-fixed coordinate system being found in the top left of the figure.

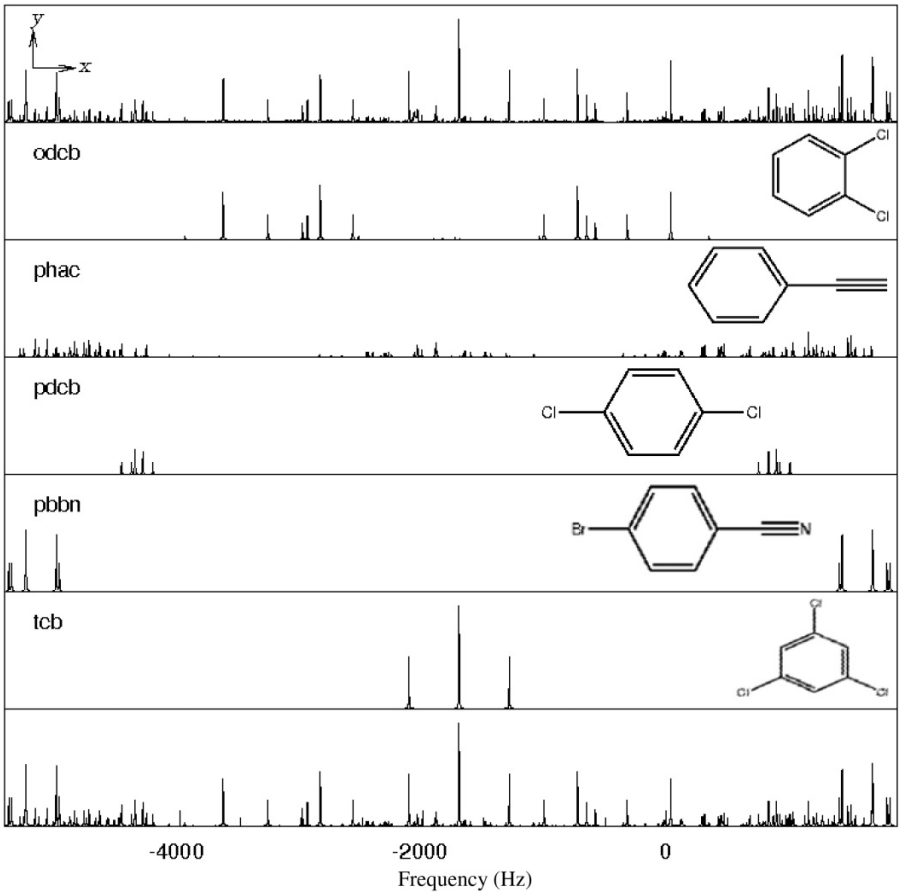

Can. J. Chem. Downloaded from www.nrcresearchpress.com by Xi'an Jiaotong University on 09/19/12
For personal use only.

SmA, and RN phases. Note that there is no detectable difference between the N and the RN phases, but the defect textures in the SmA phase are very distinct. Sample 6 was not observed to form a stable smectic phase, but exhibited clear signs of smectic fluctuations over a 3 °C temperature range. It is quite feasible that these fluctuations are present because of proximity to the critical point in the phase diagram beyond which the SmA phase no longer exists. Sample 8 showed no evidence of a smectic phase.

The set of solute order parameters obtained for each NMR experiment in both the N and SmA phases were fitted in a minimization to the MSMS nematic potential of eq. [6] to obtain G_1 and G_2 values (results not shown). In these fits the solute β parameters are taken from ref. 10. For samples that are clearly in the N phase, the two largest in absolute value order parameters for each solute recalculated from the G fit parameters agree with the experimental ones to better than 5%, except for S_{yy} (odcb) where the deviation is ~8% at lower temperatures. This excellent agreement confirms once again the validity of the MSMS potential[5] for the N phase, and that the solute β parameters are valid in the 6OCB–8OCB mixtures. However, the effect of the SmA phase on the orientational order parameters is quite small, and here we need to account for the nematic potential in as accurate a manner as possible; the 5% agreement achieved by the MSMS potential is not nearly sufficient for this purpose.

Deviations from the MSMS potential arise from a possible temperature dependence of the solute β_{ii} parameters and (or) deficiencies of the model in terms of different solutes experiencing different LC mean fields G as the temperature varies. We keep the main result of the MSMS potential, that two different MS mechanisms are sufficient to characterize the nematic potential; we arbitrarily choose to use the β_{ii} values determined earlier[10] and to obtain an exact fit to the order parameters by adjusting the G values separately for each solute in each sample at each temperature. This is an arbitrary choice, but as only the products $G\beta$ contribute to the potential (meaning that it is impossible to separate unambiguously G from β), making G values a function of both solute and solvent to get an exact fit to all solute order parameters in the N phase is as valid a choice as any. Hence, we do not need to worry about the precise nature of the $G\beta$ products involved with the MSMS potential.

Earlier studies attempted to characterize the nematic potential in the SmA phase by extrapolation of G parameters from the N into the SmA phase.[9,10] Here we use a different approach — we explore the possibility of estimating the nematic potential in the SmA phase by extrapolation as a

Fig. 2. Characterization of phase transition by optical microscopy utilizes the dramatic differences in defect textures in the nematic (N) and smectic (SmA) phases. Snapshots (at temperatures T = 317.6, 316.7, 311.8, 296.9, 292.0, and 283.7 K, respectively) from the complete time series (included as a movie in Supplementary data) show the N phase, N–SmA interface, SmA phase, SmA–RN interface, RN phase, and the RN–crystal (RN–K) interface.

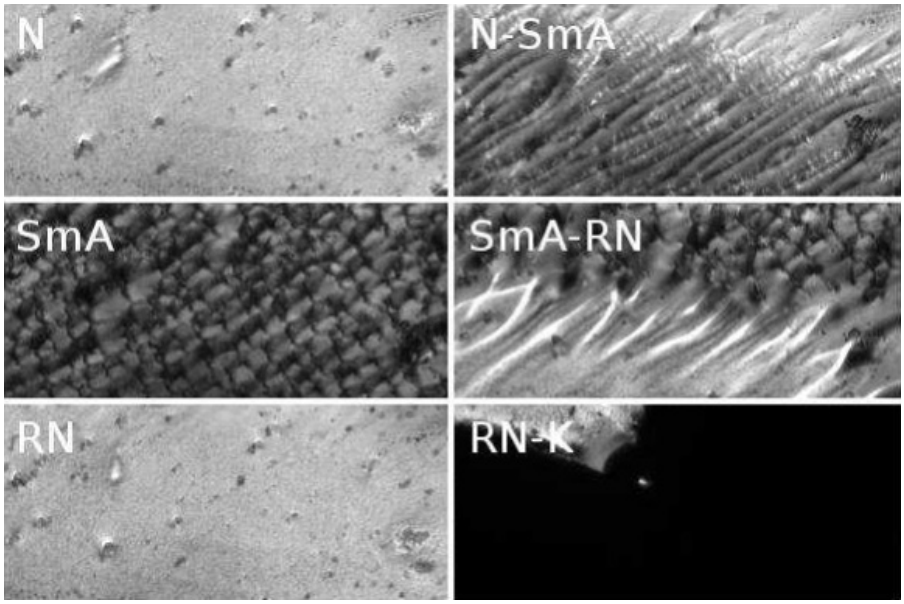

Can. J. Chem. Downloaded from www.nrcresearchpress.com by Xi'an Jiaotong University on 09/19/12
For personal use only.

function of LC composition (a different extrapolation for each temperature). We use the two order parameters for each solute s (except tcb, which has a single order parameter and therefore is not used because one order parameter cannot be used to determine two G values) and the MSMS nematic potential (eq. [6]) with the β_{ii} parameters determined earlier[10] to find values for the nematic potential parameters G_1 and G_2 for each solute in each experiment (including those for samples that show the SmA phase). The results for samples 7 (w_{60CB} = 0.301) and 8 (w_{60CB} = 0.318) (which from microscopy are clearly in the N phase at all temperatures investigated) are presented in Fig. 3. Even though w_{60CB} is different for these two samples, the G parameters are to an excellent degree equal. This is taken as affirmation that the nematic G parameters can be taken to be constant over the small concentration range (w_{60CB} = 0.270 for sample 4 to w_{60CB} = 0.318 for sample 8) spanned by the samples studied here. In other words, as samples 7 and 8 (which do not exhibit a SmA phase) give essentially equal G values for a given temperature, we assume that these values can be used as the nematic G values for the same temperatures in samples 4 and 6. To facilitate this idea, we do a polynomial fit to the G vs T values for samples 7 and 8. The lines drawn through the points in Fig. 3 are these polynomial fits.

Figure 4 presents the fitting parameters G_1 and G_2 vs T obtained by fitting the nematic potential only to order parameters obtained for solutes in samples 4 and 6, as well as the polynomial fit lines obtained from samples 7 and 8. The smectic effects are clearly seen at lower temperatures in samples 4 and 6, particularly between 296.9 and 316.7 K in sample 4 (the temperature range in which the SmA phase is observed with microscopy) where the points deviate dramatically from the lines. The most notable effects are noticed for the odcb and phac G_2 values in sample 4, but are observable elsewhere with close inspection. The broken lines in this (and other) graphs denote either the temperature range in which the SmA phase was observed with microscopy (sample 4) or a range close to the SmA phase region (sample 6). At higher temperatures the polynomials go through the points, justifying the transfer of nematic potential parameters among samples.

Fig. 3. G_1 and G_2 derived with the nematic potential (eq. [6]) only in samples 7 and 8. Lines denote polynomial fits to the G values. Sample 7 (○) and sample 8 (X).

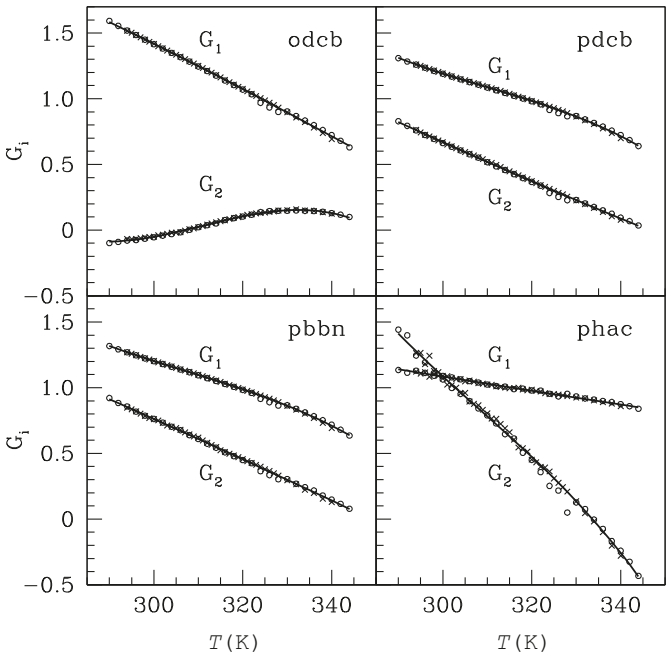

Hence, we take deviations from the lines as being caused by the smectic part of the interaction Hamiltonian. Smaller deviations are observed for sample 6 for which no smectic

Can. J. Chem. Downloaded from www.nrcresearchpress.com by Xi'an Jiaotong University on 09/19/12
For personal use only.

Fig. 4. The points are G_1 and G_2 from fits of the nematic potential only (eq. [6]) to orientational order parameters for sample 6 (*a*) and sample 4 (*b*) vs *T*. The solid lines are polynomial fits to G_1 and G_2 values determined for fits of the nematic potential to samples 7 and 8 (Fig. 3).

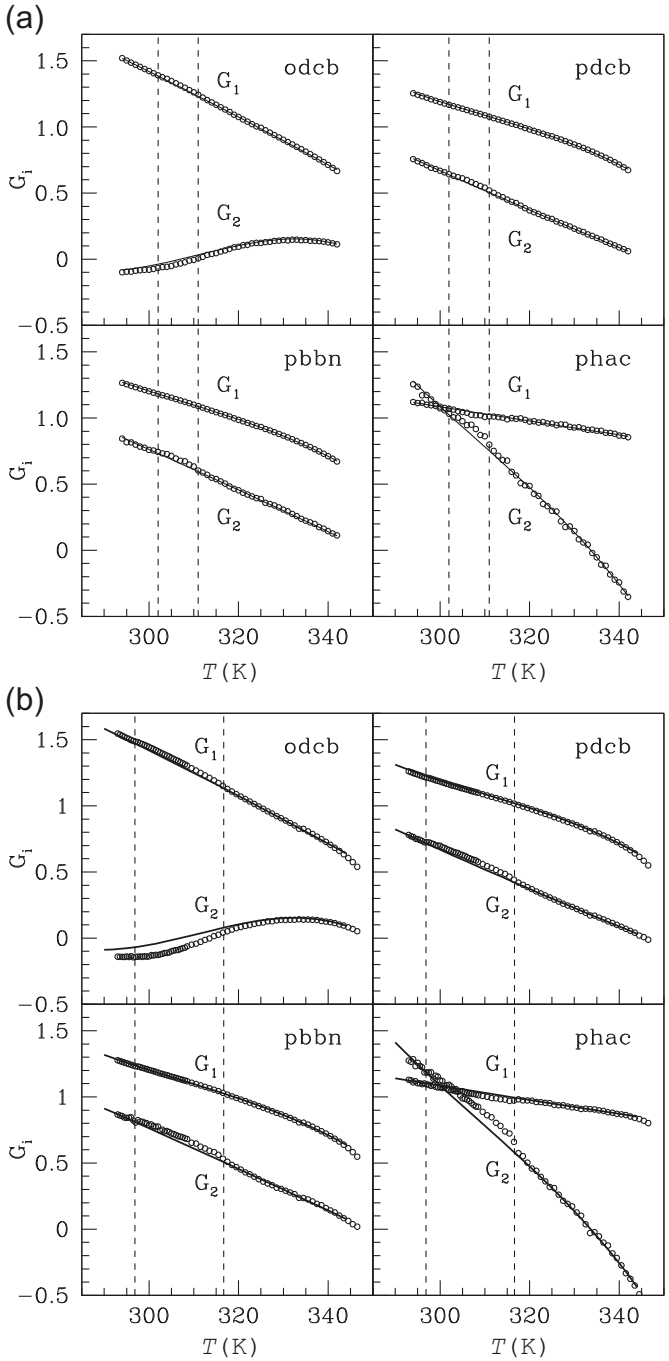

phase is observed in the microscopy experiments; however, "critical" fluctuations are observed in the region in the phase diagram that is near the smectic phase.

Thus, to fit the solute order parameters for each experiment of samples 4 and 6 to the SmA potential, the nematic G_1 and G_2 parameters in the total potential for the SmA phase (eq. [8]) are taken from the polynomial fit lines to the pure N samples 7 and 8, and the values of the smectic parameters κ_1', κ_2', τ'_{odcb}, τ'_{pdcb}, τ'_{pbbn}, and τ'_{phac} are optimized for best fits at each temperature. The κ_i' values obtained are given in Fig. 5 and the τ' values are reported in the Supplementary data. As discussed earlier, κ_1' is taken to be positive, consistent with higher shape-dependent ordering in the middle of a smectic layer. As expected, larger effects are noticed for sample 4. The phase transitions can also be noticed in Fig. 5. Values obtained from fits in the N phase should be zero: while the fitted numbers are not zero, they are associated with rather large errors, indicating the absence of the SmA phase.

The τ obtained for each solute in each experiment are given in Fig. 6. The sign of these parameters generally agrees with those determined from the earlier studies that relied on extrapolation of nematic parameters from the higher temperature N phase. It is encouraging that the essence of the analysis of the effects of a smectic phase on orientational order parameters was correct, even with the inherent dangers involved with the necessity of an extrapolation with temperature. Here we also do an extrapolation, i.e., we assume that the nematic $G\beta$ parameters are constant with sample composition.

The earlier study[10] that used the MSMS–KM theory with solutes dissolved in 8CB and 8OCB ran into difficulties with determination of τ, and in some cases limiting values had to be placed on some τ' values. The present approach does not require such restrictions. Here each SmA experiment is analysed by itself (given the nematic parameters). It is assumed that all solutes have the same κ' values, i.e., that κ' is a LC property, and that each solute has its own smectic prefactor τ'.

As is seen in Fig. 5, κ_1' and κ_2' have opposite sign, this being the same result observed in the earlier study that used the MSMS–KM approach.[10] The general trends in the results for sample 6 are quite similar to those for sample 4, but κ' absolute values are smaller and errors are larger; these observations are consistent with sample 4 exhibiting a SmA phase and sample 6 exhibiting only pretransitional effects. We note that κ_1' peaks in the centre of the SmA region, meaning that the variation in the nematic potential is maximum when deepest into the smectic phase, as might be expected. The values are not exactly zero in the N regions, especially in the RN region, indicating either a slight breakdown of the assumption that the nematic *G* parameters are identical in all samples or the existence of a correlation between κ' and τ' in the KM smectic potential. We recall that the β_{ii} parameters used in the analysis are based on mechanism 1 being associated with short-range size and shape interactions. The relatively small ($\approx$0.3) values of κ_1' are consistent with this notion, as this value means a change of roughly a factor of 2 when a solute goes from the rather rigid region in the centre of a smectic layer (large nematic potential) to the rather disordered region between layers where the nematic potential is expected to be reduced.

The N–SmA phase transitions are clear in the plot of κ_2' vs *T*. It is interesting that κ_2' becomes increasingly more negative with increasing *T* within the SmA phase. Its absolute value exceeds 1, which means there is a change in sign of the nematic potential as solutes go through a smectic layer. This same change of sign was observed in the earlier study

Can. J. Chem. Downloaded from www.nrcresearchpress.com by Xi'an Jiaotong University on 09/19/12
For personal use only.

Fig. 5. κ_1', κ_2' (including errors) vs T for sample 4 (left panel) and for sample 6 (right panel). Vertical lines indicate phase transitions as measured by microscopy. The smectic-A (SmA) phase is clearly indicated by the regions of nonzero κ' values with smaller errors.

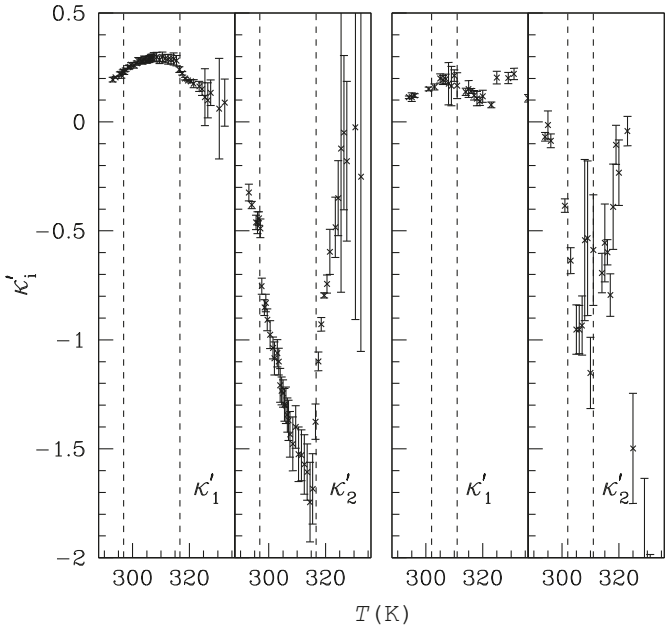

Fig. 6. τ order parameters (including errors) vs T for samples 6 (*a*) and 4 (*b*). See text for details on nonzero τ in nematic phases.

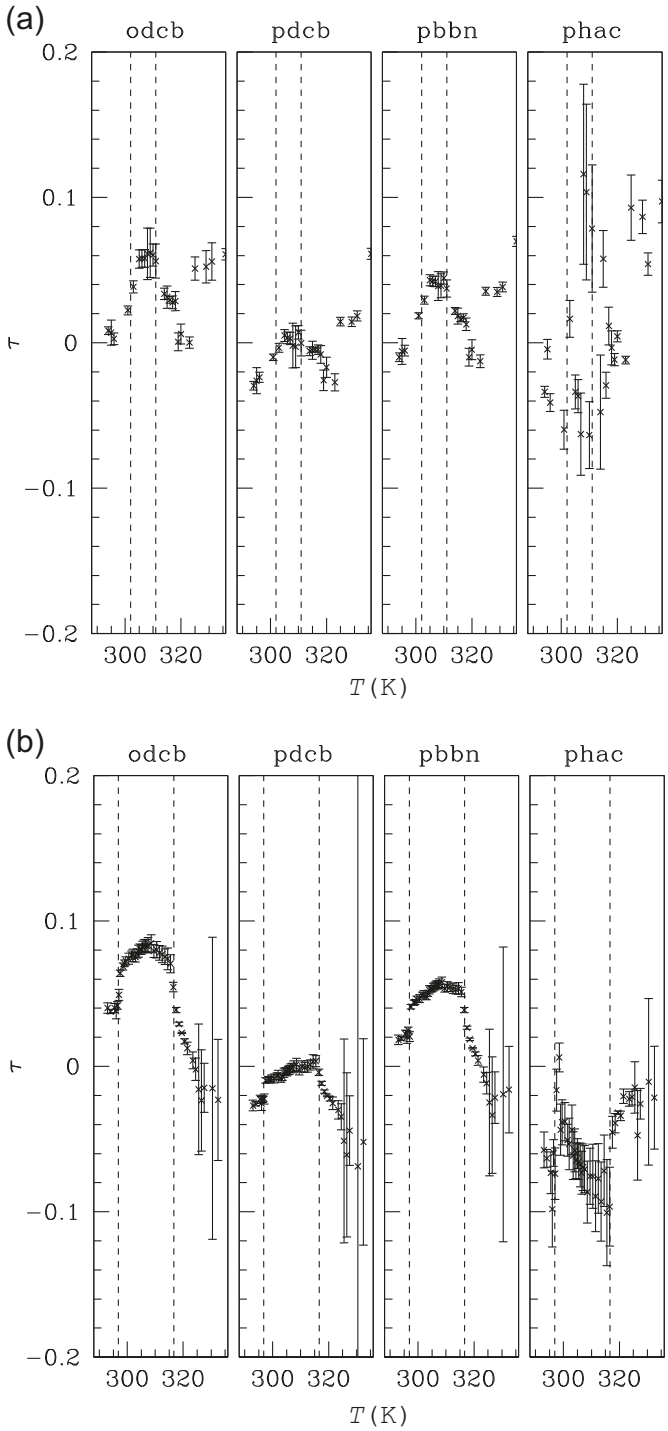

of solutes in 8CB and 8OCB,[10] where it was rationalized in terms of the angle dependence of the long-range part of the solute–solvent intermolecular interaction as a solute passes along the long axis of a solvent molecule. Possibilities for the anisotropic interactions include those involving solute and solvent quadrupoles, polarizabilities, etc. This second mechanism shows a much stronger temperature dependence than does the first (size and shape) mechanism. However, the absolute values of both G_2 and $\beta(2)$ are in general smaller than those for mechanism 1, and thus the first mechanism dominates the ordering potential. Thus, the large temperature dependence of κ_2' may well be associated with possible changes in the molecular packing. It could be interesting to explore simulations of solutes in the SmA phase (where, for example, interactions between solute and solvent quadrupoles are included[26]) to shed light on this interesting result and its temperature dependence.

The τ order parameters give information on the partitioning of a solute within the smectic layer. With our chosen sign convention (that short-range interactions lead to a stronger nematic potential within the smectic layer), a positive τ implies a preference for the solute to partition within the layer, and a negative sign implies partitioning between layers. The calculated τ values (Fig. 6) for both samples 4 and 6 are quite similar, but those for sample 4 have lower error and show less scatter. The values peak in the middle of the SmA phase, and their relatively sudden changes in values agree with the N–SmA phase transitions. The values for phac have more error than those for the other solutes. The τ values, especially in sample 4, indicate that odcb and pbbn prefer to sit within the layers and phac between the layers. The τ_{pdcb} values are interesting in that they are very close to zero deep in the SmA phase, implying an even distribution, and tend to be negative when near the N phase, thereby suggesting its likelihood to be in between layers. It should be noted that earlier studies have found pdcb to have negative τ as mentioned above when one (two) MS mechanism(s) was invoked to describe the nematic potential.[8,10]

Conclusion

NMR results were obtained for four samples of binary mixtures with compositions very close to the region in the phase diagram where a RN phase exists at low temperature.

Can. J. Chem. Downloaded from www.nrcresearchpress.com by Xi'an Jiaotong University on 09/19/12
For personal use only.

The microscopy experiments clearly show that one sample (sample 4) on cooling goes from an isotropic to a N to a SmA to a RN phase. Microscopy on sample 6 gives fluctuations in the N phase as the temperature passes close to the region where the SmA phase exists, but sample 6 is not observed to form a stable SmA phase. Evidence for smectic fluctuations in Sample 7 was not conclusive, whereas sample 8 showed no evidence whatsoever of a smectic phase.

Because for a given temperature the G parameters that describe the nematic potential are essentially identical for each solute in all four samples when they are in the N phase, we make the reasonable ansatz that in the SmA phase regions of samples 4 and 6 the nematic potential can be taken equal to that in samples 7 and 8 at the same temperature. We then analyzed samples that are in the SmA phase to extract the smectic prefactors κ_1' and κ_2' for the LC and a τ' for each solute in the smectic potential based on the KM theory of SmA phases. The values obtained are then used to calculate the smectic order parameter τ for each solute. The numbers obtained agree in general with those found in earlier studies (except odcb, which was arbitrarily set to 0.8 in the earlier studies[10]) that involved extrapolation of nematic potential parameters as a function of temperature into the SmA phase, a procedure fraught with potential error.

In the present study we gauge an interaction Hamiltonian to be incorrect in the N phase(s) (i.e., a Hamiltonian that includes the KM potential) by getting nonzero κ' and τ' values with large errors, as can be observed in Figs. 5 and 6. As a consequence, the corresponding solute smectic order parameters τ calculated from τ' values in the N phase should be taken with a grain of salt. In fact, the τ parameters should strictly vanish; the same is true for all the smectic prefactors. To summarize, the present study of binary 6OCB–8OCB mixtures that combines NMR and optical microscopy has clearly put the MSMS nematic potential in conjunction with the KM smectic potential on a firm ground for the SmA phase.

Supplementary data

Supplementary data are available with the article through the journal Web site (www.nrcresearchpress.com).

Acknowledgement

We thank W.L. Meerts for help with the CMA-ES spectral fitting, and the Natural Sciences and Engineering Research Council of Canada (NSERC) for financial support.

References

(1) Chandrasekhar, S. *Liquid Crystals;* Cambridge University Press: Cambridge, UK, 1992.
(2) Dong, R. Y. *Nuclear Magnetic Resonance of Liquid Crystals;* 1st ed.; Springer-Verlag: New York, 1994.
(3) Burnell, E. E.; de Lange, C. A., Eds. *NMR of Ordered Liquids;* Kluwer Academic: Dordrecht, The Netherlands, 2003.
(4) Dong, R. Y., Ed. *Nuclear Magnetic Resonance Spectroscopy of Liquid Crystals;* World Scientific: Singapore, 2009.
(5) Burnell, E. E.; ter Beek, L. C.; Sun, Z. *J. Chem. Phys.* **2008** *128* (16), 164901. Note that the S_{xx} values for fluorobenzene in 1132 and MM reported in Table I should both be positive. doi:10.1063/1.2900559.
(6) Yethiraj, A.; Sun, Z.; Dong, R. Y.; Burnell, E. E. *Chem. Phys. Lett.* **2004** *398* (4–6), 517. doi:10.1016/j.cplett.2004.09.108.
(7) Yethiraj, A.; Weber, A. C. J.; Dong, R. Y.; Burnell, E. E. *J. Phys. Chem. B* **2007** *111* (7), 1632. doi:10.1021/jp0670438.
(8) Yethiraj, A.; Burnell, E. E.; Dong, R. Y. *Chem. Phys. Lett.* **2007** *441* (4–6), 245. doi:10.1016/j.cplett.2007.05.043.
(9) Weber, A. C. J.; Yang, X.; Dong, R. Y.; Meerts, W. L.; Burnell, E. E. *Chem. Phys. Lett.* **2009** *476* (1–3), 116. doi:10.1016/j.cplett.2009.06.002.
(10) Weber, A. C. J.; Yang, X.; Dong, R. Y.; Burnell, E. E. *J. Chem. Phys.* **2010** *132* (3), 034503. doi:10.1063/1.3291486.
(11) Maier, W.; Saupe, A. *Z. Naturforsch. A.* **1959** *14*, 882.
(12) Maier, W.; Saupe, A. *Z. Naturforsch. A.* **1960** *15*, 287.
(13) Kobayashi, K. K. *Mol. Cryst. Liq. Cryst. (Phila. Pa.)* **1971** *13* (2), 137. doi:10.1080/15421407108084959.
(14) McMillan, W. L. *Phys. Rev. A* **1971** *4* (3), 1238. doi:10.1103/PhysRevA.4.1238.
(15) McMillan, W. L. *Phys. Rev. A* **1972** *6* (3), 936. doi:10.1103/PhysRevA.6.936.
(16) Cifelli, M.; Cinacchi, G.; De Gaetani, L. *J. Chem. Phys.* **2006** *125* (16), 164912. doi:10.1063/1.2359428.
(17) Celebre, G.; Cinacchi, G.; De Luca, G. *J. Chem. Phys.* **2008** *129* (9), 094509. doi:10.1063/1.2970074.
(18) Burnell, E. E.; de Lange, C. A. *Chem. Rev.* **1998** *98* (6), 2359 and references therein. doi:10.1021/cr941159v.
(19) Meerts, W. L.; Schmitt, M.; Groenenboom, G. *Can. J. Chem.* **2004** *82* (6), 804. doi:10.1139/v04-037.
(20) Meerts, W. L.; Schmitt, M. *Int. Rev. Phys. Chem.* **2006** *25* (3), 353. doi:10.1080/01442350600785490.
(21) Burnell, E. E.; de Lange, C. A.; Meerts, W. L. *Nuclear Magnetic Resonance Spectroscopy of Liquid Crystals;* Dong, R. Y., Ed.; World Scientific Publishing Co.: Singapore, 2009.
(22) Syvitski, R. T.; Burnell, E. E. *J. Magn. Reson.* **2000** *144* (1), 58. doi:10.1006/jmre.1999.2013.
(23) Dereppe, J. M.; Arte, E.; Van Meerssche, M. *J. Cryst. Mol. Struct.* **1974** *4* (4), 193. doi:10.1007/BF01198176.
(24) Syvitski, R. T.; Burnell, E. E. *Can. J. Chem.* **1999** *77* (11), 1761. doi:10.1139/cjc-77-11-1761.
(25) Britton, D.; Gleason, W. B. *Acta Crystallogr.* **1977** *B33*, 3926. This paper is for the structure of *p*-fluorobenzonitrile, which was used here for the proton coordinates of pbbn.
(26) Sokolovskii, R. O.; Burnell, E. E. *J. Chem. Phys.* **2009** *130* (15), 154507 and references therein. doi:10.1063/1.3104607.

Resonance assignments and secondary structure analysis of dynein light chain 8 by magic-angle spinning NMR spectroscopy

Shangjin Sun, Andrew H. Butterworth, Sivakumar Paramasivam, Si Yan, Christine M. Lightcap, John C. Williams, and Tatyana Polenova

Can. J. Chem. Downloaded from www.nrcresearchpress.com by Xi'an Jiaotong University on 09/19/12
For personal use only.

Abstract: Dynein light chain LC8 is the smallest subunit of the dynein motor complex and has been shown to play important roles in both dynein-dependent and dynein-independent physiological functions via its interaction with a number of its binding partners. It has also been linked to pathogenesis including roles in viral infections and tumorigenesis. Structural information for LC8-target proteins is critical to understanding the underlying function of LC8 in these complexes. However, some LC8-target interactions are not amenable to structural characterization by conventional structural biology techniques owing to their large size, low solubility, and crystallization difficulties. Here, we report magic-angle spinning (MAS) NMR studies of the homodimeric apo-LC8 protein as a first effort in addressing more complex, multi-partner, LC8-based protein assemblies. We have established site-specific backbone and side-chain resonance assignments for the majority of the residues of LC8, and show TALOS+-predicted torsion angles ϕ and ψ in close agreement with most residues in the published LC8 crystal structure. Data obtained through these studies will provide the first step toward using MAS NMR to examine the LC8 structure, which will eventually be used to investigate protein–protein interactions in larger systems that cannot be determined by conventional structural studies.

Key words: solid-state NMR, magic-angle spinning, MAS, dynein, LC8.

Résumé : La chaîne légère de dynéine, LC8, est la sous unité la plus petite du complexe moteur de la dynéine et il a été démontré qu'elle joue des rôles importants dans les fonctions physiologiques tant dépendantes qu'indépendantes de la dynéine par le biais de son interaction avec un certain nombre de ses partenaires de fixation. Elle a aussi été reliée à des rôles de tumorigénèse et de pathogénèse dans les infections virales. De l'information sur la structure des protéines cibles de la LC8 est critique pour comprendre la fonction sous-jacente de la LC8 dans ces complexes. Toutefois, en raison de leur grande taille, de leur faible solubilité et de difficultés de cristallisation, certaines interactions entre la LC8 et ses cibles ne peuvent pas être amenées à une caractérisation structurelle par les techniques conventionnelles de la biologie. Dans ce travail, comme premier effort en vue de comprendre les assemblages de protéines complexes, à base de LC8 avec plusieurs partenaires, on rapporte des études de RMN du ^{13}C à l'état solide dans le mode de la rotation à l'angle magique (RAM) faites sur la protéine homodimère apo-LC8. On a établi les attributions des résonances du squelette et de la chaîne latérale spécifique au site pour la majorité des résidus de la LC8 et on montre que les valeurs prédites par TALOS+ pour les angles de torsion ϕ et ψ sont en bon accord avec celles publiées pour la plupart des résidus dans des structures cristallines de la LC8. Les données obtenues par le biais de ces études serviront de premier pas dans l'utilisation de la RMN en mode RAM pour examiner la structure de la LC8 et qui pourra éventuellement être utilisée pour étudier les interactions protéine–protéine dans des systèmes plus gros qui ne peuvent pas être déterminées par des études structurales conventionnelles.

Mots-clés : RMN à l'état solide, rotation à l'angle magique (RAM), dynéine, LC8.

[Traduit par la Rédaction]

Introduction

Dynein light chain LC8 (also named DLC8, PIN, DNLC1/2, and DYNLL1/2) is an integral subunit of cytoplasmic dynein, a multisubunit microtubule-based retrograde motor.[1,2] LC8 is also found in many other protein complexes such as flagellar and axonemal dynein,[3–5] myosin-Va,[6] and nuclear pore complexes (NPCs).[7] Through interactions with diverse cellular protein partners and viral proteins, LC8 plays important roles in a broad range of dynein-dependent as well as dynein-independent cellular functions and has been implicated in viral infections and cancer progression.[8,9] The repertoire

Received 21 October 2010. Accepted 19 January 2011. Published at www.nrcresearchpress.com/cjc on 4 August 2011.

S. Sun, A.H. Butterworth, S. Paramasivam, S. Yan, and T. Polenova. Department of Chemistry and Biochemistry, University of Delaware, Newark, DE 19716, USA.
C.M. Lightcap and J.C. Williams. Department of Molecular Medicine, Beckman Research Institute of City of Hope, 1500 East Duarte Road, Duarte, CA 91010, USA.

Corresponding author: Tatyana Polenova (e-mail: tpolenov@udel.edu).

This article is part of a Special Issue dedicated to Professor Roderick E. Wasylishen.

Fig. 1. Amino acid sequence and secondary structure of *Drosophila* dynein light chain LC8 generated by PDBsum[44] from the X-ray coordinates deposited in the PDB file 2PG1.[26] Residues M1, S2, D3, and R4 are not included.

of LC8 binding partners and the roles LC8 plays in these interactions have grown substantially over the past few years. Recently, LC8 has been shown to interact with both Ebolavirus VP35[10] and bovine immunodeficiency virus BIV,[11] potentially affecting the early transcription and (or) the localization of the virus.[12,13] Studies also indicate that LC8 regulates axonal trafficking and synaptic levels of Bassoon, a core protein component of the presynaptic cytomatrix at the active zone of neurotransmitter release.[14] Lastly, LC8 has been demonstrated to be required for nuclear import of P21-activated kinase 1 (Pak1), a process critical for development of vertebrates[15] and potentially involved in cancer progression.[9]

LC8 is homodimeric under physiological conditions, but its dimer–monomer equilibrium is critical for its biological functions.[16] Several models have been proposed to explain the underlying mechanisms for this equilibrium as well as the interactions between LC8 and its diverse binding partners. Research indicates that the dimer–monomer equilibrium of LC8 can be regulated by pH changes,[17] the redox state,[18,19] and phosphorylation of S88.[9,20,21] Whether phosphorylation of S88 can occur and regulate LC8 dimerization remains controversial.[22] Moreover, the phosphomimetic LC8 mutant S88E is found to be dimeric in *Chlamydomonas* dynein, with no obvious functional deficiency caused by this mutation.[23]

The LC8 homodimer is frequently assumed to function as a cargo adaptor, linking its various binding partners to the dynein complex by binding the dynein intermediate chain and its cargo proteins simultaneously.[24,25] However, structural and thermodynamic data do not support this model. Specifically, each reported LC8 binding protein binds to the same groove as the dynein intermediate chain. In addition, all characterized LC8 binding proteins, including the dynein intermediate chain, are homodimeric.[26,27] This situation enables these targets to interact with LC8 through a bivalent–bivalent interaction, which in general is more energetically favorable than an uncoupled trivalent interaction. Instead, the LC8 dimer has been shown to stabilize weaker target dimers, particularly through the stabilization of partially disordered regions of these proteins.[8] For example, LC8 has been shown to stabilize an α-helical coiled coil within the microtubule-binding domain of syntaphilin, leading to the regulation of mitochondrial transport and retention in axons.[28]

Solution-state NMR has been extensively used to solve LC8 structures,[24,29,30] to investigate interactions between LC8 and its various protein and peptide binding partners,[22,24,25,31–34] and to probe mechanisms underlying LC8 dimerization.[17,20,21,35] In contrast, to the best of our knowledge, solid-state NMR spectroscopy has yet to be used as a tool to study the homodimeric LC8 either alone, or in complex with its binding partners, or as part of the entire dynein assembly. Solution NMR spectroscopy cannot be used to address the entire dynein assembly, since its high molecular weight (~2 MDa) broadens the resonances beyond detection owing to fast transverse relaxation. Similarly, other LC8 binding partners, such as retroviral Gag,[36] microtubule-binding protein syntaphilin[28], and nuclear pore complex,[7] cannot be studied in complex with LC8 in solution because they are also too large and (or) insoluble. Furthermore, many of these assemblies are difficult to crystallize and therefore not amenable to X-ray diffraction studies. In the solid state, the line widths are independent of the molecular weight and crystalline samples are not required. With the differential and sparse isotopic enrichment protocols as well as the recently developed pulse sequences, the structure and dynamics of large protein assemblies can be studied.[37–42]

In this work, we examine the apo-LC8 (the primary sequence and the secondary structure of the LC8 is shown in Fig. 1) by magic-angle spinning (MAS) NMR spectroscopy as the first step toward the investigations of LC8-containing protein assemblies. We report site-specific resonance assignments and the secondary structure analysis of U-^{15}N,^{13}C-enriched LC8 by a combination of two- and three-dimensional MAS NMR experiments. The secondary structure predicted by TALOS+[43]based on SSNMR resonance assignments is in close agreement with the published LC8 crystal structure 2PG1.[26] These results enable future studies including tertiary structure determination of homodimeric apo-LC8 in the solid state, as well as structural and dynamics investigations of LC8-containing protein assemblies.

Results

Resonance assignments of LC8 by MAS solid-state NMR spectroscopy

To establish the best experimental conditions, we first acquired 14.1 T 2D DARR spectra of LC8 at several temperatures ranging from 0 to –35 °C. The resolution and the signal-to-noise ratio in the DARR spectra acquired at –1.7, –6.7, –11.7, and –16.7 °C are essentially the same and no peak shifts were observed in this temperature range (Fig. S1 of the Supplementary data). Below –21.7 °C, the spectral quality deteriorates as evidenced by the disappearance or broadening of a large number of peaks. Therefore, for all experiments we have kept the sample temperature above –16.7 °C; specific conditions for the various experiments are indicated in the Experimental section.

Resonance assignments of LC8 in the solid state were derived from a combination of two- and three-dimensional homo- and hetero-nuclear correlation MAS NMR spectra acquired at 14.1 and 21.1 T. As expected for micro- and nano-crystalline protein preparations,[39,40,45–48] the homo- and hetero-nuclear spectra are of high quality with the resolution of the individual peaks of the order of 0.2–0.5 ppm. Representative 2D DARR, NCACB, and NCO spectra acquired at 14.1 T are shown in Fig. 2. An overlay of the 14.1 and

Can. J. Chem. Downloaded from www.nrcresearchpress.com by Xi'an Jiaotong University on 09/19/12
For personal use only.

Can. J. Chem. Downloaded from www.nrcresearchpress.com by Xi'an Jiaotong University on 09/19/12
For personal use only.

Fig. 2. Two-dimensional solid-state magic-angle spinning (MAS) NMR spectra of LC8; (*a*) NCO, (*b*) NCACB, (*c*) carbonyl, and (*d*) aliphatic regions of the 14.4 T DARR spectrum (mixing time, 10 ms). The first contour for the spectra is set at 5 × σ, with a multiplier of 1.2.

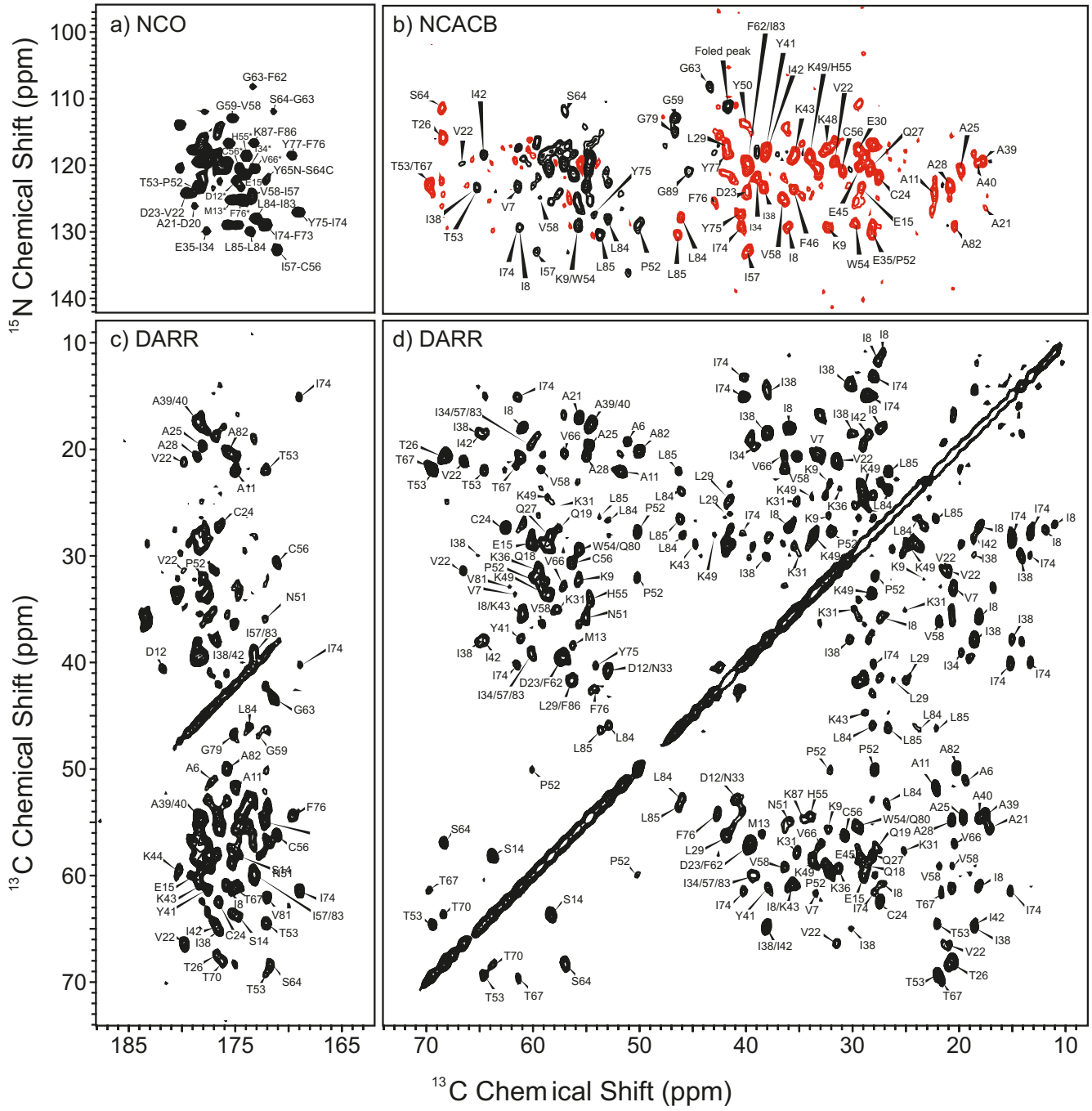

21.1 T DARR spectra is shown in Fig. 3, and the heteronuclear 2D spectra acquired at 21.1 T are demonstrated in Fig. S2 of the Supplementary data. The spectra acquired at 21.1 T exhibit superior resolution compared with the corresponding spectra acquired at 14.1 T, as expected. However, despite the resolution enhancement achieved at a high magnetic field, the 2D data sets alone are insufficient for site-specific assignments because of the intrinsic signal overlap in LC8.

To establish residue-specific backbone assignments, we used several three-dimensional data sets: dipolar coupling-based NCACB, NCACX, NCOCX, and scalar coupling-based NCOCA[49–51] experiments, the analysis of which yielded assignments for 73 out of 89 residues. A representative backbone walk for A21-E30 is illustrated in Fig. 4. For side-chain assignments, we supplemented the heteronuclear 3D data sets with 2D DARR and 3D DARR–DARR experiments, and a combination of the various spectra yielded side-chain assignments for many residues in the protein. The ^{13}C and ^{15}N chemical shifts for the assigned residues are tabulated in Table S1 of the Supplementary data.

Further analysis of the ^{13}C and ^{15}N solid-state chemical shifts indicated that these are in very good agreement with the solution NMR chemical shifts assignments established by us earlier for the LC8 sample prepared at identical pH,

Fig. 3. Overlay of the DARR spectra acquired at 14.1 T (red) and 21.1 T (blue). DARR mixing time is 10 ms for the 14.1 T data and 50 ms for the 21.1 T data (see [1]Table S2 in the Supplementary data). The spectra acquired at 21.1 T exhibit higher resolution.

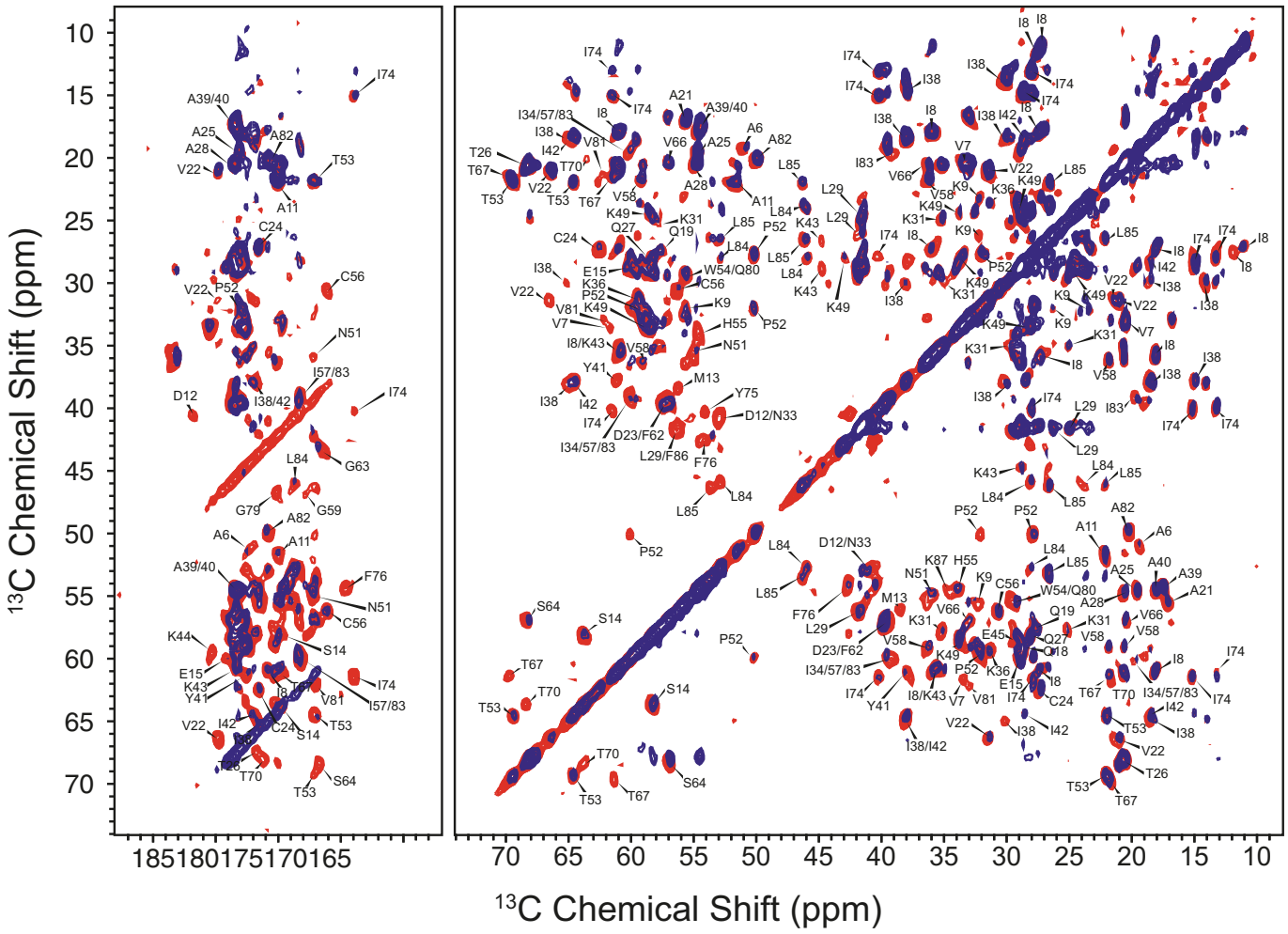

Fig. 4. Backbone walk for A21-E30 using three-dimensional experiments: dipolar-based NCACB, NCACX, NCOCX, and scalar-based NCOCA. Negative cross peaks resulting from the two-bond N–C$^{\beta}$ correlations are shown in red. The first contour in all spectra is set at 5 × σ with a multiplier of 1.2.

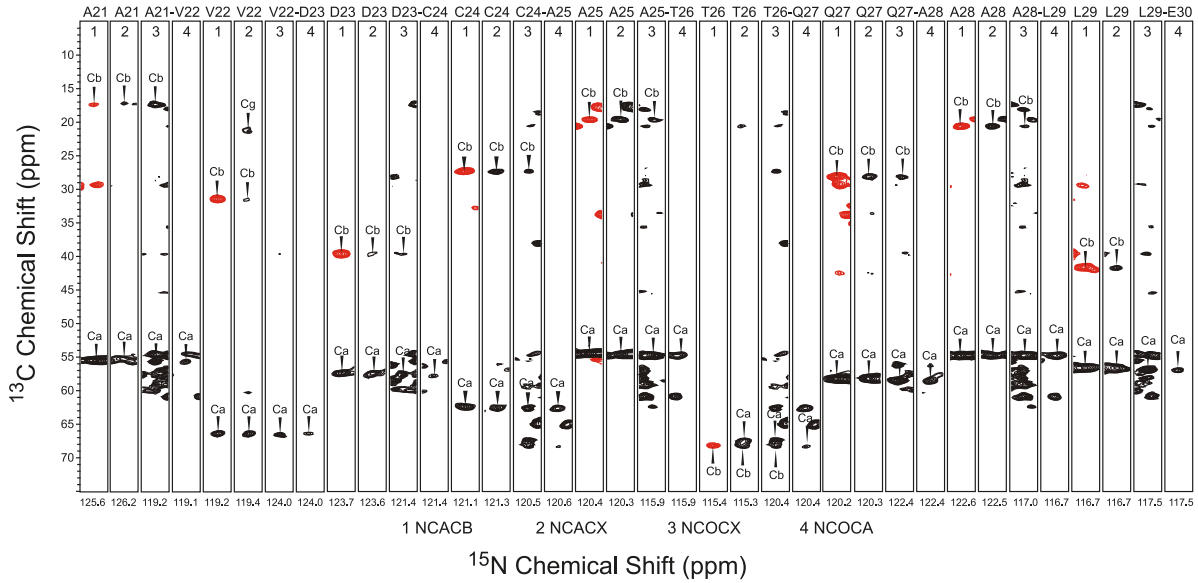

Can. J. Chem. Downloaded from www.nrcresearchpress.com by Xi'an Jiaotong University on 09/19/12
For personal use only.

Fig. 5. Differences between solid-state and solution chemical shifts plotted versus residue number in LC8 for the backbone carbon and nitrogen atoms.

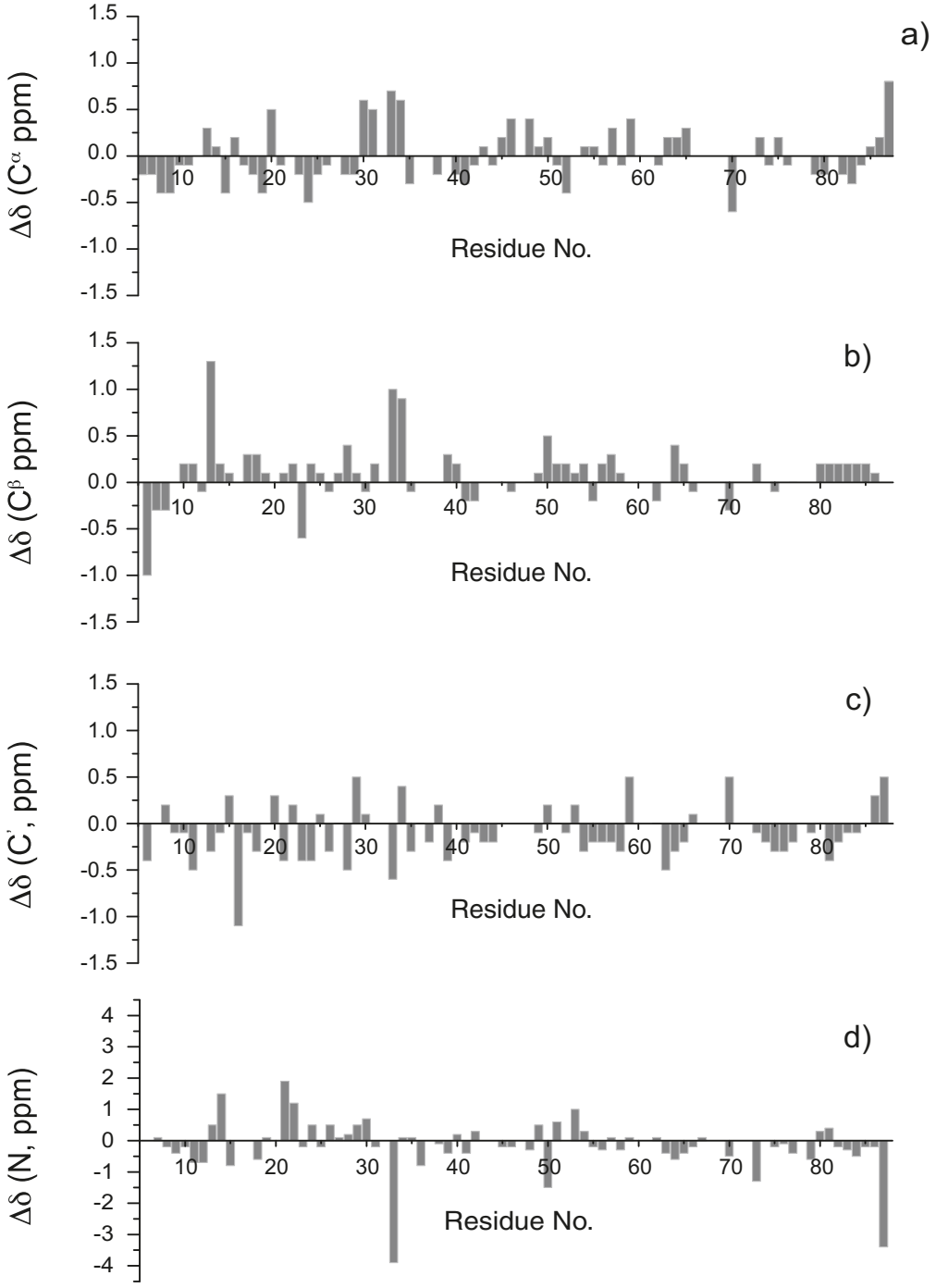

Can. J. Chem. Downloaded from www.nrcresearchpress.com by Xi'an Jiaotong University on 09/19/12
For personal use only.

with the exception of residues N33 and K87 that show a large discrepancy in the backbone ^{15}N chemical shifts. Residue-wise comparison of solid-state and solution chemical shifts is illustrated in Fig. 5 and in Table S2 of the Supplementary data. The mean chemical shift deviations are 0.3 ppm for C^{α}, C^{β}, and C', and 0.8 ppm for N^{H}. Close agreement between solid-state and solution shifts was also observed in our previous work on CAP-Gly[40] and thioredoxin,[39,52] as well as on BPTI,[45] Crh,[42] and GB1[46] from other laboratories.

Torsion angle analysis of LC8 based on chemical shift assignments by TALOS+

To predict the backbone torsion angles ϕ and ψ from the solid-state chemical shifts of LC8, we employed TALOS+.[43] Since resonance assignments are available for 73 of 89 residues of LC8, we could not derive the torsion angles for several residues (R60, N61, H68, N69, T70, R71, and H72) because TALOS+ requires resonance assignments for three consecutive residues to make predictions for the central residue. The TALOS+-predicted torsion angles yielded the

Fig. 6. (*a*) Amino acid sequence and secondary structure of dynein light chain LC8 generated by PDBsum[44] from the X-ray coordinates deposited in the PDB file 2PG1.[26] (*b*) Backbone torsion angles Φ (top) and ψ (bottom) derived from TALOS+ analysis of isotropic solid-state chemical shifts of LC8.

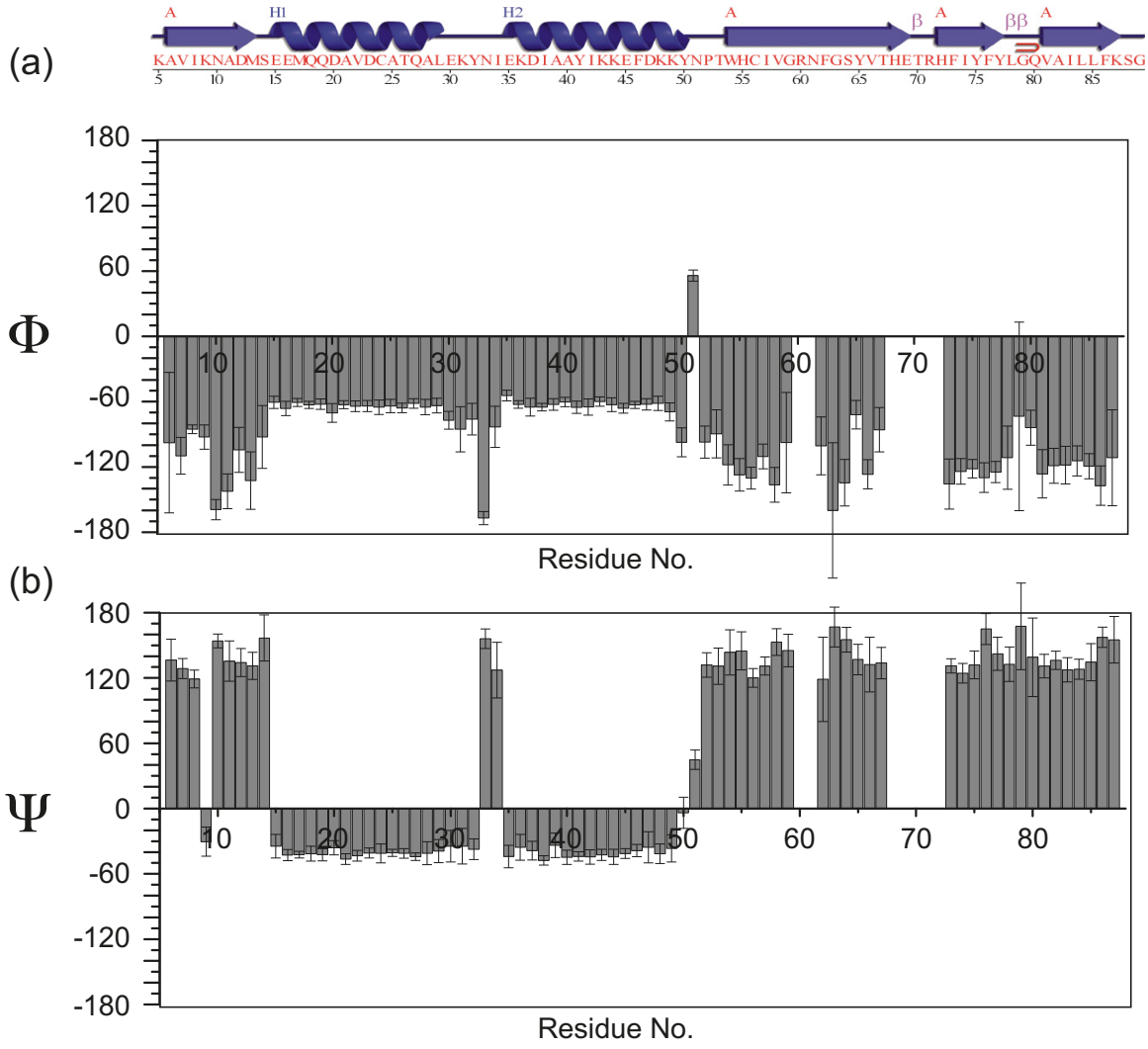

secondary structure of LC8, which is in close agreement with the crystal structure deposited in the Protein Data Bank (PDB) file 2PG1,[26] as illustrated in Figs. 6 and 7. Residue-wise comparison of the SSNMR and X-ray based torsion angles indicates that the discrepancies are small for the majority of the residues except for several residues (Y32, N33, N51, G79, and S88), which are located in loop or linker regions (as illustrated in Fig. 7).

Discussion

With the aim of investigating interactions between LC8 and its various binding partners and gaining insight into the atomic-level resolution structures of the large LC8-based multicomponent assemblies, we employed MAS solid-state NMR spectroscopy to derive site-specific resonance assignments, and predicted backbone torsion angles Φ and Ψ of LC8 based on the assigned isotropic chemical shifts. From a combination of homo- and hetero-nuclear 2D and 3D experiments, we extracted site-specific backbone resonance assignments for 73 out of 89 residues, and obtained side-chain assignments for many ^{13}C atoms in LC8 (see Table S1 of the Supplementary data). The majority of the residues that could not be unambiguously assigned from the current data sets, namely, M1, S2, D3, R4, K5, R60, N61, H68, E69, R71, H72, L78, S88, and G89, are located in loop regions. This result is consistent with our prior work and that of other laboratories,[45,47,53–55] indicating that it is generally more difficult to derive solid-state NMR assignments for residues in loop regions or at the termini, because generally these residues exhibit dynamic or static conformational heterogeneity and, therefore, give rise to broader or missing resonances. Additionally, Y32 and D47 could not be assigned; these are located in an α helix but their chemical shifts overlap with the shifts of other residues; hence, unambiguous assignments were not possible under our conditions.

A previous solution NMR study by Mohan et al.[17] indicates that pH can determine the dimer–monomer equilibrium and LC8 is in its dimeric form under pH 6. LC8 has a strong pH dependence for chemical shift patterns, indicating that dimeric and monomeric forms of LC8 have very different

Can. J. Chem. Downloaded from www.nrcresearchpress.com by Xi'an Jiaotong University on 09/19/12
For personal use only.

Fig. 7. Residue-wise comparison of Φ and Ψ torsion angles predicted by TALOS+[43] and those extracted from LC8 crystal structure (PDB file 2PG1)[26]. Differences are mapped on the 2PG1 chain A, and residues are color coded as follows: blue for $\Delta\Phi$ and $\Delta\Psi$ <50°; green for $\Delta\Phi$ and $\Delta\Psi$ ranging from 50° to 100°; and red for $\Delta\Phi$ and $\Delta\Psi$ >100°. Residues with no predicted angles owing to the lack of resonance assignments are yellow (R60, N61, H68, E69, T70, R71, and H72).

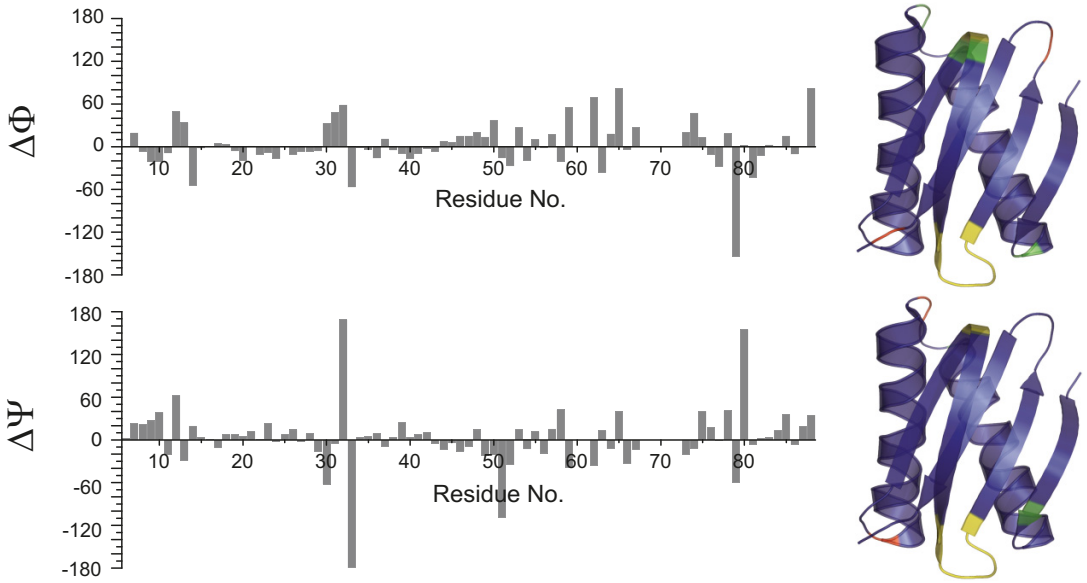

chemical shifts.[17] We noticed that SSNMR chemical shift assignments are very close to the solution NMR chemical shifts for LC8 (see Fig. 5) as both NMR samples are prepared at pH 6.0 (see the Experimental methods section). We conclude that LC8 is in its dimeric form in the SSNMR sample.

We expect that the resonance assignments for LC8 can be completed with technical improvements in sample preparation and experimental design. For instance, constant-time scalar-based experiments yield inherently higher resolution than the corresponding dipolar-based experiments and are less sensitive to global molecular motion.[49–51] However, the potential of these experiments was not fully exploited in our study because of hardware limitations on the proton decoupling powers and on the available MAS frequencies. At high MAS frequencies and high-power proton decoupling, the performance of the scalar-based experiments is enhanced dramatically.[49–51] Furthermore, under fast-MAS conditions (40 kHz or above), doping of the protein samples with paramagnetic salts at suitable concentrations and in conjunction with low-power decoupling can yield drastic enhancements in the sensitivity owing to the significantly higher spin-lattice relaxation rates (while the spin-spin relaxation rates are intact) allowing for fast recycle delays, as demonstrated recently by Ishii and co-workers.[56] Similar to their results, we indeed found that LC8 samples doped with EDTA–Cu(II) have relatively long ^{15}N T_2s, whereas the ^{1}H T_1s are dramatically shortened, indicating that this sample preparation method is beneficial for LC8 as well (data not shown). We also note that, naturally, higher resolution is afforded by recording the spectra at 21.1 T, but practical hardware limitations prevented us from being able to collect heteronuclear 3D data sets necessary for the resonance assignments. With the improvements in hardware and sample preparation, we therefore expect to achieve higher sensitivity and resolution in the future studies of LC8 at 14.1 T and higher, and to complete the resonance assignments.

Although it would be desirable to achieve complete resonance assignments, the available partial assignments already provide a platform for future studies including tertiary structure determination and characterization of protein–protein interfaces of LC8-containing protein assemblies. The close agreement between torsion angles predicted by TALOS+ on the basis of SSNMR chemical shifts and the torsion angles from the LC8 crystal structure (PDB file 2PG1) indicates that chemical shifts are assigned reliably in the solid state. Previous structural studies[22,24,26,27,57] of LC8 and its binding partners (e.g., Pak1, dynein intermediate chain IC, nNOS, etc.) revealed that residues F62–T67 form an antiparallel β sheet with a portion of the bound partner protein. It is likely that LC8 also utilizes this mechanism to interact with other proteins with fine tuning provided by global structure and dynamics of both LC8 and the binding partner. Therefore, it is of interest to examine the structure adopted by this stretch of residues when LC8 forms large assemblies. Through our current work, chemical shift assignments are available for residues F62–T67, and indicate that this stretch of residues is in a β sheet, whereas the assignments for the flanking residues are missing (see Table S1 of the Supplementary data). Therefore, even in unfavorable cases where the chemical shifts for flanking residues are unknown, such as the F62–T67 stretch above, we will still be able to investigate the functionally important interfaces of assemblies formed by LC8 and its various binding partners, through chemical shift perturbation approaches and (or) differential labeling based MAS NMR experiments.[37,41]

Experimental methods

Materials

Common chemicals were purchased from Fisher Scientific or Sigma-Aldrich. ^{15}N NH_4Cl and U-$^{13}C_6$ glucose were purchased from Cambridge Laboratories, Inc.

Can. J. Chem. Downloaded from www.nrcresearchpress.com by Xi'an Jiaotong University on 09/19/12
For personal use only.

Can. J. Chem. Downloaded from www.nrcresearchpress.com by Xi'an Jiaotong University on 09/19/12
For personal use only.

Expression and purification of isotopically enriched LC8

Subcloning of wild type *Drosophila* LC8 (Accession No. NP 525075), and the expression and purification of natural abundance or U-^{15}N, ^{13}C isotopically enriched LC8 have been described previously.[22] For isotope enrichment, the Bracken protocol[58] was followed. The yields of pure natural abundance and isotopically enriched LC8 are 34 mg (per 1 L of Luria Bertani (LB)) and 20 mg (per 1L of LB and 250 mL of M9), respectively.

Preparation of solid-state NMR samples

Eleven milligrams of pure U-^{13}C,^{15}N-enriched LC8 were dialyzed against 10 mmol/L MES buffer (10 mmol/L $MgCl_2$, pH 6.0) and concentrated to 30 mg/mL. A solution of 32% PEG-3350 (also dissolved in 10 mmol/L MES buffer) was gradually added to the LC8 solution following the controlled precipitation protocol developed previously for thioredoxin.[39] This condition was chosen from a minimal (24 well) hanging drop screen, which yielded LC8 microcrystals in a hanging drop. More than 90% of the protein was precipitated, as confirmed by the Bradford assay. The LC8–PEG-3350 mixture was centrifuged, and the pellet was used for solid-state NMR experiments. The hydrated precipitate (14.3 mg) was packed into a 3.2 mm Varian rotor and sealed using an upper spacer and a top spinner.

Solid-state NMR spectroscopy

MAS solid-state NMR spectra were acquired at 14.1 T (600 MHz) on a narrow bore Varian InfinityPlus instrument outfitted with a 3.2 mm triple resonance T3 probe; Larmor frequencies were 599.5 MHz for ^{1}H, 150.7 MHz for ^{13}C, and 60.7 MHz for ^{15}N. Dipolar-based two- and three-dimensional DARR,[59] NCA, NCO, and NCACB spectra were collected at a MAS frequency of 10.000 ± 0.001 kHz controlled by a Varian MAS controller. The dipolar NCACX and NCOCX experiments utilized the SPECIFIC-CP[60] heteronuclear magnetization transfer followed by DARR homonuclear transfer; in the NCACB experiment, the homonuclear DREAM mixing[61] with a tangent ramp was used. Scalar-based 2D NCO[51] and 3D NCOCA[49] spectra were collected at a MAS frequency of 14.705 ± 0.001 kHz controlled by a Varian MAS controller. The temperature was calibrated for this probe at different MAS frequencies using a $PbNO_3$ temperature sensor,[62] and the actual temperature at the sample was maintained to within ±0.5 °C throughout the experiments using the Varian temperature controller. The DARR spectra were acquired at temperatures of –1.7, –6.7, –11.7, –16.7, and –21.7 °C. The heteronuclear 2D and 3D spectra were acquired at –16.7 °C (with the exception of CANCO, which was acquired at –11.7 °C). ^{1}H, ^{13}C, and ^{15}N chemical shifts were referenced with respect to DSS, adamantane, and ammonium chloride used as external referencing standards.[63] The typical 90° pulse lengths were 2.7 (^{1}H), 4.5 (^{13}C), and 5 μs (^{15}N). The ^{1}H–^{13}C(^{15}N) cross polarization was performed with a linear amplitude ramp (80%–100%) on ^{13}C(^{15}N); the ^{1}H radio frequency field was 50 kHz with the center of ramp Hartmann–Hahn matched to the first spinning sideband. The ^{1}H–^{13}C and ^{1}H–^{15}N contact times were 1 ms and 1.6 ms, respectively. In the CANCO experiment, the ^{1}H–^{13}C contact time was set at 200 μs to preferentially excite the ^{13}C aliphatic region. The Z-filter time was 30 ms in all scalar-based experiments. In the dipolar-based experiments, the typical ^{15}N to ^{13}C SPECIFIC-CP transfer was performed with a 25 kHz radio frequency field for ^{15}N and ~15 kHz for the center of a tangential ramp on ^{13}C; the mixing times were 6.7 ms. The DARR mixing time was set to either 2 or 10 ms for recoupling of two ^{13}C nuclei separated by a short distance (mostly one bond), and the ^{1}H RF field strength during DARR was 10 kHz. In the DREAM mixing period (2.1 ms), a tangent ramp was applied on ^{13}C according to the condition $n\omega_r = (\omega_{rf}^2 + \omega_1^2)^{1/2} + (\omega_{rf}^2 + \omega_2^2)^{1/2}$.[56] For the scalar-based NCOCA experiment, $\tau_1 = \tau_2 = 10.9$ ms; $\tau_3 = \tau_4 = 2.72$ ms. The Z-filter time was 30 ms in all scalar-based experiments. TPPM decoupling[64] was used, and the decoupling field strengths ranged between 80 and 100 kHz in different experiments. Recycle delays in all experiments were 2 s. TPPI[65] was used for frequency discrimination in the indirect dimensions.

DARR and dipolar-based NCA and NCO spectra of LC8 were also acquired at at 21.1 T at EMSL-PNNL, on a medium bore 900 MHz Varian Inova instrument outfitted with a 3.2 mm triple resonance BioMAS probe; the Larmor frequencies were 900.575 for ^{1}H, 226.47 for ^{13}C, and 92.26 MHz for ^{15}N. The MAS frequency was 14.000 ± 0.001 kHz controlled by a Varian MAS controller. The temperature was 0 °C and was maintained to within ±0.5 °C throughout the experiments using the Varian temperature controller. The typical pulse lengths were 3.0 (^{1}H), 5.5 (^{13}C), and 6 μs (^{15}N); the ^{1}H–^{13}C and ^{1}H–^{15}N cross polarizations were performed with a tangent amplitude ramp (80%–100%); the ^{1}H radio frequency fields were 70.4 and 60.7 kHz, respectively, with the center of the ramp Hartmann–Hahn matched to the second spinning sideband; the ^{1}H–^{13}C and ^{1}H–^{15}N contact times were 2 and 1 ms, respectively. The NCA and NCO experiments were performed with a tangent amplitude ramp (80%–100%); the ^{13}C radio frequency fields were 13 and 18 kHz, respectively, with the center of the ramp Hartmann–Hahn matched to the first spinning sideband; the SPECIFIC-CP mixing times were 6.0 and 6.4 ms, respectively. TPPM decoupling (83 kHz) was applied during the evolution and acquisition periods. The ^{1}H field strength during DARR was 14 kHz; DARR mixing time was 50 ms; under these conditions predominantly one-bond correlations appeared in the spectra.

Other acquisition and processing parameters for data sets acquired at 14.1 and 21.1 T are specified in the figure captions and in the Supplementary data.

NMR data processing and analysis

The spectra were processed in NMRpipe[66] and analyzed in Sparky.[67] For 2D solid-state NMR data, 90°, 60°, or 30° shifted sine-bell apodization followed by a Lorentzian to Gaussian transformation was applied in both dimensions; forward linear prediction to twice the number of the original data points was applied in the indirect dimension for some data sets followed by zero filling to twice the total number of points. The 3D data sets were processed by using 30° or 60° shifted sine bells in all dimensions followed by a Lorentzian to Gaussian transformation (for resolution enhancement) and by using 90° shifted sine bells in all dimensions followed by a Lorentzian to Gaussian transformation (for sensitivity enhancement). The 3D spectra were also processed with

maximum entropy reconstruction as implemented in the program Roland NMR Toolkit.[68,69] Detailed information about processing parameters is specified in the Supplementary data.

Conclusions

We have established site-specific backbone and side-chain resonance assignments for the majority of the residues of LC8 through MAS solid-state NMR spectroscopy. Based on these assignments, we derived torsion angles ϕ and ψ by TALOS+. The predicted angles are in close agreement with crystal structures (2PG1) for most of the residues except for several residues located in loop or linker regions.

Supplementary data

Supplementary data (14.1 T 2D DARR, NCA, NCACB, NCACX, and NCOCX spectra of DLC8; solid-state chemical shifts of DLC8; temperature-dependent DARR spectra; and acquisition and processing parameters for solid-state and solution NMR experiments) are available with the article through the journal Web site (www.nrcresearchpress.com).

Acknowledgment

This work was supported by the National Institutes of Health (NIH Grants R01GM085396 from NIGMS and P20RR017716-08 from NCRR). The 21.1 T spectra were acquired at the Environmental Molecular Sciences Laboratory, a national scientific user facility sponsored by the United States Department of Energy's Office of Biological and Environmental Research and located at Pacific Northwest National Laboratory in Richland, Washington. A. Lipton, J. Sears, M. Froehlke, S. Burton, D. Hoyt, and J. Ford are thanked for their kind assistance during our visit to EMSL.

References

(1) King, S. M. *Biochim. Biophys. Acta* **2000** *1496* (1), 60. doi:10.1016/S0167-4889(00)00009-4.
(2) Pfister, K. K.; Shah, P. R.; Hummerich, H.; Russ, A.; Cotton, J.; Annuar, A. A.; King, S. M.; Fisher, E. M. *PLoS Genet.* **2006** *2* (1), e1. doi:10.1371/journal.pgen.0020001.
(3) Harrison, A.; Olds-Clarke, P.; King, S. M. *J. Cell Biol.* **1998** *140* (5), 1137. doi:10.1083/jcb.140.5.1137.
(4) King, S. M.; Patel-King, R. S. *J. Biol. Chem.* **1995** *270* (19), 11445. doi:10.1074/jbc.270.19.11445.
(5) Pazour, G. J.; Wilkerson, C. G.; Witman, G. B. *J. Cell Biol.* **1998** *141* (4), 979. doi:10.1083/jcb.141.4.979.
(6) Espindola, F. S.; Suter, D. M.; Partata, L. B.; Cao, T.; Wolenski, J. S.; Cheney, R. E.; King, S. M.; Mooseker, M. S. *Cell Motil. Cytoskeleton* **2000** *47* (4), 269. doi:10.1002/1097-0169(200012)47:4<269::AID-CM2>3.0.CO;2-G.
(7) Stelter, P.; Kunze, R.; Flemming, D.; Hopfner, D.; Diepholz, M.; Philippsen, P.; Bottcher, B.; Hurt, E. *Nat. Cell Biol.* **2007** *9* (7), 788. doi:10.1038/ncb1604.
(8) Barbar, E. *Biochemistry* **2008** *47* (2), 503. doi:10.1021/bi701995m.
(9) Vadlamudi, R. K.; Bagheri-Yarmand, R.; Yang, Z.; Balasenthil, S.; Nguyen, D.; Sahin, A. A.; den Hollander, P.; Kumar, R. *Cancer Cell* **2004** *5* (6), 575. doi:10.1016/j.ccr.2004.05.022.
(10) Kubota, T.; Matsuoka, M.; Chang, T. H.; Bray, M.; Jones, S.; Tashiro, M.; Kato, A.; Ozato, K. *J. Virol.* **2009** *83* (13), 6952. doi:10.1128/JVI.00480-09.
(11) Su, Y.; Qiao, W.; Guo, T.; Tan, J.; Li, Z.; Chen, Y.; Li, X.; Li, Y.; Zhou, J.; Chen, Q. *Cell. Microbiol.* **2010** *12* (8), 1098. doi:10.1111/j.1462-5822.2010.01453.x.
(12) Tan, G. S.; Preuss, M. A.; Williams, J. C.; Schnell, M. J. *Proc. Natl. Acad. Sci. U.S.A.* **2007** *104* (17), 7229. doi:10.1073/pnas.0701397104.
(13) Moseley, G. W.; Roth, D. M.; DeJesus, M. A.; Leyton, D. L.; Filmer, R. P.; Pouton, C. W.; Jans, D. A. *Mol. Biol. Cell* **2007** *18* (8), 3204. doi:10.1091/mbc.E07-01-0030.
(14) Fejtova, A.; Davydova, D.; Bischof, F.; Lazarevic, V.; Altrock, W. D.; Romorini, S.; Schone, C.; Zuschratter, W.; Kreutz, M. R.; Garner, C. C.; Ziv, N. E.; Gundelfinger, E. D. *J. Cell Biol.* **2009** *185* (2), 341. doi:10.1083/jcb.200807155.
(15) Lightcap, C. M.; Kari, G.; Arias-Romero, L. E.; Chernoff, J.; Rodeck, U.; Williams, J. C. *PLoS ONE* **2009** *4* (6), e6025. doi:10.1371/journal.pone.0006025.
(16) Barbar, E.; Kleinman, B.; Imhoff, D.; Li, M.; Hays, T. S.; Hare, M. *Biochemistry* **2001** *40* (6), 1596. doi:10.1021/bi002278+.
(17) Mohan, P. M.; Barve, M.; Chatterjee, A.; Hosur, R. V. *Protein Sci.* **2006** *15* (2), 335. doi:10.1110/ps.051854906.
(18) Jung, Y.; Kim, H.; Min, S. H.; Rhee, S. G.; Jeong, W. *J. Biol. Chem.* **2008** *283* (35), 23863. doi:10.1074/jbc.M803072200.
(19) King, S. M. *Sci. Signal.* **2008** *1* (47), pe51. doi:10.1126/scisignal.147pe51.
(20) Song, Y.; Benison, G.; Nyarko, A.; Hays, T. S.; Barbar, E. *J. Biol. Chem.* **2007** *282* (23), 17272. doi:10.1074/jbc.M610445200.
(21) Song, C.; Wen, W.; Rayala, S. K.; Chen, M.; Ma, J.; Zhang, M.; Kumar, R. *J. Biol. Chem.* **2008** *283* (7), 4004. doi:10.1074/jbc.M704512200.
(22) Lightcap, C. M.; Sun, S.; Lear, J. D.; Rodeck, U.; Polenova, T.; Williams, J. C. *J. Biol. Chem.* **2008** *283* (40), 27314. doi:10.1074/jbc.M800758200.
(23) Yang, P.; Yang, C.; Wirschell, M.; Davis, S. *J. Biol. Chem.* **2009** *284* (45), 31412. doi:10.1074/jbc.M109.050666.
(24) Fan, J.; Zhang, Q.; Tochio, H.; Li, M.; Zhang, M. *J. Mol. Biol.* **2001** *306* (1), 97. doi:10.1006/jmbi.2000.4374.
(25) Lo, K. W.; Kan, H. M.; Chan, L. N.; Xu, W. G.; Wang, K. P.; Wu, Z.; Sheng, M.; Zhang, M. *J. Biol. Chem.* **2005** *280* (9), 8172. doi:10.1074/jbc.M411408200.
(26) Williams, J. C.; Roulhac, P. L.; Roy, A. G.; Vallee, R. B.; Fitzgerald, M. C.; Hendrickson, W. A. *Proc. Natl. Acad. Sci. U.S.A.* **2007** *104* (24), 10028. doi:10.1073/pnas.0703614104.
(27) Benison, G.; Karplus, P. A.; Barbar, E. *J. Mol. Biol.* **2007** *371* (2), 457. doi:10.1016/j.jmb.2007.05.046.
(28) Chen, Y. M.; Gerwin, C.; Sheng, Z. H. *J. Neurosci.* **2009** *29* (30), 9429. doi:10.1523/JNEUROSCI.1472-09.2009.
(29) Wang, W.; Lo, K. W.; Kan, H. M.; Fan, J. S.; Zhang, M. *J. Biol. Chem.* **2003** *278* (42), 41491. doi:10.1074/jbc.M307118200.
(30) Makokha, M.; Huang, Y. J.; Montelione, G.; Edison, A. S.; Barbar, E. *Protein Sci.* **2004** *13* (3), 727. doi:10.1110/ps.03462204.
(31) Fan, J. S.; Zhang, Q.; Tochio, H.; Zhang, M. *J. Biomol. NMR* **2002** *23* (2), 103. doi:10.1023/A:1016332918178.
(32) Hall, J.; Hall, A.; Pursifull, N.; Barbar, E. *Biochemistry* **2008** *47* (46), 11940. doi:10.1021/bi801093k.
(33) Benison, G.; Karplus, P. A.; Barbar, E. *J. Mol. Biol.* **2008** *384* (4), 954. doi:10.1016/j.jmb.2008.09.083.
(34) Benison, G.; Barbar, E. *Methods Enzymol.* **2009** *455*, 237. doi:10.1016/S0076-6879(08)04209-2.
(35) Nyarko, A.; Cochrun, L.; Norwood, S.; Pursifull, N.; Voth, A.;

Can. J. Chem. Downloaded from www.nrcresearchpress.com by Xi'an Jiaotong University on 09/19/12
For personal use only.

Can. J. Chem. Downloaded from www.nrcresearchpress.com by Xi'an Jiaotong University on 09/19/12
For personal use only.

Barbar, E. *Biochemistry* **2005** *44* (43), 14248. doi:10.1021/bi0512694.
(36) Petit, C.; Giron, M.-L.; Tobaly-Tapiero, J.; Bittoun, P.; Real, E.; Jacob, Y.; Tordo, N.; de Thé, H.; Saïb, A. *J. Cell Sci.* **2003** *116* (16), 3433. doi:10.1242/jcs.00613.
(37) Yang, J.; Paramasivam, S.; Marulanda, D.; Cataldi, M.; Tasayco, M. L.; Polenova, T. *Magn. Reson. Chem.* **2007** *45* (S1), S73. doi:10.1002/mrc.2092.
(38) Yang, J.; Tasayco, M. L.; Polenova, T. *J. Am. Chem. Soc.* **2008** *130* (17), 5798. doi:10.1021/ja711304e.
(39) Marulanda, D.; Tasayco, M. L.; McDermott, A.; Cataldi, M.; Arriaran, V.; Polenova, T. *J. Am. Chem. Soc.* **2004** *126* (50), 16608. doi:10.1021/ja0464589.
(40) Sun, S.; Siglin, A.; Williams, J. C.; Polenova, T. *J. Am. Chem. Soc.* **2009** *131* (29), 10113. doi:10.1021/ja902003u.
(41) Etzkorn, M.; Bockmann, A.; Lange, A.; Baldus, M. *J. Am. Chem. Soc.* **2004** *126* (45), 14746. doi:10.1021/ja0479181.
(42) Böckmann, A.; Lange, A.; Galinier, A.; Luca, S.; Giraud, N.; Juy, M.; Heise, H.; Montserret, R.; Penin, F.; Baldus, M. *J. Biomol. NMR* **2003** *27* (4), 323. doi:10.1023/A:1025820611009.
(43) Shen, Y.; Delaglio, F.; Cornilescu, G.; Bax, A. *J. Biomol. NMR* **2009** *44* (4), 213. doi:10.1007/s10858-009-9333-z.
(44) Laskowski, R. A.; Hutchinson, E. G.; Michie, A. D.; Wallace, A. C.; Jones, M. L.; Thornton, J. M. *Trends Biochem. Sci.* **1997** *22* (12), 488. doi:10.1016/S0968-0004(97)01140-7.
(45) McDermott, A.; Polenova, T.; Bockmann, A.; Zilm, K. W.; Paulsen, E. K.; Martin, R. W.; Montelione, G. T. *J. Biomol. NMR* **2000** *16* (3), 209. doi:10.1023/A:1008391625633.
(46) Franks, W. T.; Zhou, D. H.; Wylie, B. J.; Money, B. G.; Graesser, D. T.; Frericks, H. L.; Sahota, G.; Rienstra, C. M. *J. Am. Chem. Soc.* **2005** *127* (35), 12291. doi:10.1021/ja044497e.
(47) Igumenova, T. I.; Wand, A. J.; McDermott, A. E. *J. Am. Chem. Soc.* **2004** *126* (16), 5323. doi:10.1021/ja030546w.
(48) Pauli, J.; van Rossum, B.; Forster, H.; de Groot, H. J.; Oschkinat, H. *J. Magn. Reson.* **2000** *143* (2), 411. doi:10.1006/jmre.2000.2029.
(49) Chen, L.; Kaiser, J. M.; Polenova, T.; Yang, J.; Rienstra, C. M.; Mueller, L. J. *J. Am. Chem. Soc.* **2007** *129* (35), 10650. doi:10.1021/ja073498e.
(50) Chen, L.; Olsen, R. A.; Elliott, D. W.; Boettcher, J. M.; Zhou, D. H.; Rienstra, C. M.; Mueller, L. J. *J. Am. Chem. Soc.* **2006** *128* (31), 9992. doi:10.1021/ja062347t.
(51) Chen, L. L.; Kaiser, J. M.; Lai, J. F.; Polenova, T.; Yang, J.; Rienstra, C. M.; Mueller, L. J. *Magn. Reson. Chem.* **2007** *45* (S1), S84. doi:10.1002/mrc.2107.
(52) Marulanda, D.; Tasayco, M. L.; Cataldi, M.; Arriaran, V.; Polenova, T. *J. Phys. Chem. B* **2005** *109* (38), 18135. doi:10.1021/jp052774d.
(53) Igumenova, T. I.; McDermott, A. E.; Zilm, K. W.; Martin, R. W.; Paulson, E. K.; Wand, A. J. *J. Am. Chem. Soc.* **2004** *126* (21), 6720. doi:10.1021/ja030547o.
(54) Pauli, J.; Baldus, M.; van Rossum, B.; de Groot, H.; Oschkinat, H. *ChemBioChem* **2001** *2* (4), 272. doi:10.1002/1439-7633(20010401)2:4<272::AID-CBIC272>3.0.CO;2-2.
(55) Han, Y.; Ahn, J.; Concel, J.; Byeon, I. J.; Gronenborn, A. M.; Yang, J.; Polenova, T. *J. Am. Chem. Soc.* **2010** *132* (6), 1976. doi:10.1021/ja908687k.
(56) Wickramasinghe, N. P.; Parthasarathy, S.; Jones, C. R.; Bhardwaj, C.; Long, F.; Kotecha, M.; Mehboob, S.; Fung, L. W.; Past, J.; Samoson, A.; Ishii, Y. *Nat. Methods* **2009** *6* (3), 215. doi:10.1038/nmeth.1300.
(57) Liang, J.; Jaffrey, S. R.; Guo, W.; Snyder, S. H.; Clardy, J. *Nat. Struct. Biol.* **1999** *6* (8), 735. doi:10.1038/11501.
(58) Marley, J.; Lu, M.; Bracken, C. *J. Biomol. NMR* **2001** *20* (1), 71. doi:10.1023/A:1011254402785.
(59) Takegoshi, K.; Nakamura, S.; Terao, T. *Chem. Phys. Lett.* **2001** *344* (5–6), 631. doi:10.1016/S0009-2614(01)00791-6.
(60) Baldus, M.; Petkova, A. T.; Herzfeld, J.; Griffin, R. G. *Mol. Phys.* **1998** *95* (6), 1197. doi:10.1080/00268979809483251.
(61) Verel, R.; Baldus, M.; Ernst, M.; Meier, B. H. *Chem. Phys. Lett.* **1998** *287* (3–4), 421. doi:10.1016/S0009-2614(98)00172-9.
(62) Neue, G.; Dybowski, C. *Solid State Nucl. Mag. Reson.* **1997** *7* (4), 333. doi:10.1016/S0926-2040(96)01291-X.
(63) Morcombe, C. R.; Zilm, K. W. *J. Magn. Reson.* **2003** *162* (2), 479. doi:10.1016/S1090-7807(03)00082-X.
(64) Bennett, A. E.; Rienstra, C. M.; Auger, M.; Lakshmi, K. V.; Griffin, R. G. *J. Chem. Phys.* **1995** *103* (16), 6951. doi:10.1063/1.470372.
(65) Marion, D.; Wuthrich, K. *Biochem. Biophys. Res. Commun.* **1983** *113* (3), 967. doi:10.1016/0006-291X(83)91093-8.
(66) Delaglio, F.; Grzesiek, S.; Vuister, G. W.; Zhu, G.; Pfeifer, J.; Bax, A. *J. Biomol. NMR* **1995** *6* (3), 277. doi:10.1007/BF00197809.
(67) Goddard, T. D.; Kneller, D. G. *Sparky 3 – NMR Assignment and Integration Software;* University of California: San Francisco.
(68) Stern, A. S.; Li, K. B.; Hoch, J. C. *J. Am. Chem. Soc.* **2002** *124* (9), 1982. doi:10.1021/ja011669o.
(69) Mobli, M.; Maciejewski, M. W.; Gryk, M. R.; Hoch, J. C. *J. Biomol. NMR* **2007** *39* (2), 133. doi:10.1007/s10858-007-9180-8.

Multinuclear solid-state NMR of square-planar platinum complexes — Cisplatin and related systems

Bryan E.G. Lucier, Alex R. Reidel, and Robert W. Schurko

Can. J. Chem. Downloaded from www.nrcresearchpress.com by Xi'an Jiaotong University on 09/19/12
For personal use only.

Abstract: Multinuclear solid-state nuclear magnetic resonance (SSNMR) experiments have been performed on cisplatin and four related square-planar compounds. The wideband uniform rate smooth truncation – Carr–Purcell–Meiboom–Gill (WURST–CPMG) pulse sequence was utilized in NMR experiments to acquire ^{195}Pt, ^{14}N, and ^{35}Cl ultra-wideline NMR spectra of high quality. Standard Hahn-echo and magic-angle spinning ^{195}Pt NMR experiments are also performed to refine extracted chemical shielding (CS) tensor parameters. Platinum magnetic shielding (MS) tensor orientations are calculated using both plane-wave density functional theory (DFT) and standard DFT methods. The tensor orientations are shown to be highly constrained by molecular symmetry elements, but also influenced to some degree by intermolecular interactions. ^{14}N WURST–CPMG experiments were performed on three compounds and electric field gradient (EFG) parameters (the quadrupolar coupling constant, C_Q, and the asymmetry parameter, η_Q) are reported. First principles calculations of the ^{14}N EFG tensor parameters and orientations and affirm their dependence on the local hydrogen bonding environment. ^{35}Cl WURST–CPMG experiments on cisplatin and transplatin are reported, using two different static magnetic fields to extract EFG and CS tensor parameters, and ^{35}Cl EFG tensor magnitudes and orientations are predicted using first principles calculations. Transverse (T_2) relaxation data for all nuclei are used to investigate heteronuclear dipolar relaxation mechanisms, as well as the nature of the local hydrogen bonding environments.

Key words: platinum NMR, ^{195}Pt NMR, ^{14}N NMR, ^{35}Cl NMR, cisplatin, transplatin, carboplatin, solid-state NMR, wideline NMR, WURST–CPMG, electric field gradient tensors, chemical shift tensors.

Résumé : On a effectué des expériences de résonance magnétique nucléaire à l'état solide (RMN-ES) sur le cisplatine et sur quatre composés apparentés plan carrés. Dans les expériences de RMN, on a utilise la séquence de pulsation « wideband uniform rate smooth truncation – Carr–Purcell–Meiboom–Gill (WURST–CPMG) » pour acquérir des spectres RMN du ^{195}Pt, du ^{14}N et du ^{35}Cl avec des raies ultra-larges et de grande qualité. On a aussi effectué des expériences de RMN du ^{195}Pt en écho de Hahn standard ainsi qu'à l'angle magique de rotation afin d'affiner les paramètres de tenseur du blindage chimique (BC). On a calculé les orientations du tenseur du blindage magnétique (BM) du platine en faisant appel aux méthodes de la théorie de la fonctionnelle de la densité standard (TFD) ainsi qu'avec une onde plane. On a montré que les orientations du tenseur sont grandement contraintes par les éléments de symétrie moléculaire, mais qu'ils sont aussi influencés jusqu'à un certain point par les interactions intermoléculaires. Les expériences utilisant la séquence de pulsation « WURST–CPMG » pour le ^{14}N ont été effectuées sur trois composés et on rapporte les paramètres du gradient du champ électrique (GCE; la constante de couplage quadripolaire, C_Q et le paramètre d'asymétrie, η_Q). Des calculs sur la base de premiers principes des paramètres de tenseur du GCE et des ses orientations confirment leur dépendance sur l'environnement local des liaisons hydrogènes. Opérant sur le cisplatine et le transplatine, à deux champs magnétiques différents, on a aussi réalisé des expériences utilisant la séquence de pulsation « WURST–CPMG » pour le ^{35}Cl afin d'extraire les paramètres de tenseur du GCE et du blindage chimique (BC); les amplitudes du tenseur GCE du ^{35}Cl et ses orientations peuvent être calculées correctement à partir de premiers principes. On a utilisé les données de relaxation transversale (T_2) de chacun des noyaux pour étudier les mécanismes de relaxation dipolaire hétéronucléaire ainsi que la nature des environnements des liaisons hydrogènes locales.

Mots-clés : RMN du platine, RMN du ^{195}Pt, RMN du ^{14}N, RMN du ^{35}Cl, cisplatine, transplatine, carboplatine, RMN à l'état solide, WURST–CPMG, tenseurs du gradient du champ électrique, tenseurs du déplacement chimique.

[Traduit par la Rédaction]

Received 7 January 2011. Accepted 11 February 2011. Published at www.nrcresearchpress.com/cjc on 4 August 2011.

B.E.G. Lucier, A.R. Reidel, and R.W. Schurko. Department of Chemistry and Biochemistry, University of Windsor, Windsor, ON N9B 3P4, Canada.

Corresponding author: Robert W. Schurko (e-mail: rschurko@uwindsor.ca).

This article is part of a Special Issue dedicated to Professor Roderick E. Wasylishen

Can. J. Chem. Downloaded from www.nrcresearchpress.com by Xi'an Jiaotong University on 09/19/12
For personal use only.

Introduction

Cancer is a class of diseases that affects people around the world, and in 2008 was responsible for an estimated 7.6 million deaths globally.[1] The treatment of cancer normally involves the use of several different types of chemotherapeutic drugs[2] and, of those, a prominent class are platinum-based DNA-crosslinking agents. Drugs such as cisplatin, carboplatin, and oxaliplatin are approved for use, and pharmaceutical research continues to focus on this family of compounds.[3,4] *cis*-Diamminedichloroplatinum (cisplatin or *cis*-$PtCl_2(NH_3)_2$) is one of the longest known, most effective, and oft-employed alkylating agents involved in the treatment of testicular, ovarian, bladder, head, and neck cancers.[5] Although originally reported by Peyrone in 1845 and subsequently dubbed "Peyrone's chloride",[6] more than 100 years passed before Rosenberg discovered the unique effects of cisplatin on the growth of *Escherichia coli*[7] in 1965, and its antitumor activity in mice in 1969.[8] In the time since the introduction of cisplatin, related drugs using central Pt(II) atoms such as carboplatin and oxaliplatin have been synthesized and approved to treat cancer as well.[5] Cisplatin and related platinum-based drugs are thought to kill cancerous cells via the formation of Pt–N covalent bonds between the Pt atom of the cisplatin molecule and purine bases (particularly guanine units) in DNA, which in turn triggers cell apoptosis (i.e., programmed cell death). There have been numerous reports of drug syntheses and mechanistic studies; however, the specifics regarding this mechanism are still debated.[9–11]

Studies of cisplatin and related drugs often employ one- and (or) two-dimensional solution NMR as characterization methods, since the reaction of cisplatin with DNA occurs within the aqueous environment of cells.[12,13] The majority of solution nuclear magnetic resonance (NMR) studies have focussed upon the reaction of cisplatin with relevant biomolecules and formation of intermediates in physiological (i.e., low concentration) conditions; however, even in one-dimensional experiments, the limit of detection of ^{195}Pt solution NMR (~10 mmol/L) is orders of magnitude higher than concentrations found within cells (μmol/L). Many solution NMR studies examining the reactions of these drugs must rely on ^{1}H and ^{15}N NMR experiments (as well as ^{15}N isotopic labelling), including two-dimensional inverse detection methods that allow detection of drug concentrations similar to those within the body (5 μmol/L).[5] Isotropic chemical shifts obtained from ^{195}Pt solution NMR experiments for much more concentrated systems are sometimes reported,[14–19] particularly for systems involving cisplatin hydrolysis and (or) reactions with biomolecules or DNA.[12,14,15,19–21] Detailed first principles calculations of the effects of solvents and dynamic averaging on observed ^{195}Pt NMR shieldings in cisplatin and related derivatives have also recently been reported.[22]

By comparison, there are fewer solid-state NMR (SSNMR) studies of these systems, with focus upon nuclei such as ^{1}H, ^{13}C, and ^{15}N.[23–28] Although these nuclei are very common in solution NMR work, they all have inherent drawbacks for SSNMR studies. ^{1}H NMR spectra are very broad owing to strong homonuclear dipolar couplings and not expected to be of much use in elucidating binding interactions with large DNA molecules. ^{13}C NMR experiments are of limited diagnostic use as well, since Pt–C bonds are not relevant in the interactions between Pt drugs and DNA. ^{15}N is potentially the most useful of the three nuclei for SSNMR experimentation, although owing to its low natural abundance (0.37%), expensive isotopic labelling is necessary.

The ^{195}Pt chemical shift is extremely sensitive to the local Pt environment and has a known range of ~15 000 ppm.[29,30] ^{195}Pt SSNMR powder patterns give valuable information on both the platinum isotropic chemical shift and the chemical shift anisotropy (CSA), which are extremely sensitive to structural modifications and Pt oxidation state changes. However, these powder patterns are often very broad (i.e., covering thousands of ppm / hundreds of kHz), making standard SSNMR experiments very time-consuming. The inherently low sensitivity of such experiments is of concern for the potential examination of the binding of platinum complexes to DNA chains, since the Pt content is very low in such systems. However, the recently developed wideband uniform rate smooth truncation – Carr–Purcell–Meiboom–Gill (WURST–CPMG) pulse sequence[31–37] has shown much promise for the rapid acquisition of broad powder patterns for spin-1/2 nuclei with large CSAs, including ^{195}Pt,[38] as well as quadrupolar nuclei (spin > 1/2) such as ^{14}N[39–41] and ^{35}Cl,[42,43] which are present in numerous cisplatin derivatives and may also serve as useful probes of structure and dynamics. Given the sensitivity of the ^{195}Pt CSA to subtle structural changes and the signal enhancement capabilities of the WURST–CPMG protocol, it may be possible to gain rich structural information on Pt-containing biological systems, but it is necessary to make a preliminary study of the platinum chemical shift (CS) tensors and the rapidity with which high-quality ^{195}Pt NMR spectra can be acquired.

Herein, we describe the use of the WURST–CPMG pulse sequence, in combination with frequency-stepped techniques (where necessary, vide infra),[44–47] to acquire ^{195}Pt, ^{14}N, and ^{35}Cl SSNMR spectra of cisplatin and related systems, including transplatin (its trans isomer), the second-generation chemotherapy drug carboplatin, as well as $Pt(py)_2Cl_2$ and $Pt(en)Cl_2$. The use of ultra-high magnetic fields (21.1 T) for ^{14}N and ^{35}Cl NMR experiments for distinguishing overlapping sites in spectra is also explored. The resulting data is then analysed to correlate observed ^{195}Pt, ^{14}N, and ^{35}Cl NMR parameters with the local structural environments. Density functional theory (DFT) calculations on isolated molecules and DFT plane-wave calculations on extended lattices have been applied to calculate the NMR interaction tensors and aid in this correlation. These data allow us to comment on the nature of structure and bonding which may affect the potencies of these compounds as antitumor agents. In turn, this may lead to a deeper understanding of relationships between drug–DNA interactions and drug efficacy, which may enable the rational design of new platinum-based anticancer compounds.

Experimental

Sample identities

cis-$Pt(NH_3)_2Cl_2$ (cisplatin, *cis*-diamminedichloroplatinum(II)), *trans*-$Pt(NH_3)_2Cl_2$ (transplatin, *trans*-diamminedichloroplatinum (II)), *cis*-$PtCl_2(C_5H_5N)_2$ ($Pt(py)_2Cl_2$, *cis*-dichlorobis(pyridine) platinum(II)), and $[C_4H_6(CO_2)_2]Pt(NH_3)_2$ (carboplatin, *cis*-diammine(1,1-cyclobutanedicarboxylato)platinum(II)) were

Scheme 1. Structures of compounds (*a*) cisplatin, (*b*) transplatin, (*c*) $Pt(py)_2Cl_2$, (*d*) $Pt(en)Cl_2$, and (*e*) carboplatin.

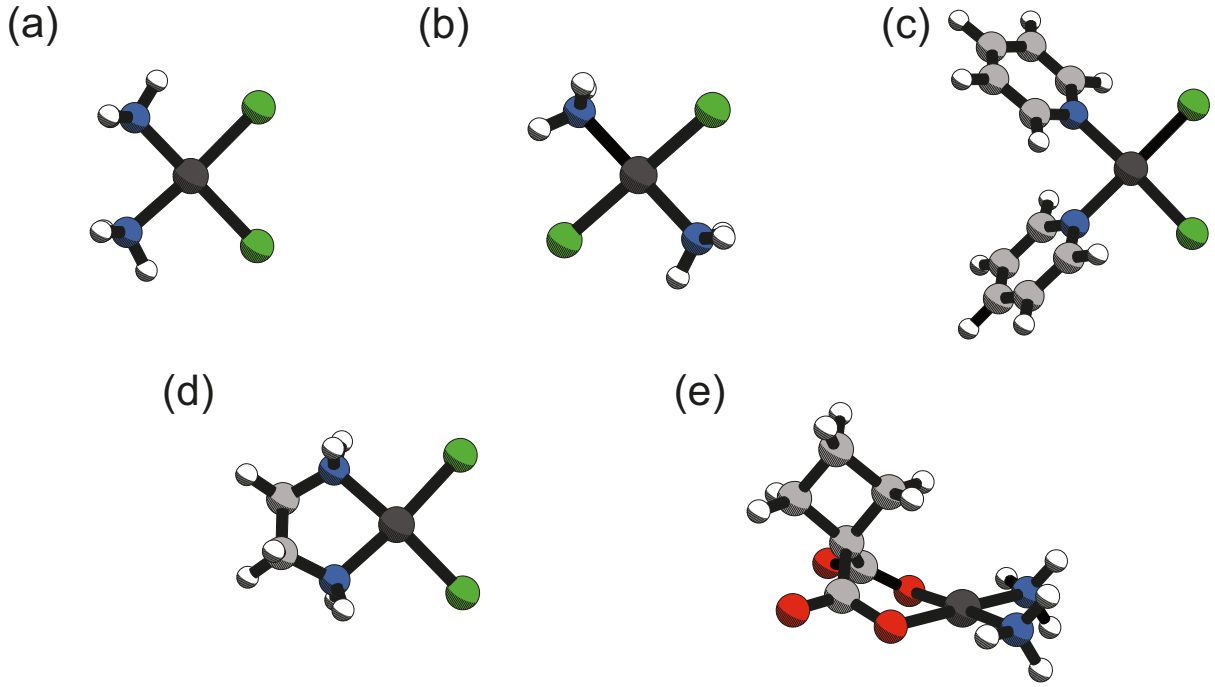

Can. J. Chem. Downloaded from www.nrcresearchpress.com by Xi'an Jiaotong University on 09/19/12
For personal use only.

purchased from Strem Chemicals, Inc., and ($H_2NCH_2CH_2NH_2$)$PtCl_2$ ($Pt(en)Cl_2$, dichloro(ethylenediamine)platinum(II)) was purchased from Sigma-Aldrich. All compounds were used without further purification (Scheme 1).

Solid-state NMR

Solid-state NMR spectra were collected on a Varian Infinity Plus NMR spectrometer with an Oxford 9.4 T ($\nu_0(^1H)$ = 399.73 MHz) wide-bore magnet with $\nu_0(^{195}Pt)$ = 85.59 MHz, $\nu_0(^{35}Cl)$ = 39.17 MHz, and $\nu_0(^{14}N)$ = 28.89 MHz. All ^1H, ^{195}Pt, and ^{14}N static experiments were conducted using a Varian/Chemagnetics 5 mm HX static probe. ^{195}Pt magic angle spinning (MAS) experiments were performed using a Varian/Chemagnetics 2.5 mm HX probe. A Chemagnetics low-γ tuning box and preamplifier were used on the X channel for all ^{14}N NMR experiments. A Varian/Chemagnetics 5 mm HXY probe was used for all ^{35}Cl experiments owing to its continuous tuning range in the ^{35}Cl Larmor frequency region. All samples were packed into 5 mm o.d. zirconia rotors or glass tubes. ^{195}Pt chemical shifts were referenced with respect to 1.0 mol/L Na_2PtCl_6 (aq) (δ_{iso} = 0.0 ppm), ^{35}Cl chemical shifts were referenced to NaCl (s) (δ_{iso} = 0.0 ppm), and ^{14}N chemical shifts were reported with respect to NH_4Cl (s) (δ_{iso} = 0.0 ppm). A proton decoupling field of either 28 or 38 kHz was employed in all experiments.

All ^{195}Pt and ^{14}N ultra-wideline static (i.e., stationary sample) NMR experiments were conducted using the WURST–CPMG pulse sequence.[31,32,35,48,49] WURST-80 pulse shapes were used with a 50 μs WURST pulse length, a sweep rate of 40 MHz/ms from high to low frequency (corresponding to a non-adiabatic π/2 pulse), and a spectral width of 2000 kHz in all cases.

^{195}Pt WURST–CPMG experiments used an experimentally optimized radio frequency (rf) power of 39 kHz. Piecewise acquisitions were generally required for ^{195}Pt WURST–CPMG experiments.[44–47] Static ^{195}Pt NMR echo spectra were acquired using a standard Hahn-echo experiment of the form $(\pi/2)_x - \tau_1 - (\pi)_y - \tau_2 -$ acq, where τ_1 and τ_2 represent interpulse delays of 40 and 20 μs, respectively. A π/2 pulse width of 2.5 μs and spectral width of 2000 kHz were used. ^{195}Pt MAS NMR spectra of transplatin were acquired using a standard Bloch-decay experiment, a π/2 pulse width of 1.0 μs and spectral width of 1500 kHz. Three different spinning speeds were employed and ^1H decoupling fields in excess of 70 kHz were applied for all experiments. See Supplementary data Tables S1–S3 for the full listing of experimental parameters.

Ultra-wideline ^{14}N NMR experiments were carried out using the WURST–CPMG pulse sequence, employing an rf power of ~30 kHz for all experiments. The first-order quadrupolar interaction dominates these spectra and results in powder patterns that are symmetric about the isotropic shift value. Therefore, the low-frequency (right) portion of the powder pattern was generated by mirroring the high-frequency (left) half of the powder pattern about the isotropic shift value (taken from either the literature or DFT calculations). Contributions from CSA are negligible in magnitude compared with the broadening from the first-order quadrupolar interaction (i.e., the effect of an extraordinarily large isotropic chemical shift (500 ppm) on a ^{14}N spectrum of $C_Q \sim 1$ MHz at 9.4 T is only ~1.5% of the width of the powder pattern), as are contributions from the second-order quadrupolar interaction.[37] See Supplementary data Table S4 for a full listing of experimental parameters.

Ultra-wideline ^{35}Cl NMR experiments at 9.4 T also utilized WURST-80 pulse shapes and 50 μs WURST pulse lengths. A spectral width of 1000 kHz, a WURST sweep rate of 20 MHz/ms from high to low frequency, and an rf power of 40 kHz were used for all experiments. High-field static NMR experiments were performed on a 21.1 T Bruker

Can. J. Chem. Downloaded from www.nrcresearchpress.com by Xi'an Jiaotong University on 09/19/12
For personal use only.

Avance II NMR spectrometer ($\nu_0(^{35}Cl)$ = 88.13 MHz) at the National Ultrahigh-field NMR Facility for Solids in Ottawa, Ontario, and samples were packed into 4 mm o.d. glass NMR tubes. Spectra were acquired on a home-built 4 mm probe using the WURST–CPMG pulse sequence. A spectral width of 1000 kHz and a WURST sweep rate of 20 MHz/ms from high to low frequency was used for all experiments at 21.1 T. See Supplementary data Table S5 for a full listing of experimental parameters.

Static ^{1}H NMR spectra were acquired using a standard Bloch decay pulse sequence, with a $\pi/2$ pulse width of 3.4 μs, a spectral width of 100 kHz, and a recycle delay of 5 s.

Simulations of all static solid-state NMR spectra were performed using the WSOLIDS software package.[50] Simulations of the ^{195}Pt MAS spectra of transplatin were performed using the DMFit software program (2007) and employed an automated iterative fit procedure, as well as manual fitting of spectra.[51] In all cases, uncertainties in extracted NMR tensor parameters were estimated using bidirectional variation within the simulation software. The uncertainties associated with individual CS tensor components (δ_{11}, δ_{22}, and δ_{33}) were calculated through propagation of error from experimental δ_{iso}, span (Ω), and skew (κ) values.

Theoretical calculations

First principles calculations of NMR tensor parameters were conducted on the SHARCNET computer network.[52] All calculations were performed on sets of coordinates derived from reported crystal structures.[53–56] Proton positions were geometry optimized using a Broyden–Fletcher–Goldfarb–Shanno algorithm[57] because of the general unreliability of the proton positions determined from X-ray diffraction experiments. The CASTEP software package[58–61] in the Materials Studio 5.0 software suite uses the gauge-including projector augmented wave algorithm (GIPAW).[60] For all calculations, revised Perdew–Burke–Ernzerhof (rPBE) functionals were used, along with the generalized gradient approximation for exchange-correlation energy. The "fine" basis set accuracy within CASTEP was used to automatically set plane-wave basis set cutoffs (400 eV for all compounds except for carboplatin, which was 550 eV) and Monkhorst–Pack *k*-space grid sizes.

DFT calculations on isolated molecules were performed using the NMR program[62] in the Amsterdam Density Functional (ADF) suite,[63,64] employing all-electron gauge including atomic orbitals (GIAO) basis sets for all atoms.[65,66] The electron exchange and correlation functionals BLYP,[67,68] VWN-BP,[69–71] and VWN-rPBE[72,73] were used with Slater-type orbitals. Calculations labelled as relativistic used the zeroth-order regular approximation (ZORA),[74,75] with either double-ζ polarized (DZP), triple-ζ polarized (TZP), triple-ζ double-polarized (TZ2P), or quadruple-ζ quadruple-polarized (QZ4P) basis sets on all atoms. For the case of ZORA/DZP, Pt atoms used a ZORA-adapted TZP basis set. For nonrelativistic calculations, DZP, TZP, TZ2P, and QZ4P basis sets were used on all atoms; however, Pt atoms used at least a ZORA-adapted TZP basis set. The Pt chemical shift reference for DFT calculations on isolated molecules was a geometry-optimized gas-phase $PtCl_6^{2-}$ molecule constrained to O_h symmetry.[76,77] No similar reference is available for plane-wave calculations.

Results and discussion

First, ^{195}Pt solid-state NMR data are presented. WURST–CPMG NMR spectra and Pt CS tensor parameters derived from analytical simulations are discussed, along with refined CS tensor data obtained via the acquisition and simulation of Hahn-echo spectra and CS tensor parameters obtained from ^{195}Pt MAS spectra of transplatin. ^{195}Pt longitudinal relaxation time (T_1) and transverse relaxation time (T_2) data are also presented. First principles calculations of the platinum nuclear magnetic shielding (MS) tensors and their orientations are presented, accompanied by discussion of their correlation to spectral appearance and molecular structure. Following this, ^{14}N SSNMR spectra and concomitant relaxation data are presented, along with ab initio calculations of ^{14}N electric field gradient (EFG) tensors. Lastly, ^{35}Cl SSNMR data for cisplatin and transplatin are discussed, along with theoretically derived ^{35}Cl EFG tensors and their orientations.

^{195}Pt WURST–CPMG SSNMR experiments — Cisplatin and transplatin

^{195}Pt NMR spectra are presented in Fig. 1 and associated CS tensor parameters are listed in Table 1 and Supplementary data Table S6. Both of the patterns are strikingly broad, each measuring ~775 kHz from end to end. Their δ_{iso} and Ω values are similar and consistent with Pt(II) centres in chemically similar, square-planar environments.[29]

The dissimilarity in spectral appearance arises from the distinct κ values. The κ for cisplatin is –0.94(2), which indicates that the CS tensor has near-axial symmetry, and that δ_{11} is the distinct component (i.e., $\delta_{22} \approx \delta_{33}$). The transplatin has a κ of –0.59(2), which indicates that the CS tensor is less axially symmetric (δ_{22} and δ_{33} are no longer almost equal), but δ_{11} is still the distinct component. Given the local square-planar geometries common to these two molecules, it is likely that the δ_{22} and δ_{33} components of the CS tensor are oriented within (or close to) the square plane, with δ_{11} perpendicular to this plane. Despite the comparable geometric parameters of these isomeric square-planar complexes (see Supplementary data Table S6), the dissimilar skew values may arise from the distinct cis- and trans-structural arrangements, and possibly intermolecular interactions (Fig. 2). The cisplatin crystal structure reveals that the molecules form columns in which the square planes are approximately parallel, with alternation of the positions of the $-NH_3$ and –Cl ligands, and relatively short intermolecular Pt–Pt interactions (Pt–Pt distance of ~3.4 Å). The transplatin molecules do not form a parallel stack; rather, the stack alternates between one unit with its square plane oriented perpendicular to the axis of propagation of the stack and another that is "tilted" with respect to this axis. The latter has a short Pt···H distance of ~2.6 Å between its own NH_3 protons and the Pt centres of the adjacent "perpendicular" units. There are some intermolecular Cl···H distances in both compounds (2.3–2.4 Å) which may also affect the CS tensor. The extended structure and packing of these compounds may affect the ^{195}Pt CS parameters, and the environment beyond the isolated molecule must be taken into consideration when rationalizing the

Can. J. Chem. Downloaded from www.nrcresearchpress.com by Xi'an Jiaotong University on 09/19/12
For personal use only.

Fig. 1. Static wideband uniform rate smooth truncation – Carr–Purcell–Meiboom–Gill (WURST–CPMG) ^{195}Pt NMR spectra (bottom trace) and simulations (top trace) of (*a*) cisplatin and (*b*) transplatin.

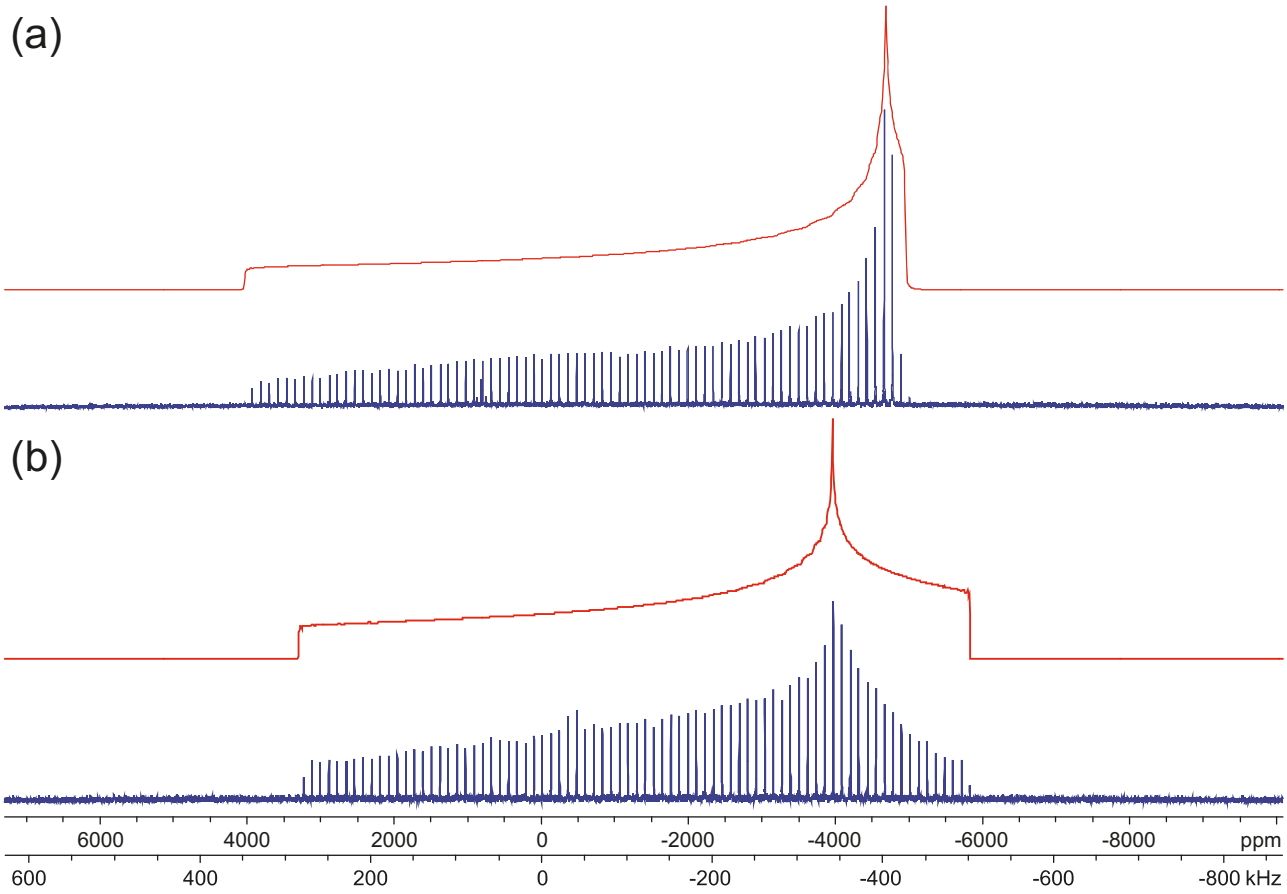

Table 1. ^{195}Pt static NMR experimental parameters.

Compound	Method[a]	δ_{11} (ppm)	δ_{22} (ppm)	δ_{33} (ppm)	δ_{iso} (ppm)[b]	Ω (ppm)[c]	κ[d]
cis-$PtCl_2(NH_3)_2$	E	4099(62)	–4697(60)	–4877(55)	–1825(50)	8975(50)	–0.96(1)
trans-$PtCl_2(NH_3)_2$	E	3260(42)	–4020(41)	–5840(35)	–2200(25)	9100(50)	–0.60(1)
	M	2884(690)	–3717(737)	–5689(544)	–2174(4)	8573(1000)	–0.54(25)
$Pt(py)_2Cl_2$	E	3705(44)	–4809(41)	–4895(33)	–2000(25)	8600(50)	–0.98(1)
$Pt(en)Cl_2$	E	3342(33)	–4900(34)	–4983(24)	–2180(15)	8325(40)	–0.98(1)
Carboplatin	E	4576(45)	–4927(44)	–4974(34)	–1775(25)	9550(50)	–0.99(1)

[a]Where E denotes that the standard Hahn-echo pulse sequence was used and M denotes that a magic-angle spinning (MAS) experiment was employed at a spinning speed of 26 kHz. For WURST–CPMG and other ^{195}Pt experimental details, see Supplementary data Tables S1–S3.

[b]Isotropic chemical shift: $\delta_{iso} = (\delta_{11} + \delta_{22} + \delta_{33})/3$.

[c]Span: $\Omega = \delta_{11} - \delta_{33}$.

[d]Skew: $\kappa = 3(\delta_{22} - \delta_{iso})/\Omega$.

origins of the ^{195}Pt CS tensors. This is discussed further in the following computational section.

Pt(py)Cl_2, Pt(en)Cl_2, and carboplatin

Much like cisplatin, these compounds yield spectra that indicate CS tensors with high degrees of axial symmetry (Fig. 3), with κ values near –1 in all cases. Span values within this series of compounds are similar to those for cisplatin and transplatin. The span of 8350(50) ppm for Pt(en)Cl_2 agrees reasonably well with the previously reported span of 8100(200) ppm determined from an MAS spectrum.[78] Although these spectra appear to be very similar, they are distinguished by their unique δ_{iso} and Ω values, which result from the extreme sensitivity of the platinum CS interaction to the local environment (i.e., bonding, ligands, intermolecular interactions, etc.). In particular, it is the δ_{11} parameters, which reflect major changes in paramagnetic shielding contributions, that show the greatest variation in this series. The tensor orientations are likely to be similar to those described for cisplatin and transplatin, with δ_{11} oriented perpendicular to the square plane in each case.

^{195}Pt Hahn-echo SSNMR experiments

CPMG-based pulse sequences yield echo trains that can be processed in two different ways: one may either Fourier transform the entire echo train to obtain a series of "spikelets", the

Fig. 2. Local structure of (*a*) cisplatin and (*b*) transplatin. Broken lines indicate Pt–Pt and Pt–H contacts. Contacts shown on bottom transplatin Pt are for clarity.

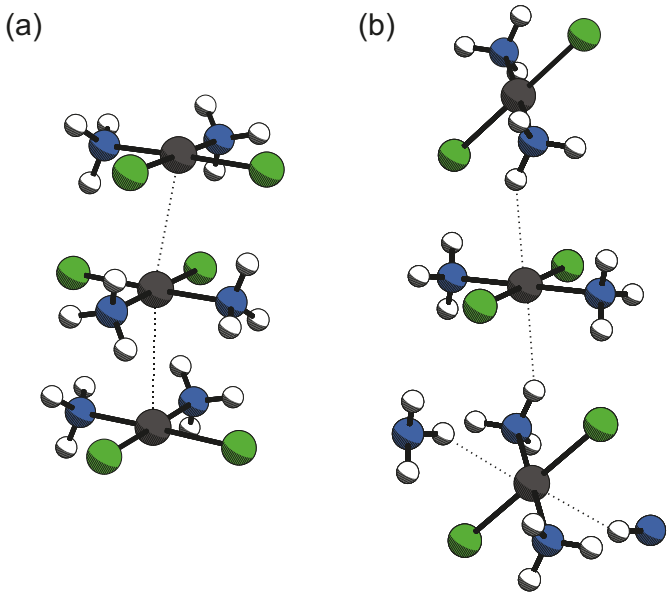

outer manifold of which matches the true static pattern, or alternatively, one may shift and co-add all of the echoes together in the time domain, and Fourier transform the resulting FID to yield a standard static pattern (see Supplementary data Fig. S1). In either case, the signal to noise ratio (S/N) is generally much higher than the corresponding static pattern obtained via routine Bloch-decay or Hahn-echo techniques (depending on favourable T_2 characteristics of the nucleus being observed); however, the resolution of the resulting CPMG pattern is limited by factors such as the number of points per echo and the inter-echo spacing in the time domain.[79]

As seen for the ^{195}Pt WURST–CPMG spectra above, localization of signal intensity under the individual spikelets yields high S/N spectra, allowing for the efficient acquisition of broad patterns; however, accurate determination of CS tensor parameters is limited by the spectral resolution of the spikelet manifold (i.e., the frequency spacings of the spikelets) and is subject to a greater degree of uncertainty than determination of parameters obtained from higher resolution static powder patterns. The reduced uncertainties, however, come at the cost of high experimental times for standard Hahn-echo experiments, since the signal is no longer concentrated into a discrete number of spikelets, but rather, spread out over a continuous pattern. Furthermore, it is important to note that the WURST component of this sequence further reduces experimental times for the acquisition of broad patterns because of the much larger excitation bandwidths.

To obtain increasingly accurate CS tensor parameters, Hahn-echo experiments were carried out, but only near the discontinuities corresponding to the principal components. Fourier transformation of these subspectra yield higher resolution patterns from which the precise locations of the discontinuities can be identified, which in turn decreases the uncertainties associated with the CS tensor parameters (Table 1 and Supplementary data Table S6 and Fig. S2). In almost all cases, acquisition of high-quality Hahn-echo spectra of spectral regions near the discontinuities took three times as along as the acquisition of the entire powder pattern (high S/N, distortion-free) using the WURST–CPMG pulse sequence (Supplementary data Tables S1 and S2). The use of fewer subspectra (i.e., a larger step size in the piecewise acquisition method) results in patterns that still yield accurate CS parameters, albeit with considerable "cosmetic" defects (i.e., systematic modulation of powder pattern intensities, Supplementary data Fig. S3). We note that the portion of the sequence can be used to sweep frequency ranges much broader than presented herein; however, the WURST excitation and detection bandwidths are limited by the Q of the probe.

From these results and similar studies we have conducted using WURST–CPMG on spin-1/2 nuclides with broad patterns,[38] we can conclude that the best manner to proceed for rapid spectral acquisition and accurate determination of CS tensor parameters is to acquire a lower resolution, high-S/N WURST–CPMG pattern to map out the total shape of the CSA-dominated pattern and obtain the CS tensor parameters, and then, if lower uncertainties are required, to acquire higher resolution, low-S/N Hahn-echo spectra in the locales of the discontinuities to refine the CS tensor parameters. We note that the differences in uncertainties in the CS tensor parameters between the two types of spectra are not large (Supplementary data Table S7), and that in most instances, the rapid WURST–CPMG experiments can be conducted independently to obtain high-quality CS tensor data.

^{195}Pt MAS SSNMR experiments

^{195}Pt MAS NMR experiments are commonly employed to acquire high S/N SSNMR spectra that can be utilized to extract CS tensor parameters. MAS experiments are of great value for determining isotropic chemical shifts associated with multiple sites and for approximate determinations of CS tensor parameters when standard rectangular pulses are unable to excite the extremely broad powder patterns. The accurate determination of CS tensor parameters utilizing Herzfeld–Berger analysis of spinning sidebands (SSBs) in MAS spectra is highly dependent upon both peak positions and intensities. While we have no issue with the SSB positions (which are established with stable MAS speeds), we are sceptical of the intensities of the SSBs on the outer limits of broad MAS patterns and their relation to the CS tensor parameters. Furthermore, we believe that there is some degree of variation in these intensities depending upon the finite pulse width, pulse power, rise/fall times, etc., that HB analysis does not take into account, which can result in large errors and (or) uncertainties in the CS tensor parameters extracted from such spectra. To further examine this, we conducted MAS NMR experiments on the transplatin complex for comparison with our static WURST–CPMG NMR spectra.

It is possible to obtain a broad high S/N pattern of transplatin with a standard Bloch-decay MAS experiment using a 2.5 mm o.d. rotor and a pulse of appropriately short length (e.g., 1.0 μs). The MAS spectrum obtained for transplatin (Fig. 4) is of roughly the same breadth as the static powder pattern, giving the impression that the pattern is uniformly excited and that only a single experiment is necessary (i.e.,

Can. J. Chem. Downloaded from www.nrcresearchpress.com by Xi'an Jiaotong University on 09/19/12
For personal use only.

Fig. 3. Static wideband uniform rate smooth truncation – Carr–Purcell–Meiboom–Gill (WURST–CPMG) ^{195}Pt NMR spectra (bottom trace) and simulations (top trace) of (*a*) $Pt(py)_2Cl_2$, (*b*) $Pt(en)Cl_2$, and (*c*) carboplatin.

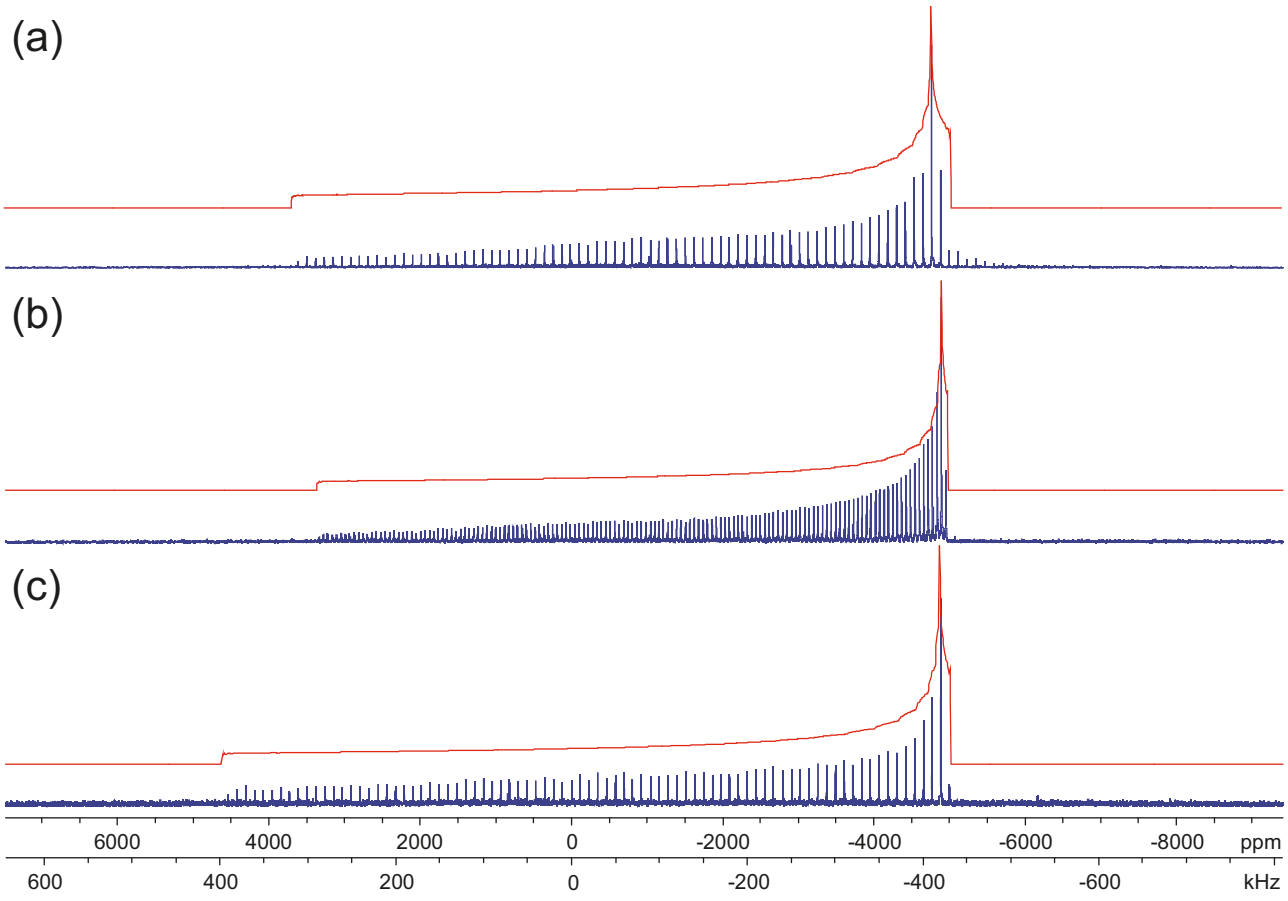

Can. J. Chem. Downloaded from www.nrcresearchpress.com by Xi'an Jiaotong University on 09/19/12
For personal use only.

no multiple subspectra). SIMPSON numerical simulations (Supplementary data Fig. S4), which consider finite pulse lengths and excitations, verify that the experimental pulse length and rf power (1.0 μs and 250 kHz, respectively) are appropriate for uniform excitation of the powder pattern. It should be noted that another set of SIMPSON simulations indicates that SSNMR pulses for routine experiments (i.e., 3.0 μs pulse length and 83.3 kHz rf power) would clearly fail to wholly excite the powder pattern (Supplementary data Fig. S5).

While the isotropic shifts can now be accurately measured (vide infra) from the MAS spectra, HB analysis yields parameters that are different than those obtained via static experiments and have much larger uncertainties (Table 1). The ambiguities associated with the HB analysis are clearly evident by an inspection of the calculated contour map (Supplementary data Fig. S6). The calculation of accurate tensor parameters relies on proper selection of the point at which the most contour lines intersect; however, there are several points in the plot that could fulfill these criteria owing to the large number of spinning sidebands (even at the high spinning speed of 26 kHz). The MAS spectrum was also simulated using parameters extracted from static experiments; however, this fit does not appear to be drastically different from the best fit of the MAS data. Therefore, the similarity of these two MAS patterns, as well as the ambiguities associated with the HBA contour map(s), suggest that anisotropic CS parameters extracted solely from this MAS spectrum are expected to have very high degrees of uncertainty compared with those obtained from analysis of corresponding static spectra.[80]

MAS experiments were conducted at three different spinning speeds to determine δ_{iso} to a high degree of accuracy and to examine changes in δ_{iso} as a result of frictional heating of the rotor at higher spinning speeds. Values for δ_{iso} of –2174(4), –2195(5), and –2178(10) ppm were determined from spectra acquired at spinning speeds of 26, 25, and 15 kHz, respectively. Each of these spectra has at least 30 SSBs and are accordingly challenging to phase; hence, prior to Fourier transformation, the FID data was left shifted to the top of the first echo. Unfortunately, the positions of sidebands (and the isotropic peak) vary slightly with the choice of phasing parameters; this issue is particularly pronounced in the 25 kHz MAS spectrum. The values of δ_{iso} do not seem to have any temperature dependence in this case; however, for similar applications to nuclei like ^{207}Pb, where the effects of temperature on δ_{iso} have been well-documented,[81–83] one must always take frictional heating into account and calibrate the MAS probe accordingly. We note that the isotropic peak of transplatin has a line width of 1030 Hz and shows no evidence of *J* coupling or residual dipolar coupling to nearby nuclei (Supplementary data Figs. S7 and S8).

^{195}Pt MAS NMR spectra of transplatin required ~20 h of experimental time by comparison with ~4–5 h for WURST–

Can. J. Chem. Downloaded from www.nrcresearchpress.com by Xi'an Jiaotong University on 09/19/12
For personal use only.

Fig. 4. Experimental ^{195}Pt magic-angle spinning (MAS) spectrum of transplatin at a speed of 26 kHz (bottom trace), analytical simulation of experimental pattern (middle trace), and analytical simulation of experimental spectrum using parameters extracted from static experiments (top trace).

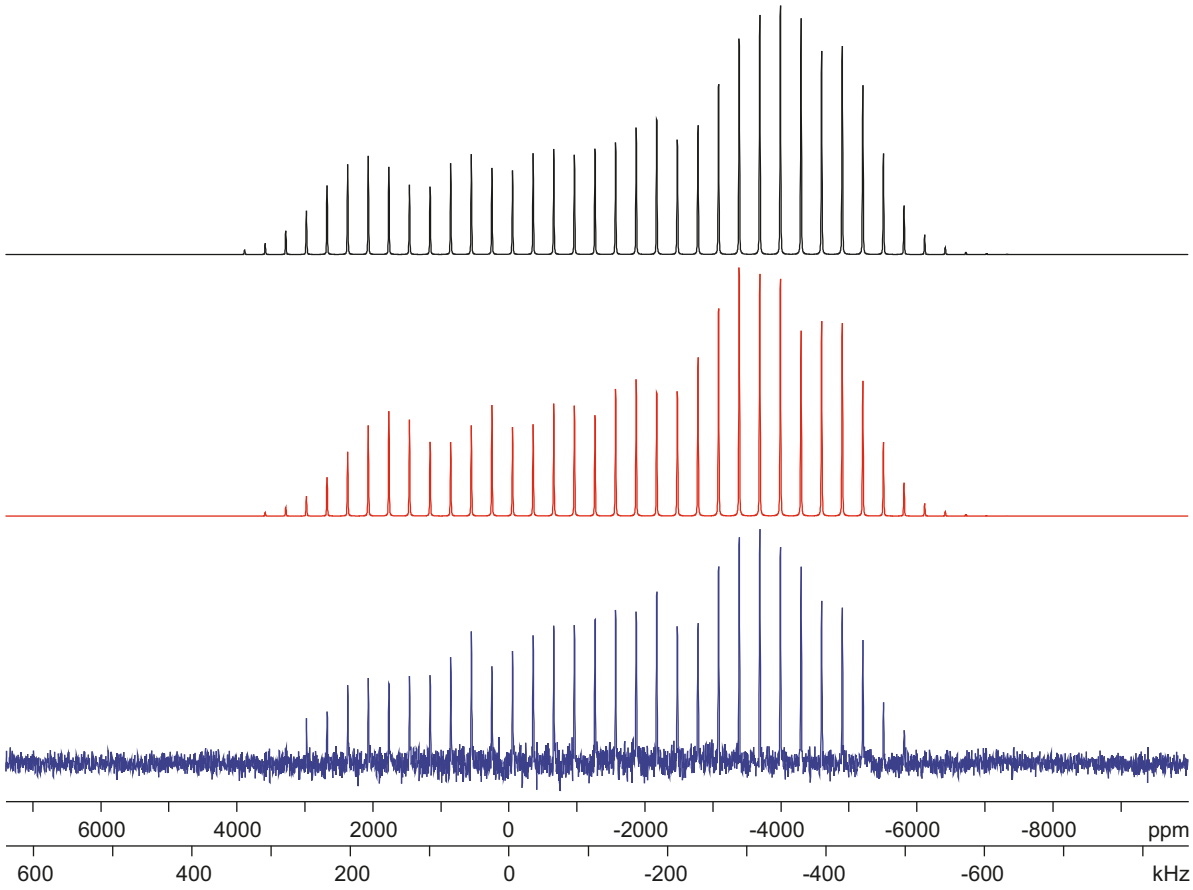

CPMG spectra. With the exception of δ_{iso}, CS tensor parameters are obtained faster and with a lower degrees of uncertainty with static WURST–CPMG experiments. In addition, static experiments are not subject to frictional heating, eliminating concerns regarding temperature dependence of the CS tensor parameters. It is clear from these sets of data that static WURST–CPMG experiments offer numerous advantages over conventional static Hahn-echo and MAS experiments, in terms of reduced experimental times, spectral quality, and accurate determination of CS tensor parameters.

First principles calculations of platinum MS tensors

Comparison of experimental and calculated results

First principles calculations of the platinum MS tensor parameters and the associated tensor orientations are integral for understanding their origins and relations to molecular structure and symmetry. We are intentionally differentiating CS (or δ, experimentally determined) and MS (or σ, theoretically derived), although they can be related to one another either by choosing an appropriate standard reference or by plotting CS vs MS, which yields a slope close to unity in cases of good agreement. We note that it is possible to compare CS and MS scales for the DFT calculations on isolated molecules, since a $PtCl_6^{2-}$ anion can be utilized as a CS reference; however, there is no similar reference molecule and (or) system for corresponding DFT plane-wave calculations. Platinum CS tensor parameters derived from first principles calculations are given in Table 2. GIPAW plane-wave DFT calculations were performed using the CASTEP software package, and standard DFT calculations were run using the ADF software package. CASTEP uses plane-wave trial functions incorporating effects of lattice periodicity to calculate NMR properties, whereas ADF calculations involve conventional MO calculations on isolated species or larger clusters. The ADF software package allows the user to include relativistic contributions to the MS tensor parameters, an option that is absent in the CASTEP program (vide infra).

Plots of δ_{iso} vs σ_{iso} for GIPAW plane-wave DFT and standard DFT calculations incorporating ZORA (Fig. 5) show that the latter exhibit slightly better agreement with experimental values, although both plots have similar correlation constant (R^2) values. The slope of the plot for the plane-wave calculations is –2.41 (far from ideal), with a $R^2 = 0.73$, whereas the slope of the plot for ZORA DFT calculations is –0.74 (if the outlier ($Pt(py)_2Cl_2$) is excluded), with an $R^2 = 0.65$. Unfortunately, there are not enough test systems to make a meaningful linear correlation between δ_{iso} and σ_{iso}; however, when the absolute magnetic shieldings are converted to chemical shifts (only for the ZORA DFT calculations, through the use of $PtCl_6^{2-}$ reference calculations, vide supra), predicted and experimental δ_{iso} values are similar. We note at this point that calculations were also conducted without taking relativistic effects into account (data not shown); in most cases, very little

Can. J. Chem. Downloaded from www.nrcresearchpress.com by Xi'an Jiaotong University on 09/19/12
For personal use only.

Table 2. ^{195}Pt experimental and calculated chemical shift (CS) tensor parameters.

Method	Level of theory	δ_{11}/σ_{11} (ppm)[a]	δ_{22}/σ_{22} (ppm)[a]	δ_{33}/σ_{33} (ppm)[a]	$\delta_{iso}/\sigma_{iso}$ (ppm)[a,b]	Ω (ppm)	κ
***cis*-$PtCl_2(NH_3)_2$**							
Experimental[c]		4099(62)	–4697(60)	–4877(55)	–1825(50)	8975(50)	–0.96(1)
Plane-wave DFT		–2323	5344	5551	2857	7874	–0.95
Standard DFT[d]	BLYP	1116	–3196	–4207	–2095	5323	–0.62
	VWN+BP	1023	–3368	–4362	–2235	5385	–0.63
	VWN+rPBE	1009	–3334	–4338	–2221	5346	–0.62
***trans*-$PtCl_2(NH_3)_2$**							
Experimental		3260(42)	–4020(41)	–5840(35)	–2200(25)	9100(50)	–0.60(1)
Plane-wave DFT		–1074	5152	6186	3421	7260	–0.72
Standard DFT	BLYP	1538	–3181	–4885	–2176	6423	–0.47
	VWN+BP	1440	–3336	–4955	–2284	6395	–0.49
	VWN+rPBE	1422	–3299	–4967	–2282	6389	–0.48
$Pt(py)_2Cl_2$							
Experimental		3705(44)	–4809(41)	–4895(33)	–2000(25)	8600(50)	–0.98(1)
Plane-wave DFT		–1636	4534	4743	2547	6379	–0.93
Standard DFT	BLYP	1457	–2500	–3009	–1351	4466	–0.77
	VWN+BP	1379	–2531	–3052	–1401	4431	–0.76
	VWN+rPBE	1382	–2562	–3057	–1413	4439	–0.78
$Pt(en)Cl_2$							
Experimental		3342(33)	–4900(34)	–4983(24)	–2180(15)	8325(40)	–0.98(1)
Plane-wave DFT		–1414	5713	5713	3338	7127	–1.00
Standard DFT	BLYP	1046	–3817	–3913	–2228	4958	–0.96
	VWN+BP	941	–3954	–4023	–2345	4964	–0.97
	VWN+rpBE	934	–3953	–4003	–2341	4936	–0.98
Carboplatin							
Experimental		4576(45)	–4927(44)	–4974(34)	–1775(25)	9550(50)	–0.99(1)
Plane-wave DFT		–3009	4631	4682	2101	7691	–0.99
Standard DFT	BLYP	2381	–3820	–3849	–1763	6230	–0.99
	VWN+BP	2262	–3969	–4015	–1907	6277	–0.99
	VWN+rPBE	2228	–3934	–3958	–1888	6187	–0.99

Note: Tabulated standard DFT calculations were all performed using a quadruple-ζ quadruple-polarized (QZ4P) basis set on all atoms and zeroth-order regular approximation (ZORA) for relativistic effects. Ω, span; κ, skew.

[a]Column refers to chemical shifts (CS, δ) for experimental values and standard DFT calculated values and magnetic shieldings (MS, σ) for plane-wave DFT calculated values.

[b]See Fig. 5 for plots of σ_{iso} vs δ_{iso}.

[c]Reported parameters and associated uncertainties are determined from simulations of Carr–Purcell–Meiboom–Gill (CPMG) spectra followed by refinement with Hahn-echo experiments near the discontinuities corresponding to the principal components.

[d]Calculated MS parameters (σ_{11}, σ_{22}, σ_{33}, and σ_{iso}) were converted to CS parameters (δ_{11}, δ_{22}, δ_{33}, and δ_{iso}) via calculations on a $PtCl_6^{2-}$ reference unit. See the Experimental section for details.

difference was observed between the two sets of calculations, with generally better agreement between experiment and theory for the ZORA DFT set (Supplementary data Table S8).

The plane-wave DFT calculations consistently predict the values of κ with greater accuracy than the corresponding DFT calculations on isolated molecules and also predict values of Ω that are closer to experimental values (although both methods underestimate the values of Ω for all systems). The underestimation of Ω values seems to stem from the out-of-plane σ_{11} components, since in most cases the σ_{22} and σ_{33} are predicted to be close to one another. The deshielding contributions to σ_{11} are the most challenging to calculate, since they involve an accurate description of the excited (virtual) orbitals involved in MS. The success of the plane-wave calculations infers that intermolecular interactions are likely to play an important role in determining the nature of the MS tensor. Unfortunately, current analyses of contributions of the individual orbitals to the MS tensors are currently limited to DFT calculations on isolated systems and large clusters.[83–85] Calculations of the Pt MS tensor for a large cluster modelled from the known crystal structure, while time consuming, would certainly yield valuable quantitative information on the intra- and inter-molecular contributions to MS; however, relativistic calculations of such large clusters would be extremely computationally intensive and is therefore beyond the scope of the current study.

Platinum MS tensor orientations

As documented previously,[78,86–91] square-planar Pt complexes normally have platinum CS tensors with large spans (i.e., >3000 ppm) and axially symmetric CS tensors (i.e., $\kappa = \pm 1$). All of the ^{195}Pt SSNMR spectra presented herein have a characteristic appearance because of κ values near –1, indicating that two principal components of the CS tensor (δ_{22} and δ_{33}) are quite similar, and the third principal component

Fig. 5. (*a*) Calculated ^{195}Pt magnetic shielding (MS) vs chemical shift (CS) values using plane-wave DFT calculations. The unbroken line corresponds to $y = -x + 800$. The broken line is a best fit to the data ($y = -2.41x - 1950$, $R^2 = 0.7301$). (*b*) Calculated ^{195}Pt MS vs CS values using standard DFT (BLYP) calculations. The unbroken line corresponds to $y = -x + 1825$. The broken line is a best fit to the data disregarding an outlier ($y = -0.74x + 2306$, $R^2 = 0.648$). The white outlier is $Pt(py)_2Cl_2$.

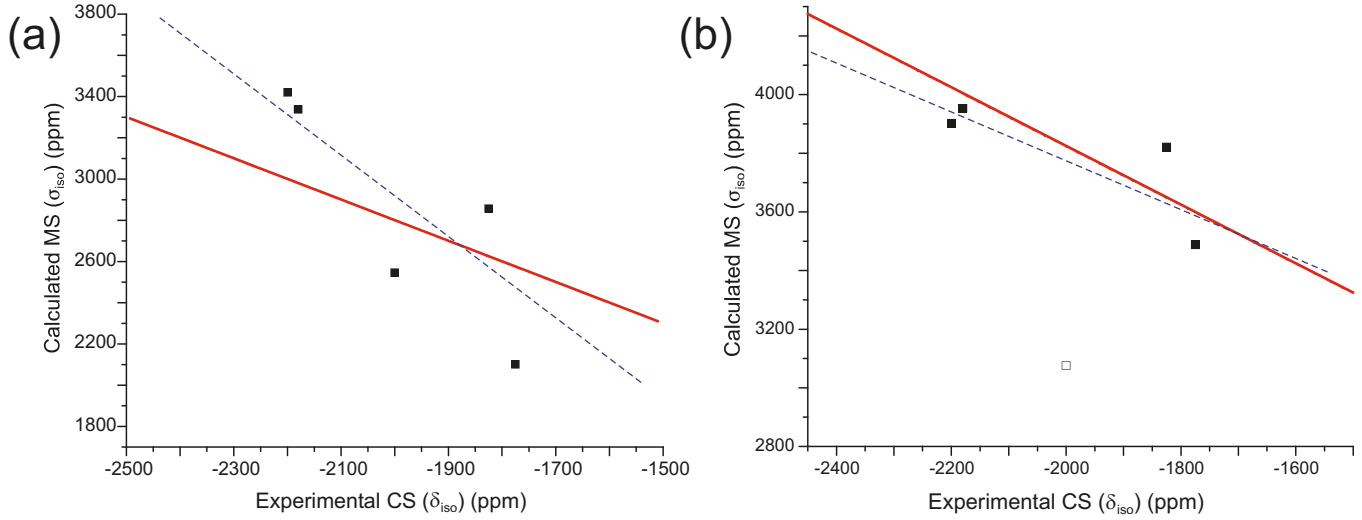

Fig. 6. Calculated platinum magnetic shielding (MS) tensor orientations from standard DFT calculations (plane-wave DFT calculations predict similar orientations). (*a*) Cisplatin, (*b*) transplatin, (*c*) $Pt(py)_2Cl_2$, (*d*) $Pt(en)Cl_2$, and (*e*) carboplatin. σ_{11} is perpendicular to the page in all instances.

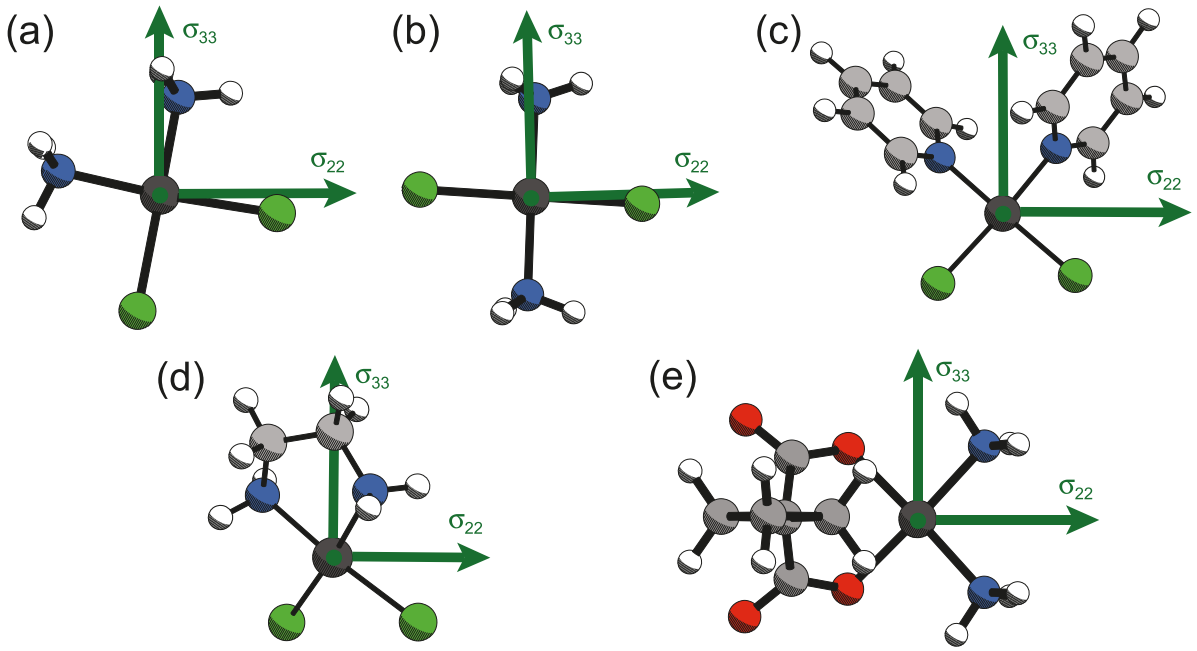

(δ_{11}) is distinct. The symmetries of these systems suggest that δ_{11} should be oriented perpendicular to the square plane in each case, with δ_{22} and δ_{33} constrained to the square plane. Since the CS tensor symmetry is so close to –1, δ_{22} and δ_{33} are very similar, and their orientations within the plane are irrelevant. Examination of the platinum MS tensor orientations for all of the systems herein reveals that, in every case, the distinct σ_{11} component corresponds to a direction perpendicular to the square plane (Fig. 6), in agreement with our predictions from experimental data. In transplatin, σ_{22} and σ_{33} lie roughly along Pt–N and Pt–Cl bonds, which coincide with mirror planes of symmetry. $Pt(py)_2Cl_2$, $Pt(en)Cl_2$, and carboplatin all have one of σ_{22} or σ_{33} located approximately along a mirror plane. Clearly, the CS tensor orientation in most square-planar Pt complexes is dictated by molecular symmetry elements, although the tensor components are not oriented precisely along (in) these symmetry elements, since these are not idealized gas-phase structures. Strangely, in cisplatin, the σ_{22} and σ_{33} components are not aligned exactly on any particular symmetry axis, with σ_{33} oriented between a Pt–NH_3 bond and a twofold rotational axis. However, roughly along the direction of σ_{33} in cisplatin lies an adjacent –NH_3 group (Pt···H distance of ~4.5 Å) and –Cl atom (Pt···Cl distance of ~4.45 Å), which may explain the peculiar MS

Can. J. Chem. Downloaded from www.nrcresearchpress.com by Xi'an Jiaotong University on 09/19/12
For personal use only.

Can. J. Chem. Downloaded from www.nrcresearchpress.com by Xi'an Jiaotong University on 09/19/12
For personal use only.

Fig. 7. Static wideband uniform rate smooth truncation – Carr–Purcell–Meiboom–Gill (WURST–CPMG) ^{14}N NMR spectra (bottom trace) and simulations (top trace) of (*a*) cisplatin, (*b*) transplatin, and (*c*) carboplatin.

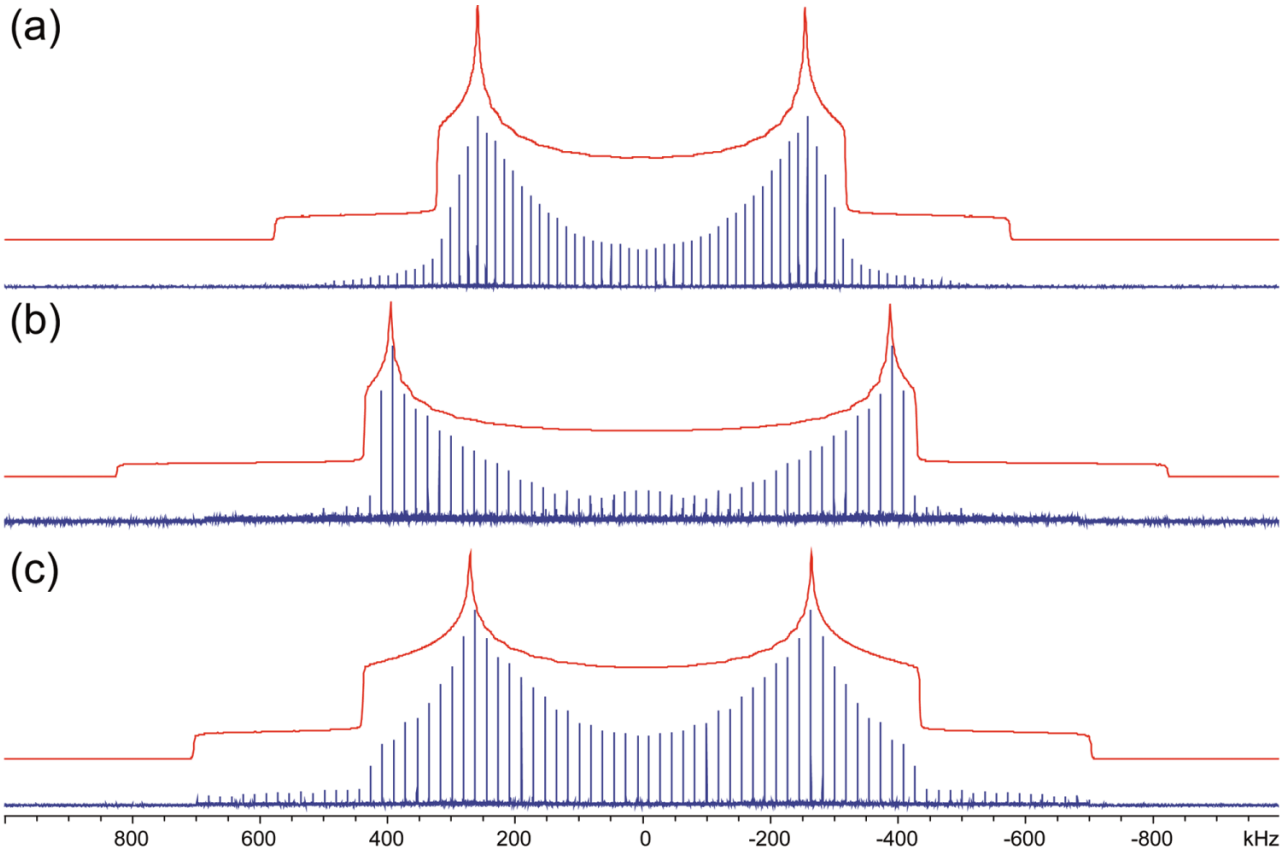

Table 3. Experimental ^{14}N electric field gradient (EFG) tensor parameters.

Compound	$\lvert C_Q \rvert$ (MHz)[a]	η_Q[b]
cis-$PtCl_2(NH_3)_2$	0.77(3)	0.11(2)
trans-$PtCl_2(NH_3)_2$	1.10(2)	0.05(3)
Carboplatin	0.94(2)	0.24(3)

Note: ^{14}N spectra were not obtained for $Pt(py)_2Cl_2$ and $Pt(en)Cl_2$ because of their small T_2 values.

[a]Quadrupolar coupling constant: $C_Q = eQV_{33}/h$, where the principal components of the EFG tensor are defined as $|V_{33}| \geq |V_{22}| \geq |V_{11}|$ and h is Planck's constant. Only the absolute value of C_Q can be obtained from NMR experiments, not its sign.

[b]Asymmetry parameter: $\eta_Q = (V_{11} - V_{22})/V_{33}$.

tensor orientation. In the absence of high molecular symmetry, the case of cisplatin illustrates that intermolecular interactions can play a role in influencing the CS tensor orientation.

^{195}Pt T_1 and T_2 relaxation measurements

While conducting WURST–CPMG ^{195}Pt NMR experiments on these five systems, we observed very different relaxation characteristics, including T_1, which determines the pulse delay required between acquisitions, and T_2, which determines how many echoes can be collected per scan (vide infra). It is possible that these relaxation parameters could also be of use in identifying and (or) distinguishing structurally similar Pt(II) complexes in cases where the CS parameters are very similar.

The difference in T_1 values is readily apparent from the optimized experimental pulse delays employed in WURST–CPMG experiments (Supplementary data Table S1). Cisplatin, transplatin, and carboplatin all required a pulse delay of 120 s between scans, while $Pt(py)_2Cl_2$ required 30 s and $Pt(en)_2Cl_2$ required only 1 s. Owing to the long interpulse delays for the majority of these systems, we could only obtain accurate measurements of the T_1 value of $Pt(en)_2Cl_2$. A standard inversion-recovery experiment revealed that $T_1 <$ 200 ms for $Pt(en)_2Cl_2$, a surprisingly small value that is due to the presence of the ethylenediamine ligand (vide infra). ^{195}Pt T_2 constants for all systems were determined by fitting the intensity of the echoes in the ^{195}Pt WURST–CPMG FIDs as a function of time and fit to mono-exponential decays (Supplementary data Table S9). Values of T_2 range across one order of magnitude from 15.2 ms (transplatin) to 3.86 ms ($Pt(en)_2Cl_2$). For all compounds, distances between the ^{195}Pt centre and the closest protons in the molecule all range between 2.5 and 3.0 Å; hence, the nature of the protons, and not simply their distance from Pt, must be carefully considered.

The extremely rapid T_1 and fast T_2 relaxation of the nuclei in $Pt(en)_2Cl_2$ may result from proton motion arising from some degree of flexibility of the bidentate ethylenediamine ligand, which forms a five-membered ring with Pt. This may cause significant variation in the local magnetic field at the Pt nucleus, perhaps resulting in efficient longitudinal and transverse relaxation. Cisplatin, transplatin, and carboplatin all possess much larger T_1 values and longer T_2 values by

Can. J. Chem. Downloaded from www.nrcresearchpress.com by Xi'an Jiaotong University on 09/19/12
For personal use only.

Table 4. Experimental and calculated ^{14}N electric field gradient (EFG) tensor parameters.

Method	Site	C_Q (MHz)[a]	η_Q
***cis*-$PtCl_2(NH_3)_2$**			
Experimental[b]	—	0.77(3)	0.11(2)
Plane-wave DFT	1	–0.79	0.14
	2	–0.96	0.05
Standard DFT[c]	1	–2.37	0.25
	2	–2.16	0.34
***trans*-$PtCl_2(NH_3)_2$**			
Experimental	—	1.10(2)	0.05(3)
Plane-wave DFT	—	–1.00	0.02
Standard DFT	1	–2.10	0.08
	2	–2.08	0.12
Carboplatin			
Experimental	—	0.94(2)	0.24(3)
Plane-wave DFT	—	–0.75	0.34
Standard DFT	—	–2.36	0.21
$Pt(py)_2Cl_2$			
Experimental	—	—	—
Plane-wave DFT	—	–1.46	0.07
Standard DFT	1	–2.56	0.24
	2	–2.61	0.19
$Pt(en)Cl_2$			
Experimental	—	—	—
Plane-wave DFT	—	–1.32	0.83
Standard DFT	—	–2.80	0.39

Note: η_Q, asymmetry parameter.

[a]Only the absolute value of the quadrupolar coupling constant (C_Q) can be obtained from NMR experiments, not its sign.

[b]No evidence of multiple ^{14}N sites were observed in the cisplatin spectrum.

[c]Calculations were performed using a triple-ζ double-polarized basis set on all atoms and the PBE exchange/correlation density functional.

comparison. Like $Pt(en)_2Cl_2$, cisplatin and transplatin also feature two Cl atoms bound to Pt; however, the latter two systems have two $–NH_3$ groups bound to Pt. Carboplatin has a rigid five-membered ring structure that includes Pt, but also has two Pt-bound $–NH_3$ groups. The $–NH_3$ protons rapidly reorient in the solid state in all of these systems, however, it is clear that this motion does not substantially affect T_1. This could be because the motion (and associated fluctuating magnetic fields) is simply too fast to make substantial dipole-dipole contributions to the T_1 (i.e., no significant contributions to spectral density at the Larmor frequency) and (or) that the Pt–H dipolar coupling constants are being partially motionally averaged.

The T_2 values should be affected by dipole–dipole relaxation. Hence, the effect of variable-field proton decoupling on ^{195}Pt T_2 values of cisplatin was also examined (Supplementary data Fig. S9 and Table S10). Increases in applied decoupling fields correlate directly with longer effective T_2 values, confirming that T_2 contributions from ^{195}Pt–^{1}H heteronuclear dipolar dephasing are important. Interestingly, analysis of WURST–CPMG echo trains from experiments conducted with transmitter frequencies positioned near the two discontinuities of the powder pattern of cisplatin indicate that ^{195}Pt T_2 anisotropy is present (Supplementary data Table S11 and Fig. S10). For instance, at the leftmost discontinuity, the T_2 is clearly larger than that measured at the rightmost discontinuity. This indicates that crystallites (and by extension, CS tensors) with particular orientations with respect to the magnetic field have ^{195}Pt nuclei that experience different secular and (or) nonsecular contributions to relaxation. The leftmost and rightmost discontinuities correspond to CS tensors that have angles of $\theta = 0°$ and 90°, respectively, where θ is the angle between the magnetic field ($\mathbf{B}_0$) and the largest component of the CS tensor (δ_{33}). Since δ_{33} is oriented within the square plane of the cisplatin units, θ may be also used to approximately describe the angle between $\mathbf{B}_0$ and the square plane. At this time, we are uncertain as to why the ^{195}Pt T_2 values are reduced for cisplatins with their square planes oriented perpendicular to $\mathbf{B}_0$ and increased for those that are parallel. Certainly, the precise origins of the ^{195}Pt T_2 anisotropy could be probed via measurements of T_2 values for various crystallite orientations at multiple fields and with variable ^{1}H decoupling field strengths, to deconvolute contributions from CSA and dipole–dipole relaxation mechanisms; however, this is beyond the scope of the current work and will be the subject of a future study.

^{14}N WURST–CPMG SSNMR experiments

^{14}N NMR spectra are shown in Fig. 7 and experimental EFG tensor parameters are listed in Table 3. Since ^{14}N is a quadrupolar nucleus with a nuclear spin of $I = 1$, the first-order quadrupolar interaction dominates the appearance of these spectra; the narrowest spectral breadth is ~1 MHz for cisplatin. The effects of the second-order quadrupolar interaction are much smaller in comparison and have no real influence on these broad spectra. Furthermore, since ^{14}N has an integer nuclear spin, there is no central transition (i.e., $+1/2 \leftrightarrow -1/2$, CT), but only satellite transitions (i.e., $+1 \leftrightarrow 0$ and $0 \leftrightarrow -1$, ST). Contributions to spectral appearance from nitrogen CSA are also negligible;[37] for example, Santos et al.[92] reported a span of 80–100 ppm for a cisplatin analogue containing a bidentate ligand and two $–NH_3$ groups. All spectra were obtained in a single experiment (i.e., piecewise acquisition was not required) by acquiring the high-frequency (left) half of the pattern using the WURST–CPMG pulse sequence, as described in the Experimental. The ^{14}N NMR spectrum of cisplatin took ~3.5 h to acquire, whereas spectra of transplatin and carboplatin were each acquired in about an hour or less (Supplementary data Table S4). Spectra could not be acquired from $Pt(py)_2Cl_2$ and $Pt(en)Cl_2$ because of unfavourable relaxation characteristics (low T_2 values) and (or) potentially larger ^{14}N C_Q values (as predicted by first principles calculations, vide infra).

The ^{14}N NMR spectra reveal moderate C_Q values (~1 MHz) and η_Q values near zero. The low η_Q values suggest, in all cases, that V_{33} is likely oriented along or near the Pt–N bond, since $|V_{33}| > |V_{22}| \approx |V_{11}|$. There are clear differences between the ^{14}N spectra for cisplatin and transplatin, with C_Qs of 1.10(2) and 0.77(3) MHz, respectively; however, measured ^{14}N T_2 values are similar (vide infra). The crystal structure for cisplatin indicates two distinct NH_3 sites, though separate patterns are not observed in the 9.4 T spectra, indicating the sites are similar and have comparable EFG tensor parameters. The sensitivity of the ^{14}N EFG tensor to nearby hydrogen bonding has been documented previously, so a closer examination of intermolecular contacts is warranted.[39]

Fig. 8. Calculated ^{14}N electric field gradient (EFG) tensor orientations of (*a*) cisplatin, (*b*) transplatin, and (*c*) carboplatin. V_{11} is perpendicular to the page in the case of cisplatin and transplatin and V_{22} is perpendicular to the page in the case of carboplatin.

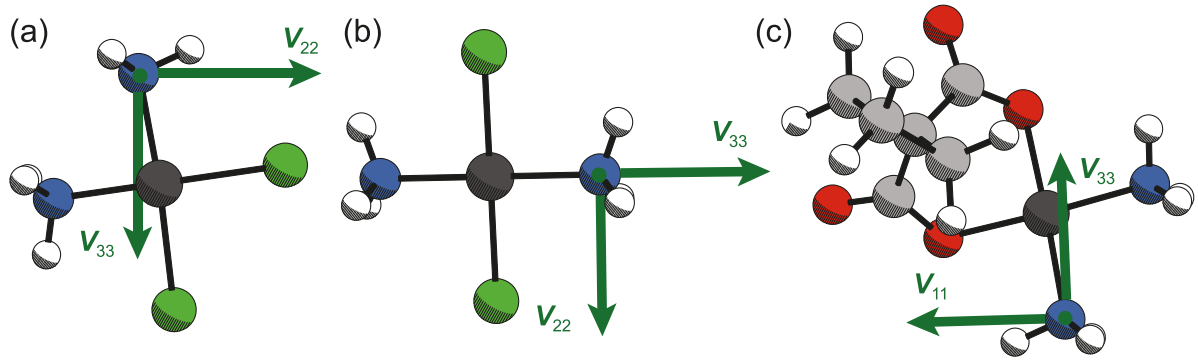

Cisplatin has intermolecular H···Cl hydrogen bonds between stacked –NH_3 and –Cl ligands (~2.3 Å from Cl to the nearest N-bound proton), whereas the transplatin has short intermolecular Pt···H (~2.6 Å) and H···Cl (~2.4 Å) distances. Hence, although the nitrogen chemical environments are superficially similar for the isolated units, it is very likely that intermolecular interactions involving –NH_3 protons result in disparate C_Q values (see the Computational section below for further discussion).

First principles calculations of ^{14}N EFG tensors

The ^{14}N EFG tensors calculated using plane-wave DFT and standard DFT methods are shown in Table 4. The plane-wave calculations are clearly superior in terms of agreement between experimental and theoretical values of C_Q, with DFT calculations resulting in overestimations of C_Q by more than double in some cases. Although the sign of C_Q cannot be obtained via static WURST–CPMG experiments, calculations predict C_Q to be negative, indicating that the electric field becomes increasingly negative as the distance from the ^{14}N nucleus increases (along the direction of V_{33}). The η_Q values for cisplatin and transplatin are better predicted by plane-wave calculations, whereas the DFT result for carboplatin is superior (however, this may be fortuitous). The success of the plane-wave calculations strengthens the argument that intermolecular interactions (e.g., hydrogen bonding) should be taken into account for ^{14}N EFG tensors in these systems.[39]

In all cases, the largest components of the ^{14}N EFG tensors (V_{33}) are directed close to the Pt–N bonds (Fig. 8), which is expected because of the C_3 rotational symmetry of the –NH_3 group and the near-zero values of η_Q. The orientations of V_{22} and V_{11} are similar in cisplatin and transplatin, with V_{22} located approximately in the square plane and V_{11} perpendicular to this plane. For carboplatin, which has a value of η_Q further from zero, V_{22} and V_{11} are predicted to be oriented out of and in the plane, respectively. Despite the difference between experimental and calculated values of η_Q for the carboplatin, this distinct tensor orientation is likely to be accurate, given that η_Q is further from zero than in the other systems, which may result from its unique organic moiety. Interestingly, both DFT and plane-wave DFT calculations predict similar EFG tensor orientations despite the dissimilar quadrupolar parameters, which indicates that the intermolecular interactions have more influence on the magnitudes of the EFG tensor components, as opposed to their orientations, which are largely dependent on intramolecular structure and bonding. Again, a full computational quantification of these contributions utilizing DFT calculations on extended cluster models is beyond the scope of the current work.[39,41,93]

^{14}N T_2 relaxation measurements

The intensity of the echoes in the ^{14}N WURST–CPMG FIDs were plotted as a function of time and fit to mono-exponential decays to determine the ^{14}N T_2 (Supplementary data Table S12 and Fig. S11). Unlike for the ^{195}Pt T_2 values, cisplatin, transplatin, and carboplatin all have similar ^{14}N T_2 values because of their similar ^{14}N environments. Since they all possess two Pt-bound NH_3 groups, this suggests that the primary mechanism of ^{14}N T_2 relaxation is governed by ^{14}N–^{1}H dipolar couplings and that the librational motions of the NH_3 groups are similar in each system. This is substantiated by a series of ^{14}N NMR experiments on cisplatin in which the strength of the ^{1}H decoupling field was varied (Supplementary data Table S13 and Fig. S12). As the decoupling field is increased, the effective T_2 value also increases, confirming that heteronuclear dipolar coupling is the dominant mechanism. Unfortunately, we were unable to increase the decoupling power past 38 kHz because of hardware restrictions, which prevented us from completely decoupling protons and measuring an effective T_2 with no contributions from the heteronuclear dipolar relaxation mechanism.

^{35}Cl WURST–CPMG SSNMR experiments

^{35}Cl NMR spectra are shown in Fig. 9 and experimental EFG tensor parameters are listed in Table 5. ^{35}Cl is a quadrupolar nucleus (I = 3/2) and the breadth of the central transition (+1/2 ↔ –1/2, CT) is dominated by second-order quadrupolar broadening, especially when the chlorine resides in a terminal environment (such as in cisplatin or transplatin).[94] The wide breadths of these spectra are such that piecewise acquisitions of individual subspectra are necessary to obtain the entire CT powder patterns.

The spectra of cisplatin and transplatin at 9.4 T are remarkably broad, with end-to-end breadths of ~4.5 and 5.0 MHz, respectively, owing to C_Q values of ~32 and 36 MHz. These C_Q values are significantly higher than those previously reported for terminal metal–Cl sites in group IV transition metal organometallic complexes.[42,94] The large breadths of the ^{35}Cl NMR spectra result in long experimental times: 14.25 h (25 subspectra) for cisplatin and 16 h (28 sub-

Can. J. Chem. Downloaded from www.nrcresearchpress.com by Xi'an Jiaotong University on 09/19/12
For personal use only.

Can. J. Chem. Downloaded from www.nrcresearchpress.com by Xi'an Jiaotong University on 09/19/12
For personal use only.

Fig. 9. Static wideband uniform rate smooth truncation – Carr–Purcell–Meiboom–Gill (WURST–CPMG) ^{35}Cl NMR spectra at a magnetic field of 9.4 T (bottom trace) and simulations (top trace) of (*a*) cisplatin and (*b*) transplatin. Static WURST–CPMG ^{35}Cl NMR spectra at a magnetic field of 21.1 T (bottom trace) and simulations (top trace) of (*c*) cisplatin and (*d*) transplatin.

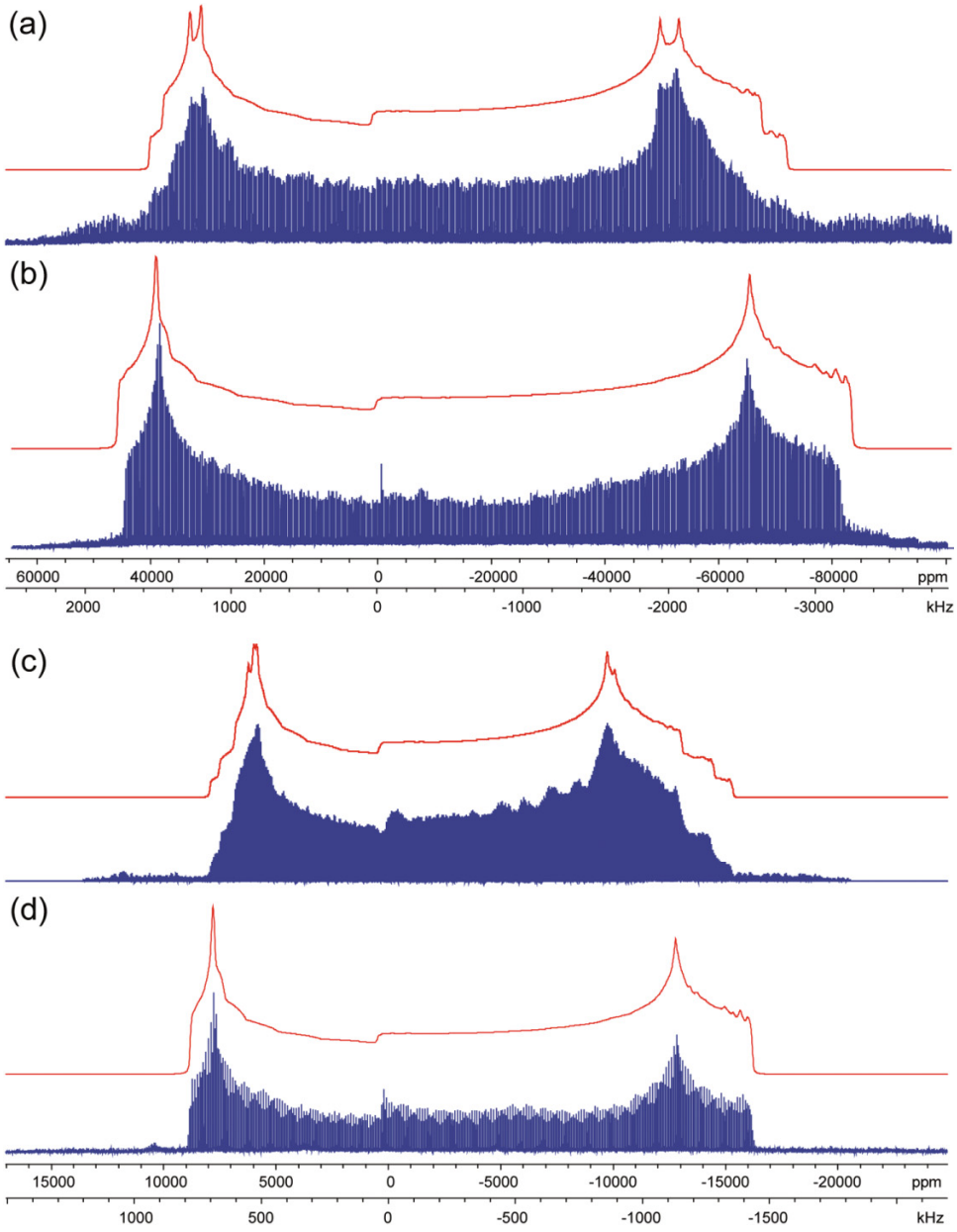

spectra) for transplatin (Supplementary data Table S5). Our C_Q values are similar to those previously obtained utilizing ^{35}Cl NQR experiments; we note that η_Q values were not reported.[95] However, several issues arise upon inspection of our EFG tensor parameters and overall spectral appearances. Firstly, although the transplatin spectrum has well-defined discontinuities (i.e., "horns" and "edges"), these same regions of the cisplatin spectrum appear "ragged" and poorly defined. The cisplatin spectrum could only be fit using two unique ^{35}Cl sites with identical η_Q values and similar C_Q values; however, the uncertainties involved with this fit are high. Secondly, neither cisplatin nor transplatin ^{35}Cl spectra showed any evidence of CSA effects (they are likely overwhelmed by the much larger effects of the second-order quadrupolar interactions).[42] If C_Q values are low and central transition powder patterns relatively narrow, CS tensor parameters may also be extracted; however, this is not possible for the broad powder patterns in this case.

To refine the ^{35}Cl EFG and CS tensor parameters, as well as to investigate the presence of multiple Cl sites and reductions in experimental time, ^{35}Cl SSNMR spectra of both compounds were acquired at a magnetic field strength of 21.1 T (Fig. 9). These spectra are much narrower than those acquired at 9.4 T owing to the inversely proportional relationship between the broadening effects of the second-order quadrupolar interaction and static magnetic field. The ^{35}Cl spectrum of cisplatin at 21.1 T took only 30 min to acquire (seven subspectra) and is of superior S/N compared with the spectrum at 9.4 T. Likewise, the spectrum of transplatin took

Can. J. Chem. Downloaded from www.nrcresearchpress.com by Xi'an Jiaotong University on 09/19/12
For personal use only.

Table 5. Experimental ^{35}Cl electric field gradient (EFG) tensor parameters.

Compound	Field strength (T)	Site	$\lvert C_Q \rvert$ (MHz)	η_Q	Ω (ppm)	β (°)
cis-$PtCl_2(NH_3)_2$	9.4	1	32.5(3)	0.15(2)	0	0
	9.4	2	31.5(3)	0.15(2)	0	0
	21.1	1	33.8(2)	0.20(1)	650(300)	90(10)
	21.1	2	32.8(2)	0.15(1)	650(300)	90(10)
	21.1	3	34.6(2)	0.21(1)	650(300)	90(10)
trans-$PtCl_2(NH_3)_2$[a]	9.4		36.6(2)	0.12(2)	0	0
	21.1		37.3(1)	0.12(1)	650(300)	90(7)

Note: These ^{35}Cl spectra are dominated by the second-order quadrupolar interaction, making quantification of the relatively much smaller chemical shift (CS) parameters (δ_{iso} and skew (κ)) impossible in almost all cases. Only the absolute value of the quadrupolar coupling constant (C_Q) can be obtained from NMR experiments, not its sign. At high field (21.1 T), the span (Ω) can be quantified, since the effects of chemical shift anisotropy (CSA) on spectral appearance scale proportionately with magnetic field strength. β describes the angle between δ_{33} and V_{33} in the molecular frame, which are the largest components of the CS and electric field gradient (EFG) tensor, respectively. Since $\upsilon_o/\upsilon_Q \approx 2$ for ^{35}Cl at 9.4 T, the high-field approximation may no longer be valid at 9.4 T, and this low-field data should be considered preliminary.

[a] A δ_{iso} value of 150 (75) ppm was required to accurately simulate this spectrum.

Fig. 10. Static wideband uniform rate smooth truncation – Carr–Purcell–Meiboom–Gill (WURST–CPMG) ^{35}Cl NMR spectra (bottom trace) and simulations (top trace) of cisplatin at a magnetic field of 21.1 T, using (*a*) three unique ^{35}Cl sites and (*b*) two unique ^{35}Cl sites. In both cases, sites are simulated with equal weighting.

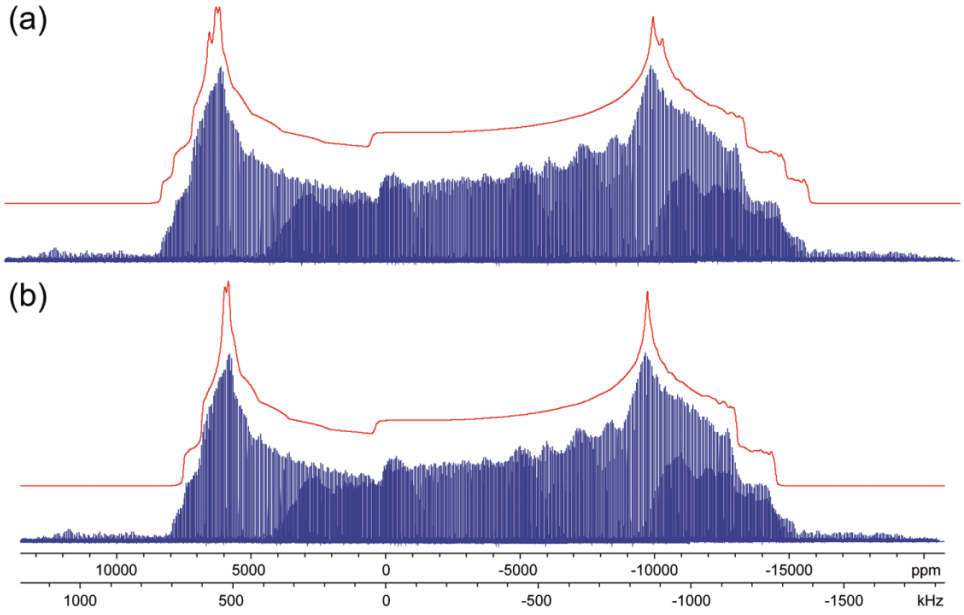

only 13 min to acquire at 21.1 T. Initial C_Q values extracted from spectra obtained at 21.1 T are ~1 MHz higher than those from spectra at 9.4 T, indicating that there may be significant chlorine CSA contribution that is unaccounted for. Simulated spectra at 21.1 T for both compounds utilizing a Ω of 650 (300) ppm seem to be in better agreement with experimental spectra, although these values are subject to high degrees of uncertainty owing to the breadth of the powder patterns. These spans have negligible effects on spectra at 9.4 T because of the proportional relationship between the broadening effects of CSA and the static magnetic field. Alternately, the disagreement in C_Q values between spectra at 9.4 and 21.1 T could also be due to a failure of the high-field approximation, which is not accounted for in the spectral simulation software, which treats the quadrupolar interaction as a first-order perturbation on the pure Zeeman Hamiltonian. Traditionally, the high-field approximation has been thought to be generally valid in cases where $\upsilon_o/\upsilon_Q \approx 10$, although Widdifield and Bryce[96] observed good agreement between experimental ^{127}I (spin = 5/2) SSNMR spectra and perturbation theory simulations in cases where $\upsilon_o/\upsilon_Q \approx 5$. In the current case, $\upsilon_o/\upsilon_Q \approx 2$ at 9.4 T; however, simulations incorporating full diagonalization of the Zeeman and quadrupolar Hamiltonians is beyond the scope of this work. To this end, the data at 9.4 T in Table 5 should be considered preliminary.

Surprisingly, simulations of the cisplatin powder pattern at 21.1 T indicate that three similar ^{35}Cl sites are present in a 1:1:1 ratio. The spectrum may also be simulated with two similar sites in an equal ratio, but the three-site fit models experimental data most accurately (Fig. 10 and Supplementary data Fig. S13). We cannot comment definitively on the

Can. J. Chem. Downloaded from www.nrcresearchpress.com by Xi'an Jiaotong University on 09/19/12
For personal use only.

Table 6. Experimental and calculated ^{35}Cl EFG tensor parameters.

Method	Field strength (T)	Site	C_Q (MHz)[a]	η_Q	Ω (ppm)	β (°)
***cis*-$PtCl_2(NH_3)_2$**						
Experimental	9.4	1	32.5(3)	0.15(2)	0	0
	9.4	2	31.5(3)	0.15(2)	0	0
	21.1	1	33.8(2)	0.20(1)	650(300)	90(10)
	21.1	2	32.8(2)	0.15(1)	650(300)	90(10)
	21.1	3	34.6(2)	0.21(1)	650(300)	90(10)
Plane-wave DFT		1	–36.2	0.14	334	
		2	–35.6	0.15	280	
Standard DFT[b]			–41.8	0.04	243	
			–40.0	0.01	273	
***trans*-$PtCl_2(NH_3)_2$**						
Experimental	9.4		36.6(2)	0.12(2)	0	0
	21.1		37.3(1)	0.12(1)	650(300)	90(7)
Plane-wave DFT			–42.4	0.12	250	
Standard DFT		1	–38.4	0.02	321	
		2	–36.7	0.11	268	

[a]Only the absolute value of the quadrupolar coupling constant (C_Q) can be obtained from NMR experiments, not its sign.

[b]Calculations were performed using a triple-ζ doubly-polarized basis set on all atoms and the PBE exchange/correlation density functional.

Fig. 11. Calculated ^{35}Cl electric field gradient (EFG) tensor orientations of (*a*) cisplatin and (*b*) transplatin. V_{11} is perpendicular to the page in both instances.

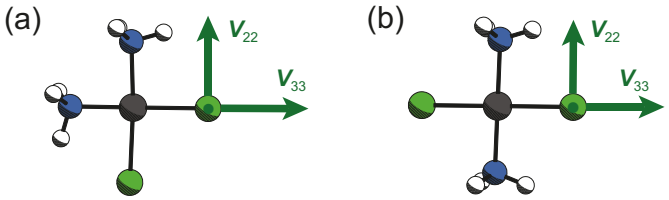

origin of these multiple powder patterns; it is possible that the third pattern represents a polymorphic form of cisplatin (perhaps from exchange of Cl for H_2O ligands), which would certainly be evident via ^{35}Cl SSNMR.[43] However, this seems implausible, given that solid-state exchange of this sort would be highly energetically unfavourable and would not readily occur for a sealed sample. Regardless of the origins of the additional powder pattern, the two sites corresponding to the crystal structure of cisplatin can be readily distinguished from an impurity by ^{35}Cl SSNMR, particularly at high magnetic fields.

First principles calculations of ^{35}Cl EFG tensors

Both plane-wave and DFT MO calculations predict two magnetically distinct ^{35}Cl sites in cisplatin, with similarly high C_Q and low η_Q values (Table 6), although values of C_Q are consistently overestimated for both compounds. Plane-wave calculations predict values of η_Q to a higher degree of accuracy than the corresponding DFT MO calculations, again indicating that intermolecular interactions (namely, Cl···H hydrogen bonding) influence the ^{35}Cl EFG tensors.[43] The calculated ^{35}Cl EFG tensor orientations are identical for both cisplatin and transplatin, with V_{33} directed along the Pt–Cl bond, V_{22} in the plane, and V_{11} perpendicular to the plane of the molecule (Fig. 11).

^{35}Cl T_2 relaxation measurements

To investigate whether ^{35}Cl T_2 values are influenced by the ^{1}H–^{35}Cl dipole–dipole relaxation mechanism, the effect of variable-field proton decoupling on the center of the cisplatin powder pattern was explored (Supplementary data Fig. S14 and Table S14). As expected, increases in the applied ^{1}H decoupling field result in increases in observed effective T_2 values, until a range of ~29 to 35 kHz, implying that the ^{35}Cl nuclei are effectively decoupled from all nearby protons. The hydrogen-bonding environment about the ^{35}Cl nuclei (Supplementary data Fig. S15) has five protons arranged in a distorted square pyramidal geometry around chlorine, with H···Cl distances ranging from 2.3 to 2.6 Å, corresponding to fairly small individual H–Cl dipolar couplings (e.g., an internuclear distance of 2 Å corresponds to a coupling constant of 1.5 kHz). This implies that it is not simply an individual ^{1}H–^{35}Cl dipolar coupling affecting the ^{35}Cl T_2 value of cisplatin, but rather, dipolar coupling between ^{35}Cl and a network of strongly dipolar-coupled protons.

Finally, the broad ^{35}Cl SSNMR spectra of cisplatin and transplatin spectra afford an opportunity to probe for T_2 anisotropy. The WURST–CPMG echo trains of two cisplatin subspectra situated over the horns of the ^{35}Cl spectrum at 9.4 T yield a T_2 value of 23.8 (3.5) ms for the high-frequency discontinuity and 15.7 (1.6) ms for the low-frequency discontinuity, which correspond to crystallite orientations where V_{33} is oriented with respect to B_0 at 88° and 30°, respectively. It follows that cisplatin molecules with V_{33} oriented perpendicular to B_o (i.e., 88°) have increased T_2 values over those with V_{33} oriented at 30°. The origins of this T_2 anisotropy are uncertain at this time and will be investigated in a forthcoming study; however, it does not appear to originate from ^{1}H–^{35}Cl dipole–dipole coupling, since these experiments were run using an applied proton decoupling field of 35 kHz (which should result in complete decoupling, vide supra).

Can. J. Chem. Downloaded from www.nrcresearchpress.com by Xi'an Jiaotong University on 09/19/12
For personal use only.

Conclusions

The WURST–CPMG pulse sequence and frequency-stepped acquisition techniques have been used to acquire ^{195}Pt, ^{14}N, and ^{35}Cl SSNMR of cisplatin and related complexes. All ^{195}Pt NMR spectra are very broad and have a characteristic appearance owing to the orientation of the CS tensor with respect to the square plane of the molecule (i.e., in each case, δ_{11} is the distinct principal component and oriented perpendicular to the square plane). From our work on these broad patterns, we suggest that the best method for accurately determining CS tensor parameters from broad patterns of spin-1/2 nuclei is to first acquire the spectrum using the WURST–CPMG pulse sequence (rapid acquisition, high S/N, and relatively high accuracy for CS tensor components). If necessary, one can utilize echo experiments of subspectra near the spectral discontinuities to refine the principal components and MAS experiments (when possible) to accurately measure the isotropic chemical shifts. Plane-wave calculations for these systems consistently predict ^{195}Pt CS tensor parameters to a high degree of accuracy, save for δ_{11}. The inconsistency of DFT calculations on isolated molecules indicates that intermolecular interactions may play a significant role in determining the origins of the ^{195}Pt CS tensor parameters and orientations. ^{195}Pt relaxation times (T_1 and T_2) show variation across this series of compounds; in particular, the T_2 time constants are facile to measure and may be of use in distinguishing different Pt sites in spectra exhibiting multiple powder patterns. ^{14}N WURST–CPMG experiments, each acquired in a matter of hours at normal magnetic fields, yielded EFG tensor parameters for three compounds. ^{35}Cl WURST–CPMG spectra of cisplatin and transplatin were acquired at two different fields, and the dominant T_2 relaxation mechanism in cisplatin was determined to arise from ^{1}H–^{35}Cl dipolar coupling. The rapid acquisition of broad powder patterns using the WURST–CPMG pulse sequence on pure compounds offers much promise for detection of nuclei in cisplatin derivatives, which are diluted in biological samples. In particular, the ^{195}Pt NMR spectra should be the most effective in this respect, owing to both the sensitivity of the ^{195}Pt CS tensor to structural changes and the rapidity with which these spectra can be acquired. We plan to further investigate systems related to cisplatin and its anticancer derivatives, and we hope that our work encourages more solid-state NMR studies in this area.

Supplementary data

Supplementary data are available with the article through the journal Web site at www.nrcresearchpress.com/cjc.

Acknowledgements

B.E.G.L. thanks the Ontario Ministry of Training, Colleges, and Universities for an Ontario Graduate Scholarship. R.W.S. thanks the Natural Sciences and Engineering Research Council of Canada (NSERC), the Canadian Foundation for Innovation, the Ontario Innovation Trust, and the University of Windsor for support. R.W.S. also thanks the Ontario Ministry of Research and Innovation for an Early Researcher Award and acknowledges the Centre for Catalysis and Materials Research at the University of Windsor for additional funding. We are also extremely grateful to Dr. K. Harris for his helpful comments during the preparation of this manuscript, and Dr. L. O'Dell, Dr. A. Rossini, Mr. M. Hildebrand, and Mr. S. Veinberg for acquiring high-field NMR data, as well as their assistance throughout the course of this study. We also thank Dr. V. Terskikh and Dr. E. Ye for technical support. Access to the 900 MHz NMR spectrometer was provided by the National Ultrahigh-Field NMR Facility for Solids in Ottawa, Ontario, a national research facility funded by the Canada Foundation for Innovation, the Ontario Innovation Trust, Recherche Québec, the National Research Council Canada, and Bruker Biospin and managed by the University of Ottawa (www.nmr900.ca).

References

(1) Ferlay, J.; Shin, H.-R.; Bray, F.; Forman, D.; Mathers, C.; Parkin, D. M. *Int. J. Cancer* **2010** *127* (12), 2893. doi:10.1002/ijc.25516.

(2) Roche, V. F. Cancer and Chemotherapy. In *Foye's Princiciples of Medicinal Chemistry;* 6th ed.; Lemke, T. L., Williams, D. A., Eds.; Lippincott Williams & Wilkins: Philadelphia, PA, 2008; pp 1147–1192.

(3) Kelland, L. *Nat. Rev. Cancer* **2007** *7* (8), 573. doi:10.1038/nrc2167.

(4) Wong, E.; Giandomenico, C. M. *Chem. Rev.* **1999** *99* (9), 2451. doi:10.1021/cr980420v.

(5) Lippert, B. *Cisplatin: Chemistry and Biochemistry of a Leading Anticancer Drug;* Wiley-VCH: Weinheim, Germany, 1999.

(6) Peyrone, M. *Justus Liebigs Ann. Chem.* **1844** *51* (1), 1. doi:10.1002/jlac.18440510102.

(7) Rosenberg, B.; Van Camp, L.; Krigas, T. *Nature* **1965** *205* (4972), 698. doi:10.1038/205698a0.

(8) Rosenberg, B.; VanCamp, L.; Trosko, J. E.; Mansour, V. H. *Nature* **1969** *222* (5191), 385. doi:10.1038/222385a0.

(9) Arnesano, F.; Natile, G. *Coord. Chem. Rev.* **2009** *253* (15–16), 2070. doi:10.1016/j.ccr.2009.01.028.

(10) Reedijk, J. *Proc. Natl. Acad. Sci. U.S.A.* **2003** *100* (7), 3611. doi:10.1073/pnas.0737293100.

(11) Jamieson, E. R.; Lippard, S. J. *Chem. Rev.* **1999** *99* (9), 2467. doi:10.1021/cr980421n.

(12) Vinje, J.; Sletten, E. *Anticancer. Agents Med. Chem.* **2007** *7* (1), 35. doi:10.2174/187152007779313982.

(13) Berners-Price, S. J.; Ronconi, L.; Sadler, P. J. *Prog. Nucl. Magn. Reson. Spectrosc.* **2006** *49* (1), 65. doi:10.1016/j.pnmrs.2006.05.002.

(14) Chen, Y.; Guo, Z.; Sadler, P. J. ^{195}Pt- and ^{15}N-NMR Spectroscopic Studies of Cisplatin Reactions with Biomolecules. In *Cisplatin: Chemistry and Biochemistry of a Leading Anticancer Drug;* Lippert, B., Ed.; Weinheim, Germany, 1999; pp 293–318.

(15) Stefanov, V. E.; Tulub, A. A. ^{195}Pt NMR-Fourier Spectroscopy in the Analysis of the Mechanism of the Cytostatic Activity of Platinum Complexes. In *NATO Science Series II: Mathematics, Physics and Chemistry;* Springer: New York, 2002; Vol. 76, pp 615–623.

(16) Tulub, A. A.; Stefanov, V. E. *Int. J. Biol. Macromol.* **2001** *28* (3), 191. doi:10.1016/S0141-8130(00)00159-8.

(17) Brière, K. M.; Goel, R.; Shirazi, F. H.; Stewart, D. J.; Smith, I. C. P. *Cancer Chemother. Pharmacol.* **1996** *37* (6), 518. doi:10.1007/s002800050423.

(18) Berners-Price, S. J.; Kuchel, P. W. *J. Inorg. Biochem.* **1990** *38* (4), 305. doi:10.1016/0162-0134(90)80005-I.

Can. J. Chem. Downloaded from www.nrcresearchpress.com by Xi'an Jiaotong University on 09/19/12
For personal use only.

(19) Miller, S. K.; Marzilli, L. G. *Inorg. Chem.* **1985** *24* (15), 2421. doi:10.1021/ic00209a021.
(20) Berners-Price, S. J.; Frey, U.; Ranford, J. D.; Sadler, P. J. *J. Am. Chem. Soc.* **1993** *115* (19), 8649. doi:10.1021/ja00072a019.
(21) Bancroft, D. P.; Lepre, C. A.; Lippard, S. J. *J. Am. Chem. Soc.* **1990** *112* (19), 6860. doi:10.1021/ja00175a020.
(22) Truflandier, L. A.; Sutter, K.; Autschbach, J. *Inorg. Chem.* **2011** *50* (5), 1723. doi:10.1021/ic102174b.
(23) Jensen, M.; Bjerring, M.; Nielsen, N. C.; Nerdal, W. *J. Biol. Inorg. Chem.* **2010** *15* (2), 213. doi:10.1007/s00775-009-0586-5.
(24) Jensen, M.; Nerdal, W. *Eur. J. Pharm. Sci.* **2008** *34* (2–3), 140. doi:10.1016/j.ejps.2008.03.002.
(25) Chupin, V.; de Kroon, A.; de Kruijff, B. *J. Am. Chem. Soc.* **2004** *126* (42), 13816. doi:10.1021/ja0468933.
(26) Guo, Z. J.; Habtemariam, A.; Sadler, P. J.; Palmer, R.; Potter, B. S. *N. J. Chem.* **1998** *22* (1), 11. doi:10.1039/a706739i.
(27) Barrie, P. J.; Austin, E. J. W.; Barbieri, A.; Clark, R. J. H. *Inorg. Chim. Acta* **1997** *264* (1–2), 81. doi:10.1016/S0020-1693(97)05599-0.
(28) Austin, E. J. W.; Barrie, P. J.; Clark, R. J. H. *Inorg. Chem.* **1992** *31* (21), 4281. doi:10.1021/ic00047a014.
(29) Pregosin, P. S. In *Annual Reports on NMR Spectroscopy;* Webb, G. A., Ed.; Academic Press: New York, 1986; Vol. 17, p 356.
(30) Goodfellow, R. J. In *Multinuclear NMR;* 1st ed.; Mason, J., Ed.; Plenum Press: New York, 1987; p 639.
(31) O'Dell, L. A.; Schurko, R. W. *Chem. Phys. Lett.* **2008** *464* (1–3), 97. doi:10.1016/j.cplett.2008.08.095.
(32) Tang, J. A.; O'Dell, L. A.; Aguiar, P. M.; Lucier, B. E. G.; Sakellariou, D.; Schurko, R. W. *Chem. Phys. Lett.* **2008** *466* (4–6), 227. doi:10.1016/j.cplett.2008.10.044.
(33) Hamaed, H.; Laschuk, M. W.; Terskikh, V. V.; Schurko, R. W. *J. Am. Chem. Soc.* **2009** *131* (23), 8271. doi:10.1021/ja901347k.
(34) Hamaed, H.; Ye, E.; Udachin, K.; Schurko, R. W. *J. Phys. Chem. B* **2010** *114* (18), 6014. doi:10.1021/jp102026m.
(35) O'Dell, L. A.; Rossini, A. J.; Schurko, R. W. *Chem. Phys. Lett.* **2009** *468* (4–6), 330. doi:10.1016/j.cplett.2008.12.044.
(36) Lucier, B. E. G.; Tang, J. A.; Schurko, R. W.; Bowmaker, G. A.; Healy, P. C.; Hanna, J. V. *J. Phys. Chem. C* **2010** *114* (17), 7949. doi:10.1021/jp907477m.
(37) O'Dell, L. A.; Ratcliffe, C. I. *Chem. Commun. (Camb.)* **2010** *46* (36), 6774. doi:10.1039/c0cc01902j.
(38) MacGregor, A. W.; O'Dell, L. A.; Schurko, R. W. *J. Magn. Reson.* **2011** *208*, 103. doi:10.1016/j.jmr.2010.10.011.
(39) O'Dell, L. A.; Schurko, R. W. *Phys. Chem. Chem. Phys.* **2009** *11* (32), 7069. doi:10.1039/b906114b.
(40) O'Dell, L. A.; Schurko, R. W. *J. Am. Chem. Soc.* **2009** *131* (19), 6658. doi:10.1021/ja901278q.
(41) O'Dell, L. A.; Schurko, R. W.; Harris, K. J.; Autschbach, J.; Ratcliffe, C. I. *J. Am. Chem. Soc.* **2011** *133* (3), 527. doi:10.1021/ja108181y.
(42) Rossini, A. J.; Mills, R. W.; Briscoe, G. A.; Norton, E. L.; Geier, S. J.; Hung, I.; Zheng, S.; Autschbach, J.; Schurko, R. W. *J. Am. Chem. Soc.* **2009** *131* (9), 3317. doi:10.1021/ja808390a.
(43) Hamaed, H.; Pawlowski, J. M.; Cooper, B. F. T.; Fu, R. Q.; Eichhorn, S. H.; Schurko, R. W. *J. Am. Chem. Soc.* **2008** *130* (33), 11056. doi:10.1021/ja802486q.
(44) Massiot, D.; Farnan, I.; Gautier, N.; Trumeau, D.; Florian, P.; Grandinetti, P. J. *J. Chim. Phys. PCB* **1995** *92*, 1847.
(45) Medek, A.; Frydman, V.; Frydman, L. *J. Phys. Chem. A* **1999** *103* (25), 4830. doi:10.1021/jp990410d.
(46) Tang, J. A.; Masuda, J. D.; Boyle, T. J.; Schurko, R. W. *ChemPhysChem* **2006** *7* (1), 117. doi:10.1002/cphc.200500343.
(47) Lipton, A. S.; Wright, T. A.; Bowman, M. K.; Reger, D. L.; Ellis, P. D. *J. Am. Chem. Soc.* **2002** *124* (20), 5850. doi:10.1021/ja0127133.
(48) Kupce, E.; Freeman, R. *J. Magn. Reson. A* **1995** *115* (2), 273. doi:10.1006/jmra.1995.1179.
(49) Bhattacharyya, R.; Frydman, L. *J. Chem. Phys.* **2007** *127*, 194503/1.
(50) Eichele, K.; Wasylishen, R. E. *WSolids1: Solid-State NMR Spectrum Simulation*, version 1.17.30; University of Tübingen: Tübingen, Germany, 2001.
(51) Massiot, D.; Fayon, F.; Capron, M.; King, I.; Le Calvé, S.; Alonso, B.; Durand, J.-O.; Bujoli, B.; Gan, Z.; Hoatson, G. *Magn. Reson. Chem.* **2002** *40* (1), 70. doi:10.1002/mrc.984.
(52) This work was made possible by the facilities of the Shared Hierarchical Academic Research Computing Network. SHARCNET. Available from www.sharcnet.ca).
(53) Milburn, G. H. W.; Truter, M. R. *J. Chem. Soc. A* **1966** 1609. doi:10.1039/j19660001609.
(54) Colamarino, P.; Orioli, P. L. *J. Chem. Soc. Dalton Trans.* **1975** (16–17), 1656. doi:10.1039/dt9750001656.
(55) Iball, J.; Macdougall, M.; Scrimgeour, S. *Acta Crystallogr. B* **1975** *31* (6), 1672. doi:10.1107/S0567740875005894.
(56) Beagley, B.; Cruickshank, D. W. J.; McAuliffe, C. A.; Pritchard, R. G.; Zaki, A. M.; Beddoes, R. L.; Cernik, R. J.; Mills, O. S. *J. Mol. Struct.* **1985** *130* (1–2), 97. doi:10.1016/0022-2860(85)85025-0.
(57) Pfrommer, B. G.; Cote, M.; Louie, S. G.; Cohen, M. L. *J. Comput. Phys.* **1997** *131* (1), 233. doi:10.1006/jcph.1996.5612.
(58) Pickard, C. J.; Mauri, F. *Phys. Rev. B* **2001** *63* (24), 245101. doi:10.1103/PhysRevB.63.245101.
(59) Profeta, M.; Mauri, F.; Pickard, C. J. *J. Am. Chem. Soc.* **2003** *125* (2), 541. doi:10.1021/ja027124r.
(60) Clark, S. J.; Segall, M. D.; Pickard, C. J.; Hasnip, P. J.; Probert, M. I. J.; Refson, K.; Payne, M. C. *Z. Kristallogr.* **2005** *220* (5–6), 567. doi:10.1524/zkri.220.5.567.65075.
(61) Yates, J. R.; Pickard, C. J.; Mauri, F. *Phys. Rev. B* **2007** *76* (2), 024401. doi:10.1103/PhysRevB.76.024401.
(62) Schreckenbach, G.; Ziegler, T. *J. Phys. Chem.* **1995** *99* (2), 606. doi:10.1021/j100002a024.
(63) *ADF 2009.01*; Amsterdam, 2009.
(64) te Velde, G. T.; Bickelhaupt, F. M.; Baerends, E. J.; Fonseca Guerra, C.; van Gisbergen, S. J. A.; Snijders, J. G.; Ziegler, T. *J. Comput. Chem.* **2001** *22* (9), 931. doi:10.1002/jcc.1056.
(65) Ditchfield, R. *Mol. Phys.* **1974** *27* (4), 789. doi:10.1080/00268974400100711.
(66) Wolinski, K.; Hinton, J. F.; Pulay, P. *J. Am. Chem. Soc.* **1990** *112* (23), 8251. doi:10.1021/ja00179a005.
(67) Becke, A. D. *Phys. Rev. A* **1988** *38* (6), 3098. doi:10.1103/PhysRevA.38.3098.
(68) Lee, C. T.; Yang, W. T.; Parr, R. G. *Phys. Rev. B* **1988** *37* (2), 785. doi:10.1103/PhysRevB.37.785.
(69) Vosko, S. H.; Wilk, L.; Nusair, M. *Can. J. Phys.* **1980** *58* (8), 1200. doi:10.1139/p80-159.
(70) Perdew, J. P. *Phys. Rev. B* **1986** *33* (12), 8822. doi:10.1103/PhysRevB.33.8822.
(71) Perdew, J. P. *Phys. Rev. B* **1986** *34* (10), 7406. doi:10.1103/PhysRevB.34.7406.
(72) Perdew, J. P.; Burke, K.; Ernzerhof, M. *Phys. Rev. Lett.* **1996** *77* (18), 3865. doi:10.1103/PhysRevLett.77.3865.
(73) Zhang, Y. K.; Yang, W. T. *Phys. Rev. Lett.* **1998** *80* (4), 890. doi:10.1103/PhysRevLett.80.890.

(74) van Lenthe, E.; Baerends, E. J.; Snijders, J. G. *J. Chem. Phys.* **1993** *99* (6), 4597. doi:10.1063/1.466059.
(75) van Lenthe, E.; Baerends, E. J.; Snijders, J. G. *J. Chem. Phys.* **1994** *101* (11), 9783. doi:10.1063/1.467943.
(76) Schefer, J.; Schwarzenbach, D.; Fischer, P.; Koetzle, T.; Larsen, F. K.; Haussuhl, S.; Rudlinger, M.; McIntyre, G.; Birkedal, H.; Burgi, H. B. *Acta Crystallogr. B* **1998** *54* (2), 121. doi:10.1107/S0108768197011956.
(77) Sterzel, M.; Autschbach, J. *Inorg. Chem.* **2006** *45* (8), 3316. doi:10.1021/ic052143y.
(78) Austin, E. J. W.; Barrie, P. J.; Clark, R. J. H. *J. Chem. Soc. Chem. Commun.* **1993** (18), 1404. doi:10.1039/c39930001404.
(79) Hung, I.; Gan, Z. H. *J. Magn. Reson.* **2010** *204* (2), 256. doi:10.1016/j.jmr.2010.03.001.
(80) Clayden, N. J.; Dobson, C. M.; Lian, L. Y.; Smith, D. J. *J. Magn. Reson.* **1986** *69*, 476.
(81) van Gorkom, L. C. M.; Hook, J. M.; Logan, M. B.; Hanna, J. V.; Wasylishen, R. E. *Magn. Reson. Chem.* **1995** *33* (10), 791. doi:10.1002/mrc.1260331005.
(82) Bielecki, A.; Burum, D. P. *J. Magn. Reson. A* **1995** *116* (2), 215. doi:10.1006/jmra.1995.0010.
(83) Briand, G. G.; Smith, A. D.; Schatte, G.; Rossini, A. J.; Schurko, R. W. *Inorg. Chem.* **2007** *46* (21), 8625. doi:10.1021/ic700738w.
(84) Sutrisno, A.; Lo, A. Y. H.; Tang, J. A.; Dutton, J. L.; Farrar, G. J.; Ragogna, P. J.; Zheng, S.; Autschbach, J.; Schurko, R. W. *Can. J. Chem.* **2009** *87* (10), 1546. doi:10.1139/V09-100.
(85) Tang, J. A.; Kogut, E.; Norton, D.; Lough, A. J.; McGarvey, B. R.; Fekl, U.; Schurko, R. W. *J. Phys. Chem. B* **2009** *113* (11), 3298. doi:10.1021/jp807530d.
(86) Thibault, M.-H.; Lucier, B. E. G.; Schurko, R. W.; Fontaine, F.-G. *Dalton Trans.* **2009** (37), 7701. doi:10.1039/b907737e.
(87) Rodina, T. A.; Lutsenko, I. A.; Gerasimenko, A. V.; Ivanov, A. V. *Russ. J. Coord. Chem.* **2009** *35* (7), 534. doi:10.1134/S1070328409070112.
(88) Sparks, S. W.; Ellis, P. D. *J. Am. Chem. Soc.* **1986** *108* (12), 3215. doi:10.1021/ja00272a009.
(89) Keller, H. J.; Rupp, H. H. *Z. Natureforsch. A* **1971** *A26*, 785.
(90) Siegel, R.; Nakashima, T. T.; Wasylishen, R. E. *J. Phys. Chem. B* **2004** *108* (7), 2218. doi:10.1021/jp031048c.
(91) Ambrosius, F.; Klaus, E.; Schaller, T.; Sebald, A. *Z. Naturforsch. A* **1995** *50*, 423.
(92) Santos, R. A.; Chien, W. J.; Harbison, G. S. *J. Magn. Reson.* **1989** *84*, 357.
(93) Autschbach, J.; Zheng, S.; Schurko, R. W. *Concepts Magn. Reson.* **2010** *36A* (2), 84. doi:10.1002/cmr.a.20155.
(94) Chapman, R. P.; Widdifield, C. M.; Bryce, D. L. *Prog. Nucl. Magn. Reson. Spectrosc.* **2009** *55* (3), 215. doi:10.1016/j.pnmrs.2009.05.001.
(95) Patterson, H. H.; Tewksbury, J. C.; Martin, M.; Krogh-Jespersen, M. B.; LoMenzo, J. A.; Hooper, H. O.; Viswanath, A. K. *Inorg. Chem.* **1981** *20* (7), 2297. doi:10.1021/ic50221a071.
(96) Widdifield, C. M.; Bryce, D. L. *J. Phys. Chem. A* **2010** *114* (40), 10810. doi:10.1021/jp108237x.

Can. J. Chem. Downloaded from www.nrcresearchpress.com by Xi'an Jiaotong University on 09/19/12
For personal use only.

Catalytic activity of Co-åkermanite and Co-pyroxene in oxidation reactions

Irena Mihailova and Dimitar Mehandjiev

Can. J. Chem. Downloaded from www.nrcresearchpress.com by Xi'an Jiaotong University on 09/19/12
For personal use only.

Abstract: Two calcium–cobalt silicates were synthesized in which cobalt occupies different structural positions. The crystal phases belong to two main structural silicate types. In the Co-åkermanite structure ($Ca_2CoSi_2O_7$), cobalt cations take tetrahedral coordination toward oxygen atoms. In the Co-pyroxene structure of $CaCoSi_2O_6$, cobalt displays octahedral coordination. $Ca_2CoSi_2O_7$ was prepared by solid-phase synthesis and $CaCoSi_2O_6$ was prepared by sol–gel method. The synthesis of the phases was confirmed by XRD, FTIR, and EPR data. On the basis of the XPS analysis, it can be concluded that Co^{2+} cations exist in the studied silicates. Thus, it is possible to study the catalytic activity of two silicate phases containing Co^{2+} cations in different coordinations: tetrahedral and octahedral. It was found that cobalt silicates with crystal structures corresponding to pyroxene and åkermanite possess catalytic activity in the reactions of complete oxidation of CO and toluene. Co-pyroxene exhibits higher catalytic activity than Co-åkermanite, but the higher cobalt content on the surface of Co-pyroxene should also be taken into account. Then, it turns out that catalytically active complexes with Co^{2+} ions in tetrahedral coordination are more efficient than those with such ions in octahedral coordination when equal concentrations of cobalt were used on the surface of the catalysts.

Key words: Co-pyroxene ($CaCoSi_2O_6$), Co-åkermanite ($Ca_2CoSi_2O_7$), cation coordination, catalytic activity, CO oxidation.

Résumé : On a réalisé la synthèse de deux silicates de calcium et de cobalt dans lesquels l'atome de cobalt occupe des positions diverses dans la structure. Les phases cristallines appartiennent à deux types principaux de structures de silicate. Dans la structure åkermanite du $Ca_2CoSi_2O_7$, les cations du cobalt occupent des positions de coordination tétraédrique par rapport aux atomes d'oxygène. Le $Ca_2CoSi_2O_7$ a été préparé par une synthèse en phase solide alors que le $CaCoSi_2O_6$ a été obtenu par méthode sol–gel. Les synthèses des phases ont été confirmées par des données de diffraction des rayons-X (DRX), d'infrarouge à transformée de Fourier (IR-TF) et résonance paramagnétique électronique (RPE). Sur la base d'analyse de données de spectroscopie photoélectronique des rayons-X (SPX), il est possible de conclure que, dans les silicates étudiés, il existe des cations Co^{2+}. Il est donc possible d'étudier l'activité catalytique des deux phases de silicate contenant des cations Co^{2+} dans des environnements de coordination différents : tétraédrique et octaédrique. On a trouvé que les silicates de cobalt avec une structure cristalline correspondant à celle du pyroxène et de l'åkermanite présentent une activité catalytique dans les réactions d'oxydation complète du CO et du toluène. Le Co-pyroxène possède une activité catalytique plus élevée que celle de la Co-åkermanite; toutefois, on doit tenir compte du fait que la teneur en cobalt est plus élevée sur la surface du Co-pyroxène. Il en découle alors que, pour des concentrations identiques de cobalt à la surface des catalyseurs, les complexes catalytiquement actifs comportant des ions Co^{2+} en coordination tétraédrique sont plus efficaces que ceux dans lesquels se trouvent dans une coordination octaédrique.

Mots-clés : Co-pyroxène ($CaCoSi_2O_6$), Co-åkermanite ($Ca_2CoSi_2O_7$), coordination d'un cation, activité catalytique, oxydation du CO.

[Traduit par la Rédaction]

Introduction

One of the important factors to consider when developing new types of catalysts is the coordination of the catalytically active ion in the final product (catalyst), since the catalytic activity is largely determined by the coordination of the ion as well as by its oxidation state. Cobalt-based catalysts are widely used in oxidation reactions mainly for disposal of CO[1–4] and harmful organic substances[5–7] and reduction of NO[8–11] in gases. The Co^{2+}–Co^{3+} ion pair and ion coordination lie at the basis of this activity.[12] These ions form the catalytically active complex (CAC). It is known that Co^{2+} and Co^{3+} prefer octahedral coordination (O_h), since the stabilization energy for such coordination is higher than that for tetrahedral (T_d) coordination.[13–16]

It is important to compare the Co^{2+} ion activity in terms of two different coordinations of the crystal field, but in similar chemical compounds. Co-åkermanite ($Ca_2CoSi_2O_7$) and Co-pyroxene ($CaCoSi_2O_6$) silicate types provide such an opportunity. $Ca_2CoSi_2O_7$ and $CaCoSi_2O_6$ are structural analogues of åkermanite and diopside minerals in the complete

Received 8 December 2010. Accepted 28 March 2011. Published at www.nrcresearchpress.com/cjc on 2 August 2011.

I. Mihailova. University of Chemical Technology and Metallurgy, 8 Kl. Ohridski, Sofia 1756, Bulgaria.
D. Mehandjiev. Institute of Catalysis, Bulgarian Academy of Sciences, Acad. G. Bonchev St, Bldg. 11, Sofia 1113, Bulgaria.

Corresponding author: Irena Mihailova (e-mail: irena66@mail.bg).

Can. J. Chem. Downloaded from www.nrcresearchpress.com by Xi'an Jiaotong University on 09/19/12
For personal use only.

Fig. 1. Crystal structure of Co-pyroxene ($CaCoSi_2O_6$) projected on the (100) plane (*a*) and (001) plane (*b*). White spheres are calcium atoms, dark polyhedra are CoO_6 octahedra, and light polyhedra are SiO_4 tetrahedra.

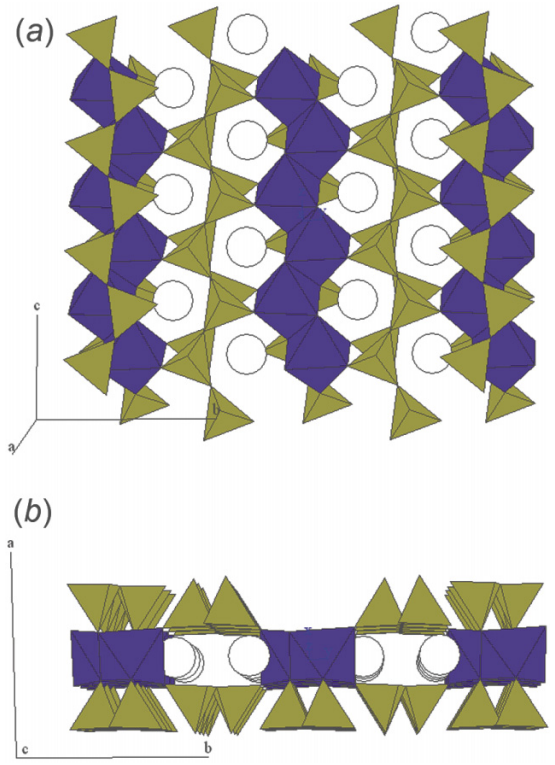

Fig. 2. Crystal structure of Co-åkermanite ($Ca_2CoSi_2O_7$) projected on the (001) plane (*a*) and the (100) plane (*b*). White spheres are calcium atoms, dark polyhedra are CoO_4 tetrahedra, and light polyhedra are SiO_4 tetrahedra.

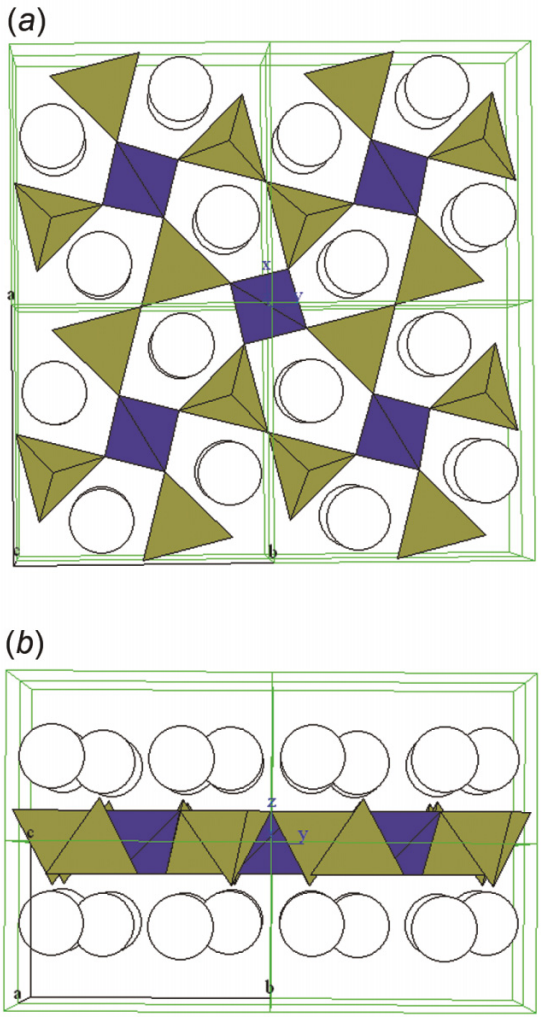

substitution of the positions of magnesium with cobalt. Such substitution is justified by the close values for ionic radii of Mg^{2+} and Co^{2+}. The crystal phases belong to two main structural silicate types: silicates with diorthogroups of silicon–oxygen tetrahedra and silicates with chains of silicon–oxygen tetrahedra. In these two phases, cobalt is expected to take different structural positions. In the åkermanite structure $Ca_2CoSi_2O_7$, cobalt cations take tetrahedral coordination toward oxygen atoms.[17–20] In pyroxene structure $CaCoSi_2O_6$, the cobalt is in octahedral coordination.[21,22] The crystal structures are presented in Figs. 1 and 2 using the software CaRIne Crystallography 3.1.[23]

Our previous study[24] on the possibilities of a synthesis of these compounds established that åkermanite may be synthesized easily via solid-state synthesis and the sol–gel method is more convenient for the synthesis of pyroxene. This allows determining the possible effect of Co^{2+} ions in such pyroxene or åkermanite crystal structure on the catalytic activity in oxidation reactions.

Therefore, the aim of the present study is to examine the catalytic activity in oxidation reactions of CO and toluene of two calcium–cobalt silicates: $Ca_2CoSi_2O_7$ and $CaCoSi_2O_6$. The catalytic activity of these phases has not yet been studied.

Experimental procedure

Synthesis

A phase $Ca_2CoSi_2O_7$ has been synthesized by solid-state reactions. The initial raw materials used were chemically pure reagents, such as $CaCO_3$, Co_3O_4, and vitreous quartz powder. The stoichiometric mixture was well-ground and homogenized. After the addition of a binding agent (3% aqueous solution of poly(vinyl alcohol)) to the mixture, samples with a diameter of 30 mm and a height of 10 mm were obtained by pressing. The prepared tablets (samples) were thermally treated at 1200 °C for 2–3 h through isothermal treatment in a corundum crucible. The sample, in which $Ca_2CoSi_2O_7$ was identified, was deep blue.

A similar scheme of pyrosynthesis was applied to synthesize $CaCoSi_2O_6$, but difficulties were met arising from the fact that the phase formation occurs in a narrow temperature range, which is close to the melting point of the composition. This was the reason for giving preference to the sol–gel synthesis method. $CaCoSi_2O_6$ pyroxene has been prepared by sol–gel technique using $Ca(NO_3)_2{\cdot}4H_2O$, $Co(NO_3)_2{\cdot}6H_2O$, and tetraethyl orthosilicate (TEOS) as precursors. The obtained gel was dried at 100 °C, and then the samples were calcined in air for 2 h. Calcinations temperature of 1200 °C was selected. The color of the obtained sample was pink. A detailed method of synthesis is described elsewhere.[24]

Can. J. Chem. Downloaded from www.nrcresearchpress.com by Xi'an Jiaotong University on 09/19/12
For personal use only.

Exeperimental methods

X-ray powder diffraction (XRD) analysis was applied for phase control. An X-ray diffractometer DRON-3M at Fe-filtered Co Kα radiation was used in the range from 8° to 70° 2θ (step size: 0.05°, counting time per step: 1 s). The Rietveld refinement was performed using DiffracPlus TOPAS v. 4.2.[25] The unit-cell parameters, the position of cobalt, and Co–O distances were refined on the basis of experimental X-ray data. The positional parameters of structure of $CaCoSi_2O_6$ (Inorganic Crystal Structure Database (ICSD) No. 202245) and those of $Ca_2CoSi_2O_7$ (ICSD No. 94131) were used as the starting parameters of the refinement of structures. PowderCell 2.4 software[26] was used to determine the size of crystallites on the basis of the experimental X-ray data.

FTIR spectroscopy was applied. Infrared transmittance spectra were recorded by using the pressed-pellet technique in KBr. The measurements were made with a FTIR spectrophotometer Bruker EQUINOX 55 in the frequency range from 4000 to 400 cm^{-1}.

Electron paramagnetic resonance (EPR) spectra have been investigated in the temperature range 100–400 K. They were registered as the first derivative using the ERS/220 spectrometer. The *g* factor was determined using the Mn^{2+}/ZnS standard.

Chemical composition was analyzed by X-ray energy dispersion spectroscopy (EDS) coupled to scanning electron microscope JEOL-JSM 6370.

X-ray photoelectron spectroscopy (XPS) studies were performed on a VG ESCALAB MkII electron spectrometer under a base pressure of 1×10^{-8} Pa. The photoelectron spectra were excited using an Al Kα X-ray source (excitation energy h_n = 1486.6 eV) with a total instrumental resolution of ~1 eV. The C1s line of adventitious carbon at 285.0 eV was used as internal standard to calibrate the binding energies. The photoelectron spectra were corrected by subtracting a Shirley-type background and were quantified using the peak area and Scofield's photoionization cross sections.

The determination of the specific surface area of the samples was carried out by nitrogen adsorption at 77.4 K. Nitrogen adsorption isotherms were used to calculate the specific surface area (A_{BET}) using the BET equation.

The catalytic activity of the samples was measured in an isothermal plug-flow reactor enabling operation under steady-state conditions without any temperature gradients. The size of the catalyst particles (0.3–0.6 mm) was chosen taking into account the reactor diameter (6 mm) and the hourly space velocity (20 000 h^{-1}) to reduce the effect of the pore diffusion. The gas feed flow rate was 4.0 L/h, the catalyst bed volume was 0.2 cm^3, and the mass of the charged catalyst was 0.5–0.55 g. The catalytic oxidation was performed within the temperature interval 200–400 °C, the oxidizing agent used being oxygen from the air (gas mixture: 21% O_2 and 79% N_2). The preliminary treatment of the catalysts included heating in air flow at 120 °C for 1 h. The flow of CO and toluene was fed into the reactor by an Ismatex M62/6 pump (Switzerland).

The initial concentration of carbon monoxide was 0.5 *v*/*v*. The carrier gas was air (a mixture of 21% O_2 and 79% N_2). A Maihak gas analyzer (O_2, CO, CO_2) was used to measure the CO and CO_2 concentrations with an accuracy of ±0.1 ppm, whereas the oxygen measurement accuracy was ±100 ppm.

The catalytic activity of the samples, with respect to the complete oxidation of toluene, were carried out in a flow reactor, with a catalyst volume of 0.2 cm^3 (0.5–0.55 g), a space velocity of 20 000 h^{-1}, and the concentration of toluene was 0.03 *v*/*v*). The inlet and outlet gas mixtures were analyzed by a THERMO-FID analyzer.

The activity of catalysts is presented as a fraction of the oxidized CO and toluene (η, %); the amount of oxidized CO and toluene per gram of catalyst per hour (I_g, mg/g h^{-1}).

Results and discussion

The XRD data confirm the synthesis of Co-åkermanite ($Ca_2CoSi_2O_7$, in accordance with PDF card 43-0005) and Co-pyroxene ($CaCoSi_2O_6$, in accordance with PDF card 84-1288) in the studied samples. As shown earlier,[17–22] åkermanite is tetragonal, space group $P\bar{4}2_1m$, whereas pyroxene is monoclinic, space group $C2/c$. Figure 3 shows the Rietveld analysis patterns of the samples. For the pyroxene sample, the *R* factors obtained were as follows: the pattern factor (R_p) = 10.42, the weighted pattern factor (R_{wp}) = 13.66, and the goodness of fit (GoF) = 1.34; and for the åkermanite sample, R_p = 11.17, R_{wp} = 14.73, and GoF = 1.34. The positional parameters of the phases do not differ from the starting models used. The refined unit-cell parameters are consistent with previous data for åkermanite: a = 7.8386(13) Å and c = 5.02390(98) Å; and those for pyroxene: a = 9.7931(20) Å, b = 8.9497(17) Å, c = 5.2447(13) Å, and β = 105.518 (13)°.[18–20,27] The size of crystallites is 104 nm for the åkermanite phase and 96 nm for pyroxene. Kimata[18] established that in the case of Co-åkermanite, the Co–O bond length (1.926 Å) is slightly shorter than the sum (1.96 Å) of the effective ionic radii of Co^{2+} (0.58 Å when four-coordinated, as in åkermanite and high spin) and O^{2-} (1.38 Å).[28] The bond distance Co–O determined in this study is 1.936 Å, and the form of tetrahedron is regular. This value is very close to the value reported by Kusaka et. al. (1.937(4) Å)[20] for the basic structure of $Ca_2CoSi_2O_7$ at room temperature. Recently, Hagiya et al.[19] succeeded in determining the incommensurate structure of synthetic $Ca_2CoSi_2O_7$. They concluded the following: the SiO_4 tetrahedron does not behave as a rigid body, the distance of Si–O tetrahedral bonds is variable throughout the crystal, and Co–O distances are simultaneously and sinusoidally modulated.

According to studies published so far,[21,22] within the pyroxene structure, all polyhedrons (including SiO_4 tetrahedron) are inherently flexible, and their absolute shapes and sizes are dependent on the interaction with the adjacent polyhedrons. The mean Co–O bond length determined in this study was 2.100 Å (there are three different Co–O distances: 2.070, 2.094, and 2.136 Å). The Co octahedron is very nearly regular. The difference between the shortest and the longest Co–O distances is 0.066 Å. Therefore, the value of the Co–O distance in pyroxene structure is very close to the sum (2.10 Å) of the effective ionic radii[28] of Co^{2+} (0.72 Å when six-coordinated) and O^{2-} (1.38 Å). Our data are consistent with the known values from the literature.[21,22]

The data for the IR spectra of Co-pyroxene and Co-åkermanite are presented in Table 1. As compared with the spectrum of $Ca_2CoSi_2O_7$ presented by Kimata,[18] the shape and the position of bands of experimental spectrum bear

Can. J. Chem. Downloaded from www.nrcresearchpress.com by Xi'an Jiaotong University on 09/19/12
For personal use only.

Fig. 3. Rietveld refinement of the diffraction pattern collected from (*a*) the Co-pyroxene ($CaCoSi_2O_6$) sample and (*b*) the Co-åkermanite ($Ca_2CoSi_2O_7$) sample. The experimental data, the calculated powder pattern, and the difference plot are reported.

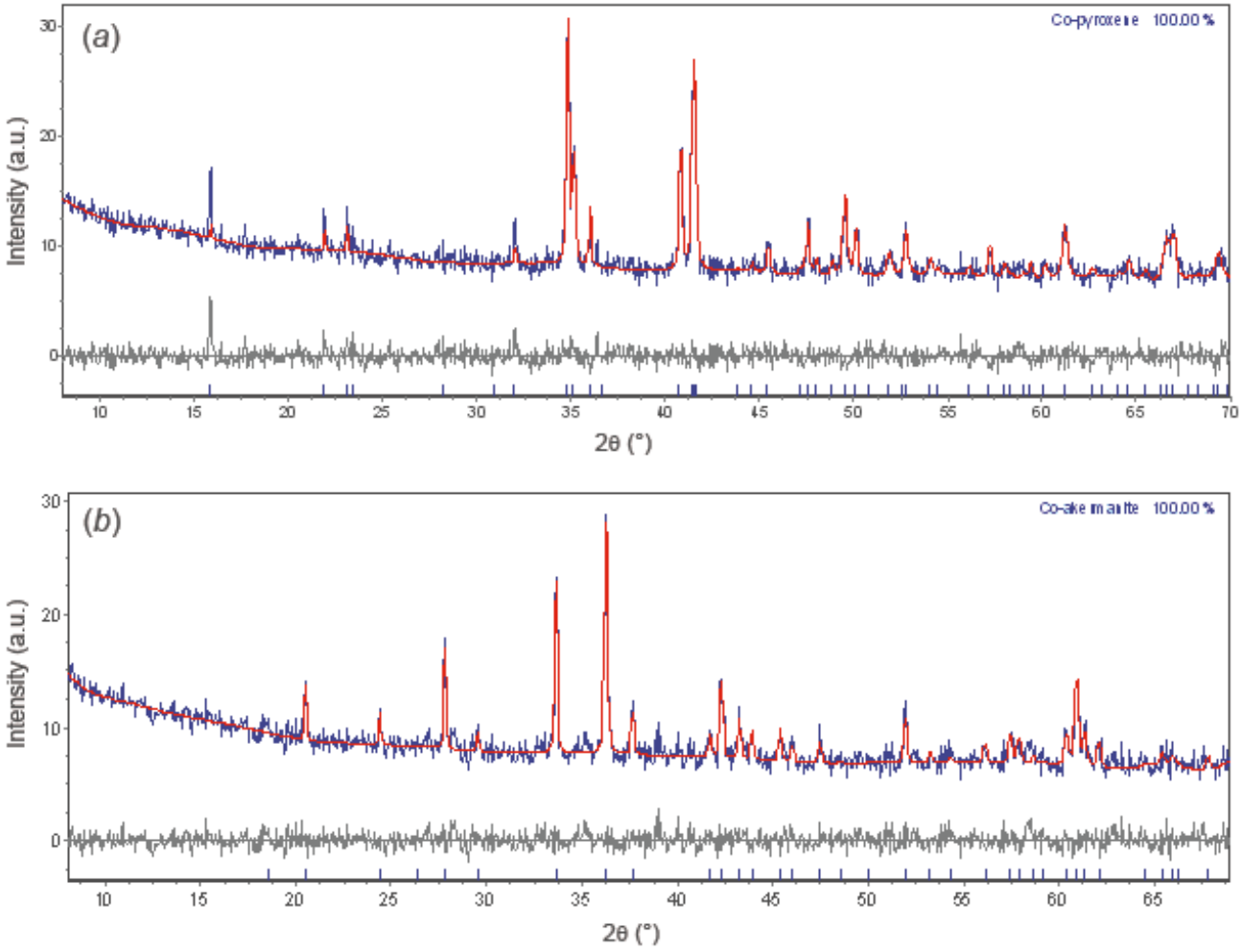

Table 1. Band frequencies and assignments for Co-åkermanite and Co-pyroxene.

Band frequencies (cm^{-1})	Tentative assignments
Co-åkermanite	
1012	ν_{as}(Si–O–Si)
964	ν_s(Si–O^-)
902	ν_s(Si–O^-)
832	
678	ν_s(Si–O–Si)
619	ν_s (Si–O–Co)
503	ν(Co–O)
455	ν(Co–O)
Co-pyroxene	
1058	ν_{as}(Si–O–Si)
965	ν_s(Si–O^-)
860	ν_{as}(Si–O^-)
673	ν_s(Si–O–Si)
627	ν_s(Si–O–Si)
502	δ(Si–O^-)
466	ν(Co–O)

striking similarities. Therefore, the FTIR spectrum confirms the structure of Co-åkermanite. This conclusion is in accordance with the XRD data. The bands near 1100–600 cm^{-1} are considered to be mainly related with the vibrations of the $Si_2O_7^{6-}$ group. In the spectrum of Co-åkermanite, the band at 678 cm^{-1} is a symmetrical stretching, ν_s(Si–O–Si) mode of bridging oxygen of the pyrosilicate anions. In the spectrum of åkermanite, the ν_s(Si–O–Si) band of the $Si_2O_7^{6-}$ group appear at 661 cm^{-1}. The bands at 902 and 964 cm^{-1} are assigned to symmetrical stretching modes of terminal oxygens, whereas the band at 1012 cm^{-1} is assigned to antisymmetric stretching of oxygens in åkermanite.[29] The FTIR data ought to show that Co^{2+} ions occur in tetrahedral coordination in the åkermanite structure. It is known that cationic substitutions in åkermanite structure change only the position of the absorption bands associated with replacement cations. In the spectrum of $Sr_2CoSi_2O_7$, the bands at 530 and 450 cm^{-1} were assigned to the vibration of CoO_4 tetrahedra.[30] A look at the frequencies of $Ca_2CoSi_2O_7$ shows that the 503 and 455 cm^{-1} bands correspond to the stretching vibrations of the CoO_4.[18]

The IR spectrum of pyroxene has a very characteristic pattern with three strong bands in the range of 1060 to 850 cm^{-1}. The five modes at high frequencies are representative of the

Can. J. Chem. Downloaded from www.nrcresearchpress.com by Xi'an Jiaotong University on 09/19/12
For personal use only.

Table 2. Results of the quantitative energy dispersion spectroscopy (EDS) analysis of the Co-åkermanite sample.

Element	Concentration (weight %)	Standard deviation (σ, weight %)	Concentration (atomic %)
Ca	27.48	0.41	17.55
Co	18.21	0.54	7.91
Si	17.95	0.32	16.36
O	36.36	0.47	58.18

Table 3. Results of the quantitative energy dispersion spectroscopy (EDS) analysis of the Co-pyroxene sample.

Element	Concentration (weight %)	Standard deviation (σ, weight %)	Concentration (atomic %)
Ca	16.30	0.25	10.60
Co	28.20	0.43	12.48
Si	19.33	0.25	17.95
O	36.18	0.36	58.97

stretching motions in the silicate chain. The chain vibrations are not particularly sensitive to the population of the cation sites.[31] The band at 1058 cm^{-1} may be attributed to the ν_{as} (Si–O–Si) mode. The bands at 965 and 860 cm^{-1} are due to the symmetrical ν_s(Si–O^-) and antisymmetric ν_{as}(Si–O^-) stretching of the terminal nonbridging oxygens in the chains. The band at 673 cm^{-1} is characteristic of pyroxene chains and corresponds to the symmetric stretch of bridging oxygen ν_s(Si–O–Si). Raman spectra of pyroxene minerals include one or two bands in the 650–680 cm^{-1} range that have been assigned to the motion of the bridging oxygens in the chains.[29] δ(Si–O^-) deformation mode appears at 502 cm^{-1}, and the band at 466 cm^{-1} corresponds to stretching vibrations of the CoO_6.

The type of EPR spectra of Co-åkermanite ($Ca_2CoSi_2O_7$) depends strongly on the temperature at which the spectra were recorded; i.e., at room temperature, signals are observed containing fine structure, whereas at low temperatures (113 K), EPR signals disappear.

The EPR spectra of Co-pyroxene ($CaCoSi_2O_6$) contain the anisotropic signal with g-tensor values $g_{\parallel} = 4.8$ and $g_{\perp} = 2.1$, respectively. At 113 K, only a broad signal owing to the exchange-connected Co^{2+} ions from $CaCoSi_2O_6$ was observed. Thus, the characterization results suggest that cobalt is present mostly as Co^{2+} ions in octahedral coordination.

We can conclude that the experimental XRD, FTIR, and EPR results are consistent with previous studies of Co-pyroxene and Co-åkermanite. Hence, they confirm the structures of the crystalline phases and, respectively, the coordination of Co^{2+} ions: tetrahedral in åkermanite and octahedral in pyroxene.

EDS analysis is needed to clarify whether the catalyst stoichiometry corresponds to that of Co-åkermanite and Co-pyroxene minerals. Data from EDS analysis for the chemical composition of synthesized åkermanite and pyroxene phases are presented, respectively, in Tables 2 and 3. The data presented are averages of five crystallites analyzed for each of the two samples. EDS analysis allowed us to determine the following chemical formulae: for Co-åkermanite, $Ca_{2.11}Co_{0.95}Si_{1.96}O_{6.98}$; and for Co-pyroxene, $Ca_{1.06}Co_{1.25}Si_{1.80}O_{5.90}$. Experimentally established composition of åkermanite contains a surplus of

Fig. 4. Amount of oxidized CO (*a*) and toluene (*b*) η (%) depending on temperature (T, °C). Samples: $CaCoSi_2O_6$ (Co-pyroxene) and $Ca_2CoSi_2O_7$ (Co-åkermanite).

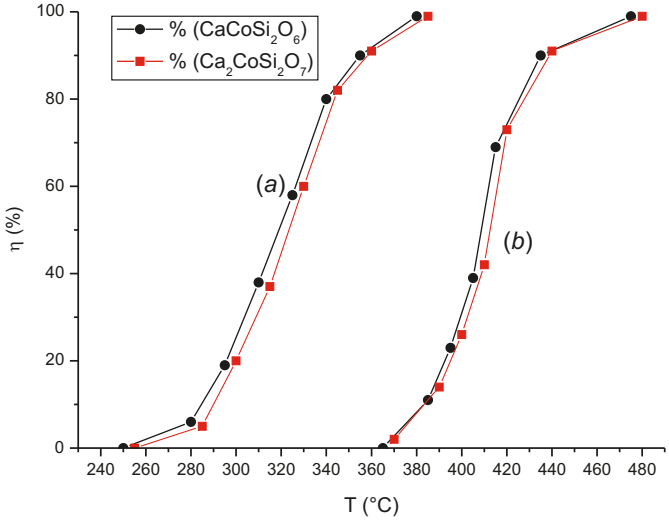

Ca versus the stoichiometric composition $Ca_2CoSi_2O_7$. Experimentally determined composition of the pyroxene phase derived by the sol–gel method deviates from the stoichiometry with an excess of Co and a decreased quantity of Si. Note that the ratio between the concentrations of cobalt in the samples is 1.58, which is significantly higher than that between the stoichiometric compositions (1.25).

The determination of the specific surface (S_0) gave the following results: $CaCoSi_2O_6$ (pyroxene sample), 24 m^2/g; and $Ca_2CoSi_2O_7$ (åkermanite sample), 23 m^2/g. Therefore, the different sample preparation methods lead to only a small change of the specific surface. The catalyst compositions exhibit a relatively high surface area for this synthesis temperature (1200 °C).

Figure 4 shows data from the catalytic activity test expressed as rates of oxidation in % for CO oxidation and complete oxidation of toluene. As shown in the figure, Co-pyroxene and Co-åkermanite exhibit catalytic activity in terms of both components. CO oxidation, as might be expected, takes place at significantly lower temperatures. Co-pyroxene shows higher activity in both reactions compared with Co-åkermanite. The quantity of oxidized CO of Co-pyroxene at 320 °C is about 7% higher than that of Co-åkermanite. In the case of the toluene oxidation at 410 °C, it is 15% higher.

The catalytic activity expressed as an amount of oxidized CO or toluene per gram of catalyst (I_g) is presented in Fig. 5. The ratio of the catalytic activities remains the same.

Can. J. Chem. Downloaded from www.nrcresearchpress.com by Xi'an Jiaotong University on 09/19/12
For personal use only.

Fig. 5. Amount of oxidized CO (*a*) and toluene (*b*) per gram of catalyst per hour (I_g) depending on temperature (T, °C). Samples: $CaCoSi_2O_6$ (Co-pyroxene) and $Ca_2CoSi_2O_7$ (Co-åkermanite).

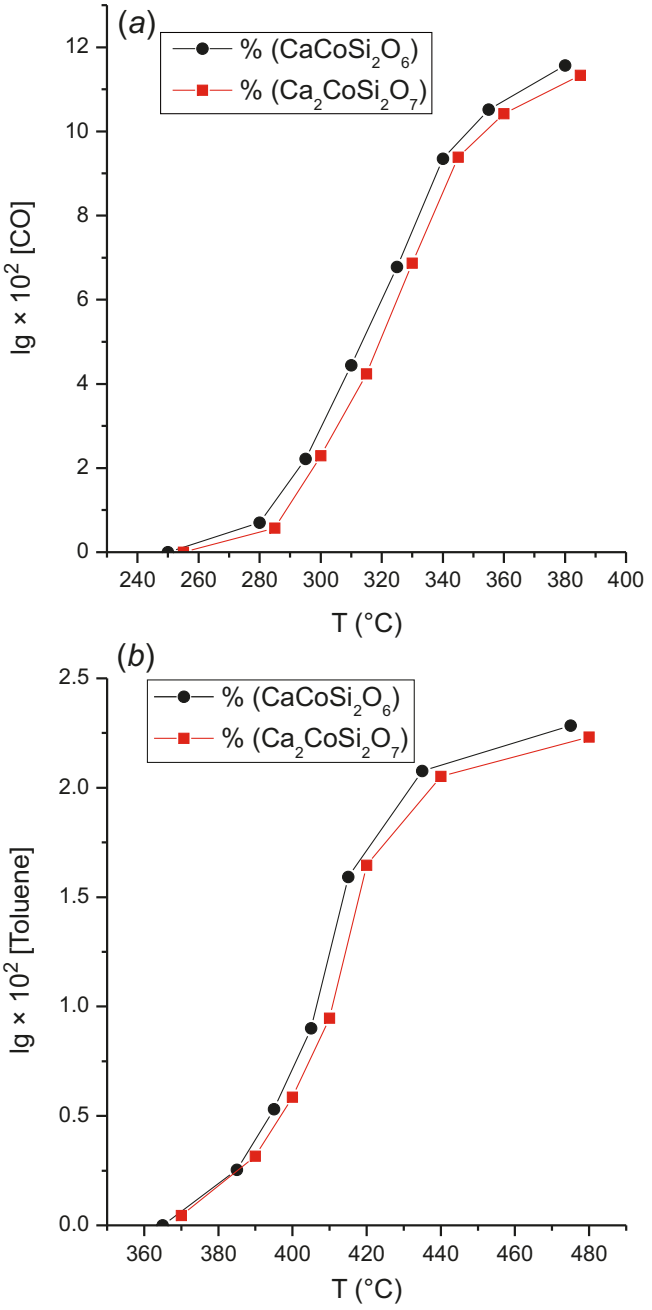

The most accurate information for the activity of massive catalysts may be obtained by comparing the activities defined as reacted substance obtained in a unit of time per unit surface area of the catalyst. This dependence is no different in nature from that of I_g because of the close values of specific surfaces of catalysts. The catalytic activity of Co-pyroxene per unit surface area of the catalyst is higher than that of Co-åkermanite. This is also evident from other representations (Figs. 4 and 5).

The obtained results show that cobalt silicates with crystal structures corresponding to pyroxene and åkermanite possess catalytic activity in reactions of complete oxidation of CO and toluene. Their catalytic activity is high enough, and under certain conditions, they can find an appropriate application. Even more interesting is the fact that Co-pyroxene exhibits a higher catalytic activity than Co-åkermanite. At the same time, we should take into account the higher Co content in pyroxene compared with åkermanite, which can also lead to higher catalytic activity. The theoretical ratio of Co content in pyroxene to åkermanite is 1.25, but on the basis of EDS data, the experimentally obtained ratio is higher. More important is the ratio of Co content on the surface of the catalysts. XPS tests were carried out to clarify the issue. The composition of the samples was investigated on the basis of the binding energies of O 1s, Si 2p, Co 2p, and Ca 2p photoelectron peaks. The obtained results are given in Fig. 6, and the calculated percentages of Co content at the surface are given in Table 4.

As shown in Table 4, the Co content at the surface is higher for Co-pyroxene. The Co-Pyroxene to Co-åkermanite ratio of Co content calculated from XPS data is 1.58 (the same value was determined by EDS analysis). This fact also contributes to the higher catalytic activity of Co-pyroxene, compared with Co-åkermanite (η, I_g).

The possible variations in the oxidation states for Co can be determined from the Co 2p peaks in the XPS spectra. The Co 2p XPS spectra of the silicates (Fig. 6*a*) consist of two main lines (i.e., $2p_{3/2}$ at ~781 eV and $2p_{1/2}$ at ~797 eV) with the spin-orbit splitting of ~16 eV, as reported in the literature.[32–35] Most of the cobalt oxides and hydroxides are not distinguishable based only on the binding energy for the Co 2p main peaks. On the other hand, the secondary features in the spectra (shake-up satellites and spin-orbit splitting) are useful in identifying the different Co types. For example, the Co spin-orbit splitting was close to 15.2 eV for Co_3O_4, but substantially larger for pure Co^{2+} oxides[35] (CoO: 16.0 eV). Moreover, CoO has a strong shake-up satellite 6 eV above the Co $2p_{3/2}$ line. The energy gap between the Co 2p main peak and the satellite peaks is related to the oxidation states of cobalt. When the energy gap is ~6.0 eV, the Co cation valence is assigned a value of 2^+. If the energy gap is 9–10 eV, the spectrum is associated with Co cations having a valence value of 3^+.[33] Another satellite peak was detected at about 6.0 eV above the Co $2p_{3/2}$ main lines (Fig. 6*a*). According to assignments reported in the literature, this satellite peak can be associated with high-spin Co^{2+} species. These results suggest that the studied samples are mainly formed by the Co^{2+} surface phase. As shown earlier for the spinels,[34] when Co^{2+} occupy tetrahedral sites, the satellite peak splitting is similar to that of divalent cobalt in an octahedral environment.

If we use data from Table 4 about the concentration of Co^{2+} ions at the surface and calculate the amount of oxidized CO and toluene from 1% surface ions, the dependencies shown in Fig. 7 are obtained. The figure shows that the Co^{2+} ions in tetrahedral coordination have a higher catalytic efficiency than those in octahedral coordination.

The basic reason for this higher catalytic efficiency is the structure of the catalytic active complex (CAC) in the catalyst.[36–38] As mentioned previously, the structure of both compounds is different. In Co-pyroxene, it is built up of chains of silicon–oxygen tetrahedra and chains of cobalt–oxygen octahedra (Fig. 1), whereas in the case of Co-åkermanite, it consists of cobalt tetrahedra connected by diorthogroups of

Can. J. Chem. Downloaded from www.nrcresearchpress.com by Xi'an Jiaotong University on 09/19/12
For personal use only.

Fig. 6. X-ray photoelectron spectroscopy (XPS) spectra for $CaCoSi_2O_6$ (Co-pyroxene) and $Ca_2CoSi_2O_7$ (Co-åkermanite). (*a*) Co 2p spectra, (*b*) O 1s spectra, (*c*) Si 2p spectra, and (*d*) Ca 2p spectra.

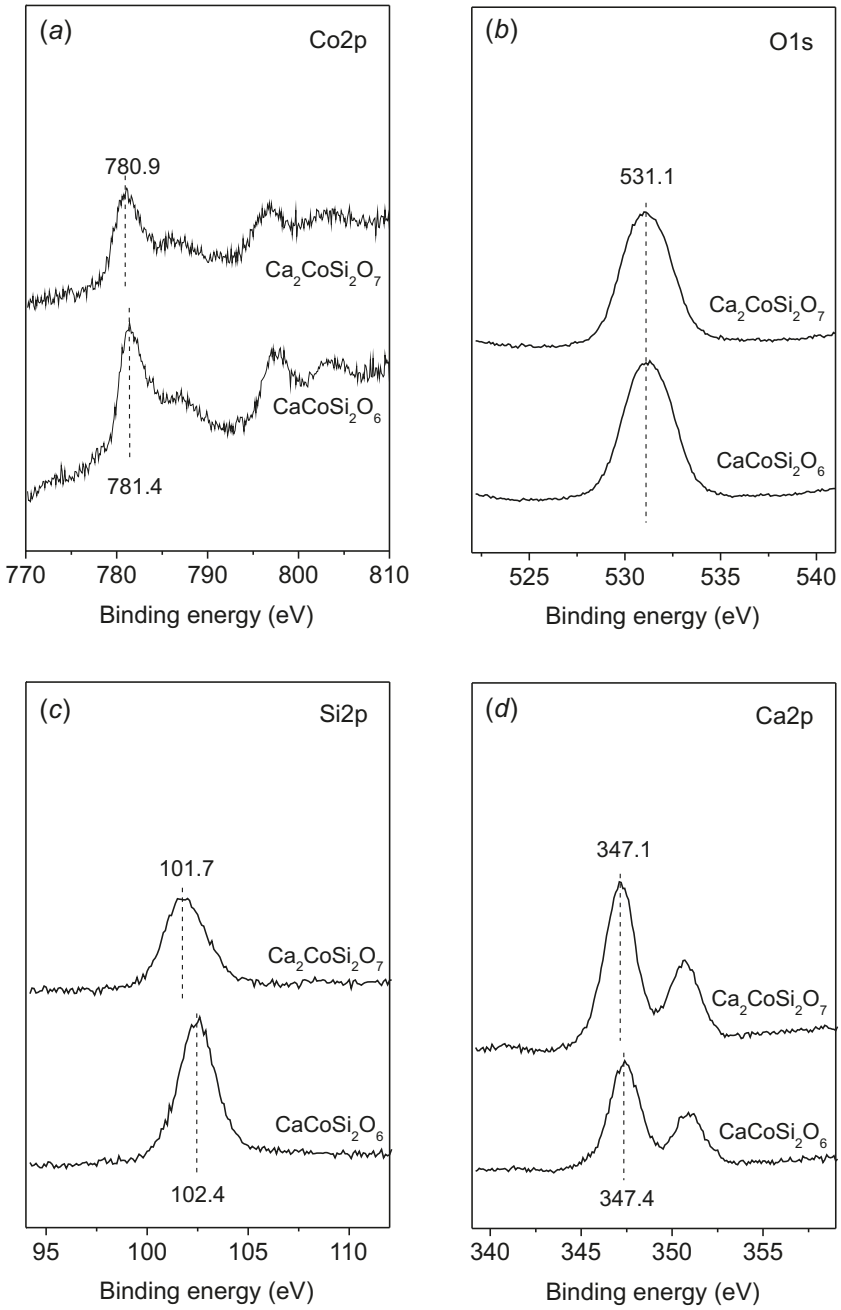

Table 4. X-ray photoelectron spectroscopy (XPS) surface elemental composition.

Samples	C (atomic %)	O (atomic %)	Ca (atomic %)	Co (atomic %)	Si (atomic %)
$CaCoSi_2O_6$	29.6	39.8	7.2	2.7	20.8
$Ca_2CoSi_2O_7$	35.4	36.7	10.5	1.6	15.8

silicon–oxygen tetrahedra (Fig. 2). The main difference in the structure of the CAC is determined by the coordination of Co^{2+} ions. In Co-pyroxene, Co^{2+} ions are in an octahedral coordination (O_h), whereas in Co-åkermanite, these ions are in a tetrahedral (T_d) coordination.

In reactions of complete oxidation within the temperature range in which the study was carried out, the reaction mechanism is probably oxidation–reduction. The cobalt ion, which is responsible for the activity in the course of the reaction, participates in the following equilibrium: $Co^{2+} \leftrightarrow Co^{3+}$. The coordination of cobalt ions in the CAC affects this process.

Conclusions

Two calcium–cobalt silicates were synthesized, in which

Can. J. Chem. Downloaded from www.nrcresearchpress.com by Xi'an Jiaotong University on 09/19/12
For personal use only.

Fig. 7. Amount of oxidized CO (*a*) and toluene (*b*) from 1% surface cobalt ions (atomic units) depending on temperature (*T*, °C). Samples: $CaCoSi_2O_6$ (Co-pyroxene) and $Ca_2CoSi_2O_7$ (Co-åkermanite).

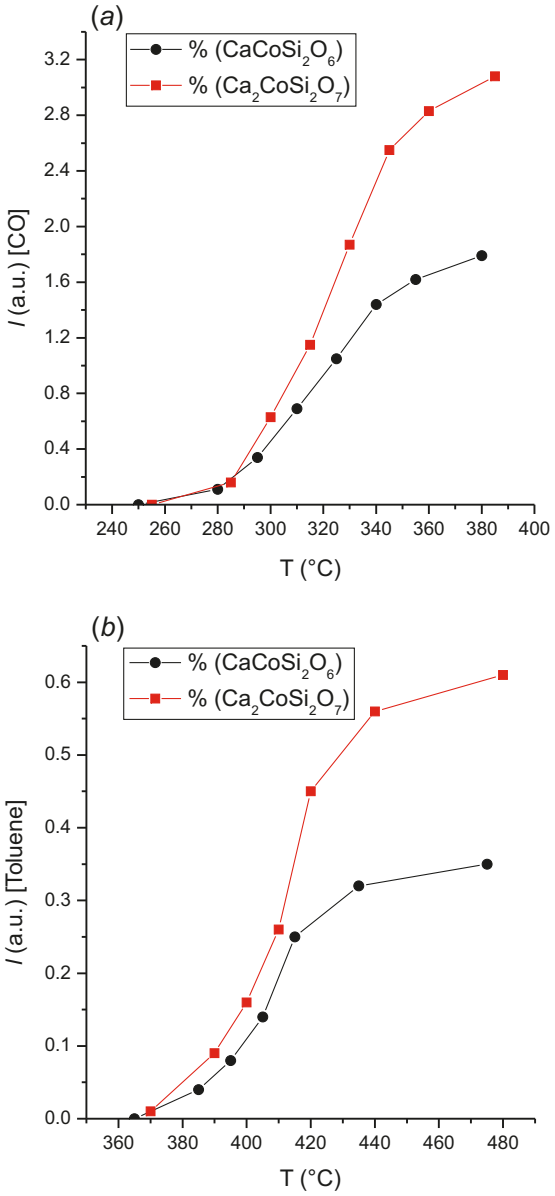

cobalt takes different structural positions. XRD, FTIR, and EPR data confirmed the synthesis of $CaCoSi_2O_6$ (Co-pyroxene) and $Ca_2CoSi_2O_7$ (Co-åkermanite). In the Co-åkermanite structure $Ca_2CoSi_2O_7$, cobalt cations take tetrahedral coordination toward oxygen atoms. In the Co-pyroxene structure $CaCoSi_2O_6$, the cobalt is in octahedral coordination.

Although different methods were used for the synthesis (e.g., the sol–gel method for $CaCoSi_2O_6$ and the solid-phase method for $Ca_2CoSi_2O_7$), only a small change in the specific surface area was observed.

The chemical composition study of the surface using EDS and XPS analyses showed a higher ratio of cobalt content in $CaCoSi_2O_6$ compared with $Ca_2CoSi_2O_7$ than what was expected on the basis of the stoichiometry of the phases.

Data from the catalytic activity test for CO oxidation and complete oxidation of toluene showed that Co-pyroxene and Co-åkermanite exhibit catalytic activity in terms of both components. Co-pyroxene showed a higher activity per gram of catalyst in both reactions than Co-åkermanite. The reason for the higher catalytic activity of Co-pyroxene compared with Co-åkermanite may be sought in the higher concentration of Co^{2+} ions at the surface of Co-pyroxene.

Catalytically active complexes with Co^{2+} ions in tetrahedral coordination are more efficient in terms of catalytic activity than those with these ions in octahedral coordination for equal concentration of cobalt on the surface of the catalysts.

References

(1) Naydenov, A.; Mehandjiev, D. *Compt. Rend. de l'Acad. Sci. Bulg.* **1992** *50*, 65.
(2) Jansson, J. *J. Catal.* **2000** *194* (1), 55. doi:10.1006/jcat.2000.2924.
(3) Xie, X.; Li, Y.; Liu, Z.; Haruta, M.; Shen, W. *Nature* **2009** *458* (7239), 746. doi:10.1038/nature07877.
(4) Sun, S.; Gao, Q.; Wang, H.; Zhu, J.; Guo, H. *Appl. Catal. B* **2010** *97* (1-2), 284. doi:10.1016/j.apcatb.2010.04.016.
(5) Jansson, J.; Palmqvist, A. E. C.; Fridell, E.; Skoglundh, M.; Österlund, L.; Thormählen, P.; Langer, V. J. *Catal.* **2002** *211*, 387.
(6) Konova, P.; Stoyanova, M.; Naydenov, A.; Christoskova, S.; Mehandjiev, D. *Appl. Catal. A Gen.* **2006** *298*, 109. doi:10.1016/j.apcata.2005.09.027.
(7) Xia, Y.; Dai, H.; Jiang, H.; Zhang, L. *Catal. Commun.* **2010** *11* (15), 1171. doi:10.1016/j.catcom.2010.07.005.
(8) Bekyarova, E.; Mehandjiev, D. *J. Colloid Interface Sci.* **1993** *161* (1), 115. doi:10.1006/jcis.1993.1448.
(9) Liotta, L. F.; Pantaleoa, G.; Macalusob, A.; Di Carlob, G.; Deganelloa, G. *Appl. Catal. A Gen.* **2003** *245* (1), 167. doi:10.1016/S0926-860X(02)00652-X.
(10) Sarellas, A.; Niakolas, D.; Bourikas, K.; Vakros, J.; Kordulis, C. *J. Colloid Interface Sci.* **2006** *295* (1), 165. doi:10.1016/j.jcis.2005.08.020.
(11) Tretyakov, V. F.; Zakirova, A. G.; Spozhakina, A. A.; Gabrovska, M. V.; Edreva-Kardzhieva, R.; Petrov, L. A. *Catal. in Industry* **2010** *2* (1), 62. doi:10.1134/S2070050410010101.
(12) Pollard, M. J.; Weinstock, B. A.; Bitterwolf, T. E.; Griffiths, P. R.; Newbery, A. P.; Paine, J. B., III. *J. Catal.* **2008** *254* (2), 218. doi:10.1016/j.jcat.2008.01.001.
(13) Paul, A.; Bagu, S. *Trans. J. Br. Ceram. Soc.* **1974** *73*, 167.
(14) Nakagawa, T.; Takada, Y.; Fukuta, Y.; Nishio, T.; Tachibana, T.; Shimada, T.; Yamamoto, T. A. *Jpn. J. Appl. Phys.* **2005** *44* (2), 994. doi:10.1143/JJAP.44.994.
(15) Lee, S. J.; Lo, C. C. H.; Matlage, P. N.; Song, S. H.; Melikhov, Y.; Snyder, J. E.; Jiles, D. C. *J. Appl. Phys.* **2007** *102* (7), 73910. doi:10.1063/1.2794711.
(16) Kale, G. M.; Pandit, S. S.; Jakob, K. T. *Trans. Jpn. Inst. Metals* **1988** *29*, 125.
(17) Kimata, M. *Naturwissenshaften* **1982** *69* (1), 40. doi:10.1007/BF00441100.
(18) Kimata, M.; Jb, N. *Miner. Abh.* **1983** *146*, 221.
(19) Hagiya, K.; Ohmasa, M.; Iishi, K. *Acta Crystallogr. B* **1993** *49* (2), 172. doi:10.1107/S0108768192008048.
(20) Kusaka, K.; Hagiya, K.; Ohmasa, M.; Okano, Y.; Mukai, M.; Iishi, K.; Haga, N. *Phys. Chem. Miner.* **2001** *28*, 150. doi:10.1007/s002690000147.
(21) Ghose, S.; Wan, C.; Okamura, F. *Am. Mineral.* **1987** *72*, 375.
(22) Durand, G.; Vilminot, S.; Rabu, P.; Derory, A.; Lambour, J. P.;

Ressouche, E. *J. Solid State Chem.* **1996** *124* (2), 374. doi:10.1006/jssc.1996.0252.
(23) Boudias, C., Monceau, D., CaRIne Crystallography 3.1, 17 rue du Moulin du Roy, F-60300 Senlis, France (1989–1998).
(24) Mihailova, I.; Stavrakeva, D.; Radev, L. *The Influence of Crystal Structure on the Position of Cobalt and the Color of Cobalt-containing Silicates,* Proceedings of the 1st National Crystallographic Symposium, Akademichno izdatelstvo, Sofia, 2009; p 64.
(25) *DiffracPlus TOPAS, version 4.2;* Bruker AXS Karlsruhe: Germany, 2009.
(26) Kraus, W.; Nolze, G. *Powdercell 2.4;* Federal Institute for Materials Research and Testing: Berlin, Germany, 2000.
(27) White, W. B.; McCarthy, G. J.; Scheetz, B. E. *Am. Mineral.* **1971** *56*, 72.
(28) Shannon, R. D. *Acta Crystallogr. A* **1976** *32* (5), 751. doi:10.1107/S0567739476001551.
(29) Sharma, S. K.; Simons, B.; Yoder, H. S. *Am. Mineral.* **1983** *68*, 1113.
(30) Gabelica-Robert, M.; Tarte, P. *Spectrochim. Acta [A]* **1979** *35A*, 649.
(31) Rutstein, M. S.; White, W. B. *Am. Mineral.* **1971** *56*, 877.
(32) Zhu, J.; Gao, Q. *Microporous Mesoporous Mater.* **2009** *124* (1–3), 144. doi:10.1016/j.micromeso.2009.05.003.
(33) Wei, W.; Chen, W.; Ivey, D. G. *Chem. Mater.* **2008** *20* (5), 1941. doi:10.1021/cm703464p.
(34) Vaz, C. A. F.; Prabhakaran, D.; Altman, E. I.; Henrich, V. E. *Phys. Rev.* **2009** *80B*, 155457.
(35) Noronha, F. B.; Perez, C. A.; Schmal, M.; Frety, R. *Phys. Chem. Chem. Phys.* **1999** *1* (11), 2861. doi:10.1039/a809963d.
(36) Greegor, R. B.; Lytle, F. W.; Chin, R. L.; Hercules, D. M. *J. Phys. Chem.* **1981** *85* (9), 1232. doi:10.1021/j150609a027.
(37) Mehandjiev, D. New Catalyst for Air Pollution Control. In *Heterogeneous Catalysis,* Proceedings of the 9th International Symposium, Varna, Bulgaria, 23–27 September, 2000; p 19.
(38) Tsoncheva, T.; Vankova, S.; Mehandjiev, D. *Fuel* **2003** *82* (7), 755. doi:10.1016/S0016-2361(02)00366-6.

Can. J. Chem. Downloaded from www.nrcresearchpress.com by Xi'an Jiaotong University on 09/19/12
For personal use only.

Cationic ruthenium(III) maltolato–imidazole complexes — Synthesis, characterization, and antiproliferatory activity*

David C. Kennedy, Brian O. Patrick, and Brian R. James

Can. J. Chem. Downloaded from www.nrcresearchpress.com by Xi'an Jiaotong University on 09/19/12
For personal use only.

Abstract: The cationic Ru^{III} complexes, *trans*-$[Ru(ma)_2(L)_2]CF_3SO_3$, where Hma = maltol = 3-hydroxy-2-methyl-4-pyrone; L = imidazole (Im) (complex **2**), 1(*N*)-methylimidazole (*N*-MeIm) (**3**), 2-methylimidazole (2-MeIm) (**4**), and 4-methylimidazole (4-MeIm) (**5**), were synthesized via the known L = EtOH (complex **1a**), and characterized by elemental analysis, ^1H NMR and IR spectroscopies, mass spectrometry, cyclic voltammetry, and (for **3** and **4**) by X-ray crystallography. The *trans*-$[Ru(ma)_2(H_2O)_2]CF_3SO_3$ complex (**1b**) was inadvertently isolated and characterized crystallographically, and the monomaltolato species $[Ru(ma)(N\text{-MeIm})_4][CF_3SO_3]_2$ (**6**) was also isolated and characterized. In vitro antiproliferatory activity of complexes **2**–**6** against human breast cancer cells (MDA-MB-435S) was tested using an MTT assay: **4** and **5** exhibit the lowest IC_{50} values, ~5 and ~15 μmol/L, respectively, whereas cisplatin exhibits an IC_{50} value of ~35 μmol/L against this cell line.

Key words: ruthenium complexes, imidazole ligands, maltolato ligand, anti-proliferatory activity.

Résumé : On a réalisé la synthèse de complexes cationiques du Ru(III), *trans*-$[Ru(ma)_2(L)_2]CF_3SO_3$ dans lesquels Hma = maltol = 3-hydroxy-2-méthylpyr-4-one; L = imidazole (Im) (complexe **2**), 1(*N*)-méthylimidazole (*N*-MeIm) (**3**), 2-méthylimidazole (2-MeIm) (**4**) et 4-méthylimidazole (4-MeIm) (**5**) à partir du complexe connu, **1a** dans lequel L = EtOH, et on les a caractérisés par leur analyse élémentaire, par les spectroscopies RMN du ^1H et IR, par la spectrométrie de masse, la voltampérométrie cyclique et, pour les composés **3** et **4**, par diffraction des rayons-X. Le complexe *trans*-$[Ru(ma)_2(H_2O)_2]CF_3SO_3$ (**1b**) a été isolé par inadvertance et caractérisé par cristallographie et l'espèce monomaltolato $[Ru(ma)(N\text{-MeIm})_4][CF_3SO_3]_2$ a aussi été isolé et caractérisé. On a évalué l'activité antiproliféatrice in vitro des complexes **2**–**6** contre les cellules du cancer du sein humain (MDA-MB-453S) en faisant appel à une méthode MTT; les composés **4** et **5** présentent les valeurs IC_{50} les plus faibles, soit environ 5 et 15 μm respectivement, alors que le cisplatine présente une valeur IC_{50} d'environ 35 μmol/L contre les cellules de cette lignée.

Mots-clés : complexes du ruthénium, ligands imidazole, ligand maltolato, activité antiproliféatrice.

[Traduit par la Rédaction]

Introduction

The area focusing on the potential use of Ru complexes as anticancer agents continues to be one of intense current interest. In a recently published article by our group on this potential of Ru(II)-4,4′-biimidazole complexes,[1] the Introduction gave leading references to the recent literature and included some articles from 2010. Now, a survey using SciFinder Scholar for the last 12 months reveals at least 200 *further* publications (excluding patents) on the "ruthenium anticancer" topic, suggesting an exponential growth in this area; only a selected number of the most recent references are quoted here. Contributions are dominated by studies from the groups of Dyson,[2,3] Keppler,[4] and Sadler,[5] often in collaborative efforts with other groups, but there were significant contributions from a myriad of other groups in 2009,[6–8] and in 2010–2011.[9–11] Studies on the pharmokinetics,[4b,12] protein interactions,[13] and DFT calculations[14] of the potential drugs KP1019 and NAMI-A continue to appear — both have successfully completed phase I clinical trials; the former complex is [HInd][*trans*-$Ru^{III}Cl_4(Ind)_2$] (Ind = indazole) and the latter is [HIm][*trans*-$Ru^{III}Cl_4(Im)(S\text{-DMSO})$] (Im = imidazole). The potential use of Ru complexes (without nitric oxide ligands) in photodynamic therapy is now attracting increasing attention.[9c,15] Finally, the glut of publications has led to generation of a plethora of recent short reviews and perspectives.[16,17] It appears that many synthetic-type coordination and organometallic researchers in the Ru chemistry area are now testing their new complexes for antiproliferatory activity!

This current paper describes the synthesis of Ru^{III} complexes containing both maltolato and imidazole ligands of the type $[Ru^{III}(O–O')_2(L)_2]^+$ or $[Ru^{III}(O–O')(L)_4]^{2+}$, where O–O′ represents the maltolato ligand and L is an imidazole (Chart 1). Their in vitro antiproliferatory activity against human

Received 4 February 2011. Accepted 6 April 2011. Published at www.nrcresearchpress.com/cjc on 2 August 2011.

D.C. Kennedy, B.O. Patrick, and B.R. James. Department of Chemistry, The University of British Columbia, Vancouver, BC V6T 1Z1, Canada.

Corresponding author: Brian R. James (e-mail: brj@chem.ubc.ca).

*Adapted from the Ph.D. thesis of D.C. Kennedy (see the References section).

Chart 1. Structures and numbering system for maltol, 4-pyridone, and imidazole.

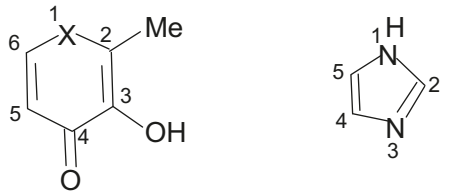

breast cancer cells (MDA-MB-435S) is also reported. We were the first to investigate such activity of Ru-maltolato complexes, specifically using the Ru^{II} species $Ru^{II}(O–O')_2(L)_2$, in which L was either a monodentate sulfoxide, or $(L)_2$ was a bidentate sulfoxide sometimes in a chiral form.[18] We later reported on the activity of *mer*-$Ru^{III}(O–O')_3$, its ethyl-substituted derivative, and a 4-pyridonato analogue (Chart 1),[19] and then on Ru^{III}(maltolato) complexes containing ancillary nitroimidazole ligands.[20] Keppler, Sadler, and co-workers have more recently also introduced maltol and pyridone (and thiopyridone) type moieties as supporting ligands in Ru-*p*-cymene complexes with anticancer potential.[4e,21] Maltol is attractive as a proligand in this area, since it is nontoxic and is used as a food additive.[22]

Experimental section

Materials for synthesis

Reagent grade solvents (Fisher Scientific) were generally dried using standard procedures under N_2 before use and deuterated solvents (Cambridge Isotope Laboratories) were used as received. The Sigma-Aldrich products imidazole (Im), 1(*N*)-methylimidazole (*N*-MeIm), 2-methylimidazole (2-MeIm), 4-methylimidazole (4-MeIm), $[^nBu_4N]PF_6$, $FeCp_2$, triflic acid, cisplatin, silica gel preparative TLC plates with fluorescent indicator (20 × 20 cm^2, Uniplate from Analtech), and maltol (3-hydroxy-2-methyl-4-pyrone, obtained from Cultor Food Science), were used as received. $RuCl_3·3H_2O$ was donated by Colonial Metals. The Ru^{III} precursor complex *mer*-$Ru(ma)_3$[19] and its conversion to *trans*-$[Ru(ma)_2(EtOH)_2]CF_3SO_3$ (**1a**) by treatment with triflic acid in EtOH[20] was reported previously; the imidazole derivatives were synthesized using standard Schlenk techniques, although this is not essential.

Physical techniques and instrumentation

^1H NMR spectra (br = broad, s = singlet, and d = doublet) were recorded at room temperature (rt, ~20 °C) on a Bruker AV300 spectrometer, chemical shifts being calibrated using residual ^1H resonances from deuterated solvents. Elemental analyses were performed by M. Lakha of this department on a Carlo Erba EA 1108 CHN-O analyzer. Mass spectral data (reported as *m*/*z* values) were acquired on a Bruker Esquire ES spectrometer in this department (c/o Y. Ling); the given M value pertains to the cationic component of the complex. IR spectra (KBr) were recorded on ATI Mattson Genesis or Bomem–Michelson MB-100 FT-IR spectrometers; selected ν values (cm^{-1}) are sometimes given with assigned functional groups. Conductivity measurements, carried out on a RCM151B Serfass conductance bridge (A.H. Thomas Co. Ltd.) with a 3403 cell (Yellow Springs Instrument Company), were calibrated using 0.01000 mol/L aq KCl solution (Λ_M = 141.3 Ω^{-1} cm^2 mol^{-1} at 25 °C, cell constant = 1.016 cm^{-1}), and data are given in units of Ω^{-1} cm^2 mol^{-1}. Cyclic voltammograms were recorded in MeCN containing 0.1 mol/L $[^nBu_4N]PF_6$ as the supporting electrolyte on a Pine Bipotentiostat (Model AFCBP1) using PineChem v2.00 software. The scan rate was 100 mV s^{-1} using a Pt working electrode, a Pt wire counter electrode, and a Ag wire reference electrode; $FeCp_2$ was used as an internal standard ($E_{1/2}$ ($Fe^{III/II}$) = 0.40 vs SCE in MeCN),[23] and $E_{1/2}$ values are reported relative to SCE.

trans-$[Ru(ma)_2(H_2O)_2]CF_3SO_3$ (1b)

A concentrated solution of the red complex *trans*-$[Ru(ma)_2(EtOH)_2]CF_3SO_3$ (**1a**) in nondried reagent grade EtOH (5 mL) was left to evaporate in air; after 2 weeks, a few red crystals of *trans*-$[Ru(ma)_2(H_2O)_2]CF_3SO_3$·EtOH (**1b**·EtOH) were deposited as determined by X-ray analysis (vide infra).

$[Ru(ma)_2(Im)_2]CF_3SO_3$ (2)

To a red solution of *mer*-$Ru(ma)_3$ (55 mg, 0.12 mmol) in EtOH (5 mL), triflic acid (22 mg, 0.14 mmol) was added under N_2 and the solution was stirred at rt for 1 h. Im (35 mg, 0.51 mmol) was then added and the solution was stirred for an additional 12 h. After 4 h the solution was checked by TLC (CH_2Cl_2–MeOH, 10:1). The band for **1a** had disappeared and was replaced by 11 minor bands; after 12 h, a single major band (R_f = 0.65) was observed with five minor bands of lower R_f. The solvent was removed under vacuum, and the dark red residue was dissolved in CH_2Cl_2 (2 mL); this solution was then applied to a 20 cm × 20 cm silica preparative TLC plate that was developed with CH_2Cl_2–MeOH (15:1, 130 mL). When the major band had clearly separated, it was cut from the plate, added to 50 mL of CH_2Cl_2 / 1 mL of MeOH, and this mixture was left stirring for 16 h. The red mixture was then filtered to remove the silica, and the filtrate was reduced in volume to ~5 mL. Hexanes (30 mL) were then added and the resulting red precipitate was collected, washed with hexanes (2 × 5 mL), and dried at 78 °C under vacuum for 48 h. Yield: 38 mg (51%). IR ν: 3145 (N–H, m), 1603 (C=O, s), 1467 (s), 1263 (s). ^1H NMR (*cis*-isomer, $CDCl_3$) δ: 62.2, 44.6 (br s, C*H*$_3$–ma), –1.5, –5.6 (br s, *H*$_5$–Im), –15.5, –24.7 (br s, *H*$_2$–Im). ^1H NMR (*trans*-isomer, $CDCl_3$) δ: 60.0 (s, C*H*$_3$–ma), –3.7 (s, *H*$_5$–Im), –19.6 (s, *H*$_2$–Im). LR-MS (+LSIMS, thioglycerol): 488 (M^+), 420 (M^+ – Im), 352 (M^+ – 2Im). $E_{1/2}$ ($Ru^{III/II}$) = –0.705 V. Λ_M (MeOH) = 119. Anal. calcd for $C_{19}H_{18}F_3N_4O_9SRu$: C 35.85, H 2.85, N 8.80; found: C 35.92, H 2.92, N 8.73.

trans-$[Ru(ma)_2(N\text{-}MeIm)_2]CF_3SO_3·CH_2Cl_2$ (3·CH_2Cl_2)

The procedure initially followed that given for **2**, but using 80 mg (0.17 mmol) of *mer*-$Ru(ma)_3$, 28 mg (0.19 mmol) of triflic acid, and 62 mg (0.76 mmol) *N*-MeIm, and the solution was stirred for a longer time (24 h). After 6 h the solution was checked by TLC (CH_2Cl_2–MeOH, 10:1): six bands were observed, the most intense being a red one at R_f = 0.60.

Can. J. Chem. Downloaded from www.nrcresearchpress.com by Xi'an Jiaotong University on 09/19/12
For personal use only.

Can. J. Chem. Downloaded from www.nrcresearchpress.com by Xi'an Jiaotong University on 09/19/12
For personal use only.

After 18 h, two major bands, a red one at $R_f = 0.64$ and a less intense blue one at $R_f = 0.35$, were seen. After 24 h, the solvent was removed and the dark red residue was dissolved in CH_2Cl_2 (~2 mL) and applied to a preparative TLC plate that was developed with CH_2Cl_2–MeOH (12:1, 130 mL). The red band was treated as described for **2** to yield a red solid. Attempts to extract the blue band were unsuccessful. Yield: 60 mg (48%). IR ν: 3458 (m), 1601 (C=O, s), 1467 (s), 1263 (s), 1031 (s). ^{1}H NMR ($CDCl_3$) δ: 62.0 (br s, CH_3–ma), 13.4 (br s, CH_3–Im, –3.8 br (s, H_5–Im), –19.0 (br s, H_2–Im). LR-MS (+LSIMS, thioglycerol): 516 (M^+), 434 (M^+ – *N*-MeIm), 352 (M^+ – 2*N*-MeIm). $E_{1/2}$ ($Ru^{III/II}$) = –0.765 V. Λ_M (MeOH) = 109. Anal. calcd for $C_{21}H_{22}F_3N_4O_9SRu{\cdot}CH_2Cl_2$: C 35.26, H 3.23, N 7.48; found: C 35.71, H 3.22, N 7.86. X-ray quality crystals were grown by slow evaporation of a CH_2Cl_2 solution of the complex layered with hexanes.

trans-[Ru(ma)$_2$(2-MeIm)$_2$]CF_3SO_3 (4)

The procedure, including the workup treatment, was as for **3**·CH_2Cl_2, but using 92 mg (0.19 mmol) of *mer*-Ru(ma)$_3$, 32 mg (0.21 mmol) of triflic acid, and 66 mg (0.80 mmol) of 2-MeIm, with just 12 h of stirring. The red band gave 63 mg of product (56% yield). IR ν: 3216 (N–H, m), 1602 (C=O, s), 1447 (s), 1265 (s). ^{1}H NMR ($CDCl_3$) δ: 67.0 (br s, CH_3–ma), 42.0 (br s CH_3–Im), –1.6 (br s, H_5–Im), –4.7 (br s, H_4–Im). LR-MS (+LSIMS, thioglycerol): 516 (M^+), 434 (M^+ – 2-MeIm), 352 (M^+– 2 × 2-MeIm). $E_{1/2}$ ($Ru^{III/II}$) = –0.844 V. Λ_M (MeOH) = 121. Anal. calcd for $C_{21}H_{22}F_3N_4O_9SRu$: C 37.95, H 3.34, N 8.43; found: C 37.61, H 3.38, N 8.20. Crystals were grown by the method used to obtain **3**·CH_2Cl_2.

trans-[Ru(ma)$_2$(4/5)-MeIm)$_2$]$CF_3SO_3{\cdot}CH_2Cl_2$ (5)

The procedure, including the work up treatment, was the same as for **3**·CH_2Cl_2, but using 50 mg (0.11 mmol) of *mer*-Ru(ma)$_3$, 20 mg (0.13 mmol) of triflic acid, and 41 mg (0.50 mmol) of 4-MeIm and only 12 h of stirring. Sampling by TLC analysis after 4 h revealed the disappearance of **1a** with production of three red bands (R_f = 0.32, 0.44, 0.54); after the 12 h, only one major red band was observed (R_f = 0.56) and this yielded 32 mg of **5** (42% yield). IR ν: 3224 (NH, m), 1601 (C=O, s), 1446 (s), 1263 (s). ^{1}H NMR ($CDCl_3$) δ: 60.0 (br s, CH_3–ma), 16.3 (br s, CH_3–Im), –4.5 (br s, H_5–Im), –20.0 (br s, H_2-Im). LR-MS (+LSIMS, thioglycerol): 516 (M^+), 434 (M^+ – 4-MeIm), 352 (M^+ – 2 × 4-MeIm). $E_{1/2}$ ($Ru^{III/II}$) = –0.738 V. Λ_M (MeOH) = 107. Anal. calcd for $C_{21}H_{22}F_3N_4O_9SRu{\cdot}CH_2Cl_2$: C 35.26, H 3.23, N 7.48; found: C 35.63, H 3.26, N 7.55.

[Ru(ma)(*N*-MeIm)$_4$][CF_3SO_3]$_2$ (6)

To a solution of *mer*-Ru(ma)$_3$ (67 mg, 0.14 mmol) in EtOH (5 mL), triflic acid (54 mg, 0.36 mmol) was added under N_2, and the solution was stirred at rt for 1 h, when *N*-MeIm (77 mg, 1.1 mmol) was added; the solution was then refluxed for 48 h. After 24 h the solution was checked by TLC (CH_2Cl_2–MeOH, 10:1): two major bands were observed, a red one at $R_f = 0.60$ and a blue one at $R_f = 0.35$. After 48 h, analysis revealed the same major blue band, several minor bands (R_f = 0.2 – 0.7), and a black spot ($R_f = 0$). The solvent was removed under vacuum and the dark blue residue was dissolved in CH_2Cl_2 (~1.5 mL) and applied to a preparative TLC plate that was developed with CH_2Cl_2–MeOH (10:1, 130 mL). The blue band was cut out, added to 50 mL of CH_2Cl_2 / 2 mL of MeOH, and the mixture was left stirring for 16 h. The blue mixture was then filtered to remove the silica and the volume was reduced to ~1 mL. Hexanes (10 mL) were then added and the resulting blue precipitate was collected, washed with hexanes (2 × 5 mL), and dried at 78 °C under vacuum for 48 h. Yield: 55 mg (46%). IR ν 3137 (m), 1601 (C=O, s), 1546 (m), 1470 (m), 1265 (s), 1031 (s). ^{1}H NMR ($CDCl_3$) δ: 81.6 (br s, CH_3–ma), 25.6, 20.4 (br s, CH_3–Im), –0.5, –5.7 (s, H_5–Im), –18.4, –24.0 (s, H_2–Im). LR-MS (+LSIMS, thioglycerol): 704 (M^{2+} + $CF_3SO_3^-$), 622 (M^{2+} + $CF_3SO_3^-$ – *N*-MeIm), 540 (M^{2+} + $CF_3SO_3^-$ – 2 × *N*-MeIm), 458 (M^{2+} + $CF_3SO_3^-$ – 3 × *N*-MeIm). $E_{1/2}$ ($Ru^{III/II}$) = –0.442 V. Λ_M (MeOH) = 273. Anal. calcd for $C_{24}H_{29}F_6N_8O_9S_2Ru$: C 33.80, H 3.43, N 13.14; found: C 33.23, H 3.34, N 12.73.

X-ray crystallographic analyses for complexes 1b·EtOH, 3·CH_2Cl_2, and 4

X-ray analyses were carried out at 173.0(1) K on a Bruker X8 APEX diffractometer with graphite-monochromated Mo Kα radiation (0.710 69 Å). The final unit-cell parameters were based on 4739 reflections with $2\theta_{max}$ = 56.5° for **1b**·EtOH, 5707 reflections with $2\theta_{max}$ = 54.2° for **3**·CH_2Cl_2, and 5269 reflections with $2\theta_{max}$ = 55.7° for **4**, in a series of ϕ and ω scans in 0.50° oscillations with respective exposures of 15.0, 49.0, and 10 s; the crystal-to-detector distance was between 37.01 and 38.79 mm. The data for **1b**·EtOH were processed using the Bruker SAINT software package[24] and the d*TREK program was used for **3**·CH_2Cl_2 and **4**.[25] The three structures were solved using direct methods[26] and expanded using Fourier techniques.[27] Data were corrected for absorption effects using the multiscan technique (SADABS)[28] for **1b**·EtOH, and the multiscan techniques (teXsan)[29] for **3**·CH_2Cl_2 and **4**, with minimum and maximum transmission coefficients in the respective ranges of 0.727–0.788 and 0.892–0.983. The data were also corrected for Lorentz and polarization effects.

All three complexes crystallize with two half-Ru moieties in the asymmetric unit, each Ru atom residing on an inversion centre. Complex **1b** crystallizes with one disordered molecule of EtOH in the asymmetric unit, the relative populations of the major and minor fragments being refined to values of 0.53 and 0.47, respectively. H atoms involved in H bonding were located in difference maps, whereas all other H atoms were included in calculated positions but not refined. In **3** there was one disordered CH_2Cl_2 in the asymmetric unit, and the CF_3SO_3 anion was also disordered; both were modeled in two orientations with restraints on bond lengths, bond angles, and anisotropic displacement parameters being used to maintain similar geometries between the disordered fragments. All non-H atoms in the three structures were refined anisotropically, whereas the C–H hydrogen atoms were included in calculated positions and not refined. The structures are shown in Figs. 1–3, and some crystallographic data are given in Table 1; selected bond lengths and angles are given in Tables 2–4. Full crystallographic data are given in the Supplementary data.

Can. J. Chem. Downloaded from www.nrcresearchpress.com by Xi'an Jiaotong University on 09/19/12
For personal use only.

Fig. 1. ORTEP diagram of *trans*-$[Ru(ma)_2(H_2O)_2]CF_3SO_3$·EtOH (**1b**·EtOH) with 50% probability thermal ellipsoids. Hydrogen atoms are omitted.

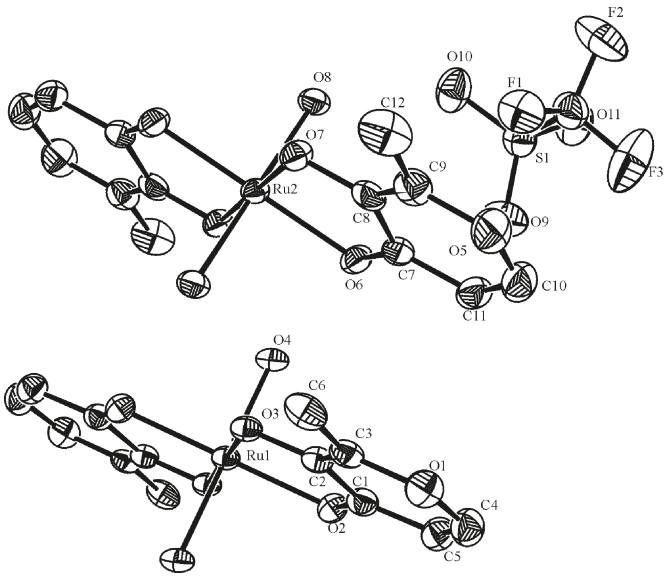

Biological assays

All reagents and cell-handling techniques, as well as experimental procedures for the MTT assay, the Ru uptake assay into cells, and DNA binding to Ru, have been described in detail in our previous publications.[18–20,30] For the MTT assay, complexes were dissolved in PBS (phosphate-buffered saline solution), and were tested against MDA-MB-435S cells in Leibovitz's L-15 medium with L-glutamine after incubation at 37 °C for 70 h. The Ru uptake in cells was studied with a Chinese hamster ovary (CHO) cell line.

Results and discussion

Reaction of *mer*-$Ru(ma)_3$ with triflic acid

As described previously, the red, paramagnetic Ru^{III} complex *trans*-$[Ru(ma)_2(EtOH)_2]CF_3SO_3$ (**1a**) was isolated from a solution made by refluxing *mer*-$Ru(ma)_3$ in EtOH with 1 equiv of triflic acid, and was well characterized by elemental analysis, mass spectrometry, ^1H NMR and IR spectroscopies, and conductivity.[20] The ^1H NMR spectrum in CD_3OD initially showed a broad singlet at δ 48.0, consistent with a single species containing *trans*-maltolato ligands in a structure with equivalent Me groups; resonances downfield of $\delta \sim 40$ can be assigned generally to this group as established previously by our detailed one- and two-dimensional NMR studies on $Ru(ma)_3$, which has a mer configuration with respect to corresponding O atoms.[19] The ^1H spectrum also showed broad singlets at 28.0 and 26.0 owing to the coordinated EtOH, but these signals were slowly replaced (>10 min) by those of free EtOH as the EtOH ligands were replaced by CD_3OD (or less likely D_2O, which would be present in trace amounts); resonances for the H(5) and H(6) protons could not be assigned.[20] In this current work, the formation of the single product, presumed to be *trans*-$[Ru(ma)_2(CD_3OD)_2]^+$ from *mer*-$Ru(ma)_3$ and triflic acid in CD_3OD solution was monitored by in situ ^1H NMR spectroscopy (see Fig. S1 in the Supplementary data) as the relatively sharp singlets of *mer*-$Ru(ma)_3$ (δ 42.0, 39.3, and 22.5)[18] were replaced by a broad singlet at δ 46 and cogeneration of signals for free maltol (δ 7.7 (d, H_6), 6.4 (d, H_5), 2.40 (s, Me)). The few X-ray quality crystals that were grown during the 2 week evaporation of an EtOH solution of **1a** in air turned out surprisingly to be those of *trans*-$[Ru(ma)_2(H_2O)_2]CF_3SO_3$·EtOH (**1b**·EtOH), the EtOH ligands having been replaced by aquo ligands (Fig. 1). The Me groups of the planar maltolato ligands are equivalent, as seen also in the ^1H NMR solution spectrum of **1a**. Attempts to grow crystals from a dry EtOH solution of **1a** (or a MeOH solution of the bis(methanol) analogue) under an inert atmosphere were unsuccessful. The same trans geometry is seen for the $[Ru(ma)_2(L)_2]CF_3SO_3$ complexes where L is an imidazole (see the following), which suggests that **1a** is the precursor to the bis(imidazole) products; indeed, these complexes can be generated by treatment of in situ formed **1a** or **1b** with the appropriate imidazole.

The structural data of **1b**·EtOH (Table 2) show that the bond lengths for the Ru–O(keto) group are about 0.05 Å longer than those for Ru–O(hydroxy), behavior that is seen in *mer*-$Ru(ma)_3$ and other maltolato complexes.[19] The $Ru–OH_2$ bond lengths, lying in between the Ru–O values of the maltolato ligands, are essentially the same as in $Ru(H_2O)_6^{3+}$,[31] and are in the range of values for other Ru^{III}–aquo complexes.[32]

Maltolato–imidazole complexes

The red *trans*-$[Ru(ma)_2(L)_2]CF_3SO_3$ complexes, where L is an *N*-bound Im (complex **2**), *N*-MeIm (**3**), 2-MeIm (**4**), and 4-MeIm (**5**), were all synthesized using the same general procedure from in situ **1a**, by displacing the EtOH ligands using a fourfold excess of the imidazole at rt over 12–24 h; the complexes were isolated in 40%–50% yield after purification by preparative TLC. The C analysis for **3** (isolated with a solvate CH_2Cl_2, as shown by X-ray analysis of the complex) was 0.45% high, and this likely results from loss of some solvate during the analysis. Attempts to speed up the synthetic reactions by a reflux procedure generally led to the formation of several side products. However, in the case of L = *N*-MeIm, a 48 h reflux procedure in which excess triflic acid was used (acid:$Ru(ma)_3$ = 2.5), as well as an eightfold excess of the imidazole, led to the formation of $[Ru(ma)(N\text{-MeIm})_4][CF_3SO_3]_2$ (**6**) in 46% yield; corresponding reactions with the other imidazoles showed no evidence for formation of a mono(maltolato)–tetrakis(imidazole) species. The measured conductivity data in MeOH for each of the complexes are consistent with their ionic formulations.[33] The C analysis for **6** was 0.57% low, but the Λ_M and $E_{1/2}$ values (see the following) and the MS and ^1H NMR data (Fig. S2*b*) support the formulation.

Complexes **3** and **4** were characterized by X-ray crystallography (Figs. 2 and 3, respectively), and they have very similar bond lengths and angles (Tables 3 and 4). As for complex **1b** in the planar equivalent maltolato ligands, the Ru–O(keto) bond lengths are ~0.05 Å longer than those for Ru–O(hydroxy). The similar Ru–N bond lengths in **3** and **4**, typical of others in Ru^{III}–imidazole systems,[34] imply the absence of any steric interactions between the imidazole–Me (adjacent to the coordinated N atom in complex **4**) and the maltolato ligands;

Fig. 2. ORTEP diagram of the cation of *trans*-[Ru(ma)$_2$(*N*-MeIm)$_2$]$CF_3SO_3 \cdot CH_2Cl_2$ (**3**·CH_2Cl_2) with 50% probability thermal ellipsoids. Hydrogen atoms are omitted.

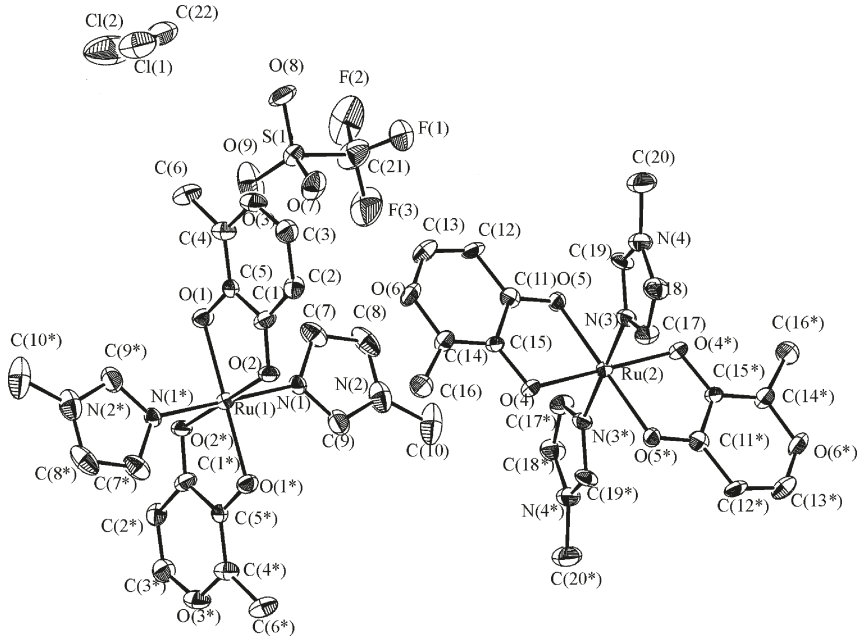

Fig. 3. ORTEP diagram of the cation of *trans*-[Ru(ma)$_2$(2-MeIm)$_2$]CF_3SO_3 (**4**) with 50% probability thermal ellipsoids; only one of the two Ru moeties is shown.

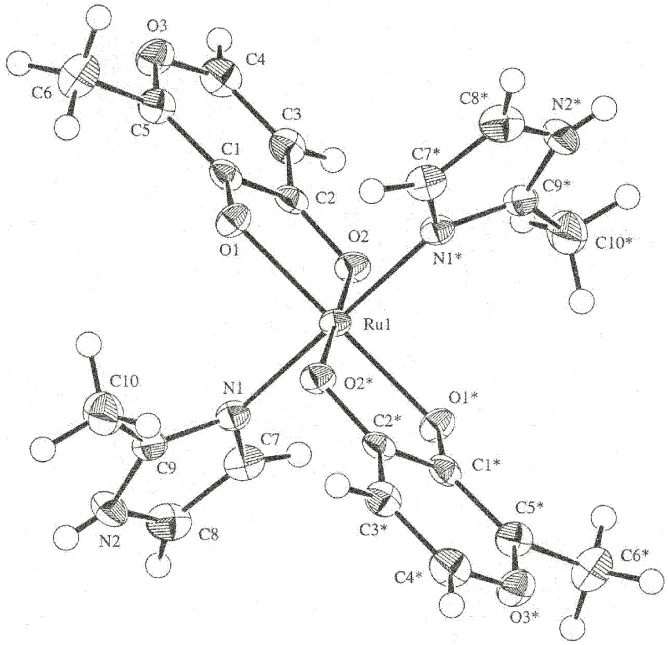

however, there is a small difference between **3** and **4** in the orientation of the imidazole ring with respect to the plane of the maltolato ligand that might relieve any such interaction in **4**. For example, for **3**, the Ru(1)–N(1)–C(9) (125.6°) and Ru (1)–N(1)–C(7) (128.0°) angles differ by 2.4°, whereas for **4**, where the Me is at C(9), the corresponding angles are 129.7° and 123.5°, a difference of 6.2°; thus, in **4**, the Me group is shifted away from the plane of the maltolato ligand rather than generating a steric interaction that could result in a lengthening of the Ru–N bond. There are no significant interactions with the triflate counteranion in **3** or **4**, or with the CH_2Cl_2 solvate in **3**.

The solution ^{1}H NMR spectra of **2**–**5** are compatible with the solid-state, trans structures determined for **3** and **4**, and assumed for **2** and **5**. Analogous to complex **1a**, a single broad resonance in the δ 67–60 region is assigned in each case to the equivalent maltolato–Me groups of the trans-isomer. For **2**, the Im complex, seen also sometimes (see the following) are two equal intensity, somewhat sharper, singlet resonances at δ 62.2 (which overlaps the broad resonance of the trans-isomer) and 44.6, and these are attributed to the maltolato–Me groups of an assumed cis-isomer; again, as for **1a**, ^{1}H resonances for the maltolato H(5) and H(6) are not observed for any of the complexes. For the *N*-MeIm and 2-MeIm complexes (**3** and **4**), the imidazole–Me resonance is seen, respectively, as a broad signal at δ 13.4 and 42.0 (see Figs. S2*a* and S3), whereas the corresponding values for the free Me–imidazoles are 3.64 and 2.35; the larger downfield shift seen for **4** results from its position closer to the paramagnetic Ru^{III} centre.[35] The imidazole–Me resonance for the 4-MeIm complex **5** is seen at δ 16.3 (the value for free 4-MeIm is 2.30); a larger shift, comparable to that seen in complex **4**, was anticipated because the 4- and 2-Me groups are both adjacent to the coordinated N atom. It is possible that complex **5** might actually contain 5-MeIm, since an initially used 4-MeIm in an attempted synthesis of [Ru(acac)$_2$(4-MeIm)$_2$]CF_3SO_3 (acac = acetylacetonate) underwent tautomerization and generated a 1:3 mixture of 4- and 5-MeIm products in solution from which the latter crystallized;[36] the more remote Me group would then be expected (as observed) to give a ^{1}H signal in the range noted for the *N*-Me complex. (Note that acac, like maltolato, is a chelating O–O′ keto-hydroxylate type ligand.). Unfortunately an X-ray quality crystal of **5** needed to test this hypothesis was not obtained. For **6**, the blue, maltolato–tetrakis(*N*-MeIm) complex, the maltolato–Me resonance, a broad singlet at δ 81.6, is downfield

Can. J. Chem. Downloaded from www.nrcresearchpress.com by Xi'an Jiaotong University on 09/19/12
For personal use only.

Can. J. Chem. Downloaded from www.nrcresearchpress.com by Xi'an Jiaotong University on 09/19/12
For personal use only.

Table 1. Crystallographic data for **1b**·EtOH, **3**·CH_2Cl_2, and **4**.

	1b·EtOH	**3**·CH_2Cl_2	**4**
Formula	$C_{15}H_{20}F_3O_{12}RuS$	$C_{22}H_{24}Cl_2F_3N_4O_9RuS$	$C_{21}H_{22}F_3N_4O_9RuS$
fw	582.44	749.48	664.55
Crystal color, habit	Red, needle	Red, platelet	Red, prism
Crystal size (mm)	0.25×0.10×0.03	0.20×0.10×0.02	0.20×0.15×0.15
Crystal system	Triclinic	Triclinic	Triclinic
Space group	*P*-1 (No. 2)	*P*-1 (No. 2)	*P*-1 (No. 2)
a (Å)	9.0433(9)	9.1784(8)	8.9512(6)
b (Å)	9.7681(10)	12.9918(3)	9.2949(7)
c (Å)	12.4972(15)	13.6855(3)	15.817(1)
α (°)	96.05(1)	64.08(2)	94.908(5)
β (°)	90.67(1)	78.77(2)	93.453(5)
γ (°)	107.00(1)	85.95(2)	93.059(4)
V (Å^3)	1048.8(2)	1439.5(13)	1306.5(2)
Z	2	2	2
D_{calcd} (cm^{-3})	1.844	1.729	1.684
μ (mm^{-1})	0.935	0.878	0.758
Total reflns.	31444	12663	11677
Unique reflns.	4739	5707	5269
R_{int}	0.047	0.084	0.041
No. of variables	310	421	363
*R*1 ($I > 2\sigma(I)$)	0.035 (3395 obs. reflns.)	0.060 (3461 obs. reflns.)	0.036 (3865 obs. reflns.)
*wR*2	0.103 (All data)[a]	0.156 (All data)[b]	0.092 (All data)[c]
GoF	1.04 (All data)	0.98 (All data)	0.97 (All data)

[a] $w = 1/[\sigma^2(F_o^2) + (0.0627\ P)^2]$.
[b] $w = 1/[\sigma^2(F_o^2) + (0.0680\ P)^2]$.
[c] $w = 1/[\sigma^2(F_o^2) + (P^2/4)F_o^2]$, where $P = (F_o^2 + 2F_c^2)/3$.

Table 2. Selected bond distances and angles for **1b**·EtOH with estimated standard deviations in parentheses.

Bond	Length (Å)	Bond	Angle (°)
Ru(1)–O(2) (keto)	2.060(2)	O(2)–Ru(1)–O(3)	81.63(8)
Ru(1)–O(3) (hydroxy)	2.0125(19)	O(6)–Ru(1)–O(7)	82.22(8)
Ru(1)–O(4) (water)	2.031(2)	O(2)–Ru(1)–O(3*)	98.37(8)
Ru(2)–O(6) (keto)	2.049(2)	O(6)–Ru(1)–O(7*)	97.78(8)
Ru(2)–O(7) (hydroxy)	2.000(2)	O(2)–Ru(1)–O(4)	91.54(9)
Ru(2)–O(8) (water)	2.026(2)	O(3)–Ru(1)–O(4)	91.71(8)
O(4)–H(4a)	0.73(2)	O(2)–Ru(1)–O(4*)	88.46(9)
O(4)–H(4b)	0.74(2)	O(3)–Ru(1)–O(4*)	88.29(8)
O(8)–H(8a)	0.78(2)	Ru(1)–O(4)–H(4A)	112(3)
O(8)–H(8b)	0.77(2)	Ru(1)–O(4)–H(4B)	115(3)

Table 3. Selected bond distances and angles for **3**·CH_2Cl_2 with estimated standard deviations in parentheses.

Bond	Length (Å)	Bond	Angle (°)
Ru(1)–O(1) (hydroxy)	2.011(4)	O(1)–Ru(1)–O(2)	82.04(17)
Ru(1)–O(2) (keto)	2.070(4)	O(1)–Ru(1)–O(2*)	97.96(17)
Ru(1)–N(1)	2.057(5)	O(1)–Ru(1)–N(1)	90.94(19)
Ru(2)–O(4) (hydroxyl)	2.012(4)	O(2)–Ru(1)–N(1)	88.15(19)
Ru(2)–O(5) (keto)	2.065(4)	O(2*)–Ru(1)–N(1)	91.85(19)
Ru(2)–N(3)	2.072(5)	Ru(1)–N(1)–C(9)	125.6(5)
C(1)–C(5)	1.425(9)	Ru(1)–N(1)–C(7)	128.0(5)
C(4)–C(5)	1.363(9)	Ru(1)–O(1)–C(5)	110.2(4)
O(3)–C(3)	1.349(8)	Ru(1)–O(2)–C(1)	110.1(4)
O(3)–C(4)	1.373(8)		

Table 4. Selected bond distances and angles for **4** with estimated standard deviations in parentheses.

Bond	Length (Å)	Bond	Angle (°)
Ru(1)–O(1) (hydroxy)	2.006(2)	O(1)–Ru(1)–O(2)	82.38(8)
Ru(1)–O(2) (keto)	2.063(2)	O(1)–Ru(1)–O(2*)	97.62(8)
Ru(1)–N(1)	2.078(3)	O(1)–Ru(1)–N(1)	88.94(9)
C(9)–C(10)	1.490(5)	O(2)–Ru(1)–N(1)	87.89(9)
C(9)–C(10)	1.490(5)	O(2*)–Ru(1)–N(1)	92.11(9)
C(5)–C(6)	1.478(5)	Ru(1)–N(1)–C(9)	129.7(2)
O(3)–C(5)	1.373(4)	Ru(1)–N(1)–C(7)	123.5(2)
O(3)–C(4)	1.346(4)	Ru(1)–O(1)–C(1)	110.0(2)
		Ru(1)–O(2)–C(2)	110.0(20)

Can. J. Chem. Downloaded from www.nrcresearchpress.com by Xi'an Jiaotong University on 09/19/12
For personal use only.

of the corresponding resonances seen for the bis(imidazole) complexes, whereas two resonances at δ 25.6 and 20.4 are observed for the Im–Me groups (Fig. S2*b*); these signals are shifted further downfield from that for the corresponding methyl group for complex **3** where only one maltolato group has been substituted. The appropriate Im–H_2, –H_4, and –H_5 resonances of complexes **2**–**6** sometimes were assigned and are found in the region δ –1.6 το –24.7 (see the Experimental section).

Attempts to separate the trans- and assumed cis-isomers of **2** were unsuccessful. The relative intensities of the relevant ^{1}H NMR signals varied between samples, suggesting the absence of a solution equilibrium and that two overlapping TLC bands are the likely source of the two isomers. Indeed, the ratio of trans to cis decreased as the silica was taken from the lower parts of the red band, but even a sample isolated from a thin section (~1 mm in width) cut from the top of the band still revealed up to 10% of the cis-isomer. The excellent elemental analysis obtained for **2** is consistent with the product being a mixture of trans- and cis-isomers of the same complex.

The studies suggest that *mer*-Ru(ma)$_3$ would be a useful general precursor for synthesis of a wide range of maltolato-containing Ru^{III} complexes.

The Ru(III/II) reduction potentials in MeCN determined for complexes **2**–**6**, together with literature data for other Ru^{III}–maltolato complexes,[19,20] are given in Table 5. Substitution of the anionic maltolato ligand of *mer*-Ru(ma)$_3$ by two neutral imidazoles, as expected, is seen to strongly stabilize the Ru^{II} oxidation state relative to Ru^{III}. The data for **6** and **3** (both *N*-MeIm species) suggest that such substitution gives a stabilization of ~300 mV. The previously reported $E_{1/2}$ value of –550 mV for *trans*-[Ru(ma)$_2$(metronidazole)$_2$]CF_3SO_3 (**7**), where metronidazole is a 2-Me–5-NO_2–1*H*-Im–1-ethanol,[20] is considered consistent with the $E_{1/2}$ values shown in Table 5, given that the electron-withdrawing NO_2 group will stabilize Ru^{II} vs Ru^{III}. Incorporation of an electron-donating Me group into imidazole (**3**–**5** vs **2**), as expected, stabilizes the higher oxidation state (by 60–140 mV). Reduction potentials can be a significant factor in the anticancer activity of transition-metal complexes (see the following).

Biological results

We previously reported on some biological activity of *mer*-Ru(ma)$_3$, the bisethanol species **1a**, and *trans*-[Ru(ma)$_2$(metronidazole)$_2$]CF_3SO_3 (**7**), and the data obtained[19,20] are summarized in Table 5, along with those from the current study of the maltolato–imidazole systems (complexes **2**–**6**) and cisplatin. The Ru complexes (except **1a**) show no sign of ligand dissociation or reactivity in MeCN (used for conductivity measurements) or in the PBS-based solutions used in the MTT assay,[18] as judged by NMR studies and TLC analyses on solutions of the complexes, and so the listed data (except for **1a**) pertain to the intact complexes. The PBS solution of **1a** changes from red to green over the 3 day incubation, presumably because of the replacement of the EtOH ligands by components other than water (likely Cl^-), since the bis(aqua) complex is also red. This imidazole-free system has the lowest antiproliferatory activity (highest IC_{50} value). Of note, in contrast to the neutral or anionic character of most reported Ru anticancer complexes, **2**–**7** are rare examples of active cationic Ru species,[37] where there is no easily labile anion to assist binding to protein residues, nucleotide bases, or other "biological" components. Indeed, to our knowledge, **4** and **5** appear to be the first reported cationic Ru^{III} complexes to show antiproliferatory activity; further, the activity is greater than that of cisplatin. It has been proposed that relatively substitution-inert Ru^{III} complexes need to be reduced in vivo to more labile Ru^{II} species for effective drug activity (e.g., see refs. 17b and 38), where ligand loss opens up coordination sites for biomolecules; however, more labile anionic chloro-containing Ru^{III} complexes can interact with DNA, cell surfaces, extracellular matrix components, and components in blood plasma such as albumin and transferrin, and such interactions are likely important in anticancer activity.[2d,4c,5d,9a,10i,11a,11d,13,17b,39] Complexes **4** and **5** show the highest antiproliferatory activities, which are greater than that of cisplatin. There is no precise correlation of activity with reduction potential, but the following data for complexes of the same formulation (**2**–**4** and **7**) argue indirectly against a required reduction to Ru^{II}: (*i*) **4**, with the "tilted" Me group, has the lowest IC_{50} value and the most negative $E_{1/2}$ (–844 mV, i.e., favors Ru^{III} vs Ru^{II} the most); (*ii*) **2**, **3**, and **7** have more positive $E_{1/2}$ values (–765 to –550 mV) and lower activities (IC_{50} = 70–80 μmol/L); and (*iii*) species **6**, although of a different type, has the most positive $E_{1/2}$, (i.e., favors Ru^{II} the most) and does have the lowest activity. If there is a general correlation between $E_{1/2}$ and activity, the potency of **5** is significantly greater than expected (cf. data for **2**, **3**, and **7**), but this could result from its uptake in cells, which is double that of **2**, **3**, and **7**. The $E_{1/2}$ value for **5** is closer to that of **3** (than that of **4**), which indirectly supports that complex **5** might be the

Table 5. Data ($E_{1/2}$ and uptake by cells, IC_{50} values) for the Ru complexes.

Complex	$E_{1/2}$ (mV)	Ru uptake (ng / 10^6 cells)[a]	IC_{50} (μmol/L)[b]
Control (no complex)	—	1	—
trans-[Ru(ma)$_2$(Im)$_2$]OTf (**2**)[c]	–705	17	70
trans-[Ru(ma)$_2$(*N*-MeIm)$_2$]OTf·CH_2Cl_2 (**3**)	–765	14	80
trans-[Ru(ma)$_2$(2-MeIm)$_2$]OTf (**4**)	–844	14	5
trans-[Ru(ma)$_2$(4/5-MeIm)$_2$]OTf·CH_2Cl_2 (**5**)[d]	–738	27	15
[Ru(ma)(*N*-MeIm)$_4$][OTf]$_2$ (**6**)	–442	13	200
trans-[Ru(ma)$_2$(metronidazole)$_2$]OTf (**7**)[e]	–550	15	80
trans-[Ru(ma)$_2$(EtOH)$_2$]OTf (**1a**)[e]	—	—	300
Mer-Ru(ma)$_3$[f]	–1130	15	140
Cisplatin	—	—	35

Note: OTf = $CF_3SO_3^-$. The free Hma and imidazole ligands have respective IC_{50} values of 1000 and >5000 μmol/L.

[a]Measured after 3 h exposure. The error limits are ±5 ng.

[b]Error limits are approx. ±10%.

[c]The sample was taken from the top of the red TLC band (see Results and discussion).

[d]See Results and discussion regarding this complex.

[e]From ref. 20.

[f]From ref. 19.

Can. J. Chem. Downloaded from www.nrcresearchpress.com by Xi'an Jiaotong University on 09/19/12
For personal use only.

5-MeIm derivative with an "innocent" Me group. The neutral Ru(ma)$_3$ species, strongly favoured in the Ru^{III} oxidation state, has relatively low activity, but the different nature of the complex makes it impossible to conclude that activity requires reduction of the metal. Of note, we recently presented MTT data on [Ru^{II}(N–N)$_3$][CF_3SO_3]$_2$ species (N–*N* = 4,4′-biimidazole and the 2,2′-Me_2 derivative; IC_{50} = 18 and 36 μmol/L, respectively),[1] these being comparable to those for [Ru^{III}(ma)$_2$(N–N)][CF_3SO_3] species (IC_{50} = 50 and 15 μmol/L),[40] and concluded that these limited findings indirectly support the concept of required metal reduction.[1] However, the reduction potentials for the bis(maltolato)–mono(biimidazole) species are in the –35 to –100 mV region, showing a much stronger preference for the Ru^{II} state than the bis(maltolato)–bis(imidazole) complexes. It should be recalled that if the intact complexes **2**–**7** are exposed to a biological reductant operating at, for example, –1.0 V, a quite feasible value,[41] then the $E_{1/2}$ values reveal that >99% of all the complexes would be present in the Ru^{II} state, a factor commonly overlooked. Thus, to consider correlations between activity and reduction potentials in such a case becomes meaningless, and factors other than reduction potentials must determine the biological activity. One clearer conclusion from the IC_{50} data for **2**–**5** is that incorporation of a Me group into an imidazole ligand adjacent to the coordinated N atom can certainly enhance antiproliferatory activity of the complex that could stem from a steric rather than electronic effect (e.g., increased substitution lability of a 2-MeIm ligand relative to the other imidazoles).

The complexes, except **5** (see the previous discussion), are transported into cells at comparable rates (Table 5), ruling out the possibility that the more potent complex, **4**, is preferentially transported. Correspondingly, the poor activity of **6** (a doubly charged cation) cannot be attributed to less effective transport, perhaps implying instead an inability to interact with some key intracellular component essential for the antiproliferatory activity of these Ru–maltolato–imidazole complexes. None of complexes **2**–**6** binds to the DNA isolated from these cells.

Even a cursory survey of the listed publications in refs. 2–12 reveals that the mechanism(s) of action of Ru anticancer agents is(are) generally different from that of cisplatin. Reported in vitro interactions of Ru species with molecules other than DNA were noted in the previous discussion, and such targets are plausible for the maltolato–imidazole complexes. The cationic nature suggests that their associated mechanism is likely to be different from those of the anionic chloro complexes involved in clinical trials (see Introduction). A wide scope of potential activity for Ru complexes seems likely and implies that a Ru-based therapy may eventually prove a viable alternative to one based on Pt.

Supplementary data

Supplementary data (^{1}H NMR data (Figs. S1–S3), MTT plots (Fig. S4), and X-ray data in CIF format) are available for this article through the journal Web site (www.nrcresearchpress.com/cjc). CCDC 823213–823215 contain the X-ray data in CIF format for this manuscript (**1b**·EtOH, **3**·CH_2Cl_2, and **4**). These data can be obtained, free of charge, via www.ccdc.cam.ac.uk/conts/retrieving.html (Or from the Cambridge Crystallographic Data Centre, 12 Union Road, Cambridge CB2 1Ez, UK; fax +44 1223 336033; or deposit @ccdc.cam.ac.uk).

Acknowledgments

We thank Dr. E. Polishchuk, Biological Services, Department of Chemistry, University of British Columbia, for assistance with the MTT assay, the Natural Sciences and Engineering Research Council of Canada (NSERC) for financial support, and Colonial Metals Inc. for the $RuCl_3·3H_2O$.

References

(1) Kennedy, D. C.; James, B. R. *Can. J. Chem.* **2010** *88* (9), 886. doi:10.1139/V10-076.

(2) For example, (a) Renfrew, A. K.; Juillerat-Jeanneret, L.; Dyson, P. J. *J. Organomet. Chem.* **2011** *696* (3), 772. doi:10.1016/j.jorganchem.2010.09.067; (b) Hanif, M.; Meier, S. M.; Kandioller, W.; Bytzek, A.; Hejl, M.; Hartinger, C. G.;

Can. J. Chem. Downloaded from www.nrcresearchpress.com by Xi'an Jiaotong University on 09/19/12
For personal use only.

Nazarov, A. A.; Arion, V. B.; Jakupec, M. A.; Dyson, P. J.; Keppler, B. K. *J. Inorg. Biochem.* **2011** *105* (2), 224. doi:10.1016/j.jinorgbio.2010.10.004; (c) Süss-Fink, G.; Khan, F.-A.; Juillerat-Jeanneret, L.; Dyson, P. J.; Renfrew, A. K. *J. Cluster Sci.* **2010** *21* (3), 313. doi:10.1007/s10876-010-0298-6; (d) Renfrew, A. K.; Scopelliti, R.; Dyson, P. J. *Inorg. Chem.* **2010** *49* (5), 2239. doi:10.1021/ic9020433; (e) Phillips, A. D.; Zava, O.; Scopelitti, R.; Nazarov, A. A.; Dyson, P. J. *Organometallics* **2010** *29* (2), 417. doi:10.1021/om900991b; (f) Pelletier, F.; Comte, V.; Massard, A.; Wenzel, M.; Toulot, S.; Richard, P.; Picquet, M.; Le Gendre, P.; Zava, O.; Edafe, F.; Casini, A.; Dyson, P. J. *J. Med. Chem.* **2010** *53* (19), 6923. doi:10.1021/jm1004804.

(3) (a) Hanif, M.; Nazarov, A. A.; Hartinger, C. G.; Kandioller, W.; Jakupec, M. A.; Arion, V. B.; Dyson, J.; Keppler, B. K. *Dalton Trans.* **2010** *39* (31), 7345. doi:10.1039/c003085f; (b) Ratanaphan, A.; Temboot, P.; Dyson, P. J. *Chem. Biodivers.* **2010** *7* (5), 1290. doi:10.1002/cbdv.200900288; (c) Egger, A. E.; Hartinger, C. G.; Renfrew, A. K.; Dyson, P. J. *J. Biol. Inorg. Chem.* **2010** *15* (6), 919. doi:10.1007/s00775-010-0654-x; (d) Casini, A.; Hartinger, C. G.; Nazarov, A. A.; Dyson, P. J. Organometallic Antitumour Agents with Alternative Modes of Action. In *Medicinal Organometallic Chemistry*; Jaoven, G., Metzler-Nolte, N., Eds.; Topics in Organometallic Chemistry, Vol. 32; Springer, New York, 2010; pp 57–80; (e) Gras, M.; Therrien, B.; Süss-Fink, G.; Zava, O.; Dyson, P. J. *Dalton Trans.* **2010** *39* (42), 10305. doi:10.1039/c0dt00887g.

(4) For example, (a) Filak, L. K.; Mühlgassner, G.; Bacher, F.; Roller, A.; Galanski, M.; Jakupec, M. A.; Keppler, B. K.; Arion, V. B. *Organometallics* **2011** *30* (2), 273. doi:10.1021/om101004z; (b) Filak, L. K.; Mühlgassner, G.; Jakupec, M. A.; Heffeter, P.; Berger, W.; Arion, V. B.; Keppler, B. K. *J. Biol. Inorg. Chem.* **2010** *15* (6), 903. doi:10.1007/s00775-010-0653-y; (c) Heffeter, P.; Böck, K.; Atil, B.; Hoda, M. A. R.; Körner, W.; Bartel, C.; Jungwirth, U.; Keppler, B. K.; Micksche, M.; Berger, W.; Koellensperger, G. *J. Biol. Inorg. Chem.* **2010** *15* (5), 737. doi:10.1007/s00775-010-0642-1; (d) Grgurić-Šipka, S.; Ivanović, I.; Rakić, G.; Todorović, N.; Gligorijević, N.; Radulović, S.; Arion, V. B.; Keppler, B. K.; Tešić, Z. L. *Eur. J. Med. Chem.* **2010** *45* (3), 1051. doi:10.1016/j.ejmech.2009.11.055; (e) Hanif, M.; Henke, H.; Meier, S. M.; Martic, S.; Labib, M.; Kandioller, W.; Jakupec, M. A.; Arion, V. B.; Kraatz, H.-B.; Keppler, B. K.; Hartinger, C. G. *Inorg. Chem.* **2010** *49* (17), 7953. doi:10.1021/ic1009785; (f) Hudej, R.; Turel, I.; Kanduser, M.; Scancar, J.; Kranjc, S.; Sersa, G.; Miklavcić, D.; Jakupec, M. A.; Keppler, B. K.; Maja, C. *Anticancer Res.* **2010** *30*, 2055; (g) Hanif, M.; Nazarov, A. A.; Hartinger, C. G.; Kandioller, W.; Jakupec, M. A.; Arion, V. B.; Dyson, P. J.; Keppler, B. K. *Dalton Trans.* **2010** *39* (31), 7345. doi:10.1039/c003085f.

(5) For example, (a) Pizarro, A. M.; Melchart, M.; Habtemariam, A.; Salassa, L.; Fabbiani, F. P. A.; Parsons, S.; Sadler, P. J. *Inorg. Chem.* **2010** *49* (7), 3310. doi:10.1021/ic902243q; (b) Novakova, O.; Malina, J.; Suchankova, T.; Kasparkova, J.; Bugarcic, T.; Sadler, P. J.; Brabec, V. *Chem.-Eur. J.* **2010** *16*, 5744; (c) Williams, J. P.; Brown, J. M.; Campuzano, I.; Sadler, P. J. *Chem. Commun. (Camb.)* **2010** *46* (30), 5458. doi:10.1039/c0cc00358a; (d) Pizarro, A. M.; Habtemariam, A.; Sadler, P. J. Activation Mechanisms for Organometallic Anticancer Complexes. In *Medicinal Organometallic Chemistry*; Jaoven, G., Metzler-Nolte, N., Eds.; Topics in Organometallic Chemistry, Vol. 32; Springer, New York, 2010; pp 21–56; (e) Liu, H.-K.; Parkinson, J. A.; Bella, J.; Wang, F.; Sadler, P. J. *Chem. Sci.* **2010** *1* (2), 258. doi:10.1039/c0sc00175a; (f) Sriskandakumar, T.; Petzold, H.; Bruijnincx, P. C. A.; Habtemariam, A.; Sadler, P. J.; Kennepohl, P. *J. Am. Chem. Soc.* **2009** *131* (37), 13355. doi:10.1021/ja903405z; (g) Bugarcic, T.; Habtemariam, A.; Deeth, R. J.; Fabbiani, F. P. A.; Parsons, S.; Sadler, P. J. *Inorg. Chem.* **2009** *48* (19), 9444. doi:10.1021/ic9013366; (h) van Rijt, S. H.; Hebden, A. J.; Amaresekera, T.; Deeth, R. J.; Clarkson, G. J.; Parsons, S.; McGowan, P. C.; Sadler, P. J. *J. Med. Chem.* **2009** *52* (23), 7753. doi:10.1021/jm900731j.

(6) For example, (a) Camm, K. D.; El-Sokkary, A.; Gott, A. L.; Stockley, P. G.; Belyaeva, T.; McGowan, P. C. *Dalton Trans.* **2009** (48): 10914. doi:10.1039/b918902e; (b) Walker, J. M.; McEwan, A.; Pycko, R.; Tassotto, M. L.; Gottardo, C.; Th'ng, J.; Wang, R.; Spivak, G. J. *Eur. J. Inorg. Chem.* **2009** *2009* (31), 4629. doi:10.1002/ejic.200900766; (c) Linares, F.; Galindo, M. A.; Galli, S.; Angustias Romero, M.; Navarro, J. A. R.; Barea, E. *Inorg. Chem.* **2009** *48* (15), 7413. doi:10.1021/ic900980y; (d) Ruiz, J.; Vicente, C.; de Haro, C.; Bautista, D. *Dalton Trans.* **2009** (26): 5071. doi:10.1039/b907296a; (e) Gao, F.; Chen, X.; Wang, J.-Q.; Chen, Y.; Chao, H.; Ji, L.-N. *Inorg. Chem.* **2009** *48* (13), 5599. doi:10.1021/ic900902f; (f) Delferro, M.; Marchio, L.; Tegoni, M.; Tardito, S.; Franchi-Gazzola, R.; Lanfranchi, M. *Dalton Trans.* **2009** (19): 3766. doi:10.1039/b823271g; (g) Giovagnini, L.; Mancinetti, E.; Ronconi, L.; Sitran, S.; Marchio, L.; Castagliuolo, I.; Brun, P.; Trevisan, A.; Fregona, D. *J. Inorg. Biochem.* **2009** *103* (5), 774. doi:10.1016/j.jinorgbio.2009.01.019; (h) Benkli, K.; Tunali, Y.; Cantürk, Z.; Artagan, Ö.; Alanyali, F. *Eur. J. Med. Chem.* **2009** *44* (6), 2601. doi:10.1016/j.ejmech.2008.09.017; (i) Harris, T. V.; Szilagyi, R. K.; McFarlane Holman, K. *J. Biol. Inorg. Chem.* **2009** *14* (6), 891. doi:10.1007/s00775-009-0501-0; (j) Vaccaro, M.; Del Litto, R.; Mangiapia, G.; Carnerup, A. M.; D'Errico, G.; Ruffo, F.; Paduano, L. *Chem. Commun. (Camb.)* **2009** (11): 1404. doi:10.1039/b820368g.

(7) (a) Reddy, V. D.; Dayal, D.; Cosenza, S. C.; Ramana Reddy, M. V.; Pearl, W. C., Jr; Adams, R. D. *J. Organomet. Chem.* **2009** *694* (6), 959. doi:10.1016/j.jorganchem.2008.11.025; (b) Prussin, A. J., II; Zhao, S.; Jain, A.; Winkel, B. S. J.; Brewer, K. J. *J. Inorg. Biochem.* **2009** *103* (3), 427. doi:10.1016/j.jinorgbio.2008.12.008; (c) Garcia, M. H.; Morais, T. S.; Florindo, P.; Piedade, M. F. M.; Moreno, V.; Ciudad, C.; Noe, V. *J. Inorg. Biochem.* **2009** *103* (3), 354. doi:10.1016/j.jinorgbio.2008.11.016; (d) Rajapakse, C. S. K.; Martinez, A.; Naoulou, B.; Jarzecki, A. A.; Suarez, L.; Deregnaucourt, C.; Sinou, V.; Schrevel, J.; Musi, E.; Ambrosini, G.; Schwartz, G. K.; Sanchez-Delgado, R. A. *Inorg. Chem.* **2009** *48* (3), 1122. doi:10.1021/ic802220w; (e) Djinovic, V. M.; Todorovic, T.; Zizak, Z.; Sabo, T. J.; Juranic, Z. D. *J. Coord. Chem.* **2009** *62* (2), 328. doi:10.1080/00958970802233128; (f) Wu, C.-H.; Wu, D.-H.; Liu, X.; Guoyiqibayi, G.; Guo, D.-D.; Lv, G.; Wang, X.-M.; Yan, H.; Jiang, H.; Lu, Z.-H. *Inorg. Chem.* **2009** *48* (6), 2352. doi:10.1021/ic900009j.

(8) (a) Wu, D.-H.; Wu, C.-H.; Li, Y.-Z.; Guo, D.-D.; Wang, X.-M.; Yan, H. *Dalton Trans.* **2009** (2): 285. doi:10.1039/b810831e; (b) Sun, R. W.-Y.; Ng, M. F.-Y.; Wong, E. L.-M.; Zhang, J.; Chui, S. S.-Y.; Shek, L.; Lau, T.-C.; Che, C.-M. *Dalton Trans.* **2009** (48): 10712. doi:10.1039/b912236b; (c) Loughrey, B. T.; Williams, M. L.; Healy, P. C.; Innocenti, A.; Vullo, D.; Supuran, C. T.; Parsons, P. G.; Poulsen, S.-A. *J. Biol. Inorg. Chem.* **2009** *14* (6), 935. doi:10.1007/s00775-009-0506-8; (d) Schmitt, F.; Govindaswamy, P.; Zava, O.; Süss-Fink, G.; Juillerat-Jeanneret, L.; Therrien, B. *J. Biol. Inorg. Chem.* **2009** *14* (1), 101. doi:10.1007/s00775-008-0427-y; (e) Beckford,

Can. J. Chem. Downloaded from www.nrcresearchpress.com by Xi'an Jiaotong University on 09/19/12
For personal use only.

F. A.; Shaloski, M., Jr; Leblanc, G.; Thessing, J.; Lewis-Alleyne, L. C.; Holder, A. A.; Li, L.; Seeram, N. P. *Dalton Trans.* **2009** *48* (48), 10757. doi:10.1039/b915081a; (f) van Rijn, J. A.; Marques-Gallego, P.; Reedijk, J.; Lutz, M.; Spek, A. L.; Bouwman, E. *Dalton Trans.* **2009** *48* (48), 10727. doi:10.1039/b909520a.

(9) For example, (a) Moreno, V.; Font-Bardia, M.; Calvet, T.; Lorenzo, J.; Aviles, F. X.; Garcia, M. H.; Morais, T. S.; Valente, A.; Robalo, M. P. *J. Inorg. Biochem.* **2011** *105* (2), 241. doi:10.1016/j.jinorgbio.2010.10.009; (b) Atilla-Gokcumen, G. E.; Di Costanzo, L.; Meggers, E. *J. Biol. Inorg. Chem.* **2011** *16* (1), 45. doi:10.1007/s00775-010-0699-x; (c) Gianferrara, T.; Bergamo, A.; Bratsos, I.; Milani, B.; Spagnul, C.; Sava, G.; Alessio, E. *J. Med. Chem.* **2010** *53* (12), 4678. doi:10.1021/jm1002588; (d) Liu, Y.-J.; Zeng, C.-H.; Yao, J.-H.; Wu, F.-H.; He, L.-X.; Huang, H.-L. *Chem. Biodivers.* **2010** *7* (7), 1770. doi:10.1002/cbdv.200900213; (e) Liu, Y.-J.; Liang, Z.-H.; Li, Z.-Z.; Zeng, C.-H.; Yao, J.-H.; Huang, H.-L.; Wu, F.-H. *Biometals* **2010** *23* (4), 739. doi:10.1007/s10534-010-9340-2; (f) Srivastava, R. S.; Fronczek, F. R.; Perkins, R. S.; Fukuyama, T.; Xu, W. *Int. J. Oncol.* **2010** *36* (6), 1591. doi:10.3892/ijo_00000646; (g) Chen, T.; Liu, Y.; Zheng, W.-J.; Liu, J.; Wong, Y.-S. *Inorg. Chem.* **2010** *49* (14), 6366. doi:10.1021/ic100277w; (h) Biersack, B.; Effenberger, K.; Knauer, S.; Ocker, M.; Schobert, R. *Eur. J. Med. Chem.* **2010** *45* (11), 4890. doi:10.1016/j.ejmech.2010.07.061; (i) Alfaro, J. M.; Prades, A.; del Carmen Ramos, M.; Peris, E.; Ripoll-Gómez, J.; Poyatos, M.; Burgos, J. *Zebrafish* **2010** *7* (1), 13. doi:10.1089/zeb.2009.0601; (j) Rubner, G.; Bensdorf, K.; Wellner, A.; Kircher, B.; Bergemann, S.; Ott, I.; Gust, R. *J. Med. Chem.* **2010** *53* (19), 6889. doi:10.1021/jm101019j.

(10) (a) Zhang, P.; Chen, J.; Liang, Y. *Acta Biochim. Biophys. Sin. (Shanghai)* **2010** *42* (7), 440. doi:10.1093/abbs/gmq040; (b) Thota, S.; Karki, S. S.; Jayaveera, K. N.; Balzarini, J.; De Clercq, E. *J. Coord. Chem.* **2010** *63* (24), 4332. doi:10.1080/00958972.2010.534140; (c) Silveira-Lacerda, E. de P.; Vilanova-Costa, C. A. S. T.; Hamaguchi, A.; Pavanin, L. A.; Goulart, L. R.; Homsi-Brandenburgo, M. I.; Santos, W. B.; Soares, A. M.; Nomizo, A. *Biol. Trace Elem. Res.* **2010** *135* (1–3), 98. doi:10.1007/s12011-009-8498-3; (d) Golfeto, C. C.; Von Poelhsitz, G.; Selistre-de-Araújo, H. S.; de Araujo, M. P.; Ellena, J.; Castellano, E. E.; Lopes, L. G. L.; Moreira, I. S.; Batista, A. A. *J. Inorg. Biochem.* **2010** *104* (5), 489. doi:10.1016/j.jinorgbio.2009.12.015; (e) Loughrey, B. T.; Williams, M. L.; Carruthers, T. J.; Parsons, P. G.; Healy, P. C. *Aust. J. Chem.* **2010** *63* (2), 245. doi:10.1071/CH09420; (f) Prajapati, R.; Dubey, S. K.; Gaur, R.; Koiri, R. K.; Maurya, B. K.; Trigun, S. K.; Mishra, L. *Polyhedron* **2010** *29* (3), 1055. doi:10.1016/j.poly.2009.11.012; (g) Ott, I.; Kowalski, K.; Gust, R.; Maurer, J.; Mücke, P.; Winter, R. F. *Bioorg. Med. Chem. Lett.* **2010** *20* (3), 866. doi:10.1016/j.bmcl.2009.12.080; (h) Ribeiro, G.; Benadiba, M.; de Oliveira Silva, D.; Colquhoun, A. *Cell Biochem. Funct.* **2010** *28* (1), 15. doi:10.1002/cbf.1626; (i) Das, S.; Sinha, S.; Britto, R.; Somasundaram, K.; Samuelson, A. G. *J. Inorg. Biochem.* **2010** *104* (2), 93. doi:10.1016/j.jinorgbio.2009.09.017; (j) Mura, P.; Camalli, M.; Casini, A.; Gabbiani, C.; Messori, L. *J. Inorg. Biochem.* **2010** *104* (2), 111. doi:10.1016/j.jinorgbio.2009.10.002.

(11) (a) Klajner, M.; Hebraud, P.; Sirlin, C.; Gaiddon, C.; Harlepp, S. *J. Phys. Chem. B* **2010** *114* (44), 14041. doi:10.1021/jp1044783; (b) Bíró, L.; Farkas, E.; Buglyó, P. *Dalton Trans.* **2010** *39* (42), 10272. doi:10.1039/c0dt00469c; (c) García-Fernández, A.; Díez, J.; Manteca, Á.; Sánchez, J.; García-Navas, R.; Sierra, B. G.; Mollinedo, F.; Gamasa, M. P.; Lastra, E. *Dalton Trans.* **2010** *39* (42), 10186. doi:10.1039/c0dt00206b; (d) Garcia, M. H.; Valente, A.; Florindo, P.; Morais, T. S.; Piedade, M. F. M.; Duarte, M. T.; Moreno, V.; Aviles, F. X.; Loreno, J. *Inorg. Chim. Acta* **2010** *363* (14), 3765. doi:10.1016/j.ica.2010.05.034; (e) Ochocki, J.; Kasprzak, M.; Checinska, L.; Erxleben, A.; Zyner, E.; Szmigiero, L.; Garza-Ortiz, A.; Reedijk, J. *Dalton Trans.* **2010** *39* (40), 9711. doi:10.1039/c0dt00535e; (f) Ke, H.; Wang, H.; Wong, W.-K.; Mak, N.-K.; Kwong, D. W. J.; Wong, K.-L.; Tam, H.-L. *Chem. Commun. (Camb.)* **2010** *46* (36), 6678. doi:10.1039/c0cc01848a.

(12) Henke, M. M.; Richly, H.; Drescher, A.; Grubert, M.; Alex, D.; Thyssen, D.; Jaehde, U.; Scheulen, M. E.; Hilger, R. A. *Int. J. Clin. Pharmacol. Ther.* **2009** *47*, 58.

(13) Liu, M.; Lim, Z. J.; Gwee, Y. Y.; Levina, A.; Lay, P. A. *Angew. Chem. Int. Ed.* **2010** *49*, 1661 and references therein. doi:10.1002/anie.200906079.

(14) For example, (a) Wu, Y.; Zhou, L. *Inorg. Chim. Acta* **2010** *363* (13), 3274. doi:10.1016/j.ica.2010.06.012; (b) Knapp-Mohammady, M.; March, N. H. *Theor. Chem. Acc.* **2010** *125* (3–6), 293. doi:10.1007/s00214-009-0686-x; (c) Chen, J.-C.; Chen, L.-M.; Liao, S.-Y.; Zheng, K.-C.; Ji, L.-N. *Phys. Chem. Chem. Phys.* **2009** *11* (18), 3401. doi:10.1039/b818023g; (d) Futera, Z.; Klenko, J.; Sponer, J. E.; Sponer, J.; Burda, J. V. *J. Comput. Chem.* **2009** *30* (12), 1758. doi:10.1002/jcc.21179; (e) Gossens, C.; Tavernelli, I.; Rothlisberger, U. *J. Phys. Chem. A* **2009** *113* (43), 11888. doi:10.1021/jp903237w.

(15) For example, (a) Liu, Y.; Chen, T.-F.; Wong, Y.-S.; Mei, W.-J.; Huang, X.-M.; Yang, F.; Liu, J.; Zheng, W.-J. *Chem. Biol. Interact.* **2010** *183* (3), 349. doi:10.1016/j.cbi.2009.11.026; (b) Zhou, Q.-X.; Lei, W.-H.; Li, C.; Hou, Y.-J.; Wang, X.-S.; Zhang, B.-W. *New J. Chem.* **2010** *34* (1), 137. doi:10.1039/b9nj00465c; (c) Zhao, R.; Hammitt, R.; Thummel, R. P.; Liu, Y.; Turro, C.; Snapka, R. M. *Dalton Trans.* **2009** (48): 10926. doi:10.1039/b913959a; (d) Zigler, D. F.; Brewer, K. J. Towards Photodynamic Therapy of Cancer with Platinum Interactions. In *Metal Complex–DNA Interactions* [Online]; Hadjiliadis, N., Sletten, E., Eds.; John Wiley and Sons, Ltd.: Chicester, UK, 2009; Chapter 9, pp 235–272. doi:10.1002/9781444312089.ch8.

(16) (a) Sakurai, H. *J. Health Sci.* **2010** *56* (2), 129. doi:10.1248/jhs.56.129; (b) Antonarakis, E. S.; Emadi, A. *Cancer Chemother. Pharmacol.* **2010** *66* (1), 1. doi:10.1007/s00280-010-1293-1; (c) Silva, D. de O. *Anticancer Agents Med. Chem.* **2010** *10*, 312.

(17) (a) Amin, A.; Buratovich, M. A. *Mini Rev. Med. Chem.* **2009** *9* (13), 1489. doi:10.2174/138955709790361566; (b) Levina, A.; Mitra, A.; Lay, P. A. *Metallomics* **2009** *1* (6), 458. doi:10.1039/b904071d; (c) Page, S. M.; Boss, S. R.; Barker, P. D. *Future Med. Chem.* **2009** *1*, 541; (d) Renfrew, A. *Chimia (Aarau)* **2009** *63* (4), 217. doi:10.2533/chimia.2009.217; (e) Moucheron, C. *New J. Chem.* **2009** *33* (2), 235. doi:10.1039/b817016a; (f) Gianferrara, T.; Bratsos, I.; Alessio, E. *Dalton Trans.* **2009** (37): 7588. doi:10.1039/b905798f; (g) Reisner, E. *Anticancer Drugs;* Spencer, P., Holt, W., Eds.; Nova Science Publishers: Hauppauge, NY, 2009; p 227.

(18) Wu, A.; Kennedy, D. C.; Patrick, B. O.; James, B. R. *Inorg. Chem.* **2003** *42* (23), 7579. doi:10.1021/ic030119j.

(19) Kennedy, D. C.; Wu, A.; Patrick, B. O.; James, B. R. *Inorg. Chem.* **2005** *44* (19), 6529. doi:10.1021/ic050034d.

(20) Kennedy, D. C.; Wu, A.; Patrick, B. O.; James, B. R. *J. Inorg. Biochem.* **2006** *100* (12), 1974. doi:10.1016/j.jinorgbio.2006.07.001.

Can. J. Chem. Downloaded from www.nrcresearchpress.com by Xi'an Jiaotong University on 09/19/12
For personal use only.

(21) (a) Kandioller, W.; Kurzwernhart, A.; Hanif, M.; Meier, S. M.; Henke, H.; Keppler, B. K.; Hartinger, C. G. *J. Organomet. Chem.* **2011** *696* (5), 999. doi:10.1016/j.jorganchem.2010.11.010; (b) Kandioller, W.; Hartinger, C. G.; Nazarov, A. A.; Kasser, J.; John, R.; Jakupec, M. A.; Arion, V. B.; Dyson, P. J.; Keppler, B. K. *J. Organomet. Chem.* **2009** *694* (6), 922. doi:10.1016/j.jorganchem.2008.10.016; (c) Kandioller, W.; Hartinger, C. G.; Nazarov, A. A.; Kuznetsov, M. L.; John, R. O.; Bartel, C.; Jakupec, M. A.; Arion, V. B.; Keppler, B. K. *Organometallics* **2009** *28* (15), 4249. doi:10.1021/om900483t; (d) Peacock, A. F. A.; Melchart, M.; Deeth, R. J.; Habtemariam, A.; Parsons, S.; Sadler, P. J. *Chem.-Eur. J.* **2007** *13* (9), 2601. doi:10.1002/chem.200601152.

(22) LeBlanc, D. T.; Akers, H. A. *Food Technol.* **1989** *43*, 78.

(23) Connelly, N. G.; Geiger, W. E. *Chem. Rev.* **1996** *96* (2), 877. doi:10.1021/cr940053x.

(24) *SAINT,* version 7.03A; Bruker AXS Inc.: Madison, WI, 1997–2003.

(25) d*TREK. *Area Detector Software,* version 4.13; Molecular Structure Corp.: The Woodlands, TX, 1996–1998.

(26) Altomare, A.; Burla, M. C.; Camalli, G.; Cascarano, M.; Giacovazzo, C.; Guagliardi, A.; Moliterni, A. G. G.; Polidori, G.; Spagna, A. *J. Appl. Crystallogr.* **1999** *32* (1), 115. doi:10.1107/S0021889898007717.

(27) Beurskens, P. T.; Admiraal, G.; Beurskens, G.; Bosman, W. P.; de Gelder, R.; Israel, R.; Smits, J. M. M. *The DIRDIF-94 Program System;* Technical Report of the Crystallography Lab; University of Nijmegen: The Netherlands, 1994.

(28) *SADABS, Bruker Nonius Area Detector Scaling and Absorption Correction,* version 2.10; Bruker AXS Inc.: Madison, WI, 2003.

(29) *teXsan, Crystal Structure Analysis Package;* Molecular Structure Corp.: The Woodlands, TX, 1985 and 1992.

(30) Yapp, D. T. T.; Rettig, S. J.; James, B. R.; Skov, K. A. *Inorg. Chem.* **1997** *36* (24), 5635. doi:10.1021/ic9606486.

(31) Bernhard, P.; Buergi, H. B.; Hauser, J.; Lehmann, H.; Ludi, A. *Inorg. Chem.* **1982** *21* (11), 3936. doi:10.1021/ic00141a016.

(32) For example, (a) Takahashi, Y.; Hikichi, S.; Moro-oka, Y.; Akita, M. *Polyhedron* **2004** *23* (2–3), 225. doi:10.1016/j.poly.2003.11.009; (b) Dinelli, L. R.; Batista, A. A.; Wohnrath, K.; de Araujo, M. P.; Queiroz, S. L.; Bonfadini, M. R.; Oliva, G.; Nascimento, O. R.; Cyr, P. W.; MacFarlane, K. S.; James, B. R. *Inorg. Chem.* **1999** *38* (23), 5341. doi:10.1021/ic990130c; (c) Gilbert, J. A.; Eggleston, D. S.; Murphy, W. R.; Geselowitz, D. A.; Gersten, S. W.; Hodgson, D. J.; Meyer, T. J. *J. Am. Chem. Soc.* **1985** *107* (13), 3855. doi:10.1021/ja00299a017; (d) Kodashova, T. S. *Zh. Strukt. Khim.* **1960** *1*, 336.

(33) Geary, W. J. *Coord. Chem. Rev.* **1971** *7* (1), 81. doi:10.1016/S0010-8545(00)80009-0.

(34) Anderson, C. *Can. J. Chem.* **2001** *79* (10), 1477 and references therein. doi:10.1139/v01-169.

(35) (a) Anderson, C.; Beauchamp, A. L. *Can. J. Chem.* **1995** *73* (4), 471. doi:10.1139/v95-062; (b) Pacheco, A.; James, B. R.; Rettig, S. J. *Inorg. Chem.* **1995** *34* (13), 3477. doi:10.1021/ic00117a016; (c) Toi, H.; La Mar, G. N.; Margalit, R.; Che, C.-M.; Gray, H. B. *J. Am. Chem. Soc.* **1984** *106* (21), 6213. doi:10.1021/ja00333a016.

(36) Baird, I. R. Fluorinated Nitroimidazoles and Their Ruthenium Complexes: Potential Hypoxia Imaging Agents. Ph.D. Dissertation, The University of British Columbia, Vancouver, BC, 1999.

(37) Mulcahy, S. P.; Gründler, K.; Frias, C.; Wagner, L.; Prokop, A.; Meggers, E. *Dalton Trans.* **2010** *39* (35), 8177. doi:10.1039/c0dt00034e.

(38) Clarke, M. J. *Coord. Chem. Rev.* **2003** *236* (1–2), 209 and references therein. doi:10.1016/S0010-8545(02)00312-0.

(39) Delmani, F. A.; Torreblanca, J.; Moreno, J.; Garcia-Herdugo, G.; Vilaplana, R.; Gonzalez-Viltchez, F. *Oncol. Res.* **2009** *17* (9), 425. doi:10.3727/096504009788912480.

(40) Kennedy, D. C. Synthesis and Characterization and Anti-Cancer Activity of New Ruthenium Maltolato and Imidazole Complexes. Ph.D. Dissertation, Department of Chemistry, The University of British Columbia, Vancouver, BC, 2003.

(41) Elving, P. J.; Bresnhan, W. T.; Moiroux, J.; Samec, Z. *Bioelectrochem. Bioenerg.* **1982** *9* (3), 365. doi:10.1016/0302-4598(82)80026-3.

Synthesis of a glycodendrimer incorporating multiple mannosides on a glucoside core

Chao Wang, Brian Sanders, and David C. Baker

Abstract: The synthesis of a glycodendrimer by incorporating repetitive mannoside units onto a glucoside core was carried out to multivalently probe fundamental carbohydrate–protein interactions. The dendritic structure was constructed by a modified procedure that utilized multiple glycosylations between a thioether glycosyl donor and five elongated spacer arms of a glycosyl acceptor. The completed dendrimer bears a full carbohydrate structure, and thus should find its potential application in the study of mannose–lectin interactions.

Key words: carbohydrate, mannose, dendrimer, glycosylation, multivalency.

Résumé : Afin d'obtenir une sonde pour effectuer des études sur les interactions multivalentes fondamentales entre les hydrates de carbone et les protéines, on a effectué la synthèse d'un glycodendrimère par l'incorporation répétitive d'unités sur une de base de glucoside. La structure dendritique a été construite par une méthode modifiée qui fait appel à des glycosylations multiples entre un thioéther donneur de glycosyle et cinq groupes intercalaires allongés d'un accepteur de glycosyle. Le dendrimère complété comporte une structure entière d'hydrate de carbone et il devrait donc trouver des applications potentielles dans l'étude des interactions entre le mannose et la lectine.

Mots-clés : hydrate de carbone, mannose, dendrimère, glycosylation, multivalence.

[Traduit par la Rédaction]

Can. J. Chem. Downloaded from www.nrcresearchpress.com by Xi'an Jiaotong University on 09/19/12
For personal use only.

Introduction

Many cell-surface events are mediated by the formation of noncovalent complexes between carbohydrate components of surface glycoconjugates and their special protein receptors known as lectins.[1] These interactions are generally weak, since dissociation constants of the formed complexes typically fall in the millimolar range.[2] Improved specificity and stability can be achieved through multivalent interactions between multiple carbohydrate ligands and corresponding protein receptors.[3] Multivalent carbohydrate–protein interactions are very important in many processes such as cell–cell adhesion,[4] immune responses,[5] inflammation,[6,7] cell degeneration,[8] and pathogenic infections.[9]

The search for simple carbohydrate-containing compounds capable of mimicking the complex natural structures has thus become an important task.[10,11] Such multivalent glycomimetics are not only valuable tools to study carbohydrate-mediated processes, but also have considerable potential as therapeutic agents.[12] Dendrimers[13–16] are especially suited for the construction of multivalent glycomimics, thanks to their highly iterative presence of ligands.[17,18] Several examples of glycodendrimers with polyamidoamine,[19,20] carbohydrate–peptide,[21] carbosilane,[22,23] and aliphatic polyether[12] architectures have been synthesized. In regard to dendrimerization methods, robust amide formation generally has been used.[24–26] More recently, the state-of-the-art "click" chemistry has also been applied to overcome the strong steric hindrance during dendrimerization.[27,28]

To study widely distributed mannose-specific bacterial adhesions[29] or some other viral infections,[30,31] we attached multiple mannose moieties to a glucose scaffold by thioether-mediated glycosylation to establish a sugar-cored glycodendrimer. Since the unusual structure contains carbohydrates at either cored or branched positions, it might give new insights when used as dendritic probe to study many mannose-involved interactions. Herein, we report the synthesis of such a mannose-branched "full-carbohydrate glycodendrimer".

Results and discussion

Synthetic approaches

Lindhorst and co-workers[32] managed to add five thiomannoside molecules to the allyl double bond of a core sugar by photoinduced thiol addition. However, precipitates that formed during the radiation process tended to block UV rays from penetrating the solution; consequently, the efficiency of this method was reduced, and the broad use of photoinitiated double bond addition reaction was thus impeded. To overcome these shortcomings and make this method more practical, we modified the Lindhorst procedure by manipulating the facile glycosylation of a mannoside donor with thioether functionality and a core glucoside acceptor bearing multiple elongated hydroxyl groups. Conventional hydrogenolysis was

Received 12 December 2010. Accepted 23 March 2011. Published at www.nrcresearchpress.com/cjc on 9 August 2011.

C. Wang. School of Material Science and Engineering, Southwest University of Science and Technology, Mianyang, Sichuan 621010, China.
B. Sanders and D.C. Baker. Department of Chemistry, the University of Tennessee, Knoxville, TN 37996-1600, USA.

Corresponding author: David C. Baker (e-mail: dcbaker@utk.edu).

Can. J. Chem. Downloaded from www.nrcresearchpress.com by Xi'an Jiaotong University on 09/19/12
For personal use only.

then applied to remove benzyl protective groups, thus furnishing the construction of the dendritic structure. By applying this strategy, the synthesis was carried out as described in the following sections.

Synthesis of sugar core 5

As Scheme 1 illustrates, known α-bromide **1**[33] was converted to its corresponding β-allyl tetraacetate **2** through a procedure developed in our laboratory.[34] Tetraacetate **2** was then deacetylated quantitatively under conventional Zemplén conditions, affording the unprotected β-allyl glucoside **3**. Tetraol **3** was fully allylated through a procedure developed by Lindhorst, and subsequent hydroboration introduced 3-hydroxypropyl spacer groups to the sugar core.[35]

Synthesis of thioether donor 8

The mannose ligand to be attached to **5** was synthesized as shown in Scheme 2. Thioether acetate **6**, prepared by ethylthiolation of the corresponding pentaacetate,[36] was subjected to deacetylation under Zemplén conditions in nearly quantitative yield. The four hydroxyls of **7** were then benzyl-protected to afford **8**. Notably, the anomeric ratio in product **8** was changed to an α:β ratio of 2.3:1 (as determined by ^{1}H NMR spectroscopy), indicating the occurrence of anomerization during this reaction. The α and β components of **8** were separated by column chromatography and characterized, respectively.

Synthesis of dendrimer 10

With a sufficient amount of benzyl-protected thioether donor **8** and pentaalcohol **5** in hand, our attention was directed to the exploration of good glycosylation conditions to install mannose moieties onto the five spacer arms of **5** (Scheme 3). Firstly, we adopted the convenience of a room-temperature reaction and a trimethylsilyl triflate (TMSOTf) catalyst based on our earlier successful experience in the synthesis of linear oligosaccharides.[37] Unfortunately, complete glycosylation was not attained because of the increased steric hindrance for such a highly branched architecture.

As a result, the catalyst was changed to a more powerful silver triflate / *N*-iodosuccinimide (AgOTf/NIS) system[38–42] and heating was also applied, in hopes of driving the glycosylation to completeness. Continuous MALDI-TOF MS monitoring of the reaction suggested that only traces of product with complete glycosylation were formed after 1 day of reflux. Over 5 consecutive days, the amount of the product was found to have reached its maximum value. No further product formation was achieved after an additional 2 days of refluxing. The resulting clustered hexasaccharide **9** was purified on a Sephadex LH-20 GPC column, followed by silica gel column chromatography.

After the dendrimerization was successfully carried out, benzyl protecting groups on **9** were removed by conventional hydrogenlysis with catalysis by $Pd(OH)_2$-on-charcoal.[43–45] Continuous MALDI-TOF MS monitoring of the reaction mixture suggested the completion point after 1 week, and subsequent GPC column purification furnished the deprotected dendrimer **10** in good yield.

Conclusions

A full-carbohydrate glycodendrimer with its first generation of repetitive mannose units was synthesized according to a modified procedure, which utilized multiple glycosylations between a thiomannosyl donor and five extended hydroxyls of a sugar acceptor. The dendritic architecture of the synthesized molecule bears potential as a multivalent mimic for the probe of fundamental carbohydrate–protein interactions.

Experimental section

General

^{1}H (300 MHz) and ^{13}C (75 MHz) NMR spectra were recorded at 25 °C with a Varian Mercury 300 instrument. Chemical shifts are given in δ units (ppm) relative to an internal standard of TMS for ^{1}H, and relative to the signal for $CDCl_3$ (δ 77.0) for ^{13}C, unless otherwise stated. Apparent first-order multiplicities are indicated by s, singlet; d, doublet; dd, doublet of doublets; t, triplet; dt, doublet of triplets; q, quartet; and m, multiplet. Column chromatography was performed on 60 Å (40–63 μm) silica gel (Sorbent Technologies), and fractions were monitored by TLC on silica gel 60 F_{254} (0.2 mm aluminum-backed plates, E. Merck) by detection with 254 nm UV light and then spray–heat development using a *p*-anisaldehyde – sulfuric acid reagent. High-resolution DART mass spectra were obtained on a JEOL AccuTOF-DART instrument with an ESI source. All solvents were dried and distilled by standard methods unless otherwise stated.

Allyl 2,3,4,6-tetra-*O*-acetyl-β-D-glucopyranoside (2)[34]

To a solution of glucosyl bromide **1**[33] (45 g, 0.11 mol) and allyl alcohol (13 mL, 0.64 mol) in dry $CHCl_3$ (150 mL) were added $HgBr_2$ (4.5 g, 12.5 mmol), HgO (24 g, 110 mmol), and $CaSO_4$ (46.2 g) at 0 °C. The reaction was allowed to stir and warm to room temperature (rt) over 10 h, after which time it was filtered, washed with aq NaBr, and extracted with CH_2Cl_2. The organic phase was dried with anhyd $MgSO_4$, filtered, and evaporated to dryness. The residue was submitted to silica gel column chromatography (3:1 hexane–EtOAc) to give allyl glucoside **2** as a colorless syrup (41.7 g, 98%). The data matched those reported in the literature.[34]

Allyl β-D-glucopyranoside (3)[46]

To a solution of **2** (25.6 g, 66.0 mmol) in dry CH_2Cl_2 (50 mL) and dry MeOH (250 mL) was added NaOMe (25% in MeOH, 0.25 mL). The reaction was stirred at rt for 2 h, after which time the reaction was neutralized with Dowex-50 × 2-100 (H^+ form). The suspension was filtered and evaporated to afford tetraol **3** as a white solid (18.2 g, 96%), which was used in the next step without further purification. The data matched those reported in the literature.[46]

Allyl 2,3,4,6-tetra-*O*-allyl-β-D-glucopyranoside (4)[35]

To a solution of tetraol **3** (2.08 g, 9.45 mmol) in 33% aq NaOH (140 mL) the phase-transfer catalyst Bu_4NBr (2.3 g) was added. Then allyl chloride (4.6 mL, 56.5 mmol) was added dropwise at rt over 1 h. The mixture was stirred for 12 h, additional allyl chloride (1.2 mL) was added, and the

Can. J. Chem. Downloaded from www.nrcresearchpress.com by Xi'an Jiaotong University on 09/19/12
For personal use only.

Scheme 1.

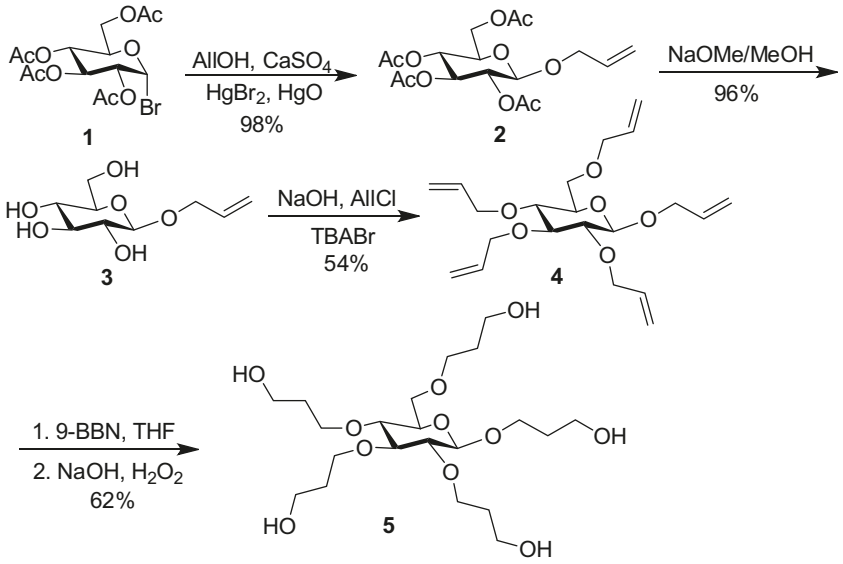

Scheme 2.

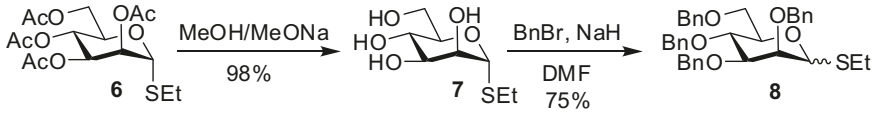

Scheme 3.

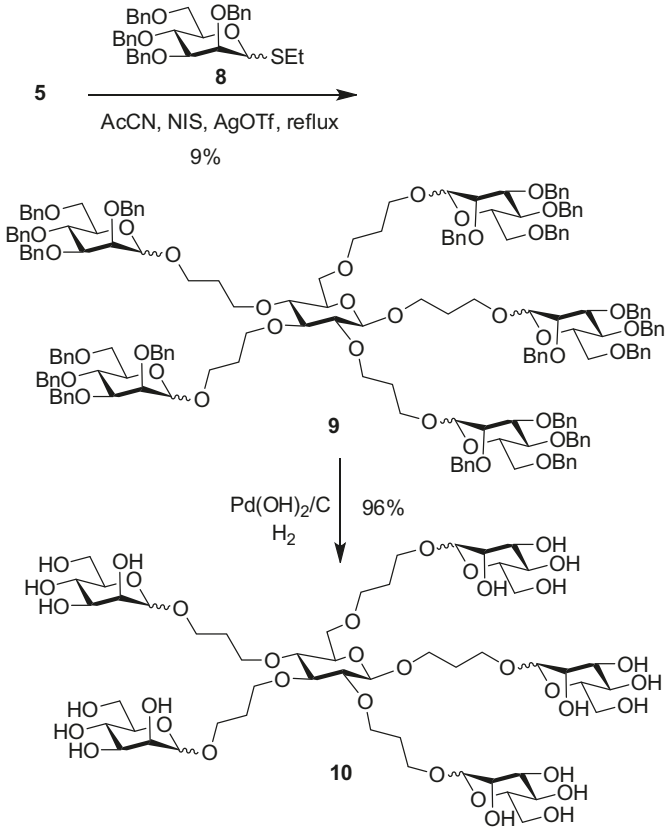

mixture was stirred for another 6 h. When the reaction was complete, toluene (100 mL) was added, and the organic layer was separated and washed five times with water. The neutral organic phase was dried with anhyd $MgSO_4$, filtered, and evaporated to dryness. The residue was submitted to silica gel column chromatography (95:1 CH_2Cl_2–EtOAc) to give per-*O*-allyl glucoside **4** as a colorless syrup (1.93 g, 54%). ^{1}H NMR (300 MHz, $CDCl_3$) δ: 6.02–5.85 (m, 5H), 5.34–5.23 (ddd, 5H), 5.22–5.12 (ddd, 5H), 4.90 (d, J = 8.4 Hz, 1H), 4.37 (ddd, 1H), 4.32 (ddd, 1H), 4.25 (ddd, 1H), 4.20–4.02 (m, 6H), 3.99 (m, 1H), 3.74 (t, J = 9.7 Hz, 1H), 3.71 (ddd, 1H), 3.65 (dd, J = 10.2 Hz, J = 3.6 Hz, 1H), 3.61 (dd, J = 2.6 Hz, 1H), 3.43 (t, J = 9.7 Hz, 1H), 3.40 (dd, J = 9.7 Hz, 1H). ^{13}C NMR (75 MHz, $CDCl_3$) δ: 135.21, 135.05, 134.78, 134.68, 134.01, 116.98, 116.93, 116.89, 116.69, 115.94, 102.45, 84.12, 81.57, 77.47, 74.72, 74.42, 73.79, 73.62, 72.43, 70.09, 68.89. The data matched those reported in the literature.[32,35]

3-Hydroxypropyl 2,3,4,6-tetra-*O*-(3-hydroxypropyl)-β-D-glucopyranoside (5)

To a solution of perallyl glucoside **4** (261 mg, 0.687 mmol) in dry THF (7 mL) was added 9-borabicyclononane (9-BBN) (0.5 mol/L solution in THF, 20.5 mL, 10.25 mmol) under an N_2 atmosphere, and the solution was stirred at reflux temperature for 6 h. Then the excess of 9-BBN was destroyed by dropwise addition of water at 0 °C. The hydroboration mixture was oxidized by adding 3 mol/L aq NaOH (10.2 mL) and 30% H_2O_2 (10.2 mL) at 0 °C, followed by stirring at rt overnight. The aqueous phase was saturated with K_2CO_3, and the THF phase was separated. The aqueous phase was extracted twice with THF. The combined organic phases were dried with anhyd $MgSO_4$, filtered, and evaporated to dryness. The residue was submitted to silica gel column chromatography (15:85 MeOH–CH_2Cl_2) to give pentaol **5** as a colorless syrup (200 mg, 62%). ^{1}H NMR

Can. J. Chem. Downloaded from www.nrcresearchpress.com by Xi'an Jiaotong University on 09/19/12
For personal use only.

(300 MHz, CD_3OD) δ: 4.24 (d, J = 7.8 Hz, 1H), 3.93–3.77 (m, 6H), 3.71–3.52 (m, 17H), 3.19 (t, J = 7.5 Hz, 2H), 2.95 (t, J = 8.1 Hz, 1H), 1.80–1073 (m, 10H). ^{13}C NMR (75 MHz, CD_3OD) δ: 104.62, 85.89, 83.64, 79.31, 75.77, 71.51, 70.85, 70.73, 70.65, 69.46, 67.62, 60.27, 60.22, 60.11, 59.97, 59.81, 34.47, 34.31, 33.77, 33.59. HR-DART-MS calcd for $C_{21}H_{42}O_{11}$ *m/z*: 470.27216; $[M + H]^+$ *m/z*: 471.27910 (calcd 471.28054).

Ethyl 1-thio-α-D-mannopyranoside (7)

To a solution of tetraacetate **6**[36] (1.57 g, 4.01 mmol) in dry CH_2Cl_2 (6 mL) and dry MeOH (30 mL) was added NaOMe (25% in MeOH, 0.3 mL). The reaction was stirred at rt for 1 h, after which time the reaction was neutralized with Dowex 50 × 2-100 (H^+ form). The suspension was filtered and evaporated to afford tetraol **7** as a slightly yellow syrup (0.879 g, 98%), which was used in the next step without further purification. ^1H NMR (300 MHz, CD_3OD) δ: 5.18 (d, J = 1.5 Hz, 1H), 3.83 (m, 2H), 3.73 (d, J = 2.1 Hz, 1H), 3.68 (d, J = 5.7 Hz, 1H), 3.57 (m, 2H), 2.68–2.46 (m, 2H), 1.21 (t, J = 7.5 Hz, 3H).

Ethyl 2,3,4,6-tetra-*O*-benzyl-1-thio-D-mannopyranoside (8)

To a suspension of tetraol **7** (1.64 g, 7.32 mmol) in dry DMF (40 mL) was added NaH (60% dispersion in mineral oil, 2.62 g) and benzyl bromide (7.5 mL, 63.1 mmol). The reaction was stirred at rt for 4 h, after which time MeOH (20 mL) was added at 0 °C to quench the NaH. Subsequently, the mixture was concentrated and filtered through a Celite bed. The filtrate was evaporated to dryness, and the residue was submitted to silica gel column chromatography (8:1 hexane–EtOAc) to give compound **8** as a yellow syrup of an α/β mixture (3.19 g, α:β = 2.3:1, 75%). α Anomer: ^1H NMR (300 MHz, $CDCl_3$) δ: 7.49–7.23 (m, 20H), 5.49 (d, J = 2.1 Hz, 1H), 4.97 (d, J = 10.8 Hz, 1H), 4.84–4.72 (m, 4H), 4.65–4.56 (m, 4H), 4.24–4.08 (m, 2H), 3.93–3.88 (m, 2H), 3.79 (dd, J = 10.8 Hz, J = 1.8 Hz, 1H), 2.77–2.57 (m, 2H), 1.32 (t, J = 7.5 Hz, 3H). ^{13}C NMR (75 MHz, $CDCl_3$) δ: 138.36, 138.21, 138.10, 137.96, 128.24–127.34, 81.66, 80.21, 76.11, 75.00, 74.86, 73.15, 71.89, 71.82, 71.75, 68.95, 25.17, 14.88. HR-DART-MS calcd for $C_{36}H_{40}O_5S$ *m/z*: 584.25910; $[M + H]^+$ *m/z*: 585.26968 (calcd 585.26692).

[3-(2,3,4,6-Tetra-*O*-benzyl-D-mannopyranosyloxy)propyl] 2,3,4,6-tetra-*O*-[3-(2,3,4,6-tetra-*O*-benzyl-D-mannopyranosyloxy)propyl]-β-D-glucopyranoside (9)

A mixture of thioether donor **8** (1.92 g, 3.28 mmol) and pentaol acceptor **5** (25 mg, 0.053 mmol) was dried on a vacuum line for at least 3 days. Then the mixture was dissolved in dry acetonitrile (300 mL) and stirred with powdered molecular sieves (4 Å) for 30 min. NIS (82 mg, 0.364 mmol) was then added, and stirring was continued for a further 30 min. After the addition of a catalytic amount of AgOTf (15 mg), the color of the reaction mixture turned deep yellow-brown. After 30 min, the reaction temperature was raised to 81 °C, which allowed the mixture to gently reflux. When MALDI-TOF MS indicated no further progression of the reaction after 1 week, triethylamine (TEA) was added to quench the reaction, and, subsequently, the mixture was diluted, filtered through a Celite bed, and concentrated. The residue was submitted to gel-permeation chromatography on Sephadex LH-20 (1:1 CH_2Cl_2–MeOH). Subsequent silica gel column chromatography (1:1 hexane–EtOAc) afforded **9** (15 mg, 9%) as a white solid. MALDI-TOF MS calcd for $C_{191}H_{212}O_{36}$ *m/z*: 3082.4787; $[M + Na]^+$ *m/z*: 3105.4226 (calcd 3105.4695).

[3-(D-Mannopyranosyloxy)propyl] 2,3,4,6-tetra-*O*-[3-(D-mannopyranosyloxy)propyl]-β-D-glucopyranoside (10)

Benzyl-protected dendrimer **9** (5 mg, 1.62 μmol) was dissolved in EtOAc–MeOH (1:1, 4 mL) and hydrogenated after the addition of $Pd(OH)_2$-on-charcoal catalyst (20%, 30 mg) at atmospheric pressure. When MALDI-TOF MS indicated the reaction was complete after 1 week, the mixture was filtered through a Celite bed, and the filtrate was concentrated and purified by gel-permeation chromatography on Sephadex LH-20 (MeOH) to yield compound **10** (2 mg, 96%) as a white solid. MALDI-MS calcd for $C_{51}H_{92}O_{36}$ *m/z*: 1280.5363; $[M + Na]^+$ *m/z*: 1303.4556 (calcd 1303.5261).

Acknowledgments

The financial support of the Natural Science Foundation of the Southwest University of Science and Technology (to C. W.) and a grant from the National Science Foundation (grant no. DMR-0906752 to D.C.B.) are gratefully acknowledged. The authors also thank W.-b. Yang and I. Abia for their laboratory assistance.

References

(1) Lis, H.; Sharon, N. *Chem. Rev.* **1998** *98* (2), 637. doi:10.1021/cr940413g.
(2) Toone, E. J. *Curr. Opin. Struct. Biol.* **1994** *4* (5), 719. doi:10.1016/S0959-440X(94)90170-8.
(3) Lee, Y. C.; Lee, R. T. *Acc. Chem. Res.* **1995** *28* (8), 321. doi:10.1021/ar00056a001.
(4) Drickamer, K. *J. Biol. Chem.* **1988** *263*, 9557.
(5) Rudd, P. M.; Elliott, T.; Cresswell, P.; Wilson, I. A.; Dwek, R. A. *Science* **2001** *291* (5512), 2370. doi:10.1126/science.291.5512.2370.
(6) Weis, W. I.; Taylor, M. E.; Drickamer, K. *Immunol. Rev.* **1998** *163* (1), 19. doi:10.1111/j.1600-065X.1998.tb01185.x.
(7) Springer, T. A. *Cell* **1994** *76* (2), 301. doi:10.1016/0092-8674(94)90337-9.
(8) Varki, A. *Glycobiology* **1993** *3* (2), 97. doi:10.1093/glycob/3.2.97.
(9) (a) Mammen, M.; Choi, S.; Whitesides, G. M. *Angew. Chem.* **1998** *110* (20), 2908. doi:10.1002/(SICI)1521-3757(19981016)110:20<2908::AID-ANGE2908>3.0.CO;2-2; (b) Mammen, M.; Choi, S.; Whitesides, G. M. *Angew. Chem. Int. Ed.* **1998** *37* (20), 2754. doi:10.1002/(SICI)1521-3773(19981102)37:20<2754::AID-ANIE2754>3.0.CO;2-3.
(10) Roy, R. *Curr. Opin. Struct. Biol.* **1996** *6* (5), 692. doi:10.1016/S0959-440X(96)80037-6.
(11) Lindhorst, T. K. *Top. Curr. Chem.* **2002** *218*, 201. doi:10.1007/3-540-45010-6_7.
(12) Boysen, M. M. K.; Elsner, K.; Sperling, O.; Lindhorst, T. K. *Eur. J. Org. Chem.* **2003** *2003* (22), 4376. doi:10.1002/ejoc.200300413.
(13) Bosman, A. W.; Janssen, H. M.; Meijer, E. W. *Chem. Rev.* **1999** *99* (7), 1665. doi:10.1021/cr970069y.
(14) (a) Fischer, M.; Vögtle, F. *Angew. Chem.* **1999** *111* (7), 934. doi:10.1002/(SICI)1521-3757(19990401)111:7<934::AID-ANGE934>3.0.CO;2-4; (b) Fischer, M.; Vögtle, F. *Angew.*

Can. J. Chem. Downloaded from www.nrcresearchpress.com by Xi'an Jiaotong University on 09/19/12
For personal use only.

Chem. Int. Ed. **1999** *38* (7), 884. doi:10.1002/(SICI)1521-3773(19990401)38:7<884::AID-ANIE884>3.0.CO;2-K.
(15) Matthews, O. A.; Shipway, A. N.; Stoddart, J. F. *Prog. Polym. Sci.* **1998** *23* (1), 1. doi:10.1016/S0079-6700(97)00025-7.
(16) Tomalia, D. A.; Durst, H. D. *Top. Curr. Chem.* **1993** *165*, 193. doi:10.1007/BFb0111285.
(17) Röckendorf, N.; Lindhorst, T. K. *Top. Curr. Chem.* **2001** *217*, 201. doi:10.1007/3-540-45003-3_6.
(18) Lundquist, J. J.; Toone, E. J. *Chem. Rev.* **2002** *102* (2), 555. doi:10.1021/cr000418f.
(19) (a) Lindhorst, T. K.; Kieburg, C. *Angew. Chem.* **1996** *108* (17), 2083. doi:10.1002/ange.19961081718; (b) Lindhorst, T. K.; Kieburg, C. *Angew. Chem. Int. Ed. Engl.* **1996** *35* (17), 1953. doi:10.1002/anie.199619531.
(20) Kieburg, C.; Lindhorst, T. K. *Tetrahedron Lett.* **1997** *38* (22), 3885. doi:10.1016/S0040-4039(97)00760-0.
(21) (a) Sadalapure, K.; Lindhorst, T. K. *Angew. Chem.* **2000** *112* (11), 2066. doi:10.1002/1521-3757(20000602)112:11<2066::AID-ANGE2066>3.0.CO;2-X; (b) Sadalapure, K.; Lindhorst, T. K. *Angew. Chem. Int. Ed.* **2000** *39* (11), 2010. doi:10.1002/1521-3773(20000602)39:11<2010::AID-ANIE2010>3.0.CO;2-1.
(22) Boysen, M. M. K.; Lindhorst, T. K. *Org. Lett.* **1999** *1* (12), 1925. doi:10.1021/ol9910619.
(23) Boysen, M. M. K.; Lindhorst, T. K. *Tetrahedron* **2003** *59* (22), 3895. doi:10.1016/S0040-4020(03)00458-7.
(24) Ashton, P. R.; Hounsell, E. F.; Jayaraman, N.; Nilsen, T. M.; Spencer, N.; Stoddart, J. F.; Young, M. *J. Org. Chem.* **1998** *63* (10), 3429. doi:10.1021/jo9804184.
(25) Kleinert, M.; Röckendorf, N.; Lindhorst, T. K. *Eur. J. Org. Chem.* **2004** *2004* (18), 3931. doi:10.1002/ejoc.200400239.
(26) Patel, A.; Lindhorst, T. K. *Carbohydr. Res.* **2006** *341* (10), 1657. doi:10.1016/j.carres.2006.01.024.
(27) Fernandez-Megia, E.; Correa, J.; Rodrı'guez-Meizoso, I.; Riguera, R. *Macromolecules* **2006** *39* (6), 2113. doi:10.1021/ma052448w.
(28) Touaibia, M.; Wellens, A.; Shiao, T. C.; Wang, Q.; Sirois, S.; Bouckaert, J.; Roy, R. *ChemMedChem* **2007** *2* (8), 1190. doi:10.1002/cmdc.200700063.
(29) Touaibia, M.; Roy, R. In *Comprehensive Glycoscience;* Kamerling, J. P., Ed.; Elsevier Press: Oxford, 2007; Vol. 3, p 781.
(30) Tabarani, G.; Reina, J. J.; Ebel, C.; Vivès, C.; Lortat-Jacob, H.; Rojo, J.; Fieschi, F. *FEBS Lett.* **2006** *580* (10), 2402. doi:10.1016/j.febslet.2006.03.061.
(31) (a) Rojo, J.; Delgado, R. *Antimicrob. J. Chemother.* **2004** *54* (3), 579. doi:10.1093/jac/dkh399; (b) Lasala, F.; Arce, E.; Otero, J. R.; Rojo, J.; Delgado, R. *Antimicrob. Agents Chemother.* **2003** *47* (12), 3970. doi:10.1128/AAC.47.12.3970-3972.2003.
(32) Köhn, M.; Benito, J. M.; Ortiz Mellet, C.; Lindhorst, T. K.; García Fernández, J. M. *ChemBioChem* **2004** *5* (6), 771. doi:10.1002/cbic.200300807.
(33) Roth, W.; Pigman, W. *Methods Carbohydr. Chem* **1963** *2*, 405.
(34) Yang, Q. Synthetic and Structural Studies on Anticancer Agents: C-/O-Linked and S-/O-Linked Hyaluronic Acid Oligosaccharide Mimetics. Ph. D. Dissertation, University of Tennessee, 2002.
(35) Dubber, M.; Lindhorst, T. K. *Carbohydr. Res.* **1998** *310* (1–2), 35. doi:10.1016/S0008-6215(98)00155-4.
(36) Tosin, M.; Murphy, P. *J. Org. Chem.* **2005** *70* (10), 4107. doi:10.1021/jo050200z.
(37) Wang, C.; Zhou, Y.; Baker, D. C. *ARKIVOC* **2009** (xiv), 171.
(38) Yun, M.; Shin, Y.; Yoon, S.; Chun, K. H.; Shin, J. E. N. *Bull. Korean Chem. Soc.* **1998** *19*, 1239.
(39) Crich, D.; Sun, S. *Tetrahedron* **1998** *54* (29), 8321. doi:10.1016/S0040-4020(98)00426-8.
(40) Baeschlin, D. K.; Green, L. G.; Hahn, M. G.; Hinzen, B.; Ince, S. J.; Ley, S. V. *Tetrahedron Asymmetry* **2000** *11* (1), 173. doi:10.1016/S0957-4166(99)00519-4.
(41) Sarbajna, S.; Roy, N. *Carbohydr. Res.* **1998** *306* (3), 401. doi:10.1016/S0008-6215(97)10083-0.
(42) Lahmann, M.; Oscarson, S. *Org. Lett.* **2000** *2* (24), 3881. doi:10.1021/ol006621e.
(43) Kötter, S.; Krallmann-Wenzel, U.; Ehlers, S.; Lindhorst, T. K. *J. Chem. Soc., Perkin Trans. 1* **1998** (14): 2193. doi:10.1039/a801985a.
(44) Lindhorst, T. K.; Kieburg, C.; Krallmann-Wenzel, U. *Glycoconjugate J.* **1998** *15* (6), 605. doi:10.1023/A:1006920027641.
(45) Lindhorst, T. K.; Dubber, M.; Krallmann-Wenzel, U.; Ehlers, S. *Eur. J. Org. Chem.* **2000** *2000* (11), 2027. doi:10.1002/1099-0690(200006)2000:11<2027::AID-EJOC2027>3.0.CO;2-L.
(46) Rich, J. R.; Wakarchuk, W. W.; Bundle, D. R. *Chem. - Eur. J.* **2006** *12* (3), 845. doi:10.1002/chem.200500518.

Automated analysis of synthesized oligorutin and oligoesculin by laccase

Julie Anthoni, Latifa Chebil, Frederic Lionneton, Jacques Magdalou, Catherine Humeau, and Mohamed Ghoul

Can. J. Chem. Downloaded from www.nrcresearchpress.com by Xi'an Jiaotong University on 09/19/12
For personal use only.

Abstract: The polymerization of phenolic species is an interesting way to generate derivatives with new or improved properties. The structural analysis of these compounds is complex and requires specific analytical techniques. The size exclusion chromatography coupled with an UV detector (SEC-UV) and matrix-assisted laser desorption ionization coupled with a time-of-flight detector (MALDI-TOF) analyses are two methods used to investigate the masses of biopolymers. To analyse the oligomers of rutin and esculin synthesized by the laccase from *Trametes versicolor*, these two techniques were used and coupled with an automated platform. The conditions of detection by MALDI-TOF were optimized. The parallel synthesis, the preparation of sample, the SEC analysis, and the MALDI spotting were realized automatically on a Chemspeed platform. The MALDI-TOF technique enables the detection of oligomers up to pentamer and nonamer, whereas the SEC-UV permits the detection of about 17-mer for rutin and esculin. The molecular mass distribution is underestimated by MALDI-TOF analysis compared with SEC-UV, but comes to the determination of absolute masses. So these two techniques would be combined to explore the masses and the oligomer distributions.

Key words: oligomers, Chemspeed, MALDI-TOF, SEC-UV.

Résumé : La polymérisation d'espèces phénoliques est une méthode intéressante de générer des dérivés possédant des propriétés nouvelles ou améliorées. L'analyse de la structure de ces composés est complexe et elle nécessite des techniques analytiques spécifiques. La chromatographie d'exclusion en fonction de la taille couplée à un détecteur ultraviolet (CET-UV) et l'ionisation par désorption au laser d'une matrice couplée à un détecteur à temps de vol (« MALDI-TOF ») sont deux méthodes d'analyse utilisées pour étudier les masses de biopolymères. On a utilisé ces deux méthodes pour analyser les oligomères de la rutine et de l'esculine par la laccase à partir du *Tramates versicolor*, et on les a couplées à une plate-forme automatisée. On a optimisé les conditions de détection dans le mode MALDI-TOF. Les synthèses parallèles, la préparation de l'échantillon, l'analyse de chromatographie d'exclusion en fonction de la taille et la détection en faisant appel à l'ionisation par désorption au laser d'une matrice ont toutes été effectuées d'une façon automatique sur une plate-forme Chemspeed. La technique de l'ionisation par désorption au laser d'une matrice couplée à un détecteur à temps de vol (MALDI-TOF) permet de détecter des oligomères allant jusqu'au pentamère et au nonamère alors que la chromatographie d'exclusion en fonction de la taille couplée à un détecteur ultraviolet (CET-UV) permet de détecter environ le 17-mère de la rutine et de l'esculine. Par comparaison avec les distributions de masses moléculaires déterminées par chromatographie d'exclusion en fonction de la taille couplée à un détecteur ultraviolet (CET-UV), la technique de l'ionisation par désorption au laser d'une matrice couplée à un détecteur à temps de vol (MALDI-TOF) conduit à une sous-évaluation de cette distribution, mais elle permet de déterminer les masses absolues. Il est donc important d'utiliser une combinaison de ces deux techniques pour examiner les masses et les distributions d'oligomères.

Mots-clés : oligomères, Chemspeed, technique de l'ionisation par désorption au laser d'une matrice couplée à un détecteur à temps de vol (« MALDI-TOF »), chromatographie d'exclusion en fonction de la taille couplée à un détecteur ultraviolet (CET-UV).

[Traduit par la Rédaction]

Introduction

The polymerization of phenolic species is an interesting way to generate derivatives with new or improved properties.[1–12] These properties could be controlled by the operating conditions of the reaction, which can affect the polymerization degree and the nature of the linkage occurring between monomers. To evaluate the effect of the operating conditions on the oligomer structure, different techniques are used: osmometry,[13] tonometry, cryometry, size exclusion chromatog-

Received 6 January 2011. Accepted 20 April 2011. Published at www.nrcresearchpress.com/cjc on 9 August 2011.

J. Anthoni, L. Chebil, C. Humeau, and M. Ghoul. Laboratoire d'ingénierie des biomolécules (LIBio), Nancy Université, 2 avenue de la forêt de Haye, 54500 Vandoeuvre-lès-Nancy, France.
F. Lionneton and J. Magdalou. Laboratoire de Pharmacologie UMR7561 CNRS-Université Henri Poincaré, Vandoeuvre les Nancy, France.

Corresponding author: Latifa Chebil (e-mail: latifa.chebil@ensaia.inpl-nancy.fr).

Can. J. Chem. Downloaded from www.nrcresearchpress.com by Xi'an Jiaotong University on 09/19/12
For personal use only.

raphy (SEC), and mass spectrometry. These last two techniques are the most used for the biopolymer characterization.

SEC is a well-known technique in the polymer field, but it needs standards with similar chemical structure to synthesize molecules. Among mass spectrometry techniques, the matrix-assisted laser desorption ionization coupled with a time-of-flight detector (MALDI-TOF) is often mentioned for the structural investigation of biopolymers. This technique avoids the fragmentation phenomena observed with other mass spectrometry techniques and ions are detected as single-charged, which facilitates spectrum identification. The TOF is adapted to a broad domain of molecular masses of polymers. However, its use for biopolymer analysis requires a judicious choice of the small organic molecules "the matrix", essential to co-crystallized with the analyte, the mode of ionization, and detection. The matrix co-crystallizes selectively with the analyte, minimizing salt contamination of the obtained crystals. The spectrum quality depends on crystal preparation, the nature of the matrix, the presence of tensioactive or buffer, the pH of the solution, and the characteristics of the analyte and solvent. The ionization could be realized in positive or negative mode. If the analyte has a proton acceptor function, the positive mode is recommended, whereas, if the molecule is a proton donor, the negative mode is selected. In the literature, flavonoids have been analyzed by mass spectrometry with negative[14,15] and positive modes.[16,17]

The detection can be carried out under linear or reflectron modes. The reflectron mode allows an increase in the time of the flight without increasing the size of the apparatus. The combination of increased flight length and conserved time distribution increases the resolution of the signal. But this mode is limited to masses <60 KDa. the linear mode is more adapted for a high molecular mass. Nevertheless, for an investigation of the whole domain of masses, these two detection modes could be combined.

The solvent proportion is also an important factor; it allows the acceleration or slowing down of the crystallization phenomena. In the same way the ratio of analyte/matrix effects the crystallization and the analyte ionization.

The objective of this work is to develop an automated platform based on the use of a Chemspeed station and two online detectors, MALDI-TOF and SEC-UV. This platform will be used to evaluate the effects of the operational conditions and the nature of the flavonoid on the properties of the synthesized oligomers. To accomplish this purpose, in a first step, the operating conditions of MALDI-TOF analysis were optimized; in a second step, the coupling of the two analytical techniques to the Chemspeed station was realized; and finally, the performance of this system was validated by the oligomerization kinetics of rutin and esculin.

Experimental

Materials

Laccase *Trametes versicolor* (E.C. 1.10.13.2., 21.4 U/mg) and esculin sesquihydrate (>98%) were purchased from Fluka and rutin (>95%) was purchased from Sigma-Aldrich. All solvents were HPLC grade and were purchased from VWR.

Parallel synthesis of oligorutin

To synthesize and analyze oligoflavonoids, a Chemspeed ASW1000 (Chemspeed Ltd., August, Switzerland) platform was used. The rutin or esculin powders (final concentration 3 g/L) were introduced in eight parallel thermostated vessels of 27 mL in total volume. All later operations were automatically realized. Methanol and water were added to each vessel (final volume 10 mL at the ratio 30:70, *v*/*v*). The reaction was started by adding an enzymatic solution of laccase (final concentration 3 U/mL). The system was stirred at 600 rpm at 20 °C. To follow the kinetics of the oligomerization, dimethylformamide (DMF) was transferred to the SEC dilution zone. Reaction media samples were added to the DMF (final ratio DMF / reaction media, 9:1, *v*/*v*). The diluted solutions were stirred and then injected online into the SEC-UV system. To avoid precipitation phenomena, the SEC dilution zone was also kept at the same temperature as the reaction. SEC analysis allowed the determination of weight average masses.

To determinate the absolute masses of rutin oligomers, samples were automatically diluted twofold in acetonitrile (ACN) / water with 0.1% trifluoroacidic acid (30:70, *v*/*v*) on the MALDI-TOF dilution zone. Homogenization was realized by a repetitive (3 times) suction/pouring. For the spotting, a needle with a 0.4 mm diameter was used in combination with a Bruker MTP 384 massive MALDI target. A special support was created to adapt this target on the Chemspeed platform. Three microlitres of the diluted solutions were spotted on line and then 1 µL of the refrigerated matrix solution (to avoid rapid degradation of the matrix) was dropped on the surface of the analyte. The spots were left for crystallization at room temperature. The positions of the samples on the MALDI target were located with *x*, *y*, *z* coordinates and programmed using the synthesizer software. All samples were automatically spotted in triplicate.

SEC analysis

Relative masses of oligomers were evaluated by SEC (HPLC LaChrom (Merck), UV 280 nm LaChrom L-7400, Tosoh TSK Gel at 3000 column, 60 °C). DMF with 1% LiBr was used as the mobile phase at a flow rate of 1 mL/min. Polystyrene standards were used to define molecular mass calibration.

MALDI-TOF analysis

Absolute masses were determinated by MALDI-TOF. Three matrices were tested: synapinic acid (SA), 2′,4′,6′-trihydroxyacetophenone (THAP), and 2,5-dihydroxybenzoic acid (DHB).

MALDI-TOF-MS experiments were performed on an Ultraflex spectrometer (Bruker) in reflectron mode. Ionization was performed with a 337 nm pulsed nitrogen laser. After time-delayed extraction, the ionic species were accelerated under a 20 kV potential for TOF MS analysis. All spectra were obtained in positive-ion mode with an accumulation of at least 600 shots. Spectra were calibrated using the statistic calibration of FlexAnalysis software (Bruker).

Results and discussion

MALDI-TOF is a very powerful analytical tool for the

Table 1. Mode of preparation of the matrix used in MALDI-TOF analysis.

Matrix	Designation	Concn of matrix	Solvent	Ref.
DHB	DHB1	5 mg/mL	ACN/water+TFA 0.1% (1:2, *v*/*v*)	18
	DHB2	20 mg/mL	ACN/water+TFA 0.1% (1:2, *v*/*v*)	
SA	SA1	1 mg/mL	ACN/water+TFA 0.1% (9:1, *v*/*v*)	19
	SA2	Step 1: saturated	ACN	
		Step 2: 0.1%	Final ratio ACN/water+TFA of 1:2 *v*/*v*	
THAP	THAP1	10 mg/mL	ACN / ammonium citrate (100 mmol/L, 1:1, *v*/*v*)	20, 21
	THAP2	saturated	Acetone	15

Note: DHB, 2,5-dihydroxybenzoic acid; SA, synapinic acid; THAP, 2′,4′,6′-trihydroxyacetophenone; ACN, acetonitrile; and TFA, trifluoroacetic acid.

Can. J. Chem. Downloaded from www.nrcresearchpress.com by Xi'an Jiaotong University on 09/19/12
For personal use only.

Fig. 1. Impact of the type of matrix, the mode of ionization, and the mode of detection on crystallization, dimer and trimer intensity, and resolution for the MALDI-TOF analysis of oligomers of rutin. Three matrices were tested: dihydroxybenzoic acid (DHB1 and DHB2) and trihydroxyacetophenone (THAP), in linear (L) or reflectron (R) mode and in positive (+) or negative (–) ionization. An analyte/matrix ratio of 3:1 was applied.

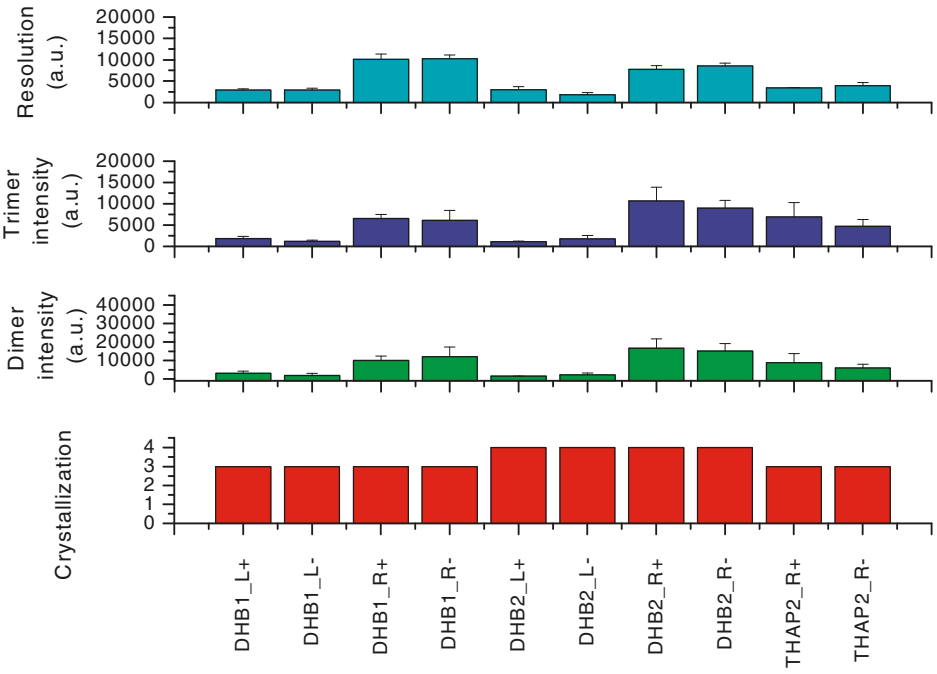

investigation of polymers. This technique leads to the determination of the mode of linkage and the mass distribution. However, its use for a given substrate needs the optimization of several factors affecting the amplitude and the reproducibility of the spectrum signal. Therefore, in a first step the effect of different parameters on MALDI-TOF analysis was investigated for oligorutin and oligoesculin obtained after 24 and 36 h of reaction, respectively.

The matrix and detection mode

To determinate the absolute mass of oligomers and, therefore, the linkage between two units of rutin, three parameters were varied offline to optimize the MALDI-TOF protocol: the matrix, the ionization mode, and the detection mode. In this work, to limit the pH influence, the analyte was diluted in a solution of ACN/water containing 0.1% TFA.

For a given polymer the choice of the matrix is crucial; some matrices are particularly sensitive to impurities, whereas for others the loss of efficiency is small, and hence such matrices are preferred when salts are available in the medium. The ideal matrix should have a high electronic absorption at the employed laser wavelength, good vacuum stability, low vapor pressure, good solubility in the solvent, and good miscibility with the analyte in the solid state. To select the most adapted matrix to rutin and esculin oligomers analysis, three matrices were tested: DHB, SA, and THAP. Various alternatives of preparation of these matrices were formulated (Table 1).

Different criteria were considered for the determination of the most appropriate conditions: the resolution, the quality of the crystallization, and the peak intensity. The quality of the crystallization was attributed arbitrarily on a scale between 0 and 4, with 4 representing high-quality.

The results show that, for all tested matrices and alternatives of preparation, only DHB1 and DHB2 in linear and reflectron modes and THAP2 in reflectron mode lead to exploitable spectra. The corresponding data are given in Fig. 1. For all tested matrices the positive and the negative modes of ionization lead to similar results.

The DHB matrix allowed a best resolution compared with

Can. J. Chem. Downloaded from www.nrcresearchpress.com by Xi'an Jiaotong University on 09/19/12
For personal use only.

Fig. 2. ASW2000 synthesizer for the oligomerization of rutin. The preparation of reaction media, SEC samples, and MALDI-TOF samples was executed online. HPLC injections and MALDI spotting were controlled by the computing interface of the synthesizer.

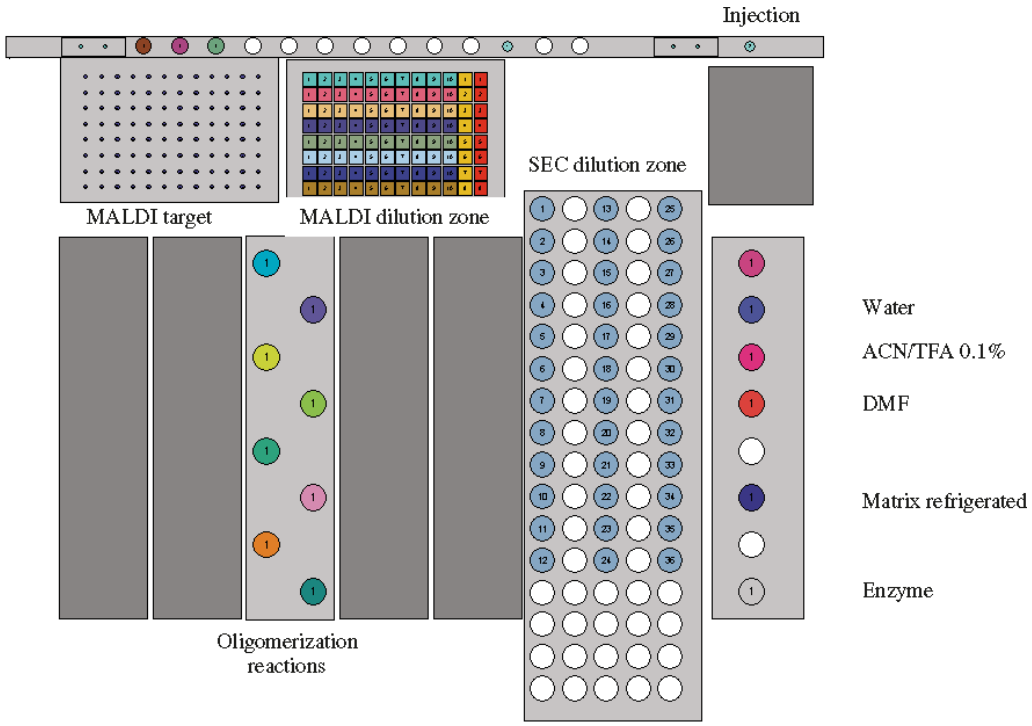

Fig. 3. Impact of the ratio of analyte/matrix (DHB1) and the proportion of solvent on resolution, intensity of the dimer and trimer, and crystallization on MALDI-TOF analysis of media containing rutin and oligomers of rutin (positive ionization mode and reflectron mode detection). ACN, acetonitrile.

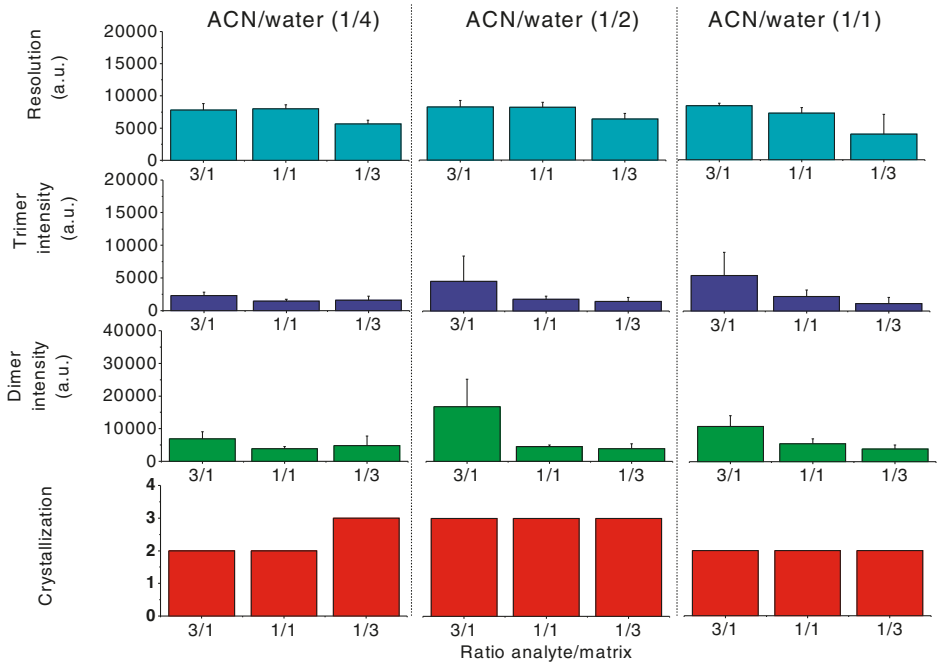

THAP2. The DHB2 matrix had the best crystallization and DHB1 had a better resolution. For the DHB matrix, a higher intensity of dimer or trimer and an enhanced resolution was obtained with the reflectron mode. Therefore, in light of these results, the effects of the other factors were analyzed in the presence of DHB1 in positive mode of ionization and in reflectron mode of detection.

Development of SEC and MALDI-TOF online analysis

MALDI-TOF and SEC analysis can be used to find the optimal reaction factors, such as optimal temperature, pH, and ratio of solvent or reactant concentration, for the production of oligomers with specific properties. To facilitate and accelerate this optimization, an online analysis was perfected. Thus, the MALDI-TOF spotting and the SEC-UV analysis

Fig. 4. Size exclusion chromatography (SEC) chromatogram of rutin oligomers (*a*) and esculin oligomers (*b*) at different times of reaction, and the molecular mass distribution determined by polystyrene standard calibration. The oligomerization reaction of flavonoid (3 g/L) was catalyzed by the laccase from *Trametes versicolor* (3 U/mL) at 20 °C in methanol/water solution (30:70, *v*/*v*).

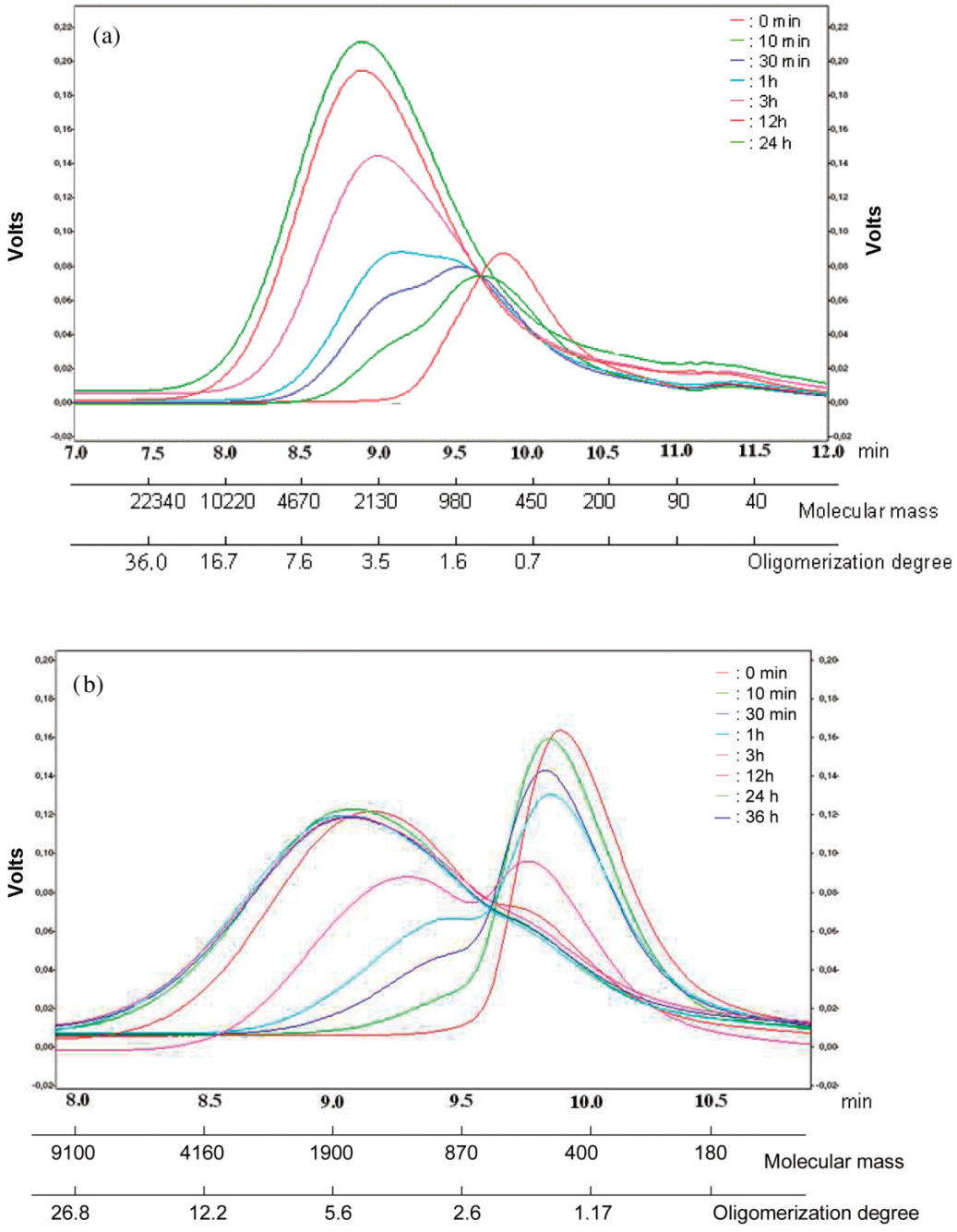

were coupled with the Chemspeed platform to be executed automatically online (Fig. 2).

This platform allows for the realization of eight parallel reactions or operating conditions and to follow the kinetics of the reaction. The stirring, the temperature, the handling of sample, the dilution, the injection, and the spotting were automatically controlled. The advantages of this automated method are the facility of implementation, the saving of time, the repeatability and reproducibility of data, and the absence of contamination. However, before being able to use this station in a routine way, the spotting conditions must be optimized. In fact, optimum results are obtained when the polymer and the matrix are soluble in the same solvent. Therefore, to solubilize the oligomers and the matrix together, a mixture of ACN/water containing 0.1% TFA was used. As the kinetics of the crystallization are affected by the solvent/water ratio, three preparations (1:4, 1:2, and 1:1, *v*/*v*) were tested. The ratio of analyte/matrix is also an important factor for the allowance of an optimal desorption of analyte. For this reason, three ratios of analyte/matrix (3:1, 1:1 and 1:3, *v*/*v*) were studied. The obtained results are summarized in Fig. 3. It appears that the highest intensity of dimer or

Can. J. Chem. Downloaded from www.nrcresearchpress.com by Xi'an Jiaotong University on 09/19/12
For personal use only.

Fig. 5. MALDI-TOF positive ion spectra ([M + Na or K]$^+$) in the reflectron mode of rutin (*a*) and esculin (*b*) oligomerization media after 24 and 36 h of reaction, respectively. Dihydroxybenzoic acid was used as the matrix.

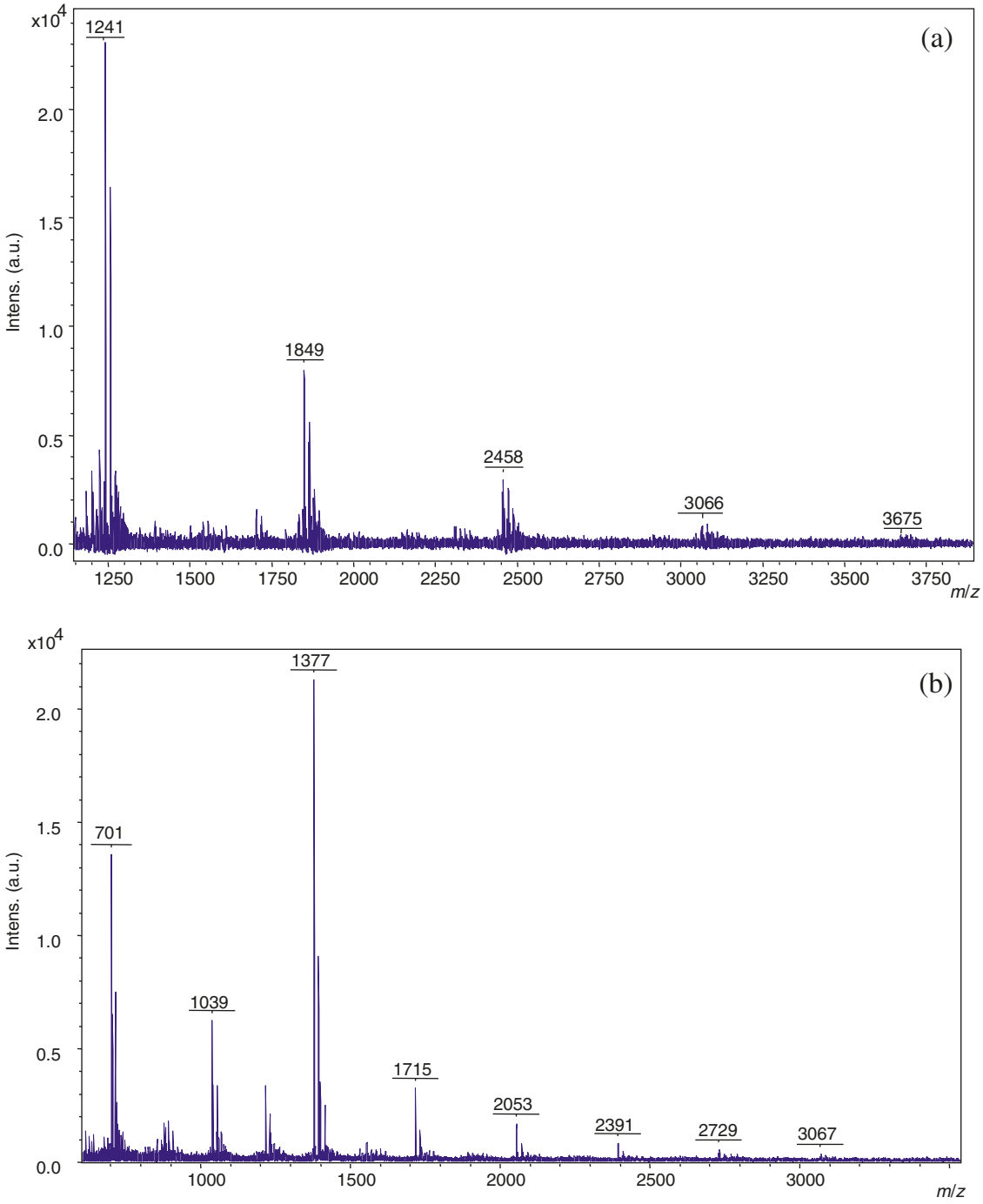

Can. J. Chem. Downloaded from www.nrcresearchpress.com by Xi'an Jiaotong University on 09/19/12
For personal use only.

trimer is reached for an analyte/matrix ratio of 3:1. In such conditions, a comparable resolution is obtained with the three proportions of diluted solutions of ACN/water (TFA 0.1%). However, the highest crystallization and dimer intensity are obtained with a ratio of 1:2 ACN/water (TFA 0.1%).

In conclusion, DHB1 as the matrix with a proportion of 1:2 (ACN/water TFA 0.1%) as a dilution solvent, an analyte/matrix ratio of 3:1, a positive ionization mode, and a reflectron detection mode were retained as optimal conditions for the oligoflavonoids characterization by MALDI-TOF.

For SEC-UV coupling with the Chemspeed platform, the samples were taken under agitation and diluted automatically in vials heated at the reaction temperature. This dilution was realized in a DMF–LiBr mixture. This solvent allows the instantaneous solubilization of the flavonoids and the synthesized oligomers. From this preparation 20 μL were injected via a rheodhyn valve. The elution solvent was DMF–LiBr at a flow rate of 1 mL/min. All steps in this procedure were supervised by the Chemspeed software.

Validation of the developed platform

This platform was validated by studying the polymeriza-

tion reaction of rutin and esculin. The oligomerization of rutin and esculin was followed over 24 and 36 h, respectively, depending on the kinetics of the reaction, by the online sampling and analysis described previously. The SEC spectra for several withdrawment samples are given on Fig. 4.

These chromatograms show that the formed oligomers can reach about 17 units for rutin and esculin.

The MALDI-TOF analysis was realized on all withdrawment samples. Figure 5 shows an example of the MALDI-TOF spectra. Dimers, trimers, and tetramers were synthesized immediately at the beginning of the reaction, thus, the enzymatic polymerization of flavonoids is not a sequential process. This technique allows the detection of oligomers up to pentamer (mass: 3044.5 g/mol) and nonamer (mass: 3044 g/mol) for rutin and esculin, respectively (Figs. 5*a* and 5*b*). However, a comparison of the SEC and MALDI-TOF results indicates that these two techniques lead to very different results. The molecular mass distribution is underestimated by MALDI-TOF analysis compared with SEC-UV. This behaviour could be due to weak ionization of oligomers having molar masses higher than 3000 Da in these conditions.

Conclusion

An automated platform allowing the realization of eight parallel syntheses or operating conditions with online sample preparation, MALDI-TOF spotting, and SEC analysis has been developed. This platform will be used to study the effect of different factors on the kinetics and structural properties of the enzymatic polymerization of flavonoids by laccase.

References

(1) Akita, M.; Tsutsumi, D.; Kobayashi, M.; Kise, H. *Biosci. Biotechnol. Biochem.* **2001** *65* (7), 1581. doi:10.1271/bbb.65.1581.

(2) Dordick, J. S.; Marletta, M. A.; Klibanov, A. M. *Biotechnol. Bioeng.* **1987** *30* (1), 31. doi:10.1002/bit.260300106.

(3) Mita, N.; Tawaki, S. I.; Uyama, H.; Kobayashi, S. *Macromol. Biosci.* **2003** *3* (5), 253. doi:10.1002/mabi.200390032.

(4) Oguchi, T.; Tawaki, S. I.; Uyama, H.; Kobayashi, M. *Bull. Chem. Soc. Jpn.* **2000** *73* (6), 1389. doi:10.1246/bcsj.73.1389.

(5) Uyama, H.; Kurioka, H.; Kobayashi, S. *Polym. J.* **1997** *29* (2), 190. doi:10.1295/polymj.29.190.

(6) Ayyagari, M.; Akkara, J. A.; Kaplan, D. L. In *ACS Symposium Series 684;* Gross, R. A.; Kaplan, D. L.; Swift, G. Eds., 1998; American Chemical Society: Washington, p 112.

(7) Bruno, F. F.; Nagarajan, S.; Nagarajan, R.; Kumar, J.; Samuelson, L. A. *J. Macromol. Sci. Pure Appl. Chem.* **2005** *42A* (11), 1547.

(8) Dubey, S.; Singh, D.; Misra, R. A. *Enzyme Microb. Technol.* **1998** *23* (7–8), 432. doi:10.1016/S0141-0229(98)00063-5.

(9) Kurisawa, M.; Chung, J. E.; Kim, Y. J.; Uyama, H.; Kobayashi, S. *Biomacromolecules* **2003** *4* (3), 469. doi:10.1021/bm034012z.

(10) Kurisawa, M.; Chung, J. E.; Uyama, H.; Kobayashi, S. *Macromol. Biosci.* **2003** *3* (12), 758. doi:10.1002/mabi.200300038.

(11) Anthoni, J.; Linneton, F.; Wieruzeski, J. M.; Magdalou, J.; Engasser, J. M.; Chebil, L.; Humeau, C.; Ghoul, M. *Rasāyan J. Chem.* **2008** *1* (4), 718.

(12) Anthoni, J.; Humeau, C.; Maia, E. R.; Chebil, L.; Engasser, J. M.; Ghoul, M. *Eur. Food Res. Technol.* **2010** *231* (4), 571. doi:10.1007/s00217-010-1298-3.

(13) Porter, L. J. *Aust. J. Chem.* **1986** *39* (4), 557. doi:10.1071/CH9860557.

(14) Foo, L. Y.; Newman, R.; Waghorn, G.; McNabb, W. C.; Ulyatt, M. J. *Phytochemistry* **1996** *41* (2), 617. doi:10.1016/0031-9422(95)00602-8.

(15) Wang, J.; Sporns, P. *J. Agric. Food Chem.* **2000** *48* (5), 1657. doi:10.1021/jf991035p.

(16) Ohnishi-Kameyama, M.; Yanagida, A.; Kanda, T.; Nagata, T. *Rapid Commun. Mass Spectrom.* **1997** *11* (1), 31. doi:10.1002/(SICI)1097-0231(19970115)11:1<31::AID-RCM784>3.0.CO;2-T.

(17) Shaikh, A. A.; Schwarz, G.; Kricheldorf, H. R. *Polymer (Guildf.)* **2003** *44* (8), 2221. doi:10.1016/S0032-3861(02)00910-2.

(18) Kéki, S.; Deák, G.; Zsuga, M. *J. Mass Spectrom.* **2001** *36* (12), 1312. doi:10.1002/jms.236.

(19) Kussmann, M.; Roepstorff, P. *Methods Mol. Cell. Biol.* **2000** *146*, 405.

(20) Kobayashi, T.; Yang, X.; Walker, L. A.; Van Breemen, R. B.; Solaro, R. J. *J. Mol. Cell. Cardiol.* **2005** *38* (1), 213. doi:10.1016/j.yjmcc.2004.10.014.

(21) Yang, X.; Wu, H.; Kobayashi, T.; Solaro, R. J.; Van Breemen, R. B. *Anal. Chem.* **2004** *76* (5), 1532. doi:10.1021/ac035203v.

Can. J. Chem. Downloaded from www.nrcresearchpress.com by Xi'an Jiaotong University on 09/19/12
For personal use only.

3,3′-*N*,*N*′-Bis(amino)-2,2′-bipyridine — An unusually methylation-resistant amine

Danielle M. Chisholm, Robert McDonald, and J. Scott McIndoe

Can. J. Chem. Downloaded from www.nrcresearchpress.com by Xi'an Jiaotong University on 09/19/12
For personal use only.

Abstract: Methylation of aromatic amino groups is usually straightforward, but the formation of two intramolecular hydrogen bonds in 3,3′-*N*,*N*′-bis(amino)-2,2′-bipyridine and (or) the potential for ring methylation prevents the clean tetramethylation of this molecule. Numerous attempts to make 3,3′-*N*,*N*′-bis(dimethylamino)-2,2′-bipyridine produced only complex mixtures of variously methylated products, and the only isolated molecule was 3,3′-*N*,*N*′-bis(methylamino)-2,2′-bipyridine, for which an X-ray crystal structure was obtained.

Key words: Proton-sponge, methylation, electrospray ionization mass spectrometry, bipyridine ligands.

Résumé : La méthylation des amines aromatiques est une réaction généralement simple mais, dans le cas de la 3,3′-*N*,*N*′-bis(amino)-2,2′-bipyridine, la formation de deux liaisons hydrogènes intramoléculaires et (ou) la possibilité de méthylation des hétérocycles empêche la réaction de tétraméthylation propre de cette molécule. Plusieurs essais de préparation de la 3,3′-*N*,*N*′-bis(diméthylamino)-2,2′-bipyridine n'ont conduit qu'à la formation de mélanges complexes de produits de degrés de méthylation divers et la seule molécule qui a pu être isolée est la 3,3′-*N*,*N*′-bis(méthylamino)-2,2′-bipyridine dont la structure a été caractérisée par diffraction des rayons-X.

Mots-clés : éponge à protons, méthylation, spectrométrie de masse avec ionisation par électronébulisation, ligands bipyridine.

[Traduit par la Rédaction]

1,8-Bis(dimethylamino)naphthalene (Proton-sponge), was first reported by Brown and Letang in 1941,[1] and in the late 1960s Alder et al.[2] drew attention to the fact that this molecule was unusually basic. Alder et al.[2] demonstrated how the sequential addition of methyl groups to 1,8-bis(amino)naphthalene increased the pK_a slowly until the fourth substitution, which increased the pK_a from 6.4 to 12.3. The high basicity is due to a number of factors. The bulky nature of the dimethylamino groups and their close proximity to one another induces steric repulsion between the lone pairs of electrons on the two nitrogen centres. To relieve some of the repulsion the naphthalene system twists out of plane by ~30°,[2] and the steric strain is easily relieved through association of a proton. The lone pairs on each nitrogen centre can become equally involved[3,4] in hydrogen bonding with the proton and are no longer repelled by one another, allowing the naphthalene ring to return to planarity.[5] The spatial arrangement of the dimethylamino groups allows access to only a proton, and anything larger will not fit comfortably (a notable exception being a highly reactive palladium fragment).[6] Many new proton sponges have since been introduced (see Fig. 1 for examples).[7–9] Staab et al.[10,11] showed that it was not just the proximity of the nitrogen centres that determined the strength of basicity but also the linearity of the resulting hydrogen bonds, hence the low basicity of structures 1(*d*) and 1(*e*). The superbase[12] 1,8-bis(hexamethyltriaminophosphazenyl)naphthalene[13] contains a combination of basic phosphazenes and proton sponge structure to achieve a pK_a of 29.9 in acetonitrile, almost 10^{12} more basic than 1,8-bis(dimethylamino)naphthalene.

The exclusive and strong association of a proton to these types of molecules makes them perfect handles for study using electrospray ionization mass spectrometry (ESI-MS).[14] Eliminating the possibility for multiple charge pathways greatly simplifies mass spectra, making this particular type of molecule very attractive. The only obstacle is adding this convenient probe to molecules of interest; in our research that equates to spectator ligands in catalytic reactions.[15–18] This end has been achieved previously in our group through altering triphenylphosphine by replacing one phenyl group with a proton sponge. (1,8-Bis[dimethylamino]naphthalene-2-yl)diphenylphosphine was synthesized and used to show that ESI-MS investigations of neutral metal complexes was possible when a chargeable ligand was employed.[19]

The direction we had envisioned for this work was toward molecules that would possess a similarly highly basic site once bound to a metal centre. We were drawn to the scaffold of the fluorene-type sponges 1(b) introduced by Staab and Saupe[8] because of the similarity they bore to the orientation of 2,2′-bipyridine ("bipy") chelating to a metal. Increasingly large atoms (O, S, Se, and Te) could replace the methylene

Received 23 February 2011. Accepted 2 March 2011. Published at www.nrcresearchpress.com/cjc on 16 August 2011.

D.M. Chisholm and J.S. McIndoe. Department of Chemistry, University of Victoria, P.O. Box 3065, Victoria, BC V8W 3V6, Canada.
R. McDonald. X-ray Crystallography Laboratory, Department of Chemistry, University of Alberta, Edmonton, AB T6G 2G2, Canada.

Corresponding author: J. Scott McIndoe (e-mail: mcindoe@uvic.ca).

Can. J. Chem. Downloaded from www.nrcresearchpress.com by Xi'an Jiaotong University on 09/19/12
For personal use only.

Fig. 1. Some of the structures developed in the course of research into proton sponges based on (*a*) naphthalene,[2] (*b*) fluorene,[8] (*c*) phenanthralene,[8] (*d*) 1,16-diaza[6]helicene,[10] (*e*) benzo[*c*]phenanthrene[11], and (*f*) phosphazene-substituted naphthalene.[13]

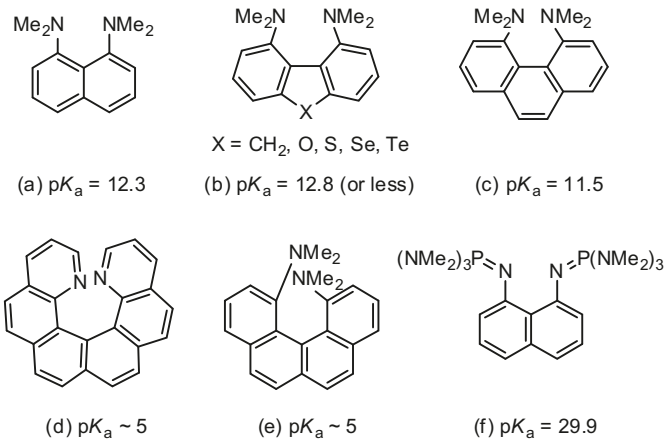

group with only minor detrimental effects on the basicity. To this end we pursued the functionalization of 2,2-bipyridine. Bipy ligands are common in coordination chemistry[20–22] so their incorporation into our investigations seemed like an appropriate choice. The idea was to substitute bipyridine at the 3 and 3′ positions to arrive at 3,3′-*N*,*N*′-bis(dimethylamino)-2,2′-bipyridine and to rely on coordination to a metal centre to orient the two groups toward each other (Fig. 2).

Once the functionalized bipyridine has coordinated to the metal and the dimethylamino groups have adopted the expected orientation, addition of a proton source should render the entire complex amenable to ESI-MS analysis and provide the first example of a metal-containing proton sponge. The effect of the relatively flexible coordination environment of the metal was also of structural interest — it is possible, of course, that the metal coordinates to one pyridine nitrogen and one dimethylamino nitrogen. In this case, an identical site would be available on the other side of the ligand, which itself could bind another metal centre or H^+.

Synthesis of the known 3,3′-bis(amino)-2,2′-bipyridine (**1**) was straightforward.[23] However, tetramethylation of the molecule to replace all N–H bonds with N–CH_3 proved anything but simple. Tetramethylation of 3,3′-bis(amino)biphenyl and 1,8-bis(amino)naphthalene is routine, but the same approach on 3,3′-bis(amino)-2,2′-bipyridine failed, and we subsequently tried nine other routes without success (Scheme 1).

Route a in Scheme 1 involved sodium hydride and dimethylsulfate, based on Staab and Staupe's[8] preparation of the fluorene-derived sponges. Route b adapted Giam and Hauck's[24] approach to the methylation of 3-aminopyridine to give 3-dimethylaminopyridine using formic acid and formaldehyde. Route c modified Sheppard's[25] methylation of *m*-trifluoromethylaniline to *m*-trifluoromethyl-*N*,*N*-dimethylaniline using trimethylphosphate and aqueous sodium hydroxide. Route d employed Charmant et al.'s[26] use of methyl iodide to methylate a benzylamine-substituted naphthalene proton sponge derivative. Route e used Shaw and Turner's[27] approach to methylating 2,2′-diaminobiphenyl to 2,2′-bis(dimethylamino)biphenyl using dimethyl sulfate and sodium hydroxide. All of these routes, to a greater or lesser extent, resulted in methylation, but always a complex mixture of

Fig. 2. Concept for a metal-containing proton sponge.

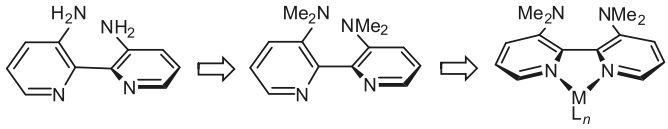

Scheme 1. Attempted routes to 3,3′-*N*,*N*′-bis(dimethylamino)-2,2′-bipyridine (**2**).

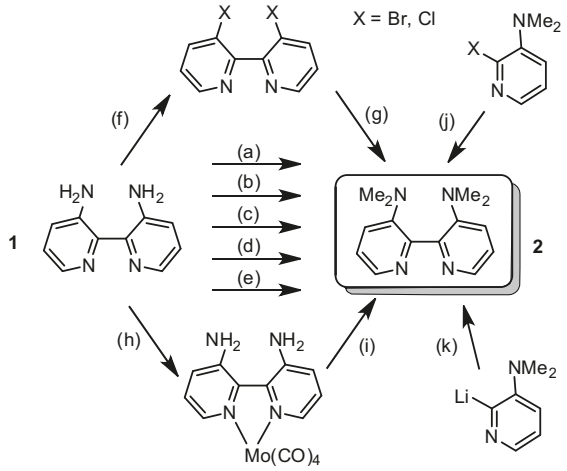

products was obtained and we were never successful in isolating the desired compound. Figure 3 illustrates a typical ESI-MS obtained from these reaction mixtures. Separating the different components by chromatography proved unsuccessful. Note that ESI-MS does not distinguish between ring methylation (+15 Da, positively charged) or replacement of one H for the Me and protonation (+15 Da, positively charged), so the following spectrum contains both series, i.e., $[C_{10}N_4Me_nH_{(4-n)}]^+$ (n = 1–5) and $[C_{10}N_4Me_nH_{(4-n)} + H]^+$ (n = 1–4). The ^{1}H NMR mixture, which showed the presence of both types of methyl groups (methylamine and methylpyridinium). Pyridines may be directly methylated by dimethylsulfate[28] or methyl iodide[29] in the absence of added strong base.

The one compound successfully isolated was the dimethylated neutral compound 3,3′-bis(methylamino)-2,2′-bipyridine (**3**) by fractional crystallization in 25% yield. Monomethylation of each amino group allows for two separate hydrogen bonds between the amine hydrogen and the pyridine nitrogen in opposite rings. Crystals of **3** were obtained from the reaction of **1** with sodium hydride and methyl iodide and were isolated by slow evaporation of diethyl ether. An X-ray crystal structure of this molecule was obtained (Fig. 4). This compound was spectroscopically characterized previously by ^{1}H and ^{15}N NMR without preparative details.[30]

The bipyridine core of **3** is very similar to unsubstituted 2,2′-bipyridine with respect to bond lengths and angles. The C–N1 and C–C bond lengths in the two equivalent pyridine rings average 1.34 and 1.40 Å, respectively, whereas the average bond angle is 120.0°. The comparative numbers for 2,2′-bipyridine are 1.36 and 1.39 Å and 120.8°, respectively.[31] As with 2,2′-bipyridine, N1 and N1 are arranged trans to one another, but whereas 2,2′-bipyridine is coplanar, the two equivalent pyridine rings of **3** lie in parallel planes separated by 0.06 Å. The presence of the hydrogen bonds

Can. J. Chem. Downloaded from www.nrcresearchpress.com by Xi'an Jiaotong University on 09/19/12
For personal use only.

Fig. 3. Positive ion ESI-MS in CH_2Cl_2 of the mixture obtained from methylation of 3,3′-bis(amino)-2,2′-bipyridine with Me_2SO_4 and NaOH.

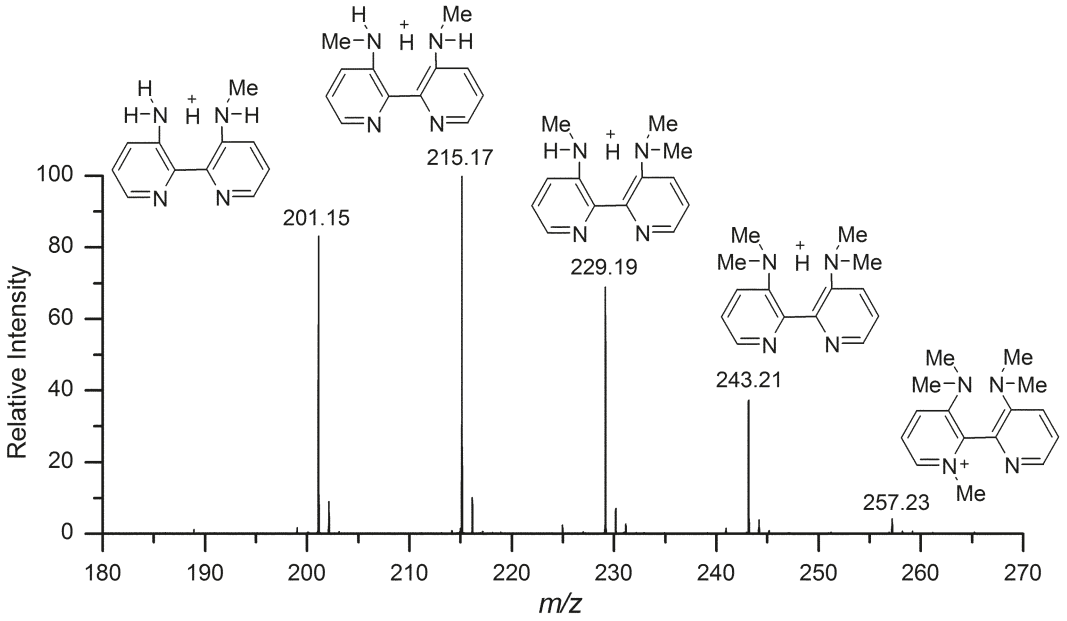

(N1–H length = 1.962 Å and N1–H–N2′ bond angle = 133.3°) is evident from the structure, and they are essentially the same as that in **1** (1.947 Å and 132.8°). A hydrogen bond can be classified as strong, moderate, or weak by evaluating factors such as bond length, bond angles, and comparison of the lengths of the hydrogen bond and the covalent bond between the hydrogen and the atom to which it is bonded,[32] and the H bonds here fall into the "moderate" category (1.5–2.2 Å and 130°–180°). There is no intermolecular H bonding evident in the packing of **3**.

Because **3** has two moderate-strength intramolecular hydrogen bonds, as does **1** (and also presumably the intermediate 3,3′-*N*,*N*′-(amino)(methylamino)-2,2′-bipyridine, although it has not been characterized), this feature may partially account for these molecules being unusually resistant to further methylation. Forcing conditions (neat MeI) seemed to be able to tri- and tetramethylate **1**, but also caused ring methylation of a pyridine nitrogen, further complicating the product mixture.

As an alternate synthetic approach, we tried cross-coupling various derivatives of 3-dimethylaminopyridine. 3-Dimethylaminopyridine[30] and 2-chloro-3-dimethylaminopyridine[31] were made from nitropyridine species, which were reduced using $SnCl_2{\cdot}2H_2O$ in HCl, and the subsequent aminopyridine was methylated using formic acid and formaldehyde to give 3-dimethylaminopyridine and 2-chloro-3-dimethylaminopyridine. The copper-catalyzed Ullmann coupling of 2 equiv of 2-chloro-3-dimethylaminopyridine (Scheme 1, route j) failed to proceed. Route k, the iron-catalyzed cross-coupling[33] of 2-chloro-3-dimethylaminopyridine and 3-dimethylamino-2-lithiopyridine (easily generated in situ using *n*-BuLi in THF and the formation verified through independent quenching experiments) did not generate a product. Several competing factors are thought to have limited the success of the coupling reactions of 2-chloro-3-dimethylaminopyridine. Whereas electron-withdrawing groups (e.g., NO_2) located ortho to the halogen activate the molecule, electron-donating groups (e.g., NMe_2) have the opposite effect. Particularly bulky substituents in this position will also hinder the formation of coupled products.[34] Similar complications seem plausible for the attempted iron-catalyzed coupling.

Fig. 4. Perspective view of **3** showing the atom-labelling scheme. Non-hydrogen atoms are represented by Gaussian ellipsoids at the 70% probability level. Hydrogen atoms are shown with arbitrarily small thermal parameters. Primed atoms are related to unprimed ones via the crystallographic inversion centre (1/2, 0, 1/2) at the midpoint of the C1–C1′ bond. Broken lines indicate hydrogen-bonded N–H···N interactions. Selected interatomic distances (Å): C1–C1′ = 1.487(2), N1–N2′ = 2.645(2), N1–C1 = 1.346(2), N1–C5 = 1.332(2), N2–C2 = 1.354(2), and N2–C6 = 1.442(2). Selected bond angles (°): N2–C2–C1 = 122.9(1) and C1–N1–C5 = 121.3(1). Selected torsion angle (°): N1–C1–C2–N2 = 178.6(1).

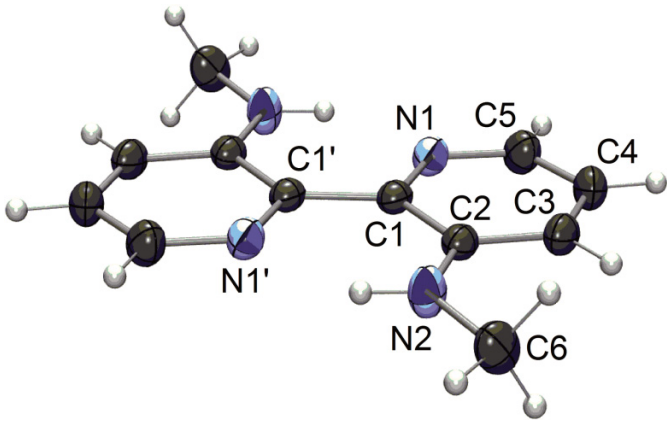

The next step was to try to inhibit the formation of the intramolecular hydrogen bonds and to block ring methylation. Coordination of **1** to a metal centre engages the lone pairs of the pyridine nitrogen so they are no longer available to form hydrogen bonds with an amine hydrogen or to be methylated. $Mo(CO)_4$ (norbornadiene) was selected for this task (Scheme 2).[35,36] Displacement of norbornadiene[37] with **1** to give $Mo(CO)_4$(**1**) (Scheme 1, step h), effectively removed the

Scheme 2. Attempted routes to 3,3′-*N*,*N*′-bis(dimethylamino)-2,2′-bipyridine (**2**).

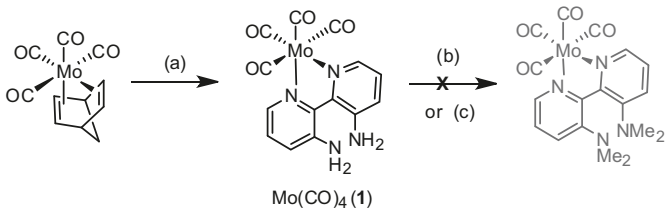

possibility of the formation of intramolecular hydrogen bonds within the bipyridine molecule. Confirmation that coordination had occurred through both pyridine nitrogen centres was obtained through comparison to the IR stretching frequencies of $Mo(CO)_4$(2,2′-bipyridine).[38,39] Sodium hydride and dimethyl sulfate were used to methylate $Mo(CO)_4$(**1**), but upon completion of step i the IR spectrum did not contain any CO-stretching frequencies, and the ESI-MS spectrum showed products containing one to four methyl groups as well as starting material. The procedure involving sodium hydride and methyl iodide described previously gave a mixture of methylated products as before.

A final attempt (Scheme 1, routes f and g) involved aminating 3,3′-bis(halo)-2,2′-bipyridines[40–42] with a lithium aminoborane reagent (LAB) made from *n*-BuLi and $BH_4{\cdot}NMe_2$ in tetrahydrofuran.[43] However, upon addition of the LAB to the bis(halogen) species none of the desired product was observed upon workup.

Conclusions

3,3′-Bis(amino)-2,2′-bipyridine (**1**) is unusually difficult to tetramethylate or to prepare by numerous other methods commonly used to construct similar molecules. The key structural feature likely to be responsible for this behaviour is the pyridine nitrogens, which can form two intramolecular hydrogen bonds in the un-, mono- and dimethylated compounds that may interfere with further methylation. These hydrogen bonds are in clear evidence in the X-ray crystal structure of 3,3′-bis(methylamino)-2,2′-bipyridine (**3**). The pyridine nitrogens are also susceptible to methylation themselves, further complicating the reactivity of **1**.

Experimental

All synthesis was performed under an inert atmosphere of N_2 using standard glovebox or Schlenk procedures. 2-Chloro-3-dimethylamino pyridine, 3,3′-diamino-2,2′-bipyridine,[23] and $Mo(CO)_4$(norbornadiene)[35,37] were made by literature methods. All other chemicals were used as obtained (Sigma-Aldrich, Oakville, Ontario). Solvents were HPLC grade and purified on an MBraun solvent purification system (SPS). Gases were obtained from Airgas (Calgary, Alberta). NMR spectra were collected on either an AV-300 or an AV-360 Bruker spectrometer. Internal reference was made to $CHCl_3$ (1H d = 7.26 ppm). All mass spectra were obtained on a Micromass Q-ToF micro hybrid quadrupole / time-of-flight mass spectrometer in positive ion mode using pneumatically assisted electrospray ionization with a capillary voltage of 2900 V, a source temperature of 100 °C, and a desolvation temperature of 180 °C. Solutions were run in dichloromethane and introduced to the mass spectrometer by a syringe pump at a rate of 2 mL/h. Internal calibrants for accurate mass experiments were protonated triphenylphosphine oxide ($[C_{15}H_{18}PO + H]^+$ = 278.0939 *m/z*), tetrapropylammonium bromide ($[C_{12}H_{28}N]^+$ = 186.2222 *m/z*), and tetrabutylammonium bromide ($[C_{16}H_{36}N^+]^+$ = 242.2848 *m/z*) as indicated where applicable. Higher mass accuracy is provided in these instances.

3,3′-Bis(methylamino)-2,2′-bipyridine (3)

Sodium hydride (0.052 g, 2.2 mmol) was added to (3,3′-diamino-2,2′-bipyridine (0.104 g, 0.55 mmol) in THF (5 mL) and stirred for 30 min resulting in bubbling and giving a yellow solution. Methyl iodide (0.31 g, 0.14 mL, 2.2 mmol) was added and the solution was refluxed for 90 min. Sodium hydroxide was added (3 mol/L, 1 mL) and the mixture extracted with diethyl ether (4 × 10 mL) until no colour remained in the aqueous phase. The organic phase was dried over magnesium sulfate and reduced in volume via a rotary evaporator. The yellow solid was redissolved with a minimal amount of diethyl ether and cooled to –5 °C to give yellow crystalline material (30 mg, 25%); mp = 148–150 °C. ^{1}H NMR (300 MHz, $CDCl_3$) δ (ppm): 2.92 (s, 6H), 7.06 (dd, $^3J_{HH}$ = 1.53, 8.37 Hz, 2H), 7.15 (dd, $^3J_{HH}$ = 4.55, 8.42 Hz, 2H), 7.91 (dd, $^3J_{HH}$ = 1.62, 4.47 Hz, 2H), 9.43 (s, 2H). ^{13}C NMR (500 MHz, $CDCl_3$) δ (ppm): 29.80, 117.69, 123.30, 133.13, 140.25, 145.81. ESI-MS (+ve, CH_2Cl_2 + formic acid) *m/z* experimental: 215.1298 $[C_{12}H_{14}N_4 + H]^+$; calcd: 215.1297.

3,3′-Dichloro-2,2′-bipyridine[40,41]

To a cold solution (0 °C) of sodium nitrite (370.2 mg, 5.4 mmol) in concentrated sulfuric acid (4 mL) was slowly added a solution of 3,3′-diamino-2,2′-bipyridine (453.2 mg, 2.4 mmol) in glacial acetic acid (4 mL) and stirred for 30 min. The ice bath was removed and the reaction stirred at room temperature for 30 min and then cooled to 0 °C. A cold solution of copper(I) chloride (2.09 g, 210 mmol) in concentrated hydrochloric acid (5 mL) was then added. The reaction was kept at low temperature to keep the evolution of gas at a slow rate. After 25 min the reaction was heated to 70 °C until the effervescence stoped, water was added (14 mL), and the reaction stirred overnight. The green-blue cloudy reaction mixture was filtered and the retrieved blue crystals dissolved in water (15 mL), made alkaline using saturated aqueous sodium hydroxide, and sodium cyanide was (0.5 g, 10 mmol) added. *CAUTION: solution must be alkaline before addition of sodium cyanide to prevent the formation of toxic hydrogen cyanide (HCN).* The aqueous mixture was extracted with dichloromethane (2 × 25 mL) that was washed once with water (50 mL), dried over magnesium sulfate, taken to near dryness on the rotary evaporator, and dried under high vacuum to give a shiny yellow solid (111.1 mg, 20% yield); mp = 125–128 °C. ^{1}H NMR (300 MHz, $CDCl_3$) δ (ppm): 7.36 (dd, $^3J_{HH}$ = 4.55, 8 Hz, 2H), 7.84 (dd, $^3J_{HH}$ = 1.41, 8 Hz, 2H), 8.64 (dd, $^3J_{HH}$ = 1.41, 4.55 Hz, 2H). ^{13}C NMR (300 MHz, $CDCl_3$) δ (ppm): 124.5, 131.0, 137.4, 147.5, 155.7. ESI-MS (+ve, CH_2Cl_2 + formic acid) *m/z* experimental: 224.9848 $[C_{10}H_6Cl_2N_2 + H]^+$; calcd: 224.9986.

Can. J. Chem. Downloaded from www.nrcresearchpress.com by Xi'an Jiaotong University on 09/19/12
For personal use only.

Can. J. Chem. Downloaded from www.nrcresearchpress.com by Xi'an Jiaotong University on 09/19/12
For personal use only.

3,3′-Dibromo-2,2′-bipyridine[40,41]

The same as for 3,3′-dichloro-2,2′-bipyridine but with CuBr in place of CuCl. 3,3′-Diamino-2,2′-bipyridine (505.7 mg, 2.72 mmol). White solid retrieved (83.6 mg, 10% yield); mp = 148–150 °C. ^{1}H NMR (300 MHz, $CDCl_3$) δ (ppm): 7.28 (dd, $^3J_{HH}$ = 4.45, 8 Hz, 2H), 8.02 (dd, $^3J_{HH}$ = 1.4, 8 Hz, 2H), 7.1 (dd, $^3J_{HH}$ = 1.4, 4.45 Hz, 2H). ^{13}C NMR (300 MHz, $CDCl_3$) δ (ppm): 120.4, 124.9, 140.7, 148.1, 157.1. ESI-MS (+ve, CH_2Cl_2 + formic acid) *m/z* experimental: 314.8899 $[C_{10}H_6Br_2N_2 + H]^+$; calcd: 314.8956.

3,3′-*N*,*N*′-Bis(dimethylamino)-2,2′-bipyridine (2), attempted syntheses

Route a — Methylation of 3,3′-diamino-2,2′-bipyridine with dimethyl sulfate[8]

Sodium hydride (320 mg, 13.33 mmol) was added to a solution of 3,3′-diamino-2,2′-bipyridine (0.392 g, 2.11 mmol) in tetrahydrofuran in four equal portions to give a cloudy yellow suspension. Dimethyl sulfate (2.4 mL, 1.80 g, 14.3 mmol) was slowly added and the mixture was refluxed for 3 h to give a brown slurry. Methanol (300 mL) was added to the room temperature reaction and the entire mixture poured over sodium hydroxide (saturated aq, 15 mL). The volume was reduced via rotary evaporator, water (200 mL) was added, and the mixture extracted with ether (200 mL, 4 × 100 mL). The volume of the bright orange organic solution was brought to ~50 mL on the rotary evaporator and then under high vacuum. The organic layer was then washed with dilute hydrochloric acid (3 × 30 mL), dried over magnesium sulfate and taken to dryness on the rotary evaporator to give an orange solid. ESI-MS analysis showed no starting material or any methylated products.

Route b — Methylation of 3,3′-diamino-2,2′-bipyridine with formaldehyde / formic acid[24]

3,3′-Diamino-2,2′-bipyridine (100 mg, 0.537 mmol) was refluxed in formic acid (8 mL) and formaldehyde (8 mL) for 8 h to give a bright yellow solution. Hydrochloric acid (4 mol/L, 20 mL) was added and the solution was taken to near dryness on high vacuum. The yellow-orange solid was taken up in distilled water (15 mL) and 18 mol/L sodium hydroxide (10 mL) was added to give a murky brown mixture. The slurry was extracted with benzene (5 × 15 mL) and the organic layer was dried with magnesium sulfate and then taken to near dryness. Starting material was recovered unchanged; no methylated products were identified.

Route c — Methylation of 3,3′-diamino-2,2′-bipyridine with trimethylphosphate[25]

3,3′-Diamino-2,2′-bipyridine (0.500 g, 2.69 mmol) was added to trimethylphosphate (0.785 g, 5.60 mmol), and the resulting yellow solution was heated at 200 °C for 2 h to give a black sticky substance. Sodium hydroxide (15% aq, 10 mL) and water (15 mL) were added and the mixture stirred for 2 h. The black mixture was extracted with diethyl ether (3 × 20 mL) and the organic layer was dried with magnesium sulfate and sodium hydroxide pellets and then dried under high vacuum. NMR of the resulting orange-brown oil showed an indistinguishable mixture of products.

Route d — Methylation of 3,3′-diamino-2,2′-bipyridine with methyl iodide[26]

Sodium hydride (0.633 g, 26.4 mmol) was added to a solution of 3,3′-diamino-2,2′-bipyridine (0.123 g, 0.659 mmol) in THF and stirred for 90 min. Methyl iodide (0.375 g, 0.16 mL, 2.64 mmol) was then added and the mixture refluxed for 1 h. After cooling to room temperature, the mixture was poured over sodium hydroxide (3 mol/L, 15 mL) and stirred for 30 min. The aqueous layer was extracted with diethyl ether (2 × 50 mL) and the organic layer was passed through an alumina plug to give a clear yellow solution. The ether was removed to give an orange-yellow oil, an inseparable mixture of the desired product and partially (and over-) methylated by-products. ESI-MS (+ve, CH_2Cl_2 + formic acid) *m/z*: 201.15 $[C_{11}H_{12}N_4 + H]^+$, 215.17 $[C_{12}H_{14}N_4 + H]^+$, 229.19 $[C_{13}H_{16}N_4 + H]^+$, 243.21 $[C_{14}H_{18}N_4 + H]^+$, 257.23 $[C_{15}H_{21}N_4]^+$.

Route e — Methylation of 3,3′-diamino-2,2′-bipyridine with dimethyl sulfate[27]

Dimethyl sulfate (0.70 mL, 0.526 g, 4.17 mmol) was added to a suspension of 3,3′-diamino-2,2′-bipyridine (0.174 g, 0.935 mmol) in water (5 mL) in portions (0.21, 0.21, and 0.28 mL), and after each addition was shaken for 10 min and made alkaline with sodium hydroxide (10% aq). The yellow solution was heated at 100 °C for 15 min. The water was removed to give an orange-yellow oil, an inseparable mixture of the desired product, and partially (and over-) methylated by-products. ESI-MS (+ve, CH_2Cl_2 + formic acid) *m/z*: 201.15 $[C_{11}H_{12}N_4 + H]^+$, 215.17 $[C_{12}H_{14}N_4 + H]^+$, 229.19 $[C_{13}H_{16}N_4 + H]^+$, 243.21 $[C_{14}H_{18}N_4 + H]^+$ 257.23 $[C_{15}H_{21}N_4]^+$.

Step f — Demethylation of 3,3′-N,N′-bis(dimethylamino)-2,2′-pyridine-pyridinium iodide

Pyridinium chloride (6.58 g, 56.9 mmol) was added to 3,3′-*N*,*N*′-bis(dimethylamino)-2,2′-pyridine-pyridinium iodide (0.170 g, 0.659 mmmol) and heated at 225 °C for 10 min. ESI-MS (+ve, CH_2Cl_2 + formic acid) *m/z*: 201.15 $[C_{11}H_{12}N_4 + H]^+$, 215.17 $[C_{12}H_{14}N_4 + H]^+$.

Step g — Halogen substitution of 3,3′-bis(chloro)-2,2′-bipyridine

$LiH_3BN(Me)_2$ was made according to literature procedures.[43] LiH_3BNMe_2 (0.95 mol/L, 0.27 mL, 0.25×10^{-4} mol) was added to 3,3′-dichloro-2,2′-bipyridine (50.8 mg, 0.22 mmol) in THF (1 mL) at 0 °C to give a deep red solution. The reaction was stirred at 0 °C for 15 min and then at room temperature for 90 min. HCl (3 mol/L, 3.3 mL) and methanol (3.3 mL) were then added at 0 °C and and the mixture was stirred for 15 min. The reaction was refluxed overnight, the volume reduced to ~5 mL, made alkaline with saturated sodium hydroxide, and extracted with CH_2Cl_2 (3 × 10 mL). The peach-coloured organic layer was dried with $MgSO_4$ and reduced to a solid that proved to be unreacted starting material. ESI-MS (+ve, CH_2Cl_2) *m/z*: 230.31 $[C_{10}H_6Cl_2N_2 + Li]^+$.

Step h — Mo(CO)$_4$(3,3′-diamino-2,2′-bipyridine)

$Mo(CO)_4$(norbornadiene) was made according to the literature preparation. $Mo(CO)_4$(nbd) (164.1 mg, 0.548 mmol) was added to a solution of 3,3′-diamino-2,2′-bipyridine

Can. J. Chem. Downloaded from www.nrcresearchpress.com by Xi'an Jiaotong University on 09/19/12
For personal use only.

(100.1 mg, 0.538 mmol) in benzene (5 mL) and the reaction was refluxed for 3 h covered in aluminum foil. The benzene was removed under high vacuum and the brown solid taken up in dichloromethane to give a red solution. Layering of hexanes over the red dichloromethane solution produced a yellow precipitate. IR (CH_2Cl_2) νCO (cm^{-1}): 2013, 1901, 1871, 1824.

Step i — Methylation of $Mo(CO)_4$(3,3′-diamino-2,2′-bipyridine) with dimethyl sulfate and methyl iodide

Reduction procedures were followed as above for sodium hydride / dimethyl sulfate[8,26] and sodium hydride / methyl iodide[26] using the metal complex in place of free 3,3′-diamino-2,2′-bipyridine. For NaH/Me_2SO_4: ESI-MS (+ve, CH_2Cl_2) *m/z*: 201.15 $[C_{11}H_{12}N_4 + H]^+$, 215.17 $[C_{12}H_{14}N_4 + H]^+$, 229.19 $[C_{13}H_{16}N_4 + H]^+$, 243.21 $[C_{14}H_{18}N_4 + H]^+$). For NaH/MeI: ESI-MS (+ve, CH_2Cl_2 + formic acid) *m/z*: 201.15 $[C_{11}H_{12}N_4 + H]^+$, 215.17 $[C_{12}N_4H_{14} + H]^+$, 229.19 $[C_{13}N_4H_{16} + H]^+$, 243.21 $[C_{14}N_4H_{18} + H]^+$, 257.23 $[C_{14}N_4H_{21}]^+$.

Route j — Homo-coupling of 2-chloro-3-dimethylaminopyridine

2-Chloro-3-dimethylaminopyridine (1.42 g, 9.14 mmol) was added to a slurry of activated copper (1.45 g, 22.79 mmol) in dry DMF (35 mL) and refluxed overnight. The hot reaction mixture was poured over H_2O (400 mL) and isolated via suction filtration and extracted with dioxane via a Soxhlet apparatus. The dioxane was removed on a rotary evaporator, the solid taken up in CH_2Cl_2, washed with aqueous ammonia followed by H_2O, and dried over $MgSO_4$. NMR (300 MHz, $CDCl_3$) showed no coupled product.

Route k — Coupling of 2-chloro-3-dimethylaminopyridine and 3-dimethylaminopyridine[33]

A 1:1 solution of *n*-BuLi/TMEDA (*n*-BuLi, 1.6 mol/L in hexanes, 4.09 mL, 6.54 mmol) was added via cannula to a solution of 3-dimethylaminopyridine (0.799 g, 6.54 mmol) in THF at –78 °C and stirred for 3 h to give a bright orange solution. In a separate Schlenk flask, 2-chloro-3-dimethylaminopyridine (0.872 g, 5.56 mmol) was added to a solution of $Fe(acac)_3$ (96.9 mg, 2.74×10^{-4} mol) and *N*-methyl-2-pyrrolidone (3.19 g, 3.1 mL, 32.15 mmol) in dry THF (30 mL) to give a deep red-orange solution that was cooled to –78 °C. The 3-dimethylaminopyridine solution was then transferred via cannula to the 2-chloro-3-dimethlyaminopyridine solution to give a deep red-purple colour and the stirred at –78 °C for 1 h before being allowed to warm to room temperature. Concentrated HCl (10 mL) was then added and the mixture stirred for 1 h. The solution was made alkaline with sodium hydroxide (1 mol/L, 10 mL), extracted with diethyl ether (4 × 50 mL), dried with $MgSO_4$, and then taken to dryness on a rotary evaporator to give a yellow-orange solid, a mixture of starting materials. ESI-MS (+ve, CH_2Cl_2 + formic acid) *m/z*: 157.05 $[C_6H_9ClN_2 + H]^+$, 123.09 $[C_6H_{10}N_2 + H]^+$.

Supplementary data

Supplementary data (full X-ray diffraction data and the ^1H NMR spectrum of the mixture of products from methylation) are available with the article through the journal Web site (www.nrcresearchpress.com/cjc).

Acknowledgements

J.S.M. thanks the Canadian Foundation for Innovation (CFI) and British Columbia Knowledge Development Fund (BCKDF) for infrastructure support, and the Natural Sciences and Engineering Research Council of Canada (NSERC) for operational funding (Discovery Grant and Discovery Accelerator Supplement).

References

(1) Brown, W. G.; Letang, N. J. *J. Am. Chem. Soc.* **1941** *63* (2), 358. doi:10.1021/ja01847a009.
(2) Alder, R. W.; Bowman, P. S.; Steele, W. R. S.; Winterman, D. R. *Chem. Commun.* **1968** *13*, 723.
(3) Glowiak, T.; Malarski, Z.; Sobczyk, L.; Grech, E. *J. Mol. Struct.* **1992** *270* (1–2), 441. doi:10.1016/0022-2860(92)85045-I.
(4) Wozniak, K.; Krygowski, T. M.; Kariuki, B.; Jones, W.; Grech, E. *J. Mol. Struct.* **1990** *240* (1–2), 111. doi:10.1016/0022-2860(90)80501-A.
(5) Truter, M. R.; Vickery, B. L. *J. Chem. Soc., Dalton Trans.* **1972** *3* (3), 395. doi:10.1039/dt9720000395.
(6) Yamasaki, T.; Ozaki, N.; Saika, Y.; Ohta, K.; Goboh, K.; Nakamura, F.; Hashimoto, M.; Okeya, S. *Chem. Lett.* **2004** *33* (7), 928. doi:10.1246/cl.2004.928.
(7) Alder, R. W. *Chem. Rev.* **1989** *89* (5), 1215. doi:10.1021/cr00095a015.
(8) Staab, H. A.; Saupe, T. *Angew. Chem. Int. Ed. Engl.* **1988** *27* (7), 865. doi:10.1002/anie.198808653.
(9) Alder, R. W.; Bryce, M. A.; Goode, N. C.; Miller, N.; Owen, J. *J. Chem. Soc., Perkin Trans. 1* **1981** *11*, 2840. doi:10.1039/p19810002840.
(10) Staab, H. A.; Diehm, M.; Krieger, C. *Tetrahedron Lett.* **1994** *35* (45), 8357. doi:10.1016/S0040-4039(00)74406-6.
(11) Staab, H. A.; Diehm, M.; Krieger, C. *Tetrahedron Lett.* **1995** *36* (17), 2967. doi:10.1016/0040-4039(95)00441-E.
(12) Caubère, P. *Chem. Rev.* **1993** *93* (6), 2317. doi:10.1021/cr00022a012.
(13) Krossing, I.; Raabe, I. *Angew. Chem. Int. Ed.* **2004** *43* (16), 2066. doi:10.1002/anie.200300620.
(14) Henderson, W.; McIndoe, J. S. *Mass Spectrometry of Inorganic and Organometallic Compounds*; John Wiley & Sons Ltd.: West Sussex, UK, 2005.
(15) Chisholm, D. M.; Oliver, A. G.; McIndoe, J. S. *Dalton Trans.* **2010** *39* (2), 364. doi:10.1039/b913225b.
(16) Chisholm, D. M.; McIndoe, J. S. *Dalton Trans.* **2008** (30): 3933. doi:10.1039/b800371h.
(17) Crawford, E.; Lohr, T.; Leitao, E. M.; Kwok, S.; McIndoe, J. S. *Dalton Trans.* **2009** *38* (42), 9110. doi:10.1039/b913492a.
(18) Farrer, N. J.; McDonald, R.; Piga, T.; McIndoe, J. S. *Polyhedron* **2010** *29* (1), 254. doi:10.1016/j.poly.2009.08.013.
(19) Farrer, N. J.; McDonald, R.; McIndoe, J. S. *Dalton Trans.* **2006** *38* (38), 4570. doi:10.1039/b609561e.
(20) Chelucci, G.; Thummel, R. P. *Chem. Rev.* **2002** *102* (9), 3129. doi:10.1021/cr0101914.
(21) Kaes, C.; Katz, A.; Hosseini, M. W. *Chem. Rev.* **2000** *100* (10), 3553. doi:10.1021/cr990376z.
(22) Malkov, A. V.; Kocovsky, P. *Curr. Org. Chem.* **2003** *7* (17), 1737. doi:10.2174/1385272033486215.
(23) Rice, R. C.; Onions, S.; Vidal, N.; Wallis, J. D.; Senna, M.; Pilkington, M.; Stoeckli-Evans, H. *Eur. J. Inorg. Chem. 2002* (8), 1985. doi:10.1002/1099-0682(200208)2002:8<1985::AID-EJIC1985>3.0.CO;2-G.

(24) Giam, C. S.; Hauck, A. E. *Org. Prep. Proced. Int.* **1977** *9* (1), 9. doi:10.1080/00304947709355653.
(25) Sheppard, W. A. *Org. Synth.* **1969** *49*, 111.
(26) Charmant, J. P. H.; Lloyd-Jones, G. C.; Peakman, T. M.; Woodward, R. L. *Eur. J. Inorg. Chem.* **1999** 2501.
(27) Shaw, F. R.; Turner, E. E. *J. Chem. Soc.* **1933** 135. doi:10.1039/jr9330000135.
(28) Prill, E. A.; McElvain, S. M. *Org. Synth.* **1935** *15*, 41.
(29) Prescott, A. B. *J. Am. Chem. Soc.* **1896** *18* (1), 91. doi:10.1021/ja02087a011.
(30) Schilf, W. *Spectrochim. Acta, Part A* **2004** *60* (12), 2695. doi:10.1016/j.saa.2004.01.025.
(31) Merritt, L. L.; Schroeder, E. D. *Acta Crystallogr.* **1956** *9* (10), 801. doi:10.1107/S0365110X56002175.
(32) Grabowski, S. J. *Hydrogen Bonding – New Insights;* Springer: Dordrecht, The Netherlands, 2006; Vol. 3.
(33) Fürstner, A.; Leitner, A.; Mendez, M.; Krause, H. *J. Am. Chem. Soc.* **2002** *124* (46), 13856. doi:10.1021/ja027190t.
(34) Hassan, J.; Sévignon, M.; Gozzi, C.; Schulz, E.; Lemaire, M. *Chem. Rev.* **2002** *102* (5), 1359. doi:10.1021/cr000664r.
(35) Kayran, C.; Okan, E. *Z. Naturforsch.* **2001** *56* (3), 218.
(36) Hirsivaara, L.; Guerricabeitia, L.; Haukka, M.; Suomalainen, P.; Laitinen, R. H.; Pakkanen, T. A.; Pursiainen, J. *Inorg. Chim. Acta* **2000** *307* (1–2), 48. doi:10.1016/S0020-1693(00)00190-0.
(37) Baxter, P. N. W.; Connor, J. A.; Wallis, J. D.; Povey, D. C.; Powell, A. K. *Polyhedron* **1992** *11* (14), 1771. doi:10.1016/S0277-5387(00)83237-4.
(38) Johnson, R.; Madhani, H.; Bullock, J. P. *Inorg. Chim. Acta* **2007** *360* (10), 3414. doi:10.1016/j.ica.2007.04.029.
(39) Braga, S. S.; Coelho, A. C.; Gonçalves, I. S.; Almeida Paz, F. A. *Acta Crystallogr. Sect. E Struct. Rep. Online* **2007** *63* (3), m780. doi:10.1107/S1600536807007234.
(40) Gunstone, F. D.; Tucker, S. H. *Org. Synth.* **1963** *4*, 160.
(41) Létinois-Halbes, U.; Hanss, D.; Beierle, J. M.; Collin, J.-P.; Sauvage, J.-P. *Org. Lett.* **2005** *7* (26), 5753. doi:10.1021/ol052051c.
(42) Truong, T.; Alvarado, J.; Tran, L. D.; Daugulis, O. *Org. Lett.* **2010** *12* (6), 1200. doi:10.1021/ol902970z.
(43) Thomas, S.; Roberts, S.; Pasumansky, L.; Gamsey, S.; Singaram, B. *Org. Lett.* **2003** *5* (21), 3867. doi:10.1021/ol035430j.

Can. J. Chem. Downloaded from www.nrcresearchpress.com by Xi'an Jiaotong University on 09/19/12
For personal use only.

A theoretical investigation of tetrahydroquinoline dyes with different spacers used for sensitized solar cells

Jie Xu, Lei Wang, Li Liu, Zikui Bai, Luoxin Wang, Guijie Liang, Xiaolin Shen, and Weilin Xu

Can. J. Chem. Downloaded from www.nrcresearchpress.com by Xi'an Jiaotong University on 09/19/12
For personal use only.

Abstract: The molecular structures and absorption spectra of three tetrahydroquinoline dyes (C2–1, C1–1, and C1–5) with a tetrahydroquinoline moiety as the electron donor, a cyanoacrylic acid moiety as the electron acceptor, and different thiophene-containing electron spacers were investigated by density functional theory (DFT) and time-dependent DFT (TD-DFT). The calculated geometries indicate that a strong conjugation is formed in the dyes and the conjugate length increases with the increase of spacer length. The interfacial charge transfer between the semiconductor electrode and the tetrahydroquinoline dyes are electron-injection processes from the excited dyes to the semiconductor conduction band. The simulated absorption bands are assigned to $\pi-\pi^*$ transitions, which exhibit appreciable red-shift with respect to the experimental bands owing to the lack of direct solute–solvent interaction and the inherent approximations in TD-DFT. Moreover, the effect of different spacers on the molecular structures, absorption spectra, and photovoltaic performance were comparatively discussed.

Key words: tetrahydroquinoline dyes, dye-sensitized solar cells, density functional theory (DFT), molecular structures, absorption spectra.

Résumé : Faisant appel à la théorie de la fonctionnelle de la densité (TFD) et à la TFD avec dépendance sur le temps (TFD-DT), on a calculé les structures moléculaires et les spectres d'absorption de trois colorants à base de la tétrahydroquinoléine (C2–1, C1–1 et C1–5) comportant une portion tétrahydroquinoléine comme donneur d'électron, une chaîne d'acide cyanoacrylique comme accepteur d'électron et divers groupes d'espacement d'électrons contenant du thiophène. Les géométries calculées indiquent qu'il se forme une forte conjugaison dans les colorants et que la longueur conjuguée augmente avec une augmentation de la longueur de l'espaceur. Le transfert de charge interfacial entre l'électrode du semiconducteur et les colorants à base de tétrahydroquinoléine sont des processus d'injection d'électron des colorants excités vers la bande de conduction du semiconducteur. Les bandes d'absorption simulées sont attribuées aux transitions $\pi-\pi^*$ qui présentent un déplacement appréciable vers le rouge par rapport aux bandes expérimentales en raison du manque d'interaction directe soluté solvant et des approximations inhérentes à la méthode (TFD-DT). On discute de plus de l'effet des divers groupes d'espacement sur les structures moléculaires, sur les spectres d'absorption et sur la performance photovoltaïque.

Mots-clés : colorants de la tétrahydroquinoléine, cellules solaires sensibilisées par des colorants, théorie de la fonctionnelle de la densité, structures moléculaires, spectres d'absorption.

[Traduit par la Rédaction]

Introduction

Nanocrystalline dye-sensitized solar cells (DSSCs) have attracted much attention as promising alternatives for the photovoltaic conversion of solar energy owing to their potentially low fabrication costs, environmentally friendly components, and relatively high conversion efficiencies.[1–6] The most successful charge-transfer sensitizers used in DSSCs are ruthenium (Ru) polypyridyl complexes, yielding solar-to-electric power conversion efficiencies up to 11%–12% under air mass (AM) 1.5 irradiation.[6] However, the Ru complexes are facing the problems of cost and environmental issues, which will limit the large-scale application of DSSCs.[7] In addition to the Ru complexes, metal-free organic dyes as sensitizers are also under intensive investigation because of their high molar extinction coefficients, flexible structural modifications, and low costs; and so far some of them have reached good efficiencies.[8–15]

In DSSCs, the dye molecules first absorb visible or near-IR light, accompanied by the excitation of electrons to the excited states. Subsequently, the excited electrons are injected into the conduction band (CB) of the semiconductor (typically TiO_2 nanoparticles), and then transfer to the anode by

Received 10 January 2011. Accepted 9 March 2011. Published at www.nrcresearchpress.com/cjc on 16 August 2011.

J. Xu, L. Wang, L. Liu, Z. Bai, L. Wang, X. Shen, and W. Xu. Key Lab of Green Processing and Functional Textiles of New Textile Materials, Ministry of Education, Wuhan Textile University, 430073 Wuhan, China.
G. Liang. College of Materials Science and Engineering, Xi'an Jiao tong University 710049, Xi'an, China.

Corresponding author: Jie Xu (e-mail: xujie0@ustc.edu).

Can. J. Chem. Downloaded from www.nrcresearchpress.com by Xi'an Jiaotong University on 09/19/12
For personal use only.

Fig. 1. Chemical structures of the tetrahydroquinoline dyes.

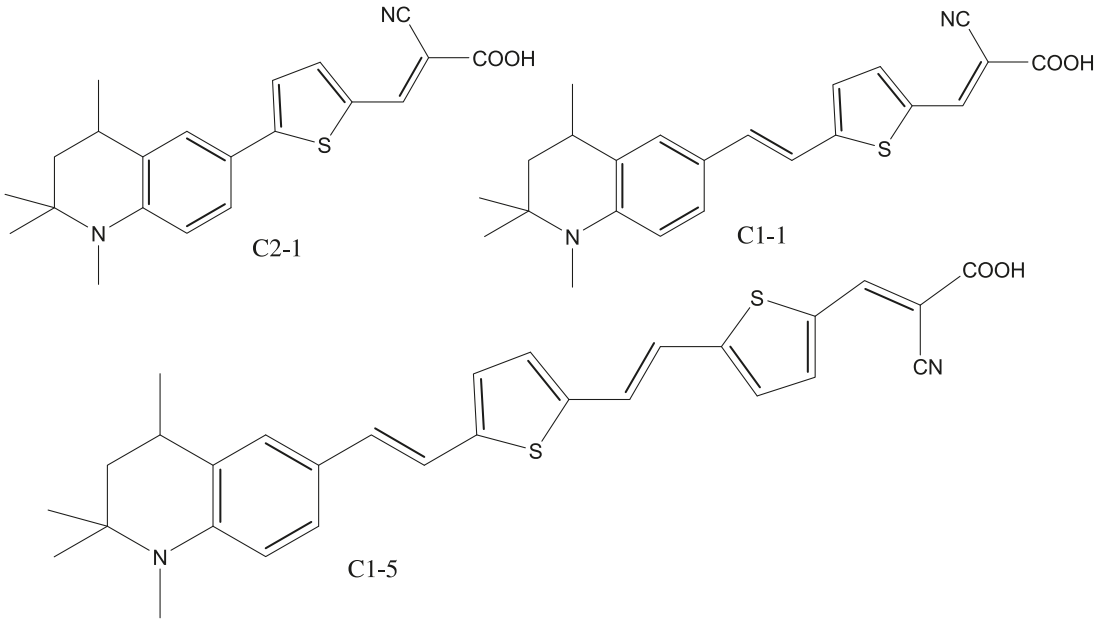

electron diffusion through the disordered network of TiO_2. The oxidized dye molecules are regenerated by the iodide redox couple or hole-transporter with the positive charge being transported from the electrolyte to the platinum counter electrode. Therefore, the performance of DSSCs strongly depends upon the following factors: (*i*) absorption efficiency of the dye sensitizer for solar light spectrum; (*ii*) electron injection probability from the excited state of the dye sensitizer to TiO_2 (efficiency of the charge separation); and (*iii*) electron transfer probability from the electrolyte to the oxidized dye.[3] All these factors are closely associated with the ground and excited electronic states of the dye sensitizer. From this point of view, the theoretical investigation of the molecular and electronic structures of the dyes is very important for better understanding the mechanism of the charge separation and transfer, which are the key working processes in this type of solar cells, as well as for the design of new dyes with improved performance.

Density functional theory (DFT) has emerged as a reliable standard tool for the theoretical treatment of the molecular and electronic structures. Its time-dependent extension, called time-dependent DFT (TD-DFT), can give reliable values for valence excitation energies with the standard exchange-correlation functionals. The computational cost of TD-DFT calculation is comparative to that of a Hartree–Fock-based single-excitation theory, such as, configuration interaction singles (CIS) or the time-dependent Hartree–Fock (TD-HF) method and maintains a uniform accuracy for open- and closed-shell systems. In recent years, DFT has been successfully used to study the structures and absorption spectra of both Ru complexes[4,16–23] and organic dye sensitizers.[24–32]

Recently, three novel organic dyes (C2–1, C1–1, and C1–5, as shown in Fig. 1), which consist of a tetrahydroquinoline moiety as the electron donor, different thiophene-containing electron spacers, and a cyanoacrylic acid moiety as the electron acceptor were designed and synthesized, yielding overall conversion efficiencies of 4.49%, 3.17%, and 2.32%, respectively.[33] Why does the C2–1 dye with a rigid and shortest π-spacer have the lowest light-absorption capability, but give the highest efficiency? To theoretically understand the spacer effect and sensitized mechanism at a molecular level in these tetrahydroquinoline dyes, the geometrical and electronic structures of them were studied in detail using DFT, and the electronic absorption spectra were investigated based on the TD-DFT calculations.

Computational method

All the calculations were performed with the Gaussian 03 program package.[34] The ground-state geometries were fully optimized without any symmetry constrains at the DFT level of theory with Becke's[35] three parameters hybrid functional and Lee, Yang, and Parr's correlational functional B3LYP[36] using a standard 6–31g(d) basis set on all atoms. A full natural bond orbital (NBO) analysis was obtained using the POP=NBO keyword. The excitation energies and oscillator strengths for the lowest 30 singlet–singlet transitions at the optimized ground-state geometry were obtained by TD-DFT using the same basis set as for the ground state and three kinds of hybrid functional PBE1PBE, MPW1B95, and BHandHLYP, respectively. From the calculated results, the UV–vis absorption spectra were simulated by means of the SWizard program (version 4.6)[37] using a Gaussian convolution with the full width at half-maximum of 3000 cm^{-1}. Solvation effects were introduced by the SCRF method via the conductor polarizable continuum model (CPCM)[38,39] implemented in the Gaussian program for both DFT and TD-DFT calculations.

Results and discussion

Geometrical structures

One of the major goals in the design of new sensitizers is to create molecular structures favouring the absorption in the visible–near-IR region and possessing an appropriate excited state able to directly inject into the CB of the semiconductor

Can. J. Chem. Downloaded from www.nrcresearchpress.com by Xi'an Jiaotong University on 09/19/12
For personal use only.

Fig. 2. Optimized ground-state geometries of the tetrahydroquinoline dyes with Cartesian axes.

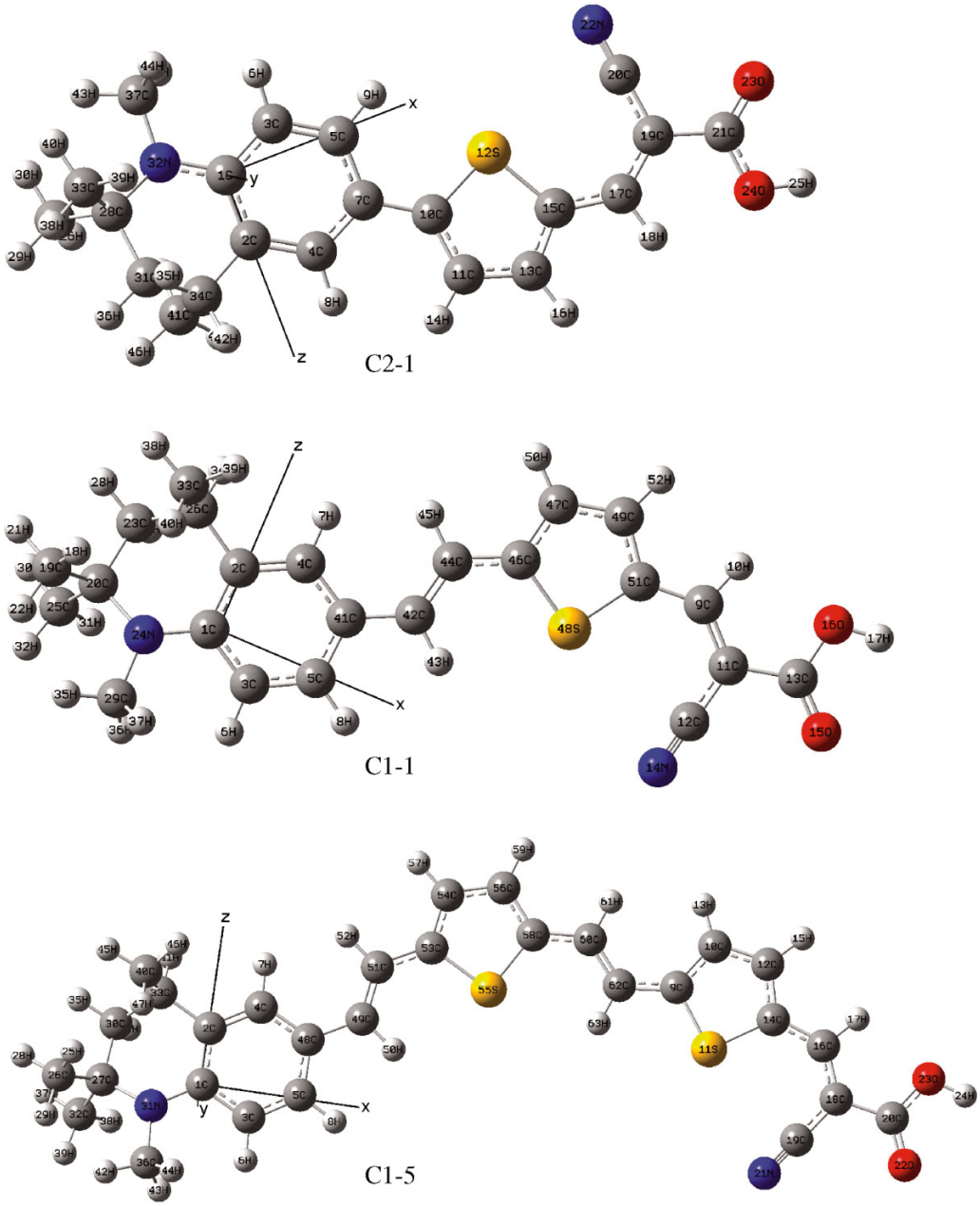

electrode (typically TiO_2). Donor–acceptor π-conjugated (D–π–A) dyes, which contain both electron-donating (D) and electron-accepting (A) groups connected by covalent links (usually π-conjugated) have been developed to enhance both the extinction coefficients and the absorption at long wavelengths (low energies). The photoabsorption properties of a D–π–A dye are associated with intramolecular charge transfer (ICT) excitation from the donor to the acceptor moiety of the dye, resulting in efficient electron transfer through the acceptor moiety (such as carboxyl or hydroxyl) from the excited dye into the semiconductor CB. The charge transfer or separation between the electron donor and acceptor moieties in the excited dye may facilitate rapid electron injection from the dye molecule into the semiconductor CB, so that it would be expected to separate the cationic charge effectively from the semiconductor surface and to restrict recombination between the photoelectron (the injected electron) and the oxidized dye sensitizer efficiently.The tetrahydroquinoline dyes C2–1, C1–1, and C1–5 in this study share the same electron donor of 1,2,2,4-tetramethyl-1,2,3,4-tetrahydroquinoline group and the same electron acceptor of cyanoacrylic acid while different types of electron spacers containing thiophene moiety are used (as illustrated in Fig. 1). The optimized ground-state geometries of the tetrahydroquinoline dyes are shown in Fig. 2, and the selected bond lengths, bond angles, and dihedral angles are listed in Table 1. From a structural point of view, at the ground state, the donor and acceptor moieties are practically identical in the three dyes, as demonstrated by the very similar calculated internal structural parameters. All the C–C lengths in the vinylene, thiophene, and phenyl groups are found to be between the distance of a single bonded C–C and a double bonded C=C, implying that

Can. J. Chem. Downloaded from www.nrcresearchpress.com by Xi'an Jiaotong University on 09/19/12
For personal use only.

Table 1. Selected bond lengths (Å), bond angles (°), and dihedral angles (°) of the tetrahydroquinoline dyes.

C2–1		C1–1		C1–5	
Bond length (Å)					
C1—C2	1.4262	C1—C2	1.4285	C1—C2	1.4265
C1—N32	1.3787	C1—N24	1.3803	C1—N31	1.3850
C2—C4	1.3834	C2—C4	1.3825	C2—C4	1.3841
C4—C7	1.4152	C4—C41	1.4161	C4—C48	1.4147
C7—C10	1.4495	C41—C42	1.4446	C48—C49	1.4503
		C42—C44	1.3644	C49—C51	1.3610
		C44—C46	1.4313	C62—C9	1.4331
C10—C11	1.3966	C46—C47	1.3986	C9—C10	1.3999
C15—C17	1.4133	C51—C9	1.4126	C14—C16	1.4135
C17—C19	1.3803	C16—C18	1.3875	C16—C18	1.3804
Bond angle (°)					
C4–C7–C10	120.8	C4–C41–C42	124.0	C4–C48–C49	124.1
C15–C17–C19	131.5	C51–C9–C11	131.5	C14–C16–C18	131.2
		C42–C44–C46	126.1	C49–C51–C53	126.2
				C56–C58–C60	126.1
Dihedral angle (°)					
C5–C7–C10–C11	170.5	C5–C41–C42–C44	179.9	C5–C48–C49–C51	179.2
		C42–C44–C46–C47	–179.6	C49–C51–C53–C54	179.7
				C56–C58–C60–C62	179.7
C13–C15–C17–C19	–179.8	C49–C51–C9–C11	–179.9	C12–C14–C16–C18	180.0
C13–C15–C19–C20	–179.5	C49–C51–C11–C12	–179.8	C12–C14–C18–C19	0.0
C13–C15–C21–O23	0.5	C49–C51–C13–O15	0.6	C12–C14–C20–O22	0.0

Table 2. Quadrupole moments (in D Å) of the tetrahydroquinoline dyes.

Dye	Q_{XX}	Q_{YY}	Q_{ZZ}	Q_{XY}	Q_{XZ}	Q_{YZ}	Q_{ii}	Q
C2–1	–254.1	–163.2	–117.9	14.2	43.0	1.67	–178.4	–90.9
C1–1	–287.6	–175.2	–114.7	4.35	43.2	–0.06	–192.5	–112.4
C1–5	–351.5	–225.6	–152.1	4.45	123.9	1.04	–243.1	–125.9

Table 3. Natural charges (e) of different groups in the tetrahydroquinoline dyes.

Dyes	Cyanoacrylic acid	Bridge	Tetrahydroquinoline
C2–1	–0.189	0.071	0.118
C1–1	–0.191	0.085	0.106
C1–5	–0.185	0.105	0.080

there exists extensive electron delocalization throughout the molecule. The calculated distances between the C atom in carboxyl and the vinyl C atom next to the thiophene group in tetrahydroquinoline are 7.6178, 9.5281, and 14.6784 Å for C2–1, C1–1, and C1–5, respectively. Thus, the distance between the electron donor and semiconductor surface is increased with the increase of spacer length, since the thiophene and vinylene groups extend the conjugate bridge length.

The cyanoacrylic acid group (acceptor) is found to be fully coplanar with the thiophene-containing π bridge, as represented by the C13–C15–C17–C19 (Fig. 2, C2–1), C49–C51–C9–C11 (Fig. 2, C1–1), and C12–C14–C16–C18 (Fig. 2, C1–5) dihedral angles, while the coplanarity between the tetrahydroquinoline group (donor) and π bridge is also apparent, although there is a distortion of ~10° in the case of C2–1 mainly owing to steric repulsion between the tetrahydroquinoline and thiophene rings. Thus, it can be concluded

Fig. 3. Frontier molecular orbital energies of the tetrahydroquinoline dyes together with the TiO_2 anatase (101) conduction band.

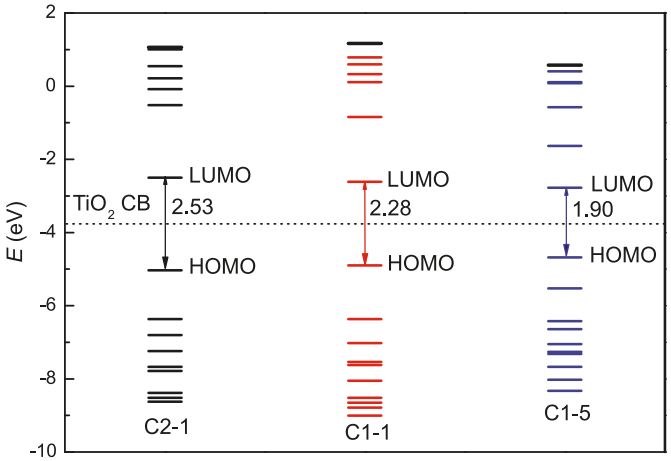

that the donor and acceptor moieties are fully conjugated through the π bridge. The delocalization in the conjugate bridge is beneficial to the ICT and to the stability of the molecule. The anchoring carboxyl group (–COOH) is coplanar with the π-extended system of the molecule, as demonstrated by the negligible C13–C15–C21–O23 (Fig. 2, C2–1), C49–C51–C13–O15 (Fig. 2, C1–1), and C12–C14–C20–O22 (Fig. 2, C1–5) values. Therefore, assuming a bidentate bind

Fig. 4. Isodensity plots (isodensity contour = 0.02 au) of the frontier orbitals of the tetrahydroquinoline dyes.

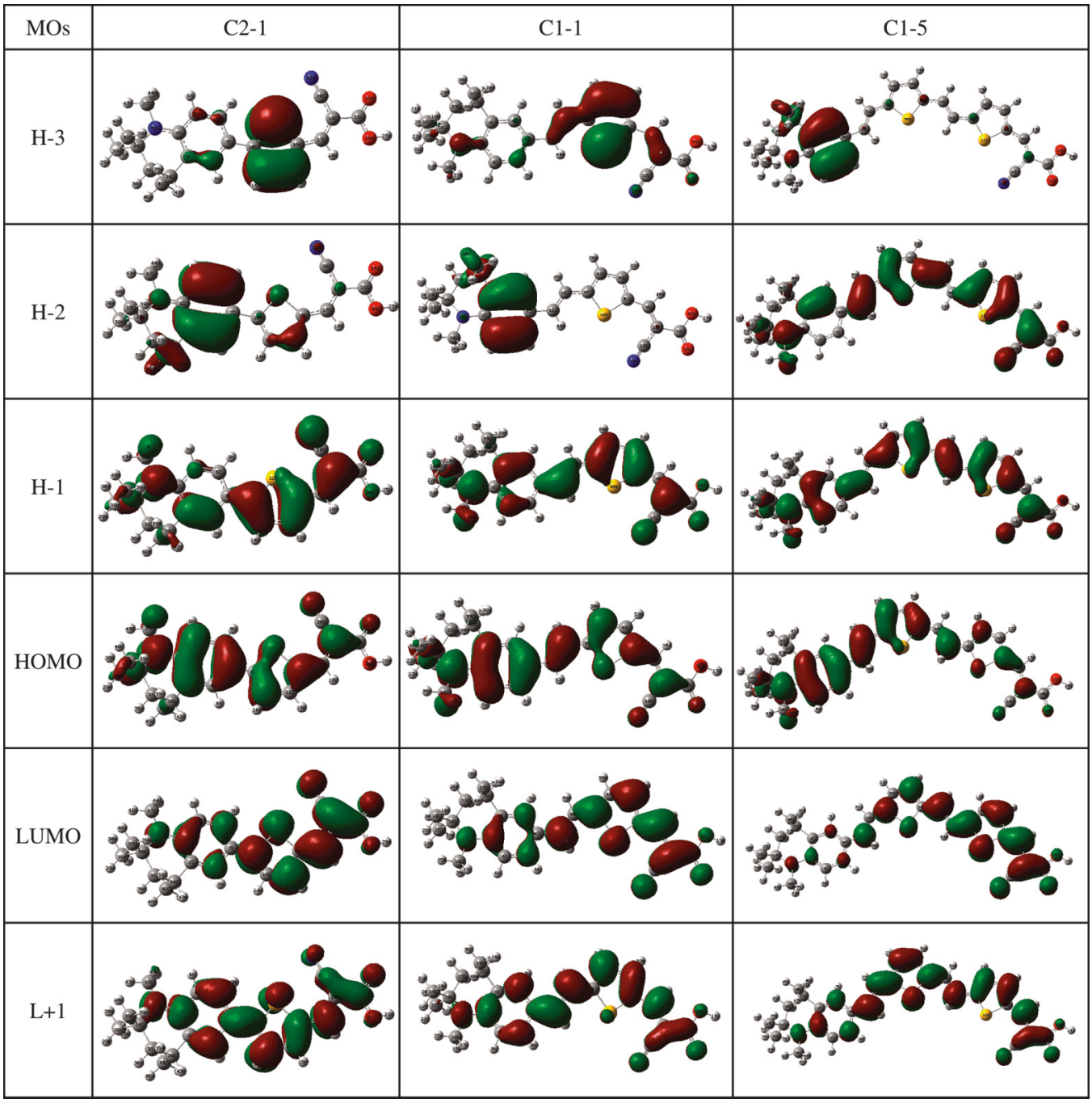

Can. J. Chem. Downloaded from www.nrcresearchpress.com by Xi'an Jiaotong University on 09/19/12
For personal use only.

of the carboxyl group to the supporting semiconductor's surface, it has been inferred that the π system of these dyes most probably lay perpendicular to the surface, thus resulting in a dense package and coverage.[40]

Electronic structures

The dipole moments for C2–1, C1–1, and C1–5 are 14.84, 15.35, and 16.03 D, respectively, indicating that these tetrahydroquinoline dyes are highly polar molecules and their polarities increase with the increase of spacer length. The values of quadrupole moments for C2–1, C1–1, and C1–5 are listed in Table 2, where the average of the diagonal quadrupole moment tensor elements Q_{ii} and unique quadrupole moment Q are defined as follows:

$$[1] \qquad Q_{ii} = (Q_{XX} + Q_{YY} + Q_{ZZ})/3$$

$$[2] \qquad Q = Q_{XX} - Q_{YY}$$

All the diagonal elements of the quadrupole moment tensors for C2–1, C1–1, and C1–5 are negative, indicating that the negative charge distribution is farther removed from the molecular centre of the nuclear charges. The off-diagonal tensor elements Q_{ij} vanish whenever the molecule has a plane of symmetry perpendicular to either one of the coordinates i or j.

Can. J. Chem. Downloaded from www.nrcresearchpress.com by Xi'an Jiaotong University on 09/19/12
For personal use only.

The values of the off-diagonal elements Q_{XY} and Q_{YZ} of C2–1, C1–1, and C1–5 are relatively lower, which can be attributed to their symmetric plane nearly perpendicular to the *y* axis, as shown in Fig. 1.

NBO analysis was employed to characterize the ICT in the tetrahydroquinoline dyes. Table 3 shows the natural charges of cyanoacrylic acid, thiophene-containing π bridge, and tetrahydroquinoline groups in the tetrahydroquinoline dyes. There are some charges transferred from the electron donor (tetrahydroquinoline) to the electron acceptor (cyanoacrylic acid) through the chemical bonds of the π bridge for the tetrahydroquinoline dyes. It was also found that the natural charges of the donor show a remarkable decrease with the increase of spacer length while the natural charges of the conjugate bridge are increased. However, the natural charges of the acceptor for the tetrahydroquinoline dyes are practically identical. These indicate that the increase of spacer length has a significant effect on the electron-donating capability of the donor, but do not significantly alter the electron-drawing capability of the acceptor.

The frontier molecular orbital (MO) contribution is very important in determining the charge-separated states of dye sensitizers. To create an efficient charge-separated state, the highest occupied MO (HOMO) must be localized on the extended donor moiety and the lowest unoccupied MO (LUMO) on the acceptor moiety. The MO energies and isodensity plots of C2–1, C1–1, and C1–5 are shown in Figs. 3 and 4, respectively. For C2–1, the HOMO, lying at –5.03 eV, is a delocalized π orbital distributed over the cyano group through the tetrahydroquinoline group, whereas the HOMO–1, lying 1.33 eV below the HOMO, is also delocalized over the entire molecule. The HOMO–2, lying 1.77 eV below the HOMO, is a π orbital mainly localized in the phenyl and thiophene groups, whereas the HOMO–3, lying 2.20 eV below the HOMO, is localized in the thiophene group with less contributions in the phenyl group. The LUMO, lying at –2.50 eV, is a π* orbital localized in the cyanoacrylic acid, thiophene, and phenyl groups. The LUMO+1, lying 1.98 eV above the LUMO, is also a π* orbital, which is similar to the LUMO. For C1–1, the HOMO and HOMO–1, lying at –4.90 and –6.37 eV, respectively, are π orbitals delocalized over the entire molecule. The HOMO–2, lying 2.12 eV below the HOMO, is localized in the phenyl group, whereas the HOMO–3, lying 2.54 eV below the HOMO, is localized in the vinylenethiophene group with sizable contributions arising from the cyanoacrylic acid group. The LUMO and LUMO+1, lying at –2.61 and –0.84 eV, respectively, are π* orbitals localized in the cyanoacrylic acid, vinylenethiophene, and phenyl groups. As to C1–5, the HOMO, lying at –4.68 eV, is delocalized over the entire molecule, and the HOMO–1 and HOMO–2 are similar to the HOMO. The LUMO, lying at –2.78 eV, is a π* orbital localized in the cyanoacrylic acid and vinylenethiophene groups, whereas the LUMO+1, lying 1.14 eV above the LUMO, is localized in the cyanoacrylic acid and vinylenethiophene groups with sizable contributions in the phenyl group.

Apparently, in these tetrahydroquinoline dyes, the HOMO is quite delocalized on the extended donor moiety, whereas the LUMO is essentially centred on the respective acceptor group. Thus, the HOMO–LUMO excitation on these dyes induced by light irradiation could move the electron distribution from the donor moiety to the anchoring–acceptor moiety, consequently favoring electron injection from the dye to the semiconductor. The computed HOMO energy increases when going from C2–1 to C1–1 (0.13 eV) and from C1–1 to C1–5 (0.22 eV), whereas the LUMO energy is computed to decrease with the increase of spacer length. The isodensity plots of LUMO exhibit a charge transfer to the anchoring acid group with the increase of spacer length, indicating that the vinylene and thiophene groups are indeed electron donors with respect to the cyanoacrylic acid group, and the insertion of more spacers results in a decreased contribution of the tetrahydroquinoline to the LUMO (in agreement with the previously discussed natural charge results). As a consequence of the variation of MOs energies, the HOMO–LUMO gap also decreases when going from C2–1 (2.53 eV) to C1–1 (2.28 eV) and C1–5 (1.90 eV), the latter molecules being expected to absorb at lower energies.

Fig. 5. Simulated absorption spectra of C2–1 using the hybrid functionals PBE1PBE, MPW1B95, and BHandHLYP.

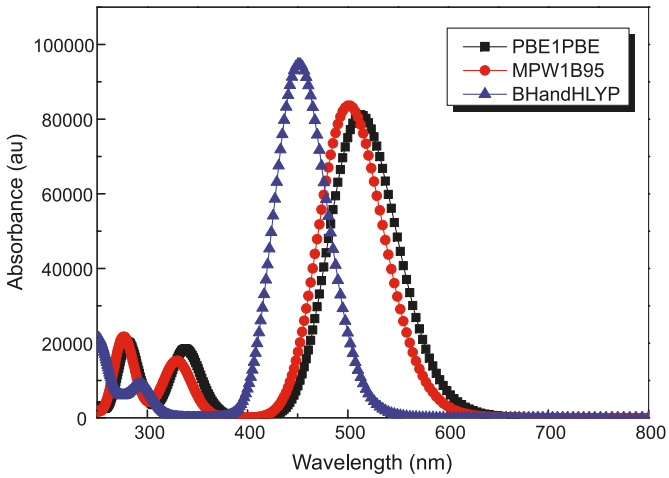

The calculated HOMO and LUMO energies of the bare $Ti_{38}O_{76}$ cluster as a model for nanocrystalline are –6.55 and –2.77 eV, respectively, resulting in a HOMO–LUMO gap of 3.78 eV; whereas the lowest transition is reduced to 3.20 eV according to TD-DFT, which is slightly smaller than the typical band gap of TiO_2 nanoparticles.[4] Furthermore, the HOMO, LUMO, and HOMO–LUMO gap values of $(TiO_2)_{60}$ cluster are –7.52, –2.97, and 4.55 eV (B3LYP/VDZ), respectively.[41] In addition, the edges of the valence band (VB) and CB of a TiO_2 anatase (101) surface are computed at –8.70 and –3.74 eV.[42] Usually, an energy gap of more than 0.2 eV between the LUMO of the dye and the CB of the TiO_2 is necessary for effective electron injection.[25] Taking the above data into account, it can be found that the HOMO energies of these tetrahydroquinoline dyes lie above the VB of TiO_2 and the LUMO energies lie above the CB of TiO_2. The above data also reveal the sensitized mechanism: the interfacial electron transfer between the TiO_2 electrode and the dye sensitizers are electron injection processes from the excited dyes to the semiconductor CB. This is a kind of typical interfacial electron-transfer reaction.[43] Relatively large energy gaps between the LUMO energies of these dyes and the semiconductor CB would be beneficial to the photovoltaic conversion efficiencies.

Can. J. Chem. Downloaded from www.nrcresearchpress.com by Xi'an Jiaotong University on 09/19/12
For personal use only.

Table 4. Electronic transition configurations, computed excitation energies, and oscillator strengths (*f*) for the optical transitions with $f > 0.01$ of the absorption bands in visible and near-UV region for the tetrahydroquinoline dyes in ethanol solution (H = HOMO, L = LUMO, L+1 = LUMO+1, and so forth).

Dye	Configuration	Excitation energy (eV/nm)	*f*	Assignment	Experimental (nm)
C2–1	H → L (+85%)	2.75/451.4	1.3082	π–π*	441
	H–1 → L (+81%)	4.21/294.2	0.1184		
	H–2 → L (+62%); H → L+2 (24%); H–2 → L+1 (6%)	4.53/273.5	0.0403		
	H–3 → L (+70%); H → L+1 (+9%); H → L+2 (9%)	4.67/265.4	0.0189		
	H → L+1 (+74%); H–3 → L (+8%)	4.89/253.8	0.1892		
C1–1	H → L (+83%)	2.48/500.7	1.5646	π–π*	468
	H–1 → L (+83%)	3.87/320.6	0.1180		
	H → L+1(+75%); H–3 → L (12%)	4.35/285.0	0.1636		
	H–3 → L (+71%); H → L+1 (+11%)	4.60/269.5	0.1673		
C1–5	H → L (+78%); H–1 → L (7%)	2.20/563.8	1.9894	π–π*	492
	H–1 → L (+71%); H → L (+6%); H–2 → L (+5%)	3.25/380.9	0.4596		
	H → L+1 (+77%); H → L (+7%)	3.49/355.6	0.3595		
	H–2 → L (+63%); H–1 → L+1 (+7%)	4.20/295.4	0.0412		
	H–1 → L+1 (+45%); H–2 → L (15%); H → L+2 (14%)	4.42/280.8	0.0783		
	H–4 → L (+34%); H–5 → L (31%); H → L+2 (+10%)	4.61/268.9	0.0611		
	H → L+2 (+48%); H–4 → L (27%); H–1 → L+1 (+6%)	4.77/260.1	0.1172		

Absorption spectra

The UV–vis absorption spectra of C2–1, C1–1, and C1–5 were measured in ethanol solution and consist of a very intense and well-isolated absorption band at 441 nm (23 000 mol/L^{-1} cm^{-1}), 468 nm (27 500 mol/L^{-1} cm^{-1}), and 492 nm (38 700 mol/L^{-1} cm^{-1}) and of less intense bands in the UV region, repectively.[33] The absorption bands are red-shifted, enhanced, and broadened when going from C2–1 to C1–1 and C1–5, which is attributed to the expansion of π-conjugation systems with the increase of spacer length.

TD-DFT calculations in ethanol solution were performed with three kinds of hybrid functional PEB1PBE, MPW1B95, and BHandHLYP based on the optimized ground-state geometries, taking the 30 lowest spin-allowed singlet–singlet transitions into account. The simulated UV–vis absorption spectra of C2–1 using the hybrid functionals PEB1PBE, MPW1B95, and BHandHLYP are shown in Fig. 5 as representative. It is found that the calculated line shapes and relative strengths are in good agreement with those of the experiment, and the overall spectral red-shift when going from C2–1 to C1–1, and C1–5 is also correctly reproduced. However, the hybrid functional BHandHLYP is more suitable than PBE1PBE and MPW1B95 for calculating absorption spectra of the tetrahydroquinoline dyes. The calculated vertical excitation energies and oscillator strengths along with the main excitation configurations of these dyes calculated by BHandHLYP are listed in Table 4. The simulated absorption spectra by BHandHLYP are shown in Fig. 6. The first band clearly corresponds to the previously described HOMO–LUMO transition, and is of charge-transfer character, thus possessing high transition intensity. As the HOMO and the LUMO are of the π and π* type, the HOMO–LUMO transition can be classified as a π–π* intramolecular charge transfer. The second and less intense band also corresponds to a π–π* transition with a strong HOMO–1 to LUMO character. Since the HOMO–1 is delocalized on the entire molecule but with a larger contribution from atomic orbitals of cyanoacrylic acid group, this band also has a charge-transfer character and consequently is computed to be red-shifted going from C2–1 to C1–1 (of 0.34 eV) and from C1–1 to C1–5 (of 0.62 eV).

Fig. 6. Simulated absorption spectra of the tetrahydroquinoline dyes at the BHandHLYP/6–31g(d) level.

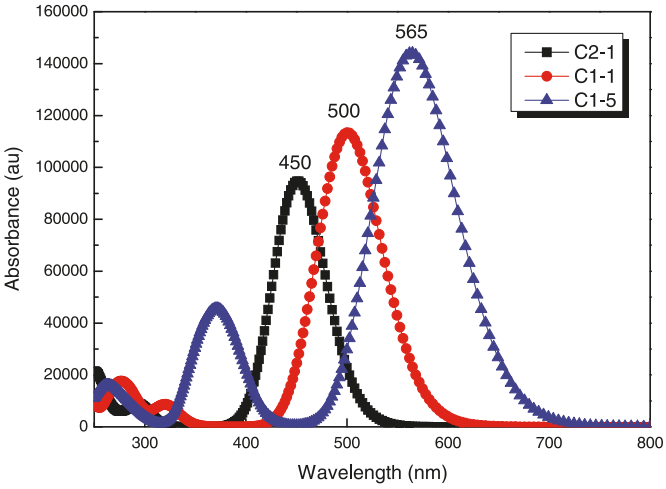

The results of the TD-DFT calculations exhibit some red-shifts with respect to the experimental spectra, which are also found for several dye sensitizers.[16,17,31,44] This discrepancy

Can. J. Chem. Downloaded from www.nrcresearchpress.com by Xi'an Jiaotong University on 09/19/12
For personal use only.

can be ascribed to the absence of explicit solvent molecules around the cyanoacrylic function in the solvation model and the inherent approximations in the TD-DFT. The LUMOs of the tetrahydroquinoline dyes significantly extend over the cyanoacrylic groups and are expected to result in direct solute–solvent interaction with the ethanol molecules through hydrogen bonding. Thus, since in the implicit solvent model used direct solute–solvent interactions are fully neglected, the large red-shift in the simulated absorption spectra for the tetrahydroquinoline dyes can be fully justified. In addition, the TD-DFT always gives a smaller energy gap,[45] and thus gives rise to smaller excitation, especially for large conjugated systems and charge-transfer complexes in excited states.[46] Therefore, it can be concluded that the TD-DFT calculations are capable of describing the spectral features because of the qualitative agreement of line shape, relative strength, and overall spectral red-shift evolution from C2–1 to C1–1 and C1–5 with respect to the experiment, although the discrepancy in absorption wavelengths exists.

Generally, the dyes with stronger and broader absorption bands are expected to give higher photo-to-current efficiency. But the experiment reported that the conversion efficiency of the tetrahydroquinoline dyes is in the following order: C2–1 > C1–1 > C1–5. The increase of spacer length in the conjugate bridge alters the absorption properties of the tetrahydroquinoline dyes more suitable for solar spectrum, but it also enlarges the distance between the electron-donor group and the semiconductor surface, and therefore reduces the probability of a dye π orbital delocalized onto the nanocrystalline surface, and decreases the electronic coupling between the chromophore and TiO_2 substrates.[47] The weak electronic coupling may slow down the electron-injection rate from the excited dyes to the semiconductor CB. On the other hand, the LUMO levels of the dyes decrease with the increase of spacer length, which would give rise to a decreased open-circuit photovoltage, according to the literature.[31] Thus, the higher efficiency of C2–1 can be mainly attributed to the shorter distance between the electron-donor group and the semiconductor surface and the higher LUMO level, despite its poorer absorption properties.

Conclusions

A quantum-chemical investigation of the geometrical and electric structures of three tetrahydroquinoline dyes with different thiophene-containing electron spacers (C2–1, C1–1, and C1–5) used for DSSC was performed. The calculated geometries indicate that strong conjugation is formed in the dyes, which is of benefit to the intramolecular charge transfer. The NBO results suggest that there are some charges transferred from the electron donor (tetrahydroquinoline group) to the electron acceptor (cyanoacrylic acid) through the chemical bonds of the conjugate thiophene-containing bridge in the dyes. The increase of spacer length gives rise to a decrease in the electron-donating strength of the donor, but has no significant effect on the electron-withdrawing ability of the acceptor. The HOMO energy levels are computed to be –5.03, –4.90, and –4.68 eV, whereas the LUMOs are –2.50, –2.61, and –2.78 eV for C2–1, C1–1, and C1–5, respectively, pointing out that the electron transfer from the excited dyes to the TiO_2 conduction band is possible. The UV–vis absorption spectra of the dyes were simulated by TD-DFT calculations. The absorption bands of the dyes are assigned to π–π^* transitions according to the qualitative agreement between the experimental and calculated results. The red-shift in the simulated absorption spectra relative to the experiment is attributed to the lack of direct solute–solvent interaction and the inherent approximations in the TD-DFT.

The comparative analysis of the geometries, electronic structures, and absorption spectra between the tetrahydroquinoline dyes reveals that the increase of spacer length in the dyes led to a better match between the absorption properties of the dyes and solar spectrum, but also enlarged the distance between the electron donor and semiconductor surface, reduced the electron injection rate, decreased the open-circuit photovoltage, and thus resulted in lower overall conversion efficiency. Therefore, the choice of the appropriate conjugate bridge is very important for the molecular design of new tetrahydroquinoline dyes with high efficiency.

Acknowledgements

This work was supported by the Foundation of Wuhan Textile University (No. 2009003), the Natural Science Foundation of Hubei Province (No. 2008CDB261), the Key Project of Science and Technology Research of Ministry of Education (No. 208089), the Educational Commission of Hubei Province (Q20101606), and the Natural Science Foundation of China (No. 51003082). The authors wish to express their thanks to the reviewers for critically reviewing the manuscript and making important suggestions.

References

(1) O'Regan, B.; Grätzel, M. *Nature* **1991** *353* (6346), 737. doi:10.1038/353737a0.
(2) Nazeeruddin, M. K.; Kay, A.; Rodicio, I.; Humphry-Baker, R.; Mueller, E.; Liska, P.; Vlachopoulos, N.; Graetzel, M. *J. Am. Chem. Soc.* **1993** *115* (14), 6382. doi:10.1021/ja00067a063.
(3) Nazeeruddin, M. K.; Péchy, P.; Renouard, T.; Zakeeruddin, S. M.; Humphry-Baker, R.; Comte, P.; Liska, P.; Cevey, L.; Costa, E.; Shklover, V.; Spiccia, L.; Deacon, G. B.; Bignozzi, C. A.; Grätzel, M. *J. Am. Chem. Soc.* **2001** *123* (8), 1613. doi:10.1021/ja003299u.
(4) Nazeeruddin, M. K.; De Angelis, F.; Fantacci, S.; Selloni, A.; Viscardi, G.; Liska, P.; Ito, S.; Takeru, B.; Grätzel, M. *J. Am. Chem. Soc.* **2005** *127* (48), 16835. doi:10.1021/ja052467l.
(5) Gao, F.; Wang, Y.; Shi, D.; Zhang, J.; Wang, M.; Jing, X.; Humphry-Baker, R.; Wang, P.; Zakeeruddin, S. M.; Grätzel, M. *J. Am. Chem. Soc.* **2008** *130* (32), 10720. doi:10.1021/ja801942j.
(6) Chen, C.-Y.; Wang, M.; Li, J.-Y.; Pootrakulchote, N.; Alibabaei, L.; Ngoc-le, C.-h.; Decoppet, J.-D.; Tsai, J.-H.; Grätzel, C.; Wu, C.-G.; Zakeeruddin, S. M.; Grätzel, M. *ACS Nano* **2009** *3* (10), 3103. doi:10.1021/nn900756s.
(7) Amao, Y.; Komori, T. *Biosens. Bioelectron.* **2004** *19* (8), 843. doi:10.1016/j.bios.2003.08.003.
(8) Horiuchi, T.; Miura, H.; Sumioka, K.; Uchida, S. *J. Am. Chem. Soc.* **2004** *126* (39), 12218. doi:10.1021/ja0488277.
(9) Hara, K.; Kurashige, M.; Dan-oh, Y.; Kasada, C.; Shinpo, A.; Suga, S.; Sayama, K.; Arakawa, H. *New J. Chem.* **2003** *27* (5), 783. doi:10.1039/b300694h.
(10) Horiuchi, T.; Miura, H.; Uchida, S. *Chem. Commun. (Camb.)* **2003** (24), 3036. doi:10.1039/b307819a.
(11) Horiuchi, T.; Miura, H.; Uchida, S. *J. Photochem. Photobiol.*

Can. J. Chem. Downloaded from www.nrcresearchpress.com by Xi'an Jiaotong University on 09/19/12
For personal use only.

Chem. **2004** *164* (1–3), 29. doi:10.1016/j.jphotochem.2003.12.018.
(12) Kitamura, T.; Ikeda, M.; Shigaki, K.; Inoue, T.; Anderson, N. A.; Ai, X.; Lian, T.; Yanagida, S. *Chem. Mater.* **2004** *16* (9), 1806. doi:10.1021/cm0349708.
(13) Hagberg, D. P.; Yum, J.-H.; Lee, H. J.; De Angelis, F.; Marinado, T.; Karlsson, K. M.; Humphry-Baker, R.; Sun, L.; Hagfeldt, A.; Grätzel, M.; Nazeeruddin, M. K. *J. Am. Chem. Soc.* **2008** *130* (19), 6259. doi:10.1021/ja800066y.
(14) Tian, H.; Yang, X.; Chen, R.; Zhang, R.; Hagfeldt, A.; Sun, L. *J. Phys. Chem. C* **2008** *112* (29), 11023. doi:10.1021/jp800953s.
(15) Mishra, A.; Fischer, M. K. R.; Bäuerle, P. *Angew. Chem. Int. Ed.* **2009** *48* (14), 2474. doi:10.1002/anie.200804709.
(16) Barolo, C.; Nazeeruddin, M. K.; Fantacci, S.; Di Censo, D.; Comte, P.; Liska, P.; Viscardi, G.; Quagliotto, P.; De Angelis, F.; Ito, S.; Gratzel, M. *Inorg. Chem.* **2006** *45* (12), 4642. doi:10.1021/ic051970w.
(17) Onozawa-Komatsuzaki, N.; Kitao, O.; Yanagida, M.; Himeda, Y.; Sugihara, H.; Kasuga, K. *New J. Chem.* **2006** *30* (5), 689. doi:10.1039/b511986c.
(18) Monat, J. E.; Rodriguez, J. H.; McCusker, J. K. *J. Phys. Chem. A* **2002** *106* (32), 7399. doi:10.1021/jp020927g.
(19) Fantacci, S.; De Angelis, F.; Selloni, A. *J. Am. Chem. Soc.* **2003** *125* (14), 4381. doi:10.1021/ja0207910.
(20) De Angelis, F.; Fantacci, S.; Selloni, A.; Nazeeruddin, M. K. *Chem. Phys. Lett.* **2005** *415* (1–3) 115. doi:10.1016/j.cplett.2005.08.044.
(21) Zhang, X.; Zhang, J.-J.; Xia, Y.-Y. *J. Photochem. Photobiol. Chem.* **2007** *185* (2–3), 283. doi:10.1016/j.jphotochem.2006.06.022.
(22) Xu, Y.; Chen, W.-K.; Cao, M.-J.; Liu, S.-H.; Li, J.-Q.; Philippopoulos, A. I.; Falaras, P. *Chem. Phys.* **2006** *330* (1–2), 204. doi:10.1016/j.chemphys.2006.08.012.
(23) Alexander, B. D.; Dines, T. J.; Longhurst, R. W. *Chem. Phys.* **2008** *352* (1–3), 19. doi:10.1016/j.chemphys.2008.05.010.
(24) Kurashige, Y.; Nakajima, T.; Kurashige, S.; Hirao, K.; Nishikitani, Y. *J. Phys. Chem. A* **2007** *111* (25), 5544. doi:10.1021/jp0720688.
(25) Hara, K.; Sato, T.; Katoh, R.; Furube, A.; Ohga, Y.; Shinpo, A.; Suga, S.; Sayama, K.; Sugihara, H.; Arakawa, H. *J. Phys. Chem. B* **2003** *107* (2), 597. doi:10.1021/jp026963x.
(26) Zhang, X.; Zhang, J.-J.; Xia, Y.-Y. *J. Photochem. Photobiol. Chem.* **2008** *194* (2–3), 167. doi:10.1016/j.jphotochem.2007.08.004.
(27) Liu, Z. *J. Mol. Struct. THEOCHEM* **2008** *862* (1–3), 44. doi:10.1016/j.theochem.2008.04.022.
(28) Xu, J.; Zhang, H.; Wang, L.; Liang, G.; Wang, L.; Shen, X.; Xu, W. *Monatsh. Chem.* **2010** *141* (5), 549. doi:10.1007/s00706-010-0298-0.
(29) Lee, C.; Sohlberg, K. *Chem. Phys.* **2010** *367* (1), 7. doi:10.1016/j.chemphys.2009.10.005.
(30) Ma, R.; Guo, P.; Cui, H.; Zhang, X.; Nazeeruddin, M. K.; Grätzel, M. *J. Phys. Chem. A* **2009** *113* (37), 10119. doi:10.1021/jp905412y.
(31) Zhang, C.-R.; Liu, Z.-J.; Chen, Y.-H.; Chen, H.-S.; Wu, Y.-Z.; Feng, W.-J.; Wang, D.-B. *Curr. Appl. Phys.* **2010** *10* (1), 77. doi:10.1016/j.cap.2009.04.018.
(32) Qin, C.; Clark, A. E. *Chem. Phys. Lett.* **2007** *438* (1–3), 26. doi:10.1016/j.cplett.2007.02.063.
(33) Chen, R.; Yang, X.; Tian, H.; Sun, L. *J. Photochem. Photobiol. Chem.* **2007** *189* (2–3), 295. doi:10.1016/j.jphotochem.2007.02.018.
(34) Frisch, M. J.; Trucks, G. W.; Schlegel, H. B.; Scuseria, G. E.; Robb, M. A.; Cheeseman, J. R.; Montgomery, J. A., Jr.; Vreven, T.; Kudin, K. N.; Burant, J. C.; Millam, J. M.; Iyengar, S. S.; Tomasi, J.; Barone, V.; Mennucci, B.; Cossi, M.; Scalmani, G.; Rega, N.; Petersson, G. A.; Nakatsuji, H.; Hada, M.; Ehara, M.; Toyota, K.; Fukuda, R.; Hasegawa, J.; Ishida, M.; Nakajima, Y.; Honda, Y.; Kitao, O.; Nakai, H.; Klene, M.; Li, X.; Knox, I. E.; Hratchian, H. P.; Cross, J. B.; Bakken, V.; Adamo, C.; Jaramillo, J.; Gomperts, R.; Stratmann, R. E.; Yazyev, O.; Austin, A. J.; Cammi, R.; Pomelli, C.; Ochterski, J. W.; Ayala, P. Y.; Morokuma, K.; Voth, G. A.; Salvador, P.; Dannenberg, J. J.; Zakrzewski, V. G.; Dapprich, S.; Daniels, A. D.; Strain, M. C.; Farkas, O.; Malick, D. K.; Rabuck, A. D.; Raghavachari, K.; Foresman, J. B.; Ortiz, J. V.; Cui, Q.; Baboul, A. G.; Clifford, S.; Cioslowski, J.; Stefanov, B. B.; Liu, G.; Liashenko, A.; Piskorz, P.; Komaromi, I.; Martin, R. L.; Fox, D. J.; Keith, T.; Al-Laham, M. A.; Peng, C. Y.; Nanayakkara, A.; Challacombe, M.; Gill, P. M. W.; Johnson, B.; Chen, W.; Wong, M. W.; Gonzalez, C.; Pople, J. A. *Gaussian 03;* Gaussian Inc., Wallingford, CT, 2004.
(35) Becke, A. D. *J. Chem. Phys.* **1993** *98* (7), 5648. doi:10.1063/1.464913.
(36) Lee, C.; Yang, W.; Parr, R. G. *Phys. Rev. B* **1988** *37* (2), 785. doi:10.1103/PhysRevB.37.785.
(37) Gorelsky, S. I. *SWizard program;* University of Ottawa, Ottawa, ON. Available from http://www.sg-chem.net, 2010.
(38) Cossi, M.; Barone, V.; Cammi, R.; Tomasi, J. *Chem. Phys. Lett.* **1996** *255* (4–6), 327. doi:10.1016/0009-2614(96)00349-1.
(39) Barone, V.; Cossi, M. *J. Phys. Chem. A* **1998** *102* (11), 1995. doi:10.1021/jp9716997.
(40) Howie, W. H.; Claeyssens, F.; Miura, H.; Peter, L. M. *J. Am. Chem. Soc.* **2008** *130* (4), 1367. doi:10.1021/ja076525+.
(41) Lundqvist, M. J.; Nilsing, M.; Persson, P.; Lunell, S. *Int. J. Quantum Chem.* **2006** *106* (15), 3214. doi:10.1002/qua.21088.
(42) Le Bahers, T. L.; Pauporté, T.; Scalmani, G.; Adamo, C.; Ciofini, I. *Phys. Chem. Chem. Phys.* **2009** *11* (47), 11276. doi:10.1039/b914626a.
(43) Watson, D. F.; Meyer, G. J. *Annu. Rev. Phys. Chem.* **2005** *56* (1), 119. doi:10.1146/annurev.physchem.56.092503.141142.
(44) Zhang, C.-R.; Liu, Z.-J.; Chen, Y.-H.; Chen, H.-S.; Wu, Y.-Z.; Yuan, L.-H. *J. Mol. Struct. THEOCHEM* **2009** *899* (1–3), 86. doi:10.1016/j.theochem.2008.12.015.
(45) Görling, A. S. A.; Vogl, P.; Majewski, J. A. *Phys. Rev. B* **1996** *53* (11), 3764. doi:10.1103/PhysRevB.53.7024.
(46) Wang, Y.; Wu, G. *Acta Phys. Chim. Sin.* **2007** *23* (12), 1831. doi:10.1016/S1872-1508(07)60086-2.
(47) Lundqvist, M. J.; Nilsing, M.; Lunell, S.; Åkermark, B.; Persson, P. *J. Phys. Chem. B* **2006** *110* (41), 20513. doi:10.1021/jp064045j.

NMR and MS study of the formation of β-D-glucopyranosylamine uronic acid in aqueous solution

Ali Ghadban, Luca Albertin, Eric Condamine, Rédéo W. Moussavou Mounguengui, and Alain Heyraud

Can. J. Chem. Downloaded from www.nrcresearchpress.com by Xi'an Jiaotong University on 09/19/12
For personal use only.

Abstract: The products of the reaction of D-glucuronic acid with various combinations of ammonia and volatile ammonium salts in water were studied by NMR and MS spectroscopy. For long reaction times (~24 h), the expected products β-D-glucopyranosylamine uronic acid and ammonium *N*-(β-D-glucopyranosyluronic acid)carbamate were obtained in good-to-high yield, whereas seven intermediate species were identified in samples taken at earlier reaction times. ^{1}H–^{1}H homonuclear and ^{1}H–^{13}C heteronuclear correlation experiments enabled a complete assignment of the ^{1}H and ^{13}C NMR spectra of the starting and final compounds, and a partial assignment of the peaks of intermediate species. Based on these results, a ^{1}H NMR protocol for the quantification of the different compounds taking part in the reaction was developed, which was used to monitor the evolution of the composition of an early reaction sample redissolved in D_2O. It was thus established that two of the observed intermediate species are actually the α anomer of the main products, whereas the others are precursors to the formation of α/β-D-glucopyranosylamine uronic acid and ammonium *N*-(α/β-D-glucopyranosyluronic acid)carbamate. The correct assignments for the ^{1}H and ^{13}C spectra of D-glucuronic acid in D_2O are also reported.

Key words: uronic acids, glycosylamines, amination, α anomer, precursor.

Résumé : La spectroscopie de résonance magnétique nucléaires (RMN) et la spectroscopie de masse (SM) ont permis d'étudier les produits de la réaction de l'acide D-glucuronique avec différentes combinaisons entre l'ammoniaque et des sels d'ammonium volatiles dans l'eau. Pour des temps de réaction longs (~24 h), les produits attendus comme l'acide β-D-glucopyranosylamine uronique et le *N*-(β-D-glucopyranosyl)carbamate d'ammonium ont été obtenus avec des rendements allant de bons à excellents. Cependant, sept espèces intermédiaires ont pu être identifiées comme étant majoritaires dans des échantillons prélevés en debut de réaction. Des expériences de corrélations ^{1}H–^{1}H homonucléaires et ^{1}H–^{13}C hétéronucléaires ont permis de faire une attribution complète des spectres RMN du ^{1}H et du ^{13}C des composés de départ et des produits finaux ainsi qu'une attribution partielle des pics des espèces intermédiaires. Sur la base de ces résultats, on a développé un protocole de RMN du ^{1}H qui permet de faire une quantification des divers composés impliqués dans la réaction et qui a été utilisé pour suivre l'évolution de la composition d'échantillons prélevés en début de réaction et redissous dans du D_2O. Il a ainsi été possible d'établir que deux des espèces observées comme intermédiaires sont en fait les anomères α des produits principaux alors que les autres sont des précurseurs dans la formation de l'acide α/β-D-glucopyranosylamine uronique et du *N*-(acide α/β-D-glucopyranosyluronique)carbamate d'ammonium. Les attributions correctes pour les spectres du ^{1}H et du ^{13}C de l'acide D-glucuronique dans le D_2O sont également reportées.

Mots-clés : acides uroniques, glycosylamines, amination, anomère α, précurseur.

[Traduit par la Rédaction]

Introduction

Glycosylamines are monosaccharides in which the hemiacetal hydroxy group has been replaced by an amino group.[1] By extension, the name is also used for oligosaccharides whose reducing end has been transformed in the same way. Glycosylamines are valuable intermediates in the synthesis of a number of glycoconjugates[2–4] such as glycopeptides,[5–11] surfactants,[8,12–14] glycopolymers,[12,15,16] and *N*-glycan probes.[17,18] Classical methods for the synthesis of glycosylamines are based on the reaction of unprotected reducing monosaccharides with ammonia in dry methanol.[19–21] These methods suffer

Received 29 November 2010. Accepted 6 March 2011. Published at www.nrcresearchpress.com/cjc on 17 August 2011.

A. Ghadban,* L. Albertin,* R.W.M. Mounguengui,* and A. Heyraud.* Centre de Recherches sur les Macromolécules Végétales (CERMAV-CNRS), BP53, 38041 Grenoble CEDEX 9, France.
E. Condamine. Institut de Biologie Structurale "Jean-Pierre Ebel", UMR5075 (CEA/CNRS/UJF), 41 rue Jules Horowitz, 38027 Grenoble, France.

Corresponding author: Luca Albertin (e-mail: luca.albertin@cermav.cnrs.fr).

*Affiliated with Université Joseph Fourier and member of the Institut de Chimie Moléculaire de Grenoble.

Table 1. Experimental protocols reported in the literature for the synthesis of glycosylamines in aqueous solution (whenever possible, the exact conditions used for uronic acids are listed).

Method	$[carb]_0$ (mol/L)	$[NH_3]_0$ (mol/L)	Salt	$[s]_0$ (mol/L)	T (°C)	Reaction time	Substrate	Yield (%)
Kochetkov[11]	≤0.2	0	NH_4HCO_3	Satd. (~3.6)[a]	30	6 days	GlcNAc	80
Lubineau[14,29]	0.2	~16	NH_4HCO_3	0.2	42	36 h	D-Glc	100
Gallop[24]	≤0.06	0	$(NH_4)_2CO_3$	Satd. (~3.3)[a]	~25[b]	5 days	D-GlcA	60
Likhosherstov[26,27]	0.8	~7.5[c]	$NH_2CO_2NH_4$	3.2	20	48 h	D-GlcA	81[d]

Note: $[s]_0$ indicates the initial concentration of species s.

[a]Solubility in water: NH_4HCO_3, 284 g/kg at 30 °C; $(NH_4)_2CO_3$, 320 g/L at 20 °C.

[b]Room temperature in the original paper.

[c]CH_3OH/NH_3 15 mol/L 1:1.

[d]Only the salt with carbamic acid was isolated.

Can. J. Chem. Downloaded from www.nrcresearchpress.com by Xi'an Jiaotong University on 09/19/12
For personal use only.

from very long reaction times (from several days to several weeks), low yields, and the concomitant formation of diglycosylamine.[22,23] Additionally, their scope is severely limited by the poor solubility of oligosaccharides and charged mono- and oligo-saccharides in alcohol, which makes them unsuitable for uronic acids.

In 1986, Kochetkov and co-workers[11] put forward an efficient method for the synthesis of β-glycopyranosylamines from 2-acetamido-2-deoxyhexoses, which is based on the use of a saturated aqueous solution of NH_4HCO_3 (Table 1). In the following years, the method was widely applied to the preparation of derivatives of hexoses, 6-deoxyhexoses, and oligosaccharides of different chain lengths.[10,16,18] Nevertheless, the considerable amount of salt used and the labour-consuming procedures needed to remove it restrict the scope of this approach in preparative synthesis. Hence, several modifications were devised in which either a lesser amount of NH_4HCO_3 was used in combination with concentrated ammonia,[14] or a saturated solution of the more volatile $(NH_4)_2CO_3$ was used instead (Table 1).[24,25] A third original variation was developed by Likhosherstov et al.,[26,27] who employed ammonium carbamate and NH_4OH in aqueous methanol solutions to prepare the relatively stable carbamic acid salt of glycosylamines. The free amine was then obtained in a second step by treatment with alcohol (e.g., CH_3OH, ethanol, or 2-propanol) containing a tertiary amine (e.g., TEA and DIPEA) followed by evaporation and (or) crystallization.[28]

The main advantage of these aqueous-based methods resides in their applicability to unprotected charged carbohydrates. Nonetheless, a detailed investigation on the formation of glycosylamines in aqueous solution is lacking. In the 1950s, Isbell and Frush[30,31] investigated the formation of glycosylamines in methanol solution and their hydrolysis, but their studies were solely based on changes in optical rotation, they assumed that the final glycosylamine was the only product of the reaction, and they did not provide any structural characterization. More recently, Campa et al.[29] applied capillary electrophoresis with indirect absorbance detection (CE–indirect UV) and high-performance anion-exchange chromatography with pulsed amperometric detection (HPAEC–PAD) to the crude reaction mixture obtained in the synthesis of D-glucosylamine, D-galactosylamine, and lactosylamine according to Lubineau et al.'s protocol.[14] Fructose (5.4 mol%) and lactulose (7.0 mol%) were identified as the only by-products in the first and last case, respectively, whereas no by-product was observed with D-galactose. Following derivatization with 9-fluorenylmethyloxycarbonyl (FMOC) chloride, the glycosylamines were quantified by micellar electrokinetic capillary chromatography (MEKC–UV), and a yield of 75% was found in the three cases. In general, the study of glycosylamines in aqueous solution is complicated by their rapid hydrolysis[30,32] in the pH range 2–8, and by the concomitant formation of diglycosylamines. At higher pH values and lower temperatures, they are rather stable and NMR spectroscopy could be used as a powerful analytical tool to study this type of compounds.

Uronic acids are monocarboxylic acids formally derived from aldoses by replacement of the hydroxymethyl group CH_2OH with a carboxy group.[1] In nature, they are found in polysaccharides fulfilling diverse biological and structural functions. Well-known examples are glycosaminoglycans, which are composed of uronic acids linked to 2-acetamido-2-deoxyglycosides in an alternating fashion (e.g., heparin, hyaluronan, and chondroitin); and homoglycuronans, which contain only uronic acid residues. Alginates, which are composed of β-D-mannuronic acid and α-L-guluronic acid units, and pectins, whose main chain is made up of α-galacturonic acid units, belong to this latter class.[33] To incorporate uronic acids into glycoconjugates, it would be advantageous to selectively functionalize their reducing end without resorting to protective-group chemistry, which can be rather cumbersome in the case of monosaccharides[34] and becomes exceedingly time-consuming in the case of oligoglycuronans.[35] A valuable alternative would be the transformation of the starting uronic acid into the corresponding glycosylamine. Although several examples of N-substituted glycosylamine uronic acids have been reported in the literature,[36] they invariably focus on monosaccharides derivatives and involve protective-group chemistry. Furthermore, only two papers claim the preparation of glycosylamine uronic acids in aqueous (from D-GlcA, D-GalA, and α-D-GalA*p*-(1→4)-D-GalA)[24] or aqueous methanolic solution (from D-GlcA).[26,37]

Faced with this dearth of information, we decided to carry out a systematic study of the formation of glycosylamine uronic acids in aqueous solution. In particular, we tried to verify whether such transformation could be conveniently performed and to identify the experimental conditions leading to the maximum yield, in the shortest time, and with the smallest amount of reagents. In this first report, we describe an NMR and MS study of the reaction of D-glucuronic acid

Scheme 1. Reactions taking place during the synthesis of β-D-glucosylamine uronic acid (**2**) in aqueous solution.

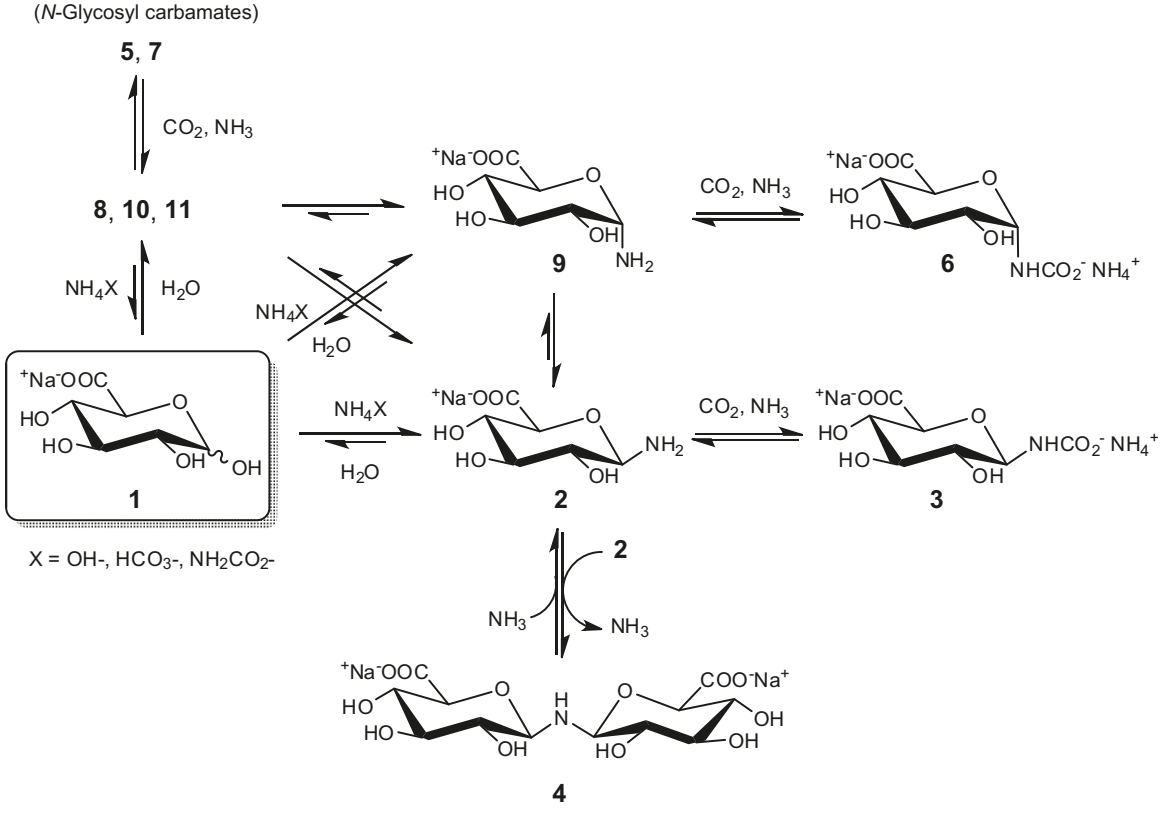

(**1**) with different ammonia sources in water (Scheme 1), and demonstrate how ^{1}H NMR spectroscopy can be routinely applied to the quantification of the different species (reactants, intermediates, and products) taking part in the reaction.

Results and discussion

NMR study

Sodium D-glucuronate (**1**) (Scheme 1) was reacted at 30 °C with ammonia and volatile ammonium salts (NH_4HCO_3 or $NH_2CO_2NH_4$) in water according to different protocols (see the Experimental section). Samples were drawn at preset reaction times, frozen in liquid nitrogen, and freeze-dried overnight to eliminate water and most of the salts. No further purification was performed and all reported analyses refer to the gross products obtained this way. To monitor the time course of the reaction, individual samples were redissolved in cold D_2O to afford clear solutions of pD ≅ 9, that were immediately analysed by ^{1}H NMR. Spectra were acquired at 278 K to inhibit hydrolysis of the products and to prevent the peak of residual HDO from interfering with integration.

Figure 1 shows an example of the evolution of the ^{1}H and ^{13}C NMR spectra when going from starting compound (Fig. 1*a*) to the gross final product (Fig. 1*c*).[38] In the proton spectrum, the disappearance of the characteristic peaks at 4.63 ($H1_\beta$), 5.23 ($H1_\alpha$), and 3.27 ppm ($H2_\beta$) proves that **1** was completely consumed during the reaction. At the same time, two new doublets appear at 4.09 ppm ($J_{1,2}$ 8.8 Hz) and 4.70 ppm ($J_{1,2}$ 8.8 Hz) that were assigned to the anomeric proton of β-D-glucopyranosylamine uronic acid (**2**) and ammonium *N*-(β-D-glucopyranosyluronic acid)carbamate (**3**), respectively. Compound **3** forms from the reaction of **2** with the CO_2 liberated by the decomposition of bicarbonate or carbamate anions.[16,18] Since it decomposes fairly easily upon standing in aqueous solution and (or) during repeated freeze-drying cycles,[18] its proportion was included in the calculation of product yields. Besides, the solution equilibrium between **2** and **3** can be easily displaced in favour of **2** by increasing the temperature. For instance, when the product obtained according to protocol A.9.06 was analysed by ^{1}H NMR at 298 K, its mole content was 37% and 52% for **2** and **3**, respectively, whereas the same sample analysed at 318 K contained 72% and 14% of the two species.[39] A complete assignment of the peaks observed in ^{1}H and ^{13}C NMR was performed via ^{1}H–^{1}H homonuclear and ^{1}H–^{13}C heteronuclear correlation experiments, and the results are summarized in Table 2. As an example, the ^{1}H–^{1}H TOCSY, ^{1}H–^{1}H COSY, and ^{1}H–^{13}C HMQC spectra are shown in Fig. 2,[40] Fig. 3,[41] and Fig. 4,[42] respectively, together with the assignment of some peaks (more spectra can be found in the Supplementary data).

The presence of 13 peaks in the ^{13}C NMR spectrum (6 for **2** and 7 for **3**) suggests that both compounds are present in a single cyclic form, and the chemical shift of C-5 (79.9 ppm) points to a hexopyranose ring.[43] Finally, values of 9.4–9.5 Hz for $J_{4,5}$ and $J_{1,2}$ are consistent with an anti orientation of the vicinal hydrogens,[44] hence a $^4C_1$ conformation and a β configuration. It is important to note the original assignment reported by Pfeffer et al.[45] for C-5α and C-6α of GlcA at pH 7.8 should

Can. J. Chem. Downloaded from www.nrcresearchpress.com by Xi'an Jiaotong University on 09/19/12
For personal use only.

Fig. 1. 1D ^{1}H (400.13 MHz, top) and ^{13}C (100.62 Hz, bottom) spectra of (*a*) **1**, (*b*) the gross product obtained after 140 min of reaction according to protocol B.5.02, and (*c*) the mixture of **2** and **3** obtained after 33 h of reaction according to protocol B.0.S. The assignments of some peaks are also shown.

Can. J. Chem. Downloaded from www.nrcresearchpress.com by Xi'an Jiaotong University on 09/19/12
For personal use only.

be exchanged with that of the β anomer, as evidenced by a three-bond ^{1}H–^{13}C correlation experiment carried out in the course of our study (see the Supplementary data). Also, 1.7–1.9 ppm should be added to the ^{13}C NMR chemical shifts originally reported to refer them to $\delta_{DSS} = 0.0$. The comparison of our results with literature data is comforting: Identical values for δ (H1) and $J_{1,2}$ were reported by Likhosherstov et al.[27] for the ^{1}H spectrum of β-D-glucopyranosylamine, the corresponding *N*-glycosylcarbamate, and the carbamic acid salt of β-D-glucopyranosylamine uronic acid[26] prepared in aqueous methanolic solution, although in those cases a complete NMR assignment was not realized.

With regard to compound **3**, a weak doublet is visible at 6.25 ppm (*J* 9.8 Hz) in the 1D ^{1}H spectrum of concentrated solutions (~15% *w/w*) acquired at 278 K. The same doublet does not couple with any carbon atom in one-bond heteronuclear correlation experiments and is displaced to 6.04 ppm in spectra acquired at 298 K. This signal correlates to the H1 (4.70 ppm) of the same molecule in three-bond homonuclear correlation experiments (Fig. 5*a*),[46] and was therefore assigned to the proton of the $NHCO_2^-$ group. Further corroboration to the structure of **3** comes from the observation that H1 correlates to a quaternary carbamate carbon (165.9 ppm) in long distance ^{1}H–^{13}C heteronuclear correlation experiments (Fig. 5*b*).[46]

When the spectra of samples taken at intermediate reaction times are examined, a more complicated picture emerges (Fig. 1*b*). In particular, five new doublets with coupling constants ranging from 3.3 to 5.6 Hz appear between 4.5 and 5.6 ppm alongside the peaks owing to the anomeric proton of the starting and final compounds. Also, an intense and complex multiplet occupies the region between 4.2 and 4.4 ppm. The nature of these new peaks was elucidated through several ^{1}H–^{1}H (gCOSY, TOCSY) and ^{1}H–^{13}C (gHSQC, gHMBC) correlation experiments and a total of seven new compounds were identified (compounds **5**–**11**). The relative abundance of these species changes significantly after a few hours at 278 K in solution, and most of them disappear within 24 h (vide infra). This is particularly true for compound **5**, whereas a small amount of compounds **6** and **9** is always observed alongside the main products **2** and **3**. To characterize these "transient" species, the use of a higher field spectrometer (800 MHz) equipped with a cryoprobe was necessary for most correlation experiments on samples taken at early reaction times. This way, the total acquisition time could be kept within 7 h per tube without sacrificing signal intensity, and a higher resolution was attained. As a result, all new doublets appearing between 4.5 and 5.6 ppm could be assigned to anomeric protons. The value of $J_{1,2}$ (3.1–5.6 Hz) for compounds **5**–**10** is consistent with a gauche orientation of the vicinal protons, and the three-bond correlation of H1 to a $NHCO_2$ proton and carbon (Fig. 5) demonstrates that **5**, **6**, and **7** are *N*-glycosylcarbamates. Additional weak doublets at 4.45 (d, 4.0 Hz), 4.77 (d, 2.9 Hz), and 5.73 ppm (d, 4.2 Hz) could not be assigned. Concerning compounds **6** and **9**, the chemical shifts of C5 (74.46 and 74.85 ppm, respectively, compared to 74.55 ppm observed for $\mathbf{1}_{\alpha}$), the values of $J_{4,5}$ (10 and 9.1 Hz), and those of $J_{1,2}$ (5.5 and 4.4 Hz) point to a hexopyranose ring in a $^{4}C_1$ conformation and to an α configuration. Based on these results, we postulate that **6** and **9** are the α anomers of compounds **3** and **2**, respectively. Interestingly, in their paper on the synthesis of 1-*N*-glycyl-β-oligosaccharide derivatives, Manger et al.[18] had already speculated that a low-intensity doublet (4.79 ppm, $J_{1,2} = 5.1$ Hz) appearing in the spectrum of β-GlcNAc-NH_2 prepared according to A.0.S was due to the α anomer of the same molecule, but they did not investigate this hypothesis any further.

The multiplet ranging from 4.2 to 4.4 ppm was particularly difficult to interpret: According to ^{1}H–^{1}H TOCSY and ^{1}H–^{1}H COSY experiments, it only correlates with itself and with species **4** (2H), **5** (2H), **7** (3H), **8** (1H), and **10** (3H), which contribute a total of 11 protons. Even so, the value of its integral indicates that other protons must be present. This is supported by one-bond ^{1}H–^{13}C correlations, which show that 15 carbon atoms are linked to this group of protons, i.e., five more than could be expected from ^{1}H–^{1}H correlations. We conclude that the multiplet at 4.2–4.4 ppm contains all proton signals of yet another compound (**11**).

Unfortunately, it was not possible to determine the exact structure of intermediates **5**, **7**, **8**, **10**, and **11** from the NMR data. The absence of secondary carbon signals in ^{13}C DEPT135 spectra excludes the formation of ketofuranoses, while the occurrence of base-catalyzed epimerization at C2 was ruled out by examining the spectra of β-D-mannopyranosylamine uronic acid (and the corresponding carbamate) prepared from D-mannurono-6,3-lactone (ManA-NH_2 C1, δ 85.17 ppm; H1, δ 4.36 ppm, $J_{1,2} = 0.84$ Hz. ManA-$NHCO_2^-$ C1, δ 83.38 ppm; H1, δ 4.94 ppm, $J_{1,2} = 0.93$ Hz).[47] The most likely hypothesis is the formation of furanose derivatives. The mechanism of formation of glycosylamines involves the opening of the starting aldose ring to give an acyclic aldehyde, which is then transformed into an imine followed by ring closure.[30,31] It is reasonable to assume that kinetically favoured furanose forms will initially be more populated than the thermodynamically favoured pyranose forms (vide infra). Unsubstituted furanose derivatives of D-glucuronic acid are not described in the literature, but assignments of ^{13}C NMR spectra are available for methyl-α/β-D-glucofuranoside[48] and β-D-glucofuranose.[49] Even so, comparison with our data is tricky. The chemical shift of C2 is the best candidate for this type of analysis; provided that the substituent on C1 is not *N*-carbamate (e.g., δ C2 is 76.6 and 76.7 ppm for $\mathbf{1}_{\beta}$ and **2**, respectively, but 74.6 ppm for **3**). This excludes its applicability to compounds **5** and **7**. Of the remaining unknown species, δ C2 was only assigned in the case of **10** (83.15 ppm), and a difference of +1.5 ppm with respect to methyl-β-D-glucofuranoside and +1.05 ppm with respect to β-D-glucofuranose is observed.

Can. J. Chem. Downloaded from www.nrcresearchpress.com by Xi'an Jiaotong University on 09/19/12
For personal use only.

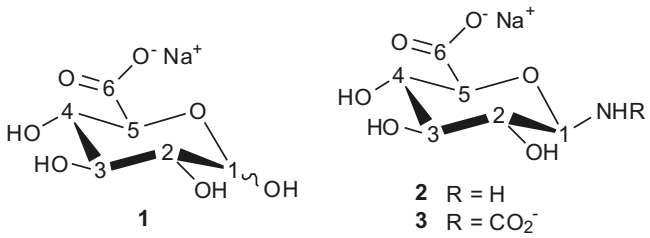

1

2 R = H
3 R = CO_2^-

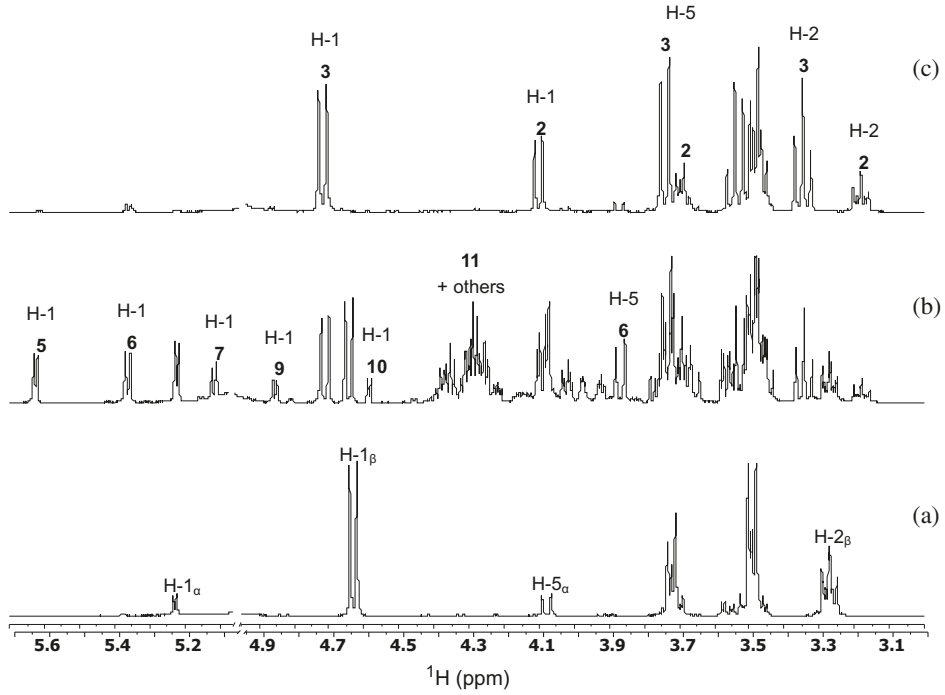

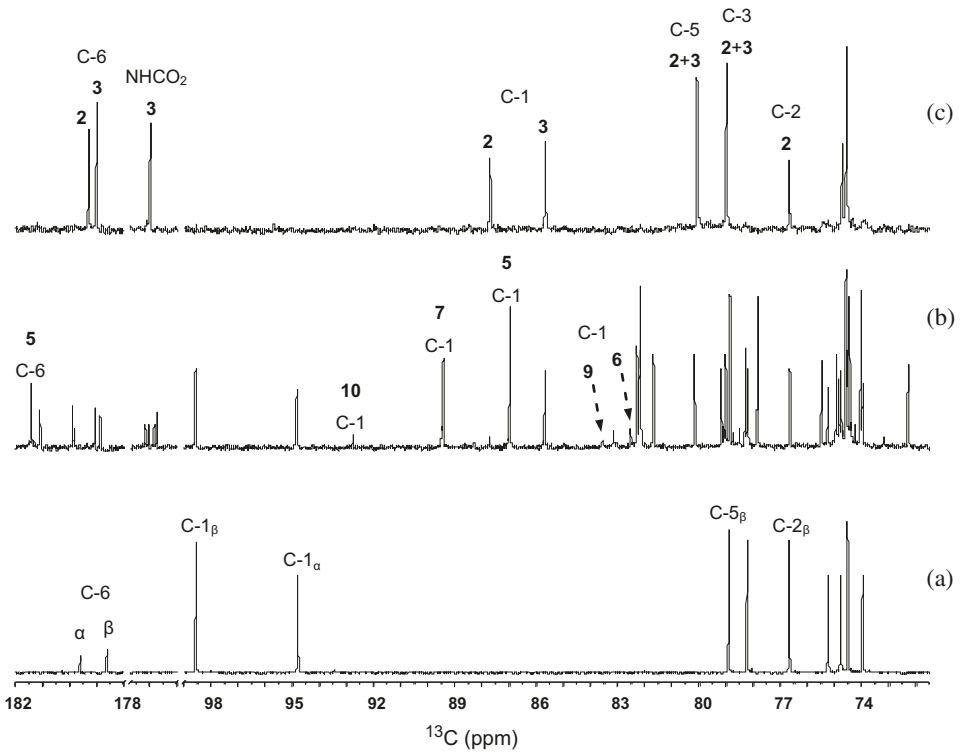

Table 2. NMR characterization of the species observed during the amination of D-glucuronic acid in aqueous solution.

Compound	Nature	δ ^{1}H (ppm) (m, *J* (Hz), assignment)	δ ^{13}C (ppm) (assignment)
$\mathbf{1}_\alpha$[a]	α-Aldopyranose	5.23 (d, 3.7, H1), 3.56 (dd, 9.8, 3.8, H2), 3.72 (m, H3), 3.48 (H4), 4.08 (d, 10.1, H5)	94.81 (C1), 73.99 (C2), 75.26 (C3), 74.79 (C4), 74.55 (C5), 179.62 (C6)
$\mathbf{1}_\beta$[a]	β-Aldopyranose	4.63 (d, 8.0, H1), 3.27 (m, H2), 3.50 (H3), 3.51 (m, H4), 3.72 (H5)	98.57 (C1), 76.70 (C2), 78.25 (C3), 74.53 (C4), 78.93 (C5), 178.64 (C6)
2[a]	β-Glycopyranosylamine	4.09 (d, 8.8, H1), 3.18 (dd, 9.0, H2), 3.48 (H3), 3.48 (d, 9.5, H4), 3.69 (m, H5)	87.68 (C1), 76.76 (C2), 79.03 (C3),74.71 (C4), 79.92 (C5), 179.14 (C6)
3[a]	*N*-(β-Glycopyranosyl)carbamate	4.70 (d, 9.1, H1), 3.34 (t, 9.0, H2), 3.52 (H3), 3.48 (H4), 3.73 (d, 9.4, H5), 6.25 (d, 9.8, $NHCO_2$)	85.68 (C1), 74.64 (C2), 79.02 (C3), 74.55 (C4), 79.87 (C5), 178.88 (C6), 165.86 ($NHCO_2$)
4[b]	Di(β-glycopyranosyl)amine	4.29 (d, 8.8, H1), 3.27 (H2)	89.51 (C1), 76.80 (C2), 179.60 (C6)
5[c]	*N*-Glycosylcarbamate	5.63 (d, 3.6, H1), 4.07 (H2), 4.27, 4.32, 5.79 (d, 10.0, $NHCO_2$)	86.97 (C1), 77.85 (C2), 181.40 (C6), 165.73 ($NHCO_2$)
6[c]	*N*-(α-Glycopyranosyl)carbamate	5.37 (d, 5.5, H1), 3.76 (H2), 3.66 (H3), 3.46 (H4), 3.86 (d, 10.0, H5) 6.15 (d, 9.5, $NHCO_2$)	82.17 (C1), 72.31, 75.49, 74.46 (C5), 179.89 (C6), 166.15 ($NHCO_2$)
7[c]	*N*-Glycosylcarbamate	5.12 (d, 5.0, H1), 4.01 (t, 4.79, H2), 4.27, 4.28, 4.36, 6.14 (d, 9.9, $NHCO_2$)	89.45 (C1), 81.69 (C2), 165.84 ($NHCO_2$)
8[d]	Unknown	5.03 (d, 3.1, H1), 3.97 (m, H2), 4.29	89.49 (C1)
9[c]	α-Glycopyranosylamine	4.84 (d, 4.4, H1), 3.67 (H2), 3.70 (H3), 3.55 (H4), 4.01 (d, 9.1, H5)	83.56 (C1), 73.21, 74.57, 74.85 (C5), 179.84 (C-6)
10[c]	Unknown	4.58 (d, 3.3, H1), 3.91 (H2), 4.23, 4.30, 4.32	92.76 (C1), 83.15 (C2)
11[c]	Unknown	4.2–4.4 (m)[e]	Five among the following: 73.21, 73.48, 73.98, 74.25, 74.40, 74.85, 77.50, 78.22, 78.76, 78.86, 79.02, 82.17, 82.29, 83.17

[a]Assignment based on spectra acquired at 298 K,

[b]Assignment based on spectra acquired at 298 (^{1}H) and 280 K (^{13}C),

[c]Assignment based on spectra acquired at 278 K.

[d]Assignment based on spectra acquired at 288 (^{1}H) and 278 K (^{13}C).

[e]Peaks owing to compounds **4** (2H), **5** (2H), **7** (3H), **8** (1H), and **10** (3H) are found in the same region. Unassigned peaks: ^{1}H (δ (ppm)) 4.45 (d, 4.0 Hz), 4.77 (d, 2.9 Hz), 5.73 (d, 4.2 Hz) visible in some concentrated solutions of intermediate samples. ^{13}C (δ (ppm)) 181.40, 181.31, 181.09.

Can. J. Chem. Downloaded from www.nrcresearchpress.com by Xi'an Jiaotong University on 09/19/12
For personal use only.

Mass spectrometry

The identity of species **5**–**11** was further investigated by mass spectrometry. To this end, freeze-dried gross products were redissolved in deionized water and immediately infused through the ESI interface at constant flow rate. Figure 6 shows the evolution of the ESI-MS spectrum when going from the starting compound (*a*) to the gross final product (*c*)[50] via a sample rich in transient species (*b*).[51] In negative-ion mode, three characteristic peaks are present for D-glucuronic acid, which correspond to the uronate anion (*m*/*z* 193, $[M - H]^-$) and to two cluster ions (*m*/*z* 387, $(\mathbf{1}_H)_2$, $[M - H]^-$; *m*/*z* 409, $(\mathbf{1}_{Na})\mathbf{1}_H$, $[M - H]^-$). Similar ions can be identified in the spectrum of **2** + **3** (*m*/*z* 192, 385, and 407) by taking into account the difference of 1 Da between the starting and the final compounds. Also, two peaks are visible that can be ascribed to di(glycosylamine) **4** (*m*/*z* 368 $\mathbf{4}_{H,H}$, $[M - H]^-$; *m*/*z* 390, $\mathbf{4}_{Na,H}$, $[M - H]^-$), whereas peaks at *m*/*z* 207, 209, and 223 could not be assigned. Concerning the sample rich in unknown species (Fig. 6*b*), its MS spectrum appears as a combination of the spectrum of **1** and of **2** + **3**, with the added complication of "mixed" cluster ions having a monoisotopic mass identical to that of the most abundant isotopologue cluster ions of **2**. For instance, *m*/*z* 386 $(\mathbf{1}_H)\mathbf{2}_H$, $[M - H]^-$ and *m*/*z* 408 $(\mathbf{1}_{Na})\mathbf{2}_H$, $[M - H]^-$. Similar considerations can be made for the spectra in positive-ion mode (Fig. 6), where the most intense peaks are those for $(\mathbf{2}_{Na})$ (*m*/*z* 216, $[M + H]^+$; *m*/*z* 238, $[M + Na]^+$). A complete list of the peaks observed for each type of sample, together with their assignment, is reported in Table 3. By examining this table, it becomes apparent that all peaks observed for the intermediate sample are also present either in the spectrum of the starting compound, or in that of the final product. This proves that species **5**–**11** are isomers of **2** and **3**, and since they have completely different NMR spectra, we conclude that they are constitutional isomers and (or) diastereomers of the major products.

Quantification of compounds

The mole fraction of each species observed during the course of the reaction was determined from the proton spectra on the basis of the assignment reported in Table 2. To this end, we assumed that each signal in the ^{1}H NMR spectrum is due to a CH group, i.e., that there was no rearrangement of C–H bonds during the reaction. This idea is supported by the absence of signals attributable to $R_2C{=}O$ or RCH_2–OH carbons in standard ^{13}C NMR and DEPT135 spectra.

Can. J. Chem. Downloaded from www.nrcresearchpress.com by Xi'an Jiaotong University on 09/19/12
For personal use only.

Fig. 2. 2D ^{1}H–^{1}H TOCSY spectrum of **2** + **3** (400.13 MHz).

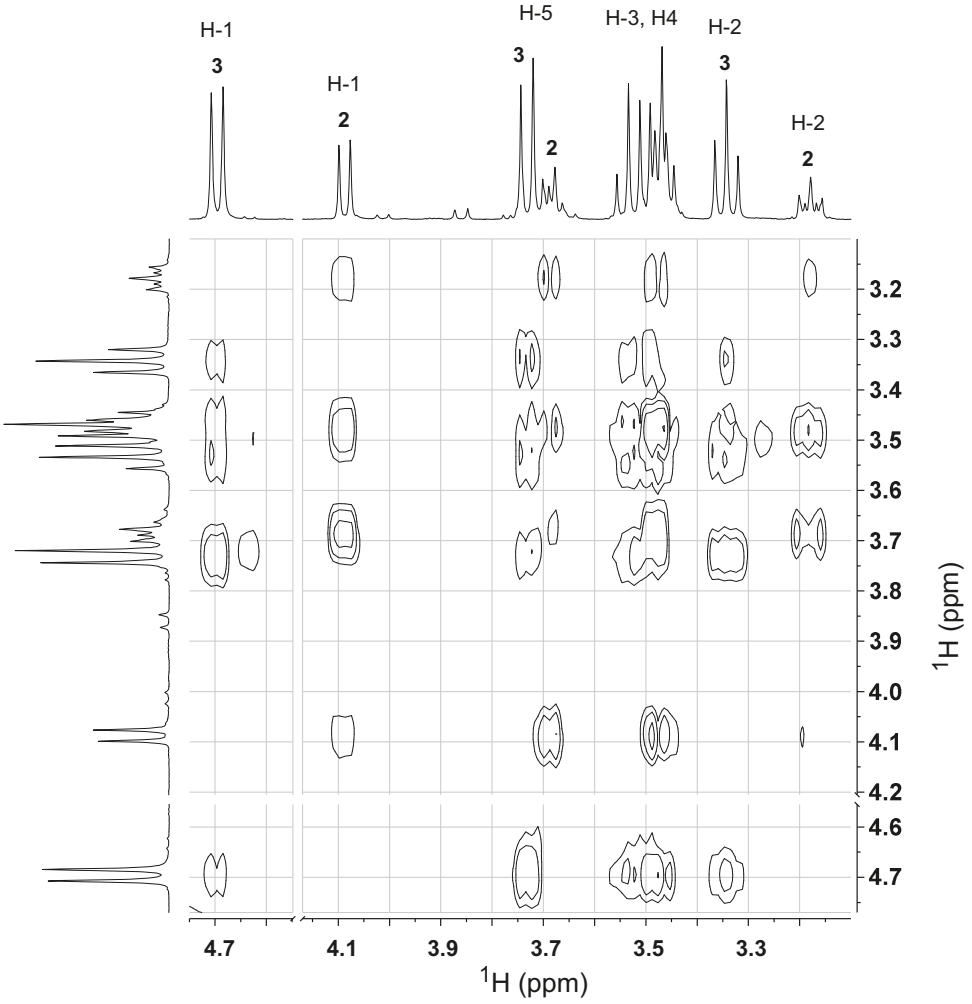

A normalizing constant S was then calculated according to the formula:

$$[1]\quad S = \sum_{i=\mathbf{1}}^{\mathbf{12}} \frac{A_\delta^i}{n_\delta^i} = A_{5.23}^{\mathbf{1}_\alpha} + A_{4.63}^{\mathbf{1}_\beta} + A_{3.18}^{\mathbf{2}} + A_{4.70}^{\mathbf{3}} + \frac{(A_{3.27} - A_{4.63}^{\mathbf{1}_\beta})}{2} + A_{5.63}^{\mathbf{5}} + A_{5.37}^{\mathbf{6}} + A_{5.13}^{\mathbf{7}} + A_{4.84}^{\mathbf{9}} + A_{4.58}^{\mathbf{10}} + \frac{(A_{4.20-4.40} - A^{\mathbf{4}} - 2A_{5.63}^{\mathbf{5}} - 3A_{5.13}^{\mathbf{7}} - 3A_{4.58}^{\mathbf{10}})}{5}$$

where A_δ^i indicates the area of the methine signal of compound i having a chemical shift δ (ppm), and n_δ^i is the number of such methine groups in species i (e.g., there are two equivalent H2 protons in diglycosylamine (**4**)). It should be noted that since the H2 signal of **4** superimposes with that of $\mathbf{1}_\beta$, the former was corrected by subtracting the integral of the anomeric proton of $\mathbf{1}_\beta$ at 4.63 ppm. Also, the contribution of species **8** and **11** was combined in the last factor, since neither can be quantified individually. The mole fraction x of each species (with the exception of **8** and **11**) is then calculated from

$$[2]\quad x^i = \frac{A_\delta^i / n_\delta^i}{S}$$

On the basis of this formula, we calculated that, depending on the protocol, between 64% (A.1.06) and 89% (B.0.S) of product **2** + **3** is obtained after 24 h of reaction at 30 °C, whereas the fraction of diglycosylamine (**4**) varies between 0% and 3%. An experiment was also carried out in which an early reaction sample (15 min) was isolated by freeze-drying, redissolved in D_2O, and monitored by ^{1}H NMR at 278 K. Figure 7 shows the evolution of its composition with time.[52] Just after dissolution, the sample was a complex mixture of all species identified in the system with the sole exception of diglycosylamine (**4**). The major single components were D-glucuronic acid (**1**, 22%), compound **5** (27%), and compound **7** (12%). In the following 7 h though, unknown species **5**, **7**, and **10** mostly disappeared; compounds **8** + **11** fell to 3%, and a small fraction of diglycosylamine (**4**) formed. At the same time, the proportion of **2** + **3** and **6** + **9** increased steadily from 12% and 11% to 39% and 30%, respectively, whereas the fraction of D-glucuronic acid (**1**) remained virtually constant. Since all sources of ammonia were removed from the sample before the beginning of the experiment, this result indicates that unknown compounds **5**, **7**, **8**, **10**, and **11** are precursors to **2**, **3**, **6**, and **9**, and that they spontaneously transform in the latter compounds upon standing in solution. Concerning species **6** and **9**, their combined proportion is

Fig. 3. ^{1}H–^{1}H COSY spectrum of **2** + **3** (100.62 MHz).

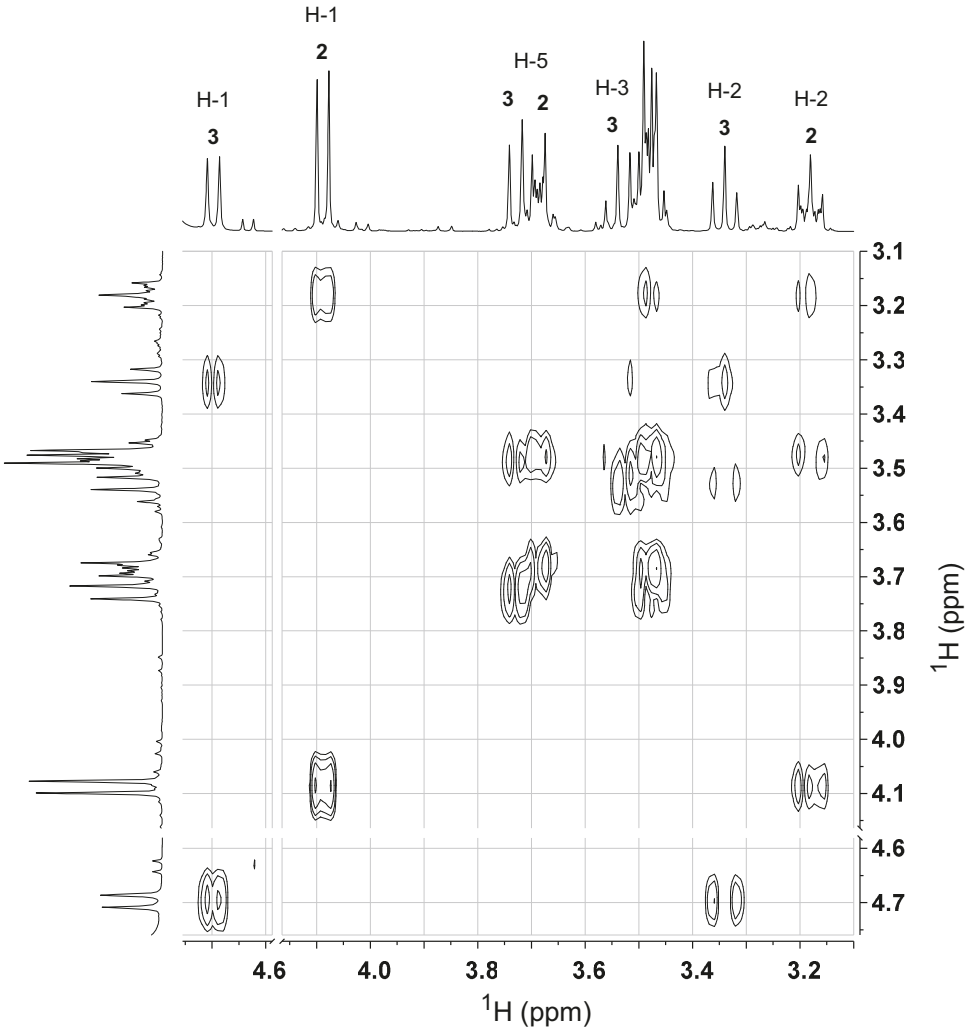

Can. J. Chem. Downloaded from www.nrcresearchpress.com by Xi'an Jiaotong University on 09/19/12
For personal use only.

initially identical to that of **2** and **3** (11%–12%), it attains a maximum around 7 h after dissolution (30%) and diminishes slowly in the following days to the advantage of **2** and **3**. This behaviour is consistent with the mutarotation of an α-glycosylamine into the more stable β anomer, both species being in equilibrium with the respective *N*-glycosylcarbamate. As a result, after 5 days at 5 °C, the sample contained 69% of product, 25% of the starting glucuronic acid, 1% of diglycosylamine, and just 5% of all other species combined. Based on this experiment, we propose the reaction scheme reported in Scheme 1.

These results show that species **5**, **7**, **8**, **10**, and **11** are kinetically favoured but thermodynamically unstable, and that they disappear after ~24 h in solution at low temperature in favour of the more stable D-glucopyranosylamine uronic acid (**2/9**) and ammonium *N*-(D-glucopyranosyluronic acid)carbamate (**3/6**). As a consequence, the occurrence of base-catalyzed epimerization as a mechanism for the formation of transient species can be safely ruled out: a catalyst only lowers the activation energy of a reaction and accelerates the formation of a product, which is more (or at least comparably) stable. To accommodate the occurrence of epimerization, we should consider that **1** is initially transformed into a more stable epimer, that the latter is aminated, and that the resulting glycosylamine is back-epimerized to the more stable α/β-D-glucopyranosylamine uronic acid (**2/9**). That is a highly unlikely reaction pathway.

Conclusions

A model uronic acid (D-glucuronic acid (**1**)) was reacted with different ammonia sources in water and the reaction was monitored by ESI-MS and solution NMR spectrometry. For long reaction times (~24 h), the expected products β-D-glucopyranosylamine uronic acid (**2**) and ammonium *N*-(β-D-glucopyranosyluronic acid)carbamate (**3**) were obtained, whereas seven other species (**5**–**11**) were identified in intermediate samples. ^{1}H–^{1}H homonuclear and ^{1}H–^{13}C heteronuclear correlation experiments enabled complete assignment of the ^{1}H and ^{13}C NMR spectra of compound $\mathbf{1}_{\alpha}$, $\mathbf{1}_{\beta}$, **2**, and **3**, whereas partial assignments were obtained for the other compounds. Based on these results, a ^{1}H NMR protocol for the quantification of the different species (reactants, intermediates, and products) taking part in the reaction was developed. It was thus calculated that after 24 h at 30 °C between 64% (A.1.06) and 89% (B.0.S) of product **2** + **3** was

Fig. 4. ^{1}H–^{13}C HMQC spectrum of **2** + **3** (400.13–100.62 MHz). The insert shows the cross peak owing to the anomeric proton and carbon of di(β-D-glucopyranosyl)amine uronic acid **4**.

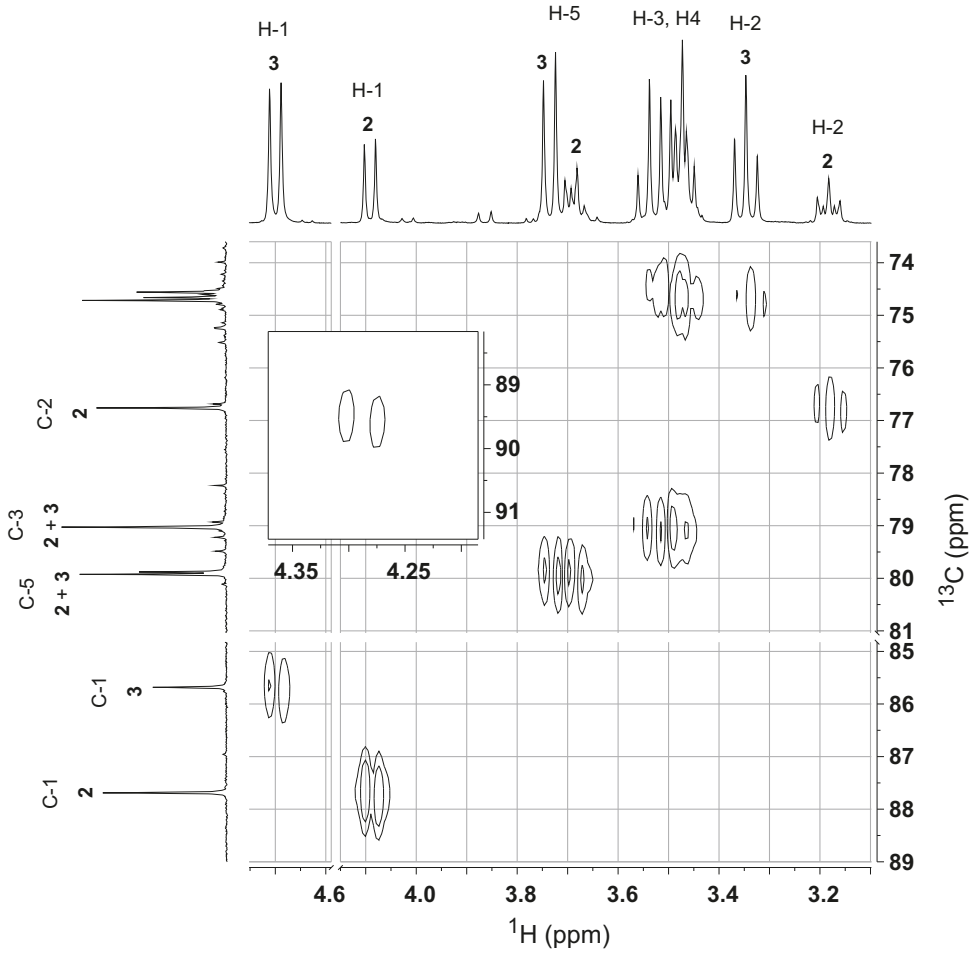

obtained, whereas the mole fraction of diglycosylamine (**4**) varied between 0% and 3%.

NMR data confirm the structure of compounds **2** and **3**, prove that **3**, **5**, **6**, and **7** are *N*-glycosylcarbamates, and indicate that **6** and **9** are indeed the α anomer of the main products **3** and **2**, respectively. Also, by combining NMR and ESI-MS results, we could prove that all intermediate species are constitutional isomers and (or) diastereomers of **2** and **3**. Finally, by monitoring the evolution of the composition of an early reaction sample redissolved in D_2O, we could prove that species **5**, **7**, **8**, **10**, and **11** are precursors of compounds **2**, **3**, **6**, and **9**, and that the α and β anomers of D-glucopyranosylamine uronic are initially formed in the same proportion, but the former gradually disappears in favour of the more stable β form. To the best of our knowledge, this is the first time that the α anomer has been observed during the formation of a β-glycosylamine. Based on these results, we propose Scheme 1 as the correct reaction scheme for the synthesis of the title compound in aqueous solution. Correct assignment for the ^{1}H and ^{13}C NMR spectra of D-glucuronic acid in D_2O were also established during the course of this study.

We are now applying the NMR protocol described herein to a kinetic study of the same reaction under different experimental conditions. The result of this study will be the object of a future communication.

Experimental

Materials and methods

Unless otherwise specified, all chemicals were reagent grade and used as received: D-glucuronic acid sodium salt monohydrate (99%, Fluka), D-glucurono-6,3-lactone (≥98.0%, Fluka), ammonium bicarbonate (≥99.0%, Fluka), ammonium carbamate (≥99.5%, Fluka), ammonia (~30% *w*/*w*, Carlo Erba), D_2O (99.9%-D, Euriso-top). Distilled or deionized water was used for all experiments.

Protocol numbering

Sodium D-glucuronate (**1**; Scheme 1) was reacted at 30 °C with ammonia and volatile ammonium salts (NH_4HCO_3 or $NH_2CO_2NH_4$) in water according to different protocols. The numbering of each protocol reveals the exact experimental conditions used. The first letter indicates the type of solid salt added (A, NH_4HCO_3; B, $NH_2CO_2NH_4$). The middle number indicates the initial formal concentration of liquid ammonia in mol/L. The last number indicates the initial formal concentration of salt in 10^{-1} mol/L. For example, A.1.06 indicates that the salt used was NH_4HCO_3 and that the initial concentration of ammonia and salt were 1 and 0.6 mol/L, respectively.

Can. J. Chem. Downloaded from www.nrcresearchpress.com by Xi'an Jiaotong University on 09/19/12
For personal use only.

Fig. 5. (*a*) Selected three bond ^{1}H–^{1}H homonuclear correlations (799.975 MHz) and (*b*) long distance ^{1}H–^{13}C heteronuclear correlations (799.975–201.172 MHz) for a sample obtained after 15 min of reaction at 30 °C according to protocol B.5.06.

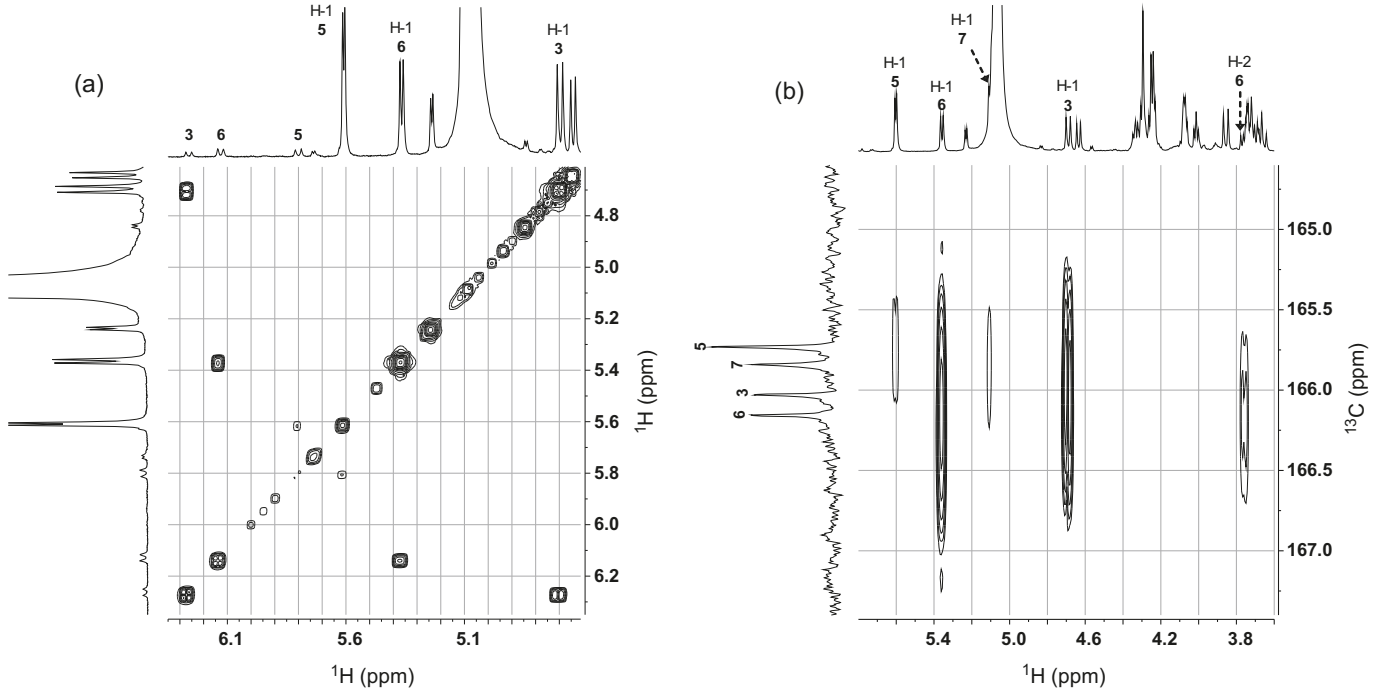

Can. J. Chem. Downloaded from www.nrcresearchpress.com by Xi'an Jiaotong University on 09/19/12
For personal use only.

MS nomenclature

In the nomenclature used to assign MS peaks, subscript symbols indicate the counterion. For example, $\mathbf{1}_{H}$ and $\mathbf{1}_{Na}$ indicate D-glucuronic acid and sodium D-glucuronate, respectively. The complete list of structures used for the interpretation of mass spectra is found in the Supplementary data.

Synthesis of β-D-glucopyranosylamine uronic acid

In a typical experiment (AG09–30_P2, protocol B.5.06), D-glucuronic acid sodium salt monohydrate (0.468 g, 2.0 mmol) and ammonium carbamate (0.468 g, 6.0 mmol) were weighed in a 25 mL round-bottomed flask. A magnetic bar was added together with 10 mL of aqueous ammonia (5 mol/L), the flask was sealed with a rubber septum, and a disposable needle (21G) was passed through the septum to prevent pressure buildup. The flask was plunged in an oil bath preheated at 30 °C and stirred at 200 rpm. At preset intervals, ~250 μL samples were drawn with a syringe, transferred to a glass vial, diluted with two volumes of water, and frozen in liquid nitrogen. All samples were then freeze-dried overnight and stored in a freezer (–18 °C) until needed. After 24 h, the molar composition as determined by ^{1}H NMR spectroscopy was **1**, 2%; **2**, 11%; **3**, 71%, **4**, 2%; **5**, 2%; **6**, 6%; **7**, 2%; **9**, 2%; **10**, 1%; and **8** + **11**, 1%.

Instrumental analyses

The composition of samples from the kinetic study was determined by NMR on a Bruker DPX400 spectrometer equipped with a variable temperature (VT) module (resonance frequency of 400.13 and 100.62 MHz for ^{1}H and ^{13}C nuclei, respectively). Two different 5 mm detection probes were used: QNP (direct) and BBIZ (inverse). Unless otherwise specified, 90° pulses and pulse sequence recycle times of 3 s were used. The probe temperature was calibrated in the range of 275–300 K using neat methanol. The NMR probe was pre-equilibrated at 278 K, individual samples were redissolved in D_2O (~3% *w*/*w*), transferred to an NMR tube, and immediately lowered into the instrument magnet for analysis. 1D ^{1}H spectra were obtained with 32 scans and 32 K data points and were reprocessed using MestReNova software (version 6.1). Sodium 3-(trimethylsilyl)propanoate (TSP) or sodium 3-(trimethylsilyl)propane-1-sulfonate (DSS) was used as an internal reference. Chemical shifts (in ppm) for ^{1}H and ^{13}C nuclei were referenced to $\delta_{TSP} = -0.017$ ppm (^{1}H) and $\delta_{TSP} = -0.149$ ppm (^{13}C) or to $\delta_{DSS} = 0.000$ ppm (^{1}H and ^{13}C).

Higher field NMR was used to identify peaks belonging to the different spin systems observed at early reaction times. Experiments were carried out on a Varian VNMRS 800 MHz spectrometer interfaced to a Dell Optiplex 755 computer using VnmrJ and equipped with a 5 mm triple-resonance (^{1}H, ^{13}C, and ^{15}N) cryoprobe including shielded z gradients. All data were processed on a Dell HP xw4400 using TopSpin software or a Dell Optiplex 755 computer using VnmrJ software. The probe was pre-equilibrated at 278 K, and samples were prepared by dissolving the starting compound in D_2O (0.600 mL) with the addition of TSP as an internal reference. Immediately after dissolution, samples were lowered into the instrument magnet and spectra were recorded at 278 K. 1D 799.975 MHz ^{1}H spectra were recorded before and after each set of 2D experiments to check medium modification with time. Each 1D ^{1}H spectrum was collected, without water suppression, with 32 scans of 32 K data points over a 9050 Hz spectral width. 1D 201.172 MHz ^{13}C spectra were obtained with power gated proton decoupling using the WALTZ-16 sequence and 1 K scans of 64 K points on

Fig. 6. ESI-MS spectrum of **1** (*a*), a sample containing 65% transient species (*b*), and **2** + **3** (*c*). Positive (top) and negative (bottom) ions are shown. In some cases, the intensity of the peaks on the right-hand side of the spectrum was magnified.

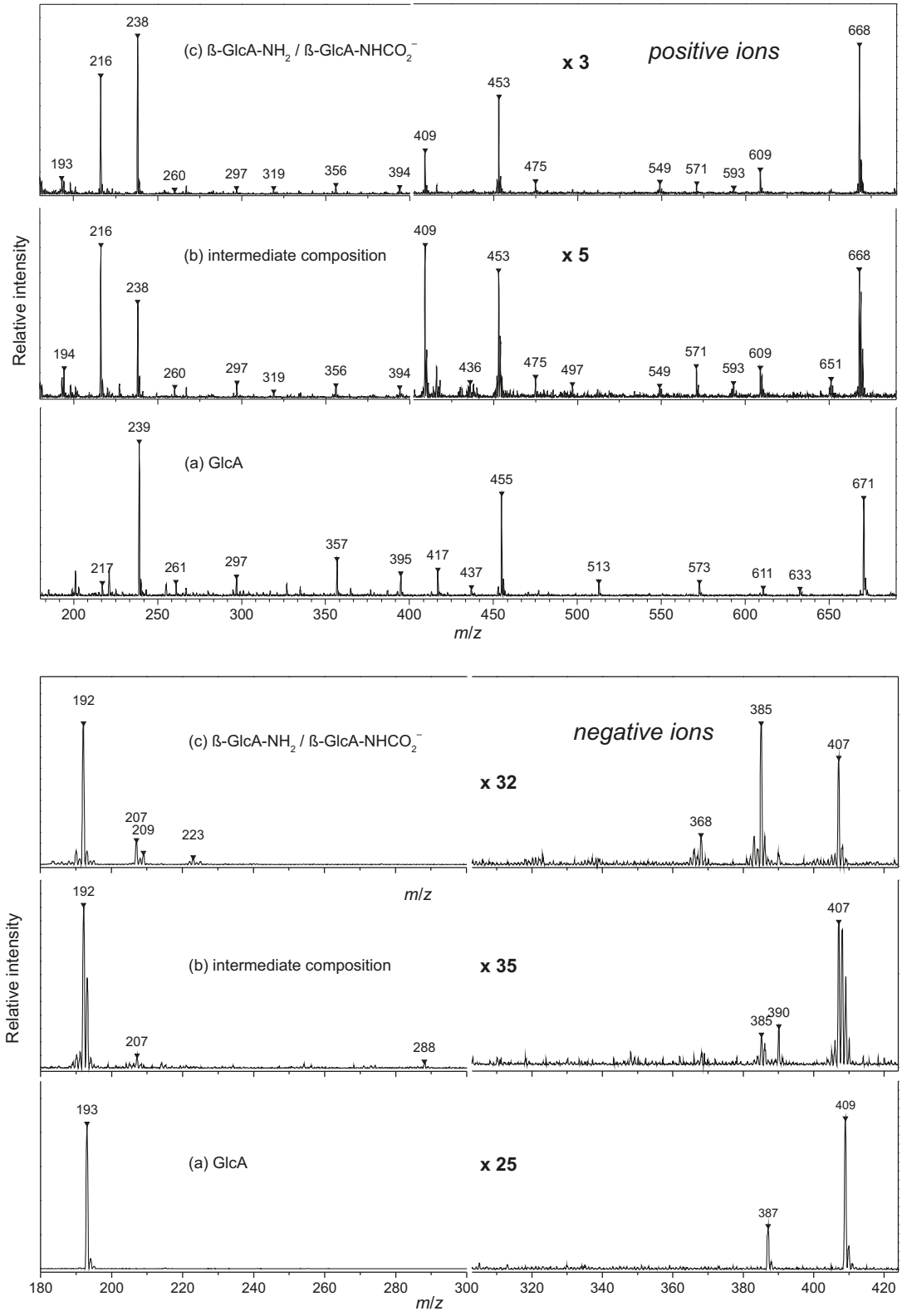

50 000 Hz of spectral width. All 2D experiments were recorded with a continuous wave pulse of 35 Hz presaturation field on the water signal during the 1.5 s relaxation delay. 2D gradient-selected 799.975 MHz ^{1}H–^{1}H COSY spectra were acquired in the absolute value mode. ^{1}H–^{1}H TOCSY spectra (799.975 MHz) used a z-filtered DIPSI-2 spin lock of 8.3 kHz power, 120 ms duration, and were acquired in the sensitive phase mode using States method for quadrature detection.

Can. J. Chem. Downloaded from www.nrcresearchpress.com by Xi'an Jiaotong University on 09/19/12
For personal use only.

Can. J. Chem. Downloaded from www.nrcresearchpress.com by Xi'an Jiaotong University on 09/19/12
For personal use only.

Table 3. List of ESI-MS peaks and their assignments.

m/z					Spectrum of observation		
Experimental	Monoisotopic ion mass	Structure	Ionization		**1**	Intermediate[a]	**2/3**[b]
192	192.1	$\mathbf{2}_{H}$	–	$[M - H]^-$		✓	✓
193	193.0	$\mathbf{1}_{H}$	–	$[M - H]^-$	✓	✓	
194	194.1	$\mathbf{2}_{H}$	+	$[M + H]^+$	✓	✓	
207		?	–	?		✓	✓
209		?	–	?			✓
216	216.0	$\mathbf{2}_{Na}$	+	$[M + H]^+$		✓	✓
217	217.0	$\mathbf{1}_{H}$	+	$[M + Na]^+$	✓		
223		?	–	?			✓
225		?	–	?			✓
238	238.0	$\mathbf{2}_{Na}$	+	$[M + Na]^+$		✓	✓
	238.0	$\mathbf{3}_{H, H}$	+	$[M + H]^+$			
239	239.0	$\mathbf{1}_{Na}$	+	$[M + Na]^+$	✓	✓	
260	260.0	$\mathbf{3}_{H, H}$	+	$[M + Na]^+$		✓	✓
261		?	+	?	✓		
267		?	+	?		✓	✓
297		?	+	?	✓	✓	✓
319		?	+	?		✓	✓
356		?	+	?		✓	✓
357		?	+	?	✓		
368	368.1	$\mathbf{4}_{H,H}$	–	$[M - H]^-$			✓
385	385.1	$(\mathbf{2}_{H})_2$	–	$[M - H]^-$		✓	✓
387	387.1	$(\mathbf{1}_{H})_2$	–	$[M - H]^-$	✓		
390	390.1	$\mathbf{4}_{Na,H}$	–	$[M - H]^-$		✓	✓
394		?	+	?		✓	✓
395		?	+	?	✓		
407	407.1	$(\mathbf{2}_{Na})\mathbf{2}_{H}$	–	$[M - H]^-$		✓	✓
409	409.2	$(\mathbf{2}_{Na})\mathbf{2}_{H}$	+	$[M + H]^+$	✓	✓	
	409.1	$\mathbf{4}_{Na,NH_4}$	+	$[M + H]^+$			
417		?	+	?	✓		
437		?	+	?	✓		
452	452.2	$\mathbf{4}_{Na, Na}$	+	$[M + K]^+$		✓	✓
453	453.1	$(\mathbf{2}_{Na})_2$	+	$[M + Na]^+$		✓	✓
455	455.0	$(\mathbf{1}_{Na})_2$	+	$[M + Na]^+$	✓		
475		?	+	?		✓	✓
497		?	+	?		✓	✓
549		?	+	?		✓	✓
513		?	+	?	✓		
571		?	+	?		✓	✓
593		?	+	?		✓	✓
609		?	+	?		✓	✓
611		?	+	?	✓		
633		?	+	?	✓		
651		?	+	?		✓	✓
668	668.1	$(\mathbf{2}_{Na})_3$	+	$[M + Na]^+$		✓	✓
671	667.1	$(\mathbf{1}_{Na})_3$	+	$[M + Na]^+$	✓		

[a]Sample obtained after 15 min of reaction at 30 °C according to protocol B.5.06 (AG10–08); the initial mole fraction of intermediate species was 65%.

[b]Sample obtained after 48 h at 30 °C according to protocol B.0.S (AG10–20_P1_end); the initial mole fraction of **2** + **3** was 89%.

For COSY and TOCSY spectra, 512 equally spaced evolution time period values were acquired, averaging 16 transients of 2 K points, with 9470 Hz of spectral width. 2D gradient-selected (799.975–201.172 MHz) ^1H–^{13}C HSQC with GARP sequence ^{13}C decoupling during acquisition was obtained in the sensitive-phase mode using echo–antiecho detection. Equally spaced evolution time period values (512) were acquired, averaging 14 transients of 1518 points, with 7300 and 3811 Hz in *F*1 and *F*2, respectively. Evolution delay for $^1J_{CH}$ amounted to 1.7 ms ($1/(4\cdot{}^1J_{CH})$). 2D gradient-selected (799.975–201.172 MHz) ^1H–^{13}C HMBC via heteronuclear zero and double quantum coherence with a low-pass J filter to suppress on-bond correlation and no ^{13}C decoupling during acquisition was achieved in the absolute mode value.

Can. J. Chem. Downloaded from www.nrcresearchpress.com by Xi'an Jiaotong University on 09/19/12
For personal use only.

Fig. 7. Evolution of the composition with time for a sample obtained after 15 min of reaction, isolated by freeze-drying, and redissolved in D_2O at 278 K. The percentage values annotated over the graph specify the mass concentration of the sample in solution.

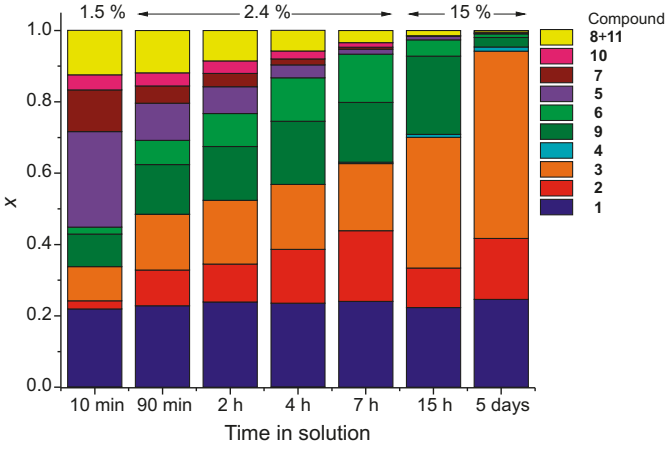

Equally spaced evolution time period values (512) were acquired, averaging 32 transients of 2426 points, with 44248 and 9470 Hz in $F1$ and $F2$, respectively. Evolution delay for low pass $^1J_{CH}$ filter and for evolution of long-range coupling amounted to 3.6 ms ($1/(2\cdot{}^1J_{CH})$) and 70 ms ($1/(2*^nJ_{CH})$), respectively.

Mass spectrometry analyses were performed with a Waters ZQ (Altrincham, UK) single quadrupole atmospheric pressure ionization mass spectrometer fitted with a Z-electrospray interface (ESI). The instrument was calibrated with mass spectra generated by ion-spray ionization of a 0.1 mol/L solution of sodium iodide in aqueous acetonitrile (50%, *v*/*v*) in the mass range of 23–1972 amu. Nitrogen was used as the drying and nebulizing gas. Samples (~1 mg/L) were dissolved in deionized water and infused to the ESI interface at constant flow rate (50 μL/min).

Supplementary data

Supplementary data (1D and 2D NMR spectra on which peak assignment and structural elucidation were based and the list of structures used for the interpretation of mass spectra) are available with the article through the journal Web site (www.nrcresearchpress.com/cjc).

Acknowledgment

We thank the French Ministère de l'Enseignement supérieur et de la Recherche, the Réseau de Recherche Chimie pour le Développement Durable (CNRS-INRA), the Région Rhône-Alpes (Cluster Chimie), the Agence Nationale de la Recherche Scientifique (ANR-09-CP2D-02), and the TGE RMN THC Fr3050 for financial support. We also thank I. Jeacomine, S. Boullanger, and Dr. B. Brasme for their assistance with NMR and MS analyses.

References

(1) McNaught, A. D. *Pure Appl. Chem.* **1996** *68* (10), 1919. doi:10.1351/pac199668101919.
(2) Kamoda, S.; Nakano, M.; Ishikawa, R.; Suzuki, S.; Kakehi, K. *J. Proteome Res.* **2005** *4* (1), 146. doi:10.1021/pr049825o.
(3) Likhosherstov, L. M.; Novikova, O. S.; Shibaev, V. N. *Russ. Chem. Bull.* **1998** *47* (6), 1214. doi:10.1007/BF02503499.
(4) Vetter, D.; Tate, E. M.; Gallop, M. A. *Bioconjug. Chem.* **1995** *6* (3), 319. doi:10.1021/bc00033a014.
(5) Ishiwata, A.; Takatani, M.; Nakahara, Y.; Ito, Y. *Synlett* **2002** *2002* (4), 634. doi:10.1055/s-2002-22716.
(6) Monsigny, M.; Quetard, C.; Bourgerie, S.; Delay, D.; Pichon, C.; Midoux, P.; Mayer, R.; Roche, A. C. *Biochimie* **1998** *80* (2), 99. doi:10.1016/S0300-9084(98)80016-3.
(7) Zeng, X.; Murata, T.; Kawagishi, H.; Usui, T.; Kobayashi, K. *Biosci. Biotechnol. Biochem.* **1998** *62* (6), 1171. doi:10.1271/bbb.62.1171.
(8) Plusquellec, D.; Brenner-Henaff, C.; Leon-Ruaud, P.; Duquenoy, S.; Lefeuvre, M.; Wroblewski, H. *J. Carbohydr. Chem.* **1994** *13* (5), 737. doi:10.1080/07328309408011677.
(9) Mellet, C. O.; Blanco, J. L. J.; Fernandez, J. M. G.; Fuentes, J. *J. Carbohydr. Chem.* **1993** *12* (4–5), 487. doi:10.1080/07328309308019403.
(10) Urge, L.; Otvos, L., Jr; Lang, E.; Wroblewski, K.; Laczko, I.; Hollosi, M. *Carbohydr. Res.* **1992** *235*, 83. doi:10.1016/0008-6215(92)80080-K.
(11) Likhosherstov, L. M.; Novikova, O. S.; Derevitskaya, V. A.; Kochetkov, N. K. *Carbohydr. Res.* **1986** *146* (1), C1. doi:10.1016/0008-6215(86)85037-6.
(12) Halila, S.; Manguian, M.; Fort, S.; Cottaz, S.; Hamaide, T.; Fleury, E.; Driguez, H. *Macromol. Chem. Phys.* **2008** *209* (12), 1282. doi:10.1002/macp.200700629.
(13) Retailleau, L.; Laplace, A.; Fensterbank, H.; Larpent, C. *J. Org. Chem.* **1998** *63* (3), 608. doi:10.1021/jo971486d.
(14) Lubineau, A.; Auge, J.; Drouillat, B. *Carbohydr. Res.* **1995** *266* (2), 211. doi:10.1016/0008-6215(94)00275-K.
(15) Tuzikov, A. B.; Gambaryan, A. S.; Juneja, L. R.; Bovin, N. V. *J. Carbohydr. Chem.* **2000** *19* (9), 1191. doi:10.1080/07328300008544143.
(16) Kallin, E.; Loenn, H.; Norberg, T.; Elofsson, M. *J. Carbohydr. Chem.* **1989** *8* (4), 597. doi:10.1080/07328308908048020.
(17) Rice, K. G. *Anal. Biochem.* **2000** *283* (1), 10. doi:10.1006/abio.2000.4644.
(18) Manger, I. D.; Rademacher, T. W.; Dwek, R. A. *Biochemistry* **1992** *31* (44), 10724. doi:10.1021/bi00159a012.
(19) Lobry de Bruyn, C. A.; Franchimont, A. P. N. *Recl. Trav. Chim. Pays Bas* **1893** *12*, 286. doi:10.1002/recl.18930121103.
(20) Lobry de Bruyn, C. A.; Van Leent, F. H. *Recl. Trav. Chim. Pays Bas* **1896** *15*, 81. doi:10.1002/recl.18960150303.
(21) Lobry de Bruyn, C. A. *Recl. Trav. Chim. Pays Bas* **1895** *14*, 98. doi:10.1002/recl.18950140305.
(22) Hodge, J. E.; Moy, B. F. *J. Org. Chem.* **1963** *28* (10), 2784. doi:10.1021/jo01045a071.
(23) Likhosherstov, L. M.; Novikova, O. S.; Shibaev, V. N.; Kochetkov, N. K. *Russ. Chem. Bull.* **1996** *45* (7), 1760. doi:10.1007/BF01431821.
(24) Vetter, D.; Gallop, M. A. *Bioconjug. Chem.* **1995** *6* (3), 316. doi:10.1021/bc00033a013.
(25) Fulks, G.; Fisher, G. B.; Rahmoeller, K.; Wu, M.-C.; D'Herde, E.; Tan, J. A Review of Solid Materials as Alternative Ammonia Sources for Lean NOx Reduction with SCR. In *Diesel Exhaust Emission Control, 2009*, SAE International: Warrendale, PA, 2009; pp 2009–2001–0907.
(26) Likhosherstov, L. M.; Novikova, O. S.; Shibaev, V. N. *Dokl. Chem.* **2003** *389* (4–6), 73. doi:10.1023/A:1023484306457.
(27) Likhosherstov, L. M.; Novikova, O. S.; Shibaev, V. N. *Dokl. Chem.* **2002** *383* (4–6), 89. doi:10.1023/A:1015428720733.
(28) For a short review on the subject seeMonsigny, M.; Quetard, C.; Bourgerie, S.; Delay, D.; Pichon, C.; Midoux, P.; Mayer,

R.; Roche, A. C. *Biochimie* **1998** *80* (2), 99. doi:10.1016/S0300-9084(98)80016-3.
(29) Campa, C.; Donati, I.; Vetere, A.; Gamini, A.; Paoletti, S. *J. Carbohydr. Chem.* **2001** *20* (3–4), 263. doi:10.1081/CAR-100104862.
(30) Isbell, H. S.; Frush, H. L. *J. Am. Chem. Soc.* **1950** *72* (2), 1043. doi:10.1021/ja01158a527.
(31) Isbell, H. S.; Frush, H. L. *J. Org. Chem.* **1958** *23* (9), 1309. doi:10.1021/jo01103a019.
(32) Frush, H. L.; Isbell, H. S. *J. Res. Natl. Bur. Stand. (U. S.)* **1951** *47* (4), 239.
(33) Vandamme, E. J.; De Baets, S.; Steinbüchel, A. *Polysaccharides II: Polysaccharides from Eukaryotes;* Wiley-VCH: Weinheim, 2002.
(34) Timoshchuk, V. A. *Russ. Chem. Rev.* **1995** *64* (7), 675. doi:10.1070/RC1995v064n07ABEH000169.
(35) van den Bos, L. J.; Codée, J. D. C.; Litjens, R. E. J. N.; Dinkelaar, J.; Overkleeft, H. S.; van der Marel, G. A. *Eur. J. Org. Chem.* **2007** *2007* (24), 3963. doi:10.1002/ejoc.200700101.
(36) Keglevic, D. *Adv. Carbohydr. Chem. Biochem.* **1979** *36*, 57. doi:10.1016/S0065-2318(08)60235-8.
(37) Only the salt with carbamic acid was isolated.
(38) Experiments (*b*) AG09–13, and (*c*) AG09–30_P1. Conditions: D_2O, 278 K, $\delta(^1H)$ TSP = –0.017 ppm, $\delta(^{13}C)$ TSP = –0.149 ppm.
(39) Experiment WM08–P2_final, 30 °C, 25 h.
(40) Conditions: D_2O, 6.4% *w/w*, 298 K, $\delta(^1H)$ TSP = –0.017 ppm. Sample obtained at 30 °C according to protocol A.0.S (WM-08_P1_final). Its initial molar composition was as follows: **1**, 12%; **2**, 42%; **3**, 37%; **4–11**, 9%. The projections do not correspond to the same sample.
(41) Conditions: D_2O, 298 K, 5.3% *w/w*, $\delta(^1H)$ TSP = –0.017 ppm. Sample obtained at 30 °C according to protocol B.9.03 (WM-08_P3 final). Its initial molar composition was as follows: **1**, 6%; **2**, 55%; **3**, 30%; **4–11**, 9%.
(42) Conditions: D_2O, 298 K, 5.3% *w/w*, $\delta(^1H)$ TSP = –0.017 ppm. Sample obtained at 30 °C according to protocol B.9.03 (WM-08_P3 final). The projections do not refer to the same sample.
(43) Bock, K.; Pedersen, C.; Tipson, R. S.; Horton, D. *Adv. Carbohydr. Chem. Biochem.* **1983** *41*, 27. doi:10.1016/S0065-2318(08)60055-4.
(44) Altona, C.; Haasnoot, C. A. G. *Org. Magn. Reson.* **1980** *13* (6), 417. doi:10.1002/mrc.1270130606.
(45) Pfeffer, P. E.; Valentine, K. M.; Parrish, F. W. *J. Am. Chem. Soc.* **1979** *101* (5), 1265. doi:10.1021/ja00499a036.
(46) 2D gradient-selected ^1H–^1H COSY (AG10–08) and ^1H–^{13}C HMBC (AG10–16) spectrum, D_2O, 15% *w/w*, 278 K.
(47) Internal results from our laboratory.
(48) Ritchie, R. G. S.; Cyr, N.; Korsch, B.; Koch, H. J.; Perlin, A. S. *Can. J. Chem.* **1975** *53* (10), 1424. doi:10.1139/v75-197.
(49) Williams, C.; Allerhand, A. *Carbohydr. Res.* **1977** *56* (1), 173. doi:10.1016/S0008-6215(00)84250-0.
(50) Experiment AG10–20_P1_end. Its initial molar composition as determined by ^1H NMR was: **1**, 2%; **2**, 25%; **3**, 63%, **4**, 1%; **5**, 1%; **6**, 5%; **7**, 0%; **9**, 2%; **10**, 0%, **8** + **11**, 1%.
(51) Experiment AG10–08. Its initial molar composition as determined by ^1H NMR was: **1**, 22%; **2**, 3%; **3**, 10%; **4**, 0%; **5**, 27%; **6**, 9%; **7**, 11%; **9**, 2%; **10**, 5%; **8** + **11**, 12%.
(52) Experiment AG10–08, protocol **B**.5.06, 30 °C. Mole fractions lower than 0.5% were disregarded.

Can. J. Chem. Downloaded from www.nrcresearchpress.com by Xi'an Jiaotong University on 09/19/12
For personal use only.

Preparation and photocatalytic activity of TiO_2 nanocomposites coated with monolayer-protected gold clusters

Piyadarsha Amaratunga, Myeongsoon Lee, Junhyung Kim, and Dongil Lee

Can. J. Chem. Downloaded from www.nrcresearchpress.com by Xi'an Jiaotong University on 09/19/12
For personal use only.

Abstract: We report the preparation and photocatalytic activity of TiO_2 nanocomposites modified with monolayer-protected gold clusters (MPCs). Highly monodisperse tiopronin-coated MPCs with core diameters of 2.2 ± 0.2 nm were pre-prepared and then anchored onto a TiO_2 surface using the bifunctional tiopronin linker. In this method, the gold core size was preserved after calcination at 260 °C as well as the anchoring process, and the gold loading on TiO_2 could be precisely controlled by the experimental condition. The photocatalytic degradation of Rhodamine 590 (Rh-590) was carried out with thus prepared MPC–TiO_2 composites. Mechanistic study of the photocatalytic reactions revealed that the degradation of Rh-590 occurs via the oxidative pathway by photogenerated holes. The photocatalytic activity of the MPC–TiO_2 composites was found to increase significantly upon calcination at 260 °C, whereas the size of gold particles remained at their initial size. The photocatalytic activity of the composites, however, drastically decreased when the composites were calcined at 400 °C. X-ray photoelectron spectroscopy analysis of the calcined composites was conducted to understand the vastly different calcination results. A significant amount of oxidized sulfur remained in the composites after calcination at 400 °C, which appears to be responsible for the drastic decrease in the photocatalytic activity.

Key words: monolayer-protected gold cluster, photocatalyst, TiO_2, tiopronin, thermal activation, nanocomposite.

Résumé : On a préparé et déterminé les propriétés photocatalytiques de nanocomposites de TiO_2 modifiés par des agrégats d'or protégés par une monocouche (APM). On a procédé en effectuant une préparation préliminaire d'APM hautement monodispersé recouverte de tiopronine dont le diamètre de la partie de coeur est de 2,2 ± 0,2 nm et on l'a ensuite ancré sur une surface de TiO_2 faisant appel à la tiopronine, un réticulant bifonctionnel. Dans cette méthode, la taille de la zone de coeur d'or est maintenue après avoir été soumise au processus d'ancrage et une calcination à 260 °C et la fixation de l'or sur le TiO_2 peut être contrôlée avec précision par les conditions expérimentales. On a procédé à la dégradation photocatalytique de la Rhodamine 590 (Rh-590) à l'aide des composites APM-TiO_2 ainsi préparés. L'étude du mécanisme des réactions photocatalytiques a permis de montrer que la dégradation de la Rh-590 se produit par le biais d'une voie oxydante impliquant des trous photogénérés. On a trouvé que l'activité catalytique des composites APM-TiO_2 augmente considérablement par calcination à 260 °C alors que la taille des particules d'or maintiennent leur taille initiale. Toutefois, l'activité catalytique des composites diminuent considérablement lorsque les composites sont calcinés à 400 °C. On a effectué des analyses par spectroscopie photoélectronique des rayons-X des composites calcinés dans le but de comprendre les résultats si différents de ces calcinations. Il semble qu'une quantité significative résiduelle de soufre oxydé dans les composites après la calcination à 400 °C soit la cause de cette diminution drastique de l'activité catalytique.

Mots-clés : agrégat d'or protégé par une monocouche (APM), photocatalyseur, TiO_2, tiopronine, activation thermique, nanocomposite.

[Traduit par la Rédaction]

Introduction

Metal-coated semiconductor nanoparticles have been the focus of numerous investigations over the last few years in photocatalysis relevant to solar energy conversion and environmental cleanup.[1–3] Contact of metal with the semiconductor indirectly influences the energetics and charge-transfer processes. For example, single-component semiconductor nanoparticles exhibit relatively poor photocatalytic efficiency, since the majority of the photogenerated charge carriers undergo recombination.[4] Semiconductor – metal composite nanoparticles on the other hand facilitate charge separation by rectifying the direction of the flow of electrons and holes in these systems.[5–7] Various preparative methods, for example, chemical, electrochemical, photochemical deposition, and deposition–precipitation methods have been used for the

Received 5 January 2011. Accepted 18 March 2011. Published at www.nrcresearchpress.com/cjc on 17 August 2011.

P. Amaratunga. Department of Chemistry, Western Michigan University, Kalamazoo, MI 49008, USA.
M. Lee and D. Lee. Department of Chemistry, Yonsei University, Seoul 120-749, Korea.
J. Kim. Department of Chemistry, Western Michigan University, Kalamazoo, MI 49008, USA; Department of Chemistry, Yonsei University, Seoul 120-749, Korea.

Corresponding author: Dongil Lee (e-mail: dongil@yonsei.ac.kr).

Scheme 1. Schematic illustration (not to scale) of photoexcitation, charge separation, and photocatalytic reactions in a monolayer-protected gold cluster (MPC) – TiO_2 nanocomposite. Only one tiopronin ligand is shown for clarity.

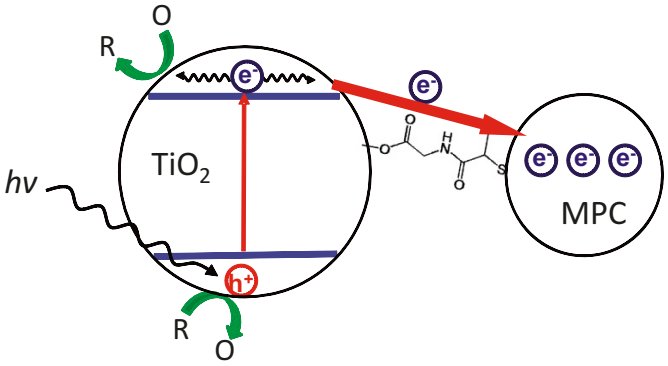

preparation of nano-sized metal deposits on metal oxide surfaces.[8] However, these methods typically produce polydisperse particles and it is very difficult to control the deposit formation experimentally.[9,10] This is the major challenge in the optimization of such semiconductor – metal composite nanoparticles that often exhibit critically size-dependent catalytic activities.[11] In this article, we present an improved method to prepare TiO_2 photocatalysts modified with uniform monolayer-protected gold clusters (MPCs).[12]

MPCs are stable, structurally and energetically well-defined nanoparticles whose size and core and ligand compositions are precisely characterized by a variety of analytical methods.[13,14] One of the most interesting properties of these has been the ability to control the transfer of electrons into and out of the metallic core.[14,15] Once charge transfer takes place, the MPC acts as a capacitor storing the charge within its core. The long-term storage of charge on the MPC core is a fundamental result of the conductive metal-core-insulating protecting shell structure.[16–20] In our previous work,[21] we investigated the photocatalytic activity of composite photocatalysts prepared by anchoring Au MPCs onto TiO_2 nanoparticles using a bifunctional linker. The MPC–TiO_2 composites showed considerably enhanced photocatalytic activity for the reduction of Uniblue A in deaerated CH_3OH–H_2O in which CH_3OH acts as an efficient hole scavenger. In another study,[22] we showed that electron transfer spontaneously occurs from the photoexcited TiO_2 nanoparticles to Au MPCs in their colloidal mixtures and that the electron transfer efficiency is determined by the MPC core size.

In the interest of utilizing the photoholes generated in MPC–TiO_2 composites, we investigate the photocatalytic activity of the composites in the absence of the hole scavenger. As illustrated in Scheme 1, band-gap illumination of TiO_2 colloids excites electrons to the conduction band and generates holes in the valence band. These photogenerated electrons and holes recombine immediately in aqueous media.[23] When MPCs are attached to the TiO_2 surface, these photoelectrons preferentially transfer to the gold cores and are stored on them.[22] It has been found that electron transfer from the photoexcited TiO_2 to Au MPC is thermodynamically favorable and it proceeds until the Fermi levels of TiO_2 and MPC are equilibrated.[5,22,24] This process would enhance the charge separation efficiency in MPC–TiO_2 composites and, as a result, more holes and electrons are available for further reactions. Both of these separated charges are capable of initiating subsequent reactions. In an aqueous environment, holes are scavenged by the hydroxyl ions on the surface of TiO_2, producing hydroxyl radicals. It is well-established that the hydroxyl radical is the primary source behind the photocatalytic activity of TiO_2.[25–27] Hydroxyl radicals are capable of oxidizing many of the organic species present.[28] Successful degradation of aliphatic compounds,[29,30] aromatic compounds,[31,32] inorganic compounds,[33,34] and surfactants[35] have been demonstrated previously.

In this work, highly monodisperse gold nanoparticles were presynthesized and then attached onto TiO_2 using a bifunctional linker (tiopronin) to form MPC–TiO_2 composites. In this method, the gold loading on TiO_2 could be facilely and precisely controlled by manipulating the experimental conditions. The photocatalytic activity of the MPC–TiO_2 composites was examined with a model dye, Rhodamine 590 (Rh-590). The degradation of Rh-590 was found to occur via an oxidative pathway and was significantly enhanced with MPC–TiO_2 composites calcined at 260 °C. The photocatalytic activity of the composites, however, drastically decreased when the composites were calcined at 400 °C. X-ray photoelectron spectroscopy analysis of the calcined composites revealed that a significant amount of oxidized sulfur remained after calcination at 400 °C, which appears to cause a drastic decrease in the photocatalytic activity. This result reveals the critical role of ligands in MPC-modified photocatalysts.

Experimental

Materials

Hydrogen tetrachloroaurate trihydrate ($HAuCl_4 \cdot 3H_2O$, ACS reagent grade), tiopronin, acetonitrile, sodium borohydride, and methanol were purchased from Sigma-Aldrich. TiO_2 nanoparticles (Aeroxide P25) was purchased from Acros Organics. Acetic acid (A.C.S. grade) was purchased from J. T. Baker. Rh-590 was purchased from Exciton. All chemicals were used as received. Water was purified using a Milli-Q system (Purelabsplus UV/UF, 18.2 MΩ cm).

Synthesis of tiopronin-protected MPCs

Tiopronin-coated MPCs were synthesized according to literature procedure[36] with some modifications. In a typical reaction, 1.85 g (4.69 mmol) of $HAuCl_4 \cdot 3H_2O$ and 4.85 g (29.7 mmol) of tiopronin were codissolved in 211 mL of a 6:1 (*v*/*v*) methanol – acetic acid mixture, giving a ruby red solution. This solution was rapidly stirred for 1 h. The color gradually disappeared and the solution became colorless. To this solution, sodium borohydride 3.59 g (94.8 mmol) dissolved in 190 mL of H_2O was added with rapid stirring, and the stirring was continued for another 45 min. The solvent was then rotary evaporated under vacuum at 38 °C to near dryness to produce a black gooey product. Monodisperse MPCs with an average core diameter of 2.2 ± 0.2 nm (Fig. S1, Supplementary data) were isolated by methanol extraction from the product.

Can. J. Chem. Downloaded from www.nrcresearchpress.com by Xi'an Jiaotong University on 09/19/12
For personal use only.

Can. J. Chem. Downloaded from www.nrcresearchpress.com by Xi'an Jiaotong University on 09/19/12
For personal use only.

Fig. 1. Transmission electron microscopy (TEM) images of (A) 1 wt% monolayer-protected gold cluster (MPC) – TiO_2 and (B) 3 wt% MPC–TiO_2. Scale bar = 50 nm.

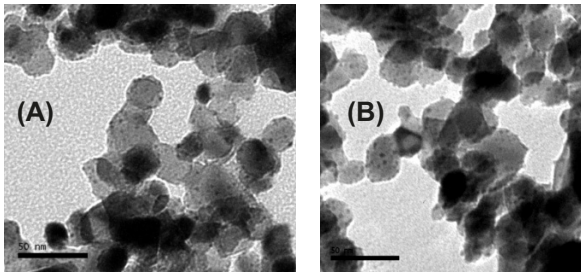

Preparation and characterization of MPC–TiO_2 composites

MPC–TiO_2 composites were prepared by anchoring tiopronin–MPCs onto TiO_2 nanoparticles. TiO_2 nanoparticles were dispersed in water by simultaneous shaking and sonicating for 30 s prior to the MPC anchoring reaction. The primary size of TiO_2 nanoparticles was ca. 20 nm as shown in Fig. 1. The anchoring of MPCs onto TiO_2 was carried out by dissolving an appropriate amount of MPC (Au/TiO_2 = 1%–6% *w*/*w*) in 20 mL of a TiO_2 aqueous suspension (5 g/L) and stirring the mixture for 3 h. After the anchoring reaction, the MPC–TiO_2 composites were centrifuged and dried. Complete anchoring of MPCs on TiO_2 was confirmed by the clear supernatant of the anchoring mixture after centrifugation. Composites were stored in a freezer and redissolved in water prior to photocatalytic reactions. To prepare calcined MPC–TiO_2 composites, the MPC–TiO_2 composites were thermally treated at 260 or 400 °C in air in a muffle furnace (heating rate = 8.3 °C/min, holding time = 30 min). Tiopronin-coated TiO_2 nanoparticles were prepared by stirring TiO_2 in an aqueous tiopronin solution that contained an equivalent amount of tiopronin to 3 wt% MPC–TiO_2.

Transmission electron microscopy (TEM) images of MPC–TiO_2 were obtained with a JEOL JEM-1230 operating at 80 kV. The TEM samples were prepared by drop casting of an MPC–TiO_2 suspension on a carbon-coated copper grid (400C-FC, Electron Microscopy Sciences, Hatfield, Pennsylvania). To enhance the interaction between the TEM grid and the hydrophilic composites, the grid was fumed with nitric acid to make it hydrophilic. Thermogravimetric analysis (TGA) was performed with a Scinco STA-1500. X-ray photoelectron spectroscopy experiments were carried out on Sigma Probe spectrometer (Thermo VG, UK) using monochromatic Al Kα X-ray source (1486.6 eV). Binding energies (BE) were calibrated with respect to carbon 1s at 284.5 eV.

Photocatalysis experiments

To an MPC–TiO_2 suspension in water (15 mg/L), Rh-590 solution was added to bring the initial concentration (C_0) to 10 μmol/L just before the photolysis experiment. Photolysis experiments were performed with a 300 W xenon lamp in a quartz cuvette while stirring the solution magnetically. Light was filtered through an UV cutoff filter (λ > 320 nm, UV-32, HOYA) and an IR filter (HA-30, HOYA). Absorption spectra of the reaction mixture was recorded in situ with a portable spectrometer (DH2000-BAL/H2000, Ocean Optics), at 1 min intervals for 30 min. A set of triplicate measurements were carried out for each photocatalytic experiment.

Results and discussion

Anchoring of MPCs onto TiO_2

It is well-known that carboxylic acid groups readily bind to the TiO_2 surface via ester- or carboxylate-type linkages.[37] Thus, tiopronin-coated MPCs were directly reacted with bare TiO_2 to produce MPC–TiO_2 composites. As can be seen in Fig. 1, after 3 h of the anchoring reaction, most of the MPCs appear to be bound to TiO_2. Therefore, the anchoring reaction of MPCs onto TiO_2 was carried out for 3 h. The MPC loading on TiO_2 can be experimentally controlled by simply varying the initial concentration of MPCs in the mixture, showing the advantage of this approach. Figures 1A and 1B, respectively, show TEM images of thus prepared 1 and 3 wt% MPC-loaded composites. It can be clearly seen in the figures that the MPC loading is indeed controlled by controlling the MPC concentration in the mixture. The MPC loading could be precisely controlled up to 6 wt%. However, there are some unbound MPCs remaining in the anchoring mixture above 6 wt%. Regardless of the loading %, the MPC core size was unchanged from its initial size of 2.2 ± 0.2 nm, and no obvious aggregation of MPC on TiO_2 was observed throughout the binding process.

Photocatalytic reaction of MPC–TiO_2 composites — Mechanistic study

In the present study, the photocatalytic activity of the MPC–TiO_2 nanoparticle composite was investigated by monitoring the degradation of Rh-590 during photocatalysis. As can be seen in Fig. 2, Rh-590 initially exhibits an intense absorption band at 525 nm. The orange color of Rh-590 gradually disappears during the reaction and turns colorless upon complete degradation. Band-gap illumination of TiO_2 colloids in water excites electrons to the conduction band, leaving holes in the valence band. While most of photoelectrons and photoholes generated in the semiconductor recombine immediately after the excitation process,[38–40] some separated electrons and holes can diffuse to the semiconductor surface and react with the molecular species adsorbed on the TiO_2 surface.[41] The Rh-590 degradation can occur via a reductive or an oxidative pathway by electrons and holes, respectively, generated in the photoexcited semiconductor.[42,43] In photocatalytic reduction and oxidation of Rhodamine B, an analog of Rh-590, in the presence of TiO_2 sols, Takahashi and coworkers[44] revealed that a new absorption band at 420 nm is observed in the reductive pathway but not in the oxidation pathway. This band was assigned to the partially reduced radical of Rhodamine B.[45] The absence of the 420 nm band in Fig. 2 suggests that the degradation of Rh-590 is likely to occur via the oxidative pathway, presumably through N-de-ethylation and (or) destruction of the conjugate structure.[43] Additionally, the degradation of Rh-590 is found to be irreversible, which is also consistent with the oxidative pathway. The oxidative pathway is further confirmed by SCN^- experiments (vide infra).

Since Rh-590 shows strong absorption in the visible region, one may speculate that Rh-590 is degraded by direct light absorption or dye-sensitization pathways.[43] In Fig. 3, there is no degradation of Rh-590 observed upon illumination in the absence of TiO_2 nanoparticles, ruling out the former possibility. In addition, no degradation was found with

Can. J. Chem. Downloaded from www.nrcresearchpress.com by Xi'an Jiaotong University on 09/19/12
For personal use only.

Fig. 2. Temporal evolution of absorbance spectra during the photocatalytic degradation of Rhodamine 590 (Rh-590) with monolayer-protected gold cluster (MPC) – TiO_2 nanocomposites.

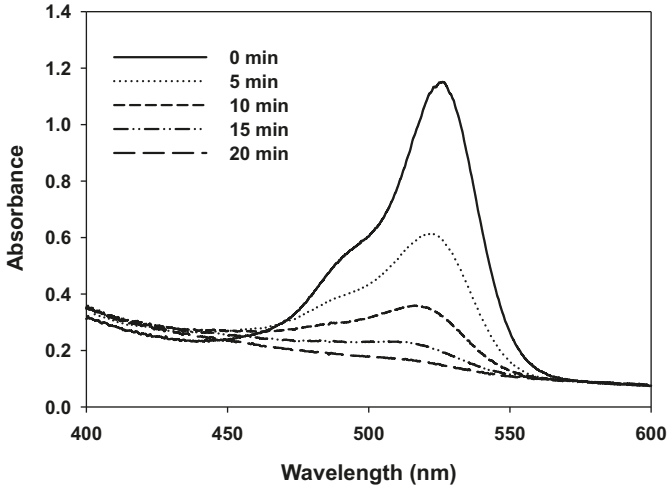

Fig. 3. Changes in Rhodamine 590 (Rh-590) concentration (C) relative to the initial concentration (C_0) during photocatalysis in the absence (A) and presence (B) of TiO_2 and in the presence of TiO_2 using a 455 nm long-pass filter (C). The Rh-590 concentration was estimated from the absorbance at 525 nm.

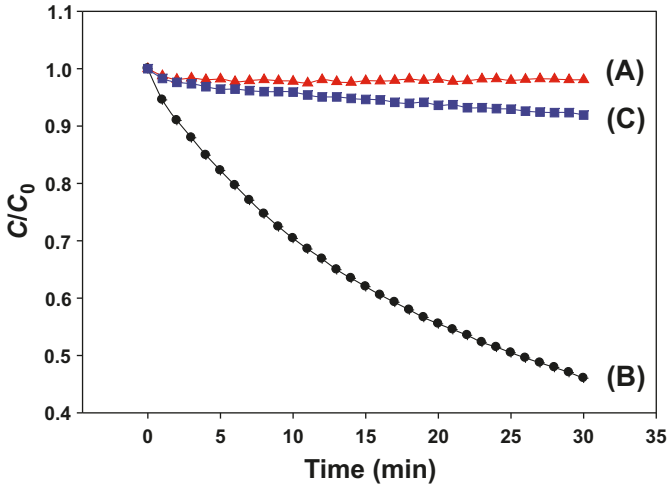

MPC alone. The possibility of dye degradation via dye sensitization was also examined. By using an additional long-pass filter ($\lambda > 455$ nm), the photoexcitation of TiO_2 was effectively blocked while Rh-590 absorption was undisturbed. This control experiment (line C in Fig. 3) shows that <8% of Rh-590 is degraded during 30 min of photolysis by the dye-sensitization mechanism. As can be seen in Fig. 3 (line B), much more Rh-590 is degraded when TiO_2 is photoexcited, confirming that the photoexcited TiO_2 plays the major role in the degradation of Rh-590.

When TiO_2 is excited with band-gap radiation (3.2 eV), electron–hole separation takes place. When the photoexcitation is carried out in an aqueous environment, the created holes can react with hydroxyl groups present on the surface, generating hydroxyl radicals. At the same time, electrons are being scavenged by oxygen.[46] Hydroxyl radicals can trigger further reactions, such as oxidation of organics.[42,47] Under the current experimental conditions, i.e., in aerated water, we thus expect the major involvement of holes toward the degradation of Rh-590. This can be confirmed by introducing SCN^-, a known hole scavenger, to the reaction mixture. The photogenerated holes can be effectively consumed by SCN^- at the semiconductor interface.[48]

Figure 4A shows the photocatalytic degradation of Rh-590 with TiO_2 in the absence and presence of a hole scavenger (SCN^-).[49] In the presence of 30 μmol/L SCN^-, the degradation rate of Rh-590 significantly decreased, suggesting that the photogenerated holes are primarily involved in the degradation of Rh-590. When the concentration of SCN^- is increased to 60 μmol/L, the degradation rate is further decreased; ca. 40% of Rh-590 is degraded after 30 min of photolysis in the absence of SCN^-, which significantly decreases to 29% and 19%, respectively, in the presence of 30 and 60 μmol/L SCN^-. The fact that the degradation rate is significantly decreased in the presence of the hole scavenger undoubtedly confirms that the photocatalytic degradation of Rh-590 occurs via oxidative photocatalytic reaction involving photogenerated holes.

In Fig. 4B, a similar trend is observed for 3 wt% MPC–TiO_2 composites calcined at 260 °C (thermal treatment of the MPC–TiO_2 composites and the effect of MPC modification are discussed later). Before the addition of SCN^-, the catalytic activity of the 3 wt% MPC–TiO_2 composite is higher than that of bare TiO_2; the Rh-590 degradation is 59% after 30 min of photolysis in the absence of SCN^-. As the addition of the hole scavenger SCN^- is increased, the catalytic degradation of Rh-590 is decreased; the Rh-590 degradation decreases to 50% and 40% when SCN^- concentration was increased to 30 and 60 μmol/L, respectively. It is interesting to note that the effect of SCN^- addition on the photocatalytic degradation of Rh-590 is very similar for both bare TiO_2 and 3 wt% MPC–TiO_2; ca. 10% and 20% decreases in the presence of 30 and 60 μmol/L SCN^-, respectively. These results suggest that the photogenerated holes are primarily involved in the photocatalytic degradation of Rh-590 for both bare TiO_2 and 3 wt% MPC–TiO_2 composites.

We next turn to the role of oxygen in oxidative photocatalytic reactions. To probe the role of oxygen in the reaction, we carried out photolysis experiments[49] in the absence of oxygen after purging with argon for 30 min to remove dissolved oxygen, prior to photolysis. As can be seen in Fig. 5 (line B), photocatalytic activity is dramatically decreased when oxygen is removed, indicating that oxygen plays a vital role in the photocatalytic degradation of Rh-590. There is still slight degradation (ca. 10%) of Rh-590 in the absence of oxygen, which is probably due to the incomplete removal of oxygen during the 30 min of purging. The role of the oxygen in photocatalytic reactions can vary. In this particular case, oxygen appears to act as an electron scavenger that facilitates electron–hole separation. To test the role of oxygen as an electron scavenger, we introduced IO_3^-, a known electron scavenger,[50] to the argon-purged reaction mixture to substitute for oxygen. As can be seen in Fig. 5, the catalytic activity for the degradation of Rh-590 was restored in the presence of IO_3^-. This confirms that oxygen acts as an electron scavenger whose presence is indispensable for the photocatalytic degradation of Rh-590.

Fig. 4. Changes in Rhodamine 590 (Rh-590) concentration (C) relative to the initial concentration (C_0) during photocatalysis with TiO_2 (A: a, b, c) and 3 wt% monolayer-protected gold cluster (MPC) – TiO_2 calcined at 260 °C (B: a, b, c) in the absence of SCN^- (a) and in the presence of 30 μmol/L (b) and 60 μmol/L (c) SCN^-.

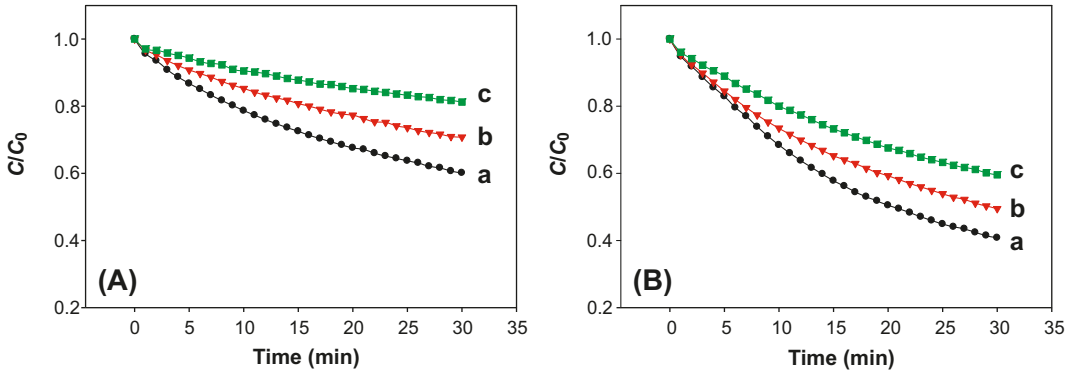

Fig. 5. Changes in Rhodamine 590 (Rh-590) concentration (C) relative to the initial concentration (C_0) during photocatalysis with TiO_2 in the presence (A) and absence (B) of oxygen, and in the absence of oxygen and in the presence of IO_3^- (C).

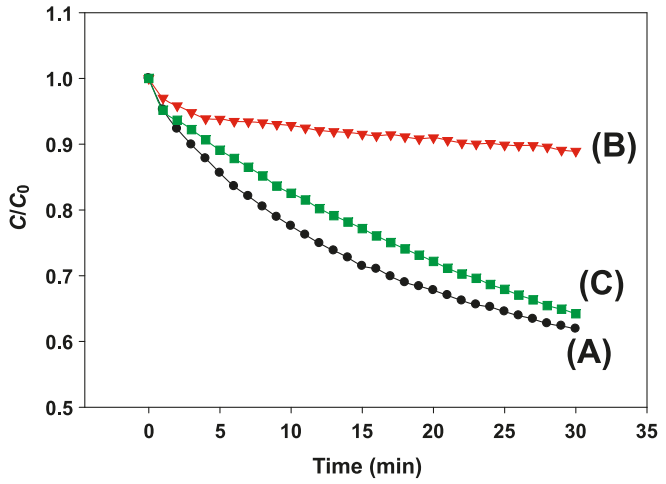

Fig. 6. Changes in Rhodamine 590 (Rh-590) concentration (C) relative to the initial concentration (C_0) during the photocatalytic reaction with (A) bare TiO_2, (B) bare TiO_2 calcined at 400 °C, (C) 3 wt% monolayer-protected gold cluster (MPC) – TiO_2, (D) 3 wt% MPC–TiO_2 calcined at 260 °C, and (E) 3 wt% MPC–TiO_2 calcined at 400 °C.

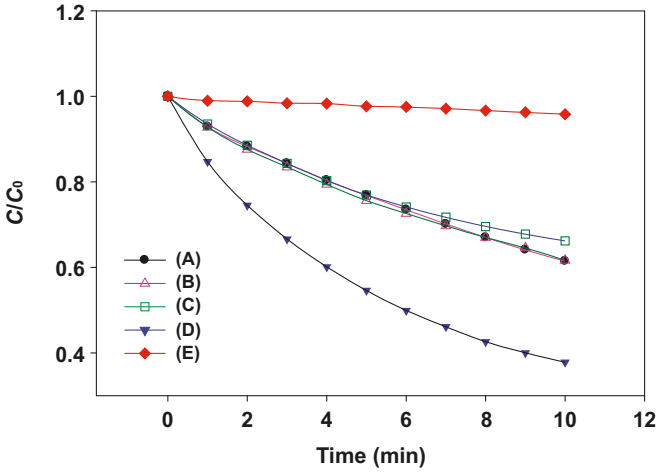

TiO_2 photocatalysts modified with MPCs

The photodegradation of Rh-590 with bare TiO_2 and 3 wt% MPC–TiO_2 are compared in Fig. 6. All nanoparticle suspensions were irradiated equally and the absorbance at 525 nm was recorded at 1 min intervals. As can be seen in Fig. 6 (lines A and C), there is no enhancement in the photocatalytic activity of 3 wt % MPC–TiO_2 compared with that of bare TiO_2. The same trend was found for other MPC–TiO_2 composites with 1, 2, and 6 wt% MPC loadings (not shown). These results suggest that the bifunctional tiopronin linker could impose a kinetic barrier for electron transfer from TiO_2 to the gold core. In fact, the distance between TiO_2 and the gold core through the tiopronin linker, which is estimated to be 0.93 nm[51], seems to be too long for the electron transfer to occur efficiently and thus the effect of MPC loading is insignificant in these MPC–TiO_2 composites.

In previous studies on supported gold catalysts employing MPCs, it was found that the catalytic activity could be greatly enhanced by removing the protecting ligands.[52–54] Electrochemical[55,56] and thermal[52,57] activation have been employed often to remove the protecting ligands. In Fig. S2A (Supplementary data), the TEM image of MPC–TiO_2 composites after calcination at 260 °C shows that the gold core size is unaltered from its initial size, and there are no detached gold clusters found on the grid. This is a promising result because it suggests that well-defined gold-modified TiO_2 nanocomposites can be prepared from MPCs through the thermal treatment. Whereas the size of gold in the nanocomposites maintained its initial size after calcination at 260 °C, the catalytic activity of the MPC–TiO_2 composite was considerably enhanced after calcination at 260 °C. As can be seen in Fig. 6 (line D), the degradation dramatically increases by more than 60% upon calcination at 260 °C. Furthermore, the results in Fig. 7 show that the photocatalytic activity of the calcined MPC–TiO_2 composites significantly increases with MPC loading; the Rh-590 degradation at 30 min is increased by more than 50% with 1 wt% MPC modification compared with the bare TiO_2. For 3 wt% MPC–TiO_2 composites, the Rh-590 degradation is completed within 25 min. The result that the photocatalytic activity can be conveniently controlled by the structural parameter (i.e., by MPC loading) of the composites clearly shows the advantage of the MPC–TiO_2 composites. Considering the degrada-

Can. J. Chem. Downloaded from www.nrcresearchpress.com by Xi'an Jiaotong University on 09/19/12
For personal use only.

Can. J. Chem. Downloaded from www.nrcresearchpress.com by Xi'an Jiaotong University on 09/19/12
For personal use only.

Fig. 7. Changes in Rhodamine 590 (Rh-590) concentration (C) relative to the initial concentration (C_0) during the photocatalytic reaction with nanocomposites calcined at 260 °C: (A) bare TiO_2, (B) 1 wt% monolayer-protected gold cluster (MPC) – TiO_2, and (C) 3 wt% MPC–TiO_2.

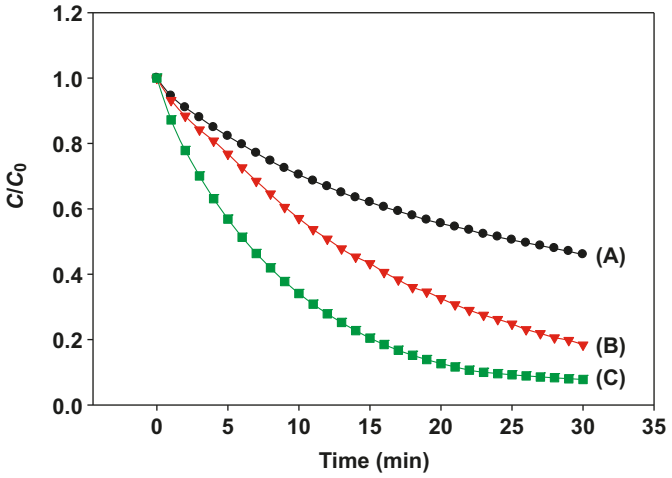

tion mechanism discussed earlier, the enhanced catalytic activity reflects the fact that more photoholes are generated in TiO_2–MPC composites calcined at 260 °C for Rh5-90 oxidation. Since TiO_2 itself exhibits the same catalytic activity after calcination at 260 °C (line A in Fig. 7), one can conclude that the enhanced catalytic activity is due to the enhanced charge separation in the presence of gold nanoparticles on TiO_2. The origin of the enhanced charge separation in the calcined composites is unclear, but it is likely that the electron transfer from TiO_2 to the gold core is significantly facilitated after calcination.

Since the photocatalytic activity of MPC–TiO_2 composites was considerably enhanced after the thermal treatment, the calcination temperature was raised to 400 °C to completely remove the ligands on the gold surface. Thermal treatment of TiO_2 at 500 °C resulted in a severe decrease in the catalytic activity, thus, the highest calcination temperature was limited to 400 °C at which the catalytic activity was maintained (line B in Fig. 6). The catalytic activities of 3 wt% MPC–TiO_2 composites calcined at 260 and 400 °C are compared in Fig. 6. Surprisingly, the catalytic activity of MPC–TiO_2 composites calcined at 400 °C decreased dramatically; the Rh-590 degradation was only 4% at 10 min and hardly increased with time. The TEM image of the composite in Fig. S2b (Supplementary data) shows that the average gold core diameter was considerably increased to 4.0 nm and that there were some detached gold particles observed, indicating significant loss of the protecting ligands after calcination at 400 °C.

XPS measurements of the MPC–TiO_2 composites were carried out to understand the drastically decreased catalytic activity after calcination at 400 °C. In Fig. 8, the sulfur S $2p_{3/2}$ BE value (162 eV) for the 3 wt% MPC–TiO_2 composite corresponds to bound thiolate, which is in agreement with previous reports.[58–60] When this composite was calcined at 260 °C, the 162 eV peak disappeared and a new peak arose at 168 eV. The 168 eV peak was assigned to the oxidized sulfur species.[59,61] When the temperature was raised to 400 °C, the 168 eV peak that corresponds to the oxidized sulfur

Fig. 8. XPS S 2p spectra of (A) monolayer-protected gold cluster (MPC) – TiO_2, (B) MPC–TiO_2 calcined at 260 °C, and (C) MPC–TiO_2 calcined at 400 °C.

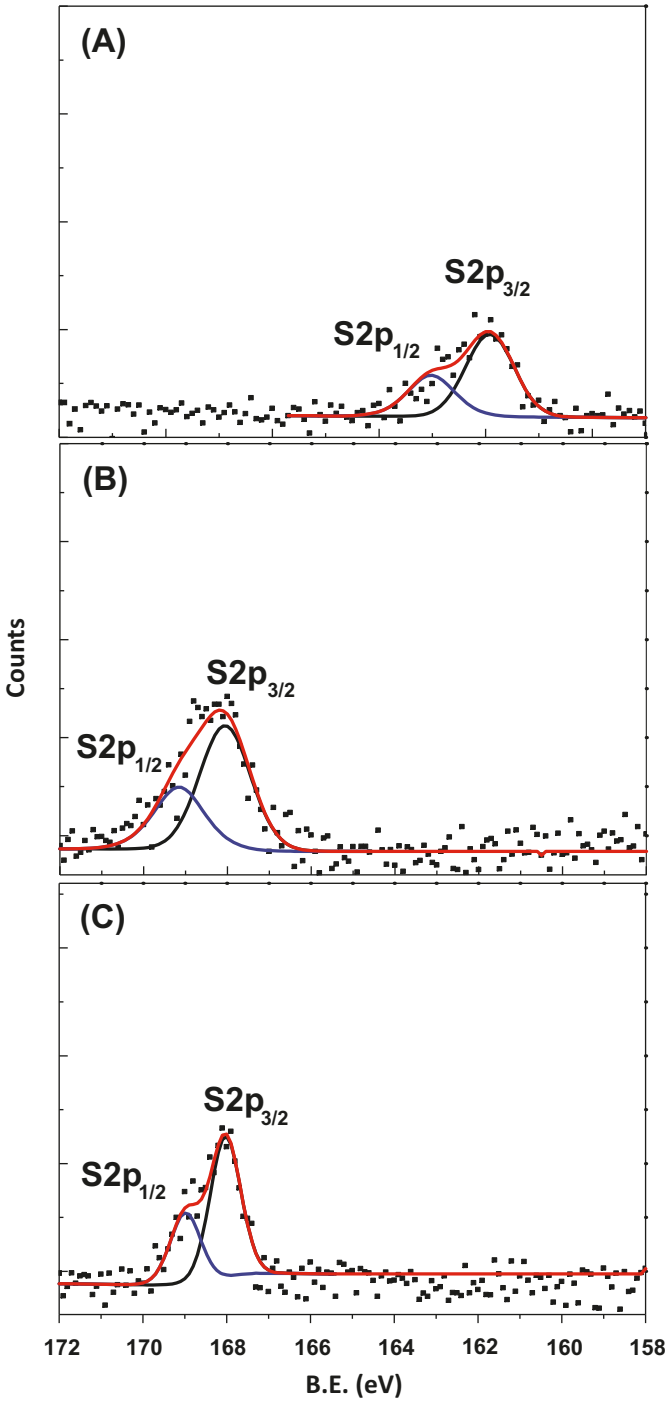

species was observed as seen for MPC–TiO_2 composites calcined at 260 °C. The XPS results of the MPC–TiO_2 composites calcined at 260 and 400 °C are similar to each other and thus one may question the origin of the vastly different photocatalytic activity between them. It could be understood by the difference in TGA results between the two calcination temperatures (Fig. S3, Supplementary data). That is, sulfur could be oxidized at 260 °C, but it is rather unlikely that sulfur directly reacts with TiO_2 considering the remaining portion of

Can. J. Chem. Downloaded from www.nrcresearchpress.com by Xi'an Jiaotong University on 09/19/12
For personal use only.

Fig. 9. Changes in Rhodamine 590 (Rh-590) concentration (C) relative to the initial concentration (C_0) during the photocatalytic reaction with (A) bare TiO_2, (B) tiopronin-coated TiO_2, (C) tiopronin-coated TiO_2 calcined at 260 °C, and (D) tiopronin-coated TiO_2 calcined at 400 °C.

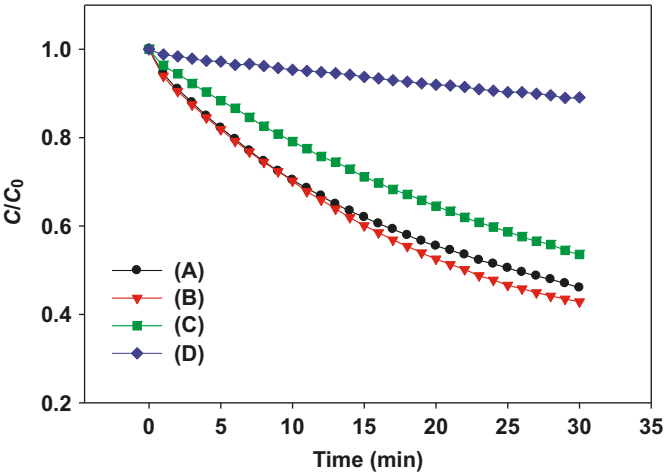

the ligand (ca. 40%) in the calcined composite. We note that there is nonetheless some minor poisoning effect observed at 260 °C (see Fig. 9). On the other hand, as most of the ligands are decomposed and removed at 400 °C, sulfur may directly react with TiO_2 and leave deposits containing oxidized sulfur on the TiO_2 surface. Such deposits appear to be responsible for the drastic decrease in photocatalytic activity found in the MPC–TiO_2 composite calcined at 400 °C by presumably acting as active recombination centers for the photogenerated electrons and holes. It has been reported that sulfur species bound to surfaces of metal oxides such as CeO_2, Al_2O_3, Cu_2O, and ZnO can lead to a poisoning effect on the metal oxides.[62,63] It has been detailed in XPS studies that sulfur-containing species can react with metal oxide surfaces at elevated temperatures, leaving highly oxidized products such as sulfites or sulfates on these metal oxides. It is thus highly probable that sulfur on tiopronin directly reacts with TiO_2 at 400 °C and leaves deposits containing oxidized sulfur on the TiO_2 surface.

Effect of the ligand on photocatalytic activity

To confirm the sulfur poisoning scenario, TiO_2 nanoparticles were coated with tiopronin alone and their catalytic activities were examined after thermal treatment at 260 and 400 °C. The photocatalytic activities of tiopronin-coated TiO_2 before and after calcination at 260 and 400 °C are compared in Fig. 9. The tiopronin-coated TiO_2 before calcination shows similar photocatalytic activity to bare TiO_2, which suggests that the tiopronin ligands do not occupy the active sites on the TiO_2 surface and do not act as recombination centers. Compared with bare TiO_2, the Rh-590 degradation is decreased by ca. 15% after calcination at 260 °C, indicating some minor poisoning effect by the tiopronin ligands after calcination. It is interesting to note that the photocatalytic activity of the MPC–TiO_2 composites increases more than 60% after calcination at 260 °C. This contrasting result suggests that the catalytic activity is enhanced in the presence of gold even though the ligand poisoning effect is nontrivial when calcined at 260 °C, confirming the active role of gold in the photocatalysis. However, the catalytic activity of the tiopronin-coated TiO_2 decreased drastically when calcined at 400 °C as observed for the MPC–TiO_2 composite calcined at 400 °C. From this result, we conclude that the drastic decrease in catalytic activity observed for MPC–TiO_2 calcined at 400 °C can be ascribed to the ligand effect.

Conclusions

We have shown that well-defined nanocomposites could be prepared by modifying TiO_2 with bifunctional tiopronin-coated MPCs. In this method, the MPC size was unaltered during the anchoring process, and the MPC loading on TiO_2 could be precisely controlled by the experimental conditions. Mechanistic studies of Rh-590 degradation with the MPC–TiO_2 composites revealed that Rh-590 degradation occurs via the oxidative pathway by photogenerated holes in the composites. The photocatalytic activity of the MPC–TiO_2 composites was found to increase significantly upon calcination at 260 °C, whereas the size of gold particles was maintained at their initial size. When the calcination temperature was raised further to 400 °C, however, the photocatalytic activity of the composites drastically decreased. XPS analyses of the calcined composites showed that a significant amount of oxidized sulfur remains after calcination that appears to act as a recombination center for the photogenerated electrons and holes, leading to a drastic decrease in the photocatalytic activity. Whereas the MPC-modified composites clearly offer an improved method for the preparation of structurally well-defined photocatalysts, these results reveal the important role of ligands in the use of MPCs in supported photocatalysts.

Supplementary data

Supplementary data are available with the article through the journal Web site (www.nrcresearchpress.com/cjc).

Acknowledgments

This research was supported by World Class University (R32-2008-000-10217-0), Priority Research Centers (2009-0093823), and Basic Science Research (2010-0009244) Programs through the National Research Foundation of Korea (NRF) funded by the Ministry of Education, Science and Technology, and the Yonsei University Research Fund. P.A. acknowledges the support from Western Michigan University.

References

(1) Bard, A. J. *J. Phys. Chem.* **1982** *86* (2), 172. doi:10.1021/j100391a008.
(2) Bard, A. J.; Fox, M. A. *Acc. Chem. Res.* **1995** *28* (3), 141. doi:10.1021/ar00051a007.
(3) Hoffmann, M. R.; Martin, S. T.; Choi, W.; Bahnemann, D. W. *Chem. Rev.* **1995** *95* (1), 69. doi:10.1021/cr00033a004.
(4) Kamat, P. V. *Chem. Rev.* **1993** *93* (1), 267. doi:10.1021/cr00017a013.
(5) Jakob, M.; Levanon, H.; Kamat, P. V. *Nano Lett.* **2003** *3* (3), 353. doi:10.1021/nl0340071.
(6) Hirakawa, T.; Kamat, P. V. *Langmuir* **2004** *20* (14), 5645. doi:10.1021/la048874c.
(7) Hirakawa, T.; Kamat, P. V. *J. Am. Chem. Soc.* **2005** *127* (11), 3928. doi:10.1021/ja042925a.

Can. J. Chem. Downloaded from www.nrcresearchpress.com by Xi'an Jiaotong University on 09/19/12
For personal use only.

(8) Subramanian, V.; Wolf, E.; Kamat, P. V. *J. Phys. Chem. B* **2001** *105* (46), 11439. doi:10.1021/jp011118k.
(9) Kamat, P. V. *J. Phys. Chem. C* **2007** *111* (7), 2834. doi:10.1021/jp066952u.
(10) Wolf, A.; Schüth, F. *Appl. Catal. A* **2002** *226*, 1.
(11) Valden, M.; Lai, X.; Goodman, D. W. *Science* **1998** *281* (5383), 1647. doi:10.1126/science.281.5383.1647.
(12) Templeton, A. C.; Wuelfing, W. P.; Murray, R. W. *Acc. Chem. Res.* **2000** *33* (1), 27. doi:10.1021/ar9602664.
(13) Hostetler, M. J.; Wingate, J. E.; Zhong, C.-J.; Harris, J. E.; Vachet, R. W.; Clark, M. R.; Londono, J. D.; Green, S. J.; Stokes, J. J.; Wignall, G. D.; Glish, G. L.; Porter, M. D.; Evans, N. D.; Murray, R. W. *Langmuir* **1998** *14* (1), 17. doi:10.1021/la970588w.
(14) Whetten, R. L.; Shafigullin, M. N.; Khoury, J. T.; Schaaff, T. G.; Vezmar, I.; Alvarez, M. M.; Wilkinson, A. *Acc. Chem. Res.* **1999** *32* (5), 397. doi:10.1021/ar970239t.
(15) Chen, S.; Ingram, R. S.; Hostetler, M. J.; Pietron, J. J.; Murray, R. W.; Schaaff, T. G.; Khoury, J. T.; Alvarez, M. M.; Whetten, R. L. *Science* **1998** *280* (5372), 2098. doi:10.1126/science.280.5372.2098.
(16) Hicks, J. F.; Zamborini, F. P.; Osisek, A. J.; Murray, R. W. *J. Am. Chem. Soc.* **2001** *123* (29), 7048. doi:10.1021/ja0106826.
(17) Lee, D.; Donkers, R. L.; DeSimone, J. M.; Murray, R. W. *J. Am. Chem. Soc.* **2003** *125* (5), 1182. doi:10.1021/ja029030n.
(18) Lee, D.; Donkers, R. L.; Wang, G.; Harper, A. S.; Murray, R. W. *J. Am. Chem. Soc.* **2004** *126* (19), 6193. doi:10.1021/ja049605b.
(19) Kim, J.; Lee, D. *J. Am. Chem. Soc.* **2006** *128* (14), 4518. doi:10.1021/ja058395f.
(20) Kim, J.; Lema, K.; Ukaigwe, M.; Lee, D. *Langmuir* **2007** *23* (14), 7853. doi:10.1021/la700753u.
(21) Lee, M.; Amaratunga, P.; Kim, J.; Lee, D. *J. Phys. Chem. C* **2010** *114* (43), 18366. doi:10.1021/jp106337k.
(22) Kim, J.; Lee, D. *J. Am. Chem. Soc.* **2007** *129* (25), 7706. doi:10.1021/ja071329o.
(23) Hurum, D. C.; Gray, K. A.; Rajh, T.; Thurnauer, M. C. *J. Phys. Chem. B* **2005** *109* (2), 977. doi:10.1021/jp045395d.
(24) Wood, A.; Giersig, M.; Mulvaney, P. *J. Phys. Chem. B* **2001** *105* (37), 8810. doi:10.1021/jp011576t.
(25) Enríquez, R.; Agrios, A. G.; Pichat, P. *Catal. Today* **2007** *120* (2), 196. doi:10.1016/j.cattod.2006.07.054.
(26) Cox, R. A.; Derwent, R. G.; Williams, M. R. *Environ. Sci. Technol.* **1980** *14* (1), 57. doi:10.1021/es60161a007.
(27) Barbeni, M.; Minero, C.; Pelizzetti, E.; Borgarello, E.; Serpone, N. *Chemosphere* **1987** *16* (10-12), 2225. doi:10.1016/0045-6535(87)90281-5.
(28) Malato, S.; Fernández-Ibáñez, P.; Maldonado, M. I.; Blanco, J.; Gernjak, W. *Catal. Today* **2009** *147* (1), 1. doi:10.1016/j.cattod.2009.06.018.
(29) Ahmed, S.; Ollis, D. F. *Sol. Energy* **1984** *32* (5), 597. doi:10.1016/0038-092X(84)90135-X.
(30) Tanguay, J. F.; Suib, S. L.; Coughlin, R. W. *J. Catal.* **1989** *117* (2), 335. doi:10.1016/0021-9517(89)90344-8.
(31) Matthews, R. W. *Sol. Energy* **1987** *38* (6), 405. doi:10.1016/0038-092X(87)90021-1.
(32) Turchi, C. S.; Ollis, D. F. *J. Catal.* **1989** *119* (2), 483. doi:10.1016/0021-9517(89)90176-0.
(33) Khalil, L. B.; Mourad, W. E.; Rophael, M. W. *Appl. Catal. B* **1998** *17* (3), 267. doi:10.1016/S0926-3373(98)00020-4.
(34) Serpone, N.; Ah-You, Y. K.; Tran, T. P.; Harris, R.; Pelizzetti, E.; Hidaka, H. *Sol. Energy* **1987** *39* (6), 491. doi:10.1016/0038-092X(87)90056-9.
(35) Topalov, A.; Molnár-Gábor, D.; Csanádi, J. *Water Res.* **1999** *33* (6), 1371. doi:10.1016/S0043-1354(98)00351-0.
(36) Templeton, A. C.; Chen, S.; Gross, S. M.; Murray, R. W. *Langmuir* **1999** *15* (1), 66. doi:10.1021/la9808420.
(37) Qu, P.; Meyer, G. J. *Langmuir* **2001** *17* (21), 6720. doi:10.1021/la010939d.
(38) Serpone, N.; Lawless, D.; Khairutdinov, R.; Pelizzetti, E. *J. Phys. Chem.* **1995** *99* (45), 16655. doi:10.1021/j100045a027.
(39) Rothenberger, G.; Moser, J.; Graetzel, M.; Serpone, N.; Sharma, D. K. *J. Am. Chem. Soc.* **1985** *107* (26), 8054. doi:10.1021/ja00312a043.
(40) Shkrob, I. A.; Sauer, M. C. *J. Phys. Chem. B* **2004** *108* (33), 12497. doi:10.1021/jp047736t.
(41) Bahnemann, D. W.; Hilgendorff, M.; Memming, R. *J. Phys. Chem. B* **1997** *101* (21), 4265. doi:10.1021/jp9639915.
(42) Aarthi, T.; Madras, G. *Ind. Eng. Chem. Res.* **2007** *46* (1), 7. doi:10.1021/ie060948n.
(43) Shinozaki, R.; Nakato, T. *Microporous Mesoporous Mater.* **2008** *113* (1–3), 81. doi:10.1016/j.micromeso.2007.11.005.
(44) Ban, T.; Kondoh, S.; Ohya, T.; Ohya, Y.; Takahashi, Y. *J. Photochem. Photobiol A* **2003** *156* (1–3), 219. doi:10.1016/S1010-6030(02)00404-5.
(45) Stevens, B.; Sharpe, R. R.; Bingham, W. S. W. *Photochem. Photobiol.* **1967** *6* (1), 83. doi:10.1111/j.1751-1097.1967.tb08792.x.
(46) Choi, W. *Catal. Surv. Asia* **2006** *10* (1), 16. doi:10.1007/s10563-006-9000-2.
(47) Gnaser, H.; Huber, B.; Ziegler, C. *Encycl. Nanosci. Nanotechnol.* **2004** *6*, 505.
(48) Kamat, P. V. *Langmuir* **1985** *1* (5), 608. doi:10.1021/la00065a017.
(49) In this experiment, an additional 455 nm short-pass filter (<455 nm) was used to avoid the direct excitation of Rh-590. As a result, the intensity of light irradiation was attenuated to some extent. The Rh-590 degradation in this experimental condition is considered to occur solely by photoexcited TiO_2 composites, not by the dye-sensitization mechanism.
(50) Glaze, W. H.; Kenneke, J. F.; Ferry, J. L. *Environ. Sci. Technol.* **1993** *27* (1), 177. doi:10.1021/es00038a021.
(51) The fully extended tiopronin length was calculated using Hyperchem 6.0 software.
(52) Luo, J.; Jones, V. W.; Han, L.; Maye, M. M.; Kariuki, N. N.; Zhong, C.-J. *J. Phys. Chem. B* **2004** *108* (28), 9669. doi:10.1021/jp037446x.
(53) Han, L.; Luo, J.; Kariuki, N.; Maye, M. M.; Jones, V. W.; Zhong, C. J. *Chem. Mater.* **2003** *15* (1), 29. doi:10.1021/cm0208051.
(54) Luo, J.; Jones, V. W.; Maye, M. M.; Han, L.; Kariuki, N. N.; Zhong, C. J. *J. Am. Chem. Soc.* **2002** *124* (47), 13988. doi:10.1021/ja028285y.
(55) Lou, Y. B.; Maye, M. M.; Han, L.; Luo, J.; Zhong, C. J. *Chem. Commun. (Camb.)* **2001** (5): 473. doi:10.1039/b008669j.
(56) Luo, J.; Lou, Y. B.; Maye, M. M.; Zhong, C. J.; Hepel, M. *Electrochem. Commun.* **2001** *3* (4), 172. doi:10.1016/S1388-2481(01)00128-X.
(57) Luo, J.; Jones, V. W.; Maye, M. M.; Han, L.; Kariuki, N. N.; Zhong, C.-J. *J. Am. Chem. Soc.* **2002** *124* (47), 13988. doi:10.1021/ja028285y.
(58) Nuzzo, R. G.; Zegarski, B. R.; Dubois, L. H. *J. Am. Chem. Soc.* **1987** *109* (3), 733. doi:10.1021/ja00237a017.
(59) Castner, D. G.; Hinds, K.; Grainger, D. W. *Langmuir* **1996** *12* (21), 5083. doi:10.1021/la960465w.
(60) Bourg, M.-C.; Badia, A.; Lennox, R. B. *J. Phys. Chem. B* **2000** *104* (28), 6562. doi:10.1021/jp9935337.

(61) Shiang, J. J.; Heath, J. R.; Collier, C. P.; Saykally, R. J. *J. Phys. Chem. B* **1998** *102* (18), 3425. doi:10.1021/jp981315s.
(62) Luo, T.; Vohs, J. M.; Gorte, R. J. *J. Catal.* **2002** *210* (2), 397. doi:10.1006/jcat.2002.3689.
(63) Lin, J.; May, J. A.; Didziulis, S. V.; Solomon, E. I. *J. Am. Chem. Soc.* **1992** *114* (12), 4718. doi:10.1021/ja00038a039.

Can. J. Chem. Downloaded from www.nrcresearchpress.com by Xi'an Jiaotong University on 09/19/12
For personal use only.

Theoretical investigation of the conformational intricacies and thermodynamic functions of noradrenaline

DongJin R. Lee, Natalie J. Galant, Donghoon M. Lee, Sean S.H. Dawson, Vanna Z.Y. Ding, David H. Setiadi, Bela Viskolcz, and Imre G. Csizmadia

Can. J. Chem. Downloaded from www.nrcresearchpress.com by Xi'an Jiaotong University on 09/19/12
For personal use only.

Abstract: Noradrenaline is a neurotransmitter that is involved in various psychological processes. In the neurotransmission process, noradrenaline binds to an adrenergic receptor by forming a complex of hydrogen bonds between its two catechol ring hydroxyl groups and the amino acid residues of adrenergic receptors. Although the two catechol ring hydroxyl groups play a crucial role in making hydrogen bonds to the binding site of the adrenergic receptor, the contribution of the catechol ring hydroxyl groups to the intramolecular stability that may affect docking has not been fully studied. To reveal the specific role that the catechol ring hydroxyl groups might play in stabilizing noradrenaline, the quantum chemical computations of geometry optimization and thermodynamic functions of N-protonated noradrenaline conformers were performed at both the B3LYP/6–31G(d,p) and G3MP2B3 levels of theory, using the Gaussian 03 program. The results were compared with those of N-protonated β-hydroxy-β-phenylethylamine, which is identical to noradrenaline except it lacks two catechol ring hydroxyl groups. For the first time, post-Hartree–Fock computations were used to obtain thermodynamic functions to establish relative stabilities of all possible conformers of N-protonated noradrenaline. In this study, 18 distinct structures of N-protonated noradrenaline were revealed, and the catechol ring hydroxyl groups were found to affect noradrenaline stability positively or negatively depending on the conformational orientations. On the basis of available experimental results, the issue that the least stable conformation of two catechol ring hydroxyl groups may be involved in the docking process has been raised. These findings may be useful in synthesis of derivatives of noradrenaline in drug design.

Key words: noradrenaline, density functional calculations, thermodynamic functions, conformational stability, intramolecular hydrogen bond.

Résumé : La noradrénaline est un neurotransmetteur impliqué dans divers processus psychologiques. Dans le processus de neurotransmission, la noradrénaline se lie à un récepteur adrénergique par formation d'un complexe de liaisons hydrogènes entre les deux groupes hydroxyles de son noyau catéchol et les résidus d'acides aminés des récepteurs adrénergiques. Même si les groupes hydroxyles de son noyau catéchol jouent un rôle important dans la formation des liaisons hydrogènes avec le site de fixation du récepteur adrénergique, la contribution des groupes hydroxyles de son noyau catéchol à la stabilité intramoléculaire qui peut affecter l'arrimage n'a pas été complètement étudié. Afin d'évaluer le rôle spécifique que les groupes hydroxyles de son noyau catéchol peuvent jouer dans la stabilisation de la noradrénaline, on a effectué des calculs de chimie quantique d'optimisation de la géométrie et des fonctions thermodynamiques des conformères de la noradrénaline N-protonée, en faisant appel au programme « Gaussian 03 », aux niveaux B3LYP/6–31G(d,p) et G3MP2B3 de la théorie. Les résultats ont été comparés à ceux obtenus avec la β-hydroxy-β-phénylethylamine N-protonée, qui est identique à la noradrénaline à l'exception de l'absence des deux groupes hydroxyles du noyau catéchol. Des calculs post-Hartree–Fock ont donc été utilisés pour la première fois pour obtenir des fonctions thermodynamiques dans le but d'établir les stabilités relatives de tous les conformères possibles de la noradrénaline N-protonée. Dans cette étude, on a mis en évidence 18 structures distinctes de la noradrénaline N-protonée et on a trouvé que les groupes hydroxyles du noyau catéchol affectent la stabilité de la noradrénaline positivement ou négativement suivant les orientations conformationnelles. Sur la base des résultats expérimentaux

Received 20 December 2010. Accepted 25 February 2011. Published at www.nrcresearchpress.com/cjc on 17 August 2011.

D.R. Lee. Department of Chemical Informatics, Faculty of Education, University of Szeged, Boldogasszony sgt. 6, Szeged, H-6725, Hungary; Department of Chemistry, Faculty of Arts and Science, University of Toronto, Toronto, ON M5S 3H6, Canada.
N.J. Galant, S.S. Dawson, and V.Z. Ding. Department of Chemistry, Faculty of Arts and Science, University of Toronto, Toronto, ON M5S 3H6, Canada.
D.M. Lee. Department of Cell & Systems Biology, Faculty of Arts and Science, University of Toronto, Toronto, ON M5S 3G5, Canada.
D.H. Setiadi. Department of Chemistry, Faculty of Arts and Science, University of Toronto, Toronto, ON M5S 3H6, Canada; Global Institute of Computational Molecular and Materials Science (www.giocomms.org).
B. Viskolcz. Department of Chemical Informatics, Faculty of Education, University of Szeged, Boldogasszony sgt. 6, Szeged, H-6725, Hungary; Drug Discovery Research Center (http://drugcent.com).
I.G. Csizmadia. Department of Chemical Informatics, Faculty of Education, University of Szeged, Boldogasszony sgt. 6, Szeged, H-6725, Hungary; Department of Chemistry, Faculty of Arts and Science, University of Toronto, Toronto, ON M5S 3H6, Canada; Global Institute of Computational Molecular and Materials Science (www.giocomms.org); Drug Discovery Research Center (http://drugcent.com).

Corresponding author: Béla Viskolcz (e-mail: viskolcz@jgypk.u-szeged.hu).

disponibles, il a été suggéré que la conformation la moins stable des deux groupes hydroxyles du noyau catéchol pourrait être impliquée dans le processus d'arrimage. Ces observations pourraient s'avérer utiles dans la planification de la synthèse de dérivés de la noradrénaline.

Mots-clés : noradrénaline, calculs de la fonctionnelle de la densité, fonctions thermodynamiques, stabilité conformationnelle, liaison hydrogène intramoléculaire.

[Traduit par la Rédaction]

Can. J. Chem. Downloaded from www.nrcresearchpress.com by Xi'an Jiaotong University on 09/19/12
For personal use only.

Introduction

A number of neurotransmitter systems, including noradrenaline, serotonin, and dopamine, are closely linked with various psychological processes, including mood regulation. Specifically, the dysfunction within noradrenaline system may lead to anxiety and mood disorders.[1–3] Neurotransmitters are released from a presynaptic cell and transmit the neural signal through successful docking to specific postsynaptic receptors, thus activating the downstream signaling pathway. In the process of docking noradrenaline to an adrenergic receptor, a complex network of hydrogen bonds is established between the catechol ring hydroxyl groups of noradrenaline and the residues of the binding site of the adrenergic receptor. The docking process through hydrogen bond formation occurs when the molecular orientation of noradrenaline is both conformationally and energetically favourable. Since the stable conformations are favoured, only a few relatively more stable conformers can be easily recognized by the adrenergic receptors.[4] Also, the molecular stability affects the ultimate degradation of the molecule.[5]

Noradrenaline is both a hormone and the simplest member of the catecholamine family of neurotransmitters. Noradrenaline contains two catechol ring hydroxyl groups, which allow flexibility of the catechol ring structure of noradrenaline with three different minimum-energy orientations.[6–8] The acidic OH protons of the catechol ring hydroxyl groups are involved in hydrogen bonding, for example, to the two serine residues of the α_{1a}-adrenergic receptors (*meta*-hydroxyl to Ser-188 and Ser-158 and *para*-hydroxyl to Ser-192) when docking.[9,10] Although the conformational landscape of noradrenaline has been characterized through ab initio computations,[6,11–13] and the intermolecular roles of the catechol ring hydroxyl group were previously studied,[11,14,15] the contribution of the catechol ring hydroxyl groups to the intrinsic intramolecular stability that may affect docking remains elusive. To address the role of the catechol ring hydroxyl groups in intramolecular stability, the quantum chemical computations of geometry optimization and thermodynamic functions of N-protonated noradrenaline conformers were performed and the results were compared with that of the model compound, N-protonated β-hydroxy-β-phenylethylamine,[16] which is identical to the noradrenaline except it lacks two catechol ring hydroxyl groups.

Scope

The first aim of this conformational study is to determine the preferred conformational structures of N-protonated noradrenaline by ab initio density functional theory (DFT) and G3-based quantum chemistry method (G3MP2B3) computation. The dihedral angles of N-protonated noradrenaline were defined (Fig. 1). The stable conformers are the minimum energy critical points of the potential energy hyper surface (eq. [1]) of five independent variables. Conformational analysis provides information about the energy change as a function of several variables as may be analyzed by the five cross sections passing through the global minimum as defined by eqs. [2]–[7].

Fig. 1. Modular atomic numbering scheme of dihedral angles for N-protonated noradrenaline. A conformation is symbolized by [ψ φ χ] [ω σ] throughout this paper. The first three characters specify the backbone and side-chain orientations and the last two characters specify the hydroxyl orientations of the catechol ring.

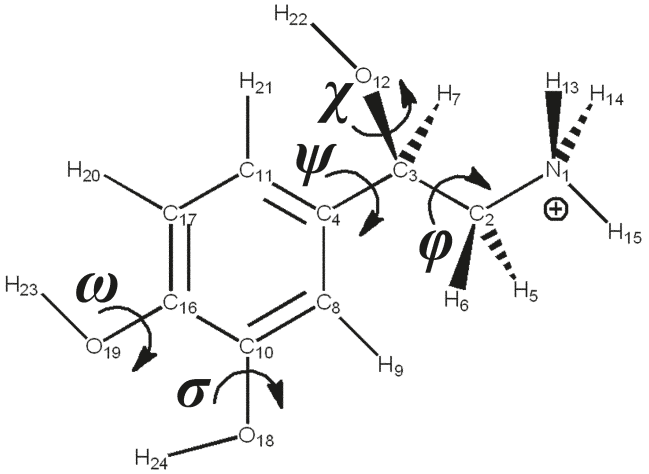

$$[1] \quad E = f(\psi, \phi, \chi, \omega, \sigma)$$

where E is the potential energy hyper surface (PEHS),

$$[2] \quad E(\psi) = f(\psi)$$

where $E(\psi)$ is the potential energy curve for tortional mode ψ,

$$[3] \quad E(\phi) = f(\phi)$$

where $E(\phi)$ is the potential energy curve for tortional mode ϕ,

$$[4] \quad E(\chi) = f(\chi)$$

where $E(\chi)$ is the potential energy curve for mode χ,

$$[5] \quad E(\omega) = f(\omega)$$

where $E(\omega)$ is the potential energy curve for the dihedral ω,

$$[6] \quad E(\sigma) = f(\sigma)$$

Fig. 2. Isodesmic reaction of N-protonated β-hydroxy-β-phenylethylamine (N-PβHβPEA) and 3,4-dihydroxytoluene forming N-protonated noradrenaline and toluene.

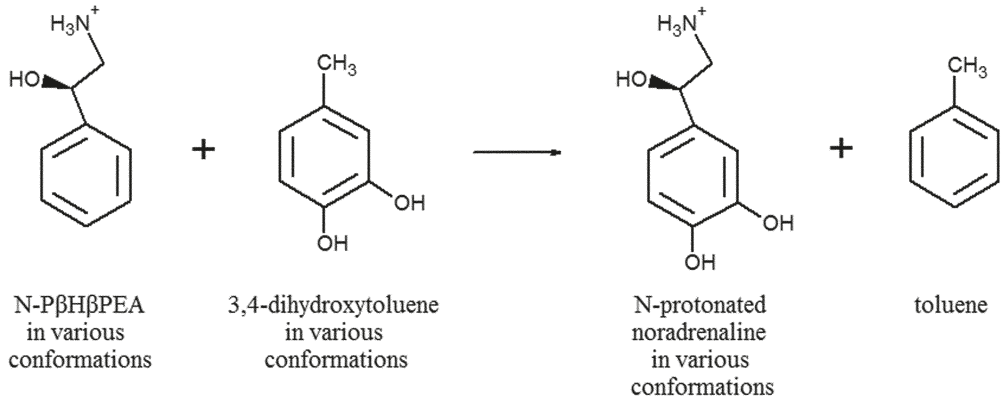

Fig. 3. Three different possible conformations of 3,4-dihydroxytoluene depending on the orientation of the catechol ring hydroxyl groups.

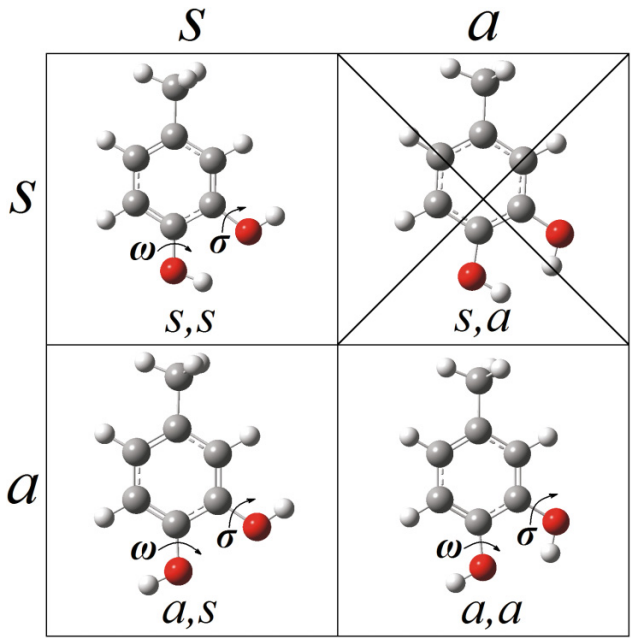

where $E(\sigma)$ is the potential energy curve for the dihedral σ,

$$[7] \qquad E(\psi, \phi) = f(\psi, \phi)$$

where $E(\psi, \phi)$ is the potential energy surface (PES).

Two torsional modes (ψ and ϕ) determine the shape of the hydrocarbon backbone and χ specifies the orientation of the hydroxyl side chain from the backbone. The dihedrals ω and σ denote the orientation of the catechol ring hydroxyl groups. This research, in its first phase, focuses on the variation of the ψ, ϕ, and χ torsional angles to determine the relative stabilities of the various conformers existing on the potential energy surface. In general, the g^+, a, or g^- conformations are considered to be stable.

The dihedral angles were defined as follows: $\psi = C_2C_3$–C_4C_8, $\phi = N_1C_2$–C_3C_4, $\chi = C_2C_3$–$O_{12}H_{22}$, $\omega = C_{10}C_{16}$–$O_{19}H_{23}$, and $\sigma = C_8C_{10}$–$O_{18}H_{24}$ (Fig. 1). To explore the conformational space of N-protonated noradrenaline, the variation of the following dihedral angles were studied: ϕ and ψ equals *gauche*$^+$ (60°), *anti* (180°) and *gauche*$^-$ (–60°); χ equals *anti* (180°); and ω and σ could be at *syn* (0°) or *anti* (180°).

The second aim of this study was to investigate the role of the various combinations of the ω and σ dihedral angles of the catechol ring hydroxyl groups that may modulate the intrinsic stability of the various side-chain conformations.

Methods

Each conformer was first optimized using the ab initio[17] restricted Hartree–Fock (RHF)[18] method and the standard split valence 3–21G basis set[19–21] incorporated in the Gaussian 03 (G03) program package.[22] Total and relative energies are tabulated in the Supplementary data (Table S1). The RHF/3–21G full geometry optimized structural parameters of conformers of N-protonated noradrenaline were used as input for a full geometry optimization and subsequent calculation of total and relative energies at the B3LYP/6–31G(d,p) level of theory.[23,24] Total and relative energies are tabulated in the Supplementary data (Table S2).

The G3-based quantum chemistry method (G3MP2B3) was employed to produce even more reliable relative energies of each geometry optimized conformer at the B3LYP/6–31G (d,p) level of theory. G3MP2B3,[25–27] denoting the Gaussian-3 based (G3) Møller–Plesset second-order (MP2) method in combination with the 6–31G(d) basis set, level of theory was used in this phase. Total and relative energies are tabulated in the Supplementary data (Table S2). The frequencies and intensities of N-protonated noradrenaline conformers were computed at the B3LYP/6–31G(d,p) and G3MP2B3 levels of theory to verify their conformations as being true minima. The frequencies and intensities of selected conformers are tabulated and graphed in the Supplementary data (Table S3 and Fig. S1, respectively).

The thermodynamic functional changes of thermally corrected energy (ΔU), enthalpy (ΔH), Gibbs free energy (ΔG), and entropy (ΔS) were calculated from the computed U, H, G, and S values obtained for the optimized conformations (Supplementary data Table S4). All the computations were carried out using the G03 program package.[22]

Isodesmic reactions have the same number of the same

Can. J. Chem. Downloaded from www.nrcresearchpress.com by Xi'an Jiaotong University on 09/19/12
For personal use only.

Table 1. The relative energy (ΔE) and thermodynamic functional changes of energy (ΔU), enthalpy (ΔH), Gibbs free energy (ΔG), and entropy (ΔS) of conformers of 3,4-dihydroxytoluene at the G3MP2B3 level of theory.

Parameters [ω σ]	ΔE (kcal/mol)	ΔU (kcal/mol)	ΔH (kcal/mol)	ΔG (kcal/mol)	ΔS (cal/mol K^{-1})
[*a a*]	0	0	0	0	0
[*a s*]	4.17	4.11	4.11	4.37	–0.88
[*s s*]	0.07	–0.52	–0.52	1.32	–6.18

Note: 1 cal = 4.184 J.

Can. J. Chem. Downloaded from www.nrcresearchpress.com by Xi'an Jiaotong University on 09/19/12
For personal use only.

Fig. 4. Single variable cross sections of the potential energy hyper surface (PEHS) demonstrating the relative energy change with respect to the changes in different dihedral angles (ψ, φ, χ, ω, and σ) from the global minimum ($\psi = g^+$, $\varphi = g^-$, $\chi = a$, $\omega = a$, and $\sigma = a$). The points were computed at the B3LYP/6–31G(d,p) level of theory. These functions correspond to eqs. [2]–[6].

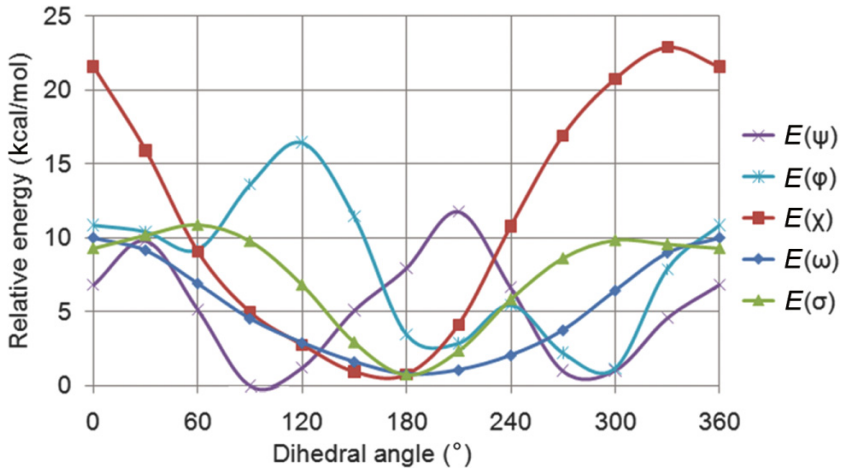

type of bonds at both sides of the equation. Consequently, their relative energy, enthalpy, or Gibbs free energy show which side of the equation is more stable. In this study, the isodesmic equation (Fig. 2) was used to assess the stabilizing or destabilizing effect of the two acidic OH groups in the catechol ring.

Results and discussion

Dihydroxytoluene

To determine the total and relative energies of N-protonated noradrenaline conformers depending on the orientation of catechol ring hydroxyl groups, the geometry optimizations of four different conformations of a model molecule (3,4-dihydroxytoluene, Fig. 3) were performed. Two possible catechol OH orientations ([*a a*] and [*s s*]) have internal hydrogen bonds, whereas the [*a s*] conformer lacks an intramolecular hydrogen bond. The [*s a*] orientation does not exist because of steric interactions.[7,8] The global energy minimum was the [*a a*] conformation (Table 1).

Relative thermodynamic functions of the three stable structures of 3,4-dihydroxytoluene (Table 1) and *U*, *H*, *G*, and *S* values (Supplementary data Table S5) were computed for later comparisons to that of N-protonated noradrenaline.

Conformation of N-protonated noradrenaline

In the study of N-protonated noradrenaline, five dihedral angles (ψ, ϕ, χ, ω, and σ) were examined to assess the free conformational space. A previous publication established the global minimum of the backbone and the side chain to be [g^+ g^- *a*],[16] where the study of 3,4-dihydroxytoluene determined the global minimum of the catechol ring hydroxyl groups to be in [*a a*] conformation. Therefore, five different 1-D cross sections were taken across [g^+ g^- a][*a a*] (Fig. 4). The total and relative energies of all five cross sections according to eqs. [2]–[6] are tabulated in Supplementary data Table S6.

The rotation about χ yields a single minimum (Fig. 4) corresponding to an *anti* orientation, consistent with previous literature.[16] On the other hand, the rotation about ω and σ yields one minimum and two minima, respectively, corresponding to both at *anti* or *syn* conformation, or pointing away from each other (one at *anti* and another at *syn*). Although the $E(\omega)$ function may exhibit two minima in a case of σ at *syn*, ω may assume *anti* orientation only where σ is already at *anti* conformation. The *R* configuration is used for the asymmetric α-carbon in all the conformers of N-protonated noradrenaline. The geometrical and energetic parameters, optimized at the B3LYP/6–31G(d,p) and G3MP2B3 levels of theory, were compiled (Supplementary data Table S2). The computations at the B3LYP/6–31G(d,p) and G3MP2B3 levels of theory yielded similar results. Since the geometries for the G3MP2B3 and B3LYP calculations were optimized using the 6–31G(d) and 6–31G(d,p) basis sets, respectively, this extra p-type polarization functions in the B3LYP calculations resulted in a small deviation between

Can. J. Chem. Downloaded from www.nrcresearchpress.com by Xi'an Jiaotong University on 09/19/12
For personal use only.

Fig. 5. (A) The contour energy map of N-protonated noradrenaline computed at the B3LYP/6–31G(d,p) level of theory with respect to changes in ψ and φ (χ, ω, and σ fixed at the *anti* position). (B) The potential energy surface (PES) cross section of the potential energy hyper surface (PEHS) associated with N-protonated noradrenaline computed at the B3LYP/6–31G(d,p) level of theory with respect to changes in ψ and φ (χ, ω, and σ fixed at the *anti* position). This 2-D cross section corresponds to eq. [7]. The energy minima are indicated with the ψ and φ conformations.

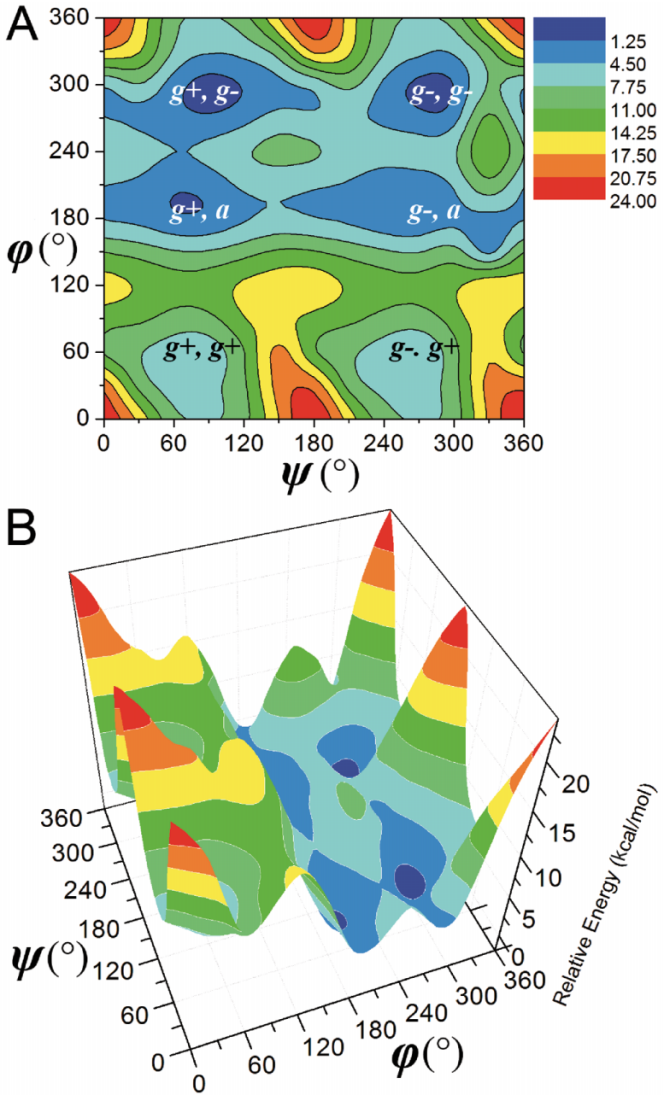

the two sets of dihedral angles. The computed results are presented using a PES cross section (Fig. 5). Having the three dihedrals (χ, ω, and σ) fixed at their corresponding lowest minimum orientation, the anticipated PEHS was simplified to a 2-D cross section (eq. [7]. This PES shows six minima (m) ($m_\psi \times m_\phi \times m_\chi = 2 \times 3 \times 1$; the same results were obtained from the N-PβHβPEA).[16] Combining all the possible orientations of the N-PβHβPEA[16] and the catechol ring hydroxyl groups (N) ($N_{[\psi\ \phi\ \chi]} \times N_{[\omega\ \sigma]} = 6 \times 3$), 18 molecular structures of N-protonated noradrenaline were constructed and the dipole moment variation of the these structures were summarized (Fig. 6 and Supplementary data Fig. S2). With the introduction of the catechol ring hydroxyl groups, the total dipole moment values, as well as their components, became slightly larger, but did not make a significant alteration in the trend from the dipole moment values of N-PβHβPEA.[16]

The optimized geometries revealed differences in the two phenolic C–O bond lengths from the various conformers of N-protonated noradrenaline as well as their shrinkages with respect to 3,4-dihydroxytoluene (Supplementary data Table S7). The two catechol ring hydroxyl groups differed in not only meta or para location, but also in their involvement in their hydrogen bonding. In the [*a s*] conformations, there is no hydrogen bonding, therefore, the two phenolic C–O bond lengths are roughly the same. However, in the [*a a*] and [*s s*] conformations, one of the catechol ring hydroxyl groups is a proton donor and the other one is a proton acceptor; the proton-donating phenolic OH had a shorter C–O bond length of 1.365 Å, whereas the proton-accepting phenolic OH had a longer C–O bond length of 1.380 Å. The C–O bond length differences were in the vicinity of 0.015 Å or 1.5 pm (Fig. 7). The shorter C–O bond length indicates strong conjugativity between the oxygen atom and the benzene ring.

Thermodynamic functions

To examine the molecular stability of noradrenaline in the 18 molecular structures, the thermodynamic functions and ΔU for the conformers of N-protonated noradrenaline at two levels of theory were computed and summarized (Supplementary data Tables S4 and S8, respectively). Their relative values are given (Table 2), showing ΔH, ΔG, and ΔS for each conformer of N-protonated noradrenaline. The ΔS for N-protonated noradrenaline was always positive compared with the entropy of the lowest energy conformation [g^+ g^- *a*] [*a a*] except for the [g^- g^- *a*][*a s*] orientation. Also, the ΔG values were significantly higher in the [*a s*] orientation for ω and σ than in the [*a a*] and [*s s*] orientations.

The distribution of the conformational ΔG values for N-protonated noradrenaline (labeled as ΔG_{NA}) was plotted as a function of the previously reported ΔG values of the dehydroxylated model compound, N-PβHβPEA[16] (labeled as ΔG_M) (Fig. 8). The three sets of catechol ring OH orientation [*a a*], [*a s*], and [*s s*] fall into three clusters. In each cluster, the [g^+ g^+ *a*] and [g^- g^+ *a*] conformers had higher ΔG values than the other conformers. The four lowest free energy conformers of the [*a s*] cluster had similar ΔG values (~6 kcal) to the highest free energy conformers of the [*a a*] and [*s s*] clusters.

Conformations 1, 7, and 13 were the highest points for $\psi = g^+$ (Fig. 8). Most of the plot lines for each cluster were close to the 45° identity line except two of those that end with conformations 7 and 13. For $\psi = g^+$, the [*s s*] and [*a s*] conformation lines were shifted up by ~2 and 6 kcal/mol (1 cal = 4.184 J), respectively, in comparison with the [*a a*] conformation. Nevertheless, conformers 7 and 13 had back-stabilization by 1.18 and 1.58 kcal/mol, respectively. Note that the 2 and 6 kcal/mol up shift of the two lines were due to the ineffectiveness of the phenolic OH hydrogen bonds of the catechol ring. These values did not deviate much from the 1.32 and 4.37 kcal/mol observed in the case of 3,4-dihydroxytoluene (Table 1). However, the back-stabilization may be due to some favourable electron distribution that occurs in conformers 7 and 13. The 0.018 Å shortening of the C–O bond length, while others were shortened only by 0.016 or

Fig. 6. Three prominent conformations (conformation Nos. 3, 9, and 15) of N-protonated noradrenaline and dipole moments (*X*, *Y*, *Z*, and total) of each conformer and model compound (in the first column), computed at the G3MP2B3 level of theory. Each dipole moment is measured in Debye, field-independent basis, and its origin is located at the center of mass, since dipole moments of charged species are not coordinate independent (see Supplementary data Fig. S2 for all the 18 structures).

	[a a]	[a s]	[s s]
[g^+ g^- a] X= -6.0 Y= -0.8 Z= 3.8	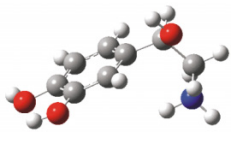 3	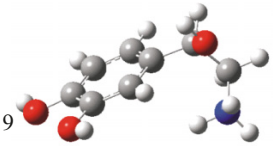 9	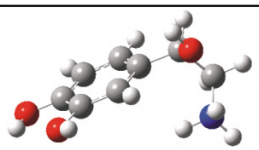 15
	X= -6.2 Y= -0.3 Z= 4.0	X= -8.7 Y= -0.5 Z= 3.6	X= -9.0 Y= -3.0 Z= 3.3
Total= 7.1	Total= 7.4	Total= 9.4	Total= 10.0

Fig. 7. An illustration depicting meta and para C–O bond lengths of phenolic hydroxyl groups in the hydrogen-bonded structure. Similar bond lengths are seen in both 3,4-dihydroxytoluene and N-protonated noradrenaline.

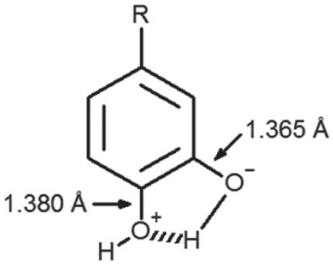

0.017 Å, also supports the notion that the oxygen lone pairs are slightly more extensively involved in stabilization (Supplementary data Table S7).

The correlation of the two μ_x components (Fig. 9) demonstrates that such a dipole moment increases upon the entrance of the two OH groups into the benzene ring. Therefore, it does appear that the back-stabilization of conformers 7 and 13 indicates a slightly more effective conjugative stabilization, involving the lone pair of the *para*-phenolic OH group and the benzene π system.

Isodesmic reaction

To assess the stabilizing or destabilizing effect of the two phenolic OH groups in the catechol ring, any thermodynamic function (Z) may be calculated for the isodesmic reaction (shown in Fig. 10) using eq. [8].

$$[8] \quad \Delta Z_{\mathrm{I}} = Z_{\mathrm{products}} - Z_{\mathrm{reactants}} = (Z_{\mathrm{NA}} + Z_{\mathrm{toluene}}) - (Z_{\mathrm{N\text{-}P\beta H\beta PEA}} + Z_{\mathrm{3,4\text{-}dihydroxytoluene}})$$

The contribution to the thermodynamic functions owing to hydrogen bonding (HB) is calculated by eqs. [9]–[11] with respect to the most stable [*a a*] phenolic OH orientation.

$$[9] \quad \Delta\Delta H_{\mathrm{HB}} = [\Delta H_{\mathrm{NA}} - \Delta H_{\mathrm{M}}] - \Delta\Delta H_{\mathrm{I}}$$

$$[10] \quad \Delta\Delta G_{\mathrm{HB}} = [\Delta G_{\mathrm{NA}} - \Delta G_{\mathrm{M}}] - \Delta\Delta G_{\mathrm{I}}$$

$$[11] \quad \Delta\Delta S_{\mathrm{HB}} = [\Delta S_{\mathrm{NA}} - \Delta S_{\mathrm{M}}] - \Delta\Delta S_{\mathrm{I}}$$

The computed relative HB values (eqs. [9]–[11]) obtained for N-protonated noradrenaline (Supplementary data Table S9) are in fact identical to those obtained for 3,4-dihydroxytoluene (Table 1). The various thermodynamic value differences of the conformations of N-protonated noradrenaline and N-PβHβPEA[16] compared with the corresponding global minimum conformation and between reactants and products in the isodesmic reaction are computed (Supplementary data Table S9). The Gibbs free energies of N-PβHβPEA[16], 3,4-dihydroxytoluene, N-protonated noradrenaline, and toluene and the added Gibbs free energies of reactants and products were also tabulated (Supplementary data Table S10).

The Born–Haber cycle for the two selected conformer pairs ([g^+ g^+ a] (conformer A) and [g^+ g^- a] (conformer B)) were graphed with molecular schematics of the isodesmic reactions (Fig. 10). The pair of phenolic hydroxyl groups was incorporated in the [*a s*] orientation. The ΔG during the isodesmic reaction differs between conformer A and conformer B, with ΔG_{I} values of –2.10 and –0.89 kcal/mol, respectively. This difference suggests that the intramolecular stabilization caused by the catechol ring hydroxyl groups is greater in the absence of the electrostatic internal hydrogen bond between the hydroxyl group on the backbone and the amine group (HO–HN) as in conformer A than in its presence as in conformer B, where the ΔG_{I} for the isodesmic reaction is negligible (–0.89 kcal/mol). A similar difference is observed between the same conformers with the phenolic hydroxyl groups in the [*s s*] orientation.

For all the conformers of N-protonated noradrenaline, the [g^- g^+ a] and [g^+ g^+ a] conformations of the [ψ, φ, χ] dihedral angles resulted in much higher change in G than any other conformations. Out of all the conformers, [*a s*] conformers of the [ω σ] dihedral angles had considerably higher changes in G than any other conformations. According to the isodesmic reaction, the catechol ring hydroxyl groups were stabilizing in conformations 13 ([g^+ g^+ a][*s s*]) and 18 ([g^- g^- a][*s s*]) only in relation to lowest energy conformation 3 ([g^+ g^- a][*a a*]). Since their $\Delta\Delta G_{\mathrm{I}}$ values were negative, and the $\Delta\Delta G_{\mathrm{I}}$ values for all the other conformers were

Can. J. Chem. Downloaded from www.nrcresearchpress.com by Xi'an Jiaotong University on 09/19/12
For personal use only.

Can. J. Chem. Downloaded from www.nrcresearchpress.com by Xi'an Jiaotong University on 09/19/12
For personal use only.

Table 2. The thermodynamic functional changes of enthalpy (ΔH), Gibbs free energy (ΔG), and entropy (ΔS) of conformers of N-protonated noradrenaline computed at the B3LYP/6–31G(d,p) and G3MP2B3 levels of theory.

		ΔH (kcal/mol)		ΔG (kcal/mol)		ΔS (cal/mol K^{-1})	
Conformer	Parameters ([ψ, φ, χ][ω σ])	G3MP2B3	B3LYP/6–31G(d,p)	G3MP2B3	B3LYP/6–31G(d,p)	G3MP2B3	B3LYP/6–31G(d,p)
1	[g^+ g^+ a][a a]	5.63	5.60	5.14	5.13	1.65	1.58
2	[g^+ a a][a a]	0.98	1.02	0.52	0.55	1.52	1.58
3	[g^+ g^- a][a a]	0.00	0.00	0.00	0.00	0.00	0.00
4	[g^- g^+ a][a a]	5.40	5.37	5.17	5.12	0.77	0.84
5	[g^- a a][a a]	1.34	1.39	0.88	0.95	1.54	1.49
6	[g^- g^- a][a a]	0.41	0.38	0.36	0.32	0.17	0.21
7	[g^+ g^+ a][a s]	10.34	10.26	10.02	9.94	1.07	1.08
8	[g^+ a a][a s]	6.47	6.48	6.14	6.13	1.10	1.18
9	[g^+ g^- a][a s]	6.28	6.22	6.20	6.06	0.27	0.56
10	[g^- g^+ a][a s]	11.43	11.39	10.82	10.82	2.04	1.90
11	[g^- a a][a s]	6.54	6.56	6.02	5.99	1.76	1.89
12	[g^- g^- a][a s]	5.47	5.41	5.48	5.41	–0.03	0.02
13	[g^+ g^+ a][s s]	6.14	6.10	5.81	5.78	1.12	1.06
14	[g^+ a a][s s]	2.56	2.60	2.16	2.17	1.36	1.45
15	[g^+ g^- a][s s]	2.59	2.56	2.39	2.35	0.69	0.70
16	[g^- g^+ a][s s]	7.60	7.63	6.60	6.68	3.35	3.19
17	[g^- a a][s s]	2.43	2.48	1.86	1.86	1.92	2.07
18	[g^- g^- a][s s]	1.33	1.30	1.30	1.27	0.10	0.11

Note: 1 cal = 4.184 J.

Published by NRC Research Press

Can. J. Chem. Downloaded from www.nrcresearchpress.com by Xi'an Jiaotong University on 09/19/12
For personal use only.

Fig. 8. Comparison plots of Gibbs free energy differences (ΔG) for the conformations of N-protonated noradrenaline (NA) and dehydroxylated model compound (M, N-PβHβPEA), computed at the G3MP2B3 level of theory. The ΔG values are compiled in Supplementary data Table S9). Reference lines, starting at the ΔG values of [g^+ g^- a] and [g^- g^- a] conformers (leftmost points in each cluster), are drawn to verify the effect of the catechol ring hydroxyl groups for NA. Also, the difference between the highest energy of each orientation of the catechol ring hydroxyl groups and the energy gained from each reference line are calculated to demonstrate the stabilizing effect of the catechol ring hydroxyl groups. The ΔG_M values are taken from Lee et al.[16]

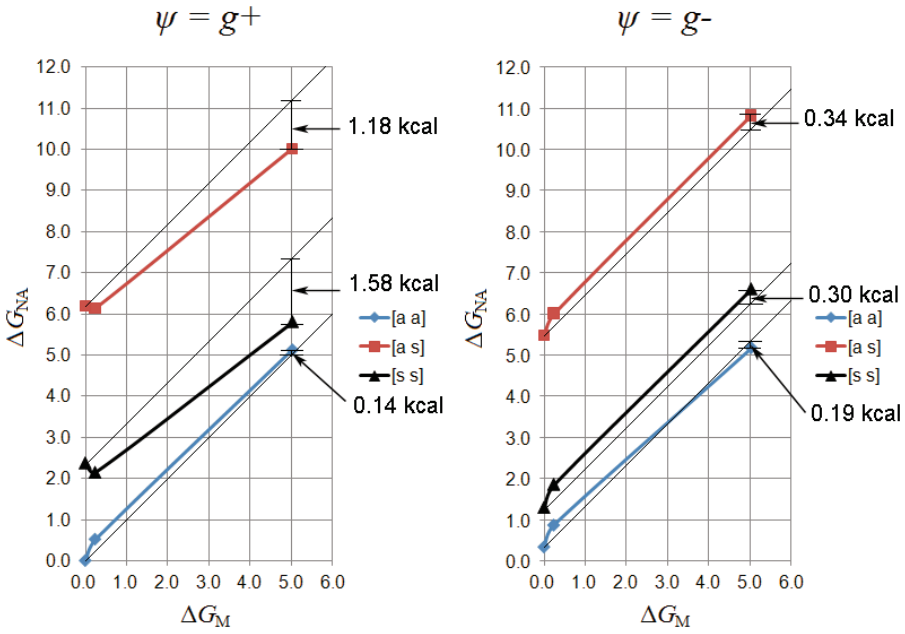

Fig. 9. The x-axis dipole moment (μ_x) comparison between the conformations of N-protonated noradrenaline (NA) and the conformations of dehydroxylated model compound (M, N-PβHβPEA), computed at the G3MP2B3 level of theory. A correlation (line of best fit) is steeper ($m > 1$) than the reference line ($m = 1$). The μ_x (M) values are taken from Lee et al.[16]

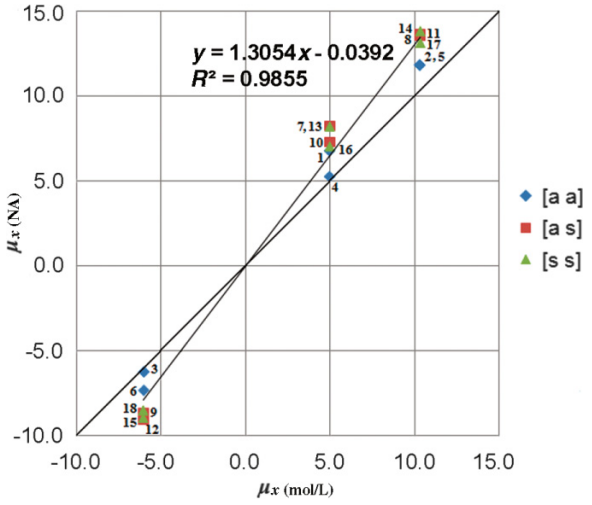

positive, the straight line obtained for four out of the six conformers in each of the three clusters (i.e., [a a], [a s], and [s s]) (Fig. 11) indicates that, with an increase in $\Delta\Delta G_I$ values, the conformational ΔG_{NA} values also increase proportionally. Note that the tangents do not differ much from unity.

Of the three possible orientations of the two catechol ring hydroxyl groups, it appears that the [a s] conformation is the least stable, lacking the internal hydrogen bond. Consequently, it is conceivable that this arrangement may form the hydrogen-bonded complexes at the two serine residues of the adrenergic receptor (Fig. 12). Although the minimum energy orientation of the phenolic OH groups in the catechol moiety is co-planar with the benzene ring, a slight distortion from the co-planarity can be seen[10] as it requires less energy than that gained from forming a hydrogen bond complex with a serine OH.

The nature of the hydrogen bonding of the catechol ring hydroxyl groups has been considered previously.[6,7,9–13] Because of the greater stability of [a a] orientation, it seemed logical to consider that the [a a] conformation is the prime candidate in the docking process of noradrenaline. Alternatively, the possibility does exist that the most stable [a a] conformation may convert to the least stable [a s] conformation (Fig. 12), but this would only be possible if new hydrogen bonds to the serine residues would compensate this docking process energetically. Either some exothermicity or at least thermoneutrality would be observed as a result of the docking process of noradrenaline to the adrenergic receptor.

Needless to say, the side chain conformation of noradrenaline molecule also plays the significant role in the docking process.[10,12] However, this paper focuses the attention to the conformation of the catechol ring hydroxyl groups.

Conclusions

The geometry optimization revealed the existence of three orientations for the catechol hydroxyl groups and six confor-

Fig. 10. Gibbs free energy (G) of a Born–Haber cycle for an isodesmic reaction with catechol ring hydroxyl groups in an [a s] conformation involving two conformers ([g^+ g^+ a] and [g^+ g^- a]; see Supplementary data Tables S9 and S10 for relative G values of the isodesmic reaction and calculated G values of the conformers, respectively). The results indicate that the incorporation of the two phenolic OH groups affects the conformational stability in a different extent.

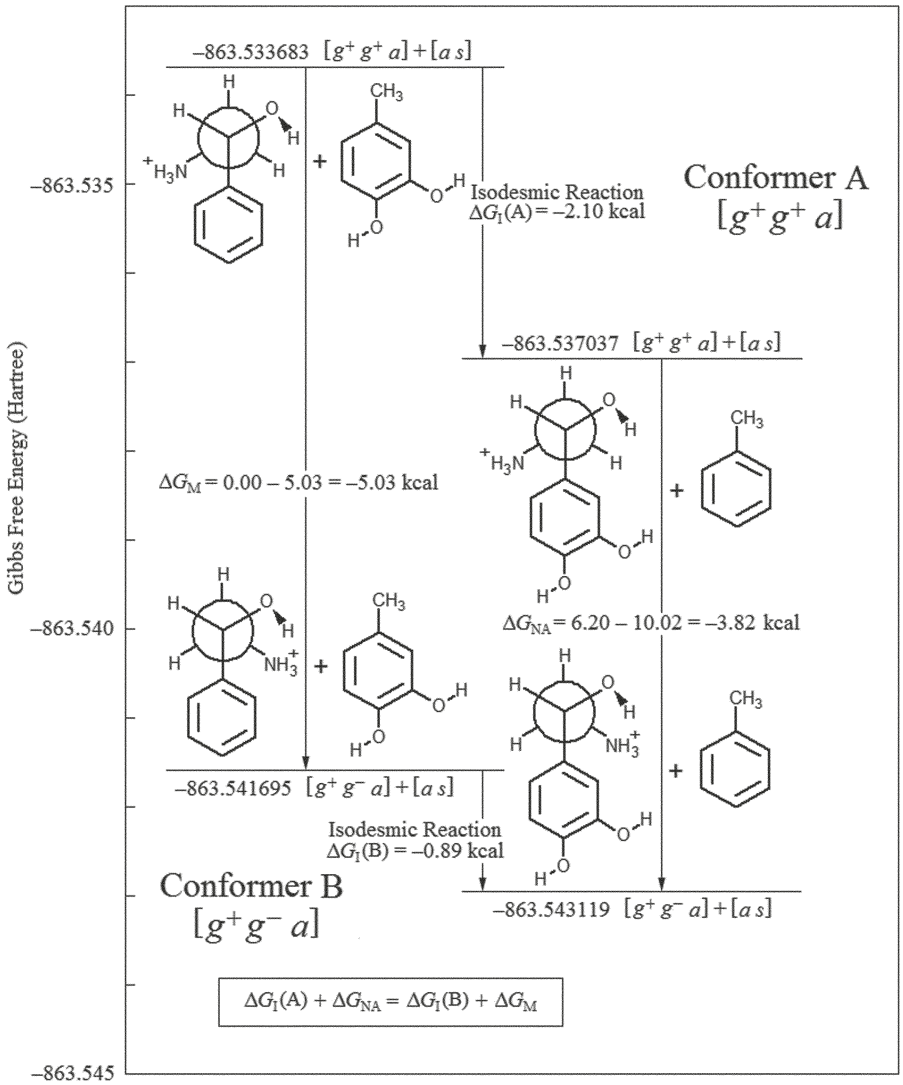

mations for the side chain of N-protonated noradrenaline, which resulted in $N_{[\omega\ \sigma]} \times N_{[\psi\ \phi\ \chi]} = 3 \times 6 = 18$ distinctly different structures. Thermodynamic functions revealed that the energetics are about the same as what might have been predicted on the basis of 3,4-dihydroxytoluene and N-protonated β-hydroxy-β-phenylethylamine[16] for 12 conformers ($N_{[\omega\ \sigma]} \times N_{[g+\ a\ a]\text{ and }[g+\ g-\ a]\text{ and }[g-\ a\ a]\text{ and }[g-\ g-\ a]} = 3 \times 4$). However, six conformers ($N_{[\omega\ \sigma]} \times N_{[g+\ g+\ a]\text{ and }[g-\ g+\ a]} = 3 \times 2$) showed some noticeable destabilization where, in two cases, the destabilization was partially compensated because of conjugative stabilization between the *para*-phenolic hydroxyl lone pair and the benzene ring. These were structure 7, i.e., [g^+ g^+ a][a s], and structure 13, i.e., [g^+ g^+ a][s s]. The issue has also been raised that the least stable conformers, i.e., [a s], may be involved in the docking process to the adrenergic receptor, and the energy requirement would need to be compensated for by the new hydrogen bonds forming in the complex.

Supplementary data

Supplementary data are available with the article through the journal Web site (www.nrcresearchpress.com/cjc).

Acknowledgements

D.J.R.L. and N.J.G. thank the Vice-Dean of the Faculty of Arts and Science, University of Toronto, for support within the Research Opportunity Program associated with their participation at the 2008 Summer Workshop held at the University of Szeged, Szeged, Hungary. The continuous support of the Global Institute of Computational Molecular and Materials Science (www.giocomms.org) and Drug Discovery Research Center (http://drugcent.com) are gratefully acknowledged. We thank L. Müller and M. Labádi for the administration of the computing systems used for this work. This work was supported by TAMOP4.2.1/B-09-1/KNOV-210-0005 and Faculty Grant CS-007/2010.

Can. J. Chem. Downloaded from www.nrcresearchpress.com by Xi'an Jiaotong University on 09/19/12
For personal use only.

Can. J. Chem. Downloaded from www.nrcresearchpress.com by Xi'an Jiaotong University on 09/19/12
For personal use only.

Fig. 11. A Gibbs free energy comparison between the conformations of N-protonated noradrenaline (ΔG_{NA}) and the changes (ΔG_I) and relative changes ($\Delta\Delta G_I$) in the isodesmic reactions, computed at the G3MP2B3 level of theory.

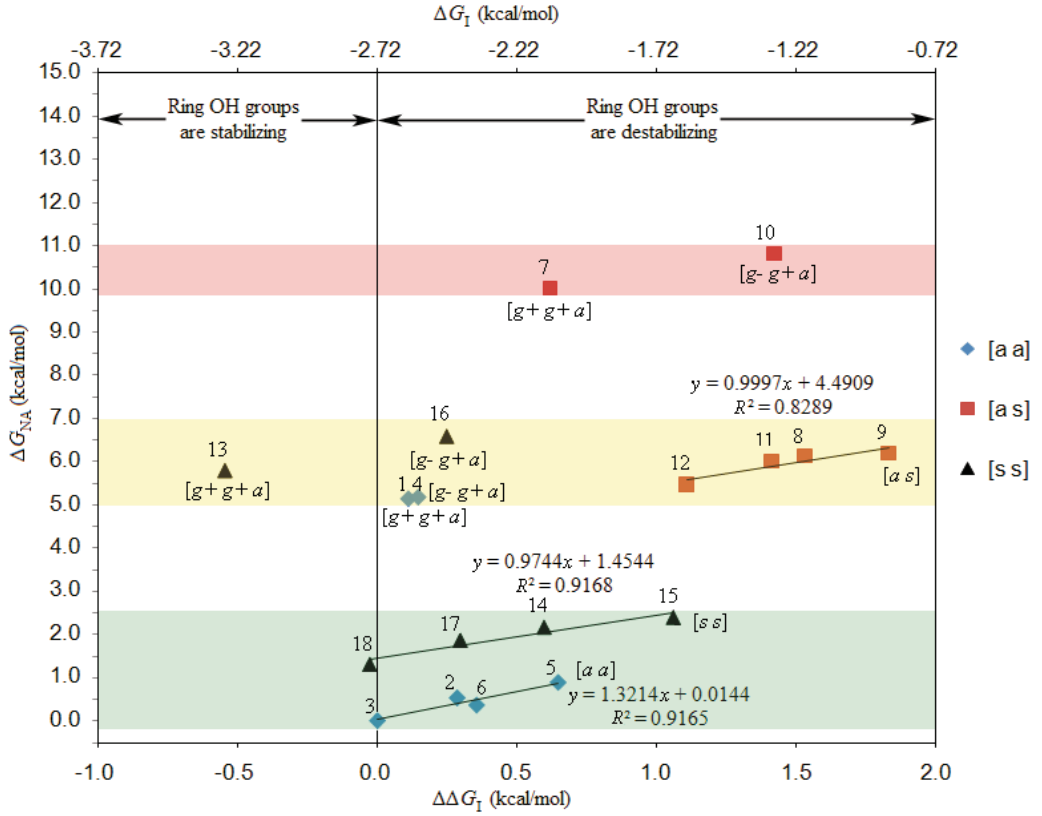

Fig. 12. A schematic illustration of the formation of hydrogen-bonded complexes at the two serine residues of the adrenergic receptor. "Ser-192 preferentially interacts with *para*-hydroxyl group, while Ser-188 (and, to minor extent, Ser-158) with *meta*-hydroxyl group",[10] where Ser-158 is not included in this figure for having only a minor interaction. The energetics of conformers 1, 7, and 13 are shown on the right-hand side in terms of ΔG (kcal/mol, 1 cal = 4.184 J), computed at the G3MP2B3 level of theory.

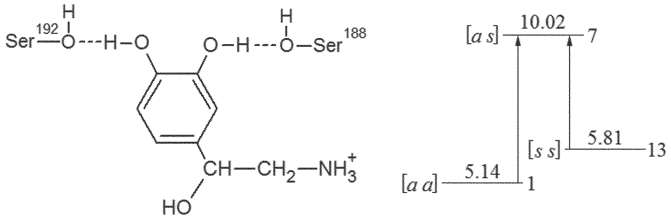

References

(1) Brunello, N.; Blier, P.; Judd, L. L.; Mendlewicz, J.; Nelson, C. J.; Souery, D.; Zohar, J.; Racagni, G. *Int. Clin. Psychopharmacol.* **2003** *18* (4), 191. doi:10.1097/00004850-200307000-00001.

(2) McClung, C. A. *Pharmacol. Ther.* **2007** *114* (2), 222. doi:10.1016/j.pharmthera.2007.02.003.

(3) Werner, F.; Covenas, R. *Int. J. Neurosci.* **2010** *120* (7), 455. doi:10.3109/00207454.2010.483651.

(4) Mitsuda, H.; Miyazaki, M.; Nielsen, I. B.; Carcabal, P.; Dedonder, C.; Jouvet, C.; Ishiuchi, S.; Fujii, M. *J. Phys. Chem. Lett* **2010** *1* (7), 1130. doi:10.1021/jz100186h.

(5) Corona-Avendano, S.; Rojas-Hernandez, A.; Romero-Romo, M. A.; Pardave, M. P.; Ramirez-Silva, M. T. *Biomol. Spec* **2005** *61* (13–14), 3139. doi:10.1016/j.saa.2004.11.047.

(6) Snoek, L. C.; van Mourik, T.; Simons, J. P. *Mol. Phys.* **2003** *101* (9), 1239. doi:10.1080/0026897031000099853.

(7) van Mourik, T.; Fruchtl, H. A. *Mol. Phys.* **2005** *103*, 1641. doi:10.1080/00268970500052338.

(8) van Mourik, T. *Chem. Phys. Lett.* **2005** *414* (4–6), 364 doi:10.1016/j.cplett.2005.08.111.

(9) Hwa, J.; Perez, D. M. *J. Biol. Chem.* **1996** *271* (11), 6322. doi:10.1074/jbc.271.11.6322.

(10) Pedretti, A.; Silva, M. E.; Villa, L.; Vistoli, G. *Biochem. Biophys. Res. Commun.* **2004** *319* (2), 493. doi:10.1016/j.bbrc.2004.04.149.

(11) Alagona, G.; Ghio, C. *Int. J. Quantum Chem.* **2002** *90* (2), 641. doi:10.1002/qua.964.

(12) Nagy, P. I.; Alagona, G.; Ghio, C.; Takacs-Novak, K. *J. Am. Chem. Soc.* **2003** *125* (9), 2770. doi:10.1021/ja028952n.

(13) Snoek, L. C.; van Mourik, T.; Çarçabal, P.; Simons, J. P. *Phys. Chem. Chem. Phys.* **2003** *5*, 4519. doi:10.1039/b307063h.

(14) Alagona, G.; Ghio, C. *Chem. Phys.* **1996** *204* (2-3), 239. doi:10.1016/0301-0104(95)00295-2.

(15) Nagy, P. I.; Alagona, G.; Ghio, C. *J. Am. Chem. Soc.* **1999** *121* (20), 4804. doi:10.1021/ja981528v.

(16) Lee, D. R.; Galant, N. J.; Wang, H.; Mucsi, Z.; Setiadi, D. H.; Viskolcz, B.; Csizmadia, I. G. *J. Phys. Chem. A* **2009** *113* (11), 2507. doi:10.1021/jp807353n.

(17) Hehre, W. J.; Radom, L.; Schleyer, P. R.; Pople, J. A. *Ab Initio Molecular Orbital Theory;* John Wiley & Sons: New York, 1986.

(18) Roothaan, C. C. J. *Rev. Mod. Phys.* **1951** *23*, 69. doi:10.1103/RevModPhys.23.69.

(19) Hehre, W. J.; Ditchfield, R.; Pople, J. A. *J. Chem. Phys.* **1972** *56* (5), 2257. doi:10.1063/1.1677527.
(20) Ditchfield, R.; Hehre, W. J.; Pople, J. A. *J. Chem. Phys.* **1971** *54* (2), 724. doi:10.1063/1.1674902.
(21) Hariharan, P. C.; Pople, J. A. *Theor. Chim. Acta* **1973** *28* (3), 213. doi:10.1007/BF00533485.
(22) Frisch, M. J.; Trucks, G. W.; Schlegel, H. B.; Scuseria, G. E.; Robb, M. A.; Cheeseman, J. R.; Montgomery, J. A., Jr.; Vreven, T.; Kudin, K. N.; Burant, J. C.; Millam, J. M.; Iyengar, S. S.; Tomasi, J.; Barone, H.; Mennucci, B.; Cossi, M.; Scalmani, G.; Rega, N.; Petersson, G. A.; Nakatsuji, H.; Hada, M.; Ehara, M.; Toyota, K.; Fukada, R.; Hasegawa, J.; Ishida, M.; Nakajima, T.; Honda, Y.; Kitao, O.; Nakai, H.; Klene, M. i, X.; Knox, J. E.; Hratchian, H. P.; Cross, J. B.; Bakken, V.; Adamo, C.; Jaramillo, J.; Gomperts, R.; Stratmann, R. E.; Yazyev, O.; Austin, A. J.; Cammi, R.; Pomelli, C.; Ochterski, J. W.; Ayala, P. Y.; Morokuma, K.; Voth, G. A.; Salvador, P.; Dannenberg, J. J.; Zakrzewski, V. G.; Dapprich, S.; Daniels, A. D.; Strain, M. C.; Farkas, O.; Maliek, D. K.; Rabuck, A. D.; Raghavachari, K.; Foresman, J. B.; Ortiz, J. V.; Cui, Q.; Baboul, A. G.; Clifford, S.; Cioslowski, J.; Stefanov, B. B.; Liu, G.; Liashenko, A.; Piskorz, P.; Komaromi, I.; Martin, R. L.; Fox, D. J.; Keith, T.; Al-Laham, M. A.; Peng, C. Y.; Nanayakkara, A.; Challacombe, M.; Gill, P. M. W.; Johnson, B.; Chen, W.; Wong, M. W.; Gonzalez, C.; Pople, J. A. *Gaussian 03*, Revision B.01; Gaussian Inc.: Wallingford, CT, 2004.
(23) Becke, A. D. *J. Chem. Phys.* **1996** *104* (3), 1040. doi:10.1063/1.470829.
(24) Lee, C. T.; Yang, W. T.; Parr, R. G. *Phys. Rev. B* **1988** *37* (2), 785. doi:10.1103/PhysRevB.37.785.
(25) Curtiss, L. A.; Redfern, P. C.; Raghavachari, K.; Rassolov, V.; Pople, J. A. *J. Chem. Phys.* **1999** *110* (10), 4703. doi:10.1063/1.478385.
(26) Curtiss, L. A.; Raghavachari, K.; Redfern, P. C.; Rassolov, V.; Pople, J. A. *J. Chem. Phys.* **1998** *109* (18), 7764. doi:10.1063/1.477422.
(27) Baboul, A. G.; Curtiss, L. A.; Redfern, P. C.; Raghavachari, K. *J. Chem. Phys.* **1999** *110* (16), 7650. doi:10.1063/1.478676.

Can. J. Chem. Downloaded from www.nrcresearchpress.com by Xi'an Jiaotong University on 09/19/12
For personal use only.

MINIREVIEW / MINISYNTHÈSE

Diffusion NMR and bicelle morphology

Peter M. Macdonald and Ronald Soong

Can. J. Chem. Downloaded from www.nrcresearchpress.com by Xi'an Jiaotong University on 09/19/12
For personal use only.

Abstract: This minireview focuses on diffusion NMR studies in bicelles. Following a discourse on diffusion fundamentals, and a comparative overview of fluorescence and NMR-based techniques for measuring diffusion, the pulsed field gradient (PFG) NMR diffusion method is introduced, emphasizing its specific advantages and limitations when applied to diffusion measurements in macroscopically oriented lamellar systems such as magnetically aligned bicelles. The utility of PFG NMR diffusion measurements in bicellar model membrane systems for examining lateral diffusion of membrane-bound molecular species is demonstrated, along with certain features of lateral diffusion that such studies illuminate. Further, those aspects of bicelle morphology that have been resolved using PFG NMR diffusion studies of various molecular weight soluble polymeric species are reviewed. The discussion concludes with an outline of future prospects for diffusion NMR studies in bicelles.

Key words: pulsed field gradient NMR, lateral diffusion, diffusion anisotropy, bicelle, PEGylated lipid, mixed bicelle model, pore size.

Résumé : Cette courte revue est focalisée sur les études par RMN de la diffusion dans les bicelles. Après une introduction sur les principes fondamentaux de la diffusion et un exposé général comparatif des techniques de mesure de la diffusion à base de fluorescence et de RMN, on introduit la méthode d'étude de la diffusion par RMN avec gradient du champ pulsé (GCP), en mettant en relief ses avantages et ses limitations spécifiques quand elle est appliquée à des mesures de diffusion dans des systèmes lamellaires macroscopiquement orientés, telles des bicelles magnétiquement alignées. On démontre l'utilité des mesures de diffusion par RMN/GCP dans des systèmes modèles de membranes bicellaires pour la détermination de la diffusion latérale d'espèces moléculaires liées à la membrane ainsi que pour la détermination de certaines caractéristiques de diffusion latérale sur lesquelles ces études jettent de la lumière. De plus, on passe en revue les aspects de la morphologie de bicelles qui ont été résolus à l'aide d'études de diffusion par RMN/GCP pour diverses espèces polymères solubles de poids moléculaires variés. La discussion se conclut par un synopsis des applications potentielles dans le futur des études par RMN de la diffusion dans des micelles.

Mots-clés : RMN avec gradient de champ pulsé, diffusion latérale, anisotropie de diffusion, bicelle, dérivés lipidiques du polyéthylèneglycol, modèle de bicelle mixte, taille des pores.

[Traduit par la Rédaction]

Introduction

Bicelles, or bilayered micelles, are model membranes widely employed as biomembrane mimics for NMR studies of membrane-associating biomolecules,[1–6] and as an orienting medium for NMR structural studies of soluble proteins and nucleic acids.[7–10] Their enduring popularity, evident from the many reviews describing their properties and uses,[11–22] stems in large part from their propensity to align in a magnetic field, and the enhanced NMR spectral resolution thus engendered.

Bicelles consist of mixtures of short-chain and long-chain amphiphiles,[23,24] as typified by the canonical mixture of dihexanoyl phosphatidylcholine (DHPC) and dimyristoyl phosphatidylcholine (DMPC) (see Fig. 1 for structures) introduced by Sanders and Shwonek.[25] In water, DMPC by itself assembles into extended lamellar bilayer sheets, whereas DHPC by itself prefers a micellar structure. Mixtures of the two, however, form single-bilayer thickness, DMPC-rich lamellae stabilized by a DHPC-rich coating at edge regions. Because bicelles are a soft material, fabricated through molecular self-assembly, they exhibit a rich, sometimes bedeviling, morphological plasticity, subject to influence by both environmental and compositional factors.

In the quest to more fully understand bicelle morphology a multitude of physical measurements have been brought to

Received 23 November 2010. Accepted 25 January 2011. Published at www.nrcresearchpress.com/cjc on 25 August 2011.

P.M. Macdonald and R. Soong.* Department of Chemistry, University of Toronto, Toronto, ON, Canada; Department of Chemical and Physical Sciences, University of Toronto Mississauga, 3359 Mississauga Road North, Mississauga, ON L5L 1C6, Canada.

Corresponding author: Peter M. Macdonald (e-mail: pm.macdonald@utoronto.ca).

*Present address: Department of Physical and Environmental Sciences, University of Toronto Scarborough, ON M1C 1A4, Canada.

Can. J. Chem. Downloaded from www.nrcresearchpress.com by Xi'an Jiaotong University on 09/19/12
For personal use only.

Fig. 1. Schematic of the morphological evolution of bicellar self-assemblies as a function of the molar ratio q = DMPC/DHPC. Pure dihexanoyl phosphatidylcholine (DHPC; black) forms micelles, whereas pure dimyristoyl phosphatidylcholine (DMPC; gray) forms lamellae. Mixtures of the two form disks at low q, or perforated lamellae at higher q, with DHPC occupying curved edge regions while DMPC forms a planar bilayer.

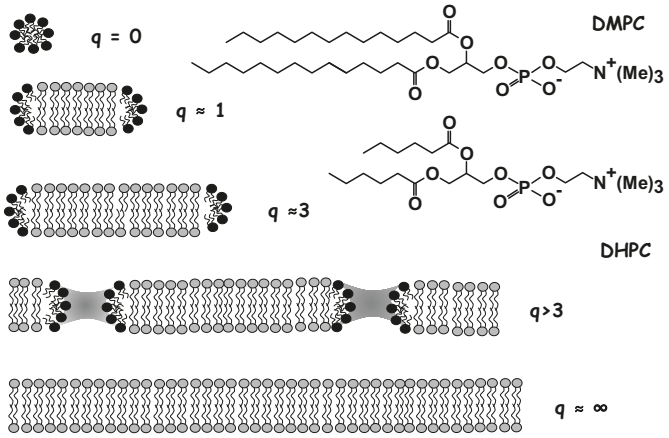

bear. These include electron microscopy (EM),[26–28] fluorescence spectroscopy,[29] NMR,[30–33] small angle X-ray scattering (SAXS),[34] and small angle neutron scattering (SANS).[18,34–39] From such studies, two of the major influences have been identified as being (*i*) the molar ratio (q) of long-chain to short-chain amphiphiles and (*ii*) temperature. Figure 1 illustrates schematically the general consensus that has emerged regarding the effects of q on bicelle morphology. At low q, bicelles adopt a discoidal morphology with DHPC occupying the edges of a DMPC-rich bilayer disk, as per the "ideal" bicelle model.[40] At higher q, the morphology evolves to a lamellar structure far larger in dimension than contemplated by the ideal bicelle model, and presumed to contain perforations stabilized by a coating of DHPC at the edges.

An NMR spectrum obtained from a bicelle sample will be influenced both by any residual anisotropic, i.e., orientation-dependent, interactions such as the chemical shift, or quadrupolar or dipolar interactions, which are present, and by the distribution of orientations across the sample. For example, as illustrated in Fig. 2, at temperatures below the DMPC gel-to-liquid-crystalline phase transition ($T_m \sim 25$ °C), bicelles cannot magnetically align, so there is a random distribution of bicelle orientations. Consequently, the ^{31}P NMR spectrum from DMPC consists of a broad resonance having a width ($\Delta\sigma = \sigma_{\parallel} - \sigma_{\perp}$) that reflects the size of the residual ^{31}P chemical shift anisotropy difference between the extrema for perpendicular ($\sigma_{\perp}$) and parallel ($\sigma_{\parallel}$) alignments of the bilayer normal relative to the direction of the magnetic field.

The line shape itself reflects the powder, i.e., random, probability distribution of bicelle orientations between those same extrema. Since DHPC is small, remains highly mobile, and favours regions of high curvature, it experiences effectively isotropic motional averaging under the identical conditions, and thus exhibits an isotropically narrow ^{31}P NMR resonance.

When the temperature is raised above the T_m of DMPC, the increased flexibility of the self-assemblies permits their reorganization, and magnetic alignment of bicelles becomes

Fig. 2. Magnetic alignment of bicelles and corresponding ^{31}P NMR spectra. (A) At temperatures below the the DMPC gel-to-liquid-crystalline phase transition (T_m) of dimyristoyl phosphatidylcholine (DMPC), bicelles do not magnetically align, thus yielding a powder pattern ^{31}P NMR spectrum for DMPC, with a width defined by the residual chemical anisotropy elements ($\Delta\sigma = \sigma_{\parallel} - \sigma_{\perp}$). Dihexanoyl phosphatidylcholine (DHPC) exhibits $\Delta\sigma = 0$ owing to its segregation into highly curved edge regions. (B) At $T > T_m$, spontaneous negative magnetic alignment can occur, wherein the normal to the bicellar planar bilayer regions are uniformly aligned perpendicular to the direction of the static magnetic field. Consequently, DMPC exhibits a ^{31}P NMR resonance at $\sigma_{\perp}$, whereas DHPC exhibits a frequency reflecting its equilibrium distribution between bilayer and edge regions. The smallest resonance visible is due to 1 mol% dimyristoylphosphatidylglycerol (DMPG), included to enhance stability. (C) Addition of lanthanides, such as Yb^{3+}, induces positive magnetic alignment, wherein the normal to the bicellar planar bilayer regions are uniformly aligned parallel to the direction of the static magnetic field. Consequently, DMPC exhibits a ^{31}P NMR resonance at $\sigma_{\parallel}$. The paramagnetic Yb^{3+} ions also cause NMR line broadening. Spectrum (B) was adapted from Soong and Macdonald.[41] Spectra (A) and (C) were provided courtesy of H. Morales.[42]

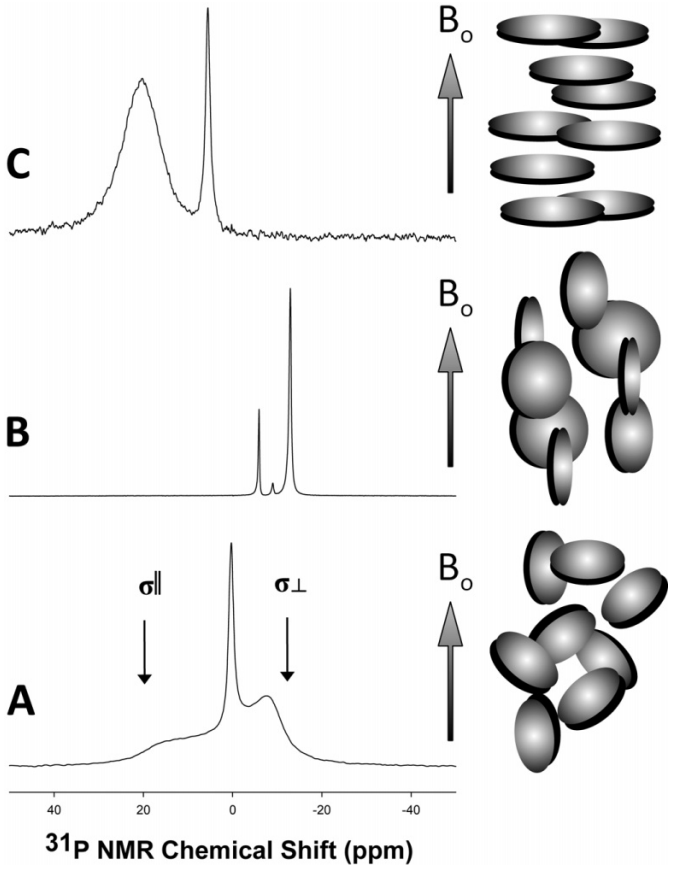

possible. The driving force is the interaction between the magnetic field and the magnetic susceptibility anisotropy of the bicelles, aided by cooperative interactions between adjacent bicellar lamellae that dampen thermal fluctuations.[43] The magnetic susceptibility anisotropy per unit volume is the sum of contributions from the individual lipids. This being a negative quantity for DMPC, the bicelles align spontaneously such that the normal to the plane of the bilayer is perpendicular

Can. J. Chem. Downloaded from www.nrcresearchpress.com by Xi'an Jiaotong University on 09/19/12
For personal use only.

to the direction of the magnetic field — the so-called negative magnetic alignment. Consequently, the ^{31}P NMR resonance from DMPC now consists of a narrow resonance, reflecting the narrow distribution of bilayer orientations under magnetic alignment, but at a frequency ($\sigma_\perp$) that still reflects the size of the residual ^{31}P chemical shift anisotropy for the perpendicular alignment. It is this combination of properties — enhanced spectral resolution while manifesting orientation-dependent interactions — that have made bicelles so attractive for NMR structural studies.

As first reported by Prosser et al.,[44–47] in the presence of surface-bound lanthanides having a positive magnetic susceptibility, examples being Tm^{3+}, Yb^{3+}, Er^{3+}, and Eu^{3+}, the direction of bicelle alignment is such that the normal to the planar lipid bilayer region lies parallel to the direction of the magnetic field — the so-called positive magnetic alignment shown schematically in Fig. 2. The corresponding ^{31}P NMR spectrum, likewise shown in Fig. 2, exhibits a narrow DMPC resonance at a frequency equal to $\sigma_\parallel$. Positive magnetic alignment of bicelles may also be achieved by incorporating phosphatidylcholines containing a biphenyl group,[48–50] peptides having phenyl ring side chains,[51] or membrane-associating aromatic amphiphiles.[52] Positively magnetically aligned bicelles are particularly useful for solid-state NMR studies of membrane proteins.

Despite these many studies, controversy persists and new aspects of bicelle morphology continue to emerge. Recently, for example, using SANS, the morphology of the magnetically alignable nematic phase of DMPC/DHPC bicelles was shown to consist of single-bilayer-thickness ribbonlike aggregates,[37,38] a result confirmed by cryo-TEM.[27] However, when the negatively charged phospholipid dimyristoylphosphatidylglycerol (DMPG) was added to such mixtures, a smectic phase was observed by SANS.[35] A smectic phase is also observed for the positively magnetically aligned state induced by lanthanide ions[53] and was proposed to consist of perforated "Swiss cheese"-like lamellae,[44] a morphology confirmed by SANS experiments[35,45] and supported by electron paramagnetic resonance[54] and NMR measurements.[55,56]

A further example concerns the location of DHPC in bicellar self-assemblies. It was originally conceived that DHPC remained strictly confined to highly curved edge regions owing to its presumed immiscibility with DMPC. A recent reinvestigation of ^{31}P NMR bicelle spectra has challenged this motion, suggesting that, on the contrary, DHPC becomes increasingly miscible with DMPC at higher temperatures, undergoing fast exchange, on the NMR time scale, between edge and planar regions of the bicelles.[57] Given the profound influence of the ratio DMPC:DHPC on bicelle morphology, the temperature-dependent redistribution of DHPC from edge to planar regions must have an equally profound effect, particularly on the size and (or) number of DHPC-lined lamellar perforations present at any one temperature.

This article provides a review of recent NMR diffusion studies in bicellar systems, emphasizing the perspectives that such studies have provided on bicelle morphology. Following a brief review of diffusion fundamentals and techniques for measuring diffusion, we describe exchange- and gradient-based NMR diffusion measurements, particularly as pertinent to lipid bilayer model membranes. The main body of the article describes results from our laboratory using pulsed field gradient (PFG) NMR diffusion measurements in magnetically aligned bicellar systems. We conclude with an outline of future prospects for NMR diffusion measurements in model membranes.

Diffusion

Diffusion is a fundamental physical property. Self-diffusion refers to thermally generated spontaneous centre-of-mass translational molecular motion occurring in the absence of any concentration gradient. It may be modeled as a random-walk process. For a spherical particle of hydrodynamic radius R_H diffusing in an isotropic medium of viscosity η, the diffusivity is quantified by the diffusion coefficient (D) given by the Stokes–Einstein equation,

$$[1] \qquad D = \frac{k_B T}{6\pi\eta R_H}$$

where k_B is the Boltzmann constant and T is the absolute temperature. Typical self-diffusion coefficients in liquid systems at room temperature range from 10^{-9} m^2 s^{-1} for small molecules to 10^{-12} m^2 s^{-1} for large polymers. Diffusion measurements are particularly useful for probing morphology in complex, disordered systems.

In many biological (and other) situations diffusion is inherently anisotropic. Examples include diffusion in the crowded cell cytoplasm, along a nerve axon, or within a biological membrane. In the most general case of anisotropic diffusion, the diffusion coefficient is described in terms of a second-rank symmetric tensor,

$$[2] \qquad \mathbf{D} = \begin{vmatrix} D_{xx} & D_{yx} & D_{zx} \\ D_{xy} & D_{yy} & D_{zy} \\ D_{xz} & D_{yz} & D_{zz} \end{vmatrix}$$

requiring that six independent tensor components D_{ij} be determined to fully specify the diffusion coefficient.[58] For the isotropic case, measuring diffusion in any one direction completely specifies the diffusion coefficient. For the specific case of lateral diffusion within a lipid bilayer membrane, a situation of central interest in this review, there are only two independent tensor components to consider: $D_\parallel$ and $D_\perp$, corresponding to diffusion parallel and perpendicular, respectively, to the bilayer normal,[59,60] as shown schematically in Fig. 3. The resulting diffusion tensor is

$$[3] \qquad \mathbf{D} = \begin{vmatrix} D_\perp & 0 & 0 \\ 0 & D_\perp & 0 \\ 0 & 0 & D_\parallel \end{vmatrix}$$

where $D_\perp$ is the lateral diffusion coefficient describing diffusion within the plane of the membrane. Generally, $D_\parallel << D_\perp$ and, therefore, can often be discounted.

From a theoretical perspective, lateral diffusion is modeled in terms of either a "free area" model[61–64] or a "hydrodynamic" model,[65,66] depending on the relative size of the diffusant versus the "solvent", i.e., the lipid molecules constituting the bilayer. For diffusants having a size comparable to the lipids, for example lipids and many drugs, the free area model predicts that lateral diffusion requires the availability

Can. J. Chem. Downloaded from www.nrcresearchpress.com by Xi'an Jiaotong University on 09/19/12
For personal use only.

Fig. 3. The diffusion tensor in the membrane frame of reference, relative to the laboratory frame of reference as defined by the magnetic field gradient direction, here assumed to lie parallel to the static magnetic field. Transforming from the membrane to the laboratory reference frame yields the relationship between the apparent diffusion coefficient and the diffusion tensor elements (see text).

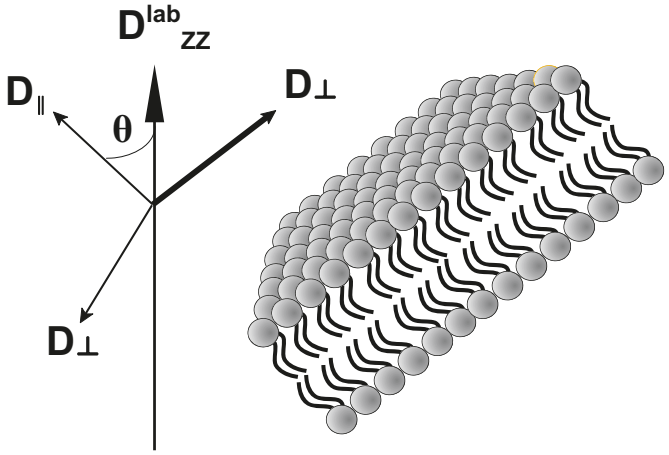

of sufficient free area per molecule at a given temperature ($a_f(T)$) relative to the close-packed area per molecule (a^*) plus a diffusant having sufficient kinetic energy to jump into the adjacent void, as per eq. [4]

$$[4] \qquad \mathbf{D} = D_0 \exp\left[\theta\frac{a*}{a_f(T)} - \frac{E_a}{RT}\right]$$

where D_0 is the instrinsic diffusion coefficient within the cage defined by the lattice, E_a is the activation energy, and θ is a scalar.[7,8] The free area model predicts an Arrhenius-type temperature dependence of lateral diffusion for diffusants in this size regime in model membrane systems.

For diffusants having a size far larger than that of the lipids, for example multi-helical transmembrane proteins, a continuum (or hydrodynamic) model was proposed by Saffman and Delbrück,[65,66] where

$$[5] \qquad \mathbf{D} \sim \left(\frac{kT}{4\pi\eta_m h}\right)\ln\left(\frac{\eta_m h}{\eta_w a} - 0.5772\right)$$

in which η_m and η_w are the viscosity of the membrane and the bathing medium, respectively, h is the membrane thickness, and a is the radius of the cylindrical membrane diffusant. The salient feature of eq. [5] is a very weak dependence on the size of the membrane diffusant in this size regime.

Fluorescence and diffusion

Of the many techniques for measuring diffusion, perhaps the most popular are those based on fluorescence, owing to the inherent advantages of speed, sensitivity, high spatial and time resolution, the ability to probe both in vitro and in vivo, and the comprehensive range of commercially available fluorophores tailored to particular applications and situations. The principal constraint is the requirement for a fluorescence signal associated with the molecule of interest having a particular photoresponse and photostability.

Fluorescence recovery after photobleaching (FRAP) is widely used to examine molecular mobility in a host of situations, and has been particularly useful in examining lateral mobility in biological membranes.[67–69] As the name implies, FRAP measures the kinetics of the recovery of fluorescence within a defined photobleached area or volume owing to diffusion of nonphotobleached molecules back into that region.

Fluorescence correlation spectroscopy (FCS), on the other hand, employs statistical analysis of fluctuations in the fluorescence signal intensity as fluorophores exit and enter a defined region to extract translational diffusion coefficients. FCS is readily used to determine diffusion coefficients in planar systems such as bilayers and biological membranes and employs a lower fluorophore concentration and lower laser power than FRAP.[70–74]

Both FRAP and FSC measure the behaviour of an ensemble of molecules. Single particle tracking (SPT), on the other hand, monitors the motion of individual fluorophore-labeled molecules using video microscopy to achieve high spatial (tens of nanometers) and temporal (tens of milliseconds) resolution.[75–77] The trajectory of an individual particle yields a net displacement (r) for a given observation period (t), which equates directly to the diffusion coefficient via the Einstein equation

$$[6] \qquad r^2 = 2dDt$$

where d is the dimensionality of the diffusion geometry, i.e., $d = 2$ for a planar lipid bilayer. From a collection of such trajectories, the statistical distribution of diffusion coefficients may be evaluated.

In model membranes, fluorescence studies of small molecule lateral diffusion confirm the Arrhenius-type temperature dependence predicted by the free area model.[67–69] For large transmembrane proteins, FCS results, for example, confirm that, as predicted by the hydrodynamic model, lateral diffusion depends only rather weakly on the number of transmembrane helices.[78]

In genuine biomembranes, FRAP and FCS results yield diffusion rates significantly slower than in model membranes for the corresponding diffusant. In cell membranes the situation is complicated by the possible presence of membrane crowding, heterogeneous lipid and protein distributions, confined and obstructed diffusion, and even directed flow. Recent SPT studies, for example, have revealed many such deviations from random diffusion in actual biomembranes, and this remains a highly active area of research, with the interpretations of the SPT observations still being the subject of controversy.[75–77]

NMR and diffusion

NMR approaches for measuring lateral diffusion in membranes can be divided broadly into two categories: those based on exchange studies in the presence of orientation-dependent interactions and those based on applying field gradients.

Exchange NMR and diffusion

In lipid bilayer membranes, residual anisotropic, i.e., orientation-dependent, interactions such as the chemical shift or quadrupolar or dipolar interactions, are generally present because of incomplete motional averaging experienced by membrane-associated molecules. Typically, in the biologically relevant liquid–crystalline state, i.e., at temperatures

Can. J. Chem. Downloaded from www.nrcresearchpress.com by Xi'an Jiaotong University on 09/19/12
For personal use only.

above T_m, there is more or less rapid free rotation about the molecule-fixed axis perpendicular to the plane of the membrane (i.e., parallel to the bilayer normal), whereas rotations about orthogonal axes are restricted because of lateral compression forces holding the membrane self-assembly together. Consequently, all such residual anisotropic interactions are reduced to the product of a scalar quantity $(\omega_{\parallel} - \omega_{\perp})$ and a simple angular dependence corresponding to the second-order Legendre polynomial $P_2(\theta) = 1/2(3\cos^2\theta - 1)$, such that

$$[7] \qquad \omega_i = \omega_{iso} + \frac{2}{3}(\omega_{\parallel} - \omega_{\perp})\frac{1}{2}(3\cos^2\theta_i - 1)$$

where ω_{iso} is the isotropic frequency, while $\omega_{\parallel}$, $\omega_{\perp}$, and θ, the angle between the bilayer normal and the magnetic field direction, are shown schematically in Fig. 4. Thus, each angle θ_i corresponds to a particular resonance frequency ω_i in the range $\Delta\omega = (\omega_{\parallel} - \omega_{\perp})$. The sin θ probability density for the distribution of angles θ on a sphere leads to the characteristic powder NMR spectral line shape.

For spherical liposomes having diameters below ~1 μm, the combination of rotational tumbling of the entire liposome plus lateral diffusion around the radius of curvature combine to produce a motional correlation time equal to, or shorter than, the inverse of the scalar $\Delta\omega = (\omega_{\parallel} - \omega_{\perp})$. The effect is to narrow the NMR line shape relative to the powder average and shorten the relaxation times. Using this effect, ^{31}P line shapes,[79,80] as well as ^{2}H transverse relaxation[81] and ^{1}H rotating frame longitudinal relaxation behaviours,[82] have been analyzed to extract lipid lateral diffusion coefficients. The method is predicated on knowledge of the mean radius and distribution of radial dimensions of the liposome population being examined, and is further limited by the poor resolution of different chemical sites inherent in the broad resonances observed plus the necessity to deconvolve the rotational tumbling correlation time from that owing to lateral diffusion.

For large diameter liposomes, exchange NMR spectroscopy (EXSY)[83] may be used to measure lateral diffusion coefficients by examining the frequency change that results from diffusion around the spherical radius of curvature as shown schematically in Fig. 4. Being a two-dimensional NMR technique, EXSY involves the usual preparation period, followed by an evolution period during which nuclear spins evolve at a frequency ω_A dictated by their initial angular position θ_A, a subsequent mixing time during which lateral diffusion may occur, and a final detection period during which nuclear spins evolve at a frequency ω_B dictated by their final angular position θ_B. In a two-dimensional NMR spectrum, therefore, lateral diffusion produces the appearance of resonance intensity at a two-dimensional frequency $\omega_A\omega_B$. The lateral diffusion coefficient is extracted from the kinetics of the spread of resonance intensity from on-diagonal ($\omega_A = \omega_B$) to off-diagonal frequencies ($\omega_A \neq \omega_B$) with increasing mixing time, taking into account the conditional probability densities of initial versus final angular positions and the radius of curvature of the spherical liposome.

EXSY has been used in this fashion to measure phospholipid lateral diffusion via ^{2}H[84] and ^{31}P resonances,[85–87] in multilamellar vesicles and in lipid bilayers on glass bead supports. The principle limitation is the considerable time required for spectral acquisition, given that separate two-dimensional powder spectra must be recorded across a sufficiently dense series of mixing times to obtain sufficiently accurate kinetics. Furthermore, the powder spectra permit only limited resolution of different species or of distributions of lateral diffusion coefficients. Finally, reasonably precise knowledge of the radius of the liposomal population being examined is essential to obtaining an accurate lateral diffusion coefficient.

Fig. 4. Exchange NMR spectroscopy (EXSY) detects lateral diffusion in spherical liposomes by virtue of changes in orientation-dependent interactions such as chemical shift anisotropy or dipolar or quadrupolar interactions. A nuclear spin initially at a position with angle θ_A corresponding to frequency ω_A, diffusing to a new position with angle θ_B corresponding to frequency ω_B, generates off-diagonal intensity at a two-dimensional frequency $\omega_A\omega_B$ in the EXSY spectrum.

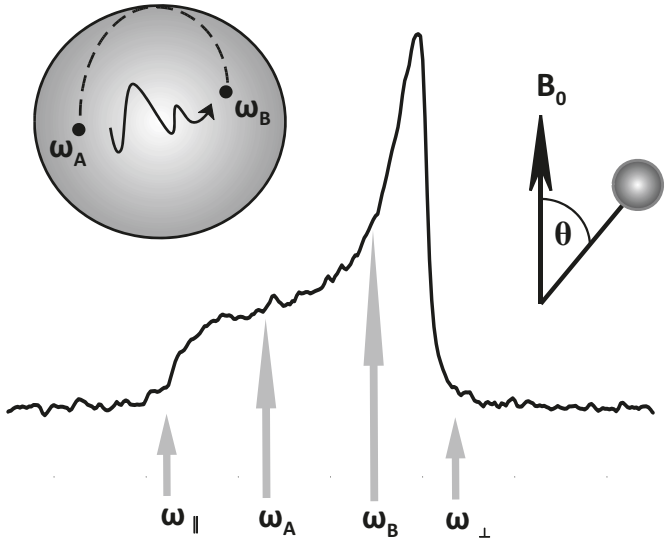

The spectral acquisition time and resolution problems associated with 2D EXSY may be overcome using 1D magic angle spinning (MAS) exchange NMR methods such as exchange induced sidebands (EIS),[88] 1D exchange spectroscopy by sideband alternation (ODESSA),[89] time-reversed ODESSA (trODESSA),[90] or centre band only detection of exchange (CODEX).[91] MAS involves spinning the sample about an axis inclined at the magic angle (54.74°) with respect to the static magnetic field. When the spinning frequency ω_r is greater than the size of the anisotropic interaction, i.e., $\omega_r \geq \Delta\omega$, only the isotropic frequency ω_{iso}, or so-called centre band, is manifest in the NMR spectrum, allowing resolution of chemically different sites. However, under slow-spinning conditions, i.e., $\omega_r \leq \Delta\omega$, a series of side bands appear in the spectrum, separated from the centre band by multiples of the spinning speed $\nu_r = \omega_r/2\pi$. The various 1D MAS exchange NMR methods employ refocusing radio frequency pulses carefully timed with respect to the rotor period ($\tau_r = 1/\nu_r$) to manipulate the phase and amplitude of these side bands. For situations where a diffusive motion has a correlation time that is long relative to the transverse relaxation time T_2, but short relative to the longitudinal relaxation time T_1, diffusion coefficients may be measured from the variation of side-band amplitudes as a function of the number of re focusing periods. While applicable in principle to the examination of lateral diffusion in membranes, to date we are not aware of any such studies using these methods.

Can. J. Chem. Downloaded from www.nrcresearchpress.com by Xi'an Jiaotong University on 09/19/12
For personal use only.

One issue is the need for a well-defined radius of curvature in the liposomal system under study.

Pulsed field gradient NMR and diffusion

Pulsed gradient-based diffusion NMR studies have flourished since their introduction more than four decades ago by Stejskal and Tanner[58] in their now classic article describing the spin echo pulsed gradient NMR diffusion experiment. The experimental diffusion time in the latter is limited by the intrinsic transverse relaxation time (T_2) of the nuclear spins being observed. Figure 5 shows the basic stimulated echo (STE) PFG NMR pulse sequence,[92] where the experimental diffusion time is limited by the longitudinal relaxation time (T_1), which is useful when, as is often the case, $T_1 >> T_2$. During the interval following the first 90° radio frequency pulse (duration $\tau_2 < T_2$) the nuclear spins precess in the transverse plane, acquiring a phase angle proportional to their intrinsic chemical shifts. The second 90° radio frequency pulse places the spin magnetization along the z axis where it may be stored for a duration $\tau_1 < T_1$. Following the third 90° radio frequency pulse, which returns the spin magnetization to the transverse detection plane, a stimulated echo forms at a time τ_2 subsequent to that pulse owing to the reversed direction of precession produced by the combination of the second and third radio frequency pulses. To render the experiment sensitive to diffusion, pulsed homogeneous field gradients, of amplitude g (T m^{-1}) and duration δ (s), are applied during the intervals following the first and third radio frequency pulses. The first gradient pulse encodes the nuclear spins according to their position along the direction of the applied field gradient by inducing an additional phase shift of angle ϕ_i

$$[8] \qquad \phi_i = \gamma g \delta z_i$$

where γ (rad T^{-1} s^{-1}) is the magnetogyric ratio and z_i is the position of an individual nuclear spin along the direction of the applied field gradient (assumed to lie parallel to the static magnetic field). The second gradient pulse decodes, i.e., reverses, the position-dependent phase shift produced by the first gradient pulse. If no diffusion occurs along the direction of the applied field gradient during the duration Δ separating the two field gradient pulses, then the nuclear spins refocus normally and the stimulated echo amplitude is unchanged. If diffusion occurs, then the echo amplitude is reduced as per eq. [9]

$$[9] \qquad I = I_0 \exp\left(\frac{-2\tau_2}{T_2}\right)\exp\left(\frac{-\tau_1}{T_1}\right) \times \exp[-\mathbf{D}(\gamma g \delta)^2(\Delta - \delta/3)]$$

where I_0 is the initial intensity and $\mathbf{D}$ is the diffusion coefficient along the direction of the applied field gradient. For simple Gaussian diffusion a plot of Ln I/I_0 vs $k = (\gamma g \delta)^2(\Delta - \delta/3)$, at constant τ_1 and τ_2 yields a linear decay with slope proportional to $\mathbf{D}$.

Given the particular focus of this review on diffusion in bicelles and related membrane systems, only the features of PFG NMR diffusion measurements most salient to membranes will be described. For a deeper presentation of the theory underlying the PFG NMR experiment, the interested reader is referred to several authoritative reviews.[94–97] Beyond the basic STE PFG NMR sequence, many innovative approaches have been developed to surmount particular challenges, such as the presence of background gradients,[98] convection,[99] or the need for solvent suppression,[100] and the interested reader is referred to the literature cited. Beyond the case of normal Gaussian diffusion, wherein the measured diffusion coefficient is independent of the observation period, there exist many situations characterized by non-Gaussian diffusive behaviour, in which the measured diffusion coefficient depends on the observation period. Typically, such situations involve complex heterogeneous systems where molecular diffusion occurs under confinements imposed by the system's morphology.[101] In such instances, PFG NMR diffusion measurements can often provide otherwise difficult to obtain morphological details.[102,103]

Fig. 5. The stimulated echo pulsed field gradient NMR pulse sequence introduced by Tanner[93] for measurement of molecular diffusion.

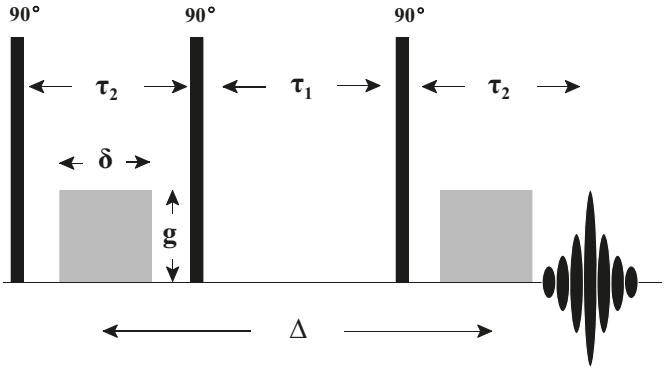

When applied to diffusion in membranes, the PFG NMR technique encounters two fundamental difficulties: first, the resonances to be observed are broad owing to residual anisotropic interactions, resulting in rapid loss of coherence during the echo delays in the PFG NMR sequence, and, second, the distribution of orientations of the membrane plane within the sample complicates the analysis of any observed intensity decays in terms of a lateral diffusion coefficient.

Gradient MAS

One innovative approach to the broad resonance issue involves subjecting the membrane sample to MAS to produce line narrowing while applying field gradients co-directional with the spinning axis.[104] Such a gradient configuration ensures that all nuclear spins experience an identical gradient strength throughout a rotor cycle. Gaede and Gawrisch[105] first employed this gradient MAS technique to examine lateral diffusion in lipid bilayers. Using multilamellar vesicles (MLVs) composed of 1-palmitoyl-2-oleoyl-phosphatidylcholine (POPC), they demonstrated that the ^{1}H NMR resonances of the POPC and the hydrophobic membrane-bound drug ibuprofen were well-resolved under MAS and that their respective lateral diffusion coefficients could be measured simultaneously.

A critical feature of the analysis is to take proper account of the powder distribution of bilayer normals in MLVs relative to the gradient axis. Extending previous work on corrections for powder samples,[59,106] it was found that, to second order, and ignoring relaxation, eq. [9] could be modified to

Can. J. Chem. Downloaded from www.nrcresearchpress.com by Xi'an Jiaotong University on 09/19/12
For personal use only.

$$[10] \qquad Ln\left(\frac{I}{I_0}\right) = -\frac{2}{3}kD + \frac{2}{45}(kD)^2$$

where k is again proportional to $(\gamma g \delta)^2$ but multiplied by a factor dependent on the pulse sequence and instrument settings, i.e., for the spin echo and stimulated echo with square gradient pulses the factor is $(\Delta - \delta/3)$. A further correction must be made to account for the curvature of the bilayers, in that an apparent diffusion coefficient is measured, which is related to the true diffusion coefficient **D** via

$$[11] \qquad \mathbf{D}_{app} = \frac{r^2}{2\Delta}\sin^2\left[\frac{(2D\Delta)^{1/2}}{r}\right]$$

where r is the radius of curvature of the bilayer vesicle.

Gaede and Gawrisch[105] demonstrated that the smaller molecule ibuprofen diffused considerably faster than the large molecule POPC, in keeping with the predictions of the free area model. The same gradient MAS diffusion NMR method was used subsequently to examine lateral diffusion of a number of membrane-associating molecules such as flavonoids,[107] cannabinoids,[108] indoles,[109] and cholesterol and its precursors,[110] and to explore domains and phase separation in model[111] and naturally occurring[112] lipid bilayers.

Macroscopically oriented membranes

One solution to the distribution of membrane orientations problem is to macroscopically align lipid bilayers by hydrating them between glass plates, a strategy first employed by Lindblom and Wennerström[113] to measure lateral diffusion. The resulting stacked uniformly aligned bilayers may be considered to have a radius of curvature approaching infinity. Inspection of eq. [11] shows that under such circumstances $\mathbf{D}_{app}$ becomes equivalent to **D**.

The issue of line broadening may also be ameliorated in macroscopically oriented bilayers. Specifically, for ^{1}H NMR diffusion studies, the principal source of line broadening in lipid bilayers is residual dipolar interactions between protons, both intermolecular and intramolecular. In the liquid–crystalline state, rapid translation diffusion eliminates intermolecular dipolar interactions, whereas rapid rotations about the lipid long axis averages the intramolecular dipolar Hamiltonians such that the angular dependence of the residual anisotropy again takes the form of the second-order Legendre polynomial $P_2(\theta)$, with θ corresponding to the angle between the bilayer normal and the direction of the static magnetic field. The key point is that when θ equals the so-called magic angle of 54.74°, $P_2(\theta) = 0$, the residual dipolar Hamiltonian disappears and the ^{1}H NMR resonance lines narrow. If the stack of macroscopically aligned lipid bilayers is oriented in the static magnetic field such that this condition applies, then the entire ensemble of lipid bilayers experiences this line narrowing.

One consequence of this arrangement is that, for the typical case in which the pulsed field gradients are applied along the z axis co-directional with the static magnetic field, the diffusion coefficient measured from a plot of Ln I/I_0 vs k (as per eq. [9]) does not directly equal the lateral diffusion coefficient, since the membrane-fixed reference frame in which the diffusion tensor is defined does not coincide with the laboratory-fixed reference frame defined by the direction of the applied field gradient. A simple rotational transformation from the membrane-fixed to the laboratory-fixed reference frame yields the relationship between the apparent diffusion coefficient $\mathbf{D_{zz}}^{\mathbf{lab}}$ and the diffusion tensor components, as shown in eq. [12][59,60]

$$[12] \qquad \mathbf{D_{zz}}^{\mathbf{lab}} = D_\perp \sin^2\theta + D_\parallel \cos^2\theta$$

where the geometry is shown in Fig. 3. As noted previously, $D_\parallel << D_\perp$ so that $\mathbf{D_{zz}}^{\mathbf{lab}} = 0.667\ D_\perp$ when $\theta = 54.74°$.

Lindblom and Orädd have been the principal proponents of this approach to measuring lateral diffusion coefficients of membrane lipids and their findings are described in several review articles.[60,114–118] A particular focus of their studies has been to describe the heterogeneity of lateral organization within a bilayer as reflected in the lateral mobility of different lipids. Especially notable achievements include the characterization of liquid-ordered and liquid-disordered domains formed in the presence of cholesterol and an elucidation of the criteria for domain formation in ternary lipid mixtures. As to the limitations of this approach, producing high-quality well-hydrated macroscopically oriented membrane samples is not a trivial matter, whereas the resolution achieved in the ^{1}H NMR spectrum is never equivalent to that obtained under MAS conditions.

Magnetically aligned bicelles

Another solution to the distribution of membrane orientations problem is to employ magnetically aligned bicelles. Two distinct situations present themselves as shown in Fig. 6. First, for negatively magnetically aligned bicelles, the bilayer normal is oriented at 90° to the static magnetic field so that, applying eq. [12], $\mathbf{D_{zz}}^{\mathbf{lab}} = D_\perp$, i.e., the lateral diffusion coefficient is measured directly. Secondly, for positively magnetically aligned bicelles, the bilayer normal is oriented parallel to the static magnetic field so that, applying eq. [12], $\mathbf{D_{zz}}^{\mathbf{lab}} = D_\parallel$, i.e., transbilayer diffusion may be measured directly. The latter quantity is largely a function of the size and number of DHPC-rich defects in the bicellar lamellae as will be discussed later.

The line width issue remains, however, since neither orientation eliminates the residual dipolar interaction, of paramount importance for the line width in ^{1}H NMR spectra of lipid bilayers, although it is reduced by a factor of 1/2 for negatively magnetically aligned bicelles as may be ascertained from eq. [7]. For a STE PFG ^{1}H NMR sequence, the residual dipolar broadening in either case is such that most lipid resonances cannot be detected owing to the loss of coherence during the echo delay periods. Nevertheless, any nuclear spins undergoing nearly isotropic motional averaging, and hence exhibiting narrow resonances, can be used to measure diffusion.

This was first demonstrated by Soong and Macdonald[56] using a PEGylated lipid incorporated into negatively magnetically aligned DMPC/DHPC bicelles. PEGylated lipids consist of a hydrophobic anchoring group, such as dimyristoyl phosphatidylethanolamine (DMPE), to which a polyethyleneglycol (PEG) group is covalently attached through the lipid's polar head group. As shown schematically in Fig. 7, the water soluble PEG becomes effectively "grafted" to the lipid bilayer surface through its DMPE hydrophobic anchor. The resulting surface coating of PEG inhibits surface binding and adhesion via steric repulsion, a property broadly useful

Can. J. Chem. Downloaded from www.nrcresearchpress.com by Xi'an Jiaotong University on 09/19/12
For personal use only.

Fig. 6. For the case of field gradients aligned parallel to the static magnetic field direction, positively magnetically aligned bicelles (left) allow measurement of the transbilayer diffusion coefficient $\mathbf{D}_{\parallel}$. Negatively magnetically aligned bicelles (right) allow measurement of the diffusion coefficient perpendicular to the bilayer normal ($\mathbf{D}_{\perp}$) corresponding to the lateral diffusion coefficient in the case of membrane-bound molecular species.

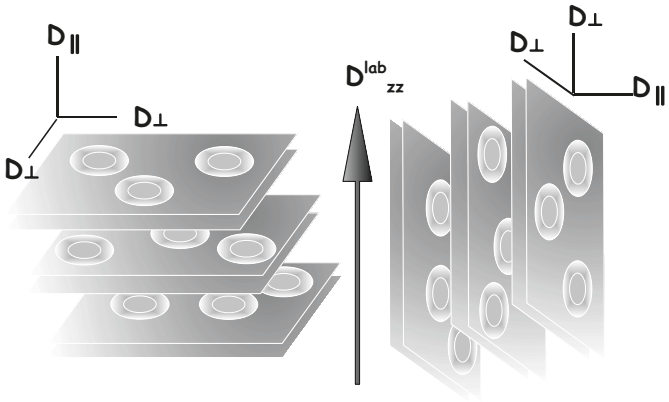

Fig. 7. The polyethyleneglycol (PEG) group of a PEGylated lipid may be regarded as a random-coil polymer grafted to the membrane surface by virtue of its hydrophobic anchoring moiety. Polymer theory[122] indicates that, for dimyristoyl phosphatidylethanolamine (DMPE) – PEG 2000, the resulting "mushroom" cap has a Flory radius (R_F) on the order of 35 Å, creating a surface "shadow" covering 60–70 dimyristoyl phosphatidylcholine (DMPC), and leading to full coverage at ~1.7 mol%.

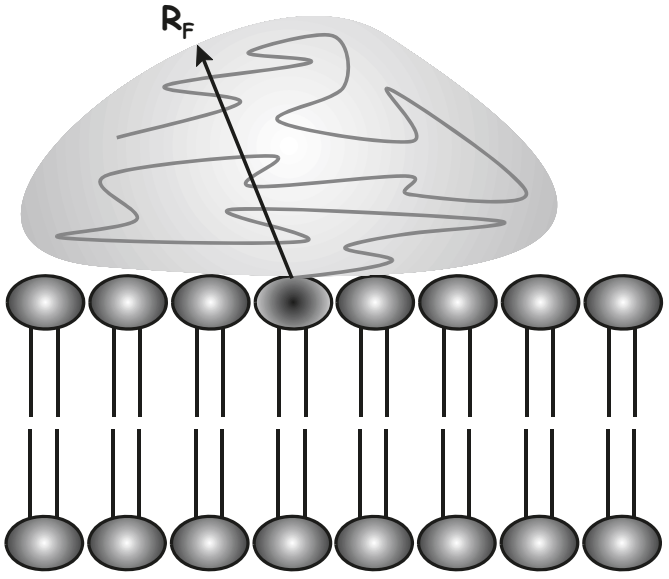

for enhancing bio-compatibility. For example, PEG-coated lipid vesicles are more effective drug delivery vehicles than vesicles lacking a PEG coating.[119] In bicelles, a surface coating of PEG enhances bicelle stability, again by virtue of steric stabilization.[120] The virtues of PEG lipids as bio-compatiblizing agents has led to intense research into their physicochemical properties, as reviewed by Marsh et al.[121]

Figure 8 show a typical series of STE PFG ^{1}H NMR spectra from which diffusion information is extracted, here for the case of negatively magnetically aligned bicelles containing DMPE–PEG 2000.[56] Any broad background lipid resonances are largely absent because of their short T_2 relative to τ_2. The two principal remaining resonances are assigned to HDO and an overlapping contribution from DHPC choline methyl plus PEG–DMPE ethylene oxide (EO) protons. The HDO resonance intensity decays rapidly with increasing k, as anticipated given water's rapid diffusion and the particular choice of gradient strength. The combined DHPC choline methyl plus PEG–DMPE EO resonance decays far more slowly, as expected for lipids constrained to diffuse laterally within a bicelle.

From plots of Ln I/I_0 vs k, such as shown in Fig. 9, the corresponding diffusion coefficient is obtained. The HDO diffusion coefficient is 1.6×10^{-9} m^2 s^{-1}, or roughly a factor of two slower water diffusion in these bicelles relative to bulk water at the same temperature,[123] the difference being attributed to the large fraction of bilayer surface-bound water in fast exchange with bulk water. Water diffusion in macroscopically oriented bilayers in general,[124] and in magnetically aligned bicelles in particular,[55,125] is anisotropic, with diffusion in the direction parallel to the bilayer normal considerably slower than in the perpendicular direction owing to slow permeation of water across the bilayer. This point will be come relevant in a later section.

In Fig. 9 diffusive intensity decays of the combined DHPC choline methyl plus DMPE–PEG 2000 EO resonance are shown for two concentrations of DMPE–PEG 2000 (1 mol% and 2 mol%) relative to DMPC. Each decay was fit as a sum of individual contributions from the DHPC and DMPE–PEG 2000, taking into account their respective initial intensity contributions, relaxation properties from independent measurements, and diffusion coefficients. Since the DHPC diffusion coefficient (5.7×10^{-10} m^2 s^{-1}) could be measured in otherwise identical bicelles lacking DMPE–PEG 2000, the sole fitting parameter was the lateral diffusion coefficient of DMPE–PEG 2000.

At larger values of k, the sole contributor to the intensity decay of this resonance is lateral diffusion of DMPE–PEG 2000. One sees that this decay is linear, i.e., monoexponential, indicating normal Gaussian diffusion. The lateral diffusion coefficient measured from the slope for 1 mol % DMPE–PEG 2000 was 1.35×10^{-11} m^2 s^{-1}, and was independent of the experimental diffusion time Δ, a further indication of normal Gaussian diffusion. For 2 mol% DMPE–PEG 2000, the lateral diffusion coefficient decreased to 1.15×10^{-11} m^2 s^{-1}.

As a comparison, Fig. 9 shows the intensity decays for free PEG 2000, i.e., nonhydrophobically modified, simply confined between the lamellae of the magnetically aligned bicelles at either 1 or 2 mol% concentrations. The measured diffusion coefficients, although reduced relative to free PEG in bulk solution, are, nevertheless, a factor of 30 times faster than the PEGylated lipid and essentially concentration independent.

Diffusion NMR and bicelle morphology

STE PFG NMR diffusion data such as that shown in Fig. 9 demonstrate the utility and ease of diffusion NMR measurements in magnetically aligned bicelle systems. In the following, we present a number of examples of the insights

Can. J. Chem. Downloaded from www.nrcresearchpress.com by Xi'an Jiaotong University on 09/19/12
For personal use only.

Fig. 8. Stimulated echo (STE) pulsed field gradient (PFG) ^{1}H NMR spectral series obtained at 35 °C with $q = 4.5$ DMPC/DHPC negatively magnetically aligned bicelles containing 1 mol% dimyristoyl phosphatidylethanolamine (DMPE) – polyethyleneglycol (PEG) 2000 as a function of increasing gradient pulse duration in the STE PFG NMR pulse sequence. The HDO resonance decays rapidly as expected given the fast diffusion of water. The ethylene oxide (EO) resonance of DMPE–PEG 20000 decays much more slowly as expected for a large molecule bound to the lipid bilayer regions of the bicelle. Other resonance are largely absent because of their fast transverse relaxation. Adapted from Soong and Macdonald.[56]

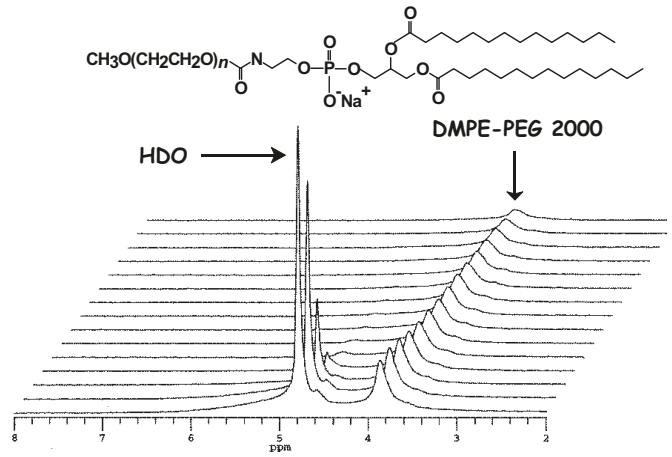

Fig. 9. Stimulated echo intensity decays as a function of dimyristoyl phosphatidylethanolamine (DMPE) – polyethyleneglycol (PEG) 2000 concentration in stimulated echo (STE) pulsed field gradient (PFG) ^{1}H NMR spectra (35 °C) of magnetically aligned dimyristoyl phosphatidylcholine (DMPC) / dihexanoyl phosphatidylcholine (DHPC) ($q = 4.5$) bicelles plus various levels of either DMPE–PEG 2000 or free (i.e., nonhydrophobically modified) PEG 2000. DMPE–PEG 2000 (1 mol%), $D_{PEG} = 1.35 \times 10^{-11}$ m^2 s^{-1} (○). DMPE–PEG 2000 (2 mol%), $D_{PEG} = 1.15 \times 10^{-11}$ m^2 s^{-1} (□). Free PEG 2000 (1 mol%), $D_{PEG} = 5.00 \times 10^{-10}$ m^2 s^{-1} (●). Free PEG 2000 (2 mol%), $D_{PEG} = 5.23 \times 10^{-10}$ m^2 s^{-1} (■). For further details see Soong and Macdonald.[56]

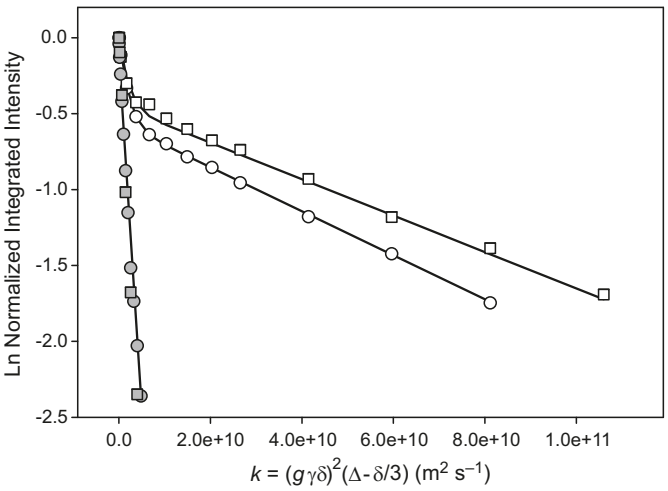

such studies can provide concerning fundamental questions of lateral diffusion in general and bicelle morphology specifically.

PEGylated lipid diffusion obeys the free area model

The lateral diffusion coefficient measured for DMPE–PEG 2000 (**D** = 1.35×10^{-11} m^2 s^{-1} for 1 mol% DMPE–PEG 2000 in $q = 4.5$ DMPC/DHPC bicelles at 35 °C) agrees closely with values reported for DMPC at a similar temperature using FRAP.[68] Hence, the lateral diffusion of this PEGylated lipid is determined primarily by the hydrophobic DMPE moiety anchoring the PEG group to the lipid bilayer, whereas the essentially extramembranous PEG group has an effect that is, at best, secondary. This conclusion is in agreement with free area models that predict that lateral diffusion is dictated by the cross-sectional area occupied within the membrane, which will be the same for DMPE–PEG 2000 and DMPC. The size of any extramembranous portion of the diffusing species, on the other hand, is secondary because the water bathing the membrane is so much less viscous than the membrane proper. Nonhydrophobically anchored PEG 2000 diffusing between bicelles, in contrast, diffuses an order of magnitude faster that DMPE–PEG 2000.[126]

Membrane crowding slows diffusion

The observation that lateral diffusion is slower when the DMPE–PEG 2000 concentration is increased from 1 to 2 mol% can be attributed directly to membrane crowding effects. Specifically, a consideration of the size of the extramembranous PEG group relative to the available space demonstrates that crowding between adjacent DMPE–PEG 2000 on the same lamellar surface must commence as the concentration rises from 1 to 2 mol%. According to polymer theory for unperturbed surface-grafted polymers,[122] the shape of the hydrophobically anchored PEG group may be modelled as a half-sphere or "mushroom" extending out from the surface a distance R_F (the Flory radius) and covering an area $A = \pi R_F^2$. This situation is shown schematically in Fig. 7. The Flory radius is calculated via the Flory equation[127]

$$[13] \qquad R_F = \mathbf{N}^{3/5}\mathbf{a}$$

where **N** is the degree of polymerization, i.e., the number of monomers, and **a** is the length of one monomer, equalling 3.5 Å for EO.[128] DMPE–PEG 2000 has 45 EO units, yielding $R_F \approx 35$ Å. Hence, assuming a footprint of 60 Å^2 for DMPC, complete coverage of the bilayer with PEG groups is achieved at 1.7 mol% DMPE–PEG 2000. Increasing the DMPE–PEG 2000 concentration from 1 to 2 mol% therefore forces overlap and entanglement of PEG groups to begin, i.e., the surface becomes crowded and lateral diffusion slows. The effect is exacerbated by higher concentrations and by higher molecular weight DMPE–PEG.[129]

Bicelle disks or perforated lamellae?

The diffusion properties of DMPE–PEG 2000 bear directly on the question of whether these bicelles under these conditions have assumed a diskoidal morphology or exist as perforated lamellae. Specifically, the fact that the diffusive decays for DMPE–PEG 2000 (as shown in Fig. 9) are linear and diffusion time independent indicates that lateral diffusion in this situation is normal, i.e., uncomplicated by restricted or anomalous diffusion. This permits a straightforward calculation of the root mean square (rms) displacement undergone during the experimental diffusion time via eq. [6]. For DMPE–PEG 2000 where $D = 1.35 \times 10^{-11}$ m^2 s^{-1} and $t = \Delta = 615$ ms,

Can. J. Chem. Downloaded from www.nrcresearchpress.com by Xi'an Jiaotong University on 09/19/12
For personal use only.

the rms displacement is on the order of 6 μm. This is a dimension far exceeding the size of an "ideal" diskoidal bicelle,[40] which is predicted to have a radius of 300 Å for the case $q = 4.5$. For situations where the experimental diffusion time would yield rms displacements exceeding the radial dimensions of such disks, any membrane-associating species confined to such a disk must exhibit restricted diffusion, characterized by a slope of zero in plots of Ln I vs k. No such behaviour was observed and, therefore, the morphology cannot be diskoidal. Instead, the perforated lamellae model of the bicelle structure must apply under these conditions, a conclusion likewise reached by Gaemers and Bax[55] from their examination of TMS diffusion in bicelles.

The mixed bicelle model

The perforations in the bicellar lamellae are formed by DHPC as a consequence of its preference for regions of high curvature. Originally, it was thought that DHPC was strictly segregated to such regions and would never mix with DMPC. Recent ^{31}P NMR results have called this view into question,[57] indicating that DHPC will in fact mix with DMPC, i.e., reside in lamellar regions, and increasingly so with increasing temperature.

Figure 10 shows the ^{31}P NMR spectra obtained in our laboratory for positively magnetically aligned DMPC/DHPC bicelles as a function of q (at constant temperature 35 °C) and as a function of temperature (at constant $q = 4.5$).[41] The key feature is the frequency of the DHPC resonance that is observed to shift progressively towards that of the DMPC resonance with either increasing q or increasing temperature. The interpretation is that DHPC is in fast exchange between regions of high curvature, where its frequency corresponds to the isotropic chemical shift, and lamellar regions, where its frequency corresponds to the anisotropic chemical shift of DMPC. Hence, the observed frequency relates to the equilibrium distribution of DHPC between these two environments, from which one may estimate an effective ratio of planar to curved phospholipid populations (q^*) via eq. [14]

$$[14] \qquad q^* = \left[\frac{q + \omega^*}{1 - \omega^*}\right]$$

where q = DMPC/DHPC as usual, and $\omega^* = \omega_{DHPC}/\omega_{DMPC}$, with ω_{DHPC} and ω_{DMPC} being the observed chemical shifts of DHPC and DMPC, respectively. Qualitatively, the ^{31}P NMR results indicate that the equilibrium distribution of DHPC shifts away from curved and towards planar regions of the bicelle upon increasing either q or temperature. This is in essential agreement with, and confirms the findings of, Triba et al.[57] and their "mixed bicelle model".

Such a mixed bicelle model has experimentally verifiable consequences for transbilayer diffusion. Specifically, the greater the amount of DHPC residing in lamellar regions, the fewer DHPC there are residing in curved regions and forming lamellar perforations. Since transbilayer diffusion will occur preferentially through such perforations, it should scale inversely with q^*.

As shown schematically in Fig. 6, diffusion in the transbilayer direction can be measured in positively magnetically aligned bicelles, with pulsed field gradients directed along the z axis, parallel to the static magnetic field.

Figure 11 shows the reduced transbilayer water diffusion

Fig. 10. ^{31}P NMR spectra of (left) positively magnetically aligned bicelles composed of 100 mol dimyristoyl phosphatidylcholine (DMPC) / 5 mol dimyristoylphosphatidylglycerol (DMPG) / 1 mol dimyristoyl phosphatidylethanolamine (DMPE) – polyethyleneglycol (PEG) 2000 + dihexanoyl phosphatidylcholine (DHPC) in the ratio q = (DMPC + DMPG + DMPE–PEG 2000) / DHPC = 4.5 as a function of temperature, and (right) at 35 °C as a function of q as indicated. All samples contained 25% *w/w* lipid–water and included ytterbium in the ratio Yb^{3+}:P = 1:75 to achieve positive magnetic alignment. Adapted from Soong and Macdonald.[41]

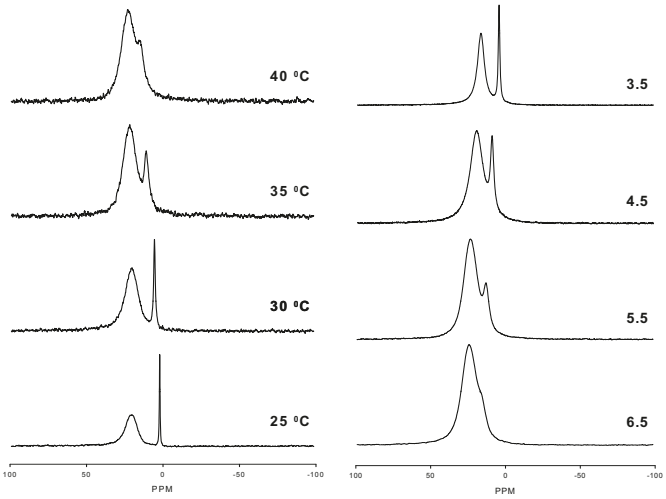

coefficient ($D_\parallel/D_0$), for the same series of positively magnetically aligned bicelles described in Fig. 10, i.e., as a function of q and of temperature, where D_0 refers to the bulk water diffusion coefficient at the corresponding temperature.[41] Because water is a small molecule, it is expected that its transbilayer diffusion will be insensitive to the size of the lamellar perforations and reflect, instead, only the the total surface area of lamellar perforations. This suggests the following simple relationship between $D_\parallel/D_0$ and q^*

$$[15] \qquad \frac{D_\parallel}{D_0} = \frac{1}{1 + \frac{A_{lam}}{A_{perf}}} = \frac{1}{1 + B \cdot q^*}$$

where A_{lam} and A_{perf} are the respective surface areas of lamellar regions and perforations and B is a model-dependent constant of proportionality relating the number of DHPC occupying perforations to the fractional surface area of those perforations.

In Fig. 11 the reduced transbilayer water diffusion coefficient is plotted as a function of $1/(1 + B{\cdot}q^*)$ for both the q-dependent (constant temperature) and the temperature-dependent (constant q) diffusion measurements using q^* values obtained from the ^{31}P NMR spectra in Fig. 10. For the q-dependent data, transbilayer water diffusion decreases as q^* increases, i.e., as DHPC decreases, supporting the supposition that water diffuses principally through DHPC-dependent lamellar perforations. For the temperature-dependent data, transbilayer water diffusion actually decreases as temperature increases, the direct converse of the Stokes–Einstein equation's expectation, but the expected result from eq. [15] given the temperature-dependent changes in q^*. The solid line indicates the idealized 1:1 relationship between the reduced transverse diffusion coefficient and the fractional

Can. J. Chem. Downloaded from www.nrcresearchpress.com by Xi'an Jiaotong University on 09/19/12
For personal use only.

Fig. 11. Reduced transbilayer water diffusion coefficient $D_{\|}/D_0$ as a function of the calculated surface fractional area of pores in bicellar lamellae. $D_{\|}$ was measured in positively magnetically aligned bicelles as a function of temperature at constant $q = 4.5$, and as a function of q at constant temperature (35 °C). The surface fractional area of pores was calculated according to eq. [15] using values of q^* obtained from ^{31}P NMR spectra as described in the text, with $B = 0.16$ as derived from the best 1:1 fit as shown by the solid line. q series at 35 °C (□). Temperature series at $q = 4.5$ (●). Adapted from Soong and Macdonald.[41]

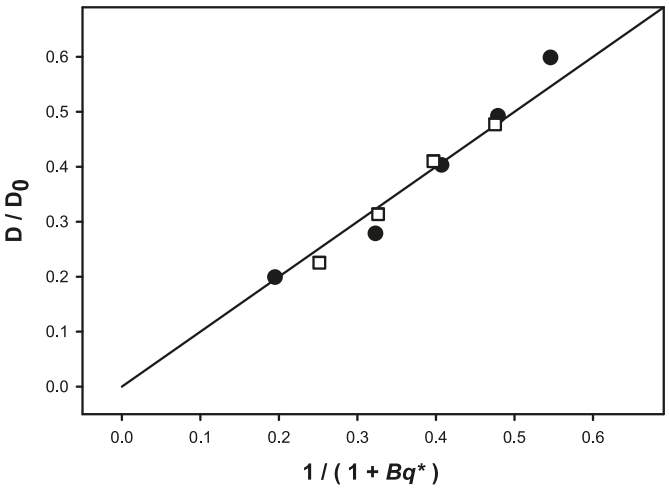

surface area of perforations and corresponds to the value $B = 0.16$. The fact that the q dependence and the temperature dependence of the transverse water diffusion coefficients fall on a common curve when treated in this fashion indicates that the common element is indeed the fraction of DHPC resident in perforations as derived assuming the mixed bicelle model. While it is possible to relate B to the number of DHPC required to form a pore, the conclusions are heavily model-dependent, require assumptions regarding pore size that cannot be obtained from water diffusion data, and do not account for other possible, albeit secondary, contributors to transbilayer water diffusion, such as bilayer fluctuations.[130]

The size of lamellar perforations

To obtain information regarding the size of the lamellar perforations, transbilayer diffusion of various molecular weight PEG was examined in positively magnetically aligned bicelles.[131] The fundamental idea is shown schematically in Fig. 12, where smaller PEG will be able to enter and traverse the DHPC-lined pores while larger PEG will be blocked. Hence, the molecular weight dependence of transbilayer PEG diffusion should reveal the pore–perforation–defect dimensions.

As shown in Fig. 13, where Ln I/I_0 is plotted vs k for various molecular weight PEG in positively magnetically aligned bicelles, transbilayer diffusion decreases with increasing PEG size, but, importantly, the diffusive decays are diffusion time independent. The latter point indicates that Tanner's asymptotic limit for diffusion across stacked, equally spaced, semipermeable barriers has been reached,[93] in that the rms diffusion displacement (several microns for PEG 4600 where $D \leq 1 \times 10^{-11}$ m^2 s^{-1}) has exceeded many multiples of the barrier spacing (roughly 100 Å),[36] so that the diffusion coefficient can be obtained simply by fitting with eq. [9], as shown by the solid curves in Fig. 13.

Fig. 12. Schematic cross-section through one defect in the perforated lamellar morphology of dimyristoyl phosphatidylcholine (DMPC) / dihexanoyl phosphatidylcholine (DHPC) bicelles. Bicelles consist of DMPC-rich (light grey) bilayer regions edged with DHPC-rich (dark gray) curved regions. The defects correspond to toroidal perforations in bicellar lamellae. Diffusants smaller than the defect dimensions can diffuse freely while larger diffusants are hindered. The NMR diffusion experiment is arranged such that the component of the molecular diffusion tensor parallel to the direction of the transverse defect axis ($D_{\|}$) is measured exclusively. Adapted from Soong et al.[131]

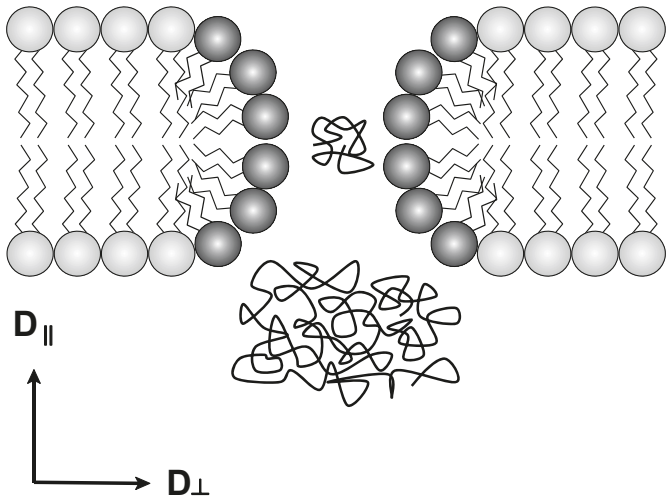

Fig. 13. Normalized diffusive intensity decays from stimulated echo (STE) pulsed field gradient (PFG) ^{1}H NMR spectra (35 °C) of various molecular weight polyethyleneglycol (PEG; as indicated) confined within positively magnetically aligned bicelles. Symbols represent different diffusion times: 210 ms (▲), 410 ms (○), 610 ms (■), 810 ms (◇), and 1010 ms (▼). The solid lines are fits using eq. [9]. Adapted from Soong et al.[131]

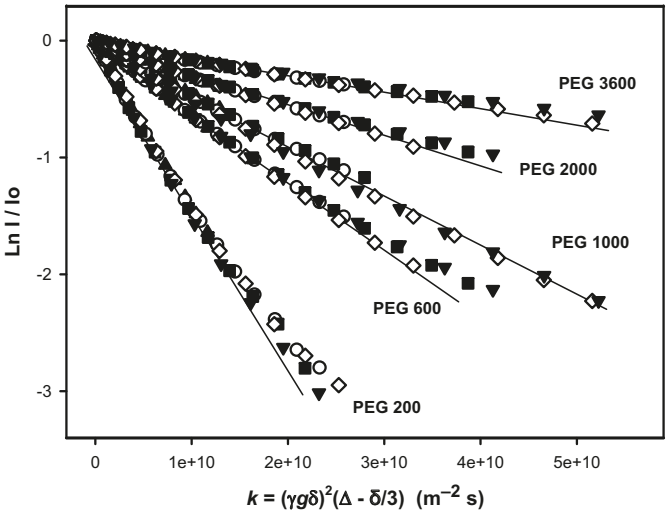

As shown in Fig. 14, the reduced transbilayer diffusion coefficient $D_{\|}/D_0$ decreases profoundly with increasing PEG size, as expressed in terms of the particular hydrodynamic,

Can. J. Chem. Downloaded from www.nrcresearchpress.com by Xi'an Jiaotong University on 09/19/12
For personal use only.

Fig. 14. Reduced transbilayer diffusion coefficients D/D_0 for various molecular weight polyethyleneglycol (PEG) in positively magnetically aligned bicelles as a function of the corresponding PEG Stokes–Einstein radius (R_s). Data are shown for three q values: 3.5 (△), 4.5 (●), and 5.5 (□). Solid curves show the best-fit Davidson and Deen model[132,133] predictions for the mean pore radii $<R_p>$ indicated in the text. Adapted from Soong et al.[131]

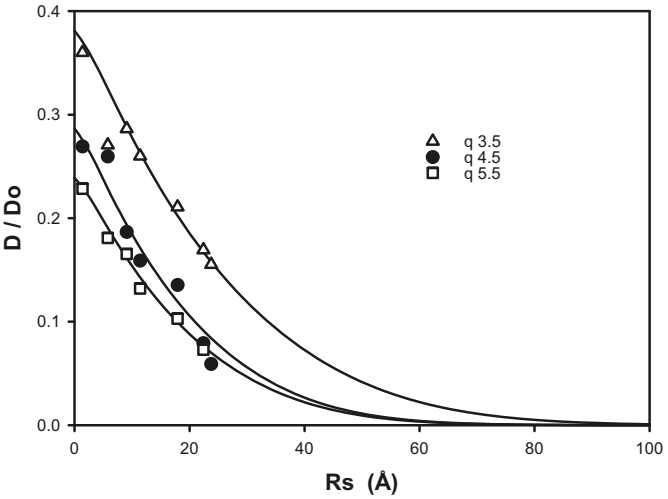

or Stokes–Einstein, radius R_S. D_0 is the diffusion coefficient of a particular PEG free in solution, from which R_S is obtained by application of eq. [1]. An average effective pore radius may be obtained by fitting such data to an appropriate model for reduced diffusion of flexible polymers through pores.

For fitting of the experimental diffusion data Davidson and Deen's hydrodynamic model is especially useful.[132,133] These authors considered the combined effects of steric exclusion from the pore and increased hydrodynamic drag within the pore, such that

$$[16] \qquad D/D_0 \sim f(\text{defect})\Phi K^{-1}$$

where Φ is the partition coefficient, describing the energetic cost, largely entropic in origin, of a polymer entering such a pore and K^{-1} accounts for the increased hydrodynamic drag on a polymer contained within such a pore. The leading term f(defect) was introduced by us to account for the fractional lamellar surface area of defects available for diffusion and is directly obtained from $D_{\|}/D_0$ for water as mentioned above. Both Φ and K^{-1} contain the term R_g/R_p relating the polymer radius of gyration to the pore radius.

For further details regarding this model and the relevant expression, a discussion of the evolution of such models and a comparison of different models, the interested reader is referred to these authors' original publications[132,133] and the comprehensive review by Deen.[134]

The solid curves in Fig. 14 show the lines of best fit of this modified Davidson and Deen model to the reduced PEG diffusion coefficients in bicelles at the three q values investigated, for the consensus values of $R_p = 165$ Å for the case $q = 3.5$ and $R_p = 125$ Å for both $q = 4.5$ and 5.5. Thus, both the number and the size of the lamellar perforations increase as q decreases (and DHPC increases). Compared with predictions derived from static geometric models of bicelle morphology,[57,131] whether disks or perforated lamellae are assumed, the apparent experimental pore sizes are consistently larger, and the trend as a function of q is diametrically opposite. A significant contributor to this discrepancy may well be fluctuations of the bicellar assemblies not considered by models such as that of Davidson and Deen, which treat the pores as static defects, but which are understood to contribute to transbilayer diffusion.[130] The fact that the discrepancy between pore size predictions from geometric models and experimental values determined from diffusion are greatest at lower q,[131] where the higher DHPC content decreases membrane ordering, implying increased fluctuations, tends to support this notion.

Conclusions and future prospects

Bicelles offer particular advantages as a model system for diffusion studies, whereas conversely, diffusion studies are a useful means to probe bicelle morphology. Whereas a number of controversies have been laid to rest as a result of diffusion measurements, new aspects of bicelle morphological plasticity continue to emerge, more complex lipid compositions than the canonical DMPC/DHPC mixtures become a focus of interest, and one always wishes to incorporate and investigate proteins.

A prerequisite for straightforward bicelle diffusion measurements is a visible NMR resonance capable of surviving the relaxation filters inherent to the PFG NMR diffusion sequence. Attaching a PEG moiety to the diffusant of interest is one strategy that has been demonstrated here, relying on the high internal mobility intrinsic to PEG. PEGylation of virtually any chemical species of interest is now possible. Alternately, many membrane-associating species, proteins in particular, may possess unstructured regions of intrinsically high flexibility such as extramembranous loops.

Emerging aspects of bicelle morphology include the nematic ribbon structure observed via SANS and PFG NMR for neutral, i.e., uncharged, bicelles, wherein diffusion is confined to a 1D path.[135] New bicelle compositions with improved alignment properties continue to be reported; for example, DHPC has been replaced with the detergent Triton 100.[136] Convincing instances of domain formation in bicelles, such as might be expected with raft-forming lipids, remain to be demonstrated, although domain formation and properties are readily characterized through diffusion measurements.

Certain aspects of the properties of membrane-associating proteins may prove amenable to study in bicelles via diffusion NMR, while others may not. The state of oligomerization of transmembrane helical proteins, for example, however important biologically, is not likely to be amenable to detailed inspection by diffusion NMR given the weak dependence of the lateral diffusion coefficient on the membrane cross-sectional area in the hydrodynamic size regime relevant to membrane proteins. On the other hand, diffusion NMR may well be able to differentiate oligomerization states of membrane-surface-associating peptides, where surface association may catalyze aggregation.

Finally, PFG NMR diffusion techniques are enormously useful for the study of ligand–protein association.[137] Membrane proteins, such as G protein coupled receptors, are extremely attractive drug targets.[138] It is conceivable, therefore, that mag-

netically aligned bicelles containing reconstituted membrane proteins could be used as a platform for diffusion NMR studies of drug – membrane protein interactions.

Acknowledgments

The research described here was supported by grants from the Natural Sciences and Engineering Research Council of Canada (NSERC). The authors wish to thank H. Morales for providing certain NMR spectra presented here.

References

(1) Sanders, C. R., II; Landis, G. C. *J. Am. Chem. Soc.* **1994** *116* (14), 6470. doi:10.1021/ja00093a072.
(2) Sanders, C. R., II; Landis, G. C. *Biochemistry* **1995** *34* (12), 4030. doi:10.1021/bi00012a022.
(3) Struppe, J.; Komives, E. A.; Taylor, S. S.; Vold, R. R. *Biochemistry* **1998** *37* (44), 15523. doi:10.1021/bi981326b.
(4) Whiles, J. A.; Brasseur, R.; Glover, K. J.; Melacini, G.; Komives, E. A.; Vold, R. R. *Biophys. J.* **2001** *80* (1), 280. doi:10.1016/S0006-3495(01)76013-4.
(5) Glover, K. J.; Whiles, J. A.; Wood, M. J.; Melacini, G.; Komives, E. A.; Vold, R. R. *Biochemistry* **2001** *40* (44), 13137. doi:10.1021/bi011485m.
(6) Marcotte, I.; Dufourc, E. J.; Ouellet, M.; Auger, M. *Biophys. J.* **2003** *85* (1), 328. doi:10.1016/S0006-3495(03)74477-4.
(7) Tjandra, N.; Bax, A. *Science* **1997** *278* (5340), 1111. doi:10.1126/science.278.5340.1111.
(8) Vold, R. R.; Deese, A. J.; Prosser, R. S. *J. Biomol. Nucl. Magn. Reson.* **1997** *9*, 329.
(9) Boyd, J.; Redfield, C. *J. Am. Chem. Soc.* **1999** *121* (32), 7441. doi:10.1021/ja9911216.
(10) Cavagnero, S.; Dyson, H. J.; Wright, P. E. *J. Biomol. Nucl. Magn. Reson.* **1999** *13*, 387.
(11) Sanders, C. R., II; Hare, B. J.; Howard, K. P.; Prestegard, J. H. *Prog. Nucl. Magn. Reson. Spectrosc.* **1994** *26*, 421. doi:10.1016/0079-6565(94)80012-X.
(12) Sanders, C. R.; Oxenoid, K. *Biochim. Biophys. Acta* **2000** *1508* (1–2), 129. doi:10.1016/S0005-2736(00)00308-4.
(13) Whiles, J. A.; Deems, R.; Vold, R. R.; Dennis, E. A. *Bioorg. Chem.* **2002** *30* (6), 431. doi:10.1016/S0045-2068(02)00527-8.
(14) Nevzorov, A. A.; Mesleh, M. F.; Opella, S. J. *Magn. Reson. Chem.* **2004** *42* (2), 162. doi:10.1002/mrc.1320.
(15) Sanders, C. R.; Kuhn Hoffmann, A.; Gray, D. N.; Keyes, M. H.; Ellis, C. D. *ChemBioChem* **2004** *5* (4), 423. doi:10.1002/cbic.200300830.
(16) De Angelis, A. A.; Jones, D. H.; Grant, C. V.; Park, S. H.; Mesleh, M. F.; Opella, S. J. *Methods Enzymol.* **2005** *394*, 350. doi:10.1016/S0076-6879(05)94014-7.
(17) Marcotte, I.; Auger, M. *Concepts Magn. Reson. A.* **2005** *24A* (1), 17. doi:10.1002/cmr.a.20025.
(18) Katsaras, J.; Harroun, T. A.; Pencer, J.; Nieh, M. P. *Naturwissenschaften* **2005** *92* (8), 355. doi:10.1007/s00114-005-0641-1.
(19) Sanders, C. R.; Sönnichsen, F. *Magn. Reson. Chem.* **2006** *44* (S1), S24. doi:10.1002/mrc.1816.
(20) Prosser, R. S.; Evanics, F.; Kitevski, J. L.; Al-Abdul-Wahid, M. S. *Biochemistry* **2006** *45* (28), 8453. doi:10.1021/bi060615u.
(21) Poget, S. F.; Girvin, M. E. *Biochim. Biophys. Acta* **2007** *1768* (12), 3098. doi:10.1016/j.bbamem.2007.09.006.
(22) Kim, H. J.; Howell, S. C.; Van Horn, W. D.; Jeon, Y. H.; Sanders, C. R. *Prog. Nucl. Magn. Reson. Spectrosc.* **2009** *55* (4), 335. doi:10.1016/j.pnmrs.2009.07.002.
(23) Ram, P.; Prestegard, J. H. *Biochim. Biophys. Acta* **1988** *940* (2), 289. doi:10.1016/0005-2736(88)90203-9.
(24) Sanders, C. R.; Prestegard, J. H. *Biophys. J.* **1990** *58* (2), 447. doi:10.1016/S0006-3495(90)82390-0.
(25) Sanders, C. R.; Schwonek, J. P. *Biochemistry* **1992** *31* (37), 8898. doi:10.1021/bi00152a029.
(26) Arnold, A.; Labrot, T.; Oda, R.; Dufourc, E. J. *Biophys. J.* **2002** *83* (5), 2667. doi:10.1016/S0006-3495(02)75276-4.
(27) van Dam, L.; Karlsson, G.; Edwards, K. *Biochim. Biophys. Acta* **2004** *1664* (2), 241. doi:10.1016/j.bbamem.2004.06.005.
(28) van Dam, L.; Karlsson, G.; Edwards, K. *Langmuir* **2006** *22* (7), 3280. doi:10.1021/la052988m.
(29) Rowe, B. A.; Neal, S. L. *Langmuir* **2003** *19* (6), 2039. doi:10.1021/la026352w.
(30) Ottiger, M.; Bax, A. *J. Biomol. NMR* **1998** *12* (3), 361. doi:10.1023/A:1008366116644.
(31) Raffard, G.; Steinbruckner, S.; Arnold, A.; Davis, J. H.; Dufourc, E. J. *Langmuir* **2000** *16* (20), 7655. doi:10.1021/la000564g.
(32) Sternin, E.; Nizza, D.; Gawrisch, K. *Langmuir* **2001** *17* (9), 2610. doi:10.1021/la001199w.
(33) Boltze, J.; Fujisawa, T.; Nagao, T.; Norisada, K.; Saito, H.; Naito, A. *Chem. Phys. Lett.* **2000** *329* (3–4), 215. doi:10.1016/S0009-2614(00)01029-0.
(34) Luchette, P. A.; Vetman, T. N.; Prosser, R. S.; Hancock, R. E.; Nieh, M. P.; Glinka, C. J.; Krueger, S.; Katsaras, J. *Biochim. Biophys. Acta* **2001** *1513* (2), 83. doi:10.1016/S0005-2736(01)00358-3.
(35) Nieh, M.-P.; Glinka, C. J.; Krueger, S.; Prosser, R. S.; Katsaras, J. *Langmuir* **2001** *17* (9), 2629. doi:10.1021/la001567w.
(36) Nieh, M.-P.; Ginka, C. J.; Krueger, S.; Prosser, R. S.; Katsaras, J. *Biophys. J.* **2002** *82* (5), 2487. doi:10.1016/S0006-3495(02)75591-4.
(37) Nieh, M. P.; Raghunathan, V. A.; Glinka, C. J.; Harroun, T. A.; Pabst, G.; Katsaras, J. *Langmuir* **2004** *20* (19), 7893. doi:10.1021/la0486411.
(38) Nieh, M.-P.; Raghunathan, V. A.; Glinka, C. J.; Harroun, T. A.; Katsaras, J. *Macromol. Symp.* **2005** *219* (1), 135. doi:10.1002/masy.200550112.
(39) Harroun, T. A.; Koslowsky, M.; Nieh, M.-P.; de Lannoy, C.-F.; Raghunathan, V. A.; Katsaras, J. *Langmuir* **2005** *21* (12), 5356. doi:10.1021/la050018t.
(40) Vold, R. R.; Prosser, R. S. *J. Magn. Reson. B.* **1996** *113* (3), 267. doi:10.1006/jmrb.1996.0187.
(41) Soong, R.; Macdonald, P. M. *Langmuir* **2009** *25* (1), 380. doi:10.1021/la801739a.
(42) Morales, H. University of Toronto Mississauga, Mississauga, Ontario, Canada. Personal communication, 2010.
(43) Boroske, E.; Helfrich, W. *Biophys. J.* **1978** *24* (3), 863. doi:10.1016/S0006-3495(78)85425-3.
(44) Prosser, R. S.; Hunt, S. A.; DiNatale, J. A.; Vold, R. R. *J. Am. Chem. Soc.* **1996** *118* (1), 269. doi:10.1021/ja953598x.
(45) Prosser, R. S.; Hwang, J. S.; Vold, R. R. *Biophys. J.* **1998** *74* (5), 2405. doi:10.1016/S0006-3495(98)77949-4.
(46) Prosser, R. S.; Bryant, H.; Bryant, R. G.; Vold, R. R. *J. Magn. Reson.* **1999** *141* (2), 256. doi:10.1006/jmre.1999.1855.
(47) Prosser, R. S.; Shiyanovskaya, I. V. *Concepts Magn. Reson.* **2001** *13* (1), 19. doi:10.1002/1099-0534(2001)13:1<19::AID-CMR3>3.0.CO;2-3.

Can. J. Chem. Downloaded from www.nrcresearchpress.com by Xi'an Jiaotong University on 09/19/12
For personal use only.

Can. J. Chem. Downloaded from www.nrcresearchpress.com by Xi'an Jiaotong University on 09/19/12
For personal use only.

(48) Cho, G.; Fung, B. M.; Reddy, V. B. *J. Am. Chem. Soc.* **2001** *123* (7), 1537. doi:10.1021/ja005605+.
(49) Tan, C.; Fung, B. M.; Cho, G. *J. Am. Chem. Soc.* **2002** *124* (39), 11827. doi:10.1021/ja027079n.
(50) Loudet, C.; Manet, S.; Gineste, S.; Oda, R.; Achard, M.-F.; Dufourc, E. J. *Biophys. J.* **2007** *92* (11), 3949. doi:10.1529/biophysj.106.097758.
(51) Picard, F.; Paquet, M. J.; Levesque, J.; Bélanger, A.; Auger, M. *Biophys. J.* **1999** *77* (2), 888. doi:10.1016/S0006-3495(99)76940-7.
(52) Sanders, C. R.; Schaff, J. E.; Prestegard, J. H. *Biophys. J.* **1993** *64* (4), 1069. doi:10.1016/S0006-3495(93)81473-5.
(53) Katsaras, J.; Donaberger, R. L.; Swainson, I. P.; Tennant, D. C.; Tun, Z.; Vold, R. R.; Prosser, R. S. *Phys. Rev. Lett.* **1997** *78* (5), 899. doi:10.1103/PhysRevLett.78.899.
(54) Cardon, T. B.; Tiburu, E. K.; Lorigan, G. A. *J. Magn. Reson.* **2003** *161* (1), 77. doi:10.1016/S1090-7807(02)00109-X.
(55) Gaemers, S.; Bax, A. *J. Am. Chem. Soc.* **2001** *123* (49), 12343. doi:10.1021/ja011967l.
(56) Soong, R.; Macdonald, P. M. *Biophys. J.* **2005** *88* (1), 255. doi:10.1529/biophysj.104.043620.
(57) Triba, M. N.; Warschawski, D. E.; Devaux, P. F. *Biophys. J.* **2005** *88* (3), 1887. doi:10.1529/biophysj.104.055061.
(58) Stejskal, E. O.; Tanner, J. E. *J. Chem. Phys.* **1965** *42* (1), 288. doi:10.1063/1.1695690.
(59) Callaghan, P. T.; Söderman, O. *J. Phys. Chem.* **1983** *87* (10), 1737. doi:10.1021/j100233a019.
(60) Lindblom, G.; Orädd, G. *Prog. Nucl. Magn. Reson. Spectrosc.* **1994** *26*, 483. doi:10.1016/0079-6565(94)80014-6.
(61) Vaz, W. L. C.; Clegg, R. M.; Hallmann, D. *Biochemistry* **1985** *24* (3), 781.. doi:10.1021/bi00324a037.
(62) Almeida, P. F. F.; Vaz, W. L. C.; Thompson, T. E. *Biochemistry* **1992** *31* (29), 6739. doi:10.1021/bi00144a013.
(63) Almeida, P. F. F.; Vaz, W. L. C.; Thompson, T. E. *Biochemistry* **1992** *31* (31), 7198. doi:10.1021/bi00146a024.
(64) Almeida, P. F. F.; Vaz, W. L. C. *Handbook of Biological Physics;* Lipovsky, R., Sackmann, E., Eds., 1995; pp 305–357.
(65) Saffman, P. G.; Delbrück, M. *Proc. Natl. Acad. Sci. U.S.A.* **1975** *72* (8), 3111. doi:10.1073/pnas.72.8.3111.
(66) Saffman, P. G. *J. Fluid Mech.* **1976** *73* (04), 593. doi:10.1017/S0022112076001511.
(67) Jovin, T. M.; Vaz, W. L. C. *Methods Enzymol.* **1989** *172*, 471. doi:10.1016/S0076-6879(89)72030-9.
(68) Tocanne, J.-F.; Dupou-Cézanne, L.; Lopez, A. *Prog. Lipid Res.* **1994** *33* (3), 203. doi:10.1016/0163-7827(94)90027-2.
(69) Rayan, G.; Guet, J.-E.; Taulier, N.; Pincet, F.; Urbach, W. *Sensors (Basel Switzerland)* **2010** *10*, 5927.
(70) Kahya, N.; Schwille, P. *Mol. Membr. Biol.* **2006** *23* (1), 29. doi:10.1080/09687860500489099.
(71) Haustein, E.; Schwille, P. *Annu. Rev. Biophys. Biomol. Struct.* **2007** *36* (1), 151. doi:10.1146/annurev.biophys.36.040306.132612.
(72) Chiantia, S.; Ries, J.; Schwille, P. *Biochim. Biophys. Acta* **2009** *1788* (1), 225. doi:10.1016/j.bbamem.2008.08.013.
(73) Macháň, R.; Hof, M. *Biochim. Biophys. Acta* **2010** *1798* (7), 1377. doi:10.1016/j.bbamem.2010.02.014.
(74) Macháň, R.; Hof, M. *Int. J. Mol. Sci.* **2010** *11* (2), 427. doi:10.3390/ijms11020427.
(75) Kusumi, A.; Sako, Y.; Yamamoto, M. *Biophys. J.* **1993** *65* (5), 2021. doi:10.1016/S0006-3495(93)81253-0.
(76) Saxton, M. J.; Jacobson, K. *Annu. Rev. Biophys. Biomol. Struct.* **1997** *26* (1), 373. doi:10.1146/annurev.biophys.26.1.373.
(77) Kusumi, A.; Nakada, C.; Ritchie, K.; Murase, K.; Suzuki, K.; Murakoshi, H.; Kasai, R. S.; Kondo, J.; Fujiwara, T. *Annu. Rev. Biophys. Biomol. Struct.* **2005** *34* (1), 351. doi:10.1146/annurev.biophys.34.040204.144637.
(78) Ramadurai, S.; Holt, A.; Krasnikov, V.; van den Bogaart, G.; Killian, J. A.; Poolman, B. *J. Am. Chem. Soc.* **2009** *131* (35), 12650. doi:10.1021/ja902853g.
(79) Cullis, P. R. *FEBS Lett.* **1976** *70* (1–2), 223. doi:10.1016/0014-5793(76)80762-4.
(80) Larsen, D. W.; Boylan, J. G.; Cole, B. *J. Phys. Chem.* **1987** *91* (22), 5631. doi:10.1021/j100306a027.
(81) Köchy, T.; Bayerl, T. M. *Phys. Rev. E* **1993** *47* (3), 2109. doi:10.1103/PhysRevE.47.2109.
(82) Lee, B. S.; Mabry, S. A.; Jonas, A.; Jonas, J. *Chem. Phys. Lipids* **1995** *78* (2), 103. doi:10.1016/0009-3084(95)02493-3.
(83) Jeener, J.; Meier, B. H.; Bachmann, P.; Ernst, R. R. *J. Chem. Phys.* **1979** *71* (11), 4546. doi:10.1063/1.438208.
(84) Dolainsky, C.; Unger, M.; Bloom, M.; Bayerl, T. M. *Phys. Rev. E* **1995** *51* (5), 4743. doi:10.1103/PhysRevE.51.4743.
(85) Fenske, D. B.; Jarrell, H. C. *Biophys. J.* **1991** *59* (1), 55. doi:10.1016/S0006-3495(91)82198-1.
(86) Fenske, D. B.; Letellier, M.; Roy, R.; Smith, I. C. P.; Jarrell, H. C. *Biochemistry* **1991** *30* (43), 10542. doi:10.1021/bi00107a025.
(87) Picard, F.; Paquet, M.-J.; Dufourc, E.; Auger, M. *Biophys. J.* **1998** *74* (2), 857. doi:10.1016/S0006-3495(98)74009-3.
(88) Yang, Y.; Schuster, M.; Blümich, B.; Spiess, H. W. *Chem. Phys. Lett.* **1987** *139* (3–4), 239. doi:10.1016/0009-2614(87)80549-3.
(89) Gérardy-Montouillout, V.; Malveau, C.; Tekely, P.; Olender, Z.; Luz, Z. *J. Magn. Reson. A* **1996** *123* (1), 7. doi:10.1006/jmra.1996.0208.
(90) Reichert, D.; Zimmermann, H.; Tekely, P.; Poupko, R.; Luz, Z. *J. Magn. Reson.* **1997** *125* (2), 245. doi:10.1006/jmre.1997.1111.
(91) deAzevedo, E. R.; Hu, W.-G.; Bonagamba, J.; Schmidt-Rohr, K. *J. Am. Chem. Soc.* **1999** *121* (36), 8411. doi:10.1021/ja992022v.
(92) Tanner, J. E. *J. Chem. Phys.* **1970** *52* (5), 2523. doi:10.1063/1.1673336.
(93) Tanner, J. E. *J. Chem. Phys.* **1978** *69* (4), 1748. doi:10.1063/1.436751.
(94) Stilbs, P. *Prog. Nucl. Magn. Reson. Spectrosc.* **1987** *19* (1), 1. doi:10.1016/0079-6565(87)80007-9.
(95) Kärger, J.; Pfeifer, H.; Heink, W. *Adv. Magn. Opt. Reson.* **1988** *12*, 1.
(96) Price, W. S. *Concepts Magn. Reson.* **1997** *9* (5), 299. doi:10.1002/(SICI)1099-0534(1997)9:5<299::AID-CMR2>3.0.CO;2-U.
(97) Price, W. S. *Concepts Magn. Reson.* **1998** *10* (4), 197. doi:10.1002/(SICI)1099-0534(1998)10:4<197::AID-CMR1>3.0.CO;2-S.
(98) Cotts, R. M.; Hoch, M. J. R.; Sun, T.; Marker, J. T. *J. Magn. Reson.* **1989** *83*, 252.
(99) Momot, K. I.; Kuchel, P. W. *J. Magn. Reson.* **2005** *174* (2), 229. doi:10.1016/j.jmr.2005.02.003.
(100) Price, W. S.; Elwinger, F.; Vigouroux, C.; Stilbs, P. *Magn. Reson. Chem.* **2002** *40* (6), 391. doi:10.1002/mrc.1029.
(101) Kärger, J. *Diffusion Fundamentals* **2005** *2*, 78.1.
(102) Mitra, P. P.; Sen, P. B.; Schwatrz, L. M. *Phys. Rev. B* **1993** *47* (14), 8565. doi:10.1103/PhysRevB.47.8565.
(103) Mitra, P. P.; Sen, P. B. *Phys. Rev. B* **1992** *45* (1), 143. doi:10.1103/PhysRevB.45.143.

(104) Maas, W. E.; Laukien, F. H.; Cory, D. G. *J. Am. Chem. Soc.* **1996** *118* (51), 13085. doi:10.1021/ja962227t.
(105) Gaede, H. C.; Gawrisch, K. *Biophys. J.* **2003** *85* (3), 1734. doi:10.1016/S0006-3495(03)74603-7.
(106) Lindblom, G.; Wennerström, H.; Arvidson, G. *Int. J. Quantum Chem.* **1977** *12*, 153.
(107) Scheidt, H. A.; Pampel, A.; Nissler, L.; Gebhardt, R.; Huster, D. *Biochim. Biophys. Acta* **2004** *1663* (1–2), 97. doi:10.1016/j.bbamem.2004.02.004.
(108) Kimura, T.; Cheng, K.; Rice, K. C.; Gawrisch, K. *Biophys. J.* **2009** *96* (12), 4916. doi:10.1016/j.bpj.2009.03.033.
(109) Gaede, H. C.; Yau, W.-Y.; Gawrisch, K. *J. Phys. Chem. B* **2005** *109* (26), 13014. doi:10.1021/jp0511000.
(110) Scheidt, H. A.; Huster, D.; Gawrisch, K. *Biophys. J.* **2005** *89* (4), 2504. doi:10.1529/biophysj.105.062018.
(111) Polozov, I. V.; Gawrisch, K. *Biophys. J.* **2004** *87* (3), 1741. doi:10.1529/biophysj.104.040725.
(112) Polozov, I. V.; Bezrukov, L.; Gawrisch, K.; Zimmerberg, J. *Nat. Chem. Biol.* **2008** *4* (4), 248. doi:10.1038/nchembio.77.
(113) Lindblom, G.; Wennerström, H. *Biophys. Chem.* **1977** *6* (2), 167. doi:10.1016/0301-4622(77)87006-3.
(114) Orädd, G.; Lindblom, G. *Magn. Reson. Chem.* **2004** *42* (2), 123. doi:10.1002/mrc.1338.
(115) Orädd, G.; Lindblom, G. *Spectroscopy* **2005** *19*, 191.
(116) Lindblom, G.; Gröbner, G. *Curr. Opin. Colloid Interface Sci.* **2006** *11* (1), 24. doi:10.1016/j.cocis.2005.09.017.
(117) Lindblom, G.; Orädd, G. *J. Dispersion Sci. Technol.* **2007** *28* (1), 55. doi:10.1080/01932690600992522.
(118) Lindblom, G.; Orädd, G. *Biochim. Biophys. Acta* **2009** *1788*, 234.
(119) Lasic, D. D.; Needham, D. *Chem. Rev.* **1995** *95* (8), 2601. doi:10.1021/cr00040a001.
(120) King, V.; Parker, M.; Howard, K. P. *J. Magn. Reson.* **2000** *142* (1), 177. doi:10.1006/jmre.1999.1928.
(121) Marsh, D.; Bartucci, R.; Sportelli, L. *Biochim. Biophys. Acta* **2003** *1615* (1–2), 33. doi:10.1016/S0005-2736(03)00197-4.
(122) de Gennes, P. G. *Macromolecules* **1980** *13* (5), 1069. doi:10.1021/ma60077a009.
(123) Mills, R. *J. Phys. Chem.* **1973** *77* (5), 685. doi:10.1021/j100624a025.
(124) Wästerby, P.; Orädd, G.; Lindblom, G. *J. Magn. Reson.* **2002** *157* (1), 156. doi:10.1006/jmre.2002.2583.
(125) Chung, J.; Prestegard, J. H. *J. Phys. Chem.* **1993** *97* (38), 9837. doi:10.1021/j100140a048.
(126) Soong, R.; Macdonald, P. M. *Langmuir* **2008** *24* (2), 518. doi:10.1021/la7022264.
(127) Flory, P. *Principles of Polymer Chemistry;* Cornell University Press: Ithaca, NY, 1971.
(128) Hristova, K.; Needham, D. *Macromolecules* **1995** *28* (4), 991. doi:10.1021/ma00108a029.
(129) Soong, R.; Macdonald, P. M. *Biochim. Biophys. Acta* **2007** *1768* (7), 1805. doi:10.1016/j.bbamem.2007.03.028.
(130) Lutti, A.; Callaghan, P. T. *Appl. Magn. Reson.* **2008** *33* (3), 293. doi:10.1007/s00723-008-0067-y.
(131) Soong, R.; Majonis, D.; Macdonald, P. M. *Biophys. J.* **2009** *97* (3), 796. doi:10.1016/j.bpj.2009.05.034.
(132) Davidson, M. G.; Suter, U.; Deen, W. M. *Macromolecules* **1987** *20* (5), 1141. doi:10.1021/ma00171a045.
(133) Davidson, M. G.; Deen, W. M. *Macromolecules* **1988** *21* (12), 3474. doi:10.1021/ma00190a022.
(134) Deen, W. M. *AIChE J.* **1987** *33* (9), 1409. doi:10.1002/aic.690330902.
(135) Soong, R.; Nieh, M.-P.; Nicholson, E.; Katsaras, J.; Macdonald, P. M. *Langmuir* **2010** *26* (4), 2630. doi:10.1021/la902795h.
(136) Park, S. H.; Opella, S. J. *J. Am. Chem. Soc.* **2010** *132* (36), 12552. doi:10.1021/ja1055565.
(137) Lucas, L. H.; Larive, C. K. *Concepts Magn. Reson. A* **2004** *20A* (1), 24. doi:10.1002/cmr.a.10094.
(138) Mustafi, D.; Palczewski, K. *Mol. Pharm.* **2009** *75* (1), 1. doi:10.1124/mol.108.051938.

Can. J. Chem. Downloaded from www.nrcresearchpress.com by Xi'an Jiaotong University on 09/19/12
For personal use only.

A multinuclear NMR and quantum chemical study of solid trimethylammonium chloride

Glenn H. Penner, Renee Webber, and Luke A. O'Dell

Abstract: The solid salt, trimethylammonium chloride (TMAC), is investigated by a combination of NMR spectroscopic techniques and quantum chemical calculations. Chemical shift and nuclear quadrupolar interaction parameters have been measured for ^{35}Cl, ^{1}H/^{2}H, and ^{15}N/^{14}N. These parameters have also been calculated as a function of the hydrogen position in the N···H···Cl fragment. Overall, the measured parameters are consistent with a structure in which the hydrogen is completely transferred to the nitrogen (i.e., N–H···Cl). The high hydrogen chemical shift (10.9 ppm by ^{2}H CP/MAS) and relatively small deuterium quadrupolar coupling constant (127 kHz) indicate a moderately strong N–H···Cl hydrogen bond. A pronounced deuterium isotope effect on the ^{35}Cl quadrupolar coupling constant is observed.

Key words: solid-state nuclear magnetic resonance, hydrogen bonding, NMR.

Résumé : On a étudié le chlorure de triméthylammonium (CTMA), à l'état de sel solide, par une combinaison de techniques de spectroscopie de RMN et de calculs de chimie quantique. On a mesuré les déplacements chimiques et les paramètres d'interaction quadripolaire nucléaire pour le ^{35}Cl, les ^{1}H/^{2}H et les ^{15}N/^{14}N. On a aussi calculé ces paramètres en fonction de la position de l'hydrogène dans le fragment N···H···Cl. Dans l'ensemble, les paramètres calculés sont en accord avec une structure dans laquelle l'hydrogène est complètement transféré à l'azote (c'est-à-dire N-H···Cl). Le déplacement chimique élevé de l'hydrogène [10,9 ppm par polarisation croisée standard avec rotation à l'angle magique (« CP/MAS ») du ^{2}H] et la constante de couplage quadripolaire relativement faible du deutérium (127 kHz) indiquent qu'il existe une liaison hydrogène N-H···Cl relativement forte. On a aussi observé un effet isotopique prononcé du deutérium sur la constante de couplage quadripolaire du ^{35}Cl.

Mots-clés : résonance magnétique nucléaire à l'état solide, liaison hydrogène, RMN.

[Traduit par la Rédaction]

Can. J. Chem. Downloaded from www.nrcresearchpress.com by Xi'an Jiaotong University on 09/19/12
For personal use only.

Introduction

Chemists have used many disparate techniques in their attempts to understand the hydrogen bond.[1] NMR spectroscopy has proven to be one of the most powerful of these methods.[2,3] NMR spectra can be used to study the effects of hydrogen bonding by directly probing the nucleus of the donor or acceptor atom, or even the hydrogen itself. Information about the hydrogen bond comes from the measurement of the chemical shift, nuclear quadrupolar, dipolar or *J*-coupling interactions through lineshapes and nuclear spin relaxation times.

Solid trimethylammonium chloride (TMAC) is an excellent example of a system with an N–H···Cl hydrogen bond. TMAC offers several magnetic nuclei (^{15}N, ^{14}N, ^{1}H, ^{2}H, ^{37}Cl, and ^{35}Cl), which are part of the hydrogen bonding structure. Yet the only reported solid-state NMR work on this solid consists of two studies of the ^{15}N–^{1}H dipolar coupling.[4,5]

Fourier transform microwave experiments carried out by Legon and Rego,[6,7] gave ^{14}N and $^{35/37}$Cl quadrupolar coupling constants (C_Q) that were consistent with a significant proton transfer from chlorine to nitrogen in the gas phase. Also in line with this conclusion is the N···Cl stretching force constant, as obtained from the centrifugal force constant, D_J. Subsequent quantum chemical calculations agree that the most stable species is the $Me_3NH^+Cl^-$ complex (see Fig. 1*a*), with a somewhat elongated N–H bond length.[8,9]

At room temperature, solid TMAC exists as crystals in the monoclinic space group $P2_1/m$, with one molecule per asymmetric unit ($Z' = 1$, see Fig. 2).[10] . At 308 K, TMAC undergoes a phase transition to a tetragonal phase with space group $P4/nmm$ (also $Z' = 1$).[11,12] Attempts to refine the structure in the tetragonal phase were only partially successful.[11,12]

In 1974, Huong and Schlaak examined the IR and Raman spectra of the series Me_3NHX, where X = Cl, Br, or I, and noted that the N–H stretching frequency increased along this series, which is consistent with a decreasing hydrogen bond interaction.[13]

Received 3 December 2010. Accepted 7 February 2011. Published at www.nrcresearchpress.com/cjc on 24 August 2011.

G.H. Penner and R. Webber. Department of Chemistry, University of Guelph, Guelph, ON N1G 2W1, Canada.
L.A. O'Dell. Steacie Institute for Molecular Sciences, National Research Council, 100 Sussex Drive, Ottawa, ON K1A 0R6, Canada.

Corresponding author: Glenn H. Penner (e-mail: gpenner@uoguelph.ca).

This article is part of a Special Issue dedicated to Professor Roderick E. Wasylishen in recognition of his immeasurable contributions to NMR spectroscopy and to the Chemistry community within Canada.

Can. J. Chem. Downloaded from www.nrcresearchpress.com by Xi'an Jiaotong University on 09/19/12
For personal use only.

Fig. 1. Three possible species of TMAC. (*a*) $Me_3NH^+Cl^-$, (*b*) $Me_3N\cdots H\cdots Cl$, and (*c*) $Me_3N\cdots HCl$.

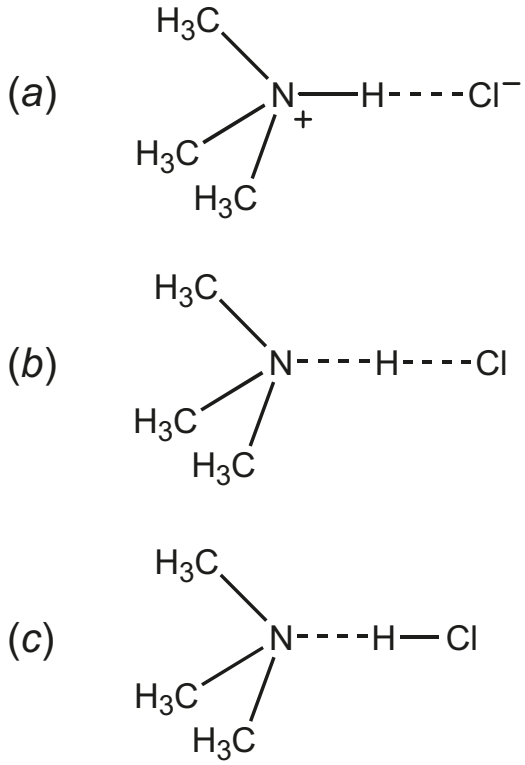

Early proton second moment and T_1 studies, and more recent ^{13}C T_1 work, concentrated on the dynamics of the trimethylammonium cation. These show fast methyl and trimethyl reorientation at room temperature.[14–17] The two NMR investigations that were most relevant to hydrogen bonding in solid TMAC measured the dipolar couplings between the ^{15}N–^1H and ^{15}N–^2H spin pairs. Roberts et al. used dipolar–chemical shift 2D MAS experiments to obtain $r(^{15}N–^1H)$ = 1.075 Å.[4] Hoelger and Limbach obtained $r(^{15}N–^1H)$ = 1.090 and 1.096 Å from CP/static and CP/MAS spectra, respectively. They also obtained $r(^{15}N–^2H)$ = 1.080 and 1.083 Å from CP/static and CP/MAS spectra, respectively, of the deuterated sample.[5] These r values are all at least 0.06 Å longer than that expected for an isolated N–H bond (1.01 Å).[18] This could be due to slight wobbling motion of the cation and (or) vibrational averaging. It could also be due to N–H···Cl hydrogen bonding.

In this investigation we present the results of a combined multinuclear (^{15}N, ^{14}N, ^1H, ^2H, and ^{35}Cl) NMR and quantum chemical study of the N–H···Cl hydrogen bond in solid TMAC.

Experimental

Sample preparation

Trimethylamine hydrochloride was purchased from Aldrich. Trimethylamine-d_9-hydrochloride was purchased from CDN isotopes with a reported isotopic purity of 99%. Trimethylamine hydrochloride-d_1 was prepared by evaporation from D_2O. Due to the extremely hygroscopic nature of trimethylamine hydrochloride, samples were heated under vacuum for at least 12 h to remove any moisture. All samples were packed in 4.0 mm o.d. zirconia rotors in a glove box, under an atmosphere of nitrogen to ensure sample dryness. All experiments were performed within a few days of sample preparation.

NMR spectroscopy

Solid-state ^{35}Cl NMR spectra were obtained at two fields, 11.75 T (ν_L = 49.06 MHz) and 18.8 T (ν_L = 78.48 MHz). The 11.75 T experiments were performed on a Bruker Avance II spectrometer using a 4 mm Bruker HFX MAS probe. Experimental setup and pulse calibrations at 11.75 T were performed using solid NaCl, and ^{35}Cl spectra were referenced to the centreband of solid NaCl at 0 ppm. The chemical shift was then corrected to NaCl at infinite dilution by subtracting 45.37 ppm.[19] The nonselective, "solution $\pi/2$" pulse length determined using NaCl was 6.5 μs. The central-transition selective, "solid $\pi/2$" pulse used was therefore 6.5 μs/(I + 1/2) = 3.25 μs. The static spectrum was collected using the $\pi/2 - \tau - \pi/2 - \tau$ – ACQ echo pulse sequence with an interpulse delay of 100 μs. A recycle delay of 1 s was used, and signal averaging was carried out over about 80 000 scans. The high-temperature spectrum (330 K) was obtained using sample heating controlled by a Bruker BVT 3000. The ^{35}Cl experiment at 18.8 T was performed on a Bruker Avance spectrometer using a 4 mm Bruker HX MAS probe. Experimental set-up, pulse calibration, and referencing were done using solid NaCl, as above. The ^{35}Cl solid $\pi/2$ pulse was 4.15 μs and a recycle delay of 1 s was used.

The ^1H NMR spectrum was acquired at 11.75T (ν_L = 500.14 MHz) using a Bruker Avance II spectrometer and a wideline probe constructed to have minimal proton background. The ^1H spectrum was referenced to the residual proton signal in pure liquid $CDCl_3$ at 7.24 ppm. The static spectrum was obtained with a single pulse.

All ^2H NMR spectra were acquired at 11.75 T (ν_L = 76.78 MHz) using a Bruker Avance II spectrometer and a 4 mm Bruker HFX MAS probe. The magic angle was set by maximizing the number of rotational echoes in the ^{23}Na FID of solid $NaNO_3$ spinning at 5 kHz. Experimental setup and pulse calibrations were performed using solid $(CD_3)_2SO_2$, and ^2H spectra were referenced to $(CD_3)_2SO_2$ at 2.77 ppm relative to TMS. The ^2H spectrum collected under stationary conditions used the $\pi/2 - \tau - \pi/2 - \tau$ – ACQ echo pulse sequence with $\pi/2$ pulses of 3.6 μs and an interpulse delay of 20 μs. The recycle delay was 30 s, and 2000 scans were collected (total experimental time of ~17 h). For the ^2H CP/MAS experiments, contact times of 10 ms were employed and 83 kHz proton decoupling was applied during acquisition. Recycle delays of 5 s were used and an average of 400 scans were collected (total experimental time of 34 min).

The ^{14}N NMR spectrum was acquired at 21.1 T (ν_L = 65.02 MHz) using a Bruker Avance II console and a 7.0 mm HX static probe built in-house (National Ultra-High Field NMR Facility for Solids, Ottawa). The WURST-QCPMG pulse sequence[20,21] was used with eight-step phase cycling and 50 μs WURST-80 pulses swept over a range of 1.0 MHz, resulting in an excitation bandwidth of approximately 850 kHz. The optimum RF power for the WURST pulses was experimentally determined as $\nu_1 \approx 30$ kHz. Continuous-wave ^1H decoupling of $\nu_2 \approx 15$ kHz power was applied for the duration of each scan. Solid NH_4Cl was used

Fig. 2. The crystal structure of TMAC in the monoclinic phase, showing a heptamer.

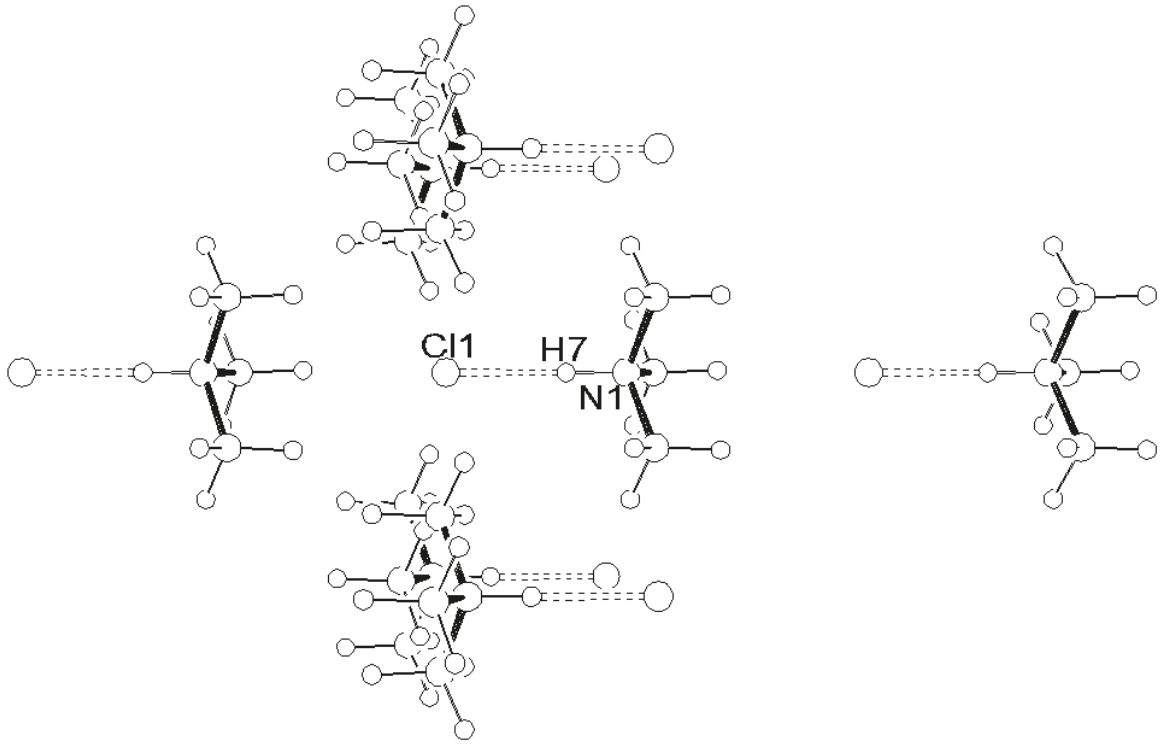

Can. J. Chem. Downloaded from www.nrcresearchpress.com by Xi'an Jiaotong University on 09/19/12
For personal use only.

as a reference and set to 0 ppm. The ultra-wideline spectrum was acquired in six pieces at transmitter offset frequencies of ±0.4, ±0.7, and ±1.0 MHz, with the WURST pulse sweep direction from low to high frequencies on the high frequency side and vice-versa.[22] For each piece, 32 echoes were acquired with 120 scans and a recycle delay of 10 s (total experiment time of 2 h). Transverse ^{14}N relaxation was observed to be relatively short compared with most crystalline organic molecules that we have previously studied,[23,24] indicating the presence of dynamics, which can cause rapid transverse dephasing via modulation of either the EFG tensor[25] or heteronuclear dipolar couplings.[24] A variation of the proton decoupling power could in principle be used to identify the latter mechanism,[24] however due to experimental time contraints this was not attempted.

A ^{15}N NMR spectrum was acquired at 11.75 T (ν_L = 50.70 MHz) using a Bruker Avance II spectrometer and a 4 mm Bruker HFX MAS probe. A RAMP cross-polarization pulse sequence was used with 5 kHz sample spinning, a contact time of 10 ms, 100 kHz proton decoupling, and a recycle delay of 2 s; 4000 scans were collected. The spectrum was referenced to the nitrate signal of solid $^{15}NH_4{}^{15}NO_3$,, which is at 4.4 ppm with respect to pure liquid nitromethane at 20 °C.

Spectral processing and simulation

Data were processed using TopSpin software (with the exception of ^{14}N data). FIDs were left-shifted where necessary, apodized using an exponential function of 10–100 Hz for MAS samples or 100–6000 Hz for static samples, and Fourier-transformed. Baseline corrections were applied to all ^{2}H CP/MAS spectra and the ^{1}H static spectrum. Spectral simulations of ^{35}Cl, ^{1}H, and ^{2}H were performed using WSOLIDS1[26] and the Solid Line Shape Guide within TOPSPIN 2.1.

For ^{14}N, spectral processing was carried out using the NUTS software (Acorn NMR). QCPMG trains were split into individual echoes, which were co-added prior to Fourier transformation. Absorptive spectra were obtained via a magnitude calculation, and complete spectra were reconstructed from the individual pieces via co-addition. EFG parameters and the isotropic chemical shift were determined by manually fitting simulations to the experimental spectra using the DMFit software.[27]

Computational details

Potential energy curves, EFG tensors, and magnetic shielding tensors were calculated using Gaussian03 (G03).[28] Single-point energy calculations were performed (r(N–H) in trimethylamine hydrochloride was stepped from 1–1.8 Å) using Hartree–Fock (HF), density-functional theory (DFT) employing the hybrid B3LYP functional, and coupled cluster singles and doubles (CCSD) methods with an augmented Dunning basis set (aug-cc-pVtz). The single-point energy calculations were performed using the X-ray structure of trimethylamine hydrochloride. The X-ray structure does not include hydrogen positions, thus, protons were inserted manually and positions were optimized using the B3LYP/6–311++G** level of theory; the heavy-atom positions were kept fixed during this optimization. Optimization of the hydrogen positions in the N–H···Cl bond and the N···H–Cl bond were performed with the three methods used to generate the PE curves. For these optimizations, all of the atoms were frozen except for the hydrogen involved in the bond; the N–H···Cl angle was forced to be linear. These optimizations allowed for accurate determination of the energy difference between the two minima

Can. J. Chem. Downloaded from www.nrcresearchpress.com by Xi'an Jiaotong University on 09/19/12
For personal use only.

in each PE curve. EFG and magnetic shielding calculations were performed with the HF and DFT methods, using Pople-type and Dunning-type basis sets. The gauge-including atomic orbitals method (GIAO) was used for calculating chemical shielding tensors. The EFG and magnetic shielding tensors contained in the G03 output files were analyzed using the EFGShield program.[29]

Plane-wave DFT calculations were performed using the CASTEP software[30–33] in the Materials Studio 4.3 software suite on an HP xw4400 Workstation with a single Intel Dual-Core 2.67 GHz processor and 8 GB DDR RAM. This software employs the gauge-including projector augmented wave algorithm (GIPAW).[30] Revised Perdew, Burke, and Ernzerhof (PBE) functionals were used with the generalized gradient approximation for the exchange-correlation energy. The plane-wave basis set cut-off was set to 300 eV and 16 k-points were sampled. Proton positions were inserted manually and optimized using a Broyden–Fletcher–Goldfarb–Shanno optimization algorithm,[34] with the lattice parameters and coordinates of all other atoms fixed. Ultrasoft ^{14}N pseudo-potentials were used for the EFG calculations.[35]

Results and discussion

Potential energy curve

The calculated potential energy curves as a function of the N···H distance in solid TMAC are shown in Fig. 3. All calculations were performed on isolated TMAC, with the exception of those employing CASTEP, which used the extended crystal structure. In all calculations the methyl groups, nitrogen atom, and chloride ion are held in positions corresponding to the solid state structure and the hydrogen position is varied while being kept colinear with the nitrogen and chloride atoms. The N···Cl distance in solid TMAC is 3.005 Å.[10] The N–H distances were varied, in steps of 0.05 Å, from that for a typical N–H bond length (1.0 Å) to that corresponding to complete transfer of the proton to the chlorine atom (1.7 Å). As one can see, the PE curve depends strongly on the method used in the calculation. Relative to structure **1a**, the energies of structure **1c** are 27.0 kJ/mol for HF/6–311++G(d,p), –2.9 kJ/mol for MP2/6–311++G(d,p), 5.3 kJ/mol for B3LYP/6–311++G(d,p), and 8.3 kJ/mol for CC(SD)/aug-cc-pvtz. Plane-wave calculations show no minimum corresponding to structure **1c**. Each isolated molecule curve has a short N–H distance minimum, corresponding to structure **1a**, and a long N–H distance minimum, corresponding to structure **1c**. These distances are, respectively, 1.060/1.657 Å for HF/6–311++G(d,p), 1.144/1.615 Å for MP2/6–311++G(d,p), 1.144/1.561 Å for B3LYP/6–311++G(d,p), and 1.11/1.63 Å for CC(SD)/aug-cc-pvtz (estimated from curve). The plane-wave calculations yield a structure **1a** minimum energy at 1.10 Å. In all cases the optimized short distance is longer than that obtained from an optimized structure of the isolated Me_3NH^+ cation (1.02 ± 0.01 Å for all isolated TMAC calculations). This is consistent with the elongation of the N–H bond expected for an N–H···Cl hydrogen bond.

Chlorine spectra and calculations

The room temperature ^{35}Cl spectra of static samples of TMAC obtained at 11.75 and 18.8 T are shown in Fig. 4. The combined results of the analyses of these spectra, to-

Fig. 3. Hydrogen atom displacement potential energy curves for TMAC with all heavy atoms fixed in their crystal structure positions, while the H atom positions were optimized. Single molecule HF/6–311++G(d,p) (◇ on green line online), single molecule CC (SD)/aug-cc-pvtz (○ on blue line online), single molecule B3LYP/6–311++G(d,p) (□ on purple line online), single molecule MP2/6–311++G(d,p) (+ on yellow line online), red triangles CASTEP (△ on red line online). The (coloured online) curves are included as a visual guide.

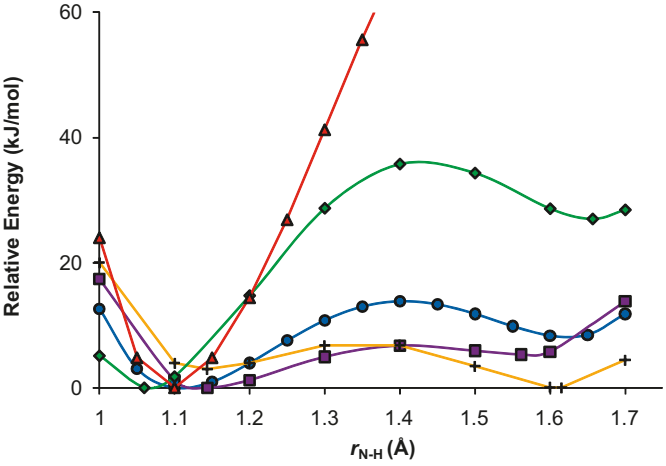

Fig. 4. (*a*) The static ^{35}Cl spectrum of TMAC at 11.75 T (upper trace) together with simulation (lower trace). (*b*) The static ^{35}Cl spectrum of TMAC-d_1 at 18.8 T (upper trace) together with simulation (lower trace). (*c*) The static ^{35}Cl spectrum of TMAC at 18.8 T (upper trace) together with simulation (lower trace).

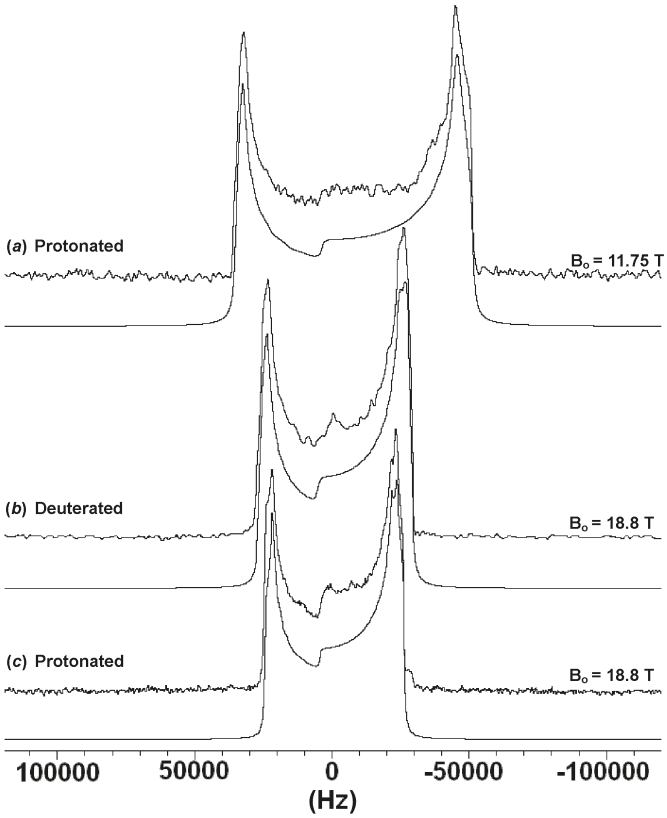

Can. J. Chem. Downloaded from www.nrcresearchpress.com by Xi'an Jiaotong University on 09/19/12
For personal use only.

Fig. 5. The ^{35}Cl spectrum (upper trace) of a static sample of solid TMAC at 11.75 T and 330 K together with simulation (lower trace).

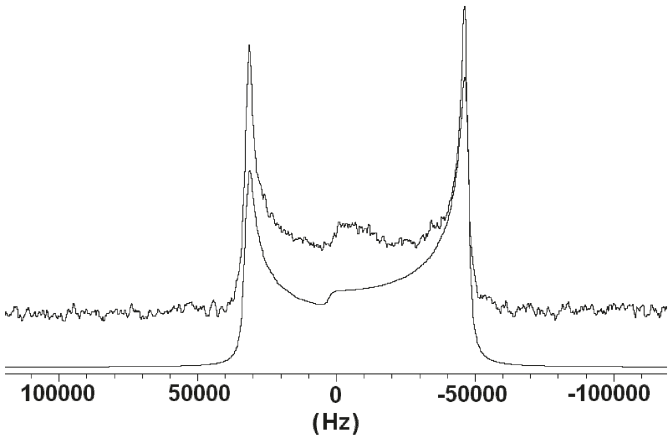

gether with the 11.75 T spectrum at 330 K (see Fig. 5), are provided in Table 1. The parameters obtained from the analyses of the 295 K spectra at two fields are in very good agreement. The point symmetry at chlorine in the room temperature phase is C_{2v}, and this is reflected in a κ value that is significantly different from ±1. However the η_Q value is still very close to 0. The shielding tensor is obviously more sensitive than the quadrupolar interaction to small deviations from C_3 symmetry due to crystallographic effects.

The phase above the transition is tetragonal, which imposes axial symmetry on the chlorine. Our simulations show that the spectrum is rather insensitive to the κ value. We can simulate the spectrum at 330 K with κ values of –0.75 to –1.0. Thus the κ value and η_Q values are within experimental error of –1 and 0, respectively, at 330 K. This is consistent with the crystallographic tetragonal symmetry and a chlorine site symmetry of C_{3v}. In addition to these changes, the Euler angle γ changes from 230°/225° to 270°. Although a previous attempt at a complete structure refinement of the tetragonal phase at 340 K was not fully successful, an N···Cl distance of 2.972(9) Å was determined.[11,12] This is 0.03(1) Å shorter than that in the monoclinic phase. Evidently, the small structural changes that occur during the phase transition result in minor changes in the chlorine quadrupolar interaction and more significant changes in the asymmetry of the shielding tensor.

It is of interest here to compare the optimized N–H distance, the ^{35}Cl C_Q, and the chlorine shielding tensor for the monomer and extended lattice structures of solid TMAC. The optimized N–H distance in the monomer is 1.124 Å (B3LYP/6–311G) and is 1.080 Å for the extended lattice (CASTEP, using revised Purdew–Burke–Ernzerhof functionals). The C_Q values for these structures are –14.9 and –9.6 MHz, respectively. In all cases the η_Q was very close to zero. The calculated Ω, κ values are 138 ppm, –0.94 and 113.5 ppm, 0.12, respectively.

There have been several $^{35/37}$Cl NMR studies of solids with N–H···Cl interactions.[19,35–38] Our observed C_Q and Ω values are consistent with these studies. Of particular interest are the results for quinuclidine hydrochloride, which is structurally similar to TMAC. Both the $|C_Q|$ value of 5.25 ± 0.02 MHz and the estimated Ω of 50 ± 30 ppm are very close to our values for TMAC.[19]

Figures 6 and 7 show the computed dependence of the ^{35}Cl C_Q and Ω values, respectively, as a function of the N–H distance in isolated TMAC (heavy atoms held at X-ray structure values). The best agreement with experiment is with the HF calculation where r(N–H) = 1.0 Å. These calculations show that the magnitude of the C_Q values steadily decrease with decreasing distance and reach a value of about –6.0 MHz at 1.0 Å. This is reasonably close to our measured values, considering that the fast rotational motion of the methyl protons and the methyl groups are not taken into account in these calculations. The computed spans of the chlorine shielding tensor steadily increase with N–H distance, reaching a maximum in the 1.5–1.6 Å range. The computed spans are in best agreement with the experimental values at 1.0 Å but are still too large.

Although the CSA values we obtained have large errors associated with them, the fact that spectral analyses at two significantly different fields yield results that are in good agreement and compare favorably with previous work implies that our values are very reliable.[15] However, the Ω and κ values we obtained from our spectra are not in very good agreement with the calculations mentioned above.

At this point it is worthwhile to briefly discuss the effect of proton transfer on the chlorine quadrupolar coupling constant in general. Gas phase ^{35}Cl C_Q values are available for HCl (–67.6 MHz), H_3N···HCl (–47.6 MHz), and TMAC, TMAC-d_1 (–21.6, –19.7 MHz).[6,7] A comparison of these values with Fig. 6 indicates that the magnitude of C_Q decreases as the proton is transferred from Cl to N. Our experimental value of (±)5.59 ± 0.03 MHz is indicative of complete proton transfer from Cl to N if one ignores intermolecular and crystal lattice contributions to the C_Q in solid TMAC.

Isotope effect on the ^{35}Cl quadrupolar coupling constant

The ^{35}Cl spectra of TMAC and TMAC-d_1 are shown in Fig. 4. Results of simulations of these spectra are provided in Table 1. The ^{35}Cl C_Q values for TMAC and TMAC-d_1 are clearly different, and the difference is easily outside the experimental error limits. This kind of isotope effect has been observed in the ^{35}Cl C_Q values of TMAC as measured by gas phase microwave spectroscopy.[6,7] In the gas phase, the C_Q of the deuterated compound is 9% lower than that of the protonated compound. This is a rather significant shift in C_Q. Our solid-state results show a 5% change, which is smaller but also quite significant.

An H vs. D isotope effect on the ^{35}Cl C_Q values in a series of long chain n-$C_xH_{2x-1}NH_3Cl$ alkylammonium salts has been reported. These show an average 2% decrease in the ^{35}Cl C_Q values on deuteration of all three N–H sites.[39] However, this effect, which is presumably attenuated by the rapid rotation of the NH_3^+ groups, is not discussed in any detail. If the stretching potential of the N–H bond is anharmonic, deuteration will very slightly decrease the bond length. As can be seen from Fig. 6, a decrease in r(N–H) should result in a decrease in the magnitude of the ^{35}Cl C_Q value. This is indeed what is observed. The degree to which deuteration affects the ^{35}Cl C_Q value will depend on the anharmonicity of the N–H stretching potential. This can be demonstrated by comparing the deuterium isotope effect in gas and solid phase TMAC. Since the C_Q is much larger in the gas phase, it is likely that

Table 1. Experimentally determined ^{35}Cl QC and CS NMR tensor parameters.

ν_L (MHz)	T (K)	$\lvert C_Q \rvert$ (MHz)	η_Q	δ_{iso} (ppm)	Ω (ppm)	κ	α, β, γ (°)
49.0	295	5.54±0.03	0.05±0.04	32±5	56±35	–0.42±0.10	150±25, 110±30, 230±15
78.4	295	5.59±0.03	0.04±0.02	35±5	47±25	–0.53±0.16	150±20, 110±15, 230±20
78.4[a]	295	5.30±0.02	0.06±0.04	34±5	48±30	–0.42±0.10	155±15, 105±10, 225±15
49.0	330	5.44±0.10	0.01±0.01	27±7	47±20	–1.0[b]	150±20, 106±35, 270±10

[a]Results for TMAC-d_1.

[b]Upper limit. This value can vary from –0.75 to –1.0 without affecting the lineshape.

Can. J. Chem. Downloaded from www.nrcresearchpress.com by Xi'an Jiaotong University on 09/19/12
For personal use only.

the N–H bond is slightly longer, with a concomitant increase in anharmonicity. The expected result is a much larger isotope effect on the ^{35}Cl C_Q in gas phase TMAC, as is observed.

Deuterium spectra and calculations

The deuterium spectra of the N–D deuteron in TMAC are expected to be quite sensitive to the degree of N–D···Cl hydrogen bonding in solid TMAC. Figure 8 shows the deuterium quadrupolar echo spectrum of a static sample of TMAC-d_1 at 295 K. The C_Q is 130 ± 5 kHz and the η_Q is 0.03 ± 0.03. The S/N was too low, and the required relaxation delay was much too long, to obtain a series of temperature-dependent spectra in a reasonable time. Instead, CP/MAS spectra were obtained at temperatures of 320, 350, and 370 K. The CP/MAS spectrum at 370 K, together with a simulation, can be found in Fig. 9. These spectra show a small component that increases in relative intensity with temperature (vide infra). It is of interest to note that the chemical shift C_Q and η_Q are essentially temperature-independent over this temperature range. For example, at 295 and at 370 K C_Q, η_Q, and δ_{iso} are 127 ± 6 kHz, 0.06 ± 0.05, and 10.9 ± 0.9 ppm and 126 ± 5 kHz, 0.05 ± 0.05, and 10.9 ± 1.0 ppm, respectively. If the deuteron was rapidly hopping between two sites with significantly different quadrupolar and shielding interactions, as would be implied by some of the potential energy curves in Fig. 3, one would expect a measurable temperature dependence of C_Q and δ_{iso}. Also, the fact that C_Q and δ_{iso} are independent of temperature suggests that there is no temperature-dependent wobbling motion of the trimethylammonium cation. This is a frequently observed phenomenon, particularly in small spheroid molecules, which causes a reduction of the observed C_Q with temperature.[40] The N–H distance dependence of the computed deuterium C_Q values are shown in Fig. 10. The HF, B3LYP, and plane-wave values match the experimental C_Q at about 1.04 Å.

The ^{2}H CP/MAS spectrum at 370 K can be seen in Fig. 9. This spectrum clearly shows a very small component with a lower chemical shift and much smaller C_Q (see Fig. 9 inset). At 370 K, C_Q, η_Q, and δ_{iso} for this component are 22 ± 1 kHz, 0.09 ± 0.05, and 2.9 ± 0.3 ppm. The relative intensity of the minor component increases with temperature, reaching a maximum relative intensity of 2% at 370 K. A plot of ln K versus $1/T$ yields a straight line with a slope corresponding to a ΔE of 16 kJ/mole. The appearance of the minor component can be interpreted as a result of the presence of a solid phase in which the Me_3NH^+ cation is undergoing large amplitude precessional motion. A wobbling, precessional, motion of the Me_3NH^+ cation would require a partial or complete breaking of the N–H···Cl hydrogen bond. In the absence of hydrogen bonding, amine proton chemical shifts are in the range of 0.5–5 ppm.[41] Our B3LYP/6–311++G(d,p) calculations on isolated Me_3NH^+ give δ_{iso} = 3.1 ppm. The observed chemical shift of the minor component at 2.9 ppm is consistent with this situation. If the cation is precessing, the ratio of the C_Q values for the two components yields an effective precessional angle of about 48°.

Fig. 6. Plots of the calculated ^{35}Cl C_Q as a function of N–H distance for TMAC with all heavy atoms fixed in their crystal structure positions, while the H atom positions were optimized. B3LYP/6–311++G(d,p) (■), HF/6–311++G(d,p) (◆), GIPAW plane-wave calculation (▲).

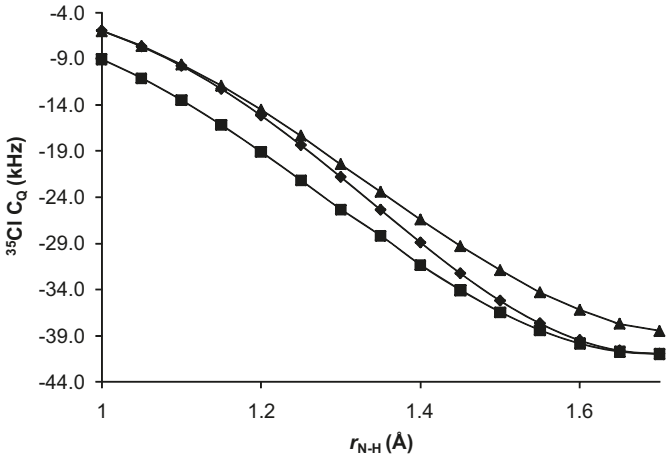

Fig. 7. Plots of the calculated span of the chlorine chemical shift tensor as a function of N–H distance for TMAC with all heavy atoms fixed in their crystal structure positions, while the H atom positions were optimized. B3LYP/6–311++G(d,p) (■), HF/6–311++G(d,p) (◆), GIPAW plane-wave calculation (▲).

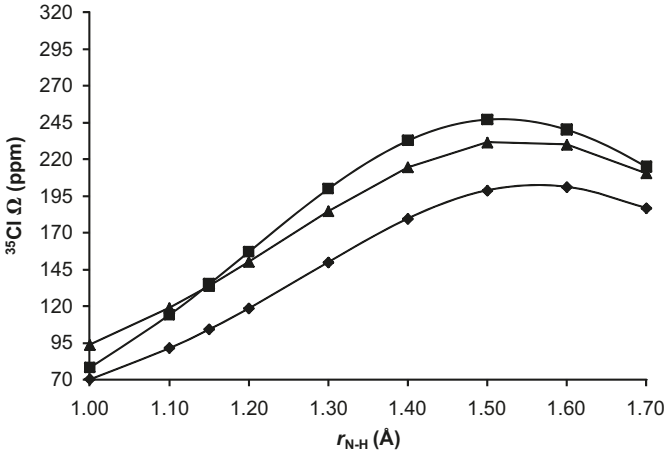

Can. J. Chem. Downloaded from www.nrcresearchpress.com by Xi'an Jiaotong University on 09/19/12
For personal use only.

Fig. 8. The quadrupolar echo spectrum of a static sample of TMAC-d_1 at 295 K, together with a simulation using $C_Q = 130$ kHz and $\eta_Q = 0.03$. Effects of CSA were not included in the simulation. The strong narrow peak at the center of the spectrum is due to traces of moisture in the sample (despite thorough drying). The lineshape is asymmetric due to an asymmetric distribution of points around the center of the echo.

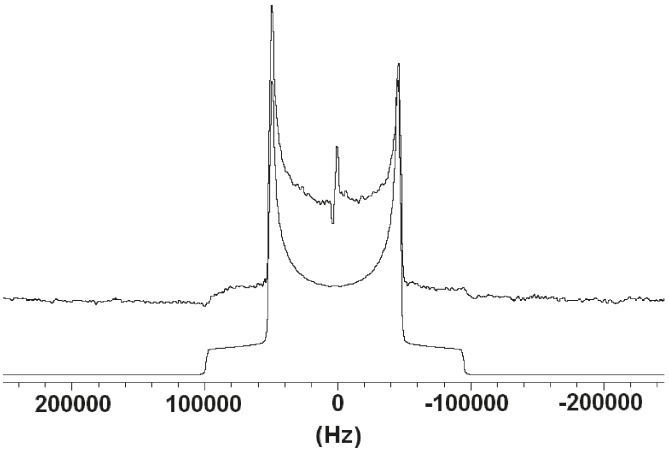

It should also be noted that the variation in peak intensity may be due to variations in CP efficiency. However, if this were the case, the intensity would be expected to decrease with an increase in temperature as a larger amplitude wobbling motion should reduce the effective ^{1}H–^{2}H dipolar interactions.

It is only through the fortuitous coincidence of the minor component having a very different chemical shift and a much smaller C_Q than the major component that we are able to see it in the ^{2}H CP/MAS spectrum. Unfortunately, the required S/N ratios in the ^{35}Cl, ^{14}N, and ^{15}N spectra are simply not achievable on our equipment with practical amounts of spectrometer time. The ^{2}H MAS spectrum of the methyl deuterated sample and the ^{13}C CP/MAS spectrum do not have the chemical shift resolution needed to observe a species with such a low relative concentration and such a small chemical shift difference from the major component. Although the ^{1}H spectrum has the sensitivity, it is not possible to observe such a relatively small resonance in the presence of two large and broad lineshapes, in addition to the significant proton background of the probe. The best chance of observing the minor component is via a ^{15}N CP/MAS spectrum of a ^{15}N enriched sample. However, such a sample is unavailable to us at this time.

Proton spectra and calculations

The proton spectra of a static sample of powdered TMAC-d_9 is shown in Fig. 11. Nearly complete deuteration of the methyl group essentially eliminates any intramolecular proton–proton dipolar coupling. The proton–deuteron dipolar coupling will be a factor of 6 smaller than proton–proton dipolar coupling, and rapid methyl and trimethyl rotation will reduce this coupling by a further factor of 9. As a result, any dipolar couplings will simply add to the broadening of the spectral lines. There are two dominant lineshapes: an intense featureless peak, which constitutes 23% of the total intensity and a broad lineshape corresponding to 77% of the total intensity.

Fig. 9. The deuterium CP/MAS spectrum of a sample of TMAC-d_1 at 370 K with sample spinning rate of 5 kHz, together with a simulation using $C_Q = 126$ kHz and $\eta_Q = 0.05$ and $\delta_{iso} = 10.9$ ppm.

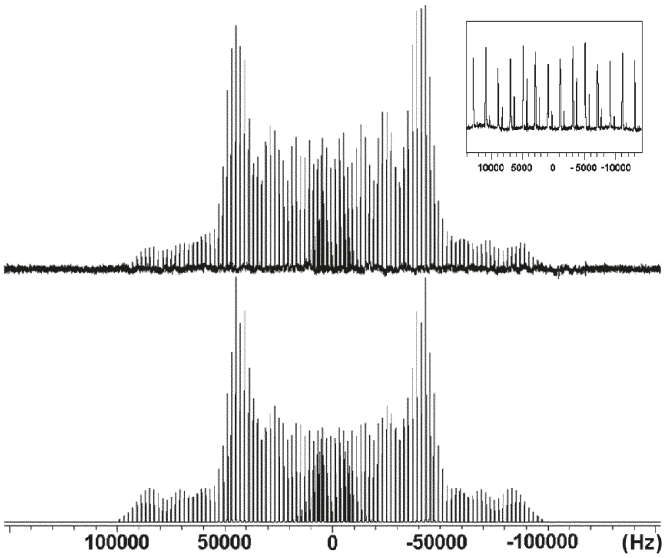

Fig. 10. Plots of the calculated ^{2}H C_Q as a function of N–H distance for TMAC with all heavy atoms fixed in their crystal structure positions, while the H atom positions were optimized. B3LYP/6–311++G(d,p) (■), HF/6–311++G(d,p) (◆), GIPAW plane-wave calculation (▲).

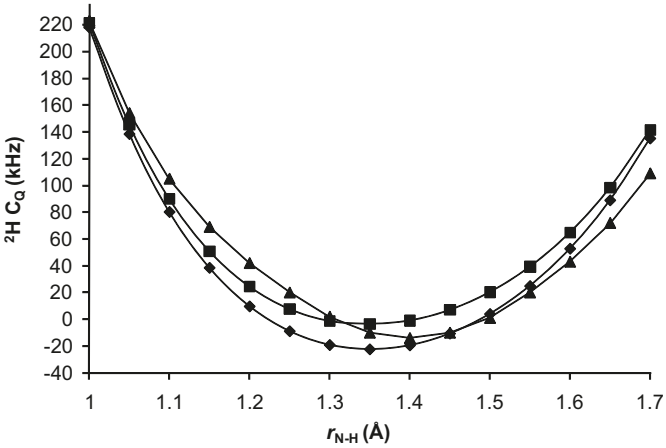

The spectrum can be deconvoluted into a component at 3.5 ± 0.8 ppm with a large linewidth and a component at 9.0 ± 1.0 ppm with a span of 45 ± 1.5 ppm and skew of –0.88 ± 0.05 (CSA = 42 ppm and $\eta = 0.13$). We assign the 3.5 ppm component to residual protons on the methyl groups and the 9.0 ppm component to the N–H proton. The relative peak areas correspond to a residual concentration of methyl protons of about 3%, due to incomplete deuteration of the sample. A plot of the calculated span of the hydrogen CS tensor (skew = –1 in all calculations) as a function of N–H distance is depicted in Fig. 12. The observed span is consistent with the isolated TMAC calculation for N–H distances ranging from 1.2–1.7 Å. The plane-wave calculations disagree with the observed span for all distances. The isotropic chemical shift, obtained from simulation of the proton spectrum, is nearly 2 ppm smaller than that obtained from the

Can. J. Chem. Downloaded from www.nrcresearchpress.com by Xi'an Jiaotong University on 09/19/12
For personal use only.

Fig. 11. Plots of the proton spectrum of a static sample of TMAC-d_9 (upper trace) together with simulations of the contributions to the lineshape of the N–H proton (red online, dark grey in print) and residual CH_3 protons (blue online, light grey in print). The convolution of the two components are combined to yield the simulated lineshape. This is shown just below the experimental spectrum.

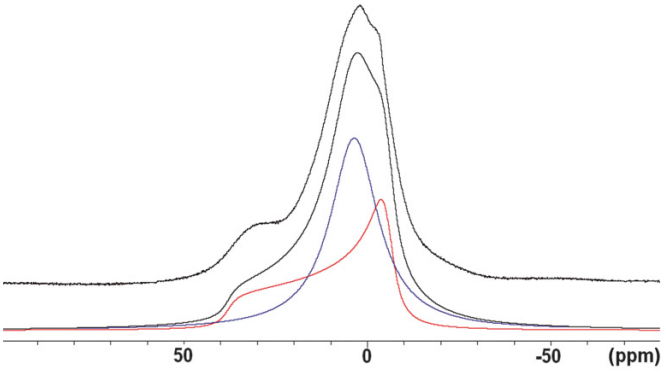

deuterium CP/MAS spectra. A primary isotope effect should move the chemical shift in the opposite direction.[42] The disagreement between the ^{2}H and ^{1}H spectra is likely due to the large error in the determination of the proton shift. Unfortunately, the severe proton background in our MAS probes made it impossible to obtain an analyzable MAS spectrum. The computed isotropic hydrogen chemical shifts are presented in Fig. 13. The curves show δ_{iso} values of 8–10 ppm for r(N–H) = 1.0 Å, typical of moderate hydrogen bonding. In the 1.3–1.4 Å range, values of 15.5–17.5 ppm were calculated, consistent with strong hydrogen bonding. The chemical shift then returns to 8–10 ppm for r(N–H) = 1.7 Å, as would be expected for a weak Cl–H···N bond. The best agreement between the computed and observed hydrogen chemical shifts occurs in the range of 1.0–1.08 Å.

Nitrogen spectra and calculations

The ^{14}N powder pattern is shown in Fig. 14. The outermost shoulders are somewhat hidden in the noise, but given the well-defined nature of the main discontinuities, it was unnecessary to obtain these features with a higher S/N, and this experimental spectrum allowed an iterative simulation to be made that resulted in the experimental parameters $|C_Q| = 1.50 \pm 0.02$ MHz, $\eta_Q = 0.02 \pm 0.02$, and $\delta_{iso} = -140 \pm 50$ ppm. CSA effects, predicted by CASTEP to be on the order of 10 ppm, were neglected in the simulation. The uncertainties were estimated visually from the quality of fit, and the very large uncertainty in the isotropic chemical shift arises from the very broad nature of the lineshape. The EFG parameters, which are measured very accurately by this technique, are in good agreement with DFT values calculated from the crystal structure using the CASTEP software. These calculations show that the ^{14}N C_Q is very insensitive to r(N–H) in the 1.0–1.2 Å range. DFT calculations of C_Q for the monomer are plotted as a function of N–H distance in Fig. 15. It has been demonstrated that these parameters can generally be calculated from crystal structures with high accuracy if the crystal structure is well-defined and dynamics are absent.[23,24] In this case, the lack of accurate proton positions and presence of dynamics will account for the discrepancy between the experimental and calculated values. The EFG tensor orientation predicted by CASTEP has the largest component of the tensor V_{33} aligned with the N–H bond, as might be expected from the crystal structure. The most shielded component of the CSA tensor (δ_{33}) is tipped away from V_{33} by 74.5°.

Fig. 12. Plots of the calculated hydrogen chemical shift as a function of N–H distance for TMAC with all heavy atoms fixed in their crystal structure positions, while the H atom positions were optimized. B3LYP/6–311++G(d,p) (■), HF/6–311++G(d,p) (◆), GIPAW plane-wave calculation (▲).

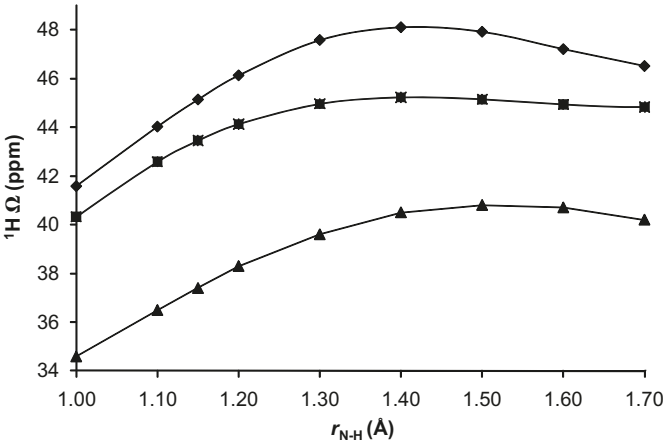

Fig. 13. Plots of the calculated span of the hydrogen chemical shift tensor as a function of N–H distance for TMAC with all heavy atoms fixed in their crystal structure positions, while the H atom positions were optimized. B3LYP/6–311++G(d,p) (■), HF/6–311++G(d,p) (◆), GIPAW plane-wave calculation (▲).

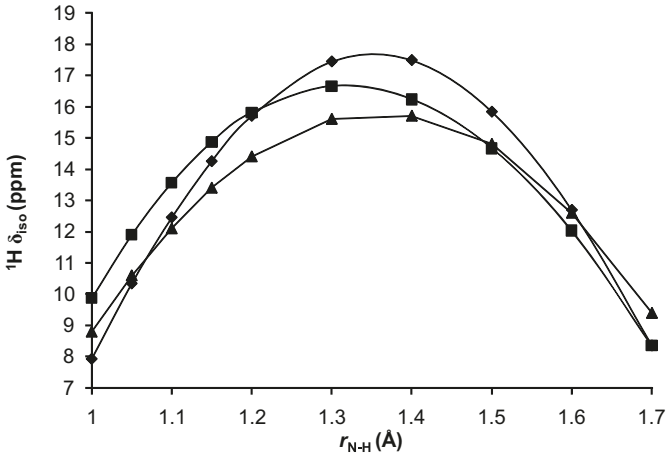

The ^{15}N CP/MAS spectrum (see Supplementary data) yields a chemical shift of –335.7 ppm with respect to liquid CH_3NO_2. Based on simulations of the featureless static ^{15}N CP spectrum, the span of the CS tensor is too small to accurately measure, and we place the upper limit at 10 ppm. All of our calculations give Ω values below 10 ppm and show very little variation with r(N–H). Analyses of the dipolar ^{15}N spectra of TMAC and TMAC-d_1 at 2.1 T completely ignored the effects of CSA.[5] The calculated isotropic chemical shift is rather dependent on the method used and also shows very little variation with r(N–H).

Table 2. Experimentally determined $^{1/2}$H and $^{14/15}$N QC and CS NMR tensor parameters.

	$\|C_Q\|$ (MHz)	η_Q	δ_{iso} (ppm)	Ω (ppm)	κ	$\Delta\delta$	η_{CS}
^{2}H[a]	0.127±0.006	0.06±0.05	10.9±1				
^{1}H	—	—	9.0±1.0	45±1.1	–0.88±0.05	42±1	0.13±0.04
^{14}N	1.50±0.02	0.02±0.02	–141±50	≤10		≤10	
^{15}N	—	—	–335.7±1	≤10		≤10	

[a]Extracted from ^{2}H spectrum recorded at room temperature.

Can. J. Chem. Downloaded from www.nrcresearchpress.com by Xi'an Jiaotong University on 09/19/12
For personal use only.

Fig. 14. (*a*) ^{14}N spectrum obtained at 21.1 T and (*b*) a fitted simulation made using parameters C_Q = 1.50 MHz, η_Q = 0.02, and δ_{iso} = 200 ppm.

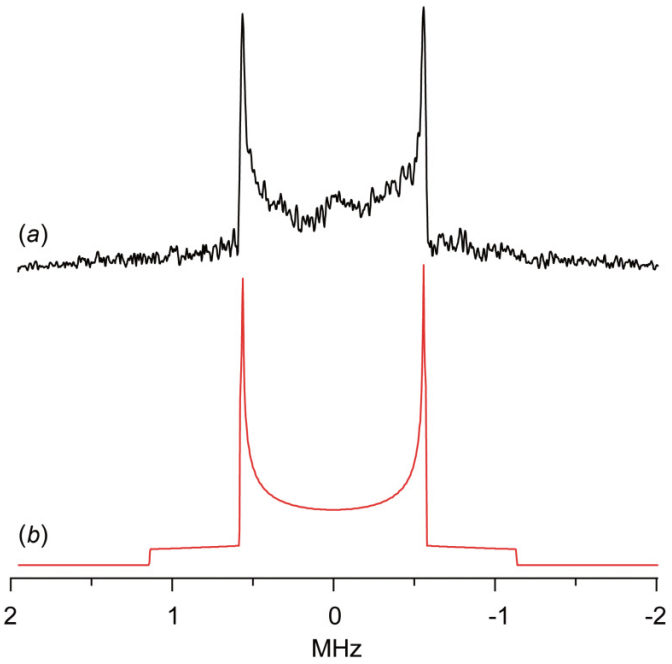

Fig. 15. Plots of the calculated ^{14}N C_Q as a function of N–H distance for TMAC with all heavy atoms fixed in their crystal structure positions, while the H atom positions were optimized. B3LYP/6–311++G(d,p) (■), HF/6–311++G(d,p) (◆), GIPAW plane-wave calculation (▲).

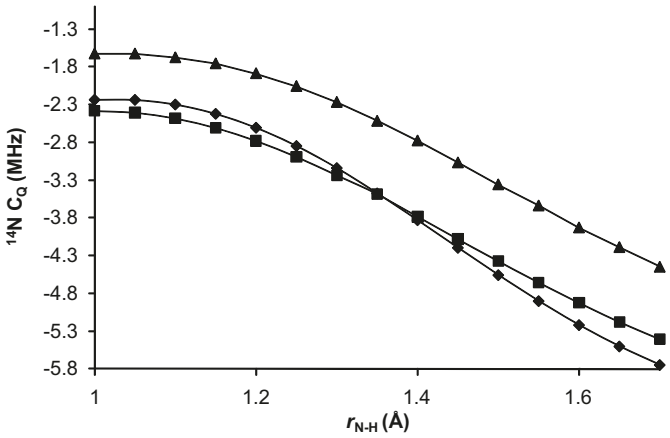

The structure of TMAC

An evolving aspect of NMR crystallography is the use of solid-state NMR spectroscopy to refine structures in crystalline solids.[43] In the case of solid crystalline TMAC this was not possible. Comparison of the measured and calculated shielding and quadrupolar parameters yield only qualitative agreement that solid TMAC exists in structure **1a**. The best determination to date of the hydrogen position in TMAC has been done through the measurement of ^{15}N–^{1}H and ^{15}N–^{2}H dipolar interactions by Hoelger and Limbach.[5] It should be noted that these are the vibrationally averaged internuclear distances. This is evident from the slight shortening of the bond length, by about 0.01 Å upon deuteration, which is consistent with what is expected for a somewhat anharmonic potential. The numbers are in good agreement with our CASTEP optimized value of 1.080 Å.

Conclusions

A multinuclear NMR and quantum chemical study of solid trimethylammonium chloride was undertaken to investigate the effects of N–H···Cl hydrogen bonding on the various observable NMR parameters. In addition, the effects of N–H internuclear distance were calculated using different quantum chemical methods.

Calculations of the energy profile, as a function of *r*(N–H), are highly dependent on the computational method used. Calculations also show that the shielding and quadrupolar interactions for $^{1/2}$H and ^{35}Cl are very sensitive to the hydrogen position in the 1.0–1.2 Å range of *r*(N–H), whereas the ^{14}N C_Q is much less dependent.

Unfortunately, it was not possible to refine the hydrogen position based on comparisons of the calculated and observed NMR parameters, as has successfully been done for the bromine position in solid $MgBr_2$ by Widdifield and Bryce.[43] With the exception of the proton chemical shift anisotropy, the measured NMR parameters are consistent with a relatively short N–H bond (structure **1a**). The high hydrogen chemical shift (10.9 ppm by ^{2}H CP/MAS) and relatively small deuterium quadrupolar coupling constant (127 kHz) indicate a moderately strong N–H···Cl hydrogen bond.

Our calculations show that the single molecule DFT and plane-wave DFT calculations are often in reasonably good agreement, the exceptions being the hydrogen span, the ^{14}N C_Q, and to a lesser degree the ^{35}Cl span. In some cases there is better agreement between the computations and experiment in the *r*(N–H) range of 1.0–1.2 Å (the interval of most interest to this study) for single molecule DFT (e.g., chlorine span), and in some cases the agreement is better for the DFT plane-wave calculations (^{14}N and ^{35}Cl C_Q values). For crystalline compounds, one would expect better agreement for the plane-wave DFT calculations. In the case of TMAC, any lack of agreement is likely due to molecular dynamics in the form of methyl and trimethyl reorientation together with uncertainty in the methyl C–H bond lengths. The latter effect can be mostly taken into account by using standard alkyl C–H bond lengths or by optimizing the methyl hydrogen positions

for every calculation. The effects of the dynamics is more difficult to deal with since this effect would have to be weighted over the rotational potential energy functions for both methyl and trimethyl rotation.

Supplementary data

Supplementary data for this article are available on the journal Web site (www.nrcresearchpress.com/cjc).

Acknowledgements

The Natural Sciences and Engineering Research Council of Canada is thanked for a Discovery grant (to GHP). The University of Guelph NMR Centre is supported by the Canada Foundation for Innovation and the Ontario Research Fund.

The National Ultra-High Field NMR Facility for Solids, Ottawa (http://nmr900.ca), is acknowledged for providing access to the 900 MHz facility and also for the use of the CASTEP software. In particular, Victor Terskikh and Eric Ye are acknowledged for assistance with the NMR experiments, and Paul Morris is thanked for help with probe construction and modifications.

One of the authors (GHP) would like to personally thank Rod Wasylishen for his hospitality during a postdoctoral fellowship (1986–1988) and a sabbatical leave (2001).

Can. J. Chem. Downloaded from www.nrcresearchpress.com by Xi'an Jiaotong University on 09/19/12
For personal use only.

References

(1) Jeffrey, G. A. *An Introduction to Hydrogen Bonding*; New York: Oxford University Press, 1997.
(2) Becker, E. D. *Hydrogen Bonding*; In *Encyclopedia of Magnetic Resonance*; R. K. Harris and R. E. Wasylishen, Eds.; Chichester, NY: John Wiley.
(3) Brown, S. P. *Hydrogen Bonding in Crystalline Organic Solids*; In *Encyclopedia of Magnetic Resonance*; R. K. Harris and R. E. Wasylishen, Eds.; Chichester, NY: John Wiley.
(4) Roberts, J. E.; Harbison, G. S.; Munowitz, M. G.; Herzfeld, J.; Griffin, R. G. *J. Am. Chem. Soc.* **1987** *109* (14), 4163. doi:10.1021/ja00248a006.
(5) Hoelger, C.-G.; Limbach, H.-H. *J. Phys. Chem.* **1994** *98* (45), 11803. doi:10.1021/j100096a028.
(6) Legon, A. C.; Rego, C. A. *J. Chem. Soc. Chem. Commun.* **1988** (22): 1496. doi:10.1039/c39880001496.
(7) Legon, A. C.; Rego, C. A. *J. Chem. Phys.* **1989** *90* (12), 6867. doi:10.1063/1.456260.
(8) Bacskay, G. B.; Craw, J. S. *Chem. Phys. Lett.* **1994** *221* (1-2), 167. doi:10.1016/0009-2614(94)87034-9.
(9) Davies, A. S.; George, W. O.; Howard, S. T. *Phys. Chem. Chem. Phys.* **2003** *5* (20), 4533. doi:10.1039/b307534f.
(10) Lindgren, J.; Olovsson, I. *Acta Crystallogr. Sect. B. Stuct. Sci.* **1968** *24*, 554.
(11) Sugiyama, M.; Machida, M.; Koyano, N.; Iwata, Y. *J. Korean Phys. Soc.* **1996** *29*, S537.
(12) Kido, J.; Machida, M.; Kobayashi, T. *J. Korean Phys. Soc.* **1996** *29*, S542.
(13) Huong, P. V.; Schlaak, M. *Chem. Phys. Lett.* **1974** *27* (1), 111. doi:10.1016/0009-2614(74)80456-2.
(14) Andrew, E. R.; Canepa, P. C. *J. Magn. Reson.* **1972** *7*, 429.
(15) Sjöblom, R.; Tegenfeldt, J.; Gramstad, T.; Songstad, J.; Pilotti, Å. *Acta Chem. Scand.* **1972** *26*, 3075. doi:10.3891/acta.chem.scand.26-3075.
(16) Sjöblom, R.; Punkkinen, M. *J. Magn. Reson.* **1975** *20*, 491.
(17) Machida, M. *Ferroelectrics* **2006** *338* (1), 205. doi:10.1080/00150190600740184.
(18) Pople, J. A.; Beveridge, D. L. *Approximate Molecular Orbital Theory*; New York: McGraw-Hill, 1970.
(19) Bryce, D. L.; Gee, M.; Wasylishen, R. E. *J. Phys. Chem. A* **2001** *105* (45), 10413. doi:10.1021/jp011962a.
(20) O'Dell, L. A.; Schurko, R. W. *Chem. Phys. Lett.* **2008** *464* (1-3), 97. doi:10.1016/j.cplett.2008.08.095.
(21) O'Dell, L. A.; Rossini, A. J.; Schurko, R. W. *Chem. Phys. Lett.* **2009** *468* (4-6), 330. doi:10.1016/j.cplett.2008.12.044.
(22) O'Dell, L. A.; Schurko, R. W. *J. Am. Chem. Soc.* **2009** *131* (19), 6658. doi:10.1021/ja901278q.
(23) O'Dell, L. A.; Schurko, R. W. *Phys. Chem. Chem. Phys.* **2009** *11* (32), 7069. doi:10.1039/b906114b.
(24) O'Dell, L. A.; Schurko, R. W.; Harris, K. J.; Autschbach, J.; Ratcliffe, C. I. *J. Am. Chem. Soc.* **2011** *133* (3), 527. doi:10.1021/ja108181y.
(25) O'Dell, L. A.; Ratcliffe, C. I. *Chem. Commun. (Camb.)* **2010** *46* (36), 6774. doi:10.1039/c0cc01902j.
(26) Eichele, K.; Wasylishen, R. E. *WSOLIDS NMR simulation package*; Version 1.19.11, 2009.
(27) Massiot, D.; Fayon, F.; Capron, M.; King, I.; Le Calvé, S.; Alonso, B.; Durand, J.-O.; Bujoli, B.; Gan, Z.; Hoatson, G. *Magn. Reson. Chem.* **2002** *40* (1), 70. doi:10.1002/mrc.984.
(28) Frisch, M. J.; Trucks, G. W.; Schlegel, H. B.; Scuseria, G. E.; Robb, M. A.; Cheeseman, J. R.; Montgomery, J. A., Jr.; Vreven, T.; Kudin, K. N.; Burant, J. C.; Millam, J. M.; Iyengar, S. S.; Tomasi, J.; Barone, V.; Mennucci, B.; Cossi, M.; Scalmani, G.; Rega, N.; Petersson, G. A.; Nakatsuji, H.; Hada, M.; Ehara, M.; Toyota, K.; Fukuda, R.; Hasegawa, J.; Ishida, M.; Nakajima, T.; Honda, Y.; Kitao, O.; Nakai, H.; Klene, M.; Li, X.; Knox, J. E.; Hratchian, H. P.; Cross, J. B.; Bakken, V.; Adamo, C.; Jaramillo, J.; Gomperts, R.; Stratmann, R. E.; Yazyev, O.; Austin, A. J.; Cammi, R.; Pomelli, C.; Ochterski, J. W.; Ayala, P. Y.; Morokuma, K.; Voth, G. A.; Salvador, P.; Dannenberg, J. J.; Zakrzewski, V. G.; Dapprich, S.; Daniels, A. D.; Strain, M. C.; Farkas, O.; Malick, D. K.; Rabuck, A. D.; Raghavachari, K.; Foresman, J. B.; Ortiz, J. V.; Cui, Q.; Baboul, A. G.; Clifford, S.; Cioslowski, J.; Stefanov, B. B.; Liu, G.; Liashenko, A.; Piskorz, P.; Komaromi, I.; Martin, R. L.; Fox, D. J.; Keith, T.; Al-Laham, M. A.; Peng, C. Y.; Nanayakkara, A.; Challacombe, M.; Gill, P. M. W.; Johnson, B.; Chen, W.; Wong, M. W.; Gonzalez, C.; Pople, J. A. *Gaussian 03, revision C.02*; Wallingford, CT: Gaussian, Inc., 2004.
(29) Adiga, S.; Aebi, D.; Bryce, D. L. *Can. J. Chem.* **2007** *85*, 496.
(30) Clark, S. J.; Segall, M. D.; Pickard, C. J.; Hasnip, P. J.; Probert, M. J.; Refson, K.; Payne, M. C. *Z. Kristallogr.* **2005** *220* (5-6-2005), 567. doi:10.1524/zkri.220.5.567.65075.
(31) Pickard, C. J.; Mauri, F. *Phys. Rev. B* **2001** *63* (24), 245101. doi:10.1103/PhysRevB.63.245101.
(32) Profeta, M.; Mauri, F.; Pickard, C. J. *J. Am. Chem. Soc.* **2003** *125* (2), 541. doi:10.1021/ja027124r.
(33) Yates, J. R.; Pickard, C. J.; Mauri, F. *Phys. Rev. B* **2007** *76* (2), 024401. doi:10.1103/PhysRevB.76.024401.
(34) Pfrommer, B. G.; Cote, M.; Louie, S. G.; Cohen, M. L. *J. Comput. Phys.* **1997** *131* (1), 233. doi:10.1006/jcph.1996.5612.
(35) Gervais, C.; Dupree, R.; Pike, K. J.; Bonhomme, C.; Profeta, M.; Pickard, C. J.; Mauri, F. *J. Phys. Chem. A* **2005** *109* (31), 6960. doi:10.1021/jp0513925.
(36) Bryce, D. L.; Sward, G. D. *J. Phys. Chem. B* **2006** *110* (51), 26461. doi:10.1021/jp065878c.

(37) Bryce, D. L.; Sward, G. D.; Adiga, S. *J. Am. Chem. Soc.* **2006** *128* (6), 2121. doi:10.1021/ja057253i.
(38) Chapman, R. P.; Bryce, D. L. *Phys. Chem. Chem. Phys.* **2007** *9* (47), 6219. doi:10.1039/b712688c.
(39) Honda, H. *Z. Naturforsch.* **2003** *58a*, 623.
(40) Sidhu, P. S.; Bell, J.; Penner, G. H.; Jeffrey, K. R. *Can. J. Chem.* **1996** *74* (10), 1784. doi:10.1139/v96-199.
(41) Pavia, D. L.; Lampman, G. M.; Kris, G. S. *Introduction to Spectroscopy*; 2nd ed.; Saunders 1996; p. 119.
(42) Perrin, C. L.; Nielson, J. B. *Annu. Rev. Phys. Chem.* **1997** *48* (1), 511. doi:10.1146/annurev.physchem.48.1.511.
(43) Widdifield, C. M.; Bryce, D. L. *Phys. Chem. Chem. Phys.* **2009** *11* (33), 7120. doi:10.1039/b911448n.

Can. J. Chem. Downloaded from www.nrcresearchpress.com by Xi'an Jiaotong University on 09/19/12
For personal use only.

Solid-state nuclear magnetic resonance (NMR) spectroscopy reveals distinctive protein dynamics in closely related spider silks

Isabelle Cloutier, Jérémie Leclerc, Thierry Lefèvre, and Michèle Auger

Can. J. Chem. Downloaded from www.nrcresearchpress.com by Xi'an Jiaotong University on 09/19/12
For personal use only.

Abstract: Structurally closely related spider silks, namely, major ampullate silk (MaS) reeled at 0.5 and 10 cm/s, minor ampullate silk (MiS), and cocoon silk have been investigated by solid-state nuclear magnetic resonance (NMR). These silks exhibit different mechanical properties that are not well explained with current structural data. NMR spectra confirm that the secondary structures of these silks are similar, but that differing relaxation dynamics exist at the alanine, glycine, and glutamine residue level. MaS reeled rapidly is made of more mobile proteins in both the β-sheet and amorphous regions, suggesting that reeling speed alters molecular rearrangement during spinning, with the chain packing being less organized in the fastpull fiber. Alanine and glycine relaxation dynamics increases as MaS < MiS < cocoon silk, showing that the whole fiber displays distinctive protein dynamics, chain packing, and intermolecular interactions. Besides molecular orientation, silk extensibility is related to a more mobile structural organization.

Key words: silk proteins, solid-state nuclear magnetic resonance (NMR), structure, dynamics, reeling speed.

Résumé : Des soies d'araignée avec des structures similaires, soit la soie de la glande ampullacée majeure (MaS) filée à 0,5 et 10 cm/s, la soie de la glande ampullacée mineure (MiS) et la soie de cocon, ont été étudiées par spectroscopie résonance magnétique nucléaire (RMN) des solides. Ces soies possèdent des propriétés mécaniques différentes qui peuvent difficilement être expliquées par les données structurales connues. Les spectres RMN obtenus dans la présente étude confirment que les structures secondaires des protéines sont similaires dans ces différents types de soie, mais que leurs dynamiques de relaxation sont différentes au niveau des résidus alanine, glycine et glutamine. La MaS filée rapidement est constituée de protéines plus mobiles à la fois dans les régions riches en feuillets β et dans les régions amorphes, ce qui suggère que la vitesse de filage influence le réarrangement moléculaire durant le filage, l'empilement des chaînes étant moins bien organisé dans la soie filée rapidement. La dynamique de relaxation des résidus alanine et glycine augmente dans l'ordre MaS < MiS < soie de cocon, suggérant que ces différentes fibres sont constituées de protéines ayant des dynamiques, des empilements de chaînes et des interactions intermoléculaires différentes. En plus de l'orientation moléculaire, l'extensibilité de la soie semble donc liée à une organisation structurale plus mobile.

Mots-clés : protéines de soie, résonance magnétique nucléaire (RMN) des solides, structure, dynamique, vitesse de filage.

Introduction

The silk filaments produced by spiders are amongst nature's most highly engineered structural materials. Their mechanical properties are particularly interesting because these biomaterials are specifically designed to fulfill specific biological functions, for example, support the weight of the spider or absorb the kinetic energy and stop flying prey.[1] Orb-weaving spiders produce six types of silk by the way of seven specialized glands.[2] More specifically, major ampullate silk (MaS) displays outstanding tensile properties due to the combination of high strength and extensibility, providing a remarkable toughness.[3] Consequently, MaS can potentially be used for industrial and medical applications,[4] such as the production of artificial tendons,[5] surgical sutures[6] or micro-electro-mechanical systems.[7] To date, the combination of strength and extensibility of natural silk has not yet been reproduced by artificial means. Therefore, to produce a high-quality synthetic silk, it is necessary to understand the structural characteristics that determine the mechanics of spider silk.

The structural model proposed for MaS includes polyalanine crystalline domains embedded in an amorphous region rich in glycine residues. In this model, the crystalline domains are responsible for the strength of silk and the amorphous regions for its elasticity.[8,9] The crystalline regions are composed of highly oriented β-sheets and the amorphous regions are made of 3_1-helices, β-turns, and random coils. Several spectroscopic studies (nuclear magnetic resonance

Received 22 December 2010. Accepted 14 February 2011. Published at www.nrcresearchpress.com/cjc on 19 August 2011.

I. Cloutier, J. Leclerc, T. Lefèvre, and M. Auger. Department of Chemistry, Regroupement québécois de recherche sur la fonction, la structure et l'ingénierie des protéines (PROTEO), Centre de recherche sur les matériaux avancés (CERMA), Université Laval, Quebec, QC G1V 0A6, Canada.

Corresponding author: Michèle Auger (e-mail: michele.auger@chm.ulaval.ca).

This article is part of a Special Issue dedicated to Professor Roderick E. Wasylishen.

Can. J. Chem. Downloaded from www.nrcresearchpress.com by Xi'an Jiaotong University on 09/19/12
For personal use only.

(NMR), X-ray, Raman, and Fourier transform infrared (FTIR)) are in agreement with this model.[10–14]

MaS is used for multiple biological functions in nature, including locomotion, safety lines, web construction, signal thread, and chemical communication.[15] Each function requires specific mechanical characteristics. Typically, the spinning rate ranges between 0.5 and 10 cm/s, corresponding to the production of the frame of the web and the lifeline, respectively.[15,16] These filaments display various tensile properties. The fastpull silk has higher breaking stress and Young modulus that are well adapted to support the spider body weight during the rapid vertical descent that allows spiders to escape predators.[17–19] The slowpull silk is more extensible, which is very efficient to support, in conjunction with the capture spiral, the kinetic energy transferred to the web when prey is captured.[17–19] Overall, the breaking energy of MaS seems to be basically constant at various reeling speeds.[19] Variability in the spinning rate seems to induce changes in the micro- and molecular structures. Usually, fibers spun at higher spinning rates have a higher global level of orientation[11,20,21] and seem to contain a lower volume of highly oriented domains.[22,23] Despite these results, the effect of the spinning speed on the structural organization of silk is sparsely documented; more work is needed to understand the relationship between the structure and the mechanical properties of silk.

The structural pattern of MaS, characterized by oriented β-sheets dispersed in an amorphous matrix, is shared by various silks that belong to the same structural family.[24–28] This class includes the cocoon silk of silkworms and the minor ampullate (MiS) and cocoon silks of spiders. As shown in Table 1, these fibers have different tensile strengths varying from 1.5 MPa for MaS, 0.9 MPa for MiS, and 0.5 MPa for cocoon silk and relatively large extensibility (21% for MaS, 33% for MiS, and 20% for cocoon silk). MaS and cocoon silk display the same level of molecular orientation.[27] In nature, MiS is used to form an auxiliary spiral that serves as a scaffold for the emerging web.[34] It has also been found in the wrapping net spun around prey.[35] Cocoon silk is produced by the tubuliform gland of female spiders during the reproductive season[36] and is used to make the cocoon outer egg sac. As shown in Table 1, MiS has a lower stress at rupture than MaS, but its extensibility is higher.[26,33] Cocoon silk has the lowest breaking stress whereas its breaking strain is located between that of MaS and MiS.

These three types of silk are made of specific proteins (Table 1), i.e., MaSpI and MaSpII for MaS,[29] MiSpI and MiSpII for MiS,[31] and TuSpI for cocoon silk.[36,37,38] Like MaS, MiS contains polyalanine motifs, but they are shorter for the latter silk (n = 3–5) than for the former one (n = 5–7).[39] MiS also contains poly(Ala-Gly) sequences that are short as compared with those found in the *Bombyx mori* cocoon silk. MaS has two glycine repetitive blocks (GXX for MaSpI and GPGXX for MaSpII)[10,40] while MiS contains only GXX modules. The repetitive sequence of cocoon silk is very different with almost no polyalanine sequences and sparsely distributed repeat motifs. It is rich in serine and glutamine residues. In contrast to their tensile properties, the structural disparities observed experimentally between these three silks are small[26,27] and actual data fail to clearly explain the structural origin of their particular responses to a mechanical drawing.

Generally speaking, despite recent advances, some silk fibers display only minor structural dissimilarities that cannot alone explain their diversified tensile behaviors. Obviously, additional data are required to unravel this paradox. We have thus investigated three closely related silks (MaS, MiS, and cocoon silk) as well as the effect of the spinning rate on MaS. Understanding structural features important for tensile properties could help with the aim of producing high quality fibers. To this end, we have used ^{13}C solid-state NMR spectroscopy since it is a powerful technique to obtain information on protein secondary structure and dynamics over a large range of timescales (kHz and MHz), in crystalline as well as in amorphous regions. Since specific resonances occur in the spectra, NMR spectroscopy has the advantage that molecular structure and dynamics can be investigated at the amino acid level.

Experimental

Silk samples

MaS, MiS, and cocoon silk samples were obtained from adult female *Nephila clavipes* spiders collected from Florida, U.S. The spiders were raised in the laboratory in 20 cm × 50 cm × 60 cm cages at 58% ± 5% relative humidity and 24 ± 2 °C. They were fed four times a week with crickets of about one centimetre in length and with 3 drops of 1% or 10% glucose solution per week. MaS was collected by forced reeling at rates of 0.5 and 10 cm/s on fully awake spiders. Samples were collected onto glass test tubes under controlled conditions as described by Ortlepp and Gosline.[41] MiS was collected by forced reeling at a rate of 0.5 cm/s. Care was taken to avoid mixing of MaS and MiS during reeling. The results presented were obtained by combining samples reeled from five different individuals. Cocoon silk was obtained from the cocoons made by the spiders in the laboratory. The eggs were removed from the cocoon. All samples were kept in a dark environment at the above controlled temperature and humidity. Typically, 25 mg of each type of silk were used to perform the NMR experiments.

NMR spectroscopy

^{13}C NMR spectra of the silk samples were recorded on a Bruker Avance 400 or Avance II 900 spectrometer (Bruker Biospin, Milton, ON) operating at ^{13}C NMR frequencies of 100 MHz and 225 MHz, respectively. The 400 and 900 MHz spectrometers were equipped with a 4 and 3.2 mm magic-angle spinning (MAS) probehead, respectively (Bruker Biospin, Milton, ON). All spectra were recorded at room temperature with MAS speeds of 10 kHz at 400 MHz and 22 kHz at 900 MHz.

Two types of ^{13}C NMR spectra were recorded: cross-polarization with magic-angle spinning (CPMAS) and Hahn echo. CPMAS spectra were recorded using 2048 complex data points and a dwell time of 5 μs. The ^{1}H 90° pulse length was typically 4 μs, the contact time was 2 ms, and the recycle delay was 4 s. A ramped CP was used on the ^{1}H channel. Typically, 2048 scans were acquired at 900 MHz and 4000 scans were acquired at 400 MHz for the CPMAS spectra. For the Hahn-echo spectra, the ^{13}C 90° pulse was typically 4.5 μs and 2048 complex points were obtained with a dwell time of 5 μs, an interpulse delay of 60 μs, and

Table 1. Comparison between the repetitive sequences and mechanical properties of MaS, MiS, and cocoon silk.

	MaS	MiS	Cocoon
Proteins	MaSpI, MaSpII	MiSpI, MiSpII	TuSpI
Repetitive sequence motifs[a]	$(A)_n$ (n = 5–7), $(GA)_n$, GGX, GPGXX	$(A)_n$ (n = 3–5), $(GA)_n$, GGX, S-rich regions	$(S)_n$, $(SA)_n$, $(SQ)_n$, GX, $(A)_n$ (n = 2–3)
Mechanical properties[b]	Strength: 1.5 MPa Extensibility: 21% Toughness: 136 J/cm^3	Strength: 0.9 MPa Extensibility: 33% Toughness: 137 J/ cm^3	Strength: 0.5 MPa Extensibility: 29% Toughness: 95 J/cm^3

[a]The sequence is given for *Nephila clavipes* and is taken from Xu and Lewis[29] and Hinman and Lewis[30] for MaS, Colgin and Lewis[31] for MiS, and Tian and Lewis[32] for cocoon silk.

[b]The mechanical properties are given for *Argiope trifasciata*[33] which, in our opinion, represents the most accurate and most complete data set regarding the tensile properties of the silks spun by a spider species

a recycle delay of 30 s. Hahn-echo spectra were acquired with 2400 scans. Two pulse phase modulation (TPPM) proton decoupling[42] was used for both the CPMAS and Hahn-echo spectra. A line broadening of 100 Hz was applied in the processing of all spectra and chemical shifts were referenced relative to external adamantane.

^{1}H T_1 relaxation times were measured at 400 MHz using an inversion-recovery ramped-CP experiment with delays of 0.05, 0.1, 0.3, 0.5, 0.8, 1, 3, and 5 s between the 180° and 90° pulses. ^{13}C $T_{1\rho}$ relaxation times were measured using a ramped-CP sequence followed by a variable carbon spin-lock time (1, 3, 5, 7.5, 10, 12.5, 15, 17.5, and 20 ms). Typically, 4000 scans were collected for each relaxation delay and all relaxation studies were repeated twice. A homemade Excel program and the relaxation program provided by Bruker were used to analyze the relaxation data.

Results and discussion

Effect of the silk spinning rate on protein secondary structure

The effect of the silk spinning rate on the secondary structure of MaS proteins was first investigated. Two extreme spinning rates were investigated, 0.5 and 10 cm/s, which are associated with the filaments made for the web frame and the safety line, respectively.[15,16] Solid-state ^{13}C NMR allows the distinction between polypeptide secondary structures since the chemical shift is sensitive to conformation.[43–45] The CPMAS spectra recorded for silk reeled at 0.5 and 10 cm/s are presented in Fig. 1. The assignment of the peaks due to alanine, glycine, glutamine, and tyrosine residues and to carbonyl groups is also indicated.

The spectra show chemical shifts typical of those associated with silk produced by the major ampullate gland.[10] The chemical shifts due to alanine residues at 49.0 ppm for C_α and 19.6–22.2 ppm for C_β are characteristic of β-sheets.[46] The small contribution at 17.4 ppm for C_β has been assigned to a 3_1-helix by Holland et al.[46] A small contribution of a 3_1-helix at 48.9 ppm is also most likely present in the Ala C_α peak but cannot be distinguished in the spectra. The current results are in agreement with the presence of at least two secondary structures for alanine residues in *N. edulis* dragline silk.[46–48] One can observe that the spectra obtained at the two spinning rates are almost identical, with no difference in the chemical shifts (except for glutamine). This result indicates that the secondary structure of the MaS protein is not significantly affected by the reeling speed.

Fig. 1. 900 MHz ^{13}C CPMAS spectra of MaS spun at 0.5 cm/s (black) and 10 cm/s (red, dark grey in print version).

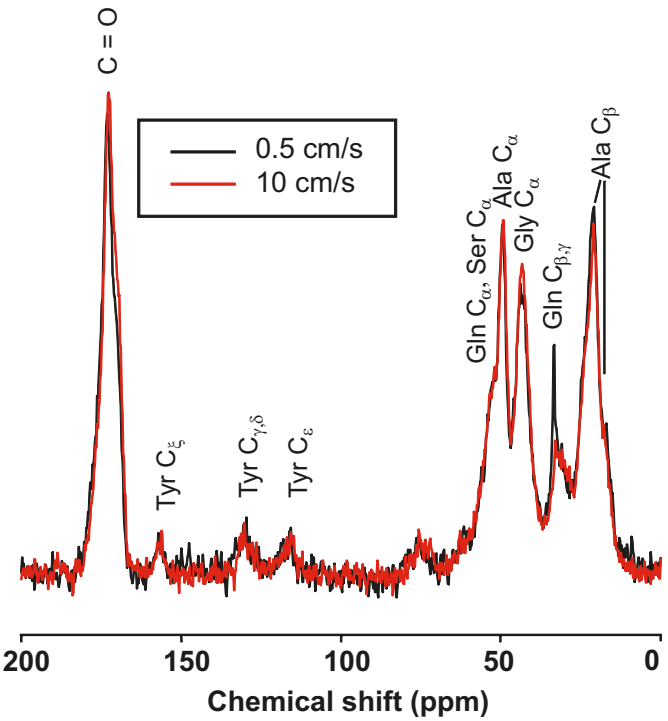

The spectra show a signal at 33 ppm due to glutamine $C_{\beta,\gamma}$, which is dramatically more resolved at 0.5 than at 10 cm/s. Thus, this amino acid has a particular behavior depending on the reeling speed. Glutamine is found in the SQGA motifs of MaSpI and in the GPGQQ motifs of MaSpII. It is the most abundant polar amino acid of MaS. The particular shape of the glutamine $C_{\beta,\gamma}$ peak as a function of reeling speed may thus reflect a specific structural arrangement or environment of these sequence motifs in the fibers. Although this line narrowing remains unclear, it may be related to a more ordered amorphous region containing the glutamine residues for silk spun at 0.5 cm/s.

We have also investigated the effect of the spinning rate on the amount of alanine residues in β-sheet regions. More specifically, Hahn-echo spectra, in which the signal is not affected by the efficiency of the CP magnetization transfer, have been recorded and are shown in Fig. 2. The proportion of alanine residues in β-sheet and 3_1-helix structures was obtained from the area of the alanine C_β peaks at 20 and 16–17 ppm,

Can. J. Chem. Downloaded from www.nrcresearchpress.com by Xi'an Jiaotong University on 09/19/12
For personal use only.

Can. J. Chem. Downloaded from www.nrcresearchpress.com by Xi'an Jiaotong University on 09/19/12
For personal use only.

Fig. 2. 900 MHz ^{13}C Hahn-echo spectra of MaS spun at 0.5 cm/s (black) and 10 cm/s (red, dark grey in print).

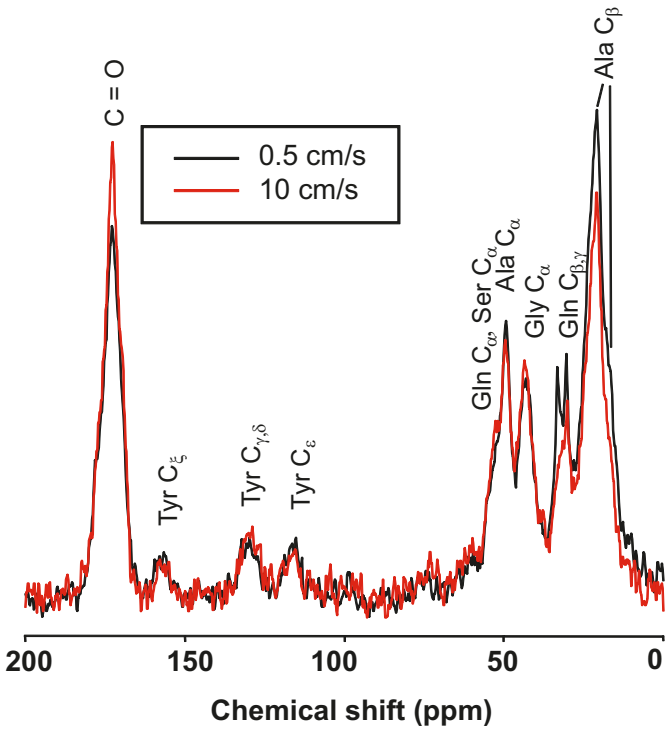

respectively. The results, presented in Table 2, show that the amount of alanine residues in β-sheets is 81% ± 5% for a reeling speed of 0.5 cm/s, a value that is very comparable to that obtained by Holland et al.[47] In addition, the proportion of alanine residues in β-sheets and 3_1-helices is the same for silk spun at 0.5 and 10 cm/s. For glycine, the chemical shift is around 43.5 ppm, in good agreement with Holland et al.,[46] and is almost identical for both samples. These results therefore confirm that the spinning rate does not have a significant influence on the secondary structure of both alanine and glycine residues. The spectra presented in Fig. 2 also reveal sharper glutamine signals at 30 and 33 ppm for the slowpull fiber, as seen in the CPMAS spectra.

Effect of the silk spinning rate on protein dynamics

Solid-state NMR is an efficient technique to characterize the dynamics of protein chains over a large range of timescales, as T_1 and $T_{1\rho}$ relaxation times report on motions in the MHz and kHz timescales, respectively.[49,50] It has been shown that the proportions of crystalline and amorphous regions in polymers such as silk can significantly influence molecular relaxation. In particular, shorter T_1 usually indicate more mobile, flexible regions. Changes in T_1 can also reflect different chain packing, which will affect the proton density and the proton dipolar interaction. On the other hand, $T_{1\rho}$ will be affected by the size of the crystallite domains and shorter $T_{1\rho}$ are usually indicative of larger amorphous components or more mobile chains. Since specific resonances in ^{13}C NMR spectra can be assigned to particular amino acids, the dynamics can be probed for various residues in crystalline or amorphous regions. Kishore et al.[51] already successfully used relaxation data to characterize the protein mobility for different hydration levels and spider species.

Table 2. Alanine residues in β-sheet and 3_1-helix structures for MaS spun at 0.5 and 10 cm/s.

Reeling speed	20 ppm (β-sheet)	16–17 ppm (3_1-helix)
0.5 cm/s	81%±5%	19%±5%
10 cm/s	82%±5%	18%±5%

The ^{1}H T_1 measured for the peaks associated with the C_α of alanine residues, mainly in β-sheet structures, the glycine C_α, and the glutamine $C_{\beta,\gamma}$ are shown in Fig. 3A. These peaks were chosen for their high resolution and intensity. Average times for ^{1}H T_1 are 1.05 s ($AlaC_\alpha$), 1.09 s ($GlyC_\alpha$), and 1.02 s ($GlnC_{\beta,\gamma}$) for silk spun at 0.5 cm/s. These values obtained for *N. clavipes* are in the same range as those measured for *N. edulis* and *Argiope keyserlingi*.[51] Compared with the ^{1}H T_1 values of the fiber spun at 0.5 cm/s, the values of the thread spun at 10 cm/s are shorter (0.79 s for $AlaC_\alpha$, 0.89 s for $GlyC_\alpha$, and for 0.73 s $GlnC_{\beta,\gamma}$), which indicates that the proteins that constitute this silk are more flexible and (or) less densely packed. The longer T_1 observed for the $GlnC_{\beta,\gamma}$ peak at a slower spinning speed is also in agreement with the line narrowing observed for this peak at 0.5 cm/s, which could be related to a more ordered amorphous region.

Figure 3B shows that the ^{13}C $T_{1\rho}$ measured for the peaks associated with the C_α of alanine residues, mainly in β-sheet structures, the glycine C_α, and the carbonyl resonance. These results indicate that the ^{13}C $T_{1\rho}$ measured for the glycine residues are shorter than those measured for the alanine residues, which is consistent with the fact that glycine residues are mainly located in the amorphous regions of the fibers. As with ^{1}H T_1, a significant decrease of the ^{13}C $T_{1\rho}$ was found for both alanine and glycine residues at a fast spinning rate. More specifically, ^{13}C $T_{1\rho}$ were 15 ms ($AlaC_\alpha$), 5 ms ($GlyC_\alpha$), and 41 ms (carbonyl) for the silk spun at 0.5 cm/s, and 3.5 ms ($AlaC_\alpha$), 0.4 ms ($GlyC_\alpha$), and 20 ms (carbonyl) for the silk spun at 10 cm/s. The decrease of ^{13}C $T_{1\rho}$ for the filament spun at 10 cm/s indicates more mobility on a slower timescale and over a longer distance,[51] which is consistent with the presence of more amorphous regions and more flexible proteins.

Overall, the present results show that, unlike the secondary structure, the dynamics of the protein chains is altered by the spinning rate at both T_1 (MHz) and $T_{1\rho}$ (kHz) timescales. Thus, it seems that the main impact of the spinning rate on the structural organization of silk occurs at a different level than the secondary structure. Alterations of the protein dynamics are significant and are observed for both alanine and glycine residues, the former amino acid being mainly representative of the β-sheets, the latter characterizing mainly the amorphous regions. This indicates that variations in the chain mobility occur in the whole fiber, indicating that the protein assembly is subtly but fundamentally affected by the spinning rate. More specifically, the dynamic relaxation data suggest that a fast spinning process leads to a less optimal packing of the proteins in the fiber with decreased intermolecular interactions between the polypeptide chains, although it leads to a higher level of orientation.[19]

The decreased mobility at a low reeling speed might in turn result from a slightly higher plasticizing effect of water. Indeed, the presence of water leads to an increased fiber plas-

Can. J. Chem. Downloaded from www.nrcresearchpress.com by Xi'an Jiaotong University on 09/19/12
For personal use only.

Fig. 3. **(A)** ^{1}H T_1 relaxation times for MaS spun at 0.5 cm/s (dark gray) and 10 cm/s (light gray). **(B)** ^{13}C $T_{1\rho}$ relaxation times for MaS spun at 0.5 cm/s (dark gray) and 10 cm/s (light gray).

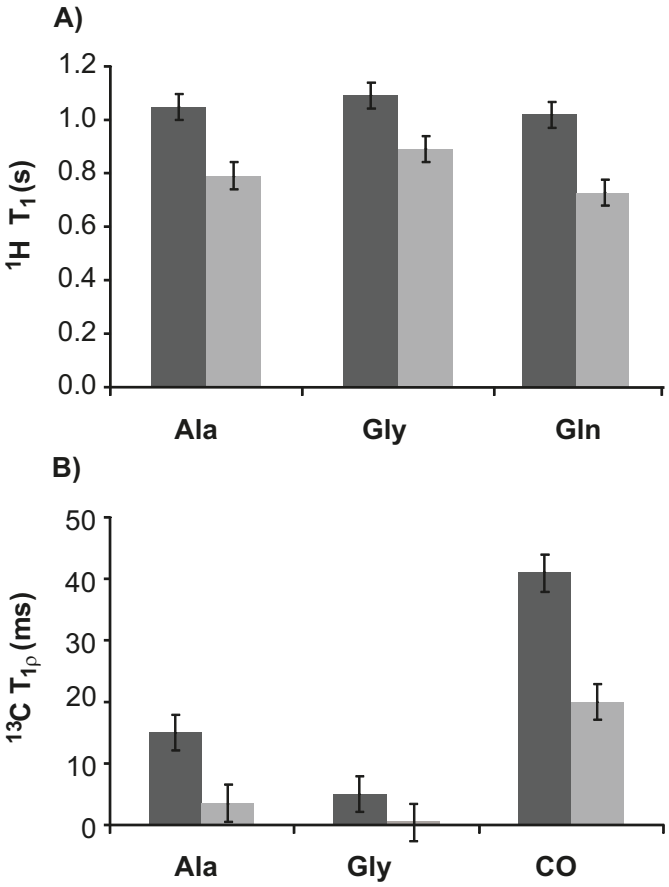

ticity leading in turn to an increase in diameter and a shrinking in length of about 50%. This allows reorientation of hydrogen bonds between the spider silk proteins[34] that could be at the origin of the increased extensibility of the silk spun at 0.5 cm/s.[19] It is also possible that the slower spinning process at 0.5 cm/s results in a more organized polypeptide alignment and packing, thus decreasing the chain dynamics. The NMR data therefore suggest that both the spinning process and protein sequence play a role in the final silk structure.

Protein secondary structure in MaS, MiS, and cocoon silk

CPMAS spectra (not shown) were first recorded and the results obtained for MaS and MiS are in agreement with those previously published.[10,39] Figure 4 displays a superposition of Hahn-echo ^{13}C spectra of MaS and MiS. The alanine C_β signal displays two contributions due to β-sheets and 3_1-helices, showing that the secondary structure of this amino acid is similar in both silks. The relative intensity of the two bands qualitatively suggests that a slightly larger proportion of alanine residues form 3_1-helices in MiS. In addition, the signals corresponding to glycine residues are basically identical for MaS and MiS, suggesting that the secondary structures of the amorphous domains are similar. The glycine C_α peak of MiS only displays a slight narrowing previously noted by Holland et al.[52] who assigned it to the fact that part of the glycine residues are involved in β-sheets. Similarly, it

Fig. 4. 400 MHz ^{13}C Hahn-echo spectra of MaS (black) and MiS (red, dark grey in print).

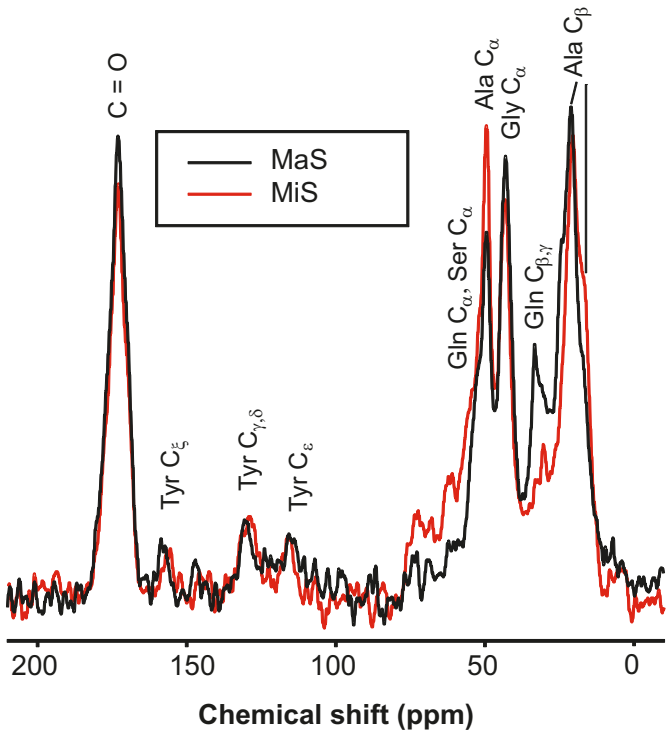

has been concluded from Raman data that poly(Ala-Gly) motifs are involved in the β-sheets.[27]

The ^{13}C CPMAS spectrum of cocoon silk is presented in Fig. 5. The alanine C_β signal displays three contributions at 16–17, 20, and 23 ppm. The contribution at 16–17 ppm is attributed to 3_1-helices, as observed for MaS and MiS, while the two contributions at 20 and 23 ppm have been attributed by Holland et al.[46] to alanine residues in β-sheet structures with packing differences of the alanine methyl groups in the β-sheet domains. The presence of the strong contribution at 23 ppm in cocoon silk therefore suggests differences in the packing of alanine residues compared to MaS and MiS. On the other hand, the presence of alanine residues in β-sheet structures in cocoon silk is in very good agreement with Raman results.[27] Therefore, alanine residues that belong to $(A)_n$ and $(SA)_n$ motifs (Table 1) are most likely involved in these β-sheets. Comparison with other NMR data of the literature suggests that the cocoon silk produced by *N. clavipes* spiders has a very similar secondary structure to that of *N. edulis* and *Araneus diadematus* spiders.[51,53]

Protein dynamics in MaS, MiS, and cocoon silk

Figure 6 shows the comparison of the relaxation parameters for the three types of silk. The relaxation times for alanine C_α in β-sheet structures, and for glycine residues and the glutamine $C_{\beta,\gamma}$ signal are shown in Fig. 6A. Average ^{1}H T_1 were 1.05 s ($AlaC_\alpha$) and 1.09 s ($GlyC_\alpha$) for MaS, 0.90 s ($AlaC_\alpha$) and 0.96 s ($GlyC_\alpha$) for MiS, and 0.42 s ($AlaC_\alpha$) and 0.45 s ($GlyC_\alpha$) for cocoon silk. The ^{1}H T_1 values indicate that protein mobility increases in the order MaS < MiS < cocoon silk. A shorter relaxation time for cocoon silk was already reported by Kishore et al.[51]

Can. J. Chem. Downloaded from www.nrcresearchpress.com by Xi'an Jiaotong University on 09/19/12
For personal use only.

Fig. 5. 400 MHz ^{13}C CPMAS spectrum of cocoon silk.

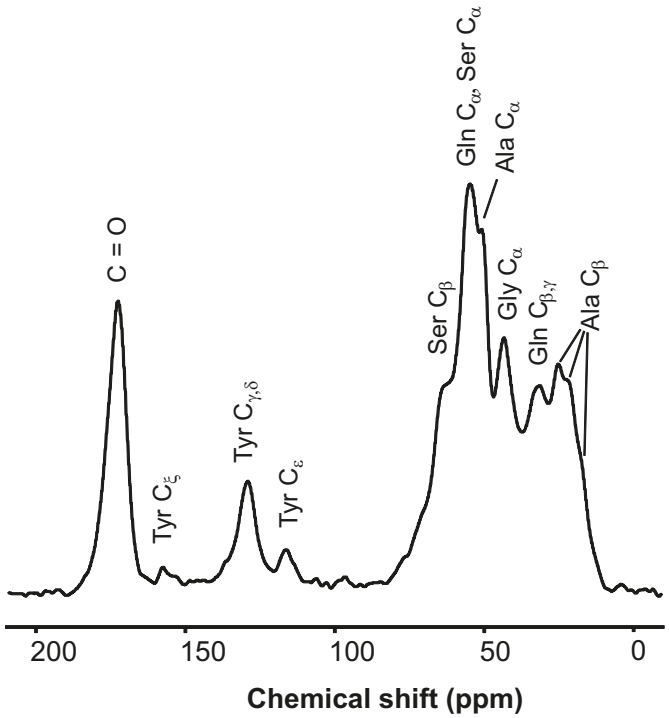

Fig. 6. **(A)** ^{1}H T_1 relaxation times for MaS (dark gray), MiS (light gray), and cocoon silk (white). **(B)** ^{13}C $T_{1\rho}$ relaxation times for MaS (dark gray), MiS (light gray), and cocoon silk (white).

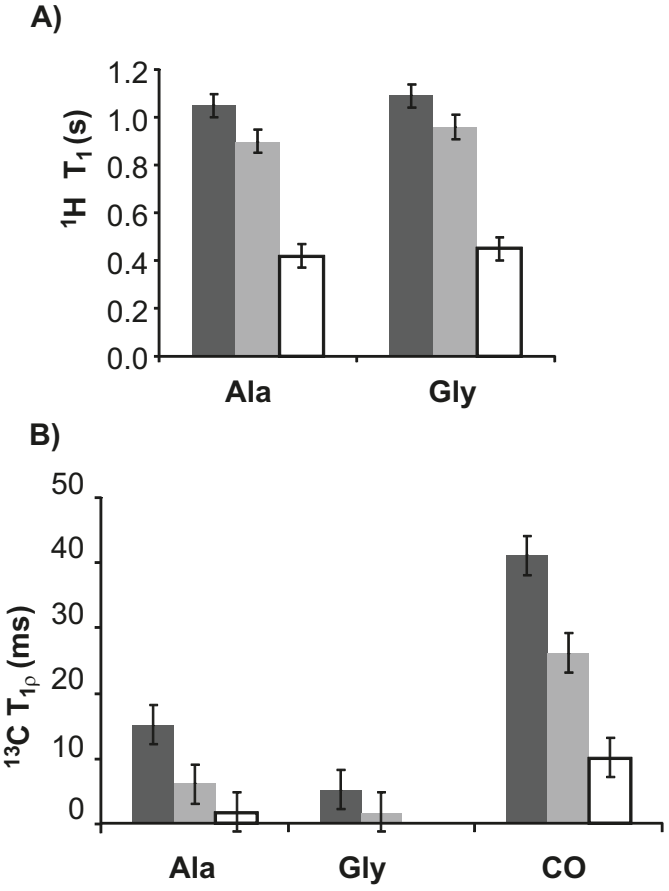

Figure 6B displays the ^{13}C $T_{1\rho}$ results for the three types of silk. Average times were 15 ms ($AlaC_\alpha$), 5 ms ($GlyC_\alpha$), and 41 ms (carbonyl) for MaS, 6 ms ($AlaC_\alpha$), 1.6 ms ($GlyC_\alpha$), and 26 ms (carbonyl) for MiS, and 1.7 ms ($AlaC_\alpha$) and 10 ms (carbonyl) for cocoon silk. The ^{13}C $T_{1\rho}$ for glycine residues in cocoon silk was too short to be measured. The results suggest that the amount of amorphous regions and molecular mobility of the different silks vary as above for the three silks. Again, the relaxation times of glycine residues are generally shorter than for the alanine residues for the three types of silk, which is consistent with the fact that glycine residues are mainly located in silk amorphous regions.

It is recognized that MaS, MiS, and cocoon silk share the same structural pattern, composed of β-sheets dispersed in an amorphous matrix.[24,26,27,39,51] In particular, the proportion of β-sheets is not significantly different for these silks.[27] NMR spectra are consistent with these observations. Structural differences appear in fact more subtle as NMR relaxation experiments reveal differences in the protein dynamics. The ^{1}H T_1 and ^{13}C $T_{1\rho}$ relaxation times show that the mobility of Ala and Gly increases in the order MaS < MiS < cocoon silk. Such a mobility of the amino acids reflects a less organized chain packing and less efficient intermolecular interactions in the fiber. This result is in good agreement with Raman experiments that have shown that these silks contain residual native polypeptide chains that are absent in MaS.[27] This higher chain flexibility of MiS and cocoon silk is consistent with their higher extensibility with respect to MaS. Thus, extensibility can be related to a less ordered structural organization of the whole fiber that cannot be necessarily detected directly by other techniques.

The comparison between MaS and MiS is particularly interesting since MiS displays shorter relaxation times for Ala and Gly, thus indicating that both the amorphous regions and β-sheets are more rigid for MaS. For MiS, the higher molecular mobility of Ala is consistent with the fact that both polyAla and poly(Ala-Gly) motifs are incorporated in the β-sheets, which may result in a less packed β-sheet structure. For cocoon silk, the even higher molecular mobility of Ala is consistent with the fact that amino acids with a large side-chain are involved in β-sheets,[24] which results in a less densely packed β-structure. This is consistent with the well-known variations displayed by the intersheet packing distance of silks produced by various sericigene glands or spun by various species.[54] Interestingly, the presence of a less densely packed β-structure in cocoon silk is also in agreement with the two contributions observed for the Ala C_β signal at 20 and 23 ppm and attributed to differently packed alanine residues.

It has been shown that the molecular orientation of MiS is lower than for MaS.[27] This characteristic can, at least partly, explain the higher extensibility of this silk (Table 1). NMR relaxation data show that the extensibility of MiS can also can be associated with a higher chain mobility. Cocoon silk has the same level of orientation than MaS.[27] However, it is even much more extensible than MiS. Cocoon silk displays the highest relaxation rate, suggesting a less rigid structure in the whole fiber that may be at the origin of the high breaking strain of this silk.

Can. J. Chem. Downloaded from www.nrcresearchpress.com by Xi'an Jiaotong University on 09/19/12
For personal use only.

Conclusions

The NMR data show almost no effect of the reeling speed on the secondary structure, but a significant effect is observed on the protein relaxation dynamics. These results suggest that the molecular rearrangement can be strongly affected during the spinning process and can lead to different chain packing and intermolecular interactions in the final fiber. The comparison between MaS, MiS, and cocoon silk shows that the secondary structure is similar but the molecular mobility is different. In this case, both the spinning process and protein primary structure can play a role on the final molecular organization. More work is clearly needed to gain a better understanding of the correlation between amino acid sequence and mechanical properties to design primary sequences with specific properties.

Acknowledgments

We thank Pierre Audet and Victor Terskikh for their technical assistance and helpful discussions. This work was supported by the Natural Sciences and Engineering Research Council of Canada (NSERC), by the Fonds québécois de la recherche sur la nature et les technologies (FQRNT), by the Regroupement stratégique sur la fonction, la structure et l'ingénierie des protéines (PROTEO), by the Centre de recherche sur les matériaux avancés (CERMA), and by the Centre québécois sur les matériaux fonctionnels (CQMF). Access to the 900 MHz NMR spectrometer was provided by the National Ultrahigh-Field NMR Facility for Solids (Ottawa, Canada), a national research facility funded by the Canada Foundation for Innovation, the Ontario Innovation Trust, Recherche Québec, the National Research Council Canada, and Bruker BioSpin and managed by the University of Ottawa (http://nmr900.ca). The Natural Sciences and Engineering Research Council of Canada (NSERC) is acknowledged for a Major Resources Support Grant.

References

(1) Porter, D.; Vollrath, F.; Shao, Z. *Eur. Phys. J. E* **2005**, *16* (2), 199. doi:10.1140/epje/e2005-00021-2.
(2) Vollrath, F.; Knight, D. P. *Nature* **2001**, *410* (6828), 541. doi:10.1038/35069000.
(3) Gosline, J. M.; Demont, M. E.; Denny, M. W. *Endeavour* **1986**, *10* (1), 37. doi:10.1016/0160-9327(86)90049-9.
(4) Kluge, J. A.; Rabotyagova, O.; Leisk, G. G.; Kaplan, D. L. *Trends Biotechnol.* **2008**, *26* (5), 244. doi:10.1016/j.tibtech.2008.02.006.
(5) Altman, G. H.; Diaz, F.; Jakuba, C.; Calabro, T.; Horan, R. L.; Chen, J.; Lu, H.; Richmond, J.; Kaplan, D. L. *Biomaterials* **2003**, *24* (3), 401. doi:10.1016/S0142-9612(02)00353-8.
(6) Meinel, L.; Hofmann, S.; Karageorgiou, V.; Kirker-Head, C.; McCool, J.; Gronowicz, G.; Zichner, L.; Langer, R.; Vunjak-Novakovic, G.; Kaplan, D. L. *Biomaterials* **2005**, *26* (2), 147. doi:10.1016/j.biomaterials.2004.02.047.
(7) Bai, J.; Ma, T.; Chu, W.; Wang, R.; Silva, L.; Michal, C.; Chiao, J. C.; Chiao, M. *Biomed. Microdevices* **2006**, *8* (4), 317. doi:10.1007/s10544-006-9820-x.
(8) Hayashi, C. Y.; Shipley, N. H.; Lewis, R. V. *Int. J. Biol. Macromol.* **1999**, *24* (2–3), 271. doi:10.1016/S0141-8130(98)00089-0.
(9) Lewis, R. V. *Chem. Rev.* **2006**, *106* (9), 3762. doi:10.1021/cr010194g.
(10) Simmons, A.; Ray, E.; Jelinski, L. W. *Macromolecules* **1994**, *27* (18), 5235. doi:10.1021/ma00096a060.
(11) Riekel, C.; Madsen, B.; Knight, D.; Vollrath, F. *Biomacromolecules* **2000**, *1* (4), 622. doi:10.1021/bm000047c.
(12) Chen, X.; Knight, D. P.; Shao, Z.; Vollrath, F. *Biochemistry* **2002**, *41* (50), 14944. doi:10.1021/bi026550m.
(13) Yamaguchi, E.; Yamauchi, K.; Gullion, T.; Asakura, T. *Chem. Commun. (Camb.)* **2009**, 4176. doi:10.1039/b906145b.
(14) Rousseau, M.-E.; Lefèvre, T.; Beaulieu, L.; Asakura, T.; Pézolet, M. *Biomacromolecules* **2004**, *5* (6), 2247. doi:10.1021/bm049717v.
(15) Foelix, R. F. *Biology of Spiders;* Oxford University Press: New York, 1996.
(16) Carmichael, S.; Viney, C. *J. Appl. Polym. Sci.* **1999**, *72* (7), 895. doi:10.1002/(SICI)1097-4628(19990516)72:7<895::AID-APP5>3.0.CO;2-4.
(17) Vollrath, F.; Porter, D. *Appl. Phys., A Mater. Sci. Process.* **2006**, *82* (2), 205. doi:10.1007/s00339-005-3437-4.
(18) Madsen, B.; Shao, Z. Z.; Vollrath, F. *Int. J. Biol. Macromol.* **1999**, *24* (2–3), 301. doi:10.1016/S0141-8130(98)00094-4.
(19) Vollrath, F.; Madsen, B.; Shao, Z. Z. *Proc. Biol. Sci.* **2001**, *268* (1483), 2339. doi:10.1098/rspb.2001.1590.
(20) Pan, Z.-J.; Liu, M. *Fibers Polym.* **2009**, *10* (3), 285. doi:10.1007/s12221-009-0285-4.
(21) Du, N.; Liu, X. Y.; Narayanan, J.; Li, L.; Lim, M. L. M.; Li, D. *Biophys. J.* **2006**, *91* (12), 4528. doi:10.1529/biophysj.106.089144.
(22) Thiel, B. L.; Viney, C. *J. Microsc.* **1997**, *185* (2), 179. doi:10.1046/j.1365-2818.1997.d01-607.x.
(23) Rousseau, M.-E.; Hernandez Cruz, D.; West, M. M.; Hitchcock, A. P.; Pézolet, M. *J. Am. Chem. Soc.* **2007**, *129* (13), 3897. doi:10.1021/ja067471r.
(24) Parkhe, A. D.; Seeley, S. K.; Gardner, K.; Thompson, L. K.; Lewis, R. V. *J. Mol. Recognit.* **1997**, *10* (1), 1. doi:10.1002/(SICI)1099-1352(199701/02)10:1<1::AID-JMR338>3.0.CO;2-7.
(25) Riekel, C.; Vollrath, F. *Int. J. Biol. Macromol.* **2001**, *29* (3), 203. doi:10.1016/S0141-8130(01)00166-0.
(26) Papadopoulos, P.; Ene, R.; Weidner, I.; Kremer, F. *Macromol. Rapid Commun.* **2009**, *30* (9–10), 851. doi:10.1002/marc.200900018.
(27) Rousseau, M.-E.; Lefèvre, T.; Pézolet, M. *Biomacromolecules* **2009**, *10* (10), 2945. doi:10.1021/bm9007919.
(28) Jenkins, J. E.; Creager, M. S.; Lewis, R. V.; Holland, G. P.; Yarger, J. L. *Biomacromolecules* **2010**, *11* (1), 192. doi:10.1021/bm9010672.
(29) Xu, M.; Lewis, R. V. *Proc. Natl. Acad. Sci. U.S.A.* **1990**, *87* (18), 7120. doi:10.1073/pnas.87.18.7120.
(30) Hinman, M. B.; Lewis, R. V. *J. Biol. Chem.* **1992**, *267* (27), 19320.
(31) Colgin, M. A.; Lewis, R. V. *Protein Sci.* **1998**, *7* (3), 667. doi:10.1002/pro.5560070315.
(32) Tian, M.; Lewis, R. V. *Biochemistry* **2005**, *44* (22), 8006. doi:10.1021/bi050366u.
(33) Blackledge, T. A.; Hayashi, C. Y. *J. Exp. Biol.* **2006**, *209* (13), 2452. doi:10.1242/jeb.02275.
(34) Heim, M.; Keerl, D.; Scheibel, T. *Angew. Chem. Int. Ed. Engl.* **2009**, *48* (20), 3584. doi:10.1002/anie.200803341.
(35) La Mattina, C.; Reza, R.; Hu, X.; Falick, A. M.; Vasanthavada, K.; McNary, S.; Yee, R.; Vierra, C. A. *Biochemistry* **2008**, *47* (16), 4692. doi:10.1021/bi800140q.
(36) Hu, X.; Vasanthavada, K.; Kohler, K.; McNary, S.; Moore, A. M.; Vierra, C. A. *Cell. Mol. Life Sci.* **2006**, *63* (17), 1986. doi:10.1007/s00018-006-6090-y.

(37) Stauffer, S. L.; Coguill, S. L.; Lewis, R. V. *J. Arachnol.* **1994**, *22*, 5.
(38) Hayashi, C. Y.; Lewis, R. V. *J. Mol. Biol.* **1998**, *275* (5), 773. doi:10.1006/jmbi.1997.1478.
(39) Liivak, O.; Flores, A.; Lewis, R. V.; Jelinski, L. W. *Macromolecules* **1997**, *30* (23), 7127. doi:10.1021/ma970834a.
(40) Scheibel, T. *Microb. Cell Fact.* **2004**, *3* (1), 14. doi:10.1186/1475-2859-3-14.
(41) Ortlepp, C. S.; Gosline, J. M. *Biomacromolecules* **2004**, *5* (3), 727. doi:10.1021/bm034269x.
(42) Bennett, A. E.; Rienstra, C. M.; Auger, M.; Lakshmi, K. V.; Griffin, R. G. *J. Chem. Phys.* **1995**, *103* (16), 6951. doi:10.1063/1.470372.
(43) Yang, M.; Nakazawa, Y.; Yamauchi, K.; Knight, D.; Asakura, T. *Biomacromolecules* **2005**, *6* (6), 3220. doi:10.1021/bm050550v.
(44) Wishart, D. S.; Sykes, B. D. *J. Biomol. NMR* **1994**, *4* (2), 171. doi:10.1007/BF00175245.
(45) Saitô, H. *Magn. Reson. Chem.* **1986**, *24* (10), 835. doi:10.1002/mrc.1260241002.
(46) Holland, G. P.; Creager, M. S.; Jenkins, J. E.; Lewis, R. V.; Yarger, J. L. *J. Am. Chem. Soc.* **2008**, *130* (30), 9871. doi:10.1021/ja8021208.
(47) Holland, G. P.; Jenkins, J. E.; Creager, M. S.; Lewis, R. V.; Yarger, J. L. *Chem. Commun. (Camb.)* **2008**, 5568. doi:10.1039/b812928b.
(48) Marcotte, I.; van Beek, J. D.; Meier, B. H. *Macromolecules* **2007**, *40* (6), 1995. doi:10.1021/ma062452n.
(49) Separovic, F.; Cornell, B.; Pace, R. *Chem. Phys. Lipids* **2000**, *107* (2), 159. doi:10.1016/S0009-3084(00)00168-7.
(50) Geppi, M.; Ciardelli, F.; Veraeini, C. A. *Polymer (Guildf.)* **1997**, *38* (23), 5713. doi:10.1016/S0032-3861(97)00134-1.
(51) Kishore, A. I.; Herberstein, M. E.; Craig, C. L.; Separovic, F. *Biopolymers* **2002**, *61* (4), 287. doi:10.1002/bip.10150.
(52) Holland, G. P.; Jenkins, J. E.; Creager, M. S.; Lewis, R. V.; Yarger, J. L. *Biomacromolecules* **2008**, *9* (2), 651. doi:10.1021/bm700950u.
(53) Bramanti, E.; Catalano, D.; Forte, C.; Giovanneschi, M.; Masetti, M.; Veracini, C. A. *Spectrochim. Acta A Mol. Biomol. Spectrosc.* **2005**, *62* (1–3), 105. doi:10.1016/j.saa.2004.12.008.
(54) Warwicker, J. O. *J. Mol. Biol.* **1960**, *2* (6), 350. doi:10.1016/S0022-2836(60)80046-0.

Can. J. Chem. Downloaded from www.nrcresearchpress.com by Xi'an Jiaotong University on 09/19/12
For personal use only.

Water molecular reorientation in ice and tetrahydrofuran clathrate hydrate from lineshape analysis of ^{17}O spin-echo NMR spectra

Yong Ba, John A. Ripmeester, and Christopher I. Ratcliffe

Can. J. Chem. Downloaded from www.nrcresearchpress.com by Xi'an Jiaotong University on 09/19/12
For personal use only.

Abstract: Lineshape analysis of ^{17}O spin-echo NMR spectra has been used to study water molecular reorientations in ice-Ih and THF Structure II clathrate hydrate. The kinetics was determined by the changes of the lineshapes of the ^{17}O central transitions at different temperatures. A model involving 12 orientations and 4-step jumps of water molecular orientations was proposed. Semi-classical exchange formalism was employed to simulate the lineshape of the central transitions of the ^{17}O nuclei. Lineshape analysis gave the quadrupolar coupling constant $C_Q = 6.43$ MHz and the asymmetry parameter $\eta = 0.935$, for both ice-Ih and THF gas hydrate. The theoretical lineshape simulations resulted in activation energies of water molecular reorientations $E_a = 55.2 \pm 2.1$ kJ mol^{-1} and $E_a = 30.5 \pm 0.8$ kJ mol^{-1} for ice-Ih and THF hydrate, respectively. The range of dynamic rates in THF clathrate hydrate is such that before melting, a pseudo-isotropic lineshape is observed that retains a second-order quadrupolar shift. The water reorientation process is discussed in light of recent results on Bjerrum defect injection obtained from molecular dynamics simulation and structural studies.

Key words: ice-Ih, THF clathrate hydrate, ^{17}O NMR, molecular reorientations of solid water, Kinetics, residual second order quadrupolar shift, dynamics of non-integer quadrupolar nuclei.

Résumé : On a fait appel à l'analyse de la forme des raies des spectres RMN du ^{17}O avec écho de spin pour étudier les réorientations moléculaires de l'eau dans la glace-Ih et dans l'hydrate du clathrate du THF de structure II. On a déterminé les cinétiques par les changements dans les formes des raies des transitions centrales du ^{17}O, à diverses températures. On propose un modèle impliquant 12 orientations et des transitions en quatre étapes des orientations moléculaires de l'eau. On a utilisé un formalisme d'échange semi-classique pour simuler la forme des raies des transitions centrales du noyau ^{17}O. Une analyse de la forme des raies permet de déterminer la constante de couplage quadripolaire $C_Q = 6{,}43$ Mhz et le paramètre d'asymétrie $\eta = 0\,935$ pour la glace-Ih et l'hydrate du THF gazeux. Les simulations des formes des raies théoriques ont permis d'évaluer les énergies d'activation des réorientations moléculaires de l'eau $E_a = 55{,}4 \pm 2{,}1$ kJ mol^{-1} et $E_a = 30{,}4 \pm 0{,}8$ kJ mol^{-1}, respectivement pour la glace-Ih et l'hydrate du THF. La plage des vitesses dynamiques pour l'hydrate du clathrate du THF est telle que, avant la fusion, il et possible d'observer une forme de raie pseudo-isotrope qui conserve un déplacement quadripolaire du deuxième ordre. On discute du processus de réorientation de l'eau à la lumière de résultats récents sur l'injection du défaut de Bjerrum obtenu à partir de simulations de la dynamique moléculaire et d'études structurales.

Mots-clés : glace-Ih, hydrate du clathrate du THF, RMN du ^{17}O, réorientations moléculaires de l'eau solide, cinétique, déplacement quadripolaire résiduel du second ordre, dynamique des noyaux quadripolaires non entiers.

[Traduit par la Rédaction]

Introduction

Water, as a substance essential for the existence of life, is one of the most important materials in nature. Also, it is one of the more difficult materials to study as it has some unusual properties and a remarkably complex phase diagram.

When frozen under normal atmospheric conditions, water molecules form a crystalline solid with hexagonal symmetry that is less dense than the water phase with which it is in equilibrium, referred to as hexagonal ice or ice-Ih.[1] Early X-ray diffraction analysis of ice-Ih showed that each oxygen atom is coordinated almost tetrahedrally by four neighboring

Received 16 November 2010. Accepted 3 February 2011. Published at www.nrcresearchpress.com/cjc on 19 August 2011.

Y. Ba. Steacie Institute for Molecular Sciences, National Research Council of Canada, 100 Sussex Drive, Ottawa, ON, K1A 0R6, Canada; Department of Chemistry and Biochemistry, California State University Los Angeles, 5151 State University Drive, Los Angeles, California 90032, USA.
J.A. Ripmeester and C.I. Ratcliffe. Steacie Institute for Molecular Sciences, National Research Council of Canada, 100 Sussex Drive, Ottawa, ON, K1A 0R6, Canada.

Corresponding author: Christopher I. Ratcliffe (e-mail: chris.ratcliffe@nrc-cnrc.gc.ca).

This paper is dedicated to professor Rod Wasylishen to honour his many outstanding contributions in the field of NMR spectroscopy and to chemistry in Canada.

Can. J. Chem. Downloaded from www.nrcresearchpress.com by Xi'an Jiaotong University on 09/19/12
For personal use only.

oxygen atoms.[2] From neutron diffraction measurements on a single crystal of D_2O solid, it was suggested that there are two half-occupied deuteron positions on the line between two neighboring oxygen atoms,[3] and the deuterons are disordered among these sites. This conclusion was later modified from the view that the O–D–O hydrogen bond should be bent by about 6.8°, since the molecular D–O–D angle is the same as that in an isolated water molecule (i.e., 104.5°).[4] Thus, each deuteron is about 0.04 Å off the line connecting the two closest oxygen atoms. These experimental data fit into Pauling's earlier statistical model for the structure of ice-Ih.[5] He proposed that (*i*) the structure of isolated water molecules is primarily preserved in ice-Ih, (*ii*) the hydrogen atoms of a water molecule are directed approximately towards two of the four oxygen atoms surrounding it tetrahedrally, (*iii*) The adjacent water molecules are oriented so that only one hydrogen atom lies between each pair of neighboring oxygen atoms, and (*iv*) the statistical orientations of water molecules generate a large number of configurations $(3/2)^n$, where n is the total number of water molecules. At any instant and under ordinary conditions, an ice-Ih crystal may exist in any one of the large number of allowed configurations. A question that follows then is whether the configuration of ice-Ih is subject to change via rotations of water molecules. Dielectric relaxation studies have suggested that the dipole moment of ice can reorient through either proton transfer or molecular rotation.[6,7] The latter was assumed based on theoretical considerations to correlate the rotational correlation time with the dielectric correlation time.[8] Bjerrum hypothesized that water molecules in ice could reorient by rotating about one hydrogen bond and form either a D defect (two hydrogen atoms between a pair of oxygen atoms) or an L defect (no hydrogen atom between a pair of oxygen atoms).[9] When these defects diffuse through the lattice, they leave a water molecule in a different orientation.

Clathrate hydrates are formed when water interacts hydrophobically with suitably small molecules (<0.9 nm), assembling via hydrogen bonding into an open framework that traps such "guest" molecules into cages of different geometries.[10–15] Three main structural types of clathrate hydrate have been identified, which form with a large number of guests, namely cubic structure I, cubic structure II, and hexagonal structure H.[10–20] Tetrahydrofuran (THF) forms a structure II hydrate popular for experimental studies as it can be made readily by freezing an aqueous solution of the correct composition.[19] The unit cell contains 136 water molecules with 16 small and 8 large cages. The large cages each encage a THF molecule. A neutron diffraction study of $3.5Xe{\cdot}8CCl_4{\cdot}136D_2O$ structure II gas hydrate shows that the local coordination of a water molecule is very similar to that in ice-Ih, although deviation from true tetrahedral coordination by four neighbouring O atoms is more marked.[20] Indeed there are three crystallographically distinct O sites. Also, as in ice-Ih, the D_2O molecules are disordered over six orientations of equal statistical weight, with deuterium atoms located in half-occupied sites, so a gas hydrate crystal also has many configurations determined by the orientations of all the water molecules.

Solid state NMR lineshapes are widely used to study dynamics.[21] Changes in the linewidth and lineshape as a function of increasing temperature reflect the effects of rapid modulation of the interaction tensors, and there are very many examples involving dipolar coupling tensors, for example of ^1H, ^{19}F, integer quadrupolar tensors, especially ^2H,[22,23], and chemical shift tensors, ^{13}C, ^{15}N, ^{19}F, etc. However, reports of cases involving dynamic averaging of the lineshapes of non-integer nuclei with second-order quadrupolar interactions are quite rare.

The reorientations of water molecules in ice-Ih and THF clathrate hydrate as a function of temperature have been observed previously using ^1H [24–30] and ^2H NMR.[28,31–36] Approaching their melting points, the spectra show isotropic lineshapes. In ^2H NMR, the results can be explained by a simple model where each O–D bond jumps between four equiprobable tetrahedral orientations, although in this model the gross approximation is made that the ^2H quadrupolar coupling tensor is axial. Unfortunately the models that can explain the experimental observables do not necessarily test the theoretical models, such as the Bjerrum model. For instance, a water molecule would have to be visited by several defects in order for it to be reoriented in such a way as to show tetrahedral averaging. Nevertheless the ^1H, ^2H and dielectric results can be explained by the presence of a single motional correlation time. One striking feature of THF clathrate hydrate is that the motions are considerably faster than in ice, and it is thought that this is due to injection of Bjerrum L-defects into the hydrate lattice by transient H-bond formation between the O atom of the THF and a water molecule.[37]

Here we present work on the central transition NMR of the spin 5/2 ^{17}O nucleus in ice and THF structure II clathrate hydrate as a function of temperature. In contrast with the four orientations visited by the ^2H quadrupole coupling tensor, the tensor of ^{17}O in the water molecule will reorient over six orientations as the arrangement of H atoms around it changes (in this case roughly octahedral orientations), and so in a sense the ^{17}O detects the motion of the whole molecule rather than of the O–D bond. Another reason for a study using ^{17}O is because the proton-shielding tensor in ice-Ih has a span of ~6 kHz, the ^1H dipolar coupling leads to spectra ~40 kHz wide, and the deuterium quadrupolar coupling constant is ~200 kHz, but the ^{17}O quadrupolar coupling constant is much larger, ~6.43 MHz. Although the ^{17}O central transitions in ice are expected to cover a spectral width of ~60 kHz, complete averaging of the quadrupolar interaction can give spectral sensitivity to a remarkably broad range of motional correlation times. Besides the problem of water molecular reorientations, there is a wide interest in the fundamental spectroscopy, that is, to observe and understand the evolution of spectral patterns for half-integer nuclei from a static pattern to one where the quadrupolar coupling is completely averaged.[38–43]

Because of the ubiquitous presence of water in its various phases, we expect considerable relevance of these results to water-containing systems.

Experimental details

Water with 45% ^{17}O (ISOTEC Inc.) and THF with 99.9% purity (Sigma-Aldrich) were used to prepare the ice and hydrate. THF is soluble in water, so that the clathrate hydrate was easily obtained by cooling its aqueous solution with 1:17 THF/H_2O stoichiometric ratio.[44] ^{17}O NMR static spectra

Can. J. Chem. Downloaded from www.nrcresearchpress.com by Xi'an Jiaotong University on 09/19/12
For personal use only.

Fig. 1. Static ^{17}O NMR ^{1}H decoupled spin-echo spectra of the central transition in ice-Ih as a function of temperature.

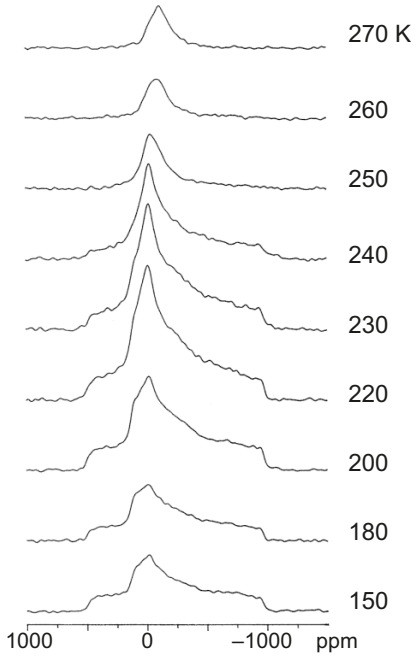

with ^{1}H decoupling were obtained at 40.68 MHz from 140 K up to the melting points, using a Bruker AMX 300 NMR spectrometer with a double resonance (^{1}H-^{17}O) high-power NMR probe (Morris Instruments Inc.). Only central transition spectra were obtained, using a spin-echo experiment with $\tau = 20$ μs.[45] ^{1}H decoupling is necessary, as the ^{17}O-^{1}H dipolar coupling is calculated to be of the order of 17 kHz, compared with ~59 kHz for the ^{17}O second-order static linewidth. The spectra are referenced to liquid $H_2{}^{17}O$ water at room temperature. Temperatures were regulated using cold nitrogen gas and a Bruker Eurotherm controller.

Results and discussion

The ^{17}O NMR central transition spectra of ice-Ih and THF clathrate hydrate as a function of temperature are shown in Figs. 1 and 2. The lowest temperature spectra correspond to essentially static quadrupolar coupling tensors. For ice-Ih at 150 K, the best theoretically fitted spectrum gave a quadrupolar coupling constant $C_Q = 6.43$ MHz and an asymmetry parameter $\eta = 0.935$. This compares favourably with previous measurements, which have given $C_Q = 6.66 \pm 0.10$ and $\eta = 0.935 \pm 0.010$ for D_2O ice-Ih at 253–263 K,[46] and $C_Q = 6.525 \pm 0.015$ and $\eta = 0.925 \pm 0.020$ at 77 K.[47] The first of these studies also determined that the principal axis components of the tensor are oriented with *yy* perpendicular to the molecular plane and *xx* along the twofold molecular axis. C_Q is moderately sensitive to the local environment of the water molecules, as seen in the different values for water-^{17}O in Ice-II ($C_Q = 6.893$ MHz, $\eta = 0.865$),[48] and crystal hydrates oxalic acid dihydrate ($C_Q = 6.8$ MHz, $\eta = 0.93$)[49] and barium chlorate monohydrate ($C_Q = 7.61$ MHz, $\eta = 0.94$).[50] For THF clathrate hydrate at 140 K, the envelope of the spectrum is somewhat noisier than that of ice-Ih, perhaps because of an inhomogeneous orientational distribution of hydrate crystallites produced

Fig. 2. Static ^{17}O NMR ^{1}H decoupled spin-echo spectra of the central transition in THF clathrate ^{17}O-hydrate as a function of temperature.

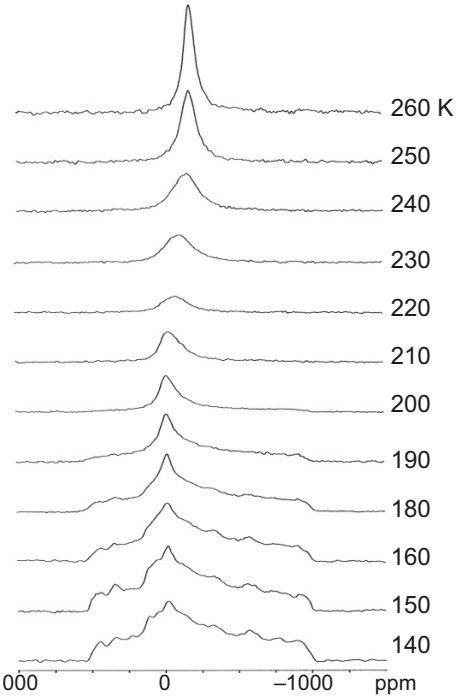

when the THF solution was frozen in the NMR probe. Nevertheless, it is clear that the lineshape is almost identical to that of ice-Ih at 150 K, and thus we conclude that the local oxygen coordination in THF clathrate hydrate is very similar to that in ice-Ih. Though there are three crystallographically distinct water oxygen sites in the THF hydrate,[19,20] these are not distinguished in the static lineshapes observed, nor even in the dynamically averaged pseudo-isotropic lineshapes observed at the highest temperatures.

One question to consider is whether the chemical shielding anisotropy (csa) of ^{17}O in ice is large enough to make a visible contribution to the central transition spectrum at 7.05 T. While there is no experimental information available on this, ab initio calculations for liquid water suggest a span of ~37 ppm.[51] This is very small (~2.5%) when compared to the observed static linewidth of ~1450 ppm but substantial enough to perhaps explain the range of experimental values. Spectra at high field would probably resolve this issue, e.g., at 21.1 T the second-order linewidth would reduce to about 161 ppm. Furthermore, at rates where the second-order quadrupolar lineshape begins to show effects of dynamic averaging, this csa will likely already be averaged to zero.

As temperature increases, the lineshapes start to show effects of dynamic averaging; their features become less well-defined, and a new shape centred around the center of gravity of the line begins to form. Comparing the spectra of the two materials, it is immediately obvious that the dynamics in the THF hydrate are considerably faster than in ice-Ih, with equivalent changes in lineshape occurring about 50 degrees lower for THF hydrate. Initially the new lineshape is asymmetric, with its peak closest to the strongest feature of the static lineshape, but then it gradually shifts to lower frequency, and in the case of THF hydrate eventually takes on

Can. J. Chem. Downloaded from www.nrcresearchpress.com by Xi'an Jiaotong University on 09/19/12
For personal use only.

Fig. 3. Static ^{17}O NMR ^{1}H decoupled spectrum of water-^{17}O in a THF clathrate hydrate sample at ~270 K, where partial melting has occurred.

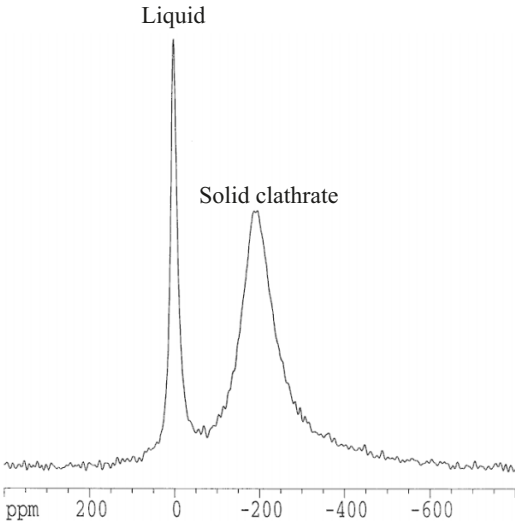

a pseudo-isotropic appearance (ice-Ih melts before this stage can be reached). That this "isotropic" line still retains a second-order shift is illustrated by the spectrum of the hydrate at 270 K, where liquid THF solution and solid THF hydrate coexist (Fig. 3). The liquid line is considerably sharper and very close to the shift of water, whereas the broader "isotropic" line of the hydrate is centred at –194 ± 3 ppm. The second-order quadrupolar shift of the central transition for a non-integer quadrupolar nucleus is given by,

$$[1] \quad \mathrm{SOQS\,(in\,ppm)} = -\left(\frac{10^5}{3}\right)\left(\frac{\omega_Q^2}{\omega_L^2}\right)\left(I(I+1)-\frac{3}{4}\right)\left(1+\frac{\eta^2}{3}\right)$$

where $\omega_Q = 6\pi C_Q/(2I(2I–1))$. Hence, for a spin I = 5/2 nucleus this becomes SOQS = $–6\,000(C_Q{}^2/\nu_L{}^2)(1+\eta^2/3)$. Substituting the C_Q and η determined from the low-temperature static lineshape, a second-order shift of –193.6 ppm is calculated, very close to that observed at the melting point.

The emergence of this pseudo-isotropic line was initially quite surprising, because the central transition lineshape depends on the second-order interaction, which is a function of the fourth-order Legendre polynomial, and therefore averaging due to rapid tetrahedral or octahedral reorientation at rates a little faster than the static central transition linewidth should *not* lead to a pseudo-isotropic lineshape (icosahedral averaging is required to achieve an isotropic line).[40] In fact, the dynamic averaging calculations described below also suggest that there should be a residual lineshape, and the initial experimental averaged shapes appear to be falling into the predicted pattern. However, the modeling does not take into account the fact that at higher rates of motion the satellite transitions will also begin to average, and for I = 5/2 the splitting of the first satellite transition $\nu_Q = 3C_Q/20$, which in this case is only 964.5 kHz.

Witschas and Eckert have studied a case for ^{23}Na NMR approaching the fast motion limit, where the first-order interaction is averaged to zero, and observed a pseudo-isotropic central transition line, which gradually shifts to the true isotropic position as the satellites also average to isotropic.[41] In the present study, although the THF hydrate residual second-order lineshape has averaged to pseudo-isotropic, the material melts before any shifting towards the true isotropic shift has begun.

Fig. 4. The 12 possible orientations of a water molecule on any one particular lattice site in ice-Ih and clathrate hydrates, if the two H atoms are distinguished. O–H chemical bonds are represented by bold bars, and O···H hydrogen bonds from neighbouring water molecules by thin lines. The arrows indicate the four single-step reorientations which can occur by rotation about each of the two O–H chemical bonds for any one particular starting orientation. Over time, all 12 orientations will be sampled.

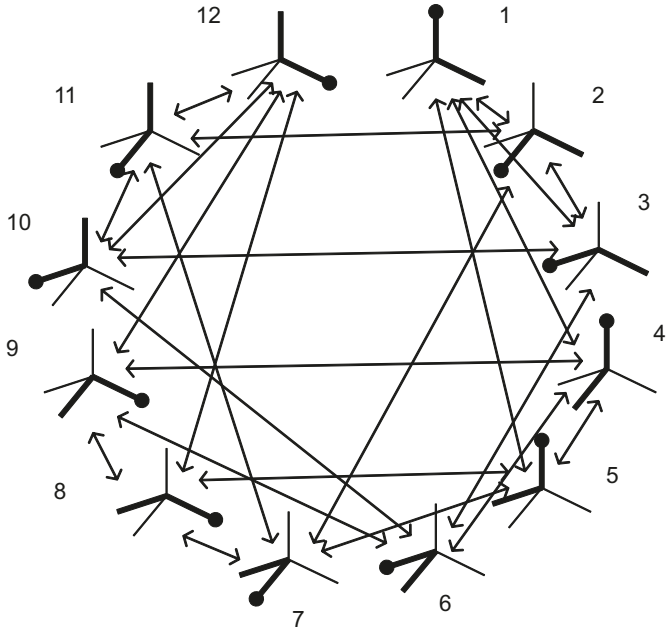

Modelling the effects of dynamic exchange on the central transition lineshape

An examination of the possible orientations for a single water molecule in ice-Ih or a clathrate hydrate shows that if the protons are distinguished, there are 12 different orientations of equal probability (Fig. 4). Assuming a single-step jump about an O-H axis only (not about O···H hydrogen bond axes) is required for the reorientational change, then each of the 12 orientations can have 4 possible single-step jumps to the other orientations. With the simplifying approximation that the coordination is perfectly tetrahedral, then all of these single-step reorientations are equivalent in terms of their kinetic parameters, as are forward and reverse exchanges. In fact this is a very reasonable assumption based on the structure of ice-Ih, but a little less so for the THF clathrate hydrate with three crystallographically distinct O atoms and some angles with larger deviations from Td. While this model provides a more complete picture of water reorientation (compared with the 4-site tetrahedral jump model used to simulate the dynamic deuterium NMR spectra of D_2O ice-Ih),[28] as far as the ^{17}O tensor is concerned, pairs of orientations related by interchange of the two proton posi-

Table 1. Euler angles of water molecular reorientations in ice-Ih.

Orientations	α	β	γ
1	0	0	0
2	215.2644	60	35.2644
3	144.7356	60	324.7356
4	35.2644	60	215.2644
5	324.7356	60	144.7356
6	90	90	90
7	270	90	270
8	324.7356	120	35.2644
9	35.2644	120	324.7356
10	144.7356	120	215.2644
11	215.2644	120	144.7356
12	0	180	180

Can. J. Chem. Downloaded from www.nrcresearchpress.com by Xi'an Jiaotong University on 09/19/12
For personal use only.

Fig. 5*a*. Calculated spin-echo NMR spectra of ^{17}O central transitions for the model of 12 reorientations and 4-step jumps of water molecules in ice-Ih with $\chi = 6.43$ MHz and the hypothetical value for $\eta = 0.9$. The exchange rate constants and spin-echo amplitudes (EA) are given along with the corresponding spectra. The intensity unit is arbitrary.

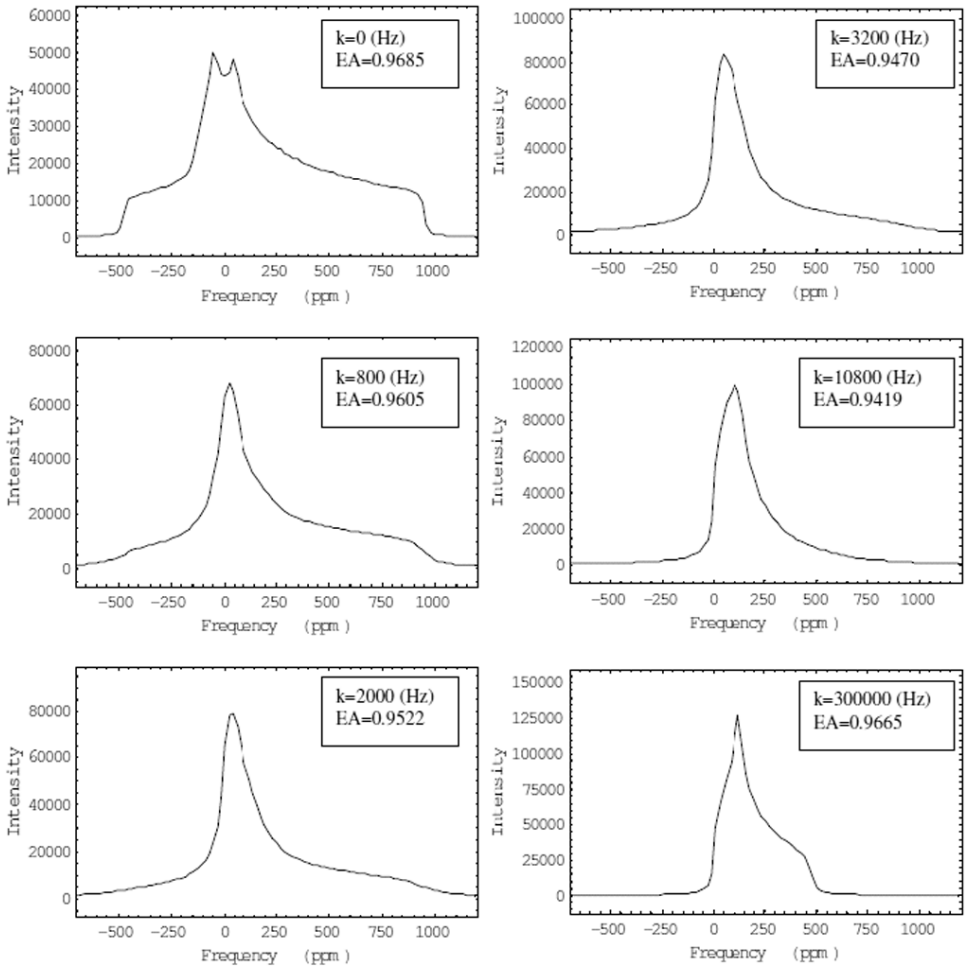

tions are equivalent. The population of these molecular orientations in an ice or a clathrate hydrate powder determines the lineshape of the NMR spectrum within the slow regime of the reorientational exchange at low temperatures, and the rate constants of the reorientations determine the lineshapes at higher temperatures.

A semi-classical exchange formalism was employed to simulate the lineshapes of the ^{17}O central transitions.[40] The relevant Hamiltonian for the exchanging quadrupolar nucleus consists of the first-order chemical shift term, and the first- and second-order quadrupolar interaction terms. Owing to the time scale of the molecular reorientations observed in the ice and the clathrate hydrate, it was assumed that the exchange rates are localized in the second-order quadrupolar term, while the effect on the lineshape by the first order quadrupolar interaction is insignificant. The calculations were further sim-

Fig. 5*b*. Calculated spin-echo NMR spectra of ^{17}O central transitions for the model of 12 reorientations and 4-step jumps of water molecules in ice-Ih with $\chi = 6.43$ MHz and the hypothetical value for $\eta = 0.5$. The exchange rate constants and spin-echo amplitudes (EA) are given along with the corresponding spectra. The intensity unit is arbitrary.

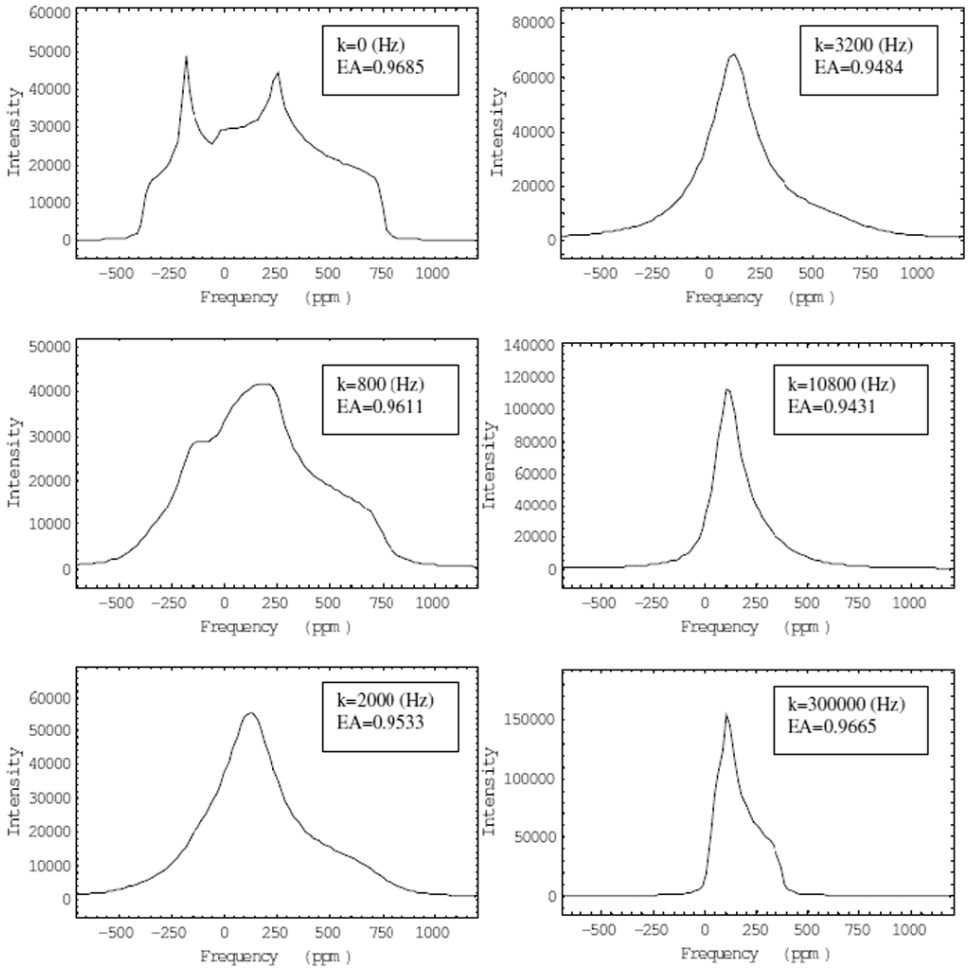

plified by ignoring the effect of chemical shift anisotropy, which as discussed earlier is likely to be negligibly small compared with the linewidth caused by the quadrupolar second-order interaction at this field, and also averaged to zero by the dynamics at quite slow rates. The relevant evolution frequency for the central transition is given as follows,[52]

$$[2]\qquad \omega_{-1/2,\,1/2}^{(2)static} = -\frac{1}{6\omega_0}\left[\frac{3C_Q}{2I(2I-1)}\right]^2\left[I(I+1)-\frac{3}{4}\right] \times [A(\alpha,\,\eta)\cos^4\beta + B(\alpha,\eta)\cos^2\beta + C(\alpha,\eta)]$$

where

$$A(\alpha,\eta) = -\frac{27}{8} + \frac{9}{4}\eta\cos 2\alpha - \frac{3}{8}(\eta\cos 2\alpha)^2$$

$$B(\alpha,\eta) = \frac{30}{8} - \frac{1}{2}\eta^2 - 2\eta\cos 2\alpha + \frac{3}{4}(\eta\cos 2\alpha)^2$$

$$C(\alpha,\eta) = -\frac{3}{8} + \frac{1}{3}\eta^2 - \frac{1}{4}\eta\cos 2\alpha - \frac{3}{8}(\eta\cos 2\alpha)^2$$

and C_Q stands for the quadrupolar coupling constant. The Euler angles α and β define the direction of the static magnetic field relative to the principal axis system of the electric field gradient.

The principal axis system of the electric field-gradient tensor of ^{17}O in the water molecule has been determined previously.[46] The *x*-axis was assigned to have the direction of the C_2 axis, the *y*-axis is perpendicular to the H–O–H plane, and the *z*-axis lies in the plane parallel to the H–H line. The twelve sets of Euler angles for water molecular orientations, as shown in Fig. 4, were derived according to this principal axis system and are listed in Table 1.

A Mathematica computer program was written to solve the equations of the kinetically modified Bloch equations,[40] and to integrate over the polar and azimuthal angles to get the powder pattern of the NMR spectrum. Figures 5*a*–5*c* show three sets of calculated ^{17}O spectra according to the exchange model shown in Fig. 4, based on a quadrupolar coupling constant of 6.43 MHz and asymmetry parameters,η = 0.9, 0.5, and 0.1, respectively. The corresponding exchange rate constants are given along with the spectra, and the spin-echo amplitudes (EA) are also shown in the figures. The transverse relaxation time $T_2 = 2.5$ ms and a spin-echo time of $\tau = 20$ μs were used in the calculations. The steps for the increments for α and β were set to be 1°, and a total of 100 points along the chemical shift axis were calculated. The chemical shifts were obtained according to the ^{17}O resonance frequency of 40.68 MHz (300 MHz for ^1H). The chemical shifts

Can. J. Chem. Downloaded from www.nrcresearchpress.com by Xi'an Jiaotong University on 09/19/12
For personal use only.

Fig. 5*c*. Calculated spin-echo NMR spectra of ^{17}O central transitions for the model of 12 reorientations and 4-step jumps of water molecules in ice-Ih with $\chi = 6.43$ MHz and the hypothetical value for $\eta = 0.1$. The exchange rate constants and spin-echo amplitudes (EA) are given along with the corresponding spectra. The intensity unit is arbitrary.

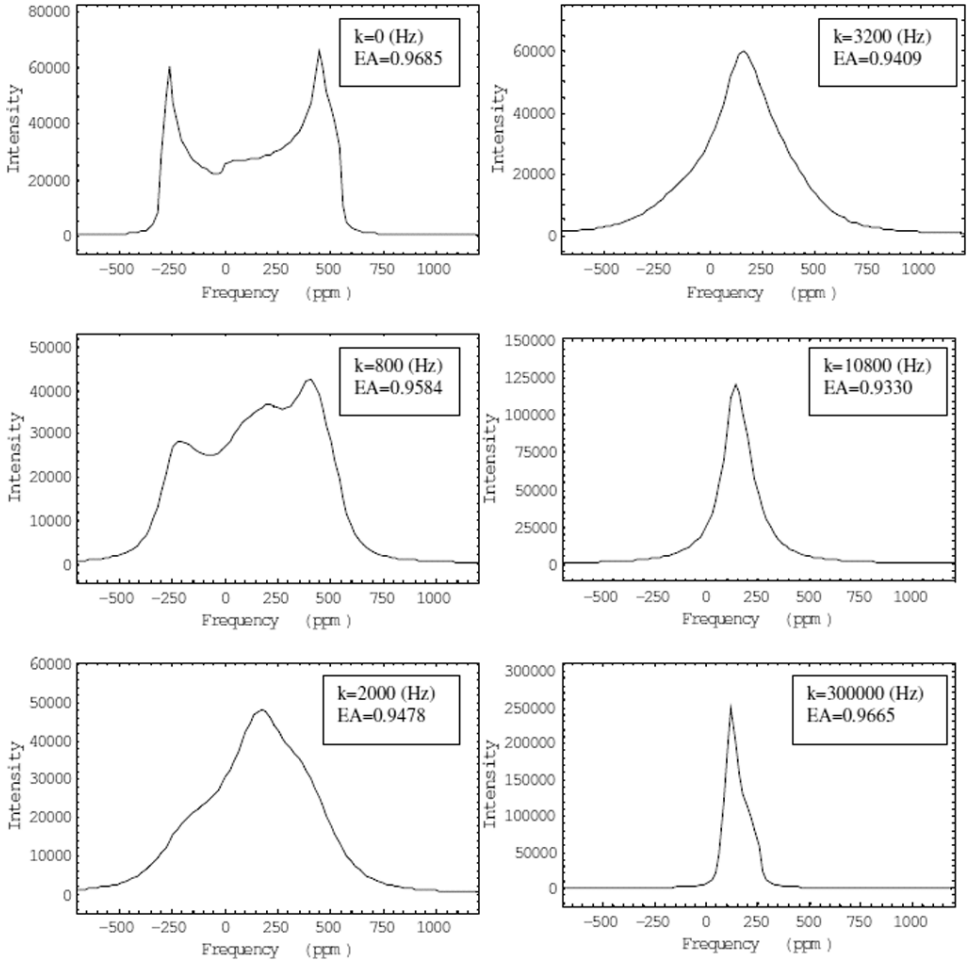

in the spectra were labeled with the opposite signs because of the convenient use of the Mathematica plotting method. The spectra at the rate constant $k = 0$ Hz show the typical powder patterns of the central transitions for spin n/2 nuclei with the corresponding hypothetical asymmetry parameters. The spectra at $k = 300\ 000$ Hz show the powder patterns in the fast-exchange regimes. Powder patterns corresponding to other intermediate exchange rates are also shown. All three sets show residual anisotropic lineshapes in the regime where rates are fast compared with the static second-order linewidth, but again it should be emphasized that these calculations do not take account of effects when the satellite lineshapes are also being averaged.

Comparison of experimental and simulated lineshapes in the exchange regime

Experimental ^{17}O spin-echo spectra acquired at several temperatures and the corresponding theoretically simulated spectra with $C_Q = 6.43$ MHz and $\eta = 0.935$ are shown in Fig. 6. Above the temperatures shown, the experimental and simulated spectra begin to diverge and comparison is no longer valid. Activation energies were determined from the set of rate constants and temperatures using the Arrhenius law,

$$[3] \qquad k = A \exp\left(-\frac{E_a}{RT}\right)$$

where A is a frequency factor (s^{-1}), E_a is the activation energy (J mol^{-1}), and R is the gas constant (8.314 JK^{-1} mol^{-1}).

Plots of $\ln(k)$ versus $1/T$ are shown in Fig. 7. The least-squares linear fit for the ice-Ih data gave an activation energy $E_a = 55.2 \pm 2.1$ kJ·mol^{-1}. This value, within error, is the same as the value of 56.5 kJ mol^{-1}, determined from the dielectric relaxation study,[6,7] showing that the activation energy measured in the dielectric relaxation arose from the water molecular reorientations. It is also equivalent to the most recent value of $E_a = 55.6$ kJ mol^{-1}, determined from ^2H NMR lineshapes.[26] Earlier studies gave values in the range 55.2 to 59.8 kJ mol^{-1}.[24–27,31] It is interesting that although the model used in the study of D_2O ice-Ih only considered the reorientations of O–D chemical bonds in a tetrahedral fashion, the activation energy is the same as that obtained in the current work for which the more rigorous model of 12 orientations and 4 single-step jumps was used. This is probably because of the nearly axially symmetric deuterium quadrupolar coupling tensor, which in principle results in nearly similar calculated ^2H NMR lineshapes when either model is used.

Can. J. Chem. Downloaded from www.nrcresearchpress.com by Xi'an Jiaotong University on 09/19/12
For personal use only.

Can. J. Chem. Downloaded from www.nrcresearchpress.com by Xi'an Jiaotong University on 09/19/12
For personal use only.

Fig. 6. Experimental ^{17}O ^{1}H decoupled spin-echo NMR spectra at several temperatures shown on the left and matching dynamic simulation spectra shown on the right, for (*a*) ice-Ih and (*b*) THF clathrate hydrate. The temperatures and rate constants are given alongside the corresponding spectra.

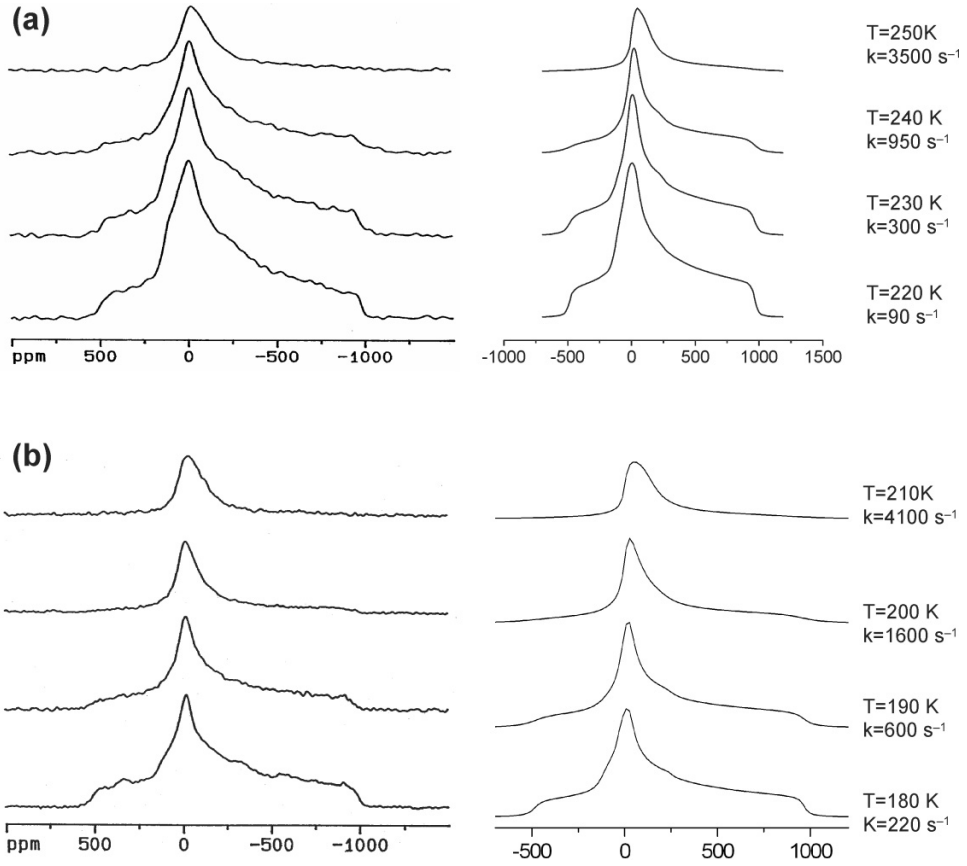

Fig. 7. Experimental plots of ln(*k*) versus 1/*T* for water reorientations in ice-Ih (■) and those in THF gas hydrate (◆) and their corresponding least-square linear fits.

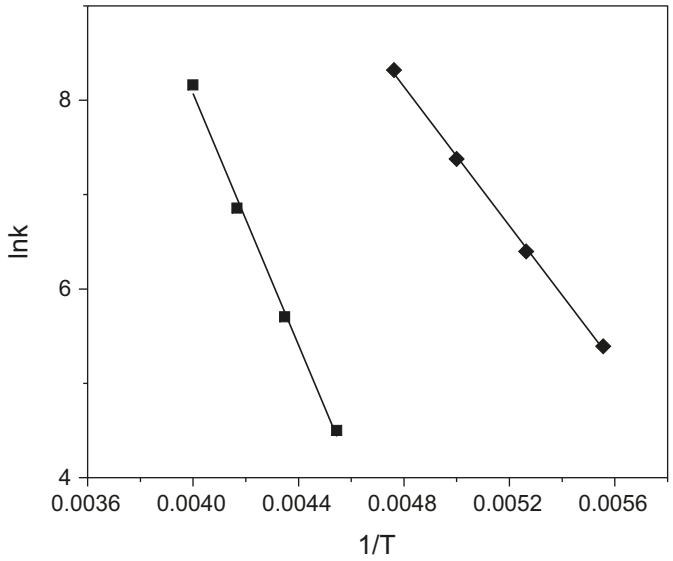

The least-squares linear fit for THF clathrate hydrate resulted in an activation energy E_a = 30.5 ± 0.8 kJ mol^{-1}, which is comparable to values of 31.0 kJ mol^{-1} from dielectric,[37] 30.12 kJ mol^{-1} from ^{1}H NMR,[30] and 31.0–32.7 kJ mol^{-1} from ^{2}H NMR.[33,34] This value is smaller than that of ice-Ih, showing that water molecular reorientations in THF gas hydrate are much more facile. As mentioned earlier, it is thought that this is due to injection of Bjerrum L-defects into the hydrate lattice by transient H-bond formation between the O atom of the THF and a water molecule.[10,15,37]

The concurrence of activation energies for both materials with values determined previously affirms the essential correctness of the model in this intermediate regime. If the Arrhenius plots are then extrapolated to 270 K the rates suggested are 2.4 × 10^4 s^{-1} for ice-Ih and 2.0 × 10^5 s^{-1} for THF hydrate. The latter value is well towards the fast limit compared with the second-order static linewidth, where the model predicts a residual anisotropic lineshape, but it is also in the range where the first satellite lineshape will be starting to average (recall that ν_Q is ~9.6 × 10^5 Hz).

It was mentioned earlier that lower activation energies for water reorientation in hydrates had been ascribed to defect injection by guest molecules containing oxygen.[10,15] Recent molecular dynamics (MD) simulation studies on nanosecond timescales have in fact observed the existence of both transient and persistent guest–host hydrogen bonds for oxygen-containing guests[53–55]. In the simplest cases, this corresponds exactly to the injection of an L-defect as there is indeed a misdirected H-bond, leaving a hydrogen vacancy in the water lattice. Such vacancies will in effect make it easier (lower barrier) for reorientation of an adjacent water molecule to

Can. J. Chem. Downloaded from www.nrcresearchpress.com by Xi'an Jiaotong University on 09/19/12
For personal use only.

occur. For the more persistent guest–host interactions, a careful study by single crystal X-ray diffraction showed that the misdirected H-bonds to guests could be seen directly (specifically in pinacolone Str.H and t-butylamine Str.II),[56] indicating that a good fraction of the guests were H-bonded at any particular instant. For stronger guest–host interactions, a water oxygen was also moved out of its usual position in the hydrate cage.[56] However, in the case of THF hydrate the MD simulations showed that these H-bonds are rather short lived (0.28 ps at 200 K), and thus no effects on the structure can be detected.[53] This *injection* of L-defects by the guest appears to be quite a different process from the *propagation* of Bjerrum defects, which governs the water reorientation process as observed by dielectric and NMR relaxation.[10,15] For instance, for THF hydrate the activation energy for L-defect *injection* was found to be ~8.3 kJ/mol from MD simulation,[53] compared with an experimental value of ~30 kJ/mol for defect *propagation* (see refs. 30, 33, 34, 37, and this work). An MD calculation of defect *propagation* will require longer simulation times, as this process barely reaches microsecond timescales at the highest temperatures of study. It may be that the limiting process for defect transport is the ease of D-defect generation.

Conclusion

This study of ^{17}O NMR lineshapes of water in ice and a clathrate hydrate has provided a remarkable picture of the effects of dynamic averaging on lineshapes of a non-integer quadrupolar nucleus over quite a broad range of jump rates. It is also quite consistent with previous studies using other nuclei and other techniques. Apparently, no new details of Bjerrum defect diffusion have come to light, although it is clear that some progress has been made in understanding the role of Bjerrum defect injection and transport in ice and hydrates in general. The observation of an apparently isotropic line that has a second-order shift is quite unusual and could have implications for reporting of shifts in other systems, if it is not recognized that dynamic effects are at play. While rapid reorientation among tetrahedral or octahedral orientations at rates faster than the full first-order linewidth will average the effective electric field gradient to zero, in which case an isotropic line at the true chemical shift is the ultimate spectrum, it is also well recognized that the second-order central transition lineshape will average to an anisotropic shape at rates comparable with its static linewidth. The current work has also partly explored a rate regime between these two situations where the anisotropically averaged second-order lineshape further averages to an isotropic shape which retains a second-order shift. In the absence of variable temperature work where this behaviour becomes apparent, it would be necessary to check whether an isotropic line has a second-order shift by measuring the shift at more than one magnetic field.

Acknowledgement

American Chemical Society Petroleum Research Fund under the award PRF#39645-GB5M is thanked for the partial support of this research.

References

(1) Hobbs, P. V. In *Ice Physics*. Clarendon Press: Oxford., 1974, p. 60–78.
(2) Bragg, W. H. *Proc. Phys. Soc.* **1922** *34*, 98.
(3) Peterson, S. W., Levy, H.A. *Acta Crystallogr.* **1957** *10*, 70. doi:10.1107/S0365110X5700016X.
(4) Chidambaram, R. *Acta Crystallogr.* **1961** *14* (5), 647. doi:10.1107/S0365110X61001509.
(5) Pauling, L. *J. Am. Chem. Soc.* **1935** *57* (12), 2680. doi:10.1021/ja01315a102.
(6) Auty, R. P.; Cole, R. H. *J. Chem. Phys.* **1952** *20* (8), 1309. doi:10.1063/1.1700726.
(7) Granicher, H.; Jaccard, C.; Scherrer, P.; Steinemann, A. *Discuss. Faraday Soc.* **1958** *23*, 50 . doi:10.1039/df9572300050.
(8) Eisenburg, D.; Kauzman, W. *The Structure and Properties of Water*. Oxford University Press, Oxford, 1969.
(9) Bjerrum, N. *Science* **1952** *115* (2989), 385. doi:10.1126/science.115.2989.385.
(10) Davidson, D. W. In *Water: A Comprehensive Treatise*, Ed. Franks, F., Plenum Press, New York, 1973, Vol.2, p115–234.
(11) Jeffrey, G. A. In *Comprehensive Supramolecular Chemistry*, Eds. MacNicol, D.D.; Toda, F.; Bishop, R., Pergamon, 1996, Vol.6, 757–788.
(12) Dyadin, Y. A.; Belosludov, V. R. In *Comprehensive Supramolecular Chemistry*, Eds. MacNicol, D.D.; Toda, F.; Bishop, R., Pergamon, 1996, Vol.6, p.789–824.
(13) Sloan, E. D.; Koh, C. A. *Clathrate Hydrates of Natural Gases*. 3rd ed., CRC Press, Boca Raton, 2008.
(14) Cox, J. L. *Natural Gas Hydrates: Properties, Occurrence and Recovery*, Butterworth Press, Woburn, Mass., 1983.
(15) Davidson, D. W.; Ripmeester, J. A. In *Inclusion Compounds*, Eds. Atwood, J.L.; Davies, J.E.D.; MacNicol, D.D., Academic Press, London,1984, Vol.3, p. 69–128.
(16) Davidson, D. W.; Desando, M. A.; Gough, S. R.; Handa, Y. P.; Ratcliffe, C. I.; Ripmeester, J. A.; Tse, J. S. *Nature* **1987** *328* (6129), 418. doi:10.1038/328418a0.
(17) Ripmeester, J. A.; Davidson, D. W. *Molecular Crystals and Liquid Crystals* **1977** *43* (3), 189. doi:10.1080/00268947708084666.
(18) Ripmeester, J. A.; Ratcliffe, C. I. *J. Phys. Chem.* **1990** *94* (25), 8773. doi:10.1021/j100388a006.
(19) Mak, T. C. W.; McMullan, R. K. *J. Chem. Phys.* **1965** *42* (8), 2732. doi:10.1063/1.1703229.
(20) McMullan, R. K.; Kvick, A. *Acta Crystallogr.* **1990** *B46*, 390.
(21) Ratcliffe, C. I.; In, N. M. R. *Crystallography*, Eds. Harris, R. K.; Wasylishen, R.E.; Duer, M.J., Wiley, Chichester UK, 2009, p. 355–373.
(22) Vega, A. J.; Luz, Z. *J. Phys. Chem.* **1987** *86* (4), 1803. doi:10.1063/1.452181.
(23) Wittebort, R. J.; Olejniczak, E. T.; Griffin, R. G. *J. Chem. Phys.* **1987** *86* (10), 5411. doi:10.1063/1.452565.
(24) Barnaal, D. E.; Lowe, I. J. *J. Chem. Phys.* **1968** *48* (10), 4614. doi:10.1063/1.1668036.
(25) Siegle, G.; Weithase, M. *Z. Phys.* **1969** *219* (4), 364. doi:10.1007/BF01395533.
(26) Weithase, M.; Noack, F.; von Schutz, J. *Z. Phys.* **1971** *246*, 91 . doi:10.1007/BF01402654.
(27) Valic, M. I.; Gornostansky, S.; Pintar, M. M. *Chem. Phys. Lett.* **1971** *9* (4), 362. doi:10.1016/0009-2614(71)80243-9.
(28) Wittebort, R. J.; Usha, M. G.; Ruben, D. J.; Wemmer, D. E.; Pines, A. *J. Am. Chem. Soc.* **1988** *110* (17), 5668. doi:10.1021/ja00225a013.

(29) Blinc, R.; Lahajnar, G.; Zupancic, I.; Granicher, H. *Chem. Phys. Lett.* **1969** *4*, 363.
(30) Garg, S. K.; Davidson, D. W.; Ripmeester, J. A. *J. Magn. Reson.* **1974** *15*, 295.
(31) Schmidt, V. H. In *Physics and Chemistry of Ice*, Ed. Whalley, E.; Jones, S.J.; Gold, L.W., Roy. Soc. Canada, Ottawa, 1973, 212–217.
(32) Davidson, D. W.; Garg, S. K.; Ripmeester, J. A. *J. Magn. Reson.* **1978** *31*, 399.
(33) Bach-Verges, M.; Kitchin, S. J.; Harris, K. D. M.; Zugic, M.; Koh, C. A. *J. Phys. Chem. B* **2001** *105* (14), 2699. doi:10.1021/jp002529o.
(34) Kirschgen, T. M.; Zeidler, M. D.; Geil, B.; Fujara, F. *Phys. Chem. Chem. Phys.* **2003** *5* (23), 5243. doi:10.1039/b212471h.
(35) Kirschgen, T. M.; Zeidler, M. D.; Geil, B.; Fujara, F. *Phys. Chem. Chem. Phys.* **2003** *5* (23), 5247. doi:10.1039/b212472f.
(36) Bach-Verges, M.; Kitchin, S. J.; Harris, K. D. M.; Zugic, M.; Koh, C. A. *Phys. Chem. Chem. Phys.* **2004** *6*, 871 . doi:10.1039/b307944a.
(37) Gough, S. R.; Hawkins, R. E.; Morris, B.; Davidson, D. W. *J. Phys. Chem.* **1973** *77* (25), 2969. doi:10.1021/j100643a009.
(38) Witschas, M.; Eckart, H.; Freiheit, H.; Putnis, A.; Korus, G.; Jansen, M.et al. *J. Phys. Chem. A* **2001** *105* (28), 6808. doi:10.1021/jp003635t.
(39) Kristensen, J. H.; Farnan, I. *J. Chem. Phys.* **2001** *114* (21), 9608. doi:10.1063/1.1368660.
(40) Schurko, R. W.; Wi, S.; Frydman, L. *J. Phys. Chem. A* **2002** *106* (1), 51. doi:10.1021/jp0130214.
(41) Witschas, M.; Eckert, H. *J. Phys. Chem. A* **1999** *103* (50), 10764. doi:10.1021/jp992763i.
(42) Muller, K. *Phys. Chem. Chem. Phys.* **2002** *4*, 5515 . doi:10.1039/b206852d.
(43) Ashbrook, S. E.; Antonijevic, S.; Berry, A. J.; Wimperis, S. *Chem. Phys. Lett.* **2002** *364* (5-6), 634. doi:10.1016/S0009-2614(02)01412-4.
(44) Ba, Y.; Ratcliffe, C. I.; Ripmeester, J. A. *Chem. Phys. Lett.* **1999** *299* (2), 201.[This is a re-interpretation of single crystal data by Waldstein, P.; Rabideau, S.W., J.Chem.Phys., 1967, 47, 5338-5342]. doi:10.1016/S0009-2614(98)01275-5.
(45) Kunwar, A. C.; Turner, G. L.; Oldfield, E. *J. Magn. Reson.* **1986** *69*, 124.
(46) Spiess, H. W.; Garrett, B. B.; Sheline, R. K.; Rabideau, S. W. *J. Chem. Phys.* **1969** *51* (3), 1201. doi:10.1063/1.1672122.
(47) Edmonds, D. T.; Zussman, A. *Phys. Lett.* **1972** *41A*, 167.
(48) Edmonds, D. T.; Goren, S. D.; Mackay, A. L.; White, A. A. L.; Sherman, W. F. *J. Magn. Reson.* **1976** *23*, 504.
(49) Zhang, Q. W.; Zhang, H. M.; Usha, M. G.; Wittebort, R. J. *Sol. Stat.NMR* **1996** *7* (3), 147. doi:10.1016/S0926-2040(96)01258-1.
(50) Schporer, M.; Achlama, A. M. *J. Chem. Phys.* **1976** *65*, 3657 . doi:10.1063/1.433553.
(51) Pennanen, T. S.; Vaara, J.; Lantto, P.; Sillanpaa, A. J.; Laasonen, K.; Jokisaari, J. *J. Am. Chem. Soc.* **2004** *126* (35), 11093. doi:10.1021/ja048049i.
(52) Man, P. P. In *Encylopedia of NMR*, Eds. Grant, D.M.; Harris, R.K., John Wiley, New York, 1996, p. 3838–47.
(53) Alavi, S.; Susilo, R.; Ripmeester, J. A. *J. Chem. Phys.* **2009** *130* (17), 174501. doi:10.1063/1.3124187.
(54) Susilo, R.; Alavi, S.; Moudrakovski, I. L.; Englezos, P.; Ripmeester, J. A. *ChemPhysChem* **2009** *10* (5), 824. doi:10.1002/cphc.200900024.
(55) Alavi, S.; Takeya, S.; Ohmura, R.; Woo, T. K.; Ripmeester, J. A. *J. Chem. Phys.* **2010** *133* (7), 074505. doi:10.1063/1.3469776.
(56) Alavi, S.; Udachin, K.; Ripmeester, J. A. *Chemistry* **2010** *16*, 1017.

Can. J. Chem. Downloaded from www.nrcresearchpress.com by Xi'an Jiaotong University on 09/19/12
For personal use only.

The refocused discrimination induced by variable amplitude minipulses (DIVAM) experiment — Improved domain selection in semicrystalline fluoropolymers by ^{19}F solid state nuclear magnetic resonance spectroscopy

Tony Montina, Paul Hazendonk, Philip Wormald, and Dinu Iuga

Can. J. Chem. Downloaded from www.nrcresearchpress.com by Xi'an Jiaotong University on 09/19/12
For personal use only.

Abstract: The discrimination induced by variable amplitude minipulses (DIVAM) filter can be tuned to select for signals from a particular domain, therefore it is possible to obtain signals specific to different domains using only one experiment. An early description of the DIVAM sequence, where the filter terminates with cross-polarization, explains this tune ability using a simple one-spin-relaxation model, thereby limiting the selection mechanism to incoherent processes. Recently, a more complete description of the selection behaviour was offered for the DIVAM filter, when it was directly applied to the observed nucleus (direct DIVAM), taking into account both the incoherent and coherent terms. Direct DIVAM experiments on poly(vinylidenefluoride) (PVDF) show significant phase distortions when large excitation angles were used. The signal from the amorphous domain is seen to nutate in a normal fashion with respect to the excitation angle, while those from the crystalline and defect units did not. The refocused DIVAM sequence is introduced to restore normal nutation for all signals. The selection behaviour is investigated using SIMPSON (simulation program for solid-state nuclear magnetic resonance (NMR) spectroscopy) simulations. These illustrate that the isotropic shift terms have been effectively removed and the dipolar term attenuated, such that the chemical shift anisotropy (CSA) leads to domain selection; however, in a different manner than seen in direct DIVAM. Therefore, this sequence provides a method to select on the basis of the CSA term in the presence of both strong dipolar couplings and a large range of isotropic shifts.

Key words: nuclear magnetic resonance (NMR), polymer, domain selection, discrimination induced by variable amplitude minipulses (DIVAM), refocusing, spin dynamics, relaxation.

Résumé : Le filtre avec discrimination induite par des minipulsations d'amplitude variable (DIMAV) peut être ajusté pour choisir des signaux à partir d'un domaine particulier; il est donc possible d'obtenir des signaux spécifiques à différents domaines au cours d'une seule expérience. Une description de la séquence DIMAV originale, dans laquelle le filtre se termine par une polarisation croisée, explique cette habilité à s'ajuster à l'aide d'un modèle simple de relaxation à un spin, limitant ainsi le mécanisme de sélection à des processus incohérents. Récemment, une description plus complète du comportement de sélection a été offerte pour le filtre avec des DIMAV qui, lorsquelle est directement appliquée au noyau observé (DIMAV directe), permet de tenir compte à la fois des termes cohérents et incohérents. Des expériences de DIMAV directe sur du poly(fluorure de vinylidène) (PFPV) montrent qu'on observe des distorsions de phase importantes quand on utilise de grands angles d'excitation. On voit que, dans le mode normal, le signal du domaine amorphe subit une nutation par rapport à l'angle d'excitation alors que ceux des unités cristallines ou défectueuses n'en subissent pas. On introduit la séquence de DIMAV refocalisée pour restaurer la nutation normale pour tous les signaux. On a étudié le comportement de sélection par des simulations à l'aide du programme de simulation pour la spectroscopie résonance magnétique nucléaire (RMN) à l'état solide (SIMPSON). Elles permettent d'illustrer que les termes de déplacement isotrope peuvent effectivement être éliminés et que le terme dipolaire peut être atténué d'une façon telle que l'anisotropie du déplacement chimique (ADC) conduit à une sélection du domaine; toutefois, cette sélection est faite d'une façon différente de celle observée par une DIMAV directe. En conséquence, cette séquence fournit une méthode de sélection sur la base du terme d'ADC en présence à la fois de forts couplages dipolaires et d'un large éventail de déplacements isotropes.

Received 23 December 2010. Accepted 11 February 2011. Published at www.nrcresearchpress.com/cjc on 24 August 2011.

T. Montina and P. Hazendonk. Department of Chemistry and Biochemistry, University of Lethbridge, Lethbridge, AB T1K 3M4, Canada.
P. Wormald. School of Chemistry, University of St Andrews, Purdie Building, St Andrews, Scotland KY16 9ST, UK.
D. Iuga. Department of Physics, University of Warwick, Coventry CV4 7AL, UK.

Corresponding authors: Paul Hazendonk (e-mail: paul.hazendonk@uleth.ca) and Philip Wormald (e-mail: pw22@st-andrews.ac.uk).

This article is part of a Special Issue dedicated to Professor Roderick E. Wasylishen.

Mots-clés : résonance magnétique nucléaire (RMN), polymère, sélection d'un domaine, discrimination induite par des mini-pulsations d'amplitude variable (DIMAV), refocalisation, dynamique des spins, relaxation.

[Traduit par la Rédaction]

Can. J. Chem. Downloaded from www.nrcresearchpress.com by Xi'an Jiaotong University on 09/19/12
For personal use only.

Introduction

Fluoropolymers see widespread commercial application, such as nonstick coatings (Teflon), textiles (GORE-TEX), and fuel cell membranes (Nafion).[1–3] Poly(vinylidenefluoride) (PVDF) is a semicrystalline fluoropolymer, which is exploited for its piezo- and pyro-electric properties in actuators, transducers, and coatings. These useful macroscopic properties are a direct result of the polymer's domain structure; therefore, a good understanding of the morphology on the atomic scale can give valuable insights into their potential applications. Fluorine solid-state nuclear magnetic resonance (SSNMR) is an ideal tool to study these polymers owing to the sensitivity of the ^{19}F nucleus to its local electronic environment.[4–7]

There are several advantages to using the ^{19}F nucleus in SSNMR. Firstly, it is 100% abundant and has the second largest gyromagnetic ratio amongst stable nuclei; hence, its sensitivity is similar to that of ^{1}H. As a consequence, it is common for fluorine to have strong homonuclear and heteronuclear dipolar couplings. These can be exploited in one- and two-dimensional techniques, giving internuclear distances, which in turn provide valuable insight into connectivity and spatial proximity.[8–11] For nonperfluorinated systems, heteronuclear couplings to protons can be easily removed by using multipulse decoupling sequences.[12,13] Secondly, fluorine is very sensitive to its local environment owing to its large chemical shift range, similar to ^{13}C, making it a very useful structural probe; furthermore, the large frequency separations suppress spin diffusion leading to high resolutions, which is extremely difficult to achieve in proton spectroscopy.

One of the benefits of SSNMR in materials science is its ability to obtain detailed information from overlapping signals corresponding to different chemical environments. Various filtering methods have been designed for domain selection, where separation is achieved via differences in relaxation, dipolar coupling (DC), and chemical shift anisotropy (CSA).[14–16] Often, it is necessary to perform several different experiments to select the signal from each domain. Relaxation methods are mainly applied to abundant nuclei, exploiting differences in their T_1, $T_{1\rho}$, or T_2[14,17–20] relaxation times. Domain selection can be achieved using differences in dipolar coupling interactions. These methods have many different implementations such as the single pulse excitation with delayed acquisition, dipolar dephasing, and dipolar filter experiments.[21–28] Selection can also be achieved using the CSA term as was recently demonstrated by Schmidt-Rohr and co-workers.[29] These aforementioned selection methods have been reviewed elsewhere and will not be elaborated upon in this work.[14]

The discrimination induced by variable amplitude minipulses (DIVAM)[17,30] and direct DIVAM[31] (Figs. 1*a* and 1*b*) experiments are domain selection methods that can be adjusted, making it possible to select the signal from each domain separately using only one pulse sequence, rather than several different pulse sequences as in the past. In the DIVAM experiment, the filtering sequence is applied to an abundant nucleus, i.e., ^{1}H, which is immediately followed by cross-polarization to the nucleus of interest, i.e., ^{19}F or ^{13}C, allowing the selection to be based on proton spin dynamics and the higher spectral resolution results from the large chemical shift dispersion of the observed nucleus.[32,33] In the case where cross-polarization is not possible from proton, i.e., for perfluorinated materials or when high mobility is present, the DIVAM sequence is applied directly to the nucleus of interest.

Fig. 1. (*a*) The DIVAM, (*b*) the direct DIVAM, and (*c*) the refocused DIVAM pulse sequences.

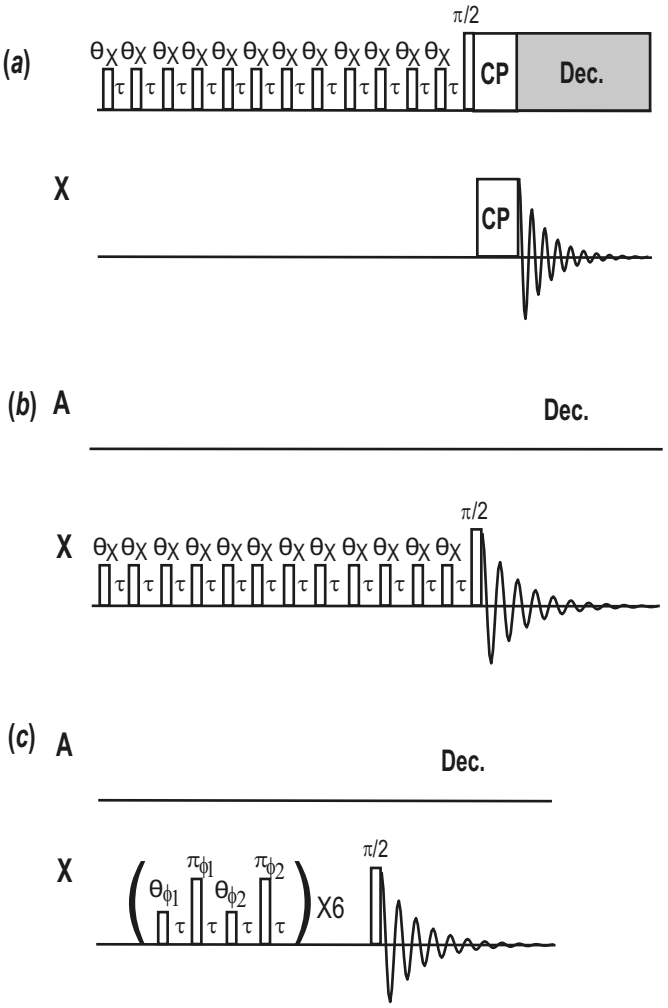

Previous work on the DIVAM sequence[30] has shown that no transient behaviour in the nutation is seen on the rotor-time scale when incrementing the interpulse delay (τ). This indicates that coherent processes of the abundant nuclei do

Can. J. Chem. Downloaded from www.nrcresearchpress.com by Xi'an Jiaotong University on 09/19/12
For personal use only.

not affect the nutation of signals from the observed nuclei. This is most likely due to rapid spin diffusion in protons, which dampens any rotor-phase dependence during the cross-polarization to the observed nucleus. Therefore, the DIVAM sequence can be thought of as selecting on the basis of differences in the transverse relaxation between domains, which was demonstrated using a one-spin relaxation model (Fig. 2*a*). With each pulse, the longitudinal components from each domain are rotated into the transverse plane. During the interpulse delay, they dephase at differing rates, resulting in a difference in their net angle of rotation along the *z*-axis. Upon each pulse-delay cycle, this phase difference accumulates resulting in a net difference in their nutation rates with respect to the excitation angle. At a specific excitation angle (θ), there is a phase difference of 90°, where the signal from one component remains positive while the other will be nulled. As a result, the signal of only one of the domains is observed.

In contrast, our previous work[31–33] has shown that nutation of the ^{19}F signals in direct DIVAM is seen to be strongly dependent on the rotor timescale. To explain the selection behaviour for the direct DIVAM sequence, a more sophisticated model combining the effects of chemical shielding, dipolar coupling, and relaxation was needed. All were seen to participate in the selection process, where the degree of each was dependant on the excitation angle and interpulse delay; therefore, it is possible to configure the sequence so that either can be the dominant selection mechanism. However, the spin dynamics terms were shown to lead to significant phase distortions for large excitation angles (θ). Also, the nutation behaviour depended strongly on the frequency offset from the radio frequency (RF) resonance, or carrier frequency, of the excitation pulses (henceforth, this will be referred to as the offset dependence of direct DIVAM). Both phase distortions and an offset dependence are undesirable as they can severely compromise effective domain selection by distorting the observed nutation behaviour; therefore, modifications to direct DIVAM are required to remove, or reduce, these effects.

At this stage, it is important to point out that although DIVAM bears a strong resemblance to DANTE (delay alternating with nutation for tailored excitation),[34,35] it is very different in its application and mode of action. On the one hand, DANTE can be thought of as a discrete version of a soft pulse, where selective excitation is achieved through the offset term; however, as it has been most extensively used in the solution state the effects of the remaining terms in the Hamiltonian are ignored. On the other hand, DIVAM is used solely on solids to select between overlapping signals, hence the offset differences are very small. This means that a combination of relaxation and the remaining terms of the solid state NMR Hamiltonian (CSA and DC) are responsible for the selection behaviour. In fact, the intention is to completely remove any residual selection resulting from the offset term during the DIVAM sequence.

In this work, the refocused DIVAM experiment (Fig. 1*c*) is introduced, which is similar to direct DIVAM, but with the addition of refocusing pulses and an appropriate phase cycle (Table 1). Refocusing pulses are added to remove the effect of coherent dephasing due to both the heteronuclear coupling and chemical shift terms of the Hamiltonian during the interpulse delay, thereby reducing both the phase distortions seen at large excitation angles (θ) and the offset dependence of direct DIVAM. Furthermore, any selection due to relaxation will be reduced as it will be governed by T_2 as opposed to T_2*. The phase cycle is implemented to ensure that the magnetization accumulates in the transverse plane in a similar manner to the previous DIVAM experiments (Fig. 2*b*). Also, the cycle makes use of EXORCYCLE (a 16-step phase cycle for spin echoes),[36] ensuring that any remaining contributions to the signal that result from the mis-setting of pulse widths are removed. The experiment is repeated with an offset alternating above and below the RF carrier frequency to ensure that any phase distortions due to the breakdown of the hard pulse approximation are minimized. All of these modifications should change the selection mechanism of the sequence by simplifying the nutation behaviour, thereby improving its prospective application in domain selection and separated local field methods. This work provides experimental and simulation results that show how these modifications affect the selection mechanism of the direct DIVAM sequence.

Fig. 2. (*a*) A vector diagram of magnetization from the two domains, with differing T_2 relaxation times, under the operation of the DIVAM pulse train illustrating the magnetization after the (*i*) first θ_x-pulse, (*ii*) first interpulse delay, (*iii*) second θ_x-pulse, (*iv*) second interpulse delay, (*v*) full DIVAM train, and (vi) the final $\pi/2$ pulse. (*b*) A similar diagram to (*a*) but for the refocused DIVAM pulse train and its first phase cycle, illustrating the magnetization after the (*i*) first θ_x-pulse and an interpulse delay, (*ii*) first π_y-pulse and an interpulse delay, (*iii*) first θ_{-x}-pulse and an interpulse delay, (*iv*) first π_{-y}-pulse and an interpulse delay, (*v*) full refocused DIVAM train, and (*vi*) final $\pi/2$ pulse.

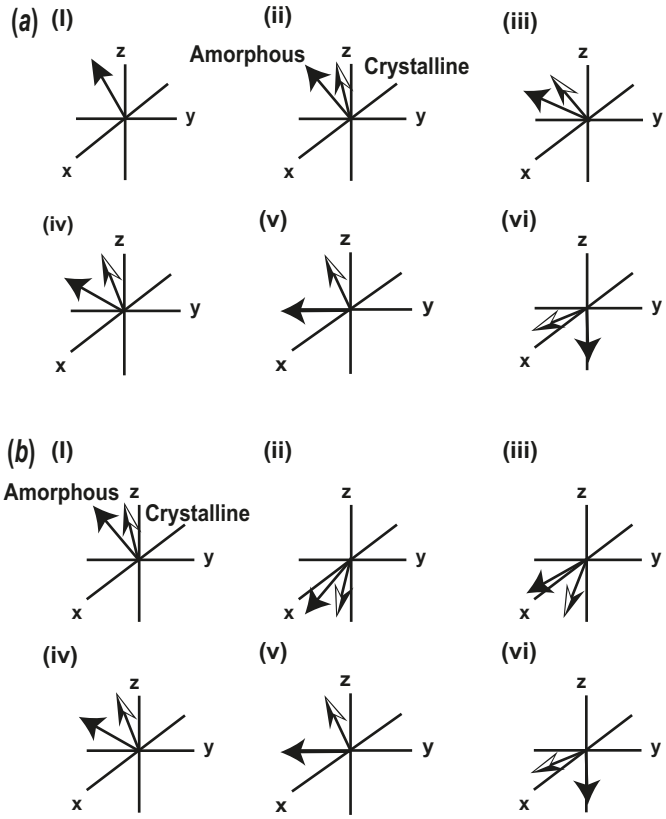

Can. J. Chem. Downloaded from www.nrcresearchpress.com by Xi'an Jiaotong University on 09/19/12
For personal use only.

Table 1. Phase cycle of the refocused DIVAM sequence.

$\theta_{\phi 1}$	$\pi_{\phi 1}$	$\theta_{\phi 2}$	$\pi_{\phi 2}$
x	y	$(-x)$	$(-y)$
x	$(-y)$	$(-x)$	y
x	x	x	$(-x)$
x	$(-x)$	x	x
$(-x)$	x	$(-x)$	$(-x)$
$(-x)$	$(-x)$	$(-x)$	x
$(-x)$	y	x	$(-y)$
$(-x)$	$(-y)$	x	y
y	y	y	$(-y)$
y	$(-y)$	y	y
y	x	$(-y)$	$(-x)$
y	$(-x)$	$(-y)$	x
$(-y)$	y	$(-y)$	$(-y)$
$(-y)$	$(-y)$	$(-y)$	y
$(-y)$	x	y	$(-x)$
$(-y)$	$(-x)$	y	x

Results and discussion

Direct and refocused DIVAM experiments on PVDF

The ^{19}F magic-angle spinning (MAS) SSNMR spectrum of PVDF (Fig. 3) contains two broad signals at –82.1 and –95.6 ppm, corresponding to the crystalline domains, and one narrow peak at –91.2 ppm that represents the amorphous domain. The crystalline signal is characterized by short T_2's and large chemical shift anisotropies (CSAs). In contrast, the signal from the amorphous region has longer T_2's and smaller CSAs, due to molecular motion. A broad signal of low intensity is composed of two signals at –118.3 and –114.9 ppm from the two adjacent CF_2 groups of the defect unit, which is formed due to reversed addition of the monomer units during polymerization. Furthermore, a lower intensity signal is present at –115 ppm and has been shown to be the CF_2H end chain signal.[6] These defect units have been associated with the amorphous region through data obtained from relaxation, radio frequency driven recoupling (RFDR), and domain filtering (i.e., dipolar filter and $T_{1\rho}$) experiments.[7]

The direct DIVAM nutation array of the ^{19}F MAS spectra of PVDF is shown in Fig. 4. Some of the aforementioned problems with direct DIVAM may not be immediately apparent, but upon closer examination they can be seen. The amorphous signal nutates for most of the excitation angles, however this nutation is lost beyond 60°. This loss of nutation is a direct result of the phase distortions created by the spin dynamics terms at large excitation angles.[31] Also, note that nutation of the crystalline signal is nearly lost and not apparent for the defect signals. This is indicative of the offset dependence of direct DIVAM as the RF is centered on the amorphous signal, which is shifted in frequency from both the crystalline and defect signals by 4.6–8.9 ppm (2.1–4.2 kHz) and 24 ppm (11.3 kHz), respectively. This offset dependence of direct DIVAM will be further investigated when looking at the application of direct and refocused DIVAM to Nafion 117.

Figure 5 shows the refocused DIVAM array of PVDF. The improved resolution in the ^{19}F spectra is due to more efficient ^{1}H decoupling during acquisition. The amorphous signal is seen to nutate at a faster rate than the crystalline signal, and passes through a null condition at $\theta \simeq 22.5°$, where positive intensity of the crystalline signal remains. Also, the crystalline signal passes through a null condition at $\theta \simeq 62.5°$, where the amorphous signal has returned to a positive intensity. Furthermore, the defect signals now nutate at a rate similar to that of the amorphous signal; this will be discussed later. It is important to point out that these selection angles are approximate. Complete selection of either the crystalline or amorphous domain is achieved by incrementing the excitation angle, around each of the approximate values, in steps that are smaller than 2.5°. In general, for any given sample the exact angles at which zero crossings occur must be determined by careful calibration of the excitation angles.

Fig. 3. The ^{19}F MAS NMR spectra of PVDF under ambient conditions, with the RF resonance set on the amorphous peak, and a MAS rate of 20 kHz.

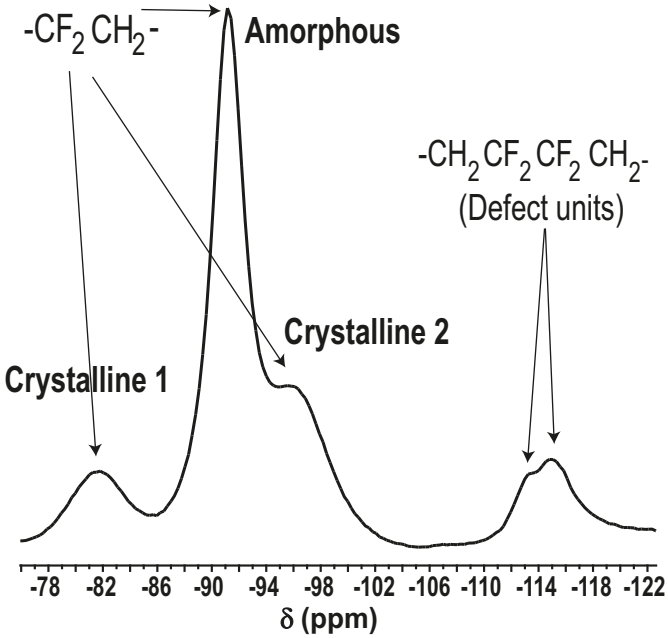

When comparing the nutation behaviour in refocused DIVAM (Fig. 5) with direct DIVAM (Fig. 4), a few observations can be made. First, note that the phase distortions in the direct DIVAM array have been reduced in the refocused DIVAM experiment. Second, the signals from all three chemical environments nutate for all excitation angles indicating that the offset dependence of direct DIVAM has been reduced. Lastly, refocused and direct DIVAM show differences in their overall rate of nutation, which can be attributed to three factors: (*i*) the interpulse delays used in direct DIVAM differ from the refocused DIVAM sequence, (*ii*) the refocused DIVAM sequence has twice as many interpulse delays due to the addition of refocusing pulses, and (*iii*) the selection mechanisms of direct and refocused DIVAM are different. As a result of the first two factors, the total filtering time of the sequence is changed and the net evolution in the transverse plain is different; therefore, differences in their nutation rates are to be expected. The selection mechanism in direct DIVAM, when off-resonance, becomes dominated by its offset dependence, while in refocused DIVAM it appears to be driven by the CSA term. This is further supported by SIMPSON (simulation program for solid-state NMR spectroscopy)[37] simula-

Fig. 4. The direct DIVAM nutation array of the ^{19}F MAS NMR spectra of PVDF using an interpulse delay of 1.67 μs and a pulse width of 2.5 μs (T_F = 50 μs). The nutation array ranges over excitation angles of 0°–90° in steps of 2.5° and was acquired with a spinning speed of 20 kHz. Enlargements of the ^{19}F MAS NMR spectra of PVDF for selected excitation angles are also shown.

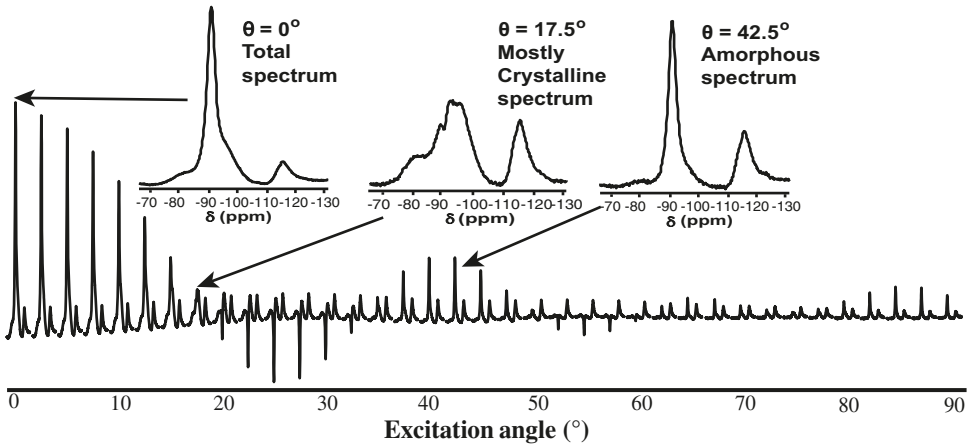

Fig. 5. The refocused DIVAM nutation array of the ^{19}F MAS NMR spectra of PVDF using an interpulse delay of 2.5 μs, a 90° pulse width of 2.5 μs, a 180° pulse width of 5 μs (T_F = 150 μs), and a pulse offset of 1 kHz. The nutation array ranges over excitation angles of 0°–90° in steps of 2.5° and was acquired with a spinning speed of 20 kHz. Enlargements of the ^{19}F MAS NMR spectra of PVDF for selected excitation angles are also shown.

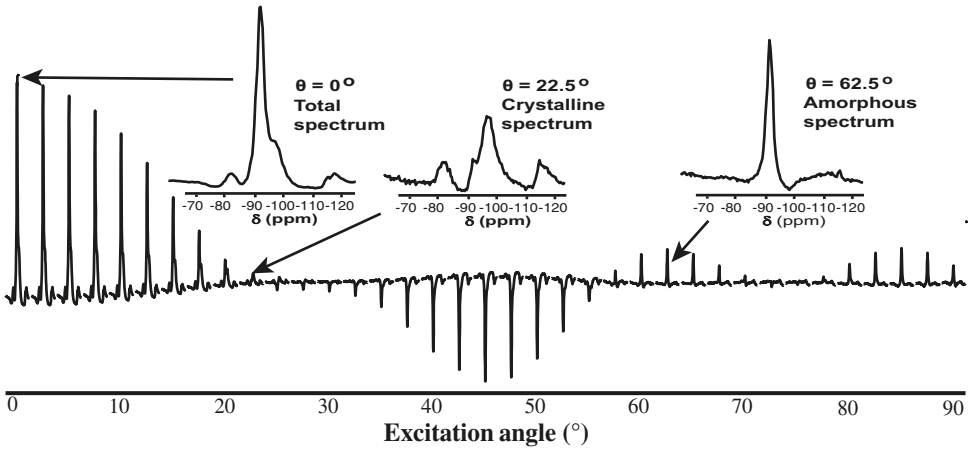

tions on refocused DIVAM, which will be shown in a later discussion (see the SIMPSON simulations section).

Although, the offset dependence of direct DIVAM has been greatly reduced, it can still be seen to a minor degree when comparing nutation rates of the amorphous and defect signals in refocused DIVAM (Fig. 5). These signals are known to be from similar environments and should have similar nutation rates. However, upon closer examination nutation of the defect signals lags slightly behind the amorphous signal. The extent of this remaining offset dependence will be examined further using Nafion 117.

The ^{19}F MAS NMR spectra of Nafion 117 and its structural assignment can be seen in Fig. 6.[38,39] Figures 7*a* and 7*b* show the nutation profile of the backbone (BB) signal (B in Fig. 6*b*) at –122 ppm and side-chain (SC) signal (E and F in Fig. 6*b*) at –82 ppm, respectively, with the RF resonance centered on the backbone (BB) signal. Similarly, Figs. 7*c* and 7*d* show analogous nutation profiles but with the RF resonance centered on the SC signal. It is clear that nutation of each signal occurs when the RF resonance is centered directly on the peak of interest (Figs. 7*a* and 7*d*) and that once the RF resonance is moved nutation is lost (Figs. 7*b* and 7*c*). This is a direct result of the aforementioned offset dependence of direct DIVAM and will be confirmed in the SIMPSON simulations section. Figure 8 illustrates the nutation profiles of the BB and SC signals in Nafion acquired using the refocused DIVAM sequence and with the RF frequency centered at –100 ppm. Refocused DIVAM recovers nutation of both the SC and BB signals and has removed the frequency offset dependence over at least a range of ~±20 ppm (~±10 kHz). The Nafion nutation arrays serve as an example of the increase in the effective frequency range of the direct DIVAM sequence by the introduction of the refocusing pulses.

SIMPSON simulations

Simulations of the refocused DIVAM sequence were performed and compared with those of direct DIVAM done previously,[31] to investigate the effect of each term in the ^{19}F Hamiltonian separately. Parallel simulations were performed using real (soft) pulses under rotor-synchronized and non-rotor-synchronized conditions (Fig. 9). Soft pulses are

Can. J. Chem. Downloaded from www.nrcresearchpress.com by Xi'an Jiaotong University on 09/19/12
For personal use only.

Can. J. Chem. Downloaded from www.nrcresearchpress.com by Xi'an Jiaotong University on 09/19/12
For personal use only.

Fig. 6. (*a*) The chemical structure of Nafion 117 and (*b*) the ^{19}F MAS NMR spectra and structural assignment of dry Nafion 117 under ambient conditions, with the RF resonance set on the backbone CF_2 peak, and a MAS rate of 24 kHz where A = SCF_2, B = $(CF_2)_n$, C = CF (backbone), D = CF (side chain), E = CF_3, F = OCF_2, and SB = spinning side band.

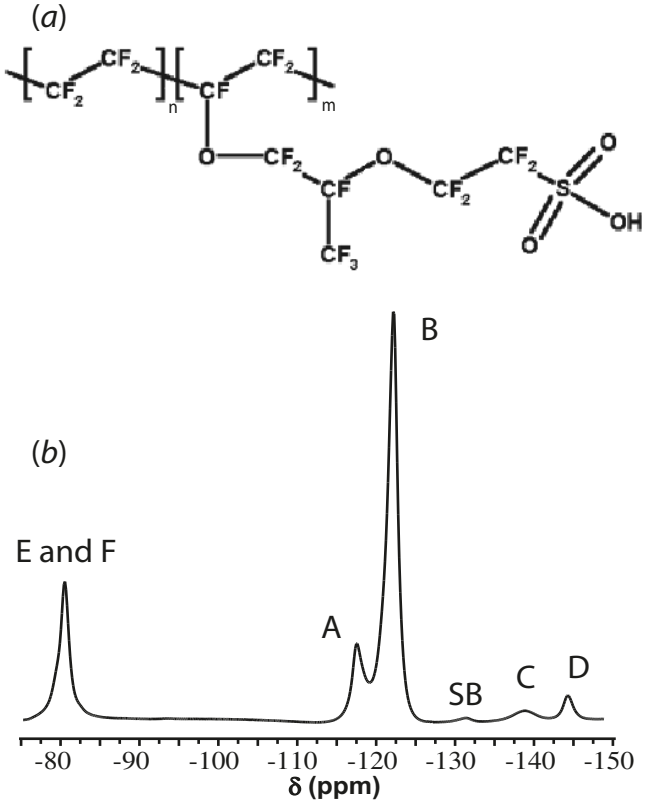

employed to avoid the use of the hard pulse approximation. The signal is computed over a range of excitation angles from 0° to 90° with an interpulse delay of 2.5 μs. The nutation of the *z*-magnetization remaining after the filter sequence is explained separately for each term in the Hamiltonian in the following text.

Isotropic shift term

Figure 9*a* shows that for a large range of frequencies the isotropic shift term of the Hamiltonian has been fully refocused in the rotor- and non-rotor-synchronized cases of refocused DIVAM. The lack of a difference between the rotor-synchronized and non-rotor-synchronized situations is to be expected, as the isotropic shift is not affected by sample rotation. Note that in the direct DIVAM simulations, the isotropic shift (offset) dependence of the nutation behaviour is obvious and has been clearly removed in refocused DIVAM. Also, the nutation of the 25 kHz curve in the direct DIVAM simulations closely resembles the nutation of the BB and SC signals in the off-resonance direct DIVAM arrays of Nafion (Figs. 7*b* and 7*c*), where the BB and SC signals are approximately 20 kHz off-resonance. This supports our earlier argument that the nutation of off-resonance signals is lost due to the offset dependence of direct DIVAM.

The chemical shift anisotropy (CSA) term

Figure 9*b* shows the nutation behaviour of the refocused and direct DIVAM sequences over a range of CSA strengths. Some interesting observations can be made when comparing the rotor-synchronized refocused and direct DIVAM simulations. For selection to occur in direct DIVAM, an anisotropy of 50 kHz or larger is required. In comparison, refocused DIVAM is sensitive to weaker anisotropies when using small excitation angles; therefore, refocused DIVAM appears to be a more sensitive CSA filter, as suggested earlier.

From the rotor-synchronized refocused DIVAM simulations, one can see that the first minimum is quite different for anisotropies of 10 kHz and above. More importantly, note that there is very little difference in the point of the first zero crossing for anisotropies up to 15 kHz. For larger excitation angles, $\theta \sim\geq 30°$, the nutation behaviour does not vary significantly for anisotropies less than 50 kHz, with a change in only the minimum but not the points of zero crossing.

The behaviour under non-rotor-synchronized conditions is substantially different and further complicated due to the rotational dependency of the CSA term. In this case, no difference in the point of the first zero crossing can be seen for anisotropies up to 25 kHz. On the other hand, differentiation in the maximum, minimum, and zero crossing of the nutation behaviour is seen for anisotropies above 10 kHz when an excitation angle greater than 30° is used. These results indicate that to achieve optimum selection conditions, rotor synchronization is of great importance and must be considered.

The effects of rotor synchronization were explored further using a range of CSA values over a series of interpulse delays, at a spinning speed of 20 kHz (Fig. 10). Rotor synchronization occurs at τ = 2.5 μs and corresponds to a T_F = 150 μs. At these conditions, a maximum difference between the curves is seen at θ = 15° and this indicates the optimum selection conditions. Upon closer examination, the selection condition becomes more favourable as the interpulse delay increases towards τ = 2.5 μs and less favourable as the difference from this value increases. Interestingly, the selection behaviour does not improve when the sequence is synchronized at either two or four rotor periods. This indicates that not only rotor synchronization, but also the number of rotor periods to which you synchronize the sequence, is important in achieving optimum selection. This suggests using interpulse delays approaching five rotor periods; however, for anisotropies of 90 kHz one can see that the signal is completely lost for longer interpulse delays (τ = 5 μs). The sequence must therefore be restricted to shorter interpulse delays to select for larger CSA values. It is important to note that the nutation curve of the 25 kHz CSA interaction, for an interpulse delay of 3 μs (top right of Fig. 10), closely resembles the nutation profile of the amorphous peak in the refocused DIVAM array (Fig. 5). This provides further support that the selection mechanism for refocused DIVAM is driven by the CSA term, but only when its strength is ≥15 kHz.

Dipolar coupling term

Figure 9*c* shows the nutation behaviour of the signal from the refocused and direct DIVAM sequences over a range of dipolar coupling interaction strengths. The comparison between the refocused and direct DIVAM rotor-synchronized simulations is quite different than what was seen for the CSA term. At the first zero crossing, differentiation is ob-

Fig. 7. The ^{19}F direct DIVAM nutation arrays of various peaks in Nafion with a MAS frequency of 24 kHz and ranging over excitation angles of 0°–90° in steps of 2.5°. Each direct DIVAM array used an interpulse delay of 1.67 μs and a pulse width of 4.44 μs (T_F = 83.3 μs). Arrays of the (*a*) backbone CF_2 peak with the RF resonance centered on the backbone CF_2 peak, (*b*) side-chain CF_3 and OCF_2 peak with the RF resonance centered on the backbone CF_2 peak, (*c*) backbone CF_2 peak with the RF resonance centered on the side-chain CF_3 and OCF_2 peaks, and (*d*) side-chain CF_3 and OCF_2 peak with the RF resonance centered on the side-chain CF_3 and OCF_2 peaks.

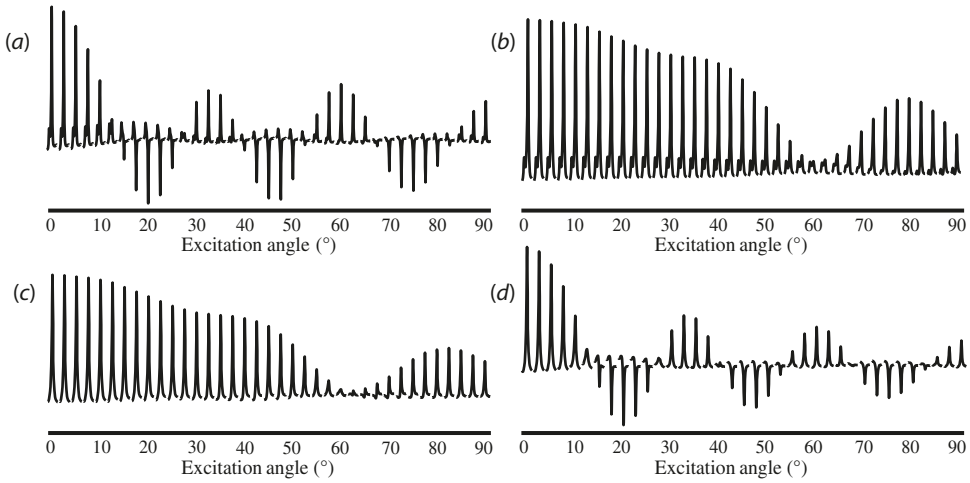

Fig. 8. The ^{19}F refocused DIVAM nutation array of Nafion at a MAS rate of 24 kHz and ranging over excitation angles of 0°–90° in steps of 2.5° of the (*a*) backbone CF_2 peak and the (*b*) side-chain CF_3 and OCF_2 peaks with the RF resonance centered at –100 ppm for both arrays. An interpulse delay of 2.5 μs, a 90° pulse width of 2.5 μs, a 180° pulse width of 5 μs (T_F = 150 μs), and a pulse offset of 1 kHz were used.

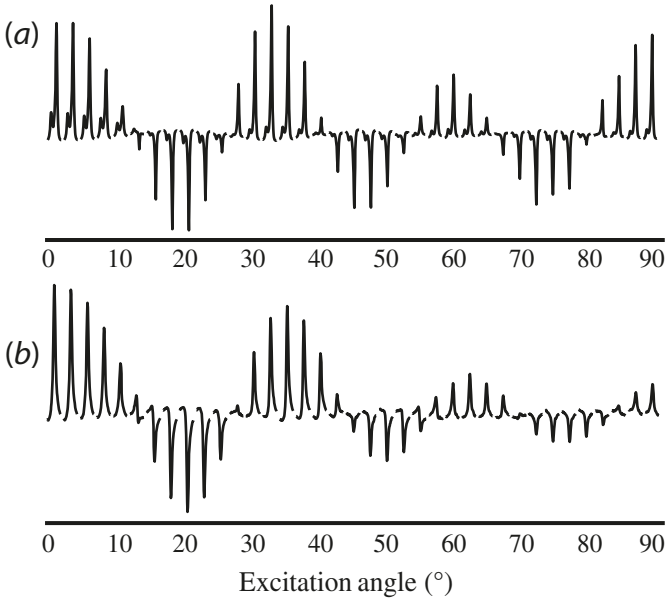

served for couplings of 25 kHz or greater in direct DIVAM, while a larger coupling of 50 kHz or greater is required for refocused DIVAM. Also, note that selection between the excitation angles of θ = 30° and 60° is not apparent in direct DIVAM, while it is quite profound in refocused DIVAM.

In the rotor-synchronized case for small excitation angles, $\theta \sim< 30°$, very little difference can be seen between the signals for dipolar couplings less than 50 kHz. This is also true in the case of excitation angles that are >60°. A dipolar coupling of 50 kHz is highly uncommon in these materials and therefore, in the small and large excitation angle regimes, the dipolar coupling should not be expected to contribute to the selection behaviour in the rotor-synchronized case. It is possible that selection could occur in the excitation angle range of θ = 30°–60° and would be based on a dipolar interaction of 15 kHz or greater.

The nutation of each signal is much more complicated in the non-rotor-synchronized case, due to the rotational dependency of the dipolar term. Similarly to the CSA term, no significant differences in the nutation behaviour are observed in the small excitation angle regimes, $\theta \sim< 30°$. In the case of the intermediate excitation angles, $\theta \simeq$ 30°–60°, the nutation behaviour varies less and now requires dipolar couplings of 25 kHz or greater for selection to occur. In the large excitation angles, $\theta \sim\geq 60°$, more differentiation is seen between signals and selection can be achieved with dipolar couplings of 15 kHz or higher. This again suggests that to achieve optimum selection conditions rotor synchronization should be employed.

Figure 11 shows a series of simulations of the dipolar term over a range of various interpulse delays and for two coupling values. For the small excitation angles, $\theta \sim< 30°$, rotor synchronization seems to be less important and no significant selection is seen between the curves. For the large excitation angles, $\theta \sim\geq 60°$, no noticeable selection occurs as we decrease the interpulse delay from 2.5 μs to 0.5 μs (T_F = 102 μs). However, selection can be seen as we increase the interpulse delay to a value of 4.5 μs (T_F = 148 μs). This indicates that for the larger excitation angles, $\theta \sim\geq 60°$, both rotor synchronization and the number of rotor periods are important. Practically speaking, rotor synchronization should be employed to ensure optimal selection; however, in general, some selection can still be achieved without it.

Simulation summary

If rotor synchronization is a requirement for domain selection then we can consider the effect of the CSA and dipolar Hamiltonian in two cases: small and large angles. In the for-

Can. J. Chem. Downloaded from www.nrcresearchpress.com by Xi'an Jiaotong University on 09/19/12
For personal use only.

Fig. 9. Simulation of the refocused and direct DIVAM sequences, which illustrate the behaviour of (*a*) the isotropic shift, (*b*) the chemical shift anisotropy, and (*c*) the dipolar coupling terms of the Hamiltonian. Each Hamiltonian varied between 1 and 50 kHz, where ○ = 1 kHz, □ = 2.5 kHz, △ = 5 kHz, ▽ = 7.5 kHz, ◇ = 10 kHz, ⬡ = 15 kHz, ⊞ = 25 kHz, and ⊕ = 50 kHz. The refocused DIVAM simulations used real 100 kHz pulses with a 90° pulse width of 2.5 μs, a 180° pulse width of 5 μs, an interpulse delay of 2.5 μs (T_F = 150 μs), and a pulse offset of 1 kHz. The direct DIVAM simulations[31] used real 100 kHz pulses with a 90° pulse width of 2.5 μs and an interpulse delay of 1.67 μs (T_F = 50 μs). In all cases, the rotor synchronized and the non-rotor-synchronized simulations used MAS rates of 20 and 25 kHz, respectively.

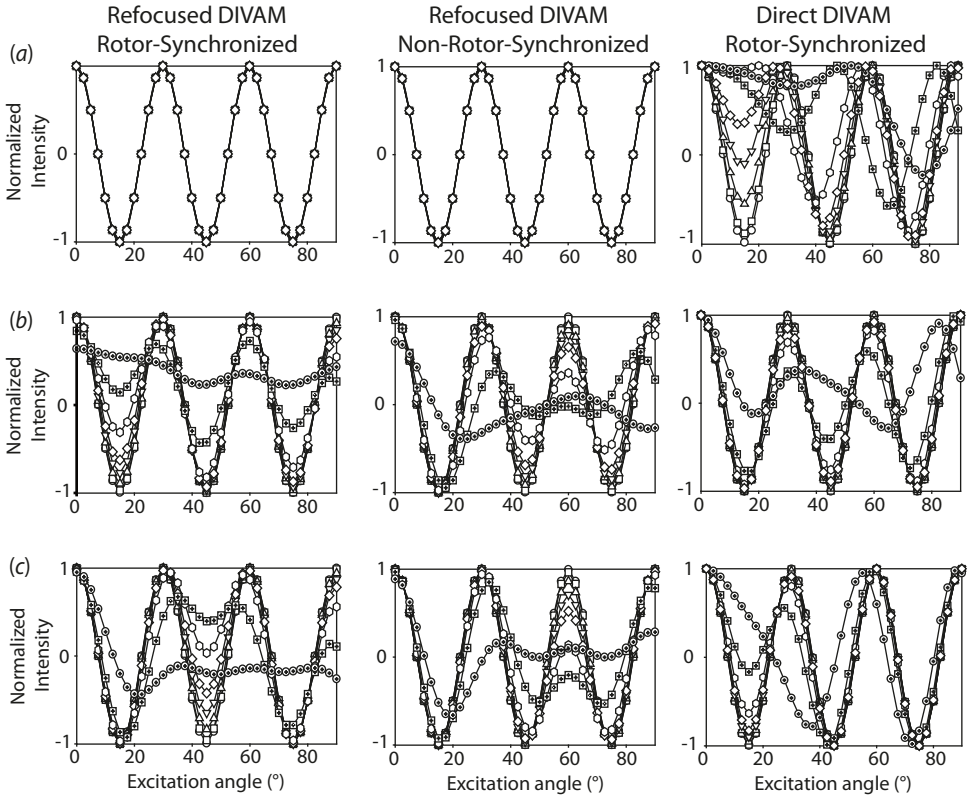

Can. J. Chem. Downloaded from www.nrcresearchpress.com by Xi'an Jiaotong University on 09/19/12
For personal use only.

mer case, CSA and dipolar interaction strengths of 15 and 50 kHz, respectively, are required for these terms to have a role in the selection. In the latter case, both rotor synchronization and the number of rotor periods over which the filter is applied are an important consideration. The total filtering time must be chosen such that no selection takes place for CSA and dipolar interaction strengths are less than 25 and 50 kHz, respectively. A total filtering time that is rotor synchronized and limited to a number of rotor periods reduces the amount of coherent dephasing that can occur during the interpulse delays, thereby ensuring minimal phase distortion in the nutation behaviour. Also, refocused DIVAM is a more sensitive CSA filter than direct DIVAM, with the latter requiring a CSA interaction strength of at least 50 kHz for selection to occur.

Conclusions

Refocused DIVAM experiments show that the phase distortions at large angles seen in the direct DIVAM experiments have been successfully removed by the addition of refocusing pulses. These experiments also demonstrate that the offset dependence of direct DIVAM has been greatly reduced and that nutation of all signals has been restored. SIMPSON simulations illustrate that the effect of the isotropic term has been removed. They also show that the effect of the CSA and dipolar terms on the selection mechanism of refocused DIVAM is profoundly different than for direct DIVAM. In fact, refocused DIVAM is more sensitive to the CSA term and less sensitive to the dipolar term. Furthermore, the refocused DIVAM experiment gives nutation behaviour, which is less complex than that of direct DIVAM, yet similar to the original CP DIVAM experiment.

The modifications made to the direct DIVAM sequence make it possible to perform CSA selection in the presence of both large isotropic shifts and dipolar interactions. In addition, this sequence is neither limited to any particular type of nucleus nor does it require any special considerations to simplify its spin dynamics; hence, the sequence is generally applicable. This is ideal for nuclei that exhibit large shielding ranges, especially with the large magnetic fields used today, such as ^{19}F, ^{31}P, ^{119}Sn, ^{117}Sn, ^{199}Hg, ^{77}Se, and ^{29}Si. These are increasingly being encountered in inorganic materials such as polymers, coordination polymers, and ceramics. Furthermore, CSA selection also has promising implications for both domain selection and separated local field methods. This is especially true when the latter is used to measure chemical shielding tensors components on systems that exhibit highly overlapped signals. This could prove to be an invaluable tool to the growing field of NMR crystallography.

Fig. 10. The effect of rotor synchronization on the selectivity of the refocused DIVAM pulse sequences for various chemical shift anisotropy and τ values where ○ = 10 kHz, ▽ = 25 kHz, and □ = 90 kHz. These simulations used real 100 kHz pulses with a MAS rate of 20 kHz, a 90° pulse width of 2.5 μs, a 180° pulse width of 5 μs, and a pulse offset of 1 kHz. The interpulse delay and total filtering time (T_F) are indicated at the top of each figure.

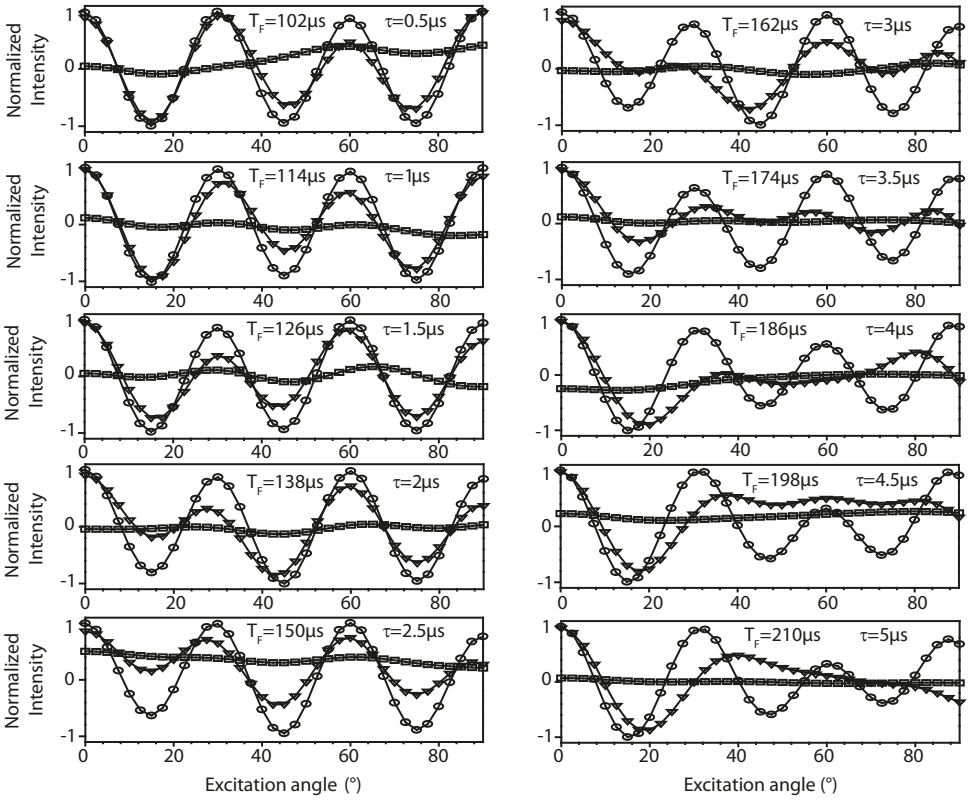

Can. J. Chem. Downloaded from www.nrcresearchpress.com by Xi'an Jiaotong University on 09/19/12
For personal use only.

Experimental

Solid-state NMR measurements

The α-PVDF sample had a molecular weight of 1×10^6 Da by gel permeation chromatography (GPC), a crystallinity of ~28%, a reverse unit content of 4.7% by NMR, and a melting point of 158 °C by differential scanning calorimetry (DSC).[3] The sample of α-PVDF was supplied by Atofina (France). The Nafion 117 sample was purchased from Dupont in the form of a commercial fuel cell membrane film. A Varian INOVA 500 MHz spectrometer with a carrier frequency of 470.18 MHz for the fluorine nucleus was used for all experimental measurements. A Varian 2.5 mm four channel HFXY probe operating at 21 °C with a MAS rate of 20 kHz for PVDF and 24 kHz for Nafion experiments was used. The 90° pulse was calibrated at 2.5 μs with the amplitude of each pulse in a full pulse train varied from 0° to 90° in 2.5° steps. The RF resonance frequency during acquisition was set to the amorphous peak of PVDF at –91.2 ppm, and is indicated in the figure captions for the Nafion experiments. Two pulse phase modulation (TPPM) decoupling was applied to ^{1}H during fluorine acquisition and also during spectral referencing so that the Bloch-Siegert shift could be neglected.[2] Spectral referencing was done using C_6F_6 (δ_F = 166.4 ppm with respect to $CFCl_3$) and zirconium oxide rotors with Vespel drive caps were used to avoid unwanted fluorine background signal.

All experimental measurements of the refocused DIVAM sequence were implemented over a minimum of 32 transients to allow for the full phase cycling of the 180° refocusing pulses. The phase cycle used (Table 1) ensures that all feedthrough terms are suppressed and effective refocusing occurs.[36] Blocks of 32 transients are required because the normal 16 step phase cycle is run twice, but with a different pulse offset used in each full cycle. The two pulse offsets used are of equal magnitude but opposite sign and the offset used for all experiments was 1 kHz.

The refocused DIVAM sequence was performed using a pulse train that consisted of twelve 2.5 μs (pulse width (pw_{90}) = 2.5 μs) pulses each followed by a 5 μs (pulse width (pw_{180}) = 5 μs) refocusing pulse, with all pulses separated by an interpulse delay (τ). After the pulse train, a terminal 90° observation pulse was applied. Measurements for the nutation series were made with the pulse excitation angle (θ) varied from 0° to 90° in 2.5° steps and both the interpulse delay and magnitude of the pulse offset fixed. The variance of the pulse excitation angle (θ) was accomplished by altering the strength of the B_1 field, whilst keeping the pulse duration constant to attain rotor synchronization. The discussion of rotor synchronization will always be with respect to the total filtering time (T_F), where $T_F = (24 \times \tau) + (12 \times pw_{90}) + (12 \times pw_{180})$.

Both the DIVAM and direct DIVAM experiments used a 90° pulse width of 2.5 μs, an interpulse delay (τ) of 1.67 μs, and a MAS rate of 20 kHz (T_F = 50 μs). These experiments were implemented in the same manner as in previously published works.[30,31]

Fig. 11. The effect of rotor synchronization on the selectivity of the refocused DIVAM pulse sequences for various dipolar coupling strengths and τ values, where ○ = 10 kHz, and ▽ = 25 kHz These simulations used real 100 kHz pulses with a MAS rate of 20 kHz, a 90° pulse width of 2.5 μs, a 180° pulse width of 5 μs, and a pulse offset of 1 kHz. The interpulse delay and total filtering time (T_F) are indicated at the top of each figure.

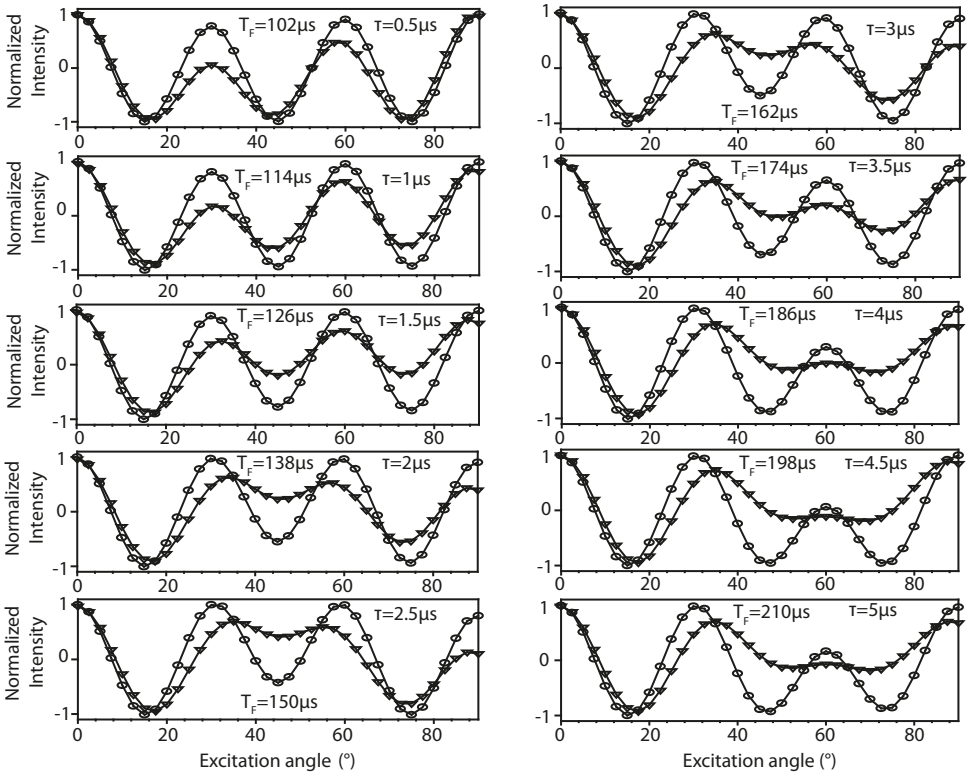

Can. J. Chem. Downloaded from www.nrcresearchpress.com by Xi'an Jiaotong University on 09/19/12
For personal use only.

Spin dynamics simulations

All simulations were carried out using SIMPSON 1.1.0[37] with an Intel Core 2 Duo 7200 processor. The refocused and direct DIVAM simulations were run separately for three different terms in the Hamiltonian corresponding to the isotropic frequency, chemical shift anisotropy (CSA), and the dipolar coupling. For each of these terms, the pulse sequence was simulated using real (soft) pulses and the strength of the Hamiltonian terms was varied in size from 0 to 50 kHz. These simulations were also run under timing conditions in which the total duration of the pulse train was either synchronized or not synchronized with the rotor. The chemical shift tensor convention used in SIMPSON is the Haeberlen–Mehring–Spiess convention,[40–42] and all discussions of simulation results are with the use of this convention.

The CSA and isotropic terms of the Hamiltonian were simulated as a one-spin system with the initial density matrix set as I_z. The dipolar coupling term of the Hamiltonian was simulated as a two-spin system with the initial density matrix set as $I_z^{(1)} + I_z^{(2)}$. At the end of the sequence, the I_z component of the density matrix was reported as a function of the pulse excitation angle (θ). For the dipolar coupling simulations, only the $I_z^{(1)}$ term of the density matrix was reported.

Simulations of the refocused and direct DIVAM sequence were implemented using the same pulse-train values as in the solid state NMR measurements (pw_{90} = 2.5 μs and pw_{180} = 5 μs). The rotor-synchronized simulations used a spinning speed of 20 kHz, while the non-rotor-synchronized simulations used a spinning speed of 25 kHz. All simulation used the direct method of calculation, 30 γ angles, 168 crystal orientations, and were powder averaged. For all simulations, two full phase cycles of the refocusing pulses were implemented (Table 1) with a pulse offset of 1 kHz.

Acknowledgements

We would like to acknowledge the assistance and expertise of Dr. David Siminovitch and the support of the Natural Sciences and Engineering Research Council of Canada (NSERC), Canadian Foundation for Innovation (CFI), The Royal Society, and the University of Lethbridge in this research.

References

(1) Dolbier, W. R., Jr. *J. Fluor. Chem.* **2005**, *126* (2), 157. doi:10.1016/j.jfluchem.2004.09.033.
(2) Park, J. W.; Seo, Y. A.; Kim, I.; Ha, C. S.; Aimi, K.; Ando, S. *Macromolecules* **2004**, *37* (2), 429. doi:10.1021/ma035402g.
(3) Nalwa, H. S. *J. Macromol. Sci. Rev. Macromol. Chem. Phys.* **1991**, *31*, 341.
(4) Harris, R. K.; Monti, G. A.; Holstein, P. Fluoropolymers. In *Solid State NMR of Polymers;* Ando, I., Asakura, T., Eds.; Elsevier: New York, 1998; pp 667–712.
(5) Harris, R. K.; Monti, G. A.; Holstein, P. ^{19}F NMR. In *Solid State NMR of Polymers;* Ando, I., Asakura, T., Eds.; Elsevier: New York, 1998; pp 253–266.
(6) Wormald, P.; Ameduri, B.; Harris, R. K.; Hazendonk, P. *Solid State Nucl. Magn. Reson.* **2006**, *30* (2), 114. doi:10.1016/j.ssnmr.2006.05.003.
(7) Wormald, P.; Apperley, D. C.; Beaume, F.; Harris, R. K.

Can. J. Chem. Downloaded from www.nrcresearchpress.com by Xi'an Jiaotong University on 09/19/12
For personal use only.

Polymer (Guildf.) **2003**, *44* (3), 643. doi:10.1016/S0032-3861(02)00821-2.
(8) Harris, R. K.; Jackson, P. *Chem. Rev.* **1991**, *91* (7), 1427. doi:10.1021/cr00007a008.
(9) Bennet, A. E.; Griffin, R. G.; Ok, J. H.; Vega, S. *J. Chem. Phys.* **1992**, *96* (11), 8624. doi:10.1063/1.462267.
(10) Caravatti, P.; Bodenhausen, G.; Ernst, R. R. *Chem. Phys. Lett.* **1982**, *89* (5), 363. doi:10.1016/0009-2614(82)80001-8.
(11) Caravatti, P.; Braunschweiler, L.; Ernst, R. R. *Chem. Phys. Lett.* **1983**, *100* (4), 305. doi:10.1016/0009-2614(83)80276-0.
(12) Bräuniger, T.; Wormald, P.; Hodgkinson, P. *Monatsh. Chem.* **2002**, *133* (12), 1549. doi:10.1007/s00706-002-0501-z.
(13) Bennett, A. E.; Rienstra, C. M.; Auger, M.; Lakshmi, K. V.; Griffin, R. G. *J. Chem. Phys.* **1995**, *103* (16), 6951. doi:10.1063/1.470372.
(14) Ando, S.; Harris, R. K.; Hazendonk, P.; Wormald, P. *Macromol. Rapid Commun.* **2005**, *26* (5), 345. doi:10.1002/marc.200400517.
(15) Schmidt-Rohr, K.; Spiess, H. W. *Multidimensional Solid State NMR and Polymers;* Academic Press: London, 1994.
(16) Ando, I., Asakura, T., Eds. *Solid State NMR of Polymers;* Elsevier: New York, 1998.
(17) Ando, S.; Harris, R. K.; Holstein, P.; Reinsberg, S. A.; Yamauchi, K. *Polymer (Guildf.)* **2001**, *42* (19), 8137. doi:10.1016/S0032-3861(01)00303-2.
(18) Ando, S.; Harris, R. K.; Reinsberg, S. A. *J. Magn. Reson.* **1999**, *141* (1), 91. doi:10.1006/jmre.1999.1866.
(19) Harris, D. J.; de Azevedo, E. R.; Bonagamba, T. J. *J. Magn. Reson.* **2003**, *162* (1), 67. doi:10.1016/S1090-7807(03)00043-0.
(20) Holstein, P.; Monti, G. A.; Harris, R. K. *Phys. Chem. Chem. Phys.* **1999**, *1* (15), 3549. doi:10.1039/a902556a.
(21) Hu, J. Z.; Taylor, C. M. V.; Pugmire, R. J.; Grant, D. M. *J. Magn. Reson.* **2001**, *152* (1), 7. doi:10.1006/jmre.2001.2380.
(22) Mao, J. D.; Schmidt-Rohr, K. *J. Magn. Reson.* **2003**, *162* (1), 217. doi:10.1016/S1090-7807(03)00012-0.
(23) Opella, S. J.; Frey, M. H. *J. Am. Chem. Soc.* **1979**, *101* (19), 5854. doi:10.1021/ja00513a079.
(24) Cai, W. Z.; Schmidt-Rohr, K.; Egger, N.; Gerharz, B.; Spiess, H. W. *Polymer (Guildf.)* **1993**, *34* (2), 267. doi:10.1016/0032-3861(93)90077-N.
(25) Clauss, J.; Schmidt-Rohr, K.; Adam, A.; Boeffel, C.; Spiess, H. W. *Macromolecules* **1992**, *25* (20), 5208. doi:10.1021/ma00046a015.
(26) Spiegel, S.; Schmidt-Rohr, K.; Boeffel, C.; Spiess, H. W. *Polymer (Guildf.)* **1993**, *34* (21), 4566. doi:10.1016/0032-3861(93)90166-8.
(27) Egger, N.; Schmidt-Rohr, K.; Blumich, B.; Domke, W. D.; Stapp, B. *J. Appl. Polym. Sci.* **1992**, *44* (2), 289. doi:10.1002/app.1992.070440213.
(28) Buda, A.; Demco, D. E.; Bertmer, M.; Blumich, B.; Reining, B.; Keul, H.; Hocker, H. *Solid State Nucl. Magn. Reson.* **2003**, *24* (1), 39. doi:10.1016/S0926-2040(03)00020-1.
(29) Liu, S. F.; Mao, J. D.; Schmidt-Rohr, K. *J. Magn. Reson.* **2002**, *155* (1), 15. doi:10.1006/jmre.2002.2503.
(30) Hazendonk, P.; Harris, R. K.; Ando, S.; Avalle, P. *J. Magn. Reson.* **2003**, *162* (1), 206. doi:10.1016/S1090-7807(03)00048-X.
(31) Hazendonk, P.; Wormald, P.; Montina, T. *J. Phys. Chem. A* **2008**, *112* (28), 6262. doi:10.1021/jp711489d.
(32) Hazendonk, P.; de Denus, C.; Iuga, A.; Cahoon, P.; Nilsson, B.; Iuga, D. *J. Inorg. Organomet. Polym. Mater.* **2006**, *16* (4), 343. doi:10.1007/s10904-006-9061-8.
(33) Borisov, A. S.; Hazendonk, P.; Hayes, P. *J. Inorg. Organomet. Polym. Mater.* **2008**, *18* (1), 163. doi:10.1007/s10904-007-9198-0.
(34) Bodenhausen, G. R.; Freeman, R.; Morris, G. A. *J. Magn. Reson.* **1976**, *23* (1), 171. doi:10.1016/0022-234(76)90150-5.
(35) Morris, G. A.; Freeman, R. *J. Magn. Reson.* **1978**, *29* (3), 433. doi:10.1016/0022-2364(78)90003-3.
(36) Rance, M.; Byrd, R. A. *J. Magn. Reson.* **1983**, *52* (2), 221. doi:10.1016/0022-2364(83)90190-7.
(37) Bak, M.; Rasmussen, J. T.; Nielsen, N. C. *J. Magn. Reson.* **2000**, *147* (2), 296. doi:10.1006/jmre.2000.2179.
(38) Liu, S. F.; Schmidt-Rohr, K. *Macromolecules* **2001**, *34* (24), 8416. doi:10.1021/ma0113576.
(39) Chen, Q.; Schmidt-Rohr, K. *Macromolecules* **2004**, *37* (16), 5995. doi:10.1021/ma049759b.
(40) Haeberlen, U. High Resolution NMR in Solids: Selective Averaging. In *Advances in Magnetic Resonance,* Suppl. 1; Academic Press: New York, 1976.
(41) Mehring, M. *Principles of High Resolution NMR in Solids;* Springer-Verlag: Berlin, 1983.
(42) Spiess, H. W. *NMR Basic Principles and Progress,* Vol. 15; Springer-Verlag: Berlin, 1978.

High-field multinuclear solid-state nuclear magnetic resonance (NMR) and first principle calculations in $MgSO_4$ polymorphs

Peter J. Pallister, Igor L. Moudrakovski, and John A. Ripmeester

Can. J. Chem. Downloaded from www.nrcresearchpress.com by Xi'an Jiaotong University on 09/19/12
For personal use only.

Abstract: A combination of solid-state nuclear magnetic resonance (NMR) and first principles calculations was applied to obtain ^{17}O, ^{25}Mg, and ^{33}S NMR parameters for two polymorphs of anhydrous magnesium sulfate. Working at the very high magnetic field of 21.14 T results in a dramatic improvement of resolution through a reduction of the effects of quadrupolar interactions and significant improvement in sensitivity. Experimental ^{25}Mg and ^{33}S spectra are dominated by quadrupolar interactions with quadrupolar parameters unique for each polymorph. In the case of ^{17}O, there is a substantial contribution of the chemical shift anisotropy. The use of multiple-quantum magic-angle spinning (MQMAS) experiments allows the resolution of distinct oxygen species and assignment of signals in the experimental ^{17}O spectrum. Chemical shielding constants and quadrupolar parameters for all three nuclei were calculated using plane wave pseudopotential density functional theory as implemented in the CASTEP computational package. The calculated NMR parameters are in very good agreement with the experimental results and help in signal assignment of the ^{17}O spectrum. The results suggest applicability of such a combined computational and experimental solid-state NMR approach for the refinement of crystallographic data.

Key words: multinuclear solid-state nuclear magnetic resonance (NMR), $MgSO_4$ polymorphs, ^{17}O, ^{25}Mg, ^{33}S, chemical shift anisotropy, electric field gradient, density functional theory (DFT) calculations.

Résumé : On a appliqué une combinaison de résonance magnétique nucléaire (RMN) à l'état solide et de calculs à partir de principes premiers pour obtenir les paramètres RMN du ^{17}O, du ^{25}Mg et du ^{33}S pour deux polymorphes du sulfate de magnésium anhydre. Opérant au champ magnétique très élevé de 21,14 T, les résultats comportent une amélioration dramatique de résolution par une réduction des effets des interactions quadripolaires et une amélioration significative de la sensibilité. Les spectres expérimentaux du ^{25}Mg et du ^{33}S sont dominés les interactions quadripolaires avec des paramètres quadripolaires uniques à chacun des polymorphes. Dans le cas du ^{17}O, une contribution substantielle de l'anisotropie du déplacement chimique est aussi observée. L'utilisation d'expériences rotation à l'angle magique à multiple quantum (RAMMQ) permet de résoudre les diverses espèces de noyaux d'oxygène et de faire une attribution aux signaux des spectres expérimentaux de ^{17}O. On a calculé les constantes de blindage chimique et les paramètres quadripolaires des trois noyaux en faisant appel à la théorie de la fonctionnelle de la densité avec pseudo-potentiel à onde plane telle que disponible dans le programme de calcul CASTEP. Les paramètres RMN calculés sont en très bon accord avec les résultats expérimentaux et ils sont utiles dans l'attribution des signaux des spectres du ^{17}O. Ces résultats suggèrent qu'une telle approche, de RMN à l'état solide expérimentale combinée à des calculs théoriques, pourrait s'appliquer au raffinement de données cristallographiques.

Mots-clés : résonance magnétique nucléaire (RMN) multinucléaire à l'état solide, $MgSO_4$ polymorphes, ^{17}O, ^{25}Mg, ^{33}S, anisotropie du déplacement chimique, gradient du champ électrique, calculs selon la théorie de la fonctionnelle de la densité (TFD).

[Traduit par la Rédaction]

Introduction

Recent developments in nuclear magnetic resonance (NMR) instrumentation, especially ultrahigh-field NMR magnets, combined with advances in computation of NMR parameters, significantly broadens the scope of solid-state (SS) NMR spectroscopy of materials. These advances are especially significant in studies concerned with low-γ, low natural abundance, and quadrupolar nuclei.[1] Another modern development that makes SS NMR an even more powerful tool in

Received 10 December 2010. Accepted 3 February 2011. Published at www.nrcresearchpress.com/cjc on 25 August 2011.

P.J. Pallister and J.A. Ripmeester. Steacie Institute for Molecular Sciences, National Research Council, 100 Sussex Drive, Ottawa, ON K1A 0R6, Canada; Department of Chemistry, Carleton University, 1125 Colonel By Drive, Ottawa, ON K1S 5B6, Canada.
I.L. Moudrakovski. Steacie Institute for Molecular Sciences, National Research Council, 100 Sussex Drive, Ottawa, ON K1A 0R6, Canada.

Corresponding author: I.L. Moudrakovski (e-mail: Igor.moudrakovski@nrc-cnrc.gc.ca).

This article is part of a Special Issue dedicated to Professor Roderick E. Wasylishen in recognition of his contribution to Solid State NMR in Canada.

Can. J. Chem. Downloaded from www.nrcresearchpress.com by Xi'an Jiaotong University on 09/19/12
For personal use only.

materials research is quantum-chemical calculations of NMR parameters. The complicated nature of interactions in solid-state NMR poses some serious challenges in the analysis of spectral data and the accurate extraction of shielding and quadrupolar parameters. Correct interpretation of the experimental spectra may require some elaborate quantum-mechanical calculations and spectral simulations. First-principles calculations may well complement experimental data and help in the interpretation and assignments of the spectra. Recent development of the gauge including projector augment wave (GIPAW)[2] formalism, implemented within the CASTEP[3] computational package, is particularly useful for solid-state NMR. Several recent studies have demonstrated that highly accurate evaluation of SS NMR parameters is possible,[4–8] with most examples coming from Earth sciences and silicates research. Thanks to the availability of more user-friendly quantum-chemical software and advances in computational hardware, today this task can be accomplished as never before.

In the current study, we explore a combination of experimental multinuclear solid-state (SS) NMR at a very high magnetic field of 21.14 T with quantum-mechanical computations to study two polymorphs of anhydrous magnesium sulphate. It is considered that magnesium sulfates are important planetary rock-forming materials in our solar system.[9,10] Specifically, $MgSO_4$ is considered to be an important mineral in putative carbonatite lavas on Venus.[9] In the outer solar system, $MgSO_4$ may well be the most important leachate from chondritic materials.[10] In many respects, the importance of magnesium sulfates as a planetary mineral resembles those of magnesium ortho- and meta-silicates in the Earth's mantle, the latter being recently studied comprehensively with a combination of multinuclear SS NMR and first principles computations.[8]

Below about 800 K, anhydrous magnesium sulfate is known to coexist in two polymorphic forms. The α-phase can be grown from a solution of MgO in H_2SO_4. The structure of the α-form is orthorhombic with space group *Cmcm* ($Z = 4$) and unit-cell dimensions $a = 5.182$ Å, $b = 7.893$ Å, and $c = 6.506$ Å.[11] The β-$MgSO_4$ can be formed either by thermal dehydration of $MgSO_4$ hydrates or by heating α-$MgSO_4$ to 868 K[12] followed by quenching to room temperature. The structure of the β-form is orthorhombic with space group *Pbnm* and unit-cell dimensions $a = 4.742$ Å, $b = 8.575$ Å, and $c = 6.699$ Å.[13] After quenching, β-$MgSO_4$ persists in this form indefinitely. The polymorphs are structurally very similar and consist of edge-sharing MgO_6 octahedra arranged in infinite ribbons and cross-linked by sheets of pseudo-close-packed SO_4 tetrahedra. The latter, however, are oriented in α- and β-forms in different planes. The structural similarities and differences of α- and β-forms were considered in some detail in a recent neutron powder diffraction study.[14] One needs to emphasize that due to the difficulties of growing single crystals of highly hygroscopic $MgSO_4$, the earlier structures were solved from X-ray powder data and were later refined using powder neutron diffraction. The first single crystal study of β-$MgSO_4$ was published only in 2007,[15] soon after the neutron powder diffraction refinement for both α- and β-polymorphs.

$MgSO_4$ poses some serious solid-state NMR challenges. All three nuclei are quadrupolar, and their SS NMR signals are broadened by quadrupolar interactions.[16–18] Two of the three nuclei (^{25}Mg and ^{33}S) have very low gammas, and only one of them has a moderate natural abundance (^{25}Mg 10%, ^{33}S 0.76%, ^{17}O 0.037%).[19] The combination of the above results in a very poor NMR receptivity (see Table 1). In this work, we report the results of a solid-state NMR study using all three nuclei in the α- and β-forms of anhydrous magnesium sulfate at a magnetic field of 21 T. At this very high magnetic field, the effects of the quadrupolar interactions are reduced significantly[16,17] and the sensitivity and accuracy in determining the NMR parameters improve dramatically. We demonstrate that for all three nuclei the quadrupolar effects dominate the NMR spectra. A complete analysis of experimental SS NMR parameters has become possible with the use of the CASTEP[2,3] computational package.

It is always of great interest to support known structural data obtained through X-ray or neutron diffraction methods with additional techniques. The use of a short-range order interaction technique such as NMR is expected to complement the existing structural data obtained through previous diffraction methods. As well, with the aid of computation, an attempt to distinguish polymorphs with the same chemical composition through SS NMR can be accomplished. The possibility of assessing the structural details in β-$MgSO_4$ obtained by two different diffraction techniques using SS NMR in conjunction with ab initio calculations is another expected outcome of this work.

Experimental

Materials

Both $MgSO_4$ polymorphs studied in this work were synthesized as ^{17}O enriched compounds. ^{17}O enriched sulfuric acid was prepared by reacting sulfuryl chloride (SO_2Cl_2, Sigma-Aldrich) with $H_2{}^{17}O$ (Cambridge Isotope Laboratories, Inc., 17.8% enrichment). The sulfuric acid obtained was added in about 20 mol% excess to a small quantity (~0.3 g) of freshly calcined MgO (Sigma-Aldrich) in a small Pt crucible and the slurry was left to evaporate over a hot plate (~300 °C). After complete evaporation of the liquid sulphuric acid, the crucible was put in an oven and kept there at a constant temperature of 450 °C overnight. The X-ray diffraction pattern of the resulting powder was that of α-MgSO4.[11,14] The β-phase of $MgSO_4$ was produced by heating the α-phase at 650 °C.[12] Because of the dilution of ^{17}O in the course of synthesis, the final enrichment was estimated to be in the range of 5%–7%.

NMR spectroscopy

All NMR measurements were performed on a Bruker Avance-II 900 MHz instrument (magnetic field of 21.14 T) at the National Ultrahigh-Field NMR Facility for Solids (Ottawa, ON). Larmor frequencies for ^{17}O, ^{25}Mg, and ^{33}S were 122.02, 55.1, and 69.09 MHz, respectively. Static powder spectra were obtained on a homebuilt 7 mm solenoid probe. A Hahn echo pulse sequence optimized to accurately reproduce the powder line shapes[20] and a quadrupolar Carr–Purcell–Meiboom–Gill (QCPMG) sequence[21] were used in static experiments. Between 250 and 2000 scans were acquired for all nuclei with relaxation delays ranging from 10 to 40 s. A dual frequency sweep (DFS) sensitivity enhancing technique[22] was

Table 1. Magnetic resonance properties of nuclei in $MgSO_4$.[19]

Isotope	Spin	Natural abundance (%)	Magnetogyric ratio γ (10^7 rad T^{-1} s^{-1})	Larmor frequency at 21.1 T (MHz)	Qudrupole moment (fm^2)	Linewidth factor (l/fm^3)	Receptivity (relative to ^{13}C)
^{17}O	5/2	0.037	–1.6388	122.02	–2.56	2.1	0.065
^{25}Mg	5/2	10.00	2.0557	55.1	19.94	130	1.58
^{33}S	3/2	0.76	–3.6281	69.09	–6.78	61	0.101

used in some of the experiments, particularly with ^{33}S. The optimal relaxation delays for each compound and nucleus were found from three to four short (16–32 scans) runs. The magic-angle spinning (MAS) experiments were performed using Bruker 4 mm (^{17}O and ^{25}Mg) and 7 mm (^{33}S) MAS probes with dry nitrogen as a carrier gas. Two-dimensional multiple-quantum (MQ) MAS experiments on ^{17}O were performed using a phase-modulated split-t_1 pulse sequence[23,24] with rotor synchronization. The spectra were externally referenced to neat H_2O (^{17}O, $\delta = 0$ ppm), 1 mol/L solution of $Mg(NO_3)_2$ (^{25}Mg, $\delta = 0$ ppm), and 2 mol/L solution of Cs_2SO_4 (^{33}S, $\delta = 333.0$ ppm from CS_2[25]).

Spectral simulations

Analytical simulations of experimental spectra were carried out with the WSolids[26] and DMFit[27] simulation packages. In all simulations, we first fitted the MAS spectra, which provided the isotropic chemical shifts (δ_{iso}), quadrupolar constants (C_Q), and quadrupolar asymmetry parameter (η_Q). These parameters were subsequently used in simulations of the static powder pattern. Special attention was given to reproducing the spectral discontinuities and shoulders in fitting the spectra.

Quantum-chemical calculations

All calculations were performed using the CASTEP[3] density functional theory code using the GIPAW[2] algorithm. The version used in this work is integrated within the Accelrys Materials Studio 4.4 suite (Accelrys, Inc., San Diego, CA). The computations use the generalized gradient approximation (GGA) and Perdew–Burke–Ernzerhof (PBE) functional,[28,29] and the core–valence interactions were described by ultrasoft pseudopotentials.[2b] Integrations over the Brillouin zone were done using a Monkhorst–Pack grid with *k*-point spacings generally being less than 0.04 $Å^{-1}$.[30] Crystallographic data used in the calculations were taken from the literature and the corresponding references are given in the text. The calculations produce the absolute shielding tensor (σ), quadrupolar coupling constant (C_Q), and asymmetry (η_Q). The later two parameters can be compared to the experimentally measured C_Q and η_Q directly. In the case of σ, however, some conversion needs to be done before comparing them with the experimentally measured chemical shifts. The isotropic chemical shift (δ_{iso}) relates to the isotropic shielding: $\sigma_{iso} = 1/3\mathrm{Tr}\{\sigma\}$ as $\delta_{iso} = -(\sigma_{iso} - \sigma_{ref})$, where σ_{ref} is the isotropic shielding calculated on the reference material with a well-defined structure and known chemical shift. The references used for the nuclei studied in this work are as follows: For ^{25}Mg, the reference shielding was obtained from a correlation of the calculated shielding constants and the experimental chemical shifts in numerous magnesium compounds, with $\sigma_{iso} = -1.072(\pm 0.036) \times \delta_{iso} + 566.06(\pm 0.99)$.[31] For ^{33}S, the reference shielding is again based on a correlation where σ_{ref} (^{33}S) = 434.1 ppm (updated data from ref. 32). For ^{17}O, the chemical shielding was referenced to the well-documented O1 site in forsterite as in ref. 8, with a σ_{ref} (^{17}O) value of 255.0 ppm.

Results and discussion

Structural details of the system studied

Table 2 shows the structural parameters for α-$MgSO_4$ and both reported structures of β-$MgSO_4$ from the most recent reports.[14,15] As can be seen in Table 2, the structures for the two polymorphs of $MgSO_4$ are somewhat similar, yet they do have significant differences. Both polymorphs crystallize with an orthorhombic lattice but α-$MgSO_4$ crystallizes in space group *Cmcm*, whereas β-$MgSO_4$ crystallizes in space group *Pbnm* or *Pnma*. The lattice volume is approximately the same for both polymorphs, yet the individual lattice parameters vary significantly. The site symmetry of the separate atoms in each cell is also quite different between the polymorphs. For Mg and S, each polymorph has only one crystallographically unique site. The most significant differences between the two polymorphs is the number of crystallographically inequivalent oxygen sites: α-$MgSO_4$ has two unique oxygen sites with a ratio of 1:1, while β-$MgSO_4$ has three sites with a ratio of 2:1:1. When examining the two reported structures of β-$MgSO_4$, it can be seen that the differences between the two are quite small. It is therefore interesting to test whether the first principle calculations are capable of distinguishing the differences and how accurately they can reproduce the experiment.

^{25}Mg results

Although ^{25}Mg has the highest natural abundance of all the nuclei examined in this work, it also has the largest quadrupole moment and the smallest magnetogyric ratio. With this in mind, one may expect that the quadrupolar interactions would dominate the NMR spectra of ^{25}Mg in $MgSO_4$. The ^{25}Mg natural abundance SS NMR spectra obtained at 21.1 T for α-$MgSO_4$ and β-$MgSO_4$ are shown in Figs. 1 and 2. Both stationary and MAS spectra are shown, obtained with Hahn echo and QCPMG pulse sequences. The parameters extracted from the experimental spectra together with the CASTEP computational results can be found in Table 3. The quadrupolar interaction indeed dominates the experimental ^{25}Mg spectra with the magnitudes differing significantly for α- and β-$MgSO_4$ polymorphs. In fact, the determined values of $C_Q = 7.41 \pm 0.05$ MHz and $C_Q = 10.4 \pm 0.1$ MHz in α- and β-$MgSO_4$, respectively, are among the largest observed for magnesium salts, where typically $C_Q < 5$ MHz for ^{25}Mg.[18,31,33–39] The quadrupolar asymmetry parameter, η_Q, is also quite different for the two polymorphs. ^{25}Mg in α-$MgSO_4$ has an $\eta_Q = 0.35 \pm 0.02$, whereas that of β-$MgSO_4$ is practically equal to 1.0. With just the ^{25}Mg quadrupolar parameters alone it is

Can. J. Chem. Downloaded from www.nrcresearchpress.com by Xi'an Jiaotong University on 09/19/12
For personal use only.

Can. J. Chem. Downloaded from www.nrcresearchpress.com by Xi'an Jiaotong University on 09/19/12
For personal use only.

Table 2. Structural details of $MgSO_4$ polymorphs.

Parameter	α-$MgSO_4$ (XPD[a])[14]	β-$MgSO_4$ (NPD[b])[14]	β-$MgSO_4$ (SCXRD[c])[15]
Lattice	Orthorhombic	Orthorhombic	Orthorhombic
a (Å)	5.1747	4.7460	8.5787
b (Å)	7.8756	8.5831	6.6953
c (Å)	6.4952	6.7093	4.7438
V (Å^3)	264.70	273.31	272.47
Z	6	4	4
Space group	*Cmcm*	*Pbnm*	*Pnma*
Mg site symmetry	C_{2h}	C_i	C_i
S site symmetry	C_{2v}	C_s	C_s
O1 site symmetry	C_s	C_s	C_1
O2 site symmetry	C_s	C_s	C_s
O3 site symmetry	—	C_1	C_s

[a]XPD: X-ray powder diffraction.
[b]NPD: neutron powder diffraction.
[c]SCXRD: single-crystal X-ray diffraction.

Fig. 1. Experimental and simulated ^{25}Mg spectra of α-$MgSO_4$: (A) stationary sample (both Hahn echo and QCPMG are shown), (B) MAS (both Hahn echo and rotor-synchronized QCPMG are shown), and (C) calculated orientations of the electric field gradient (EFG) and CSA tensors. Analytical simulations of the spectra were performed with WSolids[26] for stationary spectra and DMFit[27] for the MAS experiments.

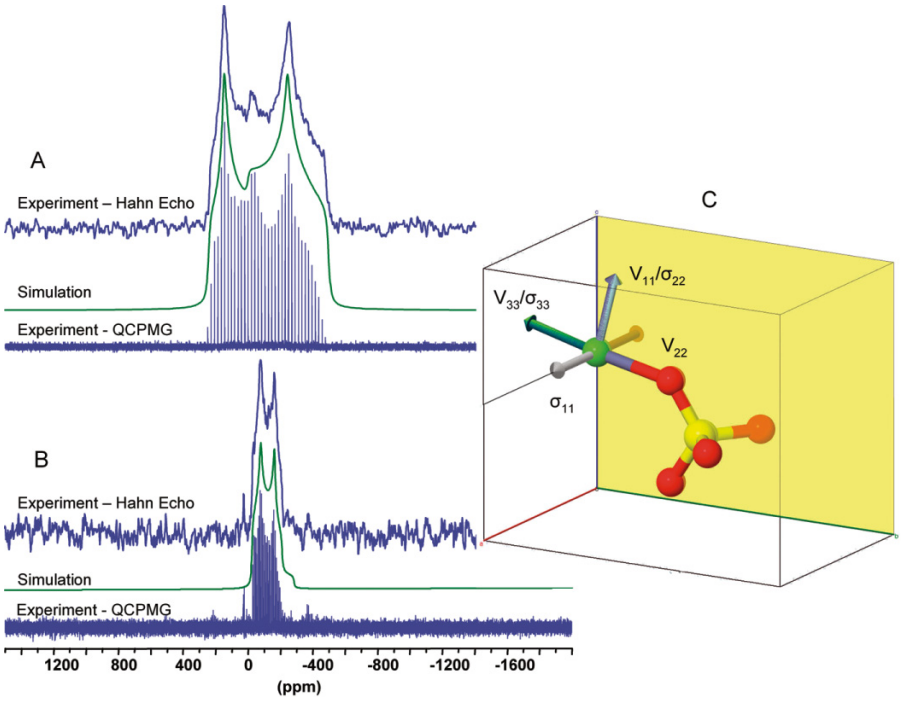

possible to differentiate these two polymorphs based on the SS NMR spectra. The isotropic chemical shifts (δ_{iso}) for α- and β-$MgSO_4$ are –8.1 ± 1.0 and 0.2 ± 2.0 ppm, respectively, which is well within the range of the shifts expected for a compound such as $MgSO_4$.[31] Typically for octahedrally oxygen-coordinated Mg compounds, the isotropic chemical shift ranges from ~ –10 ppm to ~10 ppm.[31,33,39] Since the range of ^{25}Mg chemical shifts for oxygen-coordinated magnesium is relatively small, it is not surprising that the chemical shift anisotropy (CSA) for ^{25}Mg in both α- and β-$MgSO_4$ is quite small. Considering the scale of the quadrupolar interactions for both polymorphs, the accuracy of the experimental ^{25}Mg CSA is rather low. The experimental values can found in Table 3. Due to a considerably larger magnitude of the quadrupolar interactions for β-$MgSO_4$, detection of the CSA is even more difficult, and only an estimate for the upper limit of the anisotropy (σ_{aniso}) is reported.

Data in Table 3 demonstrate very reasonable agreement between experimental and calculated ^{25}Mg NMR parameters. The isotropic chemical shift was predicted accurately for ^{25}Mg in α-$MgSO_4$, yet was slightly overestimated for both calculations in β-$MgSO_4$. CASTEP was also able to predict the scale of the ^{25}Mg CSA for both polymorphs, and the parameters match quite well with the experimental values for σ_{aniso}, η_{CSA}, and Euler angles α, β, and γ. The calculated quadrupolar parameters are also in good agreement with the experiment. Although the calculated quadrupolar coupling constant for both polymorphs was slightly overestimated, the prediction

Fig. 2. Experimental and simulated ^{25}Mg spectra of β-$MgSO_4$: (A) stationary sample with both Hahn echo and QCPMG experiments shown, (B) MAS at 16 kHz with rotor-synchronized QCPMG, and (C) calculated orientations of the EFG and CSA tensors. Analytical simulations of the spectra were performed with WSolids[26] for stationary spectra and DMFit[27] for the MAS experiments, and included both quadrupolar interactions and the CSA.

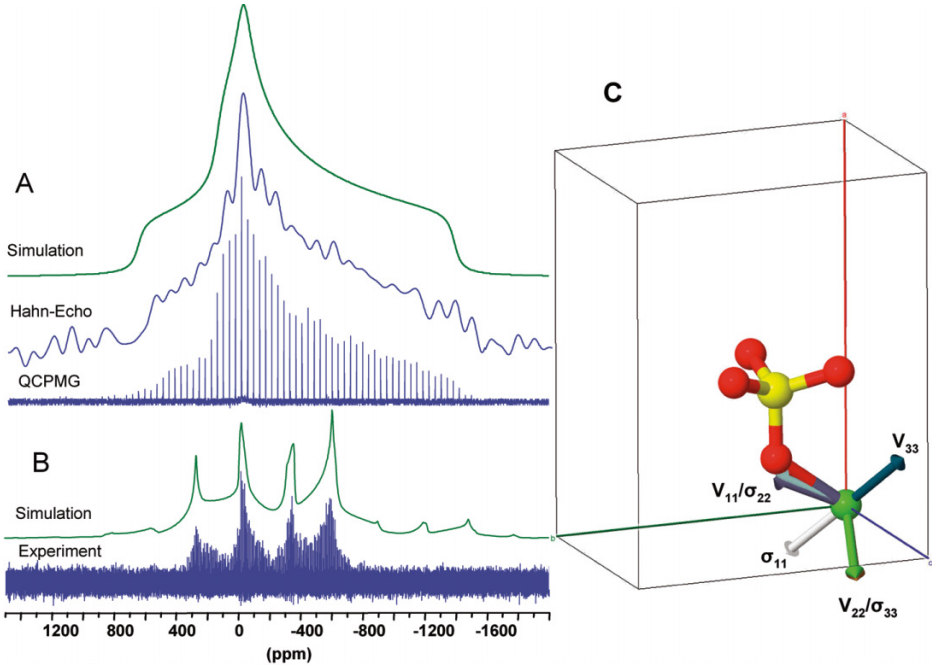

of η_Q, was good for both polymorphs. Looking at the two sets of calculated data for β-$MgSO_4$, one can see that the calculations for the NPD structure and the single crystal XRD structure produce somewhat different results. Notwithstanding, from the ^{25}Mg parameters alone it is difficult to conclude if one structure produced more accurate calculations than the other. The calculated isotropic shifts were overestimated in both cases, although the single crystal diffraction structure calculations produced a result closer to the measured shift of 0.2 ppm. The calculated quadrupolar coupling constants for the NPD and the XRD data are much the same, with both structures producing overestimated values of C_Q's. In this case, though, the neutron powder diffraction structure calculation produced a C_Q closer to the measured value of 10.4 MHz. Once again, at this stage it is hard to discern if one structure more accurately represents the actual room temperature structure of β-$MgSO_4$.

The CASTEP calculations also provide orientations of the CSA and EFG tensors for all atoms of interest. This is particularly useful for assisting in analyzing the fine structural details in a given material. For the case of magnesium in both polymorphs, the crystallographically unique magnesium site is present in an octahedral environment of oxygen atoms. However, as can be seen in Table 2, the point group symmetry of Mg sites in $MgSO_4$ is far from perfectly octahedral. For α-$MgSO_4$, magnesium is present in a C_{2h} symmetry and the relevant symmetry operations present at the magnesium site can be seen in Fig. 1B. For this type of symmetry, it has been shown that the principal components of the symmetric part of the shielding tensor are independent of each other.[40,41] Thus, one might not necessarily expect an axially symmetric shielding tensor with these restrictions on the principal components of the shielding tensor.[42] Indeed, the shielding asymmetry parameter, η_{CSA}, for ^{25}Mg in α-$MgSO_4$ shows a nonaxially symmetric tensor with $\eta_{CSA} = 0.8 \pm 0.2$. A similar argument can be made for the axially symmetric nature of the EFG tensor.[43] In agreement, the quadrupolar asymmetry parameter for ^{25}Mg in α-$MgSO_4$ shows a nonaxially symmetric EFG tensor with $\eta_Q = 0.35 \pm 0.02$. Examination of the calculated tensors for ^{25}Mg in α-$MgSO_4$ (Fig. 1B) uncovers some interesting details. The largest calculated components of the EFG and CSA tensors, V_{33} and σ_{33}, both lie in the mirror plane through the magnesium atom. CASTEP also predicts that the V_{33} and σ_{33} components are coincident with the Euler angle $\beta = 0°$, which is what is observed experimentally. The V_{33} and σ_{33} components also point directly towards one of the oxygen atoms that is part of the Mg–O pseudo-octahedron. Additionally, the V_{22} and σ_{11} components point along the C_2 proper rotation axis through the magnesium. The single unique Mg site in β-$MgSO_4$ is slightly different from that of α-$MgSO_4$. In β-$MgSO_4$, Mg is present in a C_i site, which means one would again not expect an axially symmetric CSA or EFG tensor.[41–43] Although the asymmetry parameter of the CSA tensor, η_{CSA}, could not be accurately measured due to the dominance of the EFG interaction, the quadrupolar asymmetry parameter is certainly not axially symmetric with $\eta_Q = 1.0$. The calculated EFG and CSA tensor orientations for Mg in β-$MgSO_4$ are shown in Fig. 2B. Since there is only a centre of inversion at the Mg site in β-$MgSO_4$, there is little to constrain the tensor orientations on the basis of symmetry. However, the largest component of the CSA tensor, σ_{33}, appears to point towards one of the oxygen atoms of the Mg–O pseudo-octahedron. Although it might seem that V_{33} is pointing towards another of the oxygen atoms in the octahedron, the deviation is large enough that this might not necessarily be the case.

Can. J. Chem. Downloaded from www.nrcresearchpress.com by Xi'an Jiaotong University on 09/19/12
For personal use only.

Table 3. Experimental and calculated ^{25}Mg, ^{33}S, and ^{17}O NMR parameters for $MgSO_4$ polymorphs.

	NMR parameters					
Polymorph and nucleus	$\delta_{iso}/\sigma_{iso}$ [δ_{iso}^{calcd}] (ppm)[a]	C_Q (MHz)[b]	η_Q[c]	$\Delta\sigma_{aniso}$ (ppm)[d]	η_{CSA} [e]	{α, β, γ} (°)[f]
α-$MgSO_4$ [g]						
^{25}Mg	–8.1±1.0	7.41±0.05	0.35±0.02	19.5±2.0	0.8±0.2	{0, 0, 90}
CASTEP	576.45 [–10.4]	–8.89	0.45	17.36	0.45	{0, 0, 90}
^{33}S	313.1±0.5	2.14±0.05	0.91±0.05	–51.5±5	1.0±0.2	{90, 90, 0}
CASTEP	118.81 [315.3]	–1.85	0.88	49.91	0.97	{90, 90, 180}
^{17}O (site1)	148.6±0.3	8.24±0.06	0.21±0.05	77±10	0.18±0.1	{0, 10, 0}
^{17}O (site2)	145.5±0.3	8.25±0.06	0.23±0.05	128±15	0.15±0.1	{90, 180, 270}
CASTEP (site1)	108.77 [146.23]	–8.03	0.20	80.12	0.21	{0, 10, 0}
CASTEP (site2)	111.31 [143.69]	–8.47	0.25	134.83	0.16	{90, 175, 270}
β-$MgSO_4$						
^{25}Mg	0.2±3.0	10.4±0.1	1.00±0.05	<35	—	—
CASTEP (NPD)[g]	579.59 [–13.53]	12.00	0.95	28.58	0.68	{270, 90, 180}
CASTEP (SCXRD)[h]	576.63 [–10.57]	12.54	0.91	28.25	0.74	{90, 90, 180}
^{33}S	316.8±0.5	2.00±0.05	0.11±0.05	–37.6±5	0.0±0.2	{90, 175, 10}
CASTEP (NPD)[g]	126.88 [307.22]	–1.14	0.19	–34.30	0.04	{180, 90, 270}
CASTEP (SCXRD)[h]	120.89 [313.21]	–1.84	0.33	–40.24	0.14	{180, 90, 185}
^{17}O (site1)	145.3±0.3	7.77±0.07	0.16±0.06	80±20	0.25±0.2	{–20, 5, 10}
^{17}O (site2)	145.7±0.3	8.40±0.07	0.25±0.05	115±20	0.15±0.2	{–90, 5, 10}
^{17}O (site3)	146.6±0.3	8.30±0.07	0.20±0.05	100±20	0.10±0.2	{90, 5, 90}
CASTEP (site1) (NPD)[g]	117.81 [137.19]	–7.94	0.18	97.47	0.20	{10, 5, 160}
CASTEP (site2) (NPD)[g]	121.97 [133.03]	–8.00	0.23	109.88	0.06	{90, 5, 90}
CASTEP (site3) (NPD)[g]	127.13 [127.87]	–7.89	0.29	111.98	0.12	{90, 5, 270}
CASTEP (site1) (SCXRD)[h]	115.91 [139.09]	–7.89	0.17	94.61	0.23	{190, 5, 160}
CASTEP (site2) (SCXRD)[h]	115.44 [139.56]	–8.41	0.27	130.36	0.14	{90, 5, 270}
CASTEP (site3) (SCXRD)[h]	114.55 [140.45]	–8.31	0.21	118.84	0.10	{270, 5, 90}

[a] δ_{iso}^{calcd} obtained as $\delta_{iso} = -(\sigma_{iso} - \sigma_{ref})$ with σ_{ref} defined in the experimental section.

[b] Although the calculations produce the sign of the C_Q, only the magnitude can be obtained in our experiments.

[c] η_Q is defined as $|V_{11} - V_{22}|/V_{33}$.

[d] The Haeberlen convention[44,45] is used in CASTEP with the anisotropy defined as $\sigma_{aniso} = \sigma_{33} - (\sigma_{11} + \sigma_{22})/2$.

[e] Asymmetry parameter (η_{CSA}) is defined as $\eta = (\sigma_{22} - \sigma_{11})/(\sigma_{33} - \sigma_{iso})$. Principal components of the symmetric shielding tensor are ordered as $|\sigma_{33} - \sigma_{iso}| \geq |\sigma_{11} - \sigma_{iso}| \geq |\sigma_{22} - \sigma_{iso}|$.

[f] α, β, and γ are Euler angles defining the relative orientation of the CSA and EFG tensors.[45,46] Accuracy is not expected to be better than ±10°.

[g] Calculations were performed on geometry optimized structures from NPD data.[14]

[h] Calculations were performed on geometry optimized structures from SCXRD data.[15]

^{33}S results

Sulfur-33 has a considerably lower natural abundance from that of ^{25}Mg making it quite a difficult nucleus to study. However, it has a larger magnetogyric ratio and smaller quadrupole moment than that of ^{25}Mg. As such, one might not expect the quadrupolar interaction to necessarily dominate the ^{33}S SS spectra as much as in the case of ^{25}Mg. The ^{33}S natural abundance SS NMR spectra taken at 21.1 T for α- and β-$MgSO_4$ can be seen in Figs. 3A and 3C. The NMR parameters extracted from the experimental spectra along with the calculations are summarized in Table 3. Indeed, the quadrupolar interactions do not dominate in the case of ^{33}S as they did for ^{25}Mg and CSA parameters could be reliably extracted (Table 3). The experimentally determined quadrupolar coupling constants were $C_Q = 2.14 \pm 0.05$ MHz for ^{33}S in α-$MgSO_4$ and $C_Q = 2.00 \pm 0.05$ MHz for β-$MgSO_4$. Although the magnitude of the quadrupolar interaction is quite similar for both α- and β-$MgSO_4$, the asymmetry parameters, η_Q, are quite different. For α-$MgSO_4$ it is nearly completely asymmetric with $\eta_Q = 0.91 \pm 0.05$, whereas in β-$MgSO_4$ the ^{33}S EFG tensor deviates only slightly from being axially symmetric with $\eta_Q = 0.11 \pm 0.05$. This gives another distinctive characteristic for the two polymorphs. In terms of isotropic chemical shifts for ^{33}S sites in α- and β-$MgSO_4$, the values are very similar to each other with $\delta_{iso} = 313.1 \pm 0.5$ ppm for α-$MgSO_4$ and $\delta_{iso} = 316.8 \pm 0.5$ ppm for β-$MgSO_4$. This is not surprising since the isotropic chemical shift range for ^{33}S in anhydrous sulfates is known to be quite narrow.[18,32] At high magnetic fields, the presence of the CSA can potentially complicate the spectra considerably. However, for the given case there is a discernable and measurable difference between the anisotropy in the sulfur sites of the two polymorphs. α-$MgSO_4$ has a larger chemical shielding anisotropy for ^{33}S than does β-$MgSO_4$, with $\sigma_{aniso} = -51.5 \pm 5.0$ ppm for ^{33}S α-$MgSO_4$ and $\sigma_{aniso} = -36.6 \pm 5.0$ ppm for ^{33}S in β-$MgSO_4$ (Table 3).

Can. J. Chem. Downloaded from www.nrcresearchpress.com by Xi'an Jiaotong University on 09/19/12
For personal use only.

Can. J. Chem. Downloaded from www.nrcresearchpress.com by Xi'an Jiaotong University on 09/19/12
For personal use only.

Fig. 3. Experimental and simulated ^{33}S spectra of (A) α-$MgSO_4$ and (B) β-$MgSO_4$. Traces a′ and c′ are the spectral simulations accounting only for quadrupolar interactions. Traces a″ and c″ are the fits that also include the CSA. The spectral fits to the MAS spectra account for quadrupolar interactions only. (B) and (D) demonstrate the calculated orientations of the EFG and CSA tensors of sulfur nucleus in α- and β-polymorphs, respectively. Dotted vertical lines indicate positions of singularities in the spectra. Note the discrepancies between the simulations and the experiment when only quadrupolar interaction are considered (traces a′ and c′).

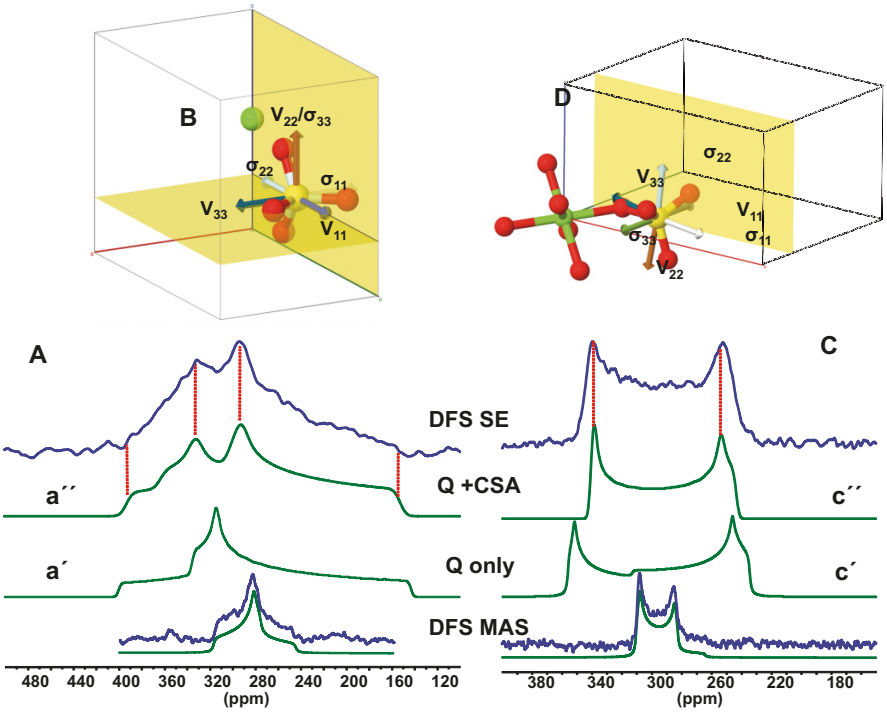

It is again of particular interest to compare the calculated NMR parameters to those obtained experimentally. It can be seen from Table 3 that overall agreement between ^{33}S experiments and calculations are very good. The CASTEP calculations for α-$MgSO_4$ reproduce quite well the isotropic chemical shift of sulfur. The quadrupolar coupling constant is only slightly underestimated and the asymmetry parameter is predicted very accurately. The magnitude of the anisotropy parameter, σ_{aniso}, was also accurately predicted for ^{33}S in α-$MgSO_4$, despite having an opposite sign (in Haeberlen convention,[45,46] when the asymmetry η_{CSA} is close to 1, the reverse of the anisotropy sign is not uncommon). The calculated value for the asymmetry of the CSA, η_{CSA}, and the Euler angles, $\{\alpha, \beta, \gamma\}$, also match the experiment well. The CASTEP calculations reproduce the ^{33}S experimental results quite accurately for the β-polymorph too. The calculated isotropic chemical shift and the quadrupolar parameters match the experimental values well. The chemical shielding anisotropy is also predicted accurately in both magnitude and sign. When examining the calculated results for ^{33}S for the two reported structures of β-$MgSO_4$, a few notable differences can be seen. Both the calculated isotropic chemical shift and the quadrupolar coupling constant for the structure determined through single crystal X-ray diffraction reproduce the experimental parameters more accurately. The only parameter from the CASTEP calculations employing the neutron powder diffraction structure, which matched the experiment more closely than that from the single crystal, was the quadrupolar asymmetry parameter, η_Q. Yet, the predicted η_Q from the single crystal structure is also well within experimental error of the experimental value. Altogether, this suggests that the atomic coordinates obtained in a single crystal study of β-$MgSO_4$ are more accurate and reliable than those from the neutron powder diffraction study. Although it is not entirely correct to compare directly *R*-factors from the SCXRD and NPD studies, we note that the single crystal XRD study of β-$MgSO_4$ reports $R = 0.017$[16], when the NPD for the same polymorph resulted in $R = 0.036$[15].

Further examination of the CASTEP calculations and structural features of sulfur in $MgSO_4$ shows some interesting details. Sulfur is, of course, in a tetrahedrally coordinated oxygen environment in the SO_4^{2-} anion. However, the symmetry present at the sulfur site is quite far from being perfectly tetrahedral. Table 2 and Figs. 3B and 3D show the point group symmetry present at the sulfur site in α- and β-$MgSO_4$. Similar to the previous case of ^{25}Mg, it is interesting to examine the relationship, if any, between the local environment and the NMR parameters for ^{33}S, both experimental and calculated. For α-$MgSO_4$ (Fig. 3B), symmetry of sulfur site is C_{2v}. For this type of symmetry there are three independent components of the symmetric part of the shielding tensor.[40,41] So again, one might not necessarily expect an axially symmetric shielding tensor with these restrictions on the principal components of the shielding tensor.[40] Indeed, the experimental results for ^{33}S in α-$MgSO_4$ show a nonaxially symmetric shielding tensor with $\eta_{CSA} = 1.0 \pm 0.2$. A similar argument can be made for the case of the EFG tensor[43] and the experimentally determined quadrupolar asymmetry parameter is far from axially symmetric with $\eta_Q = 0.91 \pm 0.05$. Examining the calculated tensor orientations for α-$MgSO_4$ in Fig. 3B

Fig. 4. Experimental and simulated ^{17}O spectra of α-$MgSO_4$ at (A) 21.1 T and (B) 9.4 T. Traces a′ and b′ are the spectral simulations accounting only for quadrupolar interactions. Traces a″ and b″ are the fits that also include the CSA. The spectral fits to the MAS spectra account for both quadrupolar interactions and the CSA. Dotted vertical lines indicate positions of singularities in the spectra. For the online colour version, red (upper) traces in the simulated spectra correspond to the sums of the contributing individual sites, shown correspondingly in green, violet, and black.

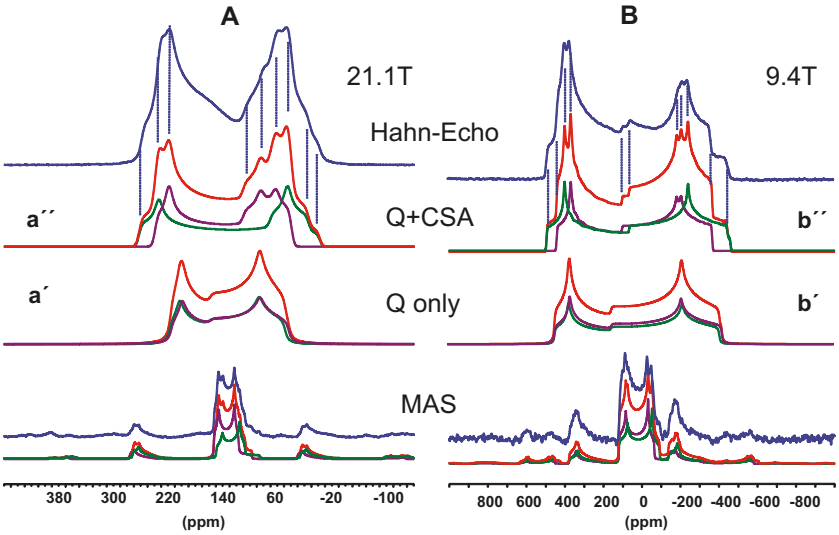

reveals some additional details. The largest component of the EFG tensor, V_{33}, is restricted to one of the mirror planes through the sulfur atom while σ_{33} lies in the other mirror plane. Additionally, V_{11} and σ_{22} are calculated to be along the C_2 proper rotation axis through the sulfur site. With these orientations, the angle between the largest components of the EFG and CSA tensor, V_{33} and σ_{33}, is 90°, which is totally in agreement with experiment (Table 3). The situation for sulfur in β-$MgSO_4$ is quite different from that of α-$MgSO_4$. The symmetry of the site is C_s with a mirror plane through the sulfur atom (Table 2 and Fig. 3D). Thus, one would expect few restrictions on the number of independent components of the CSA and EFG tensors and axial symmetry should generally not be expected. The presence of sulfur on a mirror plane, however, requires that one component of each tensor to be perpendicular to the plane, and the others must be in the plane. This inflicts limitations on possible relative orientations of two tensors. Interestingly, though, the shielding tensor for β-$MgSO_4$ is predicted by CASTEP to be close to axially symmetric and is experimentally measured to be $\eta_{CSA} = 0.0 \pm 0.2$. The EFG tensor is also experimentally close to being axially symmetric with $\eta_Q = 0.11 \pm 0.05$. Examining the calculated tensor orientations shows V_{33} is restricted to the mirror plane while σ_{33} is perpendicular to the plane. V_{33} also points to one of the oxygen atoms in the tetrahedron of the SO_4^{2-} group. This S–O axis may act as a pseudo-C_3 rotation axis in a SO_4^{2-} anion. This, together with very small differences in the S–O bond lengths in the ion, may explain the nearly axially symmetric nature of the CSA and EFG tensors. Again, a 90° angle is predicted between V_{33} and σ_{33} and this is confirmed experimentally (Table 3).

^{17}O results

The study of ^{17}O is known to be quite a challenge, in general, due to the extremely low natural abundance and quadrupolar nature of the nucleus. In this work, the samples are slightly enriched in ^{17}O, which significantly relaxes the sensitivity issues. Additionally, ^{17}O has a significantly larger magnetogyric ratio and a much smaller quadrupole moment from that of ^{25}Mg and ^{33}S. In magnesium sulfates, however, there is the additional problem of having multiple crystallographic sites for oxygen in both polymorphs studied.

The ^{17}O SS NMR spectra and spectral simulations for α- and β-$MgSO_4$ taken at 21.1 and 9.4 T can be seen in Figs. 4 and 5, respectively. To aid in the assignment and extraction of spectral parameters for the multiple oxygen sites in each polymorph, MQMAS experiments were also performed and shown in Figs. 6 and 7. The ^{17}O results for α-$MgSO_4$ are not as complicated as in the case of β-$MgSO_4$ since there are only two crystallographically unique oxygen sites in α-$MgSO_4$. The 3Q MQMAS spectrum for α-$MgSO_4$ shows two clearly resolved unique oxygen sites. Measurements of the stationary powder samples at two different fields aided by the MAS data and combined with the simulations allow for accurate extraction of parameters for both oxygen sites in α-$MgSO_4$. The ^{17}O NMR parameters obtained for the two oxygen sites in α-$MgSO_4$ are in fact quite similar (Table 3). The isotropic chemical shifts differ only by about 3 ppm and the quadrupolar coupling constants are nearly identical. Despite the small differences, however, the numerous singularities in the spectra on Fig. 4 can be resolved, aiding in the parameters evaluation. This example demonstrates the importance of using an ultrahigh field for obtaining the necessary resolution in studies of quadrupolar nuclei. The static experiments performed on α-$MgSO_4$ also show a measurable contribution of the CSA interaction. The extracted shielding anisotropy parameters are also listed in Table 3. The shielding asymmetry parameters for both sites are quite similar with $\eta_{CSA} = 0.18$ and $\eta_{CSA} = 0.15$. The anisotropy, on another hand, for one of the ^{17}O sites at $\sigma_{aniso} = 128$ ppm is much larger than that for the other site with $\sigma_{aniso} = 77$ ppm, providing a means for a better assignment of the sites.

In the case of β-$MgSO_4$, there are threee crystallographically inequivalent oxygen sites, making assignment somewhat

Can. J. Chem. Downloaded from www.nrcresearchpress.com by Xi'an Jiaotong University on 09/19/12
For personal use only.

Can. J. Chem. Downloaded from www.nrcresearchpress.com by Xi'an Jiaotong University on 09/19/12
For personal use only.

Fig. 5. Experimental and simulated ^{17}O spectra of β-$MgSO_4$ at 21.1 T and at 9.4 T. Traces a′ and b′ are the spectral simulations accounting only for quadrupolar interactions. Traces a″ and b″ are the fits that also include the CSA. The spectral fits to the MAS spectra account for both quadrupolar interactions and the CSA. Dotted vertical lines indicate positions of singularities in the spectra. For the online colour version, red (upper) traces in the simulated spectra correspond to the sums of the contributing individual sites, shown correspondingly in green, violet, and black.

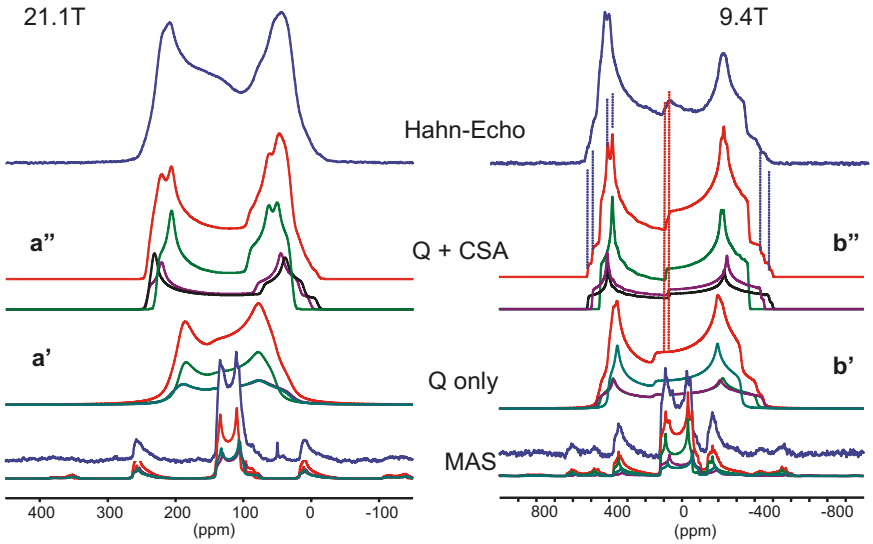

Fig. 6. ^{17}O 3Q MQMAS spectrum of α-$MgSO_4$ at 21.1 T, and calculated orientations of the main components in the EFG and CSA tensors for two oxygen sites in the crystal.

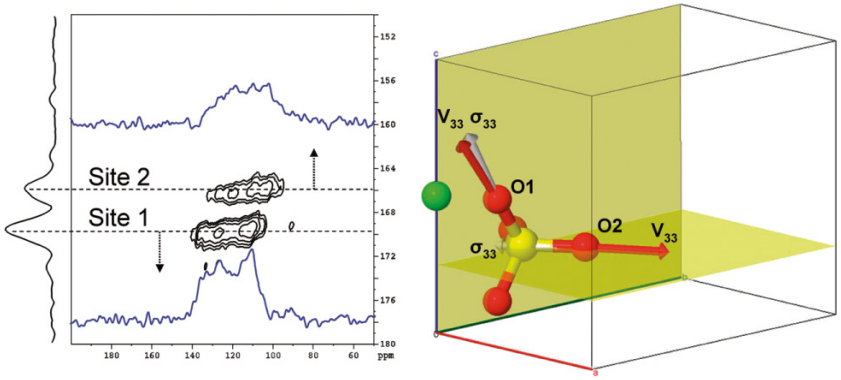

Fig. 7. ^{17}O 3Q MQMAS spectrum of β-$MgSO_4$ at 21.1 T, and calculated orientations of the main principal components in the EFG and CSA tensors for the oxygen sites in the crystal. The components V_{33}^2 , σ_{33}^2 and V_{33}^3 , σ_{33}^3 lie along the O2–S and O3–S bonds, respectively, and are all directed toward the sulfur atom.

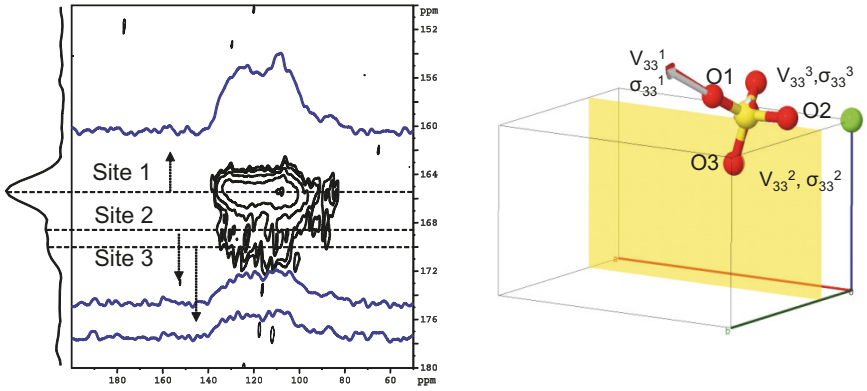

more difficult. Indeed, the MQMAS spectrum of ^{17}O in β-$MgSO_4$ was not able to completely resolve the three oxygen sites. Nevertheless, by fitting the high-field 1D MAS and static experiments and examining the lower field data, reasonable estimates for the spectral parameters for all three oxygen sites can still be accomplished, as summarized in Table 3. It

Can. J. Chem. Downloaded from www.nrcresearchpress.com by Xi'an Jiaotong University on 09/19/12
For personal use only.

should be noted that the results obtained for ^{17}O in β-$MgSO_4$ are similar to α-$MgSO_4$ in that the parameters for all sites are, in general, in the expected range and reasonably similar. Akin to the ^{25}Mg and ^{33}S results, the data obtained from ^{17}O can be used in distinguishing the two polymorphs of $MgSO_4$.

One interesting observation in regard to the ^{17}O data is that the singularities appear to be less resolved in the spectra obtained at the higher field. The main reason for this is an unfortunate interplay between the EFG and the CSA tensors. While the quadrupolar interactions clearly dominate the spectrum at 9.4 T with a relatively small input from the CSA, the situation is altered at 21.1 T. The dramatically reduced quadrupolar contribution together with an accordingly scaled up CSA result in a strong overlap of singularities and contributions from several sites. One should also note, that although the stationary spectra at 21.1 T appear visually broader than at 9.4 T, they actually spun over much narrower spectral regions (i.e., compare the scales below the spectra).

The CASTEP-calculated NMR parameters for ^{17}O in both α- and β-$MgSO_4$ match the experimentally determined values quite well. The predicted quadrupolar coupling constants for all ^{17}O sites in both α- and β-$MgSO_4$ match the experimental values accurately. As well, the magnitude of the calculated shielding anisotropy is predicted correctly for all ^{17}O sites. The only seemingly large discrepancy between the calculated results and the experimental NMR parameters is the isotropic shift of the ^{17}O sites in α- and β-$MgSO_4$. In all cases, the calculated isotropic shift for ^{17}O is systematically lower than the experimentally determined value. The issue may be due to the shielding reference for ^{17}O used in this work, which is based on a single point instead of a correlation reference as used in the case for ^{25}Mg and ^{33}S. Since the accurate prediction of ^{17}O NMR parameters is well-documented,[4,8] one might expect that if a correlation reference produced on a large set of oxygen-containing compounds, then the agreement between calculated isotropic shift and experimental isotropic shift would improve. From the ^{17}O calculations for β-$MgSO_4$ alone, it is somewhat difficult to conclude whether one structure provided more accurate NMR parameters than the other since the calculated parameters are rather similar. Still, by examining the calculated isotropic chemical shift it can be seen that the values obtained from the single crystal XRD structure provided a more accurate forecast of the experimental isotropic shifts.

Similar to ^{25}Mg and ^{33}S, a closer examination of the calculated results offers some interesting insights into the structural details of these $MgSO_4$ polymorphs. Since there are multiple oxygen sites, only the largest component of both the calculated EFG and CSA tensor are shown in Figs. 6 and 7 to avoid figure complexity. The calculated tensor orientations at both oxygen sites in α-$MgSO_4$ are shown in Fig. 6. Both oxygen sites in α-$MgSO_4$ have C_s symmetry resulting in a single mirror plane through each atom. The V_{33} and σ_{33} components for both oxygen sites lie in their respective mirror planes. One oxygen site has both principal components pointed directly away from the sulfur atom with an Euler angle β of ~10°, while the other oxygen site has V_{33} pointing directly away from the sulfur atom when the respective σ_{33} is pointing directly towards the sulfur resulting in an Euler angle β of ~180°. This result accurately matches the experiment. Given the symmetry present at these oxygen sites, one would not expect an axially symmetric EFG or CSA tensor.[40–43] Indeed, the experimental asymmetry parameters η_Q and η_{CSA} indicate the lack of axial symmetry for both tensors.

The calculated orientations for the main components of the EFG and CSA tensors in β-$MgSO_4$ are shown in Fig. 7. As for the α-form, the principal components V_{33} and σ_{33} for the oxygen atoms that have C_s symmetry, lie in the mirror plane (O2 and O3, with corresponding V_{33}^2 , σ_{33}^2 and V_{33}^3, σ_{33}^3). For both these oxygen atoms, the V_{33} and σ_{33} components also point directly towards the central sulfur atom with $\beta = \sim 5°$ in accordance with the experiment (Table 3). For the oxygen site with symmetry C_1, the largest components of the EFG and CSA tensors are also almost coincident with $\beta = \sim 5°$, which is similar to the other oxygen sites. In this case, however, V_{33} and σ_{33} point directly away from the central sulfur atom.

Conclusions

The present study has demonstrated that with the use of ultrahigh fields of 21.1 T previously unattractive nuclei such as ^{25}Mg, ^{33}S, and ^{17}O can be studied via SS NMR with relative ease. The α- and β-polymorphs of anhydrous magnesium sulfate were studied via SS NMR on all the nuclei of the material. The two polymorphs can be successfully distinguished and the spectra are in complete accordance with the crystal structures of the materials. For ^{25}Mg and ^{33}S, simple 1D MAS experiments are all that is needed to distinguish between the polymorphs, whereas enrichment and 2D experiments were required for ^{17}O. With the aid of first principles calculations, fine structural details and the relation of the EFG and CSA tensors were examined for all nuclei in both polymorphs. It was found that symmetry at the sites and character of the chemical bonds dictated specific tensor orientations. Another aspect of the study was to compare the recently reported crystal structures for β-$MgSO_4$. It was found that, at least for ^{33}S and ^{17}O, the calculations performed on a structure from single crystal XRD reproduce the experimental parameters more accurately than the calculations using the structural data from the neutron powder diffraction. This work demonstrates how previously difficult NMR nuclei can now be successfully studied, assisting in a better understanding of a material's nature. With the aid of first principles calculations, the information for each nuclei complements each other resulting in a detailed picture of the fine structural details.

Acknowledgments

This article is dedicated to Professor R. E. Wasylishen in recognition of his contribution to solid-state NMR in Canada. The authors thank Dr. Victor Terskikh for useful discussions and access to computational resources. Access to the 900 MHz NMR spectrometer was provided by the National Ultrahigh-Field NMR Facility for Solids (Ottawa, ON), a national research facility funded by the Canada Foundation for Innovation, the Ontario Innovation Trust, Recherche Québec, the National Research Council Canada, and Bruker BioSpin and managed by the University of Ottawa (http://nmr900.ca).

References

(1) Ashbrook, S. A. *Phys. Chem. Chem. Phys.* **2009**, *11* (32), 6892. doi:10.1039/b907183k.

Can. J. Chem. Downloaded from www.nrcresearchpress.com by Xi'an Jiaotong University on 09/19/12
For personal use only.

(2) (a) Pickard, C. J.; Mauri, F. *Phys. Rev. B* **2001**, *63* (24), 245101. doi:10.1103/PhysRevB.63.245101;; (b) Yates, J. R.; Pickard, C. J.; Mauri, F. *Phys. Rev. B* **2007**, *76* (2), 024401. doi:10.1103/PhysRevB.76.024401.

(3) (a) Clark, S. J.; Segall, M. D.; Pickard, C. J.; Hasnip, P. J.; Probert, M. J.; Refson, K.; Payne, M. C. *Z. Kristallogr.* **2005**, *220* (5–6), 567. doi:10.1524/zkri.220.5.567.65075;; (b) Segall, M. D.; Lindan, P. J. D.; Probert, M. J.; Pickard, C. J.; Hasnip, P. J.; Clark, S. J.; Payne, M. C. *J. Phys. Condens. Matter* **2002**, *14* (11), 2717. doi:10.1088/0953-8984/14/11/301.

(4) (a) Profeta, M.; Mauri, F.; Pickard, C. J. *J. Am. Chem. Soc.* **2003**, *125* (2), 541. doi:10.1021/ja027124r;; (b) Benoit, M.; Profeta, M.; Mauri, F.; Pickard, C. J.; Tuckerman, M. E. *J. Phys. Chem. B* **2005**, *109* (13), 6052. doi:10.1021/jp0492570;; (c) Charpentier, T.; Ispas, S.; Profeta, M.; Mauri, F.; Pickard, C. J. *J. Phys. Chem. B* **2004**, *108* (13), 4147. doi:10.1021/jp0367225.

(5) Gervais, C.; Bonhomme-Coury, L.; Mauri, F.; Babonneau, F.; Bonhomme, C. *Phys. Chem. Chem. Phys.* **2009**, *11* (32), 6953. doi:10.1039/b907450c.

(6) Griffin, J. M.; Wimperis, S.; Berry, A. J.; Pickard, C. J.; Ashbrook, S. E. *J. Phys. Chem. C* **2009**, *113* (1), 465. doi:10.1021/jp808651x.

(7) Harris, R. K.; Joyce, S. A.; Pickard, C. J.; Cadars, S.; Emsley, L. *Phys. Chem. Chem. Phys.* **2006**, *8* (1), 137. doi:10.1039/b513392k.

(8) (a) Ashbrook, S. E.; Berry, A. J.; Frost, D. J.; Gregorovic, A.; Pickard, C. J.; Readman, J. E.; Wimperis, S. *J. Am. Chem. Soc.* **2007**, *129* (43), 13213. doi:10.1021/ja074428a;; (b) Ashbrook, S. E.; Le Pollès, L.; Pickard, C. J.; Berry, A. J.; Wimperis, S.; Farnan, I. *Phys. Chem. Chem. Phys.* **2007**, *9* (13), 1587. doi:10.1039/b618211a.

(9) Kargel, J. S.; Kirk, R. L.; Fegley, B.; Treiman, A. H. *Icarus* **1994**, *112* (1), 219. doi:10.1006/icar.1994.1179.

(10) Kargel, J. S. *Icarus* **1991**, *94* (2), 368. doi:10.1016/0019-1035(91)90235-L.

(11) Rentzeperis, P. J.; Soldatos, C. T. *Acta Crystallogr.* **1958**, *11* (10), 686. doi:10.1107/S0365110X58001857.

(12) Yamaguchi, A.; Kato, E. *Yogyo Kyokai Shi* **1972**, *80*, 337.

(13) Coing-Boyat, J. *C. R. Acad. Sci. Paris* **1962**, *255*, 1962.

(14) Fortes, A. D.; Wood, I. G.; Vočadlo, L.; Brand, H. E. A.; Knight, K. S. *J. Appl. Cryst.* **2007**, *40* (4), 761. doi:10.1107/S0021889807029937.

(15) Weil, M. *Acta Crystallogr. Sect. E Struct. Rep. Online* **2007**, *63* (8), i172. doi:10.1107/S1600536807036355.

(16) Freude, D.; Haase, J. Quadrupole Effects in Solid-State Nuclear Magnetic Resonance. In *NMR Basic Principles and Progress;* Diehl, P., Fluck, E., Günther, H., Kasfeld, R., Seelig, J., Eds.; Springer-Verlag: Berlin, 1993, Vol. 29, pp 1–90.

(17) Ashbrook, S. E.; Duer, M. J. *Concepts Magn. Reson.* **2006**, *28A* (3), 183. doi:10.1002/cmr.a.20053.

(18) MacKenzie, K. J. D.; Smith, M. E. *Multinuclear Solid-State NMR of Inorganic Materials;* Pergamon: New York, 2002.

(19) Harris, R. K.; Becker, E. D.; de Menezes, S. M. C; Goodfellow, R.; Granger, P. *Pure Appl. Chem.* **2001**, *73* (11), 1795. doi:10.1351/pac200173111795.

(20) Bodart, P. R.; Amoureux, J. P.; Dumazy, Y.; Lefort, R. *Mol. Phys.* **2000**, *98* (19), 1545. doi:10.1080/00268970009483360.

(21) Larsen, F. H.; Jakobsen, H. J.; Ellis, P. D.; Nielsen, N. C. *J. Phys. Chem. A* **1997**, *101* (46), 8597. doi:10.1021/jp971547b.

(22) Kentgens, A. P. M.; Verhagen, R. *Chem. Phys. Lett.* **1999**, *300* (3–4), 435. doi:10.1016/S0009-2614(98)01402-X.

(23) Brown, S. P.; Wimperis, S. *J. Magn. Reson.* **1997**, *124* (1), 279. doi:10.1006/jmre.1996.1059.

(24) Brown, S. P.; Wimperis, S. *J. Magn. Reson.* **1997**, *128* (1), 42. doi:10.1006/jmre.1997.1217.

(25) Belton, P. S.; Cox, I. J.; Harris, R. K. *J. Chem. Soc., Faraday Trans. 2* **1985**, *81* (1), 63. doi:10.1039/f29858100063.

(26) Eichele K.; Wasylishen, R.E. *WSOLIDS NMR Simulation Package,* version 1.19.11; Solid-State NMR Group, University of Alberta: Edmonton (AB), 2009.

(27) Massiot, D.; Fayon, F.; Capron, M.; King, I.; Le Calvé, S.; Alonso, B.; Durand, J.-O.; Bujoli, B.; Gan, Z.; Hoatson, G. *Magn. Reson. Chem.* **2002**, *40* (1), 70. doi:10.1002/mrc.984.

(28) Perdew, J. P.; Burke, K.; Ernzerhof, M. *Phys. Rev. Lett.* **1996**, *77* (18), 3865. doi:10.1103/PhysRevLett.77.3865.

(29) Perdew, J. P.; Burke, K.; Ernzerhof, M. *Phys. Rev. Lett.* **1997**, *78* (7), 1396. doi:10.1103/PhysRevLett.78.1396.

(30) Monkhorst, H. J.; Pack, J. D. *Phys. Rev. B* **1976**, *13* (12), 5188. doi:10.1103/PhysRevB.13.5188.

(31) Pallister, P. J.; Moudrakovski, I. L.; Ripmeester, J. A. *Phys. Chem. Chem. Phys.* **2009**, *11* (48), 11487. doi:10.1039/b916076k.

(32) Moudrakovski, I.; Lang, S.; Patchkovskii, S.; Ripmeester, J. *J. Phys. Chem. A* **2010**, *114* (1), 309. doi:10.1021/jp908206c.

(33) Dupree, R.; Smith, M. E. *J. Chem. Soc. Chem. Commun.* **1988**, 1483. doi:10.1039/c39880001483.

(34) Bastow, T. J. *J. Phys. Condens. Matter* **1991**, *3* (6), 753. doi:10.1088/0953-8984/3/6/011.

(35) (a) Bastow, T. J.; Celotto, S. *Solid State Commun.* **1999**, *110* (5), 271. doi:10.1016/S0038-1098(99)00071-X;; (b) Bastow, T. J.; Celotto, S. *Solid State Nucl. Magn. Reson.* **2009**, *35* (4), 217. doi:10.1016/j.ssnmr.2009.02.002.

(36) MacKenzie, K. J. D.; Meinhold, R. H. *Am. Mineral.* **1997**, *82* (5–6), 479.

(37) MacKenzie, K. J. D.; Meinhold, R. H. *Am. Mineral.* **1994**, *79*, 43.

(38) Sham, S.; Wu, G. *Inorg. Chem.* **2000**, *39* (1), 4. doi:10.1021/ic991060c.

(39) Kroeker, S.; Stebbins, J. F. *Am. Mineral.* **2000**, *85* (10), 1459.

(40) Buckingham, A. D.; Malm, S. M. *Mol. Phys.* **1971**, *22* (6), 1127. doi:10.1080/00268977100103431.

(41) Weil, J. A.; Buch, T.; Clapp, J. E. In *Advances in Magnetic Resonance;* Waugh, J. S. Ed.; Academic Press: New York: 1976, Supplement 1.

(42) Robert, J. B.; Wiesenfeld, L. *Phys. Rep.* **1982**, *86* (7), 363. doi:10.1016/0370-1573(82)90164-8.

(43) Akitt, J. W.; McDonald, W. S. *J. Magn. Reson.* **1984**, *58* (3), 401.

(44) Haeberlen, U. In *Advances in Magnetic Resonance;* Waugh, J. S. Ed.; Academic Press: New York: 1976, Supplement 1.

(45) Mehring, M. *Principles of High Resolution NMR in Solids,* 2nd ed.; Springer-Verlag: Berlin, 1983.

(46) Bryce, D. L. Tensor Interplay. In *NMR Crystallography;* Harris, R. K., Wasylishen, R. E., Duer, M. J., Eds.; John Wiley & Sons, Ltd.: New York, 2009; Chapter 20, pp 289–301, and refs. cited therein.

Obtaining accurate chemical shifts for all magnetic nuclei (^{1}H, ^{13}C, ^{17}O, and ^{27}Al) in tris(2,4-pentanedionato-*O*,*O*')aluminium(III) — A solid-state NMR case study

Alan Wong, Mark E. Smith, Victor Terskikh, and Gang Wu

Can. J. Chem. Downloaded from www.nrcresearchpress.com by Xi'an Jiaotong University on 09/19/12
For personal use only.

Abstract: We report a complete set of high-resolution solid-state NMR spectra for all magnetic nuclei (^{1}H, ^{13}C, ^{17}O, and ^{27}Al) in the α-form of tris(2,4-pentanedionato-*O*,*O*')aluminium(III), α-Al(acac)$_3$. These high-resolution NMR spectra were obtained by using a host of solid-state NMR techniques: standard cross-polarization under the magic-angle spinning (CPMAS) method for ^{13}C, 1-D homonuclear decoupling using the windowed DUMBO sequence for ^{1}H, double-rotation (DOR) for ^{17}O and ^{27}Al, and multiple-quantum MAS for ^{27}Al. Some experiments were performed at multiple magnetic fields. We show that the isotropic chemical shifts obtained for ^{1}H, ^{13}C, ^{17}O, and ^{27}Al nuclei in α-Al(acac)$_3$ are highly resolved and accurate, regardless of the nature of the targeted nuclear spins (i.e., spin-1/2 or quadrupolar) and, as such, can be treated equally in comparison with computational chemical shifts obtained from a gauge-including projector-augmented wave (GIPAW) plane-wave pseudopotential DFT method.

Key words: high-resolution NMR, solid-state NMR, double rotation, chemical shift, quadrupole parameter.

Résumé : On a obtenu un ensemble complet de spectres RMN à haute résolution, à l'état solide, de tous les noyaux magnétiques (^{1}H, ^{13}C, ^{17}O, et ^{27}Al) de la forme α du tris(pentane-2,4-dionato-*O,O*'-)aluminium(III), α-Al(acac)$_3$. On a obtenu ces spectres RMN à haute résolution en utilisant un ensemble de techniques de RMN à l'état solide : polarisation croisée standard avec rotation à l'angle magique (« CPMAS ») pour le ^{13}C, découplage homonucléaire 1-D à l'aide de la séquence DUMBO avec fenêtre pour le ^{1}H et la double rotation (DOR) pour le ^{17}O et le ^{27}Al et le quantum multiple avec rotation à l'angle magique (« MAS ») pour le ^{27}Al. Diverses expériences ont été réalisées à plusieurs champs magnétiques. On démontre que les déplacements chimiques isotropes obtenus pour les noyaux de ^{1}H, ^{13}C, ^{17}O, et ^{27}Al dans le α-Al(acac)$_3$ sont très bien résolus et pré*cis* quelle que soit la nature des spins nucléaires examinés (c'est-à-dire spin-1/2 ou quadripolaire) et qu'ils peuvent ainsi être traités d'une façon égale dans une comparaison avec des déplacements chimiques calculés par la méthode de la théorie de la fonctionnelle de densité (TFD) en utilisant une onde améliorée par un opérateur de projection comportant une jauge avec un pseudopotentiel d'onde plane (« GIPAW »).

Mots-clés : RMN à haute résolution, RMN à l'état solide, double rotation, déplacement chimique, paramètre quadripolaire.

[Traduit par la Rédaction]

1. Introduction

Solid-state NMR spectroscopy has become a powerful tool for chemists to obtain detailed information about chemical bonding, structure, and the dynamics of molecules in solid materials. One emerging field in solid-state NMR is known as "NMR crystallography".[1] For organic solids, one typically examines high-resolution ^{13}C CPMAS and, to a lesser extent, ^{1}H MAS NMR spectra, from which accurate chemical shifts can often be obtained directly.[2–6] In many molecular systems, there exist magnetic nuclei other than ^{1}H and ^{13}C. In these systems, it is highly desirable that all magnetic nuclei are probed. Very often, the other magnetic nuclei are quadrupolar (spin > 1/2) for which line broadening is usually significantly greater than spin-1/2 nuclei such as ^{1}H and ^{13}C. However, because more advanced NMR techniques such as double-rotation (DOR)[7–9] and multiple-quantum magic-angle spinning (MQMAS)[10,11] are becoming increasingly available, accurate chemical shift values can also be readily obtained for many quadrupolar nuclei. Here we report a comprehen-

Received 10 January 2011. Accepted 18 February 2011. Published at www.nrcresearchpress.com/cjc on 22 August 2011.

A. Wong[†] **and M.E. Smith.** Department of Physics, University of Warwick, Coventry, CV4 7AL, UK.
V. Terskikh. Steacie Institute for Molecular Sciences, National Research Council Canada, Ottawa, ON K1A 0R6, Canada.
G. Wu. Department of Chemistry, Queen's University, 90 Bader Lane, Kingston, ON K7L 3N6, Canada.

Corresponding author: G. Wu (e-mail: gang.wu@chem.queensu.ca).

This article is part of a Special Issue dedicated to Professor Roderick E. Wasylishen in recognition of his outstanding contributions to Canadian chemistry.

[†]Present address: CEA-Saclay, DSM/IRAMIS/SIS2M/LSDRM 91191 Gif-sur-Yvette CEDEX, France.

Can. J. Chem. Downloaded from www.nrcresearchpress.com by Xi'an Jiaotong University on 09/19/12
For personal use only.

Scheme 1. Molecular structure of $Al(acac)_3$.

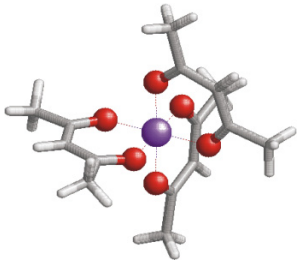

sive solid-state NMR study of the α-polymorph of crystalline tris(2,4-pentanedionato-*O*,*O*')aluminium(III), α-$Al(acac)_3$; see Scheme 1. We obtain highly accurate isotropic chemical shift values for all magnetic nuclei in α-$Al(acac)_3$: ^{1}H, ^{13}C, ^{17}O, and ^{27}Al. These experimental chemical shifts are then compared with computed chemical shifts from the density functional theory (DFT) gauge-including projector-augmented wave (GIPAW)[12,13] approach as implemented in the CASTEP code.[14] This computational method has gained considerable attention recently in the solid-state NMR community,[15–39] because it takes into account the entire unit cell and thus is ideal for dealing with solid materials for which crystal structures are known. We chose α-$Al(acac)_3$ as a target for the following reasons. First, a good-quality X-ray crystal structure was reported recently for this compound.[40] Second, although there is only one molecule in the asymmetric unit of the unit cell, the high symmetry of the acac ligand makes it challenging in solid-state NMR to resolve very similar sites (in principle, 6 CO groups, 6 CH_3 groups, 3 CH groups, and 6 O sites). Third, some limited solid-state ^{13}C, ^{2}H, and ^{27}Al NMR data are already available in the literature.[41–43] Fourth, α-$Al(acac)_3$ is a metal complex with a relatively small unit cell ($43 \times 4 = 172$ atoms, $V = 1701.96$ Å^3), which permits us to perform CASTEP computation with our currently available computing resources. This will also make an interesting comparison with the DFT results reported recently by Amini and Tafazzoli[44] who used a molecular cluster approach to calculate the NMR parameters in both α- and γ-polymorphs of $Al(acac)_3$.

2. Experimental section

Synthesis

$Al(acac)_3$ (99% purity) was obtained from Sigma-Aldrich. The ^{17}O-labeled $Al(acac)_3$ was prepared by dissolving 50 mg $Al(acac)_3$ (0.15 mmole) in 1.0 mL anhydrous CH_2Cl_2. Approximately 20 μL of acidified H_2O (70% ^{17}O, Iso-Solutions, Ottawa, Ontario) was then added to this solution. After standing at room temperature for 24 h, the solution was neutralized with NH_4OH(aq) and dried under a stream of dry nitrogen gas. This ^{17}O-enriched $Al(acac)_3$ sample (approximately 60% ^{17}O) was used for solid-state ^{17}O NMR experiments. Although all solid $Al(acac)_3$ samples were confirmed to be in the α-polymorph by powder X-ray diffraction patterns, the ^{17}O-labeled sample does contain a trace amount of NH_4Cl.

NMR experiments

Solid-state ^{1}H, ^{13}C, and ^{17}O NMR experiments were performed on a Bruker Avance II$^+$ 600 spectrometer at 14.1 T.

Fig. 1. (*a*) ^{1}H single-pulse 12.5-kHz MAS (dotted line) and windowed-DUMBO (solid line) NMR spectra of α-$Al(acac)_3$. (*b*) ^{13}C CPMAS spectrum of α-$Al(acac)_3$.

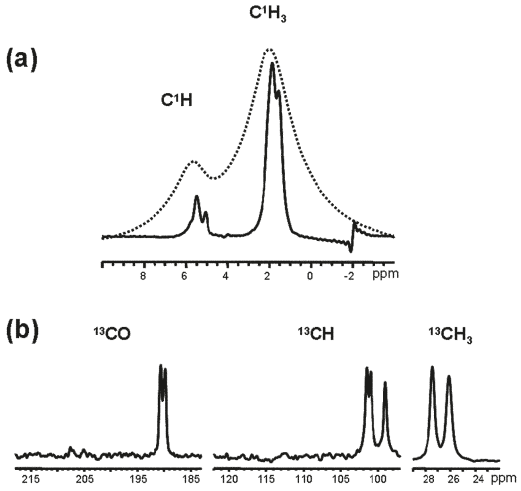

A Bruker 4-mm HX MAS probe was used. Solid-state ^{13}C NMR spectra were acquired with the standard CPMAS sequence with 100 kHz ^{1}H decoupling. High-resolution ^{1}H NMR spectra were obtained with the 1-D windowed-DUMBO sequence and a sample spinning frequency of 12.5 kHz.[45] All ^{1}H and ^{13}C chemical shifts were referenced to external TMS. ^{17}O DOR NMR spectra were acquired using a custom-built DOR probe and employing odd-order sideband suppression.[46,47] The ^{17}O excitation pulse width was 1 μs. Continuous-wave ^{1}H-decoupling (50 kHz) was applied during acquisition. The outer- and inner-rotor spinning frequencies were 1307 and 6525 Hz, respectively. The ^{17}O DOR spectrum was acquired with 30740 transients and a recycle delay of 1 s. The high-field ^{17}O DOR NMR spectrum was obtained on a Chemagnetics Varian Infinity 800 spectrometer at 18.8 T, with outer- and inner-rotor spinning frequencies of 1303 and 6515 Hz, respectively. The ^{1}H-decoupling field was approximately 27 kHz. A total of 36000 transients were collected with a recycle delay of 1 s. Similarly, ^{27}Al DOR NMR spectra were acquired at 14.1 T using odd-order sideband suppression without ^{1}H decoupling. The ^{27}Al excitation pulse width was 2.1 μs. The outer- and inner-rotor spinning frequencies were 1303 and 6420, respectively. A total of 880 transients were accumulated with a recycle delay of 1 s. ^{27}Al MQMAS (3Q and 5Q) and some ^{17}O MAS NMR experiments were performed on a Bruker Avance-II 900 spectrometer at 21.1 T operating at 234.6 MHz for ^{27}Al and 122.0 MHz for ^{17}O. A Bruker 4-mm HX MAS probe was used with a sample spinning frequency of 12 kHz for ^{27}Al and 18 kHz for ^{17}O experiments. In the MQMAS experiments, the t_1 increment was rotor-synchronized. All ^{17}O and ^{27}Al chemical shifts were referenced with respect to the signals of H_2O(liq) and 0.1 mol/L $Al(NO_3)_3$(aq), respectively. Spectral simulations were performed using WSolids[48] and DMFit.[49]

Quantum chemical computation

Calculations of the NMR shielding and electric field gradient parameters were performed using Materials Studio CASTEP software version 4.4 (Accelrys)[14,50] on a HP

Can. J. Chem. Downloaded from www.nrcresearchpress.com by Xi'an Jiaotong University on 09/19/12
For personal use only.

Table 1. Experimental and computed chemical shifts (ppm) for all magnetic nuclei in α-Al(acac)$_3$.

			δ_{castep} (ppm)		
Nucleus	Group	δ_{exptl} (ppm)	"X-ray"	"Opt-H"	"Opt-full"
^{1}H	CH	5.48±0.05	6.00	5.17	5.31
	CH	5.05±0.05	5.92	4.95	5.02
	CH_3[a]	1.84±0.05	0.44	2.21	2.02
	CH_3[a]	1.53±0.05	0.16	1.91	1.73
			(1.1)[b]	(0.3)[b]	(0.2)[b]
^{13}C	CO	189.8±0.1	202.0	185.7	191.7
	CH	101.5±0.1	108.9	100.3	106.3
	CO	190.6±0.1	203.3	187.1	191.5
	CH_3	26.1±0.1	15.1	24.2	23.7
	CH_3	27.5±0.1	13.8	25.0	25.7
	CO	189.8±0.1	201.6	185.5	190.3
	CH	101.0±0.1	108.6	99.2	105.2
	CO	190.6±0.1	199.3	184.1	191.9
	CH_3	26.1±0.1	12.3	22.8	23.5
	CH_3	27.5±0.1	15.0	25.9	25.4
	CO	189.8±0.1	201.7	184.5	190.2
	CH	99.0±0.1	107.1	97.5	103.1
	CO	190.6±0.1	202.1	187.2	192.0
	CH_3	27.5±0.1	14.8	26.0	26.6
	CH_3	26.1±0.1	13.9	24.5	24.3
			(11.4)[b]	(3.3)[b]	(2.4)[b]
^{17}O	CO	268.6±0.2	267.57	266.9	266.4
	CO	266.6±0.2	273.62	269.0	265.9
	CO	264.7±0.2	268.78	266.0	259.7
	CO	268.4±0.2	262.23	263.4	267.5
	CO	264.7±0.2	267.33	263.1	265.0
	CO	273.7±0.2	279.07	282.2	277.1
			(4.8)[b]	(4.3)[b]	(2.7)[b]
^{27}Al	Al	0.15±0.05	0.0	0.0	0.0

[a]As the 18 methyl protons of α-Al(acac)$_3$ exhibit two distinct groups of ^{1}H chemical shifts, the calculated ^{1}H chemical shifts for CH_3 are the averaged values.

[b]Root-mean-square-deviation (RMSD) between δ_{castep} and δ_{exptl} values.

xw4400 workstation with a single Intel Dual-Core 2.67 GHz processor and 8 GB DDR RAM. The Perdew, Burke, and Ernzerhof (PBE) functionals were used in all calculations in the generalized gradient approximation (GGA) for the exchange correlation energy.[51,52] On-the-fly pseudopotentials were used as supplied with NMR CASTEP with a plane wave basis set cut-off energy of 450 eV and the Monkhorst-Pack k-space grid size of 1 × 2 × 1 (0.07 Å^{-1} k-point separation) limited by the large volume of the unit cell (1701.96 Å^3). The geometry optimization was performed using the BFGS method[53] without the cell optimization and with the following convergence tolerance parameters: total energy = 5 × 10^{-5} eV/atom, maximum displacement = 0.005 Å, maximum force = 0.1 eV/Å, and maximum stress = 0.2 GPa. For the H-atom optimized structure ("opt-H"), all heavy atoms were constrained during geometry optimization. For the fully-optimized structure ("opt-full"), no atoms were constrained.

To convert the computed shielding constant to the corresponding chemical shift, we use the following equation:

$$[1] \qquad \delta_{sample} = \sigma_{ref} - \sigma_{sample}$$

where σ_{ref} is the shielding constant for a reference sample. In this study, we use the following parameters: for the "opt-full" structure, $\sigma_{ref}(^{1}H)$ = 30.6 ppm, $\sigma_{ref}(^{13}C)$ = 170.0 ppm, $\sigma_{ref}(^{17}O)$ = 259.0 ppm, and $\sigma_{ref}(^{27}Al)$ = 556.2 ppm; for the "opt-H" structure, $\sigma_{ref}(^{1}H)$ = 30.8 ppm, $\sigma_{ref}(^{13}C)$ = 170.0 ppm, $\sigma_{ref}(^{17}O)$ = 270.0 ppm, and $\sigma_{ref}(^{27}Al)$ = 555.6 ppm; for the "X-ray" structure, $\sigma_{ref}(^{1}H)$ = 34.0 ppm, $\sigma_{ref}(^{13}C)$ = 185.0 ppm, $\sigma_{ref}(^{17}O)$ = 265.0 ppm, and $\sigma_{ref}(^{27}Al)$ = 556.4 ppm. These values were chosen to optimize the agreement between experimental chemical shifts and CASTEP chemical shifts for individual structures. The calculated $C_Q(^{27}Al)$ values reported from CASTEP were corrected using a more accurate ^{27}Al quadrupole moment, $Q(^{27}Al) = 14.66 \times 10^{-30}$ m^2.[54]

3. Results and discussion

^{1}H and ^{13}C spectra

Figure 1 shows the solid-state ^{1}H and ^{13}C NMR spectra of α-Al(acac)$_3$. Using MAS alone, we were able to observe only two broad peaks in the ^{1}H NMR spectrum, attributable to the CH and CH_3 groups in α-Al(acac)$_3$. With the 1-D windowed-DUMBO sequence, significant line narrowing is achieved, leading to the observation of two different groups of signals for each of the CH and CH_3 resonances. The ^{1}H chemical

Can. J. Chem. Downloaded from www.nrcresearchpress.com by Xi'an Jiaotong University on 09/19/12
For personal use only.

Fig. 2. ^{17}O DOR spectra of α-Al(acac)$_3$ obtained at (*a*) 14.1 T and (*b*) 18.8 T. The isotropic peak is marked by *. The outer rotor spinning frequency was 1305 and 1330 Hz for (*a*) and (*b*), respectively. (*c*) The experimental (lower trace) and best-fitted (upper trace) "total ^{17}O DOR line shapes" of α-Al(acac)$_3$. The experimental "total DOR line shape" was obtained by summing up all sidebands onto the isotropic peak shown in (*b*).

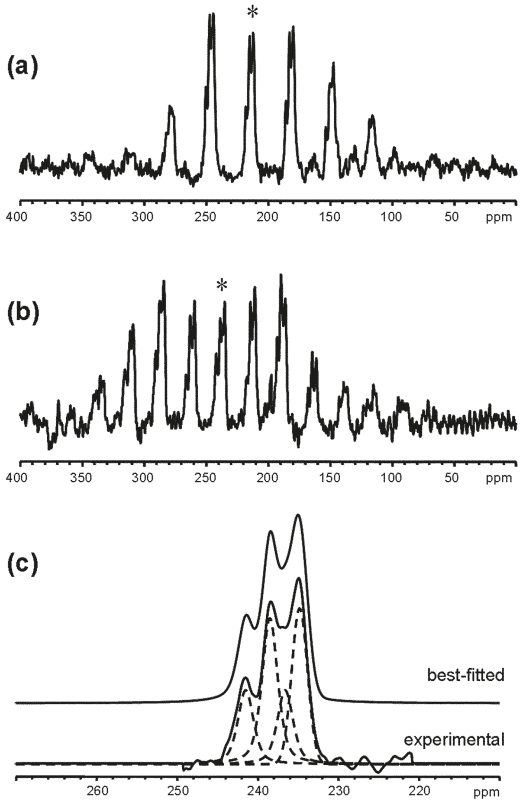

Fig. 3. Simultaneous fitting of the ^{17}O DOR data obtained at 14.1 and 18.8 T for α-Al(acac)$_3$.

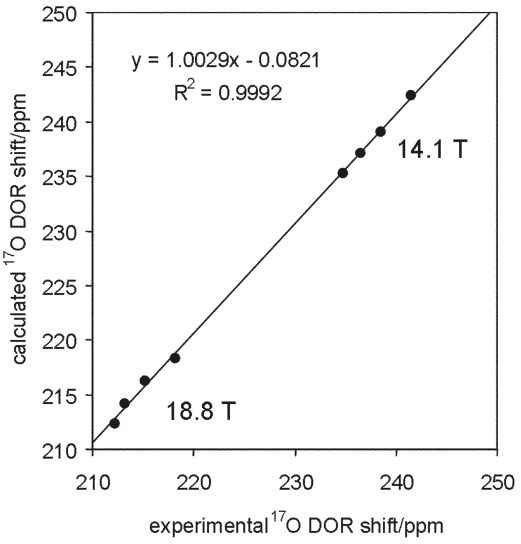

shifts observed for α-Al(acac)$_3$ are 5.48 and 5.05 ppm for the CH groups and 1.84 and 1.53 ppm for the CH_3 groups. We note that our ^{1}H chemical shifts for the CH groups are somewhat different from the 6.9 ppm previously observed in the ^{2}H MAS NMR spectrum of α-Al(acac)$_3$.[42] In the ^{13}C CPMAS spectrum, two signals are observed for each of the CO and CH_3 groups, whereas three signals are seen for the CH groups. These observations are in agreement with the earlier study of Champmartin and Rubini.[41] Because the asymmetric unit of α-Al(acac)$_3$ contains one complete molecule, there should be, in principle, six ^{13}C NMR signals for each of the CO and CH_3 groups. Clearly, each of the two ^{13}C NMR signals in the CO and CH_3 regions represents three nearly degenerate signals. All experimental ^{1}H and ^{13}C chemical shifts are listed in Table 1.

^{17}O spectra

Whereas it is straightforward to obtain and analyze ^{1}H and ^{13}C MAS NMR spectra when multiple sites are present, it is quite a different task to do the same thing for ^{17}O NMR spectra. This is because the second-order quadrupolar interactions are not averaged under MAS.[55] As a result, different types of NMR experiments such as double-rotation (DOR) can helpfully be applied to produce high-resolution ^{17}O NMR spectra. Figure 2 shows the ^{17}O DOR spectra of α-Al(acac)$_3$ obtained at 14.1 and 18.8 T. Because the spinning frequency of the outer rotor, which is at the magic angle, is usually much smaller than the frequency span of anisotropic width for the ^{17}O produced by second-order quadrupolar and chemical shift effects, a large number of spinning sidebands are present. Nonetheless, the high resolution achieved in the DOR spectra allows the observation of several resolved ^{17}O NMR signals, which is simply not possible in the corresponding ^{17}O MAS spectra (vide infra). As shown in Fig. 2*c*, the "total ^{17}O DOR line shape" can be satisfactorily analyzed by assuming four distinct peaks with integrated intensity ratios of 1:2:1:2. This is consistent with the fact that there are six crystallographically distinct CO groups in α-Al(acac)$_3$, as mentioned earlier. Next we need to analyze the observed DOR shifts to obtain fundamental NMR parameters such as chemical shifts and quadrupole parameters. It is known that the ^{17}O DOR shift, δ_{DOR}, depends on the isotropic chemical shift (δ_{iso}) and the quadrupole product parameter (P_Q) in the following manner[55,56]:

$$[2] \qquad \delta_{DOR} = \delta_{iso} - \frac{3}{500}\left(\frac{P_Q}{\nu_0}\right)^2 \times 10^6$$

where ν_0 is the Larmor frequency of ^{17}O, and $P_Q = C_Q \times (1 + \eta_Q^2/3)^{1/2}$. As shown in Fig. 3, we were able to fit simultaneously the two sets of ^{17}O DOR shifts observed at 14.1 and 18.8 T. However, we should point out that this fitting procedure is not trivial. In practice, we used the low-field MAS spectra (vide infra) to determine the initial values of C_Q and η_Q, then the DOR spectra to refine the isotropic chemical shifts. During the process, we also noticed that one of the O sites must have a slightly larger value of C_Q; see Table 2. In the end, ^{17}O MAS spectra obtained at different magnetic fields were also simulated (see Fig. 4). It should be strongly emphasized that it is important to have DOR and MAS data collected at multiple magnetic fields to extract reliable ^{17}O NMR parameters. This is particularly true when there are multiple oxygen sites with a similar environment, which is indeed the case in α-Al(acac)$_3$. Quite interestingly,

Can. J. Chem. Downloaded from www.nrcresearchpress.com by Xi'an Jiaotong University on 09/19/12
For personal use only.

Table 2. Experimental and calculated ^{17}O and ^{27}Al quadrupole parameters for α-Al(acac)$_3$. Only the CASTEP results from the "opt-full" structure are shown.

		Experimental		CASTEP	
Nucleus	Site	C_Q/MHz	η_Q	C_Q/MHz	η_Q
^{17}O	1	6.9±0.2	0.8±0.1	7.247	0.80
	2	6.9±0.2	0.8±0.1	7.243	0.81
	3	6.9±0.2	0.8±0.1	7.146	0.87
	4	6.9±0.2	0.8±0.1	7.340	0.78
	5	6.9±0.2	0.8±0.1	7.206	0.83
	6	7.1±0.2	0.8±0.1	7.455	0.72
^{27}Al	1	3.02±0.01	0.16±0.01	3.09	0.32

Fig. 4. Experimental (lower trace) and simulated (upper trace) ^{17}O MAS spectra of α-Al(acac)$_3$ at three magnetic fields. The ^{17}O NMR parameters used in spectral simulations are given in Tables 1 and 2. The inset shows the experimental (lower trace) and simulated (upper trace) "total ^{17}O MAS line shapes" for α-Al(acac)$_3$ at 21.1 T. The experimental "total ^{17}O MAS line shape" was obtained by adding spinning sidebands onto the central band of the MAS spectrum. The symbol * indicates the spectral features arising from satellite transitions.

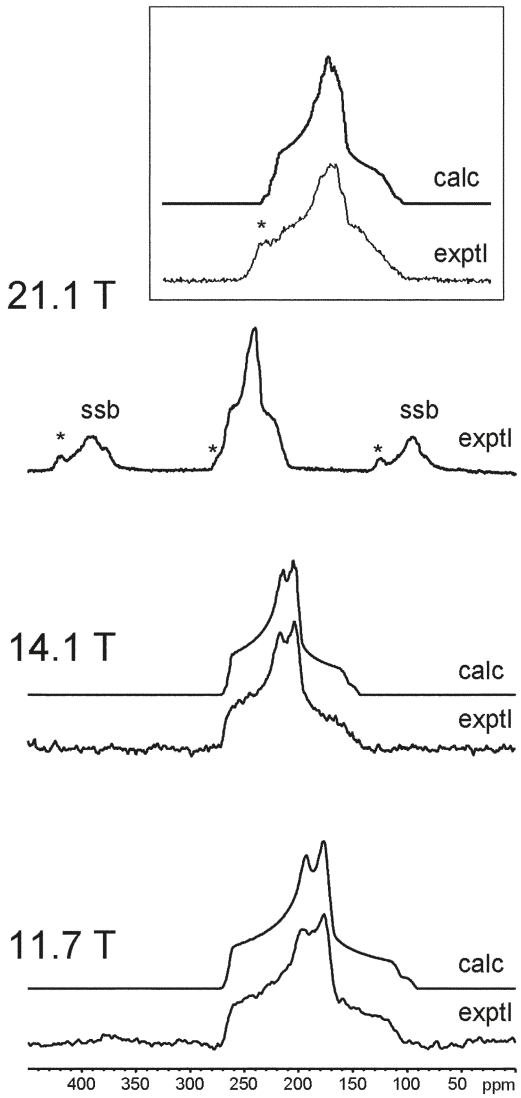

Fig. 5. Experimental (lower trace) and simulated (upper trace) ^{27}Al MAS spectra of α-Al(acac)$_3$ obtained at 21.1 T. The symbol * indicates the inner (3/2–1/2) satellite transition.

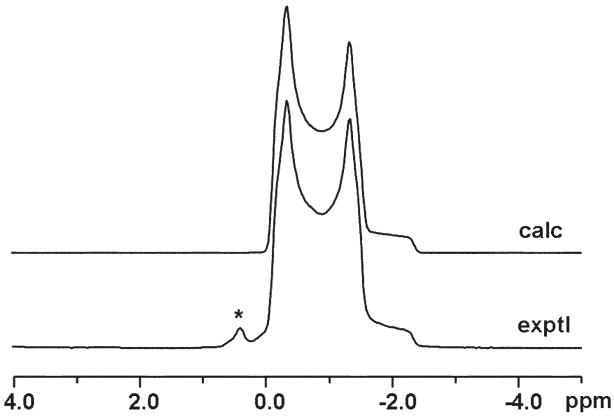

as seen in Fig. 4, while each of the ^{17}O MAS spectra obtained at 11.7 and 14.1 T seems to display just one characteristic second-order quadrupolar line shape (i.e., one oxygen site), the corresponding spectrum obtained at 21.1 T exhibits a quite complex feature suggesting that the multiple oxygen sites must have very similar ^{17}O quadrupole parameters, but slightly different chemical shifts. By combining the DOR and MAS data sets, we obtained the final set of ^{17}O NMR parameters for α-Al(acac)$_3$, as summarized in Tables 1 and 2.

^{27}Al spectra

Figure 5 shows the experimental and simulated ^{27}Al MAS spectra obtained at 21.1 T for α-Al(acac)$_3$. Because there is only one Al site in α-Al(acac)$_3$, it is straightforward to obtain accurate ^{27}Al NMR parameters from an analysis of these ^{27}Al MAS spectra. We obtained the following parameters: $\delta_{iso} = 0.15 \pm 0.05$ ppm, $C_Q = 3.02 \pm 0.01$ MHz, and $\eta_Q = 0.16 \pm 0.01$. These parameters are in excellent agreement with those reported earlier by Wasylishen and colleagues.[43] These ^{27}Al NMR parameters were further confirmed by additional MAS, DOR, 3QMAS, and 5QMAS ^{27}Al NMR spectra obtained for α-Al(acac)$_3$ at 11.7, 14.1, and 21.1 T (data not shown). It is worth noting that, in each of the ^{27}Al DOR, 3QMAS, and 5QMAS spectra, a single peak is observed without any splitting from $^1J(^{17}O, ^{27}Al)$, suggesting that this *J*-coupling is less than 20 Hz.

Chemical-shift calculations

In this section, we examine the accuracy of chemical-shift

Fig. 6. Comparison of experimental (δ_{exptl}) and calculated (δ_{castep}) chemical shifts for ^{13}C and ^{17}O in α-Al(acac)$_3$. See text for discussions on the three structures.

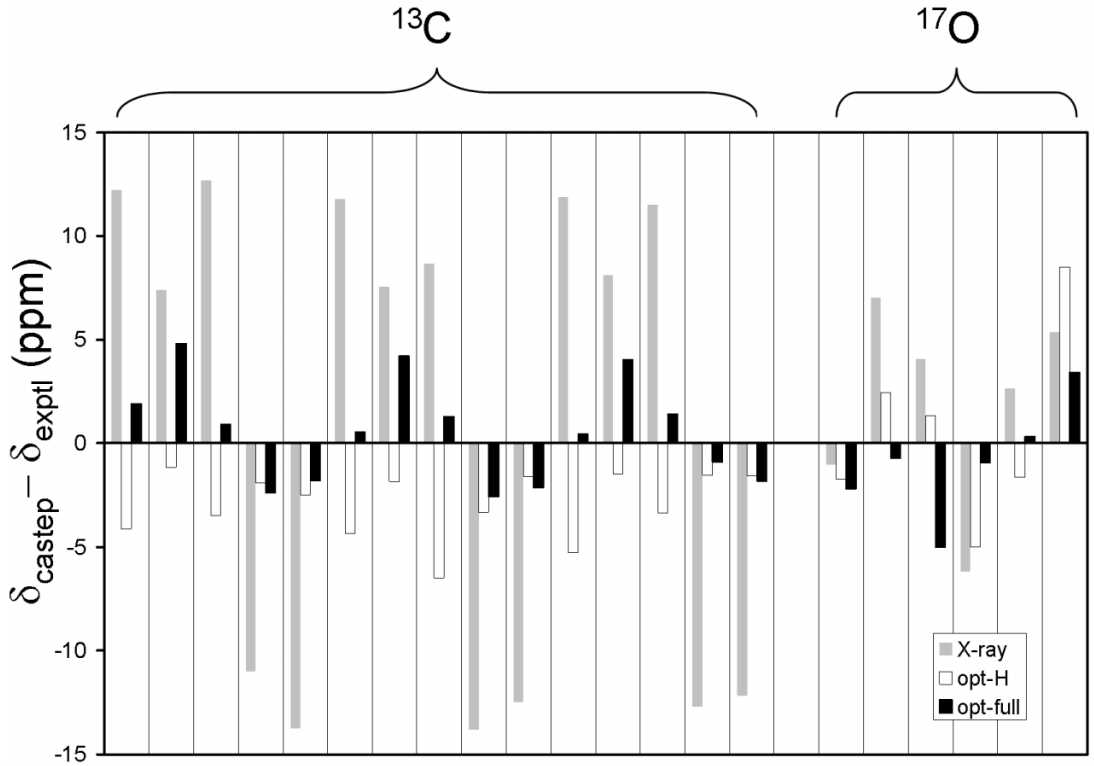

Can. J. Chem. Downloaded from www.nrcresearchpress.com by Xi'an Jiaotong University on 09/19/12
For personal use only.

calculations from the GIPAW method. To this end, we selected three α-Al(acac)$_3$ structures: (1) the original X-ray structure (R = 0.049 for 2028 reflections) as reported by Diaz-Acosta et al.[40] (denoted as the "X-ray" model), (2) the X-ray structure with the H-atom positions being optimized using CASTEP (denoted as the "opt-H" model), and (3) the X-ray structure with all atom positions being optimized (denoted as the "opt-full" model). Before discussing chemical shift results, we briefly comment on some structural differences among the three models. It is well-known that H-atom positions determined by X-ray crystal structures are not accurate and that CH bonds are typically too short (ca. 0.95 Å). Indeed, after the H-atom optimization, the CH bonds in Al(acac)$_3$ are increased by 0.14–0.16 Å for the CH and CH$_3$ groups. In the "opt-full" model, the O and C atoms change their positions slightly (O: 0.02 Å; C: 0.02–0.05 Å), in addition to the aforementioned lengthening of the CH bonds. Another useful measure of the structure is to examine the average forces given as Cartesian components for individual atoms. In the "X-ray" structure, significant forces are present on H-atoms (as large as 8 eV/Å), and the average forces on heavy atoms are also sizable (C: up to 6 eV/Å; O: up to 2 eV/Å; Al: 0.06 eV/Å). In the "opt-H" model, however, while forces on the H-atoms diminish (<0.06 eV/Å), they remain on other heavy atoms (C: 1.2 eV/Å; O: 1.6 eV/Å). In the final "opt-full" structure, average forces on all atoms are much smaller than 0.06 eV/Å.

All computational results of chemical shifts are summarized in Table 1. Figure 6 illustrates the differences in computational results for ^{13}C and ^{17}O among the three models. Because there is only one data point for ^{27}Al and because ^{1}H chemical shifts span a very narrow range, we did not include them in Fig. 6. Clearly, improvement of the "opt-H" model over the "X-ray" structure occurs primarily on the ^{1}H chemical shifts and on the ^{13}C chemical shifts for the CH and CH$_3$ groups. Interestingly, the "opt-H" model does not show any improvement for the ^{17}O chemical shifts. In the final "opt-full" model, all calculated chemical shifts show reasonable agreement with the experimental ones (with root-mean-square-deviation values of less than 3 ppm). Now we can also compare our CASTEP results with the GIAO DFT results (Gaussian 98) reported by Amini and Tafazzoli.[44] In their study, they used the same X-ray structure of α-Al(acac)$_3$, but optimized only the H-atom positions. In general, the CASTEP chemical shifts are in much better agreement with the experimental chemical shifts than the results of Amini and Tafazzoli. This is expected because they used a rather small basis set and an isolated molecule in their calculations. It can certainly be argued that α-Al(acac)$_3$ may not represent the best example to illustrate the importance of including the entire crystal lattice in chemical shift calculations. However, α-Al(acac)$_3$ is known to exhibit polymorphism. For example, while there is only one molecule in the asymmetric unit of α-Al(acac)$_3$, there are two optically active Al(acac)$_3$ molecules in the asymmetric unit of γ-Al(acac)$_3$.[57] The intermolecular contact in Al(acac)$_3$ is primarily due to CH$_3$···O interactions. It would be of interest to prepare γ-Al(acac)$_3$ and examine its solid-state NMR properties.

4. Conclusion

In this study, we have obtained accurate chemical shifts for all magnetic nuclei in α-Al(acac)$_3$ by using a variety of solid-state NMR experiments. All experimental chemical shifts are

Can. J. Chem. Downloaded from www.nrcresearchpress.com by Xi'an Jiaotong University on 09/19/12
For personal use only.

reasonably well reproduced by GIPAW chemical shift calculations, provided that a full optimization is employed to improve on the original X-ray structure. This appears to be the first attempt to treat all magnetic nuclei in a molecular crystal containing a metal centre on an equal footing regardless of the nature of their spins (i.e., spin-1/2 or quadrupolar). Although α-Al(acac)$_3$ represents a rather simple case, we anticipate that a similar approach should be applicable to more complex molecules. In addition, it is also possible in the future to combine *J*-based or dipolar-based 2-D heteronuclear correlation techniques with DOR or MQMAS to aid spectral assignment for quadrupolar nuclei.

Acknowledgements

This research was supported by the Natural Sciences and Engineering Research Council (NSERC) of Canada. We are grateful to Xin Mo for assistance in preparing ^{17}O-labeled Al(acac)$_3$ and to Irene Kwan for assistance in performing powder X-ray diffraction experiments. Access to the 900 MHz NMR spectrometer and CASTEP software was provided by the National Ultrahigh-Field NMR Facility for Solids (Ottawa, Canada), a national research facility funded by the Canada Foundation for Innovation, the Ontario Innovation Trust, Recherche Québec, the National Research Council Canada, and Bruker BioSpin and managed by the University of Ottawa (http://www.nmr900.ca). NSERC is acknowledged for a Major Resources Support grant. MES thanks the Engineering and Physical Sciences Research Council, UK (EPSRC) and the University of Warwick for contributions. NMR infrastructure, and elements of the solid-state NMR spectrometer consoles and probes used in this research were obtained through the Birmingham Science City Project, with support from Advantage West Midlands (AWM) and part funded by the European Regional Development Fund (ERDF).

References

(1) Harris, R. K.; Wasylishen, R. E.; Duer, M. J., Eds. *NMR Crystallography*. Wiley: Chichester, 2009.
(2) Harris, R. K.; Joyce, S. A.; Pickard, C. J.; Cadars, S.; Emsley, L. *Phys. Chem. Chem. Phys.* **2006** *8* (1), 137. doi:10.1039/b513392k.
(3) Harris, R. K.; Cadars, S.; Emsley, L.; Yates, J. R.; Pickard, C. J.; Jetti, R. K. R.; Griesser, U. J. *Phys. Chem. Chem. Phys.* **2007** *9* (3), 360. doi:10.1039/b614318k.
(4) Webber, A. L.; Emsley, L.; Claramunt, R. M.; Brown, S. P. *J. Phys. Chem. A* **2010** *114* (38), 10435. doi:10.1021/jp104901j.
(5) Kibalchenko, M.; Lee, D.; Shao, L.; Payne, M. C.; Titman, J. J.; Yates, J. R. *Chem. Phys. Lett.* **2010** *498* (4-6), 270. doi:10.1016/j.cplett.2010.08.077.
(6) Webber, A. L.; Elena, B.; Griffin, J. M.; Yates, J. R.; Pham, T. N.; Mauri, F.; Pickard, C. J.; Gil, A. M.; Stein, R.; Lesage, A.; Emsley, L.; Brown, S. P. *Phys. Chem. Chem. Phys.* **2010** *12* (26), 6970. doi:10.1039/c001290d.
(7) Samoson, A.; Lippmaa, E.; Pines, A. *Mol. Phys.* **1988** *65* (4), 1013. doi:10.1080/00268978800101571.
(8) Chmelka, B. F.; Mueller, K. T.; Pines, A.; Stebbins, J.; Wu, Y.; Zwanziger, J. W. *Nature* **1989** *339* (6219), 42. doi:10.1038/339042a0.
(9) Wu, Y.; Sun, B. Q.; Pines, A.; Samoson, A.; Lippmaa, E. *J. Magn. Reson.* **1990** *89* (2), 297. doi:10.1016/0022-2364(90)90236-3.
(10) Frydman, L.; Harwood, J. S. *J. Am. Chem. Soc.* **1995** *117* (19), 5367. doi:10.1021/ja00124a023.
(11) Medek, A.; Harwood, J. S.; Frydman, L. *J. Am. Chem. Soc.* **1995** *117* (51), 12779. doi:10.1021/ja00156a015.
(12) Pickard, C. J.; Mauri, F. *Phys. Rev. B* **2001** *63* (24), 245101. doi:10.1103/PhysRevB.63.245101.
(13) Yates, J. R.; Pickard, C. J.; Mauri, F. *Phys. Rev. B* **2007** *76* (2), 024401. doi:10.1103/PhysRevB.76.024401.
(14) Clark, S. J.; Segall, M. D.; Pickard, C. J.; Hasnip, P. J.; Probert, M. J.; Refson, K.; Payne, M. C. *Z. Kristallogr.* **2005** *220* (5-6-2005), 567. doi:10.1524/zkri.220.5.567.65075.
(15) Harris, R. K. *Solid State Sci.* **2004** *6* (10), 1025. doi:10.1016/j.solidstatesciences.2004.03.040.
(16) Yates, J. R.; Pickard, C. J.; Payne, M. C.; Dupree, R.; Profeta, M.; Mauri, F. *J. Phys. Chem. A* **2004** *108* (28), 6032. doi:10.1021/jp049362+.
(17) Gervais, C.; Dupree, R.; Pike, K. J.; Bonhomme, C.; Profeta, M.; Pickard, C. J.; Mauri, F. *J. Phys. Chem. A* **2005** *109* (31), 6960. doi:10.1021/jp0513925.
(18) Harris, R. K.; Hodgkinson, P.; Pickard, C. J.; Yates, J. R.; Zorin, V. *Magn. Reson. Chem.* **2007** *45* (S1), S174. doi:10.1002/mrc.2132.
(19) Ashbrook, S. E.; Le Pollès, L.; Pickard, C. J.; Berry, A. J.; Wimperis, S.; Farnan, I. *Phys. Chem. Chem. Phys.* **2007** *9*, 1587. doi:10.1039/b618211a.
(20) Zurek, E.; Pickard, C. J.; Autschbach, J. *J. Am. Chem. Soc.* **2007** *129* (14), 4430. doi:10.1021/ja069110h.
(21) Wong, A.; Thurgood, G.; Dupree, R.; Smith, M. E. *Chem. Phys.* **2007** *337* (1-3), 144. doi:10.1016/j.chemphys.2007.07.007.
(22) Bryce, D. L.; Bultz, E. B. *Chem. Eur. J.* **2007** *13* (17), 4786. doi:10.1002/chem.200700056.
(23) Joyce, S. A.; Yates, J. R.; Pickard, C. J.; Brown, S. P. *J. Am. Chem. Soc.* **2008** *130* (38), 12663. doi:10.1021/ja800419m.
(24) Johnston, J. C.; Iuliucci, R. J.; Facelli, J. C.; Fitzgerald, G.; Mueller, K. T. *J. Chem. Phys.* **2009** *131*, 144503. doi:10.1063/1.3225270.
(25) Sutrisno, A.; Terskikh, V. V.; Huang, Y. *Chem. Commun. (Camb.)* **2009**: 186. doi:10.1039/b817017g.
(26) Sutrisno, A.; Lu, C.; Lipson, R. H.; Huang, Y. *J. Phys. Chem. C* **2009** *113* (50), 21196. doi:10.1021/jp9044786.
(27) Zhu, J.; Geris, A. J.; Wu, G. *Phys. Chem. Chem. Phys.* **2009** *11* (32), 6972. doi:10.1039/b906438a.
(28) O'Dell, L. A.; Schurko, R. W. *Phys. Chem. Chem. Phys.* **2009** *11* (32), 7069. doi:10.1039/b906114b.
(29) Chapman, R. P.; Bryce, D. L. *Phys. Chem. Chem. Phys.* **2009** *11* (32), 6987. doi:10.1039/b906627f.
(30) Hung, I.; Uldry, A.-C.; Becker-Baldus, J.; Webber, A. L.; Wong, A.; Smith, M. E.; Joyce, S. A.; Yates, J. R.; Pickard, C. J.; Dupree, R.; Brown, S. P. *J. Am. Chem. Soc.* **2009** *131* (5), 1820. doi:10.1021/ja805898d.
(31) Hamaed, H.; Laschuk, M. W.; Terskikh, V. V.; Schurko, R. W. *J. Am. Chem. Soc.* **2009** *131* (23), 8271. doi:10.1021/ja901347k.
(32) Zhou, B.; Sherriff, B. L.; Wang, T. *Am. Mineral.* **2009** *94* (7), 865. doi:10.2138/am.2009.3142.
(33) Moudrakovski, I.; Lang, S.; Patchkovskii, S.; Ripmeester, J. *J. Phys. Chem. A* **2010** *114* (1), 309. doi:10.1021/jp908206c.
(34) Widdifield, C. M.; Bryce, D. L. *J. Phys. Chem. A* **2010** *114* (5), 2102. doi:10.1021/jp909106j.
(35) Sutrisno, A.; Hanson, M. A.; Rupar, P. A.; Terskikh, V. V.; Baines, K. M.; Huang, Y. *Chem. Commun. (Camb.)* **2010** *46* (16), 2817. doi:10.1039/b926071d.

(36) Widdifield, C. M.; Bryce, D. L. *J. Phys. Chem. A* **2010** *114* (40), 10810. doi:10.1021/jp108237x.
(37) Zhu, J.; Lau, J. Y. C.; Wu, G. *J. Phys. Chem. B* **2010** *114* (35), 11681. doi:10.1021/jp1055123.
(38) Griffin, J. M.; Yates, J. R.; Berry, A. J.; Wimperis, S.; Ashbrook, S. E. *J. Am. Chem. Soc.* **2010** *132* (44), 15651. doi:10.1021/ja105347q.
(39) Hanna, J. V.; Smith, M. E. *Solid State Nucl. Magn. Reson.* **2010** *38* (1), 1. doi:10.1016/j.ssnmr.2010.05.004.
(40) Diaz-Acosta, I.; Baker, J.; Cordes, W.; Pulay, P. *J. Phys. Chem. A* **2001** *105* (1), 238. doi:10.1021/jp0028599.
(41) Champmartin, D.; Rubini, P. *Inorg. Chem.* **1996** *35* (1), 179. doi:10.1021/ic950635c.
(42) Liu, K.; Ryan, D.; Nakanishi, K.; McDermott, A. E. *J. Am. Chem. Soc.* **1995** *117* (26), 6897. doi:10.1021/ja00131a011.
(43) Schurko, R. W.; Wasylishen, R. E.; Foerster, H. *J. Phys. Chem. A* **1998** *102* (48), 9750. doi:10.1021/jp982367k.
(44) Amini, S. K.; Tafazzoli, M. *Magn. Reson. Chem.* **2008** *46* (11), 1045. doi:10.1002/mrc.2324.
(45) Lesage, A.; Sakellariou, D.; Hediger, S.; Elena, B.; Charmont, P.; Steuernagel, S.; Emsley, L. *J. Magn. Reson.* **2003** *163* (1), 105. doi:10.1016/S1090-7807(03)00104-6.
(46) Samoson, A.; Lippmaa, E. *J. Magn. Reson.* **1989** *84* (2), 410. doi:10.1016/0022-2364(89)90389-2.
(47) Samoson, A.; Tegenfeldt, J. *J. Magn. Reson. A* **1994** *110* (2), 238. doi:10.1006/jmra.1994.1210.
(48) Eichele, K.; Wasylishen, R. E. *WSolids: NMR Simulation Package*, Version 1.19.11; 2009.
(49) Massiot, D.; Fayon, F.; Capron, M.; King, I.; Le Calvé, S.; Alonso, B.; Durand, J.-O.; Bujoli, B.; Gan, Z.; Hoatson, G. *Magn. Reson. Chem.* **2002** *40*, 70. doi:10.1002/mrc.984.
(50) Profeta, M.; Mauri, F.; Pickard, C. J. *J. Am. Chem. Soc.* **2003** *125* (2), 541. doi:10.1021/ja027124r.
(51) Perdew, J. P.; Burke, K.; Ernzerhof, M. *Phys. Rev. Lett.* **1996** *77* (18), 3865. doi:10.1103/PhysRevLett.77.3865.
(52) Perdew, J. P.; Burke, K.; Ernzerhof, M. *Phys. Rev. Lett.* **1998** *80* (4), 891. doi:10.1103/PhysRevLett.80.891.
(53) Pfrommer, B. G.; Cote, M. G. L. S.; Cohen, M. L. *J. Comput. Phys.* **1997** *131*, 233. doi:10.1006/jcph.1996.5612.
(54) Pyykko, P. *Mol. Phys.* **2008** *106* (16), 1965. doi:10.1080/00268970802018367.
(55) Smith, M. E.; Van Eck, E. R. H. *Prog. Nucl. Magn. Reson. Spectrosc.* **1999** *34* (2), 159. doi:10.1016/S0079-6565(98)00028-4.
(56) Wong, A.; Pike, K. J.; Jenkins, R.; Clarkson, G. J.; Anupold, T.; Howes, A. P.; Crout, D. H. G.; Samoson, A.; Dupree, R.; Smith, M. E. *J. Phys. Chem. A* **2006** *110* (5), 1824. doi:10.1021/jp055807y.
(57) McClelland, B. W. *Acta Crystallogr. Sect. B: Struct. Crystallogr. Cryst. Chem.* **1975** *31*, 2496. doi:10.1107/S056774087500787X.

Can. J. Chem. Downloaded from www.nrcresearchpress.com by Xi'an Jiaotong University on 09/19/12
For personal use only.

^{2}H double- and zero-quantum filtered NMR spectroscopy for probing the environments of water in Nafion

Jesse R. Vanderveen, Mark A. Blackburn, and Kristopher J. Ooms

Can. J. Chem. Downloaded from www.nrcresearchpress.com by Xi'an Jiaotong University on 09/19/12
For personal use only.

Abstract: Multiple quantum ^{2}H NMR spectroscopy is used to study the structure and dynamics of D_2O in Nafion membranes as a function of membrane hydration. By employing both double- and zero-quantum filtered experiments, residual quadrupolar coupling constants and T_2 relaxation values are obtained. The residual couplings vary from 240 to 20 Hz and the T_2 values range from 20 to 180 ms, with the high hydration values having smaller couplings and longer T_2 values. Analysis of the data using a water-exchange model suggests that the changes in parameters arise from a change in the fraction of time water spends in the anisotropic environments and not from changes in the order parameters that characterize the anisotropic sites. It has been found that a two-site model is needed to accurately fit the spectra above a hydration level of 10 D_2O per sulfonate, with the second site having a negligible residual quadrupolar coupling. The data supports a model with two different hydration layers at high hydration and can be understood in terms of the recently proposed parallel-channel model for Nafion hydration.

Key words: polymer electrolyte membrane, Nafion, DQF, ZQF, ^{2}H NMR, hydration models, residual quadrupolar couplings, relaxation.

Résumé : On a utilisé la RMN du ^{2}H à quantum multiple pour étudier la structure et la dynamique du D_2O dans des membranes de Nafion en fonction de l'hydratation de la membrane. En faisant appel à des expériences à filtrage à quantum double (FQD) et filtrage à quantum zéro (FQZ), on a pu obtenir les constantes de couplage quadripolaire et les valeurs des temps de relaxation, T_2. Les couplages résiduels varient de 240 à 20 Hz et les valeurs de T_2 s'étalent de 20 à 180 ms; les taux d'hydratation élevés sont associés aux couplages les plus faibles et les valeurs de T_2 les plus longues. Une analyse des données en faisant appel au modèle d'échange de l'eau suggère que les changements dans les paramètres découlent d'un changement dans la fraction de temps passé dans les environnements anisotropes et non pas de changements dans les paramètres d'ordre qui caractérisent les sites isotropes. On a trouvé qu'il est nécessaire d'utilisé un modèle à deux sites pour bien ajuster les spectres au-delà d'un niveau d'hydratation de 10 D_2O par sulfonate et que le deuxième site ne présente qu'un couplage quadripolaire résiduel. Les données sont en accord avec un modèle avec deux types différents de couches d'hydratation à hydratation élevée et il peut être compris en fonction du modèle à canaux parallèles proposé récemment pour l'hydratation du Nafion.

Mots-clés : membrane d'électrolyte polymère, Nafion, filtrage à quantum double (FQD), filtrage à quantum zéro (FQZ), modèles d'hydratation, couplages quadripolaires résiduels, relaxation.

[Traduit par la Rédaction]

Introduction

As the world attempts to reduce its dependence on hydrocarbon fuels, hydrogen, coupled to modern fuel cell technologies, can provide one alternative for meeting our requirements for clean fuel.[1] The use of hydrogen fuel cells provides the means by which some of the energy stored in the chemical bonds of the H_2 molecule can be converted to electricity with greater efficiency and safety than by combustion. The basic architecture of a hydrogen fuel cell involves a catalytic anode where H_2 gas is split into $2H^+$ and $2e^-$. Electrons are routed through an external circuit to the cathode while protons are transported through a membrane to the cathode where electrons, protons, and O_2 molecules react to form water. A key component of any fuel cell is the membrane that transports the protons from the anode to the cathode; the efficiency of the fuel cell is affected by the ability of the membrane to rapidly conduct the protons.[2] In many polymer membranes, such as Nafion, conduction occurs along water networks. Therefore, studying the structure and behaviour of water networks under different conditions is vitally important to understanding and improving fuel cell membranes.[3–6] For example, magnetic resonance imaging techni-

Received 27 December 2010. Accepted 18 February 2011. Published at www.nrcresearchpress.com/cjc on 24 August 2011.

J.R. Vanderveen, M.A. Blackburn, and K.J. Ooms. Department of Chemistry, The King's University College, 9125-50St. Edmonton, AB T6B 2H3, Canada.

Corresponding author: K.J. Ooms (e-mail: kris.ooms@kingsu.ca).

This article is part of a Special Issue dedicated to Professor Roderick E. Wasylishen.

Can. J. Chem. Downloaded from www.nrcresearchpress.com by Xi'an Jiaotong University on 09/19/12
For personal use only.

ques are increasingly being used to study water content in different parts of the membrane as a function of fuel cell operation to better understand water distribution and management.[7–17]

Current models of membrane hydration are based primarily on small-angle X-ray scattering (SAXS) and small-angle neutron scattering (SANS) studies.[5,18–20] The structure of the Nafion polymer, composed of a hydrophobic perfluoronated polymer that has hydrophilic sulfonated side chains, leads to water regions that form a reverse micelle-like structure within hydrophilic regions of the polymer matrix. Many models have been proposed to explain the experimental data and membrane properties by describing the shape and size of the water domains. The dominant model used for many years is based on the work of Gierke and expanded upon by Gebel.[18,21] This model involves three general structural motifs for the hydrated membranes below a hydration, λ, of 22 waters per sulfonate. At the lowest hydration levels, water molecules are very tightly bound to negatively charged sulfonate groups.[22] As hydration increases, pockets of water form in the swollen membrane and significant amounts of mobile water become present.[18,23] A final structural change occurs when hydration reaches approximately $\lambda = 14$ as channels form between the water pockets allowing for percolation of water through the membrane.[18]

A more recent hydration model has been proposed by Schmidt-Rohr and Chen based on predicted scattering profiles. After comparing predicted profiles for numerous models to the experimental scattering data, the authors concluded that the structure of the water environments could be best described by a parallel-channel model where channels are present at most hydration levels and simply expand in size as water is absorbed by the membrane. This model accounts for much of the experimental scattering and conductivity data. It is also based on ^{19}F and ^{13}C solid-state NMR results which suggest that the polymer backbone has rigid domains.[24,25]

The decades-long debate over the structure and behaviour of water in Nafion membranes is a result of the complex nature of the membrane–water interactions as well as the limited experimental methods by which membranes and hydration can be studied.[5,26] It is vital that new techniques be developed and used to study this important problem so that the understanding and methodologies developed for Nafion can be extended to new polymer membranes. This is particularly important now that theoretical modellers have begun to develop simulation methods to study hydration in Nafion at the molecular level.[6,26–36] When studying disordered polymer materials, NMR is a powerful technique to employ.[37] Numerous NMR studies have already been used to study the structure of the polymer,[24,25] the environment and motion of ions in the membrane,[38] and the behaviour of water in the membrane. The studies of water have focused on two regimes: the water–hydronium molecules which are tightly bound to the sulfonate groups have been studied mainly by solid-state NMR techniques,[22,39–41] whereas the more mobile water domains are studied using relaxation-based NMR techniques and NMR diffusion studies.[41–47]

The development of multiple quantum filtering (MQF) techniques has allowed researchers to study systems that fall between the extremes of solution and solid-state NMR. When nuclei exist in solution-like environments but do not experience isotropic motion, the dipolar and quadrupolar couplings may not be averaged to zero, as they are in cases of rapid isotropic motion, resulting in small residual couplings that can be measured using MQF NMR.[48–51] MQF NMR has been used to study ordered biological samples such as cartilage and spinal disc tissue, where water molecules sample anisotropic environments.[50,52–61] The same principles that have made MQF NMR valuable for studying biological materials make it potentially useful for studying hydrated membranes.

MQF techniques can be used to measure either residual dipolar couplings or residual quadrupolar couplings. Typically residual dipolar couplings are extremely small and can be difficult to detect unless the species being studied is tightly bound.[59] For example, the tightly bound protons in dry Nafion have been observed using ^1H MQF NMR.[22] To study water or ions that experience very limited ordering a more sensitive coupling must be used. The quadrupolar coupling is generally larger than the dipolar coupling and the use of MQF techniques to measure residual quadrupolar couplings has proven useful when residual dipolar couplings cannot be detected.[59] This study explores the use of MQF techniques for studying the water in the Nafion membrane as a function of hydration. The power of the quadrupolar interaction is harnessed by performing ^2H NMR studies of D_2O in the membranes and employing both double- and zero-quantum filtered experiments, DQF and ZQF, respectively.

Theory

The anisotropic nuclear magnetic resonance interactions provide ideal ways to explore the structure around a nucleus. For nuclei with spins greater than 1/2, there exists an interaction between the quadrupole moment of the nucleus, $\boldsymbol{Q}$, and the electric field gradient, EFG, set up by the charge distribution about the nucleus. The anisotropy of the EFG results in an orientation dependence of the quadrupolar-perturbed NMR energy levels. The EFG is described by a traceless second-rank tensor that can be expressed in its principal axis system by three components such that $|V_{ZZ}| \geq |V_{YY}| \geq |V_{XX}|$. The EFG is often expressed using two derived parameters, the quadrupolar coupling, C_Q (in Hz), and the asymmetry parameter, η_Q:[62,63]

$$[1] \qquad C_Q = \frac{V_{ZZ}eQ}{h}$$

$$[2] \qquad \eta_Q = \frac{(V_{XX} - V_{YY})}{V_{ZZ}}$$

The NMR spectra of a spin $I = 1$ nucleus such as deuterium in a molecule experiencing no motional averaging results in a frequency shift to the $m_I = 0 \leftrightarrow 1$ and the $m_I = -1 \leftrightarrow 0$ transitions. For a single crystal, this results in two NMR peaks separated by $2Q$, where Q is the quadrupolar half splitting which depends on C_Q, η_Q, and the orientation of the EFG in the magnetic field, defined by the angles θ and ϕ:[62]

$$[3] \qquad Q(\theta, \phi) = \frac{3\pi}{4} C_Q[3\cos^2\theta - 1 - \eta \sin^2\theta \cos 2\phi]$$

Can. J. Chem. Downloaded from www.nrcresearchpress.com by Xi'an Jiaotong University on 09/19/12
For personal use only.

In solution, where molecules can rotate freely, the quadrupolar interaction is averaged to zero and there is no effect on the peak positions in the NMR spectrum, i.e., no quadrupolar splitting. However, if the molecule is in a fluid-like environment but experiences some restriction to its motion, a small residual quadrupolar coupling C_Q^{res}, can be present. These small couplings may not be evident from one-pulse, single-quantum NMR spectra and can be easily masked by the signal from molecules experiencing isotropic motion in the sample. One experimental method for measuring these small residual couplings is MQF NMR spectroscopy. The pulse sequence used to obtain MQF NMR spectra is shown in Fig. 1.[56,59]

The MQF sequences involve two key components, an excitation pulse followed by an evolution period where spin magnetization is allowed to evolve and develop from the single quantum coherence level into the different quantum coherence levels available to the nucleus. This is followed by a set of filter pulses which select individual coherence pathways. For an isolated deuterium nucleus, $I = 1$, there are three quantum coherence levels: 0, 1, and 2. The transfer of magnetization from the single-quantum to the double- or zero-quantum coherences during the mixing time, τ, is proportional to the magnitude of the residual quadrupolar interaction and is attenuated by longitudinal relaxation, T_2. The zero-quantum and double-quantum coherences can be selected using the pulse sequence shown in Fig. 1 by varying the phase cycling of the last filter pulse and the acquisition. The spin density, which is related to the signal intensity, detected immediately after the filter pulses, is a function of τ and is given by

$$[4] \qquad \rho_{ZQF} \propto \cos(Q\tau)\exp(-\tau/T_2)$$

$$[5] \qquad \rho_{DQF} \propto \sin(Q\tau)\exp(-\tau/T_2)$$

During the acquisition, a free induction decay is observed and can be modeled using analytical equations. The signal obtained at the start of the acquisition is analogous to echo modulation where the modulation occurs due to Q and T_2. Upon Fourier transformation, ^{2}H NMR spectra are obtained that have the following form for the ZQF and DQF experiments:[56]

$$[6] \qquad S_{ZQF}(\tau,\omega_2) = \cos(Q\tau)\exp(-\tau/T_2) \times \left[\frac{1/T_2^*}{(\omega_2-\delta_0+Q)^2+(1/T_2^*)^2} + \frac{1/T_2^*}{(\omega_2-\delta_0-Q)^2+(1/T_2^*)^2}\right]$$

$$[7] \qquad S_{DQF}(\tau,\omega_2) = \sin(Q\tau)\exp(-\tau/T_2) \times \left[\frac{\omega_2-\delta_0+Q}{(\omega_2-\delta_0+Q)^2+(1/T_2^*)^2} - \frac{\omega_2-\delta_0-Q}{(\omega_2-\delta_0-Q)^2+(1/T_2^*)^2}\right]$$

where δ_0 represents the frequency offset of the peak in s^{-1}, ω_2 represents the frequency points in the spectrum and T_2^* is the relaxation that occurs during the acquisition. T_2^* is the combination of T_2 and an additional line broadening factor due to inhomogeneous broadening, W.

$$[8] \qquad 1/T_2^* = \pi W + 1/T_2$$

Equations [6] and [7] reveal that DQF and ZQF spectra provide complimentary ways of obtaining the parameters C_Q^{res}, which is related to Q by eq. [3], and T_2 based on both the signal intensity and the lineshape as a function of τ. The contribution that free water makes to the DQF and ZQF signal is also different. Since $Q = 0$ Hz for free water, the ZQF experiment contains a signal from free water, $\cos(Q\tau) = 1$, whereas the DQF signal contains no signal, $\sin(Q\tau) = 0$. It should be noted that these equations are valid when the motion of the water molecules is not in the extreme narrowing regime. As will be discussed later, if the water molecules have very short correlation times, i.e., they spend very little time in the anisotropic sites, they will enter the extreme narrowing regime where $\omega_0\tau_c \ll 1$. In this case the T_2 relaxation rate of the zero quantum signal is 3/5 that of the double quantum signal. Previous research has indicated that the water molecules may have correlation times approaching that of free water which would place them in the extreme narrowing regime.[47]

Fig. 1. The NMR pulse sequence used to acquire DQF and ZQF ^{2}H NMR spectra. A 180° refocusing pulse is placed in the middle of the mixing time, τ, to refocus any chemical shift or dipolar interactions. The four-step phase cycle for the last pulse is x, y, $-x$, $-y$ for both ZQF and DQF. The detection phase cycles for ZQF and DQF are x, y, $-x$, $-y$, and x, $-y$, $-x$, y, respectively. The delay t_1 was set to 10 ms and t_2 ranged from 1 to 3 s depending on the breadth of the peaks.

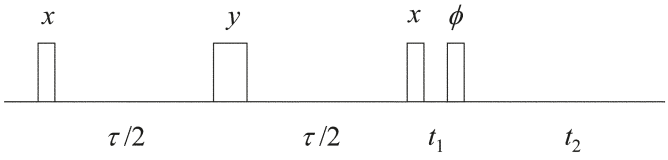

In fitting experimental spectra to the analytical expressions above, the total ZQF and DQF lineshapes of a sample are evaluated by summation of the equations over the isotropic distribution of the angles (θ, ϕ) and by weighted summation over a range of local environments having distinct values for C_Q, T_2, W, and f_0 ($f_0 = \delta_0/2\pi$).[61] This latter summation provides a powerful means of analysing multiple water environments within a specific sample. Multiple sites are often required in the fitting of experimental spectra to properly reproduce the signal intensity and line shape, suggesting the presence of different structural or kinetic water domains within the sample.[61]

Experimental

Membrane Treatment

Six different 6 cm × 1.3 cm strips of Nafion 117 (Nafion® Membrane, Fuel Cell Earth, LLC) were treated to convert the as-received membrane to the acid form.[44] The membranes were heated in a 3% H_2O_2 (Fisher) solution for one hour, washed in boiling distilled water for one hour, heated in a 0.5 mol/L H_2SO_4 (Caledon, ACS) solution for one hour, and then washed in boiling distilled water for another hour. The Nafion strips were dehydrated under vacuum and slight heat until the anhydrous weight stabilized. The anhydrous membranes were then rehydrated with D_2O (Acros, 99.5% D). Each sample was placed in a 5 mm solution NMR tube so that the membrane was coiled around the wall of the tube. The tube was then capped and sealed with Parafilm™ for the NMR experiments. Between 20 and 25 ZQF and DQF

Can. J. Chem. Downloaded from www.nrcresearchpress.com by Xi'an Jiaotong University on 09/19/12
For personal use only.

spectra were acquired for each hydration level. Sample placement was carefully monitored in an attempt to reduce the effects of magnetic susceptibility differences between the experiments. Different sample alignments were tested and did not produce significant differences in the data. Hydration values, λ, in units of D_2O per sulfonate,[23] were calculated based on the mass of water absorbed by the membrane, which was measured immediately before and after the NMR experiments were performed. The trends in hydration were also monitored by comparing the ^2H NMR signal intensities from a one-pulse experiment; a linear correlation between the signal intensities and the λ values confirmed the hydration levels. T_1 values were also measured for all samples and were comparable to those measured by others.[44]

Data Acquisition

All NMR spectra were collected on a Bruker Avance 400 MHz NMR spectrometer at The King's Center for Molecular Structure using a Bruker ATMA multinuclear probe tuned at 61.42 MHz for ^2H with a 180° pulse optimized to 40.5 μs. Experiments were referenced to liquid D_2O set at 0 Hz. The spectrometer was manually shimmed before the acquisition of each sample to reduce line shape distortions arising from sample placement; the adjustments required were typically small suggesting that the care taken during sample alignment was adequate to obtain reproducible results. T_1 relaxation measurements were made using the standard inversion recovery pulse sequence and analysed using the Bruker software. DQF and ZQF experiments were conducted using the pulse sequence shown in Fig. 1. The mixing time τ was varied from 1 ms to 120 ms depending on the experiment and the sample. The spectral fitting was performed using a home-written Matlab program based on the program developed by Polenova, Vega, and Ooms[61] which employed a multi-variable non-linear least-squares regression method to minimize the residual for a set of at least 16 calculated and experimental spectra. By including both DQF and ZQF spectra in the fitting procedure, quantitative inclusion of the water environments was ensured with very small residual quadrupole interactions.

The primary source of error in the data is experimental. Analysis of the data reveals significant variation in the parameters obtained from different samples at similar hydrations. Some of this error may be from sample alignment and field inhomogeneities during the NMR experiments, but the largest source of error arises from sample preparation. It has been noted by numerous researchers that sample preparation plays an important roll in determining Nafion membrane properties.[23] This is true for bulk property measurements and is magnified when studying molecular level properties. A detailed look at the effects of sample preparation on the measured NMR parameters is currently underway. Despite the variations arising from these experimental sources of error, the trends observed and disused below are clearly significant and important.

Results and discussion

NMR spectra

Representative DQF and ZQF ^2H NMR spectra acquired from membrane samples with λ = 5.2 (top) and λ = 19 (bottom) are shown in Fig. 2. The spectra on the left are ZQF spectra as a function of mixing time, τ, while the spectra on the right are DQF spectra. The presence of a DQF signal clearly indicates that water in the membrane is experiencing restricted motion; as discussed above, freely moving water does not produce any DQF signal. Both sets of DQF spectra (Figs. 2*b* and 2*d*) show the expected dependence on mixing time (τ); the signal starts at a reduced intensity, builds up to a maximum, and then decays. The ZQF spectra (Figs. 2*a* and 2*c*) also show the expected patterns, starting at maximum intensity and then decaying as τ is increased.

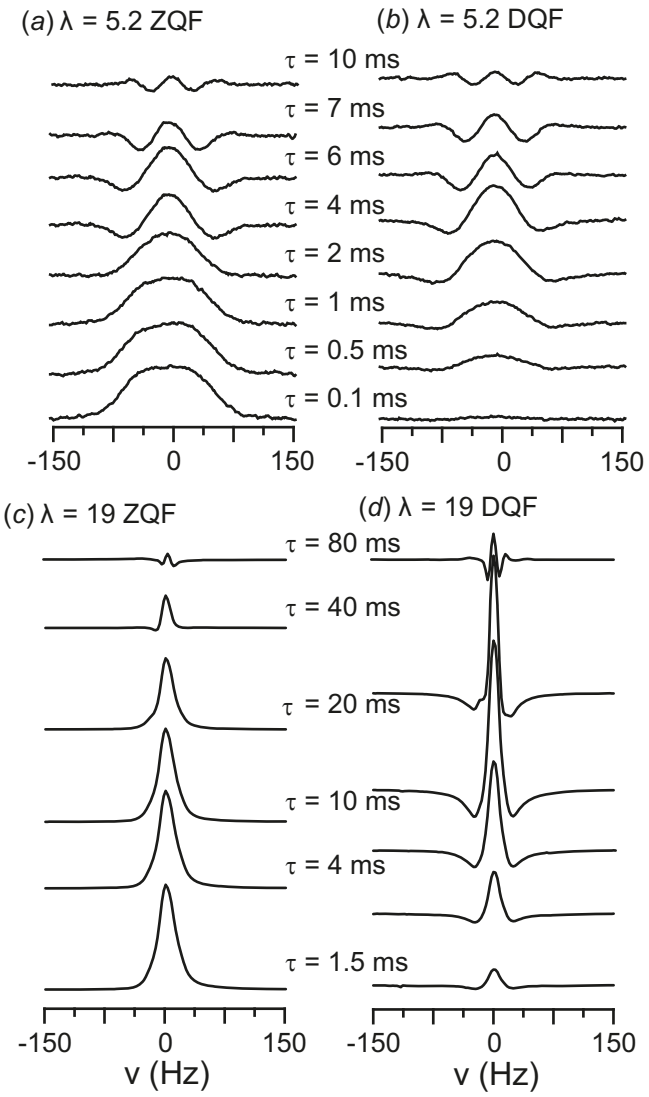

Fig. 2. Representative spectra for a Nafion membrane sample hydrated at λ = 5.2 (*a* and *b*) and λ = 19 (*c* and *d*). The spectra on the left are ZQF spectra as a function of mixing time, τ, while the spectra on the right are DQF spectra.

The linewidth-at-half-height measured at the start of the ZQF experiment changes from approximately 200 Hz at the lowest hydration level to around 20 Hz at the highest hydration level. The ZQF spectrum at the lowest τ value is approximately equivalent to the single-quantum spectrum measured

Can. J. Chem. Downloaded from www.nrcresearchpress.com by Xi'an Jiaotong University on 09/19/12
For personal use only.

using a standard single-pulse experiment. The broad lines observed at low hydration levels, Fig. 1*a*, are likely dominated by quadrupolar broadening whereas at the high hydration level, Fig. 1*c*, the narrow ZQF linewidths are dominated by T_2 relaxation as evidenced by their Lorentzian line shape.

Based on eqs. [6] and [7], significant information about the C_Q^{res} and T_2 can be inferred by examining the intensity of the DQF and ZQF signal as a function τ. The DQF spectra in particular are useful because the signal intensity is dominated by the $\sin(Q\tau)\exp(-\tau/T_2)$ part of eq. [7]; the build-up will be controlled by the quadrupolar coupling, and the signal decay will be governed by T_2. Figure 3 shows a plot of the maximum signal intensity of the DQF spectra normalized to the intensity of the single-quantum spectrum, plotted against τ for a series of hydration levels. At low hydration, the signal intensity builds up rapidly and achieves a maximum that is more than 60% the intensity of the single-quantum experiment. This indicates that most of the D_2O in the sample is experiencing some restricted motion. The T_2 relaxation values at low hydration are short, as would be expected for deuterium nuclei experiencing anisotropic motion. As the amount of water in the membrane increases, the slope of the build-up and the signal decay rate both decrease, suggesting that C_Q^{res} is being reduced and that T_2 is increasing. These changes in C_Q^{res} and T_2 are expected and confirm that the motion of the water molecules is becoming more isotropic as hydration increases.

A convenient way of representing the cumulative effect of the changing C_Q^{res} and T_2 parameters is to plot the τ value at which the signal intensity is maximum, τ_{max}, against the hydration level. Figure 4 shows a plot of τ_{max} vs λ and reveals a strong correlation between the two parameters. From a qualitative perspective, this correlation is extremely useful. Previously, researchers have used variations in τ_{max} to provide contrast for magnetic resonance imaging. By applying a DQF sequence before the imaging sequence and selecting a specific τ-value, signal intensity in the image can be correlated to the hydration level. Alternatively, τ-maps can be created where DQF signal intensity curves are acquired for each pixel in an image or point in a one dimensional cross section.[60,64,65] The results presented here suggest that using DQF to create contrast may also be useful for obtaining information at the molecular level about water distribution in membranes. Such techniques could complement magnetic resonance micro-imaging studies of water in operating fuel cells.[7,8,10–16]

Quantitative analysis

Using eqs. [6] and [7] and the multi-site fitting model discussed in the theory section, the experimental spectra were fit to calculated spectra. Typically 8 DQF and 8 ZQF spectra were selected to provide a good representation of the signal intensity curves. These 16 spectra were simultaneously fit by minimizing the difference, point-by-point, between the calculated and experimental spectra.[61] In almost all cases, good fits could be obtained for all 16 spectra. Figures 5 and 6 show typical fits. Each data set was fit using a one- and a two-site model. At low hydration most of the spectra could be fit using a single site, site **A**. However as the hydration approached $\lambda = 10$, the ZQF data could no longer be reliably

Fig. 3. Signal intensity curves for DQF spectra as a function of τ for a Nafion membrane sample at six different hydration levels. The build-up in the signal is governed by the quadrupolar coupling, $\sin(Q\tau)$, while the decay is predominantly due to T_2 relaxation, $\exp(-\tau/T_2)$.

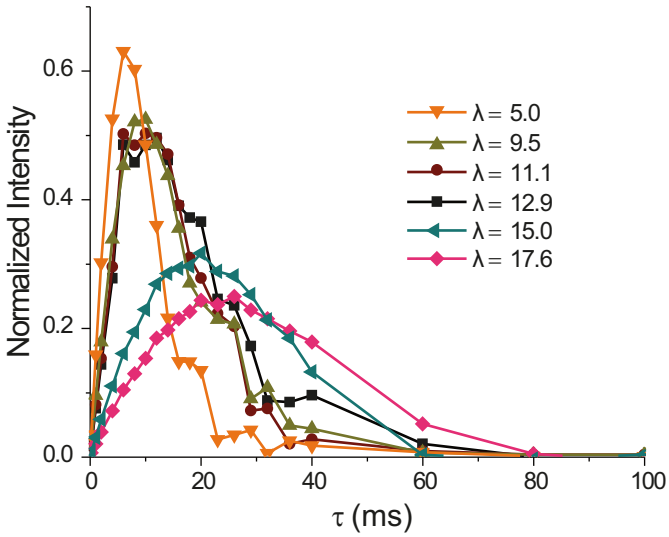

Fig. 4. A plot of the mixing time at which the maximum DQF signal intensity is observed, τ_{max}, vs the hydration level, λ, in D_2O per sulfonate.

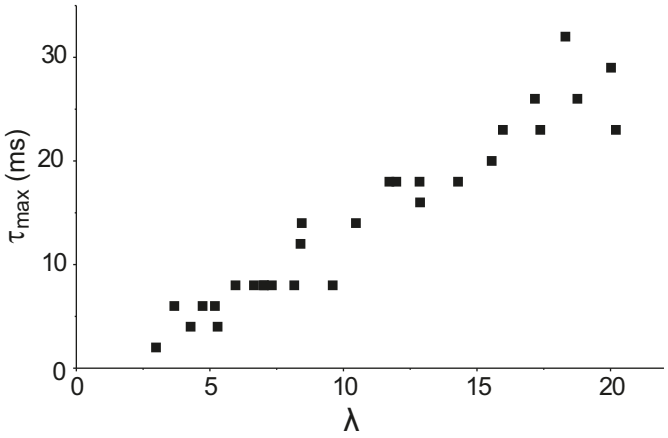

fit; specifically, the calculated ZQF spectra at longer τ values were too low in intensity (blue dot spectra in Fig. 6). This is a sign that a very small C_Q^{res} site is present in the sample. The two-site fits revealed that a second site with $C_Q^{res} <$ 20 Hz was present, site **B**. The red dashed spectra presented in Fig. 6 show the improved fit with the two-site model. The addition of a third site did not meaningfully improve the results. The results from the fitting procedure are available in the Supplementary data, Table S1.

The equation used to fit the ZQF data incorporated the 3/5 scaling of the T_2 value discussed in the theory section. Attempts to fit the data without this scaling consistently underestimated the ZQF line widths. The need to incorporate the 3/5 scaling factor indicates that the water responsible for the NMR signal is in the extreme narrowing regime where $\omega_0\tau_c \ll 1$. τ_c must therefore be much shorter than 10^{-8} s

Can. J. Chem. Downloaded from www.nrcresearchpress.com by Xi'an Jiaotong University on 09/19/12
For personal use only.

Fig. 5. Experimental (grey) and calculated (red) DQF and ZQF ^{2}H NMR spectra for a sample with a very low level of hydration, λ = 4.2. The figure demonstrates that even at low signal-to-noise ratios reasonable fits can be obtained.

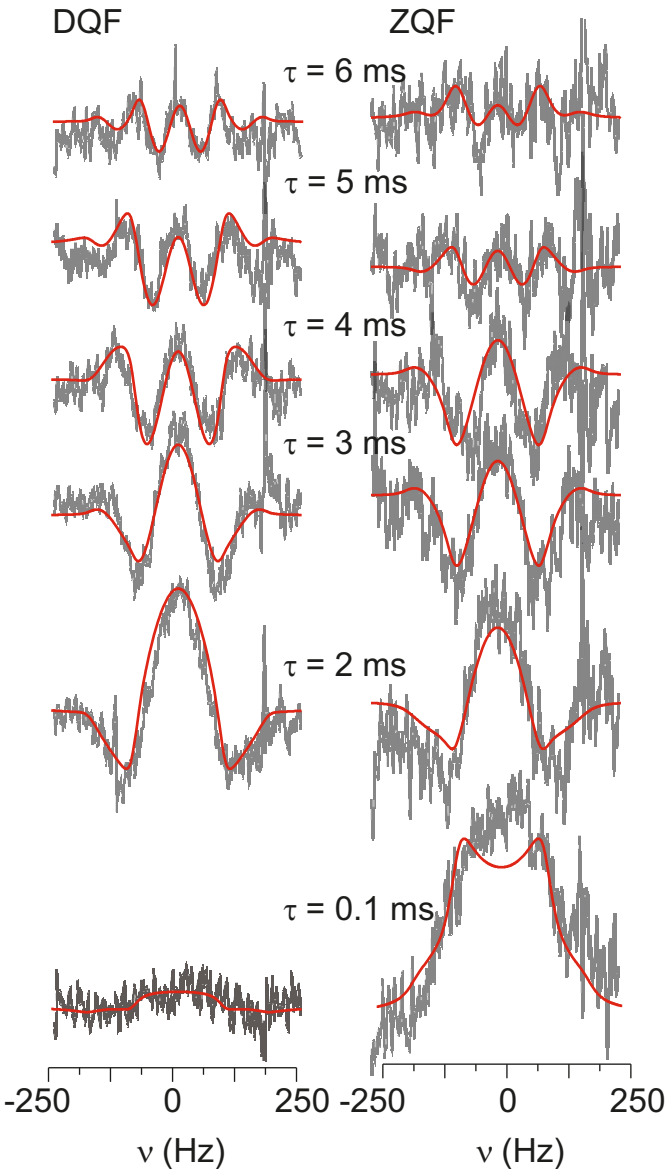

Fig. 6. Experimental (black) DQF and ZQF ^{2}H NMR spectra for a sample with an intermediate level of hydration, λ = 13.3. The blue spectra (dots) were calculated using a single-site model whereas the red spectra (dashes) demonstrate the improved fit of the ZQF spectra obtained with a two-site model.

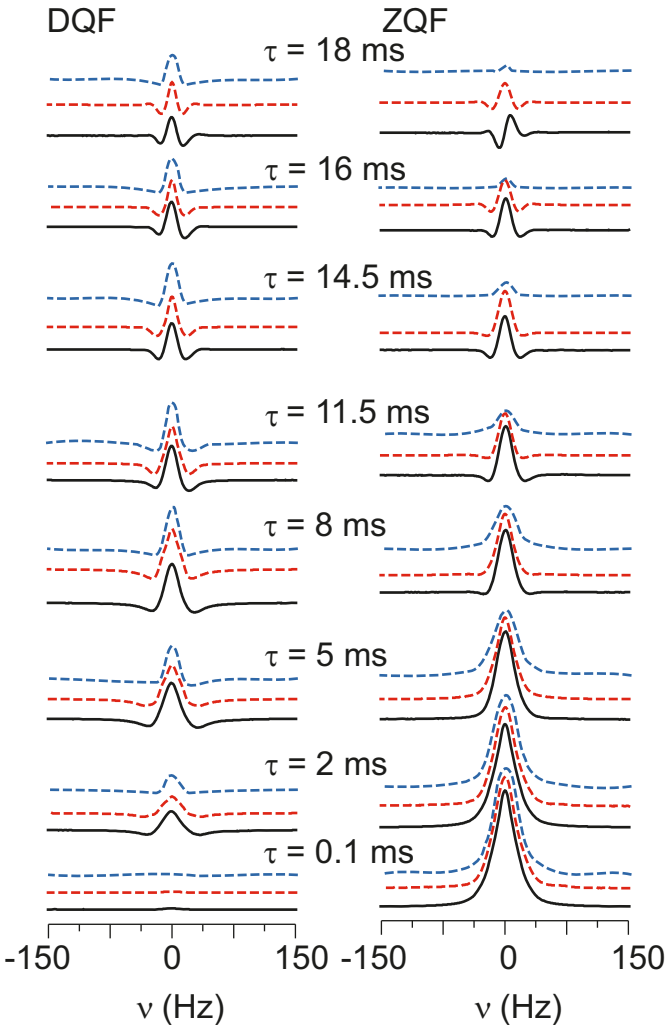

which is consistent with the correlation times reported by MacMillan and co-workers of 1.3×10^{-11} s, as well as the residence times reported by Devanathan and Perrin of 1.6×10^{-10} to 5×10^{-10} s.[6,28,47,66]

Analysis of C_Q^{res}

The C_Q^{res} values obtained as a function of hydration are plotted in Fig. 7*a* and show a non-linear decrease as the hydration increases. The C_Q^{res} values measured are small compared to those observed in other studies. For example, DQF studies of collagen hydration yield C_Q^{res} values in the kHz range at low hydration levels. In cartilage tissues, C_Q^{res} range from 100 Hz to 1500 Hz depending on the ratio of collagen to water in the tissue.[51,67]

If it is assumed that these results represent water that is in the motionally averaged regime, then the residual quadrupolar interaction is related to the quadrupolar half-splitting experienced by a water molecule when it is in an anisotropic site, Q_k, and the fraction of time it spends in the sites f_b,

$$[9] \qquad Q_{res} = \sum_k f_k Q_k = f_b \langle Q_k \rangle_b$$

where f_b is sum of all the f_k values for each site sampled by the water during the experiment. The value of $\langle Q_k \rangle_b$ is determined by the amount of motional restriction the water experiences when in an anisotropic site. The small C_Q^{res} values measured in this study arise either because the anisotropic environments sampled by the water molecules have very low degrees of order, leading to small $\langle Q_k \rangle_b$ values, or the fraction of time the water spends in the anisotropic sites, f_b, is very small, or both.

The changes in C_Q^{res} as a function of hydration are fairly smooth (Fig. 7) suggesting no large discontinuities in the structure of the water environments as hydration increases. At hydration levels above λ = 10, the C_Q^{res} values of site **A**

Can. J. Chem. Downloaded from www.nrcresearchpress.com by Xi'an Jiaotong University on 09/19/12
For personal use only.

Fig. 7. Plots of the experimental data obtained in this study vs Nafion membrane hydration (λ is in D_2O molecules per sulfonate). In the C_Q^{res} plot (*a*) the black points (closed boxes) are for site **A** while the red points (open boxes) are for site **B**. The T_2 data used corresponds to T_{2I}, see text.

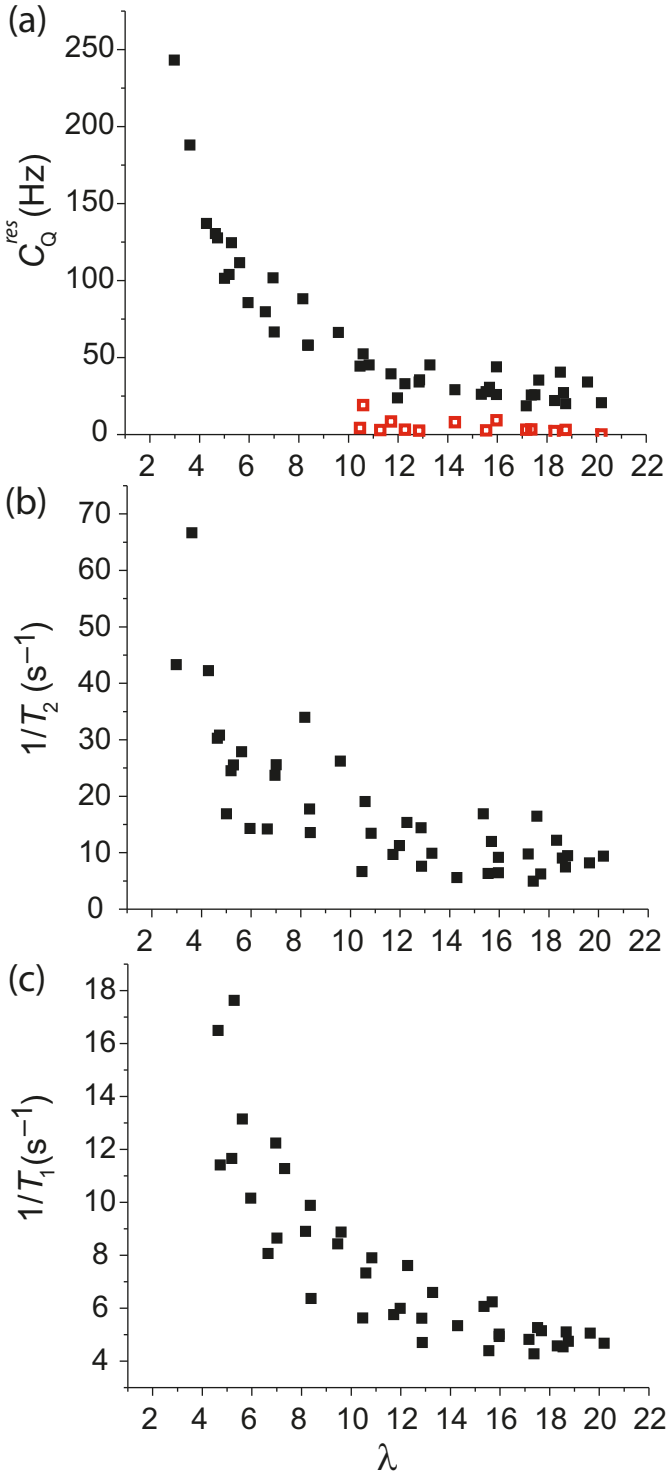

remain relatively constant at 35 ± 15 Hz, suggesting no dramatic changes in structure of the water environments. As discussed above, there are different models for the hydration of Nafion membranes. The model by Gierke proposed distinct structural regimes.[18,21] In particular, when λ was around 14 waters per sulfonate, the model proposes a structural change from isolated pockets of water to a network of channels. The parallel-channel model proposed by Schmidt-Rohr and Chen postulates that channels are created by the rigid polymer backbones.[19] Water molecules enter these and cause expansion of the channels as more water is absorbed by the membrane. This process is likely to lead to smooth changes in the water environments as hydration changes. Although the sudden formation of interconnected channels proposed by Gierke cannot be ruled out by these results, it seems unlikely that such a dramatic structural change would result in a change in C_Q^{res} less than 15 Hz, the spread of the experimental data. Our results are more consistent with the parallel channel model.

The ability of our technique to identify two sites above λ = 10 provides a valuable tool for understanding different water environments in the Nafion membrane. In addition to the C_Q^{res} and T_2 parameters, the two-site model provides relative amounts of water in the two sites. The fraction of water in site **B** increases as hydration increases, from approximately 15% near λ = 11 to 43% near λ = 20. This suggests that most of the water added to the membrane after λ = 10 undergoes nearly isotropic motion and supports a model for hydration in the parallel channels where approximately 10 water molecules per sulfonate ion form a hydration layer around the channel walls, experiencing anisotropic environments, and possessing the C_Q^{res} values observed for site **A**. Near a hydration level of λ = 10, enough water has entered the channels to form a second layer or core in the center of the channel. These water molecules do not sample anisotropic environments near the channel walls, yielding the negligible C_Q^{res} values observed for site **B**. Schmidt-Rohr and Chen indicate that at λ ≈ 12 the diameter of the channels is around 2.4 nm, much larger than that proposed by the other models.[19] This large diameter provides ample room for water molecules at the center of the channel to undergo isotropic motion and average the quadrupolar interaction to near zero values. This formation of a highly mobile core of water correlates well with the increase in the water diffusion constants and dielectric constants observed around λ = 9 to 11 and the need to have a relatively high hydration for Nafion fuel cells to function.[6,68]

Analysis of relaxation data

The $1/T_2$ and $1/T_1$ data as a function of λ are presented in Fig. 7*b* and 7*c*. The relaxation rates follow a trend similar to that for C_Q^{res} values, suggesting that the relaxation rates are strongly influenced by quadrupolar relaxation. The short correlation times for the water in the anisotropic sites suggested by this and previous studies mean that the relative orientation of the sites visited by a particular water molecule during the experiment are independent of each other. Similar assumptions for water in gels and tissues have led Halle and co-workers to propose a stochastic model of exchange-mediated orientational randomization (EMOR).[69–73] Using this model Halle has developed equations that describe the ^2H relaxation rates:

$$[10]\quad \frac{1}{T_{2I}} = (1-f_b)\frac{1}{T_{2I}^0} + \frac{3\pi^2}{20}C_{Q0}^2\sum_k f_k {S_k}^2\left[3\tau_k + \frac{5\tau_k}{1+\omega_0{}^2\tau_k{}^2} + \frac{2\tau_k}{1+4\omega_0{}^2\tau_k{}^2}\right]$$

Can. J. Chem. Downloaded from www.nrcresearchpress.com by Xi'an Jiaotong University on 09/19/12
For personal use only.

$$[11]\quad \frac{1}{T_{2J}} = (1-f_b)\frac{1}{T_{2J}^0} + \frac{3\pi^2}{20}C_{Q0}^2\sum_k f_k {S_k}^2\left[3\tau_k + \frac{\tau_k}{1+\omega_0{}^2\tau_k{}^2} + \frac{2\tau_k}{1+4\omega_0{}^2\tau_k{}^2}\right]$$

$$[12]\quad \frac{1}{T_1} = (1-f_b)\frac{1}{T_1^0} + \frac{3\pi^2}{20}C_{Q0}^2\sum_k f_k {S_k}^2\left[\frac{2\tau_k}{1+\omega_0{}^2\tau_k{}^2} + \frac{8\tau_k}{1+4\omega_0{}^2\tau_k{}^2}\right]$$

In these equations T_1^0, T_{2I}^0, and T_{2J}^0 are the respective average relaxation times of the bulk phase, i.e., for D_2O in the membrane that experiences purely isotropic motion. The *I* and *J* subscripts arise when one uses the fictitious spin-1/2 operator formalism of Vega and Pines to describe the DQF and ZQF experiments.[74] ω_0 is the resonance frequency in angular frequency units, τ_k is the mean residence time at the anisotropic site *k*, C_{Q0} is the quadrupolar coupling in the absence of motional averaging (C_{Q0} = 220 kHz),[75] S_k is an effective order parameter, and f_b and f_k are as defined above. If one assumes extreme narrowing conditions, $\omega_0\tau_c \ll 1$, eqs. [10] to [12] can be simplified to:

$$[13]\quad \frac{1}{T_{2I}} = (1-f_b)\frac{1}{T_{2I}^0} + \frac{15\pi^2}{10}f_b C_{Q0}^2\langle {S_k}^2\tau_k\rangle_b$$

$$[14]\quad \frac{1}{T_{2J}} = (1-f_b)\frac{1}{T_{2J}^0} + \frac{9\pi^2}{10}f_b\, C_{Q0}^2\langle {S_k}^2\tau_k\rangle_b$$

$$[15]\quad \frac{1}{T_1} = (1-f_b)\frac{1}{T_1^0} + \frac{15\pi^2}{10}f_b\, C_{Q0}^2\langle {S_k}^2\tau_k\rangle_b$$

where $\langle {S_k}^2\tau_k\rangle_b$ is the average of ${S_k}^2\tau_k$ over the anisotropic sites. eqs. [13] and [14] demonstrate why the T_2 relaxation time used for ZQF, T_{2I}, is 3/5 times that used for the DQF relaxation, T_{2J}.[76] The T_2 values plotted in this work and listed in the Supplementary data, Table S1, correspond to T_{2J}.

These equations show that relaxation depends on a structural parameter, describing the geometric order of the water in the anisotropic sites, as well as the fraction of time the water spends at these sites. These same considerations were used to express the quadrupolar couplings in eq. [9] where the same parameter, f_b, was used. By substituting eq. [9] into eqs. [13] and [15], a correlation between the measured relaxation rates and quadrupolar couplings can be made:

$$[16]\quad \frac{1}{T_{2J}} = \frac{1}{T_{2J}^0} + \left(\frac{9\pi^2 C_{Q0}^2\langle {S_k}^2\tau_k\rangle_b}{10\quad\langle Q_k\rangle_b} - \frac{1}{T_{2J}^0\langle Q_k\rangle_b}\right)Q_{res}$$

$$[17]\quad \frac{1}{T_{1,2I}} = \frac{1}{T_{1,2I}^0} + \left(\frac{3\pi^2 C_{Q0}^2\langle {S_k}^2\tau_k\rangle_b}{2\quad\langle Q_k\rangle_b} - \frac{1}{T_{1,2I}^0\langle Q_k\rangle_b}\right)Q_{res}$$

The plots of the $1/T_1$ and $1/T_{2I}$ against C_Q^{res} shown in Fig. 8 reveal a clear linear relationship. By assuming that C_Q^{res} is proportional to Q_{res} (assume that η_Q is constant in the various binding sites and that the distribution of orientations remains the same), the slopes and intercepts of the plots in Fig. 8 and eqs. [16] and [17] can be used to determine that the order of magnitude for $\langle {S_k}^2\tau_k\rangle_b$ is 10^{-12}. This small value suggests that, even at low hydrations, the average anisotropy that water molecules experience is small. More importantly, $\langle {S_k}^2\tau_k\rangle_b$ is constant within an order of magnitude, suggesting that the anisotropic sites water molecules experience are not changing dramatically as a function of hydration. The changes in both relaxation rates and the C_Q^{res} observed experimentally likely arise from changes in the fraction of time water spends in anisotropic environments, f_b.

Fig. 8. Plots of $1/T_1$ (top) and $1/T_2$ (bottom) vs C_Q^{res} for the Site **A** waters. Fitting the data to straight lines yields slopes of 0.08 and 0.22 and intercepts of 3.1 and 3.6 for the $1/T_1$ and $1/T_2$ data, respectively. The T_2 data used corresponds to $T_{2J;}$ see text.

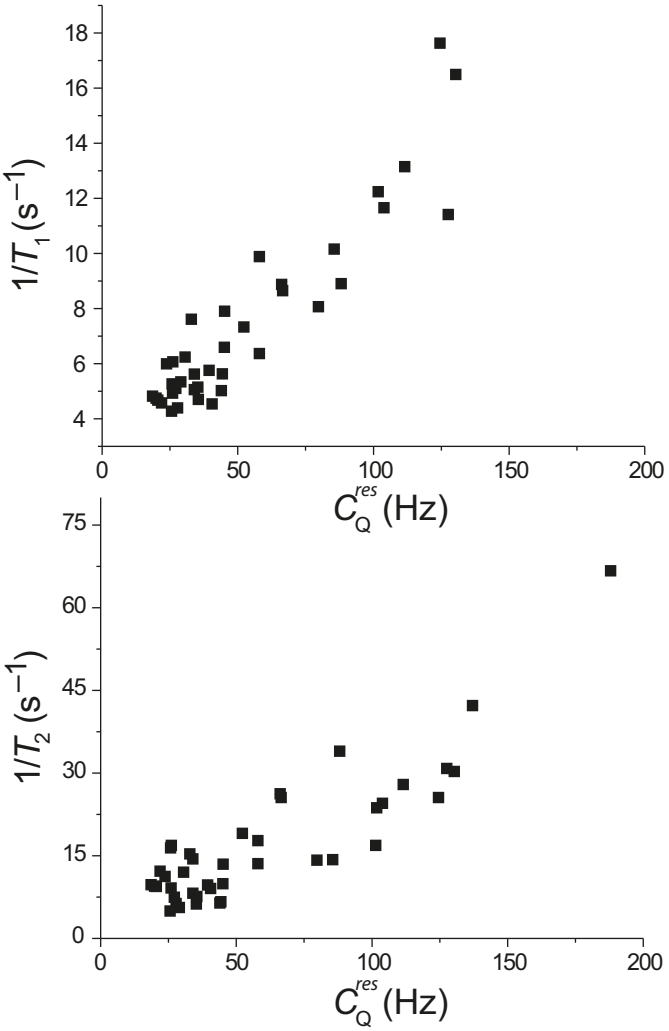

While this analysis of the relaxation data does not disprove the Gierke model of hydration, the lack of change in the anisotropic sites, suggesting limited structural changes as hydration increases, is consistent with the parallel-channel model where the structure of the anisotropic sites is controlled by the rigid backbone of the polymer and does not change significantly as the channels expand due to increasing hydration.

Can. J. Chem. Downloaded from www.nrcresearchpress.com by Xi'an Jiaotong University on 09/19/12
For personal use only.

Conclusions

Double- and zero-quantum filtered ^2H NMR spectra were acquired for D_2O in a Nafion membrane as a function of hydration. The qualitative trends observed in the spectra are consistent with a system that has expanding water domains leading to smaller residual quadrupolar couplings and longer relaxation times. The sensitivity of the signal-intensity buildup curves, particularly of the DQF spectra, may be useful as a molecular-level contrast mechanism for imaging experiments of operating fuel cells.

By fitting the experimental spectra with calculated spectra we have determine the C_Q^{res} and T_2 relaxation values for different hydration levels. It was found that above $\lambda = 10$ a two-site model was required to adequately fit the data; the second site had a negligible quadrupolar coupling, indicating that it undergoes nearly isotropic motional averaging. Using the EMOR model of Halle, the results indicate that the changes in relaxation times and C_Q^{res} as a function of hydration are likely dominated by changes in the fraction of time the water spends in the anisotropic environments and not on the structural nature of the environments. These results support a hydration model where two domains exist,[68] a first hydration layer that experiences anisotropic motion due to interaction with the polymer, and a core layer where the water molecules experience nearly isotropic motional averaging. As the sample is hydrated, the water in the first hydration layer spends less time interacting with the walls resulting in the smaller C_Q^{res} and longer relaxation times observed. This hydration model fits well with the parallel channel model proposed by Schmidt-Rohr and Chen. The ability of MQF ^2H NMR to characterize water in Nafion indicates that these methods will be useful for studying other hydrated polymer membranes.

Supplementary data

Supplementary data for this article are available on the journal Web site (www.nrcresearchpress.com/cjc).

Acknowledgments

The authors thank the members of the NMR group and the department of chemistry at The King's University College for helpful comments. Alexander Vega is also thanked for many helpful discussions and his aid in understanding the relaxation models. Natural Sciences and Engineering Research Council of Canada (NSERC) and The King's University College are thanked for financial support. MAB thanks NSERC for a USRA. Finally, KJO thanks Rod Wasylishen for his many contributions to science and his enthusiastic mentoring, teaching, and friendship.

References

(1) Nocera, D. G. *Energy. Environ. Sci.* **2010** *3*, 993. DOI: 10.1039/c003891c.
(2) Diat, O.; Gebel, G. *Nat. Mater.* **2008** *7* (1), 13. doi:10.1038/nmat2091.
(3) Weber, A. Z.; Newman, J. *Chem. Rev.* **2004** *104* (10), 4679. doi:10.1021/cr020729l.
(4) Smitha, B.; Sridhar, S.; Khan, A. A. *J. Membr. Sci.* **2005** *259* (1–2), 10. doi:10.1016/j.memsci.2005.01.035.
(5) Mauritz, K. A.; Moore, R. B. *Chem. Rev.* **2004** *104* (10), 4535. doi:10.1021/cr0207123.
(6) Devanathan, R. *Energy. Environ. Sci.* **2008** *1*, 101. DOI: 10.1039/b809492f.
(7) Dunbar, Z. W.; Masel, R. I. *J. Power Sources* **2008** *182* (1), 76. doi:10.1016/j.jpowsour.2008.03.057.
(8) Feindel, K. W.; Bergens, S. H.; Wasylishen, R. E. *ChemPhysChem* **2006** *7* (1), 67. doi:10.1002/cphc.200500504.
(9) Feindel, K. W.; LaRocque, L. P. A.; Starke, D.; Bergens, S. H.; Wasylishen, R. E. *J. Am. Chem. Soc.* **2004** *126* (37), 11436. doi:10.1021/ja0461116.
(10) Feindel, K. W.; Bergens, S. H.; Wasylishen, R. E. *J. Power Sources* **2007** *173* (1), 86. doi:10.1016/j.jpowsour.2007.04.079.
(11) Feindel, K. W.; Bergens, S. H.; Wasylishen, R. E. *Phys. Chem. Chem. Phys.* **2007** *9* (15), 1850. doi:10.1039/b617551a.
(12) Feindel, K. W.; Bergens, S. H.; Wasylishen, R. E. *J. Am. Chem. Soc.* **2006** *128* (43), 14192. doi:10.1021/ja064389n.
(13) Tsushima, S.; Hirai, S. *Fuel Cells (Weinh.)* **2009** *9* (5), 506. doi:10.1002/fuce.200800151.
(14) Tsushima, S.; Takita, S.; Hirai, S.; Kubo, N.; Aotani, K. *Exp. Heat Transfer* **2009** *22* (1), 1. doi:10.1080/08916150802530484.
(15) Wang, M. T.; Feindel, K. W.; Bergens, S. H.; Wasylishen, R. E. *J. Power Sources* **2010** *195* (21), 7316. doi:10.1016/j.jpowsour.2010.05.029.
(16) Wu, Z.; Wu, C. S.; Chu, P. P. J.; Ding, S. *Magn. Reson. Imaging* **2009** *27* (6), 871. doi:10.1016/j.mri.2008.11.001.
(17) Dunbar, Z.; Masel, R. I. *J. Power Sources* **2007** *171* (2), 678. doi:10.1016/j.jpowsour.2007.06.207.
(18) Gebel, G. *Polymer (Guildf.)* **2000** *41* (15), 5829. doi:10.1016/S0032-3861(99)00770-3.
(19) Schmidt-Rohr, K.; Chen, Q. *Nat. Mater.* **2008** *7* (1), 75. doi:10.1038/nmat2074.
(20) Schmidt-Rohr, K. *J. Appl. Cryst.* **2007** *40* (1), 16. doi:10.1107/S002188980604550X.
(21) Gierke, T. D.; Munn, G. E.; Wilson, F. C. *J. Polym. Sci. Part B: Polym. Phys.* **1981** *19*, 1687. DOI: 10.1002/pol.1981.180191103.
(22) Ye, G.; Janzen, N.; Goward, G. R. *Macromolecules* **2006** *39* (9), 3283. doi:10.1021/ma0523825.
(23) Alberti, G.; Narducci, R.; Sganappa, M. *J. Power Sources* **2008** *178* (2), 575. doi:10.1016/j.jpowsour.2007.09.034.
(24) Chen, Q.; Schmidt-Rohr, K. *Macromolecules* **2004** *37* (16), 5995. doi:10.1021/ma049759b.
(25) Chen, Q.; Schmidt-Rohr, K. *Macromol. Chem. Phys.* **2007** *208* (19–20), 2189. doi:10.1002/macp.200700200.
(26) Knox, C. K.; Voth, G. A. *J. Phys. Chem. B* **2010** *114* (9), 3205. doi:10.1021/jp9112409.
(27) Devanathan, R.; Venkatnathan, A.; Dupuis, M. *J. Phys. Chem. B* **2007** *111* (28), 8069. doi:10.1021/jp0726992.
(28) Devanathan, R.; Venkatnathan, A.; Dupuis, M. *J. Phys. Chem. B* **2007** *111* (45), 13006. doi:10.1021/jp0761057.
(29) Cui, S.; Liu, J.; Selvan, M. E.; Paddison, S. J.; Keffer, D. J.; Edwards, B. J. *J. Phys. Chem. B* **2008** *112* (42), 13273. doi:10.1021/jp8039803.
(30) Cui, S.; Liu, J.; Selvan, M. E.; Keffer, D. J.; Edwards, B. J.; Steele, W. V. *J. Phys. Chem. B* **2007** *111* (9), 2208. doi:10.1021/jp066388n.
(31) Liu, J.; Suraweera, N.; Keffer, D. J.; Cui, S.; Paddison, S. J. *J. Phys. Chem. C* **2010** *114* (25), 11279. doi:10.1021/jp911972e.
(32) Liu, J.; Selvan, M. E.; Cui, S.; Edwards, B. J.; Keffer, D. J.; Steele, W. V. *J. Phys. Chem. C* **2008** *112* (6), 1985. doi:10.1021/jp075612l.

Can. J. Chem. Downloaded from www.nrcresearchpress.com by Xi'an Jiaotong University on 09/19/12
For personal use only.

(33) Selvan, M. E.; Liu, J.; Keffer, D. J.; Cui, S.; Edwards, B. J.; Steele, W. V. *J. Phys. Chem. C* **2008** *112* (6), 1975. doi:10.1021/jp075611t.
(34) Wescott, J. T.; Qi, Y.; Subramanian, L.; Weston Capehart, T. *J. Chem. Phys.* **2006** *124* (13), 134702. doi:10.1063/1.2177649.
(35) Urata, S.; Irisawa, J.; Takada, A.; Shinoda, W.; Tsuzuki, S.; Mikami, M. *J. Phys. Chem. B* **2005** *109* (9), 4269. doi:10.1021/jp046434o.
(36) Choe, Y. K.; Tsuchida, E.; Ikeshoji, T.; Ohira, A.; Kidena, K. *J. Phys. Chem. B* **2010** *114* (7), 2411. doi:10.1021/jp906757s.
(37) Borisov, A. S.; Hazendonk, P.; Hayes, P. G. *J. Inorg. Organomet. Polym.* **2010** *20* (2), 183. doi:10.1007/s10904-010-9358-5.
(38) Rollet, A. L.; Porion, P.; Delville, A.; Diat, O.; Gebel, G. *Magn. Reson. Imaging* **2005** *23* (2), 367. doi:10.1016/j.mri.2004.11.053.
(39) Cherry, B. R.; Fujimoto, C. H.; Cornelius, C. J.; Alam, T. M. *Macromolecules* **2005** *38* (4), 1201. doi:10.1021/ma047885+.
(40) Ye, G.; Hayden, C. A.; Goward, G. R. *Macromolecules* **2007** *40* (5), 1529. doi:10.1021/ma0621876.
(41) Kidena, K.; Ohkubo, T.; Takimoto, N.; Ohira, A. *Eur. Polym. J.* **2010** *46* (3), 450. doi:10.1016/j.eurpolymj.2009.12.012.
(42) Boyle, N. G.; Mcbrierty, V. J.; Eisenberg, A. *Macromolecules* **1983** *16* (1), 80. doi:10.1021/ma00235a016.
(43) Bunce, N. J.; Sondheimer, S. J.; Fyfe, C. A. *Macromolecules* **1986** *19* (2), 333. doi:10.1021/ma00156a015.
(44) Zawodzinski, T. A.; Derouin, C.; Radzinski, S.; Sherman, R. J.; Smith, V. T.; Springer, T. E.; Gottesfeld, S. *J. Electrochem. Soc.* **1993** *140*, 1041. doi:10.1149/1.2056194.
(45) Guillermo, A.; Gebel, G.; Mendil-Jakani, H.; Pinton, E. *J. Phys. Chem. B* **2009** *113* (19), 6710. doi:10.1021/jp8110452.
(46) Nicotera, I.; Coppola, L.; Rossi, C. O.; Youssry, M.; Ranieri, G. A. *J. Phys. Chem. B* **2009** *113* (42), 13935. doi:10.1021/jp904691g.
(47) MacMillan, B.; Sharp, A. R.; Armstrong, R. L. *Polymer (Guildf.)* **1999** *40* (10), 2471. doi:10.1016/S0032-3861(98)00484-4.
(48) Schnell, I.; Spiess, H. W. *J. Magn. Reson.* **2001** *151* (2), 153. doi:10.1006/jmre.2001.2336.
(49) Knubovets, T.; Shinar, H.; Eliav, U.; Navon, G. *J. Magn. Reson. B.* **1996** *110* (1), 16. doi:10.1006/jmrb.1996.0003.
(50) Reddy, R.; Bolinger, L.; Shinnar, M.; Noyszewski, E.; Leigh, J. S. *Magn. Reson. Med.* **1995** *33* (1), 134. doi:10.1002/mrm.1910330121.
(51) Navon, G.; Shinar, H.; Eliav, U.; Seo, Y. *NMR Biomed.* **2001** *14* (2), 112. doi:10.1002/nbm.687.
(52) Navon, G.; Eliav, U.; Demco, D. E.; Blumich, B. *J. Magn. Reson. Imaging* **2007** *25* (2), 362. doi:10.1002/jmri.20856.
(53) Reddy, R.; Shinar, H.; Wang, Z.; Leigh, J. S. *J. Magn. Reson. B.* **1994** *104* (2), 148. doi:10.1006/jmrb.1994.1068.
(54) Reddy, R.; Li, S.; Noyszewski, E. A.; Kneeland, J. B.; Leigh, J. S. *Magn. Reson. Med.* **1997** *38* (2), 207. doi:10.1002/mrm.1910380208.
(55) Shinar, H.; Knubovets, T.; Eliav, U.; Navon, G. *Biophys. J.* **1993** *64* (4), 1273. doi:10.1016/S0006-3495(93)81492-9.
(56) Sharf, Y.; Eliav, U.; Shinar, H.; Navon, G. *J. Magn. Reson. B.* **1995** *107* (1), 60. doi:10.1006/jmrb.1995.1058.
(57) Eliav, U.; Navon, G. *J. Magn. Reson. B.* **1994** *103* (1), 19. doi:10.1006/jmrb.1994.1003.
(58) Eliav, U.; Navon, G. *J. Magn. Reson.* **1998** *130* (1), 63. doi:10.1006/jmre.1997.1278.
(59) Perea, W.; Cannella, M.; Yang, J.; Vega, A. J.; Polenova, T.; Marcolongo, M. *Magn. Reson. Med.* **2007** *57* (6), 990. doi:10.1002/mrm.21231.
(60) Ooms, K. J.; Cannella, M.; Vega, A. J.; Marcolongo, M.; Polenova, T. *J. Magn. Reson.* **2008** *195* (1), 112. doi:10.1016/j.jmr.2008.07.024.
(61) Ooms, K. J.; Cannella, M.; Vega, A. J.; Marcolongo, M.; Polenova, T. *Magn. Reson. Med.* **2008** *60* (2), 246. doi:10.1002/mrm.21637.
(62) Abragam, A. In *Principles of nuclear magnetism;* Oxford University Press: Oxford, 1962.
(63) Mackenzie, K. J. D.; Smith, M. E. In *Multinuclear solid-state NMR of inorganic materials;* Pergamon Materials Series; Pergamon: Amsterdam, 2002.
(64) Seo, Y.; Ikoma, K.; Takamiya, H.; Kusaka, Y.; Tsoref, L.; Eliav, U.; Shinar, H.; Navon, G. *Magn. Reson. Med.* **1999** *42* (5), 884. doi:10.1002/(SICI)1522-2594(199911)42:5<884::AID-MRM7>3.0.CO;2-0.
(65) Tsoref, L.; Eliav, U.; Seo, Y.; Shinar, H.; Navon, G. *J. Magn. Reson. Imaging* **2000** *11* (3), 336. doi:10.1002/(SICI)1522-2586(200003)11:3<336::AID-JMRI14>3.0.CO;2-V.
(66) Perrin, J. C.; Lyonnard, S.; Volino, F. *J. Phys. Chem. C* **2007** *111* (8), 3393. doi:10.1021/jp065039q.
(67) Eliav, U.; Navon, G. *J. Magn. Reson. A* **1995** *115* (2), 241. doi:10.1006/jmra.1995.1173.
(68) Lu, Z. J.; Polizos, G.; Macdonald, D. D.; Manias, E. *J. Electrochem. Soc.* **2008** *155* (2), B163. doi:10.1149/1.2815444.
(69) Chávez, F. V.; Halle, B. *J. Magn. Reson.* **2006** *56* (1), 73. doi:10.1002/mrm.20912.
(70) Vaca Chávez, F. ; Persson, E.; Halle, B. *J. Am. Chem. Soc.* **2006** *128*, 4902. doi:10.1021/ja058837n.
(71) Halle, B. *J. Magn. Reson.* **2006** *56* (1), 60. doi:10.1002/mrm.20919.
(72) Modig, K.; Liepinsh, E.; Otting, G.; Halle, B. *J. Am. Chem. Soc.* **2004** *126* (1), 102. doi:10.1021/ja038325d.
(73) Persson, E.; Halle, B. *J. Am. Chem. Soc.* **2008** *130* (5), 1774. doi:10.1021/ja0775873.
(74) Vega, S.; Pines, A. *J. Chem. Phys.* **1977** *66* (12), 5624. doi:10.1063/1.433884.
(75) Berglund, B.; Vaughan, R. W. *J. Chem. Phys.* **1980** *73* (5), 2037. doi:10.1063/1.440423.
(76) Jacobsen, J. P.; Bildsoe, H. K.; Schaumburg, K. *J. Magn. Reson.* **1976** *23*, 153.

Structural analysis of lanthanum-containing battery materials using ^{139}La solid-state NMR

Leigh Spencer, Eric Coomes, Eric Ye, Victor Terskikh, Adam Ramzy, Venkataraman Thangadurai, and Gillian R. Goward

Can. J. Chem. Downloaded from www.nrcresearchpress.com by Xi'an Jiaotong University on 09/19/12
For personal use only.

Abstract: ^{139}La solid-state NMR spectra, acquired at 21.1 and 11.7 T, have been used to evaluate the structural properties of the lithium ion battery materials, $La_{32}Li_{16}Fe_{6.4}O_{67}$ and $Li_{3x}La_{2/3-x}TiO_3$. In particular, atomic-level disorder in the second coordination sphere environment of lanthanum in these materials has been indicated by the observation of a distribution in the asymmetry parameters and the quadrupolar coupling constants derived from experimental NMR spectra, and supported by theoretical calculations. For comparison, ^{139}La NMR has been obtained for the two model compounds La_2O_3 and $LaNbO_4$, in which there is no atomic-level disorder. Quadrupolar coupling constants in the range of 17 to 59 MHz have been measured, and these values are supported by previous work as well as theoretical predictions performed in CASTEP. It has been shown that ^{139}La NMR is a useful tool for the structural analysis of lithium ion battery materials, and when combined with ^{7}Li MAS NMR and powder X-ray diffraction, can be used to determine the structure of complex solid-state electrolyte and electrode materials.

Key words: NMR, quadrupolar nuclei, lithium ion batteries, ^{139}La.

Résumé : On a utilisé les spectres RMN du ^{139}La à l'état solide, acquis à 21,1 et 11,7 T, pour évaluer les propriétés structurales des matériaux ioniques du lithium utilisés pour les batteries, $La_{32}Li_{16}Fe_{6,4}O_{67}$ et $L1_{3x}La_{2/3-x}TiO_3$. En particulier, un désordre au niveau atomique dans la deuxième sphère de coordination de l'environnement du lanthane de ces matériaux a été mis en évidence par l'observation d'une distribution dans les paramètres d'asymétrie et dans les constantes de couplage quadripolaire obtenues à partir des spectres RMN expérimentaux et confirmées par des calculs théoriques. À des fins de comparaison, on a aussi déterminé les spectres RMN du ^{139}La de deux composés modèles, La_2O_3 et $LaNbO_4$, dans lesquels on n'observe aucun désordre au niveau atomique. On a mesuré des constantes de couplage quadripolaire de l'ordre de 17 et 19 MHz; ces valeurs sont en accord avec celles rapportées dans un travail antérieur et elles correspondent aux valeurs calculées par le programme CASTEP. On a démontré que la RMN du ^{139}La est un outil utile pour l'analyse structurale des matériaux ioniques du lithium utilisés dans les batteries et que, lorsque combinée avec la RMN avec rotation à l'angle magique (RAM) et la diffraction des rayons-X, elle peut être utilisée pour déterminer la structure d'électrolytes complexes à l'état solide et de matériaux d'électrode.

Mots-clés : RMN, noyau quadripolaire, batteries aux ions lithium, ^{139}La.

[Traduit par la Rédaction]

Introduction

Lithium ion batteries play an important role in the development of environmentally friendly energy sources.[1] With applications in many portable electronic devices, lithium ion batteries are sought after in the automotive industry, as their high power and energy density make them ideal for use in electric vehicles.[1] Battery research involves the development of materials to replace current cathode, anode, and electrolyte materials with more environmentally friendly and safer materials, which have longer lifetimes and lower costs.[1] In particular, there has been much interest in replacing the traditional liquid lithium electrolyte with a solid electrolyte, capable of running at a higher voltage.[1–3] Garnet-like materials have shown great potential for this application, and research into the structure and dynamics of these materials has primarily been performed using powder X-ray diffraction and neutron diffraction.[2–4]

Received 11 December 2010. Accepted 28 January 2011. Published at www.nrcresearchpress.com/cjc on 18 August 2011.

L. Spencer, E. Coomes, and G.R. Goward. Department of Chemistry and Brockhouse Institute for Materials Research, McMaster University, 1280 Main St. W. Hamilton, ON L8S 4M1, Canada.
E. Ye. Department of Chemistry, University of Ottawa, 10 Marie Curie, Ottawa, ON K1N 6N5, Canada.
V. Terskikh. Steacie Institute of Molecular Sciences, National Research Council Canada, Ottawa, 1200 Montreal Road, M-40, Ottawa, ON K1A 0R6, Canada.
A. Ramzy and V. Thangadurai. Department of Chemistry, University of Calgary, 2500 University Dr. NW, Calgary, AB T2N 1N4, Canada.

Corresponding author: G.R. Goward (e-mail: goward@mcmaster.ca).

This article is part of a Special Issue dedicated to Professor Roderick E. Wasylishen.

Can. J. Chem. Downloaded from www.nrcresearchpress.com by Xi'an Jiaotong University on 09/19/12
For personal use only.

^{6,7}Li magic angle spinning (MAS) solid-state NMR is a useful nondestructive tool to study the structures of these materials as well as their lithium ion dynamics; however, in the absence of any paramagnetic interactions, both ^{6}Li and ^{7}Li suffer from poor chemical shift resolution and long T_1 relaxation times. Of the two, ^{6}Li is somewhat preferable, as it has smaller line widths in NMR spectral peaks. This is due to the reduction of the homonuclear dipolar coupling of this lower gamma nucleus.[5,6] In addition to electrolytes, cathode materials, aimed at replacing the currently used $LiCoO_2$, are highly sought after.[7–9] They often contain paramagnetic centers that provide unpaired electrons, which allow the lithium centers in the materials to have short T_1 relaxation times and an expanded chemical shift range.[7,10] ^{6,7}Li MAS NMR, along with powder X-ray diffraction, provides a powerful tool to study the structure as well as the nature of lithium ion dynamics in lithium ion battery materials.[6] Furthermore, many of the garnet structures proposed thus far for these applications contain significant amounts of lanthanum, an NMR active nucleus with spin 7/2, thus ^{139}La NMR may be a valuable tool in the structural analysis of these and other related materials.[6,11,12]

^{139}La NMR has been used to study highly ordered lanthanum-containing compounds, such as lanthanum halides and organometallic compounds.[13–15] It has been found that the NMR parameters obtained from simulating NMR spectra agree with calculations. These values can be used to support claims for the predicted crystal structures of these materials.

Bastow et al., in addition to the work on La_2O_3, have shown that ^{139}La NMR is capable of detecting atomic-level disorder in materials that contain atomic substitution within different crystallographic sites.[16,17] The authors used samples with high symmetry (cubic), to show that with increased doping, and thus increased complexity in the atomic distribution, the quadrupolar coupling and asymmetry parameter C_Q and η, respectively, became increasingly difficult to measure. There was evident line broadening of the ^{139}La spectrum, due to the increased distribution of C_Q and η, resulting from the induced atomic-level disorder.[16] Another challenge faced by Bastow et al. in their collection of the ^{139}La NMR spectra at 9.4 T was the extremely broad linewidth of the central transition, such that the spectrum collected with one central frequency offset did not show the full central transition. The excitation frequency was consequently moved so that several piecewise spectra were collected to observe the full lineshape of the central transition, a very time-consuming process.[16]

In this work, a ^{139}La NMR WURST approach has been used in the structural analysis of a new lithium battery cathode material and other related structures. This study has primarily focused on the ^{139}La quadrupole powder patterns obtained for these structures, with the aim of drawing a correlation between the observed powder patterns and the nature of disorder in the second coordination sphere of lanthanum.

Challenges of ^{139}La solid-state NMR

Although ^{139}La is an NMR active nucleus with high natural abundance, 99.91%, and many materials significant to the development of materials science contain large amounts of lanthanum, ^{139}La NMR is not performed routinely.[18–20] This is mainly due to the many challenges associated with the collection and interpretation of the NMR spectra. ^{139}La has a nuclear spin $I = 7/2$, with a large quadrupole moment, 0.21 b, and a moderate gyromagnetic ratio, $\gamma = 3.8085 \times 10^7$ rad T^{-1} s^{-1}.[15] The EFG-dominated spectra of ^{139}La are very broad, which makes low-field NMR measurements quite difficult. Nevertheless, it has been shown that ^{139}La NMR is sensitive to the symmetry elements of lanthanum containing structures, with resulting NMR line shapes being heavily dependent on the asymmetry parameter η, defined in eq. [1]; and the quadrupolar coupling constant C_Q, defined in eq. [2], which are known to vary according to the elements of symmetry present at the nucleus of interest.[21]

$$[1] \qquad \eta = \frac{V_{xx} - V_{yy}}{V_{zz}}$$

$$[2] \qquad C_Q = \frac{e^2qQ}{\hbar} = \frac{(eq)eQ}{\hbar}$$

where V_{xx}, V_{yy}, and V_{zz} are the three components of a electric field gradient (EFG) tensor in the principle axis frame, which is traceless[22,23]; $eq = V_{zz}$, i.e., the magnitude of the largest component of the EFG tensor; eQ = nuclear quadrupole moment; $\hbar$ = reduced Planck constant.[23] In addition, the EFG tensor components are ordered as: $|V_{xx}| \leq |V_{yy}| \leq |V_{zz}|$.

Recently introduced solid-state NMR pulse sequences, such as the WURST-QCPMG and WURST-echo, which make use of a wide adiabatic frequency-swept pulse, allow the excitation of large spectral width within a single pulse and can be employed to assist in the collection of broad NMR spectra.[24,25]

The parameters C_Q and η, which can be obtained by the simulation of the quadrupole powder patterns, are dependent on the site symmetry of the nucleus in question. More specifically C_Q depends on the spherical symmetry of the La environment in its first coordination sphere, with a large C_Q caused by a nucleus being in a nonspherical environment; η depends on the symmetry of the EFG tensor, with $\eta = 0$ resulting from the axial symmetry of the traceless EFG tensor, as defined in eq. [1]; for example, for systems with threefold (or higher) axes of rotational symmetry, if V_{zz} is oriented along the rotational axes, then $\eta = 0$ as $V_{xx} = V_{yy}$.[15] This is illustrated further in the text below for La_2O_3.

Crystalline $LaNbO_4$ and La_2O_3 are both highly ordered compounds, which show no sign of disorder in their crystal structures.[26,27] In both of these materials, lanthanum is surrounded only by oxygen in the first coordination sphere. In each case, the ^{139}La spectra is a clear representation of a single ^{139}La crystallographic site. For these reasons $LaNbO_4$ and La_2O_3 have been chosen as model compounds in this work. In contrast, the materials $Li_{16}La_{32}Fe_{6.4}O_{67}$ and $Li_{3x}La_{2/3-x}TiO_3$ ($x \leq 0.03 \leq 0.063$) are known to show disorder in the form of atomic distribution on particular crystallographic sites, which occurs as a result of vacancies present in the materials.[28,29]

The garnet-like structure $Li_{16}La_{32}Fe_{6.4}O_{67}$ is a potential cathode material for lithium ion batteries. The structure contains iron centers, which provide unpaired electrons that reduce the T_1 relaxation times of lithium that is in close proximity to the iron centers.[28] $Li_{16}La_{32}Fe_{6.4}O_{67}$ was first prepared by Mazza et al., and it was thought that the lithium in

Table 1. Crystallographic data for the materials studied.

Material	Space group	La	O-Coordination	La–O bond range (Å)	Second CS*	Ref.
$LaNbO_4$	*I2/c*	La-1	8	2.5–2.6	La, Nb	26
La_2O_3	*P-3ml*	La-1	7	2.4–2.8	La	27
$La(OH)_3$	*P63/m*	La-1	9	2.6–2.8	La	30
$Li_{3x}La_{2/3-x}TiO_3$	*Pmmm*	La-1	12	2.7–2.8	La, Ti	29
		La-2	12	2.7–2.8	La, Ti	
$La_{32}Li_{16}Fe_{6.4}O_{67}$	*Im3m*	La-1	10	2.5–2.7	La, Fe	This Work
		La-2	9	2.3–2.7	La, Fe	This Work

Note: The space group, La coordination number for each La site, La–O bond distance range, and the second coordination environment are shown. Second CS* = second coordination sphere.

Can. J. Chem. Downloaded from www.nrcresearchpress.com by Xi'an Jiaotong University on 09/19/12
For personal use only.

this compound occupied a single crystallographically unique site, while the lanthanum is distributed between two crystallographic sites, each with the lanthanum surrounded by oxygen in the first coordination sphere.[28] The source of disorder in this compound will be discussed later in this work. $Li_{3x}La_{2/3-x}TiO_3$ ($x \leq 0.03 \leq 0.063$) is a potential electrolyte material for lithium ion batteries and does not contain paramagnetic centers.[29] The disorder in this compound is attributed to the distribution of Li, La, and a vacancy, which can randomly occupy the same crystallographic site.[29]

In all of the materials mentioned, lanthanum is surrounded only by oxygen in the first coordination sphere. Thus, the ^{139}La NMR spectra can be compared directly to relate the lineshape of the spectra to the environment of the lanthanum in the crystal structures. Crystallographic information for each of these compounds is shown in Table 1, which presents the space groups, La–O bond distances, and second coordination sphere elements. In addition, the lanthanum environments in each of the structures are illustrated in Table 2. For each structure, lanthanum is shown in its oxygen environment as well as in its second coordination sphere environment.

Experimental

Synthesis

La_2O_3 was purchased from Sigma-Aldrich and exposed to air in ambient conditions. To produce La_2O_3 void of $La(OH)_3$ impurity, the purchased sample was heated at 900 °C for 24 h.[32] $LaNbO_4$ was obtained by a co-precipitation from $NbCl_5$ and $La(NO_3)_3$ by NH_3 with subsequent calcination at 800 °C.[33]

To prepare $Li_{3x}La_{2/3-x}TiO_3$ ($0.03 \leq x \leq 0.063$), stoichiometric amounts of La_2O_3, Li_2CO_3, and TiO_2 were mixed. The mixture was ball milled and heated at 500 °C. This process was repeated with temperatures of 800 and 1150 °C. A pellet was then pressed and annealed at 1350 °C to create the final product.[34] By comparing the experimental powder X-ray diffraction data to that reported by Ibarra et al., it has been determined that the content of lithium in the structure is consistent with the desired stoichiometry.[29]

To synthesize $La_{32}Li_{16}Fe_{6.4}O_{67}$, molar ratios of $LiNO_3$, La_2O_3 and Fe_2O_3 were weighed, mixed, and ball milled for 3 h, a 10% weight excess of $LiNO_3$ was used to account for lithium leaching. The mixture was sintered at 600 °C to remove nitrates and ball milled again before being pressed into a pellet and annealed at 850 °C. Phase analysis using powder X-ray diffraction determined that the correct phase was present.

NMR

^{139}La NMR spectra were acquired at two magnetic fields, 11.7 T (Larmor frequency, 70.6 MHz) and 21.1 T (Larmor frequency, 127.1 MHz). For experiments at 21.1 T, a Bruker Avance II 900 NMR spectrometer was used at the National Ultrahigh-Field NMR Facility for Solids (http://www.nmr900.ca). Experiments were performed with stationary samples using a home-built single-channel probe with a 5 mm i.d. solenoid coil. Depending on the sample, one of two pulse sequences was used: WURST-echo or WURST-QCPMG. Typically in the WURST-QCPMG experiments, 50 μs WURST pulses were applied and swept across a range of 1 MHz at a rate of 20 MHz/ms, with an RF power of 10 kHz. The spikelet-separation was set to be 2.5 kHz at 21.1 T and 5.0 kHz at 11.7 T. The number of echoes in a QCPMG train ranged from 32 to 64. Recycle delays of 0.2–0.5 s were found sufficient for complete relaxation in most samples. From 1000 to 40 000 transients were accumulated, depending on the sample. ^{139}La NMR spectra were also acquired at 11.7 T on a Bruker Avance III 500 NMR spectrometer using a 5 mm solenoid Bruker H/X probe. WURST pulse conditions were similar to those at 21.1 T. A number of spectra were obtained using a π/2–π/2 quadrupolar-echo pulse sequence, employing a 2 μs central-transition selective π/2 pulse, with RF power of 30 kHz. From 2000 to 4000 transients were accumulated. ^{139}La NMR spectra were referenced to external 1 mol/L $LaCl_3$ solution at 0 ppm. NMR spectral simulation was performed using WSolids[35] in most cases, DMFit[36] or QuadFit[37] programs were used for disordered systems (see text). Uncertainties were determined statistically by performing several simulations of each spectrum.

^{7}Li MAS NMR experiments were performed at 11.7 T (Larmor frequency, 194.4 MHz) on a Bruker Avance I 500 NMR spectrometer. Samples were spun at 20 kHz using a 2.5 mm Bruker MAS probe. A short 1 μs (π/8) excitation pulse and a sufficiently long relaxation delay of 20 s were used to ensure complete relaxation. A total of 2048 transients were accumulated. ^{7}Li NMR spectra were referenced to external 1 mol/L LiCl solution at 0 ppm, which was also used for calibrating the nonselective (π/2) pulse of 4 μs. The line-fit analysis was performed using TopSpin 2.1 software.

Powder X-Ray Diffraction

Room-temperature X-ray powder diffraction patterns were recorded on a PANalytical X'Pert Pro diffractometer with an

Can. J. Chem. Downloaded from www.nrcresearchpress.com by Xi'an Jiaotong University on 09/19/12
For personal use only.

Table 2. The lanthanum environments in materials studied in this work.

Material	Oxygen environment	Second coordination sphere
$LaNbO_4$	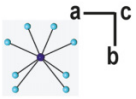	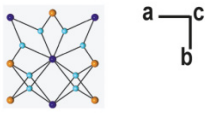
La_2O_3	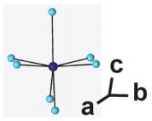	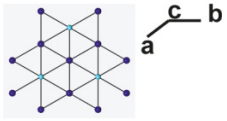
$La(OH)_3$	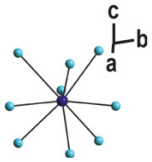	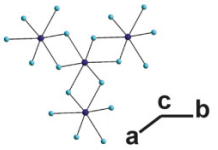
$Li_{3x}La_{2/3-x}TiO_3$ La-1	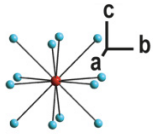	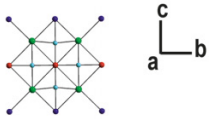
$Li_{3x}La_{2/3-x}TiO_3$ La-2	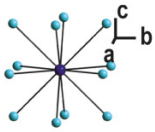	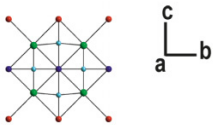
$Li_{16}La_{32}Fe_{6.4}O_{67}$ La-1	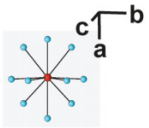	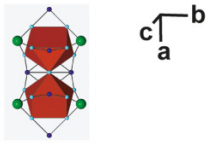
$Li_{16}La_{32}Fe_{6.4}O_{67}$ La-2	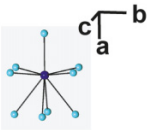	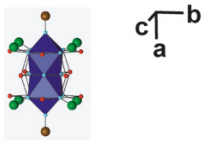

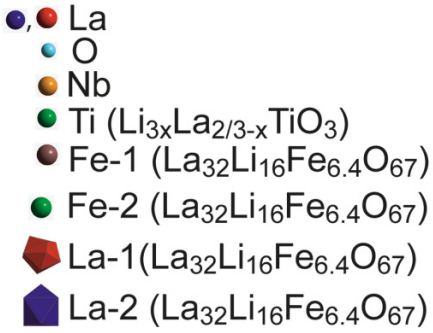

Lanthanum is represented by a dark blue or red sphere. In the $La_{32}Li_{16}Fe_{6.4}O_{67}$ structure, lanthanum is also represented by the red or blue polyhedra (very dark and dark grey in print version), for clarity, as lanthanum lies in a complex environment. In addition, oxygen is represented by light blue spheres (light grey); niobium, by orange spheres (mid grey); titanium by green spheres (light grey); in $La_{32}Li_{16}Fe_{6.4}O_{67}$ a distinction is made between iron that participates in a distribution (green spheres) with lithium, and iron that does not (brown spheres, dark grey in print). The details of the distribution are discussed in the text. All crystallographic figures were prepared in XtalDraw software.[31]

Can. J. Chem. Downloaded from www.nrcresearchpress.com by Xi'an Jiaotong University on 09/19/12
For personal use only.

X'Celerator detector and Cu $K\alpha_1$ radiation. The finely ground samples were deposited on zero background holders cut from a single crystal of silicon. The full-profile Rietveld refinement (GSAS[38]) was used for phase analyses.

Computational Methods

Quantum chemical calculations of the ^{139}La EFG and CS tensors were performed with available crystallographic data for La_2O_3,[27] $La(OH)_3$,[30], and $LaNbO_4$.[26] The original structure for $La(OH)_3$ did not contain hydrogen atoms. Before calculations, hydrogen atoms were placed in the expected positions, and the crystal structure was fully geometrically optimized.

The CASTEP NMR program[39,40] in the Accelrys Materials Studio 4.4 environment was utilized to carry out ab initio plane-wave density functional theory (DFT) calculations. Ultrasoft pseudopotentials, generated from the "on-the-fly" method in CASTEP, were used for all elements in a fine accuracy basis set, with a plane-wave basis set cut-off energy of 550 eV and with Monkhorst–Pack *k*-space grid sizes set automatically according to the fine accuracy basis set. The magnetic shielding tensors for ^{139}La were calculated using the projector gauge including augmented-wave method (GIPAW).[41,42] All calculations used the Perdew, Burke, and Ernzerhof (PBE) functionals in the generalized gradient approximation (GGA) for the exchange correlation energy.[43,44] The scalar-relativistic zero-order regular approximation (ZORA) was utilized in CASTEP calculations to take into account the relativistic effects.[45]

Results and discussion

$LaNbO_4$

In the first model compound, $LaNbO_4$, lanthanum contains only oxygen in its first coordination sphere. It has a monoclinic structure in space group *I*2/*c*. There is only one crystallographically unique lanthanum site in this compound and one niobium site. Lanthanum is coordinated to eight oxygen atoms within 2.7 Å, with a La–O bond distance range of 2.5–2.6 Å.[26] The minimum distance between La and Nb is 3.7 Å, and the minimum distance between La and another La atom is 3.9 Å.[26] Static solid-state NMR measurements were taken at 11.7 T and illustrate many of the challenges of ^{139}La solid-state NMR. Static spectra collected for $LaNbO_4$ using three different pulse sequences, quadrupolar-echo, WURST-QCPMG, and WURST-echo, are compared in Fig. 1.

This simple example already fully illustrates difficulties in obtaining high-quality ^{139}La NMR spectra for solid state samples. Even at 11.7 T, the static linewidth for this sample is in excess of 300 kHz. When the more traditional quadrupolar-echo pulse sequence is applied, the resulting spectrum shows a lineshape with attenuated intensity for outer discontinuities, compared with the simulated spectrum. This distortion is due to the limited excitation bandwidth of the rectangular $\pi/2$ pulse (2 μs). Near to the edge of the excitation bandwidth, the intensity of the excitation profile decreases significantly, resulting in the spectrum with attenuated intensity on its outer edges. To obtain a more accurate lineshape using the quadrupolar-echo pulse sequence it is often necessary to record several spectra with different central frequency offsets and then to add them together.[46,47] The WURST-echo approach affords much broader excitation bandwidth, so that the same spectrum can be correctly recorded using only a single central frequency offset in the same amount of time (Fig. 1).[25] In systems with sufficiently long T_2 relaxation times, the WURST-QCPMG approach[24] delivers all the advantages of WURST in providing broadband excitation, combined with significantly improved signal-to-noise. Because of

Fig. 1. ^{139}La WURST-QCPMG, WURST-Echo, and Quadrupole-Echo NMR spectra of $LaNbO_4$ taken at (*a*) 21.1 T and (*b*) 11.7 T. Asterisks (*) indicate a minor impurity in the sample. Simulations were performed using WSolids software.

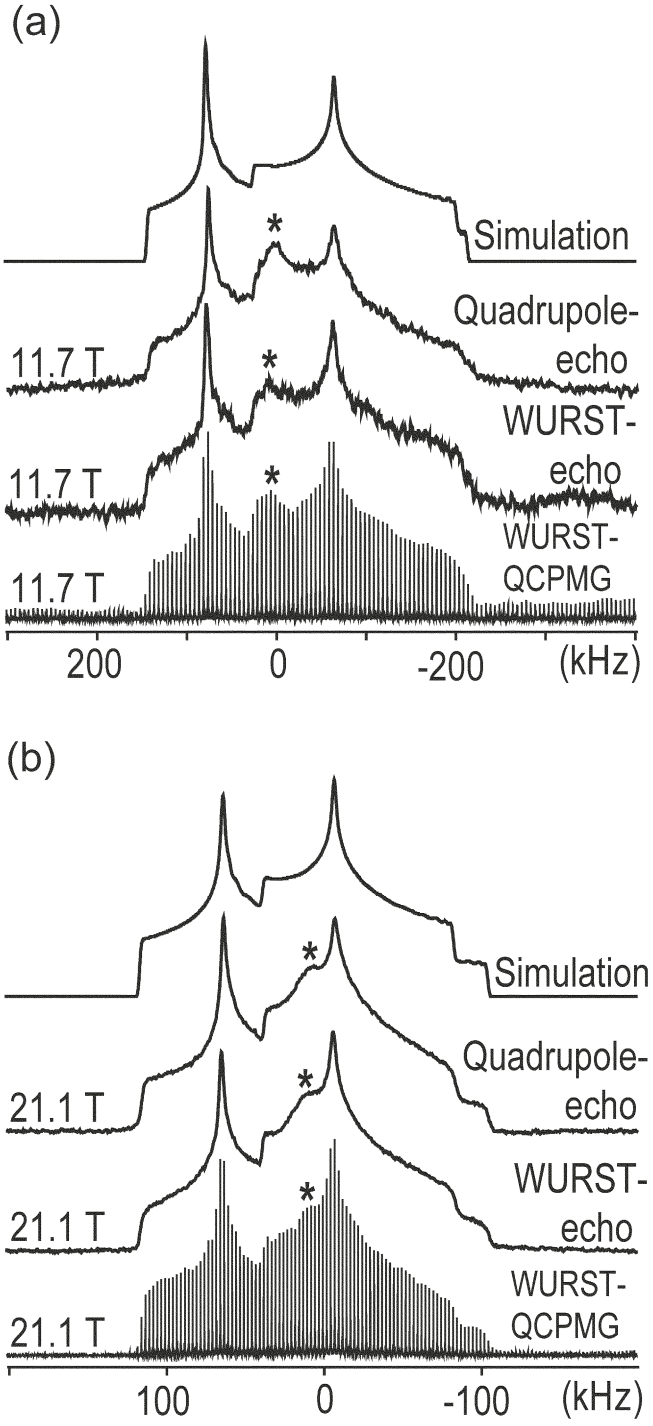

Table 3. Experimental and calculated ^{139}La NMR parameters in model compounds.

Material	Method	C_Q (MHz)	η	δ_{iso} (ppm)	Ω (ppm)	κ	α (°)	β (°)	γ (°)
$LaNbO_4$	Exptl.	36±2	0.44±0.05	295±25	255±10	0.40±0.04	90±5	50±5	270±10
	Calcd.	33.8	0.38	220[a]	490	0.11	90	27	270
La_2O_3	Exptl.	59.0±0.4	0.00±0.05	640±10	500±10	–1.0±0.1	150±30	90±10	180±10
	Calcd.	56	0.0	378[a]	260	0.44	150	88	180
$La(OH)_3$	Exptl.	22.0±0.5	0.05±0.02	260±20	80±7	0±0.1	80±7	10±10	0±10
	Calcd.	23.5	0.0	301[a]	200	0.01	92	0	0

Note: C_Q = quadrupole coupling constant; η = asymmetry parameter; δ_{iso} = isotropic chemical shift; Ω = span; κ = skew; α, β, and γ are the Euler angles.

[a]The chemical shifts were calculated using δ_{iso} (sample)–δ_{iso}(ref)= σ_{iso}(ref)–σ_{iso}(sample), where δ_{iso}(ref) and σ_{iso}(ref) are the experimental chemical shift (0.0 ppm) and the calculated chemical shielding (5022 ppm) of aqueous 1.0 mol/L $LaCl_3$, respectively.[21]

Can. J. Chem. Downloaded from www.nrcresearchpress.com by Xi'an Jiaotong University on 09/19/12
For personal use only.

spikelet oscillations in QCPMG, the finer details of the line shape are sometimes lost. Furthermore, we found that for disordered battery materials studied in this work, the T_2 relaxation times are rather short, which does not favour the use of the QCPMG method. Thus, the technique of choice in this work was the WURST-echo pulse sequence.

Simulations of the NMR spectra collected at 11.7 and 21.1 T (Fig. 1*b*) reveal a C_Q of 34 ± 2 MHz and η of 0.51 ± 0.05. Collecting the ^{139}La spectrum at two different magnetic fields allowed for the identification of a small impurity, marked with (*) in Figs. 1*a* and 1*b*. Contributions from quadrupolar interactions, as well as CSA, were considered, and the span, skew, and Euler angles, defined throughout this work as the angles that relate the CSA axis system to the EFG axis system, were determined to be 420 ± 10 ppm, 0.33 ± 0.05, $\alpha = 90° \pm 10°$, $\beta = 27° \pm 3°$, $\gamma = 270° \pm 10°$, respectively, and are in agreement with values predicted by CASTEP.[39] $LaNbO_4$ provides a good example of a system with complex NMR parameters that were challenging to simulate, and illustrates the advantage of using calculation software for NMR interpretation. CASTEP proved to be extremely beneficial in the simulation of the $LaNbO_4$ spectra obtained at 11.7 and 21.1 T, providing a starting point for the simulation: values of C_Q, η, the span, skew, and Euler angles. The values produced by CASTEP for this compound and others are shown in Table 3.

The second coordination sphere of La in $LaNbO_4$ contains both La and Nb, as shown in Table 2. The value of η obtained by simulation of the experimental spectra is 0.51 ± 0.05. Since the highest rotational symmetry element present is a two-fold rotational axis, which lies along the *b*-axis of the crystal, the experimental simulation is not sufficient to predict the respective orientation of $\boldsymbol{V}_{ZZ}$, the principle component of the EFG tensor. However, this information can be achieved by first principle calculations, which have been performed using CASTEP. The theoretically predicted orientation of the EFG tensor for $LaNbO_4$, with respect to the crystal axes, is shown in Fig. 2*a*, along with those of La_2O_3 (Fig. 2*b*) and $La(OH)_3$ (Fig. 2*c*).

^{139}La NMR powder patterns are known to be very sensitive to the environment surrounding La, often displaying high values of C_Q, as large as 105 MHz,[15] for La environments in which La has a nonspherical environment. In the case of $LaNbO_4$, the crystallographic parameters do not show disorder or partial occupancies in either the niobium or lanthanum positions, suggesting that the structure itself is ordered. This is consistent with the observed ^{139}La NMR spectrum that clearly shows a typical powder pattern for highly ordered samples with high crystalline symmetry. (The sensitivity of quadrupolar nuclei, such as lanthanum, is to the symmetry of the oxygen environment, as well as the complexity of the second coordination sphere)[15,48]

Lanthanum oxide

The second model compound, La_2O_3, is known to form a trigonal lattice structure with space group *P*-3*m1*, in which the lanthanum atoms are surrounded by seven oxygen atoms within 2.8 Å, with the La–O bond distance in the range of 2.4–2.8 Å. This structure is shown in Table 2, and the corresponding ^{139}La NMR spectra, collected at 11.7 and 21.1 T are shown in Figs. 3*a* and 3*b*. The spectra are dominated by the quadrupolar interactions, and at 11.7 T the full spectrum width is about 600 kHz. Yet even at this field, using the WURST-echo pulse, it was possible to acquire this spectrum with only a single central frequency offset. Since the second-order central-transition quadrupolar linewidth scales inversely with the field, the same spectrum recorded at 21.1 T is only about 300 kHz broad. Not only is it easier to obtain the correct line at the higher magnetic field, but the signal-to-noise is also significantly improved, which will become important when studying battery samples with lower lanthanum content. Another advantage of recording ^{139}La NMR spectra at 21.1 T is the fact that the chemical shielding interactions are proportional to the external magnetic field, and the quadrupolar interactions are inversely proportional to the external magnetic field, which facilitates the extraction of information about the chemical shielding interaction at higher magnetic fields.[13] In the La_2O_3 example (Figs. 3*a* and 3*b*), note how the singularity in the middle of the powder pattern moves to higher frequency in the high-field spectrum. The position of this singularity is directly related to the magnitude of CSA interactions, and the shift becomes more pronounced at higher magnetic field, allowing accurate quantification of CSA interactions.

The crystallographic lanthanum environment in the structure is simple, in that the major influence on lanthanum is its surrounding oxygen environment, with there being no lanthanum within 4.00 Å. Lanthanum sits in a pseudo-octahedral environment with six of the oxygen atoms, while the seventh oxygen is directly above this octahedral system, with the distance between lanthanum and the seventh oxygen being 2.555 Å. This nonspherical environment contributes to a lanthanum NMR spectrum with a large quadrupolar coupling

Can. J. Chem. Downloaded from www.nrcresearchpress.com by Xi'an Jiaotong University on 09/19/12
For personal use only.

constant C_Q of 59.0 ± 0.5 MHz. Simulations of ^{139}La NMR measurements also reveal an asymmetry parameter η of 0.00 ± 0.05, as shown in Fig. 3, which is consistent with lanthanum in an environment of three-fold or higher symmetry. This agrees with the work of Bastow, in which the ^{139}La NMR of La_2O_3 was recorded at 9.4 T, although no CSA contribution to the ^{139}La NMR spectrum was reported.[17] Nevertheless, in our ^{139}La NMR spectrum, in addition to EFG contributions, there is a contribution from the CSA, and the simulated spectrum produces a span Ω of 500 ppm ± 10 and a skew κ of –1 ± 0.1 with $\alpha = 150° \pm 30°$, $\beta = 90° \pm 10°$, and $\gamma = 180° \pm 10°$. These values were obtained by the simulation of NMR spectra collected at 21.1 and 11.7 T. The asymmetry parameter $\eta = 0$ arises from the axially symmetrical EFG tensor, which is the result of the three-fold rotational axis of the La_2O_3 crystal structure, which lies along the *c*-axis.[27] The values obtained for C_Q and η, by simulating the ^{139}La NMR spectrum, are supported by the values obtained through theoretical calculations using CASTEP: $C_Q = 56$ MHz and $\eta = 0$. In addition, CASTEP calculated a span of 260 ppm, a skew of –0.44, and Euler angles $\alpha = 150°$, $\beta = 88°$, and $\gamma = 180°$. These are shown in Table 3. The corresponding EFG tensors, as predicted by CASTEP, are shown with relation to the crystal axis in Fig. 2*b*.[39] It is clear that the major EFG tensor component, V_{zz}, is oriented along the *c*-axis of the crystal, which has three-fold rotational axis that passes through the center of the La atom. This supports the experimental finding of η being of 0.00 ± 0.05, with the axial line shape evident in the ^{139}La NMR spectra.

For comparison, the ^{139}La NMR spectra of La_2O_3 that was exposed to air in ambient conditions were measured at 21.1 T (Fig. 3*c*). An impurity is clearly visible in the ^{139}La NMR of the exposed sample.[32] (To obtain the pure La_2O_3 sample, the exposed sample was heated in air at 900 °C for 24 h.) Simulation of the NMR spectrum obtained at 21.1 T shows that the peak representing the La-impurity was found to have a C_Q of 22.0 ± 0.5 MHz and an η of 0.00 ± 0.05, with a span of 80 ± 7 ppm, skew of 0, and $\alpha = 90° \pm 30°$, $\beta = 10° \pm 10°$, $\gamma = 0° \pm 10°$. These values are also supported by measurements taken at 11.7 T. It has been shown that lanthanum oxide is reactive to air under ambient conditions, and $La(OH)_3$ is found to be formed in La_2O_3.[32] By measuring the ^{139}La NMR spectrum of $La(OH)_3$ at 9.4 T, Herreros et al.[21] reported that the C_Q and η for this compound are 20.5 MHz ± 0.5 and 0.05 ± 0.05, respectively. From the similarity in the spectra obtained, it can be concluded that the second phase present in this compound consists primarily of $La(OH)_3$. Further support is given by theoretical predictions performed in CASTEP. The theoretically predicted values are shown in Table 3, along with the experimentally obtained results. $La(OH)_3$ CASTEP predictions result in a C_Q and η of –23.5 MHz and 0.00, respectively, which support the axial shape of the spectra obtained. The value of η suggests that the EFG tensor component V_{zz} lies along the *c*-axis of the $La(OH)_3$ crystal structure. This is consistent with the crystallographic information, which places $La(OH)_3$ in the space group $P63/m$ and shows that the lanthanum atom lies at the center of a three-fold rotational axis as well as a six-fold screw axis, which are both directed along the *c*-axis of the crystal.[30] Figure 2*c* shows the orientation of the theoretically calculated EFG tensor of $La(OH)_3$ with respect to the crystal axis. In addition, CASTEP produces values of 200 ppm and 0.01 for the span and skew, respectively, with Euler angles of $\alpha = 92°$, $\beta = 0°$, and $\gamma = 0°$. Although the theoretically predicted span is larger than that observed, the predicted Euler angles are in good agreement with the observed values. Theoretically predicted and experimentally obtained values are shown in Table 3. The parameters C_Q and η are a strong indication of the structure and local symmetry in lanthanum compounds, and thus ^{139}La NMR is a valuable tool in the study of lanthanum containing compounds.[32]

$Li_{3x}La_{2/3-x}TiO_3$ ($0.03 \leq x \leq 0.063$)

The ^{139}La NMR spectra of two model lanthanum-containing compounds have been shown, and each of these structures has been highly ordered, with lanthanum in a well-defined environment with respect to its second coordination sphere elements. In contrast, the fast lithium ion electrolyte material, $Li_{3x}La_{2/3-x}TiO_3$, has an orthorhombic, perovskite type structure in space group *Pmmm* and is known to have considerable disorder, which results from the ability of lithium and lanthanum to occupy the same crystallographic site.[29,34] $Li_{3x}La_{2/3-x}TiO_3$ consists of corner-shared TiO_6 octahedra, and the lanthanum and (or) lithium is situated between TiO_6 octahedra.[29] The crystal structure predicts two lanthanum environments, as shown in Table 2. Each environment is oxygen rich, and in each case La is coordinated to 12 oxygen atoms. The difference in the lanthanum atoms is in their positions in the unit cell, with La-1 positioned on the corners of the unit cell and La-2 at the center of the *c*-axis. In addition, the La sites have different La–O bond distances; although all La–O bonds lie in the range of 2.7–2.8 Å. Interestingly, the ^{139}La NMR spectrum recorded at two magnetic fields (Fig. 4) shows only one La peak. This asymmetric lineshape, which lacks the usual sharp discontinuities typically observed in quadrupole powder patterns, is skewed to one side and is indicative of substantial quadrupolar interaction. This lineshape is due to the disorder in the second coordination sphere of lanthanum, which usually results in distribution of the quadrupolar parameters C_Q and η.[16] This distribution also makes the C_Q and the η for the two sites irresolvable at both magnetic fields (21.1 and 11.7 T), since there are many sites with different quadrupolar parameters in this sample. Nevertheless, using appropriate simulation tools, many details of this distribution can still be extracted.

To effectively simulate the spectra to extract quadrupolar information, one needs to analyze the contribution in the spectrum of chemical shielding interaction and quadrupolar coupling interaction in the spectrum. As can be seen in Fig. 4, the full-width at half-height (FWHH) for the spectrum at 11.7 T is 53.5 kHz. At 21.1 T, the FWHH is reduced significantly to 34.0 kHz. This suggests that the spectra are dominated by second-order quadrupolar interaction and can be simulated neglecting the potential chemical shielding anisotropy of lanthanum. Using QuadFit,[37] which has the capability of including a distribution in the parameters η and C_Q, the spectra at the two fields were simulated accurately by considering the distribution of quadrupolar parameters, with the resulting simulations shown in Fig. 4. As can be seen in Table 4, the quadrupolar coupling constant of La in $Li_{3x}La_{2/}$

Can. J. Chem. Downloaded from www.nrcresearchpress.com by Xi'an Jiaotong University on 09/19/12
For personal use only.

Fig. 2. EFG tensor orientations for (*a*) $LaNbO_4$, (*b*) La_2O_3, and (*c*) $La(OH)_3$. In each case V_{zz} is directed out of the page, while V_{xx} and V_{yy} lie in the a-b plane of the crystal axes. Tensor orientations are shown by green (grey in print version) arrows. Calculations of the EFG tensor orientations were performed in CASTEP. La is represented by dark blue (dark grey) spheres, O is represented by light blue spheres (light grey), and Nb is represented by orange spheres (mid grey).

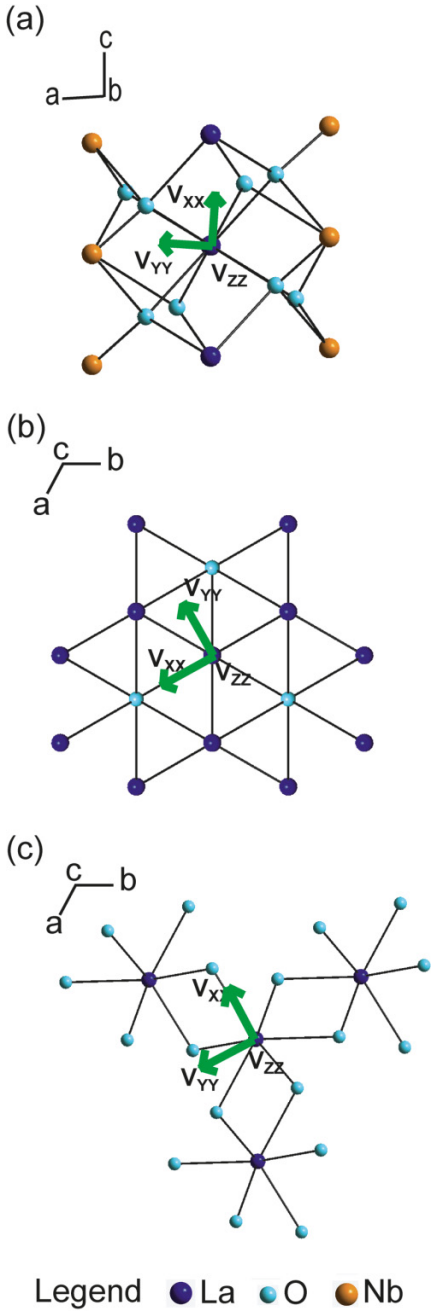

Fig. 3. ^{139}La NMR spectra of La_2O_3, heated at 900 °C to remove La $(OH)_3$ impurity: (*a*) taken at 21.1 T and (*b*) 11.7 T. (*c*) ^{139}La WURST-Echo NMR spectra at 21.1 T of La_2O_3, exposed to air in ambient conditions. Simulations were performed using WSolids Software.

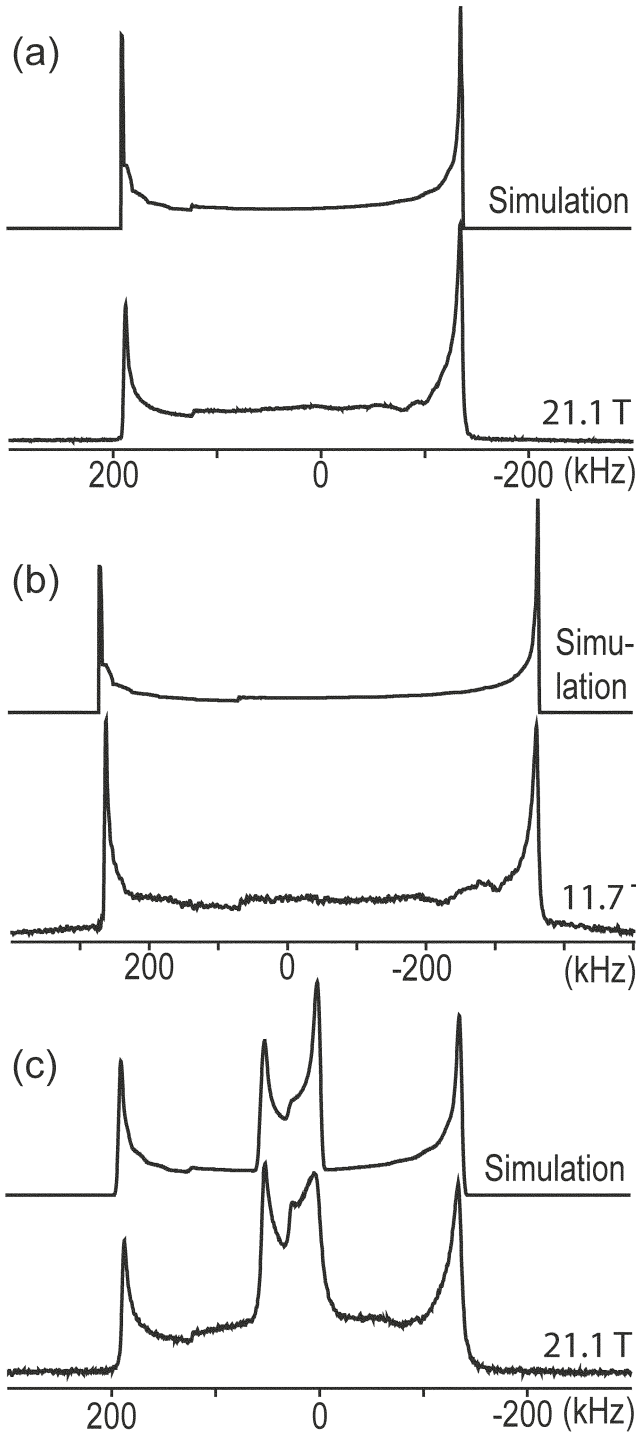

$_{3-x}TiO_3$ is ~22.5 MHz with a broad distribution of 14.5 MHz, although the asymmetry parameter is 0.75 with a narrow distribution of 0.15. It should be mentioned that almost no line broadening is needed in both simulations, which is expected for this sample, as it is highly crystalline. The extraction of quadrupolar information was also attempted by using the quadrupolar induced shift (QIS) that is inversely proportional to the external magnetic field.[49] Equation [3] is valid for a nucleus with $I = 7/2$.

Can. J. Chem. Downloaded from www.nrcresearchpress.com by Xi'an Jiaotong University on 09/19/12
For personal use only.

Fig. 4. ^{139}La WURST-Echo NMR spectra of $Li_{3x}La_{2/3-x}TiO_3$ collected at (top) 21.1 T and (bottom) 11.7 T . Simulations were performed in QuadFit and are shown above each spectrum.

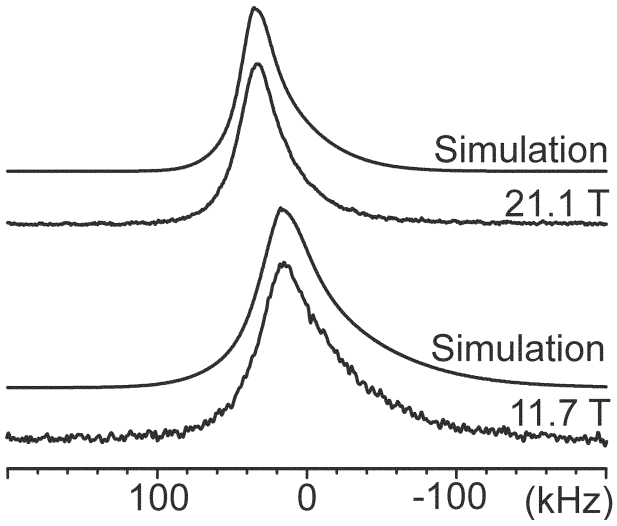

$$[3] \qquad \delta_{CG} - \delta_{iso} = -2551.02\left(\frac{C_Q^2}{\nu_z^2}\right)\left(1+\frac{\eta^2}{3}\right)$$

Where δ_{CG} is the center of gravity of the peak, δ_{iso} is the isotropic chemical shift, ν_z is the Larmor frequency, C_Q is the quadrupolar coupling constant, η is the asymmetry, and 2551.02 is a constant, which varies with the spin I of the nucleus of interest. The measured centers of gravities of peaks at 11.7 and 21.1 T are 67 ppm and 217 ppm, respectively. Using eq. [3], one can obtain δ_{iso}, 284 ± 8 ppm, as shown in Table 4. However, C_Q and η cannot be determined unambiguously using this method. Since η has the range of 0 to 1, the minimum and the maximum values of C_Q can still be determined, which are 17.8 and 20.5 MHz, respectively. Although as can be seen in Table 4, the QuadFit and the QIS calculations give very similar isotropic chemical shifts and quadrupolar coupling constants, one should note that the QIS calculation does not allow the determination of the distribution of C_Q and η, owing to the fact that the QIS calculation considers only the position of centre of gravity, not the overall lineshape. The minimum and the maximum values of C_Q are not the actual distributions of C_Q but the values corresponding to the minimum and the maximum values of the asymmetry parameter. Both spectra can be simulated with a single site without considering the distribution of C_Q and η as well, although a very high line-broadening value was necessary. The results are also presented in Table 4 for comparison. It can be seen that the simple simulation without distributions of C_Q and η gives results close to the previous methods. This may be due, coincidently, to the high asymmetry parameter of this particular sample. It has been shown previously that a featureless line shape like spectra in Fig. 4 could result from a very low asymmetry but with broad distribution of quadrupolar parameters.[50]

The distribution of quadrupolar parameters obtained above can be explained by analyzing the second coordination sphere of La in the crystal structure, which contains lanthanum, lithium, and a vacant site in a disordered distribution.[29,34] Lanthanum is in a highly symmetric environment according to the surrounding oxygen atoms, which form a cubelike arrangement around the La atoms. The highest symmetry element present is a two-fold rotational axis, which passes through both La-1 and La-2, which agrees with $\eta \neq 0$. It should be noted here that there are several possible structures of lithium lanthanum titanate materials.[51,52] Powder X-ray diffraction was used to determine that the structure of interest was in fact $Li_{3x}La_{2/3-x}TiO_3$ ($0.03 \leq x \leq 0.063$).[29] ^{139}La NMR proved to be a very useful conformational technique, in that other lithium lanthanum titanate structures are of higher symmetry, and most contain rotational axes, either three- or four-fold, that run through La. The nonzero η obtained by simulating the NMR spectrum obtained for this material confirmed that it was the correct structure, with only two-fold rotational symmetry.

The lithium atoms as well as the vacant sites in this structure are known to substitute lanthanum in its crystallographic sites, displacing a stoichiometric amount of the lanthanum from the crystal structure.[29,34] This means that for each lanthanum atom in its original place in the crystal structure, the surrounding environment is disordered by the substitution of lanthanum for lithium, or a vacant site, in the second coordination sphere. This disordered lanthanum environment is present in the same context for both lanthanum sites, which leads to the featureless ^{139}La NMR spectra of $Li_{3x}La_{2/3-x}TiO_3$ at both fields.

The CASTEP NMR calculations were performed for this compound and the results are presented in Table 4. The $Li_{3x}La_{2/3-x}TiO_3$ sample represents a certain challenge for CASTEP NMR calculations because of significant disorder in cationic positions, as disorder or partial site occupancies are not implemented in the CASTEP code. Nevertheless, we have attempted to perform CASTEP calculations for three model structures, which best represent the real $Li_{3x}La_{2/3-x}TiO_3$ structure. The results are summarized in Table 4. In the first model structure, both sites, La-1 and La-2, were fully occupied. There was no Li present. Even though there is significant charge imbalance, the CASTEP results allow the discrimination of two La sites, and obtained C_Q and η values are reasonably close to those found experimentally. In the second model structure, the La-1 site was fully occupied with La, and the La-2 site was fully occupied with Li. The third structure has the site occupations inversed, the La-1 site was fully occupied with Li, and the La-2 site was fully occupied with La. As can be seen in Table 4, for these three model structures, the CASTEP calculated C_Q values are in the same general range as found in experiments.

$Li_{16}La_{32}Fe_{6.4}O_{67}$

The garnet-related structure, $Li_{16}La_{32}Fe_{6.4}O_{67}$, considered as a potential cathode material for lithium ion batteries, has a cubic structure in space group $Im3m$. Initial studies performed using ^{7}Li MAS NMR at 11.7 T indicated that the material may contain structural disorder. It was originally determined that the compound had one crystallographically unique lithium site, two lanthanum sites and two iron sites. This number of lithium sites, however, is not supported by ^{7}Li MAS NMR performed at 11.7 T, shown in Fig. 5. The lithium peaks represent a set of paramagnetic peaks between ~4 and ~25 ppm, and a set of diamagnetic peaks at ~0 ppm.

Can. J. Chem. Downloaded from www.nrcresearchpress.com by Xi'an Jiaotong University on 09/19/12
For personal use only.

Table 4. Experimental and calculated ^{139}La NMR parameters in battery materials.

Material	Method	La	δ_{iso} (ppm)	C_Q (MHz)	η
$Li_{3x}La_{2/3-x}TiO_3$	Calcd.[a]	La-1	—	25.4	0.5
		La-2	—	18.3	0.43
	Calcd.[b]	La-2	—	34.7	0.70
	Calcd.[c]	La-1	—	17.9	0.49
	Exptl.[d]	—	284±5	19.2±1.3	
	Exptl.[e]	—	260±20	22.5±0.5	0.75±0.1
	Exptl.[f]	—	270±10	17.0±2.0	0.9±0.1
$Li_{16}La_{32}Fe_{6.4}O_{67}$	Exptl.	La-1	510±40	56.0±1.0	0.05±0.05
		La-2	290±30	29.0±2.0	0.6±0.1

[a]CASTEP, structure with two La sites, La-1 and La-2.
[b]CASTEP, structure with one La site (La-2). The La-1 site has been replaced with Li (Li-1).
[c]CASTEP, structure with one La site (La-1). The La-2 site has been replaced with Li (Li-2).
[d]Calculated using QIS (see text).
[e]Spectra were fitted using QuadFti with distributions for both C_Q (14.5 MHz) and η (0.15).
[f]Spectra were fitted using DMFit with a single site.

Here, the lithium peak that has a higher chemical shift is known to have the most paramagnetic character. This is supported by T_1 measurements that show that these peaks have T_1 relaxation values of ~11 ms, while the diamagnetic peaks have T_1 relaxation times greater than 100 s. The lithium atoms represented by the paramagnetic peaks are thus closest to one or more iron sites, while the peak at the lowest chemical shift has the least paramagnetic character because of its greater distance from iron and thus unpaired electrons in the structure.[7,10]

The different lithium environments arise from the ability of lithium to occupy vacant sites found on the Fe-2 site, represented by green (light grey in print version) spheres in Fig. 6*a*; this substitution is supported by powder X-ray analysis.[53] This Li–Fe substitution is the source of disorder in this structure, with the existence of vacant sites on the original Li sites as well as the Fe-2 sites, in which Li substitution occurs. This means that the compound contains a "variable" site, which may be occupied by Li, Fe, or a vacancy.[28] The variability of this site produces a distribution of lithium sites, which is responsible for the unique ^{7}Li MAS NMR spectrum.

To better understand the nature of the lithium distribution in this material, ^{139}La NMR was used to assign the La sites and to study their environments. There are two crystallographically unique La sites in this material: La-1 is coordinated to ten O atoms, while having La–O bond distances in the range of 2.5–2.7 Å; La-2 is coordinated to nine O atoms with La–O bond distances in the range 2.3–2.7 Å. ^{139}La NMR collected at 21.1 T, shown in Fig. 7, supports the crystallographic data and shows evidence of two lanthanum environments. Simulations of the NMR data show that La-2 has a C_Q of 56 ± 1 MHz and η of 0.05 ± 0.05. This large C_Q suggests that La-2 is in a nonspherical environment with respect to the surrounding oxygen, compared with La-1. In addition, La-2 contains little disorder in the second coordination sphere. Crystallographic information shows that the La-2 site lies on an axis of four-fold rotation, and four-fold roto-inversion, which is aligned with the *c*-axis of the crystal.[28] This high level of rotational symmetry is responsible for the experimentally obtained value of η of 0.05 ± 0.05. By comparison, simulations of NMR spectra show that La-1 has a C_Q of 29 ± 2 MHz and a η of 0.6 ± 0.1, suggesting that La-1 is in a more spherical oxygen environment and yet in a position of lower symmetry than La-2, since the highest symmetry element present for La-1 is a two-fold rotational axis. The low symmetry of this site is responsible for the observed values of η, 0.6 ± 1, which is considerably different than that of La-2. A considerable amount of line broadening was necessary to simulate this peak, which may be an indication that the NMR parameters of the La-1 site cannot be described by a single set of values of C_Q or η, or rather that there is a distribution of C_Q and (or) η for this particular site, similar to

Fig. 5. ^{7}Li MAS NMR of $Li_{16}La_{32}Fe_{6.4}O_{67}$, collected at 11.7 T with MAS 20 kHz.

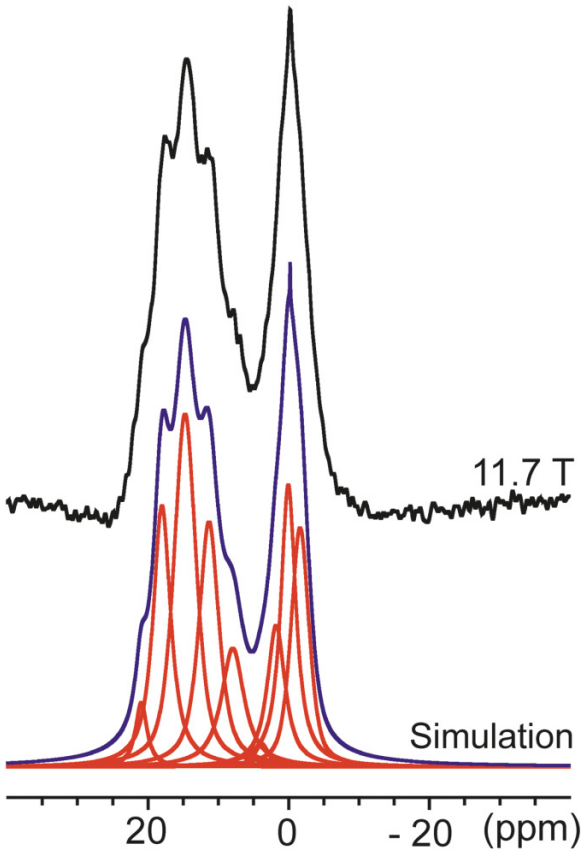

Can. J. Chem. Downloaded from www.nrcresearchpress.com by Xi'an Jiaotong University on 09/19/12
For personal use only.

Fig. 6. (*a*) Diagram of $Li_{16}La_{32}Fe_{6.4}O_{67}$ crystal structure showing a single unit cell, with La-1 and La-2 represented by red and blue spheres, respectively, Li by yellow spheres, and Fe-2 by brown polyhedra. The variable Li/Fe/vacant site is shown by green spheres. (*b*) The individual lanthanum sites showing the coordination to oxygen as well as the second coordination sphere environment around the La polyhedra. The brown spheres represent Fe-2, which does not participate in the Li–Fe disorder.

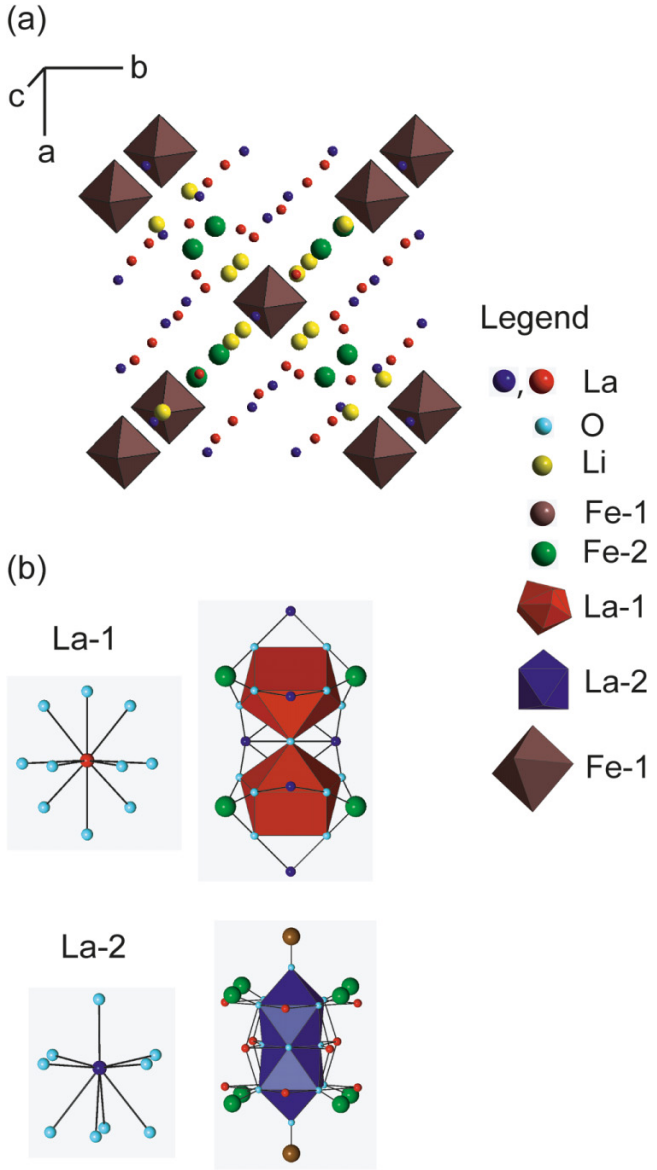

Fig. 7. ^{139}La WURST-Echo NMR spectra of $Li_{16}La_{32}Fe_{6.4}O_{67}$ collected at 21.1 T, shown with simulation. This spectrum can be represented as a superposition of two sites with La-1 having C_Q = 56.1 MHz and η = 0.05; and La-2 having C_Q = 29.8 MHz and η = 0.6. Simulations were performed using DMFit software.

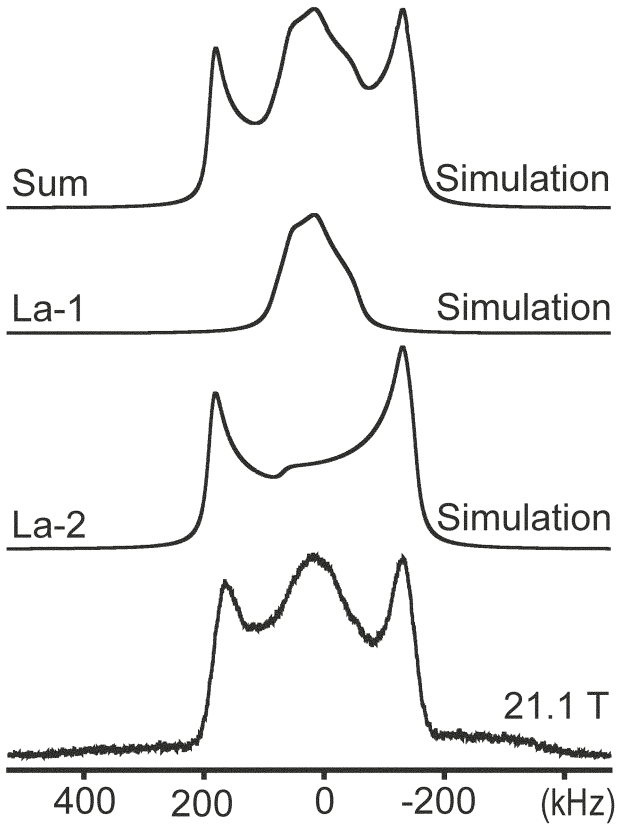

that seen in $Li_{3x}La_{2/3-x}TiO_3$. To evaluate the source of disorder in this material, the individual lanthanum environments are compared. Figure 6*b* shows the two lanthanum environments, with the respective first and second coordination sphere contents. The assignment of the ^{139}La NMR peaks was performed by analysis of the respective La environments given by crystallographic data.[28] The crystal structure shows that one of the sites, La-1, is close (3.2 Å) to the source of the disorder in the structure. This site is a variable Fe–Li–vacant site (shown in green in Fig. 6*a*). While the other lanthanum site, La-2, is much further (4.4 Å) from this site. The variable Fe–Li–vacant site provides a significant source of disorder, which accounts for the distribution in NMR parameters observed for La-1. This distribution of C_Q and η is seen clearly for La-1 but not for La-2. This can be explained by the difference in proximity to the source of disorder in the compound, as discussed above. This is further evidence that ^{139}La NMR can be used to evaluate structural features observed in complex systems containing atomic-level disorder found in the second coordination sphere of lanthanum. Theoretical calculations were not performed for $La_{32}Li_{16}Fe_{6.4}O_{67}$, because the unit cell volume is large (1830 Å^3), and the system has metallic character.[28]

The two battery materials, $Li_{16}La_{32}Fe_{6.4}O_{67}$ and $Li_{3x}La_{2/3-x}TiO_3$, each show considerable disorder in the second coordination sphere for at least one of their lanthanum environments, subsequently showing that lanthanum quadrupole parameters are sensitive to disorder in the second coordination sphere. This is reflected in the NMR spectra obtained and particularly in the values of C_Q and η extracted from simulating experimental data, with disorder being indicated by a distribution in NMR parameters. The sensitivity of the ^{139}La NMR is further pronounced when the different La sites of $Li_{16}La_{32}Fe_{6.4}O_{67}$ are considered. ^{139}La NMR can distinguish between these sites because of its sensitivity to the disorder.

Can. J. Chem. Downloaded from www.nrcresearchpress.com by Xi'an Jiaotong University on 09/19/12
For personal use only.

Conclusion

This work has compared the ^{139}La static solid-state NMR spectra of the model materials $LaNbO_4$ and La_2O_3 to the spectra of potential lithium ion battery materials $Li_{3x}La_{2/3-x}TiO_3$ and $Li_{16}La_{32}Fe_{6.4}O_{67}$. The model materials represent materials in which the ^{139}La environments are well-defined and are not in close proximity to atomic-level disorder. In contrast, $Li_{3x}La_{2/3-x}TiO_3$ and $Li_{16}La_{32}Fe_{6.4}O_{67}$ each show instances of atomic-level disorder, which can be detected by ^{139}La NMR.

It has been illustrated here that lanthanum containing lithium ion battery materials can be effectively studied using ^{139}La NMR, as it is a sensitive probe of local symmetry. Structural analysis performed using ^{139}La NMR can distinguish between different lanthanum sites by evaluating the values of C_Q and η through the measurement and subsequent simulation of ^{139}La NMR powder line shapes. Theoretical calculations performed in CASTEP were supportive of results obtained through experiments simulations. This information can be used to indicate the presence of disorder in the second coordination sphere around a specific lanthanum site, which manifests itself as a distribution of experimental values of C_Q and η for a lanthanum site in close proximity to a source of disorder. This method shows promise when applied to the understanding of complex structures. In combination with ^{7}Li MAS NMR and powder X-ray diffraction, this is a powerful tool that can be used to probe structures rich in lanthanum and subsequently help in the analysis of battery materials that contain atomic-level disorder.

Acknowledgements

We would like to thank Jim Garret in the BIMR Institute at McMaster University in Hamilton, Ontario, for advice and assistance in materials preparation. The two anonymous reviewers are thanked for valuable comments. Access to the 900 MHz NMR spectrometer and CASTEP software was provided by the National Ultrahigh-Field NMR Facility for Solids (Ottawa, Canada), a national research facility funded by the Canada Foundation for Innovation, the Ontario Innovation Trust, Recherche Québec, the National Research Council Canada, and Bruker BioSpin and managed by the University of Ottawa (www.nmr900.ca). In addition, we thank The Natural Sciences and Engineering Research Council of Canada (NSERC) in acknowledgement of a Major Resources Support grant. The authors also gratefully acknowledge funding through the AUTO21 Centers of Excellence program.

References

(1) Goodenough, J. B.; Kim, Y. *Chem. Mater.* **2010** *22* (3), 587. doi:10.1021/cm901452z.
(2) Thangadurai, V.; Weppner, W. *J. Power Sources* **2005** *142* (1–2), 339. doi:10.1016/j.jpowsour.2004.11.001.
(3) Thangadurai, V.; Schwenzel, J.; Weppner, W. *Ionics* **2005** *11* (1–2), 11. doi:10.1007/BF02430397.
(4) O'Callaghan, M. P.; Cussen, E. J. *Solid State Sci.* **2008** *10* (4), 390. doi:10.1016/j.solidstatesciences.2007.11.036.
(5) O'Callaghan, M. P.; Powell, A. S.; Titman, J. J.; Chen, G. Z.; Cussen, E. J. *Chem. Mater.* **2008** *20* (6), 2360. doi:10.1021/cm703677q.
(6) van Wullen, L.; Echelmeyer, T.; Meyer, H. W.; Wilmer, D. *Phys. Chem. Chem. Phys.* **2007** *9*, 3298 . doi:10.1039/b703179c.
(7) Lee, Y. J.; Wang, F.; Grey, C. P. *J. Am. Chem. Soc.* **1998** *120* (48), 12601. doi:10.1021/ja9817794.
(8) Cahill, L. S.; Chapman, R. P.; Britten, J. F.; Goward, G. R. *J. Phys. Chem. B* **2006** *110* (14), 7171. doi:10.1021/jp057015+.
(9) Davis, L. J. M.; Heinmaa, I.; Goward, G. R. *Chem. Mater.* **2010** *22* (3), 769. doi:10.1021/cm901402u.
(10) Cahill, L. S.; Chapman, R. P.; Kirby, C. W.; Goward, G. R. *Appl. Magn. Reson.* **2007** *32* (4), 565. doi:10.1007/s00723-007-0046-8.
(11) Cussen, E. J. *Chem. Commun. (Camb.)* **2006** (4), 412. doi:10.1039/b514640b.
(12) Thangadurai, V.; Weppner, W. *Adv. Funct. Mater.* **2005** *15* (1), 107. doi:10.1002/adfm.200400044.
(13) Ooms, K. J.; Feindel, K. W.; Willans, M. J.; Wasylishen, R. E.; Hanna, J. V.; Pike, K. J.; Smith, M. E. *Solid State Nucl. Magn. Reson.* **2005** *28* (2-4), 125. doi:10.1016/j.ssnmr.2005.07.002.
(14) Willans, M. J.; Feindel, K. W.; Ooms, K. J.; Wasylishen, R. E. *Chemistry-a European Journal* **2006** *12* (1), 159. doi:10.1002/chem.200500778.
(15) Hamaed, H.; Lo, A. Y. H.; Lee, D. S.; Evans, W. J.; Schurko, R. W. *J. Am. Chem. Soc.* **2006** *128* (39), 12638. doi:10.1021/ja0645180.
(16) Bastow, T. J.; Mathews, T.; Sellar, J. R. *Solid State Ion.* **2004** *175* (1-4), 129. doi:10.1016/j.ssi.2004.09.028.
(17) Bastow, T. J. *Solid State Nucl. Magn. Reson.* **1994** *3* (1), 17. doi:10.1016/0926-2040(94)90047-7.
(18) Lo, A. Y. H.; Sudarsan, V.; Sivakumar, S.; van Veggel, F.; Schurko, R. W. *J. Am. Chem. Soc.* **2007** *129* (15), 4687. doi:10.1021/ja068604b.
(19) Ishida, K.; Nakai, Y.; Kitagawa, S.; Kamihara, Y.; Hirano, M.; Hosono, H. *Physica B* **2009** *404* (19), 3089. doi:10.1016/j.physb.2009.07.078.
(20) Nakai, Y.; Ishida, K.; Kamihara, Y.; Hirano, M.; Hosono, H. *Phys. Rev. Lett.* **2008** *101*, 0770061.
(21) Herreros, B.; Man, P. P.; Manoli, J. M.; Fraissard, J. *J. Chem. Soc. Chem. Commun.* **1992** (6): 464. doi:10.1039/c39920000464.
(22) Ashbrook, S. E. *Phys. Chem. Chem. Phys.* **2009** *11* (32), 6892. doi:10.1039/b907183k.
(23) Duer, M. J. *Introduction to Solid-State NMR Spectroscopy.*; Blackwell Science: Oxford, UK, 2004.
(24) O'Dell, L. A.; Schurko, R. W. *Chem. Phys. Lett.* **2008** *464* (1–3), 97. doi:10.1016/j.cplett.2008.08.095.
(25) Bhattacharyya, R.; Frydman, L. *J. Chem. Phys.* **2007** *127*, 1945031.
(26) Vullum, F.; Nitsche, F.; Selbach, S. M.; Grande, T. *J. Solid State Chem.* **2008** *181* (10), 2580. doi:10.1016/j.jssc.2008.06.032.
(27) Marsella, L.; Fiorentini, V. *Phys. Rev. B* **2004** *69* (17), 1721031. doi:10.1103/PhysRevB.69.172103.
(28) Mazza, D.; Abbatista, F.; Vallino, M.; Ivaldi, G. *J. Less Common Met.* **1985** *106* (2), 277. doi:10.1016/0022-5088(85)90264-4.
(29) Ibarra, J.; Varez, A.; Leon, C.; Santamaria, J.; Torres-Martinez, L. M.; Sanz, J. *Solid State Ion.* **2000** *134* (3–4), 219. doi:10.1016/S0167-2738(00)00761-X.
(30) Djerdj, I.; Garnweitner, G.; Su, D. S.; Niederberger, M. *J. Solid State Chem.* **2007** *180* (7), 2154. doi:10.1016/j.jssc.2007.05.019.
(31) B. Downs, K. B., Kausil Simmaswamy 2003.
(32) Fleming, P.; Farrell, R. A.; Holmes, J. D.; Morris, M. A. *J. Am.*

Ceram. Soc. **2010** *93* (4), 1187. doi:10.1111/j.1551-2916.2009.03564.x.
(33) Lapina, O. B.; Khabibulin, D. F.; Romanenko, K. V.; Gan, Z. H.; Zuev, M. G.; Krasil'nikov, V. N.; Fedorov, V. E. *Solid State Nucl. Magn. Reson.* **2005** *28* (2–4), 204. doi:10.1016/j.ssnmr.2005.09.003.
(34) Inaguma, Y.; Chen, L. Q.; Itoh, M.; Nakamura, T.; Uchida, T.; Ikuta, H.; Wakihara, M. *Solid State Commun.* **1993** *86* (10), 689. doi:10.1016/0038-1098(93)90841-A.
(35) Eichele, K., Wasylishen, R. E. *WSolids1, Dalhousie University and University of Tuebingen*, 2010.
(36) Massiot, D.; Fayon, F.; Capron, M.; King, I.; Le Calve, S.; Alonso, B.; Durand, J. O.; Bujoli, B.; Gan, Z. H.; Hoatson, G. *Magn. Reson. Chem.* **2002** *40*, 70 . doi:10.1002/mrc.984.
(37) Kemp, T. F.; Smith, M. E. *Solid State Nucl. Magn. Reson.* **2009** *35* (4), 243. doi:10.1016/j.ssnmr.2008.12.003.
(38) Larson, A. C.; Dreele, R. B. V. *Los Alamos National Laboratory Report LAUR 86–748*, 1994.
(39) Clark, S. J.; Segall, M. D.; Pickard, C. J.; Hasnip, P. J.; Probert, M. J.; Refson, K.; Payne, M. C. *Z. Kristallogr.* **2005** *220* (5-6-2005), 567. doi:10.1524/zkri.220.5.567.65075.
(40) Profeta, M.; Mauri, F.; Pickard, C. J. *J. Am. Chem. Soc.* **2003** *125* (2), 541. doi:10.1021/ja027124r.
(41) Pickard, C. J.; Mauri, F. *Phys. Rev. B* **2001** *63* (24), 2451011. doi:10.1103/PhysRevB.63.245101.
(42) Yates, J. R.; Pickard, C. J.; Mauri, F. *Phys. Rev. B* **2007** *76* (2), 0244011. doi:10.1103/PhysRevB.76.024401.
(43) Perdew, J. P.; Burke, K.; Ernzerhof, M. *Phys. Rev. Lett.* **1996** *77* (18), 3865. doi:10.1103/PhysRevLett.77.3865.
(44) Perdew, J. P.; Burke, K.; Ernzerhof, M. *Phys. Rev. Lett.* **1998** *80* (4), 891. doi:10.1103/PhysRevLett.80.891.
(45) Yates, J. R.; Pickard, C. J.; Payne, M. C.; Mauri, F. *J. Chem. Phys.* **2003** *118* (13), 5746. doi:10.1063/1.1541625.
(46) Massiot, D.; Farnan, I.; Gautier, N.; Trumeau, D.; Trokiner, A.; Coutures, J. P. *Solid State Nucl. Magn. Reson.* **1995** *4* (4), 241. doi:10.1016/0926-2040(95)00002-8.
(47) Medek, A.; Frydman, V.; Frydman, L. *J. Phys. Chem. A* **1999** *103* (25), 4830. doi:10.1021/jp990410d.
(48) Hamaed, H.; Ye, E.; Udachin, K.; Schurko, R. W. *J. Phys. Chem. B* **2010** *114* (18), 6014. doi:10.1021/jp102026m.
(49) Mann, P. P. *Encyclopedia of Analytical Chemistry*; John Wiley and Sons Ltd.: Chichester, NY, 2000; pp. 12224–12265.
(50) Kentgens, A. P. M. *Geoderma* **1997** *80* (3-4), 271. doi:10.1016/S0016-7061(97)00056-6.
(51) Thangadurai, V.; Shukla, A. K.; Gopalakrishnan, J.; Joubert, O.; Brohan, L.; Tournoux, M. In *European Powder Diffraction, Pts 1 and 2*; Delhez, R., Mittemeijer, E. J., Eds. 2000; Vol. 321–3, pp. 965–970. Available from www.mf.mpg.de/de/abteilungen/mittemeijer/epdic/index.htm.
(52) Alonso, J. A.; Ibarra, J.; Paris, M. A.; Sanz, J.; Santamaria, J.; Leon, C.; Varez, A.; Fernandez, M. T. In *New Materials for Batteries and Fuel Cells*; Materials Research Society Symposia Proceedings, 5–8 April 1999, San Francisco, Calif., USA: Doughty, D. H., Nazar, L. F., Arakawa, M., Brack, H. P., Naoi, K., Eds. 2000; Vol. 575, pp. 337–342.
(53) Chen, J.; Wang, S.; Whittingham, M. S. *J. Power Sources* **2007** *174* (2), 442. doi:10.1016/j.jpowsour.2007.06.189.

Can. J. Chem. Downloaded from www.nrcresearchpress.com by Xi'an Jiaotong University on 09/19/12
For personal use only.

Reconnaissance of diverse structural and electronic environments in germanium halides by solid-state ^{73}Ge NMR and quantum chemical calculations

Brandon J. Greer, Vladimir K. Michaelis, Victor V. Terskikh, and Scott Kroeker

Can. J. Chem. Downloaded from www.nrcresearchpress.com by Xi'an Jiaotong University on 09/19/12
For personal use only.

Abstract: Solid-state ^{73}Ge nuclear magnetic resonance (NMR) is an attractive technique for the characterization of solid germanium-containing materials, but experiments can be exceedingly difficult in practice due to the unfavourable NMR properties of the ^{73}Ge nucleus. Presented herein is a series of solid-state ^{73}Ge NMR experiments on germanium halides (GeX_4 and GeX_2, where X = I, Br, and Cl) conducted at moderate (9.4 and 11.7 T) and ultrahigh (21.1 T) magnetic fields, intended to characterize the ^{73}Ge NMR response in highly symmetric and asymmetric coordination environments. Quadrupole coupling constants range from 0.16 to 35 MHz. Isotropic chemical shifts for the GeX_4 series trend with halide electronegativity, as found for the analogous silicon and tin halides. The indirect spin-spin coupling constant $^1J(^{73}Ge, ^{127}I)$ is estimated from ^{73}Ge MAS NMR to be 35 ± 10 Hz in GeI_2, with the reduced coupling constant agreeing with those of other group 14 halides. Quantum chemical calculations using GIPAW DFT are in reasonable accord with experimental quadrupole couplings, but fail for chemical shielding. A preliminary NMR crystallographic study of GeI_2 and $GeCl_2$ incorporating ^{127}I and ^{35}Cl NMR spectra has led to plausible conclusions reflecting the structural homology of these compounds, although definitive characterization remains elusive.

Key words: germanium halides, solid state nuclear magnetic resonance, ^{73}Ge NMR, GIPAW DFT, quadrupole interaction.

Résumé : La résonance magnétique nucléaire (RMN) du ^{73}Ge à l'état solide est une technique attrayante pour la caractérisation de matériaux contenant du germanium, mais les expériences peuvent être très difficiles en pratique en raison des propriétés RMN défavorables du noyau ^{73}Ge. Dans le présent travail, on présente une série d'expériences de RMN du ^{73}Ge à l'état solide effectuées sur des halogénures de germanium (GeX_4 et GeX_2, dans lesquels X = I, Br et Cl), à des champs magnétiques modérés (9,4 et 11,7 T) et extrêmement élevés (21,1 T) dans le but de caractériser la réponse de la RMN du ^{73}Ge dans des environnements de coordination très symétriques et asymétriques. Les constantes de couplage quadripolaire s'étalent de 0,16 à 35 MHz. La tendance des déplacements chimiques isotropes pour la série GeX_4 varie suivant l'électronégativité de l'halogénure, comme il avait été observé pour les analogues halogénés du silicium et de l'étain. En se basant sur la RMN du ^{73}Ge avec rotation à l'angle magique (RAM), on a évalué que la constante de couplage spin-spin indirect, $^1J(^{73}Ge,^{127}I)$, est égale à 35 ± 10 Hz, pour le GeI_2, pour lequel la constante de couplage réduite est en accord avec d'autres halogénures d'éléments du groupe 14. Des calculs de chimie quantique par la théorie de la fonctionnelle de la densité en utilisant une onde améliorée par un opérateur de projection comportant une jauge (« GIPAW-DFT ») sont en accord raisonnable avec les données expérimentales pour les couplages quadripolaires, mais elles ne donnent pas de bons résultats pour le blindage chimique. Une étude cristallographique préliminaire par RMN du GeI_2 et du $GeCl_2$ comportant des spectres RMN du ^{127}I et du ^{35}Cl conduit à des conclusions plausibles qui reflètent l'homologie structurale de ces composés, même si leur caractérisation définitive demeure incertaine.

Mots-clés : halogénures de germanium, résonance magnétique nucléaire à l'état solide, RMN du ^{73}Ge, théorie de la fonctionnelle de la densité en utilisant une onde améliorée par un opérateur de projection comportant une jauge (“GIPAW-DFT”), interaction quadripolaire.

[Traduit par la Rédaction]

Received 3 November 2010. Accepted 3 February 2011. Published at www.nrcresearchpress.com/cjc on 22 August 2011.

B.J. Greer, V.K. Michaelis,* and S. Kroeker. Department of Chemistry, University of Manitoba, Winnipeg, MB, R3T 2N2, Canada.
V.V. Terskikh. Steacie Institute for Molecular Sciences, National Research Council, Ottawa, ON, K1A 0R6, Canada.

Corresponding author: Scott Kroeker (e-mail: Scott_Kroeker@umanitoba.ca).

This article is dedicated to Professor Roderick E. Wasylishen, who, in addition to his own outstanding contributions to science, has worked tirelessly to advance research in Canada and empower many young scientists now serving in Chemistry departments across the country.

*Current address: Francis Bitter Magnet Laboratory, Massachusetts Institute of Technology, Cambridge, Massachusetts 02139 USA.

Can. J. Chem. Downloaded from www.nrcresearchpress.com by Xi'an Jiaotong University on 09/19/12
For personal use only.

Introduction

Germanium is a key element in a variety of compounds, exhibiting useful properties in mesoporous materials, semiconductors, and optical materials.[1–3] For example, germanium has been used in the development of ordered mesoporous oxide materials with tuneable properties.[4] Bearing chemical similarities to silicon, germanium is an efficient semiconductor and often finds commercial use in the biomedical field as well as in optical and telecommunication products.[5] In recent years, multifunctional nanomaterials that integrate the useful semiconducting properties of germanium into mesoporous structures have been developed.[6]

To advance research and development of these materials, various characterization tools are required to understand the interactions and structural properties present in a given system. Nuclear magnetic resonance (NMR) spectroscopy probes the local atomic environment, and appears to be an attractive technique for such characterization. However, the intrinsic properties of the ^{73}Ge nucleus (the only NMR-active stable isotope of germanium) present experimental difficulties, evidenced by the limited number of publications reporting solid-state ^{73}Ge NMR spectroscopy studies of nonmetallic germanium materials.[7–17] Germanium-73 is a quadrupolar nucleus ($I = 9/2$) with a low natural abundance (7.73%), moderately large quadrupolar moment ($Q = -19.6$ fm^2), low magnetogyric ratio ($\gamma = -0.936 \times 10^7$ rad T^{-1} s^{-1}), and correspondingly low resonance frequency (13.95 MHz at 9.4 T), with a relative receptivity of 1.09×10^{-4} compared with ^{1}H.[18] Despite the unfavourable properties, ultrahigh magnetic fields can be used to extract valuable information in many systems. At 21.1 T, for example, the resonance frequency of ^{73}Ge is 31.4 MHz, resulting in a more favourable Boltzmann population difference and a reduction in adverse probe-ringing effects, increasing the sensitivity. Furthermore, the second-order quadrupolar broadening is reduced, as it scales with the inverse-square of magnetic field strength, resulting in additional signal gains.[8] The only potential drawback of performing ^{73}Ge NMR experiments at high field is that any anisotropic shielding is amplified, however with rare exception,[14] this interaction will be eclipsed by the quadrupolar broadening.

In this study, we look at a series of germanium halides as models for the symmetrical germanium environments expected in semiconductors and mesoporous materials.[19–21] Two series of germanium halides, GeX_2 and GeX_4 (X = I, Br, and Cl), were investigated with an aim to study the electric field gradient (EFG) environments for ^{73}Ge and to observe any variations that occur between oxidation states, such as differences between the spectral features or chemical shift range. Further understanding is achieved through density functional theory (DFT) calculations, which guide experimental expectations and serve to substantiate the findings. We use the calculated parameters as a complement to the NMR experiment to provide insights on crystal structure.

Theory

In the presence of a strong magnetic field (B_0), the Zeeman effect causes splitting of spin-active nuclei ($I \geq 1/2$) into $2I + 1$ nuclear spin states, generating $2I$ possible single-quantum transitions. For quadrupolar nuclei ($I > 1/2$), multiple single-quantum frequencies must be considered: the central transition (CT; $1/2 \rightarrow -1/2$), and a total of $2I - 1$ satellite transitions ($\pm n/2 \rightarrow \pm (n - 2)/2$, where $n = 3$, 5, 7, and 9 for a spin-9/2 nucleus) appearing at a precise spacing from the CT, characteristic of the nuclear quadrupolar interaction. This quadrupolar interaction is quantified as the nuclear quadrupole coupling constant (C_Q), which describes the magnitude of the interaction between the electric quadrupole moment of the nucleus (eQ) and the surrounding electric field gradient (EFG), generated by the distribution of charge in the surrounding electronic environment and described by a second-rank tensor. This parameter is defined by the equation:

$$[1] \qquad C_Q = \frac{e^2qQ}{h}$$

where e is the charge of an electron, eQ describes the nuclear quadrupole moment of the nucleus, eq is the largest component of the EFG tensor (V_{ZZ}), and h is Planck's constant. A second term, the asymmetry parameter (η), describes the relative magnitudes of the EFG tensor principal components and hence the shape of the quadrupolar spectral pattern, defined by the equation:

$$[2] \qquad \eta = \frac{V_{XX} - V_{YY}}{V_{ZZ}}$$

where V_{XX}, V_{YY}, and V_{ZZ} are the principal components of the EFG tensor $|V_{XX}| < |V_{YY}| < |V_{ZZ}|$.[22]

In a powdered solid sample, there exists the distribution of all possible molecular orientations. If a molecule has lower than cubic symmetry, the chemical shielding around the nucleus will possess an orientational dependence in the magnetic field, termed chemical shift anisotropy (CSA). Spectra of this type will display three distinct discontinuities (chemical shifts) at δ_{11}, δ_{22}, and δ_{33}, defining the bounds and shape of the envelope. The average of these three components is the isotropic chemical shift (δ_{iso}). Two important descriptors of CSA are known as span (Ω) and skew (κ),[23] defined by the following equations:

$$[3] \qquad \Omega = \delta_{11} - \delta_{33}$$

$$[4] \qquad \kappa = \frac{3(\delta_{22} - \delta_{iso})}{\Omega}$$

While the quadrupolar coupling can often obscure the observation of CSA, it is important to consider for spectra which are not dominated by C_Q.

Experimental methods

Materials

$GeBr_2$ and GeI_4 samples were obtained from Sigma-Aldrich. $GeCl_4$, $GeBr_4$, and GeI_2 samples were obtained from Alfa Aesar. A second GeI_2 sample was obtained from Strem Chemicals. The $GeCl_2$ sample was obtained from MP Biomedicals. Liquid samples were cooled gradually or flash frozen with liquid nitrogen. All other samples were used without further modification.

Can. J. Chem. Downloaded from www.nrcresearchpress.com by Xi'an Jiaotong University on 09/19/12
For personal use only.

Nuclear magnetic resonance

Germanium-73 NMR

^{73}Ge NMR experiments for $GeCl_2$, $GeCl_4$, $GeBr_4$, GeI_2, and GeI_4 were performed on a Bruker AMX 500 NMR spectrometer (B_0 = 11.7 T) at 17.4 MHz using a 5 mm home-built low-γ solenoid probe (for $GeCl_2$, $GeBr_4$, GeI_2, and GeI_4) and a 5 mm solution inverse probe with variable temperature (VT) capabilities (for $GeCl_4$). A Hahn-echo pulse sequence was used to collect the spectra with 4 μs (90°) and 8 μs (180°) pulse lengths, ν_{rf} of 25 kHz, and recycle delays of 2–3 s, with 16 000–120 000 co-added transients. For all ^{73}Ge NMR spectra, chemical shifts are reported with respect to tetramethylgermanium, using neat germanium (IV) chloride as a secondary reference (+30.9 ppm).

^{73}Ge NMR spectra were also collected on a Bruker Avance II 900 NMR spectrometer (B_0 = 21.1 T) at 31.4 MHz for all compounds using a 7 mm magic-angle spinning (MAS) Bruker probe and a 7 mm home-built solenoid probe with VT capabilities (for $GeCl_4$). Non-spinning spectra were collected using a solid-echo pulse sequence (90°–90°) with pulse lengths of 3 μs and a recycle delay of 1 s for $GeBr_4$ and GeI_2 and 3 s for $GeCl_2$ and GeI_4, with 500–17 000 co-added transients. MAS spectra (spinning rates of 5 and 8 kHz) were collected using an echo pulse sequence with 4 μs (90°) and 8 μs (180°) pulse lengths and recycle delays of 3 s for GeI_2 and GeI_4. The $GeBr_2$ spectrum was collected in two pieces using a WURST (wideband uniform-rate and smooth truncation) quadrupolar Carr–Purcell–Meiboom-Gill (QCPMG) pulse sequence.[25,26]

Given the low melting point of $GeCl_4$ (223 K), temperature regulation was used (on both the 11.7 and 21.1 T spectrometers) to collect solid-state spectra for this compound. Additionally, $GeBr_4$ (melting point 299 K) was temperature-regulated on the 21.1 T spectrometer to ensure solidity.

A series of ^{73}Ge NMR experiments was conducted with the second GeI_2 sample (Strem Chemicals) on a Bruker Avance III 400 spectrometer (B_0 = 9.4 T) at 13.95 MHz using a 4 mm double-resonance MAS probe. Non-spinning spectra were collected using a solid-echo pulse sequence (90°–90°) with pulse lengths of 2 μs and a recycle delay of 2 s. MAS spectra (spinning rates of 3 and 15 kHz) were collected using an echo pulse sequence with 2 μs (90°) and 4 μs (180°) pulse lengths and recycle delays of 2 s. The number of scans collected ranged from 16 000–384 000.

The isotropic chemical shift, C_Q, and η for all non-spinning spectra at both fields were obtained through simulation using WSOLIDS software.[27]

Iodine-127 NMR

^{127}I NMR experiments for GeI_2 were conducted on a Varian UNITY Inova 600 spectrometer (B_0 = 14.1 T) at 120.0 MHz using a 3.2 mm MAS Varian-Chemagnetics probe with ZrO_2 rotors, referenced to solid KI (0 ppm). Non-spinning spectra were acquired using a 5 μs (90°) single pulse and 0.4 s recycle delay, with 512 co-added transients. Spectra were also acquired on a Bruker Avance II 900 at 180.1 MHz using a 7 mm home-built solenoid probe. The non-spinning spectra were acquired using a solid-echo pulse sequence with a 2 μs pulse (ν_{rf} of 42 kHz), 1 s recycle delay, and 1024 co-added transients. Spectra were simulated using WSOLIDS and STARS (implemented within VnmrJ, Varian Inc.).[28]

Chlorine-35 NMR

^{35}Cl NMR experiments (non-spinning and MAS) of $GeCl_2$ were conducted on a Varian UNITY Inova 600 at 58.8 MHz using a 5 mm DR Varian Chemagnetics MAS probe with a ZrO_2 rotor, referenced to 1 mol/L NaCl (0 ppm). All spectra were collected using a single pulse of 1 μs (13° tip, ν_{rf} of 36 kHz), and a recycle delay of 1 s, with 128–3900 co-added transients. Spinning rates of 3.2, 5.0 and 8.0 kHz were used to collect the MAS data. Spectral parameters were obtained through simulation using STARS.[28]

Quantum chemical calculations

Electric field gradient and chemical shielding calculations were completed on crystal structures (as reported from literature sources) of GeF_2, $GeCl_4$, $GeBr_2$, $GeBr_4$, GeI_2, and GeI_4 using CASTEP, a GIPAW (gauge-including projector augmented waves) DFT-based computational method that calculates electronic properties of periodic solids.[29] The Perdew–Burke–Ernzerhof (PBE) functionals were used in the generalized gradient approximation (GGA) for the exchange-correlation energy and ultrasoft pseudopotentials. All calculations were performed using ultrafine-accuracy basis sets and a maximum plane-wave energy of >550 eV with relativistic effects included using the scalar-relativistic zero-order regular approximation (ZORA).[30,31] The Monkhorst–Pack grid had a maximum density of up to 7 × 7 × 6 *k*-points. CASTEP software was used in a Materials Studio 4.4 environment, with all calculations conducted on an HP xw4400 workstation with a single Intel Dual-Core 2.67 GHz processor and 8 GB DDR RAM. Germanium C_Q values were corrected using a quadrupolar moment of –19.6 fm^2 for ^{73}Ge, as the CASTEP default is –17.3 fm^2.[32] Calculated isotropic chemical shielding values were converted to isotropic chemical shifts using the calculated shielding of solid $GeCl_4$ and its experimental chemical shift (i.e., setting σ_{iso}^{calcd} = 1424 ppm to δ_{iso}^{calcd} = 30 ppm).

Results

GeI_4

Germanium (IV) iodide packs in a cubic unit cell and belongs to the *Pa*-3 space group.[33] The tetrahedrally coordinated germanium centre exhibits Ge–I bond lengths of 2.497 ± 0.002 Å to all nearby iodine atoms, with an average I–Ge–I angle of 109.470°. The difference between the maximum and minimum Ge–I bond lengths is 0.007 Å. The closest adjacent germanium centres are separated by 6.672 Å.

Based on the positions of the ^{73}Ge satellite transitions measured at 11.7 and 21.1 T, the C_Q is determined to be 1.80 ± 0.04 MHz (Figure S1 in the Supplementary data), greater than the C_Q value of 1.34 MHz calculated by GIPAW DFT (Table 1). The asymmetry parameter is η = 0, as required by the point-group symmetry and predicted correctly by GIPAW DFT. The isotropic chemical shift (δ_{iso}) appears at –1098 ± 3 ppm, in agreement with a previously reported δ_{iso} of –1104 ppm from solution NMR.[34] Another group has reported δ_{iso} = –1171 ppm (referenced to $GeCl_4$, 30.9 ppm) and linewidth ($\Delta\delta_{1/2}$) of 950 Hz at 11.7 T for

Can. J. Chem. Downloaded from www.nrcresearchpress.com by Xi'an Jiaotong University on 09/19/12
For personal use only.

Table 1. Experimental and GIPAW DFT ^{73}Ge NMR Results for GeX_4 and GeX_2 (X = I, Br, Cl) as well as the local Ge geometry parameters (λ, σ^2, see text).

						$GeBr_2$		
		GeI_4	$GeBr_4$	$GeCl_4$	GeI_2[a]	Site 1	Site 2	$GeCl_2$
C_Q (MHz)	(11.7 T)	1.85±0.05	1.15±0.05	<1.2	0.25±0.09	n/d	n/d	<2
	(21.1 T)	1.78±0.03	1.15±0.01	<0.8	0.16±0.05[b]	34±3	35±3	1.7±0.1
	(GIPAW DFT)	1.34	0.90	0.95	1.43	30.1	36.5	n/d
η	(11.7 T)	0	0	n/d	0	n/d	n/d	n/d
	(21.1 T)	0	0	n/d	0	0.4±0.2	0.95±0.05	0
	(GIPAW DFT)	0	0	0.62	0	0.22	0.58	n/d
δ_{iso} (ppm)	(11.7 T)	–1099±3	–316±3	30±1	–216±3	n/d	n/d	–315±15
	(21.1 T)	–1097±3	–315±3	30±1	–214±3	–70±100	–320±100	–319±10
	(GIPAW DFT)	215	149	(30)[c]	–202	97	–36	n/d
λ		1.000	1.000	1.000	1.000	1.012	1.025	n/d
σ^2		0.150	0.077	0.117	0.430	109.98	292.96	n/d

[a]The non-spinning spectrum collected at 9.4 T yields C_Q = 0.22 ± 0.05 MHz, η = 0, δ_{iso} = –217 ± 5 ppm; MAS at 9.4 T gives C_Q = 0.25 ± 0.02 MHz and δ_{iso} = –216 ± 1 ppm.
[b]Based on non-spinning and MAS experiments.
[c]Fixed as chemical shift reference.

solid GeI_4.[10] The same group reported a solution value for GeI_4 of δ_{iso} = –1117 ppm, but no account was given for the discrepancy between the liquid- and solid-state chemical shifts, and no spectra were displayed within the publication. The CT linewidths observed in this work are 2200 Hz at 11.7 T and 1100 Hz at 21.1 T, mostly attributable to a reduction in the second-order quadrupolar broadening at ultrahigh field.

In these high-symmetry structures, the C_Q values are small enough that other broadening effects may become appreciable in the NMR spectrum. All the directly bonded halogens are spin-active and quadrupolar, affecting the ^{73}Ge resonance by direct-dipolar and indirect spin-spin coupling. Although these are not resolved, their presumed influence means the peakwidths should not be expected to scale predictably with the field. For example, the static dipolar coupling constant, D (^{73}Ge,^{127}I) is 54 Hz for an isolated spin-pair, using the average Ge–I bond length in GeI_4. The broadening associated with this dipolar coupling would be amplified by both the spin quantum number of the coupled spins (5/2) and the number of bonded ^{127}I atoms (4).

$GeBr_4$

Germanium (IV) bromide (α-$GeBr_4$) is isostructural with GeI_4.[35] The tetrahedrally coordinated germanium centre exhibits an average bond length of 2.265 ± 0.002 Å to bromine, with an average Br–Ge–Br angle of 109.470°. The difference between the maximum and minimum Ge–Br bond lengths is 0.004 Å. Adjacent germanium centres are separated by 6.187 Å.

^{73}Ge NMR spectra collected at both 11.7 T (Fig. 1*a*) and 21.1 T (Fig. 1*b*) can be fit with a C_Q of 1.15 ± 0.01 MHz using the prominent satellite transitions. At 11.7 T, we can only see the first set of satellite transitions (due to the narrower spectral window on the AMX spectrometer), while at 21.1 T, the first, second, and third sets may be observed. The C_Q value is in close agreement with the GIPAW DFT-predicted value of 0.90 MHz. The asymmetry parameter is η = 0, as required by point-group symmetry and verified by GIPAW DFT. The isotropic chemical shift appears at –315 ± 3 ppm (Table 1), agreeing with a previously reported solution chemical shift, δ_{iso} = –311 ppm.[34] The CT linewidths at 11.7 and 21.1 T are 1300 Hz and 650 Hz, respectively. The second-order quadrupolar broadening (of the CT) expected for a C_Q of 1.15 MHz is 550 Hz at 11.7 T and 300 Hz at 21.1 T, suggesting a broadening contribution from coupling interactions with $^{79/81}$Br; these correspond to D(^{73}Ge,^{79}Br) and D(^{73}Ge,^{81}Br) of 91 and 98 Hz, respectively, for an isolated spin-pair at the average Ge–Br bond length in $GeBr_4$.

$GeCl_4$

Unlike GeI_4 and $GeBr_4$, germanium (IV) chloride packs in a monoclinic unit cell and belongs to the $P2_1/c$ space group.[36] The tetrahedrally coordinated germanium centre exhibits an average bond length of 2.096 ± 0.002 Å to chlorine, and an average Cl–Ge–Cl angle of 109.471°. The difference between the maximum and minimum Ge–Cl bond lengths is 0.005 Å. The closest adjacent germanium centres are separated by 5.111 Å.

$GeCl_4$ is a liquid at room temperature and requires the sample to be cooled to at least –50 °C for solid-state NMR

Can. J. Chem. Downloaded from www.nrcresearchpress.com by Xi'an Jiaotong University on 09/19/12
For personal use only.

Fig. 1. (lower) Experimental solid-echo ^{73}Ge NMR spectra and (upper) simulated spectra of $GeBr_4$ at (*a*) 11.7 T, with C_Q = 1.15 MHz, η = 0, and δ_{iso} = –316 ppm, and (*b*) 21.1 T, with C_Q = 1.15 MHz, η = 0, and δ_{iso} = –315 ppm.

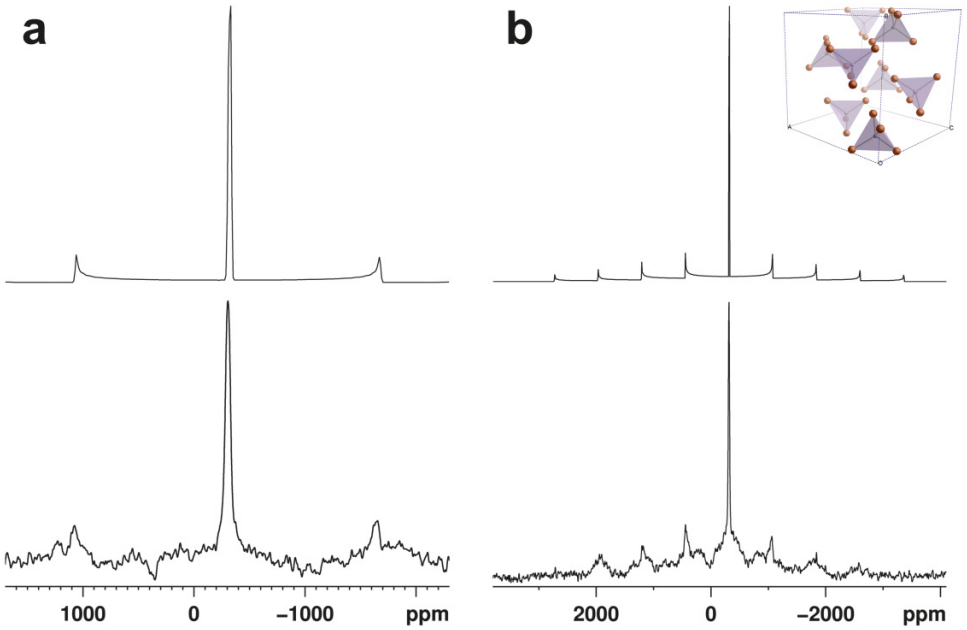

acquisition. This procedure limits the acquisition time, so the corresponding spectra have a relatively low signal-to-noise ratio (Figure S2 in the Supplementary data). No satellite transitions or characteristic peak shapes are observed; hence, no accurate determination of η can be made, and C_Q must be estimated based on peak breadth. At 11.7 T, the $\Delta\delta_{1/2}$ is 470 Hz, which predicts a C_Q no greater than 1.2 MHz. Similarly, the $\Delta\delta_{1/2}$ at 21.1 T is 320 Hz, which dictates that the C_Q cannot be greater than 0.8 MHz. These predictions assume that the entire breadth is attributable to the quadrupolar interaction, but the true value is likely to be smaller since D(^{73}Ge,^{35}Cl) and D(^{73}Ge,^{37}Cl) are 45 and 37 Hz, respectively (for an isolated spin-pair at the average Ge–Cl bond length in $GeCl_4$). The C_Q estimations are in close agreement with the GIPAW DFT-predicted value of 0.95 MHz (with predicted η = 0.62). The isotropic chemical shift (δ_{iso}) appears at +30 ppm (liquid $GeCl_4$ is the reference, +30.9 ppm) (Table 1).

GeI_2

Germanium (II) iodide packs in a trigonal cell and belongs to the *P*-3*m*1 space group.[37] The octahedrally coordinated germanium centre exhibits a Ge–I bond length of 2.990 Å to all close iodine atoms and an average I–Ge–I angle of 90.000°. Adjacent germanium centres share two iodine atoms and are separated by 4.251 Å.

The unusual-looking spectrum collected at 11.7 T (Figure S3 in the Supplementary data) shows signals on either side of the central transition that yield a C_Q of 0.25 ± 0.09 MHz if they are regarded as satellite transitions. The presumed satellite signals for the 21.1 T echo spectrum (Fig. 2*a*) place the C_Q slightly smaller, at a lower limit of 0.16 MHz, while the breadth of the CT confers an upper limit of 1.5 MHz. The C_Q predicted by GIPAW DFT is 1.43 MHz, significantly greater than the experimental average of about 0.20 MHz. The asymmetry parameter is η = 0, as required by point-group symmetry and predicted by GIPAW DFT. The isotropic chemical shift appears at –215 ± 3 ppm (Table 1), with CT linewidths of 2300 Hz at 11.7 T, 1000 Hz (quadrupolar echo) and 710 Hz (single pulse) at 21.1 T. The $\Delta\delta_{1/2}$ observed here is vastly different than the 270 Hz reported at 11.7 T for solid GeI_2 by another group,[10] although we do see a breadth of 330 Hz in the narrow portion of the CT for our GeI_2 spectrum at 11.7 T. Our measured δ_{iso} agrees with the previous report of –213.4 ppm.[10] D(^{73}Ge,^{127}I) is calculated to be 32 Hz for an isolated spin-pair, using the Ge–I bond length in GeI_2.

The non-spinning ^{73}Ge NMR spectrum at 9.4 T of the second GeI_2 sample shows δ_{iso} = –217 ± 5 ppm, while the C_Q is estimated as 0.22 ± 0.05 MHz (with η = 0) based on the presumed appearance of the first set of satellite transitions (Figure S4a in the Supplementary data). The ^{73}Ge MAS NMR spectra collected at the same field yield δ_{iso} = –216 ± 1 ppm and C_Q = 0.25 ± 0.02 MHz, based on analysis of the spinning sideband manifold (Figure S4b in the Supplementary data and see Fig. 5*b* below).

The experimental spectra for this compound are difficult to interpret, despite the simplicity of the crystal structure. The non-spinning ^{73}Ge NMR spectra of GeI_2 collected with an echo pulse sequence appear particularly complicated due to the presence of Solomon echoes, satellite transition signal coherences that appear in the free induction decay at intervals of the echo pulse spacing (τ).[38,39] Their presence may explain the discrepancy between the $\Delta\delta_{1/2}$ values for our spectrum and that from the literature and may also lead to an overestimate of C_Q for the broadened GeI_2 signal collected at 11.7 T. The time-domain signals have been transformed at the tip of the echo corresponding to the coherence of all satellite signals (τ), and should thus provide the most accurate description of all observable transitions in the quadrupolar spectrum.

Figure 2 shows a comparison between the frequency-domain calculation of the spectrum and a simulation of the spectrum

Can. J. Chem. Downloaded from www.nrcresearchpress.com by Xi'an Jiaotong University on 09/19/12
For personal use only.

Fig. 2. (*a*) Experimental solid-echo ^{73}Ge NMR spectrum of GeI_2 at 21.1 T with (*b*) SIMPSON simulation incorporating Solomon echoes using $C_Q = 0.16$ MHz and $\eta = 0$, and (*c*) simple simulation using $C_Q = 0.16$ MHz, $\eta = 0$, $\delta_{iso} = -214$ ppm.

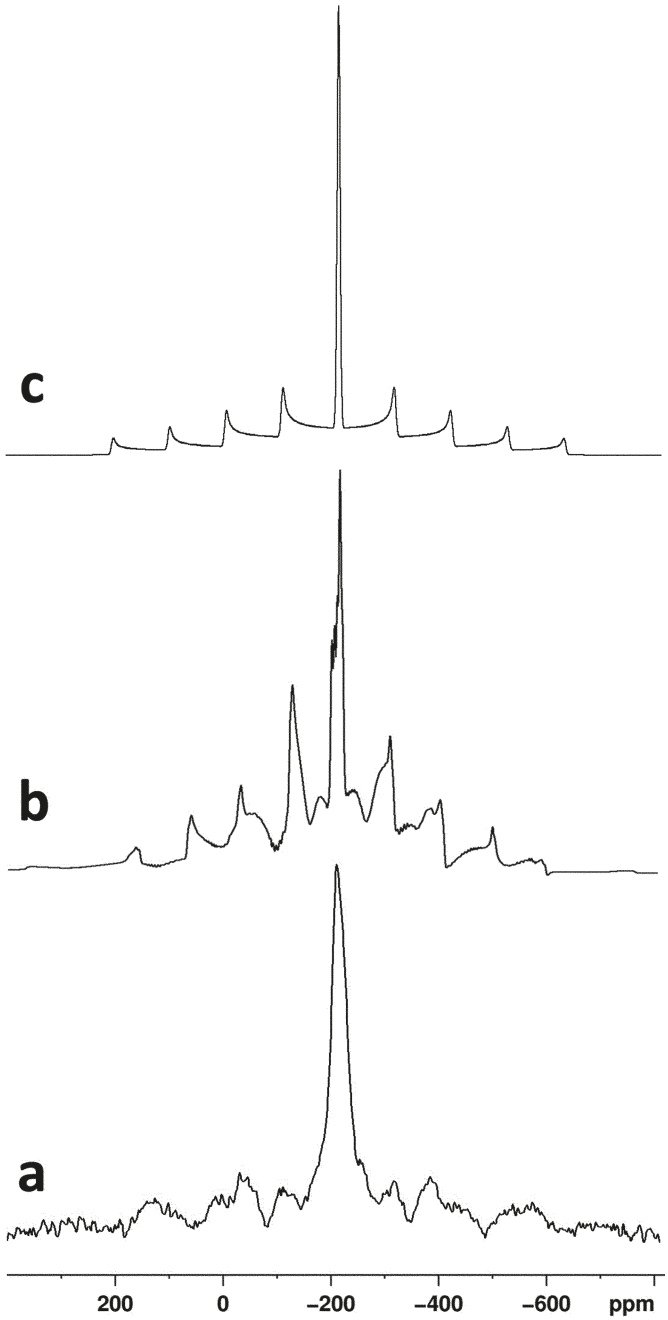

with Solomon echoes using SIMPSON.[40] While the fit is imperfect due to probe ring-down effects, the latter calculation clearly reproduces the main experimental features with greater accuracy.

$GeBr_2$

Germanium (II) bromide packs in a monoclinic cell, belonging to the $P12_1/c1$ space group. The crystal structure contains two distinct germanium sites (1:1 ratio), where the structural units are distorted $GeBr_6$ octahedra (proposed as the result of a second-order Jahn–Teller effect).[41] The first site, Ge(1), contains six bromine atoms within a 3.4 Å radius, the closest contact being 2.518 Å. The average atomic distance for these close contacts is 2.9 ± 0.3 Å. The second site, Ge(2), contains six bromine atoms within 3.7 Å, with the closest contact being 2.479 Å. The average atomic distance for the close bromine atoms is 3.0 ± 0.5 Å. Due to the octahedral distortion, both sites contain Br–Ge–Br bond angles deviating from the ideal 90°. The average Br–Ge–Br angles for Ge(1) and Ge(2) are 89.911° and 90.393°, respectively. The difference between the maximum and minimum Ge–I bond lengths is 0.130 Å for Ge(1) and 0.187 Å for Ge(2). The closest germanium atoms are separated by 3.902 Å (Ge(2)–Ge(2)).

The ^{73}Ge NMR spectrum of $GeBr_2$ (Fig. 3*a*) exhibits the largest breadth observed for either series of compounds, due to the large quadrupolar interaction arising from the asymmetric environments in which the germanium nuclei sit. The WURST-QCPMG pulse sequence[42,43] was chosen based on the large quadrupolar coupling predicted by GIPAW DFT ($C_Q > 30$ MHz).

With a large C_Q, most satellite transitions are well outside the spectral window (unless η approaches 1), thus simulation of the NMR parameters was accomplished by analysing the central transition shape using C_Q and η adjustments. The GIPAW DFT parameters ($C_{Q(1)} = 30.1$ MHz, $\eta_{(1)} = 0.22$, $C_{Q(2)} = 36.5$ MHz, $\eta_{(2)} = 0.58$) were used as a starting point in the simulation of the experimental spectrum. However, the result did not fully account for the observed breadth and shape (Fig. 3*c*). It should be noted that because of the dominating quadrupolar interaction, the inclusion of CSA parameters determined by GIPAW DFT ($\Omega_{(1)} = 204$ ppm, $\kappa_{(1)} = -0.52$, $\Omega_{(2)} = 464$ ppm, $\kappa_{(2)} = -0.44$) did not appreciably alter the appearance of the simulated spectrum. The final simulation involved incorporating both germanium sites in $GeBr_2$ ($C_{Q(1)} = 35 \pm 3$ MHz, $\eta_{(1)} = 0.4 \pm 0.2$, $\delta_{iso(1)} = -70$ ppm, $C_{Q(2)} = 34 \pm 3$ MHz, $\eta_{(2)} = 0.95 \pm 0.05$, $\delta_{iso(2)} = -310$ ppm) in addition to a 10% germanium oxide impurity identified in powder X-ray diffraction (GeO_2, $C_Q = 9.2 \pm 0.3$ MHz, $\eta = 0.5 \pm 0.1$, $\delta_{iso} = -110 \pm 20$ ppm, as previously determined).[13] The spectral evidence for the oxide impurity is based on the intensity of the tallest peak, corresponding to the chemical shift for quartz-like GeO_2.[13] There is evidence of the Ge(2) + 3/2 ↔ + 1/2 satellite transition around 5000 ppm, which appears close to the CT as this site has a high η value. The imperfect simulation in Fig. 3*b* is a consequence of three distinct Ge species in this sample, each with large and different quadrupolar parameters, illustrating the challenge of ^{73}Ge NMR in complex materials. Given the enormous size of this spectrum, the contributions from direct dipolar coupling and indirect spin-spin coupling are negligible and unobserved. For example, $D(^{73}Ge,^{79}Br)$ and $D(^{73}Ge,^{81}Br)$ are calculated to be approximately 68 and 73 Hz, respectively, for an isolated spin-pair using the average Ge–Br bond lengths in $GeBr_2$.

$GeCl_2$

The crystal structure of germanium (II) chloride has not been reported in the literature, and the experimental difficulties in preparation and stability of this compound have been noted.[44,45] A prominent GeO_2 impurity makes diffraction experiments difficult, although a space group of $P\text{-}3m1$ seems

Can. J. Chem. Downloaded from www.nrcresearchpress.com by Xi'an Jiaotong University on 09/19/12
For personal use only.

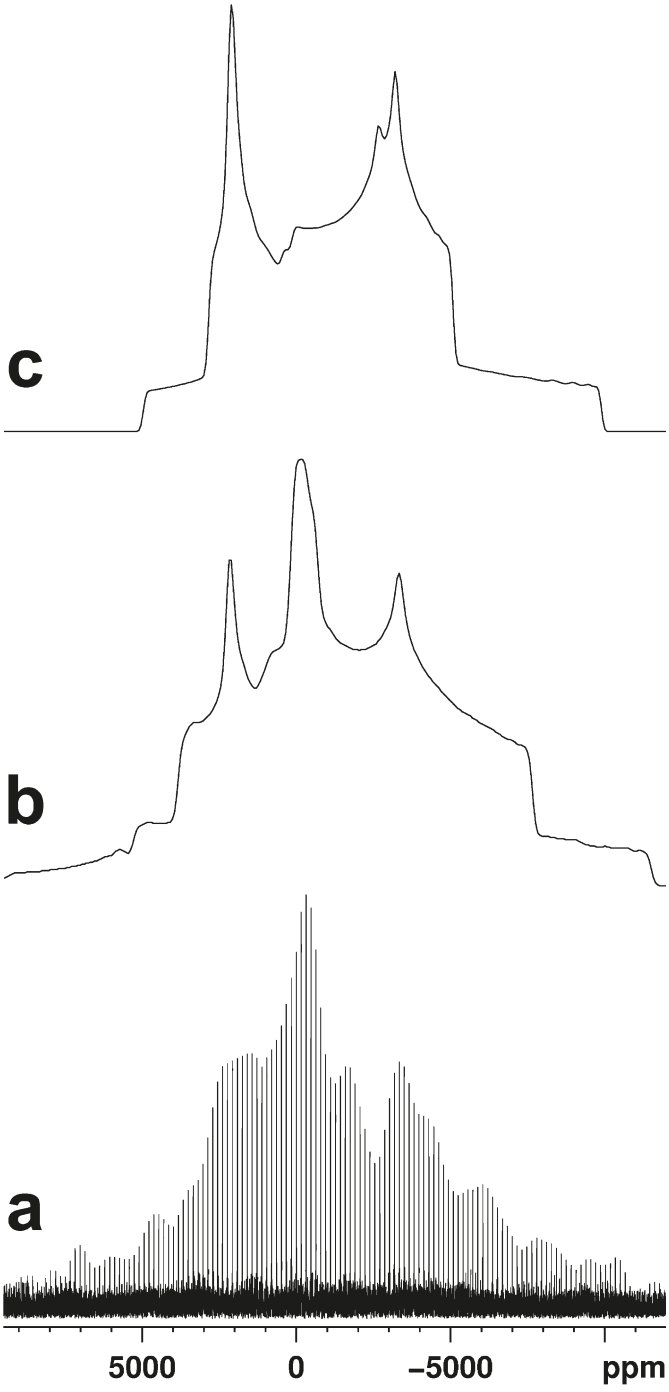

Fig. 3. (*a*) Experimental WURST-QCPMG ^{73}Ge NMR spectrum of $GeBr_2$ with (*b*) simulation of the two germanium sites using $C_{Q(1)}$ = 34 MHz, $\eta_{(1)}$ = 0.4, and $\delta_{iso(1)}$ = –70 ppm and $C_{Q(2)}$ = 1.15 MHz, $\eta_{(2)}$ = 0.95, and $\delta_{iso(2)}$ = –320 ppm, with GeO_2 impurity included at 10% using C_Q = 9.3 MHz, η = 0.5, and δ_{iso} = –110 ppm from reference 13; (*c*) simulation using GIPAW DFT parameters (Table 1).

likely from powder X-ray diffraction (Figure S5 in the Supplementary data).

It has been suggested that the crystal structure of $GeCl_2$ is similar to that of $GeBr_2$, based on the octahedral distortion observed in the known structure of a low-temperature polymorph of cesium germanium trichloride ($CsGeCl_3$, which contains distorted $GeCl_6$ units).[41,46] ^{73}Ge NMR experiments allow us to make inferences about the structure, including the similarity of $GeCl_2$ to either GeI_2 or $GeBr_2$. At 11.7 T, no satellite transitions are observed, and the signal-to-noise ratio is low (Fig. 4*a*). As a result, an estimate of the C_Q can only be accomplished by evaluating the breadth of the signal. The $\Delta\delta_{1/2}$ is 2.4 kHz, which dictates that the quadrupole coupling cannot exceed 2 MHz. No estimate of η can be accurately determined from this spectrum. At 21.1 T, we observe at least two sets of satellite transitions belonging to a single site (Fig. 4*b*), which can be fit with a C_Q of 1.7 ± 0.1 MHz and η = 0. The small signal adjacent to the central transition of $GeCl_2$ was identified through NMR spectral simulation and powder X-ray diffraction as a GeO_2 impurity.[13]

The magnitude of the quadrupole coupling observed for $GeCl_2$ and the *P*-3*m*1 space group suggested by powder X-ray diffraction indicates that the crystal structure must be closely related to GeI_2 and not to $GeBr_2$. That is, if the same octahedral distortion present in $GeBr_2$ occurred in $GeCl_2$, the Ge quadrupole coupling would be expected to be at least an order of magnitude greater than 1.7 MHz. Given the large C_Q observed for $GeBr_2$ (34–35 MHz experimental) and the calculation of GeF_2 (87.6 MHz), the $GeCl_2$ (C_Q = 1.7 ± 0.1 MHz) structure should not resemble either of these compounds, while GeI_2 shows the closest comparison ($C_Q \approx$ 0.2 MHz).

^{73}Ge MAS Spectra

Figure 5*a* shows the ^{73}Ge MAS NMR spectrum of GeI_2 at 21.1 T, where the central transition breadth is 400 Hz. Since heteronuclear dipolar coupling and chemical shift anisotropy are averaged under magic-angle spinning, only the second-order quadrupolar effect, *J*-coupling, and residual dipolar coupling broaden the peaks.[47] By contrast, a ^{73}Ge MAS spectrum of tetraphenylgermanium (not shown) yields a peak-width of 27 Hz, as expected for a Ge nucleus in a highly symmetric environment with no coupling partners. Since the quadrupolar coupling constant of ^{127}I is quite small (C_Q = 8 MHz, see below), residual dipolar coupling will have no appreciable influence on the breadth. The C_Q of 0.16 MHz determined from the non-spinning spectrum of GeI_2 at 21.1 T predicts a MAS breadth of 80 Hz, and the residual 320 Hz is attributed principally to *J*-coupling with neighbouring ^{127}I nuclei. Iodine-127 is a 100% naturally abundant spin-5/2 nucleus, which will split the ^{73}Ge signal into six sub-spectra, propagating further with coupling to each of the six bonded ^{127}I nuclei. Although no resolution is observed, the overall breadth of this coupling pattern is expected to be approximately 8 × $^1J(^{73}Ge,^{127}I)$. Hence, we estimate $^1J(^{73}Ge,^{127}I)$ to be 35 ± 10 Hz for GeI_2. It is necessary to note that if the quadrupolar relaxation of the ^{127}I is fast relative to J^{-1}, the iodines may be partially decoupled, hence the reported *J*-coupling estimates should be considered lower limits.[48]

From the spinning-sideband manifold, we can estimate the quadrupolar coupling constant with the following equations:

$$[5] \qquad \Delta\nu_{total} = |1 - 2m|\nu_Q$$

$$[6] \qquad \nu_Q = \frac{3C_Q}{2I(2I-1)}$$

Fig. 4. (lower) Experimental solid-echo ^{73}Ge NMR spectra and (upper) simulated spectra of $GeCl_2$ at (*a*) 11.7 T, with C_Q = 2 MHz, η = 0, and δ_{iso} = –315 ppm, and (*b*) 21.1 T, with C_Q = 1.7 MHz, η = 0, and δ_{iso} = –319 ppm. The additional signal between 500 and –500 ppm is a GeO_2 impurity, simulated as C_Q = 9.3 MHz, η = 0.5, and δ_{iso} = –110 ppm based on reference 13.

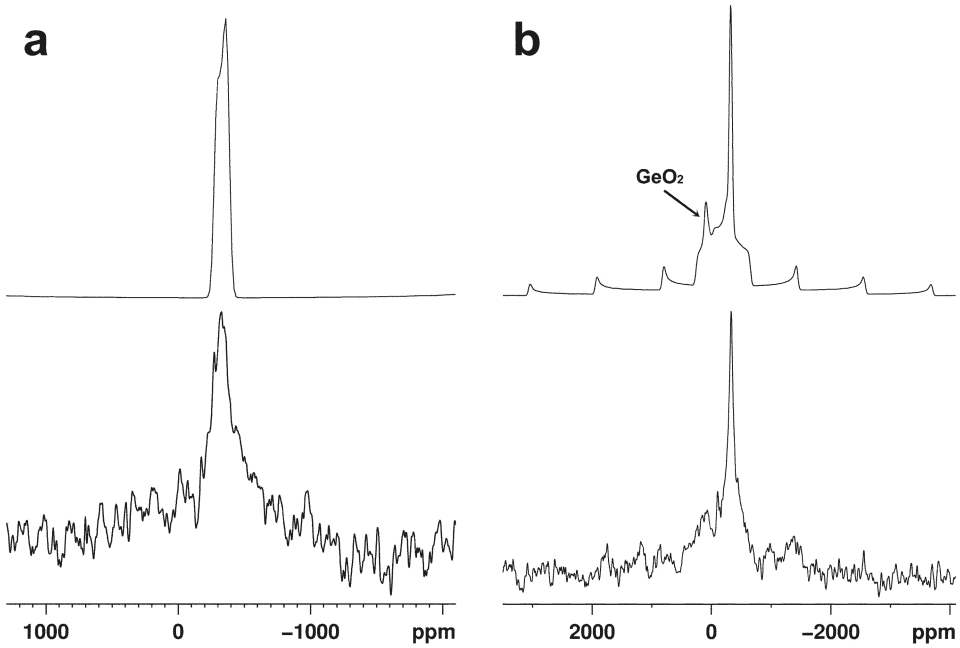

where $\Delta\nu_{total}$ denotes the breadth of the spinning-sideband manifold, *m* is the highest observed satellite transition (9/2 for ^{73}Ge), and ν_Q is the quadrupolar frequency.[49,50] At 21.1 T, $\Delta\nu_{total}$ is 41 kHz, corresponding to a ^{73}Ge C_Q of 0.12 MHz for GeI_2. The ^{73}Ge MAS NMR spectrum of GeI_2 at 9.4 T shows a $\Delta\nu_{total}$ of 84 kHz, corresponding to a C_Q of 0.25 MHz (Fig. 5*b*). These estimates support the C_Q measured in non-spinning samples.

In the ^{73}Ge MAS NMR spectrum of GeI_4 (Figure S6 in the Supplementary data), the breadth of the central transition is 400 Hz. Using the logic presented above, a C_Q of 1.78 MHz (determined from the non-spinning spectrum at 21.1 T) predicts a MAS breadth of 250 Hz from quadrupolar broadening, meaning that the remaining 150 Hz can be attributed to ^{73}Ge-^{127}I *J*-coupling. However, given the large quadrupolar coupling constant of the ^{127}I nucleus in GeI_4 (GIPAW DFT predicts C_Q = 1609 MHz for ^{127}I), significant quadrupolar distortion to the intensities and spacing of the *J*-coupling distribution prevents an accurate estimation of the *J*-coupling constant. If the MAS spectrum is simply treated as an undistorted multiplet, an estimated *J*-coupling constant of $^1J(^{73}Ge,^{127}I)$ = 25 ± 10 Hz for GeI_4 is obtained.

A $^1J(^{73}Ge,^{19}F)$ value has been reported for GeF_4 as 178.5 Hz (liquid state, 20 °C).[51] To compare these values, we must look at the reduced coupling constant ($^1K_{Ge\text{-}X}$), defined by:

$$[7] \qquad {}^1K_{XY} = \frac{4\pi^2 J_{Ge\cdot X}}{h\gamma_{Ge}\gamma_X}$$

Thus, the reduced coupling constant for ^{73}Ge-^{19}F in GeF_4 is –45.1 (× 10^{20} N A^{-2} m^{-3}), while those from GeI_4 and GeI_2 are (–30 ± 10) and (–41 ± 10) (× 10^{20} N A^{-2} m^{-3}), respectively. A DFT study predicted $^1K(^{73}Ge,^{35}Cl)$ for Ph_3GeCl

Fig. 5. ^{73}Ge MAS NMR spectra of GeI_2 at (*a*) 21.1 T (5 kHz spinning) and (*b*) 9.4 T (3 kHz spinning).

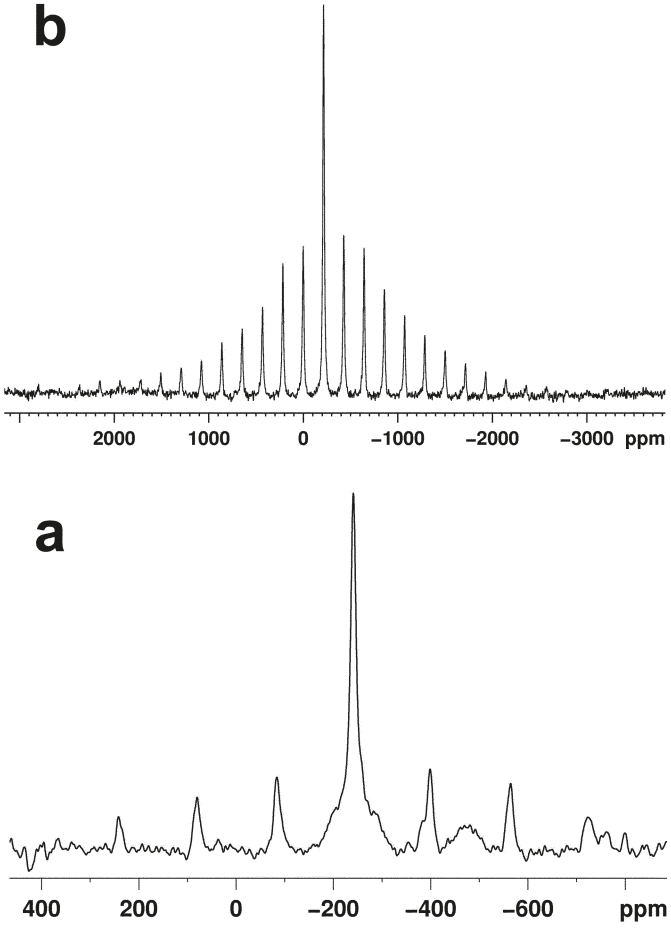

Can. J. Chem. Downloaded from www.nrcresearchpress.com by Xi'an Jiaotong University on 09/19/12
For personal use only.

Fig. 6. (lower) Experimental non-spinning ^{127}I NMR spectra and (upper) simulated spectra of GeI_2 at (*a*) 14.1 T and (*b*) 21.1 T. From both fields, C_Q = 8 MHz, η = 0, δ_{iso} = –445 ppm, Ω = 250, and κ = 1.

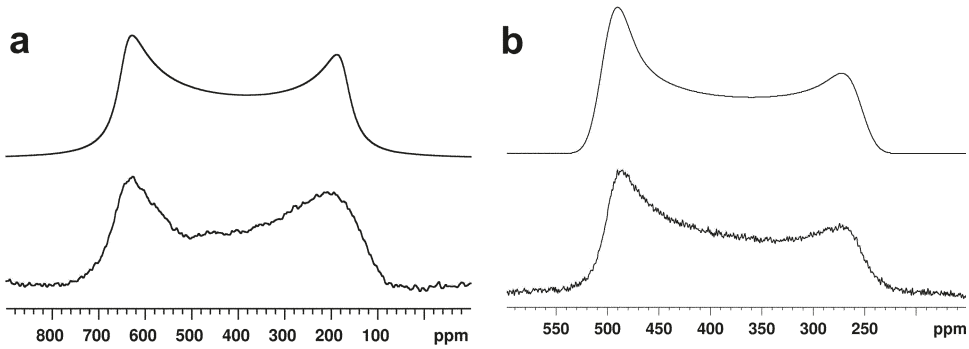

to be between –40 and –43 ($\times 10^{20}$ N $^{-2}$ m^{-3}).[52] Despite considerable error in the estimates made using MAS NMR, the reduced coupling constants are in good agreement with previous determinations.

Halogen NMR

To gain insight about the possible structure of $GeCl_2$, we look to the halogen NMR for an alternate perspective on the system, enabling a comparison with other germanium (II) halides.

Iodine-127 NMR

^{127}I NMR spectra of GeI_2 at 14.1 T (Fig. 6*a*) and 21.1 T (Fig. 6*b*) show a single site at δ_{iso} = 445 ± 5 ppm with a C_Q of 8.0 ± 0.5 MHz and η = 0. The span is Ω = 250 ± 25 with a skew of κ = 1, assuming that the EFG and chemical shielding tensor orientations are coincident. GIPAW DFT predicts C_Q = 20.3 MHz and η = 0, with Ω = 39 ppm and κ = 0.87, with Euler angles of α = 330°, β = 90°, and γ = 180°. However, when these angles are simulated, the resulting shape is in clear disagreement with the experimental spectra at both fields, and no adjustments of C_Q, η, Ω, and κ could satisfy the experimental lineshapes at both fields. Given the generally poor performance of GIPAW DFT for chemical shielding tensors in this study, there is no reason to trust the tensor orientation. Furthermore, due to relativistic effects, there is little published work on the reliability of GIPAW DFT for ^{127}I, so it is difficult to assess the agreement with the experimental parameters. The discrepancy between estimated and experimental C_Q and Ω values appears to reflect that observed for some compounds in a previous ^{127}I DFT study.[53] Given the enormous range of ^{127}I C_Q values (up to ~1000 MHz),[54,55] the relatively small measured and predicted C_Q clearly indicates that iodine is indeed present in a high-symmetry site in GeI_2.

Chlorine-35 NMR

^{35}Cl NMR of $GeCl_2$ at 14.1 T shows a single site at δ_{iso} = 75 ± 2 ppm with a narrow linewidth ($\Delta\delta_{1/2}$ = 1.5 kHz under non-spinning conditions, Fig. 7*a*). Using MAS (Figs. 7b and 7c), the C_Q is estimated to be less than 40 kHz, based on the spinning sideband manifold. Since there is a single chlorine site, it is evident that the structure of $GeCl_2$ is not similar to that of $GeBr_2$ as once postulated (which contains four crystallographically inequivalent bromine sites) or GeF_2 (which contains two distinct fluorine sites).[41,56] The structure appears to be more closely related to GeI_2, with small C_Q values observed in both ^{73}Ge and their respective halogen NMR.

Fig. 7. Experimental ^{35}Cl NMR spectra of $GeCl_2$ at 14.1 T. (*a*) Non-spinning, (*b*) 5 kHz MAS, (***c***) 8 kHz MAS.

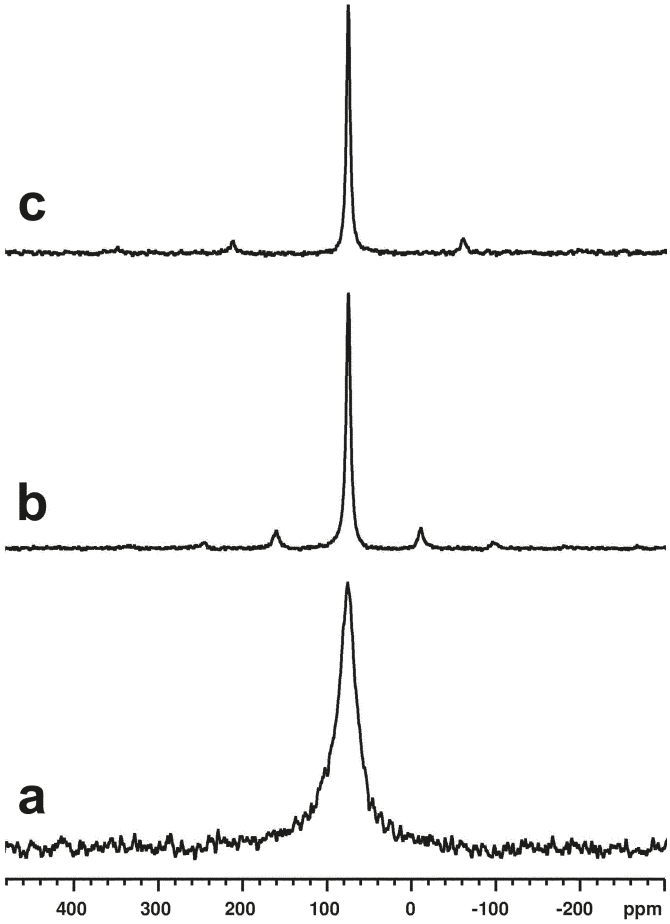

Discussion

Quadrupole couplings

The magnitude of quadrupole coupling is strongly influenced by local structure, where C_Q acts as a sensitive probe of local symmetry and allows for correlations between experimental and theoretical results. The higher symmetry species show that ^{73}Ge possesses small C_Q values, and even very

Can. J. Chem. Downloaded from www.nrcresearchpress.com by Xi'an Jiaotong University on 09/19/12
For personal use only.

Can. J. Chem. Downloaded from www.nrcresearchpress.com by Xi'an Jiaotong University on 09/19/12
For personal use only.

slight distortions from perfect symmetry result in a sharp increase in C_Q. The structural homology present in germanium (IV) halides is reflected in the much narrower range of quadrupolar constants from ^{73}Ge NMR, all falling within 1–2 MHz versus a 0–35 MHz range for germanium (II) halides.

To investigate correlations between the spectral parameters and crystal structure, a starting point is to use the well known distortion parameters as a way to quantify the local geometry about the germanium unit for each compound.[24] The mean elongation (λ) describes the variance in bond lengths, given by the equation:

$$[8] \qquad \lambda = \frac{1}{n}\sum_{i=0}^{n}\left(\frac{l_i}{l_0}\right)^2$$

where l_i values are the observed bond lengths, and l_0 is the average bond length. For tetrahedral units, $n = 4$, and for octahedral units $n = 6$. The second common parameter is known as the angle variance (σ^2), given by the equation:

$$[9] \qquad \sigma^2 = \frac{1}{n-1}\sum_{i-0}^{n}(\theta_i - \theta_0)^2$$

where θ_i values are the observed bond angles, and θ_0 is the ideal bond angle (109.47° for tetrahedral units and 90.00° for octahedral units). For tetrahedral units $n = 6$, and for octahedral units $n = 12$. No clear correlation is observed when C_Q is plotted against the λ and σ^2 distortion parameters, particularly since the former ranges narrowly from 1.000 to 1.025 (Table 1). However, if C_Q is plotted against the difference in minimum and maximum bond lengths, a stronger linear trend is observed in the region of small C_Q (0–2 MHz) (Fig. 8). The plot does not include data from $GeCl_2$, as the crystallographic information has yet to be determined, although the trend would estimate a bond length difference (maximum-minimum) of 0.012 Å. When the data from $GeBr_2$ are included, the large difference in C_Q compromises the trend. This rudimentary approach has proven reasonably successful in a series of germanium oxides, where the bond length difference provides better correlations with C_Q than conventional distortion parameters.[16]

Chemical shifts

Analysis of the ^{73}Ge chemical shifts for a given oxidation state provides some noticeable trends. First, the chemical shifts of germanium (IV) halides move to lower frequency from chlorine to bromine to iodine. This behaviour correlates with the electronegativity of the halide substituents on germanium and has been noted previously for ^{73}Ge isotropic chemical shifts of germanium halides in solution and for ^{29}Si in the analogous silicon halides (Figure S7 in the Supplementary data).[57] ^{73}Ge chemical shifts are more sensitive, ranging over 1100 ppm, whereas ^{29}Si shifts range over only 350 ppm for the same series. Similarly, ^{119}Sn chemical shifts for tin (IV) halides vary from –150 ppm ($SnCl_4$) to –1701 ppm (SnI_4), exhibiting an even larger range than ^{73}Ge chemical shifts.[57]

A conclusive determination of similar trends in germanium (II) halides is less obvious because of the unknown structure of $GeCl_2$ and the large errors associated with the measured δ_{iso} of $GeBr_2$. However, it is clear the germanium (II) halides do not exhibit the same chemical shift range as the germanium (IV) halides: the ^{73}Ge chemical shifts for GeI_2, $GeBr_2$, and $GeCl_2$ are all found within –70 to –320 ppm (Table 1) and do not show a regular trend.

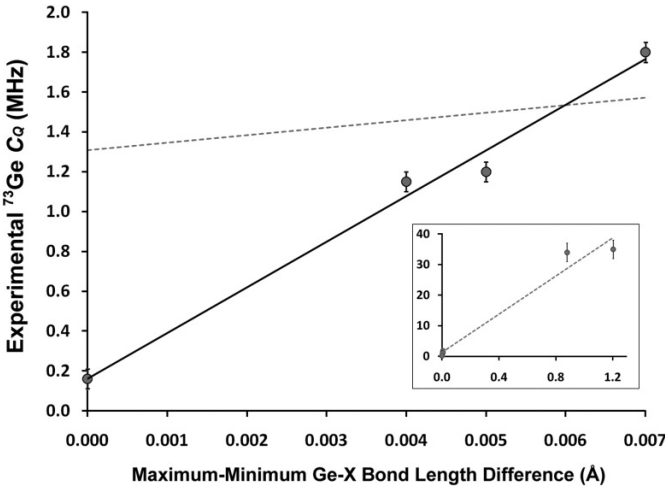

Fig. 8. Correlation between experimental ^{73}Ge C_Q and structural environment as defined by the difference in minimum and maximum Ge–X bond lengths. The solid line shows the linear trend observed for the small C_Q region while the dashed line represents the trend if $GeBr_2$ data are included (inset shows full range of C_Q).

Calculations

Quantum chemical calculations provide some complement to the parameters obtained by the experiment, although there are notable differences. In general, the GIPAW DFT quadrupole coupling calculations show reasonable agreement with our experimental results, with a slight underestimate observed in most cases (Fig. 9). This systematic underestimate has been seen in calculations for germanium oxides,[16,58] and attributed to a deficiency in the exchange-correlation functional.[16] Unsurprisingly, GIPAW DFT correctly predicts the asymmetry parameter when constrained to axial symmetry by the point-group symmetry of the germanium site. However for lower symmetry (as is the case with $GeBr_2$ and $GeCl_4$), the calculated η values are not reliable. Finally, the isotropic chemical shifts determined by GIPAW DFT do not show any particular correlation with the experimental values (Table 1).

The GeF_2 calculation shows the largest C_Q (87.6 MHz) of the series and indeed the largest calculated ^{73}Ge C_Q reported to date. Its magnitude is attributed to the two-coordinate Ge units that exist in this fluorine-bridged chain polymer structure.[56] No NMR experiment was conducted since the extreme breadth for this site would require a large number of stepwise collections and a prohibitive amount of NMR time (the CT would span over 1.8 MHz at 21.1 T).

NMR crystallography

Comparison between the experimental and GIPAW DFT results reveals that the largest disagreement exists for GeI_2 (Fig. 9, Table 1). The small C_Q observed experimentally suggests that there is a very high degree of symmetry present in the crystal structure. However, the GIPAW DFT result of 1.43 MHz does not reflect this assertion. Furthermore, this

Can. J. Chem. Downloaded from www.nrcresearchpress.com by Xi'an Jiaotong University on 09/19/12
For personal use only.

Fig. 9. Comparison of experimental and calculated ^{73}Ge C_Q values with best fit line (solid), $C_{Q(CALCD)} = 0.9629(C_{Q(EXPTL)}) + 0.098$. The inset is an expanded view of the low C_Q (0–2 MHz) region. The dashed line shows the ideal fit (experimental = calculated).

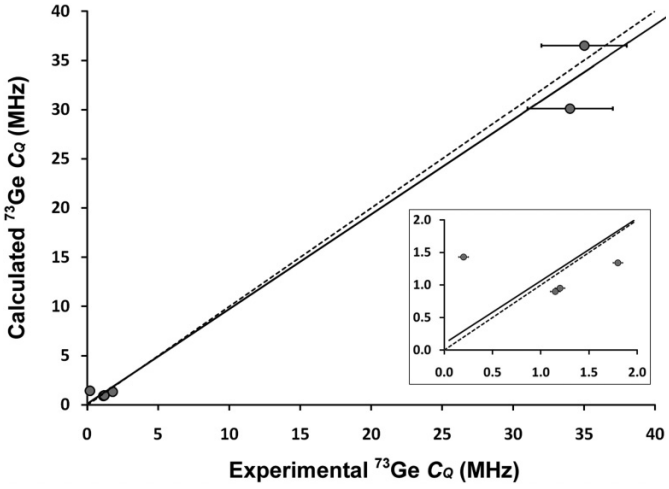

calculation breaks the observed trend that quadrupole couplings are underestimated by GIPAW DFT. Since the experimental C_Q has been determined by four independent measurements and the spectra are starkly incompatible with the GIPAW DFT-predicted value of 1.43 MHz, such a disagreement casts doubt on the validity of the crystal structure used in the calculation. This compound is an appropriate candidate for "NMR crystallography", where NMR, XRD, and quantum chemical calculations are used to refine the crystal structure.[59]

We performed initial GIPAW DFT calculations for four proposed GeI_2 structures from the literature.[37,60,61] The structure which gave the best agreement with the NMR results (calculated ^{73}Ge C_Q = 1.43 MHz) happened to be the one most recently reported (Table S1 in the Supplementary data).[37] Systematic variations of this structure were calculated, including elongation and compression of the cell axes (modification of *a* and *b* together, or *c*), or the *z* coordinate for the iodine site (the other coordinates are bound by the crystallographic space group). However, where the GIPAW DFT results (Figure S8 in the Supplementary data) showed C_Q minima for ^{73}Ge (0.31 MHz) and ^{127}I (12.3 MHz), the "crystal structure" was chemically unrealistic, with a separation between Ge and I atoms of 3.47 Å, greater than that expected based on the sum of the ionic radii (2.93 Å). Based on this one case, it appears that GIPAW DFT is not reliable in accurately predicting very small C_Q values.

Using the crystal structure of GeI_2, a test structure of $GeCl_2$ was made by substituting chlorine atoms in place of iodine, optimizing the structure using GIPAW DFT and calculating the chemical shielding and EFG parameters. The calculations yield a C_Q = 1.41 MHz for ^{73}Ge and 4.82 MHz for ^{35}Cl, with $\eta = 0$ for both. The quadrupolar coupling for ^{73}Ge is in reasonable agreement with the experimental value of 1.7 ± 0.1 MHz (especially if the GIPAW DFT underestimate is considered), while that of ^{35}Cl is strongly overestimated. While this result does not solve the unknown structure, it does provide a reasonable starting point for its determination.

Conclusion

^{73}Ge NMR experiments using three different magnetic fields have provided information about nuclear quadrupole coupling parameters and chemical shifts for two series of germanium halides. The C_Q is a sensitive probe of local symmetry, as the effect can be seen throughout the highly symmetric and less symmetric structures described here. The chemical shifts, while previously determined in solution studies (except for $GeBr_2$ and $GeCl_2$), show sensitivity to the local environment, exhibiting a range of over 1100 ppm. The quadrupolar coupling and chemical shielding information determined for $GeCl_2$ have allowed for structural predictions for this unsolved compound. Additionally, an estimate of $^1J(^{73}Ge, ^{127}I)$ has been suggested for the first time. The spectra demonstrate the advantage of ultrahigh-field NMR acquisition, but also that in some cases, moderate fields can yield interpretable ^{73}Ge NMR spectra. Having characterized the NMR parameters of both halide and oxide materials,[16] we now have a better understanding of how local environments of germanium are reflected in NMR spectra. These results demonstrate the viability of ^{73}Ge NMR as a characterization tool, and contribute to the growing knowledge in this area.

Supplementary data

Supplementary data for this article are available on the journal Web site (www.nrcresearchpress.com/cjc).

Acknowledgements

The authors thank Dr. Kirk Marat (Department of Chemistry, University of Manitoba) for technical assistance. The authors would also like to thank Dr. Frank Hawthorne and Mr. Mark Cooper (Department of Geology, University of Manitoba) and Dr. Charlotte Martineau (Tectospin, France) for helpful discussions. VKM would like to thank the Natural Sciences and Engineering Research Council of Canada (NSERC) for a PGSD3 scholarship. SK thanks the Canada Foundation for Innovation (CFI), NSERC for a Discovery grant, and the province of Manitoba for additional funding. Access to the 900 MHz NMR spectrometer and CASTEP software was provided by the National Ultrahigh-Field NMR Facility for Solids (Ottawa, Canada), a national research facility funded by CFI, the Ontario Innovation Trust, Recherche Québec, NSERC, Bruker BioSpin, and managed by the University of Ottawa (www.nmr900.ca). NSERC is acknowledged for a Major Resources Support grant.

References

(1) Davis, M. E. *Nature* **2002** *417* (6891), 813. doi:10.1038/nature00785.
(2) Henderson, E. J.; Veinot, J. G. C. *Chem. Mater.* **2007** *19* (8), 1886. doi:10.1021/cm070022l.
(3) Wu, X. C.; Song, W. H.; Zhao, B.; Sun, Y. P.; Du, J. J. *Chem. Phys. Lett.* **2001** *349* (3), 210. doi:10.1016/S0009-2614(01)01213-1.
(4) Zou, X.; Conradsson, T.; Klingstedt, M.; Dadachov, M. S.; O'Keeffe, M. *Nature* **2005** *437* (7059), 716. doi:10.1038/nature04097.
(5) Rosenberg, E. *Rev. Environ. Sci. Biotechnol.* **2009** *8* (1), 29. doi:10.1007/s11157-008-9143-x.

Can. J. Chem. Downloaded from www.nrcresearchpress.com by Xi'an Jiaotong University on 09/19/12
For personal use only.

(6) Armatas, G. S.; Kanatzidis, M. G. *Science* **2006** *313* (5788), 817. doi:10.1126/science.1130101.
(7) Takeuchi, Y.; Nishikawa, M.; Tanaka, K.; Takayama, T.; Imanari, M.; Deguchi, K.; Fujito, T.; Sugisaka, Y. *Chem. Commun. (Camb.)* **2000** (8): 687. doi:10.1039/b0010111.
(8) Stebbins, J. F.; Du, L.-S.; Kroeker, S.; Neuhoff, P.; Rice, D.; Frye, J.; Jakobsen, H. J. *Solid State Nucl. Magn. Reson.* **2001** *21* (1–2), 105.
(9) Verkhovskii, S. V.; Yakubovsky, A. Y.; Malkin, B. Z.; Saikin, S. K.; Cardona, M.; Trokiner, A.; Ozhogin, V. I. *Phys. Rev. B* **2003** *68* (10), 104201. doi:10.1103/PhysRevB.68.104201.
(10) Takeuchi, Y.; Nishikawa, M.; Yamamoto, H. *Magn. Reson. Chem.* **2004** *42* (11), 907. doi:10.1002/mrc.1486.
(11) Takeuchi, Y.; Nishikawa, M.; Hachiya, H.; Yamamoto, H. *Magn. Reson. Chem.* **2005** *43* (8), 662. doi:10.1002/mrc.1603.
(12) Takeuchi, Y.; Takayama, T. *Annu. Rep. NMR Spectrosc.* **2005** *54*, 155. doi:10.1016/S0066-4103(04)54004-8.
(13) Michaelis, V. K.; Aguiar, P. M.; Terskikh, V. V.; Kroeker, S. *Chem. Commun. (Camb.)* **2009** (31): 4660. doi:10.1039/b906642j.
(14) Sutrisno, A.; Hanson, M. A.; Rupar, P. A.; Terskikh, V. V.; Baines, K. M.; Huang, Y. *Chem. Commun. (Camb.)* **2010** *46* (16), 2817. doi:10.1039/b926071d.
(15) Sen, S.; Gan, Z. *J. Non-Cryst. Solids* **2010** *356* (28–30), 1519. doi:10.1016/j.jnoncrysol.2010.04.043.
(16) Michaelis, V. K.; Kroeker, S. *J. Phys. Chem. C* **2010** *114* (49), 21736. doi:10.1021/jp1071082.
(17) Takeuchi, Y.; Nishikawa, M.; Tanaka, K.; Takayame, T. *Chem. Lett.* **2001** *30* (6), 572. doi:10.1246/cl.2001.572.
(18) Harris, R. K.; Becker, E. D. *J. Magn. Reson.* **2002** *156* (2), 323. doi:10.1006/jmre.2002.2554.
(19) Holman, Z. C.; Kortshagen, U. R. *Langmuir* **2009** *25* (19), 11883. doi:10.1021/la9015228.
(20) Armatas, G. S.; Kanatzidis, M. G. *Nat. Mater.* **2009** *8* (3), 217. doi:10.1038/nmat2381.
(21) Armatas, G. S.; Kanatzidis, M. G. *Nature* **2006** *441* (7097), 1122. doi:10.1038/nature04833.
(22) Man, P. P. *Encyclopedia of Analytical Chemistry*; John Wiley and Sons Ltd.: Chichester, NY, 2000. pp. 12224–12265.
(23) MacKenzie, K. J. D.; Smith, M. E. *Multinuclear Solid-State NMR of Inorganic Materials*; Elsevier Science Ltd.: Oxford, UK, 2002.
(24) Robinson, K.; Gibbs, G. V.; Ribbe, P. H. *Science* **1971** *172* (3983), 567. doi:10.1126/science.172.3983.567.
(25) O'Dell, L. A.; Rossini, A. J.; Schurko, R. W. *Chem. Phys. Lett.* **2009** *486* (1–3), 97.
(26) Meiboom, S.; Gill, D. *Rev. Sci. Instrum.* **1958** *29* (8), 688. doi:10.1063/1.1716296.
(27) Eichele, K.; Wasylishen, R.E. WSOLIDS NMR simulation package. Version 1.19.11. 2009.
(28) Skibsted, J.; Nielsen, N. C.; Bildsøe, H.; Jakobsen, H. J. *J. Am. Chem. Soc.* **1993** *115* (16), 7351. doi:10.1021/ja00069a038.
(29) Pickard, C. J.; Mauri, F. *Phys. Rev. B* **2001** *63* (24), 245101. doi:10.1103/PhysRevB.63.245101.
(30) Vanderbilt, D. *Phys. Rev. B* **1990** *41* (11), 7892. doi:10.1103/PhysRevB.41.7892.
(31) Yates, J. R.; Pickard, C. J.; Payne, M. C.; Mauri, F. *J. Chem. Phys.* **2003** *118* (13), 5746. doi:10.1063/1.1541625.
(32) Kellö, V.; Sadlej, A. J. *Mol. Phys.* **1999** *96* (2), 275.
(33) Walz, L.; Thiery, D.; Peters, E.-M.; Wendel, H.; Schönherr, E.; Wojnowski, M. Z. *Z. Kristallogr.* **1993** *208* (2), 207. doi:10.1524/zkri.1993.208.Part-2.207.
(34) Yoder, C. H.; Agee, T. M.; Schaeffer, C. D.; Carroll, M. J., Jr; Feisher, A. J.; DeToma, A. S. *Inorg. Chem.* **2008** *47* (22), 10765. doi:10.1021/ic801341t.
(35) Köhler, J.; Okudera, H.; Reuter, D.; Simon, A. *Z. Kristallogr.* **2005** *220* (4), 523.
(36) Merz, K.; Driess, M. *Acta Crystallogr. C* **2002** *58* (7), i101. doi:10.1107/S0108270102010351.
(37) Urgiles, E.; Melo, P.; Coleman, C. C. *J. Cryst. Growth* **1993** *165* (3), 245. doi:10.1016/0022-0248(96)00193-5.
(38) Solomon, I. *Phys. Rev.* **1958** *110* (1), 61. doi:10.1103/PhysRev.110.61.
(39) Man, P. P. *J. Phys. Chem.* **1997** *106* (10), 3908. doi:10.1063/1.473111.
(40) Bak, M.; Rasmussen, J. T.; Nielsen, N. C. *J. Magn. Reson.* **2000** *147* (2), 296. doi:10.1006/jmre.2000.2179.
(41) Rouse, R. C.; Peacor, D. R.; Maxim, B. R. *Z. Kristallogr.* **1977** *145* (3–4), 161. doi:10.1524/zkri.1977.145.3-4.161.
(42) Larsen, F. H.; Jakobsen, H. J.; Ellis, P. D.; Nielsen, N. C. *J. Phys. Chem. A* **1997** *101* (46), 8597. doi:10.1021/jp971547b.
(43) O'Dell, L. A.; Schurko, R. W. *Chem. Phys. Lett.* **2008** *464* (1–3), 97. doi:10.1016/j.cplett.2008.08.095.
(44) Moulton, C. W.; Miller, J. G. *J. Am. Chem. Soc.* **1956** *78* (12), 2702. doi:10.1021/ja01593a014.
(45) Dennis, L. M.; Hunter, H. L. *J. Am. Chem. Soc.* **1929** *51* (4), 1151. doi:10.1021/ja01379a023.
(46) Christensen, A. N.; Ramussen, S. E. *Acta Chem. Scand.* **1965** *19* (2), 421. doi:10.3891/acta.chem.scand.19-0421.
(47) Harris, R. K.; Olivieri, A. C. *Prog. Nucl. Magn. Reson. Spectrosc.* **1992** *24* (5), 435. doi:10.1016/0079-6565(92)80004-Y.
(48) Spiess, H. W.; Haeberlen, U.; Zimmermann, H. *J. Magn. Reson.* **1977** *25* (1), 55.
(49) Samoson, A.; Kundla, E.; Lippmaa, E. *J. Magn. Reson.* **1982** *49* (2), 350.
(50) Kundla, E.; Samoson, A.; Lippmaa, E. *Chem. Phys. Lett.* **1981** *83* (2), 229. doi:10.1016/0009-2614(81)85451-6.
(51) Inglefield, P. T.; Reeves, L. W. *J. Chem. Phys.* **1964** *40* (8), 2425. doi:10.1063/1.1725540.
(52) Willans, M. J.; Demko, B. A.; Wasylishen, R. E. *Phys. Chem. Chem. Phys.* **2006** *8* (23), 2733. doi:10.1039/b603937e.
(53) Widdifield, C. M.; Bryce, D. L. *J. Phys. Chem. A* **2010** *114* (40), 10810. doi:10.1021/jp108237x.
(54) Spiess, H. W.; Sheline, R. K. *J. Chem. Phys.* **1971** *54* (3), 1099. doi:10.1063/1.1674942.
(55) Chapman, R. P.; Widdifield, C. M.; Bryce, D. L. *Prog. Nucl. Magn. Reson.* **2009** *55* (3), 215. doi:10.1016/j.pnmrs.2009.05.001.
(56) Trotter, J.; Akhtar, M.; Bartlett, N. *J. Chem. Soc. A* **1966** (1): 30. doi:10.1039/j19660000030.
(57) Mason, J. *Multinuclear NMR*; Plenum Press: New York, NY, 1987.
(58) Kibalchenko, M.; Yates, J. R.; Pasquarello, A. *J. Phys. Condens. Matter* **2010** *22* (14), 145501. doi:10.1088/0953-8984/22/14/145501.
(59) *NMR Crystallography*; Harris, R. K., Wasylishen, R. E., Duer, M. J., Eds.; John Wiley and Sons Ltd.: West Sussex, UK, 2009.
(60) Powell, H. M.; Brewer, F. M. *J. Chem. Soc.* **1938** 197. doi:10.1039/jr9380000197.
(61) Avilov, A. S.; Imamov, R. M. *Kristallografiya* **1968** *13* (1), 68.

Sensitivity enhancement in MAS NMR of half-integer quadrupolar nuclei using sideband selective double-frequency sweeps

M. Goswami, P.J.M. van Bentum, and A.P.M. Kentgens

Can. J. Chem. Downloaded from www.nrcresearchpress.com by Xi'an Jiaotong University on 09/19/12
For personal use only.

Abstract: Sensitivity enhancement of the NMR signal of the half-integer spin quadrupolar nuclei under magic angle spinning (MAS) conditions is demonstrated using the DFS (Double Frequency Sweep) enhancement scheme. It has been shown, both through numerical simulations and by experiments, that with a sinusoidal amplitude profile a narrow band DFS scheme performs much better than a DFS scheme with a large bandwidth. The total enhancement compares favorably to the hyperbolic secant (HS) pulse scheme under MAS. Finally, we report the robustness of this DFS scheme with respect to variation of different experimental parameters, making it a very attractive choice for acquiring sensitivity-enhanced NMR experiments of half-integer quadrupolar nuclei.

Key words: quadrupolar nuclei, MAS, double frequency sweeps, adiabatic pulse, CT, ST, sensitivity enhancement.

Résumé : On fait la démonstration d'une méthode d'amélioration de la sensibilité du signal RMN des noyaux quadripolaires de spins non entiers, dans les conditions de rotation à l'angle magique (« MAS »), qui utilise un schéma d'exaltation de balayage à double fréquence (BDF). Il est démontré tant par des calculs théoriques que par des données expérimentales que, avec un profil d'amplitude sinusoïdale, un schéma de BDF avec une bande étroite fonctionne beaucoup mieux qu'un schéma de BDF avec une grande largeur de bande. Dans les conditions de rotation à l'angle magique, l'amélioration totale se compare favorablement au schéma de pulsation sécante hyperbolique (SH). Enfin, on rapporte la force de ce schéma de balayage à double fréquence par rapport à la variation des différents paramètres expérimentaux qui en fait un choix très attrayant pour acquérir des données expérimentales de RMN avec une grande sensibilité pour des noyaux quadripolaires non entiers.

Mots-clés : noyau quadripolaire, rotation à l'angle magique (« MAS »), balayages à double fréquence, pulsation adiabatique, CT, ST, amélioration de la sensibilité.

[Traduit par la Rédaction]

1. Introduction

The application of nuclear magnetic resonance (NMR) to half-integer quadrupolar nuclei is widespread because of their abundant occurrence in various materials of inorganic, catalytic, and biological importance.[1,2] Extracting information about the quadrupolar interactions to which these nuclei are subjected can give valuable insights into the structural and dynamic properties of such compounds. However, the sensitivity of most quadrupolar nuclei (except for instance ^{79}Br or ^{23}Na) is notoriously low because it is affected by several factors such as low natural abundance, small values of gyromagnetic ratios, and large values of quadrupolar interaction parameters. Hence, designing efficient sensitivity enhancement schemes for quadrupolar nuclei still holds the attention of the solid-state NMR community.

In the presence of a static magnetic field, the energy levels of half-integer quadrupolar nuclei split into $2I + 1$ energy levels. At thermal equilibrium, the populations of these energy levels are governed by the Boltzmann distribution. In the high-temperature approximation, the spin levels are populated proportionally to their magnetic quantum number m. Therefore, manipulation of the satellite transitions is a useful tool to increase the polarization of the central transition (CT) levels. A subsequent inversion from the outer to the inner satellite transitions (ST) brings the population from the outer levels into the central transition levels, so that the intensity of NMR spectra of the central transition can be enhanced by a factor of $2I$.

One way to achieve this is by the application of amplitude-modulated pulses, a technique which was pioneered by Vega and Naor.[3] For a spin-3/2 nucleus contained within a single crystal, they had successfully demonstrated that an enhancement of 3 can be obtained by using amplitude-modulated pulses. However, the pulsed approach cannot achieve a similar level of enhancement in powdered samples where the satellite transitions cover a wide frequency range from 0 to $\pm\omega_Q$, where ω_Q represents the quadrupolar frequency.

Received 1 January 2011. Accepted 13 February 2011. Published at www.nrcresearchpress.com/cjc on 25 August 2011.

M. Goswami, P. van Bentum, and A. Kentgens. Radboud University Nijmegen, Institute for Molecules and Materials, Heyendaalsweg 135, 6525 AJ Nijmegen, The Netherlands.

Corresponding author: A.P.M. Kentgens (e-mail: A.Kentgens@nmr.ru.nl).

This article is part of a Special Issue dedicated to Professor Roderick E. Wasylishen.

Can. J. Chem. Downloaded from www.nrcresearchpress.com by Xi'an Jiaotong University on 09/19/12
For personal use only.

An attractive alternative approach is to use adiabatic passage schemes. It is known from classic continuous-wave NMR spectroscopy that adiabatic field or frequency sweeps can overcome the problem of a spread in resonance frequencies. The frequency sweep can invert a specific transition by sweeping the frequency of the rf field from far above resonance to far below the resonance condition of the transition under consideration. In-depth studies of the applications of these techniques to half-integer spin quadrupolar nuclei were first made by Haase et al.[5,6] and Kentgens et al.[4,7] Later adiabatic schemes like Double Frequency Sweep (DFS)[8–11] and hyperbolic secant (HS)[12–15] pulse techniques were developed which enhance the sensitivity of quadrupolar nuclei by adiabatically inverting the populations of the outer satellites to the inner ones simultaneously. To date, the DFS scheme with a large sweep range yields the best signal enhancement for the acquisition of NMR spectra of stationary powdered samples with enhancements of up to 2.5 for spin-3/2 nuclei. Similar observations were made by Schurko et al. when they applied the DFS scheme sweeping over a frequency range of ~1.6 MHz observing ^{87}Rb in a static powdered $RbClO_4$ sample.[16] Enhancements ranging from one to two orders of magnitude could be obtained by combining the broad banded DFS with the quadrupolar Carr–Purcell–Meiboom–Gill (QCPMG) pulse sequence for both static and spinning samples.

Under MAS conditions, so far the HS-based inversion results in the largest signal enhancement (up to 2.7 for spin-3/2).[13] In the optimization of the HS pulses, Wasylishen and co-workers found that optimal enhancements are obtained when the bandwidth of the pulse is confined to approximately 1 rotor period.[17] The WURST (wideband uniform-rate smooth truncation)[18] pulse is also associated with large bandwidth to invert the populations of STs and thereby increasing the population differences between CTs.[19] Recently, however, it was reported by Dey et al.[20] that a single WURST inversion pulse under MAS conditions applied to a single satellite transition spinning sideband (ssb) can effectively invert the whole ssb manifold and can achieve appreciable enhancement in the signal to noise ratio for spin-3/2 systems.

Schurko and co-workers explored the optimal control approach to obtain signal enhancements in half-integer spin quadrupolar nuclei under static conditions.[21] These pulses achieved both excitation of the central transition and signal enhancement by population transfer from the satellites. The authors reported enhancements by factors of more than 2 for the central transition of the spin-3/2 ^{87}Rb nucleus compared with a selective $\pi/2$ pulse. These optimized pulses also showed relative insensitivity to the changes made in carrier offset and RF power.

In this contribution, we analyse the behaviour of a narrowband DFS scheme under MAS. We demonstrate a new simple modification to a narrowband DFS scheme which results in greater enhancement than that of normal broadband DFS under MAS. Application of this modified DFS scheme shows enhancements both in numerical simulations as well as in experimental results which are comparable to that of the HS scheme. The new modified scheme, called sideband-selective double-frequency sweep (ssDFS), is obtained by multiplying a narrowband DFS with a sine-squared function. The motivation behind this modification is to reduce the excitation effects by smoothly increasing then decreasing the amplitude of the sweep. We examined the robustness of this scheme with respect to the RF field strength used for the DFS, carrier offset, sweep length, and bandwidth of the DFS. It is shown both numerically and experimentally that ssDFS performs better in terms of total enhancement obtained and is less dependent on experimental parameters.

2. Experimental

The experiments were performed on a Varian NMR System (VNMRS) 300 (7.05 T) and a VNMRS 400 (9.4 T) spectrometer using 2.5 and 3.2 mm HX probe heads. Experiments were performed observing the spin-5/2 ^{27}Al resonance in the Albite, $NaSi_3AlO_8$ sample. The sample was spun at 10 kHz at the magic angle. The quadrupolar coupling constant C_Q and asymmetry parameter η of the ^{27}Al nuclei in Albite were 3.29 MHz and 0.62, respectively.[22] The RF field strength and the duration of the central transition selective 90° pulse applied were 5 kHz and 16.7 μs, respectively.

2.1. DFS

We used a convergent DFS with starting (ω_s) and finishing (ω_f) resonance offsets of 1.1 MHz and 100 kHz, respectively, on the VNMRS 300 spectrometer, whereas the sweep spans from 1 MHz to 100 kHz were carried out on a VNMRS 400 spectrometer. For experiments with DFS having narrow bandwidth, we made use of a convergent DFS with bandwidth equal to the spinning frequency. The other experimental parameters are given in the respective figure captions. For experiments using the ssDFS, we multiplied a convergent DFS, with a bandwidth equalling the spinning frequency, by a sine-squared function (Fig. 1). The sine-squared function was chosen so that the resulting RF profile has a smooth build-up and decay.

2.2. HS pulse

We also made use of HS pulses with a bandwidth of 10 kHz, and offsets of ±160 kHz and ±230 kHz on the VNMRS 300 and 400 spectrometers, respectively. The other relevant pulse and acquisition parameters are given in the figure captions.

2.3. Simulation of NMR spectra using SIMPSON

All the simulations of NMR spectra were carried out using the program SIMPSON (version 3.0.1)[23] running on a Dell Optiplex 755 desktop PC under the Windows XP operating system. The shapes of the DFS and ssDFS amplitude profiles and also the hyperbolic secant pulses were created within the SIMPSON input file. Typically, the powder-averaged spectra were calculated using 4180 crystal orientations using the method of Zaremba, Conroy, and Wolfsberg[24–26] and 10 γ angles. The maximum time step over which the Hamiltonian was considered time independent was 0.5 μs which is also the time step for the DFS and the hyperbolic secant shape. The SIMPSON simulations for a spin-5/2 system with 1000 μs long DFS took around 4 h to finish. All simulations were carried out assuming a spinning frequency of 10 kHz.

3. Results and discussion

Here we present the results obtained from both numerical simulations and experiments done on an Albite ($NaSi_3AlO_8$)

Can. J. Chem. Downloaded from www.nrcresearchpress.com by Xi'an Jiaotong University on 09/19/12
For personal use only.

Fig. 1. (*a*) The RF profile of a 900-μs-long narrowband Double Frequency Sweep, (*b*) the $\sin^2 x$ shape function, and (*c*) resultant RF-amplitude profile of a 900-μs-long ssDFS.

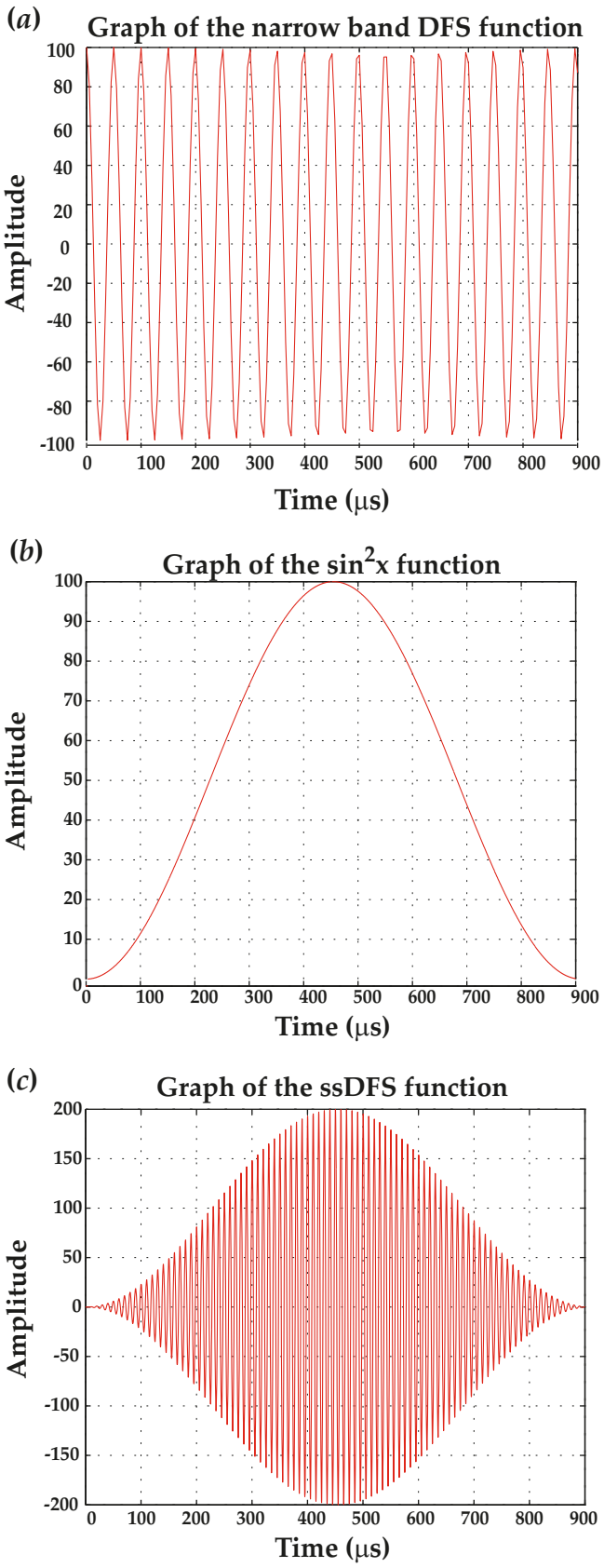

sample at two different external magnetic field strenghts (7.05 T and 9.4 T). We recorded the enhancement factors observed by applying DFS, ssDFS, and HS pulses prior to a selective 90° pulse on the central transition. We also present the behavior of the enhancement factor obtained using ssDFS as a function of different experimental parameters.

3.1. NMR experiments

One-dimensional (1D) MAS spectra of Albite obtained using a single selective 90° pulse, DFS with large bandwidth, DFS with bandwidth equal to the spinning frequency, ν_r, and the sideband-selective DFS are shown in Fig. 2. The experimental results show that the DFS with bandwidth equal to ν_r performs better than normal broadband DFS and the ssDFS performs even better. In the case of the narrowband DFS, the bandwidth was kept equal to ν_r so that the sweep affects only one set of sidebands originating from both ST2 (outer satellite transition) and ST1 (inner satellite transition) on either side of the central transition. Similar observations were made by Wasylishen et al.[17] where they applied adiabatic pulses with bandwidth less than ν_r and conditions were designed such that the sweep only affected one ST (one ST1 and one ST2) sideband on one side of the central transition called SFS (Single Frequency Sweep). They observed that SFS under this condition performs better than normal DFS. Here we observe that if we keep the bandwidth of the DFS equal to ν_r so that it affects the sidebands from both sides of the central transition, the resultant enhancement is still higher than that obtained with a DFS with large bandwidth.

We also implemented HS pulses for ^{27}Al NMR in Albite with a bandwidth equal to 10 kHz. When comparing the results obtained with the HS scheme to that of the ssDFS it turns out that the ssDFS actually performs comparably or even slightly better than that of HS (Fig. 3). Similar results were obtained when these experiments were performed at a 300 MHz spectrometer (data not shown). The enhancement factors are listed in Table 1.

To investigate the robustness of the ssDFS scheme with respect to various experimental settings such as the RF field strength of the DFS, carrier offset, sweep duration, and bandwidth of DFS, we studied the enhancement factor as a function of these variables.

At first we varied the sweep length of the DFS scheme. The enhancement factor displayed a remarkable robustness (Fig. 4*a*). The sweep length was optimized at 1 ms (10 rotor periods) and was varied from 500 μs (5 rotor period) to 1.5 ms (15 rotor period). The enhancement factor shows a flat profile when plotted against sweep length expressed in rotor periods with a maximum observed drop in enhancement by only 8% from its optimum value.

Figure 4*b* shows the signal enhancement factor for the ssDFS scheme plotted as a function of the RF field strength of the DFS, ν_{RF}^{DFS}. The DFS was optimized at an RF field strength of 17.5 kHz, and subsequently varied from 7.5 kHz to 37.5 kHz. The enhancement factor is somewhat lower at the lowest RF field strength building up to its optimum at 17.5 kHz, subsequently displaying a relatively flat profile throughout with a maximum drop of 12% of the enhancement factor from its optimum value.

Figure 4*c* displays the variation of enhancement factor as a function of carrier frequency of the DFS. Here we have var-

Can. J. Chem. Downloaded from www.nrcresearchpress.com by Xi'an Jiaotong University on 09/19/12
For personal use only.

Fig. 2. Experimental 1D MAS spectra of ^{27}Al nuclei in Albite sample obtained on a VNMRS 400 spectrometer under different pulse schemes: (*a*) selective 90° pulse, (*b*) DFS running from 1.0 MHz to 100 kHz, (*c*) narrowband DFS running from 230 kHz to 220 kHz, (*d*) ssDFS. The numbers on the right of each spectrum denote the associated enhancements. The RF on ^{27}Al during DFS was kept at 17.5 kHz and that of central-transition selective 90° pulse was 5 kHz. The sweep duration was optimized to 1000 μs to obtain maximum signal intensity. A total of 64 transients were acquired with a relaxation delay of 2 s.

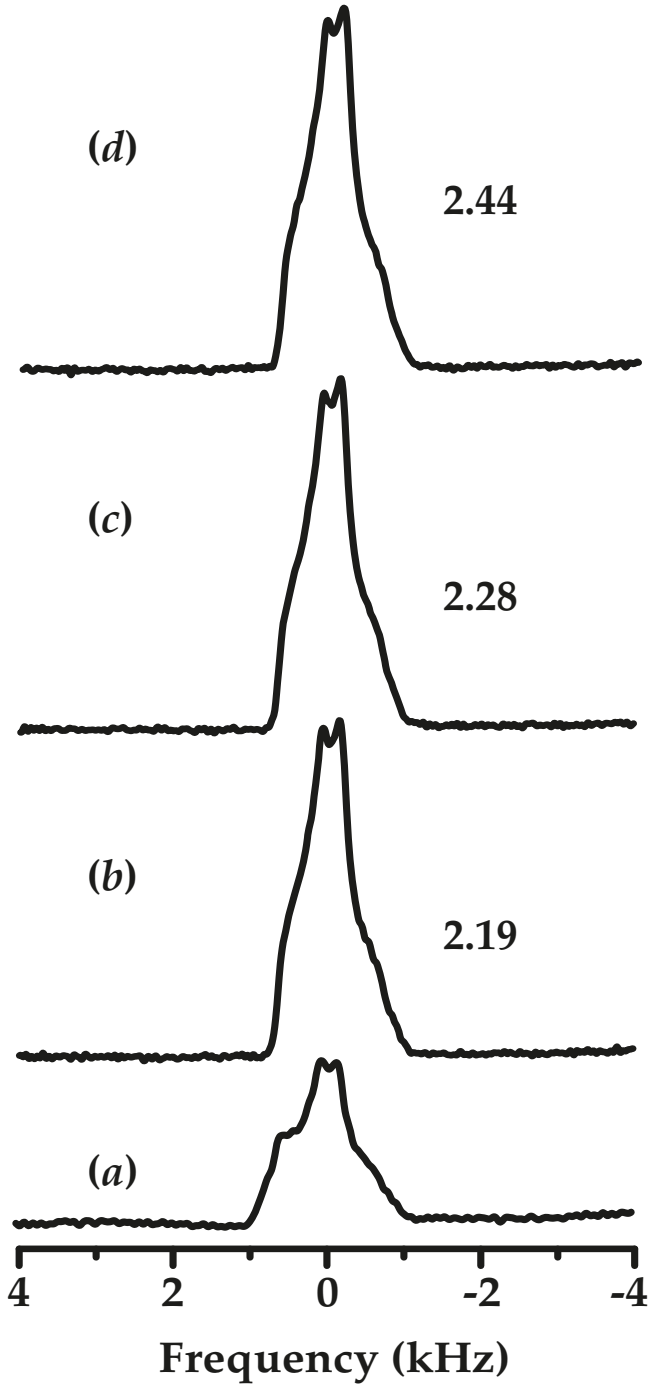

ied the position of the transmitter from the center of the central transition peak to ±100 kHz on either side of the center so that the DFS operates asymmetrically around the central

Fig. 3. Experimental 1D MAS spectra of ^{27}Al nuclei on a VNMRS 400 spectrometer using different pulse schemes: (*a*) selective 90°, (*b*) hyperbolic secant pulse, (*c*) ssDFS. The numbers on the right of each spectrum denote the associated enhancements. The HS pulse had an offset of ± 230 kHz and bandwidth of 10 kHz. The duration of the HS pulse was 2050 μs at an RF of 17.5 kHz. The RF field strength of the central-transition selective 90° pulse was 5 kHz. The number of transients and the relaxation delay time were the same asfor the DFS experiment.

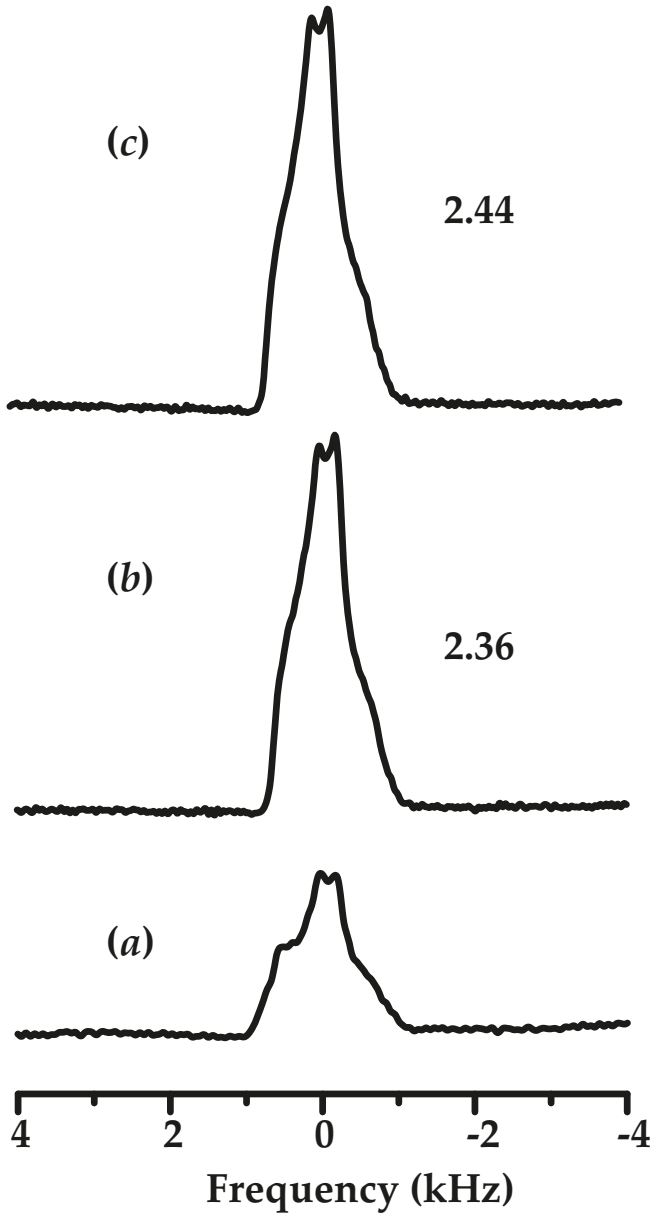

transition peak. Again, the plot of the enhancement factor versus carrier offset shows a remarkably flat profile between ±50 kHz of carrier offset. Only after ±50 kHz does the enhancement factor start to show a small decline. Again, the maximum drop in the enhancement factor was only ~8% from the optimum value.

Next we varied the bandwidth of the ssDFS from 5 kHz to 20 kHz i.e., 1/2 to 2 times spinning frequency. Interestingly, the enhancement factor now shows an oscillatory behavior

Table 1. Experimental enhancements obtained with respect to a selective 90° pulse, using different enhancement schemes at two different magnetic fields for ^{27}Al nuclei in the Albite sample.

Magnetic field	Broadband DFS	Narrowband DFS	HS	ssDFS
7.05 T	2.17±0.02	2.27±0.02	2.32±0.01	2.37±0.01
9.4 T	2.19±0.02	2.28±0.01	2.36±0.01	2.44±0.01

Fig. 4. Simulated and experimental variation of the optimized ^{27}Al NMR signal for a spinning Albite sample at 9.4 T (*a*) as a function of the sweep length (expressed in terms of rotor periods) of the DFS, (*b*) as a function of the RF field strength of the DFS, ν_{RF}^{DFS}, (*c*) as a function of the carrier offset of the DFS, (*d*) as a function of the bandwidth of the DFS.

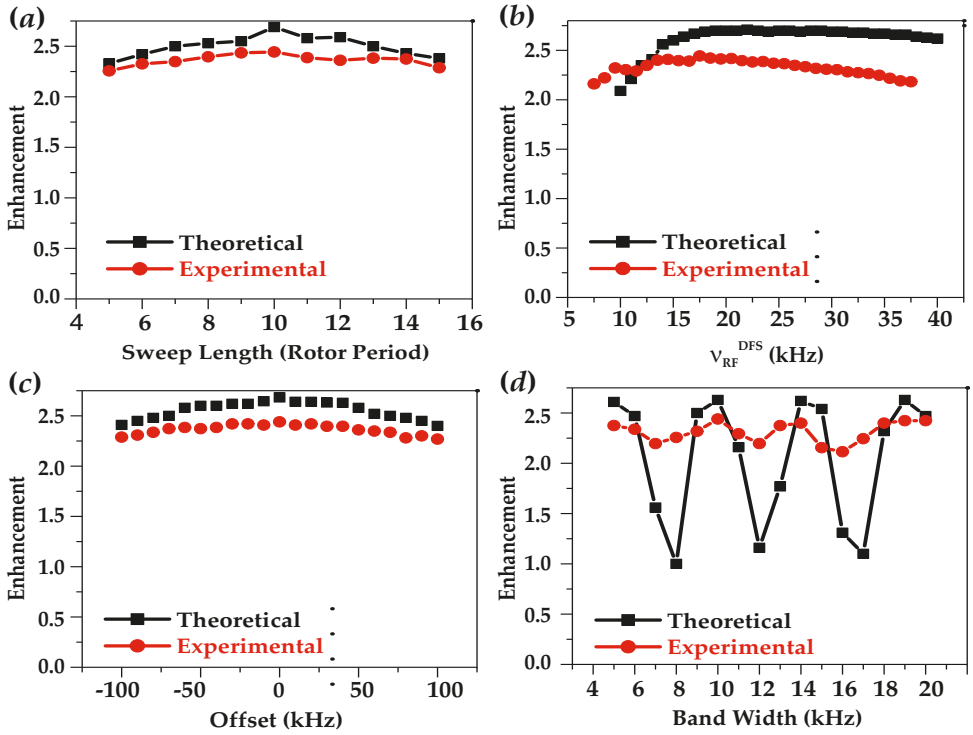

with respect to the variation of the bandwidth (Fig. 4*d*). Incidentally, similar observations were previously made by Wasylishen et al. in the case of hyperbolic secant pulses.[15] Their oscillation frequency, however, was different from ours. When we tried to rationalize this observation, we found that each and every minimum in the plot of enhancement versus bandwidth occurs when the sweep finishes on top of the spinning sidebands (ssb) of either ST1 or ST2. But when the sweep covers an entire ssb of either the inner or outer satellite transitions, the enhancement factor goes up. Hence, it can be said that when the sweep ends on top of an ssb it interferes with the inversion of that ssb which results in a cascading effect on the whole of the ssb manifold leading to smaller enhancements.

In summary, we have shown here that a narrowband DFS scheme performs much better than a broadband DFS for spinning samples. This observation confirms previous observations that narrowband adiabatic methods are best under MAS conditions.[17,20] The various adiabatic schemes perform similarly in terms of the overall enhancement effect. Small differences are attributed to the approach used to avoid *sudden* changes in the spin Hamiltonian causing unwanted excitations of the spin system. Here we have implemented a squared sinusoidal amplitude envelop to the DFS to ensure a smooth increase and decrease of the amplitude at the beginning and end of the sweep. This appears to give slightly better performance compared to other adiabatic schemes. Another favourable aspect of this DFS implementation is the robustness of its performance with respect to a great number of experimental parameters. Considering the fact that a broadband DFS is also the method of choice for enhancing the central-transition powder patterns in static samples, we argue that the DFS is the most versatile implementation for enhancing spectra of half-integer quadrupolar spins. The DFS can easily be implemented in a flexible way so that the bandwidth can be tuned to a small value for spinning conditions, whereas it can be used with a broad bandwidth under static conditions. Slowly building up and bringing down the amplitude of the sweep will avoid excitation effects. The versatility and robustness of this scheme requires very little optimization during actual experiments.

3.2. SIMPSON simulations

To validate the effect of ssDFS on the enhancement factor, we performed SIMPSON simulations on a spin-5/2 system using the quadrupolar parameters of ^{27}Al in Albite. It turned out that the simulations provided us with similar observations to those we previously made experimentally. The numerical

Can. J. Chem. Downloaded from www.nrcresearchpress.com by Xi'an Jiaotong University on 09/19/12
For personal use only.

Can. J. Chem. Downloaded from www.nrcresearchpress.com by Xi'an Jiaotong University on 09/19/12
For personal use only.

Fig. 5. Simulated 1D MAS spectra of ^{27}Al nuclei in Albite with quadrupolar coupling constant C_Q and asymmetry parameter η equal to 3.29 MHz and 0.62, respectively, using different pulse schemes. (*a*) A single 90°, (*b*) DFS running from 900 kHz to 100 kHz, (*c*) DFS running from 170 kHz to 160 kHz, (*d*) ssDFS. The numbers on the right of each spectrum denote the associated signal enhancements with respect to the single-pulse experiment.

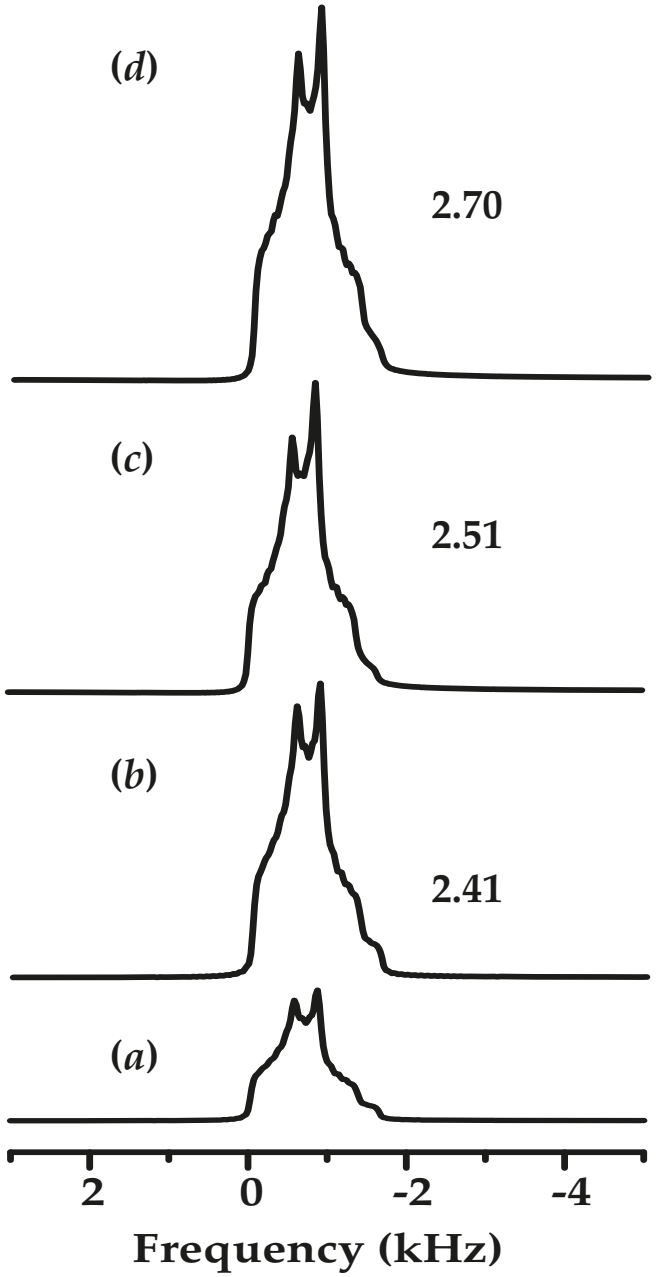

simulations show that the DFS with bandwidth equal to MAS rate, ν_r, should perform better than normal DFS whereas the ssDFS should perform even better (Fig. 5). When we further compared the ssDFS with the HS pulse, it turned out that in simulations as in experiments they behave comparably to each other (Fig. 6). Similar observations were made when we did numerical simulations for spin-3/2 and spin-7/2 systems. The results are given in Table 2. For simulations of a spin-3/2 system, we used the quadrupolar parameters of ^{87}Rb in $RbClO_4$ (C_Q = 3.29 MHz and η = 0.2) and for a spin-7/2

Fig. 6. Simulated 1D MAS spectra of ^{27}Al in Albite. (*a*) A single 90°, (*b*) hyperbolic secant pulse, and (*c*) ssDFS. The numbers on the right of each spectrum denote the associated enhancements with respect to the single-pulse experiment.

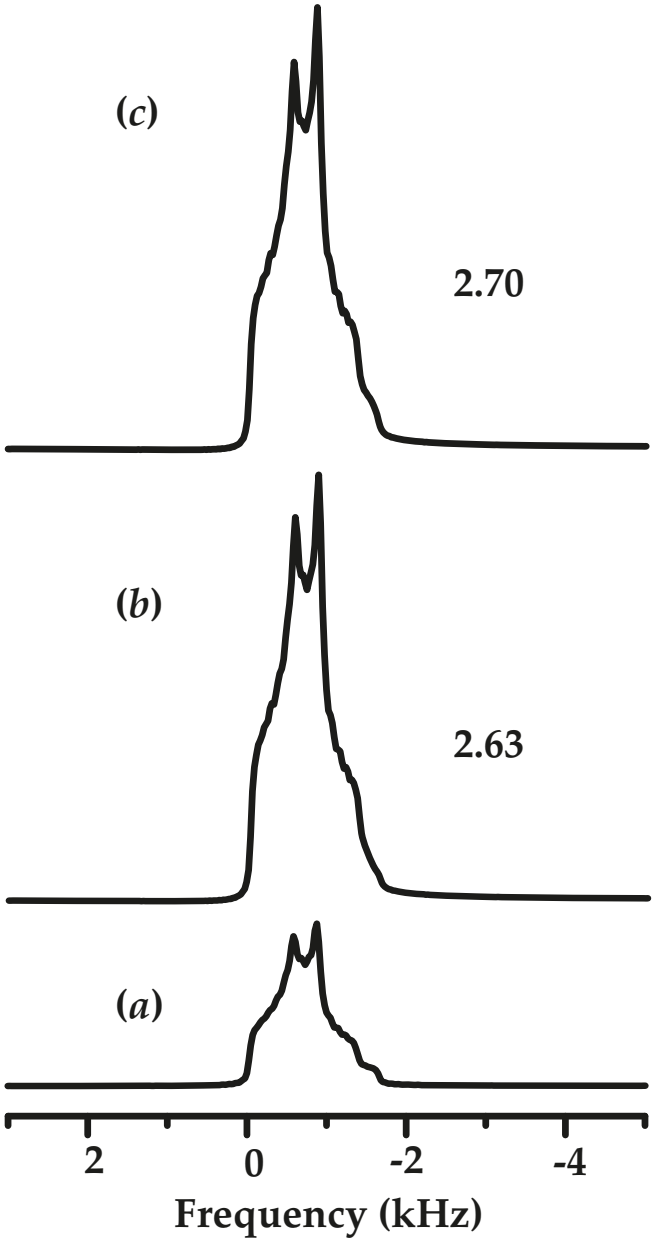

system we used the quadrupolar parameters of ^{43}Ca in $CaTiO_3$ (C_Q = 2.13 MHz and η = 0.7). The data indicate that the ssDFS scheme is universally applicable to all nuclei with half-integer quadrupolar spins.

Next we simulated the robustness of the enhancement factor obtained by the ssDFS scheme as a function of the variables such as RF field strength, sweep length, bandwidth, and carrier offset of the ssDFS scheme.

At first, we varied the length of the ssDFS. As in the experiments, the optimum sweep length was equal to 10 rotor periods i.e., 1000 μs, and was varied from the 5th to the 15th rotor period. As in the experimental results, the enhancement factor shows significant robustness with respect to the change of the sweep length(Fig. 4*a*). Next we plotted

Table 2. Simulated optimal enhancements obtained with respect to a single 90° pulse at 10 kHz MAS, using different enhancement schemes for $I = 3/2$, 5/2, and 7/2 spin systems. The quadrupolar parameters of ^{87}Rb ($I = 3/2$) in $RbClO_4$ ($C_Q = 3.2$ MHz and $\eta = 0.21$), ^{27}Al ($I = 5/2$) in Albite ($C_Q = 3.29$ MHz and $\eta = 0.62$), and ^{43}Ca ($I = 7/2$) in $CaTiO_3$ ($C_Q = 2.13$ MHz and $\eta = 0.7$) were chosen as model parameters in the simulations.

Spin system(I)	Broadband DFS	Narrowband DFS	HS	ssDFS
Spin-3/2	2.25	2.45	2.58	2.60
Spin-5/2	2.41	2.51	2.63	2.70
Spin-7/2	3.19	3.41	3.55	3.64

the variation of the enhancement factor as a function of the RF power of the DFS, ν_{RF}^{DFS}. It is evident from the plot that as in the experimental findings, the simulated enhancement factor shows an initial fast build-up as a function of ν_{RF}^{DFS}, then flattens and remains flat almost throughout the range of the plot (Fig. 4*b*). The theoretical variation of the enhancement factor as a function of carrier frequency of the DFS is shown in Fig. 4*c*. Here we mimicked the experimental condition by changing the position of the transmitter from the center of the central transition to ±100 kHz on either side of the center with an increment of 10 kHz, so that the sweep is asymmetrical around the central transition peak. It is clear from the plot that the profile of the enhancement factor remains essentially flat throughout the whole range, showing very little dependence on the variation of the carrier offset. An observation which is again similar to the experimental observation.

Next, as we varied the bandwidth of the ssDFS, we observed that here as well the simulated results follow the experimental results and the enhancement factor shows an oscillating behavior when the bandwidth is varied (Fig. 4*d*). Further, the oscillation frequency of the simulated plot remains almost identical to that of the experimental plot. However, one clear difference between the simulated and experimental plots is that the experimental oscillation displays much more damping than the simulated one. One possible reason could be the finite line widths of the experimental ssbs. This means that experimentally it may not be possible to end the sweep exactly on top of an ssb, resulting in damped oscillation.

4. Conclusions

In this report, we have provided both theoretical and experimental proof that a narrowband DFS scheme performs better than a normal broadband DFS under MAS for spin $I = 5/2$. In general, adiabatic pulses focussing on the inversion of a single sideband seem to perform best in inverting the whole sideband manifold. Subtle differences between these adiabatic schemes are attributed to differences in the amplitude profiles applied to avoid unwanted non-adiabatic excitations of the spin system. The DFS scheme possesses the flexibility to be used with a narrow bandwidth for spinning samples as well as with a large bandwidth for static samples. Further, it has been shown that the enhancement obtained with an ssDFS scheme is actually comparable with that obtained with hyperbolic secant scheme. Simulations for spin $I = 3/2$ and $I = 7/2$ indicate that the advantages of the ssDFS scheme are applicable across the whole range of half-integer spin-quantum numbers. An additional increase in the signal may be obtained by using repetitive ssDFS as has been shown using multiple RAPT,[27] repetitive DFS,[28] and multiple FAM experiments.[29] The robustness of the ssDFS scheme with respect to the (peak) RF field strength of the DFS, carrier offset, and sweep duration of the DFS has also been demonstrated. All these observations display the broad applicability of the DFS method which can be optimized once and used for all purposes. It is expected that the combination of desirable features such as higher enhancement, robustness, and the ease of implementation associated with the ssDFS scheme will make the application of this method more routine.

Acknowledgements

This work has been supported by EuroMagNET under the EU contract no 228043. We also acknowledge the support of the Netherlands Organisation for Scientific Research NWO for support of the Solid State NMR Facility for advanced materials science. We are grateful to the technical staffmembers G. Janssen, Hans Janssen, and J. van Os for their technical support.

References

(1) MacKenzie, K. J. D.; Smith, M. E. *Multinuclear Solid-State NMR of Inorganic Materials*; Pergamon Press, Oxford, 2002.
(2) Yamauchi, K.; Kuroki, S.; Ando, I.; Ozaki, T.; Shoji, A. *Chem. Phys. Lett.* **1999** *302* (3-4), 331. doi:10.1016/S0009-2614(99)00127-X.
(3) Vega, S.; Naor, Y. *J. Chem. Phys.* **1981** *75* (1), 75. doi:10.1063/1.441857.
(5) Haase, J.; Conradi, M. S. *Chem. Phys. Lett.* **1993** *209* (3), 287. doi:10.1016/0009-2614(93)80109-3.
(6) Haase, J.; Conradi, M. S.; Grey, C. P.; Vega, A. J. *J. Magn. Reson. A* **1994** *109* (1), 90. doi:10.1006/jmra.1994.1138.
(4) Kentgens, A. P. M. *J. Magn. Reson.* **1991** *95*, 619.
(7) van Veenendaal, E.; Meier, B. H.; Kentgens, A. P. M. *Mol. Phys.* **1998** *93*, 195. DOI: 10.1080/002689798169212.
(8) Kentgens, A. P. M.; Verhagen, R. *Chem. Phys. Lett.* **1999** *300* (3–4), 435. doi:10.1016/S0009-2614(98)01402-X.
(9) Iuga, D.; Schäfer, H.; Verhagen, R.; Kentgens, A. P. M. *J. Magn. Reson.* **2000** *147* (2), 192. doi:10.1006/jmre.2000.2192.
(10) Schäfer, H.; Iuga, D.; Verhagen, R.; Kentgens, A. P. M. *J. Chem. Phys.* **2001** *114* (7), 3073. doi:10.1063/1.1340576.
(11) Iuga, D.; Kentgens, A. P. M. *J. Magn. Reson.* **2002** *158* (1–2), 65. doi:10.1016/S1090-7807(02)00061-7.
(12) Siegel, R.; Nakashima, T. T.; Wasylishen, R. E. *Chem. Phys. Lett.* **2004** *388* (4–6), 441. doi:10.1016/j.cplett.2004.03.047.
(13) Siegel, R.; Nakashima, T. T.; Wasylishen, R. E. *Concepts Magn. Reson.* **2005** *26A* (2), 47. doi:10.1002/cmr.a.20037.

Can. J. Chem. Downloaded from www.nrcresearchpress.com by Xi'an Jiaotong University on 09/19/12
For personal use only.

(14) Siegel, R.; Nakashima, T. T.; Wasylishen, R. E. *Chem. Phys. Lett.* **2006** *421* (4-6), 529. doi:10.1016/j.cplett.2006.01.107.
(15) Siegel, R.; Nakashima, T. T.; Wasylishen, R. E. *J. Magn. Reson.* **2007** *184* (1), 85. doi:10.1016/j.jmr.2006.09.007.
(16) Schurko, R. W.; Hung, I.; Widdifield, C. M. *Chem. Phys. Lett.* **2003** *379* (1-2), 1. doi:10.1016/S0009-2614(03)01345-9.
(17) Nakashima, T. T.; Wasylishen, R. E.; Siegel, R.; Ooms, K. J. *Chem. Phys. Lett.* **2008** *450* (4–6), 417. doi:10.1016/j.cplett.2007.11.032.
(18) Kupce, E.; Freeman, R. *J. Magn. Reson. A* **1995** *115* (2), 273. doi:10.1006/jmra.1995.1179.
(19) Bhattacharyya, R.; Frydman, L. *J. Chem. Phys.* **2007** *127* (19), 194503. doi:10.1063/1.2793783.
(20) Dey, K. K.; Prasad, S.; Ash, J. T.; Deschamps, M.; Grandinetti, P. J. *J. Magn. Reson.* **2007** *185* (2), 326. doi:10.1016/j.jmr.2006.12.013.
(21) O'Dell, L. A.; Harris, K. J.; Schurko, R. W. *J. Magn. Reson.* **2010** *203* (1), 156. doi:10.1016/j.jmr.2009.12.016.
(22) Kirkpatrick, R. J.; Kinsey, R. A.; Smith, K. A.; Henderson, D. M.; Oldfield, E. *Am. Mineral.* **1985** *70*, 106.
(23) Bak, M.; Rasmussen, J. T.; Nielsen, N. C. *J. Magn. Reson.* **2000** *147* (2), 296. doi:10.1006/jmre.2000.2179.
(24) Zaremba, S. K. *Ann. Mat. Pura Appl.* **1966** *73*, 293. DOI: 10.1007/BF02415091.
(25) Conroy, H. *J. Chem. Phys.* **1967** *47* (12), 5307. doi:10.1063/1.1701795.
(26) Cheng, V. B.; Suzukawa, H. H., Jr; Wolfsberg, M. *J. Chem. Phys.* **1973** *59* (8), 3992. doi:10.1063/1.1680590.
(27) Kwak, H.-T.; Prasad, S.; Clark, T.; Grandinetti, P. J. *Solid State Nucl. Magn. Reson.* **2003** *24* (2–3), 71. doi:10.1016/S0926-2040(03)00051-1.
(28) Brinkmann, A.; Kentgens, A. P. M. *J. Phys. Chem. B* **2006** *110* (32), 16089. doi:10.1021/jp062809p.
(29) Goswami, M.; Madhu, P. K. *J. Magn. Reson.* **2008** *192* (2), 230. doi:10.1016/j.jmr.2008.02.020.

Can. J. Chem. Downloaded from www.nrcresearchpress.com by Xi'an Jiaotong University on 09/19/12
For personal use only.

A ^{1}H NMR study of the fatty acid distribution in developing flax bolls before and after a cooking treatment

Christopher W. Kirby, Jason L. McCallum, and Bourlaye Fofana

Can. J. Chem. Downloaded from www.nrcresearchpress.com by Xi'an Jiaotong University on 09/19/12
For personal use only.

Abstract: Flax is an important Canadian crop that contains a large percentage of fatty acids (FAs) by seed weight. Gas chromatography (GC) methods have traditionally been used to study FA distributions in oil seed crops. These methods, however, require sample preparation involving saponification and methyl ester formation. Recently, ^{1}H NMR has been shown to be an excellent way to directly measure FA distributions in edible oils using a nondestructive and experimentally faster methodology. As such, we have examined the FA profiles in developing bolls of flax cultivar AC McDuff using ^{1}H NMR and assessed the effect of cooking on FA stability and distribution. The data confirmed the high percentage of linolenic acid in mature AC McDuff flax seed compared to early stages of development and showed that FAs at early stages of boll development are more prone to thermal degradation. Triacylglycerol was found to be important to FA stability to heat. It was also observed that the FAs did not convert from cis to trans under the cooking process used herein. The usefulness of ^{1}H NMR spectroscopy in oils chemistry is highlighted.

Key words: fatty acid, flax, ^{1}H NMR, FA, triacylglycerol, omega-3, omega-6, omega-9.

Résumé : Le lin est un important produit agricole canadien contenant une grande proportion d'acides gras (AG) dans les graines. Les méthodes de chromatographie gazeuse (CG) ont traditionnellement été utilisées pour étudier la distribution des AG dans diverses cultures oléagineuses. Toutefois, ces méthodes requièrent une préparation d'échantillon impliquant une saponification et la formation d'ester. Récemment, il a été démontré que la RMN du ^{1}H est une excellente méthode pour mesurer directement la distribution des AG dans les huiles comestibles et qu'elle constitue une méthodologie non destructive et expérimentalement plus rapide. Pour cette raison, faisant appel à la RMN du ^{1}H, nous avons examiné les profiles des AG dans les capsules à graines du cultivar AC McDuff de lin et l'effet de la cuisson sur la stabilité et la distribution des AG a été évalué. Les données confirment que, par comparaison avec leurs stades précoces de développement, les graines matures du cultivar AC McDuff de lin contiennent des pourcentages élevés d'acide linolénique et que les AG des stades précoces de développement des capsules à graines de lin sont plus susceptibles à une dégradation thermique. Le triacylglycérol a été jugé important pour la stabilité des AG exposés à la chaleur. Il a été aussi observé que les AG ne sont pas convertis de cis en trans dans le processus de cuisson utilisé. L'utilité de la spectroscopie RMN du ^{1}H dans la chimie des huiles est mise en relief.

Mots-clés : acide gras, lin, RMN du ^{1}H, triacylglycérol, oméga-3, oméga-6, oméga-9.

[Traduit par la Rédaction]

Introduction

Flax (*Linum* usitatissimum L.) has emerged as a multipurpose crop with food, feed, and industrial applications.[1–4] In the food industry, flax seed is used as intact seed and (or) is processed in a variety of ways for use as food additives and for the nutraceutical market. Numerous health benefits have been associated with flax seed oil due to the large range of compounds found therein including, but not limited to, secoisolariciresinol diglucoside lignans[5,6] and omega-6 (linoleic acid) and omega-3 (linolenic acid) fatty acids (FAs).[2,7] This has recently been reviewed in detail.[8]

Flax products are increasingly being used in the functional food and nutraceutical markets, being directed, in particular, to obesity and other chronic diseases found in western societies.[1–4] As a functional food, ground flax, also known as flax meal, is found in breads and cereals, and can also be added to food matrices including juices and yoghurts to add nutritional value.[5,9] However, the question of whether the FA profiles are stable during processing remains a debate in the literature.[10] It has been reported that high levels of conjugated dienes are formed in Linola flax oil when treated at 140 °C for 40 min.[11] However, in flax seed fortified macaroni, the omega-3 level has been reported to remain unchanged after 32 weeks, both at low and elevated

Received 31 December 2010. Accepted 18 February 2011. Published at www.nrcresearchpress.com/cjc on 24 August 2011.

C.W. Kirby, J.L. McCallum, and B. Fofana. Crops and Livestock Research Centre, Agriculture and Agri-Food Canada, 550 University Avenue, Charlottetown, PEI C1A 4P3, Canada.

Corresponding author: Christopher W. Kirby (e-mail: Chris.Kirby@agr.gc.ca).

This article is part of a special issue dedicated Professor R. E. Wasylishen.

Can. J. Chem. Downloaded from www.nrcresearchpress.com by Xi'an Jiaotong University on 09/19/12
For personal use only.

temperatures.[12] In this study, the stability of the FAs, in developing AC McDuff flax bolls, mature flax seed, and flax meal, to a heating process commonly used in vegetable preparations will be examined.

There are five main fatty acids found in flax seed oil,[8] which can be broken down into four types: omega-3, omega-6, omega-9, and saturated FAs. Linolenic (omega-3, 18:3) and linoleic acids (omega-6, 18:2) are polyunsaturated FAs (PUFAs), oleic acid (omega-9, 18:1) is an unsaturated FA (UFA), while stearic (18:0) and palmitic (16:0) acids are saturated FAs (SFAs). In the A:B naming system, A tells the length of the chain (18 carbons) and B the number of double bonds in the chain. PUFAs, UFAs, and SFAs, as well as trans fats, are all contained on the labels of edible oil products.

Liquid NMR spectroscopy is used for small molecule structural elucidation, chemical purity assessment, and protein or biomolecule function and structure daily in NMR laboratories.[13] In recent years, looking at complex mixtures by NMR has become more and more common. NMR metabolomic methods for blood and urine samples have almost become routine with the commercial databases available. More recently, protocols and databases for plant extracts are in developmental stages.[14,15] In a similar way, oil mixtures can be studied quantitatively by ^{1}H NMR.[16,17] Even though the oils are not chemically pure, characteristic peaks are available to be able to completely identify the relative FA distribution in oils via ^{1}H NMR analysis. There have been reports on using such methodology in fish oils,[18–21] olive oil,[22] with particular interest in botanical origin,[23] monitoring oxidation in FAs,[24–26] studying edible oils including flax,[27–29] and recently using NMR in nutritional labeling.[30]

Gas chromatography (GC) is the method of determination of fatty acid content accepted by the American Oil Chemists' Society[31] and thus is the benchmark for the study of oils. GC methods, however, involve chemical conversion of triacylglycerol stored fatty acids to methyl esters of fatty acids before running the method. This involves cost in both chemicals and person-hours, and GC also requires standards of FAs. Using NMR, however, does not require the costs for the chemical conversion, does not require standards, and NMR has been shown to give results with accurate determination of the relative amounts of 18:3, 18:2, 18:1, and saturated fatty acids.[16] In as much, the FA profiles of developing bolls of the flax cultivar AC McDuff were examined before and after a heating treatment using a ^{1}H NMR methodology. We will show that the percentage of UFAs increases as the bolls develop, that the heating treatment has a major impact on the FA profiles during early stages of boll development, and little effect on late stage bolls as well as mature flax seed, and the heating treatment does not convert cis FAs to trans FAs.

Experimental

Plants from cultivar AC McDuff were grown in 10 pots, with 5–7 plants per pot, in a growth chamber (16/8 h light/dark and 20/18 °C day/night). At anthesis (when a flower fully blooms), individual flowers were tagged sequentially and developing bolls (the seed bearing capsules) were harvested at 4, 8, 12, and 16 d after anthesis (DAA) as well as at mature seed. Harvested bolls were immediately frozen in liquid nitrogen and then stored at –80 °C until the samples were processed.

Two grams (2 g) of developing bolls (4, 8, 12, and 16 DAA), flax seed, and ground flax seed (to be referred to as flax meal hereafter) were split into two samples with 1 g in each group. We placed one group of samples in 15 mL centrifuge tubes and heated them at 100 °C for 30 min in a water bath, hereafter referred to as cooked, while the others were untreated and will be referred to as raw. The FAs were extracted from the samples using the following protocol, which is a slight modification of that of McKillican and Sims.[32] After the cooking step, all the samples were flash-frozen in liquid nitrogen, ground to fine powder using a mortar and pestle, and extracted with 10 mL of deoxygenated hexane, in a glass tube, for 16 h on a shaker. After centrifugation at 17 500*g* for 5 min, the supernatant was collected and the hexane was evaporated under a nitrogen gas stream for 90 min. To ensure all of the hexane was removed, the samples were placed in a vacuum desiccator for 16 h. These samples were prepared in triplicate.

The dried FA samples were diluted with 600 μL of dry $CDCl_3$ and transferred to 5 mm NMR tubes. The ^{1}H NMR spectra were acquired on a Bruker Avance III 600 NMR spectrometer with a ^{1}H operating frequency of 600.28 MHz. A 5 mm inverse probe was used for all experiments with a controlled temperature set to 25.00 °C ± 0.01 °C. A 30° pulse (π/2 pulse of 7.3 μs), an acquisition time of 2.65 s (64 k-points), a recycle delay of 2 s, a spectral width of 12.3 kHz, and 16 scans were acquired for each experiment. Three independent spectra were acquired for each developmental stage for statistical analysis. The relative amount of FAs was determined quantitatively using the integrals (areas) of specific peaks as described by Knothe and Kenar.[16]

Results and discussion

^{1}H NMR spectra of the FAs extracted from developing flax bolls (raw) and mature flax seed of AC McDuff were acquired. These spectra are presented on the left side of Fig. 1. To gain an understanding of the FA distribution, Fig. 2 shows an expansion of the ^{1}H spectrum of the mature flax seed and the peaks used in the determination of the FA distribution. Using the integrals for peaks labeled A, B, C, and D in Fig. 2, the relative amounts of 18:3, 18:2, 18:1, and SFAs can be determined using the equations shown here[16]:

$$18:3 = C/(C+D) = 45.5\%$$
$$18:2 = (B/3 - 4 \times 18:3)/2 = 17.4\%$$
$$18:1 = (A/3 - 4 \times 18:2 - 6 \times 18:1)/2 = 25.1\%$$
$$\text{Saturated} = 1 - 18:3 - 18:2 - 18:1 = 12.0\%$$

Peak A are from the alkene protons only found in UFAs; peak B is unique to a methylene group located between two double bonds found in PUFAs; peak C is specific to the methyl group of linolenic acid; peak D all other methyl groups; peaks labeled G are derived from the glycerol backbone common to all storage lipids. Before numerical spectra analysis of Fig. 1, there are a number of qualitative comments that can be made from the ^{1}H NMR spectra. Since

Can. J. Chem. Downloaded from www.nrcresearchpress.com by Xi'an Jiaotong University on 09/19/12
For personal use only.

Fig. 1. [1]H NMR spectra of AC McDuff raw and cooked flax bolls at different developmental stages.

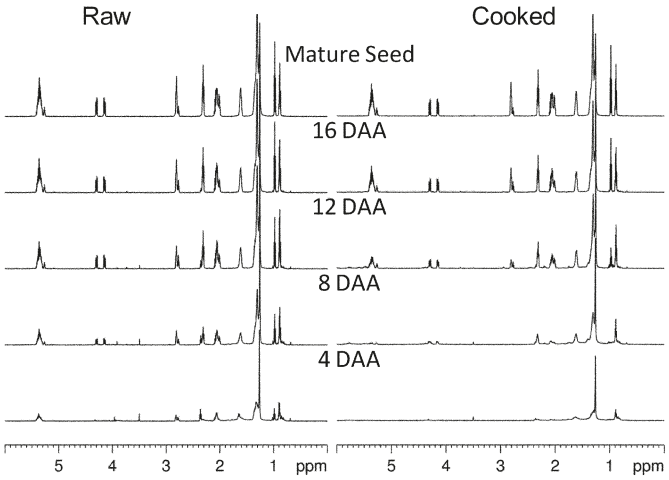

Fig. 2. Method of analysis of FA distribution from a [1]H NMR spectrum. The ratio of peaks C and D give the relative amount of 18:3 in the sample. This information and peak B give the relative amount of 18:2. These two numbers and peak A give the relative amount of 18:1. With these three numbers, the amount of SFAs is the remainder.

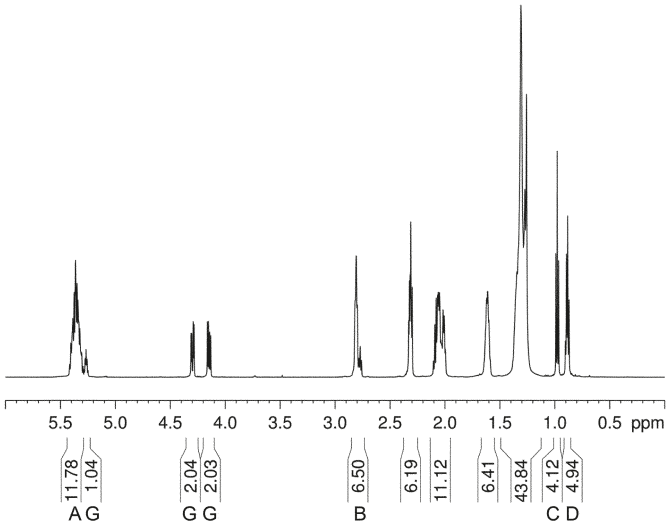

peak C is only found in omega-3 FAs, it is observed that at early stages of development there is only a small amount of 18:3. As the flax matures, a greater amount of 18:3 is present. In a similar way, peak B from PUFAs is small at early stages and is larger in relative abundance as the seed develops. These observations are in agreement with those made by Fofana et al. who reported an increased FAD2 (fatty acid desaturase 2) desaturation activity after 8 DAA leading to 18:2 which is immediately converted into 18:3 by FAD3 (fatty acid desaturase 3) activity.[33] Peaks G also grow in relative intensity as the seed develops. Thus, there are more free FAs at early stages of development and most FAs are stored as triacylglycerol esters in later stages of development which agrees with other literature reports.[34]

The FA distribution of the raw flax samples can be determined as described by Knothe and Kenar.[16] The results of the uncooked samples are given in Table 1. Even at early stages of development, there is a greater amount of UFAs than SFAs and the PUFA are two-thirds of the UFAs. As the flax boll develops, the amount PUFAs continues to increase though there is little difference between 16 DAA and mature seed. However, the amount of linolenic and linoleic acids favor the omega-3 FA in mature seed. The relative amount of SFAs continues to decrease as the flax develops until it is only ~12% in mature seed.

As described above, the flax samples were also cooked. The right side of Fig. 1 shows the [1]H NMR spectra of the cooked samples. At early stages of boll development, the cooking process almost completely degraded the UFAs (peaks A, B, and C are obliterated) that are present in the raw samples. At 12 DAA, some degradation of UFAs was observed, but at later stages of development and mature seed, the cooking process has very little effect on the FA distribution. There is a significant amount of glycerol signals (the G peaks) in 12 DAA and more developed flax bolls as compared to the earlier developmental stages. FAs are typically stored as glycerol esters in plants, which appears to provide protection from heat, at least for the conditions used in this study.

In the baking industry, flax is used both as whole seed as well as ground into a meal. In as much, a comparison of cooking the seed and the meal was done and the methyl group region of the NMR spectra are seen in Fig. 3. From a qualitative point of view, there does not appear to be any degradation in either the whole seed or the meal. Comparison of the oil distribution of raw and cooked flax bolls, seed, and meal is summarized in Table 1. There is very little UFA left (15% or less) after the cooking process at early stages in development. At 12 DAA there is a significant loss (over 50%) of PUFAs when comparing cooked and raw, however, there is still over 50% UFAs. In later stages of development, there are only minor effects on the FA distribution between cooking and raw. The greatest effect seen in 16 DAA bolls was the relative amount of 18:2 (loss of 3.7%) and 18:1 (increase of 3.8%). The seed products, both whole and meal, have very little effect of the FA profiles under the cooking conditions used here.

Recently a new [1]H NMR method has been described to study FA profiles which requires less data manipulation than that used in the current study.[17] This recent method uses the fact that in commercial edible oils the FAs are stored as triacylglycerols. The glycerol peak at 4.27 ppm is used as an internal standard to determine the levels of the different FAs. However, since we were interested in FAs during flax boll development, and the FAs are not all esterified to glycerols in a storage form at early stages as shown by the [1]H NMR spectra, the [1]H NMR analysis method we used[16] was the preferred method. Indeed, by comparing the [1]H NMR analysis method used here and the more recent method on the mature flax seed, where all the FAs are stored as triacylglycerols, the same results were obtained within a 1% error margin.

Using [1]H NMR in nutritional labeling of edible oils has recently been proposed. Labeling on nutritional labels in numerous districts require the amounts of total fats (i.e., FAs) saturated fats, and trans fats be labeled. In edible oil products like margarines, mono-unsaturated and poly-unsaturated (both omega-3 and omega-6) are also included on the nutri-

Can. J. Chem. Downloaded from www.nrcresearchpress.com by Xi'an Jiaotong University on 09/19/12
For personal use only.

Table 1. Fatty acid content in developing AC McDuff flax bolls, seed, and meal before and following a cooking treatment as determined by ^{1}H NMR.

	18:3	18:2	18:1	Saturated
4 DAA Raw	28.0% (0.5)	9.9% (2.6)	17.9% (2.8)	44.2% (1.0)
4 DAA Cooked	0.4% (0.4)	1.5% (0.7)	10.1% (2.0)	88.0% (2.5)
8 DAA Raw	34.5% (0.3)	11.9% (1.6)	23.0% (0.6)	30.6% (1.1)
8 DAA Cooked	2.3% (0.8)	1.1% (0.6)	10.9% (2.3)	85.7% (2.1)
12 DAA Raw	37.0% (0.3)	12.6% (0.8)	27.0% (0.4)	23.5% (0.6)
12 DAA Cooked	17.8% (1.3)	5.0% (2.8)	31.3% (0.4)	45.9% (3.6)
16 DAA Raw	40.5% (0.9)	22.0% (0.9)	16.5% (0.8)	21.0% (0.8)
16 DAA Cooked	39.1% (0.4)	18.3% (2.2)	20.3% (1.1)	22.3% (0.8)
Raw Seed	45.3% (0.2)	17.2% (0.7)	25.2% (0.7)	12.3% (0.4)
Cooked Seed	44.3% (0.5)	17.0% (0.5)	25.9% (0.7)	12.8% (0.5)
Raw Meal	45.2% (0.3)	16.2% (0.6)	26.8% (0.6)	11.8% (0.3)
Cooked Meal	45.0% (0.3)	16.2% (0.4)	27.0% (0.5)	11.8% (1.6)

Note: The oil percentage is given as a mean of triplicate samples. The errors given in parenthesis are one standard deviation from the mean.

Fig. 3. Comparison of the methyl regions of the ^{1}H NMR spectra of flax seed vs. flax meal with and without a cooking treatment.

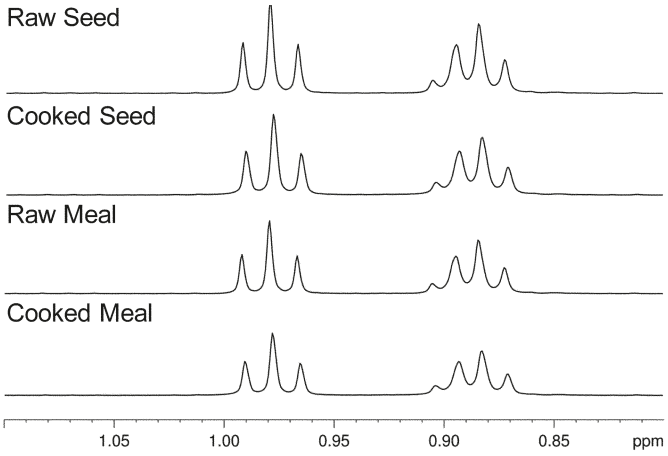

Fig. 4. Comparison of the chemical shift region of the ^{1}H NMR spectra of 12 DAA bolls raw and cooked where trans FAs would be observed if any were present.

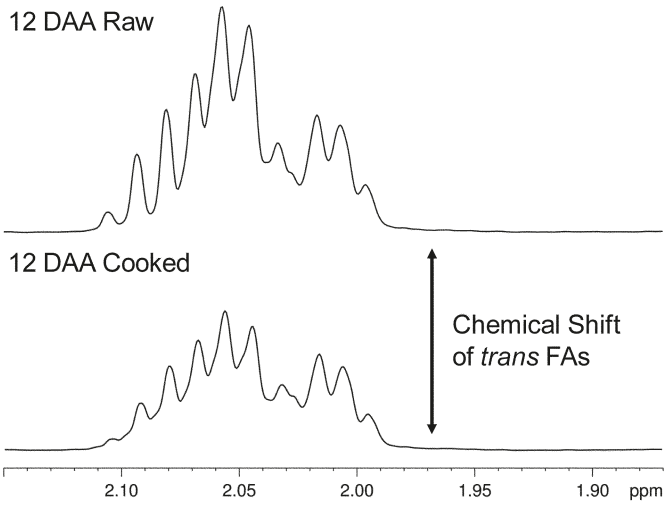

tional labels. One reason for using NMR in labeling is that trans FAs can be determined readily and quickly from a quick inspection of an ^{1}H NMR spectrum of an edible oil. Though the GC is the standard method for looking at FA distributions (including trans FAs), NMR is non-destructive and ^{1}H NMR is faster to acquire than GC methods. The cooking treatment of the bolls and seed performed in this study did not result in conversion of cis to trans FAs. Figure 4 shows an expansion of the region of the ^{1}H NMR spectrum for the 12 DAA raw and cooked bolls and no trans FAs was observed. Thus the cooking process applied here did not convert the cis FAs into trans FAs. Recently, Fofana et al.[35] have suggested the use of developing flax bolls as a fresh vegetable and the discovery that the FAs found in flax bolls do not convert from cis to trans under thermal stress adds credence to this possibility.

In this study, we did not use 90° pulses or long delay times that are usually found in quantitative NMR studies. When using 30° pulses vs. 90° pulses one can use shorter delays in particular when the number of scans is low (16 in this study) since only 50% of the magnetization gets into the x-y plane. That being said, it does introduce a small error based on previously measured T_1s in oils.[17] When we compared delay times of 4.65 s (acquisition time of 2.65 s plus 2 s delay time), 10 s, and 20 s, we found that there was a very small error in the integrals between the shorter delay times, and no difference for delays longer than 10 s. In our lab we are trying to develop rapid methodologies for the determination of metabolites in plant extracts, thus we decided to use the shorter delay time. The integration error from using shorter delay times, which when put into the equations to calculate the relative amounts of the oils, was found to be less than the error from the triplicate samples.

Conclusions

This study allowed us to determine the FA profiles of developing flax bolls of AC McDuff using a ^{1}H NMR method. As AC McDuff flax bolls develop, the relative amounts of UFAs and PUFAs increase as compared to saturated FAs. Cooking the flax bolls had little effect on FA profiles at later stages of development as consequence of their esterification to glycerol into the triacylglycerol storage form. In contrast, the cooking process had a major impact on the FA profile at early stages where, when the triacylglycerol forms are minimal. The heating process did not lead to any conversion of

cis to trans FAs at any stage in this study. These finding could have a high impact if flax bolls have to be used as a steamed vegetable.

Acknowledgements

The authors gratefully acknowledge David Main and Lloyd Kerry at the Crops and Livestock Research Centre (AAFC-Charlottetown) for their technical assistance. This research was funded by Agriculture and Agri-Food Canada through a grant allocated to BF and CK. This manuscript is in an issue dedicated to Professor Rod Wasylishen. Rod introduced CK to NMR and has had a significant impact on his career for which he is grateful.

References

(1) Hasler, C. M.; Kundrat, S.; Wool, D. *Curr. Atheroscler. Rep.* **2000** *2* (6), 467. doi:10.1007/s11883-000-0045-9.
(2) Watkins, B. A.; Devitt, A. A.; Feng, S. *World Rev. Nutr. Diet.* **2001** *90*, 162. doi:10.1159/000059814.
(3) Lemay, A.; Dodin, S.; Kadri, N.; Jacques, H.; Forest, J. C. *Obstet. Gynecol.* **2002** *100* (3), 495. doi:10.1016/S0029-7844(02)02123-3.
(4) Ogborn, M. R.; Nitschmann, E.; Bankovic-Calic, N.; Weiler, H. A.; Aukema, H. *Lipids* **2002** *37* (11), 1059. doi:10.1007/s11745-002-1001-4.
(5) Dodin, S.; Lemay, A.; Jacques, H.; Legare, F.; Forest, J. C.; Masse, B. *J. Clin. Endocrinol. Metab.* **2005** *90* (3), 1390. doi:10.1210/jc.2004-1148.
(6) Hyvärinen, H. K.; Pihlava, J.-M.; Hiidenhovi, J. A.; Hietaniemi, V.; Korhonen, H. J.; Ryhänen, E.-L. *J. Agric. Food Chem.* **2006** *54* (1), 48. doi:10.1021/jf0507590.
(7) Spence, J. D.; Thornton, T.; Muir, A. D.; Westcott, N. D. *J. Am. Coll. Nutr.* **2003** *22* (6), 494.
(8) Fofana, B.; Ragupathy, R.; Cloutier, S. *Flax Lipids: Classes, biosynthesis, genetics and the promise of applied genomics for understanding and altering of fatty acid*s; In *Lipids: Categories, Biological Functions and Metabolism, Nutrition, and Health*; Gilmore, P. L., Ed.; Nova Science Publishers, Inc., 2009; pp. 71.
(9) Dodin, S.; Cunnane, S. C.; Masse, B.; Lemay, A.; Jacques, H.; Asselin, G.; Tremblay-Mercier, J.; Marc, I.; Lamarche, B.; Legare, F.; Forest, J. C. *Nutrition* **2008** *24* (1), 23.
(10) Muir, A. D.; Westcott, N. D. *J. Agric. Food Chem.* **2000** *48* (9), 4048. doi:10.1021/jf990922p.
(11) Łukaszewicz, M.; Szopa, J.; Krasowska, A. *Food Chem.* **2004** *88* (2), 225. doi:10.1016/j.foodchem.2003.12.042.
(12) Hall, C. A., III; Manthey, F. A.; Lee, R. E.; Niehaus, M. *J. Food Sci.* **2005** *70* (8), c483. doi:10.1111/j.1365-2621.2005.tb11505.x.
(13) Jacobsen, N. E. *NMR Spectroscopy Explained: Simplified Theory, Applications and Examples for Organic Chemistry and Structural Biology*; John Wiley & Sons, Inc.: NJ, 2007.
(14) van der Kooy, F.; Maltese, F.; Choi, Y. H.; Kim, H. K.; Verpoorte, R. *Planta Med.* **2009** *75* (7), 763. doi:10.1055/s-0029-1185450.
(15) Kim, H. K.; Choi, Y. H.; Verpoorte, R. *Nat. Protoc.* **2010** *5* (3), 536. doi:10.1038/nprot.2009.237.
(16) Knothe, G.; Kenar, J. A. *Eur. J. Lipid Sci. Technol.* **2004** *106* (2), 88. doi:10.1002/ejlt.200300880.
(17) Barison, A.; da Silva, C. W.; Campos, F. R.; Simonelli, F.; Lenz, C. A.; Ferreira, A. G. *Magn. Reson. Chem.* **2010** *48* (8), 642.
(18) Sacchi, R.; Medina, I.; Aubourg, S. P.; Addeo, F.; Paolillo, L. *J. Am. Oil Chem. Soc.* **1993** *70* (3), 225. doi:10.1007/BF02545299.
(19) Aursand, M.; Rainuzzo, J. R.; Grasdalen, H. *J. Am. Oil Chem. Soc.* **1993** *70* (10), 971. doi:10.1007/BF02543023.
(20) Tyl, C. E.; Brecker, L.; Wagner, K. H. *Eur. J. Lipid Sci. Technol.* **2008** *110* (2), 141. doi:10.1002/ejlt.200700150.
(21) Igarashi, T.; Aursand, M.; Hirata, Y.; Gribbestad, I. S.; Wada, S.; Nonaka, M. *J. Am. Oil Chem. Soc.* **2000** *77* (7), 737. doi:10.1007/s11746-000-0119-0.
(22) Sacco, A.; Brescia, M. A.; Liuzzi, V.; Reniero, F.; Guillou, C.; Ghelli, S.; van der Meer, P. *J. Am. Oil Chem. Soc.* **2000** *77* (6), 619. doi:10.1007/s11746-000-0100-y.
(23) Fauhl, C.; Reniero, F.; Guillou, C. *Magn. Reson. Chem.* **2000** *38* (6), 436. doi:10.1002/1097-458X(200006)38:6<436::AID-MRC672>3.0.CO;2-X.
(24) Guillén, M. D.; Ruiz, A. *Eur. J. Lipid Sci. Technol.* **2005** *107* (1), 36. doi:10.1002/ejlt.200401056.
(25) Guillén, M. D.; Ruiz, A. *J. Sci. Food Agric.* **2005** *85* (14), 2413. doi:10.1002/jsfa.2273.
(26) Falch, E.; Anthonsen, H. W.; Axelson, D. E.; Aursand, M. *J. Am. Oil Chem. Soc.* **2004** *81* (12), 1105. doi:10.1007/s11746-004-1025-1.
(27) Guillén, M. D.; Ruiz, A. *Trends Food Sci. Technol.* **2001** *12* (9), 328. doi:10.1016/S0924-2244(01)00101-7.
(28) Guillén, M.; Ruiz, A. *J. Sci. Food Agric.* **2003** *83* (4), 338. doi:10.1002/jsfa.1317.
(29) Guillén, M. D.; Ruiz, A.; Cabo, N.; Chirinos, R.; Pascual, G. *J. Am. Oil Chem. Soc.* **2003** *80* (8), 755. doi:10.1007/s11746-003-0768-z.
(30) Sedman, J.; Gao, L.; Garcia Gonzalez, D.; Ehsan, S.; van de Voort, F. R. *Eur. J. Lipid Sci. Technol.* **2010** *112* (4), 439. doi:10.1002/ejlt.200900185.
(31) A. O. C. S. Official Methods Ce 1–62, A. O. C. S., Il USA.
(32) McKillican, M. E.; Sims, R. P. A. *J. Am. Oil Chem. Soc.* **1963** *40* (3), 108. doi:10.1007/BF02640701.
(33) Fofana, B.; Cloutier, S.; Duguid, S.; Ching, J.; Rampitsch, C. *Lipids* **2006** *41* (7), 705. doi:10.1007/s11745-006-5021-x.
(34) Ohlrogge, J. B.; Jaworski, J. G. *Annu. Rev. Plant Physiol. Plant Mol. Biol.* **1997** *48* (1), 109. doi:10.1146/annurev.arplant.48.1.109.
(35) Fofana, B.; Cloutier, S.; Kirby, C. W.; McCallum, J.; Duguid, S. *Food Res. Int.* **2011** *44*, 2459. doi:10.1016/j.foodres.2010.12.018.

Can. J. Chem. Downloaded from www.nrcresearchpress.com by Xi'an Jiaotong University on 09/19/12
For personal use only.

^{129}Xe and ^{2}H nuclear magnetic resonance (NMR) of xenon and deuterated-chloroform solutes in a thermotropic biaxial nematic liquid crystal

P. Tallavaara, A.M. Kantola, J. Jokisaari, T. Meyer, D.A. Wilson, and G.H. Mehl

Can. J. Chem. Downloaded from www.nrcresearchpress.com by Xi'an Jiaotong University on 09/19/12
For personal use only.

Abstract: Properties of a thermotropic nematic liquid crystal (LC) TM35 (organosiloxane tetrapode) were investigated by means of nuclear magnetic resonance (NMR) spectroscopy of probe atoms and molecules. ^{129}Xe isotope enriched xenon gas and ^{2}H isotope enriched chloroform were used as probes. Both ^{129}Xe and ^{2}H NMR measurements were carried out over a wide temperature range, covering isotropic, nematic, and glass phases. A clear change in the behavior of the LC is observed within the nematic phase at 289 K by changing the temperature from low to high and inspecting the spectral line width. The derivative curve of the ^{129}Xe chemical shift also reveals a change at 289 K. These changes may be an indication of hindered molecular rotation around the long axis, and the appearance of a biaxial nematic phase.

Key words: liquid crystal, biaxiality, xenon, chloroform, nuclear magnetic resonance (NMR).

Résumé : Faisant appel à la spectroscopie résonance magnétique nucléaire (RMN) d'atomes et de molécules cibles, on a étudié les propriétés du cristal liquide (CL) nématique thermotrope TM35 (organosiloxane tétrapode). Du xénon gazeux enrichi en isotope ^{129}Xe et du chloroforme enrichi en isotope ^{2}H ont été utilisés comme sondes. Les mesures de RMN du ^{129}Xe et du ^{2}H ont toutes été effectuées sur une large plage de températures couvrant les phases isotropes, nématiques et vitreuses. On observe un changement net dans le comportement du cristal liquide dans la phase nématique, à 289 K, lors du changement de température vers les températures élevées et par l'examen de la largeur de raie de la bande. La courbe dérivée du déplacement chimique du ^{129}Xe révèle aussi un changement à 289 K. Ces changements peuvent être une indication du fait qu'il existerait un empêchement à la rotation moléculaire autour de l'axe long ainsi que l'apparition d'une phase nématique biaxiale.

Mots-clés : cristal liquide, caractère biaxial, xénon, chloroforme, résonance magnétique nucléaire (RMN).

[Traduit par la Rédaction]

Introduction

The foundation of many flat-screen liquid crystal displays (LCD) is based on thermotropic uniaxial nematic (N_u) liquid crystals.[1,2] However, for example, the functionality of displays could be remarkably improved if biaxial nematic (N_b) liquid crystals were available. In fact, the first prediction of the existence of the thermotropic biaxial nematic liquid crystal was already made in 1970.[3] Biaxial nematic liquid crystals possess two directors usually marked by *n* and *m*; *n* is the same as in the uniaxial case, but *m* is the director of the secondary molecular alignment. It is predicted that the *m* responds to an electric field much faster than *n*. The response time is expected to be even 100 times faster.[4] In addition, the electric field needed for the director reorientation is estimated to be much smaller than in the case of a uniaxial nematic liquid crystal, which means a smaller power consumption by the system. Therefore, biaxial nematics have acquired a lot of theoretical as well as experimental efforts throughout the last couple of decades.

The nematic biaxiality has been observed in both lyotropic[5] and polymeric[6] liquid crystals. For thermotropic liquid crystals, however, the biaxiality has remained elusive. Many claims of the foundation of this missing phase have been proven to be wrong or at least questionable by ^{2}H nuclear magnetic resonance (NMR) spectroscopy, which is widely believed to prove whether or not biaxiality is present.[7] In this method, a fully or partially deuterated probe molecule is dissolved into the studied environment. This method has been applied to boomerang-shaped liquid crystal molecules and the results indicated small biaxiality.[8] Recently, apart from ^{2}H NMR, ^{13}C NMR was also used to investigate the biaxial phase in a V-shaped mesogen.[9] A significant breakthrough happened when it was discovered that a ^{131}Xe second-order quadrupole shift could be used to distinguish between uniaxial and biaxial nematic phases.[10] A great advantage of

Received 31 December 2010. Accepted 2 March 2011. Published at www.nrcresearchpress.com/cjc on 18 August 2011.

P. Tallavaara, A. Kantola, and J. Jokisaari. NMR Research Group, Department of Physics, University of Oulu, P.O. Box 3000, FI-90014 University of Oulu, Finland.
T. Meyer, D. Wilson, and G. Mehl. Department of Chemistry, University of Hull, Cottingham Road, Hull HU6 7RX, United Kingdom.

Corresponding author: J. Jokisaari (e-mail: Jukka.Jokisaari@oulu.fi).

This article is part of a Special Issue dedicated to Professor Roderick E. Wasylishen.

Can. J. Chem. Downloaded from www.nrcresearchpress.com by Xi'an Jiaotong University on 09/19/12
For personal use only.

this method is that the information is obtained from a static sample, i.e., no sample rotation is needed. ^{2}H NMR spectroscopy,[8,11–13] X-ray diffraction (XRD),[4,14,15] adiabatic and different scanning calorimetries (ASC and DSC),[4,16] polarizing optical microscopy (POM),[4,8,14,17] infrared absorbance,[17] dynamic light scattering,[18] and theoretical and computational studies[19–23] have proven that biaxiality arises mainly from the structure of the liquid crystal molecules. In order for a liquid crystal molecule to possess a biaxial nematic phase, its structure must deviate from cylindrical symmetry. This means that the molecule should be shaped as a boomerang[4,8,14] or a lozenge.[11,12,17,18] Another possibility is to mix rod- and disk-shaped molecules.[20,24,25] The most essential thing is that the rotation of molecules is hindered, which gives an opportunity for biaxiality to develop. In addition, the biaxial nematic phase occurs at a lower temperature than the uniaxial one. Furthermore, the phase transition from biaxial nematic to uniaxial nematic is predicted to be of the second order, whereas transition from the nematic uniaxial to isotropic phase is of the first order.[26]

In this study, we present the results derived from static ^{129}Xe and ^{2}H NMR experiments of xenon gas and chloroform dissolved into the plate-shaped organosiloxane tetrapode (TM35), which has earlier been reported to form a thermotropic biaxial nematic phase (see Fig. 1).[11,12,16] ^{129}Xe NMR has proven to be a particularly applicable approach to derive physical properties of thermotropic liquid crystals.[27–30] This method immediately reveals the sign of the anisotropy of the diamagnetic susceptibility tensor and phase transitions when spectra are taken over a sufficiently wide temperature range. Furthermore, it makes feasible the derivation of order parameters (both orientational and positional ones) in nematic and smectic A phases, and together with these, the temperature dependence of the tilt angle in smectic C and C* phases.[31] Since the ^{129}Xe chemical shift is proportional to the density, information may be obtained on this property and thus on the isobaric thermal expansion coefficient.

The molecular structure of the liquid crystal used, TM35, is shown in Fig. 1 and it is reported to posses the following four phases: glass, biaxial nematic (N_b), uniaxial nematic (N_u), and isotropic (I). All phases, especially the biaxial one, occur close to room temperature, which makes experimental measurements and possible forthcoming applications easier to perform.

Experimental

All the studied samples were prepared in standard Wilmad NMR capillary tubes (outer diameter 3.3 mm, inner diameter 2.3 mm). The liquid-crystalline compound TM35 was first placed inside the capillary tube and degassed by several heating and cooling periods while the sample tube was simultaneously attached to the vacuum line. After degassing, about 2 atm (1 atm = 101.325 kPa) of ^{129}Xe isotope enriched xenon gas (enrichment 85%, Spectra Gases, NJ, USA) was added and the sample tube was sealed by a flame. It is estimated that the concentration of xenon was about 1 mol%. Finally, temperature durability of the sample was tested in an oven and the capillary tube was placed inside a thin-walled 5 mm NMR sample tube (outer diameter 5 mm, inner diameter 4.24 mm) with spacers. The space between the two tubes

Fig. 1. The molecular structure of the organosiloxane tetrapode (TM35) used as a medium in the present study. The phase transition temperatures reported for the bulk liquid crystal are shown below the structure.[12] The nematic phase (N) may consist of both uniaxial and biaxial phases. T_g = glass phase. I = isotropic phase.

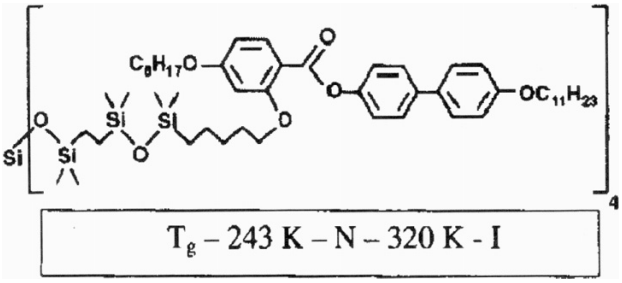

was filled with deuterated acetonitrile (CD_3CN; 99%, Stohler Isotope Chemicals, NJ, USA) and it was used as a lock substance. The sample in which deuterated chloroform ($CDCl_3$; 99.8%, MSO Isotopes, Montreal, Canada) was used as a probe was prepared in a different way. No degassing process was performed but the sample tube was directly sealed with epoxy glue and heat tested. The concentration of $CDCl_3$ was about 10 mol%. In this case, cyclohexane (C_6H_{12}; Merck, Darmstadt, Germany) was used as a substance between the sample tubes to ease shimming. Standard 1D NMR measurements were performed mainly on a Bruker Avance DRX 500 NMR spectrometer equipped with a 5 mm high-resolution BBI probe head and BVT2000 variable temperature controller. In measurements performed below room temperature, liquid nitrogen cooling was used. The sample temperatures were calibrated at the lowest and highest points of the temperature series using standard temperature calibration samples.[32] The temperature series was measured using a step of 1 K. The temperature stabilization time between experiments was 10–15 min.

Results and discussion

Figure 2 shows ^{129}Xe NMR spectra at variable temperatures from the static sample containing ^{129}Xe isotope enriched xenon gas and TM35 liquid crystal. In the isotropic state, the chemical shift changes linearly as a function of temperature, which is a consequence of the linear behavior of the density, as will be discussed below. At the transition from the isotropic to nematic phase, the chemical shift increases abruptly by about 5 ppm. From 314 to 265 K, the chemical shift behaves as it usually does in uniaxial nematic phases.[33] Obviously, the sample supercools and transforms directly from the uniaxial nematic state to a glassy state.

Figure 3 shows static ^{129}Xe NMR spectra from the same sample as those in Fig. 2. However, now the temperature series was measured from 206 K to 327 K with a step of 1 K. At the lowest temperatures no signal is seen. The most likely reason for this is that liquid crystal is frozen and xenon atoms are mostly squeezed out from the crystallized medium. Part of the xenon atoms may be captured inside the solid medium but their NMR line width is so broad that it does not stand out from the background.

As the temperature increases to about 233 K, a broad signal emerges from the background. The reason for this observation is not evident and needs further investigation. Such a

Fig. 2. Static ^{129}Xe NMR spectra from ^{129}Xe isotope enriched xenon gas in TM35. The measurements were performed by cooling the sample from the isotropic to solid phase in steps of 1 K. The small distortion at 299 K results from tuning the probe head.

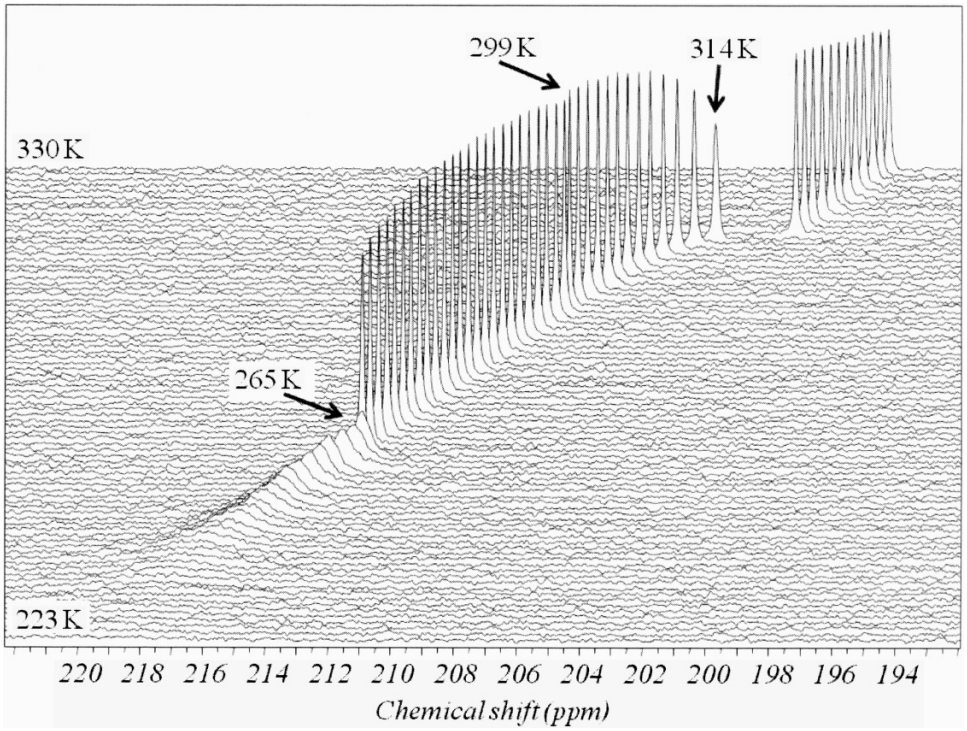

Fig. 3. Static ^{129}Xe NMR spectra from the sample containing liquid crystal TM35 and ^{129}Xe isotope enriched xenon gas. The measurements were performed by heating the sample from the solid to isotropic phase in steps of 1 K.

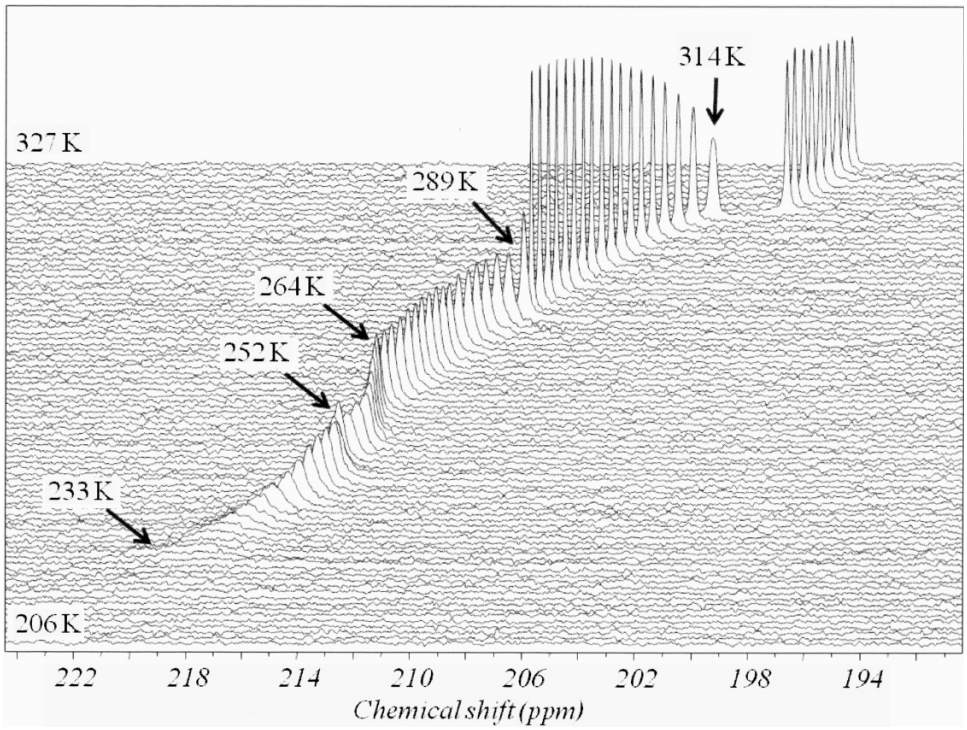

phenomenon has been found in many liquid-crystalline substances when the sample is frozen in liquid nitrogen.[34]

The transition from the uniaxial nematic (N_u) to isotropic (I) phase takes place at the same temperature as when changing temperature in the reversed order. Apart from this transition there is another transition at 289 K, which does not appear in Fig. 2. This is clearly seen as an abrupt change in the line width. The broad lines below 289 K may indicate

Can. J. Chem. Downloaded from www.nrcresearchpress.com by Xi'an Jiaotong University on 09/19/12
For personal use only.

Can. J. Chem. Downloaded from www.nrcresearchpress.com by Xi'an Jiaotong University on 09/19/12
For personal use only.

Table 1. Results of the least-squares fit of eq. [2] to the experimental ^{129}Xe chemical shifts in the isotropic and uniaxial nematic phases of TM35. Note that shielding (σ) has been replaced by chemical shift (δ). The latter is opposite in sign to the former.

Phase and parameter	Parameter value
T_o = nematic–isotropic transition temperature	315.0 K
Isotropic phase	
δ_d^o	196.78 ppm[a]
τ_1	$10.0 \cdot 10^{-4}$ 1/K
Uniaxial nematic phase	
$\Delta\delta_d^o$	13.85 ppm
τ_1	$3.8 \cdot 10^{-4}$ 1/K
τ_2	$8.0 \cdot 10^{-4}$ 1/K
y	0.998[b]
z	0.25

[a]With respect to an arbitrary external reference. Because the possible small density jump at the nematic–isotropic phase transition was neglected, this value is the same for the isotropic and nematic phases.
[b]Kept fixed.

Fig. 4. ^{129}Xe chemical shift as a function of temperature for xenon in TM35. Experimental shifts are indicated by diamonds. The sample was heated from the solid to isotropic phase in steps of 1 K. The solid line is a result of least-squares fits of eq. [2] to experimental points in the isotropic and uniaxial nematic phase. The inset shows a narrower temperature range that reveals the difference in chemical shift between extrapolated uniaxial behavior (solid curve) and experimental points below 289 K.

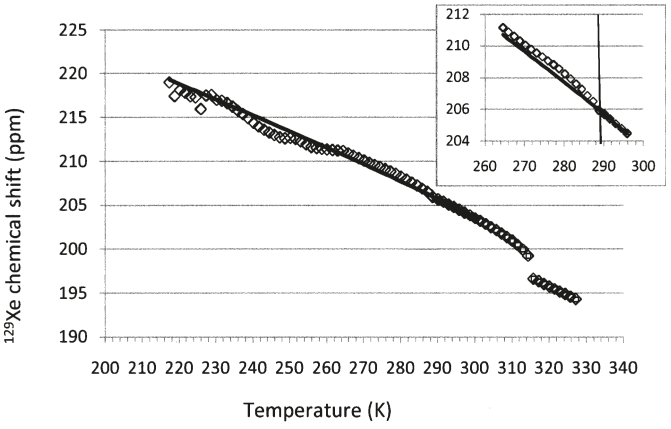

that the rotation of liquid crystal molecules around their long axes is more hindered than above 289 K. This could be regarded as a signature of a biaxial nematic phase (N_b).

Earlier NMR experiments of xenon in various uniaxial thermotropic nematic liquid crystals have indicated that the ^{129}Xe shielding is extremely sensitive to even very subtle changes in the environment of xenon. This is due to the strongly polarizable electron cloud of the atom. One observation is that the chemical shift (nuclear shielding) changes abruptly at the nematic–isotropic phase transition, and the direction of the change reveals the sign of the anisotropy of the diamagnetic susceptibility tensor of the liquid crystals. Thus, if the chemical shift decreases (shielding increases) when moving from the nematic to isotropic phase, as it does in the present case, it indicates that the sign of the anisotropy is positive and the liquid crystal director orients along the external magnetic field.

Fig. 5. Line width (full width at half -height (fwhh)) of the ^{129}Xe resonance line as a function of temperature for xenon in TM35. The vertical lines show the transition temperatures. The temperature was changed from low to high. Cr = crystal.

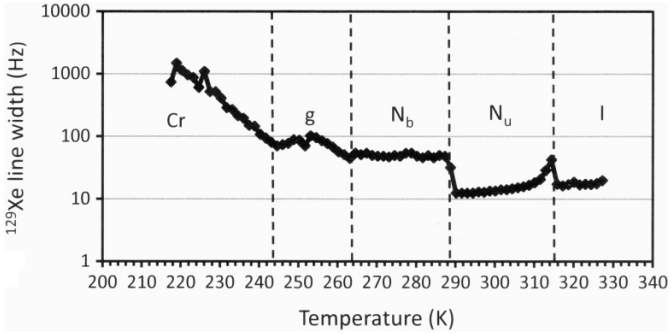

Fig. 6. Absolute derivate of the experimental ^{129}Xe chemical shift curve.

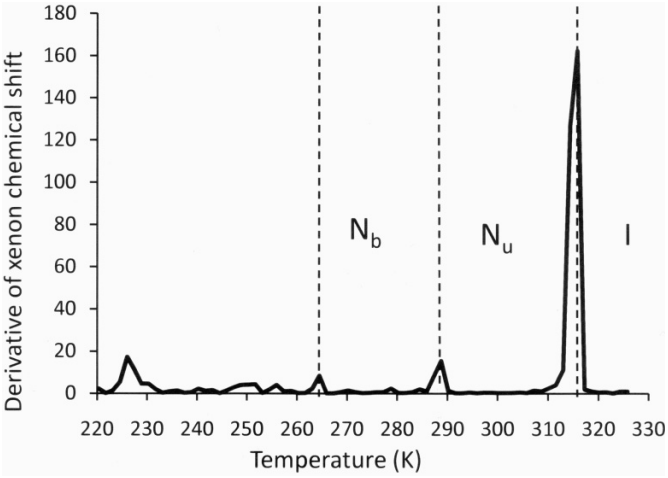

It has been shown that the ^{129}Xe shielding in a uniaxial nematic phase is proportional to the liquid crystal density, $\rho(T)$, and that both the isotropic average of the shielding tensor and its anisotropy are dependent on temperature. These temperature dependencies can be approximated to be linear and are described by the coefficients ε_1 and ε_2, as shown in eq. [1]:[35]

$$[1] \quad \sigma(T) - \sigma_o = \rho(T)\left[\sigma'_d\left(1 - \varepsilon_1(T - T_o)\right) + \frac{2}{3}\Delta\sigma'_d\left(1 - \varepsilon_2(T - T_o)\right)S(T)\right]$$

Here, σ_o is the shielding constant of a reference, σ'_d and $\Delta\sigma'_d$ are the shielding constant and shielding anisotropy, respectively, in units ppm·cm^3/g at T_o, which is a reference temperature. T_o was chosen to be the uniaxial nematic–isotropic phase transition temperature. $S(T)$ is the orientational order parameter of the LC. The temperature dependence of density can be approximated by a linear function, $\rho(T) = \rho_o[1 - \alpha(T - T_o)]$, where α is the isobaric thermal expansion coefficient and ρ_o is density at T_o. In the first-order (in T) approximation (both α and ε's are small), eq. [1] leads to

Fig. 7. Static ^{2}H NMR spectra of the sample containing $CDCl_3$ and TM35 as a function of temperature. (Left) Spectra were taken with cooling the sample from isotropic phase. (Right) The sample was first frozen in liquid nitrogen and then moved to the magnet. The small peak at zero Hz arises from cyclohexane in the annulus of the double tube system.

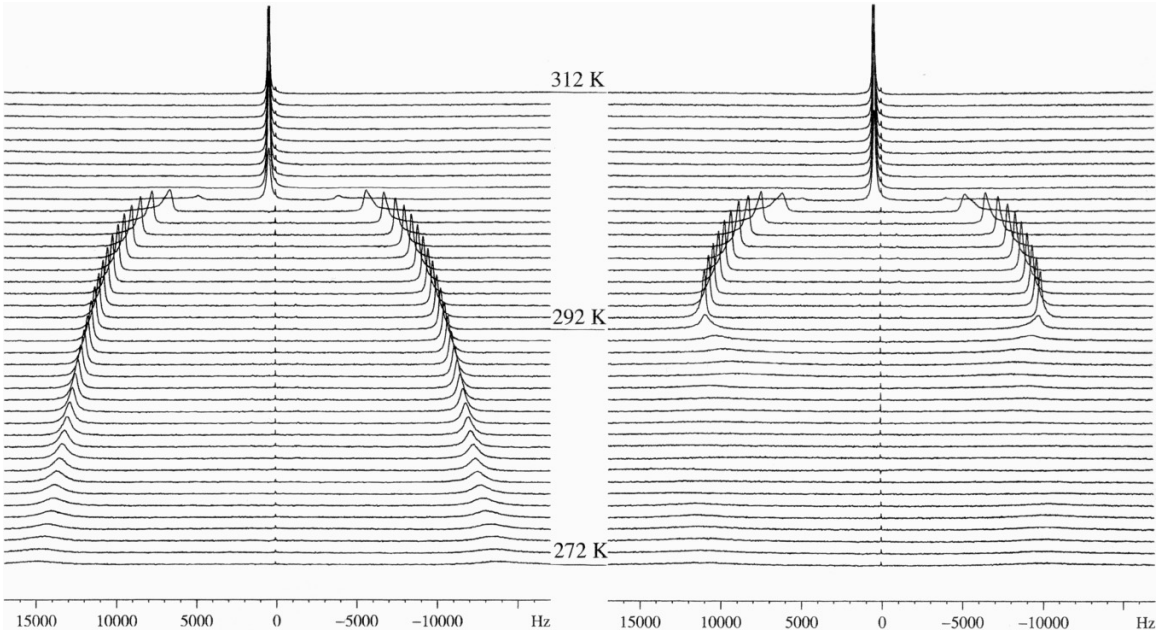

$$[2] \qquad \sigma(T) - \sigma_o = \sigma_d^o[1 - \tau_1(T - T_o)] + \frac{2}{3}\Delta\sigma_d^o[1 - \tau_2(T - T_o)]S(T)$$

where $\sigma_d^o = \rho_o\sigma_d'$ and $\Delta\sigma_d^o = \rho_o\Delta\sigma_d'$ are the shielding constant and shielding anisotropy in ppm, respectively, at the reference temperature, $\tau_1 = \alpha^{iso} + \varepsilon_1{}^{iso}$, and $\tau_2 = \alpha^{nem} + \varepsilon_2{}^{nem}$. One should note that τ_1 and τ_2 may be and usually are different in isotropic and liquid-crystalline phases. $S(T)$ can be modeled with the so-called Haller function:[36]

$$[3] \qquad S(T) = \left(1 - y\frac{T}{T_o}\right)^z$$

where y and z are adjustable parameters. One should emphasize that eq. [2] omits the effect of bulk susceptibility and the possible density change at the nematic–isotropic phase transition. This is well justified as is shown below.

The bulk susceptibility effect, σ_b, on the shielding is[35]

$$[4] \qquad \sigma_b = -\frac{1}{3}\left[\chi_d + \frac{2}{3}\Delta\chi_d S(T)\right]\frac{\rho}{M}$$

where χ_d is the isotropic part and $\Delta\chi_d$ the anisotropy of the molecular susceptibility tensor, ρ is density, and M is the molar mass (3447.23 g/mol for TM35) of the LC. Diamagnetic susceptibility of thermotropic nematogens is of the order of -10^{-9} m^3/mol, and the anisotropy of susceptibility is of the same order, the sign being positive in the present case. The density of TM35 is not known but if we use 2 Si-*n*O-CB[37] as a model system then $\rho \sim 1.2$ g/cm^3. When these typical values, together with the molar mass of TM35, are used, the bulk susceptibility effect is on average below 0.1 ppm, and thus can be omitted without an effect on the conclusions.

When evaluating the effect of a possible density change at the nematic–isotropic phase transition, we are forced to again use typical values, which are below 1%.[37,38] This is a relatively small effect and it causes only a parallel shift in the chemical shift curve without affecting the general trend.

Least-squares fits to the experimental chemical shift data in the isotropic ($S(T) = 0$ in the isotropic phase) and uniaxial nematic phase produce the parameter values shown in Table 1. Experimental and calculated chemical shifts are shown in Fig. 4. The behavior of the chemical shift in the uniaxial nematic phase was extrapolated to lower temperatures as well. Figure 4 shows that the experimental curve goes systematically above the extrapolated curve. Obviously, the slight deviation between experimental and extrapolated shift values from 289 K to lower temperatures gives a hint of a liquid crystal phase transition, which is seen as a change in line width in Fig. 3. As eq. [2] shows, ^{129}Xe shielding (chemical shift) depends on many factors. The small change detected may arise from a slight change in density and (or) orientational order parameter or transformation of the cylindrically symmetric macroscopic orientational order tensor to a biaxial one. The density change affects both isotropic shielding and shielding anisotropy, whereas the latter two contribute only to the anisotropic part of the shielding.

However, a much more pronounced change at 289 K is seen in the line broadening than in the chemical shift (see Figs. 3 and 5). An intriguing observation, however, is that the line broadening cannot be detected at 289 K when changing the temperature from high to low.

The phase transitions derived from the ^{129}Xe chemicals shifts become more clearly visible in the derivative curve shown in Fig. 6 than in the chemical shift curve in Fig. 4. The curve displayed in Fig. 6 was obtained by the numerical derivation method of three points, which is valid in cases where the abscissa values are equally spaced.[39] The peaks in Fig. 6 appear (from the left) at 226.0, 264.5, 288.7, and 315.8 K. They are supposed to be signatures of the following

Can. J. Chem. Downloaded from www.nrcresearchpress.com by Xi'an Jiaotong University on 09/19/12
For personal use only.

Can. J. Chem. Downloaded from www.nrcresearchpress.com by Xi'an Jiaotong University on 09/19/12
For personal use only.

phase transitions: Cr – 226.0 K – T_g – 264.5 K – N_b – 288.7 K – N_u – 315.8 K – I.

Apart from the ^{129}Xe chemical shifts at variable temperatures, ^{129}Xe resonance line widths were determined as well. They are shown in Fig. 5, which reveals significant changes at ~315 K, the I–N_u transition, and 289 K, supposedly the N_u–N_b transition. The broadening at the isotropic–uniaxial nematic transition is a generally observed phenomenon, reflecting slight orientational order distribution in the nematic phase at temperatures close to the phase transition temperature. It can also be seen that there is a steep increase in the line width from ~243 K towards the lower temperatures. This is the temperature reported earlier for the glass–nematic phase transition. The derivative curve in Fig. 6 does not, however, reveal any transition at this temperature. Interestingly, the line width remains practically constant with a temperature range of 265–289 K.

Apart from ^{129}Xe NMR, ^{2}H NMR experiments were carried out as well, from a sample in which deuterated chloroform ($CDCl_3$) was used as a probe in TM35. In this case, measurements were performed in the same way as in the ^{129}Xe studies described above, i.e., from high to low and from low to high temperature. The stack plots are shown in Fig. 7.

Because the relative amount of chloroform in the sample was higher than that of xenon, the I– N_u phase transition temperature has shifted to ~12 K below the value observed in the ^{129}Xe studies (315 K). Otherwise, results are quite comparable. Namely, the transition at 289 K detected in ^{129}Xe NMR seems to be completely absent when the sample temperature is decreased from the isotropic phase but it develops when the temperature is increased from the solid phase. A phase transition takes place at 291–292 K, which is close to that in xenon studies (289 K).

Conclusions

Static ^{129}Xe NMR of xenon gas and ^{2}H NMR of $CDCl_3$ were applied to study the behavior of the thermotropic liquid crystal TM35, which has been found to display a biaxial nematic phase. The results indicate that the two probes are sensitive detectors of different phases and phase transitions of the liquid crystal. Both ^{129}Xe and ^{2}H NMR experiments reveal consistent results and indicate a phase transition at 289–291 K if experiments are performed by heating the sample from the solid state. Experiments carried out from static samples do not, however, reveal direct evidence of whether a nematic phase is uniaxial or biaxial. The transition detected is most likely a transition from the biaxial to uniaxial nematic phase. Decisive experiments are under development.

Acknowledgements

The authors are grateful to the Academy of Finland (Grant No. 116824) for financial support. P.T. acknowledges the grants from the Oskar Öflund Foundation, the Emil Aaltonen Foundation, and the Oulu University Scholarship Foundation.

References

(1) Luckhurst, G. R. *Nature* **2004**, *430* (6998), 413. doi:10.1038/430413a.

(2) Luckhurst, G. R. *Thin Solid Films* **2001**, *393* (1–2), 40. doi:10.1016/S0040-6090(01)01091-4.

(3) Freiser, M. J. *Phys. Rev. Lett.* **1970**, *24* (19), 1041. doi:10.1103/PhysRevLett.24.1041.

(4) Prasad, V.; Kang, S.-W.; Suresh, K. A.; Joshi, L.; Wang, Q.; Kumar, S. *J. Am. Chem. Soc.* **2005**, *127* (49), 17224. doi:10.1021/ja052769n.

(5) Yu, L. J.; Saupe, A. *Phys. Rev. Lett.* **1980**, *45* (12), 1000. doi:10.1103/PhysRevLett.45.1000.

(6) Severing, K.; Saalwächter, K. *Phys. Rev. Lett.* **2004**, *92* (12), 125501. doi:10.1103/PhysRevLett.92.125501.

(7) Praefcke, K.; Blunk, D.; Singer, D.; Goodby, J. W.; Toyne, K. J.; Hird, M.; Styring, P.; Norbert, W. D. J. A. *Mol. Cryst. Liq. Cryst.* **1998**, *323* (1), 231. doi:10.1080/10587259808048444.

(8) Madsen, L. A.; Dingemans, T. J.; Nakata, M.; Samulski, E. T. *Phys. Rev. Lett.* **2004**, *92* (14), 145505. doi:10.1103/PhysRevLett.92.145505.

(9) Figueirinhas, J. L.; Feio, G.; Cruz, C.; Lehmann, M.; Köhn, C.; Dong, R. Y. *J. Chem. Phys.* **2010**, *133* (17), 174509. doi:10.1063/1.3496491.

(10) Jokisaari, J.; Kantola, A. M.; Lounila, J.; Ingman, P. *Phys. Rev. Lett.* **2011**, *106* (1), 017801. doi:10.1103/PhysRevLett.106.017801.

(11) Figueirinhas, J. L.; Cruz, C.; Filip, D.; Feio, G.; Ribeiro, A. C.; Frère, Y.; Meyer, T.; Mehl, G. H. *Phys. Rev. Lett.* **2005**, *94* (10), 107802. doi:10.1103/PhysRevLett.94.107802.

(12) Cruz, C.; Figueirinhas, J. L.; Filip, D.; Feio, G.; Ribeiro, A. C.; Frère, Y.; Meyer, T.; Mehl, G. H. *Phys. Rev. E* **2008**, *78* (5), 051702. doi:10.1103/PhysRevE.78.051702.

(13) Fan, S. M.; Fletcher, I. D.; Gündōan, B.; Heaton, N. J.; Kothe, G.; Luckhurst, G. R.; Praefcke, K. *Chem. Phys. Lett.* **1993**, *204* (5–6), 517. doi:10.1016/0009-2614(93)89196-O.

(14) Acharya, B. R.; Primak, A.; Kumar, S. *Phys. Rev. Lett.* **2004**, *92* (14), 145506. doi:10.1103/PhysRevLett.92.145506.

(15) Francescangeli, O.; Samulski, E. T. *Soft Matter* **2010**, *6* (11), 2413. doi:10.1039/c003310c.

(16) Cordoyiannis, G.; Apreutesei, D.; Mehl, G. H.; Glorieux, C.; Thoen, J. *Phys. Rev. E* **2008**, *78* (1), 011708. doi:10.1103/PhysRevE.78.011708.

(17) Merkel, K.; Kocot, A.; Vij, J. K.; Korlacki, R.; Mehl, G. H.; Meyer, T. *Phys. Rev. Lett.* **2004**, *93* (23), 237801. doi:10.1103/PhysRevLett.93.237801.

(18) Neupane, K.; Kang, S. W.; Sharma, S.; Carney, D.; Meyer, T.; Mehl, G. H.; Allender, D. W.; Kumar, S.; Sprunt, S. *Phys. Rev. Lett.* **2006**, *97* (20), 207802. doi:10.1103/PhysRevLett.97.207802.

(19) Peláez, J.; Wilson, M. R. *Phys. Rev. Lett.* **2006**, *97* (26), 267801. doi:10.1103/PhysRevLett.97.267801.

(20) Cuetos, A.; Galindo, A.; Jackson, G. *Phys. Rev. Lett.* **2008**, *101* (23), 237802. doi:10.1103/PhysRevLett.101.237802.

(21) De Matteis, G.; Virga, E. G. *Phys. Rev. E* **2005**, *71* (6), 061703. doi:10.1103/PhysRevE.71.061703.

(22) Mettout, B.; Tolédano, P.; Takezoe, H.; Watanabe, J. *Phys. Rev. E* **2002**, *66* (3), 031701. doi:10.1103/PhysRevE.66.031701.

(23) Shih, C.-S.; Alben, R. *J. Chem. Phys.* **1972**, *57* (8), 3055. doi:10.1063/1.1678719.

(24) Stroobants, A.; Lekkerkerker, H. N. W. *J. Phys. Chem.* **1984**, *88* (16), 3669. doi:10.1021/j150660a058.

(25) Wensink, H. H.; Vroege, G. J.; Lekkerkerker, H. N. W. *Phys. Rev. E* **2002**, *66* (4), 041704. doi:10.1103/PhysRevE.66.041704.

(26) See, for example, Wedler, W. In *Handbook of Liquid Crystals. Fundamentals;* Demus, D., Goodby, J., Gray, G. W., Spiess, H.-W., Vill, V., Eds.; Wiley & Sons: New York, 1998; Vol. 1, p 381.

(27) Raftery, D. *Annu. Rep. NMR Spectrosc.* **2006**, *57*, 205. doi:10.1016/S0066-4103(05)57005-4.
(28) Jokisaari, J. *Prog. Nucl. Magn. Reson. Spectrosc.* **1994**, *26* (Part 1), 1. doi:10.1016/0079-6565(94)80002-2.
(29) Jokisaari, J. In *NMR of Ordered Liquids;* Burnell, E.E., de Lange, C.A., Eds.; Kluwer Academic Publishers: Norwell, MA, 2003.
(30) Jokisaari, J. In *Nuclear Magnetic Resonance Spectroscopy of Liquid Crystals;* Dong, R. Y., Ed.; World Scientific: River Edge, NJ, 2009.
(31) Lounila, J.; Muenster, O.; Jokisaari, J.; Diehl, P. *J. Chem. Phys.* **1992**, *97* (12), 8977. doi:10.1063/1.463324.
(32) Van Geet, A. L. *Anal. Chem.* **1968**, *40* (14), 2227. doi:10.1021/ac50158a064.
(33) Jokisaari, J.; Diehl, P. *Liq. Cryst.* **1990**, *7* (5), 739. doi:10.1080/02678299008036755.
(34) Kekkonen, P. *Physics Research Project.* Department of Physics, University of Oulu, Finland, 2007.
(35) Ylihautala, M.; Lounila, J.; Jokisaari, J. *J. Chem. Phys.* **1999**, *110* (13), 6381. doi:10.1063/1.478541.
(36) Haller, I. *Prog. Solid State Chem.* **1975** (Part 2), *10*, 103. doi:10.1016/0079-6786(75)90008-4.
(37) Ibn-Elhaj, M.; Coles, H. J.; Guillon, D.; Skoulios, A. *J. Phys. II* **1993**, *3* (12), 1807. doi:10.1051/jp2:1993231.
(38) See, for example, Wedler, W. In *Handbook of Liquid Crystals. Fundamentals;* Demus, D., Goodby, J., Gray, G.W., Spiess, H.-W., Vill, V., Eds.; Wiley & Sons: New York, 1998; Vol. 1, p 334.
(39) See, for example, Abramowitz, M., Stegun, I., Eds. *Handbook of Mathematical Functions;* Dover Publications: Mineola, NY, 1965.

Can. J. Chem. Downloaded from www.nrcresearchpress.com by Xi'an Jiaotong University on 09/19/12
For personal use only.

An improved scheme for the calculation of NMR chemical shifts in periodic systems based on gauge including atomic orbitals and density functional theory

Dmitry Skachkov, Mykhaylo Krykunov, and Tom Ziegler

Can. J. Chem. Downloaded from www.nrcresearchpress.com by Xi'an Jiaotong University on 09/19/12
For personal use only.

Abstract: We report here on an improved first principles method that can determine NMR shielding tensors for periodic systems. Our scheme evaluates the shielding tensor as the second derivative of the total electronic energy with respect to a nuclear magnetic moment and an external magnetic field. Both the induced current density $\boldsymbol{J}^{(\alpha)}$ due to the first perturbation from the nuclear magnetic moment as well as the interaction of $\boldsymbol{J}^{(\alpha)}$ with the second perturbation in the form of an external magnetic field are evaluated analytically. Our approach is based on Kohn–Sham density functional theory and gauge-including atomic orbitals. It employs a Bloch basis set made up of Slater-type or numeric atomic orbitals and represents the Kohn–Sham potential fully without the use of effective core potentials. The method is implemented into the periodic program BAND. The new scheme represents an improvement over a previously proposed method in that use can be made of the zero-order Kohn–Sham orbitals from a calculation based on a primitive cell instead of a supercell. Further, $\boldsymbol{J}^{(\alpha)}$ is evaluated analytically rather than by a finite difference approach. The improvements reduce the required computational time by up to two orders of magnitude for three-dimensional systems. Such a reduction is made possible by the fact that we are using atomic centered basis functions. The new implementation is further able to take into account scalar relativistic effects within the zero-order regular approximation. Results from calculations of NMR shielding constants based on the present approach are presented for systems with one-, two-, and three-dimensional periodicity. The reported values are compared to experiment and results from the previously proposed scheme.

Key words: periodic NMR calculations, shielding current, diamagnetic and paramagnetic shielding tensors.

Résumé : On rapporte une méthode améliorée basée sur des principes premiers qui permet de déterminer les tenseurs de blindage de RMN pour des systèmes périodiques. Le schéma évalue le tenseur de blindage comme deuxième dérivée de l'énergie électronique totale par rapport à un moment magnétique nucléaire et un champ magnétique externe. La densité de courant induite, $\boldsymbol{J}^{(\alpha)}$, due à la première perturbation provoquée par le moment magnétique nucléaire ainsi que l'interaction de $\boldsymbol{J}^{(\alpha)}$ avec la deuxième perturbation dans la forme d'un champ magnétique externe sont toutes les deux évaluées d'une façon analytique. Cette approche est basée sur la théorie de la fonctionnelle de la densité de Kohn–Sham et sur des orbitales atomiques comportant une jauge. Cette méthode a été réalisée à l'aide du programme périodique BAND. Ce nouveau schéma représente une amélioration sur la méthode proposée antérieurement par le fait qu'il peut être utilisé dans des orbitales de Kohn–Sham d'ordre zéro à partir d'un calcul effectué à partir d'une cellule primitive plutôt que d'une supercellule. De plus, $\boldsymbol{J}^{(\alpha)}$ est évalué d'une façon analytique plutôt que par une approche de différence finie. Les améliorations réduisent les temps de calculs requis par un facteur allant jusqu'à deux ordres de grandeur pour les systèmes tridimensionnels. Cette réduction est rendue possible par le fait qu'on utilise des fonctions de base centrées sur les atomes. Avec la nouvelle approche, il est aussi possible de prendre en compte des effets relativistes scalaires à l'intérieur de l'approximation régulière d'ordre zéro. On présente des résultats de calculs de constantes de blindage en RMN effectués en utilisant la nouvelle approche pour des systèmes avec des périodicités mono-, bi- et tridimensionnelles. Les résultats de ces calculs sont comparés avec des résultats expérimentaux et des résultats obtenus à l'aide du schéma proposé antérieurement.

[Traduit par la Rédaction]

Introduction

Solid-state NMR is an active experimental field of research, and NMR is used extensively to monitor the local electronic structure around a nucleus in a periodic solid. In recent years, it has furtherbeen possible to evaluate NMR shielding tensors from first principles[1–8] with a number of computational schemes that serve as useful supplements to the experimental techniques.

Theoretically, the shielding tensor is the second derivative

Received 10 December 2010. Accepted 18 February 2011. Published at www.nrcresearchpress.com/cjc on 02 September 2011.

D. Skachkov, M. Krykunov, and T. Ziegler. Department of Chemistry, University of Calgary, Calgary, AB T2N 1N4, Canada.

Corresponding author: Tom Ziegler (e-mail: ziegler@ucalgary.ca).

This article is part of a Special Issue dedicated to Professor Roderick E. Wasylishen.

Can. J. Chem. Downloaded from www.nrcresearchpress.com by Xi'an Jiaotong University on 09/19/12
For personal use only.

of the total electronic energy with respect to an external magnetic field and a nuclear magnetic moment. In most theoretical treatments the external magnetic field is introduced as the initial perturbation, inducing a current density with which the second responding perturbation in the form of the nuclear magnetic dipole interacts. Virtually all molecular NMR codes treat the two perturbations in this order, as does the recent periodic gauge-including projector augmented-wave (GIPAW) method developed by Mauri et al.,[2,3] in which the external magnetic field further is considered as oscillating to adopt to the periodic symmetry of the solid. It is also possible in a converse picture to consider the nuclear magnetic moment as the first perturbation inducing a current density $\boldsymbol{J}^{(\alpha)}$ with which the external magnetic field $\boldsymbol{B}$ as the second responding perturbation interacts. The converse approach has been introduced by Thonhauser et al.[4,5] in conjunction with GIPAW corrections and supercell techniques. It has the advantage, in the case of systems with translational symmetry, that the first perturbation due to the magnetic dipole can be considered periodic if a supercell approach is adopted. However, due considerations must still be given to the description of the interaction between $\boldsymbol{J}^{(\alpha)}$ and the nonperiodic constant external magnetic field $\boldsymbol{B}$. Sebastiani and co-authors[6] applied an infinitesimal magnetic field and employed localized Wannier orbitals constructed from plane waves with a continuous set of gauge transformations (CSGT).[7] To obtain sufficiently localized Wannier functions, Sebastiani too employed a supercell technique. All three implementations mentioned above make use of pseudo-potentials and plane waves.

We have recently developed a method[8] for the calculation of NMR chemical shifts in periodic systems within the full potential program BAND,[9,10] in which use is made of atom-centered basis functions. In BAND, the Bloch basis set is constructed from Slater-type orbitals (STOs) and (or) numeric atomic orbitals (NAOs). The electronic density matrix near the nuclei is very important for NMR shielding, and both STOs and NAOs potentially afford an accurate description of the Kohn–Sham (KS) orbitals in this region. Atomic centered basis functions allow further for the use of gauge-included atomic orbitals (GIAOs) to ensure gauge invariant results. The calculation of other magnetic properties (EPR g- and A-tensors) has also been implemented in BAND.[11,12]

Our recently developed method[8] makes use of a supercell outside which the current density $\boldsymbol{J}^{(\alpha)}$ induced by the nuclear magnetic moment of our probe atom N falls off to zero. Further, in this approach the field-free unperturbed KS equation was solved with the supercell as the periodic unit to obtain a zero-order basis for the subsequent perturbation treatment that determines $\boldsymbol{J}^{(\alpha)}$. Such a procedure can be costly, since a supercell typically consists of five or more primitive cells. We shall now show that one can equally well make use of a zero-order basis determined by solving the field-free KS equation, with a primitive cell as the periodic unit followed by an analytic perturbation treatment involving a large supercell that includes the whole crystal. In this way the computational cost can be reduced by two orders of magnitude for 3D systems. We shall further introduce relativistic effects by adopting the scalar zero-order regular approximation (ZORA).[13,14]

We introduce in the next section our new method for calculating the NMR chemical shift in periodic systems based on atom-centered basis functions, with the computational details characteristic for BAND discussed in the following section. We have tested our new implementation on single molecules, diatomic chains, as well as one-dimensional polymers, two-dimensional sheets, and three-dimensional crystals. In the Results and discussion section we compare with experiment and other computational methods, as well as results from our previous scheme.

NMR shielding tensor in periodic systems

For a periodic system, the NMR shielding tensor $\hat{\sigma}^{\mathrm{N}}$ of nuclei N is the second derivative of the total electronic energy:

$$[1] \qquad \sigma^{\mathrm{N}}_{\alpha\beta} = \left.\frac{\partial^2 E(\boldsymbol{B}, \boldsymbol{\mu}^{\mathrm{N}})}{\partial \mu^{\mathrm{N}}_{\alpha} \partial B_{\beta}}\right|_{\substack{\boldsymbol{B}=0 \\ \boldsymbol{\mu}^{\mathrm{N}}=0}}$$

with respect to Cartesian components of the magnetic moment $\boldsymbol{\mu}^{\mathrm{N}}$ and the external magnetic field $\boldsymbol{B}$, respectively.

To calculate the second derivative of the total electronic energy, we follow the procedure by Gauss[15] and write the expression for the energy Lagrangian with the usual orthonormality constraint:

$$[2] \qquad \tilde{E} = \int \mathrm{d}\boldsymbol{k} \sum_i n_i \langle \Psi_{ik} | \boldsymbol{h} | \Psi_{ik} \rangle + \frac{1}{2} \int \mathrm{d}\boldsymbol{k} \sum_i n_i \langle \Psi_{ik} | V_{\mathrm{C}} | \Psi_{ik} \rangle + E_{\mathrm{XC}}[\rho] - \int \mathrm{d}\boldsymbol{k} \sum_i \varepsilon_{ij} n_i (\langle \Psi_{ik} | \Psi_{jk} \rangle - \delta_{ij})$$

Here, the integration over $\boldsymbol{k}$-space is introduced, E_{XC} is the exchange-correlation energy,[16], and $\boldsymbol{h}$ is given by:

$$[3] \qquad \boldsymbol{h} = \frac{K}{2}\boldsymbol{p}^2 + V_{\mathrm{NUC}} + \frac{K}{c}\boldsymbol{A}^{(\mu^{\mathrm{N}})}\boldsymbol{p} + \frac{K}{c}\boldsymbol{A}^{(B)}\boldsymbol{p} + \frac{K}{c^2}\boldsymbol{A}^{(\mu^{\mathrm{N}})}\boldsymbol{A}^{(B)}$$

contains within the scalar ZORA approximation,[13,14] the sum of the operators for the electronic kinetic energy, and the electron–nuclear attraction plus the magnetic vector potentials for the constant magnetic field,

$$[4] \qquad \boldsymbol{A}^{(B)} = \frac{1}{2}[\boldsymbol{B} \times \boldsymbol{r}]$$

and the nuclear magnetic moment of N,

$$[5] \qquad \boldsymbol{A}^{(\mu^{\mathrm{N}})}(\boldsymbol{r}) = \frac{[\boldsymbol{\mu}^{\mathrm{N}} \times (\boldsymbol{r} - \boldsymbol{R}_{\mathrm{N}})]}{|\boldsymbol{r} - \boldsymbol{R}_{\mathrm{N}}|^3}$$

where $\boldsymbol{R}_{\mathrm{N}}$ is the position of the probe atom N. We shall denote the last three (magnetic) terms in the definition of $\boldsymbol{h}$ as $\boldsymbol{h}^1$. Further, the auxiliary Kohn–Sham orbitals $\Psi_i^{(0)}$ are eigenfunctions to the set of equations:

$$[6] \qquad \boldsymbol{h}^0_{\mathrm{KS}} \Psi_i^{(0)} = \varepsilon_i^{(0)} \Psi_i^{(0)}$$

where the Kohn–Sham operator in the scalar ZORA formulation has the form:

$$[7] \qquad \boldsymbol{h}^0_{\mathrm{KS}} = \frac{K}{2}\boldsymbol{p}^2 + V^{\mathrm{KS}}$$
$$V^{\mathrm{KS}} = V_{\mathrm{XC}} + V_{\mathrm{NUC}} + V_{\mathrm{C}}$$

Can. J. Chem. Downloaded from www.nrcresearchpress.com by Xi'an Jiaotong University on 09/19/12
For personal use only.

Here V^{KS} is the effective Kohn–Sham potential, which is made up of an exchange-correlation potential V_{XC} accounting for many-body effects, an attractive potential due to nuclei V_{NUC}, and a classical electron repulsion potential V_C. The ZORA relativistic K factor is introduced as,

$$[8] \qquad K = \frac{1}{1 - V^{KS\prime}(\boldsymbol{r})/2c^2}$$

where $V^{KS\prime}$ is the model KS potential as in the molecular scalar ZORA implementation.[13,14] Finally $\varepsilon_i^{(0)}$ is an eigenvalue to eq. [6], with the eigenfunction $\Psi_i^{(0)}$ and occupation number n_i.

To obtain solutions to eq. [6] for periodic systems, the Kohn–Sham orbitals are expanded in terms of a complex Bloch basis set $\phi_{\mu k}$:

$$[9] \qquad \Psi_{ik}(\boldsymbol{r}) = \sum_{\mu} c_{\mu ik}\phi_{\mu k}(\boldsymbol{r})$$

where $\phi_{\mu k}$ is calculated as a Bloch sum of equivalent atomic orbitals $\phi_\mu(\boldsymbol{r} - \boldsymbol{R}_\mu - \boldsymbol{T})$ separated by the crystal vector $\boldsymbol{T}$ and centered on $\boldsymbol{R}_\mu + \boldsymbol{T}$:

$$[10] \qquad \phi_{\mu k}(\boldsymbol{r}) \equiv \phi_{\mu k}(\boldsymbol{r} - \boldsymbol{R}_\mu) = \sum_{\boldsymbol{T}} \phi_\mu(\boldsymbol{r} - \boldsymbol{R}_\mu - \boldsymbol{T}) e^{i\boldsymbol{k}(\boldsymbol{R}_\mu + \boldsymbol{T})}$$

To avoid gauge problems due to the use of a finite atomic basis set, we employ gauge-including atomic orbitals.[17] In this case the Bloch basis set $\phi_{\mu k}$ depends on the magnetic field $\boldsymbol{B}$:

$$[11] \qquad \phi_{\mu k}(\boldsymbol{r})^{GIAO} = \phi_{\mu k}(\boldsymbol{r}) e^{-(i/2c)([\boldsymbol{B}\times\boldsymbol{R}_\mu]\boldsymbol{r})}$$

For the second derivative we have the following expression[15,18]:

$$[12] \qquad \frac{d^2\widetilde{E}}{d\boldsymbol{B}d\boldsymbol{\mu}^N} = \int d\boldsymbol{k} \left\{ \sum_{\mu\nu} P_{\mu\nu k} \frac{\partial^2 h_{\mu\nu k}}{\partial \boldsymbol{B}\partial\boldsymbol{\mu}^N} + \frac{\partial P_{\mu\nu k}}{\partial \boldsymbol{\mu}^N} \frac{\partial h_{\mu\nu k}}{\partial \boldsymbol{B}} + \frac{\partial P_{\mu\nu k}}{\partial \boldsymbol{\mu}_N} \left[\left\langle \frac{\partial \phi_{\mu k}}{\partial \boldsymbol{B}} \middle| V_C + V_{XC} \middle| \phi_{\nu k} \right\rangle + \left\langle \phi_{\mu k} \middle| V_C + V_{XC} \middle| \frac{\partial \phi_{\nu k}}{\partial \boldsymbol{B}} \right\rangle \right] - \frac{\partial W_{\mu\nu k}}{\partial \boldsymbol{\mu}_N} \frac{\partial S_{\mu\nu k}}{\partial \boldsymbol{B}} \right\}$$

where we use the following definitions:

$$V_{XC} = \frac{\partial E_{XC}[\rho]}{\partial \rho} \qquad \text{is the exchange} - \text{correlation potential}$$

$$P_{\mu\nu k} = \sum_i n_i c^*_{\mu ik} c_{\nu ik} \qquad \text{is the density} P - \text{matrix}$$

$$W_{\mu\nu k} = \sum_i n_i c^*_{\mu ik} \varepsilon_{ik} c_{\nu ik} \qquad \text{is the energy} - \text{weighted } P \text{ - matrix}$$

$$S_{\mu\nu k} = \langle \phi_{\mu k} | \phi_{\nu k} \rangle \qquad \text{is the overlap matrix}$$

$$h_{\mu\nu k} = \langle \phi_{\mu k} | \boldsymbol{h} | \phi_{\nu k} \rangle$$

The first term in eq. [12] is the diamagnetic part of the shielding tensor, and all the other terms make up the paramagnetic shielding tensor.

The shielding tensor for nuclei N, as defined in eq. [1], is related to the interaction energy $\Delta E_{\alpha\beta}$ between the current density $\boldsymbol{J}^{(\alpha)}$ induced by the nuclear magnetic moment component $\mu_\alpha{}^N$ on N and the external magnetic field component B_β by $\Delta E_{\alpha\beta} = \sigma_{\alpha\beta}\mu_\alpha{}^N B_\beta$.[8] Unfortunately, the perturbation $\boldsymbol{A}^{(\mu^N)}(\boldsymbol{r})$ from the nuclear magnetic moment $\boldsymbol{\mu}^N$ is not periodic. As a consequence, in our previous approach we had to introduce a supercell big enough such that $\boldsymbol{J}^{(\alpha)}$ was negligible outside the cell. We were thus subsequently able to calculate the interaction energy $\Delta E_{\alpha\beta}$ between the induced current density $\boldsymbol{J}^{(\alpha)}$ and the constant magnetic field component B_β by integrating inside the supercell and thus determine $\sigma_{\alpha\beta}{}^N$.

In our previous approach,[8] the field-free KS eq. [6] was solved with the supercell as the periodic unit to obtain a zero-order basis for the subsequent perturbation treatment that would determine $\boldsymbol{J}^{(\alpha)}$ and $\sigma_{\alpha\beta}$. Such a procedure can be costly, since a supercell typically consists of five or more primitive cells. We shall now show that one can equally well make use of a zero-order basis determined by solving the KS equation with a primitive cell as the periodic unit followed by a perturbation treatment involving a large supercell including the entire crystal. To introduce our new procedure, we shall start by discussing the diamagnetic part of the shielding tensor, followed by a treatment of the paramagnetic shielding tensor. In principle, by including the entire crystal in our perturbation treatment we are ensured that $\boldsymbol{J}^{(\alpha)}$ vanishes at the edges of the supercell (crystal). In practice $\boldsymbol{J}^{(\alpha)}$ only has noticeable contributions in the first 20–40 primitive cells surrounding the perturbing nucleus ($\boldsymbol{T} = 0$).[8]

Can. J. Chem. Downloaded from www.nrcresearchpress.com by Xi'an Jiaotong University on 09/19/12
For personal use only.

Diamagnetic tensor

The shielding tensor is defined via the shielding current as,

$$[13] \qquad \sigma^{\mathrm{N}}_{\alpha\beta} = -\int\limits_{\text{crystal}} d\boldsymbol{r}[\boldsymbol{J}^{(\alpha)}(\boldsymbol{r}) \times \boldsymbol{r}]_\beta$$

The first-order change in the diamagnetic shielding current due to the μ^{N}_α perturbation in the local representation is,

$$[14] \qquad \boldsymbol{J}^{\mathrm{d}(\alpha)}(\boldsymbol{r}) = \frac{\partial}{\partial \mu^{\mathrm{N}}_\alpha}\boldsymbol{J}^{\mathrm{d}}(\boldsymbol{r})\bigg|_{\mu^{\mathrm{N}}=0} = \frac{1}{2c}\sum_{i'} n_{i'}\frac{K}{c}\boldsymbol{A}^{(\alpha)}(\boldsymbol{r}-\boldsymbol{R}_{\mathrm{N}})\left|\Psi^{(0)}_{i'}(\boldsymbol{r})\right|^2$$

where

$$[15] \qquad \boldsymbol{A}^{(\alpha)}(\boldsymbol{r}-\boldsymbol{R}_N) = \frac{\partial \boldsymbol{A}^{(\mu^{\mathrm{N}})}(\boldsymbol{r}-\boldsymbol{R}_{\mathrm{N}})}{\partial \mu^{\mathrm{N}}_\alpha}$$

is the derivative of the magnetic vector potential eq. [5] due to single nuclear moment (see Fig. 1).

Using the expansion for KS orbitals,

$$[16] \qquad \Psi_{i'}(\boldsymbol{r}) = \sum_{\mu'} c_{\mu' i'}\,\phi_{\mu'}(\boldsymbol{r})$$

affords

$$[17] \qquad \boldsymbol{J}^{\mathrm{d}(\alpha)}(\boldsymbol{r}) = \frac{1}{2c}\sum_{i'} n_{i'} c^{(0)*}_{\mu' i'} c^{(0)}_{\nu' i'}\frac{K}{c}\boldsymbol{A}^{(\alpha)}(\boldsymbol{r}-\boldsymbol{R}_{\mathrm{N}})\phi^*_{\mu'}(\boldsymbol{r})\phi_{\nu'}(\boldsymbol{r})$$

Using eq. [13] we obtain the diamagnetic shielding tensor in the local representation in the form,

$$[18] \qquad \sigma^{\mathrm{N,d}}_{\alpha\beta} = \frac{1}{2c}\sum_{i'} n_{i'}\sum_{\mu'\nu'} c^{(0)*}_{\mu' i'} c^{(0)}_{\nu' i'}\left\langle \phi_{\mu'}(\boldsymbol{r}-\boldsymbol{R}_{\mu'})\left|\left[\boldsymbol{r}\times\frac{K}{c}\mathbf{A}^{(\alpha)}(\boldsymbol{r}-\boldsymbol{R}_{\mathrm{N}})\right]_\beta\right|\phi_{\nu'}(\boldsymbol{r}-\boldsymbol{R}_{\nu'})\right\rangle$$

The integration in eq. [18] is over the whole crystal. In eq. [18] μ' and ν' numerate the atomic basis functions $\phi_{\mu'}(\boldsymbol{r}-\boldsymbol{R}_{\mu'})$ and $\phi_{\nu'}(\boldsymbol{r}-\boldsymbol{R}_{\nu'})$. Further, $\boldsymbol{R}_{\mu'}$ and $\boldsymbol{R}_{\nu'}$ are the positions of the atoms on which the basis functions are centered in the crystal. We can further write,

$$[19] \qquad \boldsymbol{R}_{\mu'} = \boldsymbol{R}_\mu + \boldsymbol{T}$$

where $\boldsymbol{T}$ is the crystal vector and $\boldsymbol{R}_\mu$ the position of atoms in the central cell of the crystal ($\boldsymbol{T} = 0$).

By using [19] we can rewrite eq. [18] as follows:

$$[20] \qquad \sigma^{\mathrm{N,d}}_{\alpha\beta} = \frac{1}{2c}\sum_{i'} n_{i'}\sum_{\boldsymbol{T}_1\boldsymbol{T}_2}\sum_{\mu\nu} c^{(0)*}_{\mu T_1 i'} c^{(0)}_{\nu T_2 i'}\left\langle \phi_\mu(\boldsymbol{r}-\boldsymbol{R}_\mu-\boldsymbol{T}_1)\left|\left[\boldsymbol{r}\times\frac{K}{c}\boldsymbol{A}^{(\alpha)}(\boldsymbol{r}-\boldsymbol{R}_{\mathrm{N}})\right]_\beta\right|\phi_\nu(\boldsymbol{r}-\boldsymbol{R}_\nu-\boldsymbol{T}_2)\right\rangle$$

To move from the local representation, where the KS orbitals are obtained from eq. [6] with the whole crystal as the periodic unit, to the crystal momentum representation,[19] where eq. [6] is solved with the primitive cell as the periodic unit, we can use the transformation formulas:

$$[21] \qquad c_{\mu T_1 i'} = \left(\frac{\Omega}{(2\pi)^3}\right)^{1/2}\int \mathrm{d}\boldsymbol{k}''\, c_{\mu i k'}\mathrm{e}^{i\boldsymbol{k}''(\boldsymbol{R}_\mu+\boldsymbol{T}_1)}, \qquad c_{\nu T_2 i'} = \left(\frac{\Omega}{(2\pi)^3}\right)^{1/2}\int \mathrm{d}\boldsymbol{k} c_{\nu j k}\mathrm{e}^{i\boldsymbol{k}(\boldsymbol{R}_\nu+\boldsymbol{T}_2)}$$

where Ω is the volume of the primitive cell, $c_{\mu i k'}$ and $c_{\nu j k}$ are the dispersion coefficients.In eq. [21] we consider an infinite crystal. The infinite crystal does not have a central cell, all cells are equal. To calculate NMR shieldings, we take from the crystal a finite region with the central cell containing the atom probed by NMR. Then we tend the size of this region to infinity.

For the non-periodic function $\boldsymbol{A}^{(\alpha)}(\boldsymbol{r}-\boldsymbol{R}_{\mathrm{N}})$ in eq. [20], we use a Fourier transform and expand $\boldsymbol{A}^{(\alpha)}(\boldsymbol{r}-\boldsymbol{R}_{\mathrm{N}}-\boldsymbol{T})$ in terms of periodic harmonics:

$$[22] \qquad \boldsymbol{A}^{(\alpha)}(\boldsymbol{r}-\boldsymbol{R}_{\mathrm{N}}-\boldsymbol{T}) = \int \mathrm{d}\boldsymbol{k}_0 \boldsymbol{A}^{(\alpha)}_{\boldsymbol{k}_0}(\boldsymbol{r}-\boldsymbol{R}_{\mathrm{N}})e^{-i\boldsymbol{k}_0(\boldsymbol{R}_{\mathrm{N}}+\boldsymbol{T})}$$

where

$$[23] \qquad \boldsymbol{A}^{(\alpha)}_{k_0}(\boldsymbol{r}-\boldsymbol{R}_{\mathrm{N}}) = \sum_{\boldsymbol{T}} \boldsymbol{A}^{(\alpha)}(\boldsymbol{r}-\boldsymbol{R}_{\mathrm{N}}-\boldsymbol{T})e^{i\boldsymbol{k}_0(\boldsymbol{R}_{\mathrm{N}}+\boldsymbol{T})}$$

Fig. 1. Model of the crystal with single dipole perturbation.

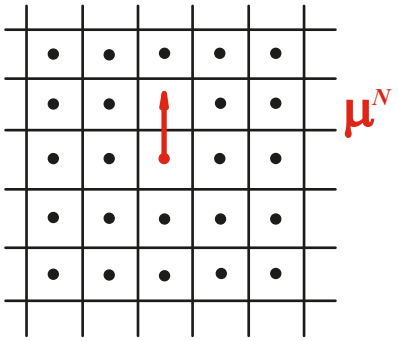

Fig. 2. Central cell and lattice vector.

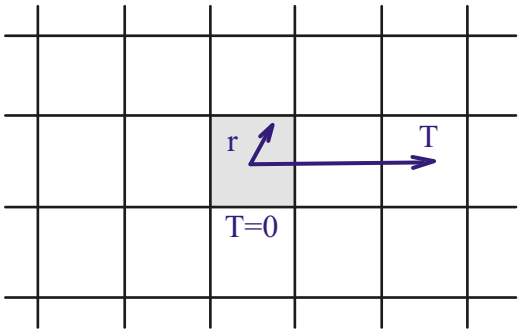

By using eqs. [18], [21], and [22] we have:

$$[24]\qquad \sigma_{\alpha\beta}^{\mathrm{N,d}} = \frac{1}{2c}\sum_{ij} n_i n_j \int \mathrm{d}\boldsymbol{k}'' \int \mathrm{d}\boldsymbol{k} \sum_{\mu\nu} c_{\mu i k''}^{(0)*} c_{\nu j k}^{(0)} \left\langle \phi_{\mu k''} \middle| \left[(\boldsymbol{r} - \boldsymbol{R}_{\mathrm{N}}) \times \frac{K}{c} \boldsymbol{A}_0^{(\alpha)} (\boldsymbol{r} - \boldsymbol{R}_{\mathrm{N}}) \right]_\beta \middle| \phi_{\nu k} \right\rangle$$

where

$$[25]\qquad \boldsymbol{A}_0^{(\alpha)} (\boldsymbol{r} - \boldsymbol{R}_{\mathrm{N}}) = \sum_{\boldsymbol{T}} \boldsymbol{A}^{(\alpha)} (\boldsymbol{r} - \boldsymbol{R}_{\mathrm{N}} - \boldsymbol{T})$$

where $\phi_{\mu k''}$ and $\phi_{\nu k}$ are Bloch functions (eq. [10]). In eq. [24], the integration is performed over the primitive cell, which is centered on $\boldsymbol{R}_{\mathrm{N}}$.

Note that the atomic functions $\phi_\mu(\boldsymbol{r} - \boldsymbol{R}_\mu - \boldsymbol{T}_1)$ with local coefficients $c_{\mu T_1 i'}$ are normalized by integration over the whole crystal, whereas the Bloch functions $\phi_{\mu k''}(\boldsymbol{r} - \boldsymbol{R}_\mu)$ with dispersion coefficients $c_{\mu i k''}$ are normalized within the primitive cell. It should be pointed out that the transformation in eq. [21] is specific to atom centered basis sets.

Using the orthonormality between Bloch functions $\Psi_{ik''}^{(0)}$ and $\Psi_{jk}^{(0)}$, we can reduce the double integration over $\boldsymbol{k}$ and $\boldsymbol{k}''$ in eq. [24] to a single integration (please see Supplementary data for complete derivation):

$$[26]\qquad \sigma_{\alpha\beta}^{\mathrm{N,d}} = \frac{1}{2c}\sum_{i} n_i \int \mathrm{d}\boldsymbol{k} \sum_{\mu\nu} c_{\mu i k}^{(0)*} c_{\nu i k}^{(0)} \left\langle \phi_{\mu k} \middle| \left[(\boldsymbol{r} - \boldsymbol{R}_{\mathrm{N}}) \times \frac{K}{c} \boldsymbol{A}_0^{(\alpha)} (\boldsymbol{r} - \boldsymbol{R}_{\mathrm{N}}) \right]_\beta \middle| \phi_{\nu k} \right\rangle$$

The diamagnetic current with GIAO corrections reads, according to eq. [18] of ref. [8] as,

$$[27]\qquad \boldsymbol{J}^{\mathrm{d}(\alpha)\mathrm{GIAO}}(\boldsymbol{r}) = \frac{1}{2c}\sum_{i'} n_{i'} \sum_{\mu'\nu'} c_{\mu' i'}^{(0)*} c_{\nu' i'}^{(0)} \frac{K}{c} \{ \phi_{\mu'}^*(\boldsymbol{r}) \boldsymbol{A}^{(\alpha)} \phi_{\nu'}(\boldsymbol{r}) + \boldsymbol{R}_{\mu'} \phi_{\mu'}^*(\boldsymbol{r}) \boldsymbol{A}^{(\alpha)} \cdot \nabla \phi_{\nu'}(\boldsymbol{r}) - \phi_{\mu'}^*(\boldsymbol{r}) \boldsymbol{A}^{(\alpha)} \cdot \nabla \left(\boldsymbol{R}_{\nu'} \phi_{\nu'}(\boldsymbol{r}) \right) \}$$

in the local representation. We have eliminated the integration over $\boldsymbol{k}$-space from eq. [18] of ref. 8, since we do not need any dispersion when we use the entire crystal as a supercell rather than n primitive cells where $n < 100$.

Using transformation in eq. [21], we will have the GIAO diamagnetic current in the crystal momentum representation,

$$[28]\qquad \boldsymbol{J}^{\mathrm{d}(\alpha)\mathrm{GIAO}}(\boldsymbol{r} - \boldsymbol{R}_{\mathrm{N}}, \boldsymbol{T}) = \frac{1}{2c} \int \mathrm{d}\boldsymbol{k}_0 \int \mathrm{d}\boldsymbol{k} \sum_i n_i \sum_{\mu\nu} c_{\mu i k}^{(0)*} c_{\nu i k}^{(0)} \frac{K}{c}$$
$$\times \left\{ \phi_{\mu k}^*(\boldsymbol{r})\, \boldsymbol{A}_{k_0}^{(\alpha)} (\boldsymbol{r} - \boldsymbol{R}_{\mathrm{N}}) \nabla \phi_{\nu k}(\boldsymbol{r}) + (-i) \frac{\partial}{\partial \boldsymbol{k}} \phi_{\mu k}^*(\boldsymbol{r}) \boldsymbol{A}_{k_0}^{(\alpha)} (\boldsymbol{r} - \boldsymbol{R}_{\mathrm{N}}) \cdot \nabla \phi_{\nu k}(\boldsymbol{r}) - \phi_{\mu k}^*(\mathbf{r}) \boldsymbol{A}_{k_0}^{(\alpha)} (\boldsymbol{r} - \boldsymbol{R}_{\mathrm{N}}) \cdot \nabla \left((-i) \frac{\partial}{\partial \boldsymbol{k}} \phi_{\nu k}(\boldsymbol{r}) \right) \right\} e^{-i \boldsymbol{k}_0 (\boldsymbol{R}_{\mathrm{N}} + \boldsymbol{T})}$$

where $\boldsymbol{r}$ runs over cell $\boldsymbol{T} = 0$ (see Fig. 2).

Using eqs. [13] and [28], we will have the diamagnetic tensor in the crystal momentum representation in the form:

$$[29]\qquad \sigma_{\alpha\beta}^{\mathrm{N,d}} = \frac{1}{2c} \int \mathrm{d}\boldsymbol{k} \sum_{\mu\nu} P_{\mu\nu k}^{(0)} \left\{ \left\langle \phi_{\mu k} \middle| \left[\left(\boldsymbol{r} - (-i) \frac{\partial^\nu}{\partial \boldsymbol{k}} \right) \times \frac{K}{c} \boldsymbol{A}_0^{(\alpha)} \right]_\beta \middle| \phi_{\nu k} \right\rangle + \left\langle \phi_{\mu k} \middle| \left[\left(\boldsymbol{r} - (-i) \frac{\partial^\nu}{\partial \boldsymbol{k}} \right) \times \left((-i) \frac{\partial^\nu}{\partial \boldsymbol{k}} - (-i) \frac{\partial^\mu}{\partial \boldsymbol{k}} \right) \right]_\beta \frac{K}{c} \boldsymbol{A}_0^{(\alpha)} \cdot \nabla \middle| \phi_{\nu k} \right\rangle \right\}$$

where $P_{\mu\nu k}^{(0)}$ is the density P-matrix. Further, the integrals over d$\boldsymbol{r}$ in eq. [29] are over the primitive central cell with $\boldsymbol{T} = 0$ only.

The operator $(-i)(\partial^\mu / \partial \boldsymbol{k})$ in eq. [29] acts on $\phi_{\mu k}$ according to:

$$\left\langle \phi_{\mu k} \middle| \left[\boldsymbol{r} \times (-i) \frac{\partial^\mu}{\partial \boldsymbol{k}} \right]_\beta \right| = \left\langle \left[\boldsymbol{r} \times (-i) \frac{\partial}{\partial \boldsymbol{k}} \phi_{\mu k} \right]_\beta \right|$$

Can. J. Chem. Downloaded from www.nrcresearchpress.com by Xi'an Jiaotong University on 09/19/12
For personal use only.

Can. J. Chem. Downloaded from www.nrcresearchpress.com by Xi'an Jiaotong University on 09/19/12
For personal use only.

In eq. [29], the first term on the right-hand side is identical to the first term on the right-hand side of eq. [12]. The second term in eq. [29] is added to obtain an expression that is gauge invariant.[8] It will be eliminated from the expression for the total shielding tensor by subtracting it from the paramagnetic shielding tensor later. The expression eq. [29] contains an infinite sum (over $\boldsymbol{T}$) of dipole terms. Fortunately the sum is conditionally convergent even in the 3D case and can be properly defined via analytic continuation techniques already implemented in BAND.[9]

Paramagnetic tensor

The first-order change in the paramagnetic current due to the μ_α^{N} perturbation in the local representation is,

$$[30]\qquad \boldsymbol{J}^{\mathrm{p}(\alpha)}(\boldsymbol{r}) = \frac{1}{2c}\sum_{i'} n_{i'}(-i)\left(\Psi_{i'}^{(\alpha,0)*}(\boldsymbol{r})K\nabla\Psi_{i'}^{(0)}(\boldsymbol{r}) + \Psi_{i'}^{(0)*}(\boldsymbol{r})K\nabla\Psi_{i'}^{(\alpha,0)}(\boldsymbol{r})\right)$$

Using the expansion eq. [16] for KS orbitals affords,

$$[31]\qquad \boldsymbol{J}^{\mathrm{p}(\alpha)}(\boldsymbol{r}) = \frac{1}{2c}(-i)\sum_{i'} n_{i'}\sum_{\mu'\nu'}\left(c_{\mu'i'}^{(\alpha,0)*}c_{\nu'i'}^{(0)} + c_{\mu'i'}^{(0)*}c_{\nu'i'}^{(\alpha,0)}\right)\phi_{\mu'}^*(\boldsymbol{r})K\nabla\phi_{\nu'}(\boldsymbol{r})$$

where $c_{\mu'i'}^{(\alpha,0)}$ is the perturbed expansion coefficients due to the α-component μ_α^{N} of the nuclear magnetic moment. The first-order perturbed expansion coefficients $c_{\mu'i'}^{(\alpha,0)}$ can be derived with the help of first-order perturbation theory (FOPT).[18,20] To that end, we first write the KS function perturbed by the α-component of a single magnetic nuclear dipole moment up to first order as:

$$[32]\qquad \Psi_{i'}^{(\mu_\alpha^{\mathrm{N}})}(\boldsymbol{r}) = \Psi_{i'}^{(0)}(\boldsymbol{r}) + \mu_\alpha^{\mathrm{N}}\sum_{j'\neq i'}\frac{h_{j'i'}^{(\alpha,0)}}{\varepsilon_{i'}^{(0)} - \varepsilon_{j'}^{(0)}}\Psi_{j'}^{(0)}(\boldsymbol{r}) + O^{(2)}[\mu_\alpha^{\mathrm{N}}]$$

where

$$[33]\qquad h_{j'i'}^{(\alpha,0)} = \left\langle \Psi_{j'}^{(0)}\middle| h^{(\alpha,0)}\middle|\Psi_{i'}^{(0)}\right\rangle$$

and $\boldsymbol{h}^{(\alpha,0)}$ is,

$$[34]\qquad \boldsymbol{h}^{(\alpha,0)} = (-i)\frac{K}{c}\boldsymbol{A}^{(\alpha)}\cdot\vec{\nabla}$$

The first-order change in the KS functions due to the magnetic dipole moment perturbation can be calculated as:

$$[35]\qquad \Psi_{i'}^{(\alpha,0)} = \frac{\partial}{\partial\mu_\alpha^{\mathrm{N}}}\left(\Psi_{i'}^{(\boldsymbol{\mu}^{\mathrm{N}})}\right)\Bigg|_{\boldsymbol{\mu}^{\mathrm{N}}=0}$$

Using the expansion eq. [16] and substituting eq. [32] into eq. [35], we obtain the perturbed expansion coefficients in the form,

$$[36]\qquad c_{\mu T_1 i'}^{(\alpha,0)} = \sum_{j'}^{\mathrm{all}}\sum_{T_3T_4}\sum_{\rho\sigma} c_{\rho T_3 j'}^{(0)*}c_{\sigma T_4 i'}^{(0)}c_{\mu T_1 j'}^{(0)}\left\langle \phi_{\rho T_3}\middle|(-i)\frac{1}{c}\boldsymbol{A}^{(\alpha)}(\boldsymbol{r}-\boldsymbol{R}_{\mathrm{N}})\cdot\nabla\middle|\phi_{\sigma T_4}\right\rangle\frac{1}{\varepsilon_{i'}^{(0)} - \varepsilon_{j'}^{(0)}}$$

Then, employing the transformations eqs. [21] and [22], the perturbed expansion coefficients in the crystal momentum representation can be expressed as,

$$[37]\qquad c_{\mu ik'}^{(\alpha,0)}(\boldsymbol{T}) = \int \mathrm{d}\boldsymbol{k}_0\int \mathrm{d}\boldsymbol{k}\int \mathrm{d}\boldsymbol{k}'\sum_{j}^{\mathrm{all}}\sum_{\rho\sigma} c_{\rho jk}^{(0)*}c_{\sigma ik'}^{(0)}c_{\mu jk''}^{(0)}\left\langle \phi_{\rho k}\middle|(-i)\frac{1}{c}\boldsymbol{A}_{k_0}^{(\alpha)}(\boldsymbol{r}-\boldsymbol{R}_{\mathrm{N}})\cdot\nabla\middle|\phi_{\sigma'}\right\rangle\frac{e^{-i\boldsymbol{k}_0(\boldsymbol{R}_{\mathrm{N}}+\boldsymbol{T})}}{\varepsilon_{ik'}^{(0)} - \varepsilon_{jk}^{(0)}}$$

The paramagnetic current in the crystal momentum representation in the point $\boldsymbol{r} + \boldsymbol{T}$ will have the form,

$$[38]\qquad \boldsymbol{J}^{\mathrm{p}(\alpha)}(\boldsymbol{r},\boldsymbol{T}) = \frac{1}{2c}(-i)\int \mathrm{d}\boldsymbol{k}\sum_{i} n_i\sum_{\mu\nu}\left(c_{\mu ik}^{(\alpha,0)*}(\mathbf{T})c_{\nu ik}^{(0)} + c_{\mu ik}^{(0)*}c_{\nu ik}^{(\alpha,0)}(\boldsymbol{T})\right)\phi_{\mu k}^*(\boldsymbol{r})K\nabla\phi_{\nu k}(\boldsymbol{r})$$

In eq. [38] we took into consideration the orthonormality of the Bloch functions and reduced the triple integration over $\boldsymbol{k}$, $\boldsymbol{k}'$, and $\boldsymbol{k}''$ in [38] with coefficients [37] to a single integration.

The paramagnetic current with GIAO corrections according to eq. [22] of ref. 8 reads as,

$$[39]\qquad \boldsymbol{J}^{\mathrm{p}(\alpha)\mathrm{GIAO}}(\boldsymbol{r}) = \frac{1}{2c}(-i)\sum_{i'} n_{i'}\sum_{\mu'\nu'}\left(c_{\mu'i'}^{(\alpha,0)*}c_{\nu'i'}^{(0)} + c_{\mu'i'}^{(0)*}c_{\nu'i'}^{(\alpha,0)}\right)$$
$$\times\left\{\phi_{\mu'}^*(\boldsymbol{r})K\nabla\phi_{\nu'}(\boldsymbol{r}) + \boldsymbol{R}_{\mu'}\phi_{\mu'}^*(\boldsymbol{r})\left(\boldsymbol{h}_{\mathrm{KS}}^0 - \varepsilon_{i'}^{(0)}\right)\phi_{\nu'}(\boldsymbol{r}) - \phi_{\mu'}^*(\boldsymbol{r})\left(\boldsymbol{h}_{\mathrm{KS}}^0 - \varepsilon_{i'}^{(0)}\right)\boldsymbol{R}_{\nu'}\phi_{\nu'}(\boldsymbol{r})\right\}$$

in the local representation. Using the transformation in eq. [21], the coefficients in eq. [37] and the formulae of eq. [19] allow us to write the GIAO based paramagnetic current in the crystal momentum representation as,

$$[40]\qquad \boldsymbol{J}^{\mathrm{p}(\alpha)\mathrm{GIAO}}(\boldsymbol{r},\boldsymbol{T}) = \frac{1}{2c}(-i)\int \mathrm{d}\boldsymbol{k}\sum_i n_i \sum_{\mu\nu}\left(c^{(\alpha,0)*}_{\mu ik}(\boldsymbol{T})c^{(0)}_{\nu ik} + c^{(0)*}_{\mu ik}c^{(\alpha,0)}_{\nu ik}(\boldsymbol{T})\right) \times \{\phi^*_{\mu k}(\boldsymbol{r})\,K\nabla\phi_{\nu k}(\boldsymbol{r}) + (-i)\frac{\partial}{\partial\boldsymbol{k}}\phi^*_{\mu k}(\boldsymbol{r})\left(\boldsymbol{h}^0_{\mathrm{KS}} - \varepsilon^{(0)}_{ik}\right)\phi_{\nu k}(\boldsymbol{r}) - \phi^*_{\mu k}(\boldsymbol{r})\left(\boldsymbol{h}^0_{\mathrm{KS}} - \varepsilon^{(0)}_{ik}\right)(-i)\frac{\partial}{\partial\boldsymbol{k}}\phi_{\nu k}(\boldsymbol{r})\}$$

Calculating the paramagnetic tensor with the help of the GIAO based paramagnetic current from eq. [39], recalling that the paramagnetic current operator in eq. [40] acts on the position operator in eq. [13], and using the relation,

$$\nabla^2\left[(-i)\frac{\partial}{\partial\boldsymbol{k}}\phi_{\nu k}(\boldsymbol{r})\times\boldsymbol{r}\right]_\beta = -\left[(-i)\frac{\partial}{\partial\boldsymbol{k}}\times\nabla\right]_\beta\phi_{\nu k}(\boldsymbol{r}) + \left[(-i)\frac{\partial}{\partial\boldsymbol{k}}\times\boldsymbol{r}\right]_\beta\nabla^2\phi_{\nu k}(\boldsymbol{r})$$

allow us finally to express the paramagnetic shielding tensor as,

$$[41]\qquad \sigma^{\mathrm{N,p}}_{\alpha\beta} = \frac{1}{2c}\int \mathrm{d}\boldsymbol{k}\sum_{\mu\nu}\left[(-i)P^{(\alpha,0)}_{\mu\nu k}\left\{\left\langle\phi_{\mu k}\middle|\left[\left(\boldsymbol{r}-(-i)\frac{\partial^\nu}{\partial\boldsymbol{k}}\right)\times K\nabla\right]_\beta\middle|\phi_{\nu k}\right\rangle - \left\langle\phi_{\mu k}\middle|\left[(\boldsymbol{r}-\boldsymbol{R}_{\mathrm{N}})\times\left((-i)\frac{\partial^\nu}{\partial\boldsymbol{k}}-(-i)\frac{\partial^\mu}{\partial\boldsymbol{k}}\right)\right]_\beta\boldsymbol{h}^0_{\mathrm{KS}}\middle|\phi_{\nu k}\right\rangle\right\}\right.$$
$$\left. + (-i)W^{(\alpha,0)}_{\mu\nu k}\left\langle\phi_{\mu k}\middle|\left[(\boldsymbol{r}-\boldsymbol{R}_{\mathrm{N}})\times\left((-i)\frac{\partial^\nu}{\partial\boldsymbol{k}}-(-i)\frac{\partial^\mu}{\partial\boldsymbol{k}}\right)\right]_\beta\middle|\phi_{\nu k}\right\rangle + P^{(0)}_{\mu\nu k}\left\langle\phi_{\mu k}\middle|\left[(-i)\frac{\partial^\nu}{\partial\boldsymbol{k}}\times(-i)\frac{\partial^\mu}{\partial\boldsymbol{k}}\right]_\beta\frac{K}{c}\boldsymbol{A}^{(\alpha)}_0(\boldsymbol{r}-\boldsymbol{R}_{\mathrm{N}})\cdot\nabla\middle|\phi_{\nu k}\right\rangle\right]$$

where

$$P^{(\alpha,0)}_{\mu\nu k} = \sum_i n_i\left(C^{(\alpha,0)*}_{\mu ik}c^{(0)}_{\nu ik} + c^{(0)*}_{\mu ik}C^{(\alpha,0)}_{\nu ik}\right)$$

is the first-order perturbed P-matrix and

$$W^{(\alpha,0)}_{\mu\nu k} = \sum_i n_i\varepsilon^{(0)}_{ik}\left(C^{(\alpha,0)*}_{\mu ik}c^{(0)}_{\nu ik} + c^{(0)*}_{\mu ik}C^{(\alpha,0)}_{\nu ik}\right)$$

is the corresponding energy-weighted P-matrix, where

$$[42]\qquad C^{(\alpha,0)}_{\mu ik} = \sum_j^{\mathrm{all}} c^{(0)}_{\mu jk}\left\langle\Psi^{(0)}_{jk}\middle|(-i)\frac{1}{c}\boldsymbol{A}^{(\alpha)}_0(\boldsymbol{r}-\boldsymbol{R}_{\mathrm{N}})\cdot\nabla\Psi^{(0)}_{ik}\right\rangle \times\frac{1}{\varepsilon^{(0)}_{ik}-\varepsilon^{(0)}_{jk}}$$

In eq. [41] we have added the term, which we subtracted from the diamagnetic tensor (see eq. [19] from ref. 8), to make both the diamagnetic and the paramagnetic tensor gauge-origin invariant. To avoid singularities in eq. [42], we separate the sum over j into two parts, involving occupied–occupied and occupied–virtual orbitals, respectively. Further, for the occupied–occupied part we use the reduced nonsingular form for the P- and W-matrices (eq. [57] from ref. 18 and eq. [28] from ref. 20).

Computational Details

The Bloch states are expanded in a mixed basis of Slater-type and numerical atomic orbitals with the radial part of each NAO stored on a grid. Such a basis has been used in our previous work.[8] Use was made of a triple zeta basis, augmented with two STO polarization functions of the BAND database. It consists of two STOs and one NAO for each *nl* sub-shell (1s, 2s, 2p, etc.). We did not have any problems with linear dependencies of the basis set functions in this work, since we used a primitive cell in our NMR calculations. Therefore, we did not have to remove any sub-shells. The numerical accuracy parameter used by BAND has been set to five. For odd *kspace* values, BAND uses quadratic integration schemes for one-, two-,[21] and three-dimensional[22] Brillouin zones. Here the *kspace* parameter of the BAND program describes the number of integration points in each $\boldsymbol{k}$ direction in reciprocal space.

All calculations are based on spin-restricted SCF calculations, employing the generalized gradient approximation (GGA) for the exchange-correlation energy. The parametrization of the exchange-correlation energy follows that of Becke[23] for the exchange and Perdew[24,25] for the correlation (BP86).

Only time-reversal symmetry is used in the integration over the Brillouin zone since magnetic perturbations do not commute with the symmetry operations.

The chemical shift is calculated as

$$[43]\qquad \delta^X = \sigma^{\mathrm{Ref}} - \sigma^X$$

where σ^{Ref} is the chemical shielding of a reference, and σ^X is the chemical shielding for the investigated system. The chemical shielding of the reference is calculated for a single molecule in a big box. We have used the following references and corresponding absolute shielding values: for the hydrogen molecule, $\sigma^{\mathrm{H}}_{\mathrm{H_2}}$ =22.2 ppm; for the water molecule, $\sigma^{\mathrm{H}}_{\mathrm{H_2O}}$ =31.8 ppm; for the tetrametilsilane (TMS) molecule, $\sigma^{\mathrm{C}}_{\mathrm{Si(CH_3)_4}}$ =180.8 ppm; for the nitromethane molecule, $\sigma^{\mathrm{N}}_{\mathrm{CH_3NO_2}}$ =–133.5 ppm; for the silane molecule, $\sigma^{\mathrm{Si}}_{\mathrm{SiH_4}}$ =440.7 ppm; for the phosphane molecule, $\sigma^{\mathrm{P}}_{\mathrm{PH_3}}$ =577.5 ppm; and for free atoms of He, Ne, Ar, Kr, Xe, and Zn, σ^{He} = 59.8 ppm, σ^{Ne} = 552.1 ppm, σ^{Ar} = 1237.9 ppm, σ^{Kr} = 3248.0 ppm, σ^{Xe} = 5647 ppm, and σ^{Zn} = 2514 ppm.

Can. J. Chem. Downloaded from www.nrcresearchpress.com by Xi'an Jiaotong University on 09/19/12
For personal use only.

Table 1. Calculated and experimental chemical shifts (in ppm).

			BAND		Calculated by other authors	
System	Type	Atom probed by NMR	Single Dipole	Supercell		Experiment
H_2 chain	1D	H[a]	2.64	2.64		
He chain	1D	He[b]	0.81	0.81		
Ne chain	1D	Ne[c]	4.18	4.18		
Ar chain	1D	Ar[d]	126.3	126.6		
Kr chain	1D	Kr[e]	554.7	554.3		
Xe chain	1D	Xe[f]	2047.	2048.		
PE	1D	C[g]	32.9	33.3		33.5[k]
PA	1D	C	137.6	142.3		137.3[l]
BN hexagonal nanoribbon	1D	N_1[h]	–258.9	–261.1		
		N_2	–217.7	–220.6		
BN hexagonal sheet	2D	N	–267.2	–272.5	–287.0[m]	–285[m]
BN cubic crystal	3D	N	–359.8		–359[m]	–358.6[m]
SiS_2	1D	Si[i]	103.4	109.2		
	3D	Si	92.5			87.3[n]
PdiFP	1D	P[j]	226.8	224.0		243.1[o]
PdiClP	1D	P	277.8	287.9		285.6[r]
PdiMeP	1D	P	280.9	275.8		282.1[s]
Black phosphorus	2D	P	267.7			288.3[t]
Ice	3D	H[p]	7.9		8.0[u]	7.4[u]
ZnS zincblende	3D	Zn[q]	1199			1068[v]

[a]Chemical shift (in ppm) with respect to free H_2.
[b]Relative to free He.
[c]Relative to free Ne.
[d]Relative to free Ar.
[e]Relative to free Kr.
[f]Relative to free Xe.
[g]With respect to TMS.
[h]With respect to nitromethane.
[i]Chemical shift with respect to SiH_4.
[j]Chemical shift with respect to PH_3.
[k]Ref.28.
[l]Ref.29.
[m]Ref.30.
[n]Ref.38.
[o]Ref.32.
[p]Relative to single H_2O.
[q]Relative to free Zn.
[r]Ref.35.
[s]Ref.37.
[t]Ref.40.
[u]Ref.41.
[v]Ref.45.

Can. J. Chem. Downloaded from www.nrcresearchpress.com by Xi'an Jiaotong University on 09/19/12
For personal use only.

Results and discussion

We have tested our BAND implementation for the calculation of NMR shielding tensors by comparing our results with estimates from a previously developed method,[8] experimental data, and other calculations reported in the literature. We shall refer to our new scheme as the single dipole method (SD), since it considers the perturbation from a single dipole in a large crystal. The old method will be referred as the supercell (SC) scheme. It considers an array of periodic supercells, each containing a magnetic dipole.

For 1D periodic systems, we have considered linear chains of H_2 molecules and He, Ne, Ar and Xe atoms. In addition, consideration was given to polymers, such as polyethylene, polyacethylene, boron nitride hexagonal nano-ribbon, poly (difluoro-phosphazene), poly(dichlorophosphazene), poly(dimethylenephosphazene), and a SiS_2 chain. The examples of two-dimensional periodic systems include a boron nitride hexagonal sheet and a 2D puckered layer of black phosphorus. As examples of three-dimensional periodic systems, we have chosen the boron nitride cubic crystal, SiS_2, ZnS zincblende, and hexagonal Ice. The results are presented in Table 1.

For all ***linear chains***, the SC method made use of 17 primitive cells and Γ-point integration only. The SD method employed for the same systems, unless otherwise stated, a single

Can. J. Chem. Downloaded from www.nrcresearchpress.com by Xi'an Jiaotong University on 09/19/12
For personal use only.

Fig. 3. Cells for (*a*) polyethylene and for (*b*) polyacethylene.

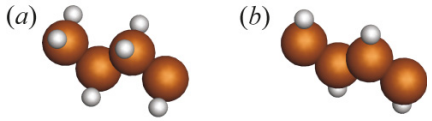

Fig. 4. (*a*) Boron nitride nanoribbon and (red, black in print version) the primitive cell of boron nitride sheet (*b*).

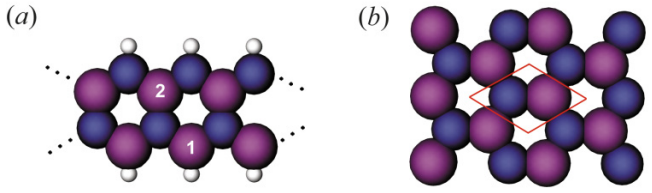

primitive cell with integration in one-half of reciprocal space using eleven ***k***-points. The H_2 linear chain with a period of 2.38 Å has, according to both methods, a chemical shift of 2.64 ppm relative to H_2 (Table 1). The chemical shifts (relative to the free atoms) for the He, Ne, Ar, and Xe linear chains with one atom in a primitive cell of 1.5 Å are calculated to be virtually identical for the two schemes (Table 1).

The **polyethylene** (PE) polymer in Fig. 3*a* has two carbon and four hydrogen atoms in each primitive cell, with a period of $T = 2.553$ Å. The bond angles and bond lengths used in the calculations were taken from experimental X-ray data.[26,27] For the C–H bond length, we adopted a value of $r_{CH} = 1.06$ Å.[26] The SD method employed integration with 11 ***k***-points in half of the reciprocal space and afforded a chemical shift value relative to TMS of 32.9 ppm. The SC approach made use of seven cells and a three-point ***k***-integration, leading to a shift value of 33.3 ppm. The experimental estimate is 33.5 ppm.[28]

The unit cell of **trans-polyacethylene** (PA) contains two atoms of carbon and two atoms of hydrogen ($T = 2.457$ Å) (see Fig. 3*b*). The SD-model with 11 ***k***-points afforded a chemical shift of 137.6 ppm, whereas the SC scheme with five primitive cells as a supercell and five ***k***-points resulted in an estimate of 142.3 ppm. The experimental value is 137.3 ppm.[29]

The **boron nitride nanoribbon** is a one-dimensional polymer with two atoms each of boron, nitrogen, and hydrogen in a primitive cell (Fig. 4*a*). The B–N bond length used in the calculation is $r_{BN} = 1.446$ Å. The results for the nitrogen-shielding shifts with respect to nitromethane are listed in Table 1. The calculated values for the SD scheme with 11 ***k***-points are –258.9 and –217.7 ppm for the first and second atoms of nitrogen (see Fig. 4*a*), respectively. SC calculations, with five primitive cells and three *k*-point integration, give –261.1 and –220.6 ppm, respectively.

Planar 2D boron nitride has a hexagonal lattice with two atoms in a primitive cell (Fig. 4*b*), where the B–N bond length is equal to 1.446 Å. We compile the isotropic ^{15}N chemical shift values with respect to nitromethane in Table 1. The SD-method with 11 *k*-point integration gives a chemical shift equal to –267.2 ppm. The converged BAND result for the SC approach is –272.5 ppm. It was obtained from a square supercell with 24 atoms and a total number 15 of ***k***-points, corresponding to the *kspace* parameter in BAND equal to three. The experimental value for hexagonal boron nitride powder is –285 ppm.[30] A molecular cluster calculation affords an estimate of –287.0 ppm.[30]

Fig. 5. Cubic BN crystal.

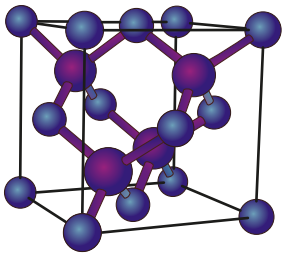

Fig. 6. Poly(difluorophosphazene) cells.

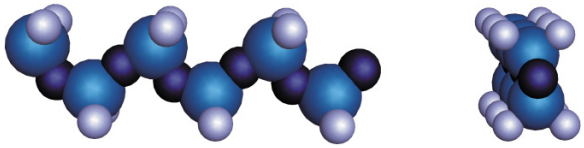

Chart 1.

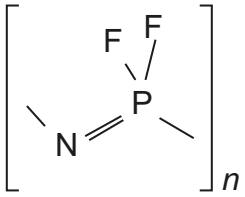

A **cubic crystal of boron nitride** has a diamond-like structure with a lattice parameter of 3.616 Å (Fig. 5). Calculations based on the SD method with 2514 ***k***-points in one-half of the first Brillouin zone (BAND *kspace* parameter equal to nine) give a chemical shift with respect to nitromethane that is equal to –359.8 ppm. The experimental value is –358.6 ppm.[30] Marian and Gastreich obtained from calculations on a H-saturated molecular cluster containing 71 atoms a value of –359.0 ppm.[30]

Poly(difluorophosphazene) (PdiFP) polymer contains two atoms of nitrogen and phosphorus and four atoms of fluorine in each primitive cell (Fig. 6 and Chart 1) with period of $T =$ 4.86 Å. Structural parameters were taken from the X-ray study from Allcock et al.[31] BAND calculations with the SD method (nine *k*-point integration) afford a chemical shift of 226.8 ppm relative to PH_3. The calculated chemical shift for the SC scheme (three primitive cells and three ***k***-points) is 224.0 ppm. The experimental chemical shift with respect to 85% aqueous H_3PO_4 is equal to –23.0 ppm.[32] By taking into account experimental absolute values for the shielding tensor for 85% aqueous H_3PO_4 and PH_3[33] in a molecular beam, we can obtain an estimate of the experimental chemical shift for PdiFP with respect to PH_3 that is equal to 243.1 ppm. This value is in fair agreement with our calculated estimates.

Poly(dichlorophosphazene) (PdiClP) polymer has a primitive cell with two atoms each of nitrogen and phosphorus and four atoms of chlorine (Fig. 7 and Chart 2) with a period of $T = 4.92$ Å. Experimental bond lengths and angles are taken from ref. 34. The calculated chemical shift, employing the SC approach (three primitive cells and three ***k***-points), amounts to 287.9 ppm relative to PH_3. The SD method with

Can. J. Chem. Downloaded from www.nrcresearchpress.com by Xi'an Jiaotong University on 09/19/12
For personal use only.

Fig. 7. Poly(dichlorophosphazene) cells.

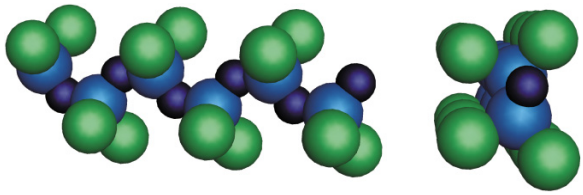

Chart 2.

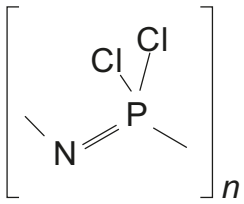

Fig. 8. Poly(dimethylphosphazene) cells.

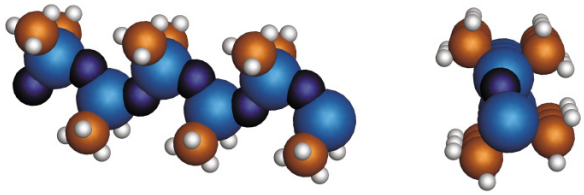

nine *k*-point integration gives 277.8 ppm. The estimated experimental chemical shift[35] relative to PH_3 is equal to 285.6 ppm .

Poly(dimethylphosphazene) (PdiMeP) polymer contains two atoms of nitrogen and phosphorus, and four methyl groups in a primitive cell (Fig. 8 and Chart 3) with period of $T = 4.887$ Å. Experimental X-ray data for bond lengths and angles are taken from the ref. 36. BAND calculations with the SD method and nine *k*-point integration give a chemical shift of 280.9 ppm with respect to PH_3. The calculated chemical shift due to the SC scheme consisting of three primitive cells and three ***k***-points affords 275.8 ppm. The estimated experimental chemical shift[37] relative to gaseous PH_3 is 282.1 ppm.

SiS_2 has a crystal of chains with a primitive cell for each chain consisting of two atoms of Si and four atoms of S (Fig. 9) with period of $T = 5.552$ Å. We have used the primitive chain cell in our 1D calculations. The experimental chemical shift for SiS_2 with respect to TMS is –19.5 ppm.[38] Using the experimental absolute values for TMS and SiH_4,[39] we obtain for the experimental chemical shift with respect to SiH_4 an estimated value of 87.3 ppm. BAND calculations based on the SD method with a five *k*-point integration give a chemical shift of 103.4 ppm with respect to the SiH_4 molecule. The calculated chemical shift for the SC scheme with three primitive cells and three ***k***-points affords 109.2 ppm. The difference between theory and experiment can be explained as due to inter chain interactions not considered in the calculations above. Thus, the distance between the chains is only 5.5 Å.

For 3D calculations (Fig. 10) with one primitive cell and a *kspace* parameter equal to 5 (total number of ***k***-points is 379), we obtain a chemical shift of 92.5 ppm, which is in much better agreement with experiment.

Chart 3.

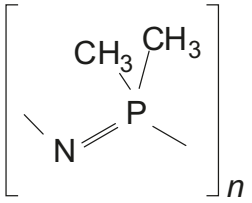

Fig. 9. SiS_2 chain.

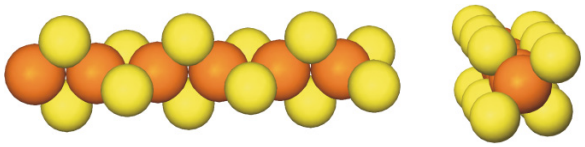

Fig. 10. SiS_2 chains packing in 3D crystal.

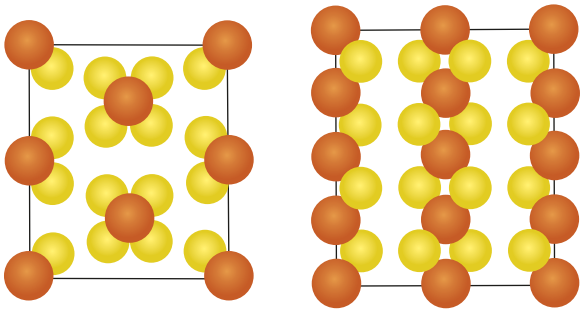

The 2D structure of **black phosphorus** consists of puckered layers and one primitive cell contains four atoms (Fig. 11). The experimental chemical shift with respect to 85% aqueous H_3PO_4 is equal to 22.2 ppm.[40] The estimated experimental chemical shift relative to gaseous PH_3 is 288.3 ppm. BAND result is 267.7 ppm, and it was obtained for primitive cell and *kspace* equal to nine (total number of ***k***-points is 153). The small difference between experiment and theory can be explained by interaction between layers in 3D crystal of black phosphorus.

The hexagonal ice 3D crystal primitive cell consists of four molecules of water (Fig. 12). The experimental chemical shift for the H atom with respect to a single molecule of water is 7.4 ppm.[41] BAND result for one primitive cell and *kspace* = 3 is 7.9 ppm. For geometry parameters we have used the experimental geometry.[42,43]

The crystal structure for **ZnS zincblende** is shown in Fig. 5. The lattice parameter was set to 5.3985 Å,[44] with a cell including four atoms of Zn and four atoms of S. The experimental chemical shift with respect to a free atom of Zn is 1068 ppm[45] compared to our estimate (*kspace* = 5) of 1199 ppm.

Conclusion

We have developed an improved Kohn–Sham DFT based approach for the calculation of NMR shielding tensors in periodic systems. As our previous formulation,[8] it is gauge-origin invariant and based on Slater type or (and) numerical atomic orbitals with the use of the complete Kohn–Sham potential without recourse to effective potentials. We can thus describe even core orbitals variationally. In our method the

Fig. 11. Black phosphorus puckered layers.

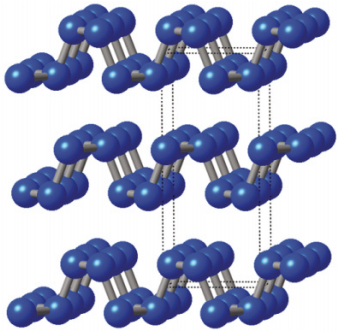

Fig. 12. Primitive cell of ice Ih.

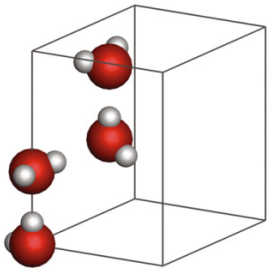

calculation of the shielding tensor $\sigma^{N}_{\alpha\beta}$ for nucleus N requires first the evaluation of the current density $\boldsymbol{J}^{(\alpha)}$ induced by the three components $(\alpha = \overline{1}, \overline{3})$ of the nuclear magnetic moment $\boldsymbol{\mu}^{N}$, followed by the response of $\boldsymbol{J}^{(\alpha)}$ to the three components $(\beta = \overline{1}, \overline{3})$ of the external magnetic field $\boldsymbol{B}$. In the previous scheme,[8] the determination of $\boldsymbol{J}^{(\alpha)}$ required a zero-order field free calculation on a supercell large enough so that $\boldsymbol{J}^{(\alpha)}$ vanishes outside. The requirement that $\boldsymbol{J}^{(\alpha)}$ should vanish at the supercell border was deemed necessary to determine the interaction between $\boldsymbol{J}^{(\alpha)}$ and the nonperiodic (and nowhere disappearing) constant magnetic field. In the current approach, use is still made of a supercell that is now extended to the entire crystal. However the determination of $\boldsymbol{J}^{(\alpha)}$ over the entire crystal is based on zero-order Kohn–Sham orbitals from SCF calculations involving only a primitive unit cell. This is made possible by the use of first-order analytic perturbation theory and the relationships for Bloch functions and their derivatives. In addition, use was made of the transformation relationships (eq. [21]) between the KS orbitals obtained with the whole crystal as the periodic unit (local representation) and the crystal momentum representation,[19] where the KS equation is solved with the primitive cell as the periodic unit. The new procedure can reduce the computational time by a factor of 10 for 1D systems to 100 for 3D systems. This improvement is made possible by the transformation in eq. [21], which is specific to atom-centered basis sets. The new implementation is further able to take into account relativistic effects within the scalar zero-order regular approximation.[13,14] The calculation of NMR chemical shifts for one-, two-, and three- dimensional periodic systems has been used to validate our new implementation, by comparison to experiment as well as other methods, including our previous scheme.[8]

Supplementary data

Supplementary data for this article are available on the journal Web site (www.nrcresearchpress.com/cjc).

Acknowledgments

T.Z. would like to thank the Canadian government for a Canada research chair in theoretical inorganic chemistry and Natural Sciences and Engineering Research Council of Canada for financial support. We would like to thank Dr. Pier Philipsen for technical help.

References

(1) Zurek, E.; Autschbach, J. *Int. J. Quantum Chem.* **2009** *109* (14), 3343. doi:10.1002/qua.22211.
(2) Mauri, F.; Pfrommer, B. G.; Louie, S. G. *Phys. Rev. Lett.* **1996** *77* (26), 5300. doi:10.1103/PhysRevLett.77.5300.
(3) Pickard, C. J.; Mauri, F. *Phys. Rev. B* **2001** *63* (24), 245101. doi:10.1103/PhysRevB.63.245101.
(4) Thonhauser, T.; Ceresoli, D.; Mostofi, A. A.; Marzari, N.; Resta, R.; Vanderbilt, D. *J. Chem. Phys.* **2009** *131* (10), 101101. doi:10.1063/1.3216028.
(5) Thonhauser, T.; Ceresoli, D.; Marzari, N. *Int. J. Quantum Chem.* **2009** *109* (14), 3336. doi:10.1002/qua.21941.
(6) Sebastiani, D.; Parinello, M. *J. Phys. Chem. A* **2001** *105* (10), 1951. doi:10.1021/jp002807j.
(7) Keith, T. A.; Bader, R. F. W. *Chem. Phys. Lett.* **1993** *210* (1–3), 223. doi:10.1016/0009-2614(93)89127-4.
(8) Skachkov, D.; Krykunov, M.; Kadantsev, E.; Ziegler, T. *J. Chem. Theory Comput.* **2010** *6* (5), 1650. doi:10.1021/ct100046a.
(9) te Velde, G.; Baerends, E. J. *Phys. Rev. B* **1991** *44* (15), 7888. doi:10.1103/PhysRevB.44.7888.
(10) te Velde, G.; Baerends, E. J.; Philipsen, P. H. T.; Wiesenekker, G.; Groeneveld, J. A.; Berger, J. A.; de Boeij, P. L.; Klooster, R.; Kootstra, F.; Romaniello, P.; Snijders, J. G.; Kadantsev, E. S.; Skachkov, D. G.; Ziegler, T. BAND 2010.01, *SCM: Theoretical Chemistry*, Vrije Universiteit, Amsterdam, The Netherlands. http://www.scm.com/.
(11) Kadantsev, E. S.; Ziegler, T. *J. Phys. Chem. A* **2008** *112* (19), 4521. doi:10.1021/jp800494m.
(12) Kadantsev, E. S.; Ziegler, T. *J. Phys. Chem. A* **2009** *113* (7), 1327. doi:10.1021/jp805466c.
(13) Schreckenbach, G.; Ziegler, T. *Int. J. Quantum Chem.* **1997** *61* (6), 899. doi:10.1002/(SICI)1097-461X(1997)61:6<899::AID-QUA3>3.0.CO;2-R.
(14) Wolff, S. K.; Ziegler, T.; van Lenthe, E.; Baerends, E. J. *J. Chem. Phys.* **1999** *110* (16), 7689. doi:10.1063/1.478680.
(15) Gauss, J. Molecular properties. In *Modern methods and algorithms of quantum chemistry, Proceedings;* Grotendorst, J., Ed.; John von Neumann Institute for Computing, Jülich, NIC series 2000, *3*, 541–592. URL: www.fz-juelich.de/nic-series/Volume3/gauss.pdf.
(16) Jones, R. O. Introduction to density functional theory and exchange-correlation energy functionals. In *Computational Nanoscience: Do It Yourself!* Grotendorst, J.; Blügel, S.; Marx, D. Eds., John von Neumann Institute for Computing, Jülich, NIC Series 2006, *31*, 45–70. URL: www2.fz-juelich.de/nic-series/volume31/jones.pdf.
(17) Ditchfield, R. *Mol. Phys.* **1974** *27* (4), 789. doi:10.1080/00268977400100711.
(18) Pople, J. A.; Krishnan, R.; Schlegel, H. B.; Binkley, J. S. *Int. J.*

Can. J. Chem. Downloaded from www.nrcresearchpress.com by Xi'an Jiaotong University on 09/19/12
For personal use only.

Quantum Chem.: Quantum Chemistry Symposium. 1979, *13*, 225.
(19) Callaway, J. *Quantum theory of the solid state.* Academic Press: New York and London, 1974, Chap. 5.
(20) O'Shea, S. F.; Santry, D. P. *Theor. Chim. Acta (Berl.)* **1975** *37* (1), 1. doi:10.1007/BF00549767.
(21) Wiesenekker, G.; te Velde, G.; Baerends, E. J. *J. Phys. Chem.* **1988** *21*, 4263. doi:10.1088/022-3719/21/23/012.
(22) Wiesenekker, G.; Baerends, E. J. *J. Phys. Condens. Matter* **1991** *3* (35), 6721. doi:10.1088/0953-8984/3/35/005.
(23) Becke, A. D. *Phys. Rev. A* **1988** *38* (6), 3098. doi:10.1103/PhysRevA.38.3098.
(24) Perdew, J. P. *Phys. Rev. B* **1986** *33* (12), 8822. doi:10.1103/PhysRevB.33.8822.
(25) Perdew, J. P. *Phys. Rev. B* **1986** *34* (10), 7406. doi:10.1103/PhysRevB.34.7406.
(26) Caminiti, R.; Pandolfi, L.; Ballirano, P. *J. Macromol. Sci.* **2000** *B39* (4), 481. doi:10.1081/MB-100100400. Preview available from http://www.tandfonline.com/doi/abs/10.1081/MB-100100400.
(27) Yamanobe, T.; Sorita, T.; Comoto, T.; Ando, I. *J. Mol. Struct.* **1985** *131* (3-4), 267. doi:10.1016/0022-2860(85)87028-9.
(28) Yamanobe, T. Structure and dynamics of crystalline and noncrystalline phases in polymers. In *Solid State NMR of Polymers*, Ando, I., Ed.; Amsterdan, NLD: Elsevier & Technology Books, 1998, pp 267–306.
(29) Terao, T.; Maeda, S.; Yamabe, T.; Akagi, K.; Shirakawa, H. *Chem. Phys. Lett.* **1984** *103* (5), 347. doi:10.1016/0009-2614(84)80318-8.
(30) Marian, C. M.; Gastreich, M. *Solid State Nucl. Magn. Reson.* **2001** *19* (1-2), 29. doi:10.1006/snmr.2000.0020.
(31) Allcock, H. R.; Kugel, R. L.; Stroh, E. G. *Inorg. Chem.* **1972** *11* (5), 1120. doi:10.1021/ic50111a041.
(32) Allcock, H. R.; Patterson, D. B.; Evans, T. L. *Macromolecules* **1979** *12* (2), 172. doi:10.1021/ma60068a002.
(33) Jameson, C. J.; De Dios, A.; Jameson, K. *Chem. Phys. Lett.* **1990** *167* (6), 575. doi:10.1016/0009-2614(90)85472-O.
(34) Chatani, Y.; Yatsuyanagi, K. *Macromolecules* **1987** *20* (5), 1042. doi:10.1021/ma00171a028.
(35) Sulkowski, W.; Sulkowska, A.; Makarucha, B.; Kireev, V. *Eur. Polym. J.* **2000** *36* (7), 1519. doi:10.1016/S0014-3057(99)00204-9.
(36) Meille, S. V.; Poletti, A. R.; Gallazzi, M. C.; Gleria, M.; Brückner, S. *Polymer (Guildf.)* **1992** *33* (11), 2364. doi:10.1016/0032-3861(92)90528-5.
(37) Panziera, N.; Pertici, P.; Barazzone, L.; Caporusso, A. M.; Vitulli, G.; Salvadori, P.; Borsacchi, S.; Geppi, M.; Veracini, C. A.; Martra, G.; Bertinetti, L. *J. Catal.* **2007** *246* (2), 351. doi:10.1016/j.jcat.2006.12.017.
(38) Tenhover, B., M.R.D.; Henderson, R.S.; Hammond, T.E.; Shreve, G.A. *Solid State Commun.* **1988** *65*, 1517. doi:10.1016/0038-1098(88)90642-4.
(39) Jameson, C. J.; Jameson, A. K. *Chem. Phys. Lett.* **1988** *149* (3), 300. doi:10.1016/0009-2614(88)85030-9.
(40) Lange, S.; Schmidt, P.; Nilges, T. *ChemInform* **2007** *38*, 4028. doi:10.1002/chin.200730015.
(41) Pfrommer, B. G.; Mauri, F.; Louie, S. G. *J. Am. Chem. Soc.* **2000** *122* (1), 123. doi:10.1021/ja991961k.
(42) Kuhs, W. F.; Lehmann, M. S. *J. Phys. Chem.* **1983** *87* (21), 4312. doi:10.1021/j100244a063.
(43) Goto, A.; Hondoh, T.; Mae, S. *J. Chem. Phys.* **1990** *93* (2), 1412. doi:10.1063/1.459150.
(44) Kopp, O. C.; Kerr, P. F. *American Minearologist* **1958** *43*, 732.
(45) Haller, M.; Hertler, W. E.; Lutz, O.; Nolle, A. *Solid State Commun.* **1980** *33* (10), 1051. doi:10.1016/0038-1098(80)90315-4.

Can. J. Chem. Downloaded from www.nrcresearchpress.com by Xi'an Jiaotong University on 09/19/12
For personal use only.

Low-energy electron-induced decarbonylation of $Fe(CO)_5$ films adsorbed on Au(111) surfaces

Christelle Hauchard and Paul A. Rowntree

Can. J. Chem. Downloaded from www.nrcresearchpress.com by Xi'an Jiaotong University on 09/19/12
For personal use only.

Abstract: The decarbonylation of $Fe(CO)_5$ adsorbed in monolayer and multilayer films on Au(111)/mica substrates has been induced by 0–20 eV electrons and studied by grazing incidence IR spectroscopy. Our results show that the cross sections for the initial stages of this process in as-deposited films range from 60–300 $Å^2$ and show considerable variations with the incident electron energy. The high sensitivity to low-energy electrons is believed to be the result of secondary reactions of anion fragments in the film with the neighbouring $Fe(CO)_5$ moieties, leading to increasingly massive heteronuclear $Fe_n(CO)_m$ species and progressive CO elimination. Continued exposure to the electron beam leads to the slower degradation of these newly created species into an Fe-rich deposit containing traces of CO. These traces are removed by subsequent heating to ~300 K. $Fe(CO)_5$ films that have been subjected to temperatures exceeding 125 K have no measurable sensitivity to the electron beam in the 0–20 eV regime; this is believed to be due to the structural transformation of the as-deposited thin film structure into 3D aggregates. This structural motif presents a very limited quantity of the adsorbed $Fe(CO)_5$ to the incident beam, and may also form a protective layer of the robust $Fe_n(CO)_m$ species during the initial stages of exposure to the electrons.

Key words: low-energy electron, $Fe(CO)_5$, CO elimination, dissociative electron attachment, surface polymerization.

Résumé : La décarbonylation du $Fe(CO)_5$ adsorbé en monocouche et en films multicouches sur des substrats de Au(III)/mica a été induite par des électrons de 0 à 20 eV et la réaction a été étudiée par spectroscopie infrarouge en incidence rasante. Les résultats obtenus montrent que les sections droites des stages initiaux de ce processus dans les films tels que déposés s'étalent de 60 à 300 $Å^2$ et varient beaucoup avec l'énergie des électrons incidents. On croit que la grande sensibilité aux électrons de faible énergie résulte de réactions secondaires des fragments ioniques dans le film avec les fractions voisines de $Fe(CO)_5$ qui conduisent à des espèces $Fe_n(CO)_m$ hétéronucléaires de plus en plus massives et à une élimination progressive de CO. Une continuation de l'exposition au faisceau d'électron conduit à une dégradation plus lente de ces espèces nouvellement créées en dépôts riches en Fe contenant des traces de CO. Il est possible d'éliminer ces traces par un chauffage subséquent à environ 300 K. Les films de $Fe(CO)_5$ qui ont été soumis à des températures supérieures à 125 K n'ont aucune sensibilité mesurable vis-à-vis du faisceau d'électron dans le régime 0 à 20 eV; on croit que cette situation est due à une transformation de la structure du film mince tel que déposé en des agrégats 3D. Ce motif structural ne représente qu'une faible quantité du $Fe(CO)_5$ adsorbé à faisceau incident et il peut agir comme couche protectrice pour les robustes espèces $Fe_n(CO)_m$ dans les étapes initiales d'exposition aux électrons.

Mots-clés : électron de faible énergie, $Fe(CO)_5$, élimination de CO, attachement dissociatif d'électron, polymérisation en surface.

[Traduit par la Rédaction]

Introduction

The growth of thin metallic films is an essential aspect in the design of reactive surfaces and in microelectronics. Among the methods of choice to deposit these films, vapour-phase depositions via thermal sources or plasmas are commonly used, as is the thermal decomposition of organometallic species via chemical vapour deposition. In both cases, energetic constraints prefer the use of relatively unstable and volatile precursors. In all cases, the cleanliness and the metallicity of the final surface film are of central importance. Metal carbonyls are useful starting reagents in this regard. The strong transition dipole moment of the carbonyls and the CO fragments make IR spectroscopy very well-suited to the characterization of these molecules in virtually all phases, as well as the determination of their decomposition pathways. More recently, the possibility of photolysis and electron-beam-induced decomposition has become attractive owing to the potential for pattern deposition on the surface and the enhanced probability of selective bond rupture in the precursor, rather than nonspecific decomposition.

One of the prototype metalcarbonyls ($Fe(CO)_5$ (IPC)) has been the object of many studies in the gas phase,[1–14] isolated in rare gas matrices,[15–19] and adsorbed onto surfaces such as Au,[20–22] Ag,[23–29] Cu,[30] Pt,[31] Ni,[32] graphite,[33,34] Si,[35–40] and silica.[41–43] A common picture has emerged that decomposition is thermally accessible on reactive metals such as Cu,[30] Pt,[31] and Ni[32]; in most other environments, IPC desorbs or

Received 16 August 2010. Accepted 20 January 2011. Published at www.nrcresearchpress.com/cjc on 2 September 2011.

C. Hauchard and P.A. Rowntree. Department of Chemistry, University of Guelph, Guelph, ON N1G 2W1, Canada.

Corresponding author: P.A. Rowntree (e-mail: rowntree@uoguelph.ca).

Can. J. Chem. Downloaded from www.nrcresearchpress.com by Xi'an Jiaotong University on 09/19/12
For personal use only.

evaporates from matrices in a molecular fashion. Thermal decomposition proceeds stepwise leading to Fe-rich adsorbates such as $Fe(CO)_4$, $Fe(CO)_3$, and $Fe(CO)_2$. The photolysis of adsorbed IPC has been studied using several substrates such as Au(111),[20] Ag(111),[24,25] and Al/SiO_2.[42] The adsorbed films are sensitive to photons in the 150–330 nm range, and the CO:Fe ratio that is produced under these conditions is typically ~4 for monolayer photolysis, and near 3 for multilayer photolysis. The decomposition products are generally less sensitive to radiation at these wavelengths than is the IPC, an effect that has been attributed to electronic de-excitation of the excited states by the surface.

Electron-induced decomposition is an attractive alternative for these systems. IPC is readily decomposed by electron impact, which has stimulated interest in using scanning tunneling microscopes as a localized electron source in surface "writing" procedures.[44–46] High-energy electron-induced (500–3000 eV) dissociation has been employed by Kunz et al.;[47–49] in these studies, the high-energy beam creates considerable decomposition of the carbonyl moieties, leading to the inclusion of unwanted C in the metal deposit. To our knowledge, there are very few studies of low-energy (0–20 eV) decomposition of adsorbed IPC; this is unfortunate, since this is the range of energies that is easily produced in STM-based experiments. In addition, this is the range of energies for secondary electrons created by high-energy electron impact onto surfaces;[50,51] electron scattering to form these low-energy secondary electrons in molecular adsorbates has been shown to be the major factor that limits the spatial resolution of electron-beam-deposited nanostructures,[50] and a better understanding of the decomposition pathways for these species on surfaces is of considerable importance. Compton and Stockdale[2] measured the gas-phase sensitivity of IPC to electrons; they found that the parent $Fe(CO)_5^-$ species is not stable, with $Fe(CO)_4^-$ being observed in high yield with electron energies from 0 to 3 eV. As the incident electron energy increases the degree of ligand elimination increases, with bare Fe^- being observed from 6 to 11 eV. In all cases, the fragment bearing the Fe atom traps the incident electron. The observation of such low-energy dissociation channels, coupled with the direct detection of anionic fragments, shows that decomposition proceeds by dissociative electron attachment (DEA);[1,2] moreover, the onset at ~0 eV shows that the repulsive anionic potential surface (upon which the dissociation takes place) crosses the neutral ground-state surface near its energetic minimum. This leads to high dissociation probabilities, since the newly created anionic species does not present a stable interaction potential well. Henderson et al.[26,27] studied the electron-induced decomposition of IPC adsorbed on Ag(111) surfaces as a function of the incident energy to extract cross sections describing the probability of the decarbonylation process; their cross sections ranged from <1 to 14 $Å^2$ in the 3–132 eV regime, with no apparent structure in the cross section versus energy profile. In view of the very high sensitivity of gas-phase IPC to low-energy electrons, and the utility of these processes in surface science, we have performed an extensive series of works to study the adsorption of IPC onto Au(111) and self-assembled monolayer (SAM) substrates,[52,53] and the present report on the sensitivity of these films to low-energy electrons as a function of the film preparation conditions. Electron-induced processes in IPC adsorbed on *n*-alkanethiol SAMs are reported elsewhere.[54]

Experimental

The IRRAS instrument used in these experiments consists of a standard ion-pumped (220 L/s) chamber with a base pressure of 2×10^{-10} torr (1 torr = 133.3224 Pa); for all results reported herein with the closed-cycle cryostat (APD-202B) being used for sample cooling, the base chamber pressure is reduced to 5×10^{-11} torr. This system is equipped with a turbomolecularly pumped load–lock system for substrate introduction and a residual gas analyzer (Stanford Research Systems RGA-200) to verify the purity of gas supplies. The IRRAS components are arranged on a single 8 in. (1 in. = 25.4 mm) OD Conflat flange containing twin differentially pumped NaCl windows. The plane of the sample is parallel to this flange; two internal adjustable room-temperature Au/glass mirrors served to reflect the incident modulated IR beam that passes through the first NaCl window onto the surface at grazing incidence (~85° from the surface normal) and to direct the reflected divergent beam out of the vacuum chamber via the second NaCl window. This internal mirror configuration was adopted to allow the measurement of transmission spectra and the use of spectral references whereby the light passes just in front of the surface without reflection; this is especially important for the IRRAS characterization of organic SAMs that are introduced onto the chamber via the load–lock. A conventional FTIR bench (Nicolet Magna 550) provided the plane-parallel modulated IR radiation, which is focused and directed into the vacuum system within a purged optical bench fixed to the IRRAS flange; the MCT-A IR detector is also within this optical accessory. Custom LabVIEW-based software was used to control the spectrometer operation, acquire data, and present the spectra for analysis and interpretation. Typical spectrometer parameters were 2 cm^{-1} resolution, (1 cm^{-1} data point spacing), ~2 cm/s moving mirror velocity, Happ–Ganzel apodization, with no zero-filling; ~128–256 mirror scans were co-added to produce each measured reflectivity versus wavenumber profile. Spectra are reported herein as absorbance spectra, whereby the reflectivity is referenced to the reflectivity of a pristine Au/mica surface, or as Δabsorbance spectra, whereby the reference is the reflectivity of the IPC/Au/mica system; this latter presentation is used to focus on the changes introduced by the electron bombardment, with the anticipated ligand removal being evidenced by negative-going peaks.[55]

The axis of a custom-built low-energy electron source is orthogonal to the IRRAS flange and the sample surface, precisely centred between the two NaCl windows. This source uses three cylindrical lenses to deliver the high-current beam from a resistively heated Ta disk filament (Kimball Physics) to the surface under consideration at normal incidence. Two orthogonal deflection fields between the final lens and the surface are used to align the beam onto the surface and to raster it across the sample along both the horizontal and vertical axes to ensure uniform irradiation. The optimum parameters to align and raster the beam were established for each electron energy according to the profile of current to the sample versus the deflection field strength in each direction.

Can. J. Chem. Downloaded from www.nrcresearchpress.com by Xi'an Jiaotong University on 09/19/12
For personal use only.

The entire surface was rastered at ~10–100 Hz. The electron energy is established by the potential difference between the centre of the filament and the surface, with an estimated accuracy of ±0.5 eV; the sample was typically maintained at –2 V (with respect to chamber ground) to prevent low-energy electrons that have scattering off the lenses or deflector plates from reaching the surface. The breadth of the energy distribution is believed to have a FWHM of ~0.3–0.4 eV. All lens potentials were fixed with respect to the filament potential and the deflector potentials were fixed with respect to the surface potential. Beam currents were measured on the biased substrate and were recorded to quantify the absorbed charge for each irradiation.

Au films (150 nm) were evaporated at a rate of 1–10 Å/s onto freshly cleaved mica sheets (Proscience-Techniglass, ASTM-V2) in an all-metal turbomolecular-pumped evaporation system used only for this purpose, based on the protocol of DeRose et al.;[56] these films have predominantly Au(111) texture owing to the heating to 300 °C before, during, and after the metal evaporation. Films were removed from the evaporator, cleaned with sulfochromic acid to eliminate adventitiously adsorbed hydrocarbons, then cut to size and mounted onto Cu sample carrier plates; copper mounting straps on the Au surface ensured good thermal contact. These sample carrier plates have a protrusion on the lower edge that is immersed in a Ga well when positioned on the sample manipulator; below the 27 °C freezing point of Ga, this provides a rigid mechanical contact with high thermal and electrical conductivity between the sample and the sample holder. This latter was supported on a five-axis manipulator system using glass beads as pivot axes, with an OFHC copper braid extending to the tip of the cryostat mentioned above to cool the sample while permitting adequate movement for optical alignment and sample exchange. Minimum sample temperatures of 45 K were routinely achieved with this system, although the heating and cooling rates were limited to ~10 K/min because of the large thermal mass of the system.

IPC (Sigma-Aldrich) was vacuum distilled and transferred to the gas manifold under Ar cover. It was freeze–thaw purified under vacuum on the manifold and changed weekly or as required if decomposition was suspected. IPC was dosed onto the surface from a background pressure of 2×10^{-8} torr; all coverages reported herein are in Langmuirs (1 Langmuir = 10^{-6} torr × s), with no corrections made for gauge sensitivity. As discussed elsewhere,[52,53] we estimate that monolayer coverages correspond to ~3–5 Langmuir; this is consistent with the 5 Langmuir estimate by other workers[20] for IPC deposition on Au(111) crystals at 80 K. Mass analysis of the gas during deposition showed no masses above the parent peak; as expected, extensive fragmentation of IPC in the ion source was observed.

Results and discussion

Electron-induced changes to the IR spectra

IPC was adsorbed onto the Au/mica substrates at 45 K; desorption occurs at 150–160 K. Figure 1A shows the IRRAS absorbance spectra of 5 Langmuir IPC/Au/mica measured at 45 K. Below ~120 K no changes are seen in the spectra of as-deposited films. They are characterized by a broad feature near 2012 cm^{-1} owing to the doubly degenerate equatorial

Fig. 1. Typical absorbance and Δabsorbance spectra for 5 Langmuir $Fe(CO)_5$ (IPC) / Au / mica films. (A) The absorbance spectrum of the as-deposited film. (B) and (C) The progressive changes to the absorbance provoked by 1 and 20 eV electrons, respectively, for cumulative doses of up to 2.5 mC/cm^2.

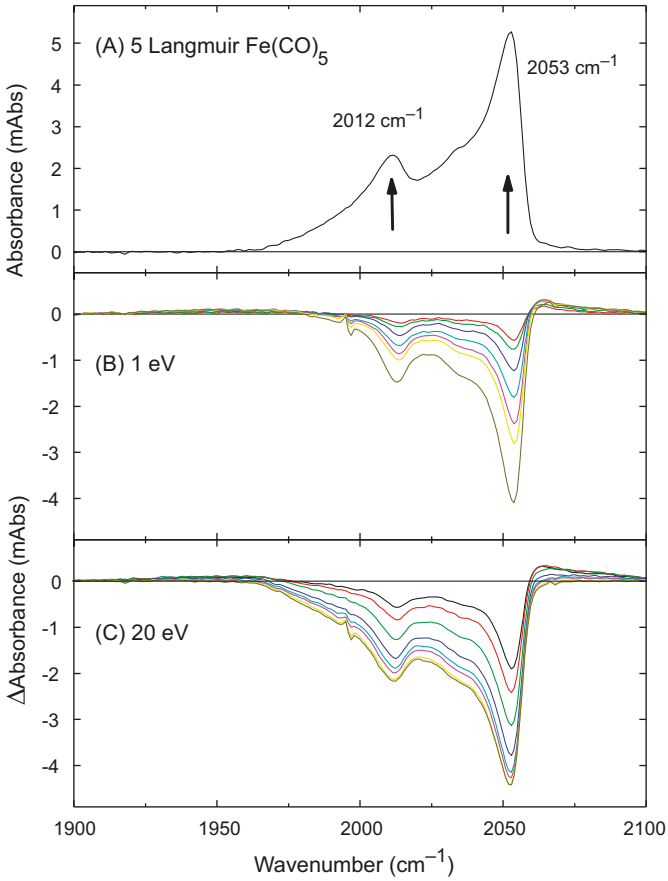

band and a sharper feature near 2053 cm^{-1} that is due to the asymmetric axial mode.[20,52] Aside from a small discrete peak near 2118 cm^{-1}, there is no significant optical absorbance below 1960 cm^{-1} or above 2062 cm^{-1}. The 2118 cm^{-1} feature has been attributed to the totally symmetric breathing mode, which appears weakly in the IRRAS spectrum because of the perturbation introduced by interaction with the metal substrate[20] or by the broken symmetry of grain boundaries.[52] These bands and the interpretation of the as-deposited monolayer structure are described in detail elsewhere.[52] Briefly, we find that the IPC layer in direct contact with the substrate is arranged with the C_3 molecular axis tilted by ~63° from the surface normal, with one axial and two equatorial CO groups directed towards the surface. This structure is consistent with the neutron diffraction results for IPC/C(0001)[33–35] and the energy minimization calculations based on semiempirical interaction potentials.[57] Similar IRRAS spectra are obtained for IPC monolayers on SAM substrates,[52] showing that specific binding to the substrate is not required to stabilize this structure.

As the exposure is increased beyond ~5 Langmuir, the equatorial band ceases to grow while the axial band narrows and shifts to higher frequencies; the high-coverage high-frequency limit is ~2062 cm^{-1} for all substrates studied, as shown in Fig. 2A. This evolution has been interpreted to be

Can. J. Chem. Downloaded from www.nrcresearchpress.com by Xi'an Jiaotong University on 09/19/12
For personal use only.

evidence that molecules in subsequent layers are adsorbed with the C_3 molecular axis more aligned with the surface normal;[52] dipolar coupling among these near-parallel transition dipoles causes the observed blue shifts.[58–60] Other structural motifs based upon strong IPC–surface interactions have been proposed to explain the shift to higher frequencies with coverage[30] for adsorbed IPC systems, but this is clearly not the case of the IPC/Au(111) or IPC/SAM systems, which are spectroscopically very similar. Equally important in the context of the present work is the observation[53] that the as-deposited films undergo a significant structural transformation when heated to 120–140 K (100–140 K on *n*-alkanethiol SAMs) that we have interpreted as the formation of solid 3D aggregates on the surface; this will be discussed in more detail in the following as it relates to the present electron-irradiation processes. With the exception of the results shown in Fig. 8B, all results presented herein are obtained for as-deposited films.

Figures 1B and 1C show the ΔAbsorbance spectra obtained when the 5 Langmuir deposits are irradiated with 1 and 20 eV electrons, respectively. Intermediate energies exhibit trends between these two limiting cases. In the limit of high delivered electron doses (~3–5 mC/cm^2), both bands can be significantly diminished for all electron energies, indicating extensive CO elimination from the surface. The extent of the band elimination under less extreme doses shows more variation with incident energy; for example, the 2053 cm^{-1} peak has lost three times more intensity at 20 eV than at 1 eV, for equivalent doses of 0.005 mC/cm^2.

The depletion structures of the ΔAbsorbance presentation are observed to be at the same positions as the structures in the original absorbance spectra, for all film thicknesses and for all electron energies. We note that the peak at 2118 cm^{-1} also suffers electron-induced CO elimination, although the weak intensity of this peak makes quantification difficult. For all electron energies impinging upon the 5 Langmuir films, the overall form of the ΔAbsorbance spectrum is almost identical to that of the initial absorbance spectrum; this indicates that there is little or no selectivity for removal of the axial versus equatorial ligands; to our knowledge, this has not been addressed in gas-phase studies. One of the most important trends shown in Figs. 1B and 1C is the initial electron-induced *increase* of IR absorbance in the regions from 1900 to 1980 cm^{-1} and from 2060 to 2100 cm^{-1}. These spectral regions are devoid of peaks associated with molecular IPC under all circumstances,[1–19] and we conclude that they are the signatures of newly created iron carbonyl species, in an unresolved structure that underlies the entire 1900–2100 cm^{-1} region. Continued irradiation at 1 eV causes the growth of these features to an asymptotic limit, whereas 20 eV bombardment causes a rapid growth followed by a slow decay of these features. The observation of a discreet absorbance feature during the electron irradiation implies that the chemical species that give rise to these features are significantly less sensitive to the incident electron flux than are the original IPC molecules; this is also consistent with the inability of the 1 eV electron beam to induce the decarbonylation of this species. In some cases, the intensity of the 2073 cm^{-1} feature increases with the beam current for a given total dose, suggesting that the rate of bombardment is important in the creation of this new species; this is the only instance that we are aware of for which low-energy electron reactive scattering displays such kinetic effects, and may be evidence of very slow surface reaction processes. In the absence of further electron irradiation or temperature changes, these structures show no temporal evolution on the seconds-to-hours timescales available in this experiment.

Fig. 2. Typical ΔAbsorbance spectra for 20 Langmuir $Fe(CO)_5$ (IPC) / Au / mica films. (A) The absorbance spectrum of the as-deposited film. (B) and (C) The progressive changes to the absorbance provoked by 1 and 20 eV electrons, respectively, for cumulative doses of up to 2.5 mC/cm^2.

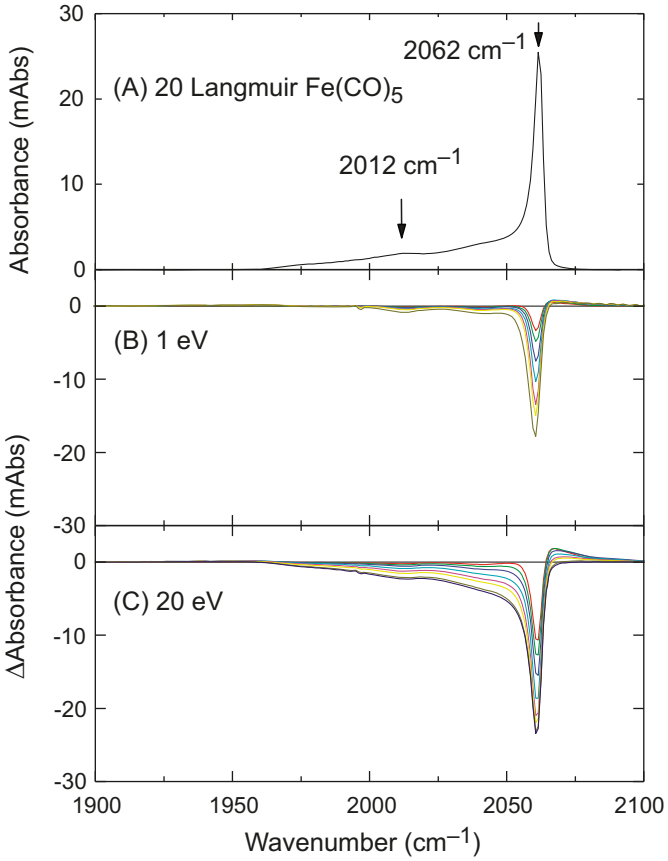

Similar results are observed for 20 Langmuir IPC/Au/mica, as shown in Figs. 2A–2C. Sharp depletions of the dominant axial-mode peak are seen for 1 and 20 eV electrons, with complete extinction possible for extended irradiation at energies above ~5 eV. Irradiation at 1 eV leads to narrower depletions, with significantly less effect on the 2012 cm^{-1} equatorial mode peak. Since this peak is the spectral signature of the tilted molecules in direct contact with the substrate,[52] this indicates that 1 eV electrons are not able to interact as strongly with this buried interface as are the 20 eV electrons. Since this behaviour was not found for the 5 Langmuir deposit (Fig. 1B), we presume that this reflects the inability of these very low-energy electrons to penetrate to the first layer of IPC, rather than a substrate-induced insensitivity of these molecules to the 1 eV excitations. This in turn indicates that the interactions of the electrons with the as-deposited film are extremely strong, with correspondingly large inelastic and reactive cross sections; weaker interactions would result in a more uniform irradiation and more uniform

Can. J. Chem. Downloaded from www.nrcresearchpress.com by Xi'an Jiaotong University on 09/19/12
For personal use only.

CO elimination within the entire 20 Langmuir film. The measurements on the 20 Langmuir films were hampered by the accumulation of negative charges in the film; it was not possible to experimentally distinguish charge trapping in interstitial sites from the creation of stable anionic molecular species, although as will be discussed in the following, we believe that latter to be an important process.

The quantitative interpretation of these results requires the measure of the IRRAS signal at a given wavenumber expressed as a function of the delivered dose per unit area (q). Irradiations have been performed in triplicate at 0.5, 1.0, 2.0, 5.0, 7.0, 9.0, 11.0, 15.0 and 20 eV for the 5 Langmuir films, and 1.0, 5.0, 10.0 and 20.0 eV for the 20 Langmuir films. Figure 3 presents the traces corresponding to the 1.0 and 20.0 eV irradiation of the 5 Langmuir IPC/Au/mica films, measured on the 2012 and 2053 cm^{-1} depletion features. For all electron energies employed, and on both peaks, the initial CO depletion is extremely rapid, again indicating that the interaction cross sections are very high. In each case, a second slower decarbonylation process follows this rapid CO elimination; semi-log plots also reveal this bi-exponential behaviour. In general, electron energies below ~5 eV inflict less decarbonylation in the first rapid process and in the slower second process than do higher energies. The break between these two regimes is below ~0.1 mC/cm^2 in all cases, corresponding to ~30% reduction in the CO band absorbance at low electron energies and as much as 80% reduction at higher energies.

Figure 4 shows the dose-dependent intensity of the 1950 and 2073 cm^{-1} "growth regions" identified previously, using 5 eV incident electrons and a 5 Langmuir IPC film. The growth and decay processes are clearly seen, and again, the break between these two regimes is always at <0.1 mC/cm^2. Although the magnitude of the 1950 cm^{-1} feature is always less than that of the 2073 cm^{-1} feature, both curves follow approximately the same profile for any given energy; as discussed previously, the profiles are energy-dependent. There is residual intensity on these features even at the maximum doses used, indicating that the newly created species are extremely resistant to the incident electron flux. Similar results are found using 20 Langmuir IPC films, with correspondingly stronger growth features, indicating that the newly created species are not preferentially formed at the IPC–metal or IPC–vacuum interfaces.

The following conclusions can be made based on the previous observations, which will guide the subsequent data analysis:

- Low-energy scattering causes rapid and extensive CO elimination from the film at all energies from 1 to 20 eV;
- The cross sections for the electron film reactive scattering events are very large;
- There is evidence of new species being created with wide and unstructured IR absorbances extending across the 1900–2100 cm^{-1} region;
- This new species is far less sensitive to electron-induced CO elimination than IPC;
- The sensitivity of the IPC and the newly formed species varies with the incident electron energy;
- There is no evidence of selective electron-induced elimination from the axial or equatorial molecular sites.

Fig. 3. Intensities at 2012 and 2053 cm^{-1} versus electron dose delivered to 5 Langmuir $Fe(CO)_5$ (IPC) / Au / mica films for 1 eV and 20 eV electrons. The solid lines are the fitted behaviours based on the extracted cross-section and compositional parameters in each case, as described in the text.

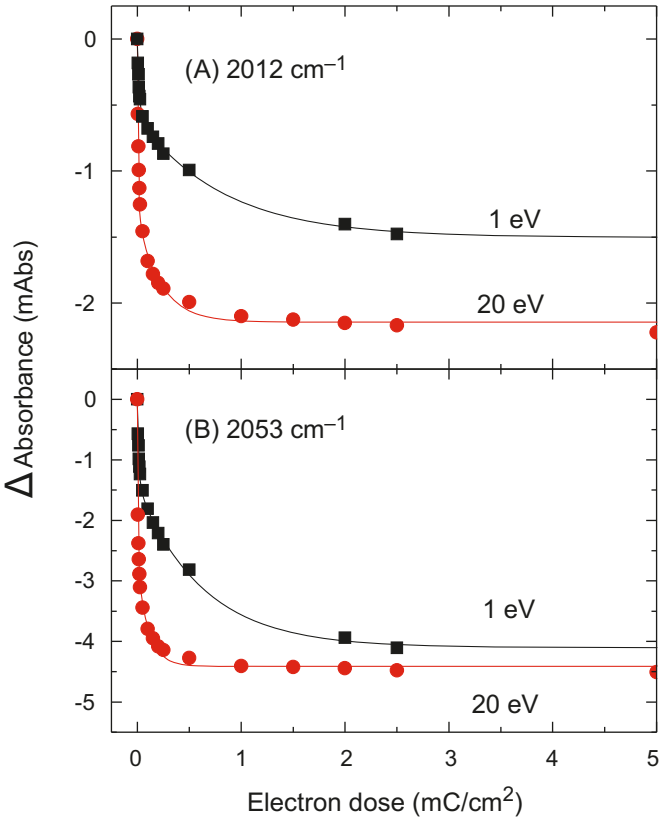

Fig. 4. Intensities at 1950 and 2073 cm^{-1} versus electron dose delivered to 5 Langmuir $Fe(CO)_5$ (IPC) / Au / mica films for 5 eV electrons. The lines are drawn to guide the eye.

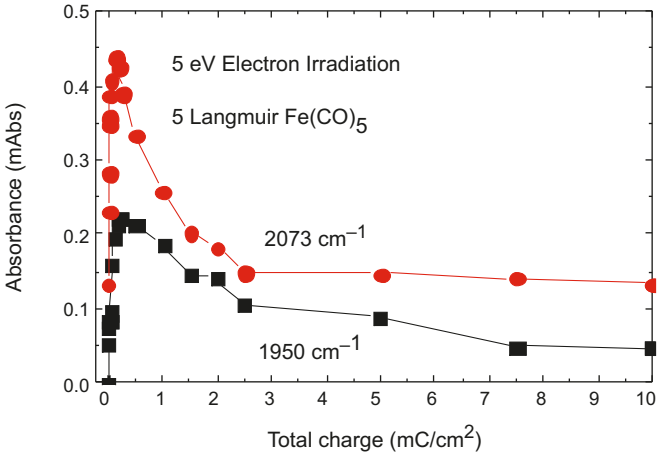

Mathematical model

To extract quantitative and transferable data from these measurements, we propose a sequential two-step irreversible reaction model involving three distinct types of surface bound species (**A**, **B**, and **C**)

Can. J. Chem. Downloaded from www.nrcresearchpress.com by Xi'an Jiaotong University on 09/19/12
For personal use only.

$$\mathbf{A} + e^- \xrightarrow{\sigma_{AB}} \mathbf{B}$$

$$\mathbf{B} + e^- \xrightarrow{\sigma_{BC}} \mathbf{C}$$

where **A** is the original IPC molecule, **B** represents the intermediate species that is formed by electron impact on the IPC, and **C** is taken to be the final material remaining following extensive irradiation at 45 K. This general scheme is not intended to imply that the fate of the incident electron is known at this point. The CO:Fe ratios that define the composition of the second and third species ($N_{\mathbf{B}}$ and $N_{\mathbf{C}}$) and the cross sections required to produce **B** and **C** ($\sigma_{\mathbf{AB}}$ and $\sigma_{\mathbf{BC}}$) are presumed to vary with the incident electron energy. Our objective was to analyse the spectral data and their dependence on the incident electron flux to have a better understanding of the initial processes taking place in these films, subject to several important caveats: in the absence of specific information, we necessarily neglect inelastic energy loss events in the adsorbed film, as well as the possible production of secondary electrons at higher incident energies. Assuming first-order dissociation dynamics, the following relationships define how the three populations ($P_{\mathbf{A}}$, $P_{\mathbf{B}}$, and $P_{\mathbf{C}}$) evolve under the influence of the incident electron dose, for a given electron energy.

$$\frac{\partial P_{\mathbf{A}}}{\partial q} = -\sigma_{\mathbf{AB}} P_{\mathbf{A}}$$

$$\frac{\partial P_{\mathbf{B}}}{\partial q} = \sigma_{\mathbf{AB}} P_{\mathbf{A}} - \sigma_{\mathbf{BC}} P_{\mathbf{B}}$$

$$\frac{\partial P_{\mathbf{C}}}{\partial q} = \sigma_{\mathbf{BC}} P_{\mathbf{C}}$$

Imposing the population constraint that the only species initially present is IPC, and that electron-stimulated desorption of the heavy iron-bearing fragments is negligible, then

$$P^0_{\mathbf{A}} = P_{\mathbf{A}}(q) + P_{\mathbf{B}}(q) + P_{\mathbf{C}}(q)$$

and the three dose-dependent populations are related as follows:

$$P_{\mathbf{A}}(q) = P^0_{\mathbf{A}} \exp(-\sigma_{\mathbf{AB}} q)$$

$$P_{\mathbf{B}}(q) = \frac{\sigma_{\mathbf{AB}} P^0_{\mathbf{A}}}{\sigma_{\mathbf{BC}} - \sigma_{\mathbf{AB}}} [\exp(-\sigma_{\mathbf{AB}} q) - \exp(-\sigma_{\mathbf{BC}} q)]$$

$$P_{\mathbf{C}}(q) = P^0_{\mathbf{A}} \left[1 - \frac{\sigma_{\mathbf{BC}}}{\sigma_{\mathbf{BC}} - \sigma_{\mathbf{AB}}} \exp(-\sigma_{\mathbf{AB}} q) + \frac{\sigma_{\mathbf{AB}}}{\sigma_{\mathbf{BC}} - \sigma_{\mathbf{AB}}} \exp(-\sigma_{\mathbf{BC}} q) \right]$$

Similar relationships are used to monitor the kinetics of two sequential reactions, whereby the rate constants determine the rate of population changes.[61] The link to the experimental results is made by assuming, consistent with the observations made previously, that the observed IR absorbance as a function of charge (Abs(q)) is simply proportional to the number of CO groups in each species multiplied by their respective populations, i.e.,

$$\mathrm{Abs}(q) = 5P_{\mathbf{A}}(q) + N_{\mathbf{B}} P_{\mathbf{B}}(q) + N_{\mathbf{C}} P_{\mathbf{C}}(q)$$

These equations were fit to the experimental data using a LabVIEW implementation of the Levenberg–Marquardt nonlinear least-squares fitting algorithm[62]; the extracted parameters were the populations and compositions of **B** and **C** during the irradiation process and the cross sections that govern the electron-induced processes. The results of these analyses are presented in Figs. 5 and 6 for the 5 Langmuir deposits based on the behaviour of the dominant 2053 cm^{-1} peak; the compositional data ($N_{\mathbf{B}}$ and $N_{\mathbf{C}}$) extracted for the 2012 cm^{-1} feature differ by <0.4 CO per Fe from the results presented herein, whereas the cross sections are usually within 20%–40% of those calculated for the 2053 cm^{-1} feature. These relatively minor discrepancies are due to the lower signal-to-noise of the equatorial peak.

The calculated cross sections for the first rapid process ($\sigma_{\mathbf{AB}}$, Fig. 5A) are indeed extremely large, revealing the high sensitivity of the IPC to the electron beam. The cross sections are always >60 $Å^2$, and typically are >100 $Å^2$, with a pronounced minimum near 2–4 eV. The cross sections for the second process leading to the **B** → **C** transformation ($\sigma_{\mathbf{BC}}$, Fig. 5B) follow the same trends as $\sigma_{\mathbf{AB}}$. As predicted, $\sigma_{\mathbf{BC}}$ is 1–2 orders of magnitude lower than $\sigma_{\mathbf{AB}}$; this disparity of the rates of creation and elimination leads to the observation of the 1950 and 2073 cm^{-1} growth and decay features during the irradiation. Although we have confidence in the approximate value of $\sigma_{\mathbf{BC}}$, the extraction of two widely different cross sections in a coupled process is mathematically difficult and the fit solutions can become unstable; the similar trends of $\sigma_{\mathbf{AB}}$ and $\sigma_{\mathbf{BC}}$ as a function of electron energy may be a consequence of this. Despite this caution, the extracted values of $\sigma_{\mathbf{BC}}$ confirm our observation that the decarbonylation of the intermediate **B** species is less probable at 1 eV than at 20 eV. Figure 6 shows the extracted CO:Fe composition ratios for the **B** and **C** species, expressed as a function of the incident electron energy. At $E_i \leq 1$ eV, the intermediate **B** species has an overall composition of $Fe(CO)_{3–4}$, and as the electron energy increases to 20 eV the average number of COs associated with each Fe atom decreases to approx. two, confirming that higher electron energies are more effective for the decarbonylation reactions involving IPC. At $E_i \leq 1$ eV, the final **C** product composition contains only 1.5–1.0 COs per Fe atom, and this low ratio decreases further to ~0.5 for $E_i \sim 20$ eV. Clearly, the final **C** product contains very little CO following extensive electron bombardment for $E_i \geq 2$ eV. The distinguishable behaviour of the high- and low-energy irradiation profiles indicates that, although inelastic scattering is certainly occurring in these films, it is unlikely that the high-energy irradiation induces decarbonylation via inelastic scattering coupled to a lower energy dissociation process.

The parameters extracted from this analysis confirm each of the qualitative conclusions outlined previously. Although we have not collected the same quantity of data for the 20 Langmuir IPC/Au/mica deposits because of sample-charging difficulties, the results extracted from this analysis are fully consistent with those extracted from the 5 Langmuir data. The agreement is encouraging in view of the approximations required

Can. J. Chem. Downloaded from www.nrcresearchpress.com by Xi'an Jiaotong University on 09/19/12
For personal use only.

Fig. 5. Cross-section parameters σ_{AB} (A) and σ_{BC} (B) extracted for electron irradiation of 5 Langmuir $Fe(CO)_5$ (IPC) / Au / mica films as a function of the incident electron energy.

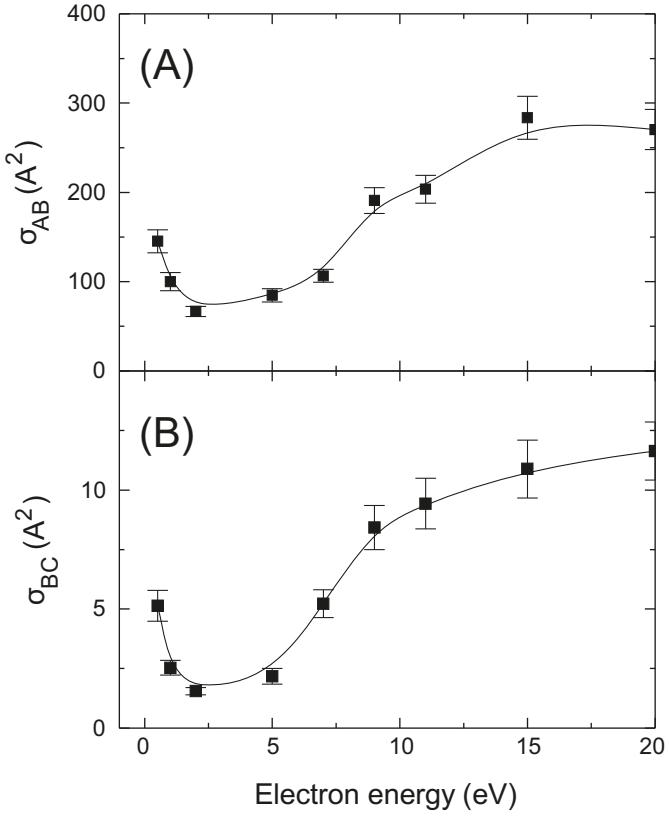

Fig. 6. Compositional parameters N_B and N_C extracted for electron irradiation of 5 Langmuir $Fe(CO)_5$ (IPC) / Au / mica films as a function of the incident electron energy.

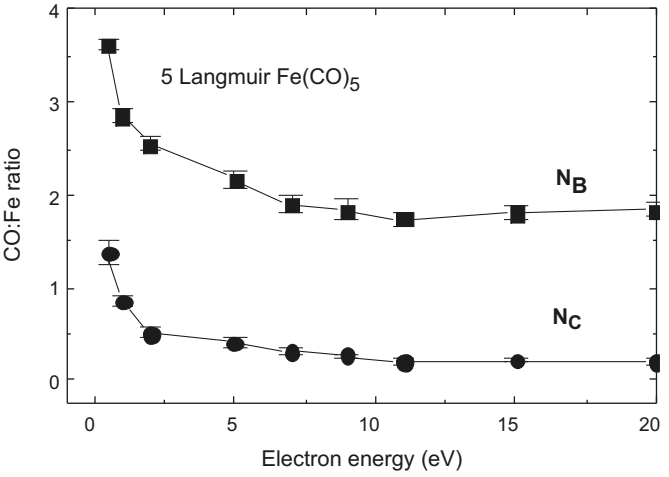

by our analysis. Table 1 shows the comparison between these sets of results and confirms the minimum of the σ_{AB} and σ_{BC} cross sections for $E_i \sim$ 2–5 eV.

Molecular interpretation

The extremely large σ_{AB} cross sections extracted by this analysis are encouraging in that they indicate that electron-induced decarbonylation of IPC is an extremely efficient process even at such low energies and may be of technological value. Their magnitude poses interesting questions concerning the mechanism of the initial electron-induced processes in the IPC films. In gas-phase electron–molecule scattering the maximum dissociative cross sections are always less than the limiting cross section for s-wave electron attachment ($\sigma_s \sim \pi\lambda^2$)[63,64] with λ being the de Broglie wavelength of the incident electron. For $E_i \sim$ 1 eV this implies an upper limit of ~100 Å^2, whereas at E_i = 12 eV the gas-phase cross sections cannot significantly exceed 1–10 Å^2. Whereas the low energy values of σ_{AB} measured above are bound by σ_s (and are consistent with the large cross sections observed for electron scattering in gas-phase IPC at low energies), the overall increase of σ_{AB} beyond $E_i \sim$ 2–5 eV cannot be directly interpreted in terms of single electron–molecule processes. The most obvious difference between the behaviour of the low-pressure gas-phase measurements and those of the present study is the possibility of secondary reactions following the initial electron-induced dissociation event. Wronka and Ridge[3] studied this process in a variable pressure ion – cyclotron resonance (ICR) gas cell containing IPC. They identified the following reaction sequences, starting with the primary dissociation of IPC to yield various fragment anions.

(1) At electron energies below ~1 eV, previous work[1,2] confirmed that the main product is $Fe(CO)_4^-$. In the ICR cell, this was found to react readily via

$$Fe(CO)_4^- + Fe(CO)_5 \xrightarrow{\sim k} Fe_2(CO)_8^- + CO, \quad N_{CO}:N_{Fe} = 4.0$$

where k is a relative rate constant that was used as a benchmark in their work. If additional reactions ensue, their reaction rates are less than k, and were not reported by Wronka and Ridge. Hence, if the primary $Fe(CO)_4^-$ product reacts with an adjacent IPC molecule, one additional CO will be released from the film, doubling the measured cross sections for decarbonylation; equally important, the final CO:Fe ratio for the surface bound species **B** will be ~4.0. This is in very good agreement with the composition of the intermediate **B** species extracted from the above analysis for $E_i \sim$ 0.5 eV as shown in Fig. 6.

(2) As the incident energy increases, the preferred fragmentation channel implies the release of more CO ligands in the primary dissociation event, with the Fe-bearing fragment always carrying the excess charge. Starting with the $Fe(CO)_3^-$ fragment, the ICR results found the following reactions to have significant rates

$$Fe(CO)_3^- + Fe(CO)_5 \xrightarrow{\sim 120k} Fe_2(CO)_6^- + 2CO, \quad N_{CO}:N_{Fe} = 3.0$$

$$Fe_2(CO)_6^- + Fe(CO)_5 \xrightarrow{\sim 16k} Fe_3(CO)_{10}^- + CO, \quad N_{CO}:N_{Fe} = 3.3$$

$$Fe_3(CO)_{10}^- + Fe(CO)_5 \xrightarrow{\sim k} Fe_4(CO)_{13}^- + 2CO, \quad N_{CO}:N_{Fe} = 3.3$$

$$Fe_4(CO)_{13}^- + Fe(CO)_5 \xrightarrow{\sim k} Fe_5(CO)_{16}^- + 2CO, \quad N_{CO}:N_{Fe} = 3.3$$

Table 1. Comparison of the electron-irradiation dissociation parameters obtained using 5 Langmuir films with those of 20 Langmuir films. The uncertainties of the cross sections are ±10%–15%, and the uncertainties on the composition parameters $N_{\mathbf{B}}$ and $N_{\mathbf{C}}$ are ±5%–10%.

	5 Langmuir films				20 Langmuir films			
Energy (eV)	$\sigma_{\mathbf{AB}}$ (Å^2)	$\sigma_{\mathbf{BC}}$ (Å^2)	$N_{\mathbf{B}}$	$N_{\mathbf{C}}$	$\sigma_{\mathbf{AB}}$ (Å^2)	$\sigma_{\mathbf{BC}}$ (Å^2)	$N_{\mathbf{B}}$	$N_{\mathbf{C}}$
1	100	2.5	2.8	0.7	137	5.0	3.1	1.4
5	85	2.0	2.4	0.5	115	2.5	1.9	0.4
10	204	9.5	1.8	0.3	267	9.0	1.8	0.4
20	270	11.5	1.8	0.2	406	10.5	2.1	0.3

If the primary product undergoes these four sequential additions to generate the final $Fe_5(CO)_{16}$ heteronuclear product shown, the incident electron will have provoked the elimination of nine CO ligands, multiplying the $\sigma_{\mathbf{AB}}$ cross sections accordingly, and producing a product that is slightly richer in Fe than observed at lower incident electron energies.

(3) Finally, if the incident electron energy is increased high enough to produce significant quantities of $Fe(CO)_2^-$, the ICR results indicate that the following reaction cascade may result

$$Fe(CO)_2^- + Fe(CO)_5 \rightarrow Fe_2(CO)_5^- + 2CO, \quad N_{CO}:N_{Fe} = 2.5$$

$$Fe_2(CO)_5^- + Fe(CO)_5 \xrightarrow{\sim 140k} Fe_3(CO)_9^- + CO, \quad N_{CO}:N_{Fe} = 3.0$$

$$Fe_3(CO)_9^- + Fe(CO)_5 \xrightarrow{\sim 150k} Fe_4(CO)_{12}^- + 2CO, \quad N_{CO}:N_{Fe} = 3.0$$

This process also eliminates a total of nine CO ligands, and the CO:Fe ratio has continued to decrease. Although the ICR experiments did not detail reactions beyond this because of the low abundance of the initial $Fe(CO)_2^-$ anion, the high rate constants measured for the last step characterized indicates that continued reactivity is a strong possibility.

The trends for the composition of the intermediate **B** species shown in these reaction sequences are consistent with those extracted from our results, although our values indicate that the intermediate **B** complex is slightly more Fe-rich than the ICR experiments would suggest. This may simply be a consequence of the higher IPC density in the condensed phase than in the gas-phase experiments, the desorption of lighter carbonyl species during electron bombardment, or it may be the result of inadequacies of the relatively simple mathematical model by which the data was interpreted. The minimum of the $\sigma_{\mathbf{AB}}$ cross sections at E_i = 2–5 eV (Fig. 5A) would appear to be the result of the decreased number of reactive anions created as the energy increases,[1,2] coupled to the increased reactivity of those anions that are formed.[3] The identification of this intermediate **B** species as a heteronuclear $Fe_n(CO)_m^-$ complex is supported by the growth of the 1950 and 2073 cm^{-1} features during the initial periods of electron irradiation. Previous work[65] has shown that such species have absorption bands at higher and lower frequencies than IPC; for example, whereas the highest IR active mode of gas-phase IPC is found at 2034 cm^{-1}, the strongest IR active modes of Fe_2CO_9 and Fe_3CO_{12} are at 2088 and 2056 cm^{-1}, respectively.[65] In all cases, bridging COs are observed at frequencies below 2000 cm^{-1},[65], which could be the origin of the growth and decay features observed herein at ~1950 cm^{-1}. Of course, these frequencies will be significantly shifted if the excess charge remains bound to the molecular core, and there is no reason to believe that the electron-induced reactions will generate oligamers with simple compositions or structures such as those studied under controlled conditions. We suggest that the relatively low values of $\sigma_{\mathbf{BC}}$ reflect the relative stability of the anionic intermediate **B** species to further electron-induced degradation; in addition, it is clear that since the growing heteronuclear material maintains the initial charge, additional electron attachment will be electrostatically hindered, further reducing the apparent $\sigma_{\mathbf{BC}}$ cross sections.

Thermal effects

In an effort to confirm the presence of the $Fe_n(CO)_m$ species following low-energy electron irradiation, we performed partial irradiation of 20 Langmuir IPC films, followed by heating of the sample at 2 K/min to induce desorption. Figure 7 shows the integrated intensity across the 1900–2100 cm^{-1} spectral region as a function of temperature for an as-deposited 20 Langmuir IPC/Au/mica film (squares) and for an identical film that has been exposed to 0.25 mC/cm^2 electron dose at 5 eV (circles). The integrated intensity of the as-deposited film shows a slow decrease up to ~120 K, presumably because of some weakly bound IPC desorption. At temperatures between 120 and 140 K, there is a marked intensity *increase* that is due to the irreversible structural transformation of the as-deposited film into compact 3D aggregates on the surface; this process has been discussed in detail elsewhere.[53] Desorption of the IPC is complete by 150–160 K, with no further spectral changes.

A very different desorption profile is seen for the partially irradiated film. More pronounced decreases are seen at low temperatures, which may be evidence of thermal desorption of lighter fragments. The 140 K thermal transformation is shifted to slightly higher temperatures and has a much less pronounced spectral signature following electron bombardment; larger polymeric species are less likely to laterally diffuse and crystallize than the original IPC. A second slight increase of integrated intensity is seen at ~210 K, which may signal another structural rearrangement; the last traces of CO in the film remain until the temperature reaches ~300 K. Bernasek[66] showed that the thermal desorption of CO

Can. J. Chem. Downloaded from www.nrcresearchpress.com by Xi'an Jiaotong University on 09/19/12
For personal use only.

Can. J. Chem. Downloaded from www.nrcresearchpress.com by Xi'an Jiaotong University on 09/19/12
For personal use only.

Fig. 7. Integrated intensity of the 1900–2100 cm^{-1} region versus temperature for 20 Langmuir $Fe(CO)_5$ (IPC) / Au / mica (squares) and for 20 Langmuir IPC/Au/mica following 0.25 mC/cm^2 irradiation at 5 eV (circles). The integrated intensities have been scaled to approximately similar values at 50 K.

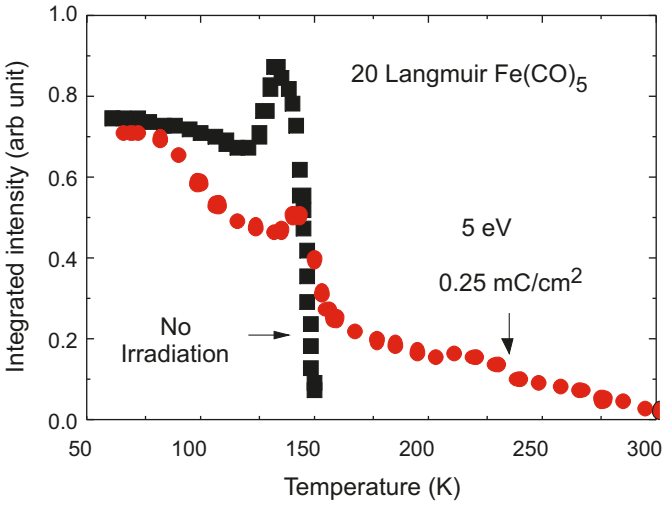

from Fe(100) surfaces takes place via multiple processes at 220, 306, 440, and 825 K; the first two peaks are from molecular CO/Fe(100) and the higher temperature peaks are due to C–O recombination processes. The close similarity of our observed temperature-induced desorption restructuring at 210 K and the final desorption temperature of ~300 K to the molecular CO/Fe(100) results suggests that our irradiated films are indeed composed of CO interacting with iron-rich regions, as proposed from our discussions and analysis.

We also explored the effect of the thermal transformation of the IPC film described previously on the apparent sensitivity to low-energy electron scattering. Figure 8 shows the effect of 5 eV irradiation on as-deposited 20 Langmuir IPC/Au/mica samples, as well as 20 Langmuir IPC/Au/mica that has been transformed by heating to ~140 K then rapidly cooled to 45 K. As discussed in detail previously, the as-deposited films are extremely sensitive to the incident electron flux; exposure to a dose of only 0.005 mC/cm^2 reduces the dominant axial band absorption by ~35%, and a total dose of 0.05 mC/cm^2 has almost completely extinguished both peaks. However, when the thermally transformed IPC/Au/mica is exposed to a 5.0 mC/cm^2 dose under identical conditions (Fig. 8B), no quantifiable changes are observed. We estimate that the heating above 120 K reduces the *apparent* cross section by *2–3 orders of magnitude* with respect to the as-deposited film.

The thermally induced structural transformations of IPC films on Au/mica and on alkanethiol self-assembled monolayer substrates have been described in detail elsewhere;[53] the thermal behaviour of the adsorbed IPC is essentially identical for these two substrates. We have shown that the IR spectra of the stretching modes associated with the terminal methyl group of self-assembled monolayers are extremely sensitive to the presence of most adsorbates, including IPC. The strong symmetric stretch at 2875 cm^{-1} suffers a systematic shift to lower wavenumbers and a decrease in intensity when in the presence of an atomic or molecular overlayer such as IPC; upon heating to ~140 K, however, this peak re-

Fig. 8. Effect of thermal pre treatments on decarbonylation processes in 20 Langmuir $Fe(CO)_5$ (IPC) / Au / mica films. (A) The absorbance spectrum of the as-deposited film and the effects of irradiating this film at 5 eV with total doses of 0.005, 0.05, and 0.5 mC/cm^2. (B) The pre-irradiation absorbance spectrum obtained by heating a 20 Langmuir IPC/Au/mica film to ~130 K. Subsequent spectra measured following doses of up to 5.0 mC/cm^2 show no significant electron-induced changes.

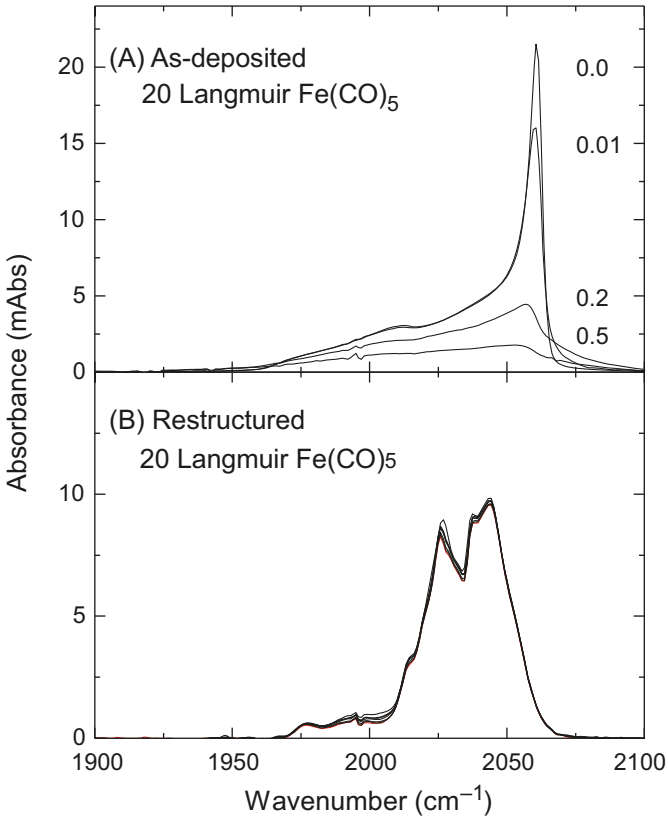

covers essentially all of its original intensity, even though the C–O stretching spectra of the carbonyl bands show that the no significant desorption of IPC has occurred at this temperature. The reduced interaction of the IPC adsorbates with the methyl-terminated surface witnesses the aggregation of the IPC into 3D islands or aggregates, since most of the SAM is no longer covered by the IPC. In fact, the newly exposed methyl terminations (in the presence of the IPC aggregates) can be exposed to additional IPC, and the IR spectra of the methyl terminations suffer the same spectral shifts that were observed during the first adsorption cycle, as the open regions of the SAM are once again covered with as-deposited IPC; reheating to 140 K causes the aggregates to grow even larger by mass transfer from the layers to the aggregates and re-exposes most of the methyl-terminated substrate. This aggregation process is irreversible, indicating that the as-deposited films are not in the thermodynamic ground state.[53] There is no evidence for thermally induced chemical changes to the IPC under the conditions of these experiments and with the substrates employed herein.

The remarkable change in the apparent sensitivity to the incident electrons upon heating is a direct consequence of the extremely large cross sections measured herein, coupled

Can. J. Chem. Downloaded from www.nrcresearchpress.com by Xi'an Jiaotong University on 09/19/12
For personal use only.

with the compact structure of the 3D IPC aggregates formed by heating. In this form most of the surface consists of exposed Au/mica regions, such that most electrons do not interact with the molecular solids; furthermore, only a very small fraction of the total IPC content of the film is on the exterior of the aggregates. Those few electrons that do interact with the IPC on the aggregate surfaces will form an electron-resistant "crust" on the aggregate that will further reduce the penetration of electrons into the solid. Previous work[41] showed that the photolysis cross sections of $Fe(CO)_5$ on silica surfaces is reduced following heating to 100 K, and this was attributed to the caging of CO fragments within the solid, followed by recombination with Fe-bearing fragments. Although caging and recombination are conceivable in the present case, we note that these electron-induced dissociation processes occur on anionic potential energy surfaces; successful recombination following DEA would require the reaction of CO with an anionic Fe-bearing fragment to be accompanied by electron emission, since the parent anion of IPC is not stable. This does not seem to be a very probable sequence of events. We conclude that the fundamental causes of the thermally induced deactivation of the IPC deposit towards low-energy electron impact are the reduced 2D surface area that is occupied by the thermally transformed IPC deposit and the lack of electron penetration into the 3D aggregates. Thus, we emphasize that it is the *apparent* sensitivity of IPC in the fully aggregated form that has been reduced by the structural transformation, and not the sensitivity of individual molecules.

To our knowledge, the only published study of low-energy electron irradiated IPC physisorbed on surfaces is that of Henderson et al.[26] for IPC/Ag(111). This work quantified the IPC and CO remaining on the surface as a function of the electron dose using temperature-programmed desorption; they too reported that the surface is transformed into $Fe_n(CO)_m$ species. However, the extent of the electron-induced decomposition is dramatically different. As shown in Fig. 3, a delivered dose of only 0.02 mC/cm^2 (~1.2×10^{14} e/cm^2) at 1 and 20 eV reduces our CO band strengths by ~30%–70%; the TPD results of Henderson et al.[26] show negligible IPC depletion for these levels of electron irradiation. As a result, their electron-induced decomposition cross sections for monolayer deposits of IPC (<1, 2.0, and 6.1 Å^2 for E_i = 3, 8, and 25 eV, respectively) are significantly lower than the results reported herein. To prepare highly uniform films, these workers heated multilayer deposits to ~157 K to desorb all but the IPC directly adsorbed onto the Ag(111) substrate, then recooled the sample to 90 K to perform the electron irradiation experiment. It is possible that this monolayer preparation protocol had the unexpected effect of transforming the remaining IPC/Ag(111) adsorbates into the compact aggregates as found above. This process is insensitive to the nature of the substrate for physisorbed IPC,[53] and once transformed, the IPC molecules appear to be resistant to the low-energy electrons.

Conclusions

This work reports the effect of low-energy electrons on films of IPC on Au/mica substrates. The decarbonylation process is described by a fast initial process that leads to a 20%–80% reduction in the CO content of the film, followed by a slower process leading to almost complete CO elimination. The decarbonylation cross sections for the first step are extremely large (~60–300 Å^2 for the 1–20 eV regime); we have interpreted this as showing that the initial process proceeds by the sequential reactions of Fe-bearing anionic species with adjacent IPC of the film to create progressively larger $Fe_n(CO)_m$ anions and progressively greater CO elimination. A simple kinetic model based on the gas-phase reactivity of anionic $Fe_n(CO)_m^-$ fragments has been shown to provide qualitative and quantitative agreement with the IR-RAS results. These apparent decarbonylation cross sections are extremely sensitive to the physical state of the IPC deposit; when arranged in compact 3D aggregates, the overall film is several orders of magnitude less sensitive to low-energy electrons. Our results suggest that this dramatic decrease is due to the small "footprint" of the aggregates on the Au/mica surface, which causes most electrons to strike pristine metal surfaces rather than the molecular adsorbates, as well as the reduced access of the electrons to the interior of the aggregates owing to their very strong interactions with the outermost IPC layers.

This study provides a quantitative framework by which to understand these highly reactive films and to develop methods by which these simple and volatile organometallics can be used to deposit metal atoms on surfaces. In the case of traditional metallic and semiconducting substrates, the use of low-energy electrons may provide a cleaner decomposition pathway than the more traditional high-energy irradiation; work in progress will quantify the C and O impurities that are trapped in the Fe overlayer during this deposition method. However, we feel that the most promising application of this approach is in the deposition of metal layers on substrates that are themselves sensitive to higher energy incident particles. Organic self-assembled monolayers are one example, since they are known to suffer large electron-induced bond rupture (C–H, C–C) for electron energies above ~6.5 eV.[55,67] As the results of this work have shown, decarbonylation of IPC is extremely efficient with incident energies well below this damage threshold for the SAM, and the deposition of metal layers on fragile organic films may be practical with this approach.[54]

Acknowledgement

The authors are grateful to the Natural Sciences and Engineering Research Council of Canada (NSERC) for their financial support of this research.

References

(1) Pignataro, S.; Foffani, A.; Grasso, F.; Cantone, B. *Z. Physik. Chem. Neue Folge* **1965** *47*, 106.
(2) Compton, R. N.; Stockdale, J. A. D. *Int. J. Mass Spectrom. Ion Phys.* **1976** *22* (1–2), 47. doi:10.1016/0020-7381(76)80106-4.
(3) Wronka, J.; Ridge, D. P. *J. Am. Chem. Soc.* **1984** *106* (1), 67. doi:10.1021/ja00313a015.
(4) Cataliotti, R.; Foffani, A.; Marchetti, L. *Inorg. Chem.* **1971** *10* (8), 1594. doi:10.1021/ic50102a010.
(5) Edgell, W. F.; Wilson, W. E.; Summitt, R. *Spectrochim. Acta* **1963** *19* (6), 863. doi:10.1016/0371-1951(63)80173-3.
(6) Edgell, W. F.; Dunkle, M. P. *J. Phys. Chem.* **1964** *68* (3), 452. doi:10.1021/j100785a002.
(7) Lundquist, R. T.; Cais, M. *J. Am. Chem. Soc.* **1962** *27*, 1167.

Can. J. Chem. Downloaded from www.nrcresearchpress.com by Xi'an Jiaotong University on 09/19/12
For personal use only.

(8) King, F. T.; Lippincott, E. R. *J. Am. Chem. Soc.* **1956** *78* (17), 4192. doi:10.1021/ja01598a003.
(9) Stammreich, H.; Sala, O.; Tavares, Y. *J. Chem. Phys.* **1959** *30* (3), 856. doi:10.1063/1.1730068.
(10) Cotton, F. A.; Danti, A.; Waugh, J. S.; Fessenden, R. W. *J. Chem. Phys.* **1958** *29* (6), 1427. doi:10.1063/1.1744746.
(11) Murata, H.; Kawai, K. *J. Chem. Phys.* **1958** *28* (3), 516. doi:10.1063/1.1744179.
(12) Nagano, Y.; Achiba, Y.; Kimura, K. *J. Chem. Phys.* **1986** *84* (3), 1063. doi:10.1063/1.450548.
(13) Baerends, E. J.; Ros, P. *Mol. Phys.* **1975** *30* (6), 1735. doi:10.1080/00268977500103261.
(14) Baev, A. K. *Russ. J. Phys. Chem.* **1993** *67*, 1783.
(15) Poliakoff, M.; Turner, J. J. *J. Chem. Soc., Dalton Trans.* **1973** *13* (13), 1351. doi:10.1039/dt9730001351.
(16) Poliakoff, M.; Turner, J. J. *J. Chem. Soc., Dalton Trans.* **1974** *20* (20), 2276. doi:10.1039/dt9740002276.
(17) Poliakoff, M.; Turner, J. J. *J. Chem. Soc., Faraday Trans. II* **1974** *70*, 93. doi:10.1039/f29747000093.
(18) Poliakoff, M. *J. Chem. Soc., Dalton Trans.* **1974** *2* (2), 210. doi:10.1039/dt9740000210.
(19) De Paoli, M. A.; De Oliveira, S. M.; Baggio-Saitovitch, E.; Guenzburger, D. *J. Chem. Phys.* **1984** *80* (2), 730. doi:10.1063/1.446779.
(20) Sato, S.; Suzuki, T. *J. Phys. Chem.* **1996** *100* (35), 14769. doi:10.1021/jp960775n.
(21) Sato, S.; Suzuki, T. *Appl. Spectrosc.* **1997** *51* (8), 1170. doi:10.1366/0003702971941692.
(22) Sato, S.; Suzuki, T. *J. Electron Spectrosc. Relat. Phenom.* **1997** *83* (1), 85. doi:10.1016/S0368-2048(96)03068-X.
(23) Sato, S.; Ukisu, Y.; Ogawa, H.; Takasu, Y. *J. Chem. Soc., Faraday Trans.* **1993** *89* (24), 4387. doi:10.1039/ft9938904387.
(24) Sato, S.; Ukisu, Y.; Ogawa, H.; Takasu, Y. *Appl. Surf. Sci.* **1994** *79–80*, 428. doi:10.1016/0169-4332(94)90449-9.
(25) Sato, S.; Tanaka, S. *Appl. Surf. Sci.* **1998** *135* (1–4), 83. doi:10.1016/S0169-4332(98)00280-3.
(26) Henderson, M. A.; Ramsier, R. D.; Yates, J. T., Jr. *Surf. Sci.* **1991** *259* (1–2), 173. doi:10.1016/0039-6028(91)90535-Z.
(27) Henderson, M. A.; Ramsier, R. D.; Yates, J. T., Jr. *J. Vac. Sci. Technol. A* **1991** *9* (3), 1563. doi:10.1116/1.577662.
(28) Henderson, M. A.; Ramsier, R. D.; Yates, J. T., Jr. *Surf. Sci.* **1992** *275* (3), 297. doi:10.1016/0039-6028(92)90802-D.
(29) Celii, F. G.; Whitmore, P. M.; Janda, K. C. *Chem. Phys. Lett.* **1987** *138* (2–3), 257. doi:10.1016/0009-2614(87)80377-9.
(30) Sun, L.; McCash, E. M. *Surf. Sci.* **1999** *422* (1–3), 77. doi:10.1016/S0039-6028(98)00881-4.
(31) Zaera, F. *Surf. Sci.* **1991** *255* (3), 280. doi:10.1016/0039-6028(91)90684-K.
(32) Xu, M.; Zaera, F. *Surf. Sci.* **1994** *315* (1–2), 40. doi:10.1016/0039-6028(94)90539-8.
(33) Wang, R.; Taub, H.; Shechter, H.; Brener, R.; Suzanne, J.; Hansen, F. Y. *Phys. Rev. B* **1983** *27* (9), 5864. doi:10.1103/PhysRevB.27.5864.
(34) Dennison, J. R.; Taub, H.; Hansen, F. Y.; Shechter, H.; Brener, R. *Phys. Rev. B* **1988** *37* (4), 2266. doi:10.1103/PhysRevB.37.2266.
(35) Foord, J. S.; Jackman, R. B. *Chem. Phys. Lett.* **1984** *112* (2), 190. doi:10.1016/0009-2614(84)85020-4.
(36) Foord, J. S.; Jackman, R. B. *J. Opt. Soc. Am. B* **1986** *3* (5), 806. doi:10.1364/JOSAB.3.000806.
(37) Foord, J. S.; Jackman, R. B. *Surf. Sci.* **1986** *171* (1), 197. doi:10.1016/0039-6028(86)90570-4.
(38) Gluck, N. S.; Ying, Z.; Bartosch, C. E.; Ho, W. *J. Chem. Phys.* **1987** *86* (9), 4957. doi:10.1063/1.452667.
(39) Swanson, J. R.; Friend, C. M.; Chabal, Y. J. *J. Chem. Phys.* **1987** *87* (8), 5028. doi:10.1063/1.452819.
(40) Thibaudau, F.; Masson, L.; Chemem, A.; Roche, J. R.; Salvan, F. *J. Vac. Sci. Technol. A* **1998** *16* (5), 2967. doi:10.1116/1.581447.
(41) Trusheim, M. R.; Jackson, R. L. *J. Phys. Chem.* **1983** *87*, 1910. doi:10.1021/j100234a017.
(42) Sato, S.; Minoura, S.; Urisu, T.; Takasu, Y. *Appl. Surf. Sci.* **1995** *90* (1), 29. doi:10.1016/0169-4332(95)00059-3.
(43) Darsillo, M. S.; Gafney, H. D.; Paquette, M. S. *J. Am. Chem. Soc.* **1987** *109* (11), 3275. doi:10.1021/ja00245a016.
(44) McCord, M. A.; Awschalom, D. D. *Appl. Phys. Lett.* **1990** *57* (20), 2153. doi:10.1063/1.103923.
(45) Kent, A. D.; Shaw, T. M.; Von Molnar, S.; Awschalom, D. D. *Science* **1993** *262* (5137), 1249. doi:10.1126/science.262.5137.1249.
(46) de Lozanne, A. *Jpn. J. Appl. Phys.* **1994** *33*, 7090. doi:10.1143/JJAP.33.7090.
(47) Kunz, R. R.; Mayer, T. M. *Appl. Phys. Lett.* **1987** *50* (15), 962. doi:10.1063/1.97999.
(48) Kunz, R. R.; Allen, T. E.; Mayer, T. M. *J. Vac. Sci. Technol. B* **1987** *5* (5), 1427. doi:10.1116/1.583629.
(49) Kunz, R. R.; Mayer, T. M. *J. Vac. Sci. Technol. B* **1988** *6* (5), 1557. doi:10.1116/1.584214.
(50) Silvis-Cividjian, N.; Hagen, C. W.; Leunissen, L. H. A.; Kruit, P. *Microelectron. Eng.* **2002** *61–62*, 693. doi:10.1016/S0167-9317(02)00515-4.
(51) Zharnikov, M.; Geyer, W.; Gölzhäuser, A.; Frey, S.; Grunze, M. *Phys. Chem. Chem. Phys.* **1999** *1*, 3163. doi:10.1039/a902013f.
(52) Hauchard, C.; Pépin, C.; Rowntree, P. *Langmuir* **2005** *21* (20), 9154. doi:10.1021/la050593x.
(53) Hauchard, C.; Pépin, C.; Rowntree, P. *Langmuir* **2005** *21* (20), 9166.
(54) Work in progress.
(55) Olsen, C.; Rowntree, P. A. *J. Chem. Phys.* **1998** *108* (9), 3750. doi:10.1063/1.475780.
(56) DeRose, J. A.; Thundat, T.; Nagahara, L. A.; Lindsay, S. M. *Surf. Sci.* **1992** *256* (1–2), 102. doi:10.1016/0039-6028(91)91204-B.
(57) Wang, R. W. Doctoral Dissertation, University of Missouri-Columbia, 1983.
(58) Ryberg, R. Infrared Spectroscopy of Molecules Adsorbed on Metal Surfaces. In *Advances in Chemical Physics: Molecule Surface Interactions;* Lawley, K. P. Ed.; John Wiley & Sons, Hoboken, NJ, 1989; Vol. 76. doi:10.1002/9780470141250.ch1.
(59) Persson, B. N. J.; Ryberg, R. *Phys. Rev. B* **1981** *24* (12), 6954. doi:10.1103/PhysRevB.24.6954.
(60) Persson, B. N. J.; Liebsch, A. *Surf. Sci.* **1981** *110* (2), 356. doi:10.1016/0039-6028(81)90644-0.
(61) Atkins, P. *Physical Chemistry;* 5th ed.; Oxford University Press, 1994; p 861–894.
(62) Press, W. H.; Flannery, B. P.; Teukolsky, S. A.; Vetterling, W. T. *Numerical Recipes in Pascal;* Cambridge University Press, 1989; Chapter 14.4, p 572–580.
(63) Christophorou, L. G.; Stockdale, J. A. D. *J. Chem. Phys.* **1968** *48* (5), 1956. doi:10.1063/1.1668997.
(64) Klar, D.; Ruf, M.-W.; Hotop, H. *Aust. J. Phys.* **1992** *45*, 263.
(65) Jang, J. H.; Lee, J. G.; Lee, H.; Xie, Y.; Schaefer, H. F., III. *J. Phys. Chem. A* **1998** *102* (27), 5298. doi:10.1021/jp981356o.
(66) Bernasek, S. L. *Annu. Rev. Phys. Chem.* **1993** *44* (1), 265. doi:10.1146/annurev.pc.44.100193.001405.
(67) Zharnikov, M.; Frey, S.; Heister, K.; Grunze, M. *Langmuir* **2000** *16* (6), 2697. doi:10.1021/la991034r.

Cobalt and nickel complexes of open-chain thioether ligands terminated by salicylaldimine functionality*

C. Robert Lucas, John M.D. Byrne, Julie L. Collins, Louise N. Dawe, and David O. Miller

Can. J. Chem. Downloaded from www.nrcresearchpress.com by Xi'an Jiaotong University on 09/19/12
For personal use only.

Abstract: Syntheses of 1,11-bis(salicylaldimine)-3,6,9-trithiaundecane (**H_2L1**), 1,11-bis(salicylaldimine)-6-oxa-3,9-dithiaundecane (**H_2L2**), and 1,8-bis(salicylaldimine)-3,6-dithiaundecane (**H_2L3**), their nickel complexes [Ni(L1)]·H_2O (**I**), [Ni(HL2)][OAc] (**II**), [Ni(L3)·HOAc]$_2$[Ni(L3)·2HOAc]·$3H_2O$ (**III**), [Ni(HL1-sal)]Cl_2·H_2O (**IV**), [Ni(HL2-sal)]Cl_2·CH_3OH (**V**), [Ni(L3-sal)Cl]·H_2O (**VI**), {[Ni(HL1-sal)]Br_2}$_2${[Ni(L1-sal)]Br}·H_2O (**VII**), {[Ni(HL2-sal)]Br_2}$_2${[Ni(L2-sal)]Br}·$2CH_3OH$ (**VIII**), {[Ni(HL3-sal)Br]Br}[Ni(L3-sal)Br]·$2CH_3OH$ (**IX**), [Ni(HL3-sal)Br]Br·CH_3OH (**X**), [Ni(HL3)Br]·$2H_2O$ (**XI**), [Ni(HL1)]$_2$[BF_4]$_2$·$5H_2O$ (**XII**), [Ni(HL2)]$_2$[BF_4]$_2$·$3H_2O$ (**XIII**), [Ni(HL3)]$_2$[BF_4]$_2$·CH_3CN (**XIV**), and [Ni(HL3)]$_2$[BF_4]$_2$·$3H_2O$ (**XV**) and their cobalt complexes [Co(L1-sal)][BF_4]$_2$ (**XVI**), [Co(L2)][OAc]·$3H_2O$ (**XVII**), [Co(L3)][OAc]·$3H_2O$ (**XVIII**), [Co(L3)][BF_4] (**XIX**), and [Co(L3-sal)(CH_3OH)][BF_4]$_2$·CH_3OH (**XX**) are reported. Single crystal X-ray structural studies for **III**, **XIV**, **XVI**, and **XIX** are described. Cyclic voltammograms of the ligands and of **I**, **II**, **III**, **VII**, **VIII**, **X**, **XIV**, and **XIX** are discussed. Electronic spectra of the ligands and complexes are discussed.

Key words: cobalt and nickel complexes, thioether, salicylaldimine ligands, X-ray structure, cyclic voltammetry, UV–vis spectra.

Résumé : On décrit les synthèses du 1,11-bis(salicylaldimine)-3,6,9-trithiaundécane (**H_2L1**), 1,11-bis(salicylaldimine)-6-oxa-3,9-dithiaundécane (**H_2L2**) et du 1,8-bis(salicylaldimine)-3,6-dithiaundécane (**H_2L3**), de leurs complexes de nickel [Ni(Ll)]·H_2O (**I**), [Ni(HL2)][OAc] (**II**), [Ni(L3)·HOAc]$_2$[Ni(L3)·2HOAc]·$3H_2O$ (**III**), [Ni(HL1-sal)]Cl_2·H_2O (**IV**), [Ni(HL2-sal)]Cl_2·CH_3OH (**V**), [Ni(L3-sal)Cl]·H_2O (**VI**), {[Ni(HL1-sal)]Br_2}$_2${[Ni(L1-sal)]Br}·H_2O (**VII**), {[Ni(HL2-sal)]Br_2}$_2${[Ni(L2-sal)]Br}·$2CH_3OH$ (**VIII**), {[Ni(HL3-sal)Br]Br}$_2$[Ni(L3-sal)Br]·$2CH_3OH$ (**IX**), [Ni(HL3-sal)Br]Br·CH_3OH (**X**), [Ni(HL3)Br]·$2H_2O$ (**XI**), [Ni(HL1)]$_2$[BF_4]$_2$·$5H_2O$ (**XII**), [Ni(HL2)$_2$[BF_4]$_2$·$3H_2O$ (**XIII**), [Ni(HL3)$_2$[BF_4]$_2$·CH_3CN (**XIV**) et [Ni(HL3)$_2$]$_2$[BF_4]$_2$·$3H_2O$ (**XV**) ainsi que de leurs complexes de cobalt [Co(L1-sal)][BF_4]$_2$ (**XVI**), [Co(L2)][OAc]·$3H_2O$ (**XVII**), [Co(L3)][OAc]·$3H_2O$ (**XVIII**), [Co(L3)][BF_4] (**XIX**) et [Co(L3-sal)(CH_3OH)][BF_4]$_2$·CH_3OH (**XX**). On décrit les structures des composés **III**, **XIV**, **XVI** et **XIX** telles que déterminées par diffraction des rayons-X. On discute des résultats obtenus par voltampérométrie cyclique des ligands **I**, **II**, **III**, **VII**, **VIII**, **X**, **XIV** et **XIX**. On discute aussi des spectres électroniques des ligands et des complexes.

Mots-clés : complexes du cobalt et du nickel, thioéther, ligands de la salicylaldimine, structure par diffraction des rayons X, voltampérométrie cyclique, spectres UV–visible.

[Traduit par la Rédaction]

Introduction

Metal complexes of salicylaldimine ligands continue to be of interest for several reasons, not the least of which is their potential for use in a variety of applications such as sensor[1] or liquid crystal[2] technology. Furthermore, future applications of metal complexes in areas such as biomodeling, materials science, catalysis, communications, and data storage require inter alia the ability to adjust properties of existing substances. To do so in a rational manner requires understanding of the consequences of structural changes at the molecular level on properties that manifest themselves primarily at the macroscopic level. Current examples could be changes observed in photoluminescence[3,4] or magnetic susceptibility[5,6] of bulk samples of matter induced by structural changes at the molecular level. As part of our continuing interest[7–9] in the influence of ligand structure on properties of thioether–metal complexes, we now report studies of complexes in which open-chain ligands (Fig. 1) are terminated by salicylaldimine functions. These ligands are related to similar open-chain ligands terminated by alkyl,[10] pyridyl,[11] thienyl,[12] pyrazolyl,[13] and benzamidazolyl[13] functionalities that we have described in earlier work and it is therefore of interest to explore

Received 5 December 2010. Accepted 14 April 2011. Published at www.nrcresearchpress.com/cjc on 7 September 2011.

C.R. Lucas, J.M. Byrne, J.L. Collins, L.N. Dawe, and D.O. Miller. Department of Chemistry, Memorial University of Newfoundland, St. John's, NL A1B 3X7, Canada.

Corresponding author: C. Robert Lucas (e-mail: rlucas@mun.ca).

*This article has a companion paper in this issue (doi: 10.1139/v11-083).

Can. J. Chem. Downloaded from www.nrcresearchpress.com by Xi'an Jiaotong University on 09/19/12
For personal use only.

Fig. 1. Ligands and their position identifiers used in this study.

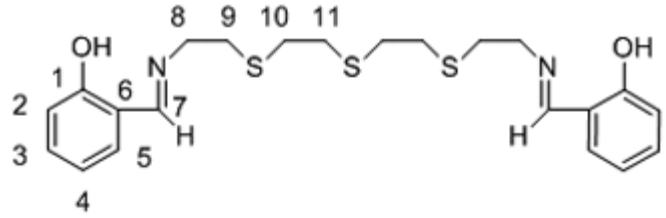

H_2L1

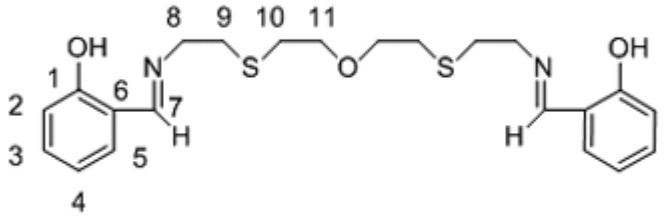

H_2L2

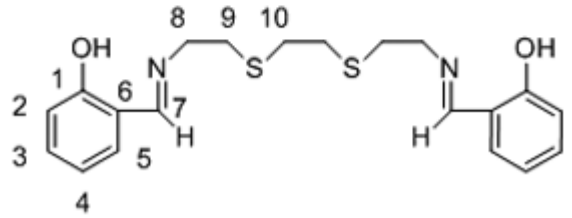

H_2L3

changes arising from alteration to salicylaldimine of the ligands' terminal groups. In a related report, we address this question for complexes of copper,[14] whereas the current paper investigates complexes of cobalt and nickel. Ligands used in this study are shown in Fig. 1.

Experimental

All reagents were obtained from the Sigma-Aldrich Chemical Co., Inc., and used without further purification. Solvents were ACS grade and were used without purification prior to use. NMR spectra were obtained on a Brüker AVANCE 500 instrument at 500.133 MHz for ^{1}H and 125.770 MHz for ^{13}C. All NMR spectra were run in $CDCl_3$ as the solvent with tetramethylsilane as the internal standard. All ^{13}C spectra were broadband decoupled. Melting points were obtained on a Fisher-Johns melting point apparatus. Electronic spectra were obtained in acetonitrile solutions that were 2.0×10^{-3} and 2.0×10^{-5} mol/L in solute using a Hewlett-Packard 8452A diode array UV–vis spectrophotometer. Other instruments used were a Brüker Tensor FTIR IR spectrometer equipped with a PIKE technologies MIRacle single reflection zinc selenide crystal HATR and an Agilent 1100 Series liquid chromatograph with either an SL MSD trap or a 1946A quadrupole detector. Electrochemical measurements were carried out under a nitrogen atmosphere at room temperature by using a Cypress Systems, Inc., CS-1087 computer-controlled potentiostat. Solution concentrations were 10^{-3} mol/L in complex and 0.1 mol/L in supporting electrolyte (tetraethylammonium perchlorate). Voltammograms were recorded in acetonitrile by using a glassy carbon working electrode that was prepolished with 0.3 mm Al_2O_3, a platinum counter electrode, and an aqueous saturated calomel reference electrode checked periodically relative to a 1.0×10^{-3} mol/L solution of ferrocene in acetonitrile containing 0.1 mol/L tetraethylammonium perchlorate for which the ferrocene/ferrocenium reduction potential was 400 mV. The reference electrode was separated from the bulk of the solution by a porous Vycor tube. Junction potential corrections were not used. X-ray diffraction data were collected on either a Rigaku AFC6S or a Rigaku AFC8 Saturn 70 diffractometer using graphite-monochromated Mo Kα radiation. Analyses were performed by Canadian Microanalytical Service, Ltd.

Preparative details — Ligands

$C_{22}H_{28}N_2O_2S_3$ (H_2L1)

Sodium (8.91 g, 0.388 mol) was dissolved in commercial absolute ethanol (400 mL) under an atmosphere of dry nitrogen, and 2-mercaptoethyl sulfide (15.0 g, 0.972 mol) was added slowly. The resulting mixture was heated to reflux and a solution of 2-chloroethylamine hydrochloride (22.6 g, 0.194 mol) in commercial absolute ethanol (20 mL) was added dropwise with stirring. Reflux was continued for 45 min, during which a white precipitate appeared. Salicylaldehyde (23.7 g, 0.194 mol) was added, instantly giving a bright yellow solution. Reflux was continued for 48 h and on cooling a thick yellow precipitate deposited. Solvent was removed under reduced pressure via rotary evaporator and the residue taken up in dichloromethane (150 mL). Undissolved sodium chloride was filtered away. The dichloromethane solution was carefully reduced in volume via a rotary evaporator until cloudy and then placed in the refrigerator overnight. The resulting crystals were collected by suction filtration, washed with ice-cold acetonitrile (3×5 mL) and crystallized from hot acetonitrile (300 mL) with storage overnight at –20 °C. The product was collected by filtration and washed with ice-cold acetonitrile (3×15 mL) to give bright yellow shiny leaflets (36.5 g, 83% yield) melting over the range 110.7–111.1 °C. UV–vis (CH_3CN) λ_{max} in nm (ε in mol^{-1} L cm^{-1}): 225 (10 800), 255 (4580), 316 (1740), 405 (450). ^{1}H NMR ($CDCl_3$, position identification from Fig. 1) δ: 2.74 (s, 8H, C10, C11), 2.88 (t, J = 7.2 Hz, 4H, C9), 3.79 (t, J = 7.2 Hz, 4H, C8), 6.88 (t, J = 8.5 Hz, 2H, C4), 6.96 (d, J = 9.5 Hz, 2H, C5), 7.26 (d, J = 7.0 Hz, 2H, C2), 7.31 (t, J = 8.5 Hz, 2H, C3), 8.37 (s, 2H, C7), 13.2 (s, 2H, O*H*). ^{13}C{^{1}H} NMR δ: 32.60 (C10), 32.82 (C9), 33.41 (C11), 59.61 (C8), 117.20 (C4), 118.83 (C6), 118.91 (C2), 131.64 (C5), 132.63 (C3), 161.26 (C1), 166.24 (C7). Mass spectrum APCI(+) calcd for M+ 1: 449.1; found: 449.2. Anal. calcd for $C_{22}H_{28}N_2O_2S_3$: C 58.89, H 6.29, N 6.24, S 21.44; found: C 58.94, H 6.44, N 6.29, S 22.21.

$C_{22}H_{28}N_2O_3S_2$ (H_2L2)

The procedure was the same as for **H_2L1** except that 2-mercaptoethyl ether was used instead of 2-mercaptoethyl sulfide. Final recrystallization was from hot acetonitrile –

Can. J. Chem. Downloaded from www.nrcresearchpress.com by Xi'an Jiaotong University on 09/19/12
For personal use only.

chloroform (150 mL : 50 mL) with storage overnight at –20 °C. The product collected by suction filtration was washed with ice-cold methanol (3 × 5 mL) and then ether (3 × 5 mL) to give bright yellow shiny needles (64% yield) melting over the range 76.8–78.0 °C. A second crop of bright yellow needles (27%) that melted over the same range was recovered from the mother liquor after further storage at –20 °C. ^{1}H NMR ($CDCl_3$, position identification from Fig. 1) δ: 2.73 (t, J = 5.5 Hz, 4H, C10), 2.89 (t, J = 8.5 Hz, 4H, C9), 3.64 (t, J = 5.5 Hz, 4H, C11), 3.79 (t, J = 5.0 Hz, 4H, C8), 6.87 (t, J = 7.0 Hz, 2H, C4), 6.95 (d, J = 8.5 Hz, 2H, C5), 7.25 (d, J = 7.5 Hz, 2H, C2), 7.31 (m, 2H, C3), 8.36 (s, 2H, C7), 13.3 (s, 2H, O*H*). ^{13}C{^{1}H} NMR δ: 32.20 (C10), 33.71 (C9), 59.65 (C8), 71.10 (C11), 117.28 (C4), 118.82 (C6), 118.89 (C2), 131.60 (C5), 132.60 (C3), 161.27 (C1), 166.12 (C7). Mass spectrum APCI(+) calcd for M + 1: 433.1; found: 433.2. Anal. calcd for $C_{22}H_{28}N_2O_3S_2$: C 61.08, H 6.52, N 6.48, S 14.82; found: C 60.89, H 6.51, N 6.49, S 14.69.

$C_{20}H_{24}N_2O_2S_2$ (H_2L3)

The procedure is similar to that for **H_2L1** except that 1,2-ethanedithiol was used instead of 2-mercaptoethyl sulfide and the initial crude residue was taken up in chloroform, filtered, reduced in volume until cloudy, and then refrigerated. The resulting solid was collected, washed with a little ice-cold chloroform, dissolved in chloroform, and washed with deionized water. The organic layer was dried over anhydrous $MgSO_4$ and filtered. Upon concentrating and storing at –20 °C a bright yellow precipitate separated was collected and then washed with ice-cold chloroform and then ether to give bright yellow shiny leaflets (86.2% yield) melting over the range 108.7–109.1 °C. UV–vis (CH_3CN) λ_{max} in nm (ε in mol^{-1} L cm^{-1}): 230 (12 630), 258 (4240), 313 (1174), 398 (350). ^{1}H NMR ($CDCl_3$, position identification from Fig. 1) δ: 2.75 (s, 4H, C10), 2.88 (t, J = 5.0 Hz, 4H, C9), 3.77 (t, J = 5.0 Hz, 4H, C8), 6.88 (t, J = 7.0 Hz, 2H, C4), 6.96 (d, J = 10.5 Hz, 2H, C5), 7.26 (d, J = 5.0 Hz, 2H, C2), 7.30 (t, J = 10.0 Hz, 2H, C3), 8.33 (s, 2H, C7), 13.2 (s, 2H, O*H*). ^{13}C{^{1}H} NMR δ: 32.82 (C10), 33.60 (C9), 59.68 (C8), 117.18 (C4), 118.79 (C6), 118.83 (C2), 131.63 (C5), 132.63 (C3), 161.28 (C1), 166.21 (C7). Mass spectrum APCI(+) calcd for M + 1 *m/z*: 389.1; found *m/z*: 389.2. Anal. calcd for $C_{20}H_{24}N_2O_2S_2$: C 61.82, H 6.23, N 7.21, S 16.51; found: C 61.72, H 6.11, N 7.41, S 16.15.

Preparative details — Complexes

[Ni(L1)]·H_2O (I)

H_2L1 (1.0 g, 2.2 mmol) dissolved in warm (~40 °C) methanol (25 mL) was mixed with nickel(II) acetate trihydrate (0.56 g, 2.4 mmol) in warm (~40 °C) methanol (25 mL) to give a dark green solution. The solvent was evaporated and the residue washed with methanol (3 × 5 mL) to give a light green powder that was dissolved in *N*,*N*′-dimethylformamide (30 mL). The solution was filtered and then added dropwise with stirring to cold deionized water (300 mL) to give a thick yellow-green precipitate that was collected in a sintered glass crucible, washed with acetone (2 × 5 mL) and then ether (5 × 5 mL), and then dried to give a brown-green powder (0.74 g, 64% yield). UV–vis (CH_3CN) λ_{max} in nm (ε in mol^{-1} L cm^{-1}): 280 (1350), 310 (1500), 408 (1400), 610 (55). Mass spectrum APCI(+) calcd for M – H_2O + 1, $[C_{22}H_{27}N_2NiO_2S_3]^+$ *m/z*: 505.0; found *m/z*: 505.0. Anal. calcd for $C_{22}H_{28}N_2NiO_3S_3$: C 50.49, H 5.39, N 5.35; found: C 50.89, H 5.09, N 5.09.

[Ni(HL2)][OAc] (II)

H_2L2 (0.72 g, 1.7 mmol) dissolved in warm (~40 °C) acetonitrile (25 mL) was mixed with nickel(II) acetate trihydrate (0.42 g, 1.8 mmol) in warm (~40 °C) methanol (25 mL) to give a dark green solution. The solvent was evaporated to give a dark green glassy film that was triturated in acetonitrile (2 mL) in which it was slightly soluble. The residue was collected by filtration and dried in air to give a fine green powder that was dissolved in chloroform (50 mL), concentrated to 20 mL via a rotary evaporator, filtered, and then added dropwise with stirring to cold ether (350 mL) to give a bright green precipitate. This was collected in a sintered glass crucible, washed with ether (3 × 5 mL), and then dried to give a green powder (0.26 g, 28% yield). UV–vis (CH_3CN) λ_{max} in nm (ε in mol^{-1} L cm^{-1}): 280 (sh), 308 (1450), 340 (sh), 400 (1500), 610 (54). Mass spectrum APCI(+) calcd for M – OAc, $[C_{22}H_{27}N_2NiO_3S_2]^+$ *m/z*: 489.1; found *m/z*: 489.0. Anal. calcd for $C_{24}H_{30}N_2NiO_5S_2$: C 52.48, H 5.50, N 5.10; found: C 52.63, H 5.41, N 5.29.

{[Ni(L3)·HOAc]$_2$[Ni(L3)·2HOAc]·3H_2O (III)

H_2L3 (0.66 g, 1.7 mmol) dissolved in warm (~40 °C) 1:1 acetonitrile/methanol (40 mL) was mixed with nickel(II) acetate trihydrate (0.42 g, 1.8 mmol) in warm (~40 °C) methanol (20 mL) to give a dark brown-green solution. Within a few hours the colour became brown-purple. The solvent was evaporated slowly in air to give a brown residue that was triturated in acetonitrile (2 mL) in which it was slightly soluble. The solid was collected by filtration, washed with cold acetonitrile (3 × 2 mL), and then dried in air to give a fine brown-green powder. The powder was dissolved in methanol (100 mL), concentrated via a rotary evaporator to 20 mL, filtered, and then the filtrate was added dropwise with stirring to cold ether to give a yellow-green precipitate. This was collected in a sintered glass crucible and washed with ether (3 × 5 mL) and then dried to give a yellow-green powder (0.50 g, 55% yield). Alternatively, slow evaporation of the methanol filtrate produced X-ray quality dark green crystals. UV–vis (CH_3CN) λ_{max} in nm (ε in mol^{-1} L cm^{-1}): 290 (1354), 345 (sh), 383 (1450), 577 (41). Mass spectrum APCI(+) calcd for [Ni(HL3)], $[C_{20}H_{23}N_2NiO_2S_2]^+$ *m/z*: 445.1; found *m/z*: 445.0. Anal. calcd for $C_{68}H_{88}N_6Ni_3O_{17}S_6$: C 50.11, H 5.44, N 5.16; found: C 49.94, H 5.31, N 5.12.

[Ni(HL1-sal)]Cl_2·H_2O (IV)

H_2L1 (1.0 g, 2.2 mmol) dissolved in warm (~40 °C) acetonitrile (25 mL) was mixed with nickel(II) chloride hexahydrate (0.52 g, 2.2 mmol) in warm (~40 °C) methanol (25 mL) to give a dark green solution. The solvent was evaporated slowly in air to give a green glassy residue that was triturated in acetonitrile (2 mL) in which it was slightly soluble. The solid, which is insoluble in acetone and chloroform, was collected by filtration and dried in air to a fine green powder. This powder was dissolved in hot methanol (100 mL). The solution was concentrated via a rotary

Can. J. Chem. Downloaded from www.nrcresearchpress.com by Xi'an Jiaotong University on 09/19/12
For personal use only.

evaporator to 20 mL, filtered, and then added dropwise with stirring to cold ether (300 mL) to give a light green precipitate. This was collected in a sintered glass crucible, washed with ether (3 × 5 mL), and then dried in air to give a light green powder (0.94 g, 86% yield). UV–vis (CH_3CN) λ_{max} in nm (ε in mol^{-1} L cm^{-1}): 293 (1500), 323 (1500), 370 (1400), 406 (sh), 602 (40). Mass spectrum APCI(+) calcd for [Ni(L1-sal)] (sal = C_7H_3O), $[C_{15}H_{23}N_2NiOS_3]^+$ *m/z*: 401.0; found *m/z*: 401.0. Anal. calcd for $C_{15}H_{26}Cl_2N_2NiO_2S_3$: C 36.61, H 5.32, N 5.69; found: C 36.70, H 4.95, N 5.41.

[Ni(HL2-sal)]Cl_2·CH_3OH (V)

The procedure is the same as for **IV** to give a green powder (0.78 g, 73% yield). UV–vis (CH_3CN) λ_{max} in nm (ε in mol^{-1} L cm^{-1}): 287 (1300), 320 (1400), 380 (1100), 595 (45). Mass spectrum APCI(+) calcd for [Ni(L2-sal)], $[C_{15}H_{23}N_2NiO_2S_2]^+$ *m/z*: 385.0; found *m/z*: 385.0. Anal. calcd for $C_{16}H_{28}Cl_2N_2NiO_3S_2$: C 39.21, H 5.76, N 5.72; found: C 38.89, H 5.23, N 5.74.

[Ni(L3-sal)Cl]·H_2O (VI)

The procedure is the same as for **III** to give a light green powder (0.59 g, 89% yield). Mass spectrum APCI(+) calcd for [Ni(L3-sal)], $[C_{13}H_{19}N_2NiOS_2]^+$ *m/z*: 341.0; found *m/z*: 341.0. Anal. calcd for $C_{13}H_{21}ClN_2NiO_2S_2$: C 39.47, H 5.35, N 7.08, Ni 14.84; found: C 39.76, H 4.84, N 6.95, Ni 14.20.

{[Ni(HL1-sal)]Br_2}$_2${[Ni(L1-sal)]Br}·H_2O (VII)

H_2L1 (1.0 g, 2.2 mmol) dissolved in warm (~40 °C) acetonitrile (25 mL) was mixed with nickel(II) bromide monohydrate (0.52 g, 2.2 mmol) in warm (~40 °C) methanol (25 mL) to give a green solution and a light green precipitate. The solid was collected by filtration and dried in air to a fine green powder. This powder was dissolved in hot methanol (80 mL). The solution was concentrated via a rotary evaporator to 15 mL, filtered, and then added dropwise with stirring to cold ether (300 mL) to give a light green precipitate that was collected, washed with ether (3 × 5 mL), and then dried in air to give a green powder (0.70 g, 59% yield). Mass spectrum APCI(+) calcd for [Ni(L1-sal)], $[C_{15}H_{23}N_2NiOS_3]^+$ *m/z*: 401.0; found *m/z*: 401.0. Calcd for [H_2L1-sal)] (sal = C_7H_3O), $[C_{15}H_{25}N_2OS_3]^+$ *m/z*: 345.1; found *m/z*: 345.1. Anal. calcd for $C_{45}H_{73}Br_5N_6Ni_3O_4S_9$: C 33.23, H 4.52, N 5.17, Br 24.57, Ni 10.83; found: C 32.87, H 4.48, N 5.19, Br 24.73, Ni 10.1.

{[Ni(HL2-sal)]Br_2}$_2${[Ni(L2-sal)]Br}·$2CH_3OH$ (VIII)

The procedure is the same as for **VII** to give a green powder (0.39 g, 33% yield). Mass spectrum APCI(+) calcd for [Ni(L2-sal)], $[C_{15}H_{23}N_2NiO_2S_2]^+$ *m/z*: 385.0; found *m/z*: 385.0. Calcd for [H_2L2-sal)], $[C_{15}H_{25}N_2O_2S_2]^+$ *m/z*: 329.1; found *m/z*: 329.1. Anal. calcd for $C_{47}H_{79}Br_5N_6Ni_3O_8S_6$: C 34.76, H 4.90, N 5.17, Br 24.60, Ni 10.8; found: C 34.37, H 4.80, N 5.08, Br 24.68, Ni 10.8.

{[Ni(HL3-sal)Br]Br}[Ni(L3-sal)Br]·$2CH_3OH$ (IX)

H_2L3 (0.65 g, 1.7 mmol) dissolved in warm (~40 °C) acetonitrile (40 mL) was mixed with nickel(II) bromide monohydrate (0.40 g, 1.7 mmol) in warm (~40 °C) methanol (20 mL) to give a small amount of white precipitate in a light brown solution. The solid was separated by filtration and discarded and the filtrate evaporated slowly in air to produce a few black crystals and a green glassy residue. The solids were washed with acetonitrile (6 × 5 mL portions), which dissolved the crystals leaving behind the glassy residue. Slow evaporation of the solution produced very dark green (nearly black) crystals analyzed as Ni(HL3)Br·$2H_2O$ (**XI**). The green glassy residue was triturated in acetonitrile (5 mL) and collected by filtration as a fine green powder analyzed as Ni(HL3-sal)Br_2·CH_3OH (**X**). This powder could be dissolved in methanol (80 mL) to give a brown solution, which when concentrated via a rotary evaporator to 10 mL, filtered, and added dropwise with stirring to cold ether (300 mL) yielded a pale-green, almost white precipitate, which was collected, washed with ether (3 × 5 mL), and then dried in air to give **IX** (0.26 g, 31% yield). UV–vis (CH_3CN) λ_{max} in nm (ε in mol^{-1} L cm^{-1}): 284 (1200), 320 (1200), 384 (1300). Mass spectrum APCI(+) calcd for [Ni(L3-sal)], $[C_{13}H_{19}N_2NiOS_2]^+$ *m/z*: 341.0; found *m/z*: 341.0. Anal. calcd for $C_{28}H_{47}Br_3N_4Ni_2O_4S_4$: C 34.00, H 4.79, N 5.66; found: C 34.18, H 4.41, N 5.70.

[Ni(HL3-sal)Br]Br·CH_3OH (X)

For preparative details see **IX**; 0.46 g, 51% yield. Mass spectrum APCI(+) calcd for [HL3-sal + 1], $[C_{13}H_{20}N_2OS_2]^+$ *m/z:* 285.1; found *m/z*: 285.1. Anal. calcd for $C_{14}H_{24}Br_2N_2NiO_2S_2$: C 31.43, H 4.52, N 5.24; found: C 31.67, H 4.36, N 5.34.

[Ni(HL3)Br]·$2H_2O$ (XI)

For preparative details see **IX**; 0.16 g, 15% yield. Mass spectrum APCI(+) calcd for [Ni(H_2L3)Br], $[C_{20}H_{24}BrN_2NiO_2S_2]^+$ *m/z*: 525.0; found *m/z*: 525.0. Calcd for [Ni(HL3)], $[C_{20}H_{23}N_2NiO_2S_2]^+$ *m/z*: 445.0; found *m/z*: 445.0. Calcd for [H_2L3 + 1], $[C_{20}H_{25}N_2O_2S_2]^+$ *m/z*: 389.1; found *m/z*: 389.1. Anal. calcd for $C_{20}H_{27}BrN_2NiO_4S_2$: C 42.73, H 4.84, N 4.98, Ni 10.44; found: C 42.66, H 4.66, N 4.90, Ni 12.20.

[Ni(HL1)]$_2$[BF_4]$_2$·$5H_2O$ (XII)

The procedure is the same as for **X** except that the fine green powder was dissolved in hot acetonitrile (100 mL), concentrated via a rotary evaporator to 20 mL, filtered, and then added dropwise with stirring to cold ether (300 mL). This produced a yellow-green precipitate that was collected, washed with ether (3 × 5 mL), and then dried in air to give a fine pale green powder (0.51 g, 36% yield). UV–vis (CH_3CN) λ_{max} in nm (ε in mol^{-1}L cm^{-1}): 283 (sh), 320 (1485), 340 (sh), 380 (1207), 420 (sh), 620 (25). Mass spectrum APCI(+) calcd for [NiHL1], $[C_{22}H_{27}N_2NiO_2S_3]^+$ *m/z*: 505.0; found *m/z*: 505.0. Calcd for [NiL1-sal], $[C_{15}H_{23}N_2NiOS_3]^+$ *m/z*: 401.0; found *m/z*: 401.0. Calcd for [H_2L1-sal], $[C_{15}H_{25}N_2OS_3]^+$ *m/z*: 345.1; found *m/z*: 345.1. Anal. calcd for $C_{44}H_{64}B_2F_8N_4Ni_2O_9S_6$: C 41.40, H 5.05, N 4.39; found: C 41.26, H 4.47, N 4.79.

[Ni(HL2)]$_2$[BF_4]$_2$·$3H_2O$ (XIII)

The procedure is the same as for **XII** except that trituration is in ether and the final product is a fine pale green powder (0.60 g, 45% yield). UV–vis (CH_3CN) λ_{max} in nm (ε in mol^{-1} L cm^{-1}): 283 (sh), 320 (1527), 378 (1431), 410 (sh), 600 (50). Mass spectrum APCI(+) calcd for [NiHL2],

Can. J. Chem. Downloaded from www.nrcresearchpress.com by Xi'an Jiaotong University on 09/19/12
For personal use only.

$[C_{22}H_{27}N_2NiO_3S_2]^+$ *m/z*: 489.1; found *m/z*: 489.0. Calcd for [H_3L2], $[C_{22}H_{29}N_2O_3S_2]^+$ *m/z*: 433.2; found *m/z*: 433.1. Calcd for [NiL2-sal] (sal = C_7H_3O), $[C_{15}H_{23}N_2NiO_2S_2]^+$ *m/z*: 385.0; found *m/z*: 385.0. Calcd for [H_2L2-sal)] (sal = C_7H_3O), $[C_{15}H_{25}N_2O_2S_2]^+$ *m/z*: 329.1; found *m/z*: 329.1. Anal. calcd for $C_{44}H_{60}B_2F_8N_4Ni_2O_9S_4$: C 43.74, H 5.00, N 4.64; found: C 43.88, H 4.63, N 4.71.

[Ni(HL3)]$_2$[BF$_4$]$_2$·CH$_3$CN (*a*) (XIV) and [Ni(HL3)]$_2$[BF$_4$]$_2$·3H$_2$O (*b*) (XV)

For (*a*), the procedure for (*b*) was followed except that the acetonitrile/ether mother liquor was saved and upon slow evaporation produced purple-black crystals suitable for structural determination by X-ray methods (0.17 g, 19% yield). UV–vis (CH_3CN) λ_{max} in nm (ε in mol^{-1} L cm^{-1}): 290 (1340), 320 (1370), 384 (1455), 580 (80). Anal. calcd for (*a*) $C_{42}H_{49}B_2F_8N_5Ni_2O_4S_4$: C 45.56, H 4.46, N 6.33; found: C 47.17, H 4.44, N 6.15.

For (*b*), **H_2L3** (0.62 g, 1.6 mmol) dissolved in warm (~40 °C) acetonitrile (40 mL) was mixed with nickel(II) tetrafluoroborate hexahydrate (0.57 g, 1.6 mmol) in warm (~40 °C) methanol (20 mL) to give a brown-purple solution. The solvent was allowed to evaporate to give a brown-purple oily residue that was triturated in ether (5 mL) and then rinsed with methanol (5 × 3 mL) until the wash solution was colourless. The light brown powder was dried in air, dissolved in hot acetonitrile (90 mL) to give a brown-pink solution, concentrated to 20 mL on a rotary evaporator, and then added dropwise with stirring to cold ether (200 mL) to produce a light-coloured precipitate. This was collected, washed with ether (3 × 5 mL), and then dried in air to give a fine powder (0.37 g, 41% yield). UV–vis (CH_3CN) λ_{max} in nm (ε in mol^{-1} L cm^{-1}): 290 (1300), 320 (1400), 385 (1390), 580 (65). Mass spectrum APCI(+) calcd for [NiHL3], $[C_{20}H_{23}N_2NiO_2S_2]^+$ *m/z*: 445.0; found *m/z*: 445.0. Calcd for [H_3L3], $[C_{20}H_{25}N_2O_2S_2]^+$ *m/z*: 389.1; found *m/z*: 389.1. Calcd for [H_2L3-sal)], $[C_{13}H_{21}N_2OS_2]^+$ *m/z*: 285.1; found *m/z*: 285.1. Anal. calcd for $C_{40}H_{52}B_2F_8N_4Ni_2O_7S_4$: C 42.89, H 4.68, N 5.00; found: C 42.45, H 4.30, N 5.18.

[Co(L1-sal)][BF$_4$]$_2$ (XVI)

H_2L1 (2.0 g, 4.5 mmol) dissolved in warm (~40 °C) chloroform (15 mL) was mixed with cobalt(II) tetrafluoroborate hexahydrate (1.5 g, 4.5 mmol) in warm (~40 °C) acetonitrile (20 mL) to produce a deep black solution and a thick black oily precipitate. This was collected by gravity filtration and dissolved in chloroform from which black crystals were obtained as the solvent slowly evaporated. These were collected and washed with ice-cold acetonitrile (3 × 2 mL). The crystals were redissolved in hot (~60 °C) acetonitrile (30 mL) and the solution was left to evaporate slowly in air. When nearly evaporated, the resulting black cubic crystals were collected, washed with ice-cold acetonitrile (3 × 2 mL), and then dried in air (0.56 g, 22% yield). UV–vis (CH_3CN) λ_{max} in nm (ε in mol^{-1} L cm^{-1}): 219 (2680), 243, (2550) 284 (3220), 388 (230), 474 (75), 637 (45). Mass spectrum APCI (+) calcd for [Co(L1-sal)], $[C_{15}H_{23}CoN_2OS_3]^+$ *m/z*: 402.0; found *m/z*: 402.0. Anal. calcd for $C_{15}H_{23}B_2F_8CoN_2OS_3$: C 31.27, H 4.02, N 4.86, Co 10.2; found: C 31.36, H 3.97, N 4.87, Co 10.1.

[Co(L2)](OAc)·3H$_2$O (XVII)

H_2L2 (0.96 g, 2.2 mmol) dissolved in warm (~40 °C) acetonitrile (25 mL) was mixed with cobalt(II) acetate tetrahydrate (0.56 g, 2.2 mmol) in warm (~40 °C) methanol (25 mL) to produce a dark orange solution that quickly became dark red. The solvent was evaporated slowly in air to give a dark red-purple film that was triturated with ether (3 mL), giving a black powder that was collected, washed with ether (3 × 5 mL), and then dried in air to a dark purple powder. The powder was dissolved in hot (~60 °C) methanol (15 mL) and the solution concentrated via a rotary evaporator to 10 mL, filtered, and then added dropwise with stirring to cold ether (300 mL) to produce a purple precipitate that was collected, washed with ether (3 × 5 mL), and then dried in air to give a light purple powder (1.05 g, 80% yield). UV–vis (CH_3CN) λ_{max} in nm (ε in mol^{-1} L cm^{-1}): 650 (40), 476 (110), 384 (600), 312 (930). Mass spectrum APCI(+) calcd for [CoL2 + H], $[C_{22}H_{27}CoN_2O_3S_2]^+$ *m/z*: 490.1; found *m/z*: 490.0. Anal. calcd for $C_{24}H_{35}CoN_2O_8S_2$: C 47.84, H 5.85, N 4.65; found: C 47.70, H 5.55, N 4.52.

[CoL3][OAc]·3H$_2$O (XVIII)

The procedure is the same as for **XVII** except that chloroform was used to dissolve the product from trituration. The final product is a brown-green powder (0.44 g, 47% yield). UV–vis (CH_3CN) λ_{max} in nm (ε in mol^{-1} L cm^{-1}): 642 (106), 476 (135), 384 (650), 297 (3580), 265 (sh). Mass spectrum APCI(+) calcd for [CoL3 + H], $[C_{20}H_{22}CoN_2O_2S_2 + H]^+$ *m/z*: 446.0; found *m/z*: 446.0. Anal. calcd for $C_{22}H_{31}CoN_2O_7S_2$: C 47.31, H 5.59, N 5.02; found: C 46.59, H 4.68, N 4.82.

[Co(L3)][BF$_4$] (XIX)

H_2L3 (1.5 g, 3.9 mmol) dissolved in warm (~40 °C) chloroform (20 mL) was mixed with cobalt(II) tetrafluoroborate hexahydrate (1.32 g, 3.9 mmol) in warm (~40 °C) acetonitrile (30 mL) to produce a dark orange solution that quickly deposited a black precipitate. This was collected and washed with ice-cold acetonitrile (3 × 3 mL). When dry, the solid was dissolved in hot (~60 °C) acetonitrile (30 mL) and the solvent evaporated slowly in air to produce black crystals. These were collected, washed with ice-cold acetonitrile (3 × 3 mL), and then dried in air (1.34 g, 65% yield). UV–vis (CH_3CN) λ_{max} in nm (ε in mol^{-1} L cm^{-1}): 252 (2900), 305 (3100), 390 (500), 475 (95), 683 (75). Mass spectrum APCI (+) calcd for [CoL3 + H], $[C_{20}H_{22}CoN_2O_2S_2 + H]^+$ *m/z*: 446; found *m/z*: 446. Anal. calcd for $C_{20}H_{22}BCoF_4N_2O_2S_2$: C 45.13, H 4.17, N 5.26; found: C 45.59, H 4.26, N 5.24.

[Co(L3-sal)(CH$_3$OH)][BF$_4$]$_2$·CH$_3$OH (XX)

H_2L3 (88 mg, 0.23 mmol) dissolved in acetonitrile (20 mL) was mixed with cobalt(II) tetrafluoroborate hexahydrate (134 mg, 0.393 mmol) in methanol (30 mL) to produce a light orange solution that quickly deposited a brown precipitate. The precipitate was collected and discarded. Solvent was allowed to evaporate slowly from the filtrate to produce black crystals that were collected, recrystallized from methanol, washed with ice-cold acetonitrile (1 mL), and then dried in air (84 mg, 63% yield). Anal. calcd for $C_{15}H_{27}B_2CoF_8N_2O_3S_2$: C 31.06, H 4.69, N 4.83; found: C 31.37, H 4.05, N 4.85.

Can. J. Chem. Downloaded from www.nrcresearchpress.com by Xi'an Jiaotong University on 09/19/12
For personal use only.

Table 1. Crystallographic data for $[Ni(L3)\cdot HOAc]_2[Ni(L3)\cdot 2HOAc]\cdot 3H_2O$ **(III)** and $[Ni(HL3)]_2[BF_4]_2\cdot CH_3CN$ (**XIV**).

	Compound	
Parameter	**III**	**XIV**
Empirical formula	$C_{68}H_{88}N_6Ni_3O_{17}S_6$	$C_{42}H_{49}B_2F_8N_5Ni_2O_4S_4$
Formula mass	1629.93	1107.13
Crystal colour, habit	Green, prism	blue/purple, prism
Crystal dimensions, mm	0.40×0.30×0.15	0.35×0.35×0.40
Crystal system	Monoclinic	Triclinic
Space group	*C*2/*c* (No. 15)	*P*-1 (No. 2)
Z	4	2
a (Å)	33.472(10)	13.568(5)
b (Å)	15.931(4)	16.166(4)
c (Å)	14.992(4)	11.757(2)
α, β, γ (°)	90, 116.159(6), 90	100.25(2), 104.41(2), 81.73(2)
V (Å^3)	7176(3)	2444(1)
D_{calcd} (g/cm^3)	1.509	1.504
T (K)	153±1	299
μ (cm^{-1})	10.26	10.17
λ	0.71069	0.71069
F(0,0,0) (electrons)	3416	1140
2θ (max.) (°)	61.4	55.2
No. reflections measured	15912	10126
No. unique reflections	7258	10126
No. variable parameters	472	611
*R*1 ($I > 2.00\sigma(I)$)[a]	0.0931	0.0608
*wR*2 (all refl.)[b]	0.2584	0.1953
Last D-map		
Highest peak (e$^-$/Å^3)	2.62	1.45
Deepest hole (e$^-$/Å^3)	–0.95	–0.76

Note: Throughout this work, esds are in parentheses and refer to the last digit printed.

[a] $R1 = \Sigma||F_o| - |F_c||/\Sigma|F_o|$.

[b] $wR2 = [\Sigma(w(F_o^2 - F_c^2)^2/\Sigma w(F_o^2)^2]^{1/2}$.

X-ray studies

A summary of crystallographic data is in Tables 1 and 2. Figures 2–5 show views of the structure and numbering schemes for **III**, **XIV**, **XVI**, and **XIX**, respectively. In all cases, non-hydrogen atoms were refined anisotropically. For **III**, atoms O8 and O9 are disordered lattice solvent water. They make up one full water molecule and were refined with the sum of their occupancies equal to one. The H atoms for the lattice solvent water molecules O8, O9, and O10 could not be located in difference map positions and were therefore omitted from the model. They were included in the formula for the calculation of intensive properties. Hydrogen atoms H5a and H7a were introduced in difference map positions. Both were refined with distance restraints and H7a was also refined with an angle restraint. All other hydrogen atoms were introduced in calculated positions and refined on a riding model.

For **XIV**, hydrogen atoms H1o and H3o were introduced in difference map positions. All other hydrogen atoms were introduced in calculated positions and refined on a riding model. Angle restraints were applied to both tetrafluoroborate anions. For **XVI** and **XIX**, hydrogen atoms were introduced in calculated positions and refined on a riding model. Descriptions of the experimental procedures, anisotropic thermal parameters, and a full listing of bond lengths and angles are available as Supplementary data.

Results and discussion

Although a two-step synthesis for $\mathbf{H_2L3}$ was reported in 1950 by Lions and Dwyer,[15] the syntheses reported herein are each one-pot processes. All three ligands, under mild conditions in the presence of a metal atom, lose one salicylaldehyde, for example, during formation of $[Co(L1\text{-}sal)][BF_4]_2$ (**XVI**) and $[Co(L3\text{-}sal)(CH_3OH)][BF_4]_2\cdot CH_3OH$ (**XX**). This appears to be simple hydrolysis via nucleophilic attack by adventitious water on the carbon atom of a metal-bound imine producing a primary amine bound to the metal and liberating salicyladehyde. A question this raises is why only one end of the chain hydrolyzes. Models suggest it is due to differences in accessibility of the site for attack. In the early stages of complexation, if only one imine nitrogen is bound to the metal, approach by a water molecule is comparatively unimpeded. However, when all coordination sites on the metal have been filled by a ligand, the remaining imino-carbon atom is shielded from nucleophilic attack both above and below the plane defined by the bent M–C=N system. Shielding of the imine system arises from sulfur nonbonding electron density on one side of the plane and from oxygen nonbonding electron density on the other. Support for this explanation is obtained from the observation that syntheses of hydrolyzed and unhydrolyzed materials sometimes occur together and must be separated during workup. Preparations for $[Ni(HL3\text{-}sal)Br]Br\cdot CH_3OH$ (**X**) and $[Ni(HL3)Br]\cdot 2H_2O$ (**XI**) illustrate this point.

Can. J. Chem. Downloaded from www.nrcresearchpress.com by Xi'an Jiaotong University on 09/19/12
For personal use only.

Table 2. Crystallographic data for $[Co(L1\text{-}sal)][BF_4]_2$ (**XVI**) and $[Co(L3)][BF_4]$ (**XIX**).

	Compound	
Parameter	**XVI**	**XIX**
Empirical formula	$C_{15}H_{23}B_2CoF_8N_2OS_3$	$C_{20}H_{22}BCoF_4N_2O_2S_2$
Formula mass	576.08	532.26
Crystal colour, habit	Dark red, prism	red-black, block
Crystal dimensions, mm	0.25×0.20×0.45	0.25×0.25×0.45
Crystal system	Monoclinic	Orthorhombic
Space group	$P2_1/n$ (No. 14)	$Pna2_1$ (No. 33)
Z	4	8
a (Å)	9.087(2)	33.773(4)
b (Å)	13.972(3)	11.183(7)
c (Å)	18.055(3)	11.397(4)
α, β, γ (°)	90, 100.02(2), 90	90, 90, 90
V (Å^3)	2257.4(9)	4304.4(30)
D_{calcd} (g/cm^3)	1.695	1.643
T (K)	299	299
μ (cm^{-1})	11.15	10.47
λ	0.71069	0.71069
F(0,0,0) (electrons)	1168	2176
2θ (max.) (°)	55.1	55.1
No. reflections measured	5222	5193
No. variable parameters	290	578
$R1$ ($I > 2.00\sigma(I)$)[a]	0.0438	0.0459
$wR2$ (all refl.)[b]	0.1207	0.1282
Last D-map		
Highest peak (e$^-$/Å^3)	0.70	0.65
Deepest hole (e$^-$/Å^3)	–0.46	–0.50

Note: Throughout this work, esds are in parentheses and refer to the last digit printed.

[a] $R1 = \Sigma||F_o| - |F_c||/\Sigma|F_o|$.

[b] $wR2 = [\Sigma(w(F_o^2 - F_c^2)^2)/\Sigma w(F_o^2)^2]^{1/2}$.

A further feature of these systems is the occurrence of complexes in which the phenolic oxygens of the ligands may or may not be deprotonated. These occurrences are likely controlled, at least in part, by solubility effects with less soluble species being more readily deposited as precipitates of complex. The simultaneous preparations of {[Ni(HL3-sal)Br]Br}[Ni(L3-sal)Br]·2CH_3OH (**IX**), [Ni(HL3-sal)Br]Br·CH_3OH (**X**), and [Ni(HL3)Br]·2H_2O (**XI**) in one synthetic batch illustrate this effect. Protonated phenolic oxygens coordinated to metals have been observed previously in salicylaldimine complexes,[16] although precipitation of both protonated and deprotonated forms when complexation is carried out in the absence of added base is less common.

Simple complexes of both Ni(II) and Cu(II)[14] can be formed from **H_2L1**, **H_2L2**, and **H_2L3**, but analogous complexes of Co(II) were not obtained under aerobic conditions. This is not surprising given the propensity of complexed Co(II), especially in presence of nitrogen donors, to oxidize to Co(III).[17]

X-ray studies

[Ni(L3)·HOAc]$_2$[Ni(L3)·2HOAc]·3H_2O **(III)** consists, per formula unit, of three similar complex molecules, four acetic acid molecules hydrogen bonded to the metal complexes and three molecules of lattice water, one of which is disordered. The crystallographic asymmetric unit of this substance is half its formula unit and, for discussion purposes, Fig. 2 presents a partial expansion of the asymmetric unit so that complete coordination spheres for the two distinct nickel complexes can be viewed. Pertinent bond lengths and angles are in Table 3.

Structural evidence for hydrogen bonding is, as usual, bond lengths and angles. Thus, the carboxylic oxygen (O(7)) and attached hydrogen (H(7a)) are 0.969(19) Å from each other, whereas phenolic oxygen (O(3)) lies 1.566(19) Å from H(7a). Both distances are consistent with hydrogen bonding[28] as is the angle O(3)–H(7a)–O(7) (177(1)°). Likewise, O(5) and H(5a) lie at 0.974(19) Å from each other, whereas O(2) lies 1.503(19) Å from H(5a) and angle O(5)–H(5a)–O(2) is 169.6(5)°. Nickel–oxygen bond distances are comparable to those in [Ni_2(Hhsae)$_2$(OAc)$_2$(CH_3OH)$_2$] (H_2hsae = 2-(5-hydroxysalicylideneamino)ethanol)[18] (2.0160(9)–2.1442(10) Å) or {[Ni_2(*trans*-tachH)$_2$(OAc)$_4$(H_2O)](OAc)$_2$·5H_2O}$_n$ (tach = *cis*,*trans*-1,3,5-triaminocyclohexane)[19] (2.061(2)–2.143(2) Å). The Ni–N lengths in **III** are comparable to those in [Ni_2(Hhsae)$_2$(OAc)$_2$(CH_3OH)$_2$] (1.9987(11) Å) and 2-(diisopropyl)-phosphinobenzyl-*N*,*N*-dimethylaminenickel(II) dibromide[20] (2.042(2) Å) and the Ni–S bonds compare well to those of [Ni(PTHD(H_2O)]$^{2+}$ (PTHD = 3,6,9,12,15-pentathiaheptadecane)[10] (2.403(2)–2.425(2) Å) or [Ni(TCS)$_2$][ClO_4]$_2$ (TCS = 1-methoxy-10-methyl-12-thia-2,9-diaza-tricyclo[8.3.1.0^{3,8}]tetradeca-3,5,7-triene)[21] (2.4055(11) Å).

The O–Ni–N angles are comparable to those in Ni(IMBF)$_2$(CH_3OH)$_2$ (IMBF = 4-(1-bromo-3,3,3-trifluoro-2-oxopropylidene)-2,2,5,5-tetramethyl-3-imidazolene-1-oxyl)[22] (84.7(2)° and 88.4(1)°) or those in Ni[(C_2H_5O)$_2$PSNHNCPh(*o*-O)OCH_3]$_2$[23] (87.69(13)°

Fig. 2. ORTEP of $[Ni(L3)\cdot HOAc]_2[Ni(L3)\cdot 2HOAc]\cdot 3H_2O$ **(III)** (see text). Thermal ellipsoids are at the 50% probability level. H_2Os are omitted for clarity.

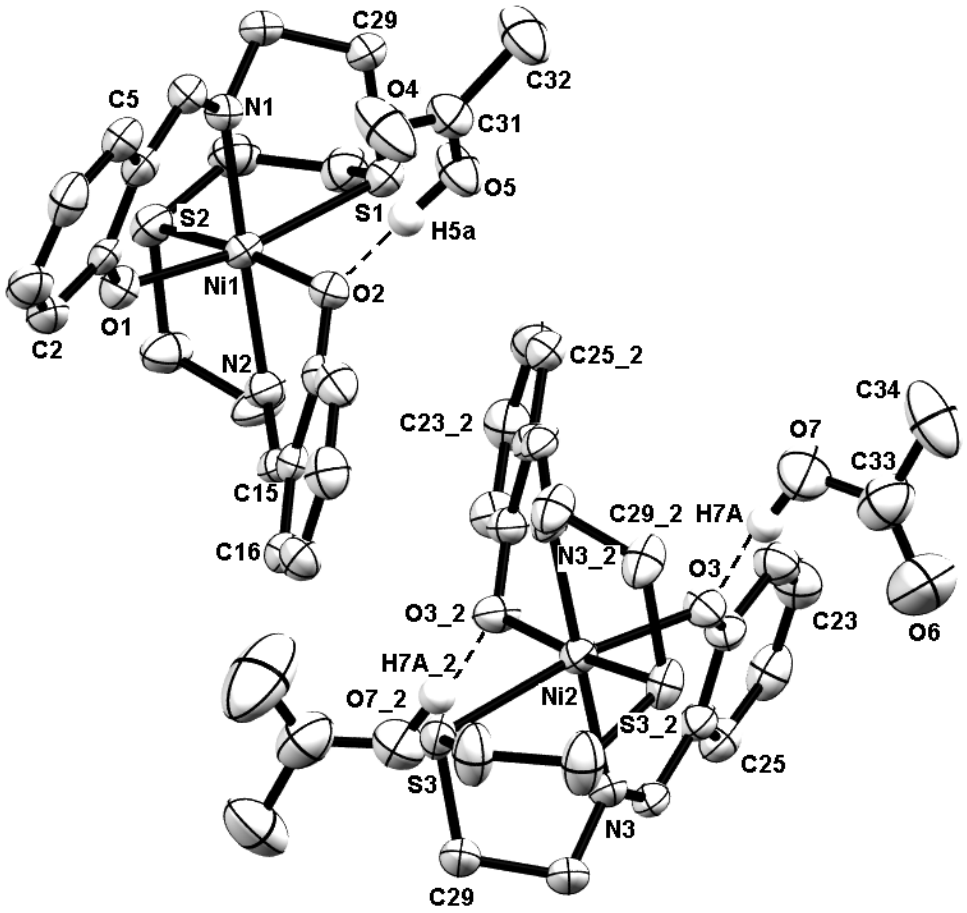

Can. J. Chem. Downloaded from www.nrcresearchpress.com by Xi'an Jiaotong University on 09/19/12
For personal use only.

and 92.31(14)°). The O–Ni–O and N–Ni–N angles are close to 90° and 180°, respectively, whereas the O–Ni–S angles are of two types representing cis- and trans-donors. The cis angles differ very little from 90°, whereas the three distinct trans-angles remain closer to 180° than those, for example, of 168.32(6)° in $[NiCl(H_2O)_2(thpd)]Cl$ (thpd = 1-(3-thia-5-hydroxypentyl)-3,5-dimethylpyrazole).[24] The six N–Ni–S angles, four on Ni(1) and two on Ni(2), all show deviations from 90° on both Ni(1) and Ni(2) of 5° ± 1° that are similar to those observed in $[Ni(aptp)(en)][NO_3]_2$ (aptp = 1-[[2-[2-aminoethyl)imino]propyl]thio]-2-propanone).[25] Finally, there are two distinct S–Ni–S angles, one at Ni(1) and one at Ni(2). Both are comparable to those in $[Ni(PDH)(CH_3CN)_2][ClO_4]_2$ (PDH = 1,6-bis(2-pyridyl)-2,5-dithiahexane)[26] (S–Ni–S = 83.2(2)° and 83.2(2)°) or $[Ni(18S_4O_2][BF_4]_2$ ($18S_4O_2$ = 1,10-dioxa-4,7,13,16-tetrathiacyclooctadecane)[27] (S–NiS = 94.52(13)°, 91.56(12)°, 88.12(12)°, and 88.37(13)°).

$[Ni(HL3)]_2[BF_4]_2\cdot CH_3CN$ (**XIV**) has in its unit cell a pair of similar but nonidentical hydrogen-bonded unipositive complex cations, two tetrafluoroborate anions, and one molecule of lattice acetonitrile. The ligand coordinates by both protonated and deprotonated phenolic oxygens, and dimers of cations are formed by hydrogen bonds involving phenolic hydrogens that were detected and refined in the crystal structure study. Pertinent bond lengths and angles are in Table 4.

The four Ni–O, four Ni–N, and four Ni–S bonds in the dimeric cation of **XIV** have lengths similar to those observed in **III** and related compounds (vide supra). Hydrogen bonds between halves of the dimeric cation have angles O(1)–H(1o)···O(4) = 173(2)° and O(3)–H(3o)···O(2) = 170(2)°. Distances O(1)–H(1o)···O(4) and O(3)–H(3o)···O(2) are both 2.44(3) Å and distances H(1o)···O(4) and H(3o)···O(2) are both 1.49(4) Å. These may be compared with literature values for strong hydrogen bonds of 2.70 Å for O–H···O and 1.70 Å for H···O.[28]

Eight O–Ni–N angles occur in the two monomers and are comparable to those in **III** and related species (vide supra). There are four N–Ni–S angles in each of the monomers with deviations between 6.9° and 8.6° from 90°. The largest is 1.1° (~14%) greater than deviations observed by Ladd et al.[25] and 2.4° (~38%) greater than the largest observed for comparable angles in **III**. There are no obvious intramolecular reasons why deviations should be larger in **XIV** than in **III**. There are, however, three contacts in **XIV** that are less than the sum of the van der Waals' radii of the atoms involved. These are N(5)···H(10a) (2.6 ± 1 Å), S(1)···H(28a_i) (3.1 ± 1 Å) and S(1)···H(29b_i) (3.1 ± 1 Å) that "lift" S(1) causing an increase in the S(1)–Ni(1)–N(2) angle. The sum of the van der Waals' radii in each case is 3.00, 3.25, and 3.25 Å.[29]

As with **III**, bond angles in **XIV** fall into two categories. There are those that lie close to ideal values for a regular octahedron and those that show significant deviation and, as with **III**, the latter category all involve a sulfur atom. This may not be coincidental in view of observations[13,30,31] that

Can. J. Chem. Downloaded from www.nrcresearchpress.com by Xi'an Jiaotong University on 09/19/12
For personal use only.

Fig. 3. ORTEP of $[Ni(HL3)]_2[BF_4]_2 \cdot CH_3CN$ (**XIV**). Thermal ellipsoids are at the 50% probability level. BF_4^- ions and CH_3CN are omitted for clarity.

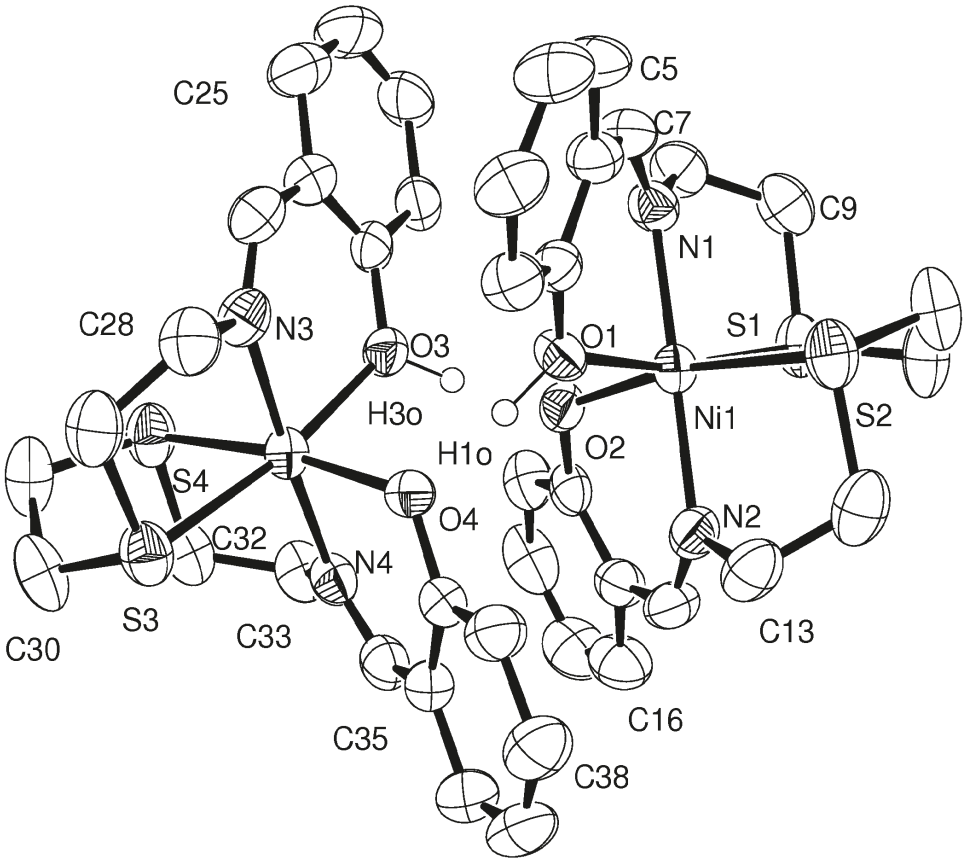

sulfur, relative to donors such as nitrogen or oxygen, is forgiving about its bond lengths and angles in a way that has been described as its bonding "plasticity". Thus, strain in complex systems is more likely to be accommodated at sulfur than at nitrogen or oxygen donors.

The structure of $[Co(L1\text{-}sal)][BF_4]_2$ (**XVI**) (Fig. 4) consists of an N_2OS_3 coordination sphere with the three sulfurs arranged facially. Pertinent bond lengths and angles are in Table 5.

The Co–O bond length in **XVI** is comparable to those in Co(III) cations such as $[Co(3\text{-}Cl\text{-}acacen)(NH_3)_2][BPh_4]$[32] (3-Cl-acacen = 3-chloro-bis(acetylacetone)ethylenediimine) (1.881(4) Å) and $[Co(L)(phen)N_3]$[33] (where H_2L = 2-hydroxy-acetophenone-N(4)-phenylsemicarbazone and phen = 1,10-phenanthroline) (1.866(4) and 1.914(3) Å). The Co–N distances compare well to those (1.8918(9), 1.951(6), and 1.960(6) Å) in $[Co(3\text{-}Cl\text{-}acacen)(NH_3)_2][BPh_4]$, where the shorter is to imino-nitrogen, or in $[Co(L)(phen)N_3]$ (1.865(4) (azomethine), 1.961(4) and 1.968(5) (phen), and 1.926(4) Å (azide)). The Co–S lengths are comparable to those in $[Co(L^4)(bipy)(N_3)]$[34] (H_2L^4 = 2-hydroxy-acetophenone-N(4)-phenylthiosemicarbazone and bipy = 2,2′-bipyridine) (2.2126(7) Å (mercaptide)) and in $[Co(tsaltp)]_2Cl_2$ ($H_2tsaltp$ = *N*,*N*′-bis(thiosalicylideneimine)-2,2′-thiobis(ethylamine))[35] (2.277(3) Å (thioether) and 2.218(3) and 2.278(3) Å (bridging mercaptide)).

The unit cell for $[Co(L3)][BF_4]$ (**XIX**) (Fig. 5) contains two similar but nonidentical $[Co(L3)][BF_4]$ units. Each of

Fig. 4. ORTEP of $[Co(L1\text{-}sal)][BF_4]_2$ (**XVI**). Thermal ellipsoids are shown at the 50% probability level.

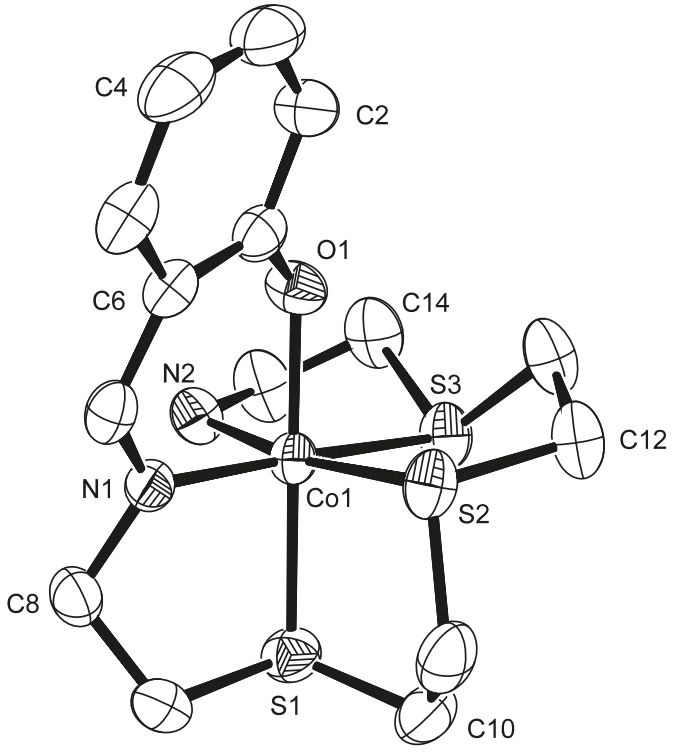

Can. J. Chem. Downloaded from www.nrcresearchpress.com by Xi'an Jiaotong University on 09/19/12
For personal use only.

Fig. 5. ORTEP of [Co(L3)][BF_4] (**XIX**). Thermal ellipsoids are shown at the 50% probability level.

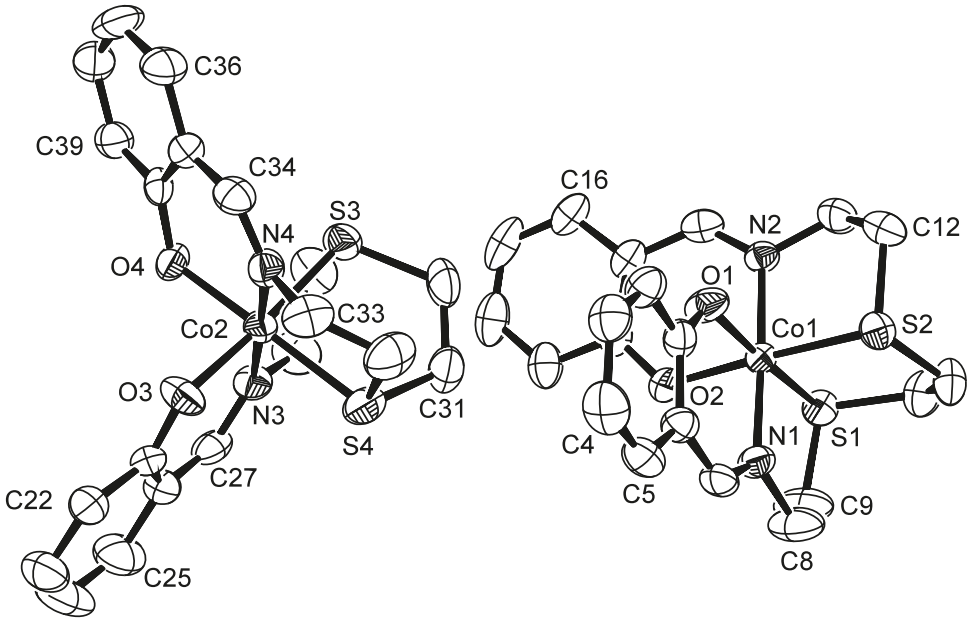

the cations consists of an $N_2O_2S_2$ coordination sphere with the nitrogens in a trans arrangement. Pertinent bond lengths and angles are in Table 6. The Co–S, Co–O, and Co–N bond lengths in both cations are similar to those in **XVI** and related species (vide supra).

Spectroscopic studies

Electronic spectra of the ligands **H_2L1** and **H_2L3** were collected in methanol and in acetonitrile and there are no significant qualitative differences in the overall appearances of the spectra with solvent. Both ligands display absorptions at ~225, ~255, and ~314 nm that can be assigned to two $\pi\rightarrow\pi^*$ transitions of the aromatic system,[36–39] and to a $\pi\rightarrow\pi^*$ transition of the –C=N– system[37,23]. In addition, a weak absorption of unknown origin occurs at ~400 nm in the spectra of both **H_2L1** and **H_2L3**.

All complexes in this study can be generalized into three related coordination sphere types. As a visual assistance to the following discussion these are presented in Fig. 6.

The IR spectrum of **XIV** in the region 3700–3000 cm^{-1} is consistent with its X-ray structure and shows a band attributable to O–H stretching that is shifted to 3250 cm^{-1} and broadened when compared with the corresponding band at 3450 cm^{-1} in the spectrum of the free ligand. The shift and broadening is expected for a hydrogen-bonded system.[40] The electronic spectrum of this compound is consistent with its solid-state structure, which suggests the coordination sphere of the nickel atoms is retained, at least in a general sense, in solution. The spectrum (Table 7) consists of bands at 290, 320, 384, and 580 nm. The first and second of these correlate with bands at 258 and 313 nm in the spectrum of the free ligand and both are shifted to longer wavelength in the complex.

All spectra of the nickel complexes (Table 7) consist of three intense bands ($\varepsilon \sim 10^3$ mol^{-1} L cm^{-1}) and one much weaker band ($\varepsilon \sim 10^1$ mol^{-1} L cm^{-1}). The former are frequently asymmetrical and display shoulders on either or both

Table 3. Selected bond lengths and angles in [Ni(L3)·HOAc]$_2$ [Ni(L3)·2HOAc]·3H_2O **(III)**.

Bond length (Å)		Bond angle (°)	
Ni(1) cation			
Ni–O(2)	2.026(4)	O(2)–Ni(1)–N(1)	92.79(17)
Ni–N(1)	2.021(3)	O(2)–Ni(1)–O(1)	91.34(17)
Ni–O(1)	2.028(4)	N(1)–Ni(1)–O(1)	86.76(17)
Ni–N(2)	2.032(4)	O(2)–Ni(1)–N(2)	86.32(17)
Ni–S(2)	2.441(2)	N(1)–Ni(1)–N(2)	179.0(2)
Ni–S(1)	2.459(2)	O(1)–Ni(1)–N(2)	93.80(17)
		O(2)–Ni(1)–S(2)	170.39(9)
		N(1)–Ni(1)–S(2)	96.26(14)
		O(1)–Ni(1)–S(2)	92.41(13)
		N(2)–Ni(1)–S(2)	84.61(14)
		O(2)–Ni(1)–S(1)	91.74(12)
		N(1)–Ni(1)–S(1)	83.98(14)
		O(1)–Ni(1)–S(1)	170.4(1)
		N(2)–Ni(1)–S(1)	95.5(1)
		S(2)–Ni(1)–S(1)	86.00(5)
Ni(2) cation			
Ni–O(3)	2.030(4)	O(3)–Ni(2)–O(3_2)	91.87(17)
Ni–O(3_2)	2.030(4)	O(3)–Ni(2)–N(3_2)	92.17(16)
Ni–N(3)	2.030(3)	O(3)–Ni(2)–N(3)	86.97(16)
Ni–N(3_2)	2.030(3)	O(3_2)–Ni(2)–N(3_2)	86.97(16)
Ni–S(3)	2.419(2)	O(3_2)–Ni(2)–N(3)	92.17(16)
Ni–S(3_2)	2.419(2)	O(3)–Ni(2)–S(3)	171.38(9)
		O(3)–Ni(2)–S(3_2)	90.96(12)
		O(3_2)–Ni(2)–S(3)	90.96(12)
		O(3_2)–Ni(2)–S(3_2)	171.38(9)
		N(3)–Ni(2)–N(3_2)	178.8(2)
		N(3)–Ni(2)–S(3)	84.8(1)
		N(3)–Ni(2)–S(3_2)	96.11(14)
		N(3_2)–Ni(2)–S(3)	96.11(14)
		N(3_2)–Ni(2)–S(3_2)	84.79(14)
		S(3)–Ni(2)–S(3_2)	87.42(6)

Can. J. Chem. Downloaded from www.nrcresearchpress.com by Xi'an Jiaotong University on 09/19/12
For personal use only.

Table 4. Selected bond lengths and angles in $[Ni(HL3)]_2[BF_4]_2{\cdot}CH_3CN$ (**XIV**).

Bond length (Å)		Bond angle (°)	
Ni(1) cation			
Ni–S(1)	2.4495(12)	S(1)–Ni–S(2)	87.10(4)
Ni–S(2)	2.4497(13)	S(1)–Ni–O(1)	168.55(10)
Ni–O(1)	2.077(3)	S(1)–Ni–O(2)	91.26(9)
Ni–O(2)	2.033(2)	S(1)–Ni–N(1)	83.12(11)
Ni–N(1)	2.025(3)	S(1)–Ni–N(2)	98.63(12)
Ni–N(2)	2.024(3)	S(2)–Ni–O(1)	91.88(9)
H(49)···O(2)	1.426(5)	S(2)–Ni–O(2)	169.95(10)
O(1)–H(48)	0.946(5)	S(2)–Ni–N(1)	96.24(10)
		S(2)–Ni–N(2)	83.06(10)
		O(1)–Ni–O(2)	91.67(12)
		O(1)–Ni–N(1)	85.66(14)
		O(1)–Ni–N(2)	92.56(15)
		O(2)–Ni–N(1)	93.41(13)
		O(2)–Ni–N(2)	87.39(13)
		N(1)–Ni–N(2)	178.07(16)
		O(1)–H(48)···O(4)	164.53(3)
Ni(2) cation			
Ni–S(3)	2.4391(11)	S(3)–Ni–S(4)	86.55(6)
Ni–S(4)	2.4790(13)	S(3)–Ni–O(3)	171.2(1)
Ni–O(3)	2.069(2)	S(3)–Ni–O(4)	91.9(1)
Ni–O(4)	2.049(2)	S(3)–Ni–N(3)	84.4(1)
Ni–N(3)	2.020(4)	S(3)–Ni–N(4)	97.7(1)
Ni–N(4)	2.015(4)	S(4)–Ni–O(3)	91.1(1)
O(3)–H(49)	1.017(5)	S(4)–Ni–O(4)	171.4(1)
H(48)···O(4)	1.515(5)	S(4)–Ni–N(3)	97.9(1)
		S(4)–Ni–N(4)	83.85(10)
		O(3)–Ni–O(4)	91.60(11)
		O(3)–Ni–N(3)	87.46(14)
		O(3)–Ni–N(4)	90.55(13)
		O(4)–Ni–N(3)	90.43(14)
		O(4)–Ni–N(4)	87.90(14)
		N(3)–Ni–N(4)	177.36(14)
		O(3)–H(49)···O(2)	177.13(3)

sides. These indicate the presence of unresolved bands that have been deconvoluted and identified by Bosnich and coworkers[37,41] as arising from either metal-to-ligand charge transfer (MLCT), intraligand $\pi\rightarrow\pi^*$ CT (charge transfer), or, at wavelengths >350 nm, from d–d processes. Unfortunately, the coordination number and geometry of the complexes cannot be determined from their electronic spectra because of overlapping absorptions.

For **III**, the IR spectrum of its free ligand exhibits a band at 3450 cm^{-1} attributable to stretching of the phenolic O–H bonds, whereas the complex exhibits no band in this region but rather a broad absorption centred at 3150 cm^{-1} attributable to stretching vibrations of the hydrogen-bonded carboxylic O–H functions and perhaps also those of the lattice water molecules. The electronic spectrum of **III** is very similar to that of **XIV** with the exception of a high-energy shoulder on the band at ~384 nm in the spectrum of **III** that is not apparent in that of **XIV**. As discussed previously, the band at ~384 nm is an envelope of unresolved bands and in **III** this is evident from its partial resolution.

The structures proposed for the remaining 13 nickel complexes in this study are based upon extrapolations from the

Table 5. Selected bond lengths and angles in $[Co(L1\text{-}sal)][BF_4]_2$ (**XVI**).

Bond lengths (Å)		Bond angles (°)	
Co–S(1)	2.235(1)	O(1)–Co–N(1)	92.8(1)
Co–S(2)	2.2393(9)	O(1)–Co–N(2)	85.7(1)
Co–S(3)	2.2337(8)	O(1)–Co–S(3)	89.60(6)
Co–O(1)	1.901(2)	O(1)–Co–S(2)	87.52(7)
Co–N(1)	1.909(2)	O(1)–Co–S(1)	179.32(7)
Co–N(2)	1.983(2)	N(1)–Co–N(2)	92.6(1)
		N(1)–Co–S(3)	177.24(8)
		N(1)–Co–S(2)	92.88(7)
		N(1)–Co–S(1)	87.35(8)
		N(2)–Co–S(3)	86.23(7)
		N(2)–Co–S(2)	171.45(8)
		N(2)–Co–S(1)	95.00(8)
		S(3)–Co–S(1)	90.27(3)
		S(3)–Co–S(2)	88.59(3)
		S(1)–Co–S(2)	91.81(3)

Table 6. Selected bond lengths and angles in $[Co(L3)][BF_4]$ (**XIX**).

Bond lengths (Å)		Bond angles (°)	
Co(1) cation			
Co(1)–S(1)	2.204(2)	S(1)–Co(1)–S(2)	92.76(7)
Co(1)–S(2)	2.224(2)	S(1)–Co(1)–O(1)	176.7(2)
Co(1)–O(1)	1.932(4)	S(1)–Co(1)–O(2)	87.94(19)
Co(1)–O(2)	1.894(4)	S(1)–Co(1)–N(1)	89.0(2)
Co(1)–N(1)	1.938(5)	S(1)–Co(1)–N(2)	93.5(2)
Co(1)–N(2)	1.922(4)	S(2)–Co(1)–O(1)	86.7(2)
		S(2)–Co(1)–O(2)	176.8(2)
		S(2)–Co(1)–N(1)	91.4(2)
		S(2)–Co(1)–N(2)	89.0(2)
		O(1)–Co(1)–O(2)	92.8(2)
		O(1)–Co(1)–N(1)	94.3(2)
		O(1)–Co(1)–N(2)	83.3(2)
		O(2)–Co(1)–N(1)	85.5(2)
		O(2)–Co(1)–N(2)	94.1(2)
		N(1)–Co(1)–N(2)	177.5(2)
Co(2) cation			
Co(2)–S(3)	2.202(2)	S(3)–Co(2)–S(4)	92.98(7)
Co(2)–S(4)	2.222(2)	S(3)–Co(2)–O(3)	174.4(2)
Co(2)–O(3)	1.924(4)	S(3)–Co(2)–O(4)	87.6(1)
Co(2)–O(4)	1.902(4)	S(3)–Co(2)–N(3)	90.1(2)
Co(2)–N(3)	1.885(5)	S(3)–Co(2)–N(4)	92.3(2)
Co(2)–N(4)	1.944(5)	S(4)–Co(2)–O(3)	89.0(2)
		S(4)–Co(2)–O(4)	179.1(1)
		S(4)–Co(2)–N(3)	91.5(2)
		S(4)–Co(2)–N(4)	88.2(2)
		O(3)–Co(2)–O(4)	90.5(2)
		O(3)–Co(2)–N(3)	95.2(2)
		O(3)–Co(2)–N(4)	82.5(2)
		O(4)–Co(2)–N(3)	87.8(2)
		O(4)–Co(2)–N(4)	92.4(2)
		N(3)–Co(2)–N(4)	177.6(2)

known structures of cobalt, copper,[14] and nickel species discussed so far plus analytical and spectroscopic evidence. Thus, the structures proposed for $[Ni(HL1)]_2[BF_4]_2{\cdot}5H_2O$ (**XII**), $[Ni(HL2)]_2[BF_4]_2{\cdot}3H_2O$ (**XIII**), and $[Ni(HL3)]_2[BF_4]_2{\cdot}3H_2O$ (**XV**) are similar to that observed by X-ray methods for **XIV**

Fig. 6. Coordination sphere types. Those in italics were determined by X-ray methods.

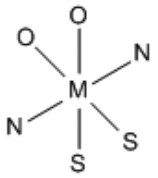

I, II, *III*, XII, XIII, *XIV*, XV, XVII, XVIII, *XIX*, XX

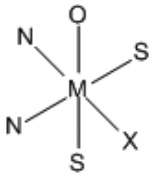

IV, V, VII, VIII, *XVI*

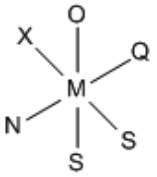

VI (X = Cl; Q = -NH_2)
IX (X = Br; Q = -NH_2)
X (X = Br; Q = -NH_2)
XI (X = Br; Q = -N=CH-C_6H_4-OH

Table 7. Electronic spectroscopy of nickel complexes.

	Electronic spectra and band assignments[a]					
Compound	Ligand π→π* (phenolic)	Ligand π→π* (C=N)		Ni→N MLCT		d–d
[Ni(HL3)]$_2$[BF_4]$_2$·CH_3CN (**XIV**)	290 (1340)	320 (1370)		384 (1455)		580 (80)
[Ni(L3)·HOAc]$_2$[Ni (L3)·2HOAc]·3H_2O (**III**)	290 (1354)		345 (sh)	383 (1450)		577 (41)
[Ni(HL2)][OAc] (**II**)	280 (sh)	308 (1450)	340 (sh)	400 (1500)		610 (54)
[Ni(HL3)]$_2$[BF_4]$_2$·3H_2O (**XV**)	290 (1300)	320 (1400)		385 (1390)		580 (65)
[Ni(L1)].H_2O (**I**)	280 (1350)	310 (1500)	340 (sh)	408 (1400)		610 (55)
[Ni(HL1-sal)]Cl_2·H_2O (**IV**)	293 (1500)	323 (1500)		370 (1400)	406 (sh)	602 (40)
[Ni(HL2-sal)]Cl_2·CH_3OH (**V**)	287 (1300)	320 (1400)		380 (1100)		595 (45)
{[Ni(HL3-sal)Br]Br}[Ni(L3-sal)Br]·2CH_3OH (**IX**)	285	319		380		
[Ni(HL2)]$_2$[BF_4]$_2$·3H_2O (**XIII**)	283 (sh)	320 (1527)	340 (sh)	378 (1431)	410 (sh)	600 (50)
[Ni(HL1)]$_2$[BF_4]$_2$·5H_2O (**XII**)	283 (sh)	320 (1485)	340 (sh)	380 (1207)	420 (sh)	620 (25)

Note: MCLT, metal-to-ligand charge transfer.
[a]In CH_3CN. δ in nm (ε in mol^{-1} L cm^{-1}).

except that the ethereal oxygen and thioether sulfur in the midpoints of L2 and L1, respectively, are not expected to be coordinated to their nickel atoms and the solvation in their crystals is water instead of acetonitrile. Thus, in all cases, the coordination sphere should be $N_2O_2S_2$ with *trans*-nitrogens and *cis*-sulfurs and -oxygens. It is anticipated that all will be hydrogen-bonded dimers and the analytical results are consistent with such formulations. There are only relatively minor differences in the various values of λ_{max} among these compounds, suggesting that a common coordination environment exists in all four cases. Finally, the IR spectra of all four compounds are similar in the region between 3000 and 3800 cm^{-1} where evidence of hydrogen bonding can be seen as described previously.

The structure proposed for [Ni(L1)]·H_2O (**I**) is similar to that observed by X-ray for [Co(L3)][BF_4] (**XIX**) except that the centre sulfur of L1 is not expected to be bound to nickel. The coordination sphere is therefore $N_2O_2S_2$ with *trans*-nitrogens and *cis*-sulfurs and -oxygens. The overall appearance of the electronic spectrum of **I** is similar to that of the other nickel compounds, although the value of λ_{max} for the band envelope near 385 nm in the other compounds is shifted to 408 nm in **I**. This amount of shift is consistent with variations owing to changes in bond angles inside the coordination sphere in related metal complexes[11,27] and may be arising from a different "fit" of the nickel atom with this ligand compared with the others. In support, it may be noted (Table 7) that **II** with a ligand of similar dimensions displays a similar shift of λ_{max}.

The formulation [Ni(HL2)][OAc] for **II** is consistent with analytical data and its infrared spectrum which shows the usual evidence of hydrogen bonding between a phenolic hydrogen and an uncoordinated acetate ion. Uncoordinated acetate is supported by the infrared spectrum's strong peaks at 1592 and 1445 cm^{-1} from $\nu_{C=O}$ of uncoordinated acetate that occur typically near 1580 and 1425 cm^{-1}.[42]

The structures of [Ni(HL1-sal)]Cl_2·H_2O (**IV**), [Ni(HL2-sal)]Cl_2·CH_3OH (**V**), and [Ni(L3-sal)Cl]·H_2O (**VI**) are proposed to have N_2OS_3, $N_2O_2S_2$ and N_2OS_2Cl donor sets, respectively. In the case of **IV**, a facial arrangement of sulfurs similar to that observed in [Co(L1-sal)][BF_4]$_2$, [Ni(PTTN)(H_2O)][ClO_4]$_2$·CH_3OH (PTTN = 1,9-bis(2-pyridyl)-2,5,8-trithianonane)[26] and [Ni(PTTD)][ClO_4]$_2$ (PTTD = 1,12-bis(2-pyridyl)-2,5,8,11-tetrathiadecane)[26] is anticipated and consistent with the compound's spectroscopic properties. Specifically, [Ni(PTTN)(H_2O)][ClO_4]$_2$·CH_3OH, which also has an N_2OS_3 coordination sphere, exhibits inter alia a d–d band at 545 nm that correlates with the 602 nm band in **IV**, the shift between the two arising from differences between the kinds of oxygen and nitrogen donors in the two compounds.[26] The IR, spectrum of **IV** shows a broad band at 3450 cm^{-1} that is unshifted and of similar shape to

Can. J. Chem. Downloaded from www.nrcresearchpress.com by Xi'an Jiaotong University on 09/19/12
For personal use only.

Table 8. Electronic spectroscopy of cobalt complexes.

	Electronic spectra and band assisgnments[a]					
Compound	Ligand π–π* (phenolic)	Ligand π–π* (C=N)		MLCT	d–d	d–d
[Co(L1-sal)][BF_4]$_2$ (**XVI**)	285 (sh)	308 (1750)	363 (sh)	389 (1560)	493 (125)	715 (42)
[Co(L2)][OAc]·3H_2O (**XVII**)	290 (sh)	310 (1800)	340 (sh)	380 (1760)	484 (105)	680 (35)
[Co(L3)][OAc]·3H_2O (**XVIII**)	289 (1240)	320 (sh)	370 (sh)	390 (1100)	488 (85)	660 (65)
[Co(L3)][BF_4] (**XIX**)	290 (sh)	308 (1890)		392 (1690)	480 (112)	680 (83)

Note: MLCT, metal-to-ligand charge transfer.
[a]In CH_3CN. λ in nm (ε in mol^{-1} L cm^{-1}).

Can. J. Chem. Downloaded from www.nrcresearchpress.com by Xi'an Jiaotong University on 09/19/12
For personal use only.

that of the free ligand suggesting no hydrogen bonding by the phenolic OH group or the molecule of water. This argues for a monomeric formulation rather than a hydrogen-bonded dimer.

For **V**, the most probable arrangement of the $N_2O_2S_2$ donors is similar to the arrangement in **IV** except that the middle donor in the ligand's aliphatic chain is now an ethereal oxygen so that the complex's two oxygen donors adopt a cis relationship. Electronic spectra of the two compounds are, as a result, similar, although the intense band at 370 nm in **IV** is shifted to 380 nm in **V** obscuring the shoulder at 406 nm in **IV**. At the same time, the shortest wavelength d–d band at 602 nm in **IV** is shifted to 595 nm in **V**, placing it very close to a similar band at 596 nm in [Ni(DTTCE)][ClO_4]$_2$ (DTTCE = 1,11-dioxa-4,8,14,18-tetrathiacycloeicosane).[43] Like the IR spectrum of **IV**, a broad band at 3450 cm^{-1} in the spectrum of **V** that is unshifted and of similar shape to that of the free ligand suggests absence of hydrogen bonding by the phenolic OH or the molecule of methanol and therefore a monomeric formulation for **V** like that of **IV**.

For **VI**, an N_2OS_2Cl coordination sphere with *trans*-nitrogens is proposed by analogy to the X-ray structure of [Co(L3)][BF_4] (**XIX**). However, in **VI** one site must be occupied by chloride instead of oxygen because of the difference between L3 and (L3-sal).

The five complexes derived from nickel bromide illustrate the versatility of these ligands. For example, from one reaction between L3 and $NiBr_2$·H_2O, three products were isolated by solvent extractions and crystallization. The first, [Ni(HL3)Br]·2H_2O (**XI**), has a mass spectrum with a peak at *m/z* 525.0 corresponding to [$C_{20}H_{24}BrN_2NiO_2S_2$]$^+$ or [Ni(HL3)Br + H^+], which suggests an N_2OS_2Br coordination sphere with t*rans*-nitrogens but with the intact phenolic group uncoordinated to the nickel atom. The second product is [Ni(HL3-sal)Br]Br·CH_3OH (**X**). Its coordination sphere is expected to consist similarly of an N_2OS_2Br donor set with *trans*-nitrogens. In this case, however, the intact phenolic group should be coordinated to the nickel atom. In the mass spectrum, there is a peak at *m/z* 285.1 corresponding to [$C_{13}H_{21}N_2OS_2$]$^+$ or [(HL3-sal) + H^+], which is consistent with the proposed organic ligand, but the spectrum contains no peaks assignable to the complete coordination sphere. The IR spectrum of the compound shows a broad band at 3450 cm^{-1} that is unshifted and of similar shape to that of the free ligand, suggesting no hydrogen bonding involving the free phenolic OH group or the molecule of methanol. For {[Ni(HL1-sal)]Br_2}$_2${[Ni(L1-sal)]Br}·H_2O (**VII**), the proposed structure is suggested by the X-ray structure for **III** plus identification by various techniques of the same or analogous cations in other species in this study. In addition, the mass spectrum of this compound exhibits a cluster of peaks from *m/z* 400 to 403, the most intense of which is at *m/z* 401 corresponding to [$C_{15}H_{23}N_2NiOS_3$]$^+$ or [Ni(L1-sal)]$^+$. Thus, a pair of cations having N_2OS_3 coordination spheres with facially disposed sulfurs is anticipated. One of these should have an intact phenol OH coordinated to nickel, whereas the other should have a deprotonated phenoxy oxygen in the analogous coordination site. The compound's IR spectrum shows a broad band at 3450 cm^{-1}, suggesting the absence of hydrogen bonding by either the phenolic group or water. Likewise, from ligand L2, which is like L1, a similar structure, {[Ni(HL2-sal)]Br_2}$_2${[Ni(L2-sal)]Br}·2CH_3OH (**VIII**), is proposed. Agreement of this formulation with the compound's analysis is good and its mass spectrum has a peak at *m/z* 385.0 corresponding to [$C_{15}H_{23}N_2NiO_2S_2$]$^+$ or [Ni(L2-sal)]$^+$. The compound's IR spectrum shows a broad band at 3450 cm^{-1}, suggesting the absence of hydrogen bonding by either phenolic groups or methanol. Finally, for {[Ni(HL3-sal)Br]Br}[Ni(L3-sal)Br]·2CH_3OH (**IX**), the proposed structure involves one [Ni(HL3-sal)Br]$^+$, as in **X**, one [Ni(L3-sal)Br]$^+$ as in **VI**, one ionic bromide, and two molecules of methanol of solvation. This agrees well with the analytical data and the mass spectrum exhibits a peak at *m/z* 341.0 consistent with [$C_{13}H_{19}N_2NiOS_2$]$^+$ or [Ni(L3-sal)]$^+$. As noted previously in this series, the IR spectrum of **IX** shows a broad band at 3450 cm^{-1}, suggesting the absence of hydrogen bonding by either phenolic groups or methanol.

The electronic spectra of **XIX** and **XVI** are similar consisting of three intense and two less intense bands. The two higher energy intense bands can be related to similar bands in the free ligand as indicated in Table 8. The third intense band at ~390 nm is probably an envelope consisting of a MLCT component similar to that in both the copper[14] and nickel complexes and a d–d component, since it is roughly coincident with the expected location of a d–d band. Support for this hypothesis is obtained from spectra of related complexes of cobalt (Table 8), where shoulders are seen emerging in several cases on the high-energy side of broad bands at ~390 nm. For six-coordinate complexes of Co(III) with less than octahedral symmetry, three d–d bands with intensities that increase as the wavelength decreases are expected,[44,45] and all spectra in Table 8 exhibit two bands with intensity suitable for classification as d–d transitions in low-symmetry six-coordinate Co(III) species. The separation between the observed bands places the anticipated third band in each case roughly where the absorptions near 390 nm are observed.

Can. J. Chem. Downloaded from www.nrcresearchpress.com by Xi'an Jiaotong University on 09/19/12
For personal use only.

Table 9. Cyclic voltammetric data for nickel complexes.

Compound	Coordination sphere	Cyclic voltammetry vs saturated calomel electrode (SCE)[a]	
		ΔE_p (mV)	$E_{1/2}$ (mV)
$[Ni(HL3)]_2[BF_4]_2 \cdot CH_3CN$ (**XIV**)	$N_2O_2S_2$	100[b]	820
$[Ni(L3) \cdot HOAc]_2[Ni(L3) \cdot 2HOAc] \cdot 3H_2O$ (**III**)	$N_2O_2S_2$		540[c]
$[Ni(L1)] \cdot H_2O$ (**I**)	$N_2O_2S_2$	110	745
[Ni(HL2)][OAc] (**II**)	$N_2O_2S_2$		675[d]
$[Ni(HL3\text{-}sal)Br]Br \cdot CH_3OH$ (**X**)	BrN_2OS_2	120	780
$\{[Ni(HL1\text{-}sal)]Br_2\}_2\{[Ni(L1\text{-}sal)]Br\} \cdot H_2O$ (**VII**)	N_2OS_3	200	788
$\{[Ni(HL2\text{-}sal)]Br_2\}_2\{[Ni(L2\text{-}sal)]Br\} \cdot 2CH_3OH$ (**VIII**)	$N_2O_2S_2$	230	800

[a]Scan rate 25 mV/s unless otherwise noted.
[b]Scan rate 200 mV/s.
[c]Irreversible oxidation only.
[d]Weak cathodic activity only.

By analogy, and because of the similarity of the electronic spectra of **XVII**, **XVIII**, and **XIX**, their coordination spheres are proposed to be similar. The ethereal oxygen donor at the midpoint of L2 in **XVII** is probably not coordinated, since the electronic spectra of **XIX**, in which the donor set is known by X-ray methods to be $O_2S_2N_2$, and of **XVII** are closely similar. Finally, **XX** is expected to have an analogous $O_2S_2N_2$ coordination sphere in which one oxygen is phenolic and the other is from methanol.

Cyclic voltammetry

Cyclic voltammetry of L1, L2, or L3 in CH_3CN reveals in all cases irreversible oxidation at potentials ≥950 mV versus the saturated calomel electrode (SCE). An irreversible reduction is observed for L1 and L2 at potentials ≤–750 mV vs SCE, whereas for L3 irreversible reduction occurs at values ≤–800 mV vs SCE. Thus, all three ligands have an electrochemical "window" from –750 to +950 mV vs SCE within which metal-centred electrochemical activity of their complexes may be observed. This window is substantially different from that observed previously[26,43] for similar chains terminated by pyridyl or ethyl groups, and the narrower window in the present case restricts observable metal-centred activity to $Ni^{III/II}$ couples (Table 9).

For **XIV**, a redox wave at $E_{1/2}$ = 820 mV vs SCE is due to a $Ni^{III/II}$ rather than a $Ni^{II/I}$ couple, since the latter typically appears near –0.7 to –0.9 V vs SCE,[26,46] whereas $[Ni(DTBO)][BPh_4]_2 \cdot CH_3CN$ (DTBO = 1,10-diaza-4,7,13,16-tetrathia-5,6:14,15-dibenzocyclooctadecane) exhibits a reversible $Ni^{III/II}$ wave at 1.29 V vs SCE.[46]

For **VIII**, $E_{1/2}$ = 800 mV vs SCE, a value close to that observed for **XIV**. For **VIII**, however, ΔE_p = 230 mV, significantly larger than for **XIV**, indicating a decrease in electrochemical reversibility for the process. The two most prevalent reasons for increased ΔE_p are slow electron transfer kinetics and chemical reactions by the oxidized or reduced forms of the electroactive species. A priori, there is no reason to expect significantly different reactivities in **VIII** compared with **XIV**. Therefore, the change in ΔE_p must derive from a change in electron transfer kinetics. Whereas sulfur is known for its ability to accommodate varying bond lengths and angles,[13,30,31] oxygen is not and it may be that slower electron transfer kinetics are experienced in **VIII** because of one of the coordination sphere oxygens being ethereal and in the middle of the hydrocarbon chain versus a terminal phenoxy oxygen in **XIV**. For outer sphere redox processes, bond lengths and angles must adjust to those of the product before electron transfer occurs and this may be more difficult in **VIII** than **XIV**. For **I**, which is expected to have an $N_2O_2S_2$ coordination sphere like **XIV** and **VIII**, the value of $E_{1/2}$ is smaller than that of either and its value of ΔE_p is comparable to that of **XIV**, suggesting a nearly reversible $Ni^{III/II}$ process. The difference in $E_{1/2}$ between **I** and the other species (**XIV** and **VIII**) is in the cathodic sense indicating **I** is less difficult to oxidize. This is consistent with the fact that it is electrically neutral, whereas in **XIV** and **VIII** the electroactive species are cations. For **II**, there is a barely discernible cathodic peak (~675 mV) at almost the same potential as comparable peaks for **XIV** and **VIII** and metal-centred oxidation is not observed. For **VII**, the value of $E_{1/2}$ = 788 mV vs SCE, when compared with **I** with $E_{1/2}$ = 745 mV vs SCE, indicates the greater ease of oxidation of **I** as anticipated from the relative overall Lewis basicity of the donor sets. The larger value of ΔE_p for **VII** relative to **I** can be attributed to the smaller flexibility of the ligand in **VII** where all donors are

Fig. 7. Cyclic voltammograms of $[Co(L3)][BF_4]$ (**IV**) vs SCE. Scan rates: 400 mV/s (– – –), 200 mV/s (– · · –), 100 mV/s (- - -), 50 mV/s (· · ·), and 25 mV/s (—).

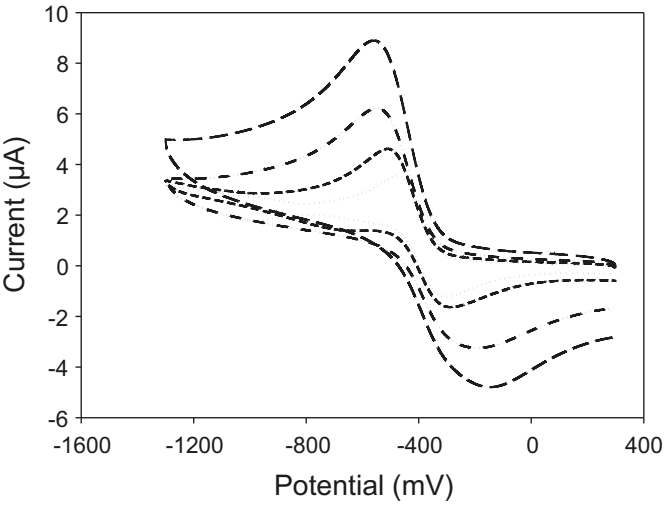

Can. J. Chem. Downloaded from www.nrcresearchpress.com by Xi'an Jiaotong University on 09/19/12
For personal use only.

bound to the metal. In **I**, a potential donor remains free allowing its ligand to adapt more readily to the changed bond lengths and angles necessary for electron transfer thereby permitting faster electron transfer kinetics and a smaller ΔE_p. For **X**, comparison may be made to **XIV**, since both have unipositive cations as the electroactive species and their coordination spheres differ only by substitution of Br for an O. Using Pauling electronegativities (Br 2.96 and O 3.44)[47] as a rough guide to donor basicity, the overall donor strength in **X** (N_2OS_2Br) is greater than that in **XIV** ($N_2O_2S_2$) and the ease of oxidation of **X** compared with **XIV** reflected in the magnitude of their relative $E_{1/2}$ values is as expected. For **III**, the only activity observed is an irreversible oxidation wave at 540 mV vs SCE from which no useful chemical information can be obtained.

For [Co(L3)][BF_4] (**XIX**), the cyclic voltammograms (Fig. 7) at scan rates varying between 25 and 400 mV/s are symmetrical about $E_{1/2}$ = –378 mV vs SCE, but show increasing cathodic and anodic wave separations with scan rate (ΔE_p = 115 mV at 25 mV/s; ΔE_p = 419 mV at 400 mV/s). This is usually taken to indicate that the $Co^{III/II}$ process is electrochemically quasi-reversible,[48] indicating that it is accompanied by a change in coordination number and (or) coordination sphere geometry.[49] Although six-coordinate $Co^{II}(S_4O_2)$ and $Co^{II}(S_4N_2)$ species such as [Co(DTC)][ClO_4]$_2$ (DTC = 1,11-dioxa-4,8,14,18-tetrathiacycloeicosane)[43] and [Co(PTTD)][ClO_4]$_2$ (PTTD = 1,12-bis(2-pyridyl)-2,5,8,11-tetrathiadecane)[50] are well known, so are five-coordinate complexes such as [Co(15O5)(H_2O)$_2$]Cl_2·H_2O) (15O5 = 1,4,7,10,13-pentaoxacyclopentadecane) with an O_5 coordination sphere[51] and [Co(Me_6tren)Br]$^+$ (Me_6tren = tris(2-dimethylaminoethyl)amine) with an N_4Br coordination sphere[17] and many four-coordinate species. Dissociation of one or more donors upon electrochemical reduction of Co (III) to Co(II) is not therefore surprising and is consistent with the tendency for Co(II) low-spin entities to undergo Jahn–Teller distortion, which, in the extreme case, would correspond to dissociation of donors at the sites of bond elongation.

The observed value of $E_{1/2}$ = –378 mV vs SCE for **XIX** can be compared to those of [Co(HTC)][ClO_4]$_2$ (HTC = 1,4,7,11,14,17-hexathiacycloeicosane)[43] ($E_{1/2}$ = +328 mV vs SCE) with its S_6 coordination sphere, [Co(HOten)][ClO_4]Cl_2 (HOten = 3-(2′-aminoethylthia)-2,2-bis((2″-aminoethylthia) methyl)propan-1-ol)[52] ($E_{1/2}$ = –177 mV vs SCE) with its N_3S_3 coordination sphere, and [Co(HOsen]Cl_3·H_2O (HOsen = 3-(2′-aminoethylamino)-2,2-bis((2″-aminoethylamino)methyl) propan-1-ol)[52] ($E_{1/2}$ = –539 mV v. SCE) with its N_6 coordination sphere. The trend in these potentials qualitatively reflects the trend in ease of reduction of the Co(III) centres and its relationship to the net σ-donor ability or Lewis basicity of the coordination sphere. Thus, the N_6 coordination sphere composed of strong σ donors exhibits the highest cathodic potential, indicating it to be the most difficult of the complexes to reduce, whereas the S_6 coordination sphere has the least cathodic potential, indicating it to be the easiest of the complexes to reduce. This trend is consistent with the abilities of N, O, and S to act as hard or soft Lewis bases, and, in particular, with the ability of sulfur to act either as an electron source or sink depending upon the requirements of the atoms to which it is bound.[26,53,54]

Conclusions

One-pot syntheses for three ligands are reported as well as for 20 of their complexes. An unexpected metal-assisted hydrolysis of just one of a pair of imine functionalities in the complexed ligands has been observed and its selectivity attributed to steric hindrance of the second coordinated imine. Electronic spectra of the ligands have been recorded and are essentially invariant with solvent. There is no evidence for solvolysis of any of the complexes and therefore by comparison of spectra of the ligands and of the complexes of known structure, assignments of structures have been made with reasonable confidence to those complexes for which X-ray data could not be obtained. Cyclic voltammetry reveals the ability of thioether sulfur to accommodate its Lewis acid–base behaviour to the demands of the metal atom to which it is attached. The ligands form complexes in which their phenoxy groups are sometimes deprotonated and sometimes not, an explanation for which has been proposed. The electrochemical behaviour of the three ligands and eight of their complexes has been measured and the ligands observed to have an electrochemically useful window from –750 to +950 mV vs SCE in CH_3CN. Alteration of the functional groups terminating the ligand chains can, in some cases, substantially change a ligand's electrochemically useful window and hence the kinds of metal-centred electrochemical activity that can be observed for its complexes. For the complexes, trends in $E_{1/2}$ and ΔE_p have been qualitatively correlated with structural parameters.

Supplementary data

Supplementary data are available for this article through the journal Web site at http://nrcresearchpress.com/doi/suppl/10.1139/v11-081. CCDC 796013 and 796014 (for Co) and 801545 and 801546 (for Ni) contain the X-ray data in CIF format for this manuscript. These data can be obtained, free of charge, via http://www.ccdc.cam.ac.uk/cgi-bin/catreq.cgi (Or from the Cambridge Crystallographic Data Centre, 12 Union Road, Cambridge CB2 1Ez, UK; fax +44 1223 336033; or deposit @ccdc.cam.ac.uk).

Acknowledgements

Funding for this work was provided by Memorial University of Newfoundland and by the Natural Sciences and Engineering Research Council of Canada (NSERC).

References

(1) Germain, M. E.; Vargo, T. R.; McClure, B. A.; Rack, J. J.; Van Patten, P. G.; Odoi, M.; Knapp, M. J. *Inorg. Chem.* **2008** *47* (14), 6203. doi:10.1021/ic702469q.
(2) Paschke, R.; Liebsch, S.; Tschierske, C.; Oakley, M. A.; Sinn, E. *Inorg. Chem.* **2003** *42* (25), 8230. doi:10.1021/ic0301021.
(3) Kwok, C.-C.; Yu, S.-C.; Sham, I. H. T.; Che, C.-M. *Chem. Commun. (Camb.)* **2004** (23): 2758. doi:10.1039/b412762e.
(4) Yang, Y.; Driesen, K.; Nockemann, P.; Van Hecke, K.; Van Meervelt, L.; Binnemans, K. *Chem. Mater.* **2006** *18* (16), 3698. doi:10.1021/cm060644r.
(5) Djukic, B.; Lemaire, M. T. *Inorg. Chem.* **2009** *48* (22), 10489. doi:10.1021/ic9015542.
(6) Koner, R.; Hazra, S.; Fleck, M.; Jana, A.; Lucas, C. R.;

Can. J. Chem. Downloaded from www.nrcresearchpress.com by Xi'an Jiaotong University on 09/19/12
For personal use only.

Mohanta, S. *Eur. J. Inorg. Chem.* **2009** *2009* (33), 4982. doi:10.1002/ejic.200900686.
(7) Mitra, K.; Biswas, S.; Lucas, C. R.; Adhikary, B. *Inorg. Chim. Acta* **2006** *359* (7), 1997. doi:10.1016/j.ica.2006.01.013.
(8) Lucas, C. R.; Liang, W.; Miller, D. O.; Bridson, J. N. *Inorg. Chem.* **1997** *36* (20), 4508. doi:10.1021/ic961536h.
(9) Lucas, C. R.; Liu, S. *Can. J. Chem.* **1996** *74* (11), 2340. doi:10.1139/v96-261.
(10) Lucas, C. R.; Liu, S. *J. Chem. Soc., Dalton Trans.* **1994** (2), 185. doi:10.1039/dt9940000185.
(11) Liu, S.; Lucas, C. R.; Hynes, R. C.; Charland, J.-P. *Can. J. Chem.* **1992** *70* (6), 1773. doi:10.1139/v92-222.
(12) Wu, H.; Lucas, C. R. *Inorg. Chem.* **1992** *31* (12), 2354. doi:10.1021/ic00038a012.
(13) Adhikary, B.; Lucas, C. R. *Inorg. Chem.* **1994** *33* (7), 1376. doi:10.1021/ic00085a027.
(14) Lucas, C. R.; Byrne, J. M. D.; J.L. Collins, J. L.; Miller, D. O. *Can. J. Chem.*, in press.
(15) Dwyer, P. J.; Lions, F. *J. Am. Chem. Soc.* **1950** *72*, 1545. doi:10.1021/ja01160a033.
(16) Kaczmarek, M. T.; Pospieszna-Markiewicz, I.; Kubicki, M.; Radecka-Paryzek, W. *Inorg. Chem. Commun.* **2004** *7*, 1247. doi:10.1016/j.inoche.2004.09.022.
(17) Cotton, F. A.; Wilkinson, G.; Murillo, C. A.; Bochmann, M. *Advanced Inorganic Chemistry;* 6th ed.; Wiley Interscience: Toronto, 1999; p 822.
(18) Hoshino, N.; Ito, T.; Nihei, M.; Oshio, H. *Chem. Lett.* **2002** *31* (8), 844. doi:10.1246/cl.2002.844.
(19) Newton, G. N.; Cooper, G. J. T.; Long, D.-L.; Körgerler, P.; Cronin, L. *J. Mol. Struct.* **2006** *796* (1–3), 23. doi:10.1016/j.molstruc.2006.03.087.
(20) Bluhm, M. E.; Folli, C.; Walter, O.; Döring, M. *J. Mol. Catal. Chem.* **2005** *229* (1–2), 177. doi:10.1016/j.molcata.2004.11.015.
(21) Tandon, S. S.; Lucas, C. R. *Can. J. Chem.* **2008** *86* (9), 912. doi:10.1139/v08-100.
(22) Sygurova, M. K.; Romanenko, G. V.; Vostrikova, K. E.; Vishnevetskaya, L. A.; Podberezskaya, N. V. *J. Struct. Chem.* **1995** *36* (5), 860. doi:10.1007/BF02579682.
(23) Xu, L.; Ye, Q.; Li, H.; Jiao, K.; Zhang, S. *J. Chem. Crystallogr.* **2000** *30* (7), 463. doi:10.1023/A:1011351500225.
(24) García-Antón, J.; Pons, J.; Solans, X.; Font-Bardia, M.; Ros, J. *Eur. J. Inorg. Chem.* **2003** *2003* (16), 2992. doi:10.1002/ejic.200300035.
(25) Ladd, M. F. C.; Larkworthy, L. F.; Leonard, G. A.; Povey, D. C.; Tandon, S. S. *J. Cryst. Spectr. Res.* **1985** *15* (1), 19. doi:10.1007/BF01185713.
(26) Adhikary, B.; Liu, S.; Lucas, C. R. *Inorg. Chem.* **1993** *32* (26), 5957. doi:10.1021/ic00078a011.
(27) Grant, G. J.; Jones, M. W.; Loveday, K. D.; VanDerveer, D. G.; Pennington, W. T.; Eagle, C. T.; Mehne, L. F. *Inorg. Chim. Acta* **2000** *300–302*, 250. doi:10.1016/S0020-1693(99)00602-7.
(28) Huheey, J. E.; Keiter, E. A.; Keiter, R. L. *Inorganic Chemistry, Principles of Structure and Reactivity;* 4th ed.; Harper Collins: New York, 1993; p 301.
(29) Huheey, J. E.; Keiter, E. A.; Keiter, R. L. *Inorganic Chemistry, Principles of Structure and Reactivity;* 4th ed.; Prentice Hall: Toronto, 1997; p 292.
(30) Lucas, C. R.; Liu, S.; Newlands, M. J.; Charland, J.-P.; Gabe, E. J. *Can. J. Chem.* **1989** *67* (4), 639. doi:10.1139/v89-096.
(31) Hartman, J. A.; Cooper, S. R. *J. Am. Chem. Soc.* **1986** *108* (6), 1202. doi:10.1021/ja00266a014.
(32) Böttcher, A.; Takeuchi, T.; Hardcastle, K. A.; Meade, T. J.; Gray, H. B.; Cwikel, D.; Kapon, M.; Dori, Z. *Inorg. Chem.* **1997** *36* (12), 2498. doi:10.1021/ic961146v.
(33) Sreekanth, A.; Kala, U. L.; Nayar, C. R.; Prathapachandra Kurup, M. R. *Polyhedron* **2004** *23* (1), 41. doi:10.1016/j.poly.2003.09.029.
(34) John, R. P.; Sreekanth, A.; Kurup, M. R. P.; Mobin, S. M. *Polyhedron* **2002** *21* (24), 2515. doi:10.1016/S0277-5387(02)01227-5.
(35) Smucker, B. W.; VanStipdonk, M. J.; Eichhorn, D. M. *J. Inorg. Biochem.* **2007** *101* (10), 1537. doi:10.1016/j.jinorgbio.2007.06.042.
(36) Solomons, T. W. G. *Organic Chemistry;* 3rd ed.; Wiley: Toronto, 1984; pp 467–468.
(37) Bosnich, B. *J. Am. Chem. Soc.* **1968** *90* (3), 627. doi:10.1021/ja01005a012.
(38) Clark, H. C.; O'Brien, R. J. *Can. J. Chem.* **1959** *37* (2), 436. doi:10.1139/v59-057.
(39) Tas, E.; Kilic, A.; Konak, N.; Yilmaz, I. *Polyhedron* **2008** *27* (3), 1024. doi:10.1016/j.poly.2007.11.038.
(40) Drago, R. S. *Physical Methods for Chemists;* 2nd ed.; Saunders College Publishing: Toronto, 1992; p 194.
(41) Fraser, C.; Ostrander, R.; Rheingold, A. L.; White, C.; Bosnich, B. *Inorg. Chem.* **1994** *33* (2), 324. doi:10.1021/ic00080a023.
(42) Ahuja, I. S. *Aust. J. Chem.* **1968** *21* (11), 2805. doi:10.1071/CH9682805.
(43) Lucas, C. R.; Liu, S.; Bridson, J. N. *Can. J. Chem.* **1995** *73* (7), 1023. doi:10.1139/v95-127.
(44) Lever, A. B. P. *Inorganic Electronic Spectroscopy;* Elsevier: New York, 1968; p 308.
(45) Cotton, F. A.; Wilkinson, G.; Murillo, C. A.; Bochmann, M. *Advanced inorganic chemistry;* 6th ed.; Wiley Interscience: Toronto, 1999; p 825.
(46) De Vries, N.; Reedijk, J. *Inorg. Chem.* **1991** *30* (19), 3700. doi:10.1021/ic00019a026.
(47) Allred, A. L. *J. Inorg. Nucl. Chem.* **1961** *17* (3–4), 215. doi:10.1016/0022-1902(61)80142-5.
(48) Bard, A. J.; Faulkner, L. R. *Electrochemical Methods, Fundamentals and Applications;* Wiley: New York, 1980.
(49) Headridge, J. B. *Electrochemical Techniques for Inorganic Chemists;* Academic Press: London, 1969.
(50) Adhikary, B.; Liu, S.; Lucas, C. R. *Inorg. Chim. Acta* **1997** *261* (1), 15. doi:10.1016/S0020-1693(96)05572-7.
(51) Streltsova, N. R.; Besky, V. K.; Bulychev, V. M.; Kireeva, O. K. *Inorg. Chim. Acta* **1991** *189*, 111. doi:10.1016/S0020-1693(00)80396-5.
(52) Bernhardt, P. V.; Kim, Y.; Sujandi. *Aust. J. Chem.* **2006** *59* (11), 783. doi:10.1071/CH06257.
(53) Lucas, C. R. *Can. J. Chem.* **1983** *61* (6), 1096. doi:10.1139/v83-194.
(54) Lucas, C. R. *Can. J. Chem.* **1986** *64* (9), 1758. doi:10.1139/v86-290.

Copper(II) complexes of open-chain thioether ligands terminated by salicylaldimine functionality*

C. Robert Lucas, John M.D. Byrne, Julie L. Collins, Louise N. Dawe, and David O. Miller

Can. J. Chem. Downloaded from www.nrcresearchpress.com by South China Agricultural University on 09/19/12
For personal use only.

Abstract: From 1,11-bis(salicylaldimine)-3,6,9-trithiaundecane (**H_2L1**), 1,11-bis(salicylaldimine)-6-oxa-3,9-dithiaundecane (**H_2L2**), and 1,8-bis(salicylaldimine)-3,6-dithiaundecane (**H_2L3**), syntheses for $[Cu(L1)]_2$ (**I**), $Cu(L2)\cdot CH_3OH$ (**II**), Cu(L3) (**III**), $[Cu(HL3)][CH_3COO]$ (**IV**), $[Cu(HL1\text{-}sal)]Cl_2$ (**V**), $Cu_4(L1)_2Br_4(H_2O)_2\cdot 2H_2O$ (**VI**) and $Cu_2(L2)Br_2\cdot xH_2O$ (**VII**) are described. Single crystal X-ray structural studies for **I**, **III** and **VII** are reported. Variable temperature magnetic susceptibility studies of **I**, **VI** and **VII** are discussed. The examination of **VII** represents the first magneto-structural study of a binuclear copper(II) species with NSO_3Br coordination spheres. This study examines perturbation by one or more of the donor atoms so that none of the known magnetostructural models predicts the copper–copper coupling.

Key words: binuclear copper(II) complexes, thioether, salicylaldimine ligands, variable temperature magnetic susceptibility, magnetostructural correlation, X-ray structure.

Résumé : Utilisant les 1,11-bis(salicylaldimine)-3,6,9-trithiaundécane (**H_2L1**), 1,11-bis(salicylaldimine)-6-oxa-3,9-dithiaundécane (**H_2L2**) et 1,8-bis(salicylaldimine)-3,6-dithiaundécane (**H_2L3**), on a réalisé les synthèses des complexes $[Cu(L1)]_2$ (**I**), $Cu(L2)\cdot CH_3OH$ (**II**), Cu(L3) (**III**), $[Cu(HL3)][CH_3COO]$ (**IV**), $[Cu(HLI\text{-}sal)]Cl_2$ (**V**), $Cu_4(L1)_2Br_5(H_2O)_2\cdot 2H_2O$ (**VI**) et $Cu_2(L2)Br_2\cdot xH_2O$ (**VII**). On a effectué la détermination des structures des composés **I**, **III** et **VII** par diffraction des rayons-X sur un cristal unique. On discute des résultats d'études de susceptibilité magnétique des composés **I**, **VI** et **VII**, à température variable. L'examen du composé **VII** correspond à la première étude magnéto-structurale d'une espèce de cuivre(II) binucléaire comportant des sphères de coordination avec du NSO_3Br. Cette étude permet d'examiner la perturbation par un ou plusieurs atomes donneurs; aucun des modèles magnéto-structuraux ne prédit le couplage cuivre–cuivre.

Mots-clés : complexes de cuivre(II) binucléaire, thioéther, ligands salicylaldimine, susceptibilité magnétique à température variable, corrélation magnéto-structurale, structure par diffraction des rayons X.

[Traduit par la Rédaction]

Introduction

Magnetostructural correlations involving multinuclear metal complexes remain of interest.[1–5] Although the nuclearity of complexes being reported continues to rise,[6,7] much that is of fundamental significance can be learned from simple systems,[8] the best representatives of which may well be binuclear copper(II) species. For example, the effects of certain specific types of ligands or atoms bridging between pairs of metal atoms are now well understood, but the list of those bridging atoms or ligands is still comparatively small. Furthermore, while it has also been apparent for some time that ligand donors not involved in bridging have an effect on the quality of superexchange phenomena, these effects remain relatively unexplored both qualitatively and quantitatively except in a small number of cases. For example, compound **VII** herein represents the first magnetostructural study of a binuclear oxygen-bridged copper(II) species with NSO_3Br coordination spheres. Thus, this paper represents part of our continuing interest[9–12] in the consequences of molecular changes upon properties that manifest themselves at the macroscopic level. Ligands in this study (Fig. 1) terminated by salicylaldimine functions are related to open-chain ligands terminated by alkyl,[13] pyridyl,[14] thienyl,[15] pyrazolyl,[16] and benzamidazolyl[16] functionalities that we have described in earlier work.

Experimental

Preparations for **H_2L1**, **H_2L2**, and **H_2L3** were carried out as reported previously.[17] Melting points were obtained on a Fisher-Johns melting point apparatus. Other instruments used include a Hewlett-Packard 8452A diode array UV–vis spectrophotometer, an Agilent 1100 series liquid chromatograph with either an SL MSD trap or a 1946A quadrupole detector and a Brüker Tensor FTIR infrared spectrometer equipped with a PIKE Technologies MIRacle single reflection zinc selenide crystal HATR. All reagents were obtained from the

Received 3 December 2010. Accepted 28 April 2011. Published at www.nrcresearchpress.com/cjc on 8 September 2011.

C.R. Lucas, J.M.D. Byrne, J.L. Collins, L.N. Dawe, and D.O. Miller. Department of Chemistry, Memorial University of Newfoundland, St. John's, NL A1B 3X7, Canada.

Corresponding author: C.R. Lucas (e-mail: rlucas@mun.ca).

*This article has a companion paper in this issue (doi: 10.1139/v11-081).

Can. J. Chem. Downloaded from www.nrcresearchpress.com by South China Agricultural University on 09/19/12
For personal use only.

Fig. 1. Ligands and their position identifiers used in this study.

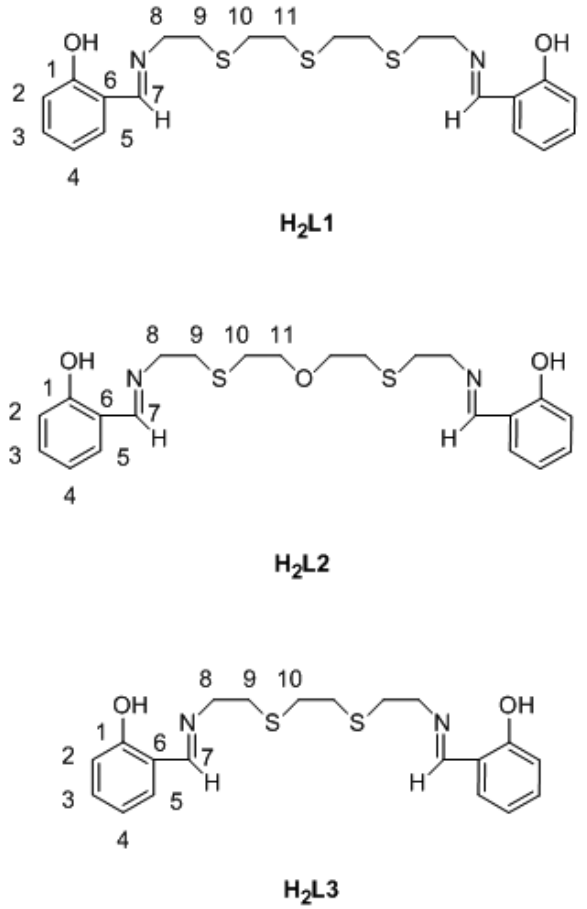

Sigma-Aldrich Chemical Co., Inc,. and were used without further purification. Solvents were ACS grade and were used without purification prior to use. Electronic spectra were obtained in acetonitrile solutions that were 2.0×10^{-3} and 2.0×10^{-5} mol/L in solute. Variable temperature (2–300 K) magnetic susceptibility measurements were made by using a Quantum Design MPMS SQUID magnetometer at a fixed field strength of 1.00 T. Diamagnetic corrections were estimated by using Pascal's constants.

Preparative details — Complexes

From acetate

[Cu(L1)]$_2$ (I)

H_2L1 (1.00 g, 2.2 mmol) dissolved in warm (~40 °C) acetonitrile (25 mL) was mixed with copper(II) acetate monohydrate (0.44 g, 2.2 mmol) in warm (~40 °C) methanol (25 mL) to give a dark green solution that quickly deposited a green precipitate. Upon cooling, a black oily solid formed. The solvent was evaporated slowly in air to produce a green residue that was triturated and rinsed in acetone (3 × 2 mL) and collected in a filter paper as a green powder. This powder was dissolved in chloroform (20 mL), filtered, and then concentrated to 10 mL via a rotary evaporator. Slow evaporation of the solvent produced X-ray quality black crystals (0.55 g, 49% yield). UV–vis (CH_3CN) λ_{max} in nm (ε in mol^{-1} L cm^{-1}): 310 (1333), 370 (1481), 390 (sh), 654 (93). Mass spectrum APCI(+) calcd for Cu(HL1), $[C_{22}H_{27}CuN_2O_2S_3]^+$, *m/z*: 510.0; found *m/z*: 510.0. Anal. calcd for $C_{44}H_{52}Cu_2N_4O_4S_6$: C 51.79, H 5.14, N 5.49, Cu 12.45; found: C 52.48, H 5.06, N 5.44, Cu 12.0.

Cu(L2)·CH$_3$OH (II)

The procedure for **I** was followed except that trituration was carried out in petroleum ether (2 mL). The dark green powder was then dissolved in chloroform (25 mL), filtered, concentrated to 10 mL via a rotary evaporator, and added dropwise with stirring to cold ether (200 mL). This produced a green precipitate that was washed with ether (3 × 5 mL) and dried in air to give a dark green powder (0.49 g, 45% yield). The petroleum ether filtrate produced black crystals after being left to evaporate slowly over a few days. These were rinsed with ether (3 × 3 mL) and dried in air (0.27 g, 25% yield). UV–vis (CH_3CN) λ_{max} in nm (ε in mol^{-1} L cm^{-1}): 318 (1613), 372 (1521), 390 (sh), 454 (sh), 620 (80). Mass spectrum APCI(+) calcd for Cu(HL2), $[C_{22}H_{27}CuN_2O_3S_2]^+$, *m/z*: 494.1; found *m/z*: 494.0. Anal. calcd for $C_{23}H_{30}CuN_2O_4S_2$: C 52.50, H 5.75, N 5.32; found: C 52.50, H 5.36, N 5.28.

Cu(L3) (III and [Cu (HL3)][OAc] (IV)

The procedure for **II** was followed. This produced a light green precipitate that was washed with ether (3 × 5 mL) and dried in air to give a dark green powder (**IV**) (48% yield). The mother liquor was saved and upon slow evaporation of solvent produced black crystals (**III**) suitable for structural determination by X-ray methods. UV–vis (CH_3CN) λ_{max} in nm (ε in mol^{-1} L cm^{-1}): 318 (1632), 374 (1547), 390 (sh), 440 (sh), 640 (88). Anal. calcd for **(III)** $C_{20}H_{22}CuN_2O_2S_2$: C 53.37, H 4.93, N 6.22; found: C 53.39, H 5.16, N 6.20. UV–vis (CH_3CN) λ_{max} in nm (ε in mol^{-1} L cm^{-1}): 316 (1741), 370 (1574), 390 (sh), 450 (sh), 592 (97). Mass spectrum **(IV)** APCI(+) calcd for Cu(HL3), $[C_{20}H_{23}CuN_2O_2S_2]^+$, *m/z*: 450.0; found *m/z*: 450.0. Anal. calcd for (**IV**) $C_{22}H_{26}CuN_2O_4S_2$: C 51.80, H 5.14, N 5.49; found: C 51.52, H 4.93, N 5.84.

From halides

[Cu(HL1-sal)]Cl$_2$ (V)

H_2L1 (1.0 g, 2.2 mmol) dissolved in warm (~40 °C) acetonitrile (25 mL) was mixed with copper(II) chloride dihydrate (0.38 g, 2.2 mmol) in warm (~40 °C) methanol (25 mL) to give a dark green solution. Solvent was evaporated slowly in air to produce dark green spheres and a brown green film. The spheres were removed by hand and triturated in ether (3 mL) to a green powder. The powder was washed with methanol (150 mL), separated by filtration, and washed with ether (3 × 5 mL). It was dried in air and collected as a dark green powder (0.70 g, 63% yield). The methanol solution was concentrated to 15 mL via a rotary evaporator and then added dropwise with stirring to cold ether (250 mL) to produce further green precipitate that was collected in a fritted glass crucible, washed with ether (3 × 5 mL), and dried in air (0.28 g, 27% yield). UV–vis (CH_3CN) λ_{max} in nm (ε in mol^{-1} L cm^{-1}): 318 (1462), 365 (1326), 654 (47). Mass spectrum APCI(+) calcd for Cu(HL1-sal) (sal = C_7H_3O), $[C_{15}H_{24}CuN_2OS_3]^+$, *m/z*: 407.0; found *m/z*: 407.0. Anal.

Can. J. Chem. Downloaded from www.nrcresearchpress.com by South China Agricultural University on 09/19/12
For personal use only.

calcd for $C_{15}H_{24}Cl_2CuN_2OS_3$: C 37.61, H 5.05, N 5.85; found: C 37.58, H 4.95, N 5.81.

Cu(L3) (III)

H_2L3 (0.65 g, 1.6 mmol) dissolved in warm (~40 °C) acetonitrile (40 mL) was mixed with copper(II) chloride dihydrate (0.28 g, 1.6 mmol) in warm (~40 °C) methanol (20 mL) to produce a dark green solution. A green-blue precipitate deposited overnight and was collected by filtration, washed with ether (3 × 5 mL), and dried in air to a green-blue powder (0.46 g, 64% yield). A portion of the solid (0.14 g, 0.3 mmol) was dissolved in hot (~70 °C) *N*,*N*-dimethylformamide (15 mL), filtered and upon slow evaporation dark crystals suitable for structural determination by X-ray methods and for analysis were produced. Mass spectrum APCI(+) calcd for Cu(HL3), $[C_{20}H_{23}CuN_2O_2S_2]^+$, *m*/*z*: 450.0; found *m*/*z*: 450.0. Note: This compound is also reported above as the result of a preparation from copper(II) acetate monohydrate. These products are indistinguishable.

$Cu_4(L1)_2Br_4(H_2O)_2{\cdot}2H_2O$ (VI)

H_2L1 (1.0 g, 2.2 mmol) dissolved in warm (~40 °C) acetonitrile (25 mL) was mixed with copper(II) bromide (0.50 g, 2.2 mmol) in warm (~40 °C) methanol (25 mL) to produce a dark green solution, which quickly deposited a dark green oily precipitate. The solvent was evaporated slowly in air to give a dark green residue that was triturated with ether (3 mL) to give a dark green powder, which was collected by filtration. This powder was dissolved in hot (~60 °C) methanol (250 mL) and filtered hot. The solution was cooled to about 30 °C and ether (50 mL) was added. The solution became slightly cloudy and a light green precipitate began to form. After precipitation was completed (~20 min), the solid was collected in a fritted glass crucible, washed with ether (3 × 5 mL), and dried in air to a green powder (0.53 g, 62% yield). UV–vis (CH_3CN) λ_{max} in nm (ε in mol^{-1} L cm^{-1}): 310 (1400), 370 (1463), 390 (sh), 658 (61). Anal. calcd for $C_{44}H_{60}Br_4Cu_4N_4O_8S_6$: C 34.34, H 3.93, N 3.64; found: C 34.56, H 3.81, N 4.02. Mass spectrum : APCI(+); calcd for [Cu(L1) + H], $[C_{22}H_{26}CuN_2O_2S_3 + H]^+$, *m*/*z*: 510.0; found *m*/*z*: 510.0. Mass spectrum: calcd for Cu(L1)Br, $[C_{22}H_{26}BrCuN_2O_2S_3]^+$, *m*/*z* (most intense peak): 590.0; found *m*/*z*: 589.9.

$Cu_2(L2)Br_2{\cdot}xH_2O$ (x = 1 or 3) (VII)

H_2L2 (0.96 g, 2.2 mmol) dissolved in warm (~40 °C) acetonitrile (25 mL) was mixed with copper(II) bromide (0.50, 2.2 mmol) in warm (~40 °C) methanol (25 mL) to produce a dark green solution. The solvent was evaporated slowly in air to give a dark green oil. Trituration in a little water produced a dark green powder that was washed with ether (3 × 5 mL) and dried in air. The powder was extracted with hot (~60 °C) methanol (50 mL), the undissolved portion being washed with ether (3 × 5 mL) and dried in air to a green powder (x = 3) (0.32 g, 38% yield). The methanol solution was then concentrated via a rotary evaporator to 10 mL and added dropwise with stirring to cold ether to produce a green precipitate that was washed with ether (3 × 5 mL) and dried in air to give more green powder (x = 3) (0.07 g, 8% yield). Alternatively, the methanol solution was left to evaporate slowly in air producing greenish crystals (x = 1) suitable for structural determination by X-ray methods. For x = 1, UV–vis (CH_3CN) λ_{max} in nm (ε in mol^{-1} L cm^{-1}): 310 (1548), 372 (1488), 390 (sh), 656 (107). Mass spectrum APCI(+) calcd for $Cu_2(L2)(H_2O)$, $[C_{22}H_{28}Cu_2N_2O_4S_2]^+$, *m*/*z*: 574.0; found *m*/*z*: 573.9. Mass spectrum calcd for Cu(HL2), $[C_{22}H_{27}CuN_2O_3S_2]^+$, *m*/*z*: 494.1; found *m*/*z*: 494.0. Mass spectral characteristics for the crystals (x = 1) and powder (x = 3) are indistinguishable. Anal. calcd for (x = 3) $C_{22}H_{32}Br_2Cu_2N_2O_6S_2$: C 34.25, H 4.18, N 3.63; found: C 34.32, H 3.88, N 3.54.

X-ray studies

A summary of crystallographic data for $[Cu(L1)]_2$ (**I**), Cu(L3) (**III**), and $Cu_2(L2)Br_2{\cdot}H_2O$ (**VII**) is in Table 1. For **I**, non-hydrogen atoms were refined anisotropically, whereas hydrogen atoms were included but not refined. For **III** and **VII**, hydrogen atoms were included in calculated or difference map positions with isotropic parameters set 20% greater than those of their bonding partners. They were refined on the riding model, whereas all non-hydrogen atoms were refined anisotropically. The model for **VII** contained one molecule of water for which the hydrogens could not be found in the difference map. Those hydrogens were not included in the model. Descriptions of the experimental procedures, anisotropic thermal parameters, a full listing of bond lengths and angles, and planes within coordination spheres are available as Supplementary data.

Results and discussion

General features of all three ligands have been discussed previously[17] and are, first, their tendency in the presence of a metal atom to lose salicylaldehyde from one end of their hydrocarbon chain as, for example, during formation of $[Cu(HL1\text{-}sal)]Cl_2$ (**V**) and, second, the solubility controlled isolation of both protonated and deprotonated forms of the ligand, as in the one-pot preparation of Cu(L3) (**III**) and [Cu(HL3)][OAc] (**IV**). Protonated phenolic oxygens coordinated to metals have been observed previously in salicylaldimine complexes,[18] although precipitation of both protonated and deprotonated forms when complexation is carried out in the absence of added base is less common.

An X-ray structural study of **I** shows the asymmetric unit contains two monometallic moieties (Fig. 2*a*), which form dinuclear complexes with their symmetry-related counterparts (Fig. 2*b*). A single ligand molecule is coordinated to each square pyramidal copper in a trans planar manner through its two phenoxy oxygens and two imine nitrogens. In addition, each ligand molecule has one of its phenoxy oxygens bridging between apical and basal sites of two symmetry-related coppers. The second phenoxy oxygen of each ligand is bound terminally to a basal site of its own copper atom. No sulfur atoms are coordinated to copper. Coordination sphere bond lengths and angles are shown in Table 2.

The two dinuclear molecules are similar but not identical. For example, the Cu(1)–Cu(1′) distance is 3.3960(3) Å and the Cu(2)–Cu(2′) distance is 3.3365(4) Å, whereas the difference in Cu–O distances at the apical sites is 0.08(1) Å. On the other hand, differences between corresponding bond lengths in the Cu(1) and Cu(2) basal sites are all ≤0.009(2) Å and on average are 0.005(2) Å. Differences within the

Can. J. Chem. Downloaded from www.nrcresearchpress.com by South China Agricultural University on 09/19/12
For personal use only.

Table 1. Crystallographic data for $[Cu(L1)]_2$ (**I**), Cu(L3) (**III**), and $Cu_2(L2)Br_2{\cdot}H_2O$ (**VII**).

Parameter	$[Cu(L1)]_2$ (**I**)	Cu(L3) (**III**)	$Cu_2(L2)Br_2{\cdot}H_2O$ (**VII**)
Empirical formula	$C_{44}H_{52}Cu_2N_4O_4S_6$	$C_{20}H_{22}CuN_2O_2S_2$	$C_{22}H_{28}Br_2Cu_2N_2O_4S_2$
Formula mass	1020,37	450,07	735,49
Crystal colour, habit	Deep red, block	Green, chunk	Orange, prism
Crystal dimensions, mm	0.48×0.36×0.30	0.25×0.21×0.18	0.20×0.10×0.10
Crystal system	Triclinic	Monoclinic	Orthorhombic
Space group	*P*-1 (No. 2)	*C*2/*c* (No. 15)	$P2_12_12_1$ (No. 19)
Z	2	8	4
a (Å)	12.8374(7)	16.6351(15)	8.7788(5)
b (Å)	13.0858(7)	22.3228(17)	16.1716(10)
c (Å)	15.5936(8)	10.7476(9)	18.5129(11)
α, β, γ (°)	91.163(1), 110.339(1), 110.983(1)	90, 99.2804(7), 90	90, 90, 90
V (Å^3)	2261.8(2)	3938.8(6)	2628.2(3)
$D_{calcd.}$ (g/cm^3)	1.498	1.518	1.859
T (K)	193±1	153±1	153±1
μ (cm^{-1})	12,64	13,389	48,587
λ	0.71073	0.71073	0.71073
F(0,0,0) (electrons)	1060	1864	1464
2θ (max.) (°)	52.8	61.4	61.4
No. reflections measured	17606	16551	46547
No. unique reflections	9186	4079	6039
No. variable parameters	542	245	309
*R*1 ($I > 2.00\sigma[I]$)[a]	0.0266	0.0416	0.0381
*wR*2 (all refl.)[b]	0.0724	0.1015	0.0965
Last D-map			
Highest peak (e$^-$/Å^3)	0.8	0.87	2.57
Deepest hole (e$^-$/Å^3)	–0.51	–0.38	–0.55

Note: Throughout this work, esds are in parentheses and refer to the last digit printed.

[a] $R1 = \sum||F_o| - |F_c||/\sum|F_o|$.

[b] $wR2 = [\sum(w(F_o^2 - F_c^2)^2/\sum w(F_o^2)^2]^{1/2}$.

coordination spheres between corresponding basal bond angles are on average 0.24(7)° and all are ≤0.67(7)°, whereas those involving the apical oxygen atoms are on average 1.99(6)° and range from 0.21(6)° to 3.48(6)°. The Cu(1)–O(2′) and the Cu(2)–O(4′) bonds define the elongated Jahn–Teller axes for Cu(1) and Cu(2) and indicate a $d_{x^2-y^2}$ ground state for each Cu with calculated τ values[19] of 0.09 and 0.08, respectively. Because these differences between the molecules are likely to be of limited impact on properties of the substance, only the molecule containing Cu(1) will be discussed further unless specifically noted.

None of the ligand's thioether sulfurs are bound to copper. The chain containing the three sulfur atoms extends in a loop that is nearly perpendicular to the plane of the copper and its donor atoms. The closest approach of a sulfur to a copper atom in its own molecule is by S(1), which lies 4.5(1) Å away. This is 1.4 times the sum (3.20 Å) of the van der Waals' radii of copper and sulfur[20], and there is therefore no bonding interaction between the two atoms. Furthermore, no sulfur atom in the loop lies near a copper atom in an adjacent molecule of the complex, the nearest sulfur (S(1)) lying 6.0(1) Å away. The bond angles at copper deviate on average 1.23(7)° from 90° and 5.14(7)° from 180°, with the largest departure from 90° being 2.52(6)° at O(1)–Cu(1)–N(2) and from 180° being 7.80(5)° at N(2)–Cu(1)–N(1). The average Cu–O and Cu–N bond lengths of 1.905(1) and 2.006(1) Å, respectively, are comparable to corresponding distances of 1.910(7) and 1.980(7) Å for Cu–O in $Cu_2(mspd)_2(CH_3COO)_2{\cdot}Cu_2(CH_3COO)_4{\cdot}2C_2H_5OH$ (Hmspd = *N*-methyl-*N*′-(4,6-dimethoxysalicylidene)-1,3-propanediamine)[21] and of 1.99(1) and 2.02(1) Å for Cu–N in $[Cu(PTN)][CF_3SO_3]_2$ (PTN = 1,9-bis(2-pyridyl)-2,5,8-trithianonane).[16] Thus, the notable aspect of this compound's structure is the absence of interactions between copper and any of the sulfurs.

The structure of **III** involves a roughly planar N_2O_2 coordination sphere with *trans*-nitrogens and *trans*-oxygens (Fig. 3). Pertinent bond lengths and angles in the copper atom's coordination sphere are shown in Table 3.

In this structure, as in that of **I**, there is no inter- or intramolecular interaction between sulfur and copper. Similarly, the chain containing the two sulfur atoms extends in a nearly perpendicular loop away from the plane defined by the copper and its coordination sphere. The closest approach of a sulfur to the copper atom within its own molecule is by S(1), which lies 4.321(2) Å away. This is 1.35 times the sum (3.20 Å) of the van der Waals' radii of copper and sulfur,[20] and there is clearly no bonding interaction between them. The sulfur lying nearest to a copper atom in an adjacent molecule is S(2), which lies 5.506(2) Å away.

The roughly planar N_2O_2 coordination sphere has a slight distortion towards tetrahedral arising from the two nitrogen atoms moving to one side of the plane and the two oxygen atoms to the other. This leaves Cu(1) lying –0.0044(1) Å outside the best plane through copper and its N_2O_2 donor set. The bond angles at copper deviate on average 3.23(7)° from 90° with the largest deviation being 4.15(7)° at O(2)–Cu–N(2).

Can. J. Chem. Downloaded from www.nrcresearchpress.com by South China Agricultural University on 09/19/12
For personal use only.

Fig. 2. (*a*) ORTEP of 1/2[Cu(L1)]$_2$ (**I**) (see text). Thermal ellipsoids are shown at the 50% probability level. (*b*) Ball and stick representation of the dimers of [Cu(L1)]$_2$ (**I**). Cu(1′) and associated atoms generated by the symmetry operation (2 – *x*, –*y*, 2 – *z*) and Cu(2′) and associated atoms generated by the symmetry operation (2 – *x*, 1 – *y*, 1 – *z*).

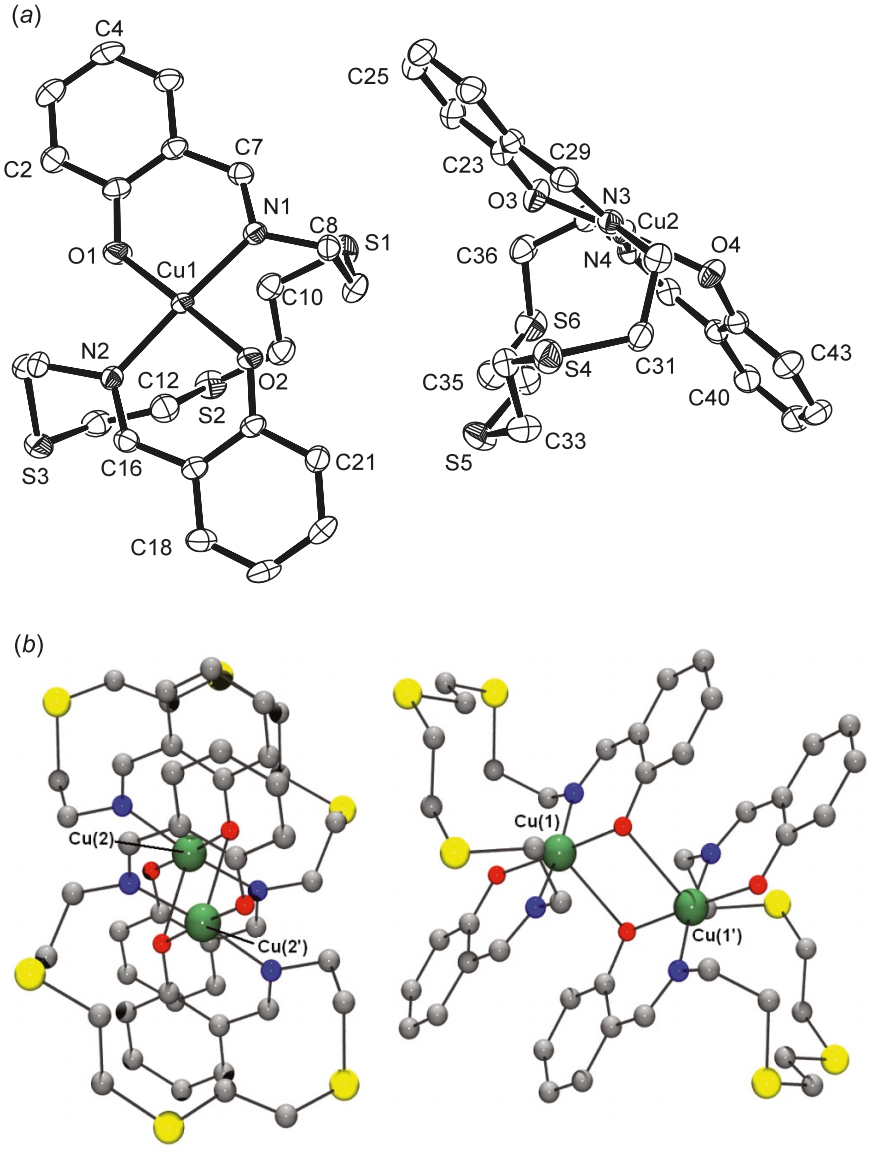

There is a larger deviation for angles expected to be close to 180° with the average being 27.65(8)° and the larger being 30.81(8)° at N(1)–Cu–N(2). These are larger deviations than those in **I** and arise presumably because of a shorter length of the loop of ligand joining N(1) and N(2) in **III** compared with **I**. The average Cu–O and Cu–N bond lengths in **III** of 1.891(2) and 1.983(2) Å, respectively, are comparable to corresponding distances in **I** and related species as discussed previously. Thus, as with **I**, the notable feature of **III** is the absence of interactions between sulfur and copper.

The X-ray structure of **VII** is in Fig. 4 and shows the phenolic oxygens and imine nitrogens again bound to copper, but in this case both sulfur atoms are also bound as is the ether oxygen, although the latter lies at the limit of what can be considered a bonding distance. It should be noted in this context that coordination by ethereal oxygen in a hydrocarbon chain also containing thioether sulfurs is well-known.[22–24] The structure of **VII** involves roughly octahedral NO_3SBr coordination spheres about each of two copper atoms. The coordination spheres share common ethereal and phenolic oxygens and as a result the pseudo-octahedra are tipped towards each other by 74.57(5)° so that the angle between their O_2NS planes is 105.43(5)°. Each of the ligand's phenolic oxygens bridges the two coppers so that those oxygens represent an intersecting or common edge of the two planes defined by a copper atom and its four NO_2S donors. The copper···copper distance in **VII** is 2.968(3) Å compared with 3.3960(3) and 3.3365(4) Å in **I**. Other coordination sphere bond lengths and angles for **VII** are shown in Table 4.

Electrical neutrality in **VII** is achieved through two deprotonated phenolic oxygens and two bromides that lie at distances Br(1)–Cu(2) = 2.6477(6) Å and Br(2)–Cu(1) = 2.6381(7) Å from the copper atoms. These distances are less than the sum of the van der Waals' radii of copper and bromine (3.20 Å),[20]

Can. J. Chem. Downloaded from www.nrcresearchpress.com by South China Agricultural University on 09/19/12
For personal use only.

Table 2. Selected bond lengths and angles in $[Cu(L1)]_2$ (**I**).

Bond lengths (Å)		Bond angles (°)	
Cu(1) molecule			
Cu–O(1)	1.8962(12)	O(1)–Cu–O(2)	177.76(6)
Cu–O(2)	1.9141(11)	O(1)–Cu–N(2)	87.48(6)
Cu–N(1)	2.0079(17)	O(2)–Cu–N(2)	91.25(6)
Cu–N(2)	2.0047(18)	Cu–O(2′)–Cu′	96.29(6)
Cu–O(2′)	2.6034(12)	O(1)–Cu–N(1)	91.09(6)
		O(2)–Cu–N(1)	89.92(6)
		N(2)–Cu–N(1)	172.19(5)
Cu(2) molecule			
Cu–O(3)	1.9055(12)	O(3)–Cu–O(4)	177.07(6)
Cu–O(4)	1.9209(12)	O(3)–Cu–N(4)	87.62(5)
Cu–N(3)	2.0104(13)	O(4)–Cu–N(4)	91.34(5)
Cu–N(4)	2.0046(14)	Cu–O(4′)–Cu′	96.49(6)
Cu–O(4′)	2.5197(16)	O(3)–Cu–N(3)	90.96(5)
		O(4)–Cu–N(3)	89.72(5)
		N(4)–Cu–N(3)	172.41(7)

suggesting a bonding interaction probably exists between copper and bromine. Because of the tendency of Cu(II) to undergo Jahn–Teller distortion, it is difficult to define a covalent radius for copper. Comparison, however, of several apical Cu–S distances to the accepted covalent radius for sulfur of 1.02 Å[20] permits one to assign a value of ~1.47 Å to copper under similar circumstances. Using this value, and the accepted value (1.14 Å)[20] for the covalent radius of bromine, the internuclear distance for a covalent bond between copper and "apical" bromine should be ~2.61 Å. Thus, the Cu···Br distances observed in this compound are consistent with bonding interactions between copper and bromine. The suggestion gains credence upon examination of the angles subtended at the coppers and involving the bromines. These angles are given in Table 5. Finally, magnetic susceptibility data (vide infra) also suggests the presence of a bonding interaction between copper and bromine.

Reminiscent of **I** and **III**, the loop of ligand containing the ethereal oxygen in **VII** stretches between coppers at a distance from them and their other donors. This places the ethereal oxygen roughly over the midpoint of the Cu_2O_2 system and at distances of 2.835(3) and 2.868(3) Å to Cu(1) and Cu(2), respectively, that are slightly less than the sum (2.90 Å) of the van der Waals' radii for copper and oxygen. Establishing copper–oxygen bonding distances in a Jahn–Teller distorted coordination sphere by the same method used above for copper–bromine distances, allows one to predict apical Cu–O bond lengths of ~2.20 Å from the published value (0.73 Å)[20] for oxygen's covalent radius. Distances to ethereal oxygen and to perchlorate oxygen in $[Cu(POT)][ClO_4]_2$ (POT = 1,9-bis(2-pyridyl)-5-oxa-2,8-dithianonane)[22] are 2.413(5) and 2.469(10) Å, respectively. This seems to suggest the ethereal oxygen in **VII** lies at a distance from the coppers that is near the limit for bonding interactions with them. It is relevant, however, that bond angles in the ligand loop produce a conformation placing the ethereal oxygen nearer rather than farther away from the coppers. This stands in contrast to the situation for the analogous thioether sulfur in **I** where there is definitely no bonding interaction between the potentially apical sulfur and copper, and where the sulfur is placed by the loop conformation further from copper rather than nearer. Finally, in **VII** the coordination spheres are tipped towards each other with a shared face involving the three oxygen atoms and the bond angles at each of the coppers (Table 4) are close to those found in an octahedron, thereby providing further evidence of a bonding interaction. The average of the eight angles lying in the rough plane of the bridging phenoxides and coppers that would ideally be 90° is 88.5(1)° with the greatest deviation being 8.60(9)° at O(1)–Cu(2)–S(1). Likewise for angles expected to be 180°, the average is 158.8(1)° with the greatest deviation being 32.28(9)° at O(1)–Cu(1)–S(2). At both coppers, the largest deviations are associated with the sulfur donors. It is reasonable to propose that those deviations are due to the ligand being too short to extend easily over the required distance leading, therefore, to the observed shift of the sulfurs from ideal positions in the copper coordination spheres. The Cu–N, Cu–O, and Cu–S distances, with average lengths of 1.939(4), 1.976(3), and 2.338(1) Å, respectively in the NO_2S planes are normal when compared with those in similar structures, as discussed above. In conclusion, consideration of the bond angles at the coppers and the apical Cu–O distances suggests a weak interaction exists between O(2) and each of the copper atoms. The structure of this dinuclear species may therefore be described as two acutely Jahn–Teller elongated NO_3SBr pseudo-octahedra sharing a face defined by three shared oxygen atoms. Magnetic susceptibility as a function of temperature for this compound (vide infra) is consistent with the structural interpretation.

Because of the similarity between ligands $\mathbf{H_2L1}$ and $\mathbf{H_2L}2$, which differ only by the identity of the central atom in their chains, the structure of $Cu_4(L1)_2Br_4(H_2O)_2\cdot 2H_2O$ (**VI**) for which crystals suitable for X-ray structural analysis could not be obtained might be expected to be analogous to that of **VII** established by X-ray methods. However, magnetic measurements (vide infra) and mass spectral fragmentation patterns suggest the structure is most likely a tetranuclear chain. The central pair of coppers in this chain are probably bridged by the organic ligands in a manner similar to that in **I** (Fig. 2*b*), whereas at each end a further copper lies surrounded by a pair of bromine atoms, thioether sulfurs, and possibly a molecule of water. Likewise, by analogy to previously established structures, that of **II** is proposed to consist of a roughly planar N_2O_2 coordination sphere. The compound's electronic spectrum consists of a single d–d band at 620 nm. Electronic spectra of **I**, **III**, and **VII** in the d–d region (Table 6) also consist, in each case, of a single absorption as expected for d^9 species.

For **IV**, the probable coordination sphere is also N_2O_2. This is proposed on the basis of anticipated similarity to the known structure for **III** (see previous). In **IV**, the oxygen donors are proposed to be the phenolic oxygens even though one of them bears a hydrogen. Precedent exists for coordinated phenolic OH.[18] Furthermore, there is no evidence for interaction of the acetate anion with copper in the IR spectrum of **IV**, which shows strong peaks at 1592 and 1445 cm^{-1}. These can be attributed to $\nu_{C=O}$ of uncoordinated acetate, which has vibrations occurring typically near 1580 and 1425 cm^{-1} that are distinguishable from those of coordinated acetate that occur near 1545 and 1405 cm^{-1}.[25]

Electronic spectroscopic evidence for **V** suggests the compound's structure involves an N_2S_3 coordination sphere.

Can. J. Chem. Downloaded from www.nrcresearchpress.com by South China Agricultural University on 09/19/12
For personal use only.

Fig. 3. ORTEP of Cu(L3) (**III**). Thermal ellipsoids are shown at the 50% probability level.

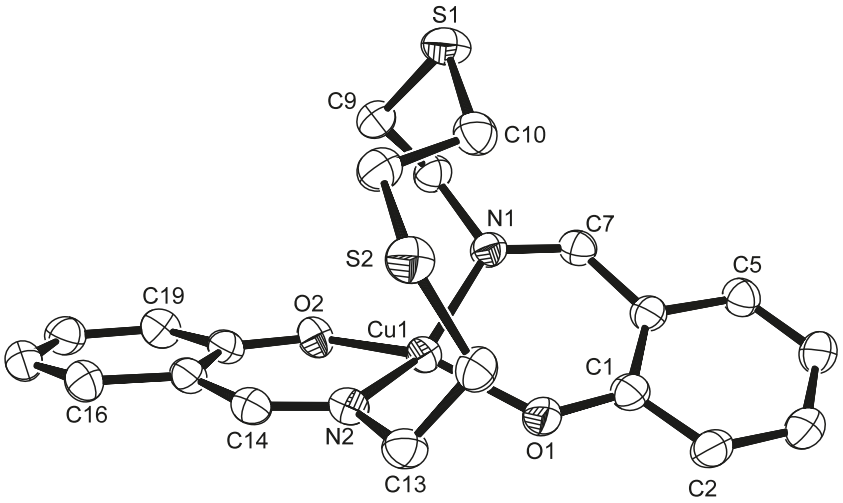

Table 3. Selected bond lengths and angles in Cu(L3) (**III**).

Bond lengths (Å)		Bond angles (°)	
Cu–O(1)	1.900(2)	O(1)–Cu–O(2)	155.52(7)
Cu–O(2)	1.882(2)	N(1)–Cu–O(2)	91.77(7)
Cu–N(1)	1.981(2)	O(1)–Cu–N(1)	93.94(7)
Cu–N(2)	1.985(2)	O(2)–Cu–N(2)	94.15(7)
		O(1)–Cu–N(2)	93.06(7)
		N(1)–Cu–N(2)	149.18(8)

Fig. 4. ORTEP of $Cu_2(L2)Br_2{\cdot}H_2O$ (**VII**). Thermal ellipsoids are shown at the 50% probability level.

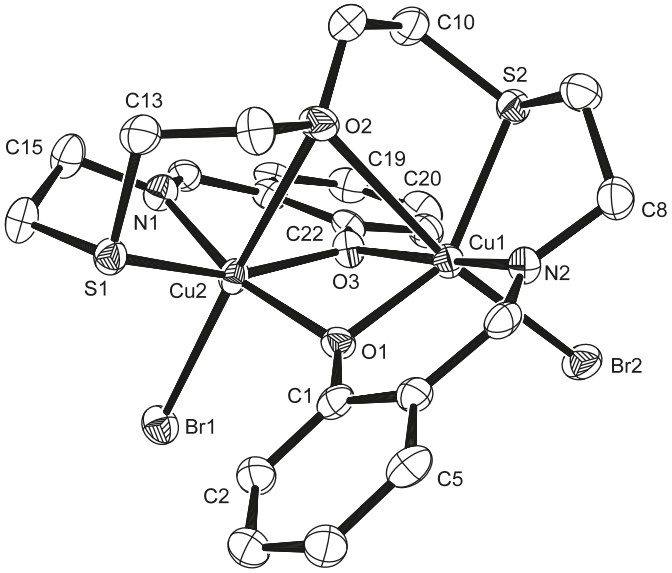

There is a strong similarity between the electronic spectrum of **V** and spectra of a series of pyrazolyl- and benzamidazolyl-trithioether complexes of copper(II)[16] having either distorted trigonal bipyramidal or square pyramidal structures in the solid state that involve N_2S_3 coordination spheres. By analogy, therefore, it is reasonable to propose a solid-state five-coordinate structure involving an N_2S_3 coordination sphere for **V** as well. In support, it is observed that at 390 nm there is a charge-transfer band appearing as an intense shoulder or broadening of another charge-transfer band at 365–374 nm in all spectra of copper complexes produced in this study except **V**. The spectral feature at 390 nm is tentatively assigned as a Cu→O metal-to-ligand charge transfer (MLCT) band. This assignment is consistent with observations by other workers. For example, Lever[26] observed Cu→O and Cu→N MLCT bands at 375 and 435 nm, respectively. Likewise, Sönmez[27] reported what appears to be a Cu→N band at 419 nm and Urbach and co-workers[28] described S→Cu charge transfer (LMCT) in the region 344–360 nm, whereas in our own laboratory examples of S→Cu charge transfer in the region 350–375 nm have been observed.[22] Finally, the relatively narrow band at 3400 cm^{-1} in the IR spectrum of the free ligand (**H_2L1**) corresponding to the stretching vibration (ν_{OH}) of the phenolic O–H bonds has been shifted in the spectrum of the complex. There ν_{OH} is centred at 3130 cm^{-1} and the band is broadened as well. This behaviour is typical of a hydrogen-bonded system and suggests the phenolic O–H in the complex is intact and free to engage in hydrogen bonding.[29] Thus, **V** represents the first example encountered in this study of a truncated ligand with its remaining phenolic OH uncoordinated to metal.

Based on precedents described previously, charge-transfer bands can be assigned as shown in Table 6. Charge transfer involving the nitrogen donors is presumably obscured by the other bands in most of the complexes, although a shoulder in the region 440–454 nm can be detected in three cases.

The room-temperature magnetic moment per mol of $Cu_2(L2)Br_2{\cdot}H_2O$ (**VII**) is 1.26 μ_B. This is reduced from the value (2.45 μ_B) that would be expected for 2 mol of uncoupled Cu(II) per mol of compound and suggests strong antiferromagnetic coupling between the copper atoms. Figure 5 shows the magnetic behaviour of **VII** as a function of temperature. The theoretical curve was obtained by least-squares fitting of the experimental data to a modified Bleaney–Bowers equation (eq. [1]).[30]

$$[1] \qquad \chi_m = \frac{N\beta^2 g^2}{3k(T-\theta)}\left[1+\frac{1}{3}\exp(-2J/kT)\right]^{-1}(1-\rho) + \frac{[N\beta^2 g^2]\rho}{4kT} + N\alpha$$

Can. J. Chem. Downloaded from www.nrcresearchpress.com by South China Agricultural University on 09/19/12
For personal use only.

Table 4. Selected bond lengths and angles in $Cu_2(L2)Br_2{\cdot}H_2O$ (**VII**).

Bond lengths (Å)		Bond angles (°)	
Cu(1)–N(2)	1.934(4)	N(2)–Cu(1)–O(3)	164.20(14)
Cu(1)–O(3)	1.974(3)	N(2)–Cu(1)–O(1)	91.86(14)
Cu(1)–O(1)	1.984(3)	N(2)–Cu(1)–S(2)	87.42(11)
Cu(1)–S(2)	2.355(1)	O(3)–Cu(1)–S(2)	95.35(9)
Cu(2)–N(1)	1.944(3)	O(3)–Cu(1)–O(1)	77.50(12)
Cu(1)–O(3)	1.964(3)	O(1)–Cu(1)–S(2)	147.72(9)
Cu(2)–O(1)	1.985(3)	Cu(1)–O(1)–Cu(2)	96.81(13)
Cu(2)–S(1)	2.322(1)	O(2)–Cu(1)–N(2)	84.72(3)
Cu(1)–O(2)	2.835(3)	O(2)–Cu(1)–S(2)	73.02(3)
Cu(2)–O(2)	2.868(3)	O(2)–Cu(1)–O(3)	81.26(3)
Cu(1)–Br2	2.6381(7)	O(2)–Cu(1)–O(1)	74.78(3)
Cu(2)–Br1	2.6477(6)	Cu(1)–O(2)–Cu(2)	62.73(1)
		N(1)–Cu(2)–O(3)	91.76(14)
		O(3)–Cu(2)–O(1)	77.68(13)
		N(1)–Cu(2)–S(1)	87.75(11)
		O(1)–Cu(2)–S(1)	98.60(9)
		N(1)–Cu(2)–O(1)	166.39(14)
		O(3)–Cu(2)–S(1)	156.99(9)
		Cu(1)–O(3)–Cu(2)	97.85(13)
		O(2)–Cu(2)–N(1)	96.04(2)
		O(2)–Cu(2)–S(1)	76.63(2)
		O(2)–Cu(2)–O(3)	80.54(2)
		O(2)–Cu(2)–O(1)	73.97(2)

Table 5. Internuclear angles involving bromine in $Cu_2(L2)Br_2{\cdot}H_2O$ (**VII**).

Angles (°)	
Br(2)–Cu(1)–O(3)	105.12(9)
Br(2)–Cu(1)–O(1)	112.87(8)
Br(2)–Cu(1)–S(2)	99.40(3)
Br(2)–Cu(1)–N(2)	89.70(11)
Br(2)–Cu(1)–O(2)	170.74(9)
Br(1)–Cu(2)–O(3)	105.92(9)
Br(1)–Cu(2)–O(1)	98.52(9)
Br(1)–Cu(2)–S(1)	97.08(3)
Br(1)–Cu(2)–N(1)	92.59(11)
Br(1)–Cu(2)–O(2)	169.08(9)

where χ_m is the molar magnetic susceptibility corrected by using Pascal's constants for diamagnetic effects, N is Avogadro's number, β is the Bohr magneton, g is the magnetogyric ratio, k is Boltzmann's constant, T is absolute temperature, θ is the Curie–Weiss correction, $-2J$ is the energy separation between the singlet and triplet energy states of the bridged two-copper system, ρ is the mole fraction of a magnetic impurity obeying Curie's Law and having the same molar mass and g as the main component, and $N\alpha$ is temperature independent paramagnetism (TIP). The best fit was obtained by using the data between 60 and 300 K to determine the floating parameters in the fitting process (g, $-2J$, $N\alpha$, ρ, and θ) and then, with the values obtained, extrapolating the theoretical curve to 2 K. The results are shown in Fig. 5 with $g = 2.14(5)$, $-2J = 585(10)$ cm^{-1}, TIP $= 120 \times 10^{-6}$ cgsu/mol, $\theta = -0.3$ K, $\rho = 0.005$, and $10^2R = 136$ ($R = [\Sigma(\chi_{obs} - \chi_{calcd})2/\Sigma\chi_{obs}{}^2]^{1/2}$). This approach is justified because antiferromagnetic coupling between the coppers is large, leading to moments at lower temperatures that are small enough for random measurement errors to become of significant relative magnitude. In fact, the suggestion of very minor ferromagnetic-like activity displayed by the experimental data between 70 and ~40 K may be derived from that source. Except for those two or three data points, the magnetic moment's trend in the low-temperature region is gently downward. This trend is consistent with the small Curie–Weiss correction of $\theta = -0.3$ K, which suggests weak intermolecular antiferromagnetic coupling that would become apparent only at very low temperatures in the face of the very strong intramolecular coupling.

It has been shown[31] for planar dinuclear copper(II) species with aromatic nitrogen ligands and a pair of hydroxo-bridges between the coppers that magnetic coupling depends upon the Cu–O–Cu angles. Furthermore, the angle between the planes containing the magnetic orbital of each copper also influences the extent of coupling,[32] and there is evidence that the nature of both the bridging and the nonbridging ligands affects the magnitude of the coupling.[33] For example, assuming a flat $L_2CuO_2CuL_2$ system with two hydroxo-bridges, the empirical equation (eq. [2])[31] that correlates Cu–O–Cu angles and $2J$ predicts values of 54.00 and –22.76 cm^{-1} by using the Cu–O–Cu bridge angles found in **VII**.

$$[2] \qquad 2J = -7453\phi + 7270 \text{ cm}^{-1}$$

These values straddle zero as expected for angles that lie either side of 97.5°, the angle at which ferromagnetic (positive) and antiferromagnetic (negative) contributions to the singlet–triplet splitting ($2J_{total} = 2J_{ferro} + 2J_{antiferro}$) become equal in Kahn's orbital model for these planar systems.[32] Neither calculated value is close to the experimentally observed value of –585(10) cm^{-1}.

A possible explanation for this discrepancy could be that for **VII** the Cu_2O_2 system is not flat. For nonplanar hydroxo-bridged systems, Kahn showed that, in general, as the planar

Can. J. Chem. Downloaded from www.nrcresearchpress.com by South China Agricultural University on 09/19/12
For personal use only.

Table 6. Electronic spectroscopy of copper complexes.

	Electronic spectra and band assignments[a]				
Compound	Ligand C=N $\pi\rightarrow\pi^*$	S→Cu LMCT	Cu→O MLCT	Cu→N MLCT	d–d
$[Cu(L1)]_2$ (**I**)	310 (1333)	370 (1481)	390 (sh)		654 (93)
$Cu(L2)\cdot CH_3OH$ (**II**)	318 (1613)	372 (1521)	390 (sh)	454 (sh)	620 (80)
Cu(L3) (**III**)	318 (1632)	374 (1547)	390 (sh)	440 (sh)	640 (88)
[Cu(HL3)][OAc] (**IV**)	316 (1741)	370 (1574)	390 (sh)	450 (sh)	592 (97)
$[Cu(HL1\text{-}sal)]Cl_2$ (**V**)	318 (1462)	365 (1326)			654 (47)
$Cu_4(L1)_2Br_4(H_2O)_2\cdot 2H_2O$ (**VI**)	310 (1400)	370 (1463)	390 (sh)		658 (61)
$Cu_2(L2)Br_2\cdot H_2O$ (**VII**)	310 (1548)	372 (1488)	390 (sh)		656 (107)

Note: MLCT, metal-to-ligand charge transfer; LMCT, ligand-to-metal charge transfer.
[a]In CH_3CN. λ in nm (ε in mol^{-1} L cm^{-1}).

Fig. 5. $\chi_m T$ vs T for $Cu_2(L2)Br_2\cdot H_2O$ (**VII**). χ_m, molar magnetic susceptibility corrected by using Pascal's constants for diamagnetic effects; T, absolute temperature.

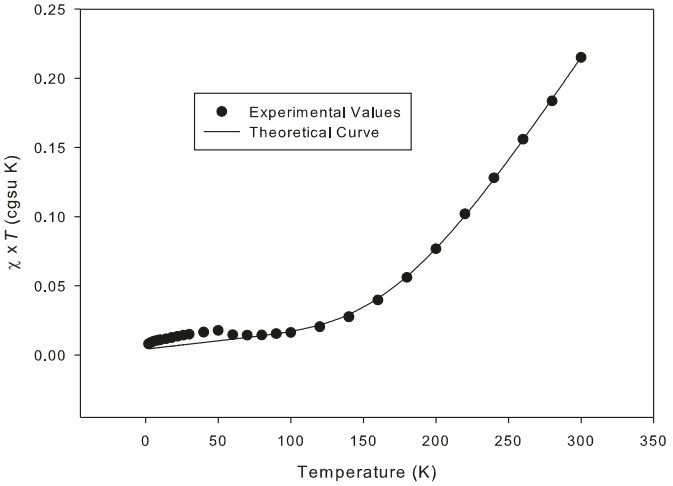

system is folded about its oxygen–oxygen axis so that the dihedral angle between the two CuO_2 planes decreases, $2J_{antiferro}$, the antiferromagnetic contribution to the coupling, also diminishes. This is driven in large part by the energy difference between the symmetric and antisymmetric molecular orbitals formed by interaction between the magnetically active atomic orbitals on the two coppers.[32,34,35] As the dihedral angle between the CuO_2 planes decreases, the energy gap between the symmetric and antisymmetric molecular orbitals also decreases until ~130°, where, in these systems, it reaches zero. Unfortunately, the dihedral angle between the two CuO_2 planes in **VII** is 105.43(5)°, which is significantly below the accidental degeneracy angle of 130°, where the antiferromagnetic contribution should become zero. The fact that at an angle of 105.43(5)° a substantial antiferromagnetic coupling is experimentally observed indicates that, quantitatively, Kahn's model for folded systems does not apply to **VII** even though its qualitative conclusions appear likely to be valid.

A possible explanation could be that the model is wrong. Thus, for **VII** the bridges are not hydroxo as in both the model systems discussed previously. In this regard, Thompson et al.[33] showed that for a series of flat or nearly flat *phenoxo*-bridged Cu_2O_2 systems that these species are all still strongly antiferromagnetic at Cu_2O bridge angles that otherwise lead to very small or zero antiferromagnetic couplings in *hydroxo*-bridged species. Their work has shown that phenoxo-bridged species generally exhibit antiferromagnetic couplings with much larger absolute values than those of alkoxo- or hydroxo-bridged species with similar bridge angles. Furthermore, the slope of the straight line correlation between $2J$ and the bridge angle is less in the phenoxo-bridged cases. By least-squares fitting of the data for 11 examples an empirical correlation (eq. [3]) for compounds of this type was obtained. By using eq. [3] and the average of the two Cu–O–Cu bridge angles (97.34°), an estimated value for $2J$ of –647.8 cm^{-1} is obtained, which is somewhat better agreement with the observed value of –585(10) cm^{-1}, suggesting that this is a more suitable model. Obviously, the model and particularly the nature of the bridge are important in development of satisfactory magnetostructural correlations and theoretical calculations[36] have suggested this should be the case.

$$[3] \qquad 2J = -31.95\alpha + 2462 \ \text{cm}^{-1}$$

In spite of a significant improvement in the efficacy of the model by replacing the hydroxo- with a phenoxo-bridge, there remains a substantial discrepancy between the experimental and predicted values of $2J$ for **VII**. This is presumably due to the failure of the model to take into account the presence and effects of the bromine, the ethereal oxygen, or the thioether sulfur atom in the coordination sphere. Unfortunately, no guidance in this matter is available because there are no examples in the literature of binuclear copper(II) compounds with NSO_3Br coordination spheres for which variable-temperature magnetic susceptibility measurements and X-ray crystal structures are available. Likewise, the literature provides only two binuclear copper(II) compounds with N_2O_2Br coordination spheres for which variable-temperature magnetic susceptibility measurements are available,[37,38] and for only one of those ($Cu_2(UPM)Br_2\cdot 4H_2O$) are both the coupling and structure known. In that compound, the macrocyclic ligand is almost flat and the N_2O_2Br coordination spheres about the coppers create a bridge angle of 103.6(3)° at the phenoxo-oxygen bridges and a value for $2J$ of –771(4) cm^{-1}. Its Cu–Br distances are both 2.737(2) Å, which is somewhat longer than the distances in **VII**. Its Cu–N distances of 1.927(6) Å are roughly comparable to those in **VII**, whereas its Cu–O distances of 1.989(4) Å are very slightly longer than those in **VII**. Thus, its major differences compared with **VII** are the absence of the ethereal oxygen donor, two nitrogen donors instead of one plus a sulfur, a slightly longer Cu–Br bond, and its core is flat as opposed to being folded along the

Can. J. Chem. Downloaded from www.nrcresearchpress.com by South China Agricultural University on 09/19/12
For personal use only.

O···O axis. Any or all of these could be the source of the diminished antiferromagnetism in **VII**. The other binuclear copper(II) compound with N_2O_2Br coordination spheres for which variable-temperature magnetic susceptibility measurements are available is $[Cu(spr)Br]_2$. For it, $2J$ has been shown to be –260 cm^{-1}, although structural details for this compound have not been determined by X-ray methods. It has been shown[32,33] that adding electronegative axial atoms and folding the system both diminish the antiferromagnetic contribution to $2J$. Furthermore, substitution of thioether sulfur for a nitrogen donor has been shown[39] to enhance antiferromagnetic coupling. Arguably, the residual discrepancy between the observed coupling in **VII** and that predicted by using the least inappropriate of the available models arises from a combination of these opposing influences. This examination of **VII** represents the first magnetostructural correlation for dinuclear copper species with NSO_3Br coordination spheres.

The magnetic susceptibilities of **I** and **VI** as a function of temperature have also been measured. The results for **I** are presented graphically in Fig. 6 and for **VI** in Fig. 7. For **I**, the theoretical curve was obtained by least-squares fitting of the experimental data to eq. [1][30] and for **VI** the theoretical curve was obtained similarly by using eq. [4] in which $\chi_{(VI)}$ is the total molar susceptibility of **VI** obtained by summing contributions described by eq. [1] from each of the four copper centres believed to be present in the molecule (vide infra).

$$[4] \qquad \chi_{(VI)} = \chi_{(dinuclear)} + 2\chi_{(Cu)}$$

The room-temperature magnetic moment per mol of **I** is 2.57 μ_B. This is slightly larger than expected for 2 mol of uncoupled Cu(II) per mol of compound, suggesting overall weak ferromagnetic coupling. The best fit of the experimental data to theory was obtained with $g = 2.08(1)$, $2J = 2.0(4)$ cm^{-1}, TIP = 105×10^{-6} cgsu/mol, $\theta = -0.6$ K, $\rho = 0.001$, and $10^2R = 1.68$ ($R = [\Sigma(\chi_{obs} - \chi_{calcd})2/\Sigma\chi_{obs}{}^2]^{1/2}$). These results suggest a very weak intramolecular ferromagnetic interaction between pairs of copper atoms and a weak but intermolecular antiferromagnetic component as well. Based on the structure of the compound, which shows the square pyramidal coordination spheres about each of the coppers are linked apex-to-base through bridging oxygen atoms thereby rendering the $d_{x^2-y^2}$ magnetic orbitals on the two coppers in each dimer roughly orthogonal, it is not surprising to find only intramolecular ferromagnetic coupling. Because overall coupling is the sum of antiferromagnetic and ferromagnetic contributions, near or complete absence of antiferromagnetic interaction will reveal ferromagnetic attributes. Weak intermolecular antiferromagnetic coupling is indicated by the negative value of the Weiss constant (θ). In the crystalline state, there are a number of intermolecular contacts along which this interaction could be propagated. Examples, inter alia, are N(2)···H(6_2), N(4)···H(33_2), and S(2)···H(51_2) at distances of 2.739, 2.592, and 3.092 Å, respectively, all of which are less than or similar to the sums of the van der Waals' radii (2.75 and 3.00 Å, respectively)[20] of the atoms involved.

The room-temperature magnetic moment per mol of **VI** is 3.77 μ_B. The best fit of the experimental data to theory was obtained with $g = 2.24(2)$, $2J = -187(11)$ cm^{-1}, TIP = 240×10^{-6} cgsu/mol, $\theta = -0.7$ K, $\rho = 0.0$, and $10^2R = 4.07$ ($R =$ $[\Sigma(\chi_{obs} - \chi_{calc})2/\Sigma\chi_{obs}{}^2]^{1/2}$). Since crystals of this compound suitable for X-ray study could not be grown, magnetostructural correlations are impossible. Because L1 and L2 are similar, one might have expected the magnetic behaviour of **VI** with an empirical formula of $Cu_2(L1)Br_2{\cdot}2H_2O$ and **VII** with a molecular formula $Cu_2(L2)Br_2{\cdot}H_2O$, established by single crystal X-ray work, to be similar. Assuming a dinuclear structure for **VI** similar to that of **VII**, superficial inspection of room-temperature magnetic moments seems to support such a conclusion. However, **VI** defies successful mathematical modelling as a dinuclear species. Bearing in mind the analytical results that require a formula unit with an even number of copper atoms, various other models, including chains and alternating chains, also appear unsuitable. On the other hand, a linear tetranuclear model with the central pair of copper atoms coupled antiferromagnetically and the terminal coppers essentially uncoupled (eq. [4]) reproduces the susceptibility profile as a function of temperature (Fig. 7). Fortunately, a plausible molecular structure can be constructed that is

Fig. 6. χ_m vs T for $[Cu(L1)]_2$ (**I**). χ_m, molar magnetic susceptibility corrected by using Pascal's constants for diamagnetic effects; T, absolute temperature.

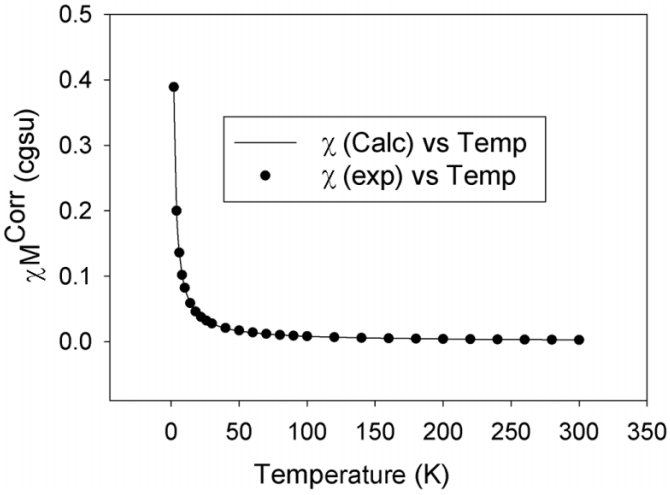

Fig. 7. χ_m vs T for $Cu_4(L1)_2Br_4(H_2O)_2{\cdot}2H_2O$ (**VI**). χ_m, molar magnetic susceptibility corrected by using Pascal's constants for diamagnetic effects; T, absolute temperature.

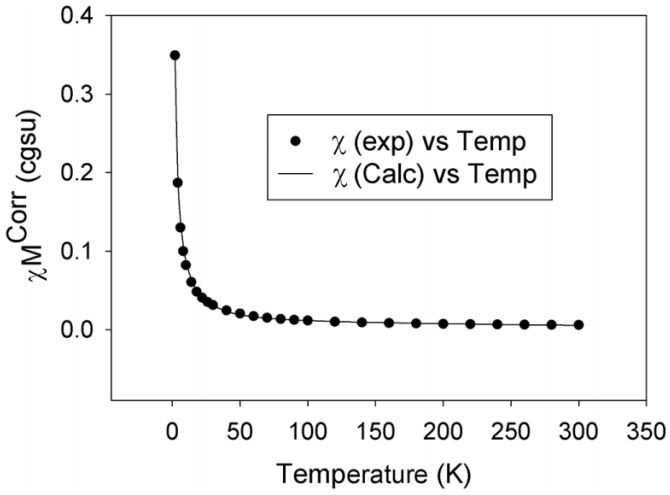

Can. J. Chem. Downloaded from www.nrcresearchpress.com by South China Agricultural University on 09/19/12
For personal use only.

consistent with this model and with known behaviour of copper complexes of similar types. Thus, one can postulate a pair of central coppers each with NO_2S_2Br coordination spheres linked by two shared phenoxy oxygens, one from each of two separate ligand molecules, and a pair of terminal coppers each also with an NO_2S_2Br coordination sphere linked to its adjacent member of the central pair by a shared sulfur on the Jahn–Teller elongated axes of both bridged atoms and also by the remaining SNO donors of the ligand on the adjacent member of the central pair of coppers. Bridging apical sulfurs would lie trans to bromines on both bridged coppers and each terminal copper would probably have a molecule of water coordinated trans to nitrogen. Coordinated water as well as water of crystallization is anticipated because analysis of aged samples of the compound show loss of varying amounts of water up to but not more than 1 mol per 2 mol of copper. The proposed structure would be consistent with antiferromagnetic coupling between the $d_{x^2-y^2}$ magnetic orbitals of the central pair of coppers linked through bridging phenoxy oxygens while leaving the corresponding magnetic orbital of each terminal copper linked to its adjacent central copper only through orthogonal d_{z^2} orbitals of each bridged copper. The structure would also have coordination spheres for each copper that are consistent with observed patterns of coordination for other compounds described in this study. Thus, based on quantitative analytical, spectroscopic, and magnetic data the formula for **VI** is proposed to be $Cu_4(L1)_2Br_4(H_2O)_2{\cdot}2H_2O$.

Conclusions

The examination of **VII** represents the first magnetostructural study of a binuclear copper(II) species with NSO_3Br coordination spheres. The observation that one or more of the bromine, thioether sulfur, and ethereal oxygen atoms perturb the system so that none of the known magnetostructural models predict the copper–copper coupling accurately suggest further work on these systems is desirable. Measurement of the variable-temperature magnetic susceptibility of **VI** has permitted a superior prediction of the probable structure of that compound than would otherwise have been possible in the absence of X-ray structural data by using analytical and other physical data alone.

Supplementary data

Supplementary data are available for this article through the journal Web site at http://nrcresearchpress.com/doi/suppl/10.1139/v11-083. CCDC 781761–781763 contain the X-ray data in CIF format for this manuscript. These data can be obtained, free of charge, via http://www.ccdc.cam.ac.uk/cgi-bin/catreq.cgi (Or from the Cambridge Crystallographic Data Centre, 12 Union Road, Cambridge CB2 1Ez, UK; fax +44 1223 336033; or deposit @ccdc.cam.ac.uk).

Acknowledgments

Dr. R. McDonald, University of Alberta, is acknowledged for the collection of the X-ray crystallographic data for $[Cu(L1)]_2$ and Dr. K, Shuvaev, Memorial University of Newfoundland, is acknowledged for the collection of the variable-temperature magnetic susceptibility data.

References

(1) Pantazis, D. A.; Krewald, V.; Orio, M.; Neese, F. *Dalton Trans.* **2010**, *39* (20), 4959. doi:10.1039/c001286f.
(2) Costa, R.; Moreira, I de P. R.; Youngme, S.; Siriwong, K.; Wannarit, N.; Illas, F. *Inorg. Chem.* **2010**, *49* (1), 285. doi:10.1021/ic902023u.
(3) Bartolome, J.; Filoti, G.; Kuncser, V.; Schinteie, G.; Mereacre, V.; Anson, C. E.; Powell, A. K.; Prodius, D.; Turta, C. *Phys. Rev. B* **2009**, *80*, 014430/1.
(4) Plass, W. *Coord. Chem. Rev.* **2009**, *253* (19-20), 2286. doi:10.1016/j.ccr.2008.12.002.
(5) McInnes, E. J. L.; Piligkos, S.; Timco, G. A.; Winpenny, R. E. P. *Coord. Chem. Rev.* **2005**, *249* (23), 2577. doi:10.1016/j.ccr.2005.02.003.
(6) Wang, J.; Zhang, Z.-C.; Wang, H.-S.; Kang, L.-C.; Zhou, H. B.; Song, Y.; You, X.-Z. *Inorg. Chem.* **2010**, *49* (7), 3101. doi:10.1021/ic100282w.
(7) Zheng, S.-T.; Zhang, J.; Clemente-Juan, J. M.; Yuan, D.-Q.; Yang, G. Y. *Angew. Chem. Int. Ed.* **2009**, *48* (39), 7176. doi:10.1002/anie.200901653.
(8) Remović-Langer, K.; Wiehl, L.; Pashchenko, V.; Wolf, B.; Schreuer, J.; Lang, M. *J. Phys. Condens. Matter* **2008**, *20* (1), 015221. doi:10.1088/0953-8984/20/01/015221.
(9) Koner, R.; Hazra, S.; Fleck, M.; Jana, A.; Lucas, C. R.; Mohanta, S. *Eur. J. Inorg. Chem.* **2009**, *2009* (33), 4982. doi:10.1002/ejic.200900686.
(10) Mitra, K.; Biswas, S.; Lucas, C. R.; Adhikary, B. *Inorg. Chim. Acta* **2006**, *359* (7), 1997. doi:10.1016/j.ica.2006.01.013.
(11) Lucas, C. R.; Liang, W.; Miller, D. O.; Bridson, J. N. *Inorg. Chem.* **1997**, *36* (20), 4508. doi:10.1021/ic961536h.
(12) Lucas, C. R.; Liu, S. *Can. J. Chem.* **1996**, *74* (11), 2340. doi:10.1139/v96-261.
(13) Lucas, C. R.; Liu, S. *J. Chem. Soc., Dalton Trans.* **1994**, (2), 185. doi:10.1039/dt9940000185.
(14) Liu, S.; Lucas, C. R.; Hynes, R. C.; Charland, J.-P. *Can. J. Chem.* **1992**, *70* (6), 1773. doi:10.1139/v92-222.
(15) Wu, H.; Lucas, C. R. *Inorg. Chem.* **1992**, *31* (12), 2354. doi:10.1021/ic00038a012.
(16) Adhikary, B.; Lucas, C. R. *Inorg. Chem.* **1994**, *33* (7), 1376. doi:10.1021/ic00085a027.
(17) Lucas, C. R.; Byrne, J. M. D.; Collins, J. L.; Dawe, L. N.; Miller, D. O. *Can. J. Chem.* **2011**, in press.
(18) Kaczmarek, M. T.; Pospieszna-Markiewicz, I.; Kubicki, M.; Radecka-Paryzek, W. *Inorg. Chem. Commun.* **2004**, *7* (12), 1247. doi:10.1016/j.inoche.2004.09.022.
(19) Addison, A. W.; Rao, T. N.; Reedijk, J.; van Rijn, J.; Verschoor, G. C. *J. Chem. Soc., Dalton Trans.* **1984**, (7), 1349. doi:10.1039/dt9840001349.
(20) Huheey, J. E.; Keiter, E. A.; Keiter, R. L. *Inorganic Chemistry, Principles of Structure and Reactivity;* 4th ed.; Harper Collins: New York, 1993; p 292.
(21) Chiari, B.; Piovesana, O.; Tarantelli, T.; Zanazzi, P. F. *Inorg. Chem.* **1988**, *27* (18), 3246. doi:10.1021/ic00291a044.
(22) Liu, S.; Lucas, C. R.; Hynes, R. C.; Charland, J.-P. *Can. J. Chem.* **1992**, *70* (6), 1773. doi:10.1139/v92-222.
(23) Lucas, C. R.; Liu, S.; Bridson, J. N. *Can. J. Chem.* **1995**, *73* (7), 1023. doi:10.1139/v95-127.
(24) Wu, H.; Lucas, C. R. *Inorg. Chem.* **1993**, *32* (5), 526. doi:10.1021/ic00057a007.
(25) Ahuja, I. S. *Aust. J. Chem.* **1968**, *21* (11), 2805. doi:10.1071/CH9682805.
(26) Lever, A. B. P. *Inorganic Electronic Spectroscopy;* Elsevier: London, 1968; p 231.

(27) Sönmez, M. *Turk. J. Chem.* **2001**, *25*, 181.
(28) Nikles, D. E.; Powers, M. J.; Urbach, F. L. *Inorg. Chem.* **1983**, *22* (22), 3210. doi:10.1021/ic00164a009.
(29) Drago, R. S. *Physical Methods for Chemists;* 2nd ed.; Saunders College Publishing: Toronto, 1992; p 194.
(30) (a) Kahn, O. *Molecular Magnetism;* VCH Publishers Inc.: New York, 1993; p 37; (b) Kahn, O. *Molecular Magnetism;* VCH Publishers Inc.: New York, 1993; p 107.
(31) Crawford, V. H.; Richardson, H. W.; Wasson, J. R.; Hodgson, D. J.; Hatfield, W. E. *Inorg. Chem.* **1976**, *15* (9), 2107. doi:10.1021/ic50163a019.
(32) Charlot, M. F.; Jeannin, S.; Jeannin, Y.; Kahn, O.; Lucrece-Abaul, J.; Martin-Frere, J. *Inorg. Chem.* **1979**, *18* (6), 1675. doi:10.1021/ic50196a056.
(33) Thompson, L. K.; Mandal, S. K.; Tandon, S. S.; Bridson, J. N.; Park, M. K. *Inorg. Chem.* **1996**, *35* (11), 3117. doi:10.1021/ic9514197.
(34) Ajò, D.; Bencini, A.; Mani, F. *Inorg. Chem.* **1988**, *27* (14), 2437. doi:10.1021/ic00287a014.
(35) Hay, P. J.; Thibeault, J. C.; Hoffmann, R. *J. Am. Chem. Soc.* **1975**, *97* (17), 4884. doi:10.1021/ja00850a018.
(36) Astheimer, H.; Haase, W. *J. Chem. Phys.* **1986**, *85* (3), 1427. doi:10.1063/1.451232.
(37) Mandal, S. K.; Thompson, L. K.; Newlands, M. J.; Gabe, E. J.; Nag, K. *Inorg. Chem.* **1990**, *29* (7), 1324. doi:10.1021/ic00332a007.
(38) Muto, Y.; Tokii, T. *Bull. Chem. Soc. Jpn.* **1978**, *51* (1), 139. doi:10.1246/bcsj.51.139.
(39) Lucas, C. R.; Liu, S.; Thompson, L. K. *Inorg. Chem.* **1990**, *29* (1), 85. doi:10.1021/ic00326a018.

Can. J. Chem. Downloaded from www.nrcresearchpress.com by South China Agricultural University on 09/19/12
For personal use only.

A partially water-soluble cationic Mn(III)–salphen complex for catalytic epoxidation

Amir Abdolmaleki and Saeed Malek-Ahmadi

Abstract: Synthesis and application of new cationic Mn(III)–salphen complexes for catalytic epoxidation of olefins to epoxides in a homogeneous reaction media have been reported. The experimental data showed that the cationic salphen is more active than its neutral form. The acceleration of the reaction rate is attributed to the phase-transfer capability of the built-in phenazinium salt of the Mn(III)–salphen catalyst.

Key words: phase transfer, phenazinium salt, cationic Mn(III)–salphen complex, epoxidation.

Résumé : On a effectué la synthèse et examiné le domaine d'application d'un nouveau complexe cationique, le Mn(III)–salphène, pour la transformation catalytique d'oléfines en époxydes, dans un milieu réactionnel homogène. Les données expérimentales montent que le salphène cationique est plus actif que sa forme neutre. L'augmentation de la vitesse de réaction est attribuée à la capacité de transfert de charge du sel de phénazinium inclus dans le catalyseur Mn(III)–salphène.

Mots-clés : transfert de phase, sel de phénazinium, complexe cationique Mn(III)–salphène, époxydation.

[Traduit par la Rédaction]

Can. J. Chem. Downloaded from www.nrcresearchpress.com by Xi'an Jiaotong University on 09/19/12
For personal use only.

Introduction

Epoxides are versatile synthetic intermediates that can be readily converted into a large variety of useful compounds by means of a regioselective ring-opening reaction.[1–3] Therefore, the design of new catalysts for epoxidation of alkenes constitutes an important strategy for the synthesis of pharmaceuticals and fine chemicals.[4–6]

In the field of homogeneous catalysis, salen and salophen ligands[4,7–11] have been investigated for many years and are among the most widely developed ligands in the catalysis toolbox of modern chemistry for a range of organic transformations. Many synthetic approaches toward metallosalen complexes are known that start off with double Schiff base precursors. These precursors commonly originate from a condensation process involving 1 equiv of a diamine and 2 equiv of salicylaldehyde or a ketone analogue. The resultant metallosalen frameworks are thermally and kinetically stable entities controlled by the presence of a tetradentate ligation mode of the N_2O_2 pocket that is characteristic of a salen ligand. This type of stabilization allows, for instance, the creation of vital catalytic intermediates generated by a change in or accommodation of a higher oxidation state of the metal ion coordinated by the salen ligand.[12–15]

In this area, Jacobsen and co-workers[16] developed a practical epoxidation procedure using a two-phase system, with an aqueous phase containing H_2O_2 and an organic phase composed of a solution of substrates.[10,17–20] For practical application, there has been a compelling interest in the development of catalytic epoxidation systems that can increase reaction activity in the aqueous H_2O_2 solution / organic biphasic system. Usually a pyridine *N*-oxide derivative is added to the aforementioned catalytic system to stabilize the catalyst by ligation and to increase the epoxidation reaction rate by drawing the active oxidant into the organic phase.[21,16] Also, the addition of some phase-transfer catalysts could accelerate the epoxidation reaction in the presence of a Mn(III)–salphen catalyst.[22] Moreover, it was reported that the epoxidation activity could be enhanced in the two-phase reaction medium using Mn (III)–salphen catalysts with a built-in phase-transfer capability, constructed by introducing tertiary amine unit(s) to the salen ligand.[23–25]

Recently, Sun and co-workers found that the internal pyridinium salt of the catalyst could play a built-in phase-transfer role for the acceleration of the epoxidation in an aqueous / organic biphasic medium as 2 mol% of external pyridinium salts and ammonium halides, with a tertiary amine unit that was used.[26,27]

In this work, the synthesis of a new phenazinium salphen and its cationic complex with Mn(III) is reported. The cationic complex Mn(III)–salphen was applied in the epoxidation of olefins to epoxides.

Experimental

General remarks

All chemicals were purchased from Merck Chemical Co. *o*-Phenylenediamine was sublimated for further purification. Other solvents and chemicals were purified by common procedures. ^{1}H NMR (500 MHz) spectra were obtained in deuterated dimethylsulfoxide (DMSO-d_6) on a Bruker Avance 500 instrument (Bruker, Rheinstetten, Germany), UV–vis absorption spectra were obtained in DMSO (ca. $\times 10^{-5}$ mol/L)

Received 2 March 2011. Accepted 4 June 2011. Published at www.nrcresearchpress.com/cjc on 7 September 2011.

A. Abdolmaleki and S. Malek-Ahmadi. Department of Chemistry, Isfahan University of Technology, Isfahan-84156/83111, Iran.

Corresponding author: Amir Abdolmaleki (e-mail: abdolmaleki@cc.iut.ac.ir).

Can. J. Chem. Downloaded from www.nrcresearchpress.com by Xi'an Jiaotong University on 09/19/12
For personal use only.

Fig. 1. ^{1}H NMR spectra of cationic salphen (**4**).

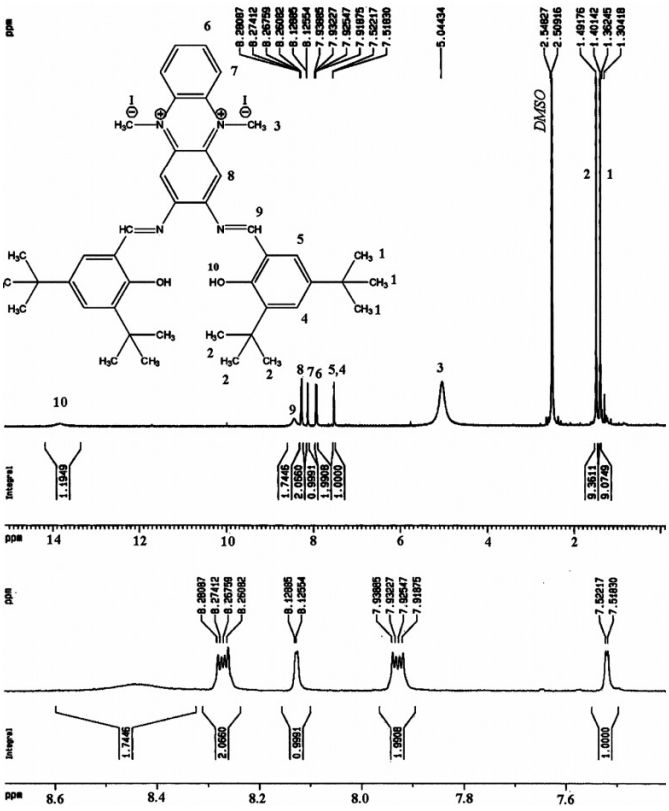

on a JASCO-570 UV–vis spectrometer, and IR spectra were obtained as KBr pellets with a 680 plus-JASCO. Elemental analysis was also performed by Malek-Ashtar University of Technology, Tehran, Iran.

Synthesis of 2,3-diaminophenazine (1)

2,3-Diaminophenazine was prepared by using a modified procedure reported in the literature.[10] In a typical experiment, 6 mL of 0.08 mol/L aq $FeCl_3$ solution was rapidly added into 30 mL of a 0.02 mol/L aqueous *o*-phenylenediamine solution with vigorous stirring. A quick color change from purple-black to reddish-brown was observed upon the addition of $FeCl_3$. After 5 h at ambient temperature, a large amount of white solid was formed. The precipitate was washed three times with deionized water, then separated by centrifugation and sublimated to afford **1** as a white needlelike crystal. Yield (%): 98; mp > 300 °C. FT-IR (KBr, cm^{-1}) ν: 3394 (s), 3313 (s), 3188 (w), 1692 (m), 1633 (m), 1531 (s), 1478 (s), 1383 (m), 1371 (m), 1240 (m), 1149 (m), 891 (w), 834 (m), 772 (m), 750 (m). ^{1}H NMR (500 MHz, DMSO-d_6, ppm) δ: 8.01 (s, 2H, aromatic H), 7.715 (s, 2H, aromatic H), 7.01 (s, 2H, aromatic H), 3.43 (br, 4H, $-NH_2$). EI/MS *m*/*z* ($C_{12}H_{10}N_4$): M^+, 210. Anal. calcd for $C_{12}H_{10}N_4$ (%): C 68.56, H 4.79, N 26.65; found: C 68.42, H 4.71, N 26.59.

Synthesis of salphen (2)

Compound (**1**) (0.21 g, 1 mmol) and 3,5-di-*tert*-butyl-2-hydroxybenzaldehyde (0.468 g, 2 mmol) were dissolved in 10 mL of absolute ethanol in a 25 mL flask equipped with a magnetic stirring bar. The reaction mixture was stirred at room temperature for 12 h. The dark brown precipitate was filtered, washed with ethanol. and was purified by column chromatography. Yield (%): 82; mp 267 °C. FT-IR (KBr, cm^{-1}) ν: 3421 (w), 2956 (s), 1636 (m), 1616 (m), 1527 (m), 1442 (s), 1398 (m), 1360 (m), 1292 (m), 1251 (m), 1144 (m), 983 (m), 847 (w), 741(m). ^{1}H NMR (500 MHz, DMSO-d_6, ppm) δ: 13.84 (s, 2H, HO–Ar), 8.43 (s, 2H, CH=N), 8.12, 7.91, 7.64, 7.54 (m, 10H, aromatic H), 1.48 (s, 18H, CH_3), 1.39 (s,18H, CH_3). Anal. calcd for $C_{42}H_{50}N_4O_2$ (%): C 78.47, H 7.84, N 8.72; found: C 78.37, H 7.73, N 7.80.

Synthesis of Mn(III) salphen (3)

In a 50 mL round-bottom flask equipped with a magnetic stirring bar, compound **1** (0.21 g, 1 mmol), 3,5-di-*tert*-butyl-2-hydroxybenzaldehyde (0.468 g, 2 mmol), $Mn(OAc)_2{\cdot}4\ H_2O$ (0.245 g, 1 mmol) and an excess amount of LiCl (0.5 g) in absolute ethanol were stirred under reflux for 12 h. For oxidation of Mn(II) to Mn(III), air was bubbled into the solution during the reaction. Then the reaction mixture was cooled to room temperature and filtered. The brown solid was washed with ethanol to remove all impurities. Yield (%): 78; mp > 300 °C. FT-IR (KBr ν, cm^{-1}): 2962 (m), 2921 (m), 1648 (m), 1610 (m), 1592 (s), 1492 (m), 1445 (m), 1220 (m), 770 (w), 643 (w), 616 (w), 488 (w). UV–vis (DMSO, nm) λ_{max}: 263, 346, 447.

Synthesis of cationic salphen (4)

In a 25 mL round-bottom flask, 15 mL of methyl iodide was added to compound **2** (0.032 g, 0.05 mmol) and refluxed for 7 days. The mixture was cooled to room temperature. The unreacted methyl iodide was removed under reduced pressure. The brown solid was obtained after the removal of methyl iodide. Yield (%): 83; mp > 300 °C (decomp.). FT-IR (KBr, cm^{-1}) ν: 3417 (w), 2958 (m), 2923 (m), 2853 (m), 1653 (m), 1624 (s), 1571 (m), 1525 (m), 1457 (m), 1384 (m), 1260 (m), 1199 (w), 1169 (w), 1097 (w), 1024 (m), 800 (w), 751 (m). ^{1}H NMR (500 MHz, DMSO-d_6, ppm) δ: 13.85 (br, 2H, HO–Ar), 8.43 (s, 2H, CH=N), 8.26, 8.12, 7.93, 7.52 (m, 10H, aromatic H), 5.04 (br, 6H, CH_3–N^+), 1.49 (s, 18H, CH_3), 1.40 (s, 18H, CH_3) (Fig. 1). Anal. calcd for $C_{44}H_{56}I_2N_4O_2$ (%): C 57.02, H 6.09, N 6.05; found: C 56.99, H 6.11, N 5.97.

Synthesis of cationic Mn(III)–salphen (5)

In a 25 mL round-bottom flask, 15 mL of methyl iodide was added to compound **3** (0.034 g, 0.02 mmol) and refluxed for 7 days; after this period of time, the reaction mixture was cooled to room temperature. After removal of the unreacted methyl iodide under reduced pressure, a brown solid was obtained. The residue was purified by chromatography on a silica gel column ($MeOH/CH_2Cl_2$, 1:8) to give the desired complex. Yield (%): 94; mp > 300 °C. FT-IR (KBr, cm^{-1}) ν: 2957 (m), 2925 (m), 2850 (m), 1650 (m), 1622 (s), 1570 (m), 1525 (m), 1460 (m), 1384 (m), 1261 (m), 1200 (w), 1171 (w), 1097 (w), 1024 (m), 799 (w), 751 (m). Anal. calcd for $C_{44}H_{54}ClI_2MnN_4O_2$ (%): C 52.06, H 5.36, N 5.52; found: C 51.93, H 5.27, N 5.50.

Epoxidation of olefins in the presence of Mn(III)–salphen (3) and cationic Mn(III)–salphen (5)

An aqueous solution of H_2O_2 (30%, 0.8 mmol) was added

Scheme 1. Reagents and conditions for catalyst syntheses.

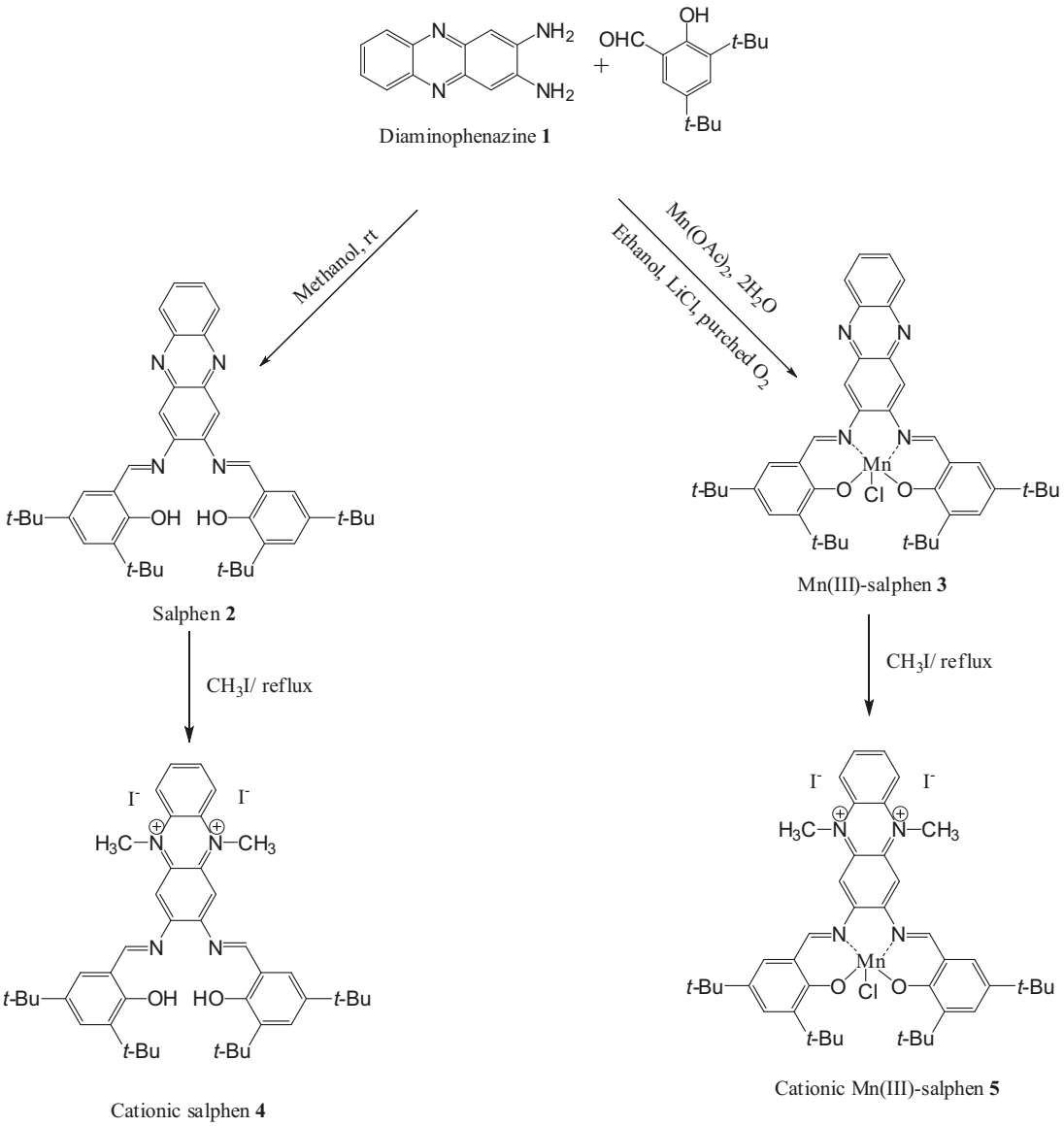

Can. J. Chem. Downloaded from www.nrcresearchpress.com by Xi'an Jiaotong University on 09/19/12
For personal use only.

portionwise to a solution of olefins (0.4 mmol) and Mn(III)–salphen complex (0.004 mmol) in CH_2Cl_2 (1 mL). The mixture was stirred at 25 °C and the progress of the reaction was monitored by gas chromatography. The aqueous and organic phases were separated and the aqueous layer was extracted twice with CH_2Cl_2 (2 × 3 mL). The combined organic layer was washed with brine (2 × 3 mL) and dried over anhydrous sodium sulfate.

Results and discussion

The procedure for catalyst preparation is depicted in the Scheme 1.

2,3-Diaminophenazine (**1**) was synthesized by oxidation of *o*-phenylenediamine. In the FT-IR spectrum, the two major peaks of 2,3-diaminophenazine are observed between 3400 and 3150 cm^{-1} owing to N–H stretching vibrations of theamino groups, which indicate the presence of NH_2 groups in the structural unit. The bands at 834 and 891 cm^{-1} are assigned to the out-of-plane bending vibrations of the C–H bonds in the 1,2,4,5-tetra-substituted benzene ring of the phenazine unit. The results obtained from the ^{1}H NMR spectrum (δ 8.01 (m, 2H), δ 7.71 (m, 2H), δ 7.01 (s, 2H), and δ 3.43 (br, 4H, $–NH_2$)) support the structure of compound **1**. The elemental analysis result is consistent with the proposed chemical formula of **1**.

Synthesis of salphen (2)

Salphen (**2**) was synthesized by using a stoichiometric ratio of 3,5-di-*tert*-butyl-2-hydroxybenzaldehyde and 2,3-diaminophenazine (2:1) (Scheme 1) and characterized by FT-IR and ^{1}H NMR spectroscopies. The ^{1}H NMR data (CH=N in δ 8.43 ppm; δ 13.84 ppm for OH; all aromatic hydrogens in δ 8.12, 7.91, 7.64, and 7.51 ppm; and two kinds of aliphatic hydrogen of the *tert*-butyl groups in δ 1.48 and 1.39 ppm) confirm the formation of compound **2**. The FT-IR spectrum of compound **2** shows vibrational peaks at 2929 and 2959 cm^{-1} (stretching of the methyl group of *tert*-butyl), at

Can. J. Chem. Downloaded from www.nrcresearchpress.com by Xi'an Jiaotong University on 09/19/12
For personal use only.

Table 1. Epoxidation of olefins catalyzed by 1% mol Mn(III)–salphen (**3**) and cationic Mn(III)–salphen (**5**).

	Mn(III)–salphen (**3**)		Cationic Mn(III)–salphen (**5**)	
Catalysts	Conversion (%)	Reaction time (min)	Conversion (%)	Reaction time (min)
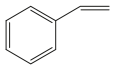	73	45	86	20
	75	45	91	20
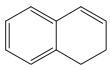	69	45	84	20
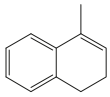	67	45	79	20
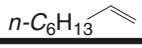	61	45	77	20

Scheme 2. Epoxidation of olefins.

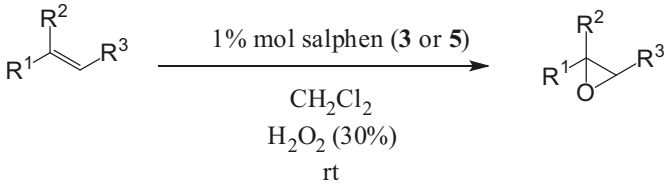

1636 cm^{-1} (stretching of the C=N bond), and at 3421 cm^{-1} for stretching of the OH group.

Preparation of Mn(III)–salphen (3)

Complex **3** was obtained according to the procedure shown in Scheme 1. The complex was synthesized in the presence of excess LiCl as a counterion. The Mn(II) was converted to Mn(III) via in situ oxidation and the progress of the oxidation reaction was monitored by UV–vis spectroscopy. The Mn (II)–salphen shows an absorption band at λ = 420 nm, whereas a maximum was observed at 447 nm for Mn(III)–salphen (**3**).

Cationic salphen (4)

As shown in Scheme 1, the cationic salphen (**4**) was prepared by reaction of salphen **2** with excess methyl iodide under reflux. The ^{1}H NMR spectrum of **4** supports the proposed structure (Fig. 1). The protons of CH_3^+–N appear at 5.04 ppm, and this evidence is important because the methyl iodide protons have no chemical shift higher than 3.5 ppm.

Cationic Mn(III)–salphen (5)

Cationic Mn(III)–salphen (**5**) was prepared by reaction of compound **3** in the presence of excess methyl iodide as a reagent and a solvent under reflux (Scheme 1). The two CH_3^+–N groups were formed in the salphen ligand and neutralized by two iodide anions.

Epoxidation of olefins

The epoxidation reaction of olefins (Scheme 2) was done using a 0.01 molar ratio of each of the catalysts, Mn(III)–salphen (**3**) and cationic Mn(III)–salphen (**5**). The conversion was measured by GC–MS spectroscopy. The results show that the cationic Mn(III)–salphen (**5**) had a higher catalytic activity than the neutral Mn(III)–salphen (**3**) (Table 1).

The addition of excess CH_3I to the 2,3-diaminophenazine moiety and formation of the cationic Mn(III)–salphen (**5**) can considerably facilitate the epoxidation reaction of olefins, which is presumably because of the formation of the more water-soluble phenazinium groups in the structure (**5**). The neutral Mn(III)–salphen is slightly soluble in water and, consequently, shows a low catalytic activity toward the epoxidation of olefins.[9]

Conclusions

We explore the synthesis of new types of salphen complexes with built-in inherent phase-transfer capability. The complexes were synthesized in good yields and applied toward two catalytic processes. The cationic Mn(III)–salphen complex with two water-soluble phenazinium groups showed an appropriate catalytic activity for the epoxidation of olefins. This method could also be useful for the preparation of other transition-metal catalysts for organic reactions.

Acknowledgements

This research was sponsored by the Isfahan University of Technology (IUT), Ishafan, Iran.

References

(1) Martinez, L. E.; Leighton, J. L.; Carsten, D. H.; Jacobsen, E. N. *J. Am. Chem. Soc.* **1995** *117* (21), 5897. doi:10.1021/ja00126a048.

(2) Rodger, A. *J. Am. Chem. Soc.* **1988** *110* (18), 5941. doi:10.1021/ja00226a002.

(3) Schurig, V.; Betschinger, F. *Chem. Rev.* **1992** *92* (5), 873. doi:10.1021/cr00013a006.
(4) Canali, L.; Sherrington, D. C. *Chem. Soc. Rev.* **1999** *28* (2), 85. doi:10.1039/a806483k.
(5) Fan, Q.-H.; Li, Y.-M.; Chan, A. S. C. *Chem. Rev.* **2002** *102* (10), 3385. doi:10.1021/cr010341a.
(6) Sato, K.; Aoki, M.; Ogawa, M.; Hashimoto, T.; Noyori, R. *J. Org. Chem.* **1996** *61* (23), 8310. doi:10.1021/jo961287e.
(7) Leung, A.; MacLachlan, M. *J. Inorg. Organometal. Polym. Mater.* **2007** *17* (1), 57. doi:10.1007/s10904-006-9092-1.
(8) McGarrigle, E. M.; Gilheany, D. G. *Chem. Rev.* **2005** *105* (5), 1563. doi:10.1021/cr0306945.
(9) Hosseinpoor, F.; Golchoubian, H. *ChemInform* **2006** *37* (43). doi:10.1002/chin.200643098.
(10) Liu, S.-Y.; Nocera, D. G. *Tetrahedron Lett.* **2006** *47* (12), 1923. doi:10.1016/j.tetlet.2006.01.074.
(11) Wei, X.; Li, J.; Zhou, B.; Qin, S. *Transition Metal Chem.* **2004** *29* (4), 457. doi:10.1023/B:TMCH.0000027463.00158.6b.
(12) Belokon, Y. N.; North, M.; Maleev, V. I.; Voskoboev, N. V.; Moskalenko, M. A.; Peregudov, A. S.; Dmitriev, A. V.; Ikonnikov, N. S.; Kagan, H. B. *Angew. Chem. Int. Ed.* **2004** *43* (31), 4085. doi:10.1002/anie.200454031.
(13) Feichtinger, D.; Plattner, D. A. *Angew. Chem. Int. Ed. Engl.* **1997** *36* (16), 1718. doi:10.1002/anie.199717181.
(14) Finney, N. S.; Pospisil, P. J.; Chang, S.; Palucki, M.; Konsler, R. G.; Hansen, K. B.; Jacobsen, E. N. *Angew. Chem. Int. Ed. Engl.* **1997** *36* (16), 1720. doi:10.1002/anie.199717201.
(15) Zheng, X.; Jones, C. W.; Weck, M. *J. Am. Chem. Soc.* **2007** *129* (5), 1105. doi:10.1021/ja0641406.
(16) Jacobsen, E. N.; Deng, L.; Furukawa, Y.; Martínez, L. E. *Tetrahedron* **1994** *50* (15), 4323. doi:10.1016/S0040-4020(01)89369-8.
(17) Krishna Mohan Kandepi, V. V.; Cardoso, J. M. S.; Royo, B. *Catal. Lett.* **2010** *136* (3–4), 222. doi:10.1007/s10562-010-0332-1.
(18) Morlanés, N.; Notestein, J. M. *J. Catal.* **2010** *275* (2), 191. doi:10.1016/j.jcat.2010.07.010.
(19) Reis, P. M.; Gamelas, C. A.; Brito, J. A.; Saffon, N.; Gómez, M.; Royo, B. *Eur. J. Inorg. Chem.* **2011** *2011* (5), 666. doi:10.1002/ejic.201001065.
(20) Stamatis, A.; Giasafaki, D.; Christoforidis, K. C.; Deligiannakis, Y.; Louloudi, M. *J. Mol. Catal. Chem.* **2010** *319* (1–2), 58.
(21) Hughes, D. L.; Smith, G. B.; Liu, J.; Dezeny, G. C.; Senanayake, C. H.; Larsen, R. D.; Verhoeven, T. R.; Reider, P. J. *J. Org. Chem.* **1997** *62* (7), 2222. doi:10.1021/jo961735i.
(22) Kureshy, R. I.; Khan, N. U. H.; Abdi, S. H. R.; Singh, S.; Ahmed, I.; Jasra, R. V. *J. Mol. Catal. Chem.* **2004** *218* (2), 141. doi:10.1016/j.molcata.2004.03.043.
(23) Kureshy, R. I.; Khan, N. U. H.; Abdi, S. H. R.; Patel, S. T.; Iyer, P. K.; Jasra, R. V. *Tetrahedron Lett.* **2002** *43* (14), 2665. doi:10.1016/S0040-4039(02)00112-0.
(24) Kureshy, R. I.; Khan, N. U. H.; Abdi, S. H. R.; Patel, S. T.; Iyer, P. K.; Subramanian, P. S.; Jasra, R. V. *J. Catal.* **2002** *209* (1), 99. doi:10.1006/jcat.2002.3558.
(25) Sun, Y.; Tang, N. *J. Mol. Catal. Chem.* **2006** *255* (1–2), 171. doi:10.1016/j.molcata.2006.03.056.
(26) He, D.; Wu, Y.; Xu, B.-Q. *Eur. Polym. J.* **2007** *43* (9), 3703. doi:10.1016/j.eurpolymj.2007.06.038.
(27) Wang, D.; Wang, M.; Wang, X.; Zhang, R.; Ma, J.; Sun, L. *J. Mol. Catal. Chem.* **2007** *270* (1–2), 278. doi:10.1016/j.molcata.2007.01.052.

Can. J. Chem. Downloaded from www.nrcresearchpress.com by Xi'an Jiaotong University on 09/19/12
For personal use only.

Can. J. Chem. Downloaded from www.nrcresearchpress.com by University of Electronic and Science Techonology of China on 09/19/12
For personal use only.

Amino-*s*-triazines — Synthesis and stereochemistry of restricted rotational phenomena — First use of a C-2-substituted serinol in tandem with masked 4-piperidone for selective amination of cyanuric chloride

Flavia Popa, Pedro Lameiras, Eric Henon, Oana Moldovan, Agathe Martinez, Carmen Bâtiu, Yvan Ramondenc, and Mircea Darabantu

Abstract: Starting from 4-piperidone monohydrate hydrochloride (or the hydrochloride of its ethylene ketal) alone, otherwise in tandem with a C-2-substituted 2-aminopropane-1,3-diol ("serinol") as amino-nucleophiles in reaction with cyanuric chloride, the synthesis of novel N-substituted amino-*s*-triazines is reported. The stereochemistry of rotational phenomena occurring about the newly created C(*s*-triazine)–N< (exocyclic) partial double bonds in the title compounds, seen as new dendritic building blocks, is discussed.

Key words: melamines, VT NMR, 4-piperidone, rotamerism, serinols.

Résumé : A partir de la 4-pipéridone monohydratée (ou le chlorhydrate de l'éthylène cétal), ou en tandem avec le 2-aminopropane-1,3-diol substitué en C-2 (« sérinol ») assimilé à un amino-nucléophile dans la réaction avec le chlorure de cyanuryle, la synthèse de nouvelles amino-*s*-triazines N-substituées est décrite. La stéréochimie des phénomènes rotationnelles autour des liaisons partiellement doubles C(*s*-triazine)–N< (exocyclique) des composés décrits dans le titre, considérés comme de nouveaux building blocks dendritique, est discutée.

Mots-clés : mélamines, TV RMN, 4-pipéridone, rotamérie, sérinols.

Introduction

Serinol is the trivial name for 2-aminopropane-1,3-diol, usually seen as the reduced form of serine and the parent term of the C-substituted commercial analogous series. We recently reviewed the continuous "serinolic" penetration in current organic synthesis.[1]

Following our previous findings in *s*-triazine chemistry,[2] particularly in chiral serinolic dendrimers and dendrons based on N-substituted 2,4,6-triamino-*s*-triazines (melamines),[2b,2c] we decided to include 4-piperidone as a challenging nucleophile with respect to cyanuric chloride. Indeed, the instability of 4-piperidone as a free base against autocondensation has been well known since 1949,[3] hence, its monohydrate hydrochloride as well as its ethylene ketal (free base or hydrochloride) are commercially available.

On the other hand, nowadays there is a noticeably focused interest in nucleophilic substitution of the remainder chlorine in chlorodiamino-*s*-triazines carried out with 4-piperidone derivatives, providing pharmaceutical compositions for treating pathological states, which arise from or are exacerbated by angiogenesis.[4]

Therefore, the aim of our work is to account for the concise synthesis of amino-*s*-triazines built entirely from 4-piperidone or in tandem with certain C-2-substituted serinols together with their rotational phenomena about the C(*s*-triazine)–N< (exocyclic) partial double bonds.

Results and discussion

Synthesis

Our synthetic approaches are depicted in Schemes 1–3. Except for our previously reported data,[2,5] no term for this new class of amino-*s*-triazines has been reported.

Received 21 October 2010. Accepted 18 April 2011. Published at www.nrcresearchpress.com/cjc on 8 September 2011.

F. Popa and O. Moldovan. "Babes-Bolyai" University, Department of Organic Chemistry, 11 Arany Jànos st, 400 028 Cluj-Napoca, Romania; University and INSA of Rouen, IRCOF–LCOFH, UMR 6014 CNRS COBRA, 76821 Mont Saint-Aignan CEDEX, France.
P. Lameiras, E. Henon, and A. Martinez. University of Reims Champagne-Ardenne, ICMR–LIS, UMR 6229, BP 1039, 51687 Reims, France.
C. Bâtiu and M. Darabantu. "Babes-Bolyai" University, Department of Organic Chemistry, 11 Arany Jànos st, 400 028 Cluj-Napoca, Romania.
Y. Ramondenc. University and INSA of Rouen, IRCOF–LCOFH, UMR 6014 CNRS COBRA, 76821 Mont Saint-Aignan CEDEX, France.

Corresponding author: Mircea Darabantu (e-mail: darab@chem.ubbcluj.ro and darabantu@cluj.astral.ro).

Can. J. Chem. Downloaded from www.nrcresearchpress.com by University of Electronic and Science Techonology of China on 09/19/12
For personal use only.

Scheme 1.

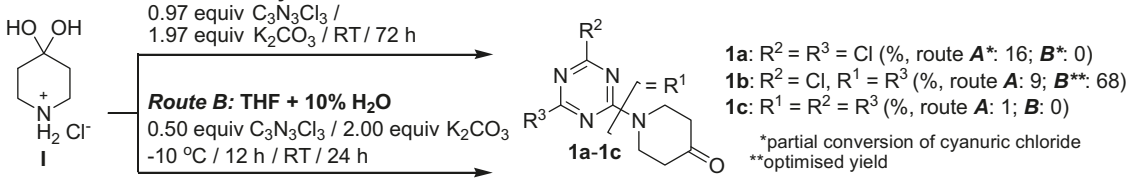

Scheme 2.

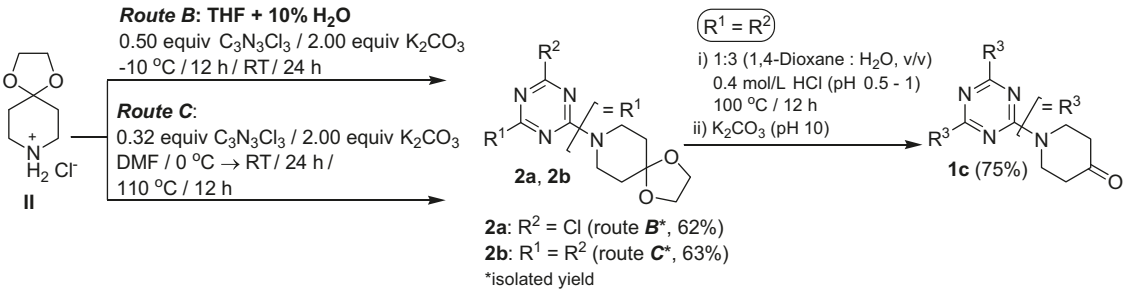

Scheme 3.

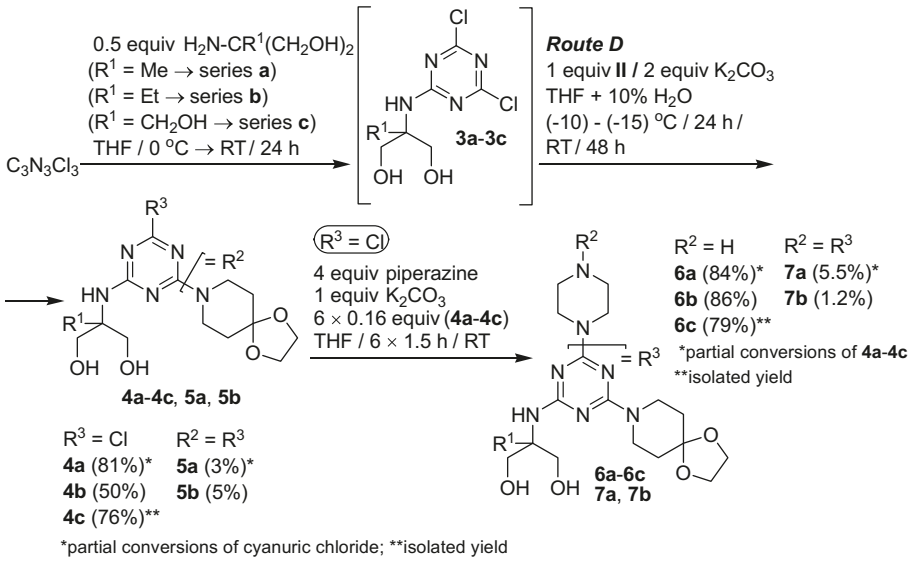

Preliminarily, we attempted the amination of cyanuric chloride with 4-piperidone monohydrate hydrochloride **I** (Scheme 1, route **A**) in the presence of anhyd potassium carbonate as a twofold proton scavenger.[5] The partial conversions and selectivity (**1a** vs **1b** vs**1c**) that we observed, indicating the overall results in anhydrous conditions, were not promising at all. Indeed, at room temperature, the hydrochloride **I** exhibited a reduced solubility in waterless solvents (THF, 1,4-dioxane, chloroform, and dichloromethane), which, combined with the insolubility of the proton scavenger, did not quickly generate the 4-piperidone free base. Moreover, during the long time reaction or upon heating (not depicted in Scheme 1, route **A**), the poorer results inferred that alteration of 4-piperidone occurred instead of the desired SN_2Ar process.

A pivotal improvement consisted of the use of 10% aq THF; this was supposed to ensure a rapid acid–base interchange between potasasium carbonate and **I** (Scheme 1, route **B**). A highly reactive nucleophile was produced, i.e., only in very mild and carefully controlled conditions, the selective double replacement of chlorine in cyanuric chloride by two 4-oxopiperidin-1-yl units could be achieved, affording the bis (ketone) **1b** with satisfactory yield.[12]

Therefore, the exploitation as a nucleophile of the freshly prepared ethylene ketal of 4-piperidone hydrochloride **II** (according to Bickelhaupt and co-workers;[6] Scheme 2) was straightforward.

As the free carbonyl analogue of **I**, **II** was also very insoluble in THF and 1,4-dioxane. Accordingly, the selectivity as a double amination of cyanuric chloride by the free base generated in situ from **II** was possible (compound **2a**, Scheme 2, route **B**) only in identical conditions as in the case of 4-piperidone itself (compound **1b**, Scheme 1, route **B**).

Can. J. Chem. Downloaded from www.nrcresearchpress.com by University of Electronic and Science Techonology of China on 09/19/12
For personal use only.

Next, DMF was determined to be a suitable solvent for **II** to perform the total substitution of chlorine in cyanuric chloride in a one-pot synthesis (compound **2b**, Scheme 2, route **C**). Deprotection of **2b** in refluxing aq 1,4-dioxane at pH 0.5–1.0 required an unexpected long time, ~12 h, as shown by its spot-to-spot evolution via TLC monitoring. Compound **1c** can be seen as a new type of melamine dendritic core.

Following up on this idea, new terminal building blocks for an iterative dendritic synthesis were successfully prepared. As depicted in Scheme 3, we accessed unsymmetrical melamine series **6a**–**6c** also based on our previous expertise with respect to the amino nucleophilicity of C-2-substituted 2-aminopropane-1,3-diols (serinols): methylserinol (R^1 = Me), ethylserinol (R^1 = Et), and TRIS (R^1 = CH_2OH).[1,5] Thus, chlorodiamino-*s*-triazines **4a**–**4c** were obtained with good yields in a one-pot synthesis[13] (route **D**), the much higher amino nucleophilicity of the azaspirane reagent (generated in situ from **II**) being taken into account. In fact, one must observe the similarity between conditions in route **B** (Schemes 1 and 2) versus route **D** (Scheme 3). Even in these mild conditions, the formation of side products (melamines **5a** and **5b**) could not be completely avoided. Next, by applying our earlier methodology[2b,2c] we did succeed in the selective amination of **4a**–**4c** with piperazine, a classic linker in dendritic melamine chemistry.[7] Our target melamines **6a**–**6c** were easily separated from the side double melamines **7a** and **7b** by column chromatography on partially deactivated silica gel.

Stereochemistry of rotational phenomena

Starting from the well-recognized herbicide atrazine (2-chloro-4-ethylamino-6-isopropylamino-*s*-triazine) as early as 1971,[8a] it is classically known that, because of the p → π conjugation involving the lone pair of the exocyclic N-atoms and the high π-deficient *s*-triazine ring, the bonds C^{sp^2}(*s*-triazine)–N^{sp^3}< manifest some double-bond character.[8,9] It strongly depends on the π-deficiency of the C-substituted *s*-triazine determining the *type of restricted rotational status* about these connections (Scheme 4).

Hereafter, we will use our recent terminology[2c] for these angularly connected molecules: at room temperature, the C(*s*-triazine)–N< (exocyclic) partial double bonds are seen as *axes of prodiastereomerism* (as in **1b** and **2a**) and *axes of diastereomerism*, including a combination of these two situations (as in **4a**–**4c**, **5a**, **5b**, **6a**–**6c**, **7a**, and **7b**). Upon heating, the acquired free rotation can be *homomeric (topomerization)* or *diastereomeric*, respectively, the whole process being suitable for VT NMR monitoring.[9,14] Except for our incipient data,[2c] no such distinct approach has been previously reported.

Homomeric rotational phenomena — Topomerizations

A first illustrative example is provided by chlorodiamino-*s*-triazines **1b** and **2a** (Scheme 5).

At room temperature (*frozen status*), the NMR discrimination between diastereotopic positions (δ(α) > δ(α′) and δ(β) > δ(β′)) was made based on the closer proximity of α and β nuclei (pro-*cis*) against α′ and β′ (pro-*trans*) with respect to the deshielding influence of the strong dipole moment of the C(2)(*s*-triazine)–Cl bond (Scheme 5; Table A1).[2c,7c] Hereafter, we will entitle this assignment as "the dipole rule". The

Scheme 4.

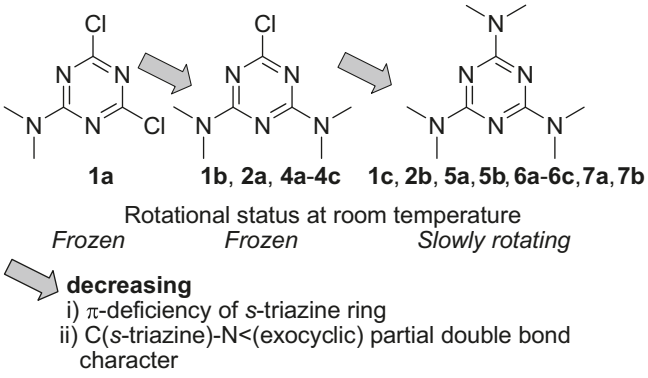

Scheme 5.

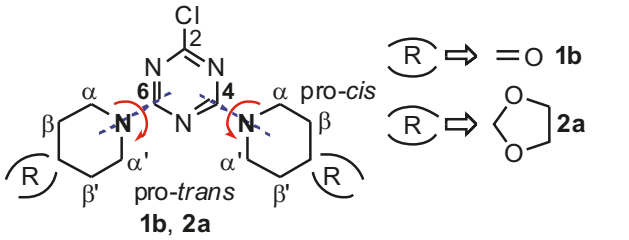

Status	Bonds **C(4 6)-N<**(exocyclic)
Frozen	➔ *Axes of prodiastereomerism* (*RT*) *
Freely rotating	➔ *Homomeric rotation* (*topomerization*) between equally populated sites

*Diastereotopic: C-α *vs.* C-α' and H-α(eq. ⇆ ax.) *vs.* H-α'(eq. ⇆ ax.) etc. (fast piperidine chair ⇆ chair flipping at RT)

frozen status was better revealed in [D_6]DMSO (ε = 46.7) than in [D_8]THF (ε = 7.58) (Table A1), to anticipate the influence of solvation effects. On heating, the rotational barriers $\Delta G^{\neq}$ (kJ/mol) referring to equilibria between two equally populated sites (*homomeric* process) were determined by applying the classic Eyring calculation algorithm (eq.[1])[10a,10b]

$$[1] \qquad \Delta G^{\neq} = 19.14 T_C [10.32 + \log (T_C/k_C)]$$

where T_C (K) is the coalescence temperature and k_C (s^{-1}) is the rate constant of the first-order kinetic exchange dynamic process occurring at T_C.

The rate constants k_C were calculated using the Gutowski–Holm equation (eq. [2])[10c]

$$[2] \qquad k_C = 2.22 \Delta\nu$$

where $\Delta\nu$ (Hz, s^{-1}) is the frequency separation between two analysed signals (e.g., H-β vs H-β′ and H-α vs H-α′; Table A1) in the absence of any exchange between the two equally populated sites.

Our $\Delta G^{\neq}$ values (Table A1) were plausible, since they are smaller with respect to those of two known normal open-chain 2-chloro-4,6-bis(di-*n*-alkylamino)-*s*-triazines (*n*-Bu, 74.22 kJ/mol; *n*-octyl, 75.17 kJ/mol) but comparable to those where the alkyl chain was branched (*i*-Pr, 65.33 kJ/mol).[9c]

We note that, in the case of **1b** and **2a**, we fortunately found "two internal clocks"[10b] because both diastereotopic methylenes (β ⇆ β′ and α ⇆ α′ (two A_2X_2 systems)) were

Can. J. Chem. Downloaded from www.nrcresearchpress.com by University of Electronic and Science Techonology of China on 09/19/12
For personal use only.

Fig. 1. ^{1}H NMR spectrum of compound **4b** (400 MHz time scale, 293 K, [D_6]DMSO); at 353 K): *pseudo freely rotating status* of the spiranic fragment about the bond C(4)(*s*-triazine)–N< (exocyclic).

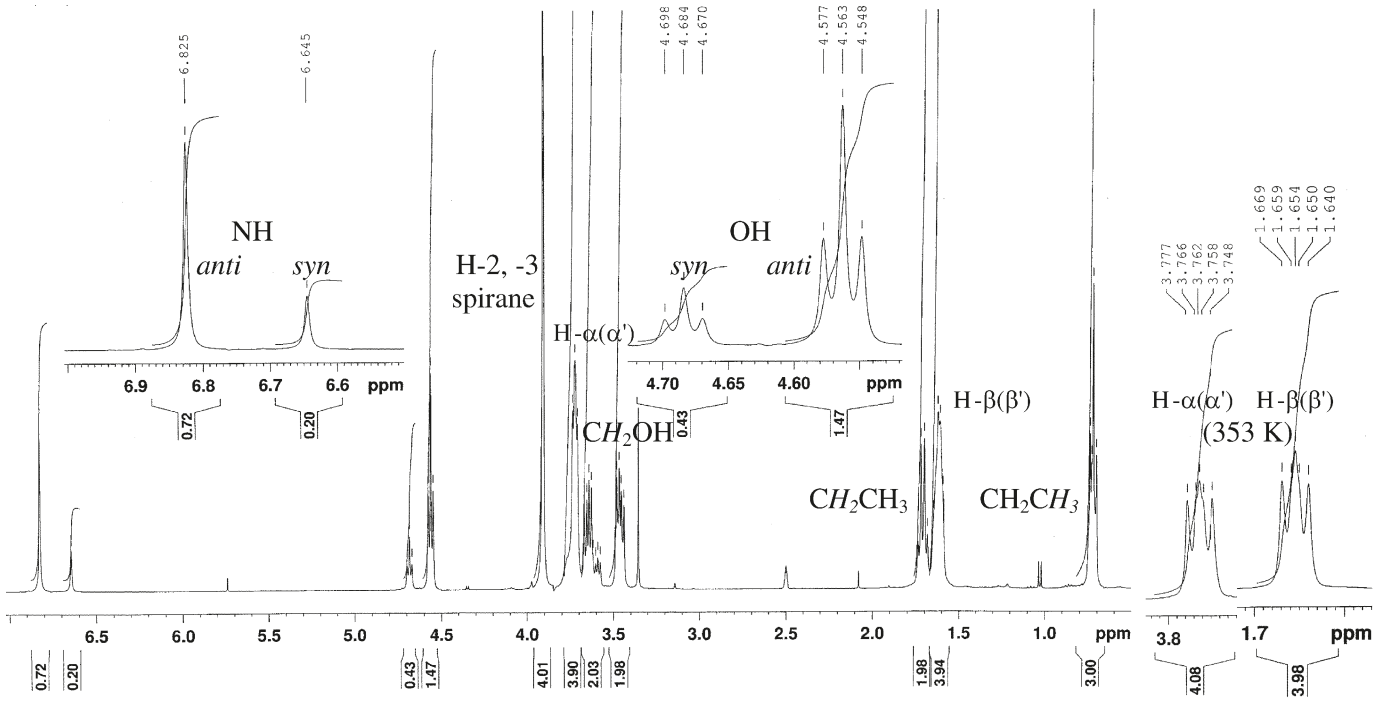

appropriate for VT NMR investigations. Since they were satisfactorily "synchronized" (ΔT_C = 5–10 K), they provided comparable kinetic results. Compound **1b** had a slightly higher $\Delta G^{\neq}$ value (~1 kJ/mol) than **2a**, the ground state of diketone **1b** being, presumably, more solvated in [D_6]DMSO than the less polar double 1,3-dioxolanic derivative **2a**.

Two additional features are worthy of mention (Table A1):

i. Upon heating, compound **2a** (at 80 °C in [D_6]DMSO) exhibited a new unexpected anisochrony between protons α ⇆ α′ (diastereotopicity as Δδ ~ 0.01 ppm, two *o*verlapped *t*riplets, "ot") that we entitled *pseudo freely rotating status*.[15] It might be consistent with some residual steric hindrance against completely free rotation between the two spiranic fragments together with the acquired pyramidal inversion of their aza-atoms.[16]

ii. At room temperature and in [D_8]THF, the rotational *frozen status* was not completely observed on both NMR (^{1}H and ^{13}C) time scales (*partially frozen status*). To our surprise, on cooling, the appearance of diastereotopicity δ(H-α) > δ(H-α′) was preceded by no detectable coalescence, e.g., the mediated α(α′)-triplet at room temperature (Δδ = 0 ppm), was progressively converted into two distinct triplets (Δδ = 0.10 ppm; Table A1). Yet, at –80 °C, (**1b**) and at –90 °C (**2a**) we were also unable to reach the frozen structure of the chair ⇆ chair piperidine ring inversion. The conformational chirality associated with this motion we discussed in detail elsewhere.[2c]

Global diastereomeric rotational phenomena

Keeping in mind the above versatile rotameric behaviour of the dioxa-azaspirane motif if linked *alone* to a chloro-*s*-triazine ring, VT NMR analysis of N,N′-unsymmetrical chlorodiamino-*s*-triazines **4a**–**4c** was performed (Scheme 6).

Scheme 6.

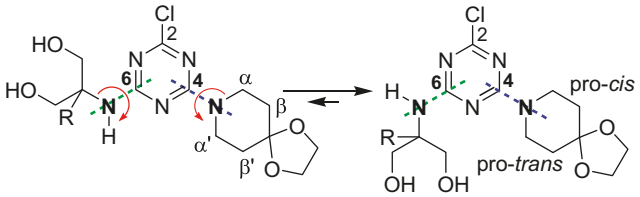

syn (*s*)* **4a-4c** (*s*) *anti* (*a*)* **4a-4c** (*a*)

R = Me (**4a**), Et (**4b**), CH_2OH (**4c**)

Status	Bonds
Frozen	➔**C(4)-N**<(exocyclic)
	Axis of prodiastereomerism (*RT*)**
	➔**C(6)-N**<(exocyclic)
	Axis of diastereomerism (*RT*)
***Local* Freely Rotating**	➔*Homomeric rotation* (*topomerization*) about the bond C(4)-N<(exocyclic)
	➔*Diastereomeric rotation* about the bond C(6)-N<(exocyclic)
***Global* Freely Rotating**	➔*Diastereomeric rotation* between unequally populated sites

*The chlorine atom and the C-2-substituted propane-1,3-diol fragment are the references for the descriptors *syn* and *anti*.
**Diastereotopic: C-α *vs.* C-α′, H-α (eq. ⇆ ax.) *vs.* H-α′(eq. ⇆ ax.) etc. (fast chair ⇆ chair flipping at RT) in each *anti vs. syn* environment.

Their diastereomeric occurrence about the bond C(6)(*s*-triazine)–N< (exocyclic) was by far nonstatistical, but in the ratio 75 (major rotamer) : 25 (minor rotamer).

At room temperature, the two blocked rotamers **4a**–**4c** *anti*

Can. J. Chem. Downloaded from www.nrcresearchpress.com by University of Electronic and Science Techonology of China on 09/19/12
For personal use only.

(*a*, major) and **4a**–**4c** *syn* (*s*, minor) were preliminarily ascertained as according to the dipole rule: the resonances of protons NH or OH positioned closer to the dipole moment of the C-2–Cl bond should be located at lower magnetic fields (Fig. 1).

However, the 2D-^{1}H, ^{1}H-NOESY experiment was unable to detect any dipolar interaction between the two sites (serinolic versus spiranic) in the assigned **4a**–**4c** *anti* rotamers. Therefore, a DFT calculation for the stereoisomers of compound **4a** was carried out, although the anti–syn difference ($\Delta\Delta G_{298} \sim -2.72$ kJ/mol) between the two species was <1 kcal/mol (1 cal = 4.184 J). The relevant results are summarized in Table 1.

In each frozen rotamer **4a**-*anti* and **4a**-*syn*, three conformers about the serinolic NH–C$^{sp^3}$ bond were optimized at the B3LYP/6–31G* and B3LYP/6–311++G** levels of theory. Furthermore, the effect of solvents (DMSO and THF) was taken into account by performing a SCRF calculation with the CPCM option implemented in Gaussian 09. The two lowest energy conformers of type **4a**-*anti* or -*syn* are depicted in Table 2. Only the B3LYP/6–311++G**/CPCM model provided results in line with our postulated dipole rule and, in DMSO, plausible $\Delta G^{\neq}_{298}$ values with respect to rotational barriers about the bond C(6)–N< (exocyclic), issued from the VT NMR calculation (see the later discussion and Table 2).

In the spiranic part of compounds **4a**–**4c**, (Table A2), diastereotopicity ($\Delta\delta$) between positions $\alpha \leftrightarrow \alpha'$ and $\beta \leftrightarrow \beta'$ was clearly distinct only in the ^{13}C NMR spectra and restricted to anti major rotamers (see Experimental).

On ^{1}H NMR spectra, unique signals were displayed by protons H-α and H-α′, but the (broad) multiplets of protons H-β and H-β′ were inappropriate for kinetic calculations (Fig. 1).

At higher temperatures, no clear coalescence was observed in the progress of methylenes α(α′). In contrast, for methylenes β(β′), the same T_C value (308 K) that was detected earlier for compounds **1b** and **2a** (Table A1) was constantly discovered in series **4a**–**4c** (Fig. 2).

Again, the *pseudo freely rotating* situation appeared in some cases, e.g., compound **4b** (two partially overlapped A_2X_2 systems for protons H-α(α′) and H-β(β′)) (Fig. 1). Therefore, we had to conclude that the *local homomeric rotation* about the C(4)(*s*-triazine)–N< (exocyclic) bond in unsymmetrical compounds **4a**–**4c** could only be estimated to be similar to that already encountered in the case of symmetric *s*-triazine **2a**; hence, $\Delta G^{\neq} = 66.11 \pm 0.25$ kJ/mol (Table A1).

In contrast, the energetic barriers about the C(6)(*s*-triazine)–N< (exocyclic) bond consisted of a rotational process between two unequally populated sites, **4a**–**4c** *anti* > **4a**–**4c** *syn*. Two $\Delta G^{\neq}$ values, $\Delta G^{\neq}_{\text{anti}}$ (anti → syn) > $\Delta G^{\neq}_{\text{syn}}$ (syn → anti), defining two first-order kinetic processes, were determined by using, comparatively, two methods, Shanan-Atidi,[10d] in tandem with Eliel and Whilen's modification of this method [10b] (Table 2).

To our knowledge, no such option has been previously reported.

First, we considered Shanan-Atidi's curve:

$$[3] \qquad \tau_C \Delta\nu = f(\Delta n)$$

where τ_C is the average critical time of life (s) at the temperature of coalescence T_C (K) of the examined rotamers, $\Delta\nu$ (Hz, s^{-1}) is the frequency separation between two analysed signals at room temperature in the absence of an exchange between sites, and $\Delta n = n_{\text{anti}} - n_{\text{syn}} > 0$ is the difference between populations of the two frozen rotamers as molar fractions (Fig. 1).

With τ_C in our hands, its reversed value, $1/\tau_C$ (s^{-1}), gave the average value of the rate constant k_C at T_C. Next, the individual rate constants at T_C, $k_{\text{C-syn}}$ (syn → anti) and $k_{\text{C-anti}}$ (anti → syn) were calculated based on the relationship of eq. [4*a*] to eq. [4*b*]:

$$[4a] \qquad k_{\text{C-syn}} = 2k_C n_{\text{anti}}$$

$$[4b] \qquad k_{\text{C-anti}} = 2k_C n_{\text{syn}}$$

Using $k_{\text{C-syn}}$ and $k_{\text{C-anti}}$ and applying the Eyring equation (eq. [1]) for each rotamer, we obtained the desired $\Delta G^{\neq}_{\text{syn}}$ (syn → anti) and $\Delta G^{\neq}_{\text{anti}}$ (anti → syn) values.

The modification of Eliel and Whilen[10b] consisted of first determining the average k_C value of the two rotamers (Gutowski–Holm equation (eq. [2])) by means of the individual rate constants, available as eqs. [5*a*] and [5*b*]

$$[5a] \qquad k_{\text{C-syn}} = k_C(1 + \Delta n)$$

$$[5b] \qquad k_{\text{C-anti}} = k_C(1 - \Delta n)$$

Equation [1] gave a second set of $\Delta G^{\neq}_{\text{syn}}$ and $\Delta G^{\neq}_{\text{anti}}$ values.

The two methods were applied to NH protons and, cautiously, OH, which at room temperature constantly exhibited the best signal separation (two synchronized internal clock $\Delta T_C = 0$ K)[10b] (Fig. 1). Since both methods gave similar kinetic values, they were averaged (errors are given in Table 2).

Our results (Table A2 and Table 2) are subjected to the following critical comments:

i. We had to use VT ^{1}H NMR parameters of the classically entitled "exchangeable protons" NH and OH. In our case, except for the OH protons in compound **4c**, at room temperature (Fig. 1 and Table A2) the analysed signals revealed, by their shape (NH, OH) and multiplicity ($^3J_{H,H} \sim 6.0$ Hz in the C*H*$_2$O*H* sequence), that these nuclei were, however, not exchangeable, but located in a chelatizing environment provided by the hydrogen bond acceptor solvent, [D_6]DMSO.[9d,10a] On heating the progressive shielding of protons NH, when passing from "amide character" (room temperature) to "amine character" (freely rotating structure, 353 K), was both expected and observed. On the other hand, the final spectral data (353 K, Table A2) also refer to the fast exchange status reached by OH and NH protons. It might obscure their relevance in rotational phenomena, since in all spectra of **4a**–**4c**, the final NH and OH resonances (353 K) ranged out of their domain of δ values at room temperature.

ii. Points of coalescence were difficult to establish properly. As for other serinolic structures reported by us, domains of coalescences were rather observed in VT ^{1}H NMR spectra.[2a–2c]

Can. J. Chem. Downloaded from www.nrcresearchpress.com by University of Electronic and Science Techonology of China on 09/19/12
For personal use only.

Table 1. Bond orders (B.O.), dipole moments (μ, D), ZPE corrected relative energies ΔH_{0K} (kJ/mol), relative free energies ΔG_{298} (kJ/mol), and transition states $\Delta G^{\neq}_{298}$ (TS) (kJ/mol) of blocked rotamers of compound **4a** vs their ^{1}H NMR abundance (%).

4a-*anti* (*a*)
75.4%

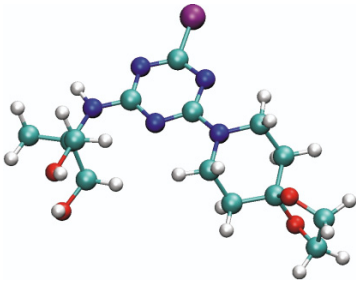

4a-*syn* (*s*)
24.6%

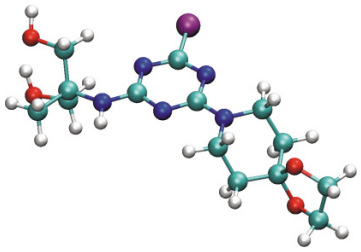

B.O.[a]						B.O.					
C(4)–N<	C(6)–N<	Dipole moment	ΔH_{0K}	ΔG_{298}	$\Delta G^{\neq}_{298}$ ($a\rightarrow s$)	C(4)–N<	C(6)–N<	Dipole moment	ΔH_{0K}	ΔG_{298}	$\Delta G^{\neq}_{298}$ ($s\rightarrow a$)
B3LYP/6–31G* (gas phase)											
—	—	5.58	2.34	2.34	74.46	—	—	5.31	0.00	0.13	76.72
B3LYP/6–31G*/CPCM/DMSO[b]											
—	—	7.20	0.08		—	—	—	7.17	0.00	0.00	72.53
B3LYP/6–311++G/CPCM/DMSO**											
1.25	1.23	7.30	0.00	0.00	69.52	1.24	1.23	7.86	1.13	0.92	68.60
B3LYP/6–311++G/CPCM/THF**											
—	—	7.03	0.00	0.00	—	—	—	7.50	0.75	0.71	—

[a]Wiberg bond order calculated within the natural bonding orbital (NBO) analysis applied to the depicted C(*s*-triazine)–N< (exocyclic) bonds.

[b]The effect of solvent was taken into account by using the implicit solvent method conductor-like polarizable continuum model (CPCM) implemented in Gaussian 09.

Can. J. Chem. Downloaded from www.nrcresearchpress.com by University of Electronic and Science Techonology of China on 09/19/12
For personal use only.

Table 2. Kinetic parameters deduced from VT ^{1}H NMR of compounds **4a**–**4c**.

	$k_{C\text{-}anti}$[a]		$\Delta G^{\neq}_{anti}$		$\Delta\Delta G^{\neq}_{syn-anti}$ (kJ/mol) at T_C		$\Delta\Delta G_{anti-syn}$ (kJ/mol) at
	$k_{C\text{-}syn}$ (s^{-1})		$\Delta G^{\neq}_{syn}$ (kJ/mol) at T_C				
Compd.	NH[b]	OH[b]	NH	OH	NH	OH	293 K
4a-*anti*	82.0±19.7	48.1±11.4	70.83±0.68	72.32±0.68			
↓↑					–3.15	–3.15	–2.73
4a-*syn*	251.2±60.3	147.5±35.0	67.68±0.69	69.17±0.68			
4b-*anti*	56.6±14.1	38.3±9.7	71.87±0.71	72.98±0.73			
↓↑					–3.53	–3.55	–3.07
4b-*syn*	199.1±50.1	135.1±33.9	68.34±0.71	69.43±0.72			
4c-*anti*	49.2±11.2	—	70.03±0.63	—			
↓↑					–2.68	—	–2.40
4c-*syn*	131.7±29.9	—	67.35±0.64	—			

[a]Rate constants at coalescence for the depicted rotamer.

[b]Protons whose frequencies were used for calculations (see Table A2 for the corresponding δ_H values).

Fig. 2. VT ^{1}H NMR spectrum of compound **4b** (400 MHz time scale, 293–323 K, [D_6]DMSO).

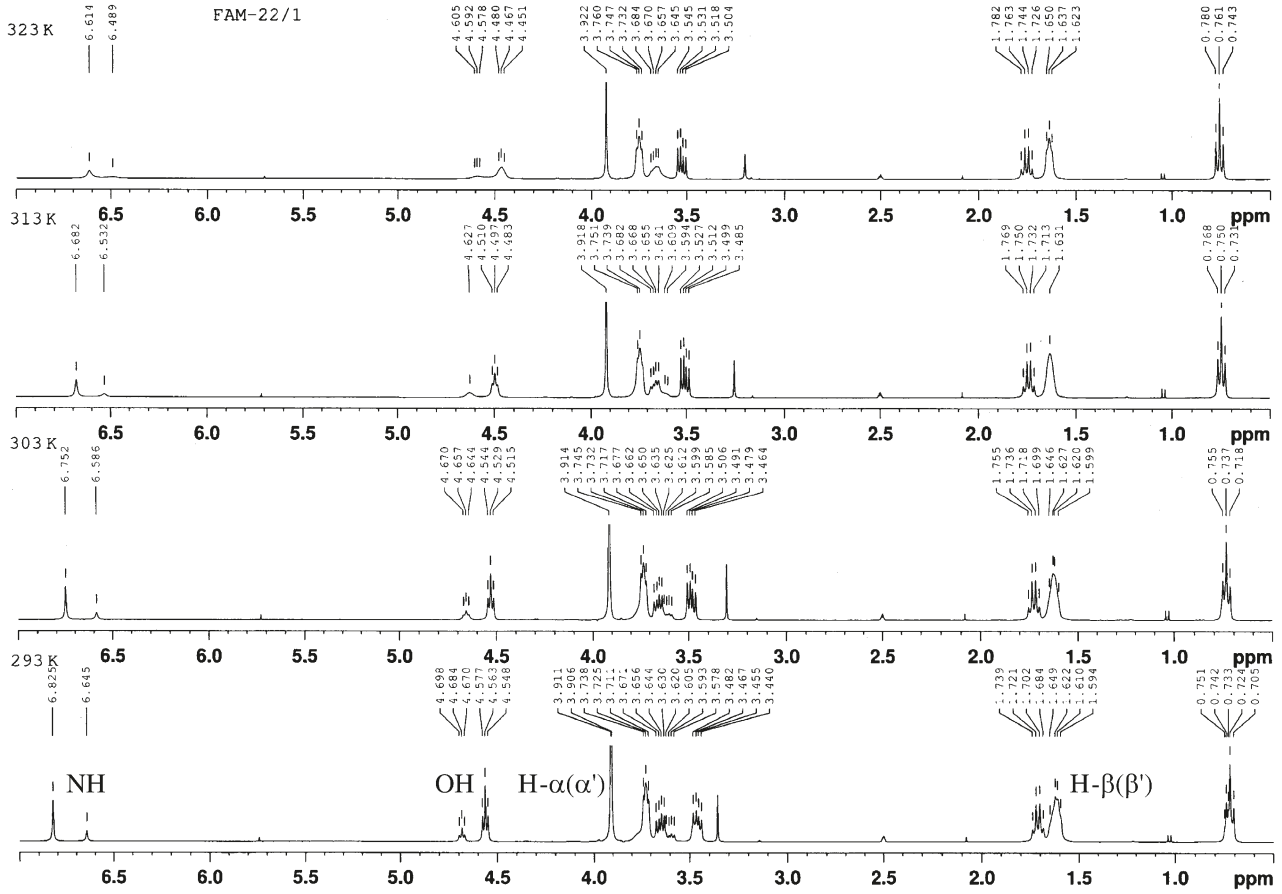

iii. In spite of the above precautions, the $\Delta G^{\neq}_{syn}$ values (kJ/mol) in Table 2 were parallel with those previously determined by us for the N,N′-symmetrically substituted chlorodiamino-*s*-triazines with the same serinolic fragments **4a** (67.68) → 68.10 and **4b** (68.34) → 68.35, but not for compound **4c** (67.35) → 69.22.

iv. Whereas the rotameric compositions were comparable, compound **4c**, the most polar, had the smallest $\Delta n = n_{anti} - n_{syn}$ difference, the smallest $\Delta G^{\neq}$ rotational barriers, and the less negative value of the temperature gradient,[17] $[\Delta\delta(NH)/\Delta T] \times 10^3$. As recently recommended by Moreno and Simanek,[9i] although this parameter is usually applied to peptides and proteins,[11] it is generally accepted and indicative that if the temperature gradient is more negative than –4 ppb/K in aqueous solution, the NH group was exposed to solvent and not involved in intramolecular hydrogen bonds. Conversely, a temperature gradient less negative than –4 ppb/K indicates that the NH protons were initially involved in intramolecular hydrogen bonding. If so, compound **4c** was the less implicated

Scheme 7.

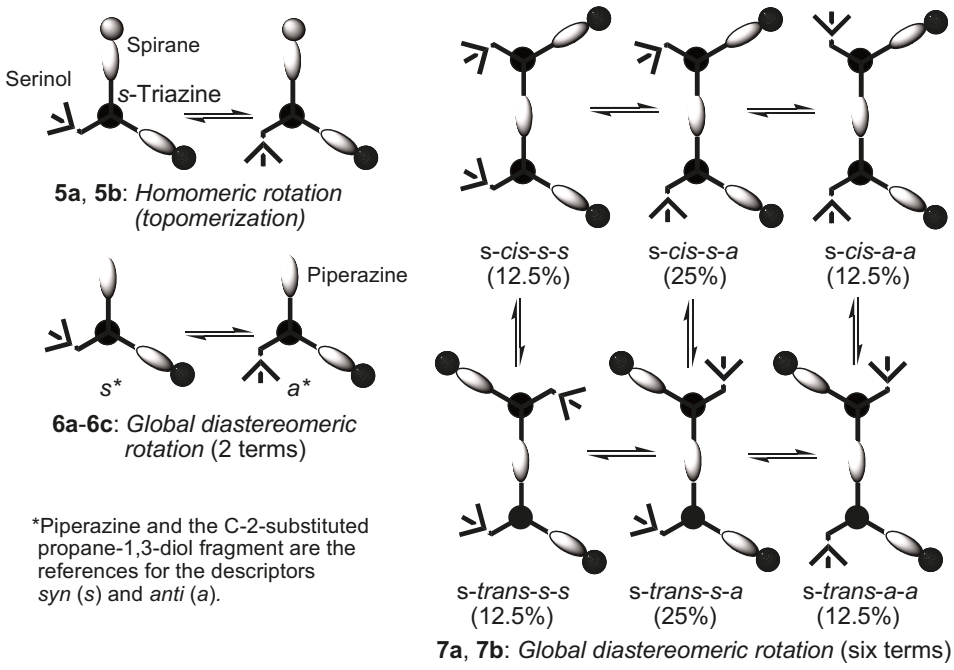

in hydrogen bonding with the solvent, presumably because of the internal strong chelating ability of its three-geminal hydroxymethyl groups associating with an important NH contribution. Consequently, its ground state was the less stabilized by the condition of the solvent (e.g., at room temperature, the OH groups of **4c** exhibited but a broad singlet, (Table A2), not useful for kinetic calculation).

v. If so, the much larger occurrence of **4a**–**4c** *anti* rotamers should be explained by a stronger NH hydrogen bonding by the solvent, $([\Delta\delta(NH)/\Delta T] \times 10^3) < -4$ ppb/K, in comparison with the syn diastereomer where $([\Delta\delta(NH)/\Delta T] \times 10^3) > -4$ ppb/K.

vi. The decreasing order of $\Delta G^{\neq}$ values as $\Delta G^{\neq}_{anti}$ (69.40–70.70 kJ/mol) > $\Delta G^{\neq}_{syn}$ (66.71–69.87 kJ/mol) > $\Delta G^{\neq}_{spirane}$ (66.10 kJ/mol) clearly discloses the order in which, on heating, compounds **4a**–**4c** are rotationally "activated" (Table 2 and Fig. 2): first, a *local homomeric rotation (topomerization)* about the C(4)(*s*-triazine)–N< (exocyclic) bond, then in tandem with a *local diastereomeric rotation* about the C(4)(*s*-triazine)–N< (exocyclic) bond, to provide a *global diastereomeric rotation*. To conclude, this order follows the increasing solvation of the N-ligands: azaspiranic < serinolic syn N-ligand < serinolic anti N-ligand.

vii. At T_C, the $\Delta\Delta G^{\neq}_{syn-anti} = \Delta G^{\neq}_{syn} - \Delta G^{\neq}_{anti} = \Delta\Delta G_{anti-syn} < 0$ values indicate small thermal dependences of $\Delta\Delta G_{anti-syn} = f(T)$ (Table 2).

Combined rotational phenomena in melamines

(VT) NMR data of the less π-deficient amino-*s*-triazines, melamines **5a**, **5b**, **6a**–**6c**, **7a**, and **7b**, described their room temperature status as a slow exchange mediating predictable (un)equally populated sites (Scheme 7 and Table A3).

As one can observe, in a series of double linearly connected melamines **7a** and **7b**, each rotamer can be generated by a single diastereomeric rotation/equilibrium: a *global s*-cis vs *s*-trans by rotation about the C(*s*-triazine)–N(piperazine) bond and the rotation about the C(*s*-triazine)–N(serinol) bond can create the local syn versus anti diastereomerism. If statistical, the occurrence of these rotamers can be predicted mathematically.

Although in all our melamines the ^{1}H NMR spectra displayed large peaks, it was in the ^{13}C NMR time scale that spiranic positions α and α′ were found throughout as diastereotopic (Δδ = 0.1–0.5 ppm, as well as, in some cases (**6b** and **6c**) those of piperazine Δδ = 0.2 and 0.6 ppm). As a general rule, C(2, 4) *s*-triazine carbons linked to piperidinic (or piperazinic) nitrogens together with carbons located in α and α′ positions exhibited broad signals. This rule did not apply to serinolic C(6)(*s*-triazine)–N< (exocyclic) connections to disclose, once more, a different rotational speed about the C(*s*-triazine)–N< versus C(*s*-triazine)–NH– bonds. However, a preferred rotamer (Scheme 7) could not be assigned.

At 353 K, all melamines were completely freely rotating structures.

The temperature gradients were less negative than –4 ppb/K, suggesting these compounds are internally NH(serinol)···OH chelated. In the **6a**–**6c** series, only the serinolic NH signal could be temperature monitored, not that of piperazine. Internal chelation increased as follows: **6a** < **6b** < **6c** (temperature gradients –2.75, –2.47, and –1.36, respectively). As in the precursor series **4a**–**4c**, TRIS derivative **6c** was the most internal chelated with respect to NH protons.

Conclusions

4-Piperidone ethylene ketal is a versatile but useful partner for C-2-substituted serinols in selective amination of cyanuric chloride directed to building blocks for potential iterative

Can. J. Chem. Downloaded from www.nrcresearchpress.com by University of Electronic and Science Techonology of China on 09/19/12
For personal use only.

Can. J. Chem. Downloaded from www.nrcresearchpress.com by University of Electronic and Science Techonology of China on 09/19/12
For personal use only.

synthesis. The VT NMR experiments showed the resulting amino-*s*-triazines exhibiting distinct types of rotamerism about the C(*s*-triazine)–N< (exocyclic) bond. Rather than steric hindrance, internal versus solvent chelation of serinolic fragments are noticeable factors of influence.

Experimental

General

Melting points are uncorrected; they were carried out on an Electrothermal instrument. Conventional NMR spectra were recorded on a Bruker AM300 instrument operating at 300 and 75 MHz for ^{1}H and ^{13}C nuclei, respectively. VT NMR experiments were performed on a Bruker AV400 instrument (Bruker DMX 500 in the case of compounds **1b**, **2a**, **4a**, and **5a**). All NMR spectra were measured in anhydrous commercially available deuteriated solvents. TLC was performed by using aluminium sheets with silica gel 60 F_{254} (Merck). Flash column chromatography was conducted on silica gel Si 60 (40–63 μm, Merck). All visualizations were realized in UV at 254 nm. IR spectra were performed on a PerkinElmer Paragom FT-IR spectrometer. Only relevant absorptions are listed (throughout in cm^{-1}: weak (w), medium (m), or (s) strong). Microanalyses were performed on a Carlo Erba CHNOS 1160 apparatus. Mass spectra (MS) were recorded on a Bruker Esquire instrument. The synthesis and data of compounds **1a**–**1c** (Scheme 1, route **A**) have been reported elsewhere.[5]

Preparation of compound 1b (Scheme 1, route B)

To a 10% *v*/*v* aqueous solution in THF suspension (100 mL) containing cyanuric chloride (0.922 g, 5.00 mmol) and anhyd K_2CO_3 (2.762 g, 20.00 mmol), cooled at –15 °C, solid piperidone monohydrate hydrochloride **I** (1.536 g, 10.00 mmol) was added portionwise within 12 h with vigorous stirring and with the temperature not exceeding –10 °C. The reaction mixture was then allowed to very slowly reach room temperature and was kept there for an additional 24 h until TLC monitoring (eluent ligroin–acetone, 1.5:1 *v*/*v*) showed completion of reaction. The reaction mixture was filtered off, minerals were well washed with dry dichloromethane (50 mL), and then dichloromethane (75 mL) was added to the filtrate with stirring. The organic layer was separated then washed with water (×50 mL) to neutrality. After drying over anhyd Na_2SO_4 and filtering off, the organic solution was evaporated to dryness under vacuum. The solid residue was crystallized from dry ether (5 mL) at –20 °C to yield 1.053 g of pure **1b** (68% yield with respect to cyanuric chloride). In a similar procedure, compound **2a** was prepared (Scheme 2, route **B**).

2-Chloro-4,6-bis(4-oxopiperidin-1-yl)-*s*-triazine (**1b**) yield 68%; white crystalline powder, mp 188.1–189.0 °C (flash column chromatography, eluent ligroin–acetone, 3.8:1 *v*/*v*). R_f 0.35 (80% ligroin–acetone); R_f 0.70 (60% ligroin–acetone). IR ν_{max} (KBr, cm^{-1}): 3007 (w), 2974 (w), 2900 (w), 1714 (s), 1592 (s), 1492 (s), 1450 (s), 1367 (m), 1331 (m), 1231 (s), 1211 (s), 1016 (m), 982 (m), 967 (m), 827 (m), 793 (m), 753 (w), 685 (w), 556 (w), 497 (w). For relevant (VT) ^{1}H NMR data see Table A1. QC NMR (125 MHz, [D_8]THF, 303 K, ppm) δ_C: 40.6, 40.3 (4 C, C-3′, -3″, -5′, -5″), 42.7, 42.6 (4 C, C-2′, -2″, -6′, -6″), 165.2 (2 C, C-4, -6, *s*-triazine), 170.3 (1 C, C-2, *s*-triazine), 205.1 (2 C, C-4′, -4′). MS (EI, 70 eV), *m*/*z* (rel. int. %): 309 [M$^+$] (100), 281 (58), 253 (78), 240 (70), 225 (40), 197 (33), 184 (29), 70 (37). Anal. calcd for $C_{13}H_{16}ClN_5O_2$ (309.10): C 50.41, H 5.21, N, 22.61%; found: C 50.79, H 4.90, N 22.71%.

2-Chloro-4,6-bis(1,4-dioxa-8-azaspiro[4.5]decan-8-yl)-*s*-triazine (**2a**) yield 62%; yellowish crystalline powder, mp 143–145 °C (Et_2O). IR ν_{max} (KBr, cm^{-1}): 2964 (m), 2932 (m), 2870 (m), 1655 (m), 1571 (s), 1492 (s), 1458 (s), 1364 (m), 1310 (m), 1230 (s), 1146 (m), 1116 (s), 1078 (s), 1034 (m), 979 (m), 944 (m), 908 (m), 796 (m), 660 (w). For relevant (VT) ^{1}H NMR data see Table A1. ^{13}C NMR (125 MHz, [D_6]DMSO, 298 K, ppm) δ_C: 34.28 (2 C, C-6′(10′), -6″(10″)), 34.33 [2 C, C-10′(6′), -10″(6″)], 41.2 (4 C, C-7′, -7″, -9′, -9″), 63.9 (4 C, C-2′, -2″, -3′, -3″), 106.4 (2 C, C-5′, -5″), 163.6 (2 C, C-4,-6, *s*-triazine), 168.9 (1 C, C-2, *s*-triazine). MS (EI, 70 eV), *m*/*z* (rel. int. %): 397 [M$^+$] (100), 354 (30), 325 (25), 310 (10), 297 (50), 284 (70), 252 (10), 225 (20), 212 (15), 197 (10), 184 (20), 170 (15), 158 (5), 142 (8), 127 (5), 99 (65), 86 (13), 70 (18). Anal. calcd for $C_{17}H_{24}ClN_5O_4$ (397.15): C 51.32, H 6.08, N 17.60%; found: C 50.98, H 5.88, N 17.31%.

Preparation of compound 2b (Scheme 2, route C)

1,4-Dioxa-8-azaspiro[4.5]decane hydrochloride **IIa** (3.60 g, 20.00 mmol) was dissolved in dry and freshly distilled DMF (125 mL) and then anhyd K_2CO_3 (5.60 g, 40.00 mmol) was added. The resulted suspension was cooled at 0 °C when solid cyanuric chloride (1.18 g, 6.35 mmol) was rapidly introduced with vigorous stirring. The reaction mixture was allowed very gently to reach room temperature (about 24 h) then heated at 110 °C until TLC monitoring (eluent ligroin–acetone, 1.5:1 *v*/*v*) indicated that there was no more evolution of the reaction and the crude product **2b** appeared as a main spot (about 12 h). The reaction mixture was poured into water (100 mL), then extracted with chloroform (100 mL). After separation, the organic layer was well washed with water (7 × 100 mL) to allow complete removal of DMF, then dried over anhyd Na_2SO_4. After filtering off and washing minerals with dry chloroform, the organic solution was evaporated under reduced pressure to dryness, yielding the crude product, which was taken with dry ether (5 mL) with stirring. The resulted suspension was cooled at –20 °C for 12 h and then filtered off and washed with dry and cooled ether to yield the title compound **2b** (2.00 g, 63% yield with respect to cyanuric chloride).

2,4,6-Tris(1,4-dioxa-8-azaspiro[4.5]decan-8-yl)-*s*-triazine (**2b**) yield 63%); yellowish crystalline powder, mp 259–263 °C (Et_2O). IR ν_{max} (KBr, cm^{-1}): 2956 (w), 2928 (w), 2878 (w), 1682 (w), 1582 (s), 1537 (s), 1494 (s), 1449 (s), 1408 (m), 1360 (m), 1310 (w), 1250 (m), 1234 (s), 1120 (s), 1081 (s), 1036 (w), 946 (s), 907 (m), 804 (w), 662 (w). ^{1}H NMR (300 MHz, $CDCl_3$, ppm) δ_H: 1.70 (12 H, t, $^3J_{H,H}$ = 5.2 Hz, H-6′, -6″, -6‴, -10′, -10″, -10‴, -a, -e), 3.86 (12 H, t, $^3J_{H,H}$ = 5.2 Hz, H-7′, -7″, -7‴, -9′, -9″, -9‴, -a, -e), 4.00 (12 H, s, H-2′, -2″, -2‴, H-3′, -3″, -3‴). ^{13}C NMR (75 MHz, $CDCl_3$, ppm) δ_C: 34.8 (6 C, C-6′, -6″, -6‴, -10′, -10″, -10‴), 41.1 (6 C, C-7′, -7″, -7‴, -9′, -9″, -9‴), 64.3 (6 C, C-2′, -2″, -2‴, -3′, -3″, -3‴), 107.8 (3 C, C-5′, -5″, -5‴), 165.3 (3 C, C-2, -4, -6, *s*-triazine). MS (EI, 70 eV), *m*/*z* (rel. int. %): 505 [M$^+$ + H] (100), 407,[10] 380 (25). Anal. calcd for $C_{24}H_{36}N_6O_6$ (504.27):

Can. J. Chem. Downloaded from www.nrcresearchpress.com by University of Electronic and Science Techonology of China on 09/19/12
For personal use only.

C 57.13, H 7.19, N 16.66%; found: C 56.98, H 7.33, N 17.01%.

Preparation of compound 1c (Scheme 2)

To 2,4,6-tris(1,4-dioxa-8-azaspiro[4.5]decan-8-yl)-*s*-triazine **2b** (1.446 g, 2.86 mmol) suspended in aqueous 1,4-dioxane (water (21 mL) + 1,4-dioxane (7 mL)), concd aqueous hydrochloric acid (1.00 mL, 1.18 g soln. 37%, 12.00 mmol HCl) was added and the reaction mixture, having the pH 0.5–1.0, was heated at reflux for 12 h. The reaction was monitored spot to spot by TLC (eluent ligroin–acetone, 1.5:1 *v*/*v*) and stopped when no more evolution was observed and the desired **1c** largely existed as a major spot. The reaction mixture was cooled at room temperature and made alkaline (pH 10) with solid K_2CO_3 and crude **1c** precipitated abundantly. After filtering off, washing with water to neutrality, and drying, pure **1c** (0.800 g, 75% yield with respect to cyanuric chloride) was obtained after crystallization from diethyl ether at –20 °C. The pure analytical sample obtained by the above methodology was identical with that obtained in route **A** (Scheme 1).

2,4,6-Tris(4-oxopiperidin-1-yl)-*s*-triazine (**1c**) yield 75%; yellowish crystalline powder, mp 234.2 °C (dec.) (flash column chromatography, eluent ligroin–acetone, 3.8:1 *v*/*v*). R_f 0.20 (80% ligroin–acetone). IR ν_{max} (KBr, cm^{-1}): 2958 (w), 2862 (w), 1709 (s), 1530 (s), 1490 (s), 1455 (s), 1371 (m), 1316 (m), 1231 (s), 1068 (m), 991 (m), 967 (m), 806 (m), 762. ^1H NMR (300 MHz, $CDCl_3$, ppm) δ_H: 2.47 (12 H, t, $^3J_{H,H}$ = 6.0 Hz, H-3′, -3″, -3‴, -5′, -5″, -5‴, -a, -e), 4.08 (12 H, t, $^3J_{H,H}$ = 6.0 Hz, H-2′, -2′, -2‴, -6′, -6″, -6‴, -a, -e). ^{13}C NMR (75 MHz, $CDCl_3$, ppm) δ_C: 41.5 (6 C, C-3′, -3″, -3‴, -5′, -5″, -5‴), 43.0 (6 C, C-2′, -2″, -2‴, -6′, -6″, -6‴), 165.8 (3 C, C-2, -4, -6, *s*-triazine), 208.9 (3 C, C-4′, -4″, -4‴). MS (EI, 70 eV), *m*/*z* (rel. int. %): 372 [M+] (100), 344 (20), 329 (18), 316 (58), 303 (75), 288 (47), 275 (45), 260 (50), 247 (60), 232 (25), 219 (28), 203 (26), 177 (25), 163 (21), 122 (33), 94 (32), 80 (46), 68 (28). Anal. calcd for $C_{18}H_{24}N_6O_3$ (372.19): C 58.05, H 6.50. N 22.57%; found: C 57.75, H 6.88, N 22.71%.

Typical procedure for the synthesis of compounds 4a–4c — Preparation of compound 4a

To a solution obtained by dissolving cyanuric chloride (1.53 g, 8.30 mmol) in dry THF (75 mL), anhyd potassium carbonate (1.15 g, 8.30 mmol) was added at room temperature with vigorous stirring. Solid 2-amino-2-methylpropane-1,3-diol ("methylserinol", 0.873 g, 8.30 mmol) was added and the resulting suspension was stirred at room temperature for an additional 24 h. After this period, TLC (eluent toluene–isopropanol, 4:1 *v*/*v*) indicated formation of the intermediate **3a** as a single major spot. Water (7.50 mL) and solid anhyd potassium carbonate (2.30 g, 16.60 mmol) was added and the reaction mixture was cooled at –10 (–15 °C). At this temperature and with vigorous stirring, solid 1,4-dioxa-8-azaspiro[4.5]decane hydrochloride **II** (1.49 g, 8.30 mmol) was added portionwise (five equal portions as 0.298 g / portion each for 90 min). The reaction mixture was kept at –10 °C (–15 °C) for an additional 24 h then allowed to reach room temperature very slowly (48 h). After the minerals were filtered, water (50 mL) and chloroform (100 mL) were added with stirring. The aqueous layer was extracted with chloroform (2 × 35 mL) and the combined organic layer was washed with water (2 × 35 mL). After drying over anhyd Na_2SO_4, the organic solution was evaporated under reduced pressure to dryness to provide 2.83 g of the crude product. This was purified by column chromatography on silica gel (eluent diethyl ether – isopropanol, 10:1 *v*/*v*, or optionally toluene–isopropanol, 4:1 *v*/*v*) to yield compound **4a** as the first fraction (2.44 g, 81% conversion with respect to cyanuric chloride), then compound **5a** as the second fraction (0.14 g, 3% conversion with respect to cyanuric chloride).

2-Chloro-6-{[1,3-dihydroxy-2-(methyl)prop-2-yl]amino}-4-(1,4-dioxa-8-azaspiro[4.5]decan-8-yl)-*s*-triazine (**4a**) yield 81%; yellowish crystalline powder, mp 135.2–138.0 °C (dec.) (flash column chromatography, eluent diethyl ether – isopropanol 10:1 *v*/*v*). R_f 0.75 (91% diethyl ether – isopropanol). IR ν_{max} (KBr, cm^{-1}): 3428 (s), 3352 (s), 3272 (s), 2929 (m), 1586 (s), 1541 (s), 1506 (s), 1460 (m), 1406 (m), 1288 (m), 1274 (m), 1241 (m), 1152 (m), 1113 (m), 1082 (s), 1053 (s), 1020 (m), 946 (m), 915 (m), 898 (m) 796 (m), 772 (w), 666 (w), 627 (w). For relevant (VT) ^1H NMR data see Table A2. ^{13}C NMR (125 MHz, [D_6]DMSO, 293 K, ppm) δ_C: 18.7, 19.1 (1 C, CH_3), 34.5, 34.8 (2 C, C-6(10) -10(6), spirane), 41.4, 41.8, 42.0 (2 C, C-7(9), -9(7), spirane), 58.9, 59.0 (1 C, C-2), 63.3, 63.8 (2 C, CH_2OH), 64.3 (2 C, C-2, -3, spirane), 106.9 (1 C, C-5, spirane), 163.5, 164.0 (1 C, C-4, *s*-triazine), 165.1, 165.7 (1 C, C-6, *s*-triazine), 168.4 (1 C, C-2, *s*-triazine). MS (ESI+), *m*/*z* (×10^5): 382.1 [M + Na^+],[8] 360.1 [M^+ + H] (3.5). Anal. calcd for $C_{14}H_{22}ClN_5ClO_4$ (359.14): C 46.73, H 6.16, N 19.46%; found: C 47.05, H 5.90, N 19.11%.

2-Chloro-6-{[1-hydroxy-2-(hydroxymethyl)but-2-yl]amino}-4-(1,4-dioxa-8-azaspiro[4.5]decan-8-yl)-*s*-triazine (**4b**) yield 50%; yellowish crystalline powder, mp 147.4–152.7 °C (flash column chromatography, eluent diethyl ether – isopropanol, 10:1 *v*/*v*). R_f 0.60 (91% diethyl ether – isopropanol). IR ν_{max} (KBr, cm^{-1}): 3290 (s), 2969 (m), 2888 (w), 1580 (s), 1548 (s), 1497 (s), 1460 (s), 1419 (s), 1366 (m), 1304 (m), 1237 (s), 1153 (m), 1115 (m), 1088 (m), 1057 (s), 1029 (m), 995 (m), 942 (w), 917 (w), 899 (w) 800 (m), 634 (w). For relevant (VT) ^1H NMR data see Table A2. ^{13}C NMR (100 MHz, [D_6]DMSO, 293 K, ppm) δ_C: 7.9, 8.1 (1 C, CH_2CH_3), 22.4, 23.0 (1 C, CH_2CH_3), 34.6, 34.8, 34.9 (2 C, C-6(10), -10(6), spirane), 41.4, 41.9, 42.1 (2 C, C-7(9), -9(7), spirane), 60.8 (1 C, C-2), 61.4, 61.5 (2 C, CH_2OH), 64.4 (2 C, C-2, -3, spirane), 106.9 (1 C, C-5, spirane), 163.6, 164.2 (1 C, C-4, *s*-triazine), 165.1, 165.8 (1 C, C-6, *s*-triazine), 168.4, 168.6 (1 C, C-2, *s*-triazine). MS (CI, *i*-BuH), *m*/*z* (rel. int. %): 430 [M^+ + *i*-BuH – 1] (15), 374 [M^+ + H] (100), 340 (45), 308 (8), 272 (9), 238 (6), 154 (6), 93 (6), 85 (10), 73 (14). Anal. calcd for $C_{15}H_{24}ClN_5O_4$ (373.15): C 48.19, H 6.47, N 18.73%; found: C 48.15, H 6.67, N 19.01%.

2-Chloro-6-{[1,3-dihydroxy-2-(hydroxymethyl)prop-2-yl] amino}-4-(1,4-dioxa-8-azaspiro[4.5]decan-8-yl)-*s*-triazine (**4c**) yield 76%; yellowish crystalline powder, mp 127.3–131.5 °C (flash column chromatography, dichloromethane–isopropanol, 8:1 *v*/*v*). R_f 0.65 (89% dichloromethane–isopropanol). IR ν_{max} (KBr, cm^{-1}): 3324 (s), 2957 (m), 2880 (m), 1591 (s), 1542 (s), 1497 (s), 1456 (s), 1412 (s), 1364 (m), 1315 (s), 1271 (m), 1218 (m), 1153 (m), 1115 (m), 1083 (m), 1083 (m), 1047 (s), 991 (m), 944 (m), 911 (m), 889 (w), 800 (m), 724

Can. J. Chem. Downloaded from www.nrcresearchpress.com by University of Electronic and Science Techonology of China on 09/19/12
For personal use only.

(w), 648 (w). For relevant (VT) ^{1}H NMR data see Table A2. ^{13}C NMR (100 MHz, [D_6]DMSO, 293 K, ppm) δ_C: 34.8, 34.9, 35.0 (2 C, C-6(10), -10(6), spirane), 41.5, 41.9, 42.1 (2 C, C-7(9), -9(7), spirane), 59.6, 60.3 (1 C, C-2), 62.6 (3 C, CH_2OH), 64.39, 64.42 (2 C, C-2, -3, spirane), 106.9 (1 C, C-5, spirane), 163.6, 164.1 (1 C, C-4, *s*-triazine), 165.3, 165.8 (1 C, C-6, *s*-triazine), 168.41, 168.44 (1 C, C-2, *s*-triazine). MS (CI, *i*-BuH), *m/z* (rel. int. %): 432 [M + *i*-BuH – 1] (15), 376 [M$^+$ + 1] (100), 342 (55), 282 (80), 272 (25), 238 (25). Found: C, 44.62; H, 5.95; N, 18.87; $C_{14}H_{22}ClN_5O_5$ (375.13) requires: C, 44.74; H, 5.90; N, 18.64%.

{6-[1,3-Dihydroxy-2-(hydroxymethyl)prop-2-yl]amino}-2,4-bis(1,4-dioxa-8-azaspiro[4.5]decan-8-yl)-*s*-triazine (**5a**) yield 3%; yellowish crystalline powder, mp 141.5–142.7 °C (flash column chromatography, eluent diethyl ether – isopropanol, 10:1 *v/v*). R_f 0.33 (91% diethyl ether – isopropanol). IR ν_{max} (KBr, cm^{-1}): 3262 (s), 2956 (m), 2889 (m), 1540 (s), 1507 (s), 1443 (s), 1361 (m), 1337 (m), 1305 (m), 1250 (m), 1234 (m), 1113 (s), 1082 (s), 1054 (m), 943 (m), 900 (m), 806 (w), 740 (w), 657 (w). For relevant (VT) NMR data see Table A3. MS (ESI+), *m/z* (×10^5): 489.3 [M + Na$^+$] (1.2), 467.3 [M$^+$ + H] (7.5). Anal. calcd for $C_{21}H_{34}N_6O_6$ (466.25): C 54.06, H 7.35, N 18.01%; found: C 49.90, H 7.50, N 18.11%.

6-{[1-Hydroxy-2-(hydroxymethyl)but-2-yl]amino-2,4-bis(1,4-dioxa-8-azaspiro[4.5]decan-8-yl)-*s*-triazine (**5b**) yield 5%; yellowish crystalline powder, mp 143.1–146.8 °C (flash column chromatography, eluent diethyl ether – isopropanol, 10:1 *v/v*). R_f 0.25 (91% diethyl ether – isopropanol). IR ν_{max} (KBr, cm^{-1}): 3405 (m), 3311 (m), 2964 (m), 2928 (m), 2878 (m), 1564 (s), 1503 (s), 1455 (s), 1360 (m), 1338 (w), 1255 (s), 1241 (m), 1122 (m), 1080 (s), 1036 (m), 946 (m), 911 (m), 808 (m), 780 (w), 663 (w). For relevant (VT) NMR data see Table A3. MS (ESI+), *m/z* (×10^5) 503.4 [M + Na$^+$] (0.3), 481.4 [M$^+$ + H] (2.2). Anal. calcd for $C_{22}H_{36}N_6O_6$ (480.27): C 54.99, H 7.55, N 17.49%; found: C 54.66, H 7.67, N 17.11.

Typical procedure for the synthesis of compounds 6a–6c — Preparation of compound 6a

In a solution obtained from dry THF (60 mL) and anhyd piperazine (2.06 g, 24.00 mmol), anhyd potassium carbonate (0.830 g, 6.00 mmol) was suspended with vigorous stirring. To this suspension, solid **4a** (2.158 g, 6.00 mmol) was added portionwise, as six equal portions, each for 90 min, at room temperature. After each addition, within 90 min TLC monitoring (eluent diethyl ether – isopropanol, 10:1 *v/v*) indicated the complete consumption of the starting material **4a**. Minerals were filtered off, washed with dry THF, and then the organic filtrate was evaporated under reduced pressure to dryness to provide 3.434 g of crude material. This was purified by column chromatography on silica gel (eluent isopropanol – aq 25% ammonia, 9:1 *v/v*) to yield the by-product **7a** (0.121 g, 5.5% conversion of **4a**), then the desired **6a** (2.064 g, 84% conversion of **4a**) as the main fraction.

6-{[1,3-Dihydroxy-2-(methyl)prop-2-yl]amino}-2-(1,4-dioxa-8-azaspiro[4.5]decan-8-yl)-4-(piperazin-1-yl)-*s*-triazine (**6a**) yield 84%; yellowish crystalline powder, mp 120.0–126.4 °C (flash column chromatography, eluent isopropanol – 25% aq ammonia 9:1 *v/v*). R_f 0.50 (90% isopropanol – 25% aq ammonia). IR ν_{max} (KBr, cm^{-1}): 3298 (m), 2931 (m), 2876 (m), 1537 (s), 1503 (s), 1445 (s), 1363 (m), 1303 (m), 1258 (m), 1148 (w), 1118 (m), 1087 (s), 1038 (m), 946 (w), 834 (w), 808 (m), 734 (w), 662 (w). For relevant (VT) NMR data see Table A3. MS (ESI+), *m/z* (×10^7): 410.2 [M$^+$ + H] (0.95). Anal. calcd for $C_{18}H_{31}N_7O_4$ (409.24): C 52.80, H, 7.63, N 23.94%; found: C 53.05, H 7.90, N 24.11%.

6-{[1-Hydroxy-2-(hydroxymethyl)but-2-yl]amino}-2-(1,4-dioxa-8-azaspiro[4.5]decan-8-yl)-4-(piperazin-1-yl)-*s*-triazine (**6b**) yield 86%; yellowish crystalline powder, mp 224–225 °C (flash column chromatography, eluent isopropanol – 25% aq ammonia, 9:1 *v/v*). R_f 0.60 (90% isopropanol – 25% aq. ammonia). IR ν_{max} (KBr, cm^{-1}): 3399 (m), 2958 (m), 2880 (m), 1562 (s), 1532 (s), 1495 (s), 1443 (s), 1363 (m), 1339 (m), 1300 (m), 1256 (m), 1117 (m), 1087 (s), 946 (w), 910 (w), 808 (m), 662 (w). For relevant (VT) NMR data see Table A3. MS (ESI+), *m/z* (×10^6): 446.1 [M + Na$^+$] (0.45), 424.1 [M$^+$ + H] (2.2). Anal. calcd for $C_{19}H_{33}N_7O_4$ (423.26): C 53.88, H 7.85, N 23.15%; found: C 54.05, H 7.67, N 22.89%.

6-{[1,3-Dihydroxy-2-(hydroxymethyl)prop-2-yl]amino}-2-(1,4-dioxa-8-azaspiro[4.5]decan-8-yl)-4-(piperazin-1-yl)-*s*-triazine (**6c**) yield 79%; yellowish crystalline powder, mp 223–229 °C (flash column chromatography, eluent isopropanol – 25% aq ammonia, 9:1 *v/v*). R_f 0.40 (90% isopropanol – 25% aq ammonia). IR ν_{max} (KBr, cm^{-1}): 3339 (m), 2948 (m), 2884 (m), 2770 (m), 1584 (s), 1565 (s), 1538 (s), 1503 (s), 1427 (s), 1368 (m), 1302 (m), 1251 (m), 1085 (s), 1017 (m), 946 (w), 808 (m), 660 (w). For relevant (VT) NMR data see Table A3. MS (ESI+), *m/z* (×10^6): 426.3 [M$^+$ + H] (6). Anal. calcd for $C_{18}H_{31}N_7O_5$ (425.24): C 50.81, H 7.34, N 23.04%; found: C 51.01, H 7.57, N 22.88%.

1,4-Bis{{6-[1,3-dihydroxy-2-(methyl)prop-2-yl]amino}-4-(1,4-dioxa-8-azaspiro[4.5]decan-8-yl)-*s*-triazin-2-yl}-piperazine (**7a**) yield 5.5%; yellowish crystalline powder, mp 199.0–200.0 °C (flash column chromatography, eluent isopropanol – 25% aq ammonia, 9:1 *v/v*). R_f 0.85 (90% isopropanol – 25% aq ammonia). IR ν_{max} (KBr, cm^{-1}): 3243 (m), 2923 (m), 2877 (m), 1532 (s), 1442 (s), 1363 (m), 1283 (m), 1258 (s), 1120 (m), 1089 (s), 1034 (m), 944 (m), 806 (m), 738 (w), 664 (w). For relevant (VT) NMR data see Table A3. MS (ESI+), *m/z* (×10^5): 733.2 [M$^+$ + H] (7.5). Anal. calcd for $C_{32}H_{52}N_{12}O_8$ (732.40): C 52.45, H 7.15, N 22.94%; found: C 52.44, H 6.90, N 22.81%.

1,4-Bis{{6-[1-hydroxy-2-(hydroxymethyl)but-2-yl]amino}-4-(1,4-dioxa-8-azaspiro[4.5]decan-8-yl)-*s*-triazin-2-yl}-piperazine (**7b**) yield 1.2%; yellowish crystalline powder, mp 197.7–200 °C (flash column chromatography, eluent isopropanol – 25% aq ammonia, 9:1 *v/v*). R_f 0.90 (90% isopropanol – 25% aq ammonia). IR ν_{max} (KBr, cm^{-1}): 3393 (m), 2966 (m), 2884 (m), 1536 (s), 1494 (s), 1442 (s), 1363 (m), 1341 (m), 1284 (m), 1261 (s), 1154 (w), 1116 (m), 1088 (s), 1033 (m), 946 (m), 805 (m), 661 (w). For relevant (VT) NMR data see Table A3. MS (ESI+), *m/z* (×10^6): 761.3 [M$^+$ + H] (2.2). Anal. calcd for $C_{34}H_{56}N_{12}O_8$ (760.43): C 53.67, H 7.42, N 22.09%; found: C 53.92, H 7.11, N 21.85%.

Acknowledgements

The financial support from a grant provided by the National Council of Scientific Research C.N.C.S.I.S. (1482) is gratefully acknowledged by Flavia Popa.

Can. J. Chem. Downloaded from www.nrcresearchpress.com by University of Electronic and Science Techonology of China on 09/19/12
For personal use only.

Oana Moldovan is grateful for an "Investing in people! Ph.D. scholarship, project co-financed by the Sectoral Operational Program for Human Resources Development 2007–2013 Priority Axis 1. "Education and training in support for growth and development of a knowledge based society". Key area of intervention 1.5: Doctoral and post-doctoral programs in support of research. Contract No.: POSDRU/88/1.5/S/60185 — Innovative Doctoral Studies in a Knowledge-Based Society, Babeş-Bolyai University, Cluj-Napoca, Romania.

The computational center of the University of Reims Champagne-Ardenne (ROMEO, http://www.romeo2.fr) is acknowledged for the CPU time donated.

References

(1) (a) Darabantu, M. *Curr Org Synth* **2010** *7* (2), 120. doi:10.2174/157017910790820300; (b) Darabantu, M. *Curr Org Synth* **2010** *7* (3), 235. doi:10.2174/157017910791162986.

(2) (a) Berghian, C.; Lamerias, P.; Toupet, L.; Condamine, E.; Plé, N.; Turk, A.; Maiereanu, C.; Darabantu, M. *Tetrahedron* **2006** *62* (31), 7319. doi:10.1016/j.tet.2006.05.031; (b) Darabantu, M.; Pintea, M.; Fazekas, M.; Lameiras, P.; Berghian, C.; Delhom, I.; Silaghi-Dumitrescu, I.; Plé, N.; Turck, A. *Lett. Org. Chem.* **2006** *3* (12), 905. doi:10.2174/157017806779467933; (c) Pintea, M.; Fazekas, M.; Lameiras, P.; Cadis, I.; Berghian, C.; Silaghi-Dumitrescu, I.; Popa, F.; Bele, C.; Plé, N.; Darabantu, M. *Tetrahedron* **2008** *64* (37), 8851. doi:10.1016/j.tet.2008.06.071.

(3) McElvain, S. M.; Mc Mahon, R. *J. Am. Chem. Soc.* **1949** *71* (3), 901. doi:10.1021/ja01171a038.

(4) Henkin, J.; Davidson, D. J.; Sheppard, G.; Woods, S.; Keith, W.; McCroskey, R. W. (Abbott Laboratories, USA), PCT Int. Appl. WO 9931088, 24 June 1999 (e.g., US Patent 6,150,362 in 2000; US Patent 6,288,228 in 2001, E.P. 1037886) cf.; *Chem. Abstr.* 1999, **131**, 58855.

(5) Popa, F.; Simioanca, I.; Pintea, M.; Fazekas, M.; Gratecap, L.; Berghian, C.; Batiu, C.; Darabantu, M. *Studia Universitatis* "*Babes-Bolyai*", *Serie Chemia* **2008** *LIII* (4), 5.

(6) Stach, K.; Thiel, M.; Bickelhaupt, F. *Monatsh. Chem.* **1962** *93* (5), 1090. doi:10.1007/BF00905909.

(7) (a) see for exampleZhang, W.; Nowlan, D. T.; Thomson, L. M.; Lackowski, M. W.; Simanek, E. E. *J. Am. Chem. Soc.* **2001** *123* (37), 8914. doi:10.1021/ja0041369; (b) Steffensen, M. B.; Simanek, E. E. *Angew. Chem. Int. Ed.* **2004** *43* (39), 5178. doi:10.1002/anie.200460031; (c) Lim, J.; Simanek, E. E. *Mol. Pharm.* **2005** *2* (4), 273. doi:10.1021/mp050030e; (d) Newkome, G. R.; Groß, J.; Moorefield, C. N.; Woosley, B. D. *Chem. Commun. (Camb.)* **1997** *6* (6), 515. doi:10.1039/a608240h; (e) Umali, A. P.; Simanek, E. E. *Org. Lett.* **2003** *5* (8), 1245. doi:10.1021/ol034161u; (f) Chen, H. T.; Neerman, M. F.; Parrish, A. R.; Simanek, E. E. *J. Am. Chem. Soc.* **2004** *126* (32), 10044. doi:10.1021/ja048548j; (g) Lai, L.-L.; Wang, L.-Y.; Lee, C.-H.; Lin, C. Y.; Cheng, K.-L. *Org. Lett.* **2006** *8* (8), 1541. doi:10.1021/ol0531076;; (h) Acosta, E. J.; Gonzalez, S. O.; Simanek, E. E. J. *Polym. Sci. Part A* **2005** *43* (1), 168. doi:10.1002/pola.20493; (i) Zhang, W.; Gonzalez, S. O.; Simanek, E. E. *Macromolecules* **2002** *35* (24), 9015. doi:10.1021/ma021101f; (j) Hollink, E.; Simanek, E. E. *Org. Lett.* **2006** *8* (11), 2293. doi:10.1021/ol060559p.

(8) (a) Drakenberg, T.; Forsen, S. *Chem. Commun.* **1971** *21*, 1404 (b) Mirvish, S. S.; Gannett, P.; Babcook, D. M.; Williamson, D.; Chen, S. C.; Weisenburger, D. D. *J. Agric. Food Chem.* **1991** *39* (7), 1205. doi:10.1021/jf00007a002.

(9) (a) Willner, I.; Rosengaus, J.; Eichen, Y. *J. Phys. Org. Chem.* **1993** *6* (1), 29. doi:10.1002/poc.610060106; (b) Katritzky, A. R.; Ghiviriga, I.; Oniciu, D. C.; Barkock, A. *J. Chem. Soc., Perkin Trans. 2* **1995** *4*, 785. doi:10.1039/p29950000785; (c) Katritzky, A. R.; Ghiviriga, I.; Steel, P. G.; Oniciu, D. C. *J. Chem. Soc. Perkin Trans.* **1996** *3*, 443. doi:10.1039/p29960000443; (d) Ghiviriga, I.; Oniciu, D. C. *Chem. Commun. (Camb.)* **2002** *22* (22), 2718. doi:10.1039/b206811g; (e) Amm, M.; Platzer, N.; Guilhem, J.; Bouchet, J. P.; Volland, J. P. *Magn. Reson. Chem.* **1998** *36* (8), 587. doi:10.1002/(SICI)1097-458X(199808)36:8<587::AID-OMR347>3.0.CO;2-B; (f) Amm, M.; Platzer, N.; Bouchet, J. P.; Volland, J. P. *Magn. Reson. Chem.* **2001** *39* (2), 77. doi:10.1002/1097-458X(200102)39:2<77::AID-MRC801>3.0.CO;2-H; (g) Birkett, H. E.; Harris, R. K.; Hodgkinson, P.; Carr, K.; Charlton, M. H.; Cherryman, J. C.; Chippendale, A. M.; Glover, R. P. *Magn. Reson. Chem.* **2000** *38* (7), 504. doi:10.1002/1097-458X(200007)38:7<504::AID-MRC710>3.0.CO;2-7; (h) Birkett, H. E.; Cherryman, J. C.; Chippendale, A. M.; Evans, J. O. S.; Harris, R. K.; James, M.; King, I. J.; Mc Pherson, G. *Magn. Reson. Chem.* **2003** *41* (5), 324. doi:10.1002/mrc.1185; (i) Moreno, X. C.; Simanek, E. E. *Macromolecules* **2008** *41* (12), 4108. doi:10.1021/ma702143f.

(10) (a) Friebolin, H. *Basic One- and Two-Dimensional NMR Spectroscopy;* VCH Verlagsgesellschaft/VCH: Weinheim, New York, 1991; p 93 and pp 263–291; (b) Eliel, E. L.; Wilen, H. S. *Stereochemistry of the Organic Compounds;* John Wiley & Sons: New York, 1994; pp 465, 503–507, 1200, 1206; (c) Gutowski, H. S.; Holm, C. H. J. *Chem. Phys.* **1956** *25* (6), 1228; (d) Shanan-Atidi, H.; Bar Eli, R. H. *J. Phys. Chem.* **1970** *74* (4), 961. doi:10.1021/j100699a054.

(11) Kessler, H. *Angew. Chem. Int. Ed. Engl.* **1982** *21* (7), 512. doi:10.1002/anie.198205121.

(12) We note that in THF + 10% *v/v* H_2O, the complete replacement of chlorine to provide a melamine built entirely from 4-piperidone (**1c**) failed; difficult separable mixtures **1a** + **1b** + **1c** were constantly obtained.

(13) Full structural data, synthesis, and stereochemistry of the intermediates **3a**–**3c** are reported elsewhere (ref. 2c).

(14) Obviously, highly symmetric compound C_{2S} (**1a**) and C_{3S} (**1c** and **2b**) were unsuitable for the C(*s*-triazine)–N< (exocyclic) rotamerism monitoring, positions C-α vs C-α′ and C-β vs C-β′ being homotopic.

(15) This anisochrony covered but 14.5 Hz (500 MHz time scale) in each case. Hence, the hypothesis that it could originate from a geminal magnetic nonequivalnce, e.g., H-α-ax. vs H-α-eq. was ruled out.

(16) At room temperature, the stable N-sp^2 hybridization, for example, that of piperazine nitrogens connected to a much less π-deficient N,N′-disubstituted (e.g., diallyl) diamino-*s*-triazine ring, is already well-documented (refs. 9e and 9f) being supported both by VT NMR and X-ray data.

(17) Calculated as $\Delta\delta(\mathrm{NH}) = [\delta(\mathrm{NH})_{353\ \mathrm{K}} - \delta(\mathrm{NH})_{\mathrm{rt}}] < 0$; $\Delta T = (353 - T_{\mathrm{rt}}) > 0$ (K).

Appendix

Can. J. Chem. Downloaded from www.nrcresearchpress.com by University of Electronic and Science Techonology of China on 09/19/12
For personal use only.

Table A1. (VT) ^{1}H NMR behavior of chlorodiamino-*s*-triazines **1b** and **2a** about the C(*s*-triazine)–N< (exocyclic) bonds on a 500 MHz time scale: the homomeric rotation.

		δ (ppm), ($^{3}J_{H,H}$, Hz)				Kinetic parameters in [D_6]DMSO		
Compd. and solvent	Rotational status at *T* (K)	H-α	H-α′	H-β	H-β′	T_C (K)	k_C (s^{-1})	$\Delta G^{\neq}$ (kJ/mol)
1b in [D_6]DMSO	Frozen (293 K)	4.03 (t, 6.3)	3.99 (t, 6.0)	2.47 (bt, 5.8)	2.44 (bt, 5.8)	313(α Δ α′)	46.6	66.78
						308(β Δ β′)	24.4	67.32
	Coalescenced							Averaged
								|
	Freely rotating (343 K)	4.03 (t, 6.3)		2.48 (t, 6.3)				67.05±0.27
1b in [D_8]THF	Partially frozen (303 K)[a]	4.10 (t, 6.5)		2.45 (bs)	2.44 (bs)			
	No coalescence							
	Frozen (233 K)	4.11 (t, 6.5)	4.07 (t, 6.0)					
	Frozen (253 K)			2.42 (t, 6.3)	2.40 (t, 6.3)			
2a in [D_6]DMSO	Frozen (293 K)	3.78 (bt, 5.3)	3.74 (bt, 5.8)	1.63 (bt, 6.0)	1.62 (bt, 5.5)	308 (α Δ α′)	43.3	65.86
						298 (β Δ β′)	14.4	66.36
	Coalescenced							Averaged
	308 K	3.77 (bs)						|
	298 K			1.63 (bs)				
	Freely rotating (343 K)	3.78 (t, 6.3)		1.65 (t, 6.0)				66.11±0.25
	Pseudo freely rotating (353 K)	3.79 (ot, 6.5)	3.78 (ot, 6.0)	1.66 (t, 6.0)				
2a in [D_8]THF	Partially frozen[b] (293 K)	3.85 (bt, 5.0)		1.64 (t, 5.3)	1.63 (t, 5.3)			
	No coalescence							
	Frozen (273 K)	3.85 (t, 5.5)	3.84 (t, 5.8)					
	Frozen (283 K)			1.64 (t, 5.8)	1.63 (t, 5.8)			

Note: Abbreviations: t (triplet), bt (broad triplet), bs (broad singlet), ot (overlapped triplet).

[a]Frozen rotamerism observed completely on a 125 MHz time scale (^{13}C NMR, ppm) as: 40.3 (C-β′), 40.6 (C-β), 42.6 (C-α′), 42.7 (C-α).

[b]Frozen rotamerism partially observed on 125 MHz time scale (^{13}C NMR, ppm) as 34.28 (C-β′), 34.33 (C-β) but 41.2 (C-α, -α′).

Published by NRC Research Press

Table A2. (VT) ^{1}H NMR behavior of compounds **4a**–**4c** about the C(*s*-triazine)–N< (exocyclic) bonds in [D_6]DMSO: the global diastereomeric rotation.

		δ_H (ppm), ($^3J_{H,H}$, Hz)				
No. (%)	Rotational status at *T* (K)	NH	OH	H-α, -α′	H-β, -β′	$\left[\frac{\Delta\delta(NH)}{\Delta T}\right] \times 10^3$ [a]
4a-*anti* (75.4)	Frozen (293 K, 500 MHz)	6.94 (s)	4.63 (t, 6.3)			–6.75 (anti)
				3.74 (bs)	1.59–1.66 (bm)	
4a-*syn* (24.6)		6.75 (s)	4.74 (t, 6.3)			–3.65 (syn)
	Coalescenced	6.59 (bs) (338 K)	4.49 (bs) (338 K)	—	1.63 (bs) (308 K)	
	Freely rotating	6.53 (bs)	4.46 (bs)	3.80 (t, 5.8)	1.66 (t, 5.8)	
4b-*anti* (77.9)	Frozen (293 K, 400 MHz)	6.83 (s)	4.56 (t, 5.8)			–6.90 (anti)
				3.72 (t, 5.4)	1.59–1.65 (m)	
4b-*syn* (22.1)		6.65 (s)	4.68 (t, 5.6)			–3.90 (syn)
	Coalescenced	6.47 (bs) (338 K)	4.43 (bs) (338 K)	—	1.63 (bs) (308 K)	
	Pseudo freely rotating (353 K)	6.41 (bs)	4.40 (bs)	3.76 (ot, 5.6)	1.65 (ot, 5.6)	
				3.77 (ot, 6.0)	1.66 (ot, 6.0)	
4c-*anti* (72.8)	Frozen (293 K, 400 MHz)	6.67 (s)				–5.36 (anti)
			4.52 (bs)	3.73 (t, 5.6)	1.60–1.67 (bm)	
4c-*syn* (27.2)		6.54 (s)				–3.28 (syn)
	Coalescenced	6.43 (bs) (328 K)	—	—	1.64 (bs) (308 K)	
	Pseudo freely rotating (353 K)	6.35 (bs)	4.33 (bs)	3.76 (ot 6.0)	1.66 (t, 5.8)	
				3.77 (ot 5.6)		

Note: Abbreviations: bm (broad multiplet), ot (overlapped triplet).

[a] As ppb/K (refs. 9i and 11).

Can. J. Chem. Downloaded from www.nrcresearchpress.com by University of Electronic and Science Techonology of China on 09/19/12
For personal use only.

Published by NRC Research Press

Can. J. Chem. Downloaded from www.nrcresearchpress.com by University of Electronic and Science Techonology of China on 09/19/12
For personal use only.

Table A3. VT NMR behavior of melamines **5a**, **5b**, **6a–6c**, **7a**, and **7b** about the C(*s*-triazine)–N< (exocyclic) bonds in [D_6]DMSO.

No.	Rotational status at T (K)	δ_{NH}	δ_H-Spirane (ppm) ($^3J_{H,H}$, Hz)		δ_H-Piperazine (ppm) ($^3J_{H,H}$, Hz)		Rotational status at T (K)	δ_C-Spirane (ppm)[a]		δ_C-Piperazine (ppm)		$\left[\frac{\Delta\delta(NH)}{\Delta T}\right] \times 10^3$
			H-α, -α′	H-β, -β′	H-α, -α′	H-β, -β′		C-α, -α′	C-β, -β′	C-α, -α′	C-β, -β′	
5a	Slow exchange (298 K, 500 MHz)	5.75	3.71 (bt, 5.5)	1.57 (bs)	—	—	Slow exchange (298 K, 125 MHz)	41.1 (bs) 41.4 (bs)	34.8	—	—	–2.56
	Freely rotating (353 K)	5.61	3.74 (bt, 5.3)	1.60 (bt, 5.3)	—	—		—	—	—	—	
5b	Slow exchange (298 K, 400 MHz)	5.60	3.71 (bt, 5.4)	1.57 (bt, 5.2)	—	—	Slow exchange (298 K, 100 MHz)	41.0 (bs) 41.5 (bs)	34.8	—	—	–2.36
	Freely rotating (353 K)	5.47	3.73 (t, 5.8)	1.60 (t, 5.6)	—	—		—	—	—	—	
6a	Slow exchange (298 K, 400 MHz)	5.70	3.71 (bt, 5.4)	1.56 (bs)	3.58 (bs)	2.70 (bs)	Slow exchange (298 K, 100 MHz)	41.1 (bs) 41.4 (bs)	34.9	44.0 (bs)	45.7	–2.75
	Freely rotating (353 K)	5.55	3.73 (t, 5.8)	1.60 (t, 5.8)	3.61 (t, 5.0)	2.74 (t, 5.2)		—	—	—	—	
6b	Slow exchange (298 K, 400 MHz)	5.57	3.71 (bt, 5.6)	1.56 (bt, 5.0)	3.55 (bt, 5.8)	2.67 (bt, 4.2)	Slow exchange (298 K, 100 MHz)	41.1 (bs) 41.5 (bs)	34.9	44.2 (bs) 44.4 (bs)	45.9	–2.47
	Freely rotating (353 K)	5.44	3.73 (t, 5.6)	1.60 (t, 5.6)	3.58 (t, 5.0)	2.71 (t, 5.6)		—	—	—	—	
6c	Slow exchange (298 K, 400 MHz)	5.68	3.71 (bs)	1.57 (bs)	3.86 (bs)	3.06 (bs)	Slow exchange (298 K, 100 MHz)	40.0 (bs) 40.1 (bs)	34.9 (bs)	41.1 (bs) 41.7 (bs)	42.9 (bs)	–1.36
	Freely rotating (353 K)	5.60	3.73 (t, 5.8)	1.61 (t, 5.6)	3.89 (bs)	3.08 (bs)		—	—	—	—	
7a	Slow exchange (298 K, 400 MHz)	5.74	3.73 (bt, 5.2)	1.57 (bt, 5.0)	3.67 (bs)		Slow exchange (298 K, 100 MHz)	41.1 (bs) 41.4 (bs)	34. (bs)	43.0 (bs)		–2.71
	Freely rotating (353 K)	5.59	3.75 (t, 5.6)	1.61 (t, 5.6)	3.70 (s)			—	—	—	—	
7b	Slow exchange (298 K, 400 MHz)	5.63	3.72 (bs)	1.57 (bt, 5.6)	3.60 (bs)		Slow exchange (298 K, 100 MHz)	41.1 (bs) 41.6 (bs)	35.0	43.1 (bs)		–2.35
	Freely rotating (353 K)	5.50	3.74 (t, 5.4)	1.60 (t, 5.6)	3.69 (s)			—	—	—	—	

[a]Labelling of nuclei as α (or α′) and β (or β′) was made with respect to the nitrogen atom linked to *s*-triazine.

Asymmetric hydroamination catalyzed by in situ generated chiral amidate and ureate complexes of zirconium — Probing the role of the tether in ligand design

Philippa R. Payne, Jason A. Bexrud, David C. Leitch, and Laurel L. Schafer

Can. J. Chem. Downloaded from www.nrcresearchpress.com by Xi'an Jiaotong University on 09/19/12
For personal use only.

Abstract: Simple chiral proligands have been synthesized from inexpensive chiral starting materials. These amidate and ureate ligands support zirconium complexes that successfully catalyze intramolecular hydroamination with up to 26% ee. Several elements necessary for successful ligand design are highlighted and discussed. In particular, the strict control of metal geometry through multidentate tethered ligands is determined to be an essential aspect of future ligand development.

Key words: ureate, amidate, hydroamination, zirconium, enantioselective.

Résumé : On a réalisé la synthèse de proligands chiraux simples à partir de produits de départ chiraux peu coûteux. Ces ligands amidates et uréates supportent des complexes du zirconium qui peut catalyseur avec succès des hydroaminations intramoléculaires avec des excès d'énantiomère allant jusqu'à 26 %. On met en évidence et on discute de plusieurs éléments nécessaires au bon développement d'un ligand. En particulier, on a déterminé qu'un aspect essentiel du développement du futur ligand est le contrôle strict de la géométrie du métal par le biais de ligands multidentates bien fixés,

Mots-clés : uréate, amidate, hydroamination, zirconium, énantiosélective.

[Traduit par la Rédaction]

Introduction

Hydroamination, the addition of an N–H bond across unsaturated C–C bonds, has shown great promise for the efficient synthesis of amines.[1] Numerous systems exist for this highly desirable transformation, encompassing alkali and alkaline earth metal,[2] actinide[3] and lanthanide,[1c,2b] early[1d,2b,4] and late[5] transition-metal complexes, and main group metal systems.[6] In particular, group 4 catalysts are attractive because of their low toxicity, low cost, and improved stability over lanthanide complexes[1d] while exhibiting excellent reactivity comparable to late transition metals. *N*,*O*-Chelating amidate,[4a,7] pyridonate,[8] and ureate[4b] ligands for group 4 transition metals have been investigated by our group and others[9] for hydroamination. The proligand that induces the most promising scope of reactivity for both inter- and intra-molecular hydroamination is a tethered urea proligand for an easily synthesized zirconium complex (Fig. 1).[4b] This ureate precatalyst is the most generally useful group 4 metal complex reported to date, promoting reactions with both primary and secondary amine substrates, exhibiting vastly expanded substrate scope and functional group tolerance, as well as excellent chemoselectivity for hydroamination. The chemoselectivity is of particular interest, as other group 4 systems can be plagued with unwanted hydroaminoalkylation side reactions to give amine-substituted carbocycles rather than heterocyclic products.[10] The development of a chiral ligand system that imparts both the high activity and selectivity of the ureates and instills high enantioselectivity is of the utmost importance for the efficient synthesis of chiral amines. Thus, the synthesis of alternate urea proligands provides valuable understanding regarding the role of the urea functionality and the tether in the unprecedented reactivity accessed by such ureate zirconium complexes.

Many chiral catalysts have been explored recently for asymmetric hydroamination[2b,5a,9d,11] and group 4 transition-metal systems have been shown to be particularly efficient.[12,9a–9c] However, excellent enantioselectivities (>90%) have only been reported for a select number of catalyst–substrate combinations, in particular those that make use of axially chiral biphenyl/binaphthyl tethered ligands.[7c,13] While these contributions illustrate the potential power of such transformations, they are only a first step toward realizing the goal of a broadly applicable asymmetric alkene hydroamination catalyst. In an effort to better understand the limitations of such catalysts, we present here our recent investigations of simple untethered, chiral amide and urea proligands that can be rapidly assembled from inexpensive, enantiopure, and commercially available starting materials to generate bis(amidate or ureate)bis(amido) zirconium complexes (eq. [1]).

Received 18 March 2011. Accepted 31 May 2011. Published at www.nrcresearchpress.com/cjc on 13 September 2011.

P.R. Payne, J.A. Bexrud, D.C. Leitch, and L.L. Schafer. Department of Chemistry, University of British Columbia, 2036 Main Mall, Vancouver, BC V6T 1Z1 Canada.

Corresponding author: Laurel L. Schafer (schafer@chem.ubc.ca).

Can. J. Chem. Downloaded from www.nrcresearchpress.com by Xi'an Jiaotong University on 09/19/12
For personal use only.

Fig. 1. Tethered bis(ureate) zirconium precatalyst for hydroamination.

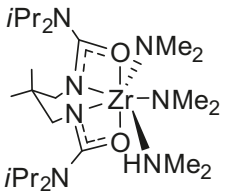

[1]

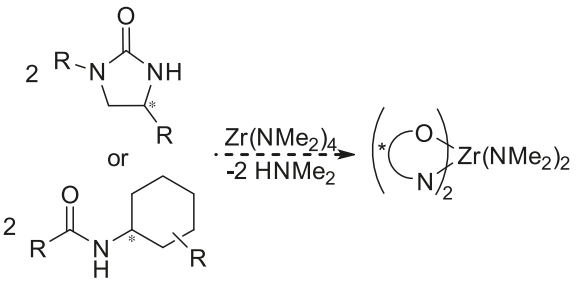

Other untethered chiral ligands have been successful as alternatives for bidentate ligands in asymmetric transformations; in particular, chiral monodentate phosphoramidite ligands have proven to be remarkably effective.[14] This versatile class of untethered ligands has exhibited excellent levels of stereocontrol for a variety of asymmetric transformations including allylic substitutions, hydrovinylations, cycloadditions, and hydrogenation of a wide variety of substrates.[14b] The parent ligand (MonoPhos) is used industrially as a ligand in the rhodium-catalyzed hydrogenation of a cinnamic acid for the production of the renin inhibitor aliskiren.[15]

Here we report the facile synthesis of new chiral urea and amide proligands from commercially available and inexpensive chiral amino acids and amines. This study compares and contrasts the reactivity and selectivity of amidate versus ureate, cyclic versus acyclic, and tethered versus untethered ligands, and explores the use of untethered chiral ligands for affecting enantioselectivity. Through the characterization of the resultant coordination complexes in these systems we can identify critical features required for improved reactivity and selectivity.

Results and discussion

Cyclic ureas, efficiently synthesized from the chiral pool of natural amino acid starting materials, are an attractive modular class of proligands for the generation of group 4 asymmetric hydroamination precatalysts. While cyclic ureas have been investigated for their medicinal properties,[16] examined for potential application as Lewis basic organocatalysts,[17] used as chiral auxiliaries for asymmetric syntheses,[18] and utilized as substrates for intermolecular hydroamination,[19] these compounds represent a new proligand motif for coordination of early transition metals. Zirconium alkyl and amido complexes supported by related achiral imidazolone ligands have recently been reported and have been shown to be effective catalysts for intramolecular hydroamination.[20]

The synthesis of proligand H**L1** proceeds in a straightforward manner, and produces H**L1** as a crystalline solid in five steps from L-valine (Scheme 1).[21] A solid-state molecular structure was obtained (see Supplementary data).

Simple chiral amide proligands can also be synthesized in minimal steps from any chiral ketone starting material[22] via reductive amination and subsequent derivatization with benzoyl chloride (eq. [2]). This modular synthetic route, like the route employed to synthesize the urea proligands, is attractive as a wide variety of proligands can be synthesized in a few steps from inexpensive starting materials. For the purpose of this investigation, (–)-menthone was chosen to synthesize chiral amide proligands.

[2]

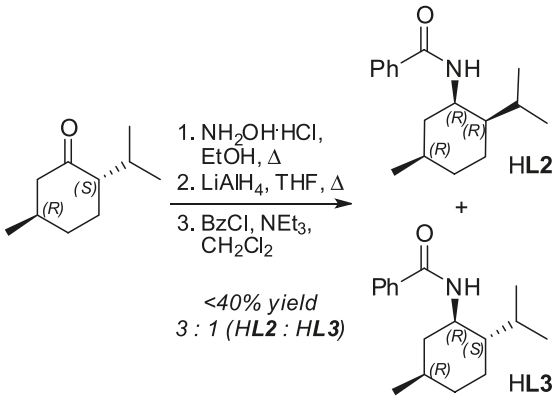

Interestingly, upon isolation it was determined that the reaction produces a mixture of compounds (1*R*,2*R*,5*R*)-H**L2** and (1*R*,2*S*,5*R*)-H**L3** (eq. [2]). As determined by X-ray crystallography (see Supplementary data), the stereochemistry of these compounds is identical in the 5-position of the cyclohexyl ring as well as the stereogenic centre adjacent to nitrogen. However, epimerization occurred over the course of the reaction resulting in differing stereochemistry at the isopropyl position. The oxime formed in the initial step of the reaction may tautomerize to allow the observed epimerization at the 2-position. Compounds H**L2** and H**L3** can be separated by selective recrystallization.

These proligands are representative examples of a large class of readily accessed auxiliary ligands. The synthetic routes employed are modular and use inexpensive enantiopure starting materials such as amino acids or chiral ketones. Notably, the urea proligands employed here are cyclic and of a defined conformation, whereas the amide proligands have two possible conformations accessible (Fig. 2), which may impact metal chelation modes.[4a]

Using urea and amide proligands, a series of zirconium complexes can be easily synthesized by a simple protonolysis route from $Zr(NMe_2)_4$ (eq. [1]). Synthesis of the bis(ureate) bis(amido) zirconium complex **1** results in crude material having elemental analysis data consistent with the target complex. However, the complicated ^1H and ^{13}C NMR spectra for this compound suggest that multiple species are present in the solution phase. Synthesis of complex **2** using the amide proligand H**L2** proceeds in an analogous manner to generate an amorphous material having elemental analysis data consistent with that of the target complex. NMR spectral data are also notably complicated, presumably because of the presence of multiple isomers in solution. No free ligand remains in either case, as is evident by loss of the diagnostic amide

Scheme 1. Modular route for synthesis of urea proligand H**L1**.

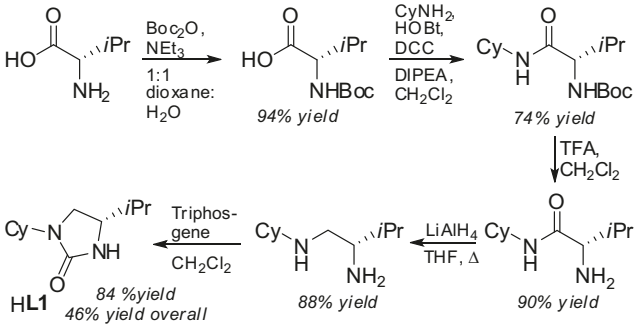

Fig. 2. Flexible cisoid and transoid configurations of amide versus rigid cyclic urea proligand.

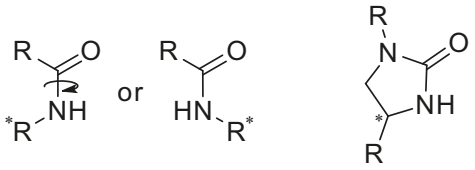

N–*H* signal at 7.18 ppm (H**L1**) and 6.15 ppm (H**L2**). Unfortunately, the product mixtures are resistant to recrystallization and high yielding crystalline material could not be obtained.

Although rigorous characterization of the resultant coordination complexes could not be achieved, the in situ prepared complexes are suitable for screening for hydroamination reactivity. Thus, the abilities of **L1**–**L3** ligated complexes to mediate enantioselective hydroamination were investigated for the cyclization of 2,2-diphenyl-1-amino-4-pentene, a standard test substrate (Table 1). The use of cyclic ureate **L1** in isolated complex **1** (Table 1, entry 1) and the in situ procedure (entry 2) generates the heterocyclic product in good yield with low enantioselectivity. The complex with amidate proligand **L2** was also tested and improved enantioselectivity is observed (entry 3). Lowering the reaction temperature does not improve the enantioselectivity (entry 4). The zirconium precatalyst with ligand **L3** showed comparable reactivity to complex **2**, but was unsuccessful in mediating enantioselectivity (entry 5). These results show that strict control of the geometry about the metal centre is required to control enantioselectivity for this reaction.

One of the exceptional elements of the tethered urea zirconium catalyst (Fig. 1), is the broadened substrate scope it displays compared with other existing group 4 catalyst systems.[4b] To discern if this improved scope of reactivity can be attributed to the urea functionality or to the tether, reactivity with a broader range of substrates was investigated using in situ prepared complex **1** (Table 2).[4b] The substrate scope using complexes prepared with proligand H**L1** is very limited; the reaction progresses in good yield to generate 5- and 6-membered heterocycles (Table 2, entries 1–5), however, no conversion to product is observed with secondary amines, internal olefins, and substrates without gem-disubstituents.

This limited reactivity profile is reminiscent of substrate scope limitations previously reported for $Zr(NMe_2)_4$ as a precatalyst for the intramolecular hydroamination of aminoalkenes.[23] We suggest that ligand redistribution could be occurring under catalytic conditions to generate $Zr(NMe_2)_4$ in solution, which could also act as a catalyst for the transformation resulting in the substrate scope limitations and poor enantioselectivities observed. Ligand redistribution and disproportionation has been observed previously with group 4 amidate systems[9b] and has been postulated to occur during the attempted synthesis of zirconium alkyl complexes supported by acyclic untethered ureate ligands.[24]

Indeed, in the only example of crystalline material obtained from a solution of complex **1**, an unexpected ligand stoichiometry (three ligands for two metal centres) is observed in the isolated product (Fig. 3). This suggests that ligand redistribution is a complicating factor under catalytic conditions and provides a rationale for both the poor ees and limited substrate scope observed. These crystals were obtained in very low yield over the course of a few weeks from a saturated pentane solution of the crude material cooled to –30 °C.

The isolated bimetallic complex has three bridging ureate ligands; the steric bulk of the ligand perhaps being insufficient to support monomeric species of the highly electrophilic metal centres. The dimeric nature of this species is not without precedent as the related zirconium imidazolone complexes reported[20] also assume dimeric solid-state structures with bridging imidazolone ligands. The isolated chiral compound is C_1 symmetric with pseudo-octahedral geometry about each zirconium atom. Selected bond lengths and angles for complex **4** (Fig. 3) are summarized in Table 3 and crystallographic parameters are summarized in Table 4. The C–N2,N4,N6 (1.317–1.325 Å) and C–O (1.271–1.290 Å) bond lengths of the metal-bound ureate fragments are consistent with moderate delocalization within the ureate backbone. The respective C–N bonds to the tertiary amine (N1,N3,N5, 1.361–1.368 Å) are slightly longer than those of the bonding moiety; however, these and the sum of 353° for the subtending angles are indicative of sp^2 hybridization and limited lone-pair donation to the π system. Interestingly, the Zr–N bonds to the ureate ligands (2.2372(9) and 2.2459(9) Å) are slightly shorter than those of the tethered ureate complex (2.279(1) Å),[4b] the exception being the Zr–N6 bond, which is presumably lengthened because of the presence of the strongly donating *trans*-dimethylamido ligand. Comparable bis(amidate)bis(amido) Zr–N(amidate) bonds are significantly longer (~2.32 Å).[25,12d] The Zr–O bond lengths in complex **4**, excluding those related to O1 (which is bridging two metal centres), are significantly shorter (by >0.1 Å), than those of related bis(amidate)bis(amido)[12e,25] and bis(ureate)bis(amido)[4b] zirconium complexes. Zr–NMe_2 (2.035–2.130 Å) bond lengths in complex **4** are slightly longer on average than Zr=N bonds reported in the literature (<2.043 Å).[25] Related tethered[12d] and untethered[25] bis(amidate)bis(amido) zirconium complexes have Zr–N(amido) bond lengths of 2.065–2.069 Å and 2.043(3) Å, respectively. The tethered bis(ureate)bis(amido)[4b] zirconium complex has Zr–NMe_2 bond lengths of 2.0292(2) Å.

Summary and conclusions

Easily prepared chiral ureate and amidate ligands can be efficiently assembled from inexpensive chiral ketones or amino acids. The in situ prepared complexes using untethered urea and amide proligands result in modestly enantioselective

Can. J. Chem. Downloaded from www.nrcresearchpress.com by Xi'an Jiaotong University on 09/19/12
For personal use only.

Can. J. Chem. Downloaded from www.nrcresearchpress.com by Xi'an Jiaotong University on 09/19/12
For personal use only.

Table 1. Enantioselectivity hydroamination studies with chiral urea and amide proligands.

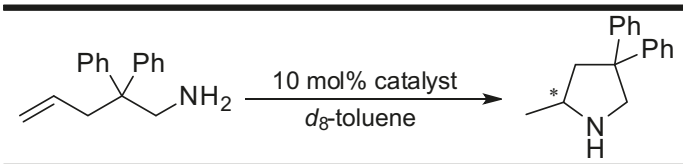

Entry	Catalyst	Conditions	Yield (%)[a]	ee (%)[b]
1	**L1**[c]	12 h, 100 °C	92	11
2	**L1**[d]	4 h, 100 °C	>98	12
3	**L2**	5 h, 110 °C	>98	26
4	**L2**	48 h, 65 °C	91	23
5	**L3**[d]	48 h, 65 °C	94	<5

[a]^{1}H NMR yield determined using 1,3,5-trimethoxybenzene as a standard.

[b]ee based on ^{1}H NMR spectroscopy of derivatized product with (+)-(*S*)-α-methoxy-α-trifluoromethylphenylacetyl chloride.

[c]Reaction time was not optimized; 5 mol% complex used.

[d]Catalyst prepared in situ using 10 mol% $Zr(NMe_2)_4$ and 20 mol% proligand.

Table 2. Reactivity studies using proligand H**L1** for intramolecular hydroamination with alkenes.

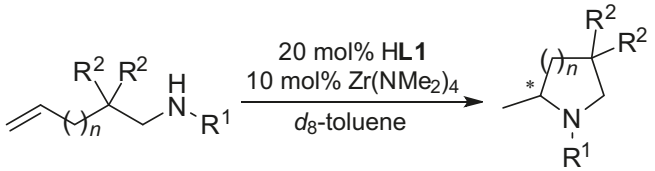

Entry	Substrate	Product	Conditions	Isolated yield (%), ee (%)[a]
1[b]	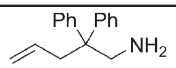	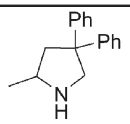	15 h, 100 °C	>98, 12[c]
2	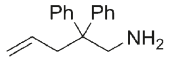	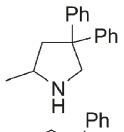	4 h, 100 °C	92, 11
3	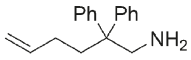	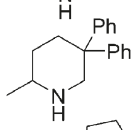	8 h, 100 °C	89, <5
4	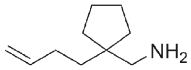	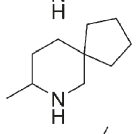	18 h, 100 °C	71, nd[d]
5	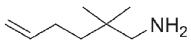	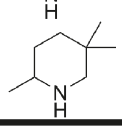	24 h, 145 °C	>95, nd[c]

[a]ee based on ^{1}H NMR spectroscopy of derivatized product with (+)-(*S*)-α-methoxy-α-trifluoromethylphenylacetyl chloride.

[b]5 mol% complex **2**.

[c]NMR yield determined by ^{1}H NMR using 1,3,5-trimethoxybenzene as internal standard owing to product volatility.

[d]Derivitized with *p*-tolylsulfonyl chloride to aid in isolation.

cyclohydroamination reactions with reactivity reminiscent of $Zr(NMe_2)_4$, suggesting that ligand redistribution may be occurring. Despite the moderate reactivity and poor selectivity observed, these results provide important insights for advanced ligand design; improvements in the state of the art for these catalyst systems must take advantage of the enhanced stability and reactivity trends of tethered amidate and ureate ligands. The role of the tether is not restricted to control of geometry at the metal centre but also dramatically improves stability by reducing the propensity for ligand redistribution. The incorporation of these design principles in a catalyst system that demonstrates the unparalleled reactivity imparted by previously reported tethered proligands[4b] with chirality integrated from inexpensive starting materials such as chiral ketones or amino acids is presently under investigation and results will be reported in due course.

Can. J. Chem. Downloaded from www.nrcresearchpress.com by Xi'an Jiaotong University on 09/19/12
For personal use only.

Fig. 3. ORTEP representation of the solid-state molecular structure of **4** (ellipsoids plotted at 50% probability; methyl groups of dimethylamido ligands (N7–11) and cyclohexyl groups attached to N1, N3, and N5 of the ureate ligands have been removed for clarity).

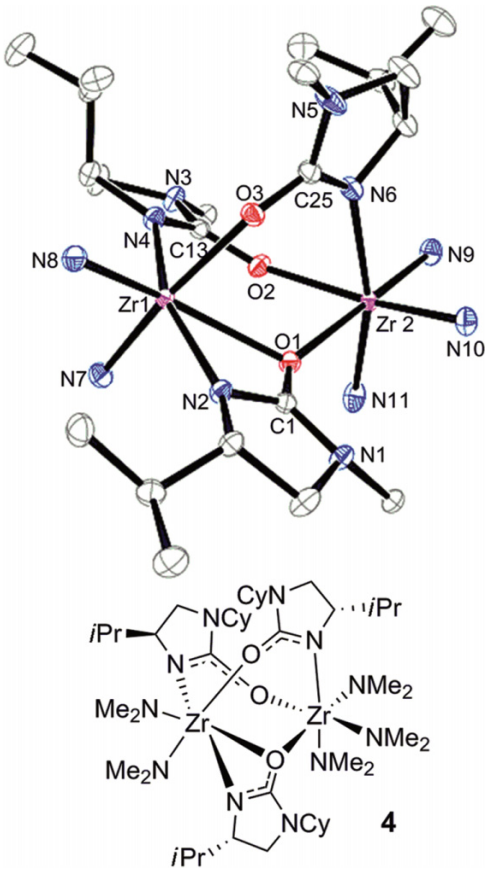

Table 3. Relevant bond lengths (Å) and angles (°) for complex **2**.

Bond lengths (Å)		Bond angles (°)	
C1–N2	1.323(1)	Sum about N1	348.7
C13–N4	1.325(1)	Sum about N3	354.3
C25–N6	1.317(1)	Sum about N5	355.6
C1–N1	1.361(1)		
C25–N5	1.368(1)		
C1–O1	1.290(1)		
C13–O2	1.271(1)		
C25–O3	1.282(1)		
C13–N3	1.362(1)		
Zr1–N2	2.2459(9)		
Zr1–N4	2.2372(9)		
Zr1–N7	2.073(1)		
Zr1–N8	2.035(1)		
Zr1–O1	2.4420(8)		
Zr1–O3	2.1386(8)		
Zr2–N6	2.3353(9)		
Zr2–N9	2.073(1)		
Zr2–N10	2.077(1)		
Zr2–N11	2.130(1)		
Zr2–O1	2.3286(8)		
Zr2–O2	2.1745(8)		

Materials and methods

Reaction materials and instrumentation

All reactions were preformed in oven-dried glassware under inert atmosphere conditions of dry nitrogen unless noted otherwise, using Schlenk line or glovebox techniques. Catalytic reactions were performed in Teflon-sealed J. Young tubes (5 mm). Toluene, pentanes, and hexanes, which were used as reaction solvents for catalyst preparation and recrystallization, were purified by passage over an activated aluminum oxide column and degassed prior to use. Dichloromethane was distilled from CaH_2 and degassed. d_8-Toluene was degassed and dried over activated 4 Å molecular sieves overnight before use. Reagents for substrate and proligand synthesis were purchased from commercial suppliers and used without further purification. $Zr(NMe_2)_4$ was purchased from Strem and used as received. 1,3,5-Trimethoxybenzene, used as an internal standard, was purchased from Sigma-Aldrich and purified by sublimation under reduced pressure. Flash chromatography was performed using SilicaFlash F60 silica gel (230–400 mesh). ^{1}H and ^{13}C NMR spectra were recorded on either a Bruker 300 MHz, 400 MHz Advance, or 600 MHz spectrometer at ambient temperature unless noted otherwise. Chemical shifts are reported in parts per million (ppm) relative to the corresponding residual solvent signal: chloroform ^{1}H 7.26 ppm, ^{13}C 77.0 ppm; benzene ^{1}H 7.16 ppm, ^{13}C 128.39 ppm; and toluene ^{1}H 2.09 ppm. Multiplicities are listed as s (singlet), d (doublet), t (triplet), q (quartet), m (multiplet), and the coupling constants are given in Hz. Single crystal X-ray structure determinations and mass spectral and elemental analyses determinations were performed at the Department of Chemistry, University of British Columbia, Vancouver, British Columbia.

Synthesis of proligands HL1–HL3

(S)-1-Cyclohexyl-4-isopropylimidazolidin-2-one HL1

The precursor (*S*)-2-amino-*N*-cyclohexyl-3-methylbutanamide was prepared by the procedure described in the literature[26] from L-valine with cyclohexylamine substituted for *tert*-butyl amine and purified by recrystallization from ethyl acetate prior to N-Boc deprotection, which proceeded cleanly. (*S*)-*N*^{1}-Cyclohexyl-3-methylbutane-1,2-diamine was prepared through reduction with $LiAlH_4$ as described in the literature.[27] (*S*)-*N*^{1}-Cyclohexyl-3-methylbutane-1,2-diamine (2.62 g, 14.176 mmol) was dissolved in dry CH_2Cl_2 and the solution was cooled to 0 °C prior to addition of triphosgene (1.472 g, 4.962 mmol) in one portion. Pyridine (2.28 mL, 28.352 mmol) was added and the solution warmed to room temperature with stirring. After 3 h the solution was diluted with 1 mol/L HCl and the organic layer was collected. The aqueous layer was extracted with CH_2Cl_2 (3 × 50 mL) and the organic layers were combined, dried over $MgSO_4$, filtered, and concentrated. Pure (*S*)-1-cyclohexyl-4-isopropylimidazolidin-2-one was obtained as colourless needles in 84% yield by recrystallization from a minimal amount of CH_2Cl_2. ^{1}H (C_6D_6, 600 MHz) δ: 0.69 (2H, d, J = 6.78 Hz, –CH_3), 0.84–0.90 (4H, m, –CH_3, CH_2 of Cy), 1.04–1.19 (4H, m, CH_2 of Cy), 1.38–1.44 (2H, m, –CH (CH$_3$)$_2$, CH_2 of Cy), 1.54–1.68 (4H, m, CH_2 of Cy), 2.68 (1H, t, J = 7.68 Hz, –N(Cy)CH_2CH–), 2.96 (1H, t, J = 8.58 Hz,

Can. J. Chem. Downloaded from www.nrcresearchpress.com by Xi'an Jiaotong University on 09/19/12
For personal use only.

Table 4. Crystallographic parameters for complex **4.**

Parameter	Complex **4**
Empirical formula	$C_{46}H_{93}N_{11}O_3Zr_2$
fw	1030.75
Colour, habit	Yellow, prism
Crystal dimensions (mm)	0.4×0.3×0.2
Crystal system	Orthorhombic
Space group	$P2_12_12_1$
Z	4
a (Å)	12.493(1)
b (Å)	20.562(2)
c (Å)	20.876(2)
α (°)	90
β (°)	90
γ (°)	90
Collection ranges	h = –17→17, k = –29→29, l = –29→29
Temperature (K)	100
Volume (Å^3)	5362(1)
D_{calcd} (Mg m^{-3})	1.277
Radiation	Mo Kα, λ = 0.71073 Å
Absorption coeff. (μ) (mm^{-1})	0.44
Absorption correction	Multiscan
F(000)	2200
θ_{min} to θ_{max} (°)	1.9–30.1
Measured reflections	231 343
Independent reflections	15 815 (R_{int} = 0.025)
Data/restraints/parameters	15 815/0/576
Maximum shift/error	0.003
Goodness-of-fit on F^2	1.087
Final R indices ($I > 2\sigma(I)$)	R_1 = 0.017,wR_2 = 0.045
R indices (all data)	R_1 = 0.0183, wR_2 = 0.0451
Absolute structure parameter	0.000(11)
Extinction coefficient	N/A
Largest diff. peak and hole (e Å^{-3})	0.447 and –0.249

–N(Cy)CH_2CH–), 3.03 (1H, q, J = 7.42 Hz, –NHC*H*–), 3.95 (1H, t, J = 11.3 Hz, C*H* of Cy), 7.18 (1H, s, –N*H*). ^{13}C (C_6D_6, 150 MHz) δ: 18.4 (*C*H$_3$), 18.9 (*C*H$_3$), 26.2 (*C*H$_2$), 26.3 (*C*H$_2$), 26.3 (*C*H$_2$), 30.4 (*C*H$_2$), 31.3 (*C*H$_2$), 34.0 (*C*H), 44.8 (*C*H$_2$), 51.3 (*C*H), 56.8 (*C*H), 162.7 (*C*). HRMS calcd for $C_{12}H_{22}N_2O$: 210.1733; found: 210.1732.

N-*((1*R*,2*R*,5*R*)-2-Isopropyl-5-methylcyclohexyl)-benzamide HL2 and* N-*((1*R*,2*S*,5*R*)-2-isopropyl-5-methylcyclohexyl)-benzamide HL3*

$NH_2OH{\cdot}HCl$ (2.11 g, 30.4 mmol), pyridine (2.50 mL, 30.9 mmol), and (–)-menthone (3.50 mL, 20.3 mmol) were dissolved in EtOH (30 mL) and the mixture was heated at reflux for 40 h. The crude reaction mixture was concentrated, dissolved in Et_2O (300 mL), washed successively with water (3 × 50 mL) and brine (50 mL), dried over Na_2SO_4, filtered, and concentrated. The crude oxime mixture was dissolved in THF (100 mL) and cooled to 0 °C prior to portionwise addition of $LiAlH_4$ (1.3 g, 34.3 mmol). The reaction mixture was heated at reflux for 40 h. After cooling the solution was quenched with sequential addition of water (1.5 mL), aqueous 1 mol/L NaOH (1.5 mL), Et_2O (100 mL), and water (4.5 mL). After stirring for 0.5 h, the mixture was filtered and the filtrate was dried over $MgSO_4$. Following concentration, dry CH_2Cl_2 (60 mL) was then added and the flask was cooled to 0 °C prior to addition of benzoyl chloride (2.60 mL, 22.6 mmol) and NEt_3 (8.0 mL, 57 mmol). After stirring for 20 h, the solution was diluted with CH_2Cl_2 (240 mL), washed successively with 1 mol/L HCl (3 × 50 mL), 1 mol/L NaOH (3 × 50 mL), water (50 mL), and brine (50 mL). The organic phase was then dried over $MgSO_4$, filtered, and concentrated. Column chromatography (18:1:1 hexanes–CH_2Cl_2–MeOH) afforded ~2 g of a mixture of crude H**L2** and H**L3** in a ratio of approximately 3:1 in favor of H**L2**. Repeated recrystallization from Et_2O afforded H**L2** as a pure compound and crystals suitable for X-ray crystallography. Repeated recrystallization from hexanes/CH_2Cl_2 (~4:1) of the residue afforded H**L3** as a pure compound and crystals suitable for X-ray crystallography.

(N-*((1*R*,2*R*,5*R*)-2-Isopropyl-5-methylcyclohexyl)-benzamide) HL2*

^{1}H NMR ($CDCl_3$, 400 MHz) δ: 0.90–1.00 (9H, m), 1.20–1.32 (1H, m), 1.53–1.72 (7H, m), 1.78–1.86 (1H, m), 4.32–4.38 (1H, m, –C*H*(NHBz)–), 6.17–6.18 (1H, br d, –N*H*Bz), 7.39–7.49 (3H, m, Ar-*H*), 7.72–7.77 (2H, m, Ar-*H*). ^{13}C NMR ($CDCl_3$, 100 MHz) δ: 21.7 (*C*H$_3$), 21.7 (*C*H$_3$), 22.3 (*C*H$_3$), 24.0 (*C*H$_2$), 27.6 (*C*H), 29.3 (*C*H), 30.4 (*C*H$_2$), 36.6 (*C*H$_2$), 44.3 (*C*H), 49.7 (*C*H), 126.7 (*C*H), 128.6 (*C*H), 131.2 (*C*H), 135.2 (*C*), 166.3 (*C*). MS (EI) *m*/*z*: 259 (M$^+$).

Anal. calcd for $C_{19}H_{25}NO$: C 78.72, H 9.71, N 5.40; found: C 79.10, H 9.76, N 5.42.

(N-((1R,2S,5R)-2-Isopropyl-5-methylcyclohexyl)-benzamide) HL3

^{1}H NMR ($CDCl_3$, 400 MHz) δ: 0.83–0. 39 (9H, m), 1.16–1.19 (2H, m), 1.45–1.60 (1H, m), 1.67–1.76 (2H, m), 1.94–2.01 (1H, m), 2.05–2.11 (1H, m), 3.95–4.04 (1H, m, –C*H* (NHBz)–), 5.82–5.85 (1H, br d, –N*H*Bz), 7.40–7.50 (3H, m, Ar-*H*), 7.74–7.76 (2H, m, Ar-*H*). ^{13}C ($CDCl_3$, 100 MHz) δ: 16.3 (*C*H_3), 21.2 (*C*H_3), 22.2 (*C*H_3), 24.0 (*C*H_2), 27.1 (*C*H), 31.9 (*C*H), 34.6 (*C*H_2), 43.2 (*C*H_2), 48.4 (*C*H), 50.4 (*C*H), 126.8 (*C*H), 128.5 (*C*H), 131.2 (*C*H), 135.2 (*C*), 166.7 (*C*). MS (EI) *m*/*z*: 259 (M^+). Anal. calcd for $C_{19}H_{25}NO$: C 78.72, H 9.71, N 5.40; found: C 78.64, H 10.00, N 5.62.

Procedure for in situ hydroamination

Proligand H**L1** (15.8 mg, 0.075 mmol) and $Zr(NMe_2)_4$ were weighed into a small vial. d_8-Toluene (0.47 mL) and 1,3,5-trimethoxybenzene (0.03 mL of a 1.25 mol/L solution in d_8-toluene) were added and the solution shaken gently.[28] The hydroamination substrate was then added (0.375 mmol) and the solution transferred to a J. Young NMR tube. The solution was then heated at reaction temperature and reaction progress was monitored by ^{1}H NMR spectroscopy.

Supplementary data

Supplementary data are available for this article through the journal Web site at http://nrcresearchpress.com/doi/suppl/10.1139/v11-091. CCDC 829545–829548 contain the X-ray data in CIF format for this manuscript. These data can be obtained, free of charge, via http://www.ccdc.cam.ac.uk/cgi-bin/catreq.cgi (Or from the Cambridge Crystallographic Data Centre, 12 Union Road, Cambridge CB2 1Ez, UK; fax +44 1223 336033; or deposit @ccdc.cam.ac.uk).

Acknowledgements

The authors gratefully acknowledge Boehringer Ingelheim (Canada) Ltd. and the Natural Sciences and Engineering Research Council of Canada (NSERC) for supporting this work. P.R.P. thanks NSERC for an Alexander Graham Bell Canada Graduate Scholarship (CGS D). J.A.B. thanks NSERC for a Postgraduate Scholarship (PGS D) award. D.C.L. thanks NSERC for a CGS D scholarship. The authors thank N. Yonson, Dr. B. Patrick, and Dr. N.C. Payne for help with the X-ray crystallography studies.

References

(1) (a) Müller, T. E.; Beller, M. *Chem. Rev.* **1998**, *98* (2), 675. doi:10.1021/cr960433d; (b) Müller, T. E.; Hultzsch, K. C.; Yus, M.; Foubelo, F.; Tada, M. *Chem. Rev.* **2008**, *108* (9), 3795. doi:10.1021/cr0306788; (c) Hong, S.; Marks, T. J. *Acc. Chem. Res.* **2004**, *37* (9), 673. doi:10.1021/ar040051r; (d) Bytschkov, I.; Doye, S. *Eur. J. Org. Chem. 2003* (6), 935. doi:10.1002/ejoc.200390149; (e) Nobis, M.; Drießen-Hölscher, B. *Angew. Chem. Int. Ed.* **2001**, *40* (21), 3983. doi:10.1002/1521-3773(20011105)40:21<3983::AID-ANIE3983>3.0.CO;2-8; (f) Pohlki, F.; Doye, S. *Chem. Soc. Rev.* **2003**, *32* (2), 104. doi:10.1039/b200386b.

(2) (a) Hultzsch, K. C.; Gribkov, D. V.; Hampel, F. *J. Organomet. Chem.* **2005**, *690* (20), 4441. doi:10.1016/j.jorganchem.2004.11.058; (b) Hultzsch, K. C. *Org. Biomol. Chem.* **2005**, *3* (10), 1819. doi:10.1039/b418521h; (c) Arrowsmith, M.; Crimmin, M. R.; Barrett, A. G. M.; Hill, M. S.; Kociok-Köhn, G.; Procopiou, P. A. *Organometallics* **2011**, *30* (6), 1493. doi:10.1021/om101063m.

(3) Barnea, E.; Eisen, M. S. *Coord. Chem. Rev.* **2006**, *250* (7–8), 855. doi:10.1016/j.ccr.2005.12.007.

(4) (a) Lee, A. V.; Schafer, L. L. *Eur. J. Inorg. Chem.* **2007** *16*, 2243; (b) Leitch, D. C.; Payne, P. R.; Dunbar, C. R.; Schafer, L. L. *J. Am. Chem. Soc.* **2009**, *131* (51), 18246. doi:10.1021/ja906955b.

(5) (a) Hii, K. K. *Pure Appl. Chem.* **2006**, *78* (2), 341. doi:10.1351/pac200678020341; (b) Widenhoefer, R. A.; Han, X. *Eur. J. Org. Chem.* **2006**, *2006* (20), 4555. doi:10.1002/ejoc.200600399; (c) Hesp, K. D.; Stradiotto, M. *ChemCatChem* **2010**, *2* (10), 1192. doi:10.1002/cctc.201000102.

(6) (a) Lehmkuhl, H.; Reinehr, D. *J. Organomet. Chem.* **1973**, *55* (2), 215. doi:10.1016/S0022-328X(00)82062-8; (b) Wei, H.; Qian, G.; Xia, Y.; Li, K.; Li, Y.; Li, W. *Eur. J. Org. Chem.* **2007**, *2007* (27), 4471. doi:10.1002/ejoc.200700483; (c) Cheng, X.; Xia, Y.; Wei, H.; Xu, B.; Zhang, C.; Li, Y.; Qian, G.; Zhang, X.; Li, K.; Li, W. *Eur. J. Org. Chem.* **2008** (11), 1929. doi:10.1002/ejoc.200701080.

(7) (a) Eisenberger, P.; Schafer, L. L. *Pure Appl. Chem.* **2010**, *82* (7), 1503. doi:10.1351/PAC-CON-09-11-27; (b) Stanlake, L. J. E.; Schafer, L. L. *Organometallics* **2009**, *28* (14), 3990. doi:10.1021/om801190t; (c) Ayinla, R. O.; Schafer, L. L. *Inorg. Chim. Acta* **2006**, *359* (9), 3097. doi:10.1016/j.ica.2005.12.041; (d) Ayinla, R. O.; Gibson, T.; Schafer, L. L. *J. Organomet. Chem.* **2011**, *696* (1), 50. doi:10.1016/j.jorganchem.2010.07.023.

(8) Bexrud, J. A.; Schafer, L. L. *Dalton Trans.* **2010**, *39* (2), 361. doi:10.1039/b913393c.

(9) (a) Gott, A. L.; Clarke, A. J.; Clarkson, G. J.; Scott, P. *Organometallics* **2007**, *26* (7), 1729. doi:10.1021/om061087l; (b) Zi, G.; Zhang, F.; Xiang, L.; Chen, Y.; Fang, W.; Song, H. *Dalton Trans.* **2010**, *39* (17), 4048. doi:10.1039/b923457h; (c) Zi, G.; Liu, X.; Xiang, L.; Song, H. *Organometallics* **2009**, *28* (4), 1127. doi:10.1021/om801061v; (d) Reznichenko, A. L.; Hultzsch, K. C. *Organometallics* **2010**, *29* (1), 24. doi:10.1021/om9008907.

(10) (a) Roesky, P. W. *Angew. Chem. Int. Ed.* **2009**, *48* (27), 4892. doi:10.1002/anie.200900735; (b) Bexrud, J. A.; Eisenberger, P.; Leitch, D. C.; Payne, P. R.; Schafer, L. L. *J. Am. Chem. Soc.* **2009**, *131* (6), 2116. doi:10.1021/ja808862w; (c) Kubiak, R.; Prochnow, I.; Doye, S. *Angew. Chem. Int. Ed.* **2009**, *48* (6), 1153. doi:10.1002/anie.200805169; (d) Prochnow, I.; Kubiak, R.; Frey, O. N.; Beckhaus, R.; Doye, S. *ChemCatChem* **2009**, *1* (1), 162. doi:10.1002/cctc.200900092; (e) Kubiak, R.; Prochnow, I.; Doye, S. *Angew. Chem. Int. Ed.* **2010**, *49* (14), 2626. doi:10.1002/anie.200906557.

(11) (a) Roesky, P. W.; Müller, T. E. *Angew. Chem. Int. Ed.* **2003**, *42* (24), 2708. doi:10.1002/anie.200301637; (b) Hultzsch, K. C. *Adv. Synth. Catal.* **2005**, *347* (2–3), 367. doi:10.1002/adsc.200404261; (c) Aillaud, I.; Collin, J.; Hannedouche, J.; Schulz, E. *Dalton Trans.* **2007**, *44* (44), 5105. doi:10.1039/b711126f; (d) Widenhoefer, R. A. *Chemistry* **2008**, *14* (18), 5382. doi:10.1002/chem.200800219; (e) Zi, G. *Dalton Trans.* **2009**, *42* (42), 9101. doi:10.1039/b906588a; (f) Chemler, S. R. *Org. Biomol. Chem.* **2009**, *7* (15), 3009. doi:10.1039/b907743j.

(12) (a) Knight, P. D.; Munslow, I.; O'Shaughnessy, P. N.; Scott, P. *Chem. Commun. (Camb.)* **2004**, (7), 894. doi:10.1039/

Can. J. Chem. Downloaded from www.nrcresearchpress.com by Xi'an Jiaotong University on 09/19/12
For personal use only.

b401493f; (b) Gott, A. L.; Clarke, A. J.; Clarkson, G. J.; Scott, P. *Chem. Commun. (Camb.)* **2008**, (12), 1422. doi:10.1039/b718373a; (c) Gribkov, D. V.; Hultzsch, K. C. *Angew. Chem. Int. Ed.* **2004**, *43* (41), 5542. doi:10.1002/anie.200460880; (d) Wood, M. C.; Leitch, D. C.; Yeung, C. S.; Kozak, J. A.; Schafer, L. L. *Angew. Chem. Int. Ed.* **2007**, *46* (3), 354. doi:10.1002/anie.200603017; (e) Xiang, L.; Song, H.; Zi, G. *Eur. J. Inorg. Chem.* **2008**, *2008* (7), 1135. doi:10.1002/ejic.200701105.

(13) A recent review:Zi, G. *J. Organomet. Chem.* **2011**, *696* (1), 68. doi:10.1016/j.jorganchem.2010.07.034.

(14) (a) Jerphagnon, T.; Renaud, J.-L.; Bruneau, C. *Tetrahedron Asymmetry* **2004**, *15* (14), 2101. doi:10.1016/j.tetasy.2004.04.037; (b) Teichert, J. F.; Feringa, B. L. *Angew. Chem. Int. Ed.* **2010**, *49* (14), 2486. doi:10.1002/anie.200904948.

(15) Boogers, J. A. F.; Felfer, U.; Kotthaus, M.; Lefort, L.; Steinbauer, G.; de Vries, A. H. M.; de Vries, J. G. *Org. Process Res. Dev.* **2007**, *11* (3), 585. doi:10.1021/op0602369.

(16) (a) Anormed Inc. Chemokine Receptor Binding Compounds. WO Patent 2007/022371 A2, 2007; (b) MacNevin, C. J.; Moore, R. L.; Liotta, D. C. *J. Org. Chem.* **2008**, *73* (4), 1264. doi:10.1021/jo7018202; (c) Rotstein, D. M.; Gabriel, S. D.; Manser, N.; Filonova, L.; Padilla, F.; Sankuratri, S.; Ji, C.; deRosier, A.; Dioszegi, M.; Heilek, G.; Jekle, A.; Weller, P.; Berry, P. *Bioorg. Med. Chem. Lett.* **2010**, *20* (11), 3219. doi:10.1016/j.bmcl.2010.04.077.

(17) (a) Hernández-Rodríguez, M.; Melgar-Fernández, M.; Juaristi, E. *J. Phys. Org. Chem.* **2005**, *18* (8), 792. doi:10.1002/poc.939; (b) Hernández-Rodríguez, M.; Avila-Ortiz, C. G.; del Campo, J. M.; Hernández-Romero, D.; Rosales-Hoz, M. J.; Juaristi, E. *Aust. J. Chem.* **2008**, *61* (5), 364. doi:10.1071/CH08116.

(18) (a) Roos, G. H. P. *S. Afr. J. Chem.* **1997** *51*, 7; (b) Nguyen, Q. P. B.; Kim, J. N.; Kim, T. H. *Tetrahedron Lett.* **2009**, *50* (28), 4015. doi:10.1016/j.tetlet.2009.01.127.

(19) Zhang, Z.; Lee, S. D.; Widenhoefer, R. A. *J. Am. Chem. Soc.* **2009**, *131* (15), 5372. doi:10.1021/ja9001162.

(20) Hu, Y.-C.; Liang, C.-F.; Tsai, J.-H.; Yap, G. P. A.; Chang, Y.-T.; Ong, T.-G. *Organometallics* **2010**, *29* (15), 3357. doi:10.1021/om100296m.

(21) Synthesis of the (*S*)-N1-cyclohexyl-3-methylbutane-1,2-diamine has been reported in the literature by analogous methodology to that used for this report and these syntheses report complete retention of chirality throughout the synthesis. Katritzky, A. R.; He, H.-Y.; Verma, A. K. *Tetrahedron Asymmetry* **2002**, *13* (9), 933. doi:10.1016/S0957-4166(02)00220-3.

(22) Bexrud, J. A. Hydroamination and C–H activation reactivity of tetrakis(amido), bis(amidate), and bis(2-pyridonate) complexes of titanium and zirconium. Ph.D. Thesis, University of British Columbia, Vancouver, British Columbia, 2008.

(23) (a) Kim, H.; Livinghouse, T.; Lee, P. H. *Tetrahedron* **2008**, *64* (11), 2525. doi:10.1016/j.tet.2008.01.031; (b) Majumder, S.; Odom, A. L. *Organometallics* **2008**, *27* (6), 1174. doi:10.1021/om700883a.

(24) Leitch, D. C.; Schafer, L. L. *Organometallics* **2010**, *29* (21), 5162. doi:10.1021/om100381d.

(25) Thomson, R. K.; Zahariev, F. E.; Zhang, Z.; Patrick, B. O.; Wang, Y. A.; Schafer, L. L. *Inorg. Chem.* **2005**, *44* (24), 8680. doi:10.1021/ic0502980.

(26) Levkin, P. A.; Ruderisch, A.; Schurig, V. *Chirality* **2006**, *18* (1), 49. doi:10.1002/chir.20219.

(27) Katritzky, A. R.; He, H.-Y.; Verma, A. K. *Tetrahedron Asymmetry* **2002**, *13* (9), 933. doi:10.1016/S0957-4166(02)00220-3.

(28) The ^{1}H NMR spectrum of this solution is consistent with ligand coordination.

Can. J. Chem. Downloaded from www.nrcresearchpress.com by Xi'an Jiaotong University on 09/19/12
For personal use only.

Theoretical investigation of some *N*-nitrosodiphenylamine biological molecules — A natural bond orbital (NBO) study

Xiao-Hong Li, Rui-Zhou Zhang, and Xian-Zhou Zhang

Can. J. Chem. Downloaded from www.nrcresearchpress.com by Xi'an Jiaotong University on 09/19/12
For personal use only.

Abstract: Theoretical study of several *N*-nitrosodiphenylamine biological molecules has been performed using quantum computational ab initio RHF and density functional B3LYP and B3PW91 methods with 6–311G++(d,p) basis set. Geometries obtained from density functional theory (DFT) calculations were used to perform Natural bond orbital (NBO) analysis. The p characters of two nitrogen natural hybrid orbitals (NHOs) $\sigma_{N3–N2}$ increase with increasing σ_p values of the substituents on the benzene, which results in a lengthening of the N3–N2 bond. The p characters of oxygen NHO $\sigma_{O1–N2}$ and nitrogen NHO $\sigma_{O1–N2}$ bond orbitals decrease with increasing σ_p values of the substituents on the benzene, which results in a shortening of the N2=O1 bond. It is also noted that decreased occupancy of the localized $\sigma_{N3–N2}$ orbital in the idealized Lewis structure, or increased occupancy of $\sigma^*_{N3-N2}$of the non-Lewis orbital, and their subsequent impact on molecular stability and geometry (bond lengths) are also related to the resulting p character of the corresponding nitrogen NHO of $\sigma_{N3–N2}$ bond orbital.

Key words: natural bond orbital (NBO), *N*-nitrosodiphenylamines, second-order delocalization energies, natural hybrid orbital (NHO).

Résumé : Faisant appel à des calculs quantiques selon la méthode ab initio de Hartree-Fock restreinte (HFR) et ceux des méthodes de la fonctionnelle de la densité B3LYP et B3PW91 avec un ensemble de base 6–311G++(d,p), on a effectué des études théoriques sur plusieurs molécules de *N*-nitrosodiphénylamines biologiquement actives. On a utilisé les géométries obtenues à l'aide de calculs de la fonctionnelle de la densité pour effectuer une analyse d'orbitales de liaison naturelle (OLN). Le caractère p des orbitales de liaison des deux atomes d'azote du NHO $\sigma_{N3–N2}$ augmente avec une augmentation des valeurs σ_p des substituants du benzène et il en résulte un allongement de la liaison N3–N2. Le caractère p des orbitales de liaison de l'oxygène NHO $\sigma_{O1–N2}$ et de l'azote NHO $\sigma_{O1–N2}$ diminue avec une augmentation des valeurs des substituants du benzène et il en résulte un raccourcissement de la liaison N2=O1. On a aussi noté qu'une diminution du taux de remplissage de l'orbitale localisée $\sigma_{N3–N2}$ dans la structure idéalisée de Lewis ou une augmentation du taux de remplissage de l'orbitale $\sigma^*_{N3–N2}$ de non-Lewis et leur impact subséquent sur la stabilité et la géométrie moléculaire (longueurs de liaison) sont aussi reliées au caractère p résultant de l'orbitale de liaison de l'orbitale hybride naturelle (OHN) de l'azote correspondant.

Mots-clés : orbitale de liaison naturelle (OLN), *N*-nitrosodiphénylamines, énergies de délocalisation du deuxième ordre, orbitale hybride naturelle (OHN).

[Traduit par la Rédaction]

Introduction

Nitric oxide (NO) is a simple intra- and inter-cellular signaling molecule playing important roles in many physiological processes.[1] Its biological functions include regulating the blood pressure, transmitting neurostimulation, and participating in the immune systems to kill tumor cells and intracellular parasites. Deficiency of nitric oxide leads to pathological and physiological complications in vivo. When the body cannot generate enough nitric oxide for normal physiological functions, exogenous supply of nitric oxide into the bloodstream in a sustained and controlled manner is essential. Many novel nitric oxide donors have been found to be useful in the treatment of various clinical conditions, particularly coronary artery diseases. So, it is noted that knowledge of NO donors and their analogues should be very important and urgently required for chemists and biochemists not only to thoroughly elucidate the detailed mechanism of NO transfer but also to scientifically design and synthesize suitable and desired nitric oxide releasing agents as NO drugs. As a unique class of such NO-carrying vehicles, *N*-nitrosodiphenylamines are generally believed to take a most active part in many biological functions of nitric oxide, especially in the processes of NO storage, transport, and delivery.[2]

N-nitrosodiphenylamines are interesting molecules in biology and medicine, which show vasodilation of veins and ar-

Received 24 February 2011. Accepted 5 May 2011. Published at www.nrcresearchpress.com/cjc on 7 September 2011.

X.-H, Li and R.-Z. Zhang. College of Physics and Engineering, Henan University of Science and Technology, Luoyang 471003, China.
X.-Z. Zhang. College of Physics and Information Engineering, Henan Normal University, Xinxiang 453007, China.

Corresponding author: Xiao-Hong Li (e-mail: lorna639@126.com).

Fig. 1. The selected *N*-nitrosodiphenylamines compounds.

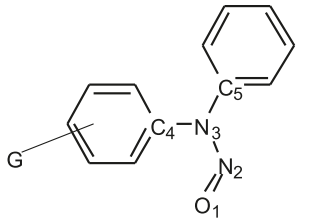

G = 4-CH_3, 4-H, 4-CH_3O, 4-NO_2

teries and inhibition of platelet aggregation through the release of NO.[2] The N–NO bonds are very weak, with an average bond dissociation energy of 28.3–33.1 kcal/mol[2], which is smaller than those of *N*-nitrosoacetanilides[3] and *N*-nitrosodiphenylamines[4] but bigger than those of *N*-nitrosophosphoramidates[2] and *N*-methyl-*N*-nitrosobenzenesulfonamides.[5] This indicates that the substituted *N*-nitrosodiphenylamines are the better NO donors among those types of NO donors.

Casado et al.[6] investigated the kinetic study of the denitrosation and hydrolysis reactions of *N*-nitrosophenylureas. Meijide et al.[7] reported that the O-nitroso compound undergoes rearrangement to *N*-nitrosophenylurea and obtained the ratio between the formation constants of benzenediazonium ion and *N*-nitrosophenylurea.

The use of *N*-nitrosodiphenylamines as NO donors in many chemical and biological reaction systems has also been recognized.[2,5] It is therefore believed that the quantitative measures of the N–NO bond information in the present study may serve as a guide for selecting efficient NO donor compounds and for a more insightful understanding of relevant NO-involving reactions.

A natural atomic orbital (NAO) is defined as a valence-shell atomic orbital derived from the diagonalization of the localized block of the full-density matrix of a given molecule, associated with basis functions χ_i(A) on that atom, and fulfilling the simultaneous requirement of ortho-normality and maximum occupancy. Although in an isolated atom, NAOs coincide simply with natural orbitals in polyatomic molecule (in contrast to natural orbitals that become delocalized over all nuclear centers); the NAOs mostly retain one-center character. Consequently, NAOs are considered optimal for describing the molecular electron density around one center in polyatomic molecules. Also, an NHO results from a symmetrically orthogonalized directed hybrid orbital derived through unitary transformation of NAO centered on a particular atom. Finally, according to the simple bond orbital picture, an NBO is defined as an orbital formed from NHOs. Therefore, for a localized σ-bond between atoms A and B, the NBO is defined as

$$[1] \qquad \sigma_{AB} = c_A h_A + c_B h_B$$

Where h_A and h_B are the natural hybrids centered on atoms A and B. So, the NBOs closely correspond to the picture of localized bonds and lone pairs as basic units of molecular structure, and therefore, it will be possible to conveniently interpret ab initio wave functions in terms of the classical Lewis structure concepts by transforming these functions to the NBO forms.[8]

In the NBO analysis,[8] to compute the span of the valence space, each valence bonding NBO (σ_{AB}) must in turn be paired with a corresponding valence antibonding NBO (σ^*_{AB}):

$$[2] \qquad \sigma^*_{AB} = c_A h_A + c_B h_B$$

Namely, the Lewis σ-type (donor) NBOs are complemented by the non-Lewis σ*-type (acceptor) NBOs that are formally empty in an idealized Lewis structure picture. Readily, the general transformation to NBOs leads to orbitals that are unoccupied in the formal Lewis structure. As a result, the filled NBOs of the natural Lewis structure are well-adapted to describe covalency effects in molecules. Since the non-covalent delocalization effects are associated with σ–σ* interactions between filled (donor) and unfilled (acceptor) orbitals, it is natural to describe them as being of donor–acceptor, charge transfer, or generalized "Lewis base – Lewis acid" type. The antibonds represent unused valence-shell capacity and spanning portions of the atomic valence space that are formally unsaturated by covalent bond formation. Weak occupancies of the valence antibonds signal irreducible departures from an idealized localized Lewis picture; i.e., true "delocalization effects".

As a result, in the NBO analysis, the donor–acceptor (bond–antibond) interactions are taken into consideration by examining all possible interactions between "filled" (donor) Lewis-type NBOs and "empty" (acceptor) non-Lewis NBOs and then estimating their energies by second-order perturbation theory. These interactions (or energetic stabilizations) are referred to as "delocalization" corrections to the zeroth-order natural Lewis structure.

Recently, we have reported the best method to compute the bond dissociation energies of the N–NO bond in *N*-nitrosodiphenylamines.[9] However, our literature survey shows that there are no published experimental or theoretical data on the structure of *N*-nitrosodiphenylamines. In addition, to the best of our knowledge, we have not seen any analysis of the nature of the bonding in *N*-nitrosodiphenylamines.

Density functional methods (especially B3P86 and B3PW91) are very reliable and economical theoretical methods to calculate molecular geometries, often give better results than the MP2 method,[10–15] thus offering an attractive alternative to study molecular structure. Csonka[16] thought that the introduction of the diffuse functions on heavy atoms is necessary for good results if B3LYP functional is used.

In the present work, we attempt to study the thermodynamic stabilities and bonding natures of a family of *N*-nitrosodiphenylamines by using RHF and density functional theory (DFT) at the B3LYP and B3PW91 levels of theory throughout with the 6–311G++(d,p) basis set implemented in the Gaussian03 program suite.[17] Geometries obtained from DFT calculations were then used to perform NBO analysis. Finally, the relative stabilities and the nature of the central bonds in some *N*-nitrosodiphenylamine compounds were systematically and quantitatively investigated by the NBO analysis method.

Computational methods

All geometry optimizations were fully carried out without any symmetry constraints using the RHF, B3LYP, and B3PW91 theoretical methods.[18–22] The quantum chemical

Can. J. Chem. Downloaded from www.nrcresearchpress.com by Xi'an Jiaotong University on 09/19/12
For personal use only.

Table 1. The related bond lengths (Å) and bond angles (°) calculated for the selected *N*-nitrosodiphenylamine compounds using RHF, B3LYP, and B3PW91 levels of theory using 6–311G++(d,p) basis set.

	RHF			B3LYP			B3PW91		
Compounds	N_3—N_2	N_2—O_1	N_3–N_2–O_1	N_3—N_2	N_2—O_1	N_3–N_2–O_1	N_3—N_2	N_2—O_1	N_3–N_2–O_1
4-CH_3O–$C_6H_4N(C_6H_5)$–NO	1.330	1.173	121.0	1.378	1.209	120.1	1.371	1.205	120.1
4-CH_3–$C_6H_4N(C_6H_5)$–NO	1.335	1.171	116.8	1.383	1.205	115.8	1.375	1.203	115.8
4-H–$C_6H_4N(C_6H_5)$–NO	1.338	1.169	116.5	1.384	1.204	115.7	1.379	1.200	115.6
4-NO_2–$C_6H_4N(C_6H_5)$–NO	1.343	1.167	120.7	1.396	1.201	119.9	1.387	1.197	120.0

Can. J. Chem. Downloaded from www.nrcresearchpress.com by Xi'an Jiaotong University on 09/19/12
For personal use only.

calculations were performed with 6–311G++(d,p) basis set implemented in Gaussian03 program.[21] The resulting geometries were then verified as minima by frequency calculations.

NBO analysis was then performed by the NBO 3.1 program[23] at the RHF, B3LYP, and B3PW91 levels of theory. The NBO analysis transforms the canonical delocalized Hartree–Fock (HF) MOs into localized orbitals that are closely tied to chemical bonding concepts. This process involves sequential transformation of non-orthogonal atomic orbitals (AOs) to the sets of natural atomic orbitals (NAOs), natural hybrid orbitals (NHOs), and NBOs. Each of these localized basis sets is complete and describes the wave functions in the most economic method, since electron density and other properties are described by the minimal amount of filled orbitals in the most rapidly convergent way. Filled NBOs describe the hypothetical, strictly localized Lewis structure. The interactions between filled and antibonding (or Rydberg) orbitals represent the deviation of the molecule from the Lewis structure and can be used as the measure of delocalization. This noncovalent bonding–antibonding interaction can be quantitatively described in terms of the NBO approach that is expressed by means of the second-order perturbation interaction energy ($E^{(2)}$).[24–27] This energy represents the estimate of the off-diagonal NBO Fock matrix elements. It can be deduced from the second-order perturbation approach[28]

$$[3] \qquad E^{(2)} = \Delta E_{ij} = q_i \frac{F(i,j)^2}{\varepsilon_j - \varepsilon_i}$$

where q_i is the ith donor orbital occupancy, ε_i and ε_j are diagonal elements (orbital energies), and $F(i, j)$ is the off-diagonal NBO Fock matrix element.

Results and discussion

Geometry optimization

The selected *N*-nitrosodiphenylamines are listed in Fig. 1. Some bond lengths and angles, calculated for the selected compounds at the RHF, B3LYP, and B3PW91 levels of theory, are reported in Table 1. 6–311G++(d,p) basis set is used.

From Table 1, it is noted that the two DFT methods used in this study result in very similar values for bond lengths and angles generally. However, their results are slightly different from those obtained by RHF method. The bond lengths calculated by RHF method are the shortest and the bond angles calculated are the largest for O_1–N_2–N_3 among the three computational methods. For the selected compounds, 4-NO_2–$C_6H_4N(C_6H_5)$–NO has the longest N_2–N_3 bond length, which is calculated by B3LYP method. 4-CH_3O–$C_6H_4N(C_6H_5)$–NO has the largest O_1–N_2–N_3 bond angle, which is calculated by RHF method. In addition, it is noted that 4-CH_3O–$C_6H_4N(C_6H_5)$–NO has the longest N_2–O_1 bond lengths, which is calculated by B3LYP method.

Interesting point observed in the selected molecules is the change of the bond length and angle with the σ_p values of the substituent on the benzene. The σ_p values[29] of OCH_3, CH_3, H, and NO_2 groups are –0.27, –0.17, 0.0, and 0.78, respectively. The experimental N_2–N_3 bond dissociation energies[30] for 4-CH_3O–$C_6H_4N(C_6H_5)$–NO, 4-CH_3–$C_6H_4N(C_6H_5)$–NO, 4-H–$C_6H_4N(C_6H_5)$–NO, and 4-NO_2–$C_6H_4N(C_6H_5)$–NO are 21.4, 21.4, 22.6, and 24.3 kcal/mol, respectively. It is noted that N_2–N_3 bond length increases with the augment of σ_p value, while N_2–O_1 bond length decreases with the augment of σ_p value. In addition, it is rather strange that the largest BDE corresponds to the longest N_2–N_3 bond. We think that for a diatomic molecule, the closer the nuclei of the bonding atoms are, a greater supply of energy is needed to separate the atoms. But for a bigger and complex molecule, BDE is controlled by the difference in ground-state and transition-structure free energies, so it is not sure that the shorter the bond length, the bigger the BDE.

Character of the natural hybrid orbital (NHO) on the selected compounds

In Table 2, we present the resulted natural atomic hybrids h_A on some atoms with the polarization coefficient c_A for each hybrid (in parentheses) in the corresponding NBO. The inspection of the results reported in Table 2 reveals that

- The p characters of two nitrogen NHO $\sigma_{N3–N2}$ bond orbitals increase with increasing σ_p value of the substituent on the benzene.
- The p characters of oxygen NHO $\sigma_{O1–N2}$ and nitrogen NHO $\sigma_{O1–N2}$ bond orbitals decrease with increasing $\sigma_p$value of the substituent on the benzene.
- The increasing p characters on two nitrogen NHO $\sigma_{N3–N2}$ bond orbitals result in a lengthening of the N_3–N_2 bond.
- The decreasing p characters on oxygen NHO $\sigma_{O1–N2}$ and nitrogen NHO $\sigma_{O1–N2}$ bond orbitals result in a shortening of the N_2=O_1 bond.
- Small and nearly equal values of the calculated d contribution of N_2 and N_3 atoms show that 3d orbitals have little importance in bonding of the *N*-nitrosodiphenylamines.

Natural bond orbital[8] (NBO) analysis shows that there is a strong hyperconjugative interaction $n_{O1} \rightarrow \sigma^*_{N3–N2}$ in the compounds studied (Table 3). For example, the second-order energy ($E^{(2)}$) for 4-H–$C_6H_4N(C_6H_5)$–NO is 25.37 kcal/mol at B3LYP level. This interaction weakens the N_2–N_3 sigma bond and elongates the N_3–N_2 bond length in *N*-nitrosodiphenylamines. In

Can. J. Chem. Downloaded from www.nrcresearchpress.com by Xi'an Jiaotong University on 09/19/12
For personal use only.

Table 2. Calculated natural hybrid (NHOs) and the polarization coefficient for each hybrid in the corresponding NBO (in parentheses) for the selected *N*-nitrosodiphenylamine compounds using the selected methods.

	Bond	$(O_1–N_2)$		$(N_2–N_3)$		$(N_3–C_4)$	
	Hybrids	O_1	N_2	N_2	N_3	N_3	C_4
4-CH_3O–$C_6H_4N(C_6H_5)$–NO	RHF	$Sp^{2.49}d^{0.01}$ (0.7404)	$sp^{2.47}d^{0.01}$ (0.6721)	$Sp^{2.71}d^{0.01}$ (0.6768)	$Sp^{2.36}d^{0.01}$ (0.7362)	$Sp^{1.91}d^{0.00}$ (0.7981)	$Sp^{2.88}d^{0.01}$ (0.6025)
	B3LYP	$Sp^{2.72}d^{0.01}$ (0.7405)	$Sp^{2.76}d^{0.01}$ (0.6721)	$Sp^{3.38}d^{0.01}$ (0.6714)	$Sp^{2.41}d^{0.00}$ (0.7411)	$Sp^{1.89}d^{0.00}$ (0.7953)	$Sp^{2.87}d^{0.00}$ (0.6062)
	B3PW91	$Sp^{2.69}d^{0.00}$ (0.7402)	$Sp^{2.74}d^{0.01}$ (0.6724)	$Sp^{3.33}d^{0.01}$ (0.6709)	$Sp^{2.40}d^{0.00}$ (0.7415)	$Sp^{1.89}d^{0.00}$ (0.7945)	$Sp^{2.85}d^{0.00}$ (0.6072)
4-CH_3–$C_6H_4N(C_6H_5)$–NO	RHF	$Sp^{2.37}d^{0.02}$ (0.7408)	$sp^{2.39}d^{0.01}$ (0.6719)	$Sp^{2.72}d^{0.02}$ (0.6647)	$Sp^{2.40}d^{0.00}$ (0.7397)	$Sp^{1.84}d^{0.00}$ (0.7919)	$Sp^{2.75}d^{0.01}$ (0.6107)
	B3LYP	$Sp^{2.66}d^{0.01}$ (0.7405)	$Sp^{2.60}d^{0.01}$ (0.6721)	$Sp^{3.41}d^{0.01}$ (0.6674)	$Sp^{2.48}d^{0.00}$ (0.7447)	$Sp^{1.79}d^{0.00}$ (0.7926)	$Sp^{2.83}d^{0.00}$ (0.6097)
	B3PW91	$Sp^{2.64}d^{0.01}$ (0.7401)	$Sp^{2.60}d^{0.01}$ (0.6725)	$Sp^{3.35}d^{0.01}$ (0.6685)	$Sp^{2.50}d^{0.00}$ (0.7437)	$Sp^{1.79}d^{0.00}$ (0.7921)	$Sp^{2.82}d^{0.00}$ (0.6104)
4-H–$C_6H_4N(C_6H_5)$–NO	RHF	$Sp^{2.28}d^{0.01}$ (0.7406)	$sp^{2.27}d^{0.01}$ (0.6719)	$Sp^{2.78}d^{0.01}$ (0.6736)	$Sp^{2.47}d^{0.00}$ (0.7391)	$Sp^{1.81}d^{0.00}$ (0.7955)	$Sp^{2.84}d^{0.01}$ (0.6059)
	B3LYP	$Sp^{2.62}d^{0.01}$ (0.7405)	$Sp^{2.57}d^{0.01}$ (0.6721)	$Sp^{3.47}d^{0.01}$ (0.6692)	$Sp^{2.51}d^{0.00}$ (0.7431)	$Sp^{1.78}d^{0.00}$ (0.7926)	$Sp^{2.84}d^{0.00}$ (0.6098)
	B3PW91	$Sp^{2.54}d^{0.01}$ (0.7411)	$Sp^{2.48}d^{0.01}$ (0.6715)	$Sp^{3.36}d^{0.01}$ (0.6686)	$Sp^{2.57}d^{0.00}$ (0.7435)	$Sp^{1.81}d^{0.00}$ (0.7885)	$Sp^{2.74}d^{0.00}$ (0.6150)
4-NO_2–$C_6H_4N(C_6H_5)$–NO	RHF	$Sp^{2.14}d^{0.01}$ (0.7415)	$sp^{2.16}d^{0.01}$ (0.6709)	$Sp^{2.86}d^{0.01}$ (0.6746)	$Sp^{2.61}d^{0.01}$ (0.7382)	$Sp^{1.88}d^{0.00}$ (0.7956)	$Sp^{2.79}d^{0.01}$ (0.6058)
	B3LYP	$Sp^{2.46}d^{0.00}$ (0.7418)	$Sp^{2.44}d^{0.01}$ (0.6707)	$Sp^{3.66}d^{0.01}$ (0.6690)	$Sp^{2.71}d^{0.00}$ (0.7433)	$Sp^{1.85}d^{0.00}$ (0.7931)	$Sp^{2.79}d^{0.01}$ (0.6091)
	B3PW91	$Sp^{2.43}d^{0.00}$ (0.7413)	$Sp^{2.44}d^{0.01}$ (0.6712)	$Sp^{3.58}d^{0.01}$ (0.6687)	$Sp^{2.70}d^{0.00}$ (0.7435)	$Sp^{1.86}d^{0.00}$ (0.7925)	$Sp^{2.79}d^{0.00}$ (0.6098)

addition, it is found that these compounds are characterized by a very strong $n_{N3} \rightarrow \sigma^*_{N2=O1}$ delocalization, which induces partial π character.

From Table 3, it is also noted that $E^{(2)}$ increases with increasing σ_p value of the substituent on the benzene, which results in a lengthening of the N_3–N_2 bond. The second-order delocalization energies for 4-CH_3O–$C_6H_4N(C_6H_5)$–NO, 4-CH_3–$C_6H_4N(C_6H_5)$–NO, 4-H–$C_6H_4N(C_6H_5)$–NO, and 4-NO_2–$C_6H_4N(C_6H_5)$–NO at B3LYP level are 24.43, 25.22, 25.37, and 30.11 kcal/mol, respectively, and the N_3–N_2 bond lengths are 1.378, 1.383, 1.384, and 1.396 Å, respectively. The above analysis indicates that the weakness in the N_2–N_3 sigma bond is due to $n_{O1} \rightarrow \sigma^*_{N3-N2}$ delocalization and is responsible for the longer N_3–N_2 bond and hence contributing to the nitro oxide releasing ability in *N*-nitrosodiphenylamines, though the N_3–N_2 bond has partial double-bond character.

The experimental N_2–N_3 bond dissociation energies [30] for 4-CH_3O–$C_6H_4N(C_6H_5)$–NO, 4-CH_3–$C_6H_4N(C_6H_5)$–NO, 4-H–$C_6H_4N(C_6H_5)$–NO, and 4-NO_2–$C_6H_4N(C_6H_5)$–NO are 21.4, 21.4, 22.6, and 24.3 kcal/mol, respectively. These values are very small compared with a simple C–C single bond dissociation energy (~70 kcal/mol) suggesting the weakness of the N_2–N_3 bond. This can be attributed to the $n_{O1} \rightarrow \sigma^*_{N3-N2}$ interaction, which weakens the N_2–N_3 bond.

To confirm that the hyperconjugation is indeed responsible for the N_2–N_3 bond weakening, calculations have been carried out on isoelectronic isomers of 4-H–$C_6H_4N(C_6H_5)$–NX (X = O, NH, or CH_2). The bond dissociation energies for the three compounds at B3LYP/6–311G++(d,p) level are 27.64, 31.05, and 37.48 kcal/mol, respectively. The hyperconjugation interactions due to the lone pair on X are 25.37, 16.02 kcal/mol, and negligible, respectively (Table 4). The gradual increase in the N–N bond dissociation energies with a decrease in the hyperconjugative interactions clearly suggests that there is a direct correlation between hyperconjugation and bond dissociation energy in these systems and show the importance of this interaction in *N*-nitrosodiphenylamines.

Donor–acceptor (bond–antibond) interactions

The most important interaction between "filled" (donor) Lewis-type NBOs and "empty" (acceptor) non-Lewis NBOs is reported in Table 5. The results of NBO analysis collected in Table 5 show that the lp(N_3) (lp: lone pair) participates as donor and the BD*(O_1–N_2) antibond acts as acceptor [lp (N3)→ BD*(O_1–N_2)], with charge transfer energy values as: 64.62, 64.05, 63.95, and 56.37 kcal/mol for 4-CH_3O–$C_6H_4N(C_6H_5)$–NO, 4-CH_3–$C_6H_4N(C_6H_5)$–NO, 4-H–$C_6H_4N(C_6H_5)$–NO, and 4-NO_2–$C_6H_4N(C_6H_5)$–NO at B3LYP level, respectively. This shows that the charge transfer energy decreases with the increasing σ_p value of the substituent on the benzene. This interaction is the most important interaction in the *N*-nitrosodiphenylamine compounds. The amount of destabilization energy calculated within the NBO approach does slightly differ in the compounds examined; thus, it can be inferred that the strength of the N–NO bond only changes slightly in the different compounds, which is consistent with our calculated results[9] and the experimental results.[30]

Table 6 shows calculated natural orbital occupancy (number of electron, or "natural population" of the orbital). It is noted that for σ_{N3-N2} bond orbital, maximum occupancy is

Can. J. Chem. Downloaded from www.nrcresearchpress.com by Xi'an Jiaotong University on 09/19/12
For personal use only.

Table 3. Second-order delocalization energies ($E^{(2)}$) in the selected compounds at various levels; all values are in kcal/mol.

Compounds	RHF/6–311G++(d,p)	B3LYP/6–311G++(d,p)	B3PW91/6–311G++(d,p)
4-CH_3O–$C_6H_4N(C_6H_5)$–NO			
$n_{O1} \rightarrow \sigma^*_{N3-N2}$	32.64	24.43	24.80
$n_{N3} \rightarrow \sigma^*_{N2=O1}$	98.80	64.62	65.44
4-CH_3–$C_6H_4N(C_6H_5)$–NO			
$n_{O1} \rightarrow \sigma^*_{N3-N2}$	33.10	25.22	25.62
$n_{N3} \rightarrow \sigma^*_{N2=O1}$	98.23	64.05	65.45
4-H–$C_6H_4N(C_6H_5)$–NO			
$n_{O1} \rightarrow \sigma^*_{N3-N2}$	33.25	25.37	31.26
$n_{N3} \rightarrow \sigma^*_{N2=O1}$	98.13	63.95	98.86
4-NO_2–$C_6H_4N(C_6H_5)$–NO			
$n_{O1} \rightarrow \sigma^*_{N3-N2}$	35.14	30.11	32.34
$n_{N3} \rightarrow \sigma^*_{N2=O1}$	85.98	56.37	58.06

Table 4. N–N bond dissociation energies and the energy due to second-order delocalizations (in kcal/mol) for the selected three compounds at B3LYP/6–311G++(d,p) level.

Parameters	4-H–$C_6H_4N(C_6H_5)$–N=O	4-H–$C_6H_4N(C_6H_5)$–N=NH	4-H–$C_6H_4N(C_6H_5)$–N=CH_2
BDE	27.64	31.05	37.48
$n_X \rightarrow \sigma^*_{N-N}$	25.37	16.02	—

Table 5. The second-order perturbation energies $E^{(2)}$ (kcal/mol) corresponding to the most important charge transfer interactions (donor–acceptor) in the compounds studied by using B3LYP/6–311G++(d,p) method.

		$E^{(2)}$ (kcal/mol)			
Donor NBO	Acceptor NBO	4-CH_3O–$C_6H_4N(C_6H_5)$–NO	4-CH_3–$C_6H_4N(C_6H_5)$–NO	4-H–$C_6H_4N(C_6H_5)$–NO	4-NO_2–$C_6H_4N(C_6H_5)$–NO
lpN_3[a]	BD*(O_1–N_2)	64.62	64.05	63.95	56.37
lpN_2	BD*(C_5–N_3)	9.01	9.70	9.62	8.40
lp O_1	BD*(N_3–C_4)	0.65	0.67	0.87	0.62

[a]lp stands for lone pair.

Table 6. The important calculated valence non-Lewis and Rydberg non-Lewis σ_{N3-N2} and $\sigma N3 = -N2*$ bond orbital occupancies at B3LYP/6–311G++(d,p)

0.00719	0.01037	0.01003	0.00661	
σ^*_{N3-N2}	0.09039	0.09698	0.09752	0.10083
Valence non-Lewis	3.18464	3.00741	2.95229	3.91897
Rydberg non-Lewis	0.23785	0.23007	0.21924	1.81999

obtained for 4-CH_3O–$C_6H_4N(C_6H_5)$–NO (1.98881); for σ^*_{N3-N2} bond orbital, the maximum occupancy is obtained for 4-NO_2–$C_6H_4N(C_6H_5)$–NO (0.10083). As we described above, small occupancies of the antibond orbitals correspond, in Hartree–Fock theory, to irreducible departure from the idealized Lewis picture, and thus to small non-covalent corrections to the picture of localized covalent bonds.

Decreased occupancy of the localized σ_{N3-N2} orbital in the idealized Lewis structure, or increased occupancy of $\sigma^*_{N3-N2}$of the non-Lewis orbital, and their subsequent impact on molecular stability and geometry (bond lengths) are also related to the resulting p character of the corresponding nitrogen natural hybrid orbital (NHO) of σ_{N3-N2} bond orbital. In Table 2, for 4-CH_3O–$C_6H_4N(C_6H_5)$–NO, 4-CH_3–$C_6H_4N(C_6H_5)$–NO, 4-H–$C_6H_4N(C_6H_5)$–NO, and 4-NO_2–$C_6H_4N(C_6H_5)$–NO at B3LYP level, the p characters of N_2 σ_{N3-N2} in selected compounds are 3.38, 3.41, 3.47, and 3.66, respectively, while the σ_{N3-N2} bond orbital occupancies are 1.98881, 1.98657, 1.98657, and 1.98809, respectively. Similarly, the N_3–N_2 bond lengths are 1.378, 1.383, 1.384, 1.396 Å, respectively, while N_2–O_1 bond lengths are 1.209, 1.205, 1.204, 1.201 Å, respectively. Therefore, the results suggest that the N_3–N_2 bond lengths of these compounds are essentially controlled by the p character of these hybrid orbitals and also by the nature of the N_3–N_2 bond.

Conclusion

According to our results, the following conclusions can be obtained for the selected *N*-nitrosodiphenylamine compounds:

1. For the selected compounds, N_2–N_3 bond length increases with the augment of σ_p value, while N_2–O_1 bond length decreases with the augment of σ_p value.
2. The p characters of two nitrogen NHO σ_{N3-N2} bond orbitals increase with increasing σ_p value of the substituent on the benzene, which results in a lengthening of the N_3–N_2 bond. The p characters of oxygen NHO σ_{O1-N2} and nitrogen NHO σ_{O3-N2} bond orbital decrease with increasing σ_p value of the substituent on the benzene, which results in a shortening of the N_2=O_1 bond.
3. There is a strong hyperconjugative interaction $n_{O1} \rightarrow \sigma^*_{N3-N2}$ in the compounds studied; this interaction weakens the N_2–N_3 sigma bond and elongates the N_3–N_2 bond length in *N*-nitrosodiphenylamines. The weakness in the N_2–N_3 sigma bond is due to $n_{O1} \rightarrow \sigma^*_{N3-N2}$ delocalization and is responsible for the longer N_3–N_2 bond length, and hence contributing to the nitro oxide releasing ability in *N*-nitrosodiphenylamines, though the N_3–N_2 bond has partial double-bond character.
4. lp(N_3) participates as donor and the BD*(O_1–N_2) antibond acts as acceptor [lp(N_3)→ BD*(O_1–N_2)] with charge transfer energy values as: 64.62, 64.05, 63.95, and 56.37 kcal/mol for 4-CH_3O–$C_6H_4N(C_6H_5)$–NO, 4-CH_3–$C_6H_4N(C_6H_5)$–NO, 4-H–$C_6H_4N(C_6H_5)$–NO, and 4-NO_2–$C_6H_4N(C_6H_5)$–NO at B3LYP level, respectively, which shows that the charge transfer energy decreases with the increasing σ_p value of the substituent on the benzene.

Acknowledge

We are grateful for the National Natural Science Foundation of China (Grant No. 10774039), the grant from Development Program in Science and Technology of Henan Province (No. 102300410114 and No. 112300410206), and Henan University of Science and Technology for Young Scholars (No. 2009QN0032) for their support of this work.

References

(1) Bulter, A. R.; Williams, D. L. H. *Chem. Soc. Rev.* **1993** *22*, 233. doi:10.1039/cs9932200233.
(2) Cheng, J.-P.; Xian, M.; Wang, K.; Zhu, X.-Q.; Yin, Z.; Wang, P.-G. *J. Am. Chem. Soc.* **1998** *120* (39), 10266. doi:10.1021/ja982086q.
(3) Cheng, J.-P.; Wang, W.; Yin, Z.; Zhu, X.-Q.; Lu, Y. *Tetrahedron Lett.* **1998** *39* (43), 7925. doi:10.1016/S0040-4039(98)01763-8.
(4) Zhu, X.-Q.; He, J.-Q.; Li, Q.; Xian, M.; Lu, J.; Cheng, J.-P. *J. Org. Chem.* **2000** *65* (20), 6729. doi:10.1021/jo000865v.
(5) Zhu, X.-Q.; Hao, W.-F.; Tang, H.; Wang, C.-H.; Cheng, J.-P. *J. Am. Chem. Soc.* **2005** *127* (8), 2696. doi:10.1021/ja0443676.
(6) Casado, J.; Castiro, A.; Manuel Lorenzo, F.; Meijide, F.; Mosquera, M. *Bull. Soc. Chim. Fr.* **1985** *4*, 597.
(7) Meijide, F.; Tato, J. V.; Casado, J.; Castro, A.; Mosquera, M. *J. Chem. Soc., Perkin Trans. 2* **1987** (12): 1759. doi:10.1039/p29870001759.
(8) Reed, A. E.; Curtiss, L. A.; Weinhold, F. *Chem. Rev.* **1988** *88* (6), 899. doi:10.1021/cr00088a005.
(9) Li, X.-H.; Tang, Z.-X.; Zhang, X.-Z. *J. Mol. Struct. THEOCHEM* **2009** *899* (1-3), 42. doi:10.1016/j.theochem.2008.12.010.
(10) Lignell, A.; Khriachtchev, L.; Lundell, J.; Tanskanen, H.; Räsänen, M. *J. Chem. Phys.* **2006** *125* (18), 184514. doi:10.1063/1.2378624.
(11) Xu, C.-X.; Chen, L.-Z. *Struct. Chem.* **2010** *21* (1), 9. doi:10.1007/s11224-009-9518-9.
(12) Fan, X.-W.; Ju, X.-H.; Xiao, H.-M.; Qiu, L. *J. Mol. Struct. THEOCHEM* **2006** *801* (1-3), 55. doi:10.1016/j.theochem.2006.08.057.
(13) Li, X.-H.; Chen, Q.-D.; Zhang, X.-Z. *Journal of Energetic Materials* **2010** *28* (4), 251. doi:10.1080/07370651003652861 .
(14) Fan, X.-W.; Ju, X.-H. *J. Comput. Chem.* **2008** *29* (4), 505. doi:10.1002/jcc.20809.
(15) Vijay, D.; Deva Priyakumar, U.; Narahari Sastry, G. *Chem. Phys. Lett.* **2004** *383* (1-2), 192. doi:10.1016/j.cplett.2003.11.021.
(16) Csonka, G. I. *J. Mol. Struct. THEOCHEM* **2002** *584* (1-3), 1. doi:10.1016/S0166-1280(02)00096-9.
(17) Frisch, M. J.; Trucks, G. W.; Schlegel, H. B.; Scuseria, G. E.; Robb, M. A.; Cheeseman, J. R.; Zakrzewski, V. G.; Montgomery, J. A.; Stratmann, R. E.; Burant, J. C.; Dapprich, S.; Millam, J. M.; Daniels, A. D.; Kudin, K. N.; Strain, M. C.; Farkas, O.; Tomasi, J.; Barone, V.; Cossi, M.; Cammi, R.; Mennucci, B.; Pomelli, C.; Adamo, C.; Clifford, S.; Ochterski, J.; Petersson, G. A.; Ayala, P. Y.; Cui, Q.; Morokuma, K.; Malick, D. K.; Rabuck, A. D.; Raghavachari, K.; Foresman, J. B.; Cioslowski, J.; Ortiz, J. V.; Baboul, A. G.; Stefanov, B. B.; Liu, G.; Liashenko, A.; Piskorz, P.; Komaromi, I.; Gomperts, R.; Martin, R. L.; Fox, D. J.; Keith, T.; Al-Laham, M. A.; Peng, C. Y.; Nanayakkara, A.; Gonzalez, C.; Challacombe, M.; Gill, P. M. W.; Johnson, B.; Chen, W.; Wong, M. W.; Andres, J. L.; Gonzalez, C.; Head Gordon, M.; Replogle, E. S.; Pople, J. A. *GAUSSIAN 03, Revision B.02,* Gaussian Inc.: Pittsburgh, PA, 2003.
(18) Becke, A. D. *J. Chem. Phys.* **1993** *98* (7), 5648. doi:10.1063/1.464913.
(19) Lee, C.; Yang, W.; Parr, R. G. *Phys. Rev. B* **1988** *37* (2), 785. doi:10.1103/PhysRevB.37.785.
(20) Miehlich, B.; Savin, A.; Stoll, H.; Preuss, H. *Chem. Phys. Lett.* **1989** *157* (3), 200. doi:10.1016/0009-2614(89)87234-3.
(21) Perdew, J. P.; Wang, Y. *Phys. Rev. B* **1992** *45* (23), 13244. doi:10.1103/PhysRevB.45.13244.
(22) Perdew, J. P. *Phys. Rev. B* **1986** *33* (12), 8822. doi:10.1103/PhysRevB.33.8822.
(23) Glendening E. D., Reed A.E., Carpenter J.E., Weinhold F., *NBO*, version 3.1, 1995. More information available from http://www.chem.wisc.edu/~nbo5/.
(24) Reed, A. E.; Weinhold, F. *J. Chem. Phys.* **1985** *83*, 1736.
(25) Reed, A. E.; Weinstock, R. B.; Weinhold, F. *J. Chem. Phys.* **1985** *83* (2), 735. doi:10.1063/1.449486.
(26) Reed, A. E.; Weinhold, F. *J. Chem. Phys.* **1983** *78* (6), 4066. doi:10.1063/1.445134.
(27) Foster, J. P.; Weinhold, F. *J. Am. Chem. Soc.* **1980** *102* (24), 7211. doi:10.1021/ja00544a007.
(28) Chocholousova, J.; Vladimir Spirko, V.; Hobza, P. *Phys. Chem. Chem. Phys.* **2004** *6*, 37. doi:10.1039/b314148a.
(29) Cao, C. Z. *Substituent Effects in Organic Chemistry;* Science Press: Beijing, 2003.
(30) Luo, Y. R. *Handbook of Bond Dissociation Energies in Organic Compounds;* CRC Press: Boca Raton, 2003.

Can. J. Chem. Downloaded from www.nrcresearchpress.com by Xi'an Jiaotong University on 09/19/12
For personal use only.

Novel bipodal, tripodal, and tetrapodal 1,4-dihydropyridines — Microwave-assisted synthesis and structural confinements

Kancherla Rajesh, Bandapalli Palakshi Reddy, and Vijayaparthasarathi Vijayakumar

Abstract: The one pot, three component reaction of *p*-hydroxy benzaldehyde, β-ketoester, and ammonium acetate afforded the corresponding monopodal 1,4-dihydropyridines as building blocks, which in turn converted into diversified novel bipodal, tripodal, and tetrapodal 1,4-dihydropyridines with different alkylating agents through conventional as well as microwave assisted reactions. The unambiguous structural confinements of the all the synthesized compounds were drawn out with the help of 2D NMR (H-H COSY and C-H COSY).

Key words: bipodal-tripodal-tetrapodal 1,4-dihydropyridines, Hantzsch pyridines, microwave irradiation.

Résumé : La réaction monotope, à trois composants, du *p*-hydroxybenzaldéhyde, d′un β-cétoester et de l′acétate d′ammonium conduit aux 1,4-dihydropyridines correspondantes, des synthons monopodes qui, par le biais de réactions normales ou assistées par des microondes, peuvent être transformées à leur tour en nouvelles 1,4-dihydropyridines bipodes, tripodes et tétrapodes portant divers agents alkylants. Les confinements structuraux non ambiguës de tous les composés synthétisés ont été délimités à l′aide de la RMN 2D (COSY H-H et COSY C-H).

Mots-clés : 1,4-dihydropyridines bipodes, tripodes ou tétrapodes, pyridines de Hantzsch, irradiation microonde.

[Traduit par la Rédaction]

Introduction

The synthesis of 1,4-dihydropyridines (1,4-DHPs) via a three-component cyclocondensation reaction of acetoacetic ester, arylaldehyde, and ammonia was first reported by Arthur Hantzsch in 1882.[1] Since then a lot of new variants of the original method have been developed, allowing the synthesis of different substituted 1,4-DHPs, which have now been recognized as vital drugs in the treatment of angina and hypertension. Some of the representatives like nifedipine,[2] felodipine,[3] nicardipine,[4] amlodipine,[5] and manidipine hydrochloride (Fig. 1), have been commercialized and have proven their pharmaceutical action in binding to the voltage dependent L-type calcium channel, thus decreasing the passage of calcium ions into the cell. The result is the relaxation of smooth muscle cells and the lowering of blood pressure.

Studies revealed that 1,4-DHPs exhibit several other medicinal applications, which include neuroprotectant[6] and platelet antiaggregatory activity,[7] in addition to acting as a cerebral anti-ischemic agent in the treatment of Alzheimer's disease[8] and as a chemosensitizer in tumor therapy.[9] The examples clearly demonstrate the potential of novel DHP derivatives as a source of valuable drug candidates. A recent computational analysis of the compressive medicinal chemistry database found that the DHP framework to be among the most prolific chemo-types. Thus, the synthesis of molecules containing this heterocyclic nucleus with diverse properties and applications has been of continuing interest, which led to the development of novel synthetic strategies. So far the attention has mainly been paid to the synthesis of monopodal 1,4-DHP derivatives, and the highly functional ones are seldom investigated. A series of *bis*-1,4-DHP derivatives was synthesized by Songlei Zhu et al. by the reaction of *p*-phenylenedialdehyde or *m*-phenylenedialdehyde and active methylene compounds.[10] Mohammad Ali Zolfigol et al. synthesized new tripodal 1,4-DHPs under solvent-free conditions by the reaction of a mixture of β-ketoester and tri-aldehydes in the presence of ammonium fluoride.[11] Although the methods described above have been beneficial in the specific examples for which they were developed, they do not show much scope for the synthesis of varyingly substituted bipodal, tripodal, and tetrapodal 1,4-DHPs, where synthesis by the former methods requires bis, tris, and tetra aldehydes, which is a costlier approach and not applicable in some cases. A retro synthetic analysis approach (Scheme 1) for target bipodal 1,4-DHPs has shown that the simple monopodal 1,4-DHPs can serve as building blocks for the construction of the target molecules.

The synthesis of monopodal 1,4-DHP building blocks involves one-pot multicomponent coupling reactions (MCRs), where several organic moieties coupled in one step for carbon–carbon and carbon–heteroatom bond formation, which is an attractive synthetic strategy for the synthesis of small molecule libraries with several degrees of structural diver-

Received 10 January 2011. Accepted 4 June 2011. Published at www.nrcresearchpress.com/cjc on 7 September 2011.

K. Rajesh, B. Palakshi Reddy, and V. Vijayakumar. Synthetic Organic Chemistry Research Laboratory, Organic Chemistry Division, School of Advanced Sciences, VIT University, Vellore 632 014, Tamil Nadu, India.

Corresponding author: Vijayaparthasarathi Vijayakumar (e-mail: kvpsvijayakumar@gmail.com).

Can. J. Chem. Downloaded from www.nrcresearchpress.com by University of Electronic and Science Techonology of China on 09/19/12
For personal use only.

Can. J. Chem. Downloaded from www.nrcresearchpress.com by University of Electronic and Science Techonology of China on 09/19/12
For personal use only.

Fig. 1. Biologically active 1,4-dihydropyridines.

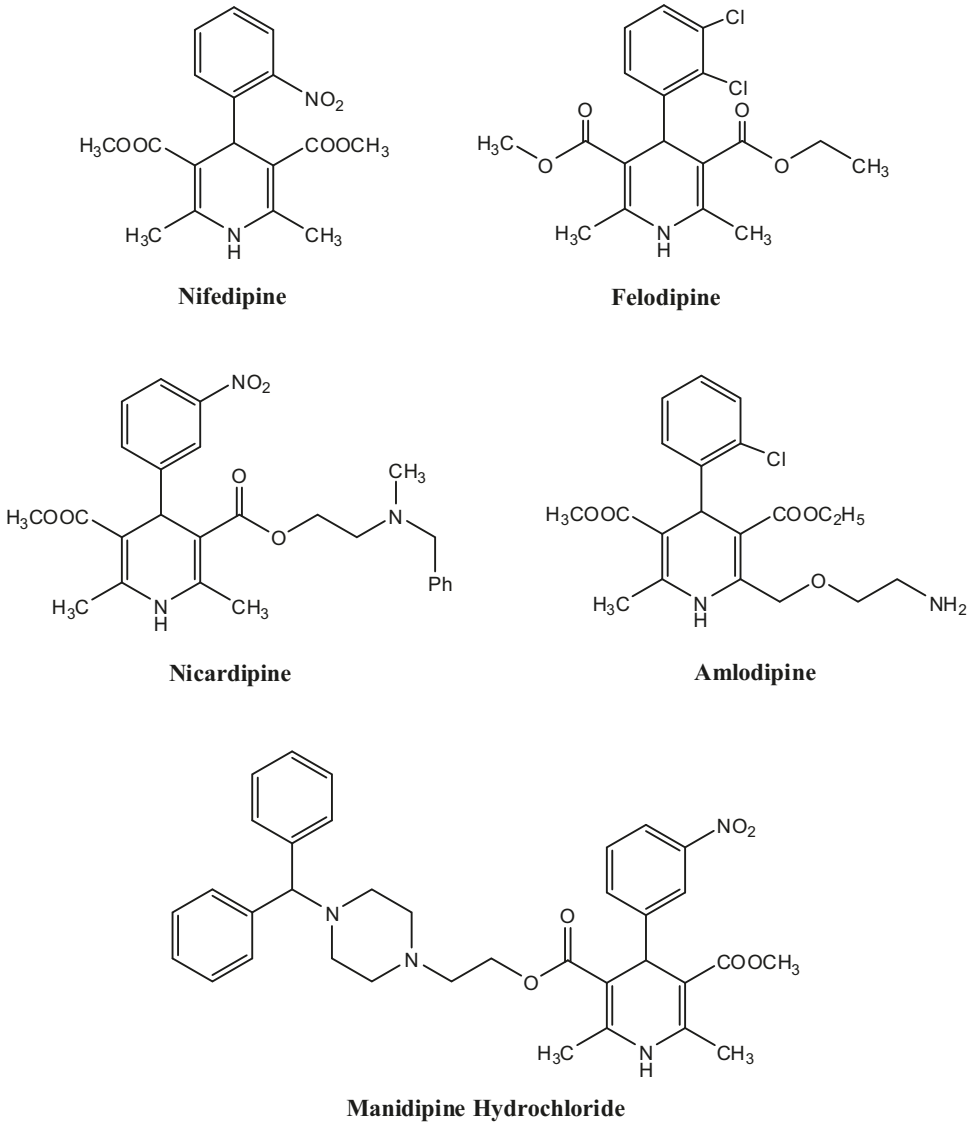

Fig. 2. Structural correlation of the synthesized bipodal 1,4-DHP **13** with the nifedipine.

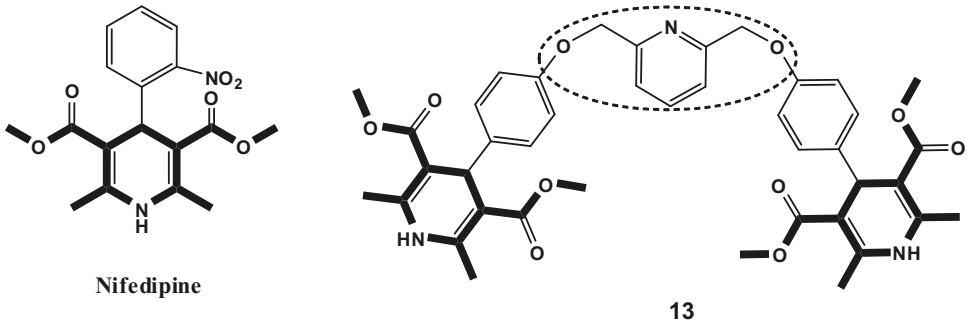

sities.[12–14] The synthesis mainly involves the dehydration of arylaldehydes, β-ketoester or diketone, and ammonium acetate.

The present work describes a direct approach, where the monofunctional 1,4-DHPs, thus synthesized according to the literature,[15,16] serve as building blocks for the construction of novel bipodal, tripodal, and tetrapodal 1,4-DHPs by the conventional methods and by microwave irradiation, which is hitherto unreported in the literature, and all the results were best executed. The structural correlation of the synthesized bipodal 1,4-DHP **13** with nifedipine (vital drug in treatment of angina and hypertension) can be seen in Fig. 2.

Can. J. Chem. Downloaded from www.nrcresearchpress.com by University of Electronic and Science Techonology of China on 09/19/12
For personal use only.

Scheme 1. Retrosynthetic analysis approach for bipodal 1,4-DHPs.

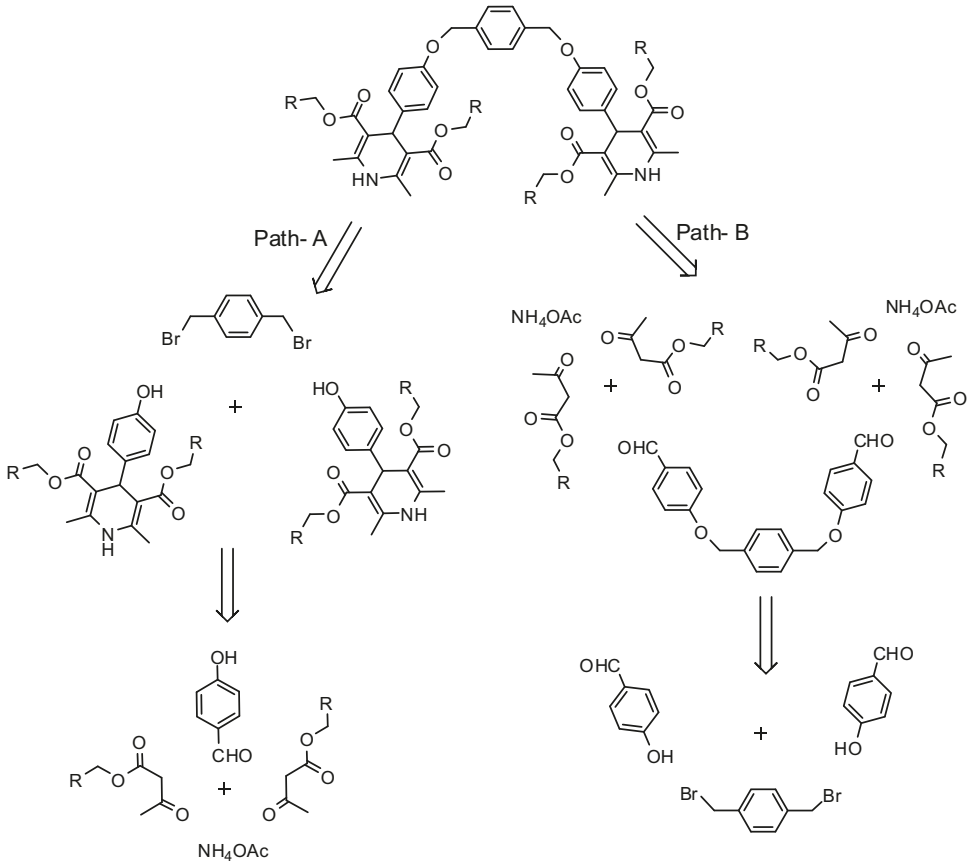

Scheme 2. Synthetic scheme for bipodal *p*-substituted 1,4-DHPs **7–8**.

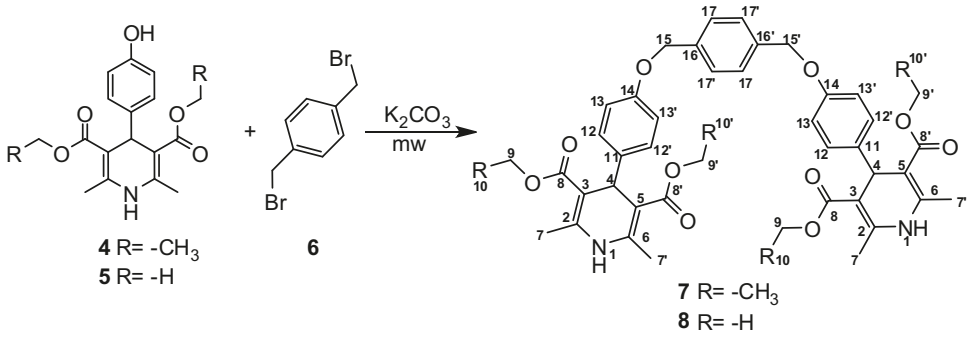

Results and discussion

As part of the continuing interest in the synthesis of 1,4-DHP nucleus[17–20] and heterocyclic compounds bearing bipodal and tripodal moieties,[21–23] we synthesized novel bipodal, tripodal, and tetrapodal 1,4-DHPs by the reaction of monofunctional 1,4-DHP (**4, 5**) with different alkylating agents by using powdered K_2CO_3 as mild base (Schemes 2–6).

The two possible retro synthetic analysis approaches, Path-A and Path-B for bipodal 1,4-DHPs, are given in Scheme 1. In case of Path-A, as a part of a first step, the desired 1,4-DHPs (**4, 5**) have to be synthesized, which may then be reacted with di-bromo, tri-bromo, or tetra-bromo benzenes to give the desired polypodals by using a mild base. Alternatively, this can also be achieved via Path-B, where bis, tris, and tetrakis aldehydes have to be synthesized in a first step using di-bromo, tri-bromo, or tetra-bromo benzenes with *p*-hydroxybenzaldehyde, which can further be reacted with β-ketoester and ammonium acetate to give the desired polypodals, but large amounts of di-bromo, tri-bromo, and tetra-bromo benzenes are needed to carry out the first step, which is a costlier approach. So, Path-A was chosen for convenience, where a mixture of *p*-hydroxy benzaldehyde, β-ketoester, and ammonium acetate in ethanol were heated to give the desired 1,4-DHPs (**4, 5**) in a first step (Table 1). The structure of the products **4** and **5** have been characterized using ^{1}H NMR and HRMS data. The melting point, retention factor, R_f (the retention factor value of the synthesized sample was compared with that of the sample commercially sourced from Sigma-Aldrich), and spectral data were found to be in accord with the literature.[15,16]

Can. J. Chem. Downloaded from www.nrcresearchpress.com by University of Electronic and Science Techonology of China on 09/19/12
For personal use only.

Scheme 3. Synthetic scheme for bipodal *m*-substituted 1,4-DHPs **10–13**.

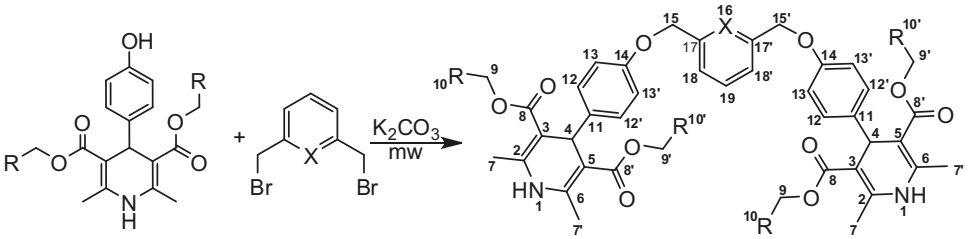

Scheme 4. Synthetic scheme for bipodal *o*-substituted 1,4-DHPs **15–16**.

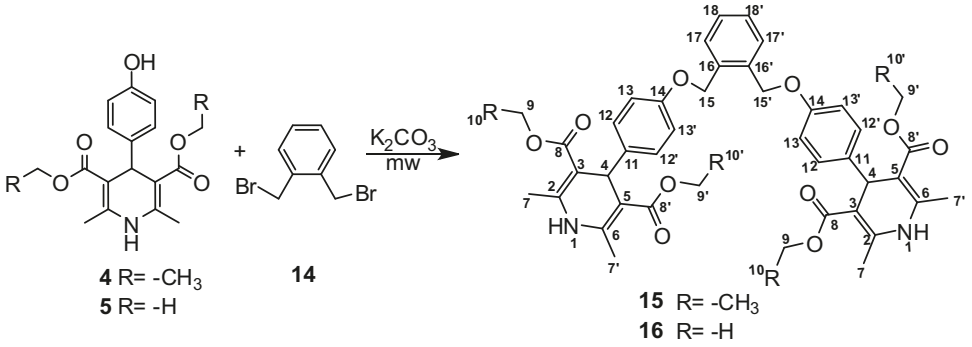

Scheme 5. Synthetic scheme for tripodal 1,4-DHPs **18–21**.

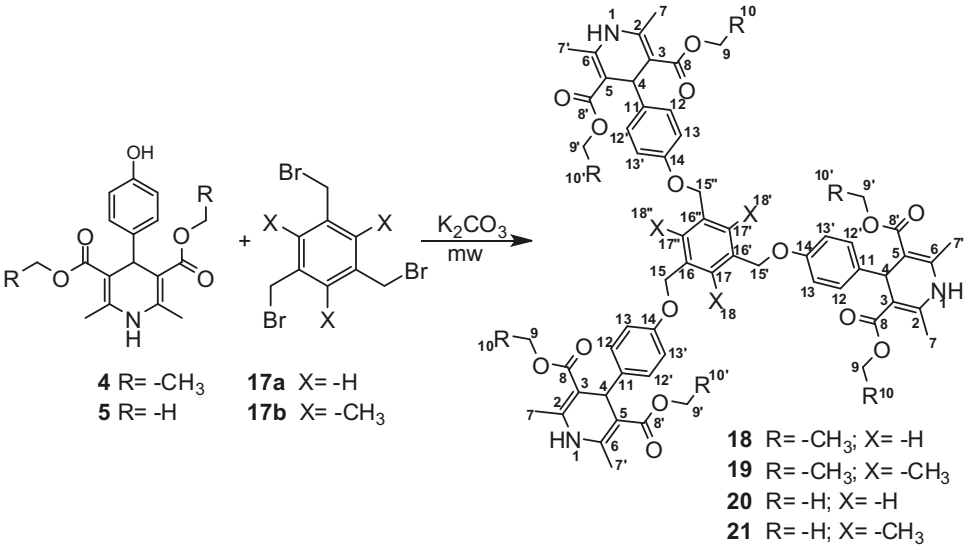

The compounds **4, 5** were converted into the desired polypodals by reacting it with di-bromo, tri-bromo, and tetra-bromo benzenes using powdered K_2CO_3/Na_2CO_3 as mild base. Initially the reaction was carried by using sodium hydride/THF, which promoted the reaction but with lowered yields (Method-A). This is because of the strong basic nature of NaH, which allows the maximum reactivity of –OH, –NH, and esters over 1,4-DHP towards **6**, resulting in undesired side products, which in turn effect the yield of the final product. This led us to quantitatively investigate an efficient approach to synthesize **7** and its derivatives. The use of powdered Na_2CO_3 or K_2CO_3 in DMF at controlled temperature (60 °C) lead to the formation of **7** and its subsequent derivatives very smoothly.

In the case of ethoxy substituent, a maximum yield of 67% was achieved for the bipodal para isomer **7**, and the other two meta substituted bipodal molecules **10** and **11** showed closely adjusted yields of 19% and 67%, respectively (Table 2). A yield of 10% was achieved for bipodal ortho isomer **15**, whereas the tripodal **18** and **19** showed yields of 67% and 50%, respectively. A yield of 49% was achieved for tetrapodal **23**. In the case of methoxy substituent, a maximum yield of 72% was achieved for the bipodal para isomer **8**, and the other two meta substituted bipodal molecules **12** and **13**

Can. J. Chem. Downloaded from www.nrcresearchpress.com by University of Electronic and Science Techonology of China on 09/19/12
For personal use only.

Scheme 6. Synthetic scheme for tetrapodal 1,4-DHPs **23–24**.

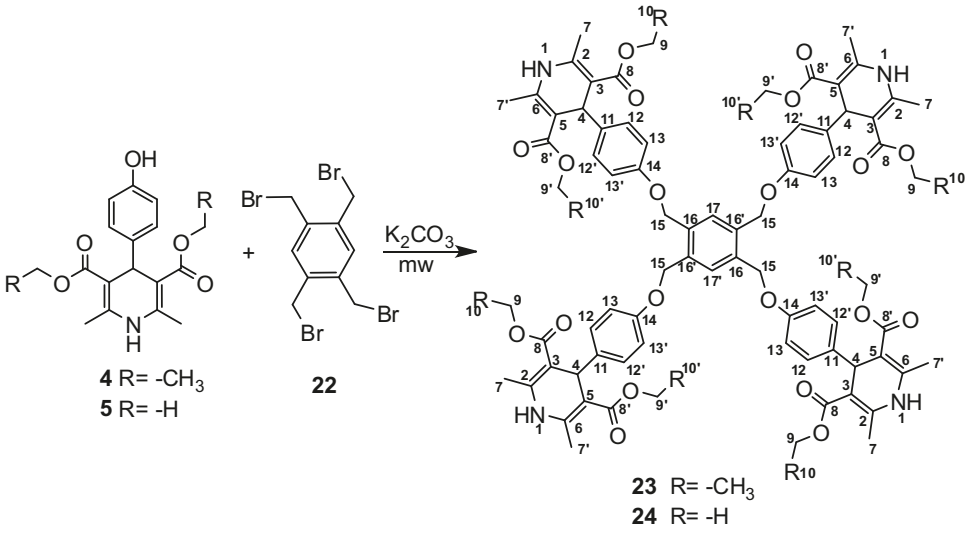

Table 1. Reaction of *p*-hydroxybenzaldehyde, ammonium acetate and β-ketoester leading to monopodal 1,4-DHPs.

				Mp (°C)	
Entry	Aldehyde	Ester	Product	Found	Reported
1	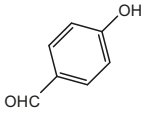	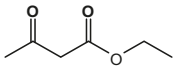	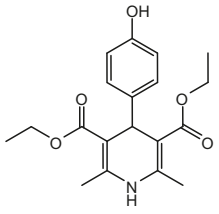 **4**	228–230	230–232[17]
2	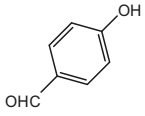	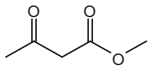	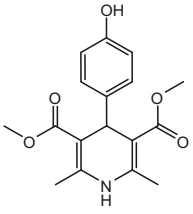 **5**	230–232	231–233[18]

showed closely adjusted yields of 64% and 59%, respectively. A yield of 52% was achieved for the bipodal ortho isomer **16**, whereas tripodal **20** and **21** showed 69% and 63% yield, respectively. A yield of 54% was achieved for tetrapodal **24**. The marked differentiation in yields was expected because of a high steric hindrance over the molecule, especially for **10** and **15**. Better results were observed in powdered Na_2CO_3 or K_2CO_3 over the granular forms because of the larger surface area, which allows maximum reactivity of the alkylating agent towards hetero atoms.

The reaction was expected to proceed via a S_N2 mechanism. The use of elevated temperatures may produce higher impurity levels, which is consistent with the carbocation mechanism. The stronger activation may result in faster generation of carbocation and has a propensity to undergo side reactions. Thus, we are confined to carry the reactions under controlled temperatures, typically at 60 °C using K_2CO_3 as mild base. Rather than changing the base and reaction temperature, we thought to change the methodology. Microwave-assisted synthesis of bipodal, tripodal, and tetrapodal 1,4-DHPs were also carried out to produce the reaction with better yield. Microwave irradiation of a mixture of diethyl or dimethyl 4-(4-hydroxyphenyl)-2,6-dimethyl-1,4-dihydropyridine-3,5-dicarboxylate, alkylating agent, powdered K_2CO_3, and 5 to 6 drops of DMF, at 30% power, was applied for 12 min (six pulses each of 2 min), resulting in product formation with good purity and yield (Table 2). The synthesized compounds were subjected to LC-MS as crude to find the presence of mono-substituted products instead of bis, tris, and tetrakis substitutions. But it was very clear that the mono-substituted compounds were not found, and the unambiguous structural confinements for the synthesized compounds were drawn out with the help of 2D NMR (H-H COSY and C-H COSY).

Conclusion

In conclusion, the mono functional 1,4-DHPs served as building blocks for the construction of novel bipodal, tripodal, and tetrapodal 1,4-DHPs by conventional method and by

Can. J. Chem. Downloaded from www.nrcresearchpress.com by University of Electronic and Science Techonology of China on 09/19/12
For personal use only.

Table 2. Reaction of 1,4-DHP with alkylating agents in the presence of K_2CO_3 under conventional and solvent free microwave Irradiation.

				Yield (%)[a]	
Entry	Alkylating agent	1,4-DHP	Product	Conv.[b]	Mw[c]
1	α,α′-Dibromo-*p*-xylene **6**	**4**	**7**	67	81
2	α,α′-Dibromo-*p*-xylene **6**	**5**	**8**	72	87
3	α,α′-Dibromo-*m*-xylene **9a**	**4**	**10**	19	39
4	2,6-Bis(bromomethyl)pyridine **9b**	**4**	**11**	67	83
5	α,α′-Dibromo-*m*-xylene **9a**	**5**	**12**	64	80
6	2,6-Bis(bromomethyl)pyridine **9b**	**5**	**13**	59	78
7	α,α′-Dibromo-*o*-xylene **14**	**4**	**15**	10	31
8	α,α′-Dibromo-*o*-xylene **14**	**5**	**16**	52	71
9	1,3,5-Tris(bromomethyl)benzene **17a**	**4**	**18**	67	82
10	2,4,6-Tris(bromomethyl)mesitylene **17b**	**4**	**19**	50	77
11	1,3,5-Tris(bromomethyl)benzene **17a**	**5**	**20**	69	85
12	2,4,6-Tris(bromomethyl)mesitylene **17b**	**5**	**21**	63	79
13	1,2,4,5-Tetrakis(bromomethyl)benzene **22**	**4**	**23**	49	72
14	1,2,4,5-Tetrakis(bromomethyl)benzene **22**	**5**	**24**	54	80

[a]The yields refer to the isolated pure products.
[b]Reaction carried under conventional heating.
[c]Reaction carried under microwave irradiation.

microwave irradiation. The microwave mehtod exhibited several advantages over conventional heating by significantly reducing the reaction time and improving the reaction yield, owing to a specific non-thermal microwave effect. The methodology employed for this synthesis shows much scope not only for the synthesis of bipodal and tripodal 1,4-DHPs but also for tetrapodal moieties, which is not possible to do by the methods in the literature.

Experimental section

General

Solvents and reagents were commercially sourced and used without further purification, with the exception of THF, which was freshly distilled over sodium. Melting points were taken with a Elchem microprocessor-based DT apparatus in open capillary tubes and are corrected with benzoic acid. IR spectra were obtained on an Avatar-330 FTIR spectrophotometer (Thermo Nicolet) using KBr pellets, and only noteworthy absorption levels (reciprocal centimetres) are listed. The NMR spectra were recorded on a Bruker 300 and 500 MHz spectrometer, using TMS as internal standard (chemical shifts δ in ppm). Mass spectra were recorded on HRMS and LCMS by an Agilent 1200 series LC and Micromass zQ spectrometer. Microwave oven used is of synthetic microwave, CATA R with the maximum power of 700 W at 100% power level. All reactions were carried at 30% power level, which produces power of 210 W. Thin-layered chromatography (TLC) was performed on preparative plates of silica gel (s.d. fine). Visualization was made with an iodine chamber. Column chromatography was performed by using silica gel (60–120 mesh).

General procedure for synthesis of 1,4-DHPs (4, 5)

A mixture of *p*-hydroxybenzaldehyde (10 mmol, 1.0 equiv.), β-ketoester (20 mmol, 2.0 equiv.) and ammonium acetate (12 mmol, 1.2 equiv.) were heated for 15 min in the presence of ethanol (10 mL). The progress of the reaction was monitored by TLC. After completion of the reaction, the reaction mixture was left aside for the formation of product, filtered to remove the insoluble solids and then the filter cake was washed with diethyl ether. The solid was recrystallized from absolute ethanol to yield respective 1,4-dihydropyridine derivatives as a yellow solid.

Diethyl 4-(4-hydroxyphenyl)-2,6-dimethyl-1,4-dihydropyridine-3,5-dicarboxylate (4)

Yellow solid (recrystallized from ethanol). R_f (pet. ether/EtOAc, 6:4) = 0.83. Mp 228–230 °C (Lit. 230–232 °C).[15] IR (KBr, cm^{-1}): 3345, 2981, 1662, 1486. ^{1}H-NMR (200 MHz, $CDCl_3$) δ: 0.88 (t, J = 7.5 Hz, 6H), 2.77 (s, 6H), 3.66–3.76 (q, J = 6.0 Hz, 4H), 4.49 (s, 1H), 6.30 (d, J = 8.0 Hz, 2H), 6.72 (d, J = 8.0 Hz, 2H), 7.60 (s, -NH, 1H), 8.27 (s, -OH, 1H). HRMS: *m/z* 345.1582 (M^+).

Dimethyl 4-(4-hydroxyphenyl)-2,6-dimethyl-1,4-dihydropyridine-3,5-dicarboxylate (5)

Yellow solid (recrystallized from ethanol). R_f (pet. ether/EtOAc, 6:4) = 0.8. Mp 230–232 °C (Lit. 231–233 °C).[16] IR (KBr, cm^{-1}): 3339, 3003, 2950, 1680, 1647, 1611. ^{1}H-NMR (200 MHz, $CDCl_3$) δ: 2.86 (s, 6H), 3.28 (s, 6H), 4.51 (s, 1H), 6.31 (d, J = 8.0 Hz, 2H), 6.70 (d, J = 8.0 Hz, 2H), 7.73 (s, -NH, 1H), 8.35 (s, -OH, 1H). HRMS: *m/z* 317.1270 (M^+).

Representative procedure for preparation of bipodal, tripodal, and tetrapodal 1,4-DHP derivatives

Method A (Classical method using NaH)

To a slurry of 22 mmol of NaH in 20 mL of dry THF in a three-necked round bottom flask under an N_2 atmosphere, 2 mmol of diethyl 4-(4-hydroxyphenyl)-2,6-dimethyl-1,4-dihydropyridine-3,5-dicarboxylate (**4**) dissolved in 30 mL of dry THF was added dropwise and the mixture was refluxed for 1 h. α,α′-Dibromo-*p*-xylene (**6**) (1.1 mmol) was dissolved in 100 mL of THF and added to the above reaction mixture

Can. J. Chem. Downloaded from www.nrcresearchpress.com by University of Electronic and Science Techonology of China on 09/19/12
For personal use only.

with stirring for 12 h and then at reflux for a further 12 h. The reaction mixture quenched with aq NH_4Cl solution to remove excess NaH, and THF was removed under reduced pressure. The residue was extracted with $CHCl_3$ and dried over anhydrous Na_2SO_4. The crude product was purified by column chromatography on silica gel, using pet. ether/EtOAc (8:2) as eluent to give tetraethyl 4,4′-(4,4′-(1,4-phenylenebis (methylene)) bis(oxy)bis(4,1-phenylene))bis(2,6-dimethyl-1,4-dihydropyridine-3,5-dicarboxylate) (**7**) in 32% yield.

Method B (Classical method using powdered K_2CO_3)

To a suspension of 1.05 equiv. of diethyl or dimethyl 4-(4-hydroxyphenyl)-2,6-dimethyl-1,4-dihydropyridine-3,5-dicarboxylate (**4** or **5**) in 10 volumes of dry DMF, 3.0 equiv. of powdered K_2CO_3 was added, stirred well for 15 min at just above room temperature (40 °C). To that, alkylating agent (0.5 equiv. in case of **6**, **9a**, **9b**, and **14**; 0.333 equiv. in case of **17a** and **17b;**; 0.25 equiv. in case of **22**) dissolved in minimum amount of DMF was added drop wise for 1 h with stirring at 50 °C. After the complete addition, the reaction mixture heated at 60 °C with stirring for 48 h. The completion of reaction was monitored by TLC. Then the reaction mixture was allowed cool to room temperature, filtered to remove the insoluble solids, and then the filter cake was washed with DMF. Excess solvents were removed under reduced pressure and then quenched with ice-cold water; the obtained crude products were purified by column chromatography (60–120 mesh), which produced the products in good to moderate yields.

Method C (Microwave irradiation)

A mixture of 1.05 equiv. of diethyl or dimethyl 4-(4-hydroxyphenyl)-2,6-dimethyl-1,4-dihydropyridine-3,5-dicarboxylate (**4** or **5**), alkylating agent (0.5 equiv. in the case of **6**, **9a**, **9b**, and **14**; 0.333 equiv. in case of **17a** and **17b;**; 0.25 equiv. in case of **22**), 3.0 equiv. of powdered K_2CO_3, and 5 to 6 drops of DMF, which acts as homogenizer were finely ground. Microwave irradiation at 30% power was applied for 12 min (six pulses each of 2 min). The progress of the reaction was followed by TLC. After the completion of reaction, the reaction mixture poured into ice-cold water; the obtained solid was filtered, washed with water, and air dried to afford the desired product. The obtained crude products were purified by column chromatography on silica gel (60–120 mesh), which obtained the products in good to moderate yields.

Tetraethyl 4,4′-(4,4′-(1,4-phenylenebis(methylene))bis(oxy) bis(4,1-phenylene))bis(2,6-dimethyl-1,4-dihydropyridine-3,5-dicarboxylate) (7)

Pale yellow solid (recrystallized from pet. ether/EtOAc, 8:2). Mp 102–104 °C. IR (KBr, cm^{-1}): 3337, 3097, 2979, 2929, 1678, 1505. ^{1}H-NMR (300 MHz, $CDCl_3$) δ_H: 1.22 (t, J = 6 Hz, 12 protons at H-10, 10′), 2.32 (s, 12 protons at H-7, 7′), 4.09 (q, 8 protons at H-9, 9′), 4.92 (s, 2 protons at H-4), 5.00 (s, 4 protons at H-15, 15′), 5.61 (bs, 2protons at -NH), 6.81 (d, J = 9 Hz, 4 arom. protons at H-13, 13′), 7.19 (d, J = 6 Hz, 4 arom. protons at H-12, 12′), 7.41 (s, 4 arom. protons at H-17, 17′). ^{13}C-NMR (75 MHz, $CDCl_3$) δ_C: 14.28 (C-10, 10′), 19.50 (C-7, 7′), 38.72 (C-4), 59.72 (C-9, 9′), 69.66 (C-15, 15′), 104.17 (C-3, 5), 114.09 (C-13, 13′), 127.69 (C-17, 17′), 128.98 (C-12, 12′), 136.93 (C-16, 16′), 140.67 (C-11), 143.85 (C-2, 6), 157.10 (C-14), 167.79 (C-8, 8′). LC-MS: m/z 793.2 (M+1). Anal. calcd. for $C_{46}H_{52}N_2O_{10}$: C, 69.68; H, 6.61; N, 3.53. Found: C, 69.50; H, 6.81; N, 3.45.

Tetramethyl 4,4′-(4,4′-(1,4-phenylenebis(methylene))bis (oxy)bis(4,1-phenylene))bis(2,6-dimethyl-1,4-dihydropyridine-3,5-dicarboxylate) (8)

White solid (recrystallized from diethyl ether/methanol, 5:5). Mp 282–284 °C; IR (KBr, cm^{-1}): 3344, 2947, 1701, 1650. ^{1}H-NMR (500 MHz, DMSO-d6) δ_H: 2.25 (s, 12 protons at H-7, 7′), 3.32 (s, 12 protons at H-9, 9′), 4.82 (s, 2 protons at H-4), 5.02 (s, 4 protons at H-15, 15′), 6.84 (d, J = 10 Hz, 4 arom.protons at H-13, 13′), 7.03 (d, J = 8.5 Hz, 4 arom. protons at H-12, 12′), 7.42 (s, 4 arom. protons at H-17, 17′), 8.82 (s, 2protons at -NH). LC-MS: m/z 735.4 (M–1), 759.4 (M+Na). Anal. calcd. for $C_{42}H_{44}N_2O_{10}$: C, 68.46; H, 6.02; N, 3.80. Found: C, 69.16; H, 5.91; N, 3.77.

Tetraethyl 4,4′-(4,4′-(1,3-phenylenebis(methylene))bis(oxy) bis(4,1-phenylene))bis(2,6-dimethyl-1,4-dihydropyridine-3,5-dicarboxylate) (10)

Pale yellow solid (recrystallized from pet. ether/EtOAc, 8:2). Mp 106–108 °C. IR (KBr, cm^{-1}): 3341, 3091, 2982, 1697, 1647. ^{1}H-NMR (300 MHz, $CDCl_3$) δ_H: 1.22 (t, J = 7.05 Hz, 12 protons at H-10, 10′), 2.32 (s, 12 protons at H-7, 7′), 4.09 (q, 8 protons at H-9, 9′), 4.93 (s, 2 protons at H-4), 5.00 (s, 4 protons at H-15, 15′), 5.64 (bs, 2 protons at -NH), 6.81 (d, J = 8.4 Hz, 4 arom. protons at H-13, 13′), 7.14–7.45 (m, 8 arom. protons at H-12, 12′, 16, 18, 18′, 19). LC-MS: m/z 793.3 (M+1). Anal. calcd. for $C_{46}H_{52}N_2O_{10}$: C, 69.68; H, 6.61; N, 3.53. Found: C, 70.24; H, 6.24; N, 3.40.

Tetraethyl 4,4′-(4,4′-(pyridine-2,6-diylbis(methylene))bis (oxy)bis(4,1-phenylene))bis(2,6-dimethyl-1,4-dihydropyridine-3,5-dicarboxylate) (11)

White solid (recrystallized from pet ether/EtOAc, 7.5:2.5). Mp 100–102 °C. IR (KBr, cm^{-1}): 3337, 3096, 2979, 1693, 1608. ^{1}H-NMR (300 MHz, $CDCl_3$) δ_H: 1.21 (t, J = 7.05 Hz, 12 protons at H-10, 10′), 2.32 (s, 12 protons at H-7, 7′), 4.08 (q, 8 protons at H-9, 9′), 4.93 (s, 2 protons at H-4), 5.14 (s, 4 protons at H-15, 15′), 5.69 (bs, 2protons at -NH), 6.82 (d, J = 8.7 Hz, 4 arom. protons at H-13, 13′), 7.20 (d, J = 8.4 Hz, 4 arom. protons at H-12, 12′), 7.43 (d, J = 7.8 Hz, 2 arom. protons at H-18, 18′), 7.71 (t, J = 7.5 Hz, 1 arom. proton at H-19). ^{13}C-NMR (75 MHz, $CDCl_3$) δ_C: 14.23 (C-10, 10′), 19.56 (C-7, 7′), 38.72 (C-4), 59.67 (C-9, 9′), 70.43 (C-15, 15′), 104.27 (C-3, 5), 114.04 (C-13, 13′), 119.99 (C-18, 18′), 129.03 (C-12, 12′), 140.17 (C-19), 140.79 (C-11), 143.58 (C-2, 6), 156.67 (C-17, 17′), 156.95 (C-14) 167.65 (C-8, 8′). LC-MS: m/z 792.5 (M–1), 816.4 (M+Na). Anal. calcd. for $C_{45}H_{51}N_3O_{10}$: C, 68.08; H, 6.47; N, 5.29. Found: C, 68.64; H, 6.90; N, 5.18.

Tetramethyl 4,4′-(4,4′-(1,3-phenylenebis(methylene))bis (oxy)bis(4,1-phenylene))bis(2,6-dimethyl-1,4-dihydropyridine-3,5-dicarboxylate) (12)

White solid (recrystallized from pet. ether/EtOAc, 8:2). Mp 116–118 °C. ^{1}H-NMR (300 MHz, $CDCl_3$) δ_H: 2.30 (s, 12 protons at H-7, 7′), 3.63 (s, 12 protons at H-9, 9′), 4.93 (s, 2 protons at H-4), 4.98 (s, 4 protons at H-15, 15′), 5.84

Can. J. Chem. Downloaded from www.nrcresearchpress.com by University of Electronic and Science Techonology of China on 09/19/12
For personal use only.

(bs, 2protons at -NH), 6.80 (d, J = 6.9 Hz, 4 arom. protons at H-13, 13′), 7.16 (d, J = 8.4 Hz, 4 arom. protons at H-12, 12′), 7.25–7.47 (m, 4 arom. protons at H-16, 18, 18′, 19). ^{13}C-NMR (75 MHz, $CDCl_3$) δ_C: 19.52 (C-7, 7′), 38.35 (C-4), 50.98 (C-9, 9′), 69.77 (C-15, 15′, 103.94 (C-3, 5), 114.28 (C-13, 13′), 126.49 (C-16), 126.96 (C-18, 18′),128.59 (C-12, 12′), 128.77 (C-19), 137.57 (C-11), 140.20 (C-17, 17′), 144.07 (C-2, 6), 157.16 (C-14), 168.11 (C-8, 8′). LC-MS: m/z 735.5 (M–1). Anal. calcd. for $C_{42}H_{44}N_2O_{10}$: C, 68.46; H, 6.02; N, 3.80. Found: C, 69.47; H, 5.70; N, 4.05.

Tetramethyl 4,4′-(4,4′-(pyridine-2,6-diylbis(methylene))bis (oxy)bis(4,1-phenylene))bis(2,6-dimethyl-1,4-dihydropyridine-3,5-dicarboxylate) (13)

White solid (recrystallized from pet. ether/EtOAc, 8:2). Mp 118–120 °C. ^{1}H-NMR (300 MHz, $CDCl_3$) δ_H: 2.31 (s, 12 protons at H-7, 7′), 3.63 (s, 12 protons at H-9, 9′), 4.93 (s, 2 protons at H-4), 5.13 (s, 4 protons at H-15, 15′), 5.75 (bs, 2protons at -NH), 6.81 (d, J = 8.4 Hz, 4 arom. protons at H-13, 13′), 7.16 (d, J = 8.1 Hz, 4 arom. protons at H-12, 12′), 7.42 (d, J = 7.8 Hz, 2 arom. protons at H-18, 18′), 7.70 (t, J = 7.5 Hz, 1 arom. proton at H-19). ^{13}C-NMR (75 MHz, $CDCl_3$) δ_C: 19.55 (C-7, 7′), 38.35 (C-4), 50.97 (C-9, 9′), 70.42 (C-15, 15′), 103.93 (C-3, 5), 114.23 (C-13, 13′), 119.99 (C-18, 18′), 128.65 (C-12, 12′), 133.99 (C-11, 11′), 135.73 (C-19), 143.99 (C-2, 6), 154.85 (C-17, 17′), 156.75 (C-14), 168.06 (C-8, 8′). LC-MS: m/z 736.5 (M–1); Anal. calcd. for $C_{41}H_{43}N_3O_{10}$: C, 66.72; H, 5.87; N, 5.70. Found: C, 66.61; H, 5.58; N, 5.46.

Tetraethyl 4,4′-(4,4′-(1,2-phenylenebis(methylene))bis(oxy) bis(4,1-phenylene))bis(2,6-dimethyl-1,4-dihydropyridine-3,5-dicarboxylate) (15)

Yellow solid (recrystallized from pet. ether/EtOAc, 8:2). Mp 112–114 °C. IR (KBr, cm^{-1}): 3347, 2986, 1661, 1635. ^{1}H-NMR (300 MHz, $CDCl_3$) δ_H: 1.22 (t, J = 6.9 Hz, 12 protons at H-10, 10′), 2.33 (s, 12 protons at H-7, 7′), 4.09 (q, 8 protons at H-9, 9′), 4.84 (s, 2 protons at H-4), 4.92 (s, 4 protons at H-15, 15′), 5.54 (bs, 2 protons at -NH), 6.66 (d, J = 8.4 Hz, 4 arom. protons at H-13, 13′), 7.14 (d, J = 8.4 Hz, 4 arom. protons at H-12, 12′), 7.26–7.28 (m, 4 arom. protons at H-17, 17′, 18, 18′). HRMS: m/z 792.3620 (M$^+$); Anal. calcd. for $C_{46}H_{52}N_2O_{10}$: C, 69.68; H, 6.61; N, 3.53. Found: C, 69.26; H, 6.46; N, 3.47.

Tetramethyl 4,4′-(4,4′-(1,2-phenylenebis(methylene))bis (oxy)bis(4,1-phenylene))bis(2,6-dimethyl-1,4-dihydropyridine-3,5-dicarboxylate) (16)

Yellow solid (recrystallized from pet. ether/EtOAc, 8:2). Mp 134–136 °C. ^{1}H-NMR (300 MHz, $CDCl_3$) δ_H: 2.31 (s, 12 protons at H-7, 7′), 3.64 (s, 12 protons at H-9, 9′), 4.94 (s, 2 protons at H-4), 5.08 (s, 4 protons at H-15, 15′), 5.97 (bs, 2 protons at -NH), 6.81 (d, J = 8.4 Hz, 4 arom. protons at H-13, 13′), 7.17 (d, J = 8.4 Hz, 4 arom. protons at H-12, 12′), 7.34–7.49 (m, 4 arom. protons at H-17, 17′, 18, 18′). ^{13}C-NMR (75 MHz, $CDCl_3$) δ_C: 19.48 (C-7, 7′), 38.30 (C-4), 50.99 (C-9, 9′), 67.72 (C-15, 15′), 103.86 (C-3, 5), 114.26 (C-13, 13′), 128.27 (C-18, 18′), 128.57 (C-12, 12′), 128.78 (C-17, 17′), 135.24 (C-16, 16′), 140.28 (C-11, 11′), 144.20 (C-2, 6), 157.03 (C-14), 168.14 (C-8, 8′). LC-MS: m/z 735.1 (M–1). Anal. calcd. for $C_{42}H_{44}N_2O_{10}$: C, 68.46; H, 6.02; N, 3.80. Found: C, 69.47; H, 5.67; N, 3.66.

Hexaethyl 4,4′,4″-(4,4′,4″-(benzene-1,3,5-triyltris (methylene))tris(oxy)tris(benzene-4,1-diyl))tris(2,6-dimethyl-1,4-dihydropyridine-3,5-dicarboxylate) (18)

White solid (recrystallized from pet. ether/EtOAc, 7:3). Mp 124–126 °C. IR (KBr, cm^{-1}): 3336, 3096, 2978, 2932, 1677. ^{1}H-NMR (300 MHz, $CDCl_3$) δ_H: 1.23 (18 protons at H-10, 10′), 2.31 (s, 18 protons at H-7, 7′), 4.09 (12 protons at H-9, 9′), 4.99 (s, 9 protons at H-4, 15, 15′, 15″), 6.34 (bs, 3 protons at -NH), 6.82–7.41 (m, 15 arom. protons at H-12, 12′, 13, 13′, 17, 17′, 17″). ^{13}C-NMR (75 MHz, $CDCl_3$) δ_C: 14.28 (C-10, 10′), 19.42 (C-7, 7′), 38.69 (C-4), 59.72 (C-9, 9′), 69.67 (C-15, 15′, 15″), 104.04 (C-3, 5), 114.13 (C-13, 13′), 125.98 (C-17, 17′, 17″), 128.94 (C-12, 12′), 137.95 (C-11), 140.72 (C-16, 16′, 16″), 144.00 (C-2, 6), 157.03 (C-14), 167.82 (C-8, 8′). HRMS: m/z 1149.5192 (M$^+$). Anal. calcd. for $C_{66}H_{75}N_3O_{15}$: C, 68.91; H, 6.57; N, 3.65. Found: C, 68.43; H, 6.86; N, 3.58.

Hexaethyl 4,4′,4″-(4,4′,4″-(2,4,6-trimethylbenzene-1,3,5-triyl)tris(methylene)tris(oxy)tris (benzene-4,1-diyl))tris (2,6-dimethyl-1,4-dihydropyridine-3,5-dicarboxylate) (19)

White solid (recrystallized from pet. ether/EtOAc, 6.5:4.5). Mp 120–122 °C. IR (KBr, cm^{-1}): 3338, 3096, 2979, 1678, 1607. ^{1}H-NMR (300 MHz, $CDCl_3$) δ_H: 1.22 (t, J = 9.4 Hz, 18 protons at H-10, 10′), 2.30 (s, 18 protons at H-7, 7′), 2.35 (s, 9 protons at H-18, 18′, 18″), 4.08 (bs,12 protons at H-9, 9′), 4.93 (s, 3 protons at H-4), 4.98 (s, 6 protons at H-15, 15′, 15″), 5.94 (bs, 3 protons at -NH), 6.83 (d, J = 6.8 Hz, 6 arom. protons at H-13, 13′), 7.20 (d, J = 6.8 Hz, 6 arom. protons at H-12, 12′). ^{13}C-NMR (75 MHz, $CDCl_3$) δ_C: 15.62 (C-10, 10′), 15.99 (C-18, 18′, 18″), 19.27 (C-7, 7′), 38.60 (C-4), 59.63 (C-9, 9′), 64.67 (C-15, 15′, 15″), 103.96 (C-3, 5), 113.79 (C-13, 13′), 128.78 (C-12, 12′), 131.37 (C-17, 17′, 17″), 139.04 (C-16, 16′, 16″), 140.52 (C-11),143.96 (C-2, 6), 157.34 (C-14), 167.76 (C-8, 8′). MS: m/z 1190.54 (M–1). Anal. calcd. for $C_{69}H_{81}N_3O_{15}$: C, 69.50; H, 6.85; N, 3.52. Found: C, 68.89; H, 7.00; N, 3.44.

Hexamethyl 4,4′,4″-(4,4′,4″-(benzene-1,3,5-triyltris (methylene))tris(oxy)tris(benzene-4,1-diyl))tris(2,6-dimethyl-1,4-dihydropyridine-3,5-dicarboxylate) (20)

Yellow solid (recrystallized from pet. ether/EtOAc, 6:4). Mp 140–142 °C. ^{1}H-NMR (300 MHz, $CDCl_3$) δ_H: 2.31 (s, 18 protons at H-7, 7′), 3.63 (s, 18 protons at H-9, 9′), 4.94 (s, 3 protons at H-4), 4.98 (s, 6 protons at H-15, 15′, 15″), 6.01 (bs, 3 protons at -NH), 6.79 (d, J = 8.4 Hz, 6 arom. protons at H-13, 13′), 7.17 (d, J = 8.1 Hz, 6 arom. protons at H-12, 12′), 7.38 (s, 3 arom. protons at H-17, 17′, 17″). ^{13}C-NMR (75 MHz, $CDCl_3$) δ_C: 19.46 (C-7, 7′), 38.31 (C-4), 50.98 (C-9, 9′), 69.64 (C-15, 15′, 15″), 103.82 (C-3, 5), 114.32 (C-13, 13′), 125.90 (C-17, 17′, 17″), 128.57 (C-12, 12′), 137.96 (C-11), 140.25 (C-16, 16′, 16″), 144.21 (C-2, 6), 157.08 (C-14), 168.15 (C-8, 8′). HRMS: m/z 1065.4260

Can. J. Chem. Downloaded from www.nrcresearchpress.com by University of Electronic and Science Techonology of China on 09/19/12
For personal use only.

(M^+). Anal. calcd. for $C_{60}H_{63}N_3O_{15}$: C, 67.59; H, 5.96; N, 3.94. Found: C, 67.71; H, 6.05; N, 3.86.

Hexamethyl 4,4′,4″-(4,4′,4″-(2,4,6-trimethylbenzene-1,3,5triyl)tris(methylene)tris(oxy)tris(benzene-4,1-diyl))tris (2,6-dimethyl-1,4-dihydropyridine-3,5-dicarboxylate)(21)

Yellow solid (recrystallized from pet. ether/EtOAc, 6:4). Mp 138–140 °C. ^{1}H-NMR (300 MHz, $CDCl_3$) δ_H: 2.32 (s, 18 protons at H-7,7′), 2.37 (s, 9 protons at H-18, 18′, 18″), 3.65 (s, 18 protons at H-9, 9′), 4.96 (s, 3 protons at H-4), 5.00 (s, 6 protons at H-15, 15′, 15″), 5.91 (bs, 3 protons at -NH), 6.86 (d, J = 7.5 Hz, 6 arom. protons at H-13, 13′), 7.21 (d, J = 6.9 Hz, 6 arom. protons at H-12, 12′). ^{13}C-NMR (75 MHz, $CDCl_3$) δ_C: 15.79 (C-18, 18′, 18″), 19.50 (C-7, 7′), 38.36 (C-4), 51.00 (C-9, 9′), 64.67 (C-15, 15′, 15″), 103.94 (C-3, 5), 114.00 (C-13, 13′), 128.55 (C-12, 12′), 131.76 (C-17, 17′, 17″), 139.16 (C-16, 16′, 16″), 140.12 (C-11), 144.12 (C-2, 6), 157.46 (C-14), 168.13 (C-8, 8′). HRMS: *m/z* 1107.4721 (M^+). Anal. calcd. for $C_{63}H_{69}N_3O_{15}$: C, 68.28; H, 6.28; N, 3.79. Found: C, 68.88; H, 6.12; N, 3.68.

Octaethyl 4,4′,4″,4‴-(4,4′,4″,4‴-(benzene-1,2,4,5-tetrayltetrakis(methylene))tetrakis(oxy) tetrakis(benzene-4,1-diyl))tetrakis(2,6-dimethyl-1,4-dihydropyridine-3,5-dicarboxylate) (23)

White solid (recrystallized from pet. ether/EtOAc, 6:4). Mp 174–176 °C. ^{1}H-NMR (300 MHz, $CDCl_3$) δ_H: 1.21 (t, J = 6 Hz, 24 protons at H-10, 10′), 2.31 (s, 24 protons at H-7, 7′), 4.08 (q, 16 protons at H-9, 9′), 4.92 (s, 4 protons at H-4), 5.07 (s, 8 protons at H-15, 15′, 15″, 15‴), 5.90 (bs, 4 protons at -NH), 6.79 (d, J = 6 Hz, 8 arom. protons at H-13, 13′), 7.18 (d, J = 7.2 Hz, 8 arom. protons at H-12, 12′), 7.61 (s, 2 arom. protons at H-17, 17′). ^{13}C-NMR (75 MHz, $CDCl_3$) δ_C: 14.25 (C-10, 10′), 19.50 (C-7, 7′), 38.60 (C-4), 59.69 (C-9, 9′), 67.52 (C-15, 15′, 15″, 15‴), 104.14 (C-3, 5), 114.12 (C-13, 13′), 127.51 (C-17, 17′), 128.91 (C-12, 12′), 136.92 (C-11), 140.68 (C-16, 16′, 16″, 16‴), 143.81 (C-2, 6), 156.89 (C-14), 167.70 (C-8, 8′). MS: *m/z* 1505.60 (M–1). Anal. calcd. for $C_{86}H_{98}N_4O_{20}$: C, 68.51; H, 6.55; N, 3.72. Found: C, 69.32; H, 6.70; N, 3.64.

Octamethyl 4,4′,4″,4‴-(4,4′,4″,4‴-(benzene-1,2,4,5-tetrayltetrakis(methylene))tetrakis(oxy) tetrakis(benzene-4,1-diyl))tetrakis(2,6-dimethyl-1,4-dihydropyridine-3,5-dicarboxylate) (24)

White solid (recrystallized from pet. ether/EtOAc, 6:4). Mp 160–162 °C. ^{1}H-NMR (300 MHz, $CDCl_3$) δ_H: 2.30 (s, 24 protons at H-7, 7′), 3.62 (s, 24 protons at H-9, 9′), 4.93 (s, 4 protons at H-4), 5.05 (s, 8 protons at H-15, 15′, 15″, 15‴), 6.11 (bs, 4 protons at -NH), 6.77 (d, J = 8.1 Hz, 8 arom. protons at H-13, 13′), 7.14 (d, J = 8.1 Hz, 8 arom. protons at H-12, 12′), 7.58 (s, 2 arom. protons at H-17, 17′). ^{13}C-NMR (75MHz, $CDCl_3$) δ_C: 19.45 (C-7, 7′), 38.27 (C-4), 51.00 (C-9, 9′), 67.51 (C-15, 15′, 15″, 15‴), 103.77 (C-3, 5), 114.33 (C-13, 13′), 124.92 (C-17, 17′, 17″, 17‴), 128.55 (C-12, 12′), 135.26 (C-11), 140.32 (C-16, 16′, 16″, 16‴), 144.32 (C-2, 6), 156.94 (C-14), 168.17 (C-8, 8′). MS: *m/z* 1393.53 (M–1). Anal. calcd. for $C_{78}H_{82}N_4O_{20}$: C, 67.13; H, 5.92; N, 4.01. Found: C, 67.86; H, 5.65; N, 3.94.

Supplementary data

Supplementary data for this article are available on the journal Web site (www.nrcresearchpres.com/cjc).

Acknowledgements

This work was supported by Department of Science & Technology, Government of India (Grant No. SR/FTP/CS-108/2006) and are gratefully acknowledged. The authors are also thankful to the VIT University management for their generous support and facilities.

References

(1) Hantzsch, A. *Chem. Ber.* **1881** *14* (2), 1637. doi:10.1002/cber.18810140214.
(2) The Merck Index. 12th ed.; Merck Research Laboratories: Rahway, NJ, 1996, 1121.
(3) Bostrom, S. L.; Ljung, B.; Mardh, S.; Forsen, S.; Thulin, E. *Nature* **1981** *292* (5825), 777. doi:10.1038/292777a0.
(4) Iwanami, M.; Shibanuma, T.; Fujimoto, M.; Kawai, R.; Tamazawa, K.; Takenaka, T.; Takahashi, K.; Murakami, M. *Chem. Pharm. Bull.* **1979** *27* (6), 1426. Available from: http://www.journalarchive.jst.go.jp/english/jnlabstract_en.php?cdjournal=cpb1958&cdvol=27&noissue=6&startpage=1426.
(5) Arrowsmith, J. E.; Campbell, S. F.; Cross, P. E.; Stubbs, J. K.; Burges, R. A.; Gardiner, D. G.; Blackburn, K. J. *J. Med. Chem.* **1986** *29* (9), 1696. doi:10.1021/jm00159a022.
(6) Klusa, V. *Drugs Future* **1995** *20* (2), 135.
(7) Bretzel, R. G.; ; Bollen, C. C.; Maeser, E.; Federlin, K. F. *Am. J. Kidney. Dis.* **1993** *21* (6), S53. Available from: http://www.ajkd.org/article/0272-6386%2893%2970125-I/abstract.
(8) Bretzel, R. G.; Bollen, C. C.; Maeser, E.; Federlin, K. F. *Drugs Future* **1992** *17*, 465.
(9) Boer, R.; Gekeler, V. *Drugs Future* **1995** *20* (5), 499.
(10) Zhu, S.; Tu, S.; Gao, Y.; Miao, C.; Li, T.; Zhang, X.; Fang, F.; Shi, D. *Synth. Commun.* **2005** *35* (8), 1011. doi:10.1081/SCC-200054183.
(11) Zolfigol, M. A.; Kolvari, E.; Abdoli, A.; Shiri, M; ., ; Mol Divers, .
(12) Hulme, C.; Gore, V. *Curr. Med. Chem.* **2003** *10* (1), 51. doi:10.2174/0929867033368600.
(13) Zhu, J. *Eur. J. Org. Chem.* **2003** *7* (7), 1133. doi:10.1002/ejoc.200390167.
(14) Orru, R. V. A.; de Greef, M. *Synthesis* **2003** *10* (10), 1471. doi:10.1055/s-2003-40507.
(15) Debache, A.; Boulcina, R.; Belfaitah, A.; Rhouati, S.; Carboni, B. *Synlett* **2008** *4* (4), 509. doi:10.1055/s-2008-1032093.
(16) Suresh; Kumar, D.; Sandhu, J. S. *Synth. Commun.* **2009** *39* (11), 1957. doi:10.1080/00397910802622762.
(17) Rajesh, K.; Vijayakumar, V.; Narasimhamurthy, T.; Suresh, J.; Tiekink, E. R. T. *Acta Crystallogr.* **2010** *E66*, o985.
(18) Rathore, R. S.; Palakshi Reddy, B.; Vijayakumar, V.; Venkat Ragavan, R.; Narasimhamurthy, T. *Acta Crystallogr.* **2009** *B65*, 375.
(19) Fun, H.-K.; Goh, J. H.; Palakshi Reddy, B.; Sarveswari, S.; Vijayakumar, V. *Acta Crystallogr.* **2009** *E65*, o2247.
(20) Mookiah, P.; Rajesh, K.; Narasimhamurthy, T.; Vijayakumar, V.; Srinivasan, N. *Acta Crystallogr.* **2009** *E65*, o2664.
(21) Vijayakumar, V.; Rajesh, K.; Suresh, J.; Narasimhamurthy, T.; Nilantha Lakshman, P. L. *Acta Crystallogr.* **2010** *E66*, o170.
(22) Rajesh, K.; Vijayakumar, V.; Sarveswari, S.; Narasimhamurthy, T.; Tiekink, E. R. T. *Acta Crystallogr.* **2010** *E66*, o1306.
(23) Rajesh, K.; Vijayakumar, V.; Sarveswari, S.; Narasimhamurthy, T.; Tiekink, E. R. T. *Acta Cryst*. **2010** *E66*, o1988.

Silver nanotubes — Biopolymer-assisted hydrothermal synthesis

Jianmao Yang, Shuyan Gao, Xiaoxia Jia, Yanli Chen, Zhigang Chen, and Junqing Hu

Abstract: In this paper, we further the biopolymer-assisted hydrothermal approach to synthesize silver nanotubes with an outer diameter of 200–300 nm, a tube wall around 50 nm, and a length of several micrometers. Here, the biopolymer is a hyaluronic acid potassium salt (HAPS). This result further verified the validity of this green biopolymer-assisted hydrothermal route for the fabrication of nanomaterials. It also gives some proof that HAPS can provide an anisotropic growth environment, which favors the formation of silver nanotubes with a nonlayered structure. The formation mechanism has been tentatively explained based on Ostwald ripening and the capping action of HAPS. In the long run, the obtained silver nanotubes can be used as a chemical template to fabricate alloyed nanotubes through the galvanic replacement reaction.

Key words: green synthesis, silver, nanotubes, hydrothermal, biopolymer.

Résumé : Dans ce travail, on préconise l'approche hydrothermale assistée par des biopolymères pour réaliser la synthèse de nanotubes d'argent avec un diamètre extérieur de 200 à 300 nm, autour d'une surface en forme de tube de 50 nm, et dont la longueur s'étend sur plusieurs micromètres. Dans cette étude, le biopolymère est le sel de potassium de l'acide hyaluronique (SPAH). Ce résultat confirme à nouveau la validité de cette voie hydrothermale assistée par des biopolymères pour la fabrication de nanomatériaux. Il apporte aussi une preuve à l'effet que le SPAH peut fournir un environnement de croissance anisotropique qui favorise la formation de nanotubes d'argent comportant une structure qui n'est pas en couche. On a expliqué provisoirement le mécanisme de formation en faisant appel à un mûrissement d'Ostwald et l'action de recouvrement du SPAH. À long terme, les nanotubes d'argent obtenus pourraient être utilisés comme moules chimiques dans la fabrication de nanotubes qui résulteraient d'alliages obtenus par le biais d'une réaction de remplacement galvanique.

Mots-clés : chimie durable, argent, nanotubes, hydrothermal, biopolymère.

[Traduit par la Rédaction]

Can. J. Chem. Downloaded from www.nrcresearchpress.com by Xi'an Jiaotong University on 09/19/12
For personal use only.

Introduction

Since the discovery of carbon nanotubes in 1991,[1] a lot of attention is currently focused on nanosized tubular materials because of their unique physical properties and potential applications as gas and fluid paths or reservoirs in catalysis, fuel cells, sensors, and separation systems.[2] For example, there have been reports on a variety of inorganic nanotubes based on boron nitride,[3] metal sulfides,[4] metal borates,[5] and metal oxides.[6] Besides harsh high-temperature processes,[1,3–5] other approaches, such as the use of physical templates, have been intensively developed for the synthesis of tubular nanomaterials. Due to the importance of noble metals in catalytic, optical, optoelectronic, magnetic, and other nanotechnological fields, gold,[7] nickel,[8] and palladium[9] nanotubes have been successfully synthesized by using nanoporous polymer and anodic aluminum films as templates. However, the templating synthesis is unfavorable to produce noble metals with tubular nanostructures at a low cost (the problems with scale-up, harsh conditions, and time and energy consumption) and high purity (the problem with impurities in the desired products originate from the templates). So, the preparation of noble metals with tubular nanostructures at low cost and high purity calls for a simpler and more tractable route.

Solution-phase syntheses may represent the most promising route to fabricate nanostructures in terms of cost, throughput, and the potential for high-volume production.[10] However, the growth of noble metals with tubular nanostructures from isotropic solutions has been a more challenging task because almost all noble metals are crystallized in the highly symmetric cubic lattices. For this system, anisotropic confinements have to be applied to induce and maintain one-dimensional (1D) growth. Recently, biomolecule-assisted synthesis of nanomaterials[11] has been developed and attracted great attention. Using this strategy, we successfully fabricated gold and silver sponges by a biopolymer-assisted hydrothermal route,[12] where hyaluronic acid potassium salt (HAPS; consisting of repeating disaccharide units of D-glucuronic acid and *N*-acetyl-D-glucosamine) was selected as the biopolymer and showed its outstanding features, which included benign water solubility, the ability to stabilize nanomaterials. and reducing properties. Fortunately, we obtained silver

Received 3 February 2011. Accepted 10 May 2011. Published at www.nrcresearchpress.com/cjc on 7 September 2011.

J. Yang. Research Center for Analysis and Measurement, Donghua University, Shanghai, 201620, P. R. China.
S. Gao, X. Jia, and Y. Chen. College of Chemistry and Environmental Science, Henan Normal University, 46 Jianshe street, Xinxiang, 453007, Henan, P. R. China.
Z. Chen and J. Hu. College of Materials Science and Engineering, Donghua University, Shanghai, 201620, P. R. China.

Corresponding author: Jianmao Yang (e-mail: yangjm@dhu.edu.cn) and Shuyan Gao (e-mail: shuyangao@htu.cn).

Can. J. Chem. Downloaded from www.nrcresearchpress.com by Xi'an Jiaotong University on 09/19/12
For personal use only.

nanotubes by modifying our previous one-step green-synthesis procedure.[12] This further verified that the selection of HAPS and the application of hydrothermal treatment are an effective strategy for the fabrication of intriguing metallic nanostructures. More importantly, this gives some evidence that HAPS can provide an anisotropic growth environment, which favors the formation of silver nanotubes. The specific advantages of this system mainly lie in the following aspects: the one-step strategy demonstrates that the process is easy to operate, the hydrothermal treatment determines that the product is well crystalline, the involvement of HAPS demonstrates that the method is environmentally benign, and the absence of a hard template avoids the time- and money-consuming post-treatment and the impurities from a template. To the best of our knowledge, there has been no report on the solution phase-based synthesis of silver nanotubes in the absence of a hard template. The formation mechanism is also tentatively proposed based on Ostwald ripening and the capping action of HAPS. Our goal was to (*i*) perfect and deepen the green biopolymer-assisted strategy for the synthesis of metal nanomaterials and (*ii*) further exploit the characteristic stabilizing, reducing, and capping capacities of HAPS under a hydrothermal condition.

Materials and methods

All chemical reagents were of analytical grade and used without further purification. All water used in this investigation was deionized by a Nanopure filtration system to a resistivity of 18 MΩ cm.

Silver nanotubes were synthesized by modifying our reported method.[12] In a typical procedure, an 8 mL aliquot of a 10 mmol/L aqueous solution of $AgNO_3$ was added to 10 mL of a 2.54 mmol/L aqueous solution of soluble HAPS (calculated by the repeating units). The mixture was then transferred into a stainless steel autoclave with a Teflon liner with a 50 mL capacity, and heated in an oven at 180 °C for 24 h. After the autoclave was air-cooled to room temperature unaided, the resulting gray-black precipitate was filtered and washed with dimethyl sulfoxide (DMSO) and distilled water. The product was redispersed in distilled water for further characterizations with X-ray diffraction (XRD) pattern, transmission electron microscopy (TEM), selected area electron diffraction (SAED), field emission scanning electron microscopy (FESEM), and energy-dispersive X-ray spectroscopy (EDS) to obtain detailed information on its phase purity, crystalline structure, and morphology.

The samples for XRD, TEM, SAED, FESEM, and EDS characterizations were prepared by placing an aliquot of the suspension on an ITO glass slide and carbon-coated copper grids, and allowing the solvent to slowly evaporate at room temperature. All the measurements were carried out at laboratory temperature. The XRD pattern was collected on a D/Max 2500 V/PC X-ray diffractometer using high-intensity Cu Kα1 radiation (λ = 1.54056 Å). TEM and SAED measurements were carried out in a JEM JEOL 2010 instrument operated at an accelerating voltage of 200 kV. The FESEM images and EDS were obtained on an XL30 ESEM FEG scanning electron microscope operated at 20 kV.

Results and discussion

Characterizations of silver nanotubes

The overall quality, phase purity, and composition of the products were assessed by XRD, which is compiled in Fig. 1. All the reflection peaks can be indexed to the face-centered cubic (fcc) unit cell structure of metallic silver with the space group *Fm*3 *m* (Joint Committee on Powder Diffraction Standards (JCPDS)card no. 87-0718). The observation of all the expected diffraction peaks substantiates the formation of crystalline silver. The intense and sharp (111) and (222) peaks in the XRD pattern also reveals that the products are anisotropically grown along the (111) plane of the fcc structure of metallic silver. The lattice constant (*a*) calculated from the XRD pattern was 4.079, which was quite consistent with the standard value of 4.077.

We observed the product through TEM by dropping the product dispersion on a carbon-coated copper grid. Figure 2a, a typical TEM image of the product, shows the 1D structure. Upon closer examination (Fig. 2*b*), the strong contrast between the dark wall and the pale centre can be clearly seen, indicating the formation of the hollow tubes with the diameter of tube wall about 50 nm and the length several micrometers. From other area (not shown), we can observe that there are silver nanoparticles with diameter of around 15 nm attached on the nanotubes' surface or dispersed in the suspension, which may provide a piece of evidence for the growth mechanism. The SAED pattern (Fig. 2*c*) of the tubular nanostructures displays strong, ordered, and linearly arranged electron diffraction spots, which are similar to single-crystal-like diffraction spots. These observations mean that these nanotubes have high crystallinity and preferred growth direction and are organized to form a specially ordered symmetry structure, which is in agreement with the XRD result.

The FESEM image (Fig. 3) reveals that the obtained materials consist of nanotubes, which are approximately 200–300 nm in outer diameter and several micrometers in length. Some nanoparticles not constituting the nanotubes can also be seen from the panorama (Fig. 2*a*), which is consistent with the results of the TEM images. Thus, it should be noted that the present synthesis conditions, such as the reactant concentrations, reactants' molar ratio, reaction time, and the experimental temperature, may not have been well optimized to produce silver nanotubes in a high yield. A much higher morphology purity and yield might be expected. The chemical compositions of the product are determined by EDS (figure not shown), which shows the peak corresponding to silver and indicates that the product is mainly the silver element.

Growth mechanism

Theoretically, the atoms in solid materials featuring a layered structure such as graphite, WS_2, and MoS_2 can be covalently bonded to form 2D layers, which can be stacked together through van der Waals interactions,[13] and rolled up into tubular structures. As a result, production of nanotubes from nonlayered materials often requires the use of templates such as carbon nanotubes (CNTs), nanowires, and porous membranes. The rolling of thin films due to residual stress has also been demonstrated to fabricate inorganic tubes with micrometer-sized openings.[14] Also, the relief from strain in the transformation from bilamellar structures to unilamellar sheets could drive the formation of tubular structures.[15]

Can. J. Chem. Downloaded from www.nrcresearchpress.com by Xi'an Jiaotong University on 09/19/12
For personal use only.

Fig. 1. XRD pattern for the silver nanotubes.

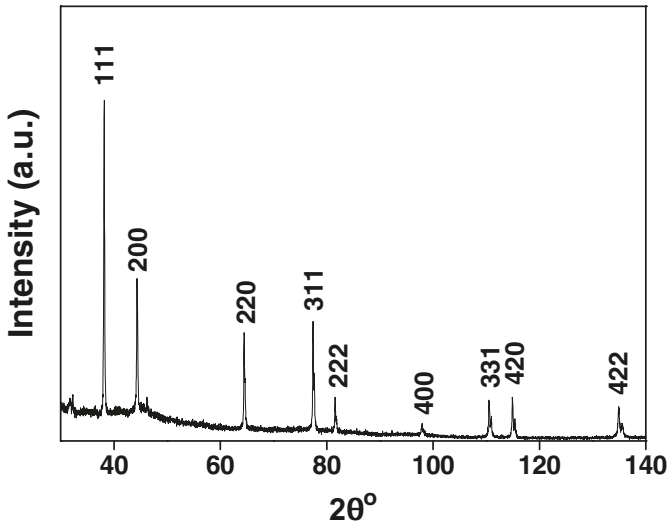

Fig. 2. (*a*) TEM images of a single silver nanotubes, (*b*) a magnified view, (*c*) and its corresponding SAED pattern.

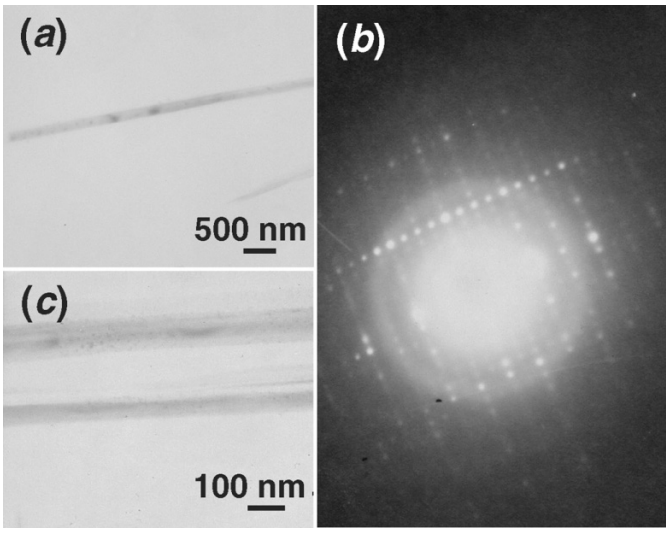

Fig. 3. (*a*) The FESEM image and (*b*) a magnified version of silver nanotubes on an ITO substrate with an initial molar ratio of 1:3 of HAPS to $AgNO_3$ for a reaction time of 24 h at 180 °C.

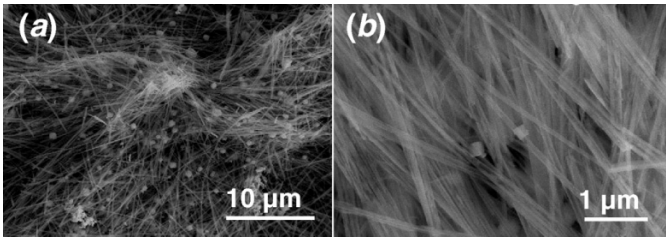

To date, nanotubes have been synthesized from a broad range of nonlayered inorganic materials, with examples including SiO_2,[16] TiO_2,[16] Al_2O_3,[17] In_2O_3,[18] Ga_2O_3,[18] CdS,[19] CdSe,[19] ZnS,[20] and Au.[21] Here, silver also belongs to nonlayered materials. However, the present synthesis conditions cannot meet the requirements of the three established approaches[13b] (i.e., nucleation-induced concentration depletion, hard templating procedures, and electrospinning technique) to fabricate tubular nanostructures from nonlayered materials. In addition, by comparing with the results reported earlier,[12] it can be seen that the participation of HAPS, the molar ratio between $AgNO_3$ and HAPS (Ag^+/HAPS), and the hydrothermal treatment determine the product's final morphology and structure, though without changing the product's crystal phase. An appropriate ratio of Ag^+/HAPS is critical to the construction of a tubular structure. With the increase of the relative concentration of silver ions, the products' structures change from discrete particle structures (not shown) to sponge-like structures[12] and then finally to nanotubes (Figs. 2 and 3). The reason may be that, at a relatively high biopolymer concentration, the biopolymer might have a stronger stabilizing capability, rather than the morphology directing the function.[22] Here, the explanation for the anisotropic formation instead of nanospheres probably involves Ostwald ripening[23] and the capping action of HAPS. Upon the reaction starting, the reduction of the silver ions would start producing small particles of silver metal, which will be stabilized by HAPS. As the reaction continued processing and heating, the small silver particles were no longer stable in solution, and they started to dissolve and contribute to the growth of larger ones. With the assistance of HAPS, some of the large nanoparticles were able to grow into a 1D structure with lateral dimensions. The exact role of HAPS in this process is not clear at the moment. One possible function for HAPS is to behave as a capping agent to kinetically control the growth rates of different crystals, just as Xia and co-workers[23a] report in exploring the poly(vinyl pyrrolidone) (PVP)-mediated silver nanowire growth mechanism, because, at an elevated temperature, the equilibrium constant for HAPS binding to certain crystal faces of silver may begin to differ, leading to selective loss of HAPS on certain crystal faces and allowing for the nanoparticle to grow along only one axis. This agrees with the "poisoning" mechanism. In this case, the "poison" adsorbed on some crystalline surfaces could significantly decrease their growth rates and lead to highly anisotropic growth.[24] In principle, the growth process would continue until all the small silver nanoparticles were completely consumed, and only nanotubes and the larger (more stable) nanoparticles survived (this also verifies that the presence of nanoparticles is reasonable). Certainly, only the above knowledge is far beyond the comprehensive and deep understanding of the growth mechanism of silver nanotubes, instead of nanowires, in our system. The underlying mechanism needs further investigation to make the synthesis of silver nanotubes controllable and their applications in nanotechnology realistic.

Conclusion

In summary, the simple procedure based on a biopolymer-assisted technique has been further developed to spontaneously fabricate silver nanotubes under hydrothermal conditions by controlling the synthesis conditions. This result further verified the validity of this green biopolymer-assisted hydrothermal route for the fabrication of nanomaterials. It also gives some proof that HAPS can provide an anisotropic growth environment, which favors the formation of silver nanotubes with a nonlayered structure. The formation mechanism has also been tentatively explained based on Ostwald ripening and the capping action of HAPS.

From the viewpoint of nanotechnology, the obtained silver nanotubes could act as a chemical template for the fabrication of alloyed nanotubes through the galvanic replacement reaction between Ag nanotubes and an aqueous solution containing the metal ions Mn^{+}, whose redox potential is higher than that of the Ag^{+}/Ag pair. So, intense work aimed at optimizing the reaction conditions for the silver nanotubes synthesis and utilizing the obtained silver nanotubes for alloyed nanotubes is in progress.

Acknowledgements

The authors are grateful to the National Natural Science Foundation of China (No. 21071047), the Program for Science & Technology Innovation Talents in Universities of Henan Province (2011HASTIT010), the Henan Provincial Natural Science Foundation of China (092300410196), the Natural Science Foundation of Educational Department of Henan Province (2008A150014), the Scientific Starting Funds For young teachers of Donghua University (No. 228-10-0044019), and the Fundamental Research Funds for the Central Universities, the National Natural Science Foundation of China (Nos. 50872020 and 50902021).

References

(1) Iijima, S. *Nature* **1991**, *354* (6348), 56. doi:10.1038/354056a0.

(2) (a) Coontz, R.; Szuromi, P. *Science* **2000**, *290* (5496), 1523. doi:10.1126/science.290.5496.1523;; (b) Brumlik, C. J.; Menon, V. P.; Martin, C. R. *J. Mater. Res.* **1994**, *9* (5), 1174. doi:10.1557/JMR.1994.1174;; (c) Tremel, W. *Angew. Chem. Int. Ed.* **1999**, *38* (15), 2175. doi:10.1002/(SICI)1521-3773(19990802)38:15<2175::AID-ANIE2175>3.0.CO;2-J;; (d) van Bommel, K. J. C.; Friggeri, A.; Shinkai, S. *Angew. Chem. Int. Ed.* **2003**, *42* (9), 980. doi:10.1002/anie.200390284.

(3) Chopra, N. G.; Luyken, R. J.; Cherrey, K.; Crespi, V. H.; Cohen, M. L.; Louie, S. G.; Zettl, A. *Science* **1995**, *269* (5226), 966. doi:10.1126/science.269.5226.966.

(4) (a) Tenne, R.; Margulis, L.; Genut, M.; Hodes, G. *Nature* **1992**, *360* (6403), 444. doi:10.1038/360444a0;; (b) Feldman, Y.; Wasserman, E.; Srolovitz, D. J.; Tenne, R. *Science* **1995**, *267* (5195), 222. doi:10.1126/science.267.5195.222.

(5) Ma, R.; Bando, Y.; Golberg, D.; Sato, T. *Angew. Chem. Int. Ed.* **2003**, *42* (16), 1836. doi:10.1002/anie.200250455.

(6) (a) Hahn, R.; Schmidt-Stein, F.; Salonen, J.; Thiemann, S.; Song, Y. Y.; Kunze, J.; Lehto, V.-P.; Schmuki, P. *Angew. Chem. Int. Ed.* **2009**, *48* (39), 7236. doi:10.1002/anie.200902207;; (b) Li, Y.; Ling, Z.; Hu, X.; Liu, Y.; Chang, Y. *Chem. Commun. (Camb.)* **2011**, *47*, 2173. doi:10.1039/c0cc04907g;; (c) Ghicov, A.; Schmuki, P. *Chem. Commun. (Camb.)* **2009**, *2009* (20), 2791. doi:10.1039/b822726h;; (d) Wang, Q.; Geng, B.; Wang, S.; Ye, Y.; Tao, B. *Chem. Commun. (Camb.)* **2010**, *46* (11), 1899. doi:10.1039/b922134d;; (e) Yada, M.; Mihara, M.; Mouri, S.; Kuroki, M.; Kijima, T. *Adv. Mater.* **2002**, *14* (4), 309. doi:10.1002/1521-4095(20020219)14:4<309::AID-ADMA309>3.0.CO;2-Q.

(7) Martin, C. R. *Science* **1994**, *266* (5193), 1961. doi:10.1126/science.266.5193.1961.

(8) Bao, J.; Tie, C.; Xu, Z.; Ma, Q.; Hong, J.; Sang, H.; Sheng, D. *Adv. Mater.* **2002**, *14* (1), 44. doi:10.1002/1521-4095(20020104)14:4<44::AID-ADMA44>3.0.CO;2-K.

(9) Steinhart, M.; Jia, Z.; Schaper, A. K.; Wehrspohn, R. B.; Gösele, U.; Wendorff, J. H. *Adv. Mater.* **2003**, *15* (9), 706. doi:10.1002/adma.200304502.

(10) (a) Alivisatos, A. P. *Science* **1996**, *271* (5251), 933. doi:10.1126/science.271.5251.933;; (b) Murphy, C. J.; Jana, N. R. *Adv. Mater.* **2002**, *14* (1), 80. doi:10.1002/1521-4095(20020104)14:4<80::AID-ADMA80>3.0.CO;2-#;; (c) El-Sayed, M. A. *Acc. Chem. Res.* **2001**, *34* (4), 257. doi:10.1021/ar960016n;; (d) Jin, R.; Cao, Y.; Mirkin, C. A.; Kelly, K. L.; Schatz, G. C.; Zheng, J. G. *Science* **2001**, *294* (5548), 1901. doi:10.1126/science.1066541;; (e) Sun, Y.; Xia, Y. *Science* **2002**, *298* (5601), 2176. doi:10.1126/science.1077229.

(11) (a) Wang, Z.; Liu, J.; Chen, X.; Wan, J.; Qian, Y. *Chemistry* **2005**, *11* (1), 160. doi:10.1002/chem.200400705;; (b) Zhou, Y. *Curr. Nanosci.* **2006**, *2* (2), 123. doi:10.2174/157341306776875785;; (c) Allred, D. B.; Sarikaya, M.; Baneyx, F.; Schwartz, D. T. *Nano Lett.* **2005**, *5* (4), 609. doi:10.1021/nl047967b;; (d) Huang, Y.; Chiang, C. Y.; Lee, S. K.; Gao, Y.; Hu, E. L.; Yoreo, J. D.; Belcher, A. M. *Nano Lett.* **2005**, *5* (7), 1429. doi:10.1021/nl050795d;; (e) Falkner, J. C.; Turner, M. E.; Bosworth, J. K.; Trentler, T. J.; Johnson, J. E.; Lin, T.; Colvin, V. L. *J. Am. Soc. Chem.* **2005**, *127* (15), 5274. doi:10.1021/ja044496m;; (f) Gao, X.; Djalali, R.; Haboosheh, A.; Samson, J.; Nuraje, N.; Matsui, H. *Adv. Mater.* **2005**, *17* (14), 1753. doi:10.1002/adma.200500357;; (g) Li, L.; Stupp, S. I. *Angew. Chem. Int. Ed.* **2005**, *44* (12), 1833. doi:10.1002/anie.200462142.

(12) Gao, S.; Zhang, H.; Wang, X.; Yang, J.; Zhou, L.; Peng, C.; Sun, D.; Li, M. *Nanotechnology* **2005**, *16* (11), 2530. doi:10.1088/0957-4484/16/11/012.

(13) (a) Tenne, R. *Angew. Chem. Int. Ed.* **2003**, *42* (42), 5124. doi:10.1002/anie.200301651;; (b) Xiong, Y.; Mayers, B. T.; Xia, Y. *Chem. Commun. (Camb.)* **2005**, *2005* (40), 5013. doi:10.1039/b509946c.

(14) Schmidt, O. G.; Eberl, K. *Nature* **2001**, *410* (6825), 168. doi:10.1038/35065525.

(15) Saupe, G. B.; Waraksa, C. C.; Kim, H.-N.; Han, Y. J.; Kaschak, D. M.; Skinner, D. M.; Mallouk, T. E. *Chem. Mater.* **2000**, *12* (6), 1556. doi:10.1021/cm981136n.

(16) Nakamura, H.; Matsui, Y. *J. Am. Chem. Soc.* **1995**, *117* (9), 2651. doi:10.1021/ja00114a031.

(17) Pu, L.; Bao, X.; Zou, J.; Feng, D. *Angew. Chem. Int. Ed.* **2001**, *40* (8), 1490. doi:10.1002/1521-3773(20010417)40:8<1490::AID-ANIE1490>3.0.CO;2-K.

(18) Cheng, B.; Samulski, E. T. *J. Mater. Chem.* **2001**, *11* (12), 2901. doi:10.1039/b108167e.

(19) Rao, C. N. R.; Govindaraj, A. G.; Deepak, F. L.; Gunari, N. A.; Nath, M. *Appl. Phys. Lett.* **2001**, *78* (13), 1853. doi:10.1063/1.1359145.

(20) Dloczik, L.; Engelhardt, R.; Ernst, K.; Fiechter, S.; Seiber, I.; Könenkamp, R. *Appl. Phys. Lett.* **2001**, *78* (23), 3687. doi:10.1063/1.1376427.

(21) Hulteen, J. C.; Jirage, K. B.; Martin, C. R. *J. Am. Chem. Soc.* **1998**, *120* (26), 6603. doi:10.1021/ja980045o.

(22) Lu, Q.; Gao, F.; Komarneni, S. *J. Am. Chem. Soc.* **2004**, *126* (1), 54. doi:10.1021/ja0386389.

(23) (a) Sun, Y.; Yin, Y. D.; Mayers, B. T.; Herricks, T.; Xia, Y. *Chem. Mater.* **2002**, *14* (11), 4736. doi:10.1021/cm020587b;; (b) Henglein, A.; Giersig, M. *J. Phys. Chem. B* **1999**, *103* (44), 9533. doi:10.1021/jp9925334;; (c) Silvert, P.-Y.; Herrera-Urbina, R.; Tekaia-Elhsissen, K. *J. Mater. Chem.* **1997**, *7* (2), 293. doi:10.1039/a605347e.

(24) (a) Almeida, M.; Alcácer, L. *J. Cryst. Growth* **1983**, *62* (1), 183. doi:10.1016/0022-0248(83)90023-4;; (b) Iguchi, M.; Murase, I. *J. Cryst. Growth* **1974**, *24–25*, 596. doi:10.1016/0022-0248(74)90386-8.

Can. J. Chem. Downloaded from www.nrcresearchpress.com by Xi'an Jiaotong University on 09/19/12
For personal use only.

Polyphosphazenes containing lactic acid ester and methoxyethoxyethoxy side groups — Thermosensitive properties and, in vitro degradation, and biocompatibility

Yunmei Bi, Xiaoying Gong, Feng He, Li Xu, Lin Chen, Xianghui Zeng, and Li Yu

Can. J. Chem. Downloaded from www.nrcresearchpress.com by Xi'an Jiaotong University on 09/19/12
For personal use only.

Abstract: The thermosensitive and hydrolytic properties and biocompatibility of polyphosphazenes containing lactic acid ester and methoxyethoxyethoxy as co-substitutents were investigated. Depending on the type of lactic acid ester, these polyphosphazenes exhibited lower critical solution temperatures (LCST) (from 33 to 52 °C), which were almost concentration-independent in the range of 1.5 to 15 wt% of the polymers in aqueous solution. The salt effect on the thermosensitivity of the polymers was studied by measuring their LCST in aqueous solutions containing various salts. Bu_4NBr and KI showed salting-in effects among the tested six salts, but NH_4Br, NaBr, NH_4Cl, and NaCl showed salting-out effects. Hydrolysis studies showed the rate of polymer hydrolysis decreased in the order of basic > acidic > neutral solution. The polyphosphazene with bulkier and more hydrophobic ester groups was more stable in hydrolysis. The results of a cytotoxicity study using an MTT assay method with HepG2 cell and K562/VCR cell showed that these polyphosphazenes and their degradation products were biocompatible. The thermoresponsiveness and biocompatibility of these biodegradable polyphosphazenes may favor the polymers as potential stimuli-responsive materials in biomedical applications.

Key words: polyphosphazenes, thermosensitive property, hydrolytic degradation, biocompatibility.

Résumé : On a étudié les propriétés de thermosensibilité et hydrolytiques ainsi que le biocompatibilité des polyphosphazènes contenant un ester de l'acide lactique et un groupement méthoxyéthoxyéthoxy comme cosubstituants. Suivant les types d'esters de l'acide lactique, ces polyphosphazènes présentent des températures critiques inférieures de solubilité (TCIS) qui s'étalent de 33 à 55 °C et qui sont pratiquement indépendantes de la concentration dans la plage de 1,5 à 15 % en poids de polymère, en solution aqueuse. On a étudié l'effet de sel sur la thermosensibilité des polymères en mesurant les TCIS de solutions aqueuses contenant divers sels. Parmi les six sels examinés, le Bu_4NBr et le KI ont pour effet d'augmenter la solubilité alors que le NH_4Br, le NaBr, le NH_4Cl et le NaCl présentent plutôt l'effet inverse de relargage. Les études d'hydrolyse montrent que la vitesse d'hydrolyse diminue dans l'ordre des solutions basique > acide > neutre. Les polyphosphazènes portant des groupes esters plus encombrants ou hydrophobes sont plus stables vis-à-vis de l'hydrolyse. Les résultats de cytotoxicité obtenus à l'aide d'une méthode MTT, aux sels de tétrazolium, avec la cellule HepGe2 et la cellule K562/VCR ont montré que ces polyphosphazènes et leurs produits de dégradation sont biocompatibles. Les propriétés de réponse thermique et de biocompatibilité de ces polyphosphazènes biodégradables pourraient favoriser les polymères comme matériaux potentiels pouvant répondre à des stimulus dans des applications biomédicales.

Mots-clés : polyphosphazènes, propriété de thermosensibilité, dégradation hydrolytique, biocompatibilité.

[Traduit par la Rédaction]

Introduction

Thermosensitive polymers have been investigated for biomedical and pharmaceutical applications.[1,2] Their solutions exhibit a phase transition known as the lower critical solution temperature (LCST), below which the polymers are soluble. When the temperature is raised above the LCST, the polymers precipitate from solution. This phenomenon is reversible and thus when the temperature is lowered, the polymers become soluble again. The most often investigated poly(N-substituted acrylamide)s, including poly(*N*-isopropylacrylamide) (PNIPAM),[3,4] poly(*N*,*N*′-diethylacrylamide),[5] and poly(2-carboxyisopropyl-acrylamide),[6] are representatives of thermosensitive polymers. PNIPAM shows a LCST around body temperature (at 32 °C) and therefore extensive studies have been performed for applications of the homopolymer or copolymers of PNIPAM to drug delivery systems.[7,8] But the

Received 21 February 2011. Accepted 24 May 2011. Published at www.nrcresearchpress.com/cjc on 7 September 2011.

Y. Bi, X. Gong, F. He, L. Xu, and L. Chen. College of Chemistry and Chemical Engineering, Yunnan Normal University, Kunming 650092, P.R. China.
X. Zeng. School of Chemical Science and Technology, Yunnan University, Kunming 650031, P.R. China.
L. Yu. College of Chemistry and Chemical Engineering, Chonqing College of Science and Technology, Chongqing 40042, P.R. China.

Corresponding author: Yunmei Bi (e-mail: yunmeibi@hotmail.com).

Can. J. Chem. Downloaded from www.nrcresearchpress.com by Xi'an Jiaotong University on 09/19/12
For personal use only.

nonbiodegradability of these polymers may be a serious limitation to their widespread use in the biomedical field.

One family of polymers where a large variability in properties is feasible is the polyphosphazenes.[9] Polyphosphazenes are hybrid polymers possessing a backbone of alternating nitrogen and phosphorus atoms with organic side groups attached to the phosphorus atoms. Polymers with a wide range of useful properties can be designed and attained by nucleophilic substitution of poly(dichlorophosphazene) (PDCP) with various organic groups.[10–12] Efforts have been made to develop thermosensitive polyphosphazenes. Allcock and co-workers,[13–15] who extensively explored the field of polyphosphazene synthesis, suggested that polyphosphazenes that bear oligoethylene oxide units exhibit a LCST in aqueous solution. Couffin-Hoarau and Leroux[16] reported that polyphosphazenes with ethylene oxide, alkyl chains, and amino butyric acid substituents presented LCSTs in the range of 32–44 °C and pH-sensitive properties. A series of thermosensitive polyphosphazenes bearing methoxy-poly(ethylene glycol) or α-amino-ω-methoxy-poly(ethylene glycol) and amino acid esters were synthesized by Song and co-workers[17–19] These polyphosphazenes were biodegradable. Thermosensitive amphiphilic graft polyphosphazenes with oligopoly(*N*-isopropylacrylamide) and amino acid esters as side groups were described by Qiu and co-workers[20] Their self-assembly behaviors were also studied in detail.[21] However, to the best of our knowledge, the reports on the biocompatibility of biodegradable thermosensitive polyphosphazenes and their degradation products are very limited.[22]

Our attention has been focused on biodegradable thermosensitive polyphosphazenes containing lactic acid ester side groups.[23] Poly(lactic acid) (PLA) is an important aliphatic polyester with degradable properties and extensive application in the biomedical area.[24] However, PLA degrades slowly and its highly concentrated degradation products have a toxic influence,[25] limiting its use to certain applications. Poly[bis(ethyl lactato) phosphazene] and poly[bis(benzyl lactato) phosphazene] hydrolyze at a faster rate than PLA.[26] In this paper, we present the results of our study on the thermosensitive and hydrolytic properties and the biocompatibility of polyphosphazenes bearing lactic acid esters and methoxyethoxyethoxy (MEE).

Results and discussion

Structural characterization

The existence of only one peak in the ^{31}PNMR spectrum of the mixed-substituent polymer **3** as indicated in the Experimental section is presumably a result of the close resonances of homogeneously substituted bis(MEE)-substituted phosphorus[13] and bis(butyl lactato)-substituted phosphorus and the expected heterogeneously substituted phosphorus. Such a result and the data of elemental analysis implied that the chlorine atoms of poly(dichlorophosphazene) were completely substituted stepwise by butyl lactato and MEE. Polymers **1**–**3** showed almost the same chemical shifts because phosphorous environments were not seriously changed.[23]

The IR spectrum of polymer **3** (Fig. 1) showed absorption bands for a carbonyl of the ester group (1739.1 cm^{-1}), P=N (1240.7 cm^{-1}), and C–O–C (1108.2 cm^{-1}). In the ^{1}H NMR spectrum of polymer **3** (Fig. 2*a*), peaks at 0.93, 1.36, 1.52, 1.61, 4.16, and 4.97 ppm are attributed to the protons of butyl lactate, whereas the protons of one methoxyl and four oxymethylene in MEE appear at 3.37 and 3.71–3.40 ppm, respectively. These results for the ^{1}H NMR spectrum were mirrored in the ^{13}C NMR spectrum (Fig. 2*b*) of polymer **3**, which added further support to the structural assignments. The integration data analyzed between the methyl protons of butyl lactato and the methoxyl protons of the MEE in the ^{1}H NMR spectrum indicated that the relative ratios of two substituents of polymer **3** is about 1:1, the same as designed. Also, the relative ratio of two pendant groups on polymers **1** and **2** is ~1:1.[23]

Fig. 1. IR spectrum of polymer **3**.

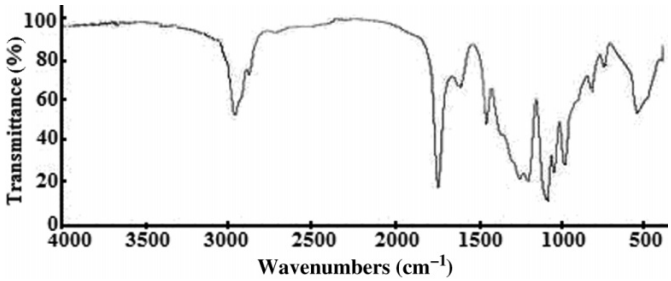

Fig. 2. (*a*) ^{1}H NMR and (*b*) ^{13}C NMR spectra of polymer **3**.

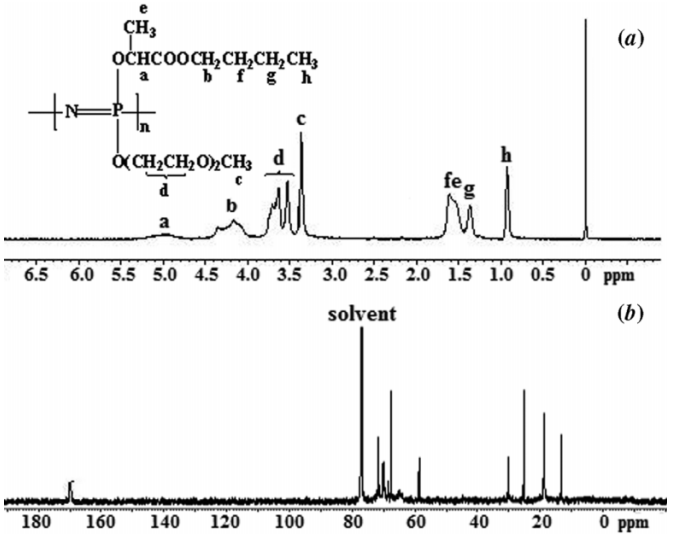

Thermal analyses reveal that the glass transition temperatures (T_g) of polymers **1**–**3** are 49.9, 44.0, and 55.7 °C, respectively.[23] These relatively low T_gs facilitated the fabrication of drug formulations in mild conditions, especially for delicate bioactive substances.[27]

Thermosensitivity

By visual inspection polymers **1**–**3** are readily soluble in water at room temperature, but the clear aqueous solutions turn turbid when heated. The LCSTs of the polymers were measured and the concentration dependence of the LCSTs was investigated in the range of 0.13–15 wt% by turbidity measurements using a UV–vis spectrophotometer. As shown in Fig. 3, the LCSTs of polymers **1**–**3** were 52, 41, and 33 °C, respectively. It has been suggested that the LCST behavior of a polymer is caused by a critical balance between hydrophilic and hydrophobic groups in the polymer and the effect of that

Can. J. Chem. Downloaded from www.nrcresearchpress.com by Xi'an Jiaotong University on 09/19/12
For personal use only.

Fig. 3. Dependence of lower critical solution temperatures (LCSTs) on concentrations of polymers **1**–**3**.

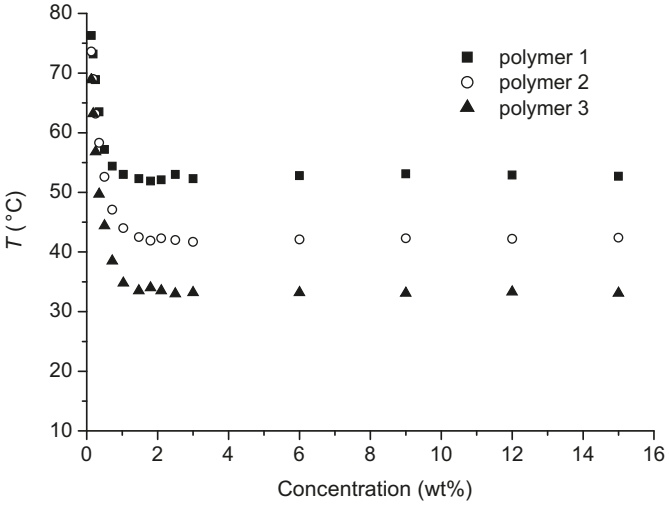

Fig. 4. The pH effect on lower critical solution temperatures (LCSTs) of polymers **1**–**3**.

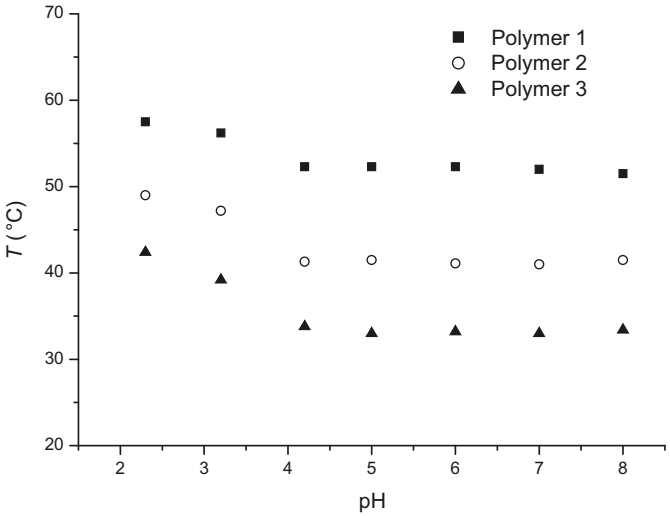

balance on the interaction through hydrogen bonding between the polymer and water molecules. Below the LCST, owing to their three oxygen atoms, the MEE groups develop strong hydrogen-bond interaction with water and thus ensure polymer hydrosolubility. As the temperature is raised, the hydrogen bonds weaken and hydrophobic interactions increase and become predominant above the LCST. Increasing the hydrophobicity of the polymer leads to a decrease in the LCST of the polymer in aqueous solution. Such a tendency was also observed in our polymer system. The LCST decreased in the following order: **1** > **2** > **3**. The more hydrophobic ester afforded the lower LCST. In addition, it was found that the LCSTs of polymers **1**–**3** were independent in the range of 1.5–15wt% of the polymer but increased at lower concentrations as observed for other thermosensitive polymers.[14,18]

The polymers were examined in citric acid / disodium hydrogen phosphate buffer solutions at different pH to determine whether the the LCSTs might be pH dependent, and the results are shown in Fig. 4. Analysis of the LCST values for each polymer showed them to be essentially independent in the buffer solutions at pH > 4. However, a slight increase in the LCST was detected in the acidic media at pH < 3 and was found for all the polymers studied. This result may be explained by the following way: in acidic media, the carbonyl oxygen atoms within lactic acid ester groups are protonated, increasing the solubility of the polymers, resulting in an increase of their LCST.

Thermosensitive polymers may be used as stimuli-responsive materials applicable in the biomedical field. The systems utilized in biological applications are usually not salt-free. It is known that salt component and content can influence the LCST of thermosensitive polymers.[18] To study the salt effect on the LCSTs of polymers **1**–**3**, different concentrations of NaCl, NaBr, KI, NH_4Br, NH_4Cl, or Bu_4NBr were added to the aqueous polymer solutions (1.5%), and their LCSTs were measured; the results are shown in Fig. 5. The LCSTs of polymer solutions in the presence of NaCl, NaBr, NH_4Br, and NH_4Cl decreased with an increase in the salt concentration, within the range used here. The salt effect on the LCSTs of polymers **1**–**3** decreased in the order of NaCl > NH_4Cl > NaBr > NH_4Br. However, the addition of Bu_4NBr caused an increase in the LCSTs of polymers **1**–**3**, and the LCSTs increased with increasing concentration of salt. When KI was added to each aqueous polymer solution, some smaller increases in LCST were observed. Such a phenomenon is known to be a general trend in the salt effect on the LCST of thermosensitive polymers.[28] It is known that the anion is important in the salt effect. The rank of the relative influence of ions on the physical behavior of aqueous systems is well-established.[29] The accepted explanation is based on the ability of a particular ion to alter the hydrogen bond networks of water.[30] Some ions, are believed to be "water structure makers", are strongly hydrated, and have stabilizing and salting-out effects on macromolecules. Others, would-be "water structure breakers", originate salting-in effects and destabilize folded macromolecules. The present results can be explained in a similar context. Cl^- and Br^-, water structure makers, weaken hydrogen bonding between molecules of water and polymers, resulting in a decrease of their LCSTs. However, I^-, a large ion, is a water structure breaker, and thus increases the interaction of water with polymers, resulting in an increase in LCST. The inorganic salts showed nearly the same effect on LCSTs of polymers **1**–**3**. This result seems to be due to lower sensitivity of the hydrophobic lactic acid ester to inorganic salts. Bu_4NBr molecules with a strongly hydrophobic nature make the polymers more soluble because of the binding of Bu_4NBr with the polymers through hydrophobic interactions, resulting in an increase in LCSTs. So it is easy to understand that the LCST of the polymers increased with the addition of Bu_4NBr more sharply because of the increasing hydrophobicity of the lactic acid ester groups.

Hydrolytic degradation

The hydrolytic degradation of polymers **1**–**3** was performed in buffer solutions at pH 3.4, 7.4, and 10.8 at 37 °C. Figure 6 shows the profiles of the time-dependent molecular weight decrease of three polymers in different buffer solutions. The polymers showed a significant decline in molecular weight, the structure of the ester groups of the lactic acids attached to the polymers affected the degradation of

Can. J. Chem. Downloaded from www.nrcresearchpress.com by Xi'an Jiaotong University on 09/19/12
For personal use only.

Fig. 5. Salt effect on lower critical solution temperatures (LCSTs) of polymers (*a*) **1**, (*b*) **2**, and (*c*) **3**.

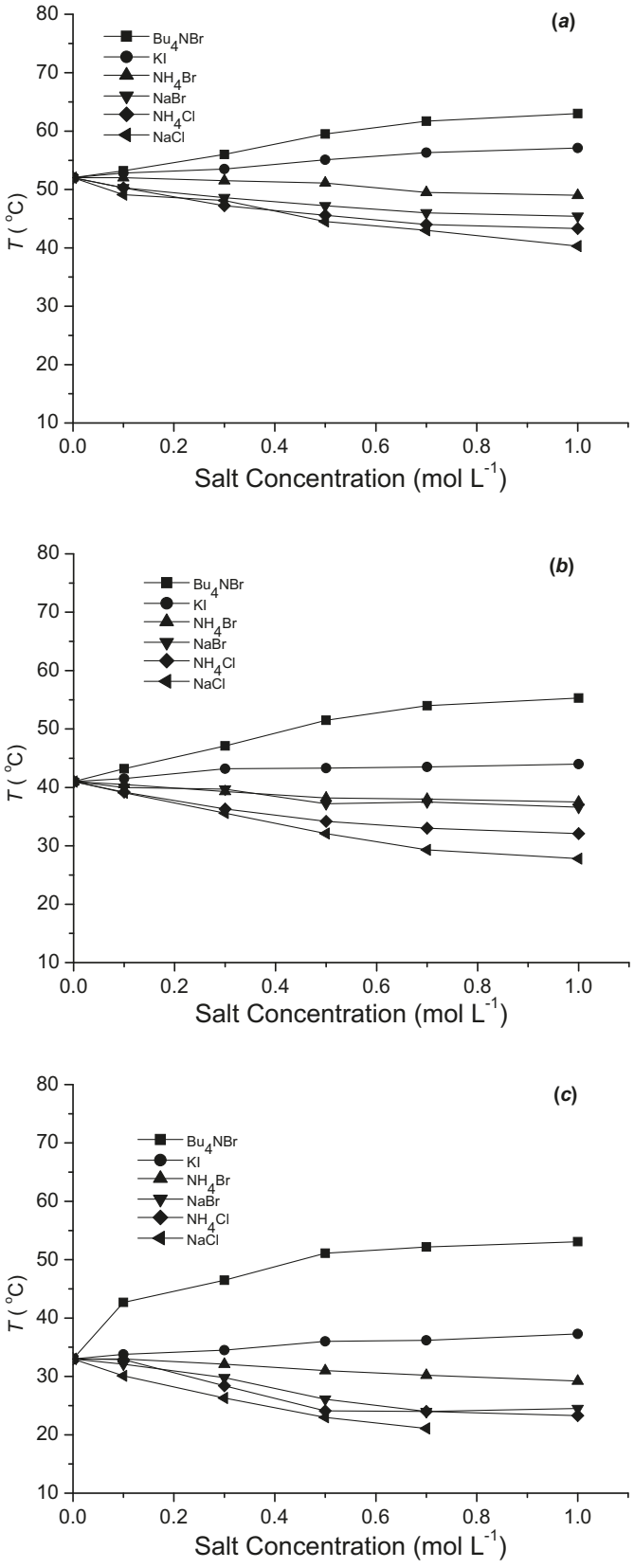

Fig. 6. Time-dependent hydrolytic degradation of polymers **1**–**3** at (*a*) pH 3.4, (*b*) pH 7.4, and (*c*) pH 10.8.

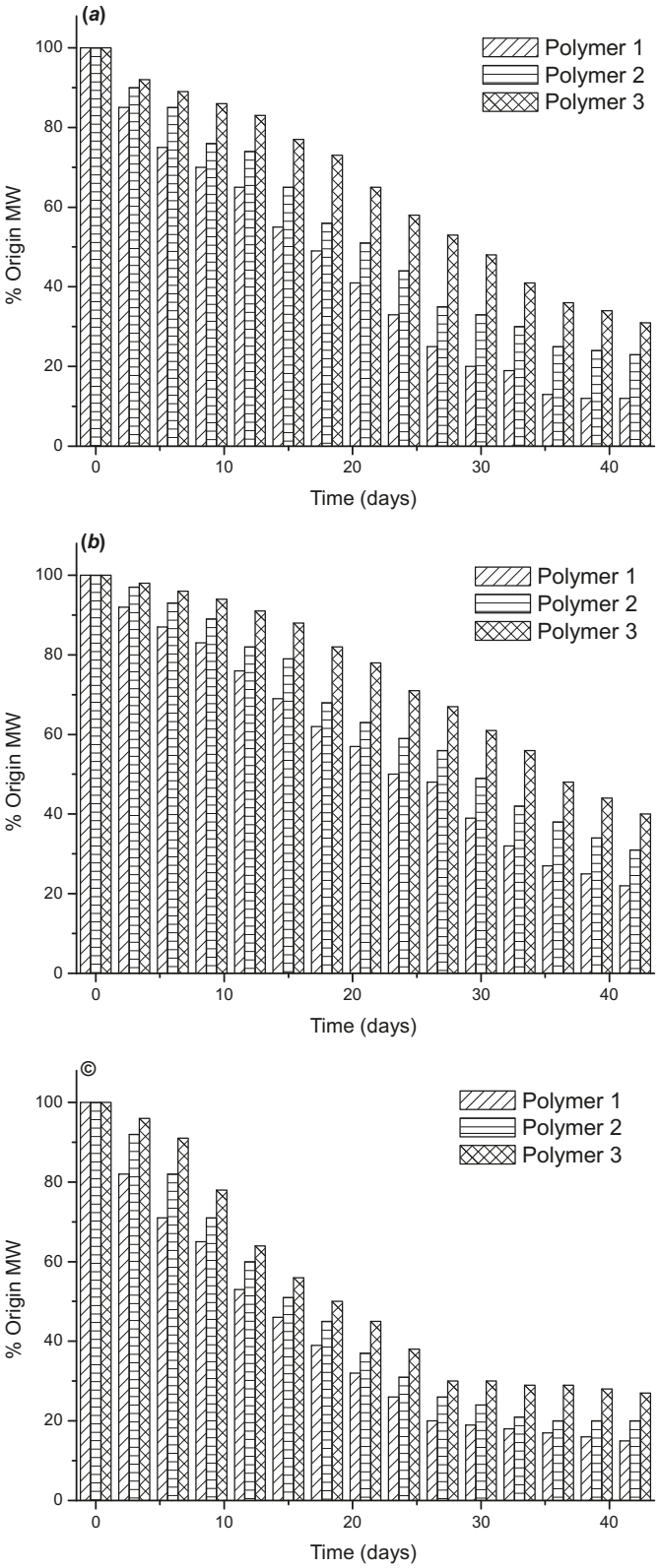

polymers, and polymer **1** showed the fastest degradation, followed by polymer **2**, and then polymer **3** in all the buffer solutions. This trend can be explained on the basis of the differences in the bulkiness and hydrophobicity of the side

Table 1. Identification of the hydrolytic products of polymers **1**–**3** after incubation for 42 days at 37 °C.

	Polymer								
	1			**2**			**3**		
pH	3.4	7.4	10.8	3.4	7.4	10.8	3.4	7.4	10.8
Phosphate[a]	+++	+	+++	+++	+	+++	++	+	+++
Ammonia	+++	+	+++	++	+	+++	+	+	++
Lactic acid	++	+	+++	++	+	+++	++	+	++
Alcohols[b]	++	+	+++	++	+	+++	+	+	++

[a]The relative amount detected.

[b]Ethanol, propanol, or butanol.

Can. J. Chem. Downloaded from www.nrcresearchpress.com by Xi'an Jiaotong University on 09/19/12
For personal use only.

groups.[18,31] For polymer **1**, co-substitution of ethyl lactato units and MEE units reduces the steric shield that can protect the polymer backbone against hydrolysis cleavage and leads to a faster loss in molecular weight. For polymer **3**, bulkier butyl lactato groups increase the overall shielding of the polymer backbone and thus result in a slower molecular weight decline. Also, the butyl lactato groups increase the hydrophobicity of the polymer, which reduces the ingress of water to the phosphazene backbone.

As shown in Fig. 6, the hydrolytic behavior of polymers **1**–**3** was dependent on the pH of the buffer solutions. The rate of their hydrolysis in aqueous solution decreased in the order base > acid > neutral solution. For instance, it took only 21 days for polymer **1** to decrease its molecular weight to almost 32% of the original one in the buffer solution of pH 10.8, 24 days at pH 3.4, but 33 days in the buffer solution at pH 7.4. This is consistent with the behavior of poly[bis(glycine ethyl ester)phospazene] where the polymer slabs disappeared faster at basic pH.[32] Thus, a possible explanation for our results is that similar mechanisms by which poly[(lactic acid ester)phospazene] and poly[(amino acid ester)phospazene] might hydrolyze. The hydrolytic mechanisms of polyphosphazenes containing amino acid ester side groups have been discussed previously.[31] Initial steps in the suggested pathways include hydrolytic cleavage of the ester groups from the amino acid or hydrolytic cleavage of the amino acid ester from the backbone. Like poly[(amino acid ester)phospazene],[33] in acidic media, the pendent ester groups of polymers **1**–**3** are hydrolyzed to generate the corresponding free carboxylic acid and then the carboxylic acid group attacks the polymer backbone, resulting in backbone cleavage, while OH^- groups in basic media preferentially displace the lactic acid esters from the phosphorus atoms to form a hydroxyphosphazene intermediate, which then undergoes chain cleavage to phosphate and ammonia. This assumption can be confirmed by the hydrolysis products of the polymers after incubation in different buffer solutions for 42 days (Table 1), which showed that phosphate was formed during hydrolysis of almost all the polymers, and its amount was larger in the buffer solutions at pH 10.8 and 3.4 than in the buffer solution of pH 7.4. A similar trend was observed during ammonia titration. Lactic acid and ethanol, propanol, or butanol derived from the ester group on the lactic acid unit during hydrolysis of all the polymers was also detected.

In vitro cytotoxicity of polymers and degradation products

To evaluate the biocompatibility of polymers **1**–**3**, the in vitro cytotoxicities to two human carcinoma cell lines, epithelial HepG2 and leukemia K562/VCR, were determined by MTT assay. The results are shown in Fig. 7. Polymers **1**–**3** showed very little cytotoxicity toward the two cell lines. The cell viabilities were >90% for HepG2 and >80% for K562/VCR at the concentrations studied. We did not observe a significant difference in the toxicity of different polymers at any of the concentrations used for both cell lines ($p > 0.05$).

Fig. 7. (*a*) Cell viability of HepG2 and K562/VCR cells versus polymers **1**–**3** and the hydrolysis products of polymer **2** after incubation in a buffer solution of pH 7.4 (**D1**) and 10.8 (**D2**).

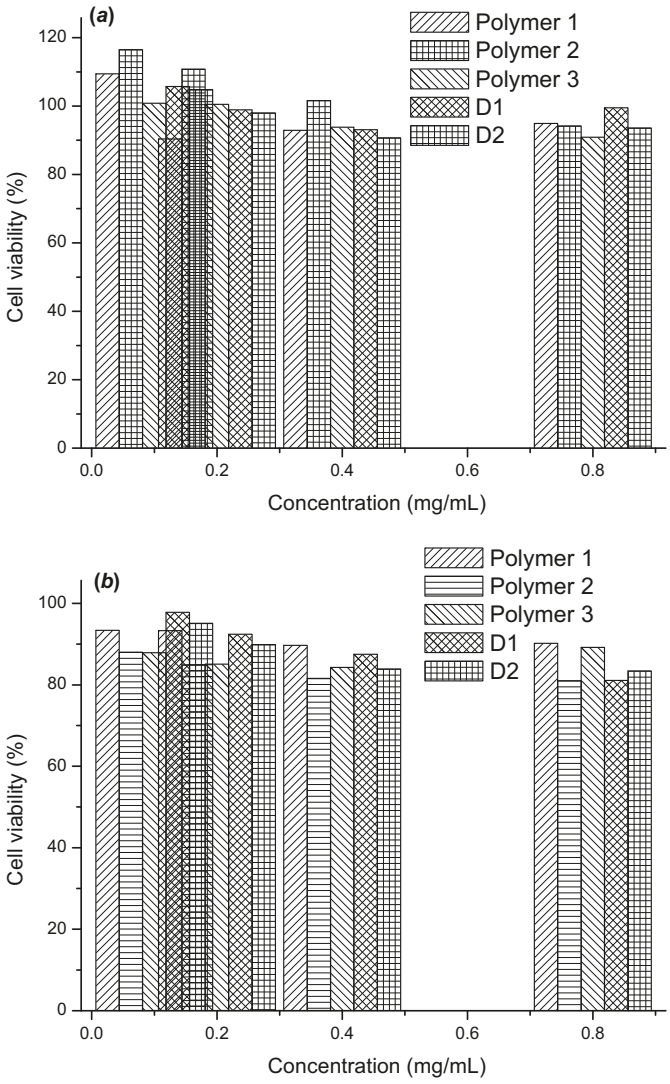

Fig. 8. Microscopic images of HepG2 cells after incubation with untreated cells (Control 1, normal saline; Control 2, buffer at pH 7.4), polymer **2**, and the hydrolysis products of polymer **2** in a buffer solution of pH 7.4 at 37 °C for 48 h.

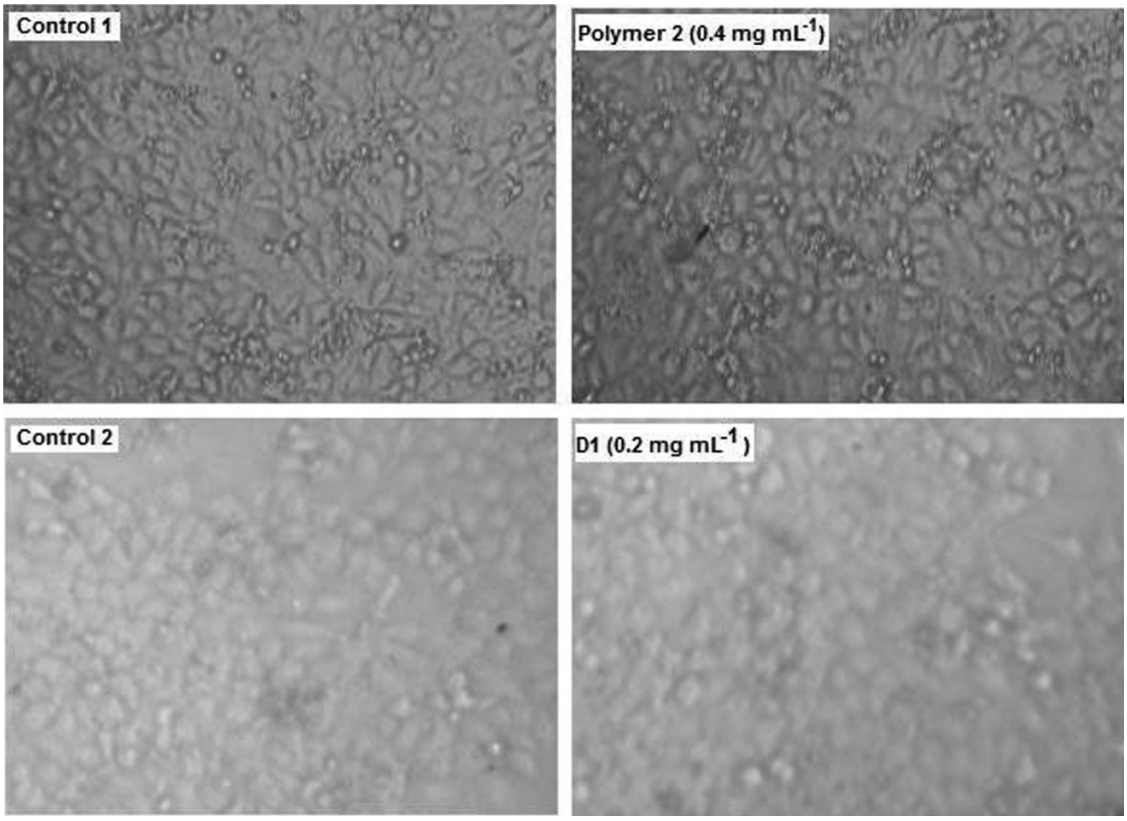

Can. J. Chem. Downloaded from www.nrcresearchpress.com by Xi'an Jiaotong University on 09/19/12
For personal use only.

Figure 8 reflects the state of cells after they were cultured in a solution of polymer **2** (0.4 mg mL^{-1}) for 48 h. The dimension, shape, and density of the cells in the solution of the polymer were very similar to those in the negative control. Both results suggest that these polymers have good biocompatibility to both cell lines.

One important factor for the evaluation of the biological safety of materials is the cytotoxicity of their degradation products.[34] As mentioned previously, poly(lactide) and poly (lactide-co-glycolide) have satisfactory biocompatibility, but their highly concentrated degradation products have a toxic influence.[25] Here, the cytotoxicity of the hydrolysis products of polymer **2** after incubation in buffer solutions of pH 7.4 and 10.8 for 42 days was also determined by the MTT method against HepG2 and K562/VCR cells. As shown in Fig. 7, cells remained viable even when the concentration of degraded products of polymer **2** was up to 0.8 mg mL^{-1} (degraded products diluted by 10 times). Furthermore, the cell morphologies (Fig. 8) after exposure to the solutions of degraded products remained virtually unchanged as compared with those of the control cells. These results indicate that the degraded products of polymer **2** also have good biocompatibility to both cell lines.

Conclusions

The UV–vis study revealed that the aqueous solution of polyphosphazenes containing lactic acid ester and MEE as co-substituents underwent thermo-induced phase transitions. The LCST of the aqueous solutions of the polymers was affected by the structures of lactic acid ester groups and kinds of salts. The more hydrophobic ester group afforded the lower LCST. NH_4Br, NaBr, NH_4Cl, and NaCl increase the LCST of the polymer solutions, whereas Bu_4NBr and KI decrease the LCST. Hydrolytic degradation of the polyphosphazenes was affected by the structures of the lactic acid ester groups and the pH of the buffer solutions. The polymers in basic solution showed the fastest hydrolysis, followed by acidic and then neutral solution. The structure of the ester groups of the lactic acids attached to the polymers affected the degradation of the polymers, and the order of sensitivity to degradation was ethyl > propyl > butyl esters in all buffer solutions. It seems possible to control the hydrolysis rate of the thermosensitive polyphosphazenes by adjustment of the lactic acid esters. In vitro cytotoxicity studies indicate that these polyphosphazenes and their hydrolysis products are well tolerated at the concentration tested in HepG2 and K562/VCR cell cultures. Therefore, on the basis of their thermoresponsiveness, biodegradability, and biocompatibility, these polyphosphazenes may be promising for biomedical applications.

Experimental

Instruments and materials

NMR spectra were obtained on a Bruker DRX-500 spectrometer. ^1H NMR and ^{13}C NMR spectra were measured in $CDCl_3$ with TMS as an internal standard. ^{31}P NMR chemical shifts were reported in ppm relative to 85% H_3PO_4 at 0 ppm. IR spectra were taken on a PerkinElmer 1640 FTIR spectrometer.

Scheme 1. Structure of polymers **1**–**3**.

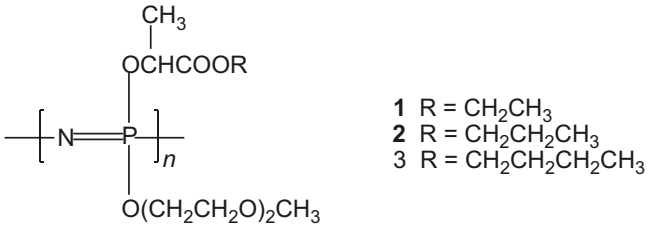

1-3

C, H, N, P, and Cl elemental analyses were carried out with a Vario EL-III instrument (Elementar, Germany), IRIS Advantage-ER /S ICP (TJA, USA), and a Metrohm MIC-IC instrument (Metrohm, Switzerland). Thermal analysis of the polymers was carried out using a Netzsch DSC 200PC. The samples were heated at a rate of 10 °C/min in the range of –100 to 200 °C. T_g was determined at half-height. Molecular weights (M_n) were estimated by a Knauer vapour pressure osmometer (VPO) in methanol at 25 °C using sucrose octaacetate (MW = 678.58) as a reference.

NaCl, NH_4Cl, NH_4Br, NaBr, Bu_4NBr, and KI were purchased from Sinopharm Chemical Reagent Co., Ltd. and were used as received. Acetic acid and sodium acetate, boronic acid and borax, and borax and sodium carbonate were dissolved in distilled deionized water to make a 0.1 mol L^{-1} buffer solution of acetic acid / sodium acetate (pH 3.4), boronic acid / borax (pH 7.4), borax / sodium carbonate (pH 10.8), respectively. 3-(4,5-Dimethylthiazol-2-yl)-2,5-diphenyltetrazolium bromide (MTT, Sigma-Aldrich) were used as received.

Poly[(butyl lactato)$_{1.0}$(MEE)$_{1.0}$ phosphazene] (3)

Polymers **1** and **2** were prepared as described in previous work,[23] and polymer **3** (Scheme 1) was synthesized by a similar procedure. The sodium salt of butyl lactate was prepared by reaction of a solution of butyl lactate (4.23 g, 29 mmol) in THF (50 mL) with a suspension of NaH (0.70 g, 29 mmol) in THF (150 mL) overnight at room temperature. The resulting solution was added dropwise to a solution of PDCP (3.36 g, 29 mmol) in THF (200 mL) under dry nitrogen. The reaction mixture was stirred and heated to 50 °C for 36 h. To a suspension of sodium hydride (1.74 g, 72.5 mmol) in THF (150 mL) was added a solution of MEE (8.70 g, 72.5 mmol) in THF (100 mL). The resulting solution was stirred overnight at room temperature and then added dropwise to the mixture containing the partially substituted polymer. The reaction was allowed to proceed at room temperature for 48 h. The completion of the reaction was checked by ^{31}P NMR spectroscopy. The polymer was isolated and purified five times by recipitations from THF into petroleum ether. A viscoelastic, light yellow-colored solid was obtained. Yield: 70%. M_n 4891. T_g 55.7 °C. ^{31}P NMR δ: –8.64 (br s). Anal. calcd (%) for $C_{12}H_{24}NO_6P$: C 46.60, H 7.83, N 4.53, P 10.02, Cl 0.00; found (%): C 46.16, H 7.79, N 4.85, P 10. 26, Cl 0.00.

Determination of phase transitions

The phase transition of each polymer was traced by monitoring the transmittance of a 500 nm light beam on a UV–vis spectrophotometer (Cary 50, Varian). The polymer was dissolved in deionized water at different concentrations. Turbidimetric experiments were performed from 20 to 95 °C with 2 °C increments every 10 min. The light intensity through the solution was measured as a function of temperature. The LCST was defined as the temperature corresponding to the initial break points in the resulting transmittance versus temperature curve.[35] The same method was used to determined the LCSTs of the polymer solutions (1.5 wt%) containing different salts. The pH dependence of LCST was examined in citric acid / disodium hydrogen phosphate buffer solutions at pH 2.3, 3.2, 4.2, 5.0, 6.0, 7.0, and 8.0.

Hydrolytic degradation studies

Polymers were dissolved in buffer solutions at a concentration of 8 mg mL^{-1}. The buffers used were acetic acid / sodium acetate (pH 3.4, 0.1 mol L^{-1}), boronic acid / borax (pH 7.4, 0.1 mol L^{-1}), and borax / sodium carbonate (pH 10.8, 0.1 mol L^{-1}). Degradation testing was carried out at 37 °C. Vials containing polymer solutions were incubated in an incubator–shaker equipped with temperature and speed controls. The molecular weight changes over a period of 3 days were determined by VPO. The hydrolysis products of the polymers were examined using the literature method.[26] Phosphates were detected semiquantitatively by treatment of the hydrolysis media with zirconyl chloride. The ninhydrin test was used to detect ammonia. Lactic acid and alcohols were detected by MS and ^1H NMR spectroscopy, respectively.

Cytotoxicity tests

In vitro cytotoxicity of polymers **1**–**3** and the hydrolysis products of polymer **2** after incubation in buffer solutions of pH 7.4 and 10.8 for 42 days against two human carcinoma cell lines, epithelial HepG2 and leukemia K562/VCR, were determined by MTT assay as described previously.[36,37] Both cell lines were obtained from Yunnan Pharmacological Laboratories of Natural Products, Kunming Medical College, Kunming, P.R. China. Polymers **1**–**3** were dissolved in normal saline at a concentration between 0.1 and 0.8 mg mL^{-1}. The solution of the hydrolysis products was diluted by 10, 20, 40, or 80 times with normal saline. The cells were seeded in 96 well plates at 4×10^4 cells mL^{-1} in 90 μL of RPMI 1640 (Gibco Brl, USA) medium containing 10% fetal bovine serum, and incubated at 37 °C in a 5% CO_2 atmosphere for 24 h. Ten microlitres of the test solutions were added to each well. After 48 h of incubation, 10 μL of MTT solution (5 mg mL^{-1}) was added to each well, followed by further incubation for 4 h. Thereafter, the medium containing unreacted MTT was carefully removed. The dissolving solution (10% sodium dodecyl sulfate (SDS), 5% isobutanol, and 0.012 mol L^{-1} HCl) was added to each well and incubated overnight at 37 °C. Negative (normal saline for polymers **1**–**3** and buffer solutions of pH 7.4 and 10.8, which were diluted similarly as was done with the degradation solution for hydrolysis products) control wells were treated as previously mentioned. Optical density values from the wells were measured at 570 nm with an ELISA Reader (Molecular Devices, USA). Cell viability (as a percentage of the negative control) was calculated from the optical density values.

Can. J. Chem. Downloaded from www.nrcresearchpress.com by Xi'an Jiaotong University on 09/19/12
For personal use only.

Can. J. Chem. Downloaded from www.nrcresearchpress.com by Xi'an Jiaotong University on 09/19/12
For personal use only.

Acknowledgments

We gratefully acknowledge support for this work by the National Natural Foundation of China (20364002, 20864003), the Program for Changjiang Scholars and Innovative Research Team in University, PCSIRT, and the Natural Science Foundation of Yunnan Province (2009ZC064M), P.R. China.

References

(1) Alvarez-Lorenzo, C.; Concheiro, A.; Dubovik, A. S.; Grinberg, N. V.; Burova, T. V.; Grinberg, V. Y. *J. Control. Release* **2005** *102* (3), 629. doi:10.1016/j.jconrel.2004.10.021.

(2) Schmaljohann, D. *Adv. Drug Deliv. Rev.* **2006** *58* (15), 1655. doi:10.1016/j.addr.2006.09.020.

(3) Dimitrov, I.; Trzebicka, B.; Müller, A. H. E.; Dworak, A.; Tsvetanov, C. B. *Prog. Polym. Sci.* **2007** *32* (11), 1275. doi:10.1016/j.progpolymsci.2007.07.001.

(4) Kopecek, J. *Eur. J. Pharm. Sci.* **2003** *20* (1), 1. doi:10.1016/S0928-0987(03)00164-7.

(5) Cai, W. S.; Gan, L. H.; Tam, K. C. *Colloid Polym. Sci.* **2001** *279* (8), 793. doi:10.1007/s003960100506.

(6) Ebara, M.; Yamato, M.; Aoyagi, T.; Kikuchi, A.; Sakai, K.; Okano, T. *Biomacromolecules* **2004** *5* (2), 505. doi:10.1021/bm0343601.

(7) Zhang, X.; Zhuo, R.; Cui, J.; Zhang, J. *Int. J. Pharm.* **2002** *235* (1–2), 43. doi:10.1016/S0378-5173(01)00976-0.

(8) Guan, J.; Hong, Y.; Ma, Z.; Wagner, W. R. *Biomacromolecules* **2008** *9* (4), 1283. doi:10.1021/bm701265j.

(9) Allcock, H. R. *Chemistry and Applications of Polyphosphazenes;* Wiley-Interscience: Hoboken: NJ, 2003.

(10) Allcock, H. R. *Adv. Mater.* **1994** *6* (2), 106. doi:10.1002/adma.19940060203.

(11) Kumbar, G. S.; Bhattacharyya, S.; Nukavarapu, S. P.; Khan, Y. M.; Nair, L. S.; Laurencin, C. T. *J. Inorg. Organomet. Polym. Mater.* **2006** *16* (4), 365. doi:10.1007/s10904-006-9071-6.

(12) Andrianov, A. K. *Polyphosphazenes for Biomedical Applications;* John Wiley & Sons, Inc.: Hoboken, NJ, 2009.

(13) Allcock, H. R.; Pucher, S. R.; Turner, M. L.; Fitzpatrick, R. J. *Macromolecules* **1992** *25* (21), 5573. doi:10.1021/ma00047a002.

(14) Allcock, H. R.; Dudley, G. K. *Macromolecules* **1996** *29* (4), 1313. doi:10.1021/ma951129+.

(15) Chang, Y.; Powell, E. S.; Allcock, H. R.; Park, S. M.; Kim, C. *Macromolecules* **2003** *36* (7), 2568. doi:10.1021/ma021490d.

(16) Couffin-Hoarau, A. C.; Leroux, J. C. *Biomacromolecules* **2004** *5* (6), 2082. doi:10.1021/bm0400527.

(17) Song, S. C.; Lee, S. B.; Jin, J. I.; Sohn, Y. S. *Macromolecules* **1999** *32* (7), 2188. doi:10.1021/ma981190p.

(18) Lee, S. B.; Song, S. C.; Jin, J. I.; Sohn, Y. S. *Macromolecules* **1999** *32* (23), 7820. doi:10.1021/ma990645n.

(19) Lee, S. B.; Song, S. C. *Polym. Int.* **2005** *54* (9), 1225. doi:10.1002/pi.1702.

(20) Zhang, J. X.; Qiu, L. Y.; Zhu, K. J.; Jin, Y. *Macromol. Rapid Commun.* **2004** *25* (17), 1563. doi:10.1002/marc.200400180.

(21) Zheng, C.; Qiu, L. Y.; Zhu, K. J. *Polymer* **2009** *50* (5), 1173. doi:10.1016/j.polymer.2009.01.004.

(22) Seong, J. Y.; Jun, Y. J.; Kim, B. M.; Park, Y. M.; Sohn, Y. *Int. J. Pharm.* **2006** *314* (1), 90. doi:10.1016/j.ijpharm.2006.02.009.

(23) Bi, Y. M.; Gong, X. Y.; Wang, W. Z.; Yu, L.; Hu, M. Q.; Shao, L. D. *Chin. Chem. Lett.* **2010** *21* (2), 237. doi:10.1016/j.cclet.2009.10.003.

(24) Fukushima, K.; Kimura, Y. *Polym. Int.* **2006** *55* (6), 626. doi:10.1002/pi.2010.

(25) Ignatius, A. A.; Claes, L. E. *Biomaterials* **1996** *17* (8), 831. doi:10.1016/0142-9612(96)81421-9.

(26) Allcock, H. R.; Pucher, S. R.; Scopelianos, A. G. *Macromolecules* **1994** *27* (1), 1. doi:10.1021/ma00079a001.

(27) Qiu, L. Y.; Zhu, K. J. *J. Appl. Polym. Sci.* **2000** *77* (13), 2987. doi:10.1002/1097-4628(20000923)77:13<2987::AID-APP24>3.0.CO;2-F.

(28) Suwa, K.; Yamamoto, K.; Akashi, M.; Takano, K.; Tanaka, N.; Kunugi, S. *Colloid Polym. Sci.* **1998** *276* (6), 529. doi:10.1007/s003960050276.

(29) Von Hippel, P. H.; Schleich, T. *Acc. Chem. Res.* **1969** *2* (9), 257. doi:10.1021/ar50021a001.

(30) Batchelor, J. D.; Olteanu, A.; Tripathy, A.; Pielak, G. J. *J. Am. Chem. Soc.* **2004** *126* (7), 1958. doi:10.1021/ja039335h.

(31) Allcock, H. R.; Pucher, S. R.; Scopelianos, A. G. *Macromolecules* **1994** *27* (5), 1071. doi:10.1021/ma00083a001.

(32) Ruiz, E. M.; Ramírez, C. A.; Aponte, M. A.; Barbosa-Cánovas, G. V. *Biomaterials* **1993** *14* (7), 491. doi:10.1016/0142-9612(93)90235-T.

(33) Allcock, H. R.; Singh, A.; Ambrosio, A. M. A.; Laredo, W. R. *Biomacromolecules* **2003** *4* (6), 1646. doi:10.1021/bm030027l.

(34) Wang, Y.; Tang, L.; Li, Y.; Wang, J. *Biomacromolecules* **2009** *10* (1), 66. doi:10.1021/bm800808q.

(35) Liu, X. Y.; Cheng, F.; Liu, H. J.; Chen, Y. *Soft Matter* **2008** *4* (10), 1991. doi:10.1039/b811012n.

(36) Hansen, M. B.; Nielsen, S. E.; Berg, K. *J. Immunol. Methods* **1989** *119* (2), 203. doi:10.1016/0022-1759(89)90397-9.

(37) Bi, Y. M.; Yin, Y. F.; Huang, R.; Li, Y. M. *Polym. Int.* **2010** *59* (2), 269. doi:10.1002/pi.2720.

A theoretical study of bipolar organic transport material: Disilanyl double-pillared bisanthracene (^{Si}DPBA)

Gui-Xia Yang, Hai-Lin Fan, Xiao-Di Niu, and Zong-Hao Huang

Can. J. Chem. Downloaded from www.nrcresearchpress.com by Xi'an Jiaotong University on 09/19/12
For personal use only.

Abstract: A novel anthracene derivative, disilanyl double-pillared bisanthracene (^{Si}DPBA), has been recently synthesized, which effectively functions as a bipolar carrier transport material in OLEDs. Its charge transport properties have been systemically investigated by band model and hopping model. Band structure calculations of ^{Si}DPBA show that the dispersions of the larger valence band and conduction band are comparable, which demonstrates that both electron and hole are favoured for transport, and that ^{Si}DPBA has the potential to be used as bipolar transport material from the viewpoint of band model. The density of states and transfer integrals in the main pathways show that it is the edge-to-face CH···π interaction that determines the charge transport property, and that the $SiMe_2$ group contibutes little to it. The calculated charge mobilities of holes and electrons are 0.461 and 0.116 $cm^2 \cdot V^{-1} \cdot s^{-1}$, respectively. They are the same order of magnitude, and the electron mobility is on the order of magnitude of perylene-3,4:9,10-tetracarboxylic acid bisimide (PBI) derivatives (0.34 $cm^2 \cdot V^{-1} \cdot s^{-1}$). Both models demonstrate that ^{Si}DPBA has the potential to be used as a bipolar transport material.

Key words: disilanyl double-pillared bisanthracene (^{Si}DPBA), charge transport, band model, hopping model.

Résumé : On a récemment réalisé la synthèse d'un nouveau dérivé de l'anthracène, un disilanyl bisanthracène à double pilier (« ^{Si}DPBA ») qui fonctionne effectivement comme un matériel de transfert de charge bipolaire dans les diodes électroluminescentes organiques (DELO). On a étudié d'une façon systématique ses propriétés de transfert de charge par le modèle de bande et le modèle des sauts. Les calculs de structure de bande pour le « ^{Si}DPBA » montrent que les dispersions de la bande de valence (BV) la plus large et de la bande de conduction (BC) sont comparables, ce qui démontre que, selon le modèle de la bande de conduction, l'électron et le trou favorisent tous les deux le transport et que le « ^{Si}DPBA » a la capacité d'être utilisé comme matériel de transfert de charge. La densité des états et les intégrales de transfert dans les voies principales montrent que la propriété de transfert de charge est déterminée par l'interaction CH···π entre l'arête et la face et que la contribution du groupe $SiMe_2$ est minime. Les mobilités de charge du trou et de l'électron sont respectivement de 0 461 et 0 116 $cm^2 \cdot V^{-1} \cdot s^{-1}$. Elles sont du même ordre de grandeur et la mobilité de l'électron est du même ordre de grandeur que celle des dérivés bisimides de l'acide pérylène-3,4 :9,10-tétracarboxylique (BIP), soit 0,34 $cm^2 \cdot V^{-1} \cdot s^{-1}$. Les deux modèles montrent que le « ^{Si}DPBA » a le potentiel pour être utilisé comme matériel de transfert de charge bipolaire.

Mots-clés : disilanyl bisanthracène à double pilier (« ^{Si}DPBA »), transfert de charge, modèle de bande, modèle des sauts.

[Traduit par la Rédaction]

Introduction

In recent years, organic semiconductors have attracted considerable attention because of their potential applications, such as organic light-emitting diodes (OLED),[1–7] organic field effect transistors (OFETs),[8–10] organic thin-film transistors (OTFTs),[11–16] and photovoltaic cells,[17,18] for which they possess great advantages such as low cost, easy fabrication, and mechanical flexibility.[19–21] A key parameter determining the performance of these devices is the charge-carrier transport mobility. Some typical oligoacene and oligothiophene derivatives have good hole or electron transport abilities. For example, field-effect hole mobilities of 1.1 and 3 $cm^2 \cdot V^{-1} \cdot s^{-1}$ have been reported for thin films of alkyl-substituted oligothiophene[22] and pentacene[23], respectively. The performance of devices using n-type semiconductors is still far from that achieved with p-type materials, because the transport in n-channel conductors is degraded easily by air.[24] An electron mobility of up to 0.6 $cm^2 \cdot V^{-1} \cdot s^{-1}$ has recently been reported for vacuum deposited films of carbonyl-functionalised quarterthiophenes[25].

The fabrication of devices exhibiting ambipolar conduction is crucial to design robust circuits of low-power consumption using organic integrated circuits,[26–32] and the most ideal

Received 16 March 2011. Accepted 7 May 2011. Published at www.nrcresearchpress.com/cjc on 9 September 2011.

G.-X. Yang. Faculty of Chemistry, Northeast Normal University, Changchun 130024, China; College of Resource and Environmental Science, Jilin Agricultural University, Changchun, Jilin 130118, China.
H.-L. Fan. College of Resource and Environmental Science, Jilin Agricultural University, Changchun, Jilin 130118, China.
X.-D. Niu. He Ping Campus Jilin University, Changchun 130062, China.
Z.-H. Huang. Faculty of Chemistry, Northeast Normal University, Changchun 130024, China.

Corresponding author: Zong-Hao Huang (e-mail:zonghaohuangnenu@gmail.com).

Fig. 1. Monomer structure (left), and packing-mode (right) parallel to the anthracene plane of ^{Si}DPBA.

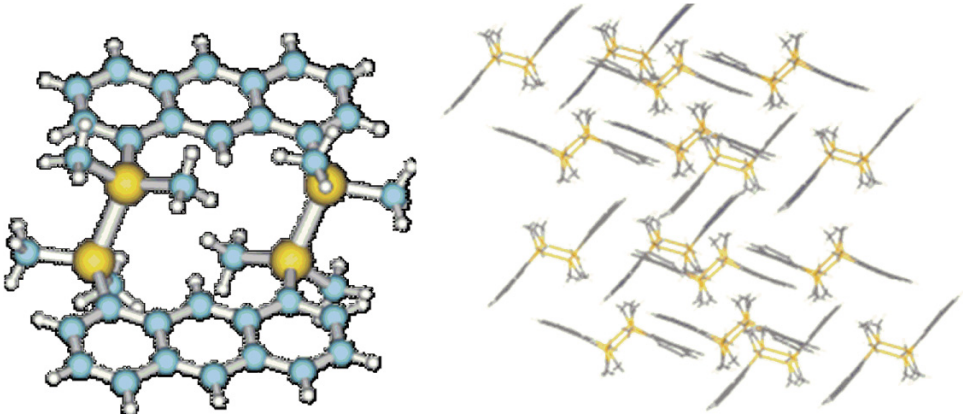

Can. J. Chem. Downloaded from www.nrcresearchpress.com by Xi'an Jiaotong University on 09/19/12
For personal use only.

ambipolar OFETs are composed of a single semiconductor material, which has high charge mobility for both hole and electron transfer, to simplify the device fabrication processes. However, due to the limitation in the range of metal work functions, most organic semiconductors show one conduction polarity, and only a few organic materials show ambipolar characteristics in a single-component molecular semiconductor. Single crystals prepared from the vapor phase of iron-phthalocyanine gave hole and electron mobilities of 0.3 and 0.03 $cm^2 \cdot V^{-1} \cdot s^{-1}$.[33] Thus, it is still a challenge to design and synthesize bipolar organic transport materials with high performance and good charge transport balance.

Quantum chemistry calculations have been widely applied in the investigation of organic semiconductors, as they provide explanations of experimental phenomenon and help to design more efficient devices.[34–38] For example, Shuai et al. carried out first-principle band-structure calculations for tris (8-hydroxyquinolinato)aluminum (Alq_3) and for the first time concluded that Alq_3 is a good electron transport material from the band structure's view.[39] Recently, Brédas et al. explored the impact of functionalization on the charge transport parameters of 37 perylene tetracarboxylic diimide (PTCDI) crystals, using density functional theory. Their results indicate that large bandwidths along with small effective masses can be obtained with the insertion of appropriate nitorgen substituents, in particular halogenated aromatic groups.[40]

Recently, there has been a report on the synthesis and characterization of a new kind of anthracene derivative, disilanyl double-pillared bisanthracene (^{Si}DPBA), shown in Fig. 1,[41] and they used a straightforward double-pillaring strategy to synthesize a series of derivatives, e.g., ^{Si}DPBAs.[42] Its glass-transition temperature T_g was recorded at 153 °C, which is higher than that found for standard OLED materials, such as α-NPD (T_g = 100 °C). The most important aspect is that the device performance using ^{Si}DPBA as both hole transport layer (HTL) and electron transport layer (ETL) is reasonably high, as the device achieved an external quantum efficiency (EQE) of 8.7%. The authors also discussed the frontier molecular orbitals and the reorganization energy of ^{Si}DPBA theoretically. However, the internal mechanism determining the transporting property is not clear. In this article, we systematically investigate the charge transport properties of ^{Si}DPBA using both band model and hopping model. We calculate the band structure and also the density of states (DOS) using the band model and obtain the charge carrier mobility using the hopping model to give an insight into the internal mechanism. It is hoped that this study can give some guidance to the design of organic transport materials.

Theoretical methodology

At low temperatures, the charge transport in a number of organic crystals can be described by a bandlike regime.[43] As temperature increases, the dynamic structure disorder may invalidate the band transport model, and transport behavior is governed by a thermally activated hopping mechanism,[44] which is usually chosen to describe charge transport at room or high temperature. However, several recent measurements indicate that the mobility decreases with temperature, which points to a bandlike mechanism of carrier transport at room temperature. For example, ultrapure single crystals of pentacene[45] (T = 225–340 K) and rubrene[46] (T = 170–300 K) show a bandlike mobility. To get a full understanding of the relative charge carrier transport properties of our system, both band model and hopping model are selected.

In a standard band-theory model, the group velocity $\boldsymbol{v}(k)$ of the delocalized electron waves or hole waves is given by the gradient of the band energy in k-space,

$$[1] \qquad \boldsymbol{v}(k) = \nabla_k E(k)/\hbar$$

where $E(k)$ is the band structure of the system, k the wave vector, and $\hbar = h/2\pi$, and h is the Planck constant. Under the constant relaxation time approximation at low temperature, the mobility can be given by,

$$[2] \qquad \mu_\alpha = e\tau m_\alpha^{-1}$$

Here, the inverse effective mass m_α^{-1} is a key parameter of the charge transport in the band-like model. The effective mass is related to the curvature of the minimum and maximum of the conductive band (CB) and valence band (VB). It reads,

$$[3] \qquad m_{\alpha\beta}^{-1} = -\frac{1}{\hbar^2}\left(\frac{\partial^2 E(k)}{\partial k_\alpha \partial k_\beta}\right)$$

Here, subscripts α and β denote the Cartesian coordinates in reciprocal space, and $E(k)$ is the band energy. The heavier the effective mass is, the smaller the mobility.

Can. J. Chem. Downloaded from www.nrcresearchpress.com by Xi'an Jiaotong University on 09/19/12
For personal use only.

Fig. 2. Band structure of ^{Si}DPBA along high-symmetry lines.

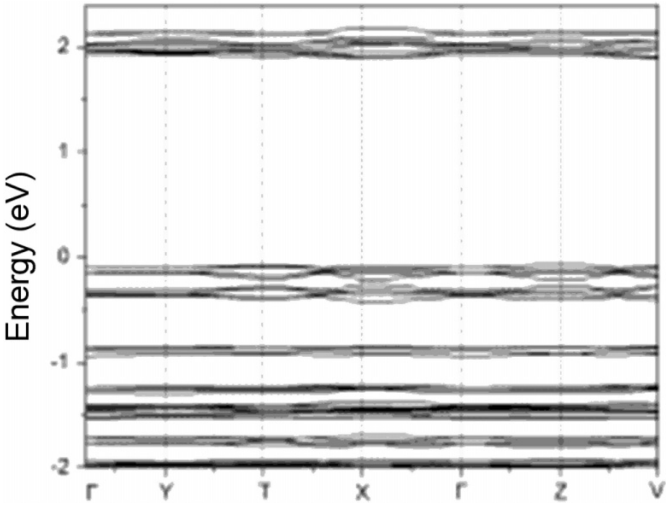

Table 1. Dispersions of valence band (VB) and conduction band (CB) along high-symmetry lines in crystal ^{Si}DPBA (in eV).

	VB	CB
ΓY	0.001	0.009
YT	0.028	0.015
TX	0.029	0.020
XΓ	0.016	0.019
ΓZ	0.022	0.001
ZV	0.035	0.030

Table 2. Calculated effective masses (m) of holes in VB and electrons in CB along different high-symmetry directions in ^{Si}DPBA crystal (in units of the electron rest mass, m_0).

	Hole (m/m_0)	Electron (m/m_0)
ΓY	114.49	11.19
YT	3.70	6.46
TX	12.60	5.41
XΓ	4.59	4.90
ΓZ	4.80	92.34
ZV	5.15	3.06

Electronic band structure and density of states calculations were performed with VASP,[47–49] using the PBE exchange-correlation functional[50] and a plane-wave basis set. The lattice parameters used here for ^{Si}DPBA are a = 12.633 Å, b = 14.510 Å, c = 18.083 Å, and α = 81.3°, β = 82.6°, γ = 81.3°. For anthracene, a = 8.562 Å, b = 6.038 Å, c = 11.184 Å, and α=γ=90°, β = 124.7°. Integrations over the Brillouin zone were sampled by 3 × 3 × 3 k points for ^{Si}DPBA, and 4 × 6 2 k points for anthracene, using the Monkhorst–Pack scheme.[51]

The hole or electronic coupling (charge transfer integral) is obtained by a direct dimer Hamiltonian evaluation method[52,53] at PW91PW91[54] /6–31G (d,p),[55–57] using the Gaussian 09 program suite.[58] A detailed computational methodology to predict the mobility is given in the Supplementary data.

Fig. 3. Band structure of anthracene crystal along high-symmetry lines.

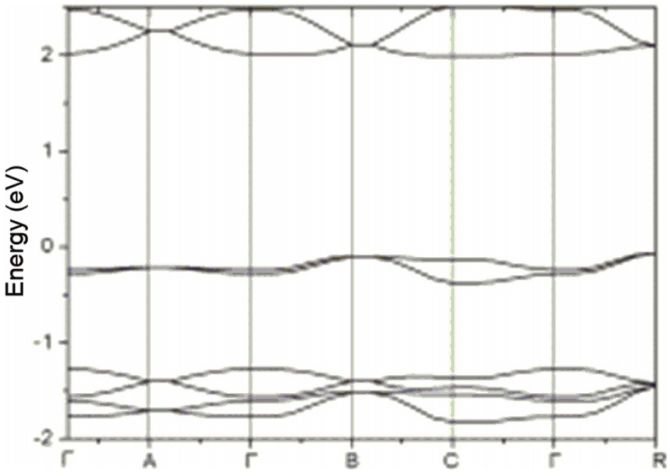

Table 3. Dispersions of valence band (VB) and conduction band (CB) along high symmetry lines in crystal anthracene (in eV).

	VB	CB
ΓA	0.027	0.230
ΓB	0.137	0.097
BC	0.029	0.022
CΓ	0.108	0.229
ΓR	0.179	0.081

Results and discussion

Geometric structure

Isobe et al. designed and synthesized ^{Si}DPBA, a new anthracene derivative.[41] The monomer and packing-mode parallel to the anthracene plane of ^{Si}DPBA are shown in Fig. 1. The $SiMe_2$ group positions two adjacent anthracene planes in an antiparallel manner, and the torsion angles between the Si–Si single bond and the anthracene plane are in the range 61°–73°, which results in a favorable σ_{Si-Si}-π conjugation. The molecules are packed with face-to-edge intermolecular contacts similar to unsubstituted anthracene. The arrangement yields a two-dimensional network of intermolecular contacts in the crystal, although the unique steplike shape of the molecule distorts the packing and hinders the formation of typical herringbone motifs.

Band structure

The crystal of ^{Si}DPBA crystallizes in the triclinic space group P-1, and there are two inequivalent molecules in the unit cell. We calculated the band structures of ^{Si}DPBA using VASP along high-symmetry directions. The high-symmetry coordinates for it are Γ(0, 0, 0), Y(0, 1/2, 0), T(0, 1/2, 1/2), X(1/2, 0, 0), Z(0,0,1/2), and V(1/2,1/2,0). The calculated band structure is shown in Fig. 2, and corresponding dispersions along high-symmetry lines are listed in Table 1. The maximum of the VB (–0.069 eV) is at point Z, and the minimum of CB (1.892 eV) is at point V. The band gap is 1.951 eV and ^{Si}DPBA is an indirect semiconductor. The larger bandwidths are along high symmetry lines T→X and

Fig. 4. Density of states (DOS) of crystals ^{Si}DPBA and anthracene.

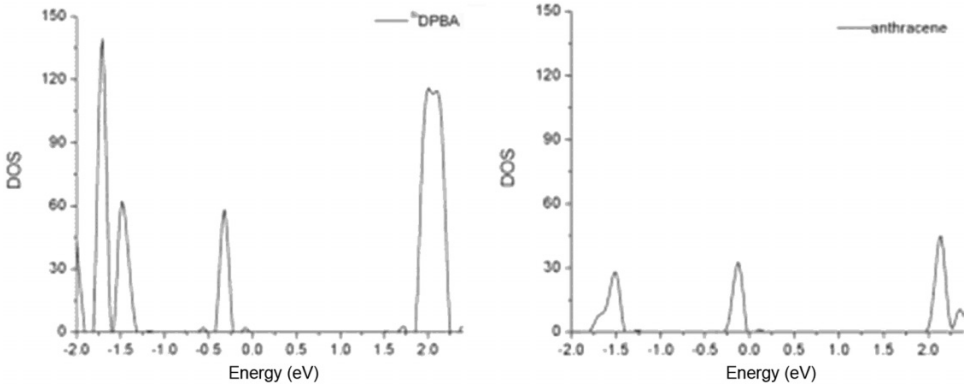

Fig. 5. Partial density of states (PDOS) of $SiMe_2$ group.

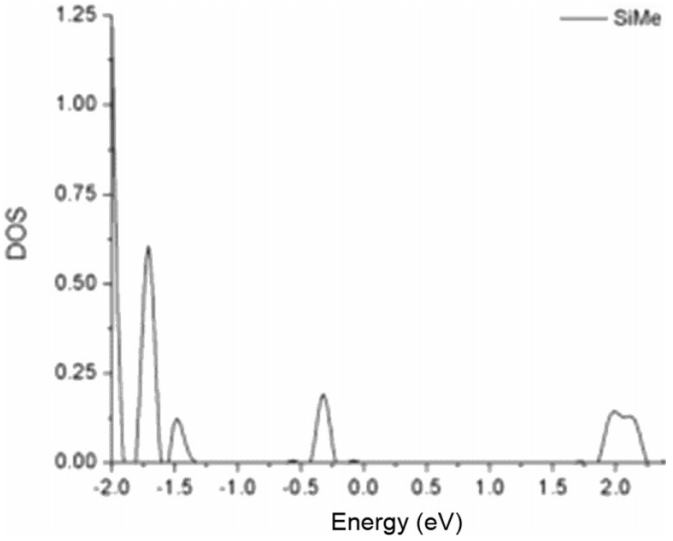

Z→V, compared with other high symmetry directions, which correspond to edge-to-face CH···π interactions between different molecular anthracene groups, and the dispersions of both VB and CB in these directions are comparable. From the viewpoint of the band model, stronger dispersion of the band gives rise to larger carrier mobility. Thus, a ^{Si}DPBA crystal could be a bipolar semiconductor.

A key parameter in the band model is the effective mass of the charge carriers; smaller effective mass gives rise to greater the mobility. We calculated the effective masses of holes in the VB and electrons in the CB along different high-symmetry lines according to the band structure of ^{Si}DPBA, and the results are listed in Table 2. As seen from the values, the results are consistent with band structure. That is, smaller effective mass leads to greater dispersion.

To compare with the band structure in ^{Si}DPBA, we calculated the band structure of anthracene crystal and discuss the differences between them. Crystal anthracene crystallizes in the monoclinic space group $P21/a$. High-symmetry k points in the Brillouin zone are selected as Γ(0, 0, 0), A(1/2, 0, 0), B(0, 1/2, 0), C(0, 1/2, 0), and R(1/2, 1/2, 0). The calculated band structure is depicted in Fig. 3, and the dispersions along different high-symmetry lines are listed in Table 3. The maximum of the VB (–0.064 eV) is at point R, and the minimum of the CB (1.988 eV) is at point C. The band gap is 2.052 eV, and anthracene is also an indirect semiconductor. The minimum of CB is higher than that of ^{Si}DPBA, which is consistent with Ref. 41, in which the LUMO of anthracene is higher than that of ^{Si}DPBA, but their VB maxima are comparable.

Generally, the dispersions of ^{Si}DPBA are smaller than those of anthracene, so the charge transport ability of ^{Si}DPBA should be weaker than in anthracene. This can be explained from the standpoint of molecular packing modes in the crystals. The introduction of Si–Si bridge breaks the coplanarity of the whole molecule, and such a change makes the π-π stacking interaction and also the CH···π hydrogen interaction weaker. As a result, the charge transport properties of ^{Si}DPBA are weaker than that of anthracene.

Density of states (DOS)

The calculated DOS of ^{Si}DPBA and anthracene are shown in Fig. 4. As seen from the plots, the total DOS of the two crystals are similar in the frontier orbital part, i.e., VB and CB. The energy of the VB peak in ^{Si}DPBA is lower than that in anthracene, but the energies of the CB are similar. This is consistent with the band structures that we analyzed above. To clarify the effect of the introduction of Si–Si bridge on the charge transport properties, we also calculated the partial density of states (PDOS) of the $SiMe_2$ group, which is shown in Fig. 5. Comparing with the total DOS of the ^{Si}DPBA crystal in Fig. 4, the DOS of the $SiMe_2$ group in both VB and CB are small, which indicates that the contribution of the $SiMe_2$ group is very small in determining the charge transport properties. On the other hand, the DOS in VB is larger than that in CB, i.e., the $SiMe_2$ group has a stronger influence on the VB than on th CB. This is consistent with the analysis of frontier molecular orbitals (FMOs) carried out by the authors in Ref. 41, in which the $SiMe_2$ group contributes to HOMO, but does not contribute to LUMO.

Transfer integral and charge mobility

Besides the band model, we also calculated the transfer integral and charge mobility using the hopping model, and the results are consistent with those from band model.

Transfer integral

The main charge hopping pathways of ^{Si}DPBA are depicted in Fig. 6, and the calculated transfer integrals in the

Can. J. Chem. Downloaded from www.nrcresearchpress.com by Xi'an Jiaotong University on 09/19/12
For personal use only.

Fig. 6. Main charge hopping pathways of ^{Si}DPBA in the *bc* plane and *ac* planes, respectively.

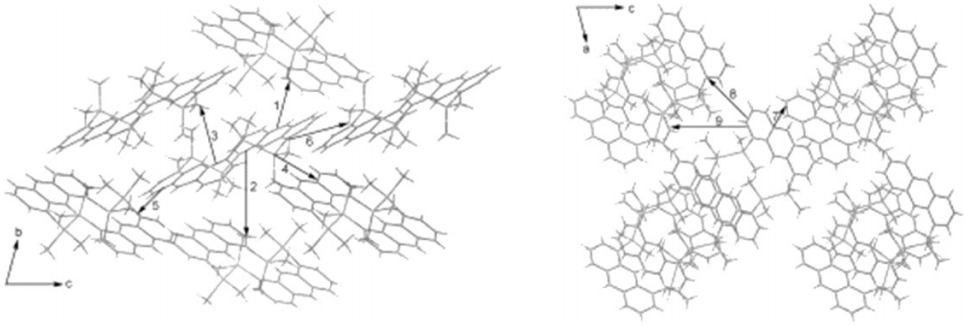

Table 4. Calculated hole (t_h) and electron (t_e) transfer integrals of ^{Si}DPBA in the main pathways.

Pathways	t_h (eV)	t_e (eV)
1	3.73×10^{-3}	-1.47×10^{-2}
2	3.45×10^{-3}	-7.98×10^{-3}
3	1.07×10^{-2}	1.16×10^{-2}
4	9.00×10^{-4}	1.24×10^{-3}
5	-1.72×10^{-2}	-1.24×10^{-2}
6	-3.12×10^{-5}	-6.00×10^{-4}
7	2.07×10^{-2}	1.28×10^{-2}
8	3.36×10^{-3}	2.92×10^{-3}
9	-6.15×10^{-4}	-4.82×10^{-4}

Fig. 7. Frontier molecular orbitals of HOMO–1/HOMO in path 7 and LUMO/LUMO+1 in path 1, respectively.

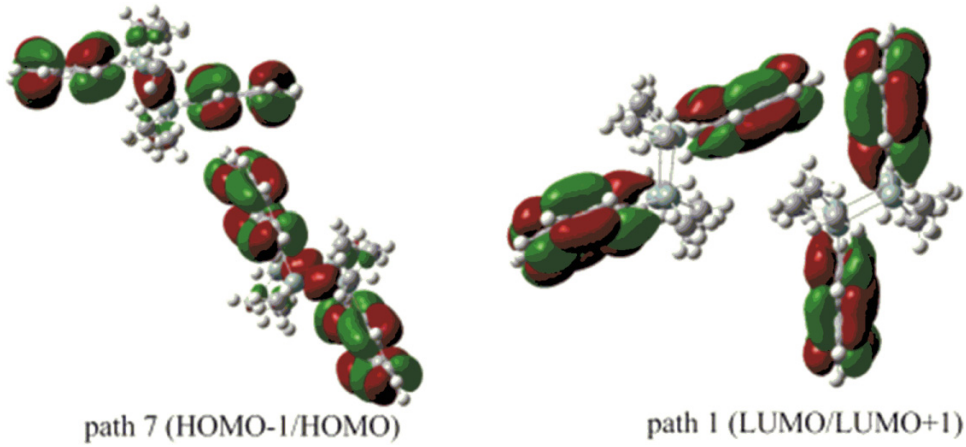

main pathways are listed in Table 4. From the results, we can see that:

1. The directions with the largest electron transfer integral in pathway 1 and largest hole transfer integral in pathway 7 are both along those with edge-to-face CH···π interactions between the anthracene groups in different molecules. This is also reflected in the band structure of ^{Si}DPBA, in which the greater dispersions of the VB and CB are also along the directions involving the CH···π interaction.
2. The pathways with greater transfer integrals are all along the directions with large dispersions in both the VB and CB. The electron transfer integral in pathway 1 is the largest, and this pathway corresponds to the TX direction in reciprocal space, which has larger CB dispersion. Pathway 7 with the largest hole transfer integral is along the ZV direction. That is, the directions with larger transfer integrals are the ones with larger dispersions in the band structure.

From the results listed in Table 4, we find that the largest transfer integral for holes is in pathway 7 and for electrons is in pathway 1. We analyzed the frontier molecular orbitals (FMOs) of HOMO/HOMO–1 for path 7 and LUMO/LUMO +1 for path 1, which are shown in Fig. 7. Clearly, both the HOMO/HOMO–1 and LUMO/LUMO+1 display a significant electronic density on the anthracene parts, and there is some contribution of $SiMe_2$ on HOMO/HOMO–1 compared with LUMO/LUMO+1. This demonstrates that the edge-to-face CH···π interaction determines the charge transport abilities.

Mobility calculation

Combining the transfer integrals and reorganization energies taken from Ref. 41, we estimated the hole (μ_h) and elec-

Can. J. Chem. Downloaded from www.nrcresearchpress.com by Xi'an Jiaotong University on 09/19/12
For personal use only.

tron (μ_e) mobilities. The calculated $\underline{\mu}_h$ is 0.461 $cm^2 \cdot V^{-1} \cdot s^{-1}$, and μ_e is 0.116 $cm^2 \cdot V^{-1} \cdot s^{-1}$. They are the same order of magnitude, and the electron mobility is the same order of magnitude as that of perylene-3,4:9,10-tetracarboxylic acid bisimide (PBIs) derivatives **1a** (0.34 $cm^2 \cdot V^{-1} \cdot s^{-1}$) calculated by Geng et al., which is a typical electron transport material.[59] The results indicate that ^{Si}DPBA has the potential to be used as bipolar organic transport material.

Conclusion

Using first-principle calculations, we investigated the charge transport properties of a new kind of anthracene derivative ^{Si}DPBA using the band and hopping models. The band structure showed that the larger dispersions in VB and CB are comparable. From the viewpoint of the band model, the charge transport abilities are also comparable. The dispersions are generally smaller than those of anthracene crystal, and this can be explained by the crystal packing. That is, introduction of a $SiMe_2$ group breaks the coplanarity of the whole molecule, and such a change weakens the π-π stacking interaction and also the hydrogen interaction. On the other hand, from the DOS analysis, we found that the $SiMe_2$ group has little contribution to the charge transport abilities of crystal ^{Si}DPBA. Larger transfer integrals and frontier molecular orbitals of HOMO–1/HOMO and LUMO/LUMO+1 both show that it is the intermolecular CH···π interaction between the anthracene groups that determine the charge transport properties. Calculated mobilities for holes and electrons are 0.461 and 0.116 $cm^2 \cdot V^{-1} \cdot s^{-1}$, respectively. Such large mobilities demonstrate that the anthracene derivative ^{Si}DPBA has the potential to be used as a new kind of organic bipolar transport material.

Supplementary data

Supplementary data for this article are available on the journal Web site (www.nrcresearchpress.com/cjc).

Acknowledgment

The authors gratefully acknowledge the National Natural Science Foundation of China (No. 20774017).

References

(1) Tang, C. W.; VanSlyke, S. A. *Appl. Phys. Lett.* **1987** *51* (12), 913. doi:10.1063/1.98799.
(2) Tang, C. W.; VanSlyke, S. A.; Chen, C. H. *J. Appl. Phys.* **1989** *65* (9), 3610. doi:10.1063/1.343409.
(3) Burroughes, J. H.; Bradley, D. D. C.; Brown, A. R.; Marks, R. N.; Mackay, K.; Friend, R. H.; Burns, P. L.; Holmes, A. B. *Nature* **1990** *347* (6293), 539. doi:10.1038/347539a0.
(4) Van Slyke, S. A.; Chen, C. H.; Tang, C. W. *Appl. Phys. Lett.* **1996** *69* (15), 2160. doi:10.1063/1.117151.
(5) Friend, R. H.; Gymer, R. W.; Holmes, A. B.; Burroughes, J. H.; Marks, R. N.; Taliani, C.; Bradley, D. D. C.; Santos, D. A. D.; Bredas, J. L.; Logdlund, M.; Salaneck, W. R. *Nature* **1999** *397* (6715), 121. doi:10.1038/16393.
(6) Pingree, L. S. C.; Russell, M. T.; Marks, T. J.; Hersam, M. C. *J. Appl. Phys.* **2006** *100* (4), 044502. doi:10.1063/1.2234544.
(7) Zaumseil, J.; Friend, R. H.; Sirringhaus, H. *Nat. Mater.* **2006** *5* (1), 69. doi:10.1038/nmat1537.
(8) Dimitrakopoulos, C. D.; Malenfant, P. R. L. *Adv. Mater. (Deerfield Beach Fla.)* **2002** *14* (2), 99.
(9) Sun, Y.; Liu, Y.; Zhu, D. *J. Mater. Chem.* **2005** *15* (1), 53. doi:10.1039/b411245h.
(10) Katz, H. E. *Chem. Mater.* **2004** *16* (23), 4748. doi:10.1021/cm049781j.
(11) Garnier, F. *Chem. Phys.* **1998** *227* (1–2), 253. doi:10.1016/S0301-0104(97)00308-X.
(12) Katz, H. E.; Bao, Z.; Gilat, S. L. *Acc. Chem. Res.* **2001** *34* (5), 359. doi:10.1021/ar990114j.
(13) Facchetti, A.; Mushrush, M.; Yoon, M.-H.; Hutchison, G. R.; Ratner, M. A.; Marks, T. J. *J. Am. Chem. Soc.* **2004** *126* (42), 13859. doi:10.1021/ja0489846.
(14) Facchetti, A.; Yoon, M.-H.; Stern, C. L.; Hutchison, G. R.; Ratner, M. A.; Marks, T. J. *J. Am. Chem. Soc.* **2004** *126* (41), 13480. doi:10.1021/ja048988a.
(15) Panzer, M. J.; Frisbie, C. D. *Appl. Phys. Lett.* **2006** *88* (20), 203504. doi:10.1063/1.2204846.
(16) Yan, H.; Yoon, M.-H.; Facchetti, A.; Marks, T. J. *Appl. Phys. Lett.* **2005** *87* (18), 183501. doi:10.1063/1.2119418.
(17) Granstrom, M.; Petritsch, K.; Arias, A. C.; Lux, A.; Andersson, M. R.; Friend, R. H. *Nature* **1998** *395* (6699), 257. doi:10.1038/26183.
(18) Roncali, J. *Chem. Soc. Rev.* **2005** *34* (6), 483. doi:10.1039/b415941c.
(19) Forrest, S. R.; Thompson, M. E. *Chem. Rev.* **2007** *107* (4), 923. doi:10.1021/cr0501590.
(20) Coropceanu, V.; Cornil, J.; da Silva Filho, D. A.; Olivier, Y.; Silbey, R.; Brédas, J.-L. *Chem. Rev.* **2007** *107* (4), 926. doi:10.1021/cr050140x.
(21) Shirota, Y.; Kageyama, H. *Chem. Rev.* **2007** *107* (4), 953. doi:10.1021/cr050143+.
(22) Halik, M.; Klauk, H.; Zschieschang, U.; Schmid, G.; Ponomarenko, S.; Kirchmeyer, S.; Weber, W. *Adv. Mater. (Deerfield Beach Fla.)* **2003** *15* (11), 917.
(23) Klauk, H.; Halik, M.; Zschieschang, U.; Schmid, G.; Radlik, W.; Weber, W. *J. Appl. Phys.* **2002** *92* (9), 5259. doi:10.1063/1.1511826.
(24) Mas-Torrent, M.; Rovira, C. *Chem. Soc. Rev.* **2008** *37* (4), 827. doi:10.1039/b614393h.
(25) Yoon, M.-H.; DiBenedetto, S. A.; Facchetti, A.; Marks, T. J. *J. Am. Chem. Soc.* **2005** *127* (5), 1348. doi:10.1021/ja045124g.
(26) Babel, A.; Wind, J. D.; Jenekhe, S. A. *Adv. Funct. Mater.* **2004** *14* (9), 891. doi:10.1002/adfm.200305180.
(27) Ye, R.; Baba, M.; Oishi, Y.; Mori, K.; Suzuki, K. *Appl. Phys. Lett.* **2005** *86* (25), 253505. doi:10.1063/1.1949731.
(28) Sakamoto, Y.; Suzuki, T.; Kobayashi, M.; Gao, Y.; Fukai, Y.; Inoue, Y.; Sato, F.; Tokito, S. *J. Am. Chem. Soc.* **2004** *126* (26), 8138. doi:10.1021/ja0476258.
(29) Dinelli, F.; Capelli, R.; Loi, M. A.; Murgia, M.; Muccini, M.; Facchetti, A.; Marks, T. J. *Adv. Mater. (Deerfield Beach Fla.)* **2006** *18* (11), 1416.
(30) Wang, J.; Wang, H.; Yan, X.; Huang, H.; Yan, D. *Chem. Phys. Lett.* **2005** *407* (1–3), 87. doi:10.1016/j.cplett.2005.03.072.
(31) Xia, Y.; Kalihari, V.; Frisbie, C. D.; Oh, N. K.; Rogers, J. A. *Appl. Phys. Lett.* **2007** *90* (16), 162106. doi:10.1063/1.2724895.
(32) Jones, B. A.; Facchetti, A.; Wasielewski, M. R.; Marks, T. J. *J. Am. Chem. Soc.* **2007** *129* (49), 15259. doi:10.1021/ja075242e.
(33) de Boer, R. W. I.; Stassen, A. F.; Craciun, M. F.; Mulder, C. L.; Molinari, A.; Rogge, S.; Morpurgo, A. F. *Appl. Phys. Lett.* **2005** *86* (26), 262109. doi:10.1063/1.1984093.

Can. J. Chem. Downloaded from www.nrcresearchpress.com by Xi'an Jiaotong University on 09/19/12
For personal use only.

(34) Delgado, M. C. R.; Kim, E.-G.; Filho, D. A. S.; Brédas, J. L. *J. Am. Chem. Soc.* **2010** *132* (10), 3375. doi:10.1021/ja908173x.
(35) Long, M.; Tang, L.; Wang, D.; Wang, L.; Shuai, Z. *J. Am. Chem. Soc.* **2009** *131* (49), 17728. doi:10.1021/ja907528a.
(36) Wang, L.; Nan, G.; Yang, X.; Peng, Q.; Li, Q.; Shuai, Z. *Chem. Soc. Rev.* **2010** *39* (2), 423. doi:10.1039/b816406c.
(37) Wu, M.; Wu, X.; Gao, Y.; Zeng, X. C. *Appl. Phys. Lett.* **2009** *94* (22), 223111. doi:10.1063/1.3143611.
(38) Delgado, M. C. R.; Pigg, K. R.; da Silva Filho, D. A.; Gruhn, N. E.; Sakamoto, Y.; Suzuki, T.; Osuna, R. M.; Casado, J.; Hernández, V.; Navarrete, J. T. L.; Martinelli, N. G.; Cornil, J.; Sánchez-Carrera, R. S.; Coropceanu, V.; Brédas, J. L. *J. Am. Chem. Soc.* **2009** *131* (4), 1502. doi:10.1021/ja807528w.
(39) Yang, Y.; Geng, H.; Yin, S.; Shuai, Z.; Peng, J. *J. Phys. Chem. B* **2006** *110* (7), 3180. doi:10.1021/jp0540252.
(40) Delgado, M. C. R.; Kim, E.-G.; Filho, D. A. S.; Brédas, J. L. *J. Am. Chem. Soc.* **2010** *132* (10), 3375. doi:10.1021/ja908173x.
(41) Nakanishi, W.; Hitosugi, S.; Piskareva, A.; Shimada, Y.; Taka, H.; Kita, H.; Isobe, H. *Angew. Chem. Int. Ed.* **2010** *49* (40), 7239. doi:10.1002/anie.201002432.
(42) Nakanishi, W.; Hitosugi, S.; Shimada, Y.; Isobe, H. *Chem. Asian J.* **2011** *6* (2), 554. doi:10.1002/asia.201000543.
(43) Troisi, A.; Orlandi, G. *Phys. Rev. Lett.* **2006** *96* (8), 086601. doi:10.1103/PhysRevLett.96.086601.
(44) Coropceanu, V.; Cornil, J.; da Silva Filho, D. A.; Olivier, Y.; Silbey, R.; Brédas, J.-L. *Chem. Rev.* **2007** *107* (4), 926. doi:10.1021/cr050140x.
(45) Jurchescu, O. D.; Baas, J.; Palstra, T. T. M. *Appl. Phys. Lett.* **2004** *84* (16), 3061. doi:10.1063/1.1704874.
(46) Ostroverkhova, O.; Cooke, D. G.; Hegmann, F. A.; Anthony, J. E.; Podzorov, V.; Gershenson, M. E.; Jurchescu, O. D.; Palstra, T. T. M. *Appl. Phys. Lett.* **2006** *88* (16), 162101. doi:10.1063/1.2193801.
(47) Kresse, G.; Hafner, J. *Phys. Rev. B* **1993** *47* (1), 558. doi:10.1103/PhysRevB.47.558.
(48) Kresse, G.; Hafner, J. *Phys. Rev. B* **1994** *49* (20), 14251. doi:10.1103/PhysRevB.49.14251.
(49) Kresse, G.; Furthmüller, J. *Phys. Rev. B* **1996** *54* (16), 11169. doi:10.1103/PhysRevB.54.11169.
(50) Perdew, J. P.; Burke, K.; Ernzerhof, M. *Phys. Rev. Lett.* **1996** *77* (18), 3865. doi:10.1103/PhysRevLett.77.3865.
(51) Pack, J. D.; Monkhorst, H. J. *Phys. Rev. B* **1977** *16* (4), 1748. doi:10.1103/PhysRevB.16.1748.
(52) Yang, X.; Wang, L.; Wang, C.; Long, W.; Shuai, Z. *Chem. Mater.* **2008** *20* (9), 3205. doi:10.1021/cm8002172.
(53) Troisi, A.; Orlandi, G. *Chem. Phys. Lett.* **2001** *344* (5–6), 509. doi:10.1016/S0009-2614(01)00792-8.
(54) Song, Y.; Di, C.; Yang, X.; Li, S.; Xu, W.; Liu, Y.; Yang, L.; Shuai, Z.; Zhang, D.; Zhu, D. *J. Am. Chem. Soc.* **2006** *128* (50), 15940. doi:10.1021/ja064726s.
(55) Ditchfield, R.; Hehre, W. J.; Pople, J. A. *J. Chem. Phys.* **1971** *54* (2), 724. doi:10.1063/1.1674902.
(56) Gordon, M. S. *Chem. Phys. Lett.* **1980** *76* (1), 163. doi:10.1016/0009-2614(80)80628-2.
(57) Zhang, Y.; Cai, X.; Bian, Y.; Li, X.; Jiang, J. *J. Phys. Chem. C* **2008** *112* (13), 5148. doi:10.1021/jp710123r.
(58) Frisch, M. J.; Trucks, G. W.; Schlegel, H. B.; Scuseria, G. E.; Robb, M. A.; Cheeseman, J. R.; Scalmani, G.; Barone, V.; Mennucci, B.; Petersson, G. A.; Nakatsuji, H.; Caricato, M.; Li, X.; Hratchian, H. P.; Izmaylov, A. F.; Bloino, J.; Zheng, G.; Sonnenberg, J. L.; Hada, M.; Ehara, M.; Toyota, K.; Fukuda, R.; Hasegawa, J.; Ishida, M.; Nakajima, T.; Honda, Y.; Kitao, O.; Nakai, H.; Vreven, T.; Montgomery, J. A. J.; Peralta, J. E.; Ogliaro, F.; Bearpark, M.; Heyd, J. J.; Brothers, E.; Kudin, K. N.; Staroverov, V. N.; Kobayashi, R.; Normand, J.; Raghavachari, K.; Rendell, A.; Burant, J. C.; Iyengar, S. S.; Tomasi, J.; Cossi, M.; Rega, N.; Millam, J. M.; Klene, M.; Knox, J. E.; Cross, J. B.; Bakken, V.; Adamo, C.; Jaramillo, J.; Gomperts, R.; Stratmann, R. E.; Yazyev, O.; Austin, A. J.; Cammi, R.; Pomelli, C.; Ochterski, J. W.; Martin, R. L.; Morokuma, K.; Zakrzewski, V. G.; Voth, G. A.; Salvador, P.; Dannenberg, J. J.; Dapprich, S.; Daniels, A. D.; Farkas, O.; Foresman, J. B.; Ortiz, J. V.; Cioslowski, J.; Fox, D. J. G. *Gaussian 09,* revision A.02; Gaussian Inc.: Wallingford Conn., USA, 2009.
(59) Geng, Y.; Wang, J.; Wu, S.; Li, H.; Yu, F.; Yang, G.; Gao, H.; Su, Z. *J. Mater. Chem.* **2011** *21* (1), 134. doi:10.1039/c0jm02119a.

Can. J. Chem. Downloaded from www.nrcresearchpress.com by Xi'an Jiaotong University on 09/19/12
For personal use only.

Shape-persistent macrocycles — Self-assembly reactions and characterization by hyperpolarized ^{129}Xe NMR spectroscopy*

Katie Campbell, Kristopher J. Ooms, Michael J. Ferguson, Peter J. Stang, Roderick E. Wasylishen, and Rik R. Tykwinski

Can. J. Chem. Downloaded from www.nrcresearchpress.com by Xi'an Jiaotong University on 09/19/12
For personal use only.

Abstract: The use of three shape-persistent, conjugated macrocycles **2a**–**2c** as ligands for self-assembly reactions is described. The macrocycles have been characterized through a combination of spectroscopic analyses and, for compounds **2b** and **2c**, X-ray crystallographic analysis. Whereas the reaction of **2a** with the *cis*-Pt(II) species **3** successfully provides the porous solid **4a**, the analogous reaction of **2b** and **2c** with **3** leads only to mixtures of products. The application of continuous-flow hyperpolarized ^{129}Xe NMR spectroscopy to investigate the solid-state pores of macrocycles **2b** and **2c** and the supramolecular complex **4a** as a function of temperature is described. All three species show permanent porosity upon removal of co-crystallized solvent molecules. Using trends in the ^{129}Xe chemical shifts and temperature-dependent dynamics of Xe atoms in the solids, information is obtained on the nature of the pores in these systems. Using the ^{129}Xe NMR data for complex **4a**, the effective heat of adsorption (ΔH_{ads}) was calculated to be ~29 kJ mol^{-1}.

Key words: macrocycles, solid-state NMR, supramolecular chemistry, xenon NMR, porous solids, metal–organic framework.

Résumé : On décrit l'utilisation des trois macrocycles conjugués à forme persistante, **2a**–**2c**, comme ligands pour des réactions d'auto-assemblage. On a caractérisé les macrocycles par une combinaison d'analyses spectroscopiques et, dans le cas des composés **2b** et **2c**, par analyse de données cristallographiques des rayons-X. Alors que la réaction du composé **2a** avec l'espèce *cis*-Pt(II), **3**, conduit avec succès à la formation du solide poreux **4a**, les réactions analogues des composés **2b** et **2c** avec le composé **3** ne conduisent qu'à des mélanges de produits. On décrit l'application de la spectroscopie RMN du ^{129}Xe en flux continu hyperpolarisé à l'étude des pores à l'état solide des macrocycles **2b** et **2c** et du complexe supramoléculaire **4a** en fonction de la température. Les trois espèces présentent chacune une porosité permanente lors de l'élimination des molécules de solvant cocristallisées. En se basant sur les tendances dans les déplacements chimiques du ^{129}Xe et sur la variation de la dynamique des atomes de xénon en fonction de la température, on a obtenu des informations sur la nature des pores dans ces systèmes. En utilisant les données de la RMN du ^{129}Xe pour le complexe **4a**, on a déterminé que la chaleur effective d'adsorption (ΔH_{ads}) est approximativement égale à 29 kJ mol^{-1}.

Mots-clés : macrocycles, RMN à l'état solide, chimie supramoléculaire, RMN du ^{129}Xe, solides poreux, squelette organométallique.

[Traduit par la Rédaction]

Introduction

The synthesis of organic and organometallic porous materials is a rapidly expanding field of synthetic chemistry.[1–5] Recent efforts to use organic and metal–organic macrocycles to form ordered materials have provided numerous systems that could potentially give rise to porous solids.[6–13] The challenges that face researchers in this field are numerous. Initial synthesis of new macrocycles is often time-consuming with only small amounts of material prepared, often <100 mg. This quantity of material makes conventional analysis techniques such as gas adsorption difficult or impossible to use, and solid-state characterization of the materials often depends almost exclusively on single-crystal X-ray diffraction. Unfortunately, however, single crystals can be difficult to grow, and even when single crystals are obtained, the solids often include guest molecules in the desired pores, typically from the solvent used for crystallization. Obtaining single-crystal

Received 9 February 2011. Accepted 17 April 2011. Published at www.nrcresearchpress.com/cjc on 8 September 2011.

K. Campbell, K.J. Ooms, M.J. Ferguson, and R.E. Wasylishen. Department of Chemistry, University of Alberta, Edmonton, AB T6G 2G2, Canada.
P.J. Stang. Department of Chemistry, University of Utah, 315 South 1400 East, RM 2020, Salt Lake City, UT 84112-0850, USA.
R.R. Tykwinski. Department of Chemistry, University of Alberta, Edmonton, AB T6G 2G2, Canada; Insitut für Organische Chemie, Friedrich-Alexander-Universität, Erlangen-Nürnberg, Henkestrasse 42, D-91054 Erlangen, Germany.

Corresponding authors: Rik R. Tykwinski (e-mail: rik.tykwinski@chemie.uni.erlangen.de) and Roderick E. Wasylishen (e-mail: roderick.wasylishen@ualberta.ca).

*In memory of Professor Michael M. Pollard.

Can. J. Chem. Downloaded from www.nrcresearchpress.com by Xi'an Jiaotong University on 09/19/12
For personal use only.

X-ray structures of the material without the guest(s) is difficult and therefore the question must be asked, is the remaining material truly porous?[14]

Inorganic-based porous materials have been studied extensively using a variety of solid-state NMR techniques. In particular, hyperpolarized ^{129}Xe NMR spectroscopy[15,16] has been used to provide information about pore size and shape, as well as the dynamics of guest molecules present within porous structures.[15,17–22] ^{129}Xe NMR spectroscopy is expected to provide important solid-state structural information about macrocyclic organic systems that cannot be obtained using other methods.[23–25]

Xenon has a van der Waals radius of 2.16 Å (approximately the same size as methane), making it an ideal probe for materials that can adsorb small molecular gases. The advantage of using ^{129}Xe NMR to explore porous solids lies in the sensitivity of the xenon atom to the local environment, as reflected in changes in chemical shift values. The chemical shift range of atomic xenon is >300 ppm.[15] The bulk gas is set as the reference (at 0 ppm) and most NMR peaks appear to high frequency of the gas peak. In general, the greater the interaction between ^{129}Xe and the host solid, the larger the observed chemical shift value, i.e., small pores or channels result in a larger chemical shift value than larger pores. For inorganic zeolites, trends between chemical shift and pore size have been established, showing that both the pore structure and Xe dynamics influence the observed ^{129}Xe chemical shift.[26–31] Although a large body of experimental and theoretical data is not yet available for organic materials,[32–45] the principles established for inorganic systems can be qualitatively used to understand the ^{129}Xe NMR spectra for metal–organic systems.[41,42,46,47]

Reported herein is the study of three conjugated macrocycles that have been developed to function as analogues of 4,4′-bipyridine in self-assembly reactions.[6a,48,49] Unlike 4,4′-bipyridine, however, these macrocycles offer the prospect of forming porous metal–organic materials in which the macrocyclic framework can contribute to the porous network. Using these macrocycles, the formation of porous solids was then explored. X-ray crystallographic analysis of some of these materials shows that the solids contain a significant number of the co-crystallized solvent molecules. The porosity of the materials is realized when the guest molecules are removed, creating cavities within the solid where other molecules might adsorb. Finally, using variable temperature ^{129}Xe NMR spectroscopy we have sought to answer two primary questions about these solids. First, from a fundamental perspective, do the solids retain porosity upon desolvation? Second, from a practical standpoint, can ^{129}Xe NMR spectroscopy be a useful tool for determining whether small quantities of a material are porous to atomic and small molecular gases such as methane?[23,24] From these NMR experiments (using as little as 15 mg of sample in the case of **4a**), general conclusions about the Xe adsorption are described and information about the porous nature of these materials in the absence of guest solvent molecules is presented.

Results and discussion

Synthesis and characterization of macrocyclic ligands

Several macrocyclic ligands were employed in this study, and their structures (**2a**–**2c**) are shown in Scheme 1. All macrocycles were prepared through the elaboration of a common starting material, tetrayne **1**. Macrocyclic ligand **2a** was synthesized via an oxidative homocoupling reaction at high dilution, as previously reported.[6a] Platinacycles featuring two pyridine moieties (**2b** and **2c**) were also targeted and their synthesis is outlined in Scheme 1. Reaction of the acyclic oligomer **1** with $PtCl_2(PPh_3)_2$ in the presence of catalytic CuI under high dilution conditions in Et_2NH leads to the formation of platinacycle **2b**, as recently communicated.[50] Macrocycle **2c** was synthesized in an analogous manner through the use of the alternative platinum source, $PtCl_2(PEt_3)_2$. Platinacycles **2b** and **2c** are both stable yellow solids and could be purified by either chromatography or selective precipitation. Compound **2b** is considerably easier to handle than the unfunctionalized derivative **2a**, but it is still only marginally soluble in common organic solvents. This leads to difficulties with respect to its isolation, and the higher isolated yield of derivative **2c** is due to its superior solubility in comparison with **2b**.[51]

Both platinacycles **2b** and **2c** are sufficiently soluble for full spectroscopic characterization. With respect to **2b**, the solution-state ^{31}P NMR spectrum shows a single resonance at δ 18.0 ppm, confirming the presence of the metal–acetylide linkage. This chemical shift value is comparable to that of previously reported macrocycles containing Pt–acetylide units.[50,52] Confirmation of the formation of **2b** comes from mass spectral analysis, in which the ESI mass spectrum shows a large signal at *m*/*z* 2498.7 (100% relative intensity) corresponding to $[M + H]^+$.

All spectroscopic data acquired for the more soluble derivative **2c** are also consistent with the proposed structure. The solution-state ^{1}H NMR spectrum of **2c** confirms the presence of the triethylphosphine ligands, with the methylene and methyl protons observed as multiplets at 1.88–1.83 and 1.10–1.00 ppm, respectively. The ^{31}P NMR spectrum of **2c** shows a single resonance at δ 13.9 ppm ($^1J_{P–Pt}$ = 2344 Hz), at slightly higher frequency relative to **2c** as a result of the ethyl groups. The solution-state ^{13}C NMR spectrum of **2c** shows 18 of the 19 expected nonequivalent carbon resonances, and the ESI mass spectrum shows a base peak at *m*/*z* 1923 ($[M + H]^+$), consistent with the constitution of **2c**.

Single crystals of the pyridine-containing macrocycle **2b**, suitable for X-ray crystallographic analysis, were grown by slow evaporation from CH_2Cl_2/$ClCH_2CH_2Cl$/acetone. The ORTEP drawing of **2b** (shown in Fig. 1) confirms the assigned trans-stereochemistry and square-planar geometry about the platinum centre (see Table 1 for crystallographic details). The macrocyclic core is nearly planar. The mean alkyne and alkylidene bond angles, 174.5° and 114.4°, respectively, show that that macrocycle is not appreciably strained. The triphenylphosphine ligands adopt a conformation in which the platinum–phosphorous bonds Pt–P(1) and Pt–P(2) are tilted by 147.1° and 36.0°, respectively, relative to the plane of the macrocycle (as defined by Pt–Pt′–C(16)–C(26)–C(16′)–C(26′). The cavity circumscribed by the enyne framework, which measures 9.0 × 9.6 (Pt–Pt) Å, is larger than that of macrocycle **2a**, but is partially obscured by the phosphine ligands of a platinum acetylide linkage. While this may initially be seen as a drawback, it is worth noting that ligand exchange at platinum offers the possibility of further opening

Can. J. Chem. Downloaded from www.nrcresearchpress.com by Xi'an Jiaotong University on 09/19/12
For personal use only.

Scheme 1. Synthesis of macrocycles **2a**–**2c**. Reagents and conditions: (a) CuI, TMEDA, CH_2Cl_2, air; (b) $PtCl_2(PPh_3)_2$, CuI, Et_2NH; and (c) $PtCl_2(PEt_3)_2$, CuI, Et_2NH.

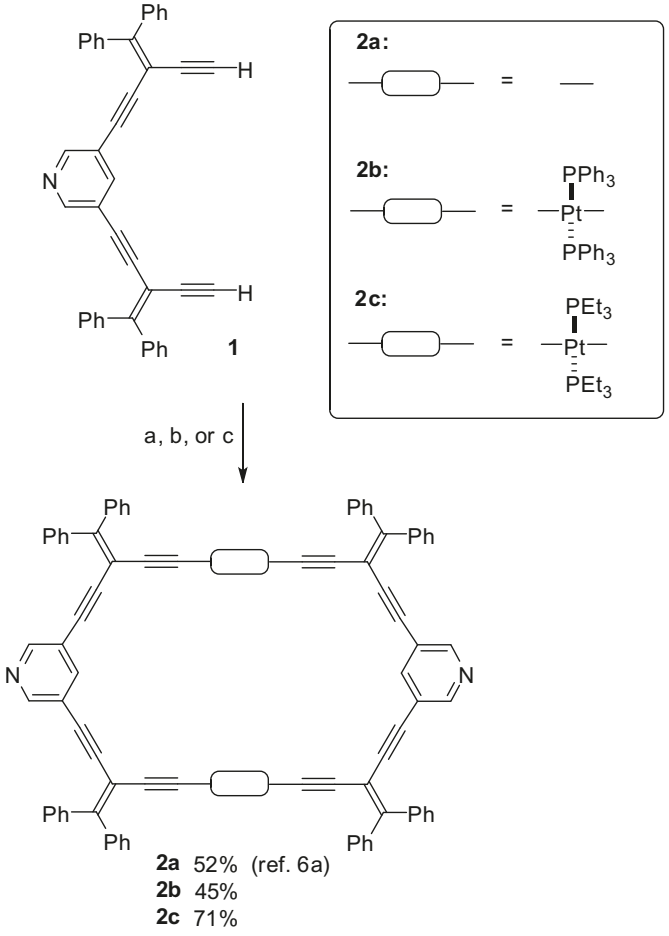

these channels and reconstruction of the macrocyclic pore structure,[50] studies of which are underway.

Single crystals of the triethylphosphine-containing platinacycle **2c** have been grown by slow evaporation from a CH_2Cl_2/acetone solution at 4 °C (see Table 1 for crystallographic details). The solid-state structure of **2c** is similar to that of the derivative **2b**, although it adopts a slight chairlike conformation. The ORTEP drawing of **2c** (Fig. 2) shows that the phosphine ligands are again "lying down" into the plane of the macrocycle. The angles between a plane defined by Pt(1)–Pt(2)–C(1)–C(17)–C(18)–C(34) and the Pt(1)–P(1), Pt(1)–P(2), Pt(2)–P(3), and Pt(2)–P(4) bonds are 59.2°, 125.0°, 127.3°, and 46.9°, respectively. Platinacycle **2c**, like **2b**, is relatively unstrained, as reflected in the mean alkyne and alkylidene bond angles, which are 174.7° and 114.2°, respectively.

Self-assembly reactions of macrocycles 2a–2c

The supramolecular assemblies targeted first were those featuring the macrocyclic ligand(s) linked to the corner piece *cis*-$(TfO)_2Pt(PEt_3)_2$ (**3**),[53] which has been well established as a component of supramolecular architectures derived from bipyridine ligands.[54,55] Thus, the reaction of **2a** with **3** gave rise to assembly **4a** (Scheme 2), the synthesis of which has been reported.[49] One equivalent of macrocyclic ligand **2a** was suspended in dry CH_2Cl_2 and then slowly added (over 15 min) to a solution of 2 equiv of *cis*-$(TfO)_2Pt(PEt_3)_2$ (**3**) in dry CH_2Cl_2. The reaction mixture was then stirred at room temperature for 18 h under a positive pressure of N_2. A second portion of the macrocycle was then suspended in dry CH_2Cl_2 and slowly added to the reaction mixture. After stirring at room temperature for a further 18 h, 80% of the solvent was allowed to evaporate in air, yielding assembly **4a** as bright orange crystals in excellent yield.

The synthesis and subsequent isolation of **4a** is only successful if several variables are carefully controlled. Most important is that all starting materials are rigorously dried, in particular, the *cis*-platinum species **3**. This prevents the formation of what is presumably the hydrated platinum species **3·$(H_2O)_2$**, as suggested by X-ray crystallography (Fig. 3; see Table 1 for crystallographic details). The hydration of **3** subsequently inhibits both binding of the pyridine-containing macrocycle to platinum, as well as the isolation of the supramolecular assembly.

Assembly **4a** has been fully characterized in solution using several NMR spectroscopic techniques in combination with IR spectroscopy and ESI mass spectral analysis. The solution-state ^1H NMR spectrum confirms the binding of macrocycles **2a** to the platinum centre(s). The solution-state ^1H NMR spectrum of free macrocyclic ligand **2a** shows resonances for the *ortho*- and *para*-pyridyl protons (H_{ortho} and H_{para}, respectively) as a doublet and a triplet at δ 8.13 and 7.83 ppm, respectively. By contrast, H_{ortho} and H_{para} appear as a second-order multiplet at δ 8.42 ppm and a triplet at δ 7.95 ppm, respectively, in the ^1H NMR spectrum of the complex **4a**. The observed splitting pattern of the ortho protons for **4a** is the result of long-range coupling to the magnetically nonequivalent phosphorous nuclei. This observation was confirmed through analysis of several solution-state NMR decoupling experiments. For example, $^1H\{^{31}P\}$ NMR spectrum of **4a** shows H_{ortho} as a doublet, albeit barely resolved. Likewise, selective decoupling of H_{ortho} from H_{para} results in the collapse of the broad second-order peaks for H_{ortho} into a simple doublet. The $^{13}C\{^1H\}$ NMR spectrum also provides convincing evidence for the formation of **4a** in solution. Signals for all 19 unique carbons for the framework of **4a** are observed (CF_3 of triflate anion not observed). In addition, the $^{31}P\{^1H\}$ and $^{19}F\{^1H\}$ NMR spectra each show only a single signal, at –1.3 and –78.2 ppm, respectively, confirming the presence of a discrete, symmetrical species in solution.

The most convincing evidence for the formation of the *dimeric* assembly **4a** in solution comes from the ESI mass spectral analysis, acquired by slow infusion of a solution of **4a** in $CH_2Cl_2/MeNO_2$. A prominent signal is observed at *m/z* 745 (24%) and assigned to $[\mathbf{4a} - 4(OTf)]^{4+}$. In addition, several peaks consistent with the fragmentation of **4a** are observed at *m/z* 1059 (9%), 492 (78%), and 429 (100%), assigned to $[\mathbf{2a} + H]^+$, $[\mathbf{3} - 2(OTf) + NO_2Me]^+$, and $[\mathbf{3} - 2(OTf)]^+$, respectively. Finally, X-ray crystallographic analysis confirmed the constitution of **4a**, as has been previously communicated.[49]

Larger supramolecular assemblies **4b** and **4c** were then targeted based on the "expanded" macrocycles **2b** and **2c** (Scheme 3). Platinacycles **2b** and **2c** were treated with identical reaction conditions as described above for **2a**, but in neither case was the desired assembly isolated. In both reactions, solution-state ^1H and ^{31}P NMR spectroscopy indicated the

Can. J. Chem. Downloaded from www.nrcresearchpress.com by Xi'an Jiaotong University on 09/19/12
For personal use only.

Fig. 1. (A) ORTEP drawing of **2b**. Selected bond lengths (Å) and angles (°): Pt–P(1) 2.3084(15), Pt–P(2) 2.3028(15), Pt–C(16) 2.000(6), Pt–C(26′) 1.985(5), P(1)–Pt–P(2) 173.82(5), C(16)–Pt–C(26′) 177.7(2), C(12)–C(13)–C(15) 114.4(5), C(22)–C(23)–C(25) 114.3(5). (B) Alternate view of **2b** highlighting the planar cyclic core (only the ipso carbons of the triphenylphosphine ligands and pendant phenyl groups are shown for clarity). Thermal ellipsoids are drawn at the 20% probability level. Co-crystallized solvent ($ClCH_2CH_2Cl$) is not shown.

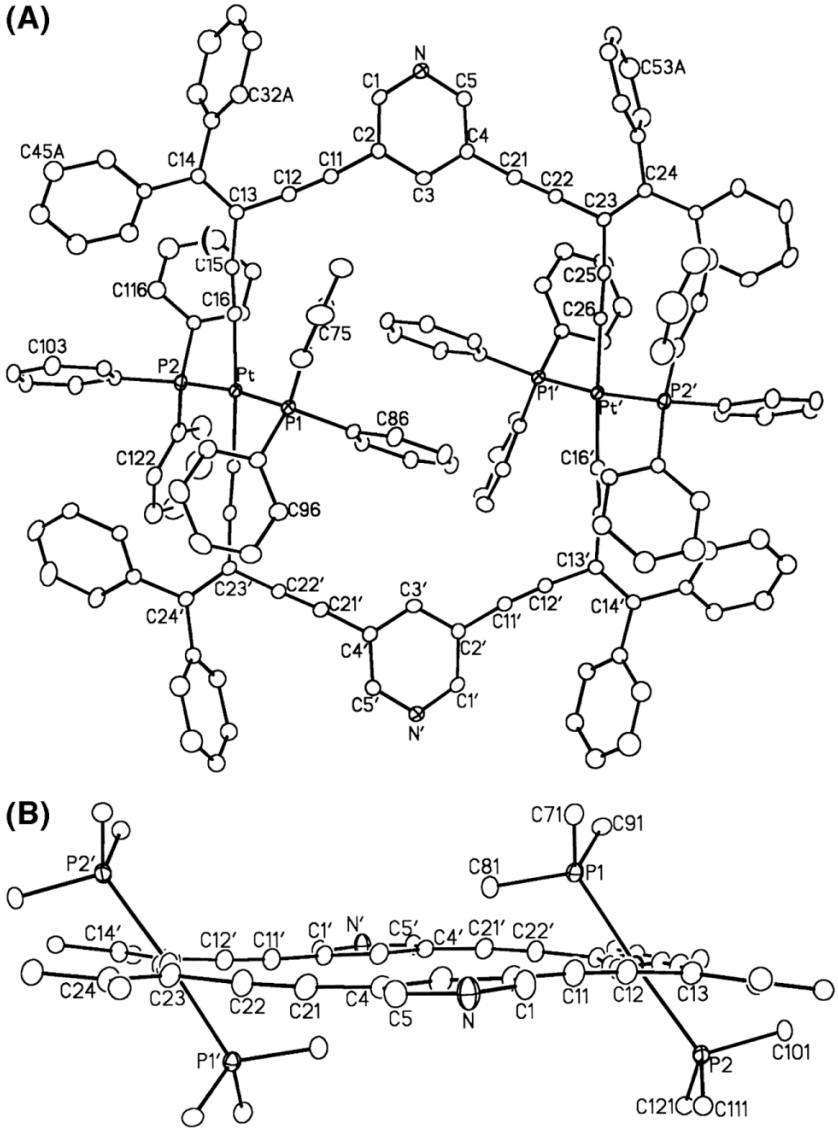

formation of a mixture of products, rather than a single discrete species. To restrict the formation of by-products, numerous NMR titration experiments were performed in which the respective macrocyclic ligand (**2b** or **2c**) was dissolved in CD_2Cl_2 and aliquots of this solution were slowly added to an NMR tube containing 1 equiv of **3** dissolved in CD_2Cl_2. Subsequent monitoring of these reactions by ^1H and ^{31}P NMR spectroscopy revealed the formation of a mixture of products. This was especially frustrating as spectroscopic analysis clearly indicated that all of the starting materials were being consumed upon addition and ESI mass spectral analysis showed signals that were attributable to fragments of the desired assemblies. Thus, these reactions demonstrated that platinacycles **2b** and **2c** were able to coordinate to the platinum species **3**, but no single distinct product could be isolated.

It was hypothesized that steric interactions between the pendant phosphine ligands of platinacycles **2b** and **2c** could be preventing the desired dimerization to form **4b** and **4c**, leading instead to a mixture of oligomeric products. Thus, the synthesis of an assembly was pursued that incorporated the extended bimetallic "spacer" **5**[56] to help mitigate steric interactions between macrocyclic units. While NMR spectroscopy as well as ESI and MALDI MS were suggestive of a supramolecular product from the reaction of **3** and **5**, the structure of this product could not be unequivocally established.

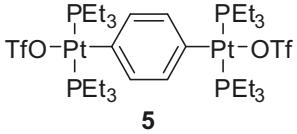

5

^{129}Xe NMR studies on porous solids

The porosity of a number of materials formed by organic

Can. J. Chem. Downloaded from www.nrcresearchpress.com by Xi'an Jiaotong University on 09/19/12
For personal use only.

Table 1. X-ray crystallographic details for compounds **2b**, **2c**, **3·(H$_2$O)$_2$**, and **4a**.

Crystal	**2b**	**2c**	**3·(H$_2$O)$_2$**	**4a** (ref. 49)
Empirical formula	$C_{154}H_{106}N_2P_4Pt_2$·2.5$ClCH_2CH_2Cl$	$C_{106}H_{106}N_2P_4Pt_2$·CH_2Cl_2	$C_{14}H_{54}F_6O_8P_2PtS_2$	$C_{192}H_{152}F_{12}N_4O_{12}P_4Pt_2S_4$ ·8$ClCH_2CH_2Cl$
Formula mass	2745.85	2006.91	765.56	4369.09
Colour, habit	Yellow, rod	Yellow, needle	Colourless, block	Red, block
Crystal dimensions (mm)	0.44×0.17×0.07	0.28×0.08×0.04	0.26×0.13×0.08	0.49×0.45×0.36
Crystal system	Triclinic	Monoclinic	Monoclinic	Triclinic
Space group	$P\bar{1}$ (No. 2)	*Ia* (an alternate setting of *Cc* (No. 9))	*I*2/*a* (an alternate setting of *C*2/*c* (No. 15))	$P\bar{1}$ (No. 2)
Z	1	4	4	1
a (Å)	12.8940(5)	29.555(2)	17.5484(10)	13.252(2)
b (Å)	14.4595(6)	13.1084(11)	9.1388(5)	20.821(3)
c (Å)	19.9990(9)	26.278(2)	16.8528(10)	21.983(3)
α (°)	104.9381(8)			102.407(3)
β (°)	97.9082(8)	105.498(2)	96.7830(10)	102.973(3)
γ (°)	99.8794(8)			95.742(3)
Collection ranges	$-16\le h\le 16$, $-18\le k\le 18$, $-20\le l\le 24$	$-35\le h\le 36$, $-16\le k\le 16$, $-32\le l\le 32$	$-21\le h\le 21$, $-10\le k\le 11$, $-21\le l\le 20$	$-16\le h\le 16$, $-25\le k\le 25$, $-27\le l\le 27$
Temperature (°C)	–80	–80	–80	–80
Volume (Å^3)	3483.9(3)	9810.3(14)	2683.8(3)	5701.9(15)
D_{calcd} (g cm^{-3})	1.309	1.359	1.895	1.272
Radiation	Mo Kα (0.71073)	Mo Kα (0.71073)	Mo Kα (0.71073)	Mo Kα (0.71073)
Absorption coeff. (μ, mm^{-1})	2.198	3.015	5.579	1.540
Absorption correction	Gaussian integration (face-indexed)	Multi-scan (SADABS)	Multi-scan (SADABS)	Gaussian integration (face-indexed)
F(000)	1385	4056	1504	2216
θ range for data collection (°)	$1.07\le\theta\le 26.39$	$1.43\le\theta\le 26.40$	$2.34\le\theta\le 26.41$	$0.98\le\theta\le 26.50$
Observed reflections	12208	15052	2553	15230
Independent reflections	13938 (R_{int} = 0.0216)	18646 (R_{int} = 0.0599)	2749 (R_{int} = 0.0295)	23153 (R_{int} = 0.0654)
Data/restraints/parameters	13938/8[a]/675	18646/17[b]/1025	2749/0/151	23153/76[c]/878
Goodness-of-fit on F^2	1.081	1.028	1.036	1.299
Flack parameter	—	0.466(7)	—	—
R_1 [$F_o^2 \ge 2\sigma(F_o^2)$]	0.0517	0.0531	0.0230	0.1216
wR_2 [$F_o^2 \ge -3\sigma(F_o^2)$]	0.1589	0.1249	0.0547	0.3645
Largest difference peak and hole (e Å^{-3})	2.414 and –0.612	1.407 and –0.587	2.122 and –0.751	4.722 and –1.982
CCDC No. (Supplementary data)	666371	666372	666373	205116

[a]The Cl–C and C–C distances of the solvent dichloroethane molecules were restrained to be 1.80(1) and 1.54(1) Å, respectively.

[b]The C–Cl and the Cl···Cl distances of the dichloromethane solvent molecules were restrained to be 1.80(1) and 2.94(1) Å, respectively. The P–CH_2, CH_2–CH_3, and CH_2···CH_2 distances within the triethylphosphine ligand P2 were restrained to be 1.80(1), 1.54(1), and 2.94(1) Å, respectively. The phenyl rings defined by carbon atoms C41B–C42B–C43B–C44B–C45B–C46B and C91B–C92B–C93B–C94B–C95B–C96B were constrained to be idealized hexagons with C–C distances of 1.39 Å.

[c]An idealized geometry was imposed upon the triflate ions by the following restraints: S–C 1.80(1) Å, S–O 1.45(1) Å, C–F 1.35(1) Å, O···O 2.37(1) Å, F···F 2.20(1) Å, and O···F (gauche interactions) 3.04(1) Å. An idealized geometry was imposed upon the dichloroethane solvent molecules by the following restraints: Cl–C 1.80(1) Å, C–C 1.54(1) Å, and Cl···C 2.73(1) Å. Distance restraints (P–C 1.83(1) Å and C–C 1.54(1) Å) were applied to the triethylphosphine ligands (all bonded distances for the P1 ligand and all but P2–C89 and C89–C90 for the P2 ligand). The phenyl rings defined by atoms C47A to C52A, C47B to C52B, C59A to C64A, C59B to C64B, C77A to C82A, and C77B to C82B were constrained to be hexagons with C–C distances of 1.39 Å.

Can. J. Chem. Downloaded from www.nrcresearchpress.com by Xi'an Jiaotong University on 09/19/12
For personal use only.

Fig. 2. (A) ORTEP drawing of **2c**. Selected bond lengths (Å) and angles (°): Pt(1)–P(1) 2.282(3), Pt(1)–P(2) 2.311(3), Pt(2)–P(3) 2.300(3), Pt(2)–P(4) 2.286(3), Pt(1)–C(1) 1.967(11), Pt(1)–C(34) 2.009(11), Pt(2)–C(17) 1.975(10), Pt(2)–C(18) 2.030(11), P(1)–Pt(1)–P(2) 175.54(12), C(1)–Pt(1)–C(34) 179.0(5), P(3)–Pt(2)–P(4) 173.32(12), C(17)–Pt(2)–C(18) 177.1(5), C(2)–C(3)–C(5) 111.1(9), C(13)–C(14)–C(16) 113.8(9), C(19)–C(20)–C(22) 115.8(9), and C(30)–C(31)–C(33) 115.9(10). (B) Alternate view of **2c** highlighting the nonplanar, cyclic core (only the methylene carbons of the triethylphosphine ligands and ipso carbons of pendent phenyl groups are shown for clarity). Thermal ellipsoids are drawn at the 20% probability level. Co-crystallized solvent (CH_2Cl_2) is not shown.

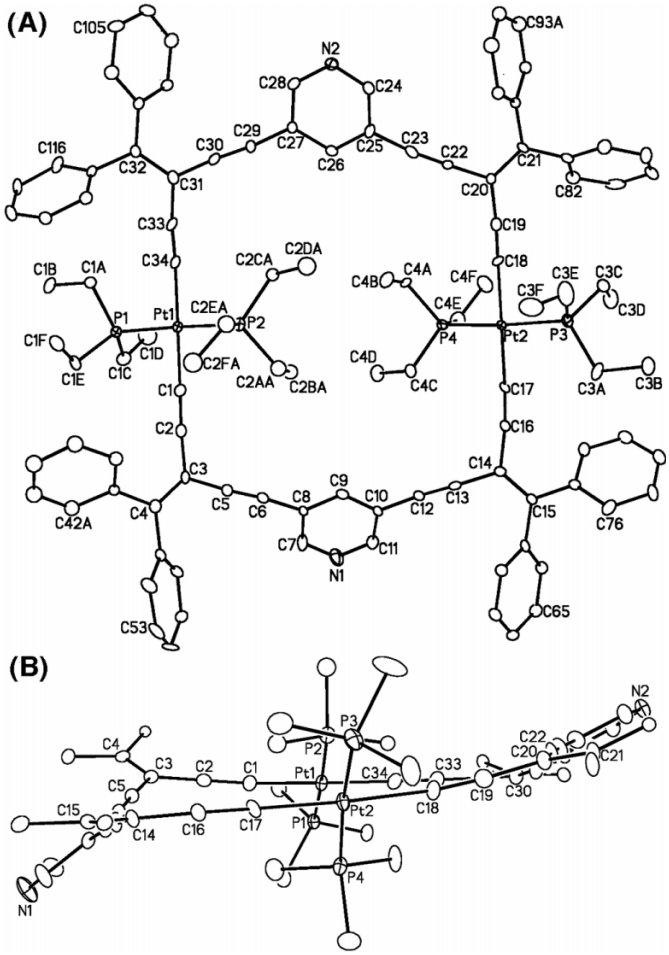

macrocycles has previously been investigated using ^{129}Xe NMR spectroscopy, including compound **2a**.[23,24] These studies have shown the solids to be porous to Xe gas after the solvent guest molecules are removed from the solid-state structure. These studies are now extended to explore the permanent porosity of the metal–organic macrocycles **2b** and **2c** using hyperpolarized Xe.

The ^{129}Xe NMR spectra for platinacycle **2b** acquired at various temperatures (Fig. 4A) show that there is little Xe adsorption at temperatures greater than –30 °C. Below this temperature, two distinct signals are observed. A peak at 128 ppm appears at –85 °C and increases in intensity as the temperature is lowered. At –67 °C, a second peak can be resolved from the gas peak; this peak appears at increasing frequencies as the temperature is decreased. The intensity of this signal also increases as the temperature is lowered, and it begins to broaden significantly at –85 °C. The chemical shift values for both signals indicate that Xe is being adsorbed into cavities that are significantly larger than the diameter of Xe.

Scheme 2. Synthesis of porous assembly **4a**.

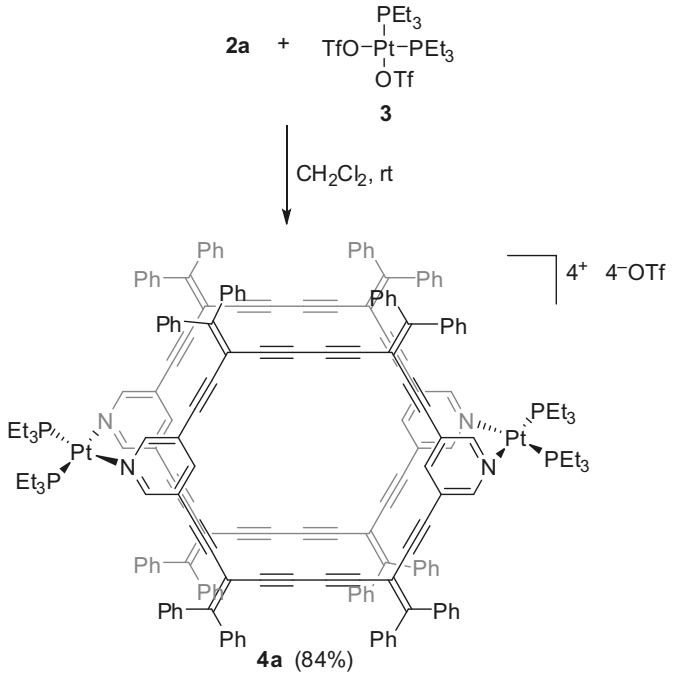

Fig. 3. ORTEP drawing of **3·(H$_2$O)$_2$**. Hydrogen atoms are shown with arbitrarily small thermal parameters for the coordinated water molecules and are not shown for the triethylphosphine groups (primed atoms are related to the unprimed ones by the twofold rotational axis at 1/4, *y*, 0).

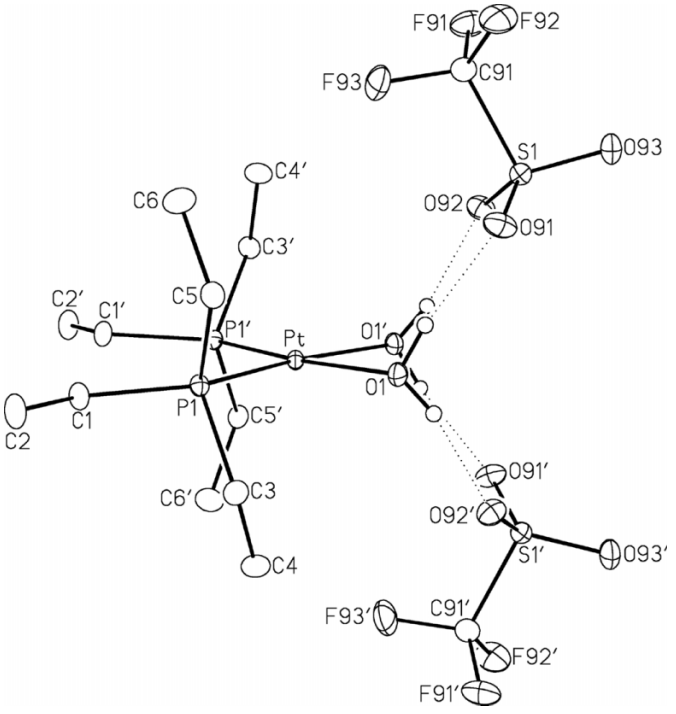

Scheme 3. Attempted synthesis of assemblies **4b** and **4c**.

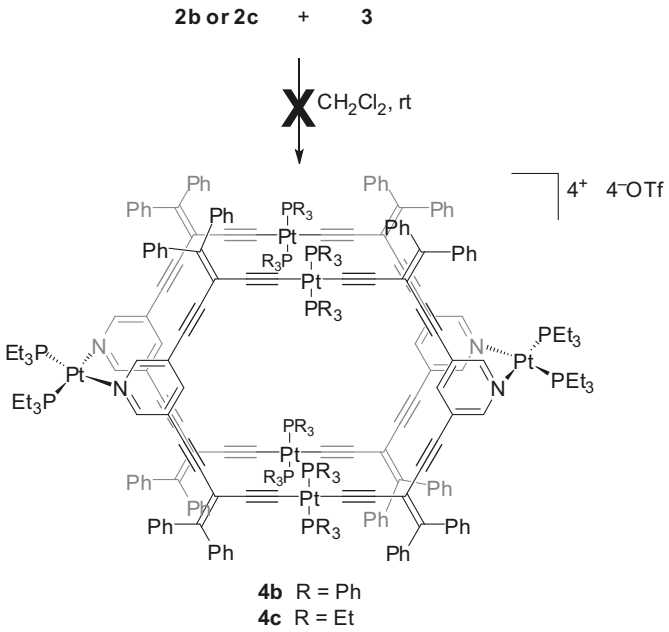

Shown in Fig. 5 is a portion of the crystal packing diagram of platinacycle **2b**. Overlaid across this structure is a representation of the interstitial void space present within the crystal lattice after the co-crystallized solvent molecules (1,2-dichloroethane) have been removed.[57] There is no obvious channel system present within the crystal lattice, although there is a significant amount of void space (18%) when the solvent molecules are removed from the structure (in the presence of co-crystallized solvent the void space is calculated to be zero). Furthermore, the two chemically nonequivalent solvent cavities are too far apart to be considered "connected". Despite the lack of channels the ^{129}Xe NMR spectra indicate that Xe is able to access these cavities. The ability of solids to adsorb small atomic or molecular gases in the absence of clear channel systems has been demonstrated for other organic materials. Calixarenes, for example, can adsorb small guest molecules such as toluene or nitrobenzene as well as larger organic molecules such as tetradecane.[58–61] Similar behaviour has also been observed for a cyclic organometallic molecule that forms stacks in the solid state.[62] The single-crystal X-ray diffraction analysis of this system revealed that there are solvent cavities in the solid with narrow openings between cages; the free diameter of the openings is 0.89 Å. Despite the lack of clear channels between the solvent cavities, the solvent molecules could readily escape from the structure, even at room temperature and ambient pressure, and other guests could be adsorbed by the solid.[62]

The behaviour of the low frequency peak observed in the ^{129}Xe NMR spectra of **2b** (Fig. 4A) is characteristic of Xe rapidly exchanging between Xe in the free gas and Xe adsorbed in the solid. If Xe atoms exchange between two nonequivalent sites at a rate that is fast with respect to the chemical shift difference (in Hz) that they experience in the two sites (i.e., in the absence of exchange), a single ^{129}Xe NMR peak will be observed with a chemical shift corresponding to the weighted population average chemical shift. The ^{129}Xe NMR spectra therefore indicate that at –30 °C

Fig. 4. Variable temperature hyperpolarized ^{129}Xe NMR spectra (55 MHz) of platinacycles (A) **2b** and (B) **2c**. The three lower spectra in Fig. 4B are scaled by 20% with respect to the upper spectra.

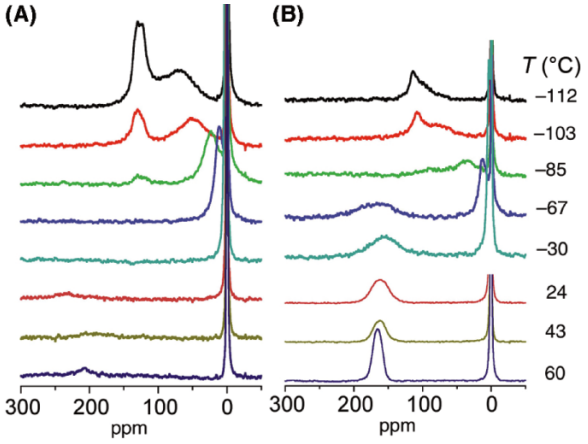

Fig. 5. Schematic representation of the crystal packing diagram of **2b**. Shown is a 2 × 2 × 2 array of unit cells as viewed down the *a* axis. A representation of the void space (when co-crystallized solvent is removed) present within the crystal lattice is shown in light gray.

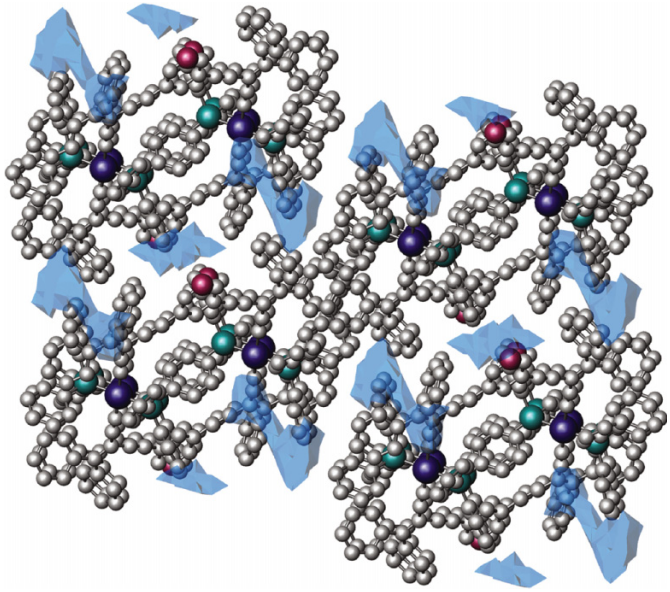

very few Xe atoms sample the cavity for a significant amount of time. As the temperature is lowered further, the Xe population inside the cavity increases, but rapid exchange still results in a narrow peak. Near –85 °C, exchange between the cavities and the free gas slows and two distinct, broad peaks are observed. The large breadth of the two peaks suggests that the adsorbed Xe atoms within the cavities experience different local environments, i.e., there is a distribution of ^{129}Xe chemical shifts. These different environments likely arise from subtle variations in the framework structure such as differences in the phenyl ring orientations or molecular packing. The narrower high frequency peak in Fig. 4A arises from Xe in smaller more uniform cavities while the broader lower frequency peak arises from larger cavities with greater structural heterogeneity; these cavities may correspond to those depicted

Can. J. Chem. Downloaded from www.nrcresearchpress.com by Xi'an Jiaotong University on 09/19/12
For personal use only.

Can. J. Chem. Downloaded from www.nrcresearchpress.com by Xi'an Jiaotong University on 09/19/12
For personal use only.

in Fig. 5. It is likely that near –103 °C exchange with the free gas has a minimal effect on the NMR peaks.

Since there is no distinct channel system for **2b** in the solid state, it is unclear why the ^{129}Xe NMR spectra show a trend that is characteristic of Xe in fast exchange with the free gas at –30 °C, with the Xe gas sampling the cavities for longer time periods as the temperature is lowered. One possible explanation is that Xe only samples cavities near the surface and then rapidly exchanges back into the free gas rather than penetrating deeper into the structure. As the temperature is lowered and the Xe atoms spend more time adsorbed in the near-surface cavities, the probability increases that the Xe will penetrate deeper into the cavities, resulting in spectra more characteristic of Xe interaction with the framework.

The ^{129}Xe NMR spectra of platinacycle **2c** acquired at various temperatures (Fig. 4B) show several differences compared with those of **2b**. At higher temperatures, a single peak is found at 166 ppm, and this signal is surprisingly intense considering the small amount of sample used, ~100 mg. The signal intensity decreases as the temperature is lowered, diminishing rapidly between 24 and –30 °C; no signal from this peak, $\delta \approx 166$ ppm, is detected at temperatures below –67 °C. Below –30 °C, a second signal separates from the free Xe gas peak at 0 ppm, and the chemical shift of this signal steadily increases as the temperature is lowered to –112 °C.

Shown in Fig. 6 is a schematic representation of the crystal packing diagram of **2c**, highlighting the channel that results along the crystallographic *b* axis when the co-crystallized CH_2Cl_2 molecules are removed from the structure. This channel has dimensions of approximately 7 Å × 5 Å. The crystal packing of platinacycle **2c** shows that the macrocycles lie nearly parallel to this channel and, in principle, the centre of the macrocycle cores provide for side pockets along the walls of the channel. Given the size of the macrocycle, Xe atoms could potentially adsorb in these pockets as they move along the main solvent channel. The chemical shift of 166 ppm is too large to be attributed to Xe in the relatively large channel and suggests Xe is indeed accessing more confined spaces within the lattice. The pocket created by the macrocycle is surrounded by the ethyl groups of the phosphine ligand and might therefore produce a highly confined alkyl environment for the Xe that would account for the observed high-frequency signal. By way of comparison, the chemical shift of Xe dissolved in ethanol is 161.1 ppm,[63] Xe in diethyl ether is 159.0 ppm,[64] and Xe in *n*-pentane is 154.1 ppm[64] (all at room temperature). Previous studies of Xe adsorbed by porous organic macrocycles shows that the chemical shift of Xe adsorbed in highly confined sites surrounded by phenyl groups is close to that of Xe dissolved in benzene, 193 ppm.[23,24,64] The line width of the peak at 166 ppm can be attributed to small differences in the structure of the pores. The ethyl groups are likely to flex as Xe is adsorbed, and different pores would therefore have slightly different chemical environments. The loss of signal as the temperature is lowered is likely due to a decrease in framework flexibility and subsequent exclusion of Xe from these cavities. The signal loss could also arise from condensation of the Xe atoms. In the hyperpolarized ^{129}Xe NMR experiment, Xe atoms can only be observed once if 90° excitation pulses are used. Therefore, if Xe atoms in the cavities do not exchange for freshly polarized Xe, no NMR signal is observed.[16] However, since there is no increase in the chemical shifts, which is also characteristic of Xe condensation, it is unlikely that condensation is the cause of the signal loss in this case.

Fig. 6. A schematic representation of the location of the channels in the solid-state structure of **2c** (ellipse). Shown is a single unit cell of **2c** as viewed down the *b* axis.

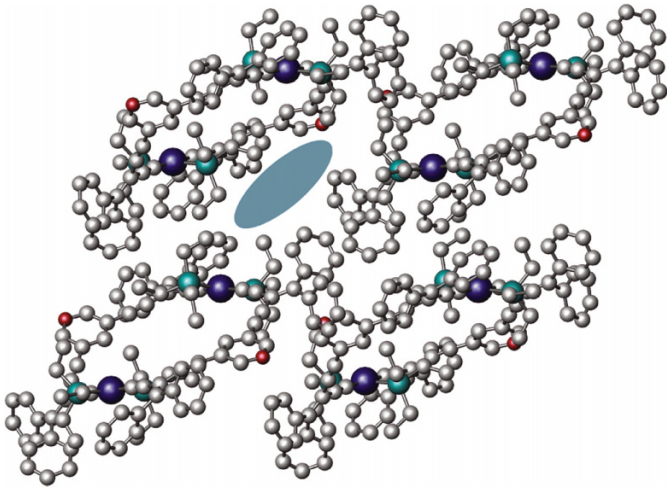

The peak that is observed to separate from the gas peak at –30 °C in the ^{129}Xe NMR spectra of **2c** shows a similar pattern versus temperature as the analogous peak observed for **2b**; the chemical shift steadily increases as the temperature is lowered, which is characteristic of Xe undergoing fast exchange between the cavity and the free gas. The low chemical shift value and, to some extent, the fast Xe exchange dynamics suggest the Xe is sampling a pore environment significantly larger than the Xe atom, i.e., the solvent channels. The broad ^{129}Xe NMR signal obtained at –103 °C suggests that different adsorption regions with different Xe populations exist within the channels, which is not surprising given the structurally varied nature of the channel walls. Above –85 °C this distribution is averaged by fast exchange between the different environments and the gas phase.

In contrast to platinacycles **2b** and **2c**, X-ray crystallography shows that supramolecular assembly **4a** stacks in the solid state such that a clear, bidirectional pore structure is realized (Fig. 7; see Table 1 for crystallographic details). The two sets of perpendicular channels result from the combined attributes of the macrocyclic building block and the supramolecular assembly. The boatlike conformation of the macrocycles bridging the Pt centres define channels that are clearly evident along the *c* axis, with dimensions of ca. 7.5 Å × 16.3 Å (Pt–Pt; Fig. 7, bottom). Stacking of the macrocyclic portion of the assembly provides a perpendicular set of channels along the *a* axis with smaller internal dimensions of 6.6 Å × 9.7 Å circumscribed by the macrocycle (Fig. 7, top). Noteworthy is the selective uptake of $ClCH_2CH_2Cl$ into the crystal lattice from the solvent mixture of $ClCH_2CH_2Cl$ and CH_2Cl_2; the unit cell of **4a** incorporates a total of eight solvent molecules. Overall, there is a significant proportion of void space in the structure, calculated at 13% with the co-crystallized solvent included. The void space in the absence of the co-crystallized solvent is a remarkable 28% of the unit cell volume.

Can. J. Chem. Downloaded from www.nrcresearchpress.com by Xi'an Jiaotong University on 09/19/12
For personal use only.

Fig. 7. Crystal packing diagrams of assembly **4a** as viewed down the *a* axis (top) and down the *c* axis (bottom). Solvent molecules have been omitted for clarity.

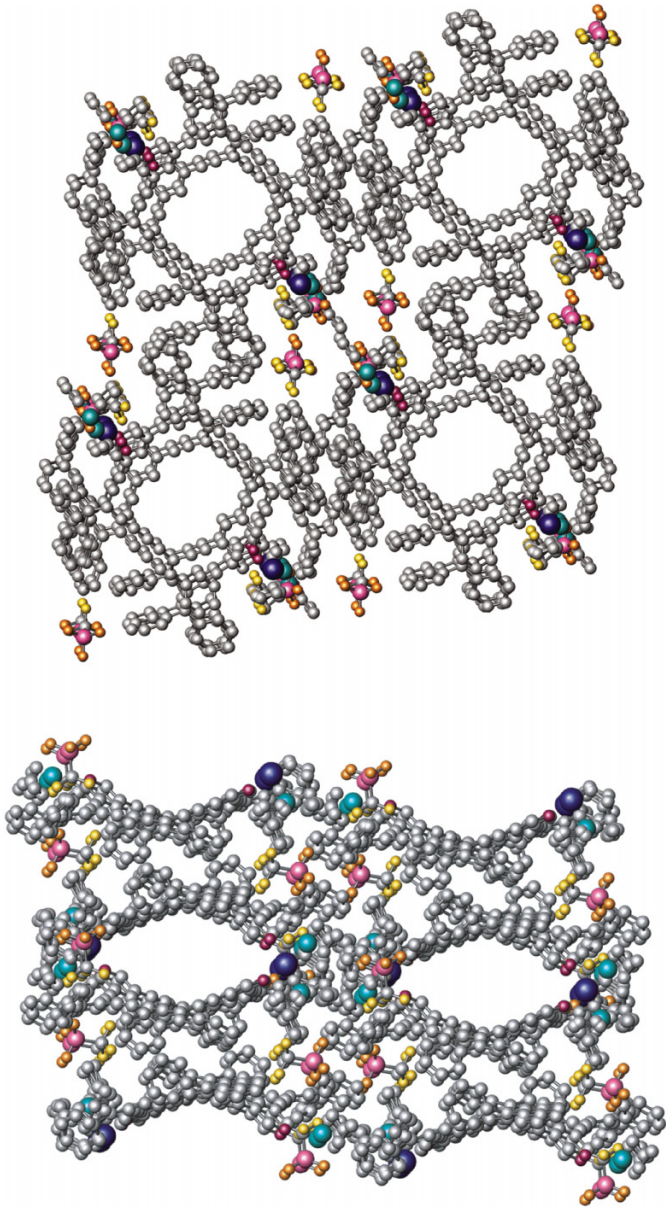

Whereas the formation of porous assembly **4a** and the inclusion of guest molecules within the structure are important, a porous material can only be useful if the guests can be removed and replaced by other molecules while retaining the host porosity. All attempts to grow crystals of **4a** from other solvents were unsuccessful and provided only noncrystalline precipitates. In the rare case in which crystals were obtained, they desolvated rapidly and shattered before X-ray analysis could be performed. The solvent was removed from crystals grown in CH_2Cl_2/$ClCH_2CH_2Cl$ mixtures by flowing N_2 over the solid at room temperature. Again, these crystals shattered upon removal of the solvent molecules and were no longer suitable for crystallographic analysis. Hyperpolarized ^{129}Xe NMR spectroscopy, therefore, seemed an ideal probe to demonstrate porosity of **4a** in the absence of guest solvent molecules.

Using the pristine crystals of **4a** (i.e., still solvated), ^{129}Xe NMR spectra were acquired at various temperatures and are shown in Fig. 8; it was assumed that the gas flow removed the solvent molecules as mentioned in the previous paragraph. These spectra were, remarkably, acquired using <15 mg of sample. It is immediately apparent that Xe atoms are able to access the channel system of **4a**, and there are two sites or pores present within the solid. First, at high temperatures, a broad resonance is just discernable in the range of 210–180 ppm. Upon cooling to room temperature, a second resonance begins to separate from the gas peak as the resonance at large chemical shift diminishes in intensity. The position of the second resonance stabilizes at 112 ppm at approximately –70 °C.

The broad peak observed near 180 ppm is similar to that observed previously for Xe adsorbed in highly confined regions of organic macrocycles, including **2a** and **2c**.[23,24] This chemical shift is too large to arise from Xe occupying the large channel and must therefore come from Xe in alternate adsorption sites. These smaller sites are likely peripheral to the channels of **4a** and would be bordered by the phenyl groups that decorate the exterior of the macrocycles. This assignment is supported by the fact that the observed chemical shift value is comparable to that of xenon dissolved in organic solvents such as benzene or toluene.[64] Based on the signal intensity, there is relatively little Xe gas accessing these highly confined sites, in contrast to **2c**. As the temperature is decreased below 6 °C the intensity of this peak decreases, possibly the result of Xe condensation into the peripheral sites. It should be re-emphasized that in the hyperpolarized ^{129}Xe NMR experiment, condensed Xe gas atoms would not be spectroscopically detectable owing to the fact that polarization is lost after a single NMR pulse sequence. An alternate explanation is that with lower temperatures, there is no longer sufficient mobility within the solid host to allow the xenon gas to enter the highly confined sites that give rise to the ^{129}Xe NMR signal at 180 ppm. For example, any restriction of slight motion of the pendant alkylidene phenyl groups could restrict access to these more confined sites within the framework.

Starting at about 24 °C, Xe atoms begin to occupy space within the channel structure of **4a** for significant amounts of time, as evidenced by the peak observed near the gas peak at 0 ppm. As with macrocycles **2b** and **2c**, this suggests that Xe is in fast exchange between the gas phase and the channels. Unlike **2b** and **2c**, however, the chemical shift of this signal remains constant at 112 ppm, over a temperature range of ca. 50° (starting at about –67 °C), shifting to 123 ppm only at the lowest temperature measured. This suggests that Xe exchange with the free gas is insignificant below –67 °C. The chemical shift in this region is therefore characteristic of Xe-framework interactions, δ_s. This value of δ_s is surprisingly similar to the values obtained for porous silica materials with pore diameters between 5 and 50 Å.[29] Assuming that the Xe loading is low, i.e., there are minimal Xe–Xe interactions, the chemical shift verses temperature profile above –112 °C can be used to obtain an effective adsorption energy (ΔH_{ads}) for Xe in **4a**. The chemical shift as a function of pore structure, temperature, adsorption energy, and δ_s can be expressed as a linear equation in the form

Can. J. Chem. Downloaded from www.nrcresearchpress.com by Xi'an Jiaotong University on 09/19/12
For personal use only.

Fig. 8. Hyperpolarized ^{129}Xe NMR spectra (55 MHz) of porous assembly **4a** acquired at various temperatures.

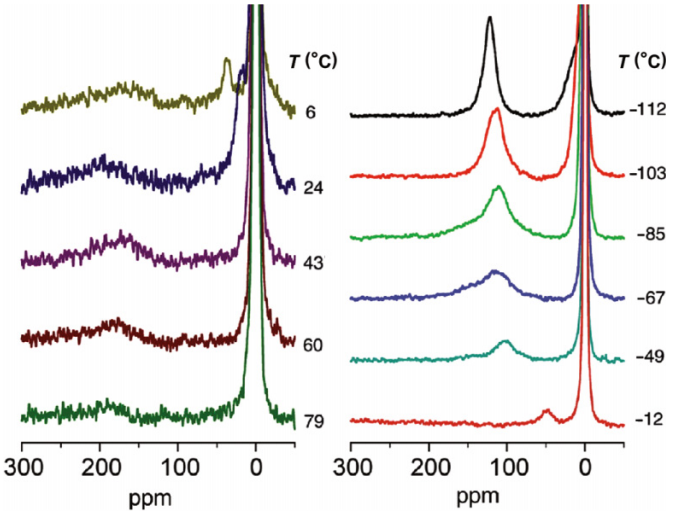

$$[1] \qquad \ln\left[\left(\frac{\delta_s}{\delta}-1\right)T^{1/2}\right] = C - \frac{\Delta H_{ads}}{RT}$$

where $C = \ln\left(\frac{D}{RK_0\eta}\right)$ and is characteristic of the pore structure, T is temperature, R is the ideal gas constant, D is the mean pore diameter, K_0 is the pre-exponential factor from the Henry's Law equation for adsorption, and η is a pore geometry factor.[65] By plotting $\ln\left[\left(\frac{\delta_s}{\delta}\right)-1\right]T^{1/2}$ vs $1/T$, the value of ΔH_{ads} is obtained from the slope.[66] On this basis, using eq. [1] to analyze the ^{129}Xe NMR spectra of **4a** provides an effective heat of adsorption of ca. 29 kJ mol^{-1}; the error is approximately ±5 kJ mol^{-1}. Clearly, it would be desirable to do the same analysis for samples **2b** and **2c** for which fast exchange is also evident between Xe in the solvent cavities and free Xe gas. Unfortunately, an estimate for δ_s for **2b** and **2c** is difficult, since there is no region where the chemical shift does not change over a significant temperature range.

Molecular dynamics simulation of Xe in **4a** indicates that, while the Xe can move freely throughout the channel system, it spends a majority of its time in the narrowest sections, between the stacked macrocyclic units that form the channel following the *c* axis; Fig. 9 shows the position.[23] The two regions depicted by the contour plots coincide with the position of two of the six 1,2-dichloroethane molecules that occupy the channels before removal of the co-crystallized solvent molecules.

Spectroscopic results have shown that assembly **4a** retains its porosity in the absence of guest solvent molecules.[67] Thus, it has been established that, while solid **4a** may be undergoing some structural changes upon removal of the guest, these changes are not as dramatic as might be expected on the basis of empirical observations of desolvation.

In summary, the appropriately substituted macrocycles **2a**–**2c** can be effectively used for the formation of supramolecular assemblies such as **4a** and **6**. Furthermore, based on the analysis of **2b**, **2c**, and **4a**, hyperpolarized ^{129}Xe NMR spectroscopy is a technique that can be successfully applied to the study of porous organic solids. Trends observed in the ^{129}Xe chemical shift, as well as the dynamic behaviour of the guest xenon gas, have provided substantial insight into the porous nature of these systems. It has also been established that, for the most part, X-ray crystallographic data acquired in the presence of guest solvent molecules can provide a reasonable model for the pore structures of these solids after the removal of the co-crystallized solvent.

Experimental section

General experimental details

Reagents were purchased reagent grade from commercial suppliers and used without further purification. CH_2Cl_2 was distilled from CaH_2 immediately prior to use. All reactions were performed in standard dry glassware under an inert atmosphere of N_2. Deoxygenation of solvents was accomplished by vigorously bubbling N_2 through the solutions for ~45 min. Evaporation and concentration in vacuo was achieved at H_2O-aspirator pressure. Column chromatography: silica gel-60 (230–400 mesh) from Silicycle. Thin layer chromatography (TLC): plastic sheets coated with silica gel G UV_{254} from Macherey-Nagel, visualization by UV light. Melting points: Gallencamp or Fisher-Johns apparatus; uncorrected. IR spectra: Nic-Plan IR microscope (as solids or cast from CH_2Cl_2 as noted). ^{1}H-, ^{13}C-, ^{31}P-, ^{19}F-NMR: Varian Gemini-300, -400, or -500 at room temperature (rt) in CD_2Cl_2; solvent peaks (5.32 ppm for ^{1}H and 53.80 ppm for ^{13}C, respectively) as reference; $CFCl_3$ as ^{19}F reference and 85% H_3PO_4 as ^{31}P reference. ESI MS (*m/z*): Micromass Zabspec oaTOF or PE Biosystems Mariner TOF instruments; solvents as noted.

Continuous-flow hyperpolarized ^{129}Xe NMR spectra were acquired on a Chemagnetics CMX Infinity 200 wide-bore spectrometer operating at a frequency of 55.36 MHz for ^{129}Xe. Hyperpolarized xenon (~7% spin polarization) was generated using a home-built continuous-flow optical pumping system.[23,24] A 60 W dual diode laser from Coherent Inc. was used. The gas mixture consisted of 1% Xe (effective pressure 7 torr (1 torr = 4.184 J)), 1% N_2, and 98% He. The sample temperatures for all spectra were determined using the Chemagnetics temperature controller and calibrated using the ^{207}Pb NMR peak of lead nitrate.[68] The spectra were referenced to the gas peak of ^{129}Xe in the gas mixture (0 ppm) prior to placing samples in the spectrometer. Bloch decay spectra were acquired using π/2 pulse widths of 2.5 μs.

Macrocycle 2a

This compound was synthesized as previously reported (see ref. 6a).

Synthesis of platinacycle 2b[50]

Oligomer **1** (43 mg, 0.082 mmol) was added to a degassed solution of $(PPh_3)_2PtCl_2$ (65 mg, 0.082 mmol) in Et_2NH (150 mL). A catalytic amount of CuI (5 mg, 0.03 mmol) was added and the mixture was sealed under N_2 and then stirred at 50 °C for 14 h. After cooling, ether/CH_2Cl_2 (150 mL, 1:1 *v/v*) was added, and the resulting solution was washed with water (2 × 50 mL) and saturated aqueous NH_4Cl (4 × 50 mL) and then dried ($MgSO_4$). Solvent removal (using *no* heat) followed by precipitation from CH_2Cl_2/acetone afforded platinacycle **2b** (45 mg, 45%) as a bright yellow solid; mp 166 °C (dec.).

Fig. 9. Contour map showing the expected distribution of Xe within the pore structure as predicted by molecular dynamics simulations (ref. 23).

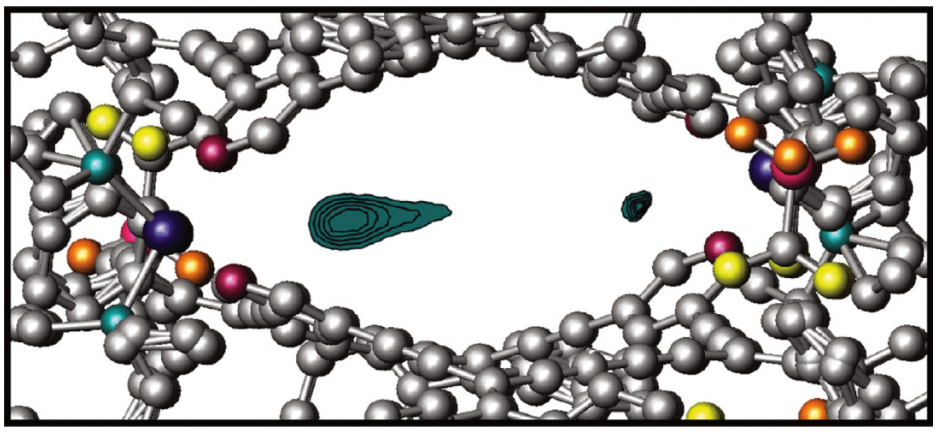

Can. J. Chem. Downloaded from www.nrcresearchpress.com by Xi'an Jiaotong University on 09/19/12
For personal use only.

R_f = 0.08 (hexanes/CH_2Cl_2 1:1, alumina). IR (CH_2Cl_2 cast, cm^{-1}): 3050, 2201, 2083, 1581, 1481. ^1H NMR (400 MHz, CD_2Cl_2) δ: 7.77 (d, J = 2.0 Hz, 4H), 7.65–7.59 (m, 24H), 7.42–7.37 (m, 12H), 7.35 (t, J = 2.0 Hz, 2H), 7.31–6.82 (m, 64H). ^{13}C {^1H} NMR (125 MHz, CD_2Cl_2) δ: 150.3, 149.1, 142.3, 140.6, 139.1, 135.4 (pseudo-t, J_{C-P} = 6.2 Hz), 131.2 (pseudo-t, J_{C-P} = 29 Hz), 130.9, 130.8, 130.4, 128.2 (pseudo-t, J_{C-P} = 6.6 Hz), 127.8 (2×), 127.5, 127.2, 120.7, 118.9 (signal too weak to observe P or Pt coupling), 111.2 (signal too weak to observe P or Pt coupling), 105.9, 95.7, 85.5. ^{31}P {^1H} NMR (162 MHz, CD_2Cl_2) δ: 18.0 (coupling to Pt not observed owing to poor signal/noise). ESI MS ($NO_2Me/ClCH_2CH_2Cl$, $C_{154}H_{106}N_2P_4Pt_2$) *m/z* (rel. intensity): 2498.7 ([M + H]$^+$, 100).

Synthesis of platinacycle 2c

Oligomer **1** (35 mg, 0.066 mmol) was added to a degassed solution of $(PEt_3)_2PtCl_2$ (33 mg, 0.066 mmol) in Et_2NH (120 mL). A catalytic amount of CuI (5 mg, 0.03 mmol) was added and the mixture was sealed under N_2 and then stirred at 40 °C for 14 h. After cooling, ether/CH_2Cl_2 (150 mL, 1:1 *v*/*v*) was added, and the resulting solution was washed with water (2 × 50 mL) and saturated aqueous NH_4Cl (4 × 50 mL) and then dried ($MgSO_4$). Solvent removal (using *no* heat) followed by purification using a gradient (CH_2Cl_2 → acetone) silica gel column afforded platinacycle **2c** (45 mg, 71%) as a pale yellow solid; mp 280 °C (dec.). R_f = 0.06 (CH_2Cl_2). IR (CH_2Cl_2 cast, cm^{-1}): 3051, 2927, 2147, 2081, 1580, 1491. ^1H NMR (400 MHz, CD_2Cl_2) δ: 8.00 (d, J = 2.0 Hz, 4H), 7.51–7.26 (m, 42H), 1.88–1.83 (br m, 24H), 1.10–1.00 (pseudo-pentet, J = 8.1 Hz, 36H). ^{13}C {^1H} NMR (100.6 MHz, CD_2Cl_2) δ: 151.1, 150.9, 142.0, 137.8, 130.6, 130.5, 128.0 (3×), 127.7, 120.7, 116.0 (t, $^1J_{C-P}$ = 15 Hz), 107.3, 106.1, 95.4, 85.5, 16.7 (pseudo-t, J_{C-P} = 17 Hz), 8.7 (one signal not observed). ^{31}P {^1H} NMR (162 MHz, CD_2Cl_2) δ: 13.9 ($^1J_{P-Pt}$ = 2344 Hz). ESI MS ($NO_2Me/ClCH_2CH_2Cl$, $C_{106}H_{106}N_2P_4Pt_2$) *m/z* (rel. intensity): 1923 ([M + H]$^+$, 100).

Synthesis of assembly 4a

cis-$(TfO)_2Pt(PEt_3)_2$ **3** (8 mg, 0.01 mmol) and macrocycle **2a** (6 mg, 0.006 mmol) were each dissolved in 10 mL of dry CH_2Cl_2. The solution containing **2a** was slowly added to the solution of **3** and the reaction was stirred at room temperature, under a positive pressure of N_2, for 18 h. A second equivalent of macrocycle **2a** (6 mg, 0.006 mmol) was dissolved in dry CH_2Cl_2 (10 mL) and added to the reaction. The mixture was stirred for a further 18 h and the majority of the solvent was then allowed to evaporate, yielding bright orange crystals, assembly **4a** (17 mg, 84% yield). Note: it is important to control both the dilution of all reactants as well as their order and rate of addition to the reaction mixture. Assembly **4a** can only be isolated in pure form via recrystallization from the reaction mixture, and the presence of excessive numbers and (or) quantities of by-products seriously inhibit the success of this purification step. Melting point 245 °C (dec.). IR (μscope, cm^{-1}): 3503, 3058, 2970, 2932, 2215, 1583, 1520. ^1H NMR (300 MHz, CD_2Cl_2) δ: 8.42 (m, 8H), 7.95 (t, J = 1.7 Hz, 4H), 7.46–7.26 (m, 80H), 1.90–1.72 (m, 24H), 1.22–1.11 (m, 36H). ^{13}C {^1H} NMR (125.3 MHz, CD_2Cl_2) δ: 163.6, 150.2, 145.1, 139.7, 139.1, 131.1, 130.7, 130.3, 130.1, 128.4, 128.3, 125.1, 99.2, 96.2, 84.1, 81.1, 77.5, 15.9 –15.5 (m), 3.3 (*C*F_3 not observed). ^{19}F NMR (400 MHz, CD_2Cl_2, ppm) –78.2. ^{31}P {^1H} NMR (162 MHz, CD_2Cl_2, ppm) –1.3. ESI MS (CH_2Cl_2/NO_2Me, $C_{192}H_{152}F_{12}N_4O_{12}P_4Pt_2S_4$) *m/z* (rel. intensity): 1059 ([**2a** + H]$^+$, 9), 745 ([M – 4(OTf)]$^{+4}$, 24), 492 ([**3** – 2(OTf) + NO_2Me]$^+$, 78), 429 ([**3** – 2(OTf)]$^+$, 100).

Supplementary data

Supplementary data are available with the article through the journal Web site at http://nrcresearchpress.com/doi/suppl/10.1139/v11-077 or as CCDC 666371–666373 and CCDC 205116, which can be obtained, free of charge, via www.ccdc.cam.ac.uk/cgi-bin/catreq.cgi (or from the Cambridge Crystallographic Data Centre, 12 Union Road, Cambridge CB2 1EZ, UK (Fax: 44-1223-336033 or e-mail: deposit@ccdc.cam.ac.uk)).

Acknowledgement

The authors wish to thank K. Feindel, Dr. G. Bernard, and Dr. D. Sears for several helpful comments, as well as Dr. C.J. Kuehl for his contributions to the initial formation of **4a**. They acknowledge Drs. S. Lang, I. Moudrakovski, and J. Ripmeester of the Steacie Institute for Molecular Sciences,

National Research Council Canada, for their advice in constructing the continuous flow diode laser system to produce the hyperpolarized xenon, and Professor T. Ueda for his assistance in constructing this apparatus. The Natural Sciences and Engineering Research Council of Canada (NSERC), the Alberta Ingenuity Fund, and the University of Alberta are gratefully thanked for financial support. R.E.W. is a Canada Research Chair in Physical Chemistry at the University of Alberta.

Can. J. Chem. Downloaded from www.nrcresearchpress.com by Xi'an Jiaotong University on 09/19/12
For personal use only.

References

(1) (a) Horike, S.; Shimomura, S.; Kitagawa, S. *Nat. Chem.* **2009** *1* (9), 695. doi:10.1038/nchem.444; (b) Kitagawa, S.; Uemura, K. *Chem. Soc. Rev.* **2005** *34* (2), 109. doi:10.1039/b313997m; (c) Kitagawa, S.; Kitaura, R.; Noro, S. *Angew. Chem. Int. Ed.* **2004** *43* (18), 2334. doi:10.1002/anie.200300610.

(2) Farrusseng, D.; Aguado, S.; Pinel, C. *Angew. Chem. Int. Ed.* **2009** *48* (41), 7502. doi:10.1002/anie.200806063.

(3) Yaghi, O. M.; O'Keeffe, M.; Ockwig, N. W.; Chae, H. K.; Eddaoudi, M.; Kim, J. *Nature* **2003** *423* (6941), 705. doi:10.1038/nature01650.

(4) (a) Wuest, J. D. *Chem. Commun. (Camb.)* **2005** (47), 5830. doi:10.1039/b512641j; (b) Perry, J. J., IV; Perman, J. A.; Zaworotko, M. J. *Chem. Soc. Rev.* **2009** *38* (5), 1400. doi:10.1039/b807086p.

(5) Mueller, U.; Schubert, M.; Teich, F.; Puetter, H.; Schierle-Arndt, K.; Pastré, J. *J. Mater. Chem.* **2006** *16* (7), 626. doi:10.1039/b511962f.

(6) (a) Campbell, K.; McDonald, R.; Tykwinski, R. R. *J. Org. Chem.* **2002** *67* (4), 1133. doi:10.1021/jo0159744; (b) Campbell, K.; McDonald, R.; Ferguson, M. J.; Tykwinski, R. R. *Organometallics* **2003** *22* (7), 1353. doi:10.1021/om020738k; (c) Campbell, K.; Johnson, C. A., II; McDonald, R.; Ferguson, M. J.; Haley, M. M.; Tykwinski, R. R. *Angew. Chem. Int. Ed.* **2004** *43* (44), 5967. doi:10.1002/anie.200461139; (d) Campbell, K.; Tiemstra, N. M.; Prepas-Strobeck, N. S.; McDonald, R.; Ferguson, M. J.; Tykwinski, R. R. *Synlett* **2004** 182.

(7) Jiang, J.; MacLachlan, M. J. *Chem. Commun. (Camb.)* **2009** (38), 5695. doi:10.1039/b914564h.

(8) Jin, Y.; Voss, B. A.; Noble, R. D.; Zhang, W. *Angew. Chem. Int. Ed.* **2010** *49* (36), 6348. doi:10.1002/anie.201001517.

(9) Xu, Y.; Smith, M. D.; Geer, M. F.; Pellechia, P. J.; Brown, J. C.; Wibowo, A. C.; Shimizu, L. S. *J. Am. Chem. Soc.* **2010** *132* (15), 5334. doi:10.1021/ja9107066.

(10) Lei, S.; Surin, M.; Tahara, K.; Adisoejoso, J.; Lazzaroni, R.; Tobe, Y.; De Feyter, S. *Nano Lett.* **2008** *8* (8), 2541. doi:10.1021/nl8016626.

(11) Zhang, W.; Moore, J. S. *Angew. Chem. Int. Ed.* **2006** *45* (27), 4416. doi:10.1002/anie.200503988; Zhao, D.; Moore, J. S. *Chem. Commun. (Camb.)* **2003** (7), 807. doi:10.1039/B207442G.

(12) Hoger, S. In *Acetylene Chemistry: Chemistry, Biology, and Material Science;* Diederich, F., Stang, P. J., Tykwinski, R. R., Eds.; Wiley-VCH: Weinheim, 2005; Chapter 10.

(13) (a) Haley, M. M. *Pure Appl. Chem.* **2008** *80* (3), 519. doi:10.1351/pac200880030519; (b) Spitler, E. L.; Johnson, C. A., II; Haley, M. M. *Chem. Rev.* **2006** *106* (12), 5344. doi:10.1021/cr050541c; (c) Nielsen, M. B.; Diederich, F. *Chem. Rev.* **2005** *105* (5), 1837. doi:10.1021/cr9903353.

(14) The topic of porosity as been discussed; see for example, Barbour, L. J. *Chem. Commun. (Camb.)* **2006** (11), 1163. doi:10.1039/b515612m; Maly, K. E. *J. Mater. Chem.* **2009** *19* (13), 1781. doi:10.1039/b816089a; McKeown, N. B. *J. Mater. Chem.* **2010** *20* (47), 10588. doi:10.1039/C0JM01867H.

(15) Berthault, P.; Huber, G.; Desvaux, H. *Prog. Nucl. Magn. Reson. Spectrosc.* **2009** *55* (1), 35. doi:10.1016/j.pnmrs.2008.11.003; Romanenko, K. V. *Annu. Rep. NMR Spectrosc.* **2010** *69*, 1. doi:10.1016/S0066-4103(10)69001-1; Ratcliffe, C. I. *Annu. Rep. NMR Spectrosc.* **1998** *36*, 123. doi:10.1016/S0066-4103(08)60007-1.

(16) Raftery, D. *Annu. Rep. NMR Spectrosc.* **2006** *57*, 205. doi:10.1016/S0066-4103(05)57005-4; Moudrakovski, I. L.; Nossov, A.; Lang, S.; Breeze, S. R.; Ratcliffe, C. I.; Simard, B.; Santyr, G.; Ripmeester, J. A. *Chem. Mater.* **2000** *12* (5), 1181. doi:10.1021/cm9908015.

(17) Goodson, B. M. *J. Magn. Reson.* **2002** *155* (2), 157. doi:10.1006/jmre.2001.2341.

(18) Bonardet, J.-L.; Fraissard, J.; Gédéon, A.; Springuel-Huet, M.-A. *Catal. Rev., Sci. Eng.* **1999** *41*, 115.

(19) Springuel-Huet, M. A.; Bonardet, J.-L.; Fraissard, J. *Appl. Magn. Reson.* **1995** *8* (3–4), 427. doi:10.1007/BF03162656.

(20) Barrie, P. J.; Klinowski, J. *Prog. Nucl. Magn. Reson. Spectrosc.* **1992** *24* (2), 91. doi:10.1016/0079-6565(92)80006-2.

(21) Brunner, E. *Magn. Reson. Chem.* **1999** *37* (13), S14. doi:10.1002/(SICI)1097-458X(199912)37:13<S14::AID-MRC534>3.0.CO;2-P.

(22) Pietrab, T. *Magn. Reson. Rev.* **2000** *17*, 263.

(23) Campbell, K.; Ooms, K. J.; Wasylishen, R. E.; Tykwinski, R. R. *Org. Lett.* **2005** *7* (16), 3397. doi:10.1021/ol050830n.

(24) Ooms, K. J.; Campbell, K.; Tykwinski, R. R.; Wasylishen, R. E. *J. Mater. Chem.* **2005** *15* (40), 4318. doi:10.1039/b507602a.

(25) Raftery, D. *Annu. Rep. NMR Spectrosc.* **2006** *57*, 205. doi:10.1016/S0066-4103(05)57005-4.

(26) Ito, T.; Fraissard, J. *J. Chem. Phys.* **1982** *76* (11), 5225. doi:10.1063/1.442917.

(27) Koskela, T.; Jokisaari, J.; Satyanarayana, C. *Microporous Mesoporous Mater.* **2004** *67* (2-3), 113. doi:10.1016/j.micromeso.2003.10.009.

(28) Demarquay, J.; Fraissard, J. *Chem. Phys. Lett.* **1987** *136* (3–4), 314. doi:10.1016/0009-2614(87)80258-0.

(29) Terskikh, V. V.; Moudrakovski, I. L.; Breeze, S. R.; Lang, S.; Ratcliffe, C. I.; Ripmeester, J. A.; Sayari, A. *Langmuir* **2002** *18* (15), 5653. doi:10.1021/la025714x.

(30) Ripmeester, J. A.; Ratcliffe, C. I. *J. Phys. Chem.* **1990** *94* (19), 7652. doi:10.1021/j100382a061.

(31) Jameson, C. J. *J. Chem. Phys.* **2002** *116* (20), 8912. doi:10.1063/1.1468884.

(32) Ooms, K. J.; Wasylishen, R. E. *Microporous Mesoporous Mater.* **2007** *103* (1–3), 341. doi:10.1016/j.micromeso.2007.01.054.

(33) Ueda, T.; Kurokawa, K.; Eguchi, T.; Kachi-Terajima, C.; Takamizawa, S. *J. Phys. Chem. C* **2007** *111* (3), 1524. doi:10.1021/jp065321x.

(34) Comotti, A.; Bracco, S.; Ferretti, L.; Mauri, M.; Simonutti, R.; Sozzani, P. *Chem. Commun. (Camb.)* **2007** (4), 350. doi:10.1039/b612002d.

(35) Simonutti, R.; Bracco, S.; Comotti, A.; Mauri, M.; Sozzani, P. *Chem. Mater.* **2006** *18* (19), 4651. doi:10.1021/cm060499h.

(36) Soldatov, D. V.; Moudrakovski, I. L.; Grachev, E. V.; Ripmeester, J. A. *J. Am. Chem. Soc.* **2006** *128* (20), 6737. doi:10.1021/ja060474j.

(37) Knagge, K.; Smith, J. R.; Smith, L. J.; Buriak, J.; Raftery, D. *Solid State Nucl. Magn. Reson.* **2006** *29* (1–3), 85. doi:10.1016/j.ssnmr.2005.10.001.

(38) Dubes, A.; Moudrakovski, I. L.; Shahgaldian, P.; Coleman, A.

Can. J. Chem. Downloaded from www.nrcresearchpress.com by Xi'an Jiaotong University on 09/19/12
For personal use only.

W.; Ratcliffe, C. I.; Ripmeester, J. A. *J. Am. Chem. Soc.* **2004** *126* (20), 6236. doi:10.1021/ja038653d.

(39) Moudrakovski, I. L.; Wang, L.-Q.; Baumann, T.; Satcher, J. H., Jr.; Exarhos, G. J.; Ratcliffe, C. I.; Ripmeester, J. A. *J. Am. Chem. Soc.* **2004** *126* (16), 5052. doi:10.1021/ja049577x.

(40) Soldatov, D. V.; Moudrakovski, I. L.; Ratcliffe, C. I.; Dutrisac, R.; Ripmeester, J. A. *Chem. Mater.* **2003** *15* (25), 4810. doi:10.1021/cm030433b.

(41) Ueda, T.; Eguchi, T.; Nakamura, N.; Wasylishen, R. E. *J. Phys. Chem. B* **2003** *107* (1), 180. doi:10.1021/jp021679r.

(42) Sozzani, P.; Comotti, A.; Simonutti, R.; Meersmann, T.; Logan, J. W.; Pines, A. *Angew. Chem. Int. Ed.* **2000** *39* (15), 2695. doi:10.1002/1521-3773(20000804)39:15<2695::AID-ANIE2695>3.0.CO;2-M.

(43) Jameson, C. J.; de Dios, A. C. *J. Chem. Phys.* **2002** *116* (9), 3805. doi:10.1063/1.1446424.

(44) Cheng, C.-Y.; Bowers, C. R. *J. Am. Chem. Soc.* **2007** *129* (45), 13997. doi:10.1021/ja074563n.

(45) Fogarty, H. A.; Berthault, P.; Brotin, T.; Huber, G.; Desvaux, H.; Dutasta, J.-P. *J. Am. Chem. Soc.* **2007** *129* (34), 10332. doi:10.1021/ja073771c.

(46) Moudrakovski, I.; Soldatov, D. V.; Ripmeester, J. A.; Sears, D. N.; Jameson, C. J. *Proc. Natl. Acad. Sci. U.S.A.* **2004** *101* (52), 17924. doi:10.1073/pnas.0405348101.

(47) Sears, D. N.; Wasylishen, R. E.; Ueda, T. *J. Phys. Chem. B* **2006** *110* (23), 11120. doi:10.1021/jp061655a.

(48) Campbell, K.; McDonald, R.; Branda, N. R.; Tykwinski, R. R. *Org. Lett.* **2001** *3* (7), 1045. doi:10.1021/ol0156087.

(49) Campbell, K.; Kuehl, C. J.; Ferguson, M. J.; Stang, P. J.; Tykwinski, R. R. *J. Am. Chem. Soc.* **2002** *124* (25), 7266. doi:10.1021/ja025773x.

(50) Campbell, K.; McDonald, R.; Ferguson, M. J.; Tykwinski, R. R. *J. Organomet. Chem.* **2003** *683* (2), 379. doi:10.1016/S0022-328X(03)00792-7.

(51) It is worth noting the importance of using no heat when removing the solvent, subsequent to workup, in reactions to form the Pt–acetylide containing macrocycles. Despite the fact that heat is applied during the transmetalation reaction, and that the platinacycles **2b** and **2c** are thermally stable solids, heating during solvent removal leads to a darkening of the solution(s) accompanied by a bad odour. This procedure results in lower overall yields, predominantly because of increased problems with respect to purification.

(52) Kaiser, A.; Bäuerle, P. *Top. Curr. Chem.* **2005** *249*, 127.

(53) Stang, P. J.; Cao, D. H.; Saito, S.; Arif, A. M. *J. Am. Chem. Soc.* **1995** *117* (23), 6273. doi:10.1021/ja00128a015.

(54) (a) Leininger, S.; Olenyuk, B.; Stang, P. J. *Chem. Rev.* **2000** *100* (3), 853. doi:10.1021/cr9601324; (b) Northrop, B. H.; Zheng, Y.-R.; Chi, K.-W.; Stang, P. J. *Acc. Chem. Res.* **2009** *42* (10), 1554. doi:10.1021/ar900077c.

(55) Seidel, S. R.; Stang, P. J. *Acc. Chem. Res.* **2002** *35* (11), 972. doi:10.1021/ar010142d.

(56) Manna, J.; Kuehl, C. J.; Whiteford, J. A.; Stang, P. J.; Muddiman, D. C.; Hofstadler, S. A.; Smith, R. D. *J. Am. Chem. Soc.* **1997** *119* (48), 11611. doi:10.1021/ja972668s.

(57) Representation of pores was generated by the Cavities option in the ATOMS program (ATOMS, Version 5.1). The surface of the pores is defined by the possible loci of a sphere of 3 Å in diameter as it rolls over the surface of the porous solid.

(58) Brouwer, E. B.; Enright, G. D.; Udachin, K. A.; Lang, S.; Ooms, K. J.; Halchuk, P. A.; Ripmeester, J. A. *Chem. Commun. (Camb.)* **2003** (12), 1416. doi:10.1039/b301739g.

(59) Brouwer, E. B.; Udachin, K. A.; Enright, G. D.; Ripmeester, J. A.; Ooms, K. J.; Halchuk, P. A. *Chem. Commun. (Camb.)* **2001** (6), 565. doi:10.1039/b009133m.

(60) Atwood, J. L.; Barbour, L. J.; Jerga, A. *Angew. Chem. Int. Ed.* **2004** *43* (22), 2948. doi:10.1002/anie.200353559.

(61) Riddle, J. A.; Bollinger, J. C.; Lee, D. *Angew. Chem. Int. Ed.* **2005** *44* (41), 6689. doi:10.1002/anie.200501888.

(62) Dobrzañska, L.; Lloyd, G. O.; Raubenheimer, H. G.; Barbour, L. J. *J. Am. Chem. Soc.* **2006** *128* (3), 698. doi:10.1021/ja057122h.

(63) Lim, Y. H.; Nugara, N.; King, A. D., Jr. *Appl. Magn. Reson.* **1995** *8* (3–4), 521. doi:10.1007/BF03162661.

(64) Stengle, T. R.; Reo, N. V.; Williamson, K. L. *J. Phys. Chem.* **1981** *85* (25), 3772. doi:10.1021/j150625a013.

(65) Conner, W. C.; Weist, E. L.; Ito, T.; Fraissard, J. *J. Phys. Chem.* **1989** *93* (10), 4138. doi:10.1021/j100347a052.

(66) Terskikh, V. V.; Mudrakovskii, I. L.; Mastikhin, V. M. *J. Chem. Soc., Faraday Trans.* **1993** *89* (23), 4239. doi:10.1039/ft9938904239.

(67) Solution-state ^{1}H NMR spectroscopy was used to confirm that all of the co-crystallized solvent had been removed from the host solid **4a** subsequent to the variable temperature ^{129}Xe NMR spectroscopy experiments.

(68) van Gorkom, L. C. M.; Hook, J. M.; Logan, M. B.; Hanna, J. V.; Wasylishen, R. E. *Magn. Reson. Chem.* **1995** *33* (10), 791. doi:10.1002/mrc.1260331005.

Triterpenoid saponins from the stem bark of *Catunaregam spinosa*

Guang-Chun Gao, Zhong-Xian Lu, Shu-Hong Tao, Si Zhang, Fa-Zuo Wang, and Qing-Xin Li

Can. J. Chem. Downloaded from www.nrcresearchpress.com by Xi'an Jiaotong University on 09/19/12
For personal use only.

Abstract: Four new triterpenoid saponins, Catunaroside E (**1**; 3-*O*-{β-D-glucopyranosyl-(1→2)-[β-D-glucopyranosyl-(1→3)]-β-D-glucopyranosyl}-siaresinolic acid), Catunaroside F (**2**; 3-*O*-{α-L-rhamnopyranosyl-(1→2)-[β-D-glucopyranosyl-(1→3)]-β-D-glucopyranosyl}-28-*O*-(β-D-glucopyranosyl)-oleanolic acid), Catunaroside G (**3**; 3-*O*-[α-L-rhamnopyranosyl-(1→2)-β-D-glucopyranosyl]- 28-*O*-(β-D-glucopyranosyl)-siaresinolic acid), and Catunaroside H (**4**; 3-*O*-{β-D-glucopyranosyl-(1→2)-[β-D-glucopyranosyl-(1→3)]-β-D-glucopyranosyl}-28-*O*-(β-D-glucopyranosyl)-siaresinolic acid), and the known triterpenoid saponin Mussaendoside J (**5**), were isolated from the stem bark of *Catunaregam* spinosa. Their structures were elucidated on the basis of their spectral data and chemical evidence.

Key words: Catunaregam spinosa, Rubiaceae, triterpenoid saponins, Catunaroside E–H.

Résumé : À partir de l'écorce du tronc de *Catunaregam spinosa,* on a isolé quatre nouvelles saponines triterpénoïdes, le catunaroside E (**1**), l'acide 3-*O*-{β-D-glucopyranosyl-(1→2)-[β-D-glucopyranosyl-(1→3)]-β-D-glucopyranosyl}siarésinolique, le catunaroside F (**2**), l'acide 3-*O*-{α-L-rhamnopyranosyl-(1→2)-[β-D-glucopyranosyl-(1→3)]-β-D-glucopyranosyl}-28-*O*-(β-D-glucopyranosyl)oléanolique, le catunaroside G (**3**), l'acide 3-*O*-{α-L-rhamnopyranosyl-(1→2)-[β-D-glucopyranosyl-(1→3)]-28-*O*-(β-D-glucopyranosyl)siarésinolique et le catunaroside H (**4**), l'acide 3-*O*-{β-D-glucopyranosyl-(1→2)-[β-D-glucopyranosyl-(1→3)]-28-*O*-(β-D-glucopyranosyl)siarésinolique et une saponine triterpénoïde connue,le mussaendoside J (**5**). Leurs structures ont été élucidées sur la base de leurs propriétés chimiques et de leurs données spectrales.

Mots-clés : Catunaregam spinosa, rubiacée, saponines triterpénoïdes, caturanoside E-H.

[Traduit par la Rédaction]

Introduction

Catunaregam spinosa T. (Rubiaceae), which is mostly distributed in tropical and semitropical areas, was used in the traditional medicinal systems of India and Brazil for its antispasmodic, antidysenteric, anti-inflammatory, immunomodulatory, and antifertility properties.[1–4] Chemical investigation of *C. spinosa* led to the isolation of triterpene and saponins,[4–6] iridoid glucosides,[1] coumarin glucosides,[7] and norneolignans.[8] In continuation of our studies on the chemical diversity of mangrove plants on Hainan Island, this plant was investigated and four new triterpenoid saponins, Catunaroside E–H, together with Mussaendoside J, were obtained from the *n*-BuOH extract of its stem bark (Fig. 1). This paper deals with the isolation and structure elucidation of those triterpenoid saponins. Mussaendoside J was first obtained from this plant.

Results and discussion

Compound **1** was obtained as a colorless amorphous powder. Its molecular formula was assigned as $C_{48}H_{78}O_{19}$ based on the high-resolution electrospray ionization mass spectrometry (HR-ESI-MS; *m/z*: 981.5080 $[M + Na]^+$). The infrared (IR) spectrum exhibited absorption bands at 3418 (OH), 1728 (C=O), and 1644 (C=C) cm^{-1}. The seven tertiary methyl groups (δ 1.26, 1.08, 0.81, 1.06, 1.66, 1.18, and 1.02 ppm) and one olefinic proton (δ 5.55, br s) were observed in the ^1H nuclear magnetic resonance (NMR) spectrum. The ^{13}C and distortionless enhanced polarization transfer (DEPT) NMR data of the aglycon part of **1** confirmed the presence of seven methyl carbons (δ 28.0, 16.7, 15.4, 17.5, 24.9, 28.9, and 24.9 ppm), two olefinic carbons (δ 123.1 and 144.9 ppm), and two oxygenated methine carbons (δ 89.5 and 81.3 ppm) (Table 2). The comparison of ^1H and ^{13}C NMR spectrum data of the aglycon part of **1** with that of Latifolioside H indicated that compound **1** possessed a 3β,19α-dihydroxyolean-12-ene-28-oic acidic aglycon.[9] The chemical shifts of C-3 (δ 89.5) and C-28 (δ 180.9) revealed that **1** was a monodesmosidic glycoside. Eighteen of

Received 16 February 2011. Accepted 10 May 2011. Published at www.nrcresearchpress.com/cjc on 22 September 2011.

G.-C. Gao and Z.-X. Lu. Institute of Plant Protection and Microbiology, Zhejiang Academy of Agriculture Science, 198 Shiqiao Road, Hangzhou 310021, P. R. China.
S.-H. Tao. Guangdong Pharmaceutical University, University City, Guangzhou 510006, P. R. China.
S. Zhang, F.-Z. Wang, and Q.-X. Li. Key Laboratory of Marine Bio-resources Sustainable Utilization, RNAM Center for Marine Microbiology, Guangdong Key Laboratory of Marine Materia Medica, South China Sea Institute of Oceanology, Chinese Academy of Sciences, 164 West Xingang Road, Guangzhou 510301, P. R. China.

Corresponding author: Si Zhang (e-mail: zhsimd@scsio.ac.cn).

Can. J. Chem. Downloaded from www.nrcresearchpress.com by Xi'an Jiaotong University on 09/19/12
For personal use only.

Table 1. ^{1}H NMR data for the sugar moieties of compounds **1–5** in pyridine-d_5 (J in parentheses in Hz).

H	**1**	**2**	**3**	**4**	**5**
3-*O*	Glc	Glc	Glc	Glc	Glc
1′	4.83 d (7.5)	4.83 d (7.5)	4.94 d (7.0)	4.83 d (7.5)	4.94 d (6.0)
2′	4.38	4.02	4.29	4.36	4.29
3′	4.25	4.20	4.28	4.23	4.28
4′	4.01	4.09	4.17	4.01	4.16
5′	3.89	4.25	4.03	3.87	4.03
6′	4.53, 4.24	4.54, 4.39	4.53, 4.37	4.52, 4.24	4.54, 4.36
3′-*O*					
1′′	5.37 d (7.6)	5.11 d (7.8)		5.36 d (8.0)	
2′′	4.08	4.00		4.02	
3′′	4.21	4.08		4.20	
4′′	4.01	4.18		4.12	
5′′	4.02	4.10		4.17	
6′′	4.47	4.24		4.45	
2′-*O*					
1′′′	5.72 d (7.6)	6.47 br s	6.56 br s	5.71 d (7.5)	6.56 br s
2′′′	4.03	4.81	4.86	4.02	4.86
3′′′	4.27	4.60	4.68	4.27	4.69
4′′′	4.13	4.29	4.34	4.14	4.34
5′′′	3.84	4.74	4.80	3.82	4.80
6′′′	4.31	1.67 d (6.0)	1.71 d (6.0)	4.31	1.71 d (6.0)
28-*O*					
1′′′′		6.31 d (8.1)	6.38 d (8.0)	6.36 d (8.0)	6.34 d (8.0)
2′′′′		4.20	4.21	4.20	4.21
3′′′′		4.28	3.98	4.01	4.03
4′′′′		4.35	4.37	4.35	4.36
5′′′′		3.95	4.10	4.06	3.94
6′′′′		4.47, 4.43	4.48, 4.43	4.45, 4.39	4.47, 4.41

Note: Glc, glucose.

48 carbons were assigned to the oligosaccharide moieties. The ^{1}H and ^{13}C NMR spectra of **1** showed three sugar anomeric protons at δ 4.83 (d, J = 7.5 Hz), 5.37 (d, J = 7.6 Hz), and 5.72 (d, J = 7.6 Hz) and carbons at δ 105.1, 104.7, and 103.8 (Tables 1 and 2). The monosaccharides were identified as glucose by comparing the retention factor (R_f) value with that of D-glucose using thin-layer chromatography (TLC) after acid hydrolysis and a combination of DEPT, heteronuclear single quantum coherence (HSQC), and heteronuclear multiple bond correlation (HMBC) experiments, respectively. All glucoses of **1** were in pyranose forms, as determined by their 1D and 2D NMR experiments. The β-anomeric configurations of the glucose units were established by its $^3J_{H1,H2}$ coupling constants (7.5–7.6 Hz). The signal at δ 88.6 in the ^{13}C NMR indicated a substitution at C-3′ of one of the glucoses. The sequence of the glycan part connected to C-3 of the aglycon was deduced from the following HMBC correlations: H-1′ (δ 4.83) of inner glucose with C-3 (δ 89.5) of sapogenin, H-1′′ (δ 5.37) of one terminal glucose with C-3′ (δ 88.6), and H-1′′′ (δ 5.72) of another terminal glucose with C-2′ (δ 79.3) (Fig. 2). The NMR data of the glycan part of **1** was in accordance with that of 3-*O*-[2′,3′-di-*O*-(β-D-glucopyranosyl)-β-D-glucopyranosyl] oleanolic acid.[10] On the basis of the above results, compound **1** was elucidated as 3-*O*-{β-D-glucopyranosyl-(1→2)-[β-D-glucopyranosyl-(1→3)]-β-D-glucopyranosyl}-siaresinolic acid, named as Catunaroside E.

Compound **2** was determined to have the molecular formula of $C_{54}H_{88}O_{22}$ by its HR-ESI-MS spectrum (*m*/*z*: 1111.5702 [M + Na]$^+$). In the ^{1}H NMR spectrum, seven methyl protons (δ 1.23, 1.15, 0.83, 1.07, 1.23, 0.89, and 0.87 ppm), one olefinic proton (δ 5.41, br s), and four sugar anomeric protons (δ 4.83, d, J = 7.5 Hz; 5.11, d, J = 7.8 Hz; 6.47, br s; and 6.31, d, J = 8.1 Hz) (Table 1) were observed. The signals of seven methyl carbons at δ 28.1, 17.1, 15.7, 17.5, 26.1, 33.1, and 23.7 ppm, two olefinic carbons at δ 122.9 and 144.1 ppm, four sugar carbons at δ 104.9, 103.9, 101.7, and 95.8 ppm, and two carbons at δ 176.4 and 88.7 ppm linked to the glycan part were also shown in the ^{13}C NMR spectrum. The above evidence revealed that **2** was a bisdesmosidic glycoside. The aglycon part of this compound was determined to be oleanolic acid by comparing the ^{1}H, ^{13}C, and DEPT NMR signals of **2** with those of 3-*O*-[β-D-glucopyranosyl-(1→3)-β-D-galactopyranosyl]-olean-12-en-3β-ol-28-oic acid.[5] Acid hydrolysis of **2** suggested that the monosaccharides of this compound were L-rhamnose and D-glucose. In combination with the characteristic proton signal at δ 1.67 (3H, d, J = 6.0 Hz) in the ^{1}H NMR spectrum, **2** could be deduced to contain one rhamnose and three glucose. By comparing with the NMR spectra of Mussaendoside J (**5**), the presence of glucose linked to C-3′ (δ 89.6) in **2** was disclosed. The sequence of the oligosaccharide chain was confirmed by HSQC, HMBC, and ^{1}H-^{1}H double quantum filtered correlation spectroscopy (DQFCOSY) experiments. The key HMBC correlations were observed: H-1′′′′ (δ 6.31) of a glucose and C-28 (δ 176.4) of the aglycon part, H-1′ (δ 4.83) of

Table 2. ^{13}C NMR data of compounds **1–5** in pyridine-d_5.

C	1	2	3	4	5	C	1	2	3	4	5
1	38.5	39.1	38.9	38.6	39.0	3-*O*	Glc	Glc	Glc	Glc	Glc
2	26.6	26.7	26.8	26.6	26.8	1′	105.1	104.9	105.4	105.1	105.4
3	89.5	88.7	88.9	89.5	88.8	2′	79.3	79.3	78.1	79.3	78.1
4	39.6	39.5	39.5	39.6	39.5	3′	88.6	89.6	79.8	88.7	79.9
5	55.9	56.1	56.2	56.0	56.1	4′	70.1	69.8	72.2	70.1	72.2
6	18.6	18.5	18.7	18.8	18.5	5′	77.7	77.0	79.3	77.7	79.3
7	33.3	33.1	33.0	33.1	33.1	6′	63.4	62.7	62.9	63.5	62.9
8	40.0	39.9	40.2	40.2	39.9	3′-*O*	Glc	Glc		Glc	
9	48.2	48.0	48.2	48.3	48.0	1′′	104.7	103.9		104.7	
10	37.1	37.0	37.1	37.1	37.0	2′′	76.4	75.2		76.4	
11	24.1	23.4	24.1	24.1	23.4	3′′	78.6	78.7		78.6	
12	123.1	122.9	123.1	123.2	122.9	4′′	71.6	71.4		71.6	
13	144.9	144.1	144.3	144.4	144.1	5′′	78.6	78.4		78.6	
14	42.1	42.2	42.1	42.2	42.2	6′′	62.6	62.3		62.6	
15	29.2	28.3	29.0	29.1	28.3	2′-*O*	Glc	Rha	Rha	Glc	Rha
16	28.4	23.8	28.0	28.1	23.8	1′′′	103.8	101.7	101.7	103.9	101.7
17	46.1	47.0	46.5	46.5	47.0	2′′′	75.4	72.4	72.4	75.4	72.4
18	44.8	41.8	44.6	44.6	41.8	3′′′	78.6	72.5	72.5	78.6	72.5
19	81.3	46.3	81.1	81.2	46.2	4′′′	72.6	73.9	74.2	72.7	74.2
20	35.7	30.8	35.5	35.6	30.8	5′′′	77.8	69.8	69.6	77.8	69.6
21	29.2	34.0	29.0	29.0	34.0	6′′′	62.4	18.6	18.7	62.2	18.7
22	33.7	32.6	33.2	33.3	32.5	28-*O*		Glc	Glc	Glc	Glc
23	28.0	28.1	28.1	28.8	28.1	1′′′′		95.8	95.9	95.9	95.8
24	16.7	17.1	17.1	16.7	17.1	2′′′′		74.1	74.2	74.2	74.2
25	15.4	15.7	15.5	15.5	15.6	3′′′′		78.9	78.9	79.0	78.9
26	17.5	17.5	17.6	17.6	17.5	4′′′′		71.1	71.1	71.2	71.1
27	24.9	26.1	24.9	25.0	26.1	5′′′′		77.8	77.8	77.8	77.8
28	180.9	176.4	177.2	177.3	176.4	6′′′′		62.3	62.2	62.4	62.2
29	28.9	33.1	28.7	28.1	33.1						
30	24.9	23.7	24.7	24.7	23.6						

Note: Glc, glucose; Rha, rhamnose.

Can. J. Chem. Downloaded from www.nrcresearchpress.com by Xi'an Jiaotong University on 09/19/12
For personal use only.

the inner glucose and C-3 (δ 88.7) of the aglycon part, H-1′′ (δ 5.11) of the terminal glucose and C-3′ (δ 89.6) of the inner glucose, and H-1′′′ (δ 6.47) of the terminal rhamnose and C-2′ (δ 78.7) of the inner glucose (Fig. 2). The β-anomeric configurations of glucose units were determined by the relatively large $^3J_{H1,H2}$ coupling constants (7.5–8.1 Hz). The $^1J_{C1,H1}$ coupling constant (168 Hz) for the rhamnosyl unit confirmed that the anomeric proton was equatorial (α-pyranoid anomeric form).[11] On the basis of this evidence, compound **2**, named as Catunaroside F, was elucidated as 3-*O*-{α-L-rhamnopyranosyl-(1→2)-[β-D-glucopyranosyl-(1→3)]-β-D-glucopyranosyl}-28-*O*-(β-D-glucopyranosyl)-oleanolic acid.

Compound **3**, also an amorphous powder, has the molecular formula of $C_{48}H_{78}O_{17}$ as indicated by its HR-ESI-MS spectrum (*m/z*: 965.5129 $[M + Na]^+$). In the ^1H NMR spectrum, seven methyl protons (δ 1.26, 1.20, 0.88, 1.13, 1.63, 1.14, and 0.98 ppm), one olefinic proton (δ 5.50, br s), and three sugar anomeric protons (δ 4.94, d, J = 7.0 Hz; 6.56, br s; and 6.38, d, J = 8.0 Hz) (Table 1) were observed. The signals of seven methyl carbons at δ 28.1, 17.1, 15.5, 17.6, 24.9, 28.,7 and 24.7 ppm, two olefinic carbons at δ 123.1 and 144.3 ppm, three sugar carbons at δ 105.4, 101.7, and 95.9 ppm, and two carbons at δ 177.2 and 88.9 ppm linked to the glycan part were also shown in the ^{13}C NMR spectrum. The signals in the NMR spectrum of **3** were in agreement with those of Mussaendoside J, except for the signals of the aglycon part at δ 81.1 (d, C-19) ppm, which was oxygenated, and 35.5 (s, C-20) ppm.[12] The aglycon part of **3** was then established as siaresinolic acid by comparing the NMR spectrum data of **3** with that of **1**. From the above evidence, compound **3** was identified as 3-*O*-[α-L-rhamnopyranosyl-(1→2)-β-D-glucopyranosyl]-28-*O*-(β-D-glucopyranosyl)-siaresinolic acid, named as Catunaroside G.

Compound **4**, obtained as an amorphous powder, was deduced to have the molecular formula of $C_{54}H_{88}O_{24}$ as indicated from the HR-ESI-MS data (*m/z*: 1143.5586 $[M + Na]^+$). Acid hydrolysis of **4** showed the existence of D-glucose. The signals at 177.3 and 89.5 ppm in the ^{13}C NMR spectrum suggested that **4** was a bisdesmosidic glycoside. In the ^1H and ^{13}C NMR spectrum, four anomeric carbon signals (δ 4.83, d, J = 7.5 Hz; 5.36, d, J = 8.0 Hz; 5.71, d, J = 7.5 Hz; and 6.36, d, J = 8.0 Hz and δ 105.1, 104.7, 103.9, 95.9 ppm) (Tables 1 and 2) were exhibited. Compound **4** had the same NMR signals as Aralia-saponin V except the signals of C-19 (δ 81.2 ppm) and C-20 (δ 35.6 ppm) of the aglycon part, which is just like the difference between compound **3** and Mussaendoside J.[13] Similarly, the aglycon moiety of **4** was determined to be siaresinolic acid. Thus, compound **4** was elucidated as 3-*O*-{β-D-glucopyranosyl-(1→2)-[β-D-glucopyranosyl-(1→3)]-β-D-glucopyranosyl}-28-*O*-(β-D-glucopyranosyl)-siaresinolic acid, named as Catunaroside H.

Can. J. Chem. Downloaded from www.nrcresearchpress.com by Xi'an Jiaotong University on 09/19/12
For personal use only.

Fig. 1. Structures of compounds **1–5.**

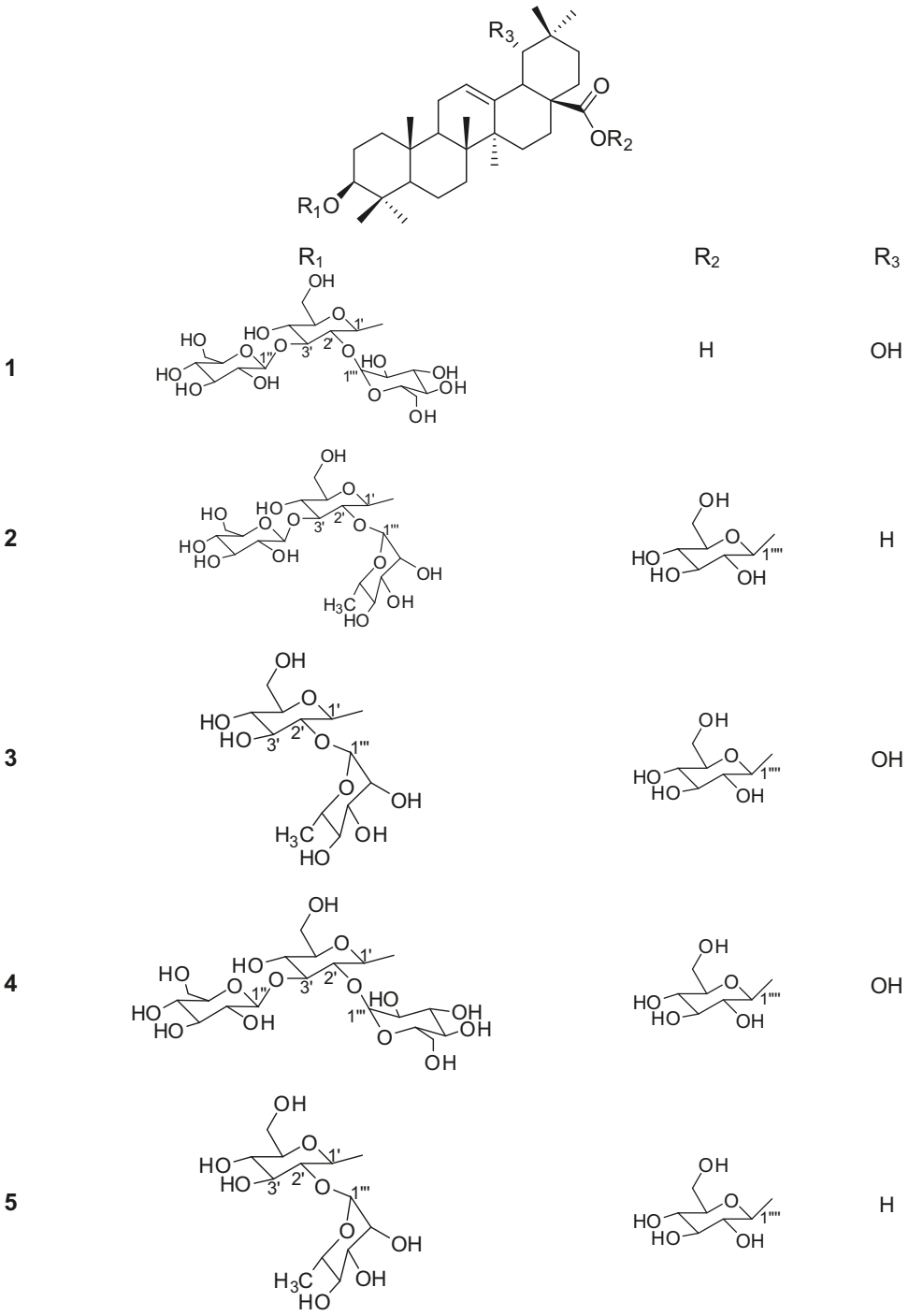

Compound **5** was elucidated as Mussaendoside J by comparing its spectra data with the data reported in the literature (IR, MS, and ^{1}H and ^{13}C NMR).[12]

Experimental

General

MS were recorded on a MDS SCIEX API 2000 LC/MS/MS instrument for ESI and a Bruker BioTOF Q spectrometer for HR-ESI. IR spectra were measured with a Bruker EQUINOX55 infrared spectrometer. ^{1}H and ^{13}C NMR spectra were acquired with a Bruker DRX-500 spectrometer ($SiMe_4$ as the internal standard). Silica gel (Qingdao Haiyang Chemical Co., Ltd., 100–200 mesh and 200–300 mesh) and LiChroprep RP-18 (Merck) were used for the silica gel column chromatography (CC) and medium-pressure liquid chromatography (MPLC). Sephadex LH-20 (Pharmacia) and macroporous resin D101 were also used for column chromatography. TLC was carried on precoated silica gel 60 F_{254} plates (Qingdao Haiyang Chemical Co., Ltd.), and detection was achieved by 10% H_2SO_4–EtOH for saponins. Semipreparative high-pressure liquid chromatography (HPLC) was performed using

Fig. 2. Key HMBC correlations for the sugar sequence of **1**–**4** (from H to C).

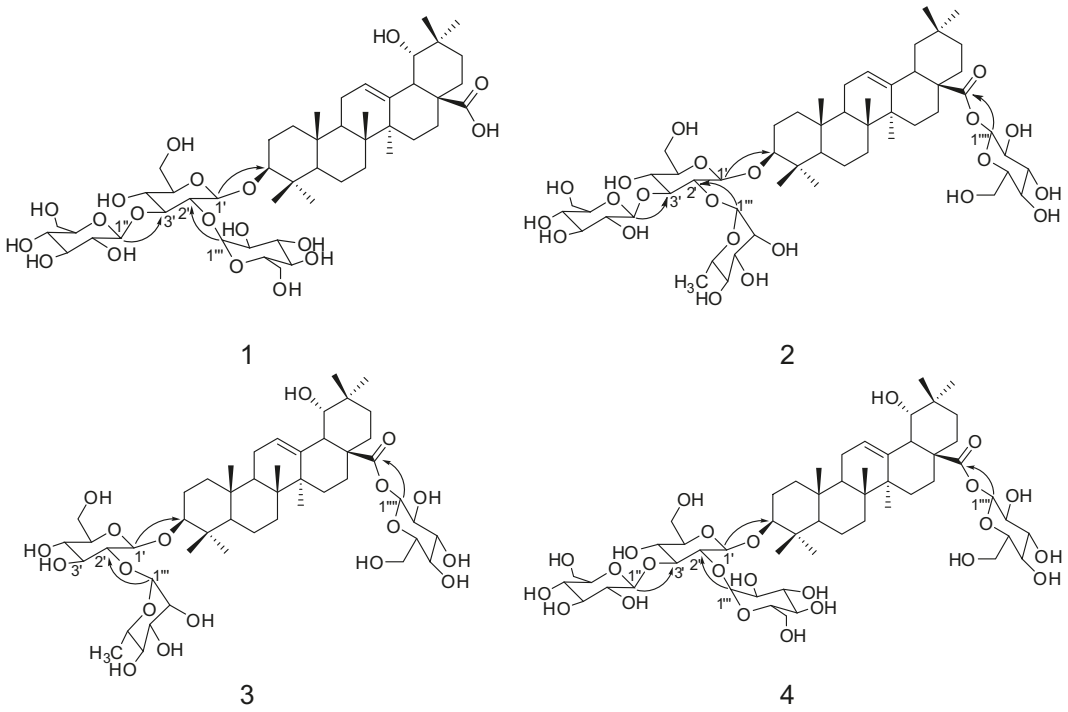

Can. J. Chem. Downloaded from www.nrcresearchpress.com by Xi'an Jiaotong University on 09/19/12
For personal use only.

an octadecylsilane (ODS) column (YMC-Pack ODS-5-A, 250 mm × 10 mm inside diameter (i.d.), 5 μm; YMC Co., Ltd.) on a Waters-600 HPLC system equipped with a Waters-996 photodiode array detector.

Plant material

The stem bark of *C. spinosa* Tirveng was collected in February 2006 from Sanya, Hainan Province, P. R. China. The specimen was identified by professor Si Zhang, South China Sea Institute of Oceanology, Chinese Academy of Sciences, Guangzhou, P. R. China. A voucher specimen has been deposited in the South China Sea Institute of Oceanology, Chinese Academy of Sciences, Guangzhou, P. R. China (accession number: GKLMMM020).

Extraction and isolation

The *n*-BuOH extract of air-dried and powdered plant material (9.0 kg) was extracted by the method as previously reported.[8] The *n*-BuOH soluble fraction (170 g) was passed through a macroporous resin (D101) column eluted with H_2O and EtOH–H_2O (3:7, 6:4, and 95:5), whereas the EtOH–H_2O (95:5, 10 g) eluted portion was subjected to silica gel CC eluted with $CHCl_3$–MeOH (98:2–50:50) to give fractions A–G. Fraction E was separated by preparative HPLC using MeOH–H_2O (68:32) to give compound **1** (10 mg). Fraction F was recrystallized to afford compound **2** (50 mg). The EtOH–H_2O (6:4, 35 g) eluted portion was subjected to silica gel CC eluted with $CHCl_3$–MeOH (90:10–50:50) to give fractions a–f. Fraction b was separated by Sephadex LH-20 (MeOH), then fractions 25–28 and 53–54 were purified by preparative HPLC eluting with MeOH–H_2O (55:45) and MeOH–H_2O (70:30) to obtain compounds **3** (22 mg) and **5** (12 mg) separately. Fraction f was rechromatographed to silica gel CC eluted with $CHCl_3$–MeOH–H_2O (80:20:5), then fraction 12 was purified by preparative HPLC using MeOH–H_2O (50:50) to yield compound **4** (70 mg).

Catunaroside E (1)

Colorless amorphous powder. IR (KBr, cm^{-1}) υ_{max}: 3418, 1728, 1644. ^{1}H NMR (500 MHz, pyridine-d_5) δ: 3.25 (1H, dd, J = 4.4, 11.5 Hz, H-3), 5.55 (1H, br s, H-12), 3.62 (1H, br s, H-18), 3.60 (1H, br s, H-19), 1.26 (3H, s, H-23), 1.08 (3H, s, H-24), 0.81 (3H, s, H-25), 1.06 (3H, s, H-26), 1.66 (3H, s, H-27), 1.18 (3H, s, H-29), 1.02 (3H, s, H-30), 4.83 (1H, d, J = 7.5 Hz, H-1′), 5.37 (1H, d, J = 7.6 Hz, H-1″), 5.72 (1H, d, J = 7.6 Hz, H-1‴). ^{13}C NMR (125 MHz, pyridine-d_5) data, see Table 2. ESI-MS *m/z*: 981 $[M + Na]^+$, 997 $[M + K]^+$. HR-ESI-MS *m/z*: 981.5080 $[M + Na]^+$. Calcd. for $C_{48}H_{78}O_{19}Na$: 981.5001.

Catunaroside F (2)

Colorless amorphous powder. IR (KBr, cm^{-1}) υ_{max}: 3426, 1739 1640. ^{1}H NMR (500 MHz, pyridine-d_5) δ: 3.38 (1H, dd, J = 3.9, 11.6 Hz, H-3), 5.41 (1H, br s, H-12), 3.18 (1H, dd, J = 3.4, 13.6 Hz, H-18), 1.23 (3H, s, H-23), 1.15 (3H, s, H-24), 0.83 (3H, s, H-25), 1.07 (3H, s, H-26), 1.23 (3H, s, H-27), 0.89 (3H, s, H-29), 0.87 (3H, s, H-30), 4.83 (1H, d, J = 7.5 Hz, H-1′), 5.11 (1H, d, J = 7.8 Hz, H-1″), 1.67 (3H, d, J = 6.0 Hz, H-6‴), 6.47 (1H, br s, H-1‴), 6.31 (1H, d, J = 8.1 Hz, H-1⁗). ^{13}C NMR (125 MHz, pyridine-d_5) data, see Table 2. ESI-MS *m/z*: 1111 $[M + Na]^+$, 1127 $[M + K]^+$. HR-ESI-MS *m/z*: 1111.5702 $[M + Na]^+$. Calcd. for $C_{54}H_{88}O_{22}Na$: 1111.5691.

Catunaroside G (3)

Colorless amorphous powder. IR (KBr, cm^{-1}) υ_{max}: 3419, 1730, 1644. ^{1}H NMR (500 MHz, pyridine-d_5) δ: 3.34 (1H, dd, J = 4.0, 11.5 Hz, H-3), 5.50 (1H, br s, H-12), 3.52 (1H, br s, H-18), 3.57 (1H, br s, H-19), 1.26 (3H, s, H-23), 1.20

(3H, s, H-24), 0.88 (3H, s, H-25), 1.13 (3H, s, H-26), 1.63 (3H, s, H-27), 1.14 (3H, s, H-29), 0.98 (3H, s, H-30), 4.94 (1H, d, J = 7.0 Hz, H-1′), 1.71 (3H, d, J = 6.0 Hz, H-6‴), 6.56 (1H, br s, H-1‴), 6.38 (1H, d, J = 8.0 Hz, H-1⁗). ^{13}C NMR (125 MHz, pyridine-d_5) data, see Table 2. ESI-MS *m/z*: 965 $[M + Na]^+$, 981 $[M + K]^+$. HR-ESI-MS *m/z*: 965.5129 $[M + Na]^+$. Calcd. for $C_{48}H_{78}O_{18}Na$: 965.5117.

Catunaroside H (4)

Colorless amorphous powder. IR (KBr, cm^{-1}) υ_{max}: 3422, 1738, 1645. ^{1}H NMR (500 MHz, pyridine-d_5) δ: 3.26 (1H, dd, J = 3.5, 11.5 Hz, H-3), 5.50 (1H, br s, H-12), 3.52 (1H, br s, H-18), 3.57 (1H, br s, H-19), 1.26 (3H, s, H-23), 1.09 (3H, s, H-24), 0.84 (3H, s, H-25), 1.12 (3H, s, H-26), 1.63 (3H, s, H-27), 1.14 (3H, s, H-29), 0.98 (3H, s, H-30), 4.83 (1H, d, J = 7.5 Hz, H-1′), 5.36 (1H, d, J = 8.0 Hz, H-1″), 5.71 (1H, d, J = 7.5 Hz, H-1‴), 6.36 (1H, d, J = 8.0 Hz, H-1⁗). ^{13}C NMR (125 MHz, pyridine-d_5) data, see Table 2. ESI-MS *m/z*: 1143 $[M + Na]^+$, 1159 $[M + K]^+$. HR-ESI-MS *m/z*: 1143.5586 $[M + Na]^+$. Calcd. for $C_{54}H_{88}O_{24}Na$: 1143.5598.

Mussaendoside J (5)

Colorless amorphous powder. IR (KBr, cm^{-1}) υ_{max}: 3422, 1736, 1643. ^{1}H NMR (500 MHz, pyridine-d_5) δ: 3.35 (1H, dd, J = 4.0, 11.5 Hz, H-3), 5.43 (1H, br s, H-12), 3.19 (1H, dd, J = 3.8, 10.5 Hz, H-18), 1.25 (3H, s, H-23), 1.19 (3H, s, H-24), 0.84 (3H, s, H-25), 1.09 (3H, s, H-26), 1.25 (3H, s, H-27), 0.91 (3H, s, H-29), 0.88 (3H, s, H-30), 4.94 (1H, d, J = 6.0 Hz, H-1′), 1.71 (3H, d, J = 6.0 Hz, H-6‴), 6.56 (1H, br s, H-1‴), 6.34 (1H, d, J = 8.0 Hz, H-1⁗). ^{13}C NMR (125 MHz, pyridine-d_5) data, see Table 2. ESI-MS *m/z*: 949 $[M + Na]^+$, 965 $[M + K]^+$. HR-ESI-MS *m/z*: 949.5178 $[M + Na]^+$. Calcd. for $C_{48}H_{78}O_{17}Na$: 949.5183.

Acid hydrolysis of 1–5

Compounds **1–5** (5 mg each) were refluxed in 5 mL of 4 N HCl for 8 h (kept sealed) in a water bath (100 °C). After cooling, the reaction mixtures were extracted with EtOAc (5 mL). The aqueous layers were adjusted to pH 6 with $NaHCO_3$. After being concentrated under reduced pressure, each H_2O layer (monosaccharide portion) was identified by comparing the R_f value with that of the authentic samples on the TLC plate (eluted with $CHCl_3$–MeOH–H_2O (8:7:1) and EtOAc–MeOH–AcOH–H_2O (13:3:4:3) solvent system, visualized with ethanol and 10% H_2SO_4 spraying and then heating).

Acknowledgments

This work was financially supported by the National Basic Research Program of China (No. 2010CB833801) and the Scientific Research Special Funds Project of the Ministry of Finance (P. R. China, KSCX2-YW-Z-1018).

References

(1) Hamerski, L.; Furlan, M.; Silva, D. H. S.; Cavalheiro, A. J.; Eberlin, M. N.; Tomazela, D. M.; Bolzani, V. D. S. *Phytochemistry* **2003**, *63* (4), 397. doi:10.1016/S0031-9422(03)00109-2.
(2) Atal, C. K.; Lamba, S. S. *Indian J. Pharm.* **1960**, *22* (5), 120.
(3) Satpute, K. L.; Jadhav, M. M.; Karodi, R. S.; Katare, Y. S.; Patil, M. J.; Rub, R.; Bafna, A. R. *J. Pharmacogn. Phytother.* **2009**, *1* (3), 036.
(4) Dubois, M.-A.; Benze, S.; Wagner, H. *Planta Med.* **1990**, *56* (5), 451. doi:10.1055/s-2006-961009.
(5) Sati, O. P.; Rana, U.; Chaukiyal, D. C.; Madhusudanan, K. P.; Bhakuni, D. S. *Planta Med.* **1987**, *53* (6), 530. doi:10.1055/s-2006-962802.
(6) Sotheeswaran, S.; Bokel, M.; Kraus, W. *Phytochemistry* **1989**, *28* (5), 1544. doi:10.1016/S0031-9422(00)97788-4.
(7) Sati, S. P.; Chaukiyal, D. C.; Sati, O. P.; Yamada, F.; Ono, M. *J. Nat. Prod.* **1989**, *52* (2), 376. doi:10.1021/np50062a026.
(8) Gao, G. C.; Luo, X. M.; Wei, X. Y.; Qi, S. H.; Yin, H.; Xiao, Z. H.; Zhang, S. *Helv. Chim. Acta* **2010**, *93* (2), 339. doi:10.1002/hlca.200900193.
(9) Ouyang, M. A.; Liu, Y. Q.; Wang, H. Q.; Yang, C. R. *Phytochemistry* **1998**, *49* (8), 2483. doi:10.1016/S0031-9422(98)00164-2.
(10) Lemmich, E.; Cornett, C.; Furu, P.; Jørstian, C. L.; Knudsen, A. D.; Olsen, C. E.; Salih, A.; Thiilborg, S. T. *Phytochemistry* **1995**, *39* (1), 63. doi:10.1016/0031-9422(94)00866-R.
(11) Bock, K.; Pedersen, C. *J. Chem. Soc. Perkin Trans. 2* **1974**, 293. doi:10.1039/p29740000293.
(12) Zhao, W.-M.; Yang, G.-J.; Xu, R.-S.; Qin, G.-W. *Nat. Prod. Lett.* **1996**, *8* (2), 119. doi:10.1080/10575639608043250.
(13) Song, S. J.; Nakamura, N.; Ma, C. M.; Hottori, M.; Xu, S. X. *Phytochemistry* **2001**, *56* (5), 491. doi:10.1016/S0031-9422(00)00379-4.

Can. J. Chem. Downloaded from www.nrcresearchpress.com by Xi'an Jiaotong University on 09/19/12
For personal use only.

Effect of vibrational and rotational excitation on the stereodynamics of the C(^{1}D) + H_2 (v, j) → CH + H reaction

Li-hua Kang, Shan-zheng Zhang, Mingyuan Zhu, and Bin Dai

Can. J. Chem. Downloaded from www.nrcresearchpress.com by Xi'an Jiaotong University on 09/19/12
For personal use only.

Abstract: The stereodynamics of the title reaction on the ab initio ^{1}A′ potential energy surface (PES) (B. Bussery-Honvault, P. Honvault, and J.-M. Launay. 2001. J. Chem. Phys. **115**: 10701) at a collision energy of 16 kJ/mol have been studied using quasi-classical trajectory (QCT) method. Vector properties including angular momentum alignment parameters and four polarization-dependent differential cross sections (PDDCS) of the product CH are presented. Furthermore, the influence of reagent vibrational and rotational excitations on the product vector properties have also been studied in the present work. The calculated results indicate that the angle distributions of the CH product are mainly dominated by backward–forward scattering.

Key words: quasi-classical trajectory, potential energy surface, stereodynamics.

Résumé : Faisant appel à la méthode de la trajectoire quasi-classique (TQC), on a étudié la stéréodynamique de la réaction mentionnée dans le titre sur une surface d'énergie potentielle (SEP) ab initio ^{1}A′ (B. Bussery-Honvault, P. Honvault, and J.-M. Launay. 2001. J. Chem. Phys. **115** : 10701), à une énergie de collision de 16 kJ/mol. On rapporte les propriétés vectorielles, dont les paramètres d'alignement de la quantité de mouvement angulaire et les quatre sections droites différentielles dépendantes de la polarisation (SDDDP) du produit CH. Dans ce travail, on a de plus étudié l'influence de l'excitation rotationnelle et vibrationnelle du réactif sur les propriétés vectorielles du produit. Les résultats calculés indiquent que les angles de distribution du produit CH sont principalement dominés par une diffusion de l'arrière ver l'avant.

Mots-clés : trajectoire quasi-classique, surface d'énergie potentielle, stéréodynamique.

[Traduit par la Rédaction]

Introduction

The gas-phase reaction C(^{1}D) + H_2 and its reverse reaction play a crucial role in astrophysics and carbon chemistry. In the last few years, the title reaction has attracted considerable attention from experimental and theoretical studies.[1–9] Being a typical atom–diatom indirect insertion reaction, it has the colliding atom in an electronically excited state and is used to test the quality of new theories and experiments. Therefore, extensive studies of the title reaction can help us explore the detailed dynamics of the other insertion-type chemical reactions, such as N(^{2}D) + H_2[10–12] and O(^{1}D) + H_2.[13–16]

Experimentally, Bergeat et al.[1] using the crossed molecular beam (CMB) scattering technique measured the product angular and time-of-flight (TOF) distributions for the C(^{1}D) + H_2 reaction. Balucani et al.[2,3] measured the product angular and velocity distributions in the crossed molecular beam experiments.

Theoretically, in 2001, Bussery-Honvault et al.[4] constructed a potential energy surface (PES) for the title reaction. Motivated by this PES, there were also a number of theoretical studies for the reaction C(^{1}D) + H_2 and its isotopic variants. Bañares et al.[5] calculated integral and differential cross sections at 80 meV collision energy with the initial H_2 rotational quantum numbers $j = 0$ and 1. In addition, they also obtained the total and vibrationally state-resolved reaction probabilities at total angular momentum $J = 0$ in the 0–0.5 eV collision energy range. Using the time-dependent real wave packet method, the state-to-state and state-to-all reactive scattering probabilities for a broad range of energies were calculated on the same PES by Gogtas et al.[17] Recently, Lin and Guo[9,18] performed quantum wave packet calculations of C(^{1}D) + H_2 reactive and inelastic scattering for $J = 0$, integral cross sections, and rate constants.

As mentioned previously, a number of experimental[1–3] and theoretical studies[4–9] on the reaction of C(^{1}D) + H_2 and its isotopic variants have been carried out for the past decades. However, most of these studies only focused on scalar properties not vector properties. The vector properties of chemical reaction can represent an interesting probe into understanding the stereodynamics.[19–21] Since the pioneering work of Fano and Macek,[22] of Case and Herschbach,[23] and of Blais and Truhlar,[24] substantial progress has been made in the field of chemical reaction stereodynamics.[25–32] With the development of new experimental techniques, such as polarized

Received 8 May 2011. Accepted 15 June 2011. Published at www.nrcresearchpress.com/cjc on 13 September 2011.

L. Kang, S. Zhang, M. Zhu, and B. Dai. School of Chemistry and Chemical Engineering/Key Laboratory for Green Processing of Chemical Engineering of Xinjiang Bingtuan, Shihezi University, Shihezi, Xinjiang, 832003, P.R. China.

Corresponding author: Li-hua Kang (e-mail: lhkang99@gmail.com).

Can. J. Chem. Downloaded from www.nrcresearchpress.com by Xi'an Jiaotong University on 09/19/12
For personal use only.

Fig. 1. The center-of-mass coordinate system used to describe the final relative velocity vector (**k**′) and the final rotational angular momentum (**j**′) correlations.

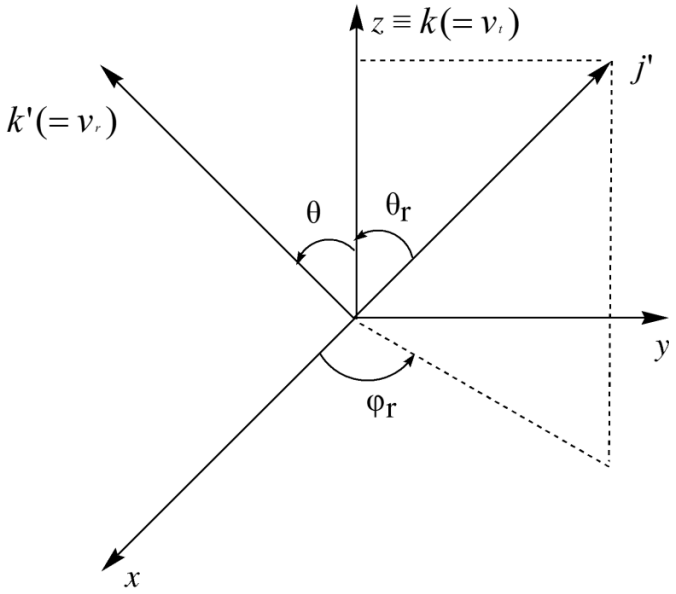

laser-induced fluorescence,[20] laser-induced chemiluminescence,[25] and Doppler-resolved laser-induced fluorescence,[28,29] it is becoming evident that product rotational polarization can provide detailed mechanistic information. One significant step in the theoretical progress is the introduction of the concept of polarization-dependent differential cross sections (PDDCSs) by Shafer-Ray et al.[30] Han and co-workers[25–27] have systematically studied the product rotational polarization of bimolecular reactions with different reagent mass combinations on attractive, mixed, and repulsive potential energy surfaces. In this paper, we focused on the vector properties of the $C(^1D) + H_2$ reaction and the influence of vibrational and rotational excitations on the stereodynamics.

Polarization-dependent differential cross sections (PDDCS)

The full three-dimensional angular distribution associated with **k**, **k**′, and **j**′ can be represented by a set of generalized PDDCSs in the center-of-mass (CM) frame,[33,34] which is shown in Fig. 1. The reagent relative velocity vector **k** is parallel to the z axis. The x–z plane is the scattering plane containing the initial and final relative velocity vectors, **k** and **k**′. The angle θ is the so-called scattering angle between the reagent relative velocity and the product relative velocity. The angles θ_r and ϕ_r are the polar and azimuthal angles of the final rotational angular momentum **j**′, respectively.

The distribution function $P(\theta_r)$ corresponding to the **k**–**j**′ correlation is expanded into a series of Legendre polynomials:[16,26]

$$[1] \qquad P(\theta_r) = \frac{1}{2}\sum_k (2k+1)\boldsymbol{a}_0^k P_k(\cos\theta_r)$$

The $\boldsymbol{a}_0^k$ coefficients (polarization parameters) are given by

Fig. 2. The distribution of $P(\theta_r)$ and $P(\phi_r)$ for the CH product from the reaction $C(^1D) + H_2$ ($v, j = 0$) → CH + H at a collision energy of 16 kJ/mol. The $P(\theta_r)$ in (*a*) describes the **k**–**j**′ correlation. The $P(\phi_r)$ in (*b*) shows the dihedral angle distribution of **j**′ with respect to the **k**–**k**′ plane.

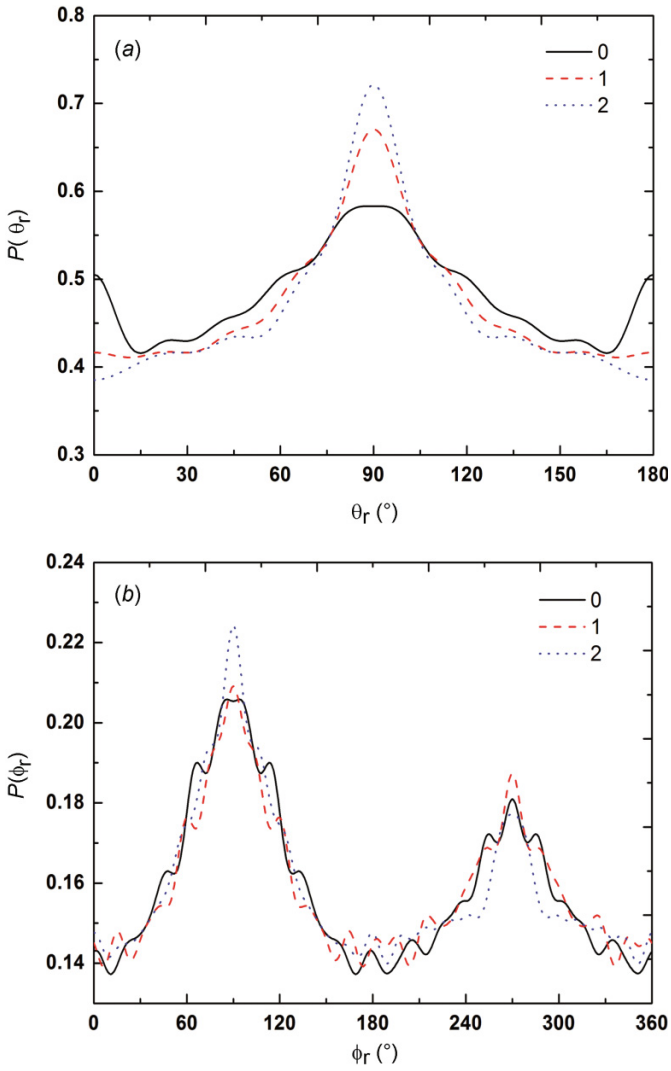

$$[2] \qquad \boldsymbol{a}_0^k = \int_0^{\pi} P(\theta_r)P_k(\theta_r)\sin\theta_r d\theta_r = < P_k(\cos\theta_r) >$$

where the angular brackets represent an average over all of the reactive trajectories. In this paper, $P(\theta_r)$ is expanded up to $k = 18$, which shows good convergence.

The dihedral angle distribution function $P(\phi_r)$ described for the **k**–**k**′–**j**′ correction can be expanded as a Fourier series:[24]

$$P(\phi_r) = \frac{1}{2}\left[1 + \sum_{n,\text{even}\geq 2} a_n \cos(\phi_r) + \sum_{n,\text{odd}\geq 2} b_n \sin(\phi_r)\right]$$

where $a_n = 2< \cos\phi_r >$ and $b_n = 2< \sin\phi_r >$. In this work, $P(\phi_r)$ is expanded up to $n = 24$, which shows good convergence.

The full three-dimensional distribution associated with **k**, **k**′, and **j**′ can be represented by a set of generalized PDDCSs. The fully correlated CM angular distribution is given as follows:[24,28]

Can. J. Chem. Downloaded from www.nrcresearchpress.com by Xi'an Jiaotong University on 09/19/12
For personal use only.

Fig. 3. Four polarization-dependent differential cross sections (PDDCSs) for the CH product from the reaction $C(^1D) + H_2$ (v, $j = 0$) → CH + H at a collision energy of 16 kJ/mol. Panel (*a*) shows the PDDCSs with (k,q) = (0,0). Panels (*b*)–(*d*) depict the PDDCSs with (k,$q\pm$) = (2,0), (2,2+), and (2,1–), respectively.

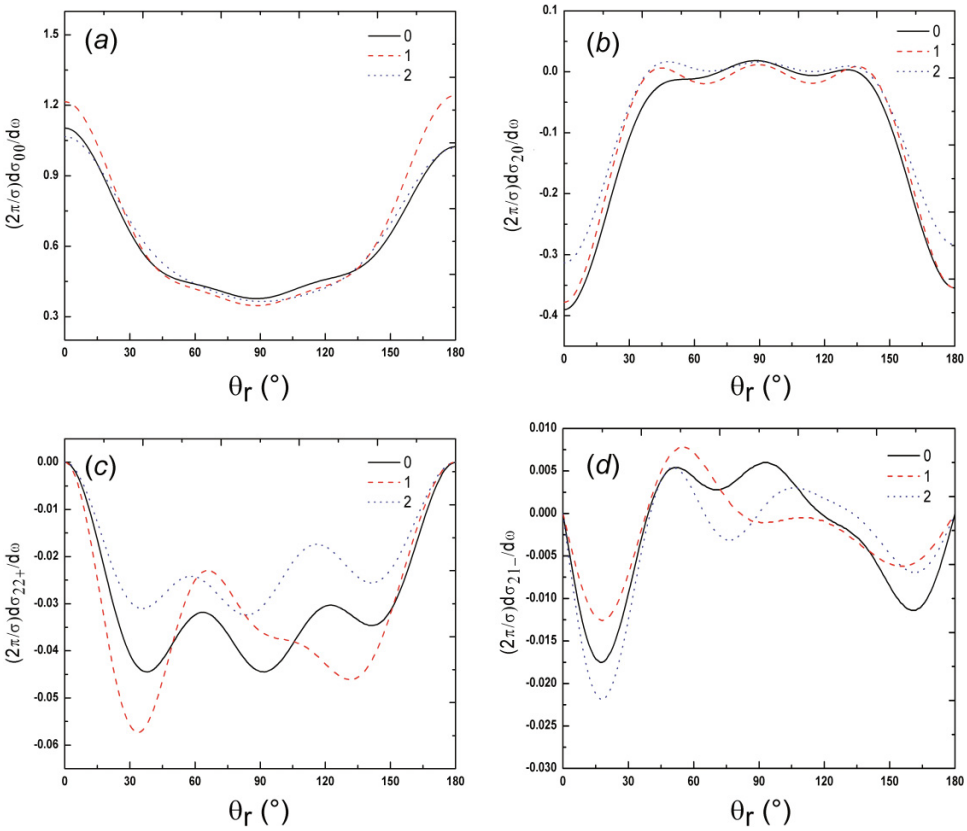

$$P(\omega_t, \omega_r) = \frac{1}{4\pi}\sum_{kq}(2k+1)\frac{1}{\sigma}\frac{d\sigma_{kq}}{d\omega t}C_{kq}(\theta_r, \phi_r)$$

where $\omega_t = \theta$ and $\omega_r = \theta_r$, and ϕ_r, $C_{kq}(\theta_r,\phi_r)$ are modified spherical harmonics, σ is the integral cross section, $\frac{1}{\sigma}\frac{d\sigma_{kq}}{d\omega t}$ are the generalized PDDCSs, and $\frac{1}{\sigma}\frac{d\sigma_{kq}}{d\omega t}$ yields

$$\frac{1}{\sigma}\frac{d\sigma_{k_0}}{d\omega t} = 0$$

where k is odd,

$$\frac{1}{\sigma}\frac{d\sigma_{kq_+}}{d\omega t} = \frac{1}{\sigma}\frac{d\sigma_{kq}}{d\omega t} + \frac{1}{\sigma}\frac{d\sigma_{k-q}}{d\omega t} = 0$$

where k is even and q is odd or k is odd and q is even,

$$\frac{1}{\sigma}\frac{d\sigma_{kq_-}}{d\omega t} = \frac{1}{\sigma}\frac{d\sigma_{kq}}{d\omega t} - \frac{1}{\sigma}\frac{d\sigma_{k+q}}{d\omega t} = 0$$

where k is even and q is even or k is odd and q is odd.

Quasi-classical trajectory (QCT) calculations

All the QCT calculations have been performed on the 1A′ CH_2 ab initio PES constructed by Bussery-Honvault et al.[4] The QCT method is described in detail elsewhere,[35–37] and the classical Hamiltonian equations are integrated numerically for motion in three dimensions with the sixth-order symplectic integration.[38] The QCT method has already proved successful in describing atom–diatom insertion reactions such as $N(^2D) + H_2 \rightarrow NH + H$[10–12] and $O(^1D) + H_2 \rightarrow OH + H$.[13–16] As pointed out by Ju et al.,[39] the QCT calculated results are in good agreement with the quantum mechanics ones for most chemical reactions. A branching of 100 000 trajectories was run for each of the $C(^1D) + H_2$ (v, j) reactions. The integration step size for the trajectories was chosen to be 10^{-17} s, which guarantees the conservation of the total energy and total angular momentum. The trajectories were started at a distance between the incoming atom and the center-of-mass of the diatom of 10 Å.

Results and discussion

The effect of vibrational excitation on stereodynamics

The $P(\theta_r)$ and $P(\phi_r)$ of the product CH from the reactions $C(^1D) + H_2$ ($v = 0$, 1, or 2, $j = 0$) → CH + H at a collision energy of 16 kJ/mol are shown in Fig. 2. Evidently, the distribution of $P(\theta_r)$ shows significant variations from the vibrational excitation of CH and displays a preference for the product rotational angular momentum vector perpendicular to the relative velocity direction. The peak of $P(\theta_r)$ at the θ_r angle is close to 90° and symmetric with respect to 90° for $v = 0$, 1, or 2, which shows that the product vibrational angular momentum vector is aligned along the direction at right angles to the relative velocity direction. In addition, the peak of $P(\theta_r)$ at 90° becomes narrower and higher with increasing vibrational excitation. $P(\phi_r)$ shown in Fig. 2*b* describes the **k**–**k**′–**j**′ correlation. The peaks of the $P(\phi_r)$ distribution and

Can. J. Chem. Downloaded from www.nrcresearchpress.com by Xi'an Jiaotong University on 09/19/12
For personal use only.

Fig. 4. The distribution of $P(\theta_r)$ and $P(\phi_r)$ for the CH product from the reaction $C(^1D) + H_2$ ($v = 0$, j) → CH + H at a collision energy of 16 kJ/mol. The $P(\theta_r)$ in (*a*) describes the **k**–**j**′ correlation. The $P(\phi_r)$ in (*b*) shows the dihedral angle distribution of **j**′ with respect to the **k**–**k**′ plane.

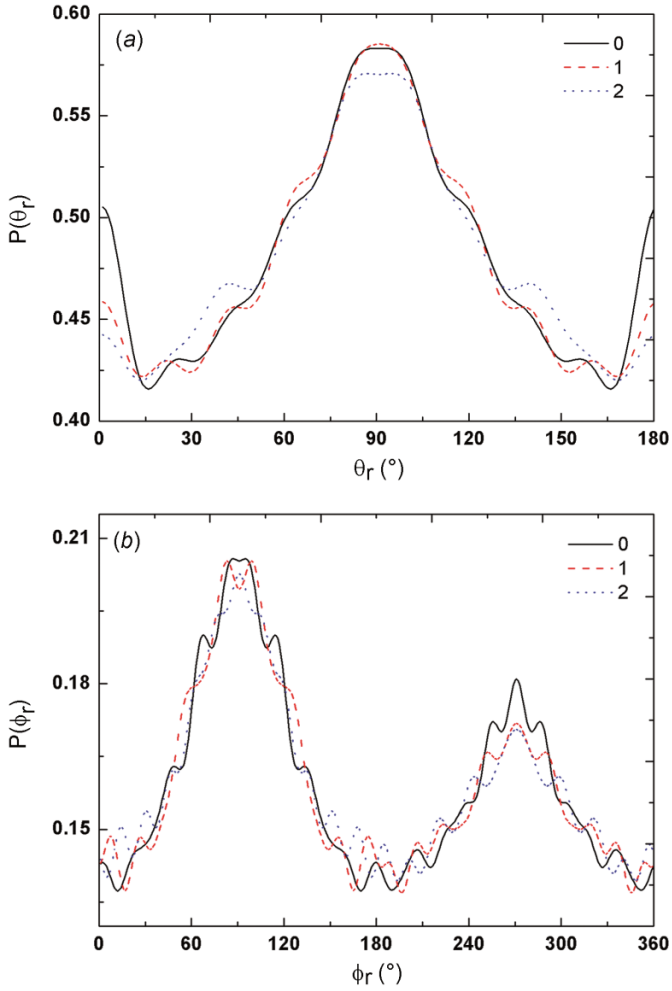

the peaks also become narrower and higher with increasing vibrational excitation. These indicate that the vibrational angular momentum vectors of the products are mainly aligned along the *y* axis of the CM frame and become stronger as the vibrational excitation increases. In addition, we can also see that the distributions of $P(\phi_r)$ tend to be asymmetric with respect to the **k**–**k**′ scattering plane (or about $\phi_r = 180°$), directly reflecting the handedness of **j**′ with respect to the **k**–**k**′ plane.[24] The peak of $P(\phi_r)$ at 90° is larger than that at 270° for $v = 0$, 1, or 2, which suggests that **j**′ is preferentially oriented along the positive direction of the *y* axis.

The PDDCSs that describe the **k**–**k**′–**j**′ correlation and the scattering direction of the product molecule are presented in Fig. 3 for the reaction $C(^1D) + H_2$ ($v = 0$, 1, or 2, $j = 0$) → CH + H at a collision energy of 16 kJ/mol. Figure 3*a* displays the PDDCSs ($(2\pi/\sigma)(d\sigma_{00}/d\omega_t)$) that describe the **k**–**k**′ correlation and the scattering direction of the product CH. The analysis of the results of $(2\pi/\sigma)(d\sigma_{00}/d\omega_t)$ indicates that the products are forward–backward symmetric scattering and are more affected by the vibrational excitation. Balucani et al.[3] studied the title reaction using a combined crossed molecular beam experimental and theoretical method. Their experimental results show the DCS at E_c (16 kJ/mol) has a pronounced preference for backward–forward symmetric scattering. It can be clearly seen that our calculated results are in good agreement with those calculated by Balucani et al.[3] The distribution of $(2\pi/\sigma)(d\sigma_{20}/d\omega_t)$ contains the alignment of **j**′ with respect to **k** as a function of the scattering angle. The behavior of $(2\pi/\sigma)(d\sigma_{20}/d\omega_t)$ (see Fig. 3*b*) shows a similar trend with $(2\pi/\sigma)(d\sigma_{00}/d\omega_t)$ and obviously is affected by the vibrational excitation. It is clearly a backward–forward scattering product owing to the negative values of $(2\pi/\sigma)(d\sigma_{20}/d\omega_t)$ and suggests that the alignment of **j**′ is preferentially polarized along the direction perpendicular to **k**. Whether the value of $(2\pi/\sigma)(d\sigma_{22+}/d\omega_t)$ is positive or negative indicates the preference of **j**′ alignment along the *x* or *y* axis, respectively. In Fig. 3*c*, we can see that the value of $(2\pi/\sigma)(d\sigma_{22+}/d\omega_t)$ is negative for all scattering angles, indicating a noticeable preference for an alignment of **j**′ along the *y* axis. It is worth mentioning that the CH product displays a stronger polarization when the CH products are scattering at about 30° for $v = 1$. However, for $v = 0$ or 2, the strongest polarization is close to 30° and 90°. The distribution of $(2\pi/\sigma)(d\sigma_{21-}/d\omega_t)$, which is related to $< \sin\theta^2 \cos 2\phi >$, is depicted in Fig. 3*d*. As seen in Fig. 3*d*, the value of $(2\pi/\sigma)(d\sigma_{21-}/d\omega_t)$ is close to zero on the surface, so $(2\pi/\sigma)(d\sigma_{21-}/d\omega_t)$ is obviously isotopic and is weakly influenced by vibrational exciation.

The effect of rotational excitation on sterodynamics

Figures 4 and 5 depict the $P(\theta_r)$, $P(\phi_r)$, and the four PDDCSs of the CH product from the reaction $C(^1D) + H_2$ ($v = 0$, $j = 0$, 1, or 2) → CH + H at a collision energy of 16 kJ/mol. Evidently, the rotational excitation of H_2 has slightly less influence on the distribution of $P(\theta_r)$ than the vibrational excitation of H_2 (see Figs. 2*a* and 4*a*). The peak of $P(\theta_r)$ at the θ_r angle is close to 90° and symmetric with respect to 90° for $j = 0$, 1, or 2, which displays a preference for the product rotational angular momentum vector perpendicular to the relative velocity direction. As can be seen, the rotational excitation also has a weak influence on the distribution of $P(\phi_r)$, which is consistent with the vibrational excitation. However, analysis of the results in Fig. 4*b* shows that the peaks of $P(\phi_r)$ at 90° are slightly larger than those at 270°, i.e., the **j**′ is preferentially oriented along the positive direction of the *y* axis.

From the results of Figs. 5*a* and 5*b*, we can conclude that the rotational excitation has a weak influence on $(2\pi/\sigma)(d\sigma_{00}/d\omega_t)$ and $(2\pi/\sigma)(d\sigma_{20}/d\omega_t)$. As we know, the PDDCS of $(2\pi/\sigma)(d\sigma_{20}/d\omega_t)$ is related to the product rotational alignment of $< P_2 (\mathbf{j}'\cdot\mathbf{k}) >$, and the expectation values of $< P_2 (\mathbf{j}'\cdot\mathbf{k}) >$ for H_2 ($v = 0$, $j = 0$, 1, or 2) are –0.345, –0.346, and –0.345, respectively, which is in good accordance with the PDDCS $(2\pi/\sigma)(d\sigma_{20}/d\omega_t)$. Whereas the PDDCS $(2\pi/\sigma)(d\sigma_{22+}/d\omega_t)$ exhibits a dependence on the rotational excitation and the scattering angle, it is clearly backward scattering owing to its negative value. Since the value of the PDDCS $(2\pi/\sigma)(d\sigma_{21-}/d\omega_t)$ is close to zero on the surface, it is obviously isotopic and is also weakly influenced by rotational excitation.

Can. J. Chem. Downloaded from www.nrcresearchpress.com by Xi'an Jiaotong University on 09/19/12
For personal use only.

Fig. 5. Four polarization-dependent differential cross sections (PDDCSs) for the CH product from the reaction $C(^1D) + H_2$ ($v = 0, j$) → CH + H at a collision energy of 16 kJ/mol. Panel (*a*) shows the PDDCSs with (k,q) = (0,0). Panels (*b*)–(*d*) depict the PDDCSs with (k,$q\pm$) = (2,0), (2,2+), and (2,1–), respectively.

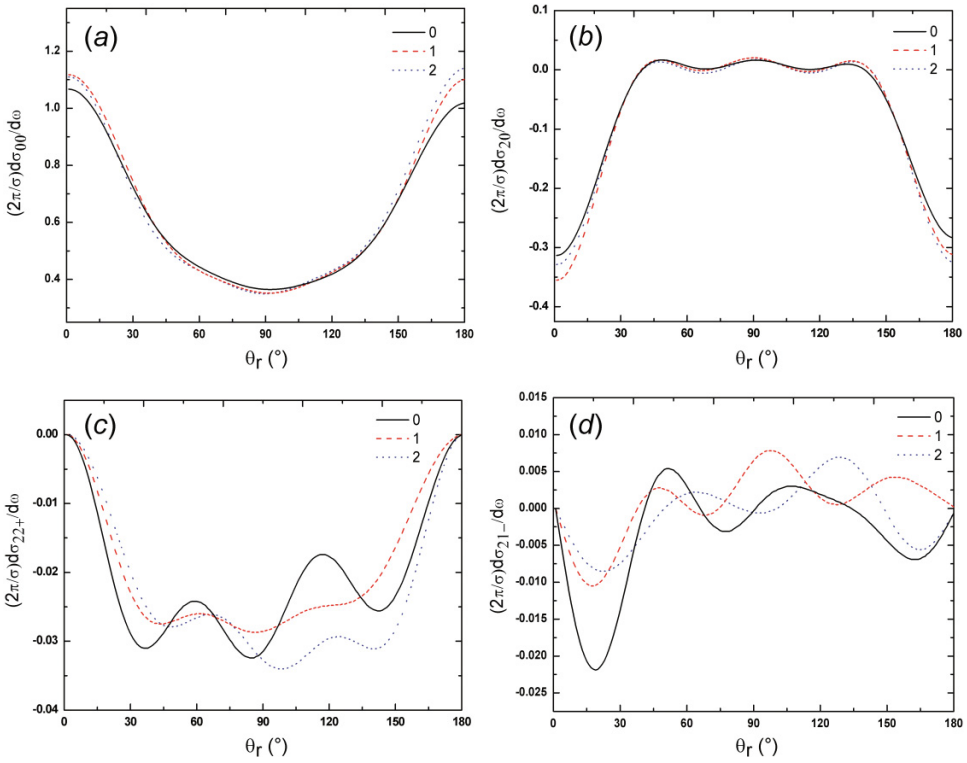

Conclusion

The major objective of this paper was to study the vector correlation for the chemical reaction $C(^1D) + H_2$ using the QCT method. To this end, the influence of the vibrational and rotational excitation of the reactant molecule (H_2) on the vector correlation was calculated. The calculated results show that the rotational angular momentum vector **j′** of CH is preferentially aligned perpendicular to k and also oriented with respect to the **k**–**k′** plane. The PDDCS of $(2\pi/\sigma)(d\sigma_{00}/d\omega_t)$ predicts that the angle distributions of the CH product are mainly dominated by backward–forward scattering, which is in agreement with the experimental results. Calculations also show that the product polarization is very sensitive to the vibrational excitation. An increase of vibrational excitation can make the peak of $P(\theta_r)$ narrower and higher, whereas the increase of rotational excitation has less effect on the peak of $P(\theta_r)$. We are looking forward to the completion of experimental studies about the stereodynamics for the title reaction system so that a reliable comparision between theory and experiment can be implemented.

Acknowledgements

The authors thank Professor K. Han for providing the code used in this calculation. This work is financially supported by the Ph.D. Programs Foundation of Shihezi University (No. RCZX200934), the Special Foundation for National Basic Research Program of China (973 Program) (No. 2010CB234605), and the Ph.D. Programs Foundation of the Xinjiang Production and Construction Corps (No. 2009JC10).

References

(1) Bergeat, A.; Cartechini, L.; Balucani, N.; Capozza, G.; Philips, L. F.; Casavecchia, P.; Volpi, G. G.; Bonnet, L.; Rayez, J. C. *Chem. Phys. Lett.* **2000** *327* (3–4), 197. doi:10.1016/S0009-2614(00)00870-8.

(2) Balucani, N.; Capozza, G.; Segoloni, E.; Russo, A.; Bobbenkamp, R.; Casavecchia, P.; Gonzalez-Lezana, T.; Rackham, E. J.; Bañares, L.; Aoiz, F. J. *J. Chem. Phys.* **2005** *122* (23), 234309. doi:10.1063/1.1930831.

(3) Balucani, N.; Capozza, G.; Cartechini, L.; Bergeat, A.; Bobbenkamp, R.; Casavecchia, P.; Aoiz, F. J.; Bañares, L.; Honvault, P.; Bussery-Honvault, B.; Launay, J.-M. *Phys. Chem. Chem. Phys.* **2004** *6*, 4957. doi:10.1039/b409327e.

(4) Bussery-Honvault, B.; Honvault, P.; Launay, J. M. *J. Chem. Phys.* **2001** *115* (23), 10701. doi:10.1063/1.1417501.

(5) Bañares, L.; Aoiz, F. J.; Honvault, P.; Bussery-Honvault, B.; Launay, J. M. *J. Chem. Phys.* **2003** *118* (2), 565. doi:10.1063/1.1527014.

(6) Bañares, L.; Aoiz, F. J.; Vázquez, S. A.; To, T. S.; Rabitz, H. *Chem. Phys. Lett.* **2003** *374* (3–4), 243. doi:10.1016/S0009-2614(03)00715-2.

(7) Gogtas, F.; Bulut, N.; Akpinar, S. *Int. J. Quantum Chem.* **2005** *105* (5), 478. doi:10.1002/qua.20722.

(8) Lin, S. Y.; Guo, H. *J. Phys. Chem. A* **2004** *108* (12), 2141. doi:10.1021/jp031184h.

(9) Lin, S. Y.; Guo, H. *J. Chem. Phys.* **2003** *119* (22), 11602. doi:10.1063/1.1624060.

(10) Chu, T. S.; Han, K. L.; Varandas, A. J. C. *J. Phys. Chem. A* **2006** *110* (4), 1666. doi:10.1021/jp054572n.

(11) Yue, X. F.; Cheng, J.; Li, H.; Zhang, Y. Q.; Wu, E. L. *Chin. Phys. B* **2010** *19*, 043401. doi:10.1088/1674-1056/19/4/043401.

Can. J. Chem. Downloaded from www.nrcresearchpress.com by Xi'an Jiaotong University on 09/19/12
For personal use only.

(12) Rackham, E. J.; Huarte-Larranaga, F.; Manolopoulos, D. E. *Chem. Phys. Lett.* **2001** *343* (3–4), 356. doi:10.1016/S0009-2614(01)00707-2.
(13) Chu, T. S.; Zhang, X.; Han, K. L. *J. Chem. Phys.* **2005** *122* (21), 214301. doi:10.1063/1.1924507.
(14) Chu, T. S.; Zhang, X.; Han, K. L. *Int. Rev. Phys. Chem.* **2006** *25* (1–2), 201. doi:10.1080/01442350600677929.
(15) Gray, S. K.; Balint-Kurti, G. G.; Schatz, G. C.; Lin, J. J.; Liu, X.; Harich, S.; Yang, X. *J. Chem. Phys.* **2000** *113* (17), 7330. doi:10.1063/1.1313785.
(16) Aoiz, F. J.; Bañares, L.; Castillo, J. F.; Herrero, V. J.; Martinez-Haya, B.; Honvault, P.; Launay, J. M.; Liu, X.; Lin, J. J.; Harich, S. A.; Wang, C. C.; Yang, X. *J. Chem. Phys.* **2002** *116* (24), 10692. doi:10.1063/1.1478693.
(17) Gogtas, F.; Bulut, N.; Akpinar, S. *Int. J. Quantum Chem.* **2005** *105* (5), 478. doi:10.1002/qua.20722.
(18) Lin, S. Y.; Guo, H. *J. Chem. Phys.* **2004** *121* (3), 1285. doi:10.1063/1.1764502.
(19) Chen, M. D.; Han, K. L.; Lou, N. Q. *Chem. Phys.* **2002** *283* (3), 463. doi:10.1016/S0301-0104(02)00768-1.
(20) Aoiz, F. J.; Brouard, M.; Enriquez, P. A. *J. Chem. Phys.* **1996** *105* (12), 4964. doi:10.1063/1.472346.
(21) Case, D. E.; Mcclelland, G. M.; Herschbach, D. R. *Mol. Phys.* **1978** *35* (2), 541. doi:10.1080/00268977800100391.
(22) Fano, U.; Macek, H. H. *Rev. Mod. Phys.* **1973** *45* (4), 553. doi:10.1103/RevModPhys.45.553.
(23) Case, D. E.; Herschbach, D. R. *Mol. Phys.* **1975** *30* (5), 1537. doi:10.1080/00268977500103061.
(24) Blais, N. C.; Truhlar, D. G. *J. Chem. Phys.* **1977** *67* (4), 1540. doi:10.1063/1.434983.
(25) Han, K. L.; Zhang, L.; Xu, D. L.; He, G. Z.; Lou, N. Q. *J. Phys. Chem. A* **2001** *105* (13), 2956. doi:10.1021/jp002181x.
(26) Chen, M. D.; Wang, M. L.; Han, K. L.; Ding, S. L. *Chem. Phys. Lett.* **1999** *301* (3–4), 303. doi:10.1016/S0009-2614(99)00052-4.
(27) Wang, M. L.; Han, K. L.; He, G. Z. *J. Phys. Chem. A* **1998** *102* (50), 10204. doi:10.1021/jp981738u.
(28) Brouard, M.; Lambert, H. M.; Rayner, S. P.; Simons, J. P. *Mol. Phys.* **1996** *89*, 403.
(29) Brouard, M.; Gatenby, S. D.; Joseph, D. M.; Vallance, C. *J. Chem. Phys.* **2000** *113* (8), 3162. doi:10.1063/1.1286971.
(30) Shafer-Ray, N. E.; Orr-Ewing, A. J.; Zare, R. N. *J. Phys. Chem.* **1995** *99* (19), 7591. doi:10.1021/j100019a045.
(31) de Miranda, M. P.; Clary, D. C. *J. Chem. Phys.* **1997** *106* (11), 4509. doi:10.1063/1.473483.
(32) de Miranda, M. P.; Aoiz, F. J.; Bañares, L.; Sáez Rábanos, V. *J. Chem. Phys.* **1999** *111* (12), 5368. doi:10.1063/1.479797.
(33) Wang, M. L.; Han, K. L.; He, G. Z. *J. Chem. Phys.* **1998** *109* (13), 5446. doi:10.1063/1.476522.
(34) Orr-Ewing, A. J.; Zare, R. N. *Rev. Phys. Chem.* **1994** *45* (1), 315. doi:10.1146/annurev.pc.45.100194.001531.
(35) Murrell, J. N.; Caner, S.; Farantos, S. C.; Huxley, P.; Varandas, A. J. C. *Molecular Potential Energy Functions;* Wiley: Chicester, UK, 1984.
(36) Truhlar, D. G.; Muckerman, J. T. In *Atom–Molecule Collision Theory;* Bernstein, R. B. Ed.; Plenum Press: New York, 1979.
(37) Raff, L. M.; Thompson, D. L. In *Theory of Chemical Reaction Dynamics;* Baer, M. Ed.; CRC Press: Boca Raton, FL, 1985.
(38) Cai, M. Q.; Zhang, L.; Tang, B. Y.; Chen, M. D.; Yang, G. W.; Han, K. L. *Chem. Phys.* **2000** *255* (2–3), 283. doi:10.1016/S0301-0104(00)00084-7.
(39) Ju, L. P.; Han, K. L.; Zhang, J. Z. H. *J. Comput. Chem.* **2009** *30* (2), 305. doi:10.1002/jcc.21032.

Hydrogen peroxide decomposition in bicarbonate solution catalyzed by ferric citrate*

Francis K. Attiogbe and Raymond C. Francis

Can. J. Chem. Downloaded from www.nrcresearchpress.com by Xi'an Jiaotong University on 09/19/12
For personal use only.

Abstract: The peroxymonocarbonate mono- and di-anions (HCO_4^- and CO_4^{2-}) are known to be generated from H_2O_2/HCO_3^-. They are promising oxidants for wood pulp bleaching, but peroxide decomposition catalyzed by ferric complexes can be significant for pulps whose lignin is highly reactive. Dicarboxylates from lignin peroxidation are believed to be the ferric chelators in the pH 8.5 range that is optimum for H_2O_2/HCO_3^-. This investigation aimed to see if HCO_3^- addition caused destabilization of the peroxygen system owing to its partial conversion to HCO_4^-. This anionic peracid is a much stronger oxidant than H_2O_2 and could lead to a higher rate of Fe(II) oxidation to Fe(III) and (or) Fe(IV). For most free radical chain mechanisms, an increase in Fe(II) oxidation results in a higher rate of peroxide decomposition. Based on the kinetic data that were obtained and theoretical analyses, it was concluded that HCO_4^- did not significantly destabilize the peroxygen system when citrate was used as a model chelator for Fe(III). Increasing the [HCO_3^-] fourfold from 0.025 to 0.10 mol/L caused the decomposition rate to increase by only 20%.

Key words: peroxymonocarbonate anions, hydrogen peroxide, ferric complexes, peroxide decomposition, pulp bleaching.

Résumé : Il est bien connu que les mono- et di-anions du peroxymonocarbonate (HCO_4^- et CO_4^{2-}) peut être générés par la réaction du H_2O_2 et du HCO_3^-. Ce sont des oxydants prometteurs pour le blanchiment de la pulpe de bois, mais la décomposition du peroxyde, catalysée par des complexes, peut être importante avec les échantillons de pulpes dont la lignine est très réactive. On croit que les dicarboxylates obtenus par peroxydation de la lignine peuvent donner une réaction de chélation avec les espèces ferriques à un pH de 8,5 optimum pour la réaction du H_2O_2 et du HCO_3^-. Cette étude a été entreprise dans le but de déterminer si l'addition de HCO_3^- provoque une déstabilisation du système de peroxygène en raison de sa conversion partielle en HCO_4^-. Ce peracide anionique est un oxydant beaucoup plus puissant que le H_2O_2 et pourrait conduire à une vitesse plus élevée d'oxydation du Fe(II) en Fe(III) et (ou) Fe(IV). Pour la plupart des mécanismes en chaîne radicalaire, une augmentation dans l'oxydation du Fe(II) conduit à une augmentation de la vitesse de décomposition du peroxyde. Sur la base des données cinétiques obtenues et d'analyses théoriques, on en conclut que le HCO_4^- ne déstabilise pas le système du peroxygène lorsqu'on utilise du citrate comme modèle pour la chélation du Fe(III). Une augmentation de la concentration du HCO_3^- par un facteur de quatre, de 0,025 à 0,10 mol/L, ne provoque qu'une augmentation de 20 % de la vitesse de décomposition.

Mots-clés : anions peroxymonocarbonates, peroxyde d'hydrogène, complexes ferriques, décomposition du peroxyde, blanchiment de la pulpe.

[Traduit par la Rédaction]

Introduction

It has been known for a long time that hydrogen peroxide reacts with the bicarbonate anion to generate the peroxymonocarbonate monoanion (HCO_4^-).[1] The equilibrium reaction and equilibrium constant associated with HCO_4^- formation are presented in eqs. [1] and [2].[1]

$$[1] \quad HCO_3^- + H_2O_2 \rightleftharpoons {}^-OC(=O)OOH + H_2O$$

$$[2] \quad K = 0.32\ (\text{mol/L})^{-1} = \frac{[HCO_4^-]}{[H_2O_2][HCO_3^-]}$$

The peroxymonocarbonate (PMC) monoanions dissociates to the dianion (CO_4^{2-}) with a pK_a ca. 10.0.[1–3] Results were recently reported where the two anions showed great promise as bleaching agents for wood pulps.[2] The results appear to indicate that the monoanion is electrophilic and the dianion is nucleophilic, and both classes of reactions occur in the pH range ca. 8.5.[2] The case of peroxide/bicarbonate (P_B) bleaching in conjunction with a non-sulfur alkaline pulping process such as soda/anthraquinone is particularly attractive. In such a situation, the pulping effluent would be concentrated by evaporation and incinerated to give a Na_2CO_3 or K_2CO_3 stream of high purity. It already has been shown that 1 mol of carbonate in solution reacts quite quickly with 1 mol of

Received 7 April 2011. Accepted 14 April 2011. Published at www.nrcresearchpress.com/cjc on 13 September 2011.

F.K. Attiogbe and R.C. Francis. Department of Paper and Bioprocess Engineering, State University of New York, College of Environmental Science and Forestry (SUNY–ESF), 1 Forestry Drive, Syracuse, NY 13210, USA.

Corresponding author: Raymond C. Francis (e-mail: francis@syr.edu and francis@esf.edu).

*This article has a companion paper in this issue (doi: 10.1139/v11-080).

Can. J. Chem. Downloaded from www.nrcresearchpress.com by Xi'an Jiaotong University on 09/19/12
For personal use only.

CO_2 at low pressure to generate 2 mol of bicarbonate.[2] Therefore, P_B bleaching would be possible without the purchase of carbonate or bicarbonate if the P_B effluent were to be recycled to the pulping chemical recovery system and Na_2CO_3 or K_2CO_3 recycled back to the P_B stage. Carbon dioxide would be obtained from the flue gas associated with combustion of the concentrated pulping and bleaching effluents.

One problem that has to be solved is the development of stabilization strategies to minimize wasteful decomposition of peroxide catalyzed by Fe and Mn species during a P_B stage. Earlier data clearly showed that these two transition metals catalyze peroxide decomposition in the bleaching slurry and that the process could be retarded by the addition of a hydroxyl radical scavenger.[2] When $Fe_2(SO_4)_3$ or $MnSO_4$ was added to bleaching effluent containing H_2O_2, the inclusion of *N*,*N*′-(5-nitro-1,3-phenylene)bisglutaramide (GAMID) as an ·OH scavenger[4,5] decreased the rate of peroxide decomposition by a factor of at least 10 for both Fe(III) and Mn(II). Because of some of its reactions with both lignin and carbohydrates, ·OH can cause considerable damage to both the optical and physical properties of pulps.[6,7]

A sizeable fraction of the Fe in wood pulps is believed to exist as ferric complexes with the lignin.[8] Some of the Fe(III) is likely to be released when some phenylpropane units in lignin are degraded to carboxylic and dicarboxylic acids by peroxidation. The dicarboxylic acids are likely to form ferric complexes capable of catalyzing peroxide decomposition. A likely redox chain mechanism to explain Fe(III) catalysis is presented in eqs. [3]–[8].[9,10] The initiation step is eq. [3], the propagation steps are eqs. [4]–[6] and eqs. [7] and [8] comprise the termination step.

$$[3]\quad \mathrm{Fe(III)L} + \mathrm{H_2O_2} \xrightarrow{k_1} \mathrm{Fe(II)L} + \cdot\mathrm{O_2^-} + 2\mathrm{H^+}$$

$$[4]\quad \mathrm{Fe(II)L} + \mathrm{H_2O_2} \xrightarrow{k_2} \mathrm{Fe(III)L} + \cdot\mathrm{OH} + \mathrm{OH^-}$$

$$[5]\quad \cdot\mathrm{OH} + \mathrm{H_2O_2} \xrightarrow{k_3} \mathrm{H_2O} + \cdot\mathrm{O_2}^- + \mathrm{H^+}$$

$$[6]\quad \cdot\mathrm{O_2}^- + \mathrm{Fe(III)L} \xrightarrow{k_4} \mathrm{Fe(II)L} + \mathrm{O_2}$$

$$[7]\quad \cdot\mathrm{O_2}^- + \mathrm{Fe(II)L} + \mathrm{H^+} \xrightarrow{k_5} \mathrm{Fe(III)L} + \mathrm{HOO^-}$$

$$[8]\quad \cdot\mathrm{OH} + \mathrm{Fe(II)L} \xrightarrow{k_5} \mathrm{OH^-} + \mathrm{Fe(III)L}$$

The difficulties associated with differentiating between ·OH and a ferryl species (eq. [9]) as the highly reactive intermediate in reaction systems containing Fe(II), Fe(III), $\cdot O_2^-$, and H_2O_2 is widely reported in the literature.[10,11] For the pulp bleaching applications that are of interest, a distinction between ·OH and a ferryl species may not be necessary. Ferryl species are reported to be capable of abstracting electrons from ethanol, *tert*-butanol and from aromatic rings.[12] Therefore, the negative attributes of ·OH towards carbohydrates and lignin are likely to also be associated with ferryl species.

$$[9]\quad \mathrm{Fe(II)L} + \mathrm{H_2O_2} \xrightarrow{k_7} \mathrm{Fe(IV)L{=}O} + \mathrm{H_2O}$$

This report is on an investigation of peroxide decomposition catalyzed by $Fe_2(SO_4)_3$ in $NaHCO_3$ solutions at pH ca. 8.5 and 40 °C and with citrate as a model chelator. Catalysis of H_2O_2 decomposition by ferrous and ferric citrate is reported to increase the rate of ·OH generation.[13,14] A key issue was whether or not HCO_4^-, a much stronger oxidant than H_2O_2,[1] significantly increased the rate of oxidation of Fe(II) to Fe(III) and (or) Fe(IV). That would be expected to accelerate peroxide decomposition because of the higher rate of formation of the highly reactive ·OH and (or) ferryl species. In a companion submission, results are presented for catalysis by Mn species in the pH range of 7.4–8.7.[15]

Experimental

The water used was purified by distillation and reverse osmosis and consistently contained <2 ppb Fe and Mn, but 10–15 ppb of Cu. Approximately 40 L of this water was collected on one occasion and used to dissolve the ferric catalysts and $NaHCO_3$ and as diluent in all of the runs where ferric catalysis was investigated. This water typically constituted >95% of the starting liquid for each run. The sodium bicarbonate used in this research was GR ACS grade from EMD Chemicals and contained 0.13 ppm Fe and 2.9 ppm Mn (determined by inductively coupled plasma - mass spectrometry, ICP-MS). The ferric citrate was prepared by dissolving $Fe_2(SO_4)_3{\cdot}H_2O$ in citric acid. The $[Fe^{3+}]$ was 0.018 mol/L (1000 ppm), and citric acid was added at a 5:1 mol ratio to Fe^{3+}. The final solution contained no particles and was nonturbid when its pH was raised from 1.9 to 7.0 with $NaHCO_3$. This solution (1000 ppm Fe) was stored at room temperature and at pH 1.9, and aliquots were taken from it and diluted to 5 or 10 ppm Fe(III). These dilute Fe(III) solutions were used for 3–5 days of research before fresh batches were made. GAMID was the same sample used before[5] and it was synthesized by the method of Singh and Hider.[4] Benzoic acid was USP grade from Fisher Scientific. Its purity was not stated on the bottle, but toluene oxidation as the means of synthesis was stated. The salicylic acid (>99.0% purity) was from ACROS Organics.

High-density polyethylene bottles (250 mL) with screw caps were used as reactors. Two holes were made in each cap, one for a pH electrode and the other for the pipettes used for liquid addition and removal. The reactor was placed in a water bath made of aluminum, maintained at 40 ± 0.5 °C, and stationed on top of two magnetic stirrers. One of the magnetic stirrers was for the reactor and the other was for the water in the bath. A reaction solution containing ferric citrate and $NaHCO_3$ was preheated to 40 °C then a concentrated H_2O_2 solution (<3% of total volume) was added to give a H_2O_2 concentration of 52–55 mmol/L. The reaction solution was given ca. 3 min to be reheated to 40 °C and then aliquots were taken for residual H_2O_2 analysis by iodometric titration at 5 or 10 min intervals.

When radical scavengers were involved, crystals or powder of the scavenger was added at the initial preheat stage, and residual H_2O_2 was determined after 0, 30, 60, and 90 min. The structures of the three scavengers are shown in Fig. 1. When benzoic acid (BA) or salicylic acid (SA) was the scavenger, the residual H_2O_2 in the solution was reduced with

Fig. 1. The three radical scavengers utilized (benzoic acid (BA), salicylic acid (SA), and *N*,*N*′-(5-nitro-1,3-phenylene)bisglutaramide (GAMID); left to right).

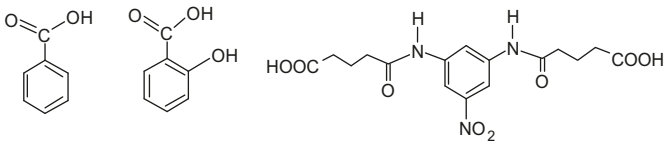

$NaHSO_3$ after 90 min. The solution was acidified to pH ca. 2, divided into two equal aliquots, and extracted with ether. Each ether extract was dried over anhydrous $MgSO_4$, decanted, and then evaporated to dryness at reduced pressure. The dry residue along with the internal standard (benzhydrol), were dissolved in 1.0 mL of dichloromethane (DCM). A fraction of the DCM solution (100 μL) was added to another vial along with 100 μL of *N*,*O*-bis(trimethylflouromethyl-silylacetamide) (BSTFA) and a drop of pyridine. The mixture was allowed to sit at room temperature overnight or for ca. 30 min at 40 °C before it was analyzed for residual amounts of the scavenger and hydrolylated products by gas chromatography with flame ionization detection (GC) or gas chromatography – mass spectrometry (GC–MS).

A HP 5890A GC equipped with a flame ionization detector (FID) and a DB-1 (dimethylpolysiloxane) capillary column (30 m × 0.25 mm; film thickness 0.25 μm) was used. Nitrogen was the carrier gas (1 mL/min), and the split ratio was 50:1. The injector temperature was 250 °C and the detector temperature was 270 °C. The following temperature profile was used: initial temperature 120 °C, holding time at initial temperature 5 min, a ramp from 120 to 270 °C at 5 °C/min, and a hold at maximum temperature for 5 min.

GC–MS analyses were performed using a Thermo Scientific Finnigan Trace GC Ultra GC coupled to a Thermo MAT95XP double focus magnetic sector mass spectrometer. The column used was a 30 m × 0.25 mm i.d., Rtx-5MS (5% diphenyl / 95% dimethylpolysiloxane) capillary column (film thickness 0.25 μm). Nitrogen at a flow rate of 1 mL/min was used as the carrier gas. About 1 μL of the sample was injected and analyzed using a split ratio of 50:1. The following temperature profile was used: initial temperature 110 °C, with a hold time of 4 min; a ramp to 260 °C at 5 °C/min followed by a 5 min hold at 260 °C; another ramp from 260 to 300 °C at 5 °C/min; and a final hold for 20 min at 300 °C. The injector and detector temperatures were 250 and 300 °C, respectively. Ionization was carried out at a 70 eV impact voltage in an ion chamber heated to 220 °C. The samples were scanned from *m*/*z* 50 to 400 at a rate of 0.6 scan/s. Peak identification was carried out on the basis of mass fragmentation patterns, comparisons of spectra with those of the authentic compounds obtained from various suppliers, and by comparing the MS data with those in the Pfleger–Mauer–Weber, Wiley, and NIST libraries.

Results and discussion

The first set of experiments was probably the most important, and these trials had to do with the selection of the source of $NaHCO_3$. A supplier was first chosen whose container stated that the crystal contained 2 ppm Fe. However, peroxide decomposition without any added transition metal salt or complex was quite variable and quite high on some occasions (50 to 40 mmol/L in 100 min). The EMD bicarbonate that listed its Fe content as 5 ppm did not cause decomposition, >8% in 100 min (50 to 46 mmol/L) in the absence of a transition metal catalyst. When the two bicarbonates were analyzed by ICP-MS it was found that the EMD sample contained only 0.13 ppm Fe and the other brand contained 0.61 ppm. All of the $NaHCO_3$ used in the investigation of metal-catalyzed peroxide decomposition was GR ACS grade from EMD. The initial concentration of H_2O_2 was ca. 50 mmol/L for all experiments in this investigation. Typically, the initial H_2O_2 concentration would be in the range of 20–40 mmol/L for a P_B stage applied to chemical pulps (0.5%–1.0% H_2O_2 on pulp at 12% consistency) and 50–130 mmol/L for mechanical pulps (1.0% H_2O_2 at 15%–30% consistency).[2] The typical concentrations for $NaHCO_3$ would be 30–50 mmol/L for chemical pulps (2%–3% $NaHCO_3$ on pulp at 12% consistency) and 60–150 mmol/L for mechanical pulps (3% $NaHCO_3$ at 15%–30% consistency).[2] A treatment pH in the range of 8.5 appears to be optimum for most pulp bleaching applications.[2]

The next set of experiments is summarized in Fig. 2 and it shows the decomposition of H_2O_2 (0.1 mol/L $NaHCO_3$, pH 8.5–8.7, 40 °C) in the absence of Fe, 0.1ppm Fe with and without citrate, and ferric citrate at 0.075ppm Fe with and without 10 mmol/L BA. The pH was monitored at 40 °C throughout each run and the readings were typically 0.1 of a unit higher than the standard pH just stated, i.e., pH 8.6–8.8 at 40 °C. In all cases where Fe (III) catalyzed peroxide decomposition to a significant degree (>25%), the disappearance of the peroxide was first-order in H_2O_2 concentration and the R^2 value on k_{OBS} (eq. [10]) was ≥0.99. The values of k_{OBS} for the five runs in Fig. 2 are presented in Table 1. It can be seen that citrate complexation significantly increased the rate of Fe(III)-catalyzed decomposition and that the mechanism responsible for ferric citrate-catalyzed decomposition was significantly retarded by BA, an ·OH scavenger. The rate constants for peroxide decomposition (k_{OBS}) with and without BA were 1.7×10^{-4} s^{-1} and 4.9×10^{-4} s^{-1}. Therefore, BA addition caused a 65% decrease in the peroxide decomposition rate.

$$[10] \qquad \frac{d[H_2O_2]}{dt} = -k_{OBS}[H_2O_2]$$

The decrease in decomposition rate (65%) caused by BA was an ambiguous result. On one hand, it is difficult to envision a mechanism of retardation other than the scavenging of ·OH, but on the other hand, BA at 10 mmol/L should have afforded a higher degree of retardation. The rate constant for benzoate anion reacting with ·OH is 5.9×10^9 $(mol/L)^{-1}$ s^{-1}, a value >200 times greater than for H_2O_2 reacting with ·OH (2.7×10^7 $(mol/L)^{-1}$ s^{-1}).[16] Therefore, 10 mmol/L of benzoate should have almost completely prevented a propagation reaction such as in eq. [5] when the initial $[H_2O_2]$ was 50 mmol/L. Analyses of residual BA and hydroxylated products were then performed. The BA concentration decreased from 10.0 to ca. 9.7 mmol/L after 90 min of reaction and the total yield of *o*-, *m*-, and *p*-hydroxybenzoic acid (HBA) was ca. 0.1 mmol/L. The ratio of *o*-HBA:*m*-HBA:*p*-HBA was approximately 3:1:1. The MS data for the three HBAs are as follows: for *o*-HBA, the major fragments were *m*/*z*:

Can. J. Chem. Downloaded from www.nrcresearchpress.com by Xi'an Jiaotong University on 09/19/12
For personal use only.

Can. J. Chem. Downloaded from www.nrcresearchpress.com by Xi'an Jiaotong University on 09/19/12
For personal use only.

Fig. 2. Effect of ferric sulfate and ferric citrate catalysis on peroxide decomposition.

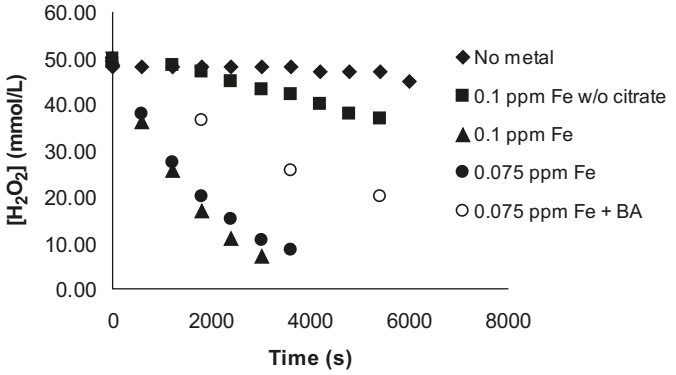

267 (100), 209 (10), 193 (10), 149 (10), 135 (15), 73 (45); for *m*-HBA, the major fragments were *m/z*: 282 (M^+, 45), 267 (100), 223 (40), 207 (30), 193 (45), 153 (25), 147 (15), 135 (20), 73 (45); and for *p*-HBA, the major fragments were *m/z*: 282 (M^+, 15), 267 (100), 223 (50), 193 (45), 147 (30), 73 (50). It is possible that *m*-HBA and *p*-HBA could act as weak catalysts for peroxide decomposition. Whereas the pK_a of the phenolic group in SA (*o*-HBA) is >13.0,[17,18] the value is ca. 9.3 for *p*-HBA[17,18] and ca. 9.9 for *m*-HBA.[17] The phenolate from *p*-HBA or *m*-HBA could slowly convert to a phenoxy radical (Fig. 3) that could participate in radical coupling and subsequent de-aromatization reactions or abstract an electron from a H_2O_2 molecule to give $\cdot O_2^-$ (Fig. 3). This would aid the propagation step in a redox chain mechanism such as that described in eqs. [3]–[8]. It should be noted that the reduction potential for the phenoxy radical in Fig. 3 has been estimated at 1.04 V at pH 7 and 0.90 V at pH > 11.[19] This species would probably be more reactive in abstracting an electron from H_2O_2 than ferric citrate in eq. [1].

When BA was replaced by 10 mmol/L GAMID the peroxide decomposition rate decreased from 4.9×10^{-4} s^{-1} (without scavenger) to $<0.1 \times 10^{-4}$ s^{-1}. Analysis of residual GAMID by UV spectrometry[4,5] showed that its recovery was close to100% with the generation of hydroxylated products being negligible (<0.1 mmol/L). It should be noted that there are convincing data showing that neither GAMID or its hydroxylated products bind either Fe(II) or Fe(III) at pH 8.[4]

A third radical scavenger, SA or *o*-HBA, was investigated. A SA concentration of 5 mmol/L was used because the rate constant for salicylate reacting with ·OH is more than twice the value for benzoate, i.e., 1.6×10^{10} vs 5.9×10^9 $(mol/L)^{-1}$ s^{-1}.[16] The 5 mmol/L concentration of SA decreased the peroxide decomposition rate from 4.9×10^{-4} to 0.2×10^{-4} s^{-1}. The SA concentration decreased from 5.0 to ca. 4.7 mmol/L after 90 min, and no hydroxylated product(s) was detected. The 0.075 ppm ferric dose was equivalent to a concentration of only 1.34×10^{-6} mol/L, and the citrate concentration was five times as high or 6.72×10^{-6} mol/L. The possibility that SA at 5.0×10^{-3} mol/L was displacing citrate as the ligand from the Fe (III) and producing a noncatalytic complex had to be investigated. If SA was indeed displacing the citrate then that process should not be affected if the SA concentration were to be decreased to 1.0×10^{-3} mol/L or 1.0 mmol/L. The mole ratio of SA to citrate would still be very high at a value of 149. The retardation effect of SA was investigated at 1.0 mmol/L and ultimate care was taken in determining the residual SA. The peroxide decomposition rate was decreased from 4.9×10^{-4} to 1.5×10^{-4} s^{-1} (69%) by 1.0 mmol/L SA. The experiment was repeated on another day and a rate constant of 1.4×10^{-4} s^{-1} was obtained. Analysis of the organic products showed a residual SA of 0.8 mmol/L for both runs and no hydroxylated product(s) was detected. It is likely that a small amount of 2,3-dihydroxybenzoic acid was generated[14], but such an intermediate, with adjacent phenolic hydroxyl groups, would likely be degraded by P_B oxidation. Based on radical scavenging by GAMID and SA at 1.0 and 5.0 mmol/L, it appears that a free radical mechanism is primarily if not totally responsible for the peroxide decomposition.

Table 1. First-order rate constants for ferric-catalyzed peroxide decomposition with various additives (according to eq. [10].

[Fe(III)Cit] (ppm Fe(III))	$[HCO_3^-]$ (mol/L)	Other additives	k_{OBS} ($s^{-1} \times 10^4$)
0	0.1		0.1
0	0.1	10 mmol/L BA	<0.1
0.1[a]	0.1		6.3, 6.5
0.1[b]	0.1		0.5
0.025	0.1		1.6
0.05	0.1		3.5
0.075	0.1		4.8, 5.0
0.075	0.1	25 mmol/L Na_2SO_4	4.9
0.075	0.1	10 mmol/L BA	1.7
0.075	0.1	10 mmol/L GAMID	<0.1
0.075	0.1	5 mmol/L SA	0.2
0.075	0.1	1.0 mmol/L SA	1.5, 1.4
0.075	0.02		3.9
0.075	0.025		4.1
0.075	0.025	25 mmol/L Na_2SO_4	4.2
0.075	0.03		4.4
0.075	0.05		4.9

Note: 50 mmol/L H_2O_2, 40 °C, initial and final pH of 8.4 and 8.6 for $[HCO_3^-] \leq 0.03$ mol/L and 8.5 and 8.7 for $[HCO_3^-] = 0.05$–0.10 mol/L. BA, benzoic acid; SA, salicylic acid; and GAMID, *N,N′*-(5-nitro-1,3-phenylene) bisglutaramide.

[a]0.1ppm Fe = 1.8×10^{-6} mol/L.

[b]No citrate.

Finally, if the peroxide decomposition mechanism is predominantly free radical in nature then the decomposition rate should not be strongly influenced by ionic strength. When ferric citrate was used at 0.075 ppm Fe the peroxide decomposition rate was unaffected by the addition of 0.025 mol/L Na_2SO_4 (Table 1).

The next step was an investigation of the effect of HCO_4^- on peroxide decomposition. At first glance it would appear that a simple approach of investigating the role of HCO_4^- would be to vary the HCO_3^- concentration and see its effect on the rate of peroxide loss. However, in a complex free radical system it would be helpful to have some idea regarding the expected reaction order for HCO_3^- in advance of initiation of a rigorous experimental protocol. Also, if a complex rate equation is obtained then appropriate concentration ranges can be chosen that would allow for simplifying assumptions to be made regarding the rate equation. Those concentration ranges would then be tested during the experimental phase. It was concluded that theoretical analysis

Fig. 3. A possible scheme to explain catalysis of H_2O_2 decomposition by *m*-hydroxybenzoic acid (HBA) and *p*-HBA.

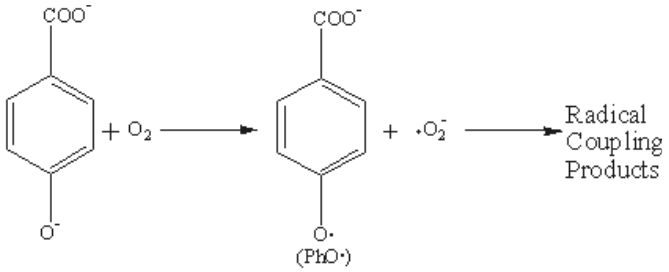

$$PhO\cdot + H_2O_2 \longrightarrow PHO^- + \cdot O_2^- + 2H^+$$

should precede the experimental research. All of the likely reactions were written in one free radical chain mechanism. The selected reactions are those shown in eqs. [3]–[7] and those in eqs. [11]–[14].

$$[11] \quad HCO_3^- + H_2O_2 \overset{K_1}{\leftrightarrow} HCO_4^- + H_2O$$

$$[12] \quad Fe(II)L + HCO_4^- \overset{k_8}{\rightarrow} Fe(III)L + \cdot OH + CO_3^{2-}$$

$$[13] \quad \cdot OH + HCO_3^- \overset{k_9}{\rightarrow} \cdot CO_3^- + H_2O$$

$$[14] \quad \cdot CO_3^- + H_2O_2 \overset{k_{10}}{\rightarrow} HCO_3^- + \cdot O_2^- + H^+$$

The reactions that were left out included eqs. [8] and [15]–[18].

$$[15] \quad HCO_3^- + Fe(II)L \rightarrow Fe(III)L + \cdot CO_3^- + OH^-$$

$$[16] \quad \cdot CO_3^- + \cdot O_2^- \rightarrow CO_3^{2-} + O_2$$

$$[17] \quad \cdot OH + HOO^- \rightarrow \cdot O_2^- + H_2O$$

$$[18] \quad \cdot CO_3^- + HOO^- \rightarrow \cdot O_2^- + HCO_3^-$$

Barb et al.[9] left out eq. [8] in cases of high H_2O_2:Fe(III) or H_2O_2:Fe(II) mole ratios. In the present case [Fe(II)] will be in the range of 10^{-8} mol/L and [H_2O_2] will be in the range of 10^{-2} mol/L and eq. [5] should dominate over eq. [8]. Equation [15] was left out because if it dominated over ·OH generation by eqs. [4] and [12] then it would be difficult to explain peroxide stabilization with BA. Based on the correlation between Hammett substituent constants and the rate constant for $\cdot CO_3^-$ reacting with aromatics,[20] BA should have a rate constant $<10^5$ (mol/L)$^{-1}$ s^{-1} for its reaction with $\cdot CO_3^-$. The rate constant for $\cdot CO_3^-$ reacting with H_2O_2 is 8.0×10^5 (mol/L)$^{-1}$ s^{-1}.[21,22] Therefore, BA at 10 mmol/L should not be able to scavenge a significant amount of $\cdot CO_3^-$ away from H_2O_2 at 50 mmol/L.

Equation [16] was left out because reaction of $\cdot CO_3^-$ with H_2O_2 (eq. [14]) should dominate over its reaction with $\cdot O_2^-$. The rate constant for eq. [16] is 2.0×10^8 (mol/L)$^{-1}$ s^{-1}.[22] Although this value is 250 times greater than the one for eq. [14], it is likely that the steady-state concentration of $\cdot O_2^-$ will be $<10^{-6}$ mol/L, whereas H_2O_2 concentrations of interest will be $>1.0 \times 10^{-2}$ mol/L (10 mmol/L). Polle[23] reported on an investigation where ascorbate and glutathione were used as scavengers for $\cdot O_2^-$. The rate constants for the two scavengers reacting with the free radical are 2.0×10^5 and 7.0×10^5 (mol/L)$^{-1}$ s^{-1}, respectively.[23] When 10 mmol/L ascorbate, 5 mmol/L of glutathione, and a $\cdot O_2^-$ feed rate of 240 μmol/L s^{-1} were used as inputs in the computer model, the steady-state $\cdot O_2^-$ concentration was estimated at 2.3×10^{-9} mol/L after 0.1 s.[23] A k_{OBS} of 6.5×10^{-4} s^{-1} was the highest observed in the present research (Table 1). Such a rate would correspond to a decrease in [H_2O_2] from 50 to 5 mmol/L over 60 min or 3600 s. A decrease in [H_2O_2] of 45 mmol/L would correspond to the generation of 22.5 mmol/L or 22 500 μmol/L of oxygen. Assuming O_2 is generated only from $\cdot O_2^-$ then the average $\cdot O_2^-$ generation rate would be only 6.25 μmol/L s^{-1} (22 500 μmol/L per 3600 s) for $k_{OBS} = 6.5 \times 10^{-4}$ s^{-1}. It is unlikely the $\cdot O_2^-$ steady-state concentration would exceed 10^{-6} mol/L in the present research because Fe(III) complexes are efficient scavengers for the free radical at pH > 4.8 (eq. [6]). Typical rate constants for eq. [6] are in the range of 1.5×10^8 (mol/L)$^{-1}$ s^{-1}.[24] Equations [17] and [18] were left out because the [HOO^-] concentration will be a thousand times lower than [H_2O_2] at pH 8.5–8.7 (pK_a of H_2O_2 = 11.6). The rate constant for ·OH reacting with HOO^- is only 278 times higher than for its reactions with H_2O_2.[16] Similarly, the rate constant for CO_3^- is only 70 times higher for HOO^- when compared with H_2O_2.[21]

The next step was to try and determine an overall rate equation for the free radical scheme, i.e., eqs. [3]–[7] and eqs. [11]–[14]. The steady-state assumption was used for the concentrations of free radicals.[5,9,10,25] By making two minor assumptions the rate law in eq. [19] was obtained. The full derivation of eq. [19] has been provided as Supplementary data and identified as Scheme 1. The first simplifying assumption was that k_3[H_2O_2] was much greater than k_9[HCO_3^-]. The respective values for k_3 and k_9 are 2.7×10^7 and 8.5×10^6 (mol/L)$^{-1}$ s^{-1}.[16] In the present investigation, the [H_2O_2] after 50% decomposition was 25 mmol/L and k_3[H_2O_2] was 3.18 times greater ($2.7 \times 10^7/8.5 \times 10^6$) than that of k_9[HCO_3^-] at a [HCO_3^-] of 25 mmol/L. This assumption was made with the intent of investigating the [HCO_3^-] of 20, 25, and 30 mmol/L experimentally. The other assumption was that k_4[Fe(III)] was much greater than k_5[Fe(II)]. Typically, k_4 is 15 times greater than k_5 at pH greater than 4.8,[24] and [Fe(III)] would be expected to be much greater than [Fe(II)]. Typical rate constants for Fe(III) oxidation of H_2O_2 (eq. [3]) are <0.01 (mol/L)$^{-1}$ s^{-1} [10,26] and the rate constants for H_2O_2 oxidation of Fe(II) complexes (eq. [4] are typically in the range of 10^3–10^4 (mol/L)$^{-1}$ s^{-1}.[12,27] Fe(II) would be converted to Fe(III) at a much higher rate than for the reverse reaction and [Fe(III)] >> [Fe(II)].

Equation [19] is quite complex with five terms on the right-hand side (RHS). However, a simple, approximate solution can be derived when both the H_2O_2 and HCO_3^-

Can. J. Chem. Downloaded from www.nrcresearchpress.com by Xi'an Jiaotong University on 09/19/12
For personal use only.

Can. J. Chem. Downloaded from www.nrcresearchpress.com by Xi'an Jiaotong University on 09/19/12
For personal use only.

concentrations are in the range of 0.025 mol/L. To begin, it will be assumed that the first term on the RHS is much less than the second term and can be ignored. The ratio k_9/k_3 in the fourth term is 0.315 ($8.5 \times 10^6/2.7 \times 10^7$) and if the assumption is made that H_2O_2 and HCO_3^- concentrations are approximately equal then the fourth term would be equal to 0.315 times the second term and it can be eliminated by multiplying the second term by 1.315. This is strictly a mathematical manipulation because the H_2O_2 concentration would vary while the HCO_3^- concentrations would be nearly constant. If the fifth term is multiplied by $k_3[H_2O_2]/k_9[HCO_3^-]$ then the third term is obtained. Therefore, the third term is 3.18 times greater than the fifth term (k_3/k_9) or the fifth term is 0.315 as large as the third term. As such, the fifth term can also be eliminated by multiplying the third term by 1.315. The simplified rate expression is eq. [20] when $[H_2O_2] \approx [HCO_3^-]$. The term $K_1[HCO_3^-][H_2O_2]$ is equivalent to $[HCO_4^-]$ by eq. [2], and the rate expression is simply the rate of Fe(II) oxidation by H_2O_2 plus that by HCO_4^-, both multiplied by 1.315.

$$[19] \quad \frac{d[O_2]}{dt} = k_1[Fe(III)L][H_2O_2] + k_2[Fe(II)L][H_2O_2] + K_1k_8[Fe(II)L][HCO_3^-][H_2O_2] + \frac{k_2k_9[Fe(II)L][HCO_3^-]}{k_3} + \frac{K_1k_8k_9[Fe(II)L][HCO_3^-]^2}{k_3}...$$

$$[20] \quad \frac{d[O_2]}{dt} = 1.315k_2[Fe(II)L][H_2O_2] + 1.315K_1k_8[Fe(II)L][HCO_3^-][H_2O_2]$$

If the second term of the RHS of eq. [20] is equal to or greater than the first then the rate of H_2O_2 decomposition (twice that of O_2 evolution) should increase noticeably when $[HCO_3^-]$ is increased from 0.02 to 0.025 to 0.03 mol/L.

The detailed experimental research on the effect of $[HCO_3^-]$ was initiated with the determination of k_{OBS} for 0.025 mol/L HCO_3^- and 0.025 mol/L each of HCO_3^- and Na_2SO_4. The rate constants observed were 4.1×10^{-4} and 4.2×10^{-4} s^{-1}, respectively. Again an increase in ionic strength appeared to have no significant impact. The rate constant for 0.02 mol/L HCO_3^- was 3.9×10^{-4} s^{-1} and the value was $4.4 \times 10^{-4}s^{-1}$ for 0.03 mol/L HCO_3^- (Table 1). If the second term on the RHS of eq. [20] was dominant over the first term then the decomposition rate should have increased by ca. 50% in going from 0.02 to 0.03 mol/L HCO_3^-. The increase observed was only 13%. When $[HCO_3^-]$ was increased to 0.05 mol/L, the decomposition rate increased only to 4.9×10^{-4} s^{-1}, which is also the value previously and reproducibly obtained for 0.1 mol/L HCO_3^-. The effect of $[HCO_3^-]$ was minor; instead of increasing nearly fourfold in going from 0.025 to 0.10 mol/L it increased by only 20%, i.e., 4.9×10^{-4} vs 4.1×10^{-4} s^{-1}. The standard initial and end pH were 8.4 and 8.6 for $[HCO_3^-]$ in the range of 0.02–0.03 mol/L, with corresponding values of 8.5 and 8.7 for the 0.05–0.10 mol/L HCO_3^- range. It did not appear that the 0.2 unit pH increase during the runs caused a significant acceleration in peroxide decomposition. The slope

Fig. 4. First-order rate plots for peroxygen decomposition in the presence of increasing concentrations of Fe(III) citrate complex at 40 °C, pH 8.5–8.7, $[HCO_3^-] = 0.10$ mol/L, and initial $[H_2O_2] = 0.05$ mol/L.

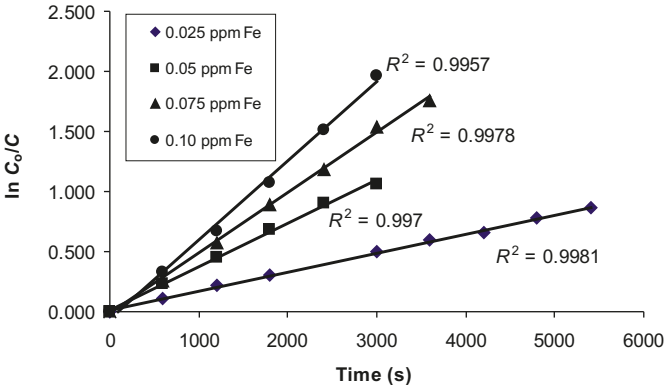

Fig. 5. Plot of $-\ln k_{OBS}$ vs $-\ln[Fe(III)L]$.

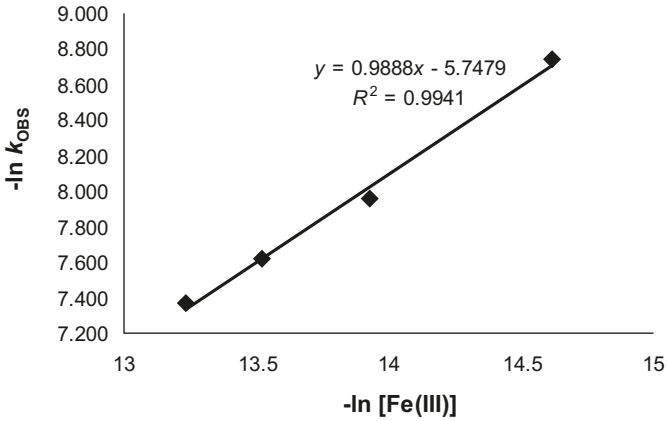

in eq. [10] was always nearly identical for data collected early and late in the runs. The R^2 value for k_{OBS} was always >0.99.

If the second term on the RHS of eq. [20] is ignored then the rate equation becomes $1.315k_2[Fe(II)L][H_2O_2]$ for oxygen generation or $-2.63k_2[Fe(II)L][H_2O_2]$ for peroxide decomposition. The rate law for eqs. [3]–[7] is given in eq. [21] and it differs from the one just stated by a factor of –2.0 instead of –2.63. The relationship between [Fe(II)L] and [Fe(III)L] is given in eq. [22] and the rate expression in terms of Fe(III)L is given in eq. [23]. The full derivations are Scheme 2 in the Supplementary data. Final relationships identical to eqs. [21]–[23] were derived by Barb et al.,[9] although their mathematical approach for the derivation of eq. [22] was different from those used in the present research. If the reactions in eqs. [3]–[7] are indeed primarily responsible for peroxide decomposition then the rate should be first order in both $[H_2O_2]$ and [Fe(III)L] in accordance with eq. [23]. The data in Figs. 4 and 5 show nearly perfect first-order fits for both variables.

$$[21] \quad \frac{d[H_2O_2]}{dt} = -2k_2[Fe(II)L][H_2O_2]$$

$$[22] \quad [Fe(II)L] = \left(\frac{k_1k_4}{k_2k_5}\right)^{\frac{1}{2}}[Fe(III)L]$$

Can. J. Chem. Downloaded from www.nrcresearchpress.com by Xi'an Jiaotong University on 09/19/12
For personal use only.

$$[23] \qquad \frac{d[H_2O_2]}{dt} = -2\left(\frac{k_1k_2k_4}{k_5}\right)^{\frac{1}{2}}[Fe(III)L][H_2O_2]$$

It appears as if HCO_4^- plays only a minor role in the ferric citrate-catalyzed decomposition of H_2O_2 in the pH 8.5 range. The likely mechanism appears to be consistent with eqs. [3]–[7] proposed by Barb et al.[9] for ferric catalysis under acidic conditions and by Walling et al.[10] for Fe(III)–EDTA in the pH 7–9 range. However, the possibility that a ferryl species is the highly reactive intermediate instead of ·OH cannot be ruled out by the present kinetic data. A ferryl species would be capable of ring hydroxylation via the formation of a radical cation.[10,28] Furthermore, if eqs. [4] and [5] were to be replaced by eqs. [9] and [24] (the ferryl alternative), a rate law similar to that in eq. [23] would be obtained with k_2 being replaced by k_7. The full derivation of this rate law is Scheme 3 in the Supplementary data. If eqs. [4] and [5] are combined the result would be eq. [25], which would also be the product if eqs. [9] and [24] are combined.

$$[9] \qquad Fe(II)L + H_2O_2 \xrightarrow{k_7} Fe(IV)L = O + H_2O$$

$$[24] \qquad Fe(IV)L = O + H_2O_2 \xrightarrow{k_{11}} Fe(III)L + \cdot O_2^- + H_2O$$

$$[25] \qquad Fe(II)L + 2H_2O_2 \rightarrow Fe(III)L + \cdot O_2^- + 2H_2O$$

Conclusion

This research was initiated with some evidence pointing to a free radical mechanism being responsible for peroxide decomposition catalyzed by ferric complexes in H_2O_2/HCO_3^- solutions at pH 8.5–8.7. This was confirmed in the present investigation. A key step in most free radical chain mechanisms is the oxidation of Fe(II) to Fe(III) and (or) Fe(IV), which results in an increase in the peroxide decomposition rate. The anionic peracid (HCO_4^-) is a much stronger oxidant than H_2O_2, and the possibility that the H_2O_2 was inherently less stable in the presence of HCO_4^- was investigated. Based on the kinetic data that were obtained and theoretical analyses, it was concluded that HCO_4^- did not significantly destabilize the peroxygen system when citrate was used as a model chelator for Fe(III).

Supplementary data

Supplementary data are available with the article through the journal Web site (http://nrcresearchpress.com/doi/suppl/10.1139/v11-078).

Acknowledgements

Financial support from Solvay Chemicals, Inc. and the Empire State Paper Research Associates (ESPRA) is deeply appreciated.

References

(1) (a) Flangan, J.; Jones, D. P.; Griffith, W. P.; Skapski, A. C.; West, A. P. *J. Chem. Soc. Commun* **1986** *1*, 20. doi:10.1039/c39860000020; (b) Richardson, D. E.; Yao, H.; Frank, K. M.; Bennett, D. A. *J. Am. Chem. Soc.* **2000** *122* (8), 1729. doi:10.1021/ja9927467; (c) Bennett, D. A.; Yao, H.; Richardson, D. E. *Inorg. Chem.* **2001** *40* (13), 2996. doi:10.1021/ic000910h.

(2) (a) Attiogbe, F. K.; Bose, S. K.; Wang, W.; McNeillie, A.; Francis, R. C. *BioResources* **2010** *5* (4), 2208 (b) Attiogbe, F. K.; Wang, W.; McNeillie, A.; Francis, R. C. *BioResources* **2010** *5* (4), 2221.

(3) Vakhitova, L. N.; Zhil'tsova, S. V.; Skrypka, A. V.; Razumova, N. G.; Taran, N.A.; Savelova, V.A.; Popov, A.F. *Theor. Exp. Chem.* **2006** *42* (5), 287. doi:10.1007/s11237-006-0055-y.

(4) Singh, S.; Hider, R. C. *Anal. Biochem.* **1988** *171* (1), 47. doi:10.1016/0003-2697(88)90123-6.

(5) Zhang, X.-Z.; Francis, R. C.; Dutton, D. B.; Hill, R. T. *Can. J. Chem.* **1998** *76*, 1064. doi:10.1139/v98-103.

(6) Gierer, J.; Jansbo, K. *J. Wood Chem. Technol.* **1993** *13* (4), 561. doi:10.1080/02773819308020534.

(7) Francis, R. C.; Zhang, X.; Froass, P. M.; Tamer, O. *Tappi J.* **1994** *77* (6), 133.

(8) Peart, C.; Ni, Y. *J. Wood Chem. Technol.* **2001** *21* (2), 113. doi:10.1081/WCT-100104222.

(9) Barb, W. G.; Buxendale, J. H.; George, P.; Hargrave, K. R. *Trans. Faraday Soc.* **1951** *47*, 591. doi:10.1039/tf9514700591.

(10) (a) Walling, C.; Goosen, A. *J. Am. Chem. Soc.* **1973** *95* (9), 2987. doi:10.1021/ja00790a042; (b) Walling, C. *Acc. Chem. Res.* **1975** *8* (4), 125. doi:10.1021/ar50088a003; (c) Walling, C.; Partch, R. E.; Weil, T. *Proc. Natl. Acad. Sci. U.S.A.* **1975** *72* (1), 140. doi:10.1073/pnas.72.1.140; (d) Walling, C.; Amarnath, K. *J. Am. Chem. Soc.* **1982** *104* (5), 1185. doi:10.1021/ja00369a005.

(11) (a) Rush, J. D.; Koppenol, W. H. *J. Biol. Chem.* **1986** *261*, 6730 (b) Rush, J. D.; Koppenol, W. H. *J. Inorg. Biochem.* **1987** *29* (3), 199. doi:10.1016/0162-0134(87)80027-2; (c) Lloyd, R. V.; Hanna, P. M.; Mason, R. P. *Free Radic. Biol. Med.* **1997** *22* (5), 885. doi:10.1016/S0891-5849(96)00432-7.

(12) (a) Yamazaki, I.; Piette, L. H. *J. Biol. Chem.* **1990** *265* (23), 13589 (b) Yamazaki, I.; Piette, L. H. *J. Am. Chem. Soc.* **1991** *113* (20), 7588. doi:10.1021/ja00020a021.

(13) (a) Gutteridge, J. M. C. *Free Radic. Biol. Med.* **1991** *11* (4), 401. doi:10.1016/0891-5849(91)90157-X; (b) Zepp, R. G.; Faust, B. C.; Hoigne, J. *Environ. Sci. Technol.* **1992** *26* (2), 313. doi:10.1021/es00026a011.

(14) Maskos, Z.; Rush, J. D.; Koppenol, W. H. *Arch. Biochem. Biophys.* **1992** *296* (2), 521. doi:10.1016/0003-9861(92)90606-W.

(15) Attiogbe, F. K., Francis, R. C. *Can. J. Chem.*, in press.

(16) Buxton, G. V.; Greenstock, C. L.; Helman, W. P.; Ross, A. *J. Phys. Chem. Ref. Data* **1988** *17*, 513. doi:10.1063/1.555805.

(17) Serjeant, E. P.; Dempsey, B. *Ionization Constants of Organic Acids in Solution;* IUPAC Chemical Data Series No. 23; Pergamon Press: Oxford, UK, 1979.

(18) Stone, A. T. *Environ. Sci. Technol.* **1987** *21* (10), 979. doi:10.1021/es50001a011.

(19) Lind, J.; Shen, X.; Eriksen, T. E.; Merenyi, G. *J. Am. Chem. Soc.* **1990** *112* (2), 479. doi:10.1021/ja00158a002.

(20) Chen, S.; Hoffman, M. Z.; Parsons, G. H., Jr. *J. Phys. Chem.* **1975** *79* (18), 1911. doi:10.1021/j100585a004.

(21) Ross, A. B.; Neta, P. *Rate Constant for Reactions of Organic Radicals in Aqueous Solution;* US Department of Commerce, 1979.

(22) Haygarth, K. S.; Marin, T. W.; Janik, I.; Kanjana, K.; Stanisky, C. M.; Bartels, D. M. *J. Phys. Chem. A* **2010** *114* (5), 2142. doi:10.1021/jp9105162.

(23) Polle, A. *Plant Physiol.* **2001** *126* (1), 445. doi:10.1104/pp.126.1.445.

(24) (a) Zuo, Y.; Hoigne, J. *Environ. Sci. Technol.* **1992** *26* (5), 1014.

doi:10.1021/es00029a022; (b) Wilson, C. L.; Hinman, N. W.; Cooper, W. J.; Brown, C. F. *Environ. Sci. Technol.* **2000** *34* (13), 2655. doi:10.1021/es9906397; (c) Rose, A. L.; Waite, T. D. *Environ. Sci. Technol.* **2002** *36* (3), 433. doi:10.1021/es0109242.

(25) Thompson, R. C. *Inorg. Chem.* **1981** *20* (4), 1005. doi:10.1021/ic50218a012.

(26) Kwan, W. P.; Voelker, B. M. *Environ. Sci. Technol.* **2002** *36* (7), 1467. doi:10.1021/es011109p.

(27) (a) Croft, S.; Gilbert, B. C.; Lindsay Smith, J. R.; Whitwood, A. C. *Free Rad. Res. Comms* **1992** *17* (1), 21. PMID:1332916; doi:10.3109/10715769209061086; (b) King, D. W.; Farlow, R. *Mar. Chem.* **2000** *70* (1–3), 201. doi:10.1016/S0304-4203(00)00026-8.

(28) Steenken, S.; O'Neill, P.; Schulte-Frohlinde, D. *J. Phys. Chem.* **1977** *81* (1), 26. doi:10.1021/j100516a007.

Can. J. Chem. Downloaded from www.nrcresearchpress.com by Xi'an Jiaotong University on 09/19/12
For personal use only.

Hydrogen peroxide decomposition in bicarbonate solution catalyzed by divalent manganese species*

Francis K. Attiogbe and Raymond C. Francis

Can. J. Chem. Downloaded from www.nrcresearchpress.com by Xi'an Jiaotong University on 09/19/12
For personal use only.

Abstract: The peroxymonocarbonate mono- and di-anions (HCO_4^- and CO_4^{2-}) are known to be generated from H_2O_2/HCO_3^-. They are promising oxidants for wood pulp bleaching, but peroxide decomposition catalyzed by Mn(II) species may be significant for pulp samples with unusually high Mn contents. This investigation aimed to see if HCO_3^- addition caused destabilization of the peroxygen system owing to its partial conversion to HCO_4^-. This anionic peracid is a much stronger oxidant than H_2O_2 and could lead to a higher rate of Mn(II) oxidation to Mn(III) and (or) Mn(IV). For most free radical chain mechanisms, an increase in Mn(II) oxidation results in a higher rate of peroxide decomposition. Peroxide decomposition catalyzed by Mn(II) was investigated in H_2O_2/HCO_3 in the pH ranges 8.5–8.7 and 7.4–7.9. The rate equation for peroxide decomposition was first order in [H_2O_2] and [Mn(II)] in both pH ranges, but close to second order in [HCO_3^-] in the higher pH range and close to third order in the lower pH range. Free radical chain mechanisms were proposed for both pH ranges and with all the correct reaction orders. Contrary to mechanisms previously proposed, it was concluded that HCO_4^- is the principal oxidizer of Mn(II) in the pH 7.4–7.9 range.

Key words: peroxymonocarbonate anions, hydrogen peroxide, divalent manganese, peroxide decomposition, pulp bleaching.

Résumé : Il est bien connu que les mono- et di-anions du peroxymonocarbonate (HCO_4^- et CO_4^{2-}) peuvent être générés par la réaction du H_2O_2 et du HCO_3^-. Ce sont des oxydants prometteurs pour le blanchiment de la pulpe de bois, mais la décomposition du peroxyde, catalysée par des espèces de Mn(II), peut être importante avec les échantillons de pulpes avec des teneurs exceptionnellement élevées de manganèse. Cette étude a été entreprise dans le but de déterminer si l'addition de HCO_3^- provoque une déstabilisation du système de peroxygène en raison de sa conversion partielle en HCO_4^-. Ce peracide anionique est un oxydant beaucoup plus puissant que le H_2O_2 et pourrait conduire à une vitesse plus élevée d'oxydation du Mn(II) en Mn(III) et (ou) Mn(IV). Pour la plupart des mécanismes en chaîne radicalaire, une augmentation dans l'oxydation du Mn(II) conduit à une augmentation de la vitesse de décomposition du peroxyde. On a étudié la décomposition du peroxyde catalysée par le Mn(II), dans le système H_2O_2/HCO_3^-, dans les plages de pH de 8,5 à 8,7 et de 7,4 à 7,9. L'équation de vitesse pour la décomposition du peroxyde est du premier ordre en [H_2O_2] et en [Mn(II)] dans les deux plages de pH, mais elle s'approche du deuxième ordre en [HCO_3^-] dans la plage élevée de pH et elle est très près du troisième ordre dans la plage de pH plus faible. On propose des mécanismes en chaîne radicalaire pour les deux plages de pH et ils correspondent aux ordres de réaction corrects. Contrairement aux mécanismes proposés antérieurement, on en conclut que l'anion HCO_4^- est l'oxydant principal du Mn(II) dans la plage de pH de 7,4 à 7,9.

Mots-clés : anions peroxymonocarbonates, peroxyde d'hydrogène, manganèse divalent, décomposition du peroxyde, blanchiment de la pulpe.

[Traduit par la Rédaction]

Introduction

It has been known for a long time that hydrogen peroxide reacts with the bicarbonate anion to generate the peroxymonocarbonate monoanion (HCO_4^-).[1] The equilibrium reaction and equilibrium constant associated with HCO_4^- formation are presented in eqs. [1] and [2].[1]

$$[1] \quad HCO_3^- + H_2O_2 \rightleftharpoons {}^-OC(=O)OOH + H_2O$$

$$[2] \quad K = 0.32\ (\text{mol/L})^{-1} = \frac{[HCO_4^-]}{[H_2O_2][HCO_3^-]}$$

The peroxymonocarbonate (PMC) monoanions dissociates to the dianion (CO_4^{2-}) with a pK_a ca. 10.0.[1–3] Results were recently reported where the two anions showed great promise as bleaching agents for wood pulps.[2] However, wasteful decomposition of peroxide catalyzed by transition metal species has to be controlled.[4] Earlier data clearly showed that Fe(III) and Mn(II) species catalyze peroxide decomposition in bleaching slurries and that such decomposition could be

Received 25 January 2011. Accepted 14 April 2011. Published at www.nrcresearchpress.com/cjc on 13 September 2011.

F.K. Attiogbe and R.C. Francis. Department of Paper and Bioprocess Engineering, State University of New York, College of Environmental Science and Forestry (SUNY–ESF), 1 Forestry Drive, Syracuse, NY 13210, USA.

Corresponding author: R.C. Francis (e-mail: francis@syr.edu and francis@esf.edu).

*This article has a companion paper in this issue (doi: 10.1139/v11-078).

Can. J. Chem. Downloaded from www.nrcresearchpress.com by Xi'an Jiaotong University on 09/19/12
For personal use only.

retarded to a very high degree by the addition of a hydroxyl radical scavenger.[2] When $Fe_2(SO_4)_3$ or $MnSO_4$ was added to bleaching effluent containing H_2O_2, the inclusion of *N*,*N*′-(5-nitro-1,3-phenylene)bisglutaramide (GAMID) as a hydroxyl radical scavenger[5] decreased the rate of peroxide decomposition by a factor of at least 10 for both Fe(III) and Mn(II). In addition to wasteful decomposition of H_2O_2, a second and probably greater concern is that ·OH is generated at a moderate to high rate by Fe (III) and Mn (II) catalysis. This free radical can retard the brightening of mechanical pulps[6] and lower the degree of polymerization of the cellulose in chemical pulps to unacceptable levels.[7]

Data in the literature suggest that carbonates and bicarbonates of Mn are the actual catalysts and rate equations for peroxide decomposition that are second order in $[HCO_3^-]$[8] and third order in $[HCO_3^-]$[9] have been reported. Thermodynamic data have been presented in support of $Mn(HCO_3)_2$ or $[Mn(CO_3)(HCO_3)]^-$ as the actual catalyst.[10–12] The one-electron oxidation potential of those species is reported to be in the range of –0.67 V up from –1.51 V for Mn^{2+} in acid.[11–13] The reduction potential for one-electron abstraction by H_2O_2 at pH 7 is given in eq. [3].[14] It can be seen that the value is only 0.46 V when compared with 0.87 V at pH 0.[14] If eq. [3] were to be combined with eq. [4] then eq. [5] would be obtained and the reaction would only be slightly endoergic.

$$[3] \quad H_2O_2 + e^- \rightarrow \cdot OH + OH^- \qquad (0.46\ V)$$

$$[4] \quad Mn(HCO_3)_2 \rightarrow Mn(HCO_3)_2^+ + e^- \qquad (-0.67\ V)$$

$$[5] \quad H_2O_2 + Mn(HCO_3)_2 \rightarrow Mn(HCO_3)_2^+ + \cdot OH + OH^- \qquad (-0.21\ V)$$

The corresponding reaction in a Mn(III)/Mn(II) cycle would be electron abstraction from H_2O_2 by Mn(III). The half-reactions and the net reactions are given in eqs. [6]–[8]. The voltage of –0.94 V (pH 7) for H_2O_2 losing an electron is from Koppenol and Butler.[14] Once again the net reaction is only slightly endoergic (–0.27 V) and the Mn(III)/Mn(II) redox cycle should be able to catalyze H_2O_2 decomposition in bicarbonate solution in the neutral pH range.

$$[6] \quad H_2O_2 \rightarrow \cdot O_2^- + 2H^+ + e^- \qquad (-0.94\ V)$$

$$[7] \quad [Mn(HCO_3)_2]^+ + e^- \rightarrow Mn(HCO_3)_2 \qquad (0.67\ V)$$

$$[8] \quad [Mn(HCO_3)_2]^+ + H_2O_2 \rightarrow Mn(HCO_3)_2 + \cdot O_2^- + 2H^+ \qquad (-0.27\ V)$$

There are two proposed free radical chain mechanisms to explain Mn(II) catalysis of peroxide decomposition in HCO_3^-, one involving Mn(II), Mn(III), and Mn(IV)[8] and the other involving only Mn(II) and Mn(III).[9] In both cases the rate of peroxide decomposition should increase with an increase in the rate of oxidation of Mn(II) by a peroxygen species. Since HCO_4^- is a much stronger oxidant than H_2O_2,[1] bicarbonate addition could lead to a higher oxidation rate for Mn(II) and an increase in the peroxide decomposition rate.

This report is on an investigation of Mn(II) catalysis of peroxide decomposition in $NaHCO_3$ solutions at pH 7.4–8.7 and 40 °C. Citrate anion was investigated as a model chelator to see if it would form complexes with Mn(II), Mn(III), and (or) Mn(IV) and interfere with the mechanism operative for Mn bicarbonates and (or) carbonates. In a companion submission, results are presented for catalysis by Fe(III) species in a pH range of 8.5–8.7.[4]

Experimental

All of the relevant chemicals are described in the companion paper.[4] Possible Mn–citrate complexes were prepared by dissolving $Mn(SO_4)\cdot H_2O$ in citric acid. The $[Mn^{2+}]$ was 0.018 mol/L (1000 ppm), and citric acid was added at a 5:1 mol ratio to Mn^{2+}. The final solution contained no particles and was nonturbid when its pH was raised from 1.9 to 7.0 with $NaHCO_3$. This solution (1000 ppm Mn) was stored at room temperature and pH 1.9 and aliquots were taken from it and diluted to 10 or 20 ppm Mn(II). These dilute Mn (II) solutions were used for 3–5 days of research before fresh batches were made. The reaction system and chemical and chromatographic analyses were identical to those used in the investigation of ferric catalysis.[4]

Results and discussion

In pulp bleaching, the initial H_2O_2 concentration is in the range of 20–40 mmol/L for a peroxide/bicarbonate (P_B) stage applied to chemical pulps (0.5%–1.0% H_2O_2 on pulp at 12% consistency) and 50–130 mmol/L for mechanical pulps (1.0% H_2O_2 at 15%–30% consistency).[2] The typical concentrations for $NaHCO_3$ are 30–50 mmol/L for chemical pulps (2%–3% $NaHCO_3$ on pulp at 12% consistency) and 60–150 mmol/L for mechanical pulps (3% $NaHCO_3$ at 15%–30% consistency).[2] Mn(II) catalysis was first investigated in the pH 8.5–8.7 range that is optimum for most P_B bleaching applications. The investigation was extended to a pH range of 7.4–7.9 because it is also applicable to P_B bleaching and because of controversies associated with the reaction mechanisms that are believed to be responsible for peroxide decomposition in that pH range. An ionic mechanism was recently proposed to explain the decomposition of hydrogen peroxide in bicarbonate solutions at pH 7.4.[13] However, most of the other proposed mechanisms in the pH range of 7–8 are dominated by free radical reactions.[8,9,15] A first-order dependence on [Mn(II)] was observed by two research groups,[8,9] whereas a second-order dependence was observed by another.[13] However, one of the groups that observed a first-order [Mn(II)] dependence observed a second-order dependence on $[HCO_3^-]$,[8] whereas the other group observed a third-order dependence.[9]

The initial set of experiments for the pH 8.5–8.7 range was aimed at seeing if the rate of peroxide decomposition decreased significantly when a radical scavenger was added. A rate constant (k_{OBS}, eq. [9]) was the basis for all comparison of decomposition rates. The R^2 associated with k_{OBS} was always >0.99 when the extent of peroxide decomposition was >25%. Catalysis of peroxide decomposition by 0.3 ppm Mn(II) (no citrate) in 0.1 mol/L HCO_3^- at 40 °C was investigated in the absence and presence of 1.0 mmol/L salicylic acid (SA). The decomposition rate decreased from 3.9×10^{-4} to 1.0×10^{-4} s^{-1} (74%) when 1.0 mmol/L SA was included

Can. J. Chem. Downloaded from www.nrcresearchpress.com by Xi'an Jiaotong University on 09/19/12
For personal use only.

(Table 1). Careful analysis for residual SA showed that it decreased to 0.5 mmol/L after 90 min of reaction. When ferric citrate catalysis was investigated under the same conditions of pH, temperature, and time, the SA concentration decreased from 1.0 to 0.8 mmol/L.[4] No hydroxylated product was observed in this case or with ferric citrate. However, the expected product (2,3-dihydroxybenzoic acid)[16] containing adjacent phenolic groups would be expected to be degraded by P_B oxidation. When 5 mmol/L SA and 10 mmol/L GAMID were used as radical scavengers, the peroxide decomposition rate decreased to ca. 0.1×10^{-4} s^{-1} for both additives (Table 1). The peroxide decomposition mechanism appeared to be dominated by a free radical mechanism(s).

$$[9] \qquad \frac{d[H_2O_2]}{dt} = -k_{OBS}[H_2O_2]$$

The concentration of Mn(II) was varied from 0.10 to 0.50 ppm in 0.1 mol/L HCO_3^-. No citrate was added along with the Mn(II). The first-order plots in terms of $[H_2O_2]$ are shown in Fig. 1 for six different [Mn(II)]. When $-\ln k_{OBS}$ was plotted against $-\ln$[Mn(II)] the slope of the regression line was 0.96, indicating a first-order dependence on [Mn(II)] (Fig. 2). The effect of $[HCO_3^-]$ was then investigated. On this occasion both $MnSO_4$ and Mn(II)citrate ($MnSO_4$ plus a 5:1 mol ratio of citrate:Mn(II)) were used as catalysts. The effects of increasing $[HCO_3^-]$ on k_{OBS} are presented in Table 1 and it can be seen that increasing $[HCO_3^-]$ from 0.10 to 0.15 mol/L caused the decomposition rate to increase more than 100%. Also, the decomposition rate was nearly equal with and without citrate. The plots of $-\ln k_{OBS}$ vs $-\ln[HCO_3^-]$ are shown in Fig. 3 for Mn(II) without and with citrate. The slope was 2.13 without citrate and 2.15 with citrate. It appears as if the major reaction mechanism that was operative in this pH range had a second-order dependence on $[HCO_3^-]$.

Research on the peroxide decomposition mechanism for the pH range 7.4–7.9 was initiated with an investigation of SA addition. The radical scavenger at 1.0 mmol/L decreased the peroxide decomposition rate from 6.8×10^{-4} to 1.3×10^{-4} s^{-1} (81%) when a [Mn(II)] of 1.0 ppm was used in 0.1 mol/L HCO_3^-. The decomposition mechanism once again appeared to be free radical in nature.

The reaction order determinations were then repeated at initial pH 7.4. The use of a buffer was avoided and the reaction pH increased from 7.4 to ca. 7.9 when ca. 75% of the H_2O_2 was decomposed. When determining the reaction order for [Mn(II)] a low HCO_3^- concentration (0.05 mol/L) was used and the peroxide residuals were determined after 0, 5, 10, 15, and 20 min. On these occasions, the pH was kept in a range of 7.4–7.7 and peroxide decomposition after 20 min varied from 8% to 35% for [Mn(II)] in the range of 1.0–5.0 ppm. However, the R^2 value on k_{OBS} (eq. [9]) was always >0.985. When $-\ln k_{OBS}$ was plotted against $-\ln$[Mn(II)] the regression line had a slope of 1.01, indicating a first-order dependence on [Mn(II)]. These data will not be shown but similar data will be shown and discussed shortly.

The HCO_3^- concentration effect was then investigated with 1.0 ppm Mn(II), and it was difficult to keep the pH in the range of 7.4–7.7 and collect enough data points when $[HCO_3^-] \geq 0.1$ mol/L. The pH would exceed 7.7 within 10–15 min. However, there did not appear to be a significant pH effect in the range 7.4–7.9. The first-order plots in terms of $[H_2O_2]$ are shown in Fig. 4 for $[HCO_3^-]$ for 0.075, 0.10, and 0.125 mol/L concentrations. If the decomposition rate increased with increasing pH during the run then one would expect the first-order plots to curve concavely upwards. This was not seen (Fig. 4). This lack of a pH dependence in the range 7.4–7.9 is in clear contradiction to Sychev et al.,[8] who observed an increase in peroxide decomposition with increasing pH: $\sim 1/[H^+]^{0.5}$.

At first glance it also appeared that Stadtman and co-workers[9] observed an increase in peroxide decomposition with increasing pH in the range 7.4–7.9. However, their increase in pH was due to an increase in $[HCO_3^-]$. The reaction order for $[HCO_3^-]$ reported by Stadtman and co-workers[9] was almost perfectly third-order. When 12 k_{OBS} (min^{-1}) values from Stadtman and co-workers[9] were plotted against their corresponding $[HCO_3^-]$,[3] a linear relationship with $R^2 > 0.99$ was observed. All 12 $[HCO_3^-]$ resulted in a reaction pH in the range 7.4–7.9. Apparently, an increase in pH does not enhance the rate of peroxide decomposition in the 7.4–7.9 range.

Now that it was known that pH had no significant effect in the range 7.4–7.9, the dependence on [Mn(II)] was repeated in 0.075 mol/L HCO_3^- solutions. The [Mn(II)] was varied from 0.5 to 2.5 ppm and peroxide decomposition after 20 min varied from 15% to 54%. The k_{OBS} values are presented in Table 2 and a plot of $-\ln k_{OBS}$ vs $-\ln$[Mn(II)] is shown in Fig. 5. The slope was 1.00 and there is definitely a first-order dependence on [Mn(II)]. This finding supports the previously reported first-order [Mn(II)] dependence[8,9] and contradicts claims of a second-order [Mn(II)] dependence.[13]

Data from the present investigation on k_{OBS} for 1.0 ppm Mn(II) and $[HCO_3^-]$ varying from 0.075 to 0.15 mol/L are given in Table 2, and a plot of $-\ln k_{OBS}$ vs $-\ln[HCO_3^-]$ is shown in Fig. 6. The reaction order was 2.88. The present results are most consistent with those of Stadtman and co-workers,[9] whose proposed mechanism contained a reaction similar to that in eq. [5].

The salient features associated with results from the literature and the present investigations are

1. Decomposition is via free radical mechanisms.
2. A mechanism that is second order in $[HCO_3^-]$ appears to be operative at pH 8.5–8.7.
3. A mechanism that is third order in $[HCO_3^-]$ appears to be operative at pH 7.4–7.9.
4. The bicarbonate dependence is higher than second order, but less than third order throughout the pH range 7.4–8.7.

A third-order dependence on $[HCO_3^-]$ can be obtained if the assumption of Stadtman and co-workers[9] is accepted that a $Mn(II)(HCO_3^-)_3$ species is involved. However, no evidence can be found in the literature for the existence of such a species at pH < 8.0. The only other approach that could be found to obtain a rate equation for a free radical chain mechanism that was first order in [Mn(II)] and $[H_2O_2]$, but third order in $[HCO_3^-]$ was to include an equilibrium reaction between H_2O_2 and HCO_3^- to produce HCO_4^- and a second equilibrium involving Mn(II) and 2 mol of HCO_3^- to produce $Mn(HCO_3)_2$ (to be discussed later). The only credible explanation that this investigation can provide is based on the

Can. J. Chem. Downloaded from www.nrcresearchpress.com by Xi'an Jiaotong University on 09/19/12
For personal use only.

Table 1. First-order rate constants for Mn(II)-catalyzed peroxide decomposition in HCO_3^- solutions at pH 8.5–8.7 with various additives (according to eq. [9]).

[Mn(II)] (ppm)	[HCO_3^-] (mol/L)	Other additives	k_{OBS} (s^{-1} $\times 10^4$)
0	0.1		0.1
0.15	0.1		2.0
0.20	0.1		2.8
0.30	0.1		3.8, 3.9
0.40	0.1		5.4
0. 50	0.1		7.5
0.30	0.1	1.0 mmol/L SA	1.0
0.30	0.1	5.0 mmol/L SA	0.1
0.30	0.1	10 mmol/L GAMID	0.1
0.10[a]	0.1		1.6
0.10	0.1	citrate	1.5
0.10	0.15		3.9, 4.0
0.10	0.15	citrate	3.6
0.10	0.20		7.9
0.10	0.20	citrate	7.7
0.10	0.30		16.4
0.10	0.30	citrate	15.5

Note: 50 mmol/L H_2O_2, 40 °C, initial and final pH of 8.5 and 8.7. SA, salicylic acid; GAMID, *N*,*N*′-(5-nitro-1,3-phenylene)bisglutaramide.

[a]0.1 ppm Mn(II) = 1.8×10^{-6} mol/L.

Fig. 1. First-order plots in terms of [H_2O_2] for peroxide decomposition catalyzed by Mn(II) in 0.1 mol/L HCO_3^- at 40 °C and pH 8.5–8.7. No citrate was added.

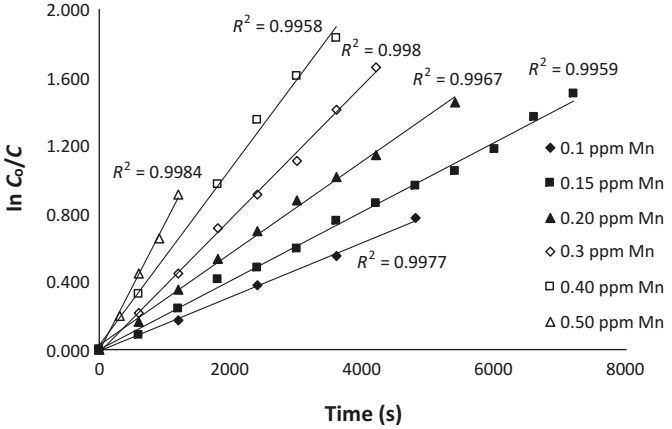

Fig. 2. Plot of $-\ln k_{OBS}$ vs $-\ln$[Mn(II)] for the data in Fig. 1.

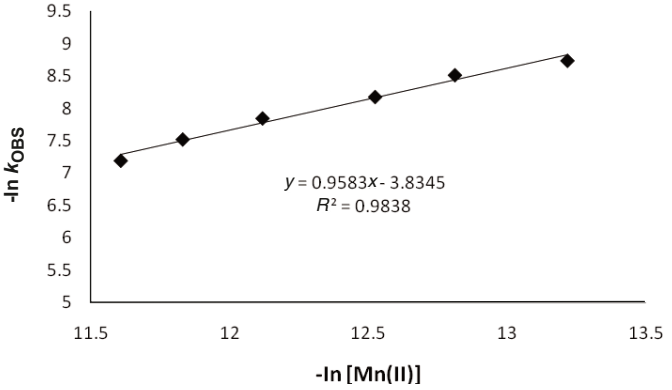

Fig. 3. Plot of $-\ln k_{OBS}$ vs $-\ln[HCO_3^-]$ for peroxide decomposition catalyzed by 0.1 ppm Mn(II) in 0.10–0.30 mol/L HCO_3^- at 40 °C and pH 8.5–8.7. When used, citrate was added at a 5:1 mol ratio to Mn(II).

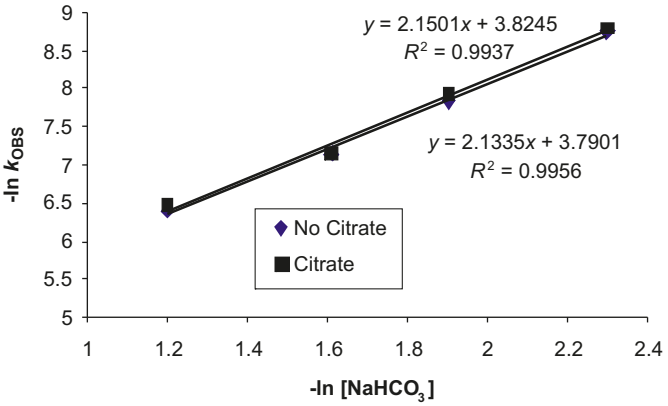

electroreduction and EPR spectroscopic study of Dasgupta et al.[12] where they observed the two species in eq. [10] in HCO_3^- solution at pH 8.3.

$$[10] \qquad Mn(HCO_3)_2 + H_2O \leftrightarrow [Mn(CO_3)(HCO_3)]^- + H_3O^+$$

Dasgupta et al.[12] estimated that the pK_a for $Mn(HCO_3)_2$, in accordance with eq. [10], should be in the range 7.5–8.5. If a pK_a of 8.5 is assumed then the dominant Mn(II) species would be $Mn(HCO_3)_2$ in the pH range 7.4–7.9, whereas the distribution would be ~50:50 between neutral and anionic Mn(II) species at pH 8.5–8.7. If it is assumed that H_2O_2 is capable of abstracting an electron from the anionic Mn(II) species at a much higher rate as compared with the neutral Mn(II) species, then the reaction scheme in eqs. [11]–[16] would give a rate equation that is first order in [H_2O_2] and [Mn(II)], but second order in [HCO_3^-]. In the derivation of

Can. J. Chem. Downloaded from www.nrcresearchpress.com by Xi'an Jiaotong University on 09/19/12
For personal use only.

Fig. 4. First-order plots in terms of $[H_2O_2]$ for peroxide decomposition catalyzed by Mn(II) in 0.075–0.125 mol/L HCO_3^- at 40 °C and pH 7.4–7.9. No citrate was added.

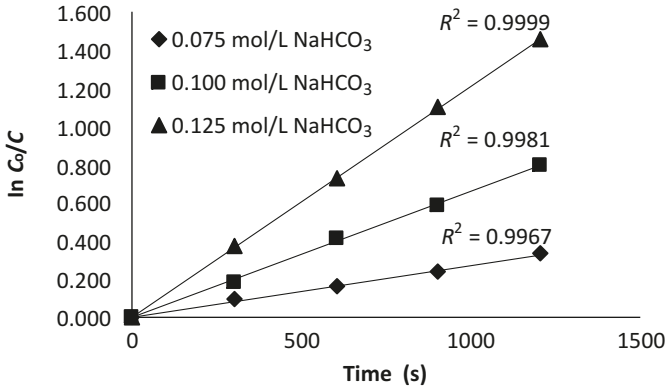

Table 2. First-order rate constants for Mn(II)-catalyzed peroxide decomposition in HCO_3^- solutions at pH 7.4–7.9 (in accordance with eq. [9]).

[Mn(II)] (ppm)	[HCO_3^-] (mol/L)	Other additives	k_{OBS} ($s^{-1} \times 10^4$)
1.0	0.1		6.7, 6.9
1.0	0.1	1.0 mmol/L SA	1.3
0.50	0.075		1.3
1.0	0.075		2.7, 2.9
1.5	0.075		4.3
2.0	0.075		5.2
2.5	0.075		6.5
1.0	0.125		12.3
1.0	0.150		20.5, 21.2

Note: 50 mmol/L H_2O_2 at 40 °C, initial pH 7.4, and final pH 7.7–7.9.

Fig. 5. Plot of $-\ln k_{OBS}$ vs $-\ln[Mn(II)]$ for peroxide decomposition catalyzed by 0.5–2.5 ppm Mn(II) in 0.075 mol/L HCO_3^- at 40 °C and pH 7.4–7.9. No citrate was added.

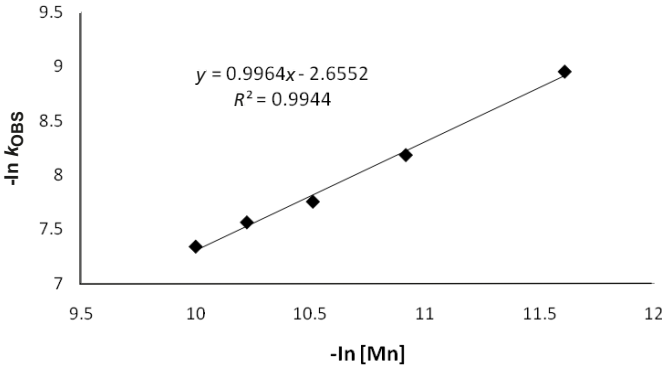

the rate equation, the reaction in eq. [16] was left out (to be discussed shortly). The redox chain mechanism is identical in form to one that is widely accepted for Fe(II)/Fe(III) catalysis of H_2O_2 decomposition.[17,18] The assumption that H_2O_2 abstracting an electron from the anionic Mn(II) species should occur at a higher rate is reasonable because the anionic Mn(II) species should be more electron-rich than the neutral Mn(II) species.

[11] $$Mn^{2+} + 2HCO_3^- \overset{K_1}{\leftrightarrow} [Mn(CO_3)(HCO_3)]^- + H^+$$

Fig. 6. Plot of $-\ln k_{OBS}$ vs $-\ln[HCO_3^-]$ for peroxide decomposition catalyzed by 1.0 ppm Mn(II) in 0.075–0.15 mol/L HCO_3^- at 40 °C and pH 7.4–7.9. No citrate was added.

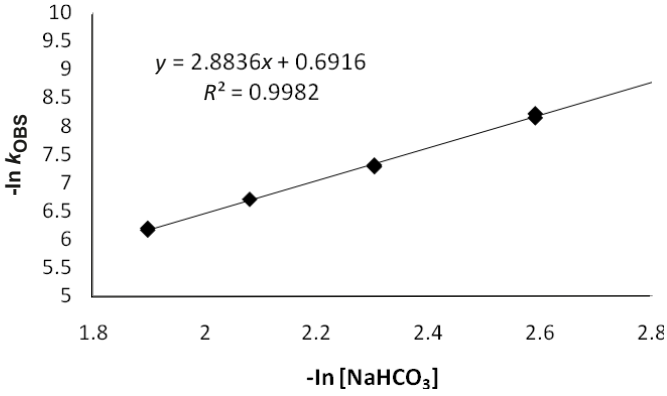

[12] $$[Mn(CO_3)(HCO_3)] + H_2O_2 \overset{k_1}{\rightarrow} [Mn(CO_3)(HCO_3)]^- + 2H^+ + \cdot O_2^-$$

[13] $$[Mn(CO_3)(HCO_3)]^- + H_2O_2 \overset{k_2}{\rightarrow} [Mn(CO_3)(HCO_3)_2] + OH^- + \cdot OH$$

[14] $$\cdot OH + H_2O_2 \overset{k_3}{\rightarrow} H_2O + \cdot O_2^- + H^+$$

[15] $$\cdot O_2^- + [Mn(CO_3)(HCO_3)] \overset{k_4}{\rightarrow} [Mn(CO_3)(HCO_3)]^- + O_2$$

[16] $$\cdot O_2^- + [Mn(CO_3)(HCO_3)]^- + H^+ \overset{k_5}{\rightarrow} Mn(CO_3)(HCO_3) + HOO^-$$

On the other hand, if it is assumed that electron abstraction from the anionic Mn(II) by HCO_4^- is retarded by anionic repulsion and that HCO_4^- is a strong enough oxidant to abstract an electron from the neutral Mn(II) species at a relatively high rate, then the reaction scheme in eqs. [17]–[20], [14], and eqs. [21] and [22] would give a rate equation that is first order in $[H_2O_2]$ and [Mn(II)], but third order in $[HCO_3^-]$. Equation [22] was left out in the rate equation derivation.

[17] $$Mn^{2+} + 2HCO_3^- \overset{K_2}{\leftrightarrow} Mn(HCO_3)_2$$

[18] $$HCO_3^- + H_2O_2 \overset{K_3}{\leftrightarrow} HCO_4^- + H_2O$$

[19] $$[Mn(HCO_3)_2]^+ + H_2O_2 \overset{k_6}{\rightarrow} Mn(HCO_3)_2 + 2H^+ + \cdot O_2^-$$

[20] $$Mn(HCO_3)_2 + HCO_4^- \overset{k_7}{\rightarrow} [Mn(HCO_3)_2]^+ + \cdot OH + CO_3^{2-}$$

[14] $$\cdot OH + H_2O_2 \overset{k_3}{\rightarrow} H_2O + \cdot O_2^- + H^+$$

Can. J. Chem. Downloaded from www.nrcresearchpress.com by Xi'an Jiaotong University on 09/19/12
For personal use only.

[21] $\cdot O_2^- + [Mn(HCO_3)_2]^+ \xrightarrow{k_8} Mn(HCO_3)_2 + O_2$

[22] $\cdot O_2^- + Mn(HCO_3)_2 + H^+ \xrightarrow{k_9} [Mn(HCO_3)_2]^+ + HOO^-$

In the derivation of the rate equations for both the high pH or anionic Mn(II) case and the low pH or neutral Mn(II) case, the termination reactions (eqs. [16] and [22]) were left out as mentioned earlier. The rate equations so derived are for oxygen generation and not peroxide decomposition. However, the simplification associated with leaving out eqs. [16] and [22] allowed for straightforward derivations of the respective rate equations. The only assumption that has to be made in the high pH case is whether $k_1[H_2O_2]$ is much greater or much less than $k_4[\cdot O_2^-]$. If it is assumed that $k_1[H_2O_2] >> k_4[\cdot O_2^-]$, the final rate equation is given in eq. [23], whereas if the reverse assumption is made the rate equation in eq. [24] is obtained. The two equations are identical in terms of reaction orders. The complete derivations of the rate equations (eqs. [23] and [24]) have been provided as Supplementary data and identified as Schemes 1*a* and 1*b*, respectively.

[23] $$\frac{d[O_2]}{dt} = \frac{2K_1k_2[Mn^{2+}][H_2O_2][HCO_3^-]^2}{[H^+]}$$

[24] $$\frac{d[O_2]}{dt} = \frac{K_1k_2[Mn^{2+}][H_2O_2][HCO_3^-]^2}{[H^+]}$$

The same assumption about relative values of $k_6[H_2O_2]$ and $k_8[\cdot O_2^-]$ is dealt with similarly in the low pH case. If it is assumed that $k_6[H_2O_2] >> k_8[\cdot O_2^-]$ then the rate equation in eq. [25] is obtained, whereas if the reverse assumption is made the rate equation in eq. [26] is obtained. The complete derivations of the rate equations (eqs. [25] and [26]) are presented as Supplementary data as Schemes 2*a* and 2*b*, respectively.

[25] $$\frac{d[O_2]}{dt} = 2K_2K_3k_7[Mn^{2+}][H_2O_2][HCO_3^-]^3$$

[26] $$\frac{d[O_2]}{dt} = K_2K_3k_7[Mn^{2+}][H_2O_2][HCO_3^-]^3$$

The experimental data showed a modest pH effect. When 0.5 ppm Mn(II) was used in 0.1 mol/L HCO_3^- at pH 8.5–8.7 a k_{OBS} of 7.5×10^{-4} s^{-1} was obtained, whereas when 1.0 ppm Mn(II) was used in 0.1 mol/L HCO_3^- at pH 7.4–7.9 a k_{OBS} of 6.8×10^{-4} s^{-1} was obtained. If it is assumed that k_{OBS} would increase to ca. 15×10^{-4} s^{-1} if the Mn(II) concentration were to be increased from 0.5 to 1.0 ppm at pH 8.5–8.7, then the peroxide decomposition rate would be >2.0 times as high at pH 8.5–8.7 as compared with pH 7.4–7.9. However, it would be extremely difficult to incorporate a pH effect into the two reaction schemes presented for high and low pH cases.

In all likelihood, reaction(s) in one scheme would compete with the corresponding reaction(s) in the other scheme. For example, the rate of Mn(III) oxidation of H_2O_2 in the high pH case is probably greater than in the low pH case (eq. [12] vs eq. [19]). It is also possible that the rate of Mn(II) oxidation by H_2O_2 is higher than the corresponding reaction with HCO_4^- (eq. [13] vs eq. [20]). It should be remembered that the ratio of $[HCO_4^-]$:$[H_2O_2]$ is only 0.032 in 0.1 mol/L HCO_3^- (eq. [2]). However, the rate of electron abstraction from $\cdot O_2^-$ in the low pH case eq. [21] may be higher than in the high pH case eq. [15]. Therefore, as pH is increased the concentrations of $[Mn(CO_3)(HCO_3)]^-$ and $Mn(CO_3)(HCO_3)$ would be expected to increase, whereas the concentrations of $Mn(HCO_3)_2$ and $[Mn(HCO_3)_2]^+$ should decrease in accordance with the equilibrium between Mn(II) species in eq. [10]. A possible outcome based on the arguments above is that the rate would increase for two reactions that are instrumental toward oxygen generation but decrease for a third. The net effect of this pH increase would be difficult to assess without having good estimates for the rate constants of the key reactions.

Conclusion

Hydrogen peroxide decomposition catalyzed by Mn(II) was investigated in HCO_3^- solutions in the pH ranges 8.5–8.7 and 7.4–7.9. The first pH range is optimum for pulp bleaching, but there are controversies in the literature regarding the mechanism of peroxide decomposition in the later pH range. It was concluded that free radical mechanisms were dominant in both pH ranges. The rate equation for peroxide decomposition was first order in $[H_2O_2]$ and [Mn(II)] in both pH ranges but close to second order in $[HCO_3^-]$ in the higher pH range and close to third order in the lower pH range. Free radical chain mechanisms were proposed that afforded rate equations that were first order in $[H_2O_2]$ and [Mn(II)]. One of the rate laws had a second-order bicarbonate dependence in the higher pH range and the other had a third-order dependence in the lower pH range.

Supplementary data

Supplementary data are available with the article through the journal Web site at http://nrcresearchpress.com/doi/suppl/10.1139/v11-080.

Acknowledgements

Financial support from Solvay Chemicals, Inc. and the Empire State Paper Research Associates (ESPRA) is deeply appreciated.

References

(1) (a) Flanagan, J.; Jones, D. P.; Griffith, W. P.; Skapski, A. C.; West, A. P. *J. Chem. Soc. Chem. Commun 1986*, 20. doi:10.1039/c39860000020; (b) Richardson, D. E.; Yao, H.; Frank, K. M.; Bennett, D. A. *J. Am. Chem. Soc.* **2000** *122* (8), 1729. doi:10.1021/ja9927467; (c) Bennett, D. A.; Yao, H.; Richardson, D. E. *Inorg. Chem.* **2001** *40* (13), 2996. doi:10.1021/ic000910h.

(2) (a) Attiogbe, F. K.; Bose, S. K.; Wang., W.; McNeillie, A.; Francis, R. C. *BioResources* **2010** *5* (4), 2208 (b) Attiogbe, F. K; Wang, W.; McNeillie, A.; Francis, R. C. *BioResources* **2010** *5* (4), 2221.

(3) Vakhitova, L. N.; Zhil'tsova, S. V.; Skrypka, A. V.; Razumova,

N. G.; Taran, N. A.; Savelova, V. A.; Popov, A. F. *Theor. Exp. Chem.* **2006** *42* (5), 287. doi:10.1007/s11237-006-0055-y.
(4) Attiogbe, F. K.; Francis, R. C. *Can. J. Chem.*, in press.
(5) (a) Singh, S.; Hider, R. C. *Anal. Biochem.* **1988** *171* (1), 47. doi:10.1016/0003-2697(88)90123-6; (b) Zhang, X.-Z.; Francis, R. C.; Dutton, D. B.; Hill, R. T. *Can. J. Chem.* **1998** *76*, 1064. doi:10.1139/v98-103.
(6) Gierer, J.; Jansbo, K. *J. Wood Chem. Technol.* **1993** *13* (4), 561. doi:10.1080/02773819308020534.
(7) Francis, R. C.; Zhang, X.; Froass, P. M.; Tamer, O. *Tappi J* **1994** *77* (6), 133.
(8) (a) Sychev, A. Y.; Isak, V. G.; Van Lap, D. *Russ. J. Phys. Chem.* **1978** *52* (1), 55; (b) Sychev, A. Y.; Isak, V. G.; Pfannmeller, U. *Russ. J. Phys. Chem.* **1983** *57* (3), 464; (c) Sychev, A. Y.; Mai, H. H.; Isak, V. G. *Russ. J. Phys. Chem.* **1984** *58* (4), 549.
(9) (a) Stadtman, E. R.; Berlett, B. S.; Chock, P. B. *Proc. Natl. Acad. Sci. U.S.A.* **1990** *87* (1), 384. doi:10.1073/pnas.87.1.384; (b) Yim, M. B.; Berlett, B. S.; Chock, P. B.; Stadtman, E. R. *Proc. Natl. Acad. Sci. U.S.A.* **1990** *87* (1), 394. doi:10.1073/pnas.87.1.394.
(10) Sychev, A. Y.; Pfannmeller, I. W.; Isak, V. G. *Russ. J. Phys. Chem.* **1981** *55* (2), 202.
(11) Kozlov, Y. N.; Zharmukhamedov, S. K.; Tikhonov, K. G.; Dasgupta, J.; Kazakova, A. A.; Dismukes, G. C.; Klimov, V. V. *Phys. Chem. Chem. Phys.* **2004** *6* (20), 4905. doi:10.1039/b406569g.
(12) Dasgupta, J.; Tyryshkin, A. M.; Kozlov, Y. N.; Klimov, V. V.; Dismukes, G. C. *J. Phys. Chem. B* **2006** *110* (10), 5099. doi:10.1021/jp055213v.
(13) Tikhonov, K. G.; Zastrizhnaya, M.; Kozlov, Y. N.; Klimov, V. V. *Biochemistry (Mosc.)* **2006** *71* (11), 1270. doi:10.1134/S0006297906110137.
(14) Koppenol, W. H.; Butler, J. *Adv. Free Radic. Biol. Med.* **1985** *1* (1), 91. doi:10.1016/8755-9668(85)90005-5.
(15) Rocha, C.; Da Costa Ferreira, A. M. *Int. J. Chem. Kinet.* **1994** *26* (11), 1121. doi:10.1002/kin.550261107.
(16) Maskos, Z.; Rush, J. D.; Koppenol, W. H. *Arch. Biochem. Biophys.* **1992** *296* (2), 521. doi:10.1016/0003-9861(92)90606-W.
(17) Barb, W. G.; Buxendale, J. H.; George, P.; Hargrave, K. R. *Trans. Faraday Soc.* **1951** *47*, 591. doi:10.1039/tf9514700591.
(18) (a) Walling, C.; Goosen, A. *J. Am. Chem. Soc.* **1973** *95* (9), 2987. doi:10.1021/ja00790a042; (b) Walling, C. *Acc. Chem. Res.* **1975** *8* (4), 125. doi:10.1021/ar50088a003; (c) Walling, C.; Partch, R. E.; Weil, T. *Proc. Natl. Acad. Sci. U.S.A.* **1975** *72* (1), 140. doi:10.1073/pnas.72.1.140; (d) Walling, C.; Amarnath, K. *J. Am. Chem. Soc.* **1982** *104* (5), 1185. doi:10.1021/ja00369a005.

Can. J. Chem. Downloaded from www.nrcresearchpress.com by Xi'an Jiaotong University on 09/19/12
For personal use only.

Theoretical calculation of the low-lying quartet states of the CrF molecule

A. Hamdan and M. Korek

Can. J. Chem. Downloaded from www.nrcresearchpress.com by Xi'an Jiaotong University on 09/19/12
For personal use only.

Abstract: The potential energy curves have been investigated for the 11 lowest quartet electronic states in the $^{2s+1}\Lambda^{\pm}$ representation below 28 000 cm^{-1} of the molecule CrF via CASSCF and MRCI (single and double excitations with Davidson correction) calculations. Eight electronic states have been studied theoretically for the first time. The harmonic frequency ω_e, the internuclear distance r_e, the rotational constant B_e, the electronic energy with respect to the ground state T_e, and the permanent dipole moment μ have been calculated. By using the canonical functions approach, the eigenvalues E_v, the rotational constant B_v, and the abscissas of the turning points r_{min} and r_{max} have been calculated for electronic states up to the vibrational level $v = 38$. The comparison of these values to the theoretical results available in the literature shows a very good agreement.

Key words: ab initio calculation, potential energy curves, spectroscopic constants, rovibrational calculation, permanent dipole moment.

Résumé : Faisant appel à des calculs de l'espace actif complet en champ autocohérent (EAC-CAC) et de l'interaction de configuration à référence multiple (IC-RM) (en excitation simple ou double, avec correction de Davidson), on a étudié les courbes d'énergie potentielle des 11 états électroniques quadruplets les plus faibles dans la $^{2s+1}\Lambda^{\pm}$ représentation en dessous de 28 000 cm^{-1} de la molécule de CrF. Huit états électroniques ont été étudiés d'une façon théorique pour la première fois. On a calculé la fréquence harmonique, ω_e, la distance internucléaire, ω_e, la constante de rotation, B_e, l'énergie électronique par rapport à l'état fondamental, T_e, et le moment dipolaire permanent, μ. Utilisant l'approche des fonctions canoniques, on a aussi calculé les valeurs eigen, E_v, la constante de rotation, B_v, et les abscisses des points de changement de sens, r_{min} et r_{max}, des états électroniques jusqu'au niveau vibrationnel $v = 38$. Une comparaison de ces valeurs avec les résultats théoriques disponibles dans la littérature présente un très bon accord.

Mots-clés : calculs ab initio, courbes d'énergie potentielle, constantes spectroscopiques, calcul rovibrationnel, moment dipolaire permanent.

[Traduit par la Rédaction]

Introduction

Diatomic molecules containing a 3d transition-metal atom and a main-group element are of considerable interest in organometalic chemistry, catalysis, high-temperature chemistry,[1,2] constituents of cool stars,[3] sunspots, and as models for the role that d-electrons play in chemical bonds involving a transition element.[4] The large number of low-lying states, often of high multiplicity, in transition-metal-containing diatomic molecules gives rise to a remarkable congestion in their spectra, which presents difficulties for both spectroscopists and theoretical chemists. Since transition-metal compounds are highly refractory, few methods are available to produce gaseous molecules efficiently for spectroscopic study at room temperature; this is the reason why few species containing a transition-metal atom have been studied with high-resolution spectroscopy, and therefore, there is a need for ab initio calculations as guidance for the experiments or analyzing the experimental results for these molecules.

In the literature, there are only few theoretical results for the quartet states $(1)^4\Sigma^+$, $(1)^4\Pi$, and $(1)^4\Delta$ of the molecule CrF. The spectroscopic constants of these states have been calculated by Harrison et al.,[4] Bencheikh et al.,[5] Koukounas et al.[6] and Koivisto et al. [7] by using, respectively, the ligand field and density functional techniques, variety of ab initio method and MRCI, and spin-orbit-configuration interaction calculation. Recently,[8] we investigated the 12 lowest sextet electronic states in the $^{2s+1}\Lambda^{\pm}$ representation below 53 000 cm^{-1} of the molecule CrF via CASSCF and MRCI (single and double excitation with Davidson correction) calculations where we found that the ground state is $X^6\Sigma^+$. In the present work, 11 low-lying quartet electronic states of CrF have been investigated by using the same procedure of ab initio method. The potential energy curves (PECs), along with the transition energy with respect to the minimum energy for the ground state T_e, the equilibrium internuclear distance r_e, the harmonic frequency ω_e, the rotational constant B_e, and the permanent dipole moment μ have been obtained for the lowest-lying quartet electronic states of the CrF molecule. Eight states have been investigated here for the first time. Taking

Received 14 January 2011. Accepted 19 April 2011. Published at www.nrcresearchpress.com/cjc on 13 September 2011.

A. Hamdan and M. Korek. Physics Department, Faculty of Science, Beirut Arab University, P.O. Box 11-5020 Riad El Solh, Beirut 1107 2809, Lebanon.

Corresponding author: M. Korek (e-mail: fkorek@yahoo.com).

Can. J. Chem. Downloaded from www.nrcresearchpress.com by Xi'an Jiaotong University on 09/19/12
For personal use only.

Fig. 1. Potential energy curves of the lowest quartet Δ and Σ states of the $^{2s+1}\Lambda^{\pm}$ representation of the molecule CrF.

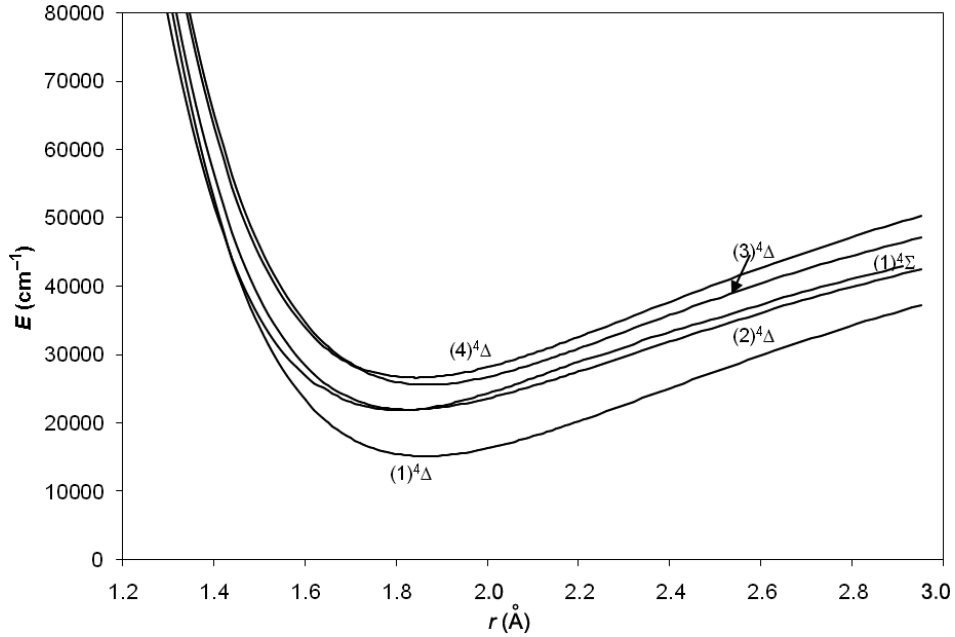

Fig. 2. Potential energy curves of the lowest quartet Π, Γ, Φ, and Σ states of the $^{2s+1}\Lambda^{\pm}$ representation of the molecule CrF.

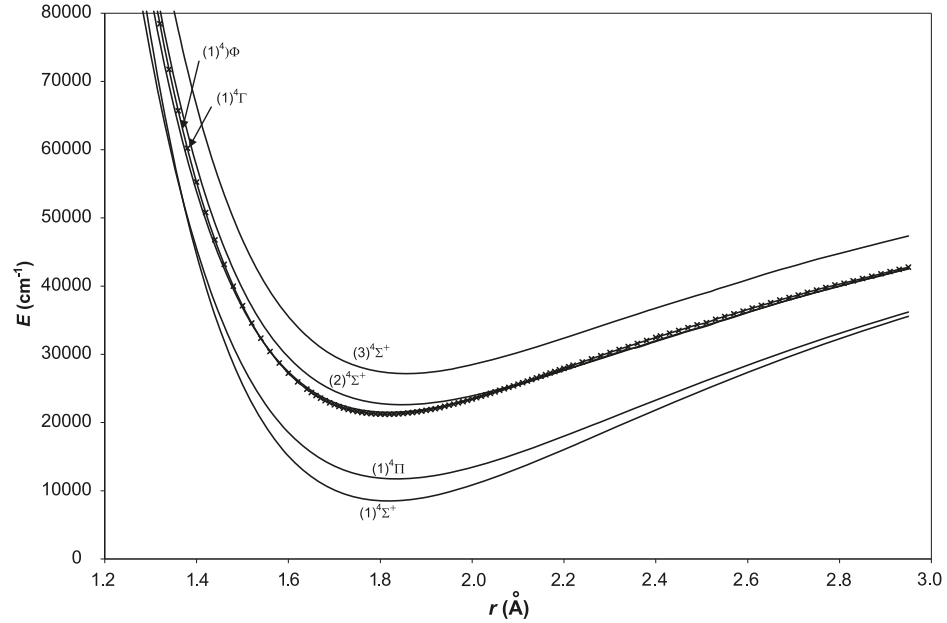

advantage of the electronic structure of the investigated electronic states of CrF and by using the canonical functions approach, the eigenvalue E_v, the rotational constant B_v, and the abscissas of the turning points r_{min} and r_{max} have been calculated for several vibrational levels of the 11 considered quartet electronic states.

Computational approach

Ab initio calculation

To test the use of ab initio calculation for the study of the transition metal – fluorine, particularly Cr atom – fluorine, we investigate in the present work the lowest-lying quartet electronic states of the CrF molecule via CASSCF method. Multireference CI calculations (single and double excitations with Davidson corrections) were performed. Chromium and fluorine atoms are treated in all electron schemes where the 24 electrons of the chromium and 9 electrons of fluorine are considered using a contracted Gaussian basis set given by Bauschlisher[9] for s, p, d, and f functions to obtain the contracted basis set [7s6p4d3f] for the Cr atom and the contracted [5s4p3d2f] Gaussian basis set aug-cc-PVQZ[10] for the F atom. By recalculating the ground state $X^6\Sigma^+$, the ab initio calculation of this molecule has been done in two ways: (*i*) 28 inner electrons were frozen in subsequence calculations so that five valance electrons were explicitly treated. The active space contains 6σ (Cr: $4s3d^04p^04d^05s$; F: 3s), 3π (Cr: $3d^{\pm1}4p^{\pm1}4d^{\pm1}$), and 2δ (Cr: $3d^{\pm2}4d^{\pm2}$) orbitals in the C_{2v}

Fig. 3. Permanent dipole moment curves of the lowest quartet Δ and Σ states of the $^{2s+1}\Lambda^{\pm}$ representation of the molecule CrF.

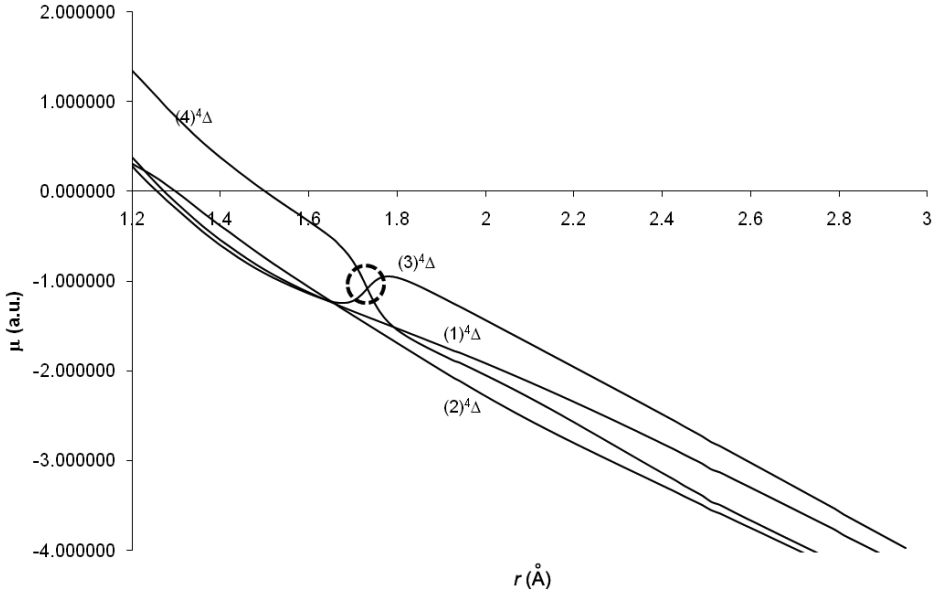

Fig. 4. Permanent dipole moment curves of the lowest quartet Π, Γ, Φ, and Σ states of the $^{2s+1}\Lambda^{\pm}$ representation of the molecule CrF.

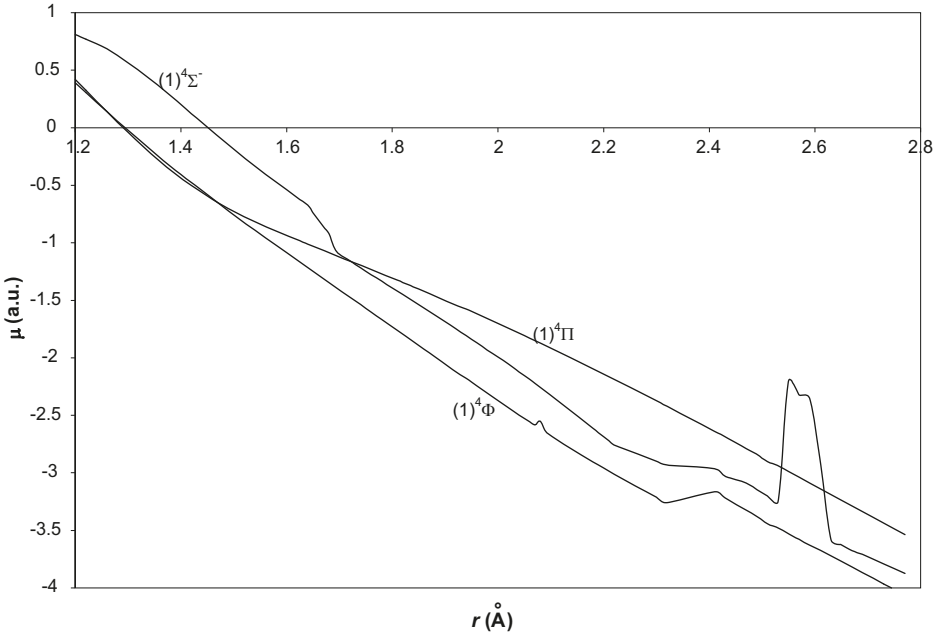

symmetry distributed into irreducible representation a_1, b_1, b_2, and a_2 in the following way $8a_1$, $3b_1$, $3b_2$, and $2a_2$ noted.[2,3,8] (*ii*) 20 inner electrons were frozen in subsequent calculations so that 13 valance electrons were explicitly treated. The active space contains 4σ (Cr: $4^s3d^04p^0$), 2π (Cr: $3d^{\pm1}4p^{\pm1}$), and 1δ (Cr: $3d^{\pm2}$) orbitals in the C_{2v} symmetry into irreducible representation a_1, b_1, b_2, and a_2 in the following way 5a1, $2b_1$, $2b_2$, and $1a_2$ noted.[1,2,5] In the range of the internuclear distance r around the equilibrium position of its ground state, the CrF molecule is assumed to be mainly ionic. This calculation has been performed via the computational chemistry program MOLPRO[11] taking advantage of the graphical user interface GABEDIT.[12]

The PECs and the dipole moment for 11 quartet states in the representation $^{2s+1}\Lambda^{\pm}$ have been calculated for 131 internuclear distances in the range 1.2 Å ≤ r ≤ 2.95 Å. These PECs, and the dipole moment in the different symmetries, in case of 13 valance electrons, are given in Figs. 1–4, respectively. In the range of r considered, some crossings between the states occur; the positions of these crossings are given in Table 1. The spectroscopic constants such as the vibrational harmonic constant ω_e, the internuclear distance at equilibrium r_e, the rotation constant B_e, and the electronic transition energy with respect to the ground state T_e have been calculated by fitting the energy values around the equilibrium position to a polynomial in terms of the internuclear distance by using the data obtained from the ab initio calculation with five and 13 valence electron. The comparison of our results with the 12 values for T_e calculated by different techniques in the literature for the states $(1)^4\Pi$, $(1)^4\Delta$, and $(1)^4\Sigma^+$ shows

Can. J. Chem. Downloaded from www.nrcresearchpress.com by Xi'an Jiaotong University on 09/19/12
For personal use only.

Can. J. Chem. Downloaded from www.nrcresearchpress.com by Xi'an Jiaotong University on 09/19/12
For personal use only.

Table 1. Positions of the crossings and avoided crossing between the different lowest electronic quartet states of the molecule CrF.

			Crossing	Avoid crossing
State 1	State 2	(n_1)state1/(n_2)state2	r_c (Å)	r_{ac} (Å)
$^4\Sigma^+$	$^4\Delta$	3/4	2.13	
	$^4\Pi$	1/1	1.37	
	$^4\Phi$	2/1	2.19	
	$^4\Phi$	2/1	2.37	
	$^4\Sigma^-$	2/1	1.96	
	$^4\Gamma$	2/1	2.10	
$^4\Sigma^-$	$^4\Delta$	1/2	1.38	
	$^4\Delta$	1/2	1.85	
$^4\Delta$	$^4\Phi$	1/1	1.34	
	$^4\Phi$	2/1	2.09	
	$^4\Gamma$	2/1	2.04	
	$^4\Delta$	3/4		1.72
$^4\Gamma$	$^4\Phi$	1/1	1.55	

that 10 values are in good agreement where the relative difference is $0.9\% \leq \delta T_e/T_e \leq 9.3\%$ for the calculation with five valence electron and $0.5\% \leq \delta T_e/T_e \leq 8.4\%$ for the calculation with 13 valence electron. For the states $(1)^4\Delta$ and $(1)^4\Sigma^+$, the comparison of our values of T_e with those calculated by using ligand field theory by Bencheikh et al.[5] and MRCI method by Koivisto et al.[7] shows that two values have larger relative difference equal 11.9% and 12.8% for the calculation with five valence electrons and 11.04% and 11.80% for the calculation with 13 valence electrons, respectively. For ω_e, and for the same states, the comparison of our values with those given in the literature showed a very good agreement for nine values where the relative difference is $0.3\% \leq \delta\omega_e/\omega_e \leq 5.2\%$ for the calculation with five valence electrons and $0.1\% \leq \delta\omega_e/\omega_e \leq 7.5\%$ for the calculation with 13 valence electrons, while the comparison with those given by ligand field theory[5] shows a larger relative difference of $12.0\% \leq \delta\omega_e/\omega_e \leq 19.2\%$ and $10.1\% \leq \delta\omega_e/\omega_e \leq 14.5\%$ for the calculations with five and 13 valence electrons, respectively. This difference in the values of ω_e can be explained by the light difference in the shape of the potential energy curves around the minimum calculated by our method and that used of Bencheikh et al.[5] For the same three states, the 12 values of r_e obtained theoretically in the literature are in very good agreement with our calculated values with a relative difference of $0.3\% \leq \delta r_e/r_e \leq 5.3\%$ and $0.0\% \leq \delta r_e/r_e \leq 3.0\%$ for the calculations with five valence electrons and 13 valence electrons, respectively.

The values of the dipole-moment operator are among the most reliably predicted physical properties; they give useful information about the degree of ionic and covalent character in the bonding, which needs to be correctly represented by the ab initio calculations. The expectation value of the dipole-moment operator is sensitive to the nature of the least energetic and most chemically relevant valence electrons. Since the dipole moment at the Hartree–Fock level is usually large, and to obtain the best accuracy, multireference configuration interaction (MRCI) wave functions were constructed using multiconfiguration self-consistent field (MCSCF) active space. By taking the Cr atom as an origin in our calculation, the permanent dipole moments of the investigated electronic states have been investigated for the 11 lowest quartet electronic states of the molecule CrF. The calculated values of the dipole moments (in Debye (D)) for these electronic states in terms of the internuclear distance r are plotted in Figs. 3 and 4. All these calculations have been performed by using the MOLPRO[11] program. The number of valence electron has a large influence on the calculation of the permanent dipole moments; the comparison of our calculated values, in case of five valence electrons, with the 6 values given in the literature[4,6] shows a relative difference (Table 2) $7.1\% \leq \delta\mu/\mu \leq 69.7\%$, while this relative difference becomes $0.6\% \leq \delta\mu/\mu \leq 15.4\%$ with the 13 valence electrons, which represents a very good agreement. One can notice the agreement between the position of the avoided crossing of the PECs (Fig. 1 and Table 1) of the $(3)^4\Delta$ and $(4)^4\Delta$ and the crossings of dipole-moment curves of these states in Fig. 3, which confirm the accuracy of the present work.

The vibration–rotation calculation

Within the Born–Oppenheimer approximation, the vibration rotation motion of a diatomic molecule in a given electronic state is governed by the radial Schrödinger equation

$$[1] \qquad \left[\frac{d^2}{dr^2} + \frac{2\mu}{\hbar^2}\Big(E_{vJ} - U(r)\Big) - \frac{\lambda}{r^2}\right]\Psi_{vJ}(r) = 0$$

where r is the internuclear distance, v and J are, respectively, the vibrational and rotational quantum numbers, $\lambda = J(J+1)$, and E_{vJ} and ψ_{vJ} are, respectively, the eigenvalue and the eigenfunction of this equation. In the perturbation theory, these functions can be expanded as

$$[2] \qquad E_{vJ} = \sum_{n=0} e_n \lambda^n$$

$$[3] \qquad \Psi_{vJ}(r) = \sum_{n=0} \Phi_n(r)\lambda^n$$

with $e_0 = E_v$, $e_1 = B_v$, $e_2 = -D_v$. ϕ_0 is the pure vibrational wave function and ϕ_n is its rotational correction. By replacing eqs. [2] and [3] into eq. [1], and since this equation is satisfied for any value of λ, one can write[13–15]

Can. J. Chem. Downloaded from www.nrcresearchpress.com by Xi'an Jiaotong University on 09/19/12
For personal use only.

Table 2. Spectroscopic constants and permanent dipole moments of the lowest quartet states of the molecule CrF.

States	T_e (cm^{-1})	$\delta T_e/T_e$ (%)	ω_e (cm^{-1})	$\delta\omega_e/\omega_e$ (%)	$B_e \times 10^2$ (cm^{-1})	r_e (Å)	$\delta r_e/r_e$ (%)	μ (D)	δμ/μ (%)
$(1)^4\Sigma^+$	8504 (a_1)		664.42 (a_1)		36.70 (a_1)	1.81 (a_1)		3.08 (a_1)	
	8598 (a_2)		678.36 (a_2)		37.48 (a_2)	1.798 (a_2)		2.12 (a_2)	
	8160 (b)	4.2 (f)	755 (b)	12.1 (f)		1.761 (b)	2.8 (f)		
		5.4 (g)		10.2 (g)			2.1 (g)		
	9748 (c)	12.8 (f)	631 (c)	5.2 (f)		1.788 (c)	1.2 (f)		
		11.8 (g)		7.5 (g)			0.6 (g)		
	8424 (d_1)	0.95 (f)	671 (d_1)	0.98 (f)		1.798 (d_2)	0.66 (f)	2.41 (d_5), (d_6)	27.8 (f)
		2.06 (g)		0.11 (g)			0.0 (g)		9.5 (g)
	8432.9 (e_1)	4.7 (f)	685.38 (e_2)	3.1 (f)		1.793 (e_3)	0.9 (f)	2.27 (e_5)	35.7 (f)
		2.0 (g)		1.0 (g)			0.3 (g)		6.6 (g)
$(1)^4\Pi$	11737 (a_1)		631.55 (a_1)		35.94 (a_1)	1.836 (a_1)		4.04 (a_1)	
	11474 (a_2)		675 (a_2)		37.52 (a_2)	1.797 (a_2)		2.41 (a_2)	
	11957 (b)	1.8 (f)	782 (b)	19.2 (f)		1.744 (b)	5.3 (f)		
		4.0 (g)		13.7 (g)			3.0 (g)		
	11903 (c)	1.4 (f)	637 (c)	0.8 (f)		1.823 (c)	0.71 (f)		
		3.6 (g)		5.6 (g)			1.4 (g)		
	12013 (d_3)	2.3 (f)	630 (d_3)	0.25 (f)		1.816 (d_1)	1.1 (f)	2.85 (d_6)	41.7 (f)
		4.5 (g)		7.1 (g)			1.0 (g)		15.4 (g)
	11413.1 (e_4)	4.6 (f)	639.6 (e_2), (e_4)	1.2 (f)		1.799 (e_2)	2.0 (f)	2.38 (e_5)	69.7 (f)
		0.5 (g)		5.5 (g)			0.1 (g)		1.3 (g)
$(1)^4\Delta$	15145 (a_1)		604 (a_1)		35.65 (a_1)	1.844 (a_1)		3.92 (a_1)	
	15290 (a_2)		618 (a_2)		36.23 (a_2)	1.828 (a_2)		3.26 (a_2)	
	17187 (b)	11.9 (f)	723 (b)	16.5 (f)		1.781 (b)	3.5 (f)		
		11.0 (g)		14.5 (g)			2.6 (g)		
	16693 (c)	9.3 (f)	608 (c)	0.7 (f)		1.813 (c)	1.7 (f)		
		8.4 (g)		1.6 (g)			0.8 (g)		
	15646 (d_1)	3.2 (f)	606 (d_4)	0.49 (f)		1.839 (d_2), (d_3)	0.27 (f)	3.66 (d_5), (d_6)	7.1 (f)
		2.3 (g)		1.8 (g)			0.6 (g)		10.9 (g)
	15179 (e_2)	3.45 (f)	608.8 (e_2)	1.06 (f)		1.830 (e_2)	0.80 (f)	3.24 (e_5)	20.98 (f)
		0.73 (g)		1.51 (g)			0.11		0.62 (g)
$(1)^4\Gamma$	21204.95 (a_1)		604 (a_1)		35.65 (a_1)	1.813 (a_1)		4.26 (a_1)	
	21865.99 (a_2)		693 (a_2)		38.28 (a_2)	1.779 (a_2)		2.41 (a_2)	
$(1)^4\Phi$	21489 (a_1)		630 (a_1)		36.58 (a_1)	1.819 (a_1)		4.56 (a_1)	
	22359 (a_2)		683 (a_2)		38.32 (a_2)	1.778 (a_2)		2.48 (a_2)	
$(1)^4\Sigma^-$	21860 (a_1)		660 (a_1)		36.78 (a_1)	1.815 (a_1)		4.21 (a_1)	
	22426 (a_2)		684 (a_2)		38.06 (a_2)	1.784 (a_2)		2.43 (a_2)	
$(2)^4\Delta$	21949 (a_1)		613 (a_1)		36.17 (a_1)	1.83 (a_1)		4.69 (a_1)	
	22849 (a_2)		704 (a_2)		38.61 (a_2)	1.771 (a_2)		2.83 (a_2)	
$(2)^4\Sigma^+$	22611 (a_1)		585 (a_1)		35.495 (a_1)	1.847 (a_1)		4.39 (a_1)	
	23700 (a_2)		696 (a_2)		38.206 (a_2)	1.781 (a_2)		3.08 (a_2)	
$(3)^4\Delta$	25589 (a_1)		620 (a_1)		34.68 (a_1)	1.869 (a_1)		2.62 (a_1)	
	27431 (a_2)		617 (a_2)		36.55 (a_2)	1.821 (a_2)		2.36 (a_2)	

Can. J. Chem. Downloaded from www.nrcresearchpress.com by Xi'an Jiaotong University on 09/19/12
For personal use only.

Table 2 (*concluded*).

States	T_e (cm^{-1})	$\delta T_e/T_e$ (%)	ω_e (cm^{-1})	$\delta\omega_e/\omega_e$ (%)	$B_e \times 10^2$ (cm^{-1})	r_e (Å)	$\delta r_e/r_e$ (%)	μ (D)	$\delta\mu/\mu$ (%)
(4) $^4\Delta$	26625 (a_1)		634 (a_1)		35.69 (a_1)	1.84 (a_1)		4.41 (a_1)	
	29060 (a_2)		891 (a_2)		39.24 (a_2)	1.755 (a_2)		2.57 (a_2)	
$(2)^4\Gamma$	26015 (a_2)		621 (a_2)		36.35 (a_2)	1.826 (a_2)		2.11 (a_2)	
$(3)^4\Sigma^+$	27174 (a_1)		621 (a_1)		35.16 (a_1)	1.856 (a_1)		3.93 (a_1)	

Note: (a_1) and (a_2) are for the present work with five valence electrons and 13 valence electrons calculations, respectively; ref. 5: (b); ref. 7: (c); ref. 6: (d_1) MRCI, (d_2) MRACPF, (d_3) MRCI+Q, (d_4) C-MRCI, (d_5) MRCI obtained by the finite field method, and (d_6) C-MRCI+Q obtained by the finite field method; ref. 4 with 21 valence electrons: (e_1) CI(R); ref. 4 with 13 valance electrons: (e_2) CI(NR), (e_3) CI(R), (e_4) CID (NR), and (e_5) MRCI; (f) and (g) represent, respectively, the relative difference between our calculated values (a_1) and (a_2) and those given in the literature.

$$[4] \qquad \phi_0'(r) + [e_0 - U(r)]\phi_0(r) = 0$$

$$[5a] \qquad \phi_1'(r) + [e_0 - U(r)]\,\phi_1(r) = -[e_1 - R(r)]\,\phi_0(r)$$

$$[5b] \qquad \phi_2'(r) + [e_0 - U(r)]\,\phi_2(r) = -[e_1 - R(r)]\,\phi_1(r) - e_2\,\phi_0(r)$$

$$[5c] \qquad \phi_n'(r) + [e_0 - U(r)]\,\phi_n(r) = R(r)\,\phi_{n-1} - \sum_{m=1}^{n} e_m\,\phi_{n-m}(r)$$

where $R(r) = 1/r^2$, the first equation is the pure vibrational Schrödinger equation, and the remaining equations are called the rotational Schrödinger equations. One may project eqs. [5*a*]–[5*c*] onto ϕ_0 and find

$$[6a] \qquad < \phi_0|\phi_0 > e_1 = < \phi_0|\frac{1}{r^2}|\phi_0 >$$

$$[6b] \qquad < \phi_0|\phi_0 > e_2 = < \phi_0|\frac{1}{r^2}|\phi_1 > -e_1 < \phi_0|\phi_1 >$$

$$[6c] \qquad < \phi_0|\phi_0 > e_n = < \phi_0|\frac{1}{r^2}|\phi_{n-1} > - \sum_{m=1}^{n-1} e_m < \phi_{n-m}|\phi_0 >$$

Once e_0 is calculated from eq. [4], e_1, e_2, e_3, …, e_n can be obtained by using alternatively eqs. [5] and [6]. By using these canonical functions and the cubic spline interpolation between each two consecutive points of the potential energy curves obtained from the ab initio calculation of the CrF molecule, the eigenvalue E_v, the rotational constant B_v, the centrifugal distortion constant D_v, and the abscissas of the turning point r_{min} and r_{max} have been calculated for all the considered electronic states up to the vibrational levels v = 38. These values for the states $(1)^4\Sigma^+$ and $(1)^4\Pi$ (as illustrated) are given in Table 3. There is no comparison of these values of with other results, since they are given here for the first time.

Conclusion

In the present work, the ab initio investigation for 11 low-lying quartet electronic states of the CrF molecule has been performed via CAS-SCF/MRCI method. The potential energy curves and the dipole moment curves have been determined along with the spectroscopic constants T_e, r_e, ω_e, and the rotational constant B_e for the considered electronic states. To the best of our knowledge, there is no experimental data for the quartet states of the molecule CrF, while the theoretical results are those of Bencheikh et al.,[5] Harrison and Hutchison,[4] Koivisto et al.,[7] and Koukounas et al.[6] By comparing our calculated values with those obtained theoretically by different techniques, one can confirm the validity and the accuracy of the ab initio MRCI calculation used in the present work with the chosen valence electrons. By using the

Table 3. Values of the eigenvalues E_v, the rotational constants B_v, the centrifugal distortion constants D_v, and the abscissas of the turning points for the different vibrational levels of $(1)^4\Sigma^+$ and $(1)^4\Pi$ states of the CrF molecule.

	$(1)^4\Sigma^+$					$(1)^4\Pi$				
v	E_v (cm^{-1})	$B_v \times 10^2$ (cm^{-1})	$D_v \times 10^7$ (cm^{-1})	r_{min} (Å)	r_{max} (Å)	E_v (cm^{-1})	$B_v \times 10^2$ (cm^{-1})	$D_v \times 10^7$ (cm^{-1})	r_{min} (Å)	r_{max} (Å)
0	336	36.542	4.333	1.7607	1.8810	314	35.834	4.712	1.7765	1.9007
1	1004	36.304	4.257	1.7225	1.9315	936	35.566	4.762	1.7371	1.9542
2	1670	36.078	4.293	1.6977	1.9676	1550	35.314	4.627	1.7116	1.9922
3	2329	35.801	4.531	1.6785	1.9999	2161	35.094	4.650	1.6918	2.0249
4	2976	35.517	4.287	1.6627	2.0287	2767	34.835	4.776	1.6752	2.0544
5	3619	35.294	4.312	1.6489	2.0554	3366	34.600	4.595	1.6608	2.0817
6	4255	35.014	4.464	1.6368	2.0806	3961	34.357	4.800	1.6481	2.1075
7	4883	34.782	4.220	1.6258	2.1046	4549	34.116	4.588	1.6367	2.1321
8	5507	34.521	4.524	1.6159	2.1278	5132	33.875	4.787	1.6263	2.1558
9	6123	34.284	4.195	1.6067	2.1502	5708	33.635	4.570	1.6168	2.1788
10	6734	34.027	4.490	1.5982	2.172	6280	33.393	4.780	1.6079	2.2011
11	7338	33.791	4.188	1.5903	2.1933	6846	33.160	4.598	1.5996	2.223
12	7936	33.531	4.431	1.5829	2.2142	7407	32.916	4.750	1.5919	2.2444
13	8529	33.305	4.297	1.5759	2.2347	7962	32.690	4.674	1.5846	2.2654
14	9115	33.046	4.321	1.5693	2.2549	8511	32.445	4.634	1.5777	2.2862
15	9696	32.823	4.428	1.5631	2.2749	9055	32.219	4.753	1.5711	2.3066
16	10271	32.572	4.153	1.5572	2.2946	9594	31.983	4.556	1.5649	2.3269
17	10841	32.337	4.494	1.5515	2.3141	10128	31.748	4.756	1.559	2.3469
18	11404	32.107	4.184	1.5461	2.3334	10656	31.525	4.664	1.5533	2.3667
19	11963	31.860	4.342	1.5409	2.3526	11179	31.289	4.592	1.5479	2.3865
20	12515	31.641	4.395	1.536	2.3834	11698	31.067	4.722	1.5427	2.406
21	13062	31.401	4.097	1.5312	2.3906	12211	30.844	4.496	1.5377	2.4255
22	13604	31.167	4.386	1.5266	2.4094	12719	30.619	4.522	1.5339	2.4445
23	14141	30.948	4.232	1.5222	2.4281	13223	30.411	4.609	1.5282	2.4635
24	14672	30.711	4.122	1.518	2.4467	13722	30.194	4.482	1.5238	2.483
25	15199	30.491	4.408	1.5139	2.4652	14217	29.966	4.685	1.5195	2.5011
26	15720	30.276	4.166	1.51	2.4838	14706	29.745	4.715	1.5153	2.5203
27	16236	30.042	4.122	1.5061	2.5019	15190	29.516	4.677	1.5113	2.5402
28	16747	29.820	4.435	1.5024	2.5205	15669	29.262	5.045	1.5074	2.5591
29	17253	29.595	4.319	1.4988	2.5393	16142	29.020	4.724	1.5036	2.578
30	17753	29.345	4.350	1.4954	2.5577	16610	28.833	3.958	1.5000	2.5972
31	18248	29.110	4.483	1.492	2.5762	17074	28.629	4.962	1.4964	2.6169
32	18736	28.895	4.237	1.4887	2.595	17533	28.345	5.378	1.493	2.6357
33	19220	28.654	4.426	1.4856	2.6146	17985	28.145	3.535	1.4897	2.6546
34	19698	28.395	4.609	1.4825	2.633	18436	28.000	4.268	1.4864	2.6736
35	20170	28.192	3.830	1.4795	2.6515	18882	27.742	5.344	1.4833	2.6926
36	20638	28.021	3.718	1.4766	2.6700					
37	21103	27.796	4.536	1.4738	2.6887					
38	21562	27.561	4.480	1.471	2.7073					

Can. J. Chem. Downloaded from www.nrcresearchpress.com by Xi'an Jiaotong University on 09/19/12
For personal use only.

Published by NRC Research Press

canonical functions approach,[13–15] the eigenvalue E_v, the rotational constant B_v, the centrifugal distortion constant D_v, and the abscissas of the turning points r_{min}, and r_{max} have been calculated up to the vibrational level $v = 38$. Eight electronic states have been investigated in the present work for the first time for the molecule CrF. We are not aiming in the present work to show the advantages of one of the theoretical techniques compared with the others, but the investigation of new valid excited electronic states to lead to the investigation of new experimental works.

References

(1) Carlson, K. D.; Claydon, C. R. In *Advances in High Temperature Chemistry;* Leroy Eyring, Ed.; Academic Press: New York, 1967; Vol. 1.

(2) Science, H. T. *Future Needs and Anticipated Developments;* (National Academy of Sciences: Washington, DC, 1979.

(3) Weltner, W., Jr. *Science* **1967** *155* (3759), 155. doi:10.1126/science.155.3759.155.

(4) Harrison, J. F.; Hutchison, J. H. *Mol. Phys.* **1999** *97* (9), 1009. doi:10.1080/00268979909482903.

(5) Bencheikh, M.; Koivisto, R.; Launila, O.; Flament, J. P. *J. Chem. Phys.* **1997** *106* (15), 6231. doi:10.1063/1.473640.

(6) Koukounas, C.; Kardahakis, S.; Mavridis, A. *J. Chem. Phys.* **2004** *120* (24), 11500. doi:10.1063/1.1738412.

(7) Koivisto, R.; Launila, O.; Schimmelpfennig, B.; Simard, B.; Wahlgren, U. *J. Chem. Phys.* **2001** *114* (20), 8855. doi:10.1063/1.1367395.

(8) Hamdan, A.; Korek, M. *Chem. Phys.* **2010** *369* (1), 13. doi:10.1016/j.chemphys.2010.01.023.

(9) Bauschlisher, C. W., Jr. *Theor. Chim. Acta* **1995** *92*, 183; (s, p, d) exponents from Partridge, H., Jr. *J. Chem. Phys.* **1989** *90*, 1043.

(10) Dunning, T. H., Jr. *J. Chem. Phys.* **1989** *90* (2), 1007. doi:10.1063/1.456153.

(11) Werner, H.-J.; Knowles, P.J.; Lindh, R.; Manby, F.R.; Schütz, M.; Celani, P.; Korona, T.; Rauhut, G.; Amos, R.D.; Bernhardsson, A.; Berning, A.; Cooper, D.L.; Deegan, M.J. O.; Dobbyn, A.J.M; Eckert, F.; Hampel, C.; Hetzer, G. Lloyd, A.W.; McNicholas, S.J.; Meyer, W.; Mura, M.E.; Nicklaß, A.; Palmieri, P.; Pitzer, R.; Schumann, U.; Stoll, H.; Stone, A.J.; Tarroni, R.; Thorsteinsson, T. *MOLPRO Package of Ab Initio Programs;* http://www.molpro.net.

(12) Allouche, A. R. *J. Comput. Chem.* **2011** *32* (1), 174. doi:10.1002/jcc.21600.

(13) Kobeissi, H.; Korek, M.; Dagher, M. *J. Mol. Spectrosc.* **1989** *138* (1), 1. doi:10.1016/0022-2852(89)90092-1.

(14) Korek, M.; Kobeissi, H. *J. Comput. Chem.* **1992** *13* (9), 1103. doi:10.1002/jcc.540130909.

(15) Korek, M. *Comput. Phys. Commun.* **1999** *119* (2–3), 169. doi:10.1016/S0010-4655(98)00180-5.

Can. J. Chem. Downloaded from www.nrcresearchpress.com by Xi'an Jiaotong University on 09/19/12
For personal use only.

A highly asymmetric direct aldol reaction catalyzed by chiral proline amide – thiourea bifunctional catalysts

Yun Li, Qing-chuan Yang, Xiao-Ying Xu, Yong Zhou, Jian-fei Bai, Fei-ying Wang, and Li-xin Wang

Can. J. Chem. Downloaded from www.nrcresearchpress.com by Xi'an Jiaotong University on 09/19/12
For personal use only.

Abstract: A series of chiral proline amide – thiourea bifunctional catalysts derived from L-proline and chiral diamine were prepared and successfully applied to highly enantioselective direct aldol reactions of cyclohexanone with various aldehydes in excellent yields (85%–97%), diastereoselectivities (anti/syn > 20:1) and enantioselectivities (up to 91% ee).

Key words: aldol reaction, bifunctional catalyst, proline, amide–thiourea.

Résumé : On a préparé une série de catalyseurs chiraux bifonctionnels amide de la proline – thiourée dérivés de la L-proline et d'une diamine chirale et on l'a appliquée avec succès à la réaction d'aldolisation directe hautement énantiosélective de la cyclohexanone avec divers aldéhydes, avec d'excellents rendements (85 %–97 %), et des diastéréosélectivités (anti/syn > 20 : 1) et énantiosélectivités (allant jusqu'à 91 % ee) élevées.

Mots-clés : réaction aldolique, catalyseur bifonctionnel, proline, amide–thiourée.

[Traduit par la Rédaction]

Introduction

The aldol reaction is considered one of the most important carbon–carbon bond-forming reactions that creates the β-hydroxy ketones frequently found in many biologically active compounds and drugs.[1,2] Since pioneering work discovered that L-proline is a highly efficient catalyst for asymmetric direct aldol reactions,[3] great advances have been made for this reaction.[2–4] The direct aldol reaction involving cyclohexanone principally generates β-hydroxyketone as a mixture of regio-, diastereo-, and enantio-isomers, and it is quite difficult to obtain a single isomer. As a result, many efforts have been made on this conversion. Xiao and co-workers[5a] developed a kind of L-prolinamide derived from L-proline and chiral diamine to catalyze this reaction and provide high entioselectivities, anti-disastereoselectivities, and yields. Since then, a series of L-prolinamides[5] have been prepared and applied to this transformation, and impressive results have been made. As well, L-proline[6] and L-prolinamides,[5] tetrazole,[7] 3-pyrrolidinecarboxylic acid,[8] 4-substituted L-proline,[9] cinchona-derived primary amines,[10] chiral phosphinyl oxide pyrrolidines,[11] prolinethioamides,[12] sulfonamide,[13] 6-APA,[14] *cis*-diamine derivatives,[15] and acyclic amino acids[16] have also been evaluated for this reaction. To the best of our knowledge, L-proline amide – thiourea bifunctional catalysts have not been reported for the catalysis of the aldol reaction of cyclohexanone with aldehydes.

Recently, chiral thiourea organocatalysts have been widely used in asymmetric catalysis because of their effective activation of carbonyl and nitro groups through double-hydrogen-bonding interactions.[17] Among them, secondary amines, especially L-proline and its structural analogues, are powerful tools for the activation of aldehydes and ketones via an enamine or imine transition state.[2,18] However, the chiral proline amide – thiourea catalysts **4a**–**4d** with two catalytic sites of chiral thiourea and L-prolic amide skeleton have not drawn enough attention.[19] Based on this background, we expected to expand the scope of the application for these bifunctional catalysts and wanted to see if these catalysts may catalyze the asymmetric direct aldol reaction of cyclohexanone with aldehydes.

Aldol reactions are typically performed in organic solvents such as DMSO, DMF, or chloroform. In recent years, water has been widely used as a substitute for conventional organic solvents in asymmetric reactions because it is safe, economical, and environment friendly.[20] Therefore, asymmetric aldol reactions using an organocatalyst in water have received considerable attention[21] since Barbas and co-workers[21a] and Hayashi et al.[9] reported the first example of a small molecule catalyzed by direct an asymmetric Aldol reaction in pure water.

As a part of our continuing interest in asymmetric synthesis,[22,23] herein, we wish to report examples of chiral proline

Received 4 May 2010. Accepted 28 January 2011. Published at www.nrcresearchpress.com/cjc on 15 September 2011.

Y. Li. Department of Chemistry, Sichuan University, Chengdu 610041, China.
Q. Yang, X.Y. Xu, Y. Zhou, J. Bai, F. Wang, and L. Wang. Key Laboratory of Asymmetric Synthesis & Chirotechnology of Sichuan Province, Chengdu Institute of Organic Chemistry, Chinese Academy of Sciences, Chengdu 610041, China.

Correspondence author: L.X. Wang (e-mail: wlxioc@cioc.ac.cn).

Can. J. Chem. Downloaded from www.nrcresearchpress.com by Xi'an Jiaotong University on 09/19/12
For personal use only.

amide – thiourea bifunctional catalyst promoted enantioselective direct aldol reaction of cyclohexanone with various aldehydes in DMSO with water as a co-solvent in excellent yields, as well as high anti-diastereoselectivities (dr > 20:1) and enantioselectivities (up to 91%). These catalysts are illustrated in Fig. 1.

Results and discussion

Chiral catalysts **4a**–**4d** may be similarly prepared as the reported procedures[19] and the catalytic activities of **4a**–**4d** were investigated in the model reaction of cyclohexanone with *p*-nitrobenzaldehyde, and the results are summarized in Table 1, which shows that chiral catalysts with different stereocompatibility and chiral centers have great effects on reactivities and selectivities. Comparatively, catalysts **4a** and **4c** gave better yields and enantioselectivities (Table 1, entries 1 and 3 versus 2 and 4). This is probably due to the compatibility of the two catalytic chiral centers. The less compatible chiral centers in **4b** and **4d** probably exert no synergic or negative effects on enantioselectivity. Catalyst **4a**, bearing a R,R linker, afforded the desired products in excellent yield (97%) and good enantioselectivity (75% ee) and was chosen for further optimization. Next, a range of solvents was screened for the model reaction catalyzed by **4a** at room temperature. As shown in Table 1, the enantioselectivities and yields were highly variable with different solvents. All the solvents delivered good yields (60%–94%), moderate to good enantioselectivities (15%–78% ee), and anti-diastereoselectivities (1:1 to 24:1). Less polar aprotic solvents such as hexane, toluene, and DCM gave good yields and moderate enantioselectivities (Table 1, entries 5–10). Protic solvents such as *i*-PrOH and water separately seemed to have an adverse influence on enantioselectivities (Table 1, entries 14 and 15). Relatively, DMSO gave an excellent yield (92%) and a good enantioselectivity (78%) and was chosen for further investigation (Table 1, entry 12).

To further improve the results, a series of additives were studied and the results are listed in Table 2. Additives have remarkable effects on catalytic activity and enantioselectivity, and the reaction time was reduced to 7 h (entries 1–8). When AcOH was used, the yield increased to 92% and the enantioselectivity was 86% ee (Table 2, entry 8). Interestingly, when water was used as a co-solvent, the reaction rate was dramatically accelerated and the reaction was completed within half an hour with increases in diastereoselectivity (Table 2, entries 9 and 10) and 81% and 87% ee were obtained. Particularly, when the volume ratio of DMSO to water reached 1:2, excellent yield (97%), good enantioselectivity (87% ee), and diastereoselectivity (96:4) were achieved (Table 2, entry 10). Through extensive screening, the optimized reaction conditions were found to be 20 mol% of catalyst **4a** and 10 equiv cyclohexanone in DMSO and water (V_{DMSO}:V_{H_2O} = 1:2) at 25 °C (Table 2, entry 10).

Having established optimized conditions for the model reaction, the scope and the limitations of the reaction with different aldehydes were examined, and the results are summarized in Table 3. All the aldehydes bearing electron-withdrawing groups in the aromatic ring either at ortho (Table 3, entries 6–8), meta (Table 3, entry 5), or para positions (Table 3, entries 1–4) gave excellent yields, diastereoselectivities, and enantioselectivities. Particularly, the strong electron-withdrawing substituents at the ortho position in the benzene ring afforded the best enantioselectivities (up to 91% ee; Table 3, entries 6 and 7). The para position also gave high yields and excellent diastereoselectivities and enantioselectivities (up to 90% ee; Table 3, entries 2 and 3). Cyclopentanone was also investigated under these optimized conditions and gave 94% yield and 71% ee.

Fig. 1. Chiral proline amide – thiourea bifunctional catalysts.

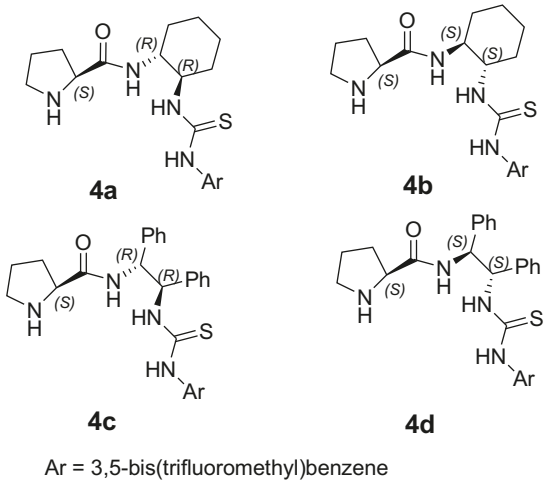

Conclusion

In conclusion, we have successfully applied the chiral proline amide – thiourea bifunctional catalysts **4a**–**4d** for the catalysis of the direct asymmetric aldol reaction of cyclohexanone with various aldehydes in the presence of water in excellent yields (85%–97%) and high anti-diastereoselectivities (dr > 20:1) and enantioselectivities (up to 91% ee). Further studies of the newly developed catalyst model and related catalysts in other organocatalyses are currently underway.

Experimental section

General

All reagents were purchased from a commercial supplier without further purification. Commercial grade solvent was dried and purified by standard procedures as specified in the *Purification of Laboratory Chemicals*;[24] NMR spectra were recorded with tetramethylsilane as the internal standard (δ = 0.0 ppm). ^{1}H NMR spectra were recorded at 300 MHz, and ^{13}C NMR spectra were recorded at 75 MHz (Bruker Avance). Chemical shifts (δ) are reported in ppm downfield from $CDCl_3$ (δ = 7.26 ppm) for ^{1}H NMR and relative to the central $CDCl_3$ resonance (δ = 77.0 ppm) for ^{13}C NMR spectroscopy. Flash column chromatography was carried out using silica gel eluting with ethyl acetate and petroleum ether. Reactions were monitored by TLC and visualized with UV light. Melting points were measured on a Büchi B-545 melting point apparatus. Enantioselectivities (ee) were determined by HPLC using Daicel Chiralpak AD, OD, WHELK, or AS

Can. J. Chem. Downloaded from www.nrcresearchpress.com by Xi'an Jiaotong University on 09/19/12
For personal use only.

Table 1. Screening of catalysts **4a**–**4d** and solvents.

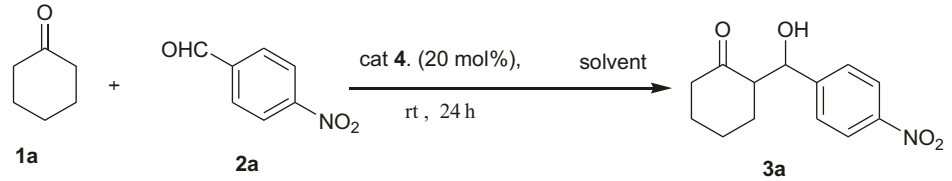

1a **2a** **3a**

Entry	Catalyst	Solvent	Yield (%)[a]	Anti / syn[b]	ee (%)[c]
1	**4a**	Neat	97	14:1	75
2	**4b**	Neat	85	11:1	41
3	**4c**	Neat	87	32:1	55
4	**4d**	Neat	35	4:1	41
5	**4a**	Toluene	94	2:1	41
6	**4a**	hexane	66	2:1	54
7	**4a**	DCM	70	2:1	44
8	**4a**	$CHCl_3$	87	9:1	62
9	**4a**	Et_2O	86	2:1	48
10	**4a**	THF	94	2:1	37
11	**4a**	CH_3CN	88	2:1	39
12	**4a**	DMSO	92	3:1	78
13	**4a**	DMF	60	24:1	64
14	**4a**	*i*-PrOH	91	1:1	15
15	**4a**	H_2O	80	4:1	57

Note: Unless otherwise specified, all reactions were carried out with catalysts **4** (0.02 mmol), **1a** (2 mmol), and **2a** (0.1 mmol) in the specified solvent (0.2 mL) at room temperature.

[a]Isolated yield.

[b]Determined by ^{1}H NMR.

[c]ee values were determined via HPLC with a Chiralpak-AD column.

Table 2. The effect of additives.

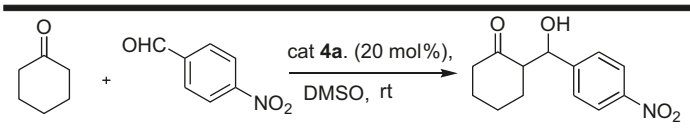

1a **2a** **3a**

Entry	Additive (20 mol%)	Time (h)	Yield (%)[a]	Anti/syn[b]	ee (%)[c]
1	4-$OHC_6H_4CO_2H$	7	84	65:35	75
2	Phenol	7	80	85:15	75
3	$PhCO_2H$	7	97	76:24	72
4	4-$NO_2C_6H_4CO_2H$	7	94	87:13	71
5	$PhCH_2CO_2H$	7	93	60:40	68
6	H_2O	7	99	79:21	66
7	$C_6H_4(CO_2H)_2$	7	80	80:20	78
8	AcOH	7	92	74:26	86
9[d]	AcOH	0.5	92	91:9	81
10[e]	AcOH	0.5	97	96:4	87

Note: Unless otherwise specified, all reactions were carried out with catalysts **4a** (0.02 mmol), **1a** (2 mmol), and **2a** (0.1 mmol) in DMSO (0.2 mL) at room temperature.

[a]Isolated yield.

[b]Determined by ^{1}H NMR.

[c]ee values were determined via HPLC with a Chiralpak-AD column.

[d]The solvent was DMSO–H_2O (2:1).

[e]The solvent was DMSO–H_2O (1:2).

columns with *i*-PrOH–hexane as the eluent. All compounds in this manuscript are known compounds. All physical and spectral data were found to be consistent with those reported.[19,22]

(*S*)-*N*-((1*R*,2*R*)-2-(3-(3,5-Bis(trifluoromethyl)phenyl) thioureido)cyclohexyl)pyrrolidine-2-carboxamide (4a)[19]

Enantiomerically pure **4a** was obtained after a single recrystallization from petroleum ether – EtOAc (*v*/*v* 1:100).

Table 3. The reaction of cyclohexanone with various aldehydes under optimized conditions.

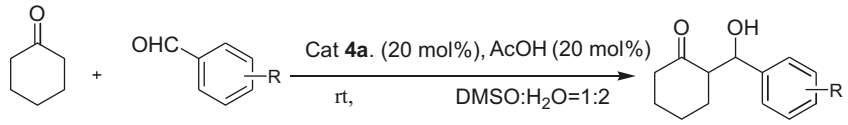

1a 2 3

Entry	R	Time (h)	Product	Yield (%)[a]	ee (%)[b]	Anti/syn[c]
1	4-NO_2	0.5	**3a**	97	87	>20:1
2	4-Br	2	**3b**	88	71	15:85
3	4-CN	2	**3c**	97	90	>20:1
4	4-F	2	**3d**	90	63	>20:1
5	3-NO_2	2	**3e**	93	90	>20:1
6	2-Br	2	**3f**	97	91	>20:1
7	2-NO_2	2	**3g**	94	91	>20:1
8	2-CN	2	**3h**	85	87	>20:1

Note: Unless otherwise specified, all reactions were carried out with catalysts **4a** (0.02 mmol), **1a** (2 mmol), and **2** (0.1 mmol) in a mixture of DMSO and water (*v*/*v* = 1:2).

[a]Isolated yield.

[b]ee values were determined by HPLC using a chiral stationary phase.

[c]Determined by ^{1}H NMR.

Can. J. Chem. Downloaded from www.nrcresearchpress.com by Xi'an Jiaotong University on 09/19/12
For personal use only.

Colorless solid, mp 176–177 °C. R_f (10% MeOH – EtOAc) 0.23. ^{1}H NMR (300 MHz $CDCl_3$) δ (ppm): 9.89–9.84 (m, 1H), 8.21 (d, J = 10.0 Hz, 1H), 8.15 (d, J = 10.8 Hz, 2H), 7.79 (d, J = 9.5 Hz, 1H), 7.55 (s, 1H), 4.63–4.60 (m, 1H), 3.74–3.67 (m, 2H), 3.01–2.96 (m, 2H), 1.99–1.94 (m, 1H), 1.68–1.22 (m, 12H). ^{13}C NMR (75 MHz, $CDCl_3$) δ: 180.9, 176.6, 141.3, 132.1, 128.6, 124.9, 122.1, 121.3, 117.7, 60.3, 56.8, 53.7, 47.1, 32.9, 32.2, 30.9, 25.8, 25.3, 24.7. HRMS (ESI-TOF) calcd for $C_{20}H_{25}F_6N_4OS$ ([M + H]$^+$): 483.1648; found: 483.1660. All physical and spectral data were found to be consistent with those reported.[19,22]

(*S*)-*N*-((1*S*,2*S*)-2-(3-(3,5-Bis(trifluoromethyl)phenyl) thioureido)cyclohexyl)pyrrolidine-2-carboxamide (4b)[19]

Enantiomerically pure **4b** was obtained after a single recrystallization from petroleum ether – EtOAc (*v*/*v* 1:100). Colorless solid, mp 149–151 °C. R_f (10% MeOH – EtOAc) 0.26. ^{1}H NMR (300 MHz, $CDCl_3$) δ (ppm): 1.03–1.35 (m, 2H), 1.47–1.57 (m, 3H), 1.63–1.70 (m, 2H), 1.89–2.01 (m, 7H), 2.97–3.03 (m,2H), 3.69–3.73 (m, 2H), 4.59–4.62 (d, J = 9 Hz, 1H), 7.55 (s, 1H), 7.77–7.80 (d, J = 9 Hz, 1H), 8.13 (s, 2H), 8.19–8.22 (d, J = 9 Hz, 1H), 9.88–9.89 (br, 1H). ^{13}C NMR (75 MHz, $CDCl_3$) δ: 180.9, 176.7, 141.4, 132.2, 128.6, 125.0, 122.1, 121.4, 117.0, 60.3, 56.9, 53.7, 47.1, 32.9, 30.9, 25.8, 25.9, 24.7. HRMS (ESI-TOF) calcd for $C_{20}H_{25}F_6N_4OS$ ([M + H]$^+$): 483.1648; found: 483.1658. All physical and spectral data were found to be consistent with those reported.[19,22]

(*S*)-*N*-((1*R*,2*R*)-2-(3-(3,5-Bis(trifluoromethyl)phenyl) thioureido)-1,2-diphenylethyl)pyrrolidine-2-carboxamide (4c)[19]

Enantiomerically pure **4c** was obtained after a single recrystallization from petroleum ether – EtOAc (*v*/*v* 1:80). Colorless solid, mp 166–168 °C. R_f (10% MeOH – EtOAc) 0.28. ^{1}H NMR (300 MHz $CDCl_3$) δ (ppm): 8.92–8.89 (m, 1H), 8.50–8.48 (m, 1H), 8.07 (s, 2H), 7.60 (s, 1H), 7.28–7.12 (m, 10 H), 6.40 (m, 1H), 5.45–5.38 (t, 1H), 3.74–3.69 (m, 1H), 3.14–3.10 (m, 1H), 3.10–2.98 (m, 1H), 2.05–1.64 (m, 6H). ^{13}C NMR (75 MHz, $CDCl_3$) δ (ppm): 181.5, 176.5, 141.0, 138.0, 131.7, 123.2, 129.0, 128.6, 128.4, 127.9, 127.7, 122.9, 122.1, 117.7, 61.9, 60.5, 58.6, 47.2, 31.1, 26.1. HRMS (ESI-TOF) calcd for $C_{28}H_{27}F_6N_4OS$ ([M + H]$^+$): 581.1804; found: 581.1823. All physical and spectral data were found to be consistent with those reported.[19,22]

(*S*)-*N*-((1*S*,2*S*)-2-(3-(3,5-Bis(trifluoromethyl)phenyl) thioureido)-1,2-diphenylethl)pyrrolidine-2-carboxamide (4d)[19]

Enantiomerically pure **4d** was obtained after a single recrystallization from petroleum ether – EtOAc (*v*/*v* 1:80). Colorless solid, mp 147–148 °C. R_f (10% MeOH – EtOAc) 0.30. ^{1}H NMR (300 MHz, $CDCl_3$) δ (ppm): 1.25–1.63 (m, 2H), 1.83–1.85 (m, 1H), 2.09–2.13 (m, 2H), 2.74–2.78 (m, 1H), 2.98–3.02 (m, 1H), 3.83–3.88 (m, 1H), 5.23–5.29 (t, J = 8.4 Hz, 9.8 Hz, 1H), 6.53–6.55 (d, J = 6 Hz, 1H), 7.08–7.19 (m, 12H), 7.43 (s, 1H), 8.65–8.68 (d, J = 9 Hz, 1H). ^{13}C NMR (75 MHz, $CDCl_3$) δ (ppm): 181.6, 176.4, 140.8, 137.8, 131.8, 129.0, 128.6, 128.2, 127.9, 127.7, 127.5, 123.1, 123.4, 122.1, 118.0, 62.9, 60.6, 59.4, 46.9, 30.4, 25.7. HRMS (ESI-TOF) calcd for $C_{28}H_{27}F_6N_4OS$ ([M + H]$^+$): 581.1804; found: 581.1812. All physical and spectral data were found to be consistent with those reported.[19,22]

Asymmetric direct aldol reactions of cyclohexanone with various aldehydes

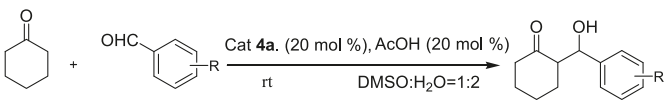

1a 2 3

Can. J. Chem. Downloaded from www.nrcresearchpress.com by Xi'an Jiaotong University on 09/19/12
For personal use only.

General procedure for direct aldol reaction of cyclohexanone with various aldehydes (Table 3)

A mixture of **2** (0.1 mmol, 1 equiv), **1a** (2 mmol, 20 equiv), **4a** (0.02 mmol, 0.2 equiv), and water–DMSO (0.2 mL, *v*/*v* 2:1) was stirred for 0.5–2 h. Then the crude product was directly purified by silica gel chromatography without workup using a mixture of EtOAc–hexanes (from 1:5 to 1:6) as the eluent and fractions were collected and concentrated in vacuo to provide the desired product.

Spectroscopic data of final products 3

2-[Hydroxy(4-nitrophenyl)methyl]cyclohexanone (3a)

The title compound was prepared according to the general procedure, as described previously, in 97% yield. HPLC (Chiralcel AD-H, *i*-PrOH–hexane = 20:80, flow rate = 1.0 mL/min, λ = 254 nm): t_{minor} = 11.25 min, t_{major} = 14.19 min, ee = 87%, dr > 20:1. Pure anti-product was obtained by silica gel chromatography (eluent: $V_{hexane}/V_{ethyl\ acetate}$ = 6:1). Furthermore, enantiomerically pure anti-product was obtained after a single recrystallization from petroleum ether – EtOAc (*v*/*v* 1.5:2). Colorless solid, mp 149–150 °C. (lit.[25] mp 149–151 °C). R_f (50% EtOAc – petroleum ether) 0.40. ^{1}H NMR (300 MHz, $CDCl_3$) δ (ppm): 1.24–1.39 (m, 1H), 1.53–1.65 (m, 3H), 1.81–1.85 (m, 1H), 2.08–2.09 (m, 1H), 2.35–2.39 (m, 1H), 2.47–2.59 (m, 2H), 4.09 (br, 1H), 4.87–4.90 (d, *J* = 9 Hz, 1H), 7.49–7.52 (d, *J* = 9 Hz, 2H), 8.19–8.22 (d, *J* = 9 Hz, 2H). All physical and spectral data were found to be consistent with those reported.[5a,9,21a,25]

2-[(4-Bromophenyl)hydroxy-methyl]cyclohexanone (3b)

The title compound was prepared according to the general procedure, as described previously, in 88% yield. HPLC (Chiralpak AD-H, *i*-PrOH–hexane = 10:90, flow rate = 1.0 mL/min, λ = 220 nm): t_{minor} = 12.98 min, t_{major} = 14.96min, ee = 71%, dr > 85:15. Pure anti-product was obtained by silica gel chromatography (eluent: $V_{hexane}/V_{ethyl\ acetate}$ = 6:1). Furthermore, enantiomerically pure anti-product was obtained after a single recrystallization from petroleum ether – EtOAc (*v*/*v* 1.8:2). Yellow solid, mp 126–128 °C. (lit.[25] mp 126–127 °C). R_f (25% EtOAc – petroleum ether) 0.27. ^{1}H NMR (300 MHz, $CDCl_3$) δ (ppm): 1.25–1.31 (m, 1H), 1.51–1.69 (m, 4H), 2.07–2.08 (m, 1H), 2.34–2.38 (m, 3H), 2.45–2.58 (m, 1H), 4.73–4.76 (d, *J* = 9 Hz, 1H), 7.17–7.26 (q, *J* = 15.39 Hz, 8.28 Hz, 5.4 Hz, 2H), 7.44–7.48 (m, 2H). All physical and spectral data were found to be consistent with those reported.[5a,9,21a,25]

2-[Hydroxy(4-oxo-cyclohexyl)methyl]benzonitrile (3c)

The title compound was prepared according to the general procedure, as described previously, in 97% yield. HPLC (Chiralcel AD-H, *i*-PrOH–hexane = 10:90, flow rate = 1.0 mL/min, λ = 220 nm): t_{minor} = 20.48 min, t_{major} = 25.34 min, ee = 90%, dr >20:1. Pure anti-product was obtained by silica gel chromatography (eluent: V_{hexane}/V_{DCM} = 1:1). Furthermore, enantiomerically pure anti-product was obtained after a single recrystallization from petroleum ether – EtOAc (*v*/*v* 1.6:2). Yellow solid, mp 72–74 °C. R_f (50% EtOAc – petroleum ether) 0.33. ^{1}H NMR (300 MHz, $CDCl_3$) δ (ppm): 1.24–1.37 (m, 1H), 1.52–1.64 (m, 3H), 2.08–2.09 (m, 2H), 2.34 (m, 1H), 2.46–2.52 (m, 2H), 2.56–2.58 (br, 1H), 4.81–4.84 (d, *J* = 9 Hz, 1H), 7.40–7.45 (m, 2H), 7.63–7.65 (d, *J* = 6 Hz, 2H). All physical and spectral data were found to be consistent with those reported.[5a,21a]

2-[Hydroxy(4-fluorophenyl)methyl]cyclohexanone (3d)

The title compound was prepared according to the general procedure, as described previously, in 90% yield. HPLC (Chiralpak WHELK, *i*-PrOH–hexane = 20:80, flow rate = 1.0 mL/min, λ = 220 nm): t_{minor} = 9.08 min, t_{major} = 7.48 min, ee = 63%, dr > 20:1. Pure anti-product was obtained by silica gel chromatography (eluent: $V_{hexane}/V_{ethyl\ acetate}$ = 6:1). Furthermore, enantiomerically pure anti-product was obtained after single recrystallization from petroleum ether – EtOAc (*v*/*v* 1:2). Colorless solid, mp 84–85 °C. (lit.[25] mp 84–85 °C). R_f (25% EtOAc – petroleum ether) 0.39. ^{1}H NMR (300 MHz, $CDCl_3$) δ (ppm): 1.26–1.30 (m, 1H), 1.52–1.68 (m, 4H), 2.07 (m, 1H), 2.34–2.57 (m, 3H), 3.99 (s, 1H), 4.76–4.78 (d, *J* = 6 Hz, 1H), 6.99–7.06 (m, 2H), 7.26–7.31 (m, 2H). All physical and spectral data were found to be consistent with those reported.[21a,26,25]

2-[Hydroxy(3-nitrophenyl)methyl]cyclohexanone (3e)

The title compound was prepared according to the general procedure, as described previously, in 93% yield. HPLC (Chiralcel OD-H, *i*-PrOH–hexane = 10:90, flow rate = 0.8 mL/min, λ = 220 nm): t_{minor} = 18.77 min, t_{major} = 14.69 min, ee = 90%, dr >20:1. Pure anti-product was obtained by silica gel chromatography (eluent: $V_{hexane}/V_{ethyl\ acetate}$ = 6:1). Furthermore, enantiomerically pure anti-product was obtained after single recrystallization from petroleum ether – EtOAc (*v*/*v* 1:3). Yellow solid, mp 102–104 °C (no literature data reported). R_f (50% EtOAc – petroleum ether) 0.50. ^{1}H NMR (300 MHz, $CDCl_3$) δ (ppm): 1.39–1.41 (m, 1H), 1.54–1.65 (m, 3H), 1.81–1.84 (m, 1H), 2.09 (m, 1H), 2.36–2.62 (m, 3H), 4.10–4.11 (s, *J* = 3 Hz, 1H), 4.87–4.91 (m, 1H), 7.49–7.54 (t, *J* = 7.89 Hz, 7.92 Hz, 1H), 7.65–7.68 (m, 1H), 8.13–8.20 (m, 2H). All physical and spectral data were found to be consistent with those reported.[5a,9,21a]

2-[(2-Bromophenyl)hydroxy-methyl]cyclohexanone (3f)

The title compound was prepared according to the general procedure, as described previously, in 91% yield. HPLC (Chiralpak AD-H, *i*-PrOH–hexane = 10:90, flow rate = 1.0 mL/min, λ = 220 nm): t_{minor} = 11.86 min, t_{major} = 10.28 min, ee = 87%, dr > 20:1. Pure anti-product was obtained by silica gel chromatography (eluent: $V_{hexane}/V_{ethyl\ acetate}$ = 6:1). Furthermore, enantiomerically pure anti-product was obtained after single recrystallization from petroleum ether – EtOAc (*v*/*v* 1.5:2). Brown solid, mp 105–106 °C (no literature data reported). R_f (50% EtOAc – petroleum ether) 0.39. ^{1}H NMR (300 MHz, $CDCl_3$) δ (ppm): 1.57–1.72 (m, 6H), 2.33–2.45 (m, 2H), 2.70 (m, 1H), 4.03–4.05 (d, *J* = 6 Hz, 1H), 5.28–5.32 (m, 1H), 7.13–7.16 (m, 1H), 7.35–7.37 (m, 1H), 7.51–7.54 (m, 2H). All physical and spectral data were found to be consistent with those reported.[27]

2-[Hydroxy(2-nitrophenyl)methyl]cyclohexanone (3g)

The title compound was prepared according to the general procedure, as described previously, in 94% yield. HPLC (Chiralcel AD-H, *i*-PrOH–hexane = 10:90, flow rate = 1.0 mL/min, λ = 220 nm): t_{minor} = 18.44 min, t_{major} =

17.34 min, ee = 91%, dr >20:1. Pure anti-product was obtained by silica gel chromatography (eluent: $V_{hexane}/V_{ethyl\ acetate}$ = 6:1). Furthermore, enantiomerically pure anti-product was obtained after single recrystallization from petroleum ether – EtOAc (*v*/*v* 1.3:2). Gray solid, mp 111–113 °C. (lit.[28] mp 126–127 °C). R_f (50% EtOAc – petroleum ether) 0.21. ^{1}H NMR (300 MHz, $CDCl_3$) δ (ppm): 1.60–1.76 (m, 4H), 2.32–2.44(m, 4H), 2.73–2.76 (m, 1H), 3.68–3.75 (br, 1H), 5.43–5.46 (d, J = 9 Hz, 1H), 7.42–7.45 (m, 1H), 7.629–7.63 (m, 1H), 7.75–7.78 (m, 1H), 7.83–7.86 (m, 1H). All physical and spectral data were found to be consistent with those reported.[5a,21a,28]

2-[Hydroxy(2-oxo-cyclohexyl)methyl]benzonitrile (3h)

The title compound was prepared according to the general procedure, as described previously, in 85% yield. HPLC (Chiralcel AS-H, *i*-PrOH–hexane = 5:95, flow rate = 1.0 mL/min, λ = 220 nm): t_{minor} = 41.79 min, t_{major} = 44.53 min, ee = 87%, dr >20:1. Pure anti-product was obtained by silica gel chromatography (eluent: $V_{hexane}/V_{ethyl\ acetate}$ = 6:1). Furthermore, enantiomerically pure anti-product was obtained after single recrystallization from petroleum ether – EtOAc (*v*/*v* 1:2). Yellow solid, mp: 185–186 °C (no literature data reported). R_f (50% EtOAc – petroleum ether) 0.50. ^{1}H NMR (300 MHz, $CDCl_3$) δ (ppm): 1.52–1.58 (m, 4H), 1.83–1.85 (m, 2H), 2.34–2.38 (m, 1H), 2.47–2.53 (m, 1H), 2.67–2.70 (m, 1H), 4.22–4.23 (d, J = 3 Hz, 1H), 5.21–5.23 (d, J = 3.18 Hz, 8.55 Hz, 1H), 7.37–7.43 (m, 1H), 7.59–7.65 (m, 3H). All physical and spectral data were found to be consistent with those reported.[29]

References

(1) Mahrwald, R., Ed. *Modern Aldol Reactions;* Wiley-VCH: Weinheim, 2004; Vols.1 and 2.

(2) (a) Sakthivel, K.; Notz, W.; Bui, T.; Barbas, C. F., III. *J. Am. Chem. Soc.* **2001** *123* (22), 5260. doi:10.1021/ja010037z; (b) Northrup, A. B.; MacMillan, D. W. C. *J. Am. Chem. Soc.* **2002** *124* (24), 6798. doi:10.1021/ja0262378; (c) Notz, W.; Tanaka, F.; Barbas, C. F., III. *Acc. Chem. Res.* **2004** *37* (8), 580. doi:10.1021/ar0300468; (d) Suri, J. T.; Ramachary, D. B.; Barbas, C. F., III. *Org. Lett.* **2005** *7* (7), 1383. doi:10.1021/ol0502533.

(3) List, B.; Lerner, R. A.; Barbas, C. F., III. *J. Am. Chem. Soc.* **2000** *122* (10), 2395. doi:10.1021/ja994280y.

(4) (a) Notz, W.; List, B. *J. Am. Chem. Soc.* **2000** *122* (30), 7386. doi:10.1021/ja001460v; (b) Dickerson, T. J.; Janda, K. D. *J. Am. Chem. Soc.* **2002** *124* (13), 3220. doi:10.1021/ja017774f; (c) Tang, Z.; Jiang, F.; Yu, L. T.; Cui, X.; Gong, L. Z.; Mi, A. Q.; Jiang, Y. Z.; Wu, Y. D. *J. Am. Chem. Soc.* **2003** *125* (18), 5262. doi:10.1021/ja034528q; (d) List, B. *Tetrahedron* **2002** *58* (28), 5573. doi:10.1016/S0040-4020(02)00516-1; (e) List, B. *Synlett* **2001** *2001* (11), 1675. doi:10.1055/s-2001-18074; (f) Xu, X. Y.; Tang, Z.; Wang, Y. Z.; Luo, S. W.; Cun, L. F.; Gong, L. Z. *J. Org. Chem.* **2007** *72* (26), 9905. doi:10.1021/jo701868t; (g) Chen, X. H.; Luo, S. W.; Tang, Z.; Cun, L. F.; Mi, A. Q.; Jiang, Y. Z.; Gong, L. Z. *Chem.-Eur. J.* **2007** *13* (2), 689. doi:10.1002/chem.200600801; (h) Xu, X. Y.; Wang, Y. Z.; Gong, L. Z. *Org. Lett.* **2007** *9* (21), 4247. doi:10.1021/ol701798x; (i) He, L.; Jiang, J.; Tang, Z.; Cui, X.; Mi, A. Q.; Jiang, Y. Z.; Gong, L. Z. *Tetrahedron Asymmetry* **2007** *18* (2), 265. doi:10.1016/j.tetasy.2007.01.028; (j) Xu, X. Y.; Wang, Y. Z.; Cun, L. F.; Gong, L. Z. *Tetrahedron Asymmetry* **2007** *18* (2), 237. doi:10.1016/j.tetasy.2007.01.021; (k) Tang, Z.; Yang, Z. H.; Chen, X. H.; Cun, L. F.; Mi, A. Q.; Jiang, Y. Z.; Gong, L. Z. *J. Am. Chem. Soc.* **2005** *127* (25), 9285. doi:10.1021/ja0510156; (l) Guo, H. M.; Cheng, L.; Cun, L. F.; Gong, L. Z.; Mi, A. Q.; Jiang, Y. Z. *Chem. Commun. (Camb.)* **2006** (4), 429. doi:10.1039/b514194j; (m) Tang, Z.; Jiang, F.; Cui, X.; Gong, L. Z.; Mi, A. Q.; Jiang, Y. Z.; Wu, Y. D. *Proc. Natl. Acad. Sci. U.S.A.* **2004** *101* (16), 5755. doi:10.1073/pnas.0307176101.

(5) (a) Chen, J. R.; Lu, H. H.; Li, X. Y.; Cheng, L.; Wan, J.; Xiao, W. J. *Org. Lett.* **2005** *7* (20), 4543. doi:10.1021/ol0520323; (b) Chen, J. R.; Li, X. Y.; Xing, X. N.; Xiao, W. J. *J. Org. Chem.* **2006** *71* (21), 8198. doi:10.1021/jo0615089; (c) Gandhi, S.; Singh, V. K. *J. Org. Chem.* **2008** *73* (23), 9411. doi:10.1021/jo8019863; (d) Tzeng, Z. H.; Chen, H. Y.; Huang, C. T.; Chen, K. *Tetrahedron Lett.* **2008** *49* (26), 4134. doi:10.1016/j.tetlet.2008.04.122; (e) Zhao, J. F.; He, L.; Jiang, J.; Tang, Z.; Cun, L. F.; Gong, L. Z. *Tetrahedron Lett.* **2008** *49* (21), 3372. doi:10.1016/j.tetlet.2008.03.131; (f) Chen, F.; Huang, S.; Zhang, H.; Liu, F. Y.; Peng, Y. G. *Tetrahedron* **2008** *64* (40), 9585. doi:10.1016/j.tet.2008.07.051; (g) Moorthy, G. N.; Saha, S. *Eur. J. Org. Chem.* **2009** 739; (h) Jia, Y. N.; Wu, F. C.; Ma, X.; Zhu, G. J.; Da, C. S. *Tetrahedron Lett.* **2009** *50* (25), 3059. doi:10.1016/j.tetlet.2009.04.013.

(6) (a) Fu, Y. Q.; Li, Z. C.; Ding, L. N.; Tao, J. C.; Zhang, S. H.; Tang, M. S. *Tetrahedron Asymmetry* **2006** *17* (24), 3351. doi:10.1016/j.tetasy.2006.12.008; (b) Puleo, G. L.; Iuliano, A. *Tetrahedron Asymmetry* **2007** *18* (24), 2894. doi:10.1016/j.tetasy.2007.11.023; (c) Wang, C.; Jiang, Y.; Zhang, X. X.; Huang, Y.; Li, B. G.; Zhang, G. L. *Tetrahedron Lett.* **2007** *48* (24), 4281. doi:10.1016/j.tetlet.2007.04.037; (d) Guizzetti, S.; Benaglia, M.; Raimondi, L.; Celentano, G. *Org. Lett.* **2007** *9* (7), 1247. doi:10.1021/ol070002p; (e) Maya, V.; Raj, M.; Singh, V. K. *Org. Lett.* **2007** *9* (13), 2593. doi:10.1021/ol071013l; (f) Sathapornvajana, S.; Vilaivan, T. *Tetrahedron* **2007** *63* (41), 10253. doi:10.1016/j.tet.2007.07.086; (g) Doherty, S.; Knight, J. G.; McRae, A.; Harrington, R. W.; Clegg, W. *Eur. J. Org. Chem.* **2008**, 1759; (h) Yang, H.; Carter, R. G. *Org. Lett.* **2008** *10* (20), 4649. doi:10.1021/ol801941j; (i) Guillena, G.; Hita, M. C.; Nájera, C.; Viózquez, S. F. *J. Org. Chem.* **2008** *73* (15), 5933. doi:10.1021/jo800773q; (j) Nyberg, A. I.; Usanp, A.; Pihko, P. M. *Synlett* **2004**, 1891.

(7) Torii, H.; Nakadai, M.; Ishihara, K.; Saito, S.; Yamamoto, H. *Angew. Chem. Int. Ed.* **2004** *43* (15), 1983. doi:10.1002/anie.200352724.

(8) Mitsumori, S.; Zhang, H.; Cheong, P. H.-Y.; Houk, K. N.; Tanaka, F.; Barbas, C. F. *J. Am. Chem. Soc.* **2006** *128* (4), 1040. doi:10.1021/ja056984f.

(9) Hayashi, Y.; Sumiya, T.; Takahashi, J.; Gotoh, H.; Urushima, T.; Shoji, M. *Angew. Chem. Int. Ed.* **2006** *45* (6), 958. doi:10.1002/anie.200502488.

(10) Zheng, B. L.; Liu, Q. Z.; Guo, C. S.; Wang, X. L.; He, L. *Org. Biomol. Chem.* **2007** *5* (18), 2913. doi:10.1039/b711164a.

(11) Liu, X. W.; Le, T. N.; Lu, Y. P.; Xiao, Y. J.; Ma, J. M.; Li, X. W. *Org. Biomol. Chem.* **2008** *6* (21), 3997. doi:10.1039/b811581h.

(12) Almaşi, D.; Alonso, D. A.; Nájera, C. *Adv. Synth. Catal.* **2008** *350*, 2467. doi:10.1002/adsc.200800430.

(13) Miura, T.; Yasaku, Y.; Koyata, N.; Murakami, Y.; Imai, N. *Tetrahedron Lett.* **2009** *50* (22), 2632. doi:10.1016/j.tetlet.2009.03.053.

(14) Emer, E.; Galletti, P.; Giacomini, G. *Eur. J. Org. Chem.* **2009** *2009* (19), 3155. doi:10.1002/ejoc.200900181.

Can. J. Chem. Downloaded from www.nrcresearchpress.com by Xi'an Jiaotong University on 09/19/12
For personal use only.

Can. J. Chem. Downloaded from www.nrcresearchpress.com by Xi'an Jiaotong University on 09/19/12
For personal use only.

(15) Nakayama, K.; Maruoka, J. *J. Am. Chem. Soc.* **2008** *130* (52), 17666. . doi:10.1021/ja807807p.

(16) Amedjkouh, M. *Tetrahedron Asymmetry* **2007** *18* (3), 390. doi:10.1016/j.tetasy.2007.01.025.

(17) (a) For inspiring discussions, see Etter, M. C. *Acc. Chem. Res.* **1990** *23* (4), 120. doi:10.1021/ar00172a005; (b) Curran, D. P.; Kuo, L. H. *J. Org. Chem.* **1994** *59* (12), 3259. doi:10.1021/jo00091a007; (c) Curran, D. P.; Kuo, L. H. *Tetrahedron Lett.* **1995** *36*, 6647; (d) Sigman, M. S.; Jacobsen, E. N. *J. Am. Chem. Soc.* **1998** *120* (19), 4901. doi:10.1021/ja980139y; (e) Sigman, M. S.; Vachal, P.; Jacobsen, E. N. *Angew. Chem. Int. Ed.* **2000** *39* (7), 1279. doi:10.1002/(SICI)1521-3773(20000403)39:7<1279::AID-ANIE1279>3.0.CO;2-U; (f) Vachal, P.; Jacobsen, E. N. *J. Am. Chem. Soc.* **2002** *124* (34), 10012. doi:10.1021/ja027246j; (g) Wenzel, A. G.; Jacobsen, E. N. *J. Am. Chem. Soc.* **2002** *124* (44), 12964. doi:10.1021/ja028353g; (h) Yoon, T. P.; Jacobsen, E. N. *Angew. Chem.* **2005** *117* (3), 470. doi:10.1002/ange.200461814.

(18) (a) Saito, S.; Nakadai, M.; Yamamoto, H. *Synlett 2001* (08), 1245. doi:10.1055/s-2001-16055; (b) Notz, W.; Sakthivel, K.; Bui, T.; Zhong, G.; Barbas, C. F., III. *Tetrahedron Lett.* **2001** *42* (2), 199. doi:10.1016/S0040-4039(00)01908-0; (c) Nakadai, M.; Saito, S.; Yamamoto, H. *Tetrahedron* **2002** *58* (41), 8167. doi:10.1016/S0040-4020(02)00965-1; (d) Saito, S.; Yamamoto, H. *Acc. Chem. Res.* **2004** *37* (8), 570. doi:10.1021/ar030064p.

(19) (a) Mei, K.; Zhang, S. L.; He, S. T.; Li, P.; Jin, M.; Xue, F.; Luo, G. S.; Zhang, H. Y.; Song, L. R.; Duan, W. H.; Wang, W. *Tetrahedron Lett.* **2008** *49* (17), 2681. doi:10.1016/j.tetlet.2008.02.164; (b) Fu, J.-Y.; Xu, X.-Y.; Li, Y.-C.; Huang, Q.-C.; Wang, L.-X. *Org. Biomol. Chem.* **2010** *8* (20), 4524. doi:10.1039/c0ob00406e.

(20) (a) Grieco, P. A., Ed. *Organic Synthesis in Water;* Blackie A & P: London, 1998; (b) Lindström, U. M. *Chem. Rev.* **2002** *102* (8), 2751. doi:10.1021/cr010122p; (c) Li, C. J. *Chem. Rev.* **2005** *105* (8), 3095. doi:10.1021/cr030009u.

(21) (a) Mase, N.; Nakai, Y.; Ohara, N.; Yoda, H.; Takabe, K.; Tanaka, F.; Barbas, C. F., III. *J. Am. Chem. Soc.* **2006** *128* (3), 734. doi:10.1021/ja0573312; (b) Teo, Y. C. *Tetrahedron Asymmetry* **2007** *18* (10), 1155. doi:10.1016/j.tetasy.2007.05.025; (c) Luo, S.; Xu, H.; Li, J.; Zhang, L.; Mi, X.; Zheng, X.; Cheng, J.-P. *Tetrahedron* **2007** *63* (46), 11307. doi:10.1016/j.tet.2007.08.096; (d) Gryko, D.; Wojciech, J.; Saletra, S. *Org. Biomol. Chem.* **2007** *5*, 2148; (e) Huang, J. M.; Zhang, X. T.; Daniel, W.; Armstrong, A. *Angew. Chem. Int. Ed.* **2007** *46*, 9073; (f) Chimni, S. S.; Singh, S.; Mahajan, D. *Tetrahedron Asymmetry* **2008** *19*, 2276. doi:10.1016/j.tetasy.2008.09.020; (g) Guizzetti, S.; Benaglia, M.; Raimondi, L.; Celentano, G. *Org. Lett. 2007*, 9; (h) Zhang, S. P.; Fu, X. K.; Fu, S. D.; Pan, J. F. *Catal. Commun.* **2009** *10* (4), 401. doi:10.1016/j.catcom.2008.10.005; (i) Lo, C. M.; Chow, H. F. *J. Org. Chem.* **2009** *74* (15), 5181. doi:10.1021/jo9006128.

(22) (a) Wang, Q.-W.; Peng, L.; Fu, J.-Y.; Huang, Q.-C.; Wang, L.-X.; Xu, X.-Y. *Arkivoc 2010*, 340; (b) Bai, J.-F.; Xu, X.-Y.; Huang, Q.-C.; Peng, L.; Wang, L. X. *Tetrahedron Lett.* **2010** *51* (21), 2803. doi:10.1016/j.tetlet.2010.03.039; (c) Peng, L.; Xu, X.-Y.; Wang, L.-L.; Huang, J.; Bai, J.-F.; Huang, Q.-C.; Wang, L.-X. *Eur. J. Org. Chem.* **2010** *2010* (10), 1849. doi:10.1002/ejoc.200901509; (d) Wang, L.-L.; Xu, X.-Y.; Huang, J.; Peng, L.; Huang, Q.-C.; Wang, L.-X. *Lett. Org. Chem.* **2010** *7* (5), 367. doi:10.2174/157017810791514652; (e) Fu, J.-Y.; Huang, Q.-C.; Wang, Q.-W.; Wang, L.-X.; Xu, X.-Y. *Tetrahedron Lett.* **2010** *51* (37), 4870. doi:10.1016/j.tetlet.2010.07.042.

(23) (a) Wang, L. X.; Tang, Y.; Chen, Y.; Tian, F. CN Patent 1927865A, 2007; Chem. Abstr. **2007,** *146*, 337870; (b) Wang, L. X.; Tang, Y.; Chen, Y.; Tian, F. CN Patent 19511940A, **2007**; Chem. Abstr. **2007,** *146*, 337870; (c) Wang, L. X.; Tang, Y.; Chen, Y.; Tian, F. CN Patent 1951941A, **2007**; Chem. Abstr. **2007,** *146*, 337870; (d) Wang, L. X.; Tang, Y.; Chen, Y.; Tian, F. EP Patent EP1942110; (e) Wang, L. X.; Tang, Y.; Chen, Y.; Tian, F. US Patent US20080249311; (f) Wang, L. X.; Tang, Y.; Chen, Y.; Tian, F. World Patent WO2007028337; (g) Wang, L. X.; Tang, Y.; Chen, Y.; Tian, F. CN Patent ZL200510060721.2, 2007; Chem. Abstr. **2007,** *146*, 337870; (h) Wang, L. X.; Tang, Y.; Chen, Y.; Tian, F. CN Patent ZL200510061230.X, 2007; Chem. Abstr. **2007,** *146*, 337870; (i) Wang, L. X.; Tang, Y.; Chen, Y.; Tian, F. CN Patent ZL200510061231.4, 2007; Chem. Abstr. **2007,** *146*, 337870; (j) Wang, L. X.; Peng, Q. H.; Du, Z. J.; Lan, H. F. CN Patent CN200610027596.X, 2006; Chem. Abstr. **2006,** *148*, 121716.

(24) Amarego, W. L. F.; Perrin, D. D. *Purification of Laboratory Chemicals,* 4th ed.; Butterworth-Heinemann: Oxford, 1997.

(25) Flowers, R.; Xu, X.; Timmons, C.; Li, G. *Eur. J. Org. Chem.* **2004** *2004* (14), 2988. doi:10.1002/ejoc.200400228.

(26) Wu, Y. Y.; Zhang, Y. Z.; Yu, M. L.; Zhao, G.; Wang, S. W. *Org. Lett.* **2006** *8* (20), 4417. doi:10.1021/ol061418q.

(27) Li, B. L.; Wang, Y. F.; Luo, S. P.; Zhong, A. G.; Li, Z. B.; Du, X. H.; Xu, D. Q. *Eur. J. Org. Chem.* **2010** *2010* (4), 656. doi:10.1002/ejoc.200900932.

(28) Sword, I. P.. *J. Chem. Soc. C* **1970**, 1916.

(29) Gu, Q.; Jiang, L. X.; Wang, Q.; Wu, X. Y. *Chin. J. Org. Chem.* **2008** *28*, 1416.

Aminomethylation of BINOL with methyleneiminium salts

Gennady Shustov and Vladimir Khlebnikov

Can. J. Chem. Downloaded from www.nrcresearchpress.com by South China Agricultural University on 09/19/12
For personal use only.

Abstract: A new method for synthesizing chiral 3,3′-bis(*N*,*N*-dialkylaminomethyl)-1,1′-bi-2-naphthols with high enantiomeric excess is described. The procedure consists of bis-lithiation of diprotected (*S*)- or (*R*)-1,1′-bis(2-naphthol) followed by treatment of the intermediate with methyleneiminium salts. Mild reaction conditions prevent racemization and provide 3,3′-bis(*N*,*N*-dialkylaminomethyl)-1,1′-bi-2-naphthols or 3-(*N*,*N*-dialkylaminomethyl)-1,1′-bi-2-naphthols with an enantiomeric excess >99%.

Key words: 3,3′-bis(*N*,*N*-dialkylaminomethyl)-1,1′-bi-2-naphthols, methyleneiminium salts, chiral, enantiomeric excess.

Résumé : On décrit une nouvelle méthode de synthèse des 3,3′-bis(*N*,*N*-dialkylaminométhyl)-1,1′-bi-2-naphthols chiraux avec des excès énantiomères élevés. Le procédé implique une bis-lithiation du (*S*)- ou (*R*)-1,1′-bis(2-naphthol) diprotégé, suivie d'un traitement de l'intermédiaire avec des sels de méthylèneiminium. Les conditions douces de la réaction permettent d'éviter la racémisation et elles permettent d'obtenir les 3,3′-bis(*N*,*N*-dialkylaminométhyl)-1,1′-bi-2-naphthols ou 3-(*N*,*N*-dialkylaminométhyl)-1,1′-bi-2-naphthols avec des excès énantiomères de plus de 99 %.

Mots-clés : 3,3′-bis(*N*,*N*-dialkylaminométhyl)-1,1′-bi-2-naphthols, sels de méthylèneiminium, chiral, excès énantiomère.

[Traduit par la Rédaction]

Introduction

Axial C_2 chirality of 3,3′-bis(*N*,*N*-dialkylaminomethyl)-1,1′-bi-2-naphthols (BINOLAMs (**1**), see Fig. 1) and their capability to form adducts with metals and some organic compounds makes them promising chiral auxiliaries in asymmetric synthesis.[1] The first use of BINOLAMs as chiral catalysts was reported[2] in the Michael addition of 2-(trimethylsilyloxy)furans to oxazolidinone enoates. Later they were used in phase-transfer α-alkylation of iminoesters of amino acids,[3] aldol[4] and nitroaldol[5] condensations, and in asymmetric addition of alkynyl-[6a] and diphenylzincs[6a,6b] to aldehydes and ketones. The major application of BINOLAMs so far is the ability of their complexes with metals to catalyze and induce enantioselectivity in various reactions of cyanosilylation,[6a,7] cyanocarbonylation,[8] and cyano-[9a,9b] or hydroxyphospholylation[9c] of aldehydes (other examples in this area are given in the review by Najera et al.[1c])

Recently, it was reported that BINOLAMs are photocytotoxic to DNA, which makes them effective against certain human tumor cell lines.[10] This BINOLAM action is based on their ability to undergo the elimination of dialkylamines under UV irradiation[11] and form highly reactive methylenequinoid structures; the latter are powerful DNA alkylating and cross-linking agents.[10]

Thus, the development of synthetic methods for producing enantiomerically pure BINOLAMs seems to be quite important. These compounds can be obtained from racemic starting material, for example, via photochemical transamination[11b] using L-proline esters as chiral auxiliaries; however, more often they are synthesized from commercial (*S*)- or (*R*)-1,1′-bis(2-naphthol) (BINOL, **2**).

Starting from BINOL, two basic synthetic approaches are described in the literature to prepare BINOLAMs containing tertiary amines in the side chain. The first one is a multistep route that starts with the introduction of the carboxylic[2a] or aldehyde[8c] groups into the 3,3′ positions of BINOL, followed by the formation of amides or imines that are subsequently reduced (a lengthier procedure from BINOL 3,3′-dialdehyde is sometimes used,[4,10] since it provides higher yields[10]). In isolated examples the required enantiomerically pure BINOL 3,3′-dicarboxylic acid was obtained via resolution[3] or enantioselective oxidative biaryl coupling.[12] Once the appropriate 3,3′-disubstituted BINOL intermediates are produced, the following steps are known to proceed without racemization and provide the enantiomerically pure BINOLAMs in 10%–30% chemical yield. The most recent publication based on this traditional approach describes a newly developed synthesis based on bis-anionic Fries rearrangement[7d] of BINOL carbamates, and it provided BINOLAM (*S*)-**1** (R = Et) with 63% yield in three steps. Unfortunately, this method can hardly be called general, because it was reported[13] that for some substrates migration of the second carbamate group is slow, and a significant amount of mono-rearranged by-product is formed.

The second known approach to the enantiomerically pure BINOLAMs utilizes the direct reaction of aminomethylation of BINOL enantiomers with *N*-hydroxymethylmorpholine (**3**, Fig. 2) at 110 °C, followed by enantiomeric enrichment of

Received 22 March 2011. Accepted 28 June 2011. Published at www.nrcresearchpress.com/cjc on 21 September 2011.

G. Shustov and V. Khlebnikov. NAEJA Pharmaceutical Inc, 4290 91A Street NW, Edmonton, AB T6E 5V2, Canada.

Corresponding author: V. Khlebnikov (e-mail: vkhlebnikov@naeja.com).

Can. J. Chem. Downloaded from www.nrcresearchpress.com by South China Agricultural University on 09/19/12
For personal use only.

Fig. 1. Chiral BINOLAMS and parent (*S*)-BINOL.

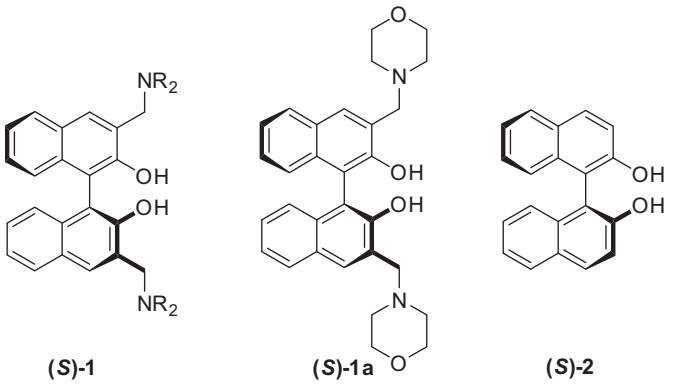

Fig. 2. Aminomethylating agents.

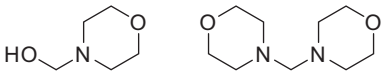

3 **4**

the product by recrystallization.[6a,7c] This is the shortest synthesis of BINOLAMs and hence it looks the most convenient. However, it suffers from several shortcomings.

First, the conversion of the starting BINOLs to BINOLAMs in this aminomethylation reaction is not very high, and usually a significant amount of monoaminomethylated product is formed along with the desired BINOLAM. Apparently, the yield in this reaction depends on the purity of the aminomethylating agent **3** and, according to our experience, the reagent **3** (normally prepared by condensation of morpholine with paraformaldehyde) often contains a significant amount of unreactive *N*,*N*-methylene–bismorpholine (**4**). The latter reaction is difficult to control, and the composition of the crude mixture may vary from experiment to experiment. The same is true for preparation of other *N*-hydroxymethyldialkylamines.

Second, since the described direct aminomethylation of BINOL is carried out at elevated temperature (110 °C), noticeable racemization could occur, resulting in the obtained BINOLAM with an ee of about 75%.[6a,7c] These results are understandable and potentially unavoidable because, as it has been demonstrated earlier, the configurational stability of BINOL decreases in the presence of bases.[14] Increasing the ee of (*S*)-**1** by recrystallization as described by other authors[6a,7c] cannot be considered to be a general method applicable to other BINOLAMs, since the recrystallization conditions need to be optimized for each individual compound. This could take significant time and may not be possible in some situations.

Based on these considerations, we thought it would be highly desirable to develop an aminomethylating agent with better reactivity, to make it possible for the aminomethylation reaction to proceed with higher yields and under milder conditions. Since the target aminomethylated BINOLs have useful practical applications and might be required in multigram quantities, we were looking at reagents that could be easily synthesized and purified.

In this study we investigated the possibility of using the methyleneiminium salts **5a**–**5b** (Fig. 3) as such reagents.

Fig. 3. Methyleneiminium salts **5a**–**5d**.

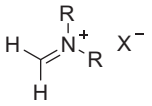

5a R+R = $(CH_2)_2O(CH_2)_2$, X = Cl
5b R+R = $(CH_2)_2O(CH_2)_2$, X = CF_3SO_3
5c R = Me X = Cl
5d R = Me X = I

Scheme 1. Synthesis of methyleneiminium salts **5a** and **5b**.

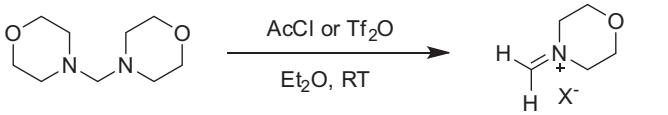

4

5a (X = Cl)
5b (X = CF_3SO_3)

Results and discussion

N,*N*-Dialkylmethyleneiminium salts can be easily generated by a reaction of acyl chlorides or anydrides with methylene–bis(dialkylamines).[15] Thus, chloride **5a** was obtained in 97% yield and triflate **5b** in 99% yield by reacting **4** with acetyl chloride or triflic anhydride accordingly (Scheme 1). Iminium salts **5c** and **5d** are commercially available.

The good reactivity of *N*,*N*-dialkylmethyleneiminium salts in aromatic electrophilic substitution reactions, which was demonstrated for anilines,[16] phenols,[17] furanes,[15c] thiophenes,[18] pyrrols,[19] and various other electron-rich heterocycles,[20] encouraged us to try this approach in the preparation of optically active BINOLAMs.

We started our experiments on BINOL aminomethylation with chloride **5a**, trying to reproduce the conditions that were reported in the literature for 3- and 4-methoxycarbonylphenols.[17] It appeared that the reaction of **2** with iminium salt **5a** in dichloromethane in the presence of K_2CO_3 at room temperature did not occur. Changing the solvent to acetonitrile, increasing the amount of **5a** to 8 equiv, and carrying out the reaction at 60 °C for 19 h did not bring positive results either. No aminomethylation reaction for **2** was observed even when stronger bases were used, such as 1 N NaOH (CH_2Cl_2–H_2O, room temperature, 16 h) or NaH (DMF, room temperature, 19 h).

Based on these results, it was concluded that to make the reaction of methyleneiminium salts with BINOL substrates successful, the increase of nucleophilicity of the latter were required. This can be done, for example, by lithiation of the 3 and 3′ positions of bis-O,O′-diprotected BINOL as described by Snieckus and co-workers.[21]

A series of experiments demonstrated that indeed MOM-protected BINOL **6**, after treatment with *n*-BuLi, reacted smoothly with methyleneiminium salts **5a**–**5d** to produce corresponding BINOLAMs **7a** and **7b** in 54%–88% yields, respectively (Scheme 2 and Table 1). Small amounts of monoaminomethyl derivatives **8a** and **8b** were also formed; however, the yields of these side products were significantly lower then in the case of the reaction of BINOL (**2**) with *N*-hydroxymethylenemorpholine (**3**).[6a,7c]

In a typical aminomethylation procedure, 3.2 equiv of methyleneiminium salt **5** relative to substrate **6** were used.

Can. J. Chem. Downloaded from www.nrcresearchpress.com by South China Agricultural University on 09/19/12
For personal use only.

Scheme 2. Synthesis of **7a** and **7b** and **8a** and **8b**.

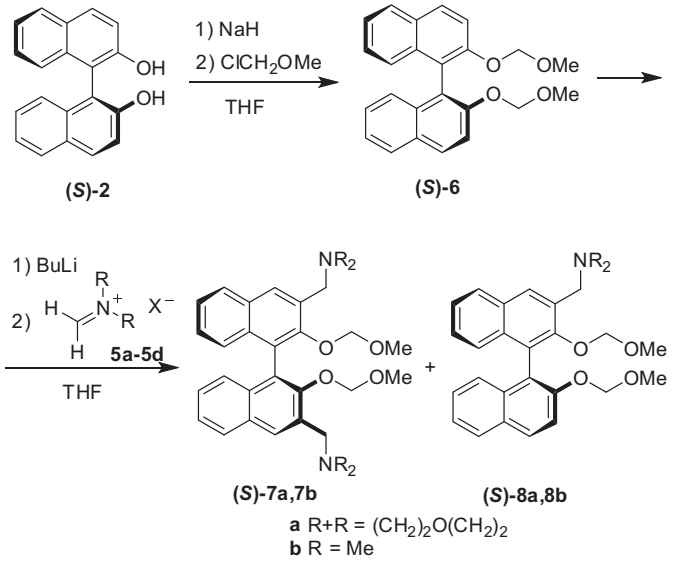

Table 1. Aminomethylation of (*S*)-**6** with methyleneiminium salts **5a**–**5d** (Scheme 2).

Entry	Methyleneiminium salt	Ratio of **7**:**8** (mol/mol)[a]	Yield (%)[b]
1	**5a**	1:0.2	54
2	**5b**	1:0.2	69
3	**5c**	1:0.2	63
4	**5d**	1:0.02	88
5	**5a**	0.2:1	69

Note: The reaction was carried out in THF at –15 °C to room temperature (1 or 2 h) with 2.6 equiv of *n*-BuLi and 3.2 equiv of **5a**–**5d** for entries 1–4 and with 1.3 equiv of *n*-BuLi and 1.6 equiv of **5a** for entry 5.

[a]In the crude mixture.

[b]Isolated yield of the major product.

Reducing this amount to 1.6 equiv allowed the monomethyleneimine compound **8** to be obtained in 69% yield.

Carrying out the reaction under mild conditions (temperature from –20 to 20 °C) helped to avoid the racemization of substrate **6** and its aminomethylated derivatives **7** and **8**. The high ee (>99%) of isolated products (*S*)-**7a** and (*S*)-**7b** and (*S*)-**8a** as well as BINOLAMs (*S*)-**1a** and (*S*)-**1b**, which were obtained after removing the MOM protective groups (Scheme 3), was confirmed by HPLC analysis using a column with a chiral stationary phase.

Conclusion

In conclusion, the investigated reaction of lithiated MOM-protected BINOL with methyleneiminium salts can be a convenient and versatile method for the synthesis of BINOLAMs with high enantiomeric excess (>99%).

Experimental

Instrumentation, analysis, and starting materials

All starting materials, solvents, and reagents were used as purchased from commercial suppliers, unless otherwise noted. Anhydrous THF was purchased from Sigma-Aldrich. Reactions were monitored by thin-layer chromatography

Scheme 3. Synthesis of 3,3′-bis(*N*,*N*-dialkylaminomethyl)-1,1′-bi-2-naphthols (BINOLAMs) **1a** and **1b**.

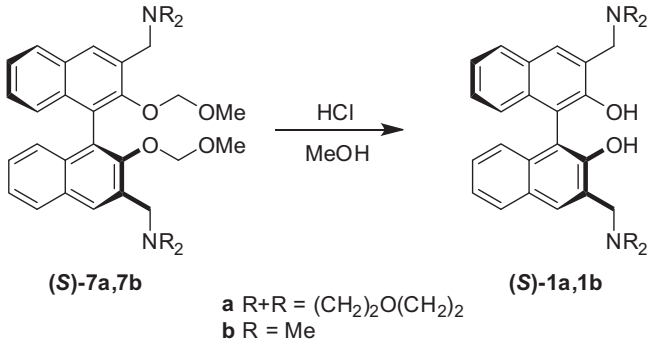

(TLC) carried out on Macherey–Nagel Alugram SIL G/UV254 silica gel 60 plates with a fluorescent indicator using phosphomolybdic acid in ethanol and heat as a developing agent. NMR spectra were recorded on a Varian Mercury 400 NMR instrument (400 MHz frequency for ^{1}H) using residual undeuterated solvent as an internal reference. Low-resolution mass spectra were recorded on a Water Micromass ZQ mass spectrometer with electrospray ionization (ESI). HPLC analyses were performed on a Waters 600 system with a Waters 2996 photodiode array detector using a C-18 reverse-phase column. For the ee determination, a Chiralcel OD-R column was used (MeCN – 0.5 N aq $NaClO_4$, 60:40 as a mobile phase). All dry column chromatography purifications were performed on silica gel 60A with a 5–15 μm particle size.

N-Methylenemorpholinium chloride (5a)

To a stirred solution of acetyl chloride (4.32 g, 55 mmol) in anhydrous Et_2O (100 mL), a solution of methylene–bismorpholine[22] (9.31 g, 50 mmol) in anhydrous Et_2O (50 mL) was added dropwise at 20–24 °C over 1.5 h. The reaction mixture was stirred for an additional 0.5 h at room temperature. The white precipitate was filtered off, washed with anhydrous Et_2O (3 × 40 mL), and dried in vacuum to provide 6.39 g (94%) of *N*-methylenemorpholinium chloride **5a**[15d] as a white powder. ^{1}H NMR (400 MHz) in $(CD_3)_2SO$ δ: 3.90 (4H, t, ^3J = 5.0 Hz, OCH_2), 4.06 (4H, t, ^3J = 5.0 Hz, NCH_2), 8.24 (2H, $^+N=CH_2$).

N-Methylenemorpholinium triflate (5b)

To a stirred solution of trifluoromethanesulfonic anhydride (9.93 g, 35.2 mmol) in anhydrous Et_2O (200 mL), a solution of methylene–bismorpholine[22] (5.96 g, 32 mmol) in anhydrous Et_2O (50 mL) was added dropwise at 20–24 °C over 1 h. The reaction mixture was stirred for an additional 2 h at room temperature. The white precipitate was filtered off, washed with anhydrous Et_2O (3 × 40 mL), and dried in vacuum to provide 7.90 g (99%) of *N*-methylenemorpholinium triflate **5b** as a highly hygroscopic white powder.[23] ^{1}H NMR (400 MHz) in $(CD_3)_2SO$ δ: 3.90 (4H, br. t, OCH_2), 4.08 (4H, br. t, NCH_2), 8.21 (2H, $^+N=CH_2$).

(*S*)-2,2′-Bis(methoxymethoxy)-1,1′-binaphthol (6)

To a stirred cooled (0–5 °C) suspension of NaH (60% in mineral oil, 15.73 g, 0.393 mol) in a mixture of anhydrous THF (660 mL) and anhydrous DMF (330 mL), a solution of **2** (50.41 g, 0.176 mol) in anhydrous THF (200 mL) was

Can. J. Chem. Downloaded from www.nrcresearchpress.com by South China Agricultural University on 09/19/12
For personal use only.

added dropwise at 5–10 °C. The resultant mixture was allowed to warm up to 15 °C and chloromethyl methyl ether (44.73 g, 0.556 mol) was added dropwise at 15–20 °C. The reaction mixture was stirred for 16 h at room temperature, quenched with water (20 mL), concentrated under reduced pressure to a volume of ~400 mL, and diluted with EtOAc (800 mL). The obtained mixture was washed with water (3 × 300 mL), 1 N HCl (300 mL), saturated aqueous $NaHCO_3$ (300 mL), and brine (300 mL) and dried over $MgSO_4$. Filtration through a pad of silica gel and removal of the solvent from the filtrate under reduced pressure provided 72.7 g of a white solid. This solid was suspended in hexanes (300 mL) and the precipitate was filtered off and washed with hexanes (2 × 150 mL). The product **6**[24] (63.2 g, 96%) was obtained as white solid after drying in vacuum. ^{1}H NMR (400 MHz) in $CDCl_3$ δ: 3.14 (6H, OMe), 4.98 (2H, d, ^2J = 6.8 Hz, OCH_A), 5.08 (2H, d, ^2J = 6.8 Hz, OCH_B), 7.15 (2H, d, J = 8.2 Hz), 7.22 (2H, t, J = 8.2 Hz), 7.35 (2H, t, J = 8.2 Hz), 7.58 (2H, d, J = 8.8 Hz), 7.87 (2H, d, J = 8.2 Hz), 7.95 (2H, d, J = 8.8 Hz).

(*S*)-3,3′-Bis(*N*-morpholinomethyl)-2,2′-bis(methoxymethoxy)-1,1′-binaphthol (7a)

To a stirred cooled (–5 °C to 0 °C) solution of **6** (1.87 g, 5 mmol) in anhydrous THF (50 mL), a 1.6 mol/L solution of *n*-butyl lithium in hexane (8.13 mL, 13 mmol) was added dropwise at –5 to 0 °C. The reaction mixture was stirred for 2 h at 0–5 °C and cooled to about –15 °C. Avoiding exposure to air, freshly prepared and dried **5b** (3.99 g, 16 mmol) was added portionwise and the reaction mixture was allowed to warm to room temperature. The stirring was continued for an additional 2 h, and the reaction was quenched by addition of water (1 mL). The resultant mixture was concentrated under reduced pressure and the oily residue was dissolved in ethyl acetate (50 mL). The obtained solution was washed with water (2 × 15 mL) and brine (20 mL). After drying over $MgSO_4$, the solution was filtered and concentrated under reduced pressure to provide 3.02 g of a light pink semisolid, which was subjected to dry flash chromatography on silica gel (50% EtOAc–hexanes to 100% EtOAc) to afford 1.98 g (69%) of **7a** as a white solid. Assayed at 98.13% by HPLC. HPLC analysis on a column with a chiral stationary phase showed an enantiomeric excess of >99.5%. ^{1}H NMR (400 MHz) in $CDCl_3$ δ: 2.62 (8H, m, NCH_2), 2.70 (6H, OMe), 3.76 (10H, m, OCH_2 + NCH_A), 3.88 (2H, d, ^2J = 13.6 Hz, NCH_B), 4.57 (2H, d, ^2J = 5.6 Hz, OCH_A), 4.74 (2H, d, ^2J = 5.6 Hz, OCH_B), 7.22 (4H, m), 7.41 (2H, t, J = 8.0 Hz), 7.88 (2H, d, J = 8.0 Hz), 8.00 (2H). MS (electrospray), *m*/*z*: 573 (M^+). Anal. calcd for $C_{34}H_{40}N_2O_6$ (%): C 71.31, H 7.04, N 4.89; found: C 71.38, H 7.10, N 4.90.

(*S*)-3,3′-Bis(*N*,*N*-dimethylaminomethyl)-2,2′-bis(methoxymethoxy)-1,1′-binaphthol (7b)

To a stirred cooled (–5 to 0 °C) solution of **6** (1.87 g, 5 mmol) in anhydrous THF (50 mL), a 1.6 mol/L solution of *n*-butyl lithium in hexane (8.13 mL, 13 mmol) was added dropwise at –5 to 0 °C. The reaction mixture was stirred for 2 h at 0–5 °C and cooled to –15 °C. Solid (*N*,*N*-dimethyl) methyleneammonium iodide (**5d**) (2.96 g, 16 mmol) was added portionwise and the reaction mixture was allowed to warm up to room temperature. The stirring was continued for an additional 2 h and the reaction was quenched by addition of water (1 mL). The resultant mixture was concentrated under reduced pressure and the oily residue was dissolved in ethyl acetate (50 mL). The obtained solution was washed with water (2 × 15 mL), a saturated aqueous solution of $Na_2S_2O_7$ (15 mL), and brine (20 mL). After drying over $MgSO_4$, the solution was filtered and concentrated under reduced pressure to provide 2.61 g of a light yellow oil, which was subjected to dry flash chromatography on silica gel (CH_2Cl_2 to 5% MeOH–CH_2Cl_2) to afford 2.15 g (88%) of **7b** as a colourless viscous oil. Assayed at 97.99% by HPLC. HPLC analysis on a column with a chiral stationary phase showed an enantiomeric excess of >99.5%. ^{1}H NMR (400 MHz) in $CDCl_3$ δ: 2.38 (12H, NMe), 2.76 (6H, OMe), 3.72 (2H, d, ^2J = 14.2 Hz, NCH_A), 3.80 (2H, d, ^2J = 14.2 Hz, NCH_B), 4.51 (2H, d, ^2J = 5.8 Hz, OCH_A), 4.66 (2H, d, ^2J = 5.8 Hz, OCH_B), 7.20 (2H, t, J = 8.2 Hz), 7.25 (2H, d, J = 8.2 Hz), 7.40 (2H, t, J = 8.2 Hz), 7.88 (2H, d, J = 8.2 Hz), 8.04 (2H). MS (electrospray), *m*/*z*: 489 (M^+ + 1). Anal. calcd for $C_{30}H_{36}N_2O_4$ (%): C 73.74, H 7.43, N 5.73; found: C 73.93, H 7.37, N 5.61.

(*S*)-3-*N*-Morpholinomethyl-2,2′-bis(methoxy-methoxy)-1,1′-binaphthol (8a)

To a stirred cooled (–5 to 0 °C) solution of **6** (13.10 g, 35 mmol) in anhydrous THF (350 mL), a 1.6 mol/L solution of *n*-butyl lithium in hexane (28.4 mL, 45.5 mmol) was added dropwise at –5 to 0 °C. The reaction mixture was stirred for 2 h at 0–5 °C and cooled to –15 °C. Solid **5a** (7.59 g, 56 mmol) was added portionwise and the reaction mixture was allowed to warm up to room temperature. The stirring was continued for additional 2 h and the reaction was quenched by addition of water (7 mL). The resultant mixture was concentrated under reduced pressure and the oily residue was dissolved in ethyl acetate (350 mL). The obtained solution was washed with water (2 × 100 mL) and brine (200 mL). After drying over $MgSO_4$, the solution was filtered and concentrated under reduced pressure to provide 16.8 g of a yellow oil, which was subjected to dry flash chromatography on silica gel (30% EtOAc–hexanes to 60% EtOAc–hexanes) to afford 11.50 g (69%) of **8a** as a white solid. Assayed at 96.81% by HPLC. HPLC analysis on a column with a chiral stationary phase showed an enantiomeric excess of >99.5%. ^{1}H NMR (400 MHz) in $CDCl_3$ δ: 2.63 (4H, m, NCH_2), 2.77 (3H, OMe), 3.16 (3H, OMe), 3.57 (4H, m, OCH_2), 3.83 (2H, NCH_2Ar), 4.64 (1H, d, ^2J = 5.6 Hz, OCH_A), 4.71 (1H, d, ^2J = 5.6 Hz, OCH_B), 5.02 (1H, d, ^2J = 7.2 Hz, OCH_A'), 5.11 (1H, d, ^2J = 7.2 Hz, OCH_B'), 7.22 (4H, m), 7.37 (2H, m), 7.58 (1H,d, J = 8.8 Hz), 7.87 (2H, m), 7.96 (2H, d, J = 8.8 Hz), 7.99 (2H). MS (electrospray), *m*/z: 474 (M^+). Anal. calcd for $C_{29}H_{31}NO_5$ (%): C 73.55, H 6.60, N 2.96; found: C 73.81, H 6.72, N 3.07.

(*S*)-3,3′-Bis(*N*-morpholinomethyl)-2,2′-dihydroxy-1,1′-binaphthol (1a)

To a stirred cooled (–5 to 0 °C) solution of **7a** (1.72 g, 3 mmol) in methanol (15 mL), a 4 mol/L solution of HCl in 1,4-dioxane (15 mL, 60 mmol) was added dropwise. The reaction mixture was allowed to warm to room temperature and was stirred for an additional 16 h. After removal of solvent under reduced pressure, the solid residue was triturated with

Can. J. Chem. Downloaded from www.nrcresearchpress.com by South China Agricultural University on 09/19/12
For personal use only.

Et_2O (2 × 30 mL) and dried in vacuum to provide 1.69 g of a white solid. The isolated solid was suspended in CH_2Cl_2 (80 mL) and saturated aqueous $NaHCO_3$ (40 mL) was added to the resultant suspension. After 15 min of stirring, the organic phase was separated and dried over $MgSO_4$. Filtration and removal of the solvent from the filtrate under reduced pressure provided 1.51 g of a yellow solid, which was subjected to dry flash chromatography on silica gel (2% EtOAc–CH_2Cl_2 to 20% EtOAc–CH_2Cl_2) to afford 1.31 g (90%) of **1a**[7c] as a white solid. Assayed at 96.53% by HPLC. HPLC analysis on a column with chiral stationary phase showed enantiomeranic excess of >99.5%. ^{1}H NMR (400 MHz) in $CDCl_3$ δ: 2.64 (8H, br. m, NCH_2), 3.69 (8H, br. m, OCH_2), 3.89 (2H, d, ^2J = 14.0 Hz, NCH_A), 4.12 (2H, d, ^2J = 14.0 Hz, NCH_B), 7.29–7.12 (6H, m), 7.66 (2H), 7.78 (2H, d, J = 8.4 Hz). MS (electrospray), m/z: 483 ($M^+ - 1$).

(*S*)-3,3′-Bis(*N*,*N*-dimethylaminomethyl)-2,2′-dihydroxy-1,1′-binaphthol (1b)

To a stirred cooled (–5 to 0 °C) solution of **7b** (1.02 g, 2.1 mmol) in methanol (2 mL), a 4 mol/L solution of HCl in methanol (10 mL, 40 mmol) was added dropwise. The reaction mixture was allowed to warm up to room temperature and was stirred for an additional 16 h. After removal of the solvent under reduced pressure, the solid residue was triturated with Et_2O (2 × 20 mL) and dried in vacuum to provide 0.96 g of a white solid. The solid was suspended in CH_2Cl_2 (50 mL) and saturated aqueous $NaHCO_3$ (25 mL) was added to the resultant suspension. After 15 min of stirring, the organic phase was separated and dried over $MgSO_4$. Filtration and removal of the solvent from the filtrate under reduced pressure provided 0.81 g of a yellow solid, which was subjected to dry flash chromatography on silica gel (CH_2Cl_2 to 6% MeOH–CH_2Cl_2) to afford 0.78 g (93%) of **1b**[2a] as a white solid. Assayed at 97.45% by HPLC. HPLC analysis on a column with a chiral stationary phase showed an enantiomeric excess of >99.5%. ^{1}H NMR (400 MHz) in $CDCl_3$ δ: 2.36 (12H, NMe), 3.76 (2H, d, ^2J = 13.6 Hz, NCH_A), 4.10 (2H, d, ^2J = 13.6 Hz, NCH_B), 7.26–7.13 (6H, m), 7.61 (2H), 7.76 (2H, d, J = 7.6 Hz). MS (electrospray), m/z: 400 (M^+).

References

(1) (a) Chen, Y.; Yekta, S.; Yudin, A. K. *Chem. Rev.* **2003** *103* (8), 3155. doi:10.1021/cr020025b; (b) Baeza, A.; Sansano, J. M.; Saá, J. M.; Nájera, C. *Pure Appl. Chem.* **2007** *79* (2), 213. doi:10.1351/pac200779020213; (c) Nájera, C.; Sansano, J. M.; Saá, J. M. *Eur. J. Org. Chem.* **2009** *2009* (15), 2385. doi:10.1002/ejoc.200801069.

(2) (a) Kitajima, H.; Ito, K.; Katsuki, T. *Tetrahedron* **1997** *53* (50), 17015. doi:10.1016/S0040-4020(97)10152-1; (b) Kitajima, H.; Katsuki, T. *Synlett* **1997** *1997* (5), 568. doi:10.1055/s-1997-3235.

(3) Casas, J.; Nájera, C.; Sansano, J. M.; González, J.; Saá, J. M.; Vega, M. *Tetrahedron Asymmetry* **2001** *12* (5), 699. doi:10.1016/S0957-4166(01)00107-0.

(4) Li, H.; Da, C.-S.; Xiao, Y.-H.; Li, X.; Su, Y.-N. *J. Org. Chem.* **2008** *73* (18), 7398. doi:10.1021/jo801182n.

(5) (a) Saá, J. M.; Tur, F.; González, J.; Vega, M. *Tetrahedron Asymmetry* **2006** *17* (1), 99. doi:10.1016/j.tetasy.2005.11.014; (b) Tur, F.; Saá, J. M. *Org. Lett.* **2007** *9* (24), 5079. doi:10.1021/ol702434t.

(6) (a) Qin, Y.-C.; Liu, L.; Sabat, M.; Pu, L. *Tetrahedron* **2006** *62* (40), 9335. doi:10.1016/j.tet.2006.06.049; (b) DeBerardinis, A. M.; Turlington, M.; Pu, L. *Org. Lett.* **2008** *10* (13), 2709. doi:10.1021/ol8008478; (c) For asymmetric addition of diethylzinc to aldehydes catalyzed by similar BINOL derivatives bearing aromatic N-heterocycles in 3,3′ positions see Guo, Q.-S.; Liu, B.; Lu, Y.-N.; Jiang, F.-Y.; Song, H.-N.; Li, J.-S. *Tetrahedron Asymmetry* **2005** *16* (22), 3667. doi:10.1016/j.tetasy.2005.09.018; (d) Ma, L.; Jin, R.-Z.; Lü, G.-H.; Bian, Z.; Ding, M.-X.; Gao, L.-X. *Synthesis* **2007** 2461; (e) Milburn, R. R.; Hussain, S. M.; Prien, O.; Ahmed, Z.; Snieckus, V. *Org. Lett.* **2007** *9* (22), 4403. doi:10.1021/ol071276f.

(7) (a) Casas, J.; Nájera, C.; Sansano, J. M.; Saá, J. M. *Org. Lett.* **2002** *4* (15), 2589. doi:10.1021/ol0262338; (b) Casas, J.; Nájera, C.; Sansano, J. M.; Saá, J. M. *Tetrahedron* **2004** *60* (46), 10487. doi:10.1016/j.tet.2004.06.137; (c) Qin, Y.-C.; Liu, L.; Pu, L. *Org. Lett.* **2005** *7* (12), 2381. doi:10.1021/ol050660e; (d) North, M.; Villuendas, P.; Williamson, C. *Tetrahedron* **2010** *66* (10), 1915. doi:10.1016/j.tet.2010.01.004.

(8) (a) Casas, J.; Baeza, A.; Sansano, J. M.; Najera, C.; Saa, J. M. *Tetrahedron Asymmetry* **2003** *14* (2), 197. doi:10.1016/S0957-4166(02)00824-8; (b) Baeza, A.; Casas, J.; Nájera, C.; Sansano, J. M.; Saá, J. M. *Eur. J. Org. Chem.* **2006** 1949. doi:10.1002/ejoc.200500939; (c) Gou, S.; Liu, X.; Zhou, X.; Feng, X. *Tetrahedron* **2007** *63* (33), 7935. doi:10.1016/j.tet.2007.05.060; (d) Baeza, A.; Najera, C.; Sansano, J. M.; Saa, J. M. *Tetrahedron Asymmetry* **2005** *16* (14), 2385. doi:10.1016/j.tetasy.2005.05.031.

(9) (a) Baeza, A.; Casas, J.; Najera, C.; Sansano, J. M.; Saa, J. M. *Angew. Chem. Int. Ed.* **2003** *42* (27), 3143. doi:10.1002/anie.200351552; (b) Baeza, A.; Najera, C.; Sansano, J. M.; Saa, J. M. *Chemistry* **2005** *11* (13), 3849. doi:10.1002/chem.200401290; (c) Gou, S.; Zhou, X.; Wang, J.; Liu, X.; Feng, X. *Tetrahedron* **2008** *64* (12), 2864. doi:10.1016/j.tet.2008.01.022.

(10) Doria, F.; Richter, S. N.; Nadai, M.; Colloredo-Mels, S.; Mella, M.; Palumbo, M.; Freccero, M. *J. Med. Chem.* **2007** *50* (26), 6570. doi:10.1021/jm070828x.

(11) (a) Richter, S. N.; Maggi, S.; Colloredo-Mels, S.; Palumbo, M.; Freccero, M. *J. Am. Chem. Soc.* **2004** *126* (43), 13973. doi:10.1021/ja047655a; (b) Colloredo-Mels, S.; Doria, F.; Verga, D.; Freccero, M. *J. Org. Chem.* **2006** *71* (10), 3889. doi:10.1021/jo060227y.

(12) Li, X.; Hewgley, B.; Mulrooney, C. A.; Yang, J.; Kozlowski, M. C. *J. Org. Chem.* **2003** *68* (14), 5500. doi:10.1021/jo0340206.

(13) Dennis, M. R.; Woodward, S. *J. Chem. Soc., Perkin Trans. 1* **1998** (6), 1081. doi:10.1039/a708436f.

(14) (a) Kyba, E. P.; Gokel, G. W.; de Jong, F.; Koga, K.; Sousa, L. R.; Siegel, M. G.; Kaplan, L.; Sogah, G. D. Y.; Cram, D. J. *J. Org. Chem.* **1977** *42* (26), 4173. doi:10.1021/jo00862a001; (b) Yudin, A. K.; Martyn, L. J. P.; Pandiaraju, S.; Zheng, J.; Lough, A. *Org. Lett.* **2000** *2* (1), 41. doi:10.1021/ol991244v.

(15) (a) Böhme, H.; Hartke, K. *Chem. Ber.* **1960** *93*, 1305. doi:10.1002/cber.19600930610; (b) Böhme, H.; Meyer-Dulheuer, K.-H. *Liebigs Ann. Chem.* **1965** *688*, 78, doi:10.1002/jlac.19656880110; (c) Heaney, H.; Papageorgiou, G.; Wilkins, R. F. *Tetrahedron Lett.* **1988** *29* (19), 2377. doi:10.1016/S0040-4039(00)86064-5; (d) Rosenau, T.; Potthast, A.; Kosma, P. *Tetrahedron* **2004** *60* (2), 301. doi:10.1016/j.tet.2003.11.015; (e) Dimmock, J. R.; Erciyas, E.; Bigam, G. E.; Kirkpatrick, D. L.; Duke, M. M. *Eur. J. Med. Chem.* **1989** *24* (4), 379. doi:10.1016/0223-5234(89)90081-0.

(16) Böhme, H.; Bomke, U.; Denis, J.-P. *Arch. Pharm.* **1982** *315*, 40. doi:10.1002/ardp.19823150110.
(17) (a) Pochini, A.; Puglia, G.; Ungaro, R. *Synthesis* **1983** *1983* (11), 906. doi:10.1055/s-1983-30560; (b) Weinert, E. E.; Dondi, R.; Colloredo-Melz, S.; Frankenfield, K. N.; Mitchell, C. H.; Freccero, M.; Rokita, S. E. *J. Am. Chem. Soc.* **2006** *128* (36), 11940. doi:10.1021/ja062948k.
(18) Dowle, M. D.; Hayes, R.; Judd, D. B.; Williams, C. N. *Synthesis* **1983** *1983* (01), 73. doi:10.1055/s-1983-30231.
(19) Biava, M.; Fioravanti, R.; Porretta, G. C.; Frachey, G.; Mencarelly, P.; Sleiter, G.; Perazzi, M. E.; Simonetti, N.; Villa, A. *Farmaco* **1995** *50*, 431.
(20) (a) Kozikowski, A. P.; Ishida, H. *Heterocycles* **1980** *14*, 55. doi:10.3987/R-1980-01-0055; (b) Sliwa, H.; Blondeau, D. *Heterocycles* **1981** *16* (12), 2159. doi:10.3987/R-1981-12-2159; (c) Tidwell, J. H.; Buchwald, S. L. *J. Am. Chem. Soc.* **1994** *116* (26), 11797. doi:10.1021/ja00105a021; (d) Pemberton, N.; Aberg, V.; Almstedt, H.; Westermark, A.; Almqvist, F. *J. Org. Chem.* **2004** *69* (23), 7830. doi:10.1021/jo048554y; (e) Schnute, M. E.; Brideau, R. J.; Collier, S. A.; Cudahy, M. M.; Hopkins, T. A.; Knechtel, M. L.; Oien, N. L.; Sackett, R. S.; Scott, A.; Stephan, M. L.; Wathen, M. W.; Wieber, J. L. *Bioorg. Med. Chem. Lett.* **2008** *18* (14), 3856. doi:10.1016/j.bmcl.2008.06.060; (f) Bayer Healthcare LLC; Dixon, J.; Magnuson, S.; Phillips, B.; Wang, Y.; Li, T.; Parcella, K.; Newcom, J.; Kluender, H.; Hong, Z.; Chandler, B.; Zhang, Z.; Allegue, K.; Liu, Z. Substituted 4-aminopyrrolotriazine derivatives useful for treating hyper-proliferative disorders and diseases associated with angiogenesis. International Patent WO 2007/064883, June 7, 2007.
(21) Cox, P. J.; Wang, W.; Snieckus, V. *Tetrahedron Lett.* **1992** *33* (17), 2253. doi:10.1016/S0040-4039(00)74182-7.
(22) Heaney, H.; Papageorgiou, G.; Wilkins, R. F. *Tetrahedron* **1997** *53* (8), 2941. doi:10.1016/S0040-4020(96)01174-X.
(23) The hygroscopicity of this material did not allow for obtaining reliable combustion analysis data. We believe that the structure of triflate **5b** is confirmed (although indirectly) by the fact that it was successfully used to prepare intermediate (*S*)-**7a**, and the latter was converted into the known compound (*S*)-**1a**.
(24) Kitajima, H.; Ito, K.; Aoki, Y.; Katsuki, T. *Bull. Chem. Soc. Jpn.* **1997** *70* (1), 207. doi:10.1246/bcsj.70.207.

Can. J. Chem. Downloaded from www.nrcresearchpress.com by South China Agricultural University on 09/19/12
For personal use only.

Systematic study of the relationships between energy levels of $(Tl^+)_2$, $(In^+)_2$, $(Ga^+)_2$ dimer centers and the crystalline environment

Qiang Sun, Lili Wang, Liangyu Gong, and Jinsheng Shi

Can. J. Chem. Downloaded from www.nrcresearchpress.com by South China Agricultural University on 09/19/12
For personal use only.

Abstract: In this paper, we present the first systematic study of correlations between energy levels of $(Tl^+)_2$, $(In^+)_2$, and $(Ga^+)_2$ dimer centers and the crystalline environment by using dielectric theory of chemical bonding for complex crystals. Our model has successfully built links between the $E_{A'}$, $E_{B'}$, and $E_{C'}$ of these centers and the environmental factor h. The h has linear relationships with $E_{A'}$, $E_{B'}$, and $E_{C'}$. The calculated results are in good agreement with the experimental values. This model can serve as a prediction tool and can be applied to assign the absorption band energies of $(Tl^+)_2$, $(In^+)_2$, and $(Ga^+)_2$ centers.

Key words: alkali halides, dimer centers, energy levels, dielectric theory, chemical bond.

Résumé : Dans ce travail, on présente la première étude systématique des corrélations entre les niveaux d'énergie des centres dimères $(Tl^+)_2$, $(In^+)_2$ et $(Ga^+)_2$ et l'environnement cristallin en faisant appel à la théorie diélectrique de la liaison chimique de cristaux complexes. Ce modèle a permis d'établir des liens entre les valeurs $E_{A'}$, $E_{B'}$ et $E_{C'}$ de ces centres et le facteur environnemental h. Ce facteur h est en relation linéaire avec les valeurs $E_{A'}$, $E_{B'}$ et $E_{C'}$. Les résultats calculés sont en bon accord avec les valeurs expérimentales. Ce modèle peut donc servir comme outil de prédiction et il peut être appliqué pour attribuer les énergies des bandes d'absorption des centres $(Tl^+)_2$, $(In^+)_2$ et $(Ga^+)_2$.

Mots-clés : halogénures de métaux alcalins, centre dimères, niveaux d'énergie, théorie diélectrique, liaison chimique.

[Traduit par la Rédaction]

Introduction

Alkali halide crystals are extremely suitable for experimental and theoretical studies of heavy-metal ions centers. They are fairly well-understood crystals with cubic lattices and outstanding transparency in a wide range from the infrared to vacuum ultraviolet (VUV).[1,2] Ions with the electronic configuration ns^2 for the ground state and $nsnp$ for the first excited state ($n = 4, 5, 6$) are called ns^2-type ions. Table 1 shows 15 ions with the outer electronic configuration s^2. Among these ions, luminescence and related optical properties of Tl^+ in KCl and other similar crystals have been most precisely studied,[3–7] and so s^2 ions are also called Tl^+-like ions.[8] A great deal of effort has been devoted to understand the optical properties of ns^2 ions embedded into alkali halides since the pioneering work of Hilsch in 1927.[9] This subject has been reviewed many times (for example, see Refs. 10–13). In principle, the spectroscopy of alkali halide phosphors doped with ns^2 ions is well understood.[11] The influence of the host lattice on these properties is drastic, a fact that is considerably less well understood.[13]

Usually, the luminescence of ns^2 ions monomer centers [Fig. 1*a*], in which a ns^2 ion is substituted for an alkali ion far from other ns^2 ions, in alkali halides is described by the $^1S_0 \rightarrow {}^3P_{1,2} + {}^1P_1$ transitions, which originate from the $6s^2 \rightarrow 6s6p$ interconfigurational transition. In an absorption spectrum, the transitions from the $^1S_0$ ground state to the $^3P_1$, $^3P_2$, and $^1P_1$ excited states are labeled in order of increasing energy by A, B, and C bands. In addition to the presence of ns^2 ion monomer centers, absorption bands coming from dimer centers (paired Tl^+, In^+, Ga^+, etc., ions) denoted by $(Tl^+)_2$, $(In^+)_2$, $(Ga^+)_2$, and so on, have been widely observed and studied (see Ref. 14 for a review). The first observation of this kind of center was made by Yuster and Delbecq from absorption spectra of KI crystals with different concentrations of Tl^+ doping.[15] They found new absorption and luminescence bands in the spectra of the most heavily doped samples, which did not appear in the spectra of lightly doped samples. Later, the presence of these dimer centers has also been observed on various Tl^+-doped alkali halides, e.g., in KCl,[16–18] KBr,[19,20] KI,[21–25] RbCl,[26,27] RbI,[28,29] NaBr,[30] and NaI.[31,32] Even in the case of small thallium concentration, there are easily formed stable dimer thallium centers, whose spectral bands may overlap with those of the main $T1^+$ centers.[33]

The number of the dimer center in a crystal depends on the geometrical structure of the center.[17] So far, two kinds of structures are possible for the dimer centers: one is a dimer with D_{2h} symmetry, where two Tl^+ ions are at the nearest

Received 24 April 2011. Accepted 1 June 2011. Published at www.nrcresearchpress.com/cjc on 21 September 2011.

Q. Sun, L. Wang, L. Gong, and J. Shi. Department of Applied Chemistry, College of Chemistry and Pharmaceutical Sciences, Qingdao Agricultural University, Qingdao 266109, China.

Corresponding author: Jinsheng Shi (e-mail: jsshiqn@yahoo.cn).

Can. J. Chem. Downloaded from www.nrcresearchpress.com by South China Agricultural University on 09/19/12
For personal use only.

Table 1. Ions with the ns^2 configuration in the ground state.

n	Ion species				
4	Cu^-	Zn^0	Ga^+	Ge^{2+}	As^{3+}
5	Ag^-	Cd^0	In^+	Sn^{2+}	Sb^{3+}
6	Au^-	Hg^0	Tl^+	Pb^{2+}	Bi^{3+}

Fig. 1. (*a*) Geometrical structure of Tl^+ monomer and ((*b*) and (*c*)) Tl^+ dimer centers in alkali halides.

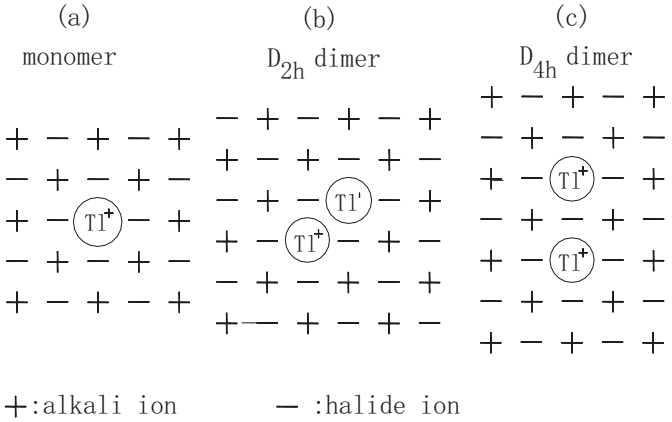

cation sites in a ⟨110⟩ direction [Fig. 1*b*], the other is a dimer with D_{4h} symmetry where two Tl^+ ions are at the second-nearest cation sites in a ⟨100⟩ direction [Fig. 1*c*].[16,17,34] In some systems, the D_{2h} dimer and the D_{4h} dimer centers may coexist. It is well established that dimers have absorption bands called A′, B′, and C′ related to A, B, and C monomer absorption bands, respectively.[22,23] The presence of these dimer centers introduces new optical-absorption bands, which may interfere with the lasing properties of the crystals.[18,27] Besides, the dimer centers have a high effective cross-section of charge carrier trapping, so they may essentially influence the character of the recombination processes in the crystal.[35] Absorption spectra of the dimer centers are similar to absorption spectra of the single centers.[36,37] In our recent synthetic studies on the sp energy levels of Pb^{2+}, Sn^{2+}, Tl^+, $Tl^0(1)$, Tl^{2+}, and In^+,[38–41] it was found that major environmental factors influencing the position of the A, B, and C bands are the chemical bond volume polarizability, fractional covalence of the chemical bond, and presented charge of the nearest anion in the chemical bonds. However, to the best of our knowledge, the relationships between the position of the absorption bands for dimer centers and the crystalline environment are still unknown. Therefore, building a theoretical model to understand the correlation between energy levels of the dimer centers for ns^2 ions and the structure of the hosts is very important and deserves further study.

In this paper, according to the experimental data and dielectric chemical bond theory, the major factors of the environment influencing the positions of A′, B′ and C′ bands are the coordination number of the central ion, the bond volume polarizability, and the fractional covalence of the chemical bond between the central ion and the nearest anion. The empirical expressions between band energies of $(Tl^+)_2$, $(In^+)_2$, and $(Ga^+)_2$ dimer centers for these three chemical bond parameters were obtained. The model calculation results are in excellent agreement with experiments. In addition, this theoretical work may also be very important for those who are investigating the optical properties of ns^2-type ion doped phosphors.

Theoretical methods

The dielectric chemical bond theory for complex crystals[42,43] is based on the bond charge model of Levine[44] and the dielectric theory of Phillips[45] and Van Vechten.[46] According to this theory, a complex crystal $E_eF_fG_gH_h$ (crystal molecular formula) can be written as a linear combination of the subformulas of various binary crystals when the crystal structure is known. The subformula of any kind of chemical bond E–F can be written as:

$$[1] \qquad \frac{N(\mathrm{F}-\mathrm{E})\cdot e}{N_{\mathrm{CE}}}\mathrm{E}\frac{N(\mathrm{E}-\mathrm{F})\cdot f}{N_{\mathrm{CF}}}\mathrm{F}$$

where E, F, G, and H represent the different constituents or different sites of the same element in the crystal formula, and e, f, g, and h represent the number of the corresponding elements. N(I–J) is the number of I ions in the coordination group of a J ion. N_{CE} and N_{CF} are the nearest-coordination numbers for each element in the crystal. Therefore in a subformula equation of a complex crystal, the charge Q presented by each coordination anion can be obtained from the valence conservation and electric neutrality of the subformula.

Having listed the subformula equation of a complex crystal and given the charge presented by each ion, we can obtain the number of effective valence electrons of each ion:

$$[2] \qquad (Z_{\mathrm{E}}^{\mu})^* = Z_{\mathrm{E}}^{\mu} q_{\mathrm{E}}^{\mu}$$

where Z_{E}^{μ} is the number of valence electrons of the E ion, and q_{E}^{μ} is the effective charge of each valence electron of each E ion. The effective valence election density associated with the bond μ is,

$$[3] \qquad (N_e^{\mu})^* = \frac{(n_e^{\mu})^*}{v_b^{\mu}}$$

The number of effective valence electrons $(n_e^{\mu})^*$ per μ bond is,

$$[4] \qquad (n_e^{\mu})^* = \frac{(Z_{\mathrm{E}}^{\mu})^*}{N_{\mathrm{CE}}^{\mu}} + \frac{(Z_{\mathrm{F}}^{\mu})^*}{N_{\mathrm{CF}}^{\mu}}$$

The chemical bond volume of the type μ bond, v_b^{μ} (in Å^3) is,

$$[5] \qquad v_b^{\mu} = (d^{\mu})^3 / \sum_{\nu} (d^{\mu})^3 N_b^{\nu}$$

where d^{μ} is the nearest-neighbor distance (in Å), and the denominator is merely the required normalization factor, where the sum over ν runs over all of the different types of bonds. N_b^{ν} is the number of bonds of type ν per cubic centimetres, which can be obtained from the crystal structural data.

According to PV. theory,[45,46] the susceptibility χ^{μ} of any bond is described as,

$$[6] \qquad \chi^{\mu} = \frac{(\hbar\Omega_p^{\mu})^2}{4\pi(E_g^{\mu})^2}$$

Can. J. Chem. Downloaded from www.nrcresearchpress.com by South China Agricultural University on 09/19/12
For personal use only.

Table 2. The chemical bond parameters and the environmental factors h of alkali halides.

Crystals	n	Bonds	d^{μ} (Å)	f_c^{μ}	α_b^{μ} (Å^3)	N	h
NaCl	1.531	Na–Cl	2.8100	0.0663	0.5462	6	0.466
NaBr	1.640	Na–Br	2.9869	0.0706	0.7639	6	0.569
NaI	1.730	Na–I	3.2350	0.0706	1.0753	6	0.675
KCl	1.488	K–Cl	3.1394	0.0483	0.7092	6	0.453
KBr	1.557	K–Br	3.2923	0.0490	0.9136	6	0.518
KI	1.658	K–I	3.5246	0.0513	1.2832	6	0.628
RbCl	1.490	Rb–Cl	3.2895	0.0445	0.8188	6	0.468
RbBr	1.550	Rb–Br	3.4384	0.0443	1.0305	6	0.523
RbI	1.640	Rb–I	3.6646	0.0457	1.4109	6	0.622
CsCl	1.631	Cs–Cl	3.5637	0.0379	0.7407	8	0.474
CsBr	1.693	Cs–Br	3.6979	0.0372	0.8909	**8**	0.515
CsI	1.789	Cs–I	3.9558	0.0372	1.2032	8	0.598

Note: n is the index of refraction; d^{μ} is the bond distance; f_c^{μ} is the fractional covalence of the chemical bond; α_b^{μ} is the polarizability of the chemical bond volume; Q^{μ} is the presented charge of the nearest anion in the chemical bond; N is the nearest-coordination numbers for each element in the crystal; h is the environmental factor of the crystals.

where Ω_p^{μ} is the plasma frequency,

$$[7] \qquad (\Omega_p^{\mu})^2 = \left[\frac{4\pi(N_e^{\mu})^* e^2}{m}\right] D_{\mu} A_{\mu}$$

where D_{μ} and A_{μ} are the correction factors defined in Refs. 46–47; e and m are the electronic charge and mass, respectively.

In eq. [6], E_g^{μ} (in eV) is the average energy band gap, and can be separated into homopolar energy E_h^{μ} (in eV) and heteropolar energy C^{μ} (in eV) as shown in the equation below,

$$[8] \qquad (E_g^{\mu})^2 = (E_h^{\mu})^2 + (C^{\mu})^2$$

where

$$[9] \qquad E_h^{\mu} = 39.74/(d^{\mu})^{2.48}$$

$$[10] \qquad C^{\mu} = 14.4 b^{\mu} \exp(-k_S^{\mu} r_o^{\mu})[(Z_E^{\mu})^* - w(Z_F^{\mu})^*]/r_o^{\mu}$$

with

$$[11] \qquad r_o^{\mu} = d^{\mu}/2$$

$$[12] \qquad k_s^{\mu} = (4k_F^{\mu}/\pi\alpha_B)^{1/2}$$

$$[13] \qquad k_F^{\mu} = [3\pi^2(N_e^{\mu})^*]^{1/3}$$

Here, b^{μ} is a correction factor that depends on the crystal structure, k_s^{μ} is the Thomas–Fermi screening factor, w is the number ratio of two elements E and F in the subformula, r_o^{μ} is the average radius between E and F atoms, and a_B is the Bohr radius. Once the refractive index n of a crystal is known, the value of b^{μ} and C^{μ} can be obtained by using eqs. [6], [8], [10] and the following equation:

$$[14] \qquad \chi = (\varepsilon - 1)/4\pi = \sum_{\mu} F^{\mu} \chi^{\mu} = \sum_{\mu} N_b^{\mu} \chi_b^{\mu}$$

where χ is the total linear susceptibility of a crystal, ε is the dielectric constant, which can be obtained from the refractive index, n (ε=n^2), F^{μ} is the fraction of bands of type μ composing the crystal, χ_b^{μ} is the susceptibility of a single bond of type μ.

The fractional ionicity f_i^{μ} and covalence f_c^{μ} of the individual bond are given by,

$$[15] \qquad f_i^{\mu} = (C^{\mu})^2/(E_g^{\mu})^2$$
$$f_c^{\mu} = (E_h^{\mu})/(E_g^{\mu})$$

According to the Lorentz formula,

$$[16] \qquad (\varepsilon^{\mu} - 1)/(\varepsilon^{\mu} + 2) = 4\pi\alpha_o^{\mu}/3$$

The polarizability coefficient of the μ bond, α_o^{μ}, can be obtained; this denotes the polarizability of the μ bond per cubic Angström. The polarizability of the type μ bond volume can be written as,

$$[17] \qquad \alpha_b^{\mu} = v_b^{\mu} \alpha_o^{\mu}$$

If the crystal structure and the refractive index n are known, the coordination number of the central ion, the bond volume polarizability α_b^{μ}, the fractional covalence f_c^{μ} of the chemical bond between the central ion and the nearest anion can be calculated by the method given above.

Results and discussion

By using the dielectric theory of chemical bonds for complex crystals, we calculated the chemical bond parameters for 12 alkali halide crystals; the results are displayed in Table 2. The second column shows the refractive index n of the crystals. Other columns in Table 2 give the chemical bond parameters: the bond distance (d^{μ}), the fractional covalence of the chemical bond (f_c^{μ}), the polarizability of the chemical bond volume (α_b^{μ}), the coordination number of the central ion (N).

The peak-positions of the dimer bands observed in absorption spectra of $(Tl^+)_2$, $(In^+)_2$, and $(Ga^+)_2$ in various alkali halides are summarized in Tables 3 and 4. For $(In^+)_2$ and $(Ga^+)_2$ dimer centers, although which of the D_{2h} and D_{4h} dimer centers is responsible for the bands in Table 4 is still uncertain. Polarized luminescence of $(In^+)_2$ and $(Ga^+)_2$ centers in KCl crystals was investigated by Tsuboi and Jacobs[19] and Ermoshkin et al.[35] Ermoshkin et al. suggested that the In^+ dimer consists of two In^+ ions with a Cl^- ion between them along ⟨100⟩ directions (i.e., the D_{4h} dimer model).[35] However,

Can. J. Chem. Downloaded from www.nrcresearchpress.com by South China Agricultural University on 09/19/12
For personal use only.

Table 3. Experimental and calculated peak positions of absorption bands due to Tl^+ dimer in various alkali halides.

		D_{2h} dimer band						D_{4h} dimer band	
Crystals	h	$E_{A',\,exptl}$	$E_{A',\,calcd}$	$E_{B',\,exptl}$	$E_{B',\,calcd}$	$E_{C',\,exptl}$	$E_{C',\,calcd}$	$E_{A',\,exptl}$	$E_{A',\,calcd}$
KCl	0.453	4.885[a]	4.880	5.770[b]	5.714	5.960[b]	5.949	4.910[a]	4.921
KBr	0.518	4.664[a]	4.650	5.426[b]	5.413	5.610[b]	5.594	4.732[a]	4.716
KI	0.628	4.265[c]	4.259	4.920[d]	4.904	4.970[d]	4.995	4.358[c]	4.368
RbCl	0.468	4.806[e]	4.827	5.585[e]	5.645		5.867		4.874
RbI	0.622	4.300[f]	4.281	4.881[f]	4.932	4.959[f]	5.027	4.390[f]	4.387
NaBr	0.569		4.469		5.177		5.316	4.558[g]	4.555
NaI	0.675	4.072[d]	4.093	4.714[d]	4.687	4.806[d]	4.738	4.220[a]	4.220

[a]Ref. 16;
[b]Ref. 17;
[c]Ref. 21;
[d]Ref. 22;
[e]Ref. 26;
[f]Refs. 14, 29;
[g]Ref. 30.

by comparing experimental results with calculations, Tsuboi and Jacobs suggest that the dimer center of In^+ in KCl has D_{2h} symmetry.[19]

From Tables 3 and 4, it is found that the position of A′, B′, and C′ bands depends not only on the alkali ion but also on the halide ion in alkali halides. For the I series in the sequence NaI→KI→RbI, the positions of the A′ band of the D_{2h} $(Tl^+)_2$ dimer center were 4.072, 4.265, and 4.300 eV, respectively. For the K series in the sequence of KCl→KBr→KI, the positions of A′ band of the D_{2h} $(Tl^+)_2$ dimer center were 4.885, 4.664, and 4.265 eV, respectively. This is because their bond lengths are different and thus the nephelanxetic effects are not the same,[48,49] therefore, the A′, B′, and C′ band energies of different dimer centers shift accordingly. Jörgensen found that the nephelanxetic ratio β can be express as: $\beta = 1 - hk$, where h relates to the ligands and k to the central metal.[48] Duffy and Ingram proposed a quantitative relation between the position of the $^1S_0 \rightarrow {}^3P_1$ transition of ns^2 ions and Jörgensen's h functions.[50] Blasse[49] and Bruce and Duffy[51] investigated the relationships between ns^2 ions $^1S_0 \rightarrow {}^3P_1$ transition, as well as Eu^{3+} charge transfer transition energy and h, and obtained some significant results. However, the detailed factors affecting h were not obtained by them. Gao and Zhang studied the mechanism of the nephelauxetic effect for the electronic structure of 3d elements and identified the main factors responsible for the effect.[43] These are: the covalency of chemical bond, polarizabilities of ligand bond volume for the host, and the valence and spin state of the center ion. Recently, the environmental factor was revised for the lanthanide ions by our group.[52,53] We successfully explained the energy difference between the spin-allowed and spin-forbidden states of Tb^{3+} in crystals,[52] as well as the barycenter of energy of lanthanide $4f^{N-1}5d$ configuration in inorganic crystals.[53]

The environmental factor designated by the symbol h[43] can be expressed as,

$$[18] \qquad h = (N f_c^{\mu} \alpha_b^{\mu})^{1/2}$$

Based on eq. [18] and the corresponding chemical bond parameters (see Table 2), the environmental factors h of the alkali halides have been calculated. The results are presented in column 8 of Table 2.

The relations between the positions of the A′, B′, and C′ bands of $(Tl^+)_2$, $(In^+)_2$, and $(Ga^+)_2$ dimer centers and h are shown in Figs. 2 and 3. It is found that all the $E_{A'}$, $E_{B'}$, and $E_{C'}$ of $(Tl^+)_2$, $(In^+)_2$, and $(Ga^+)_2$ dimer centers decrease with an increase of h.

By fitting the curves in Figs. 2 and 3, we obtained the following empirical formulas:

$$[19] \qquad D_{2h}(Tl^+)_2A' \text{ Band}: \quad E_{A'} = 6.487 - 3.547 \times h$$

$$[20] \qquad D_{2h}(Tl^+)_2B' \text{ Band}: \quad E_{B'} = 7.810 - 4.627 \times h$$

$$[21] \qquad D_{2h}(Tl^+)_2C' \text{ Band}: \quad E_{C'} = 8.419 - 5.453 \times h$$

$$[22] \qquad D_{4h}(Tl^+)_2A' \text{ Band}: \quad E_{A'} = 6.352 - 3.159 \times h$$

$$[23] \qquad (Ga^+)_2C' \text{ Band}: \quad E_{C'} = 7.816 - 5.278 \times h$$

$$[24] \qquad (In^+)_2C' \text{ Band}: \quad E_{C'} = 6.899 - 4.247 \times h$$

We should note that due to the lack of available theoretical mode to predict and assign absorption bands of monomer and dimer centers, the experimental investigation of $(Ga^+)_2$ and $(In^+)_2$ centers in alkali halides is very limited. Only $E_{C'}$ in KX (X = Cl, Br, and I) are available for $(Ga^+)_2$ and $(In^+)_2$ centers. Therefore, we think eqs. [19]–[24] are useful for investigating the absorption bands of $(Ga^+)_2$ and $(In^+)_2$ in alkali halides. $E_{A'}$, $E_{B'}$, and $E_{C'}$ of dimer centers were calculated by using eqs. [19]–[24], and the corresponding results are listed in Tables 3 and 4. The model calculation results excellently agree with the experimental data. Compared with the experimental data, the maximum error is 0.068 eV in the C′ band for D_{2h} $(Tl^+)_2$ center in NaI, the error ratio is only 1.415%. To the best of our knowledge, this is first successful quantitative investigation of the relationships between the absorption band positions of dimer ns^2 ions centers and the crystalline environment. In addition, as shown in Fig. 2, the distance of the C′ and B′ bands for the D_{2h} $(Tl^+)_2$ center decrease with increasing h. For example, $\Delta E_{C'\text{-}A'}$ of the D_{2h} $(Tl^+)_2$ center in KCl (h = 0.453) and NaI (h = 0.675) were 0.19 and 0.092 eV, respectively. This trend indicates that the distance

Table 4. Experimental and calculated peak positions of absorption bands due to Ga^+ and In^+ dimers in various alkali halides.

		$(Ga^+)_2$		$(In^+)_2$	
Crystal	h	$E_{C',exptl}$	$E_{C',calcd}$	$E_{C',exptl}$	$E_{C',calcd}$
KCl	0.453	5.438[a]	5.425	4.999[a]	4.975
KBr	0.518	5.061[a]	5.082	4.661[a]	4.699
KI	0.628	4.509[a]	4.501	4.246[a]	4.232

[a]Refs. 17, 22.

Fig. 2. The relations between A′, B′, and C′ band energies of D_{2h} and D_{4h} symmetry $(Tl^+)_2$ centers and environmental factors h.

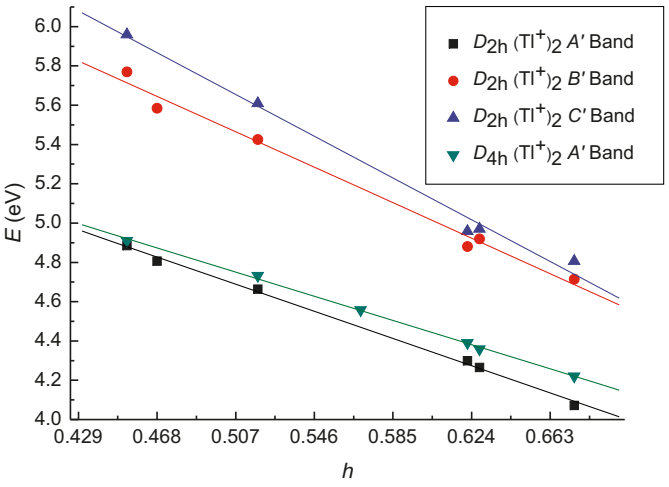

Fig. 3. The relations between C′ band energies of $(Ga^+)_2$ and $(In^+)_2$ centers and environmental factors h.

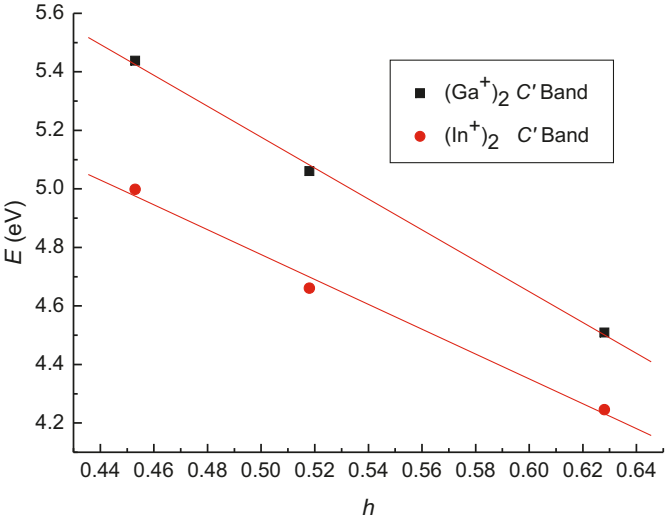

of C′ and B′ bands of Pb^{2+} will become too small to identify each band in the host for which h is very larger. Equations [19]–[21] show that the slopes increase markedly in the sequence of A′→B′→C′; the corresponding values are 3.547, 4.627, and 5.453, respectively. This means that the C′ band is the most sensitive energy level compared with the A′ and B′ bands. Moreover, as shown in Fig. 2, the distance of the A′ band for D_{4h} and D_{2h} $(Tl^+)_2$ centers increase with the increasing h. According to our model, the D_{4h} and D_{2h} symmetry of Tl^+ dimer centers can be assigned easily.

Applications

From the above discussion, it can be concluded that the $E_{A'}$, $E_{B'}$, and $E_{C'}$ of $(Tl^+)_2$, as well as $E_{C'}$ of $(In^+)_2$ and $(Ga^+)_2$ centers have direct relationships with the environmental factor h, and six good empirical formulas are obtained.

Therefore, we consider that the current model can serve as a prediction tool and can be applied to the assignments, reassignments, and predictions of the absorption band of A′, B′, and C′ bands of dimer centers in alkali halides. The applications of our model in these fields are presented in this section.

The environmental factors h of 12 alkali halides are listed in column 8 of Table 2. Using eqs. [19]–[24] we can predict $E_{A'}$, $E_{B'}$, and $E_{C'}$ of $(Tl^+)_2$, as well as $E_{C'}$ of $(In^+)_2$ and $(Ga^+)_2$ centers in these crystals. $E_{A'}$, $E_{B'}$, and $E_{C'}$ of D_{2h} $(Tl^+)_2$ in NaBr as well as $E_{C'}$ of D_{2h} $(Tl^+)_2$ and $E_{A'}$ of D_{4h} $(Tl^+)_2$ in RbCl are predicted and listed in Table 3. For other crystals, if the refractive index n and the crystal structures are known, the chemical bond parameters and environmental factors h can be calculated by using the dielectric theory of chemical bonds for complex crystals, then $E_{A'}$, $E_{B'}$, and $E_{C'}$ of dimer centers can be calculated according to our model.

The assignment of the observed absorption bands due to D_{2h} $(Tl^+)_2$ dimer centers in KCl is ambiguous. For KCl:$T1^+$, where two dimer bands peaking at 5.77 and 5.96 eV are present, an assignment is that both are related to the C′-band of the $^1T_{1u}$ state,[16] another is that the former band is related to the B′ band of the ^3E_u and $^3T_{2u}$ states, whereas the latter to the C′ band of the $(Tl^+)_2$.[17] According to our model, the calculated values of B′ and C′ bands are 5.714 and 5.949 eV, respectively. So it is concluded from our study that 5.77 and 5.96 eV of Tl^+ dimer bands in KCl mentioned above are attributable to the B′ and C′ bands, respectively, in agreement with the suggestion previously given by Tsuboi.[17]

In the case of RbCl:Tl^+, with the rise of thallium content additional absorption bands appear at 258 nm (4.806 eV) and 222 nm (5.585 eV).[26] Sharan et al. suggest that these are attributed to electronic transitions in dimers with D_{4h} symmetry: the 4.806 and 5.585 eV absorption hands have been assigned to A′ and B′ bands, respectively.[26] Unlike the suggestion by Sharan et al., however, Nistor et al.[27] suggested that the Tl^+ dimer in RbCl has D_{2h} symmetry by ESR analysis. From Table 3 it can be seen that the calculated values 4.827 eV (A′ band) and 5.645 eV (B′ band) of the D_{2h} $(Tl^+)_2$ center in RbCl:Tl^+ are in excellent agreement with the experimental data. Thus, we ascribed the 4.806 and 5.585 eV absorption bands to the A′ and B′ bands, respectively, of $(Tl^+)_2$ center with D_{2h} symmetry.

For CsBr:Tl^+, at high thallium concentration, additional absorption bands were obtained at 270 nm (4.592 eV) and

Can. J. Chem. Downloaded from www.nrcresearchpress.com by South China Agricultural University on 09/19/12
For personal use only.

Can. J. Chem. Downloaded from www.nrcresearchpress.com by South China Agricultural University on 09/19/12
For personal use only.

258 nm (4.806 eV).[54] The former was assigned to the A′ band of $(Tl^+)_2$ with D_{4h} symmetry, and the latter were not assigned by any authors.[48] Using eqs. [19] and [22], the calculated values of $(Tl^+)_2$ with D_{2h} and D_{4h} symmetries were 4.660 and 4.725 eV, respectively. Considering the fact that the two dimer centers D_{2h} and D_{4h} may coexist, we re-assign the 4.592 eV that was attributed to $(Tl^+)_2$ with D_{2h} symmetry and the 4.806 eV is assigned to $(Tl^+)_2$ with D_{4h} symmetry.

Conclusions

In this paper, we propose a semi-empirical method for predicting the absorption band positions of $(Tl^+)_2$, $(In^+)_2$ and $(Ga^+)_2$ dimer centers in alkali halides. The environmental factors affecting the absorption band positions of these dimer centers are the coordination number of the central ion, the bond volume polarizability, and the fractional covalence of the chemical bond between the central ion and the nearest anion. It was found that the environmental factors have linear relationships with the $E_{A'}$, $E_{B'}$, and $E_{C'}$ of $(Tl^+)_2$, $(In^+)_2$, and $(Ga^+)_2$ dimer centers. The calculated results are in good agreement with the experimental values. The current semi-empirical model can serve as a prediction tool and can be applied to assign and re-assign the absorption band positions of dimer centers in inorganic crystals. The model predicts that the positions of $E_{A'}$, $E_{B'}$, and $E_{C'}$ of D_{2h} $(Tl^+)_2$ in NaBr are 4.469, 5.177, 5.316 eV, respectively, and $E_{C'}$ of D_{2h} $(Tl^+)_2$ and $E_{A'}$ of D_{4h} $(Tl^+)_2$ in RbCl are 5.867, 4.874 eV, respectively. We re-assign the 5.77 and 5.96 eV bands of D_{2h} $(Tl^+)_2$ center in KCl to the B′ and C′ bands, respectively. In the case of RbCl:Tl^+, we ascribed the 4.806 and 5.585 eV to the A′ and B′ bands, respectively, of $(Tl^+)_2$ center with D_{2h} symmetry. For CsBr:Tl^+, we reassign the 4.592 eV band to $(Tl^+)_2$ with D_{2h} symmetry and the 4.806 eV was re-assigned to $(Tl^+)_2$ with D_{4h} symmetry.

Acknowledgement

This work was supported by the Project of Shandong Province Higher Educational Science and Technology Program (J10LD10).

References

(1) Zazubovich, S. *Int. J. Mod. Phys. B* **1994** *8* (8), 985. doi:10.1142/S0217979294000506.
(2) Fujita, I. *Phys. Rev. B* **1994** *49* (10), 6462. doi:10.1103/PhysRevB.49.6462.
(3) Nagarajan, S.; Sudarkodi, R. *J. Alloy. Comp.* **2009** *468* (1–2), 558. doi:10.1016/j.jallcom.2008.01.052.
(4) Yakovlev, V.; Meleshko, A.; Trefilova, L. *J. Lumin.* **2008** *128* (9), 1447. doi:10.1016/j.jlumin.2008.01.020.
(5) Voloshinovskii, A.; Zazubovich, S.; Stryganyuk, G.; Pashuk, I. *J. Lumin.* **2004** *111* (1–2), 9.
(6) Aminov, L. K.; Nikitin, S. I.; Silkin, N. I.; Shakhov, A. A.; Yusupov, R. V. *J. Phys. Condens. Matter* **2002** *14* (50), 13835. doi:10.1088/0953-8984/14/50/310.
(7) Aminov, L. K.; Kosach, A. V.; Nikitin, S. I.; Silkin, N. I.; Yusupov, R. V. *J. Phys. Condens. Matter* **2001** *13* (28), 6247. doi:10.1088/0953-8984/13/28/307.
(8) Yen, W. M.; Shionoya, S.; Yamamoto, H. Phosphor Handbook, CRC Press, Boca Raton, Boston 2006.
(9) Hilsch, R. *Z. Phys.* **1927** *44* (11–12), 860.
(10) Eppler, R. A. *Chem. Rev.* **1961** *61* (5), 523. doi:10.1021/cr60213a003.
(11) Ranfagni, A.; Mugnai, D.; Bacci, M.; Viliani, G.; Fontana, M. P. *Adv. Phys.* **1983** *32* (6), 823. doi:10.1080/00018738300101621.
(12) Jacobs, P. W. M. *J. Phys. Chem. Solids* **1991** *52* (1), 35. doi:10.1016/0022-3697(91)90059-9.
(13) Nistor, S. V.; Schoemaker, D.; Ursu, I. *Phys. Status Solidi B*, **1994** *185* (1), 9. doi:10.1002/pssb.2221850102.
(14) Tsuboi, T.; Jacobs, P. W. M. *J. Phys. Chem. Solids* **1991** *52* (1), 69. doi:10.1016/0022-3697(91)90060-D.
(15) Yuster, P. H.; Delbecq, C. J. *J. Chem. Phys.* **1953** *21* (5), 892. doi:10.1063/1.1699054.
(16) Tsuboi, T. *Phys. Rev. B* **1984** *29* (2), 1022. doi:10.1103/PhysRevB.29.1022.
(17) Tsuboi, T. *J. Phys. Soc. Jpn.* **1970** *29* (5), 1303. doi:10.1143/JPSJ.29.1303.
(18) Yang, B. R.; Goovaerts, E.; Schoemaker, D. *Phys. Rev. B* **1983** *27* (3), 1507. doi:10.1103/PhysRevB.27.1507.
(19) Tsuboi, T.; Jacobs, P. W. M. *J. Lumin.* **1976** *11* (3–4), 227. doi:10.1016/0022-2313(75)90017-4.
(20) Tsuboi, T. *Phys. Status Solidi B*, **1980** *102* (1), K7. doi:10.1002/pssb.2221020143.
(21) Ohata, T.; Hayashi, T.; Koshino, S. *J. Phys. Soc. Jpn.* **1978** *45* (2), 581. doi:10.1143/JPSJ.45.581.
(22) Fukuda, A. *J. Phys. Soc. Jpn.* **1969** *26* (4), 1006. doi:10.1143/JPSJ.26.1006.
(23) Benci, S.; Chiari, A.; Fenni, F. *Phys. Rev. B* **1986** *34* (8), 5769. doi:10.1103/PhysRevB.34.5769.
(24) Tsuboi, T. *Phys. Status Solidi B*, **1981** *106* (1), 301. doi:10.1002/pssb.2221060134.
(25) Benci, S.; Fermi, F. *Phys. Rev. B* **1985** *32* (4), 2554. doi:10.1103/PhysRevB.32.2554.
(26) Sharan, V. B.; Srivastwa, D. N. S.; Sen, S. C. *Phys. Status Solidi A*, **1979** *53* (2), 469. doi:10.1002/pssa.2210530208.
(27) Nistor, S. V.; Schoemaker, D.; Ursu, I.; Yang, B. R. *Phys. Status Solidi B*, **1985** *127* (2), 503. doi:10.1002/pssb.2221270209.
(28) Nagirnyi, V.; Soovik, T.; Vaino, P.; Zazubovich, S.; Jaanson, N. *Phys. Status Solidi B*, **1991** *164* (2), 493. doi:10.1002/pssb.2221640218.
(29) Koshino, S.; Ohata, T.; Hayashi, T. *J. Phys. Soc. Jpn.* **1980** *49* (4), 1387. doi:10.1143/JPSJ.49.1387.
(30) Joshi, R. V.; Nene, J. G. *Z. Phys. B Condens. Matter* **1982** *46* (1), 13. doi:10.1007/BF01640347.
(31) Herb, G. K.; Fontana, M. P.; Van Sciver, W. J. *Phys. Rev.* **1968** *168* (3), 1000. doi:10.1103/PhysRev.168.1000.
(32) Uchida, Y.; Matsui, E. *J. Phys. Soc. Jpn.* **1965** *20* (5), 874. doi:10.1143/JPSJ.20.874.
(33) Benci, S.; Fermi, F.; Lenzi, G. *Phys. Status Solidi B*, **1983** *119* (1), 337. doi:10.1002/pssb.2221190138.
(34) Tsuboi, T. *Phys. Rev. B* **1984** *29* (8), 4775. doi:10.1103/PhysRevB.29.4775.
(35) Ermoshkin, A.; Evarestov, R.; Gindina, R.; Maaroos, A.; Osminin, V.; Zazubovich, S. *Phys. Status Solidi B*, **1975** *70* (2), 749. doi:10.1002/pssb.2220700235.
(36) Yuster, P. H.; Delbecq, C. J. *J. Chem. Phys.* **1953** *21* (5), 892. doi:10.1063/1.1699054.
(37) Zorenko, Y.; Gorbenko, V.; Voznyak, T.; Jary, V.; Nikl, M. *J. Lumin.* **2010** *130* (10), 1963. doi:10.1016/j.jlumin.2010.05.013.
(38) Sun, Q.; Shi, J. S. *Acta Phys. Chim. Sin.* **2009** *25* (10), 2137.
(39) Sun, Q.; Shi, J. S. *J. Lumin.* **2011** *131* (5), 984. doi:10.1016/j.jlumin.2011.01.007.

(40) Sun, Q.; Qu, B. H.; Shi, J. S. *Phys. Chem. Chem. Phys.* **2010** *12* (16), 4178. doi:10.1039/b921791f.
(41) Sun, Q.; Wang, J.; Shi, J. S. *J. Solid State Chem.* **2010** *183* (5), 1174. doi:10.1016/j.jssc.2010.03.031.
(42) Zhang, S. Y. *Chin. J. Chem. Phys.* **1991** *4* (2), 109.
(43) Gao, F. M.; Zhang, S. Y. *J. Phys. Chem. Solids* **1997** *58* (12), 1991. doi:10.1016/S0022-3697(96)00139-4.
(44) Levine, B. F. *Phys. Rev. B* **1973** *7* (6), 2600. doi:10.1103/PhysRevB.7.2600.
(45) Phillips, J. C. *Rev. Mod. Phys.* **1970** *42* (3), 317. doi:10.1103/RevModPhys.42.317.
(46) Van Vechten, J. A. *Phys. Rev.* **1969** *182* (3), 891. doi:10.1103/PhysRev.182.891.
(47) Van Vechten, J. A. *Phys. Rev.* **1969** *187* (3), 1007. doi:10.1103/PhysRev.187.1007.
(48) Jörgensen, C. K. *Prog. Inorg. Chem.* **1962** *4*, 73. doi:10.1002/9780470166055.ch2.
(49) Blasse, G. *J. Solid State Chem.* **1972** *4* (1), 52. doi:10.1016/0022-4596(72)90131-4.
(50) Duffy, J. A.; Ingram, M. D. *J. Chem. Phys.* **1971** *54* (1), 443. doi:10.1063/1.1674635.
(51) Bruce, A. J.; Duffy, J. A. *J. Chem. Soc., Faraday Trans. I* **1982** *78* (3), 907. doi:10.1039/f19827800907.
(52) Shi, J. S.; Zhang, S. Y. *J. Phys. Condens. Matter* **2003** *15* (24), 4101. doi:10.1088/0953-8984/15/24/303.
(53) Shi, J. S.; Zhang, S. Y. *J. Phys. Chem. B* **2004** *108* (49), 18845. doi:10.1021/jp038001b.
(54) Sharan, V. B.; Srivastwa, D. N. S.; Sen, S. C. *Pramana* **1979** *12* (3), 291. doi:10.1007/BF02846397.

Can. J. Chem. Downloaded from www.nrcresearchpress.com by South China Agricultural University on 09/19/12
For personal use only.

A novel method to chemically bind thiazolidine-2,4-dione through cross-linked chitosan nanoparticles using malanodialdehyde as a cross-linker

Prashant Singh, Kamlesh Kumari, Vartika Tomar, Mohd. Samim, Rajan Patel, Gopal Kumar Mehrotra, Monica Dubey, Narendra Deo Pandey, and Anju Katyal

Can. J. Chem. Downloaded from www.nrcresearchpress.com by South China Agricultural University on 09/19/12
For personal use only.

Abstract: Chitosan is a biodegradable natural polymer with great potential for pharmaceutical applications because of its biocompatibility, high charge density, nontoxicity and mucoadhesion. It has been shown that it not only improves the dissolution of poorly soluble drugs but also exerts a significant effect on fat metabolism in the body. Gel formation can be obtained by interactions of chitosans with low molecular counterions such as polyphosphates, sulfates, and cross-linkers. This gelling property of chitosan allows a wide range of applications such as the coating of pharmaceuticals and food products, gel entrapment of biochemicals, plant embryos, whole cells, microorganisms, and algae. This manuscript is an insight into the exploitation of its properties for microencapsulating drugs. Herein, we report a novel method to chemically bind thiazolidine-2,4-dione through cross-linked chitosan nanoparticles using malanodialdehyde as a new cross-linker and well characterized by FT-IR, NMR, TGA, DSC, powder X-ray diffraction, TEM, and cyclic voltametry.

Key words: chitosan, nanoparticles, transmission electron microscopy (TEM), powder-X-ray diffraction (XRD), thermogravimetric analysis (TGA), differential scanning calorimetry (DSC).

Résumé : Le chitosane est un polymère naturel biodégradable qui présente un grand potentiel pour des applications pharmaceutiques en raison de sa biocompatibilité, de sa grande densité de charge, de sa non-toxicité et de sa mucoadhésion. Il a été démontré qu'en plus d'améliorer la dissolution des médicaments peu solubles, il exerce aussi un effet significatif sur le métabolisme des graisses dans le corps. La formation de gel peut être obtenue par les interactions des chitosanes avec des contre-ions de faibles masses moléculaires, tels les polyphosphates, les sulfates et les produits de réticulation. Cette propriété de gélification du chitosane permet réaliser une grande variété d'applications, tel l'enrobage de médicaments et de produits comestibles, l'encapsulation dans un gel de produits biomédicaux, d'embryons de plantes, de cellules entières, de microorganismes et d'algues. Cette présentation présente une revue des domaines dans lesquels ses propriétés pourraient être exploitées pour encapsuler des médicaments. On décrit une nouvelle méthode pour lier chimiquement la thiazolidine-2,4-dione par le biais de nanoparticules de chitosane réticulées à l'aide du dialdéhyde malonique comme nouvel agent de réticulation et bien caractérisées par infrarouge à transformée de Fourier (IR-TF), résonance magnétique nucléaire (RMN), analyse thermogravimétrique (ATG), calorimétrie différentielle à balayage (CDB), diffraction des rayons-X par une poudre, microscopie électronique à transmission (MET) et voltampérométrie cyclique.

Mots-clés : chitosane, nanoparticules, microscopie électronique à transmission (MET), diffraction des rayons X par une poudre, analyse thermogravimétrique (ATG), calorimétrie différentielle à balayage (CDB).

[Traduit par la Rédaction]

Introduction

The potential use of polymeric nanoparticles as drug carriers has led to the development of many different colloidal delivery vehicles.[1–5] The main advantages of this kind of system lie in their capacity to cross biological barriers, to protect macromolecules, such as peptides, proteins, oligonucleotides, and genes from degradation in biological media, and to deliver drugs or macromolecules to a target site followed by controlled release.[6,7] In the last few years several synthetic as

Received 28 August 2010. Accepted 3 February 2011. Published at www.nrcresearchpress.com/cjc on 21 September 2011.

P. Singh. A. R. S. D. Collage, University of Delhi, Delhi, India; Department of Chemistry, Jamia Hamdard, New Delhi 110062, India.
K. Kumari. Department of Chemistry, Jamia Hamdard, New Delhi 110062, India; MNNIT Allahabad, Uttar Pradesh, India.
V. Tomar. A. R. S. D. Collage, University of Delhi, Delhi, India.
M. Samim. Department of Chemistry, Jamia Hamdard, New Delhi 110062, India.
R. Patel. Jamia Millia Islamia, New Delhi 110025, India.
G.K. Mehrotra, M. Dubey, and N.D. Pandey. MNNIT Allahabad, Uttar Pradesh, India.
A. Katyal. ACBR, University of Delhi, Delhi 110007, India.

Corresponding author: P. Singh (e-mail: arsdchemistry@yahoo.in).

Fig. 1. Structure of chitosan.

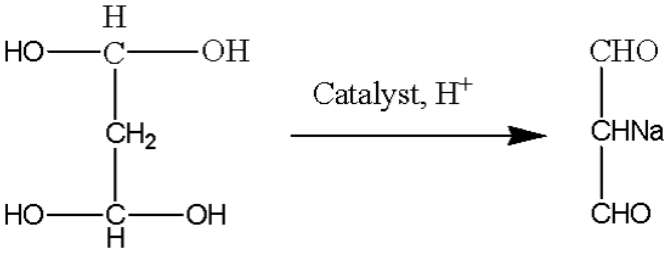

well as natural polymers have been examined for pharmaceutical applications.[8–13] The basic prerequisite for a polymer to be used as a delivery agent in an in vivo system is that it has to degrade into molecules with no toxicity for the system where it is used. A very limited number of polymers can be used to prepare biodegradable materials owing to biocompatibility problems.[14–16]

Chitosan is an interesting natural material occurring in abundance in the environment. Chitosan is a polysaccharide comparable to cellulose and it is comprised of copolymers of glucosamine and *N*-acetyl glucosamine linked by β-(1–4) linkages, which can be derived by partial deacetylation of chitin from crustacean shells as shown in Fig. 1.[17] Nanoparticles have a special role in targeted drug delivery in the sense that they have all the advantages of liposomes including the particle size, but unlike liposomes, nanoparticles have a better shelf life and can usually entrap more drugs than liposomes. Although nanoparticles made up of hydrophobic polymers encapsulating hydrophobic drugs have been reported in the literature, very few studies have been made on the preparation of drug-loaded hydrogel nanoparticles.[18–22] Preparation of nanoparticles from chitosan, a hydrogel polymer, for drug delivery can have several advantages over the use of chitosan microspheres and microcapsules.[23] Nanometer range particles have easy accessibility in the body, being transported via the circulation to different body sites. Extremely small nanoparticles of <100 nm diameter with hydrophilic surfaces have been found to have longer circulation in the blood.[24–26]

Particle size, density, viscosity, degree of deacetylation, and molecular weight are important characteristics of chitosan that influence the properties of pharmaceutical formulations based on chitosan. Properties such as biodegradability, low toxicity, and good biocompatibility make it suitable for use in biomedical and pharmaceutical formulations, e.g., it is used for hypobilirubinaemic and hypocholesterolemic effects, antacid and antiulcer activities, wound and burn healing properties, immobilization of enzymes and living cells, and in ophthalmology. Since chitosan has a capacity for forming film, it has been suggested as a biopolymer of choice for the development of contact lenses (soft and hard). Chitosan has been used for the manufacture of ocular bandage lenses used as protective devices for acutely or chronically traumatized eyes. Chitosan membranes have also been found useful as artificial kidney membranes because of their suitable permeability and high tensile strength.[8,12,15,17–19]

Chitosan has been shown to possess mucoadhesive properties owing to molecular attractive forces formed by electrostatic interaction between positively charged chitosan and negatively charged mucosal surfaces. These properties may be attributed to strong hydrogen-bonding groups like –OH, –COOH, strong charges, high molecular weight, sufficient chain flexibility, and surface-energy properties favoring spreading into mucus.

Preparation of nanoparticles with this versatile hydrogel material has been attempted by several workers with the purpose of utilizing its mucoadhesive properties to transport drugs and DNA across mucosal surfaces. The reactive free amino group on the particle surface makes it possible to chemically conjugate various other reactive groups, such as polyethylene glycol (PEG) derivatives, different ligands, antibodies, and other pH- and temperature-sensitive moieties. Considering the advantages of using ultra low sized hydrophilic nanoparticles for drug delivery, we focused on the preparation of chitosan nanoparticles of <100 nm diameter.[22–25]

The thiazolidine-2,4-diones (TZDs), also known as glitazones, are one class of chemotherapeutics that increases sensitivity to insulin and is used for the treatment of type 2 diabetes mellitus.[27,28] These agents enhance insulin action in liver, muscle, and fat tissues. TZDs bind to nuclear receptor peroxisome – proliferator-activated receptor γ (PPARγ) and activates them to trigger the expression of insulin-responsive genes responsible for the regulation of carbohydrate and lipid metabolism.[29–31]

As per Banerjee et al.,[24] the biodistribution of chitosan nanoparticles establishes that chitosan particles are RES evading and circulate in the blood for a considerable amount of time. As per Banerjee et al.,[24] chitosan nanoparticles have gained more attention as drug delivery carriers because of their better stability, low toxicity, simple and mild preparation method, and for providing versatile routes of administration. Their submicron size is not only suitable for parenteral application, but it is also applicable for mucosal routes of administration, i.e., oral, nasal, and ocular, which are noninvasive routes. The application for mucosal delivery is also facilitated by the chitosan absorption enhancing effect. Furthermore, chitosan nanoparticles also have been shown to be a good adjuvant for vaccines.[32]

Banerjee et al.[24] describe the preparation of cross-linked chitosan nanoparticles using reverse micelles as the media, but in this paper, we report a novel method for chemically binding TZD (antidiabetic in nature) for delivery through cross-linked chitosan nanoparticles using malanodialdehyde as a new cross-linker.

Experimental and method

Materials

Chitosan (MW 400 kDa) and a surfactant, i.e., sodium bis(ethylhexyl)sulfosuccinate (AOT), were purchased from Sigma-Aldrich. Sodium salt malanodialdehyde was prepared from tetraethoxypropane. All chemicals were purchased from Sigma-Aldrich and Merck and used without any purification. FT-IR spectrums were recorded on a Spectrum Bx2 IR. Electrochemical properties were determined on a Electrochemical Analyzer CH 201 instrument. Thermogravimetric analyses were done using a PerkinElmer model Pyris 6 computerized thermal analysis system. The rate of heating of the sample was kept at 10 °C/min under nitrogen flow at 20 mL/min. Copper sulfate pentahydrate was used as a calibration standard.

Can. J. Chem. Downloaded from www.nrcresearchpress.com by South China Agricultural University on 09/19/12
For personal use only.

Fig. 2. Flow chart for the synthesis of cross-linked (*a*) chitosan and (*b*) chitosan–thiazolidine-2,4-dione nanopolymers using using the sodium salt of malanodialdehyde as a cross-linker.

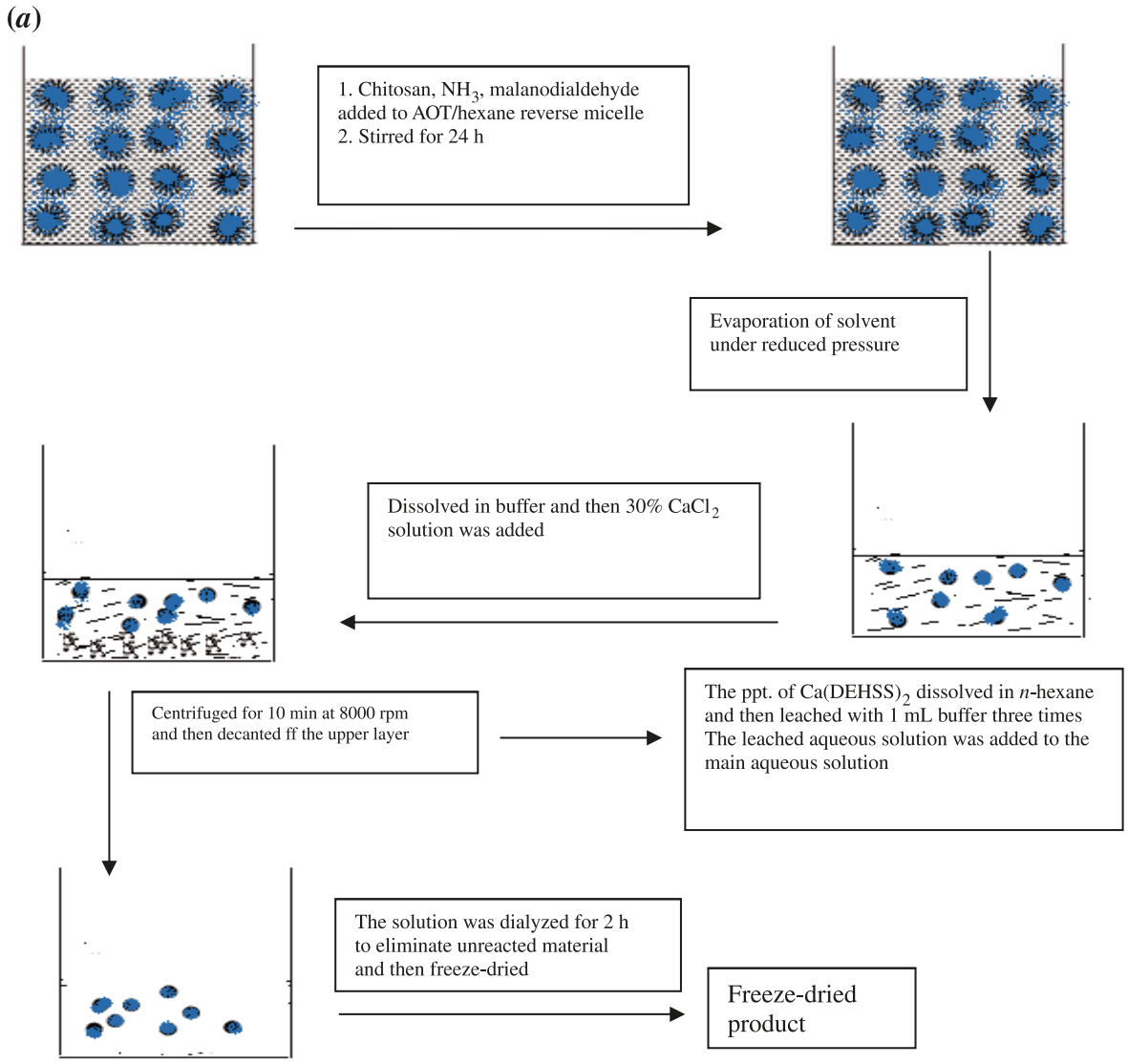

Can. J. Chem. Downloaded from www.nrcresearchpress.com by South China Agricultural University on 09/19/12
For personal use only.

NMR spectra were recorded on a Bruker Spectrospin 300 MHz spectrometer.

Preparation of the sodium salt of malanodialdehyde

Into a 50 mL flask, 4 mL of tetraethoxypropane and 5 mL of concd HCl were added and 20 mg of cation exchange resin, i.e., Amberlyst with the functionality of sulfuric acid (strong acidic), was added to the above reaction mixture. Then the reaction mixture was stirred for 5 min. The reaction mixture was filtered and the pH of the reaction mixture was made 7.2. After this the reaction mixture was precipitated with ice-cold acetone. the solution was filtered and the product was dissolved in a minimum quantity of distilled water and then precipitated out again with ice-cold acetone (Fig. 2) and then characterized by FT-IR, ^{1}H NMR, and ^{13}C NMR.

Preparation of cross-linked chitosan nanoparticles using malanodialdehyde as a cross-linker (Scheme 1*a*)

Cross-linked chitosan nanoparticles were prepared by reverse micelle medium. The surfactant (AOT) was dissolved in *n*-hexane (0.04–0.1 mol/L solution). To 200 mL of the 0.04 mol/L AOT solution, 2 mL of a 0.1% *w*/*v* chitosan solution in 6% *v*/*v* acetic acid, 880 µL of Tris–HCl buffer (0.01%, pH 8.0), 200 µL liquid ammonia, and 20 µL of a 0.01% *v*/*v* malanodialdehyde solution were added, with continuous stirring at room temperature. The solution was homogenous and optically transparent. The system was left, under stirring, overnight at room temperature. The above method produced placebo chitosan nanoparticles with 10% cross-linkage because an increase in percentage cross-linking from 10% to 100% results in an increase of particle size from 30 to ~110 nm diameter at infinite dilution. Thus, at an intermediate dilution, if the particle size is ~75 nm diameter for a 10% cross-linked polymer, then the particle size is 500–600 nm diameter for a 100% cross-linked polymer at the same dilution. The solvent was then evaporated off in a rotary evaporator and the dry mass resuspended in 40 mL of Tris–HCl buffer (pH 8.0) by sonication. Approximately 20 mL of a 30% $CaCl_2$ solution was added dropwise to precipitate the surfactant as the calcium salt of diethylhexylsulfosuccinate

Fig. 2. concluded.

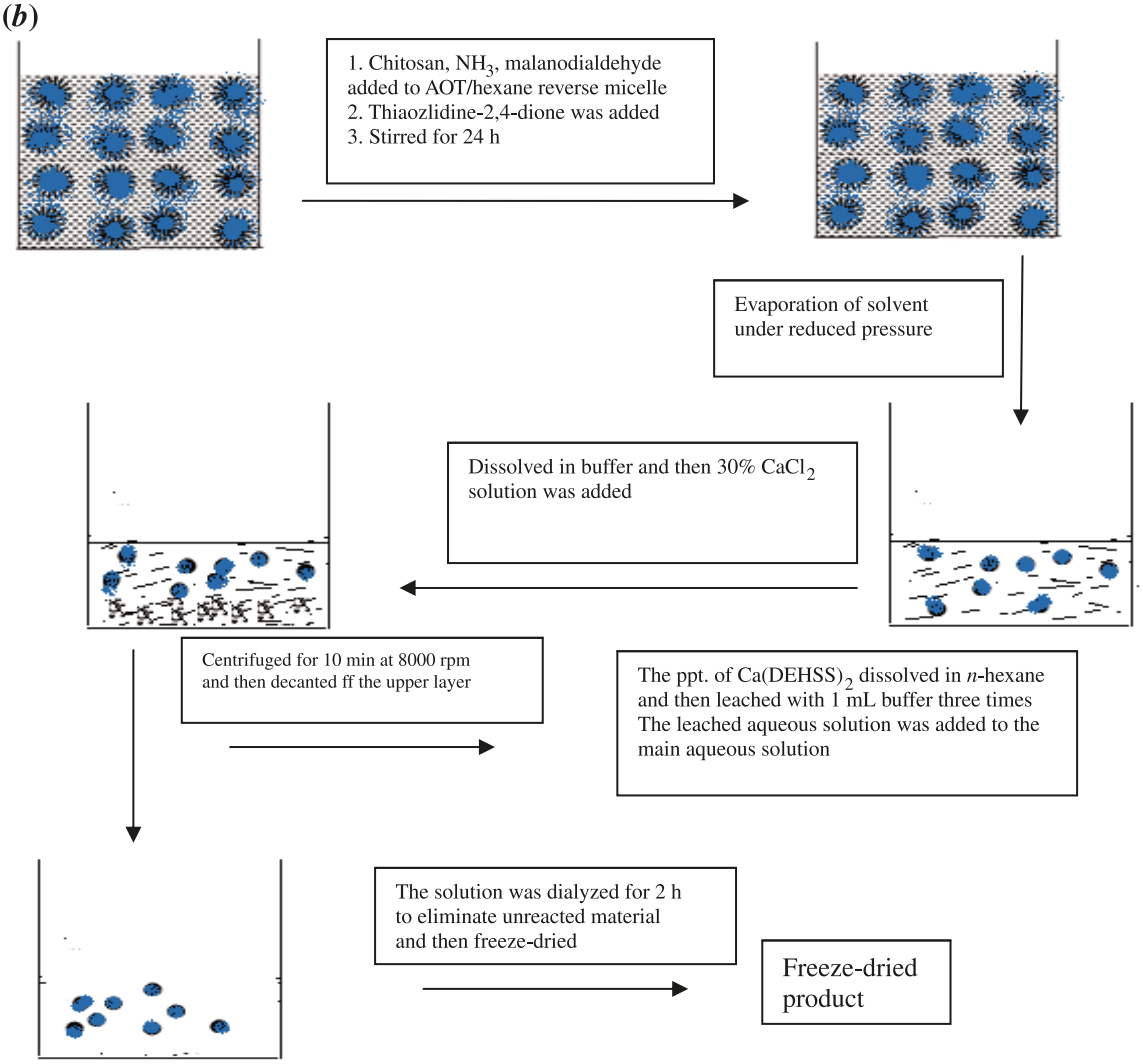

Can. J. Chem. Downloaded from www.nrcresearchpress.com by South China Agricultural University on 09/19/12
For personal use only.

($Ca(DEHSS)_2$). The precipitate was pelleted by centrifugation at 6000 rpm for 15 min at 4 °C. The cake of $Ca(DEHSS)_2$ after centrifugation contained some adsorbed nanoparticles. It was dissolved in 10 mL *n*-hexane and the hexane solution was washed two to three times, each time with 2 mL of Tris–HCl buffer. The phase-separated aqueous layer was drained out and added to the original centrifugate. The total aqueous dispersion of nanoparticles was then dialyzed for ~2–3 h using a dialysis bag. The dialyzed solution was lyophilized to dry powder for subsequent use as shown in Fig. 3*a*.

Preparation of cross-linked thiazolidine-2,4-dione–chitosan nanoparticles using MDA as a cross-linker (Scheme 1*b*)

AOT was dissolved in *n*-hexane (0.04–0.1 mol/L solution). To 200 mL of a 0.04 mol/L AOT solution, 2 mL of a 0.1% *w*/*v* chitosan solution in 6% *v*/*v* acetic acid, 880 µL of Tris–HCl buffer (0.01%; pH 8.0), 200 µL liquid ammonia, 20 µL of a 0.01% *v*/*v* malanodialdehyde solution, and 20 µL of a 0.01% *v*/*v* TZD were added, with continuous stirring at room temperature. The solution was homogenous and optically transparent. The solvent was then evaporated off in a rotary evaporator and the dry mass resuspended in 40 mL of Tris–HCl buffer (pH 8.0) by sonication. Approximately 20 mL of a 30% $CaCl_2$ solution was added dropwise to precipitate the surfactant as the calcium salt of $Ca(DEHSS)_2$. The precipitate was pelleted by centrifugation at 6000 rpm for 15 min at 4 °C. The cake of $Ca(DEHSS)_2$ after centrifugation contained some adsorbed nanoparticles. It was dissolved in 10 mL *n*-hexane and the hexane solution was washed two to three times, each time with 2 mL of Tris–HCl buffer. The phase-separated aqueous layer was drained out and added to the original centrifugate. The total aqueous dispersion of nanoparticles was then dialyzed for approximately 2–3 h using a dialysis bag. The dialyzed solution was lyophilized to dry powder for subsequent use as in Fig. 3*b*.

Size and morphology of the nanoparticles

Quasi-elastic light scattering (QELS) measurements and transmission electron microscopy (TEM) were used to establish the size and morphology of the cross-linked chitosan nanoparticles and TZD cross-linked chitosan nanoparticles.

QELS

QELS was performed using Brookhaven 8000 instrument with a BI200SM goniometer and an air-cooled argon ion laser

Can. J. Chem. Downloaded from www.nrcresearchpress.com by South China Agricultural University on 09/19/12
For personal use only.

Scheme 1. Chemical structure for the synthesis of cross-linked (*a*) chitosan nanoparticles and (*b*) chitosan–thiazolidine-2,4-dione nanopolymers using the sodium salt of malanodialdehyde as a cross-linker.

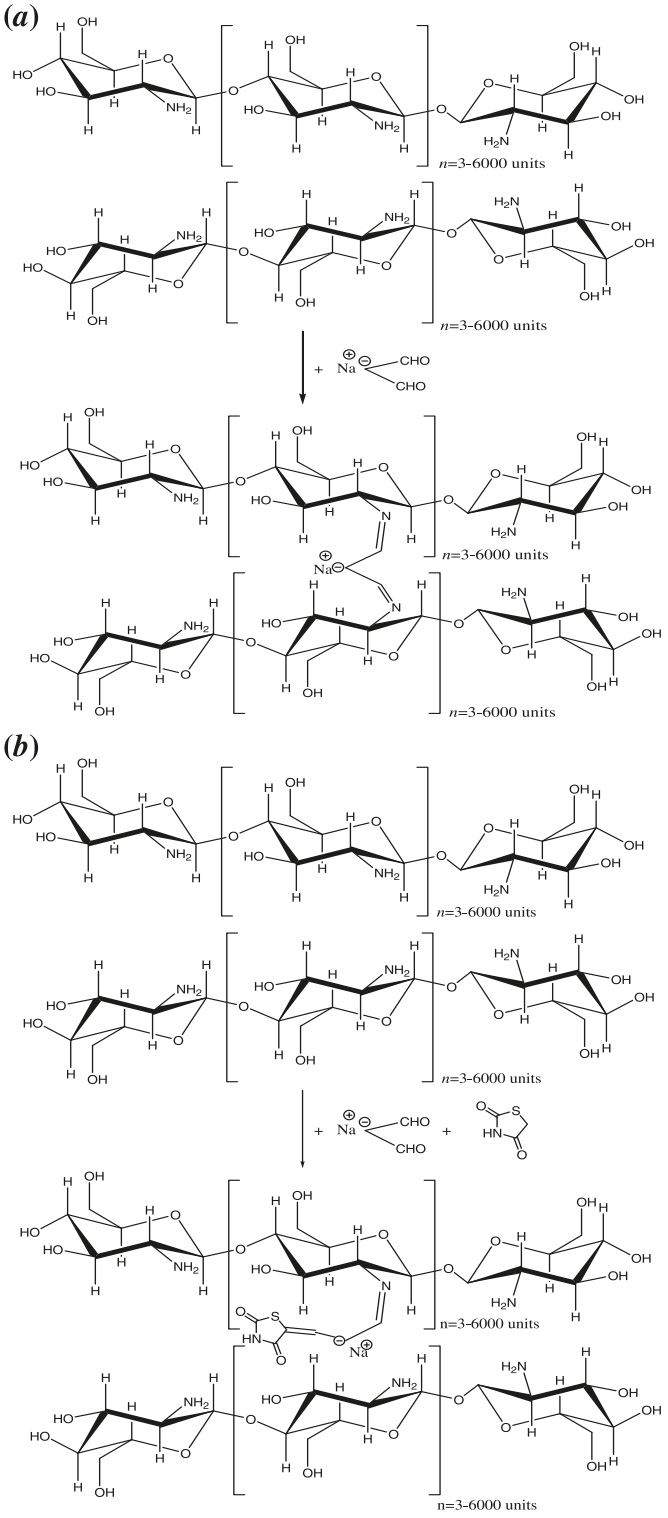

operating at 488 nm as the light source using a 128-channel digital correlator. The time dependence of the intensity autocorrelation function of the scattered intensity was derived, which gave the self-diffusion of the particles. The size of the

Fig. 3. Quasi-elastic light scattering (QELS) pictures of cross-linked (*a*) chitosan nanoparticles and (*b*) chitosan–thiazolidine-2,4-dione nanopolymers using using the sodium salt of malanodialdehyde as a cross-linker.

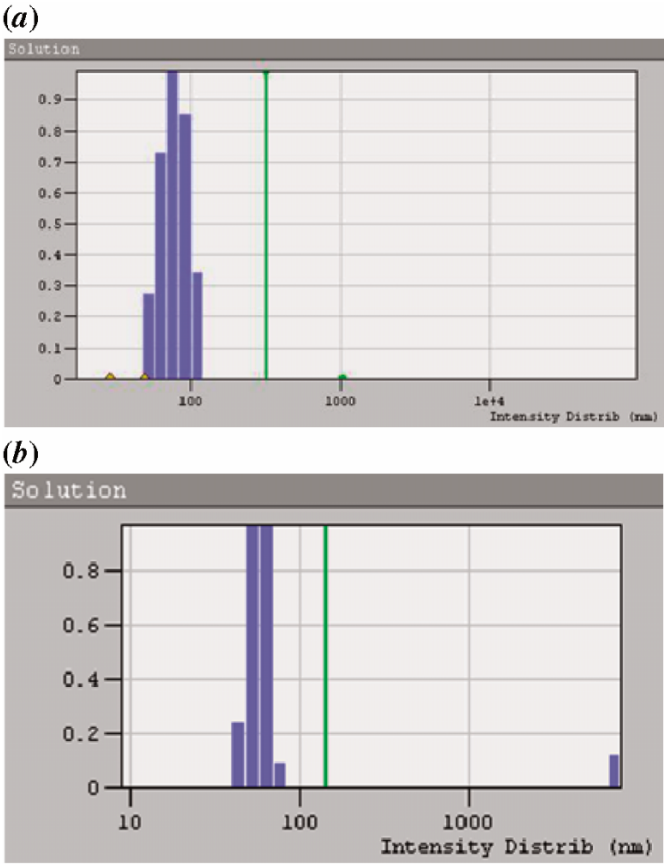

nanoparticles was determined from the diffusion of the particles (D) using the Stokes–Einstein equation

$$[1] \qquad d_h = kT/3\pi\eta D$$

where k is the Boltzmann constant, T is the absolute temperature, η is the viscosity of the medium, and d_h is the hydrodynamic diameter of the particles. Lyophilized powder (100 μg) was dispersed in 2 mL water by vortexing and used for QELS measurement. The sample was subsequently diluted to give nanoparticle solutions of known concentration and the particle size distribution was measured. Nanoparticles with different degrees of cross-linking were similarly diluted for the measurement of size distribution (Fig. 4).

TEM

Lyophilized powder (50 μg) cross-linked nanopolymer of chitosan and TZD–chitosan was dispersed in 5 mL of distilled water to have a clear solution. Samples for TEM were prepared using this clear solution. The sample solution was put on a formvar-coated grid. A clean glass slide was dipped in the formvar solution to make a formvar film on the stars, the glass slide was scratched on the edges, and the formvar film was floated on distilled water on a spherical container, and the 2090 mesh copper grids were placed upside down on the floating plastic film. A piece of water filter paper was blotted on the plastic film and lifted out from the distilled

Can. J. Chem. Downloaded from www.nrcresearchpress.com by South China Agricultural University on 09/19/12
For personal use only.

Fig. 4. TEM pictures of cross-linked (*a*) chitosan and (*b*) chitosan–thiazolidine-2,4-dione nanopolymers using the sodium salt of malanodialdehyde as a cross-linker.

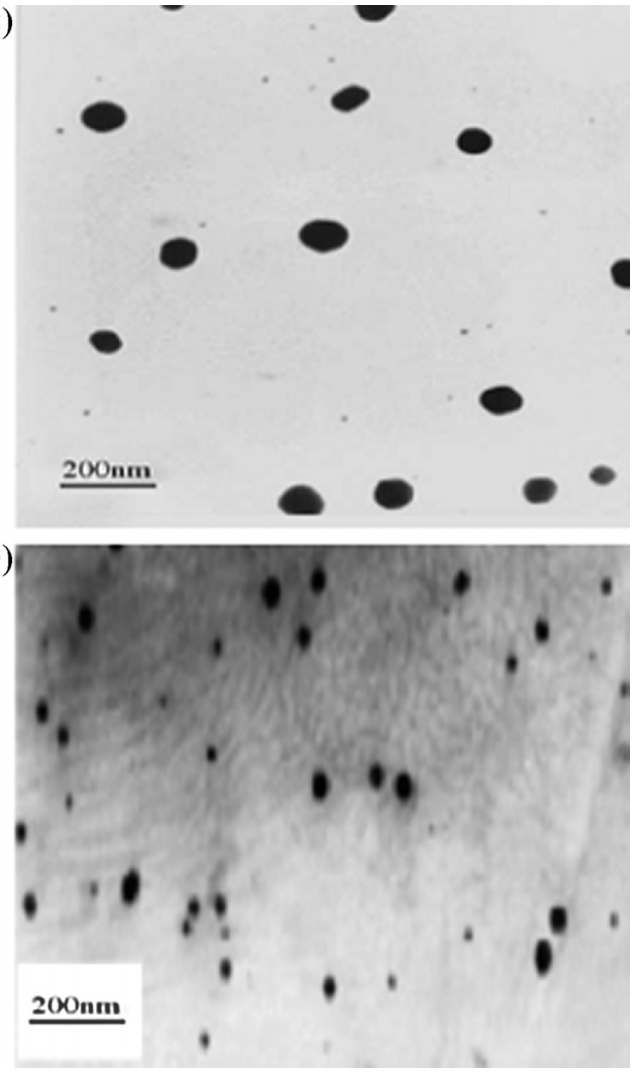

water. In this way, the plastic-coated grids were prepared. On this grid, a drop of the sample solution (containing dispersed nanoparticles) was placed and allowed to air dry. A TEM picture was taken using a JOEL JEM 2000 EX200 microscope (Fig. 5).

FT-IR studies

The IR spectra of cross-linked nanopolymer of chitosan and TZD–chitosan were taken in KBr pellets using a PerkinElmer FT-IR instrument.

NMR studies

^{1}H NMR and ^{13}C NMR spectra of cross-linked chitosan and TZD–chitosan nanopolymer in deuterated trifluroacetic acid (TFA) were obtained using a Bruker spectrospin instrument at 300 MHz.

Thermal analysis

Thermogravimetric analyses of cross-linked chitosan and TZD–chitosan nanopolymer were done using a PerkinElmer model Pyris 6 computerized thermal analysis system. The rate of heating of the sample was kept at 10 °C/min under nitrogen flow at 20 mL/min. Copper sulfate pentahydrate was used as a calibration standard.

Powder X-ray diffraction (XRD) analysis

The X-ray diffraction of cross-linked chitosan and TZD–chitosan nanopolymer patterns were recorded using a RIGAKU ROTAFLEX RAD-B (Rigaku Corporation, Japan) diffractometer using Cu target Cu Kα 1 radiation with a tube voltage of 40 kV and at 60 mA in 2θ ranging from 5° to 70°.

Cyclic voltametry analysis

Cyclic voltametry of cross-linked chitosan and TZD–chitosan nanopolymer patterns were recorded using Electrochemical Analyzer CH 201.

Results and discussion

Characterization of cross-linked chitosan and TZD–chitosan nanoparticles.

Size of the nanoparticles

We determined the particle size by QELS measurements. Chitosan is an adhesive hydrogel polymer. Therefore, in aqueous solution, these nanoparticles interact among themselves through their Brownian motion to form clusters. For interacting particles, the average particle size is always found to be higher than the actual size of the particles. The diffusion coefficient (D) of these interacting particles can be studied by QELS. In the low concentration range, D can be written as $D = D_0 (1 + \alpha\phi)$, where D_0 is the intrinsic diffusion coefficient at infinite dilution when the interaction among the particles is zero, α is the virial coefficient of diffusion, and ϕ is the volume fraction of the particles in the medium. The d_h of the dispersed particles is related to D through the Stokes–Einstein equation as mentioned earlier. Observations of TEM revealed a more or less spherical morphology for the nanoparticles having a size of ~50 nm.

FT-IR studies of cross-linked chitosan nanoparticles

The chitosan nanoparticles were prepared by cross-linking the polymer with malanodialdehyde within the reverse micelles. From the IR spectra of cross-linked chitosan and TZD–chitosan nanoparticles, the strong peaks in the range 3400–3200 cm^{-1} correspond to combined peaks of hydroxyl and intramolecular hydrogen bonding and secondary amine. Primary amines also show sharp absorption at 3500 and 3400 cm^{-1} arising from the asymmetric and symmetric stretching of two N–H bonds, but the peaks appear broad here owing to the contributed peaks from O–H stretching and hydrogen bonds. The peak at 1640 cm^{-1} (approximately) corresponds to stretching vibrations of the C=N bond. This strong peak indicates the formation of a Schiff's base as a result of the reaction between the carbonyl group of malanodialdehyde and the amine group of the chitosan chains, as well as between one carbonyl group of malanodialdehyde and one amine group of the chitosan chains and another carbonyl group of malodialdehyde with the active methylene CH_2 of TZD. The C–H stretching vibration of the polymer backbone is manifested through a strong peak at 2900 cm^{-1} (approximately). Acetyl groups absorb in the range 1300–1100 cm^{-1}. The peaks in the fingerprint region of the spectrum

Fig. 5. Thermogravimetric plot of cross-linked (*a*) chitosan and (*b*) chitosan–thiazolidine-2,4-dione nanopolymers using the sodium salt of malanodialdehyde as a cross-linker.

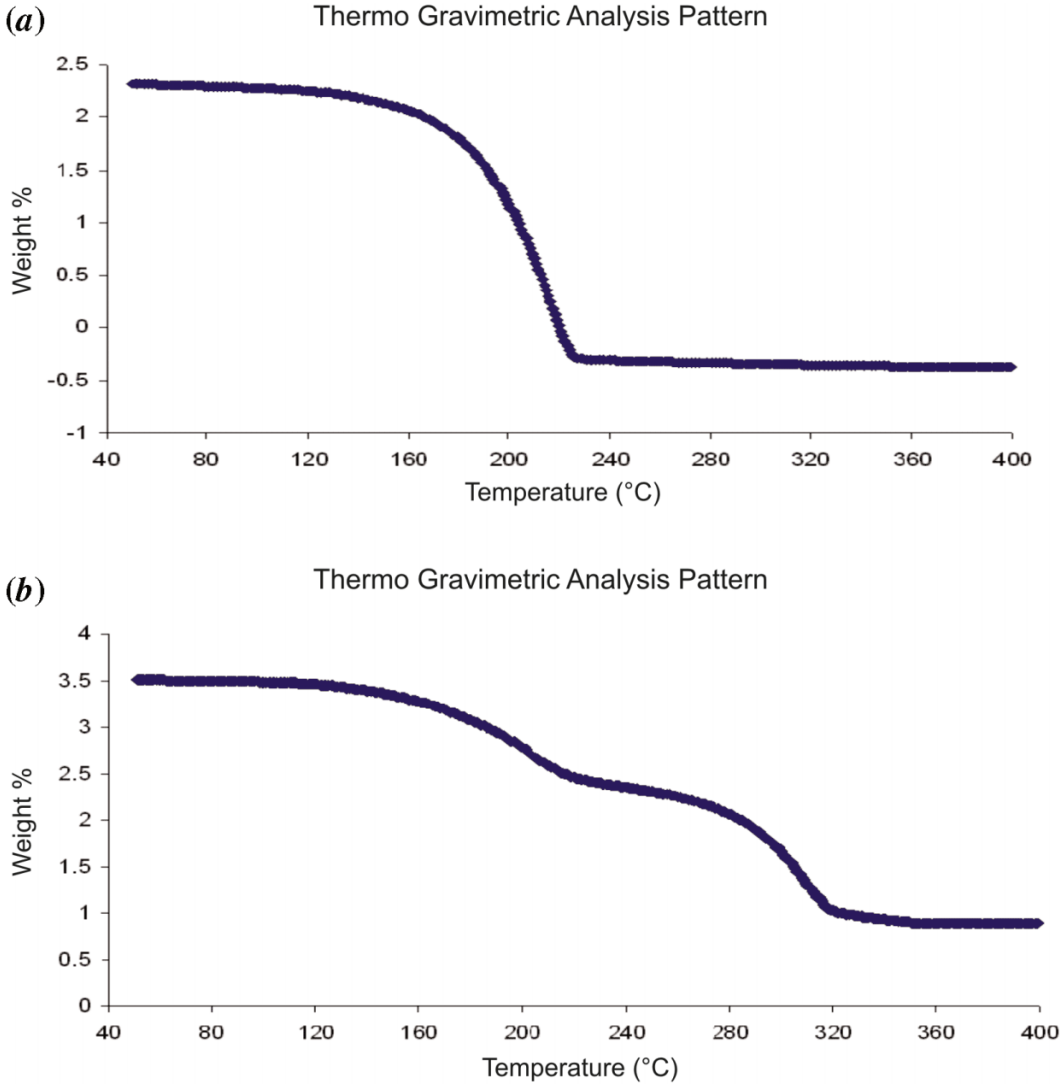

Can. J. Chem. Downloaded from www.nrcresearchpress.com by South China Agricultural University on 09/19/12
For personal use only.

are given by ethereal bonds, where the symmetric stretch of C–O–C is found around 1020–1060 cm^{-1}.

NMR studies of cross-linked chitosan and chitosan–TZD nanopolymer

^{1}H NMR study

As per the spectra, there are peaks for different types of protons. In the spectra, protons are bonded to nitrogen, carbon, and oxygen, i.e., NH, CH, CH_2, and OH. The peak at around an integral value of 9 indicates an N–H, an integral value around 2–3 indicates an aliphatic CH_2 (secondary carbon), an integral value at around 3–4 indicates an O–H, and an integral value around 4–6 also indicates a C–H (primary carbon).

^{13}C NMR study

As seen in the spectra, there are peaks for different types of carbon. The peaks with an integral value in the range of 110–120 indicate carbons that are directly doubly bonded to carbon and nitrogen. The peaks with an integral value in the range of 170–200 indicate carbonyl carbon. The peaks with an integral value in the range of 10–70 indicate aliphatic carbons.

TGA

Decomposition of cross-linked chitosan started at 90 °C and ended at 230 °C. First, the decomposition of the linker that cross-links the chitosan begins during this range of temperature. After this, elimination of small molecules from the cross-linked chitosan polymer begins. These small molecules are H_2O, NH_3, CH_2O, $HCONH_2$, and CH_2O_2, etc., (Fig. 6*a*).

Decomposition of cross-linked TZD–chitosan started at 90 °C and ended at 320 °C. We observed two stops at around 170 and 230 °C. Decomposition of the linker that cross-links the chitosan begins on increasing the temperature above 90 °C, and the decomposition continues until the second stop occurs. At 230 °C, decomposition restarts, which indicates the decomposition of the thiazolidine ring that was cross-linked with chitosan. Then, the elimination of small molecules from the cross-linked chitosan polymer begins. These small molecules are H_2O, NH_3, CH_2O, $HCONH_2$, and CH_2O_2, etc., (Fig. 6*b*).

Fig. 6. Differential scanning calorimetry plot of cross-linked (*a*) chitosan and (*b*) chitosan–thiazolidine-2,4-dione nanopolymers using malanodialdehyde as a cross-linker.

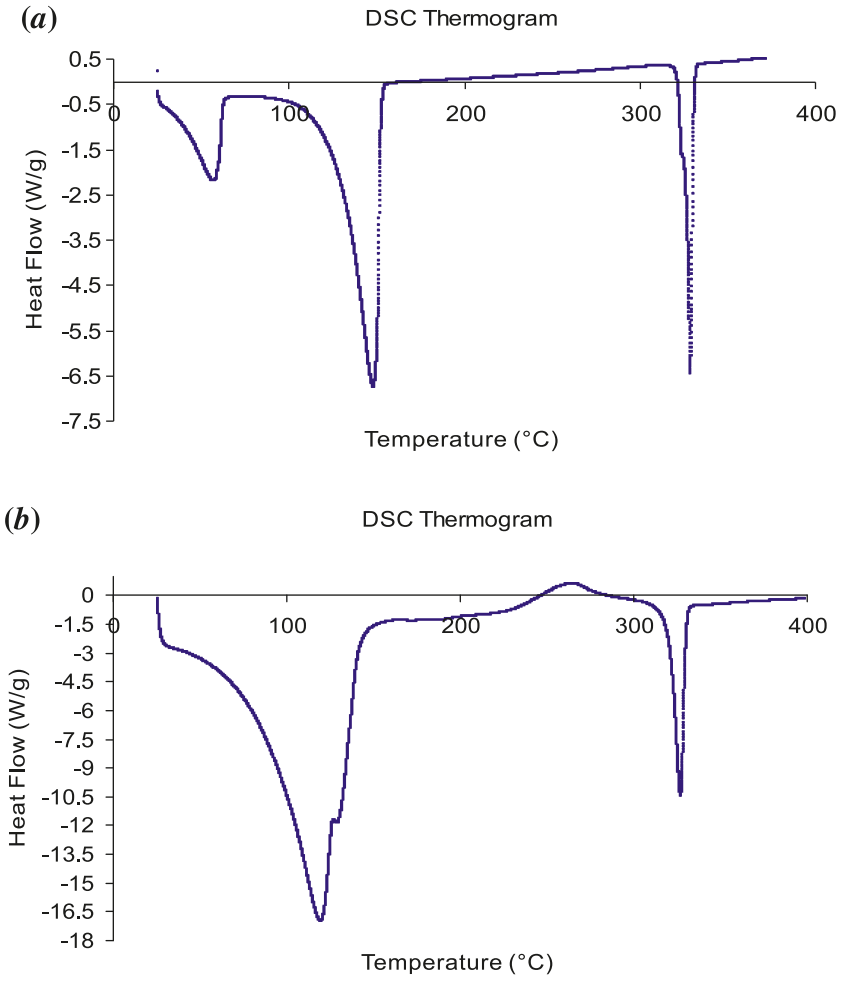

Can. J. Chem. Downloaded from www.nrcresearchpress.com by South China Agricultural University on 09/19/12
For personal use only.

Differential scaning calorimetry (DSC) analysis

DSC thermograms of amorphous polymers demonstrates the endothermic and exothermic peaks and gives an indication of the solid-state transition, the glass transition, crystallization, and fusion as well as curing the cross-linking temperature.

DSC thermogram of the cross-linked chitosan nanopolymer

The DSC thermogram indicates three peaks at 57, 147, and 327 °C. The endothermic peak starts at 26 °C and ends at 63 °C. The minimum at 57 °C indicates the solid-state transition temperature and the energy liberated was 123 J/g. The peak at 98 °C indicates the glass transition temperature and the minimum at 147 °C indicates the baseline shift temperature, which is endothermic in nature, and the energy liberated was 464 J/g. With a further increase in the temperature, the minimum at 327 °C indicates the fusion temperature and the energy liberated was 115 J/g (Fig. 7*a*).

DSC thermogram of the cross-linked chitosan nanopolymer

The DSC thermogram indicates three peaks at 119, 125, 262, and 326 °C. The endothermic peak starts at 30 °C and ends at 120 °C. The minimum at 119 °C indicates the solid-state transition temperature and with a further increase in the temperature, another minimum was observed indicating a baseline shift and the energy liberated was 505 J/g. The peak at 262 °C indicates the crystallization transition temperature, which is exothermic in nature, and the energy liberated was 32 J/g and is in the range of 231 to 300 °C. On further increasing the temperature, the minimum at 326 °C indicates the fusion temperature and the energy liberated was 50 J/g and is in the range of 300 to 330 °C, as well as being endothermic in nature (Fig. 7*b*).

Powder XRD analysis

Powder XRD is the primary technique for the determination of the degree of crystallinity of polymers. The diffraction pattern of polymers is almost a powder pattern (polycrystalline). Crystallite size in polymers is usually on the nanoscale in the thickness direction. The XRD technique is used to report about indexing, degree of crystallinity, and orientation. A synthesized cross-linked polymer is of low symmetry and orthorhombic in nature because of the asymmetry in the bonding of the crystalline lattice, i.e., the *z* axis is contains covalent bonds and the *x* and *y* axes contain van der Waals interactions or hydrogen bonds. As the cross-linking increases, crystallinity decreases, which means the amorphous character in the polymer increases. Along with this, the solubility of the polymer decreases.

Fig. 7. Powder X-ray diffraction plot of cross-linked (*a*) chitosan and (*b*) chitosan–thiazolidine-2,4-dione nanopolymers using malanodialdehyde as a cross-linker.

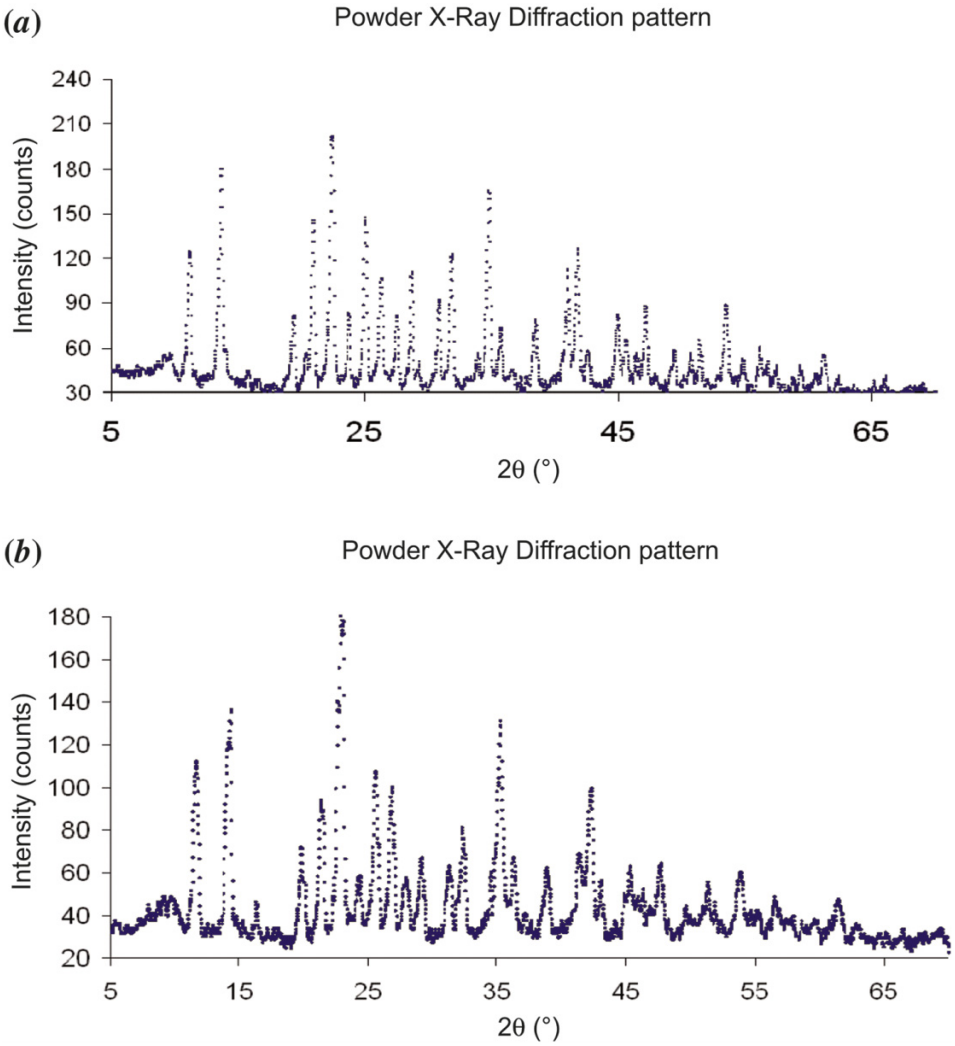

From the powder XRD curves, cross-linked chitosan nanopolymer is more crystalline in nature than the cross-linked TZD–chitosan because of more peak count intensity. This means that the greater the peak count intensity, the more it will be crystalline in nature (Figs. 8*a* and 8*b*).

Cyclic voltametry analysis

This plot was obtained from an Electrochemical Analyzer CH 201. The scalings of the plot are potential and current on the *x* and *y* axes, respectively.

The potential range is –2 to +2 V and the current range is –7 to + 8 × 10^{-3} A

The scan rate of the sample was 0.1 V/s and the sensitivity was 0.001 A/V. The number of segments were seven to provide the stability on applying voltage on the compound with time. Overlay of the segments indicates the stability of the compound. As per the plot, the overlay means that the compound attained the stability very fast. We checked other ranges of voltage on the compound, but the compound was not stable in those ranges and we found no overlay and a slow decline of the plotsappeared on application of the high voltage range to the compound. On applying this voltage range, the compound gave a current in the range of –7 to +8 × 10^{-3} A (Fig. 8*a*).

The potential range is –2 to +2 V and the current range is –10 to +10 × 10^{-3} A

The scan rate of the sample was 0.1 V/s and the sensitivitywas 0.001 A/V. The number of segments were seven to provide the stability on applying voltage on the compound with time. Overlay of the segments indicates the stability of the compound. As per the plot, the overlay means that the compound attains the stability very fast. We checked other ranges of voltage on the compound, but the compound was not stable in those ranges and we found no overlay and a slow decline of the plotsappeared on application of the high voltage range to the compound. On applying this voltage range, the compound ggave a current in the range of –10 to +10 × 10^{-3} A (Fig. 8*b*).

Conclusion

This study reports the synthesis, characterization, thermal, powder XRD, and cyclic voltametry properties of cross-linked chitosan and TZD–chitosan nanopolymer using

Can. J. Chem. Downloaded from www.nrcresearchpress.com by South China Agricultural University on 09/19/12
For personal use only.

Fig. 8. Cyclic voltametry plot of cross-linked (*a*) chitosan and (*b*) chitosan–thiazolidine-2,4-dione nanopolymers using malanodialdehyde as a cross-linker.

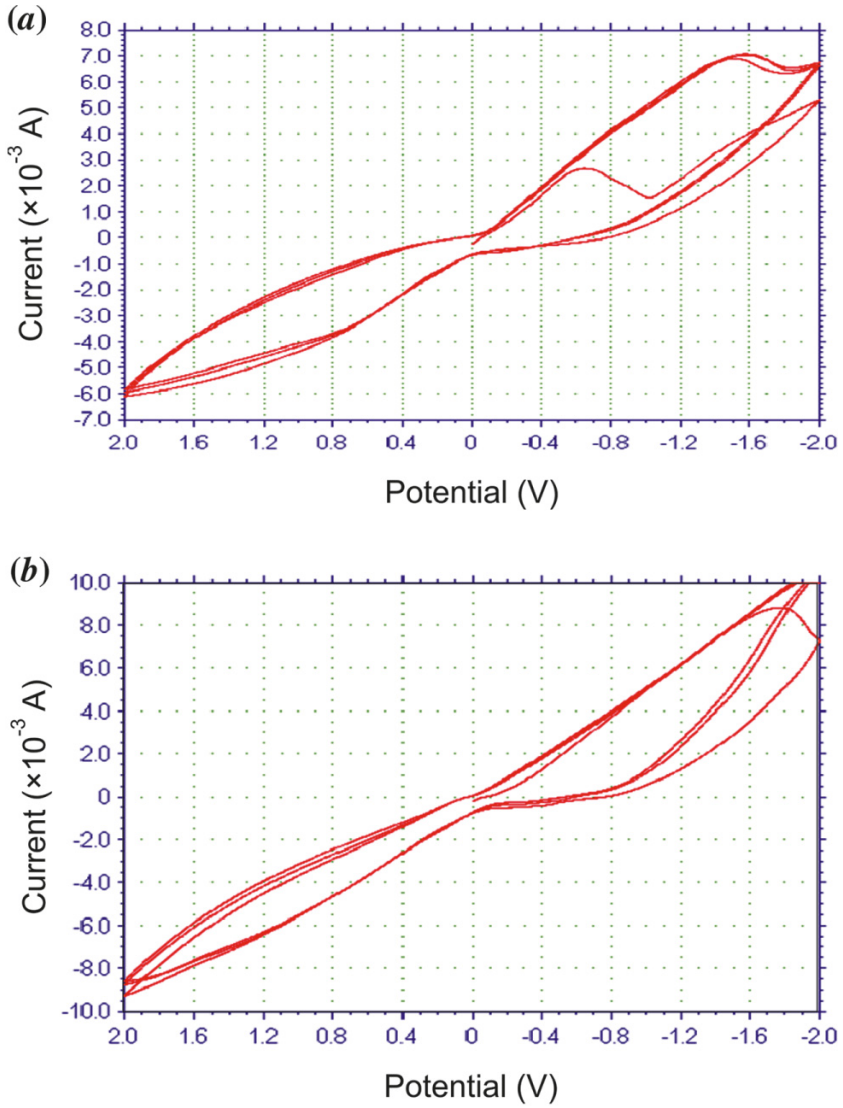

Can. J. Chem. Downloaded from www.nrcresearchpress.com by South China Agricultural University on 09/19/12
For personal use only.

malanodialdehyde as a cross-linker They have been characterized by IR, ^{1}H NMR, and ^{13}C NMR, then by thermal (TGA and DSC), powder XRD, and electrochemical studies (cyclic voltametry) to provide information on the stability on heat application, the stability for current and conductivity, and they were also characterized by TEM and QELS to provide information about the size and shape of the particle size of the crosslinked chitosan nanopolymers with drug and without drug (TZD).

Analytical data of the compounds

Cross-linked chitosan nanopolymer using malanodialdehyde as a cross-linker

White and highly crystalline. IR (υ, cm^{-1}): 3436 (O–H and N–H), 3012 (C–H), 1717 (C=O), 1639 (C=N), 1559 (C=C), 1411 (CH_2), 1271 (C–O), 1052 (=CH), 795 (CH_2), 610 (N–H). ^{1}H NMR (δ): C–H of active methylene carbon (3.72–4.53), C–H of –CH=N– (4.58–5.64), CH_2 (1.23–2.64). ^{13}C NMR (δ): carbonyl carbon (216, 181), carbon of CH=N– (121, 117, 111, 109), active methylene carbon (72, 71, 66, 63), aliphatic carbon (39, 30, 29, 24, 23, 19, 13, 10).

Cross-linked chitosan–TZD nanopolymer using malanodialdehyde as a cross-linker

White and highly crystalline. IR (υ, cm^{-1}): 3445 (O–H and N–H), 3016 (C–H), 1715 C=O), 1639 (C=N), 1559 (C=C), 1408 (CH_2), 1271 (C–O), 1029 (=CH), 787 (CH_2), 638 (N–H). ^{1}H NMR (δ): C–H of active methylene carbon (5.09–5.95), N–H (9.09–9.89), C–H of –CH=N– (6.02–6.92), CH_2 (1.46–4.64). ^{13}C NMR (δ): carbonyl carbon (181, 173, 169), carbon of –CH=N– (120, 116, 112, 108), active methylene carbon (71, 70, 62), aliphatic carbon (38, 33, 29, 28, 23, 22, 18, 12, 9).

Acknowledgement

This work is dedicated to the late Dr. N.N. Ghosh, my mentor and my guide (P.S.).

References

(1) Rhim, J.-W.; Hong, S.-I.; Park, H.-M.; Ng, P. K. W.; Agr, J. *Food Chem.* **2006**, *54* (16), 5814. doi:10.1021/jf060658h.

(2) Brenner, D. E.; Gescher, A. J. *Br. J. Cancer* **2005**, *93* (7), 735. doi:10.1038/sj.bjc.6602765.

(3) Valenta, C.; Nowack, E.; Bernkop-Schnurch, A. *Int. J. Pharm.* **1999**, *185* (1), 103. doi:10.1016/S0378-5173(99)00170-2.

(4) Zhi, J.; Wang, Y.; Luo, G. *React. Funct. Polym.* **2005**, *65* (3), 249. doi:10.1016/j.reactfunctpolym.2005.06.009.

(5) Yang, L.; Chu, J. S.; Fix, J. A. *Int. J. Pharm.* **2002**, *235* (1–2), 1. doi:10.1016/S0378-5173(02)00004-2.

(6) Rauth, M.; Mohindra, J. K. *Cancer Res.* **1983**, *43*, 4154.

(7) Mucha, M.; Pawlak, A. *Thermochim. Acta* **2005**, *427* (1–2), 69. doi:10.1016/j.tca.2004.08.014.

(8) Boyd, B. J. *Drug Delivery Report* **2005**, *63*, 22.

(9) Ramirez, H. L.; Valdivia, A.; Cao, R.; Fragoso, A.; Torres Labandeira, J. J.; Baños, M.; Villalonga, R. *Polym. Bull.* **2007**, *59* (5), 597. doi:10.1007/s00289-007-0803-8.

(10) Storm, G.; Crommelin, D. J. A. *Pharm. Sci. Technol. Today* **1998**, *1* (1), 19. doi:10.1016/S1461-5347(98)00007-8.

(11) Lee, S. *J. Appl. Polym. Sci.* **2003**, *90*, 2870. doi:10.1002/app.13070.

(12) Wang, J.; Zhang, P. C.; Mao, H. Q.; Leong, K. W. *Gene Ther.* **2002**, *9* (18), 1254. doi:10.1038/sj.gt.3301794.

(13) Igarashi, K.; Nakano, Y. *Chem. Eng. J.* **2006**, *36*, 716.

(14) Amiji, M. M.; Lai, P. K.; Shenoy, D. B.; Rao, M. *Pharm. Dev. Technol.* **2002**, *7* (2), 195. doi:10.1081/PDT-120003487.

(15) Kumbar, G. S.; Sopimath, K. S.; Abhinabhavi, M. T. *J. Appl. Polym. Sci.* **2003**, *87* (9), 1525. doi:10.1002/app.11552.

(16) Murthy, N. *Proc. Natl. Acad. Sci. U.S.A.* **2003**, *100* (9), 4995. doi:10.1073/pnas.0930644100.

(17) Igarashi, K.; Nakano, Y. *J. Appl. Polym. Sci.* **2002**, *86* (4), 901. doi:10.1002/app.11001.

(18) Akbuga, J. *Int. J. Pharm.* **1993**, *100* (1–3), 257. doi:10.1016/0378-5173(93)90100-T.

(19) Allen, T. M.; Hansen, C. *Biochim. Biophys. Acta* **1991**, *1068* (2), 133. doi:10.1016/0005-2736(91)90201-I.

(20) Hou, M. J.; Kim, M.; Shah, D. O. *J. Colloid Interface Sci.* **1988**, *123* (2), 398. doi:10.1016/0021-9797(88)90261-5.

(21) Ilium, L. *Pharm. Res.* **1998**, *15* (9), 1326. doi:10.1023/A:1011929016601.

(22) Kawashima, Y.; Lin, S. Y.; Kasai, A.; Handa, T.; Takenaka, H. *Chem. Pharm. Bull. (Tokyo)* **1985**, *33*, 2107.

(23) Leong, Y. S.; Candau, F. *J. Phys. Chem.* **1982**, *86* (13), 2269. doi:10.1021/j100210a001.

(24) Banerjee, T.; Mitra, S.; Singh, A. K.; Sharma, R. K.; Maitra, A. *Int. J. Pharm.* **2002**, *243*, 93. doi:10.1016/S0378-5173(02)00267-3.

(25) Roy, K.; Mao, H.-Q.; Huang, S.-K.; Leong, K. W. *Nat. Med.* **1999**, *5* (4), 387. doi:10.1038/7385.

(26) Storm, G.; Belliot, S. O.; Daemen, T.; Lasic, D. D. *Adv. Drug Deliv. Rev.* **1995**, *17* (1), 31. doi:10.1016/0169-409X(95)00039-A.

(27) Kaneo, Y.; Fujihara, Y.; Tanaka, T.; Kozawa, Y.; Mori, H.; Iguchi, S. *Pharm. Res.* **1989**, *6* (12), 1025. doi:10.1023/A:1015922303051.

(28) Chen, S.; Wu, G.; Zeng, H. *Carbohydr. Polym.* **2005**, *60* (1), 33. doi:10.1016/j.carbpol.2004.11.020.

(29) Singh, P.; Katyal, A.; Kalra, R.; Chandra, R. *Tetrahedron Lett.* **2008**, *49* (4), 727. doi:10.1016/j.tetlet.2007.11.106.

(30) Singh, P.; Katyal, A.; Kalra, R.; Chandra, R. *Catal. Commun.* **2008**, *9* (7), 1618. doi:10.1016/j.catcom.2008.01.010.

(31) Singh, P.; Kumari, K.; Katyal, A.; Kalra, R.; Chandra, R. *Catal. Lett.* **2009**, *127* (1–2), 119. doi:10.1007/s10562-008-9654-7.

(32) Tiyaboonchai, W. *Naresuan Uni. J.* **2003**, *11*, 51.

Can. J. Chem. Downloaded from www.nrcresearchpress.com by South China Agricultural University on 09/19/12
For personal use only.

Theoretical investigation of experimentally determined α-εffects — The role of electronics

D. Afzal and K.R. Fountain

Can. J. Chem. Downloaded from www.nrcresearchpress.com by South China Agricultural University on 09/19/12
For personal use only.

Abstract: Recent experimental reports involving both α-nucleophiles and normal nucleophiles have reported both the presence and absence of an α-effect. In ester systems, such as dimethylmethylphosphonate (DMMP), a small α-effect is reported, but the reference point is a stationary point of the potential energy surface that must rearrange to acquire the near attack conformation (NAC) necessary for the Sn2 pathway to proceed. The second type of study involves use of highly fluorinated alkoxides as normal nucleophiles and reports no α-effect. This paper employs linear free energy plots in an investigation of electronic effects in methyl formate S_N2 reactions, using high-level computations of transition states for determination of energy barriers.

Key words: AIM, valence bond, LFER, overall barrier, central barrier.

Résumé : Des données expérimentales rapportées récemment, impliquant des nucléophiles tant α que normaux, ont mis en évidence la présence ainsi que l'absence d'un effet α. Dans les systèmes impliquant des esters, tel le méthylphosphonate de diméthyle (MPDM), un faible effet α a été noté, mais la valeur de référence est une valeur stationnaire de la surface d'énergie potentielle qui doit être réorganiser pour atteindre la conformation adjacente à l'attaque (CAA) nécessaire pour que la réaction de type S_N2 puisse se produire. Le deuxième type d'étude implique l'utilisation d'alcoolates polyfluorés comme nucléophiles normaux pour lesquels aucun effet α n'a été observé. Dans le présent travail, on utilise des courbes d'énergie libre linéaire pour étudier les effets électroniques dans les réactions S_N2 du formiate de méthyle, en faisant appel à des calculs de haut niveau des états de transition pour la détermination des barrières d'énergie.

Mots-clés : atomes dans les molécules (ADM), liaison de valence, relation linéaire d'énergie libre (RLEL), barrière globale, barrière centrale.

[Traduit par la Rédaction]

Introduction and purpose

Our purpose is to compare electronic effects in two gas-phase (GP) reaction cases where experimental evidence provides interpretations favoring the existence of α-effects in methyl transfers. The GP experiments under study are the relative product ratios for displacement of methyl methylphosphonate anion (MMP^-) from dimethylmethylphosphonate (DMMP) by hydroperoxide (HOO^-) and methoxide (MeO^-) (rxn. [1A]),[1] and the GP reactions of HOO^- and HO^- displacing methyl groups from formate anion (rxn. [1B]).[2] Recent work by Ren and Yamataka[3–5] has shown the theoretical possibility of an α-effect in methyl transfers. No serious attempts to analyze potential differences in the electronic effects between normal nucleophiles and α-nucleophiles, other than one from this laboratory showing, by indirect means, a potential single electron transfer (SET) component,[6] have appeared. The α-nucleophile (HOO^-) has a lone pair of electrons (LP) adjacent to the nucleophilic atom (O^-). The α-effect is putatively an increase in nucleophilic reactivity when compared with a normal nucleophile of the same basicity (acidity).

rxn. [1]

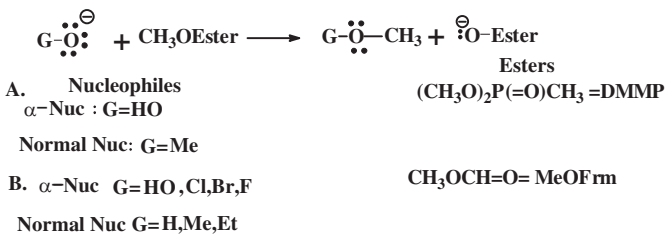

Gas-phase S_N2 reactions.

It has been generally posited for many years and in many venues that the α-effect is due to a feature or features specific to the transition states. We seek to answer several questions to ascertain which transition-state features might be responsible. Determinations of the α-effect in the gas phase (GP) have been attempted experimentally with mass spectral-SIFT tube methods and theoretically with high-level post-Hartree–Fock, highly correlated methods, as discussed and documented as follows.[1–3] Putatively GP studies simplify matters by excluding solvent effects. This paper will show that GP

Received 31 March 2011. Accepted 30 June 2011. Published at www.nrcresearchpress.com/cjc on 29 September 2011.

D. Afzal and K.R. Fountain. Department of Chemistry, Truman State University, Kirksville, MO 63501, USA.

Corresponding author: K.R. Fountain (e-mail: sc18@truman.edu).

Can. J. Chem. Downloaded from www.nrcresearchpress.com by South China Agricultural University on 09/19/12
For personal use only.

Fig. 1. A state correlation diagram for S_N2 reactions.

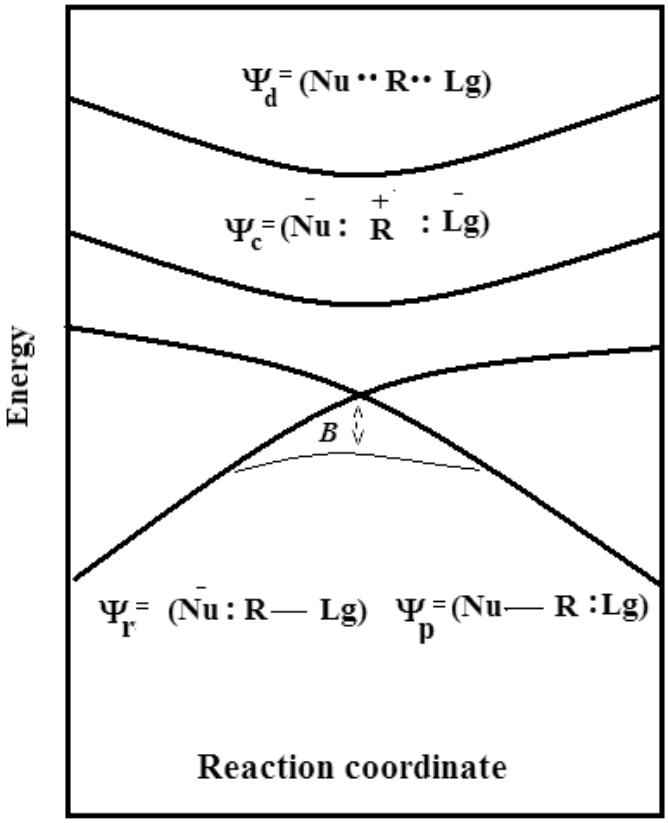

experimental results are not without complications themselves, particularly in the hermeneutic employed for interpretations of those results.

Our questions are concerned with the fundamental electronic transactions in S_N2 reactions for methyl group transfers. Such concerted nucleophilic reactions have as a settled issue the exchange of one pair of electrons by another. GP manifestations involve anions and neutrals on both sides of eq. [1]. It is natural to ask the following questions about the S_N2 process: (1) Are there differences in the electronics of normal and α-nucleophiles? (2) Can normal nucleophiles be electronically modified to behave like α-nucleophiles? (3) Can normal nucleophiles ever become more reactive than α-nucleophiles?

The early Ren and Yamataka papers ascribe the α-effect to electrostatic attractions between the α-atom and the partially charged methyl group, but their later paper retreated somewhat from that conclusion, indicating that causes for the α-effect are complex.[3] The authors of the present paper believe it is important to extract as much information as possible to answer the Mulliken question "What are electrons doing in molecules?" To this end we examine the transition-state (TS) structures of two systems where experimental results indicate the presence, or potential presence, of an α-effect, and the pathways toward the TSs in each.

Methods of study

The transition states of all the experimental methyl transfers in rxns. [1A] and [1B] (HOO^-, MeO^-, EtO^- , and HO^-) for the methyl formate case were obtained by several model chemistries. The DMMP reaction TSs were obtained at the B3LYP/6–31+G(d) model chemistry as in the original paper and the CBS-LQ(startmp2)\MP2\6–31+G(d)\HF\6–31+G(d) in the present paper.[1] The formate ester cases were obtained at the CBS-QB3(StartMP2)//mp2/6–31+G(d)/HF\6–31+G(d) model chemistry and CBS-LQ method for direct comparison between the DMMP and MeOFrm systems. This compound model chemistry conveniently gives geometries corresponding to the Ren and Yamataka G2(+) level, with a post-Hartree–Fock extrapolation to complete basis set limits. This type of model chemistry provides very highly accurate GP acidity (GPA) values for the nucleophiles. Additional sets of normal and α-nucleophiles were computed for the methylformate cases to supply information about the presence (absence) of a discernable α-effect in a linear free energy relationship plot (LFER).

Atoms-In-Molecules (AIM) results were obtained by generating wave function files with Gaussian 03W (G03W)[7,8] and performing the AIM analysis with the AIMStudio suite of programs.[9] Natural bond orbital (NBO) results were obtained from the TS geometries from the NBO segment within G03W at a HF\6–311+G(2d,p) model chemistry.

Valence bond (VB) results were obtained by copying the geometry coordinates of each TS into a template file for VB2000.[10] (A template file is available from the corresponding author on request.) The NBO results disclosed that all three of the LP electrons on the nucleophilic O atom must be considered in assessing contributions to the TS stability, therefore, all three LP electrons were included in the CASVB(x,y) computation in VB2000 (x = electron number and y = orbital number).

The results are expressed in Rumer diagrams,[11] which display the Mulliken (Coulson–Chirgin) weighting factors (λ) for each highly localized Lewis-type resonance form. Quantum mechanical resonance energy (QMRE = B) was calculated by eq. [1].[11]

$$[1] \qquad B = \mathrm{QMRE} = 0.5D_0(1 - Q_a)$$

B is the avoided crossing constant in a state correlation diagram (SCD) as in Fig. 1.

Results

The results are presented in the order of categories given in the Methods of study section.

AIM

Table 1 displays the results of the AIM determinations of both ester systems as **ρ** values (electron densities) at bond critical points (BCPs) along the bond pathways. (Details are provided in the Supplemental data).

NBO results are in Table 2 and VB results are in Table 3. An abridged Rumer diagram presentation is included in the Appendix in the Supplementary data.[12]

There are differences in how the nucleophiles store the electrons as anions then donate the electrons to the substrate in the TSs. As an example we consider the HOO^- anion, which has donor–acceptor energy (DAEn) from the donation of LP(3) on O to the BD*H–O orbital of 2.652.65 kcal/mol (1 cal = 4.184 J). In the TS HOO···Me···OFrmt (OFrmt = O–CH=O) donation is of only 1.64 kcal/mol from the LP(2) on O to the BD*HO and augmentation by 0.58 kcal/mol from BDH–O to BD*O–O.

Can. J. Chem. Downloaded from www.nrcresearchpress.com by South China Agricultural University on 09/19/12
For personal use only.

Table 1. Summary of AIM bond critical point (BCP) parameters.

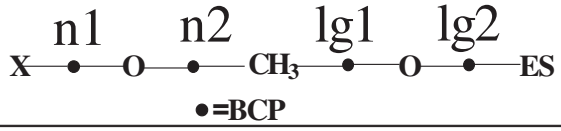

	ρ at BCP			Elipticity at BCP		
Ester systems	n1	n2	lg1	n1	n2	lg1
DMMP						
HOO(X=OH)	0.05	0.25	0.105	0.325	0.035	0.026
MeO(X=Me)	0.05	0.30	0.110	0.114	0.005	0.034
HO(X=H)	0.04	0.34	0.102	0.250	0.003	0.041
MeOFrmt						
HOOMe(X=OH)	0.05	0.25	0.105	0.089	0.026	0.082
MeO(X=CH3)	0.05	0.31	0.104	0.032	0.005	0.008
HOMe(X=H)	0.05	0.34	0.101	0.162	0.004	0.023
EtOMe(X=Et)	0.05	0.30	0.104	0.048	0.009	0.007

Note: ρ, electron density; DMMP, dimethylmethylphosphonate; MeOFrmt, methyl formate.

Table 2. Summary of natural bond order (NBO) results with donor–acceptor energy (DAEn) in kcal/mol (1 cal = 4.184 J).

System	DAEn	NBOpop BD*C-OEST	SUMBD*C-H pop
HOODMMP	62.46	0.1357	0.0272
MeODMMP	58.36	0.1334	0.0297
HODMMP	61.55	0.1450	0.0301
HOOMeOFrmt	74.38	0.1566	0.0326
HOMeOFrmt	72.65	0.1696	0.0301
MeOMeOFrmt	63.60	0.1566	0.0334
EtOMeOFrmt	69.22	0.1645	0.0340

Note: MeOfrmt, methyl formate.

Table 3. Valence bond results and *B* values (quantum mechanical resonance energy, QMRE) for transition states (TS) at mp2/6–31+G(d) geometry.

System TS	QMRE (kcal/mol)	D_o
HOO···MeOMeOP=OMe	39.5	98.2
MeO···MeOMeOP=OMe	38.8	
HO···MeOP(=O)MeOMe	36.8	
HOO···MeOFrmt	40.0	94.2
MeO···MeOFrmt	38.2	
C_2H_5O···MeOFrmt	36.7	
HO···MeOFrmt	38.6	

Note: MeO bond energy in the esters (D_o) values were determined with the Zavitsas formula, which yields nearly quantitative results from vibrational frequencies supplied by NIST.[13]

Table 1 discloses electronic differences between the α-nucleophile (HOO^-) and normal nucleophiles, such as MeO^-, in several electronic features that also show some dependence of the leaving groups. For DMMP, the size of ρ at the BCP of the nuc–OMe bond path indicates slightly larger charge transfer from the nucleophile to this point for HOO^- than for MeO^-. The ρ values at the BCPs of cleavage of the leaving group $^-$O–MMP are slightly larger for the normal nucleophile (MeO^-). The charges (*Q*) of the atoms in the X–O–DMMP TS indicate a net negative charge on HO (α-X), positive on CH_3 (X), negative *Q* (–0.904) on the nucleophile HOO^-, and less negative (–0.883) on MeO^-. On the transfer of CH_3, a slightly more positive charge exists in the HOO^- TS than for the MeO^- TS. A slightly more negative charge is transferred to the leaving O atom in the HOO^-TS than from the MeO^-. Similar values exist for the X–O–MeOFrmt case. Elipticity (*E*) values indicate the amount of π character at a particular point in a bond path display. This indicates the sense of π character in an ethylene double bond path. These differences indicate a difference in quality (i.e., hybridization) of the wave functions in these nucleophiles.

Elipticity values at BCPs for the Me and leaving O–ES groups display more *E* for the normal nucleophiles than for HOO^-. Elipticity for the DMMP case shows much larger *E* between the nucleophilic HOO^- and Me than for the MeO^- case. The BCP between X–O is larger for HOO^- than for Me–O^-. There is a difference in the MeOFrmt case compared with the DMMP case. HO^- has more *E* at the BCP to the Me group than all the other nucleophiles.

The charges on AIM atoms indicate an important electronic difference because the α-nucleophile has negative charge on the α atom, whereas all the normal nucleophiles have positive charges on their α atom. (Supplementary data) This point may be important later in sorting out the putative dependence on electrostatic effects, as shown as follows with the sulfur-containing α-nucleophiles.

The NBO results disclose the point that all three electron LPs on O contribute to the stabilization of the TS in each case. The major contributions, giving 1 kcal/mol or more stabilizations energy upon examination by a deletion routine

Fig. 2. Central barriers in the S_N2 reactions of methyl formate with *B* values (quantum mechanical resonance energy, QMRE).

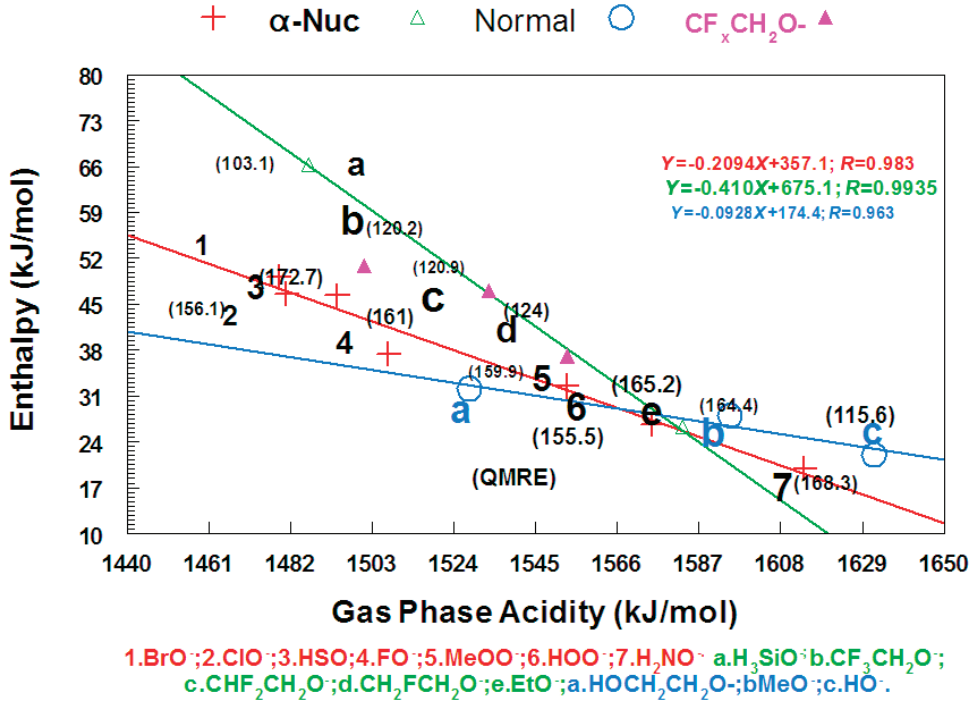

Fig. 3. Potential energy surface (PES) for a gas-phase S_N2 reaction.

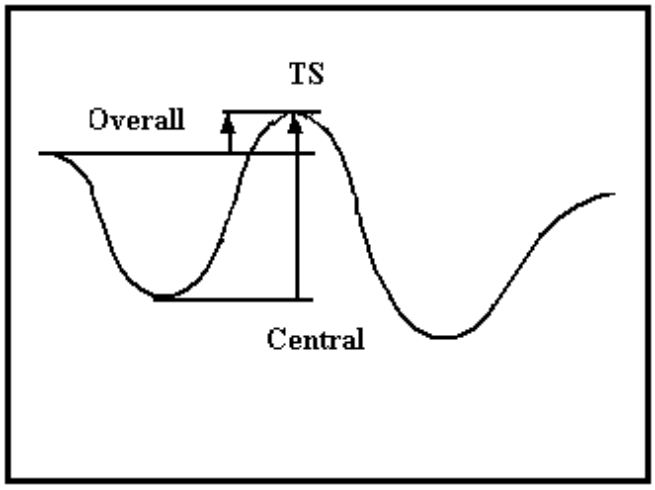

(standard with the G03W software), were retained. The major bond forming LP on O also provides DA stabilization energy by DA interactions with the C–H antibonding orbitals. For the methylformate cases, the second and sometimes the third LP on O for each nucleophile contributes 10.5 kcal/mol in MeO and 10.9 kcal/mol in EtO to the TS, and only 10.84 kcal/mol in HOO^-. The donations to C–H anti-bonding orbitals are greatest in HOO^- and EtO^-. In DMMP systems the values are HOO^-, 8.99; MeO^-, 8.26; and HO^-, 7.38. The way the LPs of the normal nucleophiles are stored in the adjacent regions of the nucleophiles depends on the identity of the atoms in those regions. The nucleophiles (HO^- and HOO^-) store energies in Rydberg orbitals only, except in HOO^-, where small energies are due to donation to the BD*H–O antibonding orbital.

The VB results in Table 3 indicate a clear distinction between HOO^- and all the normal nucleophiles in both the DMMP and MeOFrmt systems. The *B* (kcal/mol) value for the HOOMeOES TS is greater (implying greater resonance stability at the avoided crossing point in the SCD than any of the other nucleophiles) in both systems. These differences (δB, $B_{X-O} - B_{HOO^-}$) between the HOO^- anion TS and the normal nucleophiles are –0.7 kcal/mol (vs MeO^-) for DMMP and –2.7 kcal/mol (vs HO^-), which indicates more stabilizing QMRE energy for the HOO^- cases. For Frm δB is –1.8 kcal/mol(vs MeO^-), –3.3 kcal/mol (vs EtO^-), and –1.4 kcal/mol (vs HO^-). These δ *B* values order the S_N2 reactivity of the nucleophiles as $HOO^- > MeO^- > HO^-$ for DMMP and $HOO^- > HO^- > MeO^- > EtO^-$ for MeOFrmt. These differences are small and by themselves not convincing criteria for determining the α-effect. This fact changes as the LFER is considered over a wider range of GP aciditites as shown in Fig. 2.

A LFER, similar to Ren and Yamataka's[5] foundational theoretical treatment, was constructed from a series of normal and α-nucleophiles for the MeOFrmt system using the CBS-QB3 (startmp2)\mp2\6–31+G(d)\HF\6–31+G(d) model chemistry to determine TS geometries and those of the reactants and their energies.

Determinations of the theoretical α-effects depend on the reference points along the GP acidity scale (*x* axis). In solution-phase reactions, the difference in energies between the reactant complexes and the central barrier determine reactivity.[14] Differences between these barriers for normal and α-nucleophiles determine the α-effect, provided the pK_a values of the two nucleophiles are equal. In the GP reaction diagram two types of barriers are apparent (Fig. 3), an overall difference between uncomplexed reactants and the TS and the difference between the ion–dipole complex and the TS (central barrier).

This point is pertinent in the present paper because the Blanksby α-effect uses the central barrier difference between the nucleophiles, whereas the overall barrier was used by Ren

Can. J. Chem. Downloaded from www.nrcresearchpress.com by South China Agricultural University on 09/19/12
For personal use only.

Can. J. Chem. Downloaded from www.nrcresearchpress.com by South China Agricultural University on 09/19/12
For personal use only.

Fig. 4. Overall barriers for the nucleophile (Nuc) ··· methyl formate (MeOFrmt) system showing several types of normal nucleophiles.

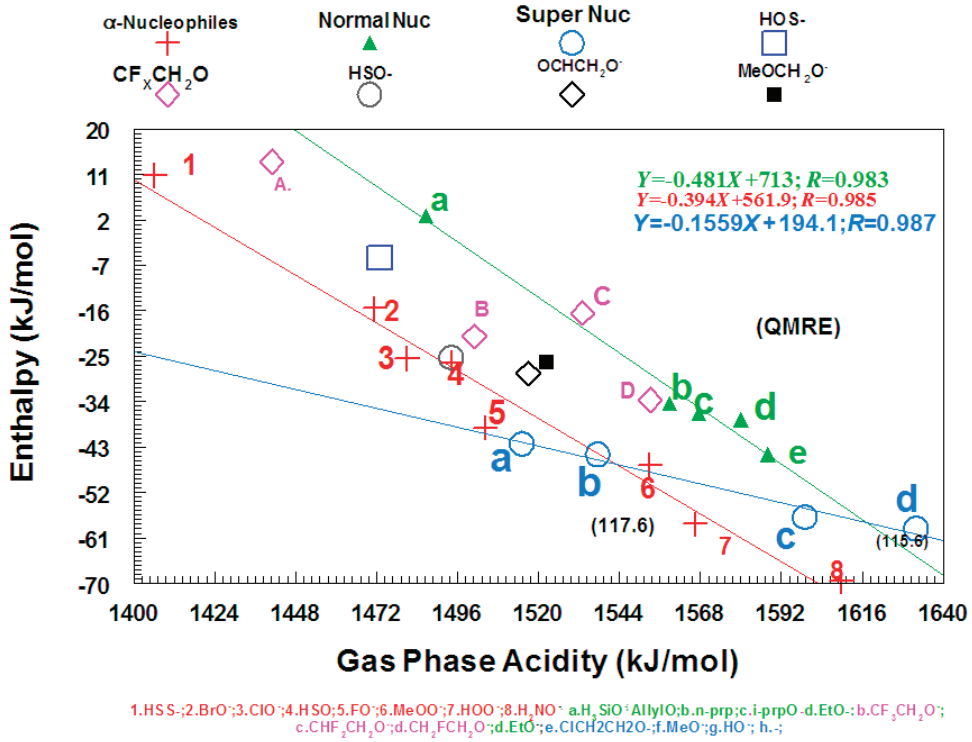

Fig. 5. A Born–Oppenheimer molecular dynamics (BOMD) scan for HOO–MeOFrmt.

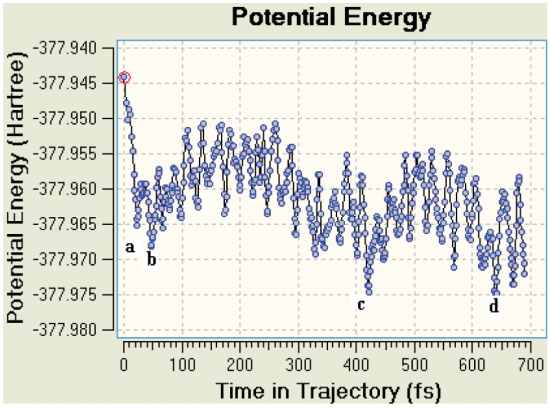

Fig. 6. A Born–Oppenheimer molecular dynamics (BOMD) scan for HOO–DMMP (dimethylmethylphosponate).

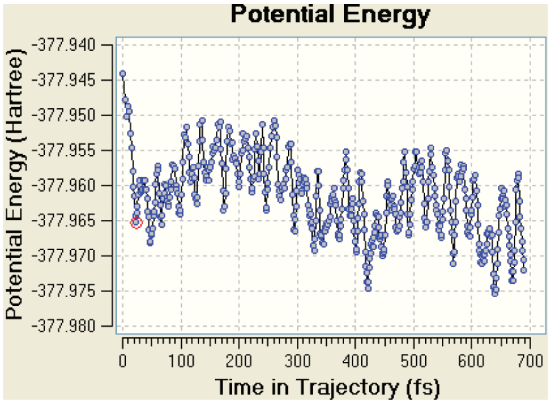

Table 4. Barriers (kcal/mol) from various points on relaxed scans at the B3LYP\6–31+G(d)model chemistry for dimethylmethylphosponate (DMMP).

System	Central NAC	Central NNAC	Overall
HOO	7.23578	43.58526	–47.8988922
MeO	13.8178	65.16129	–33.8631831
HO	11.73318	46.10833	–49.3796517

Note: Central NAC, central near attack conformation; Central NNAC, central non-NAC; Central refers to the region before the TS with or without alignment as an NAC or NNAC.

and Yamataka[5]. A reaction coordinate diagram provided in Blanksby and co-workers[1] shows values of –42 kcal/mol for the overall barrier and a 40 kcal/mol central barrier for HOO$^-$. Table 3 of their paper supplies a barrier value for the MeO–DMMPTS overall barrier of –32 kcal/mol and 47.8 kcal/mol for the central barrier. (Note: these negative values indicate greater stability for the HOO TS case.) The α-effect from the central barriers is similar to that from the overall barrier in this DMMP system (+7.8[47.8 – 40] vs +8[–32 + 40] for the central barriers). Overall barriers are mostly used to compare reactivity owing to the known existence of reactions that have zero or very small central barriers, missing their ion–dipole complexes.[14] Another such example, highly pertinent to the present paper, is a chemical dynamics trajectory study of the atomic-level mechanism of the reaction of HO$^-$ with methyl fluoride (MeF), where even a very low-energy hydrogen-bonded complex did not trap the majority of the trajectories in the channel leading to the dissociated products.[15]

The correlation LFER plot for α-nucleophiles reacting with methyl formate is shown in Fig. 4. This plot indicates that the overall barriers for the methyl formate system indicate

Can. J. Chem. Downloaded from www.nrcresearchpress.com by South China Agricultural University on 09/19/12
For personal use only.

Table 5. Barriers (kcal/mol) from various positions on the potential energy surface (PES) for the dimethylmethylphosponate (DMMP) at CBS-lq model chemistry including thermal corrections at 298.15 K.

Nucleophiles	Central NAC	Central NNAC	Overall
HOO^-	12.16113	47.99341	–47.898892
MeO^-	13.571	52.05762	–33.863183
HO^-	15.75539	42.97353	–49.379651

Note: 1 cal = 4.184 J. Central NAC, central near attack conformation; Central NNAC, central non-NAC; Central refers to the region before the TS with or without alignment as an NAC or NNAC.

Table 6. Summary of central versus overall barriers in the dimethylmethylphosponate (DMMP) and MeOFrm systems.

Nuc	Central	Overall
Nuc+DMMP		
HOO	40	–42.1
MeO	47.8	–32.4
Nuc+MeOFrmt		
HOO	25.9	–58.3
HO	29.7	–59.8
MeO	22.7	–45.1
EtO	28	–46.3

Note: Nuc, nucleophile.

α-effects for all the α-nucleophiles, analogous to those of Ren and Yamataka.[5] A companion plot showing central barriers along with *B* values appears in Fig. 2. The, rather busy, Fig. 4 provides data for a discussion of electronic factors effecting overall barriers. Figure 2 provides the information that a significant difference in *B* values between the normal and the α-nucleophile is important for detection of the presence of an α-effect.

We follow the Ren and Yamataka[5] method of using the overall barriers to express the combined experimental and theoretical α-effects in this paper, but also point to an unpublished study that shows a very good correlation between GP central barriers and the overall barriers, giving a correlation equation, $Y = 1.55X - 97.0$; $R = 0.979$ from this laboratory (available from the corresponding author on request). The role of central barriers is important in this paper because obtaining them requires distinguishing between the complex resulting from a Born–Oppenheimer molecular dynamics (BOMD) procedure or a relaxed scan, which elongates the forming C–O bond. The relaxed scan method proceeds by a systematic elongation of the nucleophile–C bond, which guarantees finding a near attack conformation (NAC). Lau and Bruice discussed such complex reaction systems in terms of correlated motions resulting in NACs for S_N2-type reactions in methyl transfers to COMT.[16] Figure 5 shows the result of the BOMD for HOO···MeO···OFrmt TS. Similar results accrue to the DMMP system. The overall result is a reaction complex that is analogous to **RC1** used by Blanksby and co-workers[1] at point **d**, (a non-NAC (NNAC) complex) with a point like a NAC complex at **a**. Transformation of the complex at point **d** in Fig. 5 to an NAC where an S_N2 reaction can begin requires overcoming a barrier of ~52 kJ/mol. With HOO the transition required was ~18 kJ/mol. From the bottom of the non-NAC curve to the TS for HOMeOFrmt is 81.6 kJ/mol, but for HOOMeOFrmt it is only 43.7 kJ/mol. At point **b**, a modified NAC complex for the HOO–MeOFrm case where the α-OH group forms a complex with H8, and the distance is actually shorter than for the C–O distance (Structure **1**). This finding plus the previous discussion indicates that determination of the α-effect, or even its observation, will depend on exactly how the barriers are designated. The overall barriers give a TS stabilization of HO relative to HOO of –0.86 kJ/mol. This is a nominally incorrect result if the experimental result using the experimental branching ratios, where the ratio HOO:HO is 1.6, favoring the reactivity of HOO over HO, can be taken as representing a rate ratio.

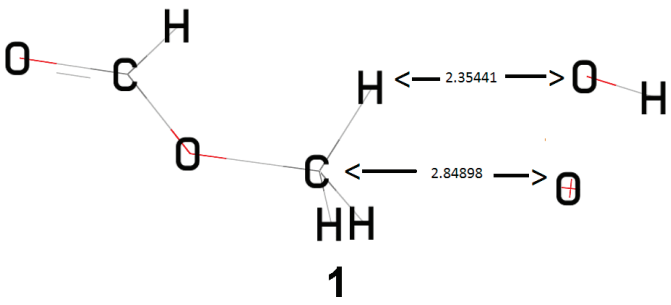

1

From the central barriers the order is $HOO^- < HO^-$, a difference of –1.42 kJ/mol and favoring HOO^-, agreeing with the branching ratios taken as indicative rate ratios.

Something similar is present in the Blanksby results.[1] Figure 6 shows the BOMD scan for the HOO···DMMP TS, elongating the HOO–C bond. The point inside a red circle indicates a NAC complex corresponding to that of the Nuc–MeOFrmt. Figure 6 shows several TSs must be similar to those in Fig. 5 for the methyl formate case to overcome the NNAC complex to form the NAC configuration. The overall appearance of Table 4 discloses the barriers from several points in the DMMP potential energy surface (PES), along with the overall barriers. The HOO and MeO anions are experimental results, with the HO anion given for comparison with the MeOFrmt system.

These results give the order of reactivity for the central barriers from NAC as $HOO^- > HO^- > MeO^-$ and from NNAC as $HOO^- > HO^- > MeO^-$. Overall barriers give (B3LYP\6–31+G(d)) $HO^- > HOO^- > MeO^-$. This difference in ordering of relativities presents a way to establish the most accurate determination of α-effects by determining their GP reactivities experimentally.

Can. J. Chem. Downloaded from www.nrcresearchpress.com by South China Agricultural University on 09/19/12
For personal use only.

Fig. 7. Linear free energy relationships (LFERs) of overall barriers for S_N2 reactions of methyl chloride.

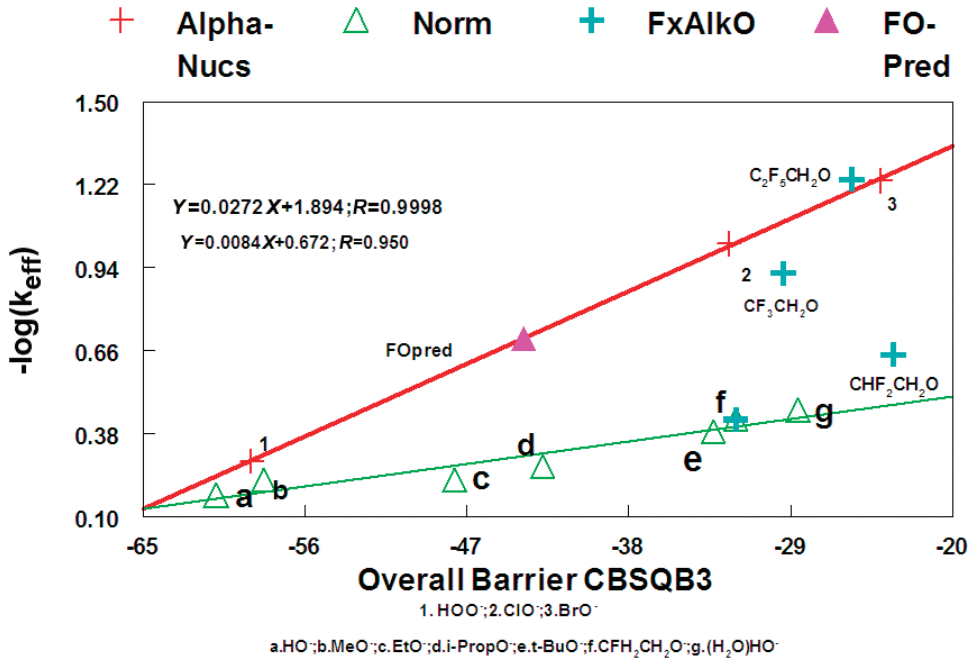

Fig. 8. Linear free energy relationships (LFERs) of central barriers for S_N2 methyl chloride reactions.

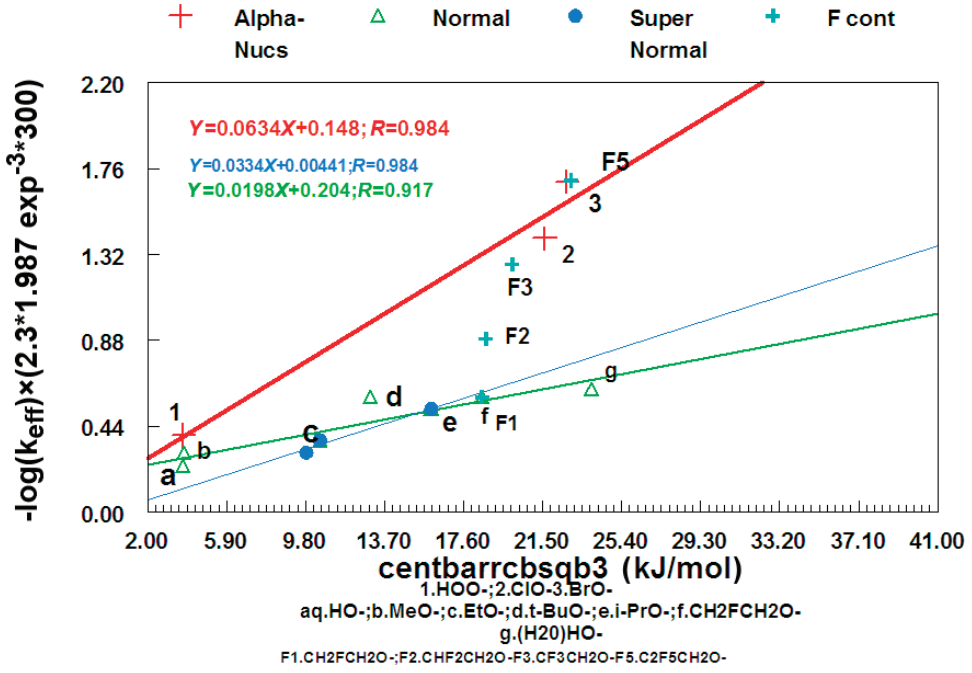

A further point deserves mention. Blanksby and co-workers[1] apparently used only the B3LYP\aug-cc-pVTZ energies at 0 K and added the ZPE energy from B3LYP\6–31+G(d), resulting in an electronic energy that lacked the thermal correction to 298.15 K. The temperature at which the reactions were done is stated as 307 K. Examination of this point to link the theoretical results to experimental ones deserves an attempt.

We examined the DMMP system using the original HOO^- anion, MeO^-, and HO^- anion, for comparison with the MeOFrm system. Likewise, the MeO^- was examined in the formate system. Thus, a direct comparison is possible between the two systems for the alleged α-effects.

A model chemistry similar to G2(+) was used by performing CBS-lq(startmp2) after the normal mp2/6–31+G(d)/HF/6–31+G(d)/ treatment in G2(+), thus, CBS-lq(startmp2)\mp2\6–31+G(d)\hf\6–31+G(d). The results are presented in Table 5. This choice of model chemistry was made because the jobs for the DMMP system at the CBS-QB3(startmp2) level were

Can. J. Chem. Downloaded from www.nrcresearchpress.com by South China Agricultural University on 09/19/12
For personal use only.

Table 7. Comparison of bond forming and bond breaking between nucleophiles and CH_3 groups in MeCl reactions.

System	Sum DAEn	NBOpop BD*C–Cl	Sumpop BD*C–H
$C_2F_5CH_2O$	83.77	0.165	0.111
CF_3CH_2O	80.18	0.162	0.111
CF_2HCH_2O	75.64	0.156	0.017
CFH_2CH_2O	54.04	0.131	0.029
EtO	53.57	0.124	0.022
MeO	55.29	0.127	0.029
HOO	78.7	0.125	0.017
HO	54.78	0.138	0.026
ClO	76.12	0.143	0.028
FO	69.25	0.140	0.278
BrO	76.46	0.152	0.029
$MeOCH_2CH_2O$	61.48	0.141	0.0284
$MeCOCH_2O$	92.17	0.198	0.0366
Cl_3CCH_2O	86.47	0.169	0.0287
CH_2ClCH_2O	70.35	0.154	0.0286
$CHCl_2CH_2O$	81.94	0.164	0.0286
$MeCF_2CH_2O$	73.64	0.154	0.029

Note: Sum DAEn, sum of donor–acceptor energy; NBOpop BD*C–Cl, electron population in an anti-bonding orbital; Sumpop BD*C–H, sum of pop in the C–H of the CH_3 group.

Fig. 9. HOO^- pole vaulting over the C–H bond barrier.

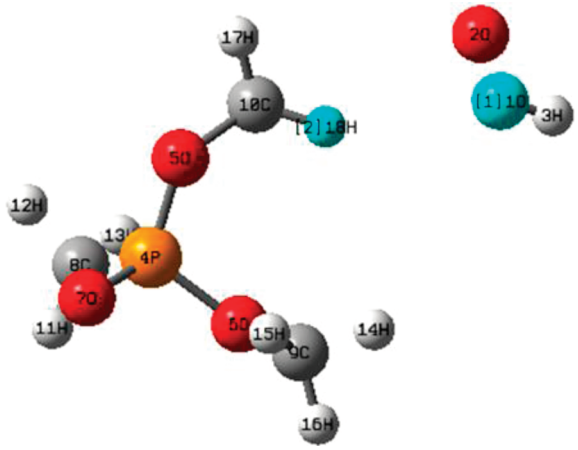

very large and very slow for our available facilities. The CBS-lq model chemistry allows easy treatment of both esters' relativities at the same modeling level and supplies thermodynamic data that is directly comparable in both systems.

The overall barriers are surprisingly the same within both B3LYP\aug-ccpVTZ and CBs-lq models. However, the central barriers are markedly different. The predicted reactivity at 298.15 K gives the order of reactivity as $HOO^- > MeO^- > HO^-$ from the NAC complex for the DMMP system. From the NNAC complex, the order is $HOO^- > HO^- > MeO^-$ at 298.15 K. This result indicates that central barriers with both NAC and NNAC complexes increase with increasing temperature, but the reactivity order is not the same from each set of barriers. Likewise, the overall barriers show $HO^- > HOO^- > MeO^-$.

Table 6 summarizes the issue of overall versus central barrier use to determine the existence or sizes of the α-effects in these two systems. Clearly, selection of the type of barrier will be crucial in the observation of an α-effect or evaluation of its size.

Combining the barrier information with either Fig. 4 or a similar plot of central barrier vs GPA discloses the fact that where one selects the normal α-nucleophile pair along the GPA axis determines both existence and size of the α-effect. An additional point was examined with BOMD trajectories to examine the question, "Is there really a pathway from the NNAC configuration, such as can be used (NAC) for determining the S_N2 α-effect?" The simplest case is for the HO–MeOFrmt system. Following a suggestion of Uggerud,[14] who used Rice–Kramers–Kassel–Marcus (RKKM) theory, we ran the BOMD trajectories backward. From the NNAC configuration for HO^-, shown as structure **2**, the BOMD trajectory was run with an input of temperature at 300 K and 1500 points. At the termination of 1500 points there was no pathway found to obtain the NAC configuration for an S_N2 reaction from the NNAC conformation. By contrast, from the S_N2 TS the NNAC configuration was attained in 326 cycles. Similarly, all the nucleophiles with MeOFrm gave no approach to their corresponding NAC configurations, nor did the nucleophiles used in the DMMP system attain the NAC S_N2 configuration from the NNAC one. Therefore, it is not possible to give credence to the α-effect for the system reported for DMMP. The G03W output files are available for examination from the corresponding author. This conclusion indicates agreement with the doubt expressed in Villano et al.[17] A recent report on S_N2 reactions with halide ions and methyl iodide modeled with trajectory simulation complementing crossbeam experiments indicated that along some trajectories the methyl halide, with sufficient energy (1.9 eV), undergoes reaction by a roundabout mechanism involving rotation of the methyl group, as well as the traditional NAC configuration.[18] When the BOMD routine was run with the anion and neutral oriented to favor S_N2 reaction with methylformate, it was observed that similar rotation of the anion–substrate pair to favor the NNAC configuration occurred in several trajectories and also for the DMMP system.

Table 8. The electrostatic energy in three S-containing α-nucleophiles and the CH_3 in S_N2 transition states.

	X–O···Me···OFrnt			
α-Nucleophile	NBO charge on X	NBO charge on Me(=CH_3)	RX–Me (nm)	*E* (kcal/mol)
HOS	–0.4781	0.4082	3.0259	–0.0645
HSS	–0.1361	0.4380	3.4642	–0.0197
HSO	0.2401	0.5244	3.0190	0.0417

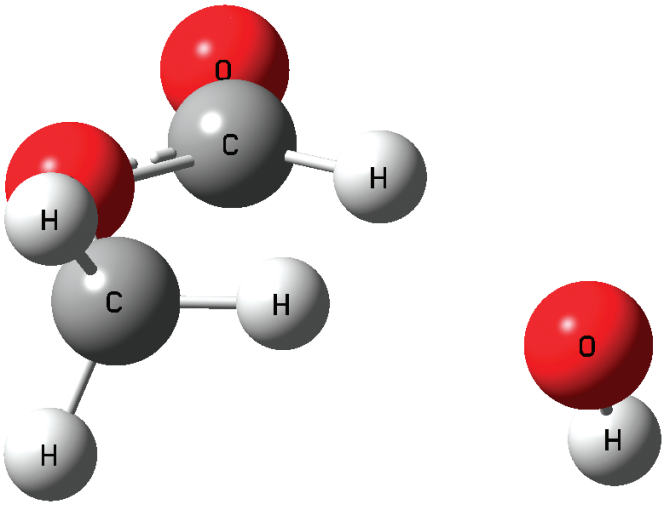

Discussion

It has been noted that the α-effect probably involves many factors. A review exists for the α-effect in solution.[19] The possibility of simplification to a small number of factors in studying the GP α-effect is at least nominally attractive. However, the present paper shows that such GP studies are not without problems. It is clear that the electronic effects differ within the nucleophiles studied in this paper, and do so in a consistent direction that indicates greater electronic reactivity for the HOO^- ion over both the HO^- and MeO^-. The method of definition, from central barriers computed from NAC, non-NAC (NNAC), or the overall barriers, is important because the energy values differ between the barrier sets. From overall barriers, as in Fig. 4, selection of a particular nucleophile at a particular GPA and a corresponding point on the other regression line denotes a difference in overall barrier for that pair of nucleophiles. This energy difference defines the size of the α-effect for that α-nucleophile – normal nucleophile pair. With no corresponding nucleophile present on the opposite line, the value of the barrier at that point still provides an estimate of the α-effect for the nucleophile selected. Similarly, the two types of central barriers (NAC or NNAC) can be determined in the corresponding two-line plots of barrier height vs GPA. The lines in Fig. 4 are similar to the LFER provided by Ren and Yamataka[3–5] for reactions with methyl halides. An intriguing comparison of the Ren and Yamataka[3–5] data plot (not shown) and the formate data is to note that the ratios of slope of the lines (slope for normal nucs/slope for α-nucs) with three different leaving groups are F = 1.07, Cl = 0.93, and Frm = 1.49. These numbers indicate that the different leaving groups cause differences in the degrees of convergence (or divergence with Cl^- leaving group) of the two lines. The point of convergence is where the size of the α-effect goes to zero, and the implication here is that this zero α-effect point depends on features in the leaving groups. In Fig. 4 the position of the point for HO^- (not included in the regression line) indicates a kind of super reactivity or basicity for this nucleophile, indicating a further complication in GP determination of the α-effect.

Employing the concept of pushing or pulling electron density via substituents along the bonding framework, the points along the blue line in Figs. 2 and 4 were obtained. The existence of these lines and the degree of correlation they exhibit have great powers of explanation about why it has been so difficult to obtain agreement, or even consistent determinations, of the α-effect in the GP. Some GP anions will behave with greater reactivity than a corresponding (GPA-matched) α-nucleophile.

Figure 2, showing central barriers for nucleophiles versus MeOFrmt S_N2 reactions, provides the QMRE (*B*) values as well as energies. The trends in *B* values indicate an electronic affect that provides interpretation of the point that where one selects the pair of normal α-nucleophiles for comparison is reflected in the QMRE energy at the avoided crossing point. When the *B* values are quite close, the detection of an α-effect becomes very difficult. At lower GPA values, the designation of an α-effect is easier, and the differences in *B* values are widely different. The findings that the electronic features of the α-nucleophiles differ markedly from the normal nucleophiles at the TSs indicates that at least one factor in the expression of the size of the α-effect involves such electronic differences. Of course, other factors may be involved, such as solvent effects, in its expression.

The AIM results indicate that electron density between the nucleophilic O atom and the displaced Me group varies only a small amount between the α-nucleophile system and the normal nucleophile system. The α-nucleophile succeeds in transferring electrons to the forming bond best, but the ethoxide case is nearly the same amount. At BCPs connecting atoms in the nucleophile to the nucleophilic atom, the α-nucleophile has the least density, although this number depends on the leaving group system. The large **ρ** numbers for the internal parts of normal nucleophiles indicate that the storage of electrons in this region is larger than for the H–O–O^- and is slightly less available to enter into forming the new bond. The net balance between donation to the forming bond and transfer into the breaking bond indicates that all the nucleophiles are approximately equal in donation to the breaking bond. The charges (*Q*) on the atoms and groups indicate positive charges on the atoms next to the O^- for all normal nucleophiles, but a negative charge on the α-atom in H–O–O^-. For HOO^-, the nucleophilic atom is actually less negative than those of the normal nucleophiles by a large amount.

Can. J. Chem. Downloaded from www.nrcresearchpress.com by South China Agricultural University on 09/19/12
For personal use only.

Can. J. Chem. Downloaded from www.nrcresearchpress.com by South China Agricultural University on 09/19/12
For personal use only.

Charges on the transferring CH_3 group are positive and largest in the HOO case with the $^-$MMP leaving group (LG), but quite similar in the –OFrm cases. Similarly, the charge on the LG O atom is very similar for all the nucleophiles, although a difference occurs between the two systems with the DMMP system having more charge on this atom than the Frm system. The elipticity at the BCP in AIM theory is related to the amount of p character, as in an ethylene double bond. In the DMMP (-lq) case, the size of the elipticity between the nucleophilic O and transferring Me group is nearly threefold that for the normal nucleophile. Similarly, the Frm (-lq) case group is greatly enhanced in elipticity at this BCP for HOO^- over the alkyl-O^- nucleophiles. HO^- as the nucleophile shows more elipticity than HOO^-. Between HO–O bonds the ellipticity ranges six- to seven-fold greater than the O atoms over the analogous BCP in the normal nucleophiles. Summarizing the AIM results we see that the quality of the electron density, as in s, p, sp, etc., seems to be the major difference between HOO^- and the normal nucleophiles.

The NBO study reveals that the LP electrons on the nucleophiles have several roles. In the DMMP system the HOO^- anion distributes electrons of LP(3) on the nucleophilic O atom into both the BD* between O5 and C10, thus, this is the breaking and making bond process, with a value of 50.37 kcal/mol. This same LP distributes to all three BD*C–H orbitals for a total of 8.64 kcal/mol. The contributions are not symmetrically disposed. The total DA energy (DAEn) sums to 59.01 kcal/mol. The MeO^- behaves quite differently, donating from two different LPs on the nucleophilic O^-. LP(2) and LP(3) each contribute for a sum of 50.47 kcal/mol to the bond-making – bond-breaking process. LP(3) also contributes two nearly symmetrical contribution and one larger one to the BD*C–H bonds, for a total of 58.73 kcal/mol. The difference of 0.28 kcal/mol marginally favors a greater TS stability to the HOO^- DMMP TS. This sum is supplemented by a DA contribution 0f 0.88 kcal/mol for LP(2) on O^- to the BD*O–H of the nucleophile. This orbital is of SP3.6-S composition, and the LP(2) orbital is 99% P. The composition of this DA contribution agrees fairly well with the size of the AIM elipticity at the BCP for this bond. The MeO–DMMP TS lacks this donation – back donation DA stabilization, although there does exist back donation into the BD*C–H bonds of the nucleophile. The Nuc–MeOFrm system NBO analysis shows a similar DA contribution from BDO–H to BD*O–O in the HOO^- anion and a back donation of the LP(2) to the BD*OH. This LP(2) is the pair that does the most important segment of the bond making – bond breaking at the CH_3 group. The total DA energy is 74.38 kcal/mol. The HOMeOFrm system lacks the extra HO bond for the DA stabilization apparent in the HOO^- case. The BD*CH_3–OFrm in the TSs for both cases are very rich in p character content, showing substantial agreement with the AIM BCP elipticites. The DA energies are considerably less for the HO^- TS case compared with the HOO^- TS, and donation into the BD*C–H bonds of the transferring CH_3 group is significantly less for HO–MeOFrm than for HOO–MeOFrm. The MeO–MeOfrm system shows a total DA stabilization energy close to the value for HO–MeOFrm, but interestingly less than EtOMeOFrm by ~3.5 kcal/mol. This DA energy for the EtOMeOfrm TS can be traced to the donation from the C–C bond of the Et group. It is helpful to recall that the wave functions used for this NBO perturbation analysis do not have any correction for electron correlation effects.

The VB treatment indicates a pattern of QMRE values consistent with the NBO analysis. The QMRE values differ as the LG changes, with the better phosphonate LG providing the larger QMRE numbers, except in the HO–DMMP TS case where the QMRE is smaller than for the HO–MeOFrmt case by 1 kcal/mol. The numbers apply only to the TSs involved. They show nothing about the pathways to those TSs. The orders of the nucleophilic reactivities are $HOO^- > MeO^- \approx HO^-$ for DMMP and $HOO^- > MeO^- \approx HO^- > EtO^-$ for MeOFrmt. The branching ratios of both systems would indicate agreement with the theoretical results. The question remains, "Do these numbers indicate an α-effect?" The murkiness of the present GP attempts to study the α-effect are illustrated by the following considerations. Mass spectroscopists, who study nucleophilic methyl transfers using SIFT tubes, such as the University of Colorado group, present their results in terms of plots of efficiencies (k_{rxn}/k_{col} = efficiency, where k_{rxn} = absolute rate and k_{col} = collision rate) on semi-log plots vs GPA.[17] Theoreticians plot barrier height vs GPA and predict an α-effect from differences in barrier heights at a particular GPA value, as in Fig. 4. These types of plots (LFERs) differ from the semi-log plots, predicting substantial α-effects or small ones depending on where one selects the GPA point. Consider Figs. 7 and 8 which plot LFERs for the published Bierbaum data for reactions with methyl chloride. In Fig. 7 the Y axis displays the –log(Eff), which is a transform of an energy term via $\Delta G = -RT \log(k_{rate})$ from TS theory. In Fig. 8 the Y axis is transformed into the same energy units as the GPA (kcal/mol). In this case the $T\Delta S$ term was neglected to use ΔH. Thus, these axes represent energy or something related by a simple transform to energy, and ensures that either central barriers or overall barriers provide a faithful correspondence of theoretical and experimental results in this case. One can then assess these plots as indicating that the –log (efficiencies) numbers reflect both overall and central barriers adequately. There are obvious differences between the α-nucleophiles and normal nucleophiles. This fact alone indicates the probable presence of the α-effect in some regions of the dual plot and near absence of one in others. We note that the behavior of the fluorine-containing nucleophiles is erratic compared with the other ones. The greater the F atom content the more nearly the barrier heights and efficiencies look like the ones on the α-effect line. Clearly, these nucleophiles would give very different conclusions for the presence or absence of an α-effect.

The fluorine-containing alkoxides deserve comment, since they seem to determine the conclusion of no α-effect in the published MS results for methyl chloride.[17] The NBO pertubation analysis of these nucleophiles and their TSs with S_N2 reactions with CH_3Cl discloses (at the 6–311+G(2d,p) model chemistry) that the DA energies of the LP electrons involved in DA interaction from the nucleophilic O^- with bond making–breaking and donation to the C–H* bonds is greatly affected by the number of F atoms in the anion. Wiberg[20] examined F-containing alkoxides with AIM theory and concluded from the AIM charges on the O atoms that increasing F content increased negative AIM charge on the O^- atom. The order was MeO^- (–1.478) > FCH_2O^- (–1.454) > F_3CO^- (–1.463), probably indicating larger nucleophilicity for the

Can. J. Chem. Downloaded from www.nrcresearchpress.com by South China Agricultural University on 09/19/12
For personal use only.

CF_3O^- nucleophile.[20] A set of full NBO calculations for all the F-containing alkoxides and their TSs show that storage of electron populations in the C–C* orbitals gives much DA (DAEn) stabilization in the anions and donation from these depots affect attaining the TSs. The most important areas are bond making and bond breaking where the DA changes between the anions and the TS energies are C_2F_5 CH_2O^- = 7.41 kcal/mol and $CF_3CH_2O^-$ = 6.45 kcal/mol, indicating that the additional F-atom content actually increases electrons in the TS as though there is an electron-pair repulsion occurring. A similar phenomenon is discussed by Burton and Wheaton[21] in the productions of difluorocarbene. Hine and Langford,[22] in the early days of halocarbene chemistry, demonstrated the concerted nature of proton abstraction from chloro and bromo halodifluromethanes and indicated that the F atoms cause this owing to repulsion of the LPs involved. A reinforcement for the notion of repulsion of LP electrons on a non-fluorine atom by LPs on F atoms involves a computational study of the conformational analysis of fluorinated dimethyl ethers where the C–O–C bond angle was increased and the C–O bond lengths were reduced in the bond to the fluorinated C atom, and increased in the opposite one, thereby increasing the computed energy with increasing F-atom content and decreasing the rotational barrier height.[23] Such considerations have significant explanatory value in assessing the anomalous behavior displayed by fluoroalkanols in Fig. 7.

Table 7 shows a revealing comparison between the fluorinated alkoxides and other nucleophiles. The DAEn summed over the contributions indicate higher values for the multiple F-substituted alkoxides to bond making by donating into the BD*C–Cl. Similarly, multiple Cl substitution allows greater contribution to bond making. Other groups also provide this additional donation. The putatively best α-nucleophile (HOO^-) is comparatively modest in both DAEn donation and population of the BD*C–Cl and BD*C–H orbitals. This may indicate that some factor related to the quality of electron donation may be working in this case.

A more complete discussion of the MeCl reactivity system is the subject of a future paper (in preparation). These plots indicate that the GPMS efficiencies correlate well with either the overall barriers or central barriers, except for the efficiencies of the fluorinated alkoxides, which may correlate, but will have very different correlation numbers. The question of which type of barrier should be used remains.

The combined results of this electronic study and the BOMD studies indicate the following scenario to explain the findings. In the MS experiments, the generation of the anions and injection of the neutrals occurs at a temperature near 300 K, resulting in a statistical spread of kinetic energies in both the anions and neutral substrates. Random collisions of these entities result in kinetic energies in pairs. The pair anion–neutral, which has a combined kinetic energy at the level of the NAC results in the S_N2 reaction, will undergo an S_N2 reaction. The sum of small attractive forces available to hold the pair close to the NAC must be matched by energies smaller than what it takes to surmount the cage of C–H bonds in the CH_3 group. The number of these complexes is probably statistically determined. The much lower energy NNAC configuration entraps more of the anion–neutral collisions, resulting in the elimination reactions of the formyl H–C from methyl formate or, in the DMMP system, oscillation between MeO groups with no escape to the NAC position for S_N2 reaction. The branching ratios in the methyl formate case indicate much larger elimination or capture by the C=O group than the S_N2 reactions for both nucleophiles. Careful examination of the method of escape of the nucleophile from the NAC approach toward the NNAC position involves many collisions between the nucleophile and the methyl C–H bonds and atoms. This situation provides a kinetic energy trap for the nucleophile at the NAC position, with a small number of substrate–anion pairs possessing less energy than necessary to pass the H atoms. Figure 9 shows the progress in passing the C–H bonds in DMMP by HOO^-. In this case the HO group is close to the H atom (2.565 Å) before the O^- atom passes the H-atom barrier (2.924 Å), as though the HO group pole vaults the rest of the nucleophile over the barrier.

The number of pathways for reaction in these two esters and the percentage of each reaction and HOS^- are shown in Fig. 4. This trio forms the basis of a Popperian risky experiment to confirm the hypothesis that the α-effect is due to electrostatic attraction between a hard electronegative atom in the α-position and a positively charged methyl group being transferred.[24] In such a risky experiment, confirmation of the theory (or hypothesis) can be granted by the result only if the entire theory is placed at risk by performing the experiment. An example of the use of this philosophical tool is provided by Berson[25] in confirming Woodward–Hoffman rules for conservation of orbital symmetry. Table 8 shows the way in which the theory of electrostatic repulsion for the cause of the α–effect is not confirmed with this trio. The lowest overall TS energy from the free reactants is due to the HSO^- nucleophile, but it has a positive (repulsive) electrostatic energy. The HSS^- case plots on the same line as the other α-nucleophiles, but the HOS^- case plots more toward the normal nucleophile line and provides a smaller difference in TS energy, although it should provide a greater (more stabilizing) energy lower than the other two S-containing α-nucleophiles.

Conclusions

Several conclusions can be drawn from this report. First, all the TS calculations showed greater favorable electronic behavior for the reactions of α-nucleophiles than for the GP-matched normal nucleophiles. The AIM results indicate larger π-type character in the forming bonds than the normal nucleophiles and indicate more involvement of electrons from bonds adjacent to the nucleophilic atom. Second, the NBO DA energies for the TSs of the α-nucleophiles indicate greater stabilization for those TSs over those involving normal nucleophiles. The exact amount of stabilizing energies involved will involve more refinement than expressed in this paper. Third, the VB results show that the QMRE found at the avoided crossing point of the wave functions of the product and reactant side of a SCD show a larger stabilization for the α-nucleophile TSs than for the normal ones. Fourth, the BOMD studies indicate that a complication of the GP reactions occurs in the pathway from ions + neutrals to NAC or NNAC complexes and between these pathways. Neither the DMMP or the methyl formate system allows a ready two-way passage between complexes, thus, the reported α-effect for the DMMP system must be re-examined. Finally, the three

questions all have the answer Yes. Sometimes normal nucleophiles are not able to be distinguished from α-nucleophiles. Sometimes normal nucleophiles possess more reactivity than GPA-matched α-nucleophiles. With the answer Yes to question 1 it follows that question 3 shows that sometimes α-nucleophiles possess reactivity less than GPA-matched normal nucleophiles. Finally, the evidence from the S-containing α-nucleophiles indicates that electrostatic attractions cannot play a major role in providing an α-effect.

Supplementary data

Supplementary data are available for this article through the journal Web site at http://nrcresearchpress.com/doi/suppl/10.1139/v11-113.

Acknowledgements

K.R.F. thanks Truman State University, Kirksville, Missouri, for continued support in the form of office space and e-mail support, as well as occasional ITS help. D.A. thanks Truman State University for travel support and for the provision of Gaussian 09, as well as upgraded computer hardware. Both authors thank our colleague and friend, Dr. E. Patterson for adding cogency to our sometimes muddled conversations.

References

(1) McAnoy, A. M.; Paine, M. R. L.; Blanksby, S. J. *Org. Biomol. Chem.* **2008**, *6* (13), 2316. doi:10.1039/b803734e.
(2) DePuy, C. H.; Della, E. W.; Filley, J.; Grabowski, J. J.; Bierbaum, V. M. *J. Am. Chem. Soc.* **1983**, *105* (8), 2481. doi:10.1021/ja00346a066.
(3) Ren, Y.; Yamataka, H. *Org. Lett.* **2006**, *8* (1), 119. doi:10.1021/ol0526930.
(4) Ren, Y.; Yamataka, H. *Chemistry* **2007**, *13* (2), 677. doi:10.1002/chem.200600203.
(5) Ren, Y.; Yamataka, H. *J. Org. Chem.* **2007**, *72* (15), 5660. doi:10.1021/jo070650m.
(6) Patterson, E. V.; Fountain, K. R. *J. Org. Chem.* **2006**, *71* (21), 8121. doi:10.1021/jo061275l.
(7) Bader, R. F. W. *Atoms in Molecules;* Oxford University Press: New York, 1990.
(8) Frisch, M. J.; Trucks, G. W.; Schlegel, H. B.; Scuseria, G. E.; Robb, M. A.; Cheeseman, J. R.; Montgomery, J. A., Jr.; Vreven, T.; Kudin, K. N.; Burant, J. C.; Millam, J. M.; Iyengar, S. S.; Tomasi, J.; Barone, V.; Mennucci, B.; Cossi, M.; Scalmani, G.; Rega, N.; Petersson, G. A.; Nakatsuji, H.; Hada, M.; Ehara, M.; Toyota, K.; Fukuda, R.; Hasegawa, J.; Ishida, M.; Nakajima, T.; Honda, Y.; Kitao, O.; Nakai, H.; Klene, M.; Li, X.; Knox, J. E.; Hratchian, H. P.; Cross, J. B.; Bakken, V.; Adamo, C.; Jaramillo, J.; Gomperts, R.; Stratmann, R. E.; Yazyev, O.; Austin, A. J.; Cammi, R.; Pomelli, C.; Ochterski, J. W.; Ayala, P. Y.; Morokuma, K.; Voth, G. A.; Salvador, P.; Dannenberg, J. J.; Zakrzewski, V. G.; Dapprich, S.; Daniels, A. D.; Strain, M. C.; Farkas, O.; Malick, D. K.; Rabuck, A. D.; Raghavachari, K.; Foresman, J. B.; Ortiz, J. V.; Cui, Q.; Baboul, A. G.; Clifford, S.; Cioslowski, J.; Stefanov, B. B.; Liu, G.; Liashenko, A.; Piskorz, P.; Komaromi, I.; Martin, R. L.; Fox, D. J.; Keith, T.; Al-Laham, M. A.; Peng, C. Y.; Nanayakkara, A.; Challacombe, M.; Gill, P. M. W.; Johnson, B.; Chen, W.; Wong, M. W.; Gonzalez, C.; Pople, J. A. *Gaussian 03, Revision C.02;* Gaussian, Inc.: Wallingford CT, 2004.
(9) Keith, T. A. *AIM Package;* Available from http://aim.tkgristmill.com.
(10) Li, J.; Duke, B.; McWeeny, R. *VB2000 2.1;* SciNet Technologies: San Diego, CA, 2009.
(11) Shaik, S. S., and Hiberty, P. C. *A Chemist's Guide to Valence Bond Theory;* Wiley-Interscience: Hoboken, NJ, 2008; p 142.
(12) Shaik, S. S., and Hiberty, P. C. *A Chemist's Guide to Valence Bond Theory;* Wiley-Interscience: Hoboken, NJ; 2008; p 118.
(13) Zavitsas, A. *J. Phys. Chem.* **1987**, *91* (22), 5573. doi:10.1021/j100306a016.
(14) Uggerud, E. *J. Chem. Soc., Perkin Trans. 2* **1999**, (7), 1465. doi:10.1039/a900380k.
(15) Sun, L.; Song, K.; Hase, Wm. L. *Science* **2002**, *296* (5569), 875. doi:10.1126/science.1068053.
(16) Lau, E. Y.; Bruice, T. C. *J. Am. Chem. Soc.* **1998**, *120* (48), 12387. doi:10.1021/ja9827447.
(17) Villano, S. M.; Eyet, N.; Lineberger, W. C.; Bierbaum, V. M. *J. Am. Chem. Soc.* **2009**, *131* (23), 8227. doi:10.1021/ja9012084.
(18) Mikosch, J.; Trippel, S.; Eichhorn, C.; Otto, R.; Lourderaj, U.; Zhang, J. X.; Hase, W. L.; Weidemüller, M.; Wester, R. *Science* **2008**, *319* (5860), 183. doi:10.1126/science.1150238.
(19) Buncel, E.; Um, I. K.-H. *Tetrahedron* **2004**, *60* (36), 7801. doi:10.1016/j.tet.2004.05.006.
(20) Wiberg, K. B. *J. Am. Chem. Soc.* **1990**, *112* (9), 3379. doi:10.1021/ja00165a019.
(21) Burton, D. J.; Wheaton, G. A. *J. Am. Chem. Soc.* **1974**, *96* (21), 6787. doi:10.1021/ja00828a055.
(22) Hine, J.; Langford, P. B. *J. Am. Chem. Soc.* **1957**, *79* (20), 5497. doi:10.1021/ja01577a046.
(23) Buono, R. A.; Zauhar, R. J.; Venanzi, C. A. *J. Mol. Struct. THEOCHEM* **1996**, *370* (2–3), 97. doi:10.1016/S0166-1280(96)04566-6.
(24) Popper, K. R. *Conjectures and Refutations;* Basic Books: New York, 1963; p 36.
(25) Berson, J. *Acc. Chem. Res.* **1972**, *5* (12), 406. doi:10.1021/ar50060a003.

Can. J. Chem. Downloaded from www.nrcresearchpress.com by South China Agricultural University on 09/19/12
For personal use only.

An efficient synthesis of 4-arylquinolin-2(1*H*)-ones and 3-alkenyl-4-arylquinolin-2(1*H*)-one using a Pd/$NiFe_2O_4$-catalyzed consecutive Heck reaction

Sanjay R. Borhade and Suresh B. Waghmode

Can. J. Chem. Downloaded from www.nrcresearchpress.com by South China Agricultural University on 09/19/12
For personal use only.

Abstract: A convenient one-pot method for the synthesis of 4-arylquinolin-2(1*H*)-ones and 4-arylcoumarins has been described. The successive Heck reaction on substituted 2-iodoaniline and 2-iodophenol catalyzed by a Pd/nickel ferrite catalyst followed by in situ cyclization was the key step. The scope of this methodology was extended to the synthesis of bioactive 3-alkenyl derivatives of 4-arylquinolin-2(1*H*)-ones.

Key words: 4-arylquinolin-2(1*H*)-ones, Pd/nickel ferrite, Heck reaction, cross-coupling reactions, heterogeneous catalysis.

Résumé : On décrit une méthode monotope commode de synthèse des 4-arylquinoléin2(1*H*)-ones et 4-arylcoumarines. L'étape clé est une réaction successive de Heck sur une 2-iodoaniline et le 2-iodophénol, catalysée de un catalyseur de Pd/ferrite de nickel, suivie par une cyclisation in situ. On a étendu la portée de cette méthodologie à la synthèse de dérivés 3-alkényles biologiquement actifs des 4-arylquinoléin-2(1*H*)-ones.

Mots-clés : 4-arylquinoléin-2(1*H*)-ones, Pd/ferrite de nickel, réaction de Heck, réactions de couplage croisé, catalyse hétérogène.

[Traduit par la Rédaction]

Introduction

Quinolin-2(1*H*)-ones constitute the basic structural fragments of many natural and synthetic biologically active molecules. They shows antiviral, antineoplastic, anti-ischemic, antiallergic, antihypertensive, and antiulcerative activity.[1] Moreover, quinolin-2(1*H*)-ones also serve as valuable synthetic intermediates because they can be easily transformed into 2-substituted quinolines (e.g., 2-Cl, 2-OTf), which can undergo further functionalization, such as nucleophillic aromatic substitutions and Pd-catalyzed coupling reactions.[2]

In particular, functionalized 4-aryl-quinolin-2(1*H*)-ones (Fig. 1) are excellent inhibitors of acyl co-enzyme A and cholesterol acyltransferase and are potent openers of high-conductance calcium-activated K+ channels.[3,4] They also show potent antibacterial activity and inhibit the replication of human immunodeficiency virus (HIV) induced by tumor necrosis factor (TNF-α) with an IC_{50} of 2.5 μm.[5] The derivatives of 3-(quinolin-3-yl) acrylates **4** and the corresponding reduced allylic alcohols have been identified by a group from Bristol-Myers Squibb (BMS) as novel and potent maxi-K channel openers useful for the treatment of male erectile dysfunction.[3a] In addition, R 115777 (Zarnestra, **5**), an orally active antitumor agent, is currently undergoing human clinical trials.[3c–3d] Although quinolinones exhibit a wide range of biological activities, only a few methods for the synthesis of 4-arylquinolinon-2(1*H*)-ones are reported in the literature.[6] In most instances, an arylquinolin-2(1*H*)-one moiety was achieved by acid–base catalyzed cyclization of *N*-acyl-*o*-amino benzophenone or via closely related procedures.[3c–3d] However, starting materials used for the cyclization approach are mostly amino ketones, which are not readily available; furthermore, these procedures suffer from the disadvantage that the aryl ring attached to the C-4 position of quinolinon-2(1*H*)-ones has to be introduced very early in the overall synthetic scheme, which limits the further laboration of this substituent.

Several research groups have recently demonstrated the successful use of a Pd-catalyzed C–C coupling reaction for the synthesis of quinolin-2(1*H*)-one as a facile, versatile, and practical route.[7,8] Xu et al.[8b] reported a solid-phase protocol (HypoGel Br resin) for the synthesis of 4-substituted quinolinones using Pd-catalyzed Suzuki and Negishi cross-coupling reactions in 63%–90% yield within 14 h. Cacchi and co-workers[8c–8d] developed a methodology for the synthesis of 4-aryl-quinolin-2(1*H*)-ones from 2-bromocinnamides and aryl iodides through Heck reaction followed by an intramolecular Buchwald–Hartwig amination sequence. In addition to this, they also reported Heck reaction and in situ cyclization of methyl β-(*o*-acetamidophenyl)acrylates with aryl iodides for the synthesis of 4-aryl-quinolin-2(1*H*)-ones in the presence of Pd $(OAc)_2$ and KOAc in DMF at 120 °C.[8g] Kappe and co-workers[8e] reported the synthesis of functionalized 4-aryl-quinolin-2(1*H*)-ones by Suzuki coupling from 4-chloroquinoline-2(1*H*)-one and boronic acid using a microwave. Although they reported a good yield in a shorter reaction time, the use of a microwave for industrial large-scale synthesis is not viable and also the

Received 27 March 2011. Accepted 29 May 2011. Published at www.nrcresearchpress.com/cjc on 7 October 2011.

S.R. Borhade and S.B. Waghmode. Department of Chemistry, University of Pune, Ganeshkhind, Pune 411 007, India.

Corresponding author: Suresh B. Waghmode (e-mail: suresh@chem.unipune.ac.in).

Fig. 1. Biologically active 4-arylquinolin-2(1*H*)-one derivatives.

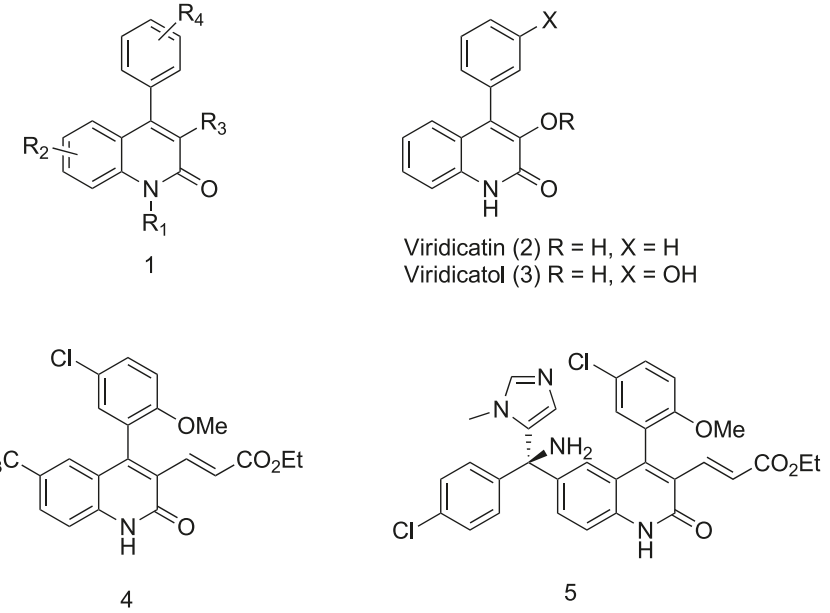

required boronic acids are costly. More recently, Inamoto et al.[8a] reported a synthetic approach through C–H bond functionalization and intramolecular amidation sequencing in the presence of a catalytic amount of $PdCl_2$ and $Cu(OAc)_2$ under an O_2 atmosphere. Although these authors have reported moderate to good yields of 4-arylquinolin-2(1*H*)-ones, nonrecovery of the precious palladium catalyst and Pd metal contamination of the final products make these processes commercially undesirable. Our ongoing interest is towards the development of new catalyst system; recently, our group[9a,9c,9d] and Manorama and co-workers[9b] reported the filtration-free magnetically separable $Pd/NiFe_2O_4$ as an efficient and inexpensive catalyst for the Heck reaction. In light of this successful methodology, we anticipated that the C–C bond formation using the Heck reaction could lead to an efficient protocol for the synthesis of 4-arylquinolin-2(1*H*)-ones. Herein we report the novel use of Pd supported on nickel ferrite as a heterogeneous and recyclable catalyst for the synthesis of functionalized 4-arylquinolin-2(1*H*)-ones and 4-arylcoumarins in one pot. We have also demonstrated the applicability of this methodology for the synthesis of (2*E*)-ethyl-3-(4-(5-chloro-2-methoxyphenyl)-6-(trifluoromethyl)-1,2-dihydro-1-methyl-2-oxoquinolin-3-yl)acrylates in four steps.

Results and discussion

Initial studies were performed using 4-(trifluoromethyl)-2-iodoaniline, acrylic acid, and iodobenzene to determine the optimal reaction conditions. We examined various palladium sources, solvents, bases, and temperatures and the results obtained are summarized in Table 1. Amongst the different Pd sources studied, palladium acetate ($Pd(OAc)_2$), tetrakistriphenylphosphine palladium(0) ($Pd(PPh_3)_4$), and tetraamminepalladium(II) chloride ($Pd(NH_3)_4Cl_2·H_2O$) gave good to moderate yields of corresponding 6-(trifluoromethyl)-4-phenyl-2-quinolinone products (Table 1, entries 5 and 6). However, 1,1-bis(diphenylphophino)ferrocene–dichloropalladium ($PdCl_2$(dppf)) and palladium chloride ($PdCl_2$) gave very poor yields (Table 1, entries 3 and 4). The presence of a Pd(IV) oxidation state in the sodiumhexachloropalladate tetrahydrate ($Na_2PdCl_6·4H_2O$) would not allow the catalyzation of the Heck reaction (entry 7).

We conclude that the Pd sources having oxidation states Pd(II) and Pd(0) were catalytically active for the Heck reaction, whereas the Pd(IV) oxidation state was not active at all. In comparison with homogeneous $Pd(OAc)_2$, a slight increase in the yield was observed for the $Pd/NiFe_2O_4$ catalyst (Table 1, entries 2 and 8). Since it was easily separable from the reaction mixture by applying an external magnetic field and no product contamination with Pd metal was observed, from this point forward $Pd/NiFe_2O_4$ catalyst was used unless otherwise stated. Among the different bases studied, triethylamine (TEA) and tributylamine (TBA) were found to be the best (Table 1, entries 8 and 9). These organic bases were superior to inorganic bases such as $NaHCO_3$, NaOAc, and Na_2CO_3 (Table 1, entries 8–12).

The effect of various solvents for consecutive Heck reaction and in situ cyclization was studied and the results showed that DMF and CH_3CN gave 75% and 66% yield, respectively, after 18 h, using TEA as a base. Nonpolar solvents such as toluene and xylene were unproductive (Table 1, entries 15 and 16). Temperature studies revealed that 85 °C was enough to activate the $Pd/NiFe_2O_4$ catalyst for the Heck reaction, whereas at higher temperature (100 °C), a lower yield was observed. Various olefins such as methyl acrylate, ethyl acrylate, butyl acrylate, and acrylic acid were reacted with 4-(trifluoromethyl)-2-iodoaniline and it was found that acrylic acid gave maximum yield.

Using the optimized reaction conditions we explored the general applicability of the $Pd/NiFe_2O_4$ catalyst for the consecutive Heck reaction of different 2-iodoanilines followed by cyclization to yield corresponding 4-arylquinolin-2(1*H*)-ones (Table 2). The transformation of various substituted aryl iodides and bromides to corresponding 4-arylquinolin-2-(1*H*)-one derivatives offered moderate to good yields. Aryl iodides gave superior yields of the desired product as

Can. J. Chem. Downloaded from www.nrcresearchpress.com by South China Agricultural University on 09/19/12
For personal use only.

Can. J. Chem. Downloaded from www.nrcresearchpress.com by South China Agricultural University on 09/19/12
For personal use only.

Table 1. Optimization of the Heck coupling and cyclization conditions for the synthesis of 4-aryl-2-quinolin-2(1*H*)-one.

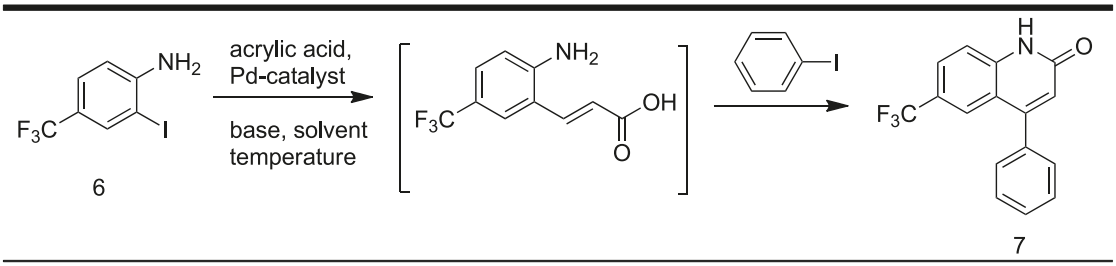

Entry	Pd source	Base	Solvent	Temp. (°C)	Yield[a]
1	—	TEA	DMF	85	—
2	$Pd(OAc)_2$	TEA	DMF	85	71
3	$PdCl_2$	TEA	DMF	85	29
4	$PdCl_2$(dppf)	TEA	DMF	85	23
5	$Pd(PPh_3)_4$	TEA	DMF	85	58
6	$Pd(NH_3)_4Cl_2{\cdot}H_2O$	TEA	DMF	85	48
7	$Na_2PdCl_6{\cdot}4H_2O$	TEA	DMF	85	—
8	$Pd/NiFe_2O_4$	TEA	DMF	85	75
9	$Pd/NiFe_2O_4$	TBA	DMF	85	72
10	$Pd/NiFe_2O_4$	NaOAc	DMF	85	8
11	$Pd/NiFe_2O_4$	$NaHCO_3$	DMF	85	12
12	$Pd/NiFe_2O_4$	Na_2CO_3	DMF	85	11
13	$Pd/NiFe_2O_4$	TEA	CH_3CN	85	69
14	$Pd/NiFe_2O_4$	TEA	DMSO	85	24
15	$Pd/NiFe_2O_4$	TEA	Xylene	85	2
16	$Pd/NiFe_2O_4$	TEA	Toluene	85	3
17	$Pd/NiFe_2O_4$	TEA	1,4-Dioxane	85	14
18	$Pd/NiFe_2O_4$	TEA	DMF	70	5
19	$Pd/NiFe_2O_4$	TEA	DMF	100	63

Note: Reaction conditions: 4-(trifluoromethyl)-2-iodoaniline (1.0 mmol), acrylic acid (1.05 mmol), Pd catalyst (2.5 mol %), base (3.25 mmol), solvent (3.0 mL) and iodobenzene (1.25 mmol) added in a second step, time 18 h. TEA, triethylamine; TBA, tributylamine.

[a]GC yields.

compared with aryl bromides. The less reactive chlorobenzene and phenylboronic acid did not couple in the second Heck reaction condition (Table 2, entries 11 and 12). The aryl iodides reacted in the second Heck coupling reaction with (*E*)-3-(2-amino-5-(trifluoromethyl)phenyl)acrylic acid containing electron-donating methoxy groups at the ortho, meta, or para positions produced the corresponding 4-arylquinolin-2-(1*H*)-one compounds **10**–**12** in 59%, 61%, and 67% yields, respectively (Table 2, entries 4–6).

We also attempted the synthesis of a biologically active flavonoid (4-aryl-2*H*-chromen-2-one, neoflavone),[10] by a similar route using 2-iodophenol and ethyl acrylates as starting materials (Table 3).

2-Iodophenol successfully reacted with ethyl acrylate and gave 96% yield of the corresponding (*E*)-3-(2-hydroxyphenyl)acrylate, but the second Heck reaction with iodobenzene and in situ cyclization was ineffective. However, after optimization of the reaction conditions we could achieve a maximum yield of up to 31% of the corresponding 4-phenyl-2*H*-chromen-2-one (Table 3, entry 1).

A hot filtration test[11] was performed to investigate Pd leaching into the reaction mixture. The test was done for the 4-(trifluoromethyl)-2-iodoaniline (Table 1, entry 8). After 18 h, the $Pd/NiFe_2O_4$ catalyst was removed from the hot reaction mixture by applying an external magnet and the clear solution was filtered to remove any dispersed particles. The filtrate was concentrated and digested in the presence of concd HNO_3 + H_2O_2. The filtrate was then diluted to 50 mL using a volumetric flask and analyzed by atomic absorption spectroscopy (AAS) analysis. The Pd content detected in the filtrate was only 2.1 ppm.

We believe that the present one-pot synthesis of 4-arylquinolin-2(1*H*)-ones proceed via the pathway shown in Scheme 1. The *trans*-2-aminocinnamic acid formed during the first Heck reaction should not cyclize without first isomerizing.[12] Oxidative addition of Pd to the aryl halide added in the second step attached to an olefinic double bond of *trans*-2-aminocinnamic acid and gave alkyl palladium species **21**. Species **21** then underwent β-hydrogen elimination to produce species **22**, which generated product **7**. Alternatively, **7** also could be formed by the route via intermediate **23** followed by the β-hydrogen elimination.

The usefulness of our methodology was extended to the synthesis of biologically important maxi-K channel opener **4** using the $Pd/NiFe_2O_4$-catalyzed Heck reaction. The synthesis of **4** has been previously described by Hewawasam et al.[3a] in 2003 starting from *N*-Boc-protected 4-(trifluoromethyl)aniline, which involves more than 10 linear steps. The key step in their synthesis was a base-catalyzed cyclization of an appropriate *N*-acyl-*O*-aminobenzophenone precursor. Kappe

Table 2. One-pot synthesis of 4-aryl-2-quinolin-2(1*H*)-one derivatives.

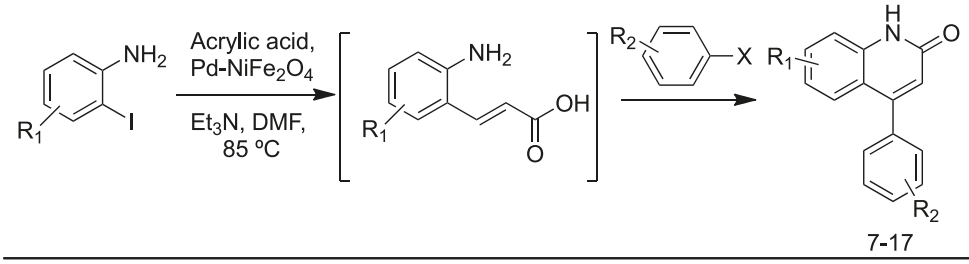

7-17

Entry	R_1	R_2	X	Yield[a]	Product
1	4-CF_3	H	I	75	**7**
2	4-CF_3	4-CH_3	I	77	**8**
3	4-CF_3	3-CH_3	I	71	**9**
4	4-CF_3	2-OCH_3	I	59	**10**
5	4-CF_3	3-OCH_3	I	61	**11**
6	4-CF_3	4-OCH_3	I	67	**12**
7	4-CF_3	H	Br	53	**7**
8	4-CF_3	4-OCH_3	Br	60	**12**
9	H	H	I	81	**13**
10	H	H	Br	47	**13**
11	H	H	Cl	—	**13**
12	H	H	$B(OH)_2$	—	**13**
13	H	3-OCH_3	I	64	**14**
14	H	4-OMe	I	65	**15**
15	H	3-CH_3	I	70	**16**
16	H	4-Me	I	67	**17**
17	H	4-OMe	Br	59	**16**

Note: Reaction conditions: substituted 2-iodoaniline (1.0 mmol), acrylic acid (1.05 mmol), triethylamine (3.25 mmol), Pd/$NiFe_2O_4$ (2.5 mol %), aryl halide (1.25 mmol), and DMF (4.0 mL) at 85 °C with a time duration of 18 h.

[a]Isolated yields after column chromatography.

Table 3. One-pot synthesis of 4-aryl-2*H*-chromen-2-one derivatives.

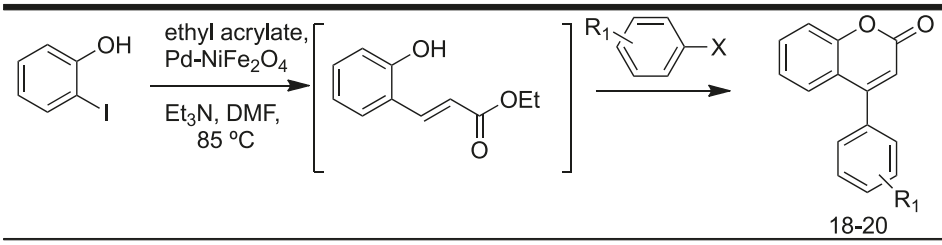

18-20

Entry	R_1	X	Yield[a]	Product
1	H	I	31	**18**
2	H	Br	13	**18**
3	4-CH_3	I	24	**19**
4	4-OCH_3	I	28	**20**

Note: Reaction conditions: 2-iodophenol (1.0 mmol), ethyl acrylate (1.05 mmol), triethylamine (3.25 mmol), Pd/$NiFe_2O_4$ (2.5 mol %), aryl halide (1.25 mmol), DMF (4.0 mL), over 18 h of heating at 85 °C.

[a]Isolated yields after column chromatography.

and co-workers[8e] reported the synthesis of **4** from *N*,*N*-bis[4-(trifluoromethyl)phenyl]malonide using Pd-catalyzed Suzuki and Heck reactions assisted by microwave, which involves six steps. Recently, Wu and co-workers[8f] also developed a general synthetic methodology for the synthesis of **4** in a combinatorial format starting from 3-bromo-4-trifloxy-quinolin-2(1*H*)-one. Although there are reported methods for the synthesis of **4**, none of the reported methods is practical, concise, or has a short synthetic route.

Our synthesis (Scheme 2) commenced with the consecutive Heck reaction of 4-(trifluoromethyl)-2-iodoaniline (**6**) with acrylic acid and 4-chloro-2-iodophenol was added in a second step in DMF at 85 °C using Pd/$NiFe_2O_4$ as the catalyst in the presence of TEA base. We observed the formation of the

Can. J. Chem. Downloaded from www.nrcresearchpress.com by South China Agricultural University on 09/19/12
For personal use only.

Can. J. Chem. Downloaded from www.nrcresearchpress.com by South China Agricultural University on 09/19/12
For personal use only.

Scheme 1. Catalytic cycle for the consecutive Heck reaction and cyclization step.

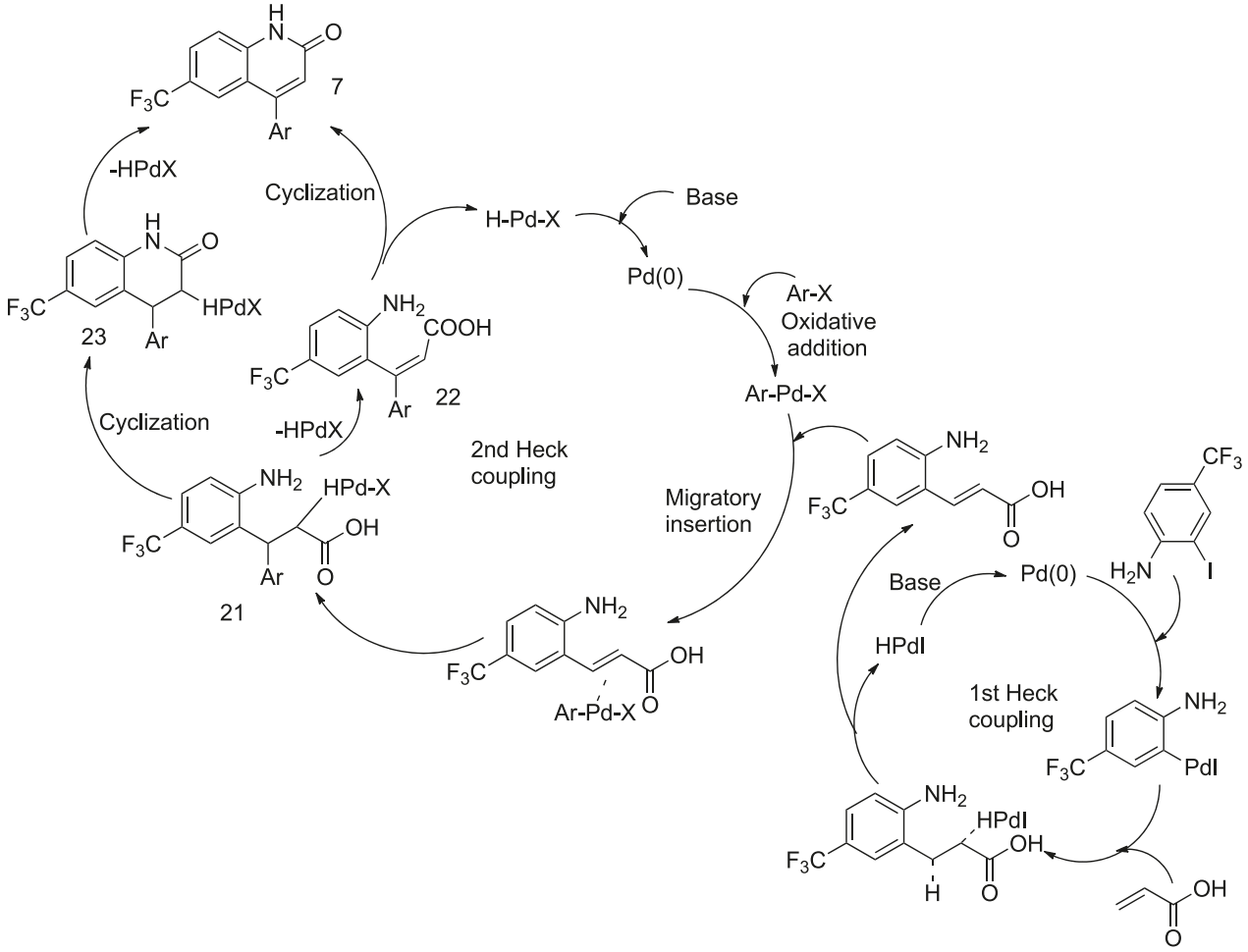

desired product (**24**) in 75% yield. The N- and O-methylation of **24** to **25** was carried out using methyl iodide in DMF at room temperature in the presence of K_2CO_3 base. We introduced the bromine moiety at the C-3 position of **25** by using our photochemical reaction approach with *N*-bromosuccinamide (NBS) in acetonitrile under UV irradiation.[13] The required 3-bromo product (**26**) was obtained in 78% yield. Further Heck vinylation of 3-bromoquinolinone (**26**) with ethyl acrylate in the presence of 2.5 mol% $Pd/NiFe_2O_4$ catalyst offered the target molecule **4** in its *N*-methyl-protected form, but in very poor yield (12%). To improve the yield of **4**, we varied the palladium precursor. The reaction carried out with $Pd(OAc)_2$ gave only 26% yield. To further improve the yield, the reaction was performed with $Pd(PPh_3)_4$ in an inert atmosphere, and this transformed into a 79% yield of the product **4**.[14]

Conclusion

In summary, we have presented a practical useful one-pot methodology for the synthesis of various 4-arylquinolin-2(1*H*)-ones from 2-iodoanilines in good yields. The heterogeneous $Pd/NiFe_2O_4$ catalyst efficiently catalyzed the successive Heck reaction in one pot and it could be easily separated from the reaction mixture by applying an external magnetic field. The scope of this methodology was successfully applied for the synthesis of biologically active 3-alkenyl-4-aryl-2-quinolinone from 4-(trifluoromethyl)-2-iodobenzamine in four linear steps in an overall yield of 42.5%.

Experimental section

General methods

Unless otherwise stated, all experiments were performed in an ambient atmosphere. All glasswares were acid and base washed and oven-dried before use. The catalytic reactions were carried out in 25 mL two-neck round-bottomed flasks equipped with a reflux condenser in an air atmosphere. The Pd salts/complexes, reactants, and solvents were obtained from Sigma-Aldrich/Merck or Spectochem and used as received without further purification or drying. The progress of the reaction was monitored by gas chromatography (GC; HP-5890, series II, equipped with a HP-5 capillary column and an FID detector) and TLC. The products were isolated by extractive work-up using ethyl acetate and were purified using silica gel (100–200) column chromatography. The products were characterized by GC–MS (Shimadzu QP-5050, DB-5 column, and FID detector), FTIR (8400 Shimadzu), and NMR (Varian 300 MHz spectrometer in $CDCl_3$ or DMSO-d_6 with TMS as an internal standard) spectroscopies. The Pd content was detected using an atomic absorption spectrophotometer (AAS), model No. Chemito AA-201.

Can. J. Chem. Downloaded from www.nrcresearchpress.com by South China Agricultural University on 09/19/12
For personal use only.

Scheme 2. Synthesis of the 3-alkenyl-4-aryl-2-quinolinone derivative.

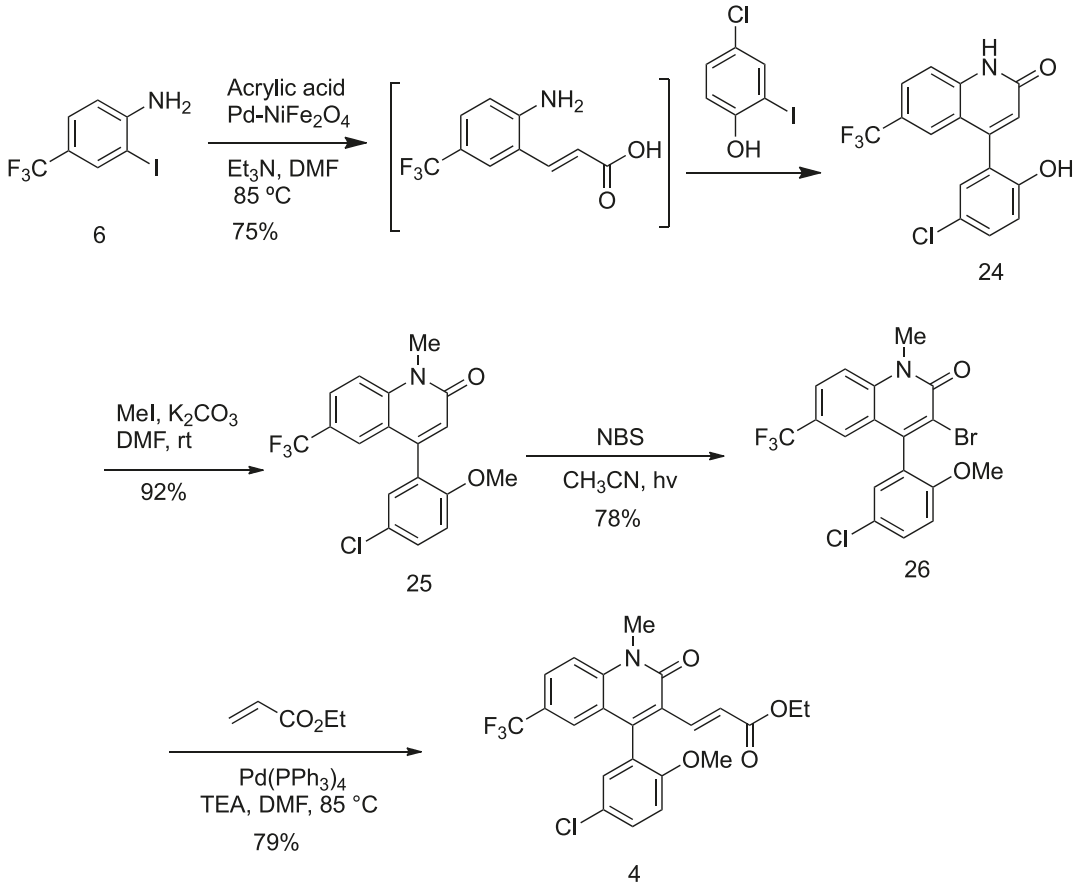

*General one-pot procedure for the synthesis of 4-arylquinolin-2(1*H*)-ones (products 7–17)*

To a 25 mL two-neck round-bottomed flask attached with a reflux condenser were added 2-iodo-aniline (1 mmol), acrylic acid (1.5 mmol), triethylamine (3.25 mmol), and Pd/$NiFe_2O_4$ (2.5 mol %) in 4 mL of DMF solvent. The reaction mixture was placed in a preheated oil bath at 85 °C for 30 min. The reactions were analyzed by GC and TLC. The reaction mixture (0.25 mL) was withdrawn by using a syringe, then diluted with water (1.0 mL), and extracted with ethyl acetate (1.0 mL). The ethyl acetate layer was separated, dried over sodium sulfate, and analyzed by GC. After the complete conversion of starting material, the new substrate, aryl halide (1.25 mmol), was added and the reaction continued for a further 16 h.

After the specified time of heating, the reaction mixture was cooled to room temperature and the catalyst was separated from the reaction mixture by applying an external magnet, and the clear solution was extracted with ethyl acetate (3 × 10 mL). The combined organic extracts were dried over anhydrous Na_2SO_4 and solvent was evaporated under reduced pressure. The crude product was then purified by silica gel column chromatography (hexane – ethyl acetate, 7:3). All products were analyzed and characterized by GC, GC–MS, IR, and NMR.

*General one-pot procedure for the synthesis of 4-aryl-2*H*-chromen-2-ones (products 18–20)*

To a 25 mL two-neck round-bottomed flask attached with a reflux condenser were added 2-iodophenol (1 mmol), ethyl acrylate (1.5 mmol), triethylamine (3.25 mmol), and Pd/$NiFe_2O_4$ (2.5 mol %) in 4 mL of DMF solvent. The reaction mixtures were heated at 85 °C for 30 min. The reactions were monitored by GC and TLC. The reaction mixture (0.25 mL) was withdrawn by using a syringe, then diluted with water (1.0 mL), and extracted with ethyl acetate (2 × 1.0 mL). The ethyl acetate layer was separated, dried over sodium sulfate, and analyzed by GC. After the complete conversion of starting material, the new substrate, aryl halide (1.25 mmol), was added and the reaction continued for a further 16 h.

After the specified time of heating, the reaction mixture was cooled to room temperature and the catalyst was separated from the reaction mixture by applying an external magnet, and the clear solution was extracted with ethyl acetate three times. The combined organic extracts were dried over anhydrous Na_2SO_4 and solvent was evaporated under reduced pressure. The crude product was then purified by silica gel column chromatography (hexane – ethyl acetate, 7:3). Purified products were analyzed and characterized by GC, GC–MS, IR, and NMR.

*Synthesis of 4-(5-chloro-2-methoxyphenyl)-6-(trifluoromethyl)-1-methylquinolin-2(1*H*)-one (25)*

To a solution of **24** (0.34 g, 1.0 mmol) in DMF (4.0 mL) were added methyl iodide (0.35 g, 2.2 mmol) and K_2CO_3 (0.44 g, 3.2 mmol) at ambient temperature. The reaction mixture was stirred for 3 h at room temperature and then diluted with ethyl acetate (3 × 20 mL). The organic layer was

Can. J. Chem. Downloaded from www.nrcresearchpress.com by South China Agricultural University on 09/19/12
For personal use only.

washed with water (2 × 10 mL) and brine (10 mL) and dried over anhydrous Na_2SO_4. The solvent was evaporated under reduced pressure, and the residue was purified by silica gel column chromatography using hexane – ethyl acetate (1:4) as the eluent to give **25** (0.36 g, 96% yield) as a white solid.

*Synthesis of 3-bromo-4-(5-chloro-2-methoxyphenyl)-6-(trifluoromethyl)-1-methyl quinolin-2(1*H*)-one (26)*

A mixture of **25** (0.37 g, 1.0 mmol) and NBS (0.35 g, 2.0 mmol) was stirred in 4 mL of acetonitrile under an N_2 atmosphere in the presence of a Philips HPL-N lamp (250 W, k_{max} = 200–600 nm) fitted with a water circulation arrangement at room temperature. After completion of the reaction (monitored by TLC and GC), the reaction mixture was quenched with cold water and extracted with ethyl acetate (3 × 25 mL). The organic phase was washed with water and brine, dried over anhydrous Na_2SO_4, and concentrated under reduced pressure to afford the crude product, which was purified by column chromatography over silica gel (60–120 mesh) using ethyl acetate and petroleum ether (1:2) as the eluent to give **26** (0.35 g, 78% yield) as a white solid.

*Synthesis of (2*E*)-ethyl 3-(4-(5-chloro-2-methoxyphenyl)-6-(trifluoromethyl)-1,2-dihydro-1-methyl-2-oxoquinolin-3-yl) acrylate (4)*

In an oven-dried 25 mL two-neck round-bottomed flask attached with a reflux condenser were added **26** (0.44 g, 1.0 mmol), $Pd(PPh_3)_4$ (0.06 g, 5.0 mol%), ethyl acrylate (0.30 g, 3.0 mmol), triethylamine (0.25 g, 2.5 mmol), and 5.0 mL of dry DMF. The reaction mixture was then heated at 85 °C for 12 h. After the completion of reaction (monitored by TLC), the heating was discontinued and the reaction was quenched by adding ice-water (25 mL). The whitish precipitate was then extracted with ethyl acetate (3 × 25 mL). The combined organic extracts was washed with brine (30 mL), dried over Na_2SO_4, and solvent was evaporated under reduced pressure. The crude product was purified by silica gel (60–120 mesh) column chromatography using ethyl acetate and petroleum ether (1:1) as the eluent to give **4** (0.37 g, 79% yield) as a white solid.

Characterization data for all products

*6-(Trifluoromethyl)-4-phenylquinolin-2(1*H*)-one (7)*

FTIR (KBr, cm^{-1}): 1265, 1475, 1573, 1685, 2918, 3315. ^{1}H NMR (DMSO-d_6) δ: 6.51 (s, 1H), 7.47–7.57 (m, 7H), 7.83 (d, 1H, J = 9.8 Hz), 12.20 (s, 1H). ^{13}C NMR (DMSO-d_6) δ: 116.0, 116.9, 118.0, 122.6, 123.1(q), 126.8, 128.5, 128.8, 129.1, 135.7, 139.8, 141.7, 150.9, 161.2. MS (EI): *m*/*z* 289 (M^+). Anal. calcd for $C_{16}H_{10}F_3NO$: C 66.44, H 3.48, N 4.84; found: C 66.47, H 3.95, N 4.83.

*6-(Trifluoromethyl)-4-*p*-tolylquinolin-2(1*H*)-one (8)*

FTIR (KBr, cm^{-1}): 1265, 1508, 1564, 1658, 3007, 3321. ^{1}H NMR (DMSO-d_6) δ: 2.30 (s, 3H), 6.39 (s, 1H), 7.28 (s, 4H), 7.45 (d, 1H, J = 8.8 Hz), 7.52 (s, 1H), 7.76 (d, 1H, J = 8.2 Hz), 12.11 (s, 1H). ^{13}C NMR (DMSO-d_6) δ: 20.7, 116.8, 118.0, 122.4, 123.1(q), 125.0, 126.7, 128.4, 129.4, 132.8, 138.7, 141.7, 150.9, 161.2, 168.7. MS (EI): *m*/*z* 303 (M^+). Anal. calcd for $C_{17}H_{12}F_3NO$: C 67.32, H 3.99, N 4.62; found: C 67.33, H 4.10, N 4.63.

*6-(Trifluoromethyl)-4-*m*-tolylquinolin-2(1*H*)-one (9)*

FTIR (KBr, cm^{-1}): 1105, 1577, 1614, 1668, 3005, 3404. ^{1}H NMR (DMSO-d_6) δ: 2.50 (s, 3H) 6.61 (s, 1H), 7.37–7.47 (m, 3H), 7.56 (t, 1H) 7.68 (t, 1H) 7.96 (dd, 1H, J = 8.2 and 1.7 Hz), 12.35 (s, 1H). ^{13}C NMR (DMSO-d_6) δ: 20.8, 116.9, 118.0, 121.8, 122.2, 122.5, 123.2(q), 125.6, 126.7, 128.6, 129.0, 129.7, 135.7, 138.3, 141.7, 151.0, 161.3. MS (EI): *m*/*z* 303 (M^+). Anal. calcd for $C_{17}H_{12}F_3NO$: C 67.32, H 3.99, N 4.62; found: C 67.32, H 4.08, N 4.62.

*6-(Trifluoromethyl)-4-(*o*-methoxyphenyl)quinolin-2(1*H*)-one (10)*

FTIR (neat, cm^{-1}): 1070, 1371, 1494, 1579, 1658, 3306. ^{1}H NMR (DMSO-d_6) δ: 3.72 (s, 3H), 6.97 (t, 1H, J = 7.4 Hz), 7.09 (d, 1H, J = 8.2 Hz), 7.27 (d, 1H, J = 7.4 Hz), 7.37 (t, 1H, J = 8.2 and 7.4 Hz), 7.47 (d, 1H, J = 8.5 Hz), 7.80 (d, 1H, J = 8.8 Hz), 7.90 (s, 1H), 8.13 (s, 1H), 12.17 (s, 1H). ^{13}C NMR (DMSO-d_6) δ: 55.8, 111.3, 115.6, 118.8, 120.0, 121.9, 122.3 (q), 125.1, 125.3, 126.1, 129.5, 130.7, 132.3, 138.3, 140.8, 156.9, 160.8. MS (EI): *m*/*z* 319 (M^+). Anal. calcd for $C_{17}H_{12}F_3NO_2$: C 63.95, H 3.79, N 4.39; found: C 63.97, H 3.88, N 4.62.

*6-(Trifluoromethyl)-4-(*m*-methoxyphenyl)quinolin-2(1*H*)-one (11)*

FTIR (KBr, cm^{-1}): 1074, 1319, 1473, 1568, 1674, 3007, 3147. ^{1}H NMR (DMSO-d_6) δ: 3.80 (s, 3H), 6.55 (s, 1H), 7.04–7.12 (m, 3H), 7.45–7.63 (m, 3H), 7.85 (d, 1H, J = 8.2 Hz), 12.24 (s, 1H). ^{13}C NMR (DMSO-d_6) δ: 55.6, 114.5, 115.2, 117.3, 118.4, 121.2, 123.0(q), 123.7, 127.2, 130.4, 137.5, 142.2, 151.2, 159.9, 161.7. MS (EI): *m*/*z* 319 (M^+). Anal. calcd for $C_{17}H_{12}F_3NO_2$: C 63.95, H 3.79, N 4.39; found: C 63.97, H 4.14, N 4.37.

*6-(Trifluoromethyl)-4-(*p*-methoxyphenyl)quinolin-2(1*H*)-one (12)*

FTIR (KBr, cm^{-1}): 1124, 1317, 1510, 1608, 1668, 2841, 3151. ^{1}H NMR (DMSO-d_6) δ: 3.84 (s, 3H), 6.48 (s, 1H), 7.13 (d, 2H, J = 7.2 Hz), 7.45 (d, 2H, J = 7.2 Hz), 7.56 (d, 1H, J = 8.3 Hz), 7.67 (s, 1H), 7.86 (d, 1H, J = 8.6 Hz), 12.19 (s, 1H). ^{13}C NMR (DMSO-d_6) δ: 55.1, 114.2, 116.8, 118.1, 121.7, 122.2, 123.1(q), 125.8, 126.7, 127.8, 130.0, 141.7, 150.6, 159.8, 161.2. MS (EI): *m*/*z* 319 (M^+). Anal. calcd for $C_{17}H_{12}F_3NO_2$: C 63.95, H 3.79, N 4.39; found: C 63.94, H 3.90, N 4.07.

*4-Phenylquinolin-2(1*H*)-one (13, 5855-57-2)[8a]*

FTIR (neat, cm^{-1}): 1072, 1265, 1433, 1496, 1568, 1654, 3306. ^{1}H NMR (DMSO-d_6) δ: 6.30 (s, 1H), 7.03–7.08 (m, 1H), 7.27–7.32 (m, 2H), 7.37–7.44 (m, 6H) 11.79 (s, 1H). MS (EI): *m*/*z* 221 (M^+).

*4-(3-Methoxyphenyl)quinolin-2(1*H*)-one (14, 65848-66-0)[8a]*

FTIR (neat, cm^{-1}): 1045, 1214, 1388, 1432, 1574, 1601, 1653, 2837, 3310. ^{1}H NMR (DMSO-d_6) δ: 3.80 (s, 3H), 6.41 (s, 1H), 7.00–7.15 (m, 4H), 7.39–7.54 (m, 4H), 11.89 (s, 1H). MS (EI): *m*/*z* 251 (M^+).

*4-(4-Methoxyphenyl)quinolin-2(1*H*)-one (15, 37118-72-2)[8a]*

FTIR (neat, cm^{-1}): 1029, 1170, 1251, 1506, 1610, 1674, 2962, 3300.^{1}H NMR (DMSO-d_6): δ 3.81 (s, 3H), 6.33 (s, 1H),

Can. J. Chem. Downloaded from www.nrcresearchpress.com by South China Agricultural University on 09/19/12
For personal use only.

7.05–7.14 (m, 3H), 7.35–7.52 (m, 5H), 11.79 (s, 1H). MS (EI): *m/z* 251 (M^+).

4*-m-*Tolylquinolin-2(1H)-one (16, 92909-30-4)[8c]

FTIR (neat, cm^{-1}): 1038, 1160, 1271, 1385, 1432, 1547, 1606, 1654, 2836, 3316. ^1H NMR (DMSO-d_6) δ: 2.36 (s, 3H), 6.34 (s, 1H), 7.08–7.13 (m, 1H), 7.20–7.41 (m, 7H), 11.85 (s, 1H). MS (EI): *m/z* 235 (M^+).

4*-p-*Tolylquinolin-2(1H)-one (17, 106015-76-3)[8c]

FTIR (neat, cm^{-1}): 1039, 1383, 1433, 1502, 1608, 1664, 2850, 3319. ^1H NMR (DMSO-d_6) δ: 2.40 (s, 3H), 6.35 (s, 1H), 7.13 (t, 1H, J = 7.7 and 7.9 Hz), 7.35–7.41 (m, 6H), 7.52 (t, 1H, J = 7.9 and 7.2 Hz), 11.82 (s, 1H). MS (EI): *m/z* 235 (M^+).

4-Phenyl-2H-chromen-2-one (18, 15185-05-4)[10]

FTIR (neat, cm^{-1}): 1365, 1444, 1491, 1560, 1606, 1734, 3072. ^1H NMR ($CDCl_3$) δ: 6.36 (s, 1H), 7.22 (t, 1H, J = 7.7 Hz), 7.40–7.57 (m, 8H). MS (EI): *m/z* 222 (M^+).

4*-p-*Tolyl-2H-chromen-2-one (19, 76103-24-7)[10]

FTIR (neat, cm^{-1}): 1365, 1510, 1608, 1726, 3070. ^1H NMR ($CDCl_3$) δ: 2.45 (s, 3H), 6.36 (s, 1H), 7.20 (d, 1H, J = 7.6 Hz), 7.23 (d, 1H, J = 7.6 Hz), 7.34 (m, 4H), 7.54 (m, 2H). MS (EI): *m/z* 236 (M^+).

4*-(4-Methoxyphenyl)-2H-*chromen-2-one (20, 170456-76-5)[10]

FTIR (neat, cm^{-1}): 1294, 1599, 1491, 1670, 1757, 3072.^1H NMR ($CDCl_3$) δ: 3.90 (s, 3H), 6.36 (s, 1H), 7.05 (d, 2H, J = 8.5 Hz), 7.25 (t, 1H), 7.42 (m, 3H), 7.56 (t, 2H, J = 8.5 Hz). MS (EI): *m/z* 252 (M^+).

***4*-(5-Chloro-2-hydroxyphenyl)-6-(trifluoromethyl)quinolin-2(1H)-one (24)**

FTIR (neat, cm^{-1}): 1437, 1558, 1653, 3311. ^1H NMR (DMSO-d_6) δ: 6.49 (s, 1H), 7.02 (d, 1H, J = 8.8 Hz), 7.30–7.35 (m, 3H), 7.52 (d, 1H, J = 8.8 Hz), 7.81 (d, 1H, J = 8.5 Hz), 10.11 (s, 1H), 12.2 (s, 1H). ^{13}C NMR (DMSO-d_6) δ: 116.5, 117.3, 117.9, 121.6, 122.0, 122.8, 123.6(q), 124.6, 126.4, 126.5, 129.6, 130.1, 141.1, 147.9, 153.2, 161.4. MS (EI): *m/z* 339 (M^+) 341 (M^++2). Anal. calcd for $C_{16}H_9ClF_3NO_2$: C 56.57, H 2.67, N 4.12; found: C 56.59, H 2.87, N 4.17.

***4*-(5-Chloro-2-methoxyphenyl)-6-(trifluoromethyl)-1-methylquinolin-2(1H)-one (25)**

FTIR (neat, cm^{-1}): 1305, 1494, 1602, 1674, 2845, 3055.^1H NMR (DMSO-d_6) δ: 3.68 (s, 3H), 3.71 (s, 3H), 6.66 (s, 1H), 7.24 (s, 1H), 7.27 (d, 1H, J = 7.0 Hz), 7.40 (d, 1H, J = 2.4 Hz), 7.58 (dd, 1H, J = 8.8 and 2.4 Hz), 7.79 (d, 1H, J = 8.8 Hz), 7.94 (d, 1H, J = 8.8 Hz). ^{13}C NMR (DMSO-d_6) δ: 29.4, 55.8, 113.5, 116.4, 119.0, 122.9, 123.6, 124.7, 125.9, 126.8, 129.7, 130.5, 141.8, 146.1, 155.0, 160.5. MS (EI): *m/z* 367 (M^+), 369 (M^+ + 2). Anal. calcd for $C_{18}H_{13}ClF_3NO_2$: C 58.79, H 3.56, N 3.81; found: C 58.81, H 3.68, N 3.81.

***3*-Bromo-4-(5-chloro-2-methoxyphenyl)-6-(trifluoromethyl)-1-methylquinolin-2(1H)-one (26)**

FTIR (neat, cm^{-1}): 1120, 1311, 1491, 1654, 2848, 2941. ^1H NMR (DMSO-d_6) δ: 3.36 (s, 3H), 3.81 (s, 3H), 7.19 (s, 1H), 7.29 (d, 1H, J = 8.8 Hz), 7.35 (d, 1H, J = 2.4 Hz), 7.58 (dd, 1H, J = 2.4 and 8.8 Hz), 7.84 (d, 1H, J = 8.8 Hz), 7.97 (d, 1H, J = 8.8 Hz). ^{13}C NMR (DMSO-d_6) δ: 31.2, 56.0, 113.8, 116.7, 119.5, 121.0, 122.6, 123.0, 123.3 (q), 124.5, 126.1, 127.0, 129.1, 130.6, 140.7, 145.8, 154.5, 157.1. MS (EI): *m/z* 445 (M^+), 447 (M^+ + 2), 449 (M^+ + 4). Anal. calcd for $C_{18}H_{12}BrClF_3NO_2$: C 48.40, H 2.71, N 3.14; found: C 48.35, H 3.02, N 3.18.

(2E)-Ethyl-3-(4-(5-chloro-2-methoxyphenyl)-6-(trifluoromethyl)-1,2-dihydro-1-methyl-2-oxoquinolin-3-yl) acrylate (4)

FTIR (neat, cm^{-1}): 1132, 1286, 1371, 1494, 1620, 1662, 1695, 3111.^1H NMR ($CDCl_3$) δ: 1.25 (t, 3H), 3.69 (s, 3H), 3.84 (s, 3H), 4.16 (q, 2H), 7.02 (d, 1H, J = 9.1 Hz), 7.08 (d, 1H, J = 2.4 Hz), 7.27 (s, 1H), 7.35 (d, 2H, J = 2.4 Hz), 7.58 (m, 2H), 7.80 (d, 1H, J = 9.1 Hz). ^{13}C NMR (75 MHz, $CDCl_3$, TMS) δ: 14.1, 30.1, 55.9, 60.3, 112.8, 114.8, 120.0, 124.1, 124.4, 125.1, 125.3, 125.4, 125.5, 126.1, 127.5(q), 130.1, 130.8, 137.4, 141.1, 147.0, 155.0, 160.4, 167.5. MS (EI): *m/z* 465 (M^+), 467 (M^+ + 2). Anal. calcd for $C_{23}H_{19}ClF_3NO_4$: C 59.30, H 4.11, N 3.01; found: C 59.29, H 4.26, N 3.08.

Acknowledgment

The authors are thankful to the Department of Science and Technology (DST) and Council of Scientific and Industrial Research (CSIR), New Delhi, India for their financial support.

References

(1) (a) Gurjar, M. K.; Sharma, G. V. M.; Ilangovan, A.; Narayanan, V. US Patent 6,191,279, 2001; (b) Thal, C.; Boye, O.; Guenard, D.; Potier, P. Int. Patent WO 9002733, 1990; (c) Hewawasam, P.; Starrett, J. E., Jr.; Swartz, S. G. Int. Patent WO 9909983, 1999; (d) Shogaki, T.; Toyoda, H.; Kakita, T.; Furukawa, M.; Nakatsugi, S.; Masai, E.; Yashima, T.; Ueda, I. Patent EP 577325, 1994; (e) Suzuki, K.; Fujiwara, S.; Machii, D.; Ochifuji, N.; Takai, H.; Oono, T.; Furuta, S.; Yamada, K. Patent JP 06092939, 1994; (f) Komatsu, M.; Uchida, M.; Nishi, T.; Ishikawa, H.; Kuroda, T.; Tsuji, K. Patent JP 08295673, 1996.

(2) (a) Goodell, J. R.; Puig Basagoiti, F.; Forshey, B. M.; Shi, P. Y.; Ferguson, D. M. *J. Med. Chem.* **2006**, *49* (6), 2127. doi:10.1021/jm051229y; (b) Arcadi, A.; Cacchi, S.; Fabrizi, G.; Manna, F.; Pace, P. *Synlett* **1998**, *1998* (4), 446. doi:10.1055/s-1998-1656; (c) Godard, A.; Fourquez, J. M.; Tamion, R.; Marsais, F.; Queguiner, G. *Synlett* **1994**, *1994* (4), 235. doi:10.1055/s-1994-22807; (d) Anzini, M.; Cappelli, A.; Vomero, S. *J. Heterocycl. Chem.* **1991**, *28* (7), 1809. doi:10.1002/jhet.5570280727.

(3) (a) Hewawasam, P.; Fan, W.; Ding, M.; Flint, K.; Cook, D.; Goggins, G. D.; Myers, R. A.; Gribkoff, V. K.; Boissard, C. G.; Dworetzky, S. I.; Starret, J. E.; Lodge, N. J. *J. Med. Chem.* **2003**, *46* (14), 2819. doi:10.1021/jm030005h; (b) Cappelli, A.; Pericot Mohr, G.; Gallelli, A.; Rizzo, M.; Anzini, M.; Vomero, S.; Mennuni, L.; Ferrari, F.; Makovec, F.; Menziani, M. C.; De Benedetti, P. G.; Giorgi, G. *J. Med. Chem.* **2004**, *47* (10), 2574. doi:10.1021/jm031100t; (c) Angibaud, P. R.; Venet, M. G.; Filliers, W.; Broeckx, R.; Ligny, Y. A.; Muller, P.; Poncelet, V. S.; End, D. W. *Eur. J. Org. Chem.* **2004**, *2004* (3), 479. doi:10.1002/ejoc.200300538; (d) Andresen, B. M.;

Can. J. Chem. Downloaded from www.nrcresearchpress.com by South China Agricultural University on 09/19/12
For personal use only.

Couturier, M.; Cronin, B.; Docchio, M.; Ewing, M. D.; Guinn, M.; Hawkins, J. M.; Jasys, V. J.; LaGreca, S. D.; Lyssikatos, J. P.; Moraski, G.; Ng, K.; Raggon, J. W.; Stewart, A. M.; Tickner, D. L.; Tucker, J. L.; Urban, F. J.; Vazquez, E.; Wei, L. *Org. Process Res. Dev.* **2004**, *8* (4), 643. doi:10.1021/op049935g; (e) Hewawasam, P.; Fan, W.; Cook, D. A.; Newberry, K. S.; Boissard, C. G.; Gribkoff, V. K.; Starrett, J.; Lodge, N. J. *Bioorg. Med. Chem. Lett.* **2004**, *14* (17), 4479. doi:10.1016/j.bmcl.2004.06.051.

(4) (a) For recent papers, see Cheng, P.; Zhang, Q.; Ma, Y. B.; Jiang, Z.-Y.; Zhang, X. M.; Zhang, F. X.; Chen, J. J. *Bioorg. Med. Chem. Lett.* **2008**, *18* (13), 3787. doi:10.1016/j.bmcl.2008.05.065; (b) Capell, B. C.; Olive, M.; Erdos, M. R.; Cao, K.; Faddah, D. A.; Tavarez, U. L.; Conneely, K. N.; Qu, X.; San, H.; Ganesh, S. K.; Chen, X.; Avallone, H.; Kolodgie, F. D.; Virmani, R.; Nabel, E. G.; Collins, F. S. *Proc. Natl. Acad. Sci. U.S.A.* **2008**, *105* (41), 15902. doi:10.1073/pnas.0807840105; (c) Wall, M. J.; Chen, J.; Meegalla, S.; Ballentine, S. K.; Wilson, K. J.; DesJarlais, R. L.; Schubert, C.; Chaikin, M. A.; Crysler, C.; Petrounia, I. P.; Donatelli, R. R.; Yurkow, E. J.; Boczon, L.; Mazzulla, M.; Player, M. R.; Patch, R. J.; Manthey, C. L.; Molloy, C.; Tomczuk, B.; Illig, C. R. *Bioorg. Med. Chem. Lett.* **2008**, *18* (6), 2097. doi:10.1016/j.bmcl.2008.01.088.

(5) (a) Kobayashi, Y.; Harayama, T. *Org. Lett.* **2009**, *11* (7), 1603. doi:10.1021/ol900255g; (b) Bracken, A.; Pocker, A.; Raistrick, H. *Biochem. J.* **1954**, *57*, 587; (c) Mohammed, Y. S.; Luckner, M. *Tetrahedron Lett.* **1963**, *4* (28), 1953. doi:10.1016/S0040-4039(01)90948-7; (d) Heguy, A.; Cai, P.; Meyn, P.; Houck, D.; Russo, S.; Michitsch, R.; Pearce, C.; Katz, B.; Bringmann, G.; Feineis, D.; Taylor, D. L.; Tyms, A. S. *Antivir. Chem. Chemother.* **1998**, *9*, 149.

(6) (a) Huang, L.; Hsieh, M.; Teng, C.; Lee, K.; Kuo, S. *Bioorg. Med. Chem.* **1998**, *6* (10), 1657. doi:10.1016/S0968-0896(98)00141-2; (b) Beier, N.; Labitzke, E.; Mederski, W. W. K. R.; Radunz, H.-E.; Rauschenbach-Ruess, K.; Schneider, B. *Heterocycles* **1994**, *39* (1), 117. doi:10.3987/COM-93-S(B)5; (c) Hauser, C. R.; Reynolds, G. A. *J. Am. Chem. Soc.* **1948**, *70* (7), 2402. doi:10.1021/ja01187a025; (d) Staskun, B. *J. Org. Chem.* **1964**, *29* (5), 1153. doi:10.1021/jo01028a038; (e) Koelsch, C. F.; Britain, J. W. *J. Org. Chem.* **1959**, *24* (10), 1551. doi:10.1021/jo01092a041; (f) Kaslow, C. E.; Cook, D. J. *J. Am. Chem. Soc.* **1945**, *67* (11), 1969. doi:10.1021/ja01227a032; (g) Hodgkinson, A. J.; Staskun, B. *J. Org. Chem.* **1969**, *34* (6), 1709. doi:10.1021/jo01258a039; (h) Park, K. K.; Lee, J. J. *Tetrahedron* **2004**, *60* (13), 2993. doi:10.1016/j.tet.2004.02.001; (i) Wang, J.; Discordia, R. P.; Crispino, G. A.; Li, J.; Grosso, J. A.; Polniaszek, R.; Truc, V. C. *Tetrahedron Lett.* **2003**, *44* (22), 4271. doi:10.1016/S0040-4039(03)00889-X; (j) Koltunov, K. Y.; Walspurger, S.; Sommer, J. *Chem. Commun. (Camb.)* **2004**, (15), 1754. doi:10.1039/b404074k.

(7) (a) Pd-catalyzed synthesis of 2-quinolinones; see, for example, Tadd, A. C.; Matsuno, A.; Fielding, M. R.; Willis, M. C. *Org. Lett.* **2009**, *11* (3), 583. doi:10.1021/ol802624e; (b) Liu, Z.; Shi, C.; Chen, Y. *Synlett* **2008**, (11), 1734; (c) Kadnikov, D. V.; Larock, R. C. *J. Org. Chem.* **2004**, *69* (20), 6772. doi:10.1021/jo049149+; (d) Mori, M.; Chiba, K.; Ohta, N.; Ban, Y. *Heterocycles* **1979**, *13* (1), 329. doi:10.3987/S-1979-01-0329; (e) Cortese, N. A.; Ziegler, C. B., Jr; Hrnjez, B. J.; Heck, R. F. *J. Org. Chem.* **1978**, *43* (15), 2952. doi:10.1021/jo00409a004.

(8) (a) Pd-catalyzed functionalizations of 2-quinolinones; see, for example, Inamoto, K.; Saito, T.; Hiroya, K.; Doi, T. *J. Org. Chem.* **2010**, *75* (11), 3900. doi:10.1021/jo100557s; (b) Xu, C.; Yang, L.; Bhandari, A.; Holmes, C. P. *Tetrahedron Lett.* **2006**, *47* (28), 4885. doi:10.1016/j.tetlet.2006.05.032; (c) Battistuzzi, G.; Bernini, R.; Cacchi, S.; De Salve, I.; Fabrizi, G. *Adv. Synth. Catal.* **2007**, *349* (3), 297. doi:10.1002/adsc.200600342; (d) Bernini, R.; Cacchi, S.; Salve, I. D.; Fabrizi, G. *Synlett* **2006**, *18*, 2947; (e) Glasnov, T. N.; Stadlbauer, W.; Kappe, C. O. *J. Org. Chem.* **2005**, *70* (10), 3864. doi:10.1021/jo0502549; (f) Wang, Z.; Wang, B.; Wu, J. *J. Comb. Chem.* **2007**, *9* (5), 811. doi:10.1021/cc7000937; (g) Bernini, R.; Cacchi, S.; Fabrizi, G.; Sferrazza, A. *Heterocycles* **2006**, *69* (1), 99. doi:10.3987/COM-06-S(O)30.

(9) (a) Borhade, S. R.; Waghmode, S. B. *Ind. J. Chem., Sect. B* **2008**, *47*, 1549; (b) Baruwati, B.; Guin, D.; Manorama, S. V. *Org. Lett.* **2007**, *9* (26), 5377. doi:10.1021/ol702064x; (c) Waghmode, S. B.; Wagholikar, S. G.; Sivasanker, S. *Bull. Chem. Soc. Jpn.* **2003**, *76* (10), 1989. doi:10.1246/bcsj.76.1989; (d) Borhade, S. R.; Waghmode, S. B. *Tetrahedron Lett.* **2008**, *49* (21), 3423. doi:10.1016/j.tetlet.2008.03.109.

(10) Yamamoto, Y.; Kirai, N. *Org. Lett.* **2008**, *10* (24), 5513 and references cited therein. doi:10.1021/ol802239n.

(11) Crudden, C. M.; Sateesh, M.; Lewis, R. *J. Am. Chem. Soc.* **2005**, *127* (28), 10045. doi:10.1021/ja0430954.

(12) Horaguchi, T.; Hosokawa, N.; Tanemura, K.; Suzuki, T. *J. Heterocyclic Chem.* **2002**, *39* (1), 61. doi:10.1002/jhet.5570390108.

(13) (a) Arbuj, S. S.; Waghmode, S. B.; Ramaswamy, A. V. *Tetrahedron Lett.* **2007**, *48* (8), 1411. doi:10.1016/j.tetlet.2006.12.101; (b) Chhattise, P. K.; Ramaswamy, A. V.; Waghmode, S. B. *Tetrahedron Lett.* **2008**, *49* (1), 189. doi:10.1016/j.tetlet.2007.10.126.

(14) $Pd(PPh_3)_4$ was freshly prepared and the reaction was conducted in an inert atmosphere: Sunagawa, M.; Matsumura, H.; Kitamura, Y. US Patent 5,226,186, 1993.

A new chemosensor based on rhodamine 101 hydrazone for Cu (II) in the red region

Puhui Xie, Fengqi Guo, Changshan Li, and Yue Xiao

Can. J. Chem. Downloaded from www.nrcresearchpress.com by South China Agricultural University on 09/19/12
For personal use only.

Abstract: A new chemosensor based on the spirolactam form of rhodamine 101 hydrazone (**III**) is found to exhibit a reversible colorimetric response toward Cu^{2+} in aqueous solutions in a selective, sensitive and rapid manner because of a formation of a Cu(II)-**III** complex. The dominating absorption maximum at 584 nm is uniquely red-shifted among rhodamine chemosensors toward Cu^{2+}. The fluorescence of **III** can be detected in a low concentration of Cu^{2+}. The results revealed that **III** is a good colorimetric sensor to Cu^{2+} in the red region.

Key words: chemosensor, rhodamine 101 hydrazone, naked-eye recognition, metal ions.

Résumé : On a observé qu'un nouveau senseur chimique à base de la forme spirolactame de l'hydrazone de la rhodamine 101 (**III**) donne lieu à une réponse colorimétrique réversible vis-à-vis de l'ion Cu^{2+} en solutions aqueuses et que cette réponse est sélective, sensible et rapide en raison de la formation d'un complexe Cu(II)-**III**. Par comparaison avec les senseurs chimiques dérivés de la rhodamine vis-à-vis du Cu^{2+}, le maximum d'absorption dominant à 584 nm est uniquement déplacé vers le rouge. La fluorescence du composé **III** peut être détectée à de faibles concentrations de Cu^{2+}. Les résultats révèlent que le composé **III** est un bon senseur colorimétrique pour le Cu^{2+} dans la région du rouge.

Mots-clés : senseur chimique, hydrazone de la rhodamine I01, reconnaissance à l'oeil nu, ions métalliques.

[Traduit par la Rédaction]

Introduction

The design and synthesis of new chemosensors for monitoring ionic species, especially heavy and transition metal cations in aqueous solutions, is of great interest because of their significance in chemical, biological, and environmental analyses.[1–3] Much attention has been paid to the design of fluorescent chemosensors, because they allow nondestructive and real-time detection of ionic species with high sensitivity by a fluorescent enhancement or quenching response.[4,5] Although Cu^{2+} plays important roles in biological process,[6] it is an environmental pollutant at high concentrations.[7] Therefore, efforts have been made to design and develop probes for the detection of Cu^{2+} in biological, toxicological, and environmental systems. Current methods for copper screening, including atomic absorption spectrometry (AAS),[8] inductively coupled plasma mass spectrometry (ICP-MS),[9] and inductively coupled plasma atomic emission spectrometry (ICP-AES),[10] often require expensive and sophisticated instrumentation or complex sample-preparation steps. Colorimetric sensing of copper ions would be more desirable, because it is less labor-intensive and highly sensitive.

Rhodamine-based dyes have found applications in complicated biological systems, such as molecular probes[7] and chemosensors,[11,12] because of their excellent spectroscopic properties with large molar extinction coefficient and high fluorescence quantum yield. The spirolactam forms of rhodamine derivatives are nonfluorescent and colorless, whereas their ring-opening forms give rise to strong fluorescence and a pink or red color.[13] Usually, the ring-opening process happens through affecting a carbonyl group in a spirolactone or spirolactam moiety by suitable metal ions or protons (Scheme 1). Consequently, addition of a specific metal ion to an appropriate host, bearing a spirolactam ring, can cause color change as well as fluorescent change of the host. Recently, the spirolactam forms for the derivatives of rhodamine B or rhodamine G have been utilized for the detection of heavy metal ions, such as Hg^{2+},[14–18] Cu^{2+},[19–23] Fe^{3+},[24] Cr^{3+} ,[25–27] and Pb^{2+}, [27] etc., in aqueous solutions via ring-opening processes of spirolactam amides or hydrazides. These cation sensors, based on rhodamine derivatives, can be potentially applied in biological and silica-mesoporous hybrid materials.[28]

However, the fluorescence enhancement or quenching based on rhodamine derivatives in the presence of Cu^{2+} occurring in the longer absorption or emission wavelength region has seldom been reported. In our previous work, rhodamine 101 hydrazide exhibited an irreversible colorimetric and fluorogenic response toward Cu^{2+} in aqueous solution in the red region.[29] The longer emission wavelengths (over 550 nm) are often preferred for the analyte, to avoid the influence of background fluorescence (below 500 nm).[30] As the absorption enhancement of a host in the presence of guests in the red region facilitates naked-eye recognition, spirolactam forms of rhodamine 101 hydrazones **III** and **IV** are

Received 26 March 2011. Accepted 19 July 2011. Published at www.nrcresearchpress.com/cjc on 13 October 2011.

P. Xie, C. Li, and Y. Xiao. College of Sciences, Henan Agricultural University, Zhengzhou 450002, P. R. China.
F. Guo. Department of Chemistry, Zhengzhou University, Zhengzhou 450001, P. R. China.

Corresponding author: Puhui Xie (e-mail: ph_xie@yahoo.com) and Fengqi Guo (e-mail: fqguo@zzu.edu.cn).

Can. J. Chem. Downloaded from www.nrcresearchpress.com by South China Agricultural University on 09/19/12
For personal use only.

Scheme 1. Ring-opening process for spirolactam form of rhodamine derivatives by proton or metal ions.

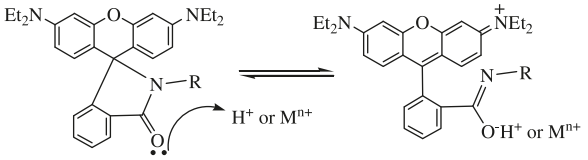

synthesized to develop reversible Cu^{2+} chemosensor in the red region in aqueous solutions. The opening of the spirolactam forms may be realized by the interaction of the Cu^{2+} with the corresponding N and O atoms in these compounds. The structural rigidity introduced by multiple *n*-propylene bridges of rhodamine 101 moieties can shift the absorption and emission maxima to longer wavelengths, with higher molar extinguishing coefficients and higher quantum yields compared with rhodamine B.[31]

Experimental

Synthesis of spirolactam rhodamine 101 derivatives III and IV

Synthesis of compound III

II was synthesized using a modified procedure from Yang et al.[32] It was recently synthesized in our group.[29] As shown in Scheme 2, 0.0892 g (0.18 mmol) of compound **II** and 0.5 mL (0.19 mmol) of 2-hydroxybenzaldehyde were dissolved in 15 mL of anhydrous ethanol. The mixture was refluxed under N_2 for 10 h. The cooled solution was partially removed upon rotary evaporation and allowed to stand overnight at 0 °C. The resulting precipitate was re-crystallized three times with ethanol to afford a pale-yellow solid (83 mg, 76%). IR (KBr, cm^{-1}, Fig. S4 in Supplementary data): 1687.83 (C=O); 1657.22 (C=N); 3433.98 (OH). ^1H NMR (DMSO-d_6, see Fig. S2 in Supplementary data) δ (ppm): 1.73 (t, 4H); 1.95 (t, 4H); 2.40 (m, 4H); 2.87 (m, 4H); 3.05 (m, 4H); 3.11 (m, 4H); 5.94 (s, 2H); 6.81 (m, 2H); 7.08 (d, 1H); 7.22 (m, 1H); 7.28 (d, 1H); 7.60 (m, 2H); 7.88 (d, 1H), 8.92 (s, 1H); 10.43 (s, 1H). ^{13}C NMR (DMSO-d_6, see Fig. S3 in Supplementary data) δ (ppm): 19.01, 21.16, 21.24, 21.74, 21.92, 27.01, 49.09, 49.52, 66.50, 105.46, 107.60, 116.95, 117.43, 119.37, 119.88, 123.46, 123.59, 129.11, 132.08, 143.97, 148.16, 151.45, 157.67. MS (ESI-MS): *m/z* calcd. for M^+, $C_{39}H_{36}N_4O_3$, 608.73; found: 609 (Fig. S1 in Supplementary data). Anal. calcd. for $C_{39}H_{36}N_4O_3 \cdot 0.6H_2O$: C, 75.61; H, 6.05; N, 9.04; found C, 75.42, H, 6.08, N, 9.00.

Synthesis of compound IV

As shown in Scheme 2, 0.1224 g (0.002 mol) of compound **II** and 0.0489 g (0.0031 mol) of quinoline-2-carbaldehyde were dissolved in 15 mL of anhydrous ethanol. The mixture was refluxed under N_2 for 10 h. The cooled solution was partially removed upon rotary evaporation and allowed to stand overnight at 0 °C. The precipitate was re-crystallized three times with ethanol to afford a pale-gray solid (0.836 g, 65%). IR (KBr, cm^{-1}): 1696.84 (C=O); 1626.30 (C=N). ^1H NMR (DMSO-d_6) δ (ppm): 1.70 (t, 4H); 1.97 (t, 4H); 2.40 (m, 4H); 2.93 (m, 4H); 3.03 (m, 4H); 3.12 (m, 4H); 6.05 (s, 2H); 7.03 (d, 1H); 7.53 (t, 1H); 7.60 (m, 2H); 7.74 (m, 2H); 7.93 (m, 3H); 7.36 (d, 1H), 8.72 (s, 1H). MS (ESI-MS): *m/z* calcd. for M^+, $C_{42}H_{37}N_5O_2$, 643.29; found: 644.4 $[M + H]^+$ (Fig. S5 in Supplementary data). Anal. calcd. for $C_{42}H_{37}N_5O_2 \cdot 0.5H_2O$: C, 77.28; H, 5.87; N, 10.73; found C, 77.03, H, 5.90, N, 10.68.

Scheme 2. Synthesis of compound **III** and **IV**.

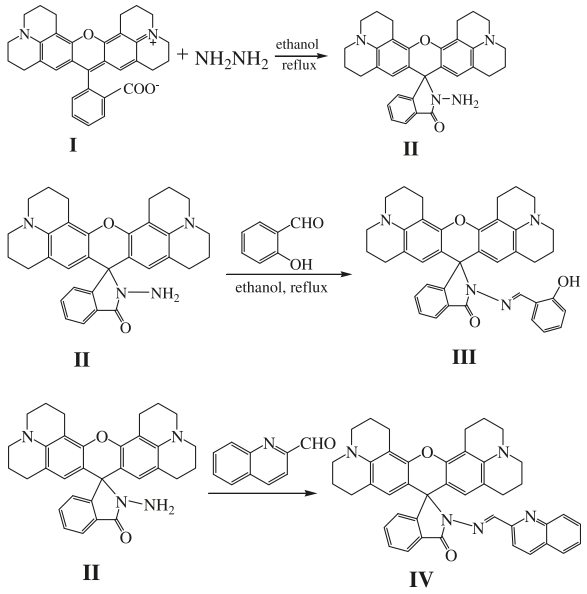

General experiments

NMR spectra were recorded with a 400 MHz Varian spectrometer. Electrospray ionization mass spectra (ESI-MS) were measured on a LC-MSD-Trap-SL system. Elemental analyses were carried on a Flash EA 1112 elemental analyzer (Thermo Electron SPA, Italy). IR spectra were recorded on a Thermo IR spectrometer. Absorption spectra were obtained on a TU1901 UV–vis spectrophotometer. The fluorescence spectra were measured with a Cary Eclipse fluorescence spectrometer. The pH values were measured with a pH S-301 pH meter.

Procedures of metal ion sensing

Nitrate salts of metal ions were used to evaluate the metal ion binding property and selectivity of compounds **III** and **IV** in ethanol-Tris-HCl buffer (0.02 mol/L, pH 7.2) (1:1, *v/v*). Stock solutions of the metal ions (5 mmol/L) were prepared in de-ionized water. Stock solutions of **III** and **IV** (1 mmol/L) were prepared in DMSO, respectively. In titration experiments, 3 mL solution of **III** or **IV**, which was diluted to a certain concentration with ethanol-Tris-HCl (0.02 mol/L, pH 7.2) (1:1, *v/v*), was added into a quartz optical cell with an optical path length of 1 cm. The stock solution of each metal ion was added into the quartz optical cell step by step via a syringe. The spectra were recorded at 2 min after the addition and mixing. For fluorescence measurements, excitation wavelength was provided at 540 nm, and emission was collected from 580 to 660 nm.

Results and discussion

Absorption spectroscopic studies

Compound **III** is proposed to chelate with metal ions via its carbonyl O, imino N, and phenol O atoms.[33] Compound

Can. J. Chem. Downloaded from www.nrcresearchpress.com by South China Agricultural University on 09/19/12
For personal use only.

Fig. 1. (*a*) Absorption spectra of **III** (27 μmol/L) upon addition of increasing amount of Cu^{2+} in ethanol-Tris-HCl (0.02 mol/L, pH 7.2) (1:1, *v*/*v*) solution. The inset shows the titration profile evaluated from the absorption at 584 nm. (*b*) Job plot (total concentration is 2×10^{-5} mol/L).

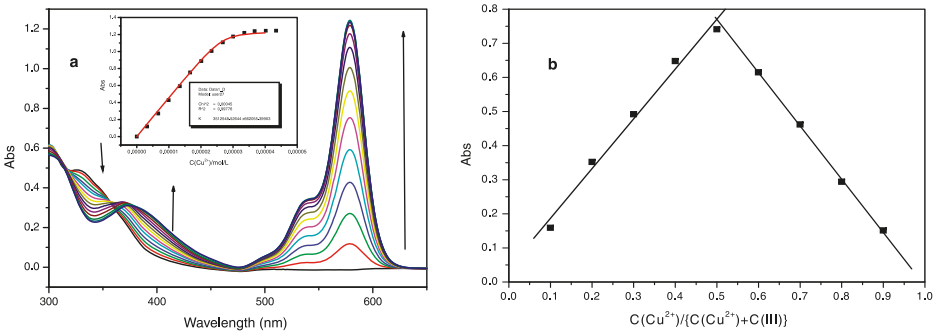

Fig. 2. Absorbance of 10 μmol/L **III** on addition of various metal ions (100 μmol/L of other metal ions) and then addition of 10 μmol/L Cu^{2+} in ethanol-Tris buffer (0.02 mol/L, pH 7.2) (1:1, *v*/*v*) solutions.

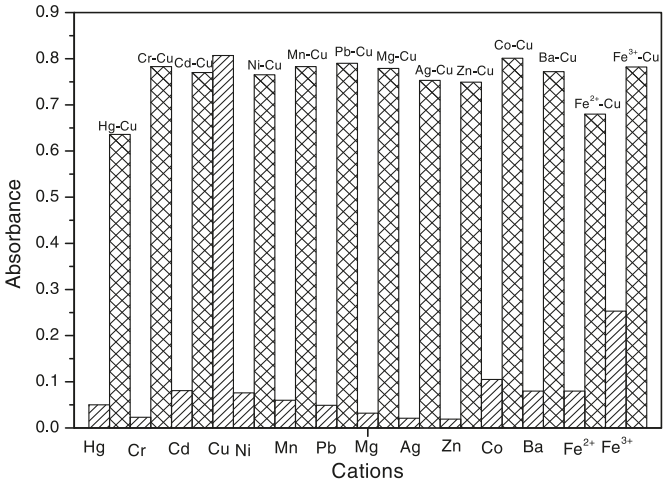

Fig. 3. Photograph of 10 μmol/L **III** as a naked-eye chemosensor for Cu^{2+} in ethanol-Tris-HCl (0.02M, pH 7.2) (1:1, *v*/*v*) solution. From left to right: 0, 2.5, 5.0, 10.0 μmol/L Cu^{2+}.

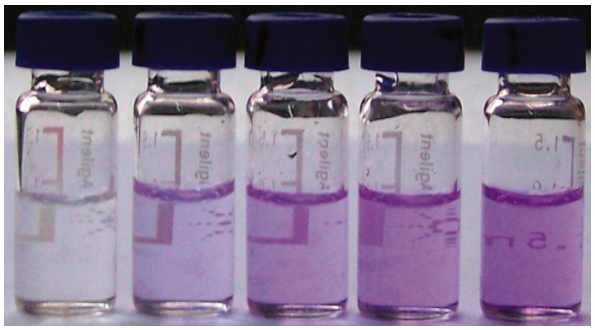

IV may also interact with metal ions via its carbonyl O, imino N, and quino N atoms. The introduction of the rhodamine framework to construct probes of the "off-on" type is a reliable method due to the well-known spirolactam ("off") to ring-opened amide ("on") equilibrium of rhodamine derivatives. The spirolactam moiety of the rhodamine framework served as a signal switcher, which was observed to turn on when the cation was bound.[34,15–27] The absorption spectra of **III**, upon titration with Cu^{2+}, are shown in Fig. 1*a*. The solution of **III** is almost colorless and exhibits almost no absorption in the visible wavelength range (300–650 nm), indicating that **III** is predominantly in the form of spirolactam. The characteristic peak of the spiro-carbon of **III** near 66.5 ppm in the ^{13}C NMR spectrum also supports this conclusion.[35] Upon addition of Cu^{2+}, a new absorption peak at 584 nm appears, and the absorption intensity increases gradually with increasing of Cu^{2+} concentration. The absorbance at 584 nm increases about 70 times upon addition of one equiv. of Cu^{2+}. At the same time, there are three concomitant isosbestic absorption points at 320, 364, and 470 nm, indicating the formation of a 1:1 complex. This stoichiometry is also supported by the Job plot evaluated from the absorption spectra of **III** and Cu (II) with a total concentration of 20 μmol/L (Fig. 1*b*). The changes in the absorption spectra of **III** upon addition of Cu^{2+} indicate the obvious interaction of Cu^{2+} and compound **III**. Nonlinear fitting based on the 1:1 stoichiometry gives a binding constant of $(3.51 \pm 0.66) \times 10^6$ L/mol (insert in Fig. 1*a*),[36] indicating a very strong binding ability of **III** to Cu^{2+}. The absorbance of **III** at 584 nm increases linearly with increasing Cu^{2+} concentration in the range of 2×10^{-7} to 8×10^{-6} mol/L (Fig. S6 in Supplementary data). The relationship between the absorbance at 584 nm and Cu^{2+} concentration was: $A = 0.0844C + 0.0955$, where A is the absorbance at 584 nm and C is the concentration of Cu^{2+} in μmol/L with a correlation coefficient of $R = 0.9999$ ($n = 18$). The detection limit, based on the definition by IUPAC was found to be 2.5×10^{-8} mol/L from 13 blank solutions. The relative standard deviation for ten repeated measurements of 0.5 μmol/L Cu^{2+} was 2.6%.

The absorbance time course of 10 μmol/L **III** to 12 μmol/L Cu^{2+} in ethanol-Tris buffer (0.02 mol/L, pH 7.2) (1:1, *v*/*v*) was investigated. The interaction of **III** with Cu^{2+} was completed in less than 2 min (Fig. S7 in Supplementary data). However, upon addition of 12 μmol/L Cu^{2+} to 10 μmol/L **IV**, no obvious variation in the absorbance at 584 nm was observed over a period of 1 h, indicating a lack of interaction between **IV** and Cu^{2+}. The acidity was chosen to be pH 7.2, because it is close to physiological pH conditions. Both the organic compound and inorganic salts must be dissolved in a suitable solvent. Compound **III** can be dissolved in strong polar solvent, such as DMSO, to prepare the stock solutions. As ethanol is more environmentally friendly and inexpensive than such solvents as acetone, acetonitrile, DMSO, DMF, the effect of ethanol fraction was investigated by using 10%, 30%, 50%, 70%, 90% (*v*/*v*) at pH 7.2 as media for Cu^{2+} determination by 10 μmol/L **III**

Can. J. Chem. Downloaded from www.nrcresearchpress.com by South China Agricultural University on 09/19/12
For personal use only.

Fig. 4. Observed ESI mass spectra of **III** (10 μmol/L) in presence of 12 μmol/L Cu^{2+}.

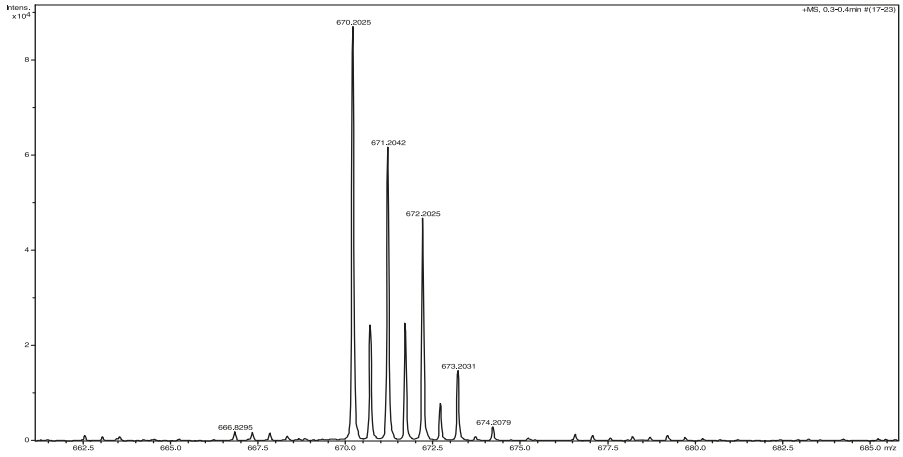

Scheme 3. Possible ring-opening process of **III** upon addition of Cu^{2+}.

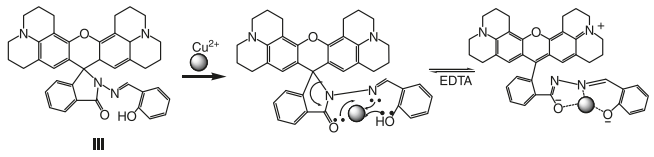

(Fig. S8 in Supplementary data). A fraction of 50% ethanol was found to efficiently monitor Cu^{2+}. Therefore, ethanol-Tris buffer (0.02 mol/L, pH 7.2) (1:1, *v*/*v*) with a trace amount of DMSO were used for each investigation.

Selectivity studies

The selective sensory studies of **III** were then extended to other metal ions. The changes in color of 10 μmol/L **III** in the presence of different cations are illustrated in Fig. S9 in the Supplementary data. Among the metal ions being investigated, the presence of 10 μmol/L Cu^{2+} brought about an obvious purple color in 10 μmol/L **III**. The presence of 100 μmol/L Co^{2+} caused a very faint pink color in 10 μmol/L **III**. The absorption spectra of 27 μmol/L **III**, upon titration with up to 270 μmol/L Co^{2+}, resulted in very small spectroscopic changes (Fig. S10 in Supplementary data). The presence of 100 μmol/L Fe^{3+} brought a pale purple color in 10 μmol/L **III**. The absorption spectra of 27 μmol/L **III**, upon titration with Fe^{3+}, indicted that Fe^{3+} would be a slight interference with Cu^{2+} detection (Fig. S11 in Supplementary data). Metal ions (100 μmol/L) such as Pb^{2+}, Mg^{2+}, Ba^{2+}, Cd^{2+}, Ag^{+}, Fe^{2+}, Mn^{2+}, Zn^{2+}, Hg^{2+}, and Cr^{3+} did not cause any color or spectral change of 10 μmol/L **III**. It is suggested that compound **III** does not bind these metal ions simply. Spectrophotometric responses of 10 μmol/L **III** in ethanol-Tris buffer (0.02 mol/L, pH 7.2) (1:1, *v*/*v*) solutions to 100 μmol/L of various metal ions before and after addition of 10 μmol/L Cu^{2+} are shown in Fig. 2. The results indicated the presence of other ions, including a 10-fold excess of Co^{2+}, did not interfere with the interaction of **III** with Cu^{2+}.

The solutions of 10 μmol/L **III** exhibited deeper and deeper color in the presence of more and more Cu^{2+} at micromolar levels (Fig. 3). The results indicate that chemosensor **III** can indeed serve as a sensitive naked-eye chemosensor for Cu^{2+} in aqueous solutions in the red region (Fig. 3 and Fig. S9 in Supplementary data). The absorption band in the red wavelength region facilitates the naked-eye recognition of Cu^{2+}. Compound **IV** cannot exert any obvious color change upon the addition of the above cations due to the poorer electron donor effect of quino N compared with phenol O atoms. As the color of **III**-Cu(II) disappears instantly upon the addition of 1-fold EDTA due to competitive binding of Cu^{2+} from **III** by EDTA, further addition of Cu^{2+} can recover the purple colour, so the response of **III** to Cu^{2+} is proposed to be a reversible complexation rather than an irreversible cation-catalyzed reaction.[29,37]

Mass spectroscopic studies

ESI mass spectra provide evidence of the formation of **III**-Cu(II) in ethanol-Tris-HCl (0.02 mol/L, pH 7.2) (1:1, *v*/*v*) solution (Fig. 4). The peak at (*m*/*z* = 670.20) for $C_{39}H_{35}CuN_4O_3$ (calcd. 670.2), corresponding to [**III** + Cu-H]$^+$, is clearly observed when 12 μmol/L Cu^{2+} is added to 10 μmol/L **III**. Whereas **III** without Cu^{2+} exhibits a peak only at *m*/*z* = 609.0 (calcd. 608.3), which corresponds to [**III** + H]$^+$ (Fig. S1 in Supplementary data). To achieve this 1:1 stoichiometry, carbonyl O, imino N, and phenol O atoms of **III** are the most likely binding sites for Cu^{2+}. The proposed mechanism is shown in Scheme 3. The phenol group of **III**, which undergoes deprotonation during the binding, plays an important role in the interaction of **III** with Cu^{2+}, because the comparing compound **IV**, which has no phenol group, displays nearly no colorimetric response to Cu^{2+} in either absorption or ESI mass spectra when treated with excess (100 μmol/L) Cu^{2+}.

Fluorescence spectroscopic studies

Fluorescent probes for copper ions have been extensively explored owing to their biological, toxicological, and environmental significance.[38–46] A solution of **III** with concentration of 2 μmol/L in ethanol or ethanol-Tris-HCl (0.02M, pH 7.2) (1:1, *v*/*v*) is nonfluorescent, indicating that the spirocyclic form is retained in solution (The slight emission band before addition of Cu^{2+} is assigned to the delocalized xanthene tautomer of the rhodamine moiety in small amount of **III**.). Upon titration of Cu^{2+}, the emission band at 600 nm appears and develops (Fig. 5*a*). A slightly amplified (nearly one time) fluorescence intensity is observed in presence of

Fig. 5. (*a*) Fluorescence responses of 2 μmol/L **III** upon addition of 0–2 μmol/L Cu^{2+} in ethanol-Tris-HCl (0.02M, pH 7.2) (1:1, *v*/*v*). The concentrations of Cu^{2+} are 0, 0.2, 0.4, 0.6, 0.8, 1.0, 1.2, 1.4, 1.6, 1.8, and 2 μmol/L, respectively. Spectra were recorded immediately after addition of Cu^{2+}. (*b*) Fluorescence enhancement factor $(F - F_0)/F_0$ at 600 nm as a function of Cu^{2+} concentration (0–2 μmol/L). Excitation was performed at 540 nm.

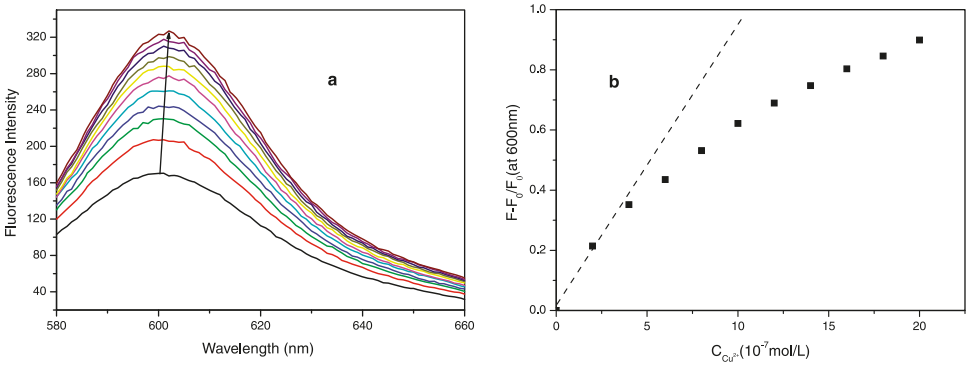

2×10^{-6} mol/L Cu^{2+}. The titration curve in Fig. 5*b* shows a slight fluorescence intensity increase in concentration range 2×10^{-7} to 2×10^{-6} mol/L of Cu^{2+}. The behaviour of the fluorescence intensity increase is nonlinear and a downward trend is observed. Although the emission spectra undergo a red shift from 600 to 605 nm, the fluorescence intensity at 600 nm has only a 1-fold enhancement, which is much weaker compared with the enhancement of the absorbance. The emission peaked at 600 nm is red-shifted compared with the reported values of 575 nm,[47] 578 nm,[37] 580 nm,[19] and 585 nm.[34] The emissions at longer wavelength may have the advantage of avoiding background signals caused by biological autofluorescence (e.g., from serum, proteins, and other macromolecular compounds) for its application in live cell imaging.

When Cu^{2+} was added to **III**, the enhancement of absorbance is found to be much more significant than that of fluorescence intensity. However, the ring-opening of the spirolactam form of rhodamine derivatives generally results in comparable amplifications of absorption and fluorescence signals.[48] In the case of compound **III**, binding to Cu^{2+} does open the spirolactam ring, but at the same time the fluorescence of the Cu(II) complex is probably quenched by Cu^{2+}. The quenching mechanism may be similar to that of some Cu^{2+} probes, displaying fluorescence quenching for the paramagnetic nature of the copper ion.[49–51] Fluorescence inner filter effects (**FIFTs**) of the **III-Cu** complex itself could reduce the observed fluorescence because of the obvious overlap of the absorption spectra and fluorescence spectra of symmetric rhodamine derivatives. Preliminary experiments found an interfering effect byFe^{3+} on the fluorescence of **III**. So **III** is not as good a fluorescence sensor as a colorimetric sensor for Cu^{2+}.[52]

Conclusions

A new spirolactam form of rhodamine 101 hydrazone (**III**) that has been synthesized as a chemosensor for the recognition of copper ion in aqueous solutions displays a selective and sensitive colorimetric change with rapid response upon addition of Cu^{2+}. The ring-opening process of spirolactam (colorless) to the delocalized hydrazone (purple) and a reversible complexation process are proposed in the spectroscopic response of **III** toward Cu^{2+}. As expected, the fluorescent maximum of this chemosensor to Cu^{2+} can be red-shifted to above 600 nm. But Cu^{2+} in high concentration will quench the fluorescence of the copper (II) complex of delocalized form of **III**. The results revealed that **III** is a sensitive and selective naked-eye chemosensor toward Cu^{2+} in the red region.

Supplementary data

Supplementary data for this article are available on the journal Web site http://www.nrcresearchpress.com/doi/suppl/10.1139/v11-111

Acknowledgments

The authors thank the Scientific Research Foundation for the Returned Overseas Chinese Scholars, State Education Ministry of People's Republic of China [No. 2009(08)] and the Education Department of Henan Province (No. 2010B150011) for the financial support.

References

(1) Amendola, V.; Fabbrizzi, L.; Licchelli, M.; Mangano, C.; Pallavicini, P.; Parodi, L.; Poggi, A. *Coord. Chem. Rev.* **1999** *190–192*, 649. doi:10.1016/S0010-8545(99)00110-1.
(2) Rurack, K. *Spectrochim. Acta A Mol. Biomol. Spectrosc.* **2001** *57* (11), 2161. doi:10.1016/S1386-1425(01)00492-9.
(3) Prodi, L.; Bolletta, F.; Montalti, M.; Zaccheroni, N. *Coord. Chem. Rev.* **2000** *205* (1), 59. doi:10.1016/S0010-8545(00)00242-3.
(4) Valeur, B.; Leray, I. *Coord. Chem. Rev.* **2000** *205* (1), 3. doi:10.1016/S0010-8545(00)00246-0.
(5) Rurack, K.; Resch-Genger, U. *Chem. Soc. Rev.* **2002** *31* (2), 116. doi:10.1039/b100604p.
(6) *Metal Ions in Biological Systems, Properties of Copper*; Vol. 12; Sigel, H., Ed.; Dekker: New York, 1981.
(7) Tapia, L.; Suazo, M.; Hodar, C.; Cambiazo, V.; Gonzalez, M. *Biometals*, **2003** *16* (1), 169. doi:10.1023/A:1020766932605.
(8) Pourreza, N.; Hoveizavi, R. *Anal. Chim. Acta*, **2005** *549* (1–2), 124. doi:10.1016/j.aca.2005.06.037.
(9) Becker, J. S.; Zoriy, M. V.; Pickhardt, C.; Palomero-Gallagher, N.; Zilles, K. *Anal. Chem.* **2005** *77* (10), 3208. doi:10.1021/ac040184q.
(10) Otero-Romaní, J.; Antonio Moreda-Piñeiro, A.; Adela Bermejo-Barrera, A.; Bermejo-Barrera, P. *Anal. Chim. Acta*, **2005** *536* (1–2), 213. doi:10.1016/j.aca.2004.12.046.

Can. J. Chem. Downloaded from www.nrcresearchpress.com by South China Agricultural University on 09/19/12
For personal use only.

Can. J. Chem. Downloaded from www.nrcresearchpress.com by South China Agricultural University on 09/19/12
For personal use only.

(11) Haugland, R. P. *Handbook of Fluorescent Probes and Research Chemicals*; 6th ed.; Molecular Probes Inc.: Eugene, 1996.
(12) Burdette, S. C.; Lippard, S. J. *Inorg. Chem.* **2002** *41* (25), 6816. doi:10.1021/ic026048q.
(13) Valeur, B. *Molecular Fluorescence: Principles and Applications*, Wiley-VCH Verlag GmbH: New York, 2001; ch. 10.
(14) Yoon, S.; Miller, E. W.; He, Q.; Do, P. H.; Chang, C. J. *Angew. Chem. Int. Ed.* **2007** *46* (35), 6658. doi:10.1002/anie.200701785.
(15) Yang, H.; Zhou, Z.; Huang, K.; Yu, M.; Li, F.; Yi, T.; Huang, C. *Org. Lett.* **2007** *9* (23), 4729. doi:10.1021/ol7020143.
(16) Huang, W.; Song, C.; He, C.; Lv, G.; Hu, X.; Zhu, X.; Duan, C. *Inorg. Chem.* **2009** *48* (12), 5061. doi:10.1021/ic8015657.
(17) Zheng, H.; Qian, Z. H.; Xu, L.; Yuan, F. F.; Lan, L. D.; Xu, J. G. *Org. Lett.* **2006** *8* (5), 859. doi:10.1021/ol0529086.
(18) Yang, Y. K.; Yook, K. J.; Tae, J. *J. Am. Chem. Soc.* **2005** *127* (48), 16760. doi:10.1021/ja054855t.
(19) Yu, M.; Shi, M.; Chen, Z.; Li, F.; Li, X.; Gao, Y.; Xu, J.; Yang, H.; Zhou, Z.; Yi, T.; Huang, C. *Chemistry*, **2008** *14* (23), 6892. doi:10.1002/chem.200800005.
(20) Chen, X.; Jou, M. J.; Lee, H.; Kou, S.; Lim, J.; Nam, S. W.; Park, S.; Kim, K. M.; Yoon, J. *Sens. Actuators B Chem.* **2009** *137* (2), 597. doi:10.1016/j.snb.2009.02.010.
(21) Huang, L.; Wang, X.; Xie, G.; Xi, P.; Li, Z.; Xu, M.; Wu, Y.; Bai, D.; Zeng, Z. *Dalton Trans.* **2010** *39* (34), 7894. doi:10.1039/c0dt00606h.
(22) Xiang, Y.; Tong, A. *Luminescence*, **2008** *23* (1), 28. doi:10.1002/bio.1012.
(23) Xiang, Y.; Li, Z.; Chen, X.; Tong, A. *Talanta*, **2008** *74* (5), 1148. doi:10.1016/j.talanta.2007.08.018.
(24) Zhang, M.; Gao, Y.; Li, M.; Yu, M.; Li, F.; Li, L.; Zhu, M.; Zhang, J.; Yi, T.; Huang, C. *Tetrahedron Lett.* **2007** *48* (21), 3709. doi:10.1016/j.tetlet.2007.03.112.
(25) Huang, K.; Yang, H.; Zhou, Z.; Yu, M.; Li, F.; Gao, X.; Yi, T.; Huang, C. *Org. Lett.* **2008** *10* (12), 2557. doi:10.1021/ol800778a.
(26) Zhou, Z.; Yu, M.; Yang, H.; Huang, K.; Li, F.; Yi, T.; Huang, C. *Chem. Commun. (Camb.)* **2008** (29): 3387. doi:10.1039/b801503a.
(27) Kwon, J. Y.; Jang, Y. J.; Lee, Y. J.; Kim, K. M.; Seo, M. S.; Nam, W.; Yoon, J. *J. Am. Chem. Soc.* **2005** *127* (28), 10107. doi:10.1021/ja051075b.
(28) Kim, H. N.; Lee, M. H.; Kim, H. J.; Kim, J. S.; Yoon, J. *Chem. Soc. Rev.* **2008** *37* (8), 1465. doi:10.1039/b802497a.
(29) Xie, P.; Guo, F.; Li, D.; Liu, X.; Liu, L. J. *J. Lumin.* **2011** *131* (1), 104. doi:10.1016/j.jlumin.2010.09.021.
(30) Liu, J.; Diwu, Z.; Leung, W. Y.; Lu, Y.; Patch, B.; Haugland, R. P. *Tetrahedron Lett.* **2003** *44* (23), 4355. doi:10.1016/S0040-4039(03)00938-9.
(31) Hougland, R. P. *Handbook of fluorescent probes and research products*; 9th ed.; Molecular Probes Inc.: Eugence, 2002.
(32) Yang, X. F.; Guo, X. Q.; Zhao, Y. B. *Talanta*, **2002** *57* (5), 883.
(33) Lee, P. F.; Yang, C. T.; Fan, D.; Vittal, J. J.; Ranford, J. D. *Polyhedron*, **2003** *22* (20), 2781. doi:10.1016/S0277-5387(03)00402-9.
(34) Xiang, Y.; Tong, A.; Jin, P.; Ju, Y. *Org. Lett.* **2006** *8* (13), 2863. doi:10.1021/ol0610340.
(35) Anthoni, U.; Christophersen, C.; Nielsen, P.; Puschl, A.; Schaumburg, K. *Struct. Chem.* **1995** *6* (3), 161. doi:10.1007/BF02286443.
(36) Connors, K. A. *Binding Constants-The Measurement of Molecular Complex Stability*; John Wiley & Sons: New York, 1987; Chapter 4.
(37) Dujols, V.; Ford, F.; Czarnik, A. W. *J. Am. Chem. Soc.* **1997** *119* (31), 7386. doi:10.1021/ja971221g.
(38) de Silva, A. P.; Gunaratne, H. Q. N.; Gunnlaugsson, T.; Huxley, A. J. M.; McCoy, C. P.; Rademacher, J. T.; Rice, T. E. *Chem. Rev.* **1997** *97* (5), 1515. doi:10.1021/cr960386p.
(39) Callan, J. F.; de Silva, A. P.; Magri, D. C. *Tetrahedron*, **2005** *61* (36), 8551. doi:10.1016/j.tet.2005.05.043.
(40) Kim, J. S.; Quang, D. T. *Chem. Rev.* **2007** *107* (9), 3780. doi:10.1021/cr068046j.
(41) Zheng, Y.; Orbulescu, J.; Ji, X.; Andreopoulos, F. M.; Pham, S. M.; Leblanc, R. M. *J. Am. Chem. Soc.* **2003** *125* (9), 2680. doi:10.1021/ja0293610.
(42) Roy, B. C.; Chandra, B.; Hromas, D.; Mallik, S. *Org. Lett.* **2003** *5* (1), 11. doi:10.1021/ol026891s.
(43) Qi, X.; Jun, E. J.; Kim, S.-J.; Hong, J. S. J.; Yoon, Y. J.; Yoon, J. *J. Org. Chem.* **2006** *71* (7), 2881. doi:10.1021/jo052542a.
(44) Kim, S. H.; Kim, J. S.; Park, S. M.; Chang, S. K. *Org. Lett.* **2006** *8* (3), 371. doi:10.1021/ol052282j.
(45) Jung, H. S.; Kwon, P. S.; Lee, J. W.; Kim, J.; Hong, C. S.; Kim, J. W.; Yan, S.; Lee, J. Y.; Lee, J. H.; Joo, T.; Kim, J. S. *J. Am. Chem. Soc.* **2009** *131* (5), 2008. doi:10.1021/ja808611d.
(46) Boiocchi, M.; Fabbrizzi, L.; Licchelli, M.; Sacchi, D.; Vázquez, M.; Zampa, C. *Chem. Commun.* **2003** (15), 1812. doi:10.1039/b305456j.
(47) Zhou, Y.; Wang, F.; Kim, Y.; Kim, S.; Yoon, J. *Org. Lett.* **2009** *11* (19), 4442. doi:10.1021/ol901804n.
(48) Xiang, Y.; Tong, A. *Org. Lett.* **2006** *8* (8), 1549. doi:10.1021/ol060001h.
(49) Varnes, A. W.; Dodson, R. B.; Wehry, E. L. *J. Am. Chem. Soc.* **1972** *94* (3), 946. doi:10.1021/ja00758a037.
(50) Torrado, A.; Walkup, G. K.; Imperiali, B. *J. Am. Chem. Soc.* **1998** *120* (3), 609. doi:10.1021/ja973357k.
(51) Li, Y.; Yang, C. M. *Chem. Commun.* **2003** (23): 2884. doi:10.1039/b310543a.
(52) Shao, N.; Zhang, Y.; Cheung, S. M.; Yang, R. H.; Chan, W. H.; Mo, T.; Li, K. A.; Liu, F. *Anal. Chem.* **2005** *77* (22), 7294. doi:10.1021/ac051010r.

Reaction of iodine with metal oxides

Marek Gliński and Urszula Ulkowska

Abstract: The reaction of iodine with various metal oxides has been studied in both vapour phase (373–873 K) and in solution in cyclohexane, under anhydrous conditions. The course of the reaction has been revised in accordance with literature and experimental data. Apart from adsorbed iodine molecules ($[I_2] < 200\ \mu mol \cdot g^{-1}$), the presence of I^- ions ($[I^-] < 50\ \mu mol \cdot g^{-1}$) has been noted. IO_n^- ions have been observed only when both water and strong basic sites, such as those on MgO or La_2O_3, are present. It has been found that the strength of interaction of iodine with metal oxide increases with basicity of the oxide.

Key words: iodine, metal oxides, iodides, basicity.

Résumé : On a étudié les réactions de l'iode avec divers oxydes métalliques, tant en phase vapeur (373–873 K) qu'en solution dans le cyclohexane, dans des conditions anhydres. On a révisé le cours de la réaction afin de le rendre en accord avec les données expérimentales et celles de la littérature. En plus des molécules d'iode absorbées, ($[I_2] < 200\ \mu mol \cdot g^{-1}$), on a aussi noté la présence d'ions I^- ($[I^-] < 50\ \mu mol \cdot g^{-1}$). On n'a observé la présence d'ions IO_n^- que lorsqu'on est en présence à la fois d'eau et de sites fortement basiques, tels ceux présents sur le MgO ou le La_2O_3. On a aussi observé que la force de l'interaction de l'iode avec l'oxyde métallique augmente avec la basicité de cet oxyde.

Mots-clés : iode, oxydes métalliques, iodures, basicité.

[Traduit par la Rédaction]

Can. J. Chem. Downloaded from www.nrcresearchpress.com by South China Agricultural University on 09/19/12
For personal use only.

Introduction

Although halogens are very potent electron acceptors, little is known about their reactivity with the surface of metal oxides. What is more, there is some controversy in the literature about the products of this reaction.

In 1974, Kibblewhite and Tench reported that halogens react at room temperature (RT) with magnesium oxide, and the effect of the reaction of a given halogen on the oxide surface strongly depends on the halogen type.[1] It has been shown that MgO treated with iodine contains the appropriate I^- ions and exhibits a lack of IO^- and IO_3^- ions. The authors stated that iodine can react with the surface oxide ions of the lowest coordination only, e.g., 3-fold coordination, which are the most reactive.

Also in 1974 a paper on the reduction of iodine in benzene solution by Al_2O_3, Al_2O_3-SiO_2, and SiO_2 surfaces was published by Flockhart et al.[2] The authors stated that hydroxyl groups on the surfaces of metal oxides can act as one-electron donor sites, and that they are responsible for the occurrence of the reaction. The authors have proposed the mechanism of the reduction based on the following equation:

$$[1] \qquad I_2 + 2OH^- \rightarrow IO^- + I^- + H_2O$$

However, they could not explain the absence of IO_3^- ions, derived from the transformations of IO^- ions, which should be formed according to:

$$[2] \qquad 3IO^- \rightarrow IO_3^- + 2I^-$$

The same type of surface reaction has been proposed for the treatment of alumina with gaseous chlorine, although no proof for the formation of ClO^- ions has been given.[3]

In a series of articles Klabunde et al. have reported that MgO-halogen adducts are reactive halogenating agents of organic molecules and exhibit noticeable biocidal character.[4,5] Moreover, magnesium oxide is found to be an active catalyst in the oxidative dehydrogenation of butane to butadiene in the presence of oxygen and iodine.[6] Based on the results of Raman spectroscopy, the authors concluded that upon adsorption of iodine on the surface of MgO, the formation of an Mg–I bond does not take place or it takes place to a negligible extent.[5]

Iodine has been used as a molecular probe of electron donor strength of Lewis base sites of various zeolites.[7,8] As has been stated, I_2 interacts with the basic framework oxygen and not the charge-balancing cation. It has also been shown that a blue shift in the visible spectrum of adsorbed iodine on zeolite increases with increasing basicity of the zeolite.[9] This technique for probing basicity of solids has been extended to classical supports like alumina, silica, and magnesia.[10] The following decreasing order of the strength of interaction has been found: MgO (very high) > Al_2O_3 (significant) > SiO_2 (weak).[10]

Very recently we have demonstrated that MgO treated with a solution of iodine in pentan-2-ol shows a significant increase in the selectivity in the hydrogen transfer reaction to cyclopentanone.[11]

Received 15 June 2011. Accepted 22 July 2011. Published at www.nrcresearchpress.com/cjc on 18 October 2011.

M. Gliński and U. Ulkowska. Warsaw University of Technology (Politechnika), Faculty of Chemistry, Noakowskiego 3, 00-664 Warsaw, Poland.

Corresponding author: Marek Gliński (e-mail: marekg@ch.pw.edu.pl.)

Can. J. Chem. Downloaded from www.nrcresearchpress.com by South China Agricultural University on 09/19/12
For personal use only.

Here, we describe the reaction of iodine with a series of metal oxides. The reactions were carried out in a broad range of conditions: with a solution of I_2 in cyclohexane at RT or with vapours of I_2 in the temperature range 373–873 K. The present study was focused on the strong interaction of iodine with metal oxides, leading to its reduction to I^- ions. We expected that our work would help to resolve the controversy found in the literature about the products of the above mentioned reaction.

Experimental

Metal oxides Al_2O_3, SiO_2, TiO_2, and ZnO

The powders of alumina (type C, Degussa), silica (Aerosil 200, Degussa), titania (P-25, Degussa), and zinc oxide (puriss p.a., Fluka) were mixed with re-distilled water, and the slurries were dried at 333 and 393 K for 24 h at each temperature. The lumps of oxide were crushed, sieved, and the grain fraction 0.4–0.63 mm was collected.

ZrO_2 and La_2O_3

The solutions of $ZrOCl_2 \cdot 8H_2O$ and $La(NO_3)_3 \cdot 6H_2O$ (both puriss p.a., Fluka) in water were treated with an aqueous ammonia solution (25%), and the precipitated hydroxides were successively washed with re-distilled water to remove all soluble salts. After filtration, metal hydroxides were treated according to the procedure described above.

MgO

Magnesium oxide was prepared by thermal decomposition of $Mg(OH)_2$, whose preparation has been described in detail elsewhere.[12] The grains of hydroxide with 0.4–0.63 mm diameter were used.

Before characterization studies and treatment with iodine or its solutions, metal oxides or hydroxides were calcined at 873 K for 1 h in a stream of air and then for 5 h at the same temperature in a stream of dry nitrogen. They were then stored under nitrogen in Schlenk-type containers.

Characterization of metal oxides

The specific surface areas were measured by nitrogen adsorption at 77 K (BET method) using a Gemini 2360 instrument (Micromeritics).

The strength of the surface acid–base sites of selected metal oxides was determined by the Hammett method, using a sequence of indicators in anhydrous toluene as the solvent.[13] The following set of indicators has been used (the values of pK_A or pK_{BH+} are given in parentheses): chalcone (–5.6), dicinnamylideneacetone (–3.0), crystal violet (0.8), methyl red (4.8), bromothymol blue (7.2), phenolphthalein (9.3), 2,4-dinitroaniline (15.0), 4-nitroaniline (18.4), diphenylamine (22.3), 4-chloroaniline (26.5), and triphenylmethane (33.0). The concentrations of acidic and basic sites of metal oxides were determined using solutions (0.01 mol/L) of triethylamine or benzoic acid in anhydrous toluene, according to a procedure described elsewhere.[14] The measurements were performed at ambient temperature under dry nitrogen, after 24 h contact of the oxides with these solutions in grease-less reactors. The results are summarized in Table 1.

Solvents and reagents

Cyclohexane (99+%, Sigma-Aldrich) was dried by filtration through a glass column containing anhydrous molecular sieves, followed by distillation over metallic potassium – benzophenone in nitrogen atmosphere directly to the Schlenk-type container. Chloroform (pure, BDH) was washed three times with distilled water to remove ethanol and dried at 273 K under nitrogen over anhydrous $CaCl_2$. A final purification of $CHCl_3$ was achieved by distillation in a stream of dry nitrogen in an all-glass apparatus. The distillate was kept under nitrogen in a Schlenk-type container, covered with metallic foil.

Potassium iodate (p.a., Merck) was dried in an oven at 423 K for 4 h and kept in a tightly closed container. Iodine (double sublimed, Merck), potassium iodide (p.a., POCh Gliwice, Poland), and sodium thiosulphate pentahydrate (99.5%, Sigma-Aldrich) were used as received. A stock solution of $Na_2S_2O_3$ was prepared (~0.1 mol/L) and stabilized by the addition of $CHCl_3$. Sodium thiosulphate solutions with lower concentrations (0.001–0.005 mol/L) were prepared by dilution of the stock solution immediately before use. Their concentrations were determined using anhydrous potassium iodate as a standard in the presence of iodide ions in an acidic solution. Sulphuric acid (p.a., 98%, Merck) was used to prepare a 1 mol/L solution in water. Starch (AR, soluble, BDH) was used as received. Its solution in water was stabilized by addition of small amounts of salicylic acid.

Reaction of metal oxides with iodine

(*All operations connected with sample preparation and handling were done in a dry nitrogen atmosphere.*) Two different procedures for the introduction of iodine on the surfaces of metal oxides were used.

In the first procedure, a weighed sample of metal oxide (250 mg), placed in an Erlenmeyer flask, was suspended in anhydrous cyclohexane (5 cm^3), and a cyclohexane solution of iodine of known concentration (0.05 mol/L, 5 cm^3) was added. A suspension of the metal oxide in the stoppered flask was stirred at RT for a certain period of time.

In the second procedure, a stream of anhydrous nitrogen (100 $cm^3 \cdot min^{-1}$) was passed through a glass saturator, filled with iodine kept at 293 K. The stream of N_2, saturated with I_2 vapours, was passed through a metal oxide bed (500 mg), placed in a tubular quartz reactor, and heated to the appropriate temperature. After a 3 h long contact with I_2 vapours, the bed of metal oxide was purged with nitrogen at the same temperature for 1 h, and cooled in a stream of N_2. It has been found in a test without a catalyst that the total amount of iodine reaching the reactor during 3 h is equal to 202 ± 6 μmol.

Analytical determinations

These are tests for the presence of I^- and IO_3^- ions. A sample of a metal oxide that had been reacted previously with an iodine solution or gaseous iodine was extracted with chloroform (5 times) to remove the free halogen, and finally the solvent was removed under reduced pressure. The resulting solid was triturated with 1 mol/L H_2SO_4. An acidic solution was treated either with 30% H_2O_2 or with a freshly prepared 0.1 mol/L KI solution in the presence of starch for

Can. J. Chem. Downloaded from www.nrcresearchpress.com by South China Agricultural University on 09/19/12
For personal use only.

Table 1. Specific surface area and acid–base properties of the studied metal oxides.

		Concentration of sites ($\mu mol \cdot g^{-1}$)		Strength	
MO_x	S_{BET} ($m^2 \cdot g^{-1}$)	Acidic	Basic	H_0	H_-
MgO	100	9	1785	[a]	<7.2; 33.0)
ZnO	3	—	—	—	—
Al_2O_3	103	132	408	(–5.6; 4.8>	<7.2; 9.3)
La_2O_3	26	–	–	–	<7.2; 15.0>[b]
SiO_2	253	30	358	(0.8; 4.8>	<7.2; 9.3)
TiO_2	38	42	130	(0.8; 4.8>	<7.2; 9.3)
ZrO_2	32	—	—	—	—

[a] $H_0 > 4.8$.
[b] Taken from Ref. 15.

the confirmation of the presence of I^- and IO_3^- ions, respectively.

I_2 on metal oxides

(*All operations were performed in a dry nitrogen atmosphere*). A weighed sample of an oxide (250 mg) was placed in an Erlenmeyer flask (100 cm^3) fitted with a ground-glass stopper, and the free iodine was extracted with anhydrous $CHCl_3$ (5 × 5 cm^3). The organic extracts were collected and treated with 10 cm^3 0.05 mol/L KI. The resulting two-phase mixture was titrated with 0.002 mol/L $Na_2S_2O_3$ in the presence of starch.

I^- ions on metal oxides

The solid left from the determination of iodine was stirred with 15 cm^3 1 mol/L H_2SO_4, and 1 cm^3 0.005 mol/L $NaIO_3$ was added. The liberated iodine was extracted with chloroform (5 × 5 cm^3). The extracts were collected, washed with water, and titrated with 0.002 mol/L $Na_2S_2O_3$, according to the procedure described earlier.

The concentrations given in Tables 2–4 are the averages of three measurements.

Results and discussion

We applied the method of Flockhart et al. to introduce iodine onto alumina using cyclohexane instead of benzene as the solvent for iodine.[2] We have found that no IO_n^- ions were formed. Moreover, the consumption of iodine can be described by the following equation:

$$[3] \quad I_2 + 2e^- \rightarrow 2I^-$$

Very small amounts of iodides, around 20 $\mu mol \cdot g^{-1}$, were found on the surface of the oxide apart from the unreacted iodine. Despite the different solvent, the concentration of iodine, the type of alumina, and analytical procedure, a quite good correlation with the results obtained by Flockhart et al. (max. $[I^-] = 76$ $\mu mol \cdot g^{-1}$) has been noted.[2] The source of electrons transferred to iodine is not established. It is said in the literature that they are derived from surface hydroxyls and (or) the lowest coordinated oxygen anions acting as one-electron donor sites.[16,17]

We have also found that stirring the suspension of alumina greatly accelerates reaching an equilibrium, and that daylight has no influence on the rate of the reaction. Stirring of the suspension for more than an hour increases the I^- concentration because of the progressive grinding of the grains of alumina. The results of preliminary measurements are collected in Table 2.

Table 2. Reaction of I_2 with Al_2O_3 in anhydrous cyclohexane.

Treatment	$[I^-]$ ($\mu mol \cdot g^{-1}$)/ Time of reaction (h)					
	0.25	0.5	1	3	10	24
—	9	12	—	12	—	14
[a]	10	12	—	13	—	13
[b]	18	19	19	21	23	29
[a,b]	20	18	19	20	24	27
[a,b,c]	0	—	0	1	—	2
[b,d]	22	20	22	23	—	24
[b,e]	20	21	—	23	—	30
[b,f]	19	18	18	20	26	33[g]

[a] In darkness.
[b] With stirring.
[c] 250 mg of quartz.
[d] 125 mg of alumina.
[e] 500 mg of alumina.
[f] 1000 mg of alumina.
[g] 33 ± 2 $\mu mol \cdot g^{-1}$ for 5 measurements.

Table 3. Reaction of I_2 with metal oxides in anhydrous cyclohexane.

MO_x	$[I^-]$ ($\mu mol \cdot g^{-1}$ MO_x) / Time of reaction (min)		
	5	15	60
SiO_2	2	3	4
La_2O_3	2	5	6[a]
MgO	5	6	8[a]
Al_2O_3	14	18	19
TiO_2	15	19	20
ZrO_2	18	21	25
ZnO	21	23	30

[a] The value increases steeply when water is present.

Other metal oxides reacted with iodine in cyclohexane in a similar manner as alumina (Table 3). A partial reduction of iodine also took place with the formation of iodide ions. No formation of IO_n^- ions was noted in the case of all studied metal oxides. Very low concentrations of iodide ions, up to 30 $\mu mol \cdot g^{-1}$, were reached. It has been found that only for strong basic oxides such as MgO or La_2O_3, the presence of water greatly accelerates the reaction of the oxide with I_2 because of the participation of a well-known disproportionation reaction of a halogen in basic media:

Can. J. Chem. Downloaded from www.nrcresearchpress.com by South China Agricultural University on 09/19/12
For personal use only.

Table 4. Reaction of I_2 with metal oxides heated to T_R for 3 h.

Metal oxide	T_R (K)	Concentration ($\mu mol \cdot g^{-1}$ MO_x)		Density ($\mu mol \cdot m^{-2}$ MO_x)	
		I_2	I^-	I_2	I^-
—[a]	473	0	0	0.0	0.0
SiO_2		0[b]	0[b]	0.0	0.0
ZrO_2		0[b]	1	0.0	0.0
TiO_2		0[b]	1	0.0	0.0[c]
ZnO		2	3	0.7	1.0
	673	0	3	0.0	1.0
Al_2O_3	373	12	2	0.1	0.0[d]
	473	4	2	0.0[e]	0.0[d]
	573	0	2	0.0	0.0[d]
La_2O_3	373	121	3	4.7	0.1
	473	49	5	1.9	0.2
	673	4	6	0.2	0.2
	873	0[b]	8	0.0	0.3
MgO	373	190	10	1.9	0.1
	473	58	12	0.6	0.1
	673	14	15	0.1	0.2
	873	0[b]	22	0.0	0.2

[a]Quartz.
[b]Less than 0.2 $\mu mol \cdot g^{-1}$.
[c]0.03 $\mu mol \cdot m^{-2}$.
[d]0.02 $\mu mol \cdot m^{-2}$.
[e]0.04 $\mu mol \cdot m^{-2}$.

$$[4] \quad 6\,Mg(OH)_2 + 6\,I_2 \rightarrow Mg(IO_3)_2 + 5\,MgI_2 + 6\,H_2O$$

However, such a reaction does not occur under the rigorous anhydrous conditions adopted in this work.

Based on the results presented above we decided to further investigate the method of introduction of iodine onto the surface of metal oxides. To simplify the reaction conditions between metal oxide and iodine, we applied a reaction method of heating the oxide to different temperatures with a stream of iodine vapour diluted with anhydrous nitrogen. In this solvent-free method, the absence of any complications connected with the use of a solvent is ensured. The results are summarized in Table 4.

Small concentrations of I^- ions, below 25 $\mu mol \cdot g^{-1}$, accompanied by various concentrations of adsorbed iodine (< 200 $\mu mol \cdot g^{-1}$) were found on the surfaces of all studied oxides. No IO_n^- ions were detected. For MgO, we have observed an excellent agreement of the surface density of I^- determined in this work (0.22 $\mu mol \cdot m^{-2}$) with that determined by Kibblewhite and Tench (0.22 $\mu mol \cdot m^{-2}$).[1] It has been found that the concentration of the adsorbed iodine depends on the temperature and the type of the oxide. After reaction at 473 K, only trace amounts of I^- ions and lack of adsorbed I_2 were found on the surfaces of SiO_2, ZrO_2, and TiO_2. In the case of weakly basic oxides (ZnO, Al_2O_3), besides very minute amounts of I^- ions, the presence of a strongly adsorbed iodine was noted. The halogen could be desorbed at temperatures higher than 473 K. For metal oxides with strong basic properties, such as MgO and La_2O_3, the adsorbed iodine could be removed only at temperatures higher than 673 K. Therefore, it has been concluded that the strength of interaction of iodine with metal oxides increases with their basicity. The results correlate well with those obtained in UV–vis spectroscopy studies.[10]

Conclusion

Iodine, both in vapour phase or in solution in anhydrous cyclohexane, reacts with the surfaces of various metal oxides. Apart from adsorbed iodine molecules ($[I_2] < 200$ $\mu mol \cdot g^{-1}$), the presence of I^- ions ($[I^-] < 50$ $\mu mol \cdot g^{-1}$) has been noted. The formation of IO_n^- ions occurs only when both water and strong basic sites, such as those on MgO or La_2O_3, are present. The strength of interaction of iodine with metal oxide increases with basicity of the oxide.

References

(1) Kibblewhite, J. F. J.; Tench, A. J. *J. Chem. Soc., Faraday Trans. I* **1974** *70*, 72. doi:10.1039/f19747000072.
(2) Flockhart, B. D.; Lieuw, K. Y.; Pink, R. C. *J. Catal.* **1974** *32* (1), 20. doi:10.1016/0021-9517(74)90154-7.
(3) Marczewski, M.; Derewiń ski, M.; Malinowski, S. *Can. J. Chem. Eng.* **1983** *61* (1), 93. doi:10.1002/cjce.5450610116.
(4) Sun, N.; Klabunde, K. J. *J. Am. Chem. Soc.* **1999** *121* (23), 5587. doi:10.1021/ja990084f.
(5) Stoimenov, P. K.; Zaikovski, V.; Klabunde, K. J. *J. Am. Chem. Soc.* **2003** *125* (42), 12907. doi:10.1021/ja030195l.
(6) Chesnokov, V. V.; Bedilo, A. F.; Heroux, D. S.; Mishakov, I. V.; Klabunde, K. J. *J. Catal.* **2003** *218* (2), 438. doi:10.1016/S0021-9517(03)00085-X.
(7) Barrer, R. M.; Wasilewski, S. *Trans. Faraday Soc.* **1961** *57*, 1140. doi:10.1039/tf9615701140.
(8) Seff, K.; Shoemaker, D. P. *Acta Crystallogr.* **1967** *22* (2), 162. doi:10.1107/S0365110X67000283.
(9) Choi, S.; Park, Y. S.; Hong, S. B.; Yoon, K. B. *J. Am. Chem. Soc.* **1996** *118* (39), 9377. doi:10.1021/ja952112+.

(10) Doskocil, E. J.; Bordawekar, S. V.; Kaye, B. G.; Davis, R. J. *J. Phys. Chem. B* **1999** *103* (30), 6277. doi:10.1021/jp991091t.
(11) Gliński, M.; Ulkowska, U. *React. Kinet. Catal. Lett.* **2008** *95* (1), 107. doi:10.1007/s11144-008-5286-6.
(12) Gliński, M.; Ulkowska, U. *Catal. Lett.* **2011** *141* (2), 293. doi:10.1007/s10562-010-0497-7.
(13) Tanabe, K.; Misono, M.; Ono, Y.; Hattori, H. *Stud. Surf. Sci. Catal.* **1989** *51*, 5. doi:10.1016/S0167-2991(08)61045-9.
(14) Yamanaka, T.; Tanabe, K. *J. Phys. Chem.* **1975** *79* (22), 2409. doi:10.1021/j100589a013.
(15) Chai, S.-H.; Wang, H.-P.; Liang, Y.; Xu, B.-Q. *Green Chem.* **2007** *9* (10), 1130. doi:10.1039/b702200j.
(16) Tench, A. J.; Nelson, R. L. *Trans. Faraday Soc.* **1967** *63*, 2254. doi:10.1039/tf9676302254.
(17) Che, M.; Naccache, C.; Imielik, B. *J. Catal.* **1972** *24* (2), 328. doi:10.1016/0021-9517(72)90077-2.

Can. J. Chem. Downloaded from www.nrcresearchpress.com by South China Agricultural University on 09/19/12
For personal use only.

Synthesis and X-ray photoelectron spectroscopy (XPS) and thermoelectric studies of ternary $Bi_2(Te_{0.5}Se_{0.5})_3$ mixed-metal chalcogenide thin films by the arrested precipitation technique

S. M. Patil, S. R. Mane, R. M. Mane, S. S. Mali, P. S. Patil, and P. N. Bhosale

Can. J. Chem. Downloaded from www.nrcresearchpress.com by South China Agricultural University on 09/19/12
For personal use only.

Abstract: Arrested precipitation technique (APT) has been successfully employed for the deposition of $Bi_2(Te_{0.5}Se_{0.5})_3$ thin films. Analytical grade bismuth nitrate complexes with triethanolamine (TEA), sodium tellurosulfite, and sodium selenosulfite were used as precursor materials. The film was obtained at 55 ± 0.5 °C in an aqueous alkaline medium (pH = 10.5 ± 0.2). As-deposited film was characterized by chemical compositional, optical, and electrical analyses. The optical absorption spectrum for the sample was recorded in the wavelength region 400–900 nm. It shows a high coefficient of absorption ($\alpha = 10^5$ cm^{-1}) with an allowed direct type of transition. X-ray diffraction (XRD) study of the film shows a nanocrystalline and rhombohedral structure. From scanning electron microscopy (SEM), atomic force microscopy (AFM), and energy dispersive X-ray analysis (EDAX) studies, the deposited film shows uniform morphology and good stoichiometry. X-ray photoelectron spectroscopy (XPS) was used to study the binding energy and surface oxidation of the material. Electrical conduction study shows that material is an n-type semiconductor and shows good thermoelectric figure of merit.

Key words: chalcogenide thin films by APT, XPS, thermoelectric study.

Résumé : On a utilisé avec succès la technique de la précipitation arrêtée (TPA) pour déposer des films minces de $Bi_2(Te_{0.5}Se_{0.5})_3$. On a utilisé des complexes de nitrate de bismuth de qualité analytique avec de la triéthanolamine (TEA), du tellurosulfite de sodium et du sélénosulfite de sodium comme produits de départ. Le film a été obtenu à 55 ± 0,5 °C, dans un milieu alcalin aqueux (pH = 10,5 ± 0,2). Le film déposé a été caractérisé par des analyses de sa composition chimique et de ses propriétés optiques et électriques. On a enregistré le spectre d'absorption optique de l'échantillon dans la plage de longueur d'onde de 400 à 900 nm. Il présente un coefficient d'absorption ($\alpha = 10^5$ cm^{-1}) correspondant à un type de transition directe permise. L'étude du film par diffraction des rayons-X (DRX) montre que la structure est nanocristalline et rhomboédrique. Les résultats obtenus par microscopie électronique à balayage (MEB), microscopie des forces atomiques (MFA) et d'une analyse par rayons-X de la dispersion d'énergie (AXDE) montrent que le film déposé possède une morphologie uniforme et une bonne stoechiométrie. On a utilisé la spectroscopie photoélectronique des rayons-X (SPX) pour étudier l'énergie de liaison et l'oxydation de la surface du matériel. Une étude de conduction électrique montre que le matériel est un semiconducteur de type n et qu'il possède un bon facteur de mérite thermoélectrique.

Mots-clés : films minces de chalcogénures, technique de la précipitation arrêtée (TPA), étude thermoélectrique, étude par spectroscopie photoélectronique des rayons X (SPX).

[Traduit par la Rédaction]

Introduction

Bi_2Te_3 with Bi_2Se_3 alloys has been an attractive thermoelectric material widely used in cooling devices and proposed for energy conversion applications at room temperature.[1] The performance of thermoelectric materials depends on the thermoelectric figure of merit of the material ZT. Recently progress has been made in improving the figure of merit of thin film. It is approximately 1 for this material at room temperature.[2] Bismuth telluride represents the parent compound of a family of technologically important semiconductor alloys that are used extensively in modern thermoelectric coolers.[3,4]

Many researchers have reported alloying bismuth telluride and bismuth selenide to increase the thermoelectric efficiency.[5–8] In our research, we deposited $Bi_2(Te_{0.5}Se_{0.5})_3$ material by a new simple developed method known as arrested precipitation technique (APT).[9–11] Deposited film was characterized for growth mechanism and optical, morphological structural, and conduction properties of $Bi_2(Te_{0.5}Se_{0.5})_3$ thin

Received 23 April 2011. Accepted 21 June 2011. Published at www.nrcresearchpress.com/cjc on 19 October 2011.

S.M. Patil, S.R. Mane, R.M. Mane, and P.N. Bhosale. Materials Research Laboratory, Department of Chemistry, Shivaji University, Kolhapur-416004, India.
S.S. Mali and P.S. Patil. Thin Film Materials Laboratory, Department of Physics, Shivaji University, Kolhapur-416004, India.

Corresponding author: P. N. Bhosale (e-mail: p_n_bhosale@rediffmail.com).

Can. J. Chem. Downloaded from www.nrcresearchpress.com by South China Agricultural University on 09/19/12
For personal use only.

Fig. 1. (*a*) X-ray diffraction patterns and (*b*) absorption coefficients and band gaps of as-deposited $Bi_2(Te_{0.5}Se_{0.5})_3$film.

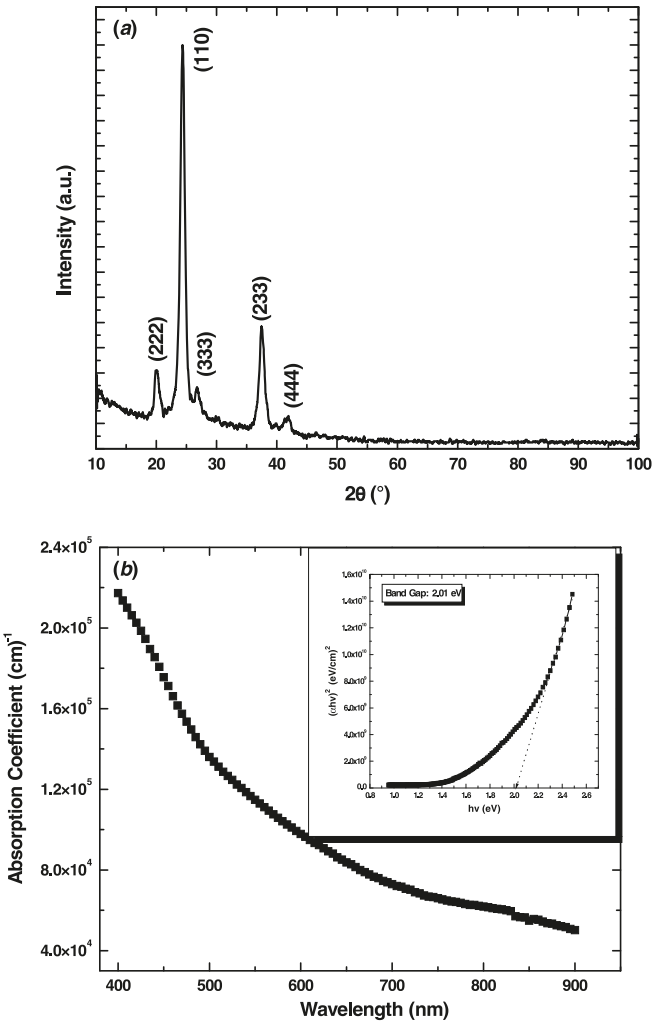

Table 1. Comparison of observed and standard *d* values of $Bi_2(Te_{0.5}Se_{0.5})_3$ thin films.

JCPDS				
Bi_2Te_3		Bi_2Se_3		Observed
d (Å)	(*hkl*)	*d* (Å)	(*hkl*)	*d* (Å)
6.64	—	—	—	6.64
5.07	(010)	—	—	5.46
4.94	—	4.57	(222)	4.94
3.67	(110)	3.37	(010)	3.57
3.21	(221)	3.30	(110)	3.21
1.83	(342)	1.82	(555)	1.81
1.80	(131)	1.79	(445)	1.79
1.60	(442)	1.62	(131)	1.61

Note: JCPDS, Joint Committee on Powder Diffraction Standards.

films. The surface morphology and binding energy was also confirmed by X-ray photoelectron spectroscopy (XPS).

Experimental details

For the deposition of the $Bi_2(Te_{0.5}Se_{0.5})_3$ composite, concentrations of bismuth nitrate, sodium selenosulfite, and sodium tellurosulfite were taken to get a 2:3 stoichiometric proportion. All chemicals were A.R. grade. Here, triethanolamine ($N(CH_2–CH_2–OH)_3$, TEA) was used as a complexing agent to arrest the bismuth ions. The $Bi_2(Te_{0.5}Se_{0.5})_3$ thin film was prepared by using APT on a ultrasonically cleaned glass substrate. Bismuth triethanolamine (Bi–TEA, 0.05 mol/L), sodium selenosulfite (Na_2SeSO_3, 0.05 mol/L), and sodium tellurosulfite (Na_2SeSO_3, 0.05 mol/L) were used as a basic source material for bismuth (Bi^{3+}), selenium (Se^{2-}), and tellurium (Te^{2-}) ions, respectively. Cleaned glass slides of dimension 75 mm × 25 mm × 1.35 mm were used as substrates mounted on a specially fabricated Bakelite holder and rotated with constant speed in the reaction mixture.The rotating speed of the glass substrate was 45 ± 2 rpm.The optimized pH temperatures were 10.5 (±0.5) and 55 (±0.5) °C. The film thickness remained constant after 1.5 h. The deposited film was washed with double distilled water, dried at 100 °C in a muffle furnace, and used for further characterization.

Growth mechanism

According to the Ostwald ripening law, if metal ions in solution are arrested using a polydentate complexing agent like TEA, the rate of reaction between metal ions and chalcogenide ions can be well controlled to avoid precipitation and obtain the desired quality of metal chalcogenide thin films. During the deposition process, owing to the Bi–TEA complex, Bi^{3+} ions are slowly released in the solution and react with Te^{2-} and Se^{2-} ions and are deposited on the cleaned glass substrate at basic pH. Deposition of film occurs when the ionic products of Bi^{3+}, Te^{2-}, and Se^{2-} exceeds the solubility product. The overall growth mechanism of the mixed composites of bismuth tellurium selenide is summarized as follows. Therefore, APT is suitable for the deposition of $Bi_2(Te_{0.5}Se_{0.5})_3$ mixed-metal thin films.

$$[1]\quad (NH_4)_3[Bi_2(CH_2-CH_2-O)_3] + 6H_2O \xrightarrow{\text{pH 10.5}} Bi^{3+} + 3NH_4OH + 3OH^- + 2[N(CH_2-CH_2-OH)_3]$$

$$[2]\quad Na_2SeSO_3 + OH^- \rightarrow Na_2SO_4 + HSe^-$$
$$HSe^- + OH^- \rightarrow H_2O + Se^2$$

$$[3]\quad Na_2TeSO_3 + OH^- \rightarrow Na_2SO_4 + HTe^-$$
$$HTe^- + OH^- \rightarrow H_2O + Te^{2-}$$

The reactions given in eqs. [1]–[3] show that the Bi^{3+}, Te^{2-}, and Se^{2-} are condensed on an ion by ion basis on the glass substrate as

$$[4]\quad Bi^{3+} + nNa_2SeO_3 + nNa_2TeO_3 \xrightarrow{\text{pH 10.5, 55(±0.5) °C,}} Bi_2(Te_{1-x}Se_x)_3 + nNa_2SO_4 + n\text{TEA}$$

Finally, the deposited $Bi_2(Te_{0.5}Se_{0.5})_3$ films are found to be uniform and well adherent to the substrate.

Fig. 2. (*a*) Scanning electron microscopy (SEM) micrograph, (*b*) atomic force microscopy (AFM) images, and (*c*) energy dispersive X-ray analysis (EDAX) spectrum for as-deposited $Bi_2(Te_{0.5}Se_{0.5})_3$ thin film.

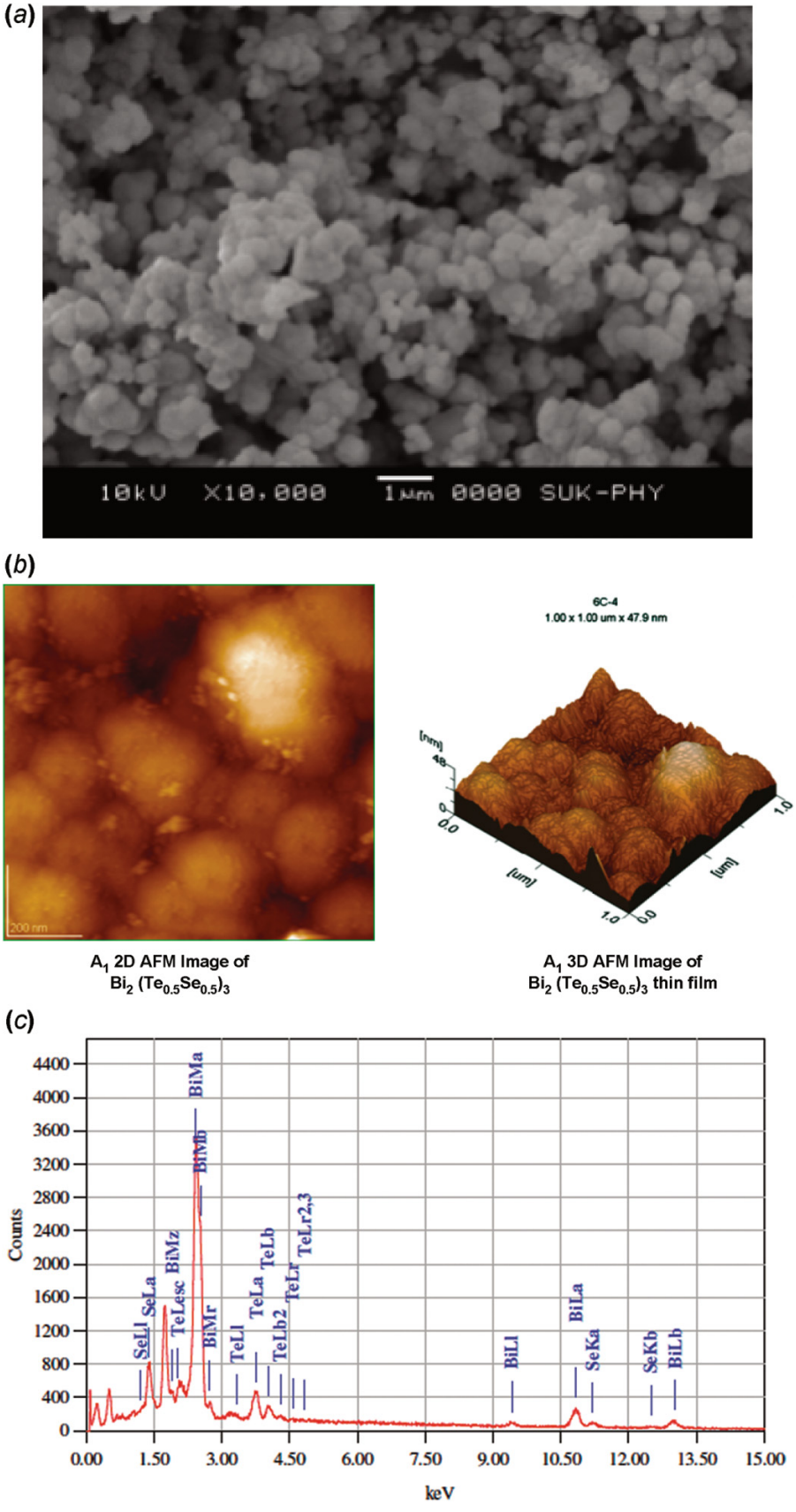

Can. J. Chem. Downloaded from www.nrcresearchpress.com by South China Agricultural University on 09/19/12
For personal use only.

Can. J. Chem. Downloaded from www.nrcresearchpress.com by South China Agricultural University on 09/19/12
For personal use only.

Characterization techniques

X-ray diffraction (XRD) analysis was carried out using a Philips PW-1710 X-ray diffractometer for 2θ ranging from 10° to 1000° with the Cu K_α line used as a beam (λ = 1.5405 Å). Optical study of $Bi_2(Te_{0.5}Se_{0.5})_3$ thin film was done by using a UV–vis–NIR spectrophotometer (Shimadzu 3600, Japan) in the wavelength range 400 to 900 nm. The film layer thickness was measured by a surface profilometer. We used an XP-1 Ambios Technology surface profilometer (contact mode) having 1.5 Å resolution. Stoichiometry of the films was studied with energy dispersive X-ray analysis (EDAX). Surface morphology was characterized using a JEOL-JSM-6360 scanning electron microscope (SEM) and atomic force microscopy (AFM) (model NSE, serial No. 245). A silicon nitride cantilever was used to probe the surface of the film. XPS was used to study the binding energy and surface oxidation of the material. Electrical conductivity of the film was studied by using the DC two-probe method at 300–500 K. The working temperature was recorded using a Chromel-Alumel thermocouple. Potential drop across the film was measured with the help of a MeCo 801 digital multimeter and current passed through sample was noted using a digital picoammeter (Scientific equipment, Roorkee DPM 111). The thermovoltage was measured using a Testronix microvoltmeter. Thermal conductivity was measured by the ring probe method using a commercial thermal conductivity measurement apparatus (C-T meter, Teleph, France) at room temperature.

Results and discussion

X-ray diffraction pattern of deposited $Bi_2(Te_{0.5}Se_{0.5})_3$ thin films

The XRD pattern of the deposited thin film is shown in Fig. 1*a*. From the XRD pattern it is seen that as-deposited films are nanocrystalline in nature. The comparison of the observed lattice spacing (*d*) values of $Bi_2(Te_{0.5}Se_{0.5})_3$ mixed composites are in good agreement with the standard *d* Joint Committee on Powder Diffraction Standards (JCPDS) data values for the rhombohedral structure JCPD data files (card Nos. 85 and 85-0519).The comparison of the observed *d* values of the deposited samples are given in Table 1. The crystallite size (*D*) of the film was calculated by using the Debye–Scherrer formula[12] and it was found to be 14.75 nm at 0.0149 half peak width β (radians).

$$[5] \qquad D = \frac{k\lambda}{\beta \cos\theta}$$

where *k* is a constant equal to 0.94, λ is the wavelength of the source, β is full-width at half-maximum (FWHM) in radians, and θ is Bragg's angle. The strongest peak for all films occurred at $2\theta = 24.13°$ with d = 5.46 Å corresponding to a (110) reflection. It indicates that the preferred orientation lies along the (110) direction for $Bi_2(Te_{0.5}Se_{0.5})_3$ thin films. The *D* for the deposits was calculated using the Debye–Scherer formula for the (110) peak assuming that microstrain can be neglected.

Optical studies

The resultant APT-deposited $Bi_2(Te_{0.5}Se_{0.5})_3$ film is continuous and adherent to the substrates. The optical absorption spectra of this sample were been studied to evaluate the absorption coefficient, optical band gap, and nature of the transition involved in the wavelength region 400–900 nm. The absorption coefficient depends on the wavelength for $Bi_2(Te_{0.5}Se_{0.5})_3$ thin film and is shown in Fig. 1*b*. It was observed that the optical absorption coefficient was high ($\alpha = 10^5$ cm^{-1}). The α, energy gap (Eg), and photon energy ($h\nu$) are related as

$$[6] \qquad \alpha = \frac{A}{h\nu}(h\nu - \mathrm{Eg})^n$$

where *A* is a constant, *h* is Planck's constant, ν is frequency, Eg is the optical energy gap of investigated sample, and *n* assumes values of 1/2, 2, 3/2, and 3 for allowed direct, allowed indirect, forbidden direct, and forbidden indirect transitions, respectively. For the allowed direct type of transition

$$[7] \qquad (\alpha h\nu)^2 = A(h\nu - \mathrm{Eg})$$

where *A* is a parameter that depends on the transition probability. Figure 1*b* shows the plot of $(\alpha h\nu)^2$ vs $h\nu$ for $Bi_2(Te_{0.5}Se_{0.5})_3$ thin films. The value of Eg was calculated by the best straight line fits in the plot and the corresponding band gap was obtained by extrapolating the straight portion of the graph of $(\alpha h\nu)^2$ vs $h\nu$ on the energy axis at $\alpha = 0$. α was observed to be 10^5 cm^{-1}

Table 2. Energy dispersive X-ray (EDAX) analysis of the as-deposited $Bi_2(Te_{0.5}Se_{0.5})_3$ thin films.

Film composition	Element	Elements (expected at %)	Elements (actual at %)
$Bi_2(Te_{0.5}Se_{0.5})_3$	Bi	40	46.28
	Te	30	25.48
	Se	30	28.24

Fig. 3. X-ray photoelectron spectroscopy (XPS) spectrum of as-deposited $Bi_2(Te_{0.5}Se_{0.5})_3$ film.

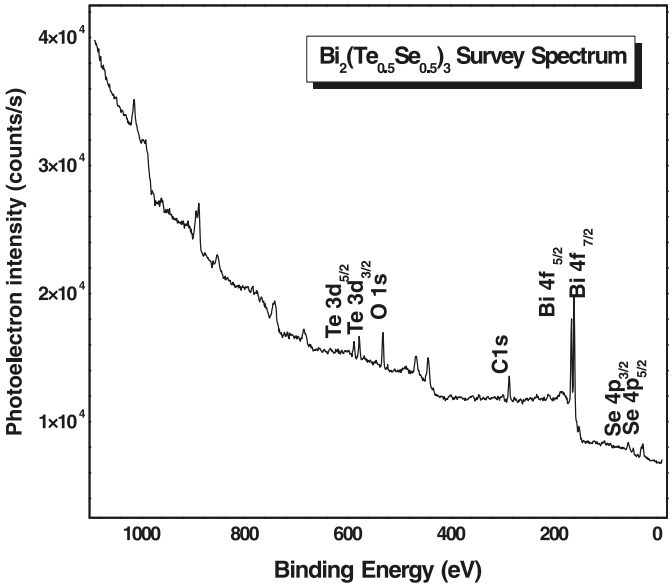

Can. J. Chem. Downloaded from www.nrcresearchpress.com by South China Agricultural University on 09/19/12
For personal use only.

Fig. 4. X-ray photoelectron spectroscopy (XPS) spectra showing (*a*) C 1s, (*b*) Te 3d, (*c*) Bi 4f, and (*d*) Se 4p states.

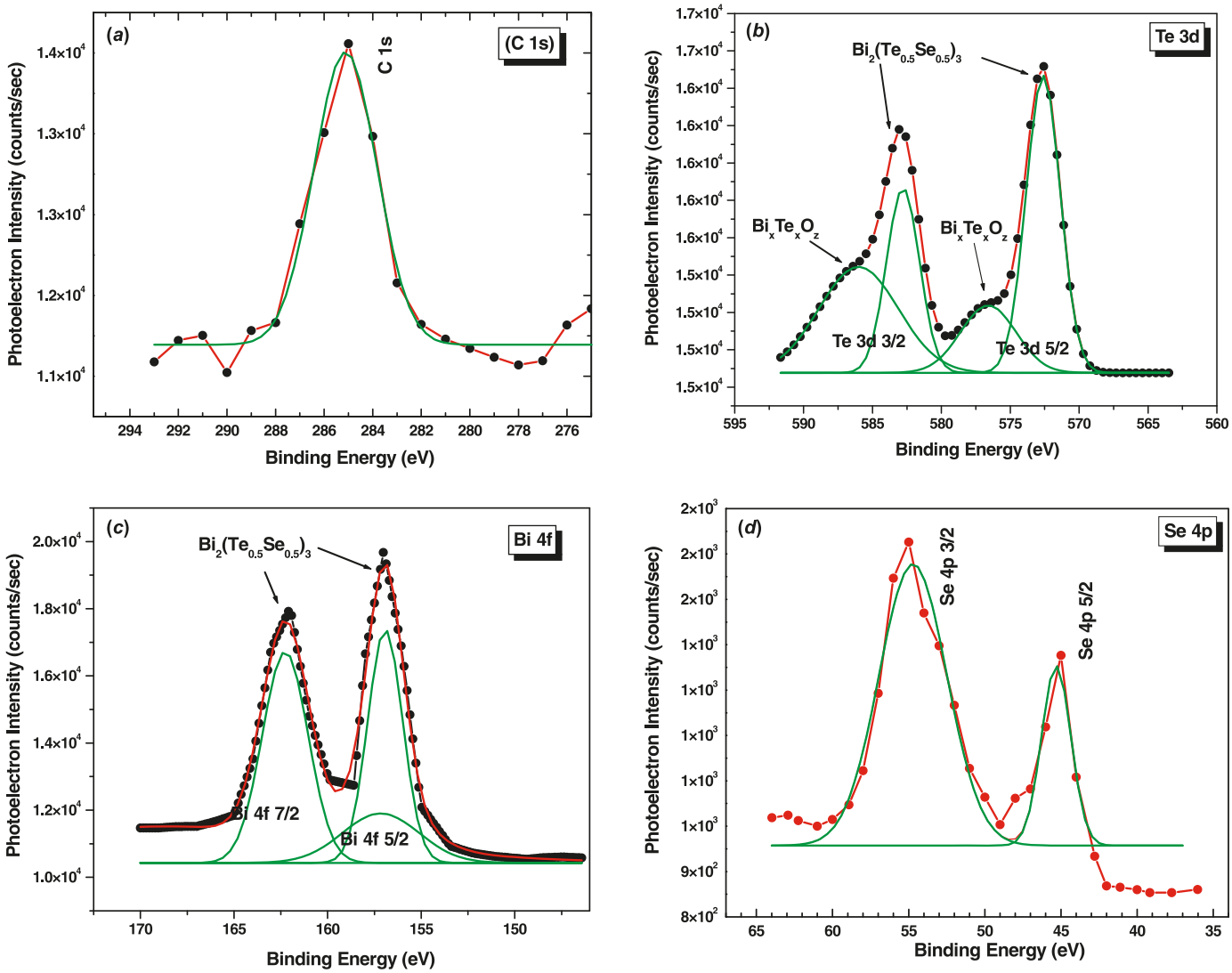

and supports that the type of transition was direct and allowed and the band gap for $Bi_2(Te_{0.5}Se_{0.5})_3$ thin film was found to be 2.01 eV.

SEM studies

Figure 2*a* shows the surface micrograph of the $Bi_2(Te_{0.5}Se_{0.5})_3$ thin film. The SEM micrograph shows that the film was compact, uniform, and adherent with a pin-hole-free nature and an average of 450 nm. This was due to less agglomeration of ions and the resultant film become nanogain-like.

AFM Studies

The surface morphology of $Bi_2(Te_{0.5}Se_{0.5})_3$ thin films was analyzed using the AFM technique. The film surface was well covered with $Bi_2(Te_{0.5}Se_{0.5})_3$ grains. Figure 2*b* shows 2D and 3D AFM images. In the 3D image, an intensity strip is shown that indicates the height of the surface grains along the *z* axis. AFM revels that granular nature of the particles. It was observed that the surface roughness of the film is 8.15 nm × 1 μm × 1 μm. The AFM images are in good agreement with the SEM image.

Table 3. Quantitative analysis of film composition by using XPS.

Film composition	Element	Elements (expected at %)	Elements by XPS (actual at %)
$Bi_2(Te_{0.5}Se_{0.5})_3$	Bi	40	42.07
	Te	30	28.13
	Se	30	27.52

EDAX studies

The elemental analyses of $Bi_2(Te_{0.5}Se_{0.5})_3$ films were done using the EDAX technique. Figure 2*c* shows the EDAX patterns of $Bi_2(Te_{0.5}Se_{0.5})_3$ thin films. For the EDAX analysis, BiLa (at 2.50 keV), TeLa (at 3.75 keV), and SeLa (at 1.45 keV) peaks were taken for Bi, Te, and Se elemental analysis, respectively. The atomic percentage ratios of Bi, Te, and Se in deposited thin films of $Bi_2(Te_{1-x}Se_x)_3$ are listed in Table 2. It clearly shows that the theoretical and practical atomic percentages of bismuth, tellurium, and selenium in the $Bi_2(Te_{0.5}Se_{0.5})_3$ thin film is in good agreement. Variation in the percentage analysis of bismuth, tellurium, and selenium might be due to an antisite effect.[13] In the present case,

Table 4. Thermoelectric (TEP) study of $Bi_2(Te_{0.5}Se_{0.5})_3$ thin films.

Film composition	S (μVK^{-1})	ρ ($\mu\Omega m^{-1}$)	Thermal conductivity (W m^{-1} K^{-1})	PF (mW K^{-2} m^{-1})	ZT at 300 K
$Bi_2(Te_{0.5}Se_{0.5})_3$	–50.05	9.784	0.409	0.256	0.1878

Note: S, Seebeck coefficient; ρ, resistivity; PF, power factor; ZT, figure of merit.

Can. J. Chem. Downloaded from www.nrcresearchpress.com by South China Agricultural University on 09/19/12
For personal use only.

EDAX analysis shows a value of 46.28 owing to antisite effect. The antisite defect consisted of Bi atoms located on the Te sublattice that carries one negative charge, Mo_{Te}' (As defect).

XPS study

To further confirm the surface composition of the $Bi_2(Te_{0.5}Se_{0.5})_3$ thin films by using XXPS. The XPS data were collected in the constant analyzer energy mode at 20 eV. Mg Kα ($h\gamma$ = 1253.6 eV) radiation was employed as the excitation source with an anode voltage of 15 kV and an emission current of 20 mA. Figure 3 shows a survey spectrum of the $Bi_2(Te_{0.5}Se_{0.5})_3$ thin-film sample. The XPS survey scans from film reveal C, Bi, Te, Se, and O peaks. The presence of the O 1s peak indicates that oxidation of the film takes place after exposure to the atmosphere. The high-resolution spectra of the Bi 4f and Te 3d are obtained using C 1s as the reference at 285 eV. It indicates that the binding energies of different states of the elements present in the films are 596.5, 174.5, and 54.5 eV for Te, Bi, and Se, respectively. The Bi $4f_{5/2}$ and $4f_{7/2}$ peaks have shoulders at higher binding energy, which indicates surface oxidation. The Bi 4f band at 158 eV corresponds to $Bi_2(Te_{0.5}Se_{0.5})_3$, consistent with the phase identified by XRD. These peaks are supported by the presence of Te 3d state at 572.2 eV (Fig. 4). The high binding energy Bi 4f state near 158.7 eV and Te 3d state at 575.8 eV indicate the presence of surface oxide on Bi_2Te_3 nanostructures.[14–16] The Te $3d_{5/2}$ and $3d_{3/2}$ peaks were located at 572.0 and 582.3 eV respecitvely, which indicates the Bi_2Te_3. These results reveal that there is no metallic tellurium impurity, which should appear at lower binding energy. This analysis of sample is consistent with the XRD data.

The quantification in XPS is determined by considering the intensity of the photoelectron. The XPS intensity (I) of a photoelectron peak from a homogeneous solid is given, in a very simplified form, by

$$[8] \qquad I = J\rho\sigma K\lambda$$

where J is the photon flux, ρ is the concentration of the atom or ion in the solid, σ is the cross-section for photoelectron production (which depends on the element and energy being considered), K is a term which covers all of the instrumental factor (0.7 for MgKα), and λ is the electron attenuation length. The intensity referred to will usually be taken as the integrated area under the peak following the subtraction of a linear or S-shaped background. Equation [8] was used for direct quantification and the analysis is summarized in Table 3.

Conduction studies

Electrical conductivity measurements were made in the temperature range 300 to 500 K at constant voltage (5 V).

Fig. 5. (*a*) The variation of ln σ (Ω^{-1} cm^{-1}) with 1000/T (K) and (*b*) temperature dependence of the Seebeck coefficient of $Bi_2(Te_{0.5}Se_{0.5})_3$ thin films.

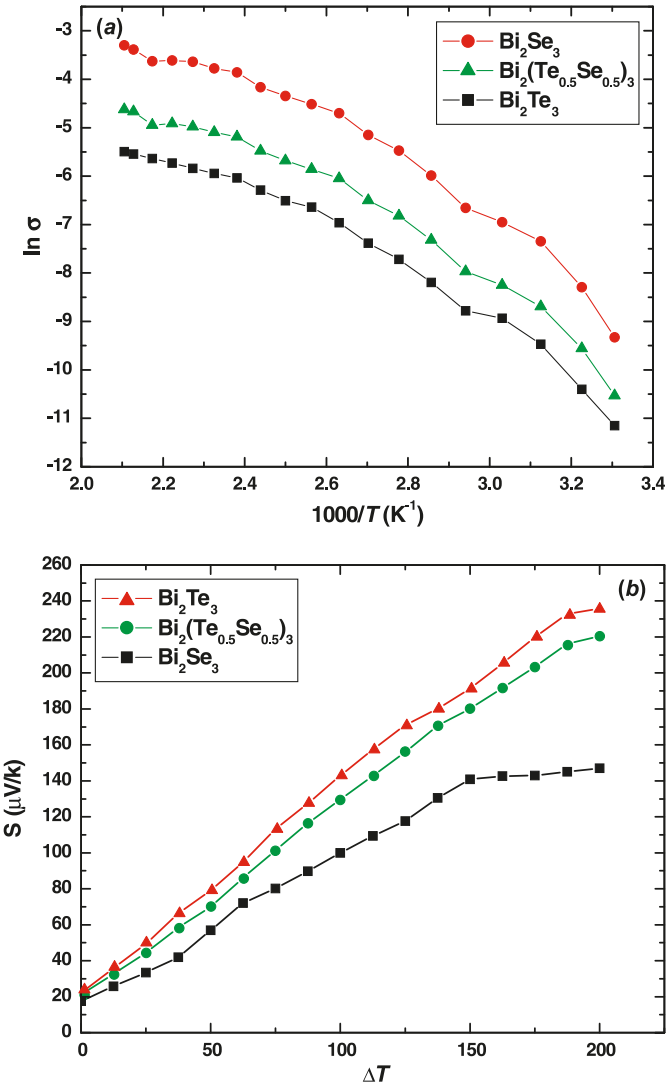

The temperature dependence of electrical conductivity of the semiconducting thin films is given by

$$[9] \qquad \sigma = \sigma_0 \exp\left(\frac{-E_a}{kT}\right)$$

where k is the Boltzmann constant, σ_0 is the temperature independent part of the conductivity, and E_a is the activation energy. The variation of ln σ with 1000/T in the temperature range 300 to 500 K is shown in Fig. 5*a*. The measurement shows an increase in electrical conductivity of the materials with an increase in temperature, indicating the films are semi-

Can. J. Chem. Downloaded from www.nrcresearchpress.com by South China Agricultural University on 09/19/12
For personal use only.

conducting in nature. For mixed-composite $Bi_2(Te_{0.5}Se_{0.5})_3$ thin films, the electrical conductivities lie between those of Bi_2Te_3 and Bi_2Se_3. From the slopes of the linear plots, activation energies were calculated for a two-temperature region. The activation energies for the low-temperature region and in the high-temperature region were found to be 0.1117 and 0.3161 eV, respectively. The temperature dependence thermo-electromotive force (emf) for all these films is shown in Fig. 5*b* at 300–500 K. Thermoelectric measurements were made using the integral method in which one end of the film was heated and the other kept at a constant low temperature and developed thermal emf was measured with respect to the temperature gradient. In the present work all the samples showed negative polarity of the generated voltage. This confirms n-type conduction of the samples.[17,18] The thermoelectric performance of $Bi_2(Te_{0.5}Se_{0.5})_3$ thin film is quantified by a dimensionless figure of merit (ZT) as

$$[10] \qquad ZT = S^2/\rho K$$

where S^2 is the Seebeck coefficient and K is the thermal conductivity. The room temperature ZT value is 0.1878 as shown in Table 4. Because of a continued increase of the Seebeck coefficient, the power factor ($S^2\sigma$) and thermoelectric performance (ZT) increase substantially at higher temperatures.[7]

Conclusions

It is concluded that $Bi_2(Te_{0.5}Se_{0.5})_3$ thin film was successfully deposited by APT and characterized by opto structural, morphological, and electrical studies. The UV–vis–NIR spectra of the film revealed that the deposited film had a band gap of 2.01 eV. The XRD of the film showed a rhombohedral structure. SEM and AFM micrographs showed that the films are compact, uniform, and adherent with a pin-hole-free nature. From EDAX, the compositions of the films are in good stoichiometric ratios. Electrical and TEP studies showed $Bi_2(Te_{0.5}Se_{0.5})_3$ mixed-metal chalcogenide thin film is semiconducting, having n-type conduction mechanism. A good thermoelectric figure of merit revealed that the $Bi_2(Te_{0.5}Se_{0.5})_3$ thin-film material is suitable for thermocooling devices at room temperature.

Acknowledgements

One of the authors (S.M.P.) wishes to acknowledge the University Grant Commission New Delhi (UGC New Delhi), India, for providing facilities under the Special Assistance Programs-Departmental Research Support (SAP-DRS) scheme. One of the authors (S.S.M.) wishes to acknowledge the Department of Atomic Energy–Board of Research In Nuclear Sciences (DAE-BRNS), Mumbai, India, for financial suppport through the DAE-BRNS (project No. 2008/37/8/BRNS/1489 for 2008–2011).

References

(1) Völklein, F.; Min, G.; Rowe, D. M. *Sens. Actuators A Phys.* **1999**, *75* (2), 95. doi:10.1016/S0924-4247(99)00002-3.
(2) Goldsmid, H. J. *Introduction to Thermoelectricity;* Springer: London, New York, 1978.
(3) Ioffe, A. F. *Semiconductor Thermoelements and Thermoelectric Cooling;* Infosearch Ltd.: London, 1957.
(4) Yim, W. M.; Rosi, F. D. J. *Solid-State Electron.* **1972**, *15* (10), 1121. doi:10.1016/0038-1101(72)90172-4.
(5) Yamashita, O.; Tomiyosh, S. J. *Appl. Phys. (Berl.)* **2004**, *95* (11), 6277. doi:10.1063/1.1712013.
(6) Fan, X. A.; Yang, J. Y.; Zhu, W.; Bao, S. Q.; Duan, X. K.; Xiao, C. J.; Li, K. *J. Phys. D Appl. Phys.* **2007**, *40* (18), 5727. doi:10.1088/0022-3727/40/18/033.
(7) Kiely, J. H.; Lee, D.-H. *Meas. Sci. Technol.* **1997**, *8* (6), 661. doi:10.1088/0957-0233/8/6/013.
(8) Hong, S.-J.; Chun, B.-S. *Mater. Res. Bull.* **2003** *38* (4), 599. doi:10.1016/S0025-5408(03)00022-9.
(9) Mane, R. K.; Ajalkar, B. D.; Bhosale, P. N. *Mater. Chem. Phys.* **2003**, *82* (3), 534. doi:10.1016/S0254-0584(03)00233-5.
(10) Patil, N. S.; Sargar, A. M.; Mane, S. R.; Bhosale, P. N. *Appl. Surf. Sci.* **2008**, *254* (16), 5261. doi:10.1016/j.apsusc.2008.02.084.
(11) Mane, R. M.; Mane, S. R.; Kharade, R. R.; Bhosale, P. N. *J. Alloy. Comp.* **2010**, *491* (1–2), 321. doi:10.1016/j.jallcom.2009.10.159.
(12) Cullity, B. D. *Elements of X-ray Diffraction;* Addison-Wesley Publishing Company: London, 1978.
(13) Horak, J.; Cermak, K.; Koudelka, L. J. *Phys. Chem. Solids* **1986**, *47* (8), 805. doi:10.1016/0022-3697(86)90010-7.
(14) Purkayastha, A.; Yan, Q. Y.; Raghuveer, M. S.; Gandhi, D. D.; Li, H. F.; Liu, Z. W.; Ramanujan, R. V.; Borca-Tasciuc, T.; Ramanath, G. *Adv. Mater. (Deerfield Beach Fla.)* **2008** (20), 2679.
(15) Bando, H.; Koizumi, K.; Oikawa, Y.; Daikohara, K.; Kulbachinskii, V. A.; Ozaki, H. *J. Phys. Condens. Matter* **2000**, *12* (26), 5607. doi:10.1088/0953-8984/12/26/307.
(16) Purkayastha, A.; Kim, S.; Gandhi, D. D.; Ganesan, P.; Borca-Tasciuc, G. T.; Ramanath, G. *Adv. Mater. (Deerfield Beach Fla.)* **2006** (18), 2958.
(17) Ufimtsev, V. B.; Osvensky, V. B.; Bublik, V. T.; Sagalova, T. B.; Jouravlev, O. E. *Adv. Perform. Mater.* **1997**, *4* (2), 189. doi:10.1023/A:1008695513708.
(18) Svechnikova, T. E.; Zemskov, V. S. *Inorg. Mater.* **2006**, *42* (7), 708. doi:10.1134/S002016850607003X.

Facile one-pot synthesis of sugar–thiazolidinone derivatives

Ali Darehkordi, Kazem Saidi, and Somayeh Ghazi

Can. J. Chem. Downloaded from www.nrcresearchpress.com by South China Agricultural University on 09/19/12
For personal use only.

Abstract: A simple, efficient, and cost-effective method for the synthesis of a series of sugar–thiazolidinone derivatives by a one-pot reaction of the corresponding thiosemicarbazone of *d*-galactose, *d*-glucose, and *d*-mannose compounds in the presence of dimethyl or diethyl acetylenedicarboxylate is described. Two different methods were used and high yields were obtained in both cases: (A) in EtOAC–H_2O at an ambient temperature and (B) microwave irradiation under solvent-free conditions.

Key words: sugar–thiazolidinone, dimethyl acetylenedicarboxylate, thiosemicarbazone.

Résumé : On a mis au point une méthode simple, efficace et économique de synthèse d'une série de dérivés de type sucre–thiazolidinone impliquant une réaction monotope des dérivés thiosemicarbazone du *d*-galactose, *d*-glucose et *d*-mannose en présence d'acétylènedicarboxylate de diméthyle ou de diéthyle. Deux méthodes différentes ont été utilisées et les deux conduisent à des rendements élevés; l'une implique l'utilisation d'un solvant formé d'eau et d'acétate d'éthyle à la température ambiante et l'autre une irradiation micro-ondes dans des conditions sans solvant.

Mots-clés : sucre–thiazolidinone, acétylènedicarboxylate de diméthyle, thiosemicarbazone.

[Traduit par la Rédaction]

Introduction

Heterocyclic compounds have acquired considerable attention in recent years in organic synthesis because of their potential for use in pharmacological activities.[1] Nitrogen, sulfur, and oxygen containing five- or six-membered heterocyclic compounds have occupied enormous significance in the field of medicinal chemistry. Several substituted thiazolidones have been found to possess hypnotic, anesthetic, sedative, anticonvulsant, and microbiological activities.[2–4] Some of the thiazolines have shown a wide range of pharmaceutical properties.[5] Recently, we reported the synthesis of thiazoline derivatives by the reaction of DMAD and DEADC with thiosemicarbazone derivatives (Scheme 1, structures **1** and **2**).[6] Reaction of thiosemicarbazide with *d*-galactose, *d*-glucose, and *d*-mannose afforded the corresponding thiosemicarbazone derivatives in either acyclic or pyranose structures depending on the solvent and the conditions of the reaction.[7]

The structure–activity relationships (SARs) in a series of thiosemicarbazone and thiosemicarbazide derivatives have been investigated by means of the electron-topological method (ETM).

All derivatives in training sets are potent inhibitors of herpes simplex virus type 1 (HSV-1) replication.[8]

In this work we have considered the reaction of different pyranose – sugar thiosemicarbazone derivatives with dimethylacetylene dicarboxylate and diethylacetylene dicarboxylate to synthesize thiazolidinone derivatives by two different methods: (A) sugar thiosemicarbazone derivatives were mixed with DMAD or DEADC in EtOAC–H_2O as a solvent at ambient temperature and (B) a microwave-assisted synthesis under solvent-free conditions.

Experimental

d-Galactose, *d*-glucose, and *d*-mannose and solvents such as EtOAC, EtOH, and Et_2OH were obtained from the Merck Chemical Co. and were used without further purification. Sugar–thiosemicarbazone derivatives were prepared according to the procedure reported in the literature.[9–12] IR spectra were obtained on a Matson-1000 FT-IR spectrometer. Peaks are reported in wavenumbers (cm^{-1}). All NMR spectra were recorded on a Bruker model DRX-500 AVANCE (^1H, 500 MHz; and ^{13}C, 125 MHz) NMR spectrometer. Chemical shifts are reported in parts per million (ppm) from tetramethylsilane (TMS) as an internal standard with DMSO-d_6 as a solvent. Elemental analyses (C, H, and N) were performed with a Heracus CHN-O-Rapid analyzer. MW irradiation was carried out using a commercial MW oven (SGO 1000 W) with a thermocouple used to monitor the temperature inside the vessel (≈100–115 °C).

A typical procedure

*Synthesis of β-*D*-galactopyranosylthiosemicarbazone (1a–1c)*

Sugar–thiosemicarbazone derivatives were prepared according to the following procedure: to a well-stirred boiling solution of *d*-galactose (10 mmol, 1.80 g) in ethanol

Received 5 February 2011. Accepted 28 July 2011. Published at www.nrcresearchpress.com/cjc on 24 October 2011.

A. Darehkordi and S. Ghazi. Department of Chemistry, Faculty of Science, Vali-e-asr University of Rafsanjan, Rafsanjan 77176, Iran.
K. Saidi. Department of Chemistry, Shahid Bahonar University of Kerman, Kerman, Iran.

Corresponding author: Ali Darehkordi (e-mail: adarehkordi@yahoo.com and darehkordi@mail.vru.ac.ir).

Can. J. Chem. Downloaded from www.nrcresearchpress.com by South China Agricultural University on 09/19/12
For personal use only.

Scheme 1.

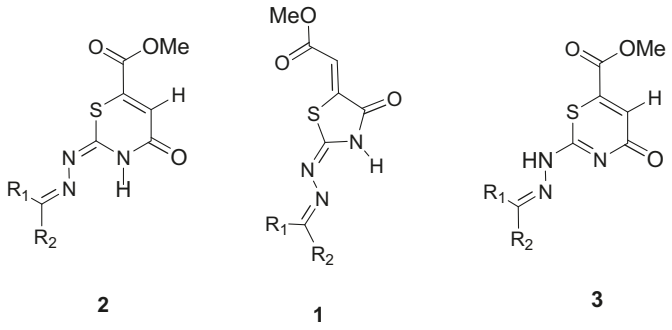

2 1 3

Scheme 2. Synthesis of sugar–thiosemicarbazone derivatives.

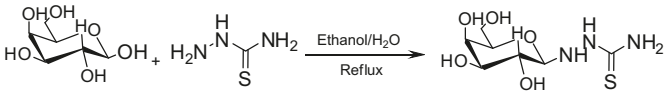

1b

(30 mL) was added thiosemicarbazide (10 mmol, 0.94 g), and boiling was continued for an additional 8 h, then the reaction mixture was cooled to room temperature and allowed to crystallize, affording a white precipitate as a pyranose (Scheme 2).[9–12]

A typical procedure

*Synthesis of ethyl 2-((***E***)-4-oxo-2-((β-*d*-galactopyranosyl) hydrazono)thiazolidinone-5-ylidene)acetate (3b)*

Method A: To a well-stirred solution of β-*d*-galactopyranosylthiosemicarbazone (4 mmol) in ethyl acetate (10 mL) and water (5 mL) was added a solution of diethyl acetylene dicarboxylate (4 mmol) in small portions. The stirring was continued at ambient temperature for an additional 3 h. The resulting mixture was filtered and recrystallized from EtOH or DMF–H_2O.

Method B: A mixture of β-*d*-galactopyranosylthiosemicarbazone (4 mmol) and DEADC (4 mmol) was subjected to microwave irradiation at a power output of 200 W for 5–7 min and after cooling the reaction mixture to room temperature, the solid residue was recrystallized from EtOH or DMF–H2O. The product was obtained as a yellow powder (Scheme 3). Table 1 shows the reaction conditions and product yields for the Aand B methods.

Yellow powder (recrystallized from EtOH or DMF–H_2O), yield: 88%; mp 189–192 °C. $[\alpha]_D^{25}$ +1.0 (*c* 1.0, DMSO). FT-IR (KBr, cm^{-1}) υ_{max}: 3200–3280 (N–H), 2955–3081 (CH, aliphatic), 1766, 1666 (C=O), 1664, 1630 (C=N) and (C=C). ^{1}H NMR (DMSO-d_6, 500 MHz), ppm) δ: 9.85 (1H, NH), 7.40 (1H, HC=C–), 6.60 (1H, NH), 3.53–5.06 (m, 4H, OH), 4.90 (1H, H-1), 4.39 (1H, H-2) 4.23 (1H, H-3), 3.72 (1H, H-4), 3.68 (m, 1H, H-5), 3.85 (1H, H-6), 3.84 (1H, H-6′) 4.23 (q, 2H, J = 7.14 Hz, –CH_2–), 1.23 (t, 3H, J = 7.14 Hz, –CH_3). ^{13}C NMR (DMSO-d_6, 125.77 MHz), ppm) δ: 168.07, 166.32, 165.74 (C=O, NC=O, C=N), 142.01, 114.53 (C=C), 82.83 (C-1), 76.83 (C-5), 74.20 (C-2), 73.20 (C-3), 70.69 (C-4), 61.66, 60.87 (C-6, –OCH_2–), 14.02 (–CH_3). Anal. calcd for $C_{13}H_{19}N_3O_8S$ (377.38) (%): C 40.38, H 5.07, N 11.13; found: C 40.22, H 5.11, N 11.45.

*Methyl 2-((***E***)-4-oxo-2-((β-*d*-galactopyranosyl)hydrazono) thiazolidinone-5-ylidene)acetate (3a)*

Yellow powder (recrystallized from EtOH or DMF–H_2O); mp 187–189 °C. $[\alpha]_D^{25}$ –2.7 (*c* 1.0, DMSO). FT-IR (KBr, cm^{-1}) υ_{max}: 3180–3285 (N–H), 2950–3080 (CH, aliphatic), 1765, 1662 (C=O), 1615, 1632 (C=N). ^{1}H NMR (DMSO-d_6, 500 MHz), ppm) δ: 8.90 (1H, NH), 6.75 (1H, HC=C–), 6.58 1H, NH), 4.00–5.12 (m, 4H, OH), 5.08 (1H, H-1), 4.92 (1H, H-2), 4.58 (1H, H-3), 4.11 (1H, H-4), 3.88 (m, 1H, H-5), 3.96 (1H, H-6), 3.95 (1H, H-6′), 3.73 (3H, –OCH_3). ^{13}C NMR (DMSO-d_6, 125.77 MHz), ppm) δ: 179.37, 176.69, 165.25 (C=O, NC=O, C=N), 147.88, 117.83 (C=C), 83.18 (C-1), 77.10 (C-5), 74.45 (C-2), 73.95 (C-3), 72.00 (C-4), 61.70 (C-6), 53.7 (–OCH_3). Anal. calcd for $C_{12}H_{17}N_3O_8S$ (363.35) (%): C 39.67, H 4.72, N 11.56; found: C 39.23, H 4.42, N 11.32.

*Methyl 2-((***E***)-4-oxo-2-((β-*d*-glucopyranosyl)hydrazono) thiazolidinone-5-ylidene)acetate (3c)*

Yellow powder (recrystallized from EtOH or DMF–H_2O); mp 126–128 °C. $[\alpha]_D^{25}$ +0.4 (*c* 1.0, DMSO). FT-IR (KBr, cm^{-1}) υ_{max}: 3210–3296 (N–H), 2955–3088 (CH, aliphatic), 1766, 1666 (C=O), 1614, 1635 (C=N). ^{1}H NMR (DMSO-d_6, 500 MHz), ppm) δ: 9.36 (1H, NH), 7.75 (1H, HC=C–), 6.63 (1H, NH), 3.55–4.90 (m, 4H, OH), 4.90 (1H, H-1), 4.42 (1H, H-2), 4.24 (1H, H-3), 3.75 (1H, H-4), 3.70 (m, 1H, H-5), 3.86 (1H, H-6), 3.86 (1H, H-6′), 3.62 (3H, –OCH_3). ^{13}C NMR (DMSO-d_6, 125.77 MHz), ppm) δ: 168.53, 166.16, 163.92 (C=O, NC=O, C=N), 142.98 115.38 (C=C), 79.96 (C-1), 76.25 (C-5), 72.27 (C-2), 71.32 (C-3), 70.30 (C-4), 61.25 (C-6), 52.62 (OCH_3). Anal. calcd for $C_{12}H_{17}N_3O_8S$ (363.35) (%): C 39.67, H 4.72, N 11.56; found: C 39.85, H 4.82, N 11.42.

*Ethyl 2-((***E***)-4-oxo-2-((β-*d*-glucopyranosyl)hydrazono) thiazolidinone-5-ylidene)acetate (3d)*

Yellow powder (recrystallized from EtOH or DMF–H_2O); mp 172–175 °C. $[\alpha]_D^{25}$ +0.1 (*c* 1.0, DMSO). FT-IR (KBr, cm^{-1}) υ_{max}: 3212–3297 (N–H), 2960–3088 (CH, aliphatic), 1767, 1665 (C=O), 1613, 1632 (C=N). ^{1}H NMR (DMSO-d_6, 500 MHz), ppm) δ: 9.14 (1H, NH), 6.95 (1H, HC=C–), 6.57 (1H, NH), 4.03–4.98 (m, 4H, OH), 5.03 (1H, H-1), 4.94 (1H, H-2), 4.62 (1H, H-3), 4.08 (1H, H-4), 3.91 (m, 1H, H-5), 3.98 (1H, H-6), 3.97 (1H, H-6′), 4.20 (q, 2H, J = 7.11 Hz, –CH_2–), 1.21 (t, 3H, J = 7.10 Hz, –CH_3). ^{13}C NMR (DMSO-d_6, 125.77 MHz), ppm) δ: 181.21, 177.90, 165.42 (C=O, NC=O, C=N), 148.27, 118.30 (C=C), 80.62 (C-1), 76.45 (C-5), 73.07 (C-2), 72.79 (C-3), 71.17 (C-4), 61.43, 60.63 (C-6, O–CH_2), 14.18 (–CH_3). Anal. calcd for $C_{12}H_{17}N_3O_8S$ (363.35) (%): C 39.67, H 4.72, N 11.56; found: C 39.23, H 4.42, N 11.32.

*Methyl 2-((***E***)-4-oxo-2-((β-*d*-mannopyranosyl)hydrazono) thiazolidinone-5-ylidene)acetate (3e)*

Yellow powder (recrystallized from EtOH or DMF–H_2O); mp 184–186 °C. $[\alpha]_D^{25}$ –1.3 (*c* 0.5, DMSO). FT-IR (KBr, cm^{-1}) υ_{max}: 3190–3280 (N–H), 2950–3080 (CH, aliphatic), 1765, 1663 (C=O), 1612, 1640 (C=N). ^{1}H NMR (DMSO-d_6, 500 MHz), ppm) δ: 9.60 (1H, NH), 7.11 (1H, NH), 6.95 (1H, HC=C–), 3.90–4.98 (m, 4H, OH), 5.60 (1H, H-1), 4.25

Scheme 3. Synthesis of sugar–thiazolidinone derivatives.

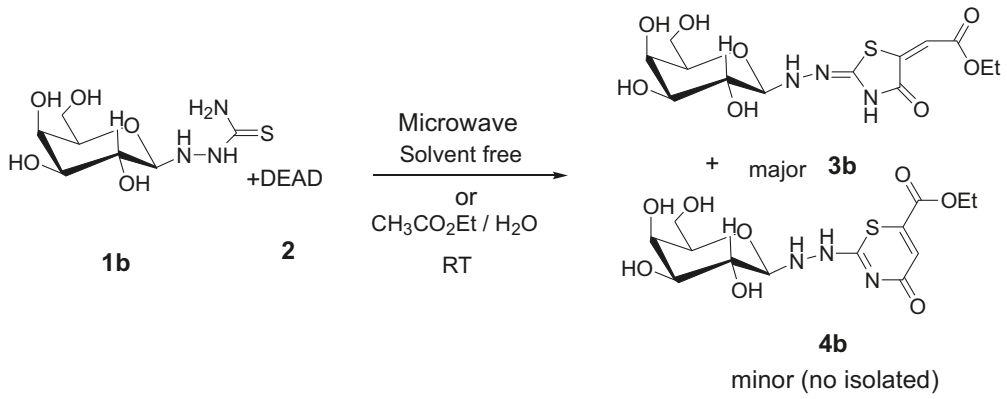

Table 1. Synthesis of sugar-thiazoline derivatives.

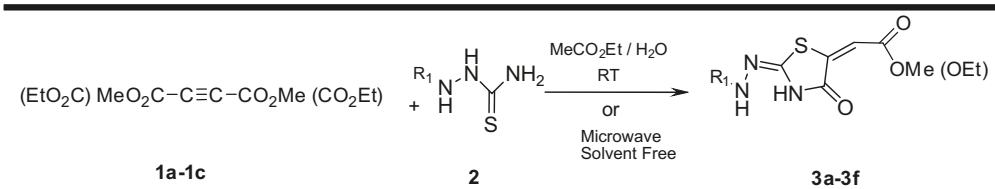

		Time		Yield (%)	
Entry	Product	Method A	Method B	Method A	Method B
3a	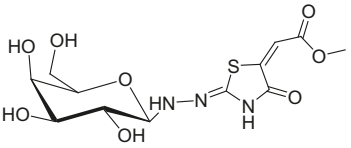	2.5 h	5 min	85	87
3b	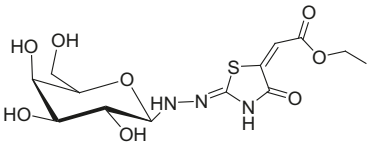	3 h	6 min	88	90
3c	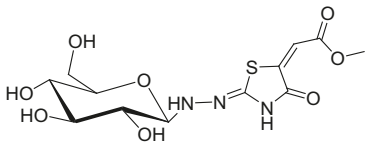	2.5 h	5 min	87	89
3d	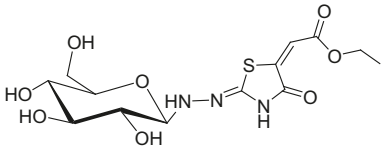	3 h	6 min	89	91
3e	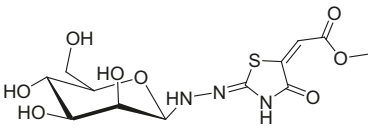	2.5 h	5 min	85	88
3f	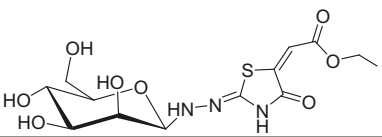	3 h	5 min	84	89

(1H, H-2), 4.11 (1H, H-3), 3.62 (1H, H-4), 3.56 (m, H-5), 4.73–4.77 (m, 2H, H-6, H-6′), 3.74 (3H, –OCH_3). ^{13}C NMR (DMSO-d_6, 125.77 MHz), ppm) δ: 176.88, 174.04, 166.32 (C=O, NC=O, C=N), 146.22, 117.90 (C=C), 82.54 (C-1), 76.48 (C-5), 74.34 (C-2), 73.80 (C-3), 72.03 (C-4), 62.20 (C-6), 53.31 (–OCH_3). Anal. calcd for $C_{12}H_{17}N_3O_8S$ (363.35) (%): C 39.67, H 4.72, N 11.56; found: C 40.01, H 4.52, N 11.33.

Can. J. Chem. Downloaded from www.nrcresearchpress.com by South China Agricultural University on 09/19/12
For personal use only.

Can. J. Chem. Downloaded from www.nrcresearchpress.com by South China Agricultural University on 09/19/12
For personal use only.

Scheme 4. A suggested mechanism for synthesis of sugar–thiazolidinone derivatives.

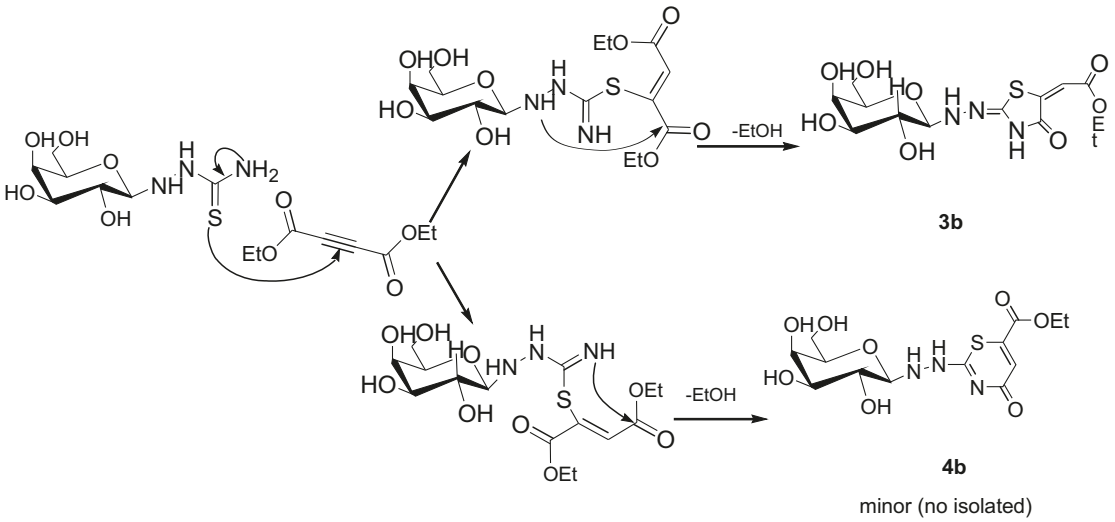

Ethyl 2-((E)-4-oxo-2-((β-d-mannopyranosyl)hydrazono) thiazolidinone-5-ylidene)acetate (3f)

Yellow powder (recrystallized from EtOH or DMF–H_2O); mp 188–189 °C. $[\alpha]_D^{25}$ +0.4 (*c* 1.0, DMSO). FT-IR (KBr), cm^{-1}) υ_{max}: 3220–3298 (N–H), 2958–3087 (CH, aliphatic), 1770, 1667 (C=O), 1619, 1645 (C=N). ^1H NMR (DMSO-d_6, 500 MHz), ppm) δ: 9.80 (1H, NH), 7.09 (1H, NH), 6.75 (1H, HC=C), 3.80–5.10 (m, 4H, OH), 5.64 (1H, H-1), 4.23 (1H, H-2), 4.07 (1H, H-3), 3.64 (1H, H-4), 3.58 (m, 1H, H-5), 4.75 (1H, H-6), 4.74 (1H, H-6′), 4.21 (q, 2H, J = 7.10 Hz, $–CH_2–$), 1.25 (t, 3H, J = 7.1 Hz, $–CH_3$). ^{13}C NMR (DMSO-d_6, 125.77 MHz), ppm) δ: 174.00, 176.55, 165.95 (C=O, NC=O, C=N), 145.77, 116.44 (C=C), 83.26 (C-1), 76.88 (C-5), 74.85 (C-2), 73.25 (C-3), 72.11 (C-4), 61.88, 62.12 (C-6, $–OCH_2–$), 14.30 ($–OCH_3$). Anal. calcd for $C_{13}H_{119}N_3O_8S$ (377.38) (%): C 40.38, H 5.07, N 11.13; found: C 39.98, H 5.23, N 10.86.

Results and discussion

In continuing our interest in the synthesis of heterocyclic compounds, such as thiazoline, from thiosemicarbazone derivatives of aldehydes and ketones and also the synthesis of other heterocyclic compounds, we would like now to report the synthesis of a different class of thiazoline compounds from sugar–thiosemicarbazone derivatives. These compounds possess N–H and S=C groups that can react with DMAD and DEADC by attack of the sulfur atom on the triple bond (Scheme 4). The resulting intermediate undergoes aminolysis of the vicinal or distal ester group to the S linkage, with respective formation of the five- or six-membered rings (compounds **3** and **4**) in an 1:1 ratio. Thus, treatment of **2** with DMAD or DEADC afforded two types of cyclic products (**3b** and **4b**, Scheme 3) in moderate to good yields. As the result of conjugate addition of the sulfur center and intermolecular N-acylation, the corresponding thiazolone (**3b**) could be isolated as a major product, which is stabilized by S–O– and S–N close-contact interactions involving the other carbomethoxy group in a quasi five-membered ring and the imino nitrogen of the hydrazone moiety in a quasi four-membered ring, respectively.[10] The reaction of sugar–thiosemicarbazone **1b** also gave one minor product (**4b**). Formation of methyl [1,3]thiazin-4-one-6-carboxylate (**4b**) can be interpreted by the conjugate addition of the sulfur center and alternative N-acylation, presumably furnishing a six-membered ring. As the product ratio **3b**:**4b** increases with longer reaction times, thiazinone **4b** seems to be an unstable kinetic product undergoing ring isomerization to **3b** catalyzed by the methanol that is released in the reaction mixture and can cleave the six-membered lactame at elevated temperature.[13,14]

In this investigation we reported two methods for the synthesis of thiazolinones: (A) β-*d*-galactopyranosyl–thiosemicarbazone was dissolved in ethyl acetate, then DMAD or DEADC is added to this solution. The reaction was carried out with stirring for 2.5–3 h at an ambient temperature and (B) β-*d*-galactopyranosyl–thiosemicarbazone was mixed with DMAD or DEADC, then the reaction was subject to microwave irradiation under solvent-free conditions for a short experimental time. The following results were obtained for the formation of **3c**, after 3 h using method A and after 5 min using method B. A plausible mechanism is shown in Scheme 4.[8]

Compound **3b** has NH groups at 3200–3280 cm^{-1}, a C–H absorption of a thiazine ring at 2955–3081 cm^{-1}, carbonyl groups at 1766 and 1666 cm^{-1}, and C=N and C=C groups at 1664 and 1630 cm^{-1}, respectively, in the FT-IR spectra. The ^1H NMR spectrum of **3b** indicate one singlet quite downfield at δ 9.85 ppm, which are the protons of the NH amide, 7.40 ppm (s, 1H, NH), 6.60 (1H, HC=C, rings), 3.53–5.06 ppm (OH, C4, C5, C6-sugar chain), 3.68–3.85 ppm (3H, C4, C5, C6, sugar), 4.23 and 1.23 ppm ($–CH_2–$ and $–CH_3$ ethoxy groups). The ^{13}C NMR spectra of **3b** indicate carbonyl group carbons (C=O and NC=O) and an imino group (C=N) at 168.07, 166.32, and 165.74 ppm, respectively, alkene groups (C=C) at 142.01 and 114.53 ppm, C-1, C-5, C-2, C-3, and C-4 pyranose cycles at 82.83, 76.83, 74.20, 73.20, and 70.69 ppm, respectively, and a C-6 pyranose cycle and $–OCH_2–$ and $–CH_3$ at 61.66, 60.87, and 14.02 ppm, respectively. Mass spectral data and elemental analyses are also in accordance with the proposed structure. In general, all of the spectral data support the structures for all of the compounds (**3a**–**3f**).

The structures of all the sugar–thiazolidinone derivatives, the reaction conditions, and the product yields are given in Table 1.

Conclusion

In conclusion, sugar–thiazolidinone derivative compounds by two different simple methods were synthesized. Since the use of microwaves is playing an increasingly pivotal role for the synthesis of organic compounds, we used a microwave-assisted method for the preparation of thiazolidinone and obtained excellent yields. No harsh conditions or cumbersome apparatus are required. A simple purification process, a short experimental time for the reaction to be completed, and solvent-free conditions (microwave-assisted) are the main advantages of this method, which make these reactions eco-friendly to the environment.

Acknowledgment

We gratefully acknowledge the financial support of a Vali-e-Asr University of Rafsanjan Faculty Research Grant.

References

(1) Martins Alho, M. A.; Baggio, R.; Garland, M. T.; D'Accorso, N. B.; Varela, O. *Carbohydr. Res.* **2002**, *337* (15), 1397. doi:10.1016/S0008-6215(02)00157-X.

(2) Berseneva, V. S.; Tkachev, A. V.; Morzherin, Yu. Yu.; Dehaen, W.; Luyten, I.; Toppet, S.; Bakulev, V. *J. Chem. Soc., Perkin Trans. 1* **1998**, *15* (14), 2133. doi:10.1039/a803543a.

(3) Shah, S. J.; Shah, S. R.; Desai, N. C.; Thaker, K. A. *J. Indian Chem. Soc.* **1984**, *61*, 648.

(4) Dave, M. P.; Patel, J. M.; Langalia, N. L.; Thaker, K. A. *J. Indian Chem. Soc.* **1984**, *61*, 891.

(5) Pereira, E. R.; Prudhomme, M.; Sancelme, M.; Ollier, M.; Severe, D.; Riou, J. F.; Crevel, H.; Savineau, J. P.; Fabbro, D.; Meyer, T. *Chem. Pharm. Bull. (Tokyo)* **1997**, *45*, 733.

(6) Darehkordi, A.; Saidi, K.; Islami, M. R. *ARKIVOC* **2007**, (i), 180.

(7) Martins Alho, M. A.; D'Accorso, N. B. *Carbohydr. Res.* **2000**, *328* (4), 481. doi:10.1016/S0008-6215(00)00127-0.

(8) Shipman, C., Jr; Smith, S. H.; Drach, J. C.; Klayman, D. L. *Antiviral Res.* **1986**, *6* (4), 197. doi:10.1016/0166-3542(86)90002-1.

(9) Tóth, M.; Somsák, L. *Carbohydr. Res.* **2003**, *338* (12), 1319. doi:10.1016/S0008-6215(03)00163-0.

(10) Nagy, P.; Csámpai, A.; Szabó, D.; Varga, J.; Harmat, V.; Ruff, F.; Kucsman, A. *J. Chem. Soc., Perkin Trans. 2* **2001** (3), 339. doi:10.1039/B008156F.

(11) Fábián, B.; Kudar, V.; Csámpai, A.; Nagy, T. Z.; Sohár, P. *J. Organomet. Chem.* **2007**, *692* (25), 5621. doi:10.1016/j.jorganchem.2007.09.017.

(12) Horton, D.; Nickol, R. G.; Varela, O. *Carbohydr. Res.* **1987**, *168* (2), 295. doi:10.1016/0008-6215(87)80032-0.

(13) Tashpulatov, A. A.; Afanas'ev, V. A.; Lidak, M. Y.; Sukhova, N. M.; Popelis, Y. Y.; Rakhmatullaev, I. *Chem. Heterocycl. Compd.* **1983**, *19* (2), 137. doi:10.1007/BF00506418.

(14) Ghosh, S.; Misra, A. K.; Bhatia, G.; Khan, M. M.; Khanna, A. K. *Bioorg. Med. Chem. Lett.* **2009**, *19* (2), 386. doi:10.1016/j.bmcl.2008.11.070.

Can. J. Chem. Downloaded from www.nrcresearchpress.com by South China Agricultural University on 09/19/12
For personal use only.

Studies on tautomerism in the triazoline dione

Alireza Salimi Beni, Zeinab Dalirnasab, Abbas Teimouri, and Alireza Najafi Chermahini

Can. J. Chem. Downloaded from www.nrcresearchpress.com by South China Agricultural University on 09/19/12
For personal use only.

Abstract: The chemical properties of the triazoline dione have been extensively studied. The relative stability of three tautomers in the gas phase and solution (using PCM model) are evaluated using HF and DFT methods and compared with MP2 level using different basis sets. The results of the calculations indicate that 4*H*-1,2,4-triazole-3,5-dione (**K** form) is more stable in the gas phase than in solution. In addition, the transition states of proton transfer reaction is calculated. The vibrational frequencies and corresponding normal mode assignments of 4*H*-1,2,4-triazole-3,5-dione and 5-hydroxy-3*H*-1,2,4-triazol-3-one (**E1** form) are also theoretically examined. In addition, the variation of dipole moments and charges on atoms with change of solvent is studied. Specific solvent effects with addition of one molecule of water near the electrophilic centers of three tautomers and the transition state of proton transfer assisted by a water molecule was investigated. Aggregation with water molecules does not change the order of stability of isomers, but proton transfer reaction assisted by a water molecule needs less energy than the intramolecular process.

Key words: triazoline dione, tautomerization, solvent effect, specific solvent effect, HOMO–LUMO energies, DFT, MP2, PCM.

Résumé : On a étudié d'une façon extensive les propriétés chimiques de la triazolinedione. On en a évalué les stabilités relatives des trois tautomères en phase gazeuse et en solution en utilisant le modèle de continuum polarisable (MCP) et les méthodes de Hartree-Fock (HF) et de la théorie de la fonctionnelle de la densité (TFD) et on les a comparées avec les valeurs obtenues par la méthode de Møller-Plesset d'ordre 2 (MP2) en utilisant divers ensembles de base. Les résultats de ces calculs indiquent que la 4*H*-1,2,4-triazole-3,5-dione (forme **K**) est la plus stable tant en phase gazeuse qu'en solution. De plus, on a calculé l'état de transition de la réaction de transfert de proton. On a aussi calculé, sur une base théorique, les fréquences vibrationnelles et les attributions des modes normaux correspondants de la 4*H*-1,2,4-triazole-3,5-dione (forme **K**) et de la 5-hydroxy-3*H*-1,2,4-triazole-3-one (forme **E1**). On a aussi étudié la variation des moments dipolaires et des charges sur les atomes avec un changement de solvant. On a aussi étudié l'effet de solvant spécifique pour l'addition d'une molécule d'eau près des centres électrophiles des trois tautomères et l'état de transition du transfert de proton assisté par une molécule d'eau. L'agrégation avec la molécule d'eau ne modifie pas l'ordre de stabilité des isomères, mais la réaction de transfert de proton assistée par une molécule d'eau nécessite moins d'énergie que le processus intramoléculaire.

Mots-clés : triazolinedione, tautomérisation, effet de solvant, effet de solvant spécifique, énergie d'orbitales moléculaires haute-occupée (OM-HO) et basse-vacante (OM-BV), théorie de la fonctionnelle de la densité (TFD), Møller–Plesset d'ordre 2 (MP2), modulation d'impulsion codée (MIC).

[Traduit par la Rédaction]

Introduction

Triazoline diones (TADs) are exceptionally strong electron acceptors and thus are among the most powerful enophiles[1–3] known as well as dienophiles in Diels–Alder reactions.[4–7] TADs are also highly reactive neutral electronphiles that exhibit reactivity smilar to singlet oxygen.[8–13] They react photochemically with compounds having easily abstracted protons and undergo self-reaction to form polymers.[14,15] Reaction with benzene,[16] naphthalene,[17] and phenanthrene[18] gives [4π+2π] adducts. In addition, they act as an aromatization agent of 1,4-dihydropyridines and pyrazolines.[19–21] In the present study, we compare HF, DFT, and MP2 results concerning tautomeric equilibria of triazolinedione molecules in the gas phase and in solution. In addition, we investigate each form when one molecule of water is placed nearby.

Computational method

The vibrational frequencies and optimized structure parameters of triazoline dione and its tautomer have been calculated by using the Hartree–Fock (HF),[22] second-order Møller–Plesset perturbation theory[23,24] and the density functional theory (DFT)[25] level by using the (B3LYP)[26,27] methods at 6–311++G(d, p), 6–311+(d), 6–31++G(d, p), and 6–311G (d) basis set levels. The tautomers were also optimized in polar solvents, and their effects have been considered by using a relatively simple self-consistent reaction field (SCRF)

Received 13 April 2011. Accepted 10 July 2011. Published at www.nrcresearchpress.com/cjc on 20 October 2011.

A.S. Beni, Z. Dalirnasab, and A.N. Chermahini. Department of Chemistry, Faculty of Science, Yasouj University, Yasouj 75918-74831, Iran.
A. Teimouri. Chemistry Department, Payame Noor University, 19395-4697 Tehran, I. R. of Iran.

Corresponding author: Alireza Najafi Chermahini (e-mail: najafi@mail.yu.ac.ir).

Fig. 1. Isomerization for the 5-hydroxy-3*H*-1,2,4-triazol-3-one and 4*H*-1,2,4-triazole-3,5-dione.

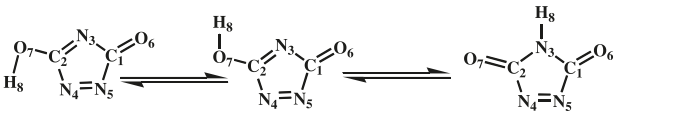

5-hydroxy-3*H*-1,2,4-triazol-3-one (**E**) 4*H*-1,2,4-triazole-3,5-dione (**K**)

method[28] based on polarizable continuum model (PCM) of Tomasi.[29,30] The electronic structures of stationary points were analyzed by the natural bond orbital (NBO) method.[31,32] All computations were performed using the Gauss-View molecular visualization program[33] and Gaussian 98 program package on a personal computer.[34]

Results and discussion

Tautomeric equilibria in the gas phase and solution

Triazoline dione can exists as two tautomeric forms (**E** and **K**) in equilibrium (see Fig. 1). Based on PES results and owing to the rotation around the C2–O7 bond, **E** form can be exist as two conformers: in the **E1** form the proton is near the N3 atom, and in the **E2** form the proton is near the N4 atom. The results of calculated total energies and relative stabilities of 5-hydroxy-3*H*-1,2,4-triazol-3-one (**E1** and **E2** forms) and 4*H*-1,2,4-triazole-3,5-dione (**K** form) in the different methods and using many basis sets (presented in Table 1).

The results of our calculations suggest that in the gas phase, **K** form is more stable and the stability order is **K** > **E1** > **E2**. For example, based on the B3LYP/6–311++G (d,p) calculations, the instability of **E1** and **E2** forms over **K** form was found to be 17.32 and 17.76 kcal/mol (1 cal = 4.184 J), respectively. Consideration of the electron correlation effects did not change the stability order, and calculations at the MP2/6–311++G(d,p) level showed **K** form favored by 15.21 and 16.08 kcal/mol over **E1** and **E2** forms, respectively. The addition of a zero-point energy correction (ZPE) does not affect the order of relative stabilities. It is notable that when using large basis sets, the difference between energies of tautomers is slightly reduced. Based on our calculations, it was found that the results of all calculations are not much different from each other, but the differences between **K** form as the most stable isomer and **E1** and **E2** forms decreased.

The results of the calculated equilibrium constants for the **K**→**E1** and **K**→**E2** conversions in the gas phase and with water as the solvent are tabulated in Table 2. As seen in the table, the **K** value for the **K**→**E1** conversion is greater than for the **K**→**E2** one. In addition, going from gas phase to the water solvent phase, the equilibrium constants decreased by a factor near 10^2.

Solvent effects are relevant in tautomer stability phenomena, since polarity differences among tautomers can induce significant changes in their relative energies in solutions. We decided to use polarizable continuum method (PCM) calculations to analyze the solvent effects on tautomerism of triazoline dione. It is important to stress that the PCM model does not consider the presence of explicit solvent molecules, hence, specific solute–solvent interactions are not described, and the calculated solvation effects arise only from mutual solute–solvent electrostatic polarization. The comparison of the results obtained for the gaseous phase and solution presented in Table 3 testify that an energy decrease in tautomers occurrs when changing from gas phase to polar solvents. This means that polar solvents increase the stability of triazoline-3,5-dione compareed with the gas phase. In addition, when going from gas phase to the more polar solvents, a regular decrease in stability of ketone form over enol forms was observed. It is notable that based on HF and DFT calculations, solvation changed the stability order to **K** > **E2** > **E1**. For example, when using HF and DFT calculations using 6–311++G(d,p) basis function, the instability of **E1** and **E2** isomers over **K** form in water was found to be 14.53 and 11.65 kcal/mol (HF), and 10.47 and 11.14 kcal/mol (DFT), respectively. However, the inclusion of electron correlation effects causes the same trends for stability in the gas phase as was observed for solvents.

The intramolecular proton transfer barriers between tautomers **K** and **E1** for title compound by using QST2 method at HF, B3LYP, and MP2 levels using 6–311++G(d,p) basis function were calculated and the results are collected in Table 4. The calculated activation energies were found to be 78.37, 62.82, and 61.47 kcal/mol at the HF, DFT, and MP2 methods, respectively. This reaction in water as solvent was investigated and activation energies were found to be 84.75, 69.63, and 68.27 kcal/mol, respectively. As seen in the table, the process needs more energy in the water solvent case.

In Fig. 2, the optimized structures and selected geometrical parameters of the transition states are presented. As seen in the figure, in the transition state the proton is slightly closer to the nitrogen atom. In addition, when comparing with results obtained from gas phase and water, it was found that the proton in the gas phase is closer to the molecule than in the water case.

Geometrical parameters

The selected geometrical parameters of the possible tautomers of triazoline dione calculated at the MP2/6–311++G (d,p) level in the gas phase and solution are summarized in Table 5.

In the case of triazoline dione (**K** form), a short N4–N5 bond (1.255 Å) is connected to two long bonds N5–C1 (1.503 Å) and C2–N4 (1.501 Å), and this suggests a highly localized N4–N5 bond. These results are with agreement with previously reported data calculated at B3LYP/6–31G* level, for which optimized lengths were found to be N4–N5 1.234 Å, C2–N4 and C2–N5 1.505 Å.[35] However, the calculated N4–N5 bond length in the **E1** and **E2** isomers was found to be 1.250 and 1.246 Å, respectively. The carbonyl bond length C1=O6, calculated for the three isomers in the gas phase, was found to be 1.192, 1.191, and 1.197 Å for **E1**, **E2** and **K** forms, respectively. The selected geometrical parameters of transition state of proton transfer reaction in the gas phase is presented Fig. 2.

The solvent interactions have a pronounced effect on the geometry of the triazoline dion molecule (**K** form). For example, when going from gas phase to polar solution, a regular decrease of the C1–N3 bond length from 1.381 to 1.370 Å was observed. In addition, when going from gas phase to polar solvents, C1–N5, and C2–N4 and N2–N4

Can. J. Chem. Downloaded from www.nrcresearchpress.com by South China Agricultural University on 09/19/12
For personal use only.

Can. J. Chem. Downloaded from www.nrcresearchpress.com by South China Agricultural University on 09/19/12
For personal use only.

Table 1. Calculated relative instabilities of **E1** and **E2** forms over **K** form in the gas phase.

		K		E1		E2	
		ΔE	ΔE +ZPE	ΔE	ΔE +ZPE	ΔE	ΔE +ZPE
HF	6–311G(d)	0	0	19.78	19.84	21.80	21.72
	6–311+G(d)	0	0	19.22	19.34	21.17	21.13
	6–311++G(d,p)	0	0	16.71	16.92	18.47	18.54
DFT	6–311G(d)	0	0	20.25	20.03	20.81	20.44
	6–311+G(d)	0	0	19.63	19.47	20.21	19.89
	6–311++G(d,p)	0	0	17.32	17.24	17.76	17.56
MP2	6–311G(d)	0	0	19.53	19.75	20.69	20.65
	6–311+G(d)	0	0	18.57	19.02	19.68	19.71
	6–311++G(d,p)	0	0	15.21	15.34	16.08	16.05

Note: Relative stabilities in kcal/mol (1 cal = 4.184 J)).

Table 2. Calculated equilibrium constants in the gas phase and water solvent phase using MP2 and DFT methods using 6–311++G(d,p) basis function.

	Gas		H_2O	
	DFT	MP2	DFT	MP2
K→E1	5.21×10^{12}	3.49×10^{11}	4.17×10^{10}	6.15×10^{9}
K→E2	8.13×10^{12}	1.09×10^{12}	$1.16\ 10^{11}$	

Table 3. Calculated total energies and relative stabilities in the gas phase and solution at different levels of theory.

	HF	Gas phase	THF	DMSO	Water
K	6–311G(d)	–389.4503415[a]	0[b]	0	0
E1			18.96	18.77	17.20
E2			12.65	10.26	14.80
K	6–311+G(d)	–389.457801	0	0	0
E1			18.45	18.28	16.76
E2			11.86	9.39	13.96
K	6–311++G(d,p)	–389.4609196	0	0	0
E1			16.09	15.92	14.53
E2			9.44	7.00	11.65
	DFT				
K	6–311G(d)	–391.5748299	0	0	0
E1			26.25	19.12	17.12
E2			19.38	10.28	14.28
K	6–311+G(d)	–391.5855847	0	0	0
E1			26.27	27.80	21.64
E2			19.03	18.45	18.26
K	6–311++G(d,p)	–391.5884381	0	0	0
E1			16.62	16.44	10.47
E2			9.36	7.10	11.14
	MP2				
K	6–311G(d)	–390 0.5885215	0	0	0
E1			17.84	17.33	17.25
E2			19.26	18.64	18.44
K	6–311+G(d)	–390.6054927	0	0	0
E1			17.09	16.62	16.54
E2			18.49	10.12	17.72
K	6–311++G(d,p)	–390.6135556	0	0	0
E1			14.11	13.73	13.77
E2			15.33	14.87	14.81

[a]Total energies in Hartree units.
[b]Relative stabilities in kcal/mol.

Can. J. Chem. Downloaded from www.nrcresearchpress.com by South China Agricultural University on 09/19/12
For personal use only.

Table 4. Calculated activation energies in the gas phase and in the water as the solvent for proton transfer reaction of K→E1 reaction using HF, DFT and MP2 methods by 6–311++G(d,p) basis function.

	HF	DFT	MP2
Gas Phase	78.37	62.82	61.47
Water	84.75	69.63	68.27

Note: Activation energies in kcal/mol.

Fig. 2. Optimized structures of transition states in the proton transfer reaction calculated at MP2, DFT, and HF methods using 6–311++G (d,p) basis set.

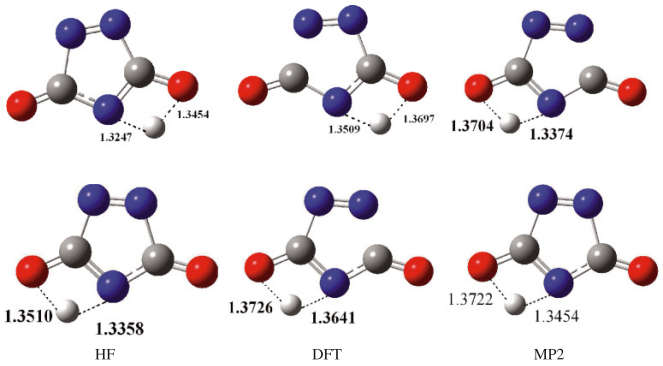

bond lengths do not change. Considering the localized nature of the N4–N5 bond, it might also show π-bond reactivity of the N4–N5 bond for cycloaddition, by acting as a dienophile in the gas phase and solution. Similar changes were found for the **E1** and **E2** isomers. For example, when going from gas phase to water, as the most polar solvent, the C1–N3 bond length changed from 1.423 and 1.421 Å to 1.403 and 1.401 Å for **E1** and **E2**, respectively. In addition, when going to polar solvents, the carbonyl bond increased from 1.192 and 1.191 Å to 1.196 and 1.197 Å for **E1** and **E2** isomers, respectively.

Vibrational analysis

To obtain the spectroscopic signature of triazoline dione and its isomers, we performed a frequency calculation analysis. It is notable that based on our literature search only one paper was found in which experimental vibrational modes were reported.[36] The results obtained in this paper are essentially different, and therefore no comparison was made.

Calculations were made for a free molecule in vacuum. The prediction of the vibrational behavior of molecules was based on B3LYP/6–31++G(d,p) results, performed on each stabilized geometry. The data are presented in Table 6.

The frequencies obtained were then scaled by using a scaling factor 0.9679,[37] which should give good agreement between experimental and theoretical results. The highest frequency in the **K** form was found to be 3577.7, 3750.3, and 3524.5 cm^{-1} for the stretching of the N–H group, calculated using the MP2, HF, and DFT methods, respectively. The symmetrical stretching of carbonyl group was found to be 1815.7, 2059.7, and 1848.5 cm^{-1}, calculated with the MP2, HF, and DFT methods, respectively. For the **E1** form, the highest frequency was found for O–H stretching. The

Table 5. Calculated geometrical parameters of triazoline dione isomers in the gas phase and solution using the MP2/6–311++G(d,p) level of theory.

	E1				**E2**				**K**			
	Gas	THF	DMSO	Water	Gas	THF	DMSO	Water	Gas	DMSO	THF	Water
C1–N3	1.423	1.408	1.404	1.403	1.421	1.405	1.401	1.401	1.381	1.370	1.372	1.370
C1–N5	1.540	1.536	1.536	1.536	1.554	1.542	1.540	1.540	1.502	1.503	1.503	1.503
C1–O6	1.192	1.195	1.196	1.196	1.191	1.195	1.196	1.196	1.197	1.200	1.200	1.200
C2–N3	1.279	1.284	1.286	1.286	1.275	1.282	1.285	1.285	1.381	1.370	1.372	1.370
C2–N4	1.491	1.495	1.496	1.496	1.505	1.506	1.507	1.507	1.502	1.503	1.503	1.503
C2–O7	1.310	1.295	1.292	1.292	1.304	1.295	1.292	1.292	1.197	1.200	1.200	1.200
N4–N5	1.250	1.249	1.249	1.249	1.246	1.246	1.247	1.247	1.255	1.253	1.253	1.253
N3–C1–O6	129.0	129.4	129.6	129.6	129.0	129.6	129.8	129.8	130.4	131.2	131.1	131.2
N3–C2–O7	129.7	131.2	131.5	131.3	128.1	127.3	127.2	127.2	130.4	131.2	131.1	131.2
N3–C1–N5	108.2	108.5	108.7	108.6	108.4	108.7	108.7	108.7	105.2	105.6	105.6	105.6
N3–C2–N4	116.0	115.1	114.9	114.9	115.6	114.7	114.7	114.5	105.2	105.6	105.6	105.6
C1–N3–C2	102.7	103.2	103.4	103.4	103.0	103.6	103.7	103.7	110.3	110.1	110.1	110.1
C1–N5–N4–C2	0	0	0	0	0	0	0	0	0	0	0	0

Note: Bond lengths are given in Å and bond angles and dihedral angles are in degrees.

Can. J. Chem. Downloaded from www.nrcresearchpress.com by South China Agricultural University on 09/19/12
For personal use only.

Table 6. Calculated vibrational frequencies of tautomeric forms of triazolin dion using the 6–311++G(d,p) basis set.

	K				**E1**			
	MP2	B3LYP	HF	Assignments	MP2	B3LYP	HF	Assignments
1	99.50	133.6	128.6	τ C2–O + C1–O6	151.9	164.4	177.3	τ C2–O7 + C1–O6
2	292.3	309.9	346.5	τ ring	291.4	308.1	341.7	τ ring
3	373.7	375.0	426.6	ρ_{asym} C2–O7 + C1–O6	354.2	354.1	401.2	ρ_{asym} C2–O7 + C1–O6
4	454.8	509.4	516.1	ρ_{sym} C2–O7 + C1–O6	476.5	473.2	571.3	ρ_{sym} C2–O7 + C1–O6
5	509.4	510.8	589.4	τ NH	558.6	568.8	593.4	τ OH
6	615.8	632.0	707.8	ω C1–N3–C2	604.9	615.2	686.3	ω C1–N3–C2
7	634.4	637.3	730.8	τ_{sym} C2–O7 + C1–O6	641.8	667.5	765.0	C1–N5
8	640.0	639.2	744.8	τ_{asym} C2–O7 + C1–O6	681.4	671.9	773.4	τ C2–O7 + C1–O6
9	731.2	762.2	848.4	τ ring	712.5	742.3	838.1	τ ring
10	778.4	769.9	910.6	υ_{sym} C2–N4 + C1–N5	745.6	749.8	890.6	τ ring
11	907.6	902.4	1012.5	υ_{asym} N4–C2 + C1–N5	886.9	892.0	1037.2	υ C1–N5 + C2–N3
12	1105.5	1076.5	1234.3	υ_{asym} C1–N3 + C2–N3	1046.4	1049.	1211.2	υ C1–N3
13	1249.0	1237.4	1402.2	υ_{sym} C1–N3 + C2–N3	1171.6	1168.7	1294.1	ρ OH
14	1286.0	1273.1	1424.5	ρ NH	1337.0	1340.9	1511.0	ρ OH + υ C2–N4
15	1434.7	1556.8	1816.1	υ N4N5	1458.2	1569.2	1788.8	υ N4–N5
16	1770.0	1788.3	1997.5	υ_{asym} C2–O7 + C1–O6	1668.6	1658.8	1848.9	υ C2–N3
17	1815.7	1848.1	2059. 9	υ_{sym} C2–O7 + C1–O6	1790.0	1832.9	2048.3	υ C1–O6
18	3577.7	3524.5	3750.3	υ NH	3642.0	3606.0	3951.4	υ OH

Note: Subscript definitions: asym (asymmetric); sym (symmetric); υ (stretching); τ (out of plane bending); ω (wagging); ρ (in-plane bending).

Table 7. Calculated dipole moments of **K**, **E1**, and **E2** isomers using various methods.

		MP2		DFT		HF	
		6–311++G(d,p)	6–31+G(d)	6–311++G(d,p)	6–31+G(d)	6–311++G(d,p)	6–31+G(d)
K	Gas	2.54	2.57	2.80	2.83	2.60	2.62
	THF	3.51	3.53	3.4506	3.94	3.12	3.11
	DMSO	3.31	3.33	3.33	3.71	3.02	3.02
	Water	3.53	3.54	3.69	3.96	3.31	3.31
E1	Gas	4.02	4.10	4.02	4.07	4.00	3.96
	THF	5.68	5.79	5.10	5.15	4.98	4.88
	DMSO	6.11	6.22	5.34	5.40	5.20	5.07
	Water	6.14	6.26	6.29	6.09	5.82	5.69
E2	Gas	4.46	7.03	4.11	4.20	4.42	4.50
	THF	6.45	6.78	6.11	6.11	6.34	6.67
	DMSO	6.98	7.10	6.66	6.78	6.85	6.96
	Water	7.04	7.29	6.71	6.84	6.91	7.11

Note: Calculated dipole moments in Debyes units.

calculated vibrational frequencies were found to be 3642, 3606, and 3951.4 cm^{-1}, calculated using the MP2, DFT, and HF methods, respectively. A comparison of the DFT, HF, and MP2 results shows that these results are strongly dependent on the methods.

Dipole moments, charge distribution, and HOMO–LUMO analysis

Dipole moment is the first derivative of the energy with respect to an applied electric field and is the measure of the asymmetry in the molecular charge distribution. The calculated dipole moments of three tautomeric forms calculated at various methods is presented in Table 7.

A close look at Table 7 indicates that order of dipole moments is **K** < **E1** < **E2** in the gas phase and in solution. The results of calculations show that dipole moments of the **K**, **E1**, and **E2** forms is affected by variation of polarity of the medium, and in all tautomers a regular increase in the dipole moment when using more polar solvents was observed. In addition, calculated dipole moments using large basis sets are slightly lower.

The calculated values of NBO charges using natural population analysis (NPA) of optimized structures of the two forms in the gas phase and solution are given in Table 8.

It can be seen that in the gas phase and in the **K** tautomer, the N3 position carries most negative charge. However in the **E1** isomer, O7 atom takes the most negative charge. The charge distributions of dipolar compounds are often altered significantly in the presence of a solvent reaction field.[38] In the compound **K** when going from gas phase to more polar solvents, the net charge on the N3 atom does not changed. However, the negative charge on the carbonyl oxygens and positive hydrogen atom increases. In addition, the negative charge on the N4 and N5 atoms slightly increases. On the

Can. J. Chem. Downloaded from www.nrcresearchpress.com by South China Agricultural University on 09/19/12
For personal use only.

Table 8. Calculated NBO charges on atoms of two tautomeric forms **K** and **E1** in the gas phase and solution using 6–311++G(d,p) basis function.

		C1	C2	N3	N4	N5	O6	O7	H8
K									
HF	Gas	0.90	0.90	–0.76	–0.16	–0.16	–0.57	–0.57	0.44
	THF	0.91	0.91	–0.76	–0.17	–0.17	–0.59	–0.59	0.46
	DMSO	0.91	0.91	–0.76	–0.17	–0.17	–0.60	–0.60	0.47
	Water	0.93	0.93	–0.76	–0.17	–0.17	–0.62	–0.62	0.49
DFT	Gas	0.76	0.76	–0.68	–0.15	–0.15	–0.48	–0.48	0.44
	THF	0.77	0.77	–0.67	–0.16	–0.16	–0.50	–0.50	0.46
	DMSO	0.77	0.77	–0.67	–0.16	–0.16	–0.51	–0.51	0.47
	Water	0.78	0.78	–0.67	–0.17	–0.17	–0.53	–0.53	0.49
MP2	Gas	0.91	0.91	–0.77	–0.16	–0.16	–0.58	–0.58	0.45
	THF	0.94	0.94	–0.77	–0.17	–0.17	–0.63	–0.63	0.50
	DMSO	0.95	0.95	–0.76	–0.18	–0.18	–0.64	–0.64	0.51
	Water	0.95	0.95	–0.76	–0.18	–0.18	–0.65	–0.65	0.51
E1									
HF	Gas	0.87	0.85	–0.69	–0.19	–0.14	–0.53	–0.67	0.51
	THF	0.88	0.87	–0.70	–0.18	–0.16	–0.57	–0.67	0.53
	DMSO	0.89	0.88	–0.71	–0.18	–0.16	–0.58	–0.67	0.53
	Water	0.90	0.90	–0.73	–0.17	–0.18	–0.60	–0.68	0.57
DFT	Gas	0.74	0.71	–0.60	–0.17	–0.14	–0.45	–0.60	0.50
	THF	0.75	0.73	–0.60	–0.17	–0.16	–0.48	–0.60	0.53
	DMSO	0.75	0.73	–0.60	–0.17	–0.16	–0.45	–0.60	0.54
	Water	0.76	0.75	–0.62	–0.17	–0.18	–0.52	0.61	0.58
MP2	Gas	0.88	0.85	–0.69	–0.19	–0.14	–0.54	–0.67	0.51
	THF	0.91	0.90	–0.73	–0.19	–0.16	–0.61	–0.69	0.56
	DMSO	0.92	0.91	–0.74	–0.17	–0.19	–0.63	–0.70	0.58
	Water	0.92	0.92	–0.74	–0.17	–0.19	–0.63	–0.70	0.58

other hand, the charge on the atoms in the **E1** form is more sensitive to the solvent. For example, the negative charge on the N3 and N5 atoms, when going to polar solvents increases. In addition, when going from gas phase to polar solvents the positive charge on the hydrogen atom increases. HOMOs and LUMOs energies, and energy gaps of two mentioned isomers calculated at HF and DFT method using 6–311++G(d,p) basis set. Three dimensional pictures of HOMO and LUMO of the studied molecules calculated at B3LYP/6–311++G (d,p) level are shown in Fig. 3. The orbital energy level analysis for the title compounds at the B3LYP and HF levels show E_{HOMO} values of –0.2902 and –0.4397 au. in the **K** form. Moreover, the E_{LUMO} values for the triazoline dion isomer were found to be –0.1620 and 0.0021 au, calculated using DFT and HF methods, respectively. These values for the **E1** form were found to be –0.2945 and –0.4478 au for the HOMO and –0.1591 and 0.0011 au for the LUMO, using B3LYP and HF methods, respectively. The HOMO–LUMO energy separation has been used as a simple indicator of kinetic stability.[39,40]

The HOMO–LUMO gaps were found to be 80.44 and 277.2 kcal/mol for **K** and 84.96 and 281.68 kcal/mol for DFT and HF methods, respectively. A large HOMO–LUMO gap implies high kinetic stability and low chemical reactivity, because it is energetically unfavorable to add an electron to a high-lying LUMO or to extract electrons from a low–lying HOMO.[40] The magnitude of the HOMO–LUMO energy separation could indicate the reactivity pattern of the molecule.[41]

The specific solvent effect

Now we investigate the tautomerization of triazoline dion tautomers assisted by a water molecule. In most recent literature studies,[42–46] particular emphasis was laid on the solvation of isolated molecules, because it was proven that explicit water molecules in their first solvation shell have a clear influence on the electronic structure and geometry of the solute and in the tautomerization processes. Selecting the hydrophilic centers on the triazoline dion ring, we searched the most stable monohydrated forms for all tautomers. All geometries were fully optimized using HF, DFT, and MP2 methods with 6–31++G (d, p) basis function. The preferred microsolvated structures optimized with the DFT method are presented in Fig. 4. In addition, the results of calculated total energies and relative stabilities of monohydrated complexes in the gas phase and water solvent case are collected in Table 9. In the **K** form, we find four hydrated complexes in which water can form hydrogen bonding with nitrogen or oxygen atoms (**KW1**, **KW2 KW3**, and **KW4**). The most stable form is the **KW1** form, in which water molecule act as both hydrogen donor and acceptor. In this complex, when oxygen acts as hydrogen acceptor the hydrogen bonding is stronger. However, the difference between the total energies of **KW1** and **KW2** form is small. If one compares the hydrogen bond lengths as a tool to estimate the power of hydrogen bonding, it is clear that in the **KW2** form the hydrogen bonding is stronger.

In addition in the **E** forms (**E1** and **E2**), four aggregations were found (see Fig. 4). The relative stabilities of all complexes were compared, and results are reported in Table 9.

Can. J. Chem. Downloaded from www.nrcresearchpress.com by South China Agricultural University on 09/19/12
For personal use only.

Fig. 3. (left) HOMO and (right) LUMO of (top) 4*H*-1,2,4-triazole-3,5-dione and (bottom) 5-hydroxy-3*H*-1,2,4-triazol-3-one (**E1** form).

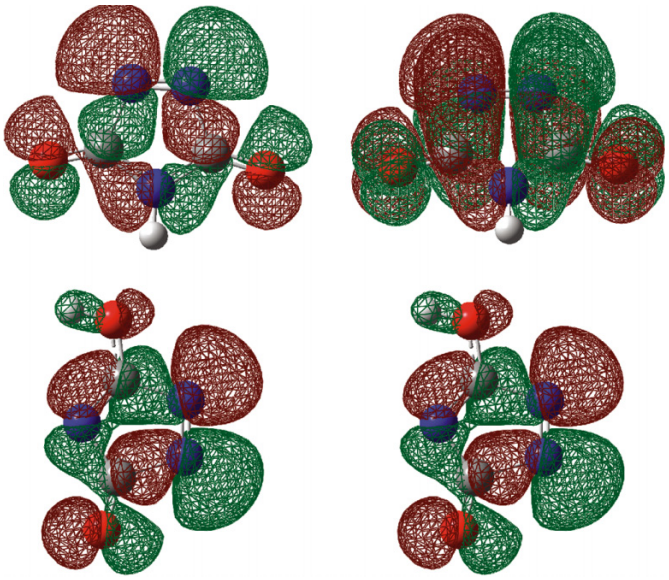

Fig. 4. The optimized geometries of monohydrated triazolinedion tautomers, their total energies (Hartree) and their relative stabilities (kcal/mol) calculated at B3LYP/6–311++G(d,p). Distances in Angstrom.

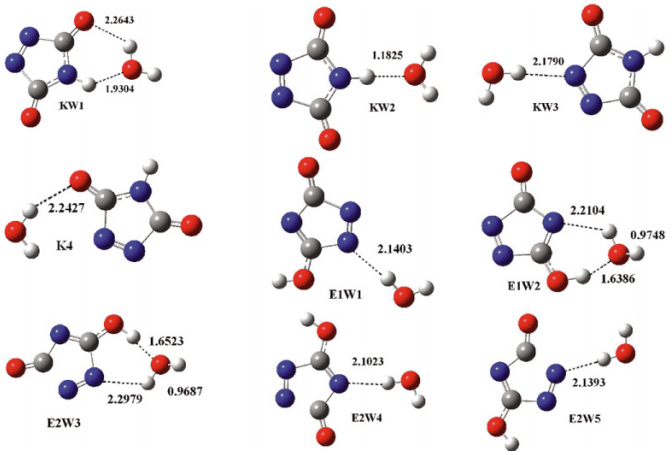

Based on our calculations, the **KW1** complex is most stable. It is clear that **E2** complexes are very unstable. In addition, a close look at Table 9 shows that the difference between stabilities in water decreased.

The optimized structures of the transition state of the proton transfer reaction assisted by a water molecule calculated at HF, DFT, and MP2 levels in the gas phase and water solvent case using 6–311++G(d,p) basis function is presented in Fig. 5. In addition, the results of calculated barriers for proton transfer in the reaction of conversion of **K→E1** assisted by a water molecule in the gas phase and water solvent case is given in Table 10. These results show that all methods predict that activation energies are reduced by the assistance of a water molecule. Interestingly, the activation energy for proton shift greatly decreased to 19.89, 20.83, and 21.93 kcal/mol in the gas phase and to 33.93, 19.46, and 21.79 kcal/mol in the water case, calculated with HF, DFT,

Table 9. Calculated total energies and relative stabilities of monohydrated triazoline dione tautomers using HF, DFT, and MP2 methods with 6–311++G(d,p) basis function.

	HF		DFT		MP2	
	Gas	Water	Gas	Water	Gas	Water
KW1	–465.5276039[a]	–465.5558938	–467.94112953	–468.0850173	–466.9048353	–4.66.9334532
	0.0[b]	0.0	0.0	0.0	0.0	0.0
KW2	1.12	0.59	1.21	0.85	1.14	0.23
KW3	6.07	4.36	6.64	2.76	6.23	3.33
KW4	5.62	1.34	6.41	2.21	5.45	2.89
E1W1	19.90	17.40	22.90	17.98	23.07	20.69
E1W2	10.34	7.98	11.99	9.12	13.38	12.41
E2W3	49.85	45.21	61.92	20.87	43.45	19.83
E2W4	43.32	30.94	52.73	15.04	37.89	21.00
E2W5	23.98	18.90	52.30	22.10	20.11	14.44

[a]Calculated total energies in Hartree units.
[b]Relative stabilities in kcal/mol.

Can. J. Chem. Downloaded from www.nrcresearchpress.com by South China Agricultural University on 09/19/12
For personal use only.

Fig. 5. Calculated transition states of reaction of proton transfer of triazoline dion, assisted by a water molecule in the gas phase (top) and water as the solvent (bellow) at HF, DFT and MP2 methods using 6–311++G(d,p) basis function.

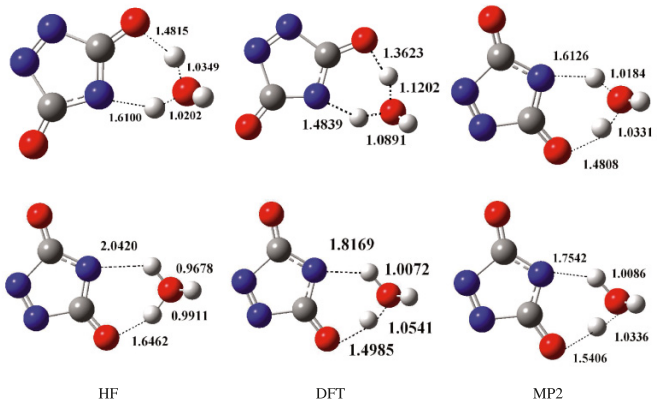

Table 10. Calculated energy barriers in the proton transfer reaction assisted by a water molecule at HF, DFT and MP2 Methods using 6–311++G (d, p) basis function.

	HF	DFT	MP2
Gas	19.89[a]	20.83	21.93
Water	33.93	19.46	21.79

[a]Energy barriers in kcal/mol.

and MP2 methods, respectively. It is clear that the water molecule apparently assists the proton transfer reaction. In addition, it was found that proton transfer assisted by a water molecule in the water solvent case is easier than in gas phase. The selected geometrical parameters in this reaction are presented in Fig. 5. As can be seen, in the gas phase and water case, the water molecule is closer to the oxygen of the carbonyl group in the transition state.

Conclusion

Molecular orbital calculations to study of tautomerism of 4*H*-1,2,4-triazole-3,5-dione and 5-hydroxy-3*H*-1,2,4-triazol-3-one were performed using different calculation levels. In the gas phase, all calculations predict that triazoline dione is more stable. The charge on all eight atoms in the three tautomers were calculated using an NBO method in the gas phase and in solution. The dipole moments of the compounds were calculated in the gas phase and the solvent case and it was observed that they are affected by the solvent. Aggregation with water molecule does not change the stability order of the isomers, but the proton transfer reaction assisted by a water molecule needs less energy than the intramolecular process. The HOMO–LUMO energy separation indicates kinetic stability of the title compound. The values of the NBO charges using the natural population analysis (NPA) are calculated. It was found that in the gas phase and in the **K** form, the N3 position carries most negative charge. However, in the **E1** isomer, O7 atom takes the most negative charge.

Acknowledgment

This work was carried out with financial support of Yasouj University (YU).

References

(1) Lai, Y. C.; Mallakpour, S. E.; Butler, G. B.; Palenik, G. J. *J. Org. Chem.* **1985** *50* (22), 4378. doi:10.1021/jo00222a036.
(2) Ohashi, S.; Leong, K.-W.; Matyjaszewski, K.; Butler, G. B. *J. Org. Chem.* **1980** *45* (17), 3467. doi:10.1021/jo01305a020.
(3) Seymour, C. A.; Greene, F. D. *J. Am. Chem. Soc.* **1980** *102* (20), 6384. doi:10.1021/ja00540a054.
(4) Gilani, S. S. H.; Triggle, D. J. *J. Org. Chem.* **1966** *31* (7), 2397. doi:10.1021/jo01345a509.
(5) Sauer, J.; Schroder, B. *Chem. Ber.* **1967** *100* (2), 678. doi:10.1002/cber.19671000238.
(6) Gillis, B. T.; Hagarty, J. D. *J. Org. Chem.* **1967** *32* (2), 330. doi:10.1021/jo01288a016.
(7) Amerva, M. G.; Lora-Tamayo, M.; Soto, J. L. *Tetrahedron Lett.* **1970** *11*,2407. doi:10.1016/S0040-4039(01)98241-3.
(8) Cheng, C. C.; Seymour, C. A.; Petti, M. A.; Greene, F. D.; Blount, J. F. *J. Org. Chem.* **1984** *49* (16), 2910. doi:10.1021/jo00190a014.
(9) Jensen, F.; Foote, C. S. *J. Am. Chem. Soc.* **1987** *109* (21), 6376. doi:10.1021/ja00255a024.
(10) Clennan, E. L.; Earlywine, A. D. *J. Am. Chem. Soc.* **1987** *109* (23), 7104. doi:10.1021/ja00257a033.
(11) Koerner von Gustrof, E.; White, D. V.; Kim, B.; Hess, D.; Leitich, L. *J. Org. Chem.* **1970** *35* (4), 1155. doi:10.1021/jo00829a065.
(12) Adam, W.; Griesbeck, A.; Klärner, F.-G.; Schröer, D. *Angew. Chem. Int. Ed. Engl.* **1986** *25* (11), 989. doi:10.1002/anie.198609891.
(13) Orfanopoulos, M.; Smonou, I.; Foote, C. *J. Am. Chem. Soc.* **1990** *112* (9), 3607. doi:10.1021/ja00165a053.
(14) Hall, J. H.; Bigard, W. E.; Fargher, J. M.; Jones, M. L. *J. Org. Chem.* **1982** *47* (8), 1459. doi:10.1021/jo00347a016.
(15) Hall, J. H. *J. Org. Chem.* **1983** *48* (10), 1708. doi:10.1021/jo00158a025.
(16) Hamrock, S. J.; Sheridan, R. S. *J. Am. Chem. Soc.* **1989** *111* (26), 9247. doi:10.1021/ja00208a028.
(17) Kjell, D. P.; Sheridan, R. S. *J. Am. Chem.* **1984** *106* (18), 5368. doi:10.1021/ja00330a065.
(18) Hamrock, S. J.; Sheridan, R. S. *Tetrahedron Lett.* **1988** *29* (43), 5509. doi:10.1016/S0040-4039(00)80799-6.
(19) Roothaan, C. C. *J. Rev. Mod. Phys.* **1951** *23* (2), 69. doi:10.1103/RevModPhys.23.69.
(20) Mallakpour, S. E.; Zolfigol, M. A. *Indian J. Chem.* **1995** *34B*, 183and references cited therein.
(21) Zolfigol, M. A.; Ghorbani Choghamarani, A.; Shahamirian, M.; Safaiee, M.; Mohammadpoor-Baltork, I.; Mallakpour, S.; Abdollahi-Alibeik, M. *Tetrahedron Lett.* **2005** *46* (33), 5581. doi:10.1016/j.tetlet.2005.06.031.
(22) Zolfigol, M. A.; Bagherzadeh, M.; Mallakpour, S.; Chehardoli, G.; Kolvari, E.; Choghamarani, A. G.; Koukabi, N. *Catal. Commun.* **2007** *8* (3), 256. doi:10.1016/j.catcom.2006.04.006.
(23) Møller, C.; Plesset, M. S. *Phys. Rev.* **1934** *46* (7), 618. doi:10.1103/PhysRev.46.618.
(24) Fletcher, G. D.; Rendell, A. P.; Sherwood, P. *Mol. Phys.* **1997** *91*, 431.
(25) Ziegler, T. *Chem. Rev.* **1991** *91* (5), 651. doi:10.1021/cr00005a001.
(26) Becke, A. D. *J. Chem. Phys.* **1993** *98* (7), 5648. doi:10.1063/1.464913.
(27) Lee, C.; Yang, W.; Parr, R. G. *Phys. Rev. B*, **1988** *37*, 785. doi:10.1103/PhysRevB.37.785.
(28) Tomasi, J.; Persico, M. *Chem. Rev.* **1994** *94* (7), 2027. doi:10.1021/cr00031a013.

(29) Cancès, E.; Mennucci, B.; Tomasi, J. *J. Chem. Phys.* **1997** *107* (8), 3032. doi:10.1063/1.474659.
(30) Barone, V.; Cossi, M.; Tomasi, J. *J. Comput. Chem.* **1998** *19* (4), 404. doi:10.1002/(SICI)1096-987X(199803)19:4<404::AID-JCC3>3.0.CO;2-W.
(31) Reed, A. E.; Weinstock, R. B.; Weinhold, F. *J. Chem. Phys.* **1985** *83* (2), 735. doi:10.1063/1.449486.
(32) Reed, A. E.; Curtiss, L. A.; Weinhold, F. *Chem. Rev.* **1988** *88* (6), 899. doi:10.1021/cr00088a005.
(33) Frisch, A.; Nielsen, A. B.; Holder, A. J. *Gauss View User Manual*; Gaussian Inc., Pittsburgh, PA, 2001.
(34) Frisch, M. J.; Trucks, G. W.; Schlegel, H. B.; Scuseria, G. E.; Robb, M. A.; Cheeseman, J. R.; Zakrzewski, V. G.; Montgomery, J. A., Jr.; Stratmann, R. E.; Burant, J. C.; Dapprich, S.; Millam, J. M.; Daniels, A. D.; Kudin, K. N.; Strain, M. C.; Farkas, O.; Tomasi, J.; Barone, V.; Cossi, M.; Cammi, R.; Mennucci, B.; Pomelli, C.; Adamo, C.; Clifford, S.; Ochterski, J.; Petersson, G. A.; Ayala, P. Y.; Cui, Q.; Morokuma, K.; Malick, D. K.; Rabuck, A. D.; Raghavachari, K.; Foresman, J. B.; Cioslowski, J.; Ortiz, J. V.; Baboul, A. G.; Stefanov, B. B.; Liu, G.; Liashenko, A.; Piskorz, P.; Komaromi, I.; Gomperts, R.; Martin, R. L.; Fox, D. J.; Keith, T.; Al-Laham, M. A.; Peng, C. Y.; Nanayakkara, A.; Gonzalez, C.; Challacombe, M.; Gill, P. M. W.; Johnson, B.; Chen, W.; Wong, M. W.; Andres, J. L.; Gonzalez, C.; Head-Gordon, M.; Replogle, E. S.; Pople, J. A. *GAUSSIAN 98, Revision A7*; Gaussian Inc., Pittsburgh, PA, 1998.
(35) Anas, S.; Syam Kishnan, K.; Sanjayan Sajisha, V.; Sasidharan Anju, K.; Radhakrishnan, K. V.; Eringathodi, S.; Suresh, C. H. *New J. Chem.* **2007** *31* (2), 237. doi:10.1039/b614533g.
(36) Wamhoff, H.; Kunz, G. *Angew. Chem.* **1981** *93* (9), 832. doi:10.1002/angew.19810930944.
(37) Andersson, M. P.; Uvdal, P. *J. Phys. Chem. A* **2005** *109* (12), 2937. doi:10.1021/jp045733a.
(38) Wong, M. W.; Wiberg, K. B.; Frisch, M. J. *J. Am. Chem. Soc.* **1992** *114* (5), 1645. doi:10.1021/ja00031a017.
(39) Kim, K. H.; Han, Y. K.; Jung, J. *Theor. Chem. Acc.* **2005** *113* (4), 233. doi:10.1007/s00214-005-0630-7.
(40) Aihara, J. *J. Phys. Chem. A* **1999** *103* (37), 7487. doi:10.1021/jp990092i.
(41) Chattopadhyay, B.; Basu, S.; Chakraborty, P.; Choudhuri, S. K.; Mukherjee, A. K.; Mukherjee, M. *J. Mol. Struct.* **2009** *932* (1–3), 90. doi:10.1016/j.molstruc.2009.05.047.
(42) Trujillo, C.; M'o, O.; Yanez, M. *Org. Biomol. Chem.* **2007** *5* (19), 3092. doi:10.1039/b708045j.
(43) Rudyk, R.; Molina, M. A. A.; Go'mez, M. I.; Blanco, S. E.; Ferretti, F. H. *J. Mol. Struct. THEOCHEM* **2004** *674* (1–3), 7. doi:10.1016/j.theochem.2003.12.019.
(44) Belkova, N. V.; Gribanova, T. N.; Gutsul, E. I.; Minyaev, R. M.; Bianchini, C.; Peruzzini, M.; Zanobini, F.; Shubina, E. S.; Epstein, L. M. *J. Mol. Struct.* **2007** *844–845*, 115. doi:10.1016/j.molstruc.2007.03.040.
(45) Chermahini, A. N.; Dabbagh, H. A.; Teimouri, A. *J. Mol. Struct. THEOCHEM* **2008** *857* (1–3), 105. doi:10.1016/j.theochem.2008.02.012.
(46) Dabbagh, H. A.; Rasti, E.; Chermahini, A. N. *J. Mol. Struct. THEOCHEM* **2010** *947* (1–3), 92. doi:10.1016/j.theochem.2010.01.044.

Can. J. Chem. Downloaded from www.nrcresearchpress.com by South China Agricultural University on 09/19/12
For personal use only.

Dual-level direct dynamics study on the hydrogen abstraction reaction of fluorine atom with 1,1-difluoro-1-chloroethane

Li Wang, Song Liu, Hongqing He, and Jinglai Zhang

Abstract: The kinetic properties of the reaction of F atoms with $CH_2H'CF_2Cl$ are investigated by a dual-level direct dynamics method. Optimized geometries and frequencies of all the stationary points and extra points along the minimum-energy path (MEP) are obtained at the MPW1K/6–311+G(d,p) level of theory. Two complexes with energy less than that of the reactants are located in the two reactant paths, respectively. The energy profiles of two reactions are refined with the interpolated single-point energies (ISPE) method at the G3(MP2)/MPW1K level. The rate constants are evaluated using the canonical variational transition state theory (CVT) with a small-curvature tunneling correction (SCT) over a wide range of temperature 200–2000 K. Agreement between the calculated CVT/SCT rate constant and the experimental value is good at 295 K. Our calculations show that the reaction path $CH_2H'CF_2Cl + F \rightarrow CH_2CF_2Cl + H'F$ (Ra) is the major reaction path below 400 K. Moreover, the contribution of $CH_2H'CF_2Cl + F \rightarrow CHH'CF_2Cl + HF$ (Rb) to the whole reaction increases with the temperature increasing and exceeds path Ra to be the major reaction path.

Key words: density functional theory, direct dynamics method, rate constants.

Résumé : On a étudié les propriétés cinétiques de la réaction des atomes de fluor avec le $CH_2H'CF_2Cl$ par une méthode dynamique directe à double niveau. On a optimisé les géométries et on a obtenu les fréquences de tous les points stationnaires et les points supplémentaires le long de la voie d'énergie minimale (VEM) au niveau MPW1K/6–311+G(d,p) de la théorie. Les deux complexes comportant moins d'énergie que les réactifs se trouvent respectivement dans les voies de ces deux réactifs. Les profils d'énergie des deux réactions ont été affinés par la méthode des énergies monoponctuelles interpolées (EMPI) au niveau G3(MP2)/MPW1K. Les constantes de vitesse ont été évaluées par la théorie de l'état de transition canonique et variationnelle (TCV) avec une correction pour l'effet tunnel à faible courbature (TFC) sur une grande plage de température allant de 200 à 2000 K. À 295 K, l'accord est bon entre la constante de vitesse calculée par la méthode TCV/TFC. et la valeur expérimentale. Les calculs effectués dans cette étude montre que la voie réactionnelle pour la réaction $CH_2H'CF_2Cl + F \rightarrow CH_2CF_2Cl + H'F$ (Ra) est la voie réactionnelle principale en-dessous de 400 K. De plus, lorsque la température réactionnelle augmente, il y a une augmentation de la contribution de la voie $CH_2H'CF_2Cl + F \rightarrow CHH'CF_2Cl + HF$ (Rb) à la réaction globale au point où elle peut devenir la voie réactionnelle principale.

Mots-clés : théorie de la fonctionnelle de la densité, méthodes dynamiques directes, constantes de vitesse.

[Traduit par la Rédaction]

Introduction

Recognition of the adverse effects of chlorofluorocarbon (CFC) release into the atmosphere has led to an international effort to replace CFCs with environmentally acceptable alternatives.[1,2] Hydrochlorofluorocarbons (HCFCs) are considered to be an important class of CFCs substitutes, since they retain many desirable properties of CFCs and have less ozone depletion potential. Moreover, the inclusion of at least one C–H bond makes them react readily with OH radicals, oxygen atoms, and other atmospheric constituents. A large number of kinetic data are available for the reactions including pure hydrocarbons, however there are limited reports on the reactions including ethane substituted by both fluorine and chlorine, particularly for 1,1-difluoro-1-chloroethane (CH_3CF_2Cl). Only one experimental kinetic study was performed on the reaction of CH_3CF_2Cl with F atoms at 295 ± 2 K.[3] No experimental values are available at other temperatures. Furthermore, only the total rate constant was measured, while the detailed mechanism as well as the branching ratio was not reported. From the mechanistic point of view, two reaction pathways are available,

$$CH_2H'CF_2CL + F \rightarrow CH_2CF_2Cl + H'F\,(Ra)$$

Received 16 May 2011. Accepted 22 July 2011. Published at www.nrcresearchpress.com/cjc on 25 October 2011.

L. Wang, S. Liu, and J. Zhang. Institute of Environmental and Analytical Sciences, College of Chemistry and Chemical Engineering, Henan University, Kaifeng, Henan 475004, P.R. China.
H. He. Wuhan Center for Magnetic Resonance, State Key Laboratory of Magnetic Resonance and Atomic and Molecular Physics, Wuhan Institute of Physics and Mathematics, Chinese Academy of Sciences, Wuhan 430071, P. R. China.

Corresponding author: Jinglai Zhang (zhangjinglai@henu.edu.cn).

Can. J. Chem. Downloaded from www.nrcresearchpress.com by University of Electronic and Science Techonology of China on 09/19/12
For personal use only.

Can. J. Chem. Downloaded from www.nrcresearchpress.com by University of Electronic and Science Techonology of China on 09/19/12
For personal use only.

Fig. 1. Optimized geometries of reactants, complexes, products, and two transition states at the MPW1K/6–311+G(d,p) level. The value in the parentheses is the experimental value.[23] Bond lengths are in angstroms and angles are in degrees.

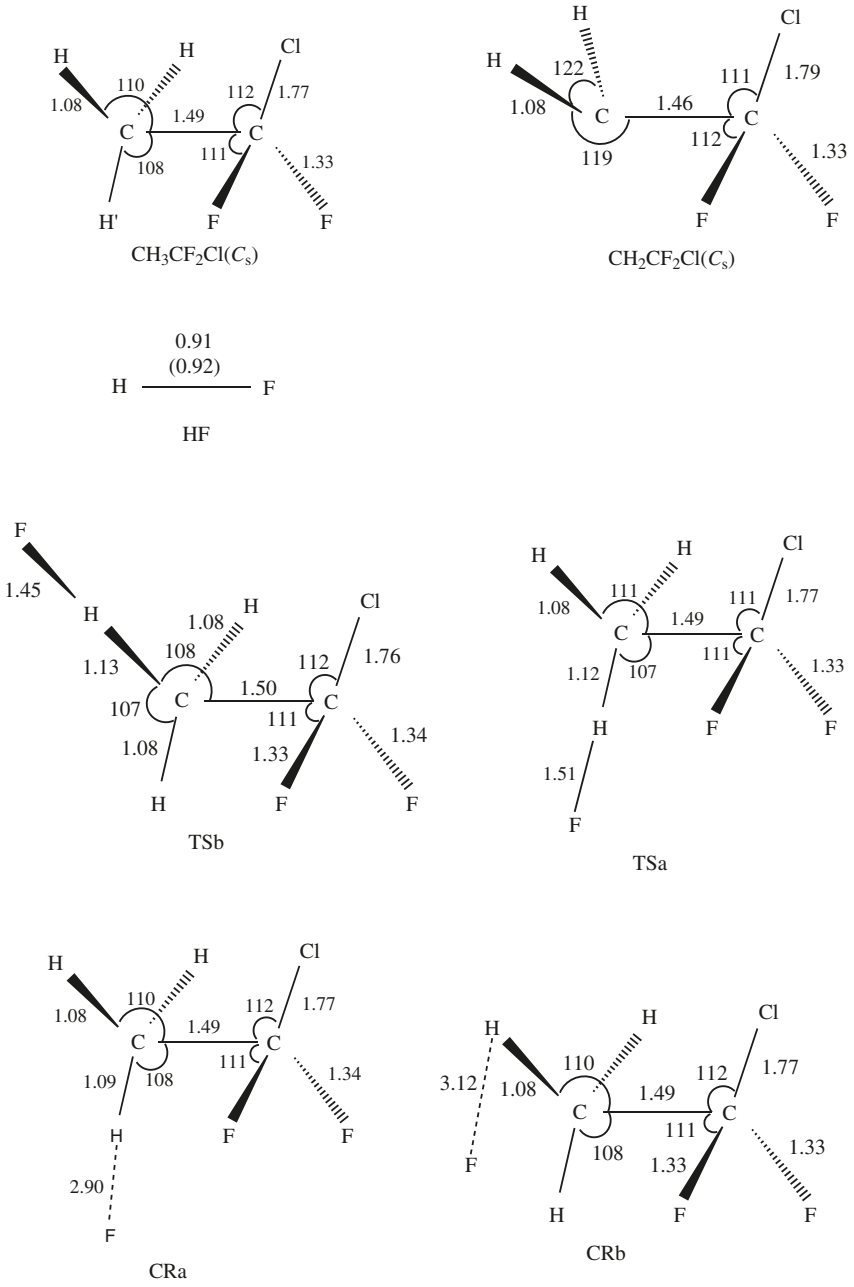

$$CH_2H'CF_2CL + F \rightarrow CH\,H'CF_2Cl + HF\,(Rb)$$

Which reaction path will be the major one? Since this problem is difficult to determine experimentally, a detailed theoretical investigation is very desirable. The aim of the present study is to provide a deep insight into the mechanism of this two-path reaction, as well as to obtain the temperature dependence of the rate constants and branching ratio over a wide temperature range. The dual-level direct dynamics method[4–6] proposed by Truhlar and co-workers are used to investigate the dynamic properties of the title reaction. In this approach, we obtain the potential energy surface (PES) information directly from density functional theory (DFT) calculations and evaluate the rate constants by the variational transition-state theory (VTST).[7–9] The comparison between theoretical and experimental results will be discussed.

Calculation methods

All electronic structure calculations involved in this work were completed using the Gaussian 03 program package.[10] The geometries and frequencies of all the stationary points (including reactants, complexes, products, and transition states) of the title reaction are calculated by modified Perdew–Wang 1-parameter model for kinetics (MPW1K),[11] with the 6–311+G(d,p) basis set (MPW1K/6–311+G(d,p)). It is well-known that hybrid Hartree–Fock density functional theory (hybrid DFT) is a very attractive alternative for many

Can. J. Chem. Downloaded from www.nrcresearchpress.com by University of Electronic and Science Techonology of China on 09/19/12
For personal use only.

Table 1. Cartesian coordinates and electronic energies for MPW1K/6–311+G(d,p) optimized geometries of all stationary points.

CH_3CF_2C, Energy = –737.939 804 4				CH_2CF_2Cl, Energy = –737. 263 571 8			
C	–0.345 676	0.004 344	0.000 000	C	–0.385 763	0.029 717	0.000 000
C	–0.805 723	1.425 026	0.000 000	C	–0.822 395	1.425 997	0.000 000
H	–1.891 599	1.432 697	0.000 000	H	–0.874 573	1.948 385	0.938 182
H	–0.436 496	1.928 443	0.885 939	H	–0.874 573	1.948 385	–0.938 182
H	–0.436 496	1.928 443	–0.885 939	Cl	1.400 071	–0.080 381	0.000 000
Cl	1.422 118	–0.131 358	0.000 000	F	–0.822 395	–0.625 810	1.074 623
F	–0.805 723	–0.646 262	1.070 717	F	–0.822 395	–0.625 810	–1.074 623
F	–0.805 723	–0.646 262	–1.070 717				
CRa, Energy = –837.671 720 6				CRb, Energy = –837.672 226 9			
C	0.403 930	–0.068 775	0.000 045	C	–0.500 431	–0.366 844	–0.056 701
C	–0.338 699	1.226 523	0.000 127	C	–0.257 437	–1.055 669	1.245 458
H	–1.402 765	1.008 958	0.000 230	H	–0.087 982	–2.110 194	1.047 260
H	–0.081 469	1.795 716	0.885 924	H	0.614 860	–0.630 042	1.727 579
H	–0.081 643	1.795 728	–0.885 714	H	–1.123 061	–0.939 108	1.887 199
Cl	2.161 004	0.162 941	–0.000 122	Cl	–0.793 101	1.368 100	0.142 238
F	0.088 230	–0.800 094	1.071 422	F	0.546 232	–0.513 567	–0.876 634
F	0.088 024	–0.800 076	–1.071 284	F	–1.553 877	–0.891 192	–0.685 877
F	–4.127 651	0.009 405	–0.000 073	F	3.077 213	0.177 729	–0.016 670
TSa, Energy = –837.668 547 6				TSb, Energy = –837.667 181			
C	0.094 553	0.322 096	0.000 000	C	0.484 106	–0.380 415	0.017 622
C	–0.60 8321	–0.995 820	0.000 000	C	–0.740 448	–0.761 824	–0.751 425
H	0.183 950	–1.790 688	0.000 000	H	–0.933 588	–1.823 779	–0.644 317
H	–1.203 648	–1.122 927	0.895 330	H	–1.623 828	–0.214 195	–0.311 807
H	–1.203 648	–1.122 927	–0.895 330	H	–0.666 094	–0.466 292	–1.790 286
Cl	–1.074 464	1.653 402	0.000 000	Cl	0.822 726	1.348 394	–0.070 246
F	0.873 031	0.452 499	1.071 053	F	0.366 887	–0.722 702	1.298 527
F	0.873 031	0.452 499	–1.071 053	F	1.540 322	–1.038 856	–0.467 011
F	0.873 031	–3.130 436	0.000 000	F	–2.932 183	0.254 337	0.095 529
HF, Energy = –100.445 678 2							
H	0.000 000	0.000 000	–0.818 294				
F	0.000 000	0.000 000	0.090 922				

applications, since its computational cost is low compared with ab initio methods. Although the good performance of hybrid DFT in structural and thermochemical applications is well documented, its usefulness in kinetics calculations has not been established. MPW1K[11] is a method developed over the past decade that shows great promise for improvement in both the calculation of reaction barrier heights and transition state geometries. To obtain more reliable reaction enthalpies and barrier heights, high level single-point calculations for the stationary points are performed by G3(MP2) theory,[12] using the MPW1K-optimized geometries. The minimum-energy path (MEP) is calculated by the intrinsic reaction coordinate (IRC) theory,[13,14] with a gradient step size of 0.05 $(amu)^{1/2}$ bohr at the MPW1K level to confirm that the TS really connects with minima along the reaction path. Also, first and second energy derivatives at geometries along the MEP are obtained to calculate the curvature of the reaction path and to calculate the generalized vibrational frequencies along the reaction path. The dual-level potential profile along the reaction path is further refined with the interpolated single-point energies (ISPE) method.[15] Four nonstationary points, i.e., ±0.05, ±1.0, for the reaction path Ra are used to correct the lower level reaction path. However, only three nonstationary points (–0.05, +0.15, +1.0) are employed for the reaction path Rb, since the points close to –1.0 in the reactant side do not converge at the G3(MP2) level. The information on the potential energy surface is used to evaluate the rate constants by means of the Polyrate 9.7 program.[16] The rate constants are calculated by using the variational transition state theory (VTST)[7–9] proposed by Truhlar and co-workers. The specific level of VTST that we used is the canonical variational transition-state theory (CVT),[17–19] and the tunneling correction is considered by the centrifugal-dominant small-curvature semiclassical adiabatic ground-state (CD-SCSAG)[20,21] method. The CD-SCSAG approximation is a generalization of the Marcus–Coltrin approximation,[22] in which the tunneling path is distorted from the MEP out to a concave-side vibrational turning point in the direction of the internal centrifugal force. In the present study, the small-curvature tunneling correction is computed with equal segments in the Boltzmann and θ integrals, and the number of Gauss–Legendre quadrature points is chosen as 40 for computing the Boltzmann average. Also, the sixth-order Lagrangian interpolation is used to obtain the values of the effective mass for the CD-SCSAG tunneling calculation. The $^2P_{1/2}$ and $^2P_{3/2}$ electronic states of the fluorine atom, with a 404 cm^{-1} splitting due to the spin-orbit coupling, are used in the calculation of the electronic partition functions. The curvature components are calculated by using a quadratic fit to obtain the derivative of the gradient with respect to the reaction coordinate. Finally, the total rate constants are obtained from the sum of the individual rate constants associated with the Ra and Rb reaction paths.

Can. J. Chem. Downloaded from www.nrcresearchpress.com by University of Electronic and Science Techonology of China on 09/19/12
For personal use only.

Table 2. Calculated and experimental frequencies (in cm^{-1}) of the reactants, complexes, products, and transition states at the MPW1K/6–311+G(d,p) level.

Species	MPW1K/6–311+G(d,p)	Exptl.[a]
CH_3CF_2Cl	257, 314, 347, 445, 454, 564, 713 947, 1012, 1176, 1258, 1290, 1460, 1510, 1511, 3141, 3234, 3248	
$CH_2CF_2Cl(C_s)$	198, 292, 353, 443, 445, 565, 590, 759, 971, 986, 1265, 1315, 1476, 3253, 3385	
HF	4293	4138
CRa	11, 13, 35, 260, 315, 347, 446, 454, 563, 713, 947, 1012, 1177, 1257, 1289, 1461, 1509, 1512, 3141, 3234, 3247	
CRb	18, 23, 59, 260, 315, 347, 446, 454, 564, 714, 947, 1011, 1177, 1253, 1288, 1461, 1511, 1512, 3140, 3233, 3249	
TSa	193*i*, 42, 50, 282, 318, 347, 444, 454, 563, 702, 939, 1006, 1137, 1247, 1259, 1364, 1376, 1483, 2375, 3196, 3273	
TSb	271*i*, 39, 50, 278, 314, 346, 444, 457, 560, 715, 921, 984, 1162, 1227, 1242, 1346, 1350, 1480, 2174, 3182, 3266	

[a]From Ref. 25.

Table 3. Reaction enthalpy at 298 K ($\Delta H_{298}{}^0$), reaction energy at 0 K (ΔE), and barrier height (ΔV) (in kcal mol^{-1}) at the MPW1K/6–311+G(d,p) and G3(MP2)//MPW1K/6–311+G(d,p) levels along with available experimental values.

	$CH_2H'CF_2Cl + F \rightarrow CH_2CF_2Cl + H'F$ (Ra)			$CH_2H'CF_2Cl + F \rightarrow CH\ H'CF_2Cl + HF$ (Rb)		
	$\Delta H_{298}{}^0$	ΔE (0 K)	ΔV	$\Delta H_{298}{}^0$	ΔE (0 K)	ΔV
MPW1K/6–311+G(d,p)	–26.4	–27.2	0.2	–26.4	–27.2	0.6
G3(MP2)// MPW1K/6–311+G(d,p)	–31.7	–32.5	0.8	–31.7	–32.5	1.0
Exptl.[a]	–32.14±4.3			–32.14±4.3		

[a]From Ref. 26

Results and discussion

1. Stationary points

The geometric parameters of all the reactants, complexes, products, and transition states optimized at the MPW1K/6–311+G(d,p) level, along with the available experimental data, are drawn in Fig. 1. The Cartesian coordinates and electronic energies for MPW1K/6–311+G(d,p) optimized geometries of all stationary points are listed in Table 1. It is seen that the theoretical values are in reasonable accord with the experimental ones, with the maximum deviation within 0.01 Å.[23] As shown in Fig. 1, both CH_3CF_2Cl and CH_2CF_2Cl radicals have C_s symmetry. For the CH_2CF_2Cl radical, C_1 symmetry conformation is not obtained. For the three hydrogen atoms in CH_3CF_2Cl, H′ (see Fig. 1) is different from the other two, as a result, two hydrogen abstraction reactions (Ra and Rb) are identified. Reactions Ra and Rb proceed via transition states TSa and TSb, leading to the same product of CH_2CF_2Cl radical with C_s symmetry. The transition states TSa and TSb resemble the reactants more than the products, with a smaller elongation of the C–H bond for 3.7% and 4.6%, compared with the C–H equilibrium bond length in isolated CH_3CF_2Cl, respectively, and a significant elongation of the H–F bond for 65.9% and 59.3% with respect to the equilibrium bond length in HF, respectively, i.e., both reactions proceed via "early" transition states. This rather early character in both transition states is in accordance with the low barrier heights and the exothermicity of both reaction paths, in keeping with Hammond's postulate.[24]

The harmonic vibrational frequencies are calculated at the same level of theory to characterize the nature of each critical point and to make zero-point energy (ZPE) corrections. The number of imaginary frequencies (0 or 1) indicates whether a minimum or a transition state has been located. The harmonic vibrational frequencies of all the reactants, complexes, products, and transition states along with the available experimental data[25] are shown in Table 2. As can be seen, our calculated frequency of HF agrees well with the experimental value with a deviation 3.7%. The transition state is identified with only one negative eigenvalue of the Hessian matrix. The imaginary frequencies are 193*i* cm^{-1} for TSa and 271*i* cm^{-1} for TSb.

The reaction energy at 298 K ($\Delta H_{298}{}^0$), the reaction energy at 0 K (ΔE), and the barrier height (ΔV) calculated at the MPW1K/6–311+G(d,p) and G3(MP2)//MPW1K/6–311+G(d,p) levels, as well as the experimental enthalpy, are summarized in Table 3. Both reaction paths (Ra and Rb) have the same products, for which the reaction energy at 298 K ($\Delta H_{298}{}^0$) of –31.7 kcal mol^{-1} (1 cal = 4.184 J) calculated at the G3(MP2)//MPW1K level agrees well with the experimental value of –32.14 ± 4.3 kcal mol^{-1}, which is derived from the experimental standard heats of formation (CH_3CF_2Cl, –127 ± 2 kcal mol^{-1}; CH_2CF_2Cl, –75 ± 2 kcal mol^{-1}; F, 19.0 ± 0.1 kcal mol^{-1}; HF, –65.14 ± 0.2 kcal mol^{-1}).[26] Since the barrier height of Ra is slightly lower than that of Rb, it is difficult to conclude which one will be the major reaction path. To express this more clearly, a schematic potential energy surface of the title reaction with zero-point energy (ZPE) corrections is plotted in Fig. 2. Note that the energy of the reactants is set to zero as a reference. For each reaction path, the complex with energy below that of the reactants is first formed, then starting from the complex, the reaction proceeds via a transition state to reach the products. The barrier height of TSa (0.8 kcal mol^{-1}) is lower than that of TSb (1.0 kcal mol^{-1}) at the G3(MP2) level. According to the barrier heights, we can tell that these two

Can. J. Chem. Downloaded from www.nrcresearchpress.com by University of Electronic and Science Techonology of China on 09/19/12
For personal use only.

Fig. 2. Schematic pathways for the reaction $CH_3CF_2Cl + F \rightarrow$ products. Relative energies with ZPE at the G3(MP2)//MPW1K/6–311+G(d,p) are in kcal mol^{-1}. The values in parentheses are those obtained at the MPW1K/6-311+G(d,p) level.

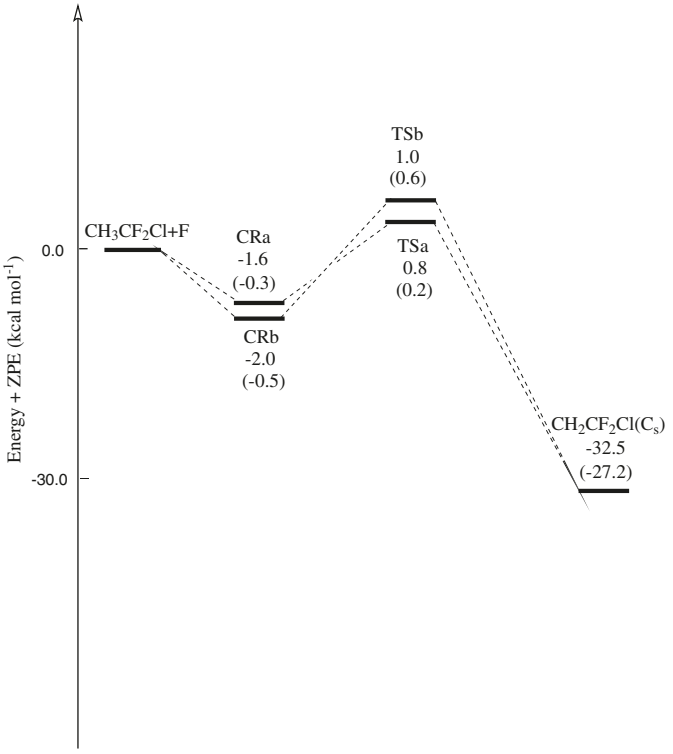

Fig. 3. Classical potential energy curve (V_{MEP}), ground-state vibrationally adiabatic energy curve (V_a^G), and zero-point energy curve (ZPE) as functions of s (amu)$^{1/2}$ bohr at the G3(MP2)//MPW1K/6–311+G(d,p) level for the CH_2H' $CF_2CL + F \rightarrow CH_2CF_2Cl + H'F$ (Ra).

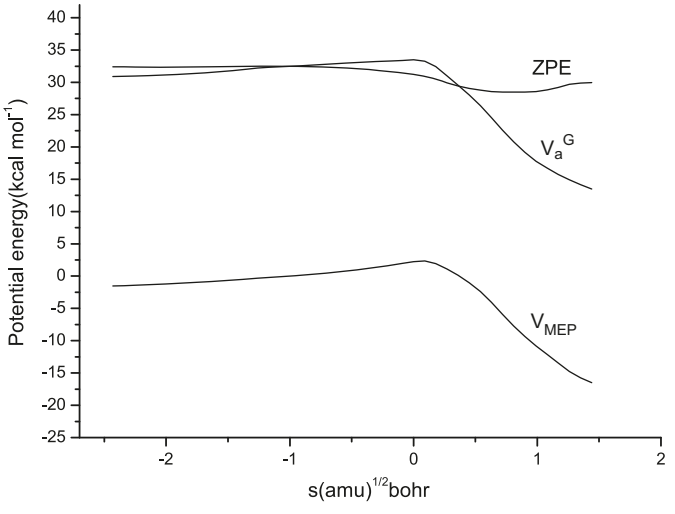

reaction paths should be competitive. Considering that two hydrogen atoms are available for Rb abstraction channel and only one hydrogen atom can be abstracted for Ra path, which reaction path will be the major one is still not clear.

2. Dynamics calculations

The MEP for each reaction path is calculated using the intrinsic reaction coordinate (IRC) theory[13,14] at the MPW1K/6–311+G(d,p) level, and the dynamics calculations of the title reaction are carried out with the VTST-ISPE[15] method at the G3(MP2)//MPW1K level. The classical potential energy ($V_{MEP}(s)$), the ground-state vibrational adiabatic potential energy ($V_a^G(s)$), and the zero-point energy (ZPE) curve of reaction Ra as functions of the intrinsic reaction coordinate (s) are plotted in Fig. 3, where $V_a^G(s) = V_{MEP}(s) + ZPE(s)$. It should be noted that the locations of the maximum on the $V_a^G(s)$ and $V_{MEP}(s)$ energy curves shift in the s-direction toward the products. Similar conclusions can be reached from the other reaction path Rb.

The PES information for each reaction path obtained at the G3(MP2)//MPW1K/6–311+G(d,p) level were put into the Polyrate 9.7 program to calculate the VTST[7–9] rate constants over the temperature range 200–2000 K. The forward rate constants are calculated using CVT[17–19] with the SCT[20,21] correction. The rate constants of k_a, k_b, and the total rate constants $k = k_a + k_b$, along with the available experimental value[3] are plotted against 1000/T (K^{-1}) in Fig. 4*a*, and the temperature dependence of the k_a/k and k_b/k branching ratios

Fig. 4. (*a*) Plot of the calculated individual rate constants k_a, k_b, the total rate constants k, and the available experimental value versus 1000/T for 200–2000 K. (*b*) Calculated branching ratio versus 1000/T for 200–2000 K.

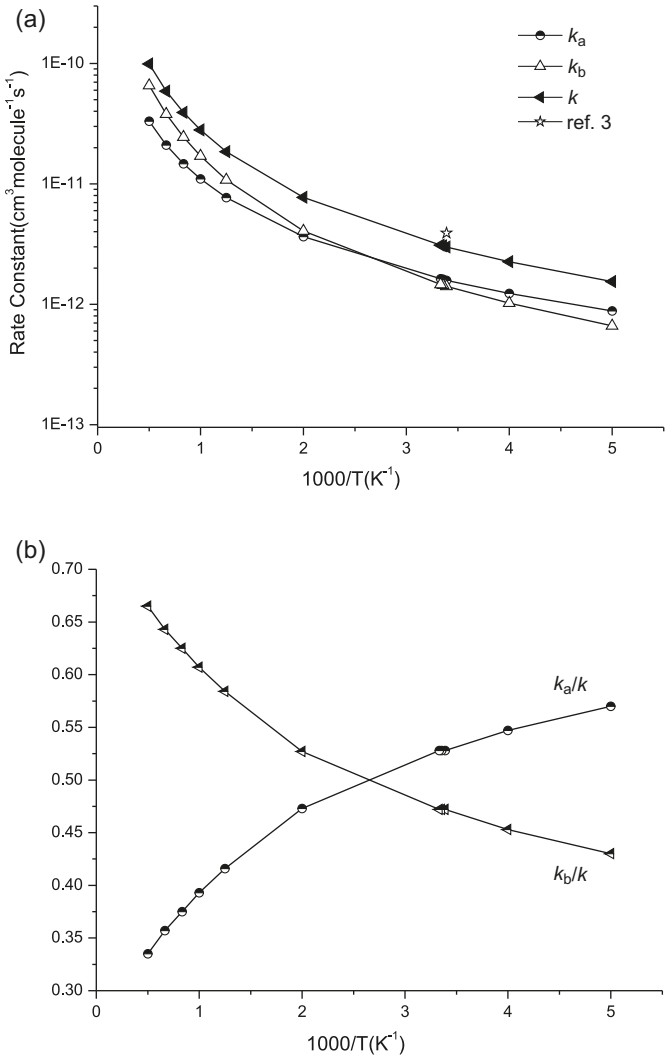

Can. J. Chem. Downloaded from www.nrcresearchpress.com by University of Electronic and Science Techonology of China on 09/19/12
For personal use only.

are shown in Fig. 4*b*. Just one experiment was performed for the title reaction at 295 ± 2 K[3], and the total rate constant was obtained. Our calculated rate constant is in reasonable agreement with the experimental one. Based on our calculations, the two reaction paths are competitive, i.e., path Ra to yield product CH_2CF_2Cl + H′F is the major reaction path below 400 K. However, the contribution from Rb leading to $CHH'CF_2Cl$ + HF increases with increasing temperature and exceeds path Ra as the major reaction path. For example, the k_b/k ratio is about 43% at 200 K, 52% at 500 K, and 66% at 2000 K. Furthermore, to achieve a good estimate for the title reaction over a wide temperature range, the CVT/SCT rate constants are fitted by the following four-parameter expression within 200–2000 K (in cm^3 $molecule^{-1}$ s^{-1}),

$$[1] \qquad k = 3.20 \times 10^{-17}\, T^{1.94} \exp\left[80.9 \times \frac{T + 111.7}{T^2 + 111.7^2}\right]$$

Conclusions

In this paper, dual-level direct dynamics method is employed to study the hydrogen abstraction reaction CH_3CF_2Cl with F atom, for which only total rate constants at one temperature is reported, and no detail reaction mechanism is performed. The rate constants calculated by the VTST at the G3(MP2)//MPW1K/6–311+G(d,p) level are observed to agree well with the available experimental value. It is shown that two reaction paths are competitive, i.e., reaction path Ra to yield the products CH_2CF_2Cl and H′F dominates the reaction below 400 K, while the contribution from path Rb increases with increasing temperature and exceeds path Ra to be the major reaction path. The four-parameter expression (in cm^3 $molecule^{-1}$ s^{-1}) for the reaction over the whole temperatures is given by eq. [1]. We hope that the theoretical results may be useful for estimating the kinetics of the reaction over a wide temperature range where no experimental data is available.

Acknowledgments

We thank Professor Donald G. Truhlar for providing the POLYRATE 9.7 program and the State Key Laboratory of Physical Chemistry of Solid Surfaces for providing computational resources. This work was supported by the National Natural Science Foundation of China (21003036), Science Foundation of Henan Province (2008A150005, 2011B150003), Science Foundation of Henan University (2009YBZR013, SBGJ090507), Doctor Foundation of Henan University.

References

(1) Scientific Assessment of Stratospheric Ozone. *World Meteorological Organization Global Ozone Research and Monitoring Project-Report No. 20*;Vol. 11, Appendix: AFEAS Report, Geneva, Switzerland, 1989.

(2) Scientific Assessment of Stratospheric Ozone Depletion. *World Meteorological Organization Global Ozone Research and Monitoring Project-Report No. 25*, 1991.

(3) Wallington, T. J.; Hurley, M. D.; Shi, J. C.; Maricq, M. M.; Sehested, J.; Nielsen, O. J.; Ellermann, T. *Int. J. Chem. Kinet.* **1993**, *25* (8), 651. doi:10.1002/kin.550250806.

(4) Truhlar, D. G. In *The Reaction Path in Chemistry: Current Approaches and Perspectives*; Heidrich, D., Ed.; Kluwer: Dordrecht, The Netherlands, 1995; p. 229.

(5) Truhlar, D. G.; Garrett, B. C.; Klippenstein, S. J. *J. Phys. Chem.* **1996**, *100* (31), 12771. doi:10.1021/jp953748q.

(6) Hu, W. P.; Truhlar, D. G. *J. Am. Chem. Soc.* **1996**, *118* (4), 860. doi:10.1021/ja952464g.

(7) Truhlar, D. G.; Garrett, B. C. *Acc. Chem. Res.* **1980**, *13* (12), 440. doi:10.1021/ar50156a002.

(8) Truhlar, D. G.; Isaacson, A. D.; Garrett, B. C. In *The Theory of Chemical Reaction Dynamics*; Baer, M., Ed.; CRC Press: Boca Raton, FL, 1985; p. 65.

(9) Truhlar, D. G.; Garrett, B. C. *Annu. Rev. Phys. Chem.* **1984**, *35* (1), 159. doi:10.1146/annurev.pc.35.100184.001111.

(10) Frisch, M. J.; Trucks, G. W.; Schlegel, H. B.; Scuseria, G. E.; Robb, M. A.; Cheeseman, J. R.; Montgomery, J. A., Jr.; Vreven, T.; Kudin, K. N.; Burant, J. C.; Millam, J. M.; Iyengar, S. S.; Tomasi, J.; Barone, V.; Mennucci, B.; Cossi, M.; Scalmani, G.; Rega, N.; Petersson, G. A.; Nakatsuji, H.; Hada, M.; Ehara, M.; Toyota, K.; Fukuda, R.; Hasegawa, J.; Ishida, M.; Nakajima, T.; Honda, Y.; Kitao, O.; Nakai, H.; Klene, M.; Li, X.; Knox, J. E.; Hratchian, H. P.; Cross, J. B.; Bakken, V.; Adamo, C.; Jaramillo, J.; Gomperts, R.; Stratmann, R. E.; Yazyev, O.; Austin, A. J.; Cammi, R.; Pomelli, C.; Ochterski, J. W.; Ayala, P. Y.; Morokuma, K.; Voth, G. A.; Salvador, P.; Dannenberg, J. J.; Zakrzewski, V. G.; Dapprich, S.; Daniels, A. D.; Strain, M. C.; Farkas, O.; Malick, D. K.; Rabuck, A. D.; Raghavachari, K.; Foresman, J. B.; Ortiz, J. V.; Cui, Q.; Baboul, A. G.; Clifford, S.; Cioslowski, J.; Stefanov, B. B.; Liu, G.; Liashenko, A.; Piskorz, P.; Komaromi, I.; Martin, R. L.; Fox, D. J.; Keith, T.; Al-Laham, M. A.; Peng, C. Y.; Nanayakkara, A.; Challacombe, M.; Gill, P. M. W.; Johnson, B.; Chen, W.; Wong, M. W.; Gonzalez, C.; Pople, J. A. *Gaussian 03, Revision B 04*; Gaussian Inc.: Pittsburgh, PA, 2003.

(11) Lynch, B. J.; Truhlar, D. G. *J. Phys. Chem. A* **2001**, *105* (13), 2936. doi:10.1021/jp004262z.

(12) Curtiss, L. A.; Redfern, P. C.; Raghavachari, K.; Rassolov, V.; Pople, J. A. *J. Chem. Phys.* **1999**, *110* (10), 4703. doi:10.1063/1.478385.

(13) Fukui, K. *Acc. Chem. Res.* **1981**, *14* (12), 363. doi:10.1021/ar00072a001.

(14) Hratchian, H. P.; Schlegel, H. B. In *Theory and Applications of Computational Chemistry: The First 40 Years*; Dykstra, C. E.; Frenking, G.; Kim, K. S.; Scuseria, G. Eds., 2005.

(15) Chuang, Y. Y.; Corchado, J. C.; Truhlar, D. G. *J. Phys. Chem.* **1999**, *103*, 1140.

(16) Corchado, J. C.; Chuang, Y. Y.; Fast, P. L.; Hu, W. P.; Liu, Y. P.; Lynch, G. C.; Nguyen, K. A.; Jackels, C. F.; Fernandez-Ramos, A.; Ellingson, B. A.; Lynch, B. J.; Zheng, J. J.; Melissas, V. S.; Villa, J.; Rossi, I.; Coitiño, E. L.; Pu, J. Z.; Albu, T. V.; Steckler, R.; Garrett, B. C.; Isaacson, A. D.; Truhlar, D. G. *POLYRATE version 9.7*; University of Minnesota, Minneapolis, MN, 2007.

(17) Garrett, B. C.; Truhlar, D. G. *J. Chem. Phys.* **1979**, *70* (4), 1593. doi:10.1063/1.437698.

(18) Garrett, B. C.; Truhlar, D. G. *J. Am. Chem. Soc.* **1979**, *101* (16), 4534. doi:10.1021/ja00510a019.

(19) Garrett, B. C.; Truhlar, D. G.; Grev, R. S.; Magnuson, A. W. *J. Phys. Chem.* **1980**, *84* (13), 1730. doi:10.1021/j100450a013.

(20) Lu, D. H.; Truong, T. N.; Melissas, V. S.; Lynch, G. C.; Liu, Y. P.; Garrett, B. C.; Steckler, R.; Issacson, A. D.; Rai, S. N.; Hancock, G. C.; Lauderdale, J. G.; Joseph, T.; Truhlar, D. G. *Comput. Phys. Commun.* **1992**, *71* (3), 235. doi:10.1016/0010-4655(92)90012-N.

(21) Liu, Y. P.; Lynch, G. C.; Truong, T. N.; Lu, D. H.; Truhlar, D. G.; Garrett, B. C. *J. Am. Chem. Soc.* **1993**, *115* (6), 2408. doi:10.1021/ja00059a041.
(22) Marcus, R. A.; Coltrin, M. E. *J. Chem. Phys.* **1977**, *67* (6), 2609. doi:10.1063/1.435172.
(23) Mason, M. G.; Vonholle, W. G.; Robinson, D. W. *J. Chem. Phys.* **1971**, *54* (8), 3491. doi:10.1063/1.1675371.
(24) Hammond, G. S. *J. Am. Chem. Soc.* **1955**, *77* (2), 334. doi:10.1021/ja01607a027.
(25) Webb, D. U.; Rao, K. N. *J. Mol. Spectrosc.* **1968**, *28* (2), 121. doi:10.1016/0022-2852(68)90001-5.
(26) DeMore, W. B.; Sander, S. P.; Golden, S. P.; Howard, C. J.; Golden, D. M.; Kolb, C. E.; Hampson, R. F.; Molina, M. J. *Chemical Kinetics and Photochemical Data for Use in Stratospheric Modeling*; Evaluation Number 9; JPL Publication 97-4, 1997.

Can. J. Chem. Downloaded from www.nrcresearchpress.com by University of Electronic and Science Techonology of China on 09/19/12
For personal use only.

Feasibility study of hydrogen-bonded nucleic acid base pairs in gas and water phases — A theoretical study

S. Arshadi, A.R. Bekhradnia, and A. Ebrahimnejad

Can. J. Chem. Downloaded from www.nrcresearchpress.com by South China Agricultural University on 09/19/12
For personal use only.

Abstract: To investigate the base pair binding probabilities for nucleic acid bases, numerous models were studied for contacts between adenine, thymine, guanine, cytosine, and uracil using density functional theory (DFT) in combination with the 6–311G* basis set. We obtained an assessment for the energy given by our calculations in gas and aqueous phases, which showed that it should be incorporated into hydrogen bonding and propeller rotational energies. The 42 complexes of base pairs (5 regular and 37 irregular base pairs) were proposed and their hydrogen-bonding (H-bonding) properties were verified. The hydrogen bonds in some irregular base pairs, including CC, UU, and TT (series 1), were stronger than in regular GC and AT base pairs. Also, the strength of the hydrogen bonds in the proposed base pairs, including CU, GG, GU, and TU (series 2), were similar to regular base pairs from an energetic point of view. The propeller rotations revealed a higher rotational barrier energy (6–7.5 kcal/mol; 1 cal = 4.184 J) for irregular base pairs (series 1 and 2) than regular GC and AT ones (1–3 kcal/mol). Nevertheless, the trend in these affinities of the complex contact probabilities and their biological properties were confirmed by our calculations.

Key words: nucleic acid bases, base pair binding probability, hydrogen-bonding energy, propeller rotational energy.

Résumé : Dans le but d'évaluer les probabilités de fixation de paires de bases pour des bases d'acide nucléique, plusieurs modèles ont été étudiés pour les contacts entre l'adénine, la thymine, la guanine, la cytosine et l'uracile à l'aide de la théorie de la fonctionnelle de la densité (TFD) en combinaison avec des ensembles de bases 6–311G*. On a pu évaluer les énergies obtenues par nos calculs en phases gazeuses et aqueuses qui montrent qu'elles devraient être incorporées dans les énergies des liaisons hydrogènes et de la rotation de l'hélice. Les 42 complexes de paires de bases (5 régulières et 37 paires de bases irrégulières) ont été proposés et on a vérifié leurs propriétés de liaisons hydrogènes. Les liaisons hydrogènes dans quelques-unes des paires de bases irrégulières, comprenant CC, UU et TT (série 1) sont plus fortes que dans les paires de bases régulières, GC et AT. De plus, d'un point de vue énergétique, les forces des liaisons hydrogènes dans les paires de bases proposées, incluant CU, GG, GU et TU (série 2) sont semblables à celles de paires de bases régulières. Les rotations de l'hélice ont mis en évidence que, pour les paires de bases irrégulières (séries 1 et 2), les barrières à l'énergie de rotation (6 à 7.5 kcal/mol ; 1 cal = 4.184 J) sont plus élevées que celles pour les bases régulières, GC et AT, par environ 1 à 3 kcal/mol. Toutefois, ces calculs confirment la tendance dans ces affinités de probabilités de complexe de contact ainsi que leurs propriétés biologiques.

Mots-clés : bases d'acides nucléiques, probabilité de fixation de paires de bases, énergie de liaison hydrogène, énergie de rotation de l'hélice.

[Traduit par la Rédaction]

Introduction

A DNA molecule is composed of two strands, running in opposite directions, which are bridged by hydrogen bonds between specific pyrimidines in one strand and purines in another (i.e., one strand runs 5′ to 3′and the complementary 3′ to 5′). Also in the RNA molecule, the hydrogen bond interactions between the nucleic acid base heterocycles are of particular importance. In fact, the bases are combined with two different interaction types: hydrogen bonding and aromatic base stacking.[1] The nature of the stabilization of these two types of pairs is different. These are stabilized by electrostatic energy as well as dispersion energy, respectively.[2] Both interactions are of equal importance in nucleic acids. The two strands of a DNA molecule are held together by the hydrogen bonding between the related bases.[3] Adenine can form two hydrogen bonds with thymine and cytosine can form three hydrogen bonds with guanine (Fig. 1).

To study the essential interaction of DNA bases experimentally, gas-phase experiments need to be performed. However, experiments on DNA base pairs are not easy to perform.[4–7] The gas-phase experiments give large amounts of

Received 14 April 2011. Accepted 2 August 2011. Published at www.nrcresearchpress.com/cjc on 24 October 2011.

S. Arshadi and A. Ebrahimnejad. Department of Chemistry, Payame Noor University, 1935-4697, I.R. of Iran.
A.R. Bekhradnia. Pharmaceutical Sciences Research Center, Department of Medicinal Chemistry, Mazandaran University of Medical Sciences, Sari, Iran.

Corresponding author: A.R. Bekhradnia (e-mail: reza_bnia@yahoo.com and abekhradnia@mazums.ac.ir).

Can. J. Chem. Downloaded from www.nrcresearchpress.com by South China Agricultural University on 09/19/12
For personal use only.

Fig. 1. The Watson–Crick DNA base pairs AT and GC.

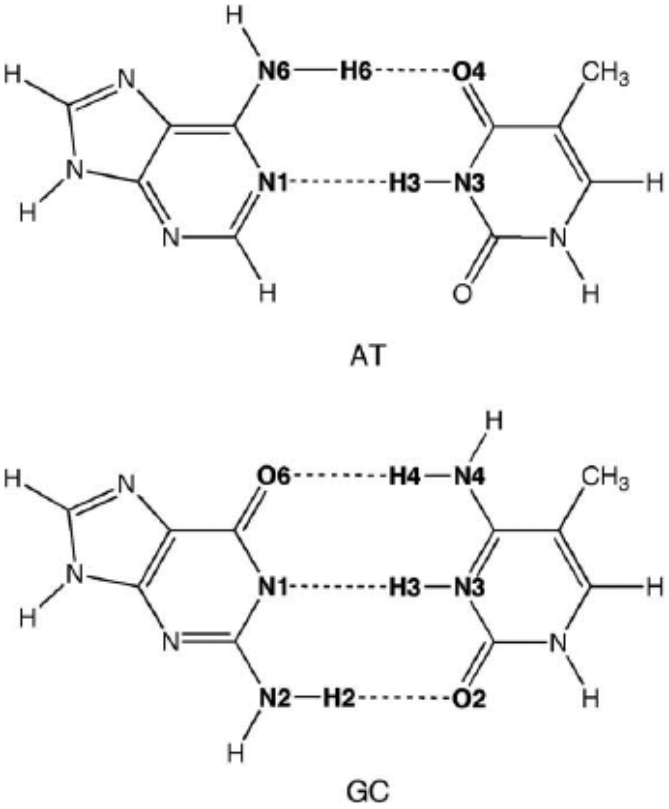

data related to the hydrogen-bonding (H-bonding) property. Also, these data are not related to the stacking of bases. For such studies, the stacked configurations might not be considered in the course of the experiment.[8,9] In recent years, theoretical study has developed into a rapid technical method and is comparable to experimental approaches in efficiency.[10] The theoretical methods can be used for simultaneous evaluation of both hydrogen bonding and aromatic base stacking. Following our previous research studies,[11–14] in this paper we investigated all contact probabilities (42 states) that might occur in the base pairs in gas and water phases (Table 1). Interestingly, the unrestricted density functional method satisfactorily confirmed the regular nucleic acid base pairs contacts (e.g., C:G and A:T).

Computational methods

Full geometry optimizations were performed without any symmetry constraints by means of hybrid functional UB3LYP and the 6–311G* basis set, employing the Gaussian 98 code.[15,16] To assess the performance of this approach, all structures were computed at higher theoretical levels, in a way that UHF/STO-3G outputs were used as inputs for the UHF/6–311G*. Also, UHF/6–311G* outputs were used as inputs for the UB3LYP/6–311G*. To improve the accuracy in estimating hydrogen-bond strengths and distances, we have done the calculations in a comparative manner and used the reasonable unrestricted B3LYP (UB3LYP) instead of the B3LYP method. This method was selected because there is significantly less spin contamination found in the DFT calculations, especially when unrestricted Kohn–Sham orbitals are used.

To evaluate the interaction between $base_1$ and $base_2$ in DNA, the basis set superposition error (BSSE) needs to be included in the binding energy calculations in the systems under consideration. For this purpose, the counterpoise method using "ghost" atoms has been used according to the following equation:

$$E_b = E(\mathrm{DNA_{base1}_DNA_{base2}}) - [E(\mathrm{DNA_{base1-ghost}_}E(\mathrm{DNA_{base2}}) + E(\mathrm{DNA_{base1}_}E(\mathrm{DNA_{base2-ghost}})]$$

where E_b is the counterpoise interaction energy and $E(\mathrm{DNA_{base1}_DNA_{base2}})$ is the total energy of $\mathrm{DNA_{base1}}$ interacting with $\mathrm{DNA_{base2}}$. The ghost molecule / $\mathrm{DNA_{base}}$ corresponds to additional basis wave functions centered at the position of the $\mathrm{DNA_{base1}}$ or the $\mathrm{DNA_{base2}}$, but without any atomic potential.

Propeller rotational energy profiles were performed around the hydrogen bonds of 42 proposed base pairs using the UB3LYP calculation and 6–311G* basis sets in the gas phase and in water as a standard biological solvent (Fig. S3 of the Supplementary data; Figs. 2 and 3). The 42 states of the proposed base pairs include 37 states of irregular and 5 states of regular base pairs (e.g., C:G and A:T). The polarizable continuum model (PCM), the polarizable conductor calculation model (PCCM), and the integral equation formalism model (IEFPCM) were applied to perform solvation analysis for structures 1–47 (5 regular, 37 irregular base pairs, and 5 separate bases) in water.

To obtain reliable results, UB3LYP/6–311G* calculations were carried out for 15 states of separated base pairs with no hydrogen bonds (nonbinding base pairs) in the gas and water phases. On the other hand, all H-bonding probabilities for Watson–Crick pairs consisting of 5 regular and 37 irregular base pairs with hydrogen bonds (binding base pairs) were verified at the same level (Tables 1–2; Tables S2 and S3 of the Supplementary data). In these tables, to facilitate the progress of comparison of separated base pairs without any hydrogen bonds (e.g., A + A and A + C) and with hydrogen bonds (e.g., AA and AC), the lowest entry in each box was set to zero and the others were adjusted accordingly. To attain a deeper insight into the nature of H-bonded interactions, Atoms In Molecules (AIM) analysis[17] was also carried out at the UB3LYP/6–311G* level. All the calculations were performed using the Gaussian 98 program package. The bond critical points of the O–H bonds and the H–N interactions were calculated and are reported.

Results and discussion

In this section we begin with listing our results followed by discussions. Therefore, thermodynamic data were calculated at UB3LYP/6–311G* level of theory for: guanine (G), adenine (A), cytosine (C), thymine (T), uracil (U), and the 42 states of the proposed base pairs (Table 1). These data include the sum of the electronic and thermal energies (E) for all complexes in gas and water phases that were obtained by the frequency option of the Gaussian 98 program (Table 2; Tables S2 and S3 of the Supplementary data).

Relative energies (E_r) for the pyrimidine–purine base pairs are presented for the gas phase (Table 2). To facilitate evaluation of the stability of the proposed base pair, the lowest

Table 1. All of the proposed 42 states of nucleic acid base pairs.

Entry	Complex	Entry	Complex	Entry	Complex	Entry	Complex	Entry	Complex	Entry	Complex
1	AA	2	AC	3	AG	4	AT	5	AU	6	CC
7	CT	8	CU	9	GC	10	GG	11	GT	12	GU
13	TT	14	TU	15	UU	16	AT1	17	CT1	18	CT2
19	CT3	20	CT4	21	CT5	22	GT1	23	GT2	24	GT3
25	GT4	26	TT1	27	TT2	28	TT3	29	TT4	30	TT5
31	TT6	32	TU1	33	TU2	34	TU3	35	TU4	36	TU5
37	TU6	38	TU7	39	TU8	40	GC1	41	GC2	42	GC3
43	A	44	C	45	G	46	T	47	U		

Note: U = uracil, T = thymine, G = guanine, A = adenine, C = cytosine.

Fig. 2. Torsional angle-scanned aromatic plane (propeller rotation) in nucleic acid base pairs at the UB3LYP/6–311G* method (in °).

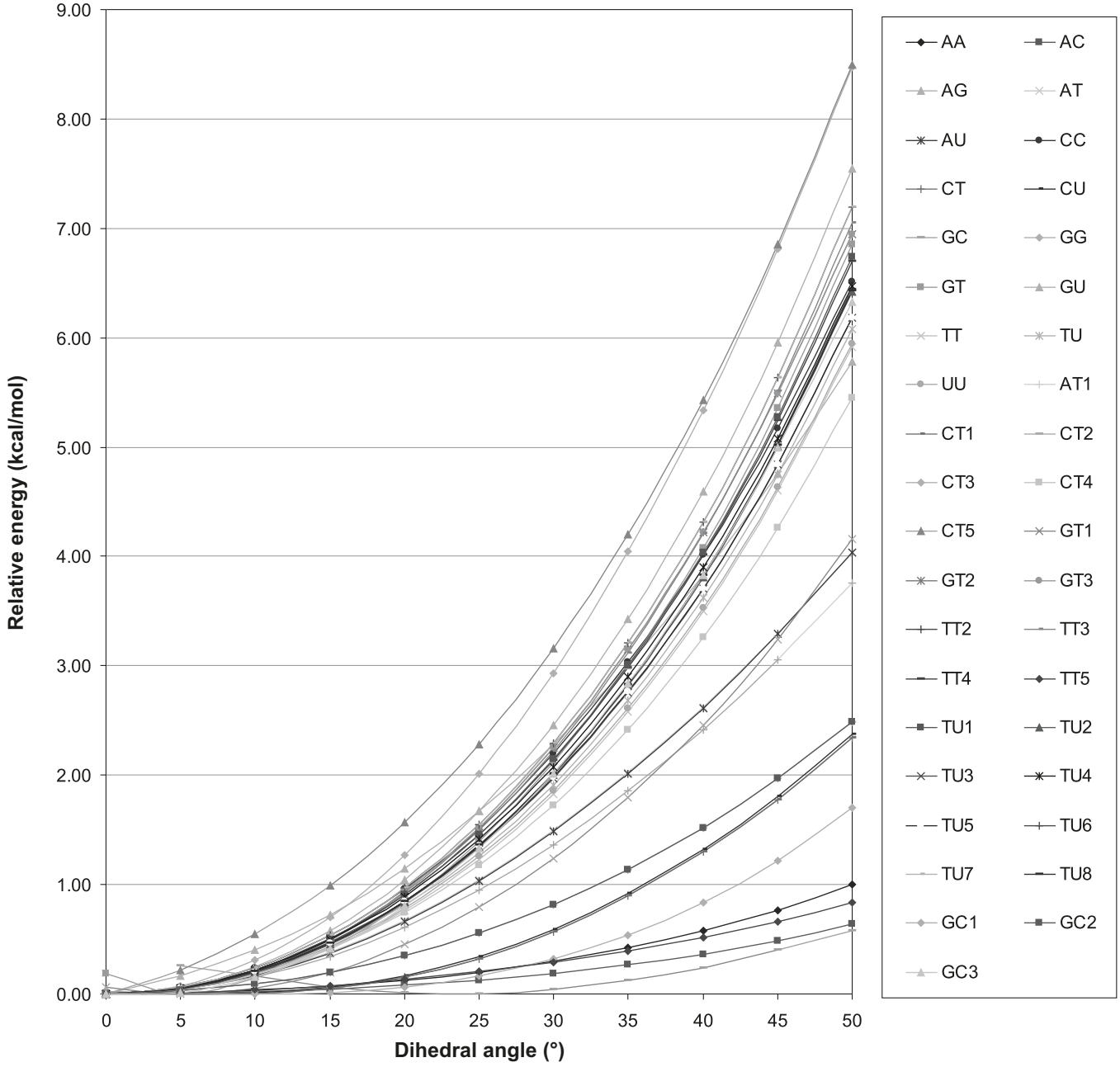

Can. J. Chem. Downloaded from www.nrcresearchpress.com by South China Agricultural University on 09/19/12
For personal use only.

Fig. 3. Torsional angle-scanned aromatic plane (propeller rotation) in the most stable nucleic acid base pairs at the UB3LYP/6–311G* method (in °).

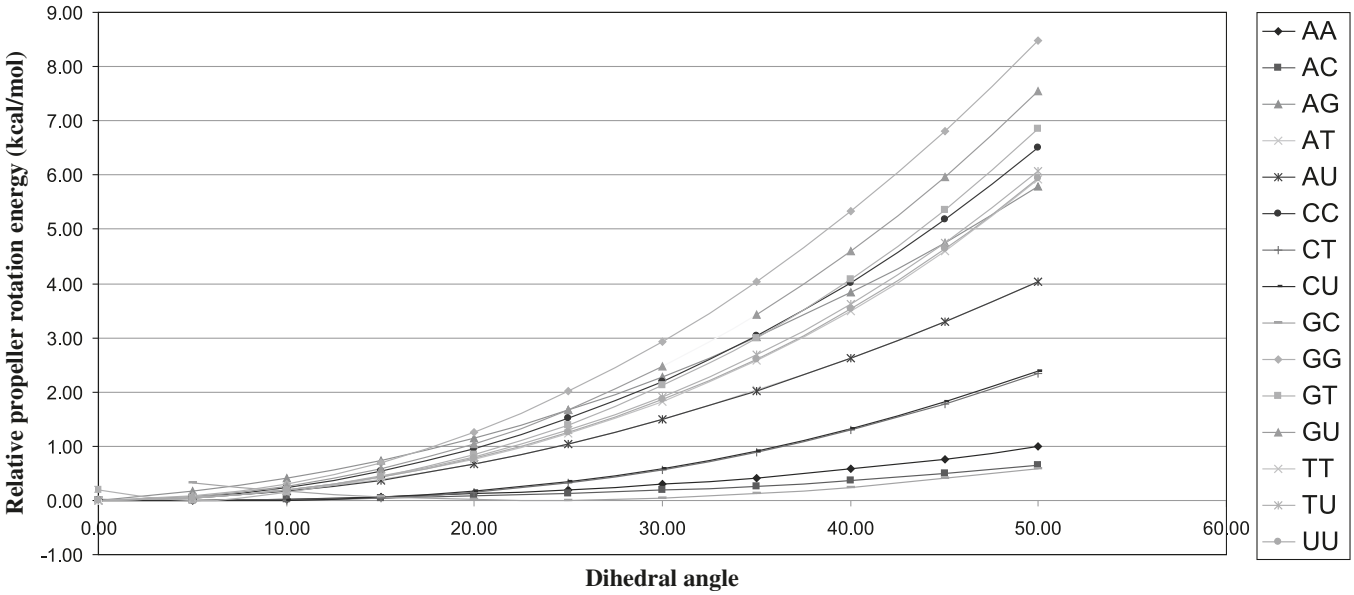

Table 2. Relative energies (E_r*) including ZPE corrections for the 42 states of the proposed base pairs with hydrogen bonds and the 15 states without hydrogen bonds in the gas phase (E_{r1}*) as well as in water (E_{r2}*) using the polarizable continuum model (PCM) method calculated at UB3LYP/6–311G* (in kcal/mol; 1 cal = 4.184 J).

Entry	Complex	E_{r1}*	E_{r2}*	Entry	Complex	E_{r1}*	E_{r2}*	Entry	Complex	E_{r1}*	E_{r2}*
1	AA	0.00	0.00	23	AT	0.00	0.19	45	TU4	0.00	0.00
2	A+A	13.11	5.08	24	CT5	0.00	0.00	46	TU3	2.88	0.63
3	AC	0.00	0.00	25	CT	8.04	4.71	47	TU1	3.53	0.82
4	A+C	16.06	8.09	26	CT3	8.10	5.08	48	TU6	3.88	1.57
5	AG	0.00	0.00	27	C+T	20.73	8.91	49	TU	5.65	2.13
6	A+G	16.15	1.32	28	CT1	22.49	4.96	50	TU8	6.01	2.07
7	AU	0.00	0.00	29	CT2	48.66	2.45	51	TU2	6.20	2.13
8	A+U	0.44	5.96	30	CT4	309.12	2.07	52	TU7	6.50	2.19
9	CC	0.00	0.00	31	GT	0.00	1.51	53	T+U	30.01	7.59
10	C+C	37.49	9.35	32	GT4	0.02	0.06	54	TU5	1.51	1.51
11	CU	0.00	0.00	33	GT3	2.43	3.70	55	GC2	28.00	0.31
12	C+U	25.25	4.08	34	G+T	15.90	9.29	56	GC3	0.00	0.00
13	GC	0.00	0.00	35	GT2	144.95	0.00	57	GC1	4.14	4.14
14	G+C	27.63	15.06	36	GT1	166.52	2.89				
15	GG	0.00	0.00	37	TT4	0.00	2.01				
16	G+G	25.78	3.58	38	TT5	25.98	0.00				
17	GU	0.00	0.00	39	TT	28.76	1.13				
18	G+U	27.24	7.53	40	TT2	32.74	1.63				
19	UU	0.00	0.00	41	TT6	38.79	10.54				
20	U+U	36.12	5.46	42	T+T	41.38	6.53				
21	AT1	12.40	0.00	43	TT1	54.89	1.26				
22	A+T	26.94	6.59	44	TT3	166.95	1.51				

Note: The counterpoise method is used for calculated relative energies.

entry for each binding base pair was set to zero and the related nonbinding base pairs were adjusted accordingly. The mentioned relative energies reflected the stability of the binding base pairs related to those nonbinding base pairs. For the propeller rotational energy, the stabilities of the proposed base pairs, including the regular and irregular ones, are depicted in Figs. 2 and 3. The propeller rotation is described as the turning around of the torsional angle of the aromatic plane in pyrimidines and purines with regard to each strand. The related torsional angles were scanned from 0° to 50° and the relative energies were obtained (Fig. 2). These were separately calculated for pyrimidine–purine, pyrimidine–pyrimidine, and purine–purine contact probabilities. The propeller rotational energy was reflective of aromatic base stacking. Thus, these figures predict the status of aromatic base stacking. The relative energy results in Table 2 indicated that among the studied base pairs AA, AC, AG, AU, CC, CU, GC, GG, GU, UU, CT5, TU4, and GC3 are more stable in

Can. J. Chem. Downloaded from www.nrcresearchpress.com by South China Agricultural University on 09/19/12
For personal use only.

Can. J. Chem. Downloaded from www.nrcresearchpress.com by South China Agricultural University on 09/19/12
For personal use only.

Table 3. The stability factors for base pairs.

Relative propeller rotation energy	Stability related to regular base pairs (GC, AT)	The most stable base pair	Proposed base pairs (series)
—	Less stable	AA	AA
—	Less stable	AC	AC
—	Less stable	AG	AG
—	Less stable	AU	AU
Less stable	More stable	CC	CC (series 1)
Less stable	Comparable	CU	CU (series 2)
More stable	Identical	GC	GC
			GC1
			GC2
			GC3
Less stable	Comparable	GG	GG (series 2)
Less stable	Comparable	GU	GU (series 2)
Less stable	More stable	UU	UU (series 1)
Approx. stable	Identical	AT	AT
			AT1
—	Less stable	CT5	CT
			CT1
			CT2
			CT3
			CT4
			CT5
—	Less stable	GT	GT
			GT1
			GT2
			GT3
			GT4
Less stable	More stable	TT4	TT (series 1)
			TT1 (series 1)
			TT2 (series 1)
			TT3 (series 1)
			TT4 (series 1)
			TT5 (series 1)
			TT6 (series 1)
Less stable	Comparable	TU4	TU (series 2)
			TU1 (series 2)
			TU2 (series 2)
			TU3 (series 2)
			TU4 (series 2)
			TU5 (series 2)
			TU6 (series 2)
			TU7 (series 2)
			TU8 (series 2)

both the gas phase (E_{r1}*) and in water (E_{r2}*) with the PCM method calculated at UB3LYP/6–311G*. On the other hand, in Fig. 2 it could be observed that the stability of the above proposed base pairs were evaluated by torsional angle-scanned aromatic plane (propeller rotation) energy at UB3LYP/6–311G* method. Accordingly, to evaluate the virtual interaction between DNA bases, both hydrogen bonding and aromatic base stacking should be considered simultaneously. On the basis of hydrogen bonding and propeller rotational energies (aromatic base stacking), the most probable nucleic acid base pairs are shown in Fig. 3. Finally, we found a rough estimate of the stability factors including hydrogen bonding and propeller rotational energies of base-pair binding probabilities (Table 3). As shown in Tables 2 and 3, the formation of the complexes were affected by relative energies (E_r*) and propeller rotational energy. Table 3 indicates that the hydrogen bonds in irregular base pairs including CC, UU, and TT4 (series 1) are stronger than those in regular GC and AT base pairs. Moreover, it can be found in Table 3 and Fig. 2 that relative propeller rotational energy parameters showed instability for three of the proposed base pairs mentioned before. Therefore, according to the relevant thermodynamic results, the regular GC and AT base pairs are form easily.

According to the topological analysis of electron density in AIM theory, ρ is used to describe the strength of a bond. In

Can. J. Chem. Downloaded from www.nrcresearchpress.com by South China Agricultural University on 09/19/12
For personal use only.

Table 4. Topological parameters of the bond critical point (BCP) in the most stable base pairs at the UB3LYP/6–311G* level (arb. units).

Structure	BCP	ρ	$\nabla^2\rho$	λ_1	λ_2	λ_3
AA	H_{10}–N_{26}	0.029	0.077	–0.039	–0.037	0.153
	H_{25}–N_{11}	0.029	0.077	–0.039	–0.037	0.153
AC	N_{11}–H_{25}	0.030	0.079	–0.041	–0.040	0.160
	N_{26}–H_{10}	0.031	0.085	–0.043	–0.041	0.169
AG	O_{23}–H_{10}	0.032	0.097	–0.046	–0.045	0.188
	N_{11}–H_{25}	0.031	0.082	–0.043	–0.041	0.165
AT	O_{26}–H_{10}	0.027	0.081	–0.037	–0.036	0.154
	N_{11}–H_{28}	0.039	0.101	–0.059	–0.056	0.217
CC	N_{11}–H_{14}	0.033	0.089	–0.047	–0.045	0.181
	N_{24}–H_{10}	0.033	0.089	–0.047	–0.045	0.181
CT_5	O_{21}–H_1	0.035	0.109	–0.052	–0.052	0.214
	O_{13}–H_{23}	0.036	0.112	–0.054	–0.054	0.219
CU	N_{11}–H_{14}	0.029	0.076	–0.039	–0.038	0.153
	O_{23}–H_{10}	0.032	0.100	–0.047	–0.047	0.194
GC	O_8–H_{25}	0.038	0.118	–0.058	–0.057	0.233
	N_{26}–H_{10}	0.033	0.089	–0.046	–0.044	0.178
	O_{28}–H_{13}	0.027	0.081	–0.037	–0.036	0.154
GG	O_{17}–H_{10}	0.040	0.119	–0.061	–0.060	0.240
	O_8–H_{26}	0.040	0.119	–0.061	–0.060	0.240
GT	O_8–H_{26}	0.032	0.096	–0.045	–0.045	0.187
	O_{28}–H_{10}	0.036	0.112	–0.053	–0.052	0.218
GU	O_8–H_{26}	0.032	0.097	–0.046	–0.046	0.189
	O_{28}–H_{10}	0.035	0.110	–0.052	–0.051	0.213
TT5	O_{23}–H_1	0.035	0.112	–0.053	–0.053	0.217
	O_{12}–H_{25}	0.031	0.096	–0.045	–0.044	0.185
TU_4	O_{15}–H_{16}	0.036	0.113	–0.055	–0.054	0.221
	O_{27}–H_1	0.035	0.109	–0.052	–0.051	0.212
UU	O_{20}–H_{10}	0.031	0.096	–0.044	–0.044	0.184
	O_8–H_{22}	0.031	0.096	–0.044	–0.044	0.184

Note: ρ, bond strength; $\nabla^2\rho$ (describes bond character) = $\lambda_1 + \lambda_2 + \lambda_3$, where λ_i is an eigenvalue of the Hessian matrix of ρ; when $\nabla^2\rho < 0$, a covalent bond is represented; when $\nabla^2\rho > 0$, an ionic bond is represented.

general, the larger the value of ρ is, the stronger the bond. The $\nabla^2\rho$ describes the character of the bond. Where $\nabla^2\rho < 0$, the bond is covalent, whereas $\nabla^2\rho > 0$ shows that the bond is ionic. Here, $\nabla^2\rho = \lambda_1 + \lambda_2 + \lambda_3$, where λ_i is an eigenvalue of the Hessian matrix of ρ. Therefore, when one of the three λ_i was positive and the other two were negative, we represented it by (3, –1) and called it the bond critical point (BCP). When one of the three λ_i was negative and the other two were positive, we represented it by (3, +1) and called it the ring critical point (RCP), indicating that a ring structure exists (Table 4).

All the BCP data for the complexes are shown in Table 4. Analysis of ρ showed two generally H-bond critical points, i.e., the O and H as well as H and N based H-bonding for each most stable base pair, characterized by values of ρ ranging from 0.027 to 0.040. These electron densities at BCPs indicated the presence of C–H···O or C–H···N bonding interactions presented in the pyrimidine and purine base pairs. It can be found that the positive values of $\nabla^2\rho$ in O and H as well as H and N based H-bonding were in the range of 0.077 to 0.119 arb units. Table 4 shows that all the ρ values are in the standard range, showing that these interactions are H-bonding interactions.

Moreover, the electrostatic and nonelectrostatic data values were obtained for binding and nonbinding proposed base pairs using UB3LYP/6–311G* via PCM, CPCM, and IEFPCM methods in the water phase (Table S1 of the Supplementary data). The differences of electrostatic and nonelectrostatic values ($\Delta G_{solvation}$) as well as repulsion, dispersion, cavitations, and polar and nonpolar solutes are shown in Tables S4–S6 of the Supplementary data.

To scrutinize the controversy between theory and experiment regarding hydrogen-bond lengths in Watson–Crick base pairs,[18,19] we have presented the selected Muliken charges along with the bond lengths of the hydrogen bonds in 42 proposed base pairs (Table S7 of the Supplementary data). Moreover, cartesian coordinates for most stable base pairs at UB3LYP/6–311G* can be found in Table S8 of the Supplementary data.

Conclusion

In summary, 42 complexes of base pairs were proposed and consequently their hydrogen-bonding and propeller rotational energies were investigated. According to UB3LYP/6–311G* data, the hydrogen bonding between regular base pairs is established as follows:

1. The hydrogen bonds in irregular base pairs including CC, UU, and TT (series 1) are stronger than those in regular GC and AT base pairs. Also, the strength of the hydrogen

Can. J. Chem. Downloaded from www.nrcresearchpress.com by South China Agricultural University on 09/19/12
For personal use only.

bonds in the proposed base pairs including CU, GG, GU, and TU (series 2) is similar to the strength of those in regular base pairs from an energetic point of view (Table 3).

2. Noticeably, the propeller rotations for the mentioned irregular base pairs in the previous case reveal higher rotational barrier energies (about 6–7.5 kcal/mol) than regular GC and AT base pairs (1–3 kcal/mol) (Figs. 1 and 2).
3. The H-bonded base pairs in AA, AC, AG, AU, CT, and GT are less stable than those in GC and AT base pairs from an energetic point of view (Table 3).
4. In the case of bond length (N-H···X), the strength of the H-bonded base pairs increases with the increasing length of the N–H covalent bond (Fig. S1 of the Supplementary data).
5. All the ρ values are in the standard range, indicating that the studied interactions are H-bonding interactions. However, each of the most stable base pair has at least two H bonds formed and considered in molecular modeling. In the proposed base pairs, the nitrogen atom plays a role as a H-bonding donator or acceptor, whereas the oxygen atom just acts as a H-bonding acceptor. The H-bonding donator and H-bonding acceptor have higher negative and higher positive muliken charges than the related free nucleic acid base, respectively. Consequently, the strength of the hydrogen bonds enhances with increasing muliken charge values (Table S7 and Fig. S3 of the Supplementary data).

Supplementary data

Supplementary data are available with the article through the journal Web site (http://nrcresearchpress.com/doi/suppl/10.1139/v11-124).

Acknowledgements

The authors gratefully acknowledge the financial support of this work by the Mazandaran University of Medical Sciences ''Professor's Projects Funds''. The authors wish to express their special thanks to N. Khaki (Mazandaran University of Medical Sciences) for her cordial co-operation in completing this research.

References

(1) (a) Hobza, P.; Sandorfy, C. *J. Am. Chem. Soc.* **1987**, *109* (5), 1302. doi:10.1021/ja00239a003; (b) Hunter, C. A. *J. Mol. Biol.* **1993**, *230* (3), 1025. doi:10.1006/jmbi.1993.1217; (c) Sponer, J.; Gabb, H. A.; Leszczynski, J.; Hobza, P. *Biophys. J.* **1997**, *73* (1), 76. doi:10.1016/S0006-3495(97)78049-4.

(2) (a) Šponer, J.; Leszczyński, J.; Hobza, P. *J. Phys. Chem.* **1996**, *100* (13), 5590. doi:10.1021/jp953306e; (b) Šponer, J.; Florián, J. L.; Ng, H.-L.; Šponer, J. E.; Špacková, N. *Nucleic Acids Res.* **2000**, *28* (24), 4893. doi:10.1093/nar/28.24.4893.

(3) Kabeláč, M.; Hobza, P. *J. Phys. Chem. B* **2001**, *105* (24), 5804. doi:10.1021/jp0104886.

(4) Desfrançois, C.; Abdoul-Carime, H.; Schulz, C. P.; Schermann, J. P. *Science* **1995**, *269* (5231), 1707. doi:10.1126/science.269.5231.1707.

(5) Schnier, P. D.; Klassen, J. S.; Strittmatter, E. F.; Williams, E. R. *J. Am. Chem. Soc.* **1998**, *120* (37), 9605. doi:10.1021/ja973534h.

(6) Nir, E.; Kleinermanns, K.; de Vries, M. S. *Nature* **2000**, *408* (6815), 949. doi:10.1038/35050053.

(7) Hoyau, S.; Norrman, K.; McMahon, T. B.; Ohanessian, G. *J. Am. Chem. Soc.* **1999**, *121* (38), 8864. doi:10.1021/ja9841198.

(8) Kratochvíl, M.; Engkvist, O.; Šponer, J.; Jungwirth, P.; Hobza, P. *J. Phys. Chem. A* **1998**, *102* (35), 6921. doi:10.1021/jp9816418.

(9) Kratochvíl, M.; Šponer, J.; Hobza, P. *J. Am. Chem. Soc.* **2000**, *122* (14), 3495. doi:10.1021/ja9936060.

(10) Chaudhuri, S.; Chakraborty, S.; Sengupta, S. K. *Biophys. Chem.* **2011**, *154* (1), 26. doi:10.1016/j.bpc.2010.12.003.

(11) Bekhradnia, A. R.; Ebrahimzadeh, M. A. *Med. Chem. Res.* [Online First]. doi:10.1007/s00044-011-9781-3. Published Online: 20 August 2011.

(12) Bekhradnia, A. R.; Arshadi, S. *Monatsh. Chem.* **2007**, *138* (8), 725. doi:10.1007/s00706-007-0657-7.

(13) Kassaee, M. Z.; Bekhradnia, A. R. *J. Biosci. Bioeng.* **2003**, *95*, 526.

(14) (a) Bekhradnia, A. R.; Arshadi, S. *Chin. J. Struct. Chem* **2011**, *30*, 906; (b) Bekhradnia, A. R.; Ebrahimzadeh, M. A.; Hejazi, V.; Gorji, R.; Vesally, E. *Asian J. Chem.* **2009**, *21*, 2110; (c) Arshadi, S.; Bekhradnia, A. R.; Ahmadi, S.; Karami, A. R.; Pourbeyram, S. *Chin. J. Chem.* **2011**, *29* (7), 1347. doi:10.1002/cjoc.201180253.

(15) Frisch, M. J.; Trucks, G. W.; Schlegel, H. B.; Scuseria, G. E.; Robb, M. A.; Cheeseman, J. R.; Zakrzewski, V. G., Jr.; Montgomery, J. A.; Stratmann, R. E.; Burant, J. C.; Dapprich, S.; Millan, J. M.; Daniels, A. D.; Kudin, K. N.; Strain, M. C.; Farkas, O.; Tomasi, J.; Barone, V.; Cossi, M.; Cammi, R.; Mennucci, B.; Pomelly, C.; Adamo, C.; Clifford, S.; Ochterski, J.; Petersson, G. A.; Ayala, P. Y.; Cui, Q.; Morokuma, K.; Malick, D. K.; Rabuck, A. D.; Raghavachari, K.; Foresman, J. B.; Cioslowski, J.; Ortiz, J. V.; Baboul, A. G.; Stefanov, B. B.; Liu, G.; Liashenko, A.; Piskorz, P.; Komaromi, I.; Gomperts, R.; Martin, R. L.; Fox, D. J.; Keith, T.; Al-Laham, M. A.; Peng, C. Y.; Nanayakkara, A.; Gonzalez, C.; Challacombe, M.; Gill, P. M. W.; Johnson, B.; Chen, W.; Wong, M. W.; Andres, J. L.; Gonzalez, C.; Head-Gordon, M.; Replogle, E. S.; Pople, J. A. *Gaussian 98;* Gaussian: Pittsburgh, PA, 1998.

(16) (a) Raghavachari, K.; Pople, J. A.; Replogle, E. S.; Head-Gordon, M. *J. Phys. Chem.* **1990**, *94* (14), 5579. doi:10.1021/j100377a033; (b) Stewart, J. J. P. *J. Comput. Chem.* **1989**, *10* (2), 209. doi:10.1002/jcc.540100208; (c) McLean, A. D.; Chandler, G. S. *J. Chem. Phys.* **1980**, *72*, 5639 doi:10.1063/1.438980; (d) Krishnan, R.; Binkley, J. S.; Seeger, R.; Pople, J. A. *J. Chem. Phys.* **1980**, *72*, 650 doi:10.1063/1.438955.

(17) Bader, R. F. W. *Atoms in Molecules: A Quantum Theory;* Oxford University Press: Oxford, 1990.

(18) Santamaria, R.; Vázquez, A. *J. Comput. Chem.* **1994**, *15* (9), 981. doi:10.1002/jcc.540150907.

(19) Šponer, J.; Sabat, M.; Burda, J. V.; Leszczynski, J.; Hobza, P. *J. Phys. Chem. B* **1999**, *103* (13), 2528. doi:10.1021/jp983744w.

Intra- and inter-molecular interactions in salicylic acid — Theoretical calculations of ^{17}O and ^{1}H chemical shielding tensors and QTAIM analysis

Mehdi D. Esrafili

Can. J. Chem. Downloaded from www.nrcresearchpress.com by South China Agricultural University on 09/19/12
For personal use only.

Abstract: A density functional theory (DFT) study was performed to examine intra- and inter-molecular hydrogen bond (HB) properties in crystalline salicylic acid (SA). BLYP, B3LYP, and M06 functionals with 6–311++G** basis set were employed to calculate NMR chemical shielding isotropy (σ_{iso}) and anisotropy ($\Delta\sigma$) at the sites of the ^{17}O and ^{1}H nuclei of SA. From this study, it appears that the intra- and inter-molecular O–H···O as well as C–H···O HBs around the SA molecule in the crystal lattice have a major influence on the chemical shielding tensors and more specifically on the carbonyl ^{17}O isotropy value. The quantum theory of atoms in molecules (QTAIM) analysis was also employed to elucidate the interaction characteristics in SA H-bonded network. Based on QTAIM results, a partial covalent character is attributed to the intra- and inter-molecular O–H···O HBs in SA.

Key words: DFT, salicylic acid, chemical shielding, intra-molecular and inter-molecular HBs, QTAIM.

Résumé : On a effectué une étude selon la théorie de la fonctionnelle de la densité (TFD) dans le but d'examiner les propriétés des liaisons hydrogènes (LH) intra- et intermoléculaires dans l'acide salicylique (AS) cristallin. On a utilisé des fonctionnelles BLYP, B3LYP et M06, avec un ensemble de base 6–311++G**, pour calculer l'isotropie (σ_{iso}) et l'anisotropie ($\Delta\sigma$) du blindage chimique en RMN aux sites des noyaux ^{17}O et ^{1}H de l'AS. Sur la base de cette étude, il semble que les liaisons hydrogènes O-H···O intra- et intermoléculaires ainsi que les LH C-H···O autour de la molécule d'AS, dans le réseau cristallin, jouent toutes un rôle important sur les tenseurs de blindage chimique, principalement sur la valeur d'isotropie du ^{17}O du carbonyle. On a aussi utilisé l'analyse par la théorie quantique des atomes dans les molécules (TQADM) pour élucider les caractéristiques de l'interaction dans le réseau de liaisons hydrogènes de l'AS. Sur la base des résultats de l'analyse par la TQADM, on peut attribuer un caractère covalent partiel aux LH intra- et intermoléculaires O-H···O de l'AS.

Mots-clés : théorie de la fonctionnelle de la densité (TFD), acide salicylique, blindage chimique, liaisons hydrogènes intramoléculaires et intermoléculaires, théorie quantique des atomes dans les molécules (TQADM).

[Traduit par la Rédaction]

Introduction

The study of hydrogen-bonding (H-bonding) interactions has long been a topic of intensive scientific research because of its relevance in biochemistry, organic chemistry, inorganic chemistry, solid-state physics, and molecular medicine.[1–4] The double helical structure of DNA, for example, is due largely to hydrogen bonds (HBs) between the base pairs, which link one complementary strand to the other and enable replication. H-bonding interactions also play an important role in determining the three-dimensional structures adopted by proteins and polypeptides. In these macromolecules, bonding between parts of the same macromolecule causes them to fold into a specific shape, which helps determine the molecule's physiological or biochemical role. Thus in recent years, much attention has been focused on HB properties using experimental and theoretical methods.[5–10]

Solid-state nuclear magnetic resonance (NMR) spectroscopy is one of the most valuable tools for studying constitution, state, and structure of compounds.[11] NMR spectra yield a wealth of information, the most commonly reported property being the chemical shielding tensor. This parameter relates an externally applied magnetic field to the resulting change in the local electronic environment of the magnetic nuclei, thereby providing key insights into the underlying atomic structure. The NMR parameters are strongly dependent on molecular structure and on the intra- and inter-molecular HBs that exist within a crystalline framework. On the other hand, the eigenvectors of the proton chemical shielding tensor give proton bond directions with an accuracy rivalled only by neutron diffraction.[12] Hence, this has resulted in numerous studies correlating the ^{17}O, ^{13}C, ^{15}N, and ^{1}H chemical shielding tensors and the structural characteristics in both experimental and theoretical fields.[13–18]

Salicylic acid (SA) and its derivatives are attractive chemicals, since their structures are of significance, particularly in phenolic anti-oxidants, medicine, and enzyme chemistry.[19,20] Like most other carboxylic acids, they exist as a cyclic H-bonded dimer in solid state and in gas phase at moderate

Received 18 April 2011. Accepted 17 June 2011. Published at www.nrcresearchpress.com/cjc on 26 October 2011.

M.D. Esrafili. Laboratory of Theoretical Chemistry, Department of Chemistry, University of Maragheh, Maragheh, Iran.

E-mail for correspondence: esrafili@maragheh.ac.ir.

Can. J. Chem. Downloaded from www.nrcresearchpress.com by South China Agricultural University on 09/19/12
For personal use only.

and high concentrations.[21,22] The existence of a relatively strong intra-molecular C=O···H–O HB in SA and its derivatives provides the possibility of intra-molecular proton transfer in the lowest state of these compounds.[23,24] In contrast to other molecules of this group, such as methylsalicylate or salicylaldehyde, the characteristics of the intra-molecular HB in SA can be essentially influenced by inter-molecular interactions, particularly by inter-molecular HBs formed by the carboxylic group. On the other hand, the interdependence of intra- and inter-molecular HBs in similar systems has been provided by experimental NMR and IR studies.[25,26] Hence, it is possible to investigate the NMR chemical shielding tensors at the sites of ^{1}H and ^{17}O nuclei in solid SA, and preferable to correlate the NMR parameters with the molecular structures, in particular, HBs geometries.

In this article, we report the use of quantum chemistry calculations to characterize the properties of intra- and inter-molecular interactions in SA. It is well known that first principles quantum mechanical calculations of shielding parameters have proven useful in assigning experimental NMR spectra.[27–30] Furthermore, correlations of computed parameters with spectroscopic observables can aid in detailed investigations of molecular and crystalline structure. For example, based on their experimental and theoretical data, Tjandra et al. found some linear correlation relationships between HB lengths and the amide proton chemical shielding isotropy value σ_{iso}.[31] They also suggest that "both the isotropic and the anisotropic components of the ^{1}H chemical shielding tensor were found to depend very strongly on the hydrogen bond length. A weaker dependence can also be observed for the hydrogen bond angle."[31]. The present work evaluates chemical shielding tensors by DFT calculations at the sites of ^{17}O and ^{1}H nuclei in the real H–bonded lattice of SA. To this aim, a seven–molecule model system of SA was created using the reported crystalline structure coordinates by earlier neutron diffraction study.[32] Hence, considering the presence of HBs in the calculations, the most probable interacting molecules with the central molecule in the crystalline structure of SA were considered in a heptamer cluster (see Fig. 1 and Table 1 for details). To study systematically the influence of the H-bonding interactions on the various nuclei, chemical shielding tensors were calculated for two molecular models: isolated gas phase (monomer) and H-bonded (heptamer).

It should be noted that NMR chemical shifts in both molecules and solids can now be performed within DFT using methods that employ periodic wave functions. The approach is based on gauge-including projector augmented waves (GIPAWs),[33] themselves derived from Blöchl's PAW electronic structure method that use pseudopotentials to describe the core-valence interactions. The use of pseudopotentials and plane waves in GIPAW provides an excellent balance of speed and accuracy. GIPAW has proved its efficiency in the study of a large range of systems containing elements of the first four rows of the periodic table. Among them, calculations of ^{17}O, ^{23}Na, ^{25}Mg, ^{27}Al, ^{29}Si, ^{31}P, and ^{43}Ca NMR parameters in various silicates,[34–36] phosphates,[37–39] and other inorganic materials[40–42] allowed a precise assignment of the corresponding spectra and exhibited general trends between NMR and structural parameters.

Theory

The chemical shielding tensor $\boldsymbol{\sigma}$ describes the electronic effect on the Zeeman energy levels of magnetic nuclei, due to the response of the electrons to a static external magnetic field B_0.[43] In closed-shell molecules this leads to a second-order change in the molecular energy:

$$[1] \qquad E = E_0 + B_0 \chi B_0 + \sum_{i=1}^{N} \mu_i \sigma_i B_0 + \cdots$$

where the summation is taken over the N nuclei in the system. Here, we are not interested in the magnetic susceptibility χ but only in the bilinear response property σ_i. Hence, the components of the $\boldsymbol{\sigma}$ tensor of nucleus i are defined as:

$$[2] \qquad \sigma_{\alpha\beta_i} = \left(\frac{\partial^2 E}{\partial \mu_{\alpha_i} \partial B_\beta} \right)_{\mu_i = B \to 0} \qquad \alpha, \beta = x, y, z$$

The σ tensor can be considered to arise from a sum of diamagnetic and paramagnetic contributions: $\sigma_i = \sigma_i^{d} + \sigma_i^{p}$. Only the diamagnetic part depends on the ground-state wave function alone; the determination of the paramagnetic term requires knowledge of the first-order wave functions, which have to be calculated using some form of perturbation theory.

In the principal axis system (PAS), the σ_i^{p} tensor is converted to a diagonal matrix with σ_{11}, σ_{22}, and σ_{33} components, where $\sigma_{33} > \sigma_{22} > \sigma_{11}$. The isotropic σ_{iso} and anisotropic $\Delta\sigma$ chemical shielding are related to the principal components by the following equations, respectively:

$$[3] \qquad \sigma_{iso} = (\sigma_{11} + \sigma_{22} + \sigma_{33})/3$$

$$[4] \qquad \Delta\sigma = \sigma_{33} - (\sigma_{11} + \sigma_{22})/2$$

Computational aspects

All calculations were performed using a modified version of the Gaussian 03 suite of programs.[44] Since the crystalline structure of SA was obtained from a neutron diffraction study,[32] geometry optimization was not needed in this work. We examined the ability of three density functionals [including one GGA (BLYP), one hybrid GGA (B3LYP), and one hybrid meta-GGA (M06)] to evaluate the chemical shielding tensors for ^{17}O and ^{1}H nuclei.[45–47] Zhao and Truhlar have recently developed the M06 family of local (M06-L) and hybrid (M06, M06-2X) meta-GGA functionals that show promising performance for noncovalent interactions.[47] For each BLYP, B3LYP, and M06 functional, 6–311++G** standard basis set was employed. Various combinations of diffuse and polarization functions are incorporated in this basis set that are necessary for computation of chemical shielding tensors of hydrogen and oxygen atoms involved in HBs. Previous studies reveal that 6–311++G** usually lead to satisfactory chemical shielding values.[48–50]

Chemical shielding calculations were performed using the gauge-included atomic orbital (GIAO) method.[51] Since quantum chemical calculations yield absolute chemical shielding values, one must establish the absolute shielding values for a particular nucleus to obtain a direct relation between the

Can. J. Chem. Downloaded from www.nrcresearchpress.com by South China Agricultural University on 09/19/12
For personal use only.

Fig. 1. (*a*) monomer and (*b*) H-bond network in the crystalline structure of SA. The target molecule (**1**) [*x*,*y*,*z*]; **2** [2–*x*, –*y*, –*z*]; **3** [1+*x*, 1/2 *y*, –1/2+*z*], **4** [*x*,1/2 *y*, –1/2+*z*], **5** [–*x*,1/2+*y*,1/2–*z*], **6** [–1+*x*,1/2 *y*,1/2+*z*], **7** [*x*,1/2 *y*,1/2+*z*]. The dashed lines show HB interactions.

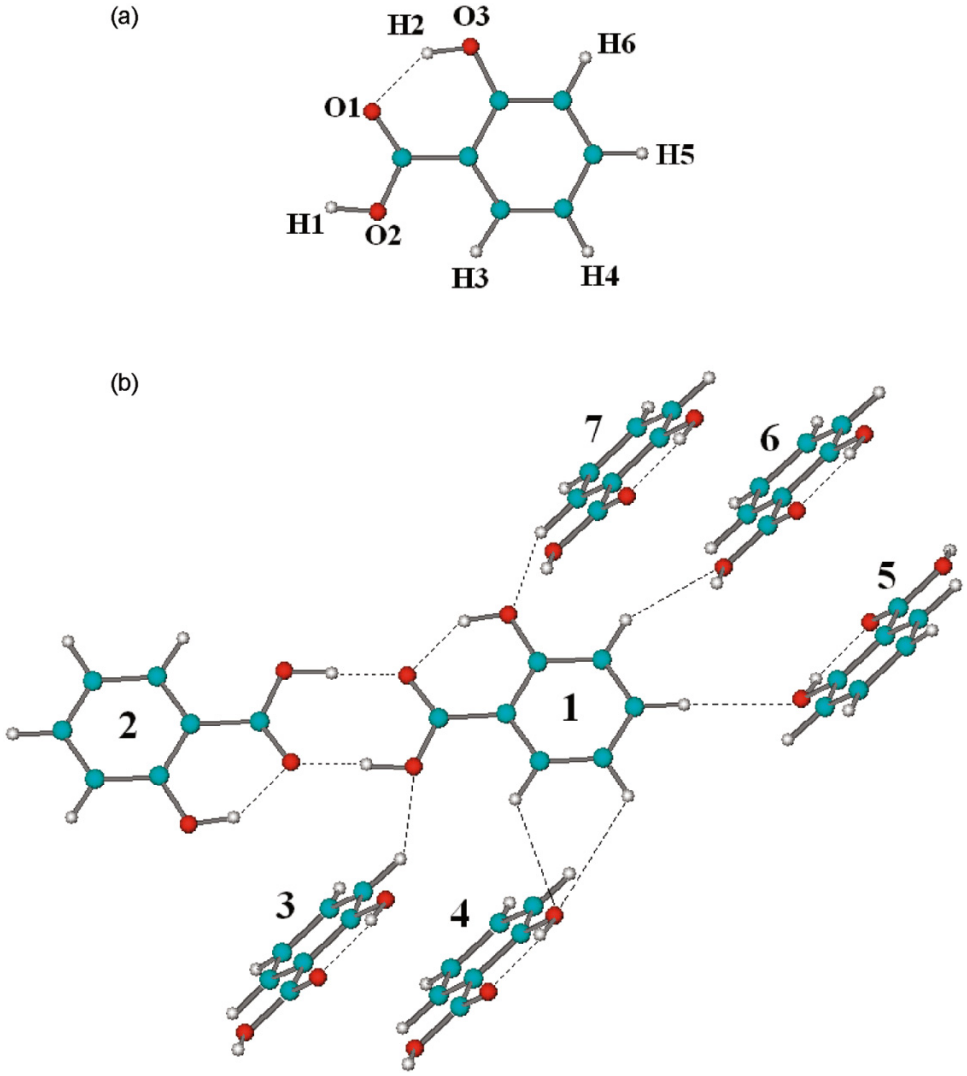

calculated results and experimentally reported data. To evaluate the chemical shift isotropy δ_{iso} from the calculated $\sigma_{iso,calcd}$ values, we used

$$[5] \qquad \delta_{iso} = \sigma_{ref} - \sigma_{iso,calcd}$$

where σ_{ref} refers to the absolute ^{17}O and ^{1}H chemical shielding of liquid water and TMS, with σ_{ref} = 307.9,[52] and 30.5 ppm,[12] respectively.

The QTAIM methodology[53] has been used to analyze the electron density of the systems considered at the M06/6–311 ++G** computational level, using AIM2000 program.[54] For atom–atom interactions such as intra- and inter-molecular contacts or valence bonds, the characteristics of the corresponding bond critical point (BCP) of molecular charge density ρ_{BCP} are very important. These are points where the electron density gradient $\nabla\rho_{BCP}$ vanishes, and additional characterization is done using the corresponding Hessian matrix (a 3 × 3 matrix of second derivatives). Diagonalization of this matrix yields the coordinate invariant eigenvalues: $\lambda_1 \leq \lambda_2 \leq \lambda_3$. The quantities Laplacian $\nabla^2\rho_{BCP}$ of charge density at the bond critical point is defined as:

$$[6] \qquad \nabla^2\rho_{BCP} = \sum_{i=1}^{3} \lambda_i$$

There are well-known relationships between energetic topological parameters and the Laplacian of electron density at BCP:

$$[7] \qquad \frac{1}{4}\nabla^2\rho_{BCP} = 2G_{BCP} + V_{BCP}$$

$$[8] \qquad H_{BCP} = G_{BCP} + V_{BCP}$$

where G_{BCP}, V_{BCP}, and H_{BCP} are the kinetic, potential, and total electron energy densities at the critical point, respectively. G_{BCP} is a positive value, whereas V_{BCP} is a negative one.

Results and discussion

The ^{17}O and ^{1}H NMR parameters, as well as electron density analysis in the H-bonded lattice of SA, are evaluated in the present computational study. To this aim, a seven-molecule

Can. J. Chem. Downloaded from www.nrcresearchpress.com by South China Agricultural University on 09/19/12
For personal use only.

Table 1. Selected H-bond distances and angles of the SA crystalline lattice.

Bond distances (Å)	
$r_{H1(1)\cdots O1(2)}$	1.626
$r_{O1(1)\cdots H1(2)}$	1.626
$r_{H2(1)\cdots O1(1)}$	1.785
$r_{H6(3)\cdots O2(1)}$	2.490
$r_{H3(1)\cdots O3(4)}$	2.640
$r_{H4(1)\cdots O3(4)}$	3.007
$r_{H5(1)\cdots O3(5)}$	2.546
$r_{H6(1)\cdots O2(6)}$	2.489
$r_{H3(7)\cdots O3(1)}$	2.639
Bond angles (°)	
O2–H1(2)···O1(1)	174.81
O2-H1(1)···O1(2)	174.81
O3-H2(1)···O1(1)	142.88
C-H6(3)···O2(1)	131.17
C-H3(1)···O3(4)	124.81
C-H4(1)···O3(4)	113.30
C-H5(1)···O3(5)	177.56
C-H6(1)···O2(6)	131.18
C-H3(7)···O3(1)	124.82

Note: The value within the parenthesis refers to the molecule number in Fig. 1*b*. The H-bond distances and angles of crystalline SA are from Ref. 32.

model system of SA was created by neutron diffraction coordinates. As seen in Table 1, the inter-molecular O–H···O HBs in SA are almost linear (the O–H···O angle equals 174.81°), and their lengths are 1.626 Å. The intra-molecular HB between the hydroxyl and the oxygen atom of the carbonyl group is strongly bent (the O–H···O angle equals 142.88°) and the O–H···O distance is 1.785 Å.

This section is divided into three subsections. First, we present the results for the ^{17}O chemical shielding tensors of SA, both in the gas phase and in solid lattice. Here we evaluate the role of intra- and inter-molecular interactions in the solid lattice, and we seek to find the main factors that differentiate calculated ^{17}O NMR parameters in SA. Second, we discuss the results for ^{1}H shielding tensors and compare them with the available experimental results for other related compounds. Finally, we present a QTAIM topological analysis of different HB interactions and evaluate their strength in crystalline SA. Unless otherwise noted, following results refer to the M06/6–311++G** level of theory.

^{17}O NMR parameters

Table 2 presents the evaluated NMR parameters from the calculated chemical shielding tensors at the sites of ^{17}O nuclei in SA. Considering the evaluated $\delta_{iso}(^{17}O)$ values, it is evident that the results obtained by different DFT methods agree with each other to within 1.14–12.70 ppm. As shown in Fig. 1, there are three crystallographically distinct oxygen sites in SA[32]: C=O, carboxylic, and phenolic O–H. From Table 2, it can be seen that all of the $\delta_{iso}(^{17}O)$ values of the monomer SA lie within the 125.92–370.62 ppm and that of phenolic O–H oxygen is relatively more shielded. Clearly, a different δ_{iso} value observed for the oxygen sites in monomer SA must arise from differences in the surrounding environment. Besides the covalent bonds (C=O or O–H) to carbon that contribute to the different ^{17}O chemical shielding regions, the phenolic oxygen also experiences an intra-molecular HB with carbonyl C=O moiety, $r_{H2(1)\cdots O1(1)}$ = 1.785 Å and angle for O3–H2(1)···O1(1) = 142.88°. It is also interesting to note that O2 and O3 exhibit somewhat similar $\Delta\sigma$ values, 145.04 and 152.42 ppm, respectively, despite the fact that the two oxygen atoms belong to quite different functional groups.

In crystal lattice, SA molecules are mainly held together in dimers by the familiar carboxylic acid dimeric linkage, involving two symmetry-equivalent HBs (Fig. 1*b*). These are of medium strength, with O···O separation of around 2.6 Å.[32] A quick look at the results reveals that inter-molecular HB interactions affect the calculated ^{17}O NMR parameters at the O1, O2, and O3 sites; however, this influence is not equivalent for the three oxygen nuclei. As seen in Table 2, M06 calculations reveal that the δ_{iso}(O1) parameter decreases by 61.30 ppm depending on whether the SA molecule is in the gas phase or in the crystal lattice. On the other hand, the corresponding anisotropy decreases about 84.49 ppm on going from the single monomer to the target molecule in the cluster. The calculated δ_{iso} parameter for O1 in crystalline SA is 309.32 ppm, which is slightly larger than that of aspirin (ca. 302.2 ppm) but quite smaller than phthalic acid (ca. 347.3 ppm) and maleic acid (ca. 343.7 ppm).[55] In contrast, the ^{17}O NMR parameters for O2 show less sensitivity to the H-bonding interactions. Figure 1 shows that O2 contributes to two HBs in crystalline SA, O–H···O (1.626 Å), and C–H···O (2.490 Å). Because of the proper HB distances, δ_{iso} increases by 12.59 ppm from the monomer to the target molecule in the cluster. The $\Delta\sigma$ also decreases by 4.71 ppm from the monomer to the cluster. These significant changes reveal the importance of the carboxylic group in contributing to the strong HBs in the crystalline SA.

It was previously reported[8] that the ^{17}O δ_{iso} values tend to decrease when the oxygen atoms are involved in stronger H-bonding environments. Recently, Smith et al[55] reported solid state ^{17}O NMR parameters for a series of carboxylic acid compounds with their C=O···H–O distance ranging from 1.2 to 2.0 Å. For C=O oxygens, δ_{iso} increases (downfield shifts) as the HB distance increases and the bond strength decreases. In contrast, δ_{iso} of O–H oxygen decreases (upfield shifts) as the HB strength decreases. Table 2 also shows correlation between the theoretical and available experimental ^{17}O NMR parameters. Compared with the ^{17}O chemical shift isotropy values for carboxylic acids in ref. 55, the calculated $\delta_{iso}(^{17}O)$ values of SA at the carboxyl site correlate well with those experimental reported of maleic acid, phthalic acid and oxalic acid.$2H_2O$ suggesting that the local environments of the oxygen sites are approximately similar from those in carboxylic acids (Table 2). The discrepancy of δ_{iso}(O–H) can be mainly attributed to the existence of C–H···O interactions, especially between O2 and molecule No.3, in crystalline SA.

As mentioned above, the phenolic O3 atom contributes to an intra-molecular interaction in monomer SA. For the NMR parameters at this site, the comparison of the isolated model and the heptamer cluster shows some discrepancies, although not as dramatic as the one seen for O1 and O2. By a quick look at Fig. 1*b*, it is found that the O3 atom of the target molecule can form an C–H···O inter-molecular HB with molecule **7**, which is located at an adjacent perpendicular sheet. From having two possibilities to formation of HBs, $r_{H2(1)\cdots O1(1)}$ = 1.785 Å

Can. J. Chem. Downloaded from www.nrcresearchpress.com by South China Agricultural University on 09/19/12
For personal use only.

Table 2. Calculated ^{17}O NMR parameters for monomer and target molecule in the heptamer cluster of SA.

Model	Method	O1		O2		O3	
		δ_{iso}	$\Delta\sigma$	δ_{iso}	$\Delta\sigma$	δ_{iso}	$\Delta\sigma$
Monomer	BLYP	358.38	414.47	196.45	143.72	132.42	149.87
	B3LYP	359.52	437.63	187.26	143.42	119.75	143.44
	M06	370.62	451.77	199.96	145.04	125.92	152.42
Heptamer	BLYP	302.16	343.29	211.19	138.24	127.75	145.95
	B3LYP	299.60	357.46	202.32	137.83	115.26	138.46
	M06	309.32	367.28	212.55	140.33	122.49	147.67
Exptl.[a]	Maleic acid	312	—	189	—	182	—
	Phthalic acid	312	—	180	—	—	—
	Oxalic acid	301	—	183	—	—	—

Note: NMR parameters calculations with 6–311++G** basis set. δ_{iso} and $\Delta\sigma$ values in ppm.
[a]Experimental values from Ref. 55.

and $r_{H3(7)\cdots O3(1)}$ = 2.639 Å, the M06 calculations reveal that δ_{iso} and $\Delta\sigma$ decrease by only 3.43 and 4.75 ppm from the monomer to the target molecule in the cluster, respectively. Besides, the evaluated δ_{iso} value at the O3 site deviates significantly from that of maleic acid (Table 2)

^{1}H NMR parameters

As shown in the previous part, H–bonding interactions affect remarkably the ^{17}O shielding parameters. In this part, we discuss the influence of H–bonding interactions on the calculated ^{1}H NMR parameters, see Table 3. Considering the evaluated $\delta_{iso}(^1H)$ values, it is found that different DFT methods agree reasonably well with each other to within 0.02–0.98 ppm.

^{1}H NMR spectroscopy is probably the most direct spectroscopic technique for investigating H-bonding. Since it is not possible to obtain absolute values of the HB strengths from experimental solid-state studies, correlations between ^{1}H NMR and HB strength have been frequently used to infer information about the HBs formed.[57] Table 3 shows the calculated δ_{iso} and $\Delta\sigma$ values of SA at the sites of six ^{1}H nuclei, both in the gas phase and solid lattice. As illustrated in Fig. 1*b*, the target molecule in the cluster is capable of participating in a variety of inter-molecular O–H···O=C, and C–H···O=C HBs with the molecules **2**–**7**; however, their strengths are not equivalent in the seven-molecule cluster. Table 3 shows that the NMR parameters of the carboxylic hydrogen atom (H1) vary considerably between the monomer and heptamer cluster, $\Delta\delta_{iso}$ = 6.80 and $\Delta(\Delta\sigma)$ = 12.55 ppm. The calculated δ_{iso} and $\Delta\sigma$ values for H1 of the target molecule have been obtained as 13.66 and 23.77 ppm at the M06 level, respectively. These values, which are obtained by taking the whole cluster into consideration, are expected to be close to the other carboxylic compounds.[57] Compared with experimental values of carboxylic acids given in Ref. 57, the smallest difference occurs for maleic acid, sqauric acid, and trichloroacetic acid (Table 3).

The correlation of the isotropic shielding and the shielding anisotropy of carboxylic hydrogen with HB distance ($r_{O\cdots O}$) has been empirically established for strong and medium strength HBs.[58] Berglund et al.[57] reported that the δ_{iso} of the H-bonded proton in an OH···O=C HB is primarily dependent on the distance between the proton and the donor atom and showed how a combined experimental and theoretical approach can be used to refine the hydrogen position. Using such a correlation equation, the δ_{iso} value of the carboxylic proton in SA falls into the category of a moderately strong HB, i.e., associated with a generic HB geometry of: O–H···O=C of ~1.6 Å. These values closely resemble those of the reported neutron diffraction structure.[32]

As seen in Table 3, the δ_{iso} value of H2 in monomer SA downshifts by 1.6 ppm from that of carboxylic H1 site. This discrepancy can be explained in terms of formation of an intra-molecular between phenolic O–H and carboxylic C=O groups. However, due to the weak nonlinear C–H3(7)···O3 interaction, 0.32 and 4.17 ppm increases in δ_{iso} and $\Delta\sigma$ parameters are observed from the monomer to the target molecule in the cluster, respectively. Table 3 also indicates that there is a reasonable agreement between the calculated shielding anisotropy of H2 in SA and the experimental value of maleic acid.[57]

The carbon-bound hydrogen atoms (H3 to H6) have almost identical positions in the monomer SA and therefore it is expected to have a quite similar ^{1}H isotropic shielding. However, the H3 atom contributes to a weak intra-molecular C–H···O=C interaction with O2, hence its δ_{iso} is slightly larger than those of others (Table 3). These hydrogen atoms also occupy a different position in the H-bonding network of the crystalline SA, so have slightly different isotropy and anisotropy values. According to the SA crystalline structure, each of the H3 to H6 atoms are involved in a single inter-molecular HB. Therefore, the variation in the calculated ^{1}H shielding tensors for these sites can be fully explained in terms of the changes in the corresponding C–H···O bond length and angle between the SA monomers. For example, both $\Delta\delta_{iso}$ = 1.43 ppm and $\Delta(\Delta\sigma)$ = 1.93 ppm for the H5 site in the heptamer structure relative to those of others arise because of the corresponding proper $r_{H5\cdots O3(5)}$ = 2.546 Å and angle for C–H5(1)···O3(5)= 177.56°. Hence, it may be deduced that such differences in hydrogen chemical shielding are attributed to the H-bonding environments mentioned above. In this context, it is to be noted that Brown et al. have observed isolated gas phase to solid-state changes of up to 1.90 ppm in the ^{1}H chemical shifts of CH and CH_2 protons in two anomeric forms of maltose, with the authors assigning these changes to weak inter-molecular C–H···O H-bonding.[59]

QTAIM analyses

A great deal of information about the nature of intra- and inter-molecular HB interactions in SA can be obtained from a

Can. J. Chem. Downloaded from www.nrcresearchpress.com by South China Agricultural University on 09/19/12
For personal use only.

Table 3. Calculated ^{1}H NMR parameters for monomer and target molecule in the heptamer cluster of SA.

Model	Method	H-1		H2		H3		H4		H5		H6	
		δ_{iso}	$\Delta\sigma$	δ_{iso}	$\Delta\sigma$	δ_{iso}	$\Delta\sigma$	δ_{iso}	$\Delta\sigma$	δ_{iso}	$\Delta\sigma$	δ_{iso}	$\Delta\sigma$
Monomer	BLYP	5.88	9.37	8.63	17.88	6.42	7.98	5.27	4.65	5.94	5.17	5.56	5.47
	B3LYP	6.21	10.42	8.60	18.72	6.56	8.12	4.35	4.73	6.07	5.26	5.66	5.62
	M06	6.86	11.22	8.48	17.90	6.36	8.42	5.19	5.04	6.11	5.77	5.48	5.95
Heptamer	BLYP	12.83	23.22	8.49	21.17	7.13	5.66	6.08	8.72	6.76	6.00	5.69	5.17
	B3LYP	13.03	24.18	8.47	21.99	7.31	5.75	6.22	8.91	6.94	6.19	5.79	5.38
	M06	13.66	23.77	8.80	22.07	7.29	5.83	6.18	9.41	7.54	7.70	6.31	5.76
Exptl.[a]	Maleic acid	16.6	22.7	14.5	19.0	—	—	—	—	—	—	—	—
	Sqauric acid	15.2	22.0	—	—	—	—	—	—	—	—	—	—
	Trichloroacetic acid	13.9	20.1	—	—	—	—	—	—	—	—	—	—

Note: NMR parameters calculations with 6–311++G** basis set. δ_{iso} and $\Delta\sigma$ values in ppm.

[a]Experimental values from Ref. 56.

topological analysis of its electron density. Based on QTAIM theory,[53] properties of BCPs serve to summarize the nature of the interaction between two atoms as shared (covalent) or closed-shell (ionic) interaction. For a set of H-bonded complexes, Koch and Popelier[60] found the correlation between the HB energy and ρ_{BCP} to be linear as long as the acceptor atom remained unchanged. In characterizing the HBs of our cluster structures, we have adopted the classification used by Rozas et al.:[61] a HB is defined as weak if $\nabla^2\rho_{BCP} > 0$ and $H_{BCP} > 0$, medium-strength if $\nabla^2\rho_{BCP} > 0$ but $H_{BCP} < 0$, and strong if $\nabla^2\rho_{BCP} < 0$ and $H_{BCP} < 0$.

A molecular graph of crystalline dimer SA is depicted in Fig. 2. For the both intra- and inter-molecular O–H···O interactions, there are corresponding bond paths and critical points (CPs) within the equilibrium structures. As indicated in previous studies, characteristics of proton···acceptor BCPs are very useful to study the nature of H-bonded systems. Parameters such as electron density at the proton···acceptor BCP, ρ_{BCP} and its Laplacian $\nabla^2\rho_{BCP}$, often correlate with the HB energy or other parameters, like proton···acceptor distance, the proton donating bond length, etc.[62] As presented in Fig. 2, there are specific bond paths and BCPs for intra- and inter-molecular OH···O connections. Therefore, the first topological criterion of the existence of H-bonding interaction is fulfilled.

Table 4 shows the ρ_{BCP}, $\nabla^2\rho_{BCP}$, the H_{BCP} and its components G_{BCP} and V_{BCP} values for the all HBs interactions examined in this work. From Table 4, it is evident that the ρ_{BCP} values are calculated to be in the range of 0.005–0.051 au, whereas the values of $\nabla^2\rho_{BCP}$ are all positive, ranging from 0.021 to 0.152 au. These values are within the common accepted values for H-bonding interactions, thus indicating closed-shell interactions in this system. As pointed out above, the electron energy density H_{BCP} is a more appropriate index to gain a deeper understanding of noncovalent interactions.[63] The sign of H_{BCP} at BCP determines whether the interaction is electrostatic dominant ($H_b > 0$) or covalent dominant ($H_{BCP} < 0$). From Table 4, it is revealed that for the all inter-molecular C–H···O interactions, the H_{BCP} values are all greater than zero, suggesting that the interactions are basically electrostatic in nature. However, negative values of H_{BCP} are predicted for both intra- and inter-molecular O–H···O, suggesting that the interactions in these HBs have some degree of covalent character. On the other hand, different contributions of various nuclei to HB interactions and observed trends of calculated NMR parameters are well justified by QTAIM analyses at the BCPs of these interactions. For example, the low values of charge density at the BCPs of C–H···O interactions suggest that δ_{iso} and $\Delta\sigma$ (H3 to H6) should not reduce considerably from the monomer to heptamer cluster. According to these results, we can conclude that strong HBs are more covalent in nature and weak HBs are mainly electrostatic interactions, which follows the electrostatic-covalent model observed for HBs (ECHBM).[64] As shown in Fig. 3, a plot of the electron densities Laplacian versus the ^{1}H isotropies are approximately linear (R^2 = 0.952). This means that, the Laplacian of electron densities is a good indication of the amount of ^{1}H shielding in SA, which reproduces the well-documented properties of HBs.

Conclusion

In this paper, we performed a systematic computational investigation on the intra- and inter-molecular HB interactions in crystalline SA by means of DFT calculations of the chemical shielding tensors at the sites of ^{17}O and ^{1}H nuclei, as well as a QTAIM analysis of charge density in two gas phase (monomer) and seven-molecule (cluster) models. Some results are listed below.

1. Our calculations indicate that NMR parameters of ^{17}O and ^{1}H nuclei are influenced by H-bonding interactions and as such are appropriate parameters to characterize the properties of these interactions.
2. Considering the calculated $\delta_{iso}(^{17}O)$ and $\delta_{iso}(^1H)$ values, it is evident that the results obtained by different DFT methods are agree with each other to within 1.14–12.70 and 0.02–0.98 ppm for the ^{17}O and ^{1}H nuclei, respectively.
3. The chemical shielding calculations reveal that inter-molecular HB interactions affect the calculated ^{17}O NMR parameters at O1, O2, and O3 sites; however, these influences are not equivalent for the three oxygen nuclei. Comparing SA monomer and heptamer clusters, it is evident that in the carboxylic group, O1 has the major role in contributing to the both intra- and inter-molecular interactionsn whereas the role of hydroxyl O–H is rather less. Moreover, the calculated ^{17}O δ_{iso} values of SA at the carboxyl site correlate well with those reported experimental data.

Can. J. Chem. Downloaded from www.nrcresearchpress.com by South China Agricultural University on 09/19/12
For personal use only.

Fig. 2. Molecular graph of SA dimer. The graph was obtained at the M06/6–311++G** level. Large circles correspond to attractors and small red (dark grey in print) and yellow (light grey) circles are bond and ring critical points, respectively. The lines are bond paths.

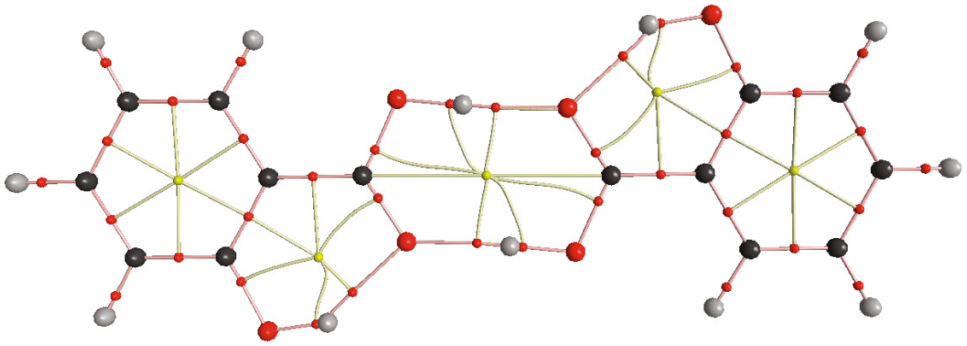

Table 4. Topological parameters of ρ for crystalline SA (electron density at BCP ρ_{BCP}, its Laplacian ∇^2_{BCP}, potential electron energy density (V_{BCP}), kinetic electron energy density (G_{BCP}), absolute ratio of V_{BCP} and G_{BCP}, total electron energy density (H_{BCP}) calculated at the M06/6–311++G** level of theory.

Interaction	ρ_{BCP}	∇^2_{BCP}	G_{BCP}	V_{BCP}	$-V_{BCP}/G_{BCP}$	H_{BCP}
H1(1)···O1(2)	0.051	0.152	0.044	–0.050	1.134	–0.006
O1(1)···H1(2)	0.051	0.151	0.044	–0.050	1.136	–0.006
H2(1)···O2(1)	0.038	0.135	0.035	–0.035	1.023	–0.001
H6(4)···O2(1)	0.008	0.030	0.006	–0.005	0.826	0.001
H3(1)···O3(4)	0.007	0.024	0.005	–0.005	0.865	0.001
H4(1)···O3(4)	0.005	0.021	0.004	–0.003	0.700	0.001
H5(1)···O3(5)	0.007	0.024	0.005	–0.004	0.840	0.001
H6(1)···O3(6)	0.008	0.030	0.006	–0.005	0.832	0.001
H3(7)···O3(1)	0.007	0.024	0.005	–0.005	0.866	0.001

Note: All ρ_{BCP}, ∇^2_{BCP}, G_{BCP}, V_{BCP}, and H_{BCP} in au.

Fig. 3. Correlation between ^{1}H shielding isotropy values and the Laplacian of electron densities at O–H···O and C–H···O BCPs of crystalline SA.

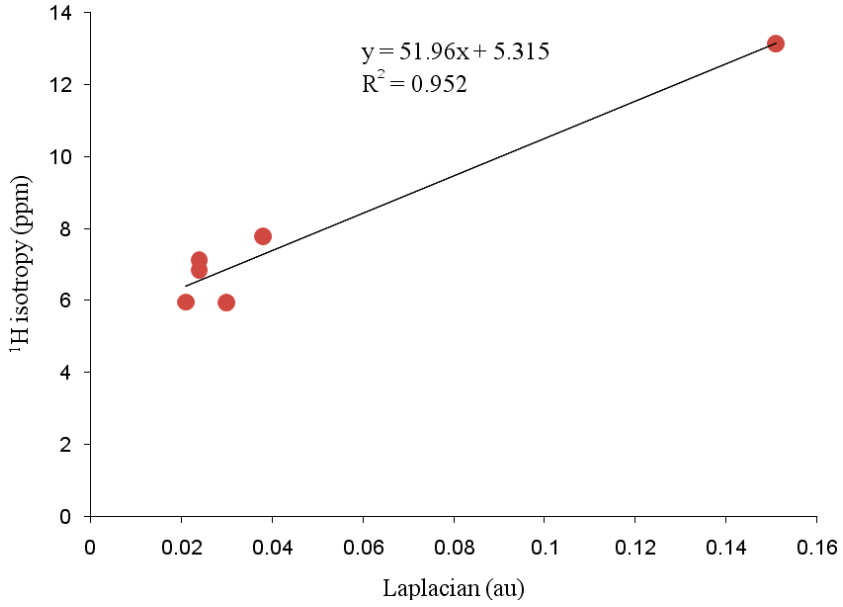

4. The NMR parameters of the carboxylic hydrogen atom (H1) vary considerably between the monomer and heptamer clusters, $\Delta\delta_{iso}$ = 6.80 and $\Delta(\Delta\sigma)$ = 12.55 ppm. The calculated δ_{iso} and $\Delta\sigma$ values for H1 of the target molecule have been obtained to be 13.66 and 23.77 ppm at the M06 level, respectively. These values, which are obtained by taking the whole cluster into consideration, are expected to be close to the other carboxylic compounds.
5. Different contributions of various nuclei to HB interactions and observed trends of calculated NMR parameters are well rationalized by QTAIM analyses at the BCPs of the interactions.

Can. J. Chem. Downloaded from www.nrcresearchpress.com by South China Agricultural University on 09/19/12
For personal use only.

References

(1) Woo, H.-K.; Wang, X.-B.; Wang, L.-S.; Lu, K.-C. *J. Phys. Chem. A* **2005**, *109* (47), 10633. doi:10.1021/jp0553277.

(2) Hobza, P.; Havlas, Z. *Chem. Rev.* **2000**, *100* (11), 4253. doi:10.1021/cr990050q.

(3) Scheiner, S. *Hydrogen bonding: A theoretical prospective*; Oxford University Press: Oxford, UK, 1997.

(4) Thar, J.; Kirchner, B. *J. Phys. Chem. A* **2006**, *110* (12), 4229. doi:10.1021/jp056133u.

(5) Waddell, K. W.; Chekmenev, E. Y.; Wittebort, R. J. *J. Phys. Chem. B* **2006**, *110* (45), 22935. doi:10.1021/jp060617o.

(6) Pike, K. J.; Lemaitre, V.; Kukol, A.; Anupold, T.; Samoson, A.; Howes, A. P.; Watts, A.; Smith, M. E.; Dupree, R. *J. Phys. Chem. B* **2004**, *108* (26), 9256. doi:10.1021/jp049958x.

(7) Kiehlmann, E.; Biradha, K.; Domasevitch, K. V.; Zaworotko, M. J. *Can. J. Chem.* **1999**, *77* (8), 1436. doi:10.1139/v99-140.

(8) Yates, J. R.; Pickard, C. J.; Payne, M. C.; Dupree, R.; Profeta, M.; Mauri, F. *J. Phys. Chem. A* **2004**, *108* (28), 6032. doi:10.1021/jp049362+.

(9) Esrafili, M. D.; Elmi, F.; Hadipour, N. L. *J. Phys. Chem. A* **2007**, *111* (5), 963. doi:10.1021/jp066761r.

(10) Wu, G.; Dong, S.; Ida, R.; Reen, N. *J. Am. Chem. Soc.* **2002**, *124* (8), 1768. doi:10.1021/ja011625f.

(11) Duer, M. J. *Solid State NMR Spectroscopy*; Blackwell Science Ltd.: London, 2002.

(12) Gerald, R., II; Bernhard, T.; Haeberlen, U.; Rendell, J.; Opella, S. *J. Am. Chem. Soc.* **1993**, *115* (2), 777. doi:10.1021/ja00055a058.

(13) Lemaître, V.; Smith, M. E.; Watts, A. *Solid State Nucl. Magn. Reson.* **2004**, *26* (3–4), 215. doi:10.1016/j.ssnmr.2004.04.004.

(14) Ooms, K. J.; Wasylishen, R. E. *Can. J. Chem.* **2006**, *84* (2), 300. doi:10.1139/v06-001.

(15) Wu, G.; Mason, P.; Mo, X.; Terskikh, V. *J. Phys. Chem. A* **2008**, *112* (5), 1024. doi:10.1021/jp077558e.

(16) Zhu, J.; Lau, J. Y. C.; Wu, G. *J. Phys. Chem. B* **2010**, *114* (35), 11681. doi:10.1021/jp1055123.

(17) Mukherjee, S.; Song, Y.; Oldfield, E. *J. Am. Chem. Soc.* **2008**, *130* (4), 1264. doi:10.1021/ja0759949.

(18) Wi, S.; Sun, H.; Oldfield, E.; Hong, M. *J. Am. Chem. Soc.* **2005**, *127* (17), 6451. doi:10.1021/ja042935b.

(19) Nagashima, U.; Nagaoka, S.; Katsumata, S. *J. Phys. Chem.* **1991**, *95* (9), 3532. doi:10.1021/j100162a020.

(20) Aruoma, O. I. *Free Radic. Biol. Med.* **1996**, *20* (5), 675. doi:10.1016/0891-5849(95)02110-8.

(21) Pant, D. D.; Joshi, H. C.; Bisht, P. B.; Tripathi, H. B. *Chem. Phys.* **1994**, *185* (1), 137. doi:10.1016/0301-0104(94)00090-5.

(22) Joshi, H. C.; Mishra, H.; Tripathi, H. B. *J. Photochem. Photobiol. Chem.* **1997**, *105* (1), 15. doi:10.1016/S1010-6030(96)04565-0.

(23) Yi, P. G.; Liang, Y. H.; Cao, C. Z. *Chem. Phys.* **2005**, *315* (3), 297. doi:10.1016/j.chemphys.2005.04.046.

(24) Douhal, A.; Lahmani, F.; Zewail, A. H. *Chem. Phys.* **1996**, *207* (2–3), 477. doi:10.1016/0301-0104(96)00067-5.

(25) Golubev, N. S.; Denisov, G. S. *J. Mol. Struct.* **1992**, *270* (1–2), 263. doi:10.1016/0022-2860(92)85033-D.

(26) Golubev, N. S.; Demsov, G. S.; Kuzina, L. A.; Smirnov, S. N. *J. General Chem. (Russ.)* **1994** *64*, 1162.

(27) Zhang, Q.; Chekmenev, E. Y.; Wittebort, R. J. *J. Am. Chem. Soc.* **2003**, *125* (30), 9140. doi:10.1021/ja034495e.

(28) Behzadi, H.; Esrafili, M. D.; Beheshtian, J.; Hadipour, N. L.; van der Spoel, D. *Chem. Phys. Lett.* **2009**, *476* (4–6), 196. doi:10.1016/j.cplett.2009.06.046.

(29) Yamada, K.; Dong, S.; Wu, G. *J. Am. Chem. Soc.* **2000**, *122* (47), 11602. doi:10.1021/ja0008315.

(30) Zhao, X.; Harbison, G. S. *J. Phys. Chem. B* **2006**, *110* (49), 25059. doi:10.1021/jp0600965.

(31) Sharma, Y.; Kwon, O. Y.; Brooks, B.; Tjandra, N. *J. Am. Chem. Soc.* **2002**, *124* (2), 327. doi:10.1021/ja016859d.

(32) Munshi, P.; Guru Row, T. N. *Acta Crystallogr. B* **2006**, *62* (4), 612. doi:10.1107/S0108768106017393.

(33) Pickard, C. J.; Mauri, F. *Phys. Rev. B* **2001**, *63* (24), 245101. doi:10.1103/PhysRevB.63.245101.

(34) Profeta, M.; Mauri, F.; Pickard, C. J. *J. Am. Chem. Soc.* **2003**, *125* (2), 541. doi:10.1021/ja027124r.

(35) Profeta, M.; Benoit, M.; Mauri, F.; Pickard, C. J. *J. Am. Chem. Soc.* **2004**, *126* (39), 12628. doi:10.1021/ja0490830.

(36) Ashbrook, S. E.; Berry, A. J.; Frost, D. J.; Gregorovic, A.; Pickard, C. J.; Readman, J. E.; Wimperis, S. *J. Am. Chem. Soc.* **2007**, *129* (43), 13213. doi:10.1021/ja074428a.

(37) Gervais, C.; Laurencin, D.; Wong, A.; Pourpoint, F.; Labram, J.; Woodward, B.; Howes, A. P.; Pike, K. J.; Dupree, R.; Mauri, F.; Bonhomme, C.; Smith, M. E. *Chem. Phys. Lett.* **2008**, *464* (1–3), 42. doi:10.1016/j.cplett.2008.09.004.

(38) Chappell, H.; Duer, M.; Groom, N.; Pickard, C. J.; Bristowe, P. *Phys. Chem. Chem. Phys.* **2008**, *10* (4), 600. doi:10.1039/b714512h.

(39) Pourpoint, F.; Kolassiba, A.; Gervais, C.; Azaïs, T.; Bonhomme-Coury, L.; Bonhomme, C.; Mauri, F. *Chem. Mater.* **2007**, *19* (26), 6367. doi:10.1021/cm7028432.

(40) Hart, R. T.; Zwanziger, J. W.; Werner-Zwanziger, U.; Yates, J. R. *J. Phys. Chem. A* **2005**, *109* (33), 7636. doi:10.1021/jp052405h.

(41) Wong, A.; Thurgood, G.; Dupree, R.; Smith, M. E. *Chem. Phys.* **2007**, *337* (1–3), 144. doi:10.1016/j.chemphys.2007.07.007.

(42) Bryce, D. L.; Bultz, E. B.; Aebi, D. *J. Am. Chem. Soc.* **2008**, *130* (29), 9282. doi:10.1021/ja8017253.

(43) Jameson, C. J. *Specialized periodical reports on NMR*; Webb, G. A., Ed.; Royal Society of Chemistry: London, 1981–1992; Vols. 10–21.

(44) Frisch, M. J.; Trucks, G. W.; Schlegel, H. B.; Scuseria, G. E.; Robb, M. A.; Cheeseman, J. R.; Montgomery, J. A., Jr.; Vreven, T.; Kudin, K. N.; Burant, J. C.; Millam, J. M.; Iyengar, S. S.; Tomasi, J.; Barone, V.; Mennucci, B.; Cossi, M.; Scalmani, G.; Rega, N.; Petersson, G. A.; Nakatsuji, H.; Hada, M.; Ehara, M.; Toyota, K.; Fukuda, R.; Hasegawa, J.; Ishida, M.; Nakajima, T.; Honda, Y.; Kitao, O.; Nakai, H.; Klene, M.; Li, X.; Knox, J. E.; Hratchian, H. P.; Cross, J. B.; Adamo, C.; Jaramillo, J.; Gomperts, R.; Stratmann, R. E.; Yazyev, O.; Austin, A. J.; Cammi, R.; Pomelli, C.; Ochterski, J. W.; Ayala, P. Y.; Morokuma, K.; Voth, G. A.; Salvador, P.; Dannenberg, J. J.; Zakrzewski, V. G.; Dapprich, S.; Daniels, A. D.; Strain, M. C.; Farkas, O.; Malick, D. K.; Rabuck, A. D.; Raghavachari, K.; Foresman, J. B.; Ortiz, J. V.; Cui, Q.; Baboul, A. G.; Clifford, S.; Cioslowski, J.; Stefanov, B. B.; Liu, G.; Liashenko, A.; Piskorz, P.; Komaromi, I.; Martin, R. L.; Fox, D. J.; Keith, T.; Al-Laham, M. A.; Peng, C. Y.; Nanayakkara, A.; Challacombe, M.; Gill, P. M. W.; Johnson, B.; Chen, W.; Wong, M. W.; Gonzalez, C.; Pople, J. A. Gaussian, Inc., Pittsburgh PA, 2003.

(45) Becke, A. D. *Phys. Rev. A* **1988**, *38* (6), 3098. doi:10.1103/PhysRevA.38.3098.

(46) Lee, C.; Yang, W.; Parr, R. G. *Phys. Rev. B* **1988**, *37* (2), 785. doi:10.1103/PhysRevB.37.785.

(47) Zhao, Y.; Truhlar, D. G. *Theor. Chem. Acc.* **2008**, *120* (1–3), 215. doi:10.1007/s00214-007-0310-x.

(48) Esrafili, M. D.; Behzadi, H.; Hadipour, N. L. *Biophys. Chem.* **2007**, *128* (1), 38. doi:10.1016/j.bpc.2007.03.002.

(49) Ida, R.; De Clerk, M.; Wu, G. *J. Phys. Chem. A* **2006**, *110* (3), 1065. doi:10.1021/jp0554947.
(50) Cheng, F.; Sun, H.; Zhang, Y.; Mukkamala, D.; Oldfield, E. *J. Am. Chem. Soc.* **2005**, *127* (36), 12544. doi:10.1021/ja051528c.
(51) Wolinski, K.; Hinton, J. F.; Pulay, P. *J. Am. Chem. Soc.* **1990**, *112* (23), 8251. doi:10.1021/ja00179a005.
(52) Wasylishen, R. E.; Mooibroek, S.; Macdonald, J. B. *J. Chem. Phys.* **1984**, *81* (3), 1057. doi:10.1063/1.447799.
(53) Bader, R. F. W. *Atoms in molecules-a quantum theory*; Oxford University Press: New York, 1990.
(54) Biegler-Konig, F.; Schonbohm, J.; Bayles, D. *J. Comput. Chem.* **2001**, *22* (5), 545. doi:10.1002/1096-987X(20010415)22:5<545::AID-JCC1027>3.0.CO;2-Y.
(55) Wong, A.; Pike, K. J.; Jenkins, R.; Clarkson, G. L.; Anupõld, T.; Howes, A. P.; Crout, D. H. G.; Samoson, A.; Dupree, R.; Smith, M. E. *J. Phys. Chem. A* **2006**, *110* (5), 1824. doi:10.1021/jp055807y.
(56) Sternberg, U.; Brunner, E. *J. Magn. Reson. A*, **1994** *108* (2), 142. doi:10.1006/jmra.1994.1104.
(57) Huelsekopf, M.; Ludwig, R. *Magn. Reson. Chem.* **2001**, *39* (S1), S127. doi:10.1002/mrc.912.
(58) Rohlfing, C. M.; Allen, L. C.; Ditchfield, R. *J. Chem. Phys.* **1983**, *79* (10), 4958. doi:10.1063/1.445589.
(59) Yates, J. R.; Pham, T. N.; Pickard, C. J.; Mauri, F.; Amado, A. M.; Gil, A. M.; Brown, S. P. *J. Am. Chem. Soc.* **2005**, *127* (29), 10216. doi:10.1021/ja051019a.
(60) Koch, U.; Popelier, P. L. A. *J. Phys. Chem.* **1995**, *99* (24), 9747. doi:10.1021/j100024a016.
(61) Rozas, I.; Alkorta, I.; Elguero, J. *J. Am. Chem. Soc.* **2000**, *122* (45), 11154. doi:10.1021/ja0017864.
(62) Jabłoński, M.; Palusiak, M. *J. Phys. Chem. A* **2010**, *114* (47), 12498. doi:10.1021/jp106740e.
(63) Lu, Y.; Zou, J.; Wang, Y.; Jiang, Y.; Yu, Q. *J. Phys. Chem. A* **2007**, *111* (42), 10781. doi:10.1021/jp0740954.
(64) Gilli, P.; Bertolasi, V.; Ferretti, V.; Gilli, G. *J. Am. Chem. Soc.* **1994**, *116* (3), 909. doi:10.1021/ja00082a011.

Can. J. Chem. Downloaded from www.nrcresearchpress.com by South China Agricultural University on 09/19/12
For personal use only.

Mechanism of OH-initiated atmospheric oxidation of diethyl phthalate

Yuan Bao, Xiaoyan Sun, Xiaomin Sun, and Jingtian Hu

Can. J. Chem. Downloaded from www.nrcresearchpress.com by South China Agricultural University on 09/19/12
For personal use only.

Abstract: Diethyl phthalate (1,2-benzenedicarboxylic acid diethyl ester, DEP) is one of a group of widely used plasticizers, which can lead to serious environmental problems. Because of manufacturing and application, DEP can be released into the atmosphere where it can undergo transport and chemical transformation. To assess the atmospheric behavior of pollutants, it is critical to know their atmospheric reactions. In this paper, the reaction mechanism and possible oxidation products for the OH-initiated atmospheric reaction of DEP were theoretically investigated by using the density functional theory (DFT) method. The geometries and frequencies of the reactants, intermediates, transition states, and products were calculated at the MPWB1K/6–31+G(d,p) level, and the energetic parameters were further refined by the MPWB1K/6–311+G(3df,2p) method. The present study shows that H abstractions from the CH_3 and CH_2 groups, as well as OH addition to the benzene ring, are energetically favorable reaction pathways for the reaction of DEP with OH radicals. Detailed degradation products are provided.

Key words: diethyl phthalate, OH radicals, atmospheric oxidation, reaction mechanism, quantum calculation, oxidation degradation.

Résumé : Le phtalate de diéthyle (ester diéthylique de l'acide benzène-1,2-dicarboxylique, PDE) est un des plastifiés les plus utilisés et il peut provoquer de sérieux problèmes environnementaux. Lors de sa fabrication et son application de PDE peut se répandre dans l'atmosphère où il peut transporter et subir des transformations chimiques. Afin de pouvoir évaluer le comportement des polluants dans l'atmosphère, il est important de connaître leurs réactions dans l'atmosphère. Dans ce travail, faisant appel à la méthode de la théorie de la fonctionnelle de la densité (TFD), on a étudié d'un point de vue théorique le mécanisme de la réaction et les produits potentiels d'oxydation résultant d'une réaction atmosphérique du PDE, initiée par des radicaux OH. Les géométries et les fréquences des réactifs, des intermédiaires, des états de transition et des produits ont été calculées au niveau MPWB1K/6–31+G(d,p) et les paramètres énergétiques ont ensuite été affinés par la méthode MPWB1K/6–311+G(3df,2p). La présente étude montre que l'enlèvement d'hydrogène à partir des groupes CH_3 et CH_2, ainsi que l'addition du radical OH sur le noyau benzénique sont des voies réactionnelles énergétiquement favorables pour la réaction du PDE avec les radicaux OH. Des produits de dégradation détaillés sont fournis.

Mots-clés : phtalate de diéthyle, radicaux OH, oxydation atmosphérique, mécanisme réactionnel, calculs quantiques, dégradation par oxydation.

[Traduit par la Rédaction]

Introduction

Diethyl phthalate (1,2-benzenedicarboxylic acid diethyl ester, DEP) is a commercially important phthalate ester. It is used extensively as an additive in the manufacture of polyvinyl chloride, polyvinyl acetates, plastics, cellulosics, and polyurethanes. It is also used in many other products such as automobile parts, paints, lubricating oils, glues, insect repellents, perfumes, and food-packaging material.[1–3] The global production volume of DEP is ~5.2 million tons per year.[4] The increasing use of DEP is causing worldwide pollution.[5–9] It has been detected in the air, water, soil, and vegetation,[10–13] as well as the issues and fluids of wildlife and people.[14] DEP may act as endocrine disruption compounds, which interfere with the normal hormone-regulated physiological processes of people and wildlife.[15,16] A response experiment in fiddler crabs showed that 7-day exposure to DEP at 50 mg/L significantly inhibited the activity of chitobiase in the epidermis and hepatopancreas.[17] DEP is known not only for its endocrine disruption and toxicity but also for its adverse reproductive effects on people and wildlife,[18–20] and its estrogenic activity has recently been documented as well.[21,22] Therefore, DEP has been categorized as a priority pollutant by the US Environmental Protection Agency.[23]

DEP can enter the atmosphere and travel many kilometres.[24] The vapor pressure of DEP is 6.48×10^{-2} Pa at 25 °C and it can vaporize quickly.[25] It is frequently detected in indoor and outdoor air.[24] In a North Sea (German Bright) field test, the atmospheric concentration of DEP was 1.6 ng/m^{-3} in the gas phase and 0.06 ng/m^{-3} in the particle phase. The

Received 19 June 2011. Accepted 14 August 2011. Published at www.nrcresearchpress.com/cjc on 26 October 2011.

Y. Bao, X. Sun, and J. Hu. Environment Research Institute, Shandong University, Jinan 250100, P. R. China.
X. Sun. Environment Research Institute, Shandong University, Jinan 250100, P. R. China; State Key Laboratory of Solid Lubrication, Lanzhou Institute of Chemical Physics, Chinese Academy Of Science, Lanzhou 730000, P. R. China.

Corresponding author: Jingtian Hu (e-mail: hjt@sdu.edu.cn).

Can. J. Chem. Downloaded from www.nrcresearchpress.com by South China Agricultural University on 09/19/12
For personal use only.

fraction of DEP in the gas phase reached up to 96%.[25] This has greatly increased the potential for human exposure to this highly toxic material. Particle-phase DEP may be removed from the atmosphere through dry or wet deposition. The tropospheric removal of gas-phase DEP involves wet and dry deposition and photolysis, oxidation reactions with OH, NO_3, or O_3. The wet and dry deposition of gaseous DEP is of relatively minor importance as a removal pathway. Among the various oxidants, OH radicals play the most essential role in determining the oxidation power of the atmosphere. The DEP reaction with OH radicals is considered to be a dominant removal process for gaseous DEP.

To assess the atmospheric behavior of pollutants, it is critical to know their atmospheric reactions. The OH-initiated degradation of phthalate esters (PAEs) in water can be found.[26,27] Blanco et al.[28] investigated the reaction mechanism of methacrylates with OH radicals in the atmosphere. Frankcombe and Smith[29] studied the mechanism of OH-initiated oxidation of toluene in the atmosphere. However, the current knowledge of the reactions of DEP in the atmosphere is very limited, and its oxidation mechanism has received little attention in experimental or computational chemistry. Quantum calculation is especially suitable for establishing whether a reaction pathway is feasible or not.[30–33] In this paper, we carried out a theoretical study of the application of quantum calculations for the OH-initiated atmospheric oxidation reaction of DEP to find favorable reaction pathways and sites. To find the formation mechanism of secondary pollutants from the OH-initiated atmospheric reactions of DEP, some possible secondary reaction pathways were also investigated. To our knowledge, this is the first study of the OH-initiated atmospheric oxidation of DEP using quantum chemistry.

Computational method

High-accuracy molecular orbital calculations for the OH-initiated atmospheric oxidation reaction of DEP were carried out in the presence of O_2 and NO. All the calculations were performed on an SGI Origin 2000 supercomputer with the Gaussian 03 package.[34] The choice of computational levels and basis sets requires a compromise between accuracy and computational time. The geometries of reactants, intermediates, transition states, and products were fully optimized at the MPWB1K[35,36] level with the 6–31+G(d,p) basis set. Zhao and Truhlar[37] compared the MPWB1K method with other DFT methods and found that the MPWB1K method gave better results for thermochemistry and gave more excellent saddle-point geometries. The MPWB1K/6–31+G(d,p) structures were employed in single-point energy calculations. The corresponding harmonic vibrational frequencies were also calculated at the MPWB1K/6–31+G(d,p) level to determine the nature of the stationary points, the zero-point energies (ZEP), and the thermal contributions to the free energy of activation. To verify that each transition state actually connected the designated reactants with products, intrinsic reaction coordinate (IRC)[38] calculations were performed. A more flexible basis set (6–311+G(3df,2p)) was used to evaluate the energetic parameters of the various species more accurately. The profile of the potential energy surface was constructed at the MPWB1K/6–311+G(3df,2p)//MPWB1K/6–31+G(d,p) level. All the relative energies quoted and discussed in this paper include ZPE corrections with unscaled frequencies obtained at the MPWB1K/6–31+G(d,p) level.

Results and discussion

The reaction of DEP with OH radicals

Since OH is strongly nucleophilic, H abstraction from DEP by OH radicals should be a possible reaction pathway. In addition, there is a benzene ring in the DEP molecule and, therefore, OH addition to the benzene ring is another possible reaction pathway. Altogether, seven possible reaction pathways (R1–R7) are presented in Fig. 1.

H-abstraction pathways

Four kinds of hydrogen atoms are found in the DEP molecule: H atoms in the CH_3 group, H atoms in the CH_2 group, H atoms bonded with the C_6 atom in the benzene ring, and H atoms bonded with the C_7 atom in the benzene ring. Thus, four primary reaction pathways (R1–R4) were identified. R1 and R2 are H abstractions from the CH_3 and CH_2 groups. R3 and R4 represent H abstractions from the benzene ring in the DEP molecule.

H abstractions from the CH_3 and CH_2 groups occur via the transition states, TS1 and TS2. The optimized structures of TS1 and TS2 are shown in Fig. 2. The transition vector of TS1 clearly shows the motion of H_1 between C_1 and O, with an imaginary frequency of 1273i cm^{-1}. The transition vector of TS2 shows the motion of H_4 between C_2 and O, with an imaginary frequency of 1269i cm^{-1}. H abstraction from the CH_3 group has a low potential barrier of 3.05 kcal/mol (1 cal = 4.184 J) and is exothermic by 14.34 kcal/mol at the MPWB1K/6–311+G(3df,2p) level. H abstraction from the CH_2 group also has a low potential barrier of 0.83 kcal/mol and is strongly exothermic by 18.14 kcal/mol. In the TS1 and TS2 structures, the breaking C_1–H_1 and C_2–H_4 bonds are elongated by 0.125 and 0.119 Å, respectively, whereas the forming O–H_1 and O–H_4 bonds are 0.328 and 0.338 Å, respectively, longer than the equilibrium value of 0.967 Å in H_2O.

H abstractions from the benzene ring in the DEP molecule require crossing potential barriers of 3.64 and 5.32 kcal/mol, respectively, via the transition states TS3 and TS4. The transition vector of TS3 shows the motion of H_6 between O and C_6, and the transition vector of TS4 shows the motion of H_7 between O and C_7. Comparison of the four H-abstraction pathways shows that H abstractions from the alkyl group have a lower barrier than H abstractions from the benzene ring. Also, H abstractions from the alkyl group are more exothermic than H abstractions from the benzene ring. The H atoms in the alkyl group are more activated than the H atoms in the benzene ring. Therefore, H abstractions from the alkyl group are expected to play an important role for the OH-initiated degradation of DEP in the atmosphere. The intermediates, denoted IM1 and IM2, produced from H abstractions from the alkyl group are open-shell activated radicals and will be further oxidized by O_2/NO and removed from the atmosphere.

OH addition to the benzene ring

Here, we analyze the reaction pathways of OH addition to the C=C bond in the benzene ring. As to the symmetry, the

Can. J. Chem. Downloaded from www.nrcresearchpress.com by South China Agricultural University on 09/19/12
For personal use only.

Fig. 1. Reaction pathways for the reaction of 1,2-benzenedicarboxylic acid diethyl ester (DEP) with OH radicals. Units: kcal/mol (1 cal = 4.184 J). ΔE, the reaction potential barrier; ΔH, the reaction enthalpy (0 K).

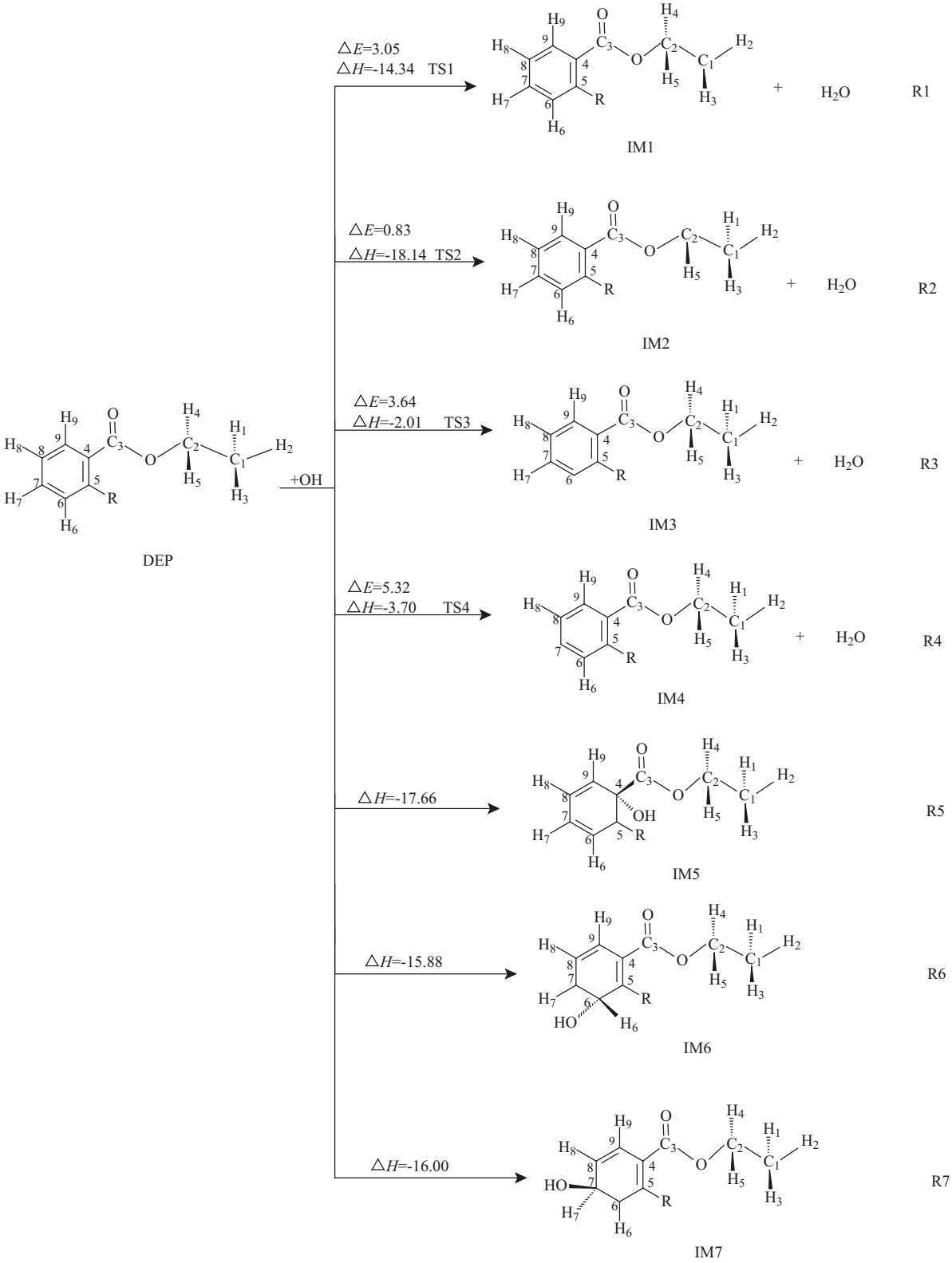

C atoms in the benzene ring fall into three groups: the C_4 and C_5 atoms are equivalent, the C_6 and C_9 atoms are equivalent, and the C_7 and C_8 are equivalent. Therefore, three different OH–DEP adduct isomers can be formed through the addition of the OH radical to the C_4, C_6, and C_7 atoms in the DEP molecule. The calculations show that OH additions to the C_4, C_6, and C_7 atoms are strongly exothermic and energetically favorable. It can be seen from Fig. 1 that addition of

Fig. 2. MPWB1K/6–31+G(d,p) optimized geometries for the transition states.

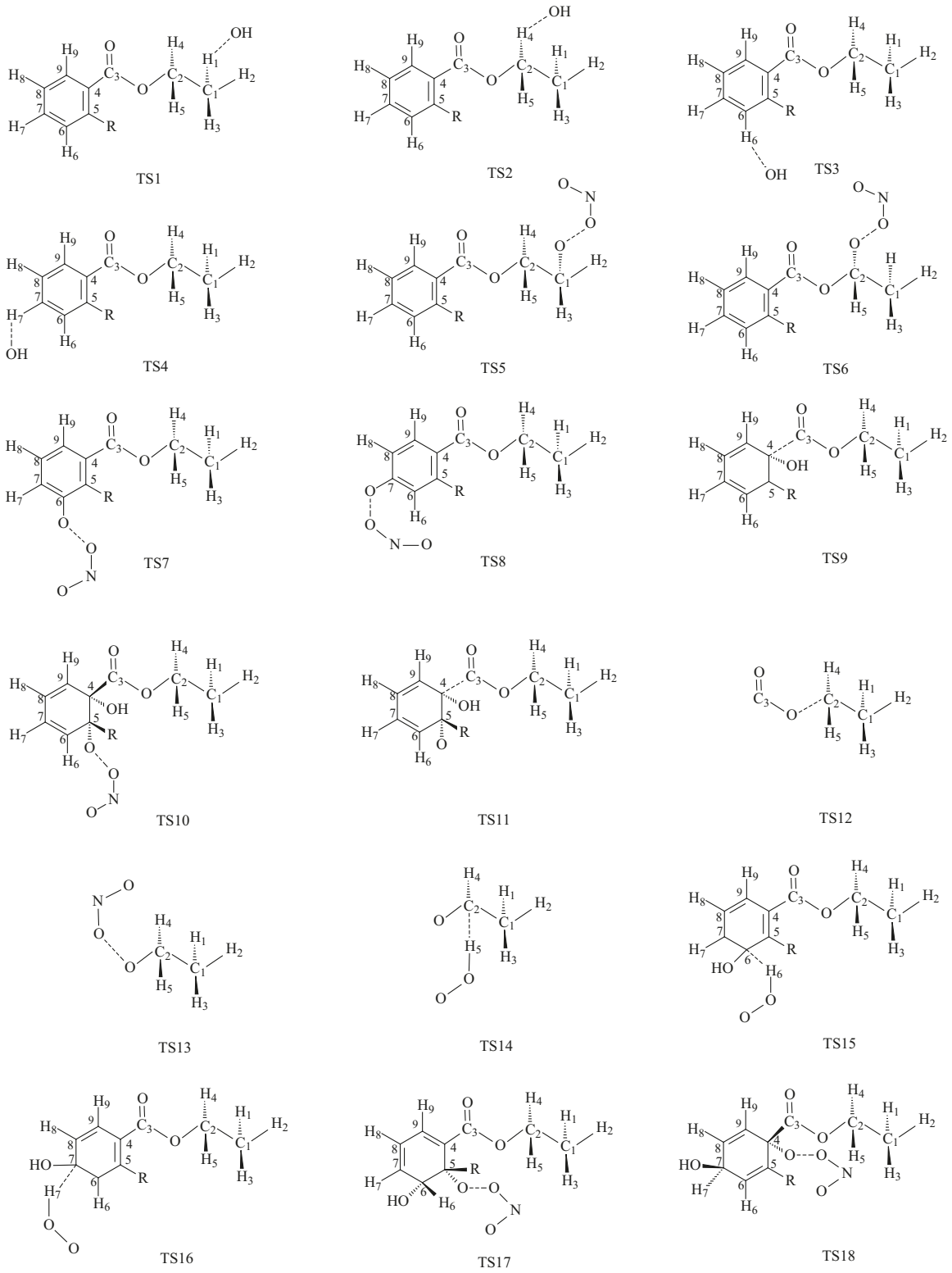

OH to the C_4, C_6, and C_7 atoms is barrierless and is a strongly exothermic processes. The high reaction energies are retained as the internal energy of the adducts. The energy-rich OH–DEP adducts (IM5, IM6, and IM7) can further react in the atmosphere.

Secondary reactions

The previous discussion shows that H abstractions from the alkyl group and OH additions to the benzene ring are energetically favorable pathways for the reactions of DEP with OH radicals. IM1–IM7 are important intermediates produced

Can. J. Chem. Downloaded from www.nrcresearchpress.com by South China Agricultural University on 09/19/12
For personal use only.

Can. J. Chem. Downloaded from www.nrcresearchpress.com by South China Agricultural University on 09/19/12
For personal use only.

from the degradation of DEP initiated by OH radicals. IM1–IM7 are open-shell activated radicals and will further react via unimolecular decomposition and (or) with O_2 or O_2/NO in the atmosphere.

Atmospheric reaction pathways of IM1 and IM2

IM1 can react with O_2 readily to form an intermediate, IM8. The calculated profile of the potential energy surface shows that the reaction of IM1 with O_2 is barrierless and strongly exothermic by 71.05 kcal/mol. In the atmosphere, IM8 will further immediately react with NO to form intermediate IM9. IM9 subsequently reacts via a direct decomposition to form P1 and NO_2 through the transition state TS5, and this reaction requires a potential barrier of 29.01 kcal/mol and is endothermic by 0.07 kcal/mol.

Similarly, IM2 can also be oxidized by O_2/NO in the atmosphere. The reaction pathways are depicted in Fig. 3.

Atmospheric reaction pathways of IM3 and IM4

The intermediates IM3 and IM4, from the H abstraction of the benzene ring, have similar atmospheric reactions. The intermediate IM3 reacts with O_2 to yield IM12 in the atmosphere and it is exothermic by 42.11 kcal/mol. Then IM12 reacts with NO to form IM13. The intermediate IM13 immediately decomposes to form product P3 and NO_2 via the transition state TS7 and it requires to cross a potential barrier of 15.17 kcal/mol.

Similar to IM3, IM4 can also be oxidized by O_2/NO in the atmosphere. The reaction pathways are depicted in Fig. 4.

Atmospheric reaction pathway of IM5

The unimolecular decomposition of IM5 results in the formation of P5 and IM16 via the transition state TS9. This process has a high potential barrier of 19.52 kcal/mol and is strongly endothermic by 9.30 kcal/mol, indicating that the decomposition is energetically unfavorable. In the troposphere, IM5 will mainly be removed by reaction with O_2.

IM5 has three possible sites to react with O_2 and three possible products (IM17, IM18, and IM19) can be formed throughthe addition of O_2 to C_5, C_7, or C_9 atoms in the IM5 molecule. The calculated profile of the potential energy surface shows that these addition reactions are barrierless and strongly exothermic by 42.07, 43.76, and 36.50 kcal/mol, respectively, indicating that these addition reactions are energetically favorable and can occur easily in the atmosphere. IM17, IM18, and IM19 have similar structures and will be removed from the atmosphere by a similar reaction mechanism. Therefore, we will just discuss the atmospheric reactions of IM17 here. IM17 could further react with NO to form IM20. IM20 will directly decompose via the transition state TS10 to form IM21 and NO_2 with a potential barrier of 15.15 kcal/mol. IM21 further decomposes to form P6 and IM16 via the transition state TS11. The O_1–C_2 bond in IM16 will rupture through the transition state TS12 with an imaginary frequency of 891i cm^{-1} to form IM22 and CO_2. This process is exothermic by 19.28 kcal/mol and a potential barrier of 15.62 kcal/mol. In the TS12 structure, the O_1–C_2 bond is elongated to 1.879 Å from 1.446 Å in IM16. IM22 subsequently readily reacts with O_2 to form an intermediate, IM23. The calculations show that the reaction of IM22 with O_2 is barrierless and strongly exothermic by 72.12 kcal/mol.

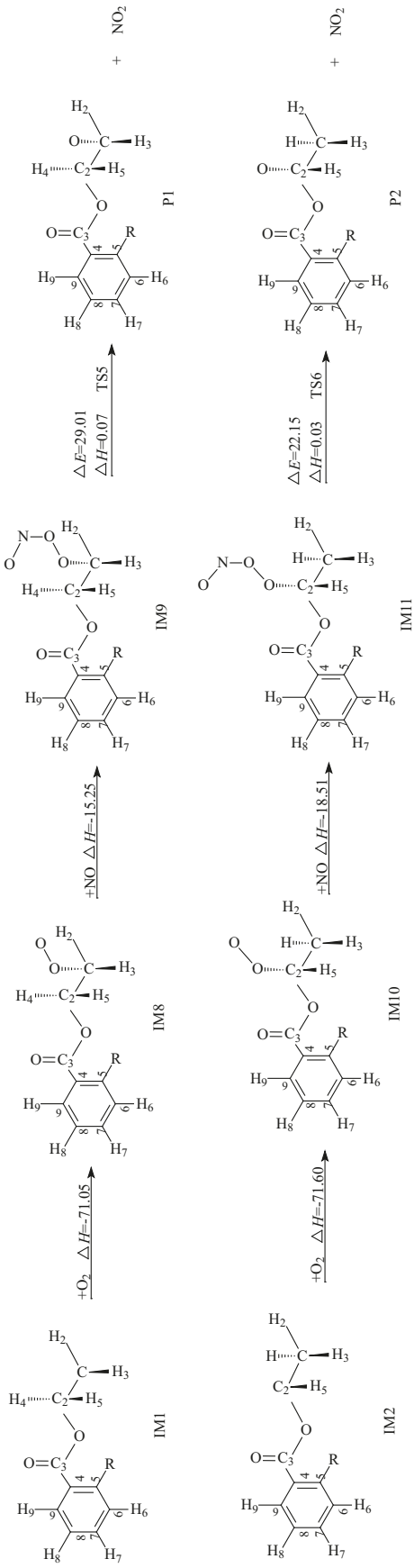

Fig. 3. Secondary reaction routes from intermediates IM1 and IM2. Units: kcal/mol (1 cal = 4.184 J). ΔE, the reaction potential barrier; ΔH, the reaction enthalpy (0 K).

Can. J. Chem. Downloaded from www.nrcresearchpress.com by South China Agricultural University on 09/19/12
For personal use only.

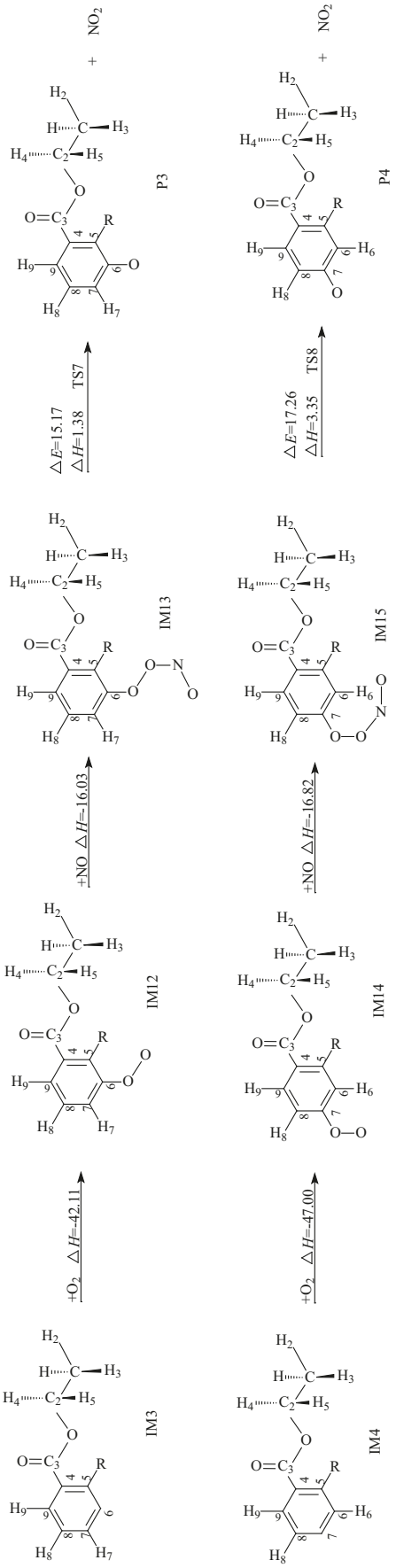

Fig. 4. Secondary reaction routes from intermediates IM3 and IM4. Units: kcal/mol (1 cal = 4.184 J). ΔE, the reaction potential barrier; ΔH, the reaction enthalpy (0 K).

In the atmosphere, IM23 will react with NO immediately to form an intermediate, IM24. IM24 subsequently reacts via a direct decomposition to form oxyl radical IM25 and NO_2 with a potential barrier of 18.83 kcal/mol, and the process is endothermic by 1.57 kcal/mol. IM25 can react with O_2 to yield P7 and HO_2 via transition state TS14. The reaction pathways are shown in Fig. 5.

Atmospheric reaction pathways of IM6 and IM7

The H atom in IM6 can be abstracted by O_2 via the transition state TS15. The process has a low potential barrier of 0.26 kcal/mol and is strongly exothermic by 71.14 kcal/mol. TS15 has an imaginary frequency of 1415i cm^{-1}. Similarly, the H atom in IM7 can be abstracted by O_2 as well. The two abstraction reactions are energetically favorable and will readily occur in the atmosphere.

Similar to IM5, IM6 can react with O_2 via an addition mechanism. There are three possible sites in IM6 to react with O_2. Three products IM26, IM27 and IM28 can be formed through addition of O_2 to C_5, C_7 and C_9 atoms in IM6. The three addition reactions are strongly exothermic by 44.45, 45.12 and 43.43 kcal/mol. IM26, IM27 and IM28 have similar structure and will be removed from the atmosphere by similar reaction mechanism. Therefore, we just discuss the atmospheric reactions of IM26 here. In the atmosphere, IM26 will further react with NO immediately to form an intermediate IM29. IM29 subsequently reacts via a direct decomposition to form oxyl radical P10 and NO_2, and this reaction requires crossing a potential barrier of 14.96 kcal/mol and is endothermic by 2.84 kcal/mol.

Similarly, IM7 can react with O_2 through the addition mechanism. The possible products are IM30, IM31, and IM32. The reaction pathways are described in Fig. 6.

Conclusion

The OH-initiated atmospheric oxidation reaction of DEP has been theoretically investigated in this paper. This study shows that the reaction of DEP with OH radicals can proceed through three energetically favorable channels: H abstraction from the CH_3 group, H abstraction from the CH_2 group, and OH addition to C_4, C_5, and C_6 atoms in the benzene ring.

On the one hand, our quantum calculations can provide a detailed degradation mechanism, which is helpful for understanding the atmospheric-chemistry transformation of the DEP. On the other hand, the quantum chemistry calculations can provide the basic information for direct kinetic studies, such as the energy, force constants, and Hessian matrices of the stationary points. The kinetic studies are planned for future work.

Acknowledgements

This work was supported financially by the National Nature Science Foundation of China (Nos. 20977059, 20903062, and 20737001), the Natural Science Foundation of Shandong Province (No. Q2008B07), the Independent Innovation Foundation of Shandong University (IIFSDU, Nos. 2009JC016 and 2010TS064), and the Open Project from the State Key Laboratory of Environmental Chemistry and Ecotoxicology, Research Center for Eco-Environmental Sciences, Chinese Academy of Sciences (No. KF2009-10).

Fig. 5. Secondary reaction routes from intermediate IM5. Units: kcal/mol (1 cal = 4.184 J). ΔE, the reaction potential barrier; ΔH, the reaction enthalpy (0 K).

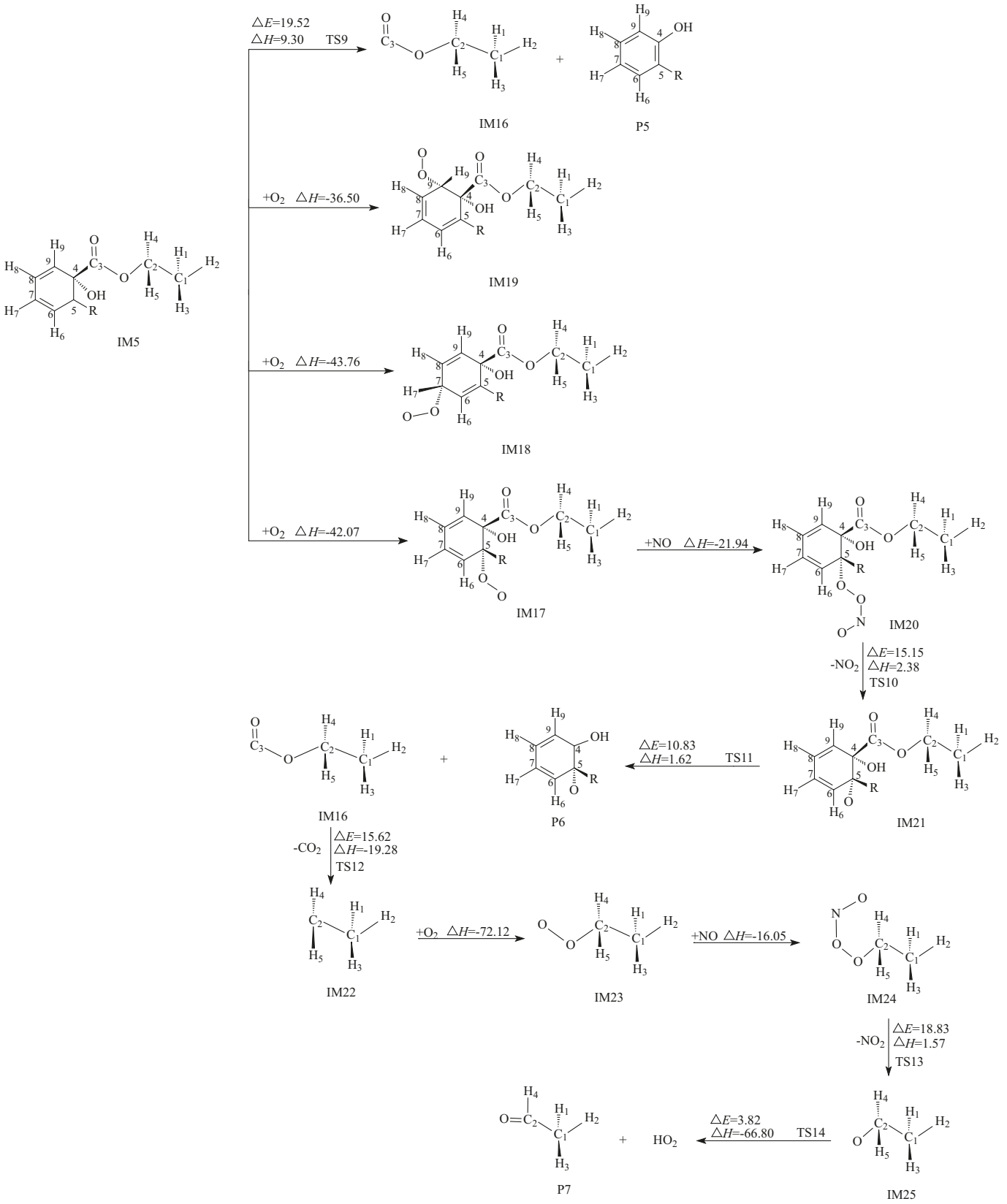

Can. J. Chem. Downloaded from www.nrcresearchpress.com by South China Agricultural University on 09/19/12
For personal use only.

Fig. 6. Secondary reaction routes from intermediates IM6 and IM7. Units: kcal/mol (1 cal = 4.184 J). ΔE, the reaction potential barrier; ΔH, the reaction enthalpy (0 K).

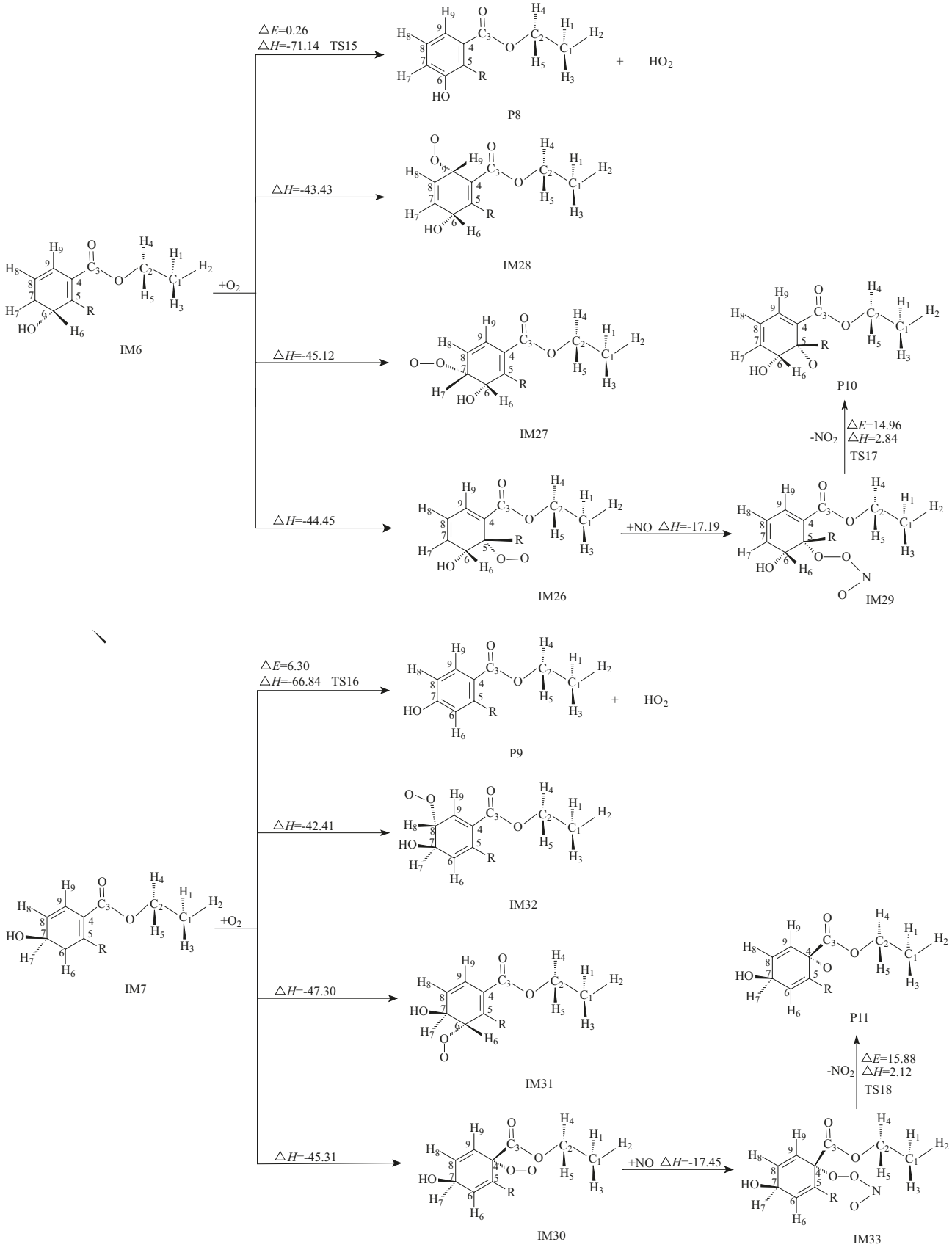

Can. J. Chem. Downloaded from www.nrcresearchpress.com by South China Agricultural University on 09/19/12
For personal use only.

Can. J. Chem. Downloaded from www.nrcresearchpress.com by South China Agricultural University on 09/19/12
For personal use only.

References

(1) Stales, C. A.; Peterson, D. R.; Parkerton, T. F.; Adams, W. J. *Chemosphere* **1997**, *35* (4), 667. doi:10.1016/S0045-6535(97)00195-1.

(2) Thomson, W. T. Insecticides, Acaricides and Avicides. In *Agricultural Chemicals, Book I;* Thomson Publications: Fresno, CA, 1976.

(3) Mackintosh, C. E.; Maldonado, J.; Hongwu, J.; Hoover, N.; Chong, A.; Ikonomou, M. G.; Gobas, F. A. P. C. *Environ. Sci. Technol.* **2004**, *38* (7), 2011. doi:10.1021/es034745r.

(4) Mackintosh, C. E.; Maldonado, J. A.; Ikonomou, M. G.; Gobas, F. A. P. C. *Environ. Sci. Technol.* **2006**, *40* (11), 3481. doi:10.1021/es0519637.

(5) Stiles, R.; Yang, I.; Lippincott, R. L.; Murphy, E.; Buckley, B. *Environ. Sci. Technol.* **2008**, *42* (8), 2976. doi:10.1021/es071804i.

(6) Blair, J. D.; Ikonomou, M. G.; Kelly, B. C.; Surridge, B.; Gobas, F. A. P. C. *Environ. Sci. Technol.* **2009**, *43* (16), 6262. doi:10.1021/es9013135.

(7) Rudel, R. A.; Camann, D. E.; Spengler, J. D.; Korn, L. R.; Brody, J. G. *Environ. Sci. Technol.* **2003**, *37* (20), 4543. doi:10.1021/es0264596.

(8) Wang, G.; Kawamura, K.; Lee, S.; Ho, K.; Cao, J. *Environ. Sci. Technol.* **2006**, *40* (15), 4619. doi:10.1021/es060291x.

(9) Kolpin, D. W.; Furlong, E. T.; Meyer, M. T.; Thurman, E. M.; Zaugg, S. D.; Barber, L. B.; Buxton, H. T. *Environ. Sci. Technol.* **2002**, *36* (18), 4007. doi:10.1021/es020136s.

(10) Suzuki, T.; Yaguchi, K.; Suzuki, S.; Suga, T. *Environ. Sci. Technol.* **2001**, *35* (18), 3757. doi:10.1021/es001860i.

(11) Psillakis, E.; Kalogerakis, N. *J. Chromatogr. A* **2003**, *999* (1–2), 145. doi:10.1016/S0021-9673(03)00390-X.

(12) Lin, Z. P.; Ikonomou, M. G.; Jing, H.; Mackintosh, C.; Gobas, F. A. P. C. *Environ. Sci. Technol.* **2003**, *37* (10), 2100. doi:10.1021/es026361r.

(13) Zhu, J.; Phillips, S. P.; Feng, Y. L.; Yang, X. *Environ. Sci. Technol.* **2006**, *40* (17), 5276. doi:10.1021/es060356w.

(14) Hogberg, J.; Hanberg, A.; Berglund, M.; Skerfving, S.; Remberger, M.; Calafat, A. M.; Filipsson, A. F.; Jansson, B.; Johansson, N.; Appelgren, M.; Håkansson, H. *Environ. Health Perspect.* **2008**, *116*, 334. doi:10.1289/ehp.10788.

(15) Jobling, S.; Reynolds, T.; White, R.; Parker, M. G.; Sumpter, J. P. *Health Perspect.* **1995**, *103* (6), 582. doi:10.1289/ehp.95103582.

(16) Liu, Y.; Guan, Y.; Yang, Z.; Cai, Z.; Mizuno, T.; Tsuno, H.; Zhu, W.; Zhang, X. *Ecotoxicology* **2009**, *18* (3), 293. doi:10.1007/s10646-008-0283-0.

(17) Available from http://en.wikipedia.org/wiki/Diethyl_phthalate.

(18) Singh, A. R.; Lawrence, W. H.; Autian, J. *J. Pharm. Sci.* **1972**, *61* (1), 51. doi:10.1002/jps.2600610107.

(19) Jobling, S.; Reynolds, T.; White, R.; Parker, M. G.; Sumpter, J. P. *Environ. Health Perspect.* **1995**, *103* (6), 582. doi:10.1289/ehp.95103582.

(20) Zhu, Y. J.; Jiang, J. T.; Ma, L.; Zhang, J.; Hong, Y.; Liao, K.; Liu, Q.; Liu, G. H. *Toxicology* **2009**, *260* (1–3), 120. doi:10.1016/j.tox.2009.03.017.

(21) Paganetto, G.; Campi, F.; Varani, K.; Piffanelli, A.; Giovannini, G.; Borea, P. A. *Pharmacol. Toxicol.* **2000**, *86* (1), 24. doi:10.1034/j.1600-0773.2000.pto860105.x.

(22) Harris, C. A.; Henttu, P.; Parker, M. G.; Sumpter, J. P. *Environ. Health Perspect.* **1997**, *105* (8), 802. doi:10.1289/ehp.97105802.

(23) Xu, Z.; Zhang, W.; Lv, L.; Pan, B.; Lan, P.; Zhang, Q. *Environ. Sci. Technol.* **2010**, *44* (8), 3130. doi:10.1021/es100058j.

(24) Otake, T.; Yoshinaga, J.; Yanagisawa, Y. *Environ. Sci. Technol.* **2001**, *35* (15), 3099. doi:10.1021/es001914o.

(25) Xie, Z.; Ebinghaus, R.; Temme, C.; Caba, A.; Ruck, W. *Atmos. Environ.* **2005**, *39* (18), 3209. doi:10.1016/j.atmosenv.2005.02.021.

(26) Vitali, M.; Guidotti, M.; Macilenti, G.; Cremisini, C. *Environ. Int.* **1997**, *23* (3), 337. doi:10.1016/S0160-4120(97)00035-4.

(27) Xu, Z.; Zhang, W.; Lv, L.; Pan, B.; Lan, P.; Zhang, Q. *Environ. Sci. Technol.* **2010**, *44* (8), 3130. doi:10.1021/es100058j.

(28) Blanco, M. B.; Taccone, R. A.; Lane, S. I.; Teruel, M. A. *Chem. Phys. Lett.* **2006**, *429* (4–6), 389. doi:10.1016/j.cplett.2006.08.088.

(29) Frankcombe, T. J.; Smith, S. C. *J. Phys. Chem. A* **2007**, *111* (19), 3686. doi:10.1021/jp067112i.

(30) Xu, F.; Yu, W.; Gao, R.; Zhou, Q.; Zhang, Q.; Wang, W. *Environ. Sci. Technol.* **2010**, *44* (17), 6745. doi:10.1021/es101794v.

(31) Zhang, Q.; Yu, W.; Zhang, R.; Zhou, Q.; Gao, R.; Wang, W. *Environ. Sci. Technol.* **2010**, *44* (9), 3395. doi:10.1021/es1004285.

(32) Qu, X.; Wang, H.; Zhang, Q.; Shi, X.; Xu, F.; Wang, W. *Environ. Sci. Technol.* **2009**, *43* (11), 4068. doi:10.1021/es802835e.

(33) Zhang, Q.; Qu, X.; Wang, H.; Xu, F.; Shi, X.; Wang, W. *Environ. Sci. Technol.* **2009**, *43* (11), 4105. doi:10.1021/es9001778.

(34) Frisch, M. J.; Trucks, G. W.; Schlegel, H. B.; Scuseria, G. E.; Robb, M. A.; Cheeseman, J. R.; Montgomery, J. A., Jr.; Vreven, T.; Kudin, K. N.; Burant, J. C.; Millam, J. M.; Iyengar, S. S.; Tomasi, J.; Barone, V.; Mennucci, B.; Cossi, M.; Scalmani, G.; Rega, N.; Petersson, G. A.; Nakatsuji, H.; Hada, M.; Ehara, M.; Toyota, K.; Fukuda, R.; Hasegawa, J.; Ishida, M.; Nakajima, T.; Honda, Y.; Kitao, O.; Nakai, H.; Klene, M.; Li, X.; Knox, J. E.; Hratchian, H. P.; Cross, J. B.; Adamo, C.; Jaramillo, J.; Gomperts, R.; Stratmann, R. E.; Yazyev, O.; Austin, A. J.; Cammi, R.; Pomelli, C.; Ochterski, J. W.; Ayala, P. Y.; Morokuma, K.; Voth, G. A.; Salvador, P.; Dannenberg, J. J.; Zakrzewski, V. G.; Dapprich, S.; Daniels, A. D.; Strain, M. C.; Farkas, O.; Malick, D. K.; Rabuck, A. D.; Raghavachari, K.; Foresman, J. B.; Ortiz, J. V.; Cui, Q.; Baboul, A. G.; Clifford, S.; Cioslowski, J.; Stefanov, B. B.; Liu, G.; Liashenko, A.; Piskorz, P.; Komaromi, I.; Martin, R. L.; Fox, D. J.; Keith, T.; Al-Laham, M. A.; Peng, C. Y.; Nanayakkara, A.; Challacombe, M.; Gill, P. M. W.; Johnson, B.; Chen, W.; Wong, M. W.; Gonzalez, C.; Pople, J. A. *GAUSSIAN 03;* Gaussian Inc.: Pittsburgh, PA, 2003.

(35) Adamo, C.; Barone, V. *J. Chem. Phys.* **1998**, *108*, 664. doi:10.1063/1.475428.

(36) Becke, A. D. *J. Chem. Phys.* **1996**, *104*, 1040. doi:10.1063/1.470829.

(37) Zhao, Y.; Truhlar, D. G. *J. Phys. Chem. A* **2004**, *108* (33), 6908. doi:10.1021/jp048147q.

(38) Fukui, K. *Acc. Chem. Res.* **1981**, *14* (12), 363. doi:10.1021/ar00072a001.

Measurement of the interaction of aqueous copper(II) with a model amyloid-β protein fragment — Interference from buffers

Michael H. Benn, Arvi Rauk, and Thomas W. Swaddle

Can. J. Chem. Downloaded from www.nrcresearchpress.com by South China Agricultural University on 09/19/12
For personal use only.

Abstract: For the formation of a complex of Cu^{2+} with the amyloid-β (Aβ) proxy *N*-α-dihydrourocanylhistamine (**L**) in unbuffered aqueous solution (pH ~ 5.7, 25.0 °C), UV spectrophotometric measurements give a stability constant of 3.8×10^5 L mol^{-1}. This stability constant is within the lower limit of the range of stability constants reported in the literature for complexes of Aβ with Cu^{2+} — as expected, in view of the smaller number of coordination sites in **L**. Computer modeling indicates that the Cu^{2+}–**L** complex is $Cu\mathbf{L}(H_2O)_2^{2+}$, with terdentate **L** bound to Cu^{2+} via two N_π atoms and the O atom of the peptide link. Attempts to make stability constant measurements for Cu^{2+} with **L** in aqueous solution buffered with Tris/$TrisH^+/ClO_4^-$ to pH near 7.2 were unsuccessful because the Tris base when in large excess over $Cu\mathbf{L}^{2+}$ promoted its dissociation to Cu^{2+} + **L** by scavenging free Cu^{2+} as $Cu(Tris)(TrisH_{-1})^+$, or when in roughly equimolar concentrations formed a ternary adduct, $Cu\mathbf{L}(Tris)^{2+}$. The interactions of Cu^{2+} with Tris buffer were re-examined spectrophotometrically and with the aid of computations that show that the most stable Cu^{2+}–Tris complexes are the syn- and anti-isomers of $Cu(Tris)_2^{2+}$, but in the experimental pH ranges these are present as $Cu(Tris)(TrisH_{-1})^+$. Since $Cu^{2+}(aq)$ is strongly complexed by almost any base capable of forming a buffer system with near-physiological pH, stability constants reported for Cu^{2+}–Aβ complexes in any buffer solution should be regarded with skepticism unless interactions of the buffer with Cu^{2+} and with $CuA\beta^{2+}$ are taken quantitatively into account. Moreover, in vivo, biological buffers will reduce the physiological importance of Aβ–Cu^{2+} complexes by competing with Aβ for Cu^{2+}.

Key words: N-α-dihydrourocanylhistamine complexes with copper(II), amyloid-β complexes with copper(II), Tris buffer complexes with copper(II), buffer interferences in biochemical measurements.

Résumé : Sur la base de mesures spectrophotométriques UV, il a pu être établi que pour la formation, en solution aqueuse non tamponnée (pH ~ 5,7, 25,0 °C) d'un complexe du Cu^{2+} avec la *N*-α-dihydrourocanylhistamine (**L**), un produit de remplacement de l'amyloïde-β (Aβ), la constante de stabilité est égale à $3{,}8 \times 10^5$ L mol^{-1}. Tel qu'on pouvait s'y attendre compte tenu du nombre plus faible de sites de coordination dans le produit **L**, cette constante de stabilité se situe à la limite inférieure de la plage des constantes de stabilité rapportées dans la littérature pour les complexes entre l'Aβ et le Cu^{2+}. La modélisation par ordinateur indique que le complexe Cu^{2+}–**L** est $Cu\mathbf{L}(H_2O)_2^{2+}$, avec un groupe **L** tridentate lié au Cu^{2+} par le biais de deux atomes N_π et un atome O de la liaison peptidique. Les essais effectués pour faire des mesures de constante de stabilité du Cu^{2+} avec le groupe **L**, en solution aqueuse tamponnée par du Tris/$TrisH^+/ClO_4^-$ à un pH d'environ 72, n'ont pas été fructueux parce que, lorsque la base tris est en grand excès par rapport au complexe $Cu\mathbf{L}^{2+}$, elle provoque sa dissociation en Cu^{2+} + **L** par épuisement du Cu^{2+} sous la forme de $Cu(Tris)(TrisH_{-1})^+$ ou, lorsque les entités sont en concentrations pratiquement équimolaires, elles forment un adduit ternaire, $Cu\mathbf{L}(Tris)^{2+}$. Les interactions du Cu^{2+} avec le tampon Tris ont été réexaminées par des études spectrophotométriques et à l'aide de calculs théoriques qui ont montré que les complexes Cu^{2+}–Tris les plus stables sont les isomères syn et anti du $Cu(Tris)_2^{2+}$; toutefois, dans les plages de pH expérimentaux, ces isomères sont présents sous la forme de $Cu(Tris)(TrisH_{-1})^+$. Considérant que le Cu^{2+} est fortement complexé par pratiquement toutes les bases capables de former un système de tampon près du pH physiologique, les constantes de stabilité rapportées pour les complexes Cu^{2+}–Aβ et mesurées dans n'importe quelle solution tampon doivent être considérées avec scepticisme à moins que les interactions du tampon avec le Cu^{2+} et le $CuA\beta^{2+}$ aient été prises en compte d'une façon quantitative. De plus, in vivo, les tampons biologiques réduisent l'importance physiologique des complexes Aβ–Cu^{2+} en étant en compétition avec Aβ pour le Cu^{2+}.

Mots-clés : complexes de la *N*-α-dihydrourocanylhistamine avec le cuivre(II), complexes de l'amyloïde β avec le cuivre(II), complexes tamponnés tris avec le cuivre(II), interférences des tampons dans les mesures biochimiques.

[Traduit par la Rédaction]

Received 13 May 2011. Accepted 27 June 2011. Published at www.nrcresearchpress.com/cjc on 14 October 2011.

M.H. Benn, A. Rauk, and T.W. Swaddle. Department of Chemistry, University of Calgary, Calgary, AB T2N 1N4, Canada.

Corresponding author: Thomas W. Swaddle (e-mail: swaddle@ucalgary.ca).

This article is part of a Special Issue to commemorate the International Year of Chemistry.

Can. J. Chem. Downloaded from www.nrcresearchpress.com by South China Agricultural University on 09/19/12
For personal use only.

Introduction

The water-soluble 4.3 kDa amyloid-β peptide (Aβ), associated with Alzheimer's disease (AD), forms complexes with aqueous metal ions such as Fe^{3+}, Al^{3+}, Zn^{2+}, and Cu^{2+}, and it is likely that such complexes of Aβ in its Aβ1–42 form are involved in the formation of the senile plaque deposits that are characteristic of AD.[1–8] The aqueous Cu^{2+} ion, which typically has the highest stability constants for complex formation among divalent transition-metal ions in the Irving–Williams series,[9] has a particular affinity for nitrogen bases, notably histidine. Indeed, Cu^{2+}(aq) evidently interacts with Aβ of various chain lengths primarily through the N_π atoms of the His13 and His14 residues.[2,4,5,10] Copper(II) has been shown to initiate the nucleated precipitation of Aβ1–40 and Aβ1–42[11] and is found in elevated concentrations in amyloid plaques.[5] Moreover, copper(II)–Aβ complexes may be responsible for the generation of reactive oxygen species that are believed to play a key role in AD.[1,3]

There is, however, no consensus on the mode of coordination of Cu^{2+} to Aβ, although it is recognized that differences in the coordination of Cu^{2+} by human and rodent Aβ may account for the absence of formation of senile Aβ plaques in rodents.[12] Because copper(II) complexes are typically highly labile in ligand substitution,[13] there may be no unique structure of a Cu^{2+}–Aβ complex; rather, the Cu^{2+} ion may be bound in dynamic equilibrium to N_π in His6, His13, His14, and a terminal $–NH_2$ site, as well as to an O atom (e.g., an O of Asp1 or Ala2) in distorted square-planar CuN_3O arrangements.[4–6,12] The populations of the alternative structures are pH dependent; at pH 7.4, there are two main coexisting forms, forms **I** and **II**, whereas at lower pH form **I** is dominant. Not surprisingly, then, the experimental stability constants $K_{A\beta}$ reported for Cu^{2+}–Aβ complexes vary widely; values ranging from 5.0×10^4 to 1.5×10^9 L mol^{-1} were tabulated by Hatcher et al.,[14] whereas Faller and Hureau[5] derived conditional $K_{A\beta}$ values of 10^7–10^{11} L mol^{-1} by reanalyzing data from the literature and expressed a preference for 10^9–10^{10} L mol^{-1}. These inconsistencies are due in part to differences in the Aβ chain length chosen (1–16 through 1–42) and to differences in the mode of calculation of the stability constants, but at least some of the discrepancies may be due to the presence of competing ligands such as buffer components, and this issue is pursued in the present article.

Elucidation of the Cu^{2+}–Aβ interaction by computational modeling is therefore very desirable, but is hindered by the size and complexity of Aβ molecules. Raffa et al.[2] therefore carried out ab initio computations on the interactions of aqueous Cu^{2+} with the model Aβ fragment 3-(1*H*-imidazol-5-yl)-*N*-[2-(1*H*-imidazol-5-ylethyl]propanamide (*N*-α-dihydrourocanylhistamine, **L**; Fig. 1), which affords two N_π bases corresponding to His13 and His14 of Aβ connected by the appropriate peptide link.

Raffa et al.[2] calculated that the most energetically favoured species were the four-coordinate 1:1 complexes $Cu\mathbf{L}(OH_2)^{2+}$ (designated species **20** by Raffa et al.[2]), in which the metal binds to terdentate **L** through the two N_π histidine atoms and the amide oxygen, and $Cu(\mathbf{L}H_{-1})(OH_2)^{+}$ (species **35**) in which Cu^{2+} again bonds through the two N_π atoms but displaces the NH proton in the peptide link to form a coordinate bond to the amido group rather than the peptide O. The amido coordination mode is feasible because the pK_a of the peptide NH was calculated to be 15.7 in free aqueous **L** but only 5.5 in species **20**.[2] The computed stability constant $K_{\mathbf{L}}$ for $Cu^{2+} + \mathbf{L} \rightarrow \mathbf{20}$ was 1.3×10^{19} L mol^{-1}, and $K_{\mathbf{L}}'$ for $Cu^{2+} + \mathbf{L} \rightarrow \mathbf{35} + H^+$ was 4.3×10^{17}. The computed value of $K_{\mathbf{L}}$ was markedly higher than the range of measured $K_{A\beta}$ noted above (although Atwood et al.[11] found $K_{A\beta} = 1.6 \times 10^{17}$ L mol^{-1} for Cu^{2+}–Aβ1–42), which is surprising because there are fewer potential donor sites in **L** relative to Aβ. In any event, an experimental value of $K_{\mathbf{L}}$ is needed. A further question to be resolved experimentally is which of the species **20** and **35** of Raffa et al. is more relevant to Cu^{2+}–**L** solution chemistry.

Fig. 1. Model amyloid-β fragment **L** (*N*-α-dihydrourocanylhistamine).

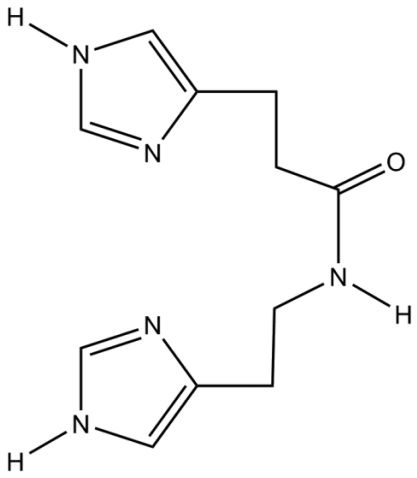

The interactions of Aβ with metal ions are known to be pH-dependent,[5] and so the use of a buffer system to maintain physiological pH is customary. However, by virtue of the position of Cu^{2+} in the Irving–Williams series,[9] it will form complexes of high stability with any ligand having a greater basicity and (or) ligand field strength than solvent water, and we recognized at the outset that this would include the base component of any practical buffer system giving pH near 7, including "Tris" (2-amino-2-(hydroxymethyl)-1,3-propanediol), which is very widely used to control pH in biochemical experiments. After we began the experimental work described here, several authors reported buffer interference in measurements on Cu^{2+}–Aβ complexation,[14–17] and in 2010 Rózga et al.[17] were particularly critical of the use of Tris, although their choice of a Hepes buffer was not necessarily better.[5]

It is surprising that the use of Tris buffers has been widespread in studies of biochemical reactions involving metal ions, particularly Cu^{2+}, as the formation of Cu^{2+}–Tris complexes has long been recognized,[18–24] although Rózga et al.[17] noted that a definitive set of stability constants for Cu^{2+}–Tris complexes is still lacking. Bai and Martell,[20] in a potentiometric study over a pH range 4–12, reported stability constants K_n for $Cu(Tris)_n^{2+}$ at 25 °C and ionic strength at 0.10 mol L^{-1}; for the assumed n = 1, 2, 3, and 4, they reported log K_n = 3.95, 3.68, 3.47, and 3.0, respectively. They also reported, however, that $Cu(Tris)^{2+}$ and $Cu(Tris)_2^{2+}$

Can. J. Chem. Downloaded from www.nrcresearchpress.com by South China Agricultural University on 09/19/12
For personal use only.

underwent deprotonation to $Cu(TrisH_{-1})^+$ and $Cu(Tris)(TrisH_{-1})^+$ with pK_a values of 6.0 and 6.32, respectively, and $Cu(Tris)(TrisH_{-1})^+$ to $Cu(TrisH_{-1})_2$ with $pK_a = 7.90$; on this basis, at our target pH of 7.20, 94% of the mono(Tris) complex would be present as $Cu(TrisH_{-1})^+$ and, if the double deprotonation is ignored, 88% of the bis(Tris) complex would exist as $Cu(Tris)(TrisH_{-1})^+$. Of the groups other than Bai and Martell that have published stability constants for the Cu^{2+}–Tris system, only Kemula et al.[19] reported potentiometric data for all of $n = 1$, 2, 3, and 4; Hall et al.[18] used visible-NIR spectrophotometry to obtain K_1, K_2, and K_3 values, whereas Takahashi et al.[21] reported only the cases $n = 1$ and 2. In general, the K_1 and K_2 data are in reasonable agreement with those of Bai and Martell.[20] Bologni et al.,[22] however, supplied further potentiometric data and analyzed all existing data statistically according to various models, finding the best fit for one which included $Cu(Tris)^{2+}$, $Cu(TrisH_{-1})^+$, and $Cu(Tris)(TrisH_{-1})^+$, plus other deprotonated species relevant only to high pH, but not $Cu(Tris)_2{}^{2+}$ or $Cu(Tris)_4{}^{2+}$; the apparent absence of $Cu(Tris)_2{}^{2+}$ may be interpreted as confirming that it is converted largely to $Cu(Tris)(TrisH_{-1})^+$ at near-physiological pH, as the pK_a reported by Bai and Martell[20] for $Cu(Tris)_2{}^{2+}$ implies. Colombo et al.[23] demonstrated the presence of Cu^{2+}–Tris complexes in solution at pH 10 by optical and ESR methods, and obtained crystal structures for solid $[Cu(TrisH_{-1})_2(OH_2)]$. Kotila[24] reported X-ray structures of solid $[Cu(Tris)(TrisH_1)OH_2]X$ (X = Cl, Br, etc.), obtained by evaporation of solutions containing CuX_2 (0.01 mol) and Tris (0.04 mol), and of other complexes containing deprotonated Tris such as $[Cu(TrisH_{-1})_2]KF{\cdot}3H_2O$.[25–28]

Thus, there is ample evidence for the existence of Cu^{2+} complexes with Tris and $TrisH_{-1}{}^-$ in solution and in the solid state. In their recent review of measurements of the Cu^{2+}–Aβ interaction in buffer systems, Faller and Hureau[5] applied corrections to Cu^{2+}–Aβ stability constants from the literature for interactions of the various buffers with Cu^{2+}, and concluded that measurements in Tris buffer systems were the most reliable relative to those with other buffers once the buffer–Cu^{2+} interactions were taken into account. One question we address here is how, and to what extent, the use of Tris or other buffers affects attempts to determine a meaningful stability constant for Cu^{2+} with the Aβ proxy **L**, either by competition between Tris and **L** for $Cu^{2+}(aq)$ or by direct complex formation between Tris and $Cu\mathbf{L}^{2+}$ or both. These complications are such, however, that we resorted to measurement of the stability constant K_{CuL} for $Cu\mathbf{L}^{2+}$ in the absence of buffers; with this information, it became possible to interpret the behavior of $Cu\mathbf{L}^{2+}$ in buffered solutions.

Experimental

Materials and methods

Synthesis of L

As the preparative method for **L** differed somewhat from that of Baures et al.,[29] it is given here in detail. Histamine dihydrochloride, urocanic acid (3-(4-imidazolyl)acrylic acid), ethyldisopropylamine(benzotriazo-1-yloxy)tripyrrolidinophosphonium hexafluorophosphate (PyBOP), and anhydrous DMF (Sigma-Aldrich) were used without further purification. Methanol and dichloromethane were from EMD, with the latter dried over 4 Å molecular sieves. Celite 545 was obtained from Fisher Scientific Canada. Column chromatography was performed on silica gel 60 (230–400 mesh Merck cat. No. 9385, Sigma-Aldrich). ^1H and ^{13}C NMR spectra were measured at 400 and 100 MHz, respectively, with a Bruker Instruments Co. DRX-400 spectrometer of solutions in MeOH-d_4 (CDN Isotopes Inc.) using the solvent signals at δ_H 3.30 and δ_C 49.0 ppm as references; the HMBC spectra were measured with a program that was optimized for a long-range coupling of 5 Hz.

N-α-Urocanylhistamine

To a solution of histamine dihydrochloride (184 mg, 1.00 mmol) dissolved in MeOH (10 mL) was added diisopropylethylamine (500 mg, 3.88 mmol) and the solvent was then removed under reduced pressure (Rotovap, bath 50 °C). The residue was dissolved in dry DMF (5 mL) and the magnetically stirred solution was cooled to 0 °C. To this, with exclusion of moisture, was added a slurry of urocanic acid (138 mg, 1 mmol), diisopropylethylamine (270 mg, 2.1 mmol), and (benzotriazo-1-yloxyphosphonium) hexafluorophosphate (520 mg, 1 mmol) in CH_2Cl_2 (10 mL). The ice bath was allowed to melt, and the mixture was stirred for a further 18 h. The suspension of finely divided solid was then concentrated (Rotovap, bath 50 °C), first at 15 and then 0.1 torr (1 torr = 133.3224 Pa) to remove the solvents. The residual pale brown oil was applied to a column of silica gel 60 (18 cm × 1.8 cm). Flash chromatography with CH_2Cl_2–MeOH (9:1 *v*/*v*; 20 mL fractions) eluted by-products in f 1–5 but little else and the eluant was then changed (f 25) to CH_2Cl_2–MeOH–NH_4OH (180:30:5 *v*/*v*), which eluted material (159 mg) in f 31–33 that crystallized upon removal of the solvents as a white solid mp 243–244 °C (uncorr.; lit.[29] mp 240–241 °C). ^1H NMR δ_H: 7.73 (1H, s), 7.60 (1H, s), 7.42 (1H, d, $J = 15.6$ Hz), 7.32 (1H, s), 6.87 (1H, s), 6.46 (1H, d, $J = 15.6$ Hz), 3.54 (2H, t, $J = 7.2$ Hz), 2.83 (2H, t, $J = 7.2$ Hz, as lit.;[29] and ^{13}C NMR δ_C: 169.2 s, 138.5 s. 136, 8 v br s, 136.2 s, 136.0 s, 132.3 s, 122.5 v br s, 119.5 s, 118.2 s, 40.7 t, 27.8 t, as lit.[29], but all signals were displaced by 2 ppm to lower field (presumably because of a difference in references). EIMS *m*/*z*: 231 (M^+, 12), 150 (27), 138 (30), 121 (100), 93 (40), 82 (40) Da. HREIMS *m*/*z*: 231.1122; req. for $C_{11}H_{13}N_5O$: 231.1120 Da.

N-α-Dihydrourocanylhistamine (L)

Urocanylhistamine (81 mg, 0.35 mmol) in MeOH (10 mL) was added to a suspension of Pd(10%)-on-C (25 mg) in MeOH (5 mL) and hydrogenated at atmospheric pressure. Hydrogen uptake was complete within 20 min. The suspension was filtered through a pad of Celite and the filter cake washed with a little MeOH. Evaporation (Rotovap, bath 50 °C) of the combined filtrate and washings gave a white solid (75 mg), which was recrystallized from MeOH, mp 176–178 °C (uncorr.; lit.[29] mp 163–164 °C). ^1H NMR δ_H: 7.59 (1H, s), 7.57 (1H, s), 6.80 (1H, s), 6.78 (1H, s), 3.40 (2H, t, $J = 7.1$ Hz), 2.85 (2H, t, $J = 7.4$ Hz), 2.73 (2H, t, $J = 7.2$ Hz), 2.47 (2H, t, $J = 7.4$ Hz) (cf. Baures et al.[29]). ^{13}C NMR δ_C: 175.0 s, 137.3 s, 136.0 d, 135.9 d, 135.7 s, 118.1 d, 117. 6 d, 40.3 t, 36.8 t, 27.7 t, 23.9 t (as Baures et al.[29]), but with those signals displaced by 1.0–1.8 ppm to lower field (presumably because of a difference in references).

Can. J. Chem. Downloaded from www.nrcresearchpress.com by South China Agricultural University on 09/19/12
For personal use only.

The connectivities of the two units within the structure was confirmed by HMBC spectra, which revealed the expected ^2J and ^3J couplings of H-2 (δ_H 2.47) to C-1, -3, and -4 (δ_C 175.1, 23.9, and 137.3, respectively); H-3 (δ_H 2.85) to C-1, -2, -4, and 5 (δ_C 175.1, 36.8, 137.3, and 117.6, respectively); H-1′ (δ_H 3.40) to C-1, -2′, and 3′ (δ_C 175.1, 27.7, and 135.7, respectively); and H-2′ (δ_H 2.73) to C-1′, 3′, and 4′ (δ_C 40.4, 135.7, and 118.1, respectively). EIMS *m/z*: 233 (M^+, 20), 140 (46), 123 (70), 95 (100), 94 (35), 82 (47), 81 (100) Da. HREIMS *m/z*: 233.1280; req. for $C_{11}H_{15}N_5O$: 233.1277.

Copper(II) interactions with L and Tris

Copper(II) perchlorate hexahydrate (Alfa; formula weight determined by cation-exchange acidimetry to be 371.7 ± 1.1), Tris (Omnipur), and standardized HCl (0.1003 mol L^{-1}, J.T. Baker) were used as received. $HClO_4$ (Baker analyzed, 69.1%) was standardized against Baker standard NaOH solution (0.250 mol L^{-1}) with accuracy better than ±0.3%. House reverse-osmosis water was further purified to >18.0 MΩ cm using a Barnstead E-Pure train.

Measurements of pH were made at room temperature (21 ± 1 °C) using an Orion Model 420 pH meter calibrated at pH 4.00, 7.20, and 10.04 with buffer solutions traceable to NIST standards. Stock Tris/$TrisH^+$ buffer solutions (50.0 mmol L^{-1} in total [Tris]) were made up for pH 7.20 from Tris and standard HCl or $HClO_4$ (0.1 mol L^{-1}) following the quantities of Bates and Bower[30]; 89.4% of the total [Tris] was then present as $TrisH^+$.

Spectrophotometric measurements were made using a 10.0 mm silica cuvette on a Cary 5E UV–vis–NIR spectrophotometer with a cell block thermostated at 25.0 ± 0.1 °C with circulating water. Spectra were automatically corrected for baselines run on each solution without the solute of interest (i.e., any absorption owing to the buffer, etc., was subtracted).

Computational methods

Geometry optimization and harmonic frequency analysis were carried out by Gaussian 03 and 09[31] calculations using the hybrid density functional method, B3LYP[32], and the 6–31+G(d) basis set, which we will refer to as the small basis set (SB). The frequency calculation confirmed that the optimized structure was at a local minimum on the potential energy hypersurface and yielded zero point energies and thermochemical parameters. The zero point energies were scaled by 0.9806.[33] However, this was not done for the thermal correction of enthalpy or entropies. Calculated entropies were adjusted in several ways. (*i*) Since we are adding the influence of solvation (see below), we interpret ΔG_{solv} values as being the free energy change that occurs when 1 mol of substrate is added to a 1 L box of water. Thus, the reference state of the entropy is modified from 24.46 L, the volume of 1 mol of ideal gas at 298 K and 1 atm pressure (1 atm = 101.325 kPa), to 1 L: S_{298} (1 mol L^{-1}) = S_{298} (1 atm) + R ln(1/24.46) = S_{298} (1 atm) – 26.585 in J mol^{-1} K^{-1}. (*ii*) Two of the species (**L** and **Tris**) exist in numerous rotameric forms of similar energy in aqueous solution. The entropy of a substance consisting of n conformers in equilibrium is given by $S = \Sigma_i\ \chi_i[S_i + R\ \ln(\chi_i)]$, where χ_i is the mol fraction of conformer i and S_i is its entropy. It is not practical to carry out a comprehensive conformer search in solution. It has been shown[34] that the entropy of a substance is well approximated as $S \approx S_i + R\ \ln(n)$, where S_i is the entropy calculated by Gaussian for the lowest energy conformer obtained by a limited conformer search in the gaseous phase and n is the number of conformers estimated by simple count of stereoisomers including rotamers. It is important to take this entropy of mixing into consideration if the number of degrees of conformational freedom changes significantly because of complex formation, as in the present case. A precise value is not important, since an error of a factor of 2 only affects the free energy change by <2 kJ mol^{-1}. Neglecting it altogether may incur a much larger error (RT ln(63) = 10 kJ mol^{-1} for the complexation of **L** with Cu^{2+}). Values used for n in this work for individual substances are listed in Supplementary data Table S2.

For more accurate enthalpies, single point energies were calculated using B3LYP with a larger basis, 6–311+(2df,2p) (= LB). To compensate for the lack of long-range dispersion at the B3LYP level,[35] single point MP2/SB calculations at the B3LYP/SB geometry were carried out to estimate MP2/LB values using the additive approximation E(MP2/LB) ≈ E('MP2/LB') = E(MP2/SB//B3LYP/SB) + E(B3LYP/LB//B3LYP/SB) – E(B3LYP/SB), where // represents "at the geometry optimized at". Computational results derived from the 'MP2/LB' level, referred to henceforth simply as MP2/LB, are tabulated and discussed in the Results section.

Details of all computed quantities and structural information are provided in Supplementary data Tables S1 and S2, respectively. Molden 4.0 was used as a visualization tool.[36]

Free energies of solvation (ΔG_{solv}) and empirical corrections

To calculate the free energy change in water ($\Delta G_{(aq)}$) the change in the free energy of solvation ($\Delta\Delta G_{solv}$) was added to the free energy change in the gaseous phase ($\Delta G_{(g)}$), corrected for a standard state of 1 mol L^{-1}. ΔG_{solv} was determined using the integral equation following polarizable continuum model (IEFPCM)[37–39] and the B3LYP/6–31+G(d) density. In our experience, charged species are undersolvated by the IEFPCM with standard scaling of the united atom Hartree–Fock (UAHF) radii, so selective scaling was applied as follows: the radii of the metal ion and atoms directly attached to it were scaled by a factor of 1.1; all other atoms were scaled by the default value, 1.2. Experimental rather than calculated relative free energies of solvation were applied where available to reduce errors further. For the proton, $\Delta G_{solv}(H^+)$ = –1107 kJ mol^{-1} was adopted.[40] In addition, for processes that liberate a proton in the buffer medium, it is important to be able to calculate the pK_a of $TrisH^+$ accurately (pK_a = 8.07).[41] As the calculated values (pK_a = 8.7 (MP2) and pK_a = 7.6 (B3LYP)) are close to the experimental value, no adjustment in the free energy of solvation of $TrisH^+$ was necessary. In summary, experimental values of ΔG_{solv} were adopted as follows (in kJ mol^{-1}): H^+, –1107; and H_2O, –16.2. For all other species, free energies of solvation were taken as calculated by the procedure described above. The largest uncertainties in the calculated numbers will be with the gaseous-phase enthalpies approximated at the MP2/LB level. However, we expect that *changes* in aqueous free energies ($\Delta G_{(aq)}$) will be accurate to ±15 kJ mol^{-1} for all of the reactions considered.

Can. J. Chem. Downloaded from www.nrcresearchpress.com by South China Agricultural University on 09/19/12
For personal use only.

Calculations of UV–vis spectra

For selected species, optical spectra in the range 200–800 nm were calculated using the time-dependent version of B3LYP[37–39] with the more flexible basis set 6–311+G(d,p) in water represented by the IEFPCM solvent reaction field. Spectra are displayed as superimposed bands with half-widths at half-height = 0.2 eV and area derived from the calculated oscillator strengths by procedures internal to Gaussview 4.07.[42]

Results

Preliminary measurements

An exploratory attempt was made to characterize the Cu^{2+}–**L** interaction using the continuous variations method of Job,[43] with pH control by a minimal amount (10.0 mmol L^{-1}) of Tris/$TrisH^+$/Cl^- buffer; attempts at such measurements with a $H_2PO_4^-$/HPO_4^{2-} buffer (9.1/20.5 mol L^{-1}, pH 7.2) failed because of precipitation. The UV absorbances of a series of solutions containing x mmol L^{-1} Cu^{2+} and $(4 - x)$ mmol L^{-1} **L** ($0 \leq x \leq 4$) were measured in the region 250–320 nm (e.g., Fig. 2 for 270 nm). All spectra were time-independent, meaning that any interactions of Cu^{2+} with **L** or Tris were complete within the time of sample preparation, as is typical of copper(II).[13,44,45] It was quickly found, however, that Job's method is not appropriate for this system because free **L** absorbs substantially in this spectral region, and moreover the apparent molar absorbance of Cu^{2+} (negligible for Cu^{2+}(aq) itself) increased markedly with [Tris], indicating the formation of Cu^{2+}–Tris species. In Fig. 2, the broken line plot shows the expected dependence of absorbance on x for formation of a 1:1 Cu^{2+}–**L** complex in absence of buffer (see below), whereas the continuous curve shows that the Tris buffer base reacts with Cu**L**$^{2+}$ and (at far right) Cu^{2+} to form Cu^{2+}–Tris and probably Cu**L**$^{2+}$–Tris complexes with higher molar absorbances in the UV than Cu**L**$^{2+}$. Detailed interpretation of Fig. 2 is not warranted because the supply of unprotonated Tris base, initially only 1.07 mmol L^{-1} at zero [Cu^{2+}], must soon have been exhausted by complex formation as [Cu^{2+}] was increased; the shape of the continuous curve implies Cu**L**$^{2+}$–Tris complex formation, but there is no obvious feature at $[Cu]_{total} \approx 1.3$ mmol L^{-1}, expected if Cu$\mathbf{L}_2^{2+}$ were important. The key point that emerges is that Tris interferes strongly with Cu^{2+}–**L** complex formation by scavenging Cu^{2+} and also by Cu**L**$^{2+}$–Tris complex formation.

The shape of Fig. 2 does, however, imply that there is a strong 1:1 interaction of **L** with Cu^{2+} when these are present in equimolar concentrations. Spectra of 1:1 mixtures of $Cu(ClO_4)_2$ + **L** (hereinafter referred to as {Cu^{2+},**L**}, to accommodate any dissociation of Cu**L**$^{2+}$) were therefore obtained in plain water and in Tris/$TrisH^+$ buffers (Figs. 3 and 4). The visible spectra of Fig. 3 quantify the obvious colour change that occurred on exposing aqueous {Cu^{2+},**L**} to Tris buffer; the absorption maximum shifted to shorter wavelengths with significant intensification. In Fig. 4, the UV spectrum of {Cu^{2+},**L**} is compared with those of Cu^{2+}(aq) and **L**; close examination of the {Cu^{2+},**L**} curve shows slight discontinuities between the segments representing 10-fold changes in concentration owing to small degrees of dissociation of Cu**L**$^{2+}$ to Cu^{2+} and **L** that increase on dilution. This effect was used as follows to estimate the stability constant of Cu**L**$^{2+}$ in the absence of a buffer.

Fig. 2. Optical absorbance at 270 nm of solutions made up with x mL $Cu(ClO_4)_2$ (4.98 mmol L^{-1}), $(4.00 - x)$ mL **L** (5.00 mmol L^{-1}), and 1.00 mL Tris/$TrisH^+$/Cl^- buffer (50.0 mmol L^{-1}), at 25.0 °C. Broken line, without buffer.

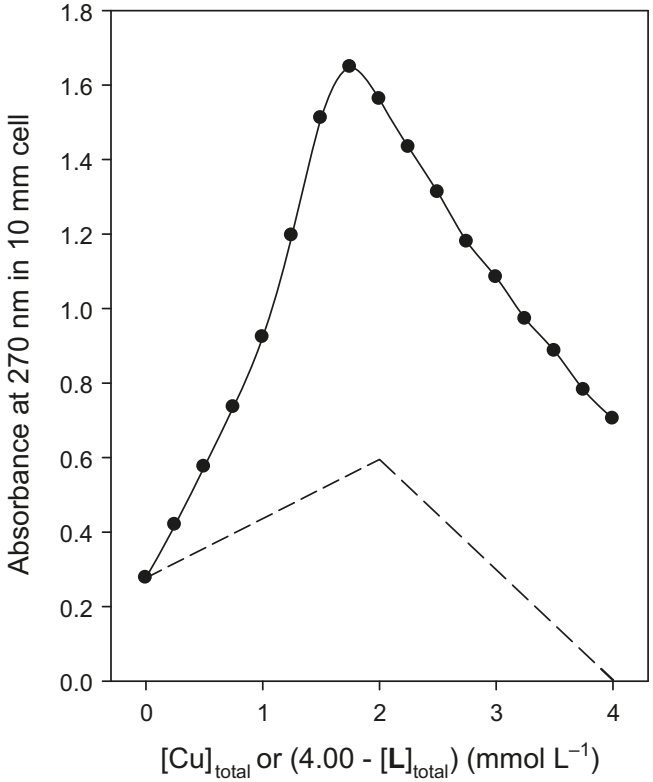

Interaction of Cu^{2+} with L in the absence of a buffer

Addition of 25.0 mL of pale sky blue $Cu(ClO_4)_2$ solution (10.01 mmol L^{-1}) to incompletely dissolved **L** (0.501 mmol) in ~20 mL water gave a clear royal blue solution; addition of a further 25.0 mL of the $Cu(ClO_4)_2$ solution caused the hue to change to a moderately intense sky blue. These respective colour changes are consistent with the formation of at least some Cu$\mathbf{L}_2^{2+}$ with excess **L** and then Cu**L**$^{2+}$ when [Cu^{2+}] = [**L**]; however, Fig. 2 and computational results (see below) indicated that Cu$\mathbf{L}_2^{2+}$ is of low stability relative to Cu**L**$^{2+}$ and was not considered further. The mixture was made to 100.0 mL with water to give a 5.0 mmol L^{-1} solution of the 1:1 complex {Cu,**L**$^{2+}$}. The measured pH of this {Cu,**L**}$(ClO_4)_2$ solution at 21 °C increased slowly from an initial 5.45 to settle at 5.69, cf. 5.23 for $Cu(ClO_4)_2$ (10 mmol L^{-1}) and 8.48 for aqueous **L** (5.0 mmol L^{-1}). From computer modeling described below, the aqueous complex is expected to be Cu$\mathbf{L}(OH_2)_2^{2+}$ with terdentate **L** (with the procedures in use in the previous study,[2] the most stable species was predicted to be Cu$\mathbf{L}(OH_2)^{2+}$). If we attribute the measured pH to acid dissociation of an aqua ligand,

$$[1] \qquad Cu\mathbf{L}(OH_2)_2{}^{2+} = Cu\mathbf{L}(OH)^+ + H_3O^+; \qquad K_{a(Cu\mathbf{L})}$$

we have $pK_{a(CuL)} \geq 9.08$ for this complex (a minimum value because of the possible presence of adventitious CO_2), cf.

Fig. 3. Visible spectra of equimolar (2.5 mmol L^{-1}) solutions of $Cu(ClO_4)_2$ + **L** without buffer (black line), in 25.0 mmol L^{-1} Tris/TrisH^+/ClO_4^- buffer (dark green line), and in 50.0 mmol L^{-1} Tris/TrisH^+/Cl^- (red line).

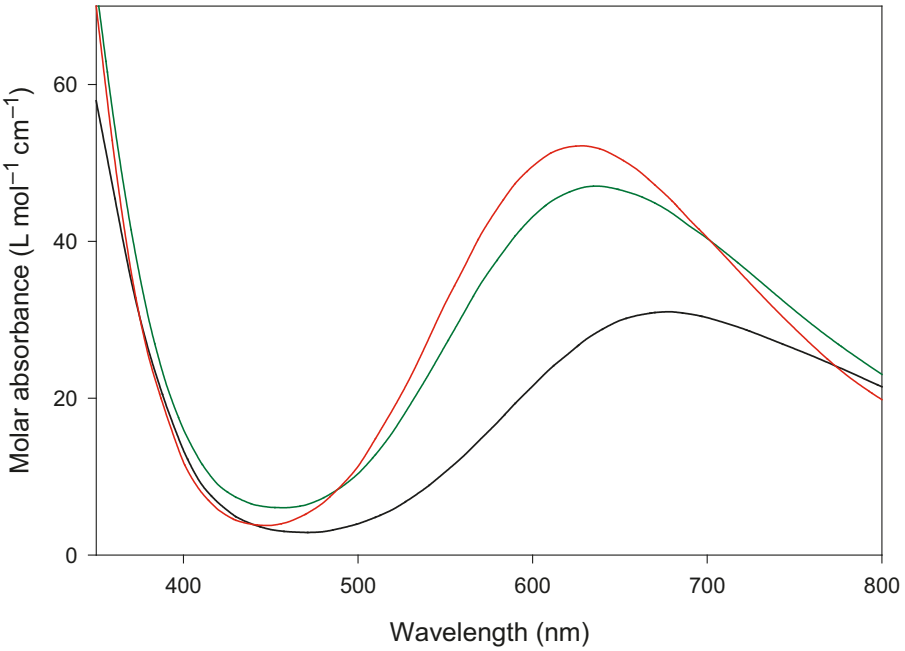

Fig. 4. Ultraviolet spectra of 1:1 $Cu(ClO_4)_2$ + **L** in water (upper curve: black segment, 0.050 mmol L^{-1}; red segment, 0.50 mmol L^{-1}; green segment, 5.0 mmol L^{-1}), and $Cu(ClO_4)_2$ in 1.0 mmol L^{-1} aqueous $HClO_4$ (blue line). The grey line is the spectrum of **L** (1.0 mmol L^{-1}) in 10.0 mmol L^{-1} Tris/TrisH^+/ClO_4^-.

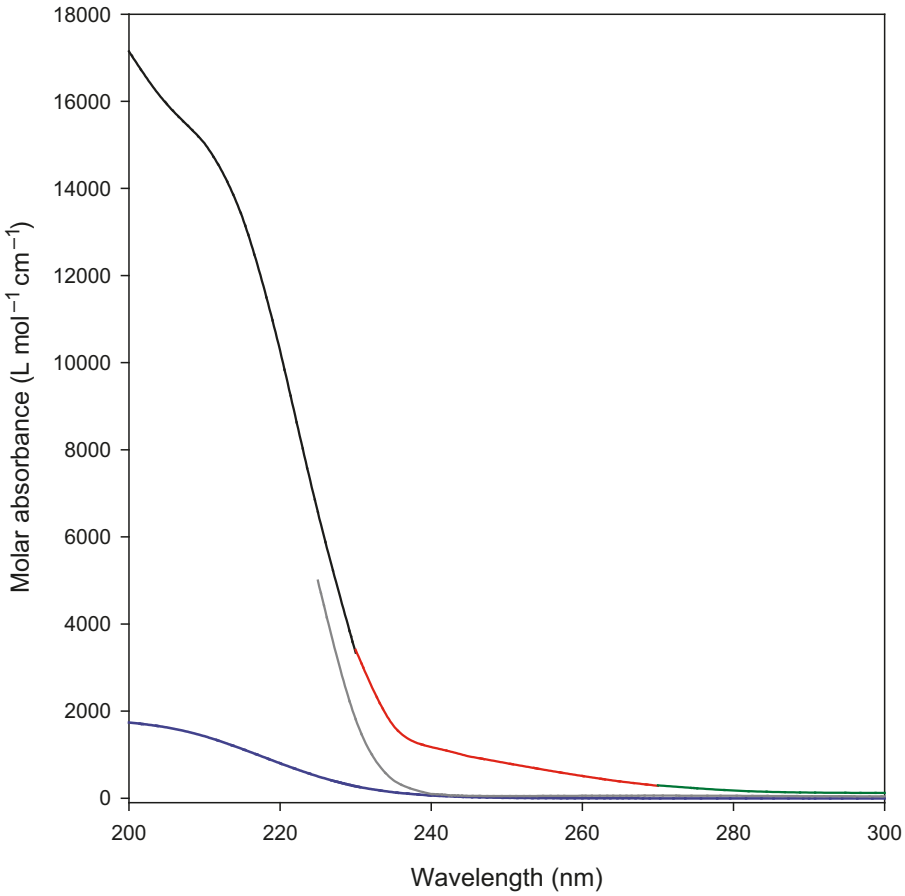

Can. J. Chem. Downloaded from www.nrcresearchpress.com by South China Agricultural University on 09/19/12
For personal use only.

Can. J. Chem. Downloaded from www.nrcresearchpress.com by South China Agricultural University on 09/19/12
For personal use only.

Fig. 5. Extrapolation of apparent molar absorbance of $\{Cu^{2+},\mathbf{L}\}$ at 250 nm in pure water to "infinite concentration".

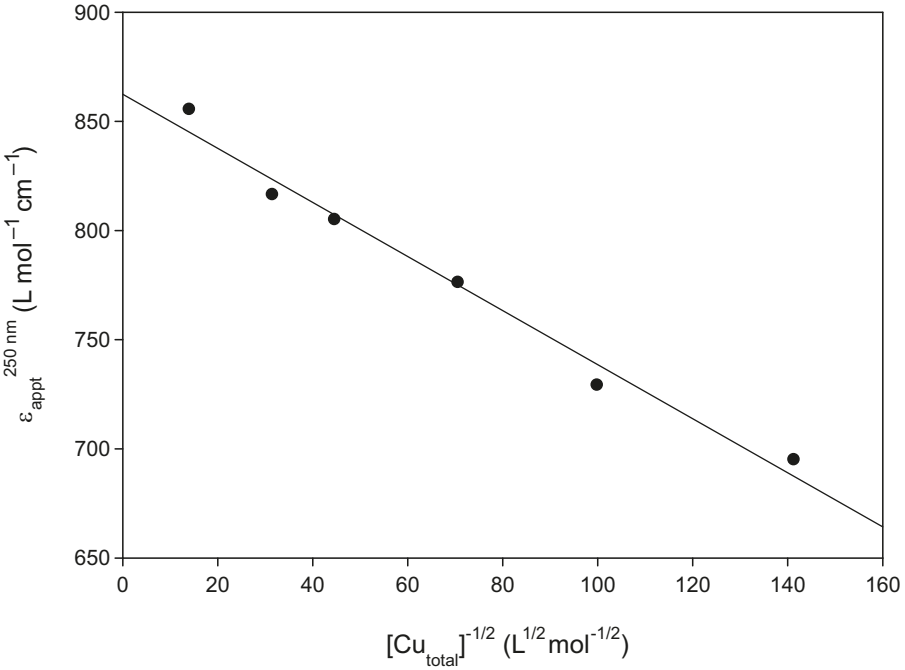

8.16 for $Cu^{2+}(aq)$ and 5.26 for aqueous $\mathbf{L}H^+$ from the pH measurements. These data indicate that the three donor atoms of **L** in $Cu\mathbf{L}(OH_2)_2^{2+}$ include the peptide O along with the two N_π bases; the alternative species **35** of Raffa et al.[2] can be ruled out as requiring release of one H^+ from the amido N per $\{Cu,\mathbf{L}H_{-1}^+\}$ formed, which on going to completion would have given pH 2.3.

The apparent UV molar absorbance ε_{appt} of $\{Cu,\mathbf{L}^{2+}\}(ClO_4)_2$ in pure water was found to decrease by about 17% with progressive dilution from 5.0 to 0.050 mmol L^{-1}. This can be confidently attributed to dissociation of $Cu\mathbf{L}^{2+}$:

$$[2]\qquad \underset{c-x}{Cu\mathbf{L}^{2+}} = \underset{x}{Cu^{2+}}(aq) + \underset{x}{\mathbf{L}};\qquad K_{Cu\mathbf{L}}{}^{-1}$$

where c is the total concentration of $\{Cu^{2+},\mathbf{L}\}$ and affords a means of determining the stability constant $K_{Cu\mathbf{L}}$ of the complex. (An alternative possibility, that the change in absorbance might be due to acid dissociation as in eq. [1], can be discounted because the minimum value found for $pK_{a(Cu\mathbf{L})}$ indicates that no more than about 0.4% of $Cu\mathbf{L}(OH_2)_2^{2+}$ would undergo acid dissociation at 0.05 mmol L^{-1}.) Fig. 4 shows that the wavelength range best suited to estimation of $K_{Cu\mathbf{L}}$ (i.e., where the absorbances of **L** and $Cu^{2+}(aq)$ are smallest relative to $Cu\mathbf{L}^{2+}$) is 235–260 nm. The molar absorbances $\varepsilon_{\mathbf{L}}$ of **L** and ε_{Cu} of $Cu^{2+}(aq)$ were measured directly at 5 nm intervals in this range, and corresponding $\varepsilon_{Cu\mathbf{L}}$ values for undissociated $Cu\mathbf{L}^{2+}$ at each wavelength were obtained with adequate precision for $x << c$ by extrapolating linear plots of ε_{appt} vs $c^{-1/2}$ (e.g., Fig. 5) to zero. Then, the concentrations x of Cu^{2+} and **L** and thence $K_{Cu\mathbf{L}}$ were obtained from eqs. [3] and [4]. The relevant data are collected in Tables 1 and 2.

$$[3]\qquad x = (\varepsilon_{Cu\mathbf{L}} - \varepsilon_{appt})c/(\varepsilon_{Cu\mathbf{L}} - \varepsilon_{\mathbf{L}} - \varepsilon_{Cu})$$

$$[4]\qquad K_{Cu\mathbf{L}} = (c - x)/x^2$$

Table 1. Apparent molar absorbances (ε_{appt}) of 1:1 Cu^{2+}–**L** solutions at 25.0 °C

	ε_{appt} (L mol^{-1} cm^{-1})				
	λ (nm)				
Total [Cu] c (mmol L^{-1})	235	240	245	250	255
1.00	1686	1195	978	816	680
0.50	1668	1176	961	804	665
0.20	1635	1136	929	776	654
0.10	1563	1075	872	729	635
0.05	1498	1015	825	695	598

Note: c, concentration; λ, wavelength.

The average value of $K_{Cu\mathbf{L}}$ (10^5 L mol^{-1}) was 3.76 ± 0.11 (standard error; ±0.31 at the 99% confidence limit). A working value of $K_{Cu\mathbf{L}} = 3.8 \times 10^5$ L mol^{-1} at 25 °C may be adopted.

Interaction of $Cu^{2+}(aq)$ with Tris

Figure 6 shows the UV spectrum of 0.10 mmol L^{-1} aqueous Cu^{2+} in the presence and absence of Tris/TrisH$^+$/ClO_4^- buffer ($[Tris]_{base} = 0.107[Tris]_{total}$) over a fourfold range of $[Tris]_{total}$; the effect of the presence of the buffer is evident (cf. spectra reported by Bai and Martell[20] for the visible region). It can be seen that the spectral shapes — in particular, the wavelengths of the absorbance maxima at 238 nm and shoulders at ~265 nm — are independent of concentration and that a limiting molar absorbance is rapidly being approached as the concentration of buffer increases, suggesting the dominance of a single Cu^{2+}–Tris species. When the maximum apparent molar absorbances ($\varepsilon_{appt}^{238} = 3054$, 3246, and 3316 L mol^{-1} cm^{-1} for [buffer] = 10, 20, and 40 mmol L^{-1}, respectively) are plotted against the concentration of uncomplexed Tris base (i.e., $\{[Tris]_{base} - n[Cu^{2+}]_{total}\}$, for $Cu(Tris)_n^{2+}$), equally good linear correlations ($r^2 = 0.9998$ and 0.9999)

Can. J. Chem. Downloaded from www.nrcresearchpress.com by South China Agricultural University on 09/19/12
For personal use only.

Table 2. Molar absorbances (ε, L mol^{-1} cm^{-1}) of Cu^{2+}(aq) and **L** obtained by direct measurement, Cu**L**$^{2+}$(aq) by extrapolation of apparent molar absorbances (ε_{appt}) as in Fig. 5, and stability constant K_{CuL} (L mol^{-1}) for Cu**L**$^{2+}$(aq) from eqs. [2]–[4].

λ (nm)	ε_{Cu}	ε_{L}	ε_{CuL}	K_{CuL} (10^5 L mol^{-1}) [a]
235	139.6	146.4	1747±7	4.03±0.30
240	66.4	101.1	1250±4	3.64±0.17
245	29.6	57.9	1025±5	3.74±0.20
250	12.8	54.8	862±7	3.32±0.19
255	5.4	56.9	695±4	4.08±0.26

Note: λ, wavelength.
[a]Average of five measurements at each wavelength; 25.0 °C.

are obtained for assumed $n = 3$ and 4, giving a limiting ε of 3376 ± 7 L mol^{-1} cm^{-1} at the 238 nm maximum. However, the pH of the 10 mmol L^{-1} Tris medium, with and without the added 0.10 mmol L^{-1} Cu^{2+}, was 7.01 and 7.15, respectively (the decrease in the pH of the buffer itself on dilution, initially 7.20 as prepared at 50 mmol L^{-1}, confirms the effect noted by Bates and Bower[30]). If this perturbation of the buffer pH by Cu^{2+} were due solely to consumption of unprotonated Tris base to form $Cu(Tris)_n^{2+}$, then eqs. [5] and [6] give the average n in that solution as 3.0 ± 0.3.

$$[5] \quad [Tris]_{free} = K_{a(TrisH)}[TrisH^+]/10^{-pH}$$

$$[6] \quad n_{average} = ([Tris]_{total} - [Tris]_{free})/[Cu^{2+}]_{total}$$

Similarly, for the solution with 20 mmol L^{-1} buffer, Cu complex formation caused a pH shift of 7.10 from 7.16, corresponding to $n_{average} = 2.8 \pm 0.6$, but in 40 mmol^{-1} buffer the pH shift was too small (7.17 from 7.19) to allow a meaningful estimate of $n_{average}$. Thus, within the error limits, the perturbation of the buffer pH corresponds to the removal of three free Tris molecules per added Cu^{2+} in both 10 and 20 mmol L^{-1} buffer.

The simplest explanation for these results is the formation of $Cu(Tris)_3^{2+}$. An alternative interpretation, however, is that the perturbation of the buffer pH was due to formation of $Cu(Tris)(TrisH_{-1})^+$ as the dominant Cu species in 10 and 20 mmol L^{-1} Tris buffer at least, each added Cu^{2+} complexing two unprotonated Tris and releasing one H^+ from the complex to protonate a third Tris. Bai and Martell[20] gave the pK_a of $Cu(Tris)^{2+}$ and $Cu(Tris)_2^{2+}$ as 6.0 and 6.32, respectively, implying that the major bis(Tris)–Cu^{2+} species at the pH values spanned by Fig. 6 would indeed be $Cu(Tris)(TrisH_{-1})^+$, which is consistent with the data analyses of Bologni et al.[22] as well as theoretical computations described as follows, and is also the complex most readily isolable as a solid salt from Cu^{2+}–Tris solutions.[24–28] Moreover, Kotila[24] showed crystallographically that Tris and $TrisH_{-1}$ in solid salts of $Cu(Tris)(TrisH_{-1})^+$ are, respectively, terdentate (O, O′, N) and bidentate (O, N), the sixth site in the distorted octahedral coordination sphere around Cu^{2+} being taken up by an aqua ligand; any additional Tris ligand would therefore be expected to replace the aqua ligand and so be only unidentate with consequent low stability. No structural information is available for the putative $Cu(Tris)_3^{2+}$ or $Cu(Tris)_4^{2+}$, but our computations (see the following) indicate that $Cu(Tris)_3^{2+}$ has limited stability in water and that $Cu(Tris)_4^{2+}$ is sterically improbable. Thus, the simplest and most probable interpretation of Fig. 6 and the pH data is that they represent nearly complete formation of $Cu(Tris)(TrisH_{-1})^+$ and that the limiting maximum ε of 3376 ± 7 L mol^{-1} cm^{-1} at 238 nm refers to this species.

Fig. 6. Ultraviolet spectra of $Cu(ClO_4)_2$ (0.10 mmol L^{-1}) in Tris/$TrisH^+/ClO_4^-$: $[Tris]_{total}$ = 40.0 (black line), 20.0 (red line), and 10.0 mmol L^{-1} (green line). Blue line: $Cu(ClO_4)_2$ (0.10 mmol L^{-1}) in $HClO_4$ (1.0 mmol L^{-1}).

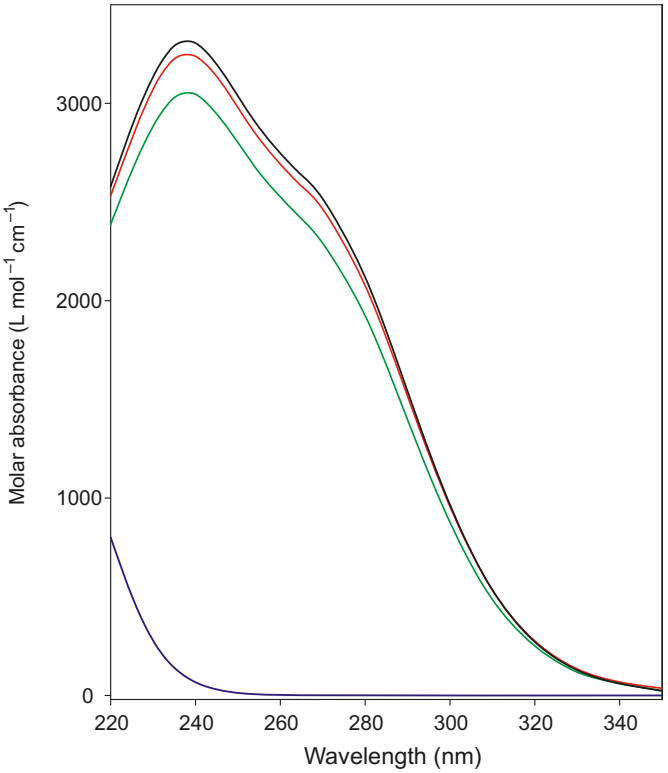

Bai and Martell[20] gave visible-region spectra (their Fig. 3) of solutions with $[Cu^{2+}]$:[Tris] ratios of 1:1 to 1:4, with various amounts of added NaOH. Interestingly, the close similarities between their spectra 4 and 7 and between their spectra 5 and 6, in which the $[Cu^{2+}]$:[Tris] ratio ranges from 2 to 4, imply that the number of Tris or $TrisH_{-1}^-$ ligands per Cu^{2+} never exceeds two at pH ~ 8 (cf. Fig. 4 of Bai and Martell). Again, this points to the dominance of $Cu(Tris)(TrisH_{-1})^+$ in the pH range 6–8.

Interaction of {Cu^{2+},L} with Tris

When aliquots of a $\{Cu,\mathbf{L}\}(ClO_4)_2$ solution were added to an excess of Tris/$TrisH^+$ buffer, the colour intensified and the hue shifted toward royal blue. This is shown in Fig. 3; the hypsochromic shift (678 to 636 nm for 25 mmol L^{-1} Tris/$TrisH^+/ClO_4^-$, to 627 nm for 50 mmol L^{-1} Tris/$TrisH^+/Cl^-$) is as expected for the replacement of aqua ligands in Cu**L**$(OH_2)_2^{2+}$ by nitrogen donor ligands (unprotonated Tris) giving Cu**L**$(Tris)^{2+}$, but could also be due to displacement of coordinated **L** by tris to form Cu^{2+}–$TrisH_{-1}^-$ complexes (cf. spectra 4–7 in Fig. 3 of Bai and Martell,[20] for which added NaOH forced deprotonation of coordinated Tris).

Can. J. Chem. Downloaded from www.nrcresearchpress.com by South China Agricultural University on 09/19/12
For personal use only.

Fig. 7. Solid lines: UV spectra of $\{Cu^{2+},\mathbf{L}\}$ perchlorate in 10.0 mmol L^{-1} Tris/$TrisH^+/ClO_4^-$; $[Cu^{2+},\mathbf{L}]$ = 1.00 mmol L^{-1} (black symbols), 0.50 mmol L^{-1} (red symbols), 0.20 mmol L^{-1} (green symbols), 0.10 mmol L^{-1} (blue symbols), 0.05 mmol L^{-1} (pink symbols), 0.04 mmol L^{-1} (grey symbols), 0.02 mmol L^{-1} (brown symbols), and 0.01 mmol L^{-1} (white symbols). Broken line: $\{Cu^{2+},\mathbf{L}\}$ in water, no buffer; red segment, $[Cu^{2+},\mathbf{L}]$ = 0.5 mmol L^{-1}; green segment, $[Cu^{2+},\mathbf{L}]$ = 5.0 mmol L^{-1}. Dotted line: **L** in buffer, pH 7.2.

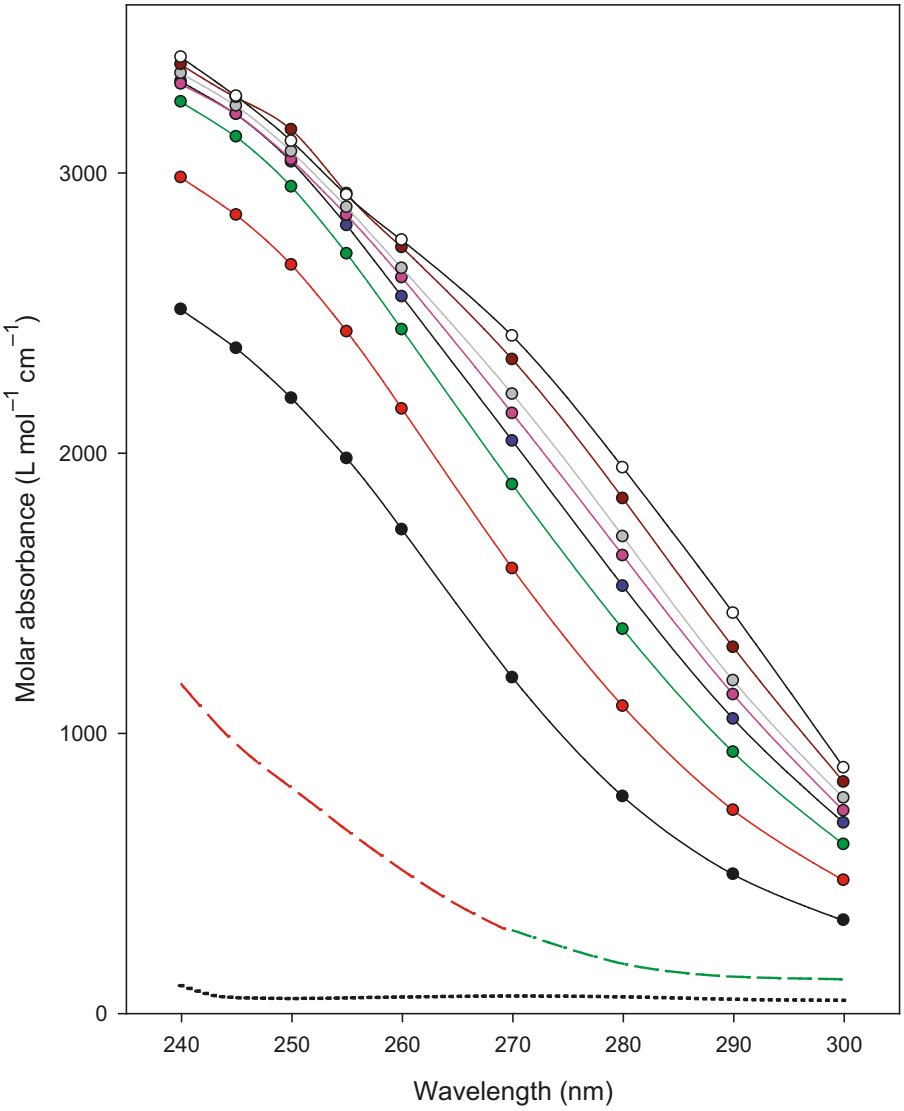

The latter interpretation is supported by computational results (see the following) that show that $Cu\mathbf{L}(Tris)^{2+}$ would be of relatively low stability in water. Detailed interpretation of the present Fig. 3 is impractical because the concentrations of free Tris base were only 1.07 and 2.14 times that of the total [Cu] for the chloride and perchlorate buffers, respectively, but the similarity of the spectrum in the 50 mmol L^{-1} chloride buffer to spectra 4 and 7 of Bai and Martell's Fig. 3[20] suggests that $Cu\mathbf{L}^{2+}$ is largely destroyed by the Tris base under these conditions to give $Cu(Tris)(TrisH_{-1})^+$. Spectra 1 and 2 of Bai and Martell's Fig. 3 rule out $Cu(Tris)^{2+}$ and $Cu(TrisH_{-1})^+$ as significant contributors to the spectra of the present Fig. 3. In any event, spectra in the visible region were unsuitable for the measurement of the dissociation of **L** from $Cu\mathbf{L}^{2+}$ on dilution because of the high concentrations of the Cu species required and were not pursued in detail.

Figure 7 shows that the apparent molar UV absorbance of the 1:1 complex $\{Cu^{2+},\mathbf{L}\}$ in 10.0 mmol L^{-1} Tris/$TrisH^+/ClO_4^-$ buffer increased as its concentration was decreased 100-fold from 1.00 mmol L^{-1}. This is attributable to an interaction between $Cu\mathbf{L}^{2+}$ and free Tris base, the concentration of which was only 1.07 mmol L^{-1} in the absence of $\{Cu^{2+},\mathbf{L}\}$ (i.e., barely in excess of $[\{Cu^{2+},\mathbf{L}\}]$ at its highest); thus, the excess of $[Tris_{free}]$ over $[\{Cu^{2+},\mathbf{L}\}]$ increased as the latter decreased. Indeed, $\{Cu^{2+},\mathbf{L}\}$ caused marked perturbations of the buffer pH through consumption of unprotonated Tris base. For the solutions represented in Fig. 7 with $[\{Cu^{2+},\mathbf{L}\}]$ = 1.00, 0.50, 0.20, and 0.10 mmol L^{-1}, the measured pH was 6.48, 6.81, 7.07, and 7.14, respectively, as compared with 7.24 for this particular buffer preparation alone, corresponding to removal of 0.9 ± 0.1, 1.3 ± 0.1, 1.7 ± 0.2, and 2.2 ± 0.4 free Tris molecules per $\{Cu^{2+},\mathbf{L}\}$ — the pH measurements were insufficiently precise to continue the calculations to lower $[\{Cu^{2+},\mathbf{L}\}]$. It could be argued that these pH data are consistent with the formation of $Cu\mathbf{L}(Tris)^{2+}$ when the free Tris supply barely exceeds $[\{Cu^{2+},\mathbf{L}\}]$, and

Can. J. Chem. Downloaded from www.nrcresearchpress.com by South China Agricultural University on 09/19/12
For personal use only.

Table 3. Relative energies of species discussed in the text: enthalpies based on MP2/LB energies.

Process	$\Delta H_{(g)}$ (kJ mol^{-1})	$T\Delta S_{(g)}$ (kJ mol^{-1})	$\Delta G_{(g)}$ (kJ mol^{-1})	$\Delta\Delta G_{solv}$ (kJ mol^{-1})	$\Delta G_{(aq)}$ (kJ mol^{-1})	$\log(K_{eq})$
$Cu(H_2O)_5^{2+}$ + Tris → $Cu(Tris)(H_2O)_2^{2+}$ + $3H_2O$	–52.2	–40.6	–92.8	84.9	–7.9	1.4
$2Cu(Tris)(H_2O)_2^{2+}$ + H_2O → $Cu(H_2O)_5^{2+}$ + *a*-$Cu(Tris)_2^{2+}$	–119.7	31.1	–88.6	33.6	–55.0	9.6
$Cu(H_2O)_5^{2+}$ + 2Tris → *a*-$Cu(Tris)_2^{2+}$ + $5H_2O$	–224.1	–50.1	–274.2	203.3	–70.9	12.4
$Cu(H_2O)_5^{2+}$ + 2Tris → *s*-$Cu(Tris)_2^{2+}$ + $5H_2O$	–224.0	–49.7	–273.8	206.4	–67.4	11.8
$Cu(H_2O)_5^{2+}$ + 2Tris → *a*-$Cu(Tris)(TrisH_{-1})^+$ + $5H_2O$ + H^+	500.9	–70.1	430.8	–407.8	23.0	(4.0)[a]
$Cu(H_2O)_5^{2+}$ + 2Tris → *s*-$Cu(Tris)(TrisH_{-1})^+$ + $5H_2O$ + H^+	496.5	–73.0	423.5	–405.6	17.9	(3.1)[a]
$Cu(H_2O)_5^{2+}$ + 3Tris → *s*-$Cu(Tris)(TrisH_{-1})^+$ + $5H_2O$ + $TrisH^+$	–469.5	–45.6	–515.1	483.4	–31.8	5.6
$Cu(H_2O)_5^{2+}$ + 3Tris → $Cu(Tris)_3^{2+}$ + $5H_2O$	–401.9	4.3	–397.6	390.5	–7.1	1.2
$Cu(H_2O)_5^{2+}$ + 4Tris → $Cu(Tris)_4^{2+}$ + $5H_2O$	–569.4	58.3	–511.1	543.6	32.6	–5.7
$Cu(H_2O)_5^{2+}$ + **L** → Cu**L**$(H_2O)_2^{2+}$ + $3H_2O$	–301.5	–29.5	–331.0	293.8	–37.1	6.5
$CuL(H_2O)_2^{2+}$ + **L** → CuL_2^{2+} + $2H_2O$	–191.8	–2.8	–194.6	184.9	–9.7	1.7
Cu**L**$(H_2O)_2^{2+}$ + Tris → Cu**L**$(Tris)^{2+}$ + $2H_2O$	–77.1	–9.3	–86.3	79.2	–7.1	1.2
Cu**L**$(H_2O)_2^{2+}$ + Tris → Cu**L**′$(Tris)^{2+}$ + $2H_2O$	–27.3	–9.4	–36.7	76.1	39.4	–6.9

[a] pK_a of $Cu(Tris)_2^{2+}$.

Cu**L**$(Tris)_2^{2+}$ or Cu**L**$(TrisH_{-1})^{+}$[20,22] for low concentrations of {Cu^{2+},**L**} when Tris is in large excess. Figures 4 and 7, however, show that the apparent ε of {Cu^{2+},**L**} in pure water continues to rise on scanning to wavelengths shorter than 250 nm, whereas the absorbance of {Cu^{2+},**L**} in Tris buffer solution, though initially higher, levels off around 240 nm as dilution progresses and shows an incipient shoulder at ~265 nm. These features correspond to the displacement of **L** from Cu$\mathbf{L}^{2+}$ or Cu**L**$(Tris)^{2+}$ by Tris base to form the Cu^{2+}–Tris complex (deduced to be $Cu(Tris)(TrisH_{-1})^+$) of Fig. 6, which has an ε maximum at 238 nm and a pronounced shoulder at 265 nm; we have seen that the Cu^{2+} ion can cause the removal of up to three Tris per Cu, most likely by forming $Cu(Tris)(TrisH_{-1})^+$ + $TrisH^+$. Although the $K_1 \times K_2$ and pK_a values for $Cu(Tris)_2^{2+}$ given by Bai and Martell[20] may be inaccurate (see the following), they may be taken together with $K_{CuL} = 3.8 \times 10^5$ L mol^{-1}, obtained in this study, to estimate the fractions of {Cu^{2+},**L**} destroyed by the free Tris base in 10.0 mmol L^{-1} Tris/$TrisH^+$/ClO_4^- buffer to be 68%, 87%, and 94% for c = 0.2, 0.1, and 0.05 mmol L^{-1}, respectively, in qualitative agreement with the progression seen in Fig. 7 (insufficient Tris base for eq. [7] was present with c = 1.0 and 0.5 mmol L^{-1}).

$$[7] \qquad Cu\mathbf{L}^{2+} + 3Tris = Cu(Tris)(TrisH_{-1})^{+} + TrisH^{+} + \mathbf{L}$$

The limiting molar absorbances of Fig. 7 approach those expected for an equimolar mixture of $Cu(Tris)(TrisH_{-1})^+$ and **L**, although difficulty in accounting quantitatively for the progression of molar absorbances on dilution suggests that a ternary Cu^{2+}–**L**–Tris complex that absorbs more strongly than Cu$\mathbf{L}^{2+}$ is formed as precursor to rxn. [7]. Indeed, computer modeling (see the following) indicates that Cu**L**$(Tris)^{2+}$ would have significant stability in aqueous solution. Rózga et al.[17] reported that there was no evidence for the formation of a ternary complex between $Cu(A\beta)^{2+}$ and the base of Hepes buffer. Whether or not ternary complexes form, the scavenging of Cu^{2+}, either from $Cu(A\beta)^{2+}$ by Hepes base or from Cu$\mathbf{L}^{2+}$ by Tris, must seriously interfere with attempts to measure the stability constants of the Cu^{2+} complexes.

The key features of Fig. 7 are seen more clearly in Fig. 8, which shows the spectrum of progressively diluted {Cu^{2+},**L**} in a fivefold more concentrated Tris/$TrisH^+$/Cl^- buffer (use of Cl^- rather than ClO_4^- made no significant difference). The ε at ~250 nm actually begins to decrease on diluting {Cu^{2+},**L**} beyond 0.10 mmol L^{-1}, even as the ε near 265 nm characteristic of $Cu(Tris)(TrisH_{-1})^+$ continues to rise, which implies that the form of Cu$\mathbf{L}^{2+}$ being destroyed must be at least in part a Cu^{2+}–**L**–Tris complex such as Cu**L**$(Tris)^{2+}$ that absorbs more strongly than Cu$\mathbf{L}^{2+}$ itself or $Cu(Tris)(TrisH_{-1})^+$. When interpreting Figs. 7 and 8, however, it should be borne in mind that the measured absorbances at the highest dilutions were small, and that the corresponding molar absorbances were therefore subject to relatively large uncertainties.

Computational results

Ab initio computational methods were applied to determine plausible structural and thermodynamic properties of the species involved in mixtures of **L**, Cu^{2+}, and Tris buffer. The calculated results are given in Table 3. The geometries and primary computed properties of all structures are listed

Can. J. Chem. Downloaded from www.nrcresearchpress.com by South China Agricultural University on 09/19/12
For personal use only.

Fig. 8. Ultraviolet spectra of {Cu^{2+},**L**} perchlorate in 50.0 mmol L^{-1} Tris/TrisH^+/Cl^-. From the bottom, [Cu^{2+},**L**] = 1.00 mmol L^{-1} (black symbols), 0.50 mmol L^{-1} (red symbols), 0.20 mmol L^{-1} (green symbols), 0.10 mmol L^{-1} (dark blue symbols), 0.05 mmol L^{-1} (pink symbols), 0.02 mmol L^{-1} (light blue symbols), and 0.01 mmol L^{-1} (white symbols).

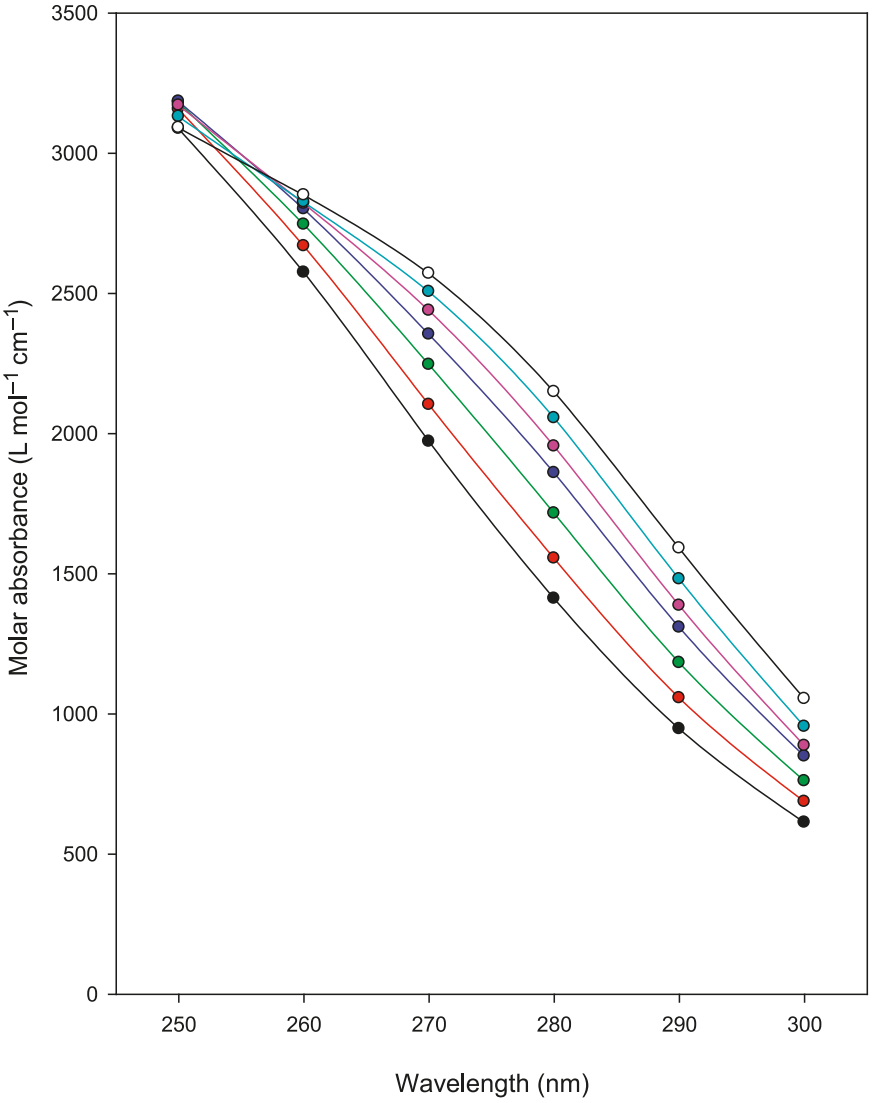

in Supplementary data Tables S1 and S2, respectively. The Cu^{2+}(aq) ion was taken to be $Cu(H_2O)_5^{2+}$, as predicted by the computational method; the burden of experimental evidence, however, indicates a tetragonally distorted octahedral Cu $(H_2O)_6^{2+}$ in aqueous solution, although some authors have argued for five-coordination.[13]

The Cu**L**$^{2+}$ coordination pattern (Fig. 9) has been previously characterized.[2] Re-evaluation of the free energy of binding of **L** to Cu^{2+} by eq. [8*a*] yielded a stability constant substantially lower than that previously determined ($\log K_{8a}$ = 19).[2] The origin of the difference lies in the improved theoretical level (MP2/LB//B3LYP/6–31+G(d) vs B3LYP/LB//B3LYP/6–31G(d)) and a renewed search of the conformational space of **L**, which yielded a structure that is 21 kJ mol^{-1} more stable than that previously found. Calculation of the pK_a value for **L**H$^+$ yielded pK_a = 5.7, in excellent agreement with the experimental value determined above, pK_a = 5.26. The value obtained at the MP2/LB level for the reaction of Cu^{2+} and **L** ($\log K_{8a}$ = 6.3) is also in good agreement with the experimental value derived above, $\log K_{CuL}$ = 5.58. At the B3LYP/LB level (Supplementary data Table S3), the calculated value is similar, $\log K_{8a}$ = 6.1.

[8*a*] $$Cu(H_2O)_5^{2+} + \mathbf{L} = Cu\mathbf{L}(H_2O)_2^{2+} + 3H_2O;$$
$$\Delta G_{(8a,aq)} = -36 \text{ kJ mol}^{-1};\ \log K_{8a} = 6.3$$

Coordination of a second **L** to Cu**L**$(H_2O)_2^{2+}$ yielding Cu$\mathbf{L}_2^{2+}$ is weakly exergonic (eq. [8*b*], $\Delta G_{(8b,aq)}$ = –10 kJ mol^{-1}). Steric crowding prevents coordination of all four imidazole groups to the copper. The second **L** in Cu$\mathbf{L}_2^{2+}$ (Fig. 9) is attached via one imidazole and the carbonyl oxygen. At the B3LYP/LB level (Supplementary data Table S3), attachment of the second **L** is strongly disfavoured, $\Delta G_{(8b,aq)}$ = 46 kJ mol^{-1}.

[8*b*] $$Cu(H_2O)_2^{2+} + \mathbf{L} = Cu\mathbf{L}_2^{2+} + 2H_2O;$$
$$\Delta G_{(8b,aq)} = -10 \text{ kJ mol}^{-1};\ \log K_{8b} = 1.7$$

The computations predict that Cu^{2+} will form 1:1, 1:2, and 1:3 complexes with Tris. The structures of the studied Cu–Tris

Can. J. Chem. Downloaded from www.nrcresearchpress.com by South China Agricultural University on 09/19/12
For personal use only.

Fig. 9. The most stable computed structures for the aqueous Cu**L**$^{2+}$ and Cu**L**$_2{}^{2+}$ complexes. Orange atoms, C; blue atoms, N; red atoms, O; yellow atoms, Cu^{II}; and white atoms, H.

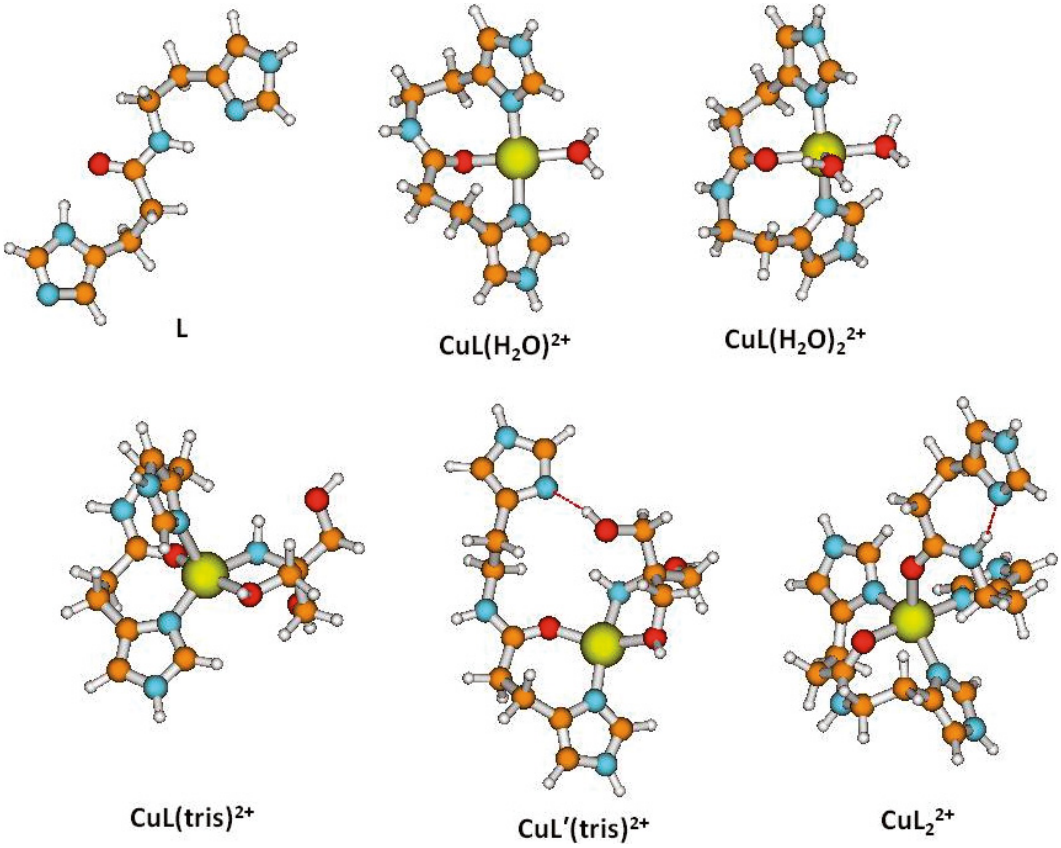

complexes, Cu(Tris)$(H_2O)_2{}^{2+}$, Cu(TrisH$_{-1}$)$(H_2O)_2{}^{+}$, *s*-Cu(Tris)$_2{}^{2+}$, *a*-Cu(Tris)$_2{}^{2+}$, Cu(Tris)$_3{}^{2+}$, Cu(Tris)$_4{}^{2+}$, *s*-Cu(Tris)(TrisH$_{-1}$)$^{+}$, and *a*-Cu(Tris)(TrisH$_{-1}$)$^{+}$, are shown in Fig. 10. The prefixes *s*- and *a*- specify the syn and anti orientation, respectively, of the two ligated NH_2 groups. Of the two bis(Tris) complexes, the anti isomer is calculated to be 4 kJ mol^{-1} more stable than the syn isomer. The opposite is true for the two singly deprotonated complexes, where the *s*-isomer is 5 kJ mol^{-1} more stable than the *a*-isomer. As these small differences are well within the anticipated uncertainties, they cannot be taken as significant. However, we note that crystal structures of Cu(Tris)(TrisH$_{-1}$)$^{+}$ are exclusively of the *s*-stereoisomer.[24,26,28] Calculated formation and acid dissociation results for all species are shown in Table 3.

The association constant (logK_9) of Cu^{2+} and Tris to form the 1:1 complex may be derived from eq. [9]:

$$[9] \quad Cu(H_2O)_5{}^{2+} + \text{Tris} = Cu(\text{Tris})(H_2O)_2{}^{2+} + 3H_2O; \quad \Delta G_{(9,aq)} = -8 \text{ kJ mol}^{-1}; \ \log K_9 = 1.4$$

The calculated association constant for the formation of Cu(Tris)$(H_2O)_2{}^{2+}$ is predicted to be considerably lower than the accepted experimental value, logK_{as} = 3.97.[20] At the B3LYP/LB level, the value is much closer, 4.8. At both the MP2/LB and B3LYP/LB theoretical levels, the computed K_{as} for both *s*-Cu(Tris)$_2{}^{2+}$ and *a*-Cu(Tris)$_2{}^{2+}$ unexpectedly exceeds that for Cu(Tris)$(H_2O)_2{}^{2+}$ (eq. [10]) by a large margin:

$$[10] \quad Cu(\text{Tris})(H_2O)_2{}^{2+} + \text{Tris} \rightarrow s\text{- or } a\text{-Cu(Tris)}_2{}^{2+} + 2H_2O; \quad \Delta G_{(10,aq)} \approx -60 \text{ kJ mol}^{-1}; \ \log K_{10} \approx 11$$

The value log K_{10} = 11 is more than seven orders of magnitude larger than the experimental value (log $K_{as2} \approx 3.7$).[18–24] At the B3LYP/LB level (Supplementary data Table S3), it is four orders of magnitude larger. These results suggest that the mono(Tris) adduct will disproportionate to Cu^{2+}(aq) and a bis(Tris) adduct, e.g., eq. [11]:

$$[11] \quad 2Cu(\text{Tris})(H_2O)_2{}^{2+} + H_2O \rightarrow s\text{- or } a\text{-Cu(Tris)}_2{}^{2+} + Cu(H_2O)_5{}^{2+}; \quad \Delta G_{(11,aq)} \approx -55 \text{ kJ mol}^{-1}$$

At the B3LYP/LB level, the exergonicity is less, –17 kJ mol^{-1}. The anomalously high computed stability of the Cu(Tris)$_2{}^{2+}$ isomers relative to other Cu(Tris)$_n{}^{2+}$ species can be attributed to the attainment of full terdentate binding by both Tris ligands in Cu(Tris)$_2{}^{2+}$ and the high symmetry of these complexes (Fig. 10).

The two isomeric conjugate bases of Cu(Tris)$_2{}^{2+}$ are *s*-Cu(Tris)(TrisH$_{-1}$)$^{+}$ and *a*-Cu(Tris)(TrisH$_{-1}$)$^{+}$ (Fig. 10). The calculated acidity constants, pK_a = 15 and pK_a = 16 (12 and 13 at the B3LYP level), respectively, are high because of the exceptional stabilities of *s*- and *a*-Cu(Tris)$_2{}^{2+}$. The influence of the positively charged metal would normally lower

Can. J. Chem. Downloaded from www.nrcresearchpress.com by South China Agricultural University on 09/19/12
For personal use only.

Fig. 10. The most stable computed structures for aqueous Cu^{2+}–Tris complexes.

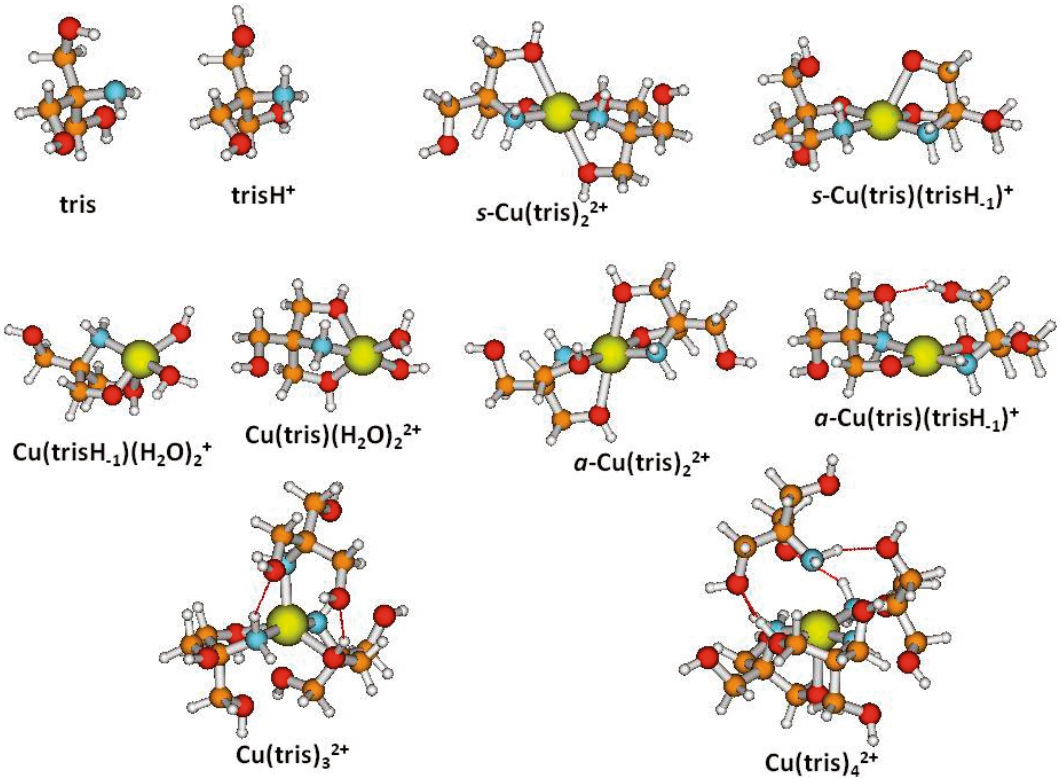

the pK_a of one of the attached OH groups to below that of an alcohol (p$K_a \approx 16$). The equation for the direct formation of either *s*-Cu(Tris)(TrisH$_{-1}$)$^+$ or *a*-Cu(Tris)(TrisH$_{-1}$)$^+$ from aqueous Cu^{2+} and Tris (Table 3) bypasses the anomalously stabilized parents and predicts that spontaneous ionization should take place with an effective p$K_a \approx 4$. In a similar vein, reaction of aqueous Cu^{2+} with three Tris to yield *s*- or *a*-Cu(Tris)(TrisH$_{-1}$)$^+$ and TrisH$^+$ is exergonic by 32 kJ mol^{-1} (by 48 kJ mol^{-1} at the B3LYP level of theory). The attachment of all three Tris to the copper, yielding $Cu(Tris)_3^{2+}$, is only weakly exergonic ($\Delta G_{(aq)} = -7$ kJ mol^{-1}) at the MP2/LB level (Table 3), but endergonic at the B3LYP/LB level, $\Delta G_{(aq)} = 41$ kJ mol^{-1} (Supplementary data Table S3). These results suggest that Cu^{2+}(aq) can consume 3 equiv of Tris to form the singly deprotonated complexes (*s*-Cu(Tris)(TrisH$_{-1}$)$^+$ and *a*-Cu(Tris)(TrisH$_{-1}$)$^+$) and a protonated Tris, in accordance with the experimental observations as interpreted above.

The most stable $Cu(Tris)_4^{2+}$ complex, optimized in the gaseous phase, is shown in Fig. 10. The fourth Tris is is only weakly bound to the Cu^{2+} and is held in place by a network of hydrogen bonds which would not persist in aqueous solution. The $Cu(Tris)_4^{2+}$ complex was found to be 33 kJ mol^{-1} higher in energy than $Cu(H_2O)_5^{2+}$ + 4 Tris. At the B3LYP level, the endergonicity is much greater, 163 kJ mol^{-1}. One must conclude that the formation of either $Cu(Tris)_3^{2+}$ or $Cu(Tris)_4^{2+}$ in water is very unlikely.

As for the interactions of $Cu\mathbf{L}^{2+}$ with Tris, we considered more than a dozen plausible structures and found one complex of the form $Cu\mathbf{L}(Tris)^{2+}$ (Fig. 9) that is weakly bound at the MP2/LB level ($\Delta G_{12} = -7$ kJ mol^{-1}), but unbound at the B3LYP/LB level ($\Delta G_{12} = 22$ kJ mol^{-1}). A second complex, $Cu\mathbf{L}'(Tris)^{2+}$, from which **L** is partially dissociated (Fig. 9), is predicted not to be bound ($\Delta G_{12} = 39$ kJ mol^{-1}). Thus, the calculations suggest that, in a 1:1:1 mixture of $Cu_{(aq)}^{2+}$, **L**, and Tris, the ternary complex, $Cu\mathbf{L}(Tris)^{2+}$ (Fig. 9) should be dominant.

[12] $$Cu\mathbf{L}(H_2O)_2^{2+} + Tris \rightarrow Cu\mathbf{L}(Tris)^{2+} + 2H_2O; \quad \Delta G_{12} = -7 \text{ kJ mol}^{-1}$$

Equations [13]–[16] examine the possible reactions of **L** with copper–Tris complexes:

[13] $$Cu(Tris)(H_2O)_2^{2+} + \mathbf{L} \rightarrow Cu\mathbf{L}(Tris)^{2+} + 2H_2O; \quad \Delta G_{13} = -36 \text{ kJ mol}^{-1}$$

[14] $$a\text{Cu(Tris)}_2^{2+} + \mathbf{L} \rightarrow Cu\mathbf{L}(Tris)^{2+} + Tris; \quad \Delta G_{14} = 27 \text{ kJ mol}^{-1}$$

[15] $$a\text{Cu(Tris)(TrisH}_{-1})^+ + \mathbf{L} + H^+ \rightarrow Cu\mathbf{L}(Tris)^{2+} + Tris; \quad \Delta G_{15} = -57 \text{ kJ mol}^{-1} \text{ (pH = 7)}$$

[16] $$Cu(Tris)_3^{2+} + \mathbf{L} \rightarrow Cu\mathbf{L}(Tris)^{2+} + 2Tris; \quad \Delta G_{16} = -37 \text{ kJ mol}^{-1}$$

These results indicate that **L** will form a ternary complex with any of the preformed Cu^{2+}–Tris complexes. The possible exception is with *a*- (or *s*-) $CuTris)_2^{2+}$ (eq. [14]).

Can. J. Chem. Downloaded from www.nrcresearchpress.com by South China Agricultural University on 09/19/12
For personal use only.

Alternatively, eqs. [17]–[20] examine the probability of reaction of a preformed Cu**L** complex with Tris:

[17] $$Cu\mathbf{L}(H_2O)_2^{2+} + Tris + H_2O \rightarrow Cu(Tris)(H_2O)_2^{2+} + \mathbf{L}; \quad \Delta G_{17} = 29 \text{ kJ mol}^{-1}$$

[18] $$Cu\mathbf{L}(H_2O)_2^{2+} + 2Tris \rightarrow a\text{-}Cu(Tris)_2^{2+} + \mathbf{L} + H_2O; \quad \Delta G_{18} = -34 \text{ kJ mol}^{-1}$$

Alternatively, one may apply eq. [19] to bypass $Cu(Tris)_2^{2+}$:

[19] $$Cu\mathbf{L}(H_2O)_2^{2+} + 3Tris \rightarrow a\text{-}Cu(Tris)(TrisH_{-1})^{+} + \mathbf{L} + H_2O + TrisH^{+}; \quad \Delta G_{19} = 0 \text{ kJ mol}^{-1}$$

[20] $$Cu\mathbf{L}(H_2O)_2^{2+} + 3Tris \rightarrow Cu(Tris)_3^{2+} + \mathbf{L} + H_2O; \quad \Delta G_{20} = 30 \text{ kJ mol}^{-1}$$

Equations [12] and [17] indicate that stoichiometric or substoichiometric amounts of Tris relative to $Cu\mathbf{L}^{2+}$ will result in the addition of Tris to $Cu\mathbf{L}^{2+}$ to form a 1:1:1 complex, rather than a displacement of **L** from the copper ion. Reaction 18 shows that **L** can be displaced by excess Tris to yield the bis(Tris) adduct of copper. Formation of the singly deprotonated form may also be possible, since reaction 19 is isoergonic. The formation of the tris(Tris) adduct, $Cu(Tris)_3^{2+}$, under these conditions is not likely by eq. [20].

The simulated TD–B3LYP/6–311+G(d,p) spectra in the visible region (350–800 nm) of the dominant species are collected in Fig. 11. The spectra are displayed as a superposition of Gaussian line shapes with half-width-at-half-height = 0.2 eV. In general, up to six low oscillatory strength transitions are predicted to fall in this region. The spectrum of $Cu\mathbf{L}(H_2O)_2^{2+}$ is relatively intense in the range 500–800 nm because of a grouping of four low-intensity transitions near 600 nm. It is of interest that none of the other doubly charged complexes is predicted to have appreciable intensity in this range. The 1:1:1 complex $Cu\mathbf{L}(Tris)^{2+}$ has a relatively strong transition at 870 nm. The highly symmetrical bis(Tris) complex (a-$Cu(Tris)_2^{2+}$) has no allowed transitions in this spectral range, and the isomeric s-$Cu(Tris)_2^{2+}$ has only weak absorbances near 600 nm and at wavelengths longer than 800 nm. The most intense spectrum, that of a-$Cu(Tris)(TrisH_{-1})^{+}$, is a superposition of two stronger transitions near 550 nm and 600 nm. The stereoisomeric deprotonated form, s-$Cu(Tris)(TrisH_{-1})^{+}$, has lower intensity in this spectral region.

Discussion

Consideration of Figs. 2–4 and 6–8, together with perturbation of the pH of Tris buffer solutions, shows that Cu^{2+} and **L** form a stable 1:1 complex in solution, but that addition of a Tris buffer to give a nominal pH of 7.2 results in displacement of **L** from $Cu\mathbf{L}^{2+}$ with formation of Cu^{2+}–Tris complexes, predominantly $Cu(Tris)(TrisH_{-1})^{+}$ when Tris base is in large excess over Cu, with about twice the molar absorbance of $\{Cu^{2+},\mathbf{L}\}$(aq) in the 235–260 nm region. When the molar concentration of Tris base is comparable to or less than that of $\{Cu^{2+},\mathbf{L}\}$, the formation of a ternary Cu^{2+}–**L**–Tris complex is indicated on the basis of computer modeling and consideration of Figs. 7 and 8, but the important result is that the presence of excess Tris seriously affects the measurement of the stability constant $K_{Cu\mathbf{L}}$ of aqueous $Cu\mathbf{L}^{2+}$ by scavenging free Cu^{2+}(aq), therefore forcing eq. [7] to the right.

In the discussion that follows, the species adopted to model $Cu\mathbf{L}^{2+}$(aq) is the five-coordinate structure with terdentate **L**, $Cu\mathbf{L}(H_2O)_2^{2+}$ (Fig. 9). A ternary complex, $Cu\mathbf{L}(Tris)^{2+}$ (Fig. 9), is predicted to be weakly stable. Attempts to model $Cu\mathbf{L}^{2+}$ complexes containing more than one Tris ligand, or involving deprotonation of the coordinated Tris to give $Cu\mathbf{L}(TrisH_{-1})^{+}$, failed to yield structures that were stable in water at pH 7.

The formation of complexes between Cu^{2+}(aq) itself and Tris has been widely studied,[18–24] but the existence of $Cu(Tris)_n^{2+}$ with $n > 2$ is not universally recognized and there is no definitive set of stability constants for Cu^{2+}–Tris species.[17] Our computer modeling accommodates two exceptionally stable species with $n = 2$ (Fig. 10) differing by the orientation of the two coordinated amino groups, with slight preference for the anti form over the syn form. A structure for $n = 3$, $Cu(Tris)_3^{2+}$, is marginally stable with respect to complete dissociation into Cu^{2+}(aq) and 3 Tris, but is unstable relative to the two bis(Tris) species. Modeling of a gaseous-phase complex with four Tris, $Cu(Tris)_4^{2+}$ (Fig. 10), revealed that there is not enough room to coordinate all four Tris to the copper. There is the additional complication that one or more Tris ligands bound to Cu^{2+} may be deprotonated in the pH range of our experiments (6.4–7.2).[20]

Although the potentiometric measurements of Bai and Martell[20] were clearly made with expertise and care over a wide range of pH, it is possible that too many species (seven) were invoked to reduce the data to a set of stability constants, especially since these constants could not have been independent of each other. Bologni et al.,[22] in a reanalysis of all the available data including their own, found the data best fit models in which neither $Cu(Tris)_2^{2+}$ nor $Cu(Tris)_4^{2+}$ were present but $Cu(Tris)(TrisH_{-1})^{+}$ was important — in other words, $Cu(Tris)_2^{2+}$ was not present in significant amounts in solutions of the pH range studied, despite the prediction of our calculations that its two isomers should be the most stable of all Cu^{2+}–Tris complexes, because it is converted to $Cu(Tris)(TrisH_{-1})^{+}$. Indeed, solid Cu^{2+}–Tris complexes isolated from solution invariably contain bidentate $TrisH_{-1}^{-}$,[23–28] with Tris, if present, in terdentate coordination. In fact, our calculations indicate that the 1:1 Cu–Tris complex is only weakly stable and will disproportionate to the 1:2 complexes. There is no definitive evidence for the independent existence of the 1:1 complex. As the spectra of Fig. 6 appear to be of a single species, with apparent ε rapidly approaching a limit as the Tris concentration increases, and whereas buffer pH data perturbations indicate complexation or protonation of up to three Tris per Cu^{2+}, that species may be taken to be $Cu(Tris)(TrisH_{-1})^{+}$, presumably with terdentate Tris and bidentate $TrisH_{-1}$ as in the solid-state structure reported by Kotila.[24] We note, however, that the Cu^{2+} complexes of neutral Tris, s- and a-$Cu(Tris)_2^{2+}$, are predicted to have very low absorbances in the visible region and therefore may have gone undetected spectroscopically at

Can. J. Chem. Downloaded from www.nrcresearchpress.com by South China Agricultural University on 09/19/12
For personal use only.

Fig. 11. Simulated spectra in the visible region of complexes of Cu^{2+}, **L**, and Tris. The vertical axis is the extinction coefficient (ε) and the horizontal axis is the wavelength in nm. Cu**L**$(H_2O)_2^{2+}$ (black line), *a*-Cu$(Tris)_2^{2+}$ (red line), *s*-Cu$(Tris)_2^{2+}$ (green line), Cu(Tris)$(TrisH_{-1})^+$ (broken red line), *s*-Cu(Tris)$(TrisH_{-1})^+$ (broken green line), and Cu**L**$(Tris)^{2+}$ (blue line).

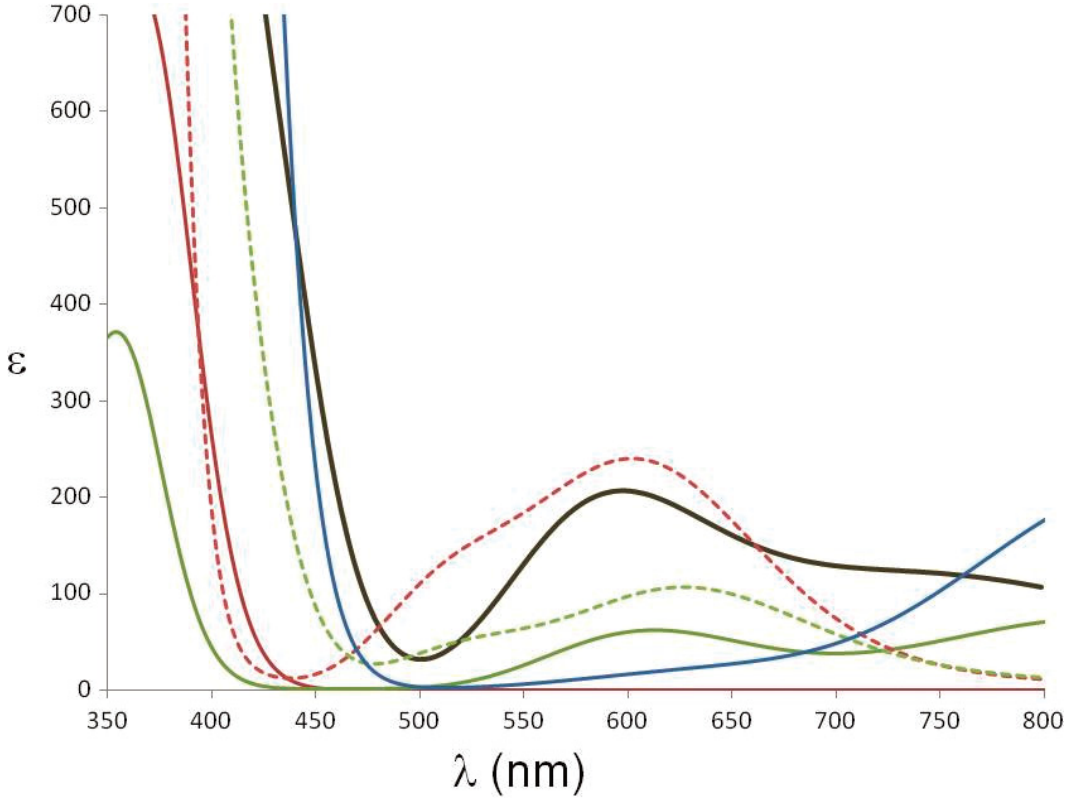

low pH, hence the assertion by Bai and Martell that "Before addition of base, little complex formation takes place".[20] The principal absorbing species is predicted to be *a*-Cu(Tris)$(TrisH_{-1})^+$ (Figs. 10 and 11).

In view of the interference of Tris in the determination of the stability constant K_{CuL} for Cu$\mathbf{L}^{2+}$, this quantity was measured in plain water, giving 3.8×10^5 L mol^{-1} at 25 °C. The pH of the unbuffered solution was 5.7, governed by the slight acid dissociation of an aqua ligand in Cu**L**$(H_2O)_2^{2+}$ or adventitious CO_2 or both, and is in the range in which form **I** Aβ–Cu^{2+} complexation is dominant — thus, in our measurements Cu$\mathbf{L}^{2+}$ is a proxy for form **I** Aβ–Cu^{2+} interactions. The measured value of K_{CuL} is close to the lower limit of the range of stability constants tabulated by Hatcher et al.[14] for Aβ–Cu^{2+}, which is as expected, since **L** represents only a fragment of the Aβ molecule and has fewer potential coordination sites.

Faller[4] makes the interesting observation that, if $K_{CuAβ}$ values are indeed around 10^9–10^{10} L mol^{-1} and the rate constant k_{on} for attachment of Cu^{2+} to Aβ is diffusion-controlled ($k_{on} \approx k_{diff} = 8000RT/3\eta = 7.4 \times 10^9$ L mol^{-1} s^{-1} at 25 °C, where η is the viscosity of water), then the rate constant k_{off} for the dissociation of Cu^{2+} from $CuAβ^{2+}$ would be on the order of $k_{on}/K_{CuAβ} \approx 1$ s^{-1}, which is 2–4 orders of magnitude smaller than those obtained from ^{1}H NMR for Cu^{2+} exchange on histidine-containing proteins by Gaggelli et al.[45] By the same reasoning, however, k_{off} for dissociation of Cu^{2+} from Cu$\mathbf{L}^{2+}$ would be $k_{diff}/K_{CuL} = 2.0 \times 10^4$ s^{-1}, which fits well with the results of Gaggelli et al.[45] for Cu^{2+} complexes with other histidine proteins.

L models only the His13–His14 dyad of Aβ. Since Aβ has additional possible Cu^{2+} binding sites at His6, terminal $–NH_2$, and aspartate and carbonyl oxygens,[6,12] it can be expected to compete with buffer bases for Cu^{2+} more effectively than does **L**. Nevertheless, since Cu^{2+}(aq) is quite strongly complexed by almost any base capable of forming a buffer system for near-physiological pH,[46,47] stability constants obtained for Cu^{2+}–Aβ complexes in any buffer solution should be regarded with skepticism. This applies regardless of whether the buffer base forms complexes directly with Cu^{2+}(Aβ) species and indeed to any measurements on chemical or biochemical systems involving reactions of copper(II) in presence of a buffer. In a living organism, it means that even a reliable value of $K_{CuAβ}$ may have limited significance, as potential ligands for Cu^{2+} include proteins and other nitrogen bases, which will be present in abundance.

Supplementary data

Supplementary data are available with the article through the Journal Web site at http://nrcresearchpress.com/doi/suppl/10.1139/v11-101.

Acknowledgements

We thank Dr. P. Baures, University of Tulsa, for his advice on the work-up of the coupling reaction; D. Fox and J. J. Li, Instrumentation Facility, Chemistry Department, University of Calgary, for the measurements of the mass spectra; and the Natural Sciences and Engineering Research Council of

Canada (NSERC) and the Chemistry Department of the University of Calgary for financial assistance.

References

(1) Bush, A. I. *Trends Neurosci.* **2003** *26* (4), 207. doi:10.1016/S0166-2236(03)00067-5.

(2) Raffa, D. F.; Gomez-Balderas, R.; Brunelle, P.; Rickard, G. A.; Rauk, A. *J. Biol. Inorg. Chem.* **2005**, *10* (8), 887. doi:10.1007/s00775-005-0038-9.

(3) Barnham, K. J.; Bush, A. I. *Curr. Opin. Chem. Biol.* **2008**, *12* (2), 222. doi:10.1016/j.cbpa.2008.02.019.

(4) Faller, P. *ChemBioChem* **2009**, *10* (18), 2837. doi:10.1002/cbic.200900321.

(5) Faller, P.; Hureau, C. *Dalton Trans.* **2009** (7), 1080. doi:10.1039/b813398k.

(6) (a) Drew, S. C.; Noble, C. J.; Masters, C. L.; Hanson, G. R.; Barnham, K. J. *J. Am. Chem. Soc.* **2009**, *131* (3), 1195. doi:10.1021/ja808073b; (b) Drew, S. C.; Masters, C. L.; Barnham, K. J. *J. Am. Chem. Soc.* **2009**, *131* (25), 8760. doi:10.1021/ja903669a.

(7) Hung, Y. H.; Bush, A. I.; Cherny, R. A. *J. Biol. Inorg. Chem.* **2010**, *15* (1), 61. doi:10.1007/s00775-009-0600-y.

(8) Lin, C.-J.; Huang, H.-C.; Jiang, Z.-F. *Brain Res. Bull.* **2010**, *82* (5-6), 235. doi:10.1016/j.brainresbull.2010.06.003.

(9) Martell, A. E.; Hancock, R. D. *Metal Complexes in Aqueous Solutions;* Plenum Press: New York, 1996; p 29.

(10) Lu, Y.; Prudent, M.; Qiao, L.; Mendez, M. A.; Girault, H. H. *Metallomics* **2010**, *2* (7), 474. doi:10.1039/c004693k.

(11) Atwood, C. S.; Scarpa, R. C.; Huang, X.; Moir, R. D.; Jones, W. D.; Fairlie, D. P.; Tanzi, R. E.; Bush, A. I. *J. Neurochem.* **2000**, *75* (3), 1219. doi:10.1046/j.1471-4159.2000.0751219.x.

(12) Hong, L.; Carducci, T. M.; Bush, W. D.; Dudzik, C. G.; Millhauser, G. L.; Simon, J. D. *J. Phys. Chem. B* **2010**, *114* (34), 11261. doi:10.1021/jp103272v.

(13) Swaddle, T. W. In *Physical Inorganic Chemistry: Reactions, Processes and Applications;* Bakac, A., Ed.; J. Wiley & Sons: Hoboken, NJ, 2010; p 339.

(14) Hatcher, L. Q.; Hong, L.; Bush, W. D.; Carducci, T.; Simon, J. D. *J. Phys. Chem. B* **2008**, *112* (27), 8160. doi:10.1021/jp710806s.

(15) Sarell, C. J.; Syme, C. D.; Rigby, S. E. J.; Viles, J. H. *Biochemistry* **2009**, *48* (20), 4388. doi:10.1021/bi900254n.

(16) Tõugu, V.; Karafin, A.; Palumaa, P. *J. Neurochem.* **2008**, *104* (5), 1249. doi:10.1111/j.1471-4159.2007.05061.x.

(17) Rózga, M.; Kloniecki, M.; Dadlez, M.; Bal, W. *Chem. Res. Toxicol.* **2010**, *23* (2), 336. doi:10.1021/tx900344n.

(18) Hall, J. L.; Swisher, J. E.; Brannon, D. G.; Liden, T. L. *Inorg. Chem.* **1962**, *1* (2), 409. doi:10.1021/ic50002a043.

(19) Kemula, W.; Brachaczek, W.; Hulanicki, A. In *Symposium: Theory and Structure of Coordination Compounds;* 1964; pp 605–610 (*Chem. Abs.* **1965**, *63*, 68967).

(20) Bai, K. S.; Martell, A. E. *J. Inorg. Nucl. Chem.* **1969**, *31* (6), 1697. doi:10.1016/0022-1902(69)80385-4.

(21) Takahashi, M.; Takano, M.; Asada, K. *J. Biochem.* **1981**, *90*, 87.

(22) Bologni, L.; Sabatini, A.; Vacca, A. *Inorg. Chim. Acta* **1983**, *69* (2), 71. doi:10.1016/S0020-1693(00)83553-7.

(23) Colombo, M. F.; Austrilino, L.; Nascimento, O. R.; Castellano, E. E.; Tabak, M. *Can. J. Chem.* **1987**, *65* (4), 821. doi:10.1139/v87-139.

(24) Kotila, S. *Acta Chem. Scand.* **1994**, *48* (9), 742. doi:10.3891/acta.chem.scand.48-0742.

(25) Kotila, S.; Valkonen, J. *Acta Chem. Scand.* **1994**, *48* (4), 312. doi:10.3891/acta.chem.scand.48-0312.

(26) Kotila, S.; Valkonen, J. *Acta Chem. Scand.* **1994**, *48* (3), 200. doi:10.3891/acta.chem.scand.48-0200.

(27) Kotila, S.; Valkonen, J. *Acta Chem. Scand.* **1993**, *47* (10), 950. doi:10.3891/acta.chem.scand.47-0950.

(28) Kotila, S.; Valkonen, J. *Acta Chem. Scand.* **1993**, *47* (10), 957. doi:10.3891/acta.chem.scand.47-0957.

(29) Baures, P. W.; Kaliyan, K.; Desper, J. *Molecules* **2002**, *7* (11), 813. doi:10.3390/71100813.

(30) Bates, R. G.; Bower, V. E. *Anal. Chem.* **1956**, *28* (8), 1322. doi:10.1021/ac60116a029.

(31) Frisch, M. J.; Trucks, G. W.; Schlegel, H. B.; Scuseria, G. E.; Robb, M. A.; Cheeseman, J. R.; Montgomery, J. A., Jr.; Vreven, T.; Kudin, K. N.; Burant, J. C.; Millam, J. M.; Iyengar, S. S.; Tomasi, J.; Barone, V.; Mennucci, B.; Cossi, M.; Scalmani, G.; Rega, N.; Petersson, G. A.; Nakatsuji, H.; Hada, M.; Ehara, M.; Toyota, K.; Fukuda, R.; Hasegawa, J.; Ishida, M.; Nakajima, T.; Honda, Y.; Kitao, O.; Nakai, H.; Klene, M.; Li, X.; Knox, J. E.; Hratchian, H. P.; Cross, J. B.; Adamo, C.; Jaramillo, J.; Gomperts, R.; Stratmann, R. E.; Yazyev, O.; Austin, A. J.; Cammi, R.; Pomelli, C.; Ochterski, J. W.; Ayala, P. Y.; Morokuma, K.; Voth, G. A.; Salvador, P.; Dannenberg, J. J.; Zakrzewski, V. G.; Dapprich, S.; Daniels, A. D.; Strain, M. C.; Farkas, O.; Malick, D. K.; Rabuck, A. D.; Raghavachari, K.; Foresman, J. B.; Ortiz, J. V.; Cui, Q.; Baboul, A. G.; Clifford, S.; Cioslowski, J.; Stefanov, B. B.; Liu, G.; Liashenko, A.; Piskorz, P.; Komaromi, I.; Martin, R. L.; Fox, D. J.; Keith, T.; Al-Laham, M. A.; Peng, C. Y.; Nanayakkara, A.; Challacombe, M.; Gill, P. M. W.; Johnson, B.; Chen, W.; Wong, M. W.; Gonzalez, C.; Pople, J. A. *Gaussian 03, Revision B04;* Gaussian: Pittsburgh, PA, 2003.

(32) Becke, A. D. *J. Phys. Chem.* **1993**, *98* (7), 5648. doi:10.1063/1.464913.

(33) Scott, A. P.; Radom, L. *J. Phys. Chem.* **1996**, *100* (41), 16502. doi:10.1021/jp960976r.

(34) Guthrie, J. P. *J. Phys. Chem. A* **2001**, *105* (37), 8495. doi:10.1021/jp010321c.

(35) Nilsson Lill, S. O. *J. Mol. Graph. Model.* **2010**, *29* (2), 178. doi:10.1016/j.jmgm.2010.06.001.

(36) Schaftenaar, G.; Noordik, J. H. *J. Comput. Aided Mol. Des.* **2000**, *14* (3), 233. doi:10.1023/A:1008163129031.

(37) Stratmann, R. E.; Scuseria, G. E.; Frisch, M. J. *J. Chem. Phys.* **1998**, *109* (19), 8218. doi:10.1063/1.477483.

(38) Bauernschmitt, R.; Ahlrichs, R. *Chem. Phys. Lett.* **1996**, *256* (4–5), 454. doi:10.1016/0009-2614(96)00440-X.

(39) Casida, M. E.; Jamorski, C.; Casida, K. C.; Salahub, D. R. *J. Chem. Phys.* **1998**, *108* (11), 4439. doi:10.1063/1.475855.

(40) Liptak, M. D.; Shields, G. C. *J. Am. Chem. Soc.* **2001**, *123* (30), 7314. doi:10.1021/ja010534f.

(41) Bates, R. G.; Hetzer, H. B. *J. Phys. Chem.* **1961**, *65* (4), 667. doi:10.1021/j100822a017.

(42) Dennington, R.; Keith, T.; Millam, J. *GaussView Version 4;* Semichem Inc.: Shawnee Mission, KS, 2009.

(43) Hill, Z. D.; MacCarthy, P. *J. Chem. Educ.* **1986**, *63* (2), 162. doi:10.1021/ed063p162.

(44) Syme, C. D.; Nadal, R. C.; Rigby, S. E. J.; Viles, J. H. *J. Biol. Chem.* **2004**, *279* (18), 18169. doi:10.1074/jbc.M313572200.

(45) Gaggelli, E.; Kozlowski, H.; Valensin, D.; Valensin, G. *Mol. Biosyst.* **2005**, *1* (1), 79. doi:10.1039/b419413f.

(46) Sillén, L. G.; Martell, A. E. *Stability Constants of Metal-Ion Complexes (Special Publication No. 17);* The Chemical Society: London, 1964.

(47) Sillén, L. G.; Martell, A. E. *Stability Constants of Metal-Ion Complexes (Supplement No. 1; Special Publication No. 25);* The Chemical Society: London, 1971.

Can. J. Chem. Downloaded from www.nrcresearchpress.com by South China Agricultural University on 09/19/12
For personal use only.

Interaction of carbon monoxide with small metal clusters: a DFT, electrochemical, and FTIR study

Brian D. Adams, Robert M. Asmussen, Aicheng Chen, and Robert C. Mawhinney

Can. J. Chem. Downloaded from www.nrcresearchpress.com by South China Agricultural University on 09/19/12
For personal use only.

Abstract: The adsorption of CO molecules onto small metal clusters was studied using density functional theory (DFT) calculations, and experimental electrochemical and attenuated total reflection-Fourier transform infrared spectroscopic (ATR-FTIR) techniques were used to examine CO adsorbed onto nanostructures of similar composition. The adsorption strengths and CO vibrational stretching frequencies were calculated and analyzed for clusters of the form M–CO for all of the period 4, 5, and 6 d-block transition metals. A direct link between the ν_{CO} and the population of d orbitals of the metal was observed. All possible binding sites for CO on clusters of the form Pd_4–CO, Pd_2Pt_2–CO, and Pd_2Au_2–CO were determined and the corresponding adsorption energies and CO stretching frequencies were examined. Pure Pd and bimetallic PdPt and PdAu nanostructures were fabricated and used as catalysts for the adsorption and electrochemical oxidation of CO. The relative quantities of CO molecules adsorbed to surface of the catalysts decrease in the order of PdPt > Pd > PdAu, consistent with our DFT results. The location of ν_{CO} bands of CO adsorbed onto the nanostructured catalysts were determined by means of ATR-FTIR spectroscopy and were found to have values close to that predicted by DFT. This paper shows that DFT calculations on very small metal clusters M_n–CO ($n \leq 4$) can be a simple but effective way of screening catalysts for their adsorbing properties.

Key words: carbon monoxide, nanoparticles, metal clusters, DFT calculations, CO adsorption.

Résumé : On a étudié l'adsorption de molécules de CO sur de petits agrégats métalliques en utilisant des calculs théoriques sur la base de la théorie de la fonctionnelle de la densité. D'un point de vue expérimental, on a utilisé des techniques électrochimiques et de la spectroscopie infrarouge à transformée de Fourier avec réflexion totale atténuée pour étudier l'adsorption du CO sur des nanostructures de compositions semblables. On a calculé et analysé les forces d'adsorption et les fréquences d'élongation vibrationnelles du CO pour des agrégats de la forme M–CO pour tous les éléments de transition des blocs 4, 5 et 6 d. On a observé une relation directe entre la valeur de ν_{CO} et la population des orbitales d du métal. On a déterminé tous les sites de liaison possibles pour le CO sur des agrégats de la forme Pd_4–CO, Pd_2Pt_2–CO et Pd_2Au_2–CO et on a examiné les énergies d'adsorption correspondantes et les fréquences d'élongation du CO. On a préparé les nanostructures de palladium pur ainsi que les structures bimétalliques PdPd et PdAu et elles ont été utilisées pour la réaction d'adsorption et d'oxydation électrochimique du CO. Les quantités relatives de molécules de CO adsorbées sur la surface des catalyseurs diminue dans l'ordre PdPt > Pd > PdAu, en accord avec les résultats des calculs à base de la théorie de la fonctionnelle de la densité (TFD). On a déterminé la position des bandes, ν_{CO}, du CO adsorbé sur les catalyseurs à nanostructures en faisant appel à la spectroscopie infrarouge à transformée de Fourier avec réflexion totale atténuée et on a trouvé que ces valeurs sont proches de celles prédites par les calculs de la TFD. Dans ce travail, on montre que des calculs selon la TFD sur de très petits agrégats métalliques M_n–CO ($n \leq 4$) peuvent s'avérer être une méthode simple et efficace d'évaluer les propriétés absorbantes de catalyseurs.

Mots-clés : monoxyde de carbone, nanoparticules, agrégats métalliques, calcules d'après la théorie de la fonctionnelle de la densité (TFD), adsorption du CO.

[Traduit par la Rédaction]

Introduction

Carbon monoxide adsorption on metallic nanoparticles has been extensively investigated because of its importance in the water–gas shift reaction, in emission control, and in fuel cell reactions.[1] In the case of fuel cells, CO is generated in the process of electrocatalytic oxidation of formic acid and other small organic compounds (often via dissociative chemisorption) and it causes substantial poisoning of the active sites on precious metal catalysts.[2] Likewise, if hydrogen gas is used as a fuel, the presence of CO at trace levels (>10 ppm) as an impurity resulting from the production of H_2 by steam reforming of methane also gives rise to catalyst poisoning and performance degradation.[3]

Received 20 May 2011. Accepted 28 July 2011. Published at www.nrcresearchpress.com/cjc on 1 November 2011.

B.D. Adams, R.M. Asmussen, A. Chen, and R.C. Mawhinney. Department of Chemistry, Lakehead University, Thunder Bay, ON P7B 5E1, Canada.

Corresponding author: Robert C. Mawhinney (robert.mawhinney@lakeheadu.ca).

This article is part of a Special Issue to commemorate the International Year of Chemistry.

Fig. 1. Possible adsorption sites for CO to a metal surface.

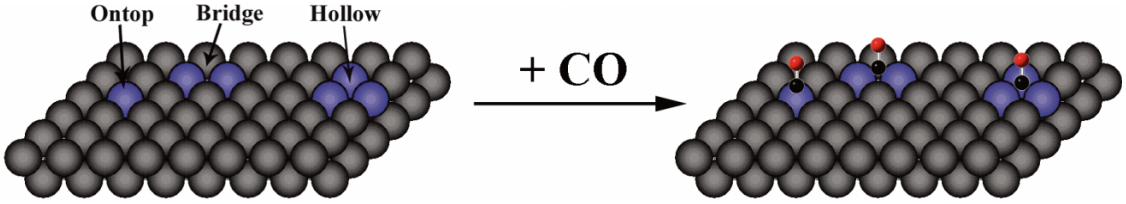

Table 1. The calculated (B3LYP/LANL2DZ for metal atoms; B3LYP/6–31G(d) for C and O) adsorption energies (E_{ads}), structural parameters, and harmonic frequencies for single metal (M) atoms bonded to CO in the lowest energy spin state.

Orbital	Molecule	Spin	E_{ads} (kcal/mol)	Bond length (Å)		M–C–O angle (°)	ν_{MC} (cm^{-1})	ν_{MCO} (cm^{-1})	ν_{CO} (cm^{-1})
				M–C	C–O				
3d	ScCO	Quartet	–17.98	2.105	1.168	180.0	397	260	1968
	TiCO	Quintet	–27.22	2.052	1.161	180.0	394	257	2011
	VCO	Sextet	–21.70	2.001	1.157	180.0	394	248	2031
	CrCO	Quintet	4.64	2.081	1.151	161.6	292	235	1987
	MnCO	Sextet	9.57	2.044	1.157	172.7	342	54	2060
	FeCO	Triplet	–24.76	1.771	1.157	180.0	437	293	2051
	CoCO	Doublet	–22.68	1.703	1.159	180.0	482	335	2025
	NiCO	Singlet	–30.12	1.669	1.160	180.0	597	347	2098
	CuCO	Doublet	–9.05	1.999	1.151	137.2	316	205	2056
	ZnCO	Singlet	1.05	3.866	1.138	117.0	19	48	2209
4d	YCO	Quartet	–17.50	2.231	1.174	180.0	367	282	1918
	ZrCO	Quintet	–36.17	2.152	1.167	180.0	387	289	1970
	NbCO	Sextet	–35.59	2.088	1.160	180.0	407	300	2017
	MoCO	Quintet	–36.11	1.948	1.171	180.0	479	349/ 329[a]	1977
	TcCO	Quartet	–46.10	1.841	1.174	180.0	557	390	1988
	RuCO	Triplet	–50.45	1.827	1.167	180.0	534	364	2031
	RhCO	Doublet	–46.20	1.819	1.161	180.0	508	333	2063
	PdCO	Singlet	–42.97	1.867	1.151	180.0	456	250	2127
	AgCO	Doublet	–1.17	2.517	1.143	127.5	82	187	2130
	CdCO	Singlet	1.12	4.026	1.138	122.7	19	47	2209
5d	LaCO	Quartet	–24.45	2.437	1.167	180.0	306	263	1951
	HfCO	Triplet	–33.72	2.076	1.170	180.0	401	313	1950
	TaCO	Quartet	–29.26	2.028	1.163	180.0	422	322	2002
	WCO	Quintet	–27.10	1.918	1.178	180.0	509	379	1940
	ReCO	Doublet	–15.43	1.818	1.176	180.0	599	439	1994
	OsCO	Triplet	–52.89	1.795	1.168	180.0	618	449	2055
	IrCO	Doublet	–69.30	1.777	1.162	180.0	622	438	2100
	PtCO	Singlet	–67.76	1.781	1.156	180.0	589	402	2132
	AuCO	Doublet	–7.96	2.080	1.148	139.2	330	205	2086
	HgCO	Singlet	1.07	4.061	1.137	140.5	7	45	2212

Note: 1 cal = 4.184 J.

[a]Renner–Teller splitting gave two π-type frequencies.

When metals are combined in an appropriate manner, the chemisorption of CO can be tuned and controlled. As catalyst design becomes more involved, alloying of various compounds becomes an attractive method to control the reaction pathway. To properly design catalysts, it is important to have an understanding of the interaction between the catalyst and the chemisorbed reactant or intermediate species. CO poisoning of alloyed PtRu and PtPb catalysts is diminished compared with pure Pt.[4,5] PtRu is possibly the most widely studied anode catalyst material for direct methanol fuel cells.[6,7] It has been proposed that the enhanced activity of PtRu towards methanol oxidation compared with Pt arises from ruthenium's ability to generate oxygen-containing species on the catalyst surface to easily oxidize the poison CO species.[8,9] In the case of PtPb, CO adsorption is avoided or very weak owing to modification of the catalyst crystal structure. This alters the reaction mechanism for formic acid oxidation, greatly enhancing its performance.[4,10]

In the past few decades, Pd-based materials have been studied rigorously to improve and extend their environmental applications for the elimination of contaminants related to automobile exhaust pipe gases like CO, NO_x, and SO_x[11] and, at one-fifth of the cost, are viewed as the most promising alternative to Pt-based catalysts.[12,13] Pd has been shown to possess superior performance as anodes for the oxidation of formic acid compared with Pt-based catalysts,[14,15] but, despite these promising properties, not nearly as much research has gone into studying them compared with Pt-based materials.

Can. J. Chem. Downloaded from www.nrcresearchpress.com by South China Agricultural University on 09/19/12
For personal use only.

Can. J. Chem. Downloaded from www.nrcresearchpress.com by South China Agricultural University on 09/19/12
For personal use only.

Fig. 2. The calculated metal–carbon bond distance (*a*) and vibrational CO-stretching frequencies (*b*) versus the number of d electrons of the metal (M) for all of the transition metal–carbonyl clusters of the form M–CO. The 3d, 4d, and 5d metals are represented by circles, squares, and triangles, respectively.

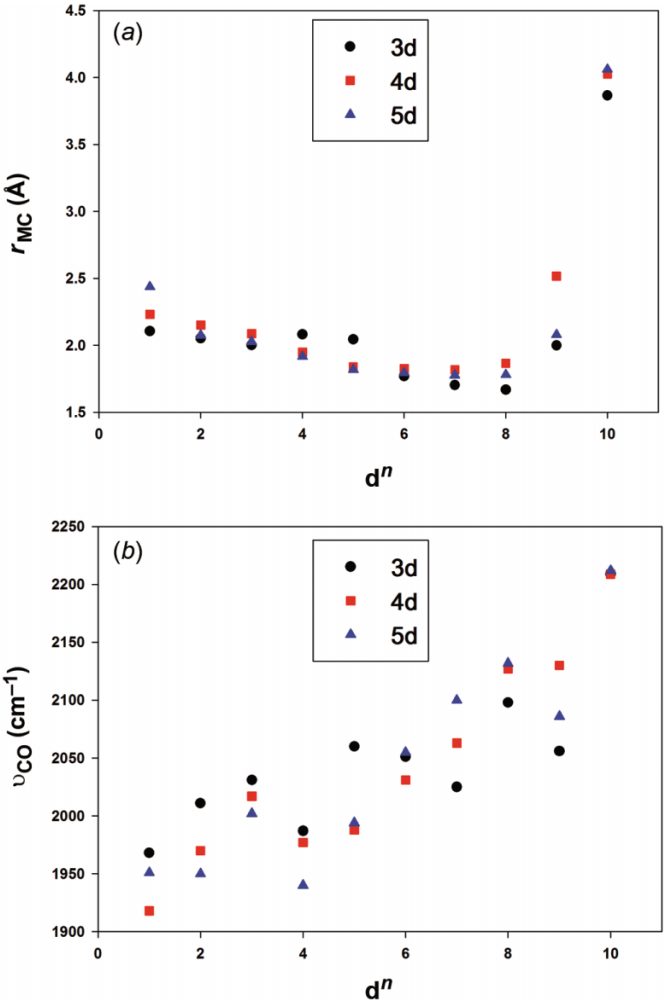

The aim of this paper is to use standard computational techniques to examine the adsorption of CO on small Pd-based metal clusters, with attempts to expand the research involving Pd-based catalytic materials.

In many studies, the adsorption energy of CO on certain transition metals is compared.[11,16–27] Zeinalipour-Yazdi et al.[16] examined several transition-metal M_2–CO and M_4–CO cluster complexes, but, to the best of our knowledge, never before has an extensive comparison been made of the CO adsorption on the entire series of transition metals. This could provide insight to new combinations of metals for catalysts involving CO as a reactant or intermediate. In this study, the CO adsorption energy is first determined for all single-atom transition-metal elements using density functional theory (DFT). Next, CO adsorption energies for Pd_4, Pd_2Au_2, and Pd_2Pt_2 clusters are calculated and compared with results from two experimental techniques: electrochemical oxidation of adsorbed CO on Pd, PdAu, and PdPt nanostructures and C–O stretch frequency analysis of CO-adsorbed nanostructures by in situ attenuated total reflection - Fourier transform infrared spectroscopy (ATR-FTIR).[10,28]

Experimental methods

Computational methods

There is an ongoing debate regarding the type of model to use for simulations of adsorption on catalytic surfaces. Periodic boundary conditions can be used to reproduce extended surfaces.[29–31] In this method one defines a unit cell that is then used to expand the cell in *x*, *y*, and (or) *z* directions, thus providing the electronic structure for linear, slab (surface), and bulk materials, respectively.[32] Alternatively, a cluster approach, where a discrete number of atoms are used to represent the active site region, has shown considerable promise.[20,21,23,24] The basic premise is that chemisorption and reactivity are local phenomena, primarily affected only by the nearby surface structure.[32–34] Several studies have shown that models based on clusters containing a very small number of atoms can obtain results for local phenomena such as CO stretches and bond distances closer to experiment than slab models for nanosized particles.[11,20,35,36]

In this work, DFT calculations were carried out using the Gaussian 03 software package[37] with the use of the Becke's three-parameter hybrid exchange functional[38] combined with the Lee–Yang–Parr nonlocal correlation functional[39] (B3LYP) and the default integration grid. The LANL2DZ effective core potential basis set[40] was employed for all transition metals and the 6–31G(d) basis set was used for C and O atoms. As shown in the literature,[16,28–30] the use of the LANL2DZ basis set significantly reduces the computational demands with minimal effect on the binding energy of CO. All considered systems were fully optimized and characterized through harmonic frequency analysis.

It is well known that CO can bond to a metal surface in three possible sites (on top, bridging, and hollow) as displayed in Fig. 1. By using a four-atom metal cluster, all of these sites can be examined with minimal computational demands.[16] Various spin multiplicities were examined for the individual metal atoms and the metal–CO (M–CO) clusters. The lowest energy spins were used in calculating the adsorption energies (E_{ads}) according to the following equation:

$$[1] \qquad E_{ads} = E_{cluster-CO} - E_{cluster} - E_{CO}$$

where $E_{cluster-CO}$, $E_{cluster}$, and E_{CO} are the total energies of the metal–carbonyl cluster, the metal cluster, and molecular CO, respectively. From this equation, as the E_{ads} becomes more negative, the adsorption of CO to the metal cluster is favoured because of the stabilization of the M–CO cluster.

Fabrication of Pd, PdAu, and PdPt catalysts

The nanostructured catalysts were fabricated using a hydrothermal-assisted reduction of Pd, Au, and Pt precursors.[41,42] For electrochemical tests, Ti plates were coated with the catalysts. The Ti substrate plates (1.25 cm × 0.80 cm × 0.5 mm) were first degreased in an ultrasonic bath of acetone for 10 min followed by 10 min in pure water (18.2 MΩ cm^{-1}) obtained from a NANOpure Diamond UV ultrapure water purification system. The substrates were then etched in 18% HCl at approximately 85 °C for 30 min. The etched Ti substrates were transferred into Teflon-lined autoclaves and 10 mL of an aqueous mixture of inorganic metal precursors and an excess amount of the reducing agent

Can. J. Chem. Downloaded from www.nrcresearchpress.com by South China Agricultural University on 09/19/12
For personal use only.

Fig. 3. Comparison of our calculated metal (M) – CO adsorption energies (E_{ads}) and those from M_2–CO and M_4–CO cluster models with the experimental values taken from ref. 27 and references therein. The metals compared were Ni, Cu, Ru, Rh, Pd, Ag, Ir, Pt, and Au. Best-fit straight lines are provided for ease of interpretation.

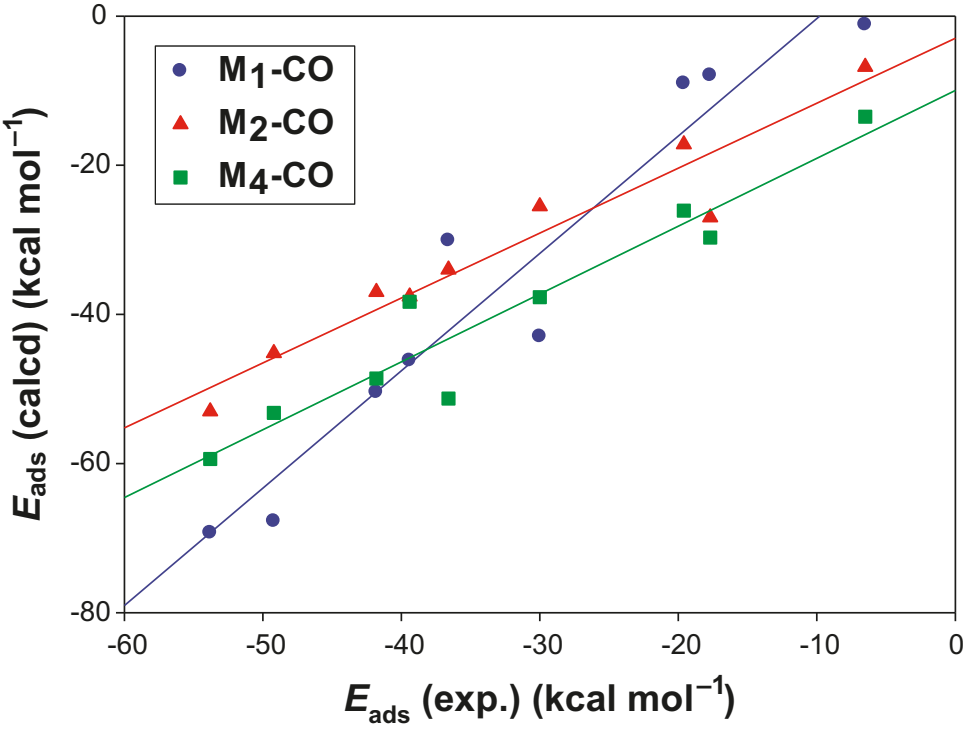

Fig. 4. Optimized structures of (*a*) Pd_4 (triplet), (*b*) Pd_4–CO on top (singlet), (*c*) Pd_4–CO on top (triplet), (*d*) Pd_4–CO bridged (triplet), and (*e*) Pd_4–CO in a hollow position (singlet). Pd, C, and O are shown in green, grey, and red, respectively (as seen in the Web version of this paper).

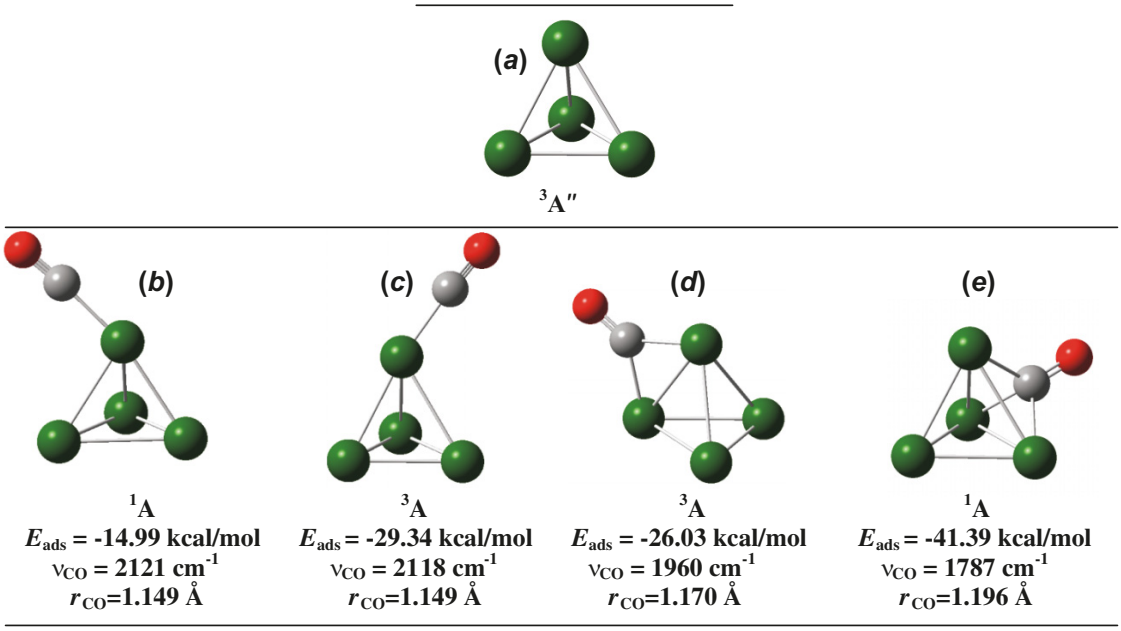

were added. Ammonium formate (Sigma-Aldrich, 99.995%) was used as the reducing agent, and the metal precursors were $PdCl_2$ (Alfa Aesar, 99.9%), $HAuCl_4{\cdot}xH_2O$ (Alfa Aesar, 99.9%), and $H_2PtCl_6{\cdot}6H_2O$ (Alfa Aesar, 99.9%). In all cases, the total amount of inorganic precursor and reducing agent added were kept constant at 5 mmol/L and 1 mol/L, respectively. Pure water was used as the solvent in all cases, with a dilute HCl solution used to aid in the solubility of $PdCl_2$. For the Pd catalyst, only $PdCl_2$ was added to the vessel, whereas for the PdAu and PdPt catalysts, stoichiometric amounts of the $PdCl_2$, $HAuCl_4{\cdot}xH_2O$, and $H_2PtCl_6{\cdot}6H_2O$ precursors were added to obtain the desired composition of Pd–Au and Pd–Pt of 50:50. The autoclaves were sealed and heated at 180 °C for 8 h. After cooling to room temperature, the Ti

Fig. 5. Optimized structures of (*a*) Pd_2Au_2 (singlet), (*b*) Pd_2Au_2–CO on-top Pd (singlet), (*c*) Pd_2Au_2–CO on-top Pd (triplet), (*d*) Pd_2Au_2–CO on-top Pd (triplet, planar), (*e*) Pd_2Au_2–CO on-top Au (singlet), (*f*) Pd_2Au_2–CO on-top Au (triplet), (*g*) Pd_2Au_2–CO bridging PdPd (singlet), and (*h*) Pd_2Au_2–CO bridging PdPd (triplet). Pd, Au, C, and O are shown in green, yellow, grey, and red, respectively (as seen in the Web version of this paper).

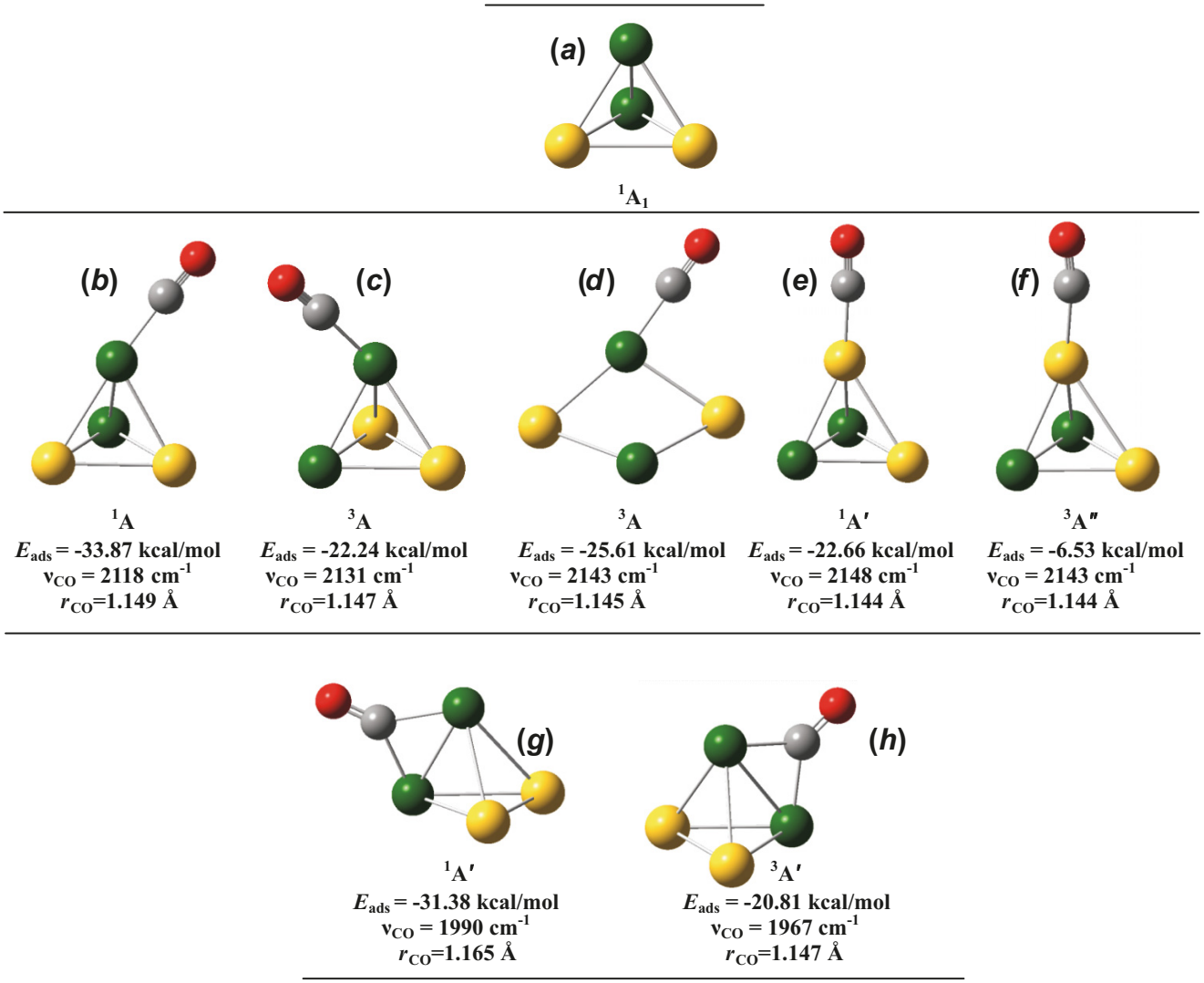

plates coated with the Pd, PdAu, and PdPt films were dried under argon and then rinsed with pure water.

Electrochemical and spectroscopic examination of the Pd, PdAu, and PdPt catalysts

The electrochemical performance of the electrodes towards the oxidation of surface-adsorbed CO was characterized using cyclic voltammetry (CV). For this, a three-electrode cell system and a VoltaLab 80 PGZ402 potentiostat were used. The counter electrode was a Pt wire coil (10 cm^2) that was cleaned before each experiment by flame annealing and quenching with pure water. The reference electrode was a saturated calomel electrode connected to the cell through a salt bridge. The working electrodes used were the prepared Ti/Pd, Ti/PdAu, and Ti/PdPt plates (1 cm^2). The coated Ti plates were annealed at 250 °C for 2 h in a tube furnace under argon to ensure a good surface adhesion of the particles. These plates were then soldered to Ti wire leads for use as working electrodes. The electrolyte for these CV studies was 0.5 mol/L H_2SO_4, and the solution was deaerated with ultrapure argon gas prior to measurements to remove any dissolved oxygen. Argon gas was continually passed over the solution throughout the experimentation. Data acquisition and analysis were performed using VoltMaster 4 software. Carbon monoxide (PRAXAIR, 99.9%) was used for the CO-stripping study. Before scanning the applied potential, the working electrode was held at –0.1 V for 360 s while a stream of pure CO was bubbled into the solution during the first 180 s. Then the solution was purged with pure Ar for the remaining 3 min holding period. Immediately following the electrode pretreatment, two cycles of CV were recorded for each electrode. All measurements were conducted at room temperature (22 ± 2 °C).

All in situ ATR-FTIR experiments were performed using a Nicolet FTIR spectrometer with a liquid N_2-cooled MCT detector. The spectro-electrochemical cell consisted of a Teflon

Can. J. Chem. Downloaded from www.nrcresearchpress.com by South China Agricultural University on 09/19/12
For personal use only.

Fig. 6. Optimized structures of (*a*) Pd_2Pt_2 (triplet), (*b*) Pd_2Pt_2–CO on-top Pd (singlet), (*c*) Pd_2Pt_2–CO on-top Pd (triplet), (*d*) Pd_2Pt_2–CO on-top Pt (singlet), (*e*) Pd_2Pt_2–CO on-top Pt (triplet), (*f*) Pd_2Pt_2–CO bridging PdPd (singlet), (*g*) Pd_2Pt_2–CO bridging PdPd (triplet), (*h*) Pd_2Pt_2–CO bridging PtPt (singlet), (*i*) Pd_2Pt_2–CO bridging PtPt (triplet), (*j*) Pd_2Pt_2–CO bridging PdPt (singlet), (*k*) Pd_2Pt_2–CO bridging PdPt (triplet), (*l*) Pd_2Pt_2–CO in a hollow PdPdPt position (singlet), (*m*) Pd_2Pt_2–CO in a hollow PtPtPd position (singlet),; and (*n*) Pd_2Pt_2–CO in a hollow PtPtPd position (triplet). Pd, Pt, C, and O shown in green, blue, grey, and red, respectively (as seen in the Web version of this paper).

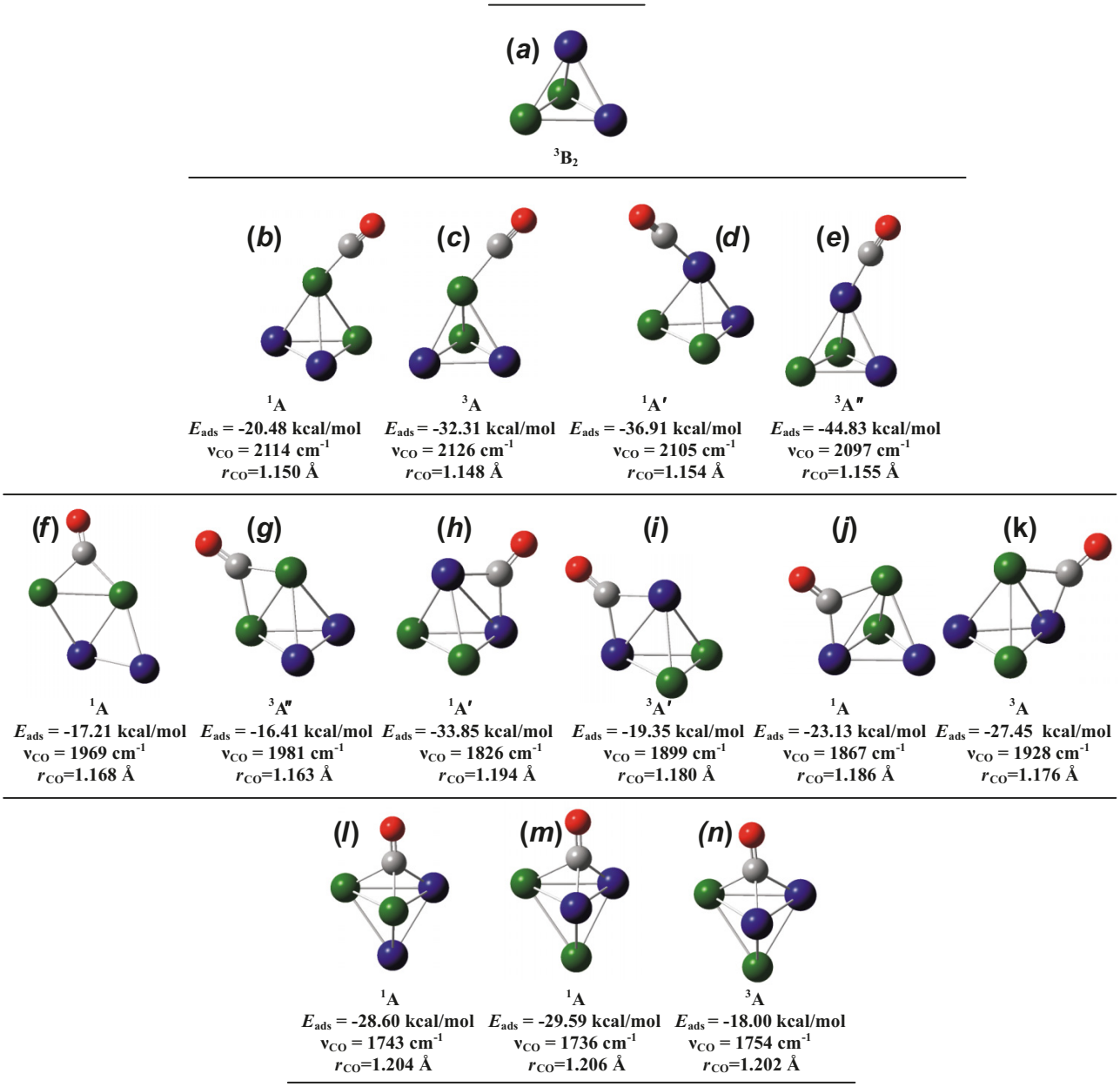

Can. J. Chem. Downloaded from www.nrcresearchpress.com by South China Agricultural University on 09/19/12
For personal use only.

chamber with a ZnSe hemisphere window sealed on the bottom. The synthesized nanoparticles were suspended in pure water with the aid of ultrasonic treatment and then coated onto the ZnSe window. The incidence angle of the IR beam was controlled with a variable angle home-made accessory and was set to 60° for all experiments. All interferograms were acquired at 4 cm^{-1} resolution, and 400 scans were added and averaged. The interferograms were shown in terms of relative change of the electrode reflectivity, which is defined as $\Delta R/R = (R(E_2) - R(E_1))/R(E_1)$, where $R(E_1)$ and $R(E_2)$ are the thin films' reflectivity at potentials E_1 and E_2, respectively. The spectra recorded at E_1 = –0.20 V was used as reference.

Results and discussion

CO adsorption onto single metal atoms

Calculations were run first on the metal atoms and CO in various spin states to determine the lowest energy spin. As expected, CO is most stable in the singlet state and the ground-state spin multiplicity for the metal atoms varies depending on the electron configuration. The energies for all

Can. J. Chem. Downloaded from www.nrcresearchpress.com by South China Agricultural University on 09/19/12
For personal use only.

Fig. 7. Scanning electron microscopic (SEM) images of the catalyst surfaces at 10000× magnification: (*a*) Pd, (*b*) PdAu, and (*c*) PdPt.

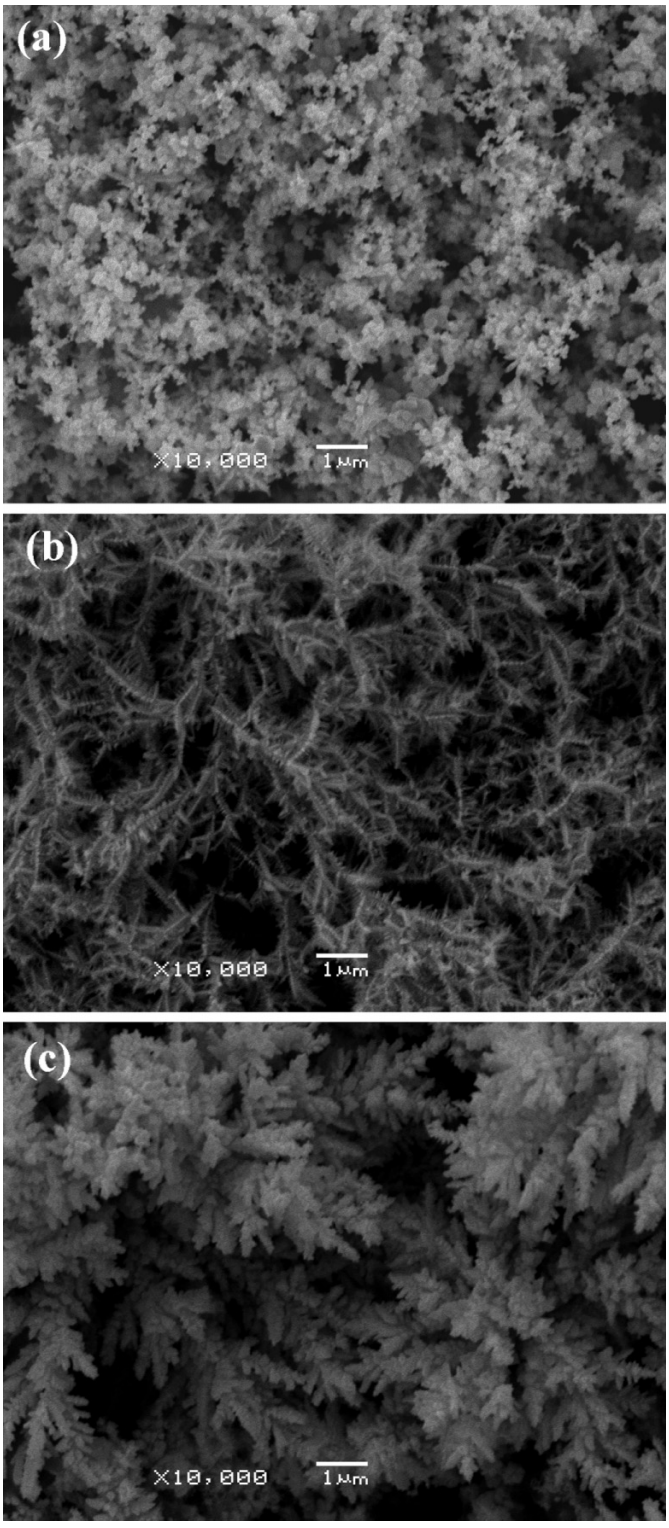

metal atoms in the different spin states can be found in the Supplementary data. For the M–CO molecules, an initial linear structure ($C_{\infty v}$) was considered and fully optimized, again assessing various spin states. The E_{ads} for the most stable species were calculated as described in the Experimental methods section and are reported in Table 1 along with the corresponding structural parameters and harmonic frequencies. It can be seen that all of the metal carbonyl molecules are linear, except those involving group 11 and 12 metals and Cr–CO and Mn–CO. In general, the smallest E_{ads} are for those that do not possess a linear geometry. As expected, the platinum group metals have the largest CO E_{ads} and, consistent with a previous DFT study that examined several transition metals,[16] iridium exhibits the largest E_{ads} followed closely by platinum. With the respect to the whole series of transition metals, CO-stretching frequencies range from 1918 (Y–CO) to 2212 cm^{-1} (Hg–CO).

There does not seem to be a good linear relationship between the E_{ads} and either the bond lengths or the vibrational frequencies over the complete set of transition metals.[16,43] On the other hand, a link between the accepted number of d electrons (d^n) on the metal and the M–C bond distances as well as the CO-stretching frequencies can be seen in Figs. 2*a* and 2*b*. The principal quantum number has little effect on either the CO-stretching frequencies or the M–C bond distances. The classical model for CO chemisorbed onto metals is the Blyholder model,[44] where there is a combination of σ donation from the carbon atom's highest occupied molecular orbital (HOMO) to the metal's lowest unoccupied molecular orbital (LUMO) along with π back-donation from the metal HOMO to the antibonding 2π* LUMO orbital of CO. This simple model does not fit well with our calculations. Instead, we suggest that the bonding of CO to metal atoms is more complex and arises primarily from metal π to CO 2π* with some repulsive σ interaction, as proposed by Bagus et al.[45] and observed by others.[46,47] As the d orbitals become more filled at a given quantum number, the M–C bond distance decreases slightly for d^1 to d^7 metals and then increases from d^7 to d^{10} (Fig. 2*a*). From d^1 to d^8, the metals can accept donation from the 5σ orbital (HOMO) of CO and there is an increasing amount of donation from the metal's HOMO to the CO's LUMO. This binding combination strengthens the M–C bond and obeys the Blyholder model. However, when the d orbitals of the metals become full, from d^7 to d^{10}, σ repulsion occurs and in turn less π back-donation, causing a very sharp increase in the M–C bond distance. Similarly, ν_{CO} increases with an increasing number of d electrons of the metals (Fig. 2*b*) owing to the effect of progressively less σ donation (and π back-donation) from the CO HOMO to the metal LUMO. This causes a weaker M–C bond, and subsequently, a stronger C–O bond, as evidenced by the ν_{CO} increase with filling of the d orbitals. There is little, if any, bonding interaction between CO and metals with filled d orbitals (d^{10} metals). The calculated ν_{CO} of free CO is 2209 cm^{-1}, which is the same as that of Zn–CO and Cd–CO, and is even slightly lower than that of Hg–CO (2212 cm^{-1}).

Shown in Fig. 3 is a comparison of our calculated M_1–CO E_{ads} with the experimental values.[17] For comparisons sake, this figure also includes the results for larger M_2–CO and M_4–CO clusters as reported by Zeinalipour-Yazdi et al.[16] It can be seen that while our work varies slightly from the experimental values, the same general trend is observed for the larger cluster models. Although CO bonded to single metal atoms does not give accurate E_{ads}, this approach can be used to compare M–CO bond strength for different elements to screen their viability as catalyst components.

Can. J. Chem. Downloaded from www.nrcresearchpress.com by South China Agricultural University on 09/19/12
For personal use only.

Table 2. Inductively coupled plasma atomic emission spectroscopy (ICP-AES) results for the final concentration of the solution after hydrothermal reduction of metal salts.

Input composition (at %)	Initial concentration[a] (ppm, mmol/L)	Final concentration[b] (ppm, mmol/L)	Actual composition[c] (at %)
Pd (100%)	Pd, 532.10, 5	Pd. 0.0550, 5.17×10^{-4}	Pd (100%)
Pd–Au (50%)	Pd, 266.05, 2.5	Pd, 0.1939, 1.82×10^{-3}	Pd–Au (50%)
	Au, 492.43, 2.5	Au, 0.0136, 6.90×10^{-5}	
Pd–Pt (50%)	Pd, 266.05, 2.5	Pd, 0.0298, 2.80×10^{-4}	Pd–Pt (50%)
	Pt, 487.70, 2.5	Pt, 0.0178, 9.12×10^{-5}	

[a]The concentration of precursors added to the reaction vessel prior to the reductions.

[b]Concentrations of metals remaining in solution after the hydrothermal reductions determined by ICP-AES.

[c]Actual composition of the nanostructures determined by subtracting the final solution concentrations from the initial concentrations.

To examine the effect of CO adsorption on combined metals ("alloys"), Pd was chosen as a base because it is a commonly used catalyst for CO oxidation and fuel cell applications. We then chose two metals to combine with Pd to assess the preferential binding sites of CO: one with a stronger affinity for CO (Pt; E_{ads} = –67.76 kcal/mol; 1 cal = 4.184 J)) and one with a weaker affinity for CO (Au; E_{ads} = –7.96 kcal/mol). These two metals were chosen because they are possibly the most widely studied catalysts on the nanoscale.[4,18,20,48–50]

CO adsorption onto a Pd_4 cluster

It is well known that CO can bind to a Pd surface via the carbon in three ways: on top of a single Pd atom, bridged between two Pd atoms, or in a hollow threefold position (see Fig. 1). Each of these binding sites, along with a Pd_4 metal cluster, were examined in the singlet and triplet spin states with the results given in Fig. 4. The known ground-state triplet spin for the metal cluster was reproduced (Fig. 4*a*).[11,51] With CO on top of a Pd atom, minima were obtained in both singlet (Fig. 4*b*) and triplet (Fig. 4*c*) states. With CO bridging two Pd atoms, only the triplet-state minimum was obtained, whereas the hollow site binding motif was located only on the singlet surface (Fig. 4*e*). The hollow site attachment has the strongest CO adsorption strength, followed by the triplet state on-top minimum, bridged site attachment, and lastly, the singlet state on-top minimum.

The E_{ads} for the two on-top minima are quite different (–14.99 kcal/mol for the singlet state vs –29.34 kcal/mol for the triplet state), yet the CO-stretching frequencies are the same (2121 and 2118 cm^{-1}, respectively). Additionally, the CO adsorption strength for the on-top sites differs from that for CO bound to a single Pd (Table 1), but the CO-stretching frequencies compare favourably. The CO stretch is a local phenomenon[35] and highly dependent on the binding motif. For example, the CO-stretching frequency for all on-top sites is ~2100 cm^{-1}, whereas for a bridging motif it is around 1900 cm^{-1}, and when bound to a hollow site the CO-stretching frequency is just under 1800 cm^{-1}. This general finding has been used extensively to identify experimental binding motifs. The reason for the variation in CO-stretching frequencies is the change in CO distance. The value of r_{CO} is 1.149–1.151 Å when CO is coordinated to one metal atom, it increases to 1.170 Å when coordinated to two metal atoms, and it elongates further (1.196 Å) when coordinated to three metal atoms. As will be evident in the following, this is an observation common to all metal clusters investigated in this study.

CO adsorption onto a Pd_2Au_2 cluster

As seen in Table 1, Au (E_{ads} = –7.96 kcal/mol) has a much lower affinity for CO than Pd (E_{ads} = –42.97 kcal/mol). To examine the effect of a metal with weaker adsorption strength for CO than Pd, a Pd_2Au_2 cluster was modeled. Our results for the binary metal complex (Fig. 5*a*) indicate that the ground state is a singlet with C_{2v} symmetry, consistent with the results of Zanti and Peeters.[52] As far as we know, this is the first study on the adsorption of CO on a Pd_2Au_2 cluster.

A total of seven adsorption sites were considered on each the singlet and triplet surfaces: CO on-top Pd, CO on-top Au, CO bridging Pd_2, CO bridging Au_2, CO bridging PdAu, CO in a Pd_2Au hollow site, and CO in a $PdAu_2$ hollow site. Of the 14 possible structures, only 7 were located (Figs. 5*b*–5*h*). The addition of Au to Pd completely hindered CO adsorption to any hollow sites and no bridging structures involving Au were located.

Unlike Pd_4–CO, the highest binding affinity in Pd_2Au_2–CO is for the singlet surface on-top Pd site (Fig. 5*b*), followed by the singlet surface Pd_2-bridged species (Fig. 5*g*), and then the triplet surface on-top Pd structure (Fig. 5*d*). All other minima have E_{ads} under 24 kcal/mol. Thus, alloying Pd with Au changes the order of site preference and reduces the overall binding affinity. However, the CO-stretching frequency (2118–2148 cm^{-1}; 1967–1990 cm^{-1}) again depends on the CO distance (1.144–1.149 Å; 1.165–1.168 Å), which is dictated by the degree of metal coordination. This can be verified by FTIR spectroscopic studies.

CO adsorption onto a Pd_2Pt_2 cluster

To examine the effect of a metal with a greater adsorption strength for CO than Pd, a Pd_2Pt_2 cluster was modeled. The optimized molecular structure of the Pd_2Pt_2 cluster is displayed in Fig. 6*a*. It has a triplet ground state and like Pd_2Au_2 is of C_{2v} symmetry. Again, all seven binding motifs were explored on each singlet and triplet surface. This time only the triplet surface Pd_2Pt hollow site was not obtained (Figs. 6*b*–6*n*). Interestingly, for CO bridging two Pd atoms, the singlet state possesses a more energetically favourable planar structure (Fig. 6*f*) that is unique compared with all other tetrahedral-like cluster geometries. The strongest adsorption site for CO is on top of a Pt atom, with an E_{ads} of

Can. J. Chem. Downloaded from www.nrcresearchpress.com by South China Agricultural University on 09/19/12
For personal use only.

Fig. 8. Cyclic voltammograms (CV) of CO stripping on the prepared electrodes: (*a*) Pd, (*b*) Pd–Au, and (*c*) Pd–Pt. Two cycles of the CV were recorded for each electrode in 0.5 mol/L H_2SO_4 at a potential scan rate of 20 mV/s. The first sweep cycle is shown with a solid line and the second with a dotted line.

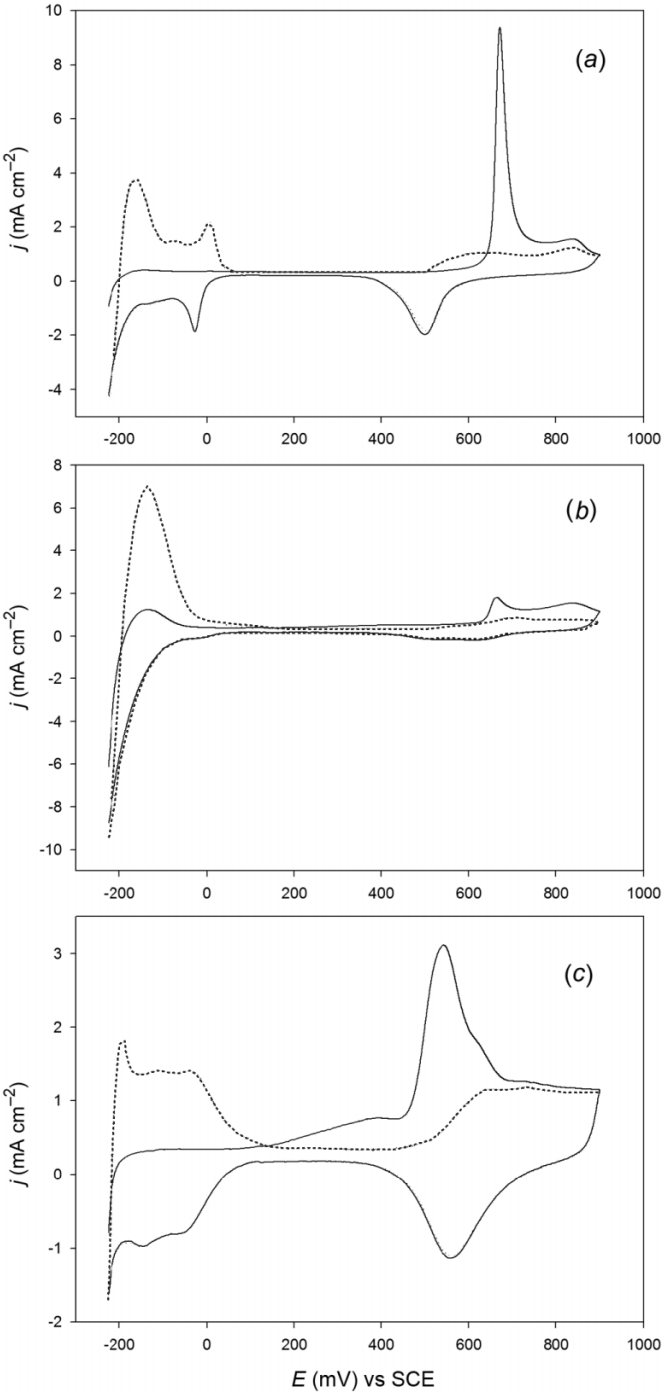

–36.91 kcal/mol in the singlet state and –44.83 kcal/mol in the triplet state. The next favoured site is CO bridging two Pt atoms in the singlet state (E_{ads}= –33.85 kcal/mol). The same binding motif in the triplet state has a much weaker CO interaction (E_{ads} = –19.35 kcal/mol). The large differences in E_{ads} between spin states emphasizes the importance of considering various spin multiplicities when performing DFT calculations on these small metal clusters to find the lowest energy configurations. Other sites, such as on top a Pd atom and a $PdPt_2$ hollow still have large E_{ads}, indicating strong interaction between CO and these sites as well.

With such a large array of structures, the previous observation that the CO-stretching frequency depends on the CO distance, which is dictated by the degree of metal coordination, is confirmed. All on-top binding minima have a ν_{CO} range between 2097 and 2126 cm^{-1} and a r_{CO} range between 1.148 and 1.155 Å, whereas bridging structures have a ν_{CO} range of 1826–1981 cm^{-1} corresponding to a r_{CO} range of 1.163–1.194 Å and hollow sites have a ν_{CO} range between 1735 and 1754 cm^{-1} and a r_{CO} range between 1.202 and 1.206 Å. Again, this demonstrates that IR spectroscopy is a valuable tool for ascertaining binding motifs.

Electrochemical oxidation of surface-adsorbed CO on Pd, PdAu, and PdPt

Scanning electron microscopic (SEM) images of the prepared nanostructures of Pd, PdPt, and PdAu are displayed in Fig. 7. It can be seen that the pure Pd exhibits nanoporous morphology with randomized small particles, which vary in size from approximately 50 to 200 nm. The PdAu and PdPt both possess a nanodendritic morphology. This is consistent with our previous work on nanodendrites and is attributed to a "foreign-particle induced mechanism" for intermetallics fabricated with the hydrothermal method used here.[10,41,42] The PdAu nanodendrites are much smaller in size, with thin trunks of approximately 1 μm in length and side branches of about 200 nm long and 50 nm wide. The PdPt nanodendrites are broader in nature and appear to be built up of particles approximately 60 nm in diameter. Although it is not realistic to compare nanostructures of these sizes with the four-atom clusters examined using DFT, it allows us to verify the general acceptance that calculations using small metal clusters compare well with experimental results for CO adsorption.[11,29,36]

The compositions of the Pd, PdPt, and PdAu nanostructures were confirmed using inductively coupled plasma atomic emission spectroscopy (ICP-AES) (Table 2). The results indicated that <0.2 ppm of metal remained in solution in all cases. Through subtraction of the final metal concentrations from the initial metal concentrations, it was found that the bulk composition of the nanostructures were exactly equal to the input compositions. This shows that the metal precursors were completely reduced by ammonium formate under the hydrothermal conditions.

Because CO is strongly adsorbed to platinum group metals, it is a major poisoning species for many catalysts in the process of the oxidation of small organic molecules. Therefore, one of the most important merits of an effective catalyst is its efficient removal of surface-adsorbed CO.[28] To compare the performance of the as-synthesized Pd, PdAu, and PdPt electrodes with CO poisoning, CO-stripping experiments were carried out in a 0.5 mol/L H_2SO_4 solution. The results are presented in Fig. 8.

There are two common characteristics in Figs. 8*a*–8*c*. First, the hydrogen desorption peaks of these electrodes are suppressed in the first positive-going scan owing to preadsorbed CO blocking the active surface sites. Second, a current peak resulting from CO oxidation appears in the potential range from 0.0 to 0.8 V. The Pd catalyst (Fig. 8*a*) displays a very sharp CO oxidation peak centred at

Fig. 9. In situ electrochemical attenuated total reflection-Fourier transform infrared spectroscopic (ATR-FTIR) spectra for the oxidation of CO adsorbed to the surfaces of Pd, PdPt, and PdAu at a potential of –0.1 V. The spectra recorded at –0.2 V were used as references.

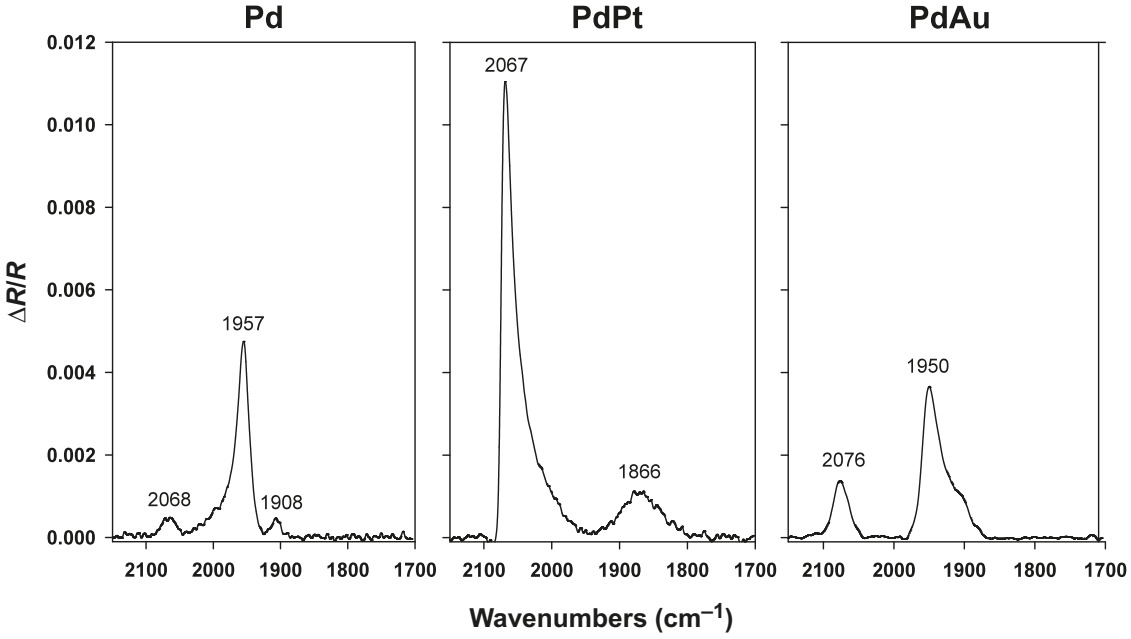

~675 mV, indicating that all of the adsorbed CO is rapidly oxidized at this potential. In the first forward scan of the PdAu CV (Fig. 8*b*), the entire hydrogen desorption peak is not suppressed. This proves that CO did not adsorb to all of the surface sites of the PdAu catalyst. Also, the CO oxidation peak is significantly smaller than the one on the pure Pd catalyst. The hydrogen adsorption–desorption peaks of PdAu are notably larger than those of Pd, indicating that Au may have the opposite adsorption energy effect on Pd for hydrogen compared with carbon monoxide. The CV for PdPt (Fig. 8*c*) shows some catalytic improvement towards the oxidation of CO compared with pure Pd. There is a shoulder beginning at around 75 mV on the broad CO oxidation peak centred at 550 mV.

The CO oxidation charge (Q_{CO}) can be determined by integrating the area under the CO oxidation peaks in the CVs along with the geometric surface area, and it is proportional to the amount of CO that has been adsorbed to the catalyst surface. Q_{CO} decreases in the order PdPt (23.18 mC/cm^2) > Pd (19.67 mC/cm^2) > PdAu (7.93 mC/cm^2), consistent with the ordering of the most stable CO bound four-atom clusters: PdPt (E_{ads} = –44.83 kcal/mol) > Pd (E_{ads} = –41.39 kcal/mol) > PdAu (E_{ads} = –33.87 kcal/mol). Additionally, the order also correlates with the number of types of possible binding sites in each cluster: PdPt (on top, bridging, and hollow), Pd (on top, bridging, and hollow), PdAu (on top, bridging) (Figs. 4–6). The preferential hollow binding site for pure Pd requires three Pd atoms per CO ligand, limiting the CO coverage on the surface as compared with the preferential on-top and bridging sites for PdPt, which require one and two atoms, respectively, per CO ligand.

In situ electrochemical ATR-FTIR study of surface-adsorbed CO

As noted earlier, the C–O stretching frequency in the four-atom clusters is sensitive to the nature of the binding site, but almost independent of the type of metal. Infrared spectroscopy, using CO as a probe, is an effective technique for investigating alloying effects of metal catalysts.[53] The presence or absence of characteristic CO stretches can be used to monitor adsorption sites on the surface, providing insight into the ensemble (geometric) effect. The CO vibrational frequency shift can be used to identify changes in the interaction between the substrate and CO molecules, which reflect the electronic modifications of the substrate surface induced by the second metal (the ligand effect).[53] By comparing the results obtained from theoretical simulations in this study with those obtained from experimental ATR-FTIR, we are able to see what sites are preferential for CO to bind to the Pd alloys.

Shown in Fig. 9 are the electrochemical ATR-FTIR spectra for CO adsorbed to Pd, PdPt, and PdAu. Because the CO frequencies are a local phenomena, we can assign the experimental peaks using the predicted values from our DFT calculations. On the pure Pd nanostructure, the largest peak at 1957 cm^{-1} is for CO in a bridge position with the smaller peaks at 2068 and 1908 cm^{-1} corresponding to CO in the on-top and hollow sites, respectively. On the PdPt surface, the most intense peak, at 2067 cm^{-1}, is for CO in the on-top position with a less intense peak at 866 cm^{-1} for CO bound in a hollow site. No peak is observed for CO bound to a bridge site. On the PdAu surface, CO adsorption occurs only at on-top sites (2076 cm^{-1}) and bridging sites (1950 cm^{-1}).

Conclusions

In conclusion, DFT calculations were carried out for CO bonded to individual atoms of the transition metals. It was found that this method is very efficient for comparing the strength of CO adsorption with different metals. To obtain accurate adsorption energies, however, other factors need to be considered. The various binding sites and the corresponding stretching frequencies for CO attachment to three metal

Can. J. Chem. Downloaded from www.nrcresearchpress.com by South China Agricultural University on 09/19/12
For personal use only.

Can. J. Chem. Downloaded from www.nrcresearchpress.com by South China Agricultural University on 09/19/12
For personal use only.

clusters (Pd_4, Pd_2Pt_2, and Pd_2Au_2) were assessed. Because of the strong CO affinity of Pt, CO was most strongly adsorbed on top Pt in the Pd_2Pt_2 cluster, but minima for nearly all possible binding sites were obtained. On the other hand, in the Pd_2Au_2 cluster, the hollow sites were completely avoided as a result of the weak interaction between Au and CO. Thus, by combining metals in an appropriate manner, the adsorption sites of CO may be controlled. Experimental electrochemical results confirmed the weaker interaction of CO with PdAu than with Pd and showed that PdPt has a greater catalytic activity for the electrochemical oxidation of CO. ATR-FTIR was used as a tool to determine CO-binding sites in the nanostructured material. Interestingly, the CO-stretching frequencies in the clusters depend almost exclusively on the CO distance, which is dictated by the degree of metal coordination and not the metal upon which it is adsorbed. The relatively simplistic approach described within may be adapted to many other catalytic adsorbate reactants or intermediates, as well as countless adsorbent catalysts, allowing for easy screening of catalyst properties.

Supplementary data

Supplementary data (energies and Cartesian coordinates of all of the optimized molecules studied here) are available with the article through the journal Web site at http://nrcresearchpress.com/doi/suppl/10.1139/v11-120.

Acknowledgement

This work was supported by a Discovery Grant from the Natural Sciences and Engineering Research Council of Canada (NSERC). A. Chen acknowledges NSERC and the Canada Foundation for Innovation (CFI) for the Canada Research Chair Award in Materials and Environmental Chemistry.

References

(1) Sadek, M. M.; Wang, L. *J. Phys. Chem. A* **2006**, *110* (51), 14036. doi:10.1021/jp065286u.
(2) Oana, M.; Hoffmann, R.; Abruña, H. D.; DiSalvo, F. J. *Surf. Sci.* **2005**, *574* (1), 1. doi:10.1016/j.susc.2004.09.045.
(3) de-los-Santos-Álvarez, N.; Alden, L. R.; Rus, E.; Wang, H.; DiSalvo, F. J.; Abruña, H. D. *J. Electroanal. Chem.* **2009**, *626* (1–2), 14. doi:10.1016/j.jelechem.2008.10.028.
(4) Ranjan, C.; Hoffmann, R.; DiSalvo, F. J.; Abruña, H. D. *J. Phys. Chem. C* **2007**, *111* (46), 17357. doi:10.1021/jp0746603.
(5) Shimodaira, Y.; Tanaka, T.; Miura, T.; Kudo, A.; Kobayashi, H. *J. Phys. Chem. C* **2007**, *111* (1), 272. doi:10.1021/jp064563u.
(6) Steigerwalt, E. S.; Deluga, G. A.; Lukehart, C. M. *J. Phys. Chem. B* **2002**, *106* (4), 760. doi:10.1021/jp012707t.
(7) Koczkur, K.; Yi, Q.; Chen, A. *Adv. Mater. (Deerfield Beach Fla.)* **2007**, *19*, 2648. doi:10.1002/adma.200602730.
(8) Park, K. W.; Sung, Y. E. *J. Phys. Chem. B* **2005**, *109* (28), 13585. doi:10.1021/jp047430m.
(9) Liu, Z.; Lee, J. Y.; Chen, W.; Han, M.; Gan, L. M. *Langmuir* **2004**, *20* (1), 181. doi:10.1021/la035204i.
(10) Wang, J.; Asmussen, R. M.; Adams, B.; Thomas, D. F.; Chen, A. *Chem. Mater.* **2009**, *21* (8), 1716. doi:10.1021/cm9000174.
(11) Bertin, V.; Agacino, E.; Lopez-Rendon, R.; Poulain, E. *J. Mol. Struct. THEOCHEM* **2006**, *769* (1–3), 243. doi:10.1016/j.theochem.2006.04.026.
(12) Liu, H.; Manthiram, A. *Electrochem. Commun.* **2008**, *10* (5), 740. doi:10.1016/j.elecom.2008.02.022.
(13) Lim, B.; Jiang, M.; Camargo, P. H. C.; Cho, E. C.; Tao, J.; Lu, X.; Zhu, Y.; Xia, Y. *Science* **2009**, *324* (5932), 1302. doi:10.1126/science.1170377.
(14) Wang, R.; Liao, S.; Ji, S. *J. Power Sources* **2008**, *180* (1), 205. doi:10.1016/j.jpowsour.2008.02.027.
(15) Jayashree, R. S.; Spendelow, J. S.; Yeom, J.; Rastogi, C.; Shannon, M. A.; Kenis, P. J. A. *Electrochim. Acta* **2005**, *50* (24), 4674. doi:10.1016/j.electacta.2005.02.018.
(16) Zeinalipour-Yazdi, C. D.; Cooksy, A. L.; Efstathiou, A. M. *Surf. Sci.* **2008**, *602* (10), 1858. doi:10.1016/j.susc.2008.03.024.
(17) Gruene, P.; Fielicke, A.; Meijer, G.; Rayner, D. M. *Phys. Chem. Chem. Phys.* **2008**, *10* (40), 6144. doi:10.1039/b808341j.
(18) Zanti, G.; Peeters, D. *Eur. J. Inorg. Chem.* **2009**, *2009* (26), 3904. doi:10.1002/ejic.200900513.
(19) Zhao, S.; Ren, Y.; Ren, Y.; Wang, J.; Yin, W. *J. Mol. Struct. THEOCHEM* **2010**, *955* (1–3), 66. doi:10.1016/j.theochem.2010.05.032.
(20) Morrow, B. H.; Resasco, D. E.; Striolo, A.; Nardelli, M. B. *J. Phys. Chem. C* **2011**, *115* (13), 5637. doi:10.1021/jp108763f.
(21) Sicolo, S.; Giordano, L.; Pacchioni, G. *J. Phys. Chem. C* **2009**, *113* (23), 10256. doi:10.1021/jp9023266.
(22) Wang, Y. L.; Zhai, H. J.; Xu, L.; Li, J.; Wang, L. S. *J. Phys. Chem. A* **2010**, *114* (3), 1247. doi:10.1021/jp903558v.
(23) Mpourmpakis, G.; Andriotis, A. N.; Vlachos, D. G. *Nano Lett.* **2010**, *10* (3), 1041. doi:10.1021/nl904299c.
(24) Popolan, D. M.; Nößler, M.; Mitrić, R.; Bernhardt, T. M.; Bonačić-Koutecký, V. *Phys. Chem. Chem. Phys.* **2010**, *12* (28), 7865. doi:10.1039/b924022e.
(25) Lin, L.; Lievens, P.; Nguyen, M. T. *Chem. Phys. Lett.* **2010**, *498* (4–6), 296. doi:10.1016/j.cplett.2010.08.068.
(26) Tian, F.-Y.; Shen, J.; Wang, Y.-X. *J. Phys. Chem. A* **2010**, *114* (4), 1616. doi:10.1021/jp910119w.
(27) Shetty, S.; Strych, S.; Jansen, A. P. J.; van Santen, R. A. *Can. J. Chem.* **2009**, *87* (7), 824. doi:10.1139/V09-015.
(28) Wang, J.; Holt-Hindle, P.; MacDonald, D.; Thomas, D. F.; Chen, A. *Electrochim. Acta* **2008**, *53* (23), 6944. doi:10.1016/j.electacta.2008.02.028.
(29) de Souza Monteiro, R.; Paes, L. W. C.; de M. Carneiro, J. W.; Aranda, D. A. G. *J. Cluster Sci.* **2008**, *19* (4), 601. doi:10.1007/s10876-008-0210-9.
(30) Lischka, M.; Mosch, C.; Groß, A. *Surf. Sci.* **2004**, *570* (3), 227. doi:10.1016/j.susc.2004.07.046.
(31) Davies, J. C.; Bonde, J.; Logadottir, Á.; Nørskov, J. K.; Chorkendorff, I. *Fuel Cells (Weinh.)* **2005**, *5* (4), 429. doi:10.1002/fuce.200400076.
(32) Neurock, M. *J. Catal.* **2003**, *216* (1–2), 73. doi:10.1016/S0021-9517(02)00115-X.
(33) Roach, P. J.; Woodward, W. H.; Castleman, A. W., Jr; Reber, A. C.; Khanna, S. N. *Science* **2009**, *323* (5913), 492. doi:10.1126/science.1165884.
(34) Johnson, G. E.; Mitrić, R.; Bonaĉić-Koutecký, V.; Castleman, A. W., Jr. *Chem. Phys. Lett.* **2009**, *475* (1–3), 1. doi:10.1016/j.cplett.2009.04.003.
(35) Neyman, K. M.; Sahnoun, R.; Inntam, C.; Hengrasmee, S.; Rösch, N. *J. Phys. Chem. B* **2004**, *108* (17), 5424. doi:10.1021/jp049830f.
(36) Chen, L.; Chen, B.; Zhou, C.; Wu, J.; Forrey, R. C.; Cheng, H. *J. Phys. Chem. C* **2008**, *112* (36), 13937. doi:10.1021/jp803504k.
(37) Frisch, M. J.; Trucks, G. W.; Schlegel, H. B.; Scuseria, G. E.;

Robb, M. A.; Cheeseman, J. R.; Montgomery, J. A., Jr.; Vreven, T.; Kudin, K. N.; Burant, J. C.; Millam, J. M.; Iyengar, S. S.; Tomasi, J.; Barone, V.; Mennucci, B.; Cossi, M.; Scalmani, G.; Rega, N.; Petersson, G. A.; Nakatsuji, H.; Hada, M.; Ehara, M.; Toyota, K.; Fukuda, R.; Hasegawa, J.; Ishida, M.; Nakajima, T.; Honda, Y.; Kitao, O.; Nakai, H.; Klene, M.; Li, X.; Knox, J. E.; Hratchian, H. P.; Cross, J. B.; Bakken, V.; Adamo, C.; Jaramillo, J.; Gomperts, R.; Stratmann, R. E.; Yazyev, O.; Austin, A. J.; Cammi, R.; Pomelli, C.; Ochterski, J. W.; Ayala, P. Y.; Morokuma, K.; Voth, G. A.; Salvador, P.; Dannenberg, J. J.; Zakrzewski, V. G.; Dapprich, S.; Daniels, A. D.; Strain, M. C.; Farkas, O.; Malick, D. K.; Rabuck, A. D.; Raghavachari, K.; Foresman, J. B.; Ortiz, J. V.; Cui, Q.; Baboul, A. G.; Clifford, S.; Cioslowski, J.; Stefanov, B. B.; Liu, G.; Liashenko, A.; Piskorz, P.; Komaromi, I.; Martin, R. L.; Fox, D. J.; Keith, T.; Al-Laham, M. A.; Peng, C. Y.; Nanayakkara, A.; Challacombe, M.; Gill, P. M. W.; Johnson, B.; Chen, W.; Wong, M. W.; Gonzalez, C.; Pople, J. A. *Gaussian 03, revision D.01;* Gaussian, Inc.: Wallingford, CT, 2004.

(38) Becke, A. D. *J. Chem. Phys.* **1993**, *98* (7), 5648. doi:10.1063/1.464913.

(39) Lee, C.; Yang, W.; Parr, R. G. *Phys. Rev. B* **1988**, *37* (2), 785. doi:10.1103/PhysRevB.37.785.

(40) Hay, P. J.; Wadt, W. R. *J. Chem. Phys.* **1985**, *82* (1), 270. doi:10.1063/1.448799.

(41) Wang, J.; Thomas, D. F.; Chen, A. *Chem. Commun. (Camb.)* **2008**, (40): 5010. doi:10.1039/b807660j.

(42) Adams, B.; Wu, G.; Nigro, S.; Chen, A. *J. Am. Chem. Soc.* **2009**, *131* (20), 6930. doi:10.1021/ja901798u.

(43) Joshi, A. M.; Tucker, M. H.; Delgass, W. N.; Thomson, K. T. *J. Chem. Phys.* **2006**, *125* (19), 194707. doi:10.1063/1.2375094.

(44) Blyholder, G. *J. Phys. Chem. B* **1964**, *68* (10), 2772. doi:10.1021/j100792a006.

(45) Bagus, P. S.; Nelin, C. J.; Bauschlicher, C. W., Jr. *Phys. Rev. B* **1983**, *28* (10), 5423. doi:10.1103/PhysRevB.28.5423.

(46) Nyberg, M.; Föhlisch, A.; Triguero, L.; Bassan, A.; Nilsson, A.; Pettersson, L. G. M. *J. Mol. Struct. THEOCHEM* **2006**, *762* (1–3), 123. doi:10.1016/j.theochem.2005.10.022.

(47) Hammer, B.; Morikawa, Y.; Nørskov, J. K. *Phys. Rev. Lett.* **1996**, *76* (12), 2141. doi:10.1103/PhysRevLett.76.2141.

(48) Zhang, J.; Jin, H.; Sullivan, M. B.; Lim, F. C. H.; Wu, P. *Phys. Chem. Chem. Phys.* **2009**, *11* (9), 1441. doi:10.1039/b814647k.

(49) Tian, N.; Zhou, Z.-Y.; Sun, S.-G. *J. Phys. Chem. C* **2008**, *112* (50), 19801. doi:10.1021/jp804051e.

(50) Moroz, B. L.; Pyrjaev, P. A.; Zaikovskii, V. I.; Bukhtiyarov, V. I. *Catal. Today* **2009**, *144* (3–4), 292. doi:10.1016/j.cattod.2008.10.038.

(51) Illas, F.; López, N.; Ricart, J. M.; Clotet, A.; Conesa, J. C.; Fernández-Garcia, M. *J. Phys. Chem. B* **1998**, *102* (41), 8017. doi:10.1021/jp982118w.

(52) Zanti, G.; Peeters, D. *J. Phys. Chem. A* **2010**, *114* (38), 10345. doi:10.1021/jp1041298.

(53) Wei, T.; Wang, J.; Goodman, D. W. *J. Phys. Chem. C* **2007**, *111* (25), 8781. doi:10.1021/jp067177l.

Can. J. Chem. Downloaded from www.nrcresearchpress.com by South China Agricultural University on 09/19/12
For personal use only.

A common synthetic route to homochiral tetracycles related to pillaromycinone and premithramycinone

Bryan Hill, Robert Jordan, Yang Qu, Abdeljalil Assoud, and Russell Rodrigo

Can. J. Chem. Downloaded from www.nrcresearchpress.com by South China Agricultural University on 09/19/12
For personal use only.

Abstract: Homochiral AB segments for (+)- and (–)-pillaromycinone were prepared in 11 steps from 2-acetylfuran. The synthesis featured an intramolecular Diels–Alder reaction of a 2,5-disubstituted furan and a hydroxyl-directed homogeneous hydrogenation of the tetrasubstituted alkene double bond of two enones. The CD segment was attached by a modified Staunton–Weinreb annulation to produce the desired homochiral tetracycle **21c** related to (+)-pillaromycinone. An unusual acetonide migration enabled the synthesis of a tetracyclic model for premithramycinone.

Key words: naphthacenone antibiotics, diastereoselective hydrogenation, Stauton–Weinreb annulation, furan Diels–Alder, regioselective dehydrogenation.

Résumé : On a préparé les segments AB homochiraux des (+)- et (–)-pillromycinone en onze étapes à partir du 2-acétylfurane. La synthèse implique une réaction de Diels–Alder intramoléculaire d'un furane 2,5-disubstitué et une hydrogénation homogène orientée par le groupe hydroxyle de la double liaison de l'alcène tétrasubstitué de deux énones. Le segment CD a été fixé par une réaction d'annelation de Staunton–Weinreb modifiée pour conduire au dérivé tétracyclique **21c** désiré, apparenté à la (+)-pillromycinone. Une réaction inusitée de migration d'un acétonide a permis de réaliser la synthèse d'un modèle tétracyclique de la prémithramycinone.

Mots-clés : antibiotiques de la naphtacénone, hydrogénation diastéréosélective, annelation de Stauton–Weinreb, réaction de Diels–Alder avec le furane, déshydrogénation régiosélective.

[Traduit par la Rédaction]

Introduction

Pillaromycin A (**1**) was isolated from a culture of *Streptomyces flavovirens* 40 years ago. Its aglycone, (+)-pillaromycinone **2**, is a linear tetracycle[1] with structural similarities to both the tetracyclines and anthracyclinones. Although it has attracted sporadic attention from the synthetic community,[2–4] no enantioselective route to (+)- or (–)-pillaromycinone has been disclosed as yet. Premithramycinone (**3**), isolated in 1998 from a blocked mutant of *Streptomyces argillaceus* ATCC 12956 is a key intermediate in the biosynthesis of the anticancer aureolic acids.[5] No synthetic work towards this compound has been recorded in the literature.

Some years ago[4a] we tested the viability of a convergent AB + CD plan, designed to provide rapid access to the tetracyclic system of **2**. Accordingly, the structurally appropriate AB intermediates, bicyclic enones (±)-**4a** and (±)-**4b**, were prepared in only 10 steps from furfural and incorporated into tetracycles (±)-**5a** and (±)-**5b** by a Staunton–Weinreb annulation. Two serious problems remained to be solved if the work was to be successfully adapted to a synthesis of any tetracycle related to (+)-pillaromycinone. The configuration at C-4a, established by heterogeneous hydrogenation of a tetrasubstituted double bond, was incorrect and no simple method existed for its correction in (±)-**4a** or (±)-**4b**. The Staunton–Weinreb annulation, although successful, needed four separate steps[4a] to form a tetracycle in an unacceptable yield of only 18% (Fig. 1).

We now report that the stereochemical deficiency has been remedied, the annulation has been profitably modified, overall yields have been improved substantially, and our basic plan[4a] has been adapted into a 14 step route to a homochiral tetracycle closely related to (+)-pillaromycinone from 2-acetylfuran. In addition, a serendipitous migration of an acetonide in one tetracyclic intermediate was discovered. Its possible application to the synthesis of premithramycinone **3** was briefly explored.

Received 22 June 2011. Accepted 23 July 2011. Published at www.nrcresearchpress.com/cjc on 1 November 2011.

B. Hill,* R. Jordan,† Y. Qu, A. Assoud,‡ and R. Rodrigo. Department of Chemistry, Unversity of Waterloo, ON N2L 3G1, Canada.

Corresponding author: Russell Rodrigo (e-mail: rrodrigo@uwaterloo.ca).

This article is part of a Special Issue to commemorate the International Year of Chemistry.

*Present address: Department of Chemistry, Brandon University, Brandon, MN R7A 6A9, Canada.
†Present address: Vibrant Pharma Inc., Brantford, ON N3P 1M1, Canada.
‡To whom enquiries about X-ray data should be addressed.

Can. J. Chem. Downloaded from www.nrcresearchpress.com by South China Agricultural University on 09/19/12
For personal use only.

Fig. 1. Summary of previous synthetic work.[4a]

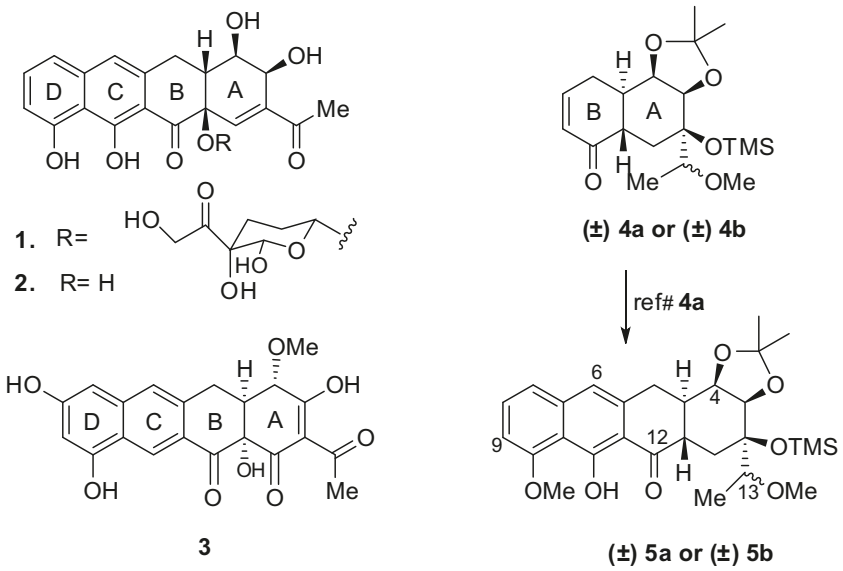

Scheme 1. Preparation of diastereomeric Diels–Alder adducts.

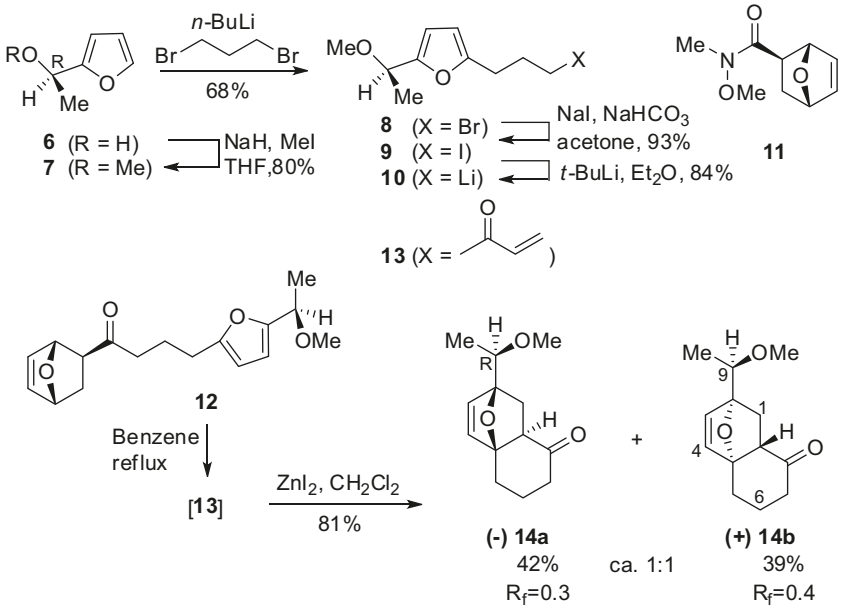

Results and discussion

The synthesis of homochiral AB units 18a–18d

The prochiral ketone 2-acetylfuran was reduced with borane in the presence of 5 mol % of the chiral ligand, diphenyl prolinol.[6] The resulting *R*(+) alcohol **6** (96% yield, >99% enantioselectivity) was methylated (NaH/MeI) to provide methyl ether (+)-**7** (80% yield). Both reactions were routinely conducted on 20 g scales and the product from each step isolated by distillation. The iodopropyl side chain was attached at the remaining furanoid α-carbon atom of **7** as before[4a] in two steps, through the bromide **8** (68%) and the iodide **9** (93%). Lithium–iodine exchange (*t*-BuLi, –78°) produced intermediate **10**, which was quenched in situ with *exo*-amide **11** to form the desired ketone **12** in 84% yield. This circuitous protocol "masks" the double bond of *N*,*O*-dimethyl acrylamide; a necessity because the conjugated amide did not react cleanly with **10**, and the 2,5-disubstituted furanoid core of these compounds was very sensitive to oxidizing agents. The enone **13** was unmasked by a retro-Diels–Alder reaction, effected by refluxing **12** in benzene overnight and removing the solvent under reduced pressure. The residue (**13**) was dissolved in dry methylene chloride and stirred at ambient temperature with 50 mol % zinc iodide for 48 h. The diastereomeric exo adducts[7] **14a** and **14b** resulting thereby were formed in an ~1:1 ratio and a combined yield of 81%. They were separated by flash column chromatography as before[4a] (Scheme 1). The three new chiral centres must have absolute configurations 2*S*,4a*S*,8a*R* and 2*R*,4a*R*,8a*S* with the already established 9*R* centre common to both. In our earlier work with racemates, X-ray crystallography of acetonide (±)-**15b** prepared from the chromatographically

Can. J. Chem. Downloaded from www.nrcresearchpress.com by South China Agricultural University on 09/19/12
For personal use only.

Scheme 2. Synthesis of hydroxy enones **16a** and **16b**.

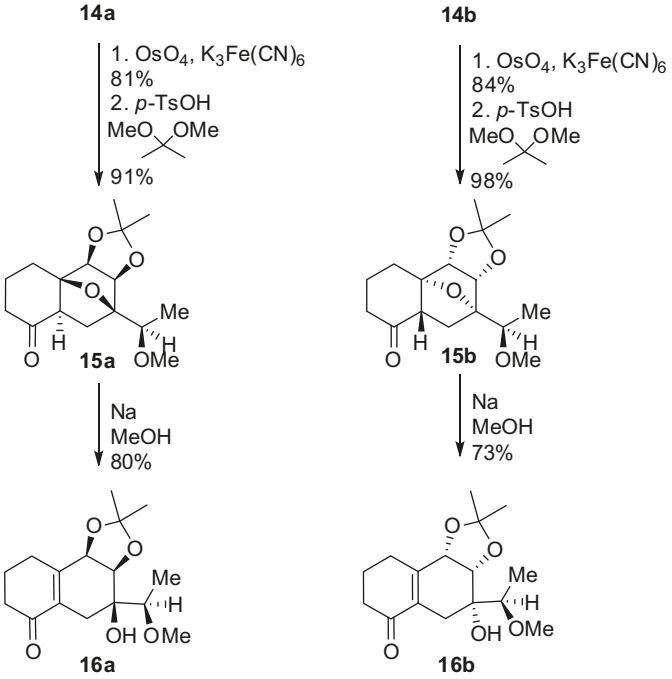

faster adduct (Scheme 2), indicated that its relative configuration was 2*S**,4a*S**,8a*R**,9*S**. It therefore follows that the absolute configuration of the faster adduct (**14b**) is 2*R*,4a*R*,8a*S*,9*R* (R_f = 0.4, $[\alpha]_D$ = +32.2) and the slower (**14a**) is 2*S*,4a*S*,8a*R*,9*R* (R_f = 0.3, $[\alpha]_D$ = –37.5). These assignments are also recorded in Scheme 1.

The 9*R* centre must be destroyed at a subsequent stage to generate the C-2 acetyl group of pillaromycinone, thereby converting the two diastereomers into enantiomers each of which can relate to (+)- or (–)-pillaromycinone. The chiral 9*R* substituent thus serves as a traditional resolving agent, but one that is also an integral part of the target molecule.

Proceeding as before,[4a] the C-3, C-4 double bond of each adduct was dihydroxylated and converted to the respective acetonides **15a** and **15b**. Each acetonide was then subjected to cleavage of the oxygen bridge by brief treatment with sodium in refluxing methanol. The resulting hydroxy enones **16a** and **16b** (higher R_f) were obtained in 10% and 9.3% overall yields, respectively, from 2-acetylfuran after nine steps (Scheme 2). We were able to separate (±)-**16a** on a chiralcell-OD column and show that our sample of **16a** was >99% enantiomerically pure (Fig. 1 of the Supplementary data).

It was now necessary to face the difficult problem of hydrogenation of the tetrasubstituted C-4a, C-8a double bond of each enone with delivery of hydrogen syn to the C-7 hydroxyl group and C_5–C_6 acetonide. Indeed, this was the step that had failed to produce the desired AB ring fusion in our earlier work.[4a] Some promising precedents[8] employing homogeneous hydrogenation techniques are available in the literature. A cationic rhodium catalyst had efficiently hydrogenated a tetrasubstituted double bond syn to a homoallylic hydroxyl group,[9] but our substrates **16a** and **16b** were unaffected by 5 or 10 mol % of $[Rh(nbd)(diphos\text{-}4)]^+BF_4^-$ at pressures of 1–50 atm (1 atm = 101.325 kPa) of hydrogen, at room temperature, after 24 or 36 h. Diimide, used earlier[10]

Scheme 3. Synthesis of *cis*-decalones **17a**–**17b**.

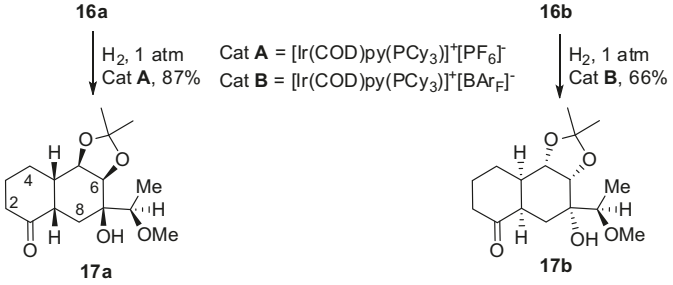

for a similar hydrogenation, also left these enones intact. The cationic iridium catalysts were evaluated next. A structural requirement for the successful hydrogenation of 3-cyclohexenols was that the hydroxyl group of the substrate be axially disposed. This ensures that both the hydroxyl group and the double bond are within reach of the metal in the putative octahedral Ir^{3+} complex resulting from oxidative addition of hydrogen[8] to the precatalyst. Our substrates did meet this criterion admirably, but they were seriously crowded around the reaction site. The homogenous hydrogenation with the Crabtree catalyst[11] was initially conducted in methylene chloride with the "slower" enone **16a** at various pressures of hydrogen, catalyst loadings, and reaction times. In general, the reaction was slow and incomplete. This was not surprising: tetrasubstituted double bonds are not easily hydrogenated. However, the desired product (the *cis*-decalone **17a**) was obtained in 87% yield after 48 h at a pressure of 1 atm of hydrogen (Scheme 3).

Surprisingly, and for reasons unknown, no conditions could be found that would hydrogenate the double bond of **16b** with the Crabtree catalyst. It has been reported that this catalyst can suffer deactivation over time by the formation of trimeric hydrogen-bridged iridium species, and this would be especially likely in slow reactions such as this. However, it is also known[12] that exchanging the PF_6^- counterion for the more lipophilic tetrakis[3,5-bis(trifluoromethyl)phenyl] borate $(BAr_F)^-$ improved catalyst performance and resistance to deactivation. We decided to prepare this catalyst by reaction of the Crabtree catalyst with $Na^+(BAr_F)^-$ in a two-phase methylene chloride – water system.[13,14] Column chromatography of the product (methylene chloride / silica) followed by crystallization from ethanol/ether gave the desired catalyst $[Ir(cod)py(PCy_3)]^+[BAr_F]^-$, whose structure was confirmed by X-ray crystallography (Supplementary data). Hydrogenation of the other diastereomeric enone (**16b**) with 10 mol % of this catalyst overnight, at a pressure of 1 atm of hydrogen produced the decalone **17b** in 66% yield. These reactions were also performed with the racemates (±)-**16a** and (±)-**16b** and the products (±)-**17a** and (±)-**17b** analysed by X-ray crystallography to establish their structures and relative stereochemistry (Supplementary data). It was gratifying indeed to observe that the difficulty with the configuration at C-4a had finally been resolved and the desired hydroxyl-directed hydrogenation had been achieved. At this stage we decided to also investigate the possibility of epimerising **17a** and **17b** at C-8a to obtain the *trans*-decalones **17c** and **17d** (Scheme 4). This was achieved in 80% yield by treatment with LiHMDS in THF (–78° → 0°), but the reactions could not be taken to completion and the products contained

Scheme 4. Synthesis of *cis*- and *trans*-enones **17a**–**17d**.

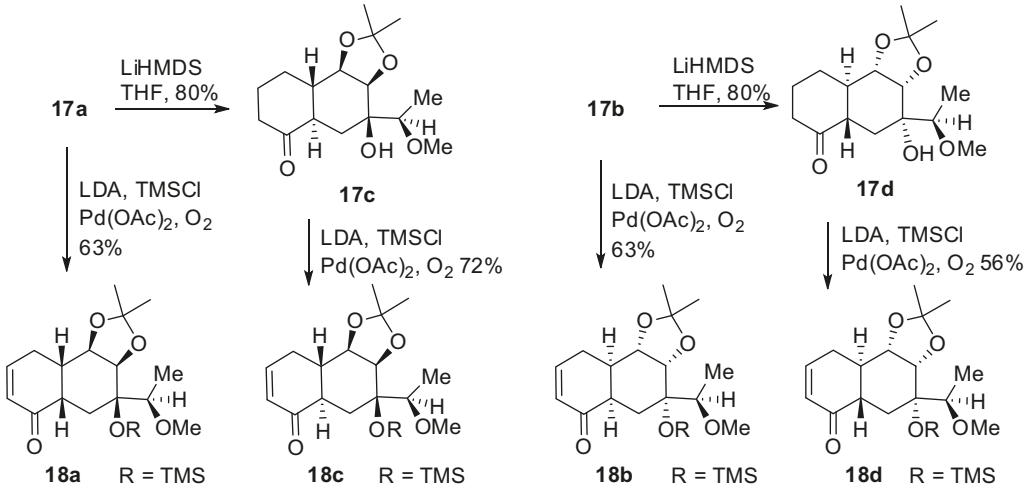

~20% of the starting *cis*-decalones **17a** and **17b**, which were separated by column chromatography. In Fig. 2 of the Supplementary data, the ^{1}H NMR spectra (500 MHz) of **17a**–**17d** are displayed. Particularly noteworthy is the small, but measureable W-coupling (found only in **17a**) between H-8α and the C-7 hydroxyl proton. This coupling is greatly reduced upon D_2O exchange. The other diagnostic feature in the figure is the lack of any signals between 2.5 and 3.2 ppm in the spectra of **17c** and **17d**. This region contains the cis-ring junction protons H-4a and H-8a in **17a** and **17b** and their absence reflects the trans-ring fusion in the former compounds.

Unlike the previous reports[2,3] that employed the Diels–Alder reaction to create the AB cis-ring fusion, our hydrogenation/epimerization sequence produces two pairs of AB intermediates cis and trans fused at will, each with a rigorously predetermined absolute configuration. The first pair (**17a** and **17c**) had stereochemistry at C-4a, C-5, and C-6 identical with that of (+)-pillaromycinone, whereas the second (**17b** and **17d**) related to the (–)-enantiomer in a similar manner. With each pair, a choice of configuration at the enolisable C-8a centre was available. We soon found that this versatility was a valuable asset in a subsequent step of the synthesis. Dehydrogenation of each decalone (**17a**–**17d**) at C-2, C-3 was achieved by the two-step Saegusa method.[15] The kinetic enolates were quenched with excess TMSCl and the resulting enol silanes were each oxidized with $Pd(OAc)_2$ in DMSO under an atmosphere of oxygen.[16] The enones (**18a**–**18d**) were isolated in 56%–72% yields. At this stage a final check on structure and stereochemistry of these AB segments was secured by a X-ray crystal structure of one of them, (±)-**18b**. We decided to continue the synthesis with the **18a**, **18c** pair only, because their configurations related to the natural antibiotic and they were produced in the highest overall yields from 2-acetylfuran (5.5% and 4.3%, respectively).

Synthesis of homochiral tetracycles

The next obstacle, the unacceptable yield of the Staunton–Weinreb annulation, was overcome by our "stannane modification" of the process.[4b] No less than seven cyclic enones, with and without[17] enolisable hydrogen atoms, were found to undergo the Michael addition – Dieckmann condensation sequence to afford polycyclic ketones in satisfactory yields. Both diastereomers **18a** and **18c** reacted with the stannane **19** after tin–lithium exchange to form ABCD tetracycles **20a** (62%) and **20c** (71%), respectively.

These homochiral tetracycles were then dehydrogenated with dicyanodichloroquinone (DDQ) in benzene. The AB cis fused heterocycle **20a** was unexpectedly resistant to the aromatisation of ring C and the reactions were difficult to complete, with product (**21a**) yields around 30%. Using other dehydrogenating agents (e.g., Pd/C or chloranil) did not improve matters.

This unfortunate setback was alleviated somewhat by testing the *trans*-enone **18c** instead, in the two-step annulation. As it happened, the AB trans tetracycle **20c** produced (71% yield) in the first step was quantitatively dehydrogenated by DDQ to (+)-**21c** ($[\alpha]_D$ = +32.4). This florescent yellow-green compound bearing the requisite substitution and absolute stereochemistry at C-3, C-4, and C-4a suitable for progressing to (+)-pillaromycinone was obtained in 14 steps and 3.95% overall yield from 2-acetylfuran (Scheme 5).

However, the configuration at the enolisable C-12a centre will have to be inverted in a subsequent hydroxylation step.

We began our effort to approach (+)-pillaromycinone by examining the possibility of O-desilylation and subsequent elimination of the tertiary hydroxyl group at C-2. Initially, treatment with TBAF in wet THF resulted in a complex mixture of products (see later), but PPTS in methanol at 0° did accomplish the desired desilylation in excellent yield. Many attempts were made to dehydrate the resulting C-2 tertiary hydroxyl group of **22**. With milder reagents like DCC, thiocarbonyl diimidazole, and mesyl chloride / DMAP, the starting material was recovered. Other reagents like thionyl chloride or triphenyl phosphine / iodine caused extensive decomposition. Acid-catalyzed dehydration with *p*-TsOH in moist THF was examined at temperatures between 0° and 25° with regular monitoring by TLC. After reaction under such conditions overnight at room temperature, the starting material **22** was consumed and two products were detected. One was the deprotected acetonide, a tetrahydroxy compound that could be eluted from a column only with neat ethyl acetate. The other, slightly slower on TLC than the starting

Can. J. Chem. Downloaded from www.nrcresearchpress.com by South China Agricultural University on 09/19/12
For personal use only.

Can. J. Chem. Downloaded from www.nrcresearchpress.com by South China Agricultural University on 09/19/12
For personal use only.

Scheme 5. Synthesis of homochiral tetracycles.

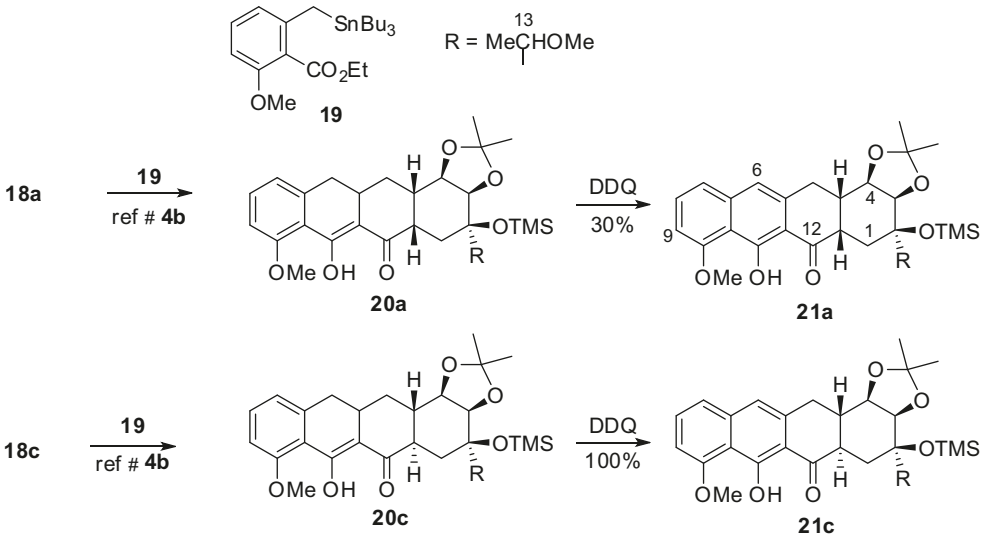

Fig. 2. Progress made towards pillaromycinone and premithramycinone.

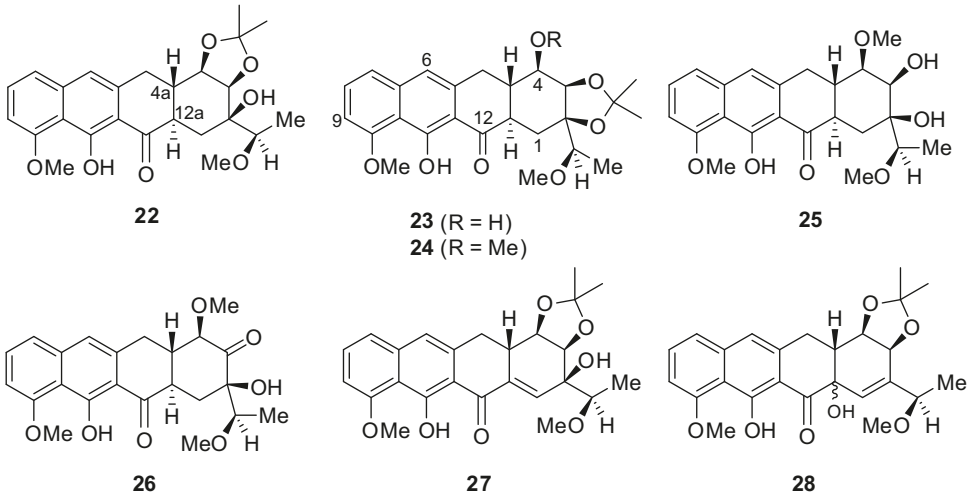

material **22**, had the same molecular formula (HRMS), but a different ^{1}H NMR spectrum, particularly in the signals of the protons on ring A (H-1, H-3, H-4, and H-4a, Table 1).[18] We were able to crystallize this product and establish its structure as **23** by X-ray crystallography. This isomeric acetonide was also formed from the silyl ether **21c** under identical conditions. Although these results were frustrating, we did not lose sight of the fact that the formation of **23** from **21c** or **22** represents the selective deprotection of the C-3, C-4 acetonide at C-4. This finding could be of much significance for a future attempt to synthesize premithramycinone **3**. To illustrate, methylation (NaH/MeI) of the now unprotected C-4 hydroxyl group afforded methyl ether **24** quantitatively. Hydrolysis of the acetonide (THF / aq HCl) left the C-2, C-3 diol **25**, which was oxidized (IBX, acetonitrile, 80°)[19] to provide the C-3 ketone **26**. These simple transformations produced a tetracycle with structure and stereochemistry not far removed from the A ring of **3** (Fig. 2).

Even though these were interesting and potentially useful reactions, they represented no advance towards pillaromycinone. In particular, we had no success in dehydrating the C-2 alcohol to generate the C-1, C-2 double bond as we had intended to do in our synthetic planning. Therefore, we decided to examine the complex mixture produced by the TBAF treatment of **21c** more carefully. Purification by chromatography provided a crystalline reddish yellow compound in an optimized yield of 60%. It had a molecular formula of $C_{25}H_{28}O_7$ (HRMS) in contrast to the starting material **21c** ($C_{28}H_{38}O_7Si$). Therefore, it must have been desilylated ($-C_3H_8Si$), but in addition had a deficiency of two hydrogen atoms. These features were confirmed by comparison of its ^{1}H and ^{13}C NMR spectra with those of **21c**.

In particular, the ^{1}H NMR signals assigned to the C-1 protons (δ 1.68, 2.67) and the C-12a proton (δ 2.95) of the starting material were absent in the spectrum of the product, but a new signal was evident as a singlet at 7.13 ppm. The ^{13}C spectrum confirmed the presence of a trisubstituted alkene with the appearance of two new signals at 135.3 and 136.5 ppm (protonated and nonprotonated, respectively). Based on these and other NMR comparisons (Table 1) we assigned the structure **27** to this compound and confirmed it by single-crystal X-ray analysis. We found that **27** was also

Can. J. Chem. Downloaded from www.nrcresearchpress.com by South China Agricultural University on 09/19/12
For personal use only.

Table 1. ^{1}H NMR data (500 MHz, δ (in ppm), *J* (in Hz)) for tetracycles **21c**, **22**, **23**, **27**, and **28** in $CDCl_3$.

	Compound				
	21c	**22**	**23**	**27**	**28**
Proton	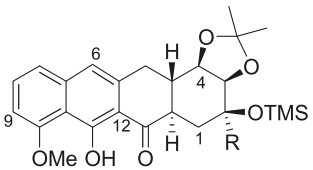	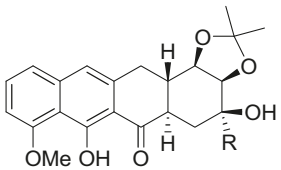	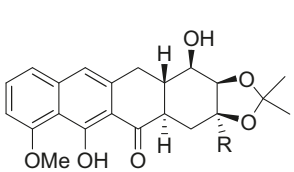	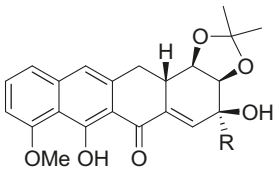	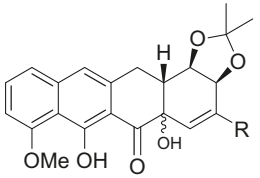
H-1	ax. 1.68(t), *J*=12.8, 12.8 eq. 2.68 overlapped by H-5	ax. 2.07(dd), *J*=15, 8.7 eq. 2.33(dd), *J*=15, 7.5	ax. 1.43(t), *J*=13.5, 13.5 eq. 2.85(dd), *J*=14.3, 3.6	7.13(d), *J*=2.9	6.9(s)
H-3	4.02(d), *J*=4.8	4.33(d), *J*=7.0	4.19(d), *J*=3.8	4.30(d), *J*=6.6	4.72(d), *J*=6.3
H-4	4.15(dd), *J*=8.6, 4.7	4.11(dd), *J*=9.0, 7.0	3.86(td), *J*=10.5, 10.5, 3.8	4.19(t), *J*=6.2, 6.2	4.49(dd), *J*=10.2, 6.3
H-4a	1.98(m), *J*=12.5, 12.5, 8.6, 3.6	2.5(m), overlapped by C-2 OH	2.2 (complex m)	3.0 (complex m)	2.16(m)
H-5	ax. 2.68 overlapped by H-leq eq. 3.3 overlapped by H-13 and C_{13}–OMe	ax. 2.68, partially overlapped by H-4a, and H-12a eq. 3.3 overlapped by H-13 and C_{13}–OMe	ax. 2.7(m) overlapped with H-12a eq. 3.49(dd), *J*=16, 3.6	ax. 2.79(t), *J*=14, 14 eq. 3.30(dd), *J*=14.8, 5.4	ax. and eq. 3.2–3.25 complex multiplet
H-12a	2.95(td), *J*=12.6, 12.6, 2.9	2.63(dt), *J*=13, 8.2, 8.0 partially overlapped by H-5_{ax}	2.7 (complex m) overlapped with H-5ax	—	—
H-13	3.3, overlapped by H-5_{eq} and C_{13}–OMe	3.32(q), *J*=6.3	3.45(q), *J*=6.2	3.34(q), *J*=6.3	4.02–4.06 overlapped by C_{10}–OMe
C_{13}-Me	1.29(d), *J*=6.3	1.29(d), *J*=6.3	1.34(d), *J*=6.2	1.29(d). *J*=6.3	1.44(d), *J*=6.4
OMe	C_{10} 4.03, C_{13} 3.31	C_{10} 4.03, C_{13} 3.37	C_{10} 4.04, C_{13} 3.33	C_{10} 4.01, C_{13} 3.36	C_{10} 4.05, C_{13} 3.4
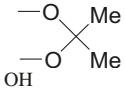	1.5, 1.43	1.53, 1.45	1.47, 1.37	1.50, 1.43	1.49, 1.38
OH	C_{11}–OH, 15.2	C_2 2.46, C_{11} 15.1	C_4 2.13(d), *J*=10.3, C_{11} 15.56	C_2 2.9, C_{11} 15.45	C_{12a} 2.21, C_{11} 14.66

Note: Aromatic H signals appeared in a narrow range in all compounds as follows: H-8(t) 7.47–7.53, H-7(d) 7.20–7.25, H-6(s) 6.90–7.01, and H-9(d) 6.80–6.84, with coupling constants *J* = 7.80–8.0 Hz.

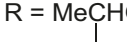

Scheme 6. Proposed mechanism for the formation of **27** from **21c** or **22**.

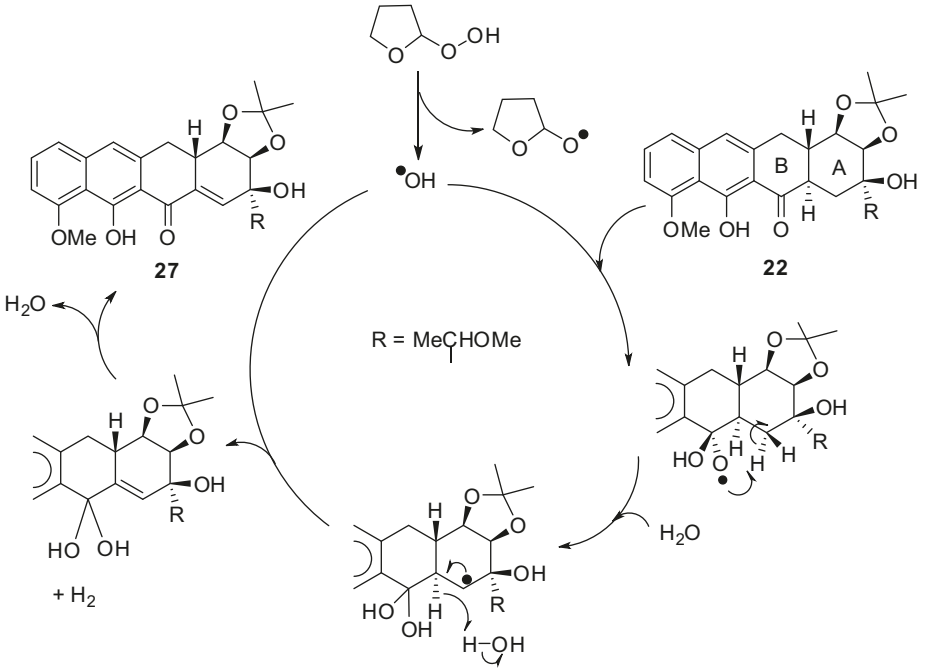

produced from the desilylated tetracycle **22** in similar yield under identical conditions. This remarkably selective dehydrogenation probably occurs by means of a radical chain process initiated by THF peroxide[20] and propagated by hydroxyl radicals. We propose a mechanism (Scheme 6) that accounts for the regioselectivity by assigning a crucial role to the carbonyl group at C-12 and avoids the intermediacy of an enolate radical at C-12a. The collapse of such a radical would result in the aromatization of ring B. The absolute configurations at every other chiral centre besides C-12a were unaffected in the transformation, and we had recognized earlier that the existing configuration at that centre would have to be corrected eventually. Consequently, we saw this γ-hydroxy enone **27** as an opportune substrate either for introducing the required hydroxyl group at C-12a in the correct orientation or for generating the desired C-2 acetyl group by dehydration at C-2, C-13.

We attempted the dehydration first by applying a simple procedure recommended specifically[21] for tertiary alcohols and illustrated with many examples of success with sensitive substrates. Under the conditions cited (mesyl chloride, triethylamine, DMAP in dry dichloromethane 0° → rt, 30 min) we obtained a green fluorescent compound that was separated from the reaction mixture by column chromatography on silica gel, first in ethyl acetate / hexane and then in dichloromethane/ether (85:15). However, even after careful chromatography, this material (a single spot on the TLC analysis) could not be obtained pure. The base peak at *m*/*z* 440 in its mass spectrum corresponded to a molecular formula $C_{25}H_{28}O_7$ (by HRMS) making it isomeric with the starting enone. In addition, the spectrum did not display an ion of significant intensity at *m*/*z* 422, thereby implying that the projected dehydration had not occurred. The ^{1}H and ^{13}C NMR spectra indicated the presence of about 10% of an impurity that appeared to be structurally similar to the major component. The ^{1}H spectrum of the green fluorescent product, when compared with the starting enone, showed many changes in the chemical shifts of protons associated with ring A. The alkene proton remained as a singlet, now at 6.9 ppm, and the signals assigned to H-3, H-4, and H-13 showed significant downfield shifts, whereas H-4a, no longer allylic, was shifted upfield considerably (Table 1). These changes taken together suggested that an allylic rearrangement[22] had occurred in ring A. The structure **28** is proposed for the fluorescent product with the double bond now at C-1, C-2 and the hydroxyl group at C-12a. The evident lack of a C-12a proton and the presence of a broad OH signal at 2.21 ppm supported the structural assignment. The configuration of the hydroxyl substituent at C-12a is still uncertain, however, and the difficulties experienced with purification of the product implies that it is an epimeric mixture of two C-12a alcohols. We have tried very hard to obtain suitable crystals of **28** for X-ray analysis without success so far, but these attempts are continuing.

Conclusion

If the configuration of **28** can be conclusively settled it would mean that we have succeeded in developing a synthesis of a very advanced intermediate for (+)-pillaromycinone requiring only minor structural adjustments for completion. It incorporates the correct absolute configuration at C-3, C-4, and C-4a and the double bond at C-1, C-2. Its synthesis required only 16 steps from 2-acetylfuran and features novel protocols for (*i*) stereochemical control at C-4a, C-4, and C-3; (*ii*) the Staunton–Weinreb annulation; (*iii*) regioselective dehydrogenation of a tetracyclic ketone at C-1, C-12a; and (*iv*) introduction of the hydroxyl group at C-12a. In addition, an interesting possibility of modifying ring A for the synthesis of premithramycinone has been created.

Can. J. Chem. Downloaded from www.nrcresearchpress.com by South China Agricultural University on 09/19/12
For personal use only.

Can. J. Chem. Downloaded from www.nrcresearchpress.com by South China Agricultural University on 09/19/12
For personal use only.

Experimental

Experimental procedures and spectroscopic data for racemic compounds **6**–**15**, stannane **19**, and chiral tetracycles **20a** and **20c** have been published previously.[4] Experimental protocols have been modified in some instances and yields improved. In such cases, the new conditions and yields are provided. See the Supplementary data for notes on general experimental methods.

R-(+)-1-Furylethanol (6)

To a stirred solution of *S*-diphenylprolinol (2.3 g, 9.08 mmol) in THF (650 mL) was added 2.0 mol/L BH_3–SMe_2 (64 mL, 128 mmol). The mixture was stirred overnight at room temperature (rt). A solution of 2-acetylfuran (20 g, 181.6 mmol) in THF (30 mL) was added slowly via a syringe pump and the mixture was stirred overnight at rt. The reaction was quenched with methanol and the solvents removed in vacuo at rt. Distillation (water aspirator) gave **6** (19.5 g, 96%) as a clear colourless liquid, bp 64°–70°. $[\alpha]_D = +21.1$ (*c* 1.06, $CHCl_3$). Optical rotation suggests >99% enantioselectivity for the reduction.[23]

R(+)-2-(1′-Methoxy)ethylfuran (7)[4a]

$[\alpha]_D = +109.9$ (*c* 1.006, $CHCl_3$), 80% yield.

R(+)-2-(3-Bromopropyl)-5-(1′-methoxy)ethylfuran (8)[4a]

$[\alpha]_D = +67.0$ (*c* 1.216, $CHCl_3$), 68% yield.

R(+)-2-(3-Iodopropyl)-5-(1′-methoxy)ethylfuran (9)[4a]

$[\alpha]_D = +59.1$ (*c* 1.482, $CHCl_3$), 93% yield.

2β-(*N*-Methyl-*N*-methoxyamido)-7-oxabicyclo[2.2.1]hept-5-ene (11)[4a] and *R*(+)4-[5-(1-methoxyethyl)furan-2-yl]-1-(7-oxabicyclo[2.2.1]hept-5-ene-2-yl)butan-1-one (12)[4a]

$[\alpha]_D = +61.0$ (*c* 1.184, $CHCl_3$), 84% yield.

2*H*-2-(1′-Methoxyethyl)-2,4a-epoxy-1,8a,5,6,7,8-hexahydronaphthalen-8-one (14a and 14b)

A solution of ketone **12** (10.98 g, 37.8 mmol) in benzene (100 mL) was heated at reflux for 48 h. The liquids were evaporated and the residue dissolved in dichloromethane (100 mL) and zinc iodide (4.82 g, 15.1 mmol) was added. The suspension was stirred for 48 h at rt and quenched with aqueous sodium bicarbonate. The mixture was extracted with dichloromethane (3 × 50 mL), the organic extracts combined and washed with brine, then dried ($MgSO_4$) and concentrated. Flash chromatography (30% ethyl acetate – hexanes) gave 6.7 g (81%) of a mixture of **14a** and **14b** and 0.23 g of unchanged starting material. The diastereomeric adducts **14a** and **14b** were separated as before[4a] by chromatography. **14b** $R_f \approx 0.4$; $[\alpha]_D = +32.2$ (*c* 1.006, $CHCl_3$); 39% yield. **14a**: $R_f \approx 0.3$; $[\alpha]_D = -37.5$ (*c* 1.004, $CHCl_3$); 42% yield.

Dihydroxylation of 14a and 14b: 2*H*-2-(1′-methoxyethyl)-3β,4β-dihydroxy-2,4a-epoxy-octahydronaphthalen-8-one[4a]

Modified procedure

A mixture of **14a** or **14b** (1 equiv), OsO_4 (0.2 equiv), $K_3Fe(CN)_6$ (3.0 equiv), K_2CO_3 (3.0 equiv), H_2O, and *tert*-butyl alcohol were stirred at rt for 48 h. The reaction was quenched with solid $NaHSO_3$ and stirred for a further 0.5 h. It was extracted with ethyl acetate (3×) and the remaining aqueous layer continuously extracted with ethyl acetate for a further 48 h. The ethyl acetate extracts were combined, dried ($MgSO_4$), and then evaporated. The residue was purified by chromatography to obtain a white solid in each case.

Dihydroxylation of 14a

13a (2.87 g, 12.9 mmol), OsO_4 (0.0714 mol/L) in water (36 mL), $K_3Fe(CN)_6$ (12.73 g, 38.7 mmol), K_2CO_3 (5.35 g, 38.7 mmol), *t*-BuOH (50 mL), and water (14 mL). Yield: 2.63 g (81%). $[\alpha]_D = -4.73$ (*c* 0.676, $CHCl_3$).

Dihydroxylation of 14b

13b (2.0 g, 9.0 mmol), OsO_4 (0.098 mol/L) in water (18 mL), $K_3Fe(CN)_6$ (8.89 g, 27 mmol), K_2CO_3 (3.73 g, 27 mmol), *t*-BuOH (35 mL), and water (17 mL). Yield: 1.934 g (84%). $[\alpha]_D = +4.44$ (*c* 0.608, $CHCl_3$).

2*H*-2-(1′-Methoxyethyl)-3β,4β-di-*O*-isopropylidene-2,4a-epoxy-octahydronaphthalen-8-one (15a and 15b)[4a]

To a refluxing solution of the diol (1.0 equiv) in 2,2-dimethoxypropane and dichloromethane was added a few crystals of TsOH. Refluxing was continued for a further 0.5 h, the mixture cooled, neutralized with solid K_2CO_3, and the solvents removed in vacuo. Flash column chromatography (3:1, hexanes / ethyl acetate) gave the pure acetonides. **15a**: Diol (5.817 g, 22.7 mmol), 2,2-dimethoxy propane (66.2 g, 636 mmol), CH_2Cl_2 (360 mL), TsOH (a few crystals). Yield: 6.09 g (91%). $[\alpha]_D = -26.8$ (*c* 0.954, $CHCl_3$). **15b**: Diol (1.774 g, 6.92 mmol), 2,2-dimethoxypropane (20 g, 194 mmol), CH_2Cl_2 (150 mL), TsOH (a few crystals). Yield: 2.0 g (98%). $[\alpha]_D = +33.2$ (*c* 1.05, $CHCl_3$).

7-(1′-Methoxyethyl)-7β-hydroxy-5β,6β-di-*O*-isopropylidene-4a,8a-dehydro-1-decalone (16a and 16b)

To a solution of sodium (5 equiv) in methanol was added the ketone **15a** or **15b** (1 equiv) in methanol. After 20–30 min the solution was cooled and poured onto dry ice. It was diluted with ether and filtered. The filtrate was evaporated to dryness and purified by flash chromatography (hexanes / ethyl acetate, 2:1). **16a**: ketone **15a** (2.0 g, 6.75 mmol), MeOH (55 mL), sodium (0.775 g, 33.7 mmol) in MeOH (55 mL), refluxed for 20 min. Yield: 1.595 g (79.8%). $[\alpha]_D = -102.7$ ($c = 0.736$, $CHCl_3$). ^{1}H NMR (300 MHz, $CDCl_3$) δ: 1.17 (3H, d, $J = 6.3$ Hz), 1.42, 1.46 (3H each, s), 1.99 (2H, m), 2.2, 2.42 (4H, m), 2.68 (2H, m), 3.25 (1H, qt), 3.31 (3H, s), 4.42 (1H, d, $J = 7.2$ Hz), 4.53 (1H, d, $J = 7.2$ Hz). ^{13}C NMR (75 MHz, $CDCl_3$) δ: 12.2, 22.1, 24.7, 24.8, 26.6, 26.9, 37.7, 57.1, 71.3, 74.6, 75.2, 78.6, 109.0, 130.1, 150.6, 198.6. EI HRMS $(M - CH_3)^+$ found: 281.1387; $C_{15}H_{21}O_5$ calcd: 281.1367. **16b**: ketone **15b** (0.485 g, 1.63 mmol) in MeOH (11 mL), sodium (0.188 g, 8.18 mmol) in MeOH (11 mL) refluxed for 30 min. Yield: 0.353 g (73%). ^{1}H NMR (300 MHz, $CDCl_3$) δ: 1.13 (3H, d, $J = 6.3$ Hz), 1.35, 1.36 (3H each, s), 1.99 (2H, m), 2.2, 2.42, 2.64 (6H, m), 3.09 (1H, qt), 3.29 (3H, s), 4.42 (1H, d, $J = 7.2$ Hz), 4.48 (1H, d, $J = 7.2$ Hz). ^{13}C NMR (75 MHz, $CDCl_3$) δ: 12.7, 22.2, 25.3, 26.6, 27.1, 27.4, 37.6, 57.1, 72.8, 75.4, 76.1, 79.9,

Can. J. Chem. Downloaded from www.nrcresearchpress.com by South China Agricultural University on 09/19/12
For personal use only.

109.3, 129.8, 151.4, 198.6. EI HRMS $(M - Me)^+$ found: 281.1386; $C_{15}H_{21}O_5$ calcd: 281.1356.

7-(1′-Methoxyethyl)-7-hydroxy-5,6-di-*O*-isopropylidene-decal-1-ones (**17a** and **17b**)

A solution of the enone **16a** or **16b** (1 equiv) with iridium catalyst (0.1 equiv) in dichloromethane was flushed with hydrogen (3×) and stirred under an atmosphere of hydrogen for 24–48 h at rt. Brine was added and the layers separated. The aqueous layer was extracted with dichloromethane (3×) and the organic layers were combined, dried ($MgSO_4$), and concentrated. Flash column chromatography (hexanes / ethyl acetate, 2:1) yielded pure products as white solids. **17a**: enone **16a** (0.332 g, 1.12 mmol), $[Ir(COD)py(PCy_3)]^+[PF_6]^-$ (0.09 g, 0.112 mmol) in CH_2Cl_2 (80 mL), stirred under H_2 for 48 h. Yield: 0.291 g (87%). $[\alpha]_D$ = +9.63 (*c* 0.114, $CHCl_3$). ^{1}H NMR (500 MHz, $CDCl_3$) δ: 1.10 (3H, d, *J* = 6.3 Hz), 1.28 (3H, s), 1.62 (1H, dd, *J* = 15.0, 8.0 Hz), 1.8–1.9 (4H, m), 2.08 (1H, ddd, *J* = 15.0, 6.5, 2.1 Hz), 2.31 (2H, m), 2.45 (1H, d, *J* = 2.1 Hz), 2.81 (2H, m), 3.08 (1H, q, *J* = 6.3 Hz), 3.28 (3H, s), 3.89 (1H, dd, *J* = 8.0, 7.6 Hz), 4.16 (1H, d, *J* = 7.6 Hz). ^{13}C NMR (75 MHz, $CDCl_3$) δ: 12.1, 22.5, 23.0, 24.6, 25.6, 26.7, 39.0, 40.7, 44.4, 57.3, 73.1, 73.3, 74.4, 80.4, 108.0, 212.7. Anal calcd for $C_{16}H_{26}O_5$: C 64.41, H 8.78; found: C 64.60, H 8.87. **17b**: enone **16b** (0.125 g, 0.421 mmol), $[Ir(COD)py(PCy_3)]^+[BAr_F]^-$ (0.064 g, 0.042 mmol) in CH_2Cl_2 (30 mL) under H_2 for 24 h. Yield: 0.0835 g (66%). ^{1}H NMR (500 MHz, $CDCl_3$) δ: 1.20 (3H, d, *J* = 6.3 Hz), 1.36 (3H, s), 1.51 (3H, s), 1.63 (1H, dd, *J* = 15.0, 8.0 Hz), 1.89 (4H, m), 2.27 (1H, ddd, *J* = 15.0, 9.4, 1.5 Hz), 2.40 (2H, m), 2.84 (1H, m), 2.91–2.93 (2H, m), 3.09 (1H, q, *J* = 6.3 Hz), 3.34 (3H, s), 3.86 (1H, dd, *J* = 9.2, 7.5 Hz), 4.11 (1H, d, *J* = 7.5 Hz). ^{13}C NMR (125 MHz, $CDCl_3$) δ: 13.0, 22.5, 25.0, 25.3, 26.3, 27.0, 38.5, 40.7, 44.2, 57.5, 73.2, 73.5, 75.1, 83.0, 108.4, 213.0. EI HRMS $(M - Me)^+$ found: 283.1548; $C_{15}H_{23}O_5$ calcd: 283.1546.

4aβ,8aα-Decal-1-one (**17c**)

cis-Decalone **17a** prepared above was dissolved in dry THF (0.25 mol/L solution) and cooled to –78°. LiHMDS (1.5 equiv) was added and the mixture stirred at –78° for 10 min. It was allowed to warm to 0° and stirred at that temperature for a further 30 min. The reaction was quenched at 0° with methanol and allowed to reach rt. The solvents were removed and the crude product purified by chromatography to leave a thick oil. Yield: 80%. $[\alpha]_D$ = –10.6 (*c* 0.46, $CHCl_3$). ^{1}H NMR (500 MHz, $CDCl_3$) δ: 1.17 (3H, d, *J* = 6.3 Hz), 1.29–1.34 (1H, m), 1.36 (3H, s), 1.45 (3H, s), 1.63 (1H, qt, *J* = 13.6, 4.0 Hz), 1.77 (1H, dd, *J* = 15.0, 7.1 Hz), 1.96–2.06 (3H, m), 2.38–2.41 (1H, m), 3.21 (1H, m), 3.21 (1H, q, *J* = 6.3 Hz), 3.29 (3H, s), 3.99 (1H, dd, *J* = 9.0, 7.1 Hz), 4.18 (1H, d, *J* = 7.1 Hz). ^{13}C NMR (125 MHz, $CDCl_3$) δ: 12.1, 24.2, 24.9, 25.8, 27.2, 30.3, 41.6, 43.5, 46.3, 57.0, 73.4, 76.2, 80.3, 80.7, 108.3, 210.1. EI HRMS M^+ found: 298.1780; $C_{16}H_{26}O_5$ calcd: 298.1779.

4aβ,8aα-Decal-1-one (**17d**)

Prepared from **17b** as above. The product was obtained in a similar yield as a 7:1 mixture of **17d**:**17b** and purified by column chromatography as before. ^{1}H NMR (500 MHz, $CDCl_3$) δ: 1.15 (3H, d, *J* = 6.3 Hz), 1.23–1.30 (1H, m), 1.35 (3H, s), 1.46 (3H, s), 1.66 (1H, br.q, *J* = 14.0 Hz), 1.81 (1H, q, *J* = 9.1 Hz), 1.98 (1H, br.q, *J* = 11.0 Hz), 2.06–2.12 (3H, m), 2.21–2.31 (2H, m), 2.42 (1H, br.d, *J* = 14.0 Hz), 2.5–2.7 (1H, br), 3.14 (1H, q, *J* = 6.0 Hz), 3.33 (3H, s), 3.90 (1H, dd, *J* = 8.4, 6.5 Hz), 4.24 (1H, d, *J* = 6.5 Hz). ^{13}C NMR (125 MHz) δ: 12.5, 25.2, 25.9, 27.5, 27.9, 29.8, 41.5, 43.6, 47.0, 57.3, 73.4, 74.8, 80.2, 81.8, 108.7, 209.7. EI HRMS (M^+) found: 298.1788; $C_{16}H_{26}O_5$ calcd: 298.1780

The ^{1}H NMR (500 MHz) spectra of **17a**–**17d** are displayed in Fig. 2 of the Supplementary data.

7-(1′-Methoxyethyl)-7-trimethylsilyloxy-5,6-di-*O*-isopropylidene-2,3-dehydrodecal-1-ones (**18a**–**18d**)

Diisopropylamine (12 equiv) in THF at 0° was stirred with *n*-BuLi (12 equiv) for 15 min. The solution was cooled to –78° and the ketone **17** (1 equiv) in THF was added slowly by a syringe. After stirring for a further 1 h at –78°, TMSCl (20 equiv) was added and the stirring was continued for a further 1.25 h. The solution was allowed to warm to 0° and was stirred for a further 15 min and then quenched with aq NH_4Cl, extracted with ether (3×), washed with brine, dried ($MgSO_4$), and concentrated. The crude bis-silylether was taken up in DMSO and $Pd(OAc)_2$ (0.5 equiv) was added and flushed with O_2 (3×). It was then stirred under an atmosphere of oxygen for 48 h at rt. The reaction was quenched with brine and extracted with EtOAc (5×) and the extracts washed with water and then brine, and then dried ($MgSO_4$). The solvents were removed and the residue purified by flash chromatography (hexanes / ethyl acetate, 8:1). **18a**: **17a** (0.336 g, 1.13 mmol in THF 12 mL), 2.0 mol/L *n*-BuLi (6.75 mL, 13.5 mmol), *i*-Pr_2NH (2.0 mL, 14.0 mmol), THF (12 mL); TMSCl (2.9 mL, 22.5 mmol), $Pd(OAc)_2$ (0.126 g, 0.563 mmol), DMSO (12 mL) yielded **18a** as an oil. Yield: 0.264 g, (63%). $[\alpha]_D$ = +13.4 (*c* 0.298, $CHCl_3$). ^{1}H NMR (300 MHz, $CDCl_3$) δ: 0.13 (9H, s) 1.16 (3H, d, *J* = 6.3 Hz), 1.30 (3H, s), 1.48 (3H, s), 1.89 (1H, dd, *J* = 14.7, 7.1 Hz), 2.08 (1H, dd, *J* = 14.7, 6.0 Hz), 2.42–2.48 (2H, m), 2.59–2.69 (2H, m), 3.12 (1H, q, *J* = 6.3 Hz), 3.16 (3H, s), 3.87 (1H, d, *J* = 6.0 Hz), 4.01 (1H, dd, *J* = 7.5, 6.2 Hz), 5.99 (1H, dt, *J* = 10.0, 1.9 Hz), 6.76 (1H, dd, *J* = 10.0, 4.3 Hz). ^{13}C NMR (75 MHz, $CDCl_3$) δ: 2.8 (3C), 12.0, 25.6, 26.5, 27.2, 27.5, 35.3, 41.9, 55.7, 76.1, 76.9, 77.5, 82.5, 107.6, 130.1, 146.3, 199.0. EI HRMS $[M - Me]^+$ found: 353.1785; $C_{18}H_{29}O_5Si$ calcd: 353.1785. **18b**: **17b** (0.171 g, 0.572 mmol in THF (6 mL)), 2.0 mol/L BuLi (3.43 mL, 6.86 mmol), *i*-Pr_2NH (1.0 mL, 7.16 mmol) in THF (6 mL), TMSCl (1.5 mL, 11.44 mmol); $Pd(OAc)_2$ (64 mg, 0.286 mmol) in DMSO (6 mL). Yield: 0.133 g (63%) of **18b** as a pale yellow oil. ^{1}H NMR (300 MHz, $CDCl_3$) δ: 0.12 (9H, s), 1.16 (3H, d, *J* = 6.3 Hz), 1.25 (3H, s), 1.45 (3H, s), 1.65 (1H, dd, *J* = 14.9, 6.8 Hz), 2.22 (1H, dd, *J* = 14.9, 7.0 Hz), 2.41–2.46, (2H, m), 2.76–2.85 (2H, m), 3.19 (3H, s), 3.15–3.21 (1H, m), 3.91 (1H, d, *J* = 6.6 Hz), 4.0 (1H, t, *J* = 6.3 Hz), 5.99 (1H, d, *J* = 10.0 Hz), 6.80 (1H, dt, *J* = 10.0, 4.0, 4.0 Hz). ^{13}C NMR (75 MHz, $CDCl_3$) δ: 2.6 (3C), 13.6, 25.8, 26.7, 27.2, 28.2, 35.1, 40.8, 56.0, 74.3, 75.7, 77.1, 81.7, 108.3, 129.7, 147.3, 199.8. **18c**: ketone **17c** (0.463 g, 1.56 mmol)

Can. J. Chem. Downloaded from www.nrcresearchpress.com by South China Agricultural University on 09/19/12
For personal use only.

in THF (17 mL), 1.6 mol/L BuLi (12.5 mL, 20 mmol), *i*-Pr_2NH (2.8 mL, 20 mmol) in THF (17 mL), TMSCl (4 mL, 30 mmol), $Pd(OAc)_2$ (0.179 g, 0.79 mmol) in DMSO (17 mL) yielded **18c** (0.415 g, 1.13 mmol, 72%). A small amount (0.03 g) of the cis fused enone **18a** was also isolated. $[\alpha]_D$ = +45.5 (*c* 1.156, $CHCl_3$). ^1H NMR (300 MHz, $CDCl_3$) δ: 0.08 (9H, s), 1.16 (3H, d), 1.34 (3H, s), 1.45 (3H, s), 1.50 (1H, t, *J* = 13.4 Hz), 1.79–1.85 (1H, m), 1.98–2.08 (1H, m), 2.38 (1H, dd, *J* = 13.9, 2.5 Hz), 2.56 (1H, td, *J* = 12.0, 12.0, 3.0 Hz), 2.67 (1H, dt, *J* ≈ 18.0, 5.0, 5.0 Hz), 3.20 (1H, q., *J* = 6.3 Hz), 3.23 (3H, s), 3.9 (1H, d, *J* = 4.5 Hz), 4.04 (1H, dd, *J* = 8.7, 4.7 Hz), 5.94 (1H, dd, *J* = 10.0, 2.4 Hz), 6.90 (1H, ddd, *J* = 10.0, 5.9, 1.9 Hz). ^{13}C NMR (125 MHz, $CDCl_3$) δ: 2.7 (3C), 12.4, 26.4, 28.2, 28.6, 30.5, 41.8, 43.9, 57.1, 77.4, 80.5, 81.3, 85.0, 107.8, 129.4, 148.5, 200.2. EI HRMS $(M - Me)^+$ found: 353.1779; $C_{18}H_{29}O_5Si$ calcd: 353.1774. **18d**: ketone **17d** (0.204 g, 0.68 mmol) in THF (6 mL), 1.6 mol/L BuLi (6.6 mL, 10.6 mmol), *i*-Pr_2NH (1.2 mL, 8.6 mmol) in THF (6 mL), TMSCl (1.8 mL, 13.73 mmol), $Pd(OAc)_2$ (82.4 mg, 0.37 mmol) in DMSO (8 mL). Yield: 98.3 mg (47%) and 27.4 mg of recovered starting material (**17d**). ^1H NMR (300 MHz, $CDCl_3$) δ: 0.08 (9H, s), 1.15 (3H, d, *J* = 6.2 Hz), 1.45 (3H, s), 1.78 (1H, dd, *J* = 14.2, 11.4 Hz), 1.94–2.22 (4H, m), 2.65–2.75 (1H, m), 3.2 (1H, q, *J* = 6.2 Hz), 3.27 (3H, s), 3.90 (1H, dd, *J* = 8.0, 5.0 Hz), 4.27 (1H, d, *J* = 5.0 Hz), 5.98 (1H, dd, *J* = 10.0, 1.8 Hz), 6.92 (1H, m). EI LRMS *m*/*z*: 353 $[M - Me]^+$ (10), 309 $[M - MeCHOMe]^+$ (90), 251 (100), 73 (30).

11-Hydroxy-10-methoxy-2-trimethylsilyloxy-2-(1′-methoxyethyl)-3,4-di-*O*-isopropylidene-1,2,3,4,4a,5,12,12a-octahydronaphthacen-12-one (21a)

A solution of tetracycle **20a**[4b] (120 mg, 0.232 mmol) and DDQ (79 mg, 0.348 mmol) in benzene (18 mL) was refluxed for 4 h. The solution was cooled, diluted with ether and water, and extracted with ether (3 × 20 mL). The organic extracts were combined, washed with water and then with brine, and dried over $MgSO_4$. The solvents were removed and the residue chromatographed (hexanes / ethyl acetate, 8:1) and the bright fluorescent band (R_f = 0.38) was separated from the starting material (R_f = 0.26), which did not fluoresce. Yield: 25.1 mg (21%); starting material recovered: 48.8 mg (41%). ^1H NMR (500 MHz, $CDCl_3$) δ: 1.20 (3H, d, *J* = 6.3 Hz), 1.31 (3H, s), 1.54 (3H, s), 1.98 (dd, *J* = 14.7, 7.4 Hz), 2.45 (1H, dd, *J* = 14.5, 4 Hz), 2.49–2.54 (1H, m), 2.80 (3H, s), 2.94 (1H, m), 3.02 (1H, dd, *J* = 15.8, 3.8 Hz), 3.05 (1H, q, *J* = 6.3 Hz), 3.08 (1H, dd, *J* =15.8, 3.8 Hz), 3.83 (1H, d, *J* = 5.3 Hz), 3.92 (1H, dd, *J* = 9, 5.3 Hz), 3.99 (3H, s), 6.76 (1H, d, *J* = 7.9 Hz), 6.97 (1H, s), 7.17 (1H, d, *J* = 7.9 Hz), 7.42 (1H, t, *J* = 8 Hz). EI HRMS M^+ found: 514.2380; $C_{28}H_{38}O_7Si$ calcd: 514.2374.

11-Hydroxy-10-methoxy-2-trimethylsilyloxy-2-(1′-methoxyethyl)-3,4-di-*O*-isopropylidene-1,2,3,4,4a,5,12,12a-octahydronaphthacen-12-one (21c)

Silyl ether **20c**[4b] (286 mg, 0.55 mmol) was dissolved in benzene (55 mL) under argon. The solution was then treated with 2,3-dichloro-5,6-dicyanobenzoquinone (197 mg, 0.87 mmol) in one portion at 25 °C. The reaction was stirred for 5 h at 25 °C and then quenched with water. The product was extracted into Et_2O and washed sequentially with saturated $NaHCO_3$ and brine. The organic layer was dried (Na_2SO_4), filtered, and concentrated to dryness under reduced pressure. The crude product was purified by silica gel chromatography (EtOAc/hexanes, 1.9) to afford the desired product **21c** (282 mg, 0.515 mmol, 100%) as a bright green amorphous solid. $[\alpha]_D$ = +32.4 ($CHCl_3$). R_f 0.36 (EtOAc/hexanes, 1:4). ^1H NMR ($CDCl_3$, 500 MHz): data are shown in Table 1. ^{13}C NMR ($CDCl_3$, 125 MHz) δ: 2.7 (3C), 12.5, 26.4, 28.6 (2C), 33.9, 41.4, 44.7, 56.1, 57.2, 77.5, 80.4, 81.3, 85.1, 105.4, 107.8, 111.1, 115.1, 116.6, 119.7, 130.8, 137.8, 140.1, 159.8, 165.7, 204.9. EI HRMS calcd for $C_{28}H_{38}O_7Si$ *m*/*z*: 514.2387; found: 514.2380.

2,11-Dihydroxy-10-methoxy-2-(1′-methoxyethyl)-3,4-di-*O*-isopropylidene-1,2,3,4,4a,5,12,12a-octahydronaphthacen-12-one (22)

To ensure complete dissolution, THF (0.60 mL) was added to a solution containing silyl ether **20c** (95.7 mg, 0.186 mmol) partially dissolved in HPLC grade MeOH (6.0 mL). The solution was cooled to 0 °C prior to adding pyridinium *p*-toluenesulfonate (52.8 mg, 0.210 mmol) as a solid in one portion. The reaction mixture was stirred in the dark under an Ar atmosphere at 0 °C for 4 h. The reaction mixture was quenched with saturated $NaHCO_3$ (0.5 mL) at 0 °C and the organic solvent removed in vacuo. The crude mixture was redissolved in CH_2Cl_2 and washed with saturated $NaHCO_3$ and saturated NaCl. The organic layer was dried over $MgSO_4$, filtered, and evaporated to dryness. The crude product was purified by flash column chromatography (EtOAc/hexanes, 2:3) to give the tetracyclic diol **22** (82.5 mg, 0.186 mmol, 100%) as a fluorescent green, amorphous solid. R_f 0.29 (EtOAc/hexanes, 3:7). ^1H NMR ($CDCl_3$, 500 MHz): data are shown in Table 1. ^{13}C NMR ($CDCl_3$, 125 MHz) δ: 12.2, 25.1, 25.6, 27.3, 34.9, 39.2, 43.9, 56.1, 57.0, 73.7, 76.2, 79.9, 80.9, 105.5, 108.6, 111.2, 115.1, 116.6, 119.7, 130.9, 137.4, 140.1, 159.8, 165.7, 204.6. EI HRMS calcd for $C_{25}H_{30}O_7$ *m*/*z*: 442.1992; found: 442.1990.

4,11-Dihydroxy-10-methoxy-2-[1′-methoxyethyl]-2β,3β,-di-*O*-isopropylidene-1,2,3,4,5,12,12a-octahydronaphthacen-12-one (23)

To a vial containing a solution of **21c** (16.6 mg, 0.032 mmol) in THF (0.40 mL) was added H_2O (0.10 mL) as a co-solvent. To the vial was then added a catalytic amount of *p*-toluenesulfonic acid monohydrate (2.0 mg, 0.011 mmol) and the reaction stirred at 25 °C for 48 h. The reaction was terminated by removal of the solvent in vacuo. The crude reaction was applied directly to silica gel and purified by flash column chromatography (EtOAc/hexanes, 2:3) to afford **23** (6.0 mg, 0.014 mmol, 42%) as a fluorescent yellow-green amorphous solid, recrystallized from CH_2Cl_2/hexane. $[\alpha]_D$ = –26.3 ($CHCl_3$). R_f 0.51 (EtOAc/hexanes, 1:1). ^1H NMR ($CDCl_3$, 500 MHz): data are shown in Table 1. ^{13}C NMR ($CDCl_3$, 125 MHz) δ: 13.6, 26.9, 28.4, 28.9, 33.0, 40.3, 46.3, 56.1, 56.7, 74.2, 81.5, 82.4, 83.3, 105.4, 108.8, 111.2, 115.1, 116.6, 119.8, 130.9, 137.6, 140.2, 159.8, 165.8, 204.5. EI HRMS calcd for $C_{25}H_{30}O_7$ *m*/*z*: 442.1992; found: 442.1988.

Can. J. Chem. Downloaded from www.nrcresearchpress.com by South China Agricultural University on 09/19/12
For personal use only.

11-Hydroxy-4,10-dimethoxy-2β,3β-di-*O*-isopropylidene-2α-(1′-methoxyethyl)-1,2,3,4,4a,5,12,12a-octahydronaphthacen-12-one (24)

Tetracyclic ketone **23** (6.0 mg, 0.014 mmol) dissolved in dry THF (1 mL) was treated with excess sodium hydride that had been previously rinsed with dry THF. Iodomethane (0.2 mL) was added and the mixture stirred at rt with occasional monitoring by TLC. After 1.5 h the starting material was completely consumed. The THF solution was poured into saturated aqueous ammonium chloride and extracted with dichloromethane (3 × 10 mL). The combined organic extracts were dried (Na_2SO_4) and evaporated. The residue was purified by chromatography (ethyl acetate / hexanes, 5:7). Yield: 6 mg (94%) ^{1}H NMR (500 MHz, $CDCl_3$) δ: 1.31 (3H, d, J = 6.2 Hz), 1.35 (3H, s), 1.43 (1H, t, $J \approx$ 1.34 Hz), 1.45 (3H, s), 2.33 (1H, qd, $J \approx$ 12.4, 12.4, 3.5 Hz), 2.59–2.69 (2H, m), 2.80 (1H, dd, $J \approx$ 14, 3.6 Hz), 3.31 (3H, s), 3.39–3.47 (3H, m), 3.56 (3H, s), 4.0 (3H, s), 4.27 (1H, d, J = 3.25 Hz), 6.77 (1H, d, J = 7.9 Hz), 6.97 (1H, s), 7.19 (1H, d, J = 8 Hz), 7.44 (1H, t, $J \approx$ 8 Hz), 15.17 (1H, s). EI HRMS M$^+$ found: 456.2155; $C_{26}H_{32}O_7$ calcd: 456.2148.

2β,3β,11-Trihydroxy-4β,10-dimethoxy-2α-[1′-methoxyethyl]-1,2,3,4,4a,5,12,12a-octahydronaphthacen-12-one (25)

Tetracycle **24** (6.0 mg, 0.013 mmol) dissolved in THF (1 mL) was treated with 1 N aq HCl (0.4 mL) and stirred at rt with monitoring by TLC. After 36 h, the solution was poured into saturated aq $NaHCO_3$ and extracted with dichloromethane (4 × 10 mL). The extracts were combined, dried (Na_2SO_4), and the solvents removed. The residue was chromatographed (ethyl acetate / hexanes, 3:1) to obtain the triol **25**. Yield: 5 mg (91%). ^{1}H NMR (500 MHz, $CDCl_3$) δ: 1.26 (3H, d, J = 6.2 Hz), 1.54 (1H, s), 1.60 (1H, t, $J \approx$ 13 Hz), 2.25 (1H, qd, $J \approx$ 12.6, 12.6, 3.4 Hz), 2.57–2.65 (2H, m), 2.69 (1H, dd, $J \approx$ 13.6, 3.55 Hz), 2.79 (1H, s), 3.31 (1H, dd, J = 10.3, 2.7 Hz), 3.34 (3H, s), 3.37 (1H, q, J = 6.3 Hz), 3.49 (3H, s), 3.97 (1H, d, J = 2 Hz), 4.0 (3H, s), 6.78 (1H, d, $J \approx$ 7.9 Hz), 6.96 (1H, s), 7.18 (1H, d, J = 8 Hz), 7.45 (1H, t, J = 8 Hz), 15.07 (1H, s). ^{13}C NMR ($CDCl_3$, 125 MHz) δ: 12.5, 28.3, 33.4, 37.3, 45.7, 56.2, 57.0, 57.3, 69.7, 75.2, 79.7, 83.3, 105.5, 111.3, 115.1, 116.8, 119.8, 130.9, 137.7, 140.2, 159.8, 165.7, 204.3. EI HRMS M$^+$ found: 416.1832; $C_{23}H_{28}O_7$ calcd: 416.1835.

2β,11-Dihydroxy-4β,10-dimethoxy-2α-[1′-methoxyethyl]-1,2,3,4,4a,5,12,12-octahydronaphthacene-3,12-dione (26)

Triol **25** (5 mg, 0.012 mmol) in acetonitrile (1 mL) was heated to 70° with *o*-iodobenzoic acid and the progress of the reaction monitored by TLC. After 18 h, almost all the starting material had been consumed. The solvents were removed and the residue was chromatographed (ethyl acetate / hexanes, 4:1). The product **26** was isolated, but a small amount of starting material **25** also remained. Yield: 3.5 mg (70%). ^{1}H NMR (500 MHz, $CDCl_3$) δ: 1.27 (3H, d, J = 6.2 Hz), 2.27–2.35 (2H, m), 2.86 (1H, td, J = 13, 13, 1 Hz), 3.17 (1H, td, J = 12.5, 12.5, 3.7 Hz), 3.35 (3H, s), 3.41 (1H, q, J = 6.2 Hz), 3.44 (1H, dd, J = 15.8, 3.5 Hz), 3.56 (3H, s), 3.88 (1H, s), 4.0 (3H, s), 4.11 (1H, d, J = 11.1 Hz), 6.80 (1H, d, J = 8 Hz), 6.97 (1H, s), 7.19 (1H, d, J = 8.3 Hz), 7.47 (1H, t, J = 8 Hz), 14.99 (1H, s). EI HRMS M$^+$ found: 414.1687; $C_{23}H_{26}O_7$ calcd: 414.1679.

2,11-Dihydroxy-10-methoxy-2-hydroxy-2-(1′-methoxyethyl)-3,4-di-*O*-isopropylidene-2,3,4,5,12-hexahydronaphthacene-12-one (27)

To an oven-dried vial containing **21c** (10.4 mg, 0.020 mmol) dissolved in anhydrous THF (0.40 mL) was added a THF solution of TBAF (1 mol/L, 0.40 mL, 0.040 mmol) at 0 °C. The reaction mixture was stirred in darkness for 4.5 h at 0 °C and then at 25 °C for 18 h. The reaction was quenched by the addition of H_2O (0.30 mL) and purified directly by flash column chromatography using silica gel. The desired product was eluted using EtOAc/hexanes (2:3) to afford intermediate **27** (6.0 mg, 0.014 mmol, 70%) as a yellow-orange solid and crystallized from methylene chloride / hexane. $[\alpha]_D$ = –345 ($CHCl_3$). R_f 0.49 (EtOAc/hexanes, 2:3). ^{1}H NMR ($CDCl_3$, 500 MHz): data are shown in Table 1. ^{13}C NMR ($CDCl_3$, 125 MHz) δ: 12.7, 25.4, 27.4, 34.5, 39.0, 56.2, 56.8, 72.6, 76.8, 79.8, 80.6, 105.8, 109.3, 111.7, 115.2, 116.5, 119.9, 131.4, 135.3, 136.5, 138.1, 140.4, 159.9, 167.2, 189.7. EI HRMS calcd for $C_{25}H_{28}O_7$ *m/z*: 440.1835; found: 440.1837.

11,12a-Dihydroxy-10-methoxy-3,4-di-*O*-isopropylidene-2-(1′-methoxyethyl)-3,4,4a,5,11,12a-hexahydronaphthacen-12-one (28)

The enone **27** (16 mg, 0.036 mmol) dissolved in dry dichloromethane (5 mL) was treated with methylamine (0.2 mL) and DMAP (4 mg). The solution was cooled to 0 °C and methanesulfoxyl chloride (0.5 mL) was added. The mixture was stirred at 0 °C for 0.5 h and monitored by TLC for the disappearance of the starting material. It was poured into cold aqueous sodium bicarbonate and the solution was extracted with dichloromethane (3 × 10 mL). The combined organic extracts were dried (Na_2SO_4) and the residue chromatographed on silica (ethyl acetate / hexanes, 1:2). The greenish yellow fluorescent fraction, slightly slower on the TLC than **22** or **27**, was collected and evaporated. Further purification by column chromatography (dichloromethane/hexane, 85:15) resulted in the collection of a product that showed a single spot on the TLC, but still appeared to be contaminated by ~10% of an impurity (^{1}H and ^{13}C NMR). ^{1}H NMR ($CDCl_3$, 500 MHz): data are shown in Table 1. ^{13}C NMR (125 MHz, $CDCl_3$) δ: 12.2, 19.2, 25.7, 27.1, 28.1, 41.8, 56.2, 56.5, 70.8, 71.7, 75.5, 77.4, 105.7, 105.9, 109.6, 109.7, 115.0, 117.2, 119.8, 124.9, 131.5, 137.3, 159.8, 163.7, 199. EI HRMS M$^+$ found: 440.1832; $C_{25}H_{28}O_7$ calcd: 440.1835.

Supplementary data

Supplementary data (general experimental methods; copies of ^{1}H NMR spectra for compounds **16a**, **16b**, **17a**–**17d**, **18a**–**18d**, **21c**, and **22**–**28**; ^{13}C or JMOD spectra for compounds **16a**, **16b**, **17a**–**17d**, **18a**, **18c**, **21c**, **22**, **23**, **25**, **27**, and **28**; H–H COSY spectrum for compound **28**; EIMS for compound **28**; and HPLC traces of compound **16a**) are available for this article through the journal Web site at http://nrcresearchpress.com/doi/suppl/10.1139/v11-119. CCDC 814893–814898 contain the X-ray data (**17a**, **17b**, **18b**, **23**, **27**, and catalyst

B) in CIF format for this manuscript. These data can be obtained, free of charge, via http://www.ccdc.cam.ac.uk/cgi-bin/catreq.cgi (Or from the Cambridge Crystallographic Data Centre, 12 Union Road, Cambridge CB2 1Ez, UK; fax +44 1223 336033; or e-mail deposit@ccdc.cam.ac.uk).

Acknowledgement

We thank the Natural Sciences and Engineering Research Council of Canada (NSERC) for support of this work and J. Shikaze for invaluable administrative assistance.

References

(1) Asai, M. *Chem. Pharm. Bull. (Tokyo)* **1970**, *18*, 1699; Asai, M. *Chem. Pharm. Bull. (Tokyo)* **1970**, *18*, 1706.

(2) Trost, B. M.; Caldwell, C. G.; Murayama, E.; Heissler, D. *J. Org. Chem.* **1983**, *48* (19), 3252. doi:10.1021/jo00167a020.

(3) (a) White, J. D.; Nolen, E. G.; Miller, C. H. *J. Org. Chem.* **1986**, *51* (7), 1150. doi:10.1021/jo00357a047; (b) White, J. D.; Demnitz, F. W.; Oda, H.; Hassler, C.; Snyder, J. P. *Org. Lett.* **2000**, *2* (21), 3313. doi:10.1021/ol000200f; (c) White, J. D.; Demnitz, F. W. J.; Xu, Q.; Martin, W. H. C. *Org. Lett.* **2008**, *10* (13), 2833. doi:10.1021/ol8009732.

(4) (a) Wang, L.; Meegalla, S. K.; Fang, C.-L.; Taylor, N.; Rodrigo, R. *Can. J. Chem.* **2002**, *80* (6), 728. doi:10.1139/v02-105; (b) Hill, B.; Rodrigo, R. *Org. Lett.* **2005**, *7* (23), 5223. doi:10.1021/ol052058u.

(5) (a) Abdelfattah, M. S.; Rohr, J. *Angew. Chem. Int. Ed.* **2006**, *45* (34), 5685. doi:10.1002/anie.200600511; (b) Lombó, F.; Menéndez, N.; Salas, J. A.; Méndez, C. *Appl. Microbiol. Biotechnol.* **2006**, *73* (1), 1. doi:10.1007/s00253-006-0511-6; (c) Rohr, J.; Weiβbach, U.; Beninga, C.; Künzel, E.; Siems, K.; Bindseil, K. U.; Lombó, F.; Rado, L.; Braña, A. F.; Méndez, C.; Salas, J. A. *Chem. Commun. (Camb.)* **1998**, (3): 437. doi:10.1039/a707446h.

(6) Prasad, K. R. K.; Joshi, N. N. *Tetrahedron Asymmetry* **1996**, *7* (11), 3147. doi:10.1016/0957-4166(96)00416-8; Quallich, G. J.; Woodall, T. M. *Synlett* **1993**, *1993* (12), 929. doi:10.1055/s-1993-22656.

(7) (a) Rogers, C.; Keay, B. A. *Can. J. Chem.* **1993**, *71* (5), 611. doi:10.1139/v93-081; (b) Rogers, C.; Keay, B. A. *Can. J. Chem.* **1992**, *70* (12), 2929. doi:10.1139/v92-375; (c) De Clercq, P. J.; Van Royen, L. A. *Synth. Commun.* **1979**, *9* (9), 771. doi:10.1080/00397917908064193.

(8) Hoveyda, A. H.; Evans, D. A.; Fu, G. C. *Chem. Rev.* **1993**, *93* (4), 1307. doi:10.1021/cr00020a002.

(9) Kuroda, T.; Takahashi, M.; Kondo, K.; Iwasaki, T. *J. Org. Chem.* **1996**, *61* (26), 9560. doi:10.1021/jo9609384.

(10) Butora, G.; Gum, A. G.; Hudlicky, T.; Abboud, K. A. *Synthesis* **1998**, *1998* (03), 275. doi:10.1055/s-1998-4529.

(11) Crabtree, R. *Acc. Chem. Res.* **1979**, *12* (9), 331. doi:10.1021/ar50141a005.

(12) Pfaltz, A.; Blankenstein, J.; Hilgoaf, R.; Hörmann, E.; McIntyre, S.; Menges, F.; Schönleber, M.; Smidt, S. P.; Wüstenberg, B.; Zimmerman, N. *Adv. Synth. Catal.* **2003**, *345* (1–2), 33. doi:10.1002/adsc.200390027.

(13) Reger, D. L.; Wright, T. D.; Little, C. A.; Lamba, J. J. S.; Smith, M. D. *Inorg. Chem.* **2001**, *40* (15), 3810. doi:10.1021/ic0100121.

(14) Lightfoot, A.; Schnider, P.; Pfaltz, A. *Angew. Chem. Int. Ed.* **1998**, *37* (20), 2897. doi:10.1002/(SICI)1521-3773(19981102)37:20<2897::AID-ANIE2897>3.0.CO;2-8.

(15) Ito, Y.; Hirao, T.; Saegusa, T. *J. Org. Chem.* **1978**, *43* (5), 1011. doi:10.1021/jo00399a052.

(16) Larock, R.; Hightower, T. *Tetrahedron Lett.* **1995**, *36* (14), 2423. doi:10.1016/0040-4039(95)00306-W.

(17) Bicyclic enones lacking a hydrogen atom at the ring junction were successfully used in the Staunton–Weinreb annulation for tetracycline synthesis. Charest, M. G.; Lerner, C. D.; Brubaker, J. D.; Siegel, D. R.; Myers, A. G. *Science* **2005**, *308* (5720), 395. doi:10.1126/science.1109755; Brubaker, J. D.; Myers, A. G. *Org. Lett.* **2007**, *9* (18), 3523. doi:10.1021/ol071377d; Also see Sun, C.; Wang, Q.; Brubaker, J. D.; Wright, P. M.; Lerner, C. D.; Noson, K.; Charest, M.; Siegel, D. R.; Wang, Y.-M.; Myers, A. G. *J. Am. Chem. Soc.* **2008**, *130* (52), 17913. doi:10.1021/ja806629e.

(18) All ^{1}H NMR assignments were made with the aid of decoupling, 2D correlations, and comparisons with spectra of similar compounds.

(19) More, J. D.; Finney, N. S. *Org. Lett.* **2002**, *4* (17), 3001. doi:10.1021/ol026427n.

(20) (a) Gangopadhyay, A. K.; Lal, B. *Synth. Commun.* **2006**, *36* (24), 3783. doi:10.1080/00397910600947940; (b) Russell, H. F.; Bremner, J. B.; Bushelle-Edghill, J.; Lewis, M. R.; Thomas, S. R.; Bates, F., II. *Tetrahedron Lett.* **2007**, *48* (9), 1637. doi:10.1016/j.tetlet.2006.12.136.

(21) Yadav, J. S.; Mysorekar, S. V. *Synth. Commun.* **1989**, *19* (5), 1057. doi:10.1080/00397918908051028.

(22) Leleti, R. R.; Hu, B.; Prashad, M.; Repic, O. *Tetrahedron Lett.* **2007**, *48* (48), 8505. doi:10.1016/j.tetlet.2007.09.156.

(23) Stepanenko, V.; De Jesus, M.; Correa, W.; Bermudez, L.; Vazquez, C.; Guzman, I.; Ortiz-Marciales, M. *Tetrahedron Asymmetry* **2009**, *20* (23), 2659. doi:10.1016/j.tetasy.2009.11.009.

Can. J. Chem. Downloaded from www.nrcresearchpress.com by South China Agricultural University on 09/19/12
For personal use only.

First-principles computational studies of the torsional potential energy surface of the *sec*-butyl radical

Ya Kun Chen and Yan Alexander Wang

Can. J. Chem. Downloaded from www.nrcresearchpress.com by South China Agricultural University on 09/19/12
For personal use only.

Abstract: First-principles calculations were carried out to investigate the torsional potential energy surface (PES) of the *sec*-butyl radical. All the wave function methods employed predict a cis-like stable conformation with a dihedral angle of about 47° in addition to the trans-like global minimum conformation and a gauche conformation. However, most of the popular density functional approaches predict only the latter two local minima and lack the cis conformation that was experimentally observed. On the other hand, some density functional methods that incorporate the exact exchange and asymptotically corrected correlation functionals can locate the cis conformation successfully. The basis-set effect was also measured using popular B3LYP and MP2 Hamiltonians: only moderate shape changes were found for PES profiles upon basis-set variations. The stationary structures and their Hessians were obtained at both MP2 and B3LYP levels, with or without incorporating the zero-point energies. Opposite to the relative stability within the Born–Oppenheimer approximation, the cis conformation is more stable than the gauche conformation upon the zero-point correction, consistent with the experiment observations.

Key words: sec-butyl, torsional potential energy surface, density functional theory, wave function theory.

Résumé : On a effectué des calculs théoriques à partir des principes premiers pour étudier la surface d'énergie potentielle (SEP) de torsion du radical *sec*-butyle. Toutes les méthodes de fonction d'onde utilisées prédisent qu'il existe sous une conformation de type cis stable avec un angle dièdre de 47° à côté d'une conformation de type trans avec minimum global et d'une conformation gauche. Toutefois, la plupart des approches populaires par la fonctionnelle de la densité ne prédisent l'existence que des deux derniers minima locaux sans prédire celle de la conformation cis observée expérimentalement. Par ailleurs, certaines méthodes de la fonctionnelle de la densité qui incorporent l'échange exact et des fonctionnelles de corrélation corrigées d'une façon asymptotique permettent de localiser avec succès la conformation cis. On a aussi mesuré l'effet de l'ensemble de base en faisant appel aux hamiltoniens populaires B3LYP et MP2 : toutefois, avec ces changements d'ensembles de base, on n'a pu observer que des changements modérés de la forme des profils de la surface d'énergie potentielle (SEP). On a obtenu les structures stationnaires et leurs matrices hessiennes aux niveaux MP2 ainsi que B3LYP, avec et sans incorporation des énergies du point zéro. Contrairement à la stabilité relative observée dans l'approximation de Born–Oppenheimer, la conformation cis est plus stable que la conformation gauche lorsqu'on introduit une correction pour l'énergie au point zéro et ceci est en accord avec les observations expérimentales.

Mots-clés : sec-butyle, surface d'énergie potentielle de torsion, théorie de la fonctionnelle de la densité, théorie de la fonction d'onde.

[Traduit par la Rédaction]

Introduction

Torsional potential energy surfaces (PESs) of many chemical species have been studied numerous times because they provide the key information for molecular thermodynamic state functions. At the same time, it is also of great interest to compare the theoretically predicted PES and available experimental data to develop and improve computational methods and to provide deep insight into the nature of torsional barriers.

Even molecules as simple as ethane have attracted much theoretical attention for the investigation of the physical nature of its torsional barrier. The rotational barriers of ethane and its congeners were mainly attributed to hyperconjugation interactions by some researchers, challenging the popular belief in many textbooks of the importance of steric repulsive interactions.[1] However, using generalized valence bond theory, a recent theoretical study, in which the torsional barrier of ethane was decomposed adiabatically into steric repulsion and hyperconjugation as well as several other insignificant contributions, manifested that the steric repulsion is the main factor to the stabilization of staggered conformation and hyperconjugation is only of a secondary effect.[2]

Received 10 February 2011. Accepted 23 June 2011. Published at www.nrcresearchpress.com/cjc on 9 November 2011.

Y.K. Chen and Y.A. Wang. Department of Chemistry, University of British Columbia, 2036 Main Mall, Vancouver, BC V6T 1Z1, Canada.

Corresponding author: Yan Alexander Wang (e-mail: yawang@chem.ubc.ca).

This article is part of a Special Issue to commemorate the International Year of Chemistry.

Can. J. Chem. Downloaded from www.nrcresearchpress.com by South China Agricultural University on 09/19/12
For personal use only.

Without the ambiguity in the physical origin of torsional barriers, it is widely accepted that conjugation effect dominates the torsional barrier of the conjugated systems. However, this well-adopted understanding does not promise good agreement between experimental results and theoretical predictions in many conformational studies. The torsional energy profile of 2,2′-bifuran was studied using various forms of Hamiltonians, in which density functional theory (DFT) methods were found inappropriate for the conformation study of this system.[3] Not only does the form of the Hamiltonian matter, but the basis set employed also plays a significant role. When biphenyl PES was studied using several wave function theory (WFT) methods, the quality of basis sets was found to be more important than that of the Hamiltonians.[4,5] Besides the individual Hamiltonian or the basis-set effect, delicate selection of certain combinations of Hamiltonians and basis sets can be critical for an accurate calculation of these (semi)rigid molecules. Theoretical study of the torsional barriers of biisothianaphthene showed that an accurate and balanced description of both conjugation and steric repulsion between nonvicinal hydrogens could be only achieved using high-level Hamiltonians and large basis sets.[6] Therefore, one must be aware of the limitations of popular theoretical tools; extensive studies are required to avoid false predictions even for small molecules based on calculations using a single Hamiltonian with a single basis set.

Other than these well-documented molecules, it might become even more challenging to study the conformations of some open-shell and complex species, including radicals whose PESs are usually so flat that an accurate description of the electronic energies involved goes beyond the reach of popular computational methods. For example, in the case of haloethyl radicals, a theoretical study showed that the DFT methods with the generalized gradient approximation (GGA) outperformed the local Møller-Plesset (MP2) method in predicting the dissociation energy of haloethyl radicals.[7] On the other hand, large spin contamination was found from DFT calculations of OOBr and OOCl, contradicting the popular view that DFT methods suffer less spin contamination than WFT methods. Sometimes, poor results can come from many different methods in a single case. In a conformational study of annulene molecules, both MP2 and DFT methods were found to fail one way or another.[8] All the uncertainties and controversies mentioned above suggest that some popular theoretical methods are still unable to work equally well for conformation studies of various molecular systems. Therefore, a convincing conclusion for the conformation studies often requires systematical benchmarking comparisons.

In this study, the torsional PES of *sec*-butyl was theoretically investigated. The available experimental data were mainly from hyperfine coupling constant (HFCC) study of its muoniated *sec*-butyl formed from muonium addition to 2-butene isomers.[9,10] As a short-lived, light isotope of hydrogen, the muonium, which is composed of a positive muon (antimuon) and an electron, is a good probing atom for the study of various systems.[11]

Before any comparison is made, it is important to point out that all *sec*-butyl isotopomers share the same PES within the Born–Oppenheimer (BO) framework, since the electronic Hamiltonian only parametrically depends on nuclear positions and has nothing to do with nuclear masses. Thus, a conformational study within the BO approximation is equally applicable for both regular (unmuoniated) and muoniated *sec*-butyl radicals (from muonium addition to 2-butene).

Based on the analysis of muon spin resonance (μSR) data, the muoniated *sec*-butyl radical formed from *cis*-2-butene has a large 0 K HFCC value on muon and this value is different from the muon HFCC from muonium addition to *trans*-2-butene. Further temperature-dependent HFCC study also supported the existence of two distinct muoniated *sec*-butyl radicals, both with large values of HFCCs on muon. However, calculations using the popular hybrid B3LYP-DFT Hamiltonian, normally believed to be well suited to predict HFCCs of small organic molecules,[12] only located two equilibrium structures on the ground-state torsional PES:[9,10] one corresponding to the radical formed from muonium addition to *trans*-2-butene and the other, a gauche conformation with HFCC on muon only about one-third of the experimental value. The absence of the experimentally observed muoniated *sec*-butyl formed from *cis*-2-butene from B3LYP calculations prompted us to carry out extensive theoretical studies of the torsional PES of the *sec*-butyl radical.

Besides providing static conformations, the PES also offers valuable information for temperature-dependent HFCC studies. The dynamic (vibrational) and thermodynamic corrections obtained based on the PES can be used to calculate the temperature-dependent behaviour of HFCCs by solving torsional Schrödinger equations. Something worrisome is that the non-BO effect may in turn be significant in a molecule containing muon, which may weaken the validity of our study based on the BO approximation. However, a study of the reaction rate of $Mu + H_2$ indicates that the non-BO effect only changes the reaction barrier height by 3.8%.[13] Therefore, we can expect much less non-BO effect in the muoniated *sec*-butyl radicals in the current study.

To our knowledge, some other experimental results from the homolysis of butyl radicals are also available. Thermodynamic and kinetic studies of the decomposition of the *sec*-butyl radical into propene and the methyl radical were performed,[14] but detailed conformational information of the *sec*-butyl radical could not be inferred from the homolysis study, since the experiment carried out at high temperature averaged out the behaviours of all distinct conformations. Therefore, theoretical calculations have to be done to illuminate possible conformations of the *sec*-butyl radical. Thus far, the first ab initio study on *sec*-butyl conformations can be traced back to the Hartree–Fock (HF) calculations in the 1980s,[15] in which the dynamic correlation effect was not taken into account. Therefore, a systematical study of the *sec*-butyl radical with various correlated Hamiltonians and different basis sets is much needed.

Computational details

All calculations in this study were carried out using the Gaussian 03 package within the BO framework.[16] Different first-principles electronic Hamiltonians, including spin-unrestricted HF, MP2, CCSD, CISD, QCISD, CCSD(T), and a variety of Kohn–Sham DFT methods were utilized. Wave functions were expanded in terms of atomic-centred one-electron basis functions including Pople-type basis sets (6–31g(d),

Can. J. Chem. Downloaded from www.nrcresearchpress.com by South China Agricultural University on 09/19/12
For personal use only.

Fig. 1. Hamiltonian and basis-set effects on the potential energy surface of the *sec*-butyl radical. (*a*)–(*d*) Hamiltonian effects using the cc-pVDZ basis set. (*e*) and (*f*) Basis-set effects based on B3LYP and MP2 Hamiltonians, respectively.

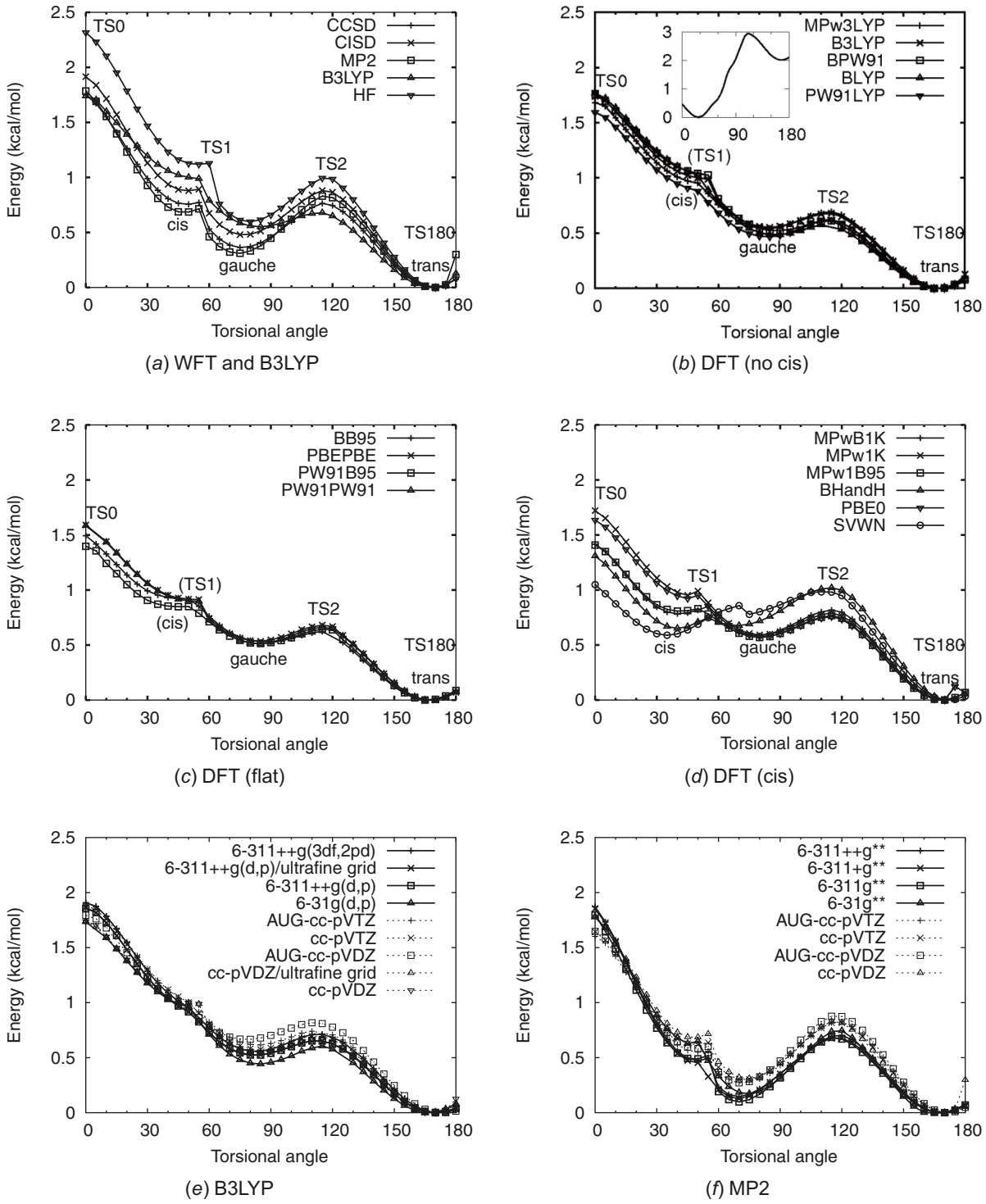

(*a*) WFT and B3LYP (*b*) DFT (no cis)

(*c*) DFT (flat) (*d*) DFT (cis)

(*e*) B3LYP (*f*) MP2

6–311++g(d,p), and 6–311++g(3df,2pd)),[17,18] and Dunning's correlation-consistent basis sets (cc-pVDZ, cc-pVTZ, AUG-cc-pVDZ, and AUG-cc-pVTZ).[19] For the DFT calculations, two-electron integrals were numerically integrated with the default grid quality in Gaussian 03 (75 radical shells and 302 angular points per shell) unless otherwise specified.

Geometry optimization was performed using the z-matrix coordinate system. Completely relaxed torsional PESs of the *sec*-butyl radical as a function of the dihedral angle (θ) of the four backbone carbon atoms were plotted using selected combinations of electronic Hamiltonians and basis sets (Fig. 1). The dihedral angle was scanned from 0° to 180° with a step size of 5°, while all the degrees of freedom other than the backbone dihedral angle were allowed to be fully optimized. The PES profile of θ in the range from 180° to 360° is essentially the mirror image of the profile from 0° to 180°, if

Can. J. Chem. Downloaded from www.nrcresearchpress.com by South China Agricultural University on 09/19/12
For personal use only.

certain symmetry constraints are applied at proper points. However, for the simplicity and uniformity of the calculations, the symmetry of the molecule was subject to no constraint throughout unless otherwise noted.

In addition, the optimized conformations were calculated at both the MP2 and B3LYP levels to obtain the diagonalized Hessian matrices to identify the nature of the stationary structures and to include the zero-point vibrational corrections. Because the harmonic approximation is usually inappropriate for the shallow minimum of the cis-structure, anharmonic vibrational calculations were also carried out at the MP2 level of theory to obtain the anharmonic zero-point corrections.

In this study, single-reference spin-unrestricted Hamiltonians were used. Spin contamination, believed to be responsible for the failure of UMP2 in determining the reaction barrier of radical formation reactions,[20,21] was found to be very small for all the spin-unrestricted Hamiltonians in the current study. This is not surprising because it is well established that the simple alkyl radical has a localized unpaired electron at the radical centre. As a result, a single-reference method should be adequate to treat alkyl radicals well. Thus, spin-unrestricted single-reference methods were utilized in this study.

Results and discussion

The torsional PES profiles calculated using different Hamiltonians and basis sets are shown in Fig. 1, with their lowest points as the common reference zero point to simplify the comparison. The cc-pVDZ basis set was utilized in Figs. 1*a*–1*d* because geometry optimization is usually carried out with a relatively small basis set and cc-pVDZ was found to be adequate for this purpose.[3]

In Fig. 1*a*, the torsional energy curve obtained from the HF calculation lies above all other potential energy profiles. The PES profiles from the CCSD, B3LYP, and MP2 calculations lie at the bottom across each other, whereas the potential energy curve obtained from the CISD calculation is situated in the middle. The PES calculated at the B3LYP level drops at a slower rate with respect to the dihedral angle increment when compared with all the WFT methods. The B3LYP calculation predicts two stable conformations when the dihedral angle θ is less than 180°, whereas all the WFT methods predict three stable conformations. The most stable conformation is uniformly predicted to be a trans-like structure at $\theta \approx 170°$ (conformation I in Fig. 2*f*). A stable gauche conformation (structure II in Fig. 2*d*) is also universally predicted at $\theta \approx 80°$. This gauche local minimum is ~0.3–0.6 kcal/mol (1 cal = 4.184 J) energetically higher than the global minimum, depending on the Hamiltonian used.

The existence of a third cis-like conformation (structure III in Fig. 2*b*) is worth some elaboration. All the WFT methods predict the existence of a stable structure on a relatively flat segment of the PES curves around $\theta \approx 50°$, whereas selected B3LYP methods predict an accelerated energy drop with increased dihedral angle in the same range. This cis-like conformation was earlier recognized as one of the three stable conformations in the very first theoretical conformation study of the *sec*-butyl radical by Chen et al.[15] The correlation effects, which are important to describe dispersion interactions for a correct prediction of stable conformations, was not included by the HF calculations performed by Chen et al.[15] though. Thus, methods taking account of correlation effects must be employed here for a reliable conformation study. Both DFT (B3LYP) and high-level post-HF WFT methods can incorporate correlation effects, but predict different torsional profiles for the *sec*-butyl radical in this study. As verified by a μSR experiment, the cis-like conformation does exist and carries a large value of HFCC on the β-muon.[9,10] In this regard, WFT methods outperform B3LYP-DFT methods decisively.

When $\theta = 0°$, the HF calculation predicts that the barrier TS0 (Fig. 2*a*), the global maximum and the transition state connecting the cis-conformation with its mirror image, is 2.3 kcal/mol higher (less stable) than the global mininum, the trans-like conformation. This indicates that the HF calculation predicts stronger bulky repulsion (by about 0.4 kcal/mol) between the two terminal methyl groups of the *sec*-butyl radical than any other correlated methods owing to the neglect of the correlation effects. The barrier separating conformations II and III, TS1 (Fig. 2*c*), is located around $\theta \approx 55°$ using correlated WFT methods and is at $\theta \approx 60°$ using the HF Hamiltonian. This TS1 barrier is very low energetically with respect to conformation III and can be easily overcome. The height of the energy barrier between conformations I and II, TS2 (Fig. 2*e*), in comparison to conformation II is about 0.5 kcal/mol from WFT calculations, whereas it drops to as low as ~0.1 kcal/mol using the B3LYP method. At $\theta \approx 180°$, the actual torsional barrier between conformation I and its mirror image was not obtained directly from the PES curve because the symmetry was not constrained during the relaxed potential energy scan. Instead, the C_s symmetry was used to help acquire the torsional barrier at $\theta \approx 180°$. Based on separate calculations, this TS180 torsional barrier is 0.13 kcal/mol at the B3LYP/cc-pVDZ level and 0.29 kcal/mol at MP2/cc-pVDZ. For the sake of simplicity, no further effort was devoted to obtain this barrier height using other methods.

Besides the comparison between WFT methods and the representative B3LYP Hamiltonian, DFT methods with various functionals were also examined using the cc-pVDZ basis set. Based on the shape of the calculated potential energy profiles between $\theta = 40°$ and 60°, where the presence of conformation III is of interest, the functionals are classified into three different categories (Figs. 1*b*–1*d*).

Figure 1*b* shows the functionals that predict no minimum within the range of interest. This group comprises some popular hybrid or pure GGA functionals. The PES profile obtained from the VSXC calculation (inset of Fig. 1*b*) is erratically different from other functionals. The VSXC functional fails to describe the potential energy needed to approach the energy maximum at $\theta = 0°$ with the big overall steric repulsion between the terminal methyl groups. The other functionals in this group yield very similar potential energy profiles with only two stable conformations (I and II). At any particular value of the dihedral angle, the energy difference between any two functionals in this group (VSXC excluded) is within 0.2 kcal/mol.

In Fig. 1*c*, the second group of functionals predict relative flat features around $\theta = 60°$ before the accelerated energy drop to conformation II. Usually, geometry optimization has a hard time to converge to a stationary point if the potential

Can. J. Chem. Downloaded from www.nrcresearchpress.com by South China Agricultural University on 09/19/12
For personal use only.

Fig. 2. Optimized stationary structures on the torsional potential energy surface of the *sec*-butyl radical.

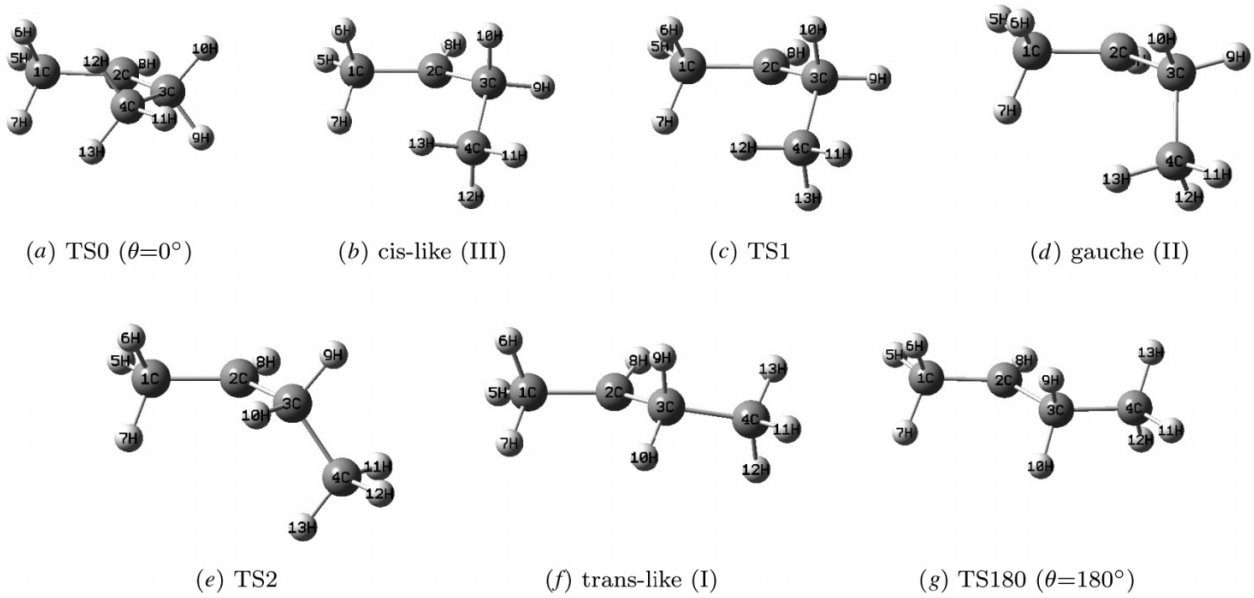

(*a*) TS0 (θ=0°) (*b*) cis-like (III) (*c*) TS1 (*d*) gauche (II)

(*e*) TS2 (*f*) trans-like (I) (*g*) TS180 (θ=180°)

gradient is very small in a case like this. Thus, further calculations to verify the existence of a minimum might not be successful. Note that some of these functionals contain components like PW_X91 or B_C95 that were designed for systems characterized by weak interactions,[22–24] which may partly compensate for the weakness of the DFT models in Fig. 1*b* so that a flat segment around $\theta = 55°$ is predicted.

In Fig. 1*d*, calculations using the third group of functionals predict a shallow potential well lying on the torsional PES around $\theta = 50°$, similar to the PES profiles obtained from MP2 and other WFT calculations. However, it is well-known that the SVWN functional, as with any other LDA-type functionals, should not be trusted unless the electron density undergoes only a small variation in space. The isolated molecular systems usually exhibit big density gradients especially around the nuclei and their electronic structure cannot be well predicted by LDA calculations. Just as in this case, the SVWN calculation predicts a distinct PES curve, quite different from its peers. This indicates that SVWN fails to capture the nonlocal exchange and correlation effects. Different from what it is usually referred to, BHandH, comprising 50% exact exchange and 50% LDA-level exchange and LYP correlation functionals as implemented in Gaussian 03,[16] is also inappropriate for the conformation study of the *sec*-butyl radical because it produces a much deeper potential well about conformation III.[25] The calculation using the PBE0 (or PBE1PBE) exchange-correlation functional, a hybrid functional with about 25% exact exchange, predicts a potential energy curve with a shallow potential well around $\theta = 50°$, in contrast to the flat surface predicted by the pure PBEPBE calculation. The other three functionals in this group combine mPW (modified PW_X91) exchange with exact exchange and PW_C91 or meta-B_C95 correlation functionals that were designed for a better long-range behaviour. PBE0 and MPW1K calculations produce similar potential energy curves to those from correlated WFT calculations. MPW1B95 and mPWB1K, on the other hand, predict low-lying curves in the range of $\theta = 0°–60°$, a clear indication of the underestimated repulsion of the terminal methyl groups compared with other Hamiltonians.

Based on the PES curves of each exchange-correlation functional combination, it is evident that incorporating the exact exchange is crucial for locating the cis-like conformation III. This implies that the nonlocal exchange-correlation effects may play an important role in this conformation study. At the same time, correlation functionals should also be carefully chosen, since mPW3LYP in group one, using a similar exchange-correlation functional as for mPW1B95, predicts a PES profile without any sign of the cis conformation III.

The basis-set effect was examined using both B3LYP and MP2 Hamiltonians. Based on some early studies,[4,5] the quality of basis functions can be more important than the form of the Hamiltonians in conformational analysis. The cc-pVDZ and 6–31g(d) basis sets were believed to be too small to include correct dispersion interaction, which lead to overstabilization of the coplanar conformer of biphenyl.[4,5] In a theoretical study of radicals, calculations using the Pople-type basis sets with various Hamiltonians approach converged results only after the size of the basis set went beyond 6–311g(d).[26] To visualize the basis-set effect, the torsional PES profiles of the *sec*-butyl radical at the B3LYP and MP2 levels with different basis sets are plotted in Figs. 1*e* and 1*f*, respectively.

Because of its single determinant nature, the Kohn–Sham DFT method is usually less sensitive to the variation of the basis set than multideterminant post-HF methods. In Fig. 1*e*, the PES profiles appear to be insensitive to the selection of the basis sets when their sizes grow bigger than cc-pVDZ or 6–31g(d,p), both of which predict the appearance of a small cusp at $\theta \approx 55°$. Calculations with larger basis sets predict smooth and high-lying potential energy curves compared with those with cc-pVDZ or 6–31g(d,p). The energy difference between calculations using any two basis sets is no more than 0.2 kcal/mol at any given dihedral angle. The convergence of basis sets is quickly achieved beyond the 6–311++g(d,p) basis set. With the size of the basis sets increased within

Can. J. Chem. Downloaded from www.nrcresearchpress.com by South China Agricultural University on 09/19/12
For personal use only.

Table 1. Relative energies (in kcal/mol; 1 cal = 4.184 J) and some geometric parameters of the stationary structures of the *sec*-butyl radical calculated at MP2 and B3LYP levels using the cc-pVDZ basis set.

Structure	Hamiltonian	C1–C2 (Å)	C2–C3 (Å)	C3–C4 (Å)	C2–H4 (Å)	C1–C2–C3 (°)	θ (°)	E_{ele} (kcal/mol)	E_{ZPC} (kcal/mol)	$E_{ZPC,Mu}$ (kcal/mol)
TS0	MP2	1.499	1.505	1.532	1.094	123.7	0.0	1.788	1.547 (1.772)	1.719 (1.906)
	B3LYP	1.493	1.500	1.532	1.094	124.4	0.0	1.740	1.694	1.891
III (cis)	MP2	1.500	1.503	1.535	1.095	120.9	47.8	0.683	0.814 (0.711)	0.819 (0.735)
	B3LYP	NA	NA	NA	NA	NA	NA	NA	NA	NA
TS1	MP2	1.499	1.501	1.539	1.093	120.6	55.2	0.779	0.476 (0.607)	0.572 (0.641)
	B3LYP	NA	NA	NA	NA	NA	NA	NA	NA	NA
II (gauche)	MP2	1.499	1.501	1.543	1.097	120.4	74.1	0.312	0.512 (0.486)	0.904 (0.854)
	B3LYP	1.492	1.497	1.546	1.096	122.0	84.6	0.553	0.788	1.308
TS2	MP2	1.497	1.500	1.539	1.095	121.6	116.7	0.841	0.509 (0.918)	0.719 (1.121)
	B3LYP	1.492	1.497	1.542	1.096	122.6	114.0	0.682	0.632	0.897
I (trans)	MP2	1.498	1.500	1.532	1.097	120.4	169.0	0.000	0.000 (0.000)	0.000 (0.000)
	B3LYP	1.492	1.495	1.532	1.096	121.5	167.9	0.000	0.000	0.000
TS180	MP2	1.497	1.498	1.531	1.094	120.4	180.0	0.299	–0.293 (–0.176)	–0.157 (–0.064)
	B3LYP	1.491	1.494	1.531	1.094	121.1	180.0	0.126	–0.283	–0.121

Note: Bond lengths are in Å. Bond angles and dihedral angles (θ) are in degrees. The relative energies are measured from the global minimal conformation III. The harmonic vibrational zero-point-corrected energy values are shown in the last two columns for hydrogen and muoniated isotopomers, respectively. For the MP2 calculation results, the anharmonic vibrational zero-point-corrected energies are shown in parentheses. NA, not available; E_{ele}, relative energy.

the Pople basis-set family, the PES curve moves upwards without exception. However, the basis-set effect within the Dunning family of basis sets is complicated. Adding diffuse functions to the cc-pVDZ or cc-pVTZ basis sets greatly raises the relative energies of the gauche conformation (II) and the TS2 barrier separating conformations I and II. On the other hand, incrementing splitting valence functions or polarization functions to the basis set results in a moderate relative energy rise (to more unstable) of conformation II and TS2, but a dramatic energy increase of TS0. This implies that, when θ is between 70° and 130°, long-range interactions may dominate the PES where diffuse basis functions play an important role. Meanwhile, adding splitting valence and polarization functions noticeably influences the PES curves at small torsion angles.

Other than the basis-set effects, the quality of numeric integration also affects the accuracy of a DFT calculation. A recent theoretical study of the *sec*-butyl cation showed that the quality of numerical integration of a DFT study that uses grid summation can be important for an accurate prediction of the equilibrium geometries.[27] Thus, an ultra-fine grid of higher quality consisting of 99 radical shells and 590 angular points per shell was also tested, but no significant difference to the default grid quality was found for the system we studied here.

Unlike the Kohn–Sham DFT and HF methods, the MP2 method, as with many other correlated WFT methods using excited configurations, is normally sensitive to the size of the basis set employed because correlated WFT methods utilize virtual orbitals that are less optimized during the SCF procedure. Thus, in most cases, MP2 calculations require a large basis set to achieve a certain level of accuracy. A study of biphenyl torsional PES indicated that the unbalanced treatment of repulsive and attractive dispersion interactions occurred if only a small Dunning correlation consisted basis set was used.[4,5] In the present study, except for those using small basis sets like cc-pVDZ and 6–31g(d,p) with which the repulsion between the terminal methyl groups is overestimated, the PES profiles obtained from other Pople basis sets lie below the potential energy profiles obtained from the Dunning correlation-consisted basis sets. The congregations of the PES profiles within each basis-set family suggest a fast convergence within each basis-set family. On the other hand, some significant difference persists between the two sets of PES curves from the two basis-set families, indicating that either or both of these basis-set families are still far away from the complete basis-set limit.

To draw a convincing conclusion, calculations using more accurate Hamiltonians with larger basis sets are always desired. Limited by our computer resources and the complexity of the open-shell systems involved, only single-point CCSD(T)/6–311++g(d,p) calculations using MP2/cc-pVTZ-optimized geometries were carried out for benchmarking purposes. In the end, the resulting "true" torsional PES profile calculated from CCSD(T) very closely resembles the MP2 one, which lends confidence to the results from the MP2 calculations.

As occurs here, disagreement between the DFT and WFT methods also took place in earlier studies. Some good agreements to the experimental data from DFT calculations were attributed to the parameterization with which the functionals

Can. J. Chem. Downloaded from www.nrcresearchpress.com by South China Agricultural University on 09/19/12
For personal use only.

were developed. DFT methods were reported to be unsuitable for the conformation study of 2,2′-bifuran for missing a shallow gauche conformation on the torsional PES curve.[8] It was also noted that MP2 and DFT gave very similar geometries, whereas DFT failed to describe the energetics of the torsional potential of biisothianaphthene.[6] In addition, many popular density functionals are believed inappropriate to describe noncovalent interactions and are difficult to improve systematically. In contrast to DFT methods, correlated WFT methods are in principle controllably adequate and, although with much higher computational cost, can be progressively improved. High-level correlated post-HF methods can then be used as a benchmark to justify low-level calculations. Alternatively, comparison between theoretical predictions and experimental data provides another way to validate the theories. Up to today, one of the most convincing ways to tell whether a theoretical method can be trusted on a specific system is to make a comparison with available experimental data. In our current study, all WFT methods predict the existance of the cis-like conformation III irrespective of the selection of the basis sets. A comparison with available experiments has confirmed the existence of the cis-like conformation III by low-temperature HFCC measurements.[9,10] Thus, the WFT methods and several DFT methods in group III (Fig. 1*d*) outperform other theoretical methods by being more in line with experimental results.

The stable geometries of the *sec*-butyl radical were optimized at both B3LYP and MP2 levels with the cc-pVDZ basis set. The optimized geometric parameters of those stable conformations are listed in Table 1. These two employed methods predict very similar bond lengths and bond angles for the same stationary structure except that the dihedral angle of the gauche conformation calculated at the B3LYP level differs by about 10° from the MP2 calculation. The C2–C3 bond length descends almost monotonically as the torsion angle increases from 0° to 180°. This indicates that the C2–C3 bond grows stronger from the cis-conformation to the trans-conformation because of decreased repulsion between the two terminal methyl groups. The hydrogen–hydrogen repulsion and hyperconjugation involving C2 and C3 exert only minor corrections to the PES profiles because the energy barrier from conformation III to conformation II is very small. Based on the optimized structures, the C1–C2 bond distance reaches maximum in TS1. This implies that the internal rotation about the C1–C2 bond plays an important role in forming the rotational barrier between conformations II and III.

In an early theoretical study by Chen et al.,[15] the shallow potential well embracing conformation III was merely regarded as a shoulder extension to the electronically more stable conformation II. If only the static electronic potential energy is considered, muoniated *sec*-butyl formed from mounium addition to *cis*-2-butene will not exist or can be easily turned into the gauche conformation II by an extremely small fluctuation (e.g., through vibration) to overcome the tiny barrier TS1, contradicting the experimental observation that the muon HFCC of this structure remained visibly strong over a wide temperature range.[9,10] There is no doubt that other effects stabilizing this molecular species must be taken into consideration.

In addition to the electronic energy, the zero-point vibrational correction also affects the relative energy difference between two structures in reality. More complete thermodynamic correction must be considered if the experiment is conducted at a higher temperature. To make a sound comparison to the experimental data at low temperatures, both harmonic and anharmonic vibrational corrections of the stable structures and the corresponding thermal corrections were calculated and are summarized in Table 1. It turns out that the zero-point corrected energy of the muoniated isotopomer of conformation III becomes lower than that of the muoniated conformation II, opposite to the prediction based on electronic energies alone. Thus, the large value of the muon HFCC of the muoniated radical formed from *cis*-2-butene can be definitely assigned after including zero-point correction. Another change in relative stability owing to the inclusion of the vibrational correction is the transition state TS180 connecting conformation I and its mirror image: the transition-state structure becomes the lowest point after the vibrational correction. Similar effects of the zero-point correction were also reported in other studies but without detailed discussion.[7]

Conclusion

First-principles calculations using spin-unrestricted HF, MP2, CCSD, and a variety of DFT Hamiltonians with different basis sets were employed to investigate the stable conformations of *sec*-butyl. Several DFT methods only predict two equilibrium structures with backbone dihedral angles of about 85° and 170°, whereas all WFT methods and some DFT methods yield an extra cis-like stable conformation with a dihedral angle of about 55°, followed by a low torsional barrier towards the gauche conformation, in agreement with existing experimental results. Inclusion of exact exchange and long-range behaviour-corrected correlation functionals is crucial to locate this elusive cis-like conformation for DFT methods. The selection of the basis sets using the B3LYP or the MP2 Hamiltonian does not affect the number of stable conformations found but only modifies the shape of the PES profiles. Noting the stable conformation of any molecular species in reality is not simply solely determined by electronic energies, calculations including the zero-point vibrational effect were further carried out. The zero-point corrected energy shows that the cis-like muoniated conformer is more stable than the gauche one, in line with the available experiment data.

Acknowledgement

Financial support for this project was provided by grants from the Natural Sciences and Engineering Research Council of Canada (NSERC).

References

(1) von Ragué Schleyer, P.; Kaupp, M.; Hampel, F.; Bremer, M.; Mislow, K. *J. Am. Chem. Soc.* **1992**, *114* (17), 6791. doi:10.1021/ja00043a026.
(2) Mo, Y.; Gao, J. *Acc. Chem. Res.* **2007**, *40* (2), 113. doi:10.1021/ar068073w.
(3) Sancho-García, J. C.; Karpfen, A. *Theor. Chem. Acc.* **2006**, *115* (5), 427. doi:10.1007/s00214-006-0123-3.
(4) Sancho-García, J. C.; Cornil, J. *J. Chem. Theory Comput.* **2005**, *1* (4), 581. doi:10.1021/ct0500242.
(5) Tsuzuki, S.; Uchimaru, T.; Matsumura, K.; Mikami, M.;

Can. J. Chem. Downloaded from www.nrcresearchpress.com by South China Agricultural University on 09/19/12
For personal use only.

Tanabe, K. *J. Chem. Phys.* **1999**, *110* (6), 2858. doi:10.1063/1.477928.
(6) Viruela, P. M.; Viruela, R.; Ortí, E.; Brédas, J. L. *J. Am. Chem. Soc.* **1997**, *119* (6), 1360. doi:10.1021/ja961586l.
(7) Ihee, H.; Zewail, A. H.; Goddard, W. A., III. *J. Phys. Chem. A* **1999**, *103* (33), 6638. doi:10.1021/jp990867n.
(8) King, R. A.; Crawford, T. D.; Stanton, J. F.; Schaefer, H. F., III. *J. Am. Chem. Soc.* **1999**, *121* (46), 10788. doi:10.1021/ja991429x.
(9) Fleming, D. G.; Bridges, M. D.; Arseneau, D. J.; Chen, Y. K.; Wang, Y. A. *J. Phys. Chem. A* **2011**, *115* (13), 2778. doi:10.1021/jp109676b.
(10) Chen, Y. K.; Fleming, D. G.; Wang, Y. A. *J. Phys. Chem. A* **2011**, *115* (13), 2765. doi:10.1021/jp1096212.
(11) Claxton, T. A. *Chem. Soc. Rev.* **1995**, *24* (6), 437. doi:10.1039/cs9952400437.
(12) Hermosilla, L.; Calle, P.; Garcia de la Vega, J. M.; Sieiro, C. *J. Phys. Chem. A* **2005**, *109* (6), 1114. doi:10.1021/jp0466901.
(13) Mielke, S. L.; Schwenke, D. W.; Peterson, K. A. *J. Chem. Phys.* **2005**, *122* (22), 224313. doi:10.1063/1.1917838.
(14) Knyazev, V. D.; Dubinsky, I. A.; Slagle, I. R.; Gutman, D. *J. Phys. Chem.* **1994**, *98* (43), 11099. doi:10.1021/j100094a018.
(15) Chen, Y.; Rauk, A.; Tschuikow-Roux, E. *J. Phys. Chem.* **1990**, *94* (16), 6250. doi:10.1021/j100379a019.
(16) Frisch, M. J.; Trucks, G. W.; Schlegel, H. B.; Scuseria, G. E.; Robb, M. A.; Cheeseman, J. R.; Montgomery, J. A., Jr.; Vreven, T.; Kudin, K. N.; Burant, J. C.; Millam, J. M.; Iyengar, S. S.; Tomasi, J.; Barone, V.; Mennucci, B.; Cossi, M.; Scalmani, G.; Rega, N.; Petersson, G. A.; Nakatsuji, H.; Hada, M.; Ehara, M.; Toyota, K.; Fukuda, R.; Hasegawa, J.; Ishida, M.; Nakajima, T.; Honda, Y.; Kitao, O.; Nakai, H.; Klene, M.; Li, X.; Knox, J. E.; Hratchian, H. P.; Cross, J. B.; Bakken, V.; Adamo, C.; Jaramillo, J.; Gomperts, R.; Stratmann, R. E.; Yazyev, O.; Austin, A. J.; Cammi, R.; Pomelli, C.; Ochterski, J. W.; Ayala, P. Y.; Morokuma, K.; Voth, G. A.; Salvador, P.; Dannenberg, J. J.; Zakrzewski, V. G.; Dapprich, S.; Daniels, A. D.; Strain, M. C.; Farkas, O.; Malick, D. K.; Rabuck, A. D.; Raghavachari, K.; Foresman, J. B.; Ortiz, J. V.; Cui, Q.; Baboul, A. G.; Clifford, S.; Cioslowski, J.; Stefanov, B. B.; Liu, G.; Liashenko, A.; Piskorz, P.; Komaromi, I.; Martin, R. L.; Fox, D. J.; Keith, T.; Al-Laham, M. A.; Peng, C. Y.; Nanayakkara, A.; Challacombe, M.; Gill, P. M. W.; Johnson, B.; Chen, W.; Wong, M. W.; Gonzalez, C.; Pople, J. A. *Gaussian 03;* Gaussian, Inc.: Wallingford, CT, 2004.
(17) Frisch, M. J.; Pople, J. A.; Binkley, J. S. *J. Chem. Phys.* **1984**, *80* (7), 3265. doi:10.1063/1.447079.
(18) Clark, T.; Chandrasekhar, J.; Spitznagel, G. W.; von Ragué Schleyer, P. *J. Comput. Chem.* **1983**, *4* (3), 294. doi:10.1002/jcc.540040303.
(19) Kendall, R. A.; Dunning, T. H., Jr; Harrison, R. J. *J. Chem. Phys.* **1992**, *96* (9), 6796. doi:10.1063/1.462569.
(20) Wong, M. W.; Radom, L. *J. Phys. Chem.* **1995**, *99* (21), 8582. doi:10.1021/j100021a021.
(21) Wong, M. W.; Radom, L. *J. Phys. Chem. A* **1998**, *102* (12), 2237. doi:10.1021/jp973427+.
(22) Perdew, J. P. Unified Theory of Exchange and Correlation Beyond the Local Density Approximation. In *Electronic Structure of Solids;* Ziesche, P., Eschrig, H., Eds.; Akademie Verlag: Berlin, 1991; pp 11–20.
(23) Burke, K.; Perdew, J. P.; Wang, Y. Derivation of a Generalized Gradient Approximation: The PW91 Density Functional. In *Electronic Density Functional Theory: Recent Progress and New Directions;* Dobson, J. F., Vignale, G., Das, M. P., Eds.; Plenum: New York, 1997; pp 81–121.
(24) Becke, A. D. *J. Chem. Phys.* **1996**, *104* (3), 1040. doi:10.1063/1.470829.
(25) Becke, A. D. *J. Chem. Phys.* **1993**, *98* (2), 1372. doi:10.1063/1.464304.
(26) Mayer, P. M.; Parkinson, C. J.; Smith, D. M.; Radom, L. *J. Chem. Phys.* **1998**, *108* (2), 604. doi:10.1063/1.476256.
(27) Vrček, V.; Kronja, O.; Saunders, M. *J. Chem. Theory Comput.* **2007**, *3* (3), 1223. doi:10.1021/ct600308b.

Density functional theory study of the vertical ionization energies of the valence and core electrons of cyclopentadiene, pyrrole, furan, and thiophene

Delano P. Chong

Can. J. Chem. Downloaded from www.nrcresearchpress.com by South China Agricultural University on 09/19/12
For personal use only.

Abstract: The procedure abbreviated as ΔPBE0(SAOP)/et-pVQZ, based on density functional theory, was developed recently for the calculation of vertical ionization energies of the valence electrons of organic and other small molecules and succeeded in giving results with an average absolute deviation of 0.21 eV from experiment for a collection of 115 reliable test cases of nonperhalo molecules. The objective of this work is to add a number of test cases to the benchmark database. We chose the set of molecules cyclo-C_4H_4X, with X = CH_2, NH, O, and S, previously studied by many workers both experimentally and theoretically. The results show that the ΔPBE0(SAOP)/et-pVQZ procedure is not only as good as ab initio methods such as SAC-CI, OVGF, and ADC(3) in performance, but also handles inner valence ionized cations more efficiently. Although the core-electron binding energies of the titled molecules have not been as well investigated theoretically, we apply the methods we developed in recent years to calculate the binding energies of C1s, N1s, O1s, S1s, and S2p, which compare well with available experimental data.

Key words: vertical ionization energies, photoelectron spectra, PES, density functional theory, cyclopentadiene, pyrrole, furan, thiophene, ESCA, XPS.

Résumé : On a développé récemment une méthode à base de la théorie de la fonctionnelle de la densité, désignée par l'acronyme ΔPBE0(SAOP)/et-pVQZ, qui permet de calculer les énergies d'ionisation verticale des électrons de valence de petites molécules organiques et autres et qui fournit des résultats avec une déviation moyenne absolue de 0,21 eV par rapport aux valeurs expérimentales pour un ensemble de 115 cas typiques de molécules qui ne sont pas perhalogénées. L'objectif de ce travail était d'ajouter un certain nombre de cas typiques à la banque de données de référence. On a choisi l'ensemble de molécules cyclo-C_4H_4X, dans lesquels CH_2, NH, O et S qui avait été étudié antérieurement par plusieurs autres auteurs, tant d'un point de vue expérimental que théorique. Les résultats montrent que la performance de la méthode ΔPBE0(SAOP)/et-pVQZ n'est pas uniquement aussi bonne que celle des méthodes ab initio SAC-CI, OVGF et ADC(3), mais qu'elle permet de manipuler d'une façon plus efficace les cations ionisés de valence interne. Même si les énergies de liaison des électrons de coeur des molécules mentionnées dans le titre n'ont pas aussi bien été étudiées d'un point de vue théorique, on leur a appliqué dans les années récentes les méthodes qu'on a développé pour calculer les énergies de liaison de C1s, N1s, O1s, S1s et S2p qui se comparent bien avec les données expérimentales disponibles.

Mots-clés : énergies d'ionisation verticale, spectres photoélectroniques (SPE), théorie de la densité fonctionnelle, cyclopentadiène, pyrrole, furane, thiophène, spectroscopie électronique pour l'analyse chimique (SEAC), spectroscopie photoélectronique des rayons X (SPX).

[Traduit par la Rédaction]

Introduction

During the last few decades, the interpretation of photoelectron spectra has evolved with the development of computer hardware and software. The early predictions of vertical ionization energies (VIEs) by semiempirical molecular orbital (MO) methods, such as CNDO, MINDO, MNDO, and AM1, based on Koopmans' theorem (KT), were surpassed by a highly parametrized semiempirical MO method known as HAM/3,[1] based on an approximate transition-state model, a concept often used in density functional theory (DFT). Although the average absolute deviation (AAD) of results from HAM/3 from observed VIEs is usually about 0.3 eV, the method is not generally applicable because it is limited to molecules containing C, N, O, F, and H only.

On the other hand, use of KT in ab initio calculations leads to larger errors. When the ordering of MOs is predicted incorrectly, the term Koopmans' breakdown is used. In any case, the AAD from KT is often around 1 eV and the procedure

Received 19 July 2011. Accepted 12 August 2011. Published at www.nrcresearchpress.com/cjc on 10 November 2011.

D.P. Chong. Department of Chemistry, 2036 Main Mall, University of British Columbia, Vancouver, BC V6T 1Z1, Canada.

E-mail for correspondence: chong@chem.ubc.ca.

This article is part of a Special Issue to commemorate the International Year of Chemistry.

Can. J. Chem. Downloaded from www.nrcresearchpress.com by South China Agricultural University on 09/19/12
For personal use only.

Table 1. Vertical ionization energies (VIEs, in eV) of cyclopentadiene.

	Observed VIE			Calculated VIE			
				1982[c]	1985[d]	2000[e]	This work
MO	1971[a]	1971[b]	Best estimate	GF	SAC-CI	SAC-CI	ΔPBE0(SAOP)
$1a_2$	8.57	8.57	8.57	8.38	8.38	8.39	8.49
$2b_1$	10.62	10.72	10.67	10.86	10.68	10.80	10.71
$6b_2$		~12.2	~12.2	12.40	12.14	12.23	12.31
$9a_1$		~12.6	~12.6	12.71	12.21	12.29	12.30
$8a_1$		13.2	13.2	13.22	12.76	12.79	12.84
$5b_2$		13.8	13.8	14.11	13.68	13.58	13.45
$1b_1$		14.8	14.8	15.02	14.82	15.26	14.65
$7a_1$		16.4	16.4		17.08	16.67	16.69
$4b_2$		17.5	17.5		17.75	17.28	17.18
$6a_1$		18.4	18.4		18.40	17.98	17.76
$5a_1$		22.3				22.70	22.07
$3b_2$						22.87	22.16
$4a_1$							26.37
AAD (N)[f]				0.1_8 (7)	0.2_3 (10)	0.2_8 (10)	0.2_6 (10)
						0.2_9 (11)	0.2_6 (11)

Note: GF, Green's function method; SAC-CI, symmetry-adapted configuration interaction method; MO, molecular orbital.

[a]Derrick et al.[48]

[b]Derrick et al.[49]

[c]Bieri et al.[50]

[d]Nakatsuji et al.[51]

[e]Wan et al.[52]

[f]Average absolute deviation for N values of VIEs.

Table 2. Experimental vertical ionization energies (VIEs, in eV) of pyrrole.

	VIE										
MO	1969[a]	1970[b]	1971[c]	1971[d]	1971[e]	1979[f]	1982[g]	1996[h]	1998[i]	2001[j]	Best estimate
$1a_2$	8.20	8.22	8.21	8.21		8.2	8.02	8.28	8.21	8.3	8.19
$2b_1$	9.16	9.22	9.20	9.20		9.2	9.05	9.26	9.20	9.3	9.18
$9a_1$	12.8	12.70		12.6		12.7	12.85	12.74	12.6	12.8	12.76
$6b_2$	13.5	12.95		13.0[k]			12.85[h]	12.94	13.0	12.8	12.91
$1b_1$		13.6		13.7[k]		13.7	13.57[h]	13.48	13.7	13.6	13.53
$5b_2$	14.3	14.4		14.3[k]		14.3	14.27[h]	14.29	14.35	14.3	14.28
$8a_1$	14.8	14.95		14.8[k]		14.8	14.80[h]	14.76	14.80	15.0	14.84
$7a_1$		17.8		17.5		17.4		17.44	17.3	17.9	17.44
$4b_2$				18.1				18.00	18.0		18.00
$6a_1$				18.8				18.8	18.8		18.8
$3b_2$				22.3	22.3						22.3
$5a_1$				23.8	23.8						23.8
$4a_1$				~29	29.5						29.5

Note: MO, molecular orbital.

[a]Eland.[53]

[b]Baker et al.[54]

[c]Derrick et al.[48]

[d]Derrick et al.[55]

[e]Gelius et al.[56]

[f]Sell and Kuppermann.[57]

[g]Klasinc et al.[58]

[h]Kishimoto et al.[59]

[i]Palmer et al.[34]

[j]Holland et al.[60] cited by Trofimov et al.[61]

[k]Wrong assignment corrected.

Can. J. Chem. Downloaded from www.nrcresearchpress.com by South China Agricultural University on 09/19/12
For personal use only.

Table 3. Theoretical vertical ionization energies (VIEs, in eV) of pyrrole.

	VIE											
		1976[b]	1977[c]	1982[d]	1985[e]	1998[f]	2001[g]	2001[g]	2005[h]	2008[i]	2008[i]	This work
MO	Observed[a]	OVGF	CI	GF	SAC-CI	GF	OVGF	ADC(3)	SAC-CI	OVGF	ADC(3)	ΔPBE0(SAOP)
$1a_2$	8.19	8.17	8.10	8.17	7.95	8.14	8.14	8.05	7.98	7.9	8.1	8.25
$2b_1$	9.18	8.92	8.94	8.92	8.73	8.88	9.01	8.95	8.78	8.7	8.8	9.19
$9a_1$	12.76	12.98		12.98	12.68	12.86	13.03	13.11	12.61	12.7	13.0	12.85
$6b_2$	12.91	13.39		13.39	13.18	13.46	13.52	13.52	13.35	13.2	13.6	13.20
$1b_1$	13.53	13.70	13.33		13.62	13.77		14.26	12.77	13.3	13.0	13.74
$5b_2$	14.28	14.37		14.37	14.12	14.54	14.58	14.53	14.49	14.3	14.5	14.21
$8a_1$	14.84	14.86		14.86	14.41	14.72	14.80	14.82	14.57	14.4	14.8	14.38
$7a_1$	17.44	18.17		*17.50*	17.94	18.06		17.63	17.51	17.8	17.9	17.68
$4b_2$	18.00	18.96		*18.26*	18.65	18.70		18.56	18.30			18.20
$6a_1$	18.8	19.64		*18.90*	19.41			19.48	19.02			19.03
$3b_2$	22.3											22.53
$5a_1$	23.8											24.10
$4a_1$	29.5											29.78
AAD (N)[j]	0.38 (10)			0.18 (6)	0.28 (8)	0.24 (6)		0.32 (8)	0.31 (8)	0.27 (8)	0.33 (8)	0.18 (8)
				0.1_7 (9)	0.3_5 (10)			0.3_8 (10)	0.3_0 (10)			0. 1_9 (10)
												0.2_0 (12)

Note: GF, Green's function method; OVGF, outer-valence Green's function method; SAC-CI, symmetry-adapted configuration interaction method; ADC(3), third-order algebraic diagrammatic construction method; MO, molecular orbital.

[a]See Table 2.

[b]von Niessen et al.[62]

[c]Tanaka et al.[63]

[d]Bieri et al.[50] Values in italics are results from 2ph-TDA.

[e]Nakatsuji et al.[51]

[f]Palmer et al.[34]

[g]Holland et al.[60]

[h]Ehara et al.[64]

[i]Trofimov et al.[61]

[j]Average absolute deviation for N values of VIEs.

Can. J. Chem. Downloaded from www.nrcresearchpress.com by South China Agricultural University on 09/19/12
For personal use only.

Table 4. Experimental vertical ionization energies (VIEs, in eV) of furan.

	VIE												
MO	1969[a]	1970[b]	1971[c]	1971[d]	1971[e]	1974[f]	1979[g]	1981[h]	1982[i]	1982[j]	1992[k]	1996[l]	Best estimate
$1a_2$	8.90	8.89	8.88	8.88		8.88	8.9	8.78	9.0	8.83	9.0	9.11	8.89
$2b_1$	10.32	10.42	10.31	10.31		10.31	10.4	10.38	10.4	10.39	10.4	10.48	10.37
$9a_1$	13.06	12.87		13.0			12.9	12.94	13.0	12.96	13.0	13.10	12.99
$8a_1$	13.8	13.70		13.8[m]			13.8	13.84	13.8	13.86	13.6	13.74	13.79
$6b_2$	14.4	14.35		14.4[m]			14.4	14.47	14.4	14.51	14.2	14.46	14.45
$5b_2$	15.2	15.02		15.1[m]			15.1	15.20	15.2_5	15.26	15.2	15.18	15.17
$1b_1$				15.6[m]					~15.6	15.26	15.6	15.44	15.35
$7a_1$		17.32		17.5			17.5	17.77	17.5		17.5	17.49	17.53
$6a_1$				19.0	18.6		~18.8		18.80		18.7	18.68	18.74
$4b_2$				19.5	19.2				~19.7		19.8		19.5
$3b_2$				~23	23.5				23		23.1		23.3
$5a_1$				~25	25.2				~24.5		24.6		24.9
$4a_1$					34.1								34.1

Note: MO, molecular orbital.

[a]Eland.[53]
[b]Baker et al.[54]
[c]Derrick et al.[48]
[d]Derrick et al.[65]
[e]Gelius et al.[56]
[f]Schweig and Thiel.[66]
[g]Sell and Kuppermann.[57]
[h]Kimura et al.[67]
[i]Bieri et al.[50]
[j]Klasinc et al.[58]
[k]Bawagan et al.[68]
[l]Kishimoto et al.[59]
[m]Misassigned.

Can. J. Chem. Downloaded from www.nrcresearchpress.com by South China Agricultural University on 09/19/12
For personal use only.

Table 5. Theoretical vertical ionization energies (VIEs, in eV) of furan.

	VIE										
		1976[b]	1977[c]	1982[d]	1985[e]	1995[f]	2001[g]	2001[g]	2005[h]	2008[i]	2008[i]	2010
MO	Observed[a]	GF	TOM	OVGF	SAC-CI	OVGF	OVGF	ADC(3)	SAC-CI	OVGF	ADC(3)	ΔPBE0(SAOP)
1a2	8.89	8.87	8.00	8.87	8.90	8.99	8.82	8.85	8.83	8.61	8.7	8.90
2b1	10.37	10.36	9.29	10.36	10.15	10.33	10.29	10.31	10.10	10.0	10.2	10.37
9a1	12.99	11.30	12.13	13.30	12.55	13.39	13.35	13.38	12.94	13.1	13.3	13.11
8a1	13.79	14.10	14.20	14.10	13.60	13.95	14.05	14.00	13.73	13.8	14.0	13.59
6b2	14.45	14.69	14.94	14.69	14.24	14.52	14.29	14.35	14.21	14.0	14.3	13.96
5b2	15.17	15.17	15.06	15.17	14.85	15.15	15.27	15.32	15.21	15.1	15.2	14.93
1b1	15.35	15.47	15.51	15.75	14.76	15.17		15.64		15.0	15.5	15.04
7a1	17.53	18.48	19.64	*17.77*	17.81	18.24		18.07	17.77		18.0	17.68
6a1	18.74	19.25	20.69	*18.60*	18.80	19.08		18.70				18.52
4b2	19.5	20.17	21.19	*19.45*	19.73	19.89		19.58				19.30
3b2	23.3		26.61									23.35
5a1	24.9		28.46									25.03
4a1	34.1		36.91									33.72
AAD (N)[j]		0.3_0 (10)		0.19 (7) 0.1_9 (10)	0.2_3 (10)	0.2_2 (10)	0.17 (6)	0.2_0 (10)	0.14 (7)	0.2_4 (7)	0.2_1 (8)	0.2_1 (10) 0.2_3 (12)

Note: GF, Green's function method; OVGF, outer-valence Green's function method; SAC-CI, symmetry-adapted configuration interaction method; ADC(3), third-order algebraic diagrammatic construction method; TOM, transition operator method; MO, molecular orbital.

[a]See Table 4.

[b]von Niessen et al.[69]

[c]Hehenberger.[70]

[d]Bieri et al.[50] Values in italics are results from 2ph-TDA.

[e]Nakatsuji et al.[51]

[f]Palmer et al.[33]

[g]Holland et al.[60]

[h]Ehara et al.[64]

[i]Trofimov et al.[61]

[j]Average absolute deviation for N values of VIEs.

Published by NRC Research Press

Table 6. Experimental vertical ionization energies (VIEs, in eV) of thiophene.

	VIE											
MO	1969[a]	1971[b]	1971[c]	1971[d]	1979[e]	1982[f]	1982[g]	1992[h]	1996[i]	2001[j]	2006[k]	Best estimate
$1a_2$	8.87	8.87	8.87			8.87	8.85	9.0	8.96	9.0	9.2	8.88
$3b_1$	9.49	9.5	9.52			9.52	9.49	9.5	9.58	9.5		9.52
$11a_1$	11.94		12.1[j]			12.1	12.00	12.0	12.04	12.1	12.9	11.99
$2b_1$	(12.39)		12.7[j]			12.7	12.46	12.5	12.49	12.5		12.48
$7b_2$	13.07		13.3				13.11	13.2	13.15	13.3		13.11
$10a_1$			13.9				13.80	13.9	13.71	13.7		13.76
$6b_2$	14.14		14.3				14.23	14.4	14.26	14.2		14.21
$9a_1$	16.4		16.6					16.6	16.52	16.6	16.6	16.52
$5b_2$	17.4		17.6	17.8				17.6	17.62			17.62
$8a_1$			~18.3	18.8				18.4	18.3		18.4	18.5
$4b_2$			~22.1	22.1[l]				22.1				22.1
$7a_1$			~22.3	22.3[l]								22.3
$6a_1$				26.1								26.1

Note: GF, Green's function method; OVGF, outer-valence Green's function method; SAC-CI, symmetry-adapted configuration interaction method; ADC(3), third-order algebraic diagrammatic construction method; MO, molecular orbital.

[a]Eland.[53]
[b]Derrick et al.[49]
[c]Derrick et al.,[71] with assignment corrected by Bieri et al.[50]
[d]Gelius et al.[56]
[e]Sell and Kuppermann.[57]
[f]Bieri et al.[50]
[g]Klasinc et al.[58]
[h]Bawagan et al.[68]
[i]Kishimoto et al.[59]
[j]Holland et al.,[60] cited by Trofimov et al.[61]
[k]Zhang et al.[72]
[l]Wrong assignment corrected.

Can. J. Chem. Downloaded from www.nrcresearchpress.com by South China Agricultural University on 09/19/12
For personal use only.

is sometimes known as Koopmans' approximation. When we used a similar method of approximating VIEs with the negative of orbital energies, but within DFT, using the exchange-correlation potential V_{xc} known as statistical average of orbital potential (SAOP),[2–4] the AAD was found to reduce to 0.4 eV.[5] This approach was named meta-Koopmans' theorem (mKT).[6] Recently, the AAD of similar mKT has been further improved by a better choice of hybrid density functional[7] based on the Baer–Neuhauser–Livshitz range separation.[8,9]

To go beyond KT, we applied the method of perturbation corrections to Koopmans' theorem from 1974[10] to 1985[11] and obtained AADs of 0.3–0.4 eV. A similar but more efficient approach using Green's function (GF) was developed by Cederbaumet al.[12] This method was later known as the outer-valence Green's function (OVGF).[13] The basis sets used were typically medium size and the AAD was usually around 0.3 eV. We tried a simplified second-order GF approach with one empirical parameter, called pGF2, to improve the efficiency and obtained AAD = 0.3 eV for a limited number of cases.[14] A method similar to OVGF called partial third order (P3) was developed by Ortiz[15] and gave slightly better results than OVGF. The OVGF method has been popular since it has been available in the Gaussian program package[16]. However, OVGF may not be as accurate as one wishes in two situations: (*i*) when the basis set, usually limited by computational facilities, is not large enough and (*ii*) when the pole strength is small owing to significant shake-up effects, in which case the method known as two-particle-hole Tamm–Dancoff approximation (2ph-TDA)[17] may be more reliable, provided a sufficiently large basis set is used. The 2ph-TDA method was used briefly but was superseded by a better approach known as third-order algebraic diagrammatic construction (ADC(3)).[18] The AADs of OVGF and ADC(3) results can be as low as 0.2 eV or better in some cases. Finally, there is the method of symmetry-adapted configuration interaction (SAC-CI)[19], also available in the Gaussian package, which can give very accurate VIEs, but the computational demand of SAC-CI calculations usually limits the size of the basis set used in practice.

We continued to look for an efficient method of predicting reliable VIEs and turned to DFT. After testing various forms of the transition-state model, with the best choice giving AAD = 0.3 eV,[20,21] we finally discovered a reliable and efficient procedure.[22] It is abbreviated as ΔPBE0(SAOP), which means the energy difference calculated with the parameter-free Perdew–Burke–Ernzerhof (PBE0) exchange-correlation functional,[23–25] using the electron density obtained with the exchange-correlation potential V_{xc} = SAOP.[2–4] It should be mentioned that, when there is a choice between maintaining symmetry and insisting on integer occupations in a cationic calculation, the latter has been found to lead to better prediction of VIEs (except for perhalo systems). This procedure of ΔPBE0(SAOP) succeeded in giving AAD = 0.21 eV for over 100 cases of nonperhalo molecules.[22] More recent studies showed that the AADs of the ΔPBE0(SAOP) method are

Can. J. Chem. Downloaded from www.nrcresearchpress.com by South China Agricultural University on 09/19/12
For personal use only.

Table 7. Theoretical vertical ionization energies (VIEs, in eV) of thiophene.

	VIE										
		1976[b]	1982[c]	1994[d]	1999[e]	2001[f]	2001[f]	2005[g]	2008[h]	2008[h]	2009[i]	2010
MO	Observed[a]	GF	GF	SDCI	GF	OVGF	ADC(3)	SAC-CI	OVGF	ADC(3)	OVGF	ΔPBE0(SAOP)
$1a_2$	8.88	8.77	8.77	8.65	8.82	8.90	8.84	8.92	8.6	8.7	8.91	8.96
$3b_1$	9.52	8.98	8.98	8.98	8.92	9.14	9.06	9.05	9.0	9.0	9.33	9.37
$11a_1$	11.99	12.01	12.01	11.77	11.88	12.02	11.91	11.70	11.9	11.9	12.09	12.00
$2b_1$	12.48	12.88	*12.48*		12.86		12.52	12.56	12.6	12.4	12.94	13.07
$7b_2$	13.11	13.29	13.29	13.32	13.17	13.37	13.35	13.32	13.1	13.3	13.37	13.17
$10a_1$	13.76	13.44	13.44		13.36	13.50	13.60	13.41	13.2	13.6	13.53	13.33
$6b_2$	14.21	14.52	14.52		14.33	14.19	14.20	14.16	13.9	14.2	14.11	13.82
$9a_1$	16.52	17.50	*16.88*		17.21		16.95	16.84		17.0	17.16	16.76
$5b_2$	17.62	18.70	18.06		18.45		18.20	18.05				17.86
$8a_1$	18.3_7	18.79			18.73		18.09	18.07				18.17
$4b_2$	22.1											22.65
$7a_1$	~22.3											22.94
$6a_1$												27.07
AAD (N)[j]			0.25 (9)	0.16 (6)	0.36 (10)		0.2_3 (10)	0.21 (8) 0.2_4 (10)	0.27 (7)	0.21 (8)	0.25 (8)	0.2_4 (10) 0.2_7 (11)

Note: GF, Green's function method; OVGF, outer-valence Green's function method; SAC-CI, symmetry-adapted configuration interaction method; ADC(3), third-order algebraic diagrammatic construction method; SDCI, singles and doubles configuration interaction; MO, molecular orbital.

[a]See Table 6.

[b]von Niessen et al.[69]

[c]Bieri et al.[50] Values in italics are results from 2ph-TDA.

[d]Takeshita and Yamamoto.[73]

[e]Palmer et al.[74]

[f]Holland et al.[60]

[g]Ehara et al.[64]

[h]Trofimov et al.[61]

[i]Singh and Mishra.[75]

[j]Average absolute deviation for N values of VIEs.

Can. J. Chem. Downloaded from www.nrcresearchpress.com by South China Agricultural University on 09/19/12
For personal use only.

Table 8. Comparison of average absolute deviation (AAD, in eV) of the first 10 vertical ionization energies (VIEs) of cyclo-C_4H_4X, calculated with various methods from experiment.

		AAD			
Year	Method	X = CH_2	X = NH	X = O	X = S
1976[a]	OVGF		0.38		
1976[b]	OVGF			0.3_0	0.4_4
1982[c]	OVGF and 2ph-TDA			0.1_9	
1985[d]	SAC-CI	0.2_3	0.3_5	0.2_3	
1995[e]	OVGF			0.2_2	
1999[f]	GF				0.36
2000[g]	SAC-CI	0.2_8			
2001[h]	ADC(3)		0.3_8	0.2_0	0.2_3
2005[i]	SAC-CI		0.3_0		0.2_4
This work	ΔPBE0(SAOP)	0.2_6	0.1_9	0.2_1	0.2_4

Note: GF, Green's function method; OVGF, outer-valence Green's function method; SAC-CI, symmetry-adapted configuration interaction method; ADC(3), third-order algebraic diagrammatic construction method.

[a]von Niessen et al.[62]
[b]von Niessen et al.[69]
[c]Bieri et al.[50]
[d]Nakatsuji et al.[51]
[e]Palmer et al.[33]
[f]Palmer et al.[74]
[g]Wan et al.[52]
[h]Holland et al.[60]
[i]Ehara et al.[64]

0.23 eV for eightVIEs of *s*-triazine,[26,27] 0.1_4 eV for 28 VIEs of naphthalene and azulene,[28] 0.1_9 eV for 16 VIEs of *p*-benzoquinone,[29] and 0.1_1 eV for nineVIEs of formamide.[30]

On the other hand, the five-membered heterocyclic aromatic molecules of pyrrole, furan, and thiophene are of considerable scientific interest to chemists. The importance of these molecules in pharmaceutical production, in coal conversion technology, and in the synthesis of pesticides and inorganic polymers, has been mentioned by Rennie et al.[31,32] Perhaps because of the industrial relevance, many studies, both theoretical and experimental, of the electron spectra have been undertaken. The UV absorption spectra of these molecules were thoroughly studied by Palmer et al.[33–35] However, the experimental data on the excited states are not as well understood as the photoelectron spectra of the valence electrons. Therefore, we concentrate on the photoelectron spectra in this study. The objective of this work is to apply the ΔPBE0(SAOP) procedure to the valence ionization of cyclopentadiene, pyrrole, furan, and thiophene, and to compare the accuracy with other theoretical methods. For core-electron ionization, we can only compare our results with available experimental data.

Method

The computational details for vertical ionization energies of valence electrons have been given previously.[22] We used the Amsterdam Density Functional (ADF) program[36] with the large basis set known as even-tempered valence quadruple-zeta (et-pVQZ) set of Slater-type orbitals.[37] The approach can be abbreviated as ΔPBE0(SAOP)/et-pVQZ. There remains only the geometry to specify. When no experimental geometry was available, we generally used the Gaussian03 program package[16] to optimize the geometry of each parent neutral molecule with the popular exchange-correlation functional known as B3LYP and the internal basis set 6–311+G(d,p). Thus, the procedure can be labelled as ΔPBE0(SAOP)/et-pVQZ//B3LYP/6–311G+(d,p). For the four molecules included in this paper, cyclo-C_4H_4X (with X = CH_2, NH, O, and S) experimental geometries are available[38–41] and were therefore employed. Thus, the procedure can be abbreviated as ΔPBE0(SAOP)/et-pVQZ//expt.

For core-electron binding energies (CEBEs) of C1s, N1s, and O1s, the method of ΔPW86-PW91+C_{rel} was developed in 1999[42] for contracted Gaussian-type orbitals. In 2003,[43] we found a more convenient alternative using the ADF program[36] with Slater-type orbitals. The procedure used in this work is ΔPW86-PW91/et-pVQZ+C_{rel}. For C1s, N1s, and O1s, we used the empirical allometric correction of

$$C_{rel} = kI_{nr}{}^n$$

where I_{nr} is the nonrelativistic value, with $k = 0.2198 \times 10^{-6}$ and $n = 2.178$ when both C_{rel} and I_{nr} are in units of eV.[44] Finally, the methods used for S2p and S1s, developed more recently, are ΔBmTau1(SAOP)/et-pVQZ+C_{re}[45] and scalar zeroth-order regular approximation (ZORA)+ΔPBE-PW91/et-pVQZ.[46] For C_{rel} for S1s, we used $k = 0.625 \times 10^{-6}$ and $n = 2.0616$, based on uncorrelated relativistic atoms.[47] Thus, the relativistic effects are approximated in different ways for the three cases. There were not enough experimental data on CEBEs of S2s to enable us to develop a reliable DFT procedure and therefore the S2s ionization energy for thiophene was not calculated.

Can. J. Chem. Downloaded from www.nrcresearchpress.com by South China Agricultural University on 09/19/12
For personal use only.

Table 9. Comparison of core-electron binding energies (CEBE, in eV) of cyclo-C_4H_4X.

	CEBE					
	This work	1971[a]	1971[b]	1977[c]	1977[d]	2002[e]
X = CH_2						
Cα	289.85					
Cβ	289.54					
Cα–Cβ	0.31					
X	290.76					
X = NH						
Cα	290.55	290.5		290.77		
Cβ	289.71	289.8		289.96		
Cα–Cβ	0.84	0.7		0.81		
N1s	405.57	406.1		406.15	406.18	
X = O						
Cα	291.48	291.5		290.81[f]		291.59
Cβ	290.44	290.3		290.61		290.32
Cα–Cβ	1.04	1.2		1.22		1.27
O1s	539.21	539.4	547.75			
X = S						
Cα	290.51	290.5		290.61		
Cβ	290.24	290.2		290.61		
Cα–Cβ	0.27	0.3				
S1s	2478.76					
S2p	169.65			170.45		

[a]Gelius et al.[56]
[b]ΔSCF/SZ calculation by Siegbahn.[79]
[c]Chambers and Thomas.[80]
[d]Cavell and Allison.[81]
[e]Rennie et al.[82]
[f]Probably 291.81 owing to typographical error.

Table 10. Vertical ionization energies (VIEs, in eV) of formamide and the ΔPBE0(SAOP) values calculated with different basis sets.

		VIE								
C_s	C_1	Observed[a]	et-pVQZ[a]	Dev	TZ2P	Dev	TZP	Dev	DZP	Dev
10a′	12a	10.35	10.39	0.04	10.42	0.07	10.42	0.07	10.66	0.31
2a″	11a	10.71	10.75	0.04	10.77	0.06	10.76	0.05	10.98	0.27
1a″	10a	14.13	14.39	0.26	14.43	0.30	14.44	0.31	14.58	0.45
9a′	9a	14.80	14.95	0.15	14.99	0.19	15.04	0.24	15.30	0.50
8a′	8a	16.36	16.61	0.25	16.64	0.28	16.68	0.32	16.91	0.55
7a′	7a	18.79	18.68	−0.11	18.71	−0.08	18.76	−0.03	19.03	0.24
6a′	6a	20.47	20.47	0.00	20.52	0.05	20.55	0.08	20.81	0.34
5a′	5a	28.6	28.59	−0.01	28.62	0.02	28.66	0.06	29.02	0.42
4a′	4a	32.8	32.64	−0.16	32.70	−0.10	32.79	−0.01	33.15	0.35
3a′	3a	294.40	294.19	−0.21	294.26	−0.14	294.33	−0.07	294.78	0.38
2a′	2a	406.38	406.55	0.17	406.58	0.20	406.61	0.23	407.70	1.32
1a′	1a	537.77	537.78	0.01	537.85	0.08	537.89	0.12	539.49	1.72
AAD (9 valence)				0.11		0.13		0.13		0.38
AAD (3 core)				0.13		0.14		0.14		1.14
AAD (all 12)				0.12		0.13		0.13		0.57

Note: AAD, average absolute deviation; dev, deviation.
[a]See Chong.[30]

Results and discussion

The results of this work are summarized in Tables 1–7 and compared with experimental and other theoretical studies.[48–75] The probable error of some of the observed VIEs is likely to be about 0.05 eV and the numbers written as subscripts in the tables are uncertain. Different workers report different numbers for the VIEs, and the AAD is presented in the

Can. J. Chem. Downloaded from www.nrcresearchpress.com by South China Agricultural University on 09/19/12
For personal use only.

tables as AAD(N) for N VIEs. It is from such comprehensive comparisons that one sees the quality of the recommended approach of ΔPBE0(SAOP)/et-pVQZ. To simplify the comparison of this work with previous ab initio studies of cyclopentadiene, pyrrole, furan, and thiophene, we select the performance of each method on the first 10 VIEs of each of the four molecules and present the results in Table 8. The difficulty of computational demands of the SAC-CI method can be seen in the AADs of over 0.3 eV in some cases. Our conclusion is that the procedure of ΔPBE0(SAOP)/et-pVQZ is as good as (if not better than) the ab initio methods of OVGF and ADC(3). Because both OVGF and ADC(3) are truncated approximations in perturbation expansions, there is a possibility of residual errors even when the basis sets approach the complete basis set limit. Moreover, the efficiency of our method enables us to use sufficiently large basis sets. Another advantage of our approach is that we can converge on cations of inner-valence ionizations. From the outstanding performance of our ΔPBE0(SAOP)/et-pVQZ procedure, we draw the tentative conclusions that (*i*) the exchange-correlation potential V_{xc} = SAOP provides excellent electron densities; (*ii*) the exchange-correlation functional PBE0 gives excellent energies from a given density; and (*iii*) the basis set of et-pVQZ is large enough for most purposes.

On the other hand, the procedure we recommend is not perfect for every molecule. When the effect of shake-up satellites is significant, the single configuration used in our DFT calculation may not be able to give an accurate enough description of the cation; and we do not have intensities like the pole strengths in OVGF and ADC(3). Another caution note must be taken into account by other users of the present method: for some unknown reason, the same procedure did not perform as well for the limited database of 13 VIEs of perhalo molecules. Instead, choosing to maintain symmetry rather than integer occupations gave a reasonable AAD of 0.25 eV.

The starting point of OVGF and ADC(3) corrections to the one-body model is the set of Hartree–Fock MOs and therefore the language used, such as terms like breakdown of one-particle picture and pole strength, refer to the Hartree–Fock model. DFT is also a one-particle model; whereas the so-called meta-Koopmans' theorem[5] models the cations by frozen Kohn–Sham holes, the present method of ΔPBE0(SAOP) models them by relaxed Kohn–Sham holes.

For the calculation of VIEs presented above, no attempt was made to include relativistic effects. Even for selenophene, the AAD of the first 10 VIEs from experiment[76,77] is only 0.2_1 eV,[78] compared with 0.3_4 eV from ADC(3).[77] However, for CEBEs, relativistic effect is unavoidable. The results of our CEBE calculations are presented in Table 9. The agreement of the calculated CEBEs with the experimental data of Gelius et al.[56] is remarkable. On the other hand, the observed values reported by Chambers and Thomas[80] appear to be 0.3 eV too high on the average. Everything considered, there are not enough experimental data to provide a reliable assessment of our computed results.

Finally, the large basis set of et-pVQZ may prohibit the study of large molecules such as nonsteroid anti-inflammation drugs. Table 10 summarizes the effect of using smaller basis sets on the performance of ΔPBE0(SAOP) for the VIEs of formamide, at the experimental slightly nonplanar geometry reported by Costain and Dowling.[83] Since many previous studies on formamide use a planar geometry, the symmetry labels in both C_1 and C_s point groups are given in Table 10. It can be seen that a small basis set such as polarized double-zeta DZP leads to serious errors and that a good compromise is the polarized triple-zeta TZP basis (which includes double-zeta core).

Summary

To further support our recommendation of ΔPBE0(SAOP)/et-pVQZ for the calculation of vertical valence ionization energies of organic and other small molecules, we show, in this study on cyclopentadiene. pyrrole, furan, and thiophene, that the recommended procedure can perform as well as, if not better than, the ab initio methods of OVGF and ADC(3). The results on core-electron binding energies also support the various procedures developed in recent years. The effect of basis set on the VIEs of formamide suggests that the large basis set of et-pVQZ may be reduced to a much smaller set of polarized triple-zeta quality without great loss of accuracy. It is therefore our hope that other workers will be encouraged to adopt our recommendation for their work.

Acknowledgment

The financial support of the Natural Sciences and Engineering Research Council of Canada (NSERC) is gratefully acknowledged.

References

(1) Lindholm, E.; Åsbrink, L. *Molecular Orbitals and their Energies, Studied by the Semiempirical HAM Method;* Springer-Verlag: Berlin, 1985.
(2) Gritsenko, O. V.; Schipper, P. R. T.; Baerends, E. J. *Chem. Phys. Lett.* **1999**, *302* (3–4), 199. doi:10.1016/S0009-2614(99)00128-1.
(3) Gritsenko, O. V.; Schipper, P. R. T.; Baerends, E. J. *Int. J. Quantum Chem.* **2000**, *76* (3), 407. doi:10.1002/(SICI)1097-461X(2000)76:3<407::AID-QUA9>3.0.CO;2-A.
(4) Schipper, P. R. T.; Gritsenko, O. V.; van Gisbergen, S. J. A.; Baerends, E. J. *J. Chem. Phys.* **2000**, *112* (3), 1344. doi:10.1063/1.480688.
(5) Chong, D. P.; Gritsenko, O. V.; Baerends, E. J. *J. Chem. Phys.* **2002**, *116* (5), 1760. doi:10.1063/1.1430255.
(6) Chong, D. P.; Takahata, Y. *Chem. Phys. Lett.* **2006**, *418* (1–3), 286. doi:10.1016/j.cplett.2005.10.091.
(7) Salzner, U.; Baer, R. *J. Chem. Phys.* **2009**, *131* (23), 231101. doi:10.1063/1.3269030.
(8) Baer, R.; Neuhauser, D. *Phys. Rev. Lett.* **2005**, *94* (4), 043002. doi:10.1103/PhysRevLett.94.043002.
(9) Livshits, E.; Baer, R. *Phys. Chem. Chem. Phys.* **2007**, *9* (23), 2932. doi:10.1039/b617919c.
(10) Chong, D. P.; Herring, F. G.; McWilliams, D. *J. Chem. Phys.* **1974**, *61* (1), 78. doi:10.1063/1.1681673.
(11) Chantranupong, L.; Chong, D. P. *J. Mol. Struct. THEOCHEM* **1985**, *133* (1–2), 37. doi:10.1016/0166-1280(85)85004-1.
(12) Cederbaum, L. S.; Hohlneicher, G.; von Niessen, W. *Mol. Phys.* **1973**, *26* (6), 1405. doi:10.1080/00268977300102581.
(13) von Niessen, W.; Schirmer, J.; Cederbaum, L. S. *Comput. Phys. Rep.* **1984**, *1* (2), 57. doi:10.1016/0167-7977(84)90002-9.

Can. J. Chem. Downloaded from www.nrcresearchpress.com by South China Agricultural University on 09/19/12
For personal use only.

(14) Hu, C.-H.; Chong, D. P.; Casida, M. E. *J. Electron Spectrosc. Relat. Phenom.* **1997**, *85* (1–2), 39. doi:10.1016/S0368-2048(97)00037-6.
(15) Ortiz, J. V. *J. Chem. Phys.* **1996**, *104* (19), 7599. doi:10.1063/1.471468.
(16) Frisch, M. J.; Trucks, G. W.; Schlegel, H. B.; Scuseria, G. E.; Robb, M. A.; Cheeseman, J. R.; Montgomery, J. A.; Vreven, T.; Kudin, K. N.; Burant, J. C.; Millam, J. M.; Iyengar, S. S.; Tomasi, J.; Barone, V.; Mennucci, B.; Cossi, M.; Scalmani, G.; Rega, N.; Petersson, G.A.; Nakatsuji, H.; Hada, M.; Ehara, M.; Toyota, K.; Fukuda, R.; Hasegawa, J.; Ishida, M.; Nakajima, T.; Honda, Y.; Kitao, O.; Nakai, H.; Klene, M.; Li, X.; Knox, J. E.; Hratchian, H. P.; Cross, J. B.; Bakken, V.; Adamo, C.; Jaramillo, J.; Gomperts, R.; Stratmann, R. E.; Yazyev, O.; Austin, A. J.; Cammi, R.; Pomelli, C.; Ochterski, J. W.; Ayala, P. Y.; Morokuma, K.; Voth, G. A.; Salvador, P.; Dannenberg, J. J.; Zakrzewski, V. G.; Dapprich, S.; Daniels, A. D.; Strain, M. C.; Farkas, O.; Malick, D. K.; Rabuck, A. D.; Raghavachari, K.; Foresman, J. B.; Ortiz, J. V.; Cui, Q.; Baboul, A. G.; Clifford, S.; Cioslowski, J.; Stefanov, B. B.; Liu, G.; Liashenko, A.; Piskorz, P.; Komaromi, I.; Martin, R. L.; Fox, D. J.; Keith, T.; Al-Laham, M. A.; Peng, C. Y.; Nanayakkara, A.; Challacombe, M.; Gill, P. M. W.; Johnson, B.; Chen, W.; Wong, M. W.; Gonzalez, C.; Pople, J. A. *Gaussian 03, Revision, C.02;* Gaussian, Inc.: Wallingford, CT, 2004.
(17) Schirmer, J.; Cederbaum, L. S. *J. Phys. B* **1978**, *11* (11), 1889. doi:10.1088/0022-3700/11/11/006.
(18) Schirmer, J.; Cederbaum, L. S.; Walter, O. *Phys. Rev. A* **1983**, *28* (3), 1237. doi:10.1103/PhysRevA.28.1237.
(19) Nakatsuji, H. *Chem. Phys. Lett.* **1978**, *59* (2), 362. doi:10.1016/0009-2614(78)89113-1.
(20) Duffy, P.; Chong, D. P. *Org. Mass Spectrom.* **1993**, *28* (4), 321. doi:10.1002/oms.1210280410.
(21) Hu, C.-H.; Chong, D. P. *J. Chinese Chem. Soc.* **2000**, *47*, 141.
(22) Segala, M.; Chong, D. P. *J. Electron Spectrosc. Relat. Phenom.* **2009**, *171* (1–3), 18. doi:10.1016/j.elspec.2008.12.006.
(23) Perdew, J. P.; Burke, K.; Ernzerhof, M. *Phys. Rev. Lett.* **1996**, *77* (18), 3865. doi:10.1103/PhysRevLett.77.3865.
(24) Perdew, J. P.; Burke, K.; Ernzerhof, M. *Phys. Rev. Lett.* **1997**, *78* (7), 1396. doi:10.1103/PhysRevLett.78.1396.
(25) Adamo, C.; Barone, V. *J. Chem. Phys.* **1999**, *110*, 6158. doi:10.1063/1.478522.
(26) Chong, D. P. *Can. J. Chem.* **2009**, *87* (8), 1148. doi:10.1139/V09-084.
(27) Chong, D. P. *Can. J. Chem.* **2010**, *88* (6), 577. doi:10.1139/V10-065.
(28) Chong, D. P. *Can. J. Chem.* **2010**, *88* (8), 787. doi:10.1139/V10-041.
(29) Chong, D. P. *Mol. Phys.* **2010**, *108* (19–20), 2459. doi:10.1080/00268976.2010.501347.
(30) Chong, D. P. *J. Electron Spectrosc. Rel. Phenom.* **2010** *184* (3–6), 164. doi:10.1016/j.elspec.2010.09.003.
(31) Rennie, E. E.; Johnson, C. A. F.; Parker, J. E.; Holland, D. M. P.; Shaw, D. A.; MacDonald, M. A.; Hayes, M. A.; Shpinkova, L. G. *Chem. Phys.* **1998**, *236* (1–3), 365. doi:10.1016/S0301-0104(98)00229-8.
(32) Rennie, E. E.; Johnson, C. A. F.; Parker, J. E.; Ferguson, R.; Holland, D. M. P.; Shaw, D. A. *Chem. Phys.* **1999**, *250* (2), 217. doi:10.1016/S0301-0104(99)00285-2.
(33) Palmer, M. H.; Walker, I. C.; Ballard, C. C.; Guest, M. F. *Chem. Phys.* **1995**, *192* (2), 111. doi:10.1016/0301-0104(94)00386-O.
(34) Palmer, M. H.; Walker, I. C.; Guest, M. F. *Chem. Phys.* **1998**, *238* (2), 179. doi:10.1016/S0301-0104(98)00285-7.
(35) Palmer, M. H.; Walker, I. C.; Guest, M. F. *Chem. Phys.* **1999**, *241* (3), 275. doi:10.1016/S0301-0104(98)00425-X.
(36) Scientific Computing and Modelling. *ADF Program System, Release 2009.01;* Scientifific Computing and Modeling NV, Vrije Universteit, Theoretical Chemistry: Amsterdam, The Netherlands, 2009. For a comprehensive description of ADF, see te Velde, G.; Bickelhaupt, F. M.; Baerends, E. J.; Fonseca Guerra, C.; van Gisbergen, S. J. A.; Snijders, J. G.; Ziegler, T. *J. Comput. Chem.* **2001**, *22* (9), 931. doi:10.1002/jcc.1056.
(37) Chong, D. P.; van Lenthe, E.; van Gisbergen, S.; Baerends, E. J. *J. Comput. Chem.* **2004**, *25* (8), 1030. doi:10.1002/jcc.20030.
(38) Damiani, D.; Ferretti, L.; Gallinella, E. *Chem. Phys. Lett.* **1976**, *37*, 265. doi:10.1016/2614(76)80212-6.
(39) Nygaard, L.; Nielsen, J. T.; Kirchheiner, J.; Maltesen, G.; Rastrup-Andersen, J.; Sorensen, G. O. *J. Mol. Struct.* **1969**, *3* (6), 491. doi:10.1016/0022-2860(69)80031-1.
(40) Mata, F.; Martin, M. C.; Sorensen, G. O. *J. Mol. Struct.* **1978**, *48* (2), 157. doi:10.1016/0022-2860(78)80018-0.
(41) Bak, B.; Christensen, D.; Hansen-Nygaard, L.; Rastrup-Andersen, J. *J. Mol. Spectrosc.* **1961**, *7* (1–6), 58. doi:10.1016/0022-2852(61)90341-1.
(42) Cavigliasso, G.; Chong, D. P. *J. Chem. Phys.* **1999**, *111* (21), 9485. doi:10.1063/1.480279.
(43) Takahata, Y.; Chong, D. P. *J. Electron Spectrosc. Relat. Phenom.* **2003**, *133* (1–3), 69. doi:10.1016/j.elspec.2003.08.001.
(44) Chong, D. P. *J. Chem. Phys.* **1995**, *103* (5), 1842. doi:10.1063/1.469758.
(45) Segala, M.; Takahata, Y.; Chong, D. P. *J. Electron Spectrosc. Relat. Phenom.* **2006**, *151* (1), 9. doi:10.1016/j.elspec.2005.09.007.
(46) Segala, M.; Chong, D. P. *J. Electron Spectrosc. Relat. Phenom.* **2010**, *182* (3), 141. doi:10.1016/j.elspec.2010.10.002.
(47) Maruani, J.; Kuleff, A. I.; Chong, D. P.; Bonnelle, C. *Int. J. Quantum Chem.* **2005**, *104* (4), 397. doi:10.1002/qua.20622.
(48) Derrick, P. J.; Åsbrink, L.; Edqvist, O.; Jonsson, B.-O.; Lindholm, E. *Spectrochim. Acta (A)* **1971**, *27A*, 2525.
(49) Derrick, P. J.; Åsbrink, L.; Edqvist, O.; Jonsson, B.-Ö.; Lindholm, E. *Int. J. Mass Spectrom. Ion Phys.* **1971**, *6* (3–4), 203. doi:10.1016/0020-7381(71)80004-9.
(50) Bieri, G.; Åsbrink, L.; von Niessen, W. *J. Electron Spectrosc. Relat. Phenom.* **1982**, *27* (2), 129. doi:10.1016/0368-2048(82)85059-7.
(51) Nakatsuji, H.; Kitao, O.; Yonezawa, T. *J. Chem. Phys.* **1985**, *83* (2), 723. doi:10.1063/1.449857.
(52) Wan, J.; Ehara, M.; Hada, M.; Nakatsuji, H. *J. Chem. Phys.* **2000**, *113* (13), 5245. doi:10.1063/1.1290004.
(53) Eland, J. H. D. *J. Mass Spectrom. Ion Phys.* **1969**, *2* (6), 471. doi:10.1016/0020-7381(69)80044-6.
(54) Baker, A. D.; Betteridge, D.; Kemp, N. R.; Kirby, R. E. *Anal. Chem.* **1970**, *42* (9), 1064. doi:10.1021/ac60291a042.
(55) Derrick, P. J.; Åsbrink, L.; Edqvist, O.; Jonsson, B.-O.; Lindholm, E. *Int. J. Mass Spectrom. Ion Phys.* **1971**, *6* (3–4), 191. doi:10.1016/0020-7381(71)80003-7.
(56) Gelius, U.; Allan, C. J.; Johansson, G.; Siegbahn, H.; Allison, D. A.; Siegbahn, K. *Phys. Scr.* **1971**, *3* (5), 237. doi:10.1088/0031-8949/3/5/008.
(57) Sell, J. A.; Kuppermann, A. *Chem. Phys. Lett.* **1979**, *61* (2), 355. doi:10.1016/0009-2614(79)80662-4.
(58) Klasinc, L.; Sabljić, A.; Kluge, G.; Rieger, J.; Scholz, M. *J. Chem. Soc.. Perkins Trans. 2* **1982**, (5), 539. doi:10.1039/p29820000539.

Can. J. Chem. Downloaded from www.nrcresearchpress.com by South China Agricultural University on 09/19/12
For personal use only.

(59) Kishimoto, N.; Yamakado, H.; Ohno, K. *J. Phys. Chem.* **1996**, *100* (20), 8204. doi:10.1021/jp960144t.
(60) Holland, D. M. P.; Karlsson, L.; von Niessen, W. *J. Electron Spectrosc. Relat. Phenom.* **2001**, *113* (2–3), 221. doi:10.1016/S0368-2048(00)00427-8.
(61) Trofimov, A. B.; Zaitseva, I. L.; Moskovskaya, T. E.; Vitkovskaya, N. M. *Chem. Heterocycl. Compd.* **2008**, *44* (9), 1101. doi:10.1007/s10593-008-0159-5.
(62) von Niessen, W.; Cederbaum, L. S.; Diercksen, G. H. F. *J. Am. Chem. Soc.* **1976**, *98* (8), 2066. doi:10.1021/ja00424a008.
(63) Tanaka, K.; Nomura, T.; Noro, T.; Tatewaki, H.; Takada, T.; Kashiwagi, H.; Sasaki, F.; Ohno, K. *J. Chem. Phys.* **1977**, *67* (12), 5738. doi:10.1063/1.434830.
(64) Ehara, M.; Ohtsuka, Y.; Nakatsuji, H.; Takahashi, M.; Udagawa, Y. *J. Chem. Phys.* **2005**, *122* (23), 234319. doi:10.1063/1.1929730.
(65) Derrick, P. J.; Åsbrink, L.; Edqvist, O.; Jonsson, B.-O.; Lindholm, E. *Int. J. Mass Spectrom. Ion Phys.* **1971**, *6* (3–4), 161. doi:10.1016/0020-7381(71)80001-3.
(66) Schweig, A.; Thiel, W. *Mol. Phys.* **1974**, *27* (1), 265. doi:10.1080/00268977400100241.
(67) Kimura, K.; Katsumata, S.; Achiba, Y.; Yamazaki, T.; Iwata, S. *Handbook 0f He I Photoelectron Spectra of Fundamental Organic Molecules;* Japan Scientific: Tokyo, 1981.
(68) Bawagan, A. D. O.; Olsson, B. J.; Tan, K. H.; Chen, J. M.; Yang, B. X. *Chem. Phys.* **1992**, *164* (2), 283. doi:10.1016/0301-0104(92)87151-X.
(69) von Niessen, W.; Kraemer, W. P.; Cederbaum, L. S. *J. Electron Spectrosc. Relat. Phenom.* **1976**, *8* (3), 179. doi:10.1016/0368-2048(76)81004-3.
(70) Hehenberger, M. *Chem. Phys. Lett.* **1977**, *46* (1), 117. doi:10.1016/0009-2614(77)85175-0.
(71) Derrick, P. J.; Åsbrink, L.; Edqvist, O.; Jonsson, B.-O.; Lindholm, E. *Int. J. Mass Spectrom. Ion Phys.* **1971**, *6* (3–4), 177. doi:10.1016/0020-7381(71)80002-5.
(72) Zhang, S. F.; Ren, X. G.; Su, G. L.; Ning, C. G.; Zhou, H.; Li, B.; Li, G. Q.; Deng, J. K. *Chem. Phys.* **2006** *327* (2–3), 269. doi:10.1016/j.chemphys.2006.05.002.
(73) Takeshita, K.; Yamamoto, Y. *Chem. Phys.* **1994**, *189* (3), 489. doi:10.1016/0301-0104(94)00292-4.
(74) Palmer, M. H.; Walker, I. C.; Guest, M. F. *Chem. Phys.* **1999**, *241* (3), 275. doi:10.1016/S0301-0104(98)00425-X.
(75) Singh, R. K.; Mishra, M. K. *J. Chem. Soc.* **2009** *121*, 867.
(76) Reineck, I.; Nohre, C.; Lodin, P.; Maripuu, R.; Lindberg, B.; Karlsson, L.; Siegbahn, K. *Chem. Scr.* **1983** *22*, 209.
(77) Powis, I.; Zaytseva, I. L.; Trofimov, A. B.; Schirmer, J.; Holland, D. M. P.; Potts, A. W.; Karlsson, L. *J. Phys. At. Mol. Opt. Phys.* **2007**, *40* (11), 2019. doi:10.1088/0953-4075/40/11/006.
(78) Chong, D. P. Unpublished work, 2011.
(79) Siegbahn, P. *Chem. Phys. Lett.* **1971**, *8* (3), 245. doi:10.1016/0009-2614(71)85001-7.
(80) Chambers, S. A.; Thomas, T. D. *J. Chem. Phys.* **1977**, *67* (6), 2596. doi:10.1063/1.435200.
(81) Cavell, R. G.; Allison, D. A. *J. Am. Chem. Soc.* **1977**, *99* (12), 4203. doi:10.1021/ja00454a072.
(82) Rennie, E. E.; Hergenhahn, U.; Kugeler, O.; Rűdel, A.; Marburger, S.; Bradshaw, A. M. *J. Chem. Phys.* **2002**, *117* (14), 6524. doi:10.1063/1.1504435.
(83) Costain, C. C.; Dowling, J. M. *J. Chem. Phys.* **1960**, *32* (1), 158. doi:10.1063/1.1700891.

Theoretical study on chemical bond parameters and properties of $LnAl_3(BO_3)_4$

Zhiping Li and Faming Gao

Can. J. Chem. Downloaded from www.nrcresearchpress.com by South China Agricultural University on 09/19/12
For personal use only.

Abstract: The detailed chemical bond parameters of $LnAl_3(BO_3)_4$ crystals were calculated using the chemical bond theory of complex crystals. Results indicated that Ln–O bonds are ionic and B–O bonds possess higher covalency. The environment factor defined by electron polarizabilities and covalency was employed to predict Racah parameters. The hardness of $YAl_3(BO_3)_4$ was predicted using Gao's model, which is also in agreement with the experimental value.

Key words: dielectric properties, hardness.

Résumé : On a calculé les paramètres détaillés des liaisons chimiques dans les cristaux de $LnAl_3(BO_3)_4$ en faisant appel à la théorie de la liaison chimique dans les cristaux. Les résultats indiquent que les liaisons Ln–O sont ioniques alors que les liaisons B–O possèdent un degré important de covalence. On a fait appel au facteur d'environnement défini par les polarisabilités et la covalence pour prédire les paramètres de Racah. La valeur de la dureté du $YAl_3(BO_3)_4$ qui a été prédite sur la base du modèle de Gao est aussi en accord avec la valeur expérimentale.

Mots-clés : propriétés diélectriques, dureté.

[Traduit par la Rédaction]

Introduction

The huntite-type borate $LnAl_3(BO_3)_4$ was synthesizd by Ballman in 1962 and the structures of $YAl_3(BO_3)_4$, $NdAl_3(BO_3)_4$, and $GdAl_3(BO_3)_4$ were reported.[1] $YAl_3(BO_3)_4$ was found to have excellent nonlinear optical properties and is widely used as a host material for solid laser crystal. The microchip laser emissions from Nd^{3+}-doped $YAl_3(BO_3)_4$ was revealed.[2] Because of their important practical applications as host materials for fluorescence and piezoelectricity materials, they have attracted considerable attention in the past few decades. For optical applications, $LnAl_3(BO_3)_4$ crystals should also possess excellent mechanical properties. The hardness of $YAl_3(BO_3)_4$ crystals is thus measured.[2] However, the effects of bond parameters on their hardness have been not studied. In addition, Racah parameters play an important role in predicting optical properties. In this paper we will employ the dielectric theory of complex structure crystals to calculate their bonding properties, and apply the obtained chemical bond parameters to predict their hardness and Racah parameters.

Theoretical method

A chemical bond theory of complex structure crystals was proposed by Zhang.[3,4] Its crucial step is decomposing the complex crystal into pseudobinary crystals, each containing only one type of chemical bond. For the multibond crystal $A_aB_b\ldots$, the subformula for any kind of chemical bond A–B can be expressed as

$$[1] \qquad \left[\frac{N(\mathrm{B}-\mathrm{A})a}{N_{\mathrm{CA}}}\right]\mathrm{A}\left[\frac{N(\mathrm{A}-\mathrm{B})b}{N_{\mathrm{CB}}}\right]\mathrm{B}$$

where A, B,… represent different elements or different sites of the same element in the crystal formula, a, b,… represent numbers of the corresponding element, N(B – A) represents the number of B ions in the coordination group of the A ion, and N_{CA} represents the nearest coordination number of the A ion. These binary crystals are related to each other, and every binary crystal includes only one type of chemical bond. However, the properties of these pseudobinary crystals are different from those of real binary crystals, although their chemical bond parameters can be calculated in a similar way. According to eq. [1], each type of bond has its corresponding subformula, and the sum of all subformulas equals the crystal formula, which is called the bond-valence equation.

On the analogy of the work of Phillips[5] and Zhang and coworkers,[3,4] the average energy gap E_g^{μ} for every μ bond in the pseudobinary crystals can be separated into homopolar $E_h^{\mu}$and heteropolar C^{μ} parts. The homopolar gap E_h^{μ} can be interpreted as being produced by the symmetric part of the total potential, whereas the ionic or charge-transfer gap C^{μ} results from the effect of the antisymmetric part. The average valence-conduction band gap is give by

$$[2] \qquad (E_g^{\mu})^2 = (E_h^{\mu})^2 + (C^{\mu})^2$$

The ionicity and covalency of any type of chemical bond is defined as follows:

Received 15 June 2011. Accepted 11 August 2011. Published at www.nrcresearchpress.com/cjc on 16 November 2011.

Z. Li and F. Gao. Key Laboratory of Applied Chemistry, Yanshan University, Qinhuangdao 066004, China.

Corresponding author: Faming Gao (e-mail: gfm0827@sina.com).

This article is part of a Special Issue to commemorate the International Year of Chemistry.

Can. J. Chem. Downloaded from www.nrcresearchpress.com by South China Agricultural University on 09/19/12
For personal use only.

Fig. 1. Crystal structure of $LnAl_3(BO_3)_4$.

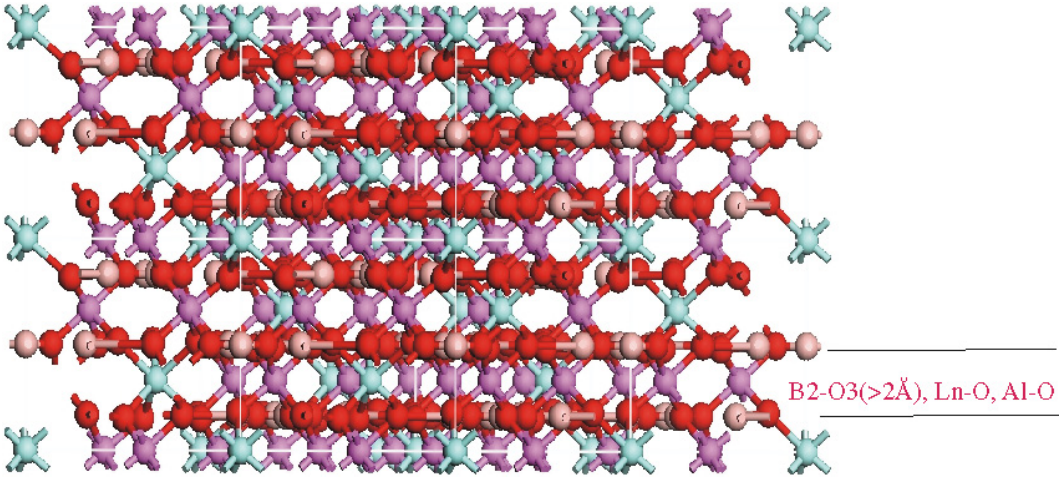

[3] $$f_i^{\mu} = (C^{\mu})^2/(E_g^{\mu})^2$$

[4] $$f_c^{\mu}(E_h^{\mu})^2/(E_g^{\mu})^2$$

and

[5] $$E_h^{\mu} = 39.74/(d^{\mu})^{2.48} \quad \text{eV}$$

where d^{μ} is the bond length. For any binary crystal, i.e., AB_n-type compounds, the heteropolar C^{μ} part is defined as

[6] $$C^{\mu} = 14.4b^{\mu}[(Z_A^{\mu})^* + \Delta Z_A^{\mu} - n(Z_B^{\mu})^*]e^{-k_s^{\mu}r_0^{\mu}}/r_0^{\mu} \quad \text{eV}$$

where $r_0^{\mu} = d^{\mu}/2$.

[7] $$k_s^{\mu} = (4k_F^{\mu}/\pi a_B)^{1/2} = 1.551(k_F^{\mu})^{1/2}$$

[8] $$(k_F^{\mu})^3 = 3\pi^2 N_e^{\mu}$$

[9] $$N_e^{\mu} = (n_e^{\mu})^*/v_b^{\mu}$$

[10] $$(n_e^{\mu})^* = [(Z_A^{\mu})^*/N_{CA}^{\mu} + (Z_B^{\mu})^*/N_{CB}^{\mu}]$$

[11] $$v_b^{\mu} = (d^{\mu})^3/\sum_{\nu}[(d^{\nu})^3 N_b^{\nu}]$$

where v_b^{μ} is the bond volume; $(n_e^{\mu})^*$ is the number of effective valence electrons per μ bond; N_e^{μ} is the number of valence electrons of the μ bond per cm^3, k_F^{μ} and k_s^{μ} are the Fermi wave number and the Thomas–Fermi screening wave number of a valence electron in a binary crystal composed of only one type of bond (μ), respectively; a_B is the Bohr radius; n is the ratio of element B to element A in the subformula; $(Z_A^{\mu})^*$ and $(Z_B^{\mu})^*$ are the number of effective valence electrons of the A and B ions, respectively; $(Z_A^{\mu})^* = Q_{AB}^{\mu} \cdot N_{CA}^{\mu}$, $(Z_B^{\mu})^* = [(Q_{AB}^{\mu} \cdot N_{CB}^{\mu})/(8 - Z_B^{\mu})] \cdot Z_B^{\mu}$; Q_{AB}^{μ} is the Pauling bond valence of the A–B bonds, Z_B^{μ} is the number of valence electrons of the B atoms; ΔZ_A^{μ} is a correction factor for the d electrons and the Jahn–Teller effect;[6,7] and b^{μ} is proportional to the square of the average coordination number N_c^{μ}.

[12] $$b^{\mu} = \beta(N_c^{\mu})^2$$

[13] $$N_c^{\mu} = N_{CA}^{\mu}/(1+n) + nN_{CB}^{\mu}/(1+n)$$

where β is a coefficient. The dielectric constant at the long wave limit (ε) can be calculated from the Kramers–Kronig relation for the dielectric function as follows:[8]

[14] $$\varepsilon = \sum_{\mu} F^{\mu}\varepsilon^{\mu}$$

[15] $$\varepsilon^{\mu} = 1 + [(4\pi N_e^{\mu} e^2/m)D^{\mu}/(E_g^{\mu})^2] \times [1 - E_g^{\mu}/4E_F^{\mu} + (E_g^{\mu})^2/48(E_F^{\mu})^2]$$

where ε^{μ} is the low-frequency dielectric constant of a binary crystal composed of only one type of μ bond, D^{μ} is the periodic dependent constant, E_F^{μ} is the Fermi energy, and F^{μ} is the fraction of the binary crystal composing the actual complex crystal.

Results and discussions

The structure of $LnAl_3(BO_3)_4$ is shown in Fig. 1. According to theory,[3,4] the crystal formula of $LnAl_3(BO_3)_4$ can be converted into a subformula equation as follows:

[16] $$LnAl_3(BO_3)_4 = LnO(3)_{3/2} + AlO(1)_2 + AlO(2)_2 + AlO(3)_{3/2} + B(1)O(1)_2 + 3/5B(2)O(2)_{5/3} + 6/5B(2)O(3)_{5/4} + 6/5B(2)O(3)_{3/2}$$

Using the theory mentioned above we can calculate the detailed bond parameters and linear optical susceptibilities of individual bonds of $LnAl_3(BO_3)_4$. The results of these calculations are listed in Table 1. The refractive indices (n_o and n_e) of $YAl_3(BO_3)_4$ are 1.773 and 1.722, respectively.[9] The average dielectric constant of $YAl_3(BO_3)_4$ is $\varepsilon = (1/3\ n_o n + 2/3 n_e)^2 = 3.024$. The calculated dielectric constants of $LnAl_3(BO_3)_4$ agree with their experimental values determined by the refractive index.[9]

Using the calculated chemical bond parameters we can estimate the hardness of these materials. The average hardness $H_{v\ av}$ of complex crystals may be calculated by a geometric

Can. J. Chem. Downloaded from www.nrcresearchpress.com by South China Agricultural University on 09/19/12
For personal use only.

Table 1. Chemical bond parameters and hardness of rare earth ferroborates.

Rare earth ferroborate	Bond type	d^{μ} (Å)	v_b^{μ} (Å^3)	N_e^{μ} (Å^{-3})	E_h^{μ} (eV)	E_g^{μ} (eV)	f_i^{μ}	χ^{μ}	ε_{av}	$\varepsilon_{av\ exp.}$[11]	h_e	B_{calcd} (cm^{-1})	$B_{exp.}$ (cm^{-1})	H_v^{μ}	$H_{v\ av}$ (GPa)
$YAl_3(BO_3)_4$	YO3	2.321	6.282	0.318	4.924	16.625	0.912	1.436	3.024	3.024				6.709	10.564
	AlO1	1.922	3.567	0.561	7.862	18.595	0.821	1.844			0.518	692	684[11]	17.473	
	AlO2	1.938	3.657	0.547	7.702	18.252	0.822	1.868						16.820	
	AlO3	1.837	3.115	0.642	8.795	28.184	0.903	0.851						19.439	
	B1O1	1.383	1.329	3.010	17.782	23.111	0.408	7.200						199.510	
	B2O2	1.367	1.283	3.117	18.303	82.513	0.951	0.479						110.139	
	B2O3	1.373	1.300	1.538	18.105	39.477	0.790	1.104						82.425	
	B2O3	2.741	10.347	0.193	3.260	8.322	0.847	3.232						3.433	
Pr $Al_3(BO_3)_4$	PrO3	2.339	6.510	0.307	4.831	16.410	0.913	1.513	3.022					6.418	9.975
	AlO1	1.937	3.697	0.541	7.712	18.348	0.823	1.824						16.692	
	AlO2	1.953	3.789	0.528	7.556	18.012	0.824	1.847						16.072	
	AlO3	1.874	3.348	0.597	8.371	27.093	0.905	0.855						17.584	
	B1O1	1.392	1.372	2.915	17.499	22.807	0.411	7.157						191.409	
	B2O2	1.376	1.325	3.018	18.008	81.721	0.951	0.471						105.972	
	B2O3	1.382	1.343	1.490	17.814	39.066	0.792	1.089						79.151	
	B2O3	2.766	10.765	0.186	3.187	8.181	0.848	3.209						3.262	
Nd $Al_3(BO_3)_4$	NdO3	2.371	6.753	0.296	4.671	15.874	0.913	1.562	3.039					6.053	9.974
	AlO1	1.932	3.654	0.547	7.761	18.430	0.823	1.830						16.946	
	AlO2	1.947	3.740	0.535	7.614	18.113	0.823	1.852						16.354	
	AlO3	1.858	3.250	0.615	8.551	27.571	0.904	0.851						18.341	
	B1O1	1.393	1.370	2.921	17.467	22.755	0.411	7.205						191.438	
	B2O2	1.424	1.463	2.734	16.540	75.793	0.952	0.498						90.960	
	B2O3	1.352	1.252	1.597	18.811	40.868	0.788	1.068						88.010	
	B2O3	2.778	10.862	0.184	3.153	8.082	0.848	3.262						3.209	
Sm $Al_3(BO_3)_4$	SmO3	2.365	6.702	0.298	4.700	15.967	0.913	1.555	3.030	3.046				6.124	10.103
	AlO1	1.927	3.625	0.552	7.811	18.537	0.822	1.823						17.151	
	AlO2	1.942	3.710	0.539	7.662	18.217	0.823	1.845						16.550	
	AlO3	1.853	3.223	0.620	8.608	27.733	0.904	0.848						18.569	
	B1O1	1.389	1.358	2.946	17.592	22.908	0.410	7.171						194.062	
	B2O2	1.427	1.472	2.717	16.453	75.445	0.952	0.499						90.103	
	B2O3	1.346	1.235	1.619	19.019	41.250	0.787	1.062						89.874	
	B2O3	2.768	10.744	0.186	3.182	8.153	0.848	3.240						3.262	
Eu $Al_3(BO_3)_4$	EuO3	2.363	6.685	0.299	4.710	15.999	0.913	1.553	3.028	3.056				6.147	10.132
	AlO1	1.926	3.619	0.553	7.821	18.559	0.822	1.822						17.192	
	AlO2	1.941	3.705	0.540	7.672	18.239	0.823	1.844						16.589	
	AlO3	1.852	3.218	0.621	8.619	27.766	0.904	0.847						18.615	
	B1O1	1.389	1.358	2.946	17.592	22.908	0.410	7.171						194.062	
	B2O2	1.426	1.469	2.723	16.482	75.560	0.952	0.499						90.390	
	B2O3	1.345	1.233	1.622	19.054	41.314	0.787	1.061						90.188	
	B2O3	2.766	10.721	0.187	3.187	8.168	0.848	3.235						3.272	

Can. J. Chem. Downloaded from www.nrcresearchpress.com by South China Agricultural University on 09/19/12
For personal use only.

Table 1 (*concluded*).

Rare earth ferroborate	Bond type	d^{μ} (Å)	v_b^{μ} (Å^3)	N_e^{μ} (Å^{-3})	E_h^{μ} (eV)	E_g^{μ} (eV)	f_i^{μ}	χ^{μ}	ε_{av}	$\varepsilon_{av\ exp.}$[11]	h_e	B_{calcd} (cm^{-1})	$B_{exp.}$ (cm^{-1})	H_v^{μ}	$H_{v\ av}$ (GPa)
Gd $Al_3(BO_3)_4$	GdO3	2.361	6.669	0.300	4.720	16.032	0.913	1.550	3.023	3.025				6.170	10.189
	AlO1	1.923	3.604	0.555	7.852	18.625	0.822	1.817						17.312	
	AlO2	1.939	3.694	0.541	7.692	18.282	0.823	1.840						16.664	
	AlO3	1.850	3.209	0.623	8.643	27.835	0.904	0.845						18.703	
	B1O1	1.387	1.352	2.958	17.655	22.986	0.410	7.151						195.335	
	B2O2	1.425	1.466	2.728	16.511	75.682	0.952	0.498						90.661	
	B2O3	1.344	1.230	1.626	19.090	41.382	0.787	1.060						90.484	
	B2O3	2.761	10.666	0.188	3.202	8.205	0.848	3.222						3.299	

Note: $H_{v\ av}$ is the calculated average Vickers hardness on prisms; B_{calcd} and B_{exp} are the calculated and experimental Racah parameters of Cr^{3+} at the Al site, respectively; ε_{av} and $\varepsilon_{av\ exp.}$ are the calculated and experimental dielectric constants, respectively; $d^{\mu}$is the bond length; v_b^{μ} is the bond volume; N_e^{μ} is the number of valence electrons of the μ bond per cm^3; E_h^{μ} is the homopolar gap; E_g^{μ} is the average energy gap; f_i^{μ} is the ionicity of the bond; $\chi^{\mu} = \varepsilon^{\mu} - 1$, where ε^{μ} is the low-frequency dielectric constant of a binary crystal composed of only one type of μ bond; and h_e is the chemical environmental factor.

average of hardness of the pseudobinary compound composed of a μ-type bond as follows:[10]

$$[17] \qquad H_{v\ av} = [\prod^{\mu}(H_v^{\mu})^{n^{\mu}}]^{1/\Sigma n^{\mu}}$$

$$[18] \qquad H_v^{\mu} = 350(N_e^{\mu})^{2/3}e^{-1.191 f_i^{\mu}}/(d^{\mu})^{2.5}$$

where n^{μ} is the number of bonds of type μ composing the actual complex crystal. From Fig. 1, we may observe the layer structure along the *c* axis in the $LnAl_3(BO_3)_4$ crystal. In these layers, B–O3 (>2Å), Ln–O, and Al–O bonds are contained. Thus, the hardness on prisms should be equal to a geometric average of hardness of the pseudobinary compound $LnO(3)_{3/2}$, $AlO(1)_2$, $AlO(2)_2$, $AlO(3)_{3/2}$, and B(2)O(3) (>2Å). Using eq. [17], the calculated hardness on prisms are listed in Table 1. For $YAl_3(BO_3)_4$, the calculated hardness on prisms is 10.564 GPa, which is in good agreement with the experimental value, 10. 5 GPa.[2]

The room-temperature excitation spectrum of the luminescence of Cr^{3+} in the $YAl_3(BO_3)_4$ single crystal has been used to estimate the crystal-field strength D_q and the Racah parameters *B* and *C*. The crystal-field strength was obtained as $10D_q = 16\,620$ cm^{-1}and $B = 684$ cm^{-1} and $C = 3194$ cm^{-1}.[11] The chemical bond parameters can also be applied to the study on nephelauxetic effect. It is known that the nephelauxetic effect depends on covalency and the polarizabilities of ligands. Jørgensen[12] found that the nephelauxetic effect can be factored into a function of just a ligand and the centre metal:

$$[19] \qquad B/B_0 = 1 - k(\text{centre ion})h_e(\text{ligand})$$

where *B* and B_0 are the Racah parameters of free ions and the ions in crystals, respectively. We introduce the chemical environmental factor(h_e) written as[13]

$$[20] \qquad h_e = \left(\sum_{\mu} \alpha_L{}^{\mu} f_c{}^{\mu}\right)^{1/2}$$

where $\alpha_L{}^{\mu}$ is the polarizability of the ligand in the μ bond.

$$[21] \qquad \alpha_L{}^{\mu} = \{(r_B{}^{\mu})^3/[(r_A{}^{\mu})^3 + (r_B{}^{\mu})^3]\}\alpha_b{}^{\mu}$$

$$[22] \qquad \alpha_b{}^{\mu} = v_b{}^{\mu}(3/4\pi)(\varepsilon^{\mu} - 1)/(\varepsilon^{\mu} + 2)$$

where $r_A{}^{\mu}$ and $r_B{}^{\mu}$ are the effective radii of the A and B ions,[14] respectively; $\alpha_b{}^{\mu}$ is the polarizability of the bond volume in the μth bond. The effect of the centre ion is expressed as[13]

$$[23] \qquad k = [(Z + 2 - S)/5]^2$$

where *Z* is the valence of the ion and *S* is the spin of the electron configuration of the ion. The *k* value of the Cr^{3+} ions is calculated as 0.49. The Racah parameter of the free Cr^{3+} ion (B_0) is 918 cm^{-1}.[15] The h_e for Fe sites in the $YAl_3(BO_3)_4$ crystals iwas obtained using eq. [22]. According to eq. [21], the calculated Racah parameter $B(Cr^{3+}$ at Al site) is 692 cm^{-1}. It is in good agreement with the experimental value, $B = 684$ cm^{-1}.[11]

Conclusion

In conclusion, the detailed chemical bond parameters of $LnAl_3(BO_3)_4$ crystals were calculated using the chemical bond theory of complex crystals. Results indicated that Ln–O bonds are ionic and B–O bonds possess higher covalency. The environment factor defined by electron polarizabilities and covalency was employed to predict Racah parameters. The hardness of $YAl_3(BO_3)_4$ was predicted using the hardness model, which is also in agreement with the experimental value.

References

(1) Ballman, A. *Am. Mineral.* **1962**, *47*, 1380.
(2) Leonyuk, N. I.; Leonyuk, L. I. *Prog. Cryst. Growth Charact. Mater.* **1995**, *31* (3–4), 179. doi:10.1016/0960-8974(96)83730-2.
(3) Zhang, S. Y. *Chin. J. Chem. Phys.* **1991**, *4*, 109.
(4) Zhang, S. Y.; Gao, F. M.; Wu, C. X. *J. Alloy. Comp.* **1998**, *275–277*, 835. doi:10.1016/S0925-8388(98)00452-6.
(5) Phillips, J. C. *Rev. Mod. Phys.* **1970**, *42* (3), 317. doi:10.1103/RevModPhys.42.317.
(6) Gao, F. M.; Zhang, S. Y. *Chin. J. Inorg. Chem.* **2000**, *16*, 751.
(7) Gao, F. M.; Li, D. C.; Zhang, S. Y. *J. Phys. Condens. Matter* **2003**, *15* (29), 5079. doi:10.1088/0953-8984/15/29/319.
(8) Levine, B. F. *J. Chem. Phys.* **1973**, *59* (3), 1463. doi:10.1063/1.1680204.
(9) Filimonov, A. A.; Leonyuk, I.; Meissner, B.; Timchenko, I.; Rez, I. S. *Kristall und Technik* **1974**, *9* (1), 63. doi:10.1002/crat.19740090111.
(10) Gao, F. M. *Phys. Rev. B* **2004**, *69* (9), 094113. doi:10.1103/PhysRevB.69.094113.
(11) Dominiak-Dzik, G.; Ryba-Romanowski, W.; Grinberg, M.; Beregi, E.; Kovacs, L. *J. Phys. Condens. Matter* **2002**, *14* (20), 5229. doi:10.1088/0953-8984/14/20/318.
(12) Jørgensen, C. K. *Prog. Inorg. Chem.* **1962**, *4*, 73. doi:10.1002/9780470166055.ch2.
(13) Gao, F. M.; Zhang, S. Y. *J. Phys. Chem. Solids* **1997**, *58* (12), 1991. doi:10.1016/S0022-3697(96)00139-4.
(14) Shannon, R. D. *Acta Crystallogr. A* **1976**, *32* (5), 751. doi:10.1107/S0567739476001551.
(15) Cole, G. M., Jr.; Garrett, B. B. *Inorg. Chem.* **1970**, *9* (8), 1898. doi:10.1021/ic50090a020.

Can. J. Chem. Downloaded from www.nrcresearchpress.com by South China Agricultural University on 09/19/12
For personal use only.

Ruthenium-catalyzed [2+2] cycloaddition reactions of a 2-oxa-3-azabicyclo[2.2.1]hept-5-ene with unsymmetrical alkynes

Robin Durham, Jérémie Mandel, Nicolas Blanchard, and William Tam

Can. J. Chem. Downloaded from www.nrcresearchpress.com by South China Agricultural University on 09/19/12
For personal use only.

Abstract: Ruthenium-catalyzed [2+2] cycloaddition reactions of a 2-oxa-3-azabicyclo[2.2.1]hept-5-ene with unsymmetrical alkynes were investigated. Yields of up to 90% were obtained though regioselectivity was modest. Select cycloadducts could be separated and used to access a highly functionalized [3.2.0] bicyclic structure through reductive cleavage of the N–O bond. These ring-opened products displayed a chemical exchange phenomenon in 1D carbon NMR and required characterization by 2D NMR techniques.

Key words: ruthenium, [2+2] cycloadditions, bicyclic alkene, ring opening, 2-oxa-3-azabicyclo[2.2.1]hept-5-enes.

Résumé : On a étudié des réactions de cycloaddition [2+2] catalysées par le ruthénium du 2-oxa-3-azabicyclo[2,2,1]hept-5-ène avec des alcynes non symétriques. On a obtenu des rendements allant jusqu'à 90 %, même si la régiosélectivité est modeste. Il a été possible de séparer des cycloadduits choisis et de les utiliser pour accéder à une structure bicyclique [3,2,0] hautement fonctionnalisée, en procédant à un clivage réducteur de la liaison N–O. Ces produits d'ouverture de cycles présentent un phénomène d'échange chimique dans la RMN du carbone 1D et leur caractérisation a nécessité l'utilisation de techniques de RMN 2D.

Mots-clés : ruthénium, cycloadditions [2+2], alcène bicyclique, ouverture de cycle, 2-oxa-3-azabicyclo[2.2.1]hept-5-ènes.

[Traduit par la Rédaction]

Introduction

The 2-oxa-3-azabicyclo[2.2.1]heptenes **1** are a group of heterobicyclic alkenes that have been extensively investigated because of their utility as synthetic intermediates. Synthesized through a nitroso hetero-Diels–Alder reaction, these relatively simple cycloadducts provide access to more complex molecular structures.[1] Though rearrangements and other chemical reactions can also occur, heterobicyclic alkene **1** is generally modified in one of four ways (Scheme 1).[2] These four categories consist of cleavage of the N–O bond, cleavage of the C–O bond, cleavage of the N–acyl bond, and modification of the alkene component.

Heterobicyclic alkene **1** is most commonly derivatized through reductive cleavage of the N–O bond to provide amino alcohol **2**. Widely used reagents include molybdenum-hexacarbonyl ($[Mo(CO)_6]$),[3,4] catalytic hydrogenation, zinc in acetic acid, samarium diiodide,[5] and titanocene(III) chloride.[6] Examples that employ enzymatic,[7] photochemical,[8] and other chemical processes to reductively cleave this bond are also present in the literature.[9]

The second area of structural modification of **1** is cleavage of the C–O bond to form compounds **3** and **4**, where the stereochemistry depends on the method used. These methods include acid-catalyzed ring-opening rearrangements,[10] palladium- and Lewis acid-catalyzed ring openings,[11] copper-catalyzed Grignard or organozinc nucleophilic ring-opening reactions;[12] ruthenium-catalyzed ring-opening reactions with alcohols,[13] and rhodium-catalyzed ring-opening reactions with arylboronic acids.[14]

The third category represents hydrolysis of the carbonyl group under mild conditions to yield compound **5**.[15] This allows removal of any chiral auxiliaries used to induce chirality during the acylnitroso hetero-Diels–Alder reaction.

In the final category, it is the alkene component of **1** that is modified to yield structures such as **6** or **7**. A number of transformations have been carried out on the alkene moiety of the related 2-oxa-3-azabicyclo[2.2.1]hept-5-ene system **8** (Scheme 2). Examples include oxidative cleavage to give diacid compound **9**, ring opening cross-metathesis providing compounds **10a** and **10b**,[16] dihydroxylation to yield diol **11**,[17] and alkylidenecyclopropanation resulting in compound **12**.[18] In addition, the dipolar cycloaddition of alkene **8** with organic azides and nitrile oxides provides regioisomeric mixtures **13a**, **13b**, and **14a** and **14b**, respectively.[19]

Received 10 June 2011. Accepted 22 September 2011. Published at www.nrcresearchpress.com/cjc on 16 November 2011.

R. Durham and W. Tam. Guelph–Waterloo Centre for Graduate Work in Chemistry and Biochemistry, Department of Chemistry, University of Guelph, Guelph, ON N1G 2W1, Canada.
J. Mandel and N. Blanchard. Université de Haute-Alsace, École Nationale Supérieure de Chimie de Mulhouse, Laboratoire de Chimie Organique et Bioorganique EA4566, 3 rue A. Werner, 68093 Mulhouse CEDEX, France.

Corresponding author: William Tam (wtam@uoguelph.ca).

This article is part of a Special Issue to commemorate the International Year of Chemistry.

Can. J. Chem. Downloaded from www.nrcresearchpress.com by South China Agricultural University on 09/19/12
For personal use only.

Scheme 1. Modification of 3-aza-2-oxabicyclo[2.2.1]heptanes.

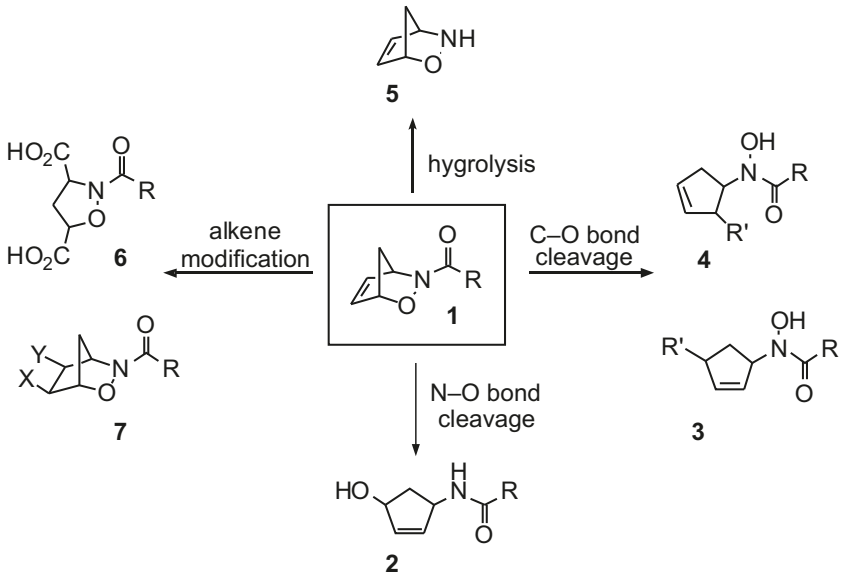

Scheme 2. Chemical transformations involving the alkene component of 3-aza-2-oxabicyclo[2.2.1]hept-5-enes.

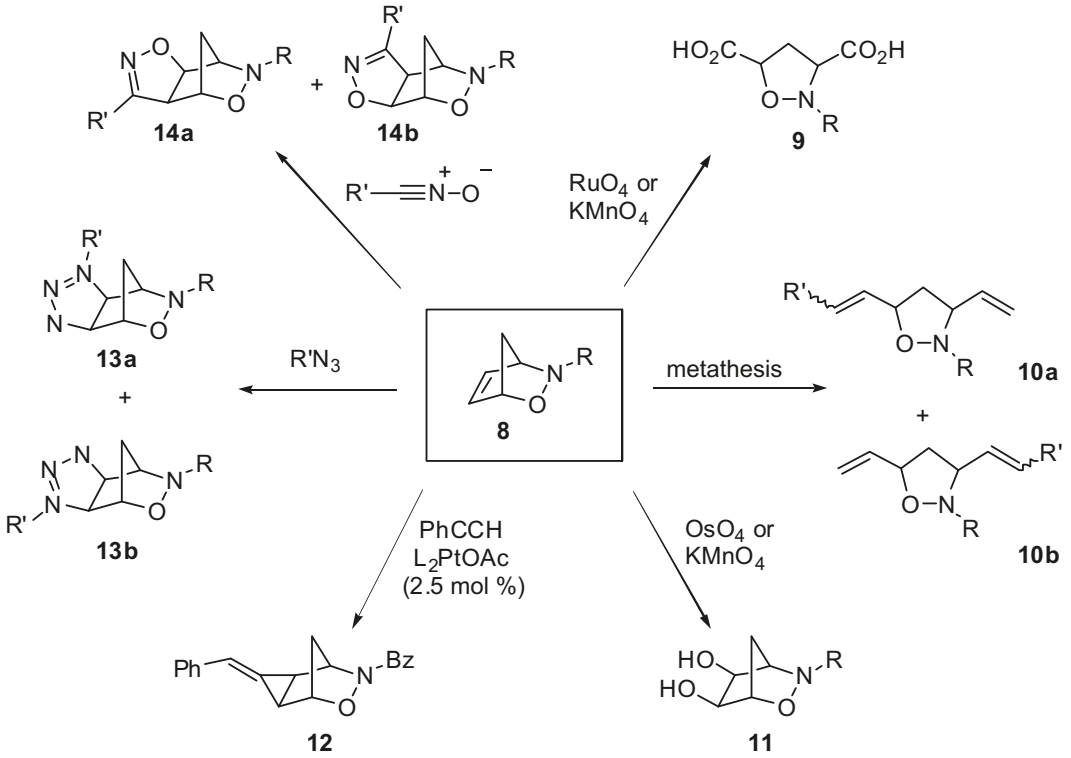

Like their heterobicyclic analogues, derivatives of norbornene are involved in a number of chemical transformations. One such example is the ruthenium-catalyzed [2+2] cycloaddition reaction between a bicyclic alkene and an alkyne. The Mitsudo group previously discovered that Cp*Ru(COD)Cl was a successful catalyst for the [2+2] cycloaddition reaction between norbornene derivatives and both aliphatic and aromatic alkynes.[20] Since then several groups have contributed to the knowledge of ruthenium-catalyzed [2+2] cycloadditions. An investigation by the Tam group focused on 2-substituted norbornenes and unsymmetrical alkynes (Scheme 3).[21] The unsymmetrical nature of both reaction partners allowed the regioselectivity of the [2+2] reaction to be studied. A variety of substituents at the C2 position of the norbornenes resulted in regioselectivities ranging from 1.2:1 to 7.5:1. Overall, the exo-2-substituted norbornenes provided higher regioselectivities than the corresponding endo-2-substituted norbornenes. The highest regioselectivites were observed when the substituent at the C2 position possessed an exocyclic double bond such as a ketone.

This and other studies on 2-substituted norbornenes demonstrate that the remote substituents at C2 are exerting an

Scheme 3. An investigation of the remote substituent effects of 2-substituted norbornenes on ruthenium-catalyzed [2+2] cycloadditions.

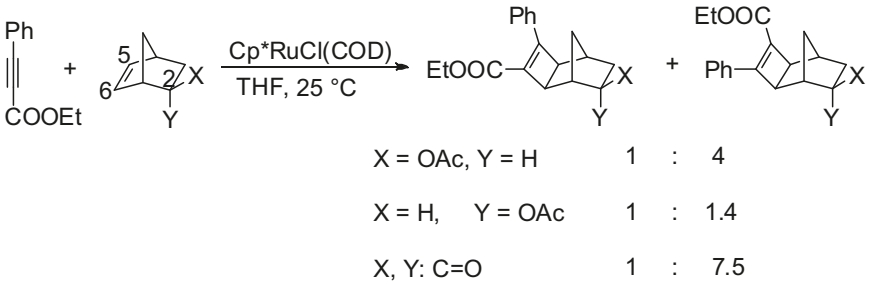

electronic effect on carbons five and six. It is the bent geometry of norbornene that causes this effect by orienting the orbitals of the alkene and the C2 substituent in such a way that through-space interactions are possible (Scheme 4). When a 2-substituted norbornene possesses a substituent Y, electron delocalization can take place between the filled π (C5–C6) orbital and the empty π* (C2–Y) or σ* (C2–Y). This causes polarization of the C5–C6 bond, which affects the stability of the transition states leading to the two possible regioisomers. If one transition state is more stable than another, one regioisomer may be formed preferentially, resulting in regioselectivity. Computational studies have revealed that an exocyclic double bond at C2 allows for more homoconjugation to occur compared with norbornenes with exo-2-substituents. Furthermore, norbornenes with endo-2-substituents do not provide any significant homoconjugation. The stronger the homoconjugation and electron delocalization, the greater the polarization of the C5–C6 double bond and the greater the effect of the remote substituent. This accounts for the trends previously observed by Tam and co-workers.[21]

In summary, a multitude of transformations involving 2-oxa-3-azabicyclo[2.2.1]hept-5-enes have been explored. In addition, many examples of ruthenium-catalyzed cycloadditions are present in the literature and investigations into the ruthenium-catalyzed [2+2] cycloadditions of 2-substituted norbornenes have demonstrated trends in regioselectivity. Like these 2-substituted norbornenes, the 2-oxa-3-azabicyclo [2.2.1]hept-5-enes possess an unsymmetrical structure yet no studies into ruthenium-catalyzed cycloaddition reactions have been carried out. The purpose of this paper is to investigate the regioselectivity of ruthenium-catalyzed [2+2] cycloaddition reactions involving 2-oxa-3-azabicyclo[2.2.1]hept-5-enes and various unsymmetrical alkynes.

Results and discussion

To evaluate the regioselectivity of the [2+2] cycloaddition reaction it was first necessary to synthesize the heterobicyclic alkene as well as the unsymmetrical alkynes. Construction of the 2-oxa-3-azabicyclo[2.2.1]hept-5-enes can be achieved in high yields under oxidizing conditions (Scheme 5).[1] Hydroxyl amine **15** is used to generate nitroso dienophile **16**, which can then undergo a hetero-Diels–Alder reaction with cyclopentadiene **17** to produce the heterobicyclic cycloadduct **18**.

A wide variety of unsymmetrical alkynes were also synthesized to explore the various electronic and steric effects of

Scheme 4. Orbital interactions of 2-substituted norbornenes.

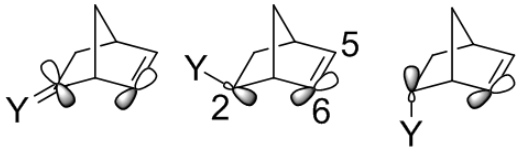

Scheme 5. Synthesis of 3-aza-2-oxabicyclo[2.2.1]hept-5-enes through a hetero-Diels–Alder reaction.

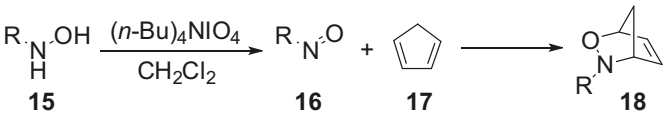

Scheme 6. General synthesis of the unsymmetrical alkynes.

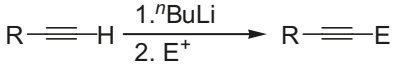

this component. In general, the alkynes were synthesized by deprotonating the appropriate terminal acetylene and subsequently trapping the resulting anion with the desired electrophile (Scheme 6). For example, 4-methoxyphenyl acetylene can be deprotonated with *n*-BuLi, followed by trapping with ethyl chloroformate to provide ethyl 4-methoxyphenylpropynoate **20c**. This strategy was altered for certain alkynes that could not be synthesized by the previous method. For instance, the construction of the haloacetylene ethyl bromopropiolate **20n** required treatment of ethyl propiolate with *N*-bromosuccinimide and silver nitrate in acetone to yield the desired acetylene.

Once prepared, heterobicyclic alkene **19** was subjected to the different unsymmetrical alkynes in the presence of ruthenium catalyst Cp*Ru(COD)Cl in THF (Table 1). Though all examples displayed modest regioselectivity (ranges from 52:48 to 76:24) of the two exo-cycloadducts, yields ranged from low to high. For the first set of alkynes, one group was fixed as an ethyl ester (R^2 = COOEt) and the other substituent was varied as different aromatic groups (R^1 = Ar) (Table 1, entries 1–9). When this substituent was a methoxyphenyl group (**20a**–**20c**), the highest yield had the methoxy moiety in the meta position (Table 1, entry 2). A similar result was observed when the aromatic substituent possessed a chlorine group (**20d**–**20e**), with *m*-chlorophenyl displaying a higher yield than the corresponding para-substituted group (Table 1, entries 4 and 5). Also following

Can. J. Chem. Downloaded from www.nrcresearchpress.com by South China Agricultural University on 09/19/12
For personal use only.

Can. J. Chem. Downloaded from www.nrcresearchpress.com by South China Agricultural University on 09/19/12
For personal use only.

Table 1. Results of ruthenium-catalyzed [2+2] reactions with different unsymmetrical alkynes.

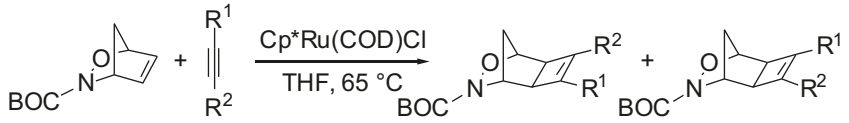

	19	20a-20r		21a-21r		22a-22r	
Entry	Alkyne	R^1	R^2	Temp. (°C)	Time (h)	Yield (%)[a]	Ratio (**22**:**21**)[b]
1	**20a**	*o*-OMe–Ph	COOEt	65	456	72	68:32
2	**20b**	*m*-OMe–Ph	COOEt	65	144	90	66:34
3	**20c**	*p*-OMe–Ph	COOEt	65	120	76	66:34
4	**20d**	*m*-Cl–Ph	COOEt	65	168	74	68:32
5	**20e**	*p*-Cl–Ph	COOEt	65	120	45	67:33
6	**20f**	*m*-Me–Ph	COOEt	65	166	85	66:34
7	**20g**	*p*-Me–Ph	COOEt	65	96	74	65:35
8	**20h**	*m*-CF_3–Ph	COOEt	65	165	32	69:31
9	**20i**	*p*-CF_3–Ph	COOEt	65	120	27	68:32
10	**20j**	*n*-Bu	COOEt	65	144	65	63:37
11	**20k**	Cy	COOEt	65	144	27	67:33
12	**20l**	CMe_2OH	COOEt	65	144	47	73:27
13	**20m**	CH_2CH_2OTBS	COOEt	65	120	51	63:37
14	**20n**	Br	COOEt	65	120	51	59:41
15	**20o**	Ph	Br	65	168	25	57:43
16	**20p**	Ph	Cl	65	96	51	52:48
17	**20q**	*n*-Bu	S–Tol	65	120	18	76:24
18	**20r**	Ph	S–CH_2CH_3	65	144	24	59:41

[a]Isolated yields after column chromatography.
[b]Ratios based on ^{1}H NMR.

this trend are the tolyl substituents (**20f**–**20g**), with the *m*-tolyl group demonstrating a higher yield than the *p*-tolyl group (Table 1, entries 6 and 7). The trifluoromethylbenzene substituents **20h**–**20i** showed higher yields with the trifluoromethyl group in the meta position (Table 1, entry 8) similar to previous aryl substituents. Although at this stage we do not have a good explanation on why meta-substituted groups always gave the highest yield with the same substituents, several points can be noted. The yields of the cycloadditions of *ortho*-methoxyphenyl-substituted alkyne (**20a**) and *para*-methoxyphenyl-substituted alkyne (**20c**) are similar, however, the *ortho*-methoxyphenyl substituted alkyne (**20a**) took almost four times longer for the reaction to go to completion (456 vs 120 h). The *ortho*-methoxyphenyl-substituted alkyne (**20a**) probably hindered the coordination of the Ru catalyst with the alkyne because of steric effect. Since both the meta and para substituents are farther away from the alkyne, steric factor should not be the one that affected the yields most. Thus, it is likely that meta substituents somehow showed a stronger electronic effect on the alkyne than the para substituents and affected the relative stability of the Ru–metallocycles intermediates, giving higher yields in the cycloadditions of the meta substituents.

When the R^1 substituent is changed to an alkyl group, higher yields are observed with primary alkyl group **20j** compared with secondary alkyl group **20k** (Table 1, entries 10 and 11). Modest yields are observed when R^1 is a propagylic alcohol (**20l**) or a TBS-protected alcohol (**20m**; Table 1, entries 12 and 13). Haloalkynes and alkynyl sulphides **20n**–**20r** result in yields that are moderate to low (Table 1, entries 14–18).

Fig. 1. exo versus endo cycloadducts.

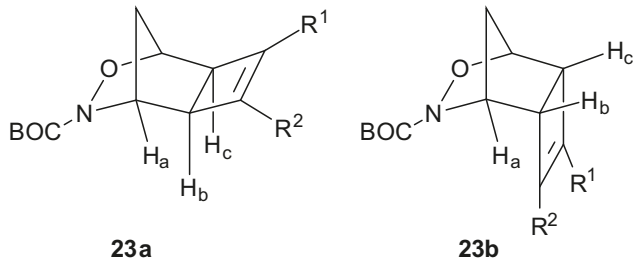

These ruthenium-catalyzed [2+2] cycloaddition could theoretically produce both exo- and endo-cycloadducts; however, because of the results of previous Tam group studies, only exo products were expected.[21] Using the coupling constant of H_b in the ^{1}H NMR it was possible to verify the exo-isomerism of the cycloadducts (Fig. 1). Computational studies show that the dihedral angle between protons H_a and H_b in an exo-addition product such as **23a** is in the range of 70°–75°.[21] The Karplus curve indicates that this corresponds to a very small coupling constant ($J \sim 0$–2 Hz). Alternatively, an endo-cycloadduct like **23b** would have a dihedral angle on the scale of 35°–40°, resulting in a coupling constant of 6–9 Hz. The cycloadducts synthesized over the course of this investigation did not display any noticeable coupling between H_a and H_b, confirming the presence of exo-cycloadducts.

Though each [2+2] reaction carried out during this study produced two exo-regioisomers, only a few examples had cycloadducts that were separable by column chromatography. Once these regioisomers were physically separated, NMR techniques, including HSQC and HCOSY, were used to

Can. J. Chem. Downloaded from www.nrcresearchpress.com by South China Agricultural University on 09/19/12
For personal use only.

Scheme 7. Ring opening of the [2+2] cycloadducts through reductive cleavage of the N–O bond.

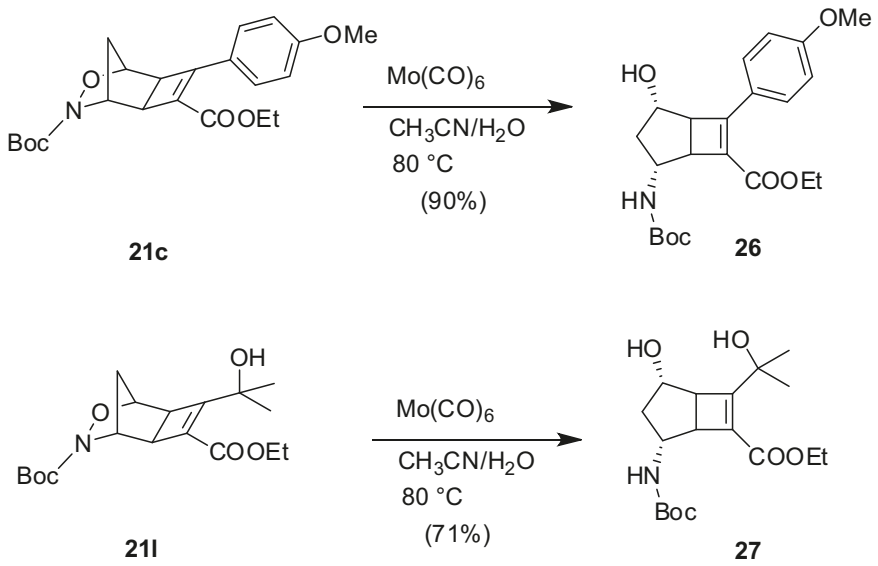

Fig. 2. Using gradient NOESY experiments to distinguish the regioisomers.

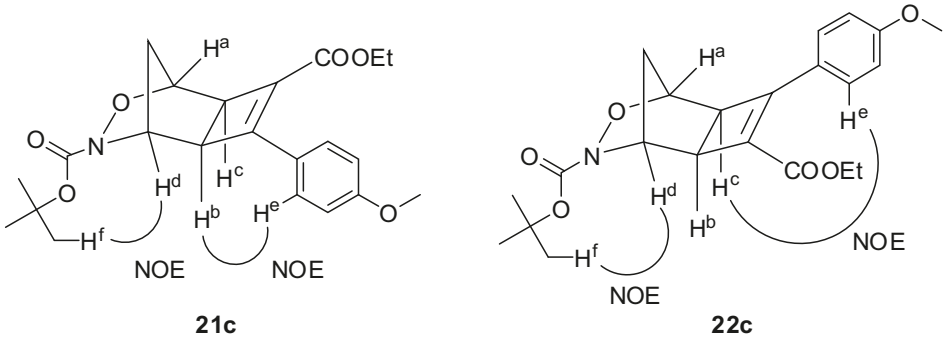

unambiguously identify each proton and carbon. The regioisomers were then distinguished using a gradient NOESY experiment (Fig. 2). In regioisomer **21c**, H_e displays an NOE with H_b, but not with H_c, whereas H_f shows an NOE with H_d, but not with H_a. Compound **22c** proves to be the opposite regioisomer with H_e showing an NOE with H_c, but not with H_b, and H_f displaying an NOE with H_d, and but not with H_a. Although the regioselectivities of the cycloadditions were low, in all cases, cycloadducts **22a**–**22r** were found to be the major regioisomers. This observation matched with our previous studies with 2-substituted norbornenes (Scheme 3).[21] With 2-substituted norbornenes, the major regioisomers formed are the ones with the aromatic group (Ph) syn to the electron-withdrawing group X (or Y) (Scheme 3). Similarly, with 2-oxa-3-azabicyclo[2.2.1]hept-5-ene **19**, the major regioisomers **22a**–**22r** formed have the aromatic groups (R^1) syn to the more electronegative atom (oxygen).

Once a [2+2] cycloadduct has been constructed and distinguished from its regioisomer, the product can then be used to synthesize more complex molecules. Ring opening of [2+2] cycloadducts to a [3.2.0] bicyclic structure is one way that these products can be used to access more complex molecular structures. Several natural products have been identified that contain a [3.2.0] heptane skeleton (Fig. 3). PC-M4 (**24**) was isolated from the fungus *Penicillium crustosum* and may

Fig. 3. Natural products containing a [3.2.0] heptane skeleton.

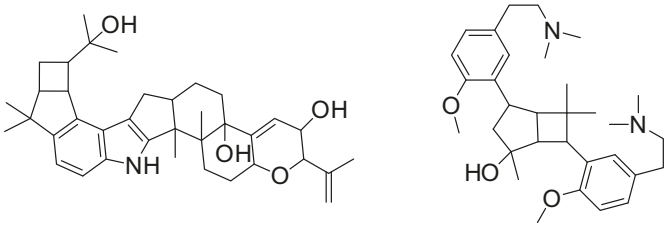

PC-M4 **24** Avicennamine **25**

be a biosynthetic precursor to the penitrems.[22] Also, avicennamine **25**, isolated from the shrub *Zanthoxylum avicennae*, acts as a platelet aggregation inhibitor and a DNA isomerize inhibitor and has antibacterial and cyctotoxic properties.[23]

One of the many transformations previously carried out on the 3-aza-2-oxa-bicyclo[2.2.1]hept-5-ene precursor was a reductive cleavage of the relatively weak N–O bond to form a cyclopentene ring-opened product. A similar reductive cleavage reaction has been applied to select [2+2] cycloadducts, resulting in the formation of highly functionalized [3.2.0] bicyclic ring systems (Scheme 7). Addition products **21c** and **21l** were subjected to molybdenumhexacarbonyl in the presence of an acetonitrile/water mixture providing ring-opened products **26** and **27**, respectively. Cycloadduct **21c** provided

Can. J. Chem. Downloaded from www.nrcresearchpress.com by South China Agricultural University on 09/19/12
For personal use only.

the corresponding [3.2.0] bicycloheptene in a higher yield of 90% compared with cycloadduct **21l** with a yield of 75%. Difficulties were encountered when attempting to characterize these ring-opened products through standard 1D NMR techniques. Several of the expected peaks appeared to be missing from the ^{13}C NMR despite a promising ^{1}H NMR spectrum. This was found to be due to intermediate chemical exchange.[24] The nitrogen atom moves from one rotamer to another, which leads to near coalescence of several ^{13}C lines in the spectrum. Although these peaks are nearly invisible in a 1D experiment, they show up clearly in a 2D correlation spectrum. These 2D experiments involve detection of the protons, whose coupling remains largely unaffected. As result, the 2D NMR techniques HSQC and HMBC were necessary to fully characterize and clearly identify the ring-opened products.

Conclusion

In summary, we have demonstrated the first examples of ruthenium-catalyzed [2+2] cycloaddition reactions of a 2-oxa-3-azabicyclo[2.2.1]hept-5-ene with unsymmetrical alkynes. Reactions in the presence of Cp*Ru(COD)Cl in THF were found to give two regioisomers of the exo-addition product. Low to appreciable yields of the cycloadducts were observed with modest regioselectivies. Ring opening of the addition products to a functionalized [3.2.0] heptene provides the opportunity to access more complex structures from relatively simple precursors.

Experimental

General information

All reactions were carried out in an atmosphere of dry nitrogen at ambient temperature unless otherwise stated. Standard column chromatography was performed on 230–400 mesh silica gel (obtained from Silicycle) using flash column chromatography techniques.[25] Analytical thin-layer chromatography (TLC) was performed on Silicycle-precoated silica gel F_{254} plates. All glassware was oven-dried. Infrared spectra were taken on a Thermo Scientific Nicolet 380 FTIR spectrophotometer. ^{1}H and ^{13}C NMR spectra were recorded on Bruker Avance-400 and -600 spectrometers. Chemical shifts for ^{1}H NMR spectra are reported in parts per million (ppm) from tetramethylsilane with the solvent resonance as the internal standard (chloroform: δ 7.26 ppm). Chemical shifts for ^{13}C NMR spectra are reported in parts per million (ppm) from tetramethylsilane with the solvent as the internal standard (deuterochloroform: δ 77.0 ppm). High-resolution mass spectra were done by Mass Spectrometry at Queen's University, Kingston, Ontario.

Reagents

Unless stated otherwise, commercial reagents were used without purification. Solvents were purified by distillation under dry nitrogen from CaH_2 (1,2-dichloroethane, hexanes) and from potassium/benzophenone (THF). Cp*Ru(COD)Cl was bought from Strem Chemicals. Alkynes **20a**–**20r** were prepared according to literature procedures and the NMR spectra obtained matched those found in the literature.[26–31] Alkene **19** was prepared according to previously described procedures.[1]

General procedure for ruthenium-catalyzed [2+2] cycloaddition reactions of 2-oxa-3-azabicyclo[2.2.1]hept-5-enes with unsymmetrical alkynes

2-Oxa-3-azabicyclo[2.2.1]hept-5-ene **19** (0.2–1.7 mmol, 1 equiv) and an unsymmetrical alkyne (1 equiv) were added to separate oven-dried vials. These vials were purged with nitrogen and transferred into a dry box. In the dry box, to a third oven-dried vial, was added Cp*Ru(COD)Cl (3 mol %). THF was added to the vial containing the bicyclic alkene and this was transferred slowly to the vial containing the ruthenium catalyst. Likewise, THF was added to the vial containing the alkyne and this was transferred to the vial containing the Ru–catalyst and bicyclic alkene. The vial was then sealed with a screw cap and removed from the dry box and heated to 65 °C. The crude products were purified by column chromatography (EtOAc–hexanes mixture) and concentrated in vacuo to give the corresponding [2+2] cycloadduct.

Cycloadducts 21a and 22a

Following the above procedure with ethyl 2-methoxyphenylpropynoate **20a** (201.1 mg, 1.02 mmol) and 2-oxa-3-azabicyclo[2.2.1]hept-5-ene **19** (209.0 mg, 1.02 mmol), the reaction was allowed to stir at 65 °C for 456 h. The crude product was purified by column chromatography (gradient of 0%–30% EtOAc in hexanes) to provide cycloadducts **21a** as a colourless viscous oil (94.7 mg, 0.236 mmol, 23%) and **22a** as a pale yellow viscous oil (201.2 mg, 0.501 mmol, 49%).

21a

R_f 0.38 (EtOAc–hexanes, 30:70). IR (neat, NaCl, cm^{-1}): 2978 (m), 1736 (m), 1704 (s), 1596 (m), 1466 (m). ^{1}H NMR ($CDCl_3$, 400 MHz) δ: 8.33 (m, 1H), 7.32 (m, 1H), 6.94 (t, 1H, J = 7.4 Hz), 6.87 (d, 1H, J = 8.4 Hz), 4.76 (m, 1H), 4.61 (br s, 1H), 4.17 (q, 2H, J = 7.1 Hz), 3.86 (s, 3H), 3.47 (m, 1H), 3.23 (m, 1H), 2.22 (d, 1H, J = 11.2 Hz), 1.68 (d, 1H, J = 11.4 Hz), 1.50 (s, 9H), 1.27 (t, 3H, J = 7.1 Hz). ^{13}C NMR (APT, $CDCl_3$, 100 MHz) δ: 162.3, 158.3, 157.1, 154.1, 132.0, 131.8, 129.8, 120.8, 120.4, 110.8, 81.8, 77.7, 60.3, 58.3, 55.1, 47.0, 45.6, 30.7, 28.2, 14.2. HREI calcd for $C_{22}H_{27}NO_6$ (M^+): m/z 401.1838; found: m/z 410.1849.

22a

R_f 0.32 (EtOAc–hexanes, 30:70). IR (neat, NaCl, cm^{-1}): 2978 (m), 1704 (s), 1596 (m), 1466 (m). ^{1}H NMR ($CDCl_3$, 400 MHz) δ: 8.35 (m, 1H), 7.32 (m, 1H), 6.94 (m, 1H), 6.85 (d, 1H, J = 8.3 Hz), 4.61 (m, 1H), 4.20 (q, 2H, J = 7.2 Hz), 3.81 (s, 3H), 3.48 (m, 1H), 3.23 (m, 1H), 2.23 (d, 1H, J = 11.5 Hz), 1.64 (br d, 1H, J = 10.5 Hz), 1.50 (s, 9H), 1.29 (t, 3H, J = 7.1 Hz). ^{13}C NMR (APT, $CDCl_3$, 100 MHz) δ: 162.3, 158.3, 157.6, 154.7, 132.0, 131.9, 129.5, 120.7, 120.4, 110.8, 82.0, 78.0, 60.3, 58.1, 55.1, 48.5, 44.3, 30.6, 28.2, 14.2. HREI calcd for $C_{22}H_{27}NO_6$ (M^+): m/z 401.1838; found: m/z 401.1851.

Cycloadducts 21b and 22b

Following the general procedure with ethyl 3-methoxyphenylpropiolate **20b** (106.8 mg, 0.542 mmol) and 2-oxa-3-

Can. J. Chem. Downloaded from www.nrcresearchpress.com by South China Agricultural University on 09/19/12
For personal use only.

azabicyclo[2.2.1]hept-5-ene **19** (110.5 mg, 0.541 mmol), the reaction was allowed to stir at 65 °C for 144 h. The crude product was purified by column chromatography (gradient of 20%–30% EtOAc in hexanes) to provide an inseparable mixture (66:34) of cycloadducts as a yellow viscous oil (195.1 mg, 0.486 mmol, 90%). R_f 0.23 (EtOAc–hexanes, 20:80). IR (neat, NaCl cm^{-1}): 2923 (s), 2853 (s), 1709(m), 1599 (w), 1460 (s), 1376 (s), 1043 (w). ^1H NMR ($CDCl_3$, 400 MHz) δ: 7.71 (m, 1H), 7.36–7.20 (m, 2H), 6.86 (m, 1H), 4.72 (m, 1H), 4.57 (s, 0.66H), 5.53 (s, 0.33H), 3.76–3.75 (m, 3H), 3.30 (m, 1H), 3.20 (m, 1H), 2.08 (m, 1H), 1.65 (m, 1H), 1.45–1.44 (m, 9H), 1.29–1.23 (m, 3H). ^{13}C NMR (APT, $CDCl_3$, 100 MHz) δ: 161.9, 161.8, 159.6, 159.5, 157.2, 157.1, 155.9, 155.4, 132.8, 132.7, 129.4, 129.1, 128.8, 120.8, 117.4, 113.3, 82.1,82.0, 77.2, 76.7, 60.3, 57.6, 57.3, 55.1, 44.8, 44.0, 43.1, 42.7, 30.7, 28.0, 14.1. HRESI calcd for $C_{22}H_{27}NO_6$ (M^+): *m/z* 401.1838; found: *m/z* 401.1845.

Cycoadducts 21c and 22c

Following the general procedure with ethyl 4-methoxyphenylpropynoate **20c** (335.4 mg, 1.63 mmol) and 2-oxa-3-azabicyclo[2.2.1]hept-5-ene **19** (326.6 mg, 1.66 mmol), the reaction was allowed to stir at 65 °C for 120 h. The crude product was purified by column chromatography (30% EtOAc in hexanes) to provide cycloadducts **21c** as a pale yellow viscous oil (170.2 mg, 0.424 mmol, 26%) and **22c** as a yellow viscous oil (325.7 mg, 0.811 mmol, 50%). Relative regio- and stereo-chemistry of each isomer was confirmed by various 2D NMR (COSY, HSQC, or HMBC) experiments and a gradient NOESY experiment preformed on a 400 MHZ NMR spectrometer.

Cycloadduct 21c

R_f 0.38 (EtOAc–hexanes, 30:70). IR (neat, NaCl, cm^{-1}): 2977 (m), 1736 (m), 1701 (s), 1603 (s), 1509 (s). ^1H NMR ($CDCl_3$, 400 MHz) δ: 7.99–7.95 (m, 2H), 6.90–6.87 (m, 2H), 4.76–4.75 (m, 1H), 4.23–4.15 (m, 2H), 3.81 (s, 3H), 3.34 (m, 1H), 3.23 (m, 1H), 2.13 (d, 1H, J = 11.4 Hz), 1.69 (d, 1H, J = 11.4 Hz), 1.50 (s, 9H), 1.29 (t, 3H, J = 7.1 Hz). ^{13}C NMR (APT, $CDCl_3$, 100 MHz) δ: 162.2, 161.6, 157.2, 155.3, 130.7, 125.9, 124.7, 113.9, 82.2, 77.5, 60.2, 57.3, 55.3, 43.8, 42.9, 30.8, 28.1, 14.2. HREI calcd for $C_{22}H_{27}NO_6$ (M^+): *m/z* 401.1838; found: *m/z* 401.1823.

Cycloadduct 22c

R_f 0.29 (EtOAc–hexanes, 30:70). IR (neat, NaCl, cm^{-1}): 2978 (m), 1737 (m), 1703 (s), 1603 (s), 1509 (s). ^1H NMR ($CDCl_3$, 400 MHz) δ: 7.91 (d, 2H, J = 8.8 Hz), 6.86 (d, 2H, J = 8.9 Hz), 4.73 (m, 1H), 4.59 (s, 1H) 4.22–4.17 (m, 2H), 3.78 (s, 3H), 3.29 (m, 1H), 3.22 (m, 1H), 2.11 (d, 1H, J = 11.4 Hz), 1.65 (d, 1H, J = 11.8 Hz), 1.47 (s, 9H), 1.29 (t, 1H, J = 7.2 Hz). ^{13}C NMR (APT, $CDCl_3$, 100 MHz) δ: 162.3, 161.6, 157.3, 155.8, 130.7, 125.5, 124.7, 113.9, 82.0, 76.8, 60.1, 57.9, 55.2, 44.6, 42.5, 30.8, 28.1, 14.2. HREI calcd for $C_{22}H_{27}NO_6$ (M^+): *m/z* 401.1838; found: *m/z* 401.1847.

Cycloadducts 21d and 22d

Following the general procedure with ethyl 3-chlorophenylpropiolate **20d** (42.0 mg, 0.206 mmol) and 2-oxa-3-azabicyclo[2.2.1]hept-5-ene **19** (41.1 mg, 0.209 mmol), the reaction was allowed to stir at 65 °C for 168 h. The crude product was purified by column chromatography (gradient of 15%–40% EtOAc in hexanes) to provide an inseparable mixture (68:32) of cycloadducts as a yellow viscous oil (60.1 mg, 0.148 mmol, 74%). R_f 0.32 (EtOAc–hexanes, 30:70). IR (neat, NaCl, cm^{-1}): 2979 (m), 1736 (m), 1705(s). ^1H NMR ($CDCl_3$, 400 MHz) δ: 8.04 (m, 1H), 7.81 (d, 0.3H, J = 7.2 Hz), 7.74 (d, 0.7H, J = 7.2 Hz), 7.37–7.30 (m, 2H), 4.78 (m, 1H), 4.63 (s, 0.68H), 4.59 (s, 0.32H), 4.28–4.21 (m, 2H), 3.36 (m, 1H), 3.28 (m, 1H), 2.10 (m, 1H), 1.72 (m, 1H), 1.51–1.50 (m, 9H), 1.36–1.30 (m, 3H). ^{13}C NMR (APT, $CDCl_3$, 100 MHz) δ: 161.9, 161.8, 157.4, 157.3, 154.3, 153.7, 134.7, 133.2, 130.8, 130.7, 130.4, 129.9, 129.8, 128.8, 128.7, 126.7, 82.5, 82.4, 77.2, 76.6, 60.7, 57.6, 57.2, 44.9, 44.3, 43.2, 43.0, 30.8, 28.2, 14.2. HRESI calcd for $C_{21}H_{24}ClNO_5$ (M + H): *m/z* 406.1421; found: *m/z* 406.1420.

Cycloadducts 21e and 22e

Following the general procedure with ethyl 4-chlorophenylpropynoate **21e** (40.3 mg, 0.19 mmol) and 2-oxa-3-azabicyclo[2.2.1]hept-5-ene **19** (40.5 mg, 0.21 mmol), the reaction was allowed to stir at 65 °C for 120 h. The crude product was purified by column chromatography (20% EtOAc in hexanes) to provide an inseparable mixture (67:33) of cycloadducts as a yellow viscous oil (38.0 mg, 0.0936 mmol, 45%). R_f 0.30 (EtOAc–hexanes, 20:80). IR (neat, NaCl, cm^{-1}): 2979 (s), 2934 (w), 1736 (m), 1706 (s), 1488 (m). ^1H NMR ($CDCl_3$, 400 MHz) δ: 7.94 (d, 0.7H, J = 8.5 Hz), 7.90–7.89 (m, 1.3H), 7.37–7.35 (m, 2H), 4.78 (s, 0.33H), 4.76 (s, 0.67H), 4.63 (s, 0.67H), 4.57 (s, 0.33H), 4.28–4.18 (m, 2H), 3.36 (m, 1H), 3.27 (m, 1H), 2.11 (m, 1H), 1.72 (m, 1H), 1.51–1.50 (m, 9H), 1.34–1.29 (m, 3H). ^{13}C NMR (APT, $CDCl_3$, 100 MHz) δ: 162.1, 162.0, 157.4, 157.3, 154.8, 154.3, 137.0, 136.9, 130.2, 130.1, 130.0, 129.6, 129.3, 129.0, 82.5, 82.4, 77.3, 76.7, 60.7, 57.7, 57.2, 44.8, 44.3, 43.2, 43.0, 30.9, 28.2, 14.3. HRESI calcd for $C_{21}H_{24}{}^{35}ClNO_5$ $(M + H)^+$: *m/z* 406.1421; found: *m/z* 406.1432.

Cycloadducts 21f and 22f

Following the general procedure with ethyl 3-tolylpropiolate **20f** (191.0 mg, 1.01 mmol) and 2-oxa-3-azabicyclo [2.2.1]hept-5-ene **19** (202.0 mg, 1.03 mmol), the reaction was allowed to stir at 65 °C for 120 h. The crude product was purified by column chromatography (20% EtOAc in hexanes) to provide an inseparable mixture (66:34) of cycloadducts as a pale yellow viscous oil (336.2 mg, 0.873 mmol, 85%). R_f 0.28 (EtOAc–hexanes, 20:80). IR (neat, NaCl, cm^{-1}): 2979 (m), 1739 (m), 1705 (s); ^1H NMR ($CDCl_3$, 400 MHz) δ: 7.76–7.74 (m, 1.34H), 7.67 (d, 0.66H, J = 7.6 Hz), 7.22 (m, 1H), 7.15 (m, 1H), 4.73 (m, 1H), 4.58 (s, 0.66H), 4.55 (0.34H), 4.23–4.13 (m, 2H), 3.32 (m, 1H), 3.21 (m, 1H), 2.31 (s, 3H), 2.08 (m, 1H), 1.65 (m, 1H), 1.46–1.45 (m, 9H), 1.30–1.24 (m, 3H). ^{13}C NMR (APT, $CDCl_3$, 100 MHz) δ: 162.1, 162.0, 157.3, 157.2, 156.1, 155.6, 138.2, 131.7, 131.6, 129.2, 128.7, 128.5, 128.4, 125.9, 82.2, 82.1, 77.4, 76.8, 60.4, 57.7, 57.3, 44.8, 44.0, 43.1, 42.7, 30.8, 28.1, 21.3, 14.2. HRESI calcd for $C_{22}H_{27}NO_5$ (M^+): *m/z* 385.1889; found: *m/z* 385.1898.

Can. J. Chem. Downloaded from www.nrcresearchpress.com by South China Agricultural University on 09/19/12
For personal use only.

Cycloadducts 21g and 22g

Following the general procedure with ethyl 4-tolylpropiolate **20g** (191.3 mg, 1.02 mmol) and 2-oxa-3-azabicyclo [2.2.1]hept-5-ene **19** (201.9 mg, 1.02 mmol), the reaction was allowed to stir at 65 °C for 96 h. The crude product was purified by column chromatography (gradient of 0%–30% EtOAc in hexanes) to provide an inseparable mixture (65:35) of cycloadducts as a yellow viscous oil (283.2 mg, 0.735 mmol, 74%). R_f 0.29 (EtOAc–hexanes, 20:80). IR (neat, NaCl, cm^{-1}): 2979 (s), 1740 (s), 1704 (s). ^1H NMR ($CDCl_3$, 400 MHz) δ: 7.89–7.83 (m, 2H), 7.20–7.17 (m, 2H), 7.46 (m, 1H), 4.61 (s, 0.65H), 4.57 (s, 0.35H), 4.25–4.19 (m, 2H), 3.35 (m, 1H), 3.24 (m, 1H), 2.35–2.34 (m, 3H), 2.12 (m, 1H), 1.68 (m, 1H), 1.50–1.49 (m, 9H), 1.33–1.28 (m, 3H). ^{13}C NMR (APT, $CDCl_3$, 100 MHz) δ: 162.2, 162.1, 157.3, 157.2, 156.1, 155.5, 141.4, 129.3, 129.0, 128.8, 128.7, 127.7, 127.4, 82.2, 82.1, 77.4, 76.8, 60.3, 57.8, 57.3, 44.7, 43.9, 43.0, 42.7, 30.8, 28.1, 21.5, 14.2. HRESI calcd for $C_{22}H_{27}NO_5Na$ $(M + Na)^+$: *m/z* 408.1787; found: *m/z* 408.1776.

Cycloadducts 21h and 22h

Following the general procedure with ethyl 3-trifluoromethylphenylpropiolate **20h** (64.2 mg, 0.265 mmol) and 2-oxa-3-azabicyclo[2.2.1]hept-5-ene **19** (52.0 mg, 0.264 mmol), the reaction was allowed to stir at 65 °C for 165 h. The crude product was purified by column chromatography (30% EtOAc in hexanes) to provide an inseparable mixture (69:31) of cycloadducts as a yellow viscous oil (29.4 mg, 0.841 mmol, 32%). R_f 0.44 (EtOAc–hexanes, 30:70). IR (neat, NaCl, cm^{-1}): 2980 (m), 2933 (w), 1736 (m), 1708 (s), 1621 (w), 1335 (s), 1306 (s), 1166 (s), 1129 (s). ^1H NMR ($CDCl_3$, 400 MHz) δ: 8.33 (m, 1H), 8.10 (d, 0.31H, J = 7.6 Hz), 8.03 (d, 0.69H, J = 7.8 Hz), 7.64 (m, 1H), 7.53 (m, 1H), 4.81 (m, 1H), 4.66 (s, 0.69H), 4.61 (s, 0.31H), 4.30–4.23 (m, 2H), 3.42 (m, 1H), 3.32 (m, 1H), 2.13 (m, 1H), 1.52–1.51 (m, 9H), 1.36–1.31 (m, 3H). ^{13}C NMR (APT, $CDCl_3$, 100 MHz) δ: 161.9, 161.8, 157.4, 157.2, 154.0, 153.4, 132.2, 131.7, 131.6, 131.4, 131.2, 131.1, 130.9, 129.3, 127.2, 125.6, 82.6, 82.4, 77.1, 76.5, 60.9, 57.5, 57.2, 44.8, 44.4, 43.2, 43.1, 30.9, 28.2, 14.2, 14.1. HREI calcd for $C_{22}H_{24}F_3NO_5$ (M^+): *m/z* 439.1607; found: *m/z* 439.1619.

Cycloadducts 21i and 22i

Following the general procedure with ethyl 4-trifluoromethylphenylpropiolate **20i** (134.8 mg, 0.682 mmol) and 2-oxa-3-azabicyclo[2.2.1]hept-5-ene **19** (152.3 mg, 0.629 mmol), the reaction was allowed to stir at 65 °C for 120 h. The crude product was purified by column chromatography (20% EtOAc in hexanes) to provide an inseparable mixture (68:32) of cycloadducts as a pale yellow viscous oil (74.5 mg, 0.170 mmol, 27%). R_f 0.28 (EtOAc–hexanes, 20:80). IR (neat, NaCl, cm^{-1}): 2981 (m), 1741 (s), 1710 (s), 1614 (m). ^1H NMR ($CDCl_3$, 400 MHz) δ: 8.11–8.04 (m, 2H), 7.65–7.63 (m, 2H), 4.79 (m, 1H), 4.65 (m, 0.68H), 4.60 (br s, 0.32H), 4.29–4.20 (m, 2H), 3.41 (m, 1H), 3.31 (m, 1H), 2.11 (m, 1H), 1.73 (m, 1H), 1.51–1.50 (m, 9H), 1.35–1.30 (m, 3H). ^{13}C NMR (APT, $CDCl_3$, 100 MHz) δ: 161.8, 161.7, 157.4, 157.2, 154.2, 153.7, 134.6, 132.3, 131.9, 131.6, 129.0, 125.6, 82.5, 82.4, 77.1, 76.5, 60.8, 57.5, 57.1, 44.9, 44.5, 43.3, 43.2, 30.8, 28.2, 14.2. HRESI calcd for $C_{22}H_{24}F_3NO_5Na$ $(M + Na)^+$: *m/z* 462.1504; found: *m/z* 462.1523.

Cycloadducts 21j and 22j

Following the general procedure with ethyl 2-heptynoate **20j** (30.6 mg, 0.198 mmol) and 2-oxa-3-azabicyclo[2.2.1] hept-5-ene **19** (39.7 mg, 0.202 mmol), the reaction was allowed to stir at 65 °C for 144 h. The crude product was purified by column chromatography (30% EtOAc in hexanes) to provide an inseparable mixture (63:37) of cycloadducts as a yellow viscous oil (48.5 mg, 0.1304 mmol, 65%). R_f 0.43 (EtOAc–hexanes, 30:70). IR (neat, NaCl, cm^{-1}): 2962 (m), 1712 (s), 1455(w), 1161 (s). ^1H NMR ($CDCl_3$, 400 MHz) δ: 4.70 (m, 0.37H), 4.59 (m, 0.63H), 4.54 (m, 0.63H), 4.41 (m, 0.37H), 4.17–4.10 (m, 2H), 3.11 (m, 1H), 2.96 (m, 1H), 2.47–2.28 (m, 2H), 2.08 (m, 1H), 1.65 (m, 1H), 1.47 (m, 9H), 1.45–1.22 (m, 7H), 0.91–0.86 (m, 3H). ^{13}C NMR (APT, $CDCl_3$, 100 MHz) δ: 164.3, 163.7, 162.1, 157.4, 157.3, 131.8, 131.3, 82.2, 82.1, 77.2, 76.4, 76.3, 60.0, 57.6, 57.5, 56.8, 46.6, 44.9, 44.2, 42.9, 30.8, 30.7, 29.1, 28.8, 28.2, 22.7. HRESI calcd for $C_{19}H_{29}NO_5$ (M + H): *m/z* 352.2124; found: *m/z* 352.2140.

Cycloadducts 21k and 22k

Following the general procedure with ethyl cyclohexanepropynoate **20k** (181.3 mg, 1.01 mmol) and 2-oxa-3-azabicyclo[2.2.1]hept-5-ene **19** (203.7 mg, 1.03 mmol), the reaction was allowed to stir at 65 °C for 144 h. The crude product was purified by column chromatography (20% EtOAc in hexanes) to provide an inseparable mixture (67:33) of cycloadducts as a yellow viscous oil (104.6 mg, 0.277 mmol, 27%). R_f 0.31 (EtOAc–hexanes, 20:80). IR (neat, NaCl, cm^{-1}): 2978 (m), 2929 (s), 2853 (m), 1740 (m), 1712(s), 1646 (w), 1449 (m), 1335 (m), 1162 (m). ^1H NMR ($CDCl_3$, 400 MHz) δ: 4.65 (s, 0.33H), 4.56 (s, 0.67H), 4.49 (s, 0.67H), 4.40 (s, 0.33H), 4.14–4.07 (m, 2H), 3.04 (m, 1H), 2.96 (m, 1H), 2.74–2.69 (m, 1H), 2.10–2.07 (m, 1H), 1.68–1.58 (m, 6H), 1.45–1.44 (m, 9H), 1.28–1.01 (m, 8H). ^{13}C NMR (APT, $CDCl_3$, 100 MHz) δ: 168.2, 167.6, 162,0, 157.3, 157.2, 129.9, 129.4, 82.1, 82.0, 77.0, 76.6, 59.9, 57.4, 57.1, 45.3, 43.8, 43.6, 42.5, 38.6, 38.4, 30.6, 30.5, 30.3, 30.2, 30.1, 28.1, 25.6, 25.5, 25.4, 14.2. HRESI calcd for $C_{21}H_{31}NO_5$ (M^+): *m/z* 377.2202; found: *m/z* 377.2210.

Cycloadducts 21l and 22l

Following the general procedure with 4-hydroxy-4-methyl-2-pentynoic acid ethyl ester **20l** (62.3 mg, 0.399 mmol) and 2-oxa-3-azabicyclo[2.2.1]hept-5-ene **19** (80.3 mg, 0.408 mmol), the reaction was allowed to stir at 65 °C for 144 h. The crude product was purified by column chromatography (gradient of 5%–50% EtOAc in hexanes) to provide cycloadducts **21l** as a pale yellow viscous oil (27.5 mg, 0.0778 mmol, 19%) and **22l** as a pale yellow viscous oil (39.7 mg, 0.1123 mmol, 28%). Relative regio- and stereo-chemistry of each isomer was confirmed by various 2D NMR (COSY, HSQC, HMBC) experiments and a gradient NOESY experiment preformed on a 400 MHZ NMR spectrometer.

Can. J. Chem. Downloaded from www.nrcresearchpress.com by South China Agricultural University on 09/19/12
For personal use only.

Cycloadduct 21l

R_f 0.30 (EtOAc–hexanes, 30:70). IR (neat, NaCl, cm^{-1}): 3436 (br, s), 2978 (m), 2929 (w), 1709 (s), 1634 (w), 1458 (w), 1369 (m), 1256 (w) 1160 (s), 1041 (m). ^1H NMR ($CDCl_3$, 400 MHz) δ: 5.18 (s, 1H), 4.69 (s, 1H), 4.46 (m, 1H), 4.26–4.13 (m, 2H), 3.12 (m, 1H), 3.04 (m, 1H), 2.17 (d, 1H, J = 11.5 Hz), 1.73 (d, 1H, J = 11.4 Hz), 1.48 (s, 9H), 1.35 (s, 3H), 1.32 (s, 3H), 1.28 (t, 3H, J = 7.1 Hz). ^{13}C NMR (APT, $CDCl_3$, 100 MHz) δ: 171.3, 163.1, 157.2, 129.4, 82.5, 76.9, 70.6, 61.4, 56.8, 44.1, 43.4, 30.7, 28.5, 28.2, 27.7, 14.1. HREI calcd for $C_{18}H_{27}NO_6$ (M^+): *m/z* 353.1838; found: *m/z* 353.1831.

Cycloadduct 22l

R_f 0.23 (EtOAc–hexanes, 30:70). IR (neat, NaCl, cm^{-1}): 3435 (br, s), 2977 (s), 2933 (m), 1709 (s), 1639 (m), 1459 (w), 1369 (m), 1161 (s), 1042 (s); ^1H NMR ($CDCl_3$, 400 MHz) δ: 5.16 (s, 1H), 4.61 (s, 1H), 4.52 (s, 1H), 4.23–4.15 (m, 2H), 3.09 (s, 1H), 3.00 (s, 1H), 2.15 (d, 1H, J = 11.5 Hz), 1.67 (d, 1H, J = 11.4 Hz), 1.46 (s, 9H), 1.31 (s, 3H), 1.27, (t, 3H, J = 7.1 Hz). ^{13}C NMR (APT, $CDCl_3$, 100 MHz) δ: 171.7, 163.2, 157.4, 128.8, 82.4, 76.2, 70.5, 61.3, 57.2, 45.7, 42.1, 30.5, 28.4, 28.1, 27.6, 14.0. HREI calcd for $C_{18}H_{27}NO_6$ (M^+): *m/z* 353.1838; found: *m/z* 353.1849.

Cycloadducts 21m and 22m

Following the general procedure with alkyne **20m** (53.2 mg, 0.207 mmol) and 2-oxa-3-azabicyclo[2.2.1]hept-5-ene **19** (41.2 mg, 0.209 mmol), the reaction was allowed to stir at 65 °C for 120 h. The crude product was purified by column chromatography (20% EtOAc in hexanes) to provide an inseparable mixture (63:37) of cycloadducts as a yellow viscous oil (48.3 mg, 0.106 mmol, 51%). R_f 0.29 (EtOAc–hexanes, 20:80). IR (neat, NaCl, cm^{-1}): 2958 (m), 2930 (m), 1712 (s), 1159 (m), 1096 (m). ^1H NMR ($CDCl_3$, 400 MHz) δ: 4.70 (s, 0.37H), 4.64 (s, 0.63H), 4.54 (s, 0.63H), 4.45 (s, 0.37H), 4.17–4.12 (m, 2H), 3.78–3.68 (m, 2H), 3.12 (m, 1H), 3.00 (m, 1H), 2.69 (m, 1H), 2.50 (m, 1H), 2.16 (m, 1H), 1.60 (m, 1H), 1.47 (m, 9H), 1.27–1.22 (m, 4H), 0.86–0.85 (m, 9H), 0.04–0.02 (m, 6H). ^{13}C NMR (APT, $CDCl_3$, 100 MHz) δ: 162.2, 161.5, 157.5, 157.3, 133.4, 132.8, 82.1, 77.0, 76.8, 60.5, 60.1, 57.5, 57.2, 47.3, 45.6, 44.7, 43.4, 33.2, 33.1, 31.0, 30.9, 29.7, 28.2, 25.9, 25.8, 18.3, 14.3, –5.3, –5.4. HRESI calcd for $C_{23}H_{39}NO_6SiNa$ ($M + Na)^+$: *m/z* 476.2444; found: *m/z* 476.2453.

Cycloadducts 21n and 22n

Following the general procedure with ethyl bromopropiolate **20n** (180.4 mg, 1.02 mmol) and 2-oxa-3-azabicyclo [2.2.1]hept-5-ene **19** (603.6 mg, 3.06 mmol), the reaction was allowed to stir at 65 °C for 120 h. The crude product was purified by column chromatography (20% EtOAc in hexanes) and recrystallized (hexanes) to provide cycloadducts **21n** as a colourless viscous oil (114.6 mg, 0.306 mmol, 30%) and **22n** as a pale yellow viscous oil (79.6 mg, 0.213 mmol, 21%).

Cycloadduct 21n

R_f 0.26 (EtOAc–hexanes, 20:80). IR (neat, NaCl, cm^{-1}): 2980 (m), 1714 (s), 1615 (m). ^1H NMR ($CDCl_3$, 400 MHz) δ: 4.68 (m, 1H), 4.62 (m, 1H), 4.21 (q, 2H, J = 7.1 Hz), 3.31 (m, 1H), 2.06 (d, 1H, J = 11.8 Hz), 1.71 (d, 1H, J = 11.7 Hz), 1.47 (s, 9H), 1.29 (t, 3H, J = 7.1 Hz). ^{13}C NMR (APT, $CDCl_3$, 100 MHz) δ: 160.3, 157.1, 138.6, 128.2, 82.6, 75.4, 60.9, 57.2, 52.2, 46.1, 30.5, 28.1, 14.1. HREI calcd for $C_{15}H_{20}{}^{79}BrNO_6$ (M^+): *m/z* 373.0525; found: *m/z* 373.0513.

Cycloadduct 22n

R_f 0.26 (EtOAc–hexanes, 20:80). IR (neat, NaCl, cm^{-1}): 2981 (s), 1713 (s), 1616 (s). ^1H NMR ($CDCl_3$, 400 MHz) δ: 4.72 (s, 1H), 4.46 (s, 1H), 4.20–4.12 (m, 2H), 2.05–2.02 (m, 1H), 1.71–1.64 (m, 1H), 1.43–1.40 (m, 9H), 1.28–1.23 (m, 3H). ^{13}C NMR (APT, $CDCl_3$, 100 MHz) δ: 160.1, 156.8, 138.9, 127.9, 82.5, 76.3, 60.7, 56.1, 50.7, 47.1, 30.4, 28.0, 14.0. HREI calcd for $C_{15}H_{20}BrNO_6$ (M^+): *m/z* 373.0525; found: *m/z* 373.0531.

Cycloadducts 21o and 22o

Following the general procedure with 1-bromo-2-phenylacetylene **20o** (185.0 mg, 1.02 mmol) and 2-oxa-3-azabicyclo [2.2.1]hept-5-ene **19** (201.5 mg, 1.02 mmol), the reaction was allowed to stir at 65 °C for 168 h. The crude product was purified by column chromatography (gradient of 5%–20% EtOAc in hexanes) to provide cycloadducts **21o** as a pale yellow viscous oil (55.1 mg, 0.145 mmol, 14%) and **22o** as a yellow viscous oil (41.5 mg, 0.110 mmol, 11%).

Cycloadduct 21o

R_f 0.37 (EtOAc–hexanes, 20:80). IR (neat, NaCl, cm^{-1}): 2977 (s), 1740 (s), 1704 (s), 1159 (s). ^1H NMR ($CDCl_3$, 400 MHz) δ: 7.65–7.63 (m, 2H), 7.41–7.35 (m, 3H), 4.72 (s, 1H), 4.62 (m, 1H), 3.49–3.48 (m, 1H), 3.37–3.36 (m, 1H), 2.18 (d, 1H, J = 11.4 Hz), 1.72 (d, 1H, J = 11.5 Hz), 1.51 (s, 9H). ^{13}C NMR (APT, $CDCl_3$, 100 MHz) δ: 157.3, 145.1, 131.3, 129.3, 128.7, 125.7, 109.1, 82.5, 76.7, 57.6, 51.5, 45.6, 30.8, 28.2. HREI calcd for $C_{18}H_{20}{}^{79}BrNO_3$ (M^+): *m/z* 377.0627; found: *m/z* 377.0613.

Cycloadduct 22o

R_f 0.34 (EtOAc–hexanes, 20:80). IR (neat, NaCl, cm^{-1}): 2977 (s), 1739 (s), 1704 (s), 1157 (s). ^1H NMR ($CDCl_3$, 400 MHz) δ: 7.60–7.57 (m, 2H), 7.40–7.32 (m, 3H), 4.79 (s, 1H), 4.54 (s, 1H), 3.48–3.47 (m, 1H), 3.37–3.36 (m, 1H), 2.17 (d, 1H, J = 11.5 Hz), 1.72 (d, 1H, J = 11.5 Hz), 1.50 (s, 9H). ^{13}C NMR (APT, $CDCl_3$, 100 MHz) δ: 157.2, 145.6, 131.2, 129.3, 128.7, 125.6, 109.2, 82.5, 77.1, 57.2, 50.3, 47.0, 30.8, 28.2. HREI calcd for $C_{18}H_{20}{}^{79}BrNO_3$ (M^+): *m/z* 377.0627; found: *m/z* 377.0616.

Cycloadducts 21p and 22p

Following the general procedure with 2-chloro-1-phenylacetylene **20p** (140.3 mg, 1.03 mmol) and 2-oxa-3-azabicyclo [2.2.1]hept-5-ene **19** (204.8 mg, 1.04 mmol), the reaction was allowed to stir at 65 °C for 96 h. The crude product was purified by column chromatography (20% EtOAc in hexanes) to provide cycloadducts **21p** as a yellow viscous oil (94.3 mg, 0.282 mmol, 27%) and **22p** as a pale yellow viscous oil (82.4 mg, 0.247 mmol, 24%).

Can. J. Chem. Downloaded from www.nrcresearchpress.com by South China Agricultural University on 09/19/12
For personal use only.

Cycloadducts 21p

R_f 0.28 (EtOAc–hexanes, 20:80). IR (neat, NaCl, cm^{-1}): 2977 (m), 1741 (s), 1702 (s), 1369 (s), 1159 (s). ^1H NMR ($CDCl_3$, 400 MHz) δ: 7.58–7.56 (m, 2H), 7.40–7.30 (m, 3H), 4.75 (m, 1H), 4.62 (s, 1H), 3.36 (m, 1H), 3.31 (m, 1H), 2.18 (d, 1H, J = 11.5 Hz), 1.72 (d, 1H, J = 11.5 Hz), 1.51 (s, 9H). ^{13}C NMR (APT, $CDCl_3$, 100 MHz) δ: 157.3, 141.1, 131.0, 129.0, 128.7, 126.0, 121.0, 82.4, 76.5, 57.8, 50.8, 42.8, 30.7, 28.2. HREI calcd for $C_{18}H_{20}{}^{35}ClNO_3$ (M^+): *m/z* 333.1132; found: *m/z* 333.1123.

Cycloadduct 22p

R_f 0.27 (EtOAc–hexanes, 20:80). IR (neat, NaCl, cm^{-1}): 2977 (s), 1740 (s), 1702 (s), 1369 (s), 1159 (s). ^1H NMR ($CDCl_3$, 400 MHz) δ: 7.53–7.51 (m, 2H), 7.39–7.30 (m, 3H), 4.79 (m, 1H), 4.57 (d, 1H, J = 1.1 Hz), 3.35–3.31 (m, 2H), 2.18 (d, 1H, J = 11.5 Hz), 1.73 (d, 1H, J = 11.5 Hz), 1.50 (s, 9H). ^{13}C NMR (APT, $CDCl_3$, 100 MHz) δ: 157.2, 141.6, 131.0, 129.0, 128.7, 126.0, 120.9, 82.0, 77.3, 57.0, 49.5, 44.3, 30.8, 28.2. HREI calcd for $C_{18}H_{20}{}^{35}ClNO_3$ (M^+): *m/z* 333.1132; found: *m/z* 333.1125.

Cycloadducts 21q and 22q

Following the general procedure with 1-(4-methylphenylthio)-1-hexyne **20q** (207.8 mg, 1.02 mmol) and 2-oxa-3-azabicyclo[2.2.1]hept-5-ene **19** (204.8 mg, 1.04 mmol), the reaction was allowed to stir at 65 °C for 120 h. The crude product was purified by column chromatography (gradient of 0%–20% EtOAc in hexanes) to provide cycloadducts **21q** as a yellow viscous oil (56.4 mg, 0.140 mmol, 14%) and **22q** as a yellow viscous oil (17.8 mg, 0.044 mmol, 4%).

Cycloadducts 21q

R_f 0.49 (EtOAc–hexanes, 20:80). IR (neat, NaCl, cm^{-1}): 2959 (s), 2925 (s), 1740 (s), 1701 (s), 1368 (s), 1161 (s). ^1H NMR ($CDCl_3$, 400 MHz) δ: 7.27 (d, 2H, J = 8.1 Hz), 7.17 (d, 2H, J = 7.9 Hz), 4.35 (s, 1H), 4.06 (m, 1H), 2.92 (d, 2H, J = 7.1 Hz), 2.32 (s, 3H), 2.14 (d, 1H, J = 11.0 Hz), 2.10–1.97 (m, 2H), 1.57 (d, 1H, J = 11.1 Hz), 1.45 (s, 9H), 1.43–1.27 (m, 4H), 0.90 (t, 3H, J = 7.2 Hz). ^{13}C NMR (APT, $CDCl_3$, 100 MHz) δ: 157.2, 147.1, 138.2, 133.2, 131.5, 129.9, 127.9, 82.0, 77.3, 58.1, 47.8, 45.3, 30.7, 29.0, 28.2, 28.0, 22.8, 21.1, 13.8. HREI calcd for $C_{23}H_{31}NO_3S$ (M^+): *m/z* 401.2025; found: *m/z* 401.2011.

Cycloadducts 22q

R_f 0.38 (EtOAc–hexanes, 20:80). IR (neat, NaCl, cm^{-1}): 2960 (s), 2930 (s), 1739 (s), 1703 (s), 1368 (m), 1160 (s). ^1H NMR ($CDCl_3$, 400 MHz) δ: 7.29–7.27 (m, 2H), 7.13–7.09 (m, 2H), 4.53 (s, 1H), 3.97 (s, 1H), 2.95–2.93 (m, 2H), 2.32 (s, 3H), 2.15 (d, 1H, J = 11.0 Hz), 2.07–2.00 (m, 2H), 1.61 (m, 1H), 1.39 (s, 9H), 1.36–1.22 (m, 4H), 0.92–0.87 (m, 3H). ^{13}C NMR (APT, $CDCl_3$, 100 MHz) δ: 157.1, 148.6, 138.0, 132.8, 130.8, 129.9, 128.1, 81.8, 77.8, 57.5, 47.1, 46.5, 30.7, 29.0, 28.1, 28.0, 22.7, 21.1, 13.8. HREI calcd for $C_{23}H_{31}NO_3S$ (M^+): *m/z* 401.2025; found: *m/z* 401.2014.

Cycloadducts 21r and 22r

Following the general procedure with ethyl phenylethynyl sulfide **20r** (166.2 mg, 1.02 mmol) and 2-oxa-3-azabicyclo[2.2.1]hept-5-ene **19** (204.5 mg, 1.02 mmol), the reaction was allowed to stir at 65 °C for 144 h. The crude product was purified by column chromatography (gradient of 5%–20% EtOAc in hexanes) to provide cycloadducts **21r** as a yellow viscous oil (35.1 mg, 0.0976 mmol, 10%) and **22r** as a pale yellow viscous oil (50.2 mg, 0.140 mmol, 14%).

Cycloadduct 21r

R_f 0.38 (EtOAc–hexanes, 20:80). IR (neat, NaCl, cm^{-1}): 2976 (m), 1739 (s), 1701 (s), 1161 (s). ^1H NMR ($CDCl_3$, 400 MHz) δ: 7.30–7.25 (m, 4H), 7.17 (m, 1H), 4.71 (m, 1H), 4.45 (m, 1H), 3.33 (m, 1H), 2.93–2.73 (m, 2H), 2.15 (d, 1H, J = 11.2 Hz), 1.67 (d, 1H, J = 11.2 Hz), 1.46 (s, 9H), 1.32 (t, 3H, J = 7.4 Hz). ^{13}C NMR (APT, $CDCl_3$, 100 MHz) δ: 157.3, 139.1, 133.3, 132.9, 128.6, 127.4, 125.6, 82.3, 78.1, 57.8, 45.7, 44.9, 31.1, 28.2, 25.8, 16.0. HREI calcd for $C_{20}H_{25}NO_3S$ (M^+): *m/z* 359.1555; found: *m/z* 359.1561.

Cycloadduct 22r

R_f 0.33 (EtOAc–hexanes, 20:80). IR (neat, NaCl, cm^{-1}): 2977 (m), 1737 (s), 1700 (s), 1368 (s), 1160 (s). ^1H NMR ($CDCl_3$, 400 MHz) δ: 7.31–7.27 (m, 4H), 7.17 (m, 1H), 4.64 (m, 1H), 4.52 (br s, 1H), 3.34 (m, 1H), 3.27 (m, 1H), 2.87–2.66 (m, 2H), 2.16 (d, 1H, J = 11.2 Hz), 1.66 (d, 1H, J = 11.2 Hz), 1.46 (s, 9H), 1.42–1.41 (m, 2H), 1.29 (t, 3H, J = 7.5 Hz). ^{13}C NMR (APT, $CDCl_3$, 100 MHz) δ: 157.3, 138.6, 133.3, 128.6, 127.4, 125.6, 82.2, 77.5, 58.4, 47.0, 43.4, 31.0, 28.2, 25.9, 16.0. HREI calcd for $C_{20}H_{25}NO_3S$ (M^+): *m/z* 359.1555; found: *m/z* 359.1564.

General procedure for oxidative ring-opening reactions of the [2+2] cycloadducts

A [2+2] cycloadduct (0.1–0.3 mmol, 1 equiv) was added to an oven-dried vial and dissolved in an acetonitrile/water mixture (94:6). $Mo(CO)_6$ (0.2–0.4 mmol, 1.1 equiv) was then added to the reaction vial. The mixture was heated to 80 °C. The crude products were purified by column chromatography (EtOAc–hexanes mixture) and concentrated in vacuo to give the corresponding [3.2.0] bicyclic product.

Ring-opened product 26

Following the above procedure with cycloadduct **21c** (131.9 mg, 0.328 mmol) and $Mo(CO)_6$ (96.2 mg, 0.364 mmol), the reaction was refluxed at 80 °C for 5 h. The crude product was purified by column chromatography (50% EtOAc in hexanes) to provide a [3.2.0] bicyclic product **26** as a pale yellow viscous oil (118.8 mg, 0.294 mmol, 90%). R_f 0.23 (EtOAc–hexanes, 50:50). IR (neat, NaCl, cm^{-1}): 3409 (br, s), 2977 (s), 1693 (s), 1603 (m), 1510 (s), 1257 (m), 1211 (m), 1176 (m). ^1H NMR ($CDCl_3$, 600 MHz) δ: 8.00 (d, 2H, J = 8.6 Hz), 6.86 (d, 2H, J = 8.6 Hz), 5.56 (br s, 1H), 4.37 (s, 1H), 4.25–4.20 (m, 3H), 3.79 (s, 3H), 3.47 (m, 1H), 3.36 (m, 1H), 2.77 (br s, 0.5H), 2.14 (br s, 1H), 1.82 (d, 1H, J = 14.7 Hz), 1.44 (s, 9H), 1.32 (t, 3H, J = 7.0 Hz). ^{13}C NMR (APT, $CDCl_3$, 150 MHz) δ: 162.9, 161.2, 158.8, 155.6, 130.9, 126.4, 124.9, 113.8, 79.5, 71.7, 60.1, 55.3, 52.3, 51.0, 50.1, 38.5, 28.5, 14.4. HREI calcd for $C_{22}H_{29}NO_6$ (M+): *m/z* 403.1995; found: *m/z* 403.1983.

Can. J. Chem. Downloaded from www.nrcresearchpress.com by South China Agricultural University on 09/19/12
For personal use only.

Ring-opened product 27

Following the general procedure with cycloadduct **21l** (46.5 mg, 0.132 mmol) and $Mo(CO)_6$ (40.3 mg, 0.153 mmol), the reaction was refluxed at 80 °C for 5 h. The crude product was purified by column chromatography (80% EtOAc in hexanes) to provide an [3.2.0] bicyclic product **27** as a yellow viscous oil (33.5 mg, 0.0943 mmol, 71%). R_f 0.39 (EtOAc–hexanes, 80:20). IR (neat, NaCl, cm^{-1}): 3415 (s), 2977 (s), 1686 (s). ^1H NMR ($CDCl_3$, 600 MHz) δ: 5.42 (d, 1H, J = 8.7 Hz), 5.37 (s, 1H), 4.34 (br d, 1H, J = 3.6 Hz), 4.24 (q, 2H, J = 7.1 Hz), 4.11 (br s, 1H), 3.24–3.16 (m, 2H), 2.22–2.15 (m, 1H), 1.84 (d, 1H, J = 14.8 Hz), 1.43 (s, 9), 1.33–1.29 (m, 9H). ^{13}C NMR (APT, $CDCl_3$, 150 MHz) δ: 171.0, 163.9, 155.2, 133.3, 82.3, 70.9, 70.5, 61.3, 54.0, 50.7, 49.2, 38.2, 28.6, 28.5, 27.7, 14.2. HREI calcd for $C_{18}H_{29}NO_6$ (M+): *m/z* 355.1995; found: *m/z* 355.1987.

Acknowledgement

This work was supported by the Natural Sciences and Engineering Research Council of Canada (NSERC), the Merck Frosst Centre for Therapeutic Research, and Boehringer Ingelheim (Canada). R.D. thanks the Ontario Government for a postgraduate scholarship (OGS).

References

(1) (a) For the synthesis of 3-aza-2-oxabicyclo[2.2.1]hept-5-enes **1**, see Zhang, D.; Ghosh, A.; Süling, C.; Miller, M. J. *Tetrahedron Lett.* **1996**, *37* (22), 3799. doi:10.1016/0040-4039(96)00692-2; (b) Dauvergne, J.; Happe, A. M.; Jadhav, V.; Justice, D.; Matos, M.-C.; McCormack, P. J.; Pitts, M. R.; Roberts, S. M.; Singh, S. K.; Snape, T. J.; Whittall, J. *Tetrahedron* **2004**, *60* (11), 2559. doi:10.1016/j.tet.2004.01.046.

(2) For a review on the synthesis and transformations of **1**, see Bodnar, B. S.; Miller, M. J. *Angew. Chem. Int. Ed.* **2011**, *50* (25), 5630. doi:10.1002/anie.201005764.

(3) Cicchi, S.; Goti, A.; Brandi, A.; Guarna, A.; De Sarlo, F. *Tetrahedron Lett.* **1990**, *31* (23), 3351. doi:10.1016/S0040-4039(00)89062-0.

(4) Nitta, M.; Kobayashi, T. *J. Chem. Soc., Perkin Trans. 1* **1985**, 1401. doi:10.1039/p19850001401.

(5) Keck, G. E.; Wager, T. T.; McHardy, S. F. *Tetrahedron* **1999**, *55* (40), 11755. doi:10.1016/S0040-4020(99)00486-X.

(6) Cesario, C.; Tardibono, L. P.; Miller, M. J. *J. Org. Chem.* **2009**, *74* (1), 448. doi:10.1021/jo802184y.

(7) Klier, K.; Kresze, G.; Werbitzky, O.; Simon, H. *Tetrahedron Lett.* **1987**, *28* (24), 2677. doi:10.1016/S0040-4039(00)96179-3.

(8) Lee, Y. H.; Choo, D. J. *Bull. Korean Chem. Soc.* **1993**, *14*, 423.

(9) Galvani, G.; Calvet, G.; Blanchard, N.; Kouklovsky, C. *Org. Biomol. Chem.* **2008**, *6* (6), 1063. doi:10.1039/b718787d.

(10) For an acid-mediated ring-opening reaction of 3-aza-2-oxabicyclo[2.2.1]heptenes **8**, see Muxworthy, J. P.; Wilkinson, J. A.; Procter, G. *Tetrahedron Lett.* **1995**, *36* (41), 7535. doi:10.1016/0040-4039(95)01525-6.

(11) (a) For palladium- and Lewis acid-catalyzed ring-opening reactions of 3-aza-2-oxabicyclo[2.2.1]heptenes **8**, see Lee, W.; Kim, K.-H.; Surman, M. D.; Miller, M. J. *J. Org. Chem.* **2003**, *68* (1), 139. doi:10.1021/jo026488z; (b) Surman, M. D.; Mulvihill, M. J.; Miller, M. J. *Org. Lett.* **2002**, *4* (1), 139. doi:10.1021/ol017036w; (c) Surman, M. D.; Miller, M. J. *J. Org. Chem.* **2001**, *66* (7), 2466. doi:10.1021/jo010094a; (d) Surman, M. D.; Miller, M. J. *Org. Lett.* **2001**, *3* (4), 519. doi:10.1021/ol006813+; (e) Mulvihill, M. J.; Surman, M. D.; Miller, M. J. *J. Org. Chem.* **1998**, *63* (15), 4874. doi:10.1021/jo980950r.

(12) (a) For copper-catalyzed Grignard or organozinc nucleophilic ring-opening reactions, see Pineschi, M.; Del Moro, F.; Crotti, P.; Macchia, F. *Pure Appl. Chem.* **2006**, *78* (2), 463. doi:10.1351/pac200678020463; (b) Pineschi, M.; Del Moro, F.; Crotti, P.; Macchia, F. *Org. Lett.* **2005**, *7* (17), 3605. doi:10.1021/ol050895q; (c) Surman, M. D.; Mulvihill, M. J.; Miller, M. J. *J. Org. Chem.* **2002**, *67* (12), 4115. doi:10.1021/jo016275u; (d) Surman, M. D.; Mulvihill, M. J.; Miller, M. J. *Tetrahedron Lett.* **2002**, *43* (7), 1131. doi:10.1016/S0040-4039(01)02353-X.

(13) Machin, B. P.; Howell, J.; Mandel, J.; Blanchard, N.; Tam, W. *Org. Lett.* **2009**, *11* (10), 2077. doi:10.1021/ol900454q.

(14) Machin, B. P.; Ballantine, M.; Mandel, J.; Blanchard, N.; Tam, W. *J. Org. Chem.* **2009**, *74* (19), 7261. doi:10.1021/jo901248w.

(15) Keck, G. E.; Webb, R. R.; Yates, J. B. *Tetrahedron* **1981**, *37* (23), 4007. doi:10.1016/S0040-4020(01)93275-2.

(16) (a) For selected examples of ring-opening metathesis of 3-aza-2-oxa bicyclo[2.2.1]heptenes **8**, see Calvet, G.; Blanchard, N.; Kouklovsky, C. *Org. Lett.* **2007**, *9* (8), 1485. doi:10.1021/ol0702066; (b) Ellis, J. M.; King, S. B. *Tetrahedron Lett.* **2002**, *43* (33), 5833. doi:10.1016/S0040-4039(02)01175-9; (c) Vincent, G.; Kouklovsky, C. *Chemistry* **2011**, *17* (10), 2972. doi:10.1002/chem.201002558.

(17) (a) For selected examples of dihydroxylation of 3-aza-2-oxabicyclo[2.2.1]heptenes **8**, see Ranganathan, S.; George, K. S. *Tetrahedron* **1997**, *53* (9), 3347. doi:10.1016/S0040-4020(97)00057-4; (b) Lin, C. C.; Wang, Y. C.; Hsu, J. L.; Chiang, C. C.; Su, D. W.; Yan, T. H. *J. Org. Chem.* **1997**, *62* (12), 3806. doi:10.1021/jo970616f; (c) Cowart, M.; Bennett, M. J.; Kerwin, J. F. *J. Org. Chem.* **1999**, *64* (7), 2240. doi:10.1021/jo981658m.

(18) Bigeault, J.; Giordano, L.; deRiggi, I.; Gimbert, Y.; Buono, G. *Org. Lett.* **2007**, *9* (18), 3567. doi:10.1021/ol071386m.

(19) (a) For selected examples of dipolar cycloadditions of 3-aza-2-oxabicyclo[2.2.1]heptenes **8**, see Quadrelli, P.; Mella, M.; Paganoni, P.; Caramella, P. *Eur. J. Org. Chem.* **2000**, *2000* (14), 2613. doi:10.1002/1099-0690(200007)2000:14<2613::AID-EJOC2613>3.0.CO;2-7; (b) Quadrelli, P.; Scrocchi, R.; Caramella, P.; Rescifina, A.; Piperno, A. *Tetrahedron* **2004**, *60* (16), 3643. doi:10.1016/j.tet.2004.02.057; (c) Bodnar, B. S.; Miller, M. J. *J. Org. Chem.* **2007**, *72* (10), 3929. doi:10.1021/jo0701987.

(20) Mitsudo, T.; Naruse, H.; Kondo, T.; Ozaki, Y.; Watanabe, Y. *Angew. Chem. Int. Ed. Engl.* **1994**, *33* (5), 580. doi:10.1002/anie.199405801.

(21) Liu, P.; Jordan, R. W.; Kibbee, S. P.; Goddard, J. D.; Tam, W. *J. Org. Chem.* **2006**, *71* (10), 3793. doi:10.1021/jo060103l.

(22) Miesch, M. *Curr Org Synth* **2006**, *3* (3), 327. doi:10.2174/157017906777934908.

(23) Zhou, J.; Xie, G.; Yan, X. *Encyclopedia of Traditional Chinese Medicine, Molecular Structures, Pharmalogical Activities, Natural Sources and Applications;* Springer: Heidelberg, 2011; Vol. 1.

(24) Robinson, V. J.; Bain, A. D. *Magn. Reson. Chem.* **1993**, *31* (9), 865. doi:10.1002/mrc.1260310914.

(25) Still, W. C.; Kahn, M.; Mitra, A. *J. Org. Chem.* **1978**, *43* (14), 2923. doi:10.1021/jo00408a041.

(26) Newman, M. S.; Merrill, S. H. *J. Am. Chem. Soc.* **1955**, *77* (21), 5552. doi:10.1021/ja01626a034.

(27) Pan, C.; Luo, F.; Wang, W.; Ye, Z.; Cheng, J. *Tetrahedron Lett.* **2009**, *50* (35), 5044. doi:10.1016/j.tetlet.2009.06.093.
(28) Eckert, T.; Ipaktschi, J. *Synth. Commun.* **1998**, *28* (2), 327. doi:10.1080/00397919808005726.
(29) Jordan, R. W.; Villeneuve, K.; Tam, W. *J. Org. Chem.* **2006**, *71* (15), 5830. doi:10.1021/jo060864o.
(30) Riddell, N.; Tam, W. *J. Org. Chem.* **2006**, *71* (5), 1934. doi:10.1021/jo052295a.
(31) Poulsen, T. B.; Bernardi, L.; Alemán, J. O.; Overgaard, J. Jørgensen, K. A. *J. Am. Chem. Soc.* **2007**, *129* (2), 441. doi:10.1021/ja067289q.

Can. J. Chem. Downloaded from www.nrcresearchpress.com by South China Agricultural University on 09/19/12
For personal use only.

Synthesis of an iridium porphyrin amido complex

Jenkins Yin Ki Tsang and Kin Shing Chan

Abstract: A synthetic route for iridium porphyrin amido complexes has been established. Treatment of a THF solution of Ir(ttp)(CO)Cl (**1**) (ttp = 5,10,15,20-tetrakis(*p*-tolyl)porphyrinato dianion) with an aqueous mixture of NaOH and $NaBH_4$, followed by 2-iodoethanol leads to the clean formation of the β-hydroxyethyl complex Ir(ttp)(C_2H_4OH) (**2**) in 92% yield. Heating a pyridine solution of complex **2** in the presence of ca. 5–10 equiv. of phthalimide ($HNC_8H_4O_2$; HPhth) leads to the formation of Ir(ttp)(C_5H_5N)(CH_2CH_2Phth) (**3**). The replacement of pyridine by THF as the reaction solvent leads to the formation of the THF adduct Ir(ttp)(THF)(Phth) (**4**), which has been characterized spectroscopically. Heating a solution of **4** in pyridine leads to the formation of Ir(ttp)(C_5H_5N)(Phth) (**5**), which has been isolated in 72% yield. Complexes **3** and **5** have been characterized by X-ray crystallographic studies. Complexes **4** and **5** are rare examples of monomeric late transition metal-amido complexes and are the first examples of iridium-amido complexes featuring a porphyrin as a supporting ligand.

Key words: porphyrin, iridium amido, phthalimide.

Résumé : On a développé une méthode de synthèse pour les complexes iridium/porphyrine amido. Le traitement d'une solution de Ir(ttp)(CO)Cl (**1**) (ttp = dianion 5,10,15,20-tétrakis(*p*-tolyl)porphyrinato) dans du THF par un mélange aqueux de NaOH et de $NaBH_4$, suivi d'une réaction avec le 2-iodoéthanol conduit à une formation propre du complexe β-hydroxyéthyle Ir(ttp)(CH_2CH_2OH) (**2**) avec un rendement de 92 %. Le chauffage du composé **2**, en solution dans la pyridine, en présence d'environ 5 à 10 équivalents de phtalimide [[$C_6H_4(C{=}O)_2NH$], PhthH] conduit à la formation du Ir(ttp)(C_5H_5N) CH_2CH_2Phth (**3**). Le remplacement de la pyridine par du THF comme solvant conduit à la formation de l'adduit Ir(ttp)(THF)Phth (**4**) qui a été caractérisé par des méthodes spectroscopiques. Le chauffage d'une solution du composé **4** dans de la pyridine conduit à la formation du complexe Ir(ttp)(C_5H_5N)Phth (**4**) qui a été isolé avec un rendement de 72 %. Les complexes **3** et **5** ont été caractérisés par des études de diffraction des rayons-X. Les complexes **4** et **5** correspondent à de rares exemples de complexes monomères amido d'un métal de la fin de la période de transition et ce sont les premiers exemples de complexes iridium-amido comportant une porphyrine comme ligand support.

Mots-clés : porphyrine, iridium-amido, phtalimide.

[Traduit par la Rédaction]

Can. J. Chem. Downloaded from www.nrcresearchpress.com by South China Agricultural University on 09/19/12
For personal use only.

Introduction

Transition metal-nitrogen covalently-bonded species are an interesting and important class of complexes.[1] They have been observed as key precursors and intermediates during important catalytic processes, such as amination of organic substrates,[2] hydroamination of olefins,[3] transfer hydrogenation,[4] amine dehydrogenation,[5] and ammoxidation.[6] In addition, metal-amidos can also effect nontrivial stoichiometric transformations such as C–H activation.[7] Late transition metal-amidos are by far less common than their early transition metal counterparts.[8] This is often rationalized by the hard-soft-acid-base theory, that hard amido or alkoxo ligands do not form strong bonds with late transition metals, which are generally considered soft. More specifically, there exists considerable electron repulsion between the filled dπ orbitals of the late transition metal and the pπ electrons of the amido ligand.[9] As a result, late transition metal-amidos are often reactive species that feature highly nucleophilic nitrogen atoms,[10] and the metal-nitrogen bonds often participate in amido exchange[11] or insertion chemistry.[10c,12] In addition, just like alkyl ligands, amido ligands are prone to undergo β-elimination.[13] Finally, amido ligands can also reductively eliminate in the presence of other suitable ligands.[14]

Our group has been researching carbon-hydrogen bond activation chemistry with iridium-porphyrin complexes to yield iridium porphyrin alkyls and acyls.[15] We have only once reported an Ir-phenoxide complex[16] but have never identified or isolated any Ir-N covalently-bonded species. This phenomenon is best explained by thermodynamics that late transition metal-carbon (alkyl or aryl) bonds are often stronger (by at least 20 kcal/mol) than the isoelectronic amido M–N bonds (1 cal = 4.184 J).[17]

Results and discussion

Our research group has attempted to construct iridium-nitrogen covalent bonds using the conventional metathesis reactions by treatment of the iridium-chloro species Ir(ttp)(CO)Cl[15] (**1**; ttp = 5,10,15,20-tetrakis(*p*-tolylporphyrinato

Received 14 April 2011. Accepted 27 June 2011. Published at www.nrcresearchpress.com/cjc on 22 November 2011.

J.Y.K. Tsang and K.S. Chan. Department of Chemistry, The Chinese University of Hong Kong, Shatin, New Territories, Hong Kong, People's Republic of China.

Corresponding author: Kin Shing Chan (e-mail: ksc@cuhk.edu.hk).

This article is part of a Special Issue to commemorate the International Year of Chemistry.

Can. J. Chem. Downloaded from www.nrcresearchpress.com by South China Agricultural University on 09/19/12
For personal use only.

Fig. 1. Structure formula for Ir(ttp)(CO)Cl (**1**) and phthalimide (HPhth).

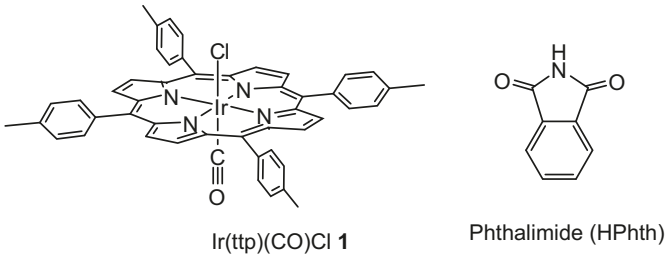

dianion; Fig. 1) with freshly-prepared lithium anilide, lithium diethylamide, or potassium phthalimide ($KC_8H_4NO_2$; KPhth). Disappointingly, these reactions only yielded mixtures of unidentifiable porphyrin-containing products without the incorporation of the amide onto the metal.

With complex **1** failing to serve as a viable source of a cationic iridium precursor for the synthesis of Ir-amidos, we decided to seek alternatives. Treatment of a THF solution of complex **1** with an aqueous solution of excess $NaBH_4$ in the presence of NaOH at 70 °C, followed by a slight excess of 2-iodoethanol, led to the formation of the β-hydroxyethyl complex Ir(ttp)(C_2H_4OH) (**2**) as a maroon solid in 92% yield (eq. [1]). The ^{1}H NMR spectrum of **2** closely resembles those of our recently reported rhodium complex Rh(ttp)(C_2H_4OH),[18] which has been demonstrated to be a precursor for the masked Rh(ttp)$^+$ cation after undergoing β-hydroxy elimination (Scheme 1).[18,19] Complex **2** is also closely related to a series of complexes with the general formula Rh(tpp)(CH_2CHROH) (tpp = 5,10,15,20-tetraphenylporphyrinato dianion), reported by Sanford et. al.,[20] as these complexes were synthesized via the reaction between the rhodium-porphyrin anion Rh(tpp)$^-$ and various epoxides.

[1] *IND, r, lf*) = ″ : 1 :: .v11 − 126eq1.gif″

Phthalimide ($HNC_8H_4O_2$; HPhth; Fig. 1) is deemed a good initial candidate as an amido precursor, because (*i*) it is quite acidic, with the pK_a of the N–H of ca. 8, a desirable feature, as the successful incorporation of the amido ligand would require the loss of this proton and (*ii*) the nitrogen lone pair is delocalized in the bicyclic aromatic system, thereby greatly reducing possible dπ–pπ electron repulsion in the target Ir-phthalimido complex.

Heating a pyridine solution of **2** in an excess (10 equiv.) of phthalimide led to formation of a new porphyrin-containing species Ir(ttp)(C_5H_5N)(CH_2CH_2Phth) (**3**) in good yields (80%, eq. [2], as evidenced by a single new β-pyrrole proton signal at 8.50 ppm). Phthalimide has been deprotonated and symmetrically incorporated onto the final product, as indicated by a pair of 2-proton doublet of doublets at 7.07 and 7.16 ppm, respectively, attributable to the two different types of aryl protons. These signals have been shifted upfield from 7.77 and 7.87 ppm of free phthalimide. The presence of coordinated pyridine is indicated also by characteristic upfield-shifted signals. Intriguingly, in addition to these expected phthalimido and pyridine signals, two sets of 2-proton multiplets appear at –6.06 and –2.19 ppm, respectively. These signals suggest that the ethylene moiety is still present in

Scheme 1. Possible reaction pathways initiated by **2**.

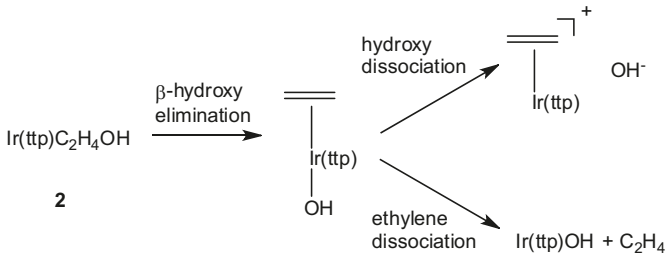

Scheme 2. Proposed mechanism for the formation of **3**.

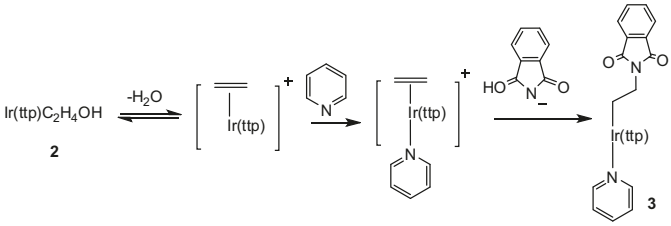

this product. Purification of this new product was achieved by chromatography on Alumina, resulting in the isolation of a red-purple powder after solvent removal. Dark-red needle-shaped single crystals were obtained by slow diffusion of layered hexanes into a concentrated CH_2Cl_2 solution. An X-ray crystallographic analysis confirms the atom connectivity in **3**, as deduced from NMR spectroscopic data (Fig. 2). Table 1 lists the crystal data and collection parameters. Regrettably, the quality of the X-ray data precludes any meaningful discussion of metrical parameters of **3**. Nevertheless, the X-ray data indicate that the ethylene moiety has been retained. A possible explanation for the formation of **3** is the nucleophilic attack by phthalimido anion on the bound ethylene (Scheme 2).[12,18,19b,21] Consistent with previous related findings, compound **3** is thermally stable and does not undergo β-elimination,[22] with the crude reaction mixture remaining unchanged upon heating for a further 3 days at 150 °C.

[2] *IND, r, lf*) = ″ : 1 :: .v11 − 126eq2.gif″

We next employed THF, a polar aprotic but less coordinating solvent than pyridine. We reasoned that a weaker σ-donor opposite to the Ir-ethylene bond would weaken the synergic interaction between the metal and the π-acceptor,[23] thereby rendering the ethylene more prone to dissociation to allow preferred nucleophilic attack on the iridium centre rather than the carbon atom. Heating a THF solution of **2** in phthalimide at 150 °C cleanly yielded a single porphyrin-containing product. Pleasingly, the ^{1}H NMR spectrum of the crude product strongly suggests the exclusive formation of Ir(ttp)(THF)(Phth) (**4**) (eq. [3]). Specifically, phthalimide has been deprotonated and symmetrically incorporated, likely directly onto the metal center, as the aryl proton resonances now appear at 6.14 and 6.51 ppm, respectively, and are further upfield-shifted compared with the corresponding signals in complex **3**. The presence of coordinated THF is indicated by distinctive upfield signals at –2.33 and –0.70 ppm, respectively. Furthermore, no ethylene signals are present in the ^{1}H

Can. J. Chem. Downloaded from www.nrcresearchpress.com by South China Agricultural University on 09/19/12
For personal use only.

Fig. 2. Solid-state molecular structure of 3 with 50% thermal ellipsoids shown. Hydrogen atoms are omitted for clarity.

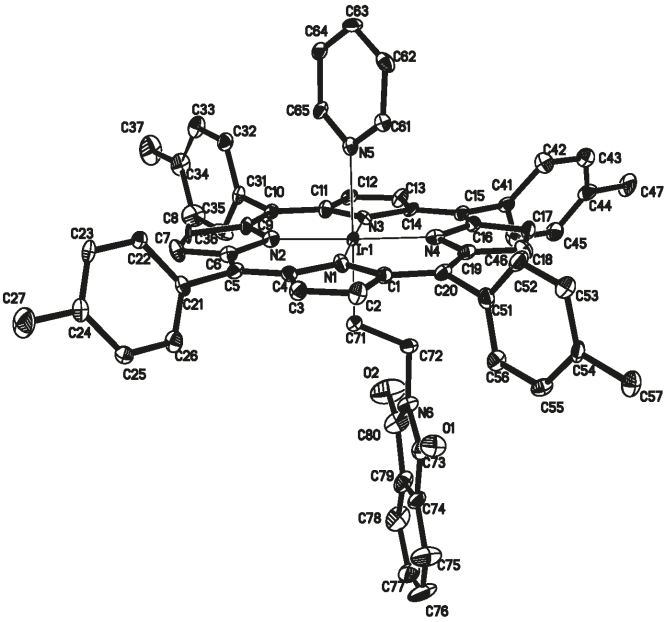

NMR spectrum of **3**. Unfortunately, the physical separation between **4** and the excess phthalimide proved to be problematic. Extraction with CH_2Cl_2–hexanes was unsatisfactory, washing with warm water led to the partial decomposition of **4** with the concomitant formation of new porphyrin-containing species, and chromatography on Alumina or silica yielded decomposition products.

[3] *IND, r, lf*) = ″ : 1 :: .v11 − 126eq3.gif″

Fortunately, under thermal conditions the THF ligand can be displaced by other ligands that yield more robust complexes. Thus, heating the crude mixture of **4** and phthalimide in neat pyridine at 100 °C for 15 h led to quantitative formation of Ir(ttp)(C_5H_5N)(Phth) (**5**), which was isolated in 78% yield as a red microcrystalline solid after chromatography on Alumina (eq. [4]). Single rod-shaped crystals were obtained from a CH_2Cl_2–hexanes bilayer, and an X-ray diffraction study confirmed the proposed structure for **5** (Fig. 3, Table 1). The distance between iridium and the phthalimido-N (Ir(1)–N(5)) is 2.083(2) Å, comparable to the iridium-pyridine distance (Ir(1)–N(6)) of 2.084(2) Å. The similarity between Ir–N covalent versus coordination bond distances has also been observed in a few other reported systems[11c,24] and could suggest low multiple-bond character between iridium and phthalimido. To our knowledge, complex **5** is the first example of an iridium porphyrin amido complex, whose structure has been studied by X-ray crystallography.

[4] *IND, r, lf*) = ″ : 1 :: .v11 − 126eq4.gif″

In conclusion, we have shown that the β-hydroxyethyl complex Ir(ttp)(C_2H_4OH) (**2**) can serve as a precursor towards novel iridium-nitrogen covalently bound species. We are currently exploring the scope of this reaction and examining the reactivity of **4** and **5**.

Experimental

General

Unless otherwise noted, all reagents were purchased from commercial suppliers and directly used without further purification. Hexanes were distilled from anhydrous $CaCl_2$. THF was distilled from sodium benzophenone ketyl. $CDCl_3$, used in the preparation of NMR samples, was distilled from CaH_2. Ir(ttp)Cl(CO) (**1**) was prepared according to the literature procedures.[15] Neutral Alumina (Merck, 70–230 mesh) / H_2O (10:1 *v*/*v*) was used for column chromatography.

NMR spectra were recorded at room temperature (RT) on Bruker DPX-300 or AV-400 spectrometers. ^{1}H NMR spectra are referenced to the residual protio isotopomer present in $CDCl_3$ (δ = 7.26 ppm) and ^{13}C NMR spectra are referenced to the natural-abundance carbon signal of the same solvent (δ = 77.23 ppm). Chemical shifts (δ) are reported as part per million (ppm) in (δ) scale downfield from TMS. Coupling constants (*J*) were reported in Hertz (Hz). High-resolution mass spectra (HRMS) were performed on a ThermoFinnigan MAT 95 XL mass spectrometer in fast atom bombardment (FAB) mode using 3-nitrobenzyl alcohol (NBA) matrix and CH_2Cl_2 as solvent or electrospray ionization (ESI) mode using MeOH:CH_2Cl_2 (1:1) as solvent.

Single X-ray crystal data were collected at 293 K using a Bruker AXS Kappa ApexII Duo diffractomter with Mo Kα radiation (λ = 0.71073 Å). Data collection and reduction were performed using ApexII software. Empirical multiscan absorption correction was applied. Structures were solved by direct method and refined by full-matrix least-squares on F^2, using the SHELXTL program package. The presence of solvent accessible void was corrected by Platon/Squeeze program. Riding refinement was used for hydrogen treatment.

Preparation of Ir(ttp)C_2H_4OH (2)

A 250-mL sealable round-bottomed flask, equipped with a Rotaflo valve, was charged with Ir(ttp)(CO)Cl (46.2 mg, 50.0 mmol) and THF (50 mL). A 10 mL Schlenk tube was charged with aqueous NaOH (1 mol/L, 3 mL) and $NaBH_4$ (20.0 mg, 529 mmol). The two solutions were degassed separately for 15 min. The $NaBH_4$/NaOH solution was added to the solution of **1** using a cannula. The resulting mixture was sealed and heated to 70 °C for 2 h, after which a color change from red to dark orange-brown was observed. The reaction mixture was cooled to RT, and 2-iodoethanol (100 mg, 581 mmol) was added via a micropipette. The mixture was stirred for 15 h at RT, after which the color of the mixture did not change significantly. Solvents were removed in vacuo and the residue was washed with water, leaving behind Ir(ttp)(C_2H_4OH) (**2**) as a maroon solid. Compound **2** was further purified by chromatography on Alumina, eluting with CH_2Cl_2/hexanes (1:1). Yield 41.7 mg (92%). ^{1}H NMR (400 MHz, $CDCl_3$) δ: –5.32 (t, $^3J_{HH}$ = 7.2, 2H, IrCH_2CH$_2$OH), –2.49 (t, $^3J_{HH}$ = 6.0, 1H, OH), –2.20 (m, 2H, IrCH$_2$CH_2OH), 2.69 (s, 12H, CH_3), 7.53 (m, 8H, Ar H), 7.97 (d, $^3J_{HH}$ = 7.2, 4H, Ar H), 8.02 (d, $^3J_{HH}$ = 8.4, 4H, Ar H), 8.54 (s, 8H, β-pyrrole H).

Can. J. Chem. Downloaded from www.nrcresearchpress.com by South China Agricultural University on 09/19/12
For personal use only.

Table 1. Crystal data and summary of data collection and refinement for **3** and **5**.

Param	**3**	**5**
Color, shape	Red needles	Red rods
Formula	$C_{63}H_{49}N_6O_2Ir$	$C_{61}H_{45}N_6O_2Ir$
Crystal size (mm)	0.40 × 0.30 × 0.20	0.40 × 0.30 × 0.20
Formula weight	1114.28	1086.23
Crystal system	triclinic	monoclinic
Space group	*P*-1	*P*2(1)/*c*
A (Å)	11.260 (2)	11.1705 (9)
B (Å)	13.461 (3)	17.3969 (14)
C (Å)	18.521 (4)	24.3961 (11)
A (°)	89.035 (4)	90
B (°)	73.592 (4)	100.4430 (10)
Y (°)	81.450 (4)	90
V (Å^3)	2662.0 (10)	4662.4 (6)
Z	2	4
D_{calcd} (Mg/m^3)	1.390	1.547
Radiation (λ) (Å)	0.71073	0.71073
θ range (°)	1.53–25.00	1.85–25.00
F(000)	1124	2184
Reflections collected	29460	32806
Independent reflections	8540	8217
Data, restraints, parameters	8540, 0, 649	8217, 0, 631
Goodness of fit	1.186	1.088
Final R_1[a] , wR_2[b] [$I > 2\sigma(I)$]	0.0735, 0.1778	0.0208, 0.0511
Final R_1[a] , wR_2[b] (all data)	0.0829, 0.1809	0.0273, 0.0565
w_1, w_2[c]	0.0000, 78.186	0.0259, 5.1729

[a] $R_1 = \sum(||F_0| - |F_c||)/\sum|F_0|$.

[b] $wR_2 = \{\sum[w(F_0^2 - F_c^2)^2]/\sum[w(F_0^2)^2]\}^{1/2}$.

[c] Weighting scheme $w^{-1} = \sigma^2(F_0^2) + (w_1P)^2 + w_2P$ where $P = (F_0^2 + 2F_c^2)/3$.

Fig. 3. Solid-state molecular structure of **5** with 50% thermal ellipsoids shown. Hydrogen atoms are omitted for clarity. Selected bond distances (Å) and angles (º): Ir(1)–N(5) 2.083(2), Ir(1)–N(6) 2.084 (2), N(5)–C(61) 1.394(4), N(5)–C(68) 1.398(4), N(5)–Ir(1)–N(6) 176.51(9), C(61)–N(5)–C(68) 109.2(2), C(61)–N(5)–Ir(1) 125.75 (18), C(68)–N(5)–Ir(1) 124.69(18).

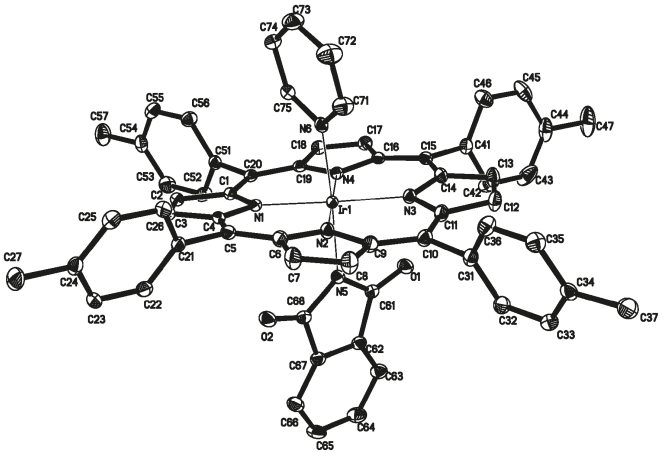

HRMS (FABMS) calcd. for $[C_{50}H_{41}N_4OIr]^+$: *m*/*z* 906.2904; found: *m*/*z* 906.2912.

Preparation of Ir(ttp)(C_5H_5N)($CH_2CH_2NC_4H_8O_2$) (3)

A glass tube equipped with a Rotaflo valve was charged with **2** (10.0 mg, 11.0 mmol), phthalimide (18.0 mg, 122 mmol), and pyridine (2 mL). The mixture was subjected to three freeze-pump-thaw cycles before being heated to 150 °C for 15 h, as the color changed from red-brown to red. Pyridine was removed in vacuo, and the mixture was analyzed by NMR spectroscopy. Hexanes were added to the $CDCl_3$ sample, and the solution was loaded onto an Alumina column, after which the column was eluted with CH_2Cl_2/hexanes (1:1). The major fraction was collected. Solvents were removed in vacuo, resulting in the deposition of **3** as a red microcrystalline powder. Yield 9.8 mg (80%). Single needle-shaped crystals suitable for X-ray crystallography were obtained from a CH_2Cl_2–hexanes bilayer. ^{1}H NMR (400 MHz, $CDCl_3$) δ: –6.06 (m, 2H, Ir$CH_2$$CH_2$), –2.19 (m, 2H, Ir$CH_2$$CH_2$), 2.18 (br d, 2H, py ortho H), 2.66 (s, 12H, CH_3), 5.31 (t, 7.53 (m, $^3J_{HH}$ = 7.2, 2H, py meta H), 6.17 (t, $^3J_{HH}$ = 7.6, 2H, py para H), 7.07 (dd, $^3J_{HH}$ = 5.4, $^4J_{HH}$ = 3.0, 2H, phthalimido Ar H), 7.16 (dd, $^3J_{HH}$ = 5.4, $^4J_{HH}$ = 3.0, 2H, phthalimido Ar H) 7.48 (m, 8H, Ar H), 7.97 (d, $^3J_{HH}$ = 7.2, 4H, Ar H), 8.05 (d, $^3J_{HH}$ = 7.6, 4H, Ar H), 8.50 (s, 8H, β-pyrrole H). ^{13}C NMR (100 MHz, $CDCl_3$) δ. HRMS (FABMS) calcd. for $[C_{63}H_{49}N_6O_2Ir - C_5H_5N]^+$: *m*/*z* 1035.3119; found: *m*/*z* 1035.3130.

Preparation of Ir(ttp)(C_4H_8O)($NC_4H_8O_2$) (4)

A glass tube equipped with a Rotaflo valve was charged with **2** (10.0 mg, 11.0 mmol), phthalimide (18.0 mg, 122 mmol), and THF (2 mL). The mixture was subjected to three freeze-pump-thaw cycles before heated to 150 °C for

Can. J. Chem. Downloaded from www.nrcresearchpress.com by South China Agricultural University on 09/19/12
For personal use only.

15 h, as the color changed from red-brown to red. THF was removed in vacuo, and the mixture was analyzed by NMR spectroscopy, which showed clean formation of **4**. Attempts to remove the excess phthalimide were not successful. ^{1}H NMR (400 MHz, $CDCl_3$) δ: –2.33 (m, 4H, THF), –0.71 (m, 4H, THF), 2.67 (s, 12H, CH_3), 6.14 (dd, $^3J_{HH}$ = 5.4, $^4J_{HH}$ = 3.0, 2H, phthalimido Ar H), 6.51 (dd, $^3J_{HH}$ = 5.4, $^4J_{HH}$ = 3.0, 2H, phthalimido Ar H), 7.49 (d, $^3J_{HH}$ = 8.0, 8H, Ar H), 7.95 (d, $^3J_{HH}$ = 7.6, 4H, Ar H), 8.11 (d, $^3J_{HH}$ = 8.0, 4H, Ar H), 8.66 (s, 8H, β-pyrrole H).

Preparation of Ir(ttp)(C_5H_5N)($NC_4H_8O_2$) (5)

To a crude mixture of Ir(ttp)(C_4H_8O)($NC_4H_8O_2$) (**4**) and phthalimide was added pyridine (2 mL). The resulting solution was subjected to three freeze-pump-thaw cycles and then heated for 15 h at 100 °C, during which little color change was observed. The resulting mixture was dried in vacuo. Compound **5** was obtained in 78% yield as a red solid after chromatography on Alumina, eluting with CH_2Cl_2/hexanes (1:1). Single rod-shaped crystals suitable for X-ray crystallography were grown from a CH_2Cl_2–hexanes bilayer. ^{1}H NMR (400 MHz, $CDCl_3$) δ: 1.13 (br d, 2H, py ortho H), 2.65 (s, 12H, CH_3), 5.05 (t, 7.53 (m, $^3J_{HH}$ = 7.2, 2H, py meta H), 6.06 (t, $^3J_{HH}$ = 7.6, 2H, py para H), 6.19 (dd, $^3J_{HH}$ = 5.4, $^4J_{HH}$ = 3.0, 2H, phthalimido Ar H), 6.54 (dd, $^3J_{HH}$ = 5.4, $^4J_{HH}$ = 3.0, 2H, phthalimido Ar H), 7.46 (m, 8H, Ar H), 7.86 (d, $^3J_{HH}$ = 7.2, 4H, Ar H), 8.10 (d, $^3J_{HH}$ = 7.6, 4H, Ar H), 8.64 (s, 8H, β-pyrrole H). HRMS (FABMS) calcd. for $[C_{61}H_{45}N_6O_2Ir]^+$: *m/z* 1086.3228; found: *m/z* 1086.3244.

Supplementary data

Text, tables, figures of crystallographic data for complexes **3** and **5** (CIF files), and ^{1}H and ^{13}C NMR spectra for complexes are available on the journal Web site (www.nrcresearchpress.com/doi/suppl/10.1139/v11-126). CCDC 831991 has also been deposited with the Cambridge Crystallographic Data Centre. These data can be obtained, free of charge, via www.ccdc.cam.ac.uk/cgi-bin/catreq.cgi (or from the Cambridge Crystallographic Data Centre, 12 Union Road, Cambridge CB2 1Ez, UK; fax +44 1223 336033; or e-mail deposit@ccdc.cam.ac.uk).

Acknowledgements

We thank the Direct Grant of the Chinese University of Hong Kong for financial support. This paper is dedicated to Professor Tak-Hang Chan for his leadership always with words of encouragement.

References

(1) For a comprehensive review of this topic, see:Fulton, J. R.; Holland, A. W.; Fox, D. J.; Bergman, R. G. *Acc. Chem. Res.* **2002**, *35* (1), 44. doi:10.1021/ar000132x.

(2) (a) For a comprehensive review of the amination of aryl halides, see:Hartwig, J. F. *Angew. Chem. Int. Ed.* **1998**, *37* (15), 2046. doi:10.1002/(SICI)1521-3773(19980817)37:15<2046::AID-ANIE2046>3.0.CO;2-L; (b) Hasegawa, Y.; Watanabe, M.; Gridnev, I. D.; Ikariya, T. *J. Am. Chem. Soc.* **2008**, *130* (7), 2158. doi:10.1021/ja710273s.

(3) (a) Glueck, D. S. *Dalton Trans.* **2008**, (39): 5276. doi:10.1039/b806138f; (b) Utsunomiya, M.; Kuwano, R.; Kawatsura, M.; Hartwig, J. F. *J. Am. Chem. Soc.* **2003**, *125* (19), 5608. doi:10.1021/ja0293608; (c) Beller, M.; Trauthwein, H.; Eichberger, M.; Breindl, C.; Herwig, J.; Muller, T. E.; Thiel, O. R. *Chemistry*, **1999**, *5* (4), 1306. doi:10.1002/(SICI)1521-3765(19990401)5:4<1306::AID-CHEM1306>3.0.CO;2-4.

(4) (a) Ito, M.; Ikariya, T. *Chem. Commun. (Cambridge)*, **2007**, (48), 5134. doi:10.1039/b709704b; (b) Heiden, Z. M.; Rauchfuss, T. B. *J. Am. Chem. Soc.* **2009**, *131* (10), 3593. doi:10.1021/ja807277s.

(5) Bernskoetter, W. H.; Brookhart, M. *Organometallics*, **2008**, *27* (9), 2036. doi:10.1021/om701148t.

(6) Burrington, J. D.; Kartisek, C. T.; Graseelli, R. K. *J. Catal.* **1982**, *75* (2), 225. doi:10.1016/0021-9517(82)90204-4.

(7) Koike, T.; Ikariya, T. *Organometallics*, **2005**, *24* (4), 724. doi:10.1021/om049205x.

(8) (a) Fryzuk, M. D.; Montgomery, C. D. *Coord. Chem. Rev.* **1989**, *95* (1), 1. doi:10.1016/0010-8545(89)80001-3; (b) Kempe, R. *Angew. Chem.* **2000**, *112* (3), 478. doi:10.1002/(SICI)1521-3757(20000204)112:3<478::AID-ANGE478>3.0.CO;2-#.

(9) (a) Caulton, K. G. *New J. Chem.* **1994**, *18*, 25; (b) Mayer, J. M.; Comments, X. *Inorg. Chem.* **1988**, *8* (4), 125. doi:10.1080/02603598808035790.

(10) (a) Gunnoe, T. B. *Eur. J. Inorg. Chem.* **2007**, *2007* (9), 1185. doi:10.1002/ejic.200601072; (b) Conner, D.; Jayaprakash, K. N.; Gunnoe, T. B.; Boyle, P. D. *Inorg. Chem.* **2002**, *41* (11), 3042. doi:10.1021/ic020163j; (c) Rahim, M.; Ahmed, K. J. *Organometallics*, **1994**, *13* (5), 1751. doi:10.1021/om00017a035.

(11) (a) Glueck, D. S.; Winslow, L. J. N.; Bergman, R. G. *Organometallics*, **1991**, *10* (5), 1462. doi:10.1021/om00051a044; (b) Hartwig, J. F.; Andersen, R. A.; Bergman, R. G. *Organometallics*, **1991**, *10* (6), 1875. doi:10.1021/om00052a037; (c) Kanzelberger, M.; Zhang, X.; Emge, T.; Goldman, A. S.; Zhao, J.; Incarvito, C.; Hartwig, J. F. *J. Am. Chem. Soc.* **2003**, *125* (45), 13644. doi:10.1021/ja037363u.

(12) Woerpel, K. A.; Bergman, R. G. *J. Am. Chem. Soc.* **1993**, *115* (17), 7888. doi:10.1021/ja00070a049.

(13) (a) Driver, M. S.; Hartwig, J. F. *J. Am. Chem. Soc.* **1996**, *118* (30), 7217. doi:10.1021/ja960937t; (b) Hartwig, J. F.; Richards, S.; Baranano, D.; Paul, F. *J. Am. Chem. Soc.* **1996**, *118* (15), 3626. doi:10.1021/ja954121o; (c) Villanueva, L. A.; Abboud, K. A.; Boncella, J. M. *Organometallics*, **1994**, *13* (10), 3921. doi:10.1021/om00022a031; (d) Zhao, P.; Hartwig, J. F. *J. Am. Chem. Soc.* **2005**, *127* (33), 11618. doi:10.1021/ja054132+; (e) Hartwig, J. F.; Bergman, R. G.; Andersen, A. *Organometallics*, **1991**, *10* (9), 3344. doi:10.1021/om00055a061.

(14) (a) Fujita, K.-i.; Yamashita, M.; Puschmann, F.; Martinez Alvarez-Falcon, M.; Incarvito, C. D.; Hartwig, J. F. *J. Am. Chem. Soc.* **2006**, *128* (28), 9044. doi:10.1021/ja062333n; (b) Yamashita, M.; Hartwig, J. F. *J. Am. Chem. Soc.* **2004**, *126* (17), 5344. doi:10.1021/ja0315107.

(15) (a) Song, X.; Chan, K. S. *Organometallics*, **2007**, *26* (4), 965. doi:10.1021/om060849+; (b) Yeung, S. K.; Chan, K. S. *Organometallics*, **2005**, *24* (26), 6426. doi:10.1021/om050661a.

(16) Cheung, C. W.; Chan, K. S. *Organometallics*, **2008**, *27* (13), 3043. doi:10.1021/om700751h.

(17) Bryndza, H. E.; Fong, L. K.; Paciello, R. A.; Tam, W.; Bercaw, J. E. *J. Am. Chem. Soc.* **1987**, *109* (5), 1444. doi:10.1021/ja00239a026.

(18) Chan, K. S.; Lau, C. M.; Yeung, S. K.; Lai, T. H. *Organometallics*, **2007**, *26* (8), 1981. doi:10.1021/om070135e.

(19) (a) Steinborn, D. *Angew. Chem. Int. Ed. Engl.* **1992**, *31* (4), 401. doi:10.1002/anie.199204011; (b) Wayland, B. B.; Van Voorhees, S. L.; Del Rossi, K. J. *J. Am. Chem. Soc.* **1987**, *109* (21), 6513. doi:10.1021/ja00255a048.

(20) Han, Y.; Sanford, M. S.; England, M. D.; Groves, J. T. *Chem. Commun. (Cambridge)*, **2006**, (5), 549. doi:10.1039/b511974j.

(21) (a) Ritter, J. C. M.; Bergman, R. G. *J. Am. Chem. Soc.* **1997**, *119* (10), 2580. doi:10.1021/ja9636653; (b) Fu, X.; Li, S.; Wayland, B. B. *J. Am. Chem. Soc.* **2006**, *128* (27), 8947. doi:10.1021/ja0583416.

(22) Yeung, S. K.; Chan, K. S. *Organometallics*, **2005**, *24* (11), 2561. doi:10.1021/om0501475.

(23) Gusev, D. G. *Organometallics*, **2009**, *28* (3), 763. doi:10.1021/om800933x.

(24) (a) Chin, C. S.; Chong, D.; Lee, B.; Jeong, H.; Won, G.; Do, Y.; Park, J. Y. *Organometallics*, **2000**, *19* (4), 638. doi:10.1021/om9908480; (b) Rahim, M.; White, C.; Rheingold, A. L.; Ahmed, K. J. *Organometallics*, **1993**, *12* (7), 2401. doi:10.1021/om00031a001.

Can. J. Chem. Downloaded from www.nrcresearchpress.com by South China Agricultural University on 09/19/12
For personal use only.

Modulation of indium–tin oxide work function by a versatile self-assembled monolayer measured with the scanning Kelvin nanoprobe

Christophe Blaszykowski, Larissa-Emilia Cheran, and Michael Thompson

Can. J. Chem. Downloaded from www.nrcresearchpress.com by South China Agricultural University on 09/19/12
For personal use only.

Abstract: In molecular optoelectronics, high-quality contacts at electrode|organics interfaces are crucial for charge carriers to efficiently flow through and therefore play a critical role on device performance. Electrode surface morphology, adhesibility, wettability, and work function are thus many parameters that must be accurately controlled, which is achievable using self-assembling monolayer (SAM) surface chemistry. Herein, we employ this technique to alter the electronic and surface energy-related properties of indium–tin oxide (ITO). In comparison to unmodified ITO, the newly introduced SAM-derivatized surface exhibits limited wettability and considerably higher work function ($\Delta\Phi$ = ~1.2 eV). Several applications are proposed for this organic coating, notably at the anode of organic light-emitting diode (OLED) devices for decreasing the hole injection barrier or as an atmospherically stable protective layer in the coatings industry.

Key words: work function, indium–tin oxide, self-assembled monolayer, scanning Kelvin nanoprobe.

Résumé : En optoélectronique moléculaire, des contacts de haute qualité sont cruciaux pour s'assurer d'un transfert efficace des porteurs de charge aux interfaces électrode|composé organique et jouent ainsi un rôle critique sur la performance des appareils optoélectroniques. La morphologie de surface, l'adhérence, la mouillabilité et travail de sortie des électrodes sont ainsi autant de paramètres qui doivent être précisément controllés, ce que permet la chimie de surface des monocouches auto-assemblées (MAA). Ici, nous utilisons cette technique afin de modifier les propriétés électroniques et celles associées à l'énergie de surface de l'oxyde d'indium–étain (OIE). En comparaison avec la surface non-modifiée d'OIE, la surface d'OIE derivatisée avec la MAA nouvellement introduite montre une mouillabilité restreinte ainsi qu'une augmentation considérable du travail de sortie ($\Delta\Phi$ = ~1,2 eV). Plusieurs applications sont proposées pour ce film organique, notamment pour diminuer la barrière de potentiel à l'anode de diodes électroluminescentes organiques (DELO) ou en tant que couche protectrice stable dans les conditions atmosphériques pour l'industrie du revêtement.

Mots-clés : travail de sortie, oxyde d'indium–étain, monocouche auto-assemblée, nanosonde de Kelvin à balayage.

Introduction

Work function is an intrinsic property of matter that is defined as the minimum amount of energy required to extract one electron from a material. With respect to energy levels, work function thus corresponds to the difference in energy between the highest populated electronic state of a material (the Fermi level, E_F) and the vacuum level. In practice, work function is extremely sensitive to very subtle surface changes of any physical or chemical nature, which makes its measurement an invaluable analysis/detection tool in many surface science fields when information about the alteration of a surface is sought.[1,2] Conversely, the ability to control work function through surface engineering has also attracted much interest, notably in molecular optoelectronics where electrodes having finely tuned energy levels are of particular importance for interfacial charge carrier flow to occur more efficiently.[3,4]

In the field of surface science, self-assembling monolayer (SAM) chemistry constitutes a powerful and versatile tool for the rapid and economical preparation of thin organic films on various solid inorganic materials such as gold, quartz, or indium–tin oxide (ITO).[5] In SAM chemistry, customizable molecules are engineered for surface modification purposes to spontaneously form ordered molecular assemblies with tailored properties usually pertaining to wettability and adhesibility. However, recent studies carried out in the field of molecular optoelectronics on organic light-emitting diodes (OLED) and organic solar cells (OSC) have shown that SAM chemistry could also be used to modulate work function.[6–16] The resulting SAM-based devices exhibited markedly improved performance, which is attributed to an enhanced charge carrier transport across the SAM-derivatized electrode | adjacent active layer junction due to higher quality contact and better frontier energy level positioning.[16–26]

At the anode of OLED devices, SAMs with appropriate dipole moment direction (pointing towards the anode) are thus used to increase the electrode work function (Φ) by imposing an interfacial dipole that permanently alters the surface

Received 7 April 2011. Accepted 1 July 2011. Published at www.nrcresearchpress.com/cjc on 21 November 2011.

C. Blaszykowski, L.-E. Cheran, and M. Thompson. Department of Chemistry, University of Toronto, 80 St. George Street, Toronto, ON M5S 3H6, Canada.

Corresponding author: Michael Thompson (e-mail: mikethom@chem.utoronto.ca).

This article is part of a Special Issue to commemorate the International Year of Chemistry.

Can. J. Chem. Downloaded from www.nrcresearchpress.com by South China Agricultural University on 09/19/12
For personal use only.

Fig. 1. Schematic energy level diagram depicting the position of the pinned Fermi level (E_F) and the local vacuum levels relative to the hole transporting layer's (HTL) and the light-emitting layer's (LEL) highest occupied molecular orbital (HOMO) levels before (left) and after (right) derivatization of an anodic material with a self-assembling monolayer (SAM) having a dipole moment pointing towards the surface. Φ_A and Φ_S are the associated work functions, HIB_A and HIB_S are the respective energy barriers to hole injection. For simplicity, Fermi level pinning and other vacuum level shifts occurring at the (SAM-derivatized) anodic material / HTL and HTL/LEL interfaces are not represented.[27–29]

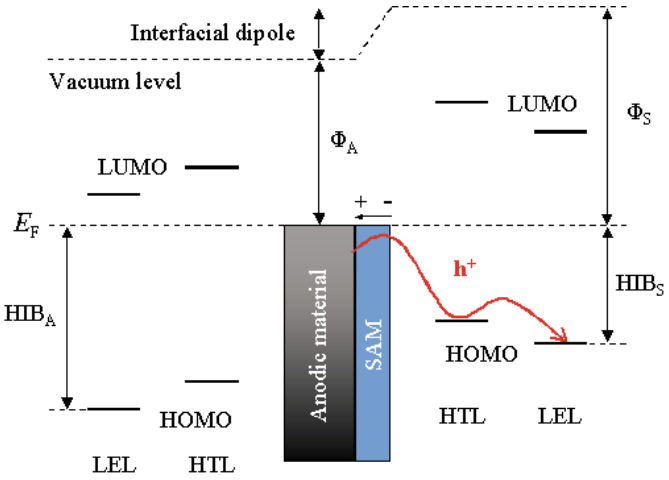

electrostatic potential and shifts the local vacuum level upwards, as illustrated in Fig. 1.[6,18,25] This in turn may allow for the hole injection barrier (HIB) to be lowered thereby enhancing hole injection (h^+) from the anode to the light-emitting layer (LEL) through the conventionally intercalated hole transporting layer (HTL).

For OLED applications where LELs having particularly low-lying HOMO levels[30] are aimed to be integrated within substrate|SAM|LEL HTL-free structures,[31,32] SAM-derivatized anodes with correspondingly high(er) work function may be required to minimize the HIB and lower the operating/driving voltages.[17,18,27] In the case of ITO, which is a commonly employed anodic material,[33] only a limited number of publications have appeared in the literature to describe SAM-derivatized ITO surfaces that display substantially higher work function than bare ITO ($\Delta\Phi > 1$ eV) and are actually operational[23,25,34,35] in an OLED device or have the potential[7,13,36,37] to be. In this context, we wish to introduce herein a new SAM-derivatized ITO surface that presents considerably higher work function than unmodified ITO ($\Delta\Phi = \sim 1.2$ eV), as determined using the scanning Kelvin nanoprobe (SKN).[1,2]

Experimental section

Materials

The following includes detailed protocols for ITO cleaning, OEG–TTTA SAM formation, and contact potential difference (CPD) measurements. SAM characterization using angle-resolved X-ray photoelectron spectroscopy (XPS) and contact angle goniometry is reported in the accompanying Supplementary data. OEG–TTTA synthesis is reported elsewhere.[5] ITO-coated glass slides (R_S = 4–8 Ω, ITO thickness of 1500–2000 Å) were purchased from Delta-Technologies Ltd. (Stillwater, Minnesota). ITO silanization was prepared in a glovebox maintained under an inert (N_2) and anhydrous (P_2O_5) atmosphere using glassware (20 mL glass scintillation vials) that had been pretreated overnight with a 1:20 (*v*/*v*) solution of octadecyltrichlorosilane (Sigma-Aldrich) in anhydrous toluene. The slides were systematically handled with thoroughly precleaned stainless steel tweezers to minimize any external contamination.

ITO cleaning procedure

ITO slides (13 mm × 13 mm × 1.1 mm) were first sonicated in concentrated dishwashing soap for 30 min, after which they were thoroughly rinsed with hot tap water followed by distilled water and then finally dried under a gentle stream of forced air. The slides were next sonicated in spectrograde methanol for 20 min, after which they were copiously rinsed with methanol, gently dried with forced air, and then N_2-plasma cleaned for 10 min. Contact angle measurements (CAM) were then performed using ultrapure water as the test liquid. The slides presenting complete wetting (CAM = 0°) were then selected and immediately transferred into a humidity chamber, maintained at 70% relative humidity (using $MgNO_3 \cdot 6H_2O$), and set aside overnight. The same procedure, with the exception of sonication, was followed for the cleaning of the Au/Pt-plated ITO slide used for measuring CPDs.

Silanization procedure (SAM formation)

Neat OEG–TTTA (10 µL) was first diluted with anhydrous toluene (10 mL). The resulting solution was portioned in six vials (1000 µL/vial) into which cleaned ITO slides were then individually soaked in a horizontal position. The vials were then tightly capped, removed from the glovebox, and placed on a spinning plate for 30 min. Next, the slides were thoroughly rinsed with toluene (3×) and then sonicated in another portion of toluene for 5 min. After a final rinse with toluene, the previous procedure was repeated with chloroform, after which the slides were dried under a gentle stream of forced air. They were then transferred into a dessicator (filled with indicating Drierite) that was subsequently high-vacuumed for 2 h. After backfilling the chamber with N_2, the surfaces were then characterized by angle-resolved XPS and contact angle goniometry. Identical preparation procedure, with the exception of the slide being vertically immersed at the desired level into the OEG–TTTA solution, was followed for the Au/Pt-plated ITO slide dedicated to CPD measurements. No protective coating mask was applied to the unsoaked part of the slide prior to immersion.

CPD measurements

CPD measurements were performed on a specially designed Au/Pt-plated ITO slide (25 mm × 25 mm × 1.1 mm) using the SKN apparatus.[1,2] CPD measurements were rapidly recorded under ambient atmospheric conditions on a freshly prepared surface immediately after its removal from the N_2-backfilled dessicator (vide supra). Data were acquired with a LabView 6 platform and then analyzed using the Origin 7 program (OriginLab Corp., Northampton, Massachusetts). Shifts in work function ($\Delta\Phi$) were calculated using the relationship $\Delta\Phi = e\Delta CPD$, where e is the elementary charge.

Scheme 1. Illustration of the formation of an OEG–TTTA SAM onto a cleaned ITO-coated glass slide.

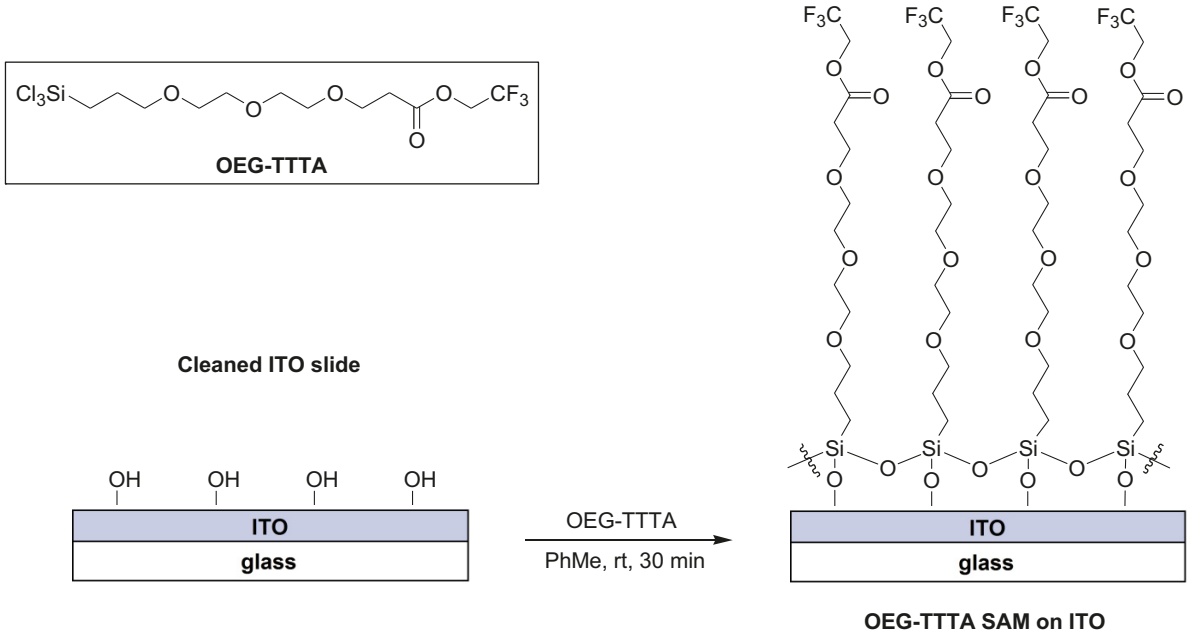

Additional information can be found in the Results and discussion section.

Results and discussion

SAM preparation and XPS characterization

Surface engineering using SAM chemistry for the development of antifouling biosensing platforms is currently the object of intense research in our laboratory.[5] Recently, we also became interested in the possibility offered by SAM chemistry to modulate electrode work function in molecular optoelectronics for the fabrication of better performing devices. Our aim was notably to develop new SAM-derivatized ITO surfaces having both tailored work function and wettability for application as anodes in photonic devices. For that purpose, we initially investigated OEG–TTTA, a molecule that had recently proven to be effective at coating hydroxylated substrates.[5]

OEG–TTTA (Scheme 1) is a bifunctional molecule that possesses a highly reactive trichlorosilyl tail function (Cl_3Si–) for strong and durable siloxane anchorage onto the underlying hydroxylated ITO surface. Another important feature of oOEG–TTTA resides in its long oligoethylene glycol (OEG) backbone that not only serves to drive self-assembly but also provides ordering and rigidity to the resulting SAM through intermolecular interactions. Lastly, OEG–TTTA possesses an electron-withdrawing trifluoroethyl ester (TFEE) head function that also participates in endowing the molecule with a dipole moment. Upon chemisorption of OEG–TTTA onto ITO, robust and polar SAMs are thus expected to form and permanently alter the surface electrostatic potential, hence work function.[6–18]

SAM-derivatized ITO surfaces (a batch of six samples) were readily prepared upon immersion of cleaned ITO slides into a 1:1000 (*v*/*v*) solution of OEG–TTTA in anhydrous toluene, for 30 min at room temperature (Scheme 1). The successful and reproducible deposition of OEG–TTTA onto ITO was determined using angle-resolved XPS. As expected for the formation of OEG–TTTA films onto bare ITO, signals for fluorine, silicon, and carbon (elements exclusively found in OEG–TTTA) appeared in the XPS profiles, as shown in Fig. 2. With respect to carbon, the peaks expected for the OEG backbone of OEG–TTTA (C–O) and TFEE head function (C=O, C–O, and CF_3) are also clearly discernible on the C1s narrow scan at ~288–294 eV.[38,39] Moreover, the signals for the characteristic elements of ITO (indium, tin, and oxygen) conversely decreased as expected for a now buried underlying ITO layer (Fig. 2). The shift to higher binding energy observed for oxygen (as well as for indium and tin) and the accompanying change in signal shape (appearance of an Si–O shoulder at ~533 eV) are also indicators that OEG–TTTA molecules are tightly bound to ITO.[34,36,40] Finally, it is important to note that XPS data showed high consistency from one sample to another (with relative standard deviations (RSDs) ranging from 2% to 13%), demonstrating that these OEG–TTTA films were prepared in a reproducible manner with respect to molecular coverage.

Contact angle measurements

Surface wettability was next determined by contact angle goniometry using ultrapure water as the test liquid (Table 1). The measurements revealed that these OEG–TTTA surfaces exhibit a quite pronounced hydrophobic character, with an average static CAM of 76°, as opposed to the complete wetting (CAM = 0°) observed for freshly cleaned hydrophilic ITO. CAM reproducibility from one sample to another was excellent (3% RSD) indicating that these OEG–TTTA surfaces were also prepared in a reproducible manner with respect to surface wettability.

Contact potential differences/work function shift

We turn now to the measurement of the shift in work function caused by the OEG–TTTA SAM using the SKN.[1,2] In practice, this instrument operates by vibrating a sharp guarded tungsten tip at close proximity over a sample placed

Can. J. Chem. Downloaded from www.nrcresearchpress.com by South China Agricultural University on 09/19/12
For personal use only.

Can. J. Chem. Downloaded from www.nrcresearchpress.com by South China Agricultural University on 09/19/12
For personal use only.

Fig. 2. Typical XPS narrow scans for bare ITO (broken line) and OEG–TTTA-coated ITO (solid line) recorded for each characteristic element of OEG–TTTA (left column) and ITO (right column). The presence of carbon in the XPS profile of bare ITO is due to contamination by adventitious carbon. The binding energy scale is calibrated to the main C1s signal at 285 eV. The take-off angle shown here is 20° relative to the surface. Complete angle-resolved XPS analysis is available in the Supplementary data.

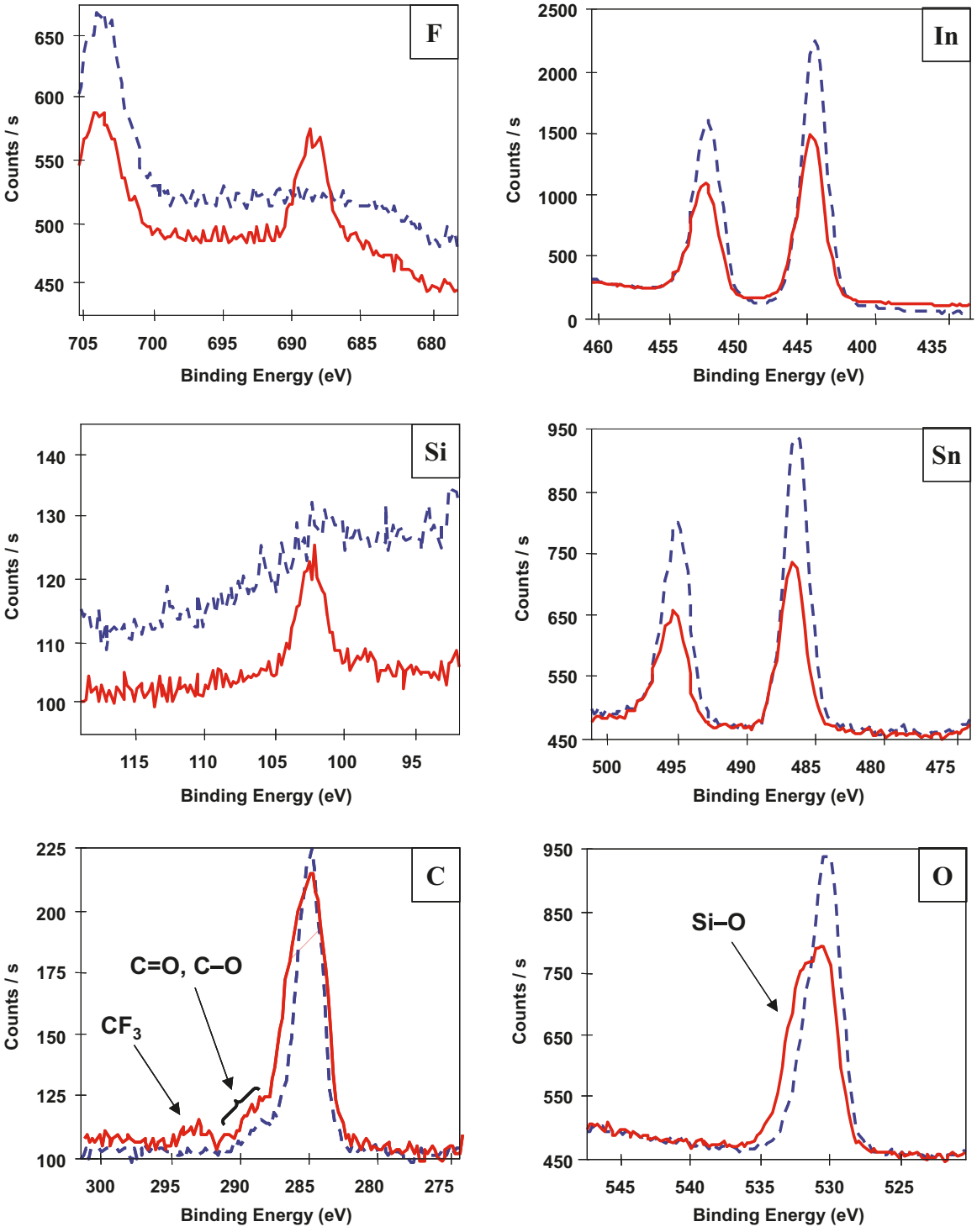

on top of a conducting table. This triggers a flow of charge between the tip and the sample (i.e., their Fermi levels), which are electrically connected via an external circuit. This movement of charge induces a difference of potential between the tip and the sample, whose amplitude depends on the nature of the sample area being scanned. In other words, SKN essentially behaves as a one-plate-varying capacitor that merely measures CPDs between the tip and the sample, with $CPD = (\Phi_{sample} - \Phi_{tip})/e$. Shifts in work function ($\Delta\Phi$) between two materials can later be calculated using the relationship $\Delta\Phi = e\Delta CPD$. However, direct access to work function requires the use of a reference material with a known and stable

Can. J. Chem. Downloaded from www.nrcresearchpress.com by South China Agricultural University on 09/19/12
For personal use only.

Table 1. Static contact angle measurements recorded for as-received ITO, freshly cleaned ITO, and OEG–TTTA SAMs on ITO using ultrapure water.

Surface	Contact angle (°)
As-received ITO	>100
Freshly cleaned ITO	0
OEG–TTTA SAM on ITO	76[a]

[a]Averaged for six slides (±2°, 3% relative standard deviation).

Fig. 3. Schematic representation of the Au/Pt-plated SAM-derivatized ITO slide used to measure CPDs. Partial SAM covering was achieved upon vertical immersion of the slide at the desired level into solution. No protective coating mask was applied to the unsoaked part beforehand, which resulted in a capillary fringe at the air/solution interface.

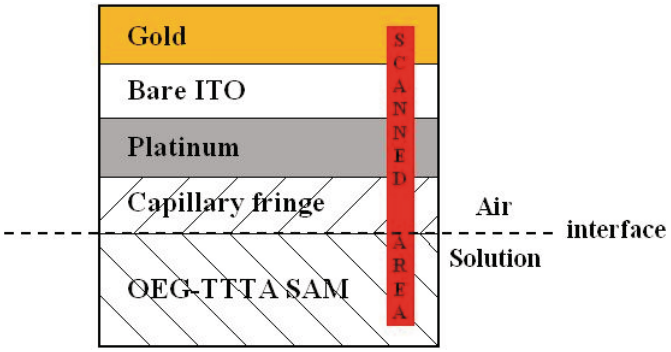

Fig. 4. CPD profile of OEG–TTTA-coated ITO vs bare ITO relative to the Au and Pt internal references. The measurement was performed under ambient atmospheric conditions on a freshly prepared surface.

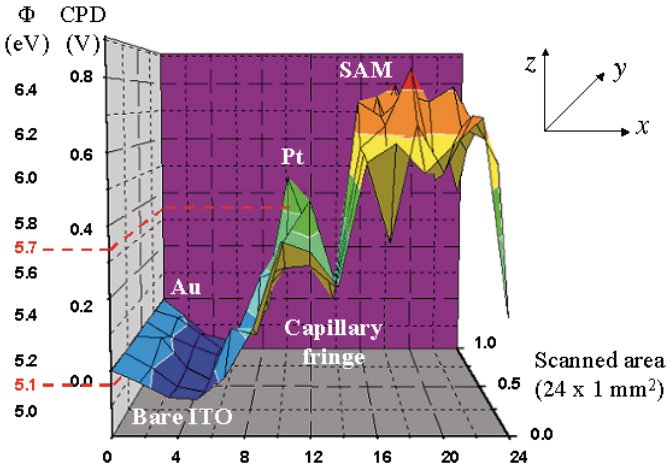

work function, such as highly ordered pyrolytic graphite (HOPG).[37] For our study, we designed an ITO-coated glass slide onto which two narrow strips of gold and platinum were plated, as illustrated in Fig. 3. These noble metals, which have respective work functions of 5.1 and 5.7 eV as measured under ultra-high vacuum (UHV) conditions,[41] can serve as internal references and offer the possibility of converting the measured CPD values into calibrated work functions. The SAM-derivatized ITO surface for CPD measurement (CAM = 76°) was prepared following the aforementioned conditions, the cleaned ITO slide being, however, only partially coated with the SAM, as shown in Fig. 3, upon vertical immersion into solution.

Upon preparation, this slide was then immediately and rapidly scanned across with the SKN under ambient atmospheric conditions, in a raster pattern of 100 μm × 200 μm step size and a total area of 24 × 1 mm^2 (Fig. 3). On the resulting CPD 3D map (Fig. 4), one can clearly recognize the successive zones depicted in Fig. 3 from (left to right) gold (lighter blue), bare ITO (darker blue), platinum (green), to the OEG–TTTA film (yellow-orange; for a colour view, please see the Web version of this paper). Capillary action at the unmasked air/solution interface during SAM formation resulted in the intermediate CPD response observed at $x \sim 14$ mm (capillary fringe).[17]

As can be seen in Fig. 4, the difference in CPD between SAM-derivatized and bare ITO is ~0.75 V under our experimental conditions, which represents a tremendous increase in work function of ~1.2 eV. Indicatively, when the scale is expressed in eV and calibrated with the Au (5.1 eV) and Pt (5.7 eV) references, the work function of bare ITO is ~4.9 eV, which is within the range reported.[13] On the other hand, the work function of the SAM-derivatized area becomes ~6.1 eV. However, we must point out that this conversion is only valid provided that the values $\Phi_{Au} = 5.1$ eV and $\Phi_{Pt} = 5.7$ eV measured under UHV still stand under our scanning conditions (ambient atmosphere), which would appear to be a reasonable assumption here. Regardless, such an increase in work function makes this hybrid material a potential anode candidate for decreasing the HIB in hole-limited OLED devices. As discussed earlier, this may also be interesting for OLED applications that aim to integrate LELs with very low-lying HOMO levels,[35] such as in the key class of blue OLEDs.[42] Another benefit anticipated is higher resistance to oxidation[35,43] that, combined with its hydrophobic character, could also make this robust molecular adlayer an atmospherically stable coating of nanometric size to prevent underlying materials or fabrics from corroding, deteriorating, or wetting.[44]

Conclusions

In this article, we have introduced new SAM chemistry for the surface modification of ITO with respect to its electronic and surface energy-related properties. It was shown that, in comparison to unmodified ITO, the novel SAM-derivatized surface exhibits limited wettability and considerably higher work function ($\Delta\Phi$ = ~1.2 eV). It was also argued that an organic coating with such attributes can be expected to draw much attention in many surface science fields, notably in molecular optoelectronics for decreasing the HIB at the anode of hole-limited OLED devices or in the coatings industry as a multipurpose, environmentally stable protective layer. Research attention is currently focused on generating a collection of surface modifiers capable of self-assembling onto various substrates and form versatile molecular coatings with customized properties.

Supplementary data

Supplementary data (including complete contact angle goniometry and angle-resolved X-ray photoelectron spectroscopy

data for SAM characterization) are available with the article through the journal Web site at http://nrcresearchpress.com/doi/suppl/10.1139/v11-140.

Acknowledgements

The authors are grateful to the Natural Sciences and Engineering Research Council of Canada (NSERC) for partial support of this work. The authors also thank E. Chak for assistance with the SKN, Dr. S.M. Ballantyne for helpful discussions regarding molecular optoelectronics, and Drs. P Brodersen and R. Sodhi at Surface Interface Ontario for XPS analysis.

References

(1) Cheran, L.-E.; Johnstone, S.; Sadeghi, S.; Thompson, M. *Meas. Sci. Technol.* **2007**, *18* (3), 567. doi:10.1088/0957-0233/18/3/005.

(2) Cheran, L.-E.; Sadeghi, S.; Thompson, M. *Analyst* **2005**, *130* (12), 1569. doi:10.1039/b509724j.

(3) Koch, N. *ChemPhysChem* **2007**, *8* (10), 1438. doi:10.1002/cphc.200700177.

(4) Ma, H.; Yip, H.-L.; Huang, F.; Jen, A. K.-Y. *Adv. Funct. Mater.* **2010**, *20* (9), 1371. doi:10.1002/adfm.200902236.

(5) Sheikh, S.; Sheng, J. C.-C.; Blaszykowski, C.; Thompson, M. *Chem. Sci.* **2010**, *1* (2), 271. doi:10.1039/c0sc00158a.

(6) de Boer, B.; Hadipour, A.; Mandoc, M. M.; van Woudenbergh, T.; Blom, P. W. M. *Adv. Mater.* **2005**, *17* (5), 621. doi:10.1002/adma.200401216.

(7) Nüesch, F.; Carrara, M.; Zuppiroli, L. *Langmuir* **2003**, *19* (12), 4871. doi:10.1021/la026962w.

(8) Alloway, D. M.; Graham, A. L.; Yang, X.; Mudalige, A.; Colorado, R., Jr; Wysocki, V. H.; Pemberton, J. E.; Lee, T. R.; Wysocki, R. J.; Armstrong, N. R. *J. Phys. Chem. C* **2009**, *113* (47), 20328. doi:10.1021/jp909494r.

(9) Gozlan, N.; Tisch, U.; Haick, H. *J. Phys. Chem. C* **2008**, *112* (33), 12988. doi:10.1021/jp803124j.

(10) Gozlan, N.; Haick, H. *J. Phys. Chem. C* **2008**, *112* (33), 12599. doi:10.1021/jp805723u.

(11) Wu, K.-Y.; Yu, S.-Y.; Tao, Y.-T. *Langmuir* **2009**, *25* (11), 6232. doi:10.1021/la900046b.

(12) Lü, J.; Delamarche, E.; Eng, L.; Bennewitz, R.; Meyer, E.; Güntherodt, H.-J. *Langmuir* **1999**, *15* (23), 8184. doi:10.1021/la9904861.

(13) Hotchkiss, P. J.; Li, H.; Paramonov, P. B.; Paniagua, S. A.; Jones, S. C.; Armstrong, N. R.; Brédas, J.-L.; Marder, S. R. *Adv. Mater.* **2009**, *21* (44), 4496. doi:10.1002/adma.200900502.

(14) Ofir, Y.; Zenou, N.; Goykhman, I.; Yitzchaik, S. *J. Phys. Chem. B* **2006**, *110* (15), 8002. doi:10.1021/jp057251k.

(15) Tseng, C.-T.; Cheng, Y.-H.; Lee, M.-C. M.; Han, C.-C.; Cheng, C.-H.; Tao, Y.-T. *Appl. Phys. Lett.* **2007**, *91* (23), 233510. doi:10.1063/1.2823579.

(16) Kim, J. S.; Park, J. H.; Lee, J. H.; Jo, J.; Kim, D.-Y.; Cho, K. *Appl. Phys. Lett.* **2007**, *91* (11), 112111. doi:10.1063/1.2778548.

(17) Appleyard, S. F. J.; Day, S. R.; Pickford, R. D.; Willis, M. R. *J. Mater. Chem.* **2000**, *10* (1), 169. doi:10.1039/a903708j.

(18) Khodabakhsh, S.; Poplavskyy, D.; Heutz, S.; Nelson, J.; Bradley, D. D. C.; Murata, H.; Jones, T. S. *Adv. Funct. Mater.* **2004**, *14* (12), 1205. doi:10.1002/adfm.200400035.

(19) Hatton, R. A.; Day, S. R.; Chesters, M. A.; Willis, M. R. *Thin Solid Films* **2001**, *394* (1–2), 292. doi:10.1016/S0040-6090(01)01191-9.

(20) Chong, L.-W.; Lee, Y.-L.; Wen, T.-C. *Thin Solid Films* **2007**, *515* (5), 2833. doi:10.1016/j.tsf.2006.05.010.

(21) Kim, D. H.; Chung, C. M.; Park, J. W.; Oh, S. Y. *Ultramicroscopy* **2008**, *108* (10), 1233. doi:10.1016/j.ultramic.2008.04.026.

(22) Cui, J.; Huang, Q.; Wang, Q.; Marks, T. J. *Langmuir* **2001**, *17* (7), 2051. doi:10.1021/la010158c.

(23) Guo, J.; Koch, N.; Schwartz, J.; Bernasek, S. L. *Mater. Res. Soc. Symp. Proc.* **2005**, *871E*, I6.52.1.

(24) Cho, C.-P.; Tao, Y.-T. *Langmuir* **2007**, *23* (13), 7090. doi:10.1021/la700648z.

(25) Ganzorig, C.; Kwak, K.-J.; Yagi, K.; Fujihira, M. *Appl. Phys. Lett.* **2001**, *79* (2), 272. doi:10.1063/1.1384896.

(26) Manna, U.; Kim, H. M.; Gowtham, M.; Yi, J.; Sohn, S.; Jung, D. *Thin Solid Films* **2006**, *495* (1–2), 380. doi:10.1016/j.tsf.2005.08.242.

(27) Zhu, L.; Tang, H.; Harima, Y.; Yamashita, K.; Aso, Y.; Otsubo, T. *J. Mater. Chem.* **2002**, *12* (8), 2250. doi:10.1039/b201391f.

(28) Hill, I. G.; Hwang, J.; Kahn, A.; Huang, C.; McDermott, J. E.; Schwartz, J. *Appl. Phys. Lett.* **2007**, *90* (1), 012109. doi:10.1063/1.2426957.

(29) Mäkinen, A. J.; Hill, I. G.; Shashidhar, R.; Nikolov, N.; Kafafi, Z. H. *Appl. Phys. Lett.* **2001**, *79* (5), 557. doi:10.1063/1.1386400.

(30) Chen, S.; Xu, X.; Liu, Y.; Qiu, W.; Yu, G.; Wang, H.; Zhu, D. *J. Phys. Chem. C* **2007**, *111* (2), 1029. doi:10.1021/jp065822i.

(31) Huang, Q.; Cui, J.; Yan, H.; Veinot, J. G. C.; Marks, T. J. *Appl. Phys. Lett.* **2002**, *81* (19), 3528. doi:10.1063/1.1517397.

(32) Morgado, J.; Barbagallo, N.; Charas, A.; Matos, M.; Alcácer, L.; Cacialli, F. *J. Phys. D Appl. Phys.* **2003**, *36* (5), 434. doi:10.1088/0022-3727/36/5/304.

(33) In the field of molecular optoelectronics, ITO constitutes a material of choice that is commonly used for the fabrication of hole injecting/transporting anodes because of its many attractive features that include high electrical conductivity, high transparency over the visible region, ease of patterning, and relatively high work function.

(34) Jee, S. H.; Kim, S. H.; Park, H.; Kim, D.-J.; Yoon, Y. S. *Jpn. J. Appl. Phys.* **2010**, *49* (2), 025701. doi:10.1143/JJAP.49.025701.

(35) For another approach towards higher work function anodes using alternative transparent conducting oxide (TCO) materials in OLED devices, see Cui, J.; Wang, A.; Edleman, N. L.; Ni, J.; Lee, P.; Armstrong, N. R.; Marks, T. J. *Adv. Mater.* **2001**, *13* (19), 1476. doi:10.1002/1521-4095(200110)13:19<1476::AID-ADMA1476>3.0.CO;2-Y.

(36) Jee, S. H.; Kim, S. H.; Ko, J. H.; Yoon, Y. S. *J. Korean Phys. Soc.* **2006**, *49* (5), 2034.

(37) See also Koh, S. E.; McDonald, K. D.; Holt, D. H.; Dulcey, C. S.; Chaney, J. A.; Pehrsson, P. E. *Langmuir* **2006**, *22* (14), 6249. doi:10.1021/la052379e.

(38) Strother, T.; Cai, W.; Zhao, X.; Hamers, R. J.; Smith, L. M. *J. Am. Chem. Soc.* **2000**, *122* (6), 1205. doi:10.1021/ja9936161.

(39) Sun, Q.-Y.; de Smet, L. C. P. M.; van Lagen, B.; Wright, A.; Zuilhof, H.; Sudhölter, E. J. R. *Angew. Chem.* **2004**, *116* (11), 1376. doi:10.1002/ange.200352137.

(40) Cossement, D.; Plumier, F.; Delhalle, J.; Hevesi, L.; Mekhalif, Z. *Synth. Met.* **2003**, *138* (3), 529. doi:10.1016/S0379-6779(02)01260-2.

(41) Michaelson, H. B. *J. Appl. Phys.* **1977**, *48* (11), 4729. doi:10.1063/1.323539.

(42) Wen, S.-W.; Lee, M.-T.; Chen, C. H. *J. Disp. Technol.* **2005**, *1* (1), 90. doi:10.1109/JDT.2005.852802.

Can. J. Chem. Downloaded from www.nrcresearchpress.com by South China Agricultural University on 09/19/12
For personal use only.

(43) Appleyard, S. F. J.; Willis, M. R. *Opt. Mater.* **1998**, *9* (1–4), 120. doi:10.1016/S0925-3467(97)00110-9.
(44) Ciampi, S.; Eggers, P. K.; Le Saux, G.; James, M.; Harper, J. B.; Gooding, J. J. *Langmuir* **2009**, *25* (4), 2530. doi:10.1021/la803710d.

Can. J. Chem. Downloaded from www.nrcresearchpress.com by South China Agricultural University on 09/19/12
For personal use only.

Theoretical study of inclusion complexes of dopamine with β-cyclodextrin based on PM6, ONIOM, and natural bonding orbital analysis

Rayenne Djemil and Djameleddine Khatmi

Can. J. Chem. Downloaded from www.nrcresearchpress.com by South China Agricultural University on 09/19/12
For personal use only.

Abstract: The inclusion process involving β-cyclodextrin (β-CD) with dopamine (DA) was investigated by using PM6, HF, and ONIOM methods. The most stable structure was obtained at the optimum position and angle. The complex orientation in which the catechol ring of dopamine penetrates into the β-CD cavity near primary hydroxyls is preferred in energy. The structures show the presence of several intermolecular hydrogen bond interactions that were studied on the basis of natural bonding orbital analysis, employed to quantify the donor–acceptor interactions between dopamine and β-CD. A study of these complexes in solution was carried out using the CPCM model to examine the influence of solvation on the stability of the dopamine β-CD complex.

Key words: dopamine, β-cyclodextrin, inclusion complexes, quantum mechanics.

Résumé : Faisant appel à des calculs théoriques suivant la méthode paramétrisée-6 (MP-6), celle de Hartree–Fock (HF) ou la méthode personnalisée « ONIOM », on a étudié le processus d'inclusion impliquant la β-cyclodextrine (CD) et la dopamine (DA). La structure la plus stable a été obtenue à la position et l'angle optimal. L'orientation du complexe dans laquelle le noyau catéchol de la dopamine pénètre dans la cavité de la β-CD près des hydroxyles primaires correspond à un minimum d'énergie. Les structures montrent la présence de plusieurs interactions de liaisons hydrogènes intermoléculaires qui ont été étudiées sur la base d'une analyse d'orbitales de liaison naturelle (OLN) pour quantifier les interactions donneur-accepteur entre la dopamine et la β-CD. Dans le but d'examiner l'influence de la solvatation sur la stabilité du complexe dopamine-β-CD, on a effectué une étude de ces complexes en solution en faisant appel au modèle du milieu continu conducteur polarisé (MCCP).

Mots-clés : dopamine, β-cyclodextrine, complexes d'inclusion, mécanique quantique.

[Traduit par la Rédaction]

Introduction

Dopamine (3,4-dihydroxyphenethylamine, DA) is an important neurotransmitter molecule of catecholamines. It plays a very important role in the functioning of central nervous, renal, hormonal, and cardiovascular systems. Its deficiency will lead to brain disorders such as Parkinson's disease and schizophrenia.[1]

Quantitative determination of DA is therefore important and has attracted much interest from neuroscientists and chemists. Dopamine can be detected by electrochemical methods, which constitute a great advantage because of their simplicity, speed, and sensitivity.[2] However, in assay of DA, these methods suffer from less selectivity owing to the presence of other species that have higher concentrations than DA in physiological fluids and for which their oxidation potential is always close to that of DA, 0.2–0.4 V. Therefore, it is important to separate the peak potential oxidation of DA from the peaks of other species present in medium. Many electrochemical approaches have been developed using pretreated electrodes, polymer-modified electrodes, and monolayer-modified electrodes to solve these problems.[3,4]

Among these methods, the electrode modifiers belonging to the cyclodextrin (CD) family[5,6] are very interesting. Naturally occurring cyclodextrins have been widely studied because of their ability to form inclusion complexes with a large variety of organic molecules. The α-, β-, and γ-cyclodextrin rings contain six, seven, and eight glucose units, respectively, and exhibit a hydrophobic conical internal cavity and a hydrophilic exterior due to the presence of hydroxyl groups. They are α-1, 4-linked cyclic oligomers of D-glucopyranose. Their well-known ability to form supramolecular complexes with suitable organic and inorganic, neutral, and ionic substances has resulted in the design of selective electrodes.[7]

CD-modified electrodes, used to determine DA, displayed excellent selectivity and sensitivity, which could separate DA and the oxidation peak potentials of other species and could detect DA at low concentration.[4–6] Therefore, it is important to clarify the structures of the inclusion complexes from a

Received 19 April 2011. Accepted 12 August 2011. Published at www.nrcresearchpress.com/cjc on 22 November 2011.

R. Djemil and D. Khatmi. Department of Chemistry, Faculty of Mathematics, Informatics and Material Sciences BP, 401 Guelma's University, Algeria.

Corresponding author: Djameleddine Khatmi (messdjem@gmail.com).

This article is part of a Special Issue to commemorate the International Year of Chemistry.

Structure 1. Molecular structures of (*a*) β-cyclodextrin and (*b*) dopamine.

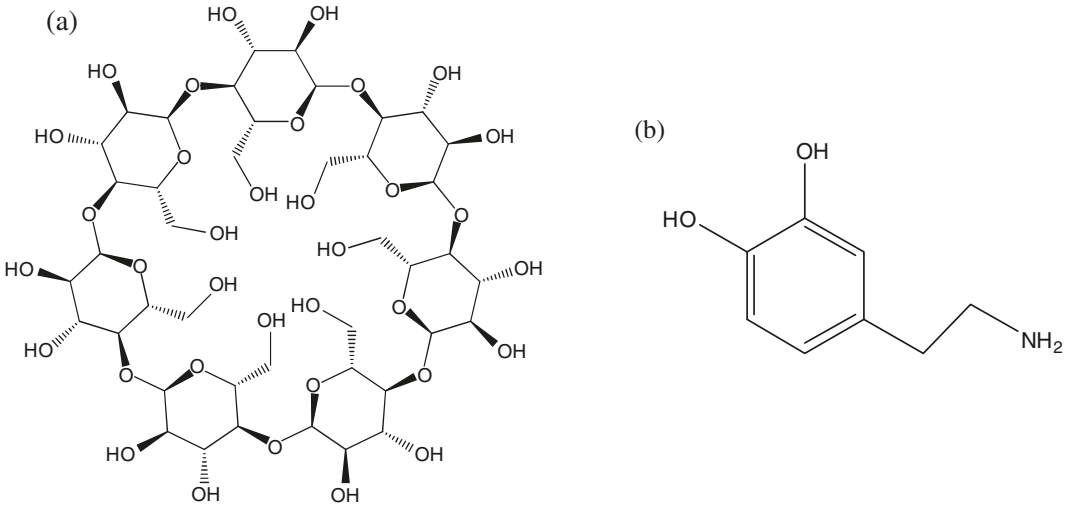

Fig. 1. The two approaches of DA from the wide secondary cyclodextrin cavity: (*a*) head orientation and *b*) tail orientation.

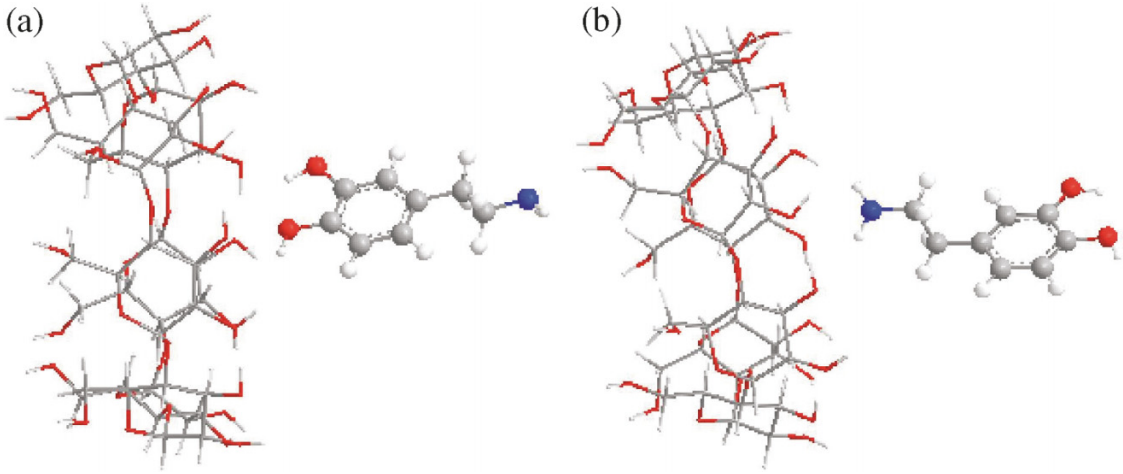

Fig. 2. Binding energies of DA–β-CD inclusion complexes at different positions of *Z* (Å) for both head and tail orientations using the PM6 method.

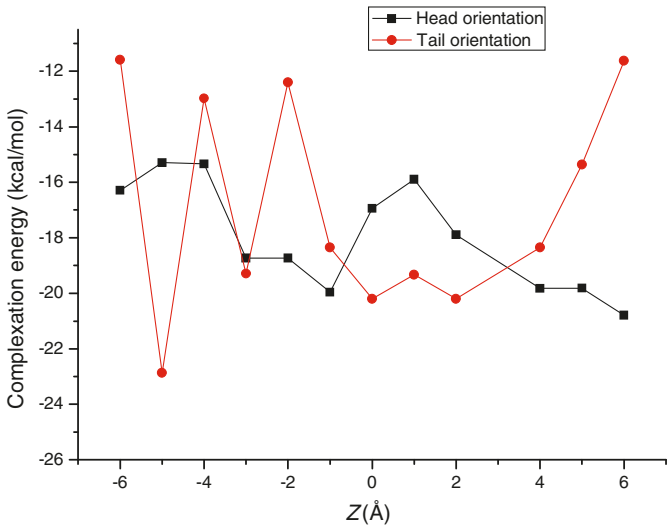

viewpoint of molecular recognition within the hydrophobic cavities of CDs. The main driving forces for the complex formation have been attributed to hydrophobic interactions, van der Waals interactions, hydrogen bonding, and release of ring strain in the CD cavity.[8]

Computer modeling studies of CD complexes are an important method to understand the mechanism of complex formation, to interpret experimental data, and to elucidate structures. Thus, in spite of its experimental detection, the geometry of the β-CD–DA complex was not elucidated due to technical difficulties related to its low solubility, not making it possible to carry out observations in NMR.[9]

In this article we propose a theoretical approach to describe the geometry of the DA–β-CD complex and to evaluate the principal intermolecular interactions between DA and β-CD.

In this paper, we first describe the formation of the host–guest complexes between β-CD and dopamine, using Parametric Model 6 (PM6)[10] semi-empirical method implemented in the MOPAC 2009 program[11] to localize the minimum energy structures, which are used as starting structures for subsequent optimizations. After that, the structures are subjected to higher level calculations, such Hartree–Fock with 3–21G*

Can. J. Chem. Downloaded from www.nrcresearchpress.com by South China Agricultural University on 09/19/12
For personal use only.

Can. J. Chem. Downloaded from www.nrcresearchpress.com by South China Agricultural University on 09/19/12
For personal use only.

Table 1. The HF/3–21G* and the ONIOM (B3LYP/6–31G(d):HF/3–21G*) complexation energies of the inclusion complexes β-CD–DA.

Orientation	$E_{complex}$ (au)	E_{CD} (au)	E_{DA} (au)	$E_{complex}$ (kcal/mol)	ΔE (kcal/mol)
PM6					
Head	–2.6418	–2.4990	–0.1096	–20.79	0.59[a]
Tail	–2.6427	–2.4990	–0.1096	–21.38	
HF/3–21G*					
Head	–4738.563	–4227.8443	–510.6553	–39.49	–11.01[a]
Tail	–4738.545	–4227.8443	–510.6553	–28.48	–10.16[b]
ONIOM					
Head	–4744.5587	–4227.8443	–516.6527	–38.71	–9.03[a]
Tail	–4744.5443	–4227.8443	–516.6527	–29.68	–8.16[b]

[a]Difference of complexation energy between the two orientations $\Delta E = E_{head} - E_{tail.}$

[b]ΔE with zero-point energy correction, using a scale factor of 0.9613 for B3LYP/6–31G(d) and 0.91671 for HF/3–21G*.

level and ONIOM (our own N-layered integrated molecular orbital mechanics) method to approach the ideal geometry and provide further insight of the complexation process of DA with β-CD. Within the ONIOM procedure, two levels are defined: (*i*) density functional theory with B3LYP functional where the 6–31G* basis set was performed on the guest molecule and (*ii*) Hartree–Fock method with 3–21G* basis set was used for the β-CD. The natural bonding orbital (NBO) population analysis procedure is employed to quantify the donor-acceptor interactions between host and guest.

Computational method

All the calculations were performed using GAUSSIAN 03 and MOPAC 2009 software packages.[12] The starting structures of β-CD and DA were constructed with the help of the Cambridge ChemBio 3D Ultra (version 11.0, Cambridge software). Dopamine was optimized with B3LYP method at the 6–31G* level, and the β-CD was used without optimization.

The method used by Liu and Guo was employed.[13] The glycosidic oxygen atoms of the β-CD were placed onto the *XY*-plane, and their center was defined as the center of the coordinate system. Then the guest was placed along the *Z*-axis of the coordinate system. The guest molecule is allowed to enter and then pass through the β-CD molecule by steps, with the ring to chain bond coincident with the *Z*-axis. The relative positions between the host and the guest was measured by the *Z*-coordinate of the common carbon atom between the cyclic part (catechol ring) and the DA chain.

For the complexation process, the β-CD molecule stays at a fixed position, while the dopamine structure approaches along the *Z*-axis toward the wide edge of the β-CD torus.[14]

To find an even more stable structure of the complex, we rotate the DA molecule to find the optimal angle at each step by scanning θ, circling around the *Z*-axis at 20° intervals from 0° to 360° and scanning the *Z*-coordinate at 1 Å intervals, where θ is the angle circling around the *Z*-axis of the system, and the bond of DA is coincident with the *Z*-axis.

Several energy expressions were used to characterize the inclusion complexes. In addition to the absolute energy of the complex (the HF value as reported by Gaussian), the binding energy ($\Delta E_{binding}$) is defined as the difference between the energy of the complex and the energy of the individual components in their optimized geometry ($E_{opt,DA}$ or $E_{opt,\ CD}$) from the complex,

$$[1] \qquad E_{binding} = E_{complex} - (E_{opt,\ \beta-CD} + E_{opt,DA})$$

The stabilization (complexation) energy upon complexation between DA and β-CD was calculated for the minimum energy structure as follows:

$$[2] \qquad E_{complexation} = E_{complex} - (E_{\beta-CD} + E_{DA})$$

where: $E_{complex}$, $E_{\beta\text{-}CD}$, and E_{DA} represent the energies of the complex, the free DA, and the free β-CD, respectively.

The gas phase full optimizations were carried out at PM6 and HF/3–21G*. To improve the precision of the theoretical results, ONIOM[15] calculations were used to optimize the CD molecule with HF at the 3–21G* level, while we treated the guest molecule using the functional of Lee et al. (B3LYP) with the split-valence 6–31G (d) basis set. The ONIOM energy is described as[16]:

$$[3] \qquad E^{ONIOM} = E(\text{high; model}) + E(\text{low; real}) - E(\text{low; model})$$

where *E*(high, model) is the energy of DA at the B3LYP/6–31g(d) level, *E*(low, real) is the energy of the complex at the HF/3–21G* level, and *E*(low, model) is the energy of β-CD at the HF/3–21G* level.

The interaction between dopamine and β-CD structures is quantified on the basis of an NBO population analysis. The NBO calculations were performed using NBO 3.1 program, as implemented in the Gaussian 03 package, to understand various second-order interactions between the filled orbitals of one subsystem and vacant orbitals of another subsystem, which is a measure of the intermolecular delocalization on hyperconjugation.[17]

The optimized structures for complexes were used for further calculations, including calculation of energies in the presence of solvent. To calculate the solvation effect, the framework of a continuum solvation model using a conductor, such as a screening model (COSMO), was used. This method, developed by Barone and Cossi, is an implementation of the COSMO model from Klamt et al. in the Gaussian software. The solvation calculations were carried out using B3LYP/3–21G*. In the CPCM (COSMO) model, the solvatation energy is partitioned into four components, including electrostatic interaction ΔG_{elec}, a cavity term ΔG_{cav}, dispersion ΔG_{dis}, and repulsion energy ΔG_{rep}, the last three terms

Table 2. The electron donor orbitals, electron acceptor orbitals, and corresponding $E^{(2)}$ energies, distances, and angles for the head orientation.

Donor	Acceptor	B3lyp/6–31g(d)		Mpw1pw91/6–31g(d)		ONIOM		
		Distance(Å)	Angle(°)	$E^{(2)}$ (kcal/mol)		Distance (Å)	Angle(°)	$E^{(2)}$ (kcal/mol)
Lp O47	BD*O154-H162	1.646	167.4	1.65	1.70	1.646	167.4	1.51
Lp O69	BD*N158-H169	2.162	166.7	3.33	3.41	2.162	166.7	2.75
Lp O155	BD*O47-H129	1.907	135.4	0.44	0.53	1.907	135.4	0.47
Lp O54	BD*C150-H160	2.570	144.9	0.70	0.69	2.570	144.9	1.05
Lp O59	BD*C157-H167	2.766	132.9	0.44	0.43	2.766	132.9	0.47
Lp O154	BD*C41-H124	2.326	167	1.42	1.43	2.326	167	1.97

Table 3. The electron donor orbitals, electron acceptor orbitals, and corresponding $E^{(2)}$ energies, distances, and angles for the tail orientation.

Donor	Acceptor	B3lyp/6–31g(d)		Mmpw1pw91/6–31g(d)		ONIOM		
		Distance (Å)	Angle(°)	$E^{(2)}$ (kcal/mol)		Distance (Å)	Angle (°)	$E^{(2)}$ (kcal/mol)
Lp O75	O155-H163	1.699	169.7	5.43	5.53	1.704	168.6	1.35
Lp O154	C23-H103	2.540	173.2	1.46	1.45	2.524	173.5	2.02
Lp O155	C35-H117	2.360	147.1	1.34	1.34	2.315	148.4	2.13

being related to the non-electrostatic interactions between solute and solvent.[18]

Results and discussion

The inclusion complex DA–β-CD has two orientations (Fig. 1), which will be denoted head and tail orientations, respectively: aromatic ring oriented to the center of mass of β-CD, namely the head orientation and aliphatic ring oriented to the center of mass of β-CD, namely the tail orientation.

The inclusion complex β-CD–DA was determined using the PM6 method to obtain the minimum energy structures. Considering the negative values of all complexation energies, we can say that the complexation process is energetically favorable. The most stable structure of DA–β-CD is reached at $Z = 6$ Å for the head orientation, and at this point the binding energy is –20.79 kcal/ mol (1 cal = 4.184 J). For the tail orientation, the optimum position was found at –5 Å, with binding energy –21.38 kcal/ mol (Fig. 2).

The energies of DA, β-CD, and the complexation energies of their inclusion complexes obtained with PM6, HF/3–21G*, and B3LYP/6–31G(d) methods are shown in Table 1. The most stable structure can be obtained by comparing energies of the two orientations of the complexes, as shown in Table 1. Thus, the complexation energies from HF/3–21G* for the head and tail orientations are –39.49 and –28.48 kcal/mol, respectively. These values show that the inclusion complex head orientation is more stable than the tail orientation. ONIOM (B3LYP/6–31G(d):HF/3–21G*) results follow the same trend as the HF data. The complexation energies from the ONIOM calculations for head and tail orientations are –38.71 and –29.68 kcal/mol, respectively. The complexation energy differences for the two complexes from HF/3–21G* and ONIOM (B3LYP/6–31 G(d):HF/3–21G*) are –11 and –9.04 kcal/mol, respectively.

The results in Table 1 indicate that for HF/3–21G(d), the zero-point energy gives energy deviation of 1.1 kcal/mol from that without corrections; for ONIOM, the zero-point energy gives an absolute deviation of 0.87 kcal/mol.

NBO analysis

To obtain additional insight into the nature of interaction between DA and β-CD, we undertook a population analysis using the NBO method. The advantages of this approach are that it concentrates almost all the molecular energy and molecular change within structures that mimic the traditional Lewis molecular model of strictly localized bonds. The very small residual energetic and charge contributions in saturated systems are largely due to the delocalization of noncovalent interactions between bonding and anti-bonding orbitals of the NBO approach. This noncovalent bonding–anti-bonding interaction gives a quantitative description of hyperconjugation. In terms of the NBO approach, this is expressed by means of a second-order perturbation interaction energy $E^{(2)}$ involving neighboring orbitals. The selected electron donor orbitals, electron acceptor orbitals, and their corresponding second-order interaction energies $E^{(2)}$ indicate the intensity of the interaction between the electron donor and electron acceptor orbitals. Thus, the greater value of $E^{(2)}$, the more tendency of a higher donor orbital.[19]

The electron donor orbitals, electron acceptor orbitals, and their corresponding $E^{(2)}$ energies, bond distances, and angles between the hydrogen bonding are also shown in Tables 2 and Table 3.

The structures of the energy minimum obtained with ONIOM calculations show the presence of several intermolecular hydrogen bond interactions, as shown in Fig. 3. In the present study the hydrogen bond analysis is carried out using an NBO approach. In the head orientation, the catechol ring of DA is included deeply in the β-CD cavity from the wide secondary hydroxyl group, so that the hydroxyl groups of DA are close to 6-OH of β-CD. This disposition allows the formation of two hydrogen bonds between the hydroxyls catechol and one hydroxyl (O47–H129) of the narrow edge

Can. J. Chem. Downloaded from www.nrcresearchpress.com by South China Agricultural University on 09/19/12
For personal use only.

Fig. 3. Geometrical structures optimized at ONIOM for DA–β-CD complexes: (*a*) tail orientation and (*b*) head orientation.

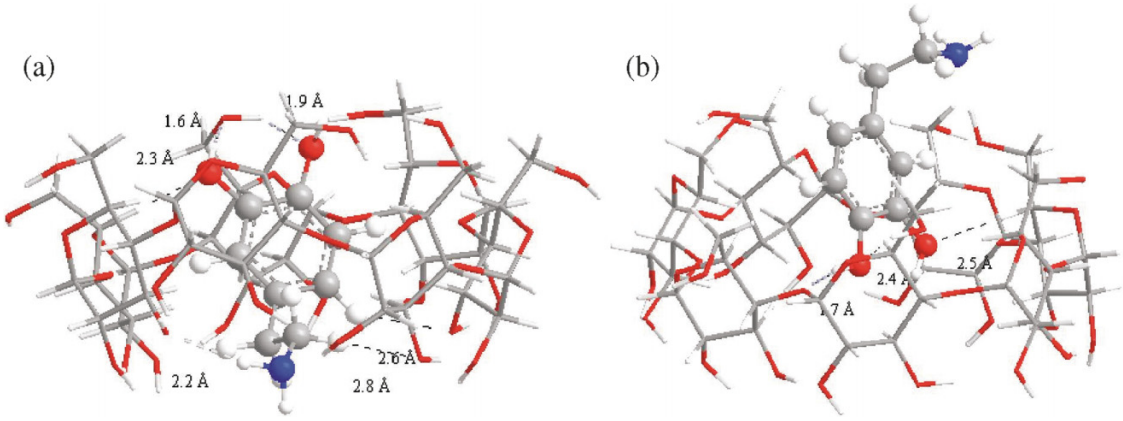

of the β-CD: the first as proton acceptor (O47···H162–O154) located at 1.646 Å with an angle equal to 167.4° and the second as proton donor (O47–H129···O155) positioned at 1.907 Å with an angle of 135.4°. The interaction energy for the second hydrogen bond (0.44 kcal/mol) was lower than the first (1.65 kcal/mol).

At the wide secondary face, one hydrogen bond is established between an oxygen atom (O69) of β-CD and a hydrogen atom (H169) of the H169–N158 bond, and that allows the chain group to remain inside the cavity; the O···H distance is about 2.16 Å, with an angle of 166.7 ° and interaction energy equal to 3.33 kcal/mol.

At the same time, several C–H···O hydrogen bonds were established between DA and β-CD. DA plays the role of donor from the carbon atoms (C157) and (C150) to the oxygen atoms (O59) and (O54) of the wide face of β-CD (C157–H167···O59 and C150–H160···O54). The DA molecule accepts a C–H···O weak hydrogen bond from hydrogen atom (H124) of the C41–H124 bond of the wide hydrophilic face (C41–H124···O154). The interaction energies of these C–H···O hydrogen bond are 0.44, 0.70, and 1.42 kcal/mol, respectively. These values are typical of weak hydrogen bonds according to the values of conventional hydrogen bonding (the C–H···O bond energies were around 0.5–2 kcal/ mol).

While in the tail orientation, we can see the guest molecule is partially incorporated in the cavity, and the chain is left out from the narrow primary face. In this structure, one strong O···H–O hydrogen bond (5.43 kcal/ mol) is established between the glycosidic oxygen atom (O75) and the hydrogen atom (H163) of the O155–H163 bond located at 1.669 Å with an angle equal to 169.7°. The oxygen atoms of the two hydroxyls of DA (O155) and (O154) accept C–H···O hydrogen bonds with (H5) C23 and C35 of the narrow face of the β-CD positioned, respectively, at 2.54 and 2.36 Å with angles equal to 173.2° and 147.1°.

The solvation energies consisting of electrostatic and non-electrostatic terms were computed using the CPCM (COSMO) model, and indicate that the head orientation is favored over the tail by 16.24 kcal/mol. This result is in agreement with those obtained in the gas phase. This is due to the difference between the mode of penetration of the guest molecule in the β-CD cavity, the full and the partial inclusions in head and tail orientations, respectively.

Conclusion

The inclusion process of DA with β-CD was studied according two orientations using quantum mechanics PM6, HF level theory with 3–21G* basis set and ONIOM (B3LYP/6–31G(d): HF/3–21G*) hybrid calculations. The minimum energy structure for each orientation was localized with the PM6 method. The affinity of these minimum energies structures was carried out with HF and ONIOM methods. The HF and ONIOM results show that the head orientation is preferred, according to complexation energy. In this configuration, the catechol ring is deeply included into the hydrophobic cavity of β-CD. However, the ONIOM method allowed better understanding the type of DA–β-CD interactions. The NBO population analysis used to quantify these interactions shows that the driving forces of DA–β-CD complexes was due to the intermolecular hydrogen bonds in addition to the hydrophobic interactions. The study in solution by using CPCM model follows the same trend as that in gas phase, thus favoring the head orientation.

Acknowledgements

This paper was supported by Algerian Ministry of Higher Education and Scientific Research and General Direction of Scientific and technologic research as a part of projects CNEPRU (No: E01520080026) and PNR (8/u24/4814). We acknowledge the department of chemistry at Guelma's university in which this work was performed.

References

(1) Liu, A.; Honma, I.; Zhou, H. S. *Biosens. Bioelectron.* **2007**, *23* (1), 74. doi:10.1016/j.bios.2007.03.019.
(2) Shervedani, R. K.; Bagherzadeh, M.; Mozaffari, S. A. *Sens. Actuators B Chem.* **2006**, *115* (2), 614. doi:10.1016/j.snb.2005.10.027.
(3) Li, J.; Lin, X. *Sens. Actuators B Chem.* **2007**, *124* (2), 486. doi:10.1016/j.snb.2007.01.021.
(4) Gao, Z.; Huang, H. *Chem. Commun. (Cambridge)*, **1998**, (19): 2107. doi:10.1039/a805915b.
(5) Izaoumen, N.; Bouchta, D.; Zejli, H.; El Kaoutit, M.; Temsamani, K. R. *Anal. Lett.* **2005**, *38* (12), 1869. doi:10.1080/00032710500230855.
(6) Fragoso, A.; Almirall, E.; Cao, R.; Echegoyen, L.; González-Jonte, R. *Chem. Commun. (Cambridge)*, **2004**, (19), 2230. doi:10.1039/b407792j.

Can. J. Chem. Downloaded from www.nrcresearchpress.com by South China Agricultural University on 09/19/12
For personal use only.

(7) Szejtli, J. *Carbohydr. Polym.* **1990**, *12* (4), 375. doi:10.1016/0144-8617(90)90088-A.
(8) Tanji, Y.; Wanzhi, W.; Jinxiang, Z. *Anal. Bioanal. Chem.* **2006**, *386* (7–8), 2087.
(9) Zhou, Y.; Liu, C.; Yu, H.; Xu, H.; Lu, Q.; Wang, L. *Spectrosc. Lett.* **2006**, *39* (5), 409. doi:10.1080/00387010600806170.
(10) Stewart, J. J. P. *J. Mol. Model.* **2007**, *13* (12), 1173. doi:10.1007/s00894-007-0233-4.
(11) Stewart, J. J. P. *J. MOPAC 2007*; Stewart Computational Chemistry, Colorado Springs, CO, USA, 2007.
(12) Frisch, M. J.; Trucks, G. W.; Schlegel, H. B.; Scuseria, G. E.; Robb, M. A.; Cheeseman, J. R.; Montgomery, J. A.; Vreven, T., Jr.; Kudin, K. N.; Burant, J. C.; Millam, J. M.; Iyengar, S. S.; Tomasi, J.; Barone, V.; Mennucci, B.; Cossi, M.; Scalmani, G.; Rega, N.; Petersson, G. A.; Nakatsuji, H.; Hada, M.; Ehara, M.; Toyota, K.; Fukuda, R.; Hasegawa, J.; Ishida, M.; Nakajima, T.; Honda, Y.; Kitao, O.; Nakai, H.; Klene, M.; Li, X.; Knox, J. E.; Hratchian, H. P.; Cross, J. B.; Adamo, C.; Jaramillo, J.; Gomperts, R.; Stratmann, R. E.; Yazyev, O.; Austin, A. J.; Cammi, R.; Pomelli, C.; Ochterski, J. W.; Ayala, P. Y.; Morokuma, K.; Voth, G. A.; Salvador, P.; Dannenberg, J. J.; Zakrzewski, V. G.; Dapprich, S.; Daniels, A. D.; Strain, M. C.; Farkas, O.; Malick, D. K.; Rabuck, A. D.; Raghavachari, K.; Foresman, J. B.; Ortiz, J. V.; Cui, Q.; Baboul, A. G.; Clifford, S.; Cioslowski, J.; Stefanov, B. B.; Liu, G.; Liashenko, A.; Piskorz, P.; Komaromi, I.; Martin, D. J.; Fox, T.; Keith, M. A.; Al-Laham, C. Y.; Peng, A.; Nanayakkara, M.; Challacombe, R. L.; Gill, P. M. W.; Johnson, B.; Chen, W.; Wong, M. W.; Gonzalez, C.; Pople, J. A. *Gaussian 03, Revision E01*; Gaussian, Inc., Pittsburgh, PA, 2003.
(13) Liu, L.; Guo, Q. X. *J. Incl. Phenom. Macro.* **2004**, *50*, 95.
(14) Yan, C. L.; Li, X. H.; Xiu, Z. L.; Hao, C. *J. Mol. Struct. THEOCHEM*, **2006**, *764* (1–3), 95. doi:10.1016/j.theochem.2006.02.008.
(15) Attoui Yahia, O.; Khatmi, D. E. *J. Mol. Struct. THEOCHEM*, **2009**, *912* (1–3), 38. doi:10.1016/j.theochem.2009.06.007.
(16) Tschumper, G. S.; Morokuma, K. *J. Mol. Struct. THEOCHEM*, **2002**, *592* (1–3), 137. doi:10.1016/S0166-1280(02)00234-8.
(17) Kavitha, E.; Sundaraganesan, N.; Sebastian, S.; Kurt, M. *Spectrochim. Acta A Mol. Biomol. Spectrosc.* **2010**, *77* (3), 612. doi:10.1016/j.saa.2010.06.034.
(18) Barone, V.; Cossi, M. *J. Phys. Chem. A*, **1998**, *102* (11), 1995. doi:10.1021/jp9716997.
(19) Chermahini, A. N.; Dabbagh, H. A.; Teimouri, A. *J. Mol. Struct. THEOCHEM*, **2008**, *857* (1–3), 105. doi:10.1016/j.theochem.2008.02.012.

Can. J. Chem. Downloaded from www.nrcresearchpress.com by South China Agricultural University on 09/19/12
For personal use only.

Density functional theory calculations for the interaction of Li^+ cations and PF_6^- anions with nonaqueous electrolytes

Mahesh Datt Bhatt, Maenghyo Cho, and Kyeongjae Cho

Can. J. Chem. Downloaded from www.nrcresearchpress.com by South China Agricultural University on 09/19/12
For personal use only.

Abstract: The interaction of lithium (Li^+) cation and hexafluorophosphate (PF_6^-) anion with nonaqueous electrolytes is studied by using density functional theory at the B3LYP/6–311++G(d,p) level in the gas phase in terms of the coordination of Li^+ and PF_6^- with these solvents. Ethylene carbonate (EC) coordinates with Li^+ and PF_6^- most strongly and reaches the anode and cathode most easily because of its highest dielectric constant among all the solvent molecules, resulting in its preferential reduction on the anode and oxidation on the cathode. For cyclic carbonates EC and propylene carbonate (PC), the structure $Li^+(S)_4$ is found to be the most stable. However, for linear carbonates dimethyl carbonate (DMC), diethyl carbonate (DEC), and ethyl methyl carbonate (EMC), the formation of $PF_6^-(S)_{n=1–3}$ is not favorable. Such analysis may be useful in applications for lithium ion batteries.

Key words: density functional theory, solvents, stability, exothermic, oxidation, heat of formation.

Résumé : Faisant appel à la théorie de la fonctionnelle de la densité au niveau B3LYP/6–311++G(d,p), on a étudié d'un point de vue théorique l'interaction du cation lithium (Li^+) et de l'anion hexafluorophosphate (PF_6^-) avec des électrolytes non aqueux, en phase gazeuse, en termes de la coordination du (Li^+) et du (PF_6^-) avec ces solvants. Le carbonate d'éthylène (CE) est celui qui donne la coordination la plus forte avec le (Li^+) et le (PF_6^-) et il atteint l'anode et la cathode le plus facilement en raison de sa constante diélectrique qui est la plus élevée de toutes les molécules de solvant; il en résulte que sa réduction à l'anode et son oxydation à la cathode sont les réactions privilégiées. Pour les carbonates cycliques, tel le CE et le carbonate de phénylène (CP), on a trouvé que la structure $Li^+(S)_4$ est la plus stable. Toutefois, pour les carbonates linéaires, tel le carbonate de diméthyle (CDM), le carbonate de diéthyle (CDE) et le carbonate d'éthyle et de méthyle (CEM), la formation de la structure $Li^+(S)_{n=1–3}$ n'est pas favorisée. Une telle analyse peut être utile dans les applications de batteries au lithium.

Mots-clés : théorie de la fonctionnelle de la densité, solvants, stabilité, exothermique, oxydation, chaleur de formation.

[Traduit par la Rédaction]

Introduction

The lithium ion battery has found wider and wider applications in electronic devices, tools, and vehicles because it provides a good combination of high-energy density and reversibility.[1] Electrolytes are of special interest because of their applications in high-energy density battery systems. The electrolytes are comprised of a lithium salt ($LiClO_4$, $LiPF_6$, $LiBF_4$, $LiAsF_6$, etc.) dissolved in an aprotic solvent with high dielectric permittivity. Progress has been made in enhancing the conductivity of solid electrolytes; however, liquid electrolytes are still the most commonly used in electrochemical systems. The common electrolytes used in electrochemical systems are ethylene carbonate (EC), propylene carbonate (PC), dimethyl carbonate (DMC), diethyl carbonate (DEC), and ethyl methyl carbonate (EMC), etc., because of their high ionic conductivity and low melting and high boiling points that can provide a suitable temperature range for the liquid state, low viscosity, as well as chemical and electrochemical stability. It is well known that some organic electrolytes decompose during the first lithium intercalation into graphite to form a solid electrolyte interphase (SEI) film on the graphite anode surface, and SEI film largely determines the performance of the graphite anode in rechargeable batteries.[2] Unlike PC, which can be cointercalated into the graphite anode with Li^+, EC is not intercalated but helps to build the SEI layer that can inhibit the decomposition of solvent molecules on the anode.[3,4] Because of the high melting point of EC (37 °C), it has resulted in products that build up a stable SEI.[5] Therefore, the mixture of linear carbonates, for

Received 15 June 2011. Accepted 18 August 2011. Published at www.nrcresearchpress.com/cjc on 21 November 2011.

M.D. Bhatt and M. Cho. WCU Multiscale Engineering Division, School of Mechanical and Aerospace Engineering, Seoul National University, Seoul 151-742, Korea.
K. Cho. WCU Multiscale Engineering Division, School of Mechanical and Aerospace Engineering, Seoul National University, Seoul 151-742, Korea; Department of Materials Science and Engineering and Department of Physics, University of Texas at Dallas, Richardson, TX 75080, USA.

Corresponding author: Mahesh Datt Bhatt (e-mail: mbhatt54@yahoo.com).

This article is part of a Special Issue to commemorate the International Year of Chemistry.

Can. J. Chem. Downloaded from www.nrcresearchpress.com by South China Agricultural University on 09/19/12
For personal use only.

Fig. 1. Optimized structure of an isolated molecule (*a*) ethylene carbonate (EC), (*b*) propylene carbonate (PC), (*c*) dimethyl carbonate (DMC), (*d*) diethyl carbonate (DEC), and (*e*) ethyl methyl carbonate (EMC).

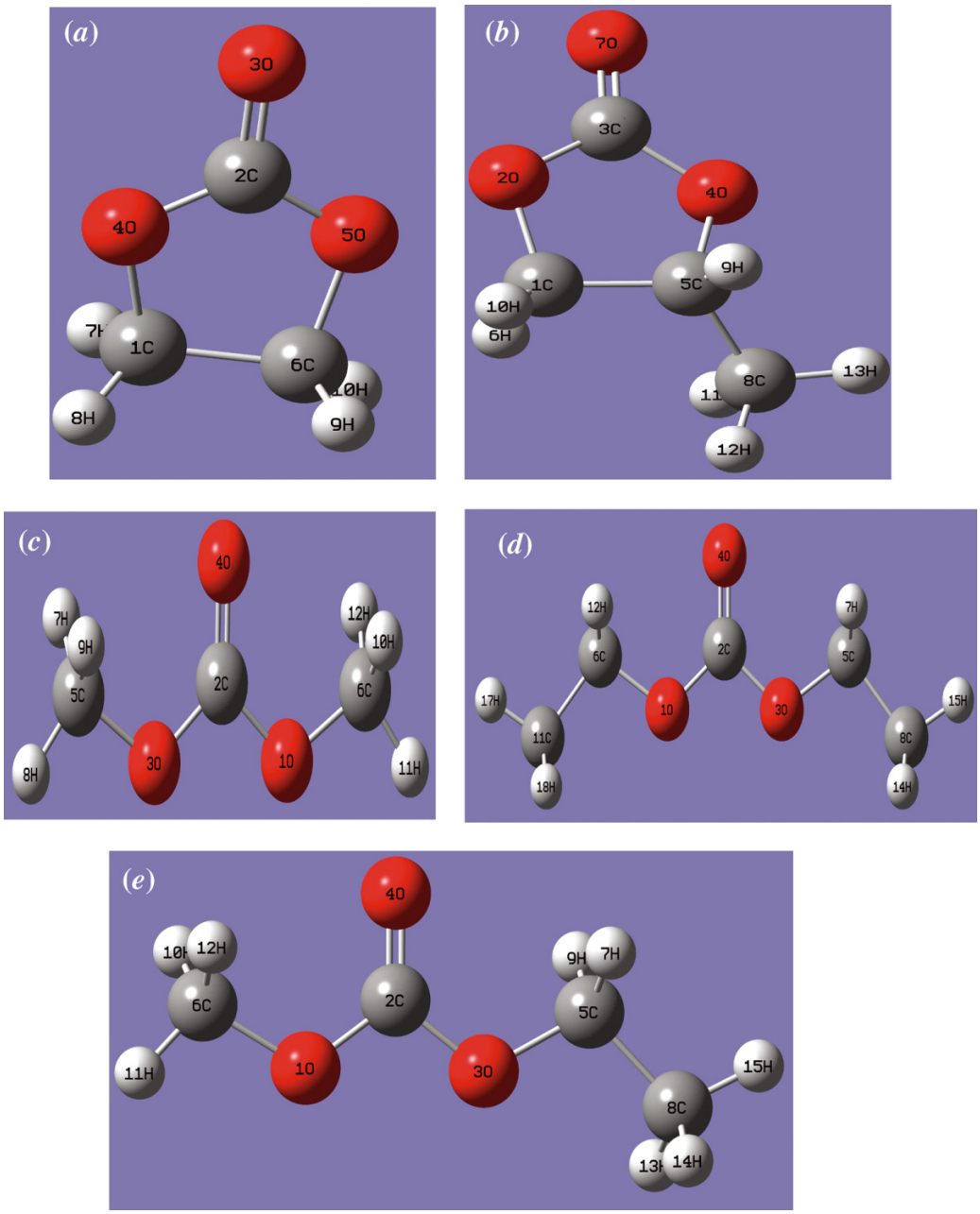

example DMC with a high-content of EC, are widely used in lithium ion batteries[6,7] because of the fact that the high dielectric permittivity of linear carbonates (DMC, DEC, or EMC) combined with the low viscosity of the cyclic carbonates (EC or PC) provides the electrolyte with a high ionic conductivity.

Much experimental work has been focused on the oxidative decomposition of solvents on the cathodes of lithium ion batteries.[8–14] Recently, a detailed mechanism on the oxidative decomposition of PC was given with theoretical calculations.[15] Similarly, a wide variety of experimental techniques have been used[5,16] to determine the reduction mechanism of EC. In addition, whereas a lithium ion battery can be cycled in an electrolyte using DMC or EMC as a solvent, this does not seem to be the case when DEC is used as an electrolyte.[17] The decomposition of the behaviors of various electrolytes apparently differs in the first cycling, and the reason for the difference remains unclear. Recently, several models have been proposed to explain the differences among the solvents.[18–20] The aim of this investigation is to understand the reductive and oxidative stability of solvents for Li^+ on the anode and PF_6^- on the cathode, respectively, by investigating the interaction between the organic solvent molecules and these ions.

In this work, the interaction of the lithium (Li^+) cation and the hexafluorophosphate (PF_6^-) anion with the nonaqueous electrolytes EC, PC, DMC, DEC, and EMC is investigated using density functional theory (DFT) at the B3LYP/6–311++G(d,p)

Can. J. Chem. Downloaded from www.nrcresearchpress.com by South China Agricultural University on 09/19/12
For personal use only.

Fig. 2. Optimized structure of (*a*) [Li^+(EC)] complex, (*b*) [Li^+(PC)] complex, (*c*) [Li^+(DMC)] complex, (*d*) [Li^+(DEC)] complex, and (*e*) [Li^+(EMC)] complex. EC, ethylene carbonate; PC, propylene carbonate; DMC, dimethyl carbonate; DEC, diethyl carbonate; and EMC, ethyl methyl carbonate.

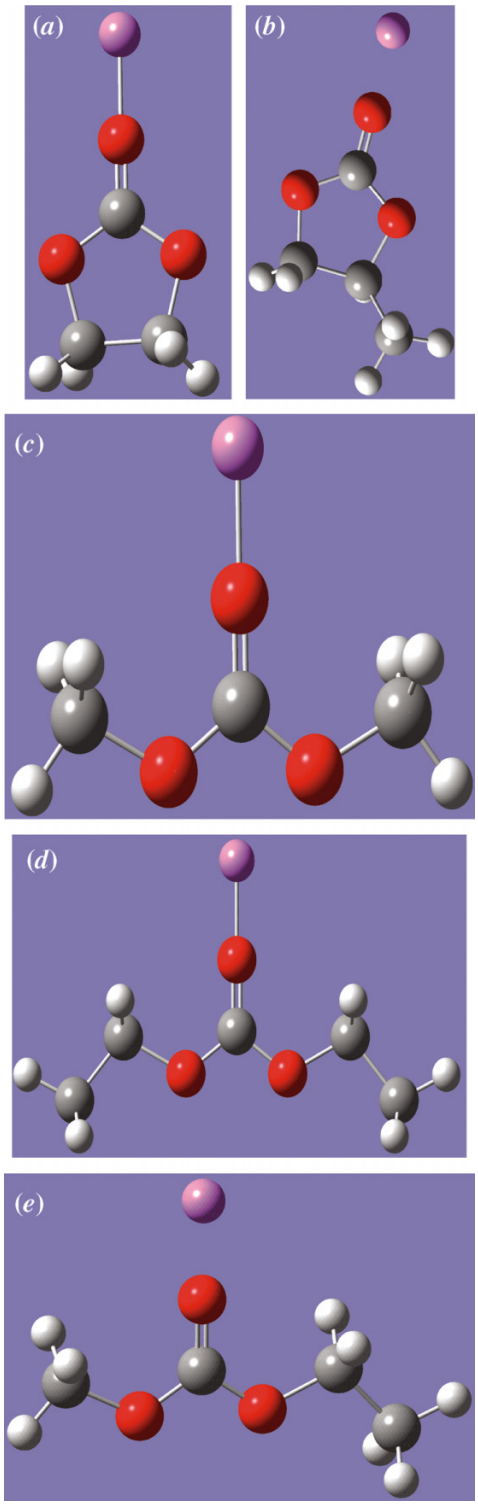

level. The optimized structure of the isolated solvent molecules with numerical labeling of the atoms is shown in Fig. 1.

Fig. 3. Optimized structure of (*a*) [PF_6^-(EC)] complex, (*b*) [PF_6^-(PC)] complex, (*c*) [PF_6^-(DMC)] complex, (*d*) [PF_6^-(DEC)] complex, and (*e*) [PF_6^-(EMC)] complex. EC, ethylene carbonate; PC, propylene carbonate; DMC, dimethyl carbonate; DEC, diethyl carbonate; and EMC, ethyl methyl carbonate.

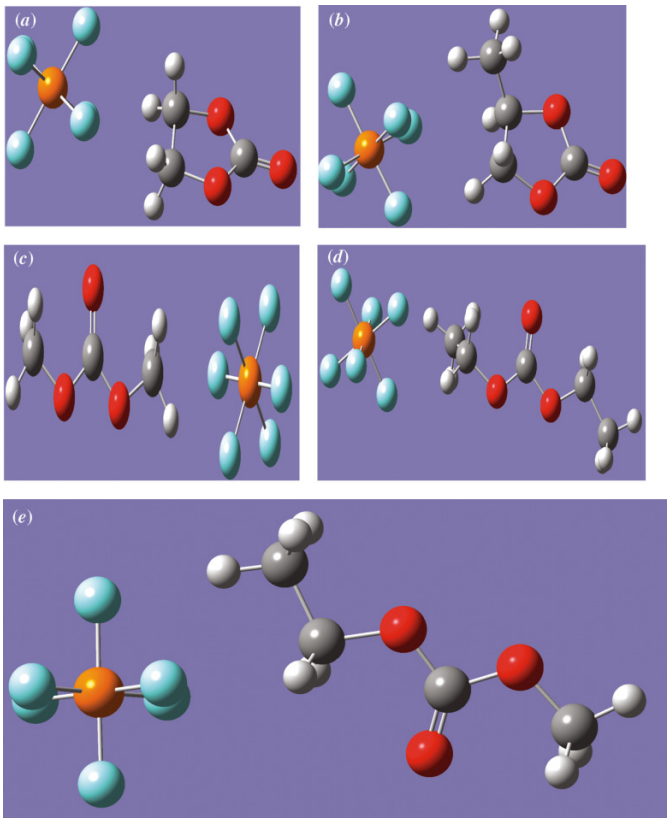

Computational details

All calculations were performed using the Gaussian 09 package[21] and PCGAMESS/Firefly package.[22] The equilibrium and transition-state structures were optimized by the B3LYP[23] method in conjunction with the 6–311++G(d,p) basis set[24] for simple solvent molecules, and one solvent molecule coordinating with Li^+ and PF_6^- and the 6–31G(d) basis set[24] for $Li^+(S)_{n=2-5}$ for S = EC or PC and $Li^+(S)_{n=2-3}$ for S = DMC, DEC, or EMC, and $PF_6^-(S)_{n=2-3}$ for S = EC, PC, DMC, DEC, or EMC. To confirm each optimized and stationary point and to make zero-point-energy (ZPE) corrections, frequency analyses were done with the same basis set. Enthalpies and Gibbs free energies were obtained at 298.15 K. The charge distribution was analyzed by the natural bond orbital (NBO) theory. The optimized structures of Li^+–S and PF_6^-–S (S = EC, PC, DMC, DEC, or EMC) complexes are shown in Figs. 2 and 3, respectively.

Results and discussion

The interaction between Li^+ and a solvent molecule was analyzed by the IR spectra, as illustrated in Fig. 4. In all cases, the asymmetric stretching frequency of C=O ($\nu_{C=O}$) is significantly decreased (1908 vs 1790 cm^{-1} for EC, 1914 vs 1772 cm^{-1} for PC, 1813 vs 1689 cm^{-1} for DMC, 1806 vs 1665 cm^{-1} for DEC, and 1801 vs 1677 cm^{-1} for EMC), indicating that C=O is weakened by the interaction of Li^+–O=C,

Can. J. Chem. Downloaded from www.nrcresearchpress.com by South China Agricultural University on 09/19/12
For personal use only.

Fig. 4. Simulated IR spectra of EC, Li^+–EC, PC, Li^+–PC, DMC, Li^+–DMC, DEC, Li^+–DEC, EMC, and Li^+–EMC systems on the basis of B3LYP/6–311++G(d,p) calculations. EC, ethylene carbonate; PC, propylene carbonate; DMC, dimethyl carbonate; DEC, diethyl carbonate; and EMC, ethyl methyl carbonate.

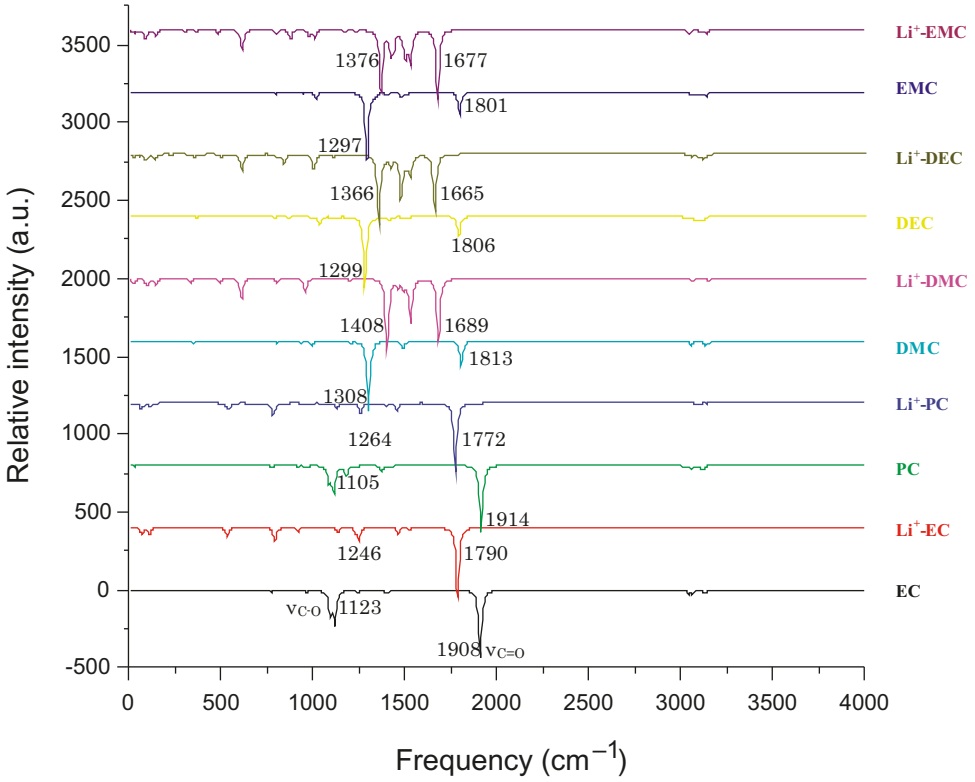

Table 1. Bond lengths R_1 and R_2 (in Å) and vibrational frequencies ν_1 and ν_2 (in cm^{-1}) of C=O before and after interaction with Li^+ calculated at the B3LYP/6–311++G(d,p) level.

Solvent	R_1	R_2	ΔR	ν_1	ν_2	$\Delta\nu$
EC	1.186	1.223	0.037	1908	1790	–118
PC	1.186	1.225	0.039	1914	1772	–142
DMC	1.205	1.243	0.038	1813	1689	–124
DEC	1.206	1.246	0.040	1806	1665	–141
EMC	1.206	1.246	0.040	1801	1677	–124

Note: EC, ethylene carbonate; PC, propylene carbonate; DMC, dimethyl carbonate; DEC, diethyl carbonate; and EMC, ethyl methyl carbonate.

whereas that of O–C (ν_{C-O}, O: linked with CH_2; C: carbonyl group) is increased (1123 vs 1246 cm^{-1} for EC, 1105 vs 1264 cm^{-1} for PC, 1308 vs 1408 cm^{-1} for DMC, 1299 vs 1366 cm^{-1} for DEC, and 1297 vs 1376 cm^{-1} for EMC). Such variations are in line with the corresponding bond changes, i.e., C=O is stretched (1.186 vs 1.223 Å for EC, 1.186 vs 1.225 Å for PC, 1.205 vs 1.243 Å for DMC, and 1.206 vs 1.246 Å for DEC and EMC), and O–C (1.362 vs 1.316 Å for EC, 1.360 vs 1.317 Å for PC, 1.338 vs 1.303 Å for DMC, and 1.339 vs 1.303 Å for DEC and EMC) is contracted. Table 1 shows that the C=O stretching is in the range of 0.037 to 0.040 Å. The interaction between PF_6^- and a solvent molecule can also be analyzed by the IR spectra, as illustrated in Fig. 5. The optimized C=O and C–O bond lengths and corresponding vibrational frequencies for EC, PF_6^-–EC, PC, PF_6^-–PC, DMC, PF_6^-–DMC, DEC, PF_6^-–EC, EMC, and PF_6^-–EMC systems are summarized in Table 2. The asymmetric stretching frequency of C=O ($\nu_{C=O}$) is significantly decreased (1908 vs 1791 cm^{-1} for EC and 1914 vs 1778 cm^{-1} for PC), indicating that C=O is weakened by the interaction of PF_6^-–O=C, whereas that of O–C (ν_{C-O}, O: linked with CH_2; C: carbonyl group) is increased (1123 vs 1256 cm^{-1} for EC and 1105 vs 1263 cm^{-1} for PC). Such variations are in line with the corresponding bond changes, i.e., C=O is stretched (1.186 vs 1.195 Å for EC and 1.186 vs 1.191 Å for PC), and O–C (1.352 vs 1.316 Å for EC and 1.355 vs 1.317 Å for PC) is contracted. However, for linear carbonates, the asymmetric stretching frequency of C=O ($\nu_{C=O}$) is slightly decreased (1813 vs 1812 cm^{-1} for DMC, 1806 vs 1804 cm^{-1} for DEC, and 1801 vs 1798 cm^{-1} for EMC), indicating very weak interaction for PF_6^-–O=C, whereas that of O–C (ν_{C-O}, O: linked with CH_2; C: carbonyl group) is also slightly increased (1308 vs 1309 cm^{-1} for DMC, 1299 vs 1301 cm^{-1} for DEC, and 1297 vs 1300 cm^{-1} for EMC). Such small variations are in line with the corresponding small bond changes, i.e., C=O is stretched (1.205 vs 1.206 Å for DMC and 1.206 vs 1.207 Å for DEC and EMC), and O–C (1.338 vs 1.336 Å for DMC and 1.339 vs 1.334 Å for DEC and EMC) is contracted. It does not favor the interaction of the PF_6^- ion with linear carbonates DMC, DEC, and EMC.

The interaction strength between Li^+ and a solvent can be quantified by calculating the binding energy of the formation of the Li^+(S) complexes (S = EC, PC, DMC, DEC, or EMC), which was defined as the difference between the product and reactant energy and can be calculated by

Can. J. Chem. Downloaded from www.nrcresearchpress.com by South China Agricultural University on 09/19/12
For personal use only.

Fig. 5. Simulated IR spectra of PF_6^-, EC, PF_6^-–EC, PC, PF_6^-–PC, DMC, PF_6^-–DMC, DEC, PF_6^-–DEC, EMC, and PF_6^-–EMC systems on the basis of B3LYP/6–311++G(d,p) calculations. EC, ethylene carbonate; PC, propylene carbonate; DMC, dimethyl carbonate; DEC, diethyl carbonate; and EMC, ethyl methyl carbonate.

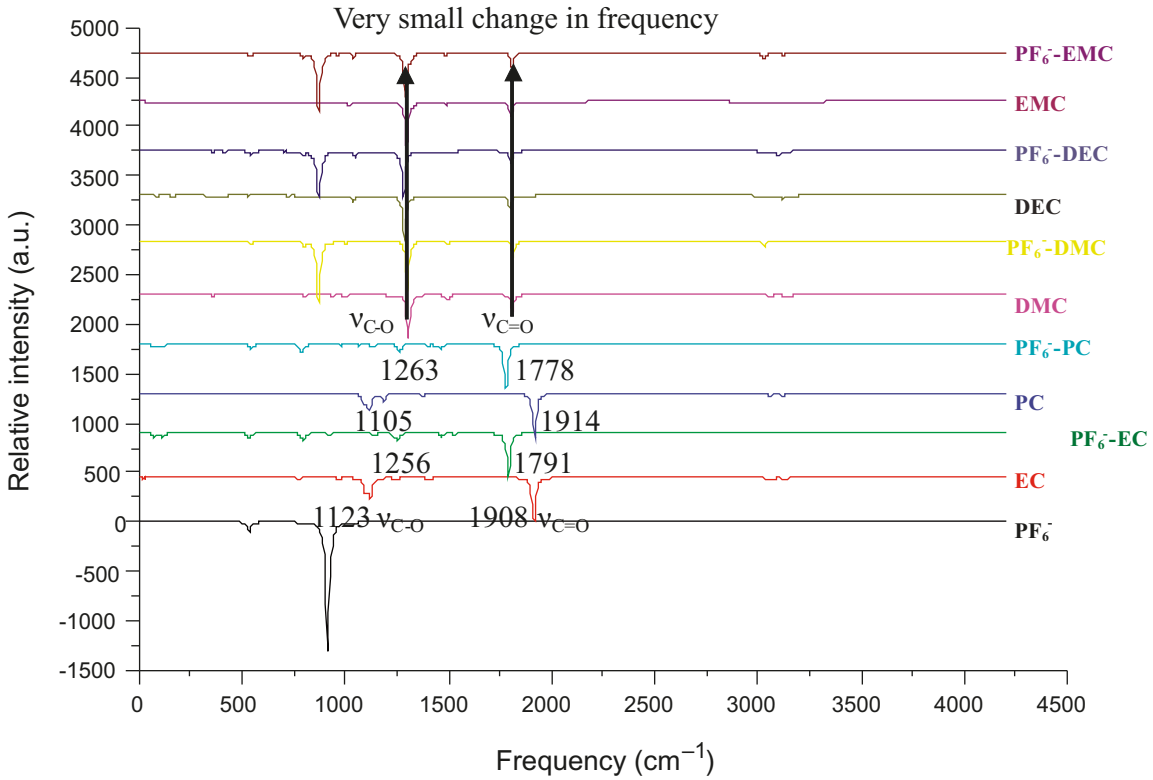

Table 2. The optimized C=O and C–O bond lengths R_1 and R_2 (in Å) and the corresponding vibrational frequencies ν_1 and ν_2 (in cm^{-1}) for EC, PF_6–EC, PC, PF_6–PC, DMC, PF_6–DMC, DEC, PF_6–DEC, EMC, and PF_6–EMC systems calculated at B3LYP/6–311++G(d,p). EC, ethylene carbonate; PC, propylene carbonate; DMC, dimethyl carbonate; DEC, diethyl carbonate; and EMC, ethyl methyl carbonate.

Solvent/complex	R_1	R_2	ν_1	ν_2
EC	1.186	1.352	1908	1123
PF_6^-–EC	1.195	1.316	1791	1256
PC	1.186	1.355	1914	1105
PF_6^-–PC	1.191	1.317	1778	1263
DMC	1.205	1.338	1813	1308
PF_6^-–DMC	1.206	1.336	1812	1309
DEC	1.206	1.339	1806	1299
PF_6^-–DEC	1.207	1.334	1804	1301
EMC	1.206	1.339	1801	1297
PF_6^-–EMC	1.207	1.334	1798	1300

$$\Delta E = E[\mathrm{Li}^+(\mathrm{S})_n] - E[\mathrm{Li}^+] - nE[\mathrm{S}]$$

where $E[\mathrm{Li}^+(\mathrm{S})_n]$, $E[\mathrm{Li}^+]$, and $E[\mathrm{S}]$ represent the total energies of the $\mathrm{Li}^+(\mathrm{S})_n$ complexes, Li^+, and the solvent molecule, respectively. The binding energies of $\mathrm{Li}^+(\mathrm{S})$ complexes are listed in Table 3. It should be noted from Table 3 that the interactions between Li^+ cation and cyclic carbonates are stronger, especially the interaction with EC, than between Li^+ and linear carbonates because of the fact that the binding energy between EC and Li^+ is higher than that of the three linear carbonates (DMC, DEC, and EMC) as well as than that of PC by a few kcal/mol (1 cal = 4.184 J). The positive charge on lithium tends to transfer to the anode when the battery is charged. Thus, Li^+–EC reaches the anode more easily than other solvent molecules, resulting in its preferential reduction on the anode when a lithium ion battery is charged. Similarly, the binding energies of the PF_6^-–S complexes (S = EC, PC, DMC, DEC, or EMC) were calculated and are listed in Table 4. This table clearly shows that the interactions between PF_6^- and cyclic carbonates are stronger, especially between PF_6^- and EC, than between PF_6^- and linear carbonates. The negative charge on hexafluorophosphate tends to transfer to the cathode when the battery is charged. Thus, PF_6^-–EC reaches the cathode more easily than other solvent molecules, resulting in its preferential oxidation on the cathode when a lithium ion battery is charged. For example, Wang and Balbeuna[25] showed that EC was more reactive than other alkyl carbonates in electrochemical reduction reactions and Moshkovich et al.[26] reported EC to be more reactive as compared with other alkyl carbonates in electrochemical oxidative reactions.

Moreover, the enthalpy of reaction for coordination is given by

$$[1] \qquad \Delta H = H[\mathrm{Li}^+(\mathrm{S})_n] - H[\mathrm{Li}^+(\mathrm{S})_{n-1}] - H(\mathrm{S})$$

where H represents the ground-state calculated enthalpies, n is the number of solvent molecules, and ΔH is the enthalpy of the coordination reaction. The coordination reaction that

Can. J. Chem. Downloaded from www.nrcresearchpress.com by South China Agricultural University on 09/19/12
For personal use only.

Table 3. The binding energies, Gibbs free energies, and heats of formation (in kcal/mol; 1 cal = 4.184 J) of solvent molecules with Li^+ in the gas phase calculated at a temperature of 298.15 K.

Energy	Li^+–EC	Li^+–PC	Li^+–DMC	Li^+–DEC	Li^+–EMC
ΔE	51.4	52.9	44.8	46.7	45.6
$\Delta E+\Delta$ZPE	53.0	54.4	45.3	47.4	46.2
ΔG	–43.5	–45.0	–36.9	–40.1	–38.6
ΔH	–49.7	–51.3	–43.5	–47.0	–45.2

Note: EC, ethylene carbonate; PC, propylene carbonate; DMC, dimethyl carbonate; DEC, diethyl carbonate; and EMC, ethyl methyl carbonate.

Table 4. The binding energies, Gibbs free energies, and heats of formation (in kcal/mol; 1 cal = 4.184 J) of solvent molecules with PF_6^- in the gas phase calculated at a temperature of 298.15 K.

Energy	PF_6^-+EC	PF_6^-+PC	PF_6^-+DMC	PF_6^-+DEC	PF_6^-+EMC
ΔE	–15.6	–15.4	–5.6	–5.0	–5.3
$\Delta E+\Delta$ZPE	–14.5	–14.4	–5.2	–4.9	–5.1
ΔG	–7.8	–5.7	–0.3	2.5	0.7
ΔH	–13.9	–14.5	–4.4	–4.5	–4.3

Note: EC, ethylene carbonate; PC, propylene carbonate; DMC, dimethyl carbonate; DEC, diethyl carbonate; and EMC, ethyl methyl carbonate.

Table 5. Calculated Gibbs free energies (in kcal/mol; 1 cal = 4.184 J), heats of formation (in kcal/mol), Li^+–O distances (in Å), and charge (q) on Li^+ (in e) for the coordination of solvent molecules with Li^+ in the gas phase at a temperature of 298.15 K.

Reactions	ΔG	ΔH	Li^+–O distance	q
$Li^+ + EC = Li^+(EC)_1$	–43.5	–49.7	1.74	0.80
$Li^+(EC)_1 + EC = Li^+(EC)_2$	–30.4	–38.2	1.79	0.63
$Li^+(EC)_2 + EC = Li^+(EC)_3$	–12.5	–23.9	1.86	0.52
$Li^+(EC)_3 + EC = Li^+(EC)_4$	–5.6	–13.5	1.92	0.38
$Li^+(EC)_4 + EC = Li^+(EC)_5$	9.0	–5.4	1.98	0.37
$Li^+ + PC = Li^+(PC)_1$	–45.0	–51.3	1.73	0.90
$Li^+(PC)_1 + PC = Li^+(PC)_2$	–31.7	–39.0	1.79	0.62
$Li^+(PC)_2 + PC = Li^+(PC)_3$	–11.6	–23.2	1.93	0.59
$Li^+(PC)_3 + PC = Li^+(PC)_4$	–1.4	–11.2	1.98	0.42
$Li^+(PC)_4 + PC = Li^+(PC)_5$	7.8	–4.6	2.01	0.38
$Li^+ + DMC = Li^+(DMC)_1$	–36.9	–43.5	1.73	0.79
$Li^+(DMC)_1 + DMC = Li^+(DMC)_2$	–27.3	–34.6	1.88	0.62
$Li^+(DMC)_2 + DMC = Li^+(DMC)_3$	–12.1	–19.5	1.92	0.53
$Li^+ + DEC = Li^+(DEC)_1$	–40.1	–47.0	1.73	0.78
$Li^+(DEC)_1 + DEC = Li^+(DEC)_2$	–27.9	–35.4	1.88	0.60
$Li^+(DEC)_2 + DEC = Li^+(DEC)_3$	–13.5	–20.2	1.93	0.51
$Li^+ + EMC = Li^+(EMC)_1$	–38.6	–45.2	1.73	0.88
$Li^+(EMC)_1 + EMC = Li^+(EMC)_2$	–27.5	–34.8	1.88	0.61
$Li^+(EMC)_2 + EMC = Li^+(EMC)_3$	–12.6	–19.7	1.93	0.52

Note: EC, ethylene carbonate; PC, propylene carbonate; DMC, dimethyl carbonate; DEC, diethyl carbonate; and EMC, ethyl methyl carbonate.

corresponds to the enthalpy of reaction can be written as $Li^+(S)_{n-1} + S = Li^+(S)_n$.

Results for the calculated heats of formation for complexes of solvents with Li^+ are presented in Table 5. The heats of formation of the first four complexes ($Li^+(EC)_{1-4}$) result in exothermic reactions, suggesting that the formation of $Li^+(EC)_4$ is favorable. These results are in full agreement with the conclusions drived from Raman intensity data.[27] The optimized structures of the $Li^+(EC)_{2-5}$ complexes are shown in Fig. 6. This is also true for the $Li^+(PC)_4$ complex. The stability of the $Li^+(S)_4$ complex (S = EC or PC) is also supported by the saturated charge on Li^+. It is evident from Table 5 that the Gibbs free energies of formation and heats of formation for $Li^+(EC)_{3-5}$ complexes are larger than those for $Li^+(PC)_{3-5}$ and $Li^+(S)_3$ (S = DMC, DEC, and EMC) complexes, indicating EC as a better electrolyte in comparison of PC, DMC, DEC, and EMC in applications of lithium ion batteries.

Can. J. Chem. Downloaded from www.nrcresearchpress.com by South China Agricultural University on 09/19/12
For personal use only.

Fig. 6. Optimized structure of (*a*) $[Li^+(EC)_2]$ complex, (*b*) $[Li^+(EC)_3]$ complex, (*c*) $[Li^+(EC)_4]$ complex, and (*d*) $[Li^+(EC)_5]$ complex. EC, ethylene carbonate; PC, propylene carbonate; DMC, dimethyl carbonate; DEC, diethyl carbonate; and EMC, ethyl methyl carbonate.

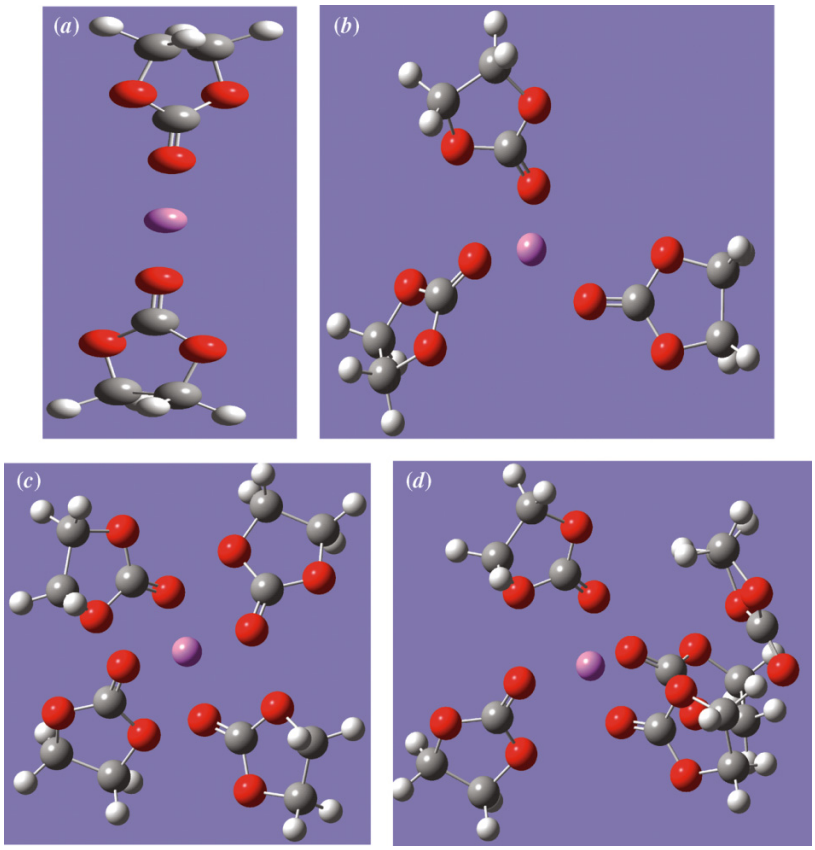

Table 6. Calculated binding energies, Gibbs free energies, and heats of formation (in kcal/mol; 1 cal = 4.184 J) for the coordination of solvent molecules with PF_6^- in the gas phase at a temperature of 298.15 K.

Reaction	ΔE	$\Delta E+\Delta ZPE$	ΔG	ΔH
$PF_6^- + EC = PF6^-(EC)_1$	–15.6	–14.5	–7.8	–13.9
$PF_6^-(EC)_1 + EC = PF6^-(EC)_2$	–30.1	–28.4	–12.7	–25.8
$PF_6^-(EC)_2 + EC = PF6^-(EC)_3$	–39.2	–37.6	–13.6	–35.1
$PF_6^- + PC = PF6^-(PC)_1$	–15.4	–14.4	–5.7	–14.5
$PF_6^-(PC)_1 + PC = PF6^-(PC)_2$	–28.2	–27.3	–11.6	–25.7
$PF_6^-(PC)_2 + PC = PF6^-(PC)_3$	–38.5	–37.3	–13.2	–34.6
$PF_6^- + DMC = PF6^-(DMC)_1$	–5.6	–5.2	–0.3	–4.4
$PF_6^-(DMC)_1 + DMC = PF6^-(DMC)_2$	–11.0	–10.5	3.5	–8.9
$PF_6^-(DMC)_2 + DMC = PF6^-(DMC)_3$	–15.8	–14.9	6.7	–12.2
$PF_6^- + DEC = PF6^-(DEC)_1$	–5.1	–4.8	2.5	–4.5
$PF_6^-(DEC)_1 + DEC = PF6^-(DEC)_2$	–10.3	–9.4	4.3	–7.7
$PF_6^-(DEC)_2 + DEC = PF6^-(DEC)_3$	–14.4	–13.5	4.4	–10.8
$PF_6^- + EMC = PF6^-(EMC)_1$	–5.3	–5.1	0.7	–4.3
$PF_6^-(EMC)_1 + EMC = PF6^-(EMC)_2$	–10.5	–9.8	4.0	–8.2
$PF_6^-(EMC)_2 + EMC = PF6^-(EMC)_3$	–14.7	–14.0	5.9	–11.3

Note: EC, ethylene carbonate; PC, propylene carbonate; DMC, dimethyl carbonate; DEC, diethyl carbonate; and EMC, ethyl methyl carbonate.

Finally, the binding energies of the $PF_6^-(S)_{n=1-3}$ complexes in the gas phase are listed in Table 6. It can be found from Table 6 that $PF_6^-(EC)_3$ and $PF_6^-(PC)_3$ are the most stable solvation structures in EC and PC electrolytes. The positive Gibbs free energies of the linear alkyl carbonates indicate that the formation of $PF_6^-(S)_n$ is not favorable. The calculated result is consistent with the reference result.[28]

Conclusions

In summary, the interaction of the lithium (Li^+) cation and the hexafluorophosphate (PF_6^-) anion with nonaqueous electrolytes EC, PC, DMC, DEC, and EMC is studied by using density functional theory at the B3LYP/6–311++G(d,p) level in the gas phase in terms of the coordination of Li^+ and PF_6^-

with these solvents. EC coordinates with Li^+ and PF_6^- most strongly and reaches the anode and the cathode most easily because of its highest dielectric constant among all the solvent molecules, resulting in its preferential reduction on the anode and oxidation on the cathode. For cyclic carbonates EC and PC, the structure $Li^+(S)_4$ is found to be the most stable. However, for linear carbonates DMC, DEC, and EMC, the formation of $PF_6^-(S)_{n=1-3}$ is not favorable. Such analysis may be useful in applications for lithium ion batteries.

Acknowledgements

This research work was supported by the World Class University (WCU) program through the Korea Research Foundation funded by the Ministry of Education, Science and Technology (R31-2008-000-10083-0).

References

(1) Armstrong, A. R.; Bruce, P. G. *Nature* **1996**, *381* (6582), 499. doi:10.1038/381499a0.
(2) Besenhard, J. O.; Winter, M.; Yang, J.; Biberacher, W. *J. Power Sources* **1995**, *54* (2), 228. doi:10.1016/0378-7753(94)02073-C.
(3) Tarascon, J. M.; Armand, M. *Nature* **2001**, *414* (6861), 359. doi:10.1038/35104644.
(4) Armstrong, A. R.; Tee, D. W.; La Mantia, F.; Novák, P.; Bruce, P. G. *J. Am. Chem. Soc.* **2008**, *130* (11), 3554. doi:10.1021/ja077651g.
(5) Arora, P.; White, R. E.; Doyle, M. *J. Electrochem. Soc.* **1998**, *145* (10), 3647. doi:10.1149/1.1838857.
(6) Aurbach, D.; Levi, M. D.; Levi, E.; Schechter, A. *J. Phys. Chem. B* **1997**, *101* (12), 2195. doi:10.1021/jp962815t.
(7) Schechter, A.; Aurbach, D.; Cohen, H. *Langmuir* **1999**, *15* (9), 3334. doi:10.1021/la981048h.
(8) Matsuta, S.; Kato, Y.; Ota, T.; Kurokawa, H.; Yoshimura, S.; Fujitani, S. *J. Electrochem. Soc.* **2001**, *148* (1), A7. doi:10.1149/1.1339025.
(9) Ufheil, J.; Wursig, A.; Schneider, O. D.; Novak, P. *Electrochem. Commun.* **2005**, *7* (12), 1380. doi:10.1016/j.elecom.2005.09.021.
(10) Arakawa, M.; Yamaki, J. *J. Power Sources* **1995**, *54* (2), 250. doi:10.1016/0378-7753(94)02078-H.
(11) Moshkovich, M.; Cojocaru, M.; Gottlieb, H. E.; Aurbach, D. *J. Electroanal. Chem.* **2001**, *497* (1–2), 84. doi:10.1016/S0022-0728(00)00457-5.
(12) Zhang, X. R.; Pugh, J. K.; Ross, P. N. *J. Electrochem. Soc.* **2001**, *148* (5), E183. doi:10.1149/1.1362546.
(13) Xu, K.; Angell, C. A. *J. Electrochem. Soc.* **1998**, *145* (4), L70. doi:10.1149/1.1838419.
(14) Xu, K.; Ding, S.; Jow, T. R. *J. Electrochem. Soc.* **1999**, *146* (11), 4172. doi:10.1149/1.1392609.
(15) Xing, L. D.; Wang, C. Y.; Li, W. S.; Xu, M. Q.; Meng, X. L.; Zhao, S. F. *J. Phys. Chem. B* **2009**, *113* (15), 5181. doi:10.1021/jp810279h.
(16) Aurbach, D. *J. Power Sources* **2000**, *89* (2), 206. doi:10.1016/S0378-7753(00)00431-6.
(17) Ota, H.; Akai, T.; Kotato, M.; Yamaguchi, S. *Abstracts of the 11th International Meeting on Lithium Batteries;* Monterey 335, CA, 2002.
(18) Jeong, S. K.; Inaba, M.; Mogi, R.; Iriyama, Y.; Abe, T.; Ogumi, Z. *Langmuir* **2001**, *17* (26), 8281. doi:10.1021/la015553h.
(19) Aurbach, D.; Zinigrad, E.; Cohen, Y.; Teller, H. *Solid State Ion.* **2002**, *148* (3–4), 405. doi:10.1016/S0167-2738(02)00080-2.
(20) Ein-Eli, Y. *Electrochem. Solid-State Lett.* **1999**, *2* (5), 212. doi:10.1149/1.1390787.
(21) Frisch, M. J.; Trucks, G. W.; Schlegel, H. B.; Scuseria, G. E.; Robb, M. A.; Cheeseman, J. R.; Scalmani, G.; Barone, V.; Mennucci, B.; Petersson, G. A.; Nakatsuji, H.; Caricato, M.; Li, X.; Hratchian, H. P.; Izmaylov, A. F.; Bloino, J.; Zheng, G.; Sonnenberg, J. L.; Hada, M.; Ehara, M.; Toyota, K.; Fukuda, R.; Hasegawa, J.; Ishida, M.; Nakajima, T.; Honda, Y.; Kitao, O.; Nakai, H.; Vreven, T.; Montgomery, J. A., Jr.; Peralta, J. E.; Ogliaro, F.; Bearpark, M.; Heyd, J. J.; Brothers, E.; Kudin, K. N.; Staroverov, V. N.; Kobayashi, R.; Normand, J.; Raghavachari, K.; Rendell, A.; Burant, J. C.; Iyengar, S. S.; Tomasi, J.; Cossi, M.; Rega, N.; Millam, N. J.; Klene, M.; Knox, J. E.; Cross, J. B.; Bakken, V.; Adamo, C.; Jaramillo, J.; Gomperts, R.; Stratmann, R. E.; Yazyev, O.; Austin, A. J.; Cammi, R.; Pomelli, C.; Ochterski, J. W.; Martin, R. L.; Morokuma, K.; Zakrzewski, V. G.; Voth, G. A.; Salvador, P.; Dannenberg, J. J.; Dapprich, S.; Daniels, A. D.; Farkas, Ö.; Foresman, J. B.; Ortiz, J. V.; Cioslowski, J.; Fox, D. J. *Gaussian 09, Revision A.1;* Gaussian Inc.: Wallingford, CT, 2009.
(22) Schmidt, M. W.; Baldridge, K. K.; Boatz, J. A.; Elbert, S. T.; Gordon, M. S.; Jensen, J. H.; Koseki, S.; Matsunaga, N.; Nguyen, K. A.; Su, S.; Windus, T. L.; Dupuis, M.; Montgomery, J. A. *J. Comput. Chem.* **1993**, *14* (11), 1347. doi:10.1002/jcc.540141112.
(23) Abbotto, A.; Streitwieser, A.; von Ragué Schleyer, P. *J. Am. Chem. Soc.* **1997**, *119* (46), 11255. doi:10.1021/ja971715d.
(24) Wang, Y.; Balbuena, P. B. *J. Phys. Chem. A* **2001**, *105* (43), 9972. doi:10.1021/jp0126614.
(25) Wang, Y.; Balbuena, P. B. *Int. J. Quant Chem.* **2005**, *102* (5), 724. doi:10.1002/qua.20466.
(26) Moshkovich, M.; Cojocaru, M.; Gottlieb, H. E.; Aurbach, D. *J. Electroanal. Chem.* **2001**, *497* (1–2), 84. doi:10.1016/S0022-0728(00)00457-5.
(27) Deng, Z.; Irish, D. E. *Can. J. Chem.* **1991**, *69* (11), 1766. doi:10.1139/v91-259.
(28) Xing, L.; Li, W.; Wang, C.; Gu, F.; Xu, M.; Tan, C.; Yi, J. *J. Phys. Chem. B* **2009**, *113* (52), 16596. doi:10.1021/jp9074064.

Can. J. Chem. Downloaded from www.nrcresearchpress.com by South China Agricultural University on 09/19/12
For personal use only.

Direct benzylation of 1,3-dicarbonyl compounds catalyzed by $Cs_{2.5}H_{0.5}PW_{12}O_{40}$ in solvent-free conditions

Ezzat Rafiee, Maryam Khodayari, and Mohammad Joshaghani

Can. J. Chem. Downloaded from www.nrcresearchpress.com by South China Agricultural University on 09/19/12
For personal use only.

Abstract: Various 1,3-dicarbonyl compounds reacted readily with benzylic alcohols in the presence of $Cs_{2.5}H_{0.5}PW_{12}O_{40}$ salt to produce 2-benzylic-1,3-dicarbonyl compounds in high yields. It was found that this catalyst could be completely recovered and reused without loss of its catalytic activities and is thus environmentally conscious especially in solvent-free conditions. The use of this method provides improved modification of the direct benzylation of 1,3-carbonyl compounds in terms of low reaction times, solvent-free conditions, usage of a small amount of the catalyst, and a clean reaction profile. Furthermore, the use of this catalyst is feasible because of its easy preparation, its easy handling, its stability, its easy recovery, its reusability, being environmentally green, its excellent activity, and its selectivity.

Key words: heteropoly salt, benzylation, 1,3-dicarbonyl compounds, nucleophilic substitution, solvent-free conditions.

Résumé : Divers composés 1,3-dicarbonylés réagissent facilement avec des alcools benzyliques, en présence du sel $Cs_{2,5}H_{0,5}PW_{12}O_{40}$, pour conduire à la formation de dérivés 2-benzylique-1,3-dicarbonylés, avec des rendements élevés. On a trouvé que ce catalyseur peut être complètement récupéré et réutilisé sans perte de ses activités catalytiques et qu'il est donc écologique, particulièrement dans des conditions expérimentales sans solvant. L'utilisation de cette méthode apporte une modification améliorée à la benzylation directe des composés 1,3-dicarbonylés en termes de temps de réaction plus courts, de conditions sans solvant, d'utilisation de quantités faibles de catalyseur et de profil réactionnel propre. De plus, l'utilisation de ce catalyseur est possible en raison de sa facilité de préparation et de manipulation, de sa stabilité, de sa facilité de récupération et de réutilisation, de son caractère écologique, de son excellente activité et de sa sélectivité.

Mots-clés : sel hétéropolaire, benzylation, composés 1,3-dicarbonylés, substitution nucléophile, conditions sans solvant.

[Traduit par la Rédaction]

Introduction

The construction of carbon–carbon bonds is a fundamental task in organic synthesis.[1,2] An important type of such reactions involves the alkylation of 1,3-dicarbonyl compounds.[3–7] The direct nucleophilic substitution of the hydroxyl group in alcohols with nucleophiles generally requires preactivation of the alcohol because of its poor leaving ability. Therefore, a promoter would be required for in situ activation of C–OH from the alcohol and C–H from the diketone for direct C–C bond formation. Recently, Lewis and Brönsted acids such as $BF_3{\cdot}OEt_2$,[8] $InCl_3$,[9] $FeCl_3$,[10,11] LnOTf (Ln = La, Yb, Sc, or Hf),[12,13] $Bi(OTf)_3$,[14] *p*-toluene sulfonic acid,[15] and *H*-montmorillonite[16] have also been reported to catalyze these reactions efficiently. Also, phosphomolibdic acid supported on silica gel has been used for the propargylation of aromatic compounds[17] and the alkylation of 1,3-dicarbonyl compounds with benzylic and propargylic alcohols.[18,19] Moreover, nucleophilic substitution reactions of different alcohols with sulfonamides, benzamides, and 4-nitroaniline have been reported in the presence of phosphotungstic acid.[20]

However, most of these methods have problems including drastic reaction conditions, long reaction times, and the use of expensive, toxic, and moisture-sensitive reagents. Therefore, the direct catalytic substitution of alcohols with 1,3-dicarbonyls using an efficient, cost-effective, and recyclable catalyst is highly desirable. Recently, the use of heteropoly acids (HPAs) as environmentally friendly and economically viable solid acids has gained increasing attention owing to their ease of handling and high catalytic activities and reactivities.[21] These compounds possess unique properties, such as well-defined structure, Brönsted acidity, the possibility of modification of their acid–base and redox properties by changing their chemical composition ability to accept and release electrons, high proton mobility, etc.[22] In view of green chemistry, the substitution of harmful liquid acids by reusable solid HPAs as catalysts in organic syntheses is a promising application of these acids.[23,24] Among HPAs,

Received 9 June 2011. Accepted 7 September 2011. Published at www.nrcresearchpress.com/cjc on 25 November 2011.

E. Rafiee and M. Joshaghani. Department of Chemistry, Faculty of Science, Razi University, Kermanshah, 67149, Iran; Kermanshah Oil Refining Company, Kermanshah, Iran.
M. Khodayari. Department of Chemistry, Faculty of Science, Razi University, Kermanshah, 67149, Iran.

Corresponding author: Ezzat Rafiee (e-mail: e.rafiei@razi.ac.ir and ezzat_rafiee@yahoo.com).

This article is part of a Special Issue to commemorate the International Year of Chemistry.

Can. J. Chem. Downloaded from www.nrcresearchpress.com by South China Agricultural University on 09/19/12
For personal use only.

$H_3PW_{12}O_{40}$ (PW), which belongs to the Keggin-type of HPAs, is the most widely used catalyst owing to their high acid strength, high thermal stability, and low reducibility. For acidic heterogeneous reactions, the bulk HPAs generally exhibit low catalytic performance because of their low surface area. Alkali-exchanged HPAs exhibit dramatic increases in surface area and profound changes in solubility over the parent HPAs; for example, salts with large monovalent ions, such as Cs^+, NH_4^+, and Ag^+, are insoluble in water. It has been demonstrated that $Cs_xH_{3-x}PW_{12}O_{40}$ possesses super acidity.[25] Cesium salts have high surface areas and thus much more acidic sites are available for catalytic reactivity.[26] This high surface area makes Cs salt a more active catalyst than the parent acid and also other known solid acids such as zeolites. Solvent-free reactions have been getting more and more attention recently, often providing clean, efficient, and high-yielding organic processes in modern synthetic chemistry. Thus, using this condition makes a clean reaction profile for organic synthesis.

We report herein the alkylation of a wide variety of 1,3-dicarbonyl compounds with benzylic alcohols catalyzed by cesium salts of PW under solventfree conditions.

Results and discussion

Reaction of benzhydrol and acetyl acetone was carried out as a model system with different solvents and temperatures and different kinds and quantities of catalysts (Scheme 1). It is obvious that the reaction does not proceed in the absence of catalysts (Table 1, entry 1). The model reaction was examined in the presence of PW and its cesium salts. The reaction was more efficient in the presence of $Cs_xH_{3-x}PW_{12}O_{40}$ compared with PW, and $Cs_{2.5}H_{0.5}PW_{12}O_{40}$ (Cs2.5) showed the best reactivity in a shorter reaction time. The efficiencies of several organic solvents for comparison with solvent-free systems were investigated (Fig. 1). Obviously, the coordinating solvents, such as acetonitrile, were unfavorable for this reaction. 1,2-Dichloroethane was found to be an effective solvent in terms of time and yield. However, a significant improvement was observed in which the product yield increased to 95% after only 1.0 h in solvent-free conditions.

The quantity of the catalyst used in this reaction was also optimized (Table 1, entries 5–7). No improvement in yield or time of the reaction was observed when catalyst loading was increased from 10 to 20 mol %. The effect of temperature was also studied. It was observed that by increasing the reaction temperature from 25 to 80 °C, the product yield was increased from 11% to 95% after 1.0 h.

Encouraged by these results, we turned our attention to various 1,3-diketones and benzylic alcohols (Table 2). It should be noted that with acetyl acetone and ketoesters, approximately the same results were obtained. Methyl acetoacetate and ethyl acetoacetate reacted smoothly with benzylic alcohols give the corresponding 2-benzylic-1,3-dicarbonyl compounds in excellent yields and with short reaction times. Other types of benzylic alcohols (Table 2, entries 3–10) underwent smooth conversion to the desired products with excellent yields.

Measurement of acidity can provide us with a better understanding of the catalytic reactivity. The acidity measurement of PW and its cesium salts by means of potentiometric titration with *n*-butylamine let us estimate the strength and the number of acid sites and their distribution. This method, based on the measured potential difference, is mainly determined by the acidic environment around the electrode membrane. The measured electrode potential is an indicator of the acidic properties of the dispersed solid particles. An aliphatic amine, such as *n*-butylamine with a basic dissociation constant of ~10^{-6}, allows a potentiometric titration of strong acids. The titration curves obtained for $Cs_xH_{3-x}PW_{12}O_{40}$ (x = 0, 1, 2, or 2.5) are presented in Fig. 2. The initial electrode potential (Ei) indicates the maximum strength of the acid sites and the value from which the plateau is reached (mequiv amine / g catalyst) indicates the total number of acid sites that are present in the titrated solid. The acidic strength of the acid sites can be classified according to the following ranges: Ei > 100 mV (very strong sites), 0 < Ei < 100 mV (strong sites), –100 < Ei < 0 mV (weak sites), and Ei < –100 mV (very weak sites).[27] According to the mentioned scale, all the catalysts present very strong acid sites. It was observed that PW is more acidic than these salts. This is

Scheme 1. Model reaction.

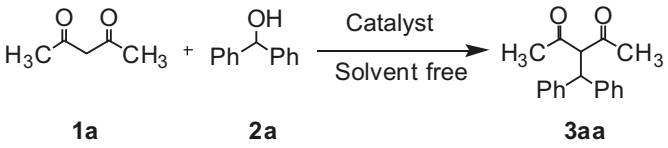

1a **2a** **3aa**

Table 1. Efficacies of $Cs_xH_{3-x}PW_{12}O_{40}$ (x = 0, 1, 2, or 2.5) in the model reaction in solvent-free conditions.

Entry	Catalyst	mol %	Time (h)	Yield (%)[a]
1	—	—	2.5	0
2	$H_3PW_{12}O_{40}$	10	2	50
3	$Cs_1H_2PW_{12}O_{40}$	10	2.5	62
4	$Cs_2H_1PW_{12}O_{40}$	10	2.5	78
5	$Cs_{2.5}H_{0.5}PW_{12}O_{40}$	10	1.0	95
6	$Cs_{2.5}H_{0.5}PW_{12}O_{40}$	5	1.0	71
7	$Cs_{2.5}H_{0.5}PW_{12}O_{40}$	20	1.0	94
8	$Cs_{2.5}H_{0.5}PW_{12}O_{40}$	10	1.0	16[b]

[a]Isolated yield.
[b]At room temperature.

Fig. 1. The effect of various solvents and solvent-free conditions.

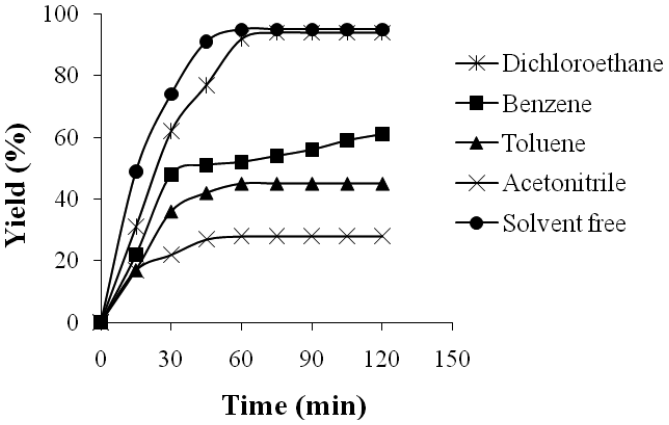

Table 2. Direct benzylation of 1,3-dicarbonyl compounds with alcohols catalyzed by $Cs_{2.5}H_{0.5}PW_{12}O_{40}$ (Cs2.5).

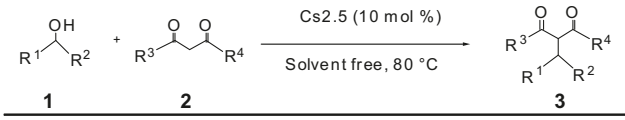

1 **2** **3**

Entry	Diketone	Alcohol	Product	Time (h)	Yield (%)[a]
1	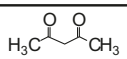 **1a**	**2a**	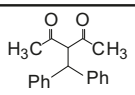 **3aa**	1.0 (2)[b]	95 (90)[b]
2	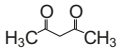 **1a**	**2b**	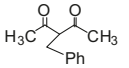 **3ab**	1.0	89
3	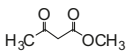 **1b**	**2a**	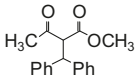 **3ba**	1.0 (2)[b]	92 (92)[b]
4	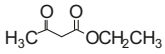 **1c**	**2a**	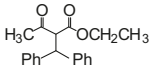 **3ca**	1.0 (2)[b]	95 (91)[b]
5	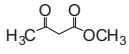 **1b**	**2b**	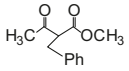 **3bb**	1.0	91
6	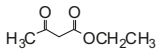 **1c**	**2b**	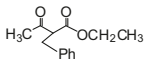 **3cb**	1.0	97
7	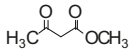 **1b**	**2c**	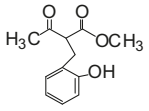 **3bc**	1.0	94
8	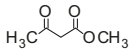 **1b**	**2d**	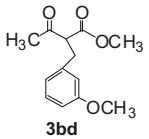 **3bd**	1.0	92
9	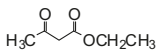 **1c**	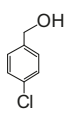 **2e**	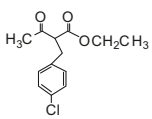 **3ce**	1.0	91

Note: All reactions were performed with 1,3-dicarbonyl compound **1** (1 mmol), benzylic alcohol **2** (1 mmol), and Cs2.5 (10 mol %) at 80 °C under solvent-free conditions.

[a]All products were fully characterized.[28,29]

[b]Results in parentheses refer to large-scale syntheses.

Can. J. Chem. Downloaded from www.nrcresearchpress.com by South China Agricultural University on 09/19/12
For personal use only.

Can. J. Chem. Downloaded from www.nrcresearchpress.com by South China Agricultural University on 09/19/12
For personal use only.

Fig. 2. Potentiometric titration curves of PW and its cesium salts.

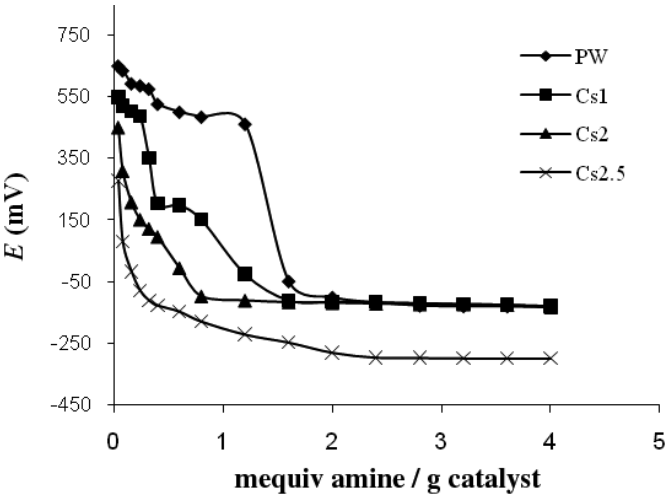

indicated by the initial electrode potential that is lower for cesium salts than for PW. As expected, the acidity decreases with increasing cesium content, but the number of acidic sites in Cs2.5 is higher than in other cesium salts and PW. So it seems that the higher reactivity of Cs2.5 is related to the higher functional acid sites that are dispersed on the surface of the solid catalyst.

The applicability of this method for large-scale operations was investigated in the reactions of **1a**–**1c** (20.0 mmol) with **2a** (20.0 mmol) under optimized conditions (Table 2, entries 1–4). Corresponding products were obtained with approximately similar yields but at higher reaction times. As can be seen, Cs2.5 is a good candidate for large-scale operations in the direct benzylation of 1,3-dicarbonyl compounds.

A suggested mechanism for this alkylation reaction is shown as Scheme 2. By the action of Cs2.5, the alcohol was protonated to generate a stable benzyl cation after dehydration. This carbocation could quickly combine with the employed 1,3-dicarbonyl compound to produce, after the release of H^+, the final alkylated product (Scheme 2). It should be noted that the GC–MS control before the complete conversion of the starting material of the reaction showed that the corresponding symmetrical ether was not detected as an intermediate or at the end of the reaction.

In addition, Cs2.5 was found to be reusable several times without loss of activity. After completion of the model reaction, the catalyst was filtered, washed with acetonitrile dried, and reused. After reusing the catalyst four times, the yield of the reaction was 90% (Fig. 3).

Conclusion

In conclusion, we have demonstrated an efficient methodology for solvent-free direct benzylation reactions of 1,3-dicarbonyl compounds catalyzed by Cs2.5. The reactions proceeded in excellent yields and avoided the usage of toxic organic solvents. No toxic reagent(s) or by-product(s) were involved. Low reactions times, an environmentally friendly procedure, low cost, and excellent selectivity are some of the salient features of this green method. Low loading of catalyst, ease of workup, ease of handling, stability, and recyclability

Scheme 2. Proposed mechanism for catalytic addition of diketones to alcohols.

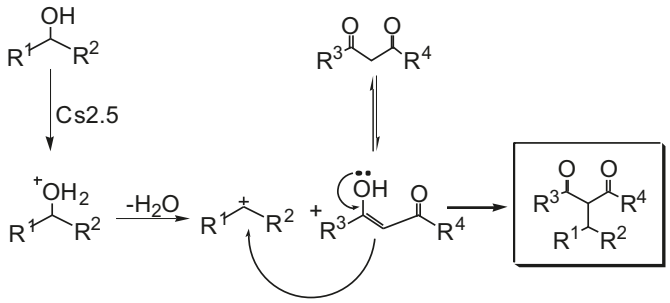

Fig. 3. Reaction profile of the five successive runs of the model reaction.

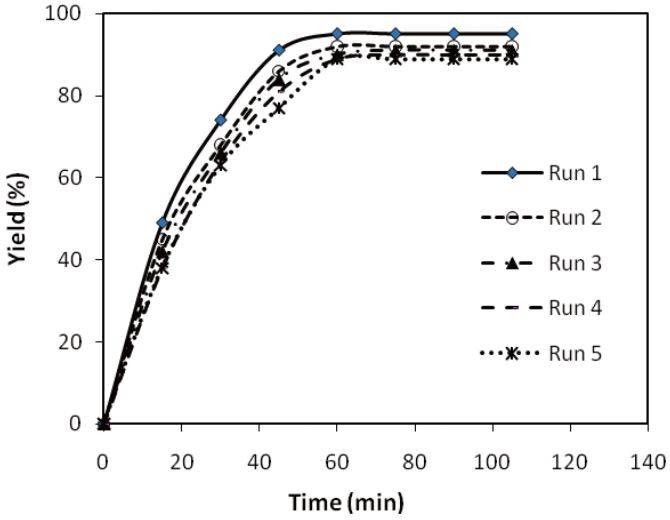

of the catalyst are other advantages of this catalyst. Large-scale synthesis is also beneficial in this method. Further applications of this catalyst to other transformations are currently under investigation.

Experimental

General remarks

All organic materials were purchased commercially from Fluka Chemical Corp. and Merck & Co., Inc. and were used without further purification. PW from Sigma-Aldrich was used. IR spectra were recorded with KBr pellets or nujol in the case of oily compounds, using a Shimadzu 470 spectrophotometer. NMR spectra were recorded on a Bruker Avance 200 MHz NMR spectrometer with $CDCl_3$ as the solvent and TMS as the internal standard. CHN compositions were measured by Hekatech elemental analysis model Euro EA 3000. Mass spectra were determined on an Agilent 6890 N GC–MS. Melting points were determined using a digital Gallenkamp apparatus.

Preparation of the catalysts ($Cs_xH_{3-x}PW_{12}O_{40}$)

The acidic salts of $Cs_xH_{3-x}PW_{12}O_{40}$ were prepared by adding the required amount of aqueous cesium carbonate to an aqueous solution of PW with stirring. An appropriate amount of the aqueous solution of Cs_2CO_3 (0.10 mol/L) was added dropwise to the aqueous solution of PW (0.08 mol/L) at

Can. J. Chem. Downloaded from www.nrcresearchpress.com by South China Agricultural University on 09/19/12
For personal use only.

room temperature with vigorous stirring. The Cs content was adjusted by the amount of Cs_2CO_3 solution added. As an example, for the synthesis of Cs2.5, the appropriate amounts of solution for Cs_2CO_3 and PW were 8.3 and 8.4 mL, respectively. From the beginning of the addition of Cs_2CO_3, very fine particles (precipitates) were formed to make the solution milky. After that the solution was aged at room temperature overnight. The precipitate obtained was dried at 40 °C in a rotary evaporator.

Acidity measurement

For the potentiometric titration, 0.05 g of solid catalyst was suspended in acetonitrile (90 mL) and stirred for 3 h. The suspension was titrated with a 0.05 N solution of *n*-butylamine in acetonitrile. The potential variation was measured with a Hanna 302 pH meter using a double junction electrode.

General procedure for benzylation of the 1,3-dicarbonyl compound

The solid acid catalyst (10 mol %) was added to a mixture of alcohol (1 mmol) and 1,3-dicarbonyl compound (1 mmol) at 80 °C. The reaction mixture was stirred for a short period of time (listed in the Table 2). The progress of the reaction was monitored by thin-layer chromatography (TLC). After completion of the reaction, the catalyst was removed by filtration and was washed with acetonitrile for reuse. The filtrate was concentrated and the product was purified by column chromatography on silica gel using EtOAc/hexane as eluent.

Recycling of the catalyst

The catalyst was separated from the reaction mixture, washed with acetonitrile, and dried at 120 °C for 2 h to give recycled Cs2.5. Isolated catalyst was reused in a subsequent reaction. The model reaction was repeated with recycled catalyst and the yields were found to remain in the range of 95%–90% for five successive runs.

Large-scale synthesis

Three entries of Table 2 (entries 1, 3, and 4) were selected for large-scale synthesis. The reactions of **1a**–**1c** (20.0 mmol) with **2a** (20.0 mmol) in the presence of Cs2.5 (10 mol %) were done at 80 °C under solvent-free conditions. As can be seen, Cs2.5 is a good candidate for large-scale synthesis and yields of the reactions were in the range of 90%–92% with longer reaction times compared with smallscale synthesis.

All products were identified by comparing their spectral data with those of the authentic samples, except for new compounds (**3ab**, **3bb**, **3cb**, **3bc**, **3bd**, and **3ce**). Analytical data for these compounds are presented in the following sections.

3-Benzylpentane-2,4-dione (compound 3ab)

Colorless oil. IR (KBr, cm^{-1}): 1695, 1715. ^1H NMR (200 MHz, $CDCl_3$) δ: 7.08–7.21 (m, 5H), 3.32–3.79 (m, 3H), 2.01 (s, 6H). ^{13}C NMR (100 MHz, $CDCl_3$) δ: 205.2, 141.3, 128.1, 127.2, 125.8, 70.5, 28.7, 27.6. Anal. calcd for $C_{12}H_{14}O_2$: C 75.76, H 7.42; found: C 75.79, H 7.39. HRMS calcd for $C_{12}H_{14}O_2$: M, 190.2384; found: 190.2382.

Methyl 2-benzyl-3-oxobutanoate (compound 3bb)

Colorless oil. IR (KBr, cm^{-1}): 1715, 1735. ^1H NMR (200 MHz, $CDCl_3$) δ: 7.08–7.30 (m, 5H), 3.91 (s, 3H), 3.30–3.81 (m, 3H), 2.05 (s, 3H). ^{13}C NMR (100 MHz, $CDCl_3$) δ: 205.2, 171.5, 141.2, 128.5, 127.6, 125.9, 51.2, 50.8, 29.8, 27.6. Anal. calcd for $C_{12}H_{14}O_3$: C 69.88, H 6.84; found: C 69.84, H 6.88. HRMS calcd for $C_{12}H_{14}O_3$: M, 206.2377; found: 206.2378.

Ethyl 2-benzyl-3-oxobutanoate (compound 3cb)

Colorless oil. IR (KBr, cm^{-1}): 1714, 1737. ^1H NMR (200 MHz, $CDCl_3$) δ: 7.10–7.31 (m, 5H), 4.00 (q, 2H, J = 7.0 Hz), 3.31–3.80(m, 3H), 2.06 (s, 3H), 1.10 (t, 3H, J = 7.0 Hz). ^{13}C NMR (100 MHz, $CDCl_3$) δ: 205.2, 171.5, 141.5, 128.5, 127.7, 126.1, 61.1, 54.4, 29.9, 27.5, 13.9. Anal. calcd for $C_{13}H_{16}O_3$: C 70.89, H 7.32; found: C 70.93, H 7.28. HRMS calcd for $C_{13}H_{16}O_3$: M, 220.2643; found: 220.2644.

Methyl 2-(2-hydroxybenzyl)-3-oxobutanoate (compound 3bc)

Pale yellow solid, mp 110–112 °C. IR (KBr, cm^{-1}): 1716, 1737. ^1H NMR (200 MHz, $CDCl_3$) δ: 6.7–7.02 (m, 4H), 5.09 (s, 1H), 3.90 (s, 3H), 3.31–3.80 (m, 3H), 2.03 (s, 3H). ^{13}C NMR (100 MHz, $CDCl_3$) δ: 205.1, 171.5, 155.6, 128.8, 127.2, 126.7, 121.0, 115.6, 51.1, 50.7, 27.6, 20.1. Anal. calcd for $C_{12}H_{14}O_4$: C 64.85, H 6.35; found: C 64.80, H 6.39. HRMS calcd for $C_{12}H_{14}O_4$: M, 222.2371; found: 222.2372.

Methyl 2-(3-methoxybenzyl)-3-oxobutanoate (compound 3bd)

Pale yellow solid, mp 67–68 °C. IR (KBr, cm^{-1}): 1715, 1736. ^1H NMR (200 MHz, $CDCl_3$) δ: 6.61–7.10 (m, 5H), 3.92 (s, 3H), 3.81 (s, 3H), 3.29–3.78 (m, 3H), 2.04 (s, 3H). ^{13}C NMR (100 MHz, $CDCl_3$) δ: 205.3, 171.4, 161.4, 142.5, 129.1, 119.2, 112.4, 111.1, 57.8, 51.2, 50.8, 30.7, 27.5. Anal. calcd for $C_{13}H_{16}O_4$: C 66.09, H 6.83; found: C 66.12, H 6.81. HRMS calcd for $C_{13}H_{16}O_4$: M, 236.2637; found: 236.2636.

Ethyl 2-(4-chlorobenzyl)-3-oxobutanoate (compound 3ce)

Pale yellow solid, mp 70–71 °C. IR (KBr, cm^{-1}): 1717, 1738. ^1H NMR (200 MHz, $CDCl_3$) δ: 7.01–7.31 (m, 4H), 4.01 (q, 2H, J = 7.0 Hz), 3.31–3.81 (m, 3H), 2.03 (s, 3H), 0.98 (t, 3H, J = 7.0 Hz). ^{13}C NMR (100 MHz, $CDCl_3$) δ: 205.3, 171.5, 137.0, 130.2, 129.0, 128.7, 61.1, 51.2, 29.8, 27.6, 13.9. Anal. calcd for $C_{13}H_{15}ClO_3$: C 61.30, H 5.94; found: C 61.34, H 5.92. HRMS calcd for $C_{13}H_{15}ClO_3$: M, 254.7094; found: 254.7095.

Acknowledgments

The authors thank the Razi University Research Council and Kermanshah Oil Refining Company for support of this work.

References

(1) March, J. *Advanced Organic Chemistry;* Wiley: New York, 1992; p 54.
(2) Scolastico, C.; Nicotra, F. *Current Trends in Organic Synthesis;* Plenum: New York, 1999; p 76.

(3) Larock, R. C. *Comprehensive Organic Transformation;* VCH: New York, 1999; p 89.
(4) Tsuji, J. *Palladium Reagents and Catalysts;* Wiley: Chichester, UK, 1995; p 109.
(5) Godleski, S. A. In *Comprehensive Organic Synthesis;* Trost, B. M.; Fleming, I., Eds.; Pergamon: Oxford, 1991; Vol. 4, pp 994–999.
(6) Tsuji, J.; Minami, I. *Acc. Chem. Res.* **1987**, *20* (4), 140. doi:10.1021/ar00136a003.
(7) Trost, B. M. *Acc. Chem. Res.* **1980**, *13* (11), 385. doi:10.1021/ar50155a001.
(8) Bisaro, F.; Pretat, G.; Vitale, M.; Poli, G. *Synlett* **2002** (11), 1823.
(9) Yasuda, M.; Somyo, T.; Baba, A. *Angew. Chem. Int. Ed.* **2006**, *45* (5), 793. doi:10.1002/anie.200503263.
(10) Jana, U.; Biswas, S.; Maiti, S. *Tetrahedron Lett.* **2007**, *48* (23), 4065. doi:10.1016/j.tetlet.2007.04.017.
(11) Salehi, P.; Iranpoor, N.; Behbahani, F. K. *Tetrahedron* **1998**, *54* (5–6), 943. doi:10.1016/S0040-4020(97)10350-7.
(12) Noji, M.; Konno, Y.; Ishii, K. *J. Org. Chem.* **2007**, *72* (14), 5161. doi:10.1021/jo0705216.
(13) Huang, W.; Wang, J.; Shen, Q.; Zhou, X. *Tetrahedron Lett.* **2007**, *48* (23), 3969. doi:10.1016/j.tetlet.2007.04.047.
(14) Rueping, M.; Nachtsheim, B. J.; Kuenkel, A. *Org. Lett.* **2007**, *9* (5), 825. doi:10.1021/ol063048b.
(15) Sanz, R.; Martinez, A.; Miguel, D.; Alvarez-Gutierrez, J. M.; Rodriguez, F. *Adv. Synth. Catal.* **2006**, *348* (14), 1841. doi:10.1002/adsc.200606183.
(16) Motokura, K.; Fujita, N.; Mori, K.; Mizugaki, T.; Ebitani, K.; Kaneda, K. *Angew. Chem. Int. Ed.* **2006**, *45* (16), 2605. doi:10.1002/anie.200504609.
(17) Srihari, P.; Reddy, J. S. S.; Mandal, S. S.; Satyanarayana, K.; Yadav, J. S. *Synthesis* **2008**, (12), 1853. doi:10.1055/s-2008-1067083.
(18) Yadav, J. S.; Subba Reddy, B. V.; Pandurangam, T.; Raghavendra Rao, K. V.; Praneeth, K.; Narayana Kumar, G. G. K. S.; Madavi, C.; Kunwar, A. C. *Tetrahedron Lett.* **2008**, *49* (27), 4296. doi:10.1016/j.tetlet.2008.04.126.
(19) Rueping, M.; Nachtsheim, B. J. *Beilstein J. Org. Chem.* **2010**, *6* (6), 1. doi:10.3762/bjoc.6.6.
(20) Wang, G. W.; Shen, Y. B.; Wu, X. L. *Eur. J. Org. Chem.* **2008**, *2008* (25), 4367. doi:10.1002/ejoc.200800413.
(21) Misono, M.; Ono, I.; Koyano, G.; Aoshima, A. *Pure Appl. Chem.* **2000**, *72* (7), 1305. doi:10.1351/pac200072071305.
(22) Kozhevnikov, I. V. *Chem. Rev.* **1998**, *98* (1), 171. doi:10.1021/cr960400y.
(23) Azizi, N.; Torkiyan, L.; Saidi, M. R. *Org. Lett.* **2006**, *8* (10), 2079 doi:10.1021/ol060498v.
(24) Baskaran, S.; Kumar, G. D. K. *Chem. Commun. (Camb.)* **2004**, 1026.
(25) Rafiee, E.; Zolfagharifar, Z.; Joshaghani, M.; Eavani, S. *Appl. Catal. A Gen.* **2009**, *365* (2), 287. doi:10.1016/j.apcata.2009.06.030.
(26) Rafiee, E.; Joshaghani, M.; Tork, F.; Fakhri, A.; Eavani, S. *J. Mol. Catal. Chem.* **2008**, *283* (1–2), 1. doi:10.1016/j.molcata.2007.11.029.
(27) (a) Rafiee, E.; Joshaghani, M.; Eavani, S.; Rashidzadeh, S. *Green Chem.* **2008**, *10* (9), 982. doi:10.1039/b803249a; (b) Cid, R.; Pecci, G. *Appl. Catal.* **1985**, *14*, 15.
(28) Funabiki, K.; Komeda, T.; Kubota, Y.; Matsui, M. *Tetrahedron* **2009**, *65* (36), 7457. doi:10.1016/j.tet.2009.07.012.
(29) Thirupathi, P.; Kim, S. S. *Tetrahedron* **2010**, *66* (16), 2995. doi:10.1016/j.tet.2010.02.063.

Can. J. Chem. Downloaded from www.nrcresearchpress.com by South China Agricultural University on 09/19/12
For personal use only.

Volatile organic compounds analyzed by direct insertion probe mass spectrometry

Jian Jun Li

Can. J. Chem. Downloaded from www.nrcresearchpress.com by South China Agricultural University on 09/19/12
For personal use only.

Abstract: A modified approach for analyzing volatile organic compounds through standard direct insertion probe mass spectrometry is presented. With aluminum oxide or silica powder packed in a capillary tube, the sample's evaporative loss in a high vacuum instrument chamber is significantly reduced and the retention time is increased accordingly. With this technique, organic compounds with lower boiling points (e.g., 2-butanol at 99 °C) can be readily detected and analyzed.

Key words: direct insertion probe, mass spectrometry, volatile compounds, packed capillary tube.

Résumé : On présente une approche modifiée pour l'analyse des composés organiques volatiles par spectrométrie de masse avec sonde à insertion directe standard. L'utilisation de tubes capillaires remplis d'oxyde d'aluminium ou de silice permet de réduire considérablement la perte d'échantillon par évaporation dans la chambre de l'instrument et il en résulte que le temps de rétention en est accru d'autant. Cette technique permet de détecter et d'analyser les composés organiques de points d'ébullition faibles, tel le 2-butanol, à 99 °C.

Mots-clés : sonde à insertion directe, spectrométrie de masse, composés volatiles, tubes capillaires remplis.

[Traduit par la Rédaction]

Introduction

Direct insertion probe mass spectrometry is a useful technique that has been routinely used for decades for the study of moderately volatile compounds in a variety of chemical laboratories.[1–5] The advantages of this technique include short analysis times (usually within 20 min) and simplicity (no need for sample preparation). However, volatile compounds are difficult to analyze directly with this method because they readily evaporate and are often lost in the high vacuum system before being detected. This results in weak signal intensity and poor quality mass spectra. To reduce the evaporation rate of the volatile sample, modifications to this probe have been made.[6–10] For example, glass wool packed into the sample crucible was found to slow down the evaporation rate.[6] However, very few applications of this technique have been reported. Another approach, subambient operation of a direct insertion probe, has been addressed more frequently.[8] In this approach, with the assistance of a cooling device, the direct insertion probe has been applied for the analysis of some volatile compounds, e.g., methyl laureate and dimethylnaphthalene. However, the cooling system is expensive and inconvenient to operate routinely. Furthermore, the samples used in these studies have relatively high boiling points (>250 °C). Generally, volatile compounds remain a class of compounds that are seldom analyzed by direct insertion probe mass spectrometry. In addition to the direct insertion probe, other early-developed types of probes for volatile compound introduction (e.g., heated reservoir inlet) have also been used to analyze volatile compounds.[11–12] However, there are disadvantages in using them. For example, some compounds may linger in the probe system long after experiment completion, causing a "memory" effect. In addition, this probe is a relatively expensive accessory and therefore not frequently used to analyze volatile compounds. As a separation instrument, GC–MS can be used to analyze volatile compounds. However, there are disadvantages in using it as well. For example, the instrument is more expensive and its operation cost is relatively higher (sample preparation, solvent consumption, and longer running times). Furthermore, some volatile compounds may overlap with the solvent peak, causing interference.

Here, an approach for the use of a standard direct insertion probe mass spectrometry to analyze volatile organic compounds without any hardware modification is described. Instead, a small amount of several inert powdered materials were packed in a capillary tube along with the sample of interest. The packing material acts as a flow restrictor that considerably reduces the sample's evaporation rate. This enables the mass spectrometric data to be recorded under normal operating conditions and a good quality sample evaporation profile to be obtained. In this paper the practical details of this method are described.

Experimental

A Finnigan SSQ7000 quadrupole mass spectrometer equipped with a standard direct insertion probe system was

Received 9 June 2011. Accepted 19 September 2011. Published at www.nrcresearchpress.com/cjc on 30 November 2011.

J.J. Li. Chemistry Instrumentation Facility, Department of Chemistry, University of Calgary, 2500 University Drive NW, Calgary, AB T2N 1N4, Canada.

E-mail for correspondence: lijj@ucalgary.ca.

This article is part of a Special Issue to commemorate the International Year of Chemistry.

Can. J. Chem. Downloaded from www.nrcresearchpress.com by South China Agricultural University on 09/19/12
For personal use only.

used. The mass spectrometer was operated in electron impact (EI) mode with electron energy at 70 eV, filament current at 400 μA, multiplier voltage at 1400 V, vacuum at 4.5×10^{-7} Torr (1 Torr = 133.3224 Pa), and filament-on delay at 1 min. The probe was inserted into the instrument's ion source 0.3 min before the filament was turned on. After insertion, the probe tip was heated from ambient temperature (holding for 2 min) to 300 °C at a rate of 15 °C/min. Disposable capillary tubes with an o.d. of 1.5–1.8 mm and a length of 8–10 mm were used for sample loading. For regular experiments, approximately 1 μg of sample (solid or liquid) was transferred to the bottom of the capillary tube with a stainless steel needle and then the capillary tube was positioned in the probe tip and inserted into the ion source of the mass spectrometer. For packing experiments, the sample was placed at the bottom of the capillary tube and inert packing materials were added to fill the tube. After packing, the capillary tube was tapped gently to ensure that the packing material was tightly packed.

Both aluminum oxide powder (Al_2O_3) and silica powder were used as packing materials in this study. Aluminum oxide powder (analytical reagent, particle size 60–70 μm) was provided by The British Drug Houses Ltd. (Poole, UK). Ultrapure silica gel (5 μm, regular) was provided by Silicycle Inc. (Quebec, Quebec). Quartz (silica) wool was provided by Elemental Microanalysis Ltd. (Okehampton, UK). All other chemicals used had purities >95%. The packing materials and quartz wool were treated in an oven overnight before being used (800 °C for aluminum oxide and 650 °C for both silica and quartz wool). The retention time is defined as the peak time of the sample evaporation profile.

For the Al_2O_3 experiments, the capillary tube containing the sample was packed solely with Al_2O_3 powder onto the sample 5–6 mm high. For the silica experiments, silica was packed first 3–4 mm high, followed by Al_2O_3 powder 2–3 mm high. This approach was taken to prevent the silica powder from being pumped out by the high vacuum, since Al_2O_3 powder is heavier than silica. Finally, the quartz wool was placed on the top of the layers in the capillary tube to hold the content in place. The details of sample loading are shown in Fig. 1.

Results and discussion

Camphor is a solid substance (molecular weight 152 Da, boiling point 204 °C) that readily sublimes. When the sample was introduced into the mass spectrometer through the vacuum interlock, most of the substance was pumped out instantly. As a result, the spectrum signal was not completely recorded. As seen in Fig. 2A, camphor shows only a small fraction of the evaporation profile in an experiment performed using a standard direct insertion probe, without any modification to the sample holder. Next, Al_2O_3 powder was packed in the capillary tube, causing the evaporation rate of camphor to be significantly reduced, thereby allowing most of the sample to remain in the source during ionization. Consequently, a complete evaporation profile of camphor was obtained, as seen in Fig. 2B.

In addition to camphor, a number of volatile organic compounds also showed promising results, yielding truncated evaporation profiles in regular experiments, but complete

Fig. 1. Sample loading and packing for different experiments. (A) Regular experiment without packing, (B) packing experiment with Al_2O_3, and (C) packing experiment with silica (primarily) plus Al_2O_3.

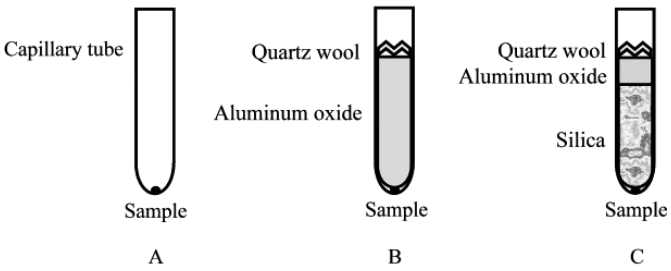

Fig. 2. Evaporation profiles of camphor obtained in different experiments. (Ion source temperature 150 °C). (A) Without packing material and (B) using Al_2O_3 as the packing material (retention time 3.3 min).

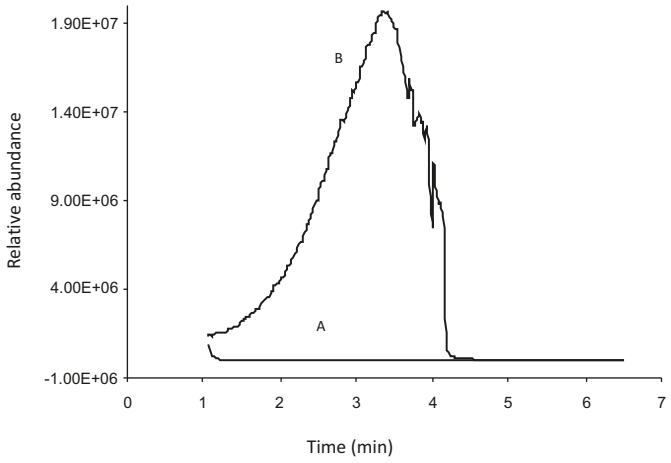

evaporation profiles in Al_2O_3-packing experiments. The compounds tested are listed in Table 1. In general, these compounds all have moderately low boiling points (~200 °C). One exception is quinoline, having the lowest boiling point (109 °C), but its retention time on Al_2O_3 packing material was not significantly different from other compounds. It is likely that there existed a stronger absorptive interaction between quinoline and Al_2O_3.

When Al_2O_3 was used as the packing material for the examination of organic compounds with even higher volatility, such as 1-butanol, the results were poor. One reason is that aluminum oxide powder has a larger particle size (more than 10 times as large as the silica) that is inefficient at preventing rapid evaporative loss. To improve this, a substance with a smaller particle size, silica powder, was chosen to partially replace Al_2O_3 in the capillary tube. In comparison experiments, silica showed a stronger ability to restrict the evaporative loss of the sample and the retention time was increased by more than 40%. Using a combination of silica and Al_2O_3 as packing material allowed complete evaporation profiles to be observed for the compounds with higher volatility. Table 2 lists several compounds of higher volatility that were successfully analyzed using combined silica and Al_2O_3 as the packing material. It is interesting to note that chlorobenzene

Can. J. Chem. Downloaded from www.nrcresearchpress.com by South China Agricultural University on 09/19/12
For personal use only.

Table 1. Volatile compounds showing complete evaporation profiles on Al_2O_3.

Chemical name	Molecular weight (Da)	Boiling point (°C)	Retention time (min)	Peak width at 1/2 peak height (min)
1-Bromo-4-nitrobenzene	201	261	5.6	0.9
Naphthalene	128	218	4.1	1.0
2,4-Dimethyl phenol	122	211	2.8	0.5
1-Octanol	130	195	8.0	1.1
2-Octanol	130	175	4.9	1.6
Quinoline	129	109	4.1	0.9

Note: Quinoline shows no signal in regular experiment. Ion source temperature, 150 °C.

Table 2. More volatile chemicals showing complete evaporation profiles on silica/Al_2O_3.

Chemical name	Molecular weight (Da)	Boiling point (°C)	Retention time (min)	Peak width at 1/2 peak height (min)
Chlorobenzene	112	131	1.5	1.0
Methyl isobutyl ketone	100	117	7.3	3.4
1-Butanol	74	117	3.6	1.4
2-Butanol	74	99	1.7	0.3

Note: All of these compounds show no signals in regular experiments. Ion source temperature, 120 °C.

had the highest boiling point in this table, but its retention time was the shortest. This may be attributed to its lower polarity.

Silica/Al_2O_3 was also used to study highly volatile and nonpolar compounds, such as toluene (boiling point 110 °C, molecular weight 92 Da) and hexane (boiling point 69 °C, molecular weight 86 Da). Although the complete evaporation profiles were not obtained in the study, the profile was sufficient to produce an adequate mass spectrum.

Conclusion

With the aid of inert packing materials, volatile organic compounds can be readily analyzed by standard direct insertion probe mass spectrometry. The evaporative loss of volatile compounds can be reduced significantly when packing material is used in the sample capillary tube. The retention time depends on the particle size of the packing material, as well as the boiling point and polarity of the compound. Our results show that this is a simple, inexpensive and convenient means of achieving direct insertion probe mass spectrometry of volatile compounds that can be implemented in any laboratory.

Acknowledgement

The author thanks Drs. M. Forgeron and K. Thurbide for their suggestions and corrections in the writing of this paper.

References

(1) Flego, C.; Zannoni, C. *Energy Fuels* **2010**, *24* (11), 6041. doi:10.1021/ef100984y.
(2) Talley, J. W.; Ghosh, U.; Furey, J. S.; Tucker, S. G.; Luthy, R. G. *Environ. Eng. Sci.* **2004**, *21* (6), 647. doi:10.1089/ees.2004.21.647.
(3) Uyar, T.; Toppare, T.; Hacaloğlu, J. *J. Anal. Appl. Pyrolysis* **2002**, *64* (1), 1. doi:10.1016/S0165-2370(01)00166-8.
(4) Puckey, D. J.; Jones, S. J. *J. Anal. Appl. Pyrolysis* **1984**, *6* (2), 157. doi:10.1016/0165-2370(84)80010-8.
(5) Robarge, T.; Phillips, E.; Conoley, M. *Application Note 10018;* Thermal Electron Corporation: Waltham, MA.
(6) Gross, J. H. *Mass Spectrometry: A Textbook;* Springer-Verlag: New York, 2004; p 208.
(7) Huang, M. W.; Chei, H. L.; Huang, J. P.; Shiea, J. *Anal. Chem.* **1999**, *71* (14), 2901. doi:10.1021/ac980516p.
(8) Sawdo, R. M.; Blumer, M. *Anal. Chem.* **1976**, *48* (4), 790. doi:10.1021/ac60368a014.
(9) Haddon, W. F.; Chait, E. M.; McLafferty, F. W. *Anal. Chem.* **1968**, *38*, 47907.
(10) Finnigan Corporation. *TSQ/SSQ 7000 Series Systems – Inlet Valve, GC, and Probes Operator's and Service Manual, Revision A, P/N 70001/97050;* Finnigan Corporation: San Jose, CA, 1993; pp 7–27.
(11) Smithson, L. D. *Anal. Chem.* **1971**, *43* (8), 1142. doi:10.1021/ac60303a050.
(12) Watson, J. T.; Sparkman, O. D. *Introduction to Mass Spectrometry;* John Wiley & Sons: New York, 2008; p 232.

NOTE OF APPRECIATION / NOTE DE RECONNAISSANCE

The success of the journal is dependent upon our reviewers. The Editors gratefully acknowledge the commitment and goodwill of all the reviewers who assisted us in the publication of Volume 89. Thank you.

Le succès du journal dépend du travail acharné de nos réviseurs. Le personnel de la rédaction est reconnaissant de leur volonté et leur nombreuses contributions qui ont rendu possible la sortie du volume 89. Merci.

Agnes, George
Al-Abadleh, Hind A.
Andersen, Raymond
Armitage, Bruce
Arndtsen, Bruce
Ashbrook, Sharon
Ata, Athar
Atkinson, Jeffrey
Aubert-Frecon, Monique
Auger, Michèle
Autschbach, Jochen
Auzanneau, France-Isabelle
Ayers, Paul
Azizi, Zahra
Back, Thomas
Bailey, William C.
Bain, Alex
Baird, Mike
Bancroft, Mike
Bandgar, Babasaheb
Barriault, Louis
Barcelo, Damia
Bartolotti, Lee
Bastow, Tim
Beaudry, Christopher
Beland, Francois
Berke, Heinz
Biris, Alexandru
Blakemore, Paul
Bodwell, Graham
Bogel-Lukasik, Rafal
Bontchev, Ranko
Borchers, Christoph
Boukherroub, Rabah
Boukouvalas, John
Boulon, Georges
Britton, Robert
Brook, Michael
Brosseau, Christa
Brouwer, Darren
Brown, Stan
Bryce, David
Buncel, Erwin
Bunton, Clifford
Burnell, Elliott
Cai, Zhengting
Chakrabarty, Manas
Chapela, G.A.
Chen, Aicheng
Chen, Maodu
Chen, Shentan
Chen, Yongjun
Chirakal, Raman
Cho, Herman
Chong, J. Michael
Chu, Tianshu
Ciufolini, Marco
Clive, Derrick
Clyburne, Jason
Cordova, A.
Corma, Avelino
Cragg, Peter
Cramb, David
Crimmins, Mike
Dabbagh, Hossein
Dake, Gregory
DaSilveira Neto, Brenno
Davis, Jeff
DeRosa, Maria
Diez, V.K.
Ding, Zhifeng
Dong, Ron
Donkor, Kingsley
Dorner, Robert
Drew, Simon
Durst, Tony
Dust, Julian
Ehara, Masahiro
Endicott, John
Erden, Ihsan
Es'haghi, Zarrin
Eswaran, P.
Fancui, Meng
Feindel, Kirk
Fernandes, Ana
Fink, Mark
Fletcher, Steven
Fokin, Valery
Foti, Mario
Gan, Zhehong
Gao, Faming
Gao, Zhiqiang
Garden, S.J.
Gauld, James
Ge, Maofa
Ghambarian, Mehdi
Ghiviriga, Ion
Giorgi, Javier B.
Giroux, Simon
Gomez-Carrasco, Susana
Górecki, Tadeusz
Goward, Gillian
Grabowski, Slawomir
Grant, David
Grant, Greg
Gravel, Michel
Gray, Christopher
Green, James
Grindley, Bruce
Gu, Xibin
Gundersen, L.L.
Hall, Dennis
Hametner, Christian
Han, Keli
Han, Sang Soo
Hansen, Jaron
Harrison, Paul
Hase, William L.
Hayes, Paul
Hazendonk, Paul
Heald, Steve
Heinekey, Michael
Heise, H.
Herr, Jason
Herring, Andrew
Hitchcock, Adam
Hocek, M.
Holder, Simon
Hong, Lian
Honvault, Pascal
Hopf, Henning
Hosmane, Narayan
Hou, X.L.
Huffman, J.
Hultin, Philip
Hureau, Christelle
Irfan, Ahmad
Ishihara, Kazuaki
Jakle, Frieder
Janecki, T.
Jang, Do
Jerschow, Alexej
Jessop, Philip
Jha, Amitabh
Johnston, Linda
Johnston, Roy
Jones, W.
Joule, John
Juaristi, Eusebio
Kar, Tapas
Karboune, Salwa
Kaszynski, Piotr
Kaufman, T.
Keefe, Dale
Keefer, Larry
Kelland, Malcolm
Kerr, Michael
Khan, Abu T.
Kim, Jun-Hyun
Kim, Soowhan
Kimmel, Gregory
Klabunde, Kenneth
Klug, D.
Kobayashi, Rika
Koenig, Burkhard
Kolandaivel, P.
Kondepudi, Dilip
Kozak, Christopher
Kozlowski, Piotr
Kroeker, Scott
Krol, Ed
Krull, Ulrich
Kulik, Dmitrii
Kundu, Bijoy
Kurth, Mark
Kusalik, Peter

Can. J. Chem. Downloaded from www.nrcresearchpress.com by 80.58.250.72 on 09/16/12
For personal use only.

Can. J. Chem. Downloaded from www.nrcresearchpress.com by 80.58.250.72 on 09/16/12
For personal use only.

Kyritsis, Panayotis
Lafleur, Michel
Lanzirotti, Antonio
Larhed, M.
Launay, Franck
Lavey, Brian
Leaist, Derek
Lessard, Jean
Lewars, Errol
Li, Chao-Jun
Li, Kecheng
Li, Liang
Li, W.
Li, Weishan
Li, Yat
Li, Yue
Li, Zhi-Ru
Ling, Chang-Chun
Liu, Jingyao
Liu, Wing-Ki
Liu, Yu
Loboda, Alexandre
Loh, Teckpeng
London, Robert
Long, Y.Q.
Loppnow, Glen
Loughlin, Wendy
Low, Paul
Luzzio, Frederick
Macartney, Donal
Macdonald, Peter
MacLachlan, Mark
Madsen, Louis
Maes, Christian
Mahwinney, Robert
Maly, Kenneth
Mar, Arthur
Marat, Kirk
Marcantoni, Enrico
Marken, Frank
Martinez, Ana
Masson, Geraldine
Mataa, Rachel
Mauzeroll, Janine
Mazyck, David
McDonald, Robert
McGrady, Sean
McIndoe, J. Scott
McNulty, James
Mehandjiev, D.
Michal, Carl
Mikkelson, Susan
Mirjalili, B.B.F.
Mirzaei, Mahmoud
Mitchell, Reg
Moghadam, Majid
Monteiro, Mario
Moreira, Jose Antonio de Sousa
Motokura, Ken
Moudrakovski, Igor
Muchall, Heidi
Mueller, Leonard
Murphy, R. Scott
Nair, Vijay
Nakano, M.
Nakashima, Tom
Narain, Ravin
Novak, Igor
Ogawa, Makoto
Ollevier, Thierry
Onchoke, Kefa
Ooms, Kristopher
Orlova, Galina
Ottolina, Gianluca
Ouellet, Stephane
Pagenkopf, Brian
Palmer, Michael H.
Pansare, Sunil
Parlar, Harun
Patchkovskii, Serguei
Paterson, David
Pedras, M. Soledade
Pekar, Miloslav
Pelton, Robert
Peng, Simon
Peng, Zhenmeng
Penner, Glenn
Phukan, P.
Piao, Hu-Ri
Pierce, Karisa
Pinhas, Allan R.
Pizzio, L.R.
Plettner, Erika
Plourde, Guy
Poirier, Raymond
Politzer, Peter
Pottie, Ian
Prevost, Sylvain
Quadrelli, Paolo
Quast, Helmut
Ragogna, Paul
Rassi, Heidar
Ratcliffe, Christopher
Rayne, Sierra
Ren, Aimin
Richardson, David
Richter, Mark M.
Ripmeester, John
Roberto-Neto, Orlando
Roohi, Hossein
Rosenberg, Lisa
Saidi, Mohammad
Salehi, Peyman
Sandhu, J.S.
Sanz, Roberto
Sartorel, Andrea
Sauers, Ronald
Sauriol, Francois
Schaper, Frank
Schlangen, Maria
Schlegel, H. Bernhard
Schmitzer, Andreea
Schreckenbach, Georg
Schulz, Bill
Schurko, Robert
Schwan, Adrian
Sdobnyakov, N.Y.
Semenikhin, Oleg
Sen, K. D.
Shahidi, Fereidoon
Shi, Jinsheng
Shi, Xiaodong Michael
Shields, George
Shimizu, M.
Shirai, Koun
Sibi, Mukund
Silber, Juana
Singer, Rob
Singh, Hari Ji
Singh, M.
Skalska, Kinga
Skene, William
Smith, Mark
Smith, Mike
Soai, K.
Spataru, Tudor
Staroverov, Viktor
Stradiotto, Mark
Straus, Suzana
Strauss, Chris
Strout, Douglas
Stubbs, Keith
Sugahara, Takeshi
Sun, Xueliang
Surman, Matthew
Sutherland, Todd
Swaddle, T.
Syvitski, Ray
Taddei, Maurizio
Takemoto, Y.
Tang, Weiping
Thompson, Alison
Thurbide, Kevin
Tian, Min
Tian, Wei Quan
Tidwell, Thomas
Toscano, John
Toth, Landy
Tsuzuki, Seiji
Urgaonkar, Sameer
Vanderwal, Christopher
Varela, O.
Vaughan, Keith
Velazquez, Carlos
Walsby, Charles
Wang, Deyun
Wang, Feng
Wang, Jin
Wang, Meishan
Wang, Mingliang
Wang, Suning
Wang, Yan-Hong
Wayland, Bradford
Wei, Y. G.
Welch, Karen Terry
Williams, Vance
Wolf, Christian
Wong, Wai-Yeung
Wright, Jim
Wu, Gang
Wu, Yundong
Wuest, James
Wujec, Monika
Xantheas, Sotiris
Xu, Charles
Xu, Qiang
Xu, Qun
Yadav, J.S.
Yamamoto, Hisashi
Yang, Zhong-Zhi
Yao, Min Liang
Yet, Larry
Zamborini, Frank
Zaragoza, Florencio
Zeng, W.
Zhang, Chi
Zhang, Jin
Zhang, Xianxi
Zimmerman, William

TRIBUTE

Can. J. Chem. Downloaded from www.nrcresearchpress.com by University of Electronic and Science Techonology of China on 09/18/12
For personal use only.

The name Juan Cesar Scaiano, of course, better known to most as Tito Scaiano, is synonymous with photochemistry and indeed chemistry in Canada. Since settling in Canada in 1979, Tito has made the Ottawa area his home and the place where he established and built his reputation as one of the world's foremost experts in photochemistry and reactive intermediates. It is a fitting tribute for the *Canadian Journal of Chemistry* to provide his friends and colleagues with the venue to present their own scientific contributions in honour of one of our country's preeminent chemists, on the occasion of his 65th birthday.

Tito was born in Buenos Aires, Argentina, in 1945. He obtained his undergraduate degree from the University of Buenos Aires in 1967 and then his Ph.D. from the University of Chile in 1970 working with Eduardo Lissi (who is a coauthor of a paper in this issue). Following a post-doc with Alwynn Davies at University College London, he returned to Chile briefly and then took a position at the University of Rio Quarto in Argentina. The stories of this part of Tito's personal and scientific life in Argentina during the years of the Peronist revolution would fill a volume on their own, and we will leave them to Tito to relate. Suffice it to say that it was this terrifying time in South American history that brought Tito to Canada in 1975, when he joined Keith Ingold (also a contributor to this issue) as a visiting scientist at the National Research Council (NRC) in Ottawa. He left Canada briefly to take up his first faculty position at the Radiation Laboratory at the University of Notre Dame, but the lure of Canada and the NRC brought him and his family back to stay in 1979. He remained at the NRC until 1991, when he gave up his position as Principal Research Officer to move to the University of Ottawa as a Professor. He is now a Distinguished University Professor and the Canada Research Chair in Applied Photochemistry, a position he has held since 2003. There is a very nice biography of Tito that appeared in the journal *Photochemistry and Photobiology* (**2006**, *82*: 1–4) that covers most aspects of his biography and his career up to 2005. This article accompanied a special issue of that journal that was dedicated to Tito after a symposium entitled *Reactive Intermediates in Photochemistry*, which celebrated his contributions on the occasion of his 60th birthday. We will not repeat much of what was so elegantly written then; instead, we summarize some of the more recent achievements that continue to highlight his remarkable career.

Tito's research interests have always been built from the foundation for which he is best known, namely, the application of laser techniques for the study of short-lived reactive intermediates and reaction mechanisms in solution, supramolecular systems, and heterogeneous media. This underlying theme led to the pioneering use of two-photon photochemistry for the study of reactive intermediates and the discovery of new photochemical pathways, and the development of novel lithographic imaging techniques. In the 1990s some of his group's focus was shifted to studying photochemical applications of biologically relevant molecules, where they examined the photostability and photodegradation mechanisms of pharmaceuticals, most notably ketoprofens. This led to the development of new photocages for the rapid and selective release of small molecules in biological systems. His extensive contributions to our knowledge of the reactivity of reaction intermediates such as radicals and biradicals has also been instrumental in the discovery of new antioxidants. In the last 6 years or so he has been a key contributor to the application of photochemical methods for the preparation and application of nanomaterials, in particular Au, Ag, and Cu nanoparticles. As one looks over his 606 (and counting) research papers, 75 in the last 5 years alone, it is evident that there is not an area of photochemistry to which Tito has not made seminal contributions. His H-index has been in the 60s over the last decade or so, making him one of Canada's most highly cited chemists. His excellence in research led to the most highly prized research awards for both Ontario and Canada, namely, the Premier's Platinum Excellence Award and the Gerhard Herzberg Canada Gold Medal in Science and Engineering. These awards cap a long list of other accolades he has earned throughout his career that are reserved for the very best in the field, including the Rutherford Memorial Medal, the Steacie Prize in Natural Sciences, the E.W.R. Steacie Award, the Inter-American Photochemical Society Award in Photochemistry, a Killam Research Fellowship, the Henry Marshall Tory Medal of the Royal Society of Canada, The Porter Medal for Photochemistry awarded jointly by the European, Japanese, and Inter-American Photochemical Societies, the Photon Award from the American Society for Photobiology, and the Sir Christopher Ingold Fellowship and Medal of the Royal Society of Chemistry. He is a Fellow of the Royal Society of Canada and the Chemical Institute of Canada, and is the University of Ottawa's first named Distinguished University Professor.

In addition to giving a number of named lectureships, in the last 5 years he has also received a number of other distinctions including Honorary Doctorates from Dalhousie University (2006) and from the Universidad de Cordoba in Argentina (2010). He was also appointed "Académico" of the National Academy of Sciences of Argentina and an Officer of the Order of Canada in 2006. The citation for the latter describes him as "*an inspiring teacher to students, nurturing their creative spirit and conveying to them a sense of community responsibility*." Tito ranks his role as a mentor to the long list of undergraduate and graduate students and post-doctoral researchers who have passed through his lab as the biggest contribution of his career. Since 2005 he has mentored 9 M.Sc. and 15 Ph.D. students, 18 post-doctoral fellows, and 19 undergraduate students, who join the more than 485 of his past collaborators and coauthors who are listed at the end of this tribute. Most of his former students and post-doctoral researchers have gone on to establish impressive careers of their own, and many have made remarkable contributions as academics or leaders in major companies and government laboratories. No less than a dozen of his former group members are faculty members at Canadian Universities. Tito's name will live on for the next generations of young chemists who may not have the good fortune to work with him directly, on the front covers of the two "bibles" of the trade — *Principles of Molecular Photochemistry: An Introduction* and *Modern Molecular Photochemistry of Organic Molecules*, published by University Science Publishers — which he coauthored with two of his longtime collaborators, Nick Turro and V. Ramamurthy.

Not surprisingly for someone of his stature, Tito has also held a number of leadership roles in national and international organizations. He served as President of both the Inter-American Photochemical Society and the American Society for Photobiology. He was the first Editor-in-Chief of *Photo-*

Can. J. Chem. Downloaded from www.nrcresearchpress.com by University of Electronic and Science Techonology of China on 09/18/12
For personal use only.

chemistry and Photobiology from outside of the United States, and has also served on the Editorial Board of many journals, including *Accounts of Chemical Research* and the *International Journal of Chemical Kinetics*.

Tito is also an entrepreneur. Anyone who has heard him give a lecture will know from his subtle "plugs" of Luzchem Research Inc., the Ottawa-based company that he started in the late 1990s with his wife, Elda. Luzchem (www.luzchem.com) specializes in the design and manufacture of instruments and equipment used in photochemistry. From its humble beginnings building photoreactors, Luzchem now offers a wide range of photochemical equipment including a miniaturized laser flash photolysis system, systems for film metrology, xenon illumination products, solar simulators, and spectroradiometers. Luzchem is a successful, family-run business (all five shareholders are Scaianos) with 13 employees, and was honored by the Ottawa Chamber of Commerce in 2007 with the award for Small Business of the Year.

Interestingly, a part of Tito's motivation for starting Luzchem was to plan for a second career once he turned 65 years of age and had to retire from academia. Tito is rarely guilty of poor planning, but as we write this in late 2010, the year Tito turned 65, there is no longer mandatory retirement in Ontario, he has recently been renewed as the CRC Chair in Applied Photochemistry at Ottawa until 2017, and he now serves as Chair of the Department of Chemistry there. It is clear that his 65th birthday is but just another milestone, and there will be much more in his career to be celebrated in the coming years.

When not "working", Tito spends time with his family — the love of his life Elda, their four grown children and their spouses, and his and Elda's grandchildren. Tito and Elda continue their adventurous spirit from the early days and now that their children are grown they can often be found traveling the world together. Recently, they have taken to adventures that involve cruising the oceans, seas, and fiords of the world. The photograph of Tito and Elda shown in this issue was taken in 2010 during a cruise of the fiords of Norway. We are honored that Elda, an accomplished artist, has agreed to allow one of her paintings to be used as the cover artwork for this Special Issue. Another painting of hers, suitably entitled "Growing in Canada" appears below. We believe that Tito has always been grateful for the opportunities that have been provided to him in his adopted country, and the cover artwork, with its distinctly Canadian theme, and "Growing in Canada" captures the essence of his career and family life.

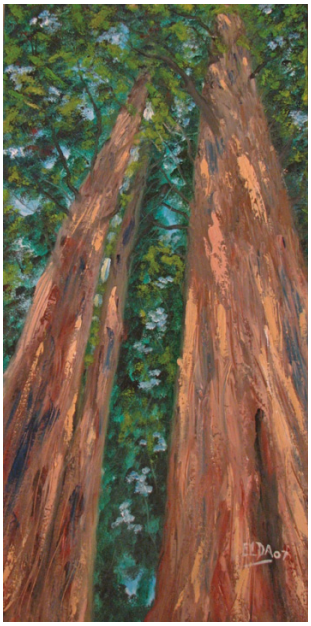

Tito is indeed a remarkable colleague and mentor. As you read the two issues dedicated to Tito, the first in February and the second in March, you will be struck by the high quality and diversity of the chemistry presented by his friends, colleagues, past students, and post-docs from across the country and around the world. They are a fitting testament to the wide-ranging impact he has had on our field, and there is something here for everyone. Tito wouldn't have it any other way.

William J. Leigh
McMaster University

Mark S. Workentin
The University of Western Ontario

HOMMAGE

Can. J. Chem. Downloaded from www.nrcresearchpress.com by University of Electronic and Science Techonology of China on 09/18/12
For personal use only.

Juan Cesar Scaiano, que la plupart connaissent mieux sous le nom de Tito Scaiano, est synonyme de photochimie et bien entendu de chimie au Canada. Depuis qu'il s'est établi au Canada en 1979, Tito a choisi de vivre dans la région d'Ottawa où il a établi et bâti sa réputation comme l'un des plus grands experts au monde dans le domaine de la photochimie et des intermédiaires réactifs. La *Revue canadienne de chimie* est l'endroit tout indiqué pour donner l'occasion à ses amis et à ses collègues de présenter leurs propres contributions scientifiques en l'honneur de l'un de nos éminents chimistes au pays, à l'occasion de son 65e anniversaire.

Tito est né à Buenos Aires (Argentine) en 1945. Il a obtenu son diplôme de premier cycle de l'Université de Buenos Aires en 1967, puis son doctorat de l'Université du Chili en 1970, sous la direction d'Eduardo Lissi (coauteur d'un article dans le présent numéro). Après avoir effectué un postdoctorat au sein du groupe d'Alwynn Davies au University College de Londres, il est retourné brièvement au Chili et a accepté par la suite un poste à l'Université de Rio Quarto en Argentine. Les récits de cet épisode de sa vie personnelle et scientifique en Argentine pendant les années de la révolution péroniste rempliraient, à eux seuls, un volume tout entier. Nous laisserons donc le soin à Tito de nous les raconter. Qu'il suffise de dire que ce sont ces moments terrifiants de l'histoire sud-américaine qui ont amené Tito au Canada en 1975, lorsqu'il a rejoint Keith Ingold (également collaborateur au présent numéro) à titre de chercheur invité au Conseil national de recherches du Canada (CNRC), à Ottawa. Il a quitté brièvement le Canada pour occuper son premier poste de professeur au laboratoire de rayonnement de l'Université Notre Dame (É.-U.), mais l'attrait du Canada et du CNRC l'a ramené s'installer au pays avec sa famille en 1979. Il a travaillé au CNRC jusqu'en 1991, année où il a renoncé à son poste d'agent principal de recherche pour occuper celui de professeur à l'Université d'Ottawa. Il est maintenant professeur distingué et titulaire de la Chaire de recherche du Canada en photochimie appliquée, poste qu'il occupe depuis 2003. Il existe une très belle biographie de Tito, parue dans la revue scientifique *Photochemistry and Photobiology* (**2006**, *82*: 1–4), qui porte sur la plupart des aspects de sa vie et de sa carrière jusqu'en 2005. Cet article accompagnait un numéro spécial de la revue consacré à Tito, à la suite d'un colloque intitulé *Reactive Intermediates in Photochemistry*, qui soulignait ses contributions à l'occasion de son 60e anniversaire. Nous ne répéterons pas ce qui a été écrit de manière si élégante à ce moment-là; nous résumerons plutôt certaines de ses plus récentes réalisations qui continuent de mettre en évidence sa carrière remarquable.

Les travaux de recherche de Tito ont toujours eu comme fondement le thème pour lequel il est le mieux connu, à savoir l'application des techniques laser pour l'étude des intermédiaires réactifs de courte durée de vie et des mécanismes de réaction en solution, dans les systèmes supramoléculaires et dans les milieux hétérogènes. Ce thème de fond a mené à l'utilisation novatrice de la photochimie à deux photons pour l'étude des intermédiaires réactifs et la découverte de nouvelles voies photochimiques, de même qu'à la création de nouvelles techniques lithographiques. Dans les années 1990, une partie des efforts de son groupe s'est tournée vers l'étude d'applications photochimiques de molécules d'intérêt biologique, où l'on a examiné la photostabilité et les mécanismes de photodégradation de médicaments, en particulier des kétoprofènes. Cette étude a mené à la création de nouvelles molécules photolabiles (« photocages ») pour la libération rapide et sélective de petites molécules dans des biosystèmes. Ses contributions considérables à l'avancement de nos connaissances sur la réactivité d'intermédiaires réactionnels comme les radicaux et les biradicaux ont également joué un rôle important dans la découverte de nouveaux antioxydants. Au cours des six dernières années, il a participé activement à l'application de méthodes photochimiques pour la préparation et l'utilisation de nanomatériaux, en particulier des nanoparticules d'or, d'argent et de cuivre. Si l'on se penche sur ses 606 articles scientifiques publiés jusqu'à maintenant, dont 75 dans les cinq dernières années seulement, il est évident qu'il n'y a aucune sphère de la photochimie à laquelle Tito n'a pas contribué de manière exceptionnelle. Son indice h a oscillé dans la soixantaine au cours de la dernière décennie, ce qui en fait l'un des chimistes canadiens les plus souvent cités. Son excellence dans la recherche l'a mené à l'obtention des prix les plus convoités en recherche en Ontario et au Canada, à savoir la Bourse du premier ministre de l'Ontario pour l'excellence en recherche et la médaille d'or Gerhard-Herzberg en sciences et en génie. Ces prix viennent couronner une longue liste d'autres récompenses remportées tout au long de sa carrière et que l'on réserve aux meilleurs du domaine, dont la médaille commémorative Rutherford, le prix Steacie en sciences naturelles, le prix E.W.R. Steacie, le prix de l'Inter-American Photochemical Society en photochimie, la bourse de recherche Killam, la médaille Henry Marshall Tory de la Société royale du Canada, la médaille Porter en photochimie décernée conjointement par l'Association européenne de photochimie, l'Inter-American Photochemical Society et la Japanese Photochemical Society, le prix Photon de l'American Society for Photobiology et le Sir Christopher Ingold and Medal de la Royal Society of Chemistry. Il est membre de la Société royale du Canada et de l'Institut de chimie du Canada et le premier à recevoir le titre de Professeur distingué de l'Université d'Ottawa.

En plus d'avoir donné un certain nombre de conférences commémoratives, il a également reçu plusieurs autres distinctions au cours des cinq dernières années, dont un doctorat honorifique de l'Université Dalhousie (2006) et un autre de l'Université de Córdoba en Argentine (2010). Il a également été nommé « Académico » de l'Académie nationale des sciences de l'Argentine et Officier de l'Ordre du Canada en 2006. La note biographique de cette dernière nomination le décrit comme « un pédagogue qui a su inspirer et guider ses étudiants en cultivant leur créativité et en leur inculquant un sens des responsabilités communautaires ». Tito classe son rôle de mentor de la longue liste d'étudiants de premier cycle, de diplômés et de chercheurs postdoctoraux qui sont passés par son laboratoire comme étant la plus grande contribution de sa carrière. Depuis 2005, il a mentoré 9 étudiants à la maîtrise et 15 autres au doctorat, 18 boursiers postdoctoraux et 19 étudiants de premier cycle, qui rejoignent les rangs de plus de 485 de ses anciens collaborateurs et coauteurs dont la liste apparaît à la fin de cet hommage. La plupart de ses anciens étudiants et chercheurs postdoctoraux ont entrepris de brillantes carrières, et beaucoup d'entre eux contribuent de façon remarquable en tant que professeurs d'université ou chefs de file dans des entreprises importantes et des labora-

Can. J. Chem. Downloaded from www.nrcresearchpress.com by University of Electronic and Science Techonology of China on 09/18/12
For personal use only.

toires gouvernementaux. Pas moins d'une douzaine d'anciens membres de son groupe font partie du corps professoral d'universités canadiennes. Le nom de Tito continuera de se perpétuer au sein des prochaines générations de jeunes chimistes qui n'auraient pas la chance de collaborer avec lui directement grâce aux deux « bibles » du domaine intitulées *Principles of Molecular Photochemistry: An Introduction* et *Modern Molecular Photochemistry of Organic Molecules*, publiées par les University Science Publishers, et qu'il a corédigées avec deux de ses collaborateurs de longue date, soit Nick Turro et V. Ramamurthy.

Comme on peut s'y attendre de la part de quelqu'un de sa stature, Tito a également assumé des rôles de leadership au sein d'organismes nationaux et internationaux. Il a été président de l'Inter-American Photochemical Society et de l'American Society for Photobiology. Il a été le premier directeur de la publication non états-unien de la revue *Photochemistry and Photobiology* et a également été membre du comité de rédaction de nombreuses revues, notamment de l'*Accounts of Chemical Research* et de l'*International Journal of Chemical Kinetics*.

Tito est également entrepreneur. Toute personne qui a déjà assisté à l'une de ses conférences aura entendu parler, en raison de ses allusions intéressées subtiles, de Luzchem Research inc., une entreprise d'Ottawa qu'il a créée avec sa femme, Elda, à la fin des années 1990. Luzchem (www.luzchem.com) se spécialise dans la conception et la fabrication d'instruments et de matériel utilisés en photochimie. De ses débuts modestes, où elle ne fabriquait que des photoréacteurs, Luzchem a prospéré et offre maintenant une vaste gamme d'appareils dont un système de photolyse éclair au laser miniaturisé, des systèmes pour l'analyse de films, des lampes au xénon, des simulateurs solaires et des spectroradiomètres. Luzchem est une entreprise familiale florissante (les cinq actionnaires sont des Scaiano) qui compte 13 employés et en 2007, elle a reçu le prix de la petite entreprise de l'année de la Chambre de commerce d'Ottawa.

Fait intéressant, l'une des raisons pour lesquelles Tito voulait fonder son entreprise était de planifier une seconde carrière en vue de sa retraite du milieu universitaire qu'il devrait prendre une fois qu'il aurait atteint 65 ans. Tito est rarement coupable d'une mauvaise planification, mais au moment où nous écrivons ces lignes, à la fin de 2010 et l'année même où il a atteint l'âge de 65 ans, il n'existe plus de retraite obligatoire en Ontario, le poste de titulaire de la Chaire de recherche du Canada en photochimie appliquée à Ottawa lui a été confié de nouveau jusqu'en 2017 et il est maintenant directeur du Département de chimie à cet endroit. Il est clair que son 65^{e} anniversaire n'est qu'une autre étape importante et que l'on soulignera encore de nombreuses réalisations professionnelles au cours des prochaines années.

Lorsqu'il ne « travaille » pas, Tito passe du temps en famille avec l'amour de sa vie, Elda, leurs quatre enfants maintenant adultes et leur conjoint ou conjointe, et les petits-enfants. Tito et Elda ont gardé leur esprit d'aventure des premiers jours, et maintenant que les enfants sont grands, on les trouve souvent parcourant le monde ensemble. Récemment, ils ont pris goût aux aventures qui touchent les croisières dans les océans, les mers et les fjords du monde. La photo de Tito et d'Elda présentée dans le présent numéro a été prise en 2010 lors d'une croisière dans les fjords de Norvège. Nous sommes très honorés qu'Elda, une artiste accomplie, ait consenti à ce que nous utilisions l'une de ses toiles comme illustration de la page couverture du présent numéro spécial. Une autre de ses œuvres, intitulée à juste titre *Growing in Canada*, apparaît ci-dessous. Nous croyons que Tito a toujours été reconnaissant des possibilités qui lui ont été offertes dans son pays d'adoption, et cette illustration de la page couverture, dont le thème est typiquement canadien, ainsi que *Growing in Canada* capturent l'essence de sa carrière et de sa vie familiale.

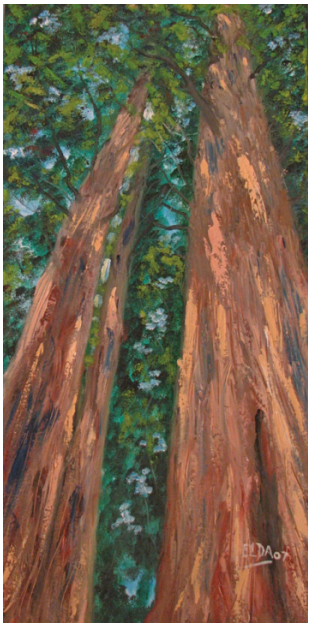

Tito est en effet un collègue et un mentor exceptionnels. En parcourant les pages des deux numéros consacrés à Tito, le premier en février et le second en avril, vous serez frappé par la grande qualité et diversité de la chimie présentée par ses amis, collègues, anciens étudiants et boursiers postdoctoraux de partout au pays et d'ailleurs dans le monde. Ils témoignent avec justesse des vastes répercussions qu'il a eues sur notre domaine, et chacun y trouve son compte ici. Tito ne voudrait pas qu'il en soit autrement.

William J. Leigh
Université McMaster

Mark S. Workentin
Université de Western Ontario

TRIBUTE

Can. J. Chem. Downloaded from www.nrcresearchpress.com by 80.58.250.72 on 09/16/12
For personal use only.

Rod was born on July 6th, 1944 in rural Alberta, approximately 250 km east of Edmonton, where his grandparents on both sides of his family homesteaded near the turn of the last century. Rod's father operated a bulk oil and gas agency together with a welding and general farming machinery repair shop in the farming community known as Landonville. When Rod was in grade one, he attended Telegraph, a one-room school, where his aunt Eunice was the teacher. Everyday he walked the 3.5 miles to school. When the winter weather was too miserable for walking, which was frequent in central Alberta, he stayed with his aunt in a small teacher's "shack" adjacent to the school. The school had only nine students, but Rod feels that he profited immensely from having his aunt as one of his first teachers in this unique environment. In 1957, Rod's family moved to Vermilion, a bustling town of approximately 2500 situated on the river of the same name, which serves the surrounding rural communities. Rod spent much of his summer "vacations" working on his grandparents' farm — repairing fences, painting, gardening, picking rocks, harvesting hay, etc. Rod's interest in chemistry was sparked by a grade 10 science teacher, Mr. Matheson, who performed a number of in-class chemistry demonstrations. To acquire a deeper understanding of chemistry, Rod constructed a laboratory in the basement of his home, much to the annoyance of his family, particularly when loud bangs from exploding hydrogen or smells of hydrogen sulfide or other noxious gases emanated from the basement.

After finishing high school, Rod spent 2 years at the Southern Alberta Institute of Technology (SAIT) in Calgary where he completed the Chemical Research Laboratory Technology program. After graduation, he took up a full-time position at Atomic Energy of Canada Limited in Pinawa, Manitoba. He quickly decided that he wanted to further his education, so he continued his move eastward to Waterloo where he obtained a B.Sc. Honours in chemistry in 1968. Forty years later, he received one of the 50 Alumni of Honour Awards to mark the 50th anniversary of the Faculty of Science at the University of Waterloo. It was here that Rod was first introduced to NMR spectroscopy while working as a summer student in the laboratory of Terry Gough. One other important discovery that Rod made in Waterloo was his future wife, Valerie, who was at the time a graduate student in Learning Psychology. Valerie hailed from the east (Kingston, Ontario, and Arvida, Quebec) so they decided to get married in the middle of the country, Winnipeg, in the fall of 1968. Rod completed his M.Sc. (1970) and Ph.D. (1972) under the supervision of Ted Schaefer at the University of Manitoba. The title of Rod's M.Sc. thesis was "A study of benzene solvent-induced shifts in the proton magnetic resonance spectra of some substituted benzenes"; the Ph.D. thesis was about "Some applications of experimental and theoretical nuclear spin-spin coupling constants to study molecular structure". Approximately 15 papers, all published in the *Canadian Journal of Chemistry*, resulted from Rod's graduate research in Schaefer's laboratory. His graduate research demonstrated the importance of performing high-precision NMR measurements (i.e., the measurement of NMR frequencies to ±0.01 Hz and line widths at half-maximum height of less than 0.10 Hz) in obtaining information on the conformations and dynamics of small molecules in solution. Another significant aspect of Rod's early research was his use of the very best theoretical methodology available at the time to interpret experimental data. For example, he used semiempirical molecular orbital theory to aid the interpretation of long-range spin-spin coupling constants; see Fig. 1. The model, while crude by today's standards, has withstood the test of time. The synergy of experiment and theory has become a hallmark of Rod's groundbreaking research in advancing our understanding of the fundamental NMR tensors.

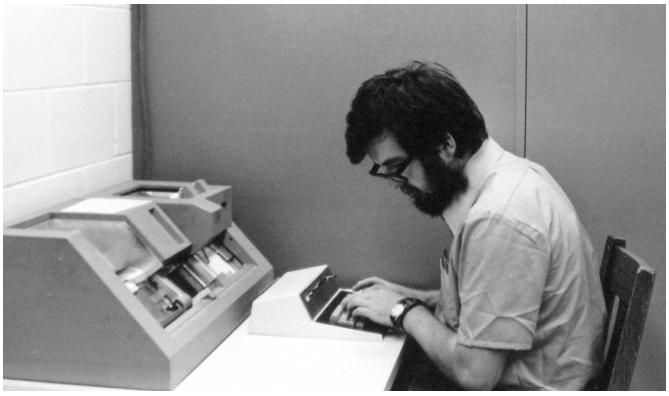

Fig. 1. Rod Wasylishen as a graduate student, ca. 1971–1972, in the old Engineering Building of the University of Manitoba. He is shown preparing punched-card computer input for John A. Pople's semi-empirical INDO program that Rod had modified to calculate spin-spin coupling constants. The FORTRAN code consisted of approximately 2000 lines (i.e., a big box of computer cards).

Between 1972 and 1974, Rod was a National Research Council postdoctoral fellow with Ted Becker at the Laboratory of Chemical Physics of the National Institutes of Health (Bethesda, Maryland). Here Rod was introduced to pulsed Fourier transform (FT) NMR spectroscopy. In 1974, Rod took up an assistant professorship at the University of Winnipeg, working on chemical applications of solution NMR spectroscopy. At Winnipeg, he also recognized the power of multinuclear NMR in studying the dynamics of orientationally disordered solids. During a one-year sabbatical (1980–1981) in Colin Fyfe's laboratory at the University of Guelph, Rod had his first opportunity to investigate rigid solids using magic-angle spinning and cross-polarization techniques.

In 1982, Rod moved to Dalhousie University, Halifax, Nova Scotia, where he established a vigorous solid-state NMR research program aimed at better understanding the relationship between NMR tensors and molecular structure. During this period, he and his research group made seminal contributions to the understanding of fundamental NMR tensors. These tensor properties and their relationships to molecular structure and chemical bonding are the foundation on which the power of NMR spectroscopy lies. He carried out extensive measurements of chemical shift tensors for a wide range of important chemical compounds. In many cases, his reports have represented the first ever measurement for a particular functional group. In the late 1980s, Rod recognized that magnetic shielding tensors and electric field gradient tensors are not necessarily coincident for quadrupolar nuclei. He developed and implemented a theoretical treatment for understanding NMR spectra of quadrupolar nuclei. This work is of paramount importance for researchers all around the world who are studying

Can. J. Chem. Downloaded from www.nrcresearchpress.com by 80.58.250.72 on 09/16/12
For personal use only.

quadrupolar nuclei by solid-state NMR. Rod reported unambiguous experimental measurements of indirect spin-spin coupling tensors, which provide important information on bonding and intramolecular conformation. Although thousands of isotropic values of indirect spin-spin coupling constants have been reported in the NMR literature, very little reliable information is available about indirect spin-spin coupling tensors. Rod's laboratory is one of very few in the world that has produced reliable experimental data to prove the existence of sizable anisotropies in ***J*** tensors. For example, Rod's group performed some beautiful single-crystal NMR measurements of ^{199}Hg–^{31}P spin-spin coupling tensors and conclusively demonstrated that *J* anisotropies are comparable to the isotropic values. Rod's group was also the first to establish absolute magnetic shielding scales for oxygen, sulfur, chlorine, and tin, making it possible for other scientists to properly understand and interpret chemical shifts observed for these nuclei. In collaboration with Jan Kwak, Rod also developed an NMR paramagnetic relaxation method to determine distribution coefficients of solubilizates in micellar systems.

In 2000, Rod returned to Alberta after 36 years, taking up a Tier 1 Canada Research Chair in Physical Chemistry at the University of Alberta. Here he established a state of the art laboratory for investigating solid materials by NMR spectroscopy and magnetic resonance imaging (MRI). His group also built a 60 W diode laser system for producing hyperpolarized Xe-129 to investigate porous materials. His group was the first to report successful MR imaging of a functional hydrogen–oxygen fuel cell. Rod's laboratory also demonstrated the advantages of using hyperbolic secant inversion pulses for the sensitivity enhancement of NMR signals from quadrupolar nuclei in solid materials. This method has become widely used by other researchers in the field. Rod has had a long-standing interest in high-resolution molecular beam and microwave spectroscopy. Most chemists are unaware of the relationship between the nuclear spin-spin coupling tensor (***J***) and the molecular beam parameters (c3 and c4). Rod's laboratory demonstrated that using high-quality molecular-beam data one could obtain the anisotropy in the indirect spin-spin coupling tensor (Δ***J***). Furthermore, he showed that first-principles multiconfigurational SCF calculations using large correlation-consistent basis sets are capable of reproducing the experimental data for first- and second-row diatomics and that, for heavier diatomics and polyatomics, Ziegler's ZORA-DFT method provides encouraging results. In recent years, Rod also demonstrated the feasibility of carrying out solid-state NMR studies on many exotic nuclei that had been seldom explored in the literature (e.g., ^{53}Cr and ^{99}Ru).

To date, Rod's prolific research program has produced more than 324 peer-reviewed publications in scientific journals and 21 invited book chapters and reviews. Since 1984, he has given over 140 invited talks and plenary lectures. He is also a co-editor of two NMR books. Rod has been recognized with many awards and honours including the Fellow of the Chemical Institute of Canada (1987), Gerhard Herzberg Award from the Spectroscopy Society of Canada (1994), Canada Council Killam Research Fellowship (1995–1997), Fellow of the Royal Society of Canada (1998), Betts Lectureship (2004), John C. Polanyi Lecture Award (2004), Fellow of the American Association for the Advancement of Science (2006), Killam Annual Professorship Award (2007), Fellow of the International Society of Magnetic Resonance (2005), and EAS Award for Outstanding Achievements in Magnetic Resonance (2011).

Rod is not only a world-class scientist, but also a great educator and mentor. Because of the nature of his research discipline, he has generally maintained a research group of moderate size, graduating a total of 30 graduate students and trained 15 PDFs, 6 visiting scientists, and numerous undergraduates. Fourteen of Rod's former group members are now faculty members in universities in Canada and worldwide. Others hold NMR-related positions across Canada and worldwide, including managers of NMR laboratories and researchers in government laboratories and in universities. Rod has the undeniable ability to inspire his students to continue in scientific research and to train them to become independent researchers. His Ph.D. students received the Canadian Association for Graduate Studies (CAGS/UMI) Distinguished Dissertation Award in natural sciences and engineering in 2003 and the Natural Sciences and Engineering Research Council of Canada (NSERC) Doctoral Prize in 1995 and 2003. Most of his Ph.D. students have held NSERC Postdoctoral Fellowships. This reflects Rod's incomparable mentoring skills. It is perhaps not an overstatement to say that Rod has educated a new generation of solid-state NMR spectroscopists in Canada.

Over the course of his career, Rod has made distinguished contributions to the Canadian and international magnetic resonance communities. He has been an associate editor of the *Canadian Journal of Chemistry* since 1998 and serves on the editorial boards of *Solid State Nuclear Magnetic Resonance, Magnetic Resonance Review*, and *Canadian Journal of Analytical Sciences and Spectroscopy*. In 2008, he joined Robin Harris as one of the two editors-in-chief for a new edition of *Encyclopedia of Magnetic Resonance* (approximately 10 000 printed pages in length, to be published by John Wiley & Sons, Inc. in 2012). He was elected to the Council of the International Society of Magnetic Resonance in 2001. Since 2004 he has been a member of the AMPERE Society. Rod has served on many NSERC committees: member of the Grant Selection Committee (1987–1990), chair of the NSERC/NMR Site Visit Committee (1991, 1992, 1995, and 2000), member of the NRC/NSERC Research Project Review Committee (1996), chair of the NSERC Accelerator Grant Program (2003–2004), and member of the Major Resources Support Committee (2007–2010). In 2003–2005, he served as secretary of the Mathematical and Physical Sciences Division of the Royal Society of Canada. It is particularly worth pointing out his continued support of this Journal. Over the years Rod has published more than 75 papers in the *Canadian Journal of Chemistry*.

Rod has demonstrated tremendous leadership and worked tirelessly on improving the NMR infrastructure in Canada. He is one of the leading founders of the National Ultrahigh-Field NMR Facility for Solids. This national facility, located in Ottawa, Ontario, features the only NMR spectrometer in Canada operating at a magnetic field of 21 T (900 MHz). This is also the first 900 MHz NMR spectrometer worldwide entirely dedicated to solid-state NMR research. Since 2005, Canadian NMR researchers from 20 universities from 7 provinces and 4 National Research Council of Canada (NRC) institutes have benefited from having access to this world-leading NMR facility. Rod was instrumental in making this unique facility a reality. This facility has provided a huge boost to the level of challenging problems that can be tackled by Canadian researchers.

In his spare time, Rod enjoys photography, astronomy, hiking, cross-country skiing, and jogging. Each summer he also tries to find time to participate in occasional 10 km running races. Although he is teased about a direct correspondence between his 10 km time in minutes and his age in the past 20 years, Rod should get credit for motivating many of his students to take up jogging. For the past 2 years, he participated in the 31 km cross-country ski race held at the Canadian Birkebeiner Ski Festival just outside of Edmonton, Alberta.

On many occasions, Rod mentioned that without Valerie's support, he would have accomplished much less in his career. Indeed, over the years, she has enjoyed getting to know

the students as well as proofreading their manuscripts. Many fond memories are associated with the group gatherings at the Wasylishens' residence, together with their children Stephen and Eric. Of course, all these group gatherings typically finished with Bob Dylan records being played on the turntable. Rod's enthusiastic fondness of Dylan's music is legendary.

Throughout his career, Rod's research contributions have always reflected his remarkably deep chemical insight. His emphasis on combining the most careful experimental measurements with the best theoretical interpretation makes his contributions of the highest quality in the literature. Rod is one of the most respected and influential scientists in Canadian chemistry. In August 2009, his former students organized an NMR Symposium in his honour at the 55th International Conference on Analytical Sciences and Spectroscopy (ICASS) in Kingston, Ontario. Now we are privileged to have this special issue of the *Canadian Journal of Chemistry* dedicated to him, to celebrate his outstanding contributions to scientific research, to science education, and his service to a broad scientific community in Canada and worldwide.

David Bryce
University of Ottawa, Ottawa, Ontario

Gang Wu
Queen's University, Kingston, Ontario

Yining Huang

The University of Western Ontario, London, Ontario

Can. J. Chem. Downloaded from www.nrcresearchpress.com by 80.58.250.72 on 09/16/12
For personal use only.